ISSN 1070-4272, Russian Journal of Applied Chemistry, 2008, Vol. 81, No. 1, pp. 1–7. © Pleiades Publishing, Ltd., 2008.
Original Russian Text © E.P. Lokshin, O.A. Tareeva, T.G. Kashulina, 2008, published in Zhurnal Prikladnoi Khimii, 2008, Vol. 81, No. 1, pp. 3–9.

INORGANIC SYNTHESIS AND INDUSTRIAL INORGANIC CHEMISTRY

Effect of Sulfuric Acid and Sodium Cations on the Solubility of Lanthanides in Phosphoric Acid

E. P. Lokshin, O. A. Tareeva, and T. G. Kashulina

Tananaev Institute of Chemistry and Technology of Rare Elements and Mineral Raw Materials, Kola Scientific Center, Russian Academy of Sciences, Apatity, Murmansk oblast, Russia

Received April 19, 2007

Abstract—Effect of introduction of sulfuric acid and sodium cations into phosphoric acid at 70°C on the solubility of lanthanides was studied.

DOI: 10.1134/S1070427208010011

In the dihydrate process of sulfuric acid decomposition of the Khibiny apatite concentrate, a noticeable part of lanthanides is contained in the wet-process phosphoric acid (WPPA) [1, 2]. Compared to the initial lanthanide composition of the apatite concentrate, these lanthanides are enriched in yttrium and elements from the middle of the lanthanide group [1], which predetermines the interest in a search for methods of their recovery.

Although the content of lanthanides in the apatite concentrate is rather constant, data on their distribution among WPPA and phosphogypsum are widely diverse. According to different reports, 20 to 40% of lanthanides pass from the Khibiny apatite concentrate into WPPA. For example, 34.6–53.0% of yttrium passes from the apatite concentrate into WPPA according to [1], and 80.6%, according to [2]. In WPPA samples from the Volkhov aluminum plant, the total content of lanthanides ΣLn_2O_3 varies from 1.42 to 2.3 g l^{-1}. The reasons for so different distributions of lanthanides among WPPA and phosphogypsum have not been analyzed.

Neutralization of the production WPPA with ammonia causes precipitation of phosphate concentrates containing the sum of lanthanides in an amount of 2.1–2.2 wt % [3]. Recovery of lanthanides from these concentrates is economically unfeasible. Therefore, a noticeable attention is being paid to the development of methods for crystallization of lanthanides directly from WPPA.

It has been suggested to crystallize the phosphate concentrate of lanthanides by thermal treatment of defluorinated WPPA in an autoclave at 200°C for 1 h [4]. This method is based on the fact that the solubility of lanthanide phosphates in phosphoric acid solutions decreases as temperature is elevated. The precipitate formed contained, on washing with a fivefold amount of water and drying, 15–24 wt % ΣLn_2O_3 and 15 wt % P_2O_5 and was strongly contaminated with calcium. The recovery of rare-earth elements (REE) into the precipitate was as high as 98%. Industrial application of this technique is unlikely because of the high energy expenditure and necessity for intricate apparatus.

According to the data of [5], lanthanides form in WPPA supersaturated solutions. Table 1 lists the calculated lanthanide concentrations that can be present in WPPA on the assumption that lanthanides from the

Table 1. Calculated and experimentally found* lanthanide concentrations in WPPA from the dihydrate process (40 wt % H_3PO_4) at ΣLn_2O_3 in the apatite concentrate equal to 0.98 wt %

Lanthanide	Concentration, g l^{-1}	
	calculation	experiment
ΣLn_2O_3	6.71	0.9–1.1
Y_2O_3	0.286	0.147
La_2O_3	1.99	0.176
Ce_2O_3	3.03	0.462
Nd_2O_3	1.05	–
Sm_2O_3	0.140	0.035
Eu_2O_3	0.037	0.011
Gd_2O_3	0.132	–
Tb_2O_3	0.014	–
Dy_2O_3	0.051	–

* Data of [1].

Table 2. Solubility of lanthanide sulfates in phosphoric–sulfuric acid solutions at different sulfuric acid concentrations (T = 70°C)

c, wt %		Solubility in terms of Ln_2O_3, g l^{-1}									
H_2SO_4	H_3PO_4	Y_2O_3	La_2O_3	Ce_2O_3	Pr_2O_3	Nd_2O_3	Sm_2O_3	Eu_2O_3	Gd_2O_3	Dy_2O_3	Er_2O_3
0	38.5	48.8	0.18	0.47	0.35	0.47	1.44	2.01	5.5	2.0	5.62
0.5	38.3	–	0.20	1.23	0.83	0.62	2.90	2.68	–	–	–
1.0	38.1	–	1.08	2.82	1.68	1.12	3.06	4.68	–	–	–
1.5	37.9	–	2.05	3.05	2.58	2.73	4.00	5.08	–	–	–
2.0	37.7	–	3.63	4.15	4.00	3.43	10.80	13.1	–	–	–
2.5	37.6	–	4.53	5.22	–	4.68	–	–	–	–	–
3.0	37.4	–	5.65	8.16	6.19	5.90	12.5	14.20	–	–	–
3.5	37.2	–	6.96	10.4	–	7.60	–	–	–	–	–
4.0	37.0	–	13.7	15.4	10.3	10.2	29.5	30.8	–	–	–
4.5	36.8	–	19.2	21.1	–	14.5	–	–	–	–	–
5.0	36.7	94.5	20.6	25.4	22.5	18.0	39.1	41.3	86.5	130	147.5
10.0	35.0	77.1	36.4	38.9	42.6	48.6	73.3	78.5	76.8	92.2	112
15.0	33.5	52.2	21.6	25.4	25.7	36.5	45.1	50.7	48.9	65.6	73.5

apatite concentrate completely dissolve in WPPA. The composition of the sum of lanthanides from the apatite concentrate is given according to [6]. The calculated lanthanide concentrations substantially exceed those experimentally found in WPPA from the dihydrate process at Ammofos Open Joint-Stock Company [1]. However, the data in Table 1 cannot serve as evidence that WPPA is supersaturated with lanthanides.

It has been reported that lanthanides can be recovered from WPPA by spontaneous crystallization on seeds composed of lanthanide phosphates or fluorides [7–9]. It has been shown that neutral lanthanide phosphate hemihydrates crystallize on phosphate seeds, and anhydrous lanthanide fluorides, on fluoride seeds. It has been found in tests of these techniques that the seeds are rapidly "poisoned" and the crystallization of lanthanides first becomes slower and then ceases at all [10, 11]. No satisfactory explanations of this effect have been found. It should be noted that hydrates of the types $YPO_4 \cdot 2H_2O$ [12], $LaPO_4 \cdot 2H_2O$ [13], and $CePO_4 \cdot xH_3PO_4 \cdot yH_2O$ [14], rather than hemihydrates, crystallize from aqueous orthophosphoric acid solutions corresponding in concentration to WPPA at 70–80°C.

To develop methods for recovery of lanthanides from WPPA by crystallization, it is necessary to study the fundamental aspects of the solubility of lanthanide compounds in phosphoric acid solutions.

The aim of our study was to examine the influence exerted by the concentrations of sulfuric acid and sodium ions on the solubility of lanthanides in phosphoric acid solutions at 70°C, the average temperature at which the apatite concentrate is subjected to hemihydrate decomposition, and to use the data obtained for recovery of a lanthanide concentrate from WPPA.

EXPERIMENTAL

We used a solution containing 38.5 wt % H_3PO_4 as a "base" solution. The solubility was studied at 70°C because the dihydrate process is commonly carried out at 70±5°C [15]. Chemicals of grade no worse than analytically pure were used. To a solution containing 38.5 wt % H_3PO_4 we added concentrated (96.5 wt %) H_2SO_4 and sodium sulfate, so that the prescribed concentrations of H_2SO_4 and Na_2SO_4 were reached. Lanthanide sulfates were introduced into the solution prepared. The resulting mixtures were kept in hermetically sealed vessels at 70±1°C until equilibrium was attained (≥168 h), which was judged from constancy of the results of analyses of liquid samples. The content of lanthanides in a separated liquid phase was found by oxalate gravimetry and atomic-emission spectroscopy with inductively coupled plasma on a Perkin–Elmer Plasma 400 instrument. The results of the analyses were in satisfactory agreement. The sodium concentration was determined by the atomic absorption method in an acetylene–air flame (Carl Zeiss AAS-30 instrument, Jena). The experimental data we obtained are listed in Tables 2 and 3.

It is known [16–23] that the solubility of lanthanide phosphates in sulfuric acid solutions depends on the kind of a lanthanide, phosphoric acid concentration, and temperature. At room temperature, the solu-

Table 3. Solubility of lanthanide sulfates and concentration of Na_2O in equilibrium phosphoric–sulfuric acid solutions at 70°C

Composition of starting solution			Solubility in terms of Ln_2O_3 (numerator) and concentration of Na_2O (denominator), g l^{-1}									
H_3PO_4	H_2SO_4	Na_2O, g l^{-1}	Y_2O_3	La_2O_3	Ce_2O_3	Nd_2O_3	Pr_2O_3	Sm_2O_3	Eu_2O_3	Gd_2O_3	Dy_2O_3	Er_2O_3
wt %												
36.7	5	0	94.5 0	20.6 0	25.1 0	18.0 0	22.5 0	39.1 0	41.3 0	86.5 0	130 0	103 0
36.7	5	5	87.2 1.5	1.03 3.41	0.81 3.20	1.79 2.32	0.94 2.9	2.93 2.7	6.64 3.6	9.3 3.5	95.5 3.5	80.6 3.3
36.7	5	10	46.3 5.3	0.30 9.05	0.26 8.80	0.32 9.10	0.27 9.1	1.07 7.80	1.87 9.5	3.2 9.0	69.7 7.8	73.8 8.4
35.0	10	0	77.1 0	36.4 0	38.9 0	48.6 0	42.6 0	73.3 0	78.5 0	76.8 0	92.2 0	134 0
35.0	10	5	69.1 1.1	0.20 3.15	0.16 3.30	0.16 3.50	0.23 4.24	0.7 3.9	1.44 3.9	2.7 3.3	33.8 3.0	96.7 3.5
35.0	10	10	22.5 5.9	0.099 8.68	0.09 8.45	0.11 9.70	0.12 9.1	0.29 9.0	0.69 8.3	1.1 8.2	11.3 7.0	75.1 5.6
33.5	15	0	52.2 0	21.6 0	25.4 0	36.5 0	25.7 0	45.1 0	50.7 0	48.9 0	65.6 0	95.8 0
33.5	15	5	27.5 1.7	0.080 3.75	0.095 3.27	0.13 4.23	0.094 3.4	0.45 3.3	0.91 3.1	1.3 2.9	10.3 2.8	66.8 2.1
33.5	15	10	6.7 7.0	0.035 9.12	0.043 9.12	0.064 8.75	0.080 8.9	0.11 9.1	0.38 8.2	0.2 9.0	4.2 8.1	30.1 5.6

bility of phosphates of the cerium-group lanthanides is considerably lower than that of yttrium and yttrium-group lanthanides at all H_3PO_4 concentrations (Fig. 1).

The solubility of yttrium [12], lanthanum [13], cerium [14, 24], and europium [25] phosphates in phosphoric acid becomes lower as temperature is elevated. It has been shown that the solubility of yttrium, lanthanum, and cerium phosphates at 70–80°C grows as the concentration of phosphoric acid increases from 10 to 50–65 wt % [12–14, 24]. As the acid concentration increases further, the solubility varies only slightly. For a solution containing 38.6 wt % H_3PO_4, the solubility was, according to different reports, 0.15–0.20 g l^{-1} La_2O_3 for lanthanum phosphate at 70°C and about 0.48 g l^{-1} Ce_2O_3 for cerium phosphate at 80°C. The solubility of $EuPO_4 \cdot 0.5H_2O$ in boiling phosphoric acid of various

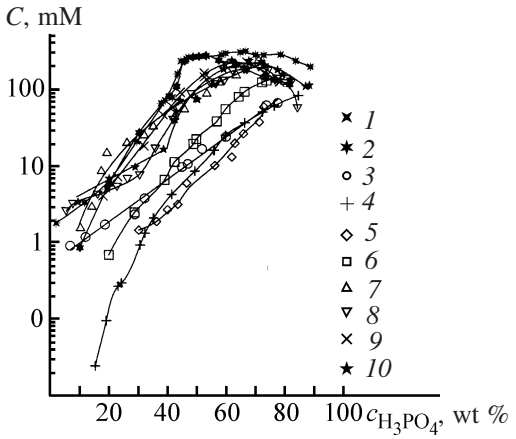


Fig. 1. Solubility c of REE phosphates in phosphoric acid vs. the phosphoric acid concentration $c_{H_3PO_4}$ at 25°C (at 20°C for Ce) according to [16–24]. (*1*) Y [16], (*2*) Y [17], (*3*) La [18], (*4*) Ce [19], (*5*) Pr [20], (*6*) Nd [21], (*7*) Gd [22], (*8*) Tb [21], (9) Dy [23], and (*10*) Ho [24].

Table 4. Solubility of $Ln_2(SO_4)\cdot nH_2O$ in water according to [26]

Lanthanide	T, °C	Solubility in terms of Ln_2O_3, g l^{-1}
La_2O_3	75	4.48
Ce_2O_3	80	6.0–8.5**
Pr_2O_3	75	18.47
Nd_2O_3	79.6	9.08
Sm_2O_3	40*	7.61
Eu_2O_3	40*	7.17

* As temperature is elevated, the solubility of lanthanide sulfates in water decreases.

** According to data of various authors.

Table 5. Solubility of $Ln_2(SO_4)\cdot nH_2O$ in sulfuric acid solutions at 25°C according to the data of [26]

$c_{H_2SO_4}$, wt %	Equilibrium concentration in terms of Ln_2O_3, g l^{-1}		
	La_2O_3	Ce_2O_3	Sm_2O_3
0	14.29	43.89	20.29
0.5	–	43.99	20.38
2.5	16.89	–	19.75
5.0	17.95	34.65	18.21
10.0	18.17	28.98	14.30
20.0	11.09	19.06	–

concentrations increases as the concentration of phosphoric acid is raised in the range 0.5–4 M and, accordingly, its boiling point grows in the interval 100.5–104°C [25].

At the same content of phosphoric acid, not exceeding 40 wt %, raising the temperature from 25 to 70–80°C reduces the solubility of lanthanide phosphates by a factor of 5–100. In more concentrated solutions, the temperature dependence becomes less pronounced.

The values obtained for the solubility of lanthanum and cerium in a sulfuric acid solution are in good agreement with the data of [13, 14, 24]. Table 2 shows that the solubility of samarium, europium, gadolinium, dysprosium, and erbium in phosphoric–sulfuric acid solutions at 70°C noticeably exceeds that of cerium-group lanthanides in solutions of the same composition. A similar dependence was also observed at 101°C [25]. It can be seen that the solubility of lanthanide phosphates hemihydrates in 2 M H_3PO_4 at 101°C increases with the atomic number of a rare-earth element and, for heavy elements, is hundreds of times the solubility of lanthanum phosphate [25]:

Lanthanide	c, g l^{-1}	Lanthanide	c, g l^{-1}
La_2O_3	0.0033	Dy_2O_3	0.186
Pr_2O_3	0.023	Ho_2O_3	0.264
Nd_2O_3	0.022	Er_2O_3	0.382
Sm_2O_3	0.031	Yb_2O_3	0.453
Eu_2O_3	0.031	Lu_2O_3	0.597
Gd_2O_3	0.094		

Introduction of sulfuric acid into a phosphoric acid solution even in an amount of 0.5 wt % makes the solubility of lanthanides substantially higher (Table 1). It rapidly grows as the content of H_2SO_4 is raised to 10 wt % and becomes comparable with, or higher than that of lanthanide sulfates in water and aqueous sulfuric acid solutions containing H_2SO_4 in the same concentration (Tables 4, 5). This fact suggests that, under the conditions studied, lanthanides can exist in phosphoric–sulfuric acid solutions as sulfuric–phosphoric acid complexes whose solubility exceeds the solubility of not only hydrated phosphates, but also lanthanide sulfates.

Table 3 shows that sulfuric acid affects the solubility of lanthanides in a phosphoric acid solution in the presence of sodium sulfate in another way: an increase in the concentration of sulfuric acid favors a dramatic decrease in the solubility of the lanthanides studied. An increase in the concentration of sodium ions in solutions with equal concentrations of phosphoric and sulfuric acids also lowers the solubility of lanthanides. When sodium ions are present, the solubility of cerium-group lanthanides is also considerably lower that the solubilities of the other lanthanides studied.

The observed decrease in the sodium content of the solutions indicates that double lanthanide sodium sulfates can be formed in phosphoric–sulfuric acid solutions. The formation of double sulfates $NaLn(SO_4)_2\cdot H_2O$ (Ln = La, Ce, Pr, Nd, Sm, Eu, Gd) was confirmed by an X-ray phase analysis of bottom phases. It was found that, at a sulfuric acid content of up to 10 wt %, yttrium, erbium, and dysprosium are present in the bottom phase as a mixture of sulfates and double sulfates (Fig. 2). At higher sulfuric acid concentrations, X-ray phase analysis revealed only double sulfates. However, in this case too, presence of minor admixtures of sulfates that are difficultly determinable because of the close similarity of crystal structures is possible.

Thus, sodium present in phosphoric–sulfuric acid solutions promotes formation of double lanthanide

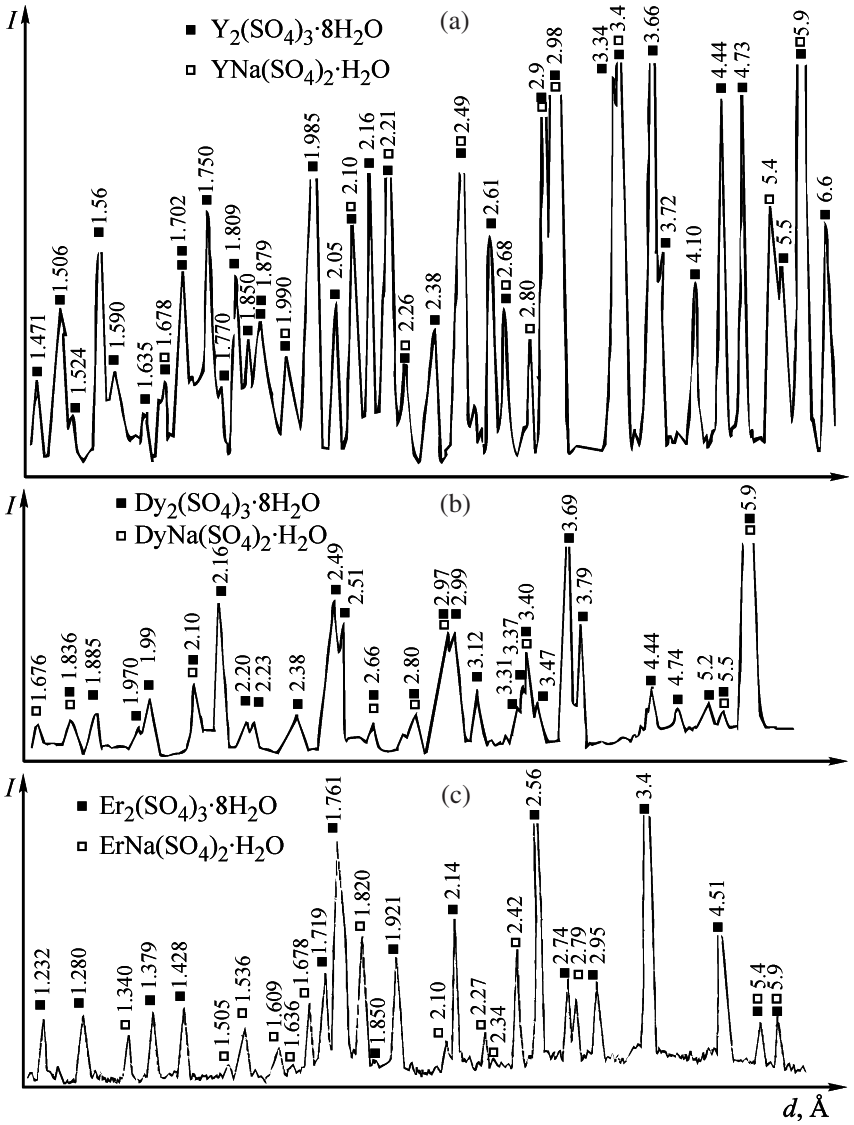


Fig. 2. X-ray diffraction patterns of bottom phases containing (a) yttrium, (b) dysprosium, and (c) erbium at $c_{H_2SO_4} < 10$ wt %. (*I*) Intensity and (*d*) interplanar spacing.

sulfates that are poorly soluble not only in sulfuric acid [27], but in phosphoric acid as well.

If it is assumed that double lanthanide sulfates dissociate by the reaction

$$NaLn(SO_4)_2 \longrightarrow Na^+ + Ln^{3+} + 2SO_4^{2-}, \quad (1)$$

then the solubility product (SP) is given by the equation

$$SP = [c_{Na^+}][c_{Ln^{3+}}][c_{SO_4^{2-}}]^2. \quad (2)$$

We used Eq. (2) and experimental data from Table 3 to calculate, taking into account that $c_{H_2SO_4}$ in Eq. (2) is found by summation of the concentration of the sulfuric acid introduced with that of sulfate ions of the dissolved lanthanide sulfates, the solubility products in sulfuric–phosphoric acid solutions in which the bottom phase is composed of only $NaLn \cdot (SO_4)_2 \cdot H_2O$ (Table 6). When calculating the volume concentrations of the components, we found the solution densities ρ by additive summation of the densities of 38.5 wt % H_3PO_4 and 96.5 wt % H_2SO_4.

The dihydrate decomposition of the apatite concentrate is commonly performed at 65–77°C. The WPPA concentration varies between different plants in the range 38.6–44 wt % [15]. The observed fluctuations of the content of lanthanides in the production WPPA from the dihydrate process cannot be attributed to

Table 6. Solubility products for $NaLn(SO_4)_2 \cdot H_2O$ (Ln = La, Ce, Nd, Pr, Sm, Eu, Gd) in phosphoric–sulfuric acid solutions

Composition of the starting solution			ρ, g cm^{-3}	Solubility product						
H_3PO_4	H_2SO_4	Na_2O, g l^{-1}		La	Ce	Nd	Pr	Sm	Eu	Gd
wt %										
36.7	5	5	1.22	2.8×10^{-4}	2.0×10^{-4}	3.2×10^{-4}	2.0×10^{-4}	5.8×10^{-4}	1.7×10^{-3}	2.2×10^{-3}
36.7	5	10	1.22	2.1×10^{-4}	1.7×10^{-4}	3.6×10^{-4}	1.9×10^{-4}	6.0×10^{-4}	1.2×10^{-3}	2.0×10^{-3}
35.0	10	5	1.25	2.0×10^{-4}	1.7×10^{-4}	2.8×10^{-4}	3.1×10^{-4}	8.2×10^{-4}	1.7×10^{-3}	2.6×10^{-3}
35.0	10	10	1.25	2.8×10^{-4}	2.4×10^{-4}	3.4×10^{-4}	3.5×10^{-4}	7.8×10^{-4}	1.7×10^{-3}	2.6×10^{-3}
33.5	15	5	1.27	2.2×10^{-4}	2.3×10^{-4}	4.0×10^{-4}	2.4×10^{-4}	10.2×10^{-4}	2.0×10^{-3}	2.5×10^{-3}
33.5	15	10	1.27	2.4×10^{-4}	2.2×10^{-4}	4.0×10^{-4}	2.7×10^{-4}	7.0×10^{-4}	2.2×10^{-3}	2.4×10^{-3}
			Average	2.4×10^{-4}	2.1×10^{-4}	3.5×10^{-4}	2.6×10^{-4}	7.5×10^{-3}	1.8×10^{-3}	2.4×10^{-3}

changes in the solubility of lanthanide phosphates at rather small differences in the concentration and temperature of WPPA.

However, the results obtained indicate that the solubility of lanthanides in a phosphoric acid solution is strongly affected by the concentration of sulfate ions and sodium cations always present in WPPA produced from the Khibiny apatite concentrate. Presumably, their varying content is the main reason why the distributions of lanthanides among WPPA and phosphogypsum are different in [1, 2].

We carried out a pilot study of the precipitation of lanthanides from WPPA (produced at Volkhov aluminum plant) with a concentration of 42.86 wt % and density of 1.276 g cm^{-3}, which contained (g l^{-1}): 2.30–2.65 ΣLn_2O_3, 19.3–22.3 CaO, 1.90 Na_2O, 0.80 K_2O, 1.82 TiO_2, 8.8 SiO_2, 6.7 Al_2O_3, 2.9 Fe_2O_3, and individual lanthanides 0.254 Y_2O_3, 0.59 La_2O_3, 0.93 CeO_2, 0.196 Pr_2O_3, 0.47 Nd_2O_3, 0.069 Sm_2O_3, 0.028 Eu_2O_3, 0.057 Gd_2O_3, 0.007 Tb_4O_7, 0.0275 Dy_2O_3, 0.0046 Ho_2O_3, 0.012 Er_2O_3, 0.008 Yb_2O_3. The experimental conditions and the data obtained are listed in Table 7.

Table 7. Residual concentration of lanthanides and calcium in WPPA in relation to increasing content of H_2SO_4 (T = 70°C)

Solution composition, wt %		Residual concentration, g l^{-1}	
H_2SO_4	H_3PO_4	ΣLn_2O_3	Ca(Sr)O
0	42.86	2.30	19.3
5	40.59	1.03	2.77
10	38.30	0.23	1.3
15	36.03	≤0.001	0.9

The composition of WPPA in the pilot study noticeably differed from that commonly obtained, but it made it possible to assess whether lanthanides can be recovered in principle. Table 7 shows that 90% of lanthanides precipitated at 70°C as the H_2SO_4 content of WPPA was raised to 10 wt % and the precipitation was complete as it was raised to 15 wt %. Thus, first, the residual content of lanthanides in WPPA containing 15 wt % H_2SO_4 was negligible and, second, not only the cerium-group lanthanides precipitated, but also the other lanthanides, whose concentration in WPPA was considerably lower than their solubility limit, i.e., a synergic effect was observed, in which more soluble double sulfates (possibly, sulfates or sulfatophosphates) cocrystallized with less soluble double sulfates. This is favored by the close crystal structures of these compounds.

It is noteworthy that the presence of 10–15 wt % H_2SO_4 in the recycle WPPA results in that 2–3 wt % H_2SO_4 is contained in the recycle sludge, which should not hinder its use for apatite decomposition, because this corresponds to the concentration range in which a well filterable phosphogypsum is obtained in the dihydrate process [15].

CONCLUSIONS

(1) Introduction of sulfuric acid into a phosphoric acid solution leads to a significant increase in the solubility of lanthanides, and introduction of sodium

cations causes a dramatic decrease in the solubility. This is due to the formation of double sulfates of lanthanides and sodium.

(2) The solubility products of double sulfates of lanthanum, cerium, praseodymium, neodymium, samarium, europium, and gadolinium in sulfuric–phosphoric acid solutions at 70°C were determined.

(3) The observed differences in the distribution of lanthanides among the liquid and solid phases can be attributed to differences in the content of free sulfuric acid and sodium cations in the wet-process phosphoric acid.

(4) Lanthanides are effectively precipitated from wet-process phosphoric acid if its content of H_2SO_4 is raised to 10–15 wt %.

ACKNOWLEDGMENTS

The study was financially supported by the Russian Foundation for Basic Research (project no. 06-08-00223-a).

REFERENCES

1. Lebedev, V.N., Masloboev, V.A., Popova, L.A., and Serkova, R.P., *Problemy effektivnogo ispol'zovaniya mineral'nogo syr'ya Kol'skogo poluostrova* (Problems of Effective Use of Mineral Raw Materials of the Kola Peninsula), Apatity: Kol'sk. Nauchn. Tsentr Ross. Akad. Nauk, 1993, pp. 43–49.
2. Kazak, V.G., Angelov, A.I., and Zaitsev, P.M., *Khim. Prom–st*., 1995, no. 9, pp. 11–19.
3. RF Patent 2132303.
4. Kijkowska, R. and Pawlowska-Kozinska, D., *Prage Nauk. Inst. Techn. Niorg. Nawoz. Mineral. P. Wroch*., 1986, no. 30, pp. 17–26.
5. Chirkst, D.E., Melikhov, I.V., Syrkin, L.N., et al., *Zh. Prikl. Khim*., 1991, vol. 64, no. 12, pp. 2576–2581.
6. Masloboev, V.A. and Lebedev, V.N., *Redkozemel'noe syr'e Kol'skogo poluostrova i problemy ego kompleksnoi pererabotki* (Rare-Earth Raw Materials of the Kola Peninsula and Problems of Its Integrated Processing), Apatity: Kol'sk. Nauchn. Tsentr Ross. Akad. Nauk, 1991.
7. USSR Inventor's Certificate no. 1595793.
8. USSR Inventor's Certificate no. 1641775.
9. USSR Inventor's Certificate no. 1656832.
10. Dibrov, I.A., Chirkst, D.E., Cheremisina, O.V., and Chaliyan, K.N., *Zh. Prikl. Khim*., 1999, vol. 72, no. 2, pp. 179–184.
11. Dibrov, I.A., Chirkst, D.E., and Cheremisina, O.V., *Zh. Prikl. Khim*., 1999, vol. 72, no. 5, pp. 739–744.
12. Tananaev, I.V., Davitashvili, E.G., Dzhabishvili, N.A., and Landiya, M.V., *Izv. Akad. Nauk SSSR, Neorg. Mater*., 1973, vol. 9, no. 12, pp. 2174–2177.
13. Sergeeva, N.M. and Kuz'menkov, M.I., *Zh. Neorg. Khim*., 1983, vol. 28, no. 8, pp. 2157–2159.
14. Sveshnikova, V.N. and Ginzburg, V.L., *Zh. Neorg. Khim*., 1962, vol. 7, no. 5, pp. 1169–1173.
15. Kopylev, B.A., *Tekhnologiya ekstraktsionnoi fosfornoi kisloty* (Technology of Wet-Process Phosphoric Acid), Leningrad: Khimiya, 1981.
16. Tananaev, I.V. and Dzhabishvili, N.A., *Izv. Akad. Nauk SSSR, Neorg. Mater*., 1969, vol. 5, no. 8, pp. 1402–1405.
17. Tananaev, I.V. and Vasil'eva, V.P., *Zh. Neorg. Khim*., 1964, vol. 9, no. 9, pp. 213–214.
18. Ul'yanov, A.I. and Kazakova, T.I., *Izv. Akad. Nauk SSSR, Ser. Khim*., 1963, no. 7, pp. 1157–1164.
19. Dzhabishvili, N.A. and Kargareteli, L.N., in *Issledovaniya v oblasti khimii kompleksnykh i prostykh soedinenii nekotorykh perekhodnykh i redkikh metallov* (Studies in Chemistry of Complex and Simple Compounds of Some Transition and Rare Metals), Tbilisi: Metsniereba, 1978, issue 3, pp. 110–115.
20. Tananaev, I.V. and Petushkova, S.M., *Zh. Neorg. Khim*., 1964, vol. 9, no. 5, pp. 1094–1098.
21. Davitashvili, E.G., Mzareulishvili, N.V., Dzhabishvili, N.A., and Landiya, M.V., *Izv. Akad. Nauk SSSR, Neorg. Mater*., 1979, vol. 15, no. 6, pp. 1112–1115.
22. Dzhabishvili, N.A. and Davitashvili, E.G., in *Issledovaniya v oblasti khimii kompleksnykh i prostykh soedinenii nekotorykh perekhodnykh i redkikh metallov* (Studies in Chemistry of Complex and Simple Compounds of Some Transition and Rare Metals), Tbilisi: Metsniereba, 1970, pp. 109–121.
23. Dzhabishvili, N.A. and Landiya, M.V., in *Issledovaniya v oblasti khimii kompleksnykh i prostykh soedinenii nekotorykh perekhodnykh i redkikh metallov* (Studies in Chemistry of Complex and Simple Compounds of Some Transition and Rare Metals), Tbilisi: Metsniereba, 1978, issue 3, pp. 116–120.
24. Vasilenko, N.A. and Chepelevetskii, M.L., *Zh. Neorg. Khim*., 1957, vol. 2, no. 10, pp. 2486–2489.
25. Kijkowska, R., *Mater. Sci*., 2003, vol. 38, pp. 229–233.
26. Komisarova, L.N., Pushkina, G.Ya., Shatskii, V.M., et al., *Soedineniya redkozemel'nykh elementov: Sul'faty, selenaty, telluraty, khromaty* (Compounds of Rare-Earth Elements: Sulfates, Selenates, Tellurates, and Chromates), Moscow: Nauka, 1986.
27. Lokshin, E.P., Tareeva, O.A., Ivlev, K.G., and Kashulina, T.G., *Zh. Prikl. Khim*., 2005, vol. 78, no. 7, pp. 1080–1084.

ISSN 1070-4272, Russian Journal of Applied Chemistry, 2008, Vol. 81, No. 1, pp. 8–13. © Pleiades Publishing, Ltd., 2008.
Original Russian Text © E.P. Lokshin, O.A. Tareeva, 2008, published in Zhurnal Prikladnoi Khimii, 2008, Vol. 81, No. 1, pp. 10–15.

INORGANIC SYNTHESIS AND INDUSTRIAL INORGANIC CHEMISTRY

Specific Features of Sulfuric Acid Leaching-out of Lanthanides from Phosphohemihydrate

E. P. Lokshin and O. A. Tareeva

Tananaev Institute of Chemistry and Technology of Rare Elements and Mineral Raw Materials, Kola Scientific Center, Russian Academy of Sciences, Apatity, Murmansk oblast, Russia

Received February 6, 2007

Abstract—Effect of raising in the range 75–95°C the temperature at which hydrated lanthanide phosphates are synthesized on the degree of their chemical activity and, accordingly, on specific features of the sulfuric acid leaching was studied. The mechanism of restoration of the chemical activity of lanthanide compounds was considered.

DOI: 10.1134/S1070427208010023

Processing of the Khibiny apatite concentrate by the hemihydrate method to obtain wet-process phosphoric acid yields dump waste calcium sulfate hemihydrate [technical name of the product is phosphohemihydrate (PHH)], from which lanthanides can be effectively leached-out with sulfuric acid solutions containing up to 30 wt % H_2SO_4 [1].

However, a study of the leaching-out of lanthanides from PHH taken directly from filters (untreated PHH) demonstrated that the process developed is efficient for the product obtained at Voskresenskie Mineral'nye Udobreniya (Voskresensk Mineral Fertilizers) Open Joint-Stock Company (OAO) (the recovery of the sum of lanthanides into solution was as high as 83.9% under the optimal conditions) but inefficient for an untreated PHH manufactured by Ammofos OAO (Table 1). As seen from Table 1, the content of alkali metal impurities in the product is low and they could not prevent the leaching-out of lanthanides by forming double sulfates poorly soluble in sulfuric acid solutions [2].

Making longer the time during which the untreated PHH manufactured by Ammofos OAO is kept in a humid medium leads to conversion of calcium sulfate hemihydrate into its dihydrate (CSD), with the leaching-out of lanthanides with sulfuric acid solutions becoming more efficient (Table 2).

According to the information provided by the Research Institute of Chemical Fertilizers and Insectofungicides (NIUIF OAO), the processing technology of the apatite concentrate is the same at both plants. Therefore, it was necessary to understand why similarly obtained products behave so differently. It was suggested that the differences in the leaching-out of lanthanides from PHH produced at these plants may be due to the following. First, this may occur because of differences in the physicochemical properties of PHH, associated with different temperatures of decomposition of the apatite concentrate and(or) different sulfuric acid introduction modes. The second reason may consist in different chemical activities of hydrated lanthanide phosphates, caused by differences in the decomposition temperatures of the apatite concentrate.

According to the first hypothesis, grains formed in the phosphoric–sulfuric acid sludge and containing celestite and lanthanide phosphates, in which form main part of lanthanides are present in PHH [3], may be encapsulated in $2CaSO_4 \cdot H_2O$ crystals at Ammofos OAO because of a slightly different mode of the acid

Table 1. Kinetics of leaching-out of lanthanides from the untreated PHH from Ammofos OAO. $c_{H_2SO_4} \approx 23$ wt %, l : s = 2 : 1

τ, min	Concentration in solution, g l^{-1}					Recovered ΣLn_2O_3, %
	ΣLn_2O_3	CaO	Na_2O	K_2O	H_3PO_4	
5	0.31	0.90	0.15	0.038	5.9	11.3
15	0.46	0.86	0.21	0.065	6.0	16.7
25	0.61	0.84	0.25	0.072	6.5	22.2
35	0.29	0.81	0.38	0.082	6.5	10.6
45	0.25	0.80	0.38	0.080	6.8	9.1

decomposition of apatite. As a result, they become inaccessible to the sulfuric acid solution. When PHH is stored in a humid medium, $CaSO_4 \cdot 0.5H_2O$ is transformed to $CaSO_4 \cdot 2H_2O$ with a noticeable increase in volume, which could lead to disruption of the integrity of the protective crust of calcium sulfate, which hinders contact with the sulfuric acid solution.

However, no more than 60 min is required for washed PHH to be completely converted to $CaSO_4 \cdot 2H_2O$ [4, 5]. Table 2 shows that this time is incomparably longer than that required to restore the "chemical activity" of lanthanide compounds present in PHH from Ammofos OAO.

The second hypothesis is based on the known fact that the chemical activity of lanthanide phosphates decreases as the degree of their hydration becomes lower. For example, anhydrous lanthanide phosphates are very chemically stable and are only sulfated at 180–200°C by concentrated H_2SO_4 [6]. In addition, the solubility of hydrated phosphates $LnPO_4 \cdot 1.5H_2O$ (Ln = La, Ce, Nd) in 1.5–5 M nitric acid solutions decreases upon partial dehydration of orthophosphate sesquihydrates at 200°C and becomes very low upon total dehydration [7].

It has been shown that hydrated crystalline lanthanide orthophosphates can be divided, as regards their thermal behavior, into two groups [8]. The first group, to which belong hexagonal orthophosphates of La to Tb and orthorhombic dysprosium orthophosphate, shows two dehydration-related endothermic effects at temperatures lower than 300°C. The second group includes tetragonal orthophosphates of yttrium and lanthanides from Ho to Tm, for which dehydration occurs in a wide temperature range 100–600°C. The onset temperatures of their dehydration are listed in Table 3.

The data in Table 3 should be considered tentative, because the products were synthesized by precipitation from boiling 2 M H_3PO_4 (bp 101°C [9]).

In the technique developed by NIUIF, the Khibiny apatite is commonly decomposed by the hemihydrate method at 90–97°C [10]. Table 3 demonstrates that partial dehydration of the hydrated phosphates $LnPO_4 \cdot H_2O$ is, in principle, possible at such temperatures.

Thus, a possible reason for differences in the behavior of lanthanides in sulfuric acid leaching is the certain difference between the temperatures of acid decomposition of the apatite concentrate at these plants, which leads to a decrease in the degree of hydration and, as a consequence, in the chemical activity of hydrated lanthanide phosphates as well.

Table 2. Efficiency of recovery of lanthanides at different storage times of PHH from Ammofos OAO. l : s = 2 : 1, leaching duration 25 min, $c_{H_2SO_4}$ = 25 wt %

τ, days	ΣLn_2O_3 concentration in solution, g l^{-1}	Recovered, %	
		in terms of PHH	in terms of CSD
4	0.84	30.0	33.0
11	1.17	41.8	46.0
18	1.30	46.4	51.0
21	1.48	52.9	58.2
24	1.50	53.6	59.0
27	1.72	61.4	67.5
40	1.90	67.9	74.5
45	1.96	71.3	78.4

Table 3. Onset temperature of $LnPO_4 \cdot H_2O$ dehydration [8]

Lanthanide	*T*, °C	Lanthanide	*T*, °C
Y	94	Gd	88
La	94	Tb	83
Ce	81	Dy	95
Pr	79	Ho	90
Nd	79	Er	85
Sm	98	Tm	90
Eu	93		

The aim of our study was to analyze reasons for the decrease in the efficiency of the sulfuric acid leaching-out of lanthanides from the untreated phosphohemihydrate from Ammofos OAO, compared with the similar product from Voskresenskie Mineral'nye Udobreniya OAO, and reasons for the improvement of leaching-out of lanthanides in dump storage of phosphohemihydrate from Ammofos OAO.

EXPERIMENTAL

We used hydrated phosphates of lanthanum, cerium, and neodymium, because these elements largely determine the composition of the sum of lanthanides in the Khibiny apatite concentrate and, according to Table 3, the onset temperatures of their dehydration noticeably differ.

Hydrated lanthanum, cerium, and neodymium orthophosphates were precipitated at 900°C from aqueous solutions of their nitrates with 20% orthophosphoric acid, taken in a 20% excess with respect to

Table 4. Fraction of lanthanides that passed into solutions under various conditions of preliminary treatment of hydrated lanthanum, cerium, and neodymium phosphates

Treatment conditions			Solubility relative to product thermally treated at 25°C, %		
run no.	*T*, °C	mode	La	Ce	Nd
1	25	1	100	100	100
2	75	1	26.8	25.8	51.5
3	85	1	12.6	12.5	36.4
4	95	1	6.3	6.4	18.2
5	25	2	100	100	100
6	75	2	24.9	10.7	40.8
7	75*	2	12.7	10.7	30.2
8	85	2	10.6	4.7	14.5
9	95	2	9.3	3.2	12.8
10	95	3	59.4	36.4	91.2
11	85	4	63.1	36.8	79.2
12	95	5	8.2	1.4	8.5

* Wet products kept in this state for 4 months.

the stoichiometry, by the reaction

$$Ln(NO_3)_3 + H_3PO_4 \rightarrow LnPO_4 + 3HNO_3. \quad (1)$$

After 12 h of keeping, gel-like precipitates were separated by centrifugation, thoroughly washed with water to remove nitrate ions and the excess amount of phosphoric acid, dried in a vacuum at 200°C, and ground in a mortar. The untreated products were amorphous. The products calcined at 900°C were orthophosphates $LnPO_4$ according to X-ray phase (XPA) and chemical analyses. According to the results of a thermogravimetric analysis (TGA), the phosphates synthesized were $LaPO_4 \cdot 1.5H_2O$, $CePO_4 \cdot 1.5H_2O$, and $NdPO_4 \cdot H_2O$.

The phosphates were additionally wetted with 70 wt % H_3PO_4 and subjected to thermal treatment at 25, 75, 85, and 95°C, with moisture not allowed to evaporate (mode 1). We assumed that this yields hydrated orthophosphates whose degree of hydration corresponds to that of orthophosphates formed in the untreated PHH under different thermal conditions of its synthesis (75, 85, and 95°C).

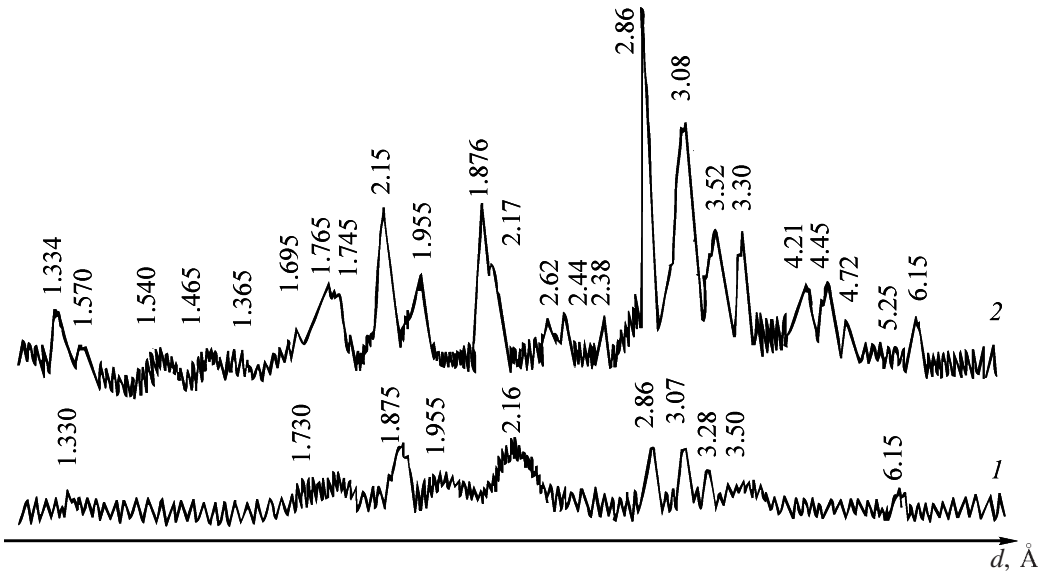
The products synthesized were subjected to various additional treatments. First, wet products thoroughly washed with water to remove orthophosphoric acid were kept for 1 month at room temperature in hermetically sealed vessels, without evaporation of the moisture that they contain (mode 2).

In addition, wet products washed with water to remove phosphoric acid in a hermetically sealed vessel for 1 month were mixed either with phosphogypsum and K_2SiF_6 taken in a mass ratio of 1 : 4 : 0.9, or only with K_2SiF_6 at a mass ratio of 1 : 0.9, or only with phosphogypsum wetted with 2 wt % H_3PO_4, taken in a mass ratio of 1 : 4. These mixtures were also kept at room temperature in hermetically sealed vessels, to give products processed in modes 3, 4, and 5, respectively.

Weighed portions were leached for 25 min with a solution containing 26 wt % H_2SO_4 and 1.5 g l^{-1} Na_2O. The solution composition and the leaching time corresponded to the optimal conditions used in sulfuric acid leaching of PHH. The s : l ratio was sufficient for providing the solubility of double lanthanide sulfates that could be formed in leaching. The amount of lanthanides that passed into solution was determined by methods described in [2]. The experimental results are listed in Table 4.

It is known that the solubility of hydrated Ce, La, and Nd orthophosphates in HNO_3 solutions with concentrations of 1.5–5 M noticeably decreases as the content of crystal hydrate water becomes lower, which is provided by elevating the thermal treatment temperature [7].

Table 4 shows that the solubility of hydrated phosphates thermally treated at 75–95°C is substantially lower than that of hydrated phosphates obtained at 25°C. We assumed that, for samples obtained in modes 1 and 2, the decrease in the solubility of hydrated phosphates thermally treated at 75–95°C, compared with the solubility of the product synthesized at 25°C, indirectly characterizes the change in the number of water molecules bound to $LnPO_4$.



X-ray diffraction patterns of hydrated cerium phosphate prepared at 75°C in mode 2. The product was (*1*) stored in a humid atmosphere for 1 month and (*2*) ground in a porcelain mortar during a short time. (*d*) Interplanar spacing.

As the thermal treatment temperature is raised from 75 to 95°C, the solubility of the phosphates in sulfuric acid solutions decreases (run nos. 2–4). The most pronounced decrease in the solubility (by a factor of 4) was observed for lanthanum and cerium phosphates. The solubility of neodymium phosphate decreases to a somewhat lesser extent, although its dehydration onset temperature is the lowest [8].

The solubility of wet products washed to remove phosphoric acid and kept for 1 month was even lower (run nos. 6–9), with an increase in the keeping time to 4 months further impairing the solubility of hydrated lanthanum and neodymium phosphates (run no. 7). The XPA data in the figure suggest that the decrease in solubility is due to aging, upon which amorphous products start to crystallize (X-ray diffraction pattern *1*). Short-term grinding of the aged products in a porcelain mortar resulted in a dramatic acceleration of the crystallization of the hydrated phosphates studied (diffraction pattern *2*).

Thus, the "spontaneous" restoration of the chemical activity of lanthanide phosphates, assumed to possibly proceed because the degree of hydration of lanthanide phosphates returns to its initial value upon their prolonged storage in a humid medium, does not occur. Consequently, the chemical activity is restored via chemical interaction of lanthanide phosphates with the PHH components. We believe that the most important of these components is phosphoric acid or SiF_6^{2-} ions present in noticeable concentrations in the dump waste PHH.

The effect of impurity components of PHH on the restoration of the chemical activity of lanthanide phosphates was studied on the least soluble samples obtained by thermal treatment at 85 and 95°C.

Phosphoric acid may find its way into dump waste PHH by two channels. First, PHH contains minor amounts of H_3PO_4 unremoved by washing. Second, silicofluorides contained in dump waste PHH are hydrolyzed if the acidity of the aqueous decreases, with the formation of hydrofluoric acid by the reactions

$$Na_2SiF_6 + (2 + n)H_2O = SiO_2 \cdot n\,H_2O\downarrow + 4HF + 2NaF, \quad (2)$$

$$K_2SiF_6 + (2 + n)H_2O = SiO_2 \cdot n\,H_2O\downarrow + 4HF + 2KF. \quad (3)$$

It can be assumed that, in storage of PHH, hydrofluoric acid reacts with $CaHPO_4$ or residual undecomposed apatite in accordance with the equations

$$CaHPO_4 + 2HF = CaF_2\downarrow + H_3PO_4, \quad (4)$$

$$Ca_5(PO_4)_3F + 9HF = 5CaF_2\downarrow + 3H_3PO_4. \quad (5)$$

As the concentration of H_3PO_4 increases, it interacts with hydrated lanthanide phosphates to give acid phosphates that are more soluble in acids by the reaction

$$LnPO_4 \cdot m\,H_2O + xH_3PO_4 = LaPO_4 \cdot x\,H_3PO_4 \cdot m\,H_2O. \quad (6)$$

However, the solubility of the samples obtained in mode 5 (run no. 12) became even lower, compared with the results of run no. 9. Thus, free phosphoric

acid does not favor restoration of the chemical activity of hydrated lanthanide phosphates.

A processing in modes 3 and 4 resulted in a substantial increase in the solubility of the hydrated phosphates. However, the solubility of cerium phosphate increased to a lesser extent, compared with lanthanum and neodymium phosphates. The results of run nos. 10 and 11 suggest that it is the hydrolysis of SiF_6^{2-} ions that restores the chemical activity of hydrated lanthanide phosphates, because the activity of the lanthanide phosphates was not restored upon storage for the same time of preliminarily dried mixtures of the same composition. Therefore, the most probable mechanism improving the solubility of the hydrated phosphates processed in modes 3 and 4 is associated with the occurrence of the reaction

$$LnPO_4 \cdot xH_2O + 3HF = LnF_3\downarrow + H_3PO_4 + xH_2O. \quad (7)$$

Lanthanide fluorides are fairly well soluble in sulfuric acid solutions. For example, the solubility of LaF_3 in 2.3 M H_2SO_4 at room temperature is 1 g l^{-1} (in terms of La_2O_3) [11] and the solubilities of CeF_3 and NdF_3 in terms of oxides are approximately 0.7 and 3 g l^{-1}, respectively.

Although the XPA method failed to confirm the formation of MF_3, probably because of the ultradispersity of the particles being formed, the fractions of lanthanides that passed into solution in run nos. 10 and 11 correlate with the above solubilities of lanthanide fluorides, which confirms this hypothesis.

CONCLUSIONS

(1) In thermal treatment of wet lanthanide orthophosphates $LnPO_4 \cdot (1–1.5)H_2O$ (Ln = La, Ce, or Nd) in the presence of 70 wt % H_3PO_4 (conditions of their formation in hemihydrate decomposition of the apatite concentrate), raising the thermal treatment temperature from 75 to 95°C lowers their solubility in a sulfuric acid solution by a factor of 3–4, probably because of a decrease in the degree of their dehydration. Consequently, a slight increase in the temperature of the hemihydrate process of phosphoric acid decomposition of the Khibiny apatite may lead to a pronounced decrease in the chemical activity of hydrated lanthanide orthophosphates.

(2) Prolonged keeping in a humid atmosphere of the hydrated lanthanide orthophosphates synthesized hinders their dissolution in a sulfuric acid solution to an even greater extent, which is due to their "aging" and the onset of crystallization of the amorphous product.

(3) Presence of SiF_6^{2-} ions in a mixture of low-active lanthanide phosphates with phosphohemihydrate or K_2SiF_6, stored for a long time in a humid medium, leads to an increase in the efficiency of sulfuric acid leaching-out of lanthanides.

(4) The results obtained make it possible to explain the experimentally observed decrease in the efficiency of sulfuric acid leaching-out of lanthanides from the untreated phosphohemihydrate from Ammofos OAO, compared with the product manufactured in a similar way at Voskresenskie Mineral'nye Udobreniya OAO, and the improvement of the leaching-out of lanthanides upon prolonged storage of the phosphohemihydrate from Ammofos OAO.

ACKNOWLEDGMENTS

The study was financially supported by the Russian Foundation for Basic Research (project no. 06-08-00223-a).

REFERENCES

1. Lokshin, E.P., Ivlev, K.G., and Tareeva, O.A., *Zh. Prikl. Khim.*, 2005, vol. 78, no. 11, pp. 1796–1800.
2. Lokshin, E.P., Ivlev, K.G., Tareeva, O.A., and Kashulina, T.G., *Zh. Prikl. Khim.*, 2005, vol. 78, no. 7, pp. 1080–1084.
3. Lokshin, E.P., Vershkov, A.V., Vershkova, Yu.A., et al., Abstracts of Papers, *Nauchnaya konferentsiya "Khimiya i khimicheskaya tekhnologiya v osvoenii prirodnykh resursov Kol'skogo poluostrova"* (Scientific Conf. "Chemistry and Chemical Technology in the Development of Natural Resources of the Kola Peninsula), Apatity: Kol'sk. Nauchn. Tsentr Ross. Akad. Nauk, 1998, pp. 31–32.
4. Pozin, M.E., Kopylev, B.A., Varshavskii, L.A., and Tokarev, G.I., in *Novye issledovaniya po tekhnologii mineral'nykh udobrenii* (New Research in Technology of Mineral Fertilizers), Leningrad: Khimiya, 1970, pp. 37–41.
5. Pozin, M.E., Kopylev, B.A., Varshavskii, L.A., and Tokarev, G.I., in *Novye issledovaniya po tekhnologii mineral'nykh udobrenii* (New Research in Technology of Mineral Fertilizers), Leningrad: Khimiya, 1970, pp. 42–45.
6. Kaplan, G.E., Uspenskaya, T.A., Zarembo, Yu.N., and Chirkov, I.V., *Torii, ego syr'evye resursy, khimiya*

i tekhnologiya (Thorium: Mineral Resources, Chemistry, and Technology), Moscow: Atomizdat, 1960.

7. Kuzina, T.I., Slivko, T.A., Zimina, G.V., and Komissarova, L.N., *Izv. Vyssh. Uchebn. Zaved., Tsvetn. Metall.*, 1994, nos. 1–2, pp. 68–70.
8. Kijkowska, R., *Thermochim. Acta*, 2003, vol. 404, pp. 81–88.
9. Kochetkov, V.N., *Fosforsoderzhashchie udobreniya: Spravochnik* (Phosphorus-Containing Fertilizers: Reference Book), Moscow: Khimiya, 1982.
10. Kopylev, B.A., *Tekhnologiya ekstraktsionnoi fosfornoi kisloty* (Technology of Wet-Process Phosphoric Acid), Leningrad: Khimiya, 1982.
11. Lokshin, E.P., Vershkova, Yu.A., Ivlev, K.G., and Tareeva, O.A., *Zh. Neorg. Khim.*, 2004, vol. 49, no. 4, pp. 707–710.

ISSN 1070-4272, Russian Journal of Applied Chemistry, 2008, Vol. 81, No. 1, pp. 14–16. © Pleiades Publishing, Ltd., 2008.
Original Russian Text © V.I. Skudaev, A.B. Solomonov, A.I. Morozovskii, N.A. Isakov, 2008, published in Zhurnal Prikladnoi Khimii, 2008, Vol. 81, No. 1, pp. 16–18.

INORGANIC SYNTHESIS AND INDUSTRIAL INORGANIC CHEMISTRY

Oxidation of Hydrogen Chloride with Hydrogen Peroxide in Aqueous Solution

V. I. Skudaev, A. B. Solomonov, A. I. Morozovskii, and N. A. Isakov

Perm State Technical University, Perm, Russia

Received June 20, 2005; in final form, October 2007

Abstract—Evolution of chlorine into the gas phase upon mixing of aqueous solutions of hydrogen chloride and hydrogen peroxide was studied. The threshold hydrogen chloride concentration corresponding to the onset of the chlorine evolution was determined.

DOI: 10.1134/S1070427208010035

From the standpoint of use of chlorine raw materials and in the environmental respect, utilization of exhaust (abgas) hydrogen chloride is one of the problems of industrial organochlorine synthesis. The basic methods for processing abgas hydrogen chloride are its deep purification and processes of hydrochlorination and oxidative chlorination [1, 2]. Certain success has been achieved in the development of chemistry and technology of the latter methods. Application of oxidative chlorination is impeded by low productivity of the method itself, which in most cases is limited by oxidation of hydrogen chloride with oxygen or air. The most commonly applied catalysts are copper(I) and copper(II) chlorides. Attempts to develop a more effective catalyst based on compounds of other metals did not ensure process intensification to an extent at which the oxidation rate of hydrogen chloride and the chlorination rate of an organic compound are comparable [3].

In this connection, efforts are made to intensify the process by applying other oxidants that are more effective than oxygen. Among the compounds tested are nitrogen(II) and nitrogen(IV) oxides, chromium(VI) oxide, ozone, and chlorine(I) and chlorine(IV) oxides. An undoubted advantage of the above oxidants is that they ensure the required rate of the hydrogen chloride oxidation even at a temperature close to 300 K. The oxidative chlorination of olefins from C_2 to C_6 and of aromatic hydrocarbons in the HCl–H_2O_2 system with the HCl conversion exceeding 70% was reported [4]. At the same time, the limiting stage of the process involving the oxidation of hydrogen chloride with hydrogen peroxide remains unknown. Therefore, for the subsequent development of the process control it is urgent to establish the formal kinetic features of chlorine evolution into the gas phase.

EXPERIMENTAL

In a temperature-controlled glass reactor with the temperature set in the range 298–348 K, 30% hydrogen peroxide (pure grade) was mixed with water, after which hydrochloric acid was added. This sequence of introducing the components ensured their fast mixing owing to high density of the latter component [5]. The released chlorine and a potassium iodide solution reacted in an absorber to form iodine, which was used for titrimetric determination of the amount of the released chlorine [6]. The oxygen formed was collected in a gas meter via rheometer to obtain data on the dynamics and amount of the released gas. The initial concentration of hydrogen peroxide before mixing with hydrochloric acid was determined by iodometric titration, and that of hydrochloric acid, by the density at 293 K. In most cases, the hydrogen chloride concentration exceeded by more than an order of magnitude the concentration of hydrogen peroxide, which made its control in the course of the reaction unnecessary. The measurements were performed only at the beginning and at the end of the experiment. Initially, when testing the procedure, we simultaneously performed the chemical analysis.

After the experiment was complete, chlorine dissolved in a solution was removed from the reactor with a gas flow and was absorbed with a potassium iodide solution. In this case, the possibility of the

oxidation of iodide ion with concomitant gases was checked when testing the procedure. In the blank experiments involving bubbling of nitrogen through a hydrogen peroxide solution and then through a solution of potassium iodide, no iodine was detected. Bubbling of oxygen through a potassium iodide solution did not result in the formation of iodine either.

Table 1 illustrates how the concentrations of hydrogen chloride c_1 and hydrogen peroxide c_2 vary with time of oxidation of hydrogen chloride with hydrogen peroxide in aqueous solution. The reaction rates are given in Table 2. The current concentrations of hydrogen chloride and hydrogen peroxide were calculated from the amounts of the forming chlorine and oxygen. The rate of chlorine evolution into the gas phase was determined as the ratio of the chlorine amount trapped by the absorber to the solution volume and time. The reaction orders, as purely formal quantities that can be used for the mathematical description of variations of rate with the concentration of the initial substances, were calculated by the Correlia 2005 computer program from data of Table 2. Four parameters can be determined simultaneously: two partial orders of reaction, activation energy, and preexponential factor [7]. The activation energy was calculated from the results of the experiments at different temperatures (Table 2). The satisfactory character of the mathematical description obtained is confirmed by good coincidence of the calculated rates with the experimental values. The rate equation obtained can be used for the analysis of variations of the rate of chlorine formation with hydrogen chloride concentration at a given concentration of hydrogen peroxide. Also, it illustrates the occurrence of the threshold hydrogen chloride concentration in a solution, below which chlorine is not released. The calculation shows that at a hydrogen chloride concentration c_1 lower than 5 M there is virtually no chlorine liberation. The formal kinetic order with respect to hydrogen chloride, estimated from these data, is larger than 8. Therefore, it may be suggested that only the concentration that is in excess over a threshold value must be put in the rate equation: $c_e = c_1 - c_0$. The experimental threshold concentration c_0 lies within 4–5 M, whereas the value calculated from the reaction order corresponding to the lowest error is 5.2 M. The activation energy E is 100 kJ mol^{-1}. The derived formal rate equation has the form

$$\nu = 4.8 \times 10^{13} \exp(-E/RT) c_e^{1.1} c_2^{2.3} \text{ mol l}^{-1} \text{ s}^{-1},$$

where c_2 is the concentration of hydrogen peroxide in solution.

Table 1. Variation of the reactant concentrations with time (sampling at 325 K)

τ, s	c_1	c_2
	M	
30	5.89	0.346
60	5.89	0.318
90	5.88	0.296
120	5.88	0.278
180	5.87	0.248
300	5.87	0.230
420	5.87	0.230

Table 2. Rate of chlorine evolution ν under different conditions

T, K	c_1	c_2	$\nu \times 10^4$	$\nu^{calc} \times 10^4$
	M		mol l^{-1} s^{-1}	
300	5.85	0.25	0.047	0.047
300	5.85	0.5	0.26	0.230
300	5.85	1	0.96	1.135
300	5.85	1.69	4.4	3.793
329	5.5	0.363	1.47	1.618
329	5.66	0.363	2.8	2.589
329	5.89	0.363	3.8	4.043
327	5.91	0.363	2.75	3.336
329	6.01	0.363	4.37	4.823
329	6.13	0.363	6.53	5.615
329	6.5	0.363	7.83	8.116
329	7.02	0.363	10.8	11.752
317	7.02	0.363	2.67	2.943
337	7.02	0.363	41.4	28.002
347	7.02	0.363	60.5	78.362

Evidently, the reaction studied is complex. The obtained formal rate equation allows us to suggest the stages that account for the experimental results. First of all, this refers to the presence of the threshold concentration of hydrochloric acid:

$$H_2O_2 + HCl \rightleftarrows H_2O_2 \cdot HCl, \quad (1)$$

$$H_2O_2 \cdot HCl \rightarrow H_2O + HOCl, \quad (2)$$

$$HOCl + HCl \rightleftarrows H_2O + Cl_2, \quad (3)$$

$$HOCl + H_2O_2 \rightarrow H_2O + HCl + O_2, \quad (4)$$

$$H_2O_2 + Cl_2 \rightarrow 2HCl + O_2 \quad (5)$$

The fact that the complex $H_2O_2 \cdot HCl$ can be

formed in the stage of the oxidation of hydrochloric acid in HOCl was reported elsewhere [5, 8].

The rate of chlorine formation by reaction (3) depends on the concentrations of hydrogen chloride and hydrogen peroxide. The dissolved chlorine is hydrolyzed by reverse reaction (3) and reduced by reaction (5).

The rate of the above reactions is proportional to chlorine concentration in the solution, which is limited by the solubility. When the solubility is exceeded, chlorine is released into gas phase. The rate of the chlorine formation in the steady-state mode is equal to the rate of its consumption up to a certain value of the HCl concentration. At a higher concentration, chlorine starts to evolve into the gas phase.

CONCLUSIONS

(1) The oxidation of hydrogen chloride with hydrogen peroxide at common temperature with the evolution of chlorine into the gas phase occurs at a hydrogen chloride concentration in a solution exceeding the threshold value (5.2 M).

(2) The obtained formal rate equation for the oxidation of hydrogen chloride with hydrogen peroxide makes it possible to calculate the rate of the chlorine evolution into the gas phase. The results are accounted for from the standpoint of the occurrence of the threshold concentration of hydrogen chloride.

REFERENCES

1. Mazanko, A.F., Romashin, O.P., Bobrin, V.S., and Treger, Yu.A., *Khim. Prom–st*., 2000, no. 9, pp. 3–6.
2. Flid, M.R., and Treger, Yu.A., *Katal. Prom–sti*., 2004, no. 2, p. 3.
3. Flid, M.R., and Treger, Yu.A., *Katal. Prom–sti*., 2004, no. 4, p. 13.
4. Muganlinskii, F.F., and Guseinov, M.M., *Zh. Vses. Khim. O–va. im. D.I. Mendeleeva*, 1985, vol. 30, no. 4, pp. 340–345.
5. *Khimiya i tekhnologiya perekisi vodoroda* (Chemistry and Technology of Hydrogen Peroxide), Seryshev, G.A., Ed., Leningrad: Khimiya, 1984, p. 16.
6. *GOST* (State Standard) *28149–89*.
7. Isakov, N.A., and Fedoseev, A.M., *Svidetel'stvo ob otraslevoi registratsii razrabotki* (Branch Development Registration Certificate) *no. 6432: Development of Regression Models of Objects with Strong Mutual Correlation between Input Parameters "Correlia 2005,"* Otraslevoi Fond Algoritmov i Programm, June 20, 2006.
8. *Perekis' vodoroda i perekisnye soedineniya* (Hydrogen Peroxide and Peroxy Compounds), Pozin, M.E., Ed., Moscow: Goskhimizdat, 1951.

ISSN 1070-4272, Russian Journal of Applied Chemistry, 2008, Vol. 81, No. 1, pp. 17–22. © Pleiades Publishing, Ltd., 2008.
Original Russian Text © M.V. Sukhanov, I.A. Shchelokov, M.M. Ermilova, N.V. Orekhova, V.I. Pet'kov, G.F. Tereshchenko, 2008, published in Zhurnal Prikladnoi Khimii, 2008, Vol. 81, No. 1, pp. 19–24.

INORGANIC SYNTHESIS AND INDUSTRIAL INORGANIC CHEMISTRY

Catalytic Properties of Sodium Zirconium Molybdate Phosphates in Methanol Transformations

M. V. Sukhanov, I. A. Shchelokov, M. M. Ermilova, N. V. Orekhova, V. I. Pet'kov, and G. F. Tereshchenko

Lobachevsky Nizhni Novgorod State University, Nizhni Novgorod, Russia
Topchiev Institute of Petrochemical Synthesis, Russian Academy of Sciences, Moscow, Russia

Received September 10, 2007

Abstract—Molybdate phosphates $Na_{1-y}Zr_2(MoO_4)_y(PO_4)_{3-y}$ (y = 0, 0.25, 0.5) having the $NaZr_2(PO_4)_3$ structure were prepared by the sol–gel method. The catalytic properties of the molybdate phosphates in dehydration and dehydrogenation of methanol in inert and oxidizing atmospheres were studied.

DOI: 10.1134/S1070427208010047

Framework phosphates that are structural analogs of sodium dizirconium orthophosphate $NaZr_2(PO_4)_3$ (NZP) have a flexible structure allowing iso- and heterovalent substitutions in both cationic and anionic positions without significant changes in the crystallographic characteristics of the basis lattice [1].

Wide isomorphism of various types of cations leads to disbalance of charges in the structure, caused by geometric features of the arrangement of the adjacent polyhedra, and to appearance of local and cooperative distortions. Thus it becomes possible to control the concentration and strength of both Brønsted and Lewis acid centers. Therefore, such phosphates show promise as heterogeneous catalysts for many acid–base (isomerization, dehydration) and redox (selective oxidation of paraffins, dehydrogenation) processes [2–11]. They are also convenient model objects for studying the correlations between the activity and chemical composition of a catalyst, structural characteristics, ionic charges and radii, surface area, acidity, etc.

Previously [12] we considered crystal-chemical features of the incorporation of Mo into various crystallographic positions of the NZP structure depending on the synthesis conditions. We noted that Mo(IV) occupies octahedral positions of the NZP framework, and Mo(VI), tetrahedral positions. In the latter case, molybdate phosphates are formed under the conditions of free air access at relatively low temperatures (873 K), and they are chemically stable. The structure of alkali metal zirconium molybdate phosphates $A_{1-y}Zr_2(MoO_4)_y(PO_4)_{3-y}$, where A = Na ($0 \le y \le 0.6$), K ($0 \le y \le 0.3$), Rb ($0 \le y \le 0.2$), Cs ($0 \le y \le 0.1$), crystallizing in the NZP structural type, was simulated in [13] by minimization of the interatomic interaction energy. The results of computer simulation of the structure were confirmed experimentally.

In this study we examined the possibility of using molybdate phosphates $Na_{1-y}Zr_2(MoO_4)_y(PO_4)_{3-y}$ as convenient objects for model studies of their catalytic properties in methanol transformations in inert (Ar) and oxidizing (air) atmospheres. The dehydration and dehydrogenation of methanol can yield dimethyl ether (promising additive to diesel fuel), formaldehyde, hydrogen, carbon oxides, and other products. Our goal was to prepare the molybdate phosphates $Na_{1-y}Zr_2 \cdot (MoO_4)_y(PO_4)_{3-y}$ (y = 0, 0.25, 0.5), characterize their surface properties, and examine their catalytic activity in methanol transformations in the inert and oxidizing atmospheres.

EXPERIMENTAL

The molybdate phosphates $Na_{1-y}Zr_2(MoO_4)_y \cdot (PO_4)_{3-y}$ were prepared from the following chemically pure grade chemicals: zirconium oxochloride $ZrOCl_2 \cdot 8H_2O$, phosphoric acid H_3PO_4, sodium chloride NaCl, and ammonium paramolybdate $(NH_4)_6 \cdot Mo_7O_{24} \cdot 4H_2O$. Weighed portions of ammonium paramolybdate were dissolved in a small amount of water, and 1 M solutions of sodium chloride and zirconium oxochloride were added in stoichiometric

Table 1. Results of microprobe analysis, surface area, and acidity of molybdate phosphates $Na_{1-y}Zr_2(MoO_4)_y(PO_4)_{3-y}$

Theoretical composition, y	Microprobe analysis	BET specific surface area, $m^2\ g^{-1}$	Acidity, $\mu mol\ g^{-1}$
0	$Na_{0.96(2)}Zr_{1.93(4)}Hf_{0.02(1)}P_{3.01(4)}O_{12}$	63.0	243.1
0.25	$Na_{0.73(3)}Zr_{1.98(3)}Hf_{0.02(0)}P_{2.79(3)}Mo_{0.22(2)}O_{12}$	22.3	107.2
0.50	$Na_{0.51(3)}Zr_{2.03(4)}Hf_{0.02(1)}P_{2.49(3)}Mo_{0.48(3)}O_{12}$	16.4	56.1

amounts. Then a stoichiometric amount of 1 M H_3PO_4 was added with continuous stirring at 343 K. The resulting gel was dried at 363 and 473 K and then heat-treated with free access of air at 873 and 923 K for no less than 24 h in each step, with intermediate grindings to ensure homogenization of the mixtures. The optimal mode of the heat treatment was chosen in accordance with the previous data [12].

The chemical composition and homogeneity of the molybdate phosphate samples were monitored with a CamScan MV-2300 scanning electron microscope (VEGA TS 5130MM), equipped with YAG detectors of secondary and reflected electrons and a Link INCA ENERGY 200C energy-dispersive X-ray microanalyzer with a Si(Li) semiconductor detector. When calculating the composition, we used the PAP correction method. The results of the microprobe analysis confirmed the homogeneity of the samples and were consistent with the theoretical composition (Table 1). The molybdate phosphates were polycrystalline powders with the prevalent crystallite size of 1–10 μm.

The phase composition of the samples was determined by X-ray phase analysis (XPA) with a DRON 3M diffractometer using Ni-filtered CuK_α radiation in the angle range $2\theta = 10°–50°$. The patterns were recorded at a rate of 2 deg min^{-1}. X-ray diffraction data for the synthesized $Na_{1-y}Zr_2(MoO_4)_y(PO_4)_{3-y}$ samples show that the positions and intensities of the diffraction maxima are close to those given in [11] and that the samples belong to the NZP structural type. The calculated unit cell parameters of the molybdate phosphates are given in Table 2.

Table 2. Unit cell parameters of molybdate phosphates $Na_{1-y}Zr_2(MoO_4)_y(PO_4)_{3-y}$

y	a	c	V
	Å		Å^3
0	8.813 (1)	22.740 (2)	1529.6 (2)
0.25	8.845 (1)	22.703 (3)	1538.2 (2)
0.50	8.871 (2)	22.670 (3)	1545.0 (2)

The specific surface area of the molybdate phosphates was calculated from the adsorption–desorption isotherms obtained with a Micrometritics ASAP 2020 installation by the method of capillary condensation of nitrogen at 77 K. The acidity of the samples was calculated from the curves of temperature-programmed desorption of ammonia. The calculation results are given in Table 1. An increase in the molybdenum content of the samples led to their sintering in the course of the synthesis and to a decrease in the surface area and acidity.

The catalytic properties of the molybdate phosphates in methanol transformations were studied in a flow-through reactor in argon or air flow at atmospheric pressure in the temperature range 450–700 K. A 0.300-g portion of molybdate phosphate was mixed with quartz (mean particle size 1 mm). Saturated methanol vapor from a temperature-controlled bubbler was fed into the reactor in a flow of a carrier gas (Ar or air) at a total rate of 1.2 l h^{-1}. The ratio of the space velocities of methanol and oxygen was 1 : 4.6. The reaction products were analyzed with an LKhM-5 chromatograph equipped with a thermal conductivity detector and with columns packed with activated carbon and Porapak T. The chromatograms were processed with a computer. From the results of the analysis, we calculated the methanol conversion x (%), selectivity S (%), and yields of target products A (mmol h^{-1} g^{-1}) by the formulas

$$x = \frac{(\varphi_0 - \varphi_1)}{\varphi_0} \times 100, \quad S = \frac{\varphi_t}{(\varphi_0 - \varphi_1)} \times 100, \quad A = \frac{FxS}{W},$$

where φ_0 and φ_1 are the initial and running volume fractions of methanol; φ_t, fraction of methanol consumed in the target reaction; F, rate of feeding methanol vapor (mmol h^{-1}); and W, catalyst weight (g).

The calculated amounts of methanol consumed and products formed in all the catalytic experiments agree with the material balance within the measurement error (±3%).

In the series of $Na_{1-y}Zr_2(MoO_4)_y(PO_4)_{3-y}$ samples, the phosphate $NaZr_2(PO_4)_3$ ($y = 0$) showed the

Table 3. Catalytic activity of zirconium-containing phosphates and known catalysts of methanol dehydration

Compound*	Methanol conversion** (573 K), %	Activity, mmol h^{-1} g^{-1}	BET specific surface area, m^2 g^{-1}	Acidity, μmol m^{-2}	References
$Zr_{0.25}Zr_2(PO_4)_3$	70	5.2	35.22	5.0	[6]
$NaZr_2(PO_4)_3$ [1]	86	6.4	63.0	3.9	This work
$NaZr_2(PO_4)_3$ [2]	87	1.6	26.81	2.4	[6]
$KZr_2(PO_4)_3$	36	2.7	–	–	[6]
$CsZr_2(PO_4)_3$	17	1.2	6.37	–	[6]
$Mg_{0.5}Zr_2(PO_4)_3$	22	1.5	6.90	7.4	[6]
$Ca_{0.5}Zr_2(PO_4)_3$	19	1.1	3.24	5.8	[6]
$Ba_{0.5}Zr_2(PO_4)_3$	7	0.5	2.50	1.6	[6]
$Al_2O_3 \cdot (0–0.3)SiO_2$	74–86	0.9–3.0	252–383	1.0–1.2	[14]
$Al_2O_3 \cdot (0.3–1.0)P_2O_5$	75–83	1.2–2.7	156–385	0.5–2.0	[15]
$(0.4–4.0)SiO_2 \cdot TiO_2$	15–20	0.2	17–60	0.9–7.0	[15]
$Ti_xZr_{1-x}O_2$, x = 0–1.0	25–83 (613 K)	0.6–2.13 (613 K)	45–225	4.2–6.1	[16]
DME–FCAT	82	1.4	168	1.7	[15]

* Methanol feeding rate, ml min^{-1}: [1] 0.88 and [2] 0.20.
** Equilibrium conversion of methanol 90%.

highest catalytic activity and nearly 100% selectivity in the dehydration of methanol to dimethyl ether (DME) in an argon flow:

$$2CH_3OH \rightleftarrows CH_3OCH_3 + H_2O. \quad (1)$$

The methanol conversion is close to the equilibrium value, 89%, at 600 K. The phosphate $NaZr_2(PO_4)_3$ well competes as methanol dehydration catalyst with other phosphates $AZr_2(PO_4)_3$ (A = K, Rb, Cs, $Mg_{0.5}$, $Ca_{0.5}$, $Ba_{0.5}$, $Zr_{0.25}$) [6], synthetic aluminosilicates, aluminophosphates, composites based on oxides of aluminum and titanium or titanium and zirconium, and commercially produced DME–FCAT catalyst (Haldor Topsoe). It shows higher productivity and ensures almost equilibrium conversion at 2–5 times higher loads (Table 3). The activity of catalysts in methanol dehydration is associated with their acid properties, which are determined by Brønsted acid centers (–OH) present on the surface of the compounds and by coordination-unsaturated cations having high charge, exerting a strong polarizing effect, and thus acting as electron density acceptors (Lewis acid centers) [15]. It was shown [5] that on the surface of the phosphate $Zr_{0.25}Zr_2(PO_4)_3$ (NZP structural type) there are strong (Zr–OH) and weak (P–OH) Brønsted acids centers and Lewis acid senters (Zr^{4+}). The schemes of formation of the adsorption complexes of methanol with acid centers of zirconium-containing phosphates are, presumably, as follows:

$$Zr–OH + O(H)CH_3 \rightleftarrows Zr–OH\text{---}O(H)CH_3,$$

$$Zr^{4+} + O(H)CH_3 \rightleftarrows Zr^{4+}\text{---}O(H)CH_3.$$

Apparently, higher activity (with respect to converted methanol) of zirconium-containing phosphates in the dehydration of methanol, compared to known alcohol dehydration catalysts, is due to higher concentration and optimal strength of acid centers on the surface.

The methanol conversion on molybdate–phosphate catalysts in an Ar atmosphere reached 93% (Fig. 1). This value is higher than the equilibrium conversion

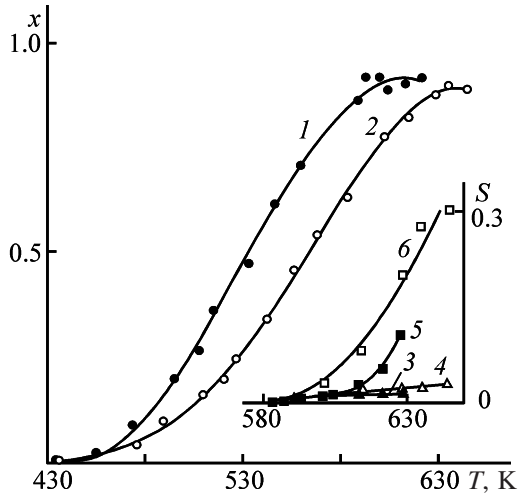


Fig. 1. (*1*, *2*) Conversion x and selectivity S of (*3*, *4*) dehydrogenation and (*5*, *6*) methanol decomposition in an inert atmosphere on molybdate phosphates $Na_{1-y}Zr_2(MoO_4)_y \cdot (PO_4)_{3-y}$ with (*1*, *3*, *5*) y = 0.25 and (*2*, *4*, *6*) y = 0.5, as functions of temperature T.

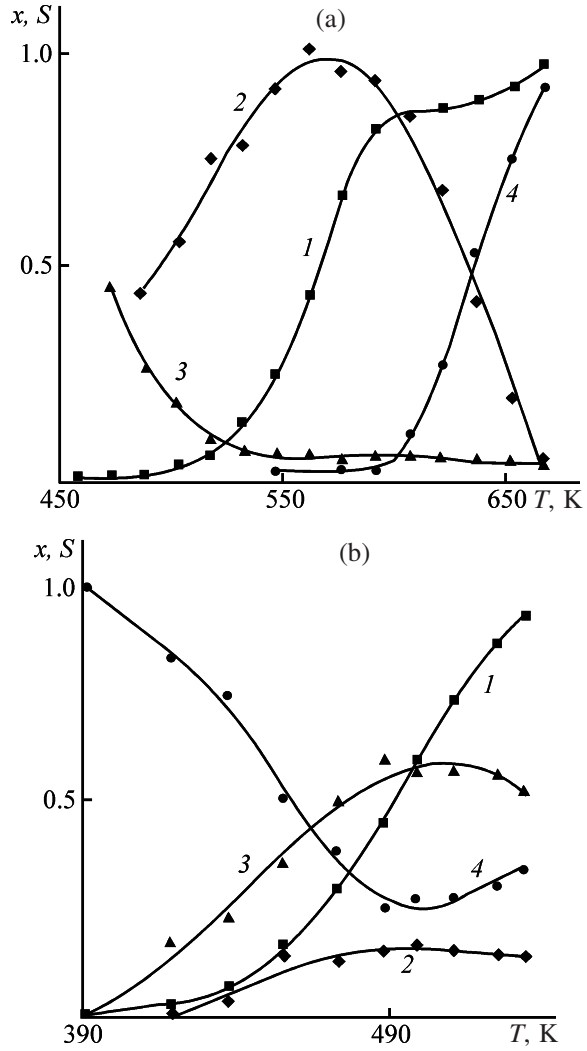


FIg. 2. (*1*) Conversion x and selectivity S of (*2*) dehydration, (*3*) dehydrogenation, and (*4*) decomposition of methanol on (a) $NaZr_2(PO_4)_3$ and (b) $Na_{0.5}Zr_2(MoO_4)_{0.5}(PO_4)_{2.5}$ in oxidizing atmosphere, as functions of temperature T.

of methanol in the dehydration (88–90%) in the examined temperature range, which is due to parallel occurrence of the dehydration (selectivity 66–100%), dehydrogenation to formaldehyde, and decomposition to carbon oxides. At temperatures above 620 K, the selectivity of methanol dehydrogenation and decomposition reached 3 and 30%, respectively (Fig. 1). With respect to the methanol conversion on molybdate phosphates at the same temperature, the most active catalyst was $Na_{0.75}Zr_2(MoO)_{0.25}(PO_4)_{2.75}$ (y = 0.25), and $Na_{0.5}Zr_2(MoO)_{0.5}(PO_4)_{2.5}$ (y = 0.5) was less active. The difference in the alcohol conversion was 20–25%. The molybdate phosphate with y = 0.25 is more active than that with y = 0.5 in methanol dehydration but less active in methanol dehydrogenation. For the sample with y = 0.25, the maximal amount of methanol converted along the dehydration pathway at 593 K was 6.5 mmol h^{-1} g^{-1}, and the dehydrogenation selectivity was 1%; for the sample with y = 0.5, the respective quantities were 4.9 mmol h^{-1} g^{-1} and 3% at the same temperature. This difference is attributable to larger specific surface area and acidity of the former sample and its lower molybdenum content, as the methanol dehydration is a typical acid-catalyzed reaction, whereas the components responsible for dehydrogenation are transition metal (Mo) atoms.

In all the experiments, the hydrogen yield was 2–10 times lower than the value corresponding to the amounts of the dehydrogenation and decomposition products. Furthermore, the hydrogen yield decreased with an increase in the molybdenum content of the catalyst. These facts are apparently due to the reduction of the Mo(VI) ions in the molybdate phosphates with the formation of water. This assumption also accounts for the observed decrease with time of the activity of the molybdate phosphates in the methanol dehydrogenation and an increase in the dehydration selectivity in the course of catalytic experiments, and also for the fact that the amount of water formed exceeds (by ~6%) the quantity corresponding to the amount of dimethyl ether formed.

When the catalytic experiments with the molybdate phosphates (y = 0.25 and 0.5) were performed in an oxidizing atmosphere, among methanol transformation products we also detected formaldehyde and carbon oxides, along with dimethyl ether and water. The temperature dependence of the selectivity of the methanol dehydration [reaction (1)] on $NaZr_2(PO_4)_3$ passes through a maximum (97%) at 570 K and gradually decreases to 5% at 670 K (Fig. 2a).

Simultaneously with a decrease in the selectivity of the methanol dehydration, the yield of water and selectivity of formation of carbon oxides increase (the latter, to 92%). The maximal conversion of methanol reached 96%, at the catalyst activity with respect to converted methanol of 7.2 mmol h^{-1} g^{-1}. We believe that the observed trend is due to the occurrence of exhaustive oxidation of both methanol [Eq. (2)] and its dehydration product, dimethyl ether [Eq. (3)]:

$$CH_3OH + 1.5O_2 \rightleftarrows CO_2 + 2H_2O, \quad (2)$$

$$CH_3OCH_3 + 3O_2 \rightleftarrows 2CO_2 + 3H_2O. \quad (3)$$

Reactions (2) and (3) are characterized by a definite ratio of the amounts of the converted reactants and formed products; therefore, to determine the tempera-

ture ranges of the occurrence of reactions (2) and (3), we plotted the ratios of the methanol consumption and product formation.

Below 550 K, according to the experimental data, the H_2O/CO_2 ratio is less than 1.5, which contradicts Eqs. (2) and (3) and suggests the occurrence of an additional pathway of the formation of carbon oxides. Apparently, such a pathway is conversion of methanol with water vapor:

$$CH_3OH + H_2O \rightleftarrows CO_2 + 3H_2, \quad (4)$$

with water formed by dehydration of methanol [reaction (1)]. Simultaneous occurrence of reactions (3) and (4) can lead to the H_2O/CO_2 ratio less than 1.5. When calculating the amount of methanol consumed for the formation of dimethyl ether that burnt out in reaction (3), we took into account the amounts of methanol consumed in reactions (2) and (4) and of water released in these reactions. In so doing, we took into account the molar ratios of the participants of reaction (1): $CH_3OH/CH_3OCH_3 = 2$, $CH_3OCH_3/H_2O = 1$.

The maximum of the formation of dimethyl ether (560–580 K) corresponds to the ratio $H_2O/CO_2 = 1.5$, suggesting the occurrence of reaction (3). With a further increase in the temperature, this ratio increased to 2, and the CH_3OH/CO_2 and CH_3OH/H_2O ratios simultaneously approached 1 and 0.5, respectively, suggesting the occurrence of reaction (2).

The selectivity of $NaZr_2(PO_4)_3$ with respect to formaldehyde formation in an oxidizing atmosphere was virtually constant, about 6%. As this phosphate contains no metals that can change the oxidation state and thus act as possible active centers of methanol dehydrogenation, the formation of formaldehyde can be accounted for as follows. On the surface of zirconium-containing phosphates there are Lewis acid centers Zr^{4+} [5]. The Zr^{4+} ion is coordination-unsaturated and has vacant 4*d* orbitals owing to which it can adsorb oxygen having free 2*p* electrons. The reaction of such adsorbed complex with a methanol molecule apparently yields formaldehyde with the regeneration of the Zr^{4+} ion:

$$Zr^{4+}O_{ads} + CH_3OH \rightarrow Zr^{4+} + CH_2O + H_2O. \quad (5)$$

The low yield of the dehydrogenation products is due to the low capability of the Zr^{4+} ion for oxygen adsorption.

On molybdate phosphates with $y = 0.25$ and 0.5 in an oxidizing medium, the rate of methanol dehydrogenation increases. The complete conversion of methanol occurs at temperatures 100 K lower than in an inert atmosphere. $Na_{0.5}Zr_2(MoO_4)_{0.5}(PO_4)_{2.5}$ is the most active (3.6 mmol h^{-1} g^{-1} of formaldehyde) and selective (56–60%) in methanol dehydrogenation, with the dehydration selectivity being less than 16% (Fig. 2b). Increased yield of the dehydrogenation products on molybdate phosphates in an oxidizing atmosphere is due to permanent regeneration of active centers, Mo(VI), whereas in an inert atmosphere, as shown above, their amount and the catalyst activity decrease with time.

CONCLUSIONS

(1) Framework molybdate phosphates of the $Na \cdot Zr_2(PO_4)_3$ structural type, $Na_{1-y}Zr_2(MoO_4)_y(PO_4)_{3-y}$ ($y = 0$, 0.25, 0.5), were prepared by the sol–gel method and characterized by X-ray diffraction, electron microprobe analysis, capillary condensation of nitrogen, and temperature-programmed desorption of ammonia.

(2) Molybdate phosphates were studied in methanol transformations in inert (Ar) and oxidizing (air) atmospheres. The main products formed in an inert atmosphere are dimethyl ether and water. In the process, $NaZr_2(PO_4)_3$ well competes with the known catalysts of methanol dehydration. Oxidative dehydrogenation of methanol in the presence of air yielded formaldehyde with up to 60% selectivity.

(3) The activity of molybdate phosphates in the dehydration and dehydrogenation of methanol depends on the surface properties and concentration of molybdenum ions in the phosphate structure.

ACKNOWLEDGMENTS

The study was financially supported by the Russian Foundation for Basic Research (project nos. 06-03-08 064, 07-03-90 808).

REFERENCES

1. Pet'kov, V.I. and Orlova, A.I., *Neorg. Mater.*, 2003, vol. 39, no. 10, pp. 1174–1185.
2. Orlova, A.I., Pet'kov, V.I., Gul'yanova, S.G., et al., *Zh. Fiz. Khim.*, 1999, vol. 73, no. 11, pp. 1965–1967.
3. Ienealem, S.N., Gul'yanova, S.G., Chekhlova, T.K., et al., *Zh. Fiz. Khim.*, 2000, vol. 74, no. 12, pp. 2281–2284.
4. Pavlova, S.N., Sadykov, V.A., Zabolotnaya, G.V., et al., *J. Mol. Catal. A: Chem.*, 2000, vol. 158, no. 1, pp. 319–323.

5. Ziyad, M., Rouimi, M., and Portefaix, J.-L., *Appl. Catal. A: Gen.*, 1999, vol. 183, no. 1, pp. 93–105.
6. Sukhanov, M.V., Ermilova, M.M., Orekhova, N.V., et al., *Vestn. Nizhegor. Gos. Univ.*, 2007, no. 1, pp. 89–94.
7. Serghini, A., Brochu, R., Olazcuaga, R., and Gravereau, P., *Mater. Lett.*, 1995, vol. 22, pp. 149–153.
8. Pylinina, A.I., Dobrova, E.P., Mikhalenko, I.I., and Yagodovskaya, T.V., *Zh. Fiz. Khim.*, 2005, vol. 79, no. 4, pp. 650–655.
9. Brik, Y., Kacimi, M., Bozon-Verduraz, F., and Ziyad, M., *Micropor. Mesopor. Mater.*, 2001, vol. 43, pp. 103–112.
10. Agaskar, P.A., Gasselli, R.K., Buttrey, D.J., and White, B., *Stud. Surf. Sci. Catal.*, 1997, vol. 110 (3rd Congr. on Oxidation Catalysis, 1997), pp. 219–226.
11. Serghini, A., Brochu, R., Ziyad, M., et al., *J. Chem. Soc., Faraday Trans.*, 1991, vol. 87, no. 15, pp. 2487–2491.
12. Pet'kov, V.I., Sukhanov, M.V., and Kurazhkovskaya, V.S., *Radiokhimiya*, 2003, vol. 45, no. 6, pp. 560–565.
13. Sukhanov, M.V., Pet'kov, V.I., Kurazhkovskaya, V.S., et al., *Zh. Neorg. Khim.*, 2006, vol. 51, no. 5, pp. 773–779.
14. Yaripour, F., Baghaei, F., Schmidt, I., and Perregaard, J., *Catal. Commun.*, 2005, vol. 6, pp. 147–152.
15. Yaripour, F., Baghaei, F., Schmidt, I., and Perregaard, J., *Catal. Commun.*, 2005, vol. 6, pp. 542–549.
16. Vishwanathan, V., Roh Hyun-Seog, Kim Jae-Woo, and Jun Ki-Won, *Catal. Lett.*, 2004, vol. 96, nos. 1–2, pp. 23–28.

ISSN 1070-4272, Russian Journal of Applied Chemistry, 2008, Vol. 81, No. 1, pp. 23–25. © Pleiades Publishing, Ltd., 2008.
Original Russian Text © K.N. Semenov, N.A. Charykov, O.V. Arapov, V.A. Keskinov, A.K. Pyartman, M.S. Gutenev, O.V. Proskurina, M.Yu. Matuzenko, V.V. Klepikov, 2008, published in Zhurnal Prikladnoi Khimii, 2008, Vol. 81, No. 1, pp. 25–27.

PHYSICOCHEMICAL STUDIES OF SYSTEMS AND PROCESSES

Polythermal Solubility of Light Fullerenes in Valeric and Caproic Acids in the Temperature Range 20–80°C

K. N. Semenov, N. A. Charykov, O. V. Arapov, V. A. Keskinov, A. K. Pyartman, M. S. Gutenev, O. V. Proskurina, M. Yu. Matuzenko, and V. V. Klepikov

St. Petersburg State University, St. Petersburg, Russia
Innovations of Leningrad Institutes and Enterprises, Private Company, St. Petersburg, Russia
St. Petersburg State Institute of Technology (Technical University), St. Petersburg, Russia

Received July 7, 2007; in final form, October 2007

Abstract—The polythermal solubility of fullerene C_{60} and a fullerene mixture (60 wt % C_{60} + 39 wt % C_{70} + 1 wt % higher fullerenes C_n, n = 76, 78, 84, 90...) in valeric and caproic acids was studied in the temperature range 20–80°C. The solubility diagrams are presented and characterized.

DOI: 10.1134/S1070427208010059

The paper completes a series of studies devoted to the polythermal solubility of fullerene C_{60} and a fullerene mixture (C_{60} + C_{70} + C_n, n = 76, 78, 84, 90...) in saturated monocarboxylic acids $C_{n-1}H_{2n-1}COOH$ (n = 1–9) that are liquid at room temperature [1–3].

Studies of the solubility of fullerenes are of primary importance for developing the crystallization and extraction methods of separation of fullerenes from a fullerene-containing carbon black, for studying chemical reactions with participation of fullerenes, and for developing methods of chromatographic and prechromatographic separation of a fullerene mixture into individual fullerene components [4–6].

EXPERIMENTAL

In the experiments we used fullerene C_{60} of 99.9% purity containing about 0.07 wt % C_{70}, a fullerene mixture 60 wt % C_{60} + 39 wt % C_{70} + 1 wt % C_n (n = 76, 78, 84, 90...) from ILIP (Innovations of Leningrad Institutes and Enterprises) Private Company (St. Petersburg), *o*-xylene (analytically pure grade), and caproic and valeric acids (chemically pure grade).

Experimentally, the polythermal solubility of both the individual fullerene C_{60} and a fullerene mixture was studied by the isothermal saturation method in the temperature range 20–80°C on a temperature-controlled shaker [1–3].

The concentrations of C_{60} and a fullerene mixture after each step of saturation were determined spectrophotometrically on a Specord M-32 spectrophotometer at λ 335.5 and 472.0 nm. The method of the analysis is reported in [7].

Hereinafter, the presence of minor amounts (about 1 wt %) of higher fullerenes C_n (n = 76, 78, 84, 90...) in the analysis was neglected.

The solvent content of crystal solvates was determined as follows. The solid phase that just precipitated from a carboxylic acid solution was washed twice with ethanol, dried at 20°C for 30 min, and weighed. Then, the resulting solid was repeatedly refluxed with ethanol in a Soxhlet apparatus (78°C, 1 atm), vacuum-dried at 200°C (0.1 mm Hg) for 1 h, and weighed again. The solvent content of the initial crystal solvate (or solid solution of fullerenes on its basis) was determined as the weight loss.

Figure 1 shows the electronic absorption spectra of the individual fullerene C_{60} and a fullerene mixture in caproic acid. Similar spectra were obtained in valeric acid. It is easily seen that the recorded spectra are stable and fully correspond to the absorption spectra of light fullerenes in one-component aromatic solvents (benzene, toluene, *o*-xylene, and *o*-dichlorobenzene) [7], so that the use of empirical relationships from [7] for calculating the concentrations of light fullerenes is quite reasonable in the given case.

Figure 2 shows six solubility polytherms of C_{60} and fullerene mixture in caproic and valeric acids.

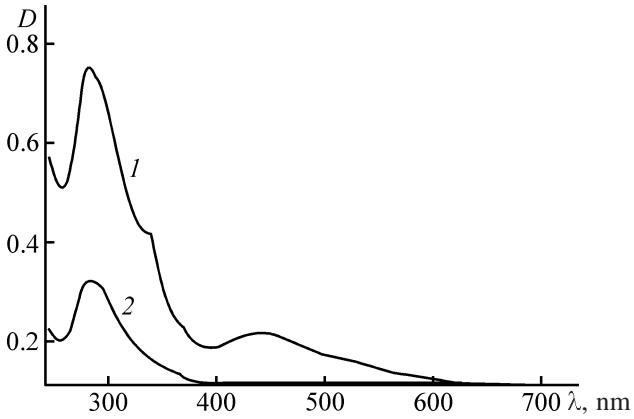


Fig. 1. Electronic absorption spectra. (*D*) Optical density and (λ) wavelength. (*1*) Fullerene mixture in caproic acid diluted with *o*-xylene in the 1 : 41 ratio and (*2*) fullerene C_{60} in caproic acid, diluted with *o*-xylene in the 1 : 61 ratio (reference solution is caproic acid diluted with *o*-xylene in the same ratio).

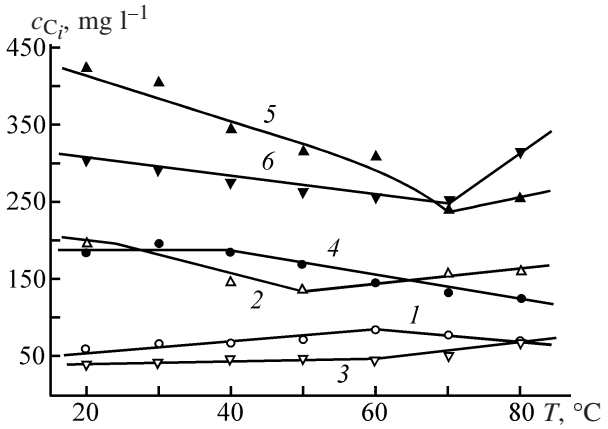


Fig. 2. Solubility polytherms. (c_{C_i}) Concentration of fullerenes and (*T*) temperature. (*1*) C_{60} in valeric acid, (*2, 3*) C_{60} and C_{70} from the fullerene mixture in valeric acid, (*4*) C_{60} in caproic acid, and (*5, 6*) C_{60} and C_{70} from the fullerene mixture in caproic acid.

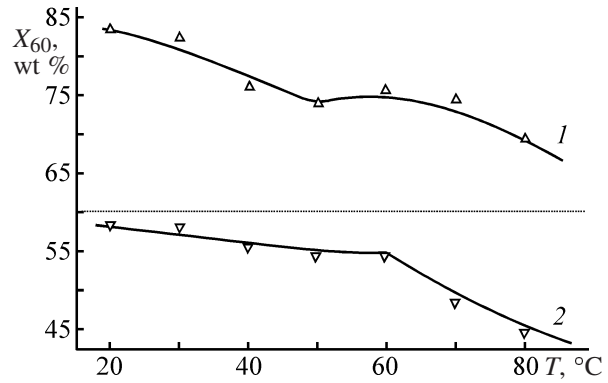


Fig. 3. Temperature dependence of the C_{60} content X_{60} in a mixture of light fullerenes C_{60} + C_{70} in the saturated liquid solution. Acid: (*1*) valeric and (*2*) caproic. The dotted line denotes the composition of the initial solid solution being dissolved.

Solubility *S* of light fullerenes in valeric and caproic acids

T, °C	Solubility, mg l^{-1}		
	C_{60}	C_{60} from mixture	C_{70} from mixture
	Valeric acid		
20	58.21	194.2	38.90
30	65.00	190.9	40.72
40	67.66	147.8	46.26
50	71.18	135.4	47.46
60	86.05	147.3	47.15
70	80.05	159.1	53.79
80	70.06	162.0	70.56
	Caproic acid		
20	184.4	423.5	303.2
30	196.7	405.1	290.9
40	186.1	344.3	275.0
50	170.4	315.4	262.6
60	146.3	310.3	257.6
70	135.2	241.2	254.3
80	127.1	257.8	315.2

The table lists experimental polythermal data on the solubility of individual C_{60} and of C_{60} and C_{70} from the fullerene mixture in these acids.

The temperature dependences of the C_{60} solubility in these acids are close: a slight monotonic increase with temperature at relatively low temperatures, then singular break point, and a monotonic decrease at high temperatures. Thus, the solubility diagrams for C_{60} in both acids consist of two solubility branches: a low-temperature branch (crystallization of fullerene monosolvate C_{60}–$C_{60} \cdot C_{n-1}H_{2n-1}COOH$) and a high-temperature branch (crystallization of unsolvated C_{60}). All diagrams contain one nonvariant through-pass point [8, 9], which corresponds to simultaneous saturation with both solid phases. This run of the polythermal dependences (Fig. 2) is rather typical of C_{60} and is in satisfactory agreement with the solubility data available from the literature [10]. Similar run is also observed for the solubility of light fullerenes C_{60} and C_{70} from the fullerene mixture in both acids. As in the previous case, each diagram consists of two solubility branches and has one nonvariant break point.

Figure 3 shows how the content (wt %) of C_{60} in a mixture of light fullerenes C_{60} + C_{70} in the saturated liquid solution varies with temperature. It can be readily seen that valeric and caproic acids exert the opposite effects. In valeric acid, the liquid phase is

always enriched in fullerene C_{60} relative to a solid solution at all temperatures, whereas in caproic acid, the liquid phase is always depleted of this fullerene. It is also seen from Fig. 3 that, with increasing temperature, the liquid phases based on both acids become richer in a more polarizable fullerene C_{70}, with the liquid solution based on caproic acid at 80°C enriched by more than 15 wt % relative to the initial solid solution being dissolved. This effect can be used in practice in cascade recrystallization for prechromatographic isolation of fullerene C_{70}.

CONCLUSIONS

(1) The solubility diagrams of the binary systems C_{60}–valeric acid and C_{60}–caproic acid were obtained; the temperature dependences of the solubility are nonmonotonic, which corresponds to the solvation mechanism of dissolution.

(2) In the case of valeric acid, the liquid phase is enriched in fullerene C_{60} in comparison with the solid solution at all temperatures, whereas in the case of caproic acid, the liquid phase is always enriched in fullerene C_{70}.

(3) The prospects for using valeric and caproic acids as solvents for prechromatographic isolation of light fullerenes were demonstrated.

REFERENCES

1. Semenov, K.N., Pyartman, A.K., Keskinov, V.A., et al., *Zh. Prikl. Khim.*, 2007, vol. 80, no. 1, pp. 39–42.
2. Semenov, K.N., Charykov, N.A., Pyartman, A.K., et al., *Zh. Prikl. Khim.*, 2007, vol. 80, no. 3, pp. 461–465.
3. Semenov, K.N., Charykov, N.A., Pyartman, A.K., et al., *Zh. Prikl. Khim.*, 2007, vol. 80, no. 4, pp. 570–574.
4. Korobov, M.V., and Smith, A.L., *Solubility of Fullerenes*, New York: Wiley, 2000, pp. 53–90.
5. Zhou, X., *Fullerene Sci. Technol.*, 1997, vol. 5, pp. 285–290.
6. Beck, M., *Pure Appl. Chem.*, 1998, vol. 70, no. 10, pp. 1881–1887.
7. Ponomarev, A.N., Yudovich, M.I., Charykov, N.A., et al., *Opt. Spektrosk.*, 2000, vol. 88, no. 2, pp. 230–232.
8. Charykov, N.A., Shakhmatkin, B.A., Charykova, M.V., et al., *Zh. Fiz. Khim.*, 2000, vol. 74, no. 9, pp. 1562–1569.
9. Charykov, N.A., Rumyantsev, A.V., and Charykova, M.V., *Zh. Fiz. Khim.*, 1998, vol. 72, no. 10, pp. 1746–1750.
10. Bezmel'nitsyn, V.N., Eletskii, A.V., and Okun', M.V., *Usp. Fiz. Nauk*, 1998, vol. 168, no. 11, pp. 1195–1218.

ISSN 1070-4272, Russian Journal of Applied Chemistry, 2008, Vol. 81, No. 1, pp. 26–29. © Pleiades Publishing, Ltd., 2008.
Original Russian Text © Yu.A. Ferapontov, M.A. Ul'yanova, T.V. Sazhneva, N.P. Kozlova, 2008, published in Zhurnal Prikladnoi Khimii, 2008, Vol. 81, No. 1, pp. 28–31.

PHYSICOCHEMICAL STUDIES OF SYSTEMS AND PROCESSES

Kinetics of Decomposition of the Liquid Phase of the Ternary System $LiOH–H_2O_2–H_2O$ in the Presence of the Solid Phase of $Li_2O_2 \cdot H_2O$

Yu. A. Ferapontov, M. A. Ul'yanova, T. V. Sazhneva, and N. P. Kozlova

Roskhimzashchita Corporation, Open Joint-Stock Company, Tambov, Russia

Received July 11, 2007

Abstract—The kinetics of decomposition of hydrogen peroxide in the liquid phase of the ternary system $LiOH–H_2O_2–H_2O$ was studied in the presence the solid phase of $Li_2O_2 \cdot H_2O$ and without it. The main kinetic parameters of the processes studied were determined.

DOI: 10.1134/S1070427208010060

To prepare peroxides of alkali and alkaline-earth metals (principal components of products for chemical regeneration of air in closed volumes), hydrogen peroxide and a hydroxide of the corresponding metal are commonly used as starting components. Peroxo solvates of varied chemical composition, obtained by crystallization from the solution, are then dehydrated to form dry peroxides (Li, Na, Ca, Ba) and superoxides (K, Rb, Cs) [1–8]. In this case, to prepare the products containing the maximum amount of the main substance, water must be removed during dehydration as quickly as possible, and its amount should be as low as possible, to avoid the reaction of the formed peroxides or superoxides with water vapor [9]. At the same time, to choose the optimal process parameters, it is necessary to determine the temperature and concentration conditions ensuring the crystallization of peroxo solvates of varied chemical composition from the $MOH–H_2O_2–H_2O$ ternary systems (M is alkali metal), which is complicated by the known experimental difficulties associated with instability of liquid and solid phases. The catalytic decomposition of peroxy compounds, occurring in the process under the action of hydroxide anions, is exothermic, which affects the temperature conditions of the study. Owing to relatively high solubility of the forming peroxo solvates, a fast shift of figurative points along the solubility curve toward lower hydrogen peroxide concentrations is observed as a consequence of the above phenomena. The decomposition rate of hydrogen peroxide solutions in the presence of hydroxides of alkali and alkaline-earth metals increases in the order $LiOH–NaOH–KOH–Ca(OH)_2–Ba(OH)_2$ [2].

At the same time, in the development of a process for the synthesis of lithium peroxide from lithium hydroxide and hydrogen peroxide [10], stabilization of a liquid phase of the ternary system $LiOH–H_2O_2–H_2O$ by the solid phase of $Li_2O_2 \cdot H_2O$ was revealed. This work continues our previous studies and concerns the kinetic parameters of the above interesting phenomenon.

EXPERIMENTAL

In all experiments, we used lithium hydroxide and 50% hydrogen peroxide (ultrapure grade). The effect exerted by the solid phase on the kinetics of decomposition of the liquid phase of the ternary system $LiOH–H_2O_2–H_2O$ was estimated experimentally in the temperature range from 21 to 33°C (hydrogen peroxide concentrations in the liquid phase 1.56–5.67 and 1.82–6.43 wt %, respectively), because the solid phase of the composition $Li_2O_2 \cdot H_2O$ crystallizes under these conditions, which was confirmed previously by chemical and qualitative X-ray phase analyses of the $LiOH–H_2O_2–H_2O$ system studied by the solubility method [10].

It is well known that the catalytic decomposition of hydrogen peroxide and peroxide-containing products in a liquid phase involves two constituents: homogeneous catalysis by ions present in the solution and heterogeneous catalysis by the reactor walls and solid phases constituting the system studied [11, 12]. To make experiments identical, all reactors had the same shape (Pyrex glass cylinders, $r = 4$ cm). In the course

of the experiments, the ratio of the surface area in contact with the liquid phase of the systems studied to their volume was the same ($S/V \approx 0.67$ cm^{-1} = const). This ensured constant contribution of the hydrogen peroxide decomposition on the reactor walls in all experiments [13].

Prior to performing the main experiments, all reactors were passivated with a solution under study at 70–75°C for 24 h. The kinetic data became reproducible after three preliminary passivations.

It was established [14] that hydrogen peroxide is accumulated in the solution in air owing to more intense evaporation of water (at 20°C, the water vapor pressure is 17.5 mm Hg, and hydrogen peroxide vapor pressure is 1.36 mm Hg). Therefore, to prevent removal of water from the solution studied and thus to decrease the experimental error, the reactors with the samples studied were closed and equipped with reflux condensers. With these precautions, the loss of water due to incomplete condensation in the examined range of temperatures was as low as 0.3 wt % throughout the experiment.

In the experiments, to hydrogen peroxide, which was thermostated on a water bath to within ±0.2°C, we added a required amount of lithium hydroxide at a rate chosen so as to avoid temperature changes exceeding 0.5°C. Thus, we prepared simultaneously two samples. Sample no. 1 was used as prepared, whereas from sample no. 2, the solid phase was separated on a Büchner funnel at the experimental temperature (the composition of the solid phase corresponded to the formula $Li_2O_2 \cdot H_2O$, as indicated by chemical and X-ray phase analyses). Samples under study were placed in a thermostat, and the kinetics of decomposition of hydrogen peroxide in the liquid phase was studied. The thermostat was in a dark room throughout the experiment. The mass of the reactors with the samples studied was also measured throughout the experiment. The liquid phase in the systems studied was analyzed by permanganatometric titration over a certain period of time, and the content of hydrogen peroxide in it was determined with an accuracy of ±0.01% [15].

Figure 1 shows the kinetics of the hydrogen peroxide decomposition in the LiOH–H_2O_2–H_2O ternary system containing 6.09 wt % hydrogen peroxide in the liquid phase at T = 30°C. The shapes of the kinetic curves of decomposition of the liquid phase in the LiOH–H_2O_2–H_2O system in the presence of the solid phase of $Li_2O_2 \cdot H_2O$ and without it at the above temperatures and concentrations are similar.

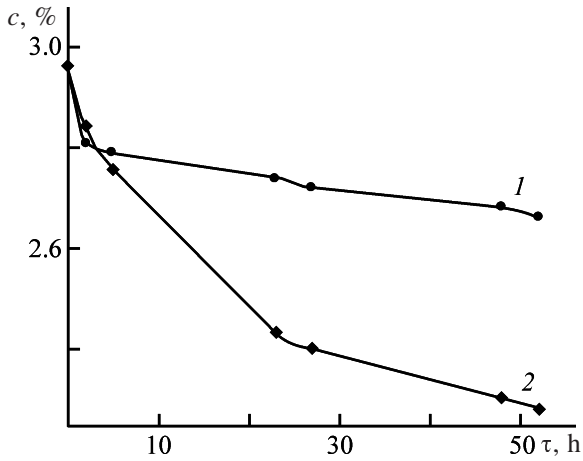


Fig. 1. Kinetic curves of decomposition of the liquid phase of the LiOH–H_2O_2–H_2O system (*1*) in the presence of the solid phase of $Li_2O_2 \cdot H_2O$ and (*2*) without it. (*c*) Content of available oxygen and (τ) time.

Curve *1* characterizes the decomposition of hydrogen peroxide in the liquid phase in the system containing the solid phase of $Li_2O_2 \cdot H_2O$, and curve *2*, the decomposition of hydrogen peroxide in the liquid phase after filtering the solid phase off. The initial section of curve *1*, wherein the concentration of available oxygen in the liquid phase of the LiOH–H_2O_2–H_2O ternary system decreases from 2.96 to 2.81% at constancy of its mass, corresponds to attainment of the phase equilibrium. The equilibrium state (compositions of liquid and solid phases are constant) can be considered to be attained 2 h after mixing the initial components. Similar results were obtained for the studied system containing from 2 to 6 wt % hydrogen peroxide in the liquid phase in the temperature range 21–33°C.

The obtained kinetic curves of the decomposition of hydrogen peroxide in the liquid phase of the LiOH–H_2O_2–H_2O system were treated by the equation for monomolecular reaction:

$$\ln(c_0/c) = k(\tau - \tau_0), \quad (1)$$

where c_0 and c are the contents of available oxygen in the solution studied at times τ_0 and τ, respectively.

In calculating the constants of hydrogen peroxide decomposition in the liquid phase of the system studied in the presence of the solid phase, the time of attainment of the phase equilibrium was assumed to be the initial point.

The temperature dependence of the rate constants of the processes studied k within the temperature

Kinetic parameters of decomposition of the liquid phase of the $LiOH–H_2O_2–H_2O$ ternary system in the presence of the solid phase of composition $Li_2O_2 \cdot H_2O$ (sample no. 1) and without it (sample no. 2)

Sample no.	T, °C	$k \times 10^{-5}$, min^{-1}	Average temperature coefficient γ	Activation energy E_a, kJ mol^{-1}, as calculated by	
				formula (4)	formula (3)
1	21	0.612	3.252	86.12	90.69
	26	1.17			
	30	1.83			
	33	2.52			
2	21	3.98	2.326	62.54	66.02
	26	5.75			
	30	8.37			
	33	10.96			

range 21–33°C is described by the Arrhenius equation

$$k = Ae^{-E_a/RT}, \quad (2)$$

where A is the Arrhenius coefficient for the given reaction, proportional to the number of collisions of active molecules, and E_a, apparent activation energy of the process.

The temperature dependence of the rate constants in Arrhenius coordinates for the decomposition of hydrogen peroxide in the liquid phase is shown in Fig. 2. The activation energy of the processes was calculated, using the presented plots, by the formula [16]

$$E_a = 19.11 \tan\alpha\xi, \quad (3)$$

where $\tan\alpha$ is the slope of the straight line and ξ, the abscissa-to-ordinate scale ratio.

The activation energy of the processes studied was also calculated using the temperature dependence of the time in which the conversion reaches a given value. For the static mode of the experiment, this method of determination of the activation energy yields more correct E_a values in comparison with the calculation based on the reaction rate constants [16, 17]. In the calculation, we used the equation

$$E_a = 4.58 \log(\tau_{T_1}/\tau_{T_2})(1/T_1 - 1/T_2)^{-1}, \quad (4)$$

where T_1 and T_2 are experimental temperatures; τ_{T_1} and τ_{T_2} are times in which 20% of hydrogen peroxide in the liquid phase of the system studied decomposes at temperatures T_1 and T_2, respectively.

The results obtained, as calculated from three replicate experiments, are listed in Table 1.

For the temperature range considered, we calculated, using formula (5), the average temperature coefficients of the rates of decomposition of hydrogen peroxide in the liquid phase of the $LiOH–H_2O_2–H_2O$ ternary system in the presence of the solid phase of $Li_2O_2 \cdot H_2O$ and without it:

$$\log k_{T_1}/k_{T_2} = \log\gamma(T_2 - T_1)/10, \quad (5)$$

where k_{T_1} and k_{T_2} are the rate constants of the reactions at temperatures T_1 and T_2, respectively.

The average temperature coefficients that we found are also listed in Table 1.

Table 1 shows that the solid phase of $Li_2O_2 \cdot H_2O$ in the $LiOH–H_2O_2–H_2O$ ternary system inhibits the decomposition of hydrogen peroxide in the liquid phase. The fact that the activation energies of decomposition of hydrogen peroxide in the liquid phase, obtained by different methods, are virtually the same

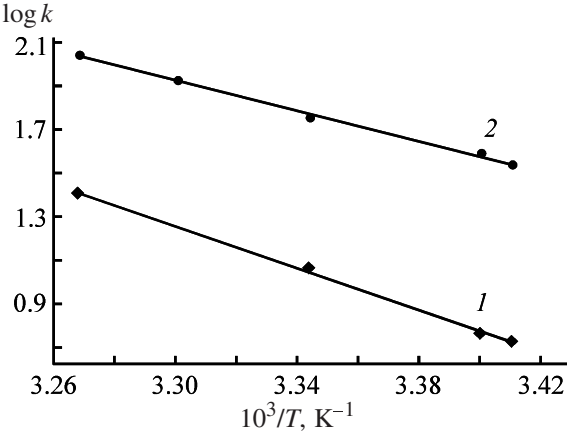


Fig. 2. Temperature dependence of rate constants k of liquid phase decomposition in the $LiOH–H_2O_2–H_2O$ system (*1*) in the presence of the solid phase of $Li_2O_2 \cdot H_2O$ and (*2*) without it.

shows that the suggested rate equation for the reaction is correct.

CONCLUSIONS

(1) The kinetics of decomposition of the liquid phase of the ternary system $LiOH–H_2O_2–H_2O$ in the temperature range from 21 to 33°C (hydrogen peroxide concentrations in the liquid phase 1.56–5.67 and 1.82–6.43 wt %, respectively) can be described by the equation for monomolecular reaction.

(2) The solid phase of the composition $Li_2O_2 \cdot H_2O$ inhibits the decomposition of peroxides in the liquid phase.

(3) The average temperature coefficients for the decomposition rate of hydrogen peroxide in the liquid phase of the $LiOH–H_2O_2–H_2O$ system in the presence of the solid phase of $Li_2O_2 \cdot H_2O$ and without it in the 21–33°C temperature range are 3.25 and 2.32, respectively.

ACKNOWLEDGMENTS

The study was supported by the Russian Foundation for Basic Research (project no. 08-08-975-18).

REFERENCES

1. Vol'nov, I.I., *Perekisnye soedineniya shchelochnykh metallov* (Peroxy Compounds of Alkali Metals), Moscow: Nauka, 1980.
2. Dobrynina, T.A., *Perekis' litiya* (Lithium Peroxide), Moscow: Nauka, 1964.
3. Makarov, S.Z., and Grigor'eva, N.K., *Izv. Akad. Nauk SSSR, Otd. Khim. Nauk*, 1955, pp. 17–24.
4. Raikhshtein, S.I., and Kazarnovskii, I.A., *Zh. Fiz. Khim.*, 1940, vol. 14, pp. 320–322.
5. Makarov, S.Z., and Grigor'eva, N.K., *Zh. Prikl. Khim.*, 1959, vol. 32, no. 10, pp. 2184–2189.
6. Dobrynina, T.A., Okhapkina, N.A., and Chernysheva, A.M., *Izv. Akad. Nauk. SSSR, Ser. Khim.*, 1967, no. 11, pp. 2569–2574.
7. Dobrynina, T.A., Dzyatkevich, B.S., and Okhapkina, N.A., *Izv. Akad. Nauk SSSR, Ser. Khim.*, 1968, no. 3, pp. 398–403.
8. Dobrynina, T.A., *Izv. Akad. Nauk SSSR, Ser. Khim.*, 1967, no. 9, pp. 1858–1863.
9. Zhdanov, D.V., Ferapontov, Yu.A., and Ul'yanova, M.A., *Zh. Prikl. Khim.*, 2005, vol. 78, no. 2, pp. 191–194.
10. Ferapontov, Yu.A., Ul'yanova, M.A., and Sazhneva, T.V., *Khim. Tekhnol.*, 2007, vol. 8, no. 5, pp. 193–196.
11. Seryshev, G.A., *Khimiya i tekhnologiya perekisi vodoroda* (Chemistry and Technology of Hydrogen Peroxide), Leningrad: Khimiya, 1984.
12. Schumb, W.C., Satterfield, C.N., and Wentworth, R.L., *Hydrogen Peroxide*, New York: Reinhold, 1955.
13. Ferapontov, Yu.A., Ul'yanova, M.A., and Zhdanov, D.V., *Khim. Tekhnol.*, 2005, no. 1, pp. 15–18.
14. Titova, K.V., Nikol'skaya, V.P., Buyanov, V.V., and Suprun, I.P., *Zh. Prikl. Khim.*, 2002, vol. 75, no. 12, pp. 1943–1946.
15. Seyb, E., and Kleinberg, J., *J. Am. Chem. Soc.*, 1951, vol. 73, pp. 2308–2315.
16. Emanuel', N.M., and Knorre, D.G., *Kurs khimicheskoi kinetiki* (A Course of Chemical Kinetics), Moscow: Vysshaya Shkola, 1962.
17. Kiperman, S.L., *Vvedenie v kinetiku geterogennykh kataliticheskikh reaktsii* (Introduction to Kinetics of Heterogeneous Catalytic Reactions), Moscow: Nauka, 1964.

ISSN 1070-4272, Russian Journal of Applied Chemistry, 2008, Vol. 81, No. 1, pp. 30–32. © Pleiades Publishing, Ltd., 2008.
Original Russian Text © A.Zh. Abil'daeva, Zh.K. Tukhmetova, Sh.B. Kasenova, S.M. Adekenov, B.K. Kasenov, T.V. Kharlamova, B.Zh. Dzhiembaev, 2008, published in Zhurnal Prikladnoi Khimii, 2008, Vol. 81, No. 1, pp. 32–34.

PHYSICOCHEMICAL STUDIES OF SYSTEMS AND PROCESSES

Thermodynamic Properties of Anthraquinone Derivatives

A. Zh. Abil'daeva, Zh. K. Tukhmetova, Sh. B. Kasenova, S. M. Adekenov, B. K. Kasenov, T. V. Kharlamova, and B. Zh. Dzhiembaev

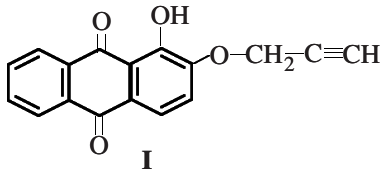
Fitokhimiya Research and Production Center, Joint-Stock Company, Ministry of Eduction and Science of Kazakhstan Republic, Karaganda, Kazakhstan
Bekturov Institute of Chemical Sciences, Almaty, Kazakhstan

Received October 3, 2007

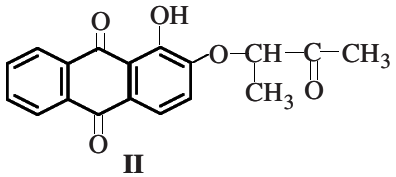
Abstract—The enthalpies of solution of a series of anthraquinone derivatives in dioxane at various dilutions were determined by isothermal calorimetry.

DOI: 10.1134/S1070427208010072

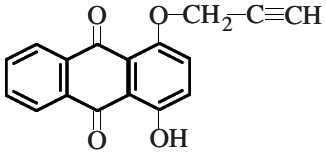
Thermodynamic and thermochemical properties of compounds are of interest for simulation of processes for preparing substances with preset properties. In this study, we determined calorimetrically the enthalpies of solution of anthraquinone derivatives: 1-hydroxy-1-(2-propyn-1-yloxy)-9,10-anthraquinone ($C_{17}H_{10}O_4$) (**I**), 1-hydroxy-2-(1-methyl-2-oxoprop-1-yloxy)-9,10-anthraquinone ($C_{18}H_{14}O_5$) (**II**), and 4-hydroxy-1-(2-propyn-1-yloxy)-9,10-anthraquinone ($C_{17}H_{10}O_4$) (**III**), and estimated their standard enthalpies of combustion ΔH^0_c, melting ΔH^0_m, and formation $\Delta_f H^0_{298.15}$:



I



II



III

The enthalpies of solution of the compounds in dioxane were measured with a DAK-I-IA isothermal calorimeter at three dilutions: 1 : 3000, 1 : 9000, and 1 : 18000 (mole of compound per mole of solvent). The experimental procedure is described in detail elsewhere [1–4]. At each dilution, we performed five replicate measurements. Their results were averaged and statistically treated. For each averaged value of the enthalpy of solution ΔH^0_s we calculated the random error using Student's test and the homogeneity of variance using Cochran's test [5]. The hypothesis of the homogeneity of variance was taken with 5% significance level.

The operation of the device was checked by measuring the enthalpy of solution of triple-recrystallized potassium chloride at dilutions of 1 : 1600, 1 : 2400, and 1 : 3200 (mole of salt per mole of water). The average enthalpy of solution of KCl in water, 17640 ± 320 J mol^{-1}, is well consistent with the recommended and reference data, J mol^{-1}: 17577 ± 34 [6] and 17489 ± 371 [7].

The enthalpies of solution of anthraquinone derivatives in dioxane at three dilutions are given in Table 1.

The obtained enthalpies of solution were extrapolated to infinite dilution using the least-squares method. Based on the known relationship $\Delta H^0_s = f(m^{1/2})$ (m is the molal concentration) [8], we obtained the following equations for each compound (kJ mol^{-1}):

$$\Delta H^m_s(\mathbf{I}) = 405.7 - 6428.8m^{1/2}, \quad (1)$$

$$\Delta H^m_s(\mathbf{II}) = 372.2 - 4437.8m^{1/2}, \quad (2)$$

$$\Delta H^m_s(\mathrm{III}) = 681.0 - 10181.4m^{1/2}, \quad (3)$$

from which we determined the standard enthalpies of

Table 1. Experimental enthalpies of solution of **I–III** in dioxane at various dilutions

Dilution	Compound **I**			Compound **II**			Compound **III**		
	weighed portion, g	ΔH_s, J	ΔH_s^0, kJ mol^{-1}	weighed portion, g	ΔH_s, J	ΔH_s^0, kJ mol^{-1}	weighed portion, g	ΔH_s, J	ΔH_s^0, kJ mol^{-1}
1 : 3000	0.0054	0.5983	30.82	0.0061	2.0112	102.90	0.0054	1.6266	83.79
	0.0054	0.6090	31.37	0.0061	1.9736	100.97	0.0054	1.6406	84.52
	0.0054	0.6122	31.54	0.0061	2.0000	102.32	0.0054	1.6243	83.68
	0.0054	0.6083	31.34	0.0061	2.0138	103.03	0.0054	1.6297	83.95
	0.0054	0.6069	31.26	0.0061	2.0136	103.02	0.0054	1.6324	84.09
		$\Delta\bar{H}_1^0 = 31.27 \pm 0.33$			$\Delta\bar{H}_1^0 = 102.45 \pm 1.1$			$\Delta\bar{H}_1^0 = 84.01 \pm 0.40$	
1 : 9000	0.0018	0.7089	109.56	0.0020	1.2941	200.71	0.0018	1.4622	225.98
	0.0018	0.7155	110.58	0.0020	1.3023	201.98	0.0018	1.4651	226.42
	0.0018	0.7076	109.36	0.0020	1.2963	201.05	0.0018	1.4663	226.61
	0.0018	0.7079	109.40	0.0020	1.2997	201.58	0.0018	1.4720	227.49
	0.0018	0.7180	110.96	0.0020	1.2941	200.71	0.0018	1.4685	226.95
		$\Delta\bar{H}_2^0 = 109.97 \pm 0.92$			$\Delta\bar{H}_2^0 = 201.21 \pm 0.70$			$\Delta\bar{H}_2^0 = 226.69 \pm 0.71$	
1 : 18 000	0.0009	0.9534	294.68	0.0010	0.8754	271.54	0.0009	1.5953	493.09
	0.0009	0.9502	293.70	0.0010	0.8758	271.67	0.0009	1.5968	493.56
	0.0009	0.9498	293.57	0.0010	0.8769	272.01	0.0009	1.5960	493.31
	0.0009	0.9489	293.30	0.0010	0.8760	271.73	0.0009	1.6009	494.82
	0.0009	0.9482	293.08	0.0010	0.8732	270.86	0.0009	1.5952	493.06
		$\Delta\bar{H}_3^0 = 293.67 \pm 0.76$			$\Delta\bar{H}_3^0 = 201.21 \pm 0.70$			$\Delta\bar{H}_3^0 = 493.57 \pm 0.90$	

solution of **I–III** in dioxane, equal to 405.7 ± 1.5, 372.2 ± 2.0, and 681.0 ± 2.2 kJ mol^{-1}, respectively.

Then the quantities ΔH_c^0 and ΔH_m^0 were determined for **I–III** using the equations suggested in [9, 10]. The results are given in Table 2.

Using the Hess cycle

$$C_{17}H_{10}O_{4(l)} + 17.5O_{2(g)} = 17CO_{2(g)} + 5H_2O_{(l)} - \Delta H_c^0, \quad (4)$$

$$C_{18}H_{14}O_{5(l)} + 19O_{2(g)} = 18CO_{2(g)} + 7H_2O_{(l)} - \Delta H_c^0, \quad (5)$$

we calculated the standard enthalpies of formation of compounds in the liquid (molten) state (Table 2). The required quantities $\Delta_f H_{298.15}^0[CO_2(g), H_2O(l)]$ were taken from [11, 12].

Table 2. Enthalpy characteristics (kJ mol^{-1}) of **I–III**

Compound	$-\Delta H_c^0$	ΔH_m^0	$-\Delta_f H_{298.15}^0$	
			liquid	solid
I	7726	78.6	398.3	472.0
II	8407	89.5	683.1	772.1
III	7726	76.6	398.3	475.0

Using ΔH_m^0, we calculated the standard enthalpies of formation of solid (crystalline) **I–III** (Table 2):

$$\Delta_f H_{298.15(s)}^0 = \Delta_f H_{298.15(l)}^0 - \Delta H_m^0. \quad (6)$$

Thus, using experimental and calculation methods of thermochemistry, we determined the previously unknown ethalpies of solution of anthraquinone derivatives in dioxane ΔH_s^0 and the enthalpies of their combustion ΔH_c^0, melting ΔH_m^0, and formation $\Delta_f H_{298.15}^0$.

CONCLUSIONS

(1) The standard enthalpies of solution of anthraquinone derivatives in dioxane were determined, and their standard enthalpies of formation, combustion, and melting were calculated.

(2) The results obtained are primary data for inclusion into data banks and handbooks of thermodynamic constants. They are of interest for physicochemical simulation of reactions involving these compounds and their analogs.

REFERENCES

1. Skuratov, S.M., Kolesov, V.P., and Vorob'ev, A.F., *Termokhimiya* (Thermochemistry), Moscow: Mosk. Gos. Univ., 1964, vol. 1.
2. Calvet, E. and Prat, H., *Mirocalorimetrie: applications physico-chimiques et biologiques*, Paris: Masson, 1956.
3. Topor, N.D. and Suponitskii, Yu.L., *Usp. Khim.*, 1984, vol. 53, no. 9, pp. 1425–1462.
4. Calvet, E., *Zh. Fiz. Khim.*, 1959, vol. 33, no. 6, pp. 1161–1175.
5. Spiridonov, V.P. and Lopatkin, A.A., *Matematicheskaya obrabotka eksperimental'nykh dannykh* (Mathematical Processing of Experimental Data), Moscow: Mosk. Gos. Univ., 1970.
6. Mishchenko, K.P. and Poltoratskii, G.M., *Termodinamika i stroenie vodnykh i nevodnykh rastvorov elektrolitov* (Thermodynamics and Structure of Aqueous and Nonaqueous Electrolyte Solutions), Leningrad: Khimiya, 1977.
7. *Termicheskie konstanty veshchestv: Spravochnik* (Thermal Constants of Substances: Handbook), Glushko, V.P., Ed., Moscow: Nauka, 1982, issue 10, part 2.
8. Krestov, G.A., *Termodinamika ionnykh protsessov v rastvorakh* (Thermodynamics of Ionic Processes in Solution), Leningrad: Khimiya, 1984.
9. Kazanskaya, A.S. and Skoblo, V.A., *Raschety khimicheskikh ravnovesii* (Calculations of Chemical Equilibria), Moscow: Vysshaya Shkola, 1974.
10. Viktorov, V.V., *Metody vychisleniya fiziko-khimicheskikh velichin i prikladnye raschety* (Methods for Calculating Physicochemical Quantities and Applied Calculations), Moscow: Khimiya, 1977.
11. *Termicheskie konstanty veshchestv: Spravochnik* (Thermal Constants of Substances: Handbook), Glushko, V.P., Ed., Moscow: VINITI, 1970, issue 4, part 1, p. 14.
12. *Termicheskie konstanty veshchestv: Spravochnik* (Thermal Constants of Substances: Handbook), Glushko, V.P., Ed., Moscow: VINITI, 1965, issue 1, p. 24.

ISSN 1070-4272, Russian Journal of Applied Chemistry, 2008, Vol. 81, No. 1, pp. 33–37. © Pleiades Publishing, Ltd., 2008.
Original Russian Text © M.V. Maslova, L.G. Gerasimova, N.V. Motina, 2008, published in Zhurnal Prikladnoi Khimii, 2008, Vol. 81, No. 1, pp. 35–40.

PHYSICOCHEMICAL STUDIES OF SYSTEMS AND PROCESSES

Sorption Properties of a Composite Material Based on Titanium Phosphate in Relation to Nonferrous Metal Ions

M. V. Maslova, L. G. Gerasimova, and N. V. Motina

Tananaev Institute of Chemistry and Technology of Rare Elements and Mineral Raw Materials, Kola Scientific Center, Russian Academy of Sciences, Apatity, Murmansk oblast, Russia

Received May 2, 2007

Abstract—Sorption of nonferrous metal ions under static conditions by a composite sorbent based on titanium phosphate was studied. The distribution coefficients and exchange constants for Cu(II), Ni(II), and Co(II) were calculated from the experimental data. The kinetics of the sorption of multiply charged ions from dilute hydrochloric acid solutions was studied, and the diffusion coefficients of exchanging ions were determined.

DOI: 10.1134/S1070427208010084

One of serious problems of plants dealing with hydrometallurgical and electrochemical productions is treatment of the wastewater containing a significant amount of heavy nonferrous metals. Harmful chemical elements penetrating in water reservoirs deteriorate their sanitary state and necessitate special deep water treatment before its household and production use.

Traditional water treatment methods, such as settling, coagulation, and flotation, do not provide the required quality of tail waters. This fact makes necessary the inclusion of a sorption refining stage in the flowsheet. As a rule, this is the final stage in a process, which makes it possible to achieve a demanded purity without application of additional chemicals.

Synthetic inorganic sorbents having certain advantages over organic resins find increasing application today for treatment of various types of polluted water. Such materials can almost completely bind metal ions in solutions with concentrations of the order of several milligrams per liter, and the possibility of their regeneration allows the ion exchanger operation life to be considerably increased.

At present, a great number of both universal and selective synthetic ion exchangers for wastewater treatment are known. Titanium phosphates of the general formula $TiOHPO_4 \cdot nH_2O$ are among highly selective ion-exchange materials. The synthesis and properties of such inorganic sorbents have been described in [1–4]. We have developed a technology of producing a new composite sorbent based on titanium phosphate [5, 6]. As a raw material we used waste from the integrated processing of apatite–nepheline ores, which considerably reduces the cost price of the end product. In this study we examined the ion-exchange properties of such sorbent in relation to ions of nonferrous metals (Cu^{2+}, Co^{2+}, and Ni^{2+}). To optimize the sorption process using the new ion exchanger, we studied the kinetics of the uptake of multiply charged ions from dilute chloride solutions under static conditions, obtained the sorption isotherms, and determined the sorption characteristics of the ion exchanger. The results obtained demonstrate the possibility for effective removal of ions of polyvalent metals.

EXPERIMENTAL

The synthetic ion exchanger used in this study has the composition $TiO_2 \cdot 0.75P_2O_5 \cdot 0.16SiO_2 \cdot 2.75H_2O$, with particles of hydrated silicon oxide fairly uniformly distributed in a titanyl phosphate matrix of a larger weight. The pH-metric titration data show that acid residues in such compound, i.e. phosphate groups, are bifunctional, and their capacity determined as described in [7] is 0.7 for strong acid groups and 3.4 mg-equiv g^{-1} for weak acid groups. Apparently, the major fraction of the sorbent is a mixture of mono- and disubstituted titanyl phosphate $TiO(HPO_4) \cdot TiO \cdot (H_2PO_4)_2 \cdot nH_2O$. Such phosphates have a layered structure with the staggered arrangement of phosphate groups of neighboring layers, forming zeolite cavities [8, 9]. One part of P–OH groups forms hydrogen bonds with phosphate groups of the neighboring layers, and another part forms hydrogen bonds with

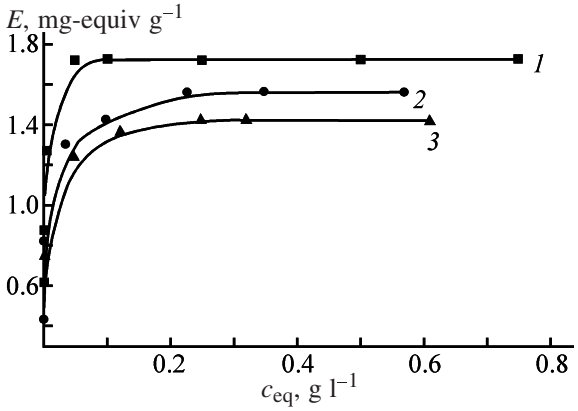


Fig. 1. Isotherms of sorption E of nonferrous metal ions by the composite sorbent. (c_{eq}) Equilibrium concentration. (*1*) Cu, (*2*) Ni, and (*3*) Co; the same for Fig. 2.

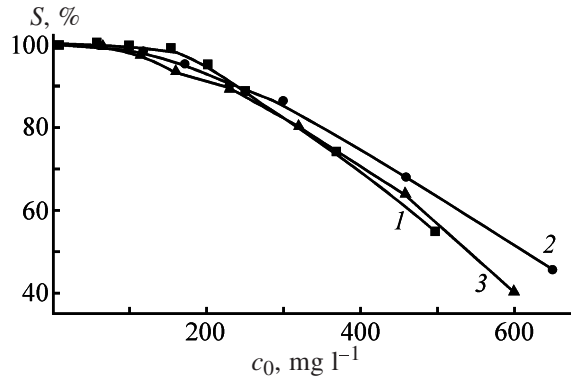
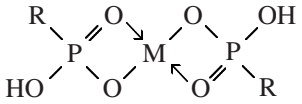


Fig. 2. Degree of sorption S as a function of metal ion concentration c_0 in the starting solution.

water molecules. In the course of an ion exchange, protons in P–OH groups bound with water molecules are replaced first, and then protons in the phosphate groups bound with the neighboring layers are replaced [10]. If ions of polyvalent metals take part in ion-exchange reactions, the following complex compounds are formed:



The relative sorbability of polyvalent metal ions, other things being equal, will be defined by the stability constant of the complex formed [11].

When studying sorption of Cu^{2+}, Co^{2+}, and Ni^{2+} ions under static conditions, 0.5 g of an ion exchanger sample in the Na^+ form was poured over with 0.01–1 g l^{-1} solutions of metal chlorides, providing the solid to liquid phase ratio of 1 : 200, and kept with intermittent stirring at 22°C until an equilibrium was attained. The pH value of starting aqueous solutions was 6–6.5. After ion exchanger removal, the equilibrium liquid phase was analyzed for the sorbate content with a Perkin–Elmer FT-IR 200 spectrophotometer. From the data obtained, the sorbent capacity (mg-equiv g^{-1}) for an ion under determination was calculated. The distribution coefficient K_d (ml g^{-1}) was calculated by the formula

$$K_d = \frac{(c_0 - c_{eq})V}{c_{eq}m},$$

where c_0 and c_{eq} are the initial and equilibrium concentrations of a metal ion in a solution; V, solution volume (ml); and m, ion exchanger sample weight (g).

To determine the concentration constant of Na^+–M^{2+} exchange, samples of the ion exchanger in the Na^+ form were poured over with 1 M NaCl solution containing certain amounts of MCl_2. After reaching an equilibrium the solution and the solid phase were analyzed for Na^+ and M^{2+}, and the exchange constants were calculated. The kinetics of sorption from MCl_2 solutions (containing 100 mg l^{-1} of M^{2+}) was studied at 20°C by the limited volume method [12]. The volume of the solution contacting with the sorbent was 50 ml, and the sorbent sample weight was 0.25 g.

Figure 1 shows that the ion exchanger under study has a good sorption capacity for nonferrous metal ions. The amount of sorbed metal cations increases as their content in the starting solution increases to 350–400 mg l^{-1}, and then it remains constant, which is due to the hindered transfer of metal cations through a product layer formed on the sorbent surface.

According to the degree of sorption (Fig. 2), the ion exchanger under study provides practically complete removal of nonferrous metal ions from solutions with an initial concentration of up to 100–150 mg l^{-1}.

All the isotherms are characterized by steep ascent in the region of low equilibrium concentrations of metal ions and by a saturation limit which allows estimation of the static sorbent capacity under the chosen conditions. The average value of the distribution coefficient at cation concentrations in the solid phase of up to 0.6 mg-equiv g^{-1} is 3×10^4 ml g^{-1} (Table 1).

It follows from the dependence of the distribution coefficient K_d of exchanging ions on their concentration in the liquid phase that a decrease in the initial concentration of metal ions in a solution favors an increase in the sorption of multiply charged ions. The K_d value decreases with increasing degree of ion exchange. This is due to the fact that large cations of

Table 1. Concentration constants K_{ex} of the exchange of nonferrous metal ions on a composite ion exchanger based on titanium phosphate. Ion exchanger weighed portion 0.5 g, solution volume 100 ml

Parameter	K_d at indicated initial concentration of metal ion in solution $c_0 \times 10^3$, mg-equiv ml^{-1}											
	Cu				Ni				Co			
	1.8	3.1	6.3	11.6	2.2	4.1	7.8	15.6	2.2	3.8	7.9	15.6
c_{eq}(s)	0.35	0.62	1.25	1.72	0.43	0.81	1.32	1.58	0.44	0.75	1.25	1.47
c_{eq}(l)	3.1×10^{-6}	2.1×10^{-5}	3.0×10^{-4}	3.0×10^{-3}	1.0×10^{-5}	8.7×10^{-5}	7.4×10^{-4}	5.0×10^{-3}	1.6×10^{-5}	1.0×10^{-4}	8.2×10^{-4}	9.9×10^{-3}
$K_d \times 10^{-3}$, ml g^{-1}	116.1	29.8	4.0	0.58	43.8	9.09	1.91	0.42	27.3	7.4	1.73	0.11
Degree of sorption, %	99.9	99.3	95.2	74.1	99.5	97.9	90.5	68.0	99.3	97.4	89.6	63.8
$K_{ex} \times 10^{-3}$	0.194	0.191	0.185	0.120	0.149	0.149	0.134	0.07	0.124	0.121	0.113	0.047

Note: c_{eq}(s), concentration in solid phase, mg-equiv g^{-1}; c_{eq}(l), concentration in liquid phase, mg-equiv ml^{-1}.

polyvalent metals, occupying surface reactive centers, block channels in the ion exchanger structure. This results in a decrease in the cation mobility and hinders the subsequent exchange in the interlayer space.

The material under study has the highest sorption capacity for the least hydrated ion, Cu^{2+}. The higher selectivity of the ion exchanger to the Ni^{2+} ion, which is more hydrated than the Co^{2+} ion, is caused by the presence of active centers of hydrated silicon oxide in the sorbent [13]. Thus, the selectivity series for sorption of nonferrous metal cations on the composite ion exchanger is as follows: $Cu^{2+} > Ni^{2+} > Co^{2+}$.

To study the exchange of these ions in more detail, we determined the Na^+–M^{2+} exchange constants by the static method at pH 5.8 (Table 1). The exchange constant allows quantitative estimation of the preferential sorption of one of two exchanging ions. The concentration exchange constants were calculated according to the exchange reaction

$$M^{2+} + 2R\text{–}Na \rightleftarrows R_2M + 2Na^+,$$

whre R is the ion exchanger matrix on which an ion is fixed,

$$K_{ex} = \frac{\bar{c}_M^{1/2} c_{Na}}{\bar{c}_{Na} c_M^{1/2}},$$

$\bar{c}_{Na}$ and $\bar{c}_M$ are concentrations of ions in the ion exchanger (mg-equiv g^{-1}), and c_{Na} and c_M are concentrations of ions in the solution (mg-equiv ml^{-1}).

The data obtained show that the exchange constant depends on the ionic composition of the ion exchanger. In the case of the Na^+–M^{2+} exchange in the region of solid phase compositions with the equivalent fraction $N_M < 0.4$, the exchange constant is practically independent of the ion exchanger ionic composition, whereas at $N_M > 0.4$ K_{ex} sharply decreases. This trend is caused by steric hindrance to entrance of cations into the interlayer space and to the action of repulsive forces between similarly charged counterions.

Apart from selectivity, sorption materials should provide a high rate of ion extraction. Kinetic characteristics of ion exchangers, which depend on their structure, play a decisive role in the choice of sorption conditions.

Time dependences of the sorption of Cu^{2+} and Co^{2+} ions are presented in Fig. 3 as semilog plots. Two linear portions (two stages) where sorption proceeds at different rates can be distinguished. In the first stage the sorption occurs on energetically

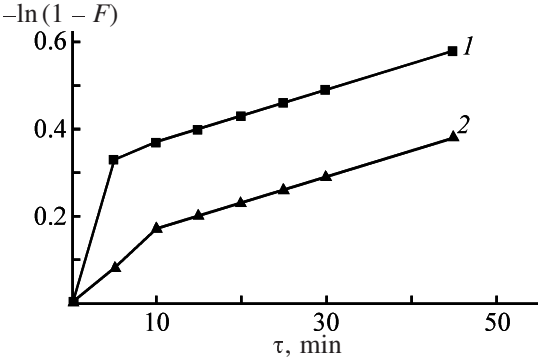


Fig. 3. Time dependence of Cu(II) and Co(II) sorption on the composite sorbent. (*F*) Degree of attainment of the sorption equilibrium and (τ) time. (*1*) Cu and (*2*) Co; the same for Fig. 4.

Table 2. Kinetic data on sorption of nonferrous metals by the composite sorbent based on titanium phosphate

t, min	Cu				Co			
	SEC, mg g^{-1}	F	Bt	$D\times 10^{11}$, $m^2\ s^{-1}$	SEC, mg g^{-1}	F	Bt	$D\times 10^{12}$, $m^2\ s^{-1}$
5	5.54	0.28	0.03	1.0	1.89	0.07	0.005	1.7
10	6.14	0.31	0.07	1.2	2.75	0.16	0.001	1.6
15	6.63	0.34	0.12	1.3	3.10	0.18	0.016	1.6
20	6.93	0.35	0.14	1.2	3.61	0.21	0.022	1.7
25	7.33	0.37	0.17	1.1	3.96	0.23	0.028	1.6
30	7.72	0.39	0.18	1.0	4.30	0.28	0.03	1.6
45	8.60	0.44	0.30	1.1	5.16	0.3	0.04	1.5
$D_{av} = 1.1\times 10^{-11}\ m^2\ s^{-1}$					$D_{av} = 1.6\times 10^{-12}\ m^2\ s^{-1}$			

favorable reactive centers located on the ion exchanger surface. Then the ion exchange is accompanied by a number of processes: rupture of hydrogen bonds between phosphate groups of neighboring layers, hydration, dehydration of a cation entering into the ion exchanger, and coordination of the cation inside the ion exchanger matrix [14]. All this requires appreciable energy expenditure, and the process rate decreases. As transition metal ions are considerably hydrated and their penetration into the sorbent bulk is hampered, the sorption as a whole proceeds rather slowly, and the equilibrium is reached in approximately 8 h.

The ion exchange kinetics is known to be controlled by either external or internal diffusion [15]. To determine the limiting stage of the sorption process, we used the interruption technique [16]. We found that after the process interruption the rate of ion absorption increases. Such a phenomenon is characteristic of gel kinetics, which is the case when the sorption rate depends on the diffusion of ions inside sorbent grains. Another indication of the gel kinetics is the linear dependence of the degree of equilibrium attainment F on $t^{1/2}$ (Fig. 4).

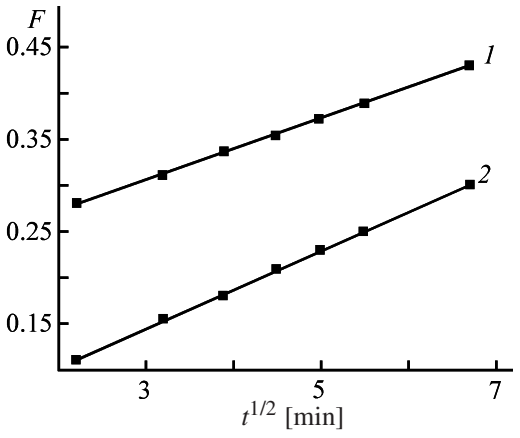


Fig. 4. Relative rate of sorption of nonferrous metals on the composite oin exchanger. (F) Degree of ion exchanger filling and (t) time.

The degree of equilibrium attainment was calculated by the formula $F = SEC_t/SEC_\infty$, where SEC_t and SEC_∞ (mg l^{-1}) are the amounts of sorbed ions at instant t and on reaching the maximal sorption. To estimate ion-exchange kinetic parameters, we used Boyd's equation for internal-diffusion processes [17]:

$$F = 1 - \frac{6}{\pi^2}\sum_{n=1}^{\infty}(1/n^2)\exp(-Dt\pi^2n^2/R^2),$$

where t is time (s); R, radius of ion exchange particles (m); D, diffusion coefficient ($m^2\ s^{-1}$); and n, natural numbers from 1 to infinity.

This series relatively rapidly converges at high degrees of filling. Having determined experimentally the degree F of equilibrium attainment for a specified time t and using the reference value of Bt [18], we calculated the diffusion coefficients D (Table 2) by the formula

$$D = \frac{Btr^2}{t\pi^2},$$

where r is the radius of sorbent particles (m).

The average radius of sorbent particles determined with a Shimadzu Sald-201V instrument is 1 mm.

It follows from Table 2 that sorbents based on titanium phosphate sorb nonferrous metal ions at a moderate rate. The diffusion coefficient of Co^{2+} cations is by an order of magnitude lower than that of Cu^{2+} cations, which is indicative of slower diffusion processes

Table 3. Sorption of nonferrous metal cations under dynamic conditions (initial concentration of metal ions in solution 100 mg l^{-1})

M^+	pH	DEC, mg-equiv g^{-1}	c_M at column outlet, mg l^{-1}
Cu^{2+}	4.98	2.27	<0.002
Ni^{2+}	6.03	1.94	<0.004
Co^{2+}	5.58	1.75	<0.005

in the case of the $Na^+ \rightarrow Co^{2+}$ exchange. This is caused by steric hindrances to the migration of more hydrated cobalt ions in the ion exchanger matrix. The value of D depends on the radius of sorbent particles. As a rule, particles of inorganic ion exchangers are agglomerates of irregular shape, consisting of nonuniform clusters of microparticles. Therefore, the diffusion takes place both in channels between microparticles and inside them. As the true size of microparticles is much smaller than the effective size of agglomerates, the measured actual diffusion rate is also lower. However, it is most probable that the established dependence between the diffusion rate and the kind of the cation will be preserved.

The results obtained can be used in the industrial practice of the sorption of nonferrous metals. Performing the sorption under dynamic conditions (flow rate 2 ml h^{-1}) allowed us to efficiently remove impurities of nonferrous metal ions from solution (Table 3).

CONCLUSIONS

(1) The ion exchanger under study provides practically complete removal of nonferrous metal ions from dilute hydrochloric acid solutions at their initial concentrations of up to 100–150 mg l^{-1} with the selectivity varying in the order $Cu^{2+} > Ni^{2+} > Co^{2+}$.

(2) The rate of ion exchange of transition metal ions is controlled by internal diffusion. The diffusion coefficient for Co^{2+} cations is by order of magnitude lower than that for Cu^{2+} cations, which is caused by steric hindrance to the migration of the more hydrated cobalt ions in an ion exchanger matrix.

REFERENCES

1. Mitchenko, T.E., Belyakov, V.N., Roitenberg, A.M., et al., *Zh. Prikl. Khim.*, 1986, vol. 59, no. 7, pp. 1440–1443.
2. Dranitsina, N.V., Egorov, Yu.V., and Fominykh, E.V., *Izv. Akad. Nauk SSSR, Neorg. Mater.*, 1970, vol. 6, no. 12, pp. 2178–2182.
3. Bortun, A., Jaimez, E., Llavona, R., et al., *Mater. Res. Bull.*, 1995, vol. 30, no. 4, pp. 413–420.
4. Bereznitski, Y., Jaroniec, M., Bortun, A., et al., *J. Colloid Interface Sci.*, 1997, vol. 191, pp. 442–448.
5. Gerasimova, L.G., Matveev, V.A., Maslova, M.V., et al., *Tsvetn. Met.*, 2005, no. 3, pp. 87–91.
6. RF Patent 2207980.
7. Tulupov, P.E., Kurakin, A.N., Gushchina, V.N., et al., *Zh. Prikl. Khim.*, 1974, vol. 47, no. 7, pp. 1663–1665.
8. Clearfield, A. and Roberts, B.D., *Inorg. Chem.*, 1988, vol. 27, p. 3237.
9. Marireles-Torres, P., Olivera-Pastor, P., Jimenez-Lopez, A., et al., *J. Mater. Chem.*, 1991, vol. 1, p. 319.
10. Materova, E.A., *Neorganicheskie ionoobmennye materialy* (Inorganic Ion-Exchange Materials), Leningrad: Leningr. Gos. Univ., 1974, issue 1, p. 56.
11. Saldadze, K.M. and Kopylova, V.D., *Zh. Fiz. Khim.*, 1971, vol. 45, no. 5, pp. 1445–1448.
12. Polyanskii, N.G., Gorbunov, G.V., and Polyanskaya, N.L., *Metody issledovaniya ionitov* (Methods of Studying Ion Exchangers), Moscow: Khimiya, 1976.
13. Maslova, M.V., Gerasimova, L.G., Okhrimenko, R.F., and Chugunov, A.S., *Zh. Prikl. Khim.*, 2006, vol. 79, no. 11, pp. 1813–1817.
14. Amphlett, C.B., *Inorganic Ion Exchangers*, Amsterdam: Elsevier, 1964.
15. Griessbach, R., *Austauschadsorption in Theorie und Praxis*, Berlin: Akademie, 1957.
16. Helfferich, F., *Ionenaustauscher*, Weinheim: Chemie, 1959, vol. 1.
17. Boyd, G.E., Adamson, A.W., and Myers, L.S., *J. Am. Chem. Soc.*, 1947, vol. 69, pp. 2834–2837.
18. Saldadze, K.M., Pashkov, A.B., and Titov, V.S., *Ionoobmennye vysokomolekulyarnye soedineniya* (Macromolecular Ion-Exchange Compounds), Moscow: Khimiya, 1960.

ISSN 1070-4272, Russian Journal of Applied Chemistry, 2008, Vol. 81, No. 1, pp. 38–41. © Pleiades Publishing, Ltd., 2008.
Original Russian Text © D.E. Chirkst, A.A. Chistyakov, O.V. Cheremisina, I.T. Zhadovskii, 2008, published in Zhurnal Prikladnoi Khimii, 2008, Vol. 81, No. 1, pp. 41–45.

PHYSICOCHEMICAL STUDIES OF SYSTEMS AND PROCESSES

Sorption of Germanium from Alkaline Solutions on Anion-Exchange Resin

D. E. Chirkst, A. A. Chistyakov, O. V. Cheremisina, and I. T. Zhadovskii

St. Petersburg State Mining Institute, St. Petersburg, Russia

Received March 16, 2007; in final form, September 2007

Abstract—Isotherm of OH^-/GeO_3^{2-} ion exchange on a synthetic sorbent is studied. The limiting sorption of the germanate ion and the apparent constant and Gibbs energy of ion exchange are estimated.

DOI: 10.1134/S1070427208010096

In non-ferrous metallurgy, particularly, in zinc and lead production, germanium-containing process solutions are formed, which should be reprocessed. Since germanium is a rare element, and its application field is being steadily extended, integrated processing of complex ores is a quite topical problem. Germanium is recovered from aqueous solutions by such methods as sorption, solvent extraction, precipitation, evaporation, and flotation. The decision on the technology is determined primarily by the germanium concentration and speciation in solution. Ion exchange is believed to be the most cost-efficient and practically feasible process. It is applicable over a wide Ge concentration range from 0.01 to 3 g l^{-1}, whereas other chemical methods are efficient only at a Ge concentration above 0.5 g l^{-1}.

Sorption of germanium on cation-exchange resins has been extensively studied. Shostak et al. [1] have demonstrated that germanium forms complexes with heterocyclic nitrogen bases, diazo compounds, aliphatic amines, phenylfluorone, dihydric phenols, carboxy derivatives of polyhydric phenols, polyhydric alcohols, and hydroxy acids. However, in practice, cation-exchange resins have no significant sorption capacity for germanium occurring in solutions, and the most of commercial cation exchangers are unsuitable for this purpose [1]. Small amounts of germanium can be sorbed from acidic solutions on KB-4P and ROAS cation exchangers (most likely via complexation), and from weakly acidic solutions on KU-21 and KU-1G cation exchangers in the presence of hydroxylamine, but not from neutral solutions. Therefore, it is advisable to use cation exchangers for treatment of Ge-containing solutions to remove concomitant metals [2]. Thus, it was recommended to use cation-exchange resins for recovery of iron, copper, lead, and zinc from acidic and sodium alkaline Ge-containing solutions. In this case, germanium practically totally remains in solution. Many methods for treating Ge-containing acidic solutions to remove Al(III), Cu(II), and some other metal cations are based on this approach [3].

Sorption of germanium from solutions on activated carbon impregnated with tartaric, oxalic, and citric acids was reported in [4–6]. Germanium complexes with tartaric and oxalic acids appeared to be readily sorbed on activated carbon. In sorption of germanium on activated carbon impregnated with tartaric acid, a germanium tartrate complex is readily formed on the sorbent surface. On the contrary, modification of activated carbon with an oxalic acid solution reduces its sorption capacity for germanium. At the same time, a germanium oxalate complex formed in a solution is readily sorbed on activated carbon. Impregnation of activated coal with citric acid considerably increases its sorption capacity for germanium, which can be attributed to the fact that, unlike the smaller tartaric acid molecules penetrating into micropores of the sorbent, bulkier citric acid molecules may penetrate only into macropores, and, as a result, they are practically totally involved in chemisorption with formation of a germanium citrate complex.

Germanium sorption on anion-exchange resins has been most thoroughly studied. Germanium dioxide speciation in solutions was determined from data on the sorption of the germanate anions on Amberlite IRA-400 strongly basic anion exchanger in the presence of chloride. Germanium is sorbed on this resin at pH 4–13, and the maximal sorption is observed at pH 9–9.2. At pH < 6 and pH > 11, germanium is only insignificantly sorbed. At pH 6.9–9.4, germanium is sorbed in the form of the pentagermanate ions $Ge_5O_{11}^{2-}$. The decrease in the germanium sorption at lower pH

is due to the formation of the monogermanate ions $HGeO_3^-$ and GeO_3^{2-}. At pH > 9.4, the adsorbed species are germanate ions of lower degree of polymerization than in $Ge_5O_{11}^{2-}$.

Meleshko and Dubrovskaya [7] reported data on the sorption of germanium from aqueous solutions on EDE-10P, AV-16G, AV-17, and AV-31G anion-exchange resins. The experiments were carried out at pH 6.0–10.0 and various Ge concentrations in solution. Regardless of the resin type, the maximal sorption was observed at pH 9.3–9.4. It was demonstrated also that, with increasing Ge concentration in solution, the exchange capacity of the resins abruptly increases by virtue of the formation of the pentagermanate ions and the fact that the large size of this ion has no negative effect on the sorption kinetics [8].

Among a number of sorbents studied, AN-31 weakly basic anion-exchange resin was found to be the most selective sorbent for germanium, and its use allowed considerable increase in the Ge recovery [3]. Furthermore, it was demonstrated that this sorbent is suitable for recovering Ge from leaching solutions formed in processing such kinds of raw materials as ashes and sublimates of power plant coal, iron ore, and nonferrous metallurgical dusts [8]. Thanks to the high selectivity of AN-31, germanium may be recovered from multicomponent solutions containing high concentrations of such elements as zinc, lead, molybdenum, arsenic, iron, etc.

EXPERIMENTAL

We studied Ge sorption on D-403 anion-exchange resin. This is a macroporous polystyrene-based weakly basic chelating resin. Its color is milk-white, and the granule size is 0.4–1.25 mm. The functionality of the resin is caused by the tertiary nitrogen atom with the hydroxy substituents in the β-, γ-, and δ-positions. The hydroxy groups reduce the mobility of the unshared electron pair of nitrogen by virtue of the negative inductive effect. The anion exchanger was converted into the OH form prior to use. The resin was charged into a column and eluted first with 2 N H_2SO_4 and then with 1 N NaOH. Finally, the resin was washed with distilled water to pH 6.

In the sorption experiments, we used the method of variable volumes in which the same samples of the resin were shaken with different volumes of the solution with a fixed element concentration. The static sorption Γ (mol kg^{-1}) of germanate ions was determined at various liquid to solid phase ratios from the difference between the initial and equilibrium solution concentrations ($c_0 - c_\infty$):

$$\Gamma = (c_0 - c_\infty)V/m.$$

The resin samples (5 ml; bulk weight of the sorbent in the swollen state 0.738 g ml^{-1}) were placed into 250-ml conical flasks, poured over with 25–100 ml of a Ge-containing solution (0.05 M with respect to Ge), and shaken until equilibration. The starting Ge solution was prepared by dissolving germanium oxide (chemically pure grade) in 5 wt % NaOH (pH 14). The time of establishment of the sorption equilibrium was 6 h. After this time elapsed, the solution was decanted, and the equilibrium germanate concentration was determined photometrically with ammonium molybdate [9]. An aliquot portion of the solution (2 to 5 ml depending on the germanate concentration) was placed into a 25-ml flask, and 5% ammonium molybdate (10 ml) and 2 N H_2SO_4 (2 ml) were added. Finally, water was added to the mark. Germanium was determined by the intensity of the adsorption band of the molybdate complex at a wavelength of 428 nm.

The equivalence of the exchange of the OH^- ions for germanate was confirmed by satisfactory agreement between the total dynamic exchange capacity (TDEC) with respect to the alkali and germanate ions. The resin was charged into a column with the sorbent bed height of 300 mm and diameter of 16 mm (sorbent volume 60 ml). A solution containing 0.04 M germanium and 5% NaOH was passed through the column at a rate of 0.5–1 ml min^{-1} using a peristaltic pump. The TDEC for Ge was determined from the Ge concentration in the eluate (50-ml samples of the eluate were analyzed by X-ray fluorescence method). Then the resin was regenerated, washed with water to pH 6, and eluted with 0.1 N NaOH. The OH^- concentration in the eluate was determined volumetrically. The TDEC for Ge was found to be 0.82 ± 0.01 equiv l^{-1}, which was well consistent with that for the OH^- ions (0.76 ± 0.01 equiv l^{-1}). These values are well consistent with the certificate data for D-403 resin (0.9 equiv l^{-1}). Therefore, not the pentagermanate ions $Ge_5O_{11}^{2-}$, but monogermanate ions $HGeO_3^-$ and GeO_3^{2-} are sorbed, since, with increasing OH^- concentration, the equilibrium

$$5GeO_3^{2-} + 4H_2O \rightleftarrows Ge_5O_{11}^{2-} + 8OH^-$$

shifts to the left. The elution curves of the OH^- and germanate ions are shown in Figs. 1a and 1b.

Figure 2 shows the isotherm of Ge sorption on the synthetic sorbent, based on data of the table. The table summarizes data on the equilibrium germanate concentrations c_∞, germanate sorption Γ and its reciprocal

Experimental results on OH^-/GeO_3^{2-} ion exchange

c_∞	Γ	$1/\Gamma$, mol^{-1} kg	ε, %	I	OH^-	$\gamma_\pm$	
mol kg^{-1}				mol kg^{-1}		Na_2GeO_3	NaOH
1.35×10^{-4}	5×10^{-5}	15.3	98.5	0.95	0.95	0.329	0.661
5.15×10^{-4}	0.065	4.98	94.5	0.95	0.95	0.329	0.661
0.003	0.201	3.14	94.4	0.95	0.95	0.328	0.661
0.006	0.318	2.50	87.1	0.96	0.96	0.327	0.661
0.011	0.399	2.37	76.4	0.97	0.97	0.326	0.660
0.016	0.422	2.25	66.0	0.98	0.98	0.325	0.660
0.022	0.445	2.13	53.7	0.99	0.99	0.324	0.659
0.025	0.470	2.09	47.4	1.00	1.00	0.323	0.659
0.030	0.479	2.07	35.8	1.01	1.01	0.322	0.658

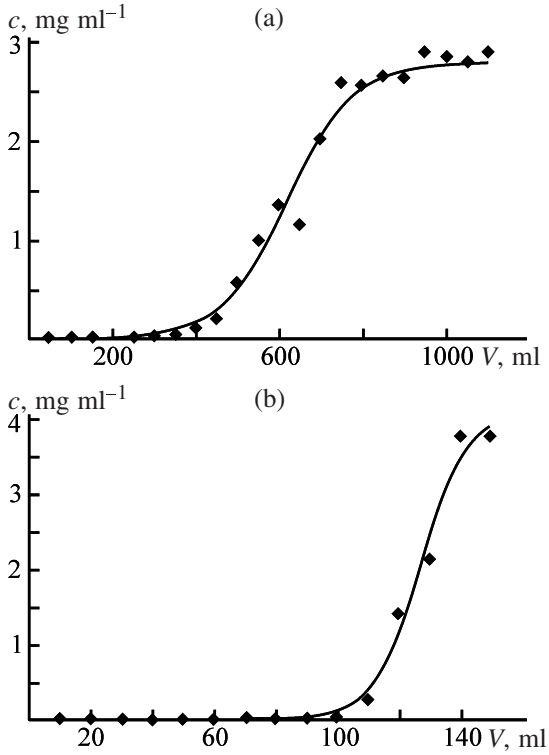


Fig. 1. Elution curves of (a) germanate and (b) OH^- ions. (c) Concentration in the solution and (V) volume of the eluate.

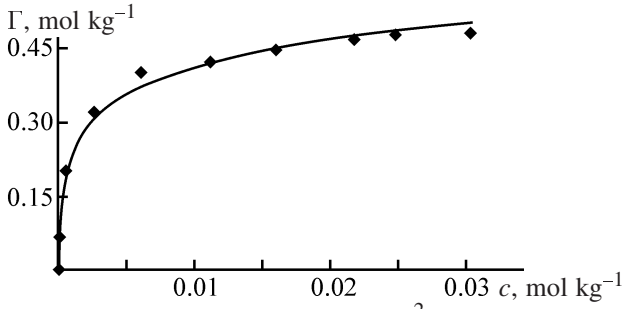


Fig. 2. Isotherms of sorption of GeO_3^{2-} on the synthetic sorbent. (Γ) Sorption of GeO_3^{2-} and (c) equilibrium germanate concentration.

values $1/\Gamma$, degree of Ge recovery ε, and mean ionic activity coefficients $\gamma_\pm$ for Na_2GeO_3 and NaOH from [10].

The thermodynamic analysis of the OH^-/GeO_3^{2-} exchange was performed on the assumption of ideality of the solid phase, i.e., without taking into account the activity coefficients of the adsorbed ionic species. The Langmuir-type equation was linearized using the procedure described in [11]. The law of mass action for the ion-exchange reaction

$$2ROH_s + 5GeO_{3aq}^{2-} \rightleftarrows R_2GeO_{3(s)} + 2OH_{aq}^-$$

takes the form

$$K = \frac{\Gamma_{GeO_3^{2-}} a_{OH^-}^2}{\Gamma_{OH^-}^2 a_{GeO_3^{2-}}}, \quad (1)$$

where K is the apparent exchange constant; $\Gamma_{GeO_3^{2-}}$ and Γ_{OH^-} are the sorptions of the ions (mol kg^{-1}); and $a_{GeO_3^{2-}}$ and a_{OH^-}, ionic activities in the solution (m).

The limiting sorption of the ions Γ_∞ (equiv kg^{-1}) is written as

$$\Gamma_\infty = \Gamma_{OH^-} + 2\Gamma_{GeO_3^{2-}}.$$

Equation (1) can be rearranged to obtain Eq. (2):

$$K = \frac{\Gamma_{GeO_3^{2-}} [OH^-]^2 \gamma_{\pm(NaOH)}^2}{\Gamma_{OH^-}^2 [GeO_3^{2-}] \gamma_{\pm(Na_2GeO_3)}}$$

$$= \frac{\Gamma_{GeO_3^{2-}} [OH^-]^2 \gamma_{\pm(NaOH)}^2}{(\Gamma_\infty - 2\Gamma_{GeO_3^{2-}})^2 [GeO_3^{2-}] \gamma_{\pm(Na_2GeO_3)}}. \quad (2)$$

Equation (2) was rearranged to Eq. (4), whose form is similar to that of the Langmuir equation (3):

$$\Gamma = \Gamma_\infty Ka/(1 + Ka), \quad (3)$$

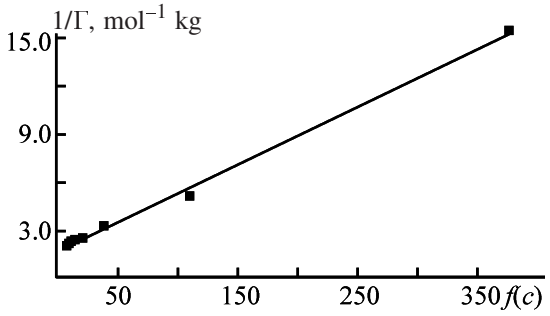


Fig. 3. Linearized isotherm of OH^-/GeO_3^{2-} ion exchange. (1/Γ) Reciprocal sorption of GeO_3^{2-} and $f(c) = [OH^-] \cdot \gamma_{\pm(NaOH)}\{\Gamma_{GeO_3^{2-}}[GeO_3^{2-}]\gamma_{\pm(Na_2GeO_3)}K\}^{-1/2}$.

$$\Gamma = \Gamma_\infty \frac{(\Gamma_{GeO_3^{2-}})^{1/2}\{[GeO_3^{2-}]\gamma_{\pm(Na_2GeO_3)}K\}^{1/2}}{[OH^-]\gamma_{\pm(NaOH)} + 2\{\Gamma_{GeO_3^{2-}}[GeO_3^{2-}]\gamma_{\pm(Na_2GeO_3)}K\}^{1/2}}. \quad (4)$$

The linearized form of Eq. (4),

$$\frac{1}{\Gamma_{GeO_3^{2-}}} = \frac{2}{\Gamma_\infty} + \frac{[OH^-]\gamma_{\pm(NaOH)}}{\Gamma_\infty\{\Gamma_{GeO_3^{2-}}[GeO_3^{2-}]\gamma_{\pm(Na_2GeO_3)}K\}^{1/2}}, \quad (5)$$

is similar to the linearized Langmuir equation (6):

$$1/\Gamma = 1/\Gamma_\infty + 1/\Gamma_\infty Ka. \quad (6)$$

In Fig. 3, the reciprocal sorption of the germanate ion $1/\Gamma_{GeO_3^{2-}}$ is plotted against $f(c)$. The linear approximation of this relationship is written as $1/\Gamma_{GeO_3^{2-}} = 0.0356f(c) + 1.6759$ (R^2 0.997). The ionic activity coefficients were determined by extrapolating the tabulated data to the Na_2GeO_3 and NaOH concentrations corresponding to a given ionic strength [10]. The ionic strength was estimated as $I = 0.5([Na^+] + 4[GeO_3^{2-}] + [OH^-])$.

Finally, the limiting sorption of GeO_3^{2-} anions was estimated to be 1.19 ± 0.01 equiv kg^{-1} (or 0.88 ± 0.01 equiv l^{-1}, taking into account the bulk density of the sorbent); apparent ion-exchange constant, $K_{OH^-/GeO_3^{2-}} = 2216$; and Gibbs energy of the exchange of the OH^- ions from the resin phase for the germanate ions from the solution, $\Delta G^0_{298} = -19.1$ kJ mol^{-1}. A negative value of the Gibbs energy reflects the selectivity of D-403 resin to germanium. The estimated limiting sorption of the germanate ions $\Gamma_\infty = 0.88 \pm 0.01$ equiv l^{-1} is above TDEC (0.82 ± 0.01 equiv l^{-1}), which can be attributed to the fact that this theoretical value is unattainable in the dynamic sorption mode.

CONCLUSIONS

(1) Capacitive characteristics of sorbent D-403 with respect to germanium are as follows (equiv l^{-1}): dynamic exchange capacity to breakthrough 0.53 ± 0.01 and total dynamic exchange capacity 0.82 ± 0.01. The total dynamic exchange capacity for germanium is consistent with that for the OH^- ions (0.76 ± 0.01 equiv l^{-1}).

(2) The isotherm of OH^-/GeO_3^{2-} ion exchange is described by a Langmuir-type relationship, which can be linearly approximated ($R^2 = 0.997$). The limiting sorption of the GeO_3^{2-} ions $\Gamma = 1.19 \pm 0.01$ equiv l^{-1}, apparent ion exchange constant $K_{OH^-/GeO_3^{2-}} = 2216$, and Gibbs energy of the exchange of the OH^- ions from the resin phase for the germanate ions from the solution $\Delta G^0_{298} = -19.1$ kJ mol^{-1}.

REFERENCES

1. Shostak, F.T., Vittikh, M.V., Sharova, A.K., and Chufarova, I.G., *Izv. Sib. Otd. Akad. Nauk SSSR*, 1960, no. 8, pp. 69–74.
2. Kalugina, V.P. and Klimenko, I.A., *Sposoby izvlecheniya germaniya iz prirodnykh vod i promyshlennykh vodnykh rastvorov* (Methods for Recovering Germanium from Natural Waters and Industrial Aqueous Solutions), Moscow, 1979.
3. Sobinyakova, N.M., Starostina, K.M., Aleksandrova, L.N., et al., *Tr. VIMS*, 1972, no. 23, pp. 59–85.
4. Kogan, E.A. and Evdokimov, D.Ya., *Zh. Prikl. Khim.*, 1966, vol. 39, no. 9, pp. 1927–1931.
5. Kogan, E.A. and Evdokimov, D.Ya., *Zh. Prikl. Khim.*, 1968, vol. 41, no. 3, pp. 579–584.
6. Evdokimov, D.Ya. and Kogan, E.A., *Zh. Prikl. Khim.*, 1970, vol. 43, no. 9, pp. 2012–2016.
7. Meleshko, V.P. and Dubrovskaya, G.E., *Zh. Prikl. Khim.*, 1969, vol. 42, no. 12, pp. 2833–2836.
8. Slobtsov, L.E., Nikol'skaya, L.L., Zastavnyi, A.N., et al., *Tsvetn. Met.*, 1977, no. 6, pp. 9–12.
9. Busev, A.I., Tiptsova, V.G., and Ivanov, V.M., *Prakticheskoe rukovodstvo po analiticheskoi khimii redkikh elementov* (Practical Manual on Analytical Chemistry of Rare Elements), Moscow: Khimiya, 1966.
10. *Kratkii spravochnik fiziko-khimicheskikh velichin* (Concise Handbook of Physicochemical Quantities), Ravdel', A.A. and Ponomareva, A.M., Eds., St. Petersburg: Khimiya, 2002.
11. Chirkst, D.E., Litvinova, T.E., Cheremisina, O.V., and Ivanov, M.V., *Zh. Prikl. Khim.*, 2004, vol. 77, no. 5, pp. 580–582.

ISSN 1070-4272, Russian Journal of Applied Chemistry, 2008, Vol. 81, No. 1, pp. 42–45. © Pleiades Publishing, Ltd., 2008.
Original Russian Text © N.M. Kozhevnikova, N.L. Tsybikova, 2008, published in Zhurnal Prikladnoi Khimii, 2008, Vol. 81, No. 1, pp. 46–49.

PHYSICOCHEMICAL STUDIES OF SYSTEMS AND PROCESSES

Sorption of Neodymium(III) Ions by Natural Mordenite-Containing Tuff

N. M. Kozhevnikova and N. L. Tsybikova

Baikal Institute of Nature Management, Siberian Branch, Russian Academy of Sciences, Ulan-Ude, Buryatia, Russia

Received September 26, 2006; in final form, August 2007

Abstract—Equilibrium in the system constituted by a mordenite-containing tuff and neodymium(III) was studied in a wide range of concentrations (10^{-5}–10^{-2} M) in sorption from neodymium sulfate solutions. Isotherms of absorption of neodymium ions were constructed and kinetic parameters of the sorption process were determined.

DOI: 10.1134/S1070427208010102

Natural zeolites modified with ions of rare-earth elements (REE) are promising for manufacture of microfertilizers and biologically active preparations [1–3].

The kinetics and equilibrium of sorption of lanthanum(III) ions by mordenite- and clinoptilolite-containing tuffs have been studied previously. It has been shown that sorption isotherms of lanthanum typically show a peak resulting from the complex nature of the interaction in the system constituted by a zeolite and lanthanum(III) ions [4]. It is of interest to study the influence exerted by the nature of REE on the equilibrium and kinetics of sorption. The insufficient understanding of the ion-exchange properties of natural zeolites with respect to REE hinders their application. For this purpose, we studied the sorption of neodymium ions by a mordenite-containing tuff in relation to the solution concentration, sorbent grain size, and solid-to-liquid mass ratio.

EXPERIMENTAL

We used as sorbent a mordenite-containing tuff from the Mukhor-Talinskoe perlite–zeolite deposit (Buryatia), with the following content of components (wt %): SiO_2 70.96, Al_2O_3 11.97, MgO 0.18, CaO 0.92, Na_2O 2.38, K_2O 5.22 [4]. The [Si]/[Al] ratio was 5.2. The content of zeolite in the rock was found by X-ray diffraction analysis with PTsL-2 [2] to be 62 wt %. To study the kinetics and equilibrium of absorption of neodymium(III) ions, the mordenite-containing tuff was crushed, grain fractions with diameters of 0.25–0.65 and 1–2 mm were selected by sieving, dust was removed, grains were dried at room temperature for 24 h, and a weighed sample was taken. The drying time of 24 h was chosen on the basis of triple control weighing every 3 h of drying.

The equilibrium was studied under static conditions in aqueous solutions of $Nd_2(SO_4)_3 \cdot 8H_2O$ by the constant-mass method [6, 7]. The content of neodymium(III) ions was determined by photometry with Arsenazo III, which is a highly sensitive and selective method [8]. The absorption capacity was calculated from the difference of the neodymium(III) ion concentrations before and after sorption, measured in three parallel runs with a relative error not exceeding 3%.

The absorption kinetics of neodymium ions was studied by the limited-volume method at s : l = 1 : 10 and 1 : 50 in sorption from neodymium(III) sulfate solutions with concentrations of 0.001–0.003 M under continuous agitation. The time of contact between a solution and the sorbent was varied from 5 min to 6 days. The effect of the sorbent grain size was studied on grains of diameters 0.25–0.5 and 1–2 mm.

The kinetic parameters were calculated from Q–τ curves [Q is the amount of sorbed neodymium(III) ions (mmol g^{-1}), and τ is time (s)] by the procedure described for the case of sorption on zeolites in the monograph [9]. For the initial period of time, when sorption occurs on the zeolite surface under outer-diffusion control, the rate constant of the outer-diffusion process, R, is calculated by the equation

$$R = dQ/d\tau(1/cK), \quad (1)$$

where c is the ion concentration in solution (M), and K is the equilibrium distribution coefficient (ml g^{-1}).

As the time of contact increases, the amount of absorbed ions is determined by the rate of exchange within a grain. The effective diffusion coefficient D and the rate constant B of the inner-diffusion process, which characterize the inner-diffusion mechanism, were calculated by the following equations derived for spherical particles:

$$F = Q_\tau/Q_\infty = (6/r)(Dr/\pi)^{1/2}, \quad (2)$$

$$B = \pi^2 D/r^2, \quad (3)$$

where F is the degree of absorption of neodymium(III) ions, and r is the average radius of sorbent grains (cm).

The results obtained are listed in the table. The equilibrium of sorption of neodymium ions on a mordenite-containing tuff was studied in a wide concentration range (10^{-5}–10^{-2} M), which made it possible to reveal changes in the initial and final portions of the equilibrium curves.

Figure 1 shows equilibrium curves for neodymium(III) ions in sorption from neodymium sulfate solutions on a natural zeolite, measured for grains with different diameters (~0.25–0.5 and 1–2 mm) at s : l = 1 : 10 and 1 : 50.

The equilibrium curves are similar and reflect a certain pattern in the nature of interaction between neodymium ions and the zeolite phase. The isotherms show an extremum, which may occur because intermediate products of the chemical reaction, toward which the sorbent exhibits an increased selectivity, are formed in solution. The processes of hydration, hydrolysis, polymerization, and complexation are characteristic of the state of aqueous solutions of neodymium(III). In neutral and acid aqueous solutions, neodymium ions form aqua and hydroxoaqua complexes of the following types: $[Nd(H_2O)_n]^{3+}$ and $[Nd(H_2O)_nOH]^{2+}$, where n = 5–8 [10, 11]. At low concentrations of sulfate ions (<0.03 M), $[Nd(SO_4)]^+$ cations are predominant [12], although anion complexes can also be formed under the same conditions [13].

The absorption of neodymium(III) ions is accompanied by a decrease in the solution pH by 0.4–0.6 unit. To find out why pH decreases, we performed control runs in which the mordenite-containing tuff was poured over with distilled water. During 20–24 h of contact, a decrease in pH also by 0.4–0.6 unit was recorded in all experiments, and this occurred via exchange between Na^+ and H^+ ions present in zeolites [10], irrespective of whether or not neodymium ions were absorbed. Possibly, the decrease in pH in contact of mordenite with distilled water occurs via hydrolysis of aluminum(III), magnesium(II), and iron(III) ions by the scheme

Kinetic parameters of sorption of neodymium(III) ions from sulfate solutions by natural mordenite-containing tuff

Parameter	Solution concentration, M		
	0.001*	0.002**	0.003**
τ, min	1540	1870	1630
$dQ/d\tau \times 10^{-5}$, mmol g^{-1} s^{-1}	5.8	3.7	4.7
K, ml g^{-1}	49.3	40.5	56.8
$R \times 10^{-4}$, s^{-1}	4.2	3.4	4.4
$D \times 10^{-8}$, cm^2 s^{-1}	4.2	2.1	3.5
$B \times 10^{-4}$, s^{-1}	8.9	7.3	8.6

* d = 0.25–0.5 mm, s : l = 1 : 50.
** d = 1–2 mm, s : l = 1 : 10.

$$M^{n+} + 2H_2O \rightleftarrows [MOH]^{(n-1)+} + H_3O^+, \quad (4)$$

$$M^{n+} = Al^{3+},\ Mg^{2+},\ Fe^{3+}.$$

The pH values for 0.005 and 0.001 M solutions of neodymium(III) sulfate are 6.4 and 6.2, respectively.

As the solution concentration increases to the point of extremum, aqua and hydroxoaqua complexes of neodymium(III) are sorbed, because these complexes have a larger ion charge and the zeolite shows an increased selectivity with respect to them. The size of windows and channels of the zeolite under study are 6–7 Å, which markedly exceeds the size of aqua and hydroxoaqua complexes of neodymium(III) and suggests that neodymium(III) is sorbed in the form of aqua and hydroxo complexes. The suggested mechanism of exchange sorption via substitution of Na^+, K^+, and H^+ by Nd^{3+} confirms the data of [7].

The grain size and s : l ratio affect the position of the peak in the isotherms in Fig. 1. The maximum of the exchange capacity (EC) on grains with d = 0.25–0.5 and s : l = 1 : 50 (Fig. 1, curve *1*) is shifted to lower equilibrium concentrations. For larger grains (d = 1–2 mm) and s : l = 1 : 10, the maximum EC lies at higher concentrations (Fig. 1, curve *2*).

Thus, the maximum CE is achieved on small-size tuff grains at a lower expenditure of the reagent.

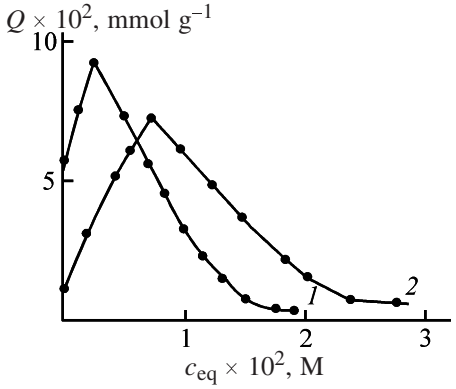


Fig. 1. Isotherms of neodymium sorption from neodymium sulfate solutions. (Q) Amount of sorbed neodymium(III) ions and (c_{eq}) equilibrium Nd(III) concentration in solution. (*1*) d = 0.25–0.5 mm, s : l = 1 : 50; (*2*) d = 1–2 mm, s : l = 1 : 10.

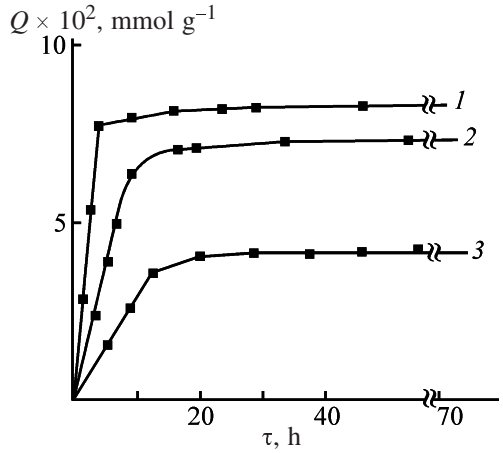


Fig. 2. Kinetic curves of neodymium(III) sorption from aqueous solutions by mordenite-containing tuff. (Q) Amount of sorbed neodymium(III) ions and (τ) sorption time. (*1*) 0.001 M, d = 0.25–0.50, s : l = 1 : 50; (*2*) 0.003 M, d = 1–2 mm, s : l = 1 : 10; and (*3*) 0.01 M, d = 1–2 mm, s : l = 1 : 10.

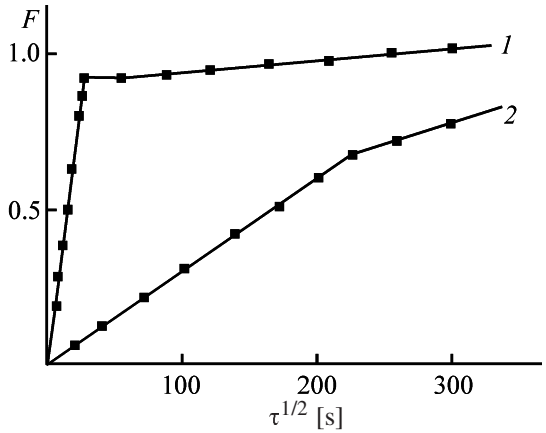


Fig. 3. Degree of exchange F vs. time τ. (*1*) 0.005 M, d = 0.25–0.50, s : l = 1 : 50; (*2*) 0.01 M, d = 1–2 mm, s : l = 1 : 10.

The kinetic curves of absorption of neodymium(III) ions are similar (Fig. 2).

The linear dependence of the degree of filling F of the zeolite phase on time τ (s), F–$(\tau)^{1/2}$, in Fig. 3 confirms the rather high contribution of the inner-diffusion sorption mechanism [7, 10].

The kinetic parameters listed in the table indicate that the absorption rate of neodymium(III) ions depends on the grain size of the mordenite-containing tuff and on the solution concentration. A decrease in the sorbent grain size leads to an increase in the surface area, which results in that the absorption rate $dQ/d\tau$ by the outer-diffusion mechanism increases. As the concentration of neodymium(III) sulfate solutions is raised, the time in which equilibrium is attained, τ_∞, becomes shorter, and the rate constants of outer- (R) and inner-diffusion (B) processes, distribution coefficient K, and effective diffusion coefficient D become larger. The constants R and B are of the same order of magnitude, which confirms that Nd^{3+} ions are sorbed by the mordenite-containing tuff by a mixed mechanism.

CONCLUSIONS

(1) The isotherms of neodymium(III) sorption by the mordenite-containing tuff exhibit a peak, which is due to the complex nature of the interaction. As the concentration of the aqueous solution increases, the selectivity of the mordenite-containing tuff with respect to neodymium(III) ions changes and its sorption capacity decreases.

(2) The sorption rate of neodymium(III) ions on the mordenite-containing tuff depends on the grain size, solution concentration, and s : l ratio. The results obtained open up prospects for production of effective microfertilizers and medicinal preparations by the sorption technology.

REFERENCES

1. Samonova, O.A., *Pochvovedenie*, 1992, no. 6, pp. 45–50.
2. Kabata-Pendias, A. and Pendias, H., *Trace Elements in Soils and Plants*, Boca Raton, FL (USA): CRC, 1984.
3. Abasheeva, N.E., Ineshina, E.G., Merkusheva, M.G., et al., *Agrokhimiya*, 2003, no. 8, pp. 39–44.
4. Kozhevnikova, N.M., Abasheeva, N.E., and Zonkhoeva, E.L., *Khim. Inter. Ustoich. Razv.*, 1999, vol. 7, no. 6, pp. 675–679.

5. Belitskii, I.A., Drobot, I.V., and Valueva, G.P., *Opyt ekspressnogo opredeleniya soderzhaniya tseolitov v gornykh porodakh s ispol'zovaniem portativnykh tseolitnykh laboratorii PTsL-1 i PTsL-2* (Experience of Proximate Determination of the Content of Zeolites in Rocks with the Use of PTsL-1 and PTsL-2 Portable Zeolite Laboratories), Novosibirsk: Nauka, 1979.
6. Kokotov, Yu.A., Zolotarev, P.P., and El'kin, G.E., *Teoreticheskie osnovy ionnogo obmena: slozhnye ionoobmennye sistemy* (Theoretical Foundations of Ion Exchange: Complex Ion-Exchange Systems), Leningrad: Khimiya, 1986.
7. Tunitskii, N.N., Kaminskii, V.A., and Timashev, S.F., *Metody fiziko-khimicheskoi kinetiki* (Methods of Physicochemical Kinetics), Moscow: Khimiya, 1972.
8. Jeffery, P.G., *Chemical Methods of Rock Analysis*, Oxford: Pergamon, 1970.
9. Chelishchev, N.F., Volodin, V.F., and Kryukov, V.L., *Ionoobmennye svoistva prirodnykh vysokokremnistykh tseolitov* (Ion-Exchange Properties of Natural High-Silica Zeolites), Moscow: Nauka, 1988.
10. Komisarova, L.N., Shatskii, V.M., Pushkina, G.Ya., et al., *Soedineniya redkozemel'nykh elementov: Sul'faty, selenaty, telluraty, khromaty (Khimiya redkikh elementov)* (Compounds of Rare-Earth Elements: Sulfates, Selenates, Tellurates, and Chromates (Chemistry of Rare Elements)), Moscow: Nauka, 1986.
11. Yatsimirskii, K.B., Kostromina, N.A., Sheka, Z.A., et al., *Khimiya kompleksnykh soedinenii redkozemel'nykh elementov* (Chemistry of Complex Compounds of Rare-Earth Elements), Kiev: Naukova Dumka, 1966.
12. Spedding, F.H. and Iaffe, S., *J. Am. Chem. Soc*., 1954, vol. 76, no. 5, pp. 882–886.
13. Secine, T., *J. Inorg. Nucl. Chem*., 1964, vol. 26, no. 7, pp. 1463–1468.

ISSN 1070-4272, Russian Journal of Applied Chemistry, 2008, Vol. 81, No. 1, pp. 46–51. © Pleiades Publishing, Ltd., 2008.
Original Russian Text © S.M. Rustamov, F.T. Makhmudov, 2008, published in Zhurnal Prikladnoi Khimii, 2008, Vol. 81, No. 1, pp. 50–55.

PHYSICOCHEMICAL STUDIES OF SYSTEMS AND PROCESSES

Dealuminated Zeolites in Sorption Treatment of Industrial Liquid Wastes to Remove Alkylbenzenesulfonates

S. M. Rustamov and F. T. Makhmudov

Institute of Chemical Problems, National Academy of Sciences of Azerbaijan, Baku, Azerbaijan

Received September 30, 2006; in final form, March 2007

Abstract—Comparative study of the fundamental aspects of the kinetics and statics (equilibrium) of sorption of alkylbenzenesulfonates from aqueous solutions and liquid wastes on industrial AV-17-OH and KAD-iodine sorbents and deeply dealuminated synthetic zeolites NaY and NaX was carried out. The kinetic curves and adsorption isotherms obtained were processed using the classical equations of the diffusion kinetics and the known Langmuir and Nikol'skii equations for equilibrium sorption processes.

DOI: 10.1134/S1070427208010114

It is known that ionic surfactants can be subdivided into anionic, cationic, and ampholytic [1, 2]. Anionic and cationic surfactants are most widely used in industry and households. In particular, alkylbenzenesulfonates (ABS) as representatives of anionic surfactants serve as a basis for fabrication of foaming and wetting agents and emulsifiers [2] and are used as detergents under the trade mark Sulfonols. In contrast to linear polymers, alkylbenzenesulfonates are rather toxic and, when they find way into natural water basins together with wastewater from various industries, they are a hazard to the flora and fauna [3].

It is recommended to purify industrial wastewater to remove ABS using, together with various physicochemical methods [4], sorption methods with solid sorbents, which are efficient and provide deep purification of water in conformity with modern regulations.

A sorption-based method for wastewater treatment to remove surfactants of various classes with activated carbons of various brands has been developed and implemented in practice [4]. A disadvantage of this technique is that these processes use only a minor fraction of the specific surface area of some of the activated carbons tested (~25–30%). Taking into account this circumstance, we consider it appropriate to use activated carbons for treatment of wastewater containing low concentrations of surfactants or, in some cases, for additional purification of wastewater after another purification method.

Solid sorbents of the class of aluminosilicates (bentonite and kaolinite clays, mixed aluminosilicate sorbent, ash from oil shales) have been successfully tested in sorption treatment of wastewater to remove ABS [2, 4–7]. Although the clays used exhibit high sorption activity with respect to ABS, their strong swelling in aqueous media prevented their wide use in wastewater treatment on sorption columns.

It is of interest to develop effective sorbents based on natural and synthetic zeolites by modification of their surface in order to remove alkylbenzenesulfonates from liquid industrial wastes. It should be noted that natural and synthetic zeolites have not been used previously to remove alkylbenzenesulfonates from liquid media because of their rigid framework and narrow-pore structure and of the lack of swelling and strong hydrophilicity in aqueous media.

Samples of natural zeolites (clinoptilolite and mordenite), modified with methylamine hydrochloride, were used for treatment of liquid wastes to remove toxic organochlorine compounds (dichloroethane, trichloroethylene, chloroform), with high sorption capacities obtained (12.0–14.5 wt %) [8].

Here we report on a study of the sorption purification of liquid industrial wastes to remove alkylbenzenesulfonates with dealuminated zeolites and on an analysis of the fundamental aspects of the kinetics and statics (equilibrium) of the process.

EXPERIMENTAL

To modify the surface by dealumination, we took natural zeolites, clinoptilolite from the Ai-Dag deposit

and mordenite from Chananab deposit (Azerbaijan), and synthetic zeolites, NaX and NaY zeolites and Na-mordenite. Samples of these zeolites were treated under dynamic conditions at room temperature with aqueous solutions of HCl (or H_2SO_4) with various concentrations (0.5–2.0 N) to give samples with various degrees of dealumination. This degree was 3 to 95–98% for NaX and NaY zeolites and 3 to 30–35% for natural clinoptilolites and mordenite.

Samples of synthetic and natural zeolites with different degrees of dealumination were preliminarily tested in wastewater treatment at a number of Sumgait detergent-manufacturing plants to remove alkylbenzenesulfonates present in a concentration of about 700 mg l^{-1} (for comparison we took commercial solid sorbents, activated carbon of KAD-iodine brand and AV-17-OH highly basic anion exchanger). Weighed portions (2 g) of sorbents (zeolites with different degrees of dealumination, KAD-iodine activated carbon, and AV-17-OH anion exchanger) were placed in glass tubes a wastewater solution was passed through these tubes, and to complete saturation of the ABS sorbents. After that, the capacities of the samples for alkylbenzenesulfonates were calculated (mg g^{-1}).

The results of experiments with dealuminated samples of synthetic zeolites NaX and NaY are listed in Table 1. For the other of the sorbents tested we obtained the following capacities for ABS (mg g^{-1}) (degrees of dealumination are given in parentheses): synthetic mordenite 27.0 (32.0), natural mordenite 28.0 (30.0), natural clinoptilolite 30.5 (35.0), KAD-iodine activated carbon 55.7, and AV-17-OH 58.2.

In accordance with the results of the experiment (Table 1), the synthetic zeolites NaY and NaX with degrees of dealumination of 63.6 and 86.4%, respectively, which exhibited high sorption activity, and natural KAD-iodine and AV-17-OH sorbents were chosen for a comparative study of the fundamental aspects of the kinetics and equilibrium of ABS sorption from a solution with concentration c_0 = 1000 mg l^{-1}. In wastewater from detergent-manufacturing plants in Sumgait, the ABS concentration varies within the range 500–1000 mg l^{-1}, which is many times the maximum permissible concentration MPC (0.1 to 5.0 mg l^{-1}, depending on a particular region) [3, 4].

The kinetic pattern of ABS sorption on the chosen sorbents was studied by the limited-volume method at l : s = 100 : 1 and temperatures of 298, 308, and 328 K. Weighed portions (0.5 g) of the sorbents were placed in flasks and poured over with 50 ml of an ABS solution with a concentration of 1000 mg l^{-1}. The flasks were transferred to a thermostat shaker and the ABS concentrations in the flask were determined at certain intervals of time by the known procedure [9]. Kinetic curves of sorption were plotted in the a_t–t coordinates, where a_t is the amount of sorbed ABS (mg g^{-1}) and t is the sorption time (s).

Table 1. Results of sorption treatment of wastewater to remove alkylbenzenesulfonates with a concentration of about 700 mg l^{-1} on dealuminated samples of synthetic zeolites NaY and NaX

NaY		NaX	
degree of dealumination, %	capacity for ABS, mg g^{-1}	degree of dealumination, %	capacity for ABS, mg g^{-1}
0	0	0	0
6.7	0	3.9	0
14.9	2.1	9.6	7.9
23.5	7.6	17.7	11.6
33.6	11.6	26.9	13.0
45.0	46.7	35.6	14.3
53.7	50.2	43.2	15.1
63.6	60.9	54.6	16.8
72.3	14.2	68.2	20.1
86.0	8.3	77.3	23.8
91.0	4.3	86.4	57.9
95.8	2.1	97.3	39.5

Isotherms of ABS sorption from a solution with a concentration of 1000 mg l^{-1} on the sorbents under study were obtained by the variable-volume method. For this purpose, 0.5-g portions of the sorbents were placed in 250-ml flasks and poured over with different volumes (20, 40, 60, 80, 100, and 120 ml) of the solution with the concentration specified above. The mixtures were agitated for 8 h (which is sufficient for the sorption equilibrium to be attained), the ABS concentrations in the equilibrium solutions were determined, and sorption isotherms were plotted in the a–c_{eq} coordinates.

It is known that, being associated in solutions, the radicals of alkylbenzenesulfonates form micelles of colloid sizes if the solution concentration exceeds a certain value named the critical micelle concentration (CMS) [2]. Formation of micelles noticeably affects the course of sorption processes, which complicates obtaining reliable values of kinetic parameters. Therefore, we processed the results of kinetic experiments at the beginning of the process (for short t) at solution concentrations below the CMC (~200–

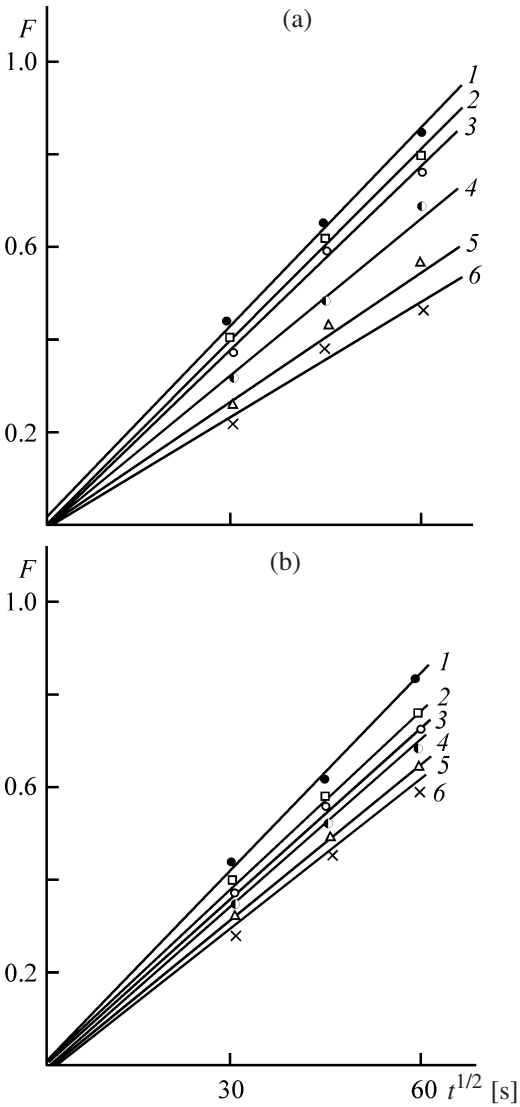


Fig. 1. Sorption parameter $F = a_t/a_\infty$ vs. t for the sorbents under study under different conditions. (t) Sorption time. Temperature, K: (*1, 2*) 323, (*3, 4*) 308, and (*5, 6*) 298. Sorbent: (a) (*1, 4, 6*) AV-17-OH and (*2, 3, 5*) KAD-iodine; (b) (*1, 3, 6*) NaY and (*2, 4, 5*) NaX.

300 mg l^{-1}) by the formula [10]

$$F = a_i/a_\infty = 6(D_{\text{eff}}t/\pi)^{1/2}r^{-1}, \quad (1)$$

where r is the average radius of sorbent particles (cm); D_{eff}, effective diffusion coefficient for alkylbenzenesulfonate ions (cm^2 s^{-1}); and a_∞, maximum equilibrium capacity of the sorbents for ABS (mg g^{-1}).

In Figs. 1a and 1b, the dependences described by formula (1) are plotted for the beginning of the process (for short t) in the coordinates F_∞–$t^{1/2}$. These dependences are linear, which made it possible to determine D_{eff}, using the known Arrhenius formula $D_{\text{eff}} = D_0 e^{-E_a/RT}$, and calculate the activation energies of diffusion for all of the sorbents under study (Table 2). Table 2 also lists values of the thermodynamic functions ΔH^0 and ΔS^0 for the diffusion stages and ΔG^0 for the equilibrium stage of the sorption process, calculated from the results of the kinetic experiments performed at different temperatures.

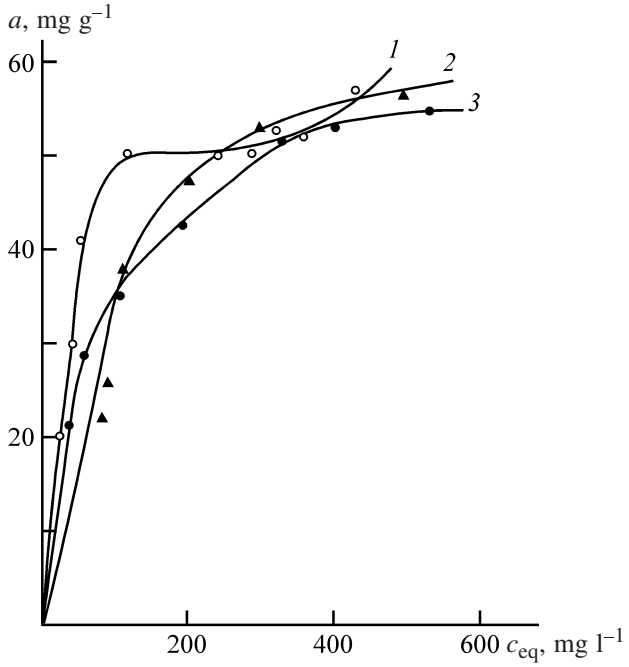


Fig. 2. Isotherms of ABS sorption from a solution with a concentration of 1000 mg l^{-1}. (*a*) Sorbed amount of ABS and (c_{eq}) equilibrium ABS concentration in solution. Sorbent: (*1*) KAD-iodine, (*2*) NaY, and (*3*) NaX.

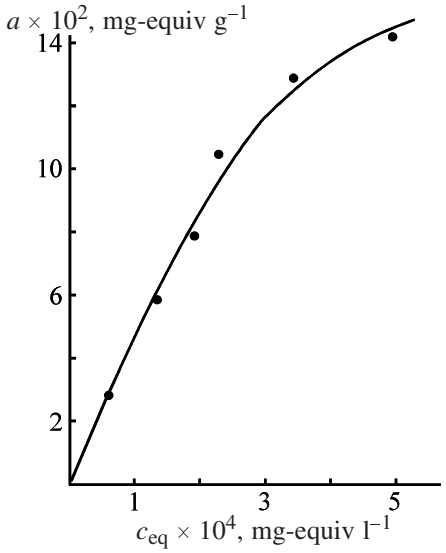


Fig. 3. Isotherm of exchange of alkylbenzenesulfonate ions from a solution of concentration 2.833 mg-equiv l^{-1} on AV-17-OH anion exchanger. (*a*) Sorbed amount of ABS and (c_{eq}) equilibrium concentration of ABS in solution.

Figures 2 and 3 show isotherms of ABS sorption

Table 2. Kinetic and thermodynamic parameters of sorption of alkylbenzenesulfonates on the sorbents under study at different temperatures T for the diffusion stage of the process

Sorbent	Radius of sorbent particles, cm	T, K	$t_\infty \times 10^{-3}$, s	D_{eff}, $cm^2\ s^{-1}$	E_a	ΔH^0	ΔG^0	ΔS^0, $J\ K^{-1}\ mol^{-1}$
					$kJ\ mol^{-1}$			
AV-17-OH	0.03	298	7.440	0.524×10^{-8}	32.320*	29.842*	2.719*	91.018*
		308	7.200	0.991×10^{-8}				
		323	6.840	1.561×10^{-8}				
KAD-iodine	0.1	298	8.100	0.771×10^{-7}	21.854	19.376	7.805	38.830
		308	7.800	1.474×10^{-7}				
		323	7.380	1.613×10^{-7}				
NaX	0.075	298	7.920	0.562×10^{-7}	22.948	20.470	10.281	34.200
		308	7.560	0.718×10^{-7}				
		323	7.020	0.767×10^{-7}				
NaX	<0.01	298	7.740	0.996×10^{-9}	25.005	22.527	9.198	44.730
		308	7.380	1.273×10^{-9}				
		323	6.900	1.754×10^{-9}				

* For AV-17-OH anion exchanger, E_a, ΔH^0, and ΔG^0 are expressed in kJ g-ion^{-1}, and ΔS^0, in J K^{-1} g-ion^{-1}.

from a solution with a concentration of 1000 g l^{-1} on the sorbents under study (KAD-iodine, NaX, and NaY) and on AV-17-OH anion exchanger, respectively.

Assuming that the sorption of ABS from solutions on KAD-iodine, NaX, and NaY sorbents must be molecular, we carried out a theoretical processing of the isotherms in Fig. 2 for the portions with $c_{eq} \leq 200$ mg l^{-1} (henceforth CMC) by the known Langmuir equation:

$$a = a_\infty K c_{eq}/(1 + K c_{eq}). \quad (2)$$

or, in linear coordinates,

$$c_{eq}/a = 1/(a_\infty K) + c_{eq}/a_\infty, \quad (3)$$

where K is the sorption equilibrium constant.

In Fig. 4, the portions with $c_{eq} \leq 200$ mg l^{-1} of the isotherms of ABS sorption on the KAD-iodine, NaX, and NaY sorbents (Fig. 2) are replotted in the coordinates (c_{eq}/a)–c_{eq} of Eq. (3). The maximum sorption capacities a_∞ of the sorbents for ABS were found from the slopes of the linear isotherms, and then the sorption equilibrium constants K were calculated (Table 3).

It is known that the sorption of alkylbenzenesulfonate ions on the surface of AV-17-OH anion exchanger in a solution is of ion-exchange nature [2, 4, 6] and occurs by substitution of mobile OH^- ions of the sorbent by the larger $C_nH_{2n+1}C_6H_4SO_3^-$ (n = 10–18) ions of the anionic surfactant. We used in experiments the fraction with an average molecular weight M = 376 g mol^{-1} (n = 14).

The isotherm in Fig. 3 was theoretically processed for the portion of isotherm with $c_{eq} \leq 5 \times 10^{-4}$ mg-equiv ml^{-1} (~200 mg l^{-1}) with the use of the Nikol'skii equation for single-charged ions [11]:

$$a_1/a_2 = K_{1.2} c_1/c_1. \quad (4)$$

On applying the exchange-equivalence law a_1 =

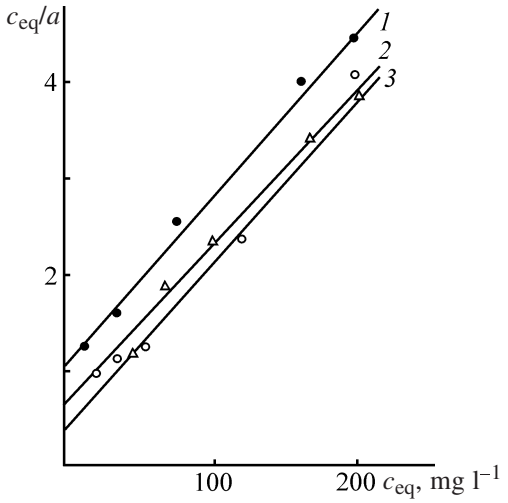


Fig. 4. Portions (for $c_{eq} \leq 200$ mg l^{-1}) of the isotherms of ABS sorption from a solution of concentration 1000 g l^{-1}, plotted in the coordinates (c_{eq}/a)–c_{eq} of Eq. (3). (c_{eq}) Equilibrium ABS concentration in solution. Sorbent: (*1*) NaX, (*2*) NaY, and (*3*) KAD-iodide.

Table 3. Values of K and a_∞, obtained from the isotherms of ABS sorption on the sorbents under study at c_0 = 1000 mg l^{-1}

Sorbent	K	a_∞	TDSC
		mg g^{-1}	
AV-17-OH	0.3334	54.170 (0.1430)*	58.204 (0.1548)*
KAD-iodine	0.0461	54.300	55.704
NaX	0.0163	56.820	57.950
NaY	0.0246	62.500	63.420

* Values of a_∞ and total dynamic sorption capacity (TDSC) for AV-17-OH anion exchanger are expressed in parentheses in mg-equiv g^{-1}.

$a_\infty - a_2$ and $c_1 = c_0 - c_2$ for the alkylbenzenesulfonate ion appearing with index 2, at $a_2 = a$ and $c_2 = c_{eq}$, Eq. (2) takes the form

$$(a_\infty - a)/a = K(c_0 - c_{eq})/c_{eq}. \quad (5)$$

Equation (5) was used in this form to find the ion-exchange equilibrium constant K. For this purpose, we determined from the data in Fig, 3, for the portion with $c_{eq} \le 5 \times 10^{-4}$ mg-equiv cm^{-3}, the maximum equilibrium ion-exchange capacity a_∞ of AV-17-OH anion exchanger for the alkylbenzenesulfonate ion. Taking several values of c_{eq} and the corresponding values of a (Fig. 3), we plotted the dependence of $(a_\infty - a)/a$ on $(c_0 - c_{eq})/c_{eq}$. In accordance with formula (5), this dependence is linear, which enabled us to find the ion-exchange equilibrium constant K. The values obtained for a_∞ and K are listed in Table 3. The same table lists TDSC values for ABS sorption on the sorbents under study, found in separate experiments at a solution concentration of 1000 mg l^{-1}.

As the temperature increases, the rate of ABS sorption on the sorbents under study grows, which leads to a steady decrease in the time t_∞ in which the equilibrium is attained. Simultaneously, the diffusion of alkylbenzenesulfonates in solution and in sorbent pores becomes faster (Table 2). It is known that sorption from solutions occurs on porous solid sorbents, including zeolites, under the mixed-diffusion control [12]. Table 2 shows that, in the case of the narrow-pore unswelling sorbents NaX and KAD-iodine, ABS is mostly adsorbed from solutions on the hydrophobic (as a result of deep dealumination for NaX) outer surface of the sorbents via mixed diffusion with prevalence of the outer diffusion. There also occurs, under inner-diffusion control, sorption in mesopores in the carbon and in secondary pores in the zeolite. This inner-diffusion hindrance in pores weakens diffusion processes to a certain extent, which is confirmed by the values of D_{eff} on the order of 10^{-7} cm^2 s^{-1}, listed in Table 2.

In contrast to the narrow-pore NaX, the synthetic zeolite NaY used in the experiment is broad-pore powder-like ($r \le 0.01$ cm) sorbent that has a developed sorption surface and is highly hydrophobized because of deep dealumination. In this case, the sorption process also occurs under mixed-diffusion control, with a noticeable influence of the inner-diffusion hindrance caused by diffusion penetration of large ABS anions into macropores of the sorbent (D_{eff} on the order of 10^{-9} cm^2 s^{-1}). Presumably, the high sorption activity of NaY (Table 3, high static and dynamic sorption capacities) with respect to large organic radicals results in that the adsorbate structure is formed early, long before the CMC region is formed [13]. In addition, aluminum hydroxide is deposited on the surface of NaY sorbent from aqueous solutions of aluminosilicates, to which NaY zeolite also belongs. ABS molecules having long hydrocarbon radicals with high van der Waals interaction energy are adsorbed not only on hydrophobic areas of the surface, but also on strongly hydrophilic areas of the powder surface with aluminum hydroxide [6, 14]. Therefore, our processing of the isotherm of ABS sorption on NaY in terms of the Langmuir equation yielded increased values of capacity, listed in Table 3.

In contrast to KAD-iodine, NaX, and NaY sorbents, on which molecular ABS is sorbed, the ABS sorption on the swelling broad-pore anion exchanger AV-17-OH is of the ion-exchange nature. It occurs in internal pores of the sorbent, where the inner-diffusion kinetics plays the most important part. In static experiments, 90.0–92.0% of the TDSC of the sorbent for alkylbenzenesulfonates could be utilized.

The values of the thermodynamic functions ΔH^0, ΔG^0, and ΔS^0, listed in Table 2, refer to the diffusion stage of the process. Therefore, they do not noticeably differ between unswelling sorbents (KAD-iodine, NaX, NaY), on which sorption mainly occurs on the outer surface of the sorbents via mixed diffusion with prevalence of the outer-sphere diffusion. Only for the broad-pore and swelling anion exchanger AV-17-OH, the substitution of the smaller hydroxide ion by the larger ABS ion is accompanied by a decrease in the content of water in the pores of the anion exchanger and, accordingly, by an increase in entropy.

The deeply dealuminated synthetic zeolites NaY and NaX, which compare well in capacity with the

commercial sorbents KAD-iodine and AV-17-OH, can be recommended for use in sorption treatment of various liquid wastes to remove toxic ions of a number of anionic surfactants.

CONCLUSIONS

(1) It was found that, among the zeolites tested, deeply dealuminated NaY and NaX compare well in capacity for alkylbenzenesulfonates (57.0–60.0 mg g^{-1}) with the commercial sorbents studied (54.0–58.0 mg g^{-1}).

(2) A theoretical processing of the kinetic curves and sorption isotherms obtained demonstrated that the sorption on the narrow-pore and unswelling sorbents NaX and KAD-iodine occurs on the hydrophobic external surface of the sorbents via mixed diffusion with prevalence of the outer-sphere diffusion, whereas the sorption on the broad-pore, powder-like, and highly hydrophobized NaY occurs also under mixed-diffusion control, but with a noticeable influence of the inner-diffusion hindrance.

(3) It was shown that, in contrast to the three sorbents mentioned above, the sorption on the swelling broad-pore anion exchanger AV-17-OH is of the ion-exchange nature and occurs in internal pores of the sorbent, where the inner-diffusion kinetics is the most important.

(4) The thermodynamic functions ΔH^0, ΔG^0, and ΔS^0 related to the diffusion stage of the sorption process were calculated.

REFERENCES

1. Abramzon, A.A., *Poverkhnostno-aktivnye veshchestva: Svoistva i primenenie* (Surfactants: Properties and Use), Leningrad: Khimiya, 1975.
2. Koganovskii, A.M. and Klimenko, N.A., *Fiziko-khimicheskie metody ochistki promyshlennykh stochnykh vod ot poverkhnostno-aktivnykh veshchestv* (Physicochemical Methods for Treatment of Industrial Wastewater To Remove Surfactants), Kiev: Naukova Dumka, 1974.
3. *Vrednye veshchestva v promyshlennosti: Spravochnik* (Noxious Substances in Industry: Reference Book), vol. 2: *Organicheskie veshchestva* (Organic Substances), Lazarev, N.V. and Levina, E.N., Eds., Leningrad: Khimiya, 1976.
4. Klimenko, N.A. and Timoshenko, M.N., *Khim. Tekhnol. Vody*, 1993, vol. 15, no. 7–8, pp. 534–566.
5. Ivanova, N.I., Volchkova, I.L., Kurbatskii, V.A., et al., *Kolloidn. Zh.*, 1990, vol. 52, no. 2, pp. 408–410.
6. Kisel'gof, G.V., Mikhailov, M.Yu., and Arkhangel'skii, L.K., *Zh. Prikl. Khim.*, 1994, vol. 67, no. 2, pp. 310–312.
7. Bartnitskii, A.E., Klimenko, N.A., and Kozhanov, V.A., *Khim. Tekhnol. Vody*, 1989, vol. 11, no. 10, pp. 898–901.
8. Rustamov, S.M., Yagubov, A.I., and Bashirova, Z.Z., *Zh. Prikl. Khim.*, 1992, vol. 65, no. 12, pp. 2716–2721.
9. Pilipenko, A.T., Kulichenko, S.A., and Dolenko, S.A., *Khim. Tekhnol. Vody*, 1990, vol. 12, no. 7, pp. 623–627.
10. Barrer, R.M., *Chem. Ind.*, 1962, no. 28, pp. 1258–1266.
11. Nikol'skii, B.P. and Paramonova, V.I., *Usp. Khim.*, 1939, vol. 8, no. 10, pp. 1535–1567.
12. Breck, D.W., *Zeolite Molecular Sieves*, New York: Wiley, 1974.
13. Smolin, S.K., Klimenko, N.A., and Timoshenko, M.N., *Khim. Tekhnol. Vody*, 1991, vol. 13, no. 10, pp. 883–887.
14. Koganovskii, A.M. and Klimenko, N.A., *Fiziko-khimicheskie osnovy izvlecheniya PAV iz vodnykh rastvorov i stochnykh vod* (Physicochemical Foundations of Surfactant Extraction from Aqueous Solutions and Wastewater), Kiev: Naukova Dumka, 1978.

ISSN 1070-4272, Russian Journal of Applied Chemistry, 2008, Vol. 81, No. 1, pp. 52–54. © Pleiades Publishing, Ltd., 2008.
Original Russian Text © S.Yu. Men'shikov, Yu.V. Mishina, Yu.V. Mikushina, A.A. Ostroushko, 2008, published in Zhurnal Prikladnoi Khimii, 2008, Vol. 81, No. 1, pp. 56–58.

PHYSICOCHEMICAL STUDIES OF SYSTEMS AND PROCESSES

A Comparative Study of Aerobic Oxidation of Turpentine

S. Yu. Men'shikov, Yu. V. Mishina, Yu. V. Mikushina, and A. A. Ostroushko

Postovskii Institute of Organic Synthesis, Ural Division, Russian Academy of Sciences, Yekaterinburg, Russia
Ural State University, Yekaterinburg, Russia

Received March 23, 2007

Abstract—The catalytic activity exhibited in turpentine oxidation at elevated pressure by cobalt coordination compounds, some transition metal compounds, in particular, polyoxometallate with spherical nanoclusters (Mo_{132}), vanadium oxide bronze, and cobalt complexes immobilized on AN-241 anion exchanger was studied.

DOI: 10.1134/S1070427208010126

It is known that oxidation of α-pinene with molecular oxygen leads to allyl oxidation products and oxygen-containing compounds formed by oxidation of the methyl group adjacent to the double bond; epoxidation products are also formed [1]. The ratio of the oxidation products can be apparently controlled by choosing appropriate catalysts. Catalytic oxidation of α-pinene still attracts researchers' attention [2–4]. At the same time, today the main source of α-pinene is sulfate turpentine, which is mainly used as solvent. Therefore, to extend the possibilities of preparing practically important α-pinene derivatives, it is appropriate to study its oxidation using as substrate commercial turpentine. Proceeding with studies in this field [5], we examined the activity of a series of homogeneous and heterogeneous catalysts in the oxidation of turpentine at elevated pressure of molecular oxygen (~1.3 atm). Apparently, slightly elevated oxygen pressure should lead to a decrease in the oxidation temperature (in contrast to [6] where the reaction was performed at reduced pressure) and in the yield of high-boiling oxidation products. As catalysts we used homogeneous complexes, including those capable of reversible oxygen binding and suitable for oxidation of sulfate turpentine because of no need in their regeneration. We also tested a series of heterogeneous catalysts containing transition metals (Cu, V, Mo, Co), taking into account successful use of these compounds, in particular, of vanadium oxide bronzes (VOBs) $Cu_{0.6} \cdot V_2O_5$ [7], for liquid-phase peroxide oxidation of aromatic compounds.

EXPERIMENTAL

The reaction mixture was analyzed with a Chrom-5 chromatograph equipped with a thermal conductivity detector and a 1.5-m glass column with DC-550 stationary phase. Carvone was used as internal reference.

Experiments were performed, in accordance with [5], in a setup with a temperature-controlled reactor fixed in a high-speed rocker. Experiments were performed at 300 rockings per minute at elevated pressure (1.3 atm) and a temperature of 50°C. We used turpentine [GOST (State Standard) 1571–82] as substrate, acetonitrile as solvent, and various homogeneous and heterogeneous catalysts.

Samples of the reaction mixture were taken at regular intervals and subjected to chromatographic analysis, and the kinetic curves of α-pinene oxidation were plotted. For each kinetic curve, we determined the initial rate by extrapolation of the measurement results after completion of the induction period, using a pseudo-first-order equation [5].

In addition, we determined the specific oxidation rate. The complexes $Co(acac)_2$ and CoSalen were prepared by procedures described in [5]. The catalyst activities were evaluated by the rate of α-pinene consumption in the reaction mixture. The α-pinene content was determined by gas chromatography. The dependence $\log c = f(t)$ is linear (see figure).

The common criterion of performance of homogeneous and heterogeneous catalysts under the examined conditions is the specific oxidation rate. This quantity is defined as the ratio of the initial rate of α-pinene oxidation to the molar concentration of the catalyst, $V_{sp} = V_0/[Cat]$ (see table).

Among the heterogeneous catalysts tested, the highest initial oxidation rate was observed with vanadium oxide bronze of the composition $Cu_{0.6}V_2O_5$.

Oxidation of α-pinene in the presence of homogeneous and heterogeneous catalysts. T = 500°C, P = 1.3 atm, solvent acetonitrile

Sample no.	Catalyst	Sample weight, g	Molar ratio α-pinene : solvent* : catalyst	V_0, mol l^{-1} min^{-1} for α-pinene	V_{sp}
	–	–	1 : 11.05 : 0	-0.00219	–
1	AN-251 + $CoCl_2$**	0.0242	1 : 11.05 : 0.0000837	-0.0217	19 700
2	$Co(acac)_2$	0.0395	1 : 11.05 : 0.0117	-0.0186	122
3	CoSalen	0.0497	1 : 11.05 : 0.0117	-0.0724	473
4	$Cu_{0.6}\cdot V_2O_5$	0.0337	1 : 11.05 : 0.0152	-0.0684	334
5	$(NH_4)_{42}[Mo^{VI}_{72}Mo^{V}_{60}O_{372}(HCO_2)_{30}\cdot (H_2O)_{72}]\cdot 30HCO_2Na\cdot 250H_2O$**	0.0337	1 : 11.05 : 0.0001169	-0.0567	37 000

* For calculation simplicity; actually the solvent also contained other turpentine components (apart from α-pinene and its oxidation products).

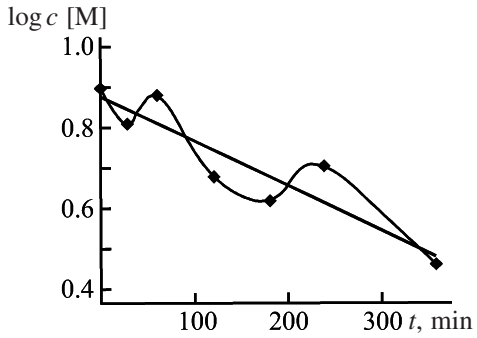
** In calculation of V_{sp} for sample nos. 1 and 5, the molecular weights of both catalysts were taken equal, 22 000.

This catalyst can be used repeatedly. Along with the compounds synthesized previously, we tested in turpentine oxidation polyoxometallate with spherical nanoclusters of the composition $(NH_4)_{42}[Mo^{VI}_{72}\cdot Mo^{V}_{60}O_{372}(HCO_2)_{30}(H_2O)_{72}]\cdot 30HCO_2Na\cdot 250H_2O$ [8].

It should be noted that the resistance of the spherical molybdenum complex to atmospheric oxygen was evaluated in [9] by spectrophotometry and by photovoltaic effect measurement, and the tendency of the complex to gradual oxidation and degradation, accelerating under the action of light, was revealed. At the same time, the oxidation of α-pinene without solvent in the presence of the polyoxometallate was slow.

A heterogeneous analog of Co(II) picoline complex, prepared by sorption of Co(II) ions on AN-251 anion exchanger, proved to be the least active among the heterogeneous catalysts, despite the fact that the corresponding homogeneous catalyst showed high selectivity in oxidation of α-pinene to verbenone [10].

According to GLC data, elevated pressure appreciably increases the α-pinene conversion. The α-pinene conversion reached 78% (at 45% conversion, the selectivity of verbenone formation was about 12%), at the highest oxidation rate, with the homogeneous Co(Salen) catalyst. It is appropriate to use this catalyst for oxidation of sulfate turpentine, as it is a one-use catalyst.



α-Pinene concentration c as a function of time t. Oxidation in the presence of $Co(acac)_2$. $\log c = -0.0011t + 0.8715$; $R^2 = 0.8375$.

CONCLUSIONS

(1) The conditions chosen for sulfate turpentine oxidation (P ~1.3 atm) ensure increased conversion of α-pinene and confirm the necessity of searching for compounds generating radical oxygen species as catalysts for α-pinene oxidation to verbenol and verbenone.

(2) The presence of other terpene hydrocarbons, along with α-pinene, in turpentine reduced the negative effect of the most active radical species on the initial oxidation process.

(3) Heterogeneous catalysts are appropriate for oxidation of oleoresin turpentine, because this raw material contains no sulfur compound and there is no risk of catalyst poisoning.

ACKNOWLEDGMENTS

The authors are grateful to V.L. Volkov for the sample of VOB of the composition $Cu_{0.6}\cdot V_2O_5$ and to V.P. Fedin for the sample of the polyoxometallate $(NH_4)_{42}[Mo^{VI}_{72}Mo^{V}_{60}O_{372}(HCO_2)_{30}(H_2O)_{72}]\cdot 30HCO_2Na\cdot 250H_2O$.

REFERENCES

1. Kislitsin, A.N., Klabukova, I.N., and Trofimov, A.N., *Khim. Rast. Syr'ya*, 2004, no. 3, pp. 109–116.

2. Bhattacharjee, S. and Anderson, J.A., *Catal. Lett.*, 2004, vol. 95, nos. 3–4, pp. 119–125.
3. Kuznetsova, N.I., Kuznetsova, L.I., Kirillova, N.V., et al., *Izv. Ross. Akad. Nauk, Ser. Khim.*, 2003, no. 7, pp. 1462–1468.
4. RF Patent 2250208.
5. Men'shikov, S.Yu., Sennikov, M.Yu., Romanova, Yu.V., et al., *Zh. Org. Khim.*, 2004, vol. 40, no. 6, pp. 830–833.
6. Patlasov, V.P., Savinykh, V.I., Kushnir, S.R., and Lukoyanov, V.P., *Izv. Vyssh. Uchebn. Zaved., Lesn. Zh.*, 1999, no. 5, pp. 74–82.
7. Men'shikov, S.Yu., Vurasko, A.V., Petrov, L.A., et al., *Neftekhimiya*, 1992, vol. 32, no. 2, pp. 162–164.
8. Muller, A., Fedin, V.P., Kuhlmann, G., et al., *Chem. Commun.*, 1999, no. 10, pp. 927–929.
9. Ostroushko, A.A., Sennikov, M.Yu., Artemov, M.Yu., et al., in *9-ya Mezhdunarodnaya konferentsiya "Fiziko-khimicheskie protsessy v neorganicheskikh materialakh"* (9th Int. Conf. "Physicochemical Processes in Inorganic Materials"), Kemerovo, September 22–25, 2004, vol. 1, pp. 422–425.
10. Volchko, K.P., Ragoza, L.N., Salakhutdinov, N.F., et al., *Preparativnaya khimiya terpenodiov* (Preparative Chemistry of Terpenoids), Novosibirsk: Sib. Otd. Ross. Akad. Nauk, 2005, book 1.

ISSN 1070-4272, Russian Journal of Applied Chemistry, 2008, Vol. 81, No. 1, pp. 55–60. © Pleiades Publishing, Ltd., 2008.
Original Russian Text © A.M. Worontsov, A.P. Patsovskii, M.N. Nikanorova, G.B. Krivtsova, 2008, published in Zhurnal Prikladnoi Khimii, 2008, Vol. 81, No. 1, pp. 59–64.

PHYSICOCHEMICAL STUDIES OF SYSTEMS AND PROCESSES

A Sonoluminescent Method for On-Line Monitoring of the Natural Water Quality

A. M. Worontsov, A. P. Patsovskii, M. N. Nikanorova, and G. B. Krivtsova

Scientific Research Center for Ecological Safety, Russian Academy of Sciences, St. Petersburg, Russia

Received December 4, 2007

Abstract—Ultrasonic impact on natural waters was applied to identify hydrochemical anomalies from the changes in the characteristics of sonoluminescence generated by ultrasonic cavitation in a flowing water sample. Sonoluminescence excitation spectra characteristic for various natural water pollutants were obtained for the first time. The suitability of changes in the sonoluminescence intensity and in the shape of the sonoluminescence excitation spectra as indicators of hydrochemical anomalies was elucidated.

DOI: 10.1134/S1070427208010138

The overwhelming majority of methods for water pollution assessment are based on comparison of the measured chemical composition, physical properties, and microbiological characteristics with the corresponding aquatic environment quality standards. Such pair-by-pair component-by-component assessment is not only awkward and hard to comprehend but also fails to meet (in ever growing extent with time going) the environmental safety requirements in the context of the hazard of chemical water pollution: There exist standards for no more than 6000 substances, while a total of 88 mln compounds were synthesized by the end of 2006 [1].

Multicriterial estimation [2] based on information compression and elimination of dimensionality of the resulting values is not suitable as an alternative to the pair-by-pair component-by-component assessment, since the resulting generalized (total property of a substance) and integrated (total amount of a substance) indicators are calculated using the results of the same single measurements of the same standardized parameters that were used previously [3]. This concerns above all such, now conventional, indicators as the water pollution index, atmosphere pollution index, soil pollution index, and waste toxicity index. Recent years have witnessed ever more extensive use of test methods for aquatic environment monitoring [4]. They can be subdivided into selective (qualitative or semiquantitative analysis of one substance) and nonselective (analysis of the total content of a substance or the total property of the medium) methods.

Clearly, nonselective test methods, in fact, provide integrated or generalized indicators without calculation of the corresponding indices. A combination of test methods with the screening methodology (elimination of obviously "blank" samples) is in line with the new analytical monitoring paradigm [5].

Development of new test methods should be focused on the search for hydrochemical anomalies, based on the "yes/no" qualitative criterion, rather than on measurement of water quality indicators (individual, generalized, or integrated). This allows designing nonselective sensors of hydrochemical anomalies, raising alarm in cases when the composition of the medium exhibits any significant deviation from the statistically normal value. These are environmental alarm sensors (EASs) which can be regarded as functional and cost analogs of widely used fire and security alarm sensors [6].

Among test methods promising for designing EASs is that based on monitoring of the total content of dissolved organic matter (DOM) in natural waters and wastewaters from ozone chemiluminescence. This method is underlain by the interrelation between the amount of DOM being ozonized in a flowing water sample and the chemiluminescence intensity [7].

Also promising is the method based on sonoluminescence (SL) effect whose intensity exhibits nonselective dependence on the content of an infinitely broad spectrum of possible components of water objects: biotic and anthropogenic dissolved organic matter of different nature, inorganic ions, dissolved

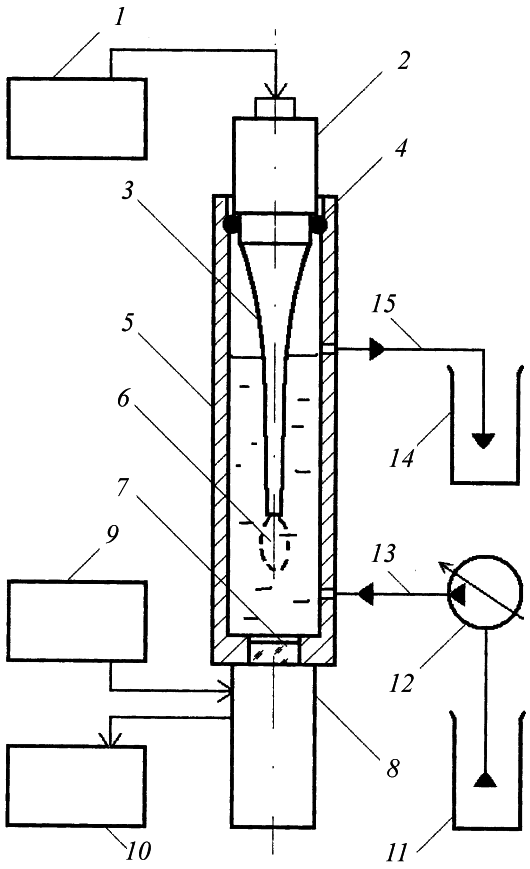


Fig. 1. Experimental setup for recording sonoluminescence in a flowing water sample (this is a functional scheme; see designations in the text).

gases, colloid particles, any kind of sonoluminescence and chemiluminescence quenchers and catalysts, and substances containing UV/Vis-absorbing chromophore groups.

Ultrasonication of water and aqueous solutions results in formation of a multibubble cavitation zone (cavitation cloud) in which specific sonochemical reactions proceed and SL arises. It has been known for already half a century that the SL intensity is proportional to the electrolyte content of water and depends on the composition and amount of dissolved gases and also that dissolved organic alcohols decrease the SL intensity [8, 9]. It is generally recognized that virtually all the dissolved organic substances act as SL quenchers, but it was recently demonstrated [10, 11] that the luminescence of aqueous solutions exhibits a complex dependence on the concentration of soluble substances.

The first examinations of sonoluminescence in a natural water flow date back to 2000 [12], when we showed that the SL effect can underlie the development of EASs. Since then, the research methodology and experimental setups were improved [13–16], which allowed us to attempt formulating the basic principles of the new method of analysis, sonoluminescence excitation spectroscopy, to underlie designing equipment to reveal chemical anomalies in the aquatic environment, in particular, sonoluminescence-based EASs.

EXPERIMENTAL

The main specific feature of the experimental setup for examination of SL in a flowing water sample (Fig. 1) is that the ultrasonication energy at a fixed ultrasonic frequency can be varied, so that the characteristic dependences of the SL intensity on the SL-exciting energy can be derived for model and natural aqueous solutions.

The setup was assembled from standard units of analytical and medical instruments. As the source of ultrasonication responsible for formation in a water flow of a multibubble cavitation zone we used a SUZA commercial medical apparatus developed in Russia [17, 18] *1* comprising one-half-wave piezo converter *2* and ultrasonication energy concentrator *3*. This system allows the specific density of acoustic energy in the ultrasonication zone to be varied discretely (in 9 steps) from 4.92 to 15.62 J cm^{-3} at a fixed frequency of 22 kHz. The ultrasonication energy concentrator *3* is introduced through shock-absorbing sealing ring *4* into the case of flow cell *5* (d_{in} = 20 mm). Ultrasonication results in formation near the end face of the concentrator of multibubble cavitation zone *6*, in which SL is generated; it passes through KU-1 melted quartz window *7* onto the photocathode of photodetector *8* (FEU-85). High-voltage board *9* supplies up to 1100 V voltage to the photomultiplier; the photocurrent comes to signal amplification and recording system *10*. Hose pump *12* with a feeding volume of 35 cm^3 min^{-1} supplies a natural water sample from reservoir *11* through line *13* (nominal diameter 2 mm) into flow cell *15*, from whence it flows down into receiver *14* through line *15* (nominal diameter 8 mm). It should be noted that this small-sized (weighing 6.5 kg) setup is essentially an SL excitation spectrometer.

A spectrometer measures the distribution function (spectrum) of some physical quantity f with respect to parameter x. Here we report on the development of a spectrometer for determination of the $f(x)$ distribution, where f is the SL intensity, and x, energy of the ultrasonication responsible for this SL (in a similar

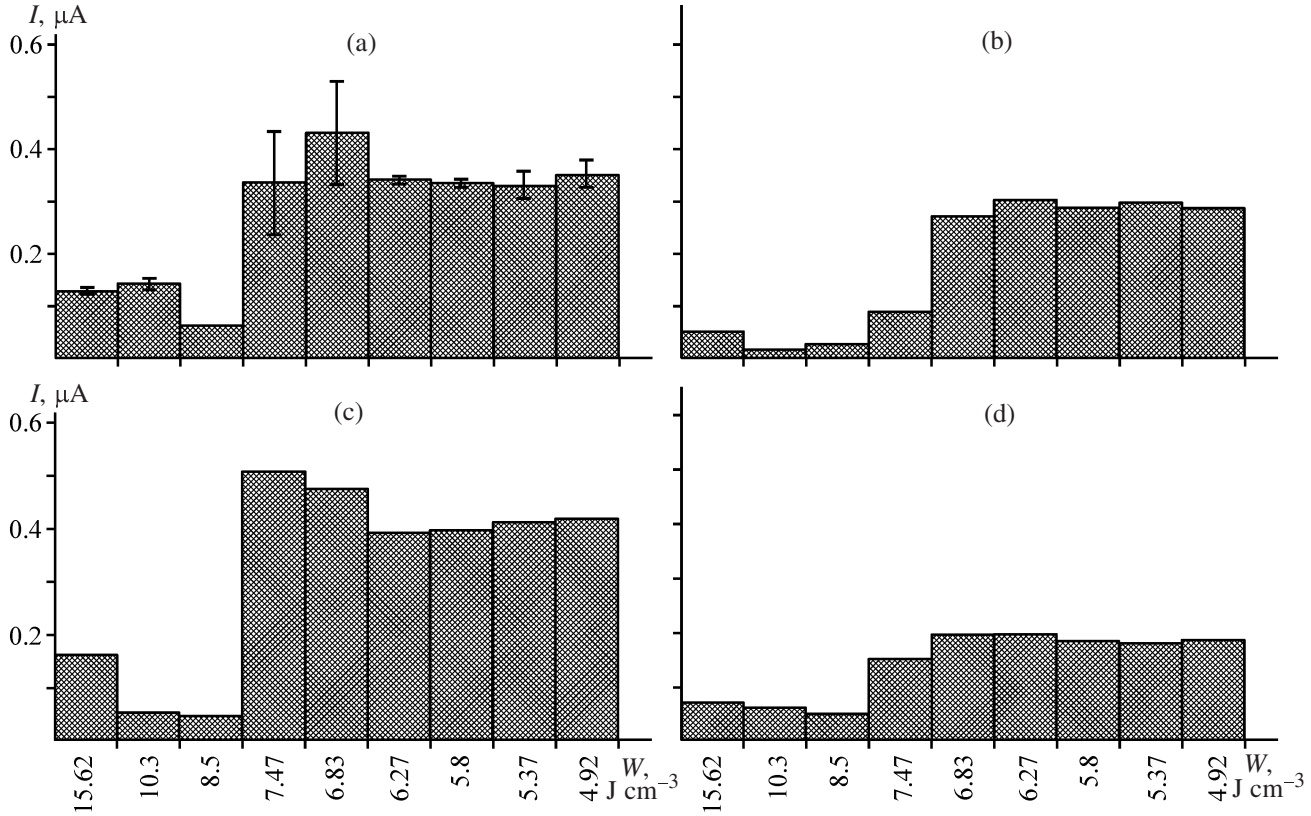


Fig. 2. Influence of various dissolved substances on the shape of the SL excitation spectrum of a flowing water sample. (*I*) Sonoluminescence intensity and (*W*) volume density of the acoustic energy. Background object: (a) distilled water; (b) sodium humate solution; 0.15 mg l^{-1}, (c) aqueous NaCl solution, 10 mg l^{-1}; and (d) aqueous solution of Ponceau 4R dye, 0.06 mg l^{-1}.

manner, e.g., spectral fluorescence instruments record the fluorescence excitation spectra).

The SL excitation spectra of aqueous solutions were recorded at different concentrations of dissolved organic and inorganic substances, salinities, and amounts of dissolved gases. Figure 2 presents the SL excitation spectrum of a background object, distilled water (Fig. 2a) and the most characteristic excitation spectra of aqueous solutions of the substances that are important indicators of the aquatic environment quality. These include humates (Fig. 2b) whose concentration largely determines the water object quality; NaCl, whose concentration governs the water environment salinity (Fig. 2c); and Ponceau 4R dye, a model natural water pollutant of organic origin (Fig. 2d).

Table presents the characteristics of the sono-

Characteristics of the sonoluminescence excitation spectrum of an aqueous NaCl solution (concentration 10.0 mg l^{-1}) at nine ultrasonication energy levels*

Characteristic	Channel no.								
	1	2	3	4	5	6	7	8	9
W_{ac}, J cm^{-3}	15.62	10.30	8.50	7.47	6.83	6.27	5.80	5.37	4.92
A, μm	15	22	29	36	43	50	57	64	70
$\bar{I}$, μA	0.13	0.13	0.08	0.32	0.45	0.33	0.34	0.32	0.33
σ, μA	0.01	0.02	0.07	0.07	0.08	0.02	0.02	0.06	0.04

* W_{ac} is the specific density of the acoustic energy in the ultrasonication zone; A, amplitude of longitudinal oscillations of the working end of the ultrasonic concentrator; I, average SL intensity at the given ultrasonic energy level; and σ, standard deviation of the output signal.

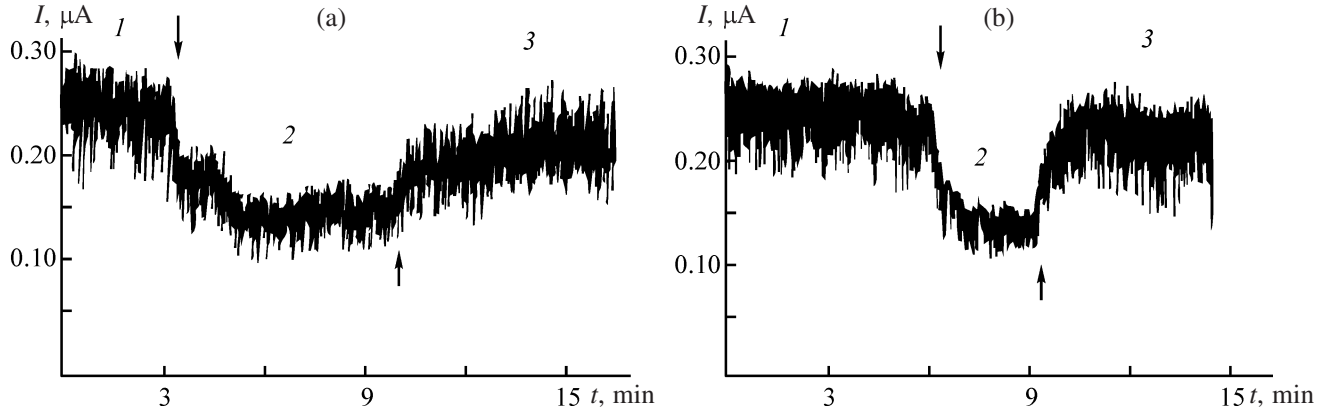


Fig. 3. Examples of variation of the SL intensity I of a natural water flow (low-mineralized source) with time t upon introduction into the flow cell of the sample (*1, 3*) without and (*2*) with additions (organic and inorganic). W_{ac} = 6.83 J cm^{-3}. (*a*) Na humate (0.2 mg l^{-1}) and (b) Cu^{2+} (10 mg l^{-1}). The moment when the solution was introduced is marked with a down-pointing arrow, and the moment when the cell washing was begun, with an up-pointing arrow.

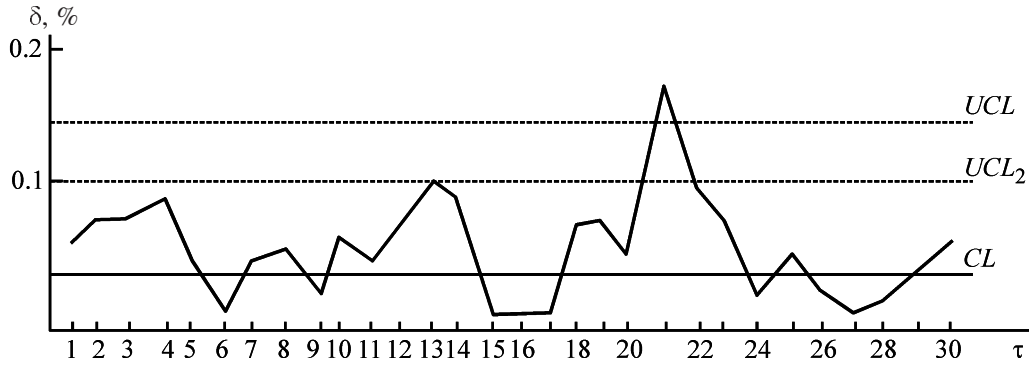


Fig. 4. A limit map for determination of the dissolved matter content of water samples taken from Chernaya Rechka river (St. Petersburg). (δ) Divergence, %, and (τ) analysis date (within April 1–30, 2007). (*CL*) Central line; (*UCL*) upper control limit, 3σ action limit; and (UCL_2) upper control limit, 2σ warning limit.

luminescence excitation spectrum of an aqueous NaCl solution.

Figure 3 shows how the SL intensity varies with time; in this case, the revealed hydrochemical anomalies were associated with the appearance in the aquatic environment of an organic (Fig. 3b) and inorganic (Fig. 3c) substance.

To check the consistency of the results of measurements and determine the action limits (the hydrochemical anomaly detection level) we used control Schuhart maps (*R*-diagrams) [19].

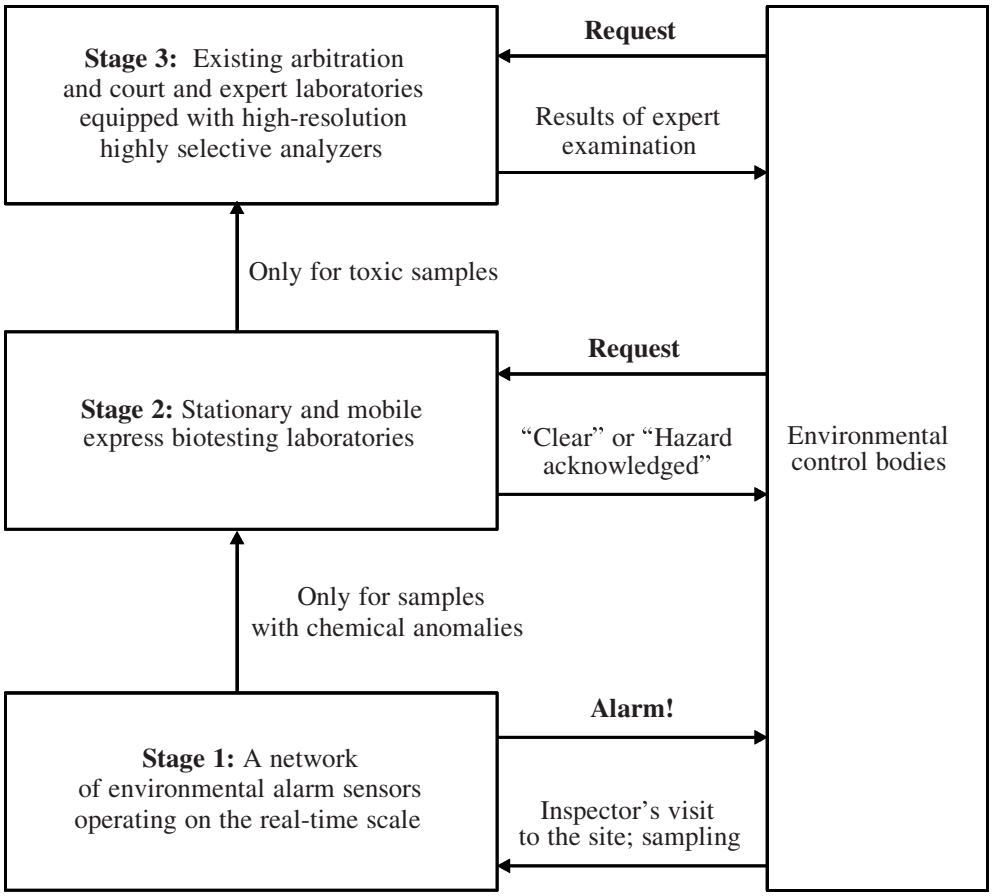
The Schuhart map is a plot of the values of certain characteristics of subgroups vs. their numbers. The map has the central line corresponding to the reference value of a characteristic. This is a long-term value of the characteristic or its nominal value derived from the previously available information about the process of interest. Schuhart maps have two statistically determined control limits relative to the central line, an upper and a lower limit.

The control limits on Schuhart maps are separated from the central line by a distance of 3σ. The ±3σ limits suggest that ca. 99.7% of the values of the subgroup characteristic will fall within these limits, provided that there will be no significant systematic errors.

The analytical application of the SL method is exemplified by Fig. 4 demonstrating the results of examinations carried out by the Laboratory of Hyphenated Methods of Environmental Control, Scientific Research Center for Ecological Safety, Russian Academy of Sciences, in the period April 1–30, 2007. The subjects of these examinations were water samples taken from Chernaya Rechka river to check the consistency of the data on the content and properties of the dissolved matter. This was done by daily analyzing three aliquots of the water sample under replication conditions. In calculation of the central line and control limits we used the coefficients from [19].

The mapped data evidence inconsistency of the

A hierarchic system of on-line environmental monitoring of water objects



results of measurements, associated with anomalies in the content of the dissolved matter: One point in the map exceeds the action limit, and the data derived from three series of measurements, each comprised of seven or more results, are located above the central line. These and similar anomalies can evidence emergent or illegal dumping or utilizing inadequate treatment technologies in water supply systems of settlements, i.e., the events that can be detected by EASs whose operation is underlain by the SL effect.

However, an EAS is able of informing only about a chemical anomaly which can be associated with natural processes and be quite harmless. Therefore, the sample taken at the time when a sensor raised an alarm needs to be promptly tested for toxicity. An ideal choice for Stage 2 can be found in simple biotesting instruments and methods suitable for identifying new and inadequately studied pollutants of unknown type and composition from the change in the total toxicity of the sample.

Only samples for which a chemical anomaly was revealed and subsequently a toxicity was identified in a biotest should be taken for analysis in Stage 3, i.e., for detailed expert examinations in laboratories equipped with expensive high-resolution highly selective instruments (chromatographs, chromato-mass-spectrometers, atomic absorption spectrometers, inductively coupled plasma atomic emission analyzers), serviced by highly skilled personnel.

This makes it possible to sharply decrease the number of expensive analytical procedures and conduct environmental monitoring at a small number of the best available arbitration and expert and criminological laboratories.

The environmental control system we proposed (see scheme) is an open hierarchic structure which can be comprised of the available components and, as soon as appropriate funding is obtained (mostly through application of the results achieved), be supplemented with new components.

CONCLUSIONS

(1) A method was proposed for the search of anomalies in the chemical composition of natural

waters, based on the sonoluminescence effect which was not earlier used for these purposes.

(2) The search for anomalies in the chemical composition using the sonoluminescence method can underlie development of a new type of environmental alarm sensors to be applied in the first stage of the natural water quality control system. Rising an alarm by such a sensor allows promptly responding to possible chemical threats, and further analytical procedures will apply only to those samples for which hydrochemical anomalies were revealed in time (stationary environmental alarm sensor in a water flow or "on the pipe") and in space (a mobile sensor onboard an over- or underwater vessel).

(3) A small-sized setup (sonoluminescence excitation spectrometer) was developed for recording the sonoluminescence intensity vs. the ultrasonication energy for a natural water flow; characteristic sonoluminescence excitation spectra of model and natural water samples were recorded.

(4) A sonoluminescence excitation spectrometer was described in a detail sufficient for replication by other research laboratories.

REFERENCES

1. Mil'man, B.L., Development of New Approaches to Mass-Spectrometric and Chromato-Mass-Spectrometric Identification of Organic Compounds, *Doctoral Dissertation*, St. Petersburg, 2006.
2. Dmitriev, V.V., in *Voprosy prikladnoi ekologii: Sbornik nauchnykh trudov* (Applied Ecology Issues: Coll. of Scientific Works), St. Petersburg: Ross. Gos. Gidrometeorol. Univ., 2002, pp. 23–30.
3. Worontsov, A.M., *Ekol. Khim*., 2004, vol. 1, no. 14, pp. 1–10.
4. Zolotov, Yu.A., Ivanov, V.M., and Amelin, V.G., *Khimicheskie test-metody analiza* (Chemical Test Methods of Analysis), Moscow: URSS, 2002.
5. Zolotov, Yu.A., *Ekol. Prom–st. Rossii*, 2006, no. 3, pp. 38–40.
6. Worontsov, A.M. and Nikanorova, M.N., in *Gos. doklad o sostoyanii okruzhayushchei sredy Sankt-Peterburga i Leningradskoi oblasti v 1998 g.* (State Report on the Condition of the Environment in St. Petersburg and Leningrad oblast in 1998), St. Petersburg: 1999, vol. 2, pp. 280–297.
7. Worontsov, A.M., Nikanorova, M.N., and Melent'ev, K.V., *Vodnye ob'ekty Sankt-Peterburga* (Water Objects of St. Petersburg), Kondrat'ev, S.A. and Frumin, G.T., Eds., St. Petersburg: Simvol, 2002, pp. 73–79.
8. Gunter, P., Zell, W., Grissar, V., and Heim, E., *Z. Elektrochem.*, 1957, vol. 61, no. 1, pp. 188–201.
9. Prevenslik, T.V., *J. Luminescence*, 2000, vols. 87–89, pp. 1210–1212.
10. Price Gareth, J. and Ashokkumar Muthupandin, *Chem. Commun*., 2002, no. 16, pp. 1740–1741.
11. Margulis, M.A. and Margulis, I.M., *Ultrasonic Sonochem*., 2002, vol. 9, no. 1, pp. 1–10.
12. Worontsov, A.M., Nikanorova, M.N., and Melent'ev, K.V., *Materialy dokladov Vserossiiskoi konferentsii "Sensor-2000"* (Proc. Russian Conf. "Sensor-2000"), St. Petersburg, June 21–23, 2000, pp. 20–21.
13. RF Useful Model Certificate 28393.
14. Worontsov, A.M., Krivtsova, G.B., and Nikanorova, M.N., in *Sbornik nauchnykh dokladov 9-i Mezhdunarodnoi konferentsii "Ekologiya i razvitie obshchestva"* (Proc. 9th Int. Conf. "Ecology and Development of Society"), St. Petersburg, July 19–24, 2005, pp. 279–280.
15. Patsovskii, A.P., Krivtsova, G.B., and Worontsov, A.M., in *Sbornik trudov Nauchno-issledovatel'skogo tsentra ekologicheskoi bezopasnosti po rezul'tatam Mezhregional'noi konferentsii molodykh uchenykh "Aktual'nye problemy ekologicheskoi bezopasnosti i ustoichivogo razvitiya regionov"* (Coll. of Works of Scientific Research Center for Ecological Safety, Based on Results of Interregional Conf. of Young Scientists "Urgent Problems of Environmental Safety and Sustainable Development of Regions"), St. Petersburg: Nauchno-Issled. Tsentr Ekolog. Bezopasnosti Ross. Akad. Nauk, November 15–16, 2006, pp. 118–125.
16. Krivtsova, G.B., Sonoluminescent Method for Express Monitoring of the Aquatic Environment, *Cand. Sci. Dissertation*, St. Petersburg, 2007.
17. RF Patent 2092120.
18. *Apparaty khirurgicheskie ul'trazvukovye "SUZA"* ("SUZA" Surgical Ultrasonic Instruments) (SPGI 941.614.000 PS Passport), St. Petersburg: Medilen, 1995.
19. *GOST* (State Standard) *R ISO 5725-6–2002*, Moscow: Izd. Standartov, 2002.

ISSN 1070-4272, Russian Journal of Applied Chemistry, 2008, Vol. 81, No. 1, pp. 61–66. © Pleiades Publishing, Ltd., 2008.
Original Russian Text © I.V. Khoruzhii, G.F. Klyakin, V.A. Taranushich, V.I. Lachin, 2008, published in Zhurnal Prikladnoi Khimii, 2008, Vol. 81, No. 1, pp. 65–70.

PHYSICOCHEMICAL STUDIES OF SYSTEMS AND PROCESSES

Electrothermal Method for Controlling the Ballistic Characteristics of Energetic Condensed Systems Based on Ammonium Nitrate

I. V. Khoruzhii, G. F. Klyakin, V. A. Taranushich, and V. I. Lachin

South-Russian State Technical University, Novocherkassk, Rostov oblast, Russia

Received April 3, 2007

Abstract—The electrothermal method for control over the combustion velocity of energetic condensed systems based on ammonium nitrate oxidizing agent at the intrachamber pressure of the gas phase of combustion products varied in the range 1–6 MPa was examined as applied to controllable solid-fuel power installations.

DOI: 10.1134/S107042720801014X

It is known that the combustion velocity of energetic condensed systems (ECS) is a function of several variables:

$$u = F[\chi,\ P_c,\ T_0,\ \nu,\ a_g],$$

where χ is the chemical composition of ECS; P_c, gas phase pressure in the combustion chamber as a function of temperature T_c; T_0, initial temperature of ECS; ν, gas-dynamic factor, e.g., the "erosion" effect determined by the Pobedonostsev criterion; and a_g, the accelerative force acting on the ECS in accelerated motion of the charge.

Because of the existence of the electrothermal effect [2, 3], which has been experimentally confirmed under atmospheric pressure, one more factor can be added to the functional dependence: power N (W) released in the reaction zone of the condensed phase (c-phase) when current flows through a continuously burning fuel.

With account of the fact that $N = IU = I^2R_x$, where I is the current strength in the reaction zone and U is the voltage across the charge, the dependence of the combustion velocity on pressure and current strength, $u(P_c, I)$, can be studied at a constant chemical composition and other factors mentioned above. The current strength obeying in steady-state combustion Ohm's law depends on the resistance related to the chemical composition and geometric dimensions of the electrically conducting zone by $R_x = \rho_0 L/S$, where ρ_0 is resistivity; L, interelectrode distance; and S, area of the conducting cross section of the reaction zone of ECS.

The electrothermal control over the combustion velocity is executed with a system of metallic electrodes built in a solid-fuel charge. These electrodes serve to pass electric current through the reaction zone of ECS from an external voltage source. All other conditions (chemical composition, initial temperature of the fuel, temperature and pressure in the chamber, etc.) being the same, the combustion velocity of a condensed system will be a function of the current flowing through the electrically conducting layer. Electrodes made of a thin metallic foil can be involved in chemical reactions as a fuel burning-out in the gas phase.

EXPERIMENTAL

To study the dependences $u(P_c, I[U, R_x])$, the procedure was chosen in which the pressure in the chamber and the current strength steadily increase in the course of combustion. In this case, the results obtained will depend on the variation rates (derivatives with respect to time) of the factors and, in the process, will become increasingly related to intrachamber transient processes and different from the results obtained under steady-state conditions $u(P_c = \text{const}_i,\ I = \text{const}_j)$.

A difficult issue is the choice of the value of the derivative dP_c/dt at which the processes occurring in the gas phase and in the reaction zone of ECS can be conditionally considered steady-state. The derivative with respect to pressure is the most important for solid fuels with a large ballistic exponent in the power law of combustion, $[u(P_c) = u_0 P_c^{\nu}]$ [1, 4]. Probably,

ECS composition and effective (control) voltage on charges

ECS composition, %	Designation	Density, g cm^{-3}	m, g	U, V
85AN + 15ED-22	a1	1.50	97.8	1.5
	a2	1.48	96.9	1.5
	a3	1.51	98.8	24
	a4	1.44	100.4	~40
	a5	1.43	96.8	~72
75AN + 10Al + 15ED-22	b1	1.53	93.0	1.5
	b2	1.55	97.8	~25
	b3	1.57	96.9	~50
	b4	1.59	97.0	~70

the dynamic properties of the reaction zones of the c-phases should be considered low-inertia, because otherwise it would be impossible for anomalous acoustic effects, such as resonant combustion of ECS at frequencies from 100 Hz to 10 kHz and more, to appear and to be maintained. For example, at harmonic pressure oscillations in the chamber, with an amplitude A = 0.1 MPa at a frequency f = 100 Hz, the absolute value of the pressure variation rate is as high as $dP_c/dt = 2\pi Af$ = 62.8 MPa s^{-1}. Therefore, the rate of the monotonic rise in pressure in the experiments was chosen to be $dP_c \le 1$ MPa s^{-1} at a free volume of the chamber equal to 1.5–1.7 l.

Under the electrothermal control, the thermal power of the electric current is released directly within the c-phase of the reaction zone of the solid fuel without any intermediate physical conversion stages or high-inertia processes and is independent of the current frequency (up to $f \le 20$ kHz).

A computerized multichannel measuring system [5] was used to record the experimental values of the chamber pressure and of the voltage and current in the

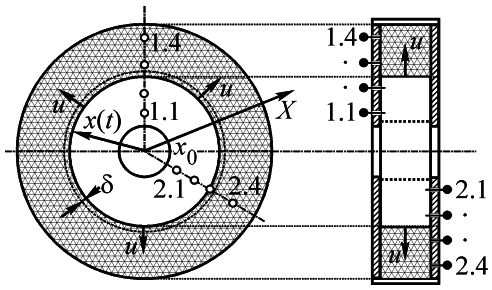


Fig. 1. Schematic of charge combustion in the inner channel. (X) Axis of radial coordinates of combustion front sensors (1.1–2.4), (u) combustion velocity vector, (δ) thickness of the reaction zone of ECS, (x_0) initial radius of the channel, and [$x(t)$] channel radius as a function of time.

reaction zone of the c-phase as functions of time and the instants of time when the ECS combustion front passed control coordinates (electrodes of the combustion front sensors, CFS). The oscillograms obtained were used to determine the values of $P_c(t)$ and $I(U, t)$ at any instant of time t in order to construct joint dependences. The function describing the combustion velocity, $u(t_i)$, was found from the derivative dx/dt of the approximated (by the least-squares method) dependence of the channel radius on time, $x(t)$, which is originally obtained in a discrete form $x(t_i)$ (at instants of time at which the control coordinates are passed by the combustion front), using CFS with known coordinates. The procedure used to determine the ECS combustion velocity has proved to be efficient in similar measurements under atmospheric pressure [6].

In the experiments, model formulations (see table) of mixed solid fuels (MSF) were used in the form of cylindrical charges (diameter 85 mm, thickness 11–12 mm) with progressive combustion in the inner channel (Fig. 1). The fuels were based on pure ammonium nitrate (AN) with addition of powdered aluminum ASD-4 (10%) at a constant content of the binder (15% ED-22 epoxy resin with urotropin as curing agent).

If the combustion front of an ECS charge is a cylindrical surface expanding in an axially symmetric manner, then the electrical resistance of the reaction zone of the c-phase can be described as a function of the channel radius x by the formula

$$R(x) = \rho_0 L/\pi(2\delta x - \delta^2), \quad (1)$$

where ρ_0 is the resistivity of the reaction zone and L is the charge thickness.

Thus, information about the ECS combustion dynamics in a wide range of automatic variation of the pressure and current strength determined by the electrical conductivity of the c-phase and the effective (const) voltage across the charge can be obtained in one experiment.

The fabrication technology of the charges included production of dried (100–200-μm) fraction of the oxidizing agent, mechanical mixing with an epoxy binder, and compaction of fuel pastes (93–100 g) in special molds under a pressure of 8 ± 0.5 MPa and polymerization of articles in a continuous mode at 75–80°C for 18–20 h. The initial diameter of the inner (cylindrical) combustion channel was x_0 = 15 mm.

A scheme illustrating the procedure used to measure the combustion velocity of the charge [5, 6], current strength, and voltage is shown in Fig. 2. The

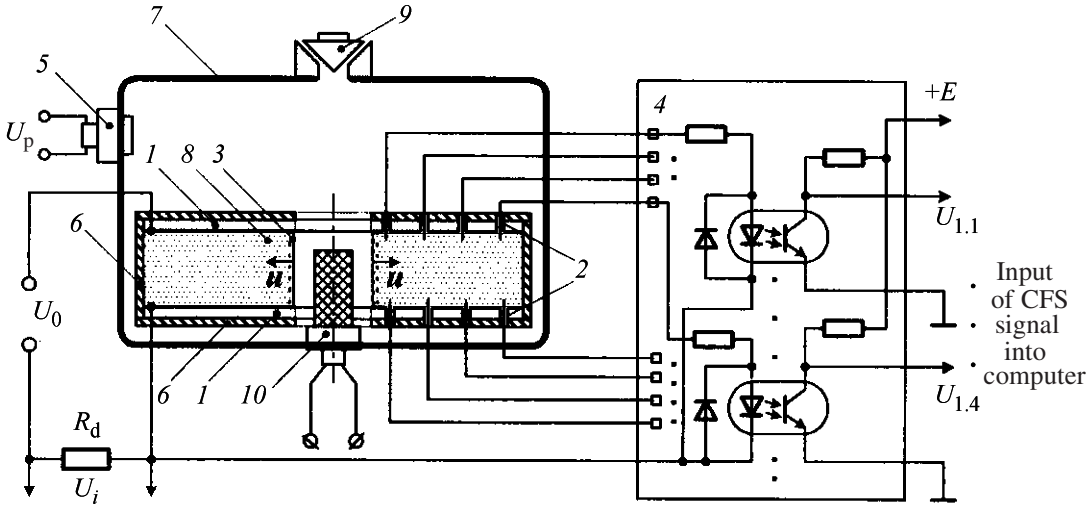


Fig. 2. Measuring unit of the experimental setup. (*1*) Electrode discs with copper foil, (*2*) CFS wire electrodes, (*3*) reaction zone (front) of combustion, (*4*) converter interface for a computer, (*5*) pressure transducer, (*6*) thermal insulation (restriction) of the charge, (*7*) combustion chamber, (*8*) MSF, (*9*) gas pressure-relief valve, (*10*) ignition device (ID), (U_p) the pressure transducer voltage, (U_0) input voltage, and (U_i) voltage across the divider R_d for measuring the current strength in the charge.

MSF charge was adhesively attached on two sides to the copper foil of round plates of foiled textolite (1) connected to a source of electric voltage U_0. These electrode discs have apertures along their radii in two directions, in which wire electrodes (2) of thickness 0.4 mm are mounted without electric contact with the copper foil. The coordinates of these electrodes (away from the longitudinal axis of the charge) and the distances x_i between them were measured with an MBS-10 microscope in the fabrication stage. Under normal conditions, when there is no adsorbed moisture on the surface of the inner channel, the fuel paste has a resistance of more than 30 MΩ (measured with V7-38 device), i.e., the resistivity of ECS is no less than 10^9 Ω cm.

Under the combustion conditions, the moving front of the electrically conducting reaction zone (3) in the condensed phase of the fuel successively passes across the wire electrodes. When touching the combustion surface (zone of molten NH_4NO_3), the electrodes are connected to the voltage source ($\sim U_0$), which opens optoelectronic switches in the electronic unit (4) of the combustion front sensors and the signals are fed via a multichannel analog-data-input interface into a computer. The dependence of the radial coordinates of the electrodes on the instants of their actuation is approximated with a continuous function $x(t)$, whose first derivative gives numerical values of the instantaneous combustion velocity in the time interval under study.

At fully closed valve, the pressure in the combustion chamber reached 10–11 MPa. Therefore, radial arrangement of CFSs was chosen in accordance with their actuation in the pressure range 1–8 MPa at the pressure derivative $dP_c/dt \leq 1$–1.2 MPa s^{-1}.

The igniting devices (ID) had the form of powder charges 12 mm in diameter, made of compacted (at pressures of up to 600 MPa) black powder, with computer-controlled electric-coil ignition. Under the action of the ID and additional powder charges, the starting gas-phase pressure of 0.8–1.0 MPa with a 30–50% excess was created in the chamber. The intrachamber gas-phase pressures were measured with a PD-150-0.4 commercial low-inertia tensoresistive transducer with the working range 0.1–15 MPa (relative error 0.4%).

Figure 3 shows prognosticated pressure dependences of the combustion velocity of an ECS with a cylindrical channel at different charge voltages U_n

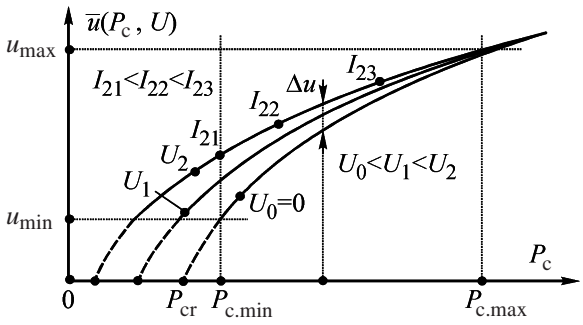


Fig. 3. Prognosticated pressure dependence of the combustion velocities, $u(P_c, U_n)$, in the pressure range under study $[P_{c.min}, P_{c.max}]$ at different voltages applied to the charges (U_1–U_3).

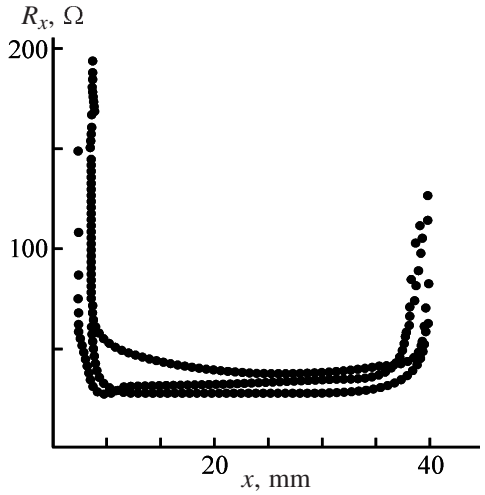


Fig. 4. Electrical resistance R_x of the reaction zones a1–a5 of ECS (85% AN + 15% ED-22) vs. the radius x of the charge combustion channels.

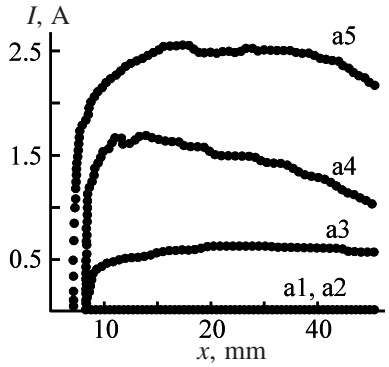


Fig. 5. Current strength I in the reaction zone of ECS vs. the radius x of the charge combustion channel.

and current strengths I_n in the reaction zone. The expected characteristics $u(P_c,\ I[U, R_x])$ are associated with the advanced rise in the mass expenditure rate of the fuel with respect to that in the electric power and with the accordingly gradually decreasing specific power (W kg^{-1} s = J kg^{-1}) in the c-phase. It is possible in this case that, as the mass expenditure rate increases, the electrothermal effect Δu will decrease and the combustion velocity will asymptotically approach its normal value under the current thermodynamic conditions, $u(P_c, 0)$.

Originally, experiments devoted to analysis of the amplitude–frequency characteristics of the c-phase were performed. For this purpose, a GZ-110 programmed sinusoidal voltage generator was used as a U_0 voltage source. This enabled multiple changes of frequency within a certain range in the course of an experiment at U_0 = const and control over the resistance of the reaction zone. At frequencies of 0–20 kHz, no changes in electrical conductivity within 5% were observed, and, therefore, both dc and ac voltages were used in experiments. This indicates that the electronic conduction predominates in the viscous-liquid (liquid-viscous) surface layer of the c-phase of ECS and the capacitive and inductive components are insignificant.

Figure 4 shows superimposed plots of the resistance of the reaction zones of five ECS (85% AN + 15% ED-22) against the combustion channel radii. The nearly rectangular shape of the curves and the increase in resistance before the complete burning-out possibly indicate that the shape of the inner channel deviates from the cylindrical [hyperbolic dependence in formula (1)] toward formation of a convex surface by the end of combustion.

These known "edge" effects [4] associated with an increase in the ECS combustion velocity in the near-wall zones probably occur in the cases in question due to the additional heating of the edge surface of the fuel across the copper foil (40–50 μm) of the electrode discs and to an increase in the initial temperature of the fuel. This factor was disregarded in data processing and its manifestation was considered to be the same in all cases and to have no effect on the general pattern of relative changes in the ballistic characteristics of ECS.

Figure 5 shows superimposed plots of the effective values of the current strength in the reaction zones of five charges (85% AN + 15% ED-22) against the combustion channel radii. At constant voltages, the currents are proportional to changes in the conductivities of the charges.

The instantaneous values of the intrachamber pressures, known from the oscillograms, and the pressure dependences of the combustion velocity, calculated for each charge, were used to obtain combustion equations for the ECS under study: $u(P_c, U)$. Figure 6 shows superimposed plots demonstrating how the ballistic characteristics of ECS vary with intrachamber pressure and discrete voltages on the charges, constructed for two experimental series (see table).

The ECS combustion equations (Fig. 6) have the form

$$u(\text{a1}) = 0.84(P_c - 10.88)^{0.405} - 0.86,$$

$$u(\text{a2}) = 0.75(P_c - 8.52)^{0.423} - 0.88,$$

$$u(\text{a3}) = 0.40(P_c - 8.99)^{0.484} - 0.01,$$

$$u(\text{a4}) = 1.03(P_c - 9.06)^{0.285} - 0.84,$$

$$u(\text{a5}) = 0.87(P_c - 12.59)^{0.240} - 0.22,$$

$$u(\text{b1}) = 0.90(P_c - 6.36)^{0.448} - 0.93,$$

$$u(\text{b2}) = 0.77(P_c - 9.22)^{0.438} - 0.23,$$

$$u(\text{b3}) = 0.74(P_c - 6.33)^{0.450} - 0.45,$$

$$u(\text{b4}) = 0.95(P_c - 8.22)^{0.315} - 0.07.$$

It is appropriate to formulate tentative conclusions based on the results obtained if the stationary model of ECS combustion, for which the characteristics shown in Fig. 6 are considered static, is adopted. In the pressure range in question, the rate of pressure buildup, dP_c/dt, did not exceed 1.0–1.2 MPa s^{-1} ($\leq$0.5 MPa s^{-1} at 1 MPa $< P_c <$ 4 MPa).

To substantiate the results (Fig. 6), it is necessary to consider comprehensively the possible processes in the gas and condensed phases. It follows from the plots that, for both ECS compositions (AN + ED-22 and AN + Al + ED-22), the functional dependences of the combustion velocity on pressure and charge voltages are similar. Metallization of ECS leads to an increase in the fuel combustion velocity, which can be attributed to a rise in the temperature of the gas phase and to the corresponding acceleration of the initial stages of the heterogeneous reactions in the viscous-liquid layer of the c-phase.

The increase in the ECS combustion velocity under the action of electric current at pressures $P_c <$ 2.5 MPa is, on the whole, in agreement with the prognosticated dependences (Fig. 3) and with the results obtained in similar studies under atmospheric pressure. The thermal power released by the electric current within the reaction zone additionally accelerates the stages of ECS decomposition and the heterogeneous reactions in accordance with the Arrhenius law. This increase in the internal energy of the reaction zone in the c-phase, independent of the inflow of heat from the gas phase, possibly corresponds to the state of the c-phase at the intrachamber pressure exceeding the current value. That is, the acceleration of the reaction kinetics in the c-phase under the action of an external source of voltage is probably equivalent to an increase in the pressure (temperature) in the gas phase in the chamber. Of interest in this case are the overall decrease in the ballistic exponent ν of the ECS, which becomes a quantity that is variable (controllable) within certain limits, and the decrease in the threshold pressures of stable combustion, P_{cr}, on raising the working voltages.

The decrease in the combustion velocity of the MSF formulations in question under the action of electric current and voltages at pressures exceeding

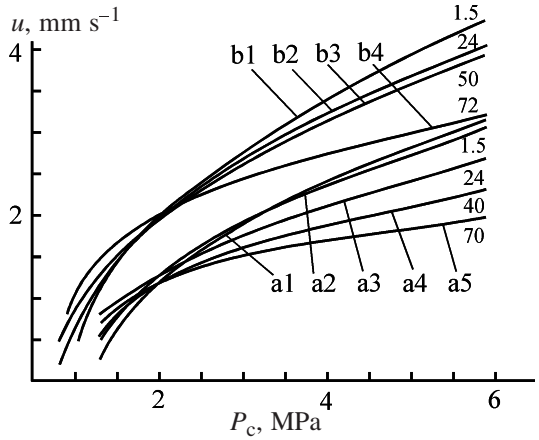


Fig. 6. ECS combustion velocity u vs. the intrachamber pressure P_c at different effective voltages on the charges. Figures at curves are charge voltages (V).

3 MPa can be, probably, accounted for by the effect of the following (one or several) factors.

(1) The decomposition rate of ammonium nitrate grows, which leads to an increase in the mass fraction of ammonia that has not enough time to react in the c-phase and is transferred into the gas phase, thereby lowering the temperature of the surface zone of the flame. The inhibiting effect of NH_3 in ammonium nitrate oxidizing agents was noted in [7].

(2) As the pressure becomes higher, the gas content of the reaction zone grows, which is accompanied by foaming (onset of boiling) of the viscous-liquid layer and by an increase in its volume, with the result that its density and, accordingly, thermal conductivity decrease and, therefore, the preliminary stages, decomposition of the oxidizing agent and thermal degradation of the binder, are decelerated. In similar experiments performed under atmospheric pressure, an intense discharge of foam-like fragments of the viscous-liquid layer of the c-phase in the form of a multitude of drops were observed at higher currents in the charge. In this case, the combustion velocity ceased to increase and its dependence on he current strength became strongly nonlinear.

(3) The decrease in the combustion velocity reflects processes that occur in natural way for these MSF formulations at considerably higher pressures (10–15 MPa), with different equivalent P_c corresponding to different voltages. Then the crossing point of the characteristics may correspond to the beginning of the exponent sign reversal ($\nu < 0$).

These effects and their possible reasons may depend on the existence (magnitude) of an intra-

chamber gas flow along the charge combustion surface and on other gas-dynamic factors.

CONCLUSIONS

(1) The increase in the combustion velocity of energetic condensed systems based on ammonium nitrate under the action of an electric current flowing in the reaction zone of the c-phase is in agreement with the prognosticated results at low intrachamber pressures of up to 2 MPa.

(2) The ballistic exponent of the energetic condensed systems (in the power law of combustion) and the critical pressure decrease under the action of an electric current. This means that the dependence of the reaction processes at the combustion surface on the inflow of heat from the gas phase becomes weaker and, accordingly, their stability at lower pressures decreases.

(3) Metallization with aluminum (10%) of mixed solid fuels based on NH_4NO_3 leads to a decrease in the conductivity of the reaction zone of the c-phase by 30–40%. This possibly means that aluminum particles are not involved in electrical conduction because, being present in the solid phase in the viscous-liquid layer, they are coated with Al_2O_3.

(4) The electronic conduction predominates in the reaction zones of the c-phases of the energetic condensed systems studied; the frequency-dependent ionic conduction of a pure ammonium nitrate melt is not manifested.

(5) The combustion velocity of the mixed solid fuel formulations studied decreases under the action of an electric current at pressures exceeding 3 MPa.

(6) The changed thermal state of the reaction zone of the c-phase, in which an electric current flows, possibly corresponds to processes that occur without any electrothermal action at higher pressures.

(7) Measurements of the electrical conductivities of the reaction zones of the c-phases of charges that should burn in strictly calculated ranges in uncontrolled modes can serve as an additional method for monitoring the intrachamber processes and revealing various deviations: appearance of acoustic oscillations, cracking (disintegration) of charges or their asymmetric burnout, and other anomalous modes.

REFERENCES

1. Gubertov, A.M., Mironov, V.V., Borisov, D.M., et al., *Gazodinamicheskie i teplofizicheskie protsessy v raketnykh dvigatelyakh tverdogo topliva* (Gas-Dynamic and Thermal Processes in Solid-Propellant Rocket Engines), Koroteev, A.S., Ed., Moscow: Mashinostroenie, 2004.
2. RF Patent 2175399.
3. Khoruzhii, I.V., Taranushich, V.A., Klyakin, G.F., and Lachin, V.I., in *Komp'yuternye tekhnologii v nauke, proizvodstve, sotsial'nykh i ekonomicheskikh protsessakh: Materialy 4-i Mezhdunarodnoi nauchno-prakticheskoi konferentsii* (Computer Technologies in Science, Industry, and Social and Economic Processes: Proc. 4th Int. Scientific and Practical Conf.), Novocherkassk: Yuzhno-Ross. Gos. Tekh. Univ. (Novocherkassk. Politekh. Inst.), November 14, 2003, part 2, pp. 53–57.
4. Sokolovskii, M.I., Petrenko, V.I., Zykov, G.A., et al., *Upravlyaemye energeticheskie ustanovki na tverdom raketnom toplive* (Controlled Power Units Working on Solid Propellants), Sokolovskii, M.I. and Petrenko, V.I., Eds., Moscow: Mashinostroenie, 2003.
5. Khoruzhii, I.V. and Lachin, V.I., in *Mikroprotsessornye, analogovye i tsifrovye sistemy: proektirovanie i skhemotekhnika, teoriya i voprosy primeneniya: Materialy 4-i Mezhdunarodnoi nauchno-prakticheskoi konferentsii* (Microprocessor, Analog, and Digital Systems: Design and Circuitry, Theory and Application Problems), Novocherkassk: Yuzhno-Ross. Gos. Tekh. Univ. (Novocherkassk. Politekh. Inst.), February 27, 2004, pp. 33–37.
6. Khoruzhii, I.V., in *Mikroprotsessornye, analogovye i tsifrovye sistemy: proektirovanie i skhemotekhnika, teoriya i voprosy primeneniya: Materialy 6-i Mezhdunarodnoi nauchno-prakticheskoi konferentsii* (Microprocessor, Analog, and Digital Systems: Design and Circuitry, Theory and Application Problems), Novocherkassk: Yuzhno-Ross. Gos. Tekh. Univ. (Novocherkassk. Politekh. Inst.), October 17, 2006, pp. 40–43.
7. Glazkova, A.P., *Kataliz goreniya vzryvchatykh veshchestv* (Catalysis of Combustion of Explosives), Moscow: Nauka, 1976.

ISSN 1070-4272, Russian Journal of Applied Chemistry, 2008, Vol. 81, No. 1, pp. 67–70. © Pleiades Publishing, Ltd., 2008.
Original Russian Text © T.M. Umarova, A.A. Khakimov, I.N. Ganiev, 2008, published in Zhurnal Prikladnoi Khimii, 2008, Vol. 81, No. 1, pp. 71–74.

APPLIED ELECTROCHEMISTRY AND CORROSION PROTECTION OF METALS

Effect of Cerium on Electrochemical and Mechanical Properties of Aluminum–Iron Alloys

T. M. Umarova, A. A. Khakimov, and I. N. Ganiev

Nikitin Institute of Chemistry, Academy of Sciences of the Republic of Tajikistan, Dushanbe, Tajikistan

Received May 16, 2007

Abstract—Effect of cerium on the corrosion-electrochemical and mechanical properties of aluminum alloys with an iron content of up to 3% was studied in order to use secondary aluminum in development of sacrificial formulations.

DOI: 10.1134/S1070427208010151

According to the fundamentals of metal science, aluminum–iron alloys are not classed with any type of alloys, being related neither to deformable, nor to castable alloys. At the same time, alloys of the Al–Fe system are of particular interest as a structural material because iron is always present in aluminum: as an impurity from the steel equipment used in melting and casting or as an alloying additive introduced to improve the heat resistance of an alloy. It is known that each percent of iron raises the modulus of elasticity by 25%, and the shear modulus, by 3%; iron improves to a certain extent the machinability of aluminum by cutting and gives rise to a damping capacity [1].

The aim of the present study is to convert off-grade aluminum to a structural material by alloying. It is known that addition of cerium in an amount of 0.25–0.5% to an alloy containing aluminum and iron leads to a decrease in the grain size and improves the hot rolling capacity [2].

EXPERIMENTAL

Because secondary aluminum may contain up to 3% iron, we preliminarily examined the effect of iron on the corrosion-electrochemical properties of aluminum. Alloys based on aluminum brands with different degrees of purity were synthesized: special-purity of A6N0 brand (TU-ANT-006–88), high-purity of A995 brand [GOST (State Standard) 11 069–74], and technical-grade of A8, A6, and A5 brands (GOST 4784–74*), whose chemical composition is listed in Table 1.

A molten aluminum alloy was poured into a steel mold to obtain cylindrical rods. The electrode thus obtained was ground, polished to mirror shine, washed, and degreased with ethanol.

Corrosion-electrochemical studies were performed on a PI 50-1 potentiostat with a PR-8 programming unit in a 3% NaCl solution at a potential sweep rate of 2 mV s^{-1} [3, 4]. A silver chloride electrode was used as reference, and the potentials given were recalculated to the standard hydrogen scale.

The corrosion current i_{corr} as the basic electrochemical characteristic of the corrosion process was calculated from the cathodic curve (with account of the slope of the Tafel portion, b_c = 0.12 V), because the pitting corrosion in neutral media is mostly controlled by the cathodic reaction of oxygen ionization [5]:

$$O_2 + 2H_2O + 4e \rightarrow 4OH^-.$$

The corrosion rate K, which is a function of the corrosion current density, was found using the formula

$$K = i_{corr}k,$$

where k is the electrochemical equivalent, equal to 0.335 g A^{-1} h^{-1} for aluminum [6].

The results of the corrosion-electrochemical tests are listed in Table 2. Rare-earth metals (REM) have specific properties and are widely used for improving the structure and properties of alloys, among which the corrosion resistance should be mentioned. For these reasons, cerium was chosen as an additional alloying component. It was introduced as a 7% alloy into an aluminum–iron melt at a temperature of 900°C.

To choose the optimal content of cerium in the

Table 1. Chemical composition of aluminum

Aluminum brand	Al, wt %	Content of impurities, wt %					
		Fe	Si	Cu	Zn	Ti	Mg, Mn
A6N0	99.9999	1×10^{-5}	1×10^{-4}	5×10^{-4}	1×10^{-6}		–
A995	99.995	1.5×10^{-3}	1.5×10^{-3}	1×10^{-3}	1×10^{-3}	1×10^{-3}	–
A8	99.80	0.15	0.15	0.02	0.05	0.03	–
A6	99.60	0.25	0.2	0.03	0.06	0.03	–
A5	99.50	0.3	0.3	0.02	0.07	0.05	0.030 Mg, 0.025 Mn

Table 2. Effect of iron on the corrosion-electrochemical characteristics* of aluminum in a 3% NaCl solution

Fe, wt %	$-E_{free\ corr}$	$-E_{pit}$	$-E_{corr}$	$-E_{repass}$	ΔE_{pass}	i_{corr}, A m^{-2}
	V					
1.0×10^{-5}	0.78	0.56	0.76	0.55	0.36	0.002
1.5×10^{-3}	0.75	0.50	0.76	0.54	0.35	0.003
0.15	0.54	0.49	0.57	–	0.33	0.004
0.20	0.53	0.43	0.56	0.50	0.30	0.024
0.30	0.55	0.49	0.58	0.52	0.30	0.026
2.18	0.58	0.41	0.55	0.52	0.36	0.040
3.00	0.50	0.40	0.54	0.52	0.35	0.050

* $-E_{free\ corr}$, $-E_{pit}$, $-E_{corr}$, and $-E_{repass}$ are the free-corrosion, pitting, corrosion, and repassivation potentials, respectively; ΔE_{pass} is the passivation interval.

Table 3. Corrosion-electrochemical characteristics of cerium-alloyed aluminum–iron alloys

Alloy component, wt %		$-E_{free\ corr}$	$-E_{corr}$	$-E_{pit}$	ΔE_{pass}	$K \times 10^3$, g m^{-2} h^{-1}
Fe*	Ce	V				
1.00	–	0.530	0.560	0.42	0.33	8.04
1.00	0.005	0.490	0.545	0.41	0.33	2.7
1.00	0.010	0.450	0.540	0.41	0.33	2.5
2.18	–	0.580	0.530	0.41	0.36	13.4
2.18	0.005	0.600	0.540	0.43	0.35	6.4
2.18	0.010	0.610	0.540	0.42	0.35	6.2
2.18	0.05	0.612	0.550	0.42	0.35	6.7
2.18	0.10	0.620	0.555	0.42	0.35	13.4
2.18	0.20	0.625	0.555	0.42	0.35	13.6
2.18	0.50	0.640	0.560	0.45	0.30	16.7
3.00	–	0.620	0.540	0.40	0.35	18.4
3.00	0.50	0.600	0.520	0.42	0.35	7.7

* A8 aluminum the rest.

alloy, we examined the electrochemical, mechanical, and technological properties of the system, which are insufficiently understood for this group of alloys. The results of a corrosion-electrochemical study of alloys of the system Al–Fe–Ce in a 3% solution of sodium chloride are listed in Table 3.

The mechanical properties were tested on a P-5 tensile machine at loads of 1000–10000 kg. The hardness of the alloys, HB, was determined by the Brinell method; strength and plasticity [ultimate strength σ_t (MPa) and relative elongation δ (%), respectively] were found in accordance with GOST 1494–84. The

Table 4. Effect of cerium on the mechanical properties of the Al–2.18Fe alloy*

Cerium content, wt %	σ_t, MPa	δ, %	HB
–	109.4	4.95	252
0.005	90.6	14.40	252
0.01	93.5	14.10	255
0.05	96.0	13.92	257
0.10	99.2	12.41	262
0.20	103.4	12.00	270
0.50	92.2	14.23	259

* Studies performed by I.T. Amonov.

results obtained in tests of cerium–modified aluminum–iron alloys of a eutectic composition (2.18%) are listed in Table 4.

It is known that one of the most reliable, available, and effective methods for control of electrochemical corrosion of metallic structures is sacrificial protection. Among the presently existing industrial sacrificial alloys based on zinc, magnesium, and aluminum, the most effective material as regards the amount of absorbed energy per unit mass is aluminum. In addition, zinc-based industrial sacrificial alloys have strict limitations on the content of impurities. A 3% NaCl solution served as the working solution, and St.3 steel rods were the protected objects. The test duration was 100 h at a current density $I = 1.5$ A m^{-2}.

The utilization coefficient (UC) of the sacrificial material was calculated using the procedure described in [7].

Table 5 lists the results of galvanostatic tests of aluminum alloys containing up to 1.5% iron and up to 1.0% Ce (cerium misch metal). Manganese has a negative equilibrium potential ($E = -1.1$ V) and its presence in an alloy reduces the adverse effect of impurities via formation of intermetallic compounds (Mn,Fe)Al and other compounds having negative electrode potentials.

It follows from the results obtained (Table 2) that iron present in amounts of up to 0.15 wt % does not affect the corrosion rate of aluminum significantly. As the amount of aluminum is raised to 15 wt %, the corrosion currents strongly increase. The free-corrosion, pitting, corrosion, and repassivation potentials are shifted to more positive values as the content of iron increases. The passivation interval ΔE_{pass} is 0.30–0.36 V.

Table 3 illustrates the effect of cerium on the corrosion-electrochemical properties of aluminum with high content of iron. For example, comparison of the characteristics of the first two alloys shows that modification with cerium shifts the free-corrosion, pitting, and corrosion potentials to more positive values. Modification with minor amounts of cerium of an alloy composed of aluminum and 1% iron reduces the corrosion rate by a factor of 3–4. Raising the content of iron to 2.18% (eutectic composition) shifts the free-corrosion, pitting, and corrosion potentials to more negative values. The passivation interval increases insignificantly. The corrosion rate of this alloy with a microscopic addition of cerium (0.005–0.05%) decreases by a factor of 2 to $(6.2–6.7) \times 10^{-4}$ g m^2 h^{-1} (Table 3). The optimal, in the corrosion regard, composition of this group of alloys is that of the alloy Al–2.18Fe–0.01Ce.

A study of the aluminum alloy with the maximum content of iron (3%) demonstrated that alloying with 0.5% cerium shifts the free-corrosion, pitting, and corrosion potentials to more positive values. In this case, the passivation interval remains unchanged, whereas the corrosion rate decreases by a factor of 2.5.

Table 5. Characteristics of aluminum alloys recommended as sacrificial materials

Alloy no.	Alloy component, wt %			$-E_w$, V	UC, %	i_{corr}, A m^{-2}
	Fe	Mn	Ce (misch metal)			
1	0.15	–	–	0.545	86.2	0.15
2	0.15	0.35	–	0.560	86.9	0.12
3	0.15	0.35	0.1	0.610	77.2	0.10
4	1.0	1.0	–	0.520	58.2	0.28
5	1.0	1.0	0.1	0.580	98.1	0.20
6	1.5	–	–	0.500	84.5	0.50
7	1.5	–	0.1	0.540	97.8	0.23

* The corrosion current densities were found from a cathodic polarization curve obtained under a sacrificial protection.

It should be noted, when analyzing the mechanical properties (hardness, strength, and plasticity) of the Al–2.18Fe alloy, that alloying with cerium exerts the strongest influence on the plasticity. The relative elongations of these alloys increase 2.5–3-fold at the same or somewhat increased hardness of the samples. The maximum hardness HB = 270 is observed for the alloy Al–2.18Fe–0.20Ce.

With account of the low electrochemcial equivalent of aluminum and aluminum-based alloys (0.335 g A^{-1} h^{-1}) and their comparatively low cost and toxicity, the possibility of further use of secondary aluminum with 0.005–0.2% cerium as low-alloy material for anodes can be considered. Table 5 shows that, at low content of iron (on the impurity level), addition of manganese affects the protective properties of technical-grade aluminum only slightly. At equal contents of iron and manganese (1 wt %), introduction of REM (cerium misch metal) into an aluminum melt results in a significant increase in the UC of the sacrificial material (to 98.1%). At the maximum content of iron (1.5%) in the absence of other components, the UC of the aluminum anode is rather high (84.5%), whereas alloying with cerium misch metal raises its value to 97.8%. Among disadvantages of these alloys can be mentioned the insufficiently negative working potential of the sacrificial material. Therefore, according to the results of this study, use of aluminum with high content of iron (up to 1.5%) as a sacrificial material is only possible if activators, such as tin, indium, or gallium, are additionally introduced, which noticeably shifts the working potential of the sacrificial material to more electronegative values [8]. For example, addition of 0.2 wt % indium to alloy nos. 3, 5, and 7 (Table 5) shifts the working potential of the sacrificial material by 300–340 mV.

CONCLUSION

The results obtained in the study enable development of alloys with enhanced corrosion resistance and plasticity on the basis of secondary aluminum with addition of cerium (cerium misch metal). These alloys can also be recommended as a sacrificial material for protection of steel from corrosion damage in aqueous chloride-containing media.

REFERENCES

1. Mondolfo, L.F., *Aluminum Alloys: Structure and Properties*, London: Butterworths, 1976.
2. *The Rare Earths*, Spedding, F.H. and Daane, A.H., Eds., New York: Wiley, 1961. Translated under the title *Redkozemel'nye metally: Sbornik statei*, 1965, p. 53.
3. Karimova, T.M., Ganiev, I.N., and Krasnoyarskii, V.V., *Zh. Prikl. Khim.*, 1988, vol. 61, no. 1, pp. 51–54.
4. Umarova, T.M. and Ganiev, I.N., *Zh. Prikl. Khim.*, 1990, vol. 63, no. 2, pp. 434–436.
5. Sinyavskii, V.S., Val'kov, V.D., and Kalinin, V.D., *Korroziya i zashchita alyuminievykh splavov* (Corrosion and Corrosion Protection of Aluminum Alloys), Moscow: Metallurgiya, 1986, p. 23.
6. Romanov, V.V., *Metody issledovaniya korrozii metallov* (Methods for Analysis of the Corrosion of Metals), Moscow: Metallurgiya, 1965.
7. Krasnoyarskii, V.V., Frenkel', G.Ya., and Nosov, R.P., *Korroziya i zashchita metallov* (Corrosion and Corrosion Protection of Metals), Moscow: Metallurgiya, 1969.
8. Lyublinskii, E.Ya., Kechin, V.A., and Demido, N.M., *Vopr. Sudostr.*, 1980, no. 26, p. 45.

ISSN 1070-4272, Russian Journal of Applied Chemistry, 2008, Vol. 81, No. 1, pp. 71–73. © Pleiades Publishing, Ltd., 2008.
Original Russian Text © I.N. Ryabova, 2008, published in Zhurnal Prikladnoi Khimii, 2008, Vol. 81, No. 1, pp. 75–77.

ORGANIC SYNTHESIS AND INDUSTRIAL ORGANIC CHEMISTRY

Nickel(II) and Copper(II) Complexes with Humic Acid Anions and Their Derivatives

I. N. Ryabova

Institute of Organic Synthesis and Coal Chemistry, Karaganda, Kazakhstan

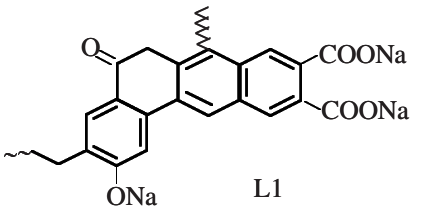
Received March 16, 2007; in final form, October 2007

Abstract—Complexation of Ni(II) and Cu(II) in aqueous solutions with anions of humic acids, extracted from naturally oxidized coal, and with their hydroxymethyl derivatives is studied spectrophotometrically and potentiometrically. The complexation stoichiometry and the stability constants of the complexes are determined.

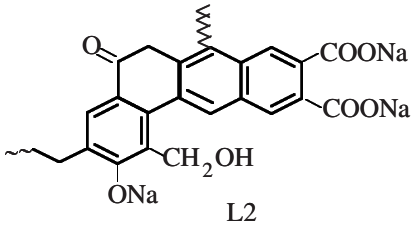
DOI: 10.1134/S1070427208010163

Humic acids (HAs) and their hydroxymethyl derivatives are insoluble in water. However, their sodium salts are water-soluble, opening the door for studying their complexation in aqueous solutions. Chuveleva et al. [1] studied complexation of HAs with Ca(II) using potentiometric titration of their aqueous suspensions. It was demonstrated that, at pH ~4, CaL and CaL_2 complexes are formed.

In this study we determined the stoichiometry and stability constants of Ni(II) and Cu(II) complexes with humic acid sodium salt L1, obtained from naturally oxidized coal, and with their hydroxymethyl derivatives L2 in aqueous solutions. The solubility of the humates in water is 0.125–0.150 M. According to the available analytical data, the structural units of L1 and L2 can be represented as follows:



L1



L2

The complexation was studied by the spectrophotometric and potentiometric methods. The electronic absorption spectra of Ni(II) and Cu(II) complexes with L1 and L2 in aqueous solutions show strong absorption bands with a maximum at 440–445 nm.

The solution pH values 4.7 and 4.2 were found to be optimal for studying complexation of Ni(II) and Cu(II) with L1, and pH values 5.4 and 5.2, with L2, respectively (Fig. 1). The stoichiometry of the complexes, formed in dilute aqueous solutions, was determined spectrophotometrically at a constant ionic strength (1 M NaCl) [2, 3].

Within the metal concentration range 1×10^{-5}–1×10^{-4} M, at a fivefold excess of the ligand, 1 : 1 complexes were found to form in the systems L1–Cu(II) and L2–Ni(II), and also 1 : 2 complex in the system L2–Cu(II). No complex was found in the system L1–Ni(II). Similar results were obtained poten-

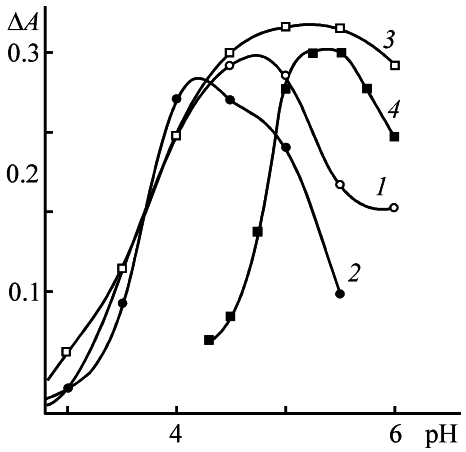


Fig. 1. Optical density ΔA as a function of the solution pH. Solution composition: (*1*) Cu(II)–L1, (*2*) Ni(II)–L1, (*3*) Cu(II)–L2, and (*4*) Ni(II)–L2 (λ = 440 nm, l = 1 cm).

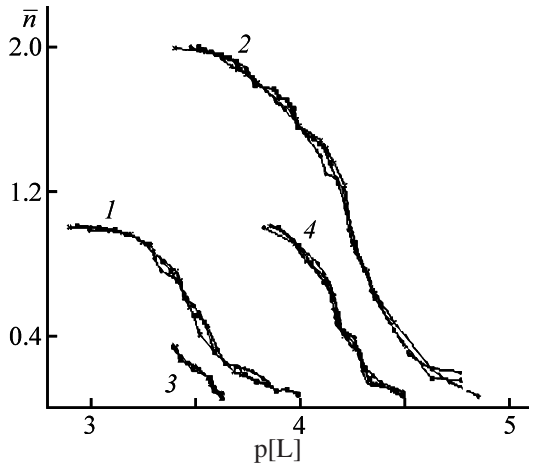


Fig. 2. Mean coordination number $\bar{n}$ as a function p[L] (negative logarithm of the concentration of ionized carboxy groups) in the systems (*1*) Cu(II)–L1, (*2*) Cu(II)–L2, (*3*) Ni(II)–L1, and (*4*) Ni(II)–L2.

tiometrically at the same ionic strength, but at the reagent concentrations 10–30 times higher than in the spectrophotometric experiments. It follows from Fig. 2 that L1 and L2 form 1 : 1 and 1 : 2 complexes with Cu(II) and Ni(II). Our previous results [4] demonstrate that, at pH < 5.5, L1 and L2 complexes exist in aqueous solutions in the form of H_nL^-. Therefore, the equilibrium ligand concentrations were estimated taking into account the first dissociation constant only (k_{a1} 4.74 and 4.53 for L1 and L2, respectively [5]).

The stoichiometry and stability constants of the complexes were estimated from the potentiometric titration curves, obtained with 0.1 M NaOH in the absence and in the presence of Ni(II) and Cu(II), using Eq. (1),

$$\bar{n} = [\mathrm{COOH}]_b/c_M, \quad (1)$$

where c_M is the initial metal concentration (M).

The results are given in the table.

The concentration of carboxy groups $[\mathrm{COOH}]_b$ bound to the metal was determined as the difference between their total concentration and the sum of the concentrations of ionized and free carboxy groups [3]. The total carboxy group concentration in the humate was estimated from the titration curve in the absence of the complexing cations. From the volume of the titrant consumed and pH, we estimated the concentration of ionized carboxy groups $[\mathrm{COO}^-]$ and then the concentration of free carboxy groups [COOH], using the Henderson–Hasselbach equation:

$$\mathrm{pH} = \mathrm{p}K - m\log\frac{1-\alpha}{\alpha}, \quad (2)$$

where m is the empirical coefficient (m 2.19 and 2.79 for L1 and L2, respectively [4]).

In the investigated systems, mononuclear complexes are essentially formed, as demonstrated by similar shapes of the curves obtained at various ligand concentrations (Fig. 2).

The stability constants were estimated from the semi-integer values of n using the least-squares method. The formation of metal hydroxo complexes within the experimental pH range was neglected. The estimated stability constants β were validated by substituting them in the Bjerrum equation [6]:

$$\bar{n} = \sum_0^N n\beta_n[\mathrm{L}]^n / \sum_0^N \beta_n[\mathrm{L}]^n$$

Our results show (see table) that Cu(II) forms medium-stability complexes with L1 and L2 (β 6.59 and 6.52, respectively). Ni(II) forms no complex with L1, but Ni(L2) is formed even at high Ni concentration in the solution (0.024 M). The stability of Ni(L2) is well comparable with that of $Cu(L2)_2$.

The mean number of the HA carboxy groups bound to Cu(II) is 1–2, which is slightly lower than the mean basicity of HA and its derivatives (2.6–2.8), as estimated by the Ostwald method [4]. Most likely, the incomplete saturation of the Cu(II) coordination sphere with the humic ligands results in formation of mixed-ligand complexes with participation of the water molecules.

Parameters of complexation of Ni(II) and Cu(II) with L1 and L2

Cation	L1		L2	
	$\bar{n}$	log β	$\bar{n}$	log β
Cu^{2+}	1	6.59	2	6.52
Ni^{2+}	–	–	1	6.46

EXPERIMENTAL

Humates L1 and L2 were synthesized from naturally oxidized coal of the Oikaragaiskoe field (Kazakhstan) using the method described in [7]. The unit molecular weight of humic acids M_r was determined ebulliometrically to be 374. The content of carboxy and phenolic hydroxy groups was 5.6 and

2.75 mg-equiv g^{-1}, respectively.

Found, wt %: C 67.81, H 3.80.
$C_{22}H_{14}O_6$.
Calculated, wt %: C 70.59, H 3.74.

IR (KBr), ν, cm^{-1}: 3450–3300, 3030, 1710, 1660–1610, 1250, 1205, 1063.

The spectrophotometric and potentiometric measurements were carried out at constant ionic strength [μ = 1 (NaCl)] and temperature (20.0±0.5°C). The spectrophotometric measurements were performed on a Shimadzu UV-2401 PC instrument, and potentiometric titration, using a Jenway 3345 ion meter. For each metal ion, the titration was carried out at three concentrations (0.8×10^{-2}, 1.6×10^{-2}, and 2.4×10^{-2} M) at a fivefold excess of the ligands.

CONCLUSIONS

(1) Humic acids and their hydroxymethyl derivatives form 1 : 1 and 1 : 2 complexes with Cu(II).

(2) Ni(II) forms a 1 : 1 complex with L2, but no complex with L1.

(3) Copper(II) forms medium-stability complexes with L1 and L2 (β 6.59 and 6.52, respectively). The stability of Ni(L2) is well comparable with that of $Cu(L2)_2$.

REFERENCES

1. Chuveleva, E.A., Nazarov, P.P., and Chmutov, K.V., *Zh. Fiz. Khim.*, 1962, vol. 36, pp. 1378–1381.
2. Bulatov, M.I. and Kalinkin, I.P., *Prakticheskoe rukovodstvo po fotokolorimetricheskim i spektrofotometricheskim metodam analiza* (Practical Manual on Photocolorimetric and Spectrophotometric Analyses), Leningrad: Khimiya, 1976.
3. Ergozhin, E.E. and Menligaziev, E.Zh., *Polifunktsional'nye ionoobmenniki* (Polyfunctional Ion Exchangers), Alma-Ata: Nauka, 1986.
4. Ryabova, I.N., Synthesis and Characterization of Humic and 2-Butenaldehyde Polymers on the Basis of Coal-Chemical Products, *Cand. Sci. Dissertation*, Almaty, 2003.
5. Ryabova, I.N., Akkulova, Z.G., and Zhubanov, B.A., *Vestn. Nats. Akad. Nauk Resp. Kaz.*, 2003, no. 3, pp. 49–53.
6. Beck, M.T., *Chemistry of Complex Equilibria*, London: Van Nostrand Reinhold, 1970.
7. Ryabova, I.N. and Mustafina, G.A., *Zh. Prikl. Khim.*, 2003, vol. 76, no. 2, pp. 269–271.

ISSN 1070-4272, Russian Journal of Applied Chemistry, 2008, Vol. 81, No. 1, pp. 74–77. © Pleiades Publishing, Ltd., 2008.
Original Russian Text © V.M. Farzaliev, A.M. Magerramov, M.R. Bairamov, I.A. Rzaeva, O.N. Dzhavadova, M.A. Allakhverdiev, 2008, published in Zhurnal Prikladnoi Khimii, 2008, Vol. 81, No. 1, pp. 78–81.

ORGANIC SYNTHESIS AND INDUSTRIAL ORGANIC CHEMISTRY

Antioxidant Properties of Sulfides Derived from 2-Propylphenol and of Their Aminomethyl Derivatives

V. M. Farzaliev, A. M. Magerramov, M. R. Bairamov, I. A. Rzaeva, O. N. Dzhavadova, and M. A. Allakhverdiev

Baku State University, Baku, Azerbaijan
Institute of Chemistry of Additives, National Academy of Sciences of Azerbaijan, Baku, Azerbaijan

Received May 16, 2007

Abstract—Antioxidant properties of sulfides derived from 2-propylphenol and of their aminomethyl derivatives were studied in a model reaction of cumene oxidation. The kinetic parameters of the reactions of these compounds with cumylperoxy radicals and cumyl hydroperoxide were determined.

DOI: 10.1134/S1070427208010175

In the modern oil-refining technology, there is a need for the development of advanced processes for production of petroleum products, including fuel and lubricating oils of optimal hydrocarbon composition, to meet the modern engineering and environmental requirements. At the same time, the use of petroleum fuels and lubricating oils is impossible without additives having various functional effects.

Among the most widely used additives to fuels and lubricating oils are alkylphenols and their various sulfur-, nitrogen-, and phosphorus-containing derivatives [1, 2].

As antioxidant properties of additives are associated with the presence of definite functional groups, it is particularly interesting to prepare organic compounds containing two or more functional groups in the molecule and to study the mechanism of their antioxidant effect, because such compounds may combine useful properties of different types of antioxidants.

Studies on the synthesis and mechanism of the antioxidant effect of compounds containing in their molecules a sulfide sulfur atom in combination with phenolic fragment (phenolic sulfides), aromatic amine (amino sulfides), and phenolic fragment + aromatic amine (aminophenolic sulfides) showed that these compounds not only combine the capabilities of sulfides to decompose hydroperoxides and of phenols and amines to terminate oxidation chains in reactions with peroxy radicals, but also exhibit a new property: They are capable to catalytically decompose hydroperoxides into molecular products [3–7].

With the aim to develop a scientific basis for the purposeful synthesis of an antioxidant of an optimal structure, exhibiting high performance, we examined in this study the antioxidant properties of new phenolic sulfides derived from 2-propylphenol and of their aminomethyl derivatives. The phenolic sulfides were prepared by homolytic thiylation of 2-propenyl- and 2-allylphenols with amyl and benzyl mercaptans, and the aminomethyl derivatives were synthesized by the Mannich condensation of the resulting phenolic sulfides with formaldehyde and dimethylamine [8–10].

Antioxidant properties of the compounds were evaluated by the well-known kinetic method based on inhibition of certain key reaction. As a model hydrocarbon we chose cumene.

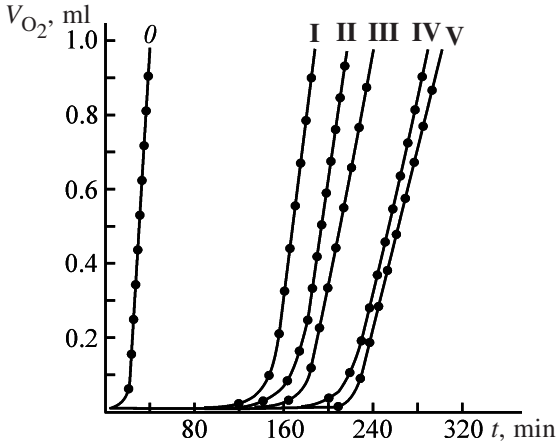
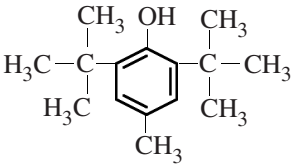
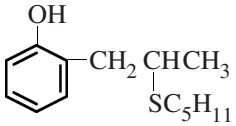
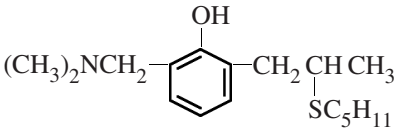
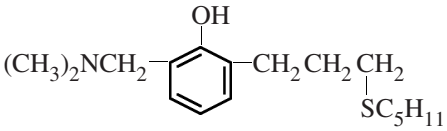
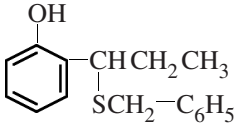
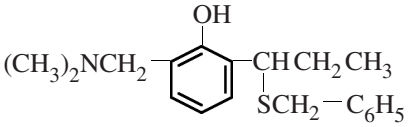


Fig. 1. Kinetic curves of cumene autooxidation (*0*) without additives and in the presence of compounds **I**–**V**. 110°C; [InH] = 5×10^{-5} M. (V_{O_2}) Oxygen uptake and (*t*) time; the same for Fig. 2.

Kinetic parameters of the reactions of **I**–**V** with cumylperoxy (CP) radicals (60°C, [AIBN] = 2×10^{-2} M) and cumyl hydroperoxide (CHP) (110°C), and induction periods of cumene autooxidation in the presence of these compounds (110°C, [InH] = 5×10^{-5} M)

Compound	Formula	CP radicals		CHP		τ, min
		f	$k_7 \times 10^{-4}$, l mol^{-1} s^{-1}	k, l mol^{-1} s^{-1}	ν	
Ionol		2.00	2.10	–	–	150
I		1.68	2.18	31	36 000	150
II		1.87	2.18	40	40 000	170
III		2.0	2.94	41	40 000	180
IV		2.88	2.85	39	45 000	220
V		2.90	2.86	40	45 000	225

Experiments on cumene autooxidation at 110°C in the presence of **I**–**V** showed (Fig. 1) that these compounds efficiently inhibit the oxidation, as judged from the long induction periods τ (see table). For comparison, we performed under the same conditions autooxidation of cumene in the presence of a widely used phenolic antioxidant, Ionol (2,6-di-*tert*-butyl-4-methylphenol). As seen from the table, only compound **I** is similar to Ionol in the induction period, whereas all the other compounds surpass Ionol. The longest induction periods are observed with **IV** and **V**.

To evaluate the capability of compounds to terminate oxidation chains in reactions with peroxy radicals, we performed initiated [with azobis(isobutyronitrile), AIBN] oxidation of cumene in the presence of these antioxidants. The reaction was performed on a manometric unit; the oxidation kinetics was monitored by the oxygen uptake in a definite time interval. The reaction temperatrue was 60°C, and initiator concentration, 2×10^{-2} M. The concentrations of **I**–**V** were varied in the range 1×10^{-4}–5×10^{-5} M. From the kinetics of the oxygen uptake, we calculated the rate constant of the reaction of the antioxidants with the cumylperoxy radicals k_7, and from the induction period, the stoichiometric coefficient of inhibition f, equal to the number of oxidation chains terminated on one molecule of the antioxidant and its transformation products [11]. The experiments showed that all the compounds tested inhibit the initiated oxidation of cumene by reacting with cumylperoxy radicals.

Figure 2 shows the kinetic curves of the initiated oxidation of cumene in the presence of **I**–**V**.

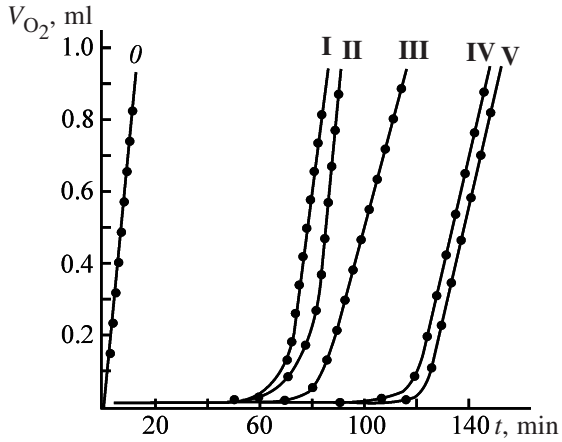


Fig. 2. Kinetic curves of the initiated oxidation of cumene (*0*) without additives and in the presence of **I**–**V**. 60°C; [AIBN] = 2×10^{-2} M.

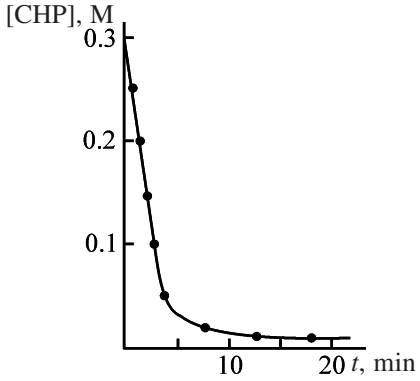


Fig. 3. Kinetic curves of CHP decomposition under the action of **I**. 110°C; [InH] = 1×10^{-4} M. (*t*) Time.

The kinetic curves of the initiated oxidation of cumene show that the rate of cumene oxidation in the presence of compounds **IV** and **V** after the end of the induction period is lower than the rate of cumene oxidation without inhibitors (curve *0*). This fact indicates that the products of the transformation of **IV** and **V** in the reaction with cumylperoxy radicals also exhibit an inhibiting effect, i.e., secondary inhibition is observed.

The kinetic parameters of the reactions of the antioxidants with the cumylperoxy radicals are given in the table. The data for Ionol, obtained under similar conditions, are also given for comparison.

It is known that for alkylphenols $f \approx 2$ [12–14], i.e., they terminate two oxidation chains. For Ionol also $f = 2$. For compounds **I**–**III**, $f \leq 2$, and for **IV** and **V** f approaches 3. The latter fact is attributable to the secondary inhibition, i.e., to partial termination of oxidation chains by products formed from **IV** and **V** in the reactions with cumylperoxy radicals. It should also be noted that, in contrast to compounds **I**–**III** with an alkyl substituent at the S atom, in **IV** and **V** the S atom is benzyl-substituted. With respect to the rate constant, compounds **I** and **II** are comparable with Ionol, and compounds **III**–**V** somewhat surpass it.

Thus, as regards the capability to terminate oxidation chains in reactions with peroxy radicals, compounds **I**–**V** behave as typical alkylphenol antioxidants. At the same time, as regards the reactivity toward peroxy radicals and the number of terminated oxidation chains, compounds **IV** and **V** surpass alkylphenolic antioxidants.

The reactions of the antioxidants with CHP were performed in chlorobenzene at 110°C in a nitrogen atmosphere at various reactant ratios. All the antioxidants studied were found to catalytically decompose CHP (Fig. 3).

The following kinetic parameters of the reaction of the antioxidants with CHP are given in the table: rate constants k and catalytic factor ν (number of CHP molecules decomposing under the action of one antioxidant molecule). It is known that dialkyl sulfides inhibit the oxidation of hydrocarbons by reacting with hydroperoxides; one sulfide molecule decomposes two hydroperoxide molecules [15]. The catalytic factors ν obtained for **I**–**V** show that one molecule of **I**–**V** is capable to decompose several tens thousands of CHP molecules. As in the reaction with cumylperoxy radicals, the highest activity in the reaction with CHP is shown by phenolic sulfide **IV** in which the sulfur atom is linked to the C atom in the α-position to the benzene ring of the phenolic fragment, and also by its aminomethyl derivative **V**.

Thus, our studies showed that sulfides derived from 2-propylphenol and their aminomethyl derivatives efficiently inhibit the oxidation of hydrocarbons and demonstrate a combined antioxidant effect: They terminate oxidation chains by reacting with peroxy radicals and catalytically decompose hydroperoxides.

CONCLUSIONS

(1) Kinetic studies of a model reaction of cumene oxidation revealed high antioxidant properties of sulfides derived from 2-propylphenol and of their aminomethyl derivatives.

(2) The mechanism of the antioxidant effect of these compounds involves termination of oxidation chains in reactions with peroxy radicals and catalytic decomposition of hydroperoxides.

(3) Among the compounds studied, the highest activity in reactions with cumylperoxy radicals and

cumyl hydroperoxide is shown by the phenolic sulfide in which the S atom is bonded to the C atom in the α-position to the benzene ring of the phenolic fragment and by its aminomethyl derivative.

(4) Introduction of the aminomethyl fragment into the molecule of phenolic sulfides somewhat enhances their antioxidant activity.

REFERENCES

1. Kuliev, A.M., *Khimiya i tekhnologiya prisadok k maslam i toplivam* (Chemistry and Technology of Additives to Oils and Fuels), Leningrad: Khimiya, 1985.
2. Bukharov, S.V., Nugumanova, G.N., and Mukmenova, N.A., *Zh. Org. Khim.*, 2004, vol. 40, no. 3, pp. 327–334.
3. Aliev, A.S., Farzaliev, V.M., Abdullaeva, F.A., and Denisov, E.T., *Neftekhimiya*, 1975, vol. 15, no. 6, pp. 890–895.
4. Farzaliev, V.M., Kuliev, F.A., and Voronkov, M.G., *Neftekhimiya*, 1981, vol. 21, no. 4, pp. 607–612.
5. Farzaliev, V.M., Kashkai, A.M., Kuliev, F.A., et al., *Neftekhimiya*, 1983, vol. 23, no. 5, pp. 684–688.
6. Farzaliev, V.M., Allakhverdiev, M.A., Khalilova, A.Z., and Guseinova, T.M., *Zh. Prikl. Khim.*, 1994, vol. 67, no. 6, p. 1049.
7. Farzaliev, V.M., Sattarzade, R.I., Rzaeva, I.A., and Allakhverdiev, M.A., *Zh. Prikl. Khim.*, 2001, vol. 74, no. 12, pp. 2023–2026.
8. Dzhavadova, O.N., Bairamov, M.R., and Magerramov, A.M., *Vestn. Bakinsk. Gos. Univ., Khim.*, 2005, no. 3, pp. 33–36.
9. Bairamov, M.R., Magerramov, A.M., and Dzhavadova, O.N., *Zh. Khim. Probl.* (Baku), 2006, no. 2, pp. 365–367.
10. Dzhavadova, O.N., Bairamov, M.R., Magerramov, A.M., and Dzhavadov, M.A., *Zh. Khim. Probl.* (Baku), 2005, no. 3, pp. 170–173.
11. Denisov, E.T., Kharitonov, V.V., and Federova, V.V., Transformation of Kinetic Curves as a Method for Evaluating the Performance of Oxidation Inhibitors, *Preprint*, Chernogolovka, 1973.
12. Emanuel', N.M. and Denisov, E.T., *Neftekhimiya*, 1976, vol. 16, no. 3, pp. 366–382.
13. Denisov, E.T., *Usp. Khim.*, 1973, vol. 42, no. 3, pp. 361–390.
14. Emanuel', N.M., *Neftekhimiya*, 1982, vol. 22, no. 4, pp. 448–453.
15. Emanuel', N.M., Denisov, E.T., and Maizus, Z.K., *Tsepnye reaktsii okisleniya uglevodorodov v zhidkoi faze* (Chain Reactions of Liquid-Phase Oxidation of Hydrocarbons), Moscow: Nauka, 1965.

ISSN 1070-4272, Russian Journal of Applied Chemistry, 2008, Vol. 81, No. 1, pp. 78–81. © Pleiades Publishing, Ltd., 2008.
Original Russian Text © A.A. Kuznetsov, G.K. Semenova, A.Yu. Tsegel'skaya, M.Yu. Yablokova, V.G. Krasovskii, 2008, published in Zhurnal Prikladnoi Khimii, 2008, Vol. 81, No. 1, pp. 82–85.

ORGANIC SYNTHESIS AND INDUSTRIAL ORGANIC CHEMISTRY

Interaction of Diamines with Benzoic Acid without a Solvent: IR Study and Phase Diagram Analysis

A. A. Kuznetsov, G. K. Semenova, A. Yu. Tsegel'skaya, M. Yu. Yablokova, and V. G. Krasovskii

Enikolopov Institute of Synthetic Polymeric Materials, Russian Academy of Sciences, Moscow, Russia
Zelinskii Institute of Organic Chemistry, Russian Academy of Sciences, Moscow, Russia

Received June 20, 2007

Abstract—The specific interaction of aromatic and aliphatic diamines with benzoic acid without a solvent was studied by IR spectroscopy and phase diagram analysis.

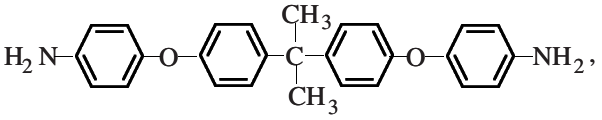
DOI: 10.1134/S1070427208010187

We have shown previously [1, 2] that a benzoic acid (BA) melt at 140–150°C can be used as catalytically active medium in the synthesis of polyimides (PI) by one-step high-temperature polycyclocondensation of diamines and dianhydrides of aromatic and tetracarboxylic acids [3, 4]. A study of this process in BA melt revealed a series of interesting kinetic features untypical of the reaction of diamines and dianhydrides under other conditions. In particular, the total rate of polycondensation in BA melt only slightly depends on the basicity of the amino group in the diamine, whereas in low-temperature polycondensation this dependence is strongly pronounced [5–7]. One of possible explanations of this effect is that the acid medium specifically interacts with the amino group and changes its reactivity. In view of these facts, in this study we examined the specific interaction of some diamines strongly differing in the basicity with molten BA in binary systems diamine–BA by phase diagram analysis in combination with IR spectroscopy.

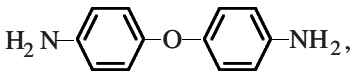
EXPERIMENTAL

The following aromatic and aliphatic diamines strongly differing in the basicity were the objects of our study:

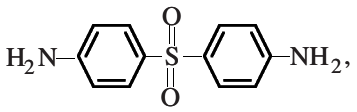
2,2-bis[4-(4-aminophenoxy)phenyl]propane (BAPP)



4,4'-diaminodiphenyl oxide (DADPO)



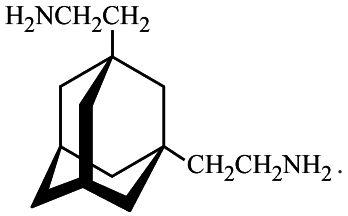
4,4'-diaminodiphenyl sulfone (DADPS)



1,6-hexamethylenediamine (HMDA)

$H_2N–(CH_2)_6–NH_2$,

1,3-bis(2-aminoethyl)adamantane (ADA)



Benzoic acid (technical grade, Russia) was recrystallized from water–ethanol mixture and dried in a vacuum at 50°C, mp 122°C; BAPP (technical grade) was purified by recrytallization from isopropyl alcohol, mp 129°C; DADPO (technical grade, Russia) was purified by sublimation in vacuum, mp 190°C; DADPS (technical grade) was purified by recrystallization from isopropyl alcohol, mp 175°C; HMDA (Aldrich) was double-distilled in a vacuum, mp 44–45°C; and ADA was distilled in a vacuum, mp 129°C.

Phase diagrams of binary mixtures were constructed from data of differential scanning calorimetry (DSC), obtained on a DTAS-1200 device (Russia) at

a heating rate of 16 deg min^{-1}. For each composition, the temperature corresponding to endothermic peak on a DSC thermogram was determined and plotted on the phase diagram. Samples for DSC were prepared by grinding in agate mortar of mixtures of the required composition, preliminarily melted and cooled to 20°C.

In the general case, interaction of nitrogen-containing organic bases with carboxylic acid can involve the dissociation of carboxylic acid dimer and formation of hydrogen-bonded complexes and even products of complete proton transfer from the acid to the base [7, 8]. To elucidate the chemical composition of products obtained by alloying the BA–diamine mixtures (in the absence of diluent), we compared the IR spectra of melts and individual components.

The IR spectra of solid binary systems containing BA and BAPP, DADPO, and DADPS are superpositions of the spectra of the individual components.

The DSC thermograms for the BA–DADPO binary system with the molar ratios of 0.9 : 0.1 (curve *1*) and 0.16 : 0.84 (curve *2*) are shown in Fig. 1. Two endothermic peaks are observed in these thermograms; the first of them is located at 108°C irrespective of the mixture composition. The temperature of the second peak depends on the composition and varies from 108°C to the melting points of the individual components. The DSC data for binary systems BA–diamine were used for construction of the corresponding phase diagrams (Figs. 2–4). In the phase diagrams of BA–BAPP (Fig. 2) and BA–DADPO (Fig. 3) systems, two curve branches bounding the homogeneity area connect the melting points of the individual components with the eutectic point. Such a pattern is characteristic of binary systems with limited mutual solubility in the absence of pronounced specific interaction. In contrast to the first two systems, in the phase diagram of the BA–DADPS system (Fig. 4) the liquidus curve for mixtures enriched in BA is the line practically parallel to the composition axis. This shape of the diagram shows that, below the BA melting point, 122°C, the components of the mixtures enriched in BA (the part of the diagram to the left of the eutectic point) are practically incompatible and crystallize separately. Above 122°C, the components are compatible at all ratios except the region bounded by the liquidus and solidus curves at compositions to the right of the eutectic point.

The phase diagrams and IR spectra of binary systems containing highly basic aliphatic diamines, BA–HMDA and BA–ADA, are essentially different. In the IR spectra of the BA–HMDA (Fig. 5) and BA–

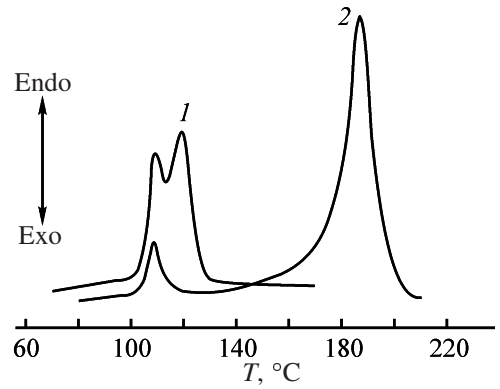


Fig. 1. DSC thermogram of BA–DADPO binary system with the component molar ratio of (*1*) 0.9 : 0.1 and (*2*) 0.16 : 0.84. (*T*) Temperature; the same for Figs. 2–4, 7, and 8.

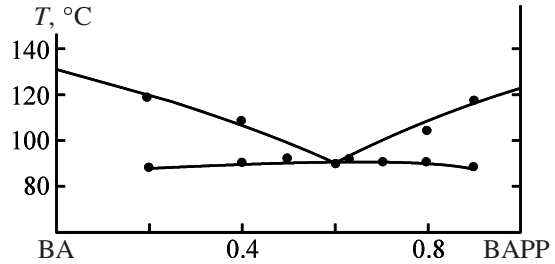


Fig. 2. Phase diagram of the BA–BAPP binary mixture (mole fraction scale).

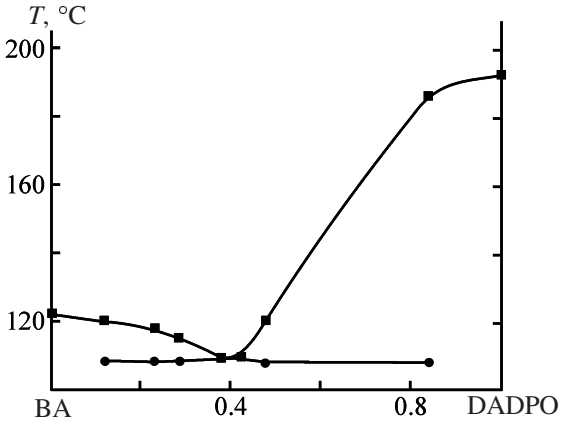


Fig. 3. Phase diagram of the BA–DADPO binary mixture (mole fraction scale).

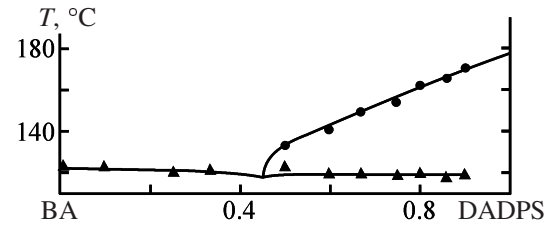


Fig. 4. Phase diagram of the BA–DADPS binary mixture (mole fraction scale).

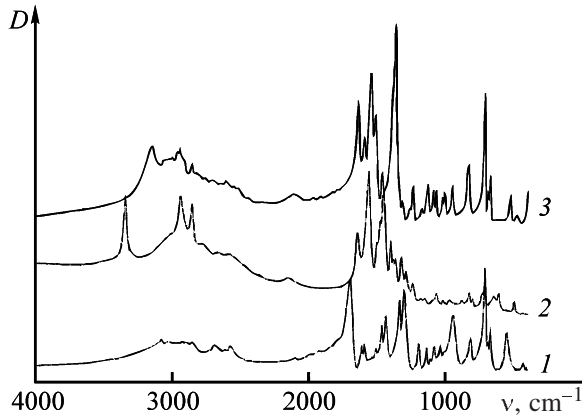


Fig. 5. IR spectrum of the BA–HMDA binary mixture with the component molar ratio of 0.7 : 0.3. (*D*) Optical density and (ν) wavenumber; the same for Fig. 6. (*1*) BA, (*2*) HMDA, and (*3*) mixture.

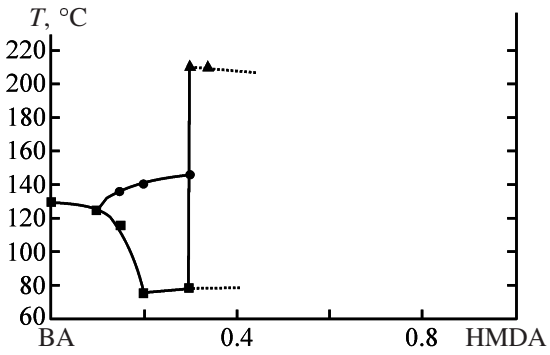


Fig. 7. Phase diagram of the BA–HMDA binary mixture (mole fraction scale).

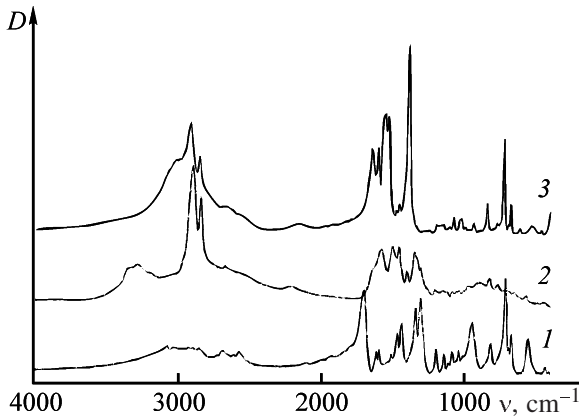


Fig. 6. IR spectrum of BA–ADA binary mixture with component molar ratio of 0.7 : 0.3. (*1*) BA, (*2*) ADA, and (*3*) mixture.

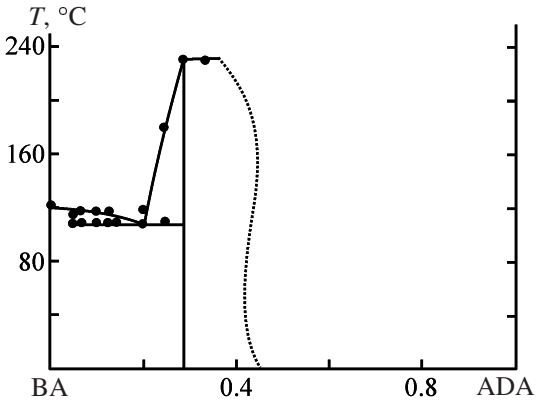


Fig. 8. Phase diagram of the BA–ADA binary mixture (mole fraction scale).

ADA systems (Fig. 6), at 2 : 1 molar ratio in both cases, new absorption bands are observed at 3154 and 3023 cm^{-1} (N–H stretching vibrations in alkylammonium ion of HMDA and ADA, respectively) and at 1550 and 1382 cm^{-1} (symmetric and antisymmetric C–O stretching vibrations of benzoate ion, respectively). At the same time, characteristic bands of the initial diamines at 3347 (N–H stretching vibrations of amino group in HMDA spectrum) and 3286 cm^{-1} (ADA) and of BA at 1690 cm^{-1} (C=O stretching vibrations) are absent.

Influence of diamine basicity on type of interaction with benzoic acid without a solvent. BA : diamine molar ratio 2 : 1

Diamine	pK_1	pK_2	Product type
HMDA	10.93	9.83	Dibenzoate salt
ADA	10.67*	9.61	Dibenzoate salt
BAPP	4.63**	4.22**	Physical mixture
DADPO	4.75	3.74	Physical mixture
DADPS	2.01	1.02	Physical mixture

* Calculated from data measured in nitromethane (pK_{a1} 17.75, pK_{a2} 16.36) using the equation $pK_a(H_2O) = 0.76pK_a(CH_3NO_2) - 2.82$.

** Data for double-hinged diamine, 4,4'-diaminodiphenoxyhydroquinone [9], structurally related to BAPP.

In phase diagrams of binary systems BA–HMDA and BA–ADA (Figs. 7 and 8, respectively), congruent point at 2 : 1 molar ratio is indicative of the formation of diamine dibenzoate.

The data in the table allow us to correlate the chemical structures of solid binary systems obtained by the reactions of diamines with BA in the absence of the solvent with the basicity of the initial diamines expressed in pK_a units (in water).

As seen from the table, only highly basic diamines with $pK_a \geq 9.5$ form BA–diamine binary systems with strong interaction, in which after melting and subsequent cooling products with complete proton transfer are formed. The resulting compounds form their own crystalline phase whose melting point is higher

than that of the initial components (congruent point). Aromatic diamines with $pK_a \leq 4.7$ show only "weak interaction" with BA. It stops in the step of formation of intermolecular complexes with amine–acid hydrogen bond in equilibrium with the initial components. On cooling of such a system, crystallization of the components can decompose the BA–amine intermolecular complex. Therefore, in the IR spectra of solid BA–aromatic diamine systems, intermolecular complexes are not manifested. With low-basic aromatic diamines with pK_a ~2, the specific interaction in the melt is virtually completely absent, and in the region of compositions rich in BA the presence of the diamine does not affect the BA melting and crystallization.

CONCLUSIONS

(1) The diamines studied can be subdivided into two groups differing in the type of the specific interaction with benzoic acid in two-component solid systems.

(2) Highly basic aliphatic diamines ($pK_a \geq 9.5$) react with benzoic acid in the melt to form products of complete proton transfer (benzoate salts), which are individual chemical compounds soluble in benzoic acid melt.

(3) Moderately and low-basic aromatic diamines with $pK_a \leq 4.7$ do not form with benzoic acid products with complete proton transfer; the phase diagrams have a shape typical for mixtures of chemical components without interaction and partial mutual or unilateral solubility.

ACKNOWLEDGMENTS

The study was financially supported by the Russian Foundation for Basic Research (project no. 05-03–32998).

REFERENCES

1. Kuznetsov, A.A., *High Perform. Polym.*, 2000, vol. 12, pp. 445–460.
2. Kuznetsov, A.A., Yablokova, M.Yu., Buzin, P.V., et al., *High Perform. Polym.*, 2004, vol. 16, pp. 89–100.
3. Vinogradova, S.V. and Vasnev, V.A., *Polikondensatsionnye protsessy i polimery* (Polycondensation Processes and Polymers), Moscow: Nauka, 2000.
4. Korshak, V.V., Vinogradova, S.V., Vygodskii, Ya.S., et al., *Izv. Akad. Nauk SSSR, Ser. Khim.*, 1967, no. 10, pp. 2267–2274.
5. Bessonov, M.I., Koton, M.M., Kudryavtsev, V.V., and Laius, L.A., *Poliimidy – klass termostoikikh polimerov* (Polyimides: A Class of Heat-Resistant Polymers), Leningrad: Nauka, 1983.
6. Svetlichnyi, V.M., Kudryavtsev, V.V., Adrova, N.A., and Koton, M.M., *Zh. Org. Khim.*, 1974, vol. 10, no. 9, pp. 1896–1900.
7. Kalnin'sh, K.K., Fedorova, E.F., Novozhilova, I.V., et al., *Dokl. Akad. Nauk SSSR*, 1970, vol. 195, no. 2, pp. 364–367.
8. Derevyanko, L.I., Tsarevskaya, M.N., and Khlevnyuk, B.S., *Zh. Obshch. Khim.*, 1972, vol. 42, no. 9, pp. 2083–2087.
9. Gol'dshtein, I.P., Gur'yanova, E.N., and Perepelkova, T.I., *Zh. Obshch. Khim.*, 1972, vol. 42, no. 9, pp. 2091–2098.

ISSN 1070-4272, Russian Journal of Applied Chemistry, 2008, Vol. 81, No. 1, pp. 82–85. © Pleiades Publishing, Ltd., 2008.
Original Russian Text © K.S. Trofimova, G.V. Bozhenkov, N.S. Shaglaeva, R.G. Sultangareev, E.A. Zabanova, G.G. Levkovskaya, 2008, published in Zhurnal Prikladnoi Khimii, 2008, Vol. 81, No. 1, pp. 86–89.

MACROMOLECULAR CHEMISTRY AND POLYMERIC MATERIALS

Radical Copolymerization of 1,2-Dichlorovinyl Propyl Ketone and Styrene

K. S. Trofimova, G. V. Bozhenkov, N. S. Shaglaeva, R. G. Sultangareev, E. A. Zabanova, and G. G. Levkovskaya

Favorskii Irkutsk Institute of Chemistry, Siberian Branch, Russian Academy of Sciences, Irkutsk, Russia
Irkutsk State Technical University, Irkutsk, Russia

Received May 30, 2007

Abstract—The possibility of synthesis of soluble copolymers by radical copolymerization of 1,2-dichlorovinyl propyl ketone with styrene in the presence of azobis(isobutyronitrile) was studied. The polymerization constants were determined and the probabilities of formation of various sequences of comonomer units were evaluated. The structure of the copolymers was studied by IR and ^{13}C NMR spectroscopy, and some characteristics of the copolymers were determined.

DOI: 10.1134/S1070427208010199

Chlorovinyl ketones are very important and promising intermediates for synthesis of numerous polyfunctional highly reactive and heterocyclic compounds [1]. Copolymers containing keto group in the backbone (polyketones, which are alternating copolymers of carbon monoxide with acyclic and cyclic olefins, dienes, styrene, and its derivatives) are thermally stable and readily processable materials and have specific gas-permeability characteristics. For example, with respect to its barrier characteristics (permeability to N_2, O_2, and CO_2), the copolymer based on carbon monoxide and ethylene is intermediate between high-density polyethylene and polyvinyl chloride, and with respect to moisture permeability it is close to polyurethane [1, 2]. The ready compatibility of polyketones with other materials (Nylon, polycarbonate, and polyvinyl alcohol) and also their chemical resistance make these substances particularly attractive in use as protective coatings and chemical containers. Due to strong adhesion to organic and inorganic materials, polyketones can be used for fabrication of structural materials. A low friction coefficient and high strength allow these polymers to be recommended for use in various gearings and similar structures [2, 3]. These copolymers containing carbonyl groups and styrene fragments can be synthesized using palladium-containing complexes as catalysts [4].

Here we suggest the simplest and convenient route to such copolymers: direct copolymerization of 1,2-dichlorovinyl propyl ketone (DCVK) and styrene (ST).

It is well known that homopolymers based on methyl 2-chlorovinyl ketone, synthesized by polycondensation under heating or in the presence of Friedel–Crafts catalysts [5, 6], are catalytically active in oxidation and dehydrogenation of alcohols [5], have extremely interesting and unusual electrical and magnetic characteristics [6], and tend to chemical transformations at elevated temperatures. There is only one paper in which the synthesis of a polymer based on phenyl 2,2-dichlorovinyl ketone in the presence of $AlCl_3$ was reported; however, the characteristics of this polymer was not studied [7]. Thus, the reactivity of chlorovinyl ketones in (co)polymerization practically was not studied.

Among the wide variety of chlorovinyl ketones, only 1,2-dichlorovinyl ketones are fairly stable. They do not become dark in storage for 1 month under ordinary conditions and are not dehydrochlorinated with formation of pyrones in prolonged storage. The presence of two chlorine atoms in the vicinal positions of vinyl and carbonyl groups in 1,2-dichlorovinyl propyl ketone offers wide possibilities for numerous polymer-analogous reactions with N-, O-, and S-nucleophiles, for dehydrochlorination, and for crotonic condensation. These transformations can lead to functionalized, polyconjugated, or aromatic condensation polymers.

EXPERIMENTAL

1,2-Dichlorovinyl propyl ketone was prepared from butyryl chloride and *cis*-1,2-dichloroethylene in the presence of aluminum chloride at 35°C within a period of 40 h. The yield of the reaction product is 90%, bp 68–70°C (9 mm Hg), n_D^{20} 1.4900, which is in good agreement with published data [8]. Styrene was purified according to the procedure described in [9]. Azobis(isobutyronitrile) (AIBN) was purified by double recrystallization from methanol.

Copolymerization of DCVK and ST was performed in hermetically sealed ampules in the bulk at 60°C in the presence of AIBN in an argon medium. The resulting reaction mixture was dissolved in DMF, and the copolymer was precipitated with methanol. Copolymers were reprecipitated two times. The copolymer composition was evaluated by the elemental analysis for chlorine using the standard procedure [9]. The turbidimetric titration was performed on a KFK-2 spectrophotometer at λ = 670 nm. DMF was used as a solvent for titration, and ethanol, as a precipitant.

The IR spectra were recorded on a Specord IR-75 spectrophotometer in KBr pellets. The ^{13}C NMR spectra were recorded on a Varian VXR-500S spectrometer (125.5 MHz, relaxation delay 2.5 s, 90° pulse, solvent DMSO-d_6). Chromium tris-acetylacetonate (0.02 M) was used as a relaxant and HMDS, as an internal reference.

The specific surface area of copolymers was determined by measurement of the volume of a gas (nitrogen) adsorbed on the surface of this solid at various pressures. The measurements were performed in a calibrated high vacuum (ASAP-2000).

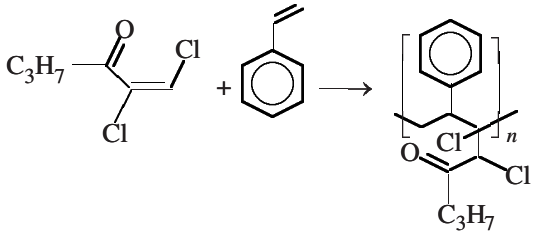
The intrinsic viscosity was determined on an Ubbelohde viscometer in DMF at 20°C; the initial concentration of the solutions was 2.6 g in 100 ml.

The copolymerization constants of monomers were evaluated by the procedure described in [10, 11] using the linear integral method modified according to [12]. The softening point (SP) was determined with a Boëtius heating table.

The radical copolymerization of DCVK and ST in the presence of AIBN was studied. Powdered products readily soluble in aromatic hydrocarbons, DMF, and DMSO and insoluble in alcohols were obtained. Homopolymerization of DCVK does not proceed under similar conditions. Variation of the reaction conditions (heating and increased AIBN concentration) does not result in formation of DCVK homopolymer. This fact can be explained by low rate constants of chain propagation in homopolymerization as a result of steric hindrance produced by two chlorine atoms.

Copolymerization via the double bond is proved by the results of turbidimetric titration and by IR and NMR (^1H, ^{13}C) data. In the IR spectra of the synthesized copolymers, there are no absorption bands typical for vinyl group, but there are characteristic bands caused by skeleton vibrations of the aromatic ring at 1601, 1584, 1500, and 1451 cm^{-1} and also stretching modes of the carbonyl group at 1695 cm^{-1}. The absorption band at 680 cm^{-1} can be assigned to the C–Cl bond. In the ^{13}C NMR spectra of copolymers, there are broad signals corresponding to carbon atoms of carbonyl (192.95 ppm), CH_2 (32.27 ppm), CH_3 (7.57 ppm), and CHCl (56.7–60.0 ppm) groups.

Based on the IR and NMR data and elemental analysis, the synthesis of the copolymer can be described by the following scheme:



As seen from Table 1, the yield and intrinsic viscosity of the resulting samples decrease with increasing concentration of DCVK in the initial mixture; however, at the equimolar ratio of comonomers in the initial mixture, the intrinsic viscosity increases to 0.165 dl g^{-1}. The dependence of SP on the copolymer composition is not linear. The turbimetric titration curve has a smooth shape corresponding to a single-component structure (Fig. 1).

From data on variation of the composition of copolymers with variation of the initial ratio of monomers in the reaction mixture (Table 1), we evaluated the copolymerization constants to be $r_{DCVK} = 0.039 \pm 0.002$ and $r_{ST} = 0.598 \pm 0.01$. As seen from the copolymerization constants, ST is by an order of magnitude more active than DCVK, which is in good agreement with the experimental data (Fig. 2). At $r_1 < 1$, $r_2 < 1$, and $r_2 \gg r_1$ a trend toward alternation of monomeric units is observed. The composition curve intersects the diagonal of the composition diagram and in the intersection point the copolymer composition is equal to the composition of the monomer mixture. In addition, the r_1 and r_2 values suggest lower activity of radicals formed from comonomers in

Table 1. Copolymerization of DCVK (M_1) and ST (M_2). AIBN concentration 0.5 wt %, temperature 60°C, reaction time 5 h

Sample no.	Composition of initial mixture, mol %		Yield, %	Copolymer composition, mol %		[η], dl g^{-1}	SP, °C
	M_1	M_2		m_1	m_2		
1	10	90	33.9	15.54	84.46	0.176	140–165
2	20	80	15.3	16.47	83.52	0.144	150–170
3	30	70	22.4	28.26	71.74	0.132	125–147
4	40	60	20.0	31.48	68.52	0.109	159–184
5	50	50	19.0	34.99	65.01	0.165	115–185
6	60	40	18.7	42.72	57.28	0.088	155–180
7	70	30	15.1	46.00	54.00	0.083	164–185
8	80	20	11.9	47.59	52.41	0.080	165–185
9	90	10	4.9	49.19	50.81	0.052	160–185

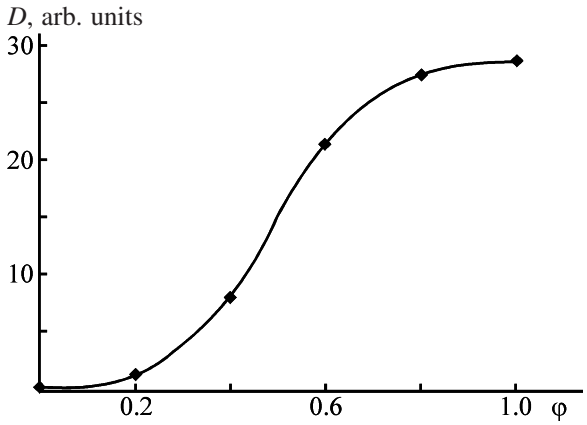


Fig. 1. Turbidimetric titration curve of the copolymer at an equimolar ratio of the monomers in the initial mixture. (D) Optical density and (φ) volume fraction of precipitant.

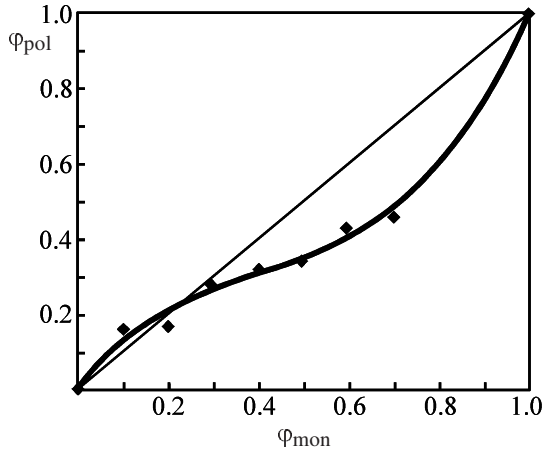


Fig. 2. Copolymer composition as a function of the composition of the monomer mixture. (φ_{pol}) Mole fraction of DCVK in the copolymer and (φ_{mon}) mole fraction of DCVK in the monomer mixture.

homopolymerization than that of radicals formed in cross chain propagation.

The distribution of monomer units in the copolymer chain was evaluated by the common statistic methods using r_1 and r_2 parameters (Table 2). At virtually all compositions of the initial mixture, alternating copolymers are formed and only at 10% content of DCVK in the reaction mixture formation of block copolymers is possible.

The reactivity of DCVK was quantitatively characterized by the Alfrey–Price method [13]; the quantities Q and e were evaluated from the experimental r_1 and r_2 values. It should be noted that the parameter e characterizing the polar properties of DCVK suggests electron-acceptor characteristics of the chlorine-containing monomer or the corresponding radical. For ST we took $Q = 1$ and $e = -0.8$. For DCVK, the calculated values are $e = 1.132$ and $Q = 0.356$.

The specific surface area S_{sp} and pore volume V_{por} of the synthesized copolymer containing 16.47 mol % DCVK (Table 1, sample no. 2) are 11.11 m^2 g^{-1} and 2.55 cm^3 g^{-1}, respectively. For comparison, we determined the similar values for emulsion polyvinyl chloride (PVC) to be $S_{sp} = 1.22$ m^2 g^{-1} and $V_{por} = 0.28$ cm^3 g^{-1}. Polyvinyl chloride had the following characteristics: Fickentscher constant $K_F = 62–63$, $T_{decomp} = 120$°C. For polystyrene in a wide range of concentration of the initial solutions, the specific surface area was found to be 20–25 m^2 g^{-1} [14].

The specific surface area of the copolymer based on DCVK and ST is intermediate between those of polystyrene and PVC. It should be noted that the polymer studied was reprecipitated two times. This

Table 2. Parameters of microstructure of copolymers based on DCVK (M_1) and ST (M_2)

M_1	m_1	M_1M_1	M_2M_2	$M_1M_2 = M_2M_1$	L_1	L_2
0.1	0.1359	0.0007	0.8428	0.1565	1	6
0.2	0.2294	0.0029	0.7033	0.2938	1	3
0.3	0.2980	0.0071	0.5785	0.4144	1	2
0.4	0.3511	0.0139	0.4665	0.5197	1	2
0.5	0.3942	0.0244	0.3652	0.6104	1	2
0.6	0.4311	0.0411	0.2734	0.6854	1	1
0.7	0.4653	0.0691	0.1900	0.7409	1	1
0.8	0.5023	0.1222	0.1142	0.7636	1	1
0.9	0.5605	0.2524	0.0466	0.7010	1	1

fact is very important in determination of the specific surface area and pore volume.

CONCLUSIONS

(1) A new convenient procedure for the synthesis of copolymers containing carbonyl groups and styrene fragments without using expensive catalysts was suggested.

(2) Copolymers based on 1,2-dichlorovinyl propyl ketone and styrene were synthesized by radical copolymerization. The copolymerization constants were determined to be $r_{DCVK} = 0.039 \pm 0.002$ and $r_{ST} = 0.598 \pm 0.010$.

(3) The probabilities of formation comonomer unit sequences M_1M_2, M_2M_2, and $M_1M_2 = M_2M_1$ were evaluated.

REFERENCES

1. Kochetkov, N.K., *Usp. Khim.*, 1955, vol. 24, no. 1, pp. 32–51.
2. Belov, G.P., *Vysokomol. Soedin., Ser. C*, 2001, vol. 43, no. 9, pp. 1651–1666.
3. Belov, G.P., *Usp. Khim.*, 2004, vol. 73, no. 3, pp. 292–319.
4. Milani, B., Anzilutti, A., Vicentini, L., et al., *Organometallics*, 1997, vol. 16, pp. 5064–5075.
5. Nesmeyanov, A.N., Rubinshtein, A.M., Dulov, A.A., et al., *Dokl. Akad. Nauk SSSR*, 1960, vol. 135, no. 3, pp. 609–612.
6. Nesmeyanov, A.N., Rybinskaya, M.I., and Slonimskii, G.L., *Vysokomol. Soedin.*, 1960, vol. 11, no. 4, pp. 526–528.
7. Mirskova, A.N., Levkovskaya, G.G., and Voronkov, M.G., *Izv. Akad. Nauk SSSR, Ser. Khim.*, 1977, no. 8, pp. 1816–1820.
8. Bozhenkov, G.V., Levkovskaya, G.G., Larina, L.I., et al., *Zh. Org. Khim.*, 2004, vol. 40, no. 11, pp. 1632–1640.
9. Toroptseva, A.M., Belogorodskaya, K.V., and Bondarenko, V.M., *Laboratornyi praktikum po khimii i tekhnologii vysokomolekulyarnykh soedinenii* (A Laboratory Guide on Chemistry and Technology of Macromolecular Compounds), Leningrad: Khimiya, 1972.
10. Deryabina, G.I., *Laboratornyi praktikum po khimii VMS: Radikal'naya polimerizatsiya–sopolimerizatsiya: Uchebnoe posobie* (Laboratory Guide on Chemistry of Macromolecular Compounds: Radical Polymerization–Copolymerization: Textbook), Kuibyshev: Samarskii Gos. Univ., 1988, p. 57.
11. Annenkov, V.V., Lebedeva, O.V., Danilovtseva, E.N., and Mikhaleva, A.I., *Vysokomol. Soedin., Ser. B*, 2001, vol. 43, no. 9, p. 1560.
12. Ezrielev, A.N., Brokhina, E.L., and Roskin, E.S., *Vysokomol. Soedin., Ser. A*, 1969, vol. 11, no. 8, p. 1670.
13. *Copolymerization*, Ham, G.E., Ed., New York: Interscience, 1964.
14. Rebinder, P.A. and Vlodavets, I.N., *Problemy fizikokhimicheskoi mekhaniki voloknistykh i poristykh dispersnykh struktur i materialov* (Problems of Physicochemical Mechanics of Fibrous and Porous Structures and Materials), Riga: Zinatne, 1967, pp. 5–40.

ISSN 1070-4272, Russian Journal of Applied Chemistry, 2008, Vol. 81, No. 1, pp. 86–90. © Pleiades Publishing, Ltd., 2008.
Original Russian Text © M.F. Galikhanov, D.E. Temnov, A.A. Kozlov, A.A. Petrova, Yu.A. Gorokhovatskii, R.Ya. Deberdeev, 2008, published in Zhurnal Prikladnoi Khimii, 2008, Vol. 81, No. 1, pp. 90–94.

MACROMOLECULAR CHEMISTRY AND POLYMERIC MATERIALS

Specific Features of the Electret Effect in Two-Layer Polymeric Films

M. F. Galikhanov, D. E. Temnov, A. A. Kozlov, A. A. Petrova, Yu. A. Gorokhovatskii, and R. Ya. Deberdeev

Kazan State Technical University, Kazan, Tatarstan, Russia
Herzen Russian State Pedagogical University, St. Petersburg, Russia

Received April 4, 2007

Abstract—Two-layer film corona-electrets based on low-density polyethylene and copolymers of ethylene with vinyl acetate of various brands were studied. The dependence of the electret characteristics of two-layer corona-electrets on the percentage content of polar groups in the copolymer constituting the bottom layer was analyzed. Data on thermally stimulated depolarization and thermally stimulated relaxation of the surface potential served as a basis for suggesting a mechanism of depolarization of two-layer corona-electrets.

DOI: 10.1134/S1070427208010205

The wide use of polymeric electrets in numerous electric instruments and devices, friction and sealing units, and gas and liquid filters [1, 2] predetermines the unremitting interest in studies of the electret effect in polymeric insulators. Particular attention is given to a search for new electret materials by combining the already known materials, i.e., by obtaining composites, to which belong multilayer electrets whose layered structure can give rise to specific features uncharacteristic of single-layer materials [3–9].

A practical application of two-layer films is their use as anticorrosive coatings whose quality is determined both by the electret properties of polymeric films and by the adhesion between a film and a metallic substrate. As shown in [6, 7], presence of a surface charge improves the anticorrosive properties of a coating, whereas an increase in the content of polar groups in the lower layer improves the adhesion, but impairs the electret properties of corona-electrets. Thus, studies of the stability of the electret state and elucidation of the depolarization mechanism are of interest and can determine the optimal content of polar groups in the lower layer to provide the best quality of anticorrosive coatings.

EXPERIMENTAL

As objects of study were chosen low-density polyethylene (LDPE) of 11503-070 brand [GOST (State Standard) 16337–77] and ethylene–vinyl acetate copolymers (EVAC) with varied content of vinyl acetate (VA) groups, of 11106-030, 11306-075, 11507-070, 11808-240 [TU (Technical Specification) 6-05-1636–78], 12306-020, and 12506-150 (TU 301-05-56–90) brands. The characteristics of the polymers are given in Table 1.

Single-layer films of thickness 0.25 mm were prepared by compaction in accordance with GOST 12019–66 at 170±5°C and compaction time of 5 min. The films were doubled at 170±5°C in a restricting frame of height 0.5 mm in the absence of pressure for 10 min. Then, the composites obtained were heated at 90°C for 10 min and cooled in the field of a negative corona discharge. The corona discharge was created with an electrode comprising 196 pointed needles evenly arranged over an area of 49 cm^2 in the form of a square. The polarization voltage and time were 35 kV and 60 s.

The electret characteristics were measured daily with an IPEP-1 meter whose working principle is based on a periodic shielding of the measuring probe situated at a certain distance from the electret surface. The error in measuring the surface potential V_e, electric field strength E, and surface density σ_{eff} of electric charges did not exceed 3%.

Spectra of thermally stimulated currents (TSC) were measured under heating at a constant rate of 5 deg min^{-1} in a special measuring cell equipped with blocking aluminum electrodes and a fluoroplastic spacer.

The films were also studied by the method of ther-

Table 1. Characteristics of the starting polymers

Polymer	Brand	Density, g cm^{-3}	Degree of crystallinity, %	VA content, %	ρ_v, Ω cm	ε at 1 kHz
LDPE	15 803-020	0.918 ± 0.002	62	0	1×10^{16}	2.23
EVAC-6	11 104-030	0.935 ± 0.005	27	6	7×10^{14}	2.42
EVAC-12	11 306-075	0.933 ± 0.003	18	13.5	1×10^{14}	2.51
EVAC-17	12 306-020	0.937 ± 0.005	12	17.5	4×10^{13}	2.70
EVAC-22	11 507-375	0.940 ± 0.005	6.8	22	1×10^{13}	3.96
EVAC-27	12 508-150	0.950 ± 0.005	4	27	9×10^{12}	4.21
EVAC-30	11 808-240	0.951 ± 0.005	3	29.1	6×10^{12}	4.37

mally stimulated relaxation of the surface potential (TSRSP), with the surface potential measured with a dynamic electrometer. The samples studied were preliminarily charged in the field of a negative corona discharge at room temperature for 60 s. After that, the samples were heated at a constant rate of 5.4 deg min^{-1}, with the temperature and the surface potential simultaneously measured. Also, temperature dependences of the potential were obtained for the same samples polarized in the field of the negative corona discharge for 60 s after preliminary heating at 90°C for 10 min.

Being a nonpolar polymer, low-density polyethylene is well electretized in a corona-discharge field. According to the phenomenological theory, the effective surface charge density is constituted by a homocharge σ_p and heterocharge P:

$$\sigma_{eff} = \sigma_p - P.$$

The homocharge in polyethylene corona-electrets is due to injected carriers (electrons and ions) and macroions (including radical ions) formed in treatment of a polymer in a corona discharge. It is quite possible that a contribution to the homocharge is made by the dipole polarization of groups (mostly oxygen-containing groups) formed on the surface of the polymeric film under the action of the corona discharge. The heterocharge is due to the dipole polarization of groups contained in the polymer itself (for polyethylene, these are "anomalous" vinylidene, vinyl, and other groups in an amount of 4–6 groups per 1000 C atoms [10]).

Ethylene–vinyl acetate copolymers are polar polymers. Their polarity is due to the presence of dipole vinyl acetate groups whose mass content varies between different EVAC brands (Table 1). It was shown in [1] that the stability of corona-electrets based on EVAC decreases as the content of vinyl acetate groups in these copolymers increases. This would be expected because depolarization involves transfer of charge to the polymer surface and relaxation of this charge. These processes are governed by the bulk resistivity ρ_v of the material, and the ρ_v of EVAC is one to three orders of magnitude lower than that in LDPE, and it is the lower, the larger the content of polar vinyl acetate groups in a polymer (Table 1). Moreover, as the mass content of vinyl acetate in EVAC increases, the degree of crystallinity decreases (Table 1), and, consequently, so does the area of the phase boundary between the amorphous and crystalline phases, which acts as a trap for injected carriers. Undoubtedly, the decrease in the number of traps leads to smaller values of the electret parameters of polymers [11].

In electretization with preliminary heating of two-layer films based on LDPE and EVAC of various brands, values of the electret parameters decrease as the content of polar groups in the lower layer increases (Table 2). This seems to be reasonable: if the amount of the homocharge remains virtually unchanged, the amount of heterocharge grows.

It should be noted that, when revealing specific features of the electret effect, two-layer LDPE + EVAC films are to be compared with cohesively connected LDPE and EVAC films, rather than with single-layer films of these types. It was shown in [12] that spectra of thermally stimulated depolarization (TSD) of polyethylene films show two positive peaks: at 80–85 and 110–115°C, which appear upon disintegration of some type of traps for injected carriers. The first of these corresponds to Vicat's softening point, and the second lies near the melting point of LDPE. At the softening point of polyethylene, the mobility of its macromolecules dramatically increases and the appearance of the TSC peak is due to the relaxation of the Maxwell–Wagner polarization at phase boundaries. At the melting point, ordered supramolecular formations constituting the crystalline phase of LDPE are thermally disintegrated and the appearance of the TSC peak is attributed to release of carriers from traps at the phase boundary between the amorphous and crystalline phases of polyethylene [12].

Table 2. Electret properties of two-layer films

Two-layer film (substrate + support)	Initial values			In 30 days		
	V_e, kV	σ_{eff}, μC m^{-2}	E, kV m^{-1}	V_e, kV	σ_{eff}, μC m^{-2}	E, kV m^{-1}
Cohesively connected films						
LDPE + LDPE	–0.80	–0.37	–42.2	–0.12	–0.07	–7.1
EVAC-6 + EVAC-6	–0.70	–0.32	–36.5	–0.03	–0.03	–3.3
EVAC-12 + EVAC-12	–0.62	–0.30	–35.2	0	0	0
EVAC-17 + EVAC-17	–0.57	–0.19	–31.1	0	0	0
EVAC-22 + EVAC-22	–0.57	–0.26	–30.7	0	0	0
EVAC-27 + EVAC-27	–0.46	–0.23	–24.2	0	0	0
EVAC-30 + EVAC-30	–0.41	–0.19	–20.9	0	0	0
Adhesively connected films						
LDPE + EVAC-6	–0.75	–0.40	–41.6	–0.08	–0.05	–5.3
LDPE + EVAC-12	–0.62	–0.33	–35.5	–0.07	–0.04	–4.9
LDPE + EVAC-17	–0.55	–0.29	–32.3	–0.04	–0.02	–2.9
LDPE + EVAC-22	–0.63	–0.33	–36.0	–0.07	–0.04	–5.0
LDPE + EVAC-27	–0.55	–0.30	–33.1	–0.06	–0.03	–3.5
LDPE + EVAC-30	–0.36	–0.19	–20.3	–0.03	–0.01	–1.8

It was found in an analysis of TSD data for a cohesively connected two-layer polyethylene film that the first, low-temperature TSC peak lies in the negative region (Fig. 1, curve *1*). On replacing the lower polyethylene layer with that of EVAC, a new low-temperature negative peak appears, and the peak at 80–85°C again becomes positive. As the fraction of vinyl acetate in EVAC increases, the position and intensity of the low-temperature negative peak change: it is shifted to lower temperatures and the thermally stimulated current increases (Fig. 1).

The data obtained can be readily understood if account is taken of the fact that there is no injected charge in EVAC and the dipole polarization can give rise to homo- and heterocharge in polymeric films. The lowered softening point of EVAC, compared with LDPE, results in that macromolecules of the copolymer become flexible to an extent sufficient for displacement of their groups and segments at lower temperatures than in the case of LDPE macromolecules. Under heating, dipole groups of the copolymer are oriented in the field of the nonequilibrium homocharge of the upper polyethylene layer. This process can be termed additional orientation, because part of the dipoles was possibly oriented in the course of electretization of two-layer films, although the time of action of the corona discharge field is short (60 s). This phenomenon is manifested in TSD spectra in the appearance of the negative peak. It can be seen (Fig. 1) that the higher the content of vinyl acetate groups in the copolymer, the lower the temperature at which the additional orientation of dipoles occurs in two-layer corona-electrets and the higher the intensity of this process.

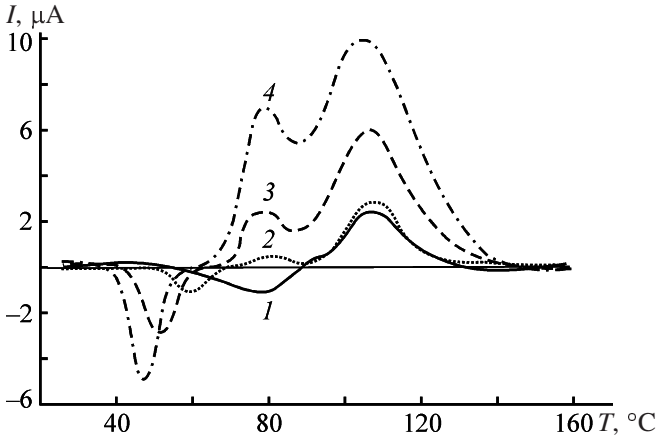


Fig. 1. Spectra of thermally stimulated depolarization currents in two-layer corona-electrets. (*I*) Current and (*T*) temperature. (*1*) LDPE + LDPE, (*2*) LDPE + EVAC-6, (*3*) LDPE + EVAC-17, and (*4*) LDPE + EVAC-27.

Then, upon further heating, there occurs the Maxwell–Wagner relaxation, which gives rise to the TSC peak at 80–85°C. An increase in the fraction of polar films in the lower layer results in that a larger amount of charge is captured at the phase boundary. It is quite probable that a part of the injected charge is released at this temperature.

When two-layer corona-electrets are heated to the melting point of LDPE, a complete charge relaxation

occurs because of the release of injected carriers from structural traps. It is the loss of the homocharge that is responsible for the final disorientation of dipole groups throughout the film volume.

The above considerations suggest that the presence of the negative peak in the spectra of the cohesively connected polyethylene films is due to the additional orientation of dipole groups present in a certain amount on the surface of polymeric films. Their presence is due to oxidation of the polymer surface, which occurs at elevated temperatures in fabrication of the two-layer structures. Connecting two LDPE films leads to appearance of an oxidized polyethylene "spacer" in the bulk of the structure, and just this spacer gives rise to the negative peak at 80–85°C.

These conclusions are confirmed by TSRP data. Figure 2 shows temperature dependences of the surface potential at a heating rate of 5.4 deg min^{-1} for two-layer films LDPE + LDPE, LDPE + EVAC-17, and LDPE + EVAC-27, preliminarily heated at 90°C for 10 min and charged in the field of a negative corona discharge. The surface potential remains unchanged up to 65–70°C and then starts to decrease (Fig. 2, curve *1*). The potential does not decrease at a constant rate as the temperature increases, and this range can be conditionally divided in two: at a temperature of 100–105°C the curve has an inflection after which the rate at which the surface potential decreases becomes higher. Comparison of the TSRP and TSD data shows that the first portion of the TSRP curve corresponds to the temperature range of the first peak of thermally stimulated currents, and the second, to the region of the high-temperature TSD peak.

A somewhat different pattern is observed for two-layer LDPE + EVAC films: the region in which the potential decreases can now be divided in three (Fig. 2, curves *2* and *3*). For example, for the LDPE + EVAC-17 film (Fig. 2, curve *2*), the first, second, and third portions lie at 50–65, 65–90, and 90–120°C. The decrease in the potential in the temperature range from 50 to 65°C is due only to the additional orientation of the dipole groups of EVAC in the lower layer and, therefore, the rate of this decrease is low. The second portion, in which the rate is the highest, corresponds to charge relaxation both in the upper polyethylene layer and in the lower layer formed by the ethylene–vinyl acetate copolymer. The third portion ends with a complete relaxation of the surface potential of two-layer corona-electrets.

Figure 3 shows how the potential depends on temperature at a heating rate of 5.4 deg min^{-1} for the same samples polarized in the field of a negative

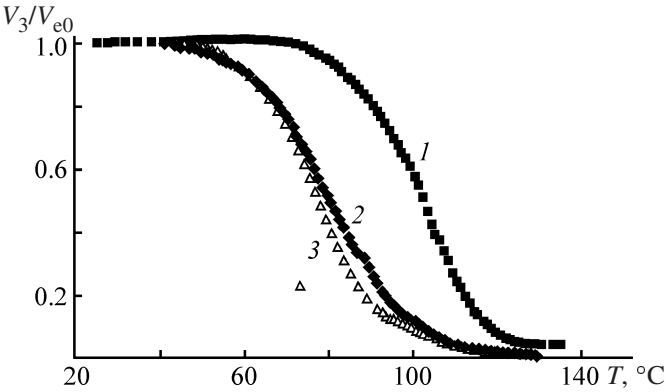


Fig. 2. Surface potential V_e/V_{e0} vs. temperature T for two-layer films charged in the field of a negative corona discharge after preliminary heating at 90°C. (*1*) LDPE + LDPE, (*2*) LDPE + EVAC-17, and (*3*) LDPE + EVAC-27.

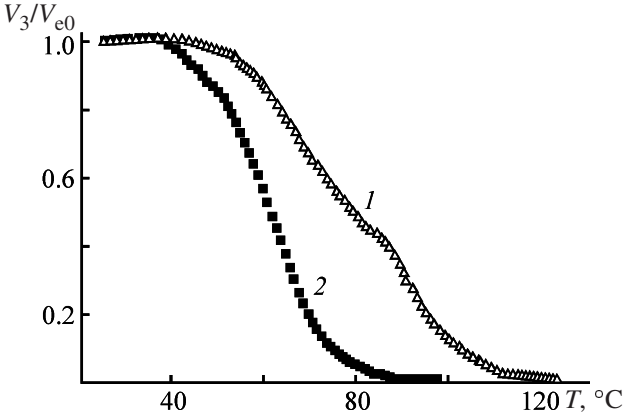


Fig. 3. Surface potential V_e/V_{e0} vs. temperature T for two-layer films charged at room temperature in the field of a negative corona discharge. (*1*) LDPE + LDPE and (*2*) LDPE + EVAC-27.

corona discharge for 60 s, but without preliminary heating. Comparison of the decaying portions of the surface potential for preliminarily heated and unheated films (Figs. 2, 3) shows that the stability of the electret state in samples preliminarily heated at 90°C before polarization exceeds that for samples polarized at room temperature. The possible reason is that, at elevated electretization temperatures, the Maxwell–Wagner polarization partly shields the field of the homocharge, which hinders the additional orientation of the polar groups of the copolymer.

The patterns revealed open up opportunities for practical use of two-layer polymeric corona-electrets based on polyethylene and an ethylene–vinyl acetate copolymer. Among the known applications are two-layer sleeves for anticorrosive insulation of edge joints of oil and gas pipelines. These sleeves are composed of polyethylene and a thermoplastic adhesive, whose role is frequently played by ethylene–vinyl acetate copolymers, and are made heat-shrinkable [13]. If the

polyethylene surface is electretized in a corona discharge, the polar groups of the polymeric adhesive will be additionally oriented in thermal treatment, which will enhance the adhesion of the sleeves to edge joints because of the contribution of electrostatic forces to the work of adhesion [14]. Undoubtedly, this suggestion needs practical verification.

CONCLUSIONS

(1) The surface potential, electric field strength, and surface electric charge density of two-layer corona-electrets based on low-density polyethylene and ethylene–vinyl acetate copolymers of various brands are adversely affected by an increase in the content of polar groups in the lower layer. This occurs because of the increase in the fraction of heterocharge.

(2) The spectra of thermally stimulated depolarization of two-layer corona-electrets based on low-density polyethylene and ethylene–vinyl acetate copolymers show three peaks: at the softening points of a copolymer and low-density polyethylene and at the melting point of the latter. The first peak points to orientation of dipole groups of the copolymer in the field of the nonequilibrium homocharge of the upper polyethylene layer (additional orientation). The second peak is indicative of the Maxwell–Wagner relaxation. The full relaxation of the charge, caused by release of carriers from structural traps that disintegrate upon melting of low-density polyethylene, gives rise to the third peak of thermally stimulated currents.

(3) Data on the thermally stimulated relaxation of the surface potential in two-layer corona-electrets confirm that the electret parameters decay in three stages corresponding to those revealed by analysis of thermally stimulated depolarization data.

(4) The stability of the electret state in two-layer corona-electrets based on low-density polyethylene and ethylene–vinyl acetate copolymers, preliminarily heated before polarization, exceeds that of samples polarized at room temperature.

REFERENCES

1. *Electrets*, Sessler, G.M., Ed., Berlin: Springer, 1980.
2. Pinchuk, L.S. and Gol'dade, V.A., *Elektretnye materialy v mashinostroenii* (Electret Materials in Machine-Building), Gomel: Infotribo, 1998.
3. Boitsov, V.G. and Rychkov, A.A., *Pis'ma Zh. Tekh. Fiz.*, 1980, vol. 6, no. 18, pp. 1139–1143.
4. Hori, Y., *J. Electrostatics*, 2000, vol. 48, pp. 127–143.
5. Shevtsova, S.A., Budarina, L.A., Arkhiereev, V.P., et al., *Vestn. Kazan. Tekhnol. Univ.* (Suppl.), Kazan: Karpol, 2001, pp. 292–303.
6. Galikhanov, M.F., Kozlov, A.A., and Deberdeev, R.Ya., *Izv. Vyssh. Uchebn. Zaved., Mater. Elektron. Tekh.*, 2005, no. 1, pp. 47–49.
7. Kozlov, A.A., Galikhanov, M.F., and Deberdeev, R.Ya., in *Struktura i dinamika molekulyarnykh sistem: Sbornik statei* (Structure and Dynamics of Molecular Systems: Coll. of Papers), Ioshkar-Ola: Mariisk. Gos. Tekh. Univ., 2005, issue 12, part 1, pp. 381–385.
8. Lushcheikin, G.A., *Polimernye elektrety* (Polymeric Electrets), Moscow: Khimiya, 1984.
9. Boev, S.G., Lopatkin, S.A., and Ushakov, V.Ya., in *Elektretnyi effekt i elektricheskaya relaksatsiya v tverdykh dielektrikakh: Mezhvuzovskii sbornik* (Electret Effect and Electrical Relaxation in Solid Insulators: Intercollegiate Coll. of Works), Moscow: MIEM, 1988, pp. 71–73.
10. Makarov, V.G. and Koptenarmusov, V.B., *Promyshlennye termoplasty: Spravochnik* (Industrial Thermoplastics: Reference Book), Moscow: Khimiya, Koloss, 2003.
11. Galikhanov, M.F. and Budarina, L.A., *Plast. Massy*, 2002, no. 1, pp. 40–42.
12. Galikhanov, M.F., Eremeev, D.A., Borisova, R.V., et al., *Izv. Vyssh. Uchebn. Zaved., Khim. Khim. Tekhnol.*, 2005, vol. 48, no. 5, pp. 89–94.
13. RF Patent 2228944.
14. Deryagin, B.V., Krotova, N.A., and Smilga, V.P., *Adgeziya tverdykh tel* (Adhesion of Solids), Moscow: Nauka, 1973.

ISSN 1070-4272, Russian Journal of Applied Chemistry, 2008, Vol. 81, No. 1, pp. 91–94. © Pleiades Publishing, Ltd., 2008.
Original Russian Text © V.A. Kraikin, N.G. Gileva, E.A. Sedova, S.I. Kuznetsov, M.S. Lobov, Yu.N. Lavreshina, A.F. Sunagatullin, S.N. Salazkin, 2008, published in Zhurnal Prikladnoi Khimii, 2008, Vol. 81, No. 1, pp. 95–98.

MACROMOLECULAR CHEMISTRY AND POLYMERIC MATERIALS

Synthesis, Microstructure, and Properties of Block Copolyarylenephthalides

V. A. Kraikin, N. G. Gileva, E. A. Sedova, S. I. Kuznetsov, M. S. Lobov, Yu. N. Lavreshina, A. F. Sunagatullin, and S. N. Salazkin

Institute of Organic Chemistry, Ufa Scientific Center, Russian Academy of Sciences, Ufa, Bashkortostan, Russia
Nesmeyanov Institute of Organoelement Compounds, Russian Academy of Sciences, Moscow, Russia

Received July 5, 2007

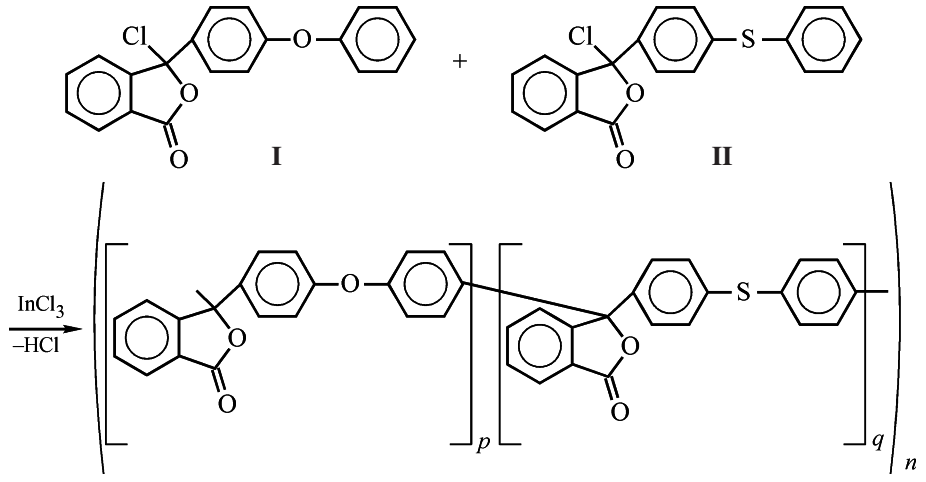
Abstract—Two-step copolycondensation of 3-chloro-3-(4-phenoxyphenyl)phthalide and 3-chloro-3-(4-phenylthiophenyl)phthalide was studied. The influence exerted by the sequence of loading the comonomers on the order of incorporation of the monomer residues into the polymer chain and on the microstructure of the resulting copolyarylenephthalides was examined.

DOI: 10.1134/S1070427208010217

Among new classes of polymers synthesized in the recent years, of much interest are polyarylenephthalides, card aromatic polymers prepared by electrophilic substitution reactions involving pseudomono- and pseudodichlorides of *o*-keto carboxylic acids [1–3]. Polyarylenephthalides combine high softening point, high heat resistance, and high chemical stability with good solubility in organic solvents and unusual electrophysical properties [1, 4].

It was demonstrated previously by the examples of 3-chloro-3-(4-phenoxyphenyl)phthalide **I** and 3-chloro-3-(4-phenylthiophenyl)phthalide **II** that pseudomonochlorides of *o*-keto carboxylic acids are capable of not only self-condensation but also copolycondensation [5]. One-step copolycondensation of these monomers yields random copolymers [6, 7].

In this study we performed two-step copolycondensation of **I** and **II**, prepared polyblock copolyarylenephthalides with different lengths of (4,4'-oxydiphenyl)phthalide and (4,4'-thiodiphenyl)phthalide sequences, and determined the microstructure and some properties of the synthesized polymers:



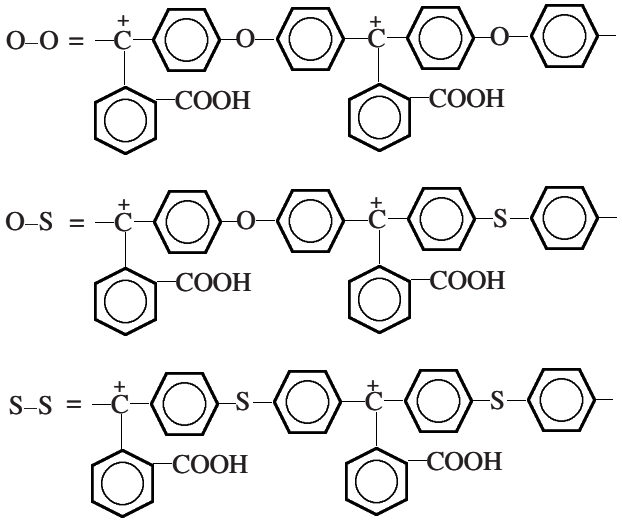
EXPERIMENTAL

Nitrobenzene and dimethylformamide were purified according to [7, 8]. $InCl_3$ was purchased from Aldrich. 3-Chloro-3-(4-phenoxyphenyl)phthalide and 3-chloro-3-(4-phenylthiophenyl)phthalide were synthesized according to [3].

Copolycondensation of **I** and **II** was performed by a two-step scheme using two procedures. In the first procedure, a 50-ml four-necked flask equipped with air-cooled reflux condenser with a bubble counter and a power-driven stirrer with a hydroseal was charged in an argon flow with 3.8 ml of a 2 M solution of **I** in nitrobenzene. Then the reaction mixture was heated with stirring to 110°C, and 0.2212 g of $InCl_3$ was added (10 mol % relative to the functional groups in both monomers). After 10, 30, or 180 min (in three different runs), 3.5 ml of a 2 M solution of **II** was added, and the synthesis was continued for 10 h. Samples of the reaction mixture (0.1–0.2 ml) were taken after 5, 10, 20, 40, 60, and 90 min. The products were isolated from the intermediate samples and final reaction mixture by precipitation into methanol. The precipitated polymers were dissolved in dimethylformamide and reprecipitated into methanol, after which they were washed with methanol and dried in air at 120°C for 24 h.

The second procedure was similar except that the self-condensation of **II** was performed first, after which compound **I** was added.

The electronic absorption spectra of sulfuric acid solutions of copolyarylenephthalides were recorded on a Shimadzu UV-3100 spectrophotometer. The optical density was measured at 533.5, 587.5, and 638.5 nm (absorption bands of the OO, OS, and SS diads, respectively):



The mole fractions of the diads in the polymer chain were determined according to [10, 11]. The experimental mole fractions of the diads P_{OO}, P_{SS}, and P_{OS} were used for calculating the microheterogeneity coefficients K_m, content of (4,4'-oxydiphenyl)phthalide (P_O) and (4,4'-thiodiphenyl)phthalide (P_S) units in the copolymer, and length of the (4,4'-oxydiphenyl)phthalide (L_O) and (4,4'-thiodiphenyl)phthalide (L_S) sequences [11]:

$$K_m = \frac{P_{OS}}{P_{OS} + P_{SS}} + \frac{P_{OS}}{P_{OS} + P_{OO}}, \quad (1)$$

$$P_O = P_{OO} + P_{OS}/2, \quad P_S = P_{SS} + P_{OS}/2,$$

$$L_O = 2P_O/P_{OS}, \; L_S = 2P_S/P_{OS}. \quad (2)$$

The softening onset temperature of the copolyarylenephthalides was determined with a thermomechanical installation at a load of 30 g mm^{-2} and a heating rate of 3 deg min^{-1}. The reduced viscosity of the polymers was measured in chloroform at 25°C and copolymer concentration of 0.5 g per 100 ml of solvent.

The microstructure of the copolyarylenephthalide prepared from **I** and **II** by two-step polycondensation depends on numerous factors: the relative reactivity of **I** and **II**, the comonomer taken in the first step for preparing the oligomeric block, the molecular weight of this block, and the time of the copolymer synthesis.

Analysis of the microstructure of the copolymers formed in the first minutes after adding the second comonomer shows that the sequence of addition of the monomeric (or oligomeric) fragments to the propagating polymer chain in the first and second procedures is different (see table).

In the first procedure (more active comonomer **I** is introduced first), the self-condensation of **I** apparently continues after addition of the second, less active comonomer **II**. This reaction is accompanied by the reactions yielding structures in which (4,4'-oxydiphenyl)phthalide units alternate with (4,4'-thiodiphenyl)phthalide units and, as the reaction goes on, with longer blocks of (4,4'-thiodiphenyl)phthalide units. This is indicated by the fact that K_m of the final copolyarylenephthalide is independent of the time of the selfcondensation of **I** (Fig. 1), and the content of heterodiads at the beginning of the copolycondensation is higher than by the end of the synthesis (see table). Thus, apparently, in the first procedure of the copolycondensation of **I** and **II** the macromolecules of the forming copolyarylenephthalide have a diagonal structure. One end of the copolymer molecule is enriched

Variation of the composition and microstructure of copolyarylenephthalides and of the mean block lengths in them

τ*	τ**	Mole fractions of diads			K_m	Mole fractions of units		P_O/P_S	Block length	
min		OO	OS	SS		P_O	P_S		L_O	L_S
First procedure										
10	5	0.619	0.061	0.320	0.133	0.650	0.350	1.86	–	–
	600	0.511	0.050	0.439	0.101	0.536	0.464	1.16	21.4	18.6
30	5	0.614	0.116	0.269	0.264	0.673	0.327	2.06	–	–
	600	0.511	0.049	0.440	0.098	0.535	0.465	1.15	21.8	18.9
180	5	0.530	0.060	0.410	0.120	0.560	0.440	1.27	–	–
	600	0.480	0.050	0.470	0.100	0.510	0.500	1.02	20.2	19.8
Second procedure										
10	5	0.442	0.057	0.501	0.114	0.471	0.529	0.89	–	–
	600	0.465	0.068	0.468	0.135	0.499	0.501	0.90	14.6	14.8
30	5	0.473	0.027	0.500	0.054	0.486	0.514	0.95	–	–
	600	0.473	0.041	0.486	0.081	0.494	0.506	0.98	24.1	24.7
180	5	0.503	0.003	0.494	0.006	0.504	0.496	1.01	–	–
	600	0.491	0.020	0.489	0.041	0.501	0.499	1.00	50.1	49.9

* Time of synthesis of the oligomeric block.
** Time of synthesis of copolyarylenephthalide after loading the second comonomer.

in (4,4'-oxydiphenyl)phthalide blocks separated by (4,4'-thiodiphenyl)phthalide units, and on the other end there are (4,4'-thiodiphenyl)phthalide blocks that are longer than in the middle of the macromolecule:

$$[-(O)_pO-S-O-(O)_p-]-[-(S)_p(O)_p-(S)_p-(O)_p-]-[-S]_q,$$

where O is (4,4'-oxydiphenyl)phthalide unit; S, (4,4'-thiodiphenyl)phthalide unit; $q > p$.

In the second synthesis procedure, after adding more active second comonomer **I**, it first undergoes self-condensation, which is followed by alternation of (4,4'-oxydiphenyl)phthalide and (4,4'-thiodiphenyl)-phthalide sequences of various lengths. This is indicated by very low content of heterodiads in the sample taken 5 min after the start of the copolymer synthesis and by gradual increase in the heterodiad content with the progress of the reaction. As the time of the self-condensation of **II** in the first step of the synthesis is increased from 10 to 30 and 90 min, K_m regularly decreases from 0.14 to 0.08 and 0.04, suggesting an increase in the mean length of the forming blocks (Fig. 2). The longer the self-condensation (i.e., the longer the oligomeric block formed in the first step of the synthesis), the lower the amount of heterodiads at block junctions and the lower the microheterogeneity coefficient of the forming copolymer (see table). It should be emphasized that the OS heterodiads (in contrast to the first procedure) are apparently localized only at block junctions. Alternation of (4,4'-thiodi-

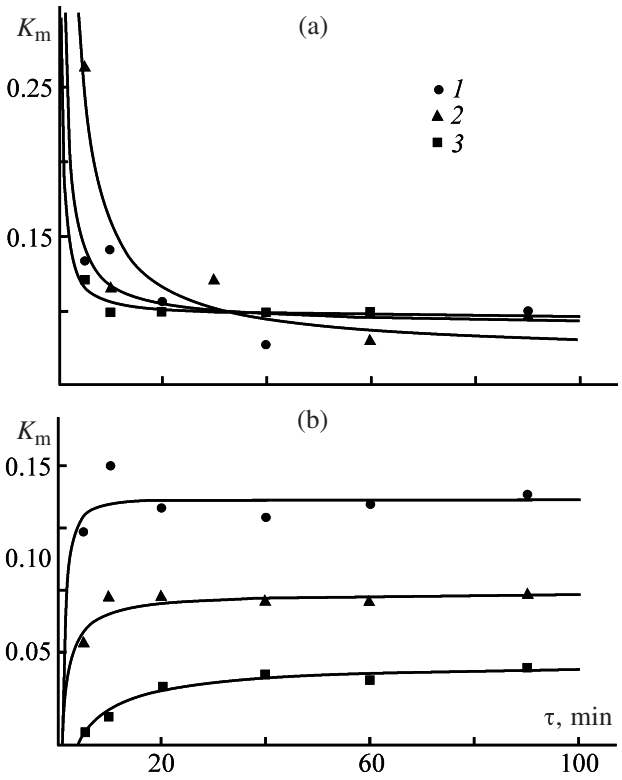


Fig. 1. Kinetic curves of variation of the microheterogeneity coefficient K_m of copolyarylenephthalides. Oligomer prepared in the first step: (a) oligo[(4,4'-oxydiphenyl)phthalide] and (b) oligo[(4,4'-thiodiphenyl)phthalide]. Second comonomer added (*1*) 10, (*2*) 30, and (*3*) 180 min after the start of the first step. Catalyst $InCl_3$, 10 mol %; 110°C; comonomer concentration 2 M; time of synthesis after adding the second comonomer 10 h; the same for Fig. 2. (τ) Time.

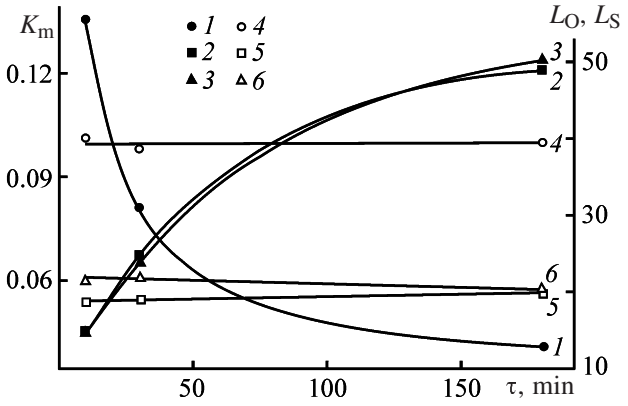


Fig. 2. (*1*, *4*) Microheterogeneity coefficient K_m and mean lengths of (*2*, *5*) (4,4'-oxydiphenyl)phthalide and (*3*, *6*) (4,4'-thiodiphenyl)phthalide blocks in copolyarylenephthalides as functions of the synthesis time τ of the oligomeric block. Procedure: (*1*–*3*) first and (*4*–*6*) second.

phenyl)phthalide units and (4,4'-oxydiphenyl)phthalide blocks with the formation of SOS triads is improbable because of the low activity of **II** and low concentration of chloride (diphenyl oxide) groups in oligo(4,4'-oxydiphenyl)phthalide.

The synthesized block copolyarylenephthalides are readily soluble in a wide range of organic solvents (chloroform, methylene chloride, tetrachloroethane, *N*-methylpyrrolidone, cyclohexanone, nitrobenzene) and form colorless transparent films (η_r = 0.45–0.64 dl g^{-1}). The flow point of copolyarylenephthalides is independent of their microstructure and amounts to 250–255°C.

CONCLUSIONS

(1) The sequence of loading the comonomers in the two-step copolycondensation of 3-chloro-3-(4-phenoxyphenyl)phthalide and 3-chloro-3-(4-phenylthiophenyl)phthalide **II** affects the order of incorporation of the monomeric fragments into the polymer chain and the microstructure of the resulting copolyarylenephthalides.

(2) The more regular structure of block copolyarylenephthalides is obtained when the less active comonomer is loaded first.

(3) Variation of the time of oligoarylenephthalide synthesis in the first step of the copolycondensation allows preparation of block copolyarylenephthalides with controllable block length.

ACKNOWLEDGMENTS

The study was financially supported by the Program no. 8 of Basic Research of the Presidium of the Russian Academy of Sciences and by the Foundation for Support of Leading Scientific Schools (project NSh-9342.2006.3).

REFERENCES

1. Salazkin, S.N., *Vysokomol. Soedin., Ser. B*, 2004, vol. 46, no. 7, pp. 1244–1269.
2. Salazkin, S.N., Rafikov, S.R., Tolstikov, G.A., et al., *Dokl. Akad. Nauk SSSR*, 1982, vol. 262, no. 2, pp. 355–359.
3. USSR Inventor's Certificate no. 704 114.
4. Zolotukhin, M.G., Lachinov, A.N., Salazkin, S.N., et al., *Dokl. Akad. Nauk SSSR*, 1988, vol. 302, no. 2, pp. 365–367.
5. Kraikin, V.A., Gileva, N.G., Sedova, E.A., et al., *Dokl. Ross. Akad. Nauk*, 2002, vol. 385, no. 3, pp. 363–366.
6. Gileva, N.G., Kraikin, V.A., Sedova, E.A., et al., *Zh. Prikl. Khim.*, 2005, vol. 78, no. 10, pp. 1712–1715.
7. Gileva, N.G., Kraikin, V.A., Kuznetsov, S.I., et al., *Bashk. Khim. Zh.*, 2005, vol. 12, no. 2, pp. 23–27.
8. Weissberger, A. and Proskauer, E.S., *Organic Solvents. Physical Properties and Methods of Purification*, Riddick, J.A. and Toops, E.E., Eds., New York: Interscience, 1955.
9. *Dictionary of Organic Compounds*, New York: Eyre and Spottiswoode, 1934.
10. Kraikin, V.A., Kuznetsov, S.I., Gileva, N.G., et al., *Dokl. Ross. Akad. Nauk*, 2002, vol. 387, no. 2, pp. 213–218.
11. Vasnev, V.A. and Kuchanov, S.I., *Usp. Khim.*, 1973, vol. 42, no. 12, pp. 2194–2220.

ISSN 1070-4272, Russian Journal of Applied Chemistry, 2008, Vol. 81, No. 1, pp. 95–99. © Pleiades Publishing, Ltd., 2008.
Original Russian Text © N.V. Lebedev, V.V. Berenblit, Yu.K. Starobin, 2008, published in Zhurnal Prikladnoi Khimii, 2008, Vol. 81, No. 1, pp. 99–103.

MACROMOLECULAR CHEMISTRY AND POLYMERIC MATERIALS

Cyclization Processes in Pyrolysis of Perfluorooxaalkanedicarboxylic Acid Derivatives

N. V. Lebedev, V. V. Berenblit, and Yu. K. Starobin

Lebedev Research Institute of Synthetic Rubber, Federal State Unitary Enterprise, St. Petersburg, Russia

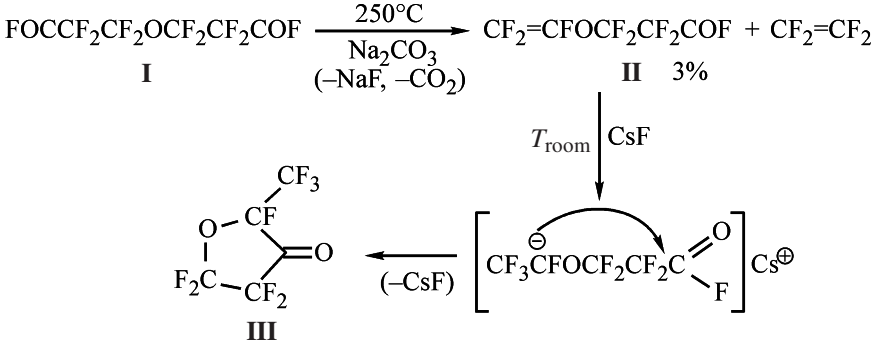
Received September 12, 2006; in final form, October 2007

Abstract—Formation of cyclic structures under the conditions of pyrolytic decarboxylation of perfluorooxaalkanedicarboxylic acids was studied.

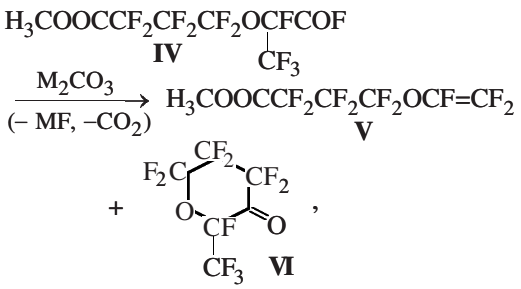
DOI: 10.1134/S1070427208010229

Pyrolytic decarboxylation of salts of perfluoro-2-alkoxypropionic acids is a known route to perfluorinated alkyl vinyl ethers [1]. However, the direction of pyrolytic processes may vary depending on the reaction conditions and substrate structure [2]. In particular, pyrolysis of perfluorooxaalkanedicarboxylic acids containing six- and seven-membered structures yields cyclic compounds.

Pyrolysis of sodium pefluoro-4-oxaheptane-1,7-dioate at 250°C gives in less than 3% yield perfluoro-3-vinyloxypropionyl fluoride **II**, which partially isomerizes under the action of CsF even at room temperature to form a cyclic product, perfluoro-2-methyloxolan-3-one **III** [3]:

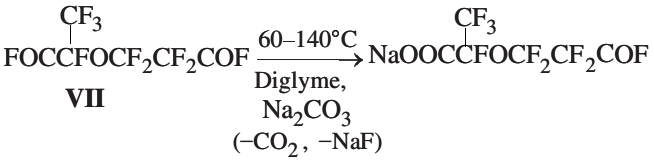


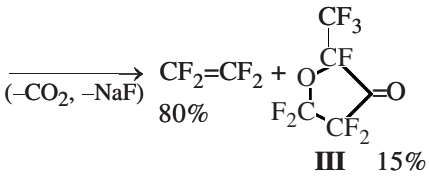
Pyrolysis of sodium and potassium salts derived from methyl perfluoro-6-methyl-5-oxa-7-oxoheptanoate **IV** yields, along with the major product, vinyl ether **V**, also perfluoro-2-methylpyran-3-one **VI** [4]:



where M = K or Na.

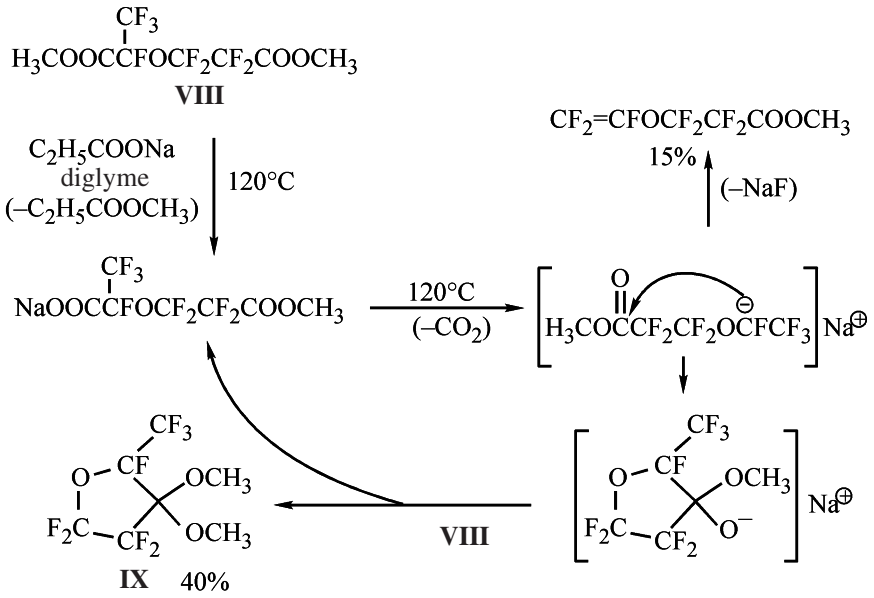
Pyrolysis of an isomer of **I**, perfluoro-2-methyl-3-oxahexane-1,6-dioyl fluoride **VII**, in diethylene glycol dimethyl ether (diglyme) at 120°C in the presence of an equimolar amount of sodium carbonate resulted in direct formation of perfluoro-2-methyloxolan-3-one **III** in approximately 15% yield [2]:





Compound **III** was identified by ^{19}F NMR spectroscopy from the characteristic signals of the magnetically nonequivalent geminal fluorine atoms with coupling constants of 125 Hz for the $–CF_2I–$ group and 295 Hz for the $–CF_2C(O)–$ group. The ^{19}F NMR spectrum also contained the signals of the –OCF< and $–CF_3$ groups (see table).

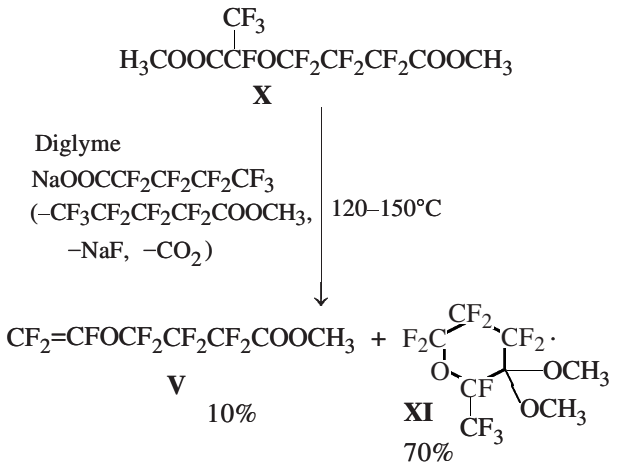
With the aim to prevent such cyclization, dimethyl perfluoro-2-methyl-3-oxahexane-1,6-dioate **VIII** was subjected to pyrolytic decomposition in diglyme in the presence of an equimolar amount of sodium perfluoropropionate [5]. At 120°C, active decarboxylation with the CO_2 evolution was observed along with the ester interchange yielding methyl perfluoropropionate. In the ^{19}F NMR spectrum of the major pyrolysis product boiling at 106°C, we failed to find the characteristic signals of the trifluorovinyl group and difluoromethylene group adjacent to the carboxyl, expected for methyl perfluoro-3-vinyloxypropionate. We managed to identify this compound only by comparing the ^{19}F NMR, ^1H NMR, and mass spectra; this compound is 3,3-dimethoxyperfluoro-2-methyloxolane **IX**. Apparently, under these conditions, stabilization of the intermediate carbanion by intramolecular cyclization with charge transfer is preferable. Apparently, the forming adduct reacts with the starting substrate **VIII**, nucleophilically attacking the ester group by the S_N2 mechanism [6] to give product **IX**, with the regeneration of the salt derived from **VIII**:



Similar results were obtained when the pyrolysis was performed in the presence of sodium perfluorobutyrate. Pyrolysis of analogs of **VIII**, diethyl (**VIIIa**) and diisopropyl (**VIIIb**) esters, yielded the corresponding cyclic ketals **IXa** and **IXb**.

An attempt to perform the pyrolysis of the related *tert*-butyl ester, di-*tert*-butyl perfluoro-2-methyl-3-oxahexane-1,6-dioate **VIIIc**, failed because of the thermal instability of this ester. Even at 80°C, compound **VIIIc** decomposes to give isobutylene, with the decarboxylation and formation of 1,2'-dihydroperfluorodiethyl ether [7].

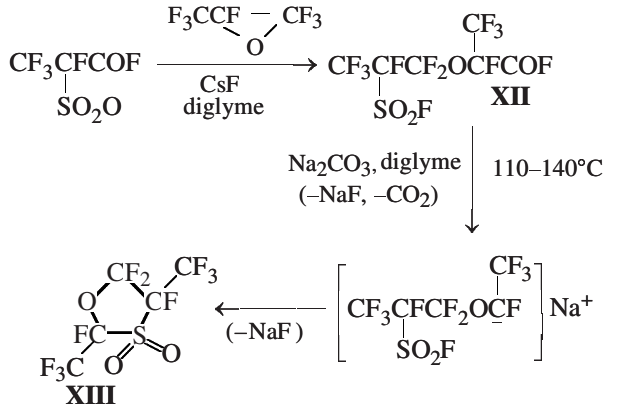
To exclude the possibility of cleavage of the C–O bond in the course of pyrolysis, characteristic of perfluoro-3-alkoxypropionic acid derivatives [2], we performed pyrolysis experiments with dimethyl perfluoro-2-methyl-3-oxaheptane-1,7-dioate **X** under similar conditions in the presence of sodium perfluorobutyrate. Along with methyl perfluorobutyrate, we obtained in approximately 10% yield methyl perfluoro-4-vinyloxybutyrate **V** and in approximately 70% yield a six-membered cyclic product boiling at 144°C and identified by the ^{19}F and ^1H NMR spectra as 3,3-dimethoxyperfluoro-2-methyloxane **XI**:



The cyclic ketals obtained are heavy liquids very resistant to acids, alkalis, and halogens under UV irradiation. Their NMR spectra are given in the table.

Without solvent, the cyclization in the course of pyrolysis occurs at a higher temperature (180–200°C), and in the case of compound **VIII** boiling below 180°C it does not occur at atmospheric pressure, probably because of the above-mentioned cleavage of the C–O bond with the elimination of tetrafluoroethylene. However, the pyrolysis of **X** gives cyclic ketal **XI** and methyl perfluoro-4-vinyloxybutyrate **V** in equal yields (~40%).

Perfluorooxaacyl fluorides containing a sulfonyl fluoride group instead of one of the carbonyl fluoride groups also underwent cyclization in the course of pyrolysis under the same conditions. For example, perfluoro-5-fluorosulfonyl-3-oxa-2-methylhexanoyl fluoride **XII** yielded exclusively perfluoro-3-oxa-2,4-dimethylsulfolane **XIII** by the scheme



The structure of **XIII** suggests the possibility of the *cis* and *trans* arrangement of the CF_3 groups relative to the ring plane, which is in agreement with the ^{19}F NMR data (see table) and corresponds to the spectrum of the isomer mixture in 1 : 1 ratio.

EXPERIMENTAL

The pyrolysis products were analyzed chromatographically with an LKhM-8MD chromatograph [model 5, thermal conductivity detector, programmed heating from 30 to 200°C at a rate of 6 deg min^{-1}, 3000 × 3 mm columns, solid support Celite-545 (0.16–0.2 mm, packing density 0.30–0.01 g cm^{-3}), stationary phase SKTFT-50 (15 wt %), carrier gas helium (40 ml min^{-1})].

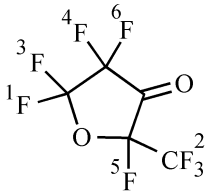
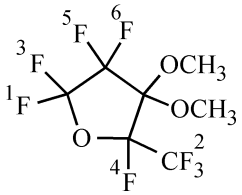
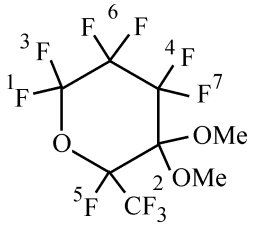
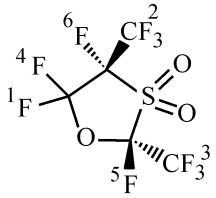
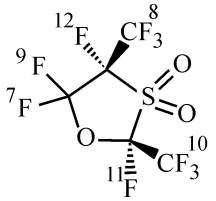
The ^{19}F NMR spectra were recorded on a Bruker Spectrospin AM-500 spectrometer at a frequency of 470.572 MHz using hexafluorobenzene or hexafluoro-*p*-xylene as internal reference and $CDCl_3$ as solvent. The ^{19}F chemical shifts were recalculated relative to CCl_3F. The ^1H NMR spectra were recorded on the same spectrometer at a frequency of 500 MHz with HMDS as external reference. The mass spectra were taken on a Chromass Varian CH-7M device.

Dimethyl, diethyl, and diisopropyl perfluoro-2-methyl-3-oxahexane-1,6-dioates were prepared by alcoholysis of perfluoro-2-methyl-3-oxahexane-1,6-dioyl fluoride **VII** with the corresponding alcohols (compound **VII** was prepared as described in [7]). Dimethyl perfluoro-2-methyl-3-oxaheptane-1,7-dioate **X** was prepared similarly.

Perfluoro-2-fluorosulfonyl-4-oxa-5-methylhexanoyl fluoride **XII** was prepared by condensation of hexafluoropropene oxide with the isomerization product of hexafluoropropene sultone [9], following the known procedure [10].

Pyrolysis of dimethyl perfluoro-2-methyl-3-oxahexane-1,6-dioate VIII. A 250-ml four-necked round-bottomed glass flask equipped with a stirrer, a thermometer, a dropping funnel, and a column (d = 10 mm, h = 40 cm) with Levin spiral packing and a reflux head was charged with 33 g (0.11 mol) of **VIII** and 50 ml of absolute diglyme. The mixture was heated to 120°C, and a solution of 19 g (0.1 mol) of sodium perfluoropropionate in 50 ml of diglyme was added dropwise with stirring over a period of 2 h. In so doing, methyl perfluoropropionate was distilled off. After adding the whole amount of sodium perfluoropropionate, the mixture was rerfluxed at 120–150°C for 6 h, and the pyrolysis products were collected successively in a receiver and in a trap cooled to –50°C. Finally the gas phase was passed through a trap with bromine, in which tetrafluoroethylene formed in small amounts was converted into 1,2-dibromoperfluoroethane. The pyrolyzate was combined, washed to remove diglyme, dried over Na_2SO_4, and subjected to fractional distillation. 3,3-Dimethoxyper-

NMR spectra of the identified compounds

Compound	Structure	NMR signal			
		atom no.	δ_F (CCl_3F, ppm)	$j_{F^*-F^*}$, Hz	*n*F
III		1	–79.1	$^{1}F–^{3}F$ 125; $^{1}F–^{5}F$ 10	1
		2	–81.0	s	3
		3	–92.5	$^{3}F–^{1}F$ 125; $^{3}F–^{4}F$ 8	1
		4	–120.2	$^{4}F–^{6}F$ 280; $^{4}F–^{3}F$ 8	1
		5	–120.9	s	1
		6	–129.8	$^{6}F–^{4}F$ 280; $^{6}F–^{1}F$ 10	1
IX		1	–80.6	$^{2}F–^{3}F$ 134; $^{2}F–^{x}F$ 13; $^{2}F–^{x}F$ 8 d.d.d	1
		2	–79.0	s	3
		3	–91.6	$^{3}F–^{2}F$ 134; $^{3}F–^{x}F$ 13; $^{3}F–^{x}F$ 3 d.d.q	1
		4	–123.3	s	1
		5	–124.6	$^{5}F–^{6}F$ 240; $^{5}F–^{2}F$ 13	1
		6	–126.6	$^{6}F–^{5}F$ 240	1
		$(OMe)_2$	(4.08)	s	6H
XI		1	–76.2	$^{1}F–^{3}F$ 150	1
		2	–77.6	s	3
		3	–88.4	$^{3}F–^{1}F$ 150	1
		4	–118.9	$^{4}F–^{7}F$ 280	1
		5	–128.0	s	1
		6	–125.1	s	2
		7	–131.6	$^{7}F–^{4}F$ 280	1
		$(OMe)_2$	(4.02)	s	6H
XIV		1	–68.8	$^{1}F–^{4}F$ 145.1; $^{1}F–^{2}F$ 15.3 d.q	1
		2	–70.1	$^{2}F–^{4x}F$ 12.8; $^{2}F–^{x}F$ 7.6 d.d	3
		3	–77.5	s	3
		4	–83.2	$^{4}F–^{x}F$ 145.1; $^{4}F–^{x}F$ 12.7 d.d	1
		5	–112.7	s	1
		6	–164.5	$^{6}F–^{1}F$ 10.2; $^{6}F–^{2}F$ 7.6 m	1
		7	–69.8	$^{7}F–^{9}F$ 142.5 d	1
		8	–70.2	$^{8}F–^{9}F$ 15.2; $^{8}F–^{12}F$ 7.6 d.d	3
		9	–76.1	$^{9}F–^{7}F$ 142.5; $^{9}F–^{12}F$ 15.3; $^{9}F–^{8}F$ 7.6 d.d.q	1
		10	–76.6	s	3
		11	–110.3	$^{11}F–^{x}F$ 5.1 d	1
		12	–167.3	$^{12}F–^{9}F$ 15.2; $^{12}F–^{8}F$ 7.6 d.q	1

fluoro-2-methyloxolane **IX** was obtained; yield 13.2 g (41%), bp 106°C, d_4^{20} 1.51 g cm^{-3}, n_D^{20} 1.3265.

Mass spectrum, *m/e* (I_{rel}, %): 290 (7.3) M^+; 271 (2.0) $M^+ – F$; 259 (10.8) $M^+ – OCH_3$; 231 (1.7) $M^+ – CO_2CH_3$; 197 (1.5) $M^+ – CF_2CO_2CH_3$; 193 (2.4) $M^+ – CF_3CO$; 181 (5.1) $M^+ – CF_2CO_2CH_3$; 174 (100) $M^+ – OCFCF_3$; 169 (7.3) $C_3F_7^+$; 159 (10.1) $C_2F_4CO_2CH_3^+$; 147 (2.9) $C_2F_5CO^+$; 143 (5.3) $C_2F_3 \cdot C(OCH_3)_2^+$; 131 (10.6) $C_3F_5^+$ [$C_2F_4OCH_3^+$]; 129 (28.4) $C_2F_4CHO^+$; 124 (21.9) $C_4F_4^+$ [$CF_2C(OCH_3)_2^+$]; 121 (7.3) $C_2F_2CO_2CH_3^+$; 119 (4.7) $C_3F_7^+$; 109 (8.9) $CF_2 \cdot CO_2CH_3^+$; 101 (20.0) $C_2F_4H^+$; 100 (16.0) $C_2F_4^+$; 97 (15.0) $C_2F_3O^+$; 93 (6.7) $C_3F_3^+$; 81 (40.0) $C_2F_3^+$; 74 (19.0) $C(OCH_3)_2^+$; 69 (24.0) CF_3^+; 59 (41.0) $CO_2CH_3^+$.

3,3-Diethoxyperfluoro-2-methyloxolane **IXa** (yield 45%), bp 136°C, d_4^{20} 1.50 g cm^{-3}, n_D^{20} 1.3276), 3,3-diisopropoxyperfluoro-2-methyloxolane **IXb** (yield 35%, bp 88°C/90 mm Hg, d_4^{20} 1.49 g cm^{-3}, n_D^{20} 1.3298), and 3,3-dimethoxyperfluoro-2-methyloxane **XI** (yield 70%, bp 144°C, d_4^{20} 1.60 g cm^{-3}, n_D^{20} 1.3315) were prepared similarly.

Pyrolysis of dimethyl perfluoro-2-methyl-3-oxaheptane-1,7-dioate X. The reactor similar to that described above was charged with 38.4 g (0.1 mol) of **X** and 28.6 g (0.1 mol) of dry sodium perfluorobutyrate. The stirring was switched on, and the mixture was heated to 180–200°C over a period of 6 h, with collection of the pyrolysis products in a receiver and a trap cooled to –60°C. The pyrolyzate was combined and subjected to fractional distillation. We isolated 13 g (40%) of 3,3-dimethoxyperfluoro-2-methyloxane **XI** and 12 g (40%) of methyl perfluoro-4-vinyloxybutyrate **V**, bp 129°C, d_4^{20} 1.57 g cm^{-3}, n_D^{20} 1.3180.

Pyrolysis of perfluoro-2-fluorosulfonyl-4-oxa-5-methylhexanoyl fluoride XII. The similar installation was charged with 22 g (0.2 mol) of dry Na_2CO_3 and 50 ml of absolute diglyme. The reaction mixture was heated with stirring to 70°C on an oil bath, and 0.79 g (0.2 mol) of **XII** was added dropwise. After the CO_2 evolution ceased, the mixture was heated to 120°C, and 56 g of the product with bp 64°C, d_4^{20} 1.64 g cm^{-3}, and n_D^{20} 1.3107 was distilled into a receiver. According to the GLC data, the content of perfluoro-3-oxa-2,4-dimethylsulfolane **XIII** was 98%. The total yield of **XIII** was 83%.

CONCLUSIONS

(1) Pyrolysis in a solvent (diglyme) of sodium salts of α,ω-perfluorooxaalkanedioic acids with the chain length n = 6–7 mainly yields five- and six-membered cyclic structures.

(2) Depending on the structure of the compound subjected to pyrolysis (fluorides or esters of perfluorooxaalkanoic acids), cyclization yields oxalanone or ketal structures.

(3) On replacement of a fluorocarbonyl group in the perfluorooxaalkanedioic acid molecule by the fluorosulfonyl group, pyrolysis also occurs along the cyclization pathway, yielding perfluoro-3-oxa-2-methylsulfolane ring.

REFERENCES

1. US Patent 3 114 778.
2. Lebedev, N.V., Berenblit, V.V., Starobin, Yu.K., and Gubanov, V.A., *Zh. Prikl. Khim.*, 2005, vol. 68, no. 10, pp. 1668–1673.
3. Ogden, P.H., *J. Chem. Soc. (C)*, 1971, no. 17, pp. 2920–2926.
4. Tiunova, T.G., Chekmeneva, T.I., Tiunov, A.V., et al., Abstracts of Papers, *VI Vsesoyuznaya konferentsiya po khimii ftororganicheskikh soedinenii* (VI All-Union Conf. on Chemistry of Organofluorine Compounds), Novosibirsk, 1990, p. 99.
5. Berenblit, V.V., Rondarev, D.S., Starobin, Yu.K., and Sokolov, S.V., Abstracts of Papers, *V Vsesoyuznaya konferentsita po khimii ftororganicheskikh soedinenii* (V All-Union Conf. on Chemistry of Organofluorine Compounds), Moscow, 1986, p. 172.
6. March, J., *Advanced Organic Chemistry. Reactions, Mechanisms, and Structure*, New York: Wiley–Interscience, 1985.
7. Buehler, C.A. and Pearson, D.E., *Survey of Organic Syntheses*, New York: Wiley–Interscience, 1970.
8. Skoblikova, V.I., Sass, V.P., Ershov, A.E., et al., *Zh. Org. Khim.*, 1973, vol. 9, no. 10, pp. 2021–2023.
9. Cheburkov, Yu. and Lamanna, W.M., *J. Fluorine Chem.*, 2003, vol. 52, pp. 147–151.
10. US Patent 3 301 893.

ISSN 1070-4272, Russian Journal of Applied Chemistry, 2008, Vol. 81, No. 1, pp. 100–103. © Pleiades Publishing, Ltd., 2008.
Original Russian Text © A.I. Bol'shakov, S.I. Kuzina, D.P. Kiryukhin, 2008, published in Zhurnal Prikladnoi Khimii, 2008, Vol. 81, No. 1, pp. 104–107.

MACROMOLECULAR CHEMISTRY AND POLYMERIC MATERIALS

Spontaneous Polymerization of Acrylamide in Preactivated Glycerol

A. I. Bol'shakov, S. I. Kuzina, and D. P. Kiryukhin

Institite of Chemical Physics Problems, Russian Academy of Sciences, Chernogolovka, Moscow oblast, Russia

Received August 30, 2007

Abstract—Spontaneous polymerization of acrylamide in acrylamide–glycerol mixture was studied.

DOI: 10.1134/S1070427208010230

It is commonly believed that spontaneous polymerization of monomers is initiated by random formation of active centers (radicals, ions, etc.) caused by various factors. The polymerization can also be initiated by impurities present in monomers and solvents. These impurities can form specific compounds capable of decomposing under certain conditions to form active intermediates. For example, the presence of hydroperoxide impurities in monomers can induce spontaneous formation of polysulfones [1, 2].

We reported previously [3] that spontaneous polymerization of acrylamide was observed in acrylamide–glycerol mixture on adding finely dispersed acrylamide monomer to glycerol without any initiatior. In this study we examined the mechanism of formation of active centers initiating the spontaneous polymerization of acrylamide in glycerol.

EXPERIMENTAL

Acrylamide recrystallized from acetone was ground in an agate mortar to 100-μm particles. Glycerol (analytically pure grade, main substance content 99.3%) was used without additional purification. The main impurities in glycerol were iron, lead, and silver sulfates and chlorides, and also fatty acid esters. Glycerol was irradiated with light [$\lambda \geq 236$ nm (intensity 7.6×10^{17} quanta $cm^2\ s^{-1}$) and $\lambda \geq 360$ nm (intensity 4.1×10^{17} quanta $cm^2\ s^{-1}$)] and with γ-rays (^{60}Co, radiation dose rate 0.5 Gy s^{-1}).

Finely dispersed acrylamide monomer (20%) was added to glycerol, and the resulting suspension was thoroughly stirred. Since dissolved atmospheric oxygen does not affect the acrylamide polymerization, the acrylamide–glycerol suspension was not degassed. After the polymerization completion, the reaction mixture was washed with ethanol to remove glycerol, and then ethanol was removed by evacuation. The ESR spectra were recorded on an EPR-21 radiospectrometer at 77 K (wavelength 3 cm, UHF field power about 10^{-4} W). The electronic absorption spectra were recorded on a Specord-40 M spectrophotometer in a 1-cm optical cell. The gaseous products of photolysis were analyzed on an MI-1201 mass spectrometer. The peroxy compounds were determined by iodometric titration.

Experiments on spontaneous polymerization of acrylamide in glycerol of various batches showed that this phenomenon was poorly reproducible. Since in glycerol of some batches polymerization was not observed, we suggested that it is the glycerol activity that is responsible for spontaneous polymerization of acrylamide. In particular, it is possible that commercial glycerol contains active species inducing polymerization. These active species can be either complexes of glycerol with impurities or other compounds formed in glycerol in its production and storage under the action of light, irradiation, heating, and other factors.

We found that glycerol is activated with both the daylight and γ-ray irradiation, and this effect occurs at small radiation doses and short exposure time. As seen from Fig. 1, the maximal yield of the polymer (70%) is reached at the irradiation dose of about 0.5 kGy or upon photolysis ($\lambda \geq 360$ nm) for 30 min. Hence, both the photolysis and radiolysis of glycerol are accompanied by formation of stabilized active intermediates initiating polymerization of acrylamide.

Figure 2 shows the dependence of the polymer yield on the wavelength of light used for preactivation

of glycerol. It is seen that commercial glycerol (analytically pure grade) used in our experiments is activated by light within wavelength range from 260 to 450 nm. It should be noted that glycerol must be optically transparent in this optical region since the C–C, C–H, C–O and OH groups absorb only in the vacuum ultraviolet range. Therefore, we believe that photoactivation of glycerol is due to photosensitizing effect of impurities. Iron, lead, and silver sulfates and chlorides, and also fatty acid esters present in commercial glycerol as impurities can acts as sensitizers. The absorption band at λ_{max} = 275 nm in the electronic absorption spectrum of glycerol (Fig. 2, curve *2*) can be caused by impurities present in glycerol.

The mechanism of activation of glycerol was examined by a common technique based on inhibition of the radical reactions by adding 2,2,6,6-tetramethylpiperidineoxyl stable radicals (nitroxyl radical, NR). The nitroxyl radicals were added to initial glycerol at 293 K and their concentration was monitored by ESR. We found that NR added to glycerol disappeared completely after irradiation for 30 min and acrylamide added to irradiated glycerol did not polymerize. Thus, in the presence of nitroxyl radicals, the active species formed in irradiation are not stabilized. The decay of NR suggests that, in irradiation of glycerol, free radicals such as $R^{\bullet}$, $HO^{\bullet}$, and $H^{\bullet}$ are formed. The peak corresponding to molecular weight 2 present in the mass spectrum of gaseous products of irradiated glycerol can be assigned to molecular hydrogen formed by rupture of CH groups in glycerol molecules. The above radicals, when reacting with glycerol molecule, generate active species.

The rate of generation of active species v in irradiation of glycerol with light ($\lambda \geq 236$ nm and $\lambda \geq 360$ nm) was determined by the inhibition technique from the experimental dependence of the active species concentration on the exposure time. The v values determined in these experiments at $\lambda \geq 236$ nm and $\lambda \geq 360$ nm were 2×10^{12} and 4.2×10^{11} $cm^{-3}\ s^{-1}$, respectively. The rate of accumulation of radicals in glycerol in the course of its irradiation at $\lambda \geq 360$ nm, determined from the initial portion of the curve of decay of nitroxyl radicals, was 4.2×10^{16} $cm^{-3}\ s^{-1}$). Thus, the fraction of the active species relative to the total amount of photolytically formed radicals was about 10^{-5}.

The active species were characterized by spectroscopic and kinetic methods. Although irradiated glycerol contained 1.4×10^{17} cm^{-3} of active species, we failed to detect paramagnetic particles by ESR spectroscopy allowing detection of 10^{14} spin cm^{-3}.

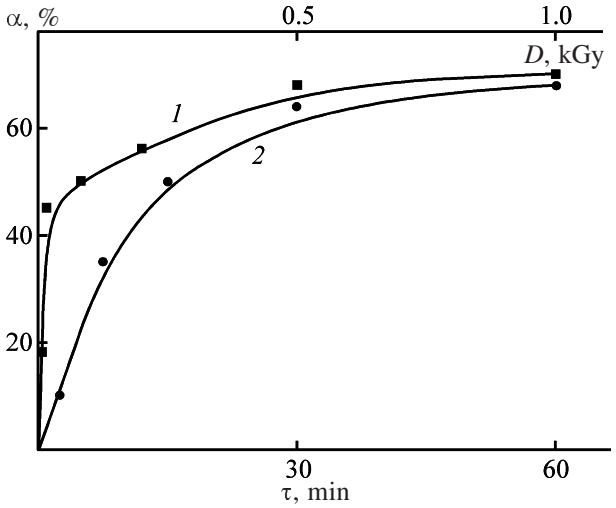


Fig. 1. Yield of polymer α in irradiation of glycerol with (*1*) light ($\lambda \geq 360$ nm) and (*2*) γ-rays vs. the exposure time and dose, respectively.

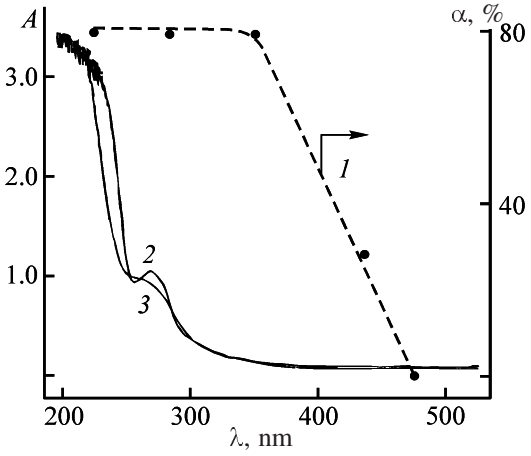


Fig. 2. Dependence of the (*1*) polymer yield α and (*2, 3*) optical absorption A (1-cm optical cell) of the (*2*) initial and (*3*) preactivated glycerol on the light wavelength λ.

The electronic absorption spectra of irradiated glycerol in the absorption range of active species (200–500 nm) also contained no additional absorption bands. These results showed that the active species are diamagnetic molecular compounds capable of dissociating to radicals initiating polymerization of acrylamide. To elucidate how the active species dissociate to induce polymerization, the nitroxyl radicals were added to a suspension of acrylamide in preactivated glycerol. We found that, under these conditions, NR rapidly disappeared, and the polymerization did not develop. This means that the active species dissociate to form radicals.

Since irradiation of glycerol generates unstable active species, they start to spontaneously decompose after the irradiation completion or on addition of

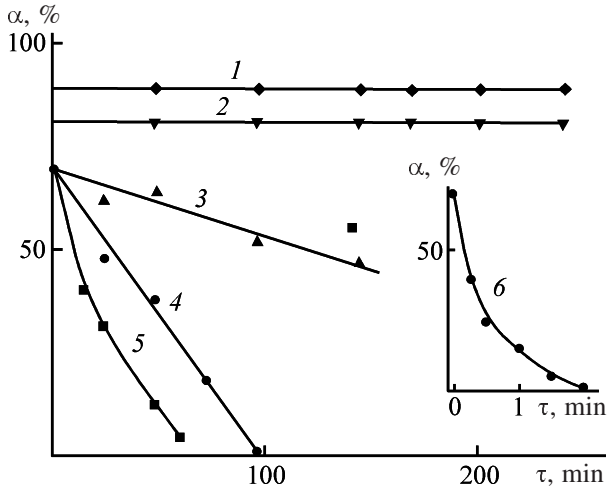


Fig. 3. Dependence of the polymer yield α on the time (τ) of keeping preactivated glycerol under temperature-controlled conditions. (*1, 2*) λ ≥ 236 nm and (*3–6*) λ ≥ 360 nm. Irradiation time, h: (*2–6*) 1 and (*1*) 5. Temperature, K: (*1–5*) 298 and (*6*) 318.

acrylamide. The initial rate of decomposition of the active species was estimated as follows. Figure 3 shows how the yield of the polymer depends on the time and temperature of keeping glycerol after completion of its photolysis. In these experiments, glycerol was irradiated with light (λ ≥ 236 nm and λ ≥ 360 nm) for different times. Since both the polymerization rate and polymer yield are in proportion with the initial content of the active species in glycerol, the decrease in the polymer yield with increasing keeping time, observed in our experiments, is apparently caused by decomposition of active species. We found that both the increase in keeping temperature of preactivated glycerol and the addition of foreign solvents (e.g., H_2O) accelerate the decomposition of the active species. The initial concentration of active species in irradiated glycerol was about 1.5×10^{15} cm^{-3}. The rate of decomposition of active species ($cm^{-3}\ s^{-1}$) increases with temperature: 273 K, 6.2×10^{8}; 293 K, 4.3×10^{9}; and 318 K, 1.7×10^{12}. On addition of water to irradiated glycerol, the rate of spontaneous decomposition of the active species was found to be 7.0×10^{9} $cm^{-3}\ s^{-1}$. The activation energy of spontaneous decomposition of active species, calculated from our experimental results, was 24 kcal mol^{-1}. This value is consistent with low thermal stability of these species.

In irradiation of glycerol by light with λ ≥ 236 nm, the polymer yield remains constant irrespective of the keeping time. At the maximal keeping time of 240 h, the concentration of active species was more than 10^{15} cm^{-3}. We suggested that under these conditions only a small portion of the active species participated in the polymerization. This hypothesis is consistent with the fact that, on removal of polymeric and monomeric acrylamide from the reaction mixture after the polymerization completion, the recycled glycerol, similar to the initial preactivated glycerol, induced effective polymerization of acrylamide (80% polymer yield).

To polymerize acrylamide in glycerol to 70% at the factor of chain transfer ~10^4 [3], the concentration of active species in the reaction mixture must be no less than 10^{14}–10^{15} cm^{-3}. In the course of polymerization for 60 min, approximately 10^{13} cm^{-3} of active species decompose in the reaction mixture. This amount is insufficient to ensure the 70% degree of polymerization of acrylamide even at complete consumption of the active species. Therefore, apparently, the spontaneous polymerization of acrylamide occurs not only due to thermal decomposition of the active species. We believe that the main amount of active centers (10^{14}–10^{15} cm^{-3}) is generated from the active species due to forces of the molecular stress caused by the concentration gradient at the solid acrylamide–glycerol interface in dissolution of acrylamide monomer.

Thus, based on the spectroscopic and kinetic data, we can suggest that the active species formed in glycerol are diamagnetic molecules slowly decomposing at room temperature with the activation energy equal to ~24 kcal mol^{-1} to give free radicals. The decomposition of active species is accelerated in dissolution of solid acrylamide monomers in glycerol. We assume that the active species are peroxy compounds. To check this hypothesis, the glycerol samples thoroughly evacuated to remove atmospheric oxygen were irradiated with light (λ ≥ 236 nm) for 20 h and then analyzed by iodometric titration for the hydroperoxy groups. These experiments showed that irradiated glycerol contains the hydroperoxy groups in the amount of ~1.2×10^{17} cm^{-3}, which is very close to the content of the active species in this system, determined by the inhibition technique (~1.4×10^{17} cm^{-3}). Thus, the irradiation of glycerol is accompanied by formation of the hydroperoxy groups, and their yield is insensitive to dissolved oxygen. On adding acrylamide to preactivated glycerol, the ROOH groups decompose to form radicals initiating the propagation of polymer chains.

The formation of the hydroperoxy groups can be described by the following scheme. On irradiation of glycerol, the impurity species absorb photons and pass

into an excited state (M)*. The excess energy of these excited species is transferred to glycerol molecules, breaking bonds in them. As a result, hydrogen atoms and glycerol radicals are formed. Although these active species rapidly decompose, a small fraction of radicals (approximately 0.001%) has time to react with glycerol to form the hydroperoxy groups ROOH.

$$(M) + UV \rightarrow (M)^* + Gl \rightarrow Gl^* + M \rightarrow R^\bullet + H^\bullet(HO^\bullet), \quad (1)$$

$$CH_2OH–CHOH–CH_2OH + H^\bullet \rightarrow CH_2OH–CHO^\bullet–CH_2OH + H_2, \quad (2)$$

$$CH_2OH–CHO^\bullet–CH_2OH + HO^\bullet \rightarrow CH_2OH–CHOOH–CH_2OH(ROOH), \quad (3)$$

$$ROOH\,(\text{decomposition}) \rightarrow RO^\bullet + HO^\bullet, \quad (4)$$

$$RO^\bullet(HO^\bullet) + \text{acrylamide(AA)} \rightarrow R_0^{AA}\,(\text{initiation}), \quad (5)$$

$$R_0^{AA} + AA \rightarrow R_p\ldots\ (\text{chain propagation}). \quad (6)$$

Since glycerol is widely used in medicine, biology, food and cosmetic industries, for producing explosives, etc., the possibility of activation of glycerol under natural factors (for example, by daylight) is important from practical viewpoint. The reaction of the photolytically induced peroxy groups with additives introduced into glycerol can produce radicals stimulating undesirable side reactions. This is particularly important for medicinal, perfume, and food products in connection with the effect of free radicals on the malignant tumor growth, aging, etc. Therefore, the production and storage of glycerol must meet stringent requirements to exclude the formation of peroxy impurities. Furthermore, in production of glycerol and glycerol-containing mixtures (pastes, creams, and solutions for medical and perfume applications), sensitizing additives should also be inadmissible because the illumination of glycerol can induce formation of peroxides and products of their spontaneous decomposition initiating undesirable radical reactions.

Thus, the development of techniques for production of glycerol free of sensitizing impurities and for purification of glycerol to remove undesirable impurities is an urgent problem. Our studies show that the determination of the degree of polymerization of acrylamide in glycerol preactivated by illumination or γ-ray irradiation is a simple, sensitive, and reliable method for determining the sensitizer content of glycerol.

CONCLUSIONS

(1) Spontaneous polymerization of acrylamide in glycerol preactivated by illumination or γ-ray irradiation is initiated by hydroperoxides formed in activated glycerol due to its photolysis (radiolysis) sensitized by trace impurities.

(2) The use of sensitizer-containing glycerol for preparing medicinal, cosmetic, and food composites can induce undesirable side reactions and formation of products dangerous to health.

(3) A method for determining the content of sensitizing impurities in glycerol was suggested.

REFERENCES

1. Kabanov, V.A., Zubov, V.P., and Semchikov, Yu.D., *Kompleksno-radikal'naya polimerizatsiya* (Complex-Radical Polymerization), Moscow: Khimiya, 1987.
2. Golubev, V.B., *Vysokomol. Soedin., Ser. A*, 1994, vol. 36, no. 2, p. 298.
3. Bol'shakov, A.I. and Kiryukhin, D.P., *Vysokomol. Soedin., Ser. A*, 2007, vol. 49, no. 9, pp. 1621–1627.

ISSN 1070-4272, Russian Journal of Applied Chemistry, 2008, Vol. 81, No. 1, pp. 104–107. © Pleiades Publishing, Ltd., 2008.
Original Russian Text © O.V. Rudometova, Zh.A. Vnutskikh, A.A. Fedorov, Yu.S. Chekryshkin, 2008, published in Zhurnal Prikladnoi Khimii, 2008, Vol. 81, No. 1, pp. 108–111.

MACROMOLECULAR CHEMISTRY AND POLYMERIC MATERIALS

Reaction of Polyvinyl Chloride with Calcium and Magnesium Oxides

O. V. Rudometova, Zh. A. Vnutskikh, A. A. Fedorov, and Yu. S. Chekryshkin

Institute of Technical Chemistry, Ural Division, Russial Academy of Sciences, Perm, Russia

Received September 17, 2007

Abstract—Reaction of polyvinyl chloride with calcium and magnesium oxides was studied. The dependence of binding with metal oxides of hydrogen chloride formed by polyvinyl chloride dehydrochlorination on the oxide to polymer weight ratio and on temperature was examined. The activation energies and specific rates of formation of the corresponding metal chlorides were calculated. Conditions of complete chloride binding into environmentally safe products were found.

DOI: 10.1134/S1070427208010242

The use of plastics grows at appreciably higher rate compared to other materials, which results in accumulation of enormous amounts of the polymeric waste (both household and industrial). The traditional methods of waste incineration or disposal are extremely unhealthy from the environmental point of view because of penetration into the atmosphere, water, and soil of toxic substances, dioxins, which are strong carcinogens. The method of deep oxidation of solid polymeric materials containing halogens by heating these materials mixed in the finely ground state with oxides and hydroxides of calcium, magnesium, and barium with formation of harmless products has been reported [1].

The dehydrochlorination of polyvinyl chloride (PVC) (which is the primary reaction of PVC thermal degradation), producing polyene sequences in the degraded polymer, and the secondary reaction of crosslinking of macrochains, proceeding parallel-successively, are fairly comprehensively studied [2, 3]. At the same time, the data on PVC reaction with inorganic compounds are very limited. The effect of copper(I) chloride on formation of polychlorinated dibenzo-*p*-dioxins and polychlorodibenzofurans in the course of PVC incineration was noted [4]. The PVC pyrolysis in the presence of zinc and barium chlorides decreases the dehydrochlorination temperature and formation of high-molecular-weight products [5]. The 11%, on the average, increase in the efficiency of hydrogen chloride trapping at PVC reprocessing with sorbents based on calcium carbonate, hydroxide, and acetate was reported in [6].

The goal of this study is determination of the effect of calcium and magnesium oxides on PVC dehydrochlorination, examination of the kinetics of PVC reaction with calcium and magnesium oxides under isothermal conditions, and optimization of conditions of complete binding of PVC chlorine into the corresponding metal chlorides.

EXPERIMENTAL

Powder of emulsion PVC of E-6250Zh brand and analytically pure grade calcium and magnesium oxides were used. The reaction of the components was studied by differential-thermal and thermogravimetric methods on a Q-1500D derivatograph in alundum crucibles at a heating rate of 2.5 deg min^{-1}. The reaction kinetics was studied under isothermal conditions by introduction of polymer and metal oxide mixture (taken in definite weight ratio) into a crucible heated to preset temperature. The samples were prepared by prolonged trituration of the suspension of the components in acetone in an agate mortar. The content of alkaline-earth metal chlorides was determined by volumetric Mohr titration after dissolution of the mixture sample in distilled water. Similarly, the chlorine content of the gas phase was determined after absorption of hydrogen chloride with water.

The degree of binding of polymer chlorine α was calculated as the ratio of chlorine weight in metal chloride to chlorine weight in the initial PVC sample.

It was found that the thermal oxidative degradation of PVC and reaction of the degradation products with

calcium and magnesium oxides occur step by step within the range 200–500°C interval and involve PVC dehydrochlorination, the subsequent reaction of hydrogen chloride with metal oxide, and oxide carbonation.

The PVCh dehydrochlorination, irrespective of the composition of the gas phase, starts at 200°C, and a maximal rate of the weigh loss is observed at 250°C (Fig. 1 a). At 280°C, 90% of chlorine contained in PVC is eliminated. An endothermic effect at 255°C corresponding to reaction [7, 8]

$$[CH_2–CHCl]_n \rightarrow [–CH=CH–]_n + HCl$$

is observed in the derivatogram.

Within the range 280–340°C, two processes occur: The PVC dehydrochlorination is complete, and gradual decomposition of the hydrocarbon residue starts. Above 340°C, the decomposition is accompanied by oxidation of the decomposition products, which is confirmed by exothermic effects at 425 and 500°C. In an inert gas (nitrogen, helium) flow, the thermal effects corresponding to oxidation substantially decrease.

The reaction of PVC with magnesium oxide is complex and multistage (Fig. 1b). Similarly to thermal degradation of straight PVC, the first stage is PVC dehydrochlorination with the maximal rate of hydrogen chloride evolution at 250°C. The released hydrogen chloride reacts with magnesium oxide, as indicated by disappearance of the endothermic effect of HCl release at 255°C and appearance of an exothermic peak in the DTA curve at 270°C. At MgO/PVC ratio increased from 2 to 3, the reaction surface area increases, which accounts for the difference in the weight loss associated with the larger amount of magnesium chloride formed. Within the range 300–400°C, the PVC degradation products decompose. The exothermic effect within the range 410–470°C corresponds to carbonation of magnesium oxide [9]. The further increase in the temperature leads to reverse reaction of magnesium carbonate decomposition, which is accompanied by an endothermic effect in the DTA curve (this effect is not detected at low heating rates). The analysis of the residue after heating the reaction mixture to 500°C showed the absence of magnesium carbonate.

The behavior of PVC–CaO mixture at heating substantially differs from that of the mixture with MgO (Fig. 1c). After the stage of dehydrochlorination and subsequent reaction of HCl with calcium oxide, the sample weight increases. This feature is also observed

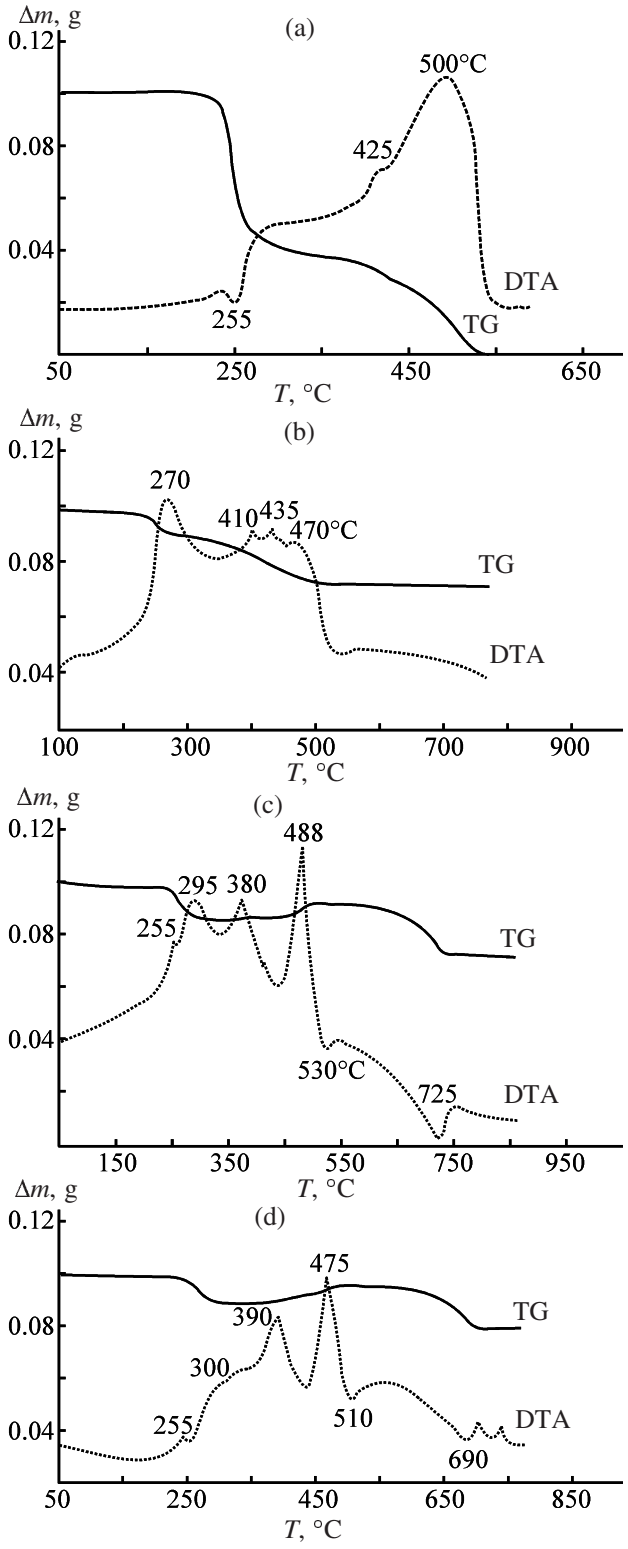


Fig. 1. DTA and TG curves of (a) PVC, (b) PVC + MgO, and (c, d) PVC + CaO. Heating: (a–c) in air and (d) in helium atmosphere. M = 3. (Δm) Weight loss and (T) temperature.

Table 1. Degree of chlorine binding and activation energies of formation of calcium and magnesium chlorides in reaction of PVC with CaO and MgO. Temperature 290°C, contact time 6 min

Oxide	Degree of PVC chlorine binding α, %		Activation energy, kJ mol^{-1}			
			α = 15%		α = 20%	
	M = 2	*M* = 3	*M* = 2	*M* = 3	*M* = 2	*M* = 3
CaO	25.9	37.6	86.2 ± 13.3	88.8 ± 7.1	93.9 ± 11.5	92.7 ± 6.8
MgO	21.0	35.4	44.8 ± 1.7	38.7 ± 0.6	48.3 ± 3.1	42.5 ± 1.6

when the experiment is performed in a flow of an inert gas (Fig. 1d). This fact suggests probable formation in this stage of calcium hydroxide and carbonate in the reaction of PVC degradation products with CaO. The decrease in the sample weight at the temperature higher than 500°C is due to dehydration of $Ca(OH)_2$ and decarbonation of $CaCO_3$, which is confirmed by endothermic effects at 530 (510) and 725 (690)°C in air (helium). The degree of polymer carbon binding amounts to 55%.

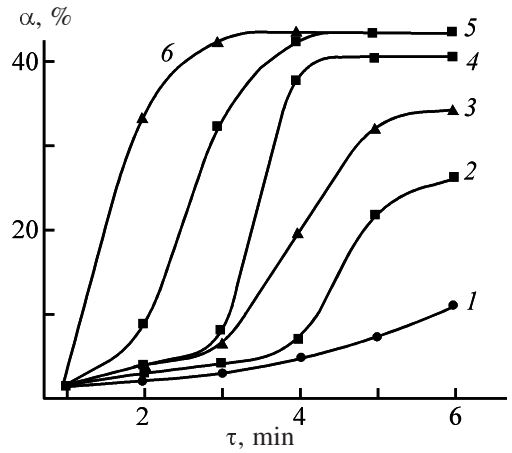


Fig. 2. Time dependence of the degree of PVC chlorine binding α. Heating with MgO (*M* = 3). Temperature, °C: (*1*) 274, (*2*) 290, (*3*) 300, (*4*) 310, (*5*) 320, and (*6*) 350.

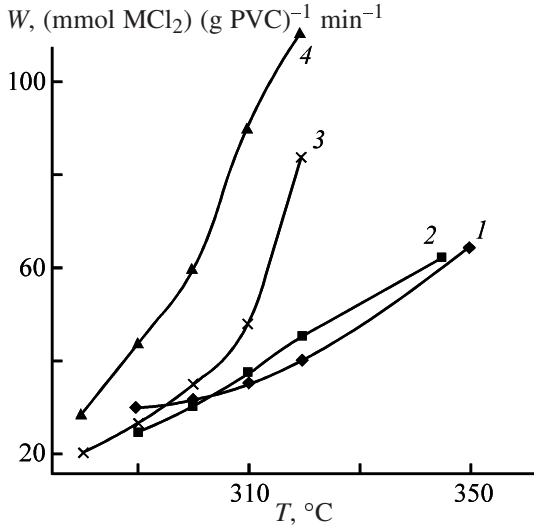


Fig. 3. Temperature dependence of the specific rate of calcium and magnesium chloride formation *W* in mixtures: (*1*) PVC : MgO = 1 : 3, (*2*) PVC : MgO = 1 : 2, (*3*) PVC : CaO = 1 : 2, and (*4*) PVC : CaO = 1 : 3.

The kinetics of formation of metal chlorides was studied within the range 270–350°C at metal oxide/polymer weight ratio *M* 2 and 3. The dependence of the degree of the polymer chlorine binding on time has double-bend shape (Fig. 2), demonstrating acceleration of formation of metal chlorides in the initial period, caused by autoacceleration of PVC dehydrochlorination [7].

The calculated values of the degree of PVC chlorine binding in the reactions with calcium and magnesium oxides are listed in Table 1. They show that, with increasing oxide/polymer weight ratio, the degree of PVC chlorine binding increases and that the degree of PVC chlorine binding in the mixture with CaO under any conditions is higher than that in the PVC–MgO mixture. The specific rates of formation of metal chlorides per gram of PVC (initial amount in the mixture) were calculated for the period up to reaction deceleration. The dependence of the specific rate of metal chloride formation on the temperature at 20% binding of PVC chlorine is shown in Fig. 3. With increasing temperature, the rate of metal chloride formation increases, and the specific rate of calcium chloride formation is in all cases higher than that of magnesium chloride formation.

From data obtained, we calculated the effective activation energy of the formation of calcium and magnesium chlorides at the degree of PVC chlorine binding α equal to 15 and 20% (Table 1). As can be seen, the activation energy is independent of the metal oxide/polymer weight ratio. At the same time, the activation energy increases in going from magnesium to calcium.

In experiments on optimization of conditions of

Table 2. Chlorine amount in the solid (metal chlorides) and gas (HCl) phase in reaction of PVC reaction with CaO and MgO. Temperature 290°C, M = 3

Reaction mixture	Phase	Chlorine amount, %
PVC + CaO	Solid	94.6
		99.3*
	Gas	5.3
		1.5*
PVC + MgO	Solid	72.1
		96.8*
	Gas	18.2
		3.1*

* PVC–oxide mixture, 0.2 g + oxide, 0.1 g.

PVC chlorine binding into the corresponding metal chlorides, to increase the time of contact of HCl formed with the solid phase, a sample of the reaction mixture was introduced into a narrow reactor (inner diameter 4 mm) heated to a required temperature, and then the air flow was passed. The results of calculation of α are listed in Table 2. As can be seen, α is fairly high, 95% for calcium oxide, while for magnesium oxide this value is 72% under the similar conditions.

To additionally increase α, a bed of pure metal oxide of equal weight was charged over the reaction mixture bed. As follows from Table 2, in this case 99% of PVC chlorine can be bound with calcium oxide and 97%, with magnesium oxide.

CONCLUSIONS

(1) The reactivity of calcium oxide with respect to PVC chlorine binding under conditions of PVC dehydrochlorination is higher than that of magnesium oxide.

(2) At 290–300°C, the metal oxide/polymer weight ratio equal to 3, and time of the contact of HCl formed with the solid phase of 6 min, PVC chlorine reacted with CaO or MgO to form the corresponding chlorides to 97–99%.

ACKNOWLEDGMENTS

The study was supported by the Grant of the President of the Russian Federation for young Russian scientists (MK-2102.2007.3) and by the Program for State Support of Leading Scientific Schools (NSh-5812.2006.3).

REFERENCES

1. RF Patent 2 100 702.
2. Yanborisov, V.M. and Minsker, K.S., *Vysokomol. Soedin., Ser. A*, 2002, vol. 44, no. 5, pp. 857–862.
3. Jordan, K.J., Suib, S.L., and Koberstein, J.T., *J. Phys. Chem. B*, 2001, vol. 105, no. 16, pp. 3174–3181.
4. Wang Pong-Li, Xu Xiao-Bai, Zheng Ming-Hui, and Chung, H., *Acta Chim. Sin.*, 2000, vol. 58, no. 12, pp. 1681–1684.
5. Cheng Wu Hsun and Liang, Y.C., *J. Appl. Polym. Sci.*, 2000, vol. 77, no. 11, pp. 2464–2471.
6. Li Shuiquing, Chi Yong, Li Weiwu, et al., *J. Environ. Sci.*, 2001, vol. 22, no. 2, pp. 95–100.
7. Minsker, K.S., Kolesov, S.V., and Zaikov, G.E., *Starenie i stabilizatsiya polimerov na osnove vinilkhlorida* (Aging and Stabilization of Polymers Based on Vinyl Chloride) Moscow: Nauka, 1982.
8. Vrandecic, N.S., Klaric, I., and Kovacic, T., *Polym. Degrad. Stab.*, 2004, vol. 84, no. 1, pp. 31–39.
9. Berg, L.G., *Vvedenie v termografiyu* (Introduction to Thermography), Moscow: Akad. Nauk SSSR, 1961.

ISSN 1070-4272, Russian Journal of Applied Chemistry, 2008, Vol. 81, No. 1, pp. 108–113. © Pleiades Publishing, Ltd., 2008.
Original Russian Text © Yu.V. Shulevich, O.Yu. Kovaleva, A.V. Navrotskii, V.G. Skrebneva, I.A. Novakov, 2008, published in Zhurnal Prikladnoi Khimii, 2008, Vol. 81, No. 1, pp. 112–117.

MACROMOLECULAR CHEMISTRY AND POLYMERIC MATERIALS

Influence of the Lyophilizing Power of the Polymer Chain on the Relationships in Formation of Polyelectrolyte–Surfactant Complexes

Yu. V. Shulevich, O. Yu. Kovaleva, A. V. Navrotskii, V. G. Skrebneva, and I. A. Novakov

Volgograd State Technical University, Volgograd, Russia

Received July 23, 2007

Abstract—Viscometry and turbidimetry were applied to examine the relationships in formation of complexes by poly-1,2-dimethyl-5-vinylpyridinium methyl sulfate, poly-*N,N,N,N*-trimethyl(methacryloyloxyethyl)ammonium methyl sulfate, and poly[*N*-benzyl-*N,N*-dimethyl-*N*-(methacryloyloxyethyl)]ammonium chloride with sodium dodecyl sulfate.

DOI: 10.1134/S1070427208010254

Complexes formed by polyelectrolytes (PEs) with oppositely charged surfactants, polymer–colloid complexes (PCs), belong to a special class of amphiphilic compounds with variable lyophilic–lyophobic balance controllable by varying the composition of the complex [1]. Numerous studies of PCs showed that complexing is driven by electrostatic interactions of oppositely charged ions of PEs and surfactants, as well as by hydrophobic interactions of the alkyl moieties of surfactants, responsible for micellization in the body of the macromolecule [2]. The critical association concentration (CAC) of surfactants in the presence of PE is by 1.5–2 orders of magnitude lower than the critical micellization concentration (CMC) of surfactants in water [1]. Depending on the composition and reaction conditions, PCs can be soluble or insoluble in water and water–salt media. The solubility of complex species is provided by free PE units which are not bound to the surfactant ions [1]. When the content of surfactant in the complex species exceeds some critical level, so-called limiting composition of soluble complexes, the lyophilizing power of the free segments of the polymer chains proves to be insufficient, and phase segregation occurs in the system [3]. Thus, the range of existence of soluble complexes is determined by the hydrophilic–hydrophobic balance of the PC species, which, in turn, depends both on the hydrophobicity of the components of the complex (e.g., length of the aliphatic moiety of the surfactant) and on the lyophilizing power of the macromolecule. The lyophilizing power of the PE is governed by the effective charge of the polymer chain, as well as by the polar and nonpolar groups in the composition of the macromolecule, which can cause the lyophilizing power to increase or decrease.

The growth of interest in PCs is dictated by the fact that they contain surfactant micelles linked to the polymer coil by salt bonds and exhibiting a significant solubilizing power with respect to different classes of organic compounds [4]. This makes them suitable for solving various environmental, medicinal, and engineering problems. In particular, high-performance flocculants for wastewater treatment can be synthesized from PCs.

We examined here complexation of polyelectrolytes with sodium dodecyl sulfate (DDS) as influenced by their lyophilizing power.

EXPERIMENTAL

Polymerization of monomers, 1,2-dimethyl-5-vinylpyridinium methyl sulfate (M-1), *N,N,N,N*-trimethyl(methacryloyloxyethyl)ammonium methyl sulfate (M-2), and [*N*-benzyl-*N,N*-dimethyl-*N*-(methacryloyloxyethyl)]ammonium chloride (M-3), was carried out in aqueous solutions at 20 ± 0.5°C by the ampule method. To this end, the initiator in the form of an aqueous solution with the concentration of 0.001–0.1 M was introduced into the monomer solution of

Table 1. Synthesis conditions for the polyelectrolytes

Monomer	$[M_0]$, M	Initiator, M, chain-transfer agent, M	$[\eta]$, dl g^{-1}	Polyelectrolyte
M-1	2.5	TBPP, 10^{-4}	5.05	P-1-1
	2.0	TBPP, 10^{-3}; ethanol, 0.03	3.45	P-1-2
	2.5	TBPP, 10^{-3}; hydroquinone, 0.01	0.78	P-1-3
	2.5	TBPP, 10^{-3}; hydroquinone, 0.05	0.40	P-1-4
M-2	4.0	TBPP, 0.001; HCl, 0.001	15.83	P-2-1
	2.0	TBPP, 0.001; HCl, 0.001	7.70	P-2-2
	1.5	TBPP, 0.001; HCl, 0.001	6.10	P-2-3
	2.5	TBPP, 0.001; hydroquinone, 0.1	2.19	P-2-4
M-3	2.0	TBPP, 0.001; HCl, 0.001	4.00	P-3

* $[M_0]$ is the initial concentration of the monomer, and $[\eta]$, intrinsic viscosity of the PE solution in 0.05 M NaCl at 30°C.

a definite concentration. The initial monomers were purified by recrystallization from organic solvents. Polymerization was run to 96–98% conversion, whereupon the polymerization product was dissolved in methanol and precipitated with diethyl ether. The polymers were additionally purified by reprecipitation from methanol solutions with diethyl ether and vacuum-dried (p_{res} = 1.5–2.0 mm Hg, T = 20 ± 0.5°C) to constant weight. The polyelectrolytes with different molecular weights (MWs) were synthesized using *tert*-butylperoxy-2-propanol (TBPP) as initiator and ethanol or hydroquinone as the chain-transfer agent [5, 6]. Table 1 presents the synthesis conditions for the polyelectrolytes.

The surfactant, sodium dodecyl sulfate available from Merck, was used without additional purification.

The PC solutions were prepared by mixing the initial solutions of the PE and DDS in 0.05 M aqueous solution of a low-molecular-weight electrolyte (sodium chloride, sodium bromide, sodium fluoride, or potassium iodide). To this end, a DDS solution of the known concentration was added dropwise to a PE solution under vigorous stirring. The properties of the solutions were examined no earlier that 1 day after the preparation. The composition of the complexes was presumed to be identical to that of the reaction mixture Z, expressed through the ratio of the molar concentrations of DDS and PE in the system.

The molecular-weight characteristics of the PE were determined by static laser light scattering. The scattered light intensity was measured on a PhotoCor (PhotoCor, USA) wide-angle laser light scattering photometer using a PhotoCor 280-channel logic correlometer. The increment of the refractive index of the solutions dn/dc was determined on a Chromatix KMX-16 (Milton Roy) differential refractometer with a He–Ne laser (2 mW power, wavelength 630 nm) as the light source. The reference solution in measurements of dn/dc was the solvent brought into the dialysis balance with the solution. The weight-average molecular weight M_w was determined by the Zimm's double extrapolation method accurately to within 15%. Before measurements, the solutions were thoroughly freed from dust by filtering through Millipore membrane filters with the pore size of 0.45 μm.

The intrinsic viscosity $[\eta]$, dl g^{-1}, of the solutions of the polymers was measured in an Ubbelohde viscometer at 30°C in 0.05 M aqueous solution of a low-molecular-weight salt (sodium chloride, sodium bromide, sodium fluoride, or potassium iodide). The intrinsic viscosity was determined by double extrapolation of the specific viscosity η_{sp} and the logarithm of the ratio of the relative viscosity η_{rel} to the polymer concentration c, g dl^{-1}, to the zero concentration of the polymer. The η_{sp} parameter of the polymer solutions in the presence of different amounts of DDS was determined as the ratio of the times of flow of the corresponding solution of the polymer τ and of the solvent τ_0.

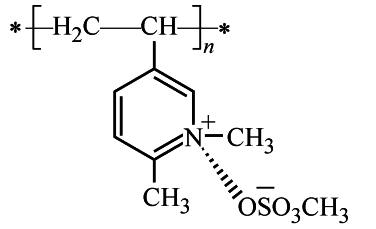
To determine the limiting compositions of the complexes, dilute solutions of the PEs were titrated with a DDS solution of the known concentration, which was added dropwise under vigorous stirring. After each portion of DDS was added, the optical density of the solution A was measured at the wavelength of 490 nm on a KFK-3 photoelectrocolorimeter. The turbidity of the solutions D was calculated by the formula $D = 2.3A/l$, where l = 3 cm is the cell length. We presumed that the limiting composition of the reaction mixture at which the system remains transparent (the

Table 2. Molecular-weight characteristics of the initial polyelectrolytes

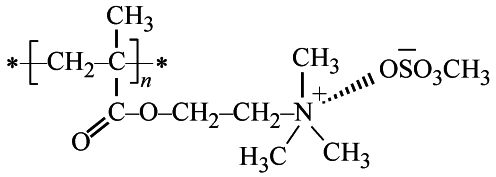
Polyelectrolyte	$M \times 10^{-6}$	$A_2 \times 10^4$, cm^3 mol g^{-2}	R_g, nm	α	*a*
P-1-2	3.6	4.56	127	2.67	0.78
P-2-2	6.5	4.65	141	3.35	0.79
P-3	4.4	1.60	139	1.43	0.72

turbidity is close to zero) corresponds to the limiting composition of water-soluble complexes, i.e., to the maximal content of DDS in the system at which the complexes remain soluble in aqueous media.

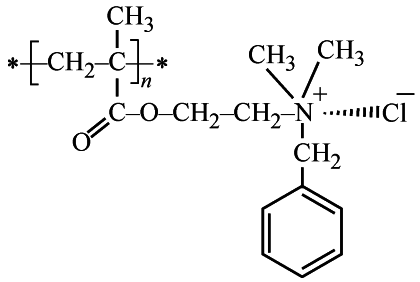
The limiting composition of soluble PCs corresponds to the maximal content of the ions of surfactants in the bulk of the macromolecule and is determined by the hydrophilic–lipophilic balance of the complex species. When the composition of the complex exceeds the limiting level, phase segregation occurs in the system. We examined here the complexes formed by a series of polymers with the same surfactant; hence, the hydrophilic–lipophilic balance of the complex species can be largely determined by the lyophilizing power of the polymer chain, which depends both on the hydrophobicity of the polymer backbone and the degree of binding of the counterions. To examine the structure and properties of the resulting PCs as influenced by the chemical structure of the PEs, we synthesized a series of polymers with essentially different structures of the lateral substituents, namely: poly-1,2-dimethyl-5-vinylpyridinium methyl sulfate (P-1), poly-*N,N,N,N*-trimethyl(methacryloyloxyethyl)ammonium methyl sulfate (P-2), and poly[*N*-benzyl-*N,N*-dimethyl-*N*-(methacryloyloxyethyl)]ammonium chloride (P-3):



P-1



P-2



P-3

This choice was dictated by the excellent flocculation properties exhibited by these polymers with respect to various model and real disperse systems [7, 8]; some of them are produced commercially (P-1 under the trade name KF-91, and P-2–acrylamide copolymer, KF-99).

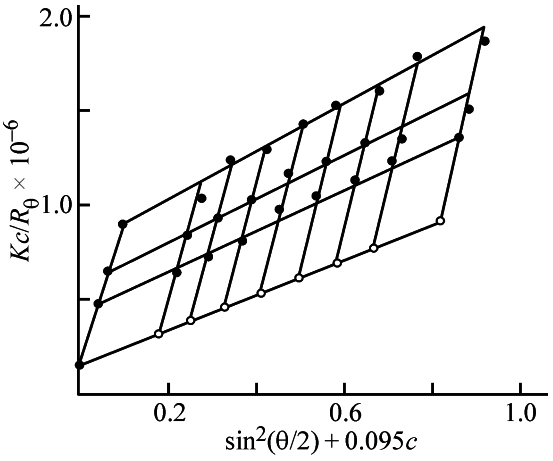


Fig. 1. Zimm's diagram for P-2-2. [NaCl] = 0.05 M, T = 20°C.

The characteristics of the PEs synthesized were derived from the static light scattering data. Figure 1 presents as an example the Zimm's diagram for P-2-2, and Table 2, the basic molecular-weight characteristics of the PEs.

It is seen from Table 2 that the PEs have high molecular weights M_W. Positive values of the second virial coefficients A_2 suggest that 0.05 M solution of sodium chloride is a thermodynamically good solvent for all the PEs. Also, they suggest that the PE macromolecules occur in solution as swollen coils. This is confirmed by the rms radii of gyration R_g of the macromolecules of the polymers examined [9]. Not-

Table 3. Hydrodynamic parameters of the polyelectrolytes in a water–salt medium

[NaCl], M	Polyelectrolyte					
	P-1-2		P-2-2		P-3	
	$[\eta]$, dl g^{-1}	k_H^*	$[\eta]$, dl g^{-1}	k_H^*	$[\eta]$, dl g^{-1}	k_H^*
0.1	5.07	0.31	6.70	0.36	5.83	0.45
0.2	3.56	0.35	4.98	0.38	4.33	0.45
0.5	2.67	0.53	3.33	0.39	2.47	0.54
0.6	2.27	0.96	3.25	0.42	1.92	0.67
$[\eta]^{0.1}/[\eta]^{0.6}$	2.23		2.06		3.04	
$k_H^{0.6}/k_H^{0.1}$	3.1		1.1		1.5	

* k_H is the Huggins constant, T = 30°C.

ably, the A_2 coefficient for P-3 is much smaller than those for P-1-2 and P-2-2. The unit of this polyelectrolyte contains a bulky hydrophobic benzyl substituent; hence, the hydrophobic interactions for P-3 are presumably stronger than those for P-1-2 and P-2-2.

Based on the known relationship between A_2 and the intrinsic viscosity of the solution, we can estimate the coefficient of polyelectrolyte swelling of the coils α. It can be used, in turn, for determining the exponent a at the molecular weight in the Mark–Kuhn–Houwink equation from the relationship [10]

$$\ln[1 + \pi^{1/2}(\alpha^2 - 1)/2] = \frac{27\Phi}{(32)^{1/2}\pi N_a}\frac{M_w A^2}{[\eta]},$$

$$a = \frac{4\alpha^2 - 3}{5\alpha^2 - 3},$$

where $\Phi = 2.1 \times 10^{21}$ mol^{-1}.

The calculated parameters α and a are also presented in Table 2. It is seen that, for P-3, the polyelectrolyte swelling coefficient is also much smaller than those for P-1-2 and P-2-2.

The conformation assumed by the macromolecular coil in a dilute solution is determined, on the one hand, by the electrostatic interactions associated with the occurrence in the polymer chain of charged units, and, on the other, with intramolecular interactions, characteristic for PEs whose macromolecules comprise hydrophobic groups. An increase in the concentration of a low-molecular-weight electrolyte will result in shielding of the electrostatic interactions. Hence, the size of the macromolecules will be determined to a greater extent by hydrophobic interactions. The intensity of the intramolecular interactions in the macromolecule can be estimated by examining how the intrinsic viscosity and the Huggins constant vary with increasing concentration of the low-molecular-weight electrolyte (Table 3). It is seen that, with increasing ionic strength, the intrinsic viscosity of the PEs examined naturally tends to decrease, and the Huggins constant, to increase.

Another way to characterize the lyophilicity of the macromolecular chain is via changing the nature of the low-molecular-weight electrolyte (Table 4). By varying the nature of the low-molecular-weight anion without changing essentially the nature of the cation, it is possible to elucidate the influence exerted by the degree of binding of the low-molecular-weight counterions with the macromolecular chain.

As known, the strength of binding of halide ions with the polycation containing a quaternized nitrogen atom decreases as $I^- > Br^- > Cl^- > F^-$ [11]. Table 4 shows that the increase in the degree of binding of counterions with the polymer chain tends to decrease the lyophilizing power of PE, thereby decreasing the intrinsic viscosity of their solutions.

Thus, combined analysis of the viscometric and

Table 4. Hydrodynamic parameters of the polyelectrolytes in water–salt media of different nature

Polyelectrolyte	$[\eta]$, dl g^{-1}			
	NaF	NaCl	NaBr	KI
P-1-2	5.12	3.45	3.31	I/s*
P-2-2	10.88	7.70	7.12	4.52
P-3	8.14	4.00	3.92	I/s

* (I/s) The polyelectrolyte is insoluble.

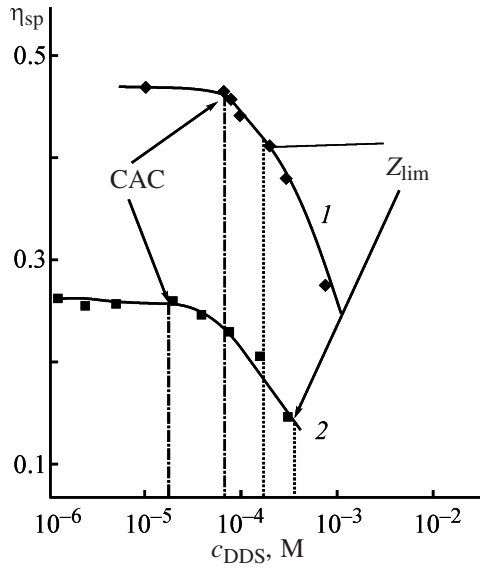


Fig. 2. Specific viscosity η_{sp} of the PE solutions vs. the DDS concentration c_{DDS}. [NaCl] = 0.05 M, c_{PE} = 0.001 M, T = 30°C. (*1*) P-1-2 and (*2*) P-2-2.

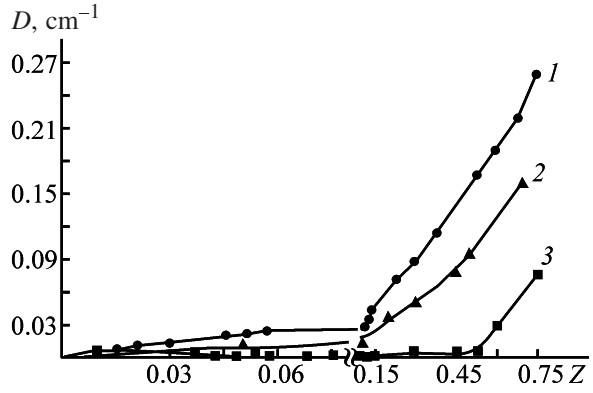


Fig. 3. Turbidity D of the PC solutions vs. the reaction medium composition Z. (c_{PE}) = 0.001 M, [NaCl] = 0.05 M. (*1*) P-1, (*2*) P-3, and (*3*) P-2.

Table 5. Limiting composition of the water-soluble complexes in relation to the molecular weight of the polyelectrolyte

Polyelectrolyte	[η], dl g^{-1}	Z^*_{lim}
P-1-1	5.05	0.17
P-1-2	3.45	0.15
P-1-3	0.78	0.20
P-1-4	0.40	0.14
P-2-1	15.83	0.55
P-2-2	7.70	0.52
P-2-3	6.10	0.60
P-2-4	2.19	0.60

* [NaCl] = 0.05 M, c_{PE} = 0.001 M, T = 20°C.

light-scattering data suggests that the contribution from the hydrophobic interactions to the size of the macromolecules varies for the PEs examined as P-2-2 ≪ P-1-2 ≈ P-3. It can be expected that different lyophilizing powers of the macromolecules will be manifested in the features of in their interaction with the surfactant ions.

Examination of the complexation of P-1-2 and P-2-2 with DDS revealed common relationships for these PCs. For example, Fig. 2 shows that, starting from some critical DDS concentration of about 10^{-5}–10^{-4} M, the viscosity of the solutions of the polymers sharply decreases due to binding of the DDS ions by the PE macromolecules. The CAC of sodium dodecyl sulfate in the presence of the polymers is by nearly two orders of magnitude smaller than the CMC of sodium dodecyl sulfate in water (8×10^{-3} M), which reasonably agrees with the published data [1].

It should be noted that the DDC concentration range within which the viscosity is reduced because of complexation is enclosed in Fig. 2 by two points, of which one corresponds to CAC, and the other, to the limiting composition of the soluble complex. A decrease in viscosity of the PE solutions with further increase in Z is associated with a decrease in the polymer concentration in the system.

Indeed (Fig. 3), up to a certain composition of the reaction mixture, the turbidity of the system remains virtually unchanged. An increase in Z beyond this value sharply increases the turbidity of the system owing to formation of insoluble complexes. It should be noted that the P-2-2 solution remains transparent up to Z = 0.5, while P-1-2 and P-3 are characterized by an appreciable change in the turbidity starting from Z = 0.1–0.15.

The reason for this substantial difference in the limiting compositions of the complex can be found in the molecular weight of the polymer. However, examination of the limiting composition as influenced by the molecular weight of the PE showed that the limiting composition of soluble complexes is virtually unaffected by the degree of polymerization of the PE over a wide range of molecular weights (Table 5).

The limiting composition of the complex is also determined by the effective charge of the macromolecule. In real solutions, a significant proportion of the counterions in PE is condensed on a macromolecule, and the remaining ionized units determine its effective charge and, hence, the lyophilizing power. Table 6 shows that, in the series of salts NaF → NaCl → NaBr → KI, the limiting composition of the water-

Table 6. Limiting compositions of the PCs in water–salt media of different nature

Polyelectrolyte	Composition			
	F^-	Cl^-	Br^-	I^-
P-2-2	0.70	0.50	0.50	0.10
P-1-2	0.30	0.15	0.15	N/f*
P-3	0.25	0.10	0.10	N/f

* (N/f) Water-soluble complexes are not formed.

soluble complexes tends to decrease with decreasing degree of binding of the anions in the series I > Cl > Br > F. The degree of binding of the iodide ions with P-3 and P-1-2 proves to be so high that, in the presence of NaI, soluble complexes are not formed. This is consistent with the measured viscosities of the solutions of the polyelectrolytes in solutions of these salts. The fact that the limiting composition remains unaffected by the change from NaCl to NaBr for all the PEs examined is explained by comparable degrees of binding for the chloride and bromide anions.

Evidently, a decrease in the lyophilizing power of the polymer chain causes the range of existence of water-soluble complexes to narrow, and in the case of hydrophobic PEs water-soluble complexes are not formed.

CONCLUSION

The lyophilizing power of a polyelectrolyte affects substantially the relationships in formation of water-soluble complexes. In the presence of hydrophobic moieties in the composition of the polyelectrolyte macromolecules, the limiting composition of the complexes decreases owing to a decrease in the lyophilizing power of the macromolecular chain.

ACKNOWLEDGMENTS

The authors are deeply grateful to A.B. Zezin and Yu.A. Zakharova for the opportunity to carry out light-scattering experiments.

This study was financially supported by the Russian Foundation for Basic Research (project no. 07-03-97630-r_ofi).

REFERENCES

1. Goddard, E.D. and Ananthapadmanabhan, K.P., *Interactions of Surfactants with Polymers and Proteins*, New York: CRC, 1993.
2. Kasaikin, V.A., Efremov, V.A., Zakharova, Yu.A., et al., *Dokl. Ross. Akad. Nauk*, 1997, vol. 354, no. 4, pp. 498–501.
3. Zakharova, Yu.A., Otdel'nova, M.V., Aliev, I.I., et al., *Kolloidn. Zh.*, 2002, vol. 64, no. 2, pp. 170–175.
4. Kabanov, V.A., Zezin, A.B., and Kasaikin, V.A., *Usp. Khim.*, 1991, no. 3, pp. 595–601.
5. Novakov, I.A., Navrotskii, A.V., Starovoitova, Ya.M., et al., *Zh. Prikl. Khim.*, 2003, vol. 76, no. 7, pp. 1200–1206.
6. Novakov, I.A. and Navrotskii, A.V., *Vysokomol. Soedin., Ser. C.*, 2002, vol. 44, no. 9, pp. 1660–1676.
7. Novakov, I.A., Navrotskii, A.V., Navrotskii, V.A., et al., *Nauka – Proizv.*, 2000, no. 1, pp. 40–43.
8. Panarin, E.F., *Usp. Khim.*, 1991, vol. 60, no. 3, pp. 629–630.
9. Eskin, V.E., *Rasseyanie sveta rastvorami polimerov* (Light Scattering by Polymer Solutions), Moscow: Nauka, 1973.
10. Tanford, Ch., *Physical Chemistry of Macromolecules*, New York: Wiley, 1963.
11. Satoh, M., Yoda, E., and Komiyama, J., *Macromolecules*, 1991, vol. 24, no. 5, pp. 1123–1127.

ISSN 1070-4272, Russian Journal of Applied Chemistry, 2008, Vol. 81, No. 1, pp. 114–122. © Pleiades Publishing, Ltd., 2008.
Original Russian Text © O.A. Dudarko, Yu.L. Zub, A. Dabrowski, M. Barczak, 2008, published in Zhurnal Prikladnoi Khimii, 2008, Vol. 81, No. 1, pp. 118–126.

MACROMOLECULAR CHEMISTRY AND POLYMERIC MATERIALS

Polysiloxane Xerogels with a Bifunctional Surface Layer Containing O/N, O/S, S/N, and S/S Donor Centers

O. A. Dudarko, Yu. L. Zub, A. Dabrowski, and M. Barczak

Chuiko Institute of Surface Chemistry, National Academy of Sciences of Ukraine, Kiev, Ukraine
Faculty of Chemistry, Maria Curie-Sklodowska University, Lublin, Poland

Received May 14, 2007

Abstract—Formation of bifunctional xerogels containing $-NH_2$, –SH, $-P(O)(OEt)_2$, and $-NHP(O,S)(OEt)_2$ complexing groups in the surface layer was studied using sol–gel method (fluoride ion catalyst, ethanol solvent) and three-component systems.

DOI: 10.1134/S1070427208010266

The possibility of using multicomponent systems is a principal advantage of sol–gel synthesis of functionalized polysiloxane materials. This makes it possible to vary the nature and ratio of both cross-linking [$E(OR)_n$, E = Si, Al, Ti, etc.] and functionalizing agents [in the simplest case, trifunctional silanes $(RO)_3SiR'$]. In the latter case, polysiloxane xerogels with a complex surface layer containing various functional groups R' can be prepared in one step. The possibility of changing conditions of hydrolytic polycondensation allows, to a large extent, direct control of the properties of the final xerogels, primarily their structural-sorption characteristics. Thus, using sol–gel method, one can control the design of both the resulting materials and their surface.

However, whereas the use of one- and two-component systems for preparing monofunctionalized xerogels with complexing groups has been studied rather extensively [1–3], there are only a few papers on preparing bifunctional polysiloxane xerogels using three-component systems. In these papers [4–7] the procedures of sol–gel synthesis of such materials are developed and their structures are studied by spectral methods. It should be noted that the design of polyfunctional surface layer suggests a finer effect on the xerogel properties (e.g., sorption) by changing both the nature and ratio of the functional groups in this layer [7–9]. At the same time, apparently, participation of alkoxysilanes with ligand groups of various chemical and steric structures in the hydrolytic polycondensation will strongly affect both the structure of the resulting xerogels and their surface. Therefore, it becomes necessary to determine the decisive factors affecting the composition, structure, and properties of xerogels with a bifunctional surface layer. In this study we attempted to analyze some of these factors using as example xerogels containing both (thio)phosphoryl and amine (or thiol) functional groups in the surface layer.

EXPERIMENTAL

In our study we used tetraethoxysilane $Si(OC_2H_5)_4$ (TEOS, 99%, Aldrich), diethoxyphosphorylethyltriethoxysinlane $(C_2H_5O)_3Si(CH_2)_2P(O)(OC_2H_5)_2$ (DPTS, 95%, Gelest), 3-aminopropyltriethoxysilane $(C_2H_5O)_3Si(CH_2)_3NH_2$ (APTES, 98%, Aldrich), 3-mercaptopropyltrimethoxysilane $(CH_3O)_3Si(CH_2)_3 \cdot SH$ (MPTMS, 95%, Aldrich), ammonium fluoride NH_4F (Fluka, ≥98%), and absolute ethanol. Diethyl 3-(triethoxysilyl)propylphosphoramidate $(C_2H_5O)_3 \cdot Si(CH_2)_3NHP(O)(OC_2H_5)_2$ (DEPPA) and *O,O'*-diethyl 3-(triethoxysilyl)propylphosphoramidothioate $(C_2H_5O)_3Si(CH_2)_3NHP(S)(OC_2H_5)_2$ (DEPPAT) were prepared by the procedure given elsewhere [10]. The procedures of the xerogel synthesis were as follows.

DO-1. DPTS (0.025 mol), APTES (0.025 mol), and TEOS (0.1 mol) were dissolved in 12.5, 12.5, and 10 ml of ethanol, respectively. Then, a solution of ammonium fluoride (0.0463 g, 0.00125 mol) in water (4.28 ml, 0.2375 mol) was added dropwise with stirring to a DPTS solution cooled on an ice bath. After stirring for 5 min, solutions of APTES and TEOS were added dropwise. After formation of a clear solu-

tion, the stirring was terminated. A gel formed in 1 min, which was confirmed by opalescence. After aging for 24 h, the gel was dispersed and dried in a vacuum at room temperature for 1 h, and then at 50 and 105°C for 1 and 4 h, respectively. Then, the resulting xerogel was ground in an agate mortar, washed with water (800 ml), and dried by the above procedure. A white compound was obtained, yield 13.67 g.

DO-2. Compound was prepared by the above procedure, using MPTMS (0.005 mol) instead of APTES (0.02 mol of TEOS, 0.005 mol of DPTS). The reaction was performed using a solution of ammonium fluoride (0.0093 g, 0.00025 mol) in water (0.86 ml, 0.0525 mol). The gel was formed in 5 min; the yield of the xerogel was 2.73 g.

DO-3. The xerogel was prepared by the procedure given for DO-1 using TEOS (0.03 mol), DPTS (0.005 mol), and APTES (0.005 mol) dissolved in ethanol (2.5 ml in each solution) and a solution of ammonium fluoride (0.0148 g, 0.0004 mol) in water (1.35 ml, 0.075 mol). The gel was formed in 1 min; the yield of the xerogel was 2.87 g.

DO-4. The xerogel was prepared by the procedure given for DO-3 using MPTMS instead of APTES. The gel was formed in 5 min; the yield of the xerogel was 3.28 g.

DO-5. The xerogel was prepared by the procedure given for DO-1 using DEPPA (0.01 mol) instead of DPTS, TEOS (0.04 mol), and APTES (0.01 mol) dissolved in ethanol (5 ml in each solution) and a solution of ammonium fluoride (0.0222 g, 0.0006 mol) in water (1.98 ml, 0.11 mol). The gel was formed in 1 min; the yield of the xerogel was 5.06 g.

DO-6. The xerogel was prepared by the procedure given for DO-5 using MPTMS instead of APTES. The gel was formed in 1 h; the yield of the xerogel was 5.66 g.

DO-7. The xerogel was prepared by the procedure given for DO-5 using DEPPAT instead of DEPPA. The gel was formed in 1 min; the yield of the xerogel was 5.36 g.

DO-8. The xerogel was prepared by the procedure given for DO-6 using DEPPAT instead of DEPPA. The gel was formed in 20 min; the yield of the xerogel was 6.12 g.

DO-9. The xerogel was prepared by the procedure given for DO-3 using DEPPA (0.01 mol) instead of DPTS, APTES (0.01 mol), and TEOS (0.06 mol) dissolved in ethanol (12.5, 12.5, and 10 ml in each solution, respectively) and a solution of ammonium fluoride (0.0296 g, 0.0008 mol) in water (2.71 ml, 0.15 mol). The gel was formed in 5 min; the yield of the xerogel was 6.84 g.

DO-10. The xerogel was prepared by the procedure given for DO-9 using MPTMS instead of APTES. The gel was formed in 10 min; the yield of the xerogel was 7.18 g.

DO-11. The xerogel was prepared by the procedure given for DO-9 using DEPPAT instead of DEPPA. The fine gel was formed immediately on mixing; the yield of the xerogel was 5.97 g.

DO-12. The xerogel was prepared by the procedure given for DO-11 using MPTMS instead of APTES. The gel was formed in 10 min; the yield of the xerogel was 7.36 g.

DO-13. The xerogel was prepared by the procedure given for DO-12 using 0.08 mol of TEOS and 0.001 mol of ammonium fluoride. The gel was formed in 5 min; the yield of the xerogel was 6.12 g.

The composition of the resulting xerogels was determined in the analytical laboratory (Institute of Organic Chemistry, National Academy of Sciences of Ukraine). The particle shape and size were determined using a Tesla BS301 scanning electron microscope. The thermal analysis was performed on an MOM Q-15000 derivatograph (Hungary) in the 20–1000°C range at a heating rate of 10 deg min^{-1}. The sensitivity of the thermal balance was ± 0.1 mg, and the sensitivities of DTA, DTG, and TG were 1/5, 1/5, and 100, respectively. The IR spectra were recorded on a Nicolet NEXUS FTIR spectrophotometer in the 400–4000 cm^{-1} range in the reflection mode with 4 cm^{-1} resolution. The IR spectra of the initial alkoxysilanes were recorded from thin film between RS-5 plates. The solid-state NMR spectra were recorded on a Bruker Avance spectrometer (300 MHz); the ^{13}C and ^{29}Si CP/MAS NMR (cross-polarization under fast magic angle spinning) spectra were recorded at 121.6 and 59.7 MHz, respectively. The rate of spinning of the ampule with the sample was 7–8 kHz, and the scan number was 1024–4096. Tetramethylsilane and 85% orthophosphoric acid were used as references.

The structural and sorption characteristics of the resulting xerogels were calculated using the isotherms of low-temperature adsorption of nitrogen (Kelvin-1042). The samples were preliminarily degassed in a helium flow at 100°C for 2 h. The specific surface area of the sorbents was studied by the BET procedure [11], and the size distribution were determined by

Composition and structural and sorption properties of bifunctional xerogels*

Sample	Reactant ratio	Composition, wt %						C/P	Si/P	$c^1_{f.gr}$	$c^2_{f.gr}$	S_{sp}, $m^2\ g^{-1}$	V_{sorb}, $cm^3\ g^{-1}$	d_{eff}, nm
		C	H	N	P	S	Si			mmol g^{-1}				
DO-1	4TEOS/DPTS/APTES	19.1	4.4	2.2	5.6	–	29.8	8.9	5.9	1.9a, 1.6b	1.9a 1.8b	205	0.14	3.8
DO-2	4TEOS/DPTS/MPTMS	–	–	–	–	–	–	–	–	–	–	<1	–	–
DO-3	6TEOS/DPTS/APTES	14.2	3.6	2.2	3.8	–	31.9	9.8	9.4	1.3a 1.6b	1.5a 1.5b	230	0.21	3.6
DO-4	6TEOS/DPTS/MPTMS	14.3	3.5	–	3.9	4.4	30.5	9.4	8.6	1.3a 1.5c	1.5a 1.5c	315	0.21	3.6
DO-5	4TEOS/DEPPA/APTES	–	–	–	–	–	–	–	–	–	–	<1	–	–
DO-6	4TEOS/DEPPA/MPTMS	–	–	–	–	–	–	–	–	–	–	<1	–	–
DO-7	4TEOS/DEPPAT/APTES	15.0	3.9	4.7	5.5	4.2	29.5	7.1	6.0	1.9a 1.7b	1.7a 1.7b	88	0.13	4.7
DO-8	4TEOS/DEPPAT/MPTMS	–	–	–	–	–	–	–	–	–	–	<1	–	–
DO-9	6TEOS/DEPPA/APTES	16.9	3.6	4.0	4.2	–	30.7	10.3	8.0	1.4a 1.6b	1.4a 1.5b	280	0.31	4.6
DO-10	6TEOS/DEPPA/MPTMS	–	–	–	–	–	–	–	–	–	–	<1	–	–
DO-11	6TEOS/DEPPAT/APTES	15.7	3.8	3.8	4.3	3.8	30.8	9.5	8.0	1.5a 1.3b	1.4a 1.4b	220	0.83	15.0**
DO-12	6TEOS/DEPPAT/MPTMS	–	–	–	3.8	8.1	–	–	–	1.3a 1.5c	1.4a 1.5c	<1	–	–
DO-13	8TEOS/DEPPAT/MPTMS	12.1	3.4	1.6	3.4	6.5	31.6	9.1	10.3	1.1a 1.1c	1.2a 1.3c	<1	–	–

* Amount of functional groups: $c^1_{f.gr}$, calculated from the data of chemical analysis; $c^2_{f.gr}$, calculated from the reactant ratio (a, b, and c refer to PO(S), NH_2, and SH groups, respectively).

** Calculated from the Gurvich equation ($d_{eff} = 4V_{sorb}/S_{sp}$) [13].

BJH method [12] and from the Gurvich equation ($d_{eff} = 4V_{sorb}/S_{sp}$) [13].

Our preliminarily experiments showed that hydrolytic polycondensation proceeds rather rapidly in most of the three-component systems studied. Therefore, the reaction was performed at decreased temperature using ethanol. Without ethanol solvent, heterogeneous gelation was often observed in these systems. As catalyst we used fluoride ion [6, 10] (F/Si ratio 1/100), which hinders breakdown of the sulfur-containing ligand groups:

$$Si(OEt)_4 + (EtO)_3Si(CH_2)_2L + (MO)_3Si(CH_2)_3L' \xrightarrow[-EtOH,\ -MOH]{+H_2O/F^-} [(SiO_2)_x(O_{3/2}Si(CH_2)_2L/O_{3/2}Si(CH_2)_3L')],$$

where L = $-3P(O)(OEt)_2$ and $-CH_2NHP(O,S)(OEt)_2$; and L' = $-NH_2$ and $-SH$.

After vacuum drying we obtained white powder compounds; some sulfur-containing compounds were yellowish. As a rule, all the xerogels are easily suspended in air.

The content of the functional groups in the resulting xerogels, determined from the data of chemical analysis, is given in the table. As can be seen, the contents of the phosphorus-containing, amino, and mercapto groups vary within 1.0–1.9, 1.3–1.7, and 1.0–1.5 mmol g^{-1}, respectively, which is determined by the ratio of TEOS and trifunctional silane in the initial mixture. With increasing relative content of TEOS, it naturally decreases. It should also be noted that the molar ratio of trifunctional silanes in the initial solution (1 : 1) is, as a rule, preserved in the final xerogel. The C/P ratio in the final samples in most cases is often slightly higher than that calculated from the ratio of the initial componenta (see table). This is due to the presence of residual alkoxysilyl groups (no chemical analysis was performed for virtually nonporous materials). Analysis of the Si/P ratio and comparison of the content of the introduced groups with their content in xerogels (chemical analysis) suggests that only an insignificant amount of oligomeric siloxanes is removed by washing.

The thermogravimetric curves for samples DO-3, DO-4, DO9, and DO-11 are shown in Fig. 1. As can

be seen, the DTA curves for all the samples exhibit small endothermic effect at 80–130°C, which can be due to the loss of water (and residual solvent). The exothermic effects observed at higher temperatures (270–600°C) suggest degradation of the surface layer. The weight changes at 220–400°C are primarily due to the removal of ethoxy groups and oxidation of the sulfur-containing fragments. Two exothermic effects with smaller weight changes can be due to oxidation of NH and CH groups. It is obvious that samples DO-3, DO-4, and DO-9 are more thermally stable than DO-11, because intense weight loss for these samples is observed only above 200°C, whereas in the case of sample DO-11 breakdown of the surface layer starts already at 160°C. This is probably due to the different composition of substituents at the phosphorus atom in the functional groups. In the 440–460°C range, for all the samples an exothermic effect is observed, which is not accompanied by a significant weight loss (Fig. 1). This effect is probably due to exothermic intrastructural processes. Analysis of the TG curves shows that, for all the samples, the weight loss in the range 160–700°C is 22–28%, which agrees with the data of chemical analysis assuming that nonvolatile phosphates are formed upon burn-out of the organic fraction of the gel.

The composition and structure of the surface layer in the samples were first studied by IR spectroscopy. The IR spectra of all the samples (Fig. 2) contain weak bands at 1350–1490 cm^{-1} and three medium-intensity bands at 2800–3000 cm^{-1}. The latter bands are typical of the stretching vibrations $\nu_{s,as}(CH)$, whereas the absorption bands at 1364–1372, 1392, 1442–1446, and 1478 cm^{-1} belong, respectively, to the vibrations $\omega(CH_2)$, $\delta_s(CH_3)$, $\delta_{as}(CH_3)$, and $\delta(CH_2)$ of the ethoxy groups bound to the phosphorus atom [14]. The absorptions bands of the fragments $\equiv Si(CH_2)_2-$ [and/or $\equiv Si(CH_2)_3-$] occurring in the same region are weak, except the absorption band of $\delta[(Si)CH_2]$ [14] at 1409–1417 cm^{-1} (Fig. 2). The absorption band of $\nu(P=O)$, which in the IR spectra of individual trifunctional silanes is observed at 1240 (DPTS) [15] and 1233 cm^{-1} (DEPPA) [10], in the corresponding xerogels shifts toward lower frequencies and is observed as either a pronounced shoulder or as a separate strong band at ~1200 cm^{-1} (Fig. 2). This fact suggests that the phosphoryl group participates in formation of a hydrogen bond.

The IR spectra of the samples prepared using DEPPAT contain a weak band at 556–642 cm^{-1}, belonging to the $\nu(P=S)$ vibration (Fig. 2). The IR spectra of the xerogels prepared using such trifunctional silanes as DEPPA and DEPPAT contain two strong bands at 790–800 and 960–965 cm^{-1} belonging probably to $\nu_s(PN)$ and $\nu_{as}(PN)$, respectively [10]. The IR spectra of samples DO-2, DO-4, DO-6, DO-8, DO-10, DO-12, and DO-13 have a weak absorption band at 2565 cm^{-1} belonging to $\nu(SH)$ (Fig. 2).

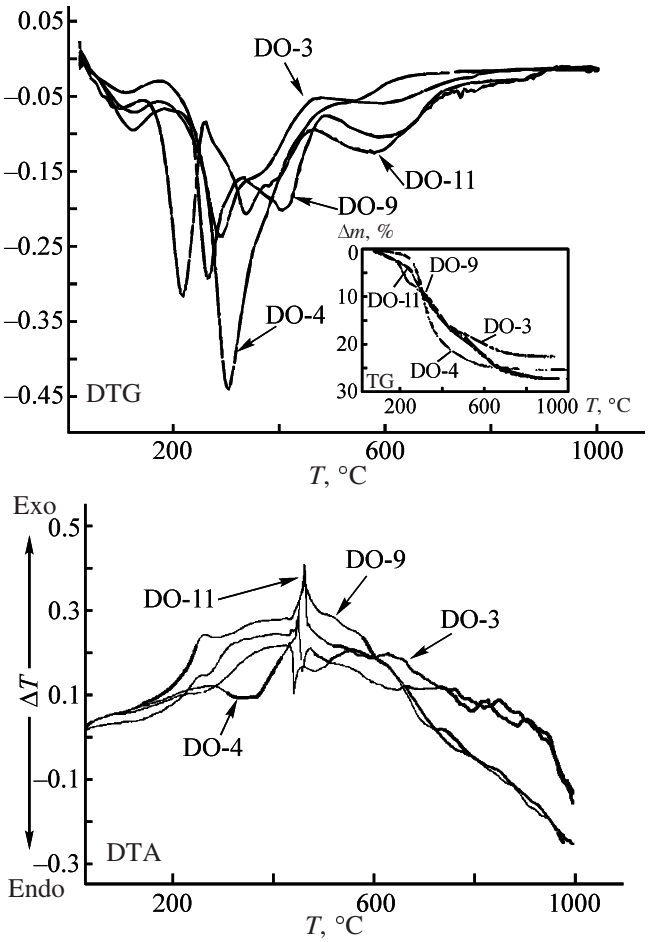


Fig. 1. Thermogravimetric curves of xerogels. (Δm) Weight loss and (T) temperature.

It should be noted that the IR spectra of all the samples exhibit the strongest absorption band at 1045–1065 cm^{-1}, which suggests formation of a three-dimensional system of the siloxane bonds [16]. The presence of water in the samples is confirmed by IR absorption bands at 1630 and 3100–3400 cm^{-1} [14]. In the 3100–3400 cm^{-1} range, the absorption bands $\nu(OH)$ overlap with the absorption band $\nu(NH)$, which is fairly strong in the IR spectra of the initial amides (DEPPA and DEPPAT). As for APTES, the absorption bands $\nu_{s,as}(NH)$ occurring in the same region are weak and are not observed in the IR spectra of the resulting xerogels (Fig. 2). At the same time, the absorption band $\delta(NH_2)$ at 1540 cm^{-1} suggests the presence of amino groups participating in formation of

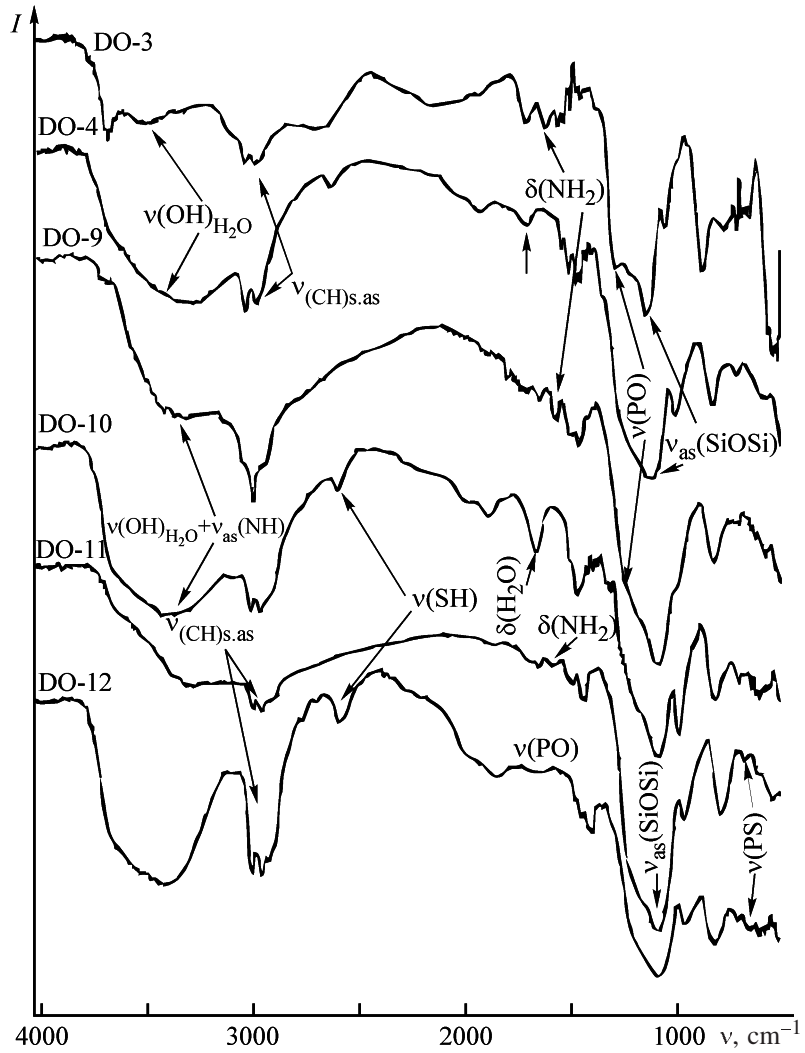


Fig. 2. IR spectra of xerogels prepared at the ratio TEOS : phosphorus-containing alkoxysilane : APTES (or MPTMS) = 6 : 1 : 1. (*I*) Intensity and (ν) wavenumber.

a hydrogen bond (in the IR spectra of neat APTES, this absorption band is observed at 1600 cm^{-1}). It should be noted that the IR spectra of the xerogels studied exhibit a broad shoulder at 3635–3660 cm^{-1}, which probably belongs to the stretching vibrations of the silanol groups. Thus, the IR data confirm the presence of the introduced functional groups, water, silanol groups, and polysiloxane bonds in the resulting xerogels.

The ^{13}C CP/MAS NMR spectra of xerogels DO-3 and DO-4 are shown in Fig. 3. Both spectra exhibit a signal at 5 ppm, which belongs to the carbon atom of the ethyl chain directly bound to the silicon atom ≡Si$\underline{C}H_2$–CH_2–P(O)= [17]. The signal of the second carbon atom in this chain, which is bound to the phosphorus atom and should be observed at 16 ppm, was not identified because it is obscured by the signal of the methyl carbon atom of the ethoxy group. The presence of the ethoxy groups in DO-3 and DO-4 is also confirmed by the signal at 62 ppm belonging to the methylene carbon atom of these groups (Fig. 3). The ^{13}C CP/MAS NMR spectra of sample DO-3 also exhibit three signals at 9.9, 19.8, and 42.6 ppm, which belong to the carbon atom of the propyl fragment (≡$SiCH_2$–, –C[CH_2]C–, and –CH_2NH_2, respectively [18]). The signal of the middle carbon atom of the propyl group at 20–23 ppm suggests that the amino group participates in formation of a strong hydrogen bond [19], which agrees with the conclusion based on the IR data. As for sample DO-4, only two signals of the propyl fragment were identified in its ^{13}C CP/MAS NMR spectrum (Fig. 3), which is typical for the 3-mercaptopropyl fragment [18] and is due to

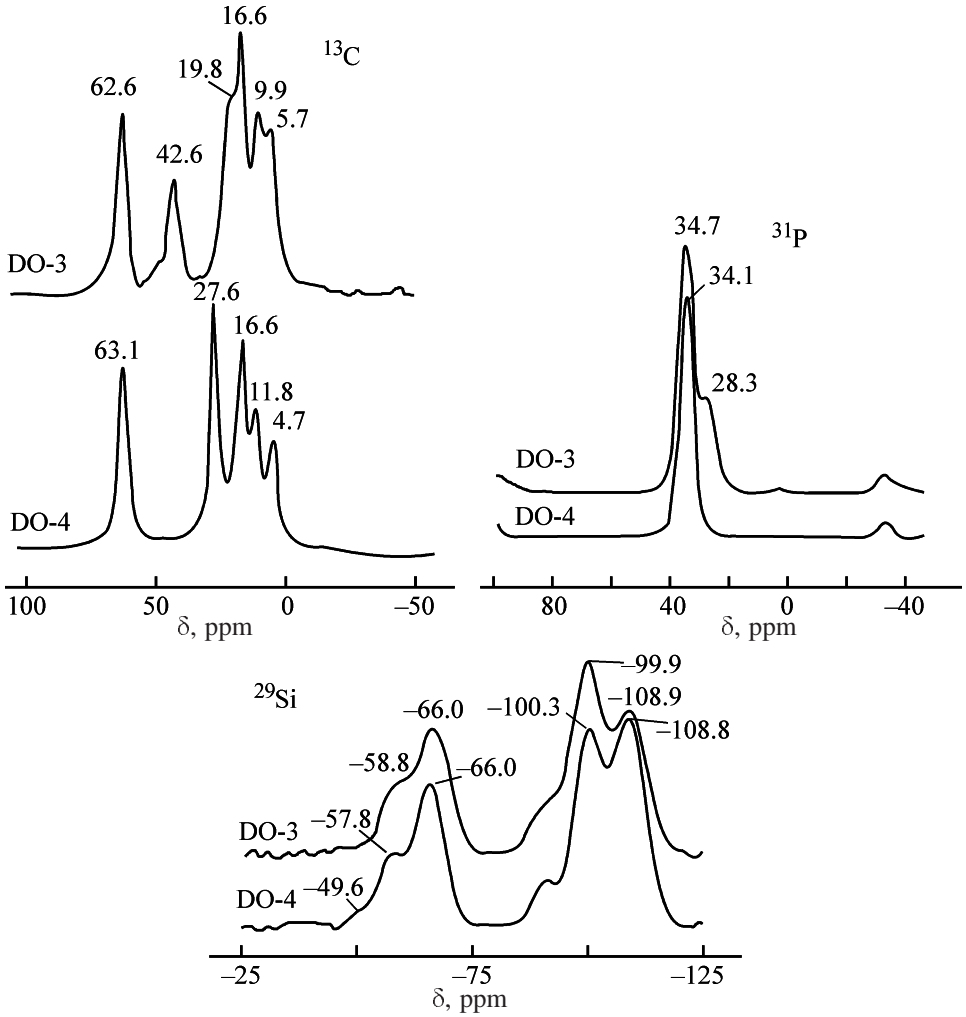


Fig. 3. CP/MAS NMR spectra of samples DO-3 and DO-4. (δ) Chemical shift.

the overlap of the signals of two carbon atoms: –C[$\underline{C}H_2$]C– and –$\underline{C}H_2NH_2$.

As seen from Fig. 3, the ^{13}C CP/MAS NMR spectra of the samples prepared under similar conditions differ from each other. For example, for sample DO-4 only one signal is identified at 34 ppm, whereas for sample DO-3, along with a strong signal at 35 ppm, an additional weaker signal at 28 ppm is observed. This second signal is probably due to interaction of the phosphorus-containing group with the xerogel surface with the formation of bridges like ≡Si$(CH_2)_2$P(O)–(OC_2H_5)OSi≡, which can appear in the course of prolonged drying of the samples under reduced pressure. In other words, one of the ethoxy groups bound with the phosphorus atom interacts with the silanol group to form ethanol, which is removed from the sample upon drying. A similar phenomenon was observed for xerogels with a monofunctional surface layer [20, 21].

The ^{29}C Si/MAS NMR spectra of samples DO-3 and DO-4 are similar, and their shapes are typical of polysiloxane xerogels (Fig. 3). In the range from –45 to –70 ppm, the spectrum of sample DO-3 exhibits only two signals, which are due to the presence of structural units T^2 and T^3 in the xerogel [18]. Thus, the xerogel surface layer contains no readily hydrolyzable structural units of T^1 type, i.e., there are no structural units which are linked to the polysiloxane skeleton by a single siloxane bond. However, the signal of this structural unit is observed in the ^{29}Si CP/MAS NMR spectrum of sample DO-4 (Fig. 3). Three other signals in the range from –90 to –110 ppm belong to the structural units of Q^n type (n = 2, 3, or 4) [22]. Thus, the data of solid-state NMR spectroscopy not only confirm but also supplement the conclusions based on the IR data.

The isotherms of the low-temperature adsorption–desorption of nitrogen on porous xerogels are shown

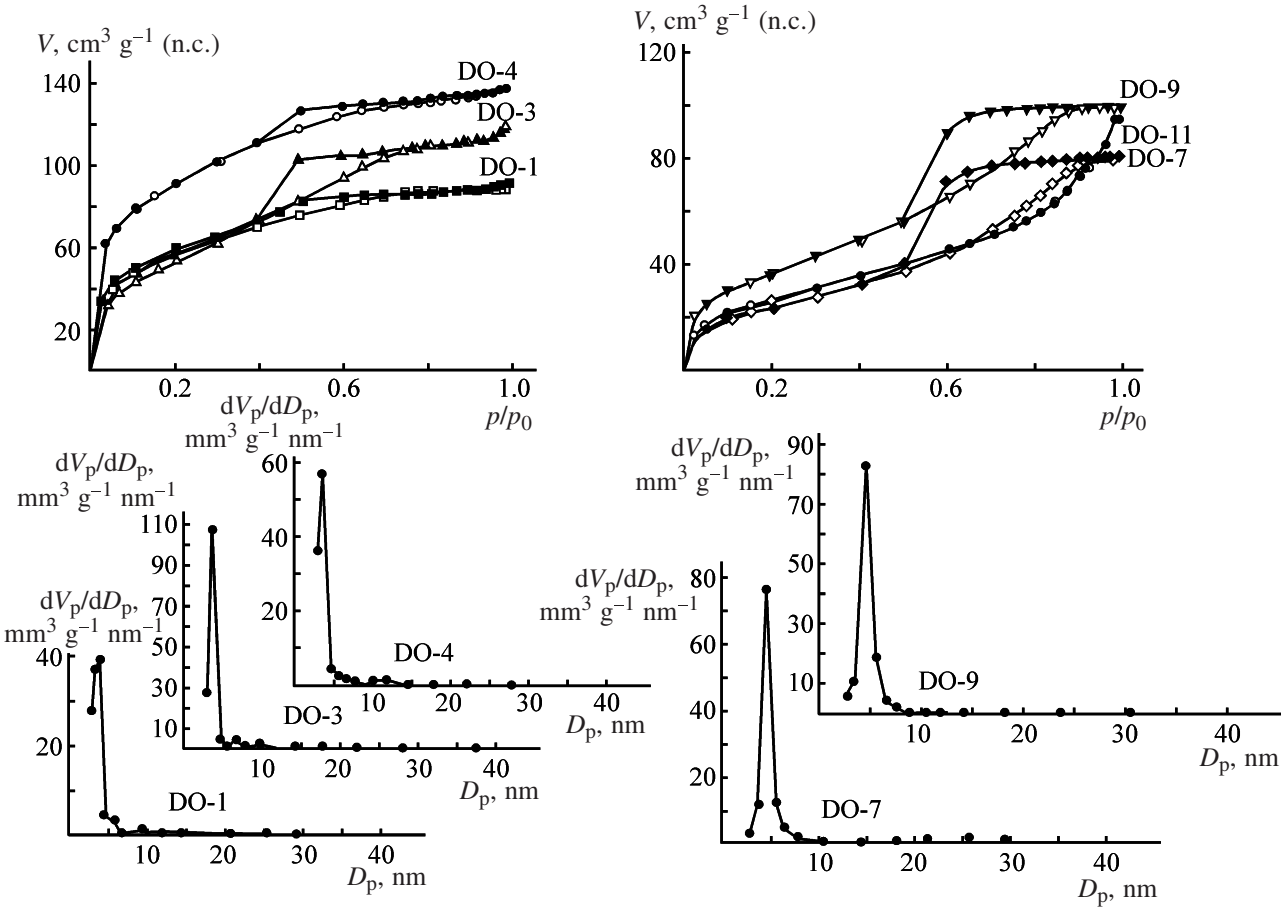


Fig. 4. Sorption–desorption isotherms of nitrogen and pore size D_p distribution dV_p/dD_p of the xerogels studied. (V) Volume of adsorbed nitrogen and (p/p_0) relative pressure.

in Fig. 4. The isotherms of samples DO-1, DO-3, DO-4, DO-7, and DO-9 belong to type IV in accordance with the IUPAC classification [23] and exhibit a hysteresis in the relative pressure range 0.4–0.8. They are also characterized by relatively narrow pore diameter distribution (Fig. 4). The pore sizes evaluated from these curves (see table) suggest that all the xerogels studied have the mesopore structure. The shape of the sorption isotherm of sample DO-11 differs from that of the above samples (Fig. 4); this also concerns the pore structure parameters (see table). This result can be attributed to the fact that in the course of synthesis of the given xerogel a precipitate rather than a gel is formed throughout the solution bulk.

The structural and adsorption parameters given in the table allow the following conclusions. In the systems prepared using DPTS at the molar ratio TEOS : trifunctional silanes = 2 : 1 (0.5 + 0.5), porous xerogel was formed only on addition of the amino group (sample DO-1). With increasing molar ratio to 3 : 1 (0.5 + 0.5), porous xerogels were formed on introduction of both 3-aminopropyl and 3-mercaptopropyl groups (samples DO-3 and DO-4). It should be noted that the xerogels prepared in [15] at the TEOS : DPTS ratios of 2 : 1 and 3 : 1 were nonporous. However, the conditions for preparing these samples and those described above were similar. The same phenomenon was observed for xerogels containing thiourea group $\equiv Si(CH_2)_3NHC(S)NHC_3H_7$-$n$ in the surface layer [6]. This fact confirms our previous conclusion on the noticeable effect of the size of the introduced functional groups on the structural and sorption parameters of the resulting xerogels. In general, the parameters of the pore structure of samples DO-5–DO-8 do not contradict this conclusion (see table). For example, replacement of DPTS by DEPPA and DEPPAT with bulkier functional groups (molar ratio of the reacting alkoxysilanes 2 : 1) provides formation of almost nonporous or weakly porous (in the case of DO-7) samples. With an increase in this ratio to 3 : 1, a xerogel with the developed surface containing additional amino group (sample DO-9) was prepared. With the amino group replaced by the

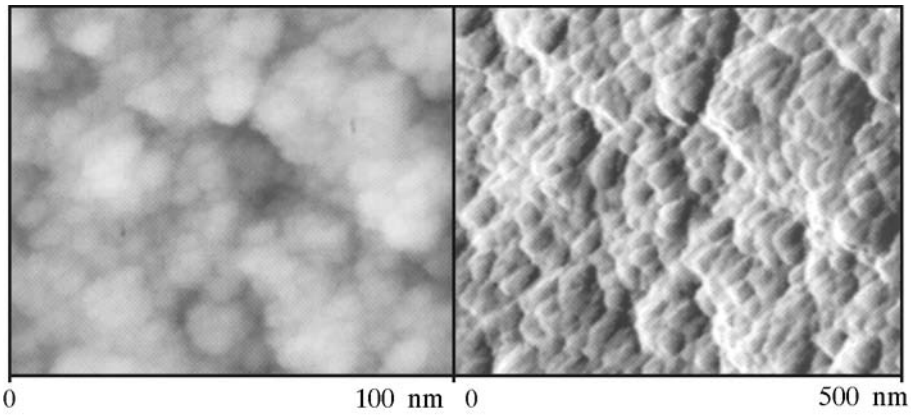


Fig. 5. Photomicrographs of xerogel DO-4, obtained by atomic force microscopy.

mercapto group, only nonporous samples were prepared at any molar ratio (2 : 1–4 : 1) of the reactants (see table). Probably, in this case the pore structure parameters are determined not only by an increase in the size of functional groups, but also by changes in the medium in which the hydrolytic polycondensation occurs (it changes from alkaline to nearly neutral).

The photomicrographs of xerogel DO-4 shown in Fig. 5 indicate that the sample surface is nonuniform. As can be seen, the xerogel particles are nearly spherical and they are probably aggregates of primary particles (globules). As we found, the sizes of these aggregates are similar and vary within 40–50 nm.

CONCLUSIONS

(1) The sol–gel procedure allows one-step preparation of the xerogels with a bifunctional surface layer and a relatively high total content of functional groups (3.6 mmol g^{-1}).

(2) The replacement of such complexing groups as $\equiv Si(CH_2)_3P(O)(OC_2H_5)_2$ by bulkier functional groups such as $\equiv Si(CH_2)_3NHP(O)(OC_2H_5)_2$ and $\equiv Si(CH_2)_3 \cdot NHP(S)(OC_2H_5)_2$ leads to the formation of nonporous compounds.

(3) The replacement of 3-aminopropyl groups in the bifunctional surface layer by 3-mercaptopropyl groups does not lead to the formation of porous xerogels even when the ratio of the reacting alkoxysilanes (tetraethoxysilane/mixture of trifunctional silanes) reaches $4 : 1(0.5 + 0.5)$. This fact suggests that the pore structure is determined not only by the size of functional groups but also by changes in the medium in which the hydrolytic polycondensation occurs.

REFERENCES

1. Zub, Yu.L. and Chuiko, A.A., *Colloidal Silica: Fundamentals and Applications*, Bergna, H.E. and Roberts, W.O., Eds., Boca Raton: CRC, 2006, pp. 397–424.
2. Zub, Yu.L. and Chuiko, A.A., *Combined and Hybrid Adsorbents: Fundamental and Applications* (ARW NATO), Loureiro, J.M. and Kartel, M., Eds., Springer, 2006, pp. 3–21.
3. Voronkov, M.G., Vlasova, N.N., and Pozhidaev, Yu.N., *Appl. Organomet. Chem.*, 2000, vol. 14, pp. 287–303.
4. El-Nahhal, I.M., Yang, J.J., Chuang, I.-C., and Maciel, G.E., *J. Non-Cryst. Solids*, 1996, vol. 208, pp. 105–118.
5. Yang, J.J., El-Nahhal, I.M., Chuang, I.-C., and Maciel, G.E., *J. Non-Cryst. Solids*, 1997, vol. 212, pp. 281–291.
6. Zub, Yu.L., Melnyk, I.V., Chuiko, A.A., et al., *Chem. Phys. Technol. Surf.*, 2002, no. 7, pp. 35–45.
7. Melnyk (Seredyuk), I.V., Zub, Yu.L., Chuiko, A.A., and van der Voort, P., *Chem. Phys. Technol. Surf.*, 2002, no. 8, pp. 125–133.
8. Zub, Yu.L., Gorochovatskaya, M.Ya., Chuiko, A.A., and Nesterenko, A.M., Extended Abstracts, *Fourth Int. Conf. on Fundamentals of Adsorption*, Kyoto (Japan), 1992, pp. 461–463.
9. Zub, Yu.L., Drozd, L.S., and Chuiko, A.A., Abstracts of Papers, *IUPAC Symp. on the Characterization of Porous Solids*, Marseille (France), 1993, p. 95.
10. Dudarko, O.A., Zub, Yu.L., Semenii, V.Ya., and Dabrowski, A., *Kolloid. Zh.*, 2007, vol. 69, no. 1, pp. 72–80.
11. Brunauer, S., *The Adsorption of Gases and Vapors*, Princeton: Princeton Univ., 1943.
12. Barret, E.P., Joyner, L.C., and Halenda, P.P., *J. Am. Chem. Soc.*, 1951, vol. 73, pp. 373–380.

13. Gregg, S.J. and Sing, K.S.W., *Adsorption, Surface Area and Porosity*, London: Academic, 1982.
14. Li n-Vien, D., Colthup, N.B., Fateley, W.G., and Grasselli J.G., *The Handbook of Infrared and Raman Characteristic Frequencies of Organic Molecules*, London: Academic, 1991.
15. Dudarko, O.A., Mel'nik, I.V., Zub, Yu.L., et al., *Kolloidn. Zh.*, 2005, vol. 67, no. 6, pp. 753–758.
16. Finn, L.P. and Slinyakova, I.B., *Kolloidn. Zh.*, 1975, vol. 37, no. 4, pp. 723–729.
17. Aliev, A., Ou, D.L., Ormsby, B., and Sullivan, A.C., *J. Mater. Chem.*, 2000, vol. 10, pp. 2758–2764.
18. Maciel, G.E., in *Solid State NMR of Polymers*, Amsterdam: Elsevier, 1998, pp. 923–984.
19. Zub, Yu.L., Mel'nik, I.V., Stolyarchuk, N.V., et al., *Khimiya, fizika i tekhnologiya poverkhnosti* (Chemistry, Physics, and Technology of Surfaces), Kiev: Naukova Dumka, 2006, issues 11–12, pp. 185–203.
20. Dabrowski, A., Barczak, M., Dudarko, O.A., and Zub, Yu.L., *Pol. Chem. J.*, 2007, vol. 81, pp. 475–483.
21. Dudarko, O.A., Mel'nik, I.V., Zub, Yu.L., et al., *Neorg. Mater.*, 2006, vol. 42, no. 4, pp. 413–420.
22. Enhelhardt, G. and Mishel, D., *High-Resolution Solid-State NMR of Silicates and Zeolites*, Chichester: Wiley, 1987.
23. Sing, K.S.W., Everett, D.H., Haul, R.A.W., et al., *Pure Appl. Chem.*, 1985, vol. 57, no. 4, pp. 603–619.

ISSN 1070-4272, Russian Journal of Applied Chemistry, 2008, Vol. 81, No. 1, pp. 123–127. © Pleiades Publishing, Ltd., 2008.
Original Russian Text © R.Z. Khairullin, V.P. Arkhireev, 2008, published in Zhurnal Prikladnoi Khimii, 2008, Vol. 81, No. 1, pp. 127–131.

MACROMOLECULAR CHEMISTRY AND POLYMERIC MATERIALS

Modification of High-Density Polyethylene with Binary Mixtures of ε-Caprolactone and ε-Caprolactam

R. Z. Khairullin and V. P. Arkhireev

Kazan State Technological University, Kazan, Tatarstan, Russia

Received August 13, 2007

Abstract—Modification of high-density polyethylene with binary mixtures of ε-caprolactone and ε-caprolactam was performed. The composition–property diagrams reflecting the dependences of the physicomechanical, rheological, and optical properties of the resulting polymeric compounds on the content of modifying mixture components were constructed, and the thermal oxidative degradation of the blend samples was studied. Based on the results obtained, the optimal modifier concentrations were suggested.

DOI: 10.1134/S1070427208010278

Progress of engineering requires the development of new types of polymeric materials with a set of properties that are not exhibited by the known plastics. This problem can be largely solved by modification of polymers with the aim to adjust their properties to a level required by the conditions of processing and operation. Much success has been gained in the modification of polymers. Diverse modifying compounds were tested, either as fillers or as chemically active additives, in a wide concentration range with virtually all the known commercial polymers [1].

Modification of polymers with individual compounds allows improvement of many of their processing and service characteristics. However, in some cases the use of binary mixtures leads to an effect significantly exceeding that produced by the components taken separately, i.e., to a synergistic effect [2]. From this viewpoint, modification with binary systems opens wide prospects for improving the properties of polymeric materials. At the same time, it is difficult to find among the diversity of chemical compounds the components that would enhance the effect of each other.

In this study we chose as modifying additives the heterocyclic compounds that are capable to chemically react with each other to form various copolymers and with the polymer subjected to modification (high-density polyethylene, HDPE) at temperatures close to that of HDPE processing. The products formed in these reactions can significantly affect the properties of the modified polymer.

We chose HDPE as one of large-tonnage products of polymer chemistry. In the world production of polymerization plastics, polyethylene (PE) occupies the first place thanks to a combination of valuable properties with the feasibility of processing by all the known highly productive methods used in the technology of thermoplastics. In addition, PE is one of the cheapest polymers, which also makes its use economically sound.

The goal of this study was to evaluate the efficiency of HDPE modification with ε-caprolactam (ε-CLM) and ε-caprolactone (ε-CLN) taken both separately and as binary mixtures, and also to determine the optimal concentrations of the modifying additives.

EXPERIMENTAL

Experiments were performed with HDPE of 277-73 brand [GOST (State Standard) 16338–85], produced by the Organicheskii Sintez Joint-Stock Company (Kazan) and widely used for production of various articles. The modifying additives were ε-CLN and ε-CLM, widely used as monomers for the commercial production of the corresponding polyesters and polyamides.

The components were compounded in a melt on a Brabender rotary mixer at 170°C, with simultaneous introduction of the modifying components. Additionally, 0.1 wt % 2,4-toluene diisocyanate, an activator of anionic polymerization of ε-CLN and ε-CLM, was introduced into the melt.

To optimize the search for effective compositions of modifying mixtures, we used the simplex–lattice experimental design [3–5]. As approximating polynomial we chose third- (maximal content of the addi-

Table 1. Some physicomechanical characteristics of HDPE modified with binary mixtures of ε-CLM and ε-CLN in the presence of SL (numerator) and without it (denominator)

Composition, wt %			σ_t^*, MPa	E, MPa
HDPE	ε-CLN	ε-CLM		
100	–	–	29.0	786
97	1	–	30.2/28.5	831/1022
97	–	1	27.2/27.9	722/1058
97	2	1	32.9/27.7	883/1035
97	1	2	26.8/26.4	788/983
98	2	–	26.4/27.5	808/984
99	1	–	28.5/30.0	826/1133
98	–	2	29.3/27.8	810/1050
99	–	1	28.1/29.6	861/1074
98	1	1	28.8/30.4	1085/1128

* (ε_t) Breaking tensile stress and (E) elastic modulus.

tive 3 wt %) and fourth-order (maximal content of the additive 12 wt %) Scheffe models. To construct the composition–property diagrams, we used the program developed at the Kazan State University.

The mid-IR spectra of the reaction products of HDPE and the binary mixture were recorded on a Bruker FT-IR spectrophotometer from the preliminarily prepared films. Quantitative treatment of the IR spectra was performed with an internal reference [6].

The physicomechanical characteristics were determined in accordance with GOST (State Standard) 11262–80 at 20±2°C (samples of type 1) on an Inspekt mini tensile-testing machine (Trilogica) at a clamp velocity of 100 mm min^{-1}. Samples were cut out from plates prepared by direct hot pressing in accordance with GOST 12019–66.

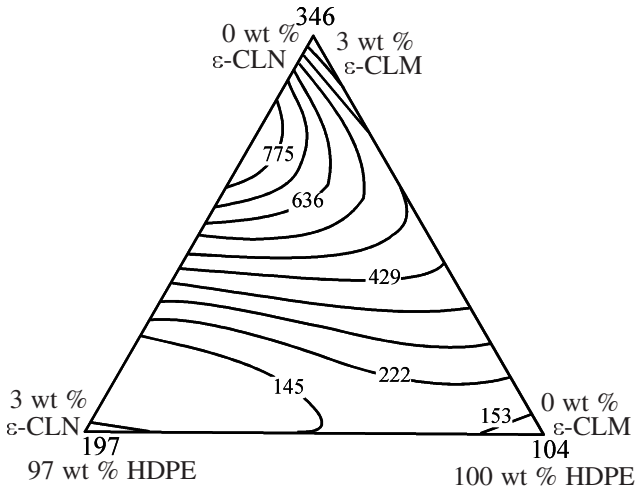


Fig. 1. Isolines of ε of the system HDPE–ε-CLN–ε-CLM.

The melt flow index (MFI) was determined in accordance with GOST 11645–83 on an IIRT-type capillary viscometer at 190°C and a load of 5 kg.

The optical density of polymer samples, preliminarily pressed and having equal thickness, was measured with an SF-2000 spectrophotometer.

To evaluate the stabilizing effect of the modifiers, we studied the autooxidation of HDPE. The method is based on the determination of the amount of oxygen taken up by the polymer at high temperatures. Tests were performed on an installation consisting of differential manometers to which the test tubes containing the modified samples were connected. The test tubes were placed in a thermostat kept at 200°C. The amount of oxygen taken up by the polymer was evaluated from the pressure change.

It is known that ε-CLM and ε-CLN copolymerize to form the corresponding poly(amido esters) (PAEs) [7]. The composition of the copolymers depends on the content of the monomers in the starting mixture. The activators of the anionic polymerization of these compounds are isocyanates, and the reaction rate increases in the presence of lactamates of various alkali metals [8].

It was of certain interest to examine the effect of the modifiers and their transformation products on the whole set of HDPE properties, and also to estimate how sodium lactamate (SL) acting as accelerator of the anionic polymerization affects the properties of the polymeric compounds. For this purpose, we additionally examined the effect of SL on the properties of modified HDPE. We obtained two series of polymeric compounds, one of which contained SL in catalytic concentrations and ther other was prepared without the catalyst.

The physicomechanical tests showed that the catalyst exerts a certain effect on the properties of the polymeric compound (Table 1). It should be noted that, on the whole, there is no rigorous relationship between the presence of SL in the polymeric compound and the physicomechanical properties. This result can be accounted for by the fact that the presence of SL favors more complete passing of both homo- and copolymerization of ε-CLM and ε-CLN and that the copolymers formed in the process strongly affect the physicomechanical properties of HDPE.

It should be noted that the alkali metal present in the HDPE matrix may somewhat accelerate the thermal oxidative degradation of HDPE. Therefore, our further experiments were performed with the samples containing no catalyst.

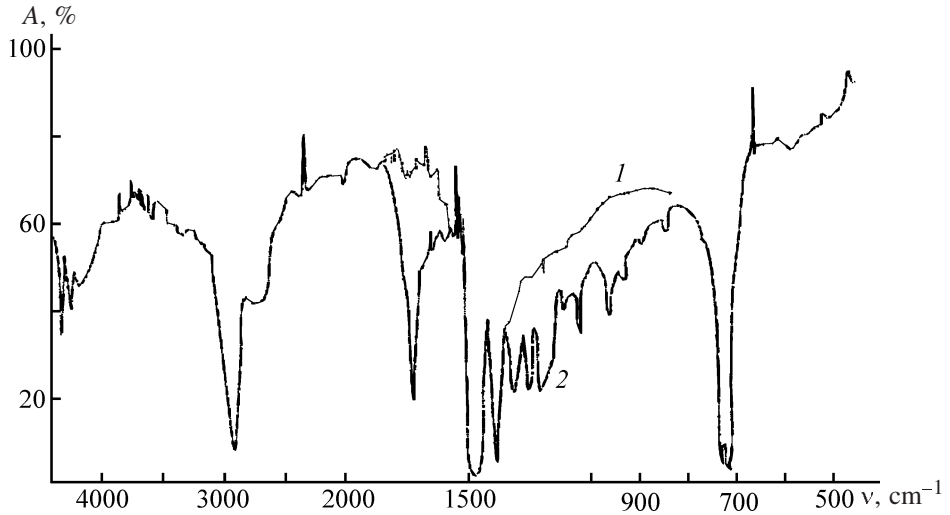


Fig. 2. IR spectra of (*1*) initial HDPE and (*2*) HDPE modified with a binary mixture of ε-CLM and ε-CLN. Molar ratio of the modifiers 1 : 1. (*A*) Absorption and (ν) wavenumber.

We should also note a considerable incrase in the relative breaking elongation ε upon modification of HDPE with small concentrations of ε-CLN and ε-CLM. However, the highest ε is observed with the binary mixtures, rather than with the individual modifiers (Fig. 1). For example, modification of HDPE with a binary mixture of 1 wt % ε-CLN and 2 wt % ε-CLM increased ε by a factor of more than 8, compared to unmodified HDPE, with the strength properties remaining on the same level as for straight HDPE.

Our results can be attributed to the occurrence of the anionic polymerization in the course of compounding at elevated temperatures, with opening of the lactam ring of ε-CLM and lactone ring of ε-CLN. As a result, poly(amido esters) are formed, which interact with defects of the HDPE amorphous phase, altering its structure and ultimately increasing ε. The occurrence of the copolymerization was confirmed by comparison of the IR spectra of the initial and modified HDPE (Fig. 2).

Figure 2 shows that new bands appear at about 1730 (vibrations of ester carbonyl group), 1470 (methylene C–H bending vibrations), and 1170 cm^{-1} (C–O stretching vibrations). These facts show that ε-CLM and ε-CLN undergo anionic copolymerization with opening of the corresponding heterorings.

The formation of PAEs can also be indirectly confirmed by an increase in the optical density *D* of the modified polymeric compounds. The products formed from ε-CLN and ε-CLM are incompatible with HDPE because of their essentially different polarity, and it can be expected that they will form a separate phase and thus increase *D* to the greater extent, the more heterogeneous is the polymer blend. In our case, the highest optical densities are observed with HDPE modified specifically with binary mixtures of ε-CLN and ε-CLM. This fact suggests that the forming copolymers are less compatible with HDPE than the homopolymers of ε-CLN and ε-CLM. Data on *D* of the HDPE-based polymeric compounds are given in Table 2.

One of the main processing characteristics of a polymer is the melt flow index. This quantity deter-

Table 2. Optical density of HDPE modified with binary mixtures of ε-CLN and ε-CLM

Composition, wt %			*D* at indicated wavelength, nm		
HDPE	ε-CLN	ε-CLM	400	600	800
100	–	–	2.3359	2.1188	1.6236
99	1	–	2.6152	2.2773	1.7969
99	–	1	2.5365	2.2846	1.9375
98	2	–	2.6654	2.2996	2.7149
98	–	2	2.8264	2.3515	1.9216
97	3	–	2.7650	2.4580	2.9942
97	–	3	2.5882	2.3464	2.0257
97	2	1	2.6455	2.2997	1.9427
97	1	2	2.9270	2.4811	2.2988
98	1	1	2.4951	2.3359	2.0287
97	1	2	2.9270	2.4811	2.2988
97	2	1	2.6435	2.2997	1.9427
94	3	3	2.5659	2.3421	2.1548
91	6	3	2.5699	2.4021	2.2976
91	3	6	2.9834	2.4771	2.3238
88	6	6	2.4859	2.2986	2.1563

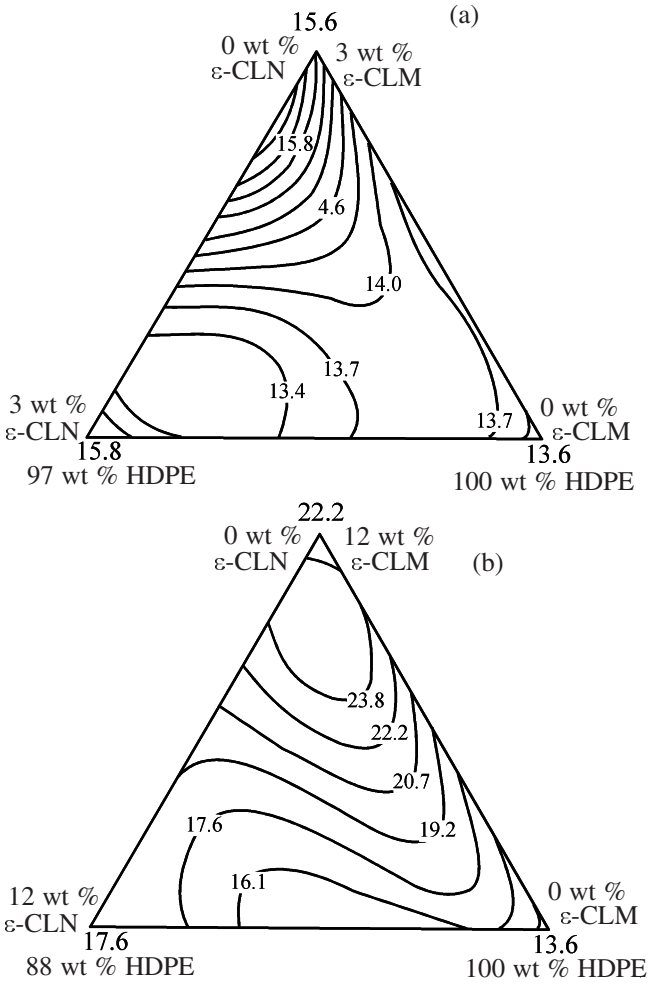


Fig. 3. Isolines of MFI of the HDPE–ε-CLN–ε-CLM system at the maximal content of the modifying additive of (a) 3 and (b) 12 wt %.

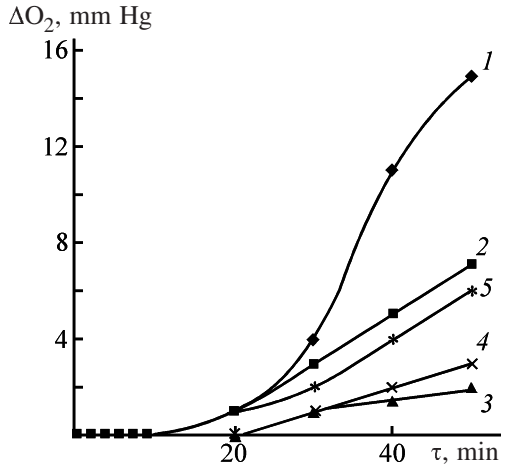


Fig. 4. Oxygen uptake ΔO_2 by HDPE modified with ε-CLN, ε-CLM, and their binary mixtures. (τ) Time. Additive, wt %: (*1*) none, (*2*) 6 ε-CLN, (*3*) 6 ε-CLM, (*4*) 6 ε-CLN + 6 ε-CLM, and (*5*) 1 ε-CLN + 1 ε-CLM.

mines the feasibility and optimal procedure of plastic deformation (extrusion, die casting, etc.) for polymer processing. A decrease in the viscosity of the polymer melt, with the other characteristic preserved, allows considerable saving of power for heating the equipment and reduction of the equipment wear.

Measurement of the rheological characteristics of HDPE blend modified with binary mixtures of ε-CLM and ε-CLN demonstrated the efficiency of these substances as additives decreasing the temperature of polymer processing (Fig. 3).

A study of the effect of modifiers on the viscosity of the HDPE melt showed that the maximal decrease in the melt viscosity is also provided by binary mixtures of ε-CLN and ε-CLM. Addition of even small amounts of the modifiers (Fig. 3a) leads to a noticeable decrease in the melt viscosity. A stronger effect is observed with larger amounts of the modifiers. The most pronounced decrease in the viscosity is provided by the binary mixture of 3 wt % ε-CLN + 9 wt % ε-CLM. When introduced into HDPE, this mixture increases its MFI to 23.4 g/10 min, i.e., by a factor of almost 2 relative to staight HDPE.

The effects observed can be accounted for by the fact that the PAEs formed from ε-CLN and ε-CLM exhibit a certain plasticizing effect.

One of the main causes of limited use of polymers as structural materials is aging, namely, changes in the polymer characteristics with time under the action of various factors of the environment. From this viewpoint, it is important to enhance the resistance of a polymer to these factors.

To evaluate how the additives in hand affect the resistance of the polymer to thermal oxidative aging, we examined HDPE samples modified with binary mixtures of ε-CLN and ε-CLM. The results are given in Fig. 4. It was found that the oxidation curves have a combined shape, i.e., both the induction period and autoacceleration are obseved. It should be noted that the oxidation curves of HDPE samples modified with ε-CLN, ε-CLM, and their binary mixtures lie below the oxidation curve of staight HDPE. Thus, ε-CLN and ε-CLM at high temperatures exhibit a certain stabilizing effect.

CONCLUSIONS

(1) The use of binary mixtures of ε-caprolactone and ε-caprolactam as modifiers for high-density polyethylene is preferable over separate use of these modifiers.

(2) Modification of high-density polyethylene with binary mixtures of ε-caprolactone and ε-caprolactam, on the one hand, appreciably decreases the viscosity of the polymer melt and, on the other hand, increases the relative breaking elongation, with the breaking tensile stress remaining essentially the same as for straight high-density polyethylene.

(3) The effects observed are associated with the occurrence of the anionic copolymerization of ε-caprolactone and ε-caprolactam at elevated temperature in the presence of isocyanate activator. The poly(amido esters) formed, interacting with defects of the amorphous phase of high-density polyethylene, alter its structure, causing a sharp increase in the relative breaking elongation.

REFERENCES

1. Sirota, A.G., *Modifikatsiya struktury i svoistv poliolefinov* (Modification of the Structure and Properties of Polyolefins), Moscow: Khimiya, 1969.
2. Kochnev, A.M., Zaikin, A.E., Galibeev, S.S., and Arkhireev, V.P., *Fizikokhimiya polimerov* (Physical Chemistry of Polymers), Kazan: Fen, 2003.
3. Zergenidze, I.G., *Planirovanie eksperimenta dlya issledovaniya mnogokomponentnykh sistem* (Experimental Design for Studying Multicomponent Systems), Moscow: Nauka, 1976.
4. Adler, Yu.A., Markova, E.V., and Granovskii, Yu.V., *Planirovanie eksperimenta pri poiske optimal'nykh uslovii* (Experimental Design in Searching for Optimal Conditions), Moscow: Nauka, 1976.
5. *Novye idei v planirovanii eksperimenta* (New Ideas in Experimental Design), Nalimov, V.V., Ed., Moscow: Nauka, 1969.
6. *Praktikum po khimii i fizike polimerov* (Practical Course of Polymer Chemistry and Physics), Kurenkov, V.F., Ed., Moscow: Khimiya, 1995.
7. Goodman, I., *Eur. Polym. J.*, 1984, vol. 20, no. 6, pp. 549–557.
8. *Entsiklopediya polimerov* (Polymer Encyclopedia), Kargin, V.A., Ed., Moscow: Sov. Entsiklopediya, 1977.

ISSN 1070-4272, Russian Journal of Applied Chemistry, 2008, Vol. 81, No. 1, pp. 128–130. © Pleiades Publishing, Ltd., 2008.
Original Russian Text © N.A. Gushchin, G.U. Ostrovidova, E.A. Sosnov,2008, published in Zhurnal Prikladnoi Khimii, 2008, Vol. 81, No. 1, pp. 132–135.

MACROMOLECULAR CHEMISTRY AND POLYMERIC MATERIALS

Antimicrobial Polymeric Composite Films for Medical Use

N. A. Gushchin, G. U. Ostrovidova, and E. A. Sosnov

St. Petersburg State Institute of Technology (Technical University), St. Petersburg, Russia

Received June 28, 2007

Abstract—Preparation of prolonged-action antimicrobial polymeric films based on polyvinyl alcohol and carboxymethyl cellulose sodium salt (Na-CMC), modified with chlorohexidine, is studied. The effects of Na-CMC on the adsorption capacity, degradability, and specific weight of the electrodeposited film are examined.

DOI: 10.1134/S107042720801028X

Modification of polymers with bioactive compounds (BACs) has attracted a great interest in view of the development of immobilized biocatalysts, bioregulators, and prolonged-action drug dosage forms.

Many up-to-date therapeutic agents are characterized by a short durability because of ineffective drug formulation. Therefore, one has to repeatedly take a medicine, increasing the hazard of overdose and side effects [1].

The use of BACs immobilized on biocompatible polymers allows solution of this problem by increasing duration of prolonged action through controlled degradation of the polymeric support, by ensuring desired BAC liberation kinetics via control of the chemical composition of the carrier, and by providing a convenient drug dosage form via optimization of the polymer matrix.

The existing methods for modification of polymeric films with BACs do not always provide a prolonged effect of the immobilized BACs. For example, polyvinyl alcohol (PVA) films modified with immobilized protease C and polyhexamethyleneguanidine hydrochloride lose their enzymatic activity in 2–3 h and antimicrobial activity, in a day [2].

Electroforming shows promise as a method for preparing films of water-soluble polymers with simultaneous immobilization of bioactive components [3]. The method allows thickness-controlled preparation of film coatings of a complex composition. Furthermore, this is a time-saving method, which can be realized under mild conditions. The latter is particularly significant for BACs, as they are sensitive to elevated temperature and immobilization time.

Water-soluble polymers commonly used for film formation showed themselves for many years in medicine and pharmaceutics as nontoxic and highly biocompatible materials [4–6].

Here we report on preparation and characterization of prolonged-action antimicrobial polymeric films based on polyvinyl alcohol (PVA) and carboxymethyl cellulose.

EXPERIMENTAL

Polymeric films were prepared from polyvinyl alcohol [PVA, 16/1 grade; MW ~40000; GOST (State Standard) 10779–78] and carboxymethyl cellulose sodium salt [Na-CMC, Kamtsel-0 grade; MW ~120 000; TU (Technical Specifications) 2231-002-50277563-00]. Boric acid (GOST 9656–75) was used as a cross-linking agent. To impart antimicrobial activity, chlorohexidine (CH) (000 P no. 000734/01) was introduced into the formulation. The hydrogel was electroformed on a Si(111) support.

Chlorohexidine is widely used in medicine [7–9]. This antiseptic agent, taken in a concentration above 0.01%, demonstrates a strong bactericidal activity against most gram-positive and gram-negative aerobes and anaerobes, and fungicidal and antiviral activities as well.

The CH concentration was determined spectrophotometrically at $\lambda = 253$ nm. The antimicrobial activity of immobilized CH was measured in the agar-diffusion test [10] using *Staphylococcus citreus* as a test culture.

To improve the elastic characteristic of the films, 3 wt % glycerol (GOST 6259–75) was added into the formulation as a plasticizer [11].

The basic film-forming component is PVA [12, 13]. The film cannot be electroformed from a formulation containing only Na-CMC.

The presence of Na-CMC considerably increases the specific weight of the film deposited on the electrode (Fig. 1, curves *2, 3*). In aqueous Na-CMC, asso-

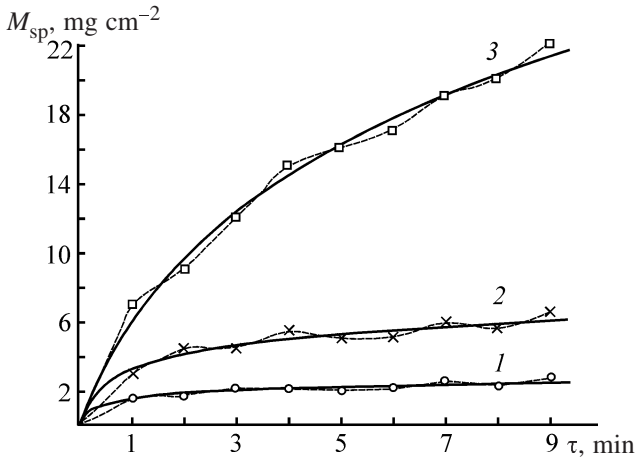


Fig. 1. Specific weight of the electroformed film M_{sp} as a function of the deposition time τ: (*1*) 1% CMC, (*2*) 3% PVA, and (*3*) 1% CMC + 3% PVA.

ciation of macromolecules occurs through intermolecular hydrogen bonding [6]. Evidently, similar interactions take place in the composite solution between free hydroxy groups of Na-CMC and PVA. In the electric field, the resulting associates move to the cathode to form a polymeric film. Na-CMC, used in this study, has a molecular weight three times that of PVA, thus increasing the specific weight of the electroformed film.

It was experimentally demonstrated that addition of Na-CMC increases the adsorption capacity of the resulting material with respect to chlorohexidine by virtue of electrostatic binding of the CH cations to COO^- groups of the Na-CMC molecules [14, 15] (Fig. 2).

The films were formed in the electric field of a 15–20 V cm^{-1} strength for 1–5 min. All the components of the composite solution are involved in the electrophoretic motion. On the cathode, a hydrogel of PVA, cross-linked with boric acid, is formed. Na-CMC also enters the composition of the hydrogel, but via hydrogen bonding with the hydrogel network. The chlorohexidine cation also moves to the cathode, which allows control of its concentration in the hydrogel by changing the film formation time (Fig. 2) [8].

The degradability of the polymeric films was characterized by the sample weight loss in water (Fig. 3). Addition of Na-CMC to the starting composite solution facilitates degradation. The reason is that Na-CMC does not form a strong chemical bond with the PVA hydrogel, but disturbs its structure, thus promoting degradation of the film. Heat treatment at 50°C improves the adhesion of the film to the electrode surface, decelerating the degradation (Fig. 3). In this case, the bioactivity of CH remains unchanged [8].

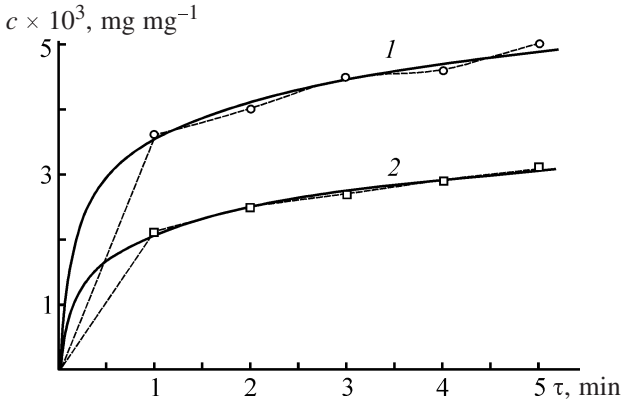


Fig. 2. Chlorohexidine content of the film as a function of the deposition time τ: (*1*) CMC + PVA and (*2*) PVA. CH content of the initial solution 0.01%.

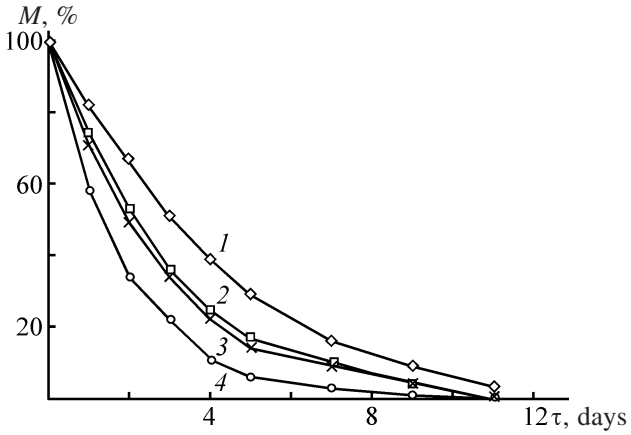


Fig. 3. Kinetic curves of the film degradation. (*M*) Weight loss and (τ) time. (*1*) 6% PVA, heat-treated; (*2*) 6% PVA, (*3*) 1% CMC + 6% PVP, heat-treated; and (*4*) 1% CMC + 6% PVA.

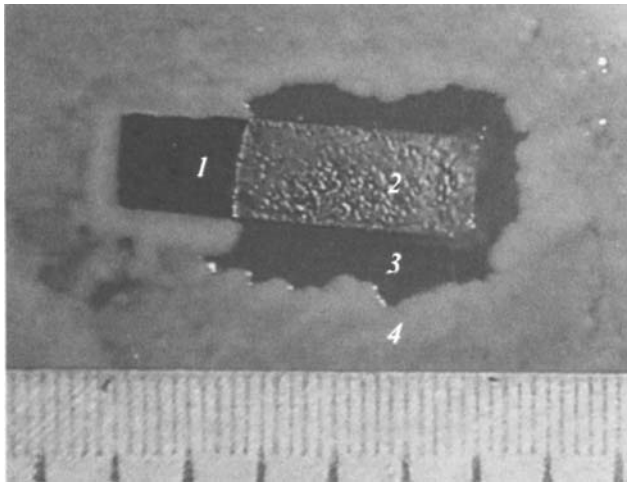


Fig. 4. Inhibition zone against the growth of *Staphylococcus citreus*. Chlorohexidine content about 0.005 mg mg^{-1}. (*1*) Coating-free electrode, (*2*) antimicrobial film, (*3*) growth inhibition zone, and (*4*) test culture of *Staphylococcus citreus* (3-day age).

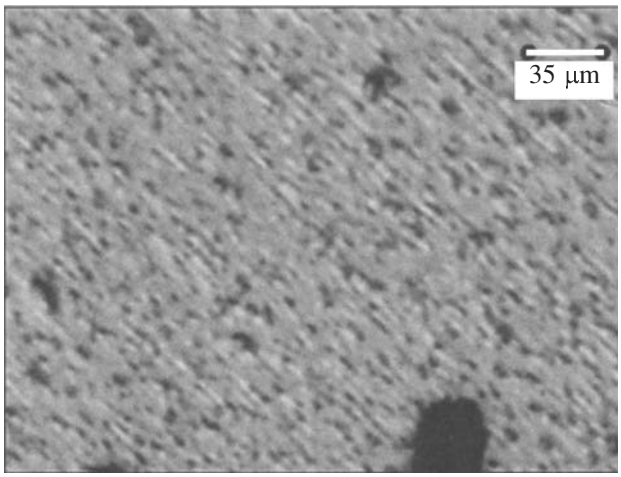


Fig. 5. Optical image of the film surface (cantilever width 35 μm).

The antimicrobial activity of the CH-doped films was demonstrated to be high even at a relatively low CH concentration (about 0.005 mg mg^{-1}) [7]. The inhibition zone against the test microorganisms was at least 15 mm (Fig. 4, zone *3*). The antimicrobial durability of the film was at least 7 days.

The surface morphology of the polymeric films was examined using a scanning tunneling microscope (Optem Int.) with an atomic-force probe. Figure 5 shows that the film surface is oriented (textured).

Finally, taking into account the biocompatibility of the polymeric matrix of the film and bactericidal properties of chlorohexidine, one may recommend the investigated films for use in local treatment of coverlets and mucous coats, particularly, for disinfection of postoperative stitches, wounds, and other injuries; and for treatment and infection prophylaxis of the oral cavity and parodentium [7–9].

CONCLUSIONS

(1) Modification of polyvinyl alcohol based films with carboxymethyl cellulose sodium salt improves their performance, including the specific weight of the film, adsorption capacity for bioactive substances, and degradability.

(2) The degradability of the films can be controlled by changing the composite formulation and by heat treatment.

(3) The films doped with chlorohexidine demonstrate a prolonged antimicrobial effect. The chlorohexidine content of the film can be controlled by changing the film electroforming parameters. The efficiency and duration of the antimicrobial action depend on the concentration of immobilized chlorohexidine and degradability of the matrix. The duration of the antimicrobial effect of the investigated films was at least 7 days.

REFERENCES

1. Marychev, S.N. and Kalinin, B.A., *Polimery v meditsine: Uchebnoe posobie* (Polymers in Medicine: A Handbook), Vladimir: Vladimir. Gos. Univ., 2001.
2. Yudanova, T.N., Skokova, I.F., Aleshina, E.U., and Gal'braikh, L.S., *Khim. Volokna*, 2001, no. 1, pp. 19–22.
3. USSR Inventor's Certificate no. 1 308 329.
4. Rozenberg, M.E., *Polymery na osnove vinilatsetata* (Vinyl Acetate Based Polymers), Leningrad: Khimiya, 1983.
5. Ushakov, S.N., *Polivinilovyi spirt i ego proizvodnye* (Polyvinyl Alcohol and Its Derivatives), Moscow: Akad. Nauk SSSR, 1960, vols. 1, 2.
6. *Cellulose and Cellulose Derivatives*, Bikales, N.M. and Segal, L., Eds., New York: Wiley, 1971.
7. *Lekarstvennye preparaty, primenyaemye v stomatologii: Spravochnik* (Medical Products for Dental Use: A Handbook), Yasnetsov, V.V. and Efremova, G.N., Eds., Moscow: GEOTAR MED, 2004.
8. Afinogenov, G.E. and Blinov, N.P., *Antiseptiki v khirurgii* (Antiseptics in Surgery), Leningrad: Meditsina, 1987.
9. *Antibiotic and Antimicrobial Use in Dental Practice*, Newman, M.G. and Winkelhoff, A.J. van, Eds., Chicago: Quintessence, 2001.
10. Vorob'ev, A.A., *Meditsinskaya i sanitarnaya mikrobiologiya: Uchebnoe posobie* (Medical and Sanitary Microbiology: A Handbook), Moscow: Akademiya, 2003.
11. Barshtein, R.S., Kirillovich, V.I., and Nosovskii, Yu.E., *Plastifikatory dlya polimerov* (Plasticizers for Polymers), Moscow: Khimiya, 1982.
12. Ostrovidova, G.U., Makeev, A.V., and Shamtsian, M.M., *J. Mater. Sci. Eng., Ser. C*, 2003, vol. 23, pp. 545–550.
13. Ostrovidova, G.U. and Makeev, A.V., *Zh. Prikl. Khim.*, 2002, vol. 75, no. 9, pp. 1509–1512.
14. Rogovin, Z.A., *Khimiya tsellulozy* (Cellulose Chemistry), Moscow: Khimiya, 1972.
15. Petropavlovskii, G.A., *Gidrofil'nye chastichno zameshchennye efiry tsellyulozy i ikh modifikatsiya putem khimicheskogo sshivaniya* (Hydrophilic Partly Substituted Cellulose Ethers and Esters and Their Modification by Chemical Cross-Linking), Leningrad: Nauka, 1988.

ISSN 1070-4272, Russian Journal of Applied Chemistry, 2008, Vol. 81, No. 1, pp. 131–134. © Pleiades Publishing, Ltd., 2008.
Original Russian Text © N.S. Shaglaeva, R.T. Sultangareev, E.A. Zabanova, O.V. Lebedeva, K.S. Trofimova, 2008, published in Zhurnal Prikladnoi Khimii, 2008, Vol. 81, No. 1, pp. 136–139.

MACROMOLECULAR CHEMISTRY AND POLYMERIC MATERIALS

Nucleophilic Substitution of Chlorine Atoms in Polyvinyl Chloride

N. S. Shaglaeva, R. T. Sultangareev, E. A. Zabanova, O. V. Lebedeva, and K. S. Trofimova

Favorskii Institute of Chemistry, Siberian Division, Russian Academy of Sciences, Irkutsk, Russia
Irkutsk State Technical University, Irkutsk, Russia

Received May 15, 2007

Abstract—To modify properties of polyvinyl chloride, its chlorine atoms were substituted using sodium salts of pyrazole, 3,5-dimethylpyrazole, and 2-mercaptobenzimidazole.

DOI: 10.1134/S1070427208010291

Polyvinyl chloride (PVC) is one of the most important polymers produced on a large scale. High cost efficiency of production and application of PVC in different branches of industry caused fast growth in its production in many countries, which is due to availability and low cost of the initial raw material, valuable physical and physicochemical properties of materials and articles made of PVC, and advances in stabilization of PVC and its processing.

However, PVC has a number of significant drawbacks. The most serious drawback is that the straight polymer cannot be processed. The presence of C–Cl bonds determining many properties of PVC is the main cause of its poor solubility in organic solvents, very high viscosity of its melts, and low thermal stability at temperatures required for its effective processing.

The most widely used method for modifying PVC properties is copolymerization of vinyl chloride (VC) with one or several monomers. The PVC properties can also be improved by nucleophilic substitution of chlorine atoms in the polymer. Copolymerization of VC was extensively studied [1, 2], whereas substitution of chlorine in PVC was given much less attention.

In this study we examined nucleophilic substitution of chlorine atoms in PVC. For this purpose we used sodium salts of pyrazole (pz), 3,5-dimethylpyrazole (dpz), and 2-mercaptobenzimidazole (mbi).

EXPERIMENTAL

Commercial pz, dpz, and mbi were recrystallized from ethanol.

Sodium and potassium salts of pz, dpz, and mbi were prepared as follows. The initial pz, dpz, or mbi (1 mol) were dissolved in ethanol (30 ml). To this solution, an aqueous solution of NaOH or KOH (1 mol) was added. The reaction mixture was kept for 3 h at room temperature. The solvent was removed and the resulting salt was dried by azeotropic distillation with benzene. The purity of the salt was determined by potentiometric titration.

Substitution of chlorine atoms was performed in solvents purified by known methods [3]. To a 4% PVC solution, Na or K salts of pz, dpz, and mbi were added in portions at a definite temperature. The salts were isolated by dialysis or precipitation into water. The product was filtered off, washed with water, and dried. The viscosity of polymer solutions was measured on an Ubbelohde viscometer at 25°C. Elemental analysis of the reaction products was performed on a Thermo Finnigan gas analyzer.

The IR spectra of the copolymers in the form of KBr pellets or mulls in mineral oil were recorded on a Specord IR-75 or Bruker IFS-25 spectrophotometer. The ^{13}C NMR spectra of the copolymers were taken on a Varian VXR-500S spectrometer operating at 125.5 MHz with relaxation delay of 2.5 s and 90° pulse in DMSO-d_6 solutions. Chromium(III) acetylacetonate (0.02 M) was used as a relaxation agent. The relative integration error was 3%. The ^{1}H NMR spectra were recorded on a Bruker DPX-400 spectrometer operating at 400.13 MHz in C_6D_6 and DMSO-d_6. The concentration of the polymer solutions was 1%.

The specific surface area of the composites was de-

Table 1. Nucleophilic substitution of chlorine atoms in PVC with sodium salts of pz and dpz

Run no.	Reactant ratio	Solvent	T, °C	Elemental analysis, %				Yield, %	Solubility
				C	H	N	Cl		
1	PVC : Na-pz = 1 : 1	DMF	0–2	42.69	4.68	1.47	50.68	24	Soluble
2	PVC : Na-pz = 1 : 1	DMF	10–12	45.42	5.17	1.84	44.36	27	Insoluble
3	PVC : Na-pz = 1 : 1	DMF	20–22	59.54	6.24	3.99	16.00	27	Insoluble
4	PVC : Na-pz = 1 : 1	DMF	40–45	47.46	6.45	1.36	38.08	29	Insoluble
5	PVC : Na-pz = 1 : 2	DMF	0–2	67.00	5.94	4.73	8.25	14	Insoluble
6	PVC : Na-dpz = 1 : 1	DMF	(–10)–(–15)	41.03	5.90	0.85	53.76	35	Soluble
7	PVC : Na-dpz = 1 : 1	DMF	10–12	39.47	4.92	1.61	53.89	38	Insoluble
8	PVC : Na-dpz = 1 : 1	DMF	20–22	45.57	5.26	1.81	35.71	22	Insoluble
9	PVC : Na-dpz = 1 : 1	DMSO	20–22	48.34	5.59	2.04	36.49	23	Insoluble
10	PVC : Na-pz = 1 : 1	CH	40–45	47.12	5.70	1.29	42.54	20	Insoluble
11	PVC : Na-dpz = 1 : 1	CH	40–45	49.84	5.94	1.53	32.98	19	Insoluble
12	PVC : K-pz = 1 : 1	DMF	0–2	39.23	5.02	1.34	56.31	23	Soluble
13	PVC : K-dpz = 1 : 1	DMF	20–22	45.84	5.58	4.25	38.50	23.7	Insoluble
14	PVC : K-pz = 1 : 1	CH	20–22	43.16	5.46	0.26	49.53	23	Insoluble

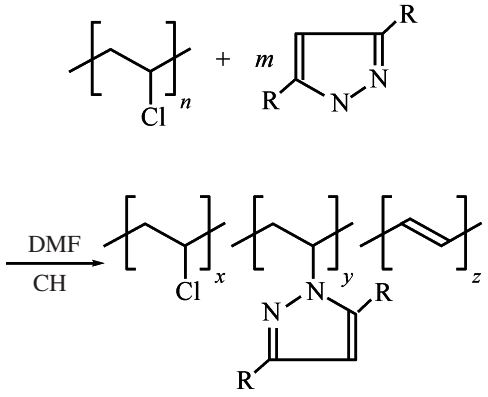
termined by nitrogen adsorption at different pressures. The measurements were performed in a graduated high vacuum.

We used emulsion PVC soluble in dimethylformamide (DMF), dimethyl sulfoxide (DMSO), and cyclohexanone (CH). The polymer has the following properties: Fickentscher constant K_F = 62–63, T_{dec} = 120°C, and specific surface area of 1.81 $cm^2 g^{-1}$.

Nucleophilic substitution of chlorine atoms in PVC with pz and dpz anions in the form of sodium and potassium salts was performed in different solvents at temperatures from 0 to 45°C. The presence of nitrogen in the reaction products confirms substitution of chlorine atoms. The results are presented in Table 1.

As seen from Table 1, reaction of PVC with sodium and potassium salts of pz and dpz at temperatures above 0–2°C yields insoluble products. It is known

Scheme 1.



[2] that the chromophore effect is observed after elimination of only 0.1–0.2% of HCl. Substitution of chlorine atoms in PVC is accompanied by dehydrochlorination: signals of the ~CH=CH– fragment (128.03–127.58 ppm) appear in the ^{13}C NMR spectra of the examined solutions, and a new band at 1640 cm^{-1} appears in the IR spectra. Substitution of chlorine atoms in PVC is described by Scheme 1.

Double bonds of the macromolecule form cross-links, which makes the polymer insoluble. The maximal nitrogen content is approximately 4% (Table 1, run nos. 3, 5, and 11). At low temperature (0–2°C), the substitution is insignificant (the maximal nitrogen content is as low as 1.48%, Table 1, run no. 1). However, PVC modified under these conditions is soluble in DMF and DMSO. The degree of chlorine substitution under the similar reaction conditions depends on the solvent: the maximal nitrogen content (2.04 %) is observed in a DMSO solution (Table 1, run no. 9; cf. samples modified in DMF, run no. 8). As the Na-pz concentration is increased by a factor of 2, insoluble samples are formed even when the modification is performed at 0–2°C (Table 1, run no. 5).

Nucleophilic substitution of chlorine in PVC is accompanied, as a rule, by cyclization and cross-linking [1, 2]. For example, the polymer treated with lithium or potassium contains small amount of chlorine, cyclopropane rings, and cross-links.

It is known that reactivity of the –SNa group in nucleophilic substitution is higher that that of the >NH group. To check this fact, we studied the reac-

Table 2. Nucleophilic substitution of chlorine in PVC by sodium salt of mbi

Run no.	Solvent	T, °C	τ, h	Elemental analysis, %					Yield, %
				C	H	N	S	Cl	
1	CH	80	8	51.40	6.04	7.52	10.02	25.02	53
2	CH	100	2	55.44	5.48	8.21	9.95	20.92	74
3	CH	100	4	58.09	5.72	8.47	10.10	17.62	69
4	CH	100	6	57.96	6.27	9.65	11.00	15.12	65
5	CH	100	8	58.34	5.53	10.86	11.65	13.62	67
6	CH	120	8	59.58	5.54	9.30	11.68	13.90	70
7*	DMF	80	8	60.12	6.13	10.55	12.49	10.71	52

* Analytical data for the soluble product.

Table 3. Relative hydrogen content in different fragments of the copolymer (Table 2, run no. 5)

Structural fragment	Hydrogen fraction q	Range of ^{1}H and ^{13}C chemical shifts, ppm, assignment
		^{1}H NMR spectrum
H_{ar}	0.222	7.0–7.8; H-4,5,6,7 atoms of mbi
H_{ol}	0.111	5.0–6.7; hydrogen atoms of olefin fragments
CHCl	0.167	4.0–5.0; hydrogen atoms of CHCl group of VC
CH_2 + CH	0.500	2.0–4.0; hydrogen atoms of CH_2 groups of VC, CH and CH_2 groups of CH_2–CH fragment, and low-molecular-weight impurities
		^{13}C NMR spectrum
C_{ar}	0.539	110–156; carbon atoms of mbi
C_{ol}	0.151	128–138; carbon atoms of olefin fragments
CHCl	0.100	58.0–64.0; carbon atoms of CHCl group of VC
CH_2 + CH	0.210	46.0–48.4; carbon atoms of CH_2CH_2 group of VC and CH and CH_2 groups of CH_2–CH fragment

tion of PVC with sodium salt of 2-mercaptobenzimidazole. The results are presented in Table 2.

The reaction in CH yields only soluble products, whereas in DMF both soluble and insoluble polymers are formed. As the reaction temperature increases from 80 to 100°C, the nitrogen content of the polymers increases from 7.52 to 10.86% (Table 2, run nos. 1–5). At 120°C, the nitrogen content of the samples does not increase further (Table 2, run no. 6).

The presence of strongly broadened signals of CHCl and CH_2 groups of PVC (4.0–5.0 and 2.0–2.9 ppm, respectively [4]) and signals of H-4,7 and H-5,6 atoms of mbi (7.6 and 7.1 ppm, respectively [5]) suggests formation of the copolymer by the reaction of PVC with sodium salt of mbi (Table 2, run no. 5). Broadened strongly overlapped lines in the resonance region of hydrogen atoms of olefin fragments (5.0–6.7 ppm [6]) are also present in the ^{1}H NMR spectrum.

The presence of olefin fragments in the copolymer structure was confirmed by ^{13}C NMR spectroscopy. Significantly overlapped strong signals of carbon atoms of the olefin fragments HC=CH are observed in the range 128–138 ppm along with signals of carbon atoms of vinyl chloride fragments (58.0–64.0 and 46.0–48.4 ppm for CHCl and CH_2 groups, respectively) and broad signals of 2-mercaptobenzimidazole [110–118 (C-4,7); 122 and 126 (C-5,6); ~140 (C-8,9); and 142–150 ppm (C-2)].

The results of quantitative analysis of the ^{1}H and ^{13}C NMR spectra of the copolymer are presented in Table 3. The ratio of the main structural elements in the copolymer calculated from these data is mbi : VC : (HC=CH) = 1 : 1.32 : 1.

The elemental composition of the copolymer, calculated from the ^{13}C NMR data and results of chemical analysis, is presented in Table 4. It is seen that

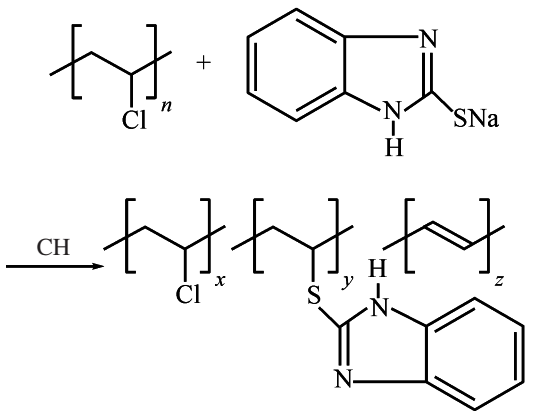
Table 4. Elemental composition of the copolymer (Table 2, run no. 5) calculated from the ^{1}H and ^{13}C NMR data and the results of chemical analysis

Element	Content, wt %	
	NMR data	chemical analysis
C	58.9	58.34
H	4.9	5.53
N	10.6	10.86
S	12.1	11.65
Cl	13.4	13.62

the data obtained by two different methods are well consistent.

Thus, nucleophilic substitution of chlorine atoms in PVC under the cation of sodium salt of mbi can be described by the Scheme 2:

Scheme 2.



The decomposition temperature of the reaction products of PVC with mbi (Table 2, run nos. 4–6) is as high as 160–180°C. Relatively strong and stable composite films are formed by application of solutions of these compounds to metal or polyethylene surface. The specific surface area and pore volume of the VC copolymers are higher by a factor of 6.7 (8.23 $m^2 g^{-1}$ and 1.89 $cm^3 g^{-1}$, respectively, Table 2, run nos. 4 and 5) than those of the initial PVC.

This is of fundamental importance for plasticization of VC copolymers.

Thus, nucleophilic substitution of chlorine atoms in polyvinyl chloride is one of the most interesting reactions from the theoretical and practical viewpoints, allowing improvement of physical properties of PVC polymers. To obtain polymers with required properties, the influence of different factors on the reaction course should be studied.

ACKNOWLEDGMENTS

This study was financially supported by the Russian Foundation for Basic Research (project no. 06-08-00320-a).

CONCLUSIONS

(1) Only insignificant fraction of chlorine atoms is substituted in polyvinyl chloride by the reaction with sodium pyrazolate or sodium 3,5-dimethylpyrazolate. The maximal nitrogen content of the soluble reaction products is 5.90%.

(2) When sodium salt of 2-mercaptobenzimidazole is used as a nucleophile, the degree of substitution of chlorine atoms increases and the nitrogen content of the reaction products reaches 7.52–10.86%.

(3) The ratio of the main structural fragments of the copolymer was calculated from the ^{1}H and ^{13}C NMR data.

REFERENCES

1. *Poluchenie i svoistva polivinilkhlorida* (Preparation and Properties of Polyvinyl Chloride), Zil'berman, E.N., Ed., Moscow: Khimiya, 1968.
2. Kropacheva, E.N., *Entsiklopediya polimerov* (Encyclopedia of Polymers), Moscow: Sov. Entsiklopediya, 1972, vol.1, p. 814.
3. *Laboratorni technica organicke chemie*, Keil, B., Ed., Prague: Ceskoslov. Akad. Ved, 1963.
4. Larina, L.I., NMR Spectroscopy and Structure of Substituted Azoles, *Doctoral Dissertation*, Irkutsk, 2003.
5. Kalabin, G.A., Kanitskaya, L.V., and Kushnarev, D.F., *Kolichestevnnaya spektroskopiya YaMR prirodnogo organicheskogo syr'ya i produktov ego pererabotki* (Quantitative NMR Spectroscopy of Natural Organic Raw Materials and Their Processing Products), Moscow: Khimiya, 2000.
6. Kalynowsky, H.O., Berger, S., and Braun, S., *Carbon-13 NMR Spectroscopy*, New York: Wiley, 1988.

ISSN 1070-4272, Russian Journal of Applied Chemistry, 2008, Vol. 81, No. 1, pp. 135–143. © Pleiades Publishing, Ltd., 2008.
Original Russian Text © Ya.I. Estrin, V.V. Komratova, G.A. Estrina, V.P. Lodygina, B.A. Rozenberg, 2008, published in Zhurnal Prikladnoi Khimii, 2008, Vol. 81, No. 1, pp. 140–147.

MACROMOLECULAR CHEMISTRY AND POLYMERIC MATERIALS

Selectivity of Acylation of Ethanolamines with (Meth)acryloyl Chlorides

Ya. I. Estrin, V. V. Komratova, G. A. Estrina, V. P. Lodygina, and B. A. Rozenberg

Institute of Chemical Physics Problems, Russian Academy of Sciences, Chernogolovka, Moscow oblast, Russia

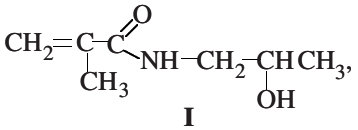
Received May 30, 2007; in final form, October 2007

Abstract—The selectivity with respect to N-acylation of the reactions of *N*,*N*-bis(2-hydroxyethyl)amine and *N*-methyl(2-hydroxyethyl)amine with acryloyl and methacryloyl chlorides was examined.

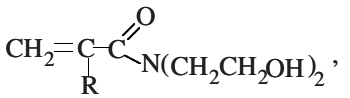
DOI: 10.1134/S1070427208010308

The majority of polymers derived from acrylamides are water-soluble. Aqueous solutions of these polymers, in particular, of poly(*N*-isopropyl)acrylamide, can be sensitive to external effects. For example, variation of the temperature in a narrow range strongly affects their solubility. Therefore, such polymers are widely used in various branches of engineering and medicine [1, 2]. Expansion of the assortment of such polymers and study of their behavior are of both scientific and practical interest. This particularly concerns acrylamide polymers containing hydroxyalkyl groups in monomeric units. For example, Laschewsky et al. [3] studied in detail the phase equilibria in solutions of polymers and copolymers of mono-, di-, and trihydroxyalkyl(meth)acrylamides: *N*-(2-hydroxypropyl)methacrylamide **I**, *N*,*N*-bis(2-hydroxyethyl)acrylamide **IIa**, *N*-tris[(hydroxymethyl)methyl]acrylamide, and their partially and fully acylated derivatives.

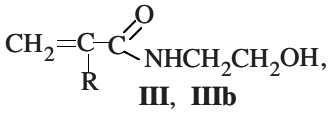
The synthesis and polymerization of *N*-hydroxyalkyl(meth)acrylamides (HAAs), namely, of *N*-(2-hydroxyethyl)acrylamide **IIIa**, *N*-(2-hydroxyethyl)methacrylamide **IIIb**, *N*-methyl-*N*-(2-hydroxyethyl)acrylamide **IVa**, and *N*-methyl-*N*-(2-hydroxyethyl)methacrylamide **IVa** were described for the first time in patents [4, 5]:



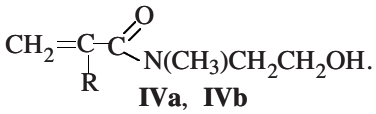
I



IIa, **IIb**



III, **IIIb**



IVa, **IVb**

where R = H (**IIa**–**IVa**) or CH_3 (**IIb**–**IVb**).

Procedures for preparing **IIa** and **IIIa** are also given in a patent [6], and the synthesis and polymerization of **I** are described in [7]. A modified procedure for preparing amide **IIa** in a tetrahydrofuran (THF) solution is given in [3]. In all the cases, HAAs were prepared by the reactions of appropriate hydroxyalkylamines [2-hydroxyethylamine (ethanolamine), 2,2'-bis(hydroxyethyl)amine (diethanolamine, **V**), *N*-methyl-*N*-(2-hydroxyethyl)amine **VI**] with acryloyl chloride **VIIa** or methacryloyl chloride **VIIb** in acetonitrile or in THF at low temperature. At the same time, Mohamed and Abd El-Hai [8] reported on the preparation of **IIa** by the reaction of diethanolamine with acrylic acid **VIII** in refluxing xylene with azeotropic distillation of water.

In patent [4], the monomers were isolated by vacuum distillation and characterized by the boiling point, refractive index, density, and nitrogen content. Product **I** was isolated by low-temperature crystallization from acetone and was characterized by the melting point only [7]. In all these cases, the target product yield did not exceed 60%. In the other cases, the monomers were used for the subsequent polymeriza-

tion without isolation and purification; therefore, their physicochemical characteristics were not given (amide **IIa** was characterized only by the ^{1}H NMR spectrum [3]). Data on the composition of the reaction mixture obtained were not reported either.

At the same time, the presence in hydroxyalkylamine molecules of two or three centers capable of reacting with acylating agents creates prerequisites for the occurrence of the reaction along more than one pathway, as both N- and O-acylation are possible. Hence, evaluation of the selectivity of such syntheses and of the purity of the monomers obtained is a topical problem. It is particularly important to determine whether the reaction mixture contains compounds polyfunctional with respect to double bonds (ester amides), as such compounds can cause undesirable gelation due to cross-linking of the macromolecules. Furthermore, along with undesirable O-acylation, addition of the amine across the acrylate double bond (Michael reaction [9, 10]) is also possible.

The goals of this study were to evaluate the selectivity of various methods for HAA synthesis, determine the content of undesirable impurities, find possible ways of their removal, and develop procedures for preparing the monomers of the required high purity.

N-Hydroxyalkyl(meth)acrylamides are a particular case of N-substituted amides which are usually prepared by the following procedures [11]: (1) condensation of primary or secondary amines with acyl chlorides in the presence of bases (tertiary amines or inorganic bases) as HCl acceptors; (2) oxidation of Schiff bases formed by reactions of primary amines with aromatic aldehydes; (3) addition of alcohols to nitriles; (4) amide interchange in reactions of primary or secondary amides with esters at elevated temperature, with the release of the corresponding alcohol; (5) condensation of primary or secondary amines with carboxylic acids at elevated temperature, usually with azeotropic distillation of water; (6) alkylation of primary amides with alcohols or alkyl halides at elevated temperature (up to 180°C).

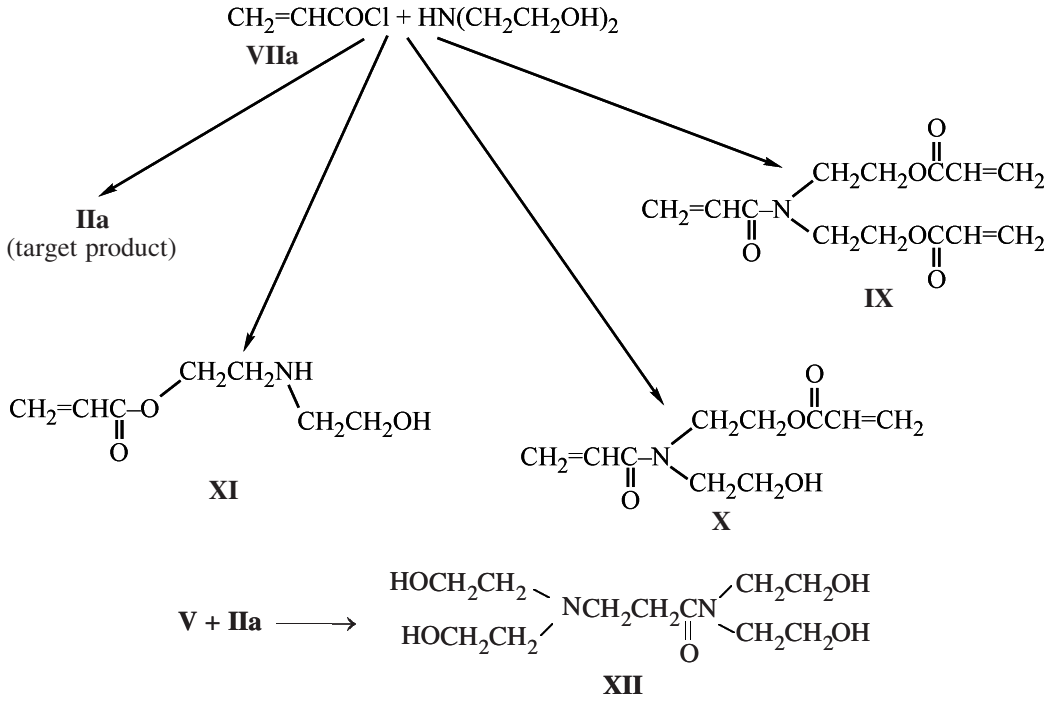
The synthesis procedure via Schiff bases is by no means suitable for preparing (meth)acrylamides. Addition of alcohols to nitriles is also a specific route, hardly suitable for this purpose. The amide interchange (fourth route) readily occurs only in cases when esters derived from relatively acidic alcohols (e.g., nitrophenol) react with highly basic amines. With (meth)acrylates as starting esters, the Michael reaction will be the major pathway, especially with low-basicity amines such as hydroxyalkylamines. Furthermore, this route, like all the other routes starting from the fourth route, requires, as a rule, elevated temperatures significantly exceeding 100°C. The same is true for the synthesis of *N*-hydroxyalkyl- or *N*,*N*-dihydroxyalkylamines by reactions of epoxides (ethylene oxide, epichlorohydrin, glycidyl alcohol) with primary amides (acetamide, formamide) at 140–150°C in the presence of base or acid catalysts [12, 13]. Apparently, in synthesis of (meth)acrylate derivatives under these conditions, it is virtually impossible to prevent the polymerization of both the starting compounds and the target products. Although in [8] the polymerization in the course of the synthesis of **IIa** seems to be avoided, our attempt to reproduce this procedure led to oligomers as major products (see below).

Thus, the first route seems to be the only suitable for preparing HAAs, and we chose this route in our experiments.

Amines very rapidly react with acyl halides at low temperatures, which allows the polymerization to be excluded. However, the polyfunctional structure of both reagents gives rise to certain problems in the selective synthesis of HAAs. Indeed, the starting hydroxyalkylamines contain not only amino groups but also hydroxy groups, which are also capable of acylation. (Meth)acryloyl chlorides contain, along with the reactive acyl chloride group, fairly active C=C bonds. In our case, apparently, the major side reaction will be O-acylation (formation of esters), occurring instead of, or along with N-acylation. As for the Michael reaction, it probability, at first glance, is low when the reaction is performed quickly and at low temperature, but it cannot be fully ruled out a priori. Thus, the reaction of (meth)acryloyl chloride with HAA may yield a mixture of products, as illustrated in Scheme 1 by the example of **VIIa** and **V**.

An ingenious procedure for preparing **IIa**, circumventing the problem of selectivity in the acylation step, was used by Miyabe et al. [14]: Diethanolamine **V** was exhaustively acylated with acryloyl chloride **VIIa** at the reactant molar ratio of 1 : 3 in the presence of triethylamine (TEA), after which the ester groups in acryloyliminodiethane-1,1'-diyl bisacrylate **IX** thus obtained (Scheme 1) were subjected to base alcoholysis with a saturated solution of Na_2CO_3 in methanol. However, whereas the yield of the target product based on the starting amine **V** is about 95%, the yield based on the starting chloride **VIIa** does not exceed 32%. This procedure apparently deserves at-

Scheme 1. Possible side processes in reactions of hydroxyalkylamines with acryloylchloride



tention as a preparative route, but for the synthesis of large amounts of monomers it is preferable to use a one-step procedure with the minimal consumption of expensive acid chlorides.

To elucidate how the condensation conditions affect the reaction selectivity, we studied the products of the reaction of **V** with **VIIa**, performed under different conditions. The relative contributions of the N- and O-acylation pathways can be readily evaluated by IR spectroscopy. Formation of ester groups leads to appearance of a strong absorption band of the carbonyl group in the range 1740–1720 cm^{-1} and of bands at about 1180 and 1120 cm^{-1} (C–O–C vibrations), whereas the amide C=O groups absorb at approximately 1600 cm^{-1} [15].

The reaction of amine **V** with equimolar amounts of acid chloride **VIIa** and TEA was performed in toluene (in this case, the system was heterogeneous, as compound **V** is insoluble in toluene), 1,4-dioxane (DO), and THF. In all the cases, along with bands at 1640 (vibrations of C=C bond in acrylic derivatives) and ~1610 cm^{-1} (vibrations of amide C=O group), the IR spectrum of the reaction mixture contained strong bands at 1740, 1180, and 1120 cm^{-1}, belonging to ester groups (Fig. 1, spectrum *1*). The same result was obtained when the reaction was performed in the phase-transfer mode, when a toluene solution of **VIIa** was added dropwise with vigorous stirring to an aqueous solution of amine **V** and sodium carbonate.

A different IR pattern is obtained when the reaction is performed with excess amine **V** (and not TEA) as HCl acceptor, both in DO and in THF. The bands at 1740, 1180, and 1120 cm^{-1} become weak, whereas the bands at 1640 and ~1600 cm^{-1} are fairly strong (Fig. 1, spectrum *2*). Spectrum *3* in Fig. 1 belongs to

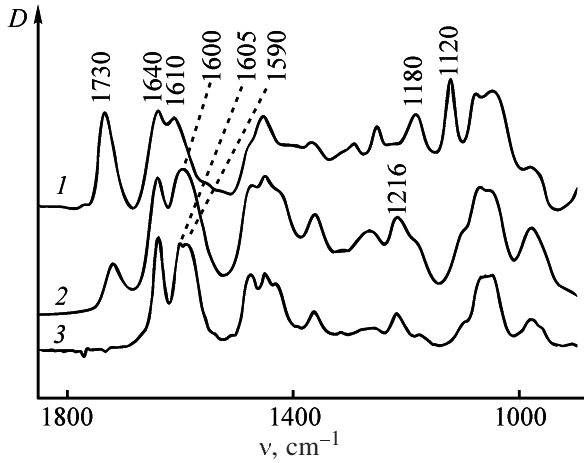


Fig. 1. IR spectra of products prepared by the reaction of **V** with **VIIa**. (*D*) Optical density and (ν) wavenumber; the same for Figs. 2, 3, and 5. (*1*) In the presence of acrylic acid **VIII** and (*2*, *3*) with excess amine **V**; (*2*) before and (*3*) after purification.

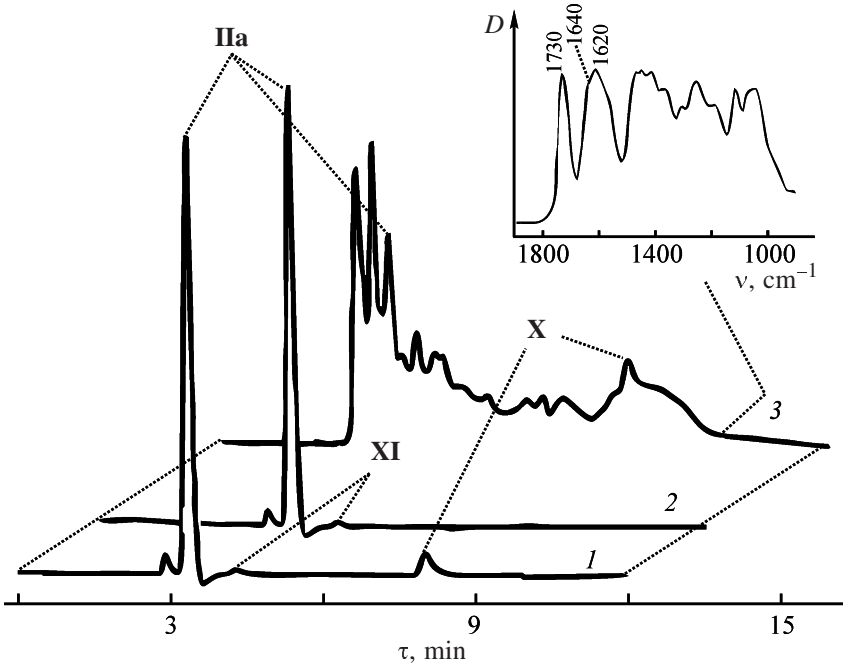


Fig. 2. Reversed-phase chromatogram of reaction products. (τ) Time; the same for Fig. 4. (*1*) Crude amide **IIa**, (*2*) product **IIa** after purification, and (*3*) product of condensation of **V** and **VIII** by the procedure from [8] (tenfold magnification of signal intensities). The IR spectrum of the latter product is shown in the insert. Products **X** and **XI** were identified by retention times and UV spectra.

the same product after purification. The bands at 1740, 1180, and 1120 cm^{-1} in the latter spectrum are fully absent, but a doublet band at 1605–1590 cm^{-1} belonging to the C=O groups of the disubstituted amide can be observed. Hence, under these conditions N-acylation is the major reaction pathway. The reaction mixture after adding a solution of chloride **VIIa** to a solution of amine **V** in a 1 : 2 ratio is a low-viscosity turbid solution over a highly viscous precipitate. The yield of crude **IIa** after distilling off the solvent is approximately 60% based on converted chloride **VIIa**.

Similarly, we prepared *N*,*N*-bis(2-hydroxyethyl)-2-methacrylamide **IIb** by the reaction of a twofold excess of amine **V** with chloride **VIIb** in THF. The yield of the crude product was up to 90% based on **VIIb**. By reactions of a twofold excess of amine **VI** with chlorides **VIIa** and **VIIb** in THF, we prepared amides **IVa** and **IVb**; the yields of the crude products were 67 and 95%, respectively.

To evaluate the reaction selectivity, the composition of the reaction mixture was determined by reversed-phase HPLC. It should be noted that chromatography (especially in combination with spectroscopic methods) is the most efficient, sensitive, and reliable method for determining compositions of complex mixtures. Chromatograms of crude (pattern *1*) and purified (pattern *2*) amide **IIa** are shown in Fig. 2 (their IR spectra are given in Fig. 1). Chromatogram *3* (Fig. 2) belongs to the product obtained by condensation of amine **V** with an equimolar amount of acrylic acid **VIII** in refluxing xylene with azeotropic distillation of water, as described in [8].

Crude product **IIa** contains as major impurity approximately 2–5% 2-[acryloyl(2-hydroxyethyl)amino]ethyl acrylate **X**, the product of simultaneous N- and O-acylation. This impurity is undesirable, as it can cause formation of an insoluble gel in the course of synthesis of linear polymers. Fortunately, compound **X**, in contrast to amide **IIa**, is better soluble in organic solvents than in water. Chromatogram *2* (Fig. 2) belongs to a sample of amide **IIa** isolated after treatment of its aqueous solution with methylene chloride. In this case, the content of the target product is approximately 96.5%. However, a small peak with a retention time of 4.3 min does not disappear after the extraction with methylene chloride. This peak apparently belongs to the O-acylation product, 2-[(2-hydroxyethyl)amino]ethyl acrylate **XI**, which is similar in polarity to **IIa**. The UV spectra of amide **IIa** (major peak) and product **X** (peak with a retention time of about 8 min) have maxima at 220 and 246 nm, characteristic of acrylamides [16]. Product **XI** (peak

with a retention time of 4.3 min) has a UV spectrum with only one maximum at approximately 220 nm, characteristic of acrylic acid ester [17]. The peak at 2.86 min was not identified. This product shows no UV absorption, i.e., it is neither an esters nor an amide and is apparently a nonreactive water-soluble impurity in **V**. The exhaustive acylation product **IX** shown in the scheme present in trace amounts or absent at all in the reaction mixture and is absent in the purified product.

Chromatogram *3* in Fig. 2 essentially differs from chromatograms *1* and *2*. The product prepared by condensation of amine **V** with acrylic acid **VIII** in refluxing xylene following the procedure from [8] is a dark semisolid mass consisting of numerous compounds (most likely polymers or oligomers). Peaks of several individual substances can be seen against irregular background. The content of target amide **IIa** (identified by the retention time) in this mixture is as low as 10%. The IR data also show that N-acylation is not the major reaction pathway under these conditions: The spectrum given in [8] is almost identical to the spectrum of the product obtained in our experiment but differs essentially from the spectrum of pure amide **IIa** in the range of vibrations of carbonyl groups and C=C double bonds (see insert in Fig. 2).

The IR spectrum and chromatogram of amide **IIb** prepared by condensation of chloride **VIIb** with a twofold excess of amine **V** in THF are shown in Figs. 3 and 4. Similar results were obtained in the reactions of **VIIa** and **VIIb** with excess **VI** in THF, as seen from the IR spectra and chromatograms of products **IVa** and **IVb** (Figs. 3 and 4, respectively). All these spectra contain a C=C absorption band at 1644 (for methacrylic derivatives) or 1640 cm^{-1} (for acrylic derivatives), and also bands at 1600 cm^{-1} belonging to C=O groups in unsaturated amides. Crude products were purified by extraction of less polar impurities containing two C=O bonds with methylene chloride from aqueous solutions in all the cases except **IVb**. Compound **IVb** was fairly pure (~95%) without additional treatment. According to the IR spectra (Fig. 3, spectrum *3*, lack of absorption at ~1720 cm^{-1}) and chromatograms (Fig. 4, pattern *4*, lack of peaks after the major peak), it contains no impurities of O-acylation products.

Thus, with a twofold excess of hydroxyalkylamine in the absence of other HCl acceptors, the N-acylation selectivity exceeds 90% for amine **V** and reaches almost 100% for amine **VI**. Specifically this procedure, suggested and substantiated for the first time in

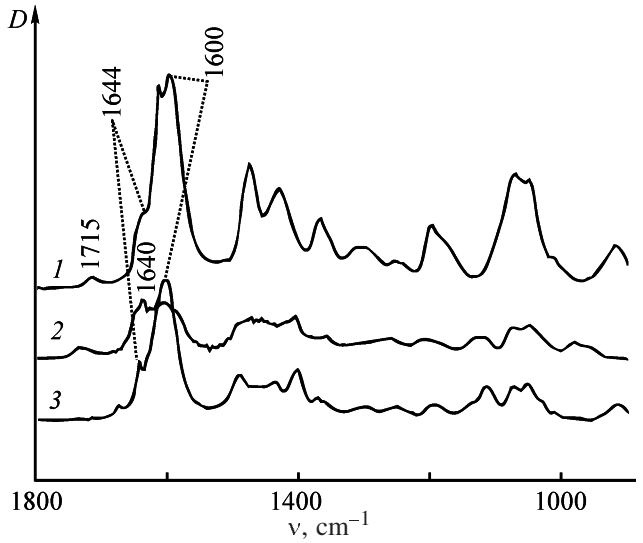


Fig. 3. IR spectra of crude amides (*1*) **IIb**, (*2*) **IVa**, and (*3*) **IVb**.

[4], was subsequently used by other authors for preparing the corresponding HAAs whose polymerization yielded water-soluble polymers. An exception is patent [6] whose authors prepared amide **IIa** by the reaction of amine **V** with acid chloride **VIIa** in the presence of TEA in THF. The solution after separation from the precipitate of triethylamine hydrochloride was used, without isolating the target product, for preparing polymers and copolymers. The polymers described in [6] are insoluble in water and become soluble only after boiling in aqueous NaOH. Apparently, in this case the reaction yields a mixture of N- and O-acylation products with a high content of bi- and, possibly, trifunctional (with respect to double bonds) compounds (Scheme 1). Dissolution of polymers prepared from such a mixture occurs under the action of alkali, apparently due to hydrolysis of cross-links formed via ester groups.

Nevertheless, partial O-acylation takes place even when an HAA is prepared with excess of the amine component. Isolation and complete identification of the by-products were beyond the scope of this study. However, data on the structures of the starting compounds and the reactivities of their functional groups suggest that the main by-products in the synthesis of HAAs are formed by simultaneous N- and O-acylation. These are amido esters (compound **X** and its analogs) containing two double bonds in the molecule and aminoalkyl acrylates (compound **XI** and its analogs). This conclusion follows from the IR spectra and chromatograms of the crude products (presence of absorption bands of ester carbonyl groups

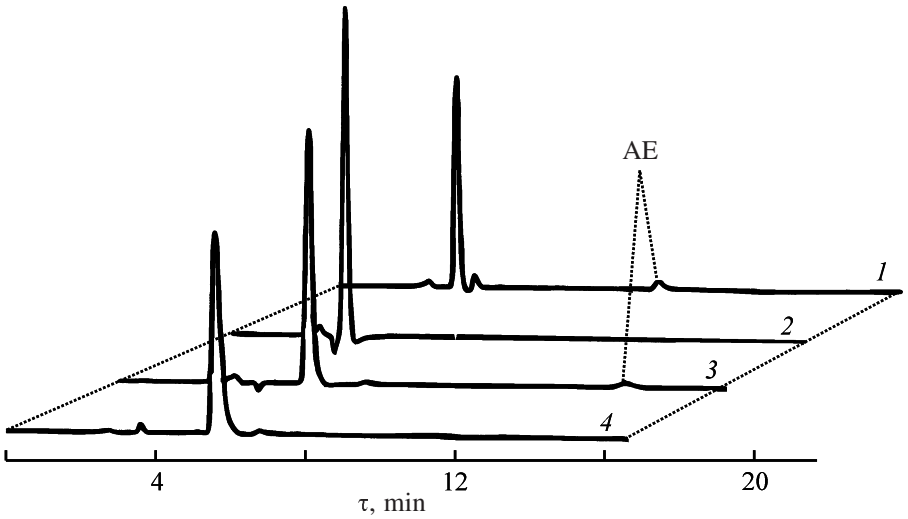


Fig. 4. Chromatograms of (*1*) crude **IIb**, (*2*) purified **IIb**, (*3*) crude **IVa**, and (*4*) crude **IVb**. (AE) Impurities of amido esters.

and of minor peaks that have longer retention times and hence belong to less polar, compared to the target products, compounds), and also from the characteristic UV spectra of the impurities.

Along with side O-acylation, the Michael reaction also takes place, especially with acrylamides. This conclusion is based on the following observations. First, the yields of amides **IIb** and **IVb** are almost quantitative, whereas the yields of **IIa** and **IVa** are considerably lower. Second, the volume of the salt precipitate formed in the course of the reaction is considerably larger in the case of the synthesis of **IIa**, compared to **IIb**. It is known that acrylic derivatives add primary and secondary amines after Michael considerably faster than do methacrylic derivatives. If the rate of the Michael reaction is sufficiently high, the reaction of amide **V** with chloride **VIIa** can yield a large amount of 3-[bis(2-hydroxyethyl)amino]-*N*,*N*-bis(2-hydroxyethyl)propanamide **XII** (Scheme 1), because the free amine is present in the reaction mixture almost up to the end of the process along with growing concentration of the target product **IIa**. Apparently, the Michael reaction can occur in the synthesis of acrylamides to a greater extent than in the synthesis of methacrylamides. It should be noted that, even if the target product contains an impurity of the product of this reaction, its amount is very low, because by the end of the reaction it virtually fully transforms into the hydrochloride insoluble in THF. Furthermore, this impurity should not affect the polymerization of the monomers, because it contains no double bonds. An additional evidence for the possible formation of this adduct is the fact that, on mixing equimolar amounts of **V** and **IIa** at room temperature, the IR spectrum of the mixture rapidly takes the form shown in Fig. 5. The spectrum does not contain the absorption band of the C=C bond at 1640 cm^{-1} but contains a strong band at 1610 cm^{-1}, belonging to the amide group [15].

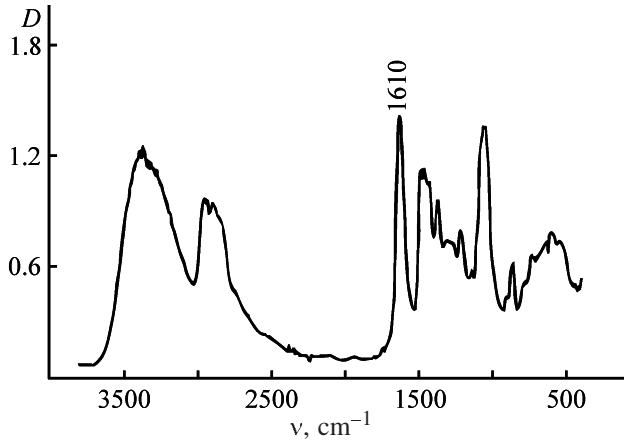


Fig. 5. IR spectrum of the product formed by the reaction of equimolar amounts of **V** and **IIa** at room temperature.

One more evidence for the noticeable contribution of the Michael reaction in the case of acrylamides is the fact that, at a threefold excess of the amine, the yield of the target product under the same conditions does not exceed 20%. Apparently, the major fraction of amide **IIa** formed subsequently adds the unchanged amine.

Thus, addition of amines **V** and **VI** to amides **IIa** and **IVa**, respectively, occurs fairly actively, despite

low temperature and relatively short reaction time (taking into account the fact that the yields of amides **IVa** and **IIa** are considerably lower than the theoretical value, in contrast to amide **IVb**). Acylation of amines with acid chlorides is strongly exothermic. Therefore, the reaction time is determined by the rate of addition of acid chloride solution to the amine solution, which should not be high to avoid overheating of the reaction mixture. Thus, to reduce the contribution of the Michael reaction and increase the yield of the target products, it is necessary to perform the reaction in an apparatus providing efficient heat removal.

The high selectivity of N-acylation of hydroxyalkylamines with acid chlorides in the absence of a "foreign" hydrogen chloride acceptor is apparently due to the fact that the first step of the reaction is formation of complexes of acid chlorides with bases present in the reaction mixture. If an amine containing an N–H bond is used as a base, the second step predominantly occurs as an intramolecular rearrangement with the formation of the C–N bond and release of HCl. If a more basic tertiary amine is present in the system, specificially this component forms the related complex in the first step. In the second step, this complex reacts along a bimolecular pathway with any proton-donor groups present in the reaction mixture. The reaction either is nonselective or predominantly involves more acidic (in particular, hydroxy) groups. Thus, without tertiary amine, O-acylation of hydroxyalkylamines is improbable, whereas in the presence of a tertiary amine it becomes even more probable than N-acylation.

The suggested mechanism can also account for the higher contribution of O-acylation in the synthesis of acrylamides, compared to methacrylamides. Indeed, as shown above, the occurrence of the Michael reaction with the acrylic derivative leads to the formation of a large amount of tertiary amine **XII**, which becomes a "foreign" HCl acceptor and thus decreases the reaction selectivity.

EXPERIMENTAL

Diethanolamine **V** (Aldrich, 98.5%) was distilled in a vacuum, bp 115–118°C/1 mm Hg. Acryloyl chloride **VIIa** (Aldrich, 96%) and methacryloyl chloride **VIIb** (Aldrich, 80%) were distilled at atmospheric pressure with the addition of tetramethylpiperidine-*N*-oxyl (TEMPO) as inhibitor. Triethylamine (Aldrich, 99%) and *N*-methylhydroxyethylamine **VI** (Aldrich, 99%) were used without additional purification. The solvents DO, THF, and toluene were distilled from KOH (THF), P_2O_5 (DO), or Na (toluene) and were then stored over CaH_2 (THF, under argon). Xylene was distilled without drying. Methylene chloride (Aldrich, 99.6%) was distilled just before use.

The reaction of diethanolamine **V** with acryloyl chloride **VIIa** in the presence of TEA was performed as follows.

(a) Compound **VIIa** (0.6 ml) was slowly added to a mixture of 1 ml of TEA, 0.5 g of amine **V**, and 10 ml of toluene under vigorous stirring with a magnetic stirrer. The solution was filtered to remove the precipitate, and the solvent was distilled off. The remaining viscous nonvolatile liquid has an IR spectrum shown in Fig. 1 (spectrum *1*).

(b) Acryloyl chloride **VIIa** (0.5 ml) was slowly added under vigorous stirring with a magnetic stirrer to a mixture of 2.5 ml of TEA, 0.76 g of amine **V**, and 10 ml of DO. The solution was filtered to remove the precipitate, and the solvent was evaporated. The remaining viscous nonvolatile liquid has an IR spectrum similar to that in procedure (a).

To perform phase-transfer condensation of diethanolamine **V** with acryloyl chloride **VIIa**, a solution of **VIIa** (0.5 ml) in toluene (7 ml) was added dropwise under vigorous stirring with a magnetic stirrer to a mixture of 0.65 g of **V** and 0.7 g of Na_2CO_3 in 10 ml of water. After the reaction completion, the aqueous layer was separated, KCl was added to the aqueous solution to obtain a saturated salt solution, and the organic products were extracted with diethyl ether. The IR spectrum of the viscous nonvolatile residue after distillation of the solvent was similar to those in procedures (a) and (b).

The condensation of diethanolamine **V** with acrylic acid **VIII** in xylene was performed under the same conditions as in [8], except that NaA zeolite treated with 1 N HCl and washed with water to neutral reaction was used as catalyst instead of mordenite.

Amides IIa, IIb, IVa, and IVb. Amine **V** (31.1 g, ~0.3 mol) was placed in a three-necked flask equipped with a thermometer, a dropping funnel, and a power-driven stirrer. Then the flask was charged with 200 ml of THF, and the mixture was cooled to 8–10°C on a water–ice bath. A solution of 12.5 g (~0.14 mol) of acid chloride **VIIa** in 20 ml of THF was added dropwise with vigorous stirring over a period of 12 min. In the process, the temperature of the reaction mixture did not exceed 15°C. The resulting solution was decanted from the viscous residue. The precipitate was extracted with 200 ml of THF, the second solution

was also decanted, and both solutions were combined. The mixture, which had alkaline reaction, was acidified to weakly acidic reaction by dropwise addition of concentrated sulfuric acid. The solution was filtered, TEMPO was added, and the solvent was distilled off. Crude amide **IIa** was obtained in an amount of 12.5 g (0.078 mol, yield 56%). The product was dissolved in 120 ml of water; the solution was extracted with seven 100-ml portions of methylene chloride. After distillation of water, 10.1 g of the purified product (yield 45% based on acid chloride **VIIa**) was obtained; d_4^{20} = 1.163, n_D^{20} = 1.5135.

Found, %: C 51.33, H 8.18, N 8.46.
$C_7H_{13}NO_3$.
Calculated, %: C 52.82, H 8.23, N 8.80.

The same procedure was used for preparing amide **IIb**. From 0.28 mol of amine **V** and 0.12 mol of acid chloride **VIIb**, 19 g (0.11 mol, yield >90%) of crude amide **IIb** was obtained. Yield of the purified product after extraction with methylene chloride 15.0 g (72% based on acid chloride **VIIb**); d_4^{20} = 1.135, n_D^{20} = 1.497.

Found, %: C 55.30, H 8.60, N 7.76.
$C_8H_{15}NO_3$.
Calculated, %: C 55.47, H 8.73, N 8.09.

Similarly, from 28.3 g (0.377 mol) of amine **VI** and 17.3 g (0.191 mol) of acid chloride **VIIa** in 200 ml of THF at 7–10°C, we prepared 16.6 g (0.128 mol) of amide **VIa** (67% based on acid chloride **VIIa**). After single extraction of an aqueous solution of crude **IVa** with methylene chloride, 11.0 g (0.085 mol) of pure amide **IVa** was obtained; d_4^{20} = 1.099, n_D^{20} = 1.5015.

Found, %: C 54.23, H 8.50, N 9.83.
$C_6H_{11}NO_2$.
Calculated, %: C 55.80, H 8.58, N 10.84.

By adding a solution of 20.3 g (0.194 mol) of acid chloride **VIIb** in 20 ml of THF to a solution of 30.7 g (0.409 mol) of amine **VI** in 200 ml of THF at 8–10°C, we obtained 26.2 g (0.183 mol) of amide **IVb** (94.3% based on acid chloride **VIIb**); d_4^{20} = 1.0645, n_D^{20} = 1.4879.

Found, %: C 58.37, H 8.44, N 8.69.
$C_7H_{13}NO_2$.
Calculated, %: C 58.72, H 9.15, N 9.78.

The IR spectra were recorded on a Specord M82 spectrophotometer from neat substances as thin films between KBr plates.

Liquid chromatography was performed with a Waters chromatograph equipped with a refractometric detector and a spectrophotometric detector with a photodiode matrix. Column Diaspher 110 C18, 250 × 4 mm; eluent water–methanol, 30 : 70 for **IIa** and **IVa**, 40 : 60 for **IIb** and **IVb**, 0.7 ml min^{-1}; column temperature 35°C. The chromatograms were recorded and processed with Millennium 32 software.

CONCLUSIONS

(1) The use of liquid chromatography in combination with spectroscopic methods shows that, in reaction of carboxylic acid chlorides of the acrylic series with hydroxyalkylamines, the selectivity with respect to N-acylation exceeds 90% and can reach virtually 100% provided that the amine reagent acts as the only acceptor of hydrogen chloride. Correspondingly, the contribution of the side O-acylation reaction can be reduced to a minimum.

(2) The possibility of virtually complete removal of impurity O-acylation products and preparation of 95–97% pure monomers was demonstrated.

(3) In the synthesis of acrylamides, in contrast to methacrylamides, Michael addition of the amine across the double bond occurs fairly actively, leading to a substantial decrease in the target product yield.

ACKNOWLEDGMENTS

The study was supported by the International Science and Technology Center (project no. 1918), Russian Foundation for Basic Research (project no. 04-03-32674-a), and Russian Academic Scientific Program (no. 10002-251/BCMS-04/12-131/060603-540).

REFERENCES

1. Swift, G., *Polym. Degrad. Stab.*, 1994, vol. 45, pp. 215–231.
2. Schild, H.G., *Prog. Polym. Sci.*, 1992, vol. 17, pp. 163–249.
3. Laschewsky, A., Rekay, E.D., and Wischerhoff, E., *Macromol. Chem. Phys.*, 2001, vol. 202, pp. 276–286.
4. US Patent 2593888.
5. US Patent 2508717.
6. US Patent 3285886.
7. Strohalm, J. and Kopeček, J., *Angew. Makromol. Chem.*, 1978, vol. 70, pp. 109–118.
8. Mohamed, M.M. and Abd El-Hai, F., *Mol. Catal. A: Chemical*, 2004, vol. 211, pp. 199–208.

9. Mather, B.D., Viswanathan, K., Miller, K.M., and Long, T.E., *Prog. Polym. Sci.*, 2006, vol. 31, pp. 487–531.
10. Liu, M. and Sibi, M.P., *Tetrahedron*, 2002, vol. 58, pp. 7991–8035.
11. Tolstikov, G.A., Borisova, E.Ya., Cherkashin, M.I., et al., *Usp. Khim.*, 1991, vol. 60, pp. 852–880.
12. Petrenko, L.P., *Tr. Khim. Fak. Voronezh. Gos. Univ.*, 1953, vol. 32, pp. 17–19.
13. Petrenko, L.P., *Tr. Khim. Fiz.-Mat. Fak. Voronezh. Gos. Univ.*, 1956, vol. 42, no. 2, pp. 45–47.
14. Miyabe, H., Ueda, M., Fujii, K., et al., *J. Org. Chem.*, 2003, vol. 68, pp. 5618–5626.
15. Bellamy, L.J., *The Infra-Red Spectra of Complex Molecules*, New York: Wiley, 1957.
16. Gur'eva, L.L., Tkachuk, A.I., Dzhavadyan, E.A., et al., *Vysokomol. Soedin., Ser. A*, 2007, vol. 49, no. 9, pp. 1635–1648.
17. Estrina, G.A., Komarov, B.A., Estrin, Ya.I., and Rozenberg, B.A., *Vysokomol. Soedin., Ser. A*, 2004, vol. 46, pp. 207–216.

ISSN 1070-4272, Russian Journal of Applied Chemistry, 2008, Vol. 81, No. 1, pp. 144–147. © Pleiades Publishing, Ltd., 2008.
Original Russian Text © N.V. Volkova, D.N. Emel'yanov, A.A. Molodova, 2008, published in Zhurnal Prikladnoi Khimii, 2008, Vol. 81, No. 1, pp. 148–151.

MACROMOLECULAR CHEMISTRY AND POLYMERIC MATERIALS

Adhesion of Butyl Methacrylate Copolymers to Cellulose Fabrics

N. V. Volkova, D. N. Emel'yanov, and A. A. Molodova

Lobachevsky State University, Nizhni Novgorod, Russia

Received May 31, 2007

Abstract—The influence of physicochemical properties of polyacrylate binder on adhesion properties of cellulose fabrics glued by its melt was examined.

DOI: 10.1134/S107042720801031X

A common step of restoration of paintings and applied art pieces made of fabric is their bonding to a new fabric with the aid of adhesives. These substances should strongly glue the initial and backing material at minimal pressure and temperature but should be free of solvents that dissolve paint, should not deform the article being restored owing to shrinkage in the course of formation of the adhesive joint, and should not change the elasticity and strength of the joint in the course of prolonged storage [1]. Adhesives most widely used in the world for fabric-to-fabric bonding are water-base acryl dispersions and an analog of Beva 371 wax–resin formulation [composite of ethylene–vinyl acetate (VA) copolymer, Keton N resin, paraffin, benzine, and toluene]. Bonding with both adhesives is performed at elevated temperature and pressure on a vacuum apparatus equipped with a heater [1]. Frequently, foreign methods cannot be used in Russian restoration practice because of economic and technical reasons. Therefore, development of new Russian adhesives and procedures for their application is an urgent problem.

The aim of this study was to prepare butyl methacrylate (BMC) copolymers with a number of vinyl monomers, whose melts would be suitable for gluing canvases of paintings and cotton fabric with a backing material.

EXPERIMENTAL

We used BMC as the main component for preparing copolymers. This choice is caused by the fact that its homopolymer, poly(butyl methacrylate) (PBMA), is widely used in Russian restoration practice for preservation and restoration of masterpieces, including those on a fabric base [2, 3]. The copolymer composition is presented in Table 1. The copolymers were prepared by radical polymerization at 80°C in a solution of isopropanol which is a chain-transfer agent. Low-molecular-weight copolymers with flow points T_f below 100°C were prepared. Melts of these copolymers can be used to glue fabrics. The molecular weight M of these copolymers was estimated by comparison of the intrinsic viscosity $[\eta]$ (dl g^{-1}) of their acetone solutions with that of a solution of PBMA in the same solvent. The flow point of the copolymers was determined on a Hoeppler consistometer.

Fabrics, coarse calico produced in Ivanovo [GOST (State Standard) 29298–92], were glued (bonded) as follows. Copolymer solutions of definite concentration were applied with a brush to a fabric sample. Then the second and third polymer layers were applied onto the first layer at intervals of 1 h. The sample was dried to constant weight by convection exchange at ambient temperature. Thus we obtained a sample of backing fabric. The sample of backing fabric was put by the polymer-coated side onto the sample of the initial fabric. The fabrics were glued at a small force for 3 min with the aid of an iron heated to 120°C. The glued fabrics were cooled under a load of 0.8 kg. The viscosity $[\eta]$ (mPa s) of copolymer solutions applied onto the backing fabric was measured with the aid of a Hoeppler ball viscometer at 23°C; the viscosity of melts η_m (kPa s) was measured with a modified device for measuring thermoplastic melt indices (TMIM). The tensile strength σ_t (Pa) and relative elongation ε (%) were measured on an RMI-5 tensile-testing machine. The main parameter determining the suitability of the copolymers as

Table 1. Thermal and physicomechanical properties, viscosity, and adhesion to fabric of copolymers with different composition

Composition of (co)polymers, mol %	μ,* D	[η], dl g^{-1}	$M \times 10^{-4}$	T_f, °C	η_m, kPa m	$\sigma_t \times 10^5$, Pa	ε, %	γ, g cm^{-1}
Suspension PBMA		0.57	43	142	–	111	254	500
PBMA		0.20	8.5	136	–	13	240	2500
PBMA	2.16	0.07	1.4	43	29	8	450	528
90 BMA–10 VA	1.75	0.06		44	28	Friable		500
90 BMA–10 BA	1.85	0.05		33	5	0.5	2500	700
95 BMA–5 (2-EHA)	2.19	0.06		35	7	Plastic		850
95 BMA–5 MAA	1.79	0.07		55	2000	4	0	130
85 BMA–10 VA–5 BA		0.20		67		22	570	2000
85 BMA–10 VA–5 BA		0.06		35	25	3	2000	520

* μ is the dipole moment of the monomer [7].

Table 2. Influence of paraffin content on the adhesion of 85 BMA–10 VA–5 BA (mol %) composite to coarse calico

[η], dl g^{-1}	Paraffin content of adhesive	Concentration of solution	γ, g cm^{-1}, at indicated number of layers n		$\gamma_{COP}/\gamma_{comp}$*
	wt %		3	4	
0.20	0	40	2000	–	
	10	40	300	–	6.6
	20	40	270	–	7.0
	30	40	150	–	13.0
0.07	0	40	300	–	
	5	40	55	–	5.5
	5	40	–	190	1.6
	10	40	8	–	38.0
	10	50	150	–	2.0

* γ_{COP} is the plybond strength measured after application of one copolymer layer to the fabric; γ_{comp} is the plybond strength measured after application of copolymer–paraffin composite to the fabric.

adhesives is their adhesion to the fabric. To estimate the adhesion of the copolymers used for restoration of fabric articles, the plybond strength γ (g cm^{-1}) [4] was measured at room temperature on an RMI-5 tensile-testing machine at an extension rate of 50 mm min^{-1}.

It is known [4, 5] the adhesion of macromolecular compounds containing polar functional groups to a macromolecular substrate also containing such groups is high. Therefore, vinyl polymers containing along with BMA polar (μ, D) units should exhibit the maximal adhesion to polar cellulose fibers [4–6]. This is confirmed by the data presented in Table 1. As seen from Table 1, the adhesion of copolymers to the fabric is also determined by the viscosity of their melts during gluing. The lower the viscosity of a copolymer melt, the higher the adhesion to the fabric. This is due to the fact that a low-viscous copolymer melt penetrates faster and deeper from the backing fabric into interthread cells and into the threads of the doubled fabric, thus providing deeper junction. However, if the viscosity of the melt is too low, it can penetrate into the paint layer of the article being restored, which is strictly forbidden by the requirements to adhesives used in restoration. Hence, an adhesive should have good fluidity and high adhesion but should be held on the internal side of the doubled fabric. For this purpose, a higher-molecular-weight copolymer should be used. Indeed, the main components of adhesive melts are high-molecular-weight polymers providing sufficiently high cohesion strength of the adhesive [5]. However, as M of the copolymer increases, the fluidity of its melt decreases and hence the adhesion of the polymer to the fabric decreases (Table 1).

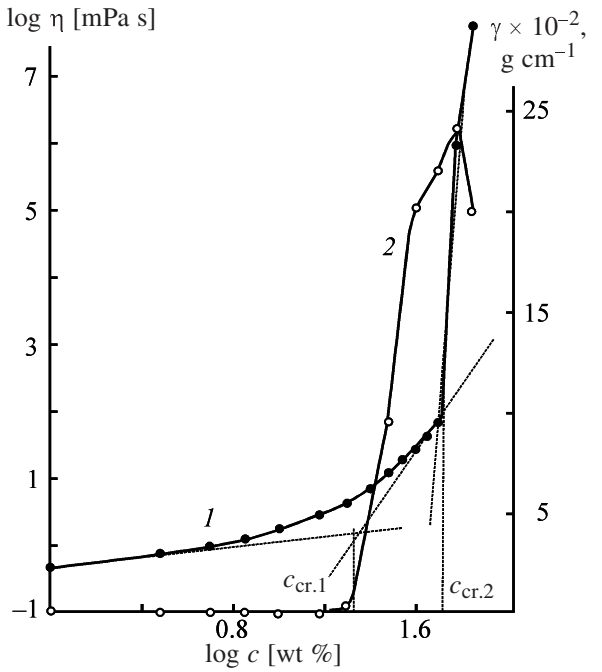
To increase the fluidity of a polymer melt, waxes (e.g., paraffin) are added to the adhesive [5]. As seen from Table 2, the adhesion of adhesive compound to the fabric sharply decreases after introduction of

Table 3. Influence of the solution concentration c and number n of polymer layers applied to the backing fabric on the adhesion of glued fabrics

Copolymer composition, mol %	[η], dl g^{-1}	c, wt %	γ, g cm^{-1}, at indicated n		
			1	2	3
65 BMA–30 BA–5 MAA	0.17	30	0	500	650
		40	0	675	1350
		50	400	900	1500
85 BMA–10 VA–5 BA	0.20	20	0	0	120
		30	0	600	950
		40	0	1000	2000
		50	900	1700	2200
85 BMA–10 VA–35 BA	0.07	40	0	0	300
		50	0	0	430

paraffin. The lower M of the copolymer and the higher the paraffin content of the compound, the lower the plybond strentgh. To prevent sharp decrease in the plybond strength with a low-molecular-weight copolymer adhesive, the more concentrated solution should be used or the number of polymer layers applied to the backing fabric should be increased.

Fabric fibers are porous. The pore volume of natural cellulose fibers of cotton is 35–45% of the fiber volume. In addition, there is a space between threads of the first and second twists [4]. Therefore, interaction of a polymer adhesive with a textile substrate is controlled by diffusion and is determined by the adhesive amount. The larger the adhesive amount in the glue joint, the larger amount of the adhesive can penetrate into fabric interstice. The adhesive amount on the backing fabric can be increased either by an increase in the concentration of a polymer solution applied to the fabric or by application of several layers of the polymer solution. As seen from Table 3, both methods increase the adhesion.



(*1*) Viscosity η of a solution of 85 BMA–10 VA–5 BA copolymer with [η] = 0.20 dl g^{-1} and (*2*) plybond strength γ of glued coarse calico as functions of the polymer concentration c in the solution. Three layers of the copolymer solution were applied to the backing fabric.

As seen from the figure, the fabrics are glued with a measurable adhesion when the polymer concentration in the solution reaches $C_{cr.1}$ = 20 wt %. At this concentration, a Newtonian liquid transforms into a structured-viscous liquid [8]. In the latter case, macromolecular associates are formed. Penetration of large associates into fiber interstice of the backing fabric is complicated, and these associates are located on the fiber surface to form an adhesive layer. Therefore, solutions in the structured-viscous rheological state should be applied onto the backing fabric. As seen from the figure (curve *2*), the adhesives prepared from solutions with a concentration close to $C_{cr.2}$ (50–60 wt %) have the best adhesive properties. At higher concentration, the solution transforms from the structured-viscous to hyperelastic state [8]. At $c \cong c_{cr.2}$, the associates are closely packed in the solution. A polymer film prepared from this solution shrinks to a lesser extent. In this case, the internal stresses in the adhesive film decrease and the adhesion-strength properties are improved. At $c > c_{cr.2}$, a fluctuation network of macromolecular contacts is formed [8]. When a continuous fluctuation network of contacts is formed in a solution, its viscosity sharply increases (Fig. 1, curve *1*). This solution is difficult to apply to a fabric. It does not noticeably penetrate into pores of fabric fibers and is located on the filament surface. As a result, adhesion of the composite decreases owing to poor adhesion of the polymer molecules to fibers of both backing and doubled fabric, since the structure of the polymer solution is retained in the film prepared from this solution [9].

It is known than the unfolded conformation of the polymer chain is favorable for interaction of the polymer with the substrate surface, whereas the globular conformation formed, e.g., in a "bad" solvent prevents formation of sufficiently large number of contacts, thus decreasing the adhesion. As seen from Table 4, the adhesion of the copolymer applied from a solution in a bad solvent (isopropanol) is lower. The quality of solvents with respect to the copolymers was estimated

Table 4. Influence of the solvent on the plybond strength γ of BMA copolymers. Copolymer concentration in the solution applied to the backing fabric (coarse calico) 50 wt %; three layers applied

Copolymer composition, wt %	δ_{COP},* $(cal\ cm^{-3})^{1/2}$	Ethyl acetate, δ = 9.1 $(cal\ cm^{-3})^{1/2}$		Isopropanol, δ = 12.06 $(cal\ cm^{-3})^{1/2}$**	
		η, mPa s	γ, g cm^{-1}	η, mPa s	γ, g cm^{-1}
100 BMA	8.70	107	528	251	388
90 BMA–10 VA	8.75	91	500	184	120
90 BMA–10 BA	8.70	77	700	166	560
95 BMA–5 (2–EHA)	–	56	850	191	500
85 BMA–10 VA–5 BA	8.74	67	520	180	348

* $\delta_{COP} = \Sigma \delta_i \varphi_i$, where φ_i is the volume fraction of the monomer in the copolymer and δ_i is the solubility parameter of the homopolymer [10].

** δ for propanol.

by comparison of the solubility parameters of the copolymer and solvent [10]. As seen from Table 4, the viscosity of a solution in a bad solvent is higher than that in a good solvent (ethyl acetate). As noted above, the more structured solution is nonuniformly applied onto the fabric and lower amount of the polymer penetrates into pores of fabric fibers.

CONCLUSIONS

(1) To increase the adhesion to cellulose fabric (coarse calico) of butyl methacrylate copolymer applied from a copolymer melt, hydroxyl-containing vinyl acetate and acrylic units should be introduced into the copolymer macromolecules, the copolymer molecular weight should be higher, the polymer amount in the adhesive layer should be larger, and the viscosity of the adhesive melt should be lower.

(2) The structural rheological state of a copolymer solution applied to the backing fabric affects the adhesion of cellulose fabrics glued by copolymer melts. Adhesive melts prepared from solutions being in the transition from the structured-viscous to hyperelastic states have the best adhesion to cellulose fabrics.

(3) Copolymer solution in solvent good for the copolymer should be used to prepare adhesives with high adhesion to fabrics.

REFERENCES

1. Fedoseeva, T.S., Application of Synthetic Materials to Restoration of Easel Oil Paintings, *Konservatsiya i restavratsiya muzeinykh khudozhestvennykh tsennostei. Obzor informatsii* (Conservation and Restoration of Art Masterpieces in Museums. Information Review), 1989, issue 5, p. 40.
2. Emel'yanov, D.N. and Volkova, N.V., *Available from ONIITEI*, Cherkassy, July 30, 1981, no. 665 khp-D-81.
3. Antonyan, A.S., in *Skul'ptura: Prikladnoe iskusstvo* (Sculpture: Applied Art), Moscow: VKhRNTs, 1993, pp. 16–24.
4. Berlin, A.A. and Basin, V.E., *Osnovy adgezii polimerov* (Foundations of Polymer Adhesion), Moscow: Khimiya, 1969.
5. Kovacic, L., *Skleivanie metallov i plastmass* (Gluing of Metals and Plastics), Moscow: Khimiya, 1985.
6. Prytkin, L.M., Kardamov, D.A., and Vakula, V.L., *Monomernye klei* (Monomeric Adhesives), Moscow: Khimiya, 1988.
7. *Spravochnik po dipol'nym momentam* (Handbook of Dipole Moments), Osipov, O.A., Minkin, V.I., and Garnovskii, A.D., Eds., Moscow: Vysshaya Shkola, 1971.
8. Yemelyanov, D.N., Smetanina, I.E., and Vinogradov, G.V., *Rheol. Acta*, 1982, vol. 221, pp. 280–287.
9. Tager, A.A., *Fizikokhimiya polimerov* (Physical Chemistry of Polymers), Moscow: Khimiya, 1978.
10. Krause, S., *Polymer Blends*, Paul, D.R. and Newman, S., Eds., New York: Academic, 1978, vol. 1. Translated under the title *Polimernye smesi*, Moscow: Mir, 1981, vol. 1, p. 26.

ISSN 1070-4272, Russian Journal of Applied Chemistry, 2008, Vol. 81, No. 1, pp. 148–152. © Pleiades Publishing, Ltd., 2008.
Original Russian Text © S.V. Frolova, V.A. Demin, 2008, published in Zhurnal Prikladnoi Khimii, 2008, Vol. 81, No. 1, pp. 152–156.

MACROMOLECULAR CHEMISTRY AND POLYMERIC MATERIALS

Degradation of Wood Cellulose with Lewis Acids with the Aim to Prepare Powder Cellulose

S. V. Frolova and V. A. Demin

Institute of Chemistry, Komi Scientific Center, Ural Division, Russian Academy of Sciences, Syktyvkar, Komi Republic, Russia

Received May 2, 2007

Abstract—The influence of various factors on degradation of wood cellulose with Lewis acids was studied. The physicochemical characteristics of the resulting products were analyzed.

DOI: 10.1134/S1070427208010321

Reactions of monosaccharides catalyzed by Lewis acids (MX_n) are well studied and widely used [1]. In chemistry of polysaccharides, Lewis acids are used less extensively. They are mainly used as highly effective catalysts for cellulose degradation. Previously [2, 3] conversion of cotton cellulose in the presence of Lewis acids was studied and possible application fields for the synthesized powder celluloses were outlined. The use of water-free procedures is a promising pathway for production of powder celluloses. The use of organic solvents in the course of the reaction and their subsequent regeneration allows a decrease in the expenditure of pure water and in the volume of wastewaters.

Wood cellulose differs from cotton cellulose by the presence of residual hemicelluloses and lignin. It is used for production of powder cellulose for technical purpose. For this purpose, it is degraded in an aqueous medium at a high liquid-to-solid ratio and an excess of sodium hypochlorite. The use of Lewis acids and anhydrous media for production of powder celluloses can essentially improve the product purity. The use of wood raw materials for this purpose can significantly reduce the cost of the process and impart new properties to the cellulose material.

Here we studied the influence of various factors on degradation of wood cellulose with the use of Lewis acids and analyzed physicochemical characteristics of the resulting products.

EXPERIMENTAL

The object of the study was deciduous kraft bleached cellulose produced by the Syktyvkar Timber Industry Association, Joint-Stock Company. Before treatment, the cellulose was separated into single fibers to provide the highest homogeneity in size. Aluminum chloride, aluminum bromide, and titanium tetrachloride were used as Lewis acids (MX_n). $AlCl_3$ and $AlBr_3$ were synthesized by the standard procedure [4]. Before use, the sample stored for more than one year was purified by sublimation at atmospheric pressure. The sample stored for more than two years was purified by simple distillation. To prepare $TiCl_4$ we used commercial titanium tetrachloride of pure grade, which was purified by simple distillation at atmospheric pressure [4]. The reaction was performed in anhydrous organic solvents (carbon tetrachloride, hexane, and ethanol) at their boiling points. A weighed portion of cellulose dried at 105°C was placed into a conical flask and poured over with a solution of freshly prepared Lewis acid for a certain period of time. Aluminum chloride: a 1.99-g weighed portion of cellulose was treated with 50 ml of 0.1–0.005% solution in CCl_4. Titanium chloride: a 1.65-g weighed portion of cellulose was treated with 100 ml of 1.0–0.005% solution in CCl_4. Depending on the concentration of Lewis acid in the solution, the weight ratio MX_n : cellulose was from 1 : 2.5 to 1 : 500 (Table 1). After a lapse of time, cellulose was transferred onto a glass frit, the solution was filtered, and the residual catalyst was washed out with the same solvent, included with ethanol, and dried in an oven. The degree of degradation was judged from variation of the average degree of polymerization (DP) of the samples determined from their viscosity in aqueous solutions of Cadoxen [5].

In the experiments we varied the concentration of Lewis acids, treatment duration, weight ratio

Table 1. Influence of the concentration of Lewis acid on the degree of polymerization of cellulose

Catalytic system, reaction temperature, °C	DP at indicated concentration of Lewis acid, wt % (numerator) and MX_n : cellulose ratio, g (denominator)					
	1.0/1 : 2.5	1.0/1 : 25	0.05/1 : 50	0.025/1 : 100	0.010/1 : 250	0.005/1 : 500
$AlCl_3$–CCl_4, 76.7	–	135	180	190	200	310
$TiCl_4$–C_6H_{14}, 68.8	–	83	137	190	350	370
$TiCl_4$–CCl_4, 76.7	180	260	320	350	360	380
$AlCl_3$–C_2H_5OH, 78.3	120	150	230	330	420	–
$TiCl_4$–C_2H_5OH, 78.3	160	240	360	–	–	–
$AlBr_3$–C_2H_5OH, 78.3	240	330	–	–	–	–

MX_n : cellulose, and conditions of drying the samples. Data on the influence of Lewis acid concentration on the degree of polymerization of cellulose powders (treatment duration 120 min) are presented in Table 1. The degree of polymerization of the initial cellulose was 580.

All systems of metal halides with a concentration of 1.0% exhibit high catalytic activity. The degree of polymerization of cellulose is 180–240, which corresponds to the limiting value for microcrystalline cellulose prepared by the "classic" procedure [6]. After treatment the cellulose samples are in the form of powders.

At low concentrations of the catalysts (0.01–0.10%), the most active degrading agents are metal chlorides: $AlCl_3$ in CCl_4 and $TiCl_4$ in C_6H_{14}. The less active catalyst is $AlBr_3$ in C_2H_5OH: at its concentration lower than 1.0% the attempts to prepare powder cellulose failed, because at DP higher than 330 the cellulose particles preserved the structure of microfibers and were not friable.

The solvent significantly affects cellulose degradation (Table 1). The DP reaches the smallest values in nonpolar solvents (C_6H_{14} and CCl_4) and the largest values, in a protic solvent (C_2H_5OH). These results are in good agreement with data for cotton cellulose [7].

The kinetic curves of cellulose degradation are presented in Fig. 1. For comparison, data on degradation of the same raw materials in hydrolytic treatment are also presented. These data suggest that the degree of cellulose degradation, compared to the hydrolytic treatment, is higher in nonpolar solvents and lower in polar solvents.

It was shown previously [8] that an increase in the contact time of cellulose with Lewis acid leads to a certain increase in the product weight, because washing of the samples with solvent does not ensure complete removal of the catalyst from cellulose. In subsequent additional drying of cellulose in an oven, metal chlorides induce its further degradation. This fact made it necessary to study the effect of metal chlorides on the degradation process. As follows from Table 2, the choice of drying conditions significantly affects DP of cellulose. An increase in DP was observed for the samples obtained as a result of cellulose degradation in CCl_4 and then subjected to drying in a chamber with removal of the $AlCl_3$ residue.

Washing with the solvent decreases DP of cellulose with subsequent drying in a chamber. The use of additional heating for the powders obtained after cellulose treatment in the $AlCl_3$–CCl_4 medium at two levels of the catalyst concentration increased the degree of degradation by a factor of 2, and samples with very low values of DP (60 and 100) were obtained. In the systems with ethanol, DP of the samples decreased at any modes of additional heating.

The reuse of the catalytic solution after filtration showed that the reagent dissolved in nonpolar solvents

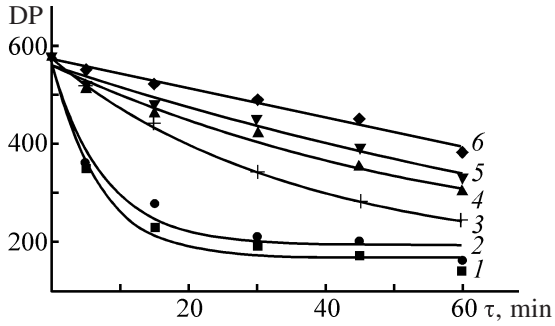


Fig. 1. Degree of polymerization of powder cellulose DP as a function of conditions of catalytic degradation. (τ) Time. Catalytic system, temperature (°C): (*1*) $AlCl_3$–CCl_4 (0.1 wt %), 76.7; (*2*) $TiCl_4$–C_6H_{14} (0.1 wt %), 68.8; (*3*) HCl 1 N (3.65 wt %), 78.3; (*4*) $AlCl_3$–C_2H_5OH (0.1 wt%), 78.3; (*5*) $TiCl_4$–C_2H_5OH (0.1 wt %), 78.3; and (*6*) $AlBr_3$–C_2H_5OH (0.1 wt %), 78.3.

Table 2. Influence of conditions of additional drying of the cellulose samples on their DP

Degradation medium	Treatment time, min	Degree of polymerization of samples			
		drying in air at 20°C	additional heating at 100°C for 120 min		reuse of degrading solution
			without washing off the catalyst	after washing off the catalyst	
Initial cellulose	0	580	580	580	580
0.1% $AlCl_3$ in CCl_4	30	190	310	130	540
	45	170	300	90	520
	60	140	290	70	510
	120	135	280	60	500
0.01% $AlCl_3$ in CCl_4	30	420	480	240	560
	60	380	440	200	550
	120	200	400	100	540
1.0% $AlCl_3$ in C_2H_5OH	30	320	280	190	340
	60	240	200	150	300
	120	120	180	110	260
0.1% $AlCl_3$ in C_2H_5OH	30	420	380	340	460
	60	300	220	170	420
	120	150	200	120	400

is consumed practically completely, whereas the reagents dissolved in ethanol react significantly more slowly and in reuse the system exhibits weak catalytic activity, probably due to dehydration of the treated polysaccharides.

Whiteness is a significant factor of the cellulose quality. The results of studying the influence of temperature on the DP and whiteness of the powder cellulose samples obtained in anhydrous organic media after washing off the acid catalyst are presented in Table 3. For comparison, data on cellulose subjected to hydrolytic treatment are presented. The whiteness of cellulose was measured on an FKTsSh-M double-beam photometer. Under these conditions, the hydrolysis duration does not noticeably affect the whiteness of powder cellulose, and additional heating at 100°C has virtually no effect on its DP.

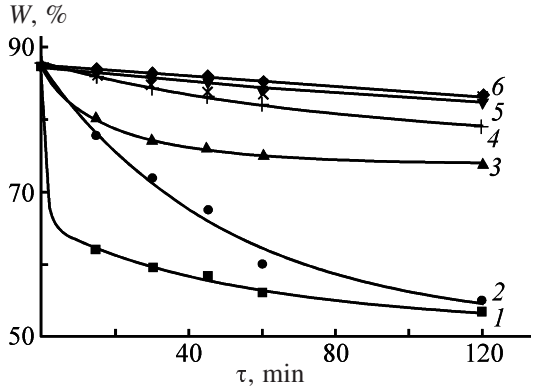


Fig. 2. Whiteness of powder cellulose W as a function of treatment duration τ. Catalytic system (content 0.1 wt %), temperature, °C: (*1*) $TiCl_4$–CCl_4, 76.7; (*2*) $AlCl_3$–CCl_4, 76.7; (*3*) $TiCl_4$–C_6H_{14}, 68.8; (*4*) $AlCl_3$–C_2H_5OH, 78.3; (*5*) $TiCl_4$–C_2H_5OH, 78.3; and (*6*) $AlBr_3$–C_2H_5OH, 78.3.

As a rule, in treatment of cellulose with Lewis acids, its degradation is accompanied by decrease in whiteness. This trend is particularly pronounced for the samples of powder cellulose prepared with using $TiCl_4$. The apparent change in color can be explained by formation of the complex MX_n–cellulose. The decrease in whiteness of cellulose as a result of the action of $TiCl_4$ and $AlCl_3$ is particularly significant with catalysts in CCl_4. This is illustrated by Fig. 2.

An increase in the MX_n concentration from 0.01 to 1.00 wt% is favorable for faster and deeper decrease in cellulose whiteness. The darkest samples of cellulose powders were obtained after treatment of cellulose in the $TiCl_4$–CCl_4 medium throughout the entire range of catalyst concentrations (Fig. 3).

To evaluate the influence of Lewis acid expenditure on the DP of cellulose, we varied the liquid-to-solid ratio ($cm^3\ g^{-1}$) at the initial concentration of $TiCl_4$ in C_6H_{14} equal to 0.1%. The reaction was carried out in a thermostat at the boiling point of the solvent. In one case, the weighed portion of cellulose (1.65 g) was placed into a conical flask containing 100 ml of degrading solution, and, in the other case, a weighed portion of cellulose (0.34 g) was placed

Table 3. Influence of additional thermal treatment on the depth of degradation and whiteness of cellulose powders in various catalytic systems

Degrading medium	Treatment time, min	Degree of polymerization of samples		Whiteness,* %
		drying in air at 20°C	additional heating for 120 min at 100°C	
Initial cellulose	0	580	580	87
0.1% $AlCl_3$ in CCl_4	5	350	300	72
	15	230	150	61
	30	190	130	59
	45	170	90	58
	60	140	70	56
	120	135	60	53
0.1% $TiCl_4$ in CCl_4	5	380	260	81
	15	170	140	80
	30	180	160	71
	45	190	170	66
	60	230	180	60
	120	260	250	50
0.1% $AlCl_3$ in C_2H_5OH	30	420	340	86
	60	300	170	84
	120	150	120	82
0.1% $TiCl_4$ in C_2H_5OH	30	450	380	85
	60	290	170	82
	120	240	150	80
0.1% $AlBr_3$ in C_2H_5OH	30	490	430	87
	60	380	300	86
	120	330	270	85
1 N HCl	60	210	200	87
	120	180	170	87
0.1 N HCl	60	380	360	84
	120	350	340	83

* After treatment and drying in air.

into an ampule and impregnated with 1 ml of the degrading solution. In this case, the liquid-to-solid ratios were 60 : 1 and 3 : 1, and the ratios MX_n : cellulose were 1 : 25 and 1 : 500, respectively (Fig. 4).

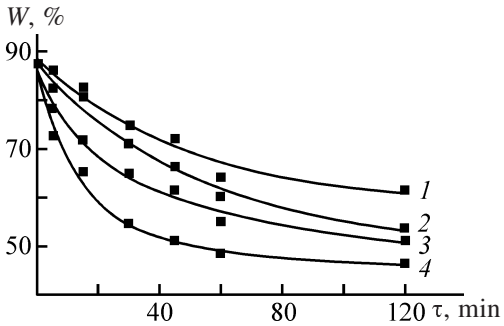


Fig. 3. Whiteness of powder cellulose W as a function of treatment duration τ in the system $TiCl_4$–CCl_4 at various catalyst concentrations c. Degradation at T = 76.7°C, the samples were dried at T = 100.0°C for 120 min. Catalyst concentration, wt %: (*1*) 0.01, (*2*) 0.10, (*3*) 0.30, and (*4*) 1.0.

Figure 4 shows that an increase in the liquid-to-solid ratio is favorable for significant decrease in the DP of cellulose. The minimum value of DP reaches 85 (curve *1*) and 390 (curve *2*).

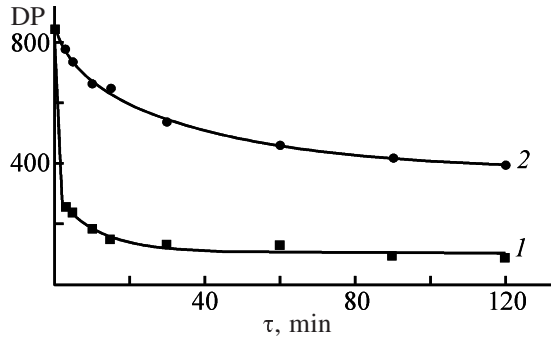


Fig. 4. Degree of polymerization DP of powder celluloses as a function of duration τ of treatment with 0.1% $TiCl_4$ in hexane at liquid-to-solid ratio of (*1*) 60 : 1 and (*2*) 3 : 1.

CONCLUSIONS

(1) Lewis acids $AlCl_3$ and $TiCl_4$ in CCl_4 and C_6H_{14} exhibit high catalytic activity at catalyst concentration of 0.01–0.1 wt%. As a result of treatment of cellulose in nonpolar solvents for a short time, products with the degree of polymerization two times lower than that after acid hydrolysis can be obtained.

(2) In drying of the samples, excess Lewis acid leads to an increase in the degree of polymerization due to probable cross-linking of cellulose chains. The formation of the complex MX_n–cellulose is accompanied by darkening of the product and depends on the acid concentration.

REFERENCES

1. Sarybaeva, R.I., Afanas'ev, V.A., Zaikov, G.E., et al., *Usp. Khim.*, 1977, vol. 46, no. 8, pp. 1395–1410.
2. Sarybaeva, R.I., Vasil'kova, T.V., and Afanas'ev, V.A., *Izv. Akad. Nauk Kirg. SSR*, 1979, no. 2, pp. 42–48.
3. Sultankulova, A.S., Sarybaeva, R.I., and Afanas'ev, V.A., *Khim. Drev.*, 1992, nos. 4–5, pp. 114–115.
4. Karyakin, Yu.V. and Angelov, I.I., *Chistye khimicheskie veshscestva* (Pure Chemical Substances), Moscow: Khimiya, 1974.
5. Bolotnikova, L.S., Danilov, S.N., and Samsonova, T.I., *Zh. Prikl. Khim.*, 1966, vol. 39, no. 1, pp. 176–180.
6. Battista, O.A., *Cellulose and Cellulose Derivatives*, Bikales, N.M. and Segal, L., Eds., New York: Wiley–Interscience, 1971, part IV. Translated under the title *Mikrokristallicheskaya tsellyuloza*, Moscow: Mir, 1974, pp. 412–423.
7. USSR Inventor's Certificate no. 730692.
8. Frolova, S.V., Kuchin, A.V., Demin, V.A., et al., in *Khimiya drevesiny, lesokhimiya i organicheskii sintez: Trudy Komi Nauchnogo Tsentra Ural'skogo Otd. Ross. Akad. Nauk* (Wood Chemistry and Organic Synthesis: Proc. Komi Scientific Center, Russian Acad. Sci.), Syktyvkar, 1999, no. 162, pp. 113–116.

ISSN 1070-4272, Russian Journal of Applied Chemistry, 2008, Vol. 81, No. 1, pp. 153–157. © Pleiades Publishing, Ltd., 2008.
Original Russian Text © D.V. Novikov, 2008, published in Zhurnal Prikladnoi Khimii, 2008, Vol. 81, No. 1, pp. 157–161.

MACROMOLECULAR CHEMISTRY AND POLYMERIC MATERIALS

Adsorption of Gold Nanoparticles Obtained by Vacuum Deposition on an Amorphous Polymer Surface

D. V. Novikov

Bonch-Bruevich St. Petersburg State University of Telecommunications, St. Petersburg, Russia

Received July 3, 2007

Abstract—Spatial distribution of gold nanoparticles obtained by vacuum deposition on the surface of amorphous polymers was studied within the limits of the cluster lattice model.

DOI: 10.1134/S1070427208010333

The formation of condensed phase particles on a solid surface can be random, independent of the topological structure of the substrate, or can preferentially occur on active centers of the surface interacting with adsorbed particles [1, 2]. Such centers can be presented by structural defects of the surface and also sites with an enhanced energy and noncompensated electric charge, where, as a rule, essential local fluctuations of electron density take place [2]. The preferential formation of particles on active centers results in decoration of the substrate surface, i.e., special features of its microstructure are revealed. This finds use in the analysis of the topology of solid surfaces [3].

Of special interest is the use of vacuum deposition of gold for the decoration of the surface of amorphous and semicrystalline polymers [4]. The decoration of nano- and microdefects on the surface of polymers favors revealing both well pronounced irregularities of a geometrical microrelief, e.g., dislocations on a surface of polymeric crystals [5], and heterogeneity of an energy microrelief, e.g., impurity inclusions, sites of localization of reactive functional groups, density fluctuations of macromolecular packing, etc. [4].

At present, structural microheterogeneity of amorphous polymers is associated either with density fluctuations or with a cluster structure of an object [6]. Usually by clusters are meant fractal aggregates of structural units (in case of polymers, blocks of segments of macromolecules) having a higher local density compared to an average density of a substance [7, 8]. Amorphous films obtained from solutions of flexible-chain polymers are characterized by heterogeneity of the supramolecular scale, caused by density fluctuations arising owing to the irreversible transition from a solution to a solid state of the polymer [9]. Density fluctuations have a scale-invariant character and can be described within the limits of the model of fractal clusters [10, 11].

Cluster microheterogeneous structure of amorphous polymers causes the heterogeneous character of the surface energy microrelief and substantially influences initial stages of the formation and growth of decorating gold particles [12, 13]. Most of defects of amorphous polymers are associated with density fluctuations of packing of macromolecules and are localized on boundaries of the clusters [8]; therefore, the topography of decorating particles is connected with the profile of a planar density distribution on the polymeric support surface.

The character of the adsorption defines the dependence of density fluctuations $\langle\sigma^2\rangle/\langle N\rangle$ of a spatial distribution of adsorbed particles on the degree of filling of the substrate surface with these particles [14]. The dependences of $\langle\sigma^2\rangle/\langle N\rangle$ on the fraction θ of the surface area covered by adsorbed particles were determined by computer simulation of various mechanisms of the adsorption of dispersed phase particles on a solid surface [14, 15]. The random surface filling with the particles corresponds to the random adsorption (RA) model [16], for which dependence [14] is valid:

$$\langle\sigma^2\rangle/\langle N\rangle = 1 - 4\theta + 3^{1/2}/\pi\theta^2 + o(\theta^3), \qquad (1)$$

where $o(\theta^3)$ is a value of the third infinitesimal order.

This dependence was confirmed experimentally by studying the adsorption of small particles of polymeric latexes from dilute solutions on a solid substrate [15].

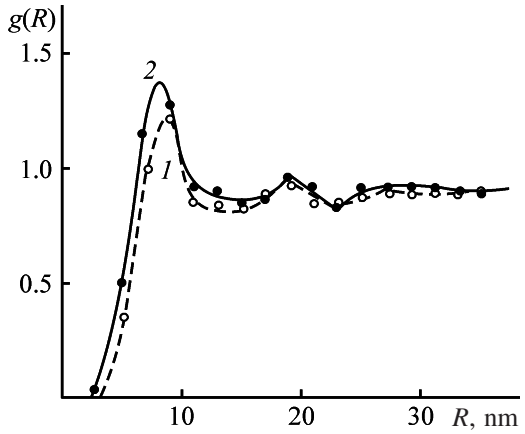


Fig. 1. Distribution functions $g(R)$ of gold nanoparticles on the surfaces of (*1*) PS and (*2*) CTA films.

In the case of adsorption in an external potential field, e.g., the adsorption of heavy particles in a gravitational field, the ballistic adsorption model [17] is valid. According to this model, the dependence of $\langle\sigma^2\rangle/\langle N\rangle$ on θ is of form (2) [14]:

$$\langle\sigma^2\rangle/\langle N\rangle = 1 - 3.16\theta^3 + 2.3\theta^4 + o(\theta^5). \qquad (2)$$

In this study we used the cluster lattice model to study the spatial distribution of gold nanoparticles of size 1–15 nm, obtained by vacuum deposition on a surface of films formed from polystyrene (PS) and cellulose triacetate (CTA) solutions. The aim of the study was to examine the effect of the cluster structure of the polymer surface in the steps of the formation and growth of decorating gold particles.

EXPERIMENTAL

In the work we used samples of X-ray amorphous PS and CTA films of 60 μm thickness. The films of linear atactic PS (molecular weight $M_n = 9 \times 10^6$) and partially hydrolyzed CTA (degree of polymerization 300, degree of substitution 2.85) were obtained from solutions of the polymers in chloroform (PS concentration 0.72 g dl^{-1}) and in a 9 : 2 methylene chloride : ethanol mixture (CTA concentration 10 wt %) on a leveled plate glass at 298 K. According to the capillary viscometry, the concentration of polymers in the solution corresponded to the formation of a continuous fluctuational network of macromolecular contacts [18].

Polystyrene belongs to typical flexible-chain polymers, whereas CTA macromolecules, in turn, are rigid-chain polymers and form anisotropic ordered assemblies of the microdomain type in boundary layers [19].

Single vacuum depositions of gold (vacuum 0.00133 Pa, flux level 10^{15}–10^{16} cm^{-2} s^{-1}, effective layer thickness 0.4 nm) were carried out on the surface of films formed on the boundary with air. Gold particles, which were separated from the films using supporting carbon replicas, were studied with an EMV-100L electron microscope. The electron micrographs for computer treatment were obtained at a 500 000 magnification.

The radial distribution function $g(R)$ of gold nanoparticles was determined by step-by-step scanning of the density ρ of particle distribution (at δ = 2 nm steps) on a micrograph [4, 12].

Aggregates of gold nanoparticles on the surface of films were represented as clusters on a two-dimensional lattice [10] with an interstitial distance corresponding to the most probable distance r between particles. The coordination number m of the quasilattice was determined from the $g(R)$ functions as an average number of the nearest neighbors around an arbitrarily selected particle [20].

According to [13], the relative distribution function ρ_l of m for points of a two-dimensional regular lattice is expressed as

$$\left.\begin{aligned} \rho_l &= 0.77/r^2 \text{ for } m = 3, \\ \rho_l &= 1/r^2 \text{ for } m = 4. \end{aligned}\right\} \qquad (3)$$

The functions $g(R)$ for the distribution of gold nanoparticles on the surfaces of PS and CTA films are shown in Fig. 1. The coordination number m of the two-dimensional quasilattice takes the value m = 3 for PS (hexagonal lattice) and m = 4 for CTA (square lattice). The density ρ of the distribution of the complete ensemble of nanoparticles practically corresponds to the density ρ_l of two-dimensional regular lattice points calculated by relationships (3), which allows us to use the lattice model for the description of the spatial distribution of particles.

In this study we have carried out a computer simulation of the process of sequential filling of a lattice (surface) with gold nanoparticles as their size increases. For this purpose an ensemble of particles on micrographs was separated into classes according to their maximum linear size l at 1-nm intervals. For each group of classes limited by a value of l, we calculated the degree $\rho_s(l)$ of filling of a two-dimensional quasilattice with particles, or the lattice density of clusters: $\rho_s(l) = \rho(l)/\rho$, where $\rho(l)$ is the density func-

tion of particles with sizes not exceeding l, and ρ is the density function of the complete ensemble of particles.

To analyze the character of surface filling with gold nanoparticles, we used the scheme of the percolation along bound circles with centers located in particles [20]. Figure 2 shows the dependences of the weight-average size $\langle n^2\rangle/\langle n\rangle$ of the clusters of bound circles with centers in particles on the dimensionless radius of circles $R\rho(l)^{1/2}$. These dependences were obtained for isolated groups of separated classes of particles. At l = 1–11 nm for a PS sample and l = 1–5 nm for CTA, the semilog plots of $\langle n^2\rangle/\langle n\rangle$ vs. $R\rho(l)^{1/2}$ have a break point which shows that gold nanoparticles are distributed on the substrate surface as separate aggregates, i.e., discrete clusters. At $l \geq 12$ (PS) and $l \geq 6$ nm (CTA), infinite clusters of particles exist, and the dependences monotonically ascend according to the law $\langle n^2\rangle/\langle n\rangle \sim (R_p - R)^{-\gamma}$, where n is the number of circles in a cluster; R_p, radius of a circle corresponding to the percolation cluster; the critical exponent $\gamma = 2.4 \pm 0.2$ [21].

The transition from finite clusters to an infinite cluster takes place at the $\rho_s(l)$ value equal to the percolation threshold p_c. For the lattice clusters of gold nanoparticles on the PS film surface (m = 3), the percolation threshold, $p_c \approx 0.65$, corresponds to that in the case of the random filling of a hexagonal lattice [10]. In the case of CTA sample, $p_c \sim 0.75$. This value is higher than the percolation threshold at random filling of the square lattice (p_c = 0.59 [10]). In this case, the positions of "point" gold nanoparticles of a size $l \leq 5$ nm are correlated with each other (nanoparticles are localized as separate chains) and form discrete fractal clusters with the correlaton radius $\xi \approx 20$ nm and fractal dimension $D = 1.25 \pm 0.05$.

The fractal dimension D of clusters was calculated from the slope of the log–log plot of the average lattice density $\rho_s(l, R)$ of gold nanoparticle clusters in a circle of radius R with the center in the particle vs. R. Such dependences obtained for separate groups of classes of particles with sizes limited by the l value are shown in Fig. 3. The density of the lattice clusters decreases as the radius R of a scale increases according to the law $\rho_s(l, R) \sim R^{D-2}$. The scale value of R corresponding to the position of the break point of the dependences fits the average correlation radius ξ of clusters [10].

Clusters of the "point" gold nanoparticles are localized inside a set of homogeneously distributed larger particles. The presence of clusters (chains) of

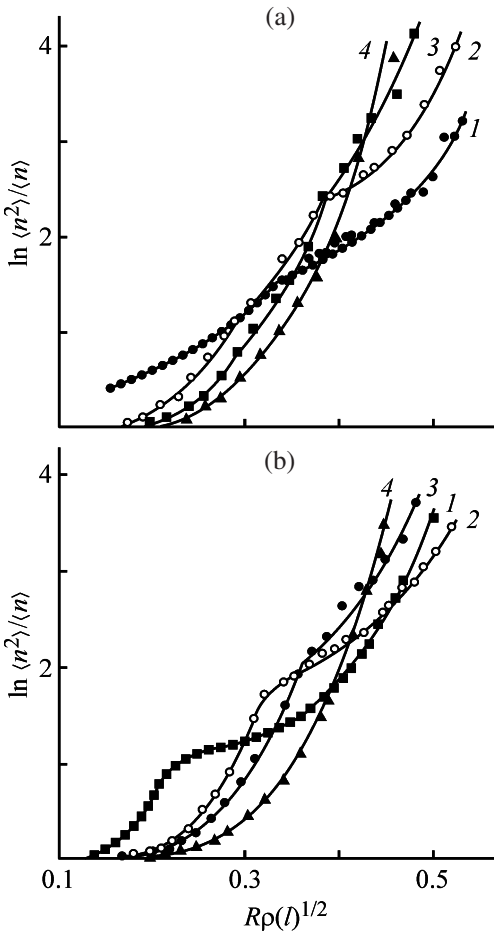


Fig. 2. Semilog plots of the weight-average size $\langle n^2\rangle/\langle n\rangle$ of clusters of bound circles vs. the dimensionless radius of circles $R\rho(l)^{1/2}$. Centers of circles correspond to the positions of nanoparticles on the surfaces of films. (a) PS and (b) CTA. l, nm: (a) (*1*) 6, (*2*) 8, (*3*) 10, and (*4*) 12; (b) (*1*) 2, (*2*) 4, (*3*) 5, and (*4*) 6.

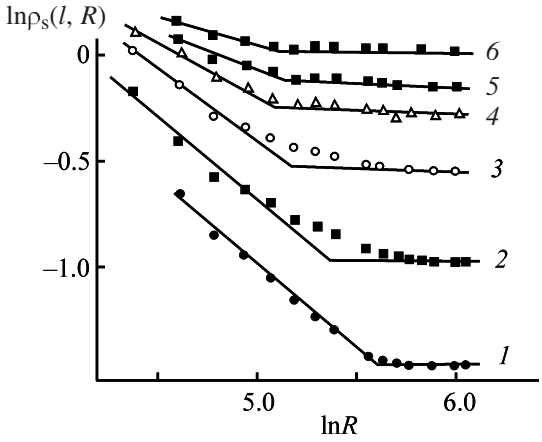


Fig. 3. Dependence of the lattice density $\rho_s(l, R)$ of clusters of gold nanoparticles on the scale R in log–log coordinates for the CTA film surface. l, nm: (*1*) 2, (*2*) 3, (*3*) 4, (*4*) 5, (*5*) 6, and (*6*) 8.

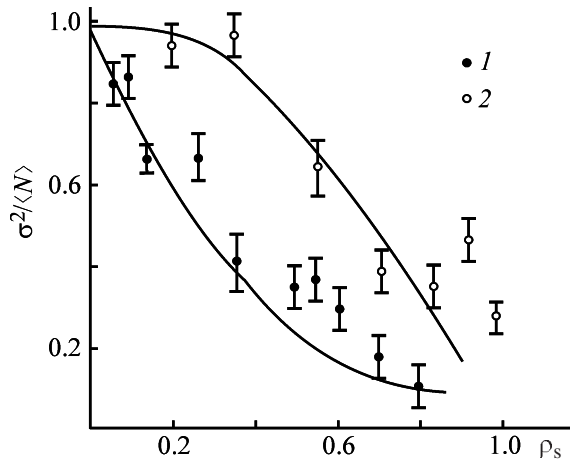


Fig. 4. Dependence of fluctuations $\langle\sigma^2\rangle/\langle N\rangle$ of the density function of gold nanoparticle on the degree ρ_s of lattice filling with the particles for the films of (*1*) PS and (*2*) CTA. Lower line: dependence (*4*) for the RA adsorption model; upper line: dependence (*5*) for the ballistic adsorption model.

point gold nanoparticles is caused by their preferential formation on the structural defects located on boundaries of close-packed aggregates of macromolecules or microdomains with the average size of about 20 nm. This size of microdomains corresponds to the size of scattering particles in the CTA film (16–26 nm), calculated from the data of small-angle X-ray scattering [22]. The size of microdomains is close to the value of Kuhn's segment for cellulose acetates (25–30 nm [23]). Defects on the polymer surface stabilize gold nanoparticles formed by vacuum deposition and hinder their further coalescence.

The value of fluctuations $\langle\sigma^2\rangle/\langle N\rangle(l)$ of the density function of particles for each set of the separated classes was calculated by the procedure from [14], and, to compare the resulting dependences of $\langle\sigma^2\rangle/\langle N\rangle(l)$ on $\rho_s(l)$ with model dependences (1) and (2), these latter were reduced to the form $\langle\sigma^2\rangle/\langle N\rangle(\rho_s)$ as follows. When the relationships $\theta/\theta_{max} = \rho_s$ (θ_{max} is the maximal degree of coverage of the surface by adsorbed particles), $\theta_{max} = 0.547$ for the RA model, and $\theta_{max} = 0.611$ [14, 15] for the ballistic adsorption model are taken into account, dependences (1) and (2) take forms (4) and (5) for RA and ballistic models, respectively:

$$\langle\sigma^2\rangle/\langle N\rangle = 1 - 2.19\rho_s + 1.32\rho_s^2, \quad (4)$$

$$\langle\sigma^2\rangle/\langle N\rangle = 1 - 0.72\rho_s^3 + 0.32\rho_s^4. \quad (5)$$

The dependences of the fluctuations $\langle\sigma^2\rangle/\langle N\rangle(l)$ of the density of the spatial distribution of gold nanoparticles on the degree $\rho_s(l)$ of the filling of PS and CTA film surfaces with these nanoparticles are shown in Fig. 4. The dependence of $\langle\sigma^2\rangle/\langle N\rangle(l)$ on $\rho_s(l)$ for the PS film corresponds to the RS adsorption model and random filling of the surface with particles. In the case of the CTA film, this dependence corresponds to the ballistic adsorption model in an external potential field. Such a field is the potential field of the surface defining the character of the interaction of adsorbed gold nanoparticles with CTA macromolecules. Deviations from model dependences (4) and (5) in Fig. 4 appear when the size of gold nanoparticles increases. They are caused by a change of the mechanism of their growth during the vacuum deposition of the metal on transition from the particle–adsorbed atom interactions to the particle–particle interactions, resulting in the coalescence of particles.

CONCLUSIONS

(1) The profile of the energy microrelief of the amorphous polymer surface, defined by its cluster microheterogeneous structure, predetermines the features of the spatial distribution of decorating gold nanoparticles obtained by vacuum deposition on the surface under study. The ballistic adsorption mechanism and the cluster type of the spatial distribution of particles correspond to the preferential formation of nanoparticles on active surface centers (structural defects).

(2) The mechanism of the adsorption of decorating nanoparticles defines the character of the dependence of density fluctuations of nanoparticle ensembles selected according to their values on the degree of filling of the surface with these nanoparticles.

(3) The smoothed energy microrelief of a polymer surface leads to random adsorption and random distribution of nanoparticles, which was shown by the example of a polystyrene film. In this case, to reveal in detail the topology of the cluster surface structure, a modification of the surface by additional active centers of the decorating particle formation is required.

REFERENCES

1. Lewis, B. and Anderson, J.C., *Nucleation and Growth of Thin Films*, New York: Academic, 1978.
2. Distler, G.I., *Aktivnaya poverkhnost' tverdykh tel* (Active Surface of Solids), Available from VINITI, Moscow, 1976, pp. 96–112.
3. Distler, G.I., Vlasov, V.P., and Gerasimov, Yu.M., *Dekorirovanie poverkhnosti tverdykh tel* (Decoration of Surfaces of Solids), Moscow: Nauka, 1976.

4. Novikov, D.V. and Varlamov, A.V., *Zh. Prikl. Khim*., 1995, vol. 68, no. 10, pp. 1718–1726.
5. Wunderlich, B., *Macromolecular Physics*, New York: Academic, 1973.
6. Svergun, D.I. and Feigin, L.A., *Rentgenovskoe i neitronnoe malouglovoe rasseyanie* (X-ray and Neutron Small-Angle Scattering), Moscow: Nauka, 1986.
7. Perepechko, I.I., *Vvedenie v fiziku polimerov* (Introduction to Polymer Physics), Moscow: Khimiya, 1978.
8. Kozlov, G.V. and Novikov, V.U., *Usp. Fiz. Nauk*, 2001, no. 7, pp. 717–764.
9. Matveev, Yu.I. and Askadskii, A.A., *Vysokomol. Soedin., Ser. A*, 1986, vol. 28, no. 7, pp. 1365–1372.
10. Feder, J., *Fractals*, New York: Plenum, 1988.
11. Smirnov, B.M., *Fizika fraktal'nykh klasterov* (Physics of Fractal Clusters), Moscow: Nauka, 1991.
12. Novikov, D.V., Varlamov, A.V., and Mnatsakanov, S.S., *Zh. Prikl. Khim*., 1990, vol. 63, no. 9, pp. 2013–2018.
13. Novikov, D.V. and Varlamov, A.V., *Poverkhnost'*, 1992, no. 6, pp. 117–120.
14. Wojtaszczyk, P., Mann, E.K., Senger, B., et al., *J. Chem. Phys*., 1995, vol. 103, no. 18, pp. 8285–8295.
15. Schaaf, P., Wojtaszczyk, P., Mann, E.K., et al., *J. Chem. Phys*., 1995, vol. 102, no. 12, pp. 5077–5086.
16. Hinrichsen, E.L., Feder, J., and Jossang, T., *J. Stat. Phys*., 1986, vol. 44, nos. 5/6, pp. 793–827.
17. Jullien, R. and Meakin, P., *Physica A*, 1991, vol. 175, no. 2, pp. 211–221.
18. Krasovskii, A.N., Nikolaev, V.P., Shlyakov, A.M., and Mnatsakanov, S.S., *Vysokomol. Soedin., Ser. A*, 1995, vol. 37, no. 2, pp. 273–282.
19. Polyakov, D.N., Krasovskii, A.N., and Odlyanitskii, L.A., *Kolloidn. Zh*., 1993, vol. 55, no. 6, pp. 90–94.
20. Ziman, J.M., *Models of Disorder: The Theoretical Physics of Homogeneously Disordered Systems*, Cambridge: Cambridge Univ. Press, 1979.
21. Stanley, H., *J. Phys. A*, 1977, vol. 10, no. 11, pp. L211–L234.
22. Varlamov, A.V., Kenarov, A.V., Dyshlevskaya, O.S., and Mnatsakanov, S.S., *Khimicheskaya tekhnologiya, svoistva i primenenie plastmass: Mezhvuzovskii sbornik* (Chemical Technology, Properties, and Application of Plastics: Intercollegiate Coll.), St. Petersburg: Tekhnol. Univ., 1992, pp. 131–133.
23. Tsvetkov, V.N., *Zhestkotsepnye polimernye molekuly* (Rigid-Chain Polymer Molecules), Leningrad: Nauka, 1986.

ISSN 1070-4272, Russian Journal of Applied Chemistry, 2008, Vol. 81, No. 1, pp. 158–159. © Pleiades Publishing, Ltd., 2008.
Original Russian Text © V.N. Zaichenko, G.Ya. Kolbasov, Yu.S. Krasnov, 2008, published in Zhurnal Prikladnoi Khimii, 2008, Vol. 81, No. 1, pp. 162–163.

BRIEF COMMUNICATIONS

Separation of Impurities from Cobalt with Complexing Agents

V. N. Zaichenko, G. Ya. Kolbasov, and Yu. S. Krasnov

Institute of General and Inorganic Chemistry, National Academy of Sciences of Ukraine, Kiev, Ukraine

Received July 23, 2007

Abstract—Chemical purification of cobalt powders to remove iron, silicon, copper, and sodium with complexing oxalate ions was studied.

DOI: 10.1134/S1070427208010345

Modern industrial processes employing powdered cobalt impose stringent requirements to its purity. Therefore, development of processes for cobalt purification to remove iron, silicon, manganese, copper, sodium, and calcium is exceedingly important. Most frequently, processes of this kind are employed in reprocessing of secondary raw materials (worked-out hard-alloy tools, catalysts, contaminated powders, etc.).

The known, in hydrometallurgy of cobalt, practice of cobalt treatment to remove iron, with lime or soda used to neutralize acid solutions and atmospheric oxygen serving as an agent that oxidizes Fe(II) [1], cannot be employed to obtain an ultrapure cobalt powder because of its contamination with sodium and calcium. Moreover, oxidation of iron with atmospheric oxygen is prolonged and inefficient.

The known technique for processing of secondary raw materials to obtain a cobalt powder employs soda for neutralization of the working solution [2]. In [3], the procedure by which powders were obtained from worked-out cobalt cathodes in deposition of iron and manganese used sodium chlorate and hypochlorite, caustic soda, and soda ash. In this case, the final product is also contaminated with sodium. In the techniques developed, iron is separated from solution in the form of a poorly filterable Fe(III) hydroxide, which poses certain technological difficulties. In addition, the freshly precipitated Fe(III) hydroxide sorbs cobalt from solutions, which leads to its loss.

This study was devoted to a search for new ways to solve the problem of cobalt refining. A possible way was to use complexing agents. Substances of this kind make it possible to obtain complex metal compounds with widely diverse physicochemical properties. It was necessary to determine whether Co can be recovered from an acid solution by choosing such a complexing agent with which Fe and other impurities would remain in solution, i.e., by reversing the order in which two basic procedures of the process are performed. This cannot be done using the hydroxide technique, whereas complexing agents can probably provide the desired effect.

It was found that the complexing agents best suitable for resolving this problem are carboxylic acids and their salts, e.g., oxalic acid and ammonium oxalate. These compounds cannot contaminate the cobalt powder with sodium, and Fe(III) oxalate is a stable complex well soluble in water. Carbon monoxide released in thermal reduction of cobalt oxalate to a metallic powder is involved in the reduction process, which saves hydrogen.

To perform the process, it was necessary to choose an oxidizing agent appropriate for Fe(II) oxidation to Fe(III) in an acid medium. Hydrogen peroxide was found to be the best suitable. Comparison of the standard potentials of the redox reactions

$$H_2O_2 + 2H^+ + 2e \rightarrow 2H_2O, \quad E_0 = 1.77\ V, \quad (1)$$

$$Fe^{2+} \rightarrow Fe^{3+} + e, \quad E_0 = 0.77\ V, \quad (2)$$

$$Co^{2+} \rightarrow Co^{3+} + e, \quad E_0 = 1.81\ V \quad (3)$$

shows that hydrogen peroxide is an effective agent for Fe(II) oxidation in an acid medium, with the potential of Co(II) → Co(III) oxidation not reached. Furthermore, hydrogen peroxide does not contaminate the final product and its excess amount is easily removed from solution. If oxalate ions are used as a complexing agent, it is important to analyze the state and mutual influence of the forming oxalates CoC_2O_4 and $Fe_2(C_2O_4)_3$.

Content of impurity elements in the starting cobalt powder and that after refining

Powder	Precipitant	Content of impurities, wt %				
		Fe	Ni	Si	Cu	Na
Starting	–	3.5	≤0.01	0.01	0.03	0.04
After refining	$(NH_4)_2C_2O_4$	<0.01	≤0.01	≤0.05	Trace amounts	Not found
	$H_2C_2O_4$	<0.01	≤0.01	≤0.05		

It is known that CoC_2O_4 is a poorly soluble substance (SP = 6.3×10^{-8}), whereas $Fe_2(C_2O_4)_3$ is well soluble in water [4]. Therefore, the former precipitates, whereas the latter remains in solution. Presence of free oxalic acid in solution makes lower the solubility of cobalt oxalate in an acid medium [5]. It should be noted that, in an acid medium, oxalic acid is a weak reducing agent:

$$H_2C_2O_4 + 6H^+ + 6e \rightarrow 2H_2O + CH_3COOH,\ E_0 = 0.31\ V, \quad (4)$$

but in the presence of a strong oxidizing agent (H_2O_2) it cannot reduce Fe(III) to Fe(II). For the same reason, the photochemical reaction of Fe(III) reduction by $C_2O_4^{2-}$, used in manufacture of photographic paper, is impossible. Hydrolysis of Fe^{3+} ions does not occur, either, because of the sufficiently acid medium and the stability of the complex $Fe_2(C_2O_4)_3$.

If secondary cobalt is contaminated with manganese, it can be seen from a comparison of the solubility products of their oxalates, equal to 2.0×10^{-6} and 6.3×10^{-8}, respectively, that the solid phase of cobalt oxalate will be the first to precipitate from solution, and the relative content of Mn in the solid phase will be lower than that in solution.

These facts demonstrate that cobalt can be purified by using oxalate ions as a complexing agent and hydrogen peroxide as an oxidizing agent. A test in cobalt refining confirmed this suggestion.

A cobalt powder contaminated with iron was chosen as object of study. The contents of impurities are listed in the table.

The experiments wee carried out as follows. Weighed portions of cobalt (10.0 g), containing 3.5 wt % Fe, were dissolved in 85 ml of HCl (1 : 1) under agitation with a magnetic stirrer. After complete dissolution, 2.5 ml of a 30% hydrogen peroxide solution was added to each sample and the mixtures were agitated and kept for 0.5 h (solution 1). Then, 16.7 g of ammonium oxalate was dissolved in hot water (solution 2), which constitutes a 20% excess with respect to stoichiometry (in terms of Co and Fe), and solution 2 was slowly poured into a solution 1, heated to 80 ± 5°C. The cobalt oxalate precipitate formed was filtered off on a nutsch filter and thrice washed first with water acidified with oxalic acid and then with pure warm water, and dried at 120 ± 5°C for 0.5 h. The precipitate obtained was thermally reduced in hydrogen at 750 ± 20°C. The final product was finely dispersed pure cobalt powder, whose impurity content is presented in the table. It can be seen that the procedure developed allows cobalt purification to remove iron, silicon, copper, and sodium to residual concentrations lower than those regulated by GOST (State Standard) 9722–97 for a powder of PK-1u brand, which makes it possible to class the product with ultrapure powders. The content of nickel cannot be lowered because the solubility product of its oxalate is two orders of magnitude smaller than that of cobalt oxalate.

CONCLUSIONS

(1) A technique for chemical refining of cobalt with complexing oxalate ions was developed.

(2) The technique does not use any sodium- or calcium-containing reagents that could contaminate cobalt.

(3) The cobalt refining is performed in two steps, which simplifies it to the maximum possible extent.

REFERENCES

1. Reznik, I.D., Sobol', S.I., and Khudyakov, V.M., *Kobal't* (Cobalt), Moscow: Metallurgiya, 1995, vol. 2.
2. Kurochkina, I.A., Polyakov, M.L., and Samsonov, A.S., *Tsvetn. Met.*, 2002, no. 10, pp. 28–30.
3. Hester, A.S., Mitchell, A.D., and Rees, R.W., *Ind. Eng. Chem.*, 1960, vol. 52, no. 2, pp. 94–100.
4. *Handbook of Chemistry and Physics*, Cleveland, 1955, 37th ed.
5. Serebrennikov, V.V., *Khimiya redkozemel'nykh elementov* (Chemistry of Rare-Earth Elements), vol. 1, book 1: *Redkozemel'nye metally i ikh soedineniya* (Rare-Earth Metals and Their Compounds), Tomsk: Tomsk. Univ., 1959.

ISSN 1070-4272, Russian Journal of Applied Chemistry, 2008, Vol. 81, No. 1, pp. 160–161. © Pleiades Publishing, Ltd., 2008.
Original Russian Text © S.O. Eshbekova, A.A. Kholmuminov, 2008, published in Zhurnal Prikladnoi Khimii, 2008, Vol. 81, No. 1, pp. 164–165.

BRIEF COMMUNICATIONS

Structuring of Fibrillar Proteins in Electrodialysis of Ions in a Shear Flow

S. O. Eshbekova and A. A. Kholmuminov

Dzhizak Polytechnic Institute, Dzhizak, Uzbekistan
Institute of Polymer Chemistry and Physics, Academy of Sciences of the Republic of Uzbekistan, Tashkent, Uzbekistan

Received October 23, 2007

Abstract—Possibility of using electrodialysis for controlling the content of ions in structuring of silk fibroin in a shear flow was studied.

DOI: 10.1134/S1070427208010357

Fibrous wastes of fibrillar proteins can be processed into polymeric materials in solutions in the presence of ions of salts, acids, and alkalis [1]. However, presence of ions in solution hinders formation of bonds between macromolecules when a three-dimensional structure of proteins is formed in a flow. The ions can be subsequently removed from the solutions by electrodialysis, and application of this technique is of practical interest [2].

The present study was concerned with the effect of electrodialysis of salt ions on the structuring of fibrillar proteins in a shear flow for the example of the fibroin of real silk.

EXPERIMENTAL

An installation for carrying out the experiments was fabricated on the basis of the Rheotest-2 instrument (Germany) with a cylinder–cylinder working unit (Fig. 1). A cylindrical cellulose hydrate membrane (*2*) was mounted between carbon electrodes (*1, 1'*) fixed in parallel in a glass cylinder. A glass cylinder (*3*) rotated by electric motor (M) was coaxially mounted within the membrane cylinder. The spacing between the cylinders, filled with a solution of silk fibroin (*4*), was about 3 mm. A polarization beam was passed through this space in order to determine the macromolecule orientation factor β in the flow with a polarization microscope (PM):

$$\beta = (\Delta n/\Delta n_\infty)^{0.5}, \quad (1)$$

where Δn is the current birefringence, and Δn_i, the maximum possible birefringence [3].

The direction in which ions *6* move across the membranes toward the electrodes submerged in the dialyzate coincides with the direction in which protein molecules are deformed by the centrifugal force $F_c = V\rho\omega^2 r$ (V is the volume of the solution; ρ, its density; ω, angular rate of rotation; and r, distance from the rotation axis).

The fluidity ρ_r of the fibroin solution was found by the Margules formula [2], with the rate of cylinder rotation controlled by the electric motor

$$\tau_r = 1/\eta_r \approx 2\pi\omega h R^3/bM, \quad (2)$$

where η_r is the solution viscosity; h, cylinder height; $R = (R_1 + R_2)/2$, hydrodynamic cell parameter (R_1 is the radius of the inner glass cylinder, and R_2, that of the outer membrane cylinder); b, distance between the cylinders; and $M = rF_c$, torque.

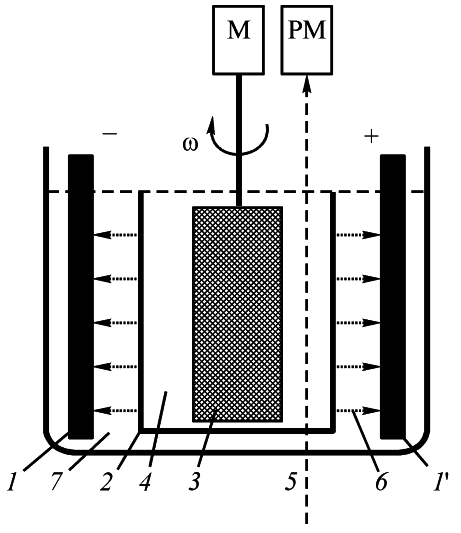


Fig. 1. Schematic of electrodialysis of ions in a shear flow of ion-containing solutions of fibrillar proteins. For explanations, see text.

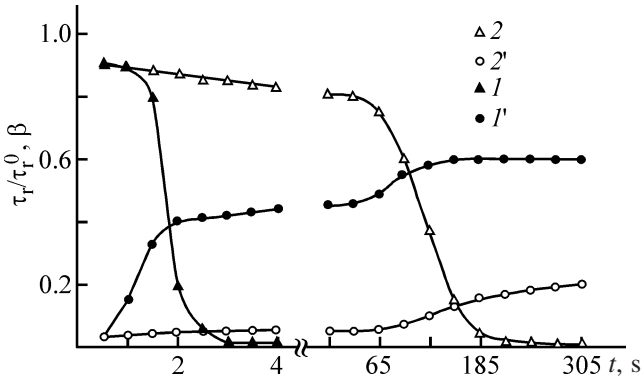


Fig. 2. (*1, 2*) Relative fluidity τ_r/τ_r^0 and (*1'*, *2'*) orientation factor β vs. time *t* of (*1, 1'*) electrodialysis and (*2, 2'*) dialysis of ions in a shear flow of the fibroin solution.

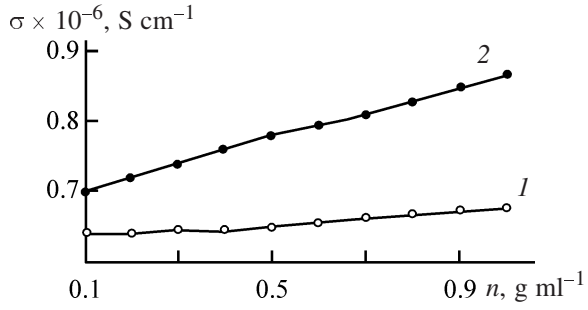


Fig. 3. Electrical conductivity σ vs. concentration *n* of residal ions in gel-plastics of fibroin at (*1*) 25 and (*2*) 50°C.

The variation of the dynamics of solution fluidity was found by comparison with the initial fluidity τ_r^0. The ratio $\tau_r/\tau_r^0 \to 0$ characterizes the loss of the independent flow of solutions on their transformation to the gel-like state.

The electrodialysis was performed for a 10% solution of fibroin in 2.5 M LiCl–DMF, with water used as a dialyzate. The efficiency of electrodialysis was evaluated by comparison with an ordinary dialysis of ions in a flow.

Figure 2 shows how the relative fluidity τ_r/τ_r^0 and the orientation factor β depend on the electrodialysis time. The curves are S-shaped, which is characteristic of a non-Newtonian flow of the solutions.

It was found that, in the course of electrodialysis ($I \approx 5$ mA) of solutions ($V \approx 50$ cm^3) subjected to a permanent shear stress (100 N m^{-2}), the fluidity steeply decreases in the time interval 100–150 s, to become zero at $t > 180$ s (Fig. 2). The results of birefringence measurements demonstrated that the macromolecule orientation factor starts to grow considerably earlier in the case of electrodialysis of ions (curves *1'*), compared with ordinary dialysis (curves *2'*). Consequently, electrodialysis accelerates the formation of intermolecular interactions of the chains being deformed in the shear field, with a controlled content of ions in solution.

Because the gelation of the solutions in electrodialysis of ions develops in the course of 120 min, the value $\beta \approx 0.4$, reached during this time, indicates that macromolecules are contained in gels in a rather ordered state. Further action of the shear field markedly raised the degree of deformation-induced ordering of proteins and resulted in that a value $\beta \approx 0.6$ was reached, with phase separation occurring in the solution. A compressed gel-like phase was formed near the membrane wall as a gel-plastic. This sample preserved its structure after the shear flow was stopped. The content of residual ions in the gel-plastics was found by extraction in a Soxhlet apparatus. It was found that 0.1 to 1 g of residual ions is contained in 10 ml of the gel plastic and this amount depends on the dc current passed in electrodialysis.

The residual ions make gel-plastics electrically conducting. The results obtained when determining the electrical conductivity at different temperatures are presented in Fig. 3. It can be seen that the electrical conductivity is higher for samples containing residual ions in a larger amount. An increase in temperature to 50°C results in that the curves are linearly shifted to higher σ. The shifts and electrical conductivities observed are characteristic of ion-containing polymeric formulations [5]. The electrical conduction mechanism is mixed, with both the ionic and electronic components, because ions are readily separated from the proteins under the action of the electric field.

CONCLUSIONS

Electrodialysis enables control over the content of ions in structuring of fibrillar proteins in a flow. The gel-plastics obtained are ion-containing electrically conducting formulations with a medium degree of chain ordering.

REFERENCES

1. Frenkel', S.Ya. and Tsygol'nyi, I.M., *Molekulyarnaya kibernetika* (Molecular Cybernetics), Lvov: Svit, 1990, p. 167.
2. Eliseeva, T.V., Lushchik, I.G., Tekuchev, A.Yu., et al., *Elektrokhimiya*, 2001, vol. 37, no. 4, pp. 492–495.
3. Kholmuminov, A.A., Sattarov, Kh.A., and Urinov, E.U., *Polym. Sci*., 1994, no. 5 (36), pp. 726–728.
4. Zakharchenko, V.N., *Kolloidnaya khimiya* (Colloid Chemistry), Moscow: Vysshaya Shkola, 1989.
5. Elias, H.G., *Mega Molecules*, Berlin: Springer, 1987.

ISSN 1070-4272, Russian Journal of Applied Chemistry, 2008, Vol. 81, No. 1, pp. 162–164. © Pleiades Publishing, Ltd., 2008.
Original Russian Text © T.A. Bal'burova, V.G. Shiretorova, E.V. Zoltoev, G.I. Khanturgaeva, 2008, published in Zhurnal Prikladnoi Khimii, 2008, Vol. 81, No. 1, pp. 166–168.

BRIEF COMMUNICATIONS

Production of Activated Carbons from Pine Nutshells

T. A. Bal'burova, V. G. Shiretorova, E. V. Zoltoev, and G. I. Khanturgaeva

Baikal Institute of Nature Management, Siberian Branch, Russian Academy of Sciences, Ulan-Ude, Buryatia, Russia

Received February 26, 2007; in final form, September 2007

Abstract—Optimal conditions for obtaining activated carbons from pine nutshells were determined. Their sorption properties were studied.

DOI: 10.1134/S1070427208010369

Solving the problems associated with integrated processing of the vegetable biomass into valuable food and technological products is a particularly topical issue for the Siberian region, on whose territory is situated up to 19% of world's resources of wood. The resources of cedar in East Siberia are vast, with cedar forests occupying 18.7 million hectares. Purely cedar forests (kedrachs) cover the territory of Tyva, Krasnoyarsk krai, Altai, and Buryatia [1]. Annually, more than one million tons of pine nuts are harvested in Siberia, so that large amounts of wastes in the form of nutshells, which constitute 51–59% of the mass of nuts, will be accumulated at places of industrial processing of the nuts. Nutshells are a valuable raw material for obtaining nutritional substances and tanning agents (tannins), essential oils, and activated carbons (AC). So far, the problem of large-tonnage utilization of pine nutshells (PNS) has not been resolved. The PNS belong to renewable raw materials and are an environmentally cleaner product than artificial polymers and natural coals. Moreover, the availability of the raw material and the low content of mineral admixtures, comparatively high strength, and developed porous structure of the resulting AC make nutshells a promising material for manufacture of low-cost high-quality carbon sorbents [2].

EXPERIMENTAL

Activated carbon was produced from the starting pine nutshells and shells extracted with an aqueous–alcoholic solution (PNSE) to recover tanning agents (tannins). Removal of extractive substances leads to additional opening of pores in solid nutshell residues, which allows further use of extracted nutshells to obtain activated carbons.

PNS and PNSE crushed to 0.1–0.2 mm were used. To intensify the recovery of tannins from PNS, a microwave electromagnetic field (MEF) was additionally used, with aqueous solutions of highest-purity ethanol of Ekstra brand serving as an extractive agent [3]. This kind of treatment gives rise to cooperative processes in the system: rapid bulk warming-up of the reaction mixture, formation of micropores, and release of extractive substances because of the appearing temperature gradient and excess pressure. After drying, the tannins obtained have the form of a dark brown powder with a specific odor of pine nuts.

Carbon adsorbents were produced from PNS and PNSE by the conventional technology including stages of carbonization and steam activation.

The carbonization and activation of pine nutshells were performed in a tubular reactor placed in a shaft furnace. The installation enables gradual heating of samples under study to 1200°C. First, the carbonization was carried out with heating to 550°C at a rate of 2–3 deg min^{-1} and keeping at this temperature for 30 min. The carbonizate yield was 78–88 wt % relative to the starting weighed portion. The carbonizate obtained was steam-activated at 750–800°C for 30 min. After the activation was complete, the activated carbon was cooled in the reactor to room temperature. The burn-off mass loss X_m (%) was found as the ratio $(m_0 - m)/m_0$, where m_0 and m are the initial and final masses of the product [4], and the carbon yield R (%) after thermal treatment stages was determined.

The sorption properties of the AC obtained were determined with respect to iodine, benzene, and Methylene Blue by the standard methods [5]. As a ref-

Properties of carbonizates and activates produced from PNS and PNSE

Parameter	Carbonizate at 550°C		Activate at 800°C		Activated carbon (pellets)
	PNS	PNSE	PNS	PNSE	
Burn-off mass loss X_m, %	70.5	65.0	83.4	80.5	–
Carbon yield R, %	34.5	35.0	16.6	19.5	–
Pore volume V_s, $cm^3\ g^{-1}$	0.07	0.12	0.23	0.38	0.41
Specific surface area $S_{BET}(N_2)$, $m^2\ g^{-1}$	80.0	120.0	600.0	800.0	800.0
Sorption activity:					
for iodine, %	10.5	12.4	62.0	79.0	58.42
for Methylene Blue, $mg\ g^{-1}$	29.1	36.6	76.6	100.2	112.8

erence sample was used commercially available activated carbon (in pellets) conforming to the requirements of FS (Pharmacopoeia Item) 42-3246–95 "Activated Carbon Pellets."

It is known that PNS (PNSE) belongs to the class of cellulose materials [6], contains more than 90% carbohydrates (of which 38.6% is cellulose), and possesses an "open" porous structure and enhanced adsorption properties. Additional treatment with selective removal of a part of components enables purposeful development of, and control over the porous structure of the carbon material and manufacture of a product with high specific surface area.

The loss of mass in carbonization of PNS (PNSE) (Fig. 1) occurs for the most part because of the release of carbon-containing low-molecular-weight volatile compounds and heavy tarry products during pyrolysis [1].

The main loss of mass occurs in the temperature range 200–250°C, being accompanied by vigorous gas evolution. The gas evolution is complete at 550°C, with the mass loss of 75–88%.

The lower yield of AC from the starting nutshells, compared with ethanol-treated nutshells, is due to removal, in the course of thermal treatment at elevated temperatures, of a large amount of tarry substances and the corresponding decrease in the yield of the final carbon product.

Preliminary removal of extractive substances from PNS leads to a slight increase in the pore volume in the material obtained from 0.01 to 0.02 $cm^3\ g^{-1}$. After the carbonization, the total pore volume for benzene increases to 0.12 and 0.07 $cm^3\ g^{-1}$ for the nutshells subjected to extraction and the initial nutshells, respectively. In the course of carbonization, there occurs loss of mass: by 65 and 70.5% by PNSE and starting PNS, respectively.

After activation of the carbonizate from PNSE to a mass loss of 81.0%, the resulting AC has a pore volume for benzene of 0.38 $cm^3\ g^{-1}$ and its yield is 19.0%. The yield of the activate from the starting nutshells is 16.6% and its pore volume for benzene is 0.23 $cm^3\ g^{-1}$.

When tannins are recovered from PNS with MEF, cellulose degrades to give oxycellulose containing carboxy groups. Thermolysis of oxycellulose is typically accompanied by an increase in the number of phenol and carboxy groups on the nutshell surface.

Carbonization and activation of the starting and preliminarily extracted nutshells yielded samples whose properties are listed in the table in comparison with those of activated carbon (FS 42-3246–95).

The table shows that the pore volume of the carbonizate increases in the stage of carbonization of materials obtained both from the initial PNS and from the preliminarily extracted PNSE. The activation stage introduces strong differences in the properties of materials obtained from PNS and PNSE. For example, the yields of the activate from PNSE and PNS are 19.5 and 1.66%, respectively.

After preliminary extraction, nutshell samples have a large BET specific surface area (800 $m^2\ g^{-1}$) [8].

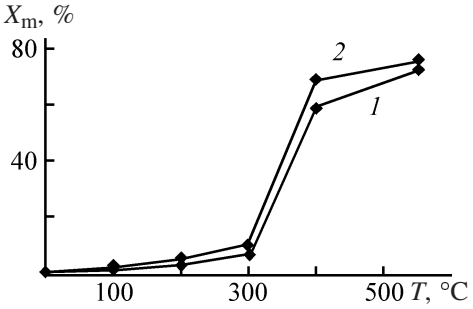


Fig. 1. Mass loss X_m by nutshells vs. carbonization temperature T. (*1*) Extracted PNSE and (*2*) unextracted PNS.

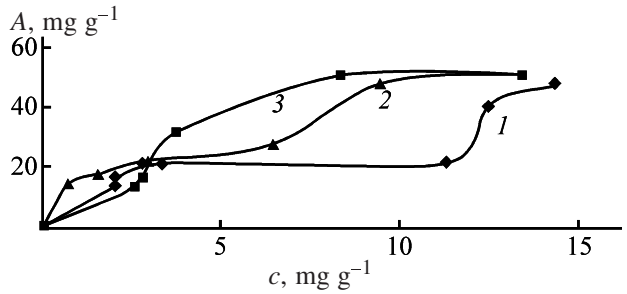


Fig. 2. Sorption isotherm of Fe(III) ions at different temperatures. (*A*) Sorption capacity and (*c*) concentration. *T*, °C: (*1*) 20, (*2*) 40, and (*3*) 60.

The adsorption capacity of the resulting activated carbons for iodine varies within the range 62.0–79.0%. These values correspond to parameters of modern industrial carbon sorbents [9]. The sorption properties of the activate produced from PNSE are comparable with those of pelletized activated carbon, a known enterosorbent.

The sorption properties of the activated carbons obtained from PNSE were studied by the method of sorption of iron(III) ions under static conditions at various temperatures. It has been found that, in sorption on microporous sorbents of substances whose molecular sizes are close to the effective pore sizes, the penetration of these molecules into the pores is temperature-dependent. At a sufficient temperature, sorbate molecules penetrate into pore windows and are sorbed, otherwise there occurs only a slight absorption on the surface of meso- and macropores. In the case in question, the maximum sorption capacities were obtained at 40°C (Fig. 2).

The spent activated carbon was regenerated after the sorption with 0.1 N HCl. On being treated with the acid, a sample was washed with distilled water to neutral reaction. The sorption capacity of the regenerated carbons for benzene was 0.20 $cm^3 g^{-1}$.

CONCLUSIONS

(1) The possibility of obtaining high-porosity activated carbons from pine nutshells and residues of their extractive processing was demonstrated.

(2) It was found that preliminary separation of extractive substances from nutshells can yield activated carbons with better sorption properties. These activated carbons have properties satisfying the requirements to modern industrial carbon sorbents.

REFERENCES

1. Nevzorov, V.N., *Tekhnika i tekhnologiya zagotovki kedrovogo orekha* (Technology of Pine Nut Harvesting), Krasnoyarsk: KGTA, 1996.
2. Bagreev, A.A., Broshnik, A.P., Strelko, V.V., and Tarasenko, Yu.A., *Zh. Prikl. Khim.*, 1999, vol. 72, no. 6, pp. 942–946.
3. Shiretorova, V.G., Development of Principles of a Technology for Production of Cedarwood Oil by Microwave Extraction with Ethanol, *Cand. Sci. Dissertation*, Ulan-Ude, 2002.
4. Kolyshkin, D.A. and Mikhailov, K.K., *Aktivnye ugli* (Activated Carbons), Leningrad: Khimiya, 1972.
5. Sklyar, M.G. and Tyutyunnikov, Yu.B., *Khimiya tverdykh goryuchikh iskopaemykh* (Chemistry of Solid Fossil Fuels), Kiev: Vyshcha Shkola, 1985.
6. Bagreev, A.A., Broshnik, A.P., Strelko, V.V., and Tarasenko, Yu.A., *Zh. Prikl. Khim.*, 2001, vol. 74, no. 9, pp. 1413–1416.
7. Offan, K.B., Transformations of Pine Nutshells under Thermal and Chemical Treatments, *Cand. Sci. Dissertation*, Krasnoyarsk, 2001.
8. Gregg, S.J. and Sing, K.S.W., *Adsorption, Surface Area and Porosity*, London: Academic, 1982.
9. Smirnov, A.V., *Sorbtsionnaya ochistka vody* (Sorption Purification of Water), Leningrad: Khimiya, 1982.

ISSN 1070-4272, Russian Journal of Applied Chemistry, 2008, Vol. 81, No. 2, pp. 165–169. © Pleiades Publishing, Ltd., 2008.
Original Russian Text © E.P. Lokshin, M.L. Belikov, 2008, published in Zhurnal Prikladnoi Khimii, 2008, Vol. 81, No. 2, pp. 177–181.

INORGANIC SYNTHESIS AND INDUSTRIAL INORGANIC CHEMISTRY

On Purification of Wastewater Containing Complex Aluminum and Silicon Fluorides To Remove Fluorine

E. P. Lokshin and M. L. Belikov

Tananaev Institute of Chemistry and Technology of Rare Elements and Mineral Raw Materials, Kola Scientific Center, Russian Academy of Sciences, Apatity, Murmansk oblast, Russia

Received January 31, 2007

Abstract—Possibility of sorption-precipitation purification of wastewater to remove admixtures of fluorine with titanium compounds was studied.

DOI: 10.1134/S1070427208020018

Previously, it has been suggested to purify wastewater containing F^- ions by using titanium compounds [1, 2]. However, a number of plants (e.g., those manufacturing mineral fertilizers from an apatite concentrate, metallic aluminum by electrolysis, etc.) produce wastewater in which fluorine can be present in the form of fluorosilicate and fluoroaluminate complexes.

The goal of this study was to examine the possibility of removing fluorine in the form of complexes with silicon and aluminum from wastewater.

EXPERIMENTAL

Wastewater can be purified if fluorine contained in the anionic complexes SiF_6^{2-} or AlF_6^{3-} can be bound into poorly soluble more stable hydroxo fluoride complexes with titanium or zirconium. We took into account published data according to which the stability of complex fluorides in solution increases in the order: $FeF_6^{3-} < SiF_6^{2-} < AlF_6^{3-} < BF_4^- < BeF_6^{4-} < ZrF_6^{2-}$ [3] and also the results of our earlier study [1] which demonstrated that F^- anions can be effectively removed from wastewater with titanium compounds.

The results of a potentiometric titration of H_2SiF_6, Na_3AlF_6, K_2TiF_6, and K_2ZrF_6 solutions are shown in Fig. 1. It can be seen in Fig. 1a that hydrolysis of H_2SiF_6 occurs without formation of stable intermediate complexes and is complete at pH about 7 at an initial concentration $c_{SiF_6^{2-}} = 0.003258$ N.

A stepwise change in pH is observed in the initial stage of titration in the curve of Na_3AlF_6 titration (Fig. 1b), which points to an increased hydrolytic stability of the AlF_3 species predominant at this concentration of fluorine [4]. At pH exceeding 7, hydrolysis readily occurs without formation of stable intermediate complexes, being complete at pH ~8.4.

In potentiometric titration of a K_2TiF_6 solution (Fig. 1c), a break is observed at pH 4.7–4.8, which may indicate, judging from the NaOH consumption corresponding to this break, that $TiOF_2 \cdot nH_2O$ is formed. The hydrolysis is complete at pH ~8.

In titration of more concentrated K_2TiF_6 solutions (0.0104–0.0208 N) with sodium or ammonium hydroxide, precipitation of $TiO(OH)F \cdot nH_2O$ at pH 5.75–6.48 was also observed, together with the formation of $TiOF_2 \cdot nH_2O$ at pH 5.3–5.75. The hydrolysis was complete at pH 10.45 [5].

The titration of K_2ZrF_6 occurs similarly to that of K_2TiF_6 (Fig. 1d). Here, a break is also observed, which indicates that an intermediate form $ZrOF_2 \cdot nH_2O$ is formed. The hydrolysis is complete at pH 8.6.

Effective purification to remove an admixture of fluorine is possible under conditions for preferential hydrolysis of complex fluorine-containing anions of silicon and aluminum to give F^- ions, whereas poorly soluble variable-composition hydroxide complexes of fluorine with titanium or zirconium are still stable.

Therefore, we carried out a preliminary study of the hydrolytic behavior of SiF_6^{2-}, AlF_6^{3-}, TiF_6^{2-}, and ZrF_6^{2-} anions in solutions. We used solutions with an equivalent fluorine concentration of 10 mg l^{-1}, because the total concentration of fluorine in various

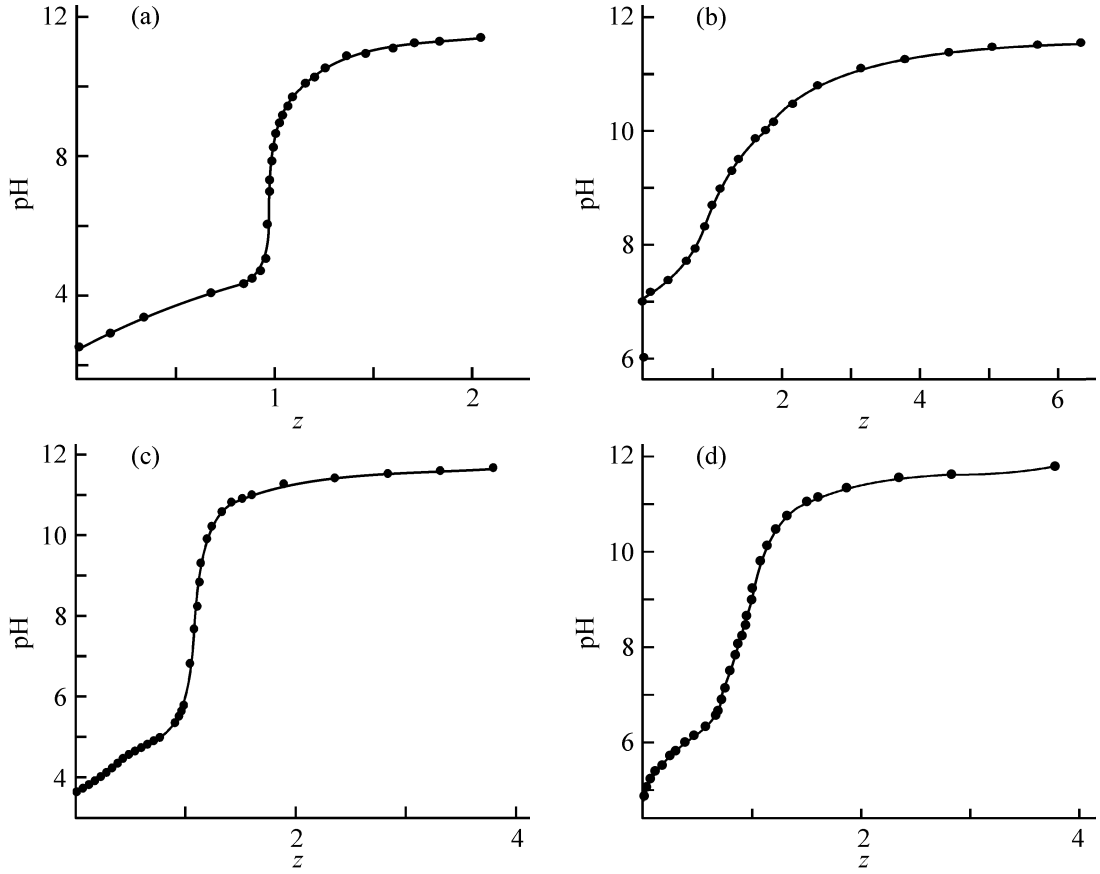


Fig. 1. Titration curves of (a) 0.003258 N H_2SiF_6, (b) 0.000263 N Na_3AlF_6, (c) 0.000438 N K_2TiF_6, and (d) 0.000441 N K_2ZrF_6 solutions with a 0.01 N NaOH solution. (z) Ratio between gram-equivalents of NaOH and F^-.

anionic forms in wastewater from numerous factories and fluorine-contaminated underground water from artesian wells does not exceed this value.

We determined the dependence of the degree of hydrolysis on the solution pH by the ionometric method, with the concentrations of H^+ and F^- ions measured using an I-160 ionometer with an ESL-43-07 electrode and a Volta-3000 fluorine-selective electrode, respectively. It was found that, on adding a next NaOH portion, equilibrium was attained in 15 min.

According to the data [6], the hydrolysis of SiF_6^{2-}, AlF_6^{3-}, TiF_6^{2-}, and ZrF_6^{2-} anions is described by the reactions

$$SiF_6^{2-} + 2H_2O = \downarrow SiO_2 + 4H^+ + 6F^-, \quad (1)$$

$$AlF_6^{3-} + 3H_2O = \downarrow Al(OH)_3 + 3H^+ + 6F^-, \quad (2)$$

$$TiF_6^{2-} + 3H_2O = \downarrow TiO(OH)_2 + 4H^+ + 6F^-, \quad (3)$$

$$ZrF_6^{2-} + 4H_2O = \downarrow Zr(OH)_4 + 4H^+ + 6F^-. \quad (4)$$

Experimental dependences of the degree x of hydrolysis at room temperature on pH are listed for the ions SiF_6^{2-}, AlF_6^{3-}, TiF_6^{2-}, and ZrF_6^{2-} in the table.

We calculated the hydrolysis constants K from the experimental data. The calculation scheme is presented for the example of the SiF_6^{2-} ion.

If the fraction of hydrolyzed SiF_6^{2-} ions is x, the amount of SiF_6^{2-} ions remaining in solution is $(1 - x)$, and that of F^- ions formed, $6x$. On the assumption that the activities of ions in dilute solutions are equal to their concentrations, we obtain the following expression for calculating the hydrolysis constant:

$$K = \frac{6^6 x^6 a_{H^+}^4 a_{SiF_6^{2-}}^5}{1 - x}. \quad (5)$$

Equation (5) is also applicable to calculation of the hydrolysis constants of reactions (3) and (4). Similar reasoning for the equilibrium constant of reaction (2) leads to Eq. (6).

$$K = \frac{3^3 6^6 a_{H^+}^3 x^6 c_{AlF_6^{3-}}^5}{1-x}. \quad (6)$$

Hydrolysis constants K calculated by Eqs. (5) and (6) are listed in the table, which shows that K depends on pH. The hydrolysis constants for the SiF_6^{2-} anion markedly differ from the values 8.3×10^{-28}–1.7×10^{-27} reported in [6]. It can be assumed that the scatter of the hydrolysis constants K is due to the fact that the solubility of metal hydroxides (oxohydroxides) formed in the hydrolysis was disregarded in the calculations.

The solubility of amorphous silica at room temperature in the pH range 2–9 is 0.1–0.15 g l^{-1} SiO_2, with the minimum solubility observed at pH ≈ 7 [7]. It is assumed in this case that the monomer $Si(OH)_4$ is formed in solutions.

At low concentrations of the SiF_6^{2-} ion, examined in this study, the maximum concentration of the hydrated form of silica in solution was 0.007 g l^{-1}. It can be considered that hydrolysis of anions occurs by the reaction

$$SiF_6^{2-} + 2H_2O = Si(OH)_4 + 4H^+ + 6F^-, \quad (7)$$

and the equilibrium constant is given by

$$K_1 = \frac{a_{Si(OH)_4} a_{H^+}^4 a_{F^-}^6}{a_{SiF_6^{2-}}}. \quad (8)$$

If we assume that the activity coefficient of the hydrated form of silica in the solutions under study is unity, then $a_{SiO_2} = x a_{SiF_6^{2-}}$ and the expression for the equilibrium constant takes the form

$$K_1 = \frac{6^6 x^7 a_{H^+}^4 a_{SiF_6^{2-}}^6}{1-x}. \quad (9)$$

It can be seen in the table, which lists K_1 values calculated by Eq. (9), that the K_1 value for SiF_6^{2-} anions is sufficiently invariable and equal to $(3.1 \pm 1.2) \times 10^{-32}$.

The solubilities of $Al(OH)_3$, $TiO(OH)_2$, and $Zr(OH)_4$, estimated using the data of [8–10], are 0.0034, 0.0061, and 0.001 mg l^{-1}, respectively. Therefore, it seems justified to neglect these solubilities when calculating the equilibrium constants of reactions (2)–(4). Presumably, the scatter of the K values for the reactions of hydrolysis of the AlF_6^{3-} and TiF_6^{2-} anions indicates that the forming $Al(OH)_3$, $TiO(OH)_2$, and $Zr(OH)_4$ react in parallel with sodium cations even at low concentrations of reagents:

$$Al(OH)_3 + xNa^+ \rightarrow Al(OH)_{3-x}(ONa)_x + xH^+, \quad (10)$$

$$TiO(OH)_2 + xNa^+ \rightarrow TiO(OH)_{2-x}(ONa)_x + xH^+, \quad (11)$$

$$Zr(OH)_4 + xNa^+ \rightarrow Zr(OH)_{4-x}(ONa)_x + xH^+, \quad (12)$$

which affect the equilibria in solutions.

Effect of pH on the degree of hydrolysis of the SiF_6^{2-}, AlF_6^{3-}, TiF_6^{2-}, and ZrF_6^{2-} ions and the hydrolysis constants K and K_1 (c_{F^-} = 10 mg l^{-1})

pH	F^- found, mg l^{-1}	x	K	K_1
$T = 18.85 \pm 0.05$°C, $c_{K_2SiF_6} = 8.77 \times 10^{-5}$ M, SiF_6^{2-} ion				
3.40*	6.5	0.65	3.4×10^{-28}	1.9×10^{-32}
3.56	8.2	0.82	1.1×10^{-28}	4.3×10^{-32}
4.00	9.8	0.98	5.5×10^{-30}	2.4×10^{-32}
4.35	10.0	1.00	–	–
$T = 18.45 \pm 0.05$°C, $c_{Na_3AlF_6} = 8.77 \times 10^{-5}$ M, AlF_6^{3-} ion				
5.65*	6.0	0.60	8.6×10^{-33}	–
6.80	6.8	0.68	8.0×10^{-36}	–
7.06	8.0	0.80	5.8×10^{-36}	–
7.45	9.2	0.92	2.2×10^{-36}	–
7.70	10.0	1.00	–	–
$T = 18.1 \pm 0.1$°C, $c_{K_2TiF_6} = 8.77 \times 10^{-5}$ M, TiF_6^{3-} ion				
3.61*	7.6	0.76	7.1×10^{-31}	–
4.00	8.8	0.88	9.4×10^{-32}	–
4.40	9.6	0.96	1.2×10^{-32}	–
5.02	9.8	0.98	8.9×10^{-35}	–
5.25	10.0	1.00	–	–
$T = 17.1 \pm 0.1$°C, $c_{K_2ZrF_6} = 8.77 \times 10^{-5}$ M, ZrF_6^{2-} ion				
4.35*	3.6	0.36	2.1×10^{-36}	–
4.60	5.2	0.52	1.9×10^{-36}	–
5.40	8.0	0.80	1.6×10^{-38}	–
6.71	8.8	0.88	1.6×10^{-42}	–
6.92	9.6	0.96	4.0×10^{-44}	–
7.20	10	1.00	–	–

* pH of the starting solution.

It can be seen from the table that, at room temperature and equal initial concentrations in solution, the SiF_6^{2-}, AlF_6^{3-}, TiF_6^{2-}, and ZrF_6^{2-} anions are completely hydrolyzed at pH 4.35, 7.70, 5.25, and 7.20, respectively. Therefore, the hydrolytic stability series differs, at least at low concentrations, from that found

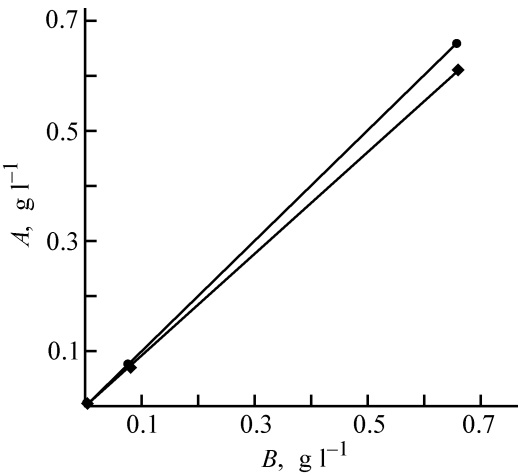


Fig. 2. Effect of impurity anions on the efficiency of fluorine determination in solutions of alkali element fluorides by the ionometric method. (*A*) Fluorine found and (*B*) fluorine introduced. Impurity anion: (*1*) Cl^-, NO_3^- and (*2*) SO_4^{2-}.

previously [9], and aluminum, rather than zirconium, is the strongest fluorine acceptor among the anions under study.

Thus, effective precipitation of fluorine from the AlF_6^{3-} anion with titanium or zirconium compounds cannot be reached.

We studied water purification to remove fluorine present in the form of SiF_6^{2-} with titanium sulfate compounds. Model solutions containing 8.77×10^{-5} M K_2SiF_6 (10 mg l^{-1} of fluorine) were used. A prescribed amount of a titanium-containing reagent (titanyl sulfate dihydrate $TiOSO_4 \cdot 2H_2O$) was introduced into fluorine-containing solutions. The pH value was maintained in the interval 4–4.5 by addition of a concentrated sodium hydroxide solution and, upon agitation, the precipitate formed was separated by centrifugation. The degree of fluorine removal was estimated from the residual content of fluorine in the solution and from the amount of fluorine in the precipitate, found as follows.

The fluorine concentration in a solution after treatment was measured by ionometry at pH 4 and 8. The precipitate was treated with a sodium hydroxide solution, the solid and liquid phases were separated by centrifugation, and then the fluorine concentration in the resulting alkaline solution was measured by the ionometric method.

The fluorine-selective electrode used in the study is suitable for operation in solutions with pH 4–8. Therefore, the alkaline solution was preliminary neutralized with hydrochloric or nitric acid, because it was found that the ionometric determination of fluorine with sulfuric acid gives a content approximately 7.5% lower than the actual value (Fig. 2). Consequently, a part of fluorine is present in sulfate solutions, together with the F^- ion determined by ionometry, in the form that cannot be determined with a fluorine-selective electrode. Probably, this form is the complex fluorosulfate anion FSO_4^{3-}. It has been shown previously [11–13] that this anion exists at 50–75°C in solutions containing 44–60 wt % H_2SO_4 and 6–10% HF and appreciable concentrations of lanthanides and titanium, with the phases $LnFSO_4 \cdot nH_2O$ (Ln = Y, Ce, Nd) isolated from the solutions.

The increased solubility of LaF_3 and YbF_3 fluorides at room temperature in sulfate solutions of lower concentrations (9.5–20 wt %), compared with their solubility in monobasic acids, was attributed to formation of FSO_4^{3-} ([14]).

When $TiOSO_4 \cdot 2H_2O$ (800 mg l^{-1}) was added to a K_2SiF_6 solution containing 10 mg l^{-1} of fluorine, the residual concentration of fluorine in the treated solution was 0.64 at pH 4 and 2.7–2.8 mg l^{-1} at pH 8. This suggests that the remaining fluorine is in a complex form in solution. The solutions produced by alkali treatment of the precipitate contained 7.2–7.32 mg of fluorine, which points to a good agreement of the results obtained. Upon introduction of an additional amount of $TiOSO_4 \cdot 2H_2O$ (200 mg l^{-1}) into the solution, the residual concentration of fluorine was 0.75 mg l^{-1}.

The results of a calculation show that the $TiO_2 : F^-$ molar ratio in the precipitate is 10.5 and its composition can be represented by the formula $TiO(OH)_{1.905}F_{0.095} \cdot nH_2O$.

CONCLUSIONS

(1) It was shown that the hydrolytic stability in dilute solutions increases in the order $SiF_6^{2-} < TiF_6^{2-} < ZrF_6^{2-} < AlF_6^{3-}$. Therefore, use of titanium compounds for efficient wastewater purification to remove fluorine in complexes with aluminum is unpromising.

(2) The hydrolysis constant of the SiF_6^{2-} anion was found to be $(3.1 \pm 1.2) \times 10^{-32}$ at room temperature. It was shown that a scatter of the calculated values of hydrolysis constants for the AlF_6^{3-}, TiF_6^{2-}, and ZrF_6^{2-} is observed. This is due to the necessity for taking into account the interaction of the alkaline element cation with the forming hydroxides (oxohydroxides).

(3) It was found experimentally that wastewater containing up to 10 mg l^{-1} of fluorine in the form

of the complex anion SiF_6^{2-} can be purified with titanium sulfate compounds to satisfy regulations concerning the content of fluorine in fish-farming ponds. In the presence of sulfate ions, fluorine forms complex fluorosulfate anions.

ACKNOWLEDGMENTS

The study was financially supported by the Russian Foundation for Basic Research (project no. 06-08-00223-a).

REFERENCES

1. Lokshin, E.P. and Belikov, M.L., *Zh. Prikl. Khim.*, 2003, vol. 76, no. 9, pp. 1505–1510.
2. RF Patent 2228911.
3. Chepelevetskii, M. and Bol'ts, Ts., *Zh. Prikl. Khim.*, 1937, vol. 10, no. 7, pp. 1183–1193.
4. Kleiner, K.E., *Zh. Obshch. Khim.*, 1950, vol. 20, no. 10, pp. 1747–1759.
5. Lastochkina, A.A. and Sheka, I.A., *Ukr. Khim. Zh.*, 1964, vol. 30, no. 9, pp. 896–900.
6. Ryss, I.G., *Khimiya ftora i ego neorganicheskikh soedinenii* (Chemistry of Fluorine and Its Inorganic Compounds), Moscow: Goskhimizdat, 1956.
7. Iler, R.K., *The Chemistry of Silica*, New York: Wiley-Interscience, 1979.
8. Dickerson, R.E., Gray, H.B., and Haight, G.P., *Chemical Principles*, Menlo Park, Calif.: Benjamin, 1979, 3d ed.
9. Babko, A.K., Gridchina, G.I., and Nabivanets, B.I., *Zh. Neorg. Khim.*, 1962, vol. 7, no. 1, pp. 132–138.
10. Kirgintsev, A.N., Trushnikova, L.N., and Lavrent'ev, V.G., *Rastvorimost' neorganicheskikh veshchestv v vode* (Solubility of Inorganic Substances in Water), Leningrad: Khimiya, 1972.
11. Belokoskov, V.I., Zaginaichenko, N.I., Akhmetova, T.V., et al., *Khimiya i tekhnologiya mineral'nogo syr'ya Kol'skogo poluostrova* (Chemistry and Technology of Mineral Raw Materials of the Kola Peninsula), St. Petersburg: Nauka, 1992, pp. 94–104.
12. Belokoskov, V.I., Zaginaichenko, N.I., Akhmetova, T.V., et al., *Khimiya i tekhnologiya mineral'nogo syr'ya Kol'skogo poluostrova* (Chemistry and Technology of Mineral Raw Materials of the Kola Peninsula), Mineral Raw Materials of the Kola Peninsula), St. Petersburg: Nauka, 1992, pp. 85–94.
13. Panasenko, E.B., Zaginaichenko, N.I., Belokoskov, V.I., et al., *Zh. Neorg. Khim.*, 1988, vol. 33, no. 12, pp. 3171–3175.
14. Lokshin, E.P., Vershkova, J.A., Ivlev, K.G., and Tareeva, O.A., *Zh. Neorg. Khim.*, 2004, vol. 49, no. 4, pp. 707–710.

ISSN 1070-4272, Russian Journal of Applied Chemistry, 2008, Vol. 81, No. 2, pp. 170–173. © Pleiades Publishing, Ltd., 2008.
Original Russian Text © D.V. Shilo, E.Yu. Buinitskaya, 2008, published in Zhurnal Prikladnoi Khimii, 2008, Vol. 81, No. 2, pp. 182–185.

INORGANIC SYNTHESIS AND INDUSTRIAL INORGANIC CHEMISTRY

Effect of the Method of Magnesium Dispersion on the Process of Hydrogen Absorption by the Metal

D. V. Shilo and E. Yu. Buinitskaya

Mendeleev Russian University of Chemical Engineering, Moscow, Russia
NIIgrafit Research Institute, Moscow, Russia

Received April 27, 2007

Abstract—Absorption of hydrogen by carbon-magnesium composites synthesized by mechanochemical treatment and arc spraying was studied and methods for optimization of the process of hydrogen absorption were suggested.

DOI: 10.1134/S107042720802002X

Owing to the high content of hydrogen (7.66 wt %), magnesium hydride (MgH_2) is one of the most promising materials for accumulation of hydrogen. However, the high temperature of hydrogen absorption and release hinders its practical use [1].

Intermetallic compounds of magnesium, primarily with nickel and rare-earth metals, obtained by classical metallurgical methods, exhibit a high rate of interaction with hydrogen. However, the mass content of hydrogen in these compounds markedly decreases because of the increase in their density, caused by introduction of heavy elements.

An alternative to the conventional metallurgical methods for improvement of the properties of most of the hydride-forming metals is their mechanochemical treatment in high-energy ball mills.

Mechanochemical treatment of a mixture of magnesium and graphite has been used to obtain carbon-magnesium composites [2]. Composites of this kind are hydrogenated at lower temperatures (the hydrogenation temperature decreases by nearly 200°C). A subsequent analysis of a thermal desorption spectrum allowed the authors to record a shift of the hydrogen evolution onset to lower temperatures, compared with pure magnesium hydride [1].

The authors of [3] obtained carbon-magnesium composites with nanosize particles by grinding metallic magnesium in liquid hydrocarbons. It was found that hydrogenation occurs at a higher rate on nanosize magnesium particles. Already in the first cycle, magnesium absorbs hydrogen at a rate of 6 wt % per hour, which exceeds by a factor of 1.5 that for magnesium ground together with graphite to only a micrometer size (4 wt % per hour). This value is 60 times that for magnesium with nanosize particles, unmodified with graphite (0.1 wt % per hour).

Use of graphite instead of heavy elements, combined with mechanochemical treatment, made it possible to obtain magnesium-based composites that have lower density and can be hydrogenated (dehydrogenated) at lower temperatures.

In [4], a nickel-magnesium alloy was ground in a solution of fullerenes in toluene. It was found that the time of hydrogen desorption from the composite obtained decreased by a factor of 2–3, compared with composites produced by grinding in the presence of graphite.

One more method for dispersion of various materials is, in addition to mechanical grinding, their evaporation in an electric arc. It is known that this method of dispersion of carbon materials and, in particular, graphite can yield carbon nanostructures: fullerenes, nanofibers, and nanotubes. The application of this technique in the present study yielded a carbon-magnesium composite in a highly dispersed state.

The goal of the study was to determine how methods for dispersion of magnesium together with carbon, namely, joint grinding with graphite and sputtering of a magnesium-graphite composite in a dc arc, affect the activation of the carbon-magnesium composites obtained. The composites were also compared with the starting magnesium and magnesium ground without carbon additives.

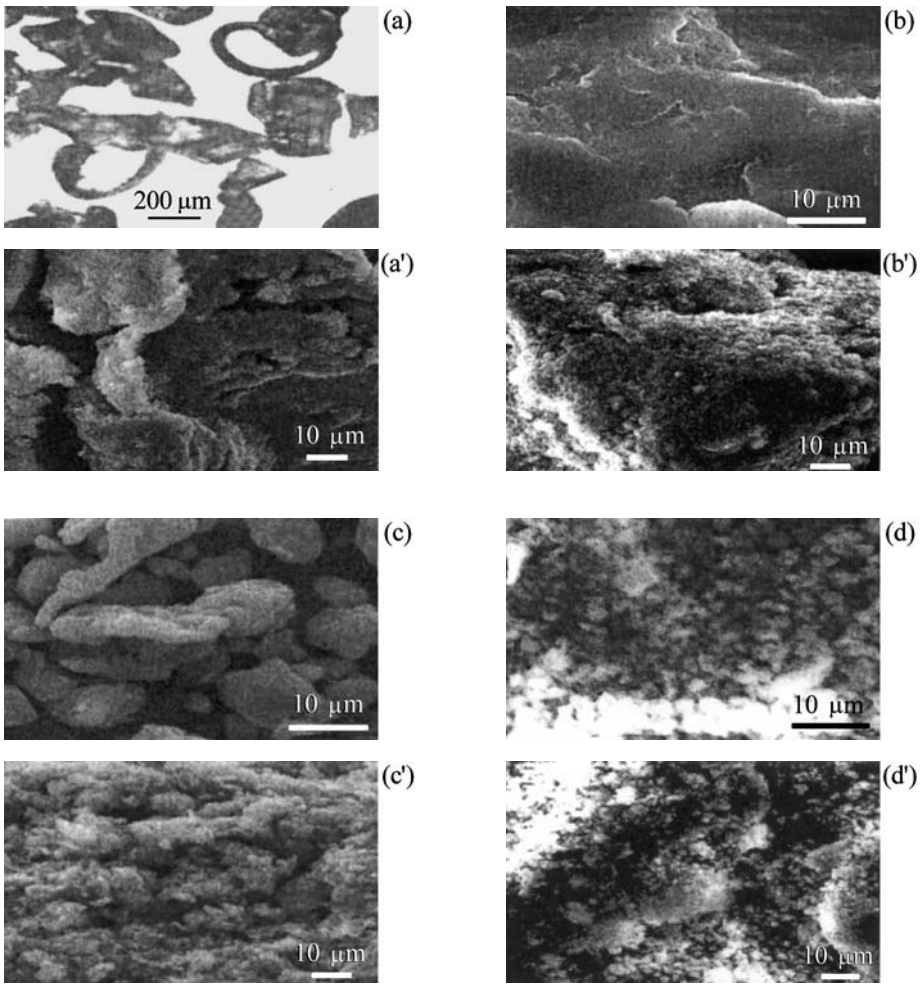


Fig. 1. Particles of a material (a–d) before and (a'–d') after five cycles of hydrogenation. Material: (a, a') starting magnesium powder, (b, b') ground magnesium, (c, c') ground magnesium with graphite), and (d, d') magnesium sputtered in an arc with carbon. (b–d, a'–d') Electron microscopy and (a) optical microscopy.

EXPERIMENTAL

The mechanochemical synthesis was performed with powdered magnesium (99.98%) with particles having an average size of 100 μm and low-ash medium-grain graphite of GMZ brand [5]. Graphite had the following properties: density 1.6 g cm^{-3}, compression strength 300 kg cm^{-2}, bending strength 120 kg cm^{-2}, electrical resistivity 10 Ω mm^2 m^{-1}, porosity ≤25%. The grinding was carried out in an IVCh vibration grinder. The grinding time was 30 min.

A composite magnesium-carbon electrode was sputtered in an electric arc on the installation described in [6]. The composite electrode was fabricated by compaction of a mixture of magnesium (70 wt %) and novolak with addition of urotropin (30 wt %) at 180°C under a pressure of 200 kg cm^{-2}.

The electrode was calcined in a graphite charge in a muffle furnace at 500°C. The heating rate was 0.5 deg min^{-1}. The composite electrode was sputtered in the atmosphere of helium at a pressure of 13.33 kPa and temperature of 2000°C. The content of carbon in the sputtered sample, found from the difference of sample masses before and after dissolution of magnesium in hydrochloric acid, was 13.2 wt %.

The processes of hydrogenation and dehydrogenation were studied using hydrogen of purity 99.9999%. The amount of absorbed gas was measured on a volumetric installation at 350°C and a constant pressure of 65 atm. The amount of absorbed hydrogen was found from the decrease in pressure in the measuring

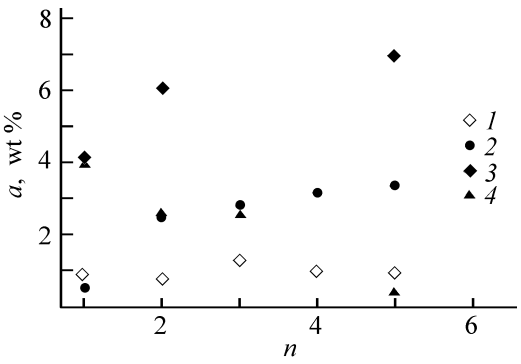


Fig. 2. Amount of hydrogen absorbed by magnesium vs. the number *n* of cycles at 350°C (*a*) Amount of absorbed hydrogen per 1 g of Mg; the same for Fig. 3. Magnesium: (*1*) starting powder, (*2*) ground, (*3*) with 10 wt % graphite, and (*4*) obtained in arc discharge.

volume of the installation, and that of released hydrogen, from the volume of water displaced from the gas meter under the ambient pressure. The absorption of hydrogen by each sample was examined in five cycles of hydrogenation–dehydrogenation. The samples were vacuum-treated at 1.33 Pa before the first cycle, and taken without vacuum treatment in the subsequent cycles.

The particle size of the materials obtained was measured with a Polyvar-Met optical microscope with a Quantimet analytical system and by electron microscopy.

The amount of absorbed hydrogen was measured for the following samples: unground (starting) magnesium, ground magnesium without carbon additives, and magnesium ground with graphite and modified with carbon by sputtering in an electric arc. According to optical-microscopic data, the starting magnesium powder was composed of irregularly shaped particles 200 to 600 μm in size (Fig. 1a).

According to electron-microscopic data, magnesium particles had an average size of about 145 μm after grinding in a vibration grinder (Fig, 1b). Upon grinding of magnesium together with graphite (10 wt %), the particle size decreased to 10 μm (Fig. 1c).

It can be seen in Figs. 1a and 1c that some particles of ground magnesium are agglomerates composed of finer particles. Introduction of graphite in the grinding stage makes smaller both the agglomerates themselves and the particles constituting these agglomerates. The magnesium powder produced by arc sputtering is composed of spherical particles of size not exceeding 1–2 μm (Fig. 1d).

It is known that, in hydrogenation of magnesium, its absorption capacity does not reach maximum values immediately. Of high importance in this case are the duration and temperature of hydrogenation.

Figure 2 shows how the number of hydrogenation–dehydrogenation cycles in activation of samples affects their absorption capacity. It can be seen that, at 350°C, the maximum amount of absorbed hydrogen by the unground (starting) magnesium powder reaches a value of about 1–1.5% relative to the mass of magnesium and remains virtually unchanged during five repeated cycles of hydrogenation-dehydrogenation. The amount of hydrogen absorbed by ground magnesium increases, compared with the starting magnesium. It reaches a value of 3 wt % in the third cycle and slightly increases (to 3.5 wt %) in the fourth and fifth hydrogenation–dehydrogenation cycles.

The volume of hydrogen absorbed by a sample produced by grinding of magnesium together with graphite reaches the maximum value of 7 wt %, close to that theoretically possible, already by the fourth cycle.

The hydrogenation of a sample produced by arc sputtering markedly differs from that of other samples. The volume of absorbed hydrogen, which varies from cycle to cycle, reaches a certain maximum value by the third cycle (approximately 3 wt %) and then substantially decreases to less than 1 wt %.

Figure 3A shows how the amount of hydrogen absorbed in the first cycle depends on the hydrogenation time. It can be seen that, initially, all the samples are hydrogenated at a high rate, with the limiting values rapidly reached. In this case, all the samples containing no graphite absorb a substantially smaller volume of hydrogen, compared with samples containing graphite.

In the second cycle (Fig. 3B), the rate of hydrogenation in the initial stage still remains high; however, the maximum volume of absorbed hydrogen increases only for samples ground in the vibration grinder. It decreases to 2 wt % for the sample produced by the arc method and remains unchanged for unground magnesium.

In the fifth cycle, magnesium ground together with graphite reaches the maximum capacity, and the sample produced by the arc method absorbs an even smaller amount of hydrogen than that in the preceding cycles (Fig. 3C).

These data suggest that, in grinding with graphite, the oxide film hindering the hydrogenation process is disintegrated. The cyclic hydrogenation–dehydrogenation at a sufficiently high temperature also improves the absorption capacity of magnesium.

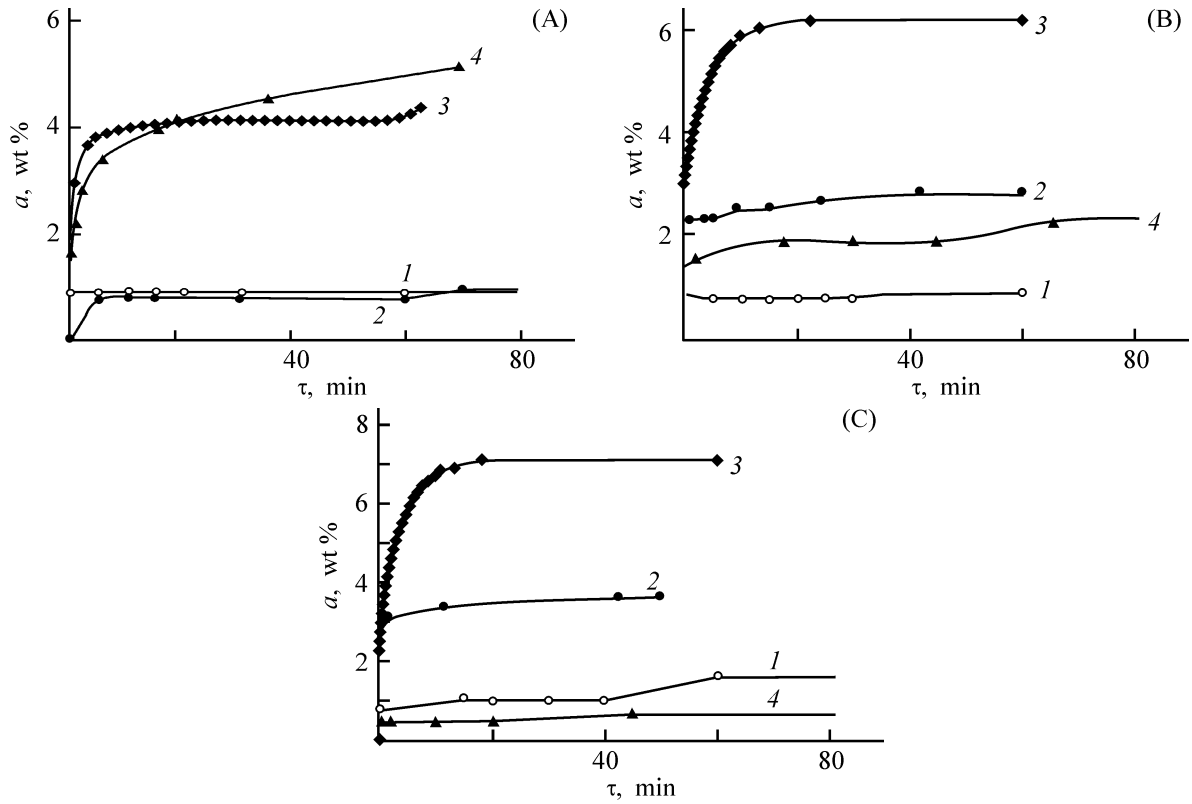


Fig. 3. Amount of hydrogen absorbed by various composites vs. the hydrogenation time τ in (A) first, (B) second, and (C) fifth cycles.

The sample produced by arc sputtering possibly contains not only magnesium, but also its carbides. As a consequence, carbide particles are shifted, from cycle to cycle in hydrogenation and dehydrogenation processes, from the bilk of a sample to its surface. It is these carbide particles that prevent further hydrogenation of magnesium and, accordingly, its dehydrogenation.

The surface morphology of samples subjected to hydrogenation-dehydrogenation cycles (Figs. 1a'–1d') shows that strong changes are observed for all the samples except that produced by arc sputtering (Fig. 1d'). Changes for a sample produced in an electric arc are difficult to observe because of the insufficient resolution of the microscope.

CONCLUSIONS

(1) Grinding of magnesium strongly affects the hydrogenation rate and is a necessary stage in magnesium preparation for use in hydrogen accumulators.

(2) A sample with a particle size of about 0.02 μm, produced by sputtering in an electric arc, is deactivated already after the second cycle and ceases to absorb hydrogen, whereas the composite produced by grinding in a vibration grinder to a particle size of several tens of micrometers, retains its absorption and desorption capacity.

REFERENCES

1. Klyamkin, S.N. and Tarasov, B.P., Abstracts of Papers, *VIII mezhdunarodnaya konferentsiya "Vodorodnoe materialovedenie i khimiya uglerodnykh nanomaterialov," ICHMS'2003. Sudak, 14–20 sentyabrya 2003 goda* (VIII Int. Conf. "Hydrogen Materials Science and Chemistry of Carbon Materials," ICHMS'2003, Sudak, September 14–20, 2003), pp. 22–23.
2. Imamura, H., Tabata, S., Sihitomi, N., et al., *J. Alloys Comp.*, 2002, no. 330–332, pp. 579–583.
3. Bouaricha, S., Dodelet, J.P., Guay, D., et al., *J. Alloys Comp.*, 2001, no. 325, pp. 245–251.
4. Bouaricha, S., Dodelet, J.P., Guay, D., et al., *J. Alloys Comp.*, 2000, no. 307, pp. 226–233.
5. *TU* (Technical Specifications) *48-20-86–81*.
6. Trefilov, V.I., Shchur, D.V., Tarasov, B.P., et al., *Fullereny – osnova materialov budushchego* (Fullerenes, a Basis for Materials of the Future), Kiev: IPM Nats. Akad. Nauk Ukr., IPKhF Ross. Akad. Nauk, 2001.

ISSN 1070-4272, Russian Journal of Applied Chemistry, 2008, Vol. 81, No. 2, pp. 174–177. © Pleiades Publishing, Ltd., 2008.
Original Russian Text © G.V. Bychko, V.D. Koshevar, I.P. Kazhuro, 2008, published in Zhurnal Prikladnoi Khimii, 2008, Vol. 81, No. 2, pp. 186–189.

INORGANIC SYNTHESIS AND INDUSTRIAL INORGANIC CHEMISTRY

Synthesis of Colored Cobalt-containing Shell Powders from Silicon Oxide Particles

G. V. Bychko, V. D. Koshevar, and I. P. Kazhuro

Institute of General and Inorganic Chemistry, National Academy of Sciences of Belarus, Minsk, Belarus

Received April 10, 2007

Abstract—Possibility of synthesizing core microstructures composed of a core-forming material (silicon dioxide micrograins) and shell of cobalt oxides, formed as a result of precipitation of the corresponding hydroxides from a cobalt(II) chloride solution and their subsequent thermal decomposition, was studied.

DOI: 10.1134/S1070427208020031

Synthesis of core microstructures of the "core in the shell" type is an efficient method for controlling the surface properties of composite materials, which enables wide variation of their physicochemical and service properties. It consists in deposition of inorganic, organic, and polymeric shells onto inert carriers, cores [1, 2]. This is a way to obtain colored powders that can be used as pigments-fillers for decorative and protective coatings for various purposes, with a considerable amount of nonferrous maetals saved [3, 5].

The goal of this study was to examine whether core microstructures can be produced using silicon dioxide particles synthesized from wastes formed in manufacture of orthophosphoric acid at Gomel chemical combine [TU (Technical Specifications) RB 00 203 714.006] as a core-forming material, and hydrated cobalt(II)oxide obtained from a salt solution by chemical precipitation, as a shell.

Silicon dioxide particles have a large surface energy content and readily form cellular coagulation structures. The potential of an aqueous dispersion of such SiO_2, ξ, is –12.2 mV, and the average particle radius, 5 μm. Silanol groups of the acid type are present on the surface of SiO_2 micrograins. These groups can dissociate in water and enter into ion-exchange reactions with metal cations. In synthesis at pH 8–9, metal hydroxides are poorly soluble compounds and, therefore, the equilibrium is shifted toward their precipitation in solution and on the active surface of SO_2 as an X-ray-amorphous hydroxo complex. Positively charged adsorbed metal complexes electrostatically interacting with negatively charged SO_2 particles can further undergo hydrolysis and polymerization localized in the surface layer. The polymerization presumably occurs between bulk and surface complexes by the polycondensation mechanism [6]. The final stages of shell formation on the particles are drying and thermal treatment. In dehydration of hydroxo compounds of metals and removal of bound water, the cohesion of the shell with the surface of carrier-core particles increases.

The components forming the outer shell are used in the given case in amounts of 5–25% relative to the mass of the carrier core, which is economically profitable because nonferrous metals are saved. Thus, formation of shell powders of this composition is of scientific and practical interest.

EXPERIMENTAL

The synthesis process was studied by FTIR spectroscopy on a Midac M200 spectrophotometer (USA). The IR spectra were recorded in the spectral range 4000–400 cm^{-1} (resolution 4 cm^{-1}) and processed using GRAMSS/32 software (Galactic, USA). A differential-thermal analysis (DTA) was made on an MOM derivatograph (Hungary), with calcined aluminum oxide as reference and a heating rate of 5 deg min^{-1}. An X-ray phase analysis (XPA) was performed on a DRON-2 instrument with a Cu anode. The granulometric composition of the powders was determined on a FSKh-4 photosedimentometer. A computer unit calculated, using a specially developed software, the integral and differential size distribution functions of the mass and number of particles and a number

Color characteristics of the powders synthesized in relation to the $CoCl_2$ concentration

Composition no.	$CoCl_2$ concentration, M	$CoCl_2$ solution volume, ml	$SiO_2 : CoCl_2$ mass ratio	Powder color		
				initial	after calcination at T, °C	
					600	800
s : l phase ratio 1 : 2						
1	1.5	50	6 : 1	Gray-pink	Blue	Dark blue
2	1.0	50	9 : 1	Gray	Light blue	Blue
3	0.5	50	19 : 1	Gray	Light blue	Light blue
s : l phase ratio 1 : 10						
4	1.5	50	1.1 : 1	Pale pink	Gray-green	Green
5	1.0	50	1.6 : 1	Pale pink	Green	Bright green
6	0.5	50	3.3 : 1	Gray-pink	Light green	Light green
7	1.0	50	1 : 1.18	Pink	Green	Dark green
8	0.25	200	1 : 1.18	Pink	Gray	Gray
9	0.5	50	1.69 : 1	Gray-pink	Green	Bright green
10	0.25	100	1.69 : 1	Light pink	Gray-green	Green
11	2.0	75	1 : 1.78	Pale green	Black	Black

of statistical parameters of the distributions. The reflectances of the colored powders at various wavelengths in the visible spectral range were measured with a FMSh-56M photoelectric sphere photometer, with the subsequent calculation by the method of weighted ordinates of color characteristics [6].

In the first stage of synthesis, silicon dioxide micrograins were dispersed, for purification, in water at room temperature on an LDU-3MPR laboratory installation at a cutter rotation rate of 500 rpm for 30 min. After filtration and drying, 0.5–2 M solutions of cobalt(II) chloride were added to the resulting SiO_2 powder at s : l = 1 : 2 or 1 : 10. In the second stage, the precipitating agent (NaOH, 50 g l^{-1}) was added to the resulting suspension under heating (80°C) and constant agitation, with the pH of the mixture brought to 8–9. The precipitate obtained was subjected to centrifugation, filtration, multiple decantation with water, and drying at 60°C and then was thermally treated at 200–800°C for 1–3 h.

To optimize the synthesis, the dependence of the color tone of the powders of the given system on the concentration of the $CoCl_2$ solution, precipitation pH, ratio between the amounts of the core-forming (SiO_2 particles) and shell-forming phases [cobalt(II) chloride solution], temperature, and calcination duration was studied. The data obtained are listed in the table and presented in Fig. 1.

As follows from the data in the table, a higher cobalt(II) chloride concentration favors, irrespective of the phase ratio, formation of powders with an increasing fraction of the green color component. At a phase ratio of 1 : 2 and calcination temperature of 800°C, blue powders are formed, with the intensity of their coloration decreasing as the SiO_2 content becomes higher. If the concentration of the $CoCl_2$ solution is lowered at the same solution volume and components ratio (composition nos. 7–10), the intensity of the color tone decreases. At a high content of $CoCl_2$ (>25%), black powders was synthesized (composition no. 11). Raising the calcination temperature from 600 to 800°C is accompanied in most cases by an increase in the coloration intensity.

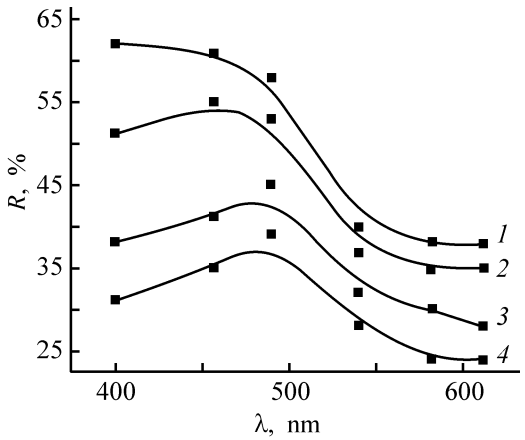


Fig. 1. Reflectance curves for cobalt-containing core powders. (R) Reflectance and (λ) wavelength in the visible spectral range. Co(II) content (wt %): (*1*) 5, (*2*) 10, (*3*) 15, and (*4*) 20.

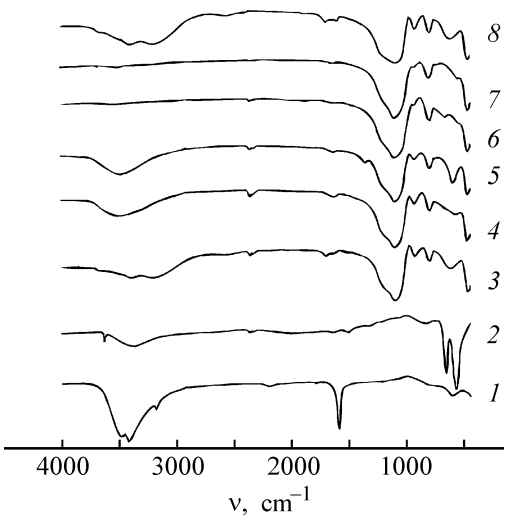


Fig. 2. IR spectra of individual substances and core powders. (ν) Wave number. (*1*) Starting $CoCl_2 \cdot 5H_2O$; (*2*) experimentally obtained CoOOH; (*3*) starting SiO_2; (*4*) SiO_2 : CoOOH (aqueous ammonia as precipitating agent); (*5*) SiO_2 : CoOOH (NaOH as precipitating agent); (*6*) SiO_2 : CoOOH, calcination at 800°C for 1 h; (*7*) mechanical mixture of SiO_2 and $CoCl_2$, calcination at 800°C for 1 h; and (*8*) mechanical mixture before calcination.

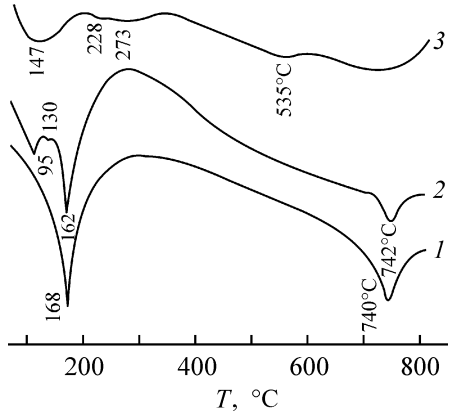


Fig. 3. DTA curves of the starting SiO_2 and powders produced by impregnation or precipitation. (*T*) Heating temperature. (*1*) Starting SiO_2, (*2*) SiO_2 impregnated with a cobalt(II) chloride solution, and (*3*) SiO_2 : CoOOH (NaOH as precipitating agent).

As the content of the shell-forming phase increases, the reflectance curves of the powders (Fig. 1) are characterized by a gradual shift of the maximum reflectance from the blue part of the visible spectral range (465 nm) to the blue-green part (496 nm). At wavelengths of 540–660 nm, there appears a strong absorption of Co(II) ions in the tetrahedral coordination. As a result, the powder color changes from light blue to blue-green.

Powders synthesized at low $CoCl_2$ solution pH (1.2, 4.0, 5.0) form no colored precipitates before and after thermal calcination. This occurs because hydroxo forms of the $[CoOH(H_2O)_5]^+$ type and, possibly, $–Si–OH \cdot Co(OH)_2$ or $–Si–OCo(OH)_2$ complexes are formed in solution only at pH 9.0. It was found that raising the calcination time from 1 to 3 h at a fixed temperature does not exert any further noticeable influence on the intensity of the color tone.

It follows from the IR spectra in Fig. 2 that the samples under study are characterized by the following absorption bands (AB): 3100–3500 cm^{-1}, deformation vibrations of molecular and adsorbed water and hydroxo groups incorporated into the layer from solutions; 1400–1500 cm^{-1}, deformation vibrations of bonds of OH^- groups contained in cobalt hydroxide; and 500–700 cm^{-1}, stretching vibrations of the Co–O bond. The absorption bands at 1100–1110 cm^{-1} are identified as Si^{4+}-related stretching vibrations, and AB at 927–933 and 472–475 cm^{-1} can presumably be assigned to vibrations of Si–O groups (bonds with a nonbridging oxygen atom) and deformation vibrations of Si–O–Si, respectively.

As is known [7], $Co(OH)_2$ formed in precipitation exists in two forms: unstable blue and stable pink, which appears at a high alkalinity and elevated temperatures (80°C). This form is intensively oxidized in air, to give CoOOH as a result of aging. This compound characteristically shows AB in the form of shoulders at 578 and 662 cm^{-1}, associated with stretching vibrations of Co–O groups. Comparison of the spectra of the individual CoOOH (spectrum *2*) and of the resulting core powders before their calcination (spectra *4*, *5*) shows that the AB at 568, 599, and 668 cm^{-1}, which are presumably associated with vibrations of the Co–O bond, are somewhat shifted under the action of the energy field of SiO_2. XPA data also confirm the presence of CoOOH (weak peak at 2θ = 22.56°). These AB (spectrum *8*) are not present in the spectrum of a mechanical mixture SiO_2 : $Co(OH)_2$. The observed doubled AB at 3391–3486 and 3181–3196 cm^{-1} in the range of stretching vibrations of H_2O and AB at 1699 and 1602 cm^{-1} in the range of deformation vibrations of H_2O suggest that, in the case in question, $CoCl_2 \cdot 3Co(OH)_2 \cdot [Co(OH)_{1.5}Cl_{0.5}]$ is formed in addition to $Co(OH)_2$. After thermal treatment of the powders at 800°C, all the AB in the spectra lie in the range 400–1200 cm^{-1} (spectrum *6*) because of the removal of OH^- groups, and are shifted to higher frequencies.

Figure 3 shows DTA data for the starting SiO_2 powder and that impregnated with a cobalt(II) salt solution, and for the product obtained by precipitation of cobalt(II) hydroxide on the surface of SiO_2 particles. The starting SiO_2 shows two endothermic ef-

fects: strong at 168°C, associated with desorption of adsorbed water, and that of medium intensity, related to removal of surface OH^- groups. In this case, the loss of mass was 8 and 19% in the first and second stages, respectively. The following changes were observed for SiO_2 impregnated with a cobalt(II) chloride solution: weak endothermic effect at 95°C, which is probably due to partial loss of the hydration water of the aqua complex of cobalt; medium-intensity effect at 162°C, associated with desorption of water adsorbed by the SiO_2 surface; and endothermic effect related to loss of surface hydroxides. This suggests that the impregnation of SiO_2 with a $CoCl_2$ solution is not accompanied by any chemical transformations. For shell powders (curve *3*), the endothermic effect associated with transformations of hydrated water is shifted to higher temperatures (117°C), the endothermic effect associated with desorption of water bound to the SiO_2 surface decreases in intensity and is shifted by nearly 100°C, and a slight endothermic effect corresponding to loss of surface OH^- groups is observed. These changes indicate that the energy state of the SiO_2 surface affects thermal processes occurring in the given product.

Thus, the differences observed in the IR absorption spectra of the mechanical mixture $SiO_2 : Co(OH)_2$ and the synthesized shell powders, as well as the differences in the derivatograms, confirm that cobalt hydroxo compounds interact with active surface centers of SiO_2 particles and these centers are involved in the control over the color tone of colored products. XPA data demonstrated that these powders are X-ray-amorphous. However, X-ray diffraction patterns of the samples synthesized by precipitation from concentrated $CoCl_2$ solutions (composition nos. 7 and 8) and thermally treated at 800°C for 2 h show reflections associated with CoO (2θ 21.2, 36.8°) and Co_3O_4 (2θ 18.45, 19.30, 22.4, 29.7°). Just this circumstance can account for the fact that black powders are obtained.

The most intense coloration is observed for powders synthesized at pH 9 at s : l = 1 : 10 from a 0.5 M $CoCl_2$ solution and calcined at 800°C for 1 h. The calculated photometric chromaticity coordinates *X*, *Y*, *Z* and the dominant wavelength λ (nm) and color purity *P* (%), found from the color triangle, have the following values: $X = 32$, $Y = 37$, $Z = 31$, $\lambda = 558$, and $P = 30$ for green powders and $X = 26$, $Y = 30$, $Z = 44$, $\lambda = 490$, and $P = 10$ for blue powders. The granulometric composition of the colored powders synthesized does not change significantly, compared with the starting aerosil particles (average particle diameter 2–5 μm). As regards their service characteristics, the powders have a satisfactory chemical stability against water (the color purity does not change on keeping the powders in water for 30 days or boiling for 1 h), hiding power of 60 g cm^{-2} [GOST (State Standard) 8784–75], and oil absorption of 37 g per 100 g of oil (GOST 211 119.8–75, section 1). The powders are easily dispersed in aqueous media to give comparatively stable suspensions.

CONCLUSIONS

(1) Shell powders with various color tones were produced by precipitation of cobalt(II) hydroxo compounds on the surface of SiO_2 particles. The main factors affecting the coloration of the powders is the concentration of a cobalt(II) salt in solution, ratio between the solid and liquid phases, and calcination temperature.

(2) It was found that, during precipitation, cobalt(II) hydroxo compounds interact with active centers of the surface of silicon dioxide particles. This gives rise to a "prestructure" of the future material with a shell in the form of an X-ray-amorphous hydroxo complex.

(3) It was shown that the colored powders synthesized are somewhat inferior in coloration intensity to cobalt pigments produced by the conventional methods. However, the process of their synthesis is less energy-intensive and saves expensive cobalt salts. Powders of this kind may be of interest as filler pigments in manufacture of paint-and-varnish materials, ceramics with magnetic properties, and various products for building purposes.

REFERENCES

1. Tolstoi, V.P., *Usp. Khim.*, 2006, vol. 75, no. 2, pp. 183–199.
2. Yurkov, G.Yu., Baranov, D.A., Kozinkin, A.V., et al., *Neorg. Mater.*, 2006, vol. 42, no. 9, pp. 1112–1119.
3. Medovoi, O.V., Morozov, S.M., and Indeikin, E.A., *Lakokras. Mater.*, 2005, no. 3, pp. 3–6.
4. Pfaff, G., *Neorg. Mater.*, 2003, vol. 39, no. 2, pp. 170–174.
5. Tsukanova, V.M. and Tikhomolova, K.P., *Zh. Prikl. Khim.*, 1997, vol. 70, no. 3, pp. 353–370.
6. Gorlovskii, I.A., Indeikin, E.A., and Tolmachev, I.A., *Laboratornyi praktikum po pigmentam i pigmentirovannym lakokrasochnym materialam* (Laboratory Course of Pigments and Pigmented Paint-and-Varnish Materials), Leningrad: Khimiya, 1990.
7. Chalyi, V.P., *Gidrookisi metallov* (Metal Hydroxides), Kiev: Naukova Dumka, 1972.

ISSN 1070-4272, Russian Journal of Applied Chemistry, 2008, Vol. 81, No. 2, pp. 178–182. © Pleiades Publishing, Ltd., 2008.
Original Russian Text © A.A. Andreev, A.N. D'yachenko, R.I. Kraidenko, 2008, published in Zhurnal Prikladnoi Khimii, 2008, Vol. 81, No. 2, pp. 190–194.

INORGANIC SYNTHESIS AND INDUSTRIAL INORGANIC CHEMISTRY

Fluorination of Beryllium Concentrates with Ammonium Fluorides

A. A. Andreev, A. N. D'yachenko, and R. I. Kraidenko

Tomsk Polytechnic University, Tomsk, Russia

Received August 30, 2007

Abstract—New method for processing of beryllium ores to beryllium oxide was suggested and studied. The method is based on decomposition of bertrandite or phenacite with ammonium chloride, with the subsequent leaching of ammonium tetrafluoroberyllate and precipitation from a beryllium hydroxide solution. The thermodynamic characteristics were calculated and a thermogravimetric analysis of the process was made. The kinetics of beryllium oxide fluorination with ammonium fluoride was experimentally studied. A technological scheme of a closed cycle for processing of beryllium-containing raw materials with ammonium fluoride was suggested.

DOI: 10.1134/S1070427208020043

Russia possesses vast resources of beryllium ores [1], but beryllium is not manufactured in our country. The only plant manufacturing beryllium plants on the CIS territory is Ul'ba metallurgical plant (Ust'-Kamenogorsk, Kazakhstan). At present, work is in progress on restoring the mining and smelting combine at the Ermakovskoe deposit (Buryatiya), where mining of the beryllium concentrate is to be resumed. Two kinds of beryllium ore are predominant at the Ermakovskoe deposit, bertrandite $Be_4[Si_2O_7](OH)_2$ and phenacite Be_2SiO_4.

The most widely used method for processing of beryllium concentrates is their sulfuric acid decomposition, followed by recovery of beryllium compounds from solution. The main technological procedures used in processing of beryllium concentrates have been described in the literature [2–4]. The applicability of these methods to the concentrate from the Ermakovskoe deposit is limited because this concentrate contains a large amount of fluorite (calcium fluoride), which is the carrier rock. Fluorite reacts with sulfuric acid to give gaseous hydrogen fluoride and gypsum (calcium sulfate). Present-day problems of, and prospects for processing of the beryllium concentrates from the Ermakovskoe deposit were described in [5–7].

The goal of this study was develop a virtually waste-free industrial technology for decomposition of fluorite-beryllium concentrates with ammonium fluorides. In [8–10], physicochemical foundations of the processes of fluoroammonium processing of mineral substances, such as zircon, ilmenite, and topaz were described; the same procedures were used when studying the interaction of beryllium-containing minerals with ammonium fluorides.

Melts of ammonium fluoride (NH_4F) and ammonium hydrofluoride ($NH_4F \cdot HF$) are strong fluorinating agents with reactivity exceeding that of fluorine and hydrogen fluoride. The fluorinating capacity is exhibited by these substances in melts in the temperature range 126–240°C. At room temperature, ammonium fluorides are nonvolatile and sufficiently ecologically safe crystalline substances.

Processing of silicon-containing minerals {Be_2SiO_4, $Be_4[Si_2O_7](OH)_2$}, is hindered by their chemical stability. The quartz component of the mineral can be decomposed under the action of fluoride ions. Ammonium fluorides form with silicon oxide a complex compound $(NH_4)_2SiF_6$. The convenience of use of ammonium hexafluorosilicate in the technology consists in its physicochemical properties. At temperatures above 320°C, this compounds sublimes and leaves the reaction mass; in another apparatus, ammonium hexafluorosilicate can be condensed and subjected to ammonia hydrolysis, with the regenerated ammonium fluoride recycled and a commercial product, silicon oxide of "carbon white" brand, obtained [11–13].

Thermodynamic characteristics of the process of phenacite fluorination with NH_4F and $NH_4F \cdot HF$

Reaction	ΔG, kJ mol^{-1} K^{-1}, at indicated T, K						ΔH_{298}, kJ mol^{-1}
	298	400	500	600	700	800	
(1)	20	–181	–384	–588	–793	–999	32
(2)	–224	–297	–353	–394	–424	–443	620

The thermodynamic probability of the occurrence of reactions was calculated for the interaction of components of a beryllium concentrate (phenacite) with ammonium fluorides

$$Be_2SiO_4 + 14NH_4F = 2(NH_4)_2BeF_4 + (NH_4)_2SiF_6 + 8NH_3 + 4H_2O, \quad (1)$$

$$Be_2SiO_4 + 7NH_4F \cdot HF = 2(NH_4)_2BeF_4 + (NH_4)_2SiF_6 + NH_3 + 4H_2O. \quad (2)$$

The results of the thermodynamic calculation are listed in the table.

The calculated temperature dependence of the Gibbs energy suggests that the reaction of phenacite NH_4F fluorination [reaction (1)] proceeds toward formation of ammonium hexafluoroberyllate at temperatures exceeding 400 K, and $NH_4F \cdot HF$ interacts with phenacite by reaction (2) at room temperature and above. As the temperature is elevated, the completeness of fluorination increases for both the reactions in proportion to the decrease in the Gibbs energy of the processes.

After the thermodynamic possibility of the fluorination reaction was confirmed, a thermogravimetric study of the process was performed. In this experiment, ammonium hydrofluoride was used instead of ammonium fluoride to eliminate the heat-flux DTA peaks corresponding to melting of ammonium fluoride and its conversion to ammonium hydrofluoride, with ammonia released. The peak corresponding to this conversion overlapped in the DTA curve with the peaks related to reactions between the components. After melting and decomposition of ammonium fluoride, the reaction occurs just with ammonium hydrofluoride. The experiments were carried out on an SDT Q600 combined TGA/DSC/DTA analyzer-derivatograph, with data processing by TA instruments Universal v. 4.2E software. The samples were heated at rate of 1 deg min^{-1} in a flow of air.

Figure 1 shows gravimetric (TG) and differential-thermal (DTA) dependences for the interaction of beryllium oxide with ammonium hydrofluoride introduced in a twofold excess with respect to stoichiometry.

The reaction starts to proceed at room temperature to give a fluoroammonium complex of beryllium, $(NH_4)_2BeF_4 \cdot nNH_4F$, with release of gaseous ammonia and water. Upon further heating, the fluoroammonium complex of beryllium decomposes. At 126°C, ammonium hydrofluoride melts. At 200°C, $(NH_4)_2BeF_4 \cdot NH_4F$ is formed, which decomposes to $(NH_4)_2BeF_4$ on heating to 240°C. As the temperature is elevated to 280°C, $(NH_4)_2BeF_4$ decomposes to NH_4BeF_4, which, in turn, decomposes to BeF_2 at 385°C. The fluoroammonium complexes decompose with release of gaseous ammonia and hydrogen fluoride.

The thermogravimetric study of the reaction of beryllium oxide with ammonium fluoride yielded the same results, but the thermograms obtained were complicated by peaks related to decomposition of ammonium fluoride to the hydrofluoride.

The results of an analysis of the thermogravimetric data suggest the following scheme of chemical trans-

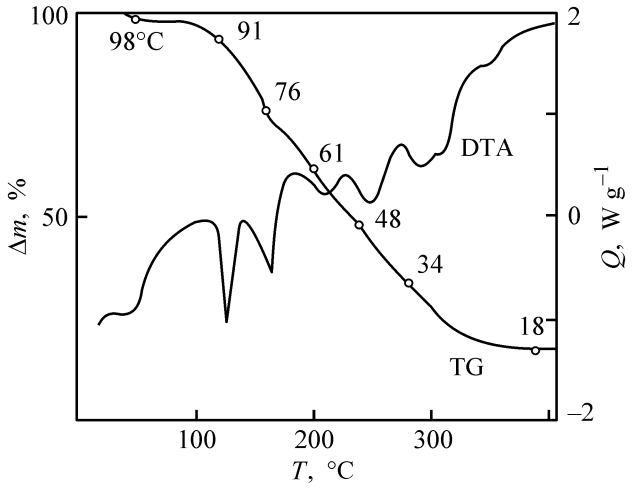


Fig. 1. Thermogram of the interaction of beryllium oxide with ammonium hydrofluoride. (Δm) Change in mass, (Q) heat flux, and (T) temperature.

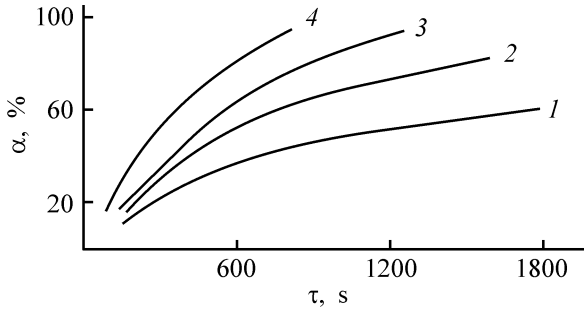


Fig. 2. Kinetic curves of the reaction between beryllium oxide and ammonium fluoride. (α) Degree of conversion and (τ) time. Temperature (°C): (*1*) 140, (*2*) 160, (*3*) 180, and (*4*) 200.

formations that occur in the reaction of beryllium oxide with ammonium fluoride and hydrofluoride:

$$BeO + NH_4F \cdot nHF \xrightarrow{200^\circ C} (NH_4)_2BeF_4 \cdot NH_4F$$

$$\xrightarrow{240^\circ C} (NH_4)_2BeF_4 \xrightarrow{280^\circ C} NH_4BeF_3 \xrightarrow{385^\circ C} BeF_2.$$

The thermogravimetry of the reaction between silicon oxide (as the second component of phenacite) with ammonium fluorides was described in detail in [15].

The results of thermodynamic and thermal analyses of the system under consideration, which confirmed the theoretical possibility of the process, made necessary a study of the rate of beryllium oxide fluorination by ammonium fluoride

$$BeO + 4NH_4F = (NH_4)_2BeF_4 + 2NH_3 + H_2O. \quad (3)$$

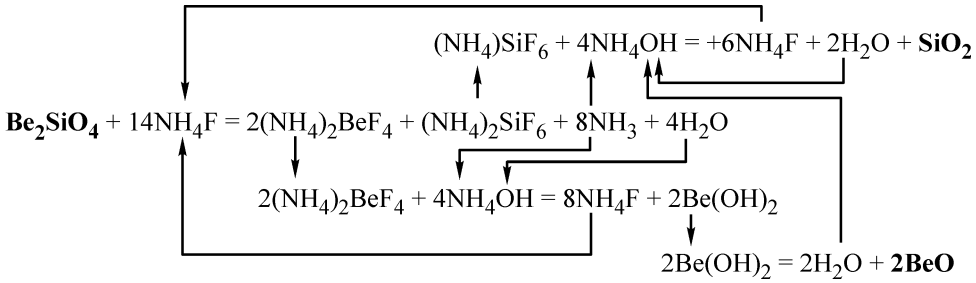
A kinetic experiment was performed by uninterrupted weighing of the reacting mixture, with automatic recording of the mass. The mass loss determined by the formation of gaseous ammonium and water was used to find the degree of conversion. Preliminarily, the decomposition rate of ammonium hydrofluoride at these same temperatures was experimentally determined, with appropriate corrections introduced into the final results. The kinetic curves of beryllium oxide decomposition are shown in Fig. 2.

The experimental data are described with sufficient accuracy by the equation of a contracting sphere, and the following dependence of the conversion α on time τ and temperature T was derived:

$$\alpha = 1 - \left(1 - 1.8e^{\frac{31\,000}{8.31T}}\tau\right)^3.$$

The rate constant of the chemical reaction is 1.8 s^{-1}. The activation energy of the process was 31 kJ mol^{-1}, which indicates that the reaction occurs under mixed diffusion and kinetic control. This means that not only temperature, but also the intensity of agitation of the reaction mass affect the rate of the chemical reaction. The kinetic study demonstrated that more than 95% of beryllium oxide decomposes in 20 min at 200°C.

The general scheme of a closed fluoroammonium cycle of phenacite decomposition into silicon oxide and beryllium oxide, with ammonium fluoride regenerated, is as follows:

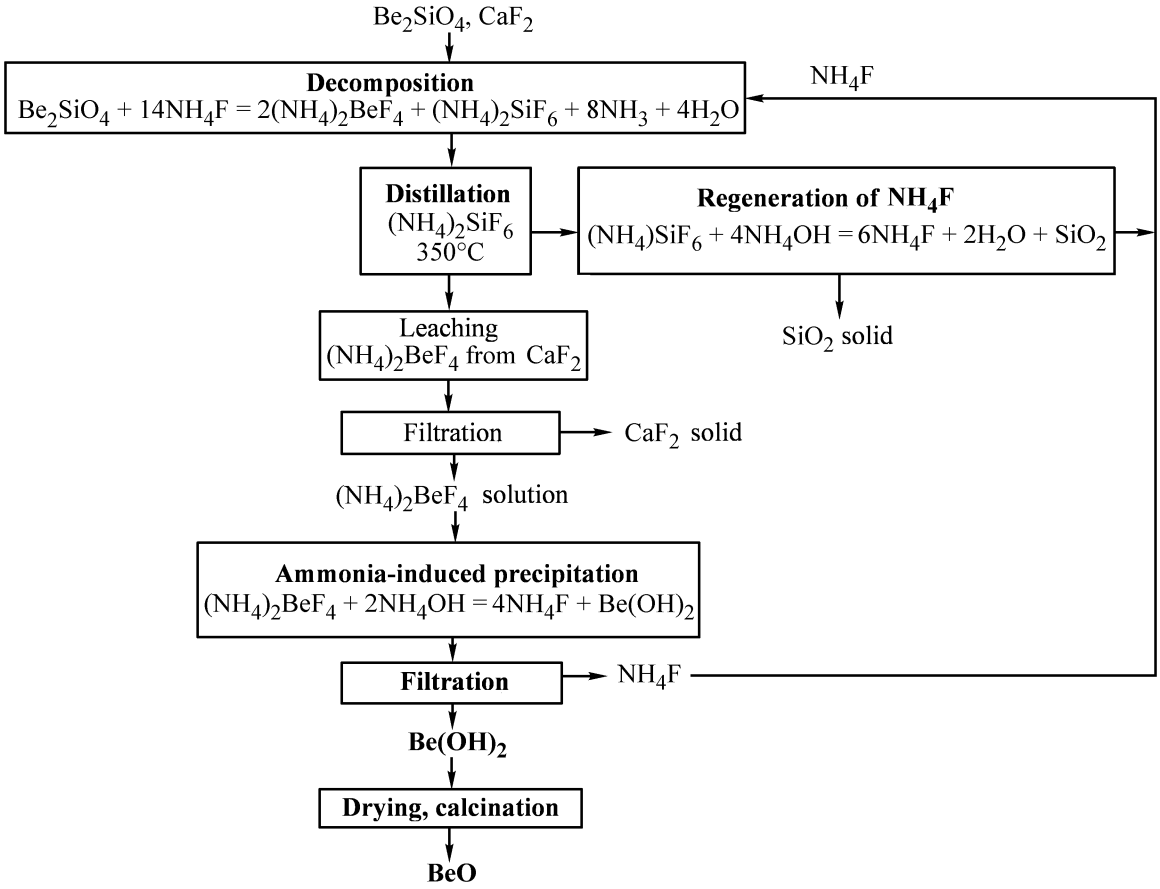


(4)

Scheme (4) clearly demonstrates that the flows are closed and the material balance are equal. A scheme of a closed fluoroammonium cycle of beryllium oxide decomposition by ammonium hydrofluoride can be composed in the same way.

The calculated and experimental data presented here suggest the technological sequence of operations in the fluoroammonium method for beryllium oxide recovery from the fluorite-phenacite concentrate (see scheme).

In accordance with the technological scheme suggested, the starting fluorite-phenacite concentrate (phenacite content 30%) is mixed with ammonium fluoride and heated to 200°C. Phenacite reacts with



Technological scheme of fluoroammonium processing of the fluorite-phenacite concentrate.

ammonium fluoride to give ammonium fluoroberyllate and ammonium hexafluorosilicate, with gaseous ammonium and water released in accordance with reaction (1). After the hydrofluorination, the resulting mixture of fluorides is heated to 320°C, with silicon sublimed in the form of gaseous ammonium hexafluorosilicate $(NH_4)_2SiF_6$. Thus, silicon is removed from the mixture as ammonium hexafluorosilicate. Ammonium tetrafluoroberyllate and unfluorinated fluorite remain in the solid fraction. Leaching-out of ammonium tetrafluoroberyllate with water enables its complete recovery from the carrier rock, because the solubility of $(NH_4)_2BeF_4$ is as high as 32% and calcium fluoride is virtually insoluble. After the ammonium tetrafluoroberyllate solution is separated, it is purified to remove admixtures of aluminum and iron by the method of ammonium-induced increase in the solution pH to 8.5. At pH 8.5, aluminum and iron hydroxides precipitate from the solution. The separation of aluminum impurity by ammonium precipitation enables application of the fluoroammonium technique in processing of beryl ($2BeO \cdot Al_2O_3 \cdot 6SiO_2$), too. As the solution pH is raised further to 12, beryllium hydroxide precipitates. Beryllium hydroxide separated by filtration is converted to the oxide form after calcination.

An important economical factor of the process is the possibility of regeneration of a major part of ammonium fluoride from ammonium hexafluorosilicate. The sublimed ammonium hexafluorosilicate was subjected to ammonia hydrolysis:

$$(NH_4)_2SiF_6 + 4NH_4OH = SiO_2\downarrow + 6NH_4F + 2H_2O. \quad (5)$$

Ammonium tetrafluoroberyllate is also subjected to ammonia hydrolysis with regeneration of ammonium fluoride:

$$(NH_4)_2BeF_4 + 2NH_4OH = Be(OH)_2 + 4NH_4F. \quad (6)$$

Thus, the fluorite-phenacite rock is decomposed using ammonium fluoride and beryllium hydroxide is recovered and separated from impurities.

The advantages of the method suggested are the following: possibility of complete regeneration of

ammonium fluoride or hydrofluoride, virtually waste-free mode, and possibility of using the standard chemical apparatus for setting-up commercial production.

CONCLUSIONS

(1) A thermodynamic analysis of the reactions of phenacite with ammonium fluorides demonstrated that the reaction equilibrium is shifted toward product formation.

(2) A thermogravimetric analysis revealed the mechanism of beryllium oxide fluorination by ammonium fluorides. The fluorination occurs to give intricate fluoroammonium complexes, which decompose to beryllium difluoride at temperatures exceeding 380°C.

(3) The kinetic study demonstrated that more than 95% of beryllium oxide is fluorinated in 20 min at 200°C. The rate constant of the chemical reaction is 1.8 s^{-1}, and the activation energy of the process, 31 kJ mol^{-1}.

(4) A technological scheme was suggested for fluoroammonium processing of the fluorite-phenacite concentrate, with ammonium fluoride recycled and beryllium oxide, silicon oxide, and calcium fluoride recovered.

REFERENCES

1. *Metodicheskie rekomendatsii po primeneniyu klassifikatsii zapasov k mestorozhdeniyam berillievykh rud* (Methodological Recommendations for Application of the Resources Classification to Beryllium Ore Deposits), Moscow: Min. Prirodn. Resurs. Ross. Feder., 2005.
2. Beryllium Science and Technology, Webster, D. and London, G.J., Eds., *New York: Plenum*, 1979.
3. Everest, D.A.: *The Chemistry of Beryllium*, Amsterdam: Elsevier, 1964.
4. Fridlyander, I.N. et al., *Berillii–material sovremennoi tekhniki: Spravochnik* (Beryllium, a Material of Modern Technology: Reference Book), Moscow: Metallurgiya, 1992.
5. Samoilov, V.I. and Borsuk, A.N., *Metody sovmestnoi pererabotki bertrandita, fenakita i berilla v gidrometallurgii berilliya* (Methods for Joint Processing of Bertrandite, Phenacite, and Beryl in Hydrometallurgy of Beryllium), Ust'-Kamenogorsk: MediaAl'yans, 2005.
6. Samoilov, V.I., *Zh. Prikl. Khim.*, 2006, vol. 79, no. 6, pp. 889–895.
7. Samoilov, V.I., Borsuk, A.N., and Kishlyanova, A.A., *Zh. Prikl. Khim.*, 2006, vol. 79, no. 6, pp. 896–901.
8. D'yachenko, A.N., *Khim. Prom–st. Segodnya*, 2006, no. 7, pp. 22–27.
9. Andreev, A.A., Buinovskii, A.S., D'yachenko, A.N., and Kraidenko, R.I., *Nov. Ogneupory*, 2006, no. 5, pp. 8–11.
10. Andreev, A.A., D'yachenko, A.N., and Kraidenko, R.I., *Khim. Prom–st. Segodnya*, 2007, no. 3, pp. 6–11.
11. Rakov, E.G., *Khimiya i tekhnologiya neorganicheskikh ftoridov* (Chemistry and Technology of Inorganic Fluorides), Moscow: Mosk. Khim. Tekhnol. Inst. im. D.I. Mendeleeva, 1990.
12. Mel'nichenko, E.I., *Ftoridnaya pererabotka redkometall'nykh rud Dal'nego Vostoka* (Fluoride Processing of Rare-Metal Ores of the Far East), Vladivostok: Dal'nauka, 2002.
13. Mel'nichenko, E.I, Epov, D.G., Krysenko, G.F., et al., *Zh. Prikl. Khim.*, 1996, vol. 69, no. 8, pp. 1248–1251.

ISSN 1070-4272, Russian Journal of Applied Chemistry, 2008, Vol. 81, No. 2, pp. 183–187. © Pleiades Publishing, Ltd., 2008.
Original Russian Text © I.A. Massalimov, I.N. Vikhareva, M.S. Kireeva, 2008, published in Zhurnal Prikladnoi Khimii, 2008, Vol. 81, No. 2, pp. 195–199.

INORGANIC SYNTHESIS AND INDUSTRIAL INORGANIC CHEMISTRY

Use of Polysulfides of Alkali and Alkaline-Earth Metals To Obtain Highly Dispersed Sulfur

I. A. Massalimov, I. N. Vikhareva, and M. S. Kireeva

Research Institute of Low-Tonnage Chemical Products and Reagents, Ufa, Bashkortostan, Russia

Received May 15, 2007

Abstract—Possibilities of obtaining polysulfides of alkali and alkaline-earth metals in aqueous solutions were considered. The composition of the polysulfides and their concentration in solutions were found. The efficiencies of application of highly dispersed sulfur, produced from calcium polysulfide, and colloid sulfur as a fungicide were compared.

DOI: 10.1134/S1070427208020055

Sulfur widely occurs in nature in a free state, in various sulfide ores, and as various sulfates, such as gypsum ($CaSO_4$), barite ($BaSO_4$), etc. The diversity of the application fields of sulfur is due to its bactericide and fungicide properties. Brimstone deposits had been industrially developed beginning in the XIX century till mid-XX century [1, 2]. However, the intensive exploitation of sulfur-containing-oil and -gas fields yielded a new source of sulfur. The amount of sulfur in wastes from oil-and-gas processing plants started to rapidly increase. By now, the accumulated resources of these products are so vast that considerable amounts of high-quality raw materials remain unused. In this context, a search for new ways to use elementary sulfur is a rather topical task.

The effective utilization of its bactericide properties can be achieved by grinding sulfur in various devices, micronizers and colloid mills [3]. A prolonged mechanical treatment with addition of various surfactants can yield sulfur with micrometer particles, which is commonly used under the name "colloid sulfur" as a means for plant protection [4]. It has been found that the activity (chemical, catalytic, and biological) of highly dispersed substances markedly increases on passing to submicrometer, nanosize particles [5]. The preparative chemistry employs various precipitation methods that can yield sulfur in a sufficiently dispersed submicrometer state. However, these methods of sulfur isolation (with hydrochloric acid from calcium sulfide and sodium thiosulfate solutions) can only be used to obtain chemically pure sulfur in comparatively small amounts [6].

According to published data [7], ammonium, potassium, sodium, barium and calcium polysulfides have been tested at different times as chemical means of plant protection, but failed to find use because of the lack of preparative forms convenient for practical purposes.

The aim of our study was to examine the possibility of obtaining stable compounds of sulfur with alkali (sodium, potassium) and alkaline-earth (calcium, strontium, barium) metals with subsequent isolation of high-dispersity (submicrometer) sulfur from these compounds. The efficiency of practical application of sulfur recovered from solutions of its compounds and colloid sulfur was tested by comparison of their fungicide properties.

We chose as a basis the polysulfide form containing a comparatively large amount of sulfur, from which, as demonstrated by experiments, highly dispersed sulfur can be produced. We examined the possibility of obtaining polysulfides of varied chemical nature in aqueous solutions and determined their composition. We analyzed, for the example of calcium polysulfide, the possibility of converting sulfur into the polysulfide form by its mechanical activation in a disintegrator and tested it as a plant protection means.

EXPERIMENTAL

Polysulfides of alkali and alkaline-earth metals were synthesized in aqueous solutions in a flask with

a reflux and stirrer. To prevent the possible evolution of hydrogen sulfide, the outlet of the reflux was connected with a solution of lead acetate.

To a weighed portion of a metal hydroxide or oxide was added a certain amount of water, with the mixture heated to boiling. Separately, we prepared a hand-ground sulfur powder, from which a paste was prepared by addition of water and mixed with the boiling solution of the metal hydroxide. Them the mixture was boiled and then cooled and filtered. The filtrate is a dark cherry liquid whose coloration intensity grows as the solution concentration increases. The solution concentration can be controlled in the subsequent evaporation of water. Being subjected to a nucleophilic attack by ions of hydroxide-containing compounds, chains of sulfur molecules are ruptured to give S_n^{2-} ions of various lengths, with polysulfides of the corresponding metals formed as a result.

It was found that elementary sulfur is converted to the polysulfide form in aqueous solutions in different ways in all cases (see table). The synthesis of polysulfides is the easiest for alkali metals:

$$10S + 6NaOH = 2Na_2S_4 + Na_2S_2O_3 + 3H_2O.$$

The process goes rapidly, in 1–1.5 h; by the end of an experiment, the reaction mass contains in the precipitate only sulfur taken in an excess (10% with respect to the stoichiometry) and the content of the target polysulfide reaches high values (35–40 wt % dry substance).

A different situation is observed when alkali metal polysulfides are obtained. For example, in the reaction of synthesis of calcium polysulfide

$$10S + 3CaO = 2CaS_4 + CaS_2O_3,$$

with the use of hand-ground sulfur, the main part (70–75%) of the starting reagents enters into the reaction in the course of 3–4 h of thermal treatment at 100°C. At the same time, a considerable part (up to 25–30%) of the starting reagents is not involved in the reaction even upon prolonged thermal treatment (up to 60–70 h). To obtain a concentrated (with 20% dry substance and more) solution, it is necessary to evaporate water and add stabilizers [8].

It is known that preliminary mechanical treatment of reagents [9] leads to a substantial acceleration of chemical reactions in solid and liquid phases. To improve the synthesis of calcium polysulfide, we used a disintegrator that, as shown previously, strongly changes the thermodynamic [10] and structural characteristics [11, 12]. We obtained in our study samples with different numbers of treatments in the disintegrator and subjected these samples to an X-ray diffraction analysis. The samples were used in the reaction of synthesis of calcium polysulfide. With sulfur once treated in the disintegrator, the time of boiling of a mixture of sulfur and calcium hydroxide decreased from 3–4 to 1 h, and the amount of the precipitate, from 30 to 5%. It was also found that use of sulfur twice treated in the disintegrator leads to complete interaction of the starting reagents. Thus, intensive mechanical treatment changes the equilibrium solubility of sulfur, enables full use of the starting reagents, and markedly facilitates preparation of its concentrated aqueous solutions in the form of polysulfides. Synthesis of calcium polysulfide with mechanically activated sulfur and polysulfide stabilizers (glycerol, sugar, ethylene glycol, etc.) can give concentrated solutions with density $\rho = 1.18–1.32$ g cm^{-3}.

To study how the particle size and structural parameters vary in mechanical treatment, we performed sedimentation and X-ray diffraction analyses of the starting and mechanically treated sulfur samples. Because the disintegrator is a flow-through grinding device, the duration of the mechanical treatment was varied by carrying out repeated treatments.

The particle size distribution (Lumosed sedimentograph) demonstrated that the process of sulfur particle grinding virtually ceased after two treatments. The particle size of the starting hand-ground powder was in the range 0.1–3 mm; immediately after the first treatment the particle size distribution corresponded to the range 1–12 μm.

The integral intensities and diffraction angles were measured on a DRON-3M diffractometer. The experimental results were processed using a special-purpose software package developed at Moscow Institute of Steel and Alloys. It was found that the X-ray diffraction patterns of the starting and mechanically treated samples exhibit reflections that correspond only to the orthorhombic phase of elementary sulfur, but their parameters (width and position) change in the course of mechanical treatment. The basic parameter characterizing deviations of the crystal lattice from the ideal order is the integral linewidth. It is known [9, 11, 12] that just this quantity is correlated with practically important parameters, such as the solubility and chemical activity of solid substances.

The figure shows how the integral linewidth for reflections from the (313), (135), and (026) planes depends on the treatment duration. It should be noted that sample 2 corresponds to the stage of a double

Results of chemical analyses of polysulfides of alkali and alkaline-earth metals (M)

M polysulfide	Initial content, wt %		Content according to the results of analyses, wt %						Formula
	S*	M	S_{tot}	S_{thios}	S_{sulf}	$S_{polysulf}$	M	S_{Σ}	
Na	23.33	10.06	24.90	4.00	2.67	18.23	10.09	25.00	$Na_2S_{4.2}$
K	21.85	16.02	17.70	3.65	1.55	12.50	16.36	21.32	K_2S_3
Ca	21.77	8.18	12.84	2.19	1.23	9.42	4.81	13.15	$CaS_{3.9}$
Ba	7.92	10.20	5.64	0.12	1.24	4.28	5.18	5.82	$BaS_{4.8}$
Sr	11.78	9.68	4.40	1.42	0.55	2.43	4.03	5.00	$SrS_{3.3}$

* The weighed portion of sulfur corresponds to the mass of sulfur with account of the stoichiometric coefficients in the equation describing the synthesis of a polysulfide.

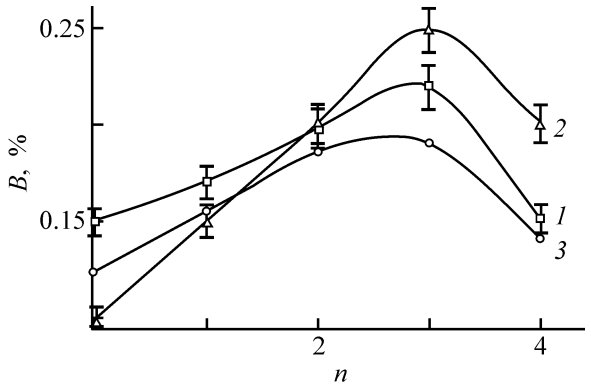
treatment, in which the grinding process is complete. It can be seen from the figure that, despite the grinding is complete, the linewidth increases as the treatment duration becomes longer, untill the third treatment, and the linewidth slightly decreases for sample 4. Thus, these dependences demonstrate that the level of structural disruption within particles (samples 3 and 4) changes even in the absence of comminution. Comparison of the results of X-ray studies with data on dissolution of elementary sulfur in a calcium hydroxide solution shows that a gradual increase in the linewidth is correlated with a rise in the solubility of sulfur. In this case, the increase in the linewidth, observed for sample 2, is sufficient for complete dissolution of sulfur.

It was found experimentally that a 20–30-fold dilution of the starting solution with density ρ = 1.18–1.20 g cm^{-3} results in that the solution loses transparence and a precipitate composed of finely dispersed sulfur and calcium carbonate, hydroxide, and thiosulfate is formed in 24 h. A sedimentation analysis of the precipitate demonstrated that 95% of precipitate particles are less than 1 μm in size, and 80%, less than 0.1 μm. Thus, the method of sulfur isplation from a calcium polysulfide solution can give highly dispersed sulfur, which is difficult to obtain by mill grinding.

Further, we performed a chemical analysis of the solutions obtained. In samples of polysulfide solutions, the amount of ions of alkaline-earth metals was determined by chelatometry, and that of alkali metals, by acid-base titration.

The amount of sulfur in the thiosulfate form was found by iodometric titration after separating the polysulfide and sulfide sulfur in the form of cadmium sulfide and sulfur. A part of sulfur, which is in the sulfide form, was determined by back redox titration with iodine [13], with the subsequent subtraction of the previously found amount of thiosulfate sulfur. The content of sulfur in the polysulfide form was found by conversion of the polysulfide sulfur to thiosulfate under the action of a sodium sulfite solution, separation of the sulfide sulfur in the form of cadmium sulfide, and titration with iodine thiosulfate in an acid medium [14, 15]. The sum of these three constituents, S_{Σ}, is presented in the table. The value of S_{tot} was found experimentally by redox titration with a potassium bromide-bromate solution [16, 17]. The data obtained were used to calculate the formulas of the polysulfides.

It can be seen in the table that, depending on the nature of a metal atom, the number of sulfur atoms in the molecule ranges from 3 for K_2S_4 to 4.8 for $BaS_{4.8}$. The difference between the initial amounts of a metal and sulfur and those experimentally found in alkaline-earth polysulfides is observed because part of reagents in the latter are in the precipitate.



Linewidth *B* for reflections from the planes (*1*) (313), (*2*) (135), and (*3*) (026) vs. the number *n* of mechanical treatments.

To determine the fungicide activity[1], we performed industrial tests of the new preparative form of sulfur, which contained, together with calcium polysulfide, solution stabilizers (glycerol) and polyvinyl alcohol as a film-forming agent. The analysis demonstrated that spraying with the preparation enables effective distribution over the surface of plants (pine trunks and needles) of highly dispersed sulfur formed in decomposition of calcium polysulfide. It was found that hydrophobic sulfur is fixed on the surface of plants upon the subsequent drying, which makes it possible to reduce the number of treatments.

Tests were carried out in three variants, with concentrations of 10, 5, and 2.5% in terms of the preparation or 2.0, 1.0, and 0.5% in terms of pure sulfur and an application rate of 400 l of the working liquid per 1 ha. As a reference for treatment of pine yearlings served a 2% solution of colloid sulfur at the same application rate of the working liquid. The treatments were performed on a total area of 2 ha. An examination of the treated seedlings demonstrated the following.

(1) The average number of infested seedlings on treated plots was 0.67, 0.97, and 2.8% with 10, 5, and 2.5% solutions, respectively. The number of infested seedlings in the control was 3.7%. A comparison of the effect of the preparation under study, with concentrations of 10 and 2% in terms of pure sulfur, and of the reference 2% solution of colloid sulfur demonstrated that the efficiency of the form we developed is 5.5 times higher.

(2) Laboratory tests aimed to evaluate the activities of different doses of the preparative form of sulfur as an aqueous solution were performed on pure cultures of the most harmful and widely occurring agents causing diseases in conifer seedlings. The colloid sulfur conventionally used as a fungicide was used as reference. The preparations were introduced into a not-yet-solidified nutritional medium and the fungus cultures *Phacidium infestans Karst* (snow blight) and *Lophodermium pinastri Chev* (pine needle cast) were applied to its already solidified surface. As controls served nutritional media with fungus cultures, but without addition of the preparations. The fungicide effect of the preparations tested was judged from the occurrence or absence of mycelium growth and from the colony diameter after 7 days of growth of the mycelium of the fungi. The results obtained demonstrated that the preparation exhibits a fungicide effect.

The preparation suppressed the growth of colonies of the agent causing show blight, whose diameters were 25, 20, and 12.5 mm after 7 days of growth in media with 4, 6, and 10% aqueous solutions of the preparation, respectively. This diameter was 47 mm with the reference preparation, and 59 mm in the control.

An even more pronounced fungicide effect was produced by the preparation on the growth of colonies of agents of pine needle cast, whose diameters were 18, 14, and 8.5 mm after 7 days of growth in media with 4, 6, and 10% aqueous solutions of calcium polysulfide, respectively. This diameter was 52 mm with the reference preparation, and 60 mm in the control. Thus, the preparation tested under industrial conditions exhibited a stronger fungicide effect for forest cultures, compared with colloid sulfur.

CONCLUSIONS

(1) It was found that elementary sulfur can be used upon its conversion to the polysulfide form, followed by isolation in the highly dispersed (submicrometer) state.

(2) The possibility of intensifying the reaction of polysulfide formation by using sulfur mechanically activated in a disintegrator was demonstrated.

(3) Tests of calcium polysulfide as a means of plant protection from fungal diseases demonstrated that the preparative form suggested is more efficient than ground, colloid sulfur, which makes it possible to recommend its use as a component of an integrated scheme for protection of cultivated plants and forest plantations.

REFERENCES

1. Menkovskii, M.A. and Yavorskii, V.T., *Tekhnologiya sery* (Technology of Sulfur), Moscow: Khimiya, 1983.
2. Hurlbut, C. S., Jr. and Klein, C., *Manual of Mineralogy (after J.D. Dana)*, New York: John Wiley and Sons, 1977.
3. *Entsiklopediya vinogradarstva* (Encyclopedia of Viticulture), Kishinev, 1987, vol. 3.
4. Mel'nikov, N.N., *Pestitsidy: Khimiya, tekhnologiya i primenenie* (Pesticides: Chemistry, Technology, and Application), Moscow: Khimiya, 1987.
5. Sergeev, G.B., *Nanokhimiya* (Nanochemistry), Moscow: Mosk. Gos. Univ., 2003.
6. Karyakin, V.I., *Khimicheski chistye reaktivy* (Chemically Pure Reagents), Moscow: Goskhimizdat, 1947.
7. Berim, N.G., *Khimicheskaya zashchita rastenii* (Chemical Plant Protection), Leningrad: Kolos, 1972.

[1] The fungicide activity was determined at a station of the Center for forest protection of the Republic of Bashkortostan (Bishindin arboretum, Tuimazy test forestry).

8. Massalimov, I.A. and Kireeva, M.S., *Nauchnye issledovaniya vysshei shkoly v oblasti khimii i khimicheskie produkty* (Research in Chemistry in Higher School and Chemical Products), Moscow: Ross. Khim.-Tekhnol. Univ. im. D.I. Mendeleeva, 2002, p. 112.
9. Avvakumov, E.G., *Mekhanicheskie metody aktivatsii khimicheskikh protsessov* (Mechanical Methods for Activation of Chemical Processes), Novosibirsk: Nauka, 1986.
10. Massalimov, I.A. and Sangalov, Yu.A., *Zh. Prikl. Khim.*, 2001, vol. 74, no. 4, pp. 545–548.
11. Massalimov, I.A. and Sangalov, Yu.A., *Khim. Prom–st. Segodnya*, 2004, no. 5, pp. 11–20.
12. Massalimov, I.A., *Neorg. Mater.*, 2003, vol. 39, no. 11, pp. 1–7.
13. Légrádi, L., *Analyst*, 1961, vol. 86, pp. 854 – 857.
14. Papp, J. and Havas, J., Mag. kė m. Folyoirat., 1970, vol. 76, pp. 307–309.
15. *Unifitsirovannye metody analiza* (Unified Analytical Methods), Lur'e, Yu.Yu., Ed., Moscow: Khimiya, 1971.
16. Szekeres, L., *Z. anal. Chem.*, 1960, vol. 178, pp. 81–83.
17. Szekeres, L., *Pharm. Zentralhalle*, 1963, vol. 102, pp. 6 – 9.

ISSN 1070-4272, Russian Journal of Applied Chemistry, 2008, Vol. 81, No. 2, pp. 188–195. © Pleiades Publishing, Ltd., 2008.
Original Russian Text © O.B. Dormeshkin, N.I. Vorob'ev, G.Kh. Cherches, A.N. Gavrilyuk, 2008, published in Zhurnal Prikladnoi Khimii, 2008, Vol. 81, No. 2, pp. 200–206.

INORGANIC SYNTHESIS AND INDUSTRIAL INORGANIC CHEMISTRY

Effect of Carbamide on Sulfuric Acid Decomposition of Phosphate Raw Materials in Nonthickening Suspensions in Production of Integrated Fertilizers

O. B. Dormeshkin, N. I. Vorob'ev, G. Kh. Cherches, and A. N. Gavrilyuk

Belarussian State Technological University, Minsk, Belarus

Received June 8, 2007

Abstract—Effect of carbamide on sulfuric acid decomposition of phosphate raw materials in nonthickening suspensions in production of integrated fertilizers was studied. The mechanism and phase composition of the intermediate and final products of the decomposition process in the presence of carbamide were examined. The results obtained served as a theoretical basis for development of a new technological process for manufacture of integrated sulfur-containing fertilizers.

DOI: 10.1134/S1070427208020067

Processes of acid decomposition of phosphate materials in nonthickening suspensions are of fundamental importance in the technology of inorganic substances, because they are employed to obtain a number of most important chemical products and, in particular, extractive phosphoric acid (EPA) and simple and double superphosphate. At the same time, a stable tendency is conversion of shops for production of simple single-component fertilizers to manufacture of integrated NP and NPK fertilizers. For example, the fraction of simple phosphate fertilizers in Russia is only 1.6% of the total [1]. About 200 brands of phosphorus-containing integrated fertilizers are offered at present by the European market. The main way to optimize the assortment of mineral fertilizers in the Republic of Belarus is, according to the data obtained by agrochemists [2], a substantial increase in volume of manufacture and application of complete integrated fertilizers. This will diminish by 65–70% the expenditure for introduction of fertilizers and optimize the mineral feeding of plants, which is extremely difficult with simple forms and existing application techniques.

At present, a considerable researchers' and manufacturers' attention is given to production of integrated fertilizers with introduction of carbamide. The use of carbamide in synthesis of complex fertilizers based on products of acid processing of phosphates is advisable from the agrochemical standpoint. The interest in systems constituted by carbamide and superphosphate, and carbamide and ammonium phosphates is also due to the fact that reactions of adduct formation occur between the components of these systems. Fertilizers containing adducts of carbamide with calcium sulfate and hydrosulfate release nitrogen into soils at a considerably slower rate than carbamide, which enables their use in production of prolonged-action integrated fertilizers and diminishes the loss of nutritive components in soils. However, production of integrated fertilizers with introduction of carbamide is a rather difficult task. Direct mixing of carbamide and superphosphate (ammonium phosphates) is undesirable because the differences in the physical properties and, in particular, bulk density result in that the mixture is inhomogeneous in composition and separate components are nonuniformly distributed over fields. Introduction of carbamide in the industrial process of superphosphate synthesis and, in particular, that together with the recycle is not simple, either, because it involves release of water and formation of a large amount of an additional liquid phase, increase in the extent of recycling, higher energy expenditure, and stronger caking of the final product.

It seems appropriate to introduce carbamide directly into the acid, or partly ammonized suspension before the granulation stage. This will diminish the amount of the liquid phase introduced into the process together with the starting reagents and, accordingly, will make lower the expenditure for its subsequent drying because of the improvement of the rheological properties

of the suspensions upon introduction of carbamide. However, the available data on the effect of carbamide on the process of sulfuric acid decomposition of phosphate raw materials are of unsystematic nature and frequently contradictory and give no way of making an unambiguous conclusion about the optimal method and place of carbamide introduction into the technological cycle in production of integrated fertilizers.

The goal of this study was to examine specific features of the process of sulfuric acid decomposition of phosphate raw materials in nonthickening suspensions in the presence of carbamide and to determine the chemical and phase composition of the products formed. The results obtained were used to develop a new low-waste technology for manufacture of sulfur-containing integrated NPKS fertilizers.

EXPERIMENTAL

The effect of carbamide on the process of sulfuric acid decomposition of phosphate raw materials was studied under conditions corresponding to the dihydrate mode of extraction in manufacture of EPA from the apatite concentrate as the phosphate raw material. The necessary amount of sulfuric acid, calculated from the stoichiometry and corresponding to the molar ratio P : S = 3 : 5, was 89.4 mass fractions of H_2SO_4 per 100 mass fractions of apatite. The content of $CO(NH_2)_2$ was varied within the range 10–40 wt % relative to the mass of the liquid fraction. The duration of decomposition was 30 min.

The decomposition yields well-fluid suspensions; however, separation of the solid and liquid phases is difficult, and, therefore, the suspensions obtained were diluted with water and filtered for further analyses. The precipitate was washed with water to pH 5–6 and dried at 95°C to constant weight. In parallel, in order to study the additional decomposition of apatite in drying, the forming suspensions were dried at 95°C to constant weight without preliminary separation. The content of biologically available and total P_2O_5 was determined in the dried sulfur and precipitate, and that of water-soluble P_2O_5 and carbamide, in an aqueous extract from the dried sulfur and in the filtrate. The chemical analysis was performed by the standard procedures [3].

The results of these analyses were used to find the basic technological parameters of the process. The decomposition coefficients were calculated both from the amount of P_2O_5 soluble in water and citric acid, i.e., biologically available P_2O_5 (K_1), and from the difference between the total P_2O_5 and that soluble in citric acid, i.e., from the amount of biologically unavailable P_2O_5 (K_2). After the dilution with water, filtration, and washing and drying of the precipitate

$$K_{1f} = (P_2O_{5\,aq} + P_2O_{5\,b.a}^{pr})/P_2O_{5\,init}, \quad (1)$$

$$K_{2f} = 1 - (P_2O_{5\,tot}^{pr} - P_2O_{5\,b.a}^{pr})/P_2O_{5\,init}; \quad (2)$$

and after drying of the suspension

$$K_{1s} = P_2O_{5\,b.a}/P_2O_{5\,init}, \quad (3)$$

$$K_{2s} = 1 - (P_2O_{5\,tot} - P_2O_{5b.a})/P_2O_{5\,init}, \quad (4)$$

with the following designations for the content of phosphorus(V) oxide: $P_2O_{5\,init}$, in a weighed portion of apatite; $P_2O_{5\,aq}$, water-soluble; $P_2O_{5b.a}^{pr}$ and $P_2O_{5tot}^{pr}$, biologically available and total in dried precipitate; and $P_2O_{5\,b.a}$ and $P_2O_{5\,tot}$, biologically available and total in dried suspension; the contents of all forms of phosphorus(V) oxide can be expressed in any identical units.

Data on the loss of mass in drying and the results obtained in analysis of dried suspensions for the content of carbamide were used to estimate the mass of water remaining in the suspension (H_2O_{res}) on the assumption that the loss of mass in drying is constituted by loss of H_2O and CO_2 formed in conversion of carbamide:

$$m(H_2O_{res}) = m(H_2O_{init}) - \Delta m + m(CO_2) - m(H_2O_r), \quad (5)$$

where $m(H_2O_{init})$ is the total mass of water in the mixture of the starting substances (g); Δm, loss of the suspension mass in drying (g); $m(CO_2)$, mass of CO_2 formed in conversion of carbamide (g); and $\Delta m(H_2O_r)$, mass of water entering into the reaction of carbamide hydrolysis (g).

The resulting samples of dried suspensions and precipitates were studied by the methods of X-ray phase analysis (XPA) and IR spectroscopy. The X-ray study was performed using a Bruker D8 Advance X-ray diffractometer. The phase composition of the samples was determined using the database [4]. IR bands were assigned using the reference book [5]. The results of chemical analyses of the filtrates and precipitates and the process parameters calculated from these data are listed in Table 1.

The deviation of the total amount of P_2O_5 found in the filtrate and precipitate from the initial amount of P_2O_5 in apatite is 0.1–2.5%, the decomposition

Table 1. Results of a study of the apatite decomposition by sulfuric acid, followed by dilution of the suspension with water, filtration, and washing and drying of the precipitate

Process parameter	Initial content of $CO(NH_2)_2$ in the liquid phase, wt %					Process parameter	Initial content of $CO(NH_2)_2$ in the liquid phase, wt %				
	0	10	20	30	40		0	10	20	30	40
Filtration of the suspension immediately after the dilution						Filtration of the suspension 5 days after the dilution					
Content of phosphorus forms (%) relative to $P_2O_{5\,init}$:						Content of phosphorus forms (%) relative to $P_2O_{5\,init}$:					
$P_2O_{5\,aq}$	43.7	29.7	22.3	17.5	20.6	$P_2O_{5\,aq}$	69.5	76.0	66.4	66.2	50.1
$P_2O_{5\,b.a}^{pr}$	0.4	0.2	0.5	2.4	0.6	$P_2O_{5\,b.a}^{pr}$	0.9	0.7	1.4	1.4	1.7
$P_2O_{5\,tot}^{pr}$	56.6	67.9	75.2	84.2	80.1	$P_2O_{5\,tot}^{pr}$	31.5	26.0	35.8	34.9	49.8
$P_2O_{5\,tot}^{pr} - P_2O_{5\,b.a}^{pr}$	56.2	67.7	74.7	81.8	79.5	$P_2O_{5\,tot}^{pr} - P_2O_{5\,b.a}^{pr}$	30.6	25.3	34.4	33.5	48.1
$P_2O_{5\,aq} + P_2O_{5\,tot}^{pr}$	100.3	97.6	97.5	101.7	100.7	$P_2O_{5\,aq} + P_2O_{5\,tot}^{pr}$	100.9	102.0	102.2	101.1	99.9
Content of $CO(NH_2)_2$ (%) relative to the initial value		103.0	104.0	104.2	103.6	Content of $CO(NH_2)_2$ (%) relative to the initial value		97.0	95.4	97.3	97.7
K_{1f}, %	44.1	29.9	22.8	19.9	21.2	K_1, %	70.4	76.7	67.8	67.6	51.8
K_{2f}, %	43.8	32.3	25.3	18.2	20.5	K_2, %	69.4	74.7	65.6	66.5	51.9

coefficients calculated from analytical data for the filtrates (K_1) and precipitates (K_2) differ by 0.1–2.2%; the amount of carbamide in the filtrate differs from the initial value by 2.3–4.6%, which confirms the reliability of the results obtained.

Comparison of the data obtained in filtration of suspensions immediately after the end of decomposition and a week after the dilution shows that further decomposition of apatite occurs in the diluted suspension. Therefore, the process of separation of the solid and liquid phases was evaluated immediately after the decomposition was complete.

As follows from an analysis of the data in Fig. 1a, the distribution of phosphorus among various forms strongly varies with the content of carbamide. As the amount of carbamide grows, the fraction of P_2O_5 in the liquid phase decreases, and that in the solid phase, increases, which indicates that the content of water-soluble forms becomes lower. In this case, the content of biologically available phosphates in

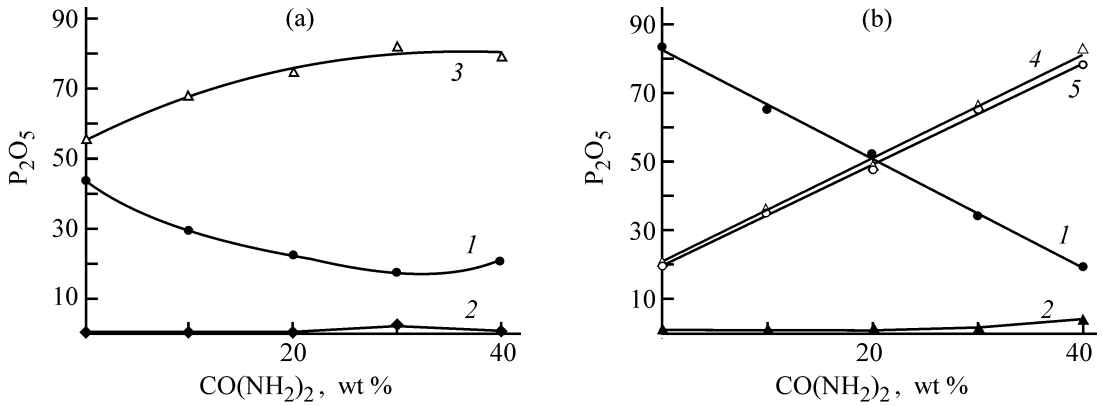


Fig. 1. Effect of the content of carbamide on the phosphorus distribution (in percent relative to P_2O_{5init}) among various forms in apatite decomposition by sulfuric acid. Suspension: (a) filtered immediately after the dilution and (b) dried. Form of phosphorus: (*1*) P_2O_{5aq}, (*2*) $P_2O_{5\,b.a}^{pr}$, (*3*) $P_2O_{5\,tot}^{pr} - P_2O_{5\,b.a}^{pr}$, (*4*) $P_2O_{5tot} - P_2O_{5aq}$, and (*5*) $P_2O_{5tot} - P_2O_{5b.a}$.

Table 2. Results of a study of apatite decomposition by sulfuric acid, followed by drying of the suspension

Process parameter	Initial content of $CO(NH_2)_2$ in the liquid phase, wt %				
	0	10	20	30	40
Drying duration, h	24	24	20	20	16
Loss of mass in drying, % relative to the suspension mass	30.2	25.9	20.1	10.3	4.3
Content of $CO(NH_2)_2$, % relative to the initial value		97.8	95.3	96.5	92.0
Loss of $CO(NH_2)_2$ in drying, g		0.04	0.18	0.21	0.64
Loss of H_2O, % relative to H_2O_{init}	84.8	86.8	85.6	60.8	34.6
H_{2res}, g	1.67	1.18	1.00	1.95	1.95
Content of phosphorus forms, % relative to $P_2O_{5\,init}$:					
$P_2O_{5\,aq}$	82.7	65.5	52.4	34.1	19.5
$P_2O_{5\,b.a}$	83.8	66.6	53.6	35.9	23.8
$P_2O_{5\,tot}$	103.2	101.8	101.3	100.8	101.9
$P_2O_{5\,b.a} - P_2O_{5\,aq}$	1.1	1.1	1.2	1.8	4.3
$P_2O_{5\,tot} - P_2O_{5\,b.a}$	19.4	35.2	47.7	64.9	78.1
$K_{1\,s}$, %	83.8	66.6	53.6	35.9	23.8
$K_{2\,s}$, %	80.6	64.8	52.3	35.1	21.9

the precipitate is low and independent of the presence of carbamide. As can be seen from an analysis of the curves (Fig. 2) describing the variation of the extent to which raw materials decompose, the decomposition coefficient K_{1f} decreases from 44.1 to 21.2%, and K_{2f}, from 43.8 to 20.5%, i.e., by more than a factor of 2, as the content of carbamide increases to 40%. This suggests that the decomposition is impaired in the presence of carbamide.

It is known that a strong change in the phase composition and basic process parameters is observed in the stage of drying of phosphoric acid suspensions in flow production of phosphorus-containing fertilizers: in particular, in an apparatus with a drum granulator-drier. Therefore, analysis of how carbamide affects the composition and basic technological parameters of dried phosphoric acid suspensions is of scientific and practical interest. Dried carbamide-containing suspensions are tarry products, which is natural in view of their high acidity. The results of the analysis and the process parameters calculated from these data are listed in Table 2.

It was found that the loss of carbamide increases as its initial content in the system becomes higher and this dependence is nonlinear, which indicates that hydrolysis partly proceeds by the scheme

$$CO(NH_2)_2 + 2H_2O \rightarrow (NH_4)_2CO_3.$$

The data obtained confirm that additional decomposition of phosphate raw material occurs in drying of phosphoric acid suspensions, which is indicated by the increase in the decomposition coefficient. However, the tendency toward a decrease in the degree of its decomposition and in the content of water-soluble forms of phosphorus in the presence of carbamide is preserved (Table 2, Figs. 1b and 2), and, at a carbamide content of 40 wt %, the additional decomposition of the raw material in the course of drying virtually ends.

It is known that a decrease in the solubility of calcium phosphates is promoted by all cations neutraliz-

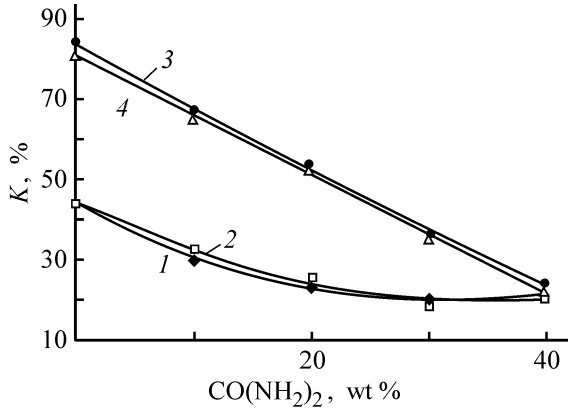


Fig. 2. Effect of the content of carbamide on the process of sulfuric acid decomposition of natural phosphates (*K*) Decomposition coefficient. Calculation of *K* from the amount of P_2O_5: (*1*) biologically available immediately after decomposition (K_{1f}), (*2*) biologically unavailable immediately after decompositions (K_{2f}), (*3*) biologically available in dried suspensions (K_{1s}), and (*4*) biologically unavailable in dried suspensions (K_{2s}).

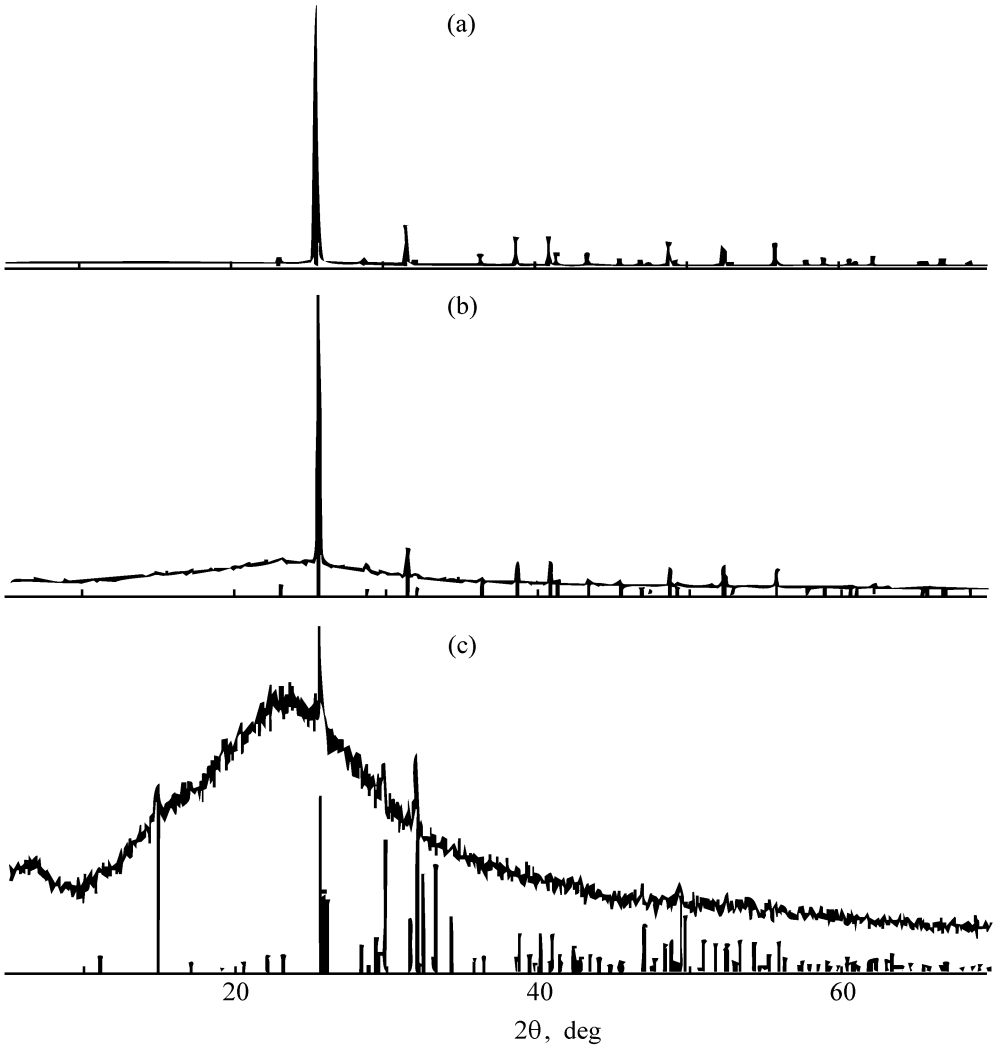


Fig. 3. X-ray diffraction patterns of suspensions obtained in sulfuric acid decomposition of apatite. (2θ) Bragg angle. Amount of carbamide introduced in the decomposition stage (wt %): (a) 10, (b) 20, and (c) 40.

ing the acid, which leads to an increase in pH and decrease in the activity of hydrogen ions, a_{H^+} [6]. According to [7], the rate of apatite dissolution is directly proportional to a_{H^+}. Because carbamide is a weak base, the solution pH increases in its presence, which leads to a decrease in the rate and degree of decomposition. Additional neutralization of the acid in the course of the process is possible as a result of partial hydrolysis of carbamide to give ammonium ions in the stage of drying of the phosphoric acid suspension.

It is known that carbamide can form salt-like compounds with acids and complex compounds with salts. Carbamide can react with components present in the system in decomposition of apatite with sulfuric acid to give the following compounds: $H_2SO_4 \cdot CO(NH_2)_2$, $H_2SO_4 \cdot 2CO(NH_2)_2$ [8]; $H_3PO_4 \cdot CO(NH_2)_2$ [9]; $H_2SiF_6 \cdot 2CO(NH_2)_2$, $H_2SiF_6 \cdot 4CO(NH_2)_2$ [10]; $CaSO_4 \cdot 4CO(NH_2)_2$ [11]; $MgSO_4 \cdot CO(NH_2)_2 \cdot 2H_2O$, $MgSO_4 \cdot 4CO(NH_2)_2 \cdot H_2O$ [12]; $Al_2(SO_4)_3 \cdot CO(NH_2)_2 \cdot 2H_2O$ [13]. In the opinion of the authors of [8], when carbamide sulfates are formed, the strong inorganic acid neutralizes the weak base via protonation or direct addition to its molecule. If the formation of the above compounds in the system under study is confirmed, this phenomenon is the main reason why the degree of sulfuric acid decomposition of phosphate raw material decreases in the presence of carbamide. However, not all of these compounds will equally affect the process of acid decomposition of natural phosphates. In particular, carbamide phosphate dissolves in water incongruently [8], and, therefore, the formation of the compound $H_3PO_4 \cdot CO(NH_2)_2$ probably has no direct negative effect on the process

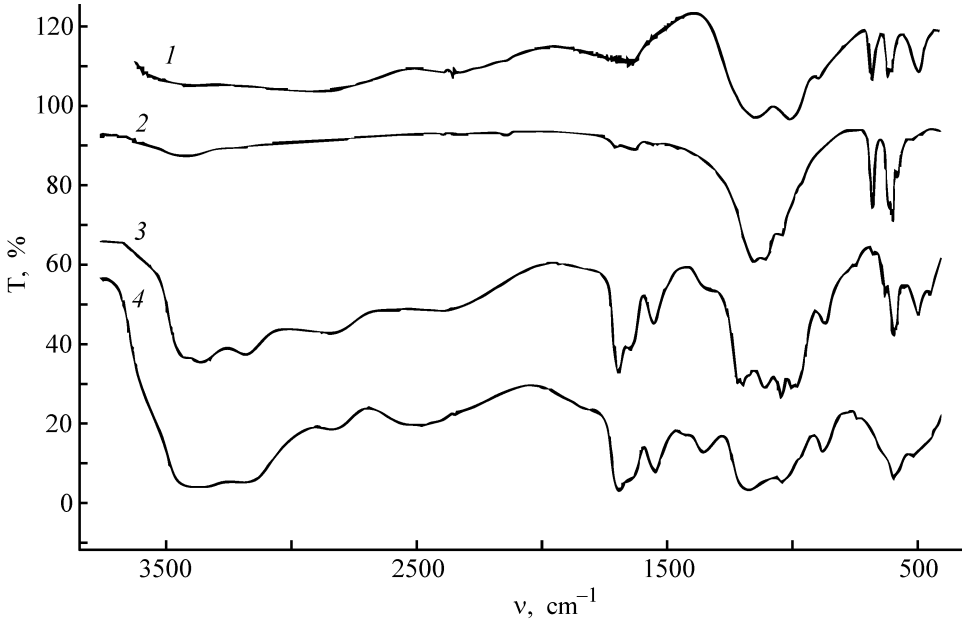


Fig. 4. IR spectra of products formed in apatite decomposition with sulfuric acid (dried suspensions) with introduction of carbamide. (T) Transmission and (ν) wave number; the same for Fig. 5. Amount of carbamide introduced in the decomposition stage (wt %): (*1*) 0, (*2*) 10, (*3*) 20, and (*4*) 40.

of apatite decomposition. An admixture of H_2SiF_6 makes larger the decomposition coefficient [14]. In the system H_2SiF_6–$CO(NH_2)_2$–H_2O, two congruently soluble compounds, $H_2SiF_6 \cdot 2CO(NH_2)_2$ and $H_2SiF_6 \cdot 4CO(NH_2)_2$, are formed [10], with the result that the positive effect of H_2SiF_6 on the decomposition process can be weakened. The process of sulfuric acid decomposition of apatite is strongly affected by the size and shape of the forming crystals of calcium sulfate and its solubility. Of particular interest in this context is the compound $CaSO_4 \cdot 4CO(NH_2)_2$ [11], whose formation can change the equilibrium conditions and the suspension properties. With other sulfates, carbamide forms adducts of different compositions; in particular, carbamide can react with impurities present in the system to give the compounds $MgSO_4 \cdot CO(NH_2)_2 \cdot 2H_2O$, $MgSO_4 \cdot 4CO(NH_2)_2 \cdot H_2O$ [12], and $Al_2(SO_4)_3 \cdot CO(NH_2)_2 \cdot 2H_2O$ [13]. The compounds of magnesium and aluminum mostly affect the size and shape of calcium sulfate crystals [15], and, therefore, formation of these adducts can change these parameters; however, their effect on the decomposition process will be insignificant.

To understand the observed specific features of the acid decomposition of natural phosphates in the presence of carbamide, samples of precipitates and suspensions obtained in the decomposition stage were subjected to an X-ray phase analysis and studied by IR spectroscopy. According to the XPA data, the main crystalline phase present in washed and dried precipitates after dilution and filtration of suspensions formed in apatite decomposition with sulfuric acid is $CaSO_4$, which seems to be natural. In addition, the precipitates contain the starting apatite, whose relative amount increases with the content of carbamide because of the decrease in the degree of decomposition of the raw material. No carbamide or its compounds were found in the precipitates, which confirms its presence in the suspensions under study in the liquid phase.

The X-ray diffraction patterns of samples of dried sulfuric acid suspensions with an initial carbamide content of up to 20 wt % contain $CaSO_4$ reflections (Fig. 3). The reflections related to apatite have an exceedingly low intensity. In the X-ray diffraction pattern of a sample containing 40% carbamide, the presence of apatite is manifested to a greater extent and, in addition, there are reflections associated with $CaSO_4 \cdot 0.5H_2O$. As the content of carbamide grows, the background peaked at around $2\theta = 23°$ becomes more pronounced as a result of the increase in the amount of the amorphous phase.

Similar changes are also observed in analysis of the IR spectra of these suspensions. The application of IR spectroscopy made it possible to reveal changes occurring in the course of sulfuric acid decomposition in the presence of carbamide and to explain why the degree of decomposition of phosphate raw materials decreases (Figs. 4 and 5).

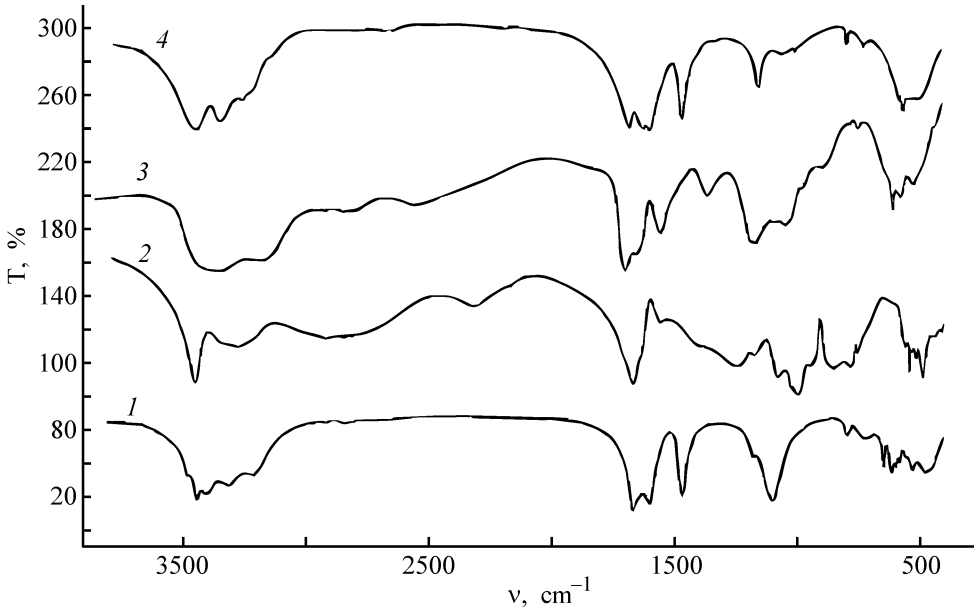


Fig. 5. IR spectra of carbamide adducts. (*1*) $4CO(NH_2)_2 \cdot CaSO_4$, (*2*) $CO(NH_2)_2 \cdot H_3PO_4$, (*3*) $2CO(NH_2)_2 \cdot H_2SO_4$, and (*4*) $CO(NH_2)_2$.

The frequency range best suitable for analysis is 1700–1400 cm^{-1}. In this range, carbamide shows absorption at 1680, 1625, 1598, and 1467 cm^{-1}. The IR spectra of a carbamide-free sample and that with 10% $CO(NH_2)_2$ contain bands characteristic of $CaSO_4$ (1153, 674, 615, 595 cm^{-1}) [5]. The IR spectra of samples with a higher content of carbamide show, in addition to the bands characteristic of calcium sulfate and apatite, also bands in the frequency range of vibrations of the N–H, C=O, and C–N bonds (3500–3200 and 1700–1400 cm^{-1}) and, in particular, bands at 1699, 1650–1655, 1557 cm^{-1} (Fig. 4), which differ from the bands characteristic of carbamide and its adducts with calcium sulfate and phosphoric acid. For interpretation of these data, model compounds of carbamide with H_2SO_4, H_3PO_4, and $CaSO_4$ were synthesized and their IR spectra were recorded (Fig. 5). A comparison of the IR spectra of these compounds led to a conclusion that dried suspensions contain carbamide sulfate (3358, 3185, 1700, 1655, and 1558 cm^{-1}), whose formation is the main reason why the degree of apatite decomposition with sulfuric acid decreases in the presence of carbamide.

CONCLUSIONS

(1) The rate and degree of sulfuric acid decomposition of natural phosphates in nonthickening suspensions decrease if carbamide is introduced together with the acid in the initial stage of the process.

(2) The main reason for the decrease in the degree of decomposition is that an adduct of carbamide sulfate is formed.

(3) When organizing a technological process for production of sulfur-containing integrated fertilizers, it is recommended to introduce carbamide after the stage of acid decomposition into acid or partly ammonized suspensions.

(4) Introduction of carbamide strongly affects changes in the phase composition of the forming products and the content and distribution of various forms of phosphorus. The process of adduct formation leads to deceleration of nitrogen dissolution from the fertilizers obtained, which allows their classification with prolonged-action fertilizers.

REFERENCES

1. Zhmai, L.A. and Sidenko, O.M., *Nauch.-Tekhn. Nov.*, 2004, Special issue 5(8), pp. 76–81.
2. Lapa, V.V., *Materialy Respublikanskoi nauchno-prakticheskoi konferentsii, Minsk, 29 sentyabrya 2005 goda* (Proc. Republ. Sci.-Pract. Conf., Minsk, September 29, 2005), Minsk, 2005, pp. 5–9.
3. Vinnik, M.M. et al., *Metody analiza fosfatnogo syr'ya, fosfornykh i kompleksnykh udobrenii, kormovykh fosfatov* (Methods for Analysis of Phosphate Raw Materials, Phosphate and Integrated Fertilizers, and Forage Phosphates), Moscow: Khimiya, 1975.
4. CPDS International Centre for Diffraction Data 2003.

5. Zharskii, I.M., Vorob'ev, N.I., Mel'nikova, R.Ya., et al., *Svoistva i metody identifikatsii veshchestv v neorganicheskoi tekhnologii* (Properties and Methods for Identification of Substances in Inorganic Technology), Minsk: Fond Fundament. Issled., 1996.
6. Shapkin, M.A., Zavertyaeva, T.I., Zinyuk, R.Yu., and Guller, B.D., *Dvoinoi superfosfat: Tekhnologiya i primeneniya* (Double Superphosphate: Technology and Application), Leningrad: Khimiya, 1987.
7. Orekhov, I.I. and Vlasova, T.L., *Izv. Vyssh. Uchebn. Zaved., Khim. Khim. Tekhnol.*, 1976, vol. 19, no. 4, pp. 615–617.
8. Nurakhmetov, N.N. and Beremzhanov, B.A., *Zh. Neorg. Khim.*, 1978, vol. 23, no. 2, pp. 504–514.
9. Kaganskii, I.M., Mukhlya, G.S., Khardamova, V.M., and Naumov, V.A., *Zh. Prikl. Khim.*, 1964, vol. 37, no. 5, pp. 1111–1116.
10. Beremzhanov, B.A., Nurakhmetov, N.N., Tashenov, A., and Suyundikova, F.O., *Zh. Neorg. Khim.*, 1987, vol. 32, no. 1, pp. 256–259.
11. Lehr, J.R., Brown, E.H., Frazier, A.W., et al., *Chem. Eng. Bull.*, 1967, no. 6, pp. 37.
12. Tembatov, B.K., *Uchen. Zapis. Mosk. Obl. Pedagog. Ins–ta*, 1969, no. 236, pp. 22–25.
13. Safiulin, N.Sh., Moshoshina, M.N., and Bobyrenko, Yu.Ya., *Zh. Prikl. Khim.*, 1973, vol. 46, no. 7, pp. 1625–1627.
14. Karmyshev, V.F., *Khimicheskaya pererabotka fosforitov* (Chemical Processing of Phosphorites), Moscow: Khimiya, 1983.
15. Pozin, M.E., *Tekhnologiya mineral'nykh solei, v 2 chastyakh* (Technology of Mineral Salts, in 2 parts), Leningrad: Khimiya, 1974, part 2.

ISSN 1070-4272, Russian Journal of Applied Chemistry, 2008, Vol. 81, No. 2, pp. 196–201. © Pleiades Publishing, Ltd., 2008.
Original Russian Text © A.K. Trofimchuk, T.G. Maglevanaya, I.M. Shkoda, A.Ya. Gritzkiv, 2008, published in Zhurnal Prikladnoi Khimii, 2008, Vol. 81, No. 2, pp. 207–212.

INORGANIC SYNTHESIS AND INDUSTRIAL INORGANIC CHEMISTRY

Optimization of the Conditions of Sorption of Molybdenum(VI), Tungsten(VI), and Vanadium(V) on Modified Silica Gels with the Use of Bromopyrogallol Red and Surfactants

A. K. Trofimchuk, T. V. Maglevanaya, I. M. Shkoda, and A. Ya. Gritzkiv

Shevchenko National University, Kiev, Ukraine

Ovcharenko Institute of Biocolloid Chemistry, National Academy of Sciences of Ukraine, Kiev, Ukraine

Received May 14, 2007

Abstract—Sorption of molybdenum(VI), tungsten(VI), and vanadium(V) on amino silica gels in the presence of an anionic dye, bromopyrogallol red, and cationic surfactants fixed on the sorbent surface or present in solution was studied.

DOI: 10.1134/S1070427208020079

Basic principles of interactions in a system constituted by a metal, an organic dye, and a surfactant in solution have been described in the literature [1–6]. They primarily consist in that the hydrate shell of a metal (M) ion is loosened, i.e., the interaction between water molecules becomes stronger, and the binding between water and the metal, weaker. This leads to an increase in the number of coordinated ligands, and addition of a larger number of ions of the cationic surfactant to the organic dye bound into a complex with the metal ion. These factors cause an increase in the absorption intensity and, as a rule, lead to a bathochromic shift of the absorption spectra of the solutions and to a shift of the complexation pH into a more acid region.

It would be expected that these factors will be also manifested in a system constituted by M, organic dye, and surfactant in the case when complexation processes occur at the surface of dispersed silicas. At the same time, limitations on the degrees of freedom of fixed molecules of a surfactant and(or) an organic dye may result in that interactions in the heterogeneous system under consideration will differ from those in a homogeneous system.

The aims of this study were as follows: (1) to find the optimal conditions of sorption of molybdenum(VI), tungsten(VI), and vanadium(V) on silica gels with aminopropyl (NH_2-C) or ethylenediamine (en-C) groups covalently bound to the surface, with bromopyrogallol red (BPR) dye fixed on the surface or present in solution together with the metal being sorbed and a cationic surfactant, dodecylpyridinium chloride (DPC); and (2) to determine the optimal conditions of sorption of molybdenum(VI), tungsten(VI), and vanadium(V) on a silica gel with a polymeric cationic surfactant, polyhexamethyleneguanidinium chloride (PHMGC), deposited on its surface, in the presence of BPR fixed on the surface or present in solution together with the metal being sorbed.

The choice of PHMGC is due to its high sorption capacity on the silica gel surface and to the combination of properties of a surfactant and an anion exchanger.

Thus, the following systems were studied in order to optimize complexation-related sorption of metals: systems with amino silica gels (Am-C): Am-C (surface) and M^{n+} (solution), [Am-C + BPR] (surface) and M^{n+} (solution), Am-C (surface) and [BPR + M^{n+}] (solution), Am-C (surface) and [BPR + DPC + M^{n+}] (solution); and those with a silica gel modified with PHMGC (PHMGC-C): [PHMGC-C + BPR] (surface) and M^{n+} (solution), PHMGC-C surface) and [BPR + M^{n+}] (solution).

The charges and forms of existence of the metal ions are omitted for the sake of simplicity.

EXPERIMENTAL

The starting solutions of molybdenum(VI), tungsten(VI), and vanadium(V) were prepared by dissolu-

tion of precisely weighed portions of $(NH_4)_6Mo_7O_{24} \cdot 4H_2O$, $Na_2WO_4 \cdot 2H_2O$, and $Na_3VO_4 \cdot 12H_2O$ in distilled water by the procedures described in [7]. The working solutions with lower metal concentrations were obtained by dilution of the starting solutions. Aqueous solutions of BPR (1×10^{-4} M) and DPC (1×10^{-3} M) were prepared with twice-distilled water immediately before use.

Amino silica gels were synthesized by the method described in [8] from Silica Gel 60 (Merck), with a specific surface area found from low-temperature adsorption of nitrogen by the Brunauer–Emmett–Teller (BET) technique to be 260 $m^2 g^{-1}$ and average pore size of 12 nm. As modifiers served 3-aminopropyltriethoxysilane and 3-diethyldiaminopropyltroethoxysilane (Merck) without additional purification. The concentrations of grafted amino groups, found by elemental analysis for nitrogen and potentiometric titration with HCI on the surface of NH_2-C and en-C, were 0.88 and 0.70 mmol g^{-1}, respectively.

The concentration of the metals in the aqueous solution was found using a Spectroflame Modula optical atomic-emission spectrometer with inductively coupled plasma, from the lines of molybdenum (281.615 nm), tungsten (207.911 nm), and vanadium (311.071 nm).

The acidity of the solutions was monitored with an Ionometr I-130.2m.1 pH-meter with a glass electrode.

Diffuse reflection spectra of the sorbates in the spectral range 12 000–27 000 cm^{-1} were recorded with a UV-VIS Specord M40 spectrophotometer.

BPR was fixed on amino silica gels by bringing them in contact with a 0.05 M solution of BPR in H_2SO_4 under vigorous agitation for 10 min (quantitative sorption of BPR on amino silica gels occurs at pH 0.8–5.6 in 2–3 min). The samples obtained were filtered off; air-dry samples were used for further sorption of the metals from solution.

The sorption of the metals on the modified silica gels was studied under static conditions. For this purpose, precisely weighed portions of a sorbent (0.2 g) were placed in vessels with ground-in stoppers and poured-over with 25 ml of a metal salt solution of a known concentration with necessary ingredients. The resulting suspensions were agitated with a magnetic stirrer for a required time. The sorbent was separated from the solution by filtration and the equilibrium metal concentrations and solution pH values were measured in the filtrate.

The generalized experimental data on the sorption of Mo(VI), W(VI), and V(V) on NH_2-C (Figs. 1a–1c,

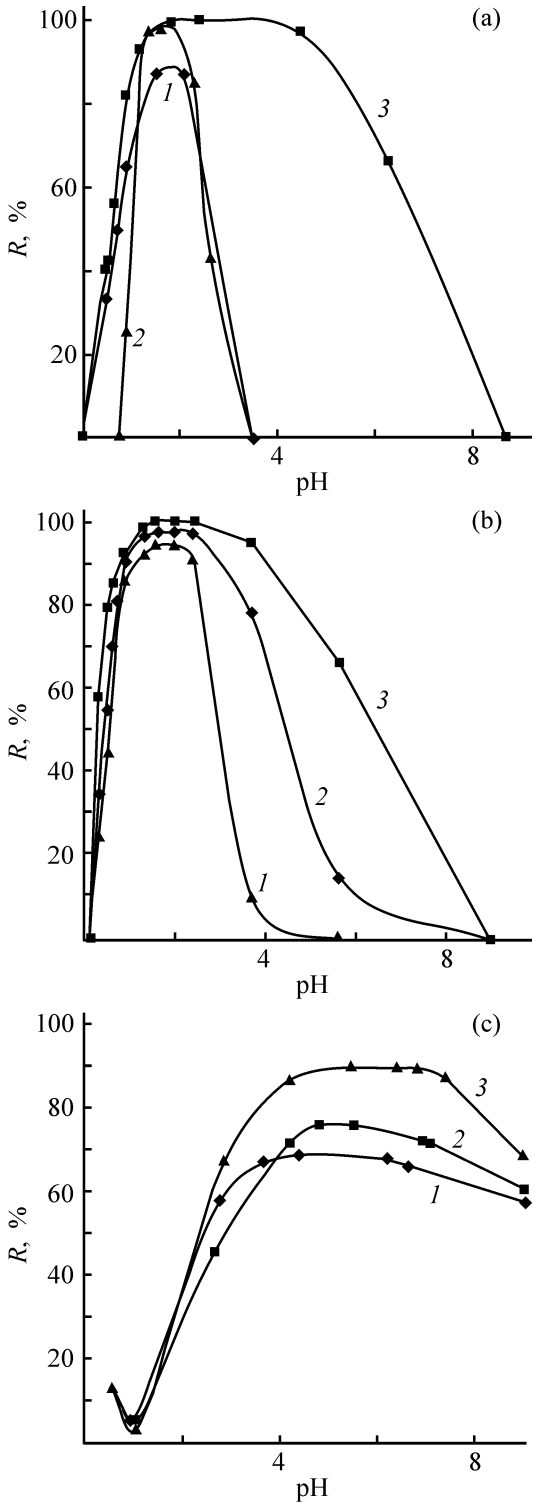


Fig. 1. Degree R of sorption of (a) Mo(VI), (b) W(VI), and (c) V(V) on NH_2-C in the presence of BPR and DPC vs. pH. $c_{Mo} = 2.0 \times 10^{-5}$ M, $c_{BPR} = 4.0 \times 10^{-5}$ M, $c_{DPC} = 4.0 \times 10^{-5}$ M, $m_{sorb} = 0.2$ g. (a) (*1*) Mo(VI), (*2*) Mo(VI)–BPR, (*3*) Mo(VI)–BPR–DPC; (b) (*1*) W(VI), (*2*) W(VI)–BPR, (*3*) W(VI)–BPR–DPC; (c) (*1*) V(V), (*2*) V(V)–BPR, (*3*) V(V)–BPR–DPC.

Sorption of Mo(VI), W(VI), and V(V) on en-C in relation to modification of the sorbent and chemical composition of the solution

Sorption conditions	Optimal-sorption pH	Degree of sorption under the optimal conditions
Mo(VI):		
solution of the metal (M) on Am-C	1.8–2.1	89
M solution on Am-C with sorbed BPR	1–3	90
M solution on DPC–Am-C with sorbed BPR	1–3	95
M solution on BPR–Am-C	0.8–3	>99
M solution on BPR and DPC–Am-C	1–5	>99
W(VI):		
solution of the metal (M) on Am-C	1.8–2.2	92
M solution on Am-C with sorbed BPR	0.5–3.5	93
M solution on DPC–Am-C with sorbed BPR	1–3	>99
M solution on BPR–Am-C	0.8–3.0	>99
M solution on BPR and DPC–Am-C	0.5–5	>99
V(V):		
solution of the metal (M) on Am-C	5–9	89
M solution on Am-C with sorbed BPR	6–9	90
M solution on DPC–Am-C with sorbed BPR	7–9	95
M solution on BPR–Am-C	6–9	96
M solution on BPR and DPC–Am-C	6–9	>99

respectively) and on en-C (see table) show that the degree of metal recovery on NH_2-C is lower, compared with NH_2-C with fixed BPR. This points to a somewhat higher stability of complex compounds of the metals with BPR, compared with aminopropyl groups grafted to the silica gel surface.

Upon introduction of DPC into solutions of metals, the sorption activity of Am-C with fixed BPR grows further. This increase is due to the possible formation, in the presence of DPC, of more stable complexes of metals with BPR on the surface of silicon dioxide for the same reasons why this occurs in solution, when a cationic surfactant has no less than 12 carbon atoms in the hydrophobic chain.

The complexes Mo(VI)–BPR and W(VI)–BPR are not sorbed on the surface of unmodified silica gel and do not color it. The strongest effect of sorption concentration is observed in sorption of Mo(VI), W(VI), and V(V) on amino silica gels from metal solutions in the presence of BPR and DPC. In all probability, this is due to the optimal conditions of metal complexation with BPR and to the specific effect of DPC on their hydrate shell, which improves the stability of the complexes being formed and, consequently, extends the pH range of complexation.

As can be seen in Fig. 1c, the degree of vanadium sorption on NH_2-C decreases as pH grows in the range 0–1 and, as the acidity decreases further, again starts to increase. The same pattern is observed in the case of V(V) sorption on en-C. This occurs because V(V) exists in strongly acidic solutions as mononuclear particles. At pH > 2, the overwhelming majority of vanadium(V) is in the form of VO_2^+, VO_3^-, and $H_2V_{10}O_{28}^{4-}$. According to [9], BPR forms under these conditions complexes with VO_2^+ and $H_2V_{10}O_{28}^{4-}$. As pH increases, coordination of BPR to vanadium(V), which also exists in the form of other polynuclear species, becomes possible. It should be noted that both in sorption of metal ions on amino silica gels with BPR fixed on their surface, which occurs by the scheme

$$\text{–}NH_3^+ \cdot {}^-O_3S\text{–BPR} + M^{n+} = \text{–}NH_3^+ \cdot {}^-O_3S\text{–BPR}\cdots M^{n+}, \quad (1)$$

and in sorption of metal complexes with BPR

$$\text{–}NH_3^+ + {}^-O_3S\text{–BPR}\cdots M^{n+} = \text{–}NH_3^+ \cdot {}^-O_3S\text{–BPR}\cdots M^{n+}, \quad (2)$$

or

$$\text{–}NH_3^+ + {}^-O_3S\text{–BPR}\cdots M^{n+}\cdots {}^-O_3S\text{–BPR} = \text{–}NH_3^+ \cdot {}^-O_3S\text{–BPR}\cdots M^{n+}\cdots {}^-O_3S\text{–BPR}, \quad (3)$$

the time in which the sorption equilibrium is attained is 5–7 min. This enables sorption concentration of metals from the solutions under consideration in both static and dynamic conditions.

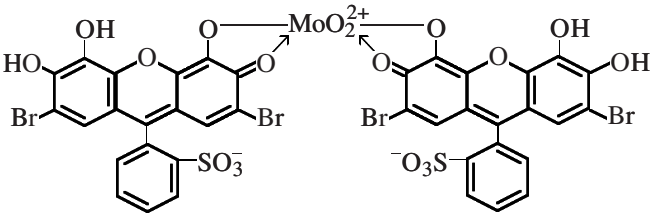
It is known [10] that, on passing from strongly acidic to strongly alkaline media, the coloration of BPR in solution successively changes from yellow, to orange, red, violet, and blue, with the peak of the absorption spectra of BPR shifted from 450 to 600 nm. The peaks of the absorption spectra of Mo(VI), W(VI), and V(V) complexes with BPR in solution virtually coincide with those of the absorption spectra of the dye itself. The diffuse-reflection spectra of the BPR sorbates on amino silica gels have a peak at 17000–18000 cm^{-1} (λ = 555–588 nm), which is shifted with pH to a lesser extent, compared with aqueous solutions. Introduction of DPC into solution leads to formation of different-ligand complexes characterized by a shift to longer wavelengths (16000 cm^{-1}, λ = 625 nm). A similar pattern is observed in diffuse-reflection spectra of complexes with tungsten(VI), which are shifted to longer wavelengths upon introduction of DPC (17000 cm^{-1}, λ = 588 nm).

The bathochromic effect is due to the influence of surfactants on the auxochromic groups of BPR, which are bound by a common system of conjugated bonds of the reagent and are not involved in the complexation with a metal [11]. The formation of associates at ionized auxochromic groups of the reagents may also be accompanied by hypsochromic effects. The reason is that the complexation occurs in the hydrophobic core of a micelle and is accompanied by a pronounced dehydration of the components in the surface layer of the sorbent. In particular, such a hypsochromic effect is observed in the case of V(V) complexation. The diffuse-reflection spectra of V(V)–BPR complexes preliminarily obtained in solution and adsorbed on the surface of amino silica gels are peaked at around 17000 cm^{-1} (λ = 588 nm). Introduction of DPC into solution gives rise to a complex that shows, in sorption on amino silica gels, an absorption peak at 21000 cm^{-1} (λ = 476 nm). This phenomenon is nontrivial and can be observed in other systems [6].

Molybdenum and tungsten exist in the form of ions MoO_2^{2+} and WO_2^{2+} in acid solutions (pH < 1) and as $MoO_2(OH)^+$ and $WO_2(OH)^+$, $MoO_2(OH)_2$ and $WO_2(OH)_2$, $HMoP_4^-$ and HWO_4^- in weakly acidic solutions (pH 1–4); at pH > 5, MoO_4^{2-} and WO_4^{2-} ions predominate [12].

The method of the equilibrium shift was used to determine the ratios between a metal and BPR in complexes with W(VI) and V(V) in the presence of DPC on the Am-C surface. For the complexes of tungsten and vanadium, M : BPR = 1 : 1 was found. Introduction of a surfactant does not change the ratio between the components of a metal and the dye. BPR interacts with Mo(VI) to give two complexes with λ_{max} = 540 and 630 nm and molar ratios of the components equal to 1 : 1 and 1 : 2, respectively. According to the data of [11], the 1 : 1 complexes are formed by MoO_2OH^+ ions, and the 1 : 2 complexes, by MoO_2^{2+} ions.

With account of the state of the reagent and molybdenum(VI), the following formula can be suggested for the complex formed in a 1 : 2 ratio:

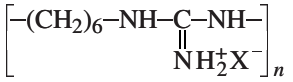


For BPR solvated with dodecylpyridinium chloride, a second complex with absorption peak at ν = 16000 cm^{-1} (625 nm) is characteristically formed.

Thus, use of amino silica gels favors fixation on their surface of anionic dyes or complex compounds of these dyes with metals [Eq. (3)], and introduction of a cationic surfactant with a carbon radical containing no less than 12 carbon atoms into solution improves the strength of the forming mixed-ligand complexes, with their spectral characteristics changed.

It should be noted that Am-C are rather expensive sorbents. Because, in addition, molecules of organic dyes are comparatively large, there fixation on the surface will always leave "free" amino groups, which themselves possess ligand properties and can affect the properties of the resulting analytical form of the reagent. Therefore, anionic dyes are frequently fixed with a quaternary ammonium salt (QAS). Silica gel is modified with QAS under static conditions in toxic organic solvents, for the most part hexane, toluene, or a mixture of these [13], which is an important disadvantage of this sorbate. In addition, QAS are partly soluble in water, especially in acid media, which restricts their applicability area and affects the reproducibility of analytical determinations.

It was suggested to use for fixation on the silica gel surface the salt form of polyhexamethyleneguanidinium (PHMG) of general formula



where n = 30–90, and X is the anion of an inorganic or organic acid.

PHMG salts are macromolecular derivatives of a specific base of guanidine and cationic surfactants.

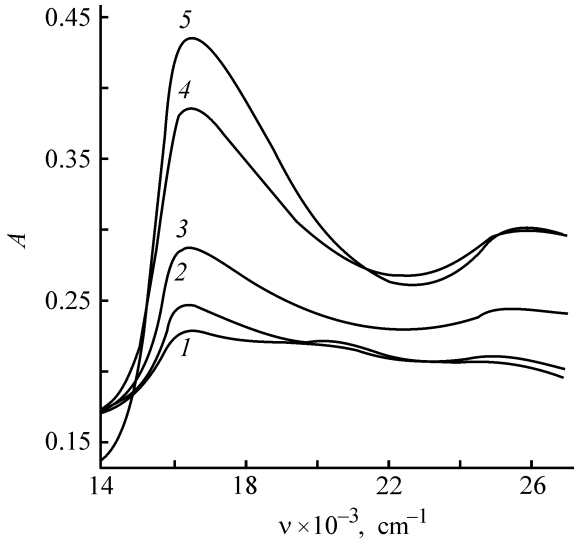


Fig. 2. Diffuse-reflection spectra $A = f(\nu)$ of Mo(VI)–BPR complexes on the surface of silica gels modified with PHMGC on the background of 0.1 N H_2SO_4. $c_{Mo} = 2.0 \times 10^{-5}$ M, $c_{BPR} = 4.0 \times 10^{-5}$ M, $m_{sil} = 0.2$ g. c_{PHMGC} (μg ml^{-1}): (*1*) 0, (*2*) 0.1, (*3*) 0.3, (*4*) 0.5, and (*5*) 0.7.

The convenient spatial arrangement of atoms in the guanidine group creates favorable conditions for formation of multicenter hydrogen bonds, and, therefore, PHMG salts containing a hydrophobic polymethylene chain can serve as good anion exchangers. In view of the aforesaid, it would be expected that PHMG sorption on the silica gel surface will be efficient in aqueous solutions and the sorbate obtained will be convenient for creating an analytical form of the reagent via fixation of anionic dyes. The PHMG sorbate fixed as a salt form on the silica surface has an important advantage over polyamine sorbates, which possess both anion-exchange and ligand properties. Because of the incomplete interaction of amino centers with organic dyes as a result of steric hindrances, silica gels of this kind have the same disadvantages as chemically modified Am-C.

Of the salt forms, it is most appropriate to use PHMGC, which is well soluble in water (50 wt % at 250°C) and is readily available and widely used bactericidal preparation, for modifying the silica gel surface. It was found that quantitative sorption of PHMGC on silica gel occurs in the pH range 0–9 as a result of a corporative interaction of charged PHMG macromolecules with active groups on the silica gel surface. The time in which the sorption equilibrium is attained does not exceed 3 min. The sorbate formed is so stable that it cannot be removed by washing with water in a Soxhlet apparatus for several days.

It is quite understandable that only part of guanidine groups of the polymer are involved in multicenter interaction with the silanol groups of the surface in modification of the silica gel surface with PHMGC (PHMGC-C). "Free" groups of guanidine on the PHMGC-C surface are involved in formation of ionic associates in interaction with anionic dyes by the scheme

$$\left[-(CH_2)_6-NH-\underset{\underset{NH_2^+X^-}{\|}}{C}-NH-\right]_n + {}^-O_3S-R$$

$$\rightarrow \left[-(CH_2)_6-NH-\underset{\underset{NH_2^+\ {}^-O_3S-R}{\|}}{C}-NH-\right]_n \qquad (4)$$

The time in which the adsorption equilibrium is attained is 3–5 min. The complexes of Mo(VI), W(VI), and V(V) with BPR are sorbed on the PHMGC-C surface at the same rate, with the sorption of these metals under the optimal conditions being quantitative.

When the complexes Mo(VI)–BPR and W(VI)–BPR are brought in contact with PHMGC-C, intensely colored ionic associates are formed. These associates are blue, with the maximum absorption at 16 000 cm^{-1} (λ = 625 nm), for molybdenum(VI) and violet, with the maximum absorption at 17 000 cm^{-1} (λ = 588 nm), for tungsten(VI). Thus, PHMGC fixed on the silica gel surface behaves as a cationic surfactant with a hydrocarbon radical containing no less than 12 atoms, despite that 6 methylene units alternate with guanidine groups in the polymeric chain of PHMGC.

As can be seen in Fig. 2, the intensity of absorption by Mo(VI)–BPR complexes increases with the PHMGC concentration sorbed on the surface. The same behavior is observed in sorption of W(VI)–BPR on PHMGC-C. The dependence was found to be linear for Mo(VI)–BPR and W(VI)–BPR complexes at PHMGC concentrations of 0–40 and 0–25 μg per 0.2 g of silica gel, respectively. This fact was used to develop a procedure for sorption-photometric determination of microscopic amounts of PHMGC in aqueous solutions, with sorption processes performed under static or dynamic conditions.

Thus, PHMGC-C is a simple and convenient form for sorption of BPR and its complexes with Mo(VI), W(VI), and V(V). The formation of ionic associates on the surface of PHMGC-C enables fixation of other anionic dyes without changes in their ligand (*o*-oxyquinone groups) centers to create new analytical forms for analysis of inorganic and organic compounds.

CONCLUSIONS

(1) In sorption of molybdenum(VI), tungsten(VI), and vanadium(V) on amino silica gels in the presence of an anionic dye BPR at pH 0.6–7.8, complexes of the metals with BPR are formed on the surface, with M : BPR = 1 : 1 [M = W(VI), V(V)] and 1 : 2 [Mo(VI)].

(2) It is advisable to use polyhexamethyleneguanidinium chloride as a cationic surfactant. This compound also acts as an ion exchanger and favors fixation of anionic dyes, including BPR. Quantitative recovery of molybdenum(VI) and tungsten(VI) on silica gels impregnated with polyhexamethyleneguanidinium chloride occurs at pH 0.5–3.5.

(3) The coloration intensity of sorbed Mo(VI) and W(VI) complexes with BPR depends both on their surface concentration and on the concentration of polyhexamethyleneguanidinium chloride itself, which can be used to develop a procedure for determining microscopic amounts of this compound in water.

REFERENCES

1. Savvin, S.B., Chernova, R.K., Belousova, V.V., et al., *Zh. Anal. Khim.*, 1978, vol. 33, no. 8, pp. 1473–1480.
2. Ivanova, V.I., Mamedova, A.M., and Akhmedov, S.A., *Vestn. Mosk. Gos. Univ.*, 2003, vol. 44, no. 4, pp. 253–257.
3. Ivanova, V.I., Mamedova, A.M., and Akhmedov, S.A., *Vestn. Mosk. Gos. Univ.*, 2004, vol. 45, no. 2, pp. 117–123.
4. Ivanov, V.M. and Mamedova, A.M., *Vestn. Mosk. Gos. Univ.*, 2002, vol. 43, no. 5, pp. 291–296.
5. Chernova, R.K., Amelin, V.G., and Shtykov, S.N., *Zh. Fiz. Khim.*, 1983, vol. 57, no. 6, pp. 1482–1485.
6. Savvin, S.B., Chernova, R.K., and Shtykov, S.N., *Poverkhnostno-aktivnye veshchestva (Analiticheskie reagenty)* [Surfactants (Analytical Reagents)], Moscow: Nauka, 1991.
7. Korostylev, P.P., *Prigotovlenie rastvorov dlya khimiko-analiticheskikh rabot* (Preparation of Solutions for Chemical-Analytical Studies), Moscow: Nauka, 1962.
8. Tarasevich, Yu.I., Trofimchuk, A.K., Legenchuk, A.V., and Ivanova, Z.G., *Kolloid. Zh.*, 2004, vol. 64, no. 1, pp. 78–84.
9. Fadeeva, V.I., Tikhomirova, T.I., Kudryavtsev, G.V., and Yuferova, I.B., *Zh. Anal. Khim.*, 1992, vol. 47, no. 3, pp. 466–477.
10. Ivanov, V.M. and Mamedova, A.M., *Vestn. Mosk. Gos. Univ., 2, Khim.*, 2002, vol. 43, no. 3, pp. 168–173.
11. Savvin, S.B., Chernova, R.K., and Beloliptseva, G.M., *Zh. Anal. Khim.*, 1980, vol. 35, no. 6, pp. 1128–1137.
12. Mokhosoev, M.V. and Shevtsova, N.A., *Sostoyanie ionov molibdena i vol'frama v vodnykh rastvorakh* (State of Molybdenum and Tungsten Ions in Aqueous Solutions), Ulan-Ude: Buryat. Knizhn. 1977.
13. Savvin, S.B. and Mikhailova, A.V., *Zh. Anal. Khim.*, 1996, vol. 51, no. 1, pp. 49–56.

ISSN 1070-4272, Russian Journal of Applied Chemistry, 2008, Vol. 81, No. 2, pp. 202–206. © Pleiades Publishing, Ltd., 2008.
Original Russian Text © L.L. Lobanova, E.V. Batalova, Yu.P. Khranilov, 2008, published in Zhurnal Prikladnoi Khimii, 2008, Vol. 81, No. 2, pp. 213–217.

INORGANIC SYNTHESIS AND INDUSTRIAL INORGANIC CHEMISTRY

Reagent Techniques for Nickel Recovery from Spent Electroless Nickel-Plating Solutions

L. L. Lobanova, E. V. Batalova, and Yu. P. Khranilov

Vyatka State University, Kirov, Russia

Received May 15, 2007

Abstract—A technique for nickel recovery from spent electroless nickel-plating solutions was developed. The process yields nickel sulfate, a source for preparing an electroless nickel-plating solution, and a nickel-containing concentrate.

DOI: 10.1134/S1070427208020080

Many Russian machine-building companies use the high-temperature (90–95°C) electroless nickel-plating in weak-acid solutions. During the process, the solutions are continuously adjusted with respect to nickel sulfate and sodium hypophosphite by introducing a concentrated solution of these salts; simultaneously, the evaporation loss of water is replenished. Because the electroless nickel-plating is accompanied by acidification of the working solution, its pH is maintained by addition of ammonia. The concentration of sodium phosphite steadily increases during the apparatus operation, which makes necessary frequent (approximately once a week) discharges of spent electroless nickel-plating solutions (SENPS) to sewage-purification facilities. In wastewater purification, nickel is mixed with other toxic metals and irretrievably lost, with the presence of a large quantity of the ammonium nitrogen in SENPS making difficult high-quality purification of wastewater to remove of many metals.

The results of a four-month study[1] [1] allowed us to compose a material balance of nickel transfer in electroless nickel-plating. It was found that 58.3% of nickel coming into the process with nickel sulfate is consumed for plating of articles, and 22.5% for coating of technological pallets (grid baskets). The loss of nickel with SENPS sewage volleys is 16.1%, and that with washing water, only 3.1%. These data indicate that it is advisable to separately collect and accumulate SENPS, with composition averaging and subsequent utilization of nickel from SENPS.

[1] The study was carried out at Velkont plant (Kirovo-Chepetsk, Kirov oblast).

EXPERIMENTAL

When developing the utilization technique, we chose the reagent method which is more economical than ion exchange and electrolysis. However, the presence of ammonium nitrogen in the sewage volley demanded a preliminary calculation of ionic equilibria in the Ni^{2+}–NH_4^+–NH_3–OH^- system with account of the range of actual NH_4^+ concentrations in SENPS (0.32–1.13 M).

The accumulation of the ammonium nitrogen in solution in electroless nickel-plating results in that the ammonium nitrogen is converted to ammonia nitrogen in the subsequent neutralization of SENPS with alkaline reagents:

$$NH_4^+ + OH^- \rightarrow NH_4OH \rightarrow NH_3 + H_2O. \quad (1)$$

The ammonia nitrogen, in turn, binds nickel ions into stable complexes:

$$Ni^{2+} + nNH_3 \rightarrow Ni(NH_3)_n^{2+} \quad (n = 1–6). \quad (2)$$

This results in an appreciable increase in the total solubility of nickel as compared with SENPS, which contain no ammonium nitrogen. Disintegration of ammine complexes and precipitation of nickel requires a considerable excess of an alkali [to shift equilibrium (3) to the right]:

$$Ni(NH_3)_n^{2+} + 2OH^- \rightleftarrows Ni(OH)_2\downarrow + nNH_3. \quad (3)$$

The total activity of nickel in a solution, [Ni], has the following constituents: the activity of simple Ni^{2+}

ions, found from the solubility product (SP) of nickel hydroxide and dependent on pH; activity of nickel in the form of hydroxo complexes with stability constants K_m; and activity of nickel in the form of ammine complexes with stability constants K_n [2]:

$$[\mathrm{Ni}] = [\mathrm{Ni}^{2+}] + [\mathrm{Ni}^{2+}]\sum_{1-3}^{m} K_m [\mathrm{OH}^-]^m + [\mathrm{Ni}^{2+}]\sum_{1-6}^{m} K_n [\mathrm{NH_3}]^n$$

$$= [\mathrm{Ni}^{2+}]\left(1 + \sum_{1-3}^{m} K_m [\mathrm{OH}^-]^m + \sum_{1-6}^{m} K_n [\mathrm{NH_3}]^n\right). \quad (4)$$

To calculate the nickel solubility by Eq. (4), we took values of SP, K_m, and K_n from the handbook [3]. The value of SP for freshly precipitated $Ni(OH)_2$ was used. Because there are no published data on the activity coefficients of various forms of nickel ions and ammonia nitrogen in SENPS subjected to neutralization, we replaced in our calculations the activities of the equilibrium participants with their concentrations (except for hydroxide ions whose activities are determined by the pH values in neutralization).

In the calculations, we varied the pH values in the range 7–13.5. The initial concentration of the ammonium nitrogen was set in the range 0–1.2 M with a step of 0.2 M. At pH 3.1–5.6, which corresponds to the real SENPS (see table), virtually the whole amount of nitrogen is in the ammonium form. The total concentration of nitrogen remains constant in the conversion of the ammonium nitrogen to the ammonia nitrogen and to nitrogen bound into complexes by reactions (1) and (2). Therefore, Eq. (4) gives us the total molar concentration of nitrogen compounds (with account of the equilibrium constant of reaction (1), equal to 1.76×10^{-5} [3]). Using the method of successive approximations, we found such a value of $[NH_3]$ at which the total concentration of nitrogen compounds is equal to the initial concentration of NH_4^+ ions in SENPS, with a discrepancy not exceeding 0.0001 M. The calculations were carried out using a specially written computer program.

SENPS composition and NaOH consumption for their neutralization

SENPS no.	Concentration			pH	Consumption of solid NaOH, kg m^{-3} of SENPS for adjusting pH to 13
	Ni, g l^{-1}	NH_4^+			
		g l^{-1}	M		
1	3.5	12.6	0.7	4.4	113
2	22.1	5.76	0.32	3.2	132
3	4.48	20.34	1.13	4.2	129
4	9.23	17.82	0.99	3.8	157
5	9.0	19.26	1.07	4.0	139
6	2.74	19.98	1.11	5.6	160
7	14.1	10.08	0.56	4.0	132
8	11.03	10.8	0.6	3.1	125
9	14.15	20.16	1.12	3.5	118
Average					134

The calculated data (Fig. 1) show that the pH value corresponding to the minimum solubility of nickel is determined by the NH_4^+ content of SENPS and falls within the range 11.9–13.1. In view of the fact that SENPS mainly contain about 1 M of NH_4^+ ions (see table), the precipitation of nickel hydroxide should be finished at pH 13.

The calculated nickel solubility is compared in Fig. 2 with the residual nickel concentration determined by chemical analysis during neutralization

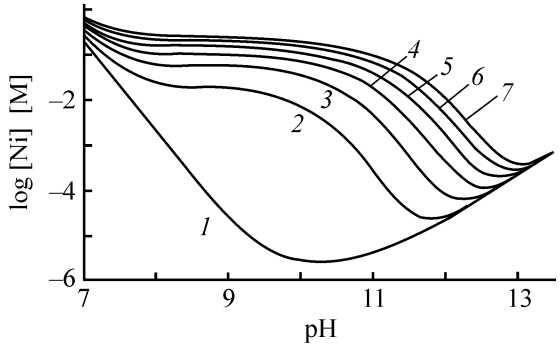


Fig. 1. Calculated curves of the effect of pH on the nickel solubility log [Ni] at various total concentrations of the ammonium nitrogen. NH_4^+ concentration (M): (*1*) 0, (*2*) 0.2, (*3*) 0.4, (*4*) 0.6, (*5*) 0.8, (*6*) 1.0, (*7*) 1.2.

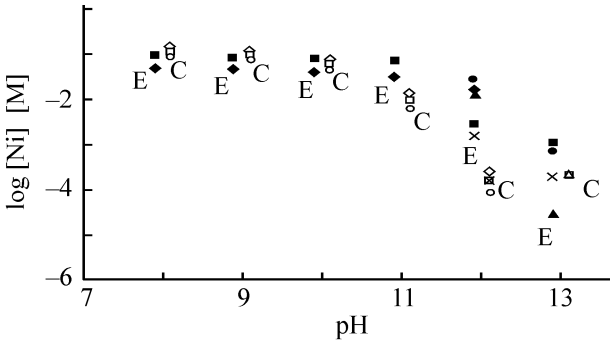


Fig. 2. Calculated (C) values of the nickel solubility and experimental (E) values of the residual nickel concentration in titration with a 10% NaOH solution to various final pH values of SENPS. [Ni] is the nickel concentration.

of SENPS with a NaOH solution. The nickel content was determined by trilonometry or photocolorimetry. When calculating the nickel solubility, we took into account that the solution is diluted in SENPS neutralization and the total concentration of all forms of nitrogen decreases.

The calculated data agree with the experimental values at pH 8–10 and 13, which indicates that the assumptions made in the calculations are correct. A certain excess of the experimental nickel concentrations over the values calculated for pH 11–12 may be due to formation of polynuclear hydroxo and mixed hydroxo-ammine complexes in this range. $Fe_2(OH)_2^{4+}$ and $Co(NH_3)_4(OH)_2^+$ can serve as an example of such complexes [2]. However, this discrepancy does not refute the above conclusion that pH should be brought to 13.

To determine the consumption of sodium hydroxide for the SENPS neutralization, we recorded potentiometric titration curves for several SENPS taken from two plants of Kirov oblast with a 10% NaOH solution (with pH brought to 13). The solution compositions and the NaOH consumption are listed in the table. It is necessary to note that the consumption of the alkali cannot be calculated theoretically, because the reagent neutralization of SENPS is complicated by the presence in their composition of lactic acid, phosphites formed in electroless nickel plating, and ammonium salts. This leads to a sharp increase in the total consumption of the precipitating agent because of the occurrence of the following side reactions [4]: neutralization of lactic acid, reaction of alkali with sodium phosphite, conversion of ammonium nitrogen to ammonia nitrogen, and reaction of alkali with a buffer additive. Under industrial conditions, the alkali consumption can be determined in a simpler way by preliminary recording of potentiometric titration curves after the accumulation of a SENPS mixture.

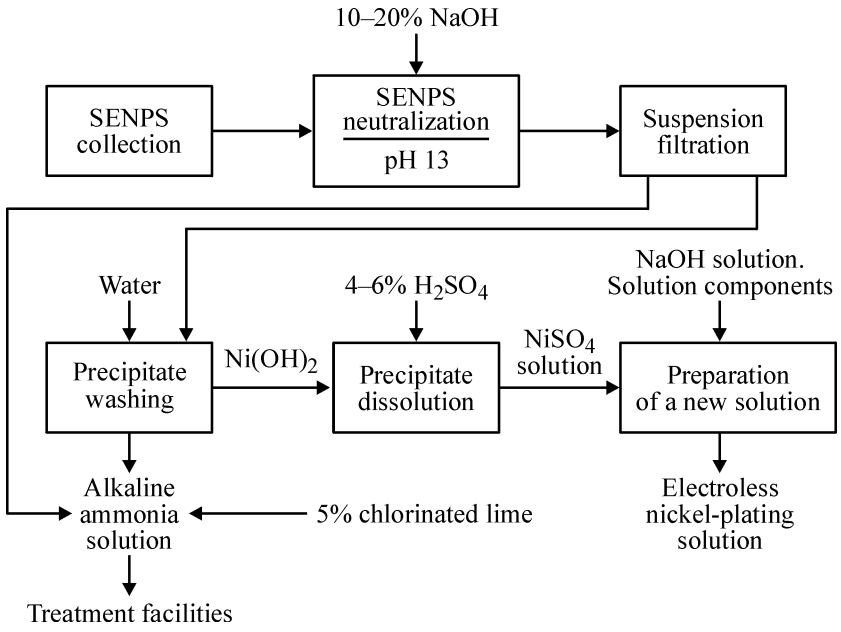
The first variant of the technique for nickel recovery [5] assumed the following technological sequence of SENPS processing: accumulation of SENPS, with averaging of their composition and addition of a stabilizer $\rightarrow$ neutralization of the SENPS mixture with a NaOH solution $\rightarrow$ thermal desorption of ammonia by heating of a $Ni(OH)_2$ suspension $\rightarrow$ filtering of the $Ni(OH)_2$ suspension and thorough washing of the precipitate with water to remove water-soluble salts $\rightarrow$ dissolution of the precipitate in a weak sulfuric acid solution for the subsequent preparation of new solutions for electroless nickel-plating (ENP). A critical consideration of this technique enabled its improvement.

The introduction of the stabilizer (sodium thiosulfate, ~2 g l^{-1}) into SENPS was aimed to prevent partial spontaneous decomposition of SENPS to give a powdered Ni–P alloy upon neutralization. However, the use of a stabilizer requires a very thorough washing of nickel hydroxide to remove water-soluble salts. The absence of the stabilizer imposes less stringent requirements on the quality of washing of the $Ni(OH)_2$ precipitate. Our experiments demonstrated that, when a 10% alkali solution is slowly introduced (within 0.5 h in small portions) under continuous stirring, nickel hydroxide can be precipitated without self-decomposition of the solution (warming-up is weak, SENPS does not decompose, and no Ni–P alloy powder is formed). Thus, the addition of the stabilizer is not obligatory.

The thermal desorption of ammonia from the alkaline suspension of $Ni(OH)_2$ was aimed to remove ammonia from wastewater after filtering the suspension. Calculations of the percentage ratio of various forms of nitrogen demonstrated that, at pH 12 and higher, the main part of nitrogen is in the ammonia form. For example, even at pH 12, the fractions of ammonia in nickel complexes and ammonium ions are as low as 0.95 and 0.17%, respectively. The ammonia nitrogen can be removed from the filtrate by heating the solution at $80 \pm 5°C$ for 3 h (or at $100 \pm 2°C$ for 1 h), which was confirmed by special experiments with three SENPS.

Washed $Ni(OH)_2$ precipitates were dissolved in 5% H_2SO_4 to form $NiSO_4$ solutions, a basis for new SCNP. High-quality nickel coatings on steel articles were obtained in these solutions.

However, an insignificant amount of a gelatinous precipitate was formed in one of the three solutions in the bottom part. An analysis of the possible reasons for the appearance of this precipitate allowed us to conclude that, during a long-term thermal desorption of ammonia, phosphites from SENPS are oxidized to phosphates, with the subsequent binding of a part of phosphate ions into nickel phosphate contaminating the $Ni(OH)_2$ precipitate. In view of this assumption, we reprocessed SENPS without ammonia desorption, by the following scheme: neutralization with a NaOH solution $\rightarrow$ filtration $\rightarrow$ washing of the precipitate $\rightarrow$ dissolution of the precipitate in 5% sulfuric acid $\rightarrow$ preparation of a new ENPS. The solution obtained using this scheme contained no gelatinous precipitate. High-quality nickel coatings were also obtained in this solution.



Technological scheme of nickel sulfate recovery from SENPS.

In view of the aforesaid, we suggested the second variant of nickel recovery (see scheme). Because this scheme does not assume thermal desorption of NH_3, an alkaline ammonia solution appears in the sewage. Its ammonia can be oxidized with chlorinated lime (as confirmed by separate experiments).

Economical calculations demonstrated that the price of recycled nickel sulfate is 2.5 times the expenditure for sodium hydroxide and sulfuric acid. Furthermore, plants can cut expenses for purification of SENPS volleys and burial of the slimes formed.

The presented techniques for nickel recovery from SENPS, with recycling of nickel sulfate are cost-effective even though they require the expensive sodium hydroxide. In this context, it is important to search for less expensive precipitating agents for SENPS neutralization. We tested spent degreasing solutions from a galvanic production line and CaO suspensions as precipitating agents of this kind.

Spent degreasing solutions contain NaOH, Na_2CO_3, and Na_3PO_4. Our experiments demonstrated that presence of soda brings no complications in the process of SENPS neutralization. However, the presence of trisodium phosphate in this process results in precipitation of nickel phosphate, which hinders deposition of a nickel coating on articles in a new solution. Therefore, use of spent degreasing solutions for SENPS neutralization is only advisable for obtaining a nickel-containing concentrate. The sequence of operations in this variant of technology is as follows: accumulation of SENPS with averaging of their composition → neutralization of the SENPS mixture with a spent degreasing solution → desorption of ammonia by heating of the suspension → filtering of the suspension of poorly soluble nickel compounds → washing of the precipitate with water to remove water-soluble salts → drying of the precipitate. This technique makes it possible not only to obtain a concentrate of nickel salts (with a nickel content of no less than 23%), but also to diminish the volume of toxic galvanic slimes formed at a plant.

Experiments on SENPS neutralization with a CaO suspension were carried out by the following scheme: neutralization of SENPS with a 5% CaO suspension → filtering and washing of the precipitate with water to remove water-soluble salts → $Ni(OH)_2$ dissolution in a weak solution of sulfuric acid with heating for 0.5–2 h → filtering of the solution to remove $CaSO_4$ → preparation of a new electroless nickel-plating solution.

The experimental results demonstrate that the 5% CaO suspension sufficiently completely transfers nickel from SENPS to $Ni(OH)_2$ on reaching a pH value close to 13 (concentrations of nickel ions in the filtrate 0.0016–0.008 g l^{-1}). The highest degrees of nickel extraction (DE_{Ni}) into a sulfate solution were reached upon dissolution of the precipitate for 2 h at 50–70°C (DE_{Ni} = 98–99%). A simplification of the technological procedure (temperature lowered to 20°C or a shorter dissolution time) results in a less

complete extraction of nickel (DE_{Ni} = 92–93%). A rather important factor determining the efficiency of the process is the time during which the $Ni(OH)_2$ precipitate is stored before dissolution in the acid. This was confirmed by an experiment in which a precipitate was dissolved at 70°C for 2 h, but a week after SENPS neutralization and filtering of the resulting suspension. During this time, crystals were coarsened and the precipitate was solidified, which resulted in a low degree of nickel extraction (about 24%). Therefore, a freshly precipitated $Ni(OH)_2$ should be dissolved in sulfuric acid.

The $NiSO_4$ solutions obtained in SENPS neutralization with a CaO suspension were used to prepare new ENPS, in which electroless nickel coatings of the required industrial quality were obtained.

An additional variant of a technique for nickel recovery from SENPS, with a CaO suspension used as a precipitating agent, was suggested on the basis of the experiments we performed. It differs from the second variant (see scheme) in that a $Ni(OH)_2$ precipitate is dissolved in a heated sulfuric acid (50°C, 0.5 h) not later than 24 h after the precipitation. Furthermore, an operation of filtration of the sulfuric acid solution to remove calcium sulfate is added after the dissolution.

An economical analysis of the process demonstrated that the price of nickel sulfate recycled in this way is, on average, three times the expenditure for lime hydrate and sulfuric acid.

CONCLUSIONS

(1) A procedure for calculation of ionic equilibria in the system Ni^{2+}–NH_4^+–NH_3–OH^- for the conditions of neutralization of spent electroless nickel-plating solutions was suggested. Systematic calculations by this procedure were carried out. This allowed substantiation of the pH values to be reached by the end of the neutralization, which were confirmed experimentally.

(2) Techniques for nickel recovery from spent electroless nickel-plating solutions with the use of an alkali solution and a CaO suspension as precipitating agents were developed. Recycling of the above-mentioned solutions gives a nickel sulfate solution that can serve as a basis for preparation of a new electroless nickel-plating solution providing high-quality coatings.

(3) It was shown that neutralization of spent electroless nickel-plating solutions with spent degreasing solutions is accompanied by precipitation of a mixture of poorly soluble nickel compounds, including nickel phosphate, which gives no way of using the precipitate for preparation of new solutions. A procedure for recovery of nickel from spent electroless nickel-plating solutions into a concentrate with a nickel content of about 23% was developed.

REFERENCES

1. Lobanova, L.L. and Khranilov, Yu.P., Abstracts of Papers, *XII Vserossiiskoe soveshchanie "sovershenstvovanie tekhnologii gal'vanicheskikh pokrytii"* (XII All-Russia Conf. "Development of a Technology of Metal Plating"), Kirov, 2003, pp. 64–65.
2. Butler, J.N., *Ionic Equilibrium (A Mathematical Approach)*, Massachusetts: Addison-Wesley, 1964.
3. Lur'e, Yu.Yu., *Spravochnik po analiticheskoi khimii* (Handbook of Analytical Chemistry), Moscow: Khimiya, 1989.
4. Khranilov, Yu.P., *Nekotorye osobennosti neitralizatsii otrabotannykh rastvorov khimicheskogo nikelirovaniya* (Specific Features of Neutralization of Spent Electroless Nickel-Plating Solutions), Available from VINITI, 1995, Kirov, no. 2480-V95.
5. Khranilov, Yu.P. and Lobanova, L.L., *Gal'vanotekhn. Obrab. Pov–sti*, 2002, vol. 10, no. 1, pp. 41–44.

ISSN 1070-4272, Russian Journal of Applied Chemistry, 2008, Vol. 81, No. 2, pp. 207–211. © Pleiades Publishing, Ltd., 2008.
Original Russian Text © V.V. Voitylov, A.V. Voitylov, E.N. Korytkova, V.P. Romanov, S.V. Ul'yanov, V.V. Gusarov, 2008, published in Zhurnal Prikladnoi Khimii, 2008, Vol. 81, No. 2, pp. 218–222.

INORGANIC SYNTHESIS AND INDUSTRIAL INORGANIC CHEMISTRY

Structure of Aqueous Dispersions of $Mg_3Si_2O_5(OH)_4$ Nanotubes

V. V. Voitylov, A. V. Voitylov, E. N. Korytkova, V. P. Romanov, S. V. Ul'yanov, and V. V. Gusarov

St. Petersburg State University, St. Petersburg, Russia

Grebenshchikov Institute of Silicate Chemistry, Russian Academy of Sciences, St. Petersburg, Russia

Received September 26, 2007

Abstract—Behavior of hydrosilicate nanotubes of composition $Mg_3Si_2O_5(OH)_4$ in aqueous dispersions was studied. Experiments devoted to observation of steady-state and relaxation electro-optical effects demonstrated that, irrespective of their initial concentration in water, nanotubes form stable bulk aggregates with weak anisotropy, rather than a homogeneous system of separate suspended nanosize cylinders.

DOI: 10.1134/S1070427208020092

The unique properties of substances with a nanotubular structure [1–3] have initiated systematic studies of the possibility of their use for developing new materials and technologies [4–7]. Recently, there have been numerous reports devoted to nanomaterials based on carbon nanotubes [8, 9] and heterostructural nanorolls [10] synthesized by the method suggested in [11]. At the same time, there exists, together with the above-mentioned types of nanotubes, a vast class of inorganic and, in particular, silicate nanotubes with various chemical compositions and morphologies [12–19], formed by twisting of layers of chemical compounds with layered structure [20]. The experience of application of silicate nanotubes in, e.g., the development of polymer-inorganic nanocomposites has shown that their introduction into a polymeric matrix improves the mechanical and pervaporation characteristics of materials [21–23]. A promising field of application of these nanotubes is water purification to remove impurities, including radionuclides [24].

Purposeful use of nanotubes in the above-listed and many other practical areas requires that their behavior in aqueous dispersions and dispersions based on other liquids should be understood. This is necessary because the structure of dispersions of nanotubes largely determines the efficiency of their use in composite materials and technologies involving contact of nanotubes with liquid media of various compositions.

EXPERIMENTAL

Nanotube hydrosilicates of composition $Mg_3Si_2O_5 \cdot (OH)_4$ were synthesized under hydrothermal conditions. As precursors served mixtures of magnesium and silicon oxides, as well as magnesium silicates and hydrosilicates of varied structure and composition and, in particular, $MgSiO_3$ having a chain structure and $Mg_3Si_4O_{10}(OH)_2$ with layered structure. All the mixtures were prepared in terms of the stoichiometry $MgO : SiO_2 = 3 : 2$, for which purpose magnesium oxide was added to the starting mixtures based on magnesium silicates. The starting mixtures were subjected to hydrothermal treatment with distilled water and aqueous solutions of NaOH (0.3–3 wt %) at temperatures of 200–500°C and pressures of 10–100 MPa by the method described in [25]. The products of this treatment were washed to remove alkaline components and dried. After that their chemical composition, morphological parameters, and optical and electro-optical characteristics were determined.

It was found that nanotubes of hydrosilicates with a chrysotile structure and chemical composition close to that given by the theory, $Mg_3Si_2O_5(OH)_4$, were synthesized from all the precursors under the hydrothermal conditions at temperatures of 250–450°C and pressures of 10–100 MPa. The refractive indices of the hydrosilicates synthesized, found by optical microscopy in immersion liquids, are as follows: n_g =

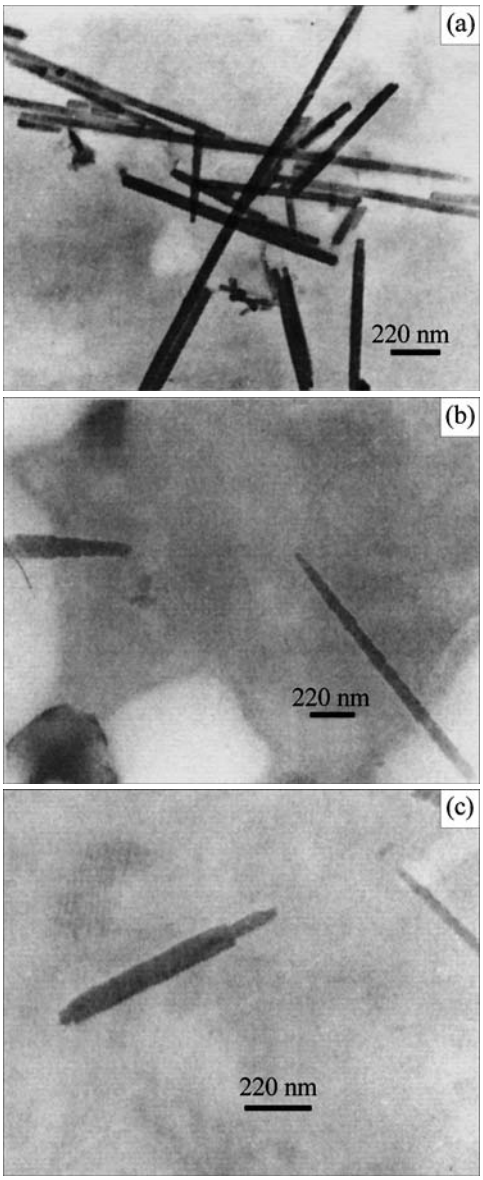


Fig. 1. Electron micrographs of nanotubes of various forms: (a) cylindrical, (b) conical, and (c) socket-like.



Fig. 2. Electron micrograph of an ensemble of nanotubes.

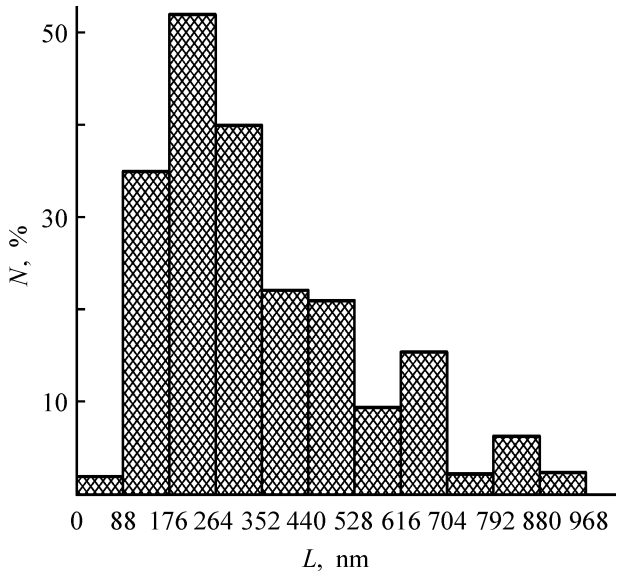


Fig. 3. Histogram of the nanotube distribution over length *L*. (*N*) Number of nanotubes.

1.545–1.551, n_p = 1.539–1.545, $n_g - n_p$ = 0.006. An electron-microscopic study revealed a wide variety of morphological forms of nanotubes: cylinders, cones, socket tubes (Fig. 1). The outer diameter varies from 20 to 70 nm for cylindrical nanotubes and from 20 to 50 nm for conical nanotubes. The inner diameter of cylindrical nanotubes is 3–5 nm. It was shown that prevalence of some morphological forms of nanotubes depends on synthesis conditions: composition of the hydrothermal solution, temperature and duration of the hydrothermal treatment of precursors.

The hydrothermal synthesis of nanotubes of composition $Mg_3Si_2O_5(OH)_4$ at temperatures of 300–350°C and pressures of 30–100 MPa for 12–24 h in a hydrothermal solution containing 0.8–1 wt % NaOH can give, with a 100% yield of the final product, exclusively cylindrical nanotubes with weakly varying inner and outer diameters of about 3 and 25 nm, respectively.

Aqueous dispersions of $Mg_3Si_2O_5(OH)_4$ nanotubes, whose electron micrograph is shown in Fig. 2, were studied. The histogram of the length distribution for such nanotubes is shown in Fig. 3. As follows from an analysis of the data presented in the form of a histogram, the length of most of nanotubes falls within the range 100–500 nm and their outer diameters vary

from 10 to 25 nm. Even a minor addition of nanotubes to water (no more than 10 μg cm^{-3}) and shaking leads to a noticeable light scattering by the dispersion. In several days, a loose white precipitate is formed at the bottom of the test tube and the aqueous solution over this precipitate becomes virtually transparent. The precipitate is easily destroyed by repeated shaking and ultrasonic treatment of suspensions of this kind. These observations of the behavior of suspensions suggest that nanotubes form aggregates in water. Then these aggregates become larger, which leads to their sedimentation.

To evaluate the geometric and electrical parameters of nanotube aggregates, electro-optical studies of their aqueous suspensions were carried out. In these studies, an external electric field induced an optical anisotropy of the dispersion and characteristics of this anisotropy were measured. The nanotubes shown in Fig. 2 have lengths comparable with the wavelength of the electromagnetic radiation in the visible spectral range. The scattering of linearly polarized light by tubes of this kind strongly depends on their orientation with respect to the propagation direction of the light wave and its polarization. The contribution made by a separate tube to the total optical anisotropy of the suspension can be defined as the difference between the energies of light propagating perpendicularly to the tube axis and polarized along or perpendicularly to this axis. This difference is proportional to the tube length and its changes with the tube orientation can be described theoretically [26].

The experimental setup for studies of this kind, described in detail in [27], comprises the electrical and optical parts. It includes a sound generator, field pulse-forming unit, power amplifier, and a transparent cuvette with electrodes, filled with a system under study. The setup enables orientation of nanoparticles suspended in the liquid between the electrodes of the cuvette along the force lines of the external field. The optical part of the setup includes the following components: white-light source; movable polarizer, which can pass light whose polarization plane is parallel or perpendicular to the electric field strength vector; and a system for recording the intensity of light that passes through the cuvette. In the experiment, relative changes in the intensity of transmitted light, $\Delta J_{\|}/J$ and $\Delta J_{\perp}/J$, polarized along and perpendicularly to the field that gives rise to the optical anisotropy of the suspension in the cuvette, were measured. It is the difference between these relative changes in the intensity of light that determines the magnitude of

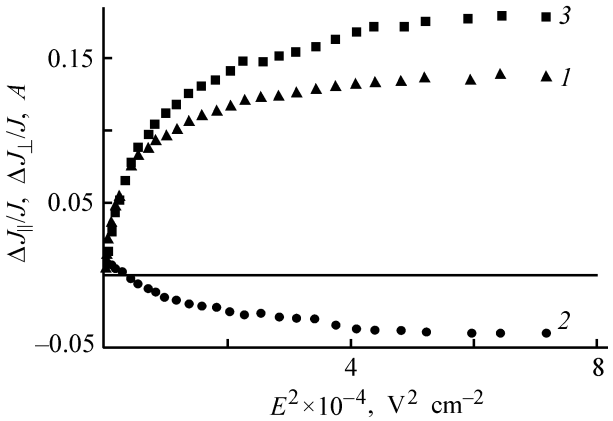


Fig. 4. Relative changes (*1*) $\Delta J_{\|}/J$ and (*2*) $\Delta J_{\perp}/J$ in the light flux and (*3*) their difference A vs. the field strength E in the cuvette. (E^2) Squared electric field strength.

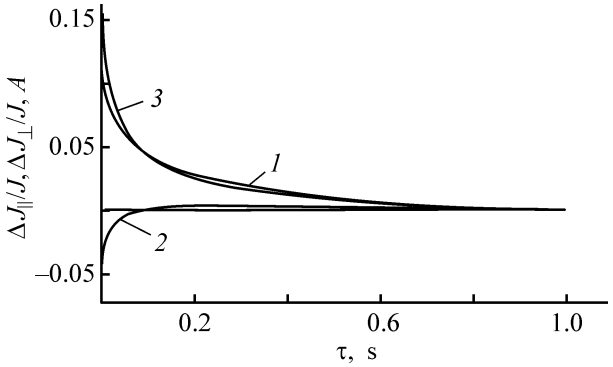


Fig. 5. Experimentally measured relaxation dependences of (*1*) $\Delta J_{\|}/J$, (*2*) $\Delta J_{\perp}/J$, and (*3*) A on time τ.

the electro-optical effect, $A = \Delta J_{\|}/J - \Delta J_{\perp}/J$. Dependences of A on the strength E of a sinusoidal radio-frequency field (field dependences) make it possible to evaluate the anisotropy of polarizability of separate independent nanotubes or their aggregates, which are oriented along the field in the cuvette. The type of the time dependence of A after switching-off the field (relaxation dependences) can be used to determine the length of noninteracting nanotubes or the size of their aggregates.

In the study, the field and relaxation dependences of $\Delta J_{\|}/J$, $\Delta J_{\perp}/J$, and A were measured for a diluted suspension of $Mg_3Si_2O_5(OH)_4$ nanotubes in water, with a concentration of 100 μg cm^{-3}. The measurement results are presented in Figs. 4 and 5. As follows from these data, $\Delta J_{\|}/J$ and $\Delta J_{\perp}/J$ have different signs, with the applied field clarifying the system under study if light is oriented along the field in the cuvette and, by contrast, making it less transparent to light polarized perpendicularly to the field. It follows from the dependence of the steady-state electro-optical ef-

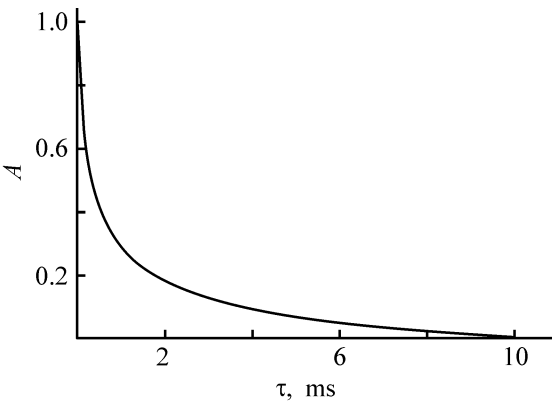


Fig. 6. Relaxation dependence of A, calculated for noninteracting nanotubes. (τ) Relaxation time.

fect on the strength of the 10-kHz sinusoidal electric field (Fig. 4) the induced optical anisotropy reaches a constant value ("saturates") at field strengths of 250–300 V cm^{-1}. It is interesting to note that nanoparticles of length 100–500 nm, which constitute the majority of dispersion particles according to the histogram, must have an unrealistically high anisotropy of polarizability, γ. Indeed, the limiting values of $\Delta J_{\parallel}/J$, $\Delta J_{\perp}/J$, and A, corresponding to the saturated orientation of particles along the field are reached at $\gamma E^2/2k_B T \approx 3$, where γ is the anisotropy of particle polarizability and $k_B T$ is the thermal energy [27]. Hence follows an estimate for the average anisotropy of polarizability, $\gamma \approx 5 \times 10^{-13}$ cm^3. At the same time, a calculation of γ for a separate nanotube of medium length, assumed to be dielectric and possessing a broadened double layer, gives $\gamma \approx 10^{-15}$ cm^3 [28]. This discrepancy between the model and experimental values of γ may be due either to an exceedingly high intrinsic anisotropy of the polarizability of nanotubes, which is unlikely, or to formation by these nanotubes of large aggregates suspended in water. As follows from the data in Fig. 4, the optical anisotropy induced by electric field remains invariable at field strengths E of 300 to 700 V cm^{-1}.

The process of free relaxation of the induced optical anisotropy is illustrated by Fig. 5. As follows from an analysis of the curves in Fig. 5, the characteristic relaxation time is close to 0.1 s. If the free relaxation of A is calculated for nanotubes as a system of independent thin cylinders [28], a value on the order of fractions of a millisecond is obtained for the characteristic time of transition of the system from the ordered-orientation state to the chaotic state. A more detailed calculation based on the histogram shown in Fig. 3 yields a relaxation dependence $A(\tau)$, with amplitude normalized to unity. This dependence is shown in Fig. 6. The experimentally observed relaxation time is found to be two orders of magnitude larger than that calculated on the assumption of rotation of the long axes of independent cylinders.

Thus, the results of the experiments in which steady-state and relaxation electro-optical effects were observed suggest that a system of $Mg_3Si_2O_5(OH)_4$ nanotubes suspended in water is aggregated in all the three directions, with the size of the aggregates exceeding the average length of the nanotubes by approximately a factor of 4–5.

In order to obtain a dispersion composed of separate nanotubes, the starting system was diluted by a factor of 10–100 and more and treated with ultrasound. However, measurements demonstrated that, in this case, the relaxation time of the electro-optical effect remains virtually unchanged and fields leading to saturation are close for diluted and undiluted systems. This points to a rather high stability of the aggregates.

In fields of strength exceeding 700 V cm^{-1}, the optical anisotropy starts to grow again, which is due to elongation of the aggregates in the field. It was found that, if separate pulses of a sinusoidal field (pulse width 0.2 s, amplitude 2 kV cm^{-1}) are applied at intervals of 10 s, the relaxation time of the electro-optical effect markedly increases. This indicates that nanotube aggregates become coarser. The action of longer pulses, with width of about 10 s, leads to nonmonotonic time dependences, both for the rise in the optical anisotropy and for its decay after switching-off the field. This may be due to a pronounced influence of strong fields on the process of formation of nanostructured dispersions.

CONCLUSIONS

(1) Aqueous dispersions of $Mg_3Si_2O_5(OH)_4$ nanotubes are composed of aggregates with a size exceeding the average nanotube length by a factor of 4–5.

(2) Aggregates of nanotubes do not change their size upon dilution of the suspension with water and its ultrasonic treatment, i.e., are rather stable formations.

(3) Under the action of an electric field, the aggregates in an aqueous medium change their shape (are elongated) and become coarser.

ACKNOWLEDGMENTS

The study was supported by the Russian Foundation for Basic Research (grant no. 06-08-01202-a).

REFERENCES

1. Ivanovskii, A.L., *Usp. Khim.*, 2002, vol. 71, no. 3, pp. 203–224.
2. Rao, C.N.R. and Nath, M., *Dalton Trans.*, 2003, pp. 1–24.
3. Eletskii, A.V., *Usp. Fiz. Nauk*, 2002, vol. 172, no. 4, pp. 401–438.
4. Ivanovskaya, V.V., Enyashin, A.N., Makurin, Yu.N., and Ivanovskii, A.L., *Nanotekhnika*, 2006, no. 1(5), pp. 126–140.
5. Zakharova, G.S., Volkov, V.L., Ivanovskaya, V.V., and Ivanovskii, A.L., *Usp. Khim.*, 2005, vol. 74, no. 7, pp. 651–685.
6. Harris, P.J.F., *Carbon Nanotubes and Related Structures: New Materials for the Twenty-First Century*, Cambridge: Cambridge Univ., 1999.
7. Ajayan, R.M., *Chem. Rev.*, 1999, vol. 99, no. 7, pp. 1787–1799.
8. Lordi, V. and Nan, Y., *J. Mater. Res.*, 2000, vol. 15, pp. 2770–2779.
9. Che, G., Lakshmi, B.B., Fisher, E.R., and Martin, C.R., *Nature*, 1998, vol. 393, pp. 346–349.
10. Aseev, A.L., *Vestnik Ross. Akad. Nauk*, 2006, vol. 76, no. 7, pp. 603–611.
11. Prinz, V.Ya., *Microelectr. Eng.*, 2003, vol. 69, pp. 466–475.
12. Korytkova, E.N., Maslov, A.V., Pivovarova, L.N., et al., *Fiz. Khim. Stekla*, 2004, vol. 30, no. 1, pp. 72–78.
13. Korytkova, E.N., Maslov, A.V., Pivovarova, L.N., et al., *Neorg. Mater.*, 2005, vol. 41, no. 7, pp. 849–855.
14. Korytkova, E.N., Pivovarova, L.N., Semenova, O.E., et al., *Zh. Neorg. Khim.*, 2007, vol. 52, no. 3, pp. 388–394.
15. Korytkova, E.N., Pivovarova, L.N., Drozdova, I.A., and Gusarov, V.V., *Zh. Obshch. Khim.*, 2007, vol. 77, no. 10, pp. 1269–1277.
16. Jancar, B. and Suvorov, D., *Nanotechnology*, 2006, vol. 17, pp. 25–29.
17. Falini, G., Foresti, F., Lesci, G., and Roveri, N., *Chem. Commun.*, 2002, vol. 14, pp. 1512–1513.
18. Wilson, M.A., Lee, G.S.H., and Taylor, R.C., *J. Non-Cryst. Solids*, 2001, vol. 296, pp. 172–181.
19. Ohashi, F., Tomura, S., Akaku, K., et al., *J. Mater. Sci.*, 2004, vol. 39, pp. 1799–1801.
20. Chivilikhin, S.A., Popov, I.Yu., and Gusarov, V.V., *Dokl. Akad. Nauk*, 2007, vol. 412, no. 2, pp. 201–203.
21. Yudin, V.E., Gladchenko, S., Otaigbe, J., et al., *Polymer*, 2007, vol. 48, pp. 1306–1315.
22. Gofman, I., Svetlichniy, V., Yudin, V., et al., *Czech. Compos. Carbon Mater. Soc.*, 2007, no. 1, pp. 32–37.
23. Kononova, S.V., Korytkova, E.N., Romashkova, K.A., et al., *Zh. Prikl. Khim.*, 2007, vol. 80, no. 12, pp. 2064–2070.
24. Maslennikova, T.P., Korytkova, E.N., and Gusarov, V.V., Abstracts of Papers, *VII Mezhdunarodnaya nauchnaya konferentsiya "Khimiya tverdogo tela i sovremennye mikro- i nanotekhnologii"* (VII Int. Sci. Conf. "Solid-State Chemistry and Modern Micro- and Nanotechnologies"), Kislovodsk, 2007, pp. 186–187.
25. Korytkova, E.N., Maslov, A.V., and Gusarov, V.V., *Khimiya poverkhnosti i sintez nizkorazmernykh sistem: Sbornik nauchnykh trudov* (Surface Chemistry and Synthesis of Low-Dimension Systems: Coll. of Sci. Works), St. Petersburg: RIO SPbGTI(TU), 2002, pp. 54–59.
26. Spartakov, A.A, Trusov, A.A., Voitylov, A.V., and Voitylov, V.V., *Molecular and Colloidal Electro-optics*, Stoylov, S.P. and Stoimenova, M.V., Eds., CRC, Taylor & Francis Group, *Surfactant Science Series*, 2007, vol. 134, part 7, pp. 193–227.
27. Voitylov, V.V., Pochtareva, T.V., Spartakov, A.A., and Trusov, A.A., *Kolloid. Zh.*, 1978, vol. 40, no. 6, pp. 1085–1090.
28. Stoilov, S., Shilov, V.N., Dukhin, S.S., et al., *Elektrooptika kolloidov* (Electro-optics of Colloids), Dukhin, S.S., Ed., Kiev: Naukova Dumka, 1977.

ISSN 1070-4272, Russian Journal of Applied Chemistry, 2008, Vol. 81, No. 2, pp. 212–217. © Pleiades Publishing, Ltd., 2008.
Original Russian Text © Kh.Kh. Gil'manov, A.A. Lamberov, E.V. Shatokhina, E.V. Dement'eva, 2008, published in Zhurnal Prikladnoi Khimii, 2008, Vol. 81, No. 2, pp. 223–228.

PHYSICOCHEMICAL STUDIES OF SYSTEMS AND PROCESSES

Transformation of the Phase Structure of an Iron Oxide Catalyst for Dehydrogenation of Methyl Butenes under Industrial Exploitation Conditions

Kh. Kh. Gil'manov, A. A. Lamberov, E. V. Shatokhina, and E. V. Dement'eva

Nizhnekamskneftekhim Open Joint-Stock Company, Nizhekamsk, Tatartstan, Russia

Kazan State University, Kazan, Tatarstan, Russia

Received August 6, 2007

Abstract—X-ray phase, differential-thermal, and elemental analyses were used to study the transformation of the phase structure of an iron oxide catalyst for dehydrogenation of methyl butenes after exploitation.

DOI: 10.1134/S1070427208020109

Isoamylenes are dehydrated in a flow-through adiabatic reactor in a fixed bed of an iron oxide catalyst at a temperature of 600–640°C in the presence of steam [1]. Industrial exploitation of the catalyst under severe conditions (low dilution of raw materials with steam, high temperature) leads to its gradual deactivation [2], with the result that the basic catalytic parameters of the catalyst fall in 1–2 years. Accordingly, its reloading and utilization becomes necessary after this period of time.

It is known [3] that the main reason for the irreversible deactivation of the iron oxide catalyst is the loss of potassium promoter. However, there are no data on the distribution of potassium along the height and diameter of the catalyst bed. Issues associated with the efficiency of the regeneration performed and with the uniform operation of the whole catalyst bed remain unclear.

The goal of this study was to examine the transformation of the phase structure of the iron oxide catalyst for dehydrogenation of methyl butenes under industrial conditions to determine the efficiency of its operation in high-power adiabatic reactors.

EXPERIMENTAL

As objects of study served fresh and spent (8000 h) samples of the domestic KDO catalyst [4], taken at different places along the height and diameter of the adiabatic reactor.

An X-ray phase analysis (XPA) of all the samples was performed on a modified automatic X-ray diffractometer based on a standard DRON-2 instrument, with independent rotation of a sample and the counter and with Cu_{K_α} radiation. A graphite monochromator was used in the diffracted beam. The angles 2θ were recorded in the range 5–60° with a step of 0.5°. The X-ray diffraction patterns were recorded at 30 kV and 15 mA with an exposure time of 3 s. The average size of the coherent-scattering region (CSR) was found from the broadening of diffraction lines.

The thermal behavior and thermal transformations under nonisothermal conditions were studied on a Netzsch CTA-409 PC Luxx synchronous thermal analyzer (Germany) in air in the temperature range 25–1100°C at a heating rate of 10–40 deg min^{-1}. The accuracy of determining the loss of mass was ±0.5%.

An analysis for the content of carbon was made on a HORIBA EMIA-510 instrument with a heat-conductivity detector by the ASTM method, with a 1-g catalyst sample burnt at 1450°C in the course of 60 s.

The elemental composition of the catalyst (iron, calcium, magnesium, potassium, and cerium oxides) was determined on a Hitachi Z-6100 atomic-absorption spectrometer with an acetylene–air flame by the method of a calibration plot.

Table 1. XPA data for fresh and spent catalyst samples

Sample no.	Catalyst	CSR size at indicated *d*, Å			Area under the strongest reflections, arb. units, at indicated *d*, Å			Phases present
		2.70 (hematite)	11.90 (polyferrite)	3.12 (cerium oxide)	2.70 (hematite)	11.90 (polyferrite)	3.12 (cerium oxide)	
1	Fresh	612	396	155	21	69	84	$K_xFe_{22}O_{34}$, α-Fe_2O_3, CeO_2
	Spent:							
2	from the upper part of the bed	312	–	416	169	–	68	α-Fe_2O_3, CeO_2, Fe_3O_4
3	from the middle of the bed	136	–	375	126	–	72	α-Fe_2O_3, CeO_2, Fe_3O_4
4	from the lower part of the bed	265	–	452	36	–	57	α-Fe_2O_3, CeO_2, Fe_3O_4

It can be seen from the X-ray diffraction patterns in Fig. 1 that the phase compositions of the fresh and spent samples are markedly different.

The fresh catalyst contains phases of potassium polyferrite (*d* 11.90, 5.95, 2.98, 2.66 Å, etc.), hematite (*d* 3.66, 2.70, 2.51 Å), and cerianite (*d* 3.11 Å), and spent samples, the phases of magnetite (*d* 2.53, 2.96, 4.84 Å, etc.), cerianite, and trace amounts of hematite. The observed transformation of the phase structure is due to reduction of Fe^{3+} to Fe^{2+}, with the phase of hematite converted to magnetite and that of potassium polyferrite decomposed into hematite and potassium compounds. The crystal lattice of iron oxide changes from hexagonal to cubic. As can be seen in Table 1, hematite present in spent catalyst samples has smaller crystallites in the CSR.

A detailed analysis of samples taken from different points along the reactor height demonstrated that the hematite phase predominates in the upper layer of the catalyst bed, which is indicated by the areas under the diffraction lines (Fig. 1). This is due to partial oxidation of magnetite to hematite during preliminary regeneration of the catalyst before its being discharged.

During the operation of the catalyst, the content of potassium in the upper layer decreases as a result of decomposition of potassium polyferrite to hematite and potassium compounds, which are present in the form of a liquid film on the catalyst surface [5].

To determine the potassium distribution throughout the reactor, samples taken not only along the height of the catalyst bed, but also along its diameter were analyzed. It was shown that potassium is nonuniformly carried away along both the height and diameter of

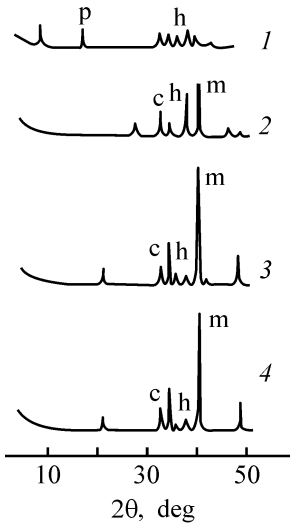


Fig. 1. X-ray diffraction patterns of (*1*) fresh catalyst and spent samples from (*2*) upper, (*3*) middle, and (*4*) lower parts of the catalyst bed in the adiabatic reactor. (2θ) Bragg angle; the same for Fig. 5.

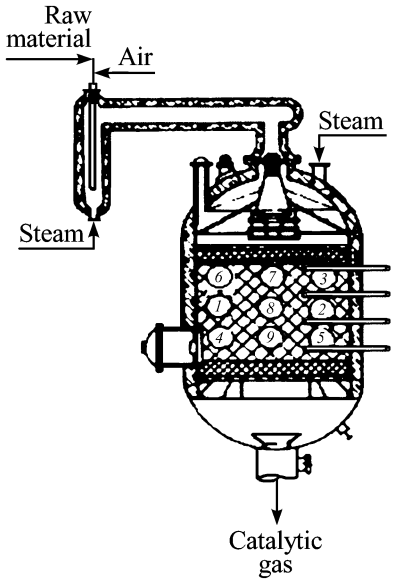


Fig. 2. Points of sampling from (*3*, *6*, *7*) upper, (*1*, *2*, *8*) middle, and (*4*, *5*, *9*) lower layer of the catalyst bed in the adiabatic reactor (frontal section).

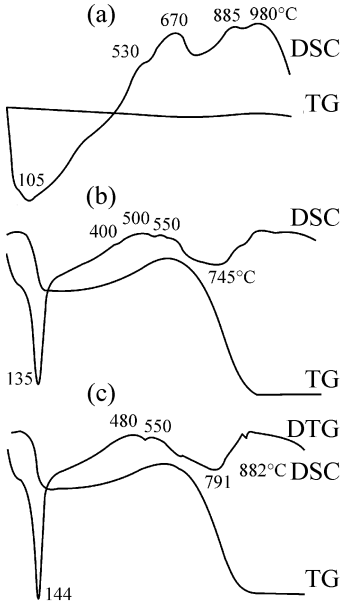


Fig. 3. DSC and TG curves for spent samples from (a) upper, (b) middle, and (c) lower parts of the catalyst bed.

the catalyst bed (Fig. 2), although the content of other components does not change significantly (Table 2).

It can be assumed that, in the course of exploitation, channeling of the raw material flow is observed within the catalyst bed because of the unsatisfactory operation of the distributing device.

Regeneration is performed under industrial conditions with steam at a temperature of 630–660°C in the course of 5–10 h. To test the quality of the steam regeneration and determine the conditions of burning-out of carbon deposits, spent samples were subjected to differential-thermal analysis. Figure 3 shows DSC, DTG, and TG curves for samples from the upper, middle, and lower parts of the catalyst bed after preliminary regeneration with overheated steam. The endothermic effects in the temperature range 24–200°C are due to removal of physically adsorbed water. The exothermic effects at 200–530°C are associated with oxidation of magnetite to hematite, with a gain in mass. The exothermic effects in the temperature range 530–700°C are associated with burning-out of carbon deposits to give CO_2. According to XPA data, the hematite phase is predominant in the sample from the upper layer, and, therefore, no gain in mass is observed. In the TG curves for other samples, the gain in mass is 1.18 wt % (for medium layer) and 1.11 wt % (for lower layer). Because of the superposition of the exothermic effects of magnetite oxidation and burning-out of carbon deposits, the loss of mass cannot be determined for each particular sample.

In contrast to the sample from the upper layer, the DSC curves for other samples show endothermic effects in the temperature range 650–850°C, associated with formation of potassium ferrites. This can be understood as follows: according to the results of elemental analysis, the content of potassium is virtually zero in a sample from the upper layer and considerably higher in other layers (Table 2). It follows

Table 2. Absolute content of the components in the ionic form in spent catalyst samples

Sampling point (Fig. 2)	Sample no.	Content, wt %					Sampling point (Fig. 2)	Sample no.	Content, wt %				
		K^+	Fe^{3+}	Ca^{2+}	Mg^{2+}	Ce^{2+}			K^+	Fe^{3+}	Ca^{2+}	Mg^{2+}	Ce^{2+}
–	1	4.30	–	8.72	9.06	5.25	*2*	3	0.02	69.13	6.07	7.48	5.50
6	2	1.05	71.69	5.22	4.97	5.69	*8*		4.14	69.00	4.73	5.33	5.24
3		4.23	73.12	4.17	6.34	5.84	*4*	4	3.60	70.52	4.58	10.23	5.80
7		0.01	78.87	4.21	6.27	5.78	*5*		4.42	66.63	6.13	10.39	5.80
1	3	0.03	68.06	5.84	8.35	5.29	*9*		4.32	68.89	5.47	10.83	6.94

Table 3. Results of a derivatographic analysis of spent samples of the dehydrogenation catalyst

Sample no.	Effects in the temperature range, °C						
	endo-, 24–200		*exo*-, 200–700		*endo*-, 650–850		24–1000 $\Sigma\Delta G$, %
	T_{min}, °C	ΔG, %	T_{max}, °C	ΔG, %	T_{min}, °C	ΔG, %	
1	105	–0.05	530 670	–0.2	–	–	–0.26
2	135	–2.21	400 500 550	1.18	745	–5.07	–6.09
3	144	–2.70	480 550	1.11	791	–6.48	–8.15

Table 4. Results of a quantitative determination of the content of potassium carbonate in spent catalyst samples by the methods of titration and burning-out of carbon

Sample no.	Content, wt %			Sample no.	Content, wt %		
	K_2CO_3, titration	C	K_2CO_3		K_2CO_3, titration	C	K_2CO_3
		burning-out				burning-out	
1	0.60	–	–	3	0.87	0.98	0.27
2	0.00	0.15	0.00	4	0.89	0.80	0.39

from the data presented that samples from the middle and upper layers contain free potassium carbonate, which again forms, in reaction with hematite, potassium ferrites, the active components of iron oxide catalysts. A distinctive feature of these samples is that, upon heating, the endothermic dip is shifted from 745°C (for the middle layer) to 791°C (for the lower layer) and the loss of mass in the temperature range 650–850°C increases from 5.07 to 6.48 wt %, respectively (Table 3). Probably, this occurs because the concentration of potassium carbonate in the lower layers is high and, consequently, a larger amount of potassium ferrites is formed. These data are confirmed by the results of titration (Table 4). The DSC curve for a sample from the lower layer (Fig. 3) shows a distinct endothermic effect at T_{min} = 882°C, which is associated with decomposition of potassium carbonate to the oxide and cannot be determined quantitatively.

The amount of carbon formed in the course of catalyst operation was determined using an analyzer for sulfur and coke; the corresponding kinetic curves are shown in Fig. 4. The kinetic curve describing the sample burning-out at the upper layer exhibits a single peak in the interval 0–30 s. According to DTA and elemental analysis data, this range is related to burning-out of carbon deposits, which is confirmed by the results of titration and quantitative determination of carbon deposits and potassium carbonate in spent catalyst samples (Table 4).

The kinetic curves of carbon burning-out (Fig. 4) show two peaks for samples from the middle and

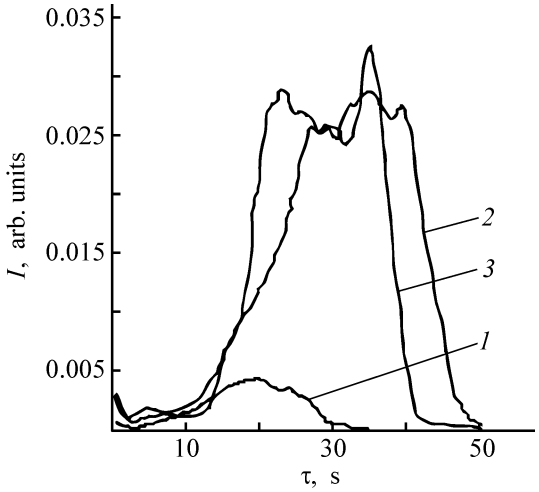


Fig. 4. Kinetic curves of carbon burning-out in spent catalyst samples taken from (*1*) upper, (*2*) middle, and (*3*) lower layers. (*I*) Signal and (τ) burning-out time.

Table 5. XPA data for calcined spent catalyst samples

Sample no.	CSR size at indicated d, Å			Area under the strongest reflections, arb. units, at indicated d, Å			Phases present
	2.70 (hematite)	11.90 (polyferrite)	3.12 (cerium oxide)	2.70 (hematite)	11.90 (polyferrite)	3.12 (cerium oxide)	
2	419.26	–	382.92	273.59	–	98.29	α-Fe_2O_3, CeO_2, Trace amounts of Fe_3O_4
3	273.92	245.28	382.92	92.98	70.28	88.68	$K_xFe_{22}O_{34}$, α-Fe_2O_3, CeO_2, trace amounts of Fe_3O_4
4	222.40	211.44	372.56	68.41	44.67	82.44	The same

Table 6. Results of tests of fresh and calcined spent catalyst samples

Sample no.	A, %	S, %	Sample no.	A, %	S, %
1	42.0	88.4	3	36.4	88.4
2	17.9	82.6	4	35.9	88.5

lower layers. The carbon deposits burn-out to the maximum extent in 30 s. The first peak is formed before the end of this period and belongs to burning-out of carbon deposits, and the second in the range 35–40 s, to decomposition of potassium carbonate, because K_2CO_3 decomposes at higher temperatures and, accordingly, its burning-out takes a longer time.

Thus, the concentration of potassium in the middle and lower layers is close to that in a fresh sample, with ferrites formed in repeated calcination of the samples under study. To verify the formation of potassium ferrites with certain parameters, the samples were repeatedly calcined at 750°C for 1 h and 850°C for 30 min and subjected to XPA. The X-ray diffraction patterns of the calcined samples are shown in Fig. 5.

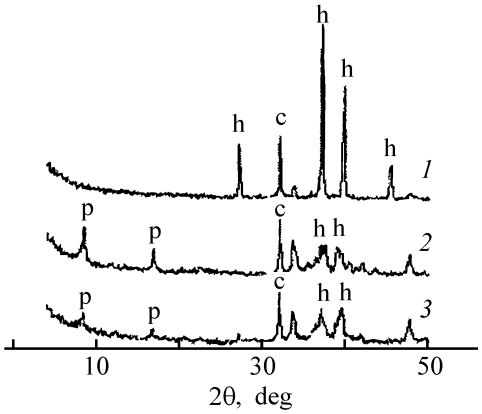
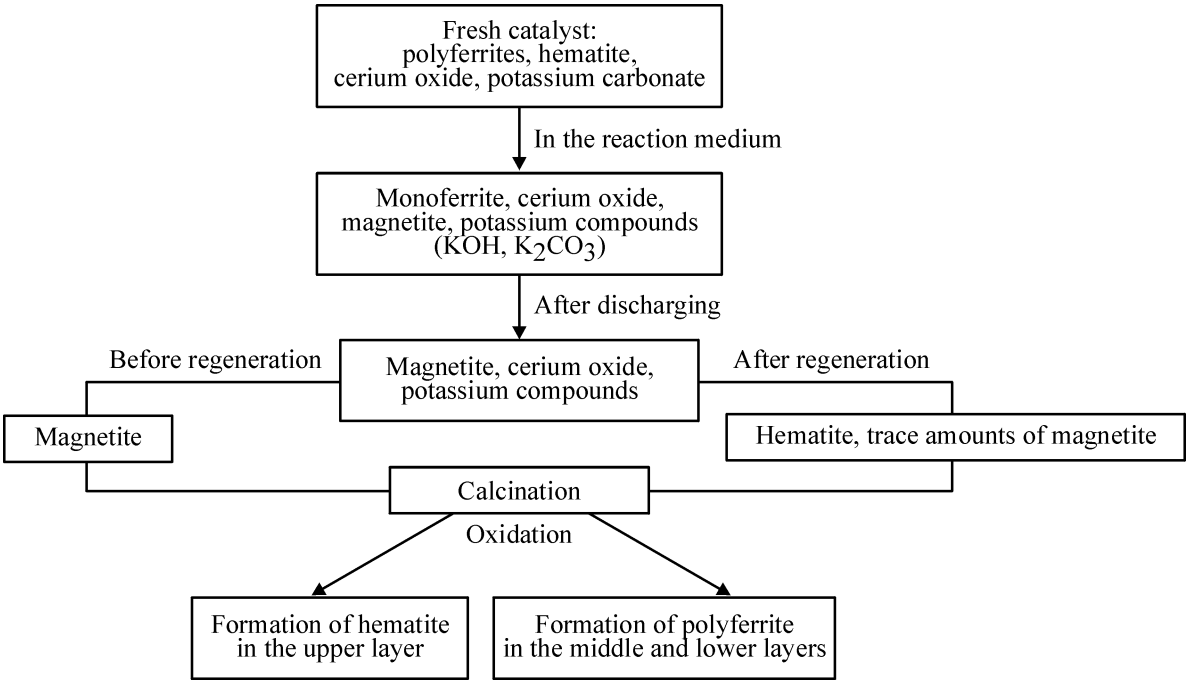


Fig. 5. X-ray diffraction patterns of calcined spent samples from (*1*) upper, (*2*) middle, and (*3*) lower layer of the catalyst bed in an adiabatic reactor.

It can be seen from the X-ray diffraction patterns in Fig. 5 that the phase composition of calcined samples differs from that of spent samples. In calcined spent samples, the following phases are observed: hematite (d = 2.70 Å), potassium polyferrite (d = 11.90 Å), cerianite (d = 3.12 Å), and magnetite (d = 2.53 Å). The calcined samples are characterized, in contrast to the spent samples, by the presence of the polyferrite phase in the middle and lower layers, because, in sample calcination, magnetite is oxidized to hematite and interacts with potassium carbonate. In this case, the quantitative content of potassium polyferrites and hematite is, respectively, lower and higher than that in the fresh sample. This is indicated by the XPA data in Tables 1 and 5.

Probably, the less intensive ferrite formation is due to healing of defects in iron oxide in the course of catalyst operation. According to XPA data, spent calcined samples from the upper, middle, and lower layers are characterized by a smaller CSR in hematite (Table 5), compared with that for the fresh catalyst (Table 1). The CSR of hematite in samples from middle and lower layers is nearly two times smaller in size than the CSR of hematite from the upper layer. Probably, this is due to the effect of potassium compounds on the crystallization of hematite.



Block diagram of transformations of the phase composition of the iron oxide catalyst in exploitation and reactivation.

Thus, the phase component of the catalyst changes both in the course of exploitation and in reactivation at different points of the reactor (see scheme).

To determine the catalytic activity of spent samples, they were tested under laboratory conditions. In the course of exploitation, the catalyst is deactivated, with its catalytic parameters under laboratory conditions impaired.

As can be seen in Table 6, the fresh catalyst has high activity *A* and selectivity *S*, in contrast to the spent sample from the upper layer, although samples from the lower and middle layers have rather high values of the catalytic parameters. Under industrial conditions, the catalyst is completely discharged from all the layers, which is not quite advisable because the capacity of the middle and lower layer is not fully exhausted. Therefore, further use of the catalyst from lower layers is possible.

CONCLUSIONS

(1) The phase composition of the catalyst changes in the course of its exploitation, with the CSR size for hematite decreasing.

(2) According to the results of a differential-thermal analysis, the steam regeneration of the catalyst under industrial conditions fails to fully remove carbon deposits and to oxidize magnetite to hematite.

(3) The distribution of the residual potassium along the height and diameter of the catalyst bed is not uniform because of the inefficient operation of the distributing device.

(4) Spent catalysts from lower layers have sufficiently high catalytic parameters. Consequently, the spent catalyst can be repeatedly used as a precatalyst or in the main bed.

REFERENCES

1. Mukhlenov, I.P., Dobkina, E.I., Deryuzhkina, V.I., and Soroko, V.E., *Tekhnologiya katalizatorov* (Technology of Catalysts), Leningrad: Khimiya, 1979.
2. Kolesnikov, I.M., *Kataliz i proizvodstvo katalizatorov* (Catalysis and Manufacture of Catalysts), Moscow: Tekhnika TUMA GRUPP, 2004.
3. Rossetti, I., Bencini, E., Trentini, L., and Forni, L., *Appl. Catal. A: General*, 2005, vol. 292, pp. 118–123.
4. RF Patent 2266785.
5. *J. Catal.*, 211.265-272 doi:10.1006\jcat.2002.3725.

ISSN 1070-4272, Russian Journal of Applied Chemistry, 2008, Vol. 81, No. 2, pp. 218–222. © Pleiades Publishing, Ltd., 2008.
Original Russian Text © D.G. Cherkasov, M.P. Smotrov, K.K. Il'in, 2008, published in Zhurnal Prikladnoi Khimii, 2008, Vol. 81, No. 2, pp. 229–233.

PHYSICOCHEMICAL STUDIES OF SYSTEMS AND PROCESSES

Equilibrium in the Liquid–Liquid System and Critical Phenomena in the Ternary System Constituted by Water, Pyridine, and Butyric Acid in the Temperature Range 5–55°C

D. G. Cherkasov, M. P. Smotrov, and K. K. Il'in

Chernyshevsky State University, Saratov, Russia

Received May 2, 2007

Abstract—Visual-polythermic method was used to study the mutual solubility of the components and critical phenomena in the system constituted by water, pyridine, and butyric acid in the temperature range 5.0–55.0°C. The temperature dependence of the composition of the critical solubility point was determined.

DOI: 10.1134/S1070427208020110

Extractive methods of extraction, separation, and concentration of substances are widely used in the technological practice. These methods have a number of disadvantages, the main of which is use of easily volatile and combustible solvents, hydrocarbons. This problem can be solved by using unconventional ternary extractive systems [1] containing no hydrocarbons. System of this kind are frequently characterized by a closed binodal curve, whose appearance was attributed by Mertslin [2] and, later, by his followers [3–5] to chemical interaction of the components of a binary boundary system. In this system, a new compound with limited solubility in water is formed. The wide diversity of stratifying systems and the simplicity and high selectivity of methods for recovery of various substances indicate that these methods are promising.

The most complete pattern of phase equilibria, necessary for optimization of extractive processes, can be obtained by constructing solubility diagrams and determining the coordinates of the critical point of the stratification region. The position of the critical point on a stratification isotherm characterizes the interaction of components in a system, and, therefore the problem of its coordinates and factors affecting its composition are rather important in a study of the mutual solubility of liquids. As temperature is raised or lowered, the closed stratification region may disappear via, respectively, the upper or lower three-component critical solubility point (UTCSP or LTCSP) [2–5]. Unfortunately, the compositions of the critical points in the solubility isotherms are unknown for the overwhelming majority of systems with a closed stratification region and the coordinates of UTCSP and LTSCP have been occasionally determined inaccurately and not for all systems.

In [4], the system constituted by water, pyridine, and butyric acid was studied by the method of isothermal titration and closed binodal curves were plotted in the concentration triangle at 12, 25, 38, and 50°C. The area of the stratification field decreased as temperature was elevated. The mutual solubility minima in the binodals demonstrated that an unstable compound was formed in the system with pyridine and butyric acid, with the component ratio of 1 : 2, respectively. The dissociation of this compound became stronger upon heating. The authors suggested that the given system has a UTCSP at 53°C and provided an approximate critical composition (wt %): C_5H_5N 19, $C_4H_8O_2$ 26, and H_2O 55. However, the compositions of the critical points in the solubility isotherms were not determined and the UTCSP coordinates were found approximately.

In the present study, the effect of temperature on the mutual solubility of the components and the composition of the critical solution for the system constituted by water, pyridine, and butyric acid in the temperature range 5.0–55.0°C was analyzed in order to reveal fundamental aspects of the topological transformation of the solubility diagrams of ternary systems with a closed stratification region.

EXPERIMENTAL

The solvents used in the study were thoroughly purified. Water was obtained using a DEM-20 MERA-POLNA redistiller. An analytically pure preparation of pyridine (content of main substance > 99%) was dried and distilled by the procedure described in [6]. A butyric acid preparation of pure grade was purified using the procedure developed in this study: it was first dried over calcined magnesium sulfate for one week, the filtrate was distilled on an installation with a herringbone dephlegmator of height 0.3 m, and the fraction boiling in the range 163.0–164.0°C was taken. The solvents were identified by the boiling points, refractive indices, and densities; their physical constants are in good agreement with reference data [7].

The polythermic study of the phase equilibria in the ternary system was performed by the visual-polythermic method, and the solution compositions corresponding to the critical solubility points were found by the method of phase volume ratio [8]. The method used to process the results of the polythermic study and to construct isothermal phase diagrams of the ternary system was described in [8]. The relative error in determining the mixture compositions corresponding to the phase transition points at the chosen temperature was ±0.5%.

The compositions of the component mixtures were varied along 11 sections of the concentration triangle of the system. The component mixtures for sections *I–V* had a variable content of pyridine and constant mass ratio between butyric acid and water: *I* 24.00 : 76.00, *II* 30.00 : 70.00, *III* 37.00 : 63.00, *IV* 44.00 : 56.00, and *V* 52.00 : 48.00. The component mixtures along sections *VI–XI* had a variable content of water and constant mass ratio between butyric acid and pyridine: *VI* 77.00 : 23.00, *VII* 68.00 : 32.00, *VIII* 61.00 : 39.00, *IX* 58.30 : 41.70, *X* 57.00 : 43.00, and *XI* 56.00 : 44.00.

It was found that the polytherms of mutual solubility of the components of the system are similar for all the sections: the parabola-shaped solubility curve separates the stratification field $l_1 + l_2$ from the field of homogeneous solutions, *l*. Of particular interest were the polytherms for sections *III* and *VI–XI*, some of whose mixtures exhibited critical phenomena between two liquid phases. In each of these sections, as well as in a number of additional sections, the mixture composition and the temperature corresponding to the critical solubility point were determined. Temperature dependences of the content of butyric acid and pyridine in critical solutions are shown in Fig. 1. At 50.7°C, these curves exhibit a temperature maximum at the point *K*' corresponding to a mixture of composition (wt %): $C_4H_8O_2$ 27.97, C_5H_5N 20.00, and H_2O 52.03.

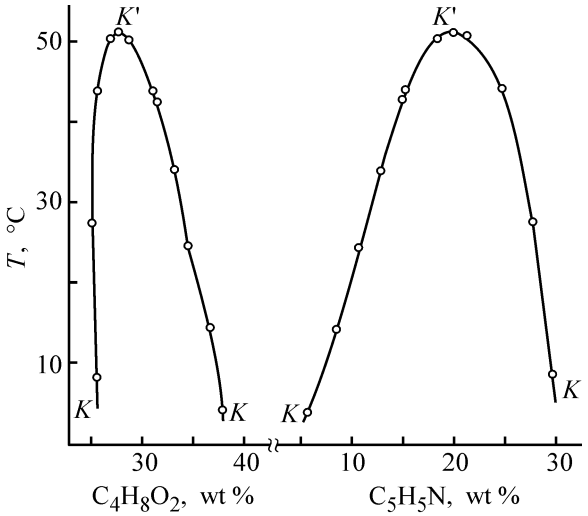


Fig. 1. Content of $C_4H_8O_2$ and C_5H_5N in the mixtures corresponding to the critical solubility points of the system H_2O–C_5H_5N–$C_4H_8O_2$ vs. temperature *T*.

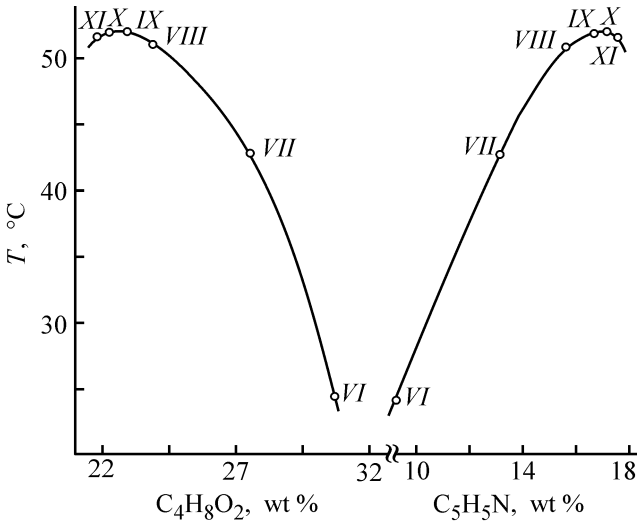


Fig. 2. Content of $C_4H_8O_2$ and C_5H_5N in the mixtures corresponding to the maximum coexistence temperatures of two liquid phases along sections *VI–XI* of the system H_2O–C_5H_5N–$C_4H_8O_2$ vs. temperature *T*.

The polytherms of mutual solubility of the components were used to construct dependences of the content of butyric acid and pyridine in mixtures corresponding to the coexistence temperatures of two liquid phases along sections *VI–XI* of the ternary system (Fig. 2). The coordinates of peaks in these curves correspond to the maximum coexistence temperature

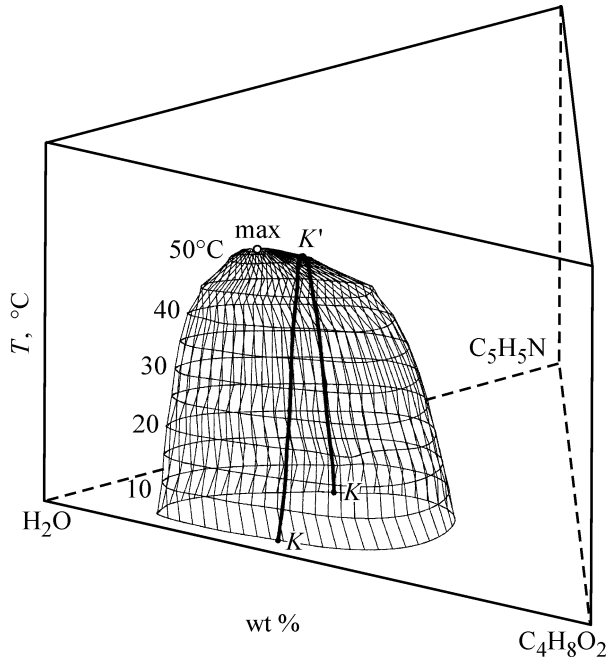


Fig. 3. Volume of two liquid phases delimited by the surface with a line of critical solubility points *KK'K* of the system H_2O–C_5H_5N–$C_4H_8O_2$ in the temperature–concentration prism. (*T*) Temperature.

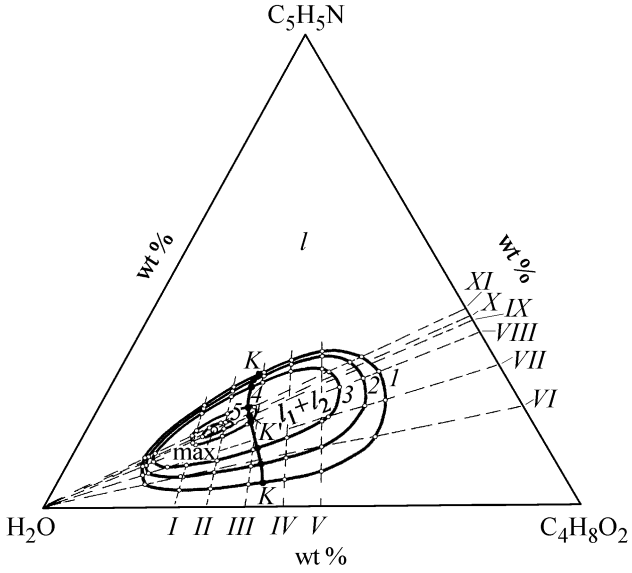


Fig. 4. Orthogonal projections of isothermal sections of the volume of two liquid phases in the system H_2O–C_5H_5N–$C_4H_8O_2$ onto the base of the temperature–concentration prism at different temperatures. Temperature (°C): (*1*) 5.0, (*2*) 20.0, (*3*) 35.0, (*4*) 50.0, and (*5*) 51.5. *KK'K* curve is the orthogonal projection of the line of critical solubility points on the binodal surface.

of two liquid phases in the given system (52.0°C) and to the composition (wt %): $C_4H_8O_2$ 22.77, C_5H_5N 17.17, and H_2O 60.06.

The method of graphical interpolation was used to determine, from the solubility polytherms and critical curves (Fig. 1), the mutual solubility of the components and the compositions of the critical points at 5.0, 10.0, 15.0, 20.0, 25.0, 30.0, 35.0, 40.0, 45.0, 50.0, and 51.5°C. The table lists data for 5.0, 20.0, 25.0, 35.0, 40.0, 50.0, and 51.5°C. To determine the fundamental aspects of the topological transformation of the volume of two liquid phases at different temperatures, the binodal surface (Fig. 3) along which passes the line of critical solubility points *KK'K* was constructed. This surface has a temperature maximum at the point *K'* at 50.7°C. There is a point (designated as max) on the binodal surface, to which corresponds a mixture with the maximum existence temperature of equilibrium between two phases in the system (52.0°C).

Figure 4 shows orthogonal projections of isothermal sections of the volume of two liquid phases of the system to the base of the temperature–concentration prism (solubility isotherms) at 5.0, 20.0, 35.0, 50.0, and 51.5°C. Each solubility isotherm is a closed binodal curve separating the field of the two-phase liquid phase, $l_1 + l_2$, from that of homogeneous solutions, *l*. The binodal curve at 5.0°C runs near the H_2O–$C_4H_8O_2$ side of the concentration triangle from the vertex corresponding to water toward the C_5H_5N–$C_4H_8O_2$ side. As temperature is elevated, the area of the field of two liquid phases decreases because of the increase in the mutual solubility of the components. At a higher temperature the stratification field lies within the stratification field for a lower temperature. In each binodal curve for 5.0, 20.0, 35.0, and 50.0°C (Fig. 4), there are two critical solubility points denoted by black circles. The critical points lie against those sides of the composition triangle which correspond to binary systems water + pyridine and water + butyric acid, which points to a weaker interaction between the components of these binary systems, compared with the chemical interaction of the components in the system constituted by pyridine and butyric acid. In the last binary system, there occurs an acid–base interaction of the components to give a molecular compound with a hydrogen bond [9]. According to Mertslin's concept [10], the boundary binary system pyridine + butyric acid is a system with a predominant interaction between the components in the ternary system under study.

The *KK'K* curve in Fig. 4 is an orthogonal projection of the line of critical points *KK'K* on the binodal surface delimiting the volume of two liquid phases that are in equilibrium (Fig. 3). The point *K'* in this curve corresponds to the composition of a mixture with the maximum critical temperature of equilibrium

Mutual solubility of the components of the ternary system H_2O–C_5H_5N–$C_4H_8O_2$

Composition of the saturated solution, wt %								
H_2O	$C_4H_8O_2$	C_5H_5N	H_2O	$C_4H_8O_2$	C_5H_5N	H_2O	$C_4H_8O_2$	C_5H_5N
				T = 5.0°C				
79.0	16.2	4.8	44.5	26.1	29.4	44.2	47.9	7.9
78.2	14.8	7.0	37.9	29.8	32.3	52.7	41.4	5.9
77.2	13.9	8.9	31.5	34.2	34.3	56.9*	37.7*	5.4*
75.7	13.6	10.7	24.8	42.1	33.1	59.8	35.2	5.0
59.0	18.6	22.4	23.1	46.9	30.0	67.2	28.8	4.0
51.7	22.1	26.2	24.8	51.1	24.1	73.0	23.1	3.9
45.2*	25.6*	29.2*	30.8	53.3	15.9	–	–	–
				T = 20.0°C				
77.2	15.5	7.3	38.4	30.1	31.5	50.0	39.3	10.7
76.6	14.3	9.1	32.1	34.8	33.1	55.1*	35.5*	9.4*
75.3	13.8	10.9	27.6	40.5	31.9	57.4	33.7	8.9
59.4	18.8	21.8	26.7	44.7	28.6	64.7	27.8	7.5
52.1	22.4	25.5	29.3	48.1	22.6	71.0	22.4	6.6
46.7*	25.4*	27.9*	41.5	45.0	13.5	71.7	21.8	6.5
44.9	26.3	28.8	41.7	45.1	13.2	–	–	–
				T = 25.0°C				
76.2	14.5	9.3	38.6	30.3	31.1	49.2	38.7	12.1
75.2	13.9	10.9	32.4	35.1	32.5	54.6*	34.7*	10.7*
59.7	18.8	21.5	28.7	39.9	31.4	56.6	33.3	10.1
52.4	22.4	25.2	28.2	43.8	28.0	64.1	27.5	8.4
47.2*	25.3*	27.5*	31.4	46.7	21.9	70.2	22.2	7.6
45.1	26.5	28.4	40.8	44.3	14.9	74.5	17.9	7.6
				T = 35.0°C				
74.7	15.4	9.9	39.3	30.9	29.8	47.5	37.4	15.1
73.6	14.8	11.6	33.6	36.3	30.1	54.0*	33.0*	13.0*
60.3	19.0	20.7	32.3	37.9	29.8	55.1	32.3	12.6
53.1	22.7	24.2	32.0	41.5	26.5	62.9	26.9	10.2
48.2*	25.4*	26.4*	37.3	42.6	20.1	68.9	21.8	9.3
45.9	26.9	27.2	39.0	42.2	18.8	72.7	18.6	8.7
				T = 40.0°C				
73.3	16.3	10.4	39.9	31.3	28.8	46.6	36.6	16.8
72.1	15.6	12.3	34.8	37.7	27.5	53.7*	32.0*	14.3*
60.8	19.2	20.0	35.0	36.4	28.6	54.1	31.8	14.1
53.5	23.0	23.5	34.8	39.8	25.4	62.0	26.6	11.4
49.1*	25.5*	25.4*	44.8	37.5	17.7	69.0	21.1	9.9
46.4	27.2	26.4	37.4	40.6	22.0	69.3	20.7	10.0
				T = 50.0°C				
65.4	20.6	14.0	51.3*	27.2*	21.5*	59.2	25.4	15.4
65.2	19.5	15.3	50.0	28.0	22.0	65.2	21.2	13.6
63.3	20.0	16.7	52.5*	29.0*	18.5*	–	–	–
55.8	23.9	20.3	53.3	28.5	18.2	–	–	–
				T = 51.5°C				
63.0	21.6	15.4	58.0	23.5	18.5	55.5	25.9	18.6
60.7	22.0	17.3	57.0	24.4	18.6	57.9	24.8	17.3

* Critical solubility point.

between the two liquid phases (50.7°C) in the system (Fig. 1). Within the stratification field at 51.5°C, there is a point (designated by a large circle and an inscription max) corresponding to the composition of a mixture with the maximum coexistence temperature of two liquid phases (52.0°C) in the given system (Fig. 2). Thus, the volume of two liquid phases in the system constituted by water, pyridine, and butyric acid disappears as temperature is elevated via the noncritical point. This conclusion disagrees with the results of [4]. Such a transformation of the closed stratification region, with its disappearance via the noncritical point, is observed for the first time.

The transversal line passed from the H_2O vertex of the concentration triangle via the extremum points of the binodal points at 5.0 and 20.0°C intersects the C_5H_5N–$C_4H_8O_2$ size (Fig. 4) at the point corresponding to the composition of the rational compound between the components of this binary system, in a ratio of 2 : 3, respectively. This compound has a limited solubility in water, in contrast to pyridine and butyric acid exhibiting unlimited solubility. As temperature increases, the solubility extrema are shifted from this composition to an irrational component ratio. It can be assumed that the mutual solubility of the components of the ternary system increases, as temperature is elevated, because of the decomposition of the chemical compound formed.

CONCLUSIONS

(1) The mutual solubility of the components was determined in the range 5.0–55.0°C and the temperature dependence of the critical solution was found for the ternary system constituted by water, pyridine, and butyric acid. It was shown that the solubility of the components increases with temperature.

(2) The mixture compositions corresponding to the maximum coexistence temperature of two liquid phases in the system under study (52.0°C) and to the maximum critical temperature (50.7°C) were determined. On the basis of these data, it was found for the first time that, in systems with a closed stratification region, the volume of two liquid phases can disappear via the noncritical point as temperature is elevated.

(3) A polythermic study of the solubility diagram of the system constituted by water, pyridine, and butyric acid yielded results that can be used in extractive practice as reference data.

REFERENCES

1. Yakovleva, T.P., Lesnov, A.E., Petrov, B.I., et al., *Izbrannye glavy fiziko-khimicheskogo analiza, v 2-kh chastyakh* (Selected Chapters of Physicochemical Analysis, in 2 parts), Perm: Perm. Univ.; ENI pri Perm. Univ., 2003, part 1, pp. 135–171.
2. Mertslin, R.V., *Zh. Obshch. Khim.*, 1936, vol. 6, no. 12, pp. 1828–1840.
3. Zhuravlev, E.F., *Zh. Obshch. Khim.*, 1959, vol. 29, no. 10, pp. 3178–3183.
4. Krupatkin, I.L. and Rozhentsova, P.O., *Zh. Fiz. Khim.*, 1970, vol. 44, no. 4, pp. 1036–1039.
5. Sergeeva, V.F. and Matyushinskaya, L.B., *Zh. Obshch. Khim.*, 1977, vol. 47, no. 6, pp. 1215–1218.
6. *Laboratorni Technica organicke Chemie*, Keil, B., Ed., Praha: Ceskoslovenske Akademie ved, 1963.
7. *Khimicheskaya entsiklopediya* (Chemical Encyclopedia), Knunyants, I.L., Ed., Moscow: Sovertskaya Entsiklopediya, 1988–1998, vols. 1–5.
8. Sinegubova, S.I., Il'in, K.K., and Cherkasov, D.G., *Zh. Prikl. Khim.*, 2005, vol. 78, no. 3, pp. 394–397.
9. Gusakova, G.V., Denisov, G.S., and Smolyanskii, A.P., *Zh. Prikl. Spektrosk.*, 1972, vol. 10, no. 3, pp. 503–505.
10. Nikurashina, N.I. and Mertslin, R.V., *Metod sechenii: Prilozhenie ego k izucheniyu mnogofaznogo sostoyaniya mnogokomponentnykh sistem* (Method of Sections Applied to a Study of the Multiple-Phase State of Multicomponent Systems), Saratov: Saratov. Univ., 1969.

ISSN 1070-4272, Russian Journal of Applied Chemistry, 2008, Vol. 81, No. 2, pp. 223–230. © Pleiades Publishing, Ltd., 2008.
Original Russian Text © M.A. Toikka, B.I. Gorovits, A.M. Toikka, 2008, published in Zhurnal Prikladnoi Khimii, 2008, Vol. 81, No. 2, pp. 234–240.

PHYSICOCHEMICAL STUDIES OF SYSTEMS AND PROCESSES

Solubility in the System Constituted by Acetic Acid, *n*-Propanol, Water, and *n*-Propyl Acetate

M. A. Toikka, B. I. Gorovits, and A. M. Toikka

St. Petersburg State University, St. Petersburg, Russia

Received September 17, 2007

Abstract—Experimental data on the solubility in the system constituted by acetic acid, *n*-propanol, water, and *n*-propyl acetate at 313.15 K are presented. The position of the critical curve for the liquid–liquid equilibrium, including that of the critical points on the chemical equilibrium surface, is discussed.

DOI: 10.1134/S1070427208020122

Studies of the compositions of equilibrium liquid phases in stratifying systems are highly important both for the development of the fundamental theory of phase equilibria and for practical purposes, e.g., for performing extraction processes. In recent years, a particular practical interest has aroused in combined reactive mass-exchange processes in which a chemical reaction and a phase transition occur simultaneously. An example of the related applications most widely used in chemical technology is the reactive rectification [1–5], i.e., a combined process involving a liquid–vapor phase transition. Theoretical studies are also mostly devoted to problems of equilibrium of chemically reacting liquid phases with a vapor [1–9]. A considerably smaller attention is given in the literature to extraction processes accompanied by chemical reactions. In this context, of certain importance for the development of the theory of reactive mass-exchange processes are studies of chemically reacting systems with stratifying liquid phases. In this communication, we present and discuss the results of an experimental study of the solubility of liquid phases in a system with an etherification reaction.

As object of study served the system constituted by acetic acid, *n*-propanol, water, and *n*-propyl acetate at 313.15 K. Our choice of the system was governed by the availability of detailed experimental data on the chemical equilibrium for the reaction of etherification-hydrolysis of the ester in this system [10], which enable construction of the chemical equilibrium surface in the concentration tetrahedron. Also, there are published data on the liquid–liquid equilibrium in both stratifying ternary subsystems: acetic acid + *n*-propyl acetate + water at 313.15 K [11] and *n*-propanol + *n*-propyl acetate + water under isothermal and isobaric conditions [12, 13]. Because the temperature in [12, 13] differed from 313.15 K, we experimentally studied the solubility at this temperature. In addition, data on certain compositions of the equilibrium liquid–liquid phases of the quaternary system have been obtained previously [14–16], with a gas-chromatographic analysis used.

All the reagents used in the study were thoroughly purified and their physicochemical constants (refractive index and boiling point) were in agreement with published data [17, 18]. The refractive index was determined with an IRF-454B2M refractometer at a temperature of 293.15 K, maintained by a TZh-TS-01 liquid thermostat. The boiling points were determined with a Sventoslavskii ebulliometer at several pressures close to the atmospheric pressure and then were recalculated to a pressure of 101 kPa. Also, the purity of the substances was additionally monitored by gas chromatography. The chromatographic analysis was performed with an LKhM-8MD chromatograph, model 2. Its fluoroplastic column with a length of about 2.5 m and inner diameter of 3 mm was packed with Chromaton N-Super with grain size of 0.3–0.4 mm, impregnated with 7 wt % dinonylphthalate and 1 wt % 1,2,3-tris(β-cyanoetoxy)-propane relative to the mass of the solid carrier. The working thermostating temperature was about 370 K for the columns and 390 K for the heat-conductivity detector. These conditions enable separation of the components of the system and provide sensitivity to possible impurities and primarily to products of the etherification-hydrolysis reaction [15].

Table 1. Experimental data on the solubility in the three-component system constituted by (2) *n*-propanol, (3) water, and (1) *n*-propyl acetate at 313.15 K

Concentration, mole fraction			Concentration, mole fraction		
x_2	x_3	x_1	x_2	x_3	x_1
0.150	0.821	0.029	0.279	0.548	0.174
0.164	0.793	0.043	0.287	0.527	0.186
0.187	0.759	0.054	0.288	0.494	0.218
0.224	0.701	0.075	0.281	0.453	0.266
0.235	0.681	0.084	0.273	0.388	0.339
0.232	0.680	0.088	0.210	0.288	0.502
0.251	0.647	0.102	0.089	0.895	0.016
0.256	0.632	0.112	0.131	0.839	0.030
0.262	0.618	0.120	0.166	0.791	0.043
0.267	0.604	0.130	0.153	0.195	0.652
0.271	0.592	0.137	0.092	0.891	0.017
0.272	0.585	0.143	0.062	0.930	0.008
0.275	0.574	0.151	0.049	0.945	0.006
0.278	0.565	0.157	0.062	0.117	0.821

The solubility (stratification limits) was determined by isothermal titration. As is known, this method can, in most cases, most accurately determine the position of the binodal [19–21]. We carried out the experiment in two ways; (a) by titration of a stratifying solution with a solvent until a homogeneous state was reached (titration to "clarification") and (b) by titration of a homogeneous solution until stratification occurred (titration to "turbidization"). The starting solutions were prepared by the gravimetrical method on an HF0-200 analytical balance with an accuracy as good as 0.001 g. The titration was performed in a thermostat (313.15 K) under continuous stirring with a magnetic stirrer. The titrating liquid was introduced into the mixture with microburettes (2 and 5 ml). The titrant volume was measured with an accuracy of 0.05 ml; when determining the amount of the liquid spent for the titration, its density was taken into account (commonly, the microburette temperature was about 298 K). As the final point of titration (both to clarification and to turbidization) and, accordingly, the solubility (stratification) limit were taken clarification or turbidization of a solution being titrated during no less than 2 min. With account of the volume of the mixture being titrated and the drop size of the titrating liquid (0.02 ml in the case of titration with twice-distilled water and 0.01 ml in titration with *n*-propanol), the accuracy with which the concentrations were determined was not worse than 0.001 mol %. With account of all the other possible factors affecting the accuracy of the results (purity of reagents, thermostating errors), the maximum error of the data obtained can be estimated as not exceeding ±0.002 mole fractions of a component.

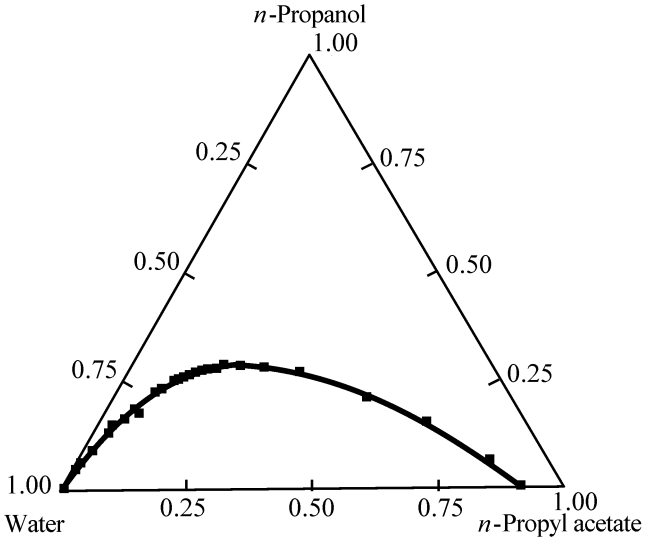


Fig. 1. Solubility curve for the three-component system constituted by *n*-propanol, water, and *n*-propyl acetate at 313.15 K.

When studying the three-component system constituted by *n*-propanol, water, and *n*-propyl acetate, we titrated binary stratifying mixtures of water and ester with *n*-propanol. The starting compositions were chosen in such a way that the points were, on the whole, uniformly distributed along the binodal; at the same time, the density of the points near the critical point was considerably higher. The data we obtained for the solubility in the ternary system constituted by *n*-propanol, water, and *n*-propyl acetate are listed in Table 1, and the solubility curve is shown in Fig. 1.

Table 2. Experimental data on the solubility in the system constituted by (1) acetic acid, (2) *n*-propanol, (3) water, and (4) *n*-propyl acetate at 313.15 K

Concentration ratio, mole fraction	Concentration on the solubility surface of the system, mole fraction				Concentration ratio, mole fraction	Concentration on the solubility surface of the system, mole fraction			
	x_1	x_2	x_3	x_4		x_1	x_2	x_3	x_4
Titration with water Acid : alcohol									
3 : 1	0.173	0.058	0.543	0.226	1 : 3	0.052	0.157	0.709	0.082
	0.166	0.055	0.607	0.173		0.064	0.192	0.594	0.150
	0.174	0.058	0.497	0.272		0.068	0.203	0.518	0.211
	0.148	0.049	0.687	0.116		0.065	0.195	0.437	0.304
	0.117	0.039	0.783	0.061		0.057	0.172	0.366	0.404
	0.167	0.056	0.428	0.349		0.043	0.130	0.286	0.541
	0.146	0.049	0.349	0.456					
	0.133	0.045	0.335	0.487	1 : 4	0.015	0.062	0.911	0.012
	0.115	0.038	0.306	0.540		0.033	0.133	0.781	0.052
						0.048	0.192	0.648	0.113
4 : 1	0.138	0.035	0.747	0.081		0.053	0.211	0.571	0.165
	0.160	0.040	0.675	0.125		0.054	0.216	0.478	0.253
	0.175	0.044	0.610	0.172		0.050	0.200	0.398	0.353
	0.183	0.046	0.557	0.215		0.043	0.172	0.315	0.470
	0.183	0.046	0.486	0.286		0.033	0.132	0.266	0.568
	0.168	0.042	0.397	0.393		0.008	0.008	0.979	0.005
	0.146	0.036	0.335	0.484		0.047	0.047	0.890	0.017
	0.117	0.029	0.282	0.572		0.016	0.016	0.962	0.006
					0 : 0*	0.000	0.000	0.082	0.918
						0.000	0.000	0.995	0.006
Titration with *n*-propanol Acid : ester									
1 : 1	0.140	0.087	0.634	0.140	1 : 2	0.020	0.127	0.812	0.040
	0.081	0.112	0.726	0.081		0.015	0.109	0.847	0.029
	0.058	0.109	0.776	0.058		0.010	0.093	0.876	0.021
	0.045	0.097	0.814	0.045		0.180	0.052	0.408	0.360
	0.038	0.092	0.833	0.038					
	0.020	0.081	0.880	0.020	2 : 1	0.165	0.013	0.740	0.082
	0.010	0.062	0.917	0.010		0.117	0.041	0.784	0.059
	0.170	0.058	0.602	0.170		0.091	0.052	0.811	0.045
	0.218	0.014	0.551	0.218		0.074	0.059	0.830	0.037
						0.055	0.062	0.856	0.027
1 : 2	0.114	0.155	0.503	0.228		0.040	0.061	0.878	0.020
	0.069	0.183	0.611	0.137		0.029	0.057	0.900	0.014
	0.050	0.183	0.667	0.100		0.021	0.052	0.917	0.010
	0.039	0.171	0.711	0.079		0.013	0.041	0.940	0.007
	0.029	0.150	0.765	0.057					

* System of water and *n*-propyl acetate.

As noted above, data on phase equilibria in this ternary system have also been obtained previously [12, 13] for temperatures other than 313.15 K. To compare these results with our experiment and to make additional correlations, we interpolated polythermic (from 309.22 to 357.5 K) data from [12, 13] to the temperature of 313.15 K. The results of this interpolation and our experimental data for 313.15 K are in good agreement: the maximum discrepancy is about 0.01 mole fraction of a component.

The solubility in the four-component system constituted by acetic acid, *n*-propanol, water, and *n*-propyl acetate were studied with account of the subsequent possibility of a sufficiently full representation of the stratification surface in the concentration tetrahedron on the basis of the experimental data. To achieve an ordered arrangement of the composition points, the set of solutions under study was prepared with a constant ratio between the concentrations of two components in the mixture. Simultaneously, this choice of the starting compositions facilitates evaluation of the accuracy of the data with respect to accidental errors. Because stratification is observed in two of the four ternary subsystems, the ternary mixtures (acid, alcohol, ester) were titrated with water at a constant ratio between the concentrations of *n*-propanol and acetic acid.

As is known, the choice of a variant of isothermal titration (to turbidization or clarification) depends on the physicochemical properties of the system, including the concentration interval. Based on the results of the experiments performed, we established for the system under consideration that the stratification limit is more distinctly determined in titration to clarification. In this case, we chose the tetrahedron-cutting planes corresponding to a constant ratio between the concentrations of the ester and acetic acid. The compositions of the ternary mixtures (water, ester, and acid) to be subjected to titration belonged to the heterogeneous region.

The results of an experimental determination of the solubility in the system constituted by (1) acetic acid, (2) *n*-propanol, (3) water, and (4) *n*-propyl acetate at 313.15 K are listed in Table 2. The triangular diagrams corresponding to the tetrahedron sections under study, with compositions x_i/x_k = const (where x_i and x_k are the mole fractions of *i*th and *k*th components) are shown in Fig. 2; the positions of the corresponding solubility curves rather fully reflect the shape of the stratification surface of the quaternary system as a whole.

Figure 3 shows the stratification surface at 313.15 K, constructed using the experimental data obtained in our study and the data reported in [16] for the cutting planes with x_1/x_2 = 0.5, 1, and 2. In addition, we

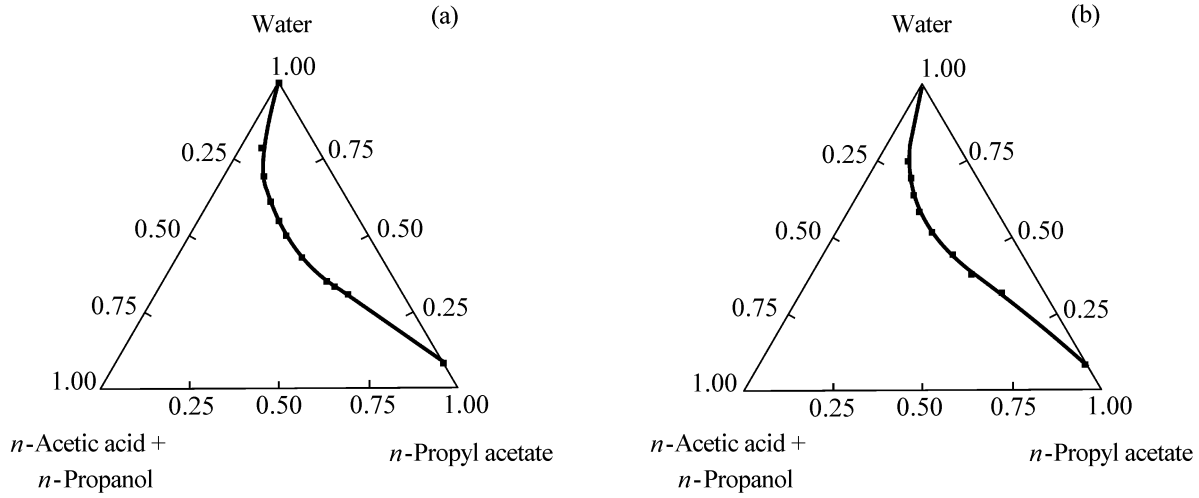


Fig. 2. Composition points belonging to the solubility surface in the system constituted by (1) acetic acid, (2) *n*-propanol, (3) water, and (4) *n*-propyl acetate at 313.15 K. Cutting planes of the concentration tetrahedron, which correspond to a constant ratio between the concentrations (mole fraction) of the components: (a) $x_1 : x_2 = 1 : 3$ (titration with water), (b) $x_1 : x_2 = 4 : 1$ (titration with water), (c) $x_1 : x_2 = 1 : 3$ (titration with water), (d) $x_1 : x_2 = 1 : 4$ (titration with water), (e) $x_1 : x_4 = 1 : 1$ (titration with alcohol), (f) $x_1 : x_4 = 1 : 2$ (titration with alcohol), and (g) $x_1 : x_4 = 2 : 1$ (titration with alcohol).

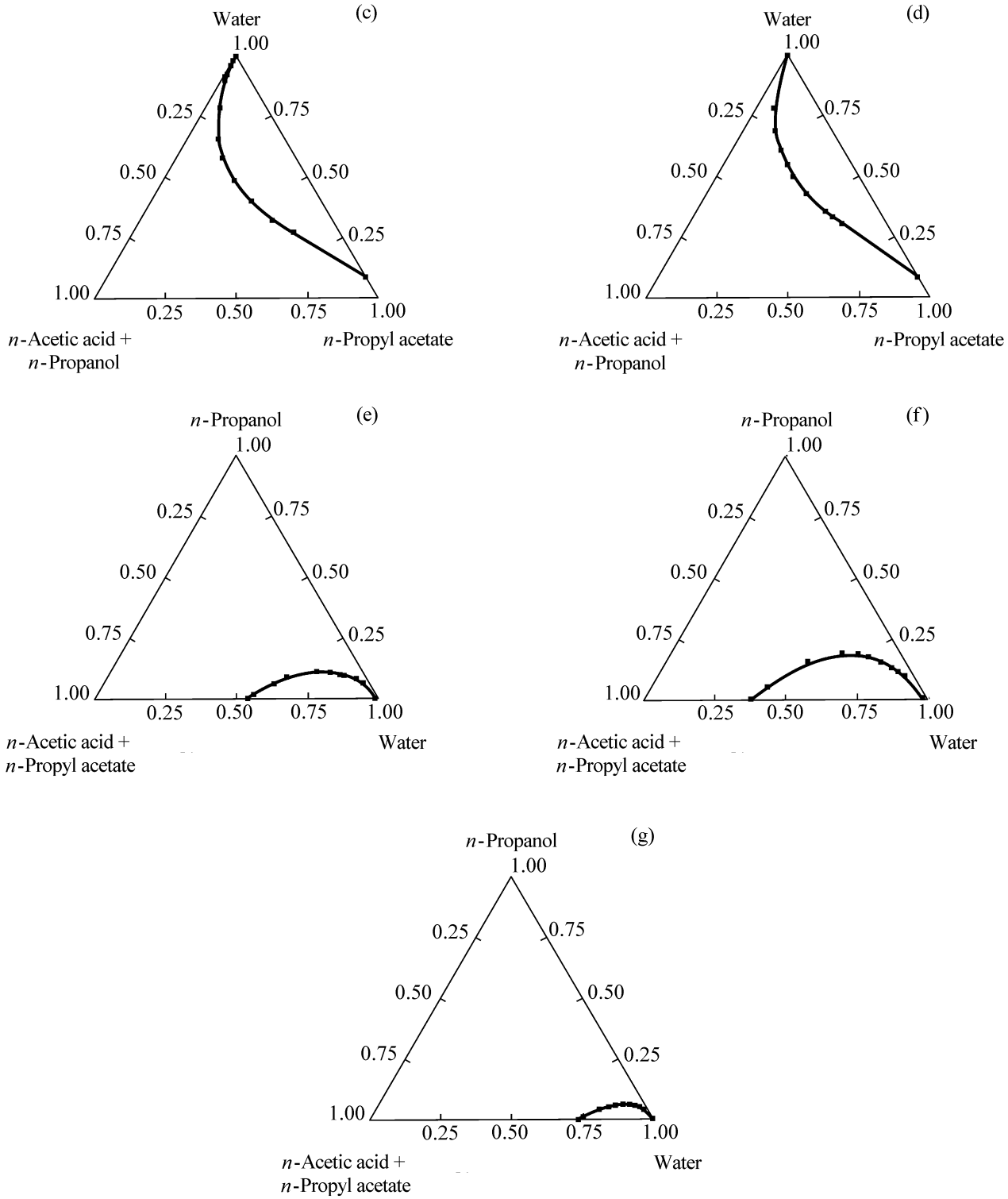


Fig. 2. (Contd.)

invoked, when analyzing the run of the critical curve and the position of the stratification surface, the data of [14, 15] on the liquid–liquid–vapor equilibrium (their thermodynamic consistency was preliminarily estimated using the Gibbs–Duhem equation). The stratification surface in Fig. 3 is presented in the concentration space having the form of an irregular tetrahedron.

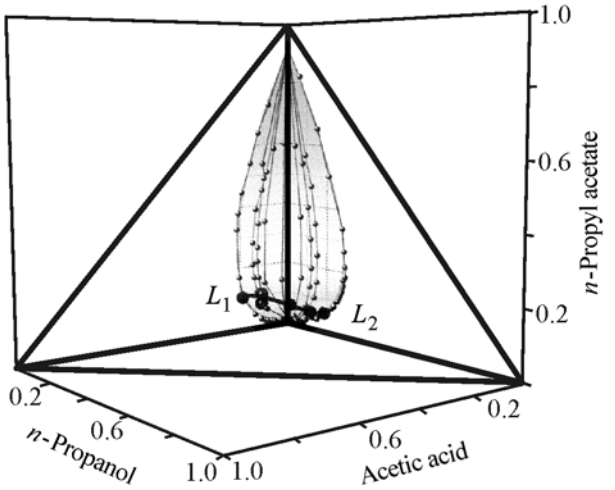


Fig. 3. Solubility surface of the system (mole fraction) constituted by acetic acid, *n*-propanol, water, and *n*-propyl acetate at 313.15 K. L_1L_2 is the critical curve for the liquid–liquid equilibrium.

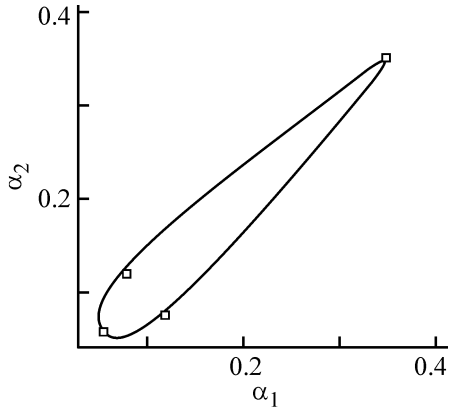


Fig. 4. Region of intersection of the solubility surface with the chemical equilibrium surface in the space of α-variables at 313.15 K. *Solid curve*, closed line; *points*, chemically equilibrium compositions belonging to the stratification surface (according to the experimental data obtained in this study).

Figure 3 also qualitatively shows the run of the liquid–liquid critical curve in the quaternary system. To analyze the run of the critical curve, we used, in addition to the results of the present study, data of [14, 15] on the liquid–liquid equilibrium in the four-component system. The compositions corresponding to the critical points and the critical curve in the quaternary system were found from data on the liquid–liquid equilibrium and monitored in the course of isothermal titration. The composition of the critical point in the ternary subsystem constituted by water, acetic acid, and *n*-propyl acetate was determined using the data of [11]. The composition of the critical point of the ternary subsystem constituted by *n*-propyl acetate, *n*-propanol, and water at 313.15 K was found experimentally (x_1 = 0.187, x_2 = 0.054, x_3 = 0.759). The composition of the same critical point was determined by processing the data of [12, 13], interpolated to 313.15 K using the geometric Coolidge method [21]. The compositions of the critical point, found by these two methods, are in good agreement. The data for constructing the critical curve in the quaternary system are listed in Table 3.

Table 3. Compositions belonging to the liquid–liquid critical curve in the system constituted by (1) acetic acid, (2) *n*-propanol, (3) water, and (4) *n*-propyl acetate at 313.15 K

Concentration, mole fraction			
x_1	x_2	x_3	x_4
0	0.187	0.759	0.054
0.190	0	0.710	0.100
0.148	0.049	0.687	0.116
0.138	0.035	0.747	0.081
0.081	0.112	0.726	0.081
0.029	0.150	0.764	0.057

The results obtained in determining the solubility and the run of the critical curve were compared with data on the chemical equilibrium of the reaction of etherification-hydrolysis of the ester at 313.15 K [10]. To the chemical equilibrium of the reactions of the type

$$R_1 + R_2 \rightleftarrows R_3 + R_4, \quad (1)$$

whose stoichiometry is similar to that of the reactions of ester synthesis, corresponds the surface in the composition tetrahedron. This surface is delimited by the ribs of the given concentration simplex, which correspond to chemically inert mixtures (acid–water, acid–ester, alcohol–water, alcohol–ester). The chemical equilibrium surface for the system constituted by acetic acid, *n*-propanol, water, and *n*-propyl acetate at 313.15 K was reported in [22]. To represent the thermodynamic properties of chemically equilibrium systems, Zharov suggested new composition variables (transformed concentration variables, or α-variables) [6, 23], which can be represented, in the case of reaction (1), as

$$\left.\begin{aligned}\alpha_1 &= x_1 + x_4,\\ \alpha_2 &= x_2 + x_4,\\ \alpha_3 &= x_3 - x_4.\end{aligned}\right\} \quad (2)$$

These variables furnish a compact and clearly understandable representation of properties for states of chemical equilibrium: the concentration space is transformed into a 2*D* complex, square of α-variables.

Based on the results of our study, we established that the chemical equilibrium surface intersects the stratification surface for the system constituted by acetic acid, *n*-propanol, water, and *n*-propyl acetate at 313.15 K in the composition tetrahedron. In other words, the states of chemical equilibrium of the given reaction include not only the region of homogeneous solutions, but also the heterogeneous region. In Fig. 4, the boundaries of this region are represented in the square of α-variables. Two points in Fig. 4 for the stratification surface and for the chemical equilibrium surface ($\alpha_1 = 0.16$, $\alpha_2 = 0.199$ and $\alpha_1 = 0.19$, $\alpha_2 = 0.14$) correspond to the critical state of the liquid–liquid equilibrium [the corresponding concentrations are as follows (mole fraction): $x_1 = 0.12$, $x_2 = 0.09$, $x_3 = 0.07$ and $x_1 = 0.07$, $x_2 = 0.12$, $x_3 = 0.07$]. These compositions can also be interpreted as points at which the critical curve intersects the chemical equilibrium surface. Thus, the results obtained in the study can be of use both for development of solubility a database for four-component liquid-phase systems and for studies of critical phenomena in chemically reacting systems. Previously, the related issues, including the topology of diagrams with reactions of another stoichiometry, were discussed only theoretically in some publications of recent years [24–28].

CONCLUSIONS

(1) Detailed experimental data on the solubility of liquid phases in the system constituted by acetic acid, *n*-propanol, water, and *n*-propyl acetate at 313.15 K were obtained. These data were used to establish that the stratification surface intersects the chemical equilibrium surface (reactions of synthesis of *n*-propyl acetate) in the composition tetrahedron. To the chemical equilibrium in the system constituted by acetic acid, *n*-propanol, water, and *n*-propyl acetate at 313.15 K corresponds not only a homogeneous region, but also a heterogeneous liquid-phase region. This region is represented in the square of transformed composition variables.

(2) It was demonstrated that the critical curve of the liquid–liquid equilibrium intersects the chemical equilibrium surface in the concentration space; accordingly, the system constituted by acetic acid, *n*-propanol, water, and *n*-propyl acetate at 313.15 K has two liquid–liquid critical points corresponding to chemically equilibrium states.

ACKNOWLEDGMENTS

The study was financially supported by the Russian Foundation for Basic Research (grant no. 06-03-32 698-a).

REFERENCES

1. Serafimov, L.A. and Balashov, M.I., *Massoperedacha s khimicheskoi reaktsiei* (Mass Transfer Involving a Chemical Reaction), Leningrad: Khimiya, 1971, chapter 17, p. 186.
2. Pisarenko, Yu.A., Kardona, K.A., and Serafimov, L.A., *Reaktsionno-rektifikatsionnye protsessy: dostizheniya v oblasti issledovaniya i prakticheskogo ispol'zovaniya* (Reactive-Rectification Processes: Advances in Research and Practical Application), Moscow: Luch, 2001.
3. Serafimov, L.A., Pisarenko, Yu.A., and Kulov, N.N., *Chem. Eng. Sci.*, 1999, vol. 54, pp. 1383–1388.
4. Doherty, M.F. and Malone, M.F., *Conceptual Design of Distillation Systems*, New York: McGraw–Hill, 2001.
5. *Reactive Distillation: Status and Future Directions*, Sundmacher, K. and Kienle, A., EDs., Weinheim: WILEYVCH Verlag GmbH & Co. KGaA, 2003.
6. Zharov, V.T., *Voprosy termodinamiki geterogennykh sistem i poverkhnostnykh yavlenii* (Problems of Thermodynamics of Heterogeneous Systems and Surface Phenomena), Storonkin, A.V., Ed., Leningrad: Len. Gos. Univ., 1973, issue 2, pp. 35–53.
7. Pervukhin, O.K. and Zharov, V.T., *Voprosy termodinamiki geterogennykh sistem i teorii poverkhnostnykh yavlenii* (Problems of Thermodynamics of Heterogeneous Systems and Surface Phenomena), Leningrad: Len. Gos. Univ., 1979, issue 5, pp. 3–29.
8. Barbosa, D. and Doherty, M.F., *Chem. Eng. Sci.*, 1988, vol. 43, no. 3, pp. 529–540.
9. Taylor, R. and Krishna, R., *Chem. Eng. Sci.*, 2000, vol. 55, pp. 5183–5229.
10. Sokolov, V.A. and Markuzin, N.P., *Eksperimental'nye dannye o ravnovesii mezhdu zhidkost'yu i parom i o khimicheskoi reaktsii v sisteme uksusnaya kislota–propilovyi spirt–voda–propilatsetat* (Experimental Data on the Liquid–Vapor Equilibrium and on the Chemical Reaction in the System Constituted by Acetic Acid, *n*-Propanol, Water, and *n*-Propyl Acetate), Available from VINITI, 1982, Leningrad, no. 35–82.
11. Toikka, A.M., Gorban', Yu.P., Ivanova, Zh.V., and Kocherbitov, V.V., *Zh. Prikl. Khim.*, 1997, vol. 70, no. 1, pp. 44–46.

12. Smirnova, N.A., Morachevskii, A.G., and Storonkin, A.V., *Vestn. Len. Gos. Univ.*, 1959, no. 22, pp. 70–76.
13. Smirnova, N.A., Morachevskii, A.G., and Storonkin, A.V., *Vestn. Len. Gos. Univ.*, 1963, no. 22, pp. 97–104.
14. Kocherbitov, V.V. and Toikka, A.M., *Zh. Prikl. Khim.*, 1999, vol. 72, no. 10, pp. 1615–1617.
15. Kocherbitov, V.V., Thermodynamic Stability and Phase Equilibrium in the system Constituted by Acetic Acid, *n*-Propanol, Water, and *n*-Propyl Acetate, *Cand. Sci. Dissertation*, St. Petersburg, 1997.
16. Toikka, M., *Distillation & Absorption 2006*, Sorensen, E., Ed., Rugby, UK: IChemE, 2006, pp. 563–573.
17. *Spravochnik khimika* (Chemist's Handbook), Nikol'skii, B.P., Ed., Leningrad: GNTIKhL, 1963.
18. *Khimicheskaya entsiklopediya v 5-ti tomakh* (Chemical Encyclopedia in 5 vols.), Knunyants, L.I., Chief Ed., Moscow: Sovetskaya Entsiklopediya–Bol'shaya Rossiiskaya Entsiklopediya, 1988–1998.
19. Letcher, T.M., Wooten, S., Shuttleworth, B., and Heward, C., *J. Chem. Thermodyn.*, 1986, vol. 18, pp. 1037–1042.
20. Letcher, T.M. and Siswana, P.M., *Fluid Phase Equilib.*, 1992, vol. 74, pp. 203–217.
21. Novak, J.P., Matous, J., and Pick, J., *Liquid–Liquid Equilibrium*, Prague: Academia, 1987.
22. Toikka, A.M. and Jenkins, J.D., *Chem. Eng. J.*, 2002, vol. 89, pp. 1–27.
23. Zharov, V.T., *Zh. Fiz. Khim.*, 1970, vol. 44, pp. 1967–1974.
24. Kocherbitov, V.V. and Toikka, A.M., *Vestn. SPb. Gos. Univ., Ser. 4, Fiz., Khim.*, 1998, issue 3 (no. 18), pp. 120–124.
25. Furzer, I.A., *Chem. Eng. Sci.*, 1994, vol. 49, pp. 2544–2549.
26. Wasylkiewicz, S.K. and Ung, S., *Fluid Phase Equilib.*, 2000, vol. 175, pp. 253–272.
27. Qi, Z., Kolah, A., and Sundmacher, K., *Chem. Eng. Sci.*, 2002, vol. 57, pp. 163–178
28. Qi, Z. and Sundmacher, K., *Comp. Chem. Eng.*, 2002, vol. 26, pp. 1459–1471.

ISSN 1070-4272, Russian Journal of Applied Chemistry, 2008, Vol. 81, No. 2, pp. 231–235. © Pleiades Publishing, Ltd., 2008.
Original Russian Text © N.N. Chopabaeva, E.E. Ergozhin, 2008, published in Zhurnal Prikladnoi Khimii, 2008, Vol. 81, No. 2, pp. 241–245.

PHYSICOCHEMICAL STUDIES OF SYSTEMS AND PROCESSES

Sorption of Pt(IV) Chloride Complexes with a Chelating Resin Based on Modified Lignin

N. N. Chopabaeva and E. E. Ergozhin

Bekturov Institute of Chemical Sciences, Ministry of Education and Science of the Republic of Kazakhstan, Almaty, Kazakhstan

Received June 22, 2007

Abstract—Sorption of hexachloroplatinic(IV) acid on a new phytosorbent based on lignin modified with thioamide groups was studied. The sorption capacity of the sorbent for Pt(IV) was examined in relation to the Pt(IV) concentration in the aqueous phase, pH, temperature, and sorption time. The kinetic characteristics of sorption of Pt(IV) on the lignin sorbent were studied.

DOI: 10.1134/S1070427208020134

As compared to common ion-exchange resins, chelating sorbents are characterized by higher sorption capacity and selectivity to chemical elements with similar properties. Therefore, these sorbents find growing use for separation and preconcentration of metals. The high selectivity of chelating resins is controlled not only by the chemical composition of the polymeric matrix and sorption sites, but also by their steric arrangement. An important role in this respect is played by both the remoteness of functional groups from the matrix and the uniformity of the sorbent framework.

A wide variety of commercial chelating sorbents are available today. The techniques for preparation of chelating sorbents and physicochemical characteristics of these resins have been described in detail in numerous reviews and monographs [1–6]. These sorbents are mainly prepared by polycondensation of the initial compounds containing chelating groups or by polymeryzation of vinyl monomers containing complexing groups. Chelating sorbents can also be prepared by modification of the initial nonchelating resins with chelating agents. The latter approach is the most promising since it allows preparation of chelating sorbents not only from common macrocellular (polystyrene, polyacrylate, etc.) or fibrous (e.g., polyacrylonitrile, polyvinyl alcohol) polymers, but also from natural porous hydrophilic polyelectrolytic matrices (cellulose, chitin, tannin, and gelatin) [4, 7, 8].

In this study, we examined the sorption of Pt(IV) from aqueous hydrochloric acid solutions on a new chelating phytosorbent prepared from commercial hydrolytic lignin by its modification with thioamide functional groups.

EXPERIMENTAL

The phytosorbent was prepared from lignin of cotton peel from the Chimkent hydrolytic plant. This raw material was subjected to catalytic alkylation with ED-20 bifunctional epoxy oligomer [9], followed by modification with the thiourea α-oxide derivative [10]. The resulting resin contains the chelating thioamide groups (SEC_{HCl} 3.70 mg-equiv g^{-1}, N 6.72, and S 9.02 wt %). This sorbent is an analog of SRAFION NMRR commercial poly(styrene–divinylbenzene) complexone [4, 11] and MSPVS [4, 12–15], MTILON-T [4, 7, 8, 16–21] and TIOPAN-4 [22] complexing sorbents based on graft copolymers of polyvinyl alcohol, cellulose, and polyacrylonitrile.

The sorption of Pt(IV) on the modified lignin sorbent from aqueous and aqueous HCl solutions of hexachloroplatinic(IV) acid hexahydrate was carried out under static conditions at 20, 40, and 60°C without stirring. The weighed portion of the phytosorbent was 0.05 g. The liquid phase volume was 100 ml. A stock solution was prepared by dissolving a weighed portion of $H_2[PtCl_6] \cdot 6H_2O$ (pure grade) in water [23]. The correct concentration of platinum in this solution was determined gravimetrically with Thionalide [24–27]. The working solutions were prepared by accurate dilution of the stock solution. The content of platinum(IV) in the initial and equilibrium solutions in

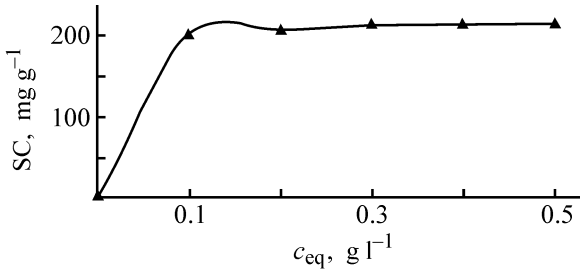


Fig. 1. Isotherm of Pt(IV) sorption from aqueous solutions with modified lignin sorbent. Contact time τ 3 days; the same for Figs. 2 and 3. (SC) Sorption capacity of modified lignin sorbent for Pt and (c_{eq}) equilibrium concentration of Pt(IV).

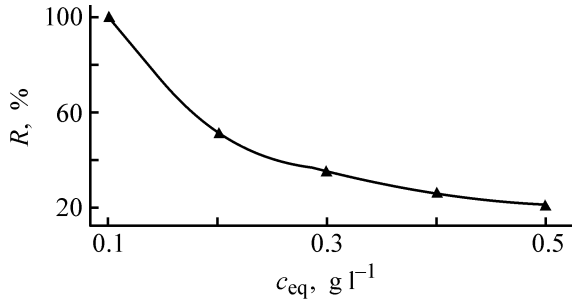


Fig. 2. Degree of Pt(IV) sorption, R, on modified lignin sorbent vs. the equilibrium concentration of Pt(IV) in the aqueous phase c_{eq}.

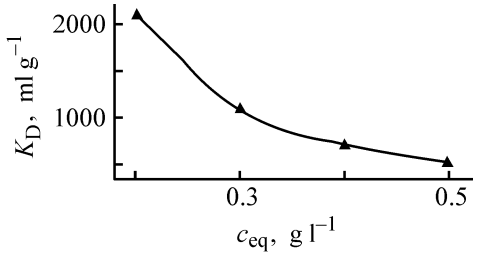


Fig. 3. Distribution ratio of Pt(IV) between modified lignin and aqueous phase K_D vs. the equilibrium concentration of Pt(IV) in the aqueous phase c_{eq}.

the sorption systems was determined photocolorimetrically with $SnCl_2$ on a KFK-2MP photocolorimeter (λ = 440 nm, l = 10.07 mm, V = 5 ml) [23]. The calibration curve was processed by the least-squares technique. The sorption capacity of the phytosorbent for Pt(IV) (SC) and the distribution ratio K_D were calculated by the procedure described in [28, 29]. The degree of platinum sorption, R, was determined according to [30]. The degree of sorption completion, F, was determined as the ratio of SC at a certain time to the equilibrium SC. The IR spectra of the initial sorbent and that after the sorption of Pt were recorded on a Nicolet FT-IR spectrophotometer (KBr pellets).

Effect of pH of the liquid phase on the sorption capacity of the modified lignin for platinum (c_{Pt} = 0.1 g l^{-1}, τ = 3 days)

pH	SC, mg g^{-1}	R, %	K_D, ml g^{-1}
1	145	72.5	5272
2	150	75	6000
3	160	80	8000
4	178	89	16181
5	200	100	∞
6	200	100	∞

The sorption isotherm shows (Fig. 1) that the sorption of Pt(IV) is the most efficient from dilute aqueous solutions. With increasing Pt(IV) concentration in the aqueous phase, the degree of sorption of Pt(IV) (Fig. 2) and the distribution ratio of Pt(IV) between the sorbent and aqueous phase (Fig. 3) decrease.

The table shows that modified lignin exhibits strong sorption capacity for Pt(IV) within a wide pH range. It is seen that, with increasing pH, the sorption of Pt(IV) grows. This trend is typical of complexing sorbents containing sulfamide groups, e.g., Movinex [31] and SRAFION NMRR [21] sorbents based on macroporous copolymers of styrene and divinylbenzene.

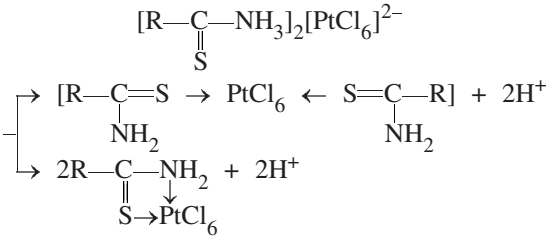
Presumably [32], sorbents containing the sulfamide groups sorb chloroplatinate anions from weakly acidic (pH > 2) and neutral solutions by the coordination mechanism to form chelate compounds. This sorption mechanism is favored by the fact that, under these conditions, the amino groups of the sorbent are present in the deprotonated state and the aquated chloroplatinate anions formed in this case undergo the ligand substitution more readily than do the initial chloroplatinate complexes [21]. It is also suggested [33] that the sorbable chelate compound can be formed by Anderson's rearrangement of onium complexes containing NH_3^+ groups protonated in the neutral pH range by protons of water molecules.

In acidic media, the amide groups are protonated, and thermodynamically stable and kinetically inert hexachloroplatinate complexes are weakly hydrolyzed [24, 25]. Under these conditions, hexachloroplatinate anions are apparently sorbed by the following heterogeneous reaction [21]:

$$2R{-}\underset{\underset{S}{\|}}{C}{-}NH_2HCl + [PtCl_6]^{2-} \leftrightarrows [R{-}\underset{\underset{S}{\|}}{C}{-}NH_3^+]_2[PtCl_6]^{2-} + 2Cl^-.$$

We found that chloroplatinate anions sorbed on modified lignin are not eluted with 1–5 N solutions

of nitric, hydrochloric, and oxalic acids. This means that chloroplatinate anions form very strong, not salt-like, complexes with the thioamide groups of the sorbent. We believe that the initially formed outer-sphere ionic associates are converted to donor–acceptor complexes between hexachloroplatinate anions and the thioureide groups of the sorbent. This rearrangement is accompanied by incorporation of the polymer ligands into the inner coordination sphere of Pt(IV). Under these conditions, the chelate thioamide complexes of the sorbent with chloroplatinate anions are formed. In these complexes, the donor atoms of sulfur or of sulfur and nitrogen simultaneously are coordinated with Pt(IV) [21]:



This complexation pattern is in agreement with published data [21, 30, 33]. In sorption of Pt(IV) from 1–6 M aqueous HCl with a sorbent containing bidentate thioamide functional groups [34], the ion-exchange mechanism of sorption is complicated by strong complexation of Pt(IV) with the sulfur donor atoms. As a result, the desorption of Pt(IV) from the resin saturated with Pt(IV) becomes impossible.

The strong covalent binding of Pt(IV) with modified lignin is confirmed by the IR spectra of the modified lignin sorbent saturated with Pt(IV) from its acidic and neutral solutions. In these spectra, the absorption band of the bending vibrations of the thioamide groups >C(NH)=S at 1606 cm^{-1} (1471–1613 cm^{-1} [35]) is shifted toward higher frequencies and is split in two peaks at 1616 and 1636 cm^{-1}. In the range of stretching vibrations of the NH groups (3500–3200 cm^{-1}), new bands at 3276 and 3178 cm^{-1} appear. The absorption band of the C–S stretching vibrations at 767 cm^{-1} is shifted toward lower frequencies and is split in two bands at 710 and 730 cm^{-1}. On the whole, these changes in the IR spectra suggest the complexation of Pt(IV) with the nitrogen and sulfur atoms of the thioamide functional groups of the modified lignin.

The limiting stage of sorption of Pt(IV) with modified lignin was elucidated by analysis of the kinetic curves of Pt(IV) sorption from solutions of $H_2[PtCl_6]$ at pH 1 (Fig. 4) and the curves plotted in the coordinates F vs. $\tau^{1/2}$ (Fig. 5a) [hypothesis that sorption of Pt(IV) is controlled by internal diffusion] and

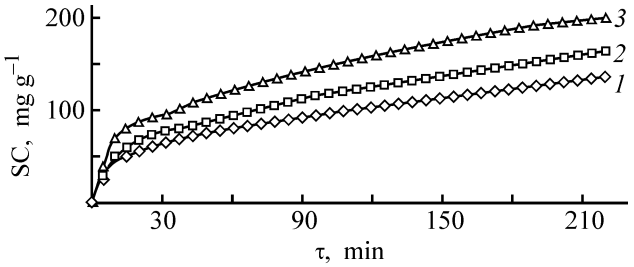


Fig. 4. Kinetic curves of sorption of Pt(IV) with modified lignin. pH 1, c_{Pt} = 0.1 g l^{-1}; the same for Fig. 5. (SC) Sorption capacity of sorbent (mg g^{-1}) and (τ) time. Temperature, °C: (*1*) 20, (*2*) 40, and (*3*) 60; the same for Fig. 5.

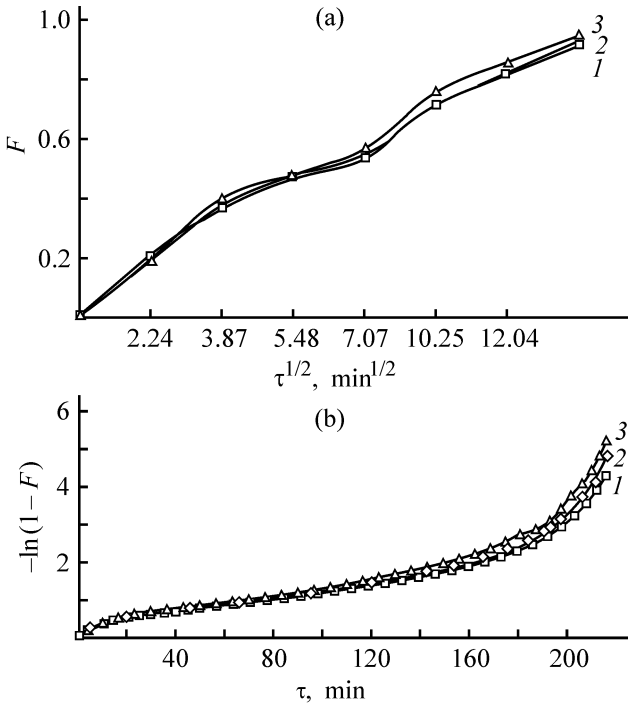


Fig. 5. Kinetic curves of sorption of Pt(IV) on modified lignin from aqueous hydrochloric acid, plotted in the coordinates (a) F vs. $\tau^{1/2}$ and (b) $-\log(1 - F)$ vs. τ. (F) Degree of sorption completeness and (τ) time.

$-\log(1 - F)$ vs. τ (Fig. 5b) [hypothesis that sorption of Pt(IV) is controlled by external diffusion] at different temperatures. The complicated shape of the curves and the lack of distinct linearity in their initial portion suggest that the sorption of Pt(IV) is characterized by mixed diffusion-controlled kinetics.

Figure 4 shows that, irrespective of temperature, the equilibrium in sorption of Pt(IV) on modified lignin is attained within 220 min. The half-sorption time is also temperature-independent. This parameter is 35, 40, and 35 min at 20, 40, and 60°C, respectively. It should be noted that the sorption kinetic

curves are also independent of temperature. Both the increase in the sorption capacity of modified lignin for Pt(IV) in acidic solutions with increasing temperature and the decelerated sorption kinetics suggest that Pt(IV) is sorbed on modified lignin by the coordination mechanism rather than by the faster anion-exchange mechanism.

CONCLUSIONS

(1) A phytosorbent containing the chelating thioamide groups was prepared by chemical modification of hydrolytic lignin with ED-20 commercial epoxy resin and thiourea. This sorbent quantitatively recovers chloroplatinate anions from weakly acidic and neutral aqueous solutions at $c_{Pt} = 0.1$ g l^{-1}.

(2) Sorption of Pt(IV) on modified lignin increases with temperature.

(3) Pt(IV) is irreversibly sorbed on modified lignin by complexation of chloroplatinate anions with the thioamide functional groups.

REFERENCES

1. Hering, R., *Chelatbildende Ionenaustauscher*, Berlin: Akademie, 1967.
2. Sinyavskii, V.G., *Selektivnye ionity* (Selective Ion Exchangers), Kiev: Tekhnika, 1967.
3. Myasoedova, G.V., Eliseeva, O.P., and Savvin, S.B., *Zh. Anal. Khim.*, 1971, vol. 26, no. 11, pp. 2472–2487.
4. Myasoedova, G.V. and Savvin, S.B., *Khelatoobrazuyushchie sorbenty* (Chelating Sorbents), Moscow: Nauka, 1984.
5. Dyatlova, N.M., Temkina, V.Zh., and Popkov, K.I., *Kompleksony i kompleksonaty metallov* (Complexones and Metal Complexonates), Moscow: Khimiya, 1988.
6. Ergozhin, E.E. and Utkelov, B.A., *Khelatnye polimernye reagenty* (Chelating Polymeric Reagents), Almaty: Gylym, 1998.
7. Rogovin, Z.A. and Gal'braikh, L.S., *Khimicheskie prevrashcheniya i modifikatsiya tsellyulozy* (Chemical Transformations and Modification of Cellulose), Moscow: Khimiya, 1979.
8. Myasoedova, G.V. and Savvin, S.B., *Zh. Anal. Khim.*, 1982, vol. 37, no. 3, pp. 499–519.
9. Ergozhin, E.E., Chopabaeva, N.N., and Tasmagambet, A.T., *Khim. Zh. Kaz.*, 2006, no. 3, pp. 100–108.
10. Ergozhin, E.E., Chopabaeva, N.N., and Tairova, B.T., *Khim. Prirodn. Soedin.*, 2006, no. 5, pp. 480–483.
11. Nadkarni, R.A. and Morrison, G.N., *Anal. Chem.*, 1974, vol. 46, pp. 232–236.
12. Simanova, S.A. and Kukushkin, Yu.N., *Izv. Vyssh. Uchebn. Zaved., Khim. Khim. Tekhnol.*, 1986, vol. 29, no. 5, pp. 3–14.
13. Simanova, S.A., Kalontarov, I.Ya., Bobritskaya, L.S., et al., *Zh. Prikl. Khim.*, 1978, vol. 51, no. 8, pp. 1871–1874.
14. Simanova, S.A., Bobritskaya, L.S., Kukushkin, Yu.N., et al., *Zh. Prikl. Khim.*, 1981, vol. 54, no. 4, pp. 764–771.
15. Simanova, S.A., Bobritskaya, L.S., Kukushkin, Yu.N., and Kalontarov, I.Ya., *Zh. Prikl. Khim.*, 1981, vol. 54, no. 4, pp. 514–517.
16. Orobinskaya, V.A., Chulkova, N.E., Nazarenko, G.N., et al., *Analiz i tekhnologiya blagorodnykh metallov* (Analysis and Technology of Noble Metals), Moscow: Metallurgiya, 1971.
17. Tolmachev, V.N., Gubenko, E.P., Lishevskaya, M.O., and Ishchenko, I.K., *Izv. Vyssh. Uchebn. Zaved., Khim. Khim. Tekhnol.*, 1976, vol. 19, no. 1, pp. 97–100.
18. Tolmachev, V.N., Gubenko, E.P., Lishevskaya, M.O., and Ishchenko, I.K., *Izv. Vyssh. Uchebn. Zaved., Khim. Khim. Tekhnol.*, 1976, vol. 19, no. 3, pp. 444–447.
19. Tolmachev, V.N., Gubenko, E.P., Lishevskaya, M.O., and Ishchenko, I.K., *Izv. Vyssh. Uchebn. Zaved., Khim. Khim. Tekhnol.*, 1976, vol. 19, no. 9, pp. 1460–1463.
20. Myasoedova, G.V. and Malofeeva, G.I., *Zh. Anal. Khim.*, 1979, vol. 34, no. 8, pp. 1626–1636.
21. Myasoedova, G.V. and Komozin, P.N., *Zh. Neorg. Khim.*, 1994, vol. 39, no. 2, pp. 280–288.
22. Zamorova, I.N., Kazakevich, Yu.E., Danilova, E.Ya., and Emets, L.V., *Zh. Prikl. Khim.*, 1992, vol. 65, no. 3, pp. 686–691.
23. *Sintez kompleksnykh soedinenii platinovoi gruppy: Spravochnik* (Synthesis of Complex Compounds of Platinum Group Metals: Handbook), Chernyaev, I.I., Ed., Moscow: Nauka, 1964.
24. Ginzburg, S.I., Ezerskaya, N.A., Prokof'eva, I.V., et al., *Analiticheskaya khimiya elementov: Platinovye metally* (Analytical Chemistry of Elements: Platinum Metals), Moscow: Nauka, 1972.
25. Ginzburg, S.I., Gladyshevskaya, K.A., Ezerskaya, N.A., et al., *Rukovodstvo po khimicheskomu analizu platinvykh metallov i zolota* (Manual on Chemical Analysis of Platinum Metals and Gold), Moscow: Nauka, 1965.

26. Pshenitsyn, N.K. and Prokof'eva, I.V., *Zh. Neorg. Khim.*, 1957, no. 2, pp. 569–573.
27. Pshenitsyn, N.K. and Prokof'eva, I.V., *Zh. Neorg. Khim.*, 1962, no. 7, pp. 258–262.
28. Amelina, Zh.S., Amelin, A.N., and Leikin, Yu.A., *Zh. Prikl. Khim.*, 1979, vol. 52, no. 1, pp. 128–131.
29. Kholmogorov, A.G., Kononova, O.N., Kachin, S.V., et al., *Zh, Fiz. Khim.*, 1998, vol. 72, no. 2, pp. 318–321.
30. Simanova, S.A., Kuznetsov, T.V., Belyaev, A.N., et al., *Zh. Prikl. Khim.*, 1999, vol. 72, no. 4, pp. 580–586.
31. Warshawsky, A. and Fieberg, M., *Sep. Purif. Meth.*, 1980, vol. 9, no. 2, p. 209.
32. Saldadze, K.M. and Kopylova-Valova, V.D., *Kompleksoobrazhuyushchie ionity (kompleksity)* (Complexing Ion Exchangers (Complexites)), Moscow: Khimiya, 1980.
33. Simanova, S.A., Knyaz'kov, O.V., Belyaev, A.N., et al., *Zh. Prikl. Khim.*, 1998, vol. 71, no. 2, pp. 220–226.
34. Skobeleva, V.I., Gribanova, I.N., Villeval'd, G.V., et al., *Zh. Fiz. Khim.*, 1982, vol. 56, no. 5, pp. 1212–1216.
35. Bellamy, L.J., *The Infra-Red Spectra of Complex Molecules*, London: Methuen, 1954.

ISSN 1070-4272, Russian Journal of Applied Chemistry, 2008, Vol. 81, No. 2, pp. 236–240. © Pleiades Publishing, Ltd., 2008.
Original Russian Text © G.A. Polotskaya, A.V. Pen'kova, N.N. Sudareva, A.E. Polotskii, A.M. Toikka, 2008, published in Zhurnal Prikladnoi Khimii, 2008, Vol. 81, No. 2, pp. 246–250.

PHYSICOCHEMICAL STUDIES OF SYSTEMS AND PROCESSES

Polyamide Ultrafiltration Membranes Modified with Nanocarbon Additives

G. A. Polotskaya, A. V. Pen'kova, N. N. Sudareva, A. E. Polotskii, and A. M. Toikka

Institute of Macromolecular Compounds, Russian Academy of Sciences, St. Petersburg, Russia
St. Petersburg State University, St. Petersburg, Russia
State Research Institute of Ultrapure Biopreparations, St. Petersburg, Russia

Received July 24, 2007

Abstract—Possibility of modification of polyphenyleneisophthalamide with 5 wt % nanocarbon additive (fullerene, astralene, or graphite soot) was studied. The resulting composites were used to prepare asymmetric membranes, and the effect of carbon additives on the performance of these membranes was examined. Finally, the membranes were tested using a mixture of proteins of various molecular weights.

DOI: 10.1134/S1070427208020146

Ultrafiltration membrane processes are widely used in microbiology, food industry, pharmaceutics, and other branches of industry, and also for solving environmental problems [1]. The diversity of systems to be separated requires extension of the spectrum of membrane materials. Modification of polymers commonly used as membrane materials shows promise as a way to develop novel membranes.

Among the common commercial polymers used for production of fibers and membranes, a firm place is held by aromatic polyamides and, in particular, products of condensation of isoterephthaloyl chloride with *p*- and *m*-phenylenediamine. The structure and properties of polyphenyleneisophthalamide (PA), as well as some features of supramolecular structures in its concentrated solutions, were reported in [2, 3]. The formation of polyamide-based ultrafiltration membranes was studied by Bil'dyukevich et al. [4–6].

In this study, we modified PA with nanocarbon additives: fullerene C_{60}, astralene, and graphite soot, which are essentially different in their structure and properties. Graphite soot is a chemically inert amorphous form of carbon. Fullerene C_{60}, prepared by laser ablation of graphite, has a closed-shell spheroid configuration consisting of 20 hexagons and 12 pentagons [7]. It is this configuration that is responsible for the high chemical activity and noticeable solubility of C_{60} in organic solvents [8, 9]. Astralene is a carbonaceous nanomaterial formed in synthesis of fullerene soot. This material contains 20 to 90 wt % fulleroid nanoparticles (primarily with cage structure): multi- and single-wall nanotubes, nanobarrels, nanobulbs, and nanocones [10].

There is scarce information on gas-separation and pervaporation membranes based on polymer nanocomposites with fullerene [11–13]. Preparation and characterization of ultrafilters with membranes of fullerene-containing polyphenylene oxide were reported in [14]. Despite that fullerenes are produced on a commercial scale in a number of countries, only proton-conducting Nafion 117 fuel-cell membranes with addition of C_{60} fullerene are ready for commercial introduction [15].

The goals of this study were to prepare polyamide composites with nanocarbon additives, to form asymmetric membranes on their basis, and to examine the effect of nanocarbon additives (graphite soot, C_{60}, and astralene) on the ultrafiltration performance of the membranes.

EXPERIMENTAL

Polyphenyleneisophthalamide (Fenilon®) (PA) was used as a test subject. Composites of PA with 5 wt % nanoadditive (fullerene C_{60}, astralene, or graphite soot) were prepared by mixing PA and nanocarbon in a porcelain mortar. The resulting mixture was dissolved in *N*,*N*-dimethylacetamide. A 0.12% polymer

solution was cast onto a glass plate using a draw die with a 0.30-mm passageway. Finally, the glass plate was immersed in a precipitation bath to form an asymmetric porous membrane through phase inversion.

The rigidity of the structure of the membranes was monitored when passing solvent across them in the order ethanol, water, isopropanol, hexane, i.e., in accordance with their mutual solubility. The experiments on determination of the solvent flux across the membranes and on ultrafiltration of protein solutions were carried out in stirred cells under a pressure of 0.1 MPa.

The rejection curves of the ultrafiltration membranes were obtained according to the procedure described in [16], using a 0.4 wt % aqueous solution of a model mixture of proteins of various molecular weights: vitamin B_{12} (MW 1340), cytochrome C (MW 12 500), chemotrypsinogen (MW 24 000), egg albumin (MW 44 500), bovine serum albumin (MW 67 000), and γ-globulin (MW 160 000). The selectivity of the membranes was characterized by the rejection factor φ, which was estimated as $\varphi = 1 - c_p/c_f$, where c_p and c_f are the concentrations of the permeate and feed solution, respectively.

The experiments on static sorption of proteins on the membranes were carried out in hermetically sealed weighing bottles by immersing the membranes into 4 ml of the solution of protein mixture, with intermittent stirring. The protein concentration in the solution was monitored by the optical density at 280 and 415 nm at fixed intervals. The equilibrium concentration was established in 4 h, and the total experiment time was 20 h.

The contact angles of the membrane surface with water were determined by the Wilhelmy method on a KRUSS contact-angle-measuring system with computer-controlled sample immersion rate and data processing.

To gain insight into the effect of a modifier, we performed a comparative study of the PA-based membranes containing 5 wt % of various nanocarbon additives. The membrane morphology was examined by scanning electron microscopy (SEM). The SEM results revealed that nanocarbon additives had virtually no effect on the pore structure. Figure 1 shows a cross-sectional SEM micrograph of a PA membrane modified with 5 wt % fullerene. It should be pointed out that the performance characteristics of membranes are not always manifested on the morphological level as judged from SEM data. For example, polysulfone gas-separation membranes modified with various carbonaceous additives have similar morphology, but demonstrate considerable differences in their transport characteristics [17].

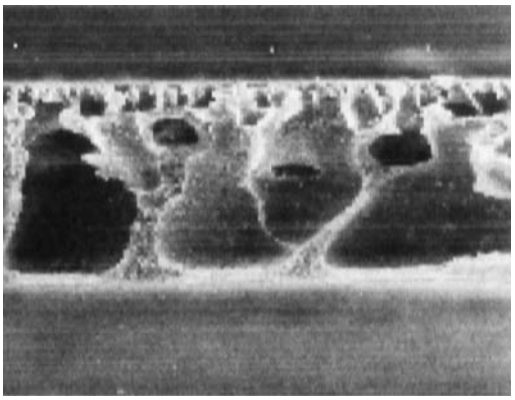


Fig. 1. Cross-sectional SEM image of a polyimide membrane modified with 5 wt % fullerene C_{60}.

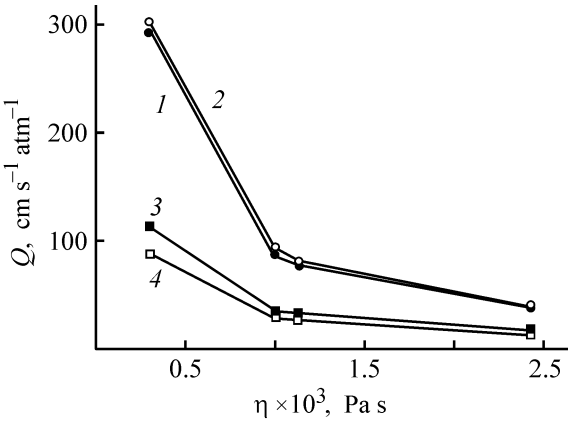


Fig. 2. Flux Q vs. the solvent viscosity η for asymmetric membranes: (*1*) PA, (*2*) PA + 5 wt % graphite soot, (*3*) PA + 5 wt % fullerene, and (*4*) PA + 5 wt % astralene; the same for Figs. 3 and 4.

The modifier nature affects the structure of the skin layer. The skin porosity can be characterized by the solvent flux across the membrane. In this study, the durability of the membranes and their resistance with respect to various media were characterized by the flux of water and several organic solvents (hexane, ethanol, and isopropanol) across the ultrafiltration membranes modified with 5 wt % nanocarbon additives. The solvents used were different in their viscosity ($\eta_{hexane} = 0.30 \times 10^{-3}$, $\eta_w = 1.0 \times 10^{-3}$, $\eta_{EtOH} = 1.13 \times 10^{-3}$, and $\eta_{i\text{-PrOH}} = 2.43 \times 10^{-3}$ Pa s) and, therefore, in their flux across the membranes.

Figure 2 shows that, in accordance with the Hagen–Poiseuille law [18], the flux decreases with increasing viscosity of the fluid for all the membranes studied. It is noteworthy that, for all the solvents studied,

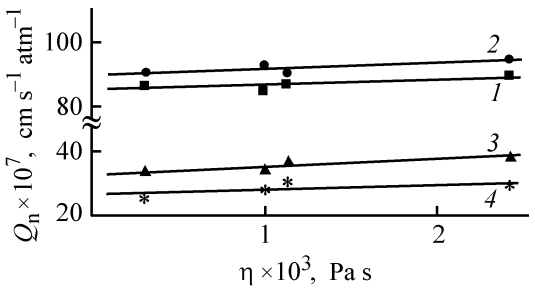


Fig. 3. Normalized flux Q_n (cm Pa atm^{-1}) vs. the fluid viscosity η (Pa s) for the asymmetric membranes.

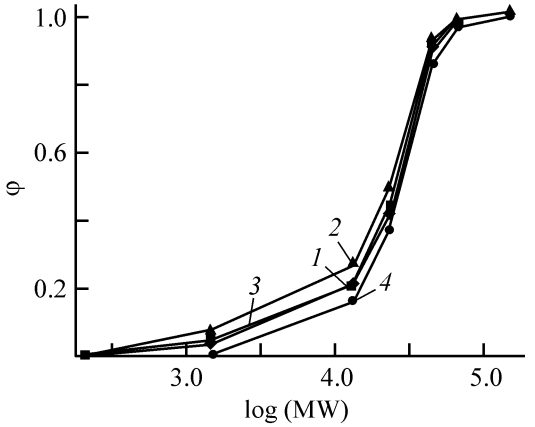


Fig. 4. Rejection factors of the membranes φ vs. the molecular weight of proteins.

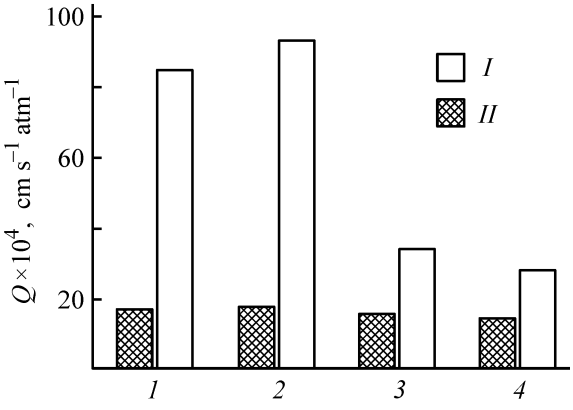


Fig. 5. Flux Q (cm s^{-1} atm^{-1}) of (*I*) water and (*II*) protein mixture across the membranes.

the flux across the PA membrane modified with 5 wt % graphite soot was slightly higher as compared to the unmodified membrane, suggesting that this chemically inert additive serves as a filler for both the casting solution and the resulting membrane. For all the solvents, the flux across the fullerene-modified membranes considerably decreased as compared to the PA membrane, which can be attributed to formation of donor–acceptor and maybe covalent bonds, thus influencing the polymer structure [19, 20]. With the astralene-modified membranes, the flux of all the solvents decreased even stronger than with the fullerene additive, which is probably due to the high reactivity of the fulleroid particles with respect to the PA matrix.

In addition to the solvent flux Q, we estimated the normalized flux Q_n written as a product $Q_n = Q\eta$, where η is the solvent viscosity. The normalized flux is intended to characterize the stability of the membranes in the media investigated. Our results show (Fig. 3) that the normalized fluxes of all the solvents are similar, suggesting an insignificant swellability of the membranes in solvents of varied chemical nature.

The modified PA membranes were tested with a solution of a protein mixture. The data obtained in the ultrafiltration experiments were then used to construct the rejection curves, which represent the dependences of the rejection factor on the molecular weight of proteins (Fig. 4). An important characteristic of the rejection curves is the molecular weight corresponding to the rejection factor of 0.9, which is known as the molecular-weight cut-off (M_L). All the membranes studied are characterized by similar values of M_L [(40–50) × 10^{3}g mol^{-1}].

As can be seen from Fig. 5, the flux of the protein solution is considerably lower than that of water. The primary factors responsible for the increase in the hydraulic resistance and the corresponding decrease in the flux are considered to be concentration polarization, formation of a deposit layer on the membrane, and adsorption. The last factor depends primarily on the chemical nature of the molecules to be filtered and on the polymer material of the membrane. It is the adsorption that essentially causes the decrease in the flux in the case of filtration of hydrophilic compounds [21], among them proteins.

The suggestion that the adsorption of proteins on the surface and in the pores of the membranes is responsible for the flux decrease was checked by comparison of the water flux restoration after the membranes were in contact with protein mixture under the ultrafiltration conditions and also under the static sorption conditions, when the membranes were held in a solution of protein mixture for 20 h. In both cases, the water flux restoration ratio (FRR) was estimated as FRR = Q_1/Q_0, where Q_0 and Q_1 are the water fluxes before and after contacting the membranes with the protein solution.

Figure 6 shows data on the water flux restoration in the ultrafiltration and static sorption modes. The membranes modified with fullerene and astralene show high FRR in the range 0.8–0.9. For PA membranes unmodified and modified with graphite soot, FRR was below 0.45. Such a low FRR suggests that these membranes strongly absorb proteins in both ultrafiltration and static sorption modes. It should be pointed out that such a behavior is typical of most of the existing polymeric membranes.

For the membranes modified with fullerene C_{60} and astralene, the sorption of proteins is considerably lower, which can be attributed to the fact that these additives block the sorption sites of PA. This suggestion is supported by data on the contact angles of the membranes with water. The contact angle increases from 81° for unmodified PA membranes to 85° for the membranes modified with 5 wt % fullerene, suggesting an increase in the hydrophobicity.

Finally, modification of PA membranes with fullerene C_{60} and astralene improves such an important performance characteristic as the water flux restoration ratio, which facilitates regeneration of the membranes and reduces the loss of the target products.

CONCLUSIONS

(1) Modification of polyphenyleneisophthalamide with nanocarbon additives has no significant effect on the initial porous sponge-like structure of the membranes. The modifier nature is manifested in a change in the surface porosity and sorption activity of the membranes.

(2) The membrane permeability depends on the modifier nature. For each of the membranes studied, the normalized fluxes of hexane, water, ethanol, and isopropanol are similar, suggesting virtually no swelling of the membranes in these solvents.

(3) The membranes modified with fullerene and astralene demonstrate good water flux restoration after being in contact with a protein mixture (FRR ≈ 0.8–0.9), in contrast to straight polyphenyleneisophthalamide membranes and those modified with carbon black (FRR < 0.45). This is due to the fact that addition of fullerene and astralene increases the hydrophobicity of the membrane matrix and decreases its sorption capacity for proteins. Modification of the polyamide with fullerene and astralene improves the ultrafiltration performance of the membranes.

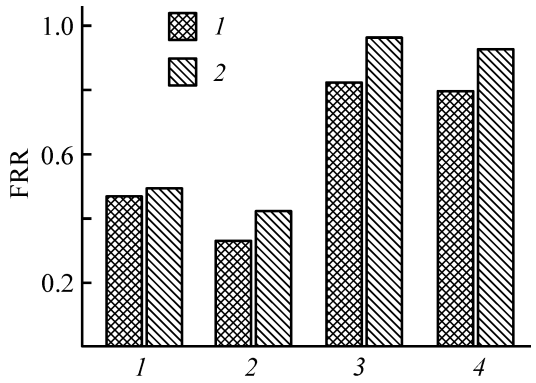


Fig. 6. Water flux restoration ratio FRR in (*1*) ultrafiltration and (*2*) static sorption modes.

ACKNOWLEDGMENTS

The study was financially supported by the Russian Foundation for Basic Research (project no. 06-03-32493).

REFERENCES

1. Baker, R.W., *Membrane Technology and Applications*, New York: McGraw–Hill, 2000.
2. Kazaryan, L.G., Ivankin, D.Ya., Vasil'ev, V.M., et al., *Vysokomol. Soedin., Ser. A*, 1975, vol. 17, no. 7, pp. 1560–1568.
3. Klenin, V.I., Prozorov, L.V., and Zhizdyuk, B.I., *Vysokomol. Soedin., Ser. A*, 1974, vol. 16, no. 7, pp. 1665–1672.
4. Bil'dyukevich, A.V., Soldatov, V.S., and Kaputskii, F.N., *Khim. Tekhnol. Vody*, 1990, vol. 12, no. 6, pp. 542–548.
5. Pratsenko, S.A. and Bil'dyukevich, A.V., *Vysokomol. Soedin., Ser. A*, 1994, vol. 36, no. 3, pp. 457–460.
6. Pratsenko, S.A., Bil'dyukevich, A.V., Varslovan, E.S., et al., *Zh. Prikl. Khim.*, 1995, vol. 68, no. 3, pp. 453–456.
7. Kerl, R.F., *Usp. Fiz. Nauk*, 1998, vol. 168, no. 3, pp. 331–342.
8. Bezmel'nitsyn, V.N., Eletskii, A.V., and Okun', M.V., *Usp. Fiz. Nauk*, 1998, vol. 168, no. 11, pp. 1195–1234.
9. Konarev, D.V. and Lyubovskaya, R.N., *Usp. Khim.*, 1999, vol. 68, no. 1, pp. 23–42.
10. Harris, P.J., *Carbon Nanotubes and Related Structures*, Cambridge: Cambridge Univ., 2003.
11. Gladchenko, S.V., Polotskaya, G.A., Gribanov, A.V., and Zgonnik, V.N., *Zh. Tekh. Fiz.*, 2002, vol. 72, no. 1, pp. 105–109.
12. Higuchi, A., Agatsuma, T., Uemiya, S., et al., *J. Appl. Polym. Sci.*, 2000, vol. 77, pp. 529–537.
13. Polotskaya, G.A., Penkova, A.V., Toikka, A.M., et al.,

Sep. Sci. Technol., 2007, vol. 42, no. 2, pp. 333–348.

14. Ong, S.L., Hu, J.Y., Biryulin, Yu.F., and Polotskaya, G.A., *Fullerenes, Nanotubes, Carbon Nanostruct.*, 2006, vol. 14, nos. 2–3, pp. 463–466.
15. Tasaki, K., De Sousa, R., Wang, H., et al., *J. Membrane Sci.*, 2006, vol. 281, nos. 1–2, pp. 570–580.
16. Cherkasov, A.N., *Sep. Sci. Technol.*, 2005, vol. 40, pp. 2775–2801.
17. Bhardwaj, V., Macintosh, A., Sharpe, I.D., et al., *Adv. Membr. Technol.*, 2003, vol. 984, no. 1, pp. 318–328.
18. Cherkasov, A.N. and Pasechnik, V.A., *Membrany i sorbenty v biotekhnologii* (Membranes and Sorbents in Biotechnology), Leningrad: Khimiya, 1991.
19. Janaki, J., Premila, M., Gopalan, P., and Sundarm C.S., *Thermochim. Acta*, 2000, vol. 356, nos. 1–2, pp. 109–116.
20. Isobe, H., Tomita, N., and Nakamura, E., *Org. Lett.*, 2000, vol. 2, no. 23, pp. 3663–3665.
21. Zularisam, A.W., Ismail, A.F., Salim, M.R., et al., *Desalination*, 2007, vol. 212, pp. 191–208.

ISSN 1070-4272, Russian Journal of Applied Chemistry, 2008, Vol. 81, No. 2, pp. 241–246. © Pleiades Publishing, Ltd., 2008.
Original Russian Text © Yu.G. Vlasov, S.S. Levichev, A.A. Kruchinin, Yu.E. Ermolenko, Bing-Joe Hwang, 2008, published in Zhurnal Prikladnoi Khimii, 2008, Vol. 81, No. 2, pp. 251–257.

PHYSICOCHEMICAL STUDIES OF SYSTEMS AND PROCESSES

Dye Molecules as Nanosize Sensors for Low-Temperature Fuel Cells

Yu. G. Vlasov, S. S. Levichev, A. A. Kruchinin, Yu. E. Ermolenko, and Bing-Joe Hwang

St. Petersburg State University, St. Petersburg, Russia
National Taiwan University of Science and Technology, Taiwan, China

Received December 26, 2007

Abstract—Dye molecules were suggested as a sensitive element for an optical sensor of parameters determining the efficiency of a fuel cell with a proton-exchange membrane, in which a water–methanol mixture is used as a fuel. The sensitivity of representatives of three different types of dyes to the concentrations of protons and methanol was examined.

DOI: 10.1134/S1070427208020158

Extensive research and development activities have been aimed recently to make fuel cells (FCs) a source of power supply for various purposes, such as microelectronic devices [1], automobiles [2], industrial plants [3], etc. One of the most attractive low-power devices is a low-temperature FC with a water–methanol mixture as a fuel, a membrane with proton conductivity [4], and catalysts of electrode reactions [5].

The studies showed that, among the parameters determining the FC efficiency, the proton conductivity of a membrane and its permeability to methanol are the most important [6]. The membrane conductivity should be at a maximum, and the permeability to methanol, at a minimum. FC efficiency can be optimized in different ways. Monitoring of membrane parameters with a warning issued upon their deviation beyond the admissible range is possible. Optimization of parameters in real time through a control system capable of controlling the composition of the fuel mixture and the FC temperature is also possible. However, in both cases, a sensor that transforms the optimization parameters into a signal convenient for recording (e.g., into an optical and then electric signal) is required. For FCs of the type under consideration, the concentration of methanol that penetrated into the membrane from the fuel mixture and the proton concentration inside the membrane can be such parameters. The mechanism of the proton concentration effect on the FC efficiency is determined by the fact that protons are charge carriers and provide current transport across the membrane. Hence, the membrane conductivity should be proportional to the proton concentration. The mechanism of the methanol concentration effect can be more complex. For instance, the penetration of methanol in the molecular (not deprotonated) form can suggest an insufficient performance of the anodic catalyst. Methanol that penetrated across the membrane can also negatively affect the cathodic catalyst.

At present, main attention is focused on indirect estimation of the membrane conductivity through the methanol concentration in the fuel mixture. There have been reports of ammetric [7], ultrasonic [8], and optical [9] sensors for this purpose. The common feature of these sensors is that they do not allow measurement of the proton concentration. The measurement of the proton concentration in the membrane by traditional potentiometric sensors [10, 11] is problematic. The use of potentiometric sensors (ion-selective electrodes and field-effect transistors [12]) in FC is complicated by the fact that FC is a power electricity-generating device in which the current across the membrane can amount to amperes or even tens of amperes. Such a current may produce a parasitic drop potential across electrodes of the potentiometric sensor of hundreds of millivolts, which can chaotically change in time. Under such conditions, the error in proton concentration measured using a potentiometric sensor can amount to several orders of magnitude, which makes such type of sensors useless for this purpose.

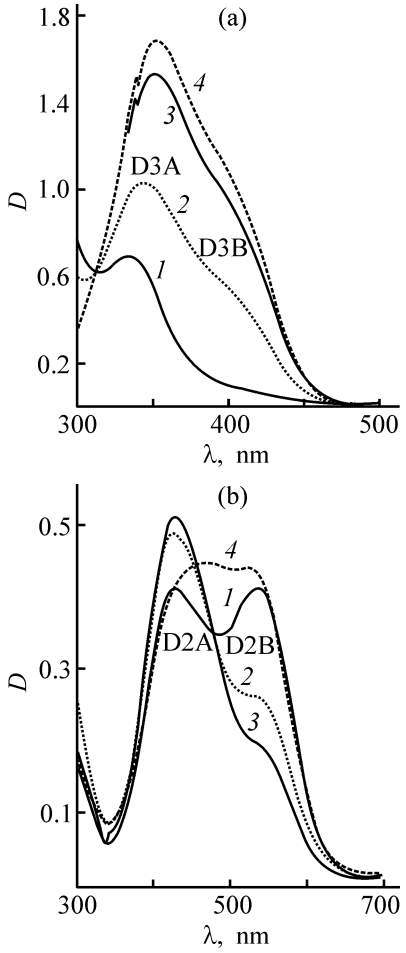


Fig. 1. Absorption spectra of (a) picric acid at various pH values and methanol concentration of 90 vol % and (b) Tropeolin OO at pH 1.1 and various methanol concentrations. (a) pH: (*1*) 0.1, (*2*) 1.1, (*3*) 2.1, and (*4*) 3.1. (b) Methanol concentration, vol %: (*1*) 90, (*2*) 85, (*3*) 80, and (*4*) 50.

Segregation of the proton-conducting membrane into hydrophilic and hydrophobic phases of microscopic size [13] gives rise to additional problems.

It follows from the aforesaid that, to measure the proton concentration inside a membrane, we should have very small sensor (micro- or even nano-size) whose response is independent of the electric current passing through the membrane. As such a sensor we suggest dye molecules whose optical spectrum depends on the proton concentration in the solution. The experimental part of this study is devoted to examination of such dyes in solutions simulating the internal medium of a proton-conducting membrane of the most widespread type. In so doing, a question arises as to how methanol affects the molecular sensor response to the proton concentration, because detailed data on the dye behavior in membrane media are lacking, and the results to be obtained can be used in further studies with real membranes.

EXPERIMENTAL

Today, membranes based on perfluorinated hydrocarbons with readily dissociating sulfonate groups are the most widespread (e.g., Nafion or its analog, MF4SK). The internal medium of such membrane contains water, an analog of sulfuric acid in the form of sulfonate groups covalently bonded to a polymeric matrix, and, probably, methanol, which can penetrate into the membrane from the fuel mixture. Correspondingly, our simulating solutions contain water, sulfuric acid, and methanol. It should be taken into consideration that the proton concentration is usually expressed as $pH = -\log[H^+]$, where $[H^+]$ is the proton concentration expressed in moles per liter. Correspondingly, we hereinafter use pH units as a measure of proton concentration in model solutions.

Chemically pure methanol and sulfuric acid and distilled water were used. Dyes Malachite Green (D1), Tropeolin OO (D2), and picric acid (D3) served as molecular sensors. Their optical absorption spectra can be used to determine pH in the strongly acidic region. The structural formulas of these dyes were reported in [14]. The dyes belong to three different groups, namely, triphenylmethane dyes, diazo dyes, and dyes based on nitro compounds, respectively. Such a choice is made for two reasons: (1) to provide the maximal conductivity of the FC membrane, the maximal proton concentration should be supported (i.e., the medium inside the membrane should be highly acidic) and (2) in a multicomponent solution, selective solvation is possible, and it can differently affect the molecules with different structures [15].

The optical spectra of the dyes were recorded on an SF-56 spectrophotometer within the 300–700 nm range. For each dye, spectra of 24 solutions with six fixed values of methanol concentrations and four fixed pH values were measured. The methanol concentrations were 0, 20, 50, 80, 85, and 90 vol %. In the region of high methanol concentrations, measurements were performed at a 5% interval because methanol at concentrations higher than 80% starts to strongly affect the pH of water–methanol mixtures [16]. The pH values of model solutions were 0.1, 1.1, 2.1, and 3.1. The acidity of a water–methanol mixture prepared in advance was brought to the required value with sulfuric acid; in so doing, pH was measured with a glass electrode with an accuracy of ±0.1 pH unit.

The spectra of D3 and D2 in water–methanol mixtures are shown in Fig. 1. As can be seen, they have two broad bands *A* and *B*, whose intensity can depend

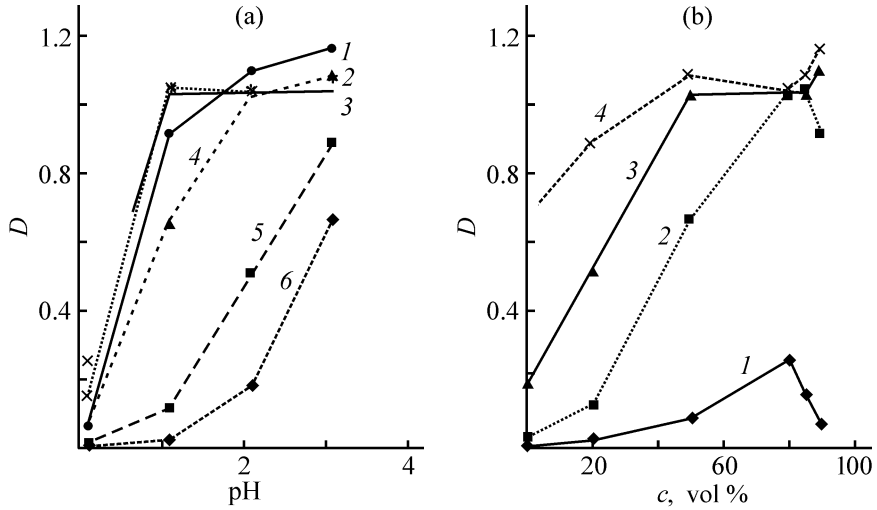


Fig. 2. Dependences of the optical density on (a) pH at various methanol concentrations and (b) methanol concentration at various pH values. Malachite Green (dye D1), band D1B. (a) Methanol concentration, vol %: (*1*) 90, (*2*) 85, (*3*) 80, (*4*) 50, (*5*) 20, and (*6*) 0; the same for Figs. 3–5. (b) pH: (*1*) 0.1, (*2*) 1.1, (*3*) 2.1, and (*4*) 3.1; the same for Figs. 3–5.

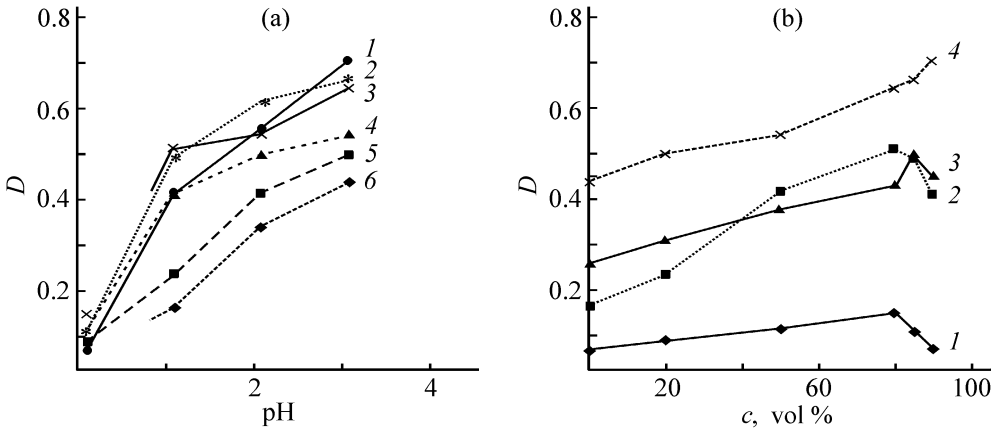


Fig. 3. Dependences of the optical density on (a) pH at various methanol concentrations and (b) methanol concentration at various pH values. Tropeolin OO (dye D2), band D2A.

on pH (Fig. 1a) and methanol concentration (Fig. 1b). In Fig. 1, each band is designated by a three-character index. The first two characters unambiguously refer to the dye to which the given band belongs. We will use this index hereinafter. In the spectrum of D1 (not shown because of the limited volume of this paper), there are also two readily identifiable bands whose intensity may depend on the proton and/or methanol concentration. Let us consider in detail the behavior of the dye bands behave as the pH or methanol concentration in model solutions is varied.

The dependence of the intensity of D1B band on pH and methanol concentration is shown in Fig. 2. As can be seen, the intensity of D1 bands depends on both parameters of the model solution, i.e., this dye can be regarded as a sensor of both pH and methanol concentration.

The intensity of the D1B band increases with pH. Its sensitivity to pH is different in different pH intervals and depends on the methanol concentration. As can be seen from Fig. 2a, at low methanol concentration (0–20 vol %) it is advisable to use D1 as a pH sensor within the pH range 1.1–3.1, in which the pH response is fairly strong. At higher methanol concentrations (50–90 vol %), the range of the pH response of this dye shifts toward the acid region (0.1–1.1).

It also follows from Fig. 2b that, in solutions with pH 0.1–1.1, the intensity of the D1B band monotonically increases as the methanol concentration is raised from 0 to 80 vol %. In the spectra of the solutions with pH 2.1–3.1, the intensity of the D1B band tends to a constant value at methanol concentrations exceeding 50 vol %.

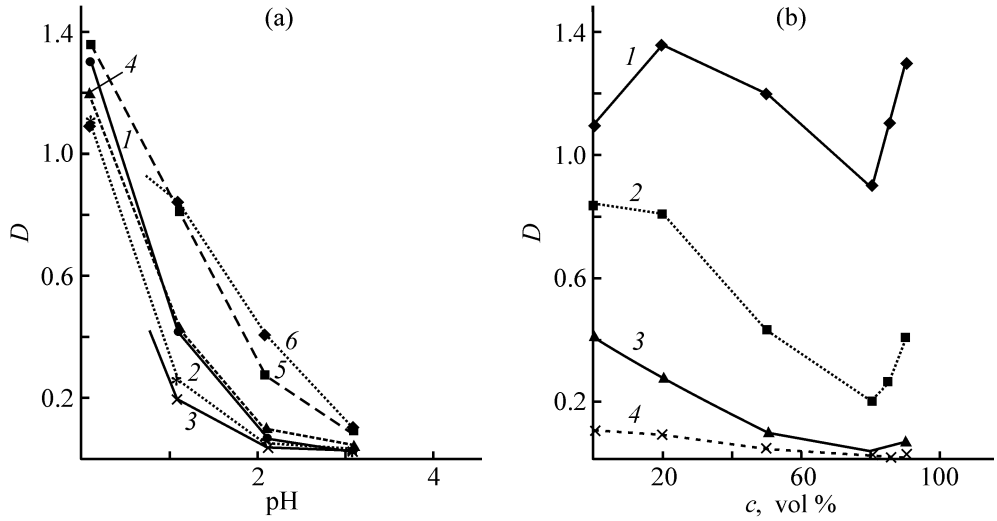


Fig. 4. Dependences of the optical density on (a) pH at various methanol concentrations and (b) methanol concentration at various pH values. Tropeolin OO (dye D2), band D2B.

The D1A band as an acidity sensor and sensor of the methanol concentration behaves similarly; however, its intensity is several times lower. Thus, both D1A and D1B bands give a combined response to both parameters of the model solution.

The pH dependences of the intensity of D2A and D2B bands are shown in Figs. 3a and 4a, and those on the methanol concentration, in Figs. 3b and 4b. As can be seen, the intensity of D2 bands depends on both parameters of the model solution, i.e., this dye is a sensor of both pH and methanol concentration. The specific feature of D2 as a pH sensor is that the D2A band intensity increases and the D2B band intensity decreases as the acidity becomes higher. The pH sensitivity of D2 bands is different in different intervals of the pH range studied and depends on the methanol concentration. Figure 3a shows that the working range of the D2A band as pH sensor covers the whole pH range studied, from 0.1 to 3.1, in the methanol concentration range 0–20 vol %. At higher methanol concentrations (50–90 vol %), the response of the D2A band within pH 1.1–3.1 is lower than the response in the more acidic region (pH 0.1–1.1). The behavior of the D2B band as a pH sensor differs from the behavior of the D2A band (Fig. 4a). An approximately uniform distribution of the pH sensitivity throughout the pH range studied, pH 0.1–3.1, is attained only at a methanol concentration of 20 vol %. For the solution without methanol, the pH response in the strongly acidic region (pH 0.1–1.1) decreases. An increase in the methanol concentration from 50 to 90 vol % strongly diminishes the pH response within the pH 2.1–3.1 range.

The responses of the D2A and D2B bands to the methanol concentration also substantially differ (Figs. 3b and 4b). The intensity of the D2A band monotonically increases as the methanol concentration is raised from 0 to 80 vol % within the entire pH range studied, pH 0.1–3.1. The dependence of the intensity of the D2B band on the methanol concentration becomes nonmonotonic in the strongly acidic region (pH 0.1–1.1). In less acid solutions (pH 2.1–3.1), the intensity of the D2B band decreases with increasing methanol concentration.

Thus, D2A and D2B bands give a combined response to pH and methanol concentration. The behavior of these bands as both pH sensors and sensors of the methanol concentration substantially differs.

The dependence of the intensity of the D3A band on pH and methanol concentration is plotted in Fig. 5. As can be seen, at a methanol concentration less than 80 vol %, D3 dye is mainly a pH sensor, and it gives only a weak response to changes in the methanol concentration. The maximal response to pH change is observed in the pH interval 0.1–1.1. Nevertheless, at fairly high accuracy of measurements, the working interval of the D3A band as pH sensor can be extended to pH 2.1, since in the interval from pH 1.1 to pH 2.1 the intensity of this band continues to monotonically increase with pH, but the trend is less pronounced.

The D3B band as a sensor of acidity and methanol concentration behaves similarly, although its intensity is lower and it overlaps with the D3A band. An appropriate mathematical processing is required for its separation from the total spectrum.

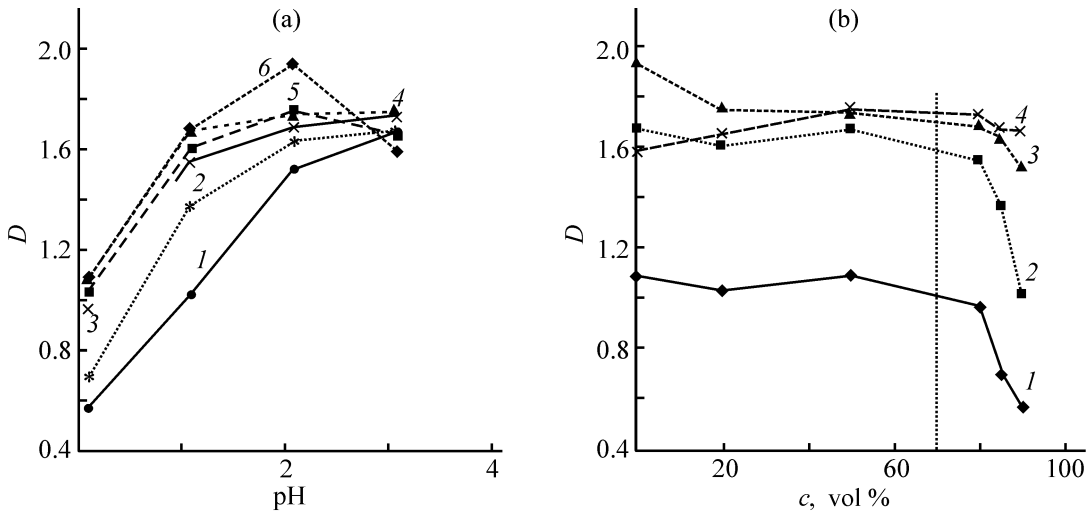


Fig. 5. Dependences of the optical density on (a) pH at various methanol concentrations and (b) methanol concentration at various pH values. Picric acid (dye D3), band D3A.

Thus, D3A and D3B bands give the response mainly to pH of the model solution when the methanol concentration does not exceed 80 vol %.

In should be noted that the reported FCs use a fuel mixture with a low methanol concentration, from 0.5 to 20 vol % [17, 18]. Fuel mixtures with a higher methanol content have also been reported, but, in any case, the methanol fraction does not exceed 70 vol % [19]. The published data allow determination of the upper boundary of the methanol content (which is of interest for FC) as 70 vol %. This boundary is designated by the dotted vertical line in Fig. 5b. As can be seen, dye D3 can be used as pH sensor within the entire range of methanol concentrations of practical interest.

It follows from the experimental data that none of the dyes studied, taken separately, can be regarded as a sensor of simultaneously two parameters of the model solution, pH and methanol concentration. However, we may suggest that the combination of D3 + D1 or D3 + D2 can be used for this purpose, provided that the dyes exert no interfering effect on each other.

To confirm this assumption, let us consider the D3 + D1 combination. The absorption bands D3A and D1B are situated so that they can be observed without additional processing to improve the spectral resolution. The D3B band overlaps with the D1A band so strongly that their use as sensors is seriously complicated. The behavior of the D3A band as a pH sensor in the solution containing the D3 + D1 combination does not substantially differ from its behavior in a model solution containing D3 only. The weak sensitivity of the D3A band to methanol concentration within the 0–80 vol % range is also preserved for the D3 + D1 combination. The response of the D1B band to the methanol concentration is preserved for the D3 + D1 combination within the same methanol concentration range.

Consideration of the D3 + D2 combination shows that the D3A and D2B bands do not require any additional processing for their resolution. The D3B band overlaps with the D2A band so strongly that their use as sensors is seriously complicated. The behavior of the D3A band as a pH sensor in the solution containing the D3 + D2 combination does not substantially differ from its behavior in a model solution containing D3 only. The weak sensitivity of the D3A band to methanol concentration within the 0–80 vol % range is also preserved for the D3 + D2 combination. The response of the D2B band to the methanol concentration is preserved for the D3 + D2 combination within the same methanol concentration range. It should be noted that the properties of the D2A and D2B bands as sensors of the methanol concentration are substantially different. The D2A band is more convenient because of its monotonic response to the methanol concentration up to 80 vol % at all pH values studied. The impossibility of using the D2A band for the D3 + D2 combination makes this combination less convenient in the combined monitoring of pH and methanol concentration as compared to the D3 + D1 combination.

The mechanism of formation of the combined or selective response of the molecular sensor to parameters of the model solution is unknown. However, we

can suggest that the primary response to pH observed for D3 and the combined response to pH and methanol concentration observed for D1 and D2 are determined by the formation of the dye molecule solvate core consisting of water or water + methanol. This assumption can be verified by quantum-chemical simulation of the absorption spectrum in the solutions with different compositions, which will be the topic of our further study. An analysis of the mechanism of the molecular sensor response to pH and methanol concentration may be useful in the development of molecular sensors whose properties are adapted to specific conditions of application.

CONCLUSIONS

(1) Examination of the optical spectra of dyes in water–methanol mixtures simulating the internal medium of Nafion type membranes for fuel cells shows that picric acid and Malachite Green can be used as optical sensors.

(2) Dyes of different type (triphenylmethane derivatives, diazo compounds, phenol nitro derivatives) can give response mainly to proton concentration or to proton and methanol concentrations simultaneously.

ACKNOWLEDGMENTS

The study was in part financially supported by the National Taiwan University of Science and Technology (grant no. RP07-1).

REFERENCES

1. Gottesfeld, S., *Fuel Cell Rev.*, 2004, vol. 1, no. 2, pp. 25–29.
2. Wilson, D. and Walter, T., *Automotive Eng. Int.*, 2001, March, pp. 85–88.
3. King, J.M. and O'Day, M.J., *J. Power Sources*, 2000, vol. 86, no. 1–2, pp. 16–22.
4. Sarma, L.S. and Hwang, B.J., *Adv. Fuel Cells*, 2005, pp. 1–43.
5. Sarma, L.S., Lin, T.D., Tsai, Y.-W., et al., *J. Power Sources*, 2005, vol. 139, pp. 44–54.
6. Tsivadze, A.Yu., Tarasevich, M.R., Andreev, V.N., and Bogdanovskaya, V.A., *Ross. Khim. Zh.*, 2006, vol. 50, no. 6, pp. 109–114.
7. US Patent 6836123.
8. Asada, T., *Asia Electron. Ind.*, 2006, September, pp. 33–34.
9. US Patent 6998185.
10. Morf, W.E., *The Principles of Ion-Selective Electrodes and of Membrane Transport*, Budapest: Akad. Kiado, 1981.
11. Bergveld, P., and Sibbald, A., *Analytical and Biomedical Applications of Ion-Selective Field-Effect Transistors*, Amsterdam: Elsevier, 1988.
12. Vlasov, Yu., Levichev, S., and Bratov, A., *Sens. Actuators B*, 1994, vols. 18–19, pp. 625–628.
13. Dobrovol'skii, Yu.A., Volkov, E.V., Pisareva, A.V., et al., *Ross. Khim. Zh.*, 2006, vol. 50, no. 6, pp. 95–104.
14. Lur'e, Yu.Yu., *Spravochnik po analiticheskoi khimii* (Handbook of Analytical Chemistry), Moscow: Khimiya, 1989.
15. Reichardt, C., *Solvents and Solvent Effects in Organic Chemistry*, Weinheim: VCH, 1988.
16. Canals, I., Oumada, F.Z., Roses, M., and Bosch, E., *J. Chromatogr. A*, 2001, vol. 911, pp. 191–202.
17. US Patent 5523177.
18. US Patent 6727016.
19. US Patent 6890672.

ISSN 1070-4272, Russian Journal of Applied Chemistry, 2008, Vol. 81, No. 2, pp. 247–253. © Pleiades Publishing, Ltd., 2008.
Original Russian Text © I.V. Sheveleva, L.A. Zemskova, S.V. Zheleznov, A.V. Voit, N.N. Barinov, V.G. Kuryavyi, V.I. Sergienko, 2008, published in Zhurnal Prikladnoi Khimii, 2008, Vol. 81, No. 2, pp. 258–264.

PHYSICOCHEMICAL STUDIES OF SYSTEMS AND PROCESSES

Correlation of Electrochemical and Structural Characteristics of Chitosan-Carbon Fibrous Materials

I. V. Sheveleva, L. A. Zemskova, S. V. Zheleznov, A. V. Voit, N. N. Barinov, V. G. Kuryavyi, and V. I. Sergienko

Institute of Chemistry, Far-Eastern Branch, Russian Academy of Sciences, Vladivostok, Russia
Far-Eastern Geological Institute, Far-Eastern Branch, Russian Academy of Sciences, Vladivostok, Russia

Received July 17, 2007

Abstract—Changes in the electrochemical properties and morphology of the surface of fibrous materials in the course of their modification with chitosan were studied in relation to the conditions of biopolymer deposition. The capacitances of the electrical double layer of the chitosan-carbon materials in NaCl solutions of various concentrations were determined by of cyclic voltammetry and the method of charging curves. The parameters of charging of the modified electrodes were calculated.

DOI: 10.1134/S107042720802016X

Carbon materials (CMs) with highly developed surface, thermal and electrical conductivity, and high chemical and electrochemical stability are used as sorbents and electrode materials for electrosorption processes and energy storage [1–3]. Various properties of CMs allowing their use as sorbents and electrodes are actually interrelated, The common property of CMs is their highly developed surface providing sorption of molecules and ions in the electrical double layer or its charging and discharge [2].

To enhance the properties of CMs (i.e., to raise the surface area, make the surface more accessible to electrolyte ions, and enhance the capacity and selectivity), they are modified by oxidation and deposition of metal oxides [4–7], hydrolyzed antimony compounds [8], and natural and synthetic polymers [4, 9]. Natural chitosan is one of promising modifying agents. It can form membranes and is characterized by mechanical strength and susceptibility to chemical modification owing to the presence of amino and hydroxy groups [10]. Deposition on a solid biopolymer matrix provides the highest development of its surface [11] and enables preparation of carbon materials that combine the porous structure of the matrix with the ion-exchange and complexing properties of chitosan.

Along with common procedures [12], the properties of carbon materials are often analyzed using electrochemical methods for studying carbon electrodes with a highly developed surface [1, 13, 14]. Electrochemical properties of a carbon material, including a fibrous material, brought in contact with an electrolyte solution allow evaluation of changes in the structural and surface properties of the material. One of the main characteristics of electrode is the capacitance of the electrical double layer (EDL), which is determined by the conditions of EDL formation in the pores of a carbon material. The EDL capacitance can be determined by electrochemical impedance spectroscopy, cyclic voltammetry, and the method of charging curves [1]. Data on the EDL capacitance of porous electrodes allow determination of the conditions of their charging [15], which determines the efficiency of using modified fibrous materials as electrodes in various processes occurring at electrode polarization.

In this study, we examined the correlation between the electrochemical properties of carbon fibers modified with chitosan natural biopolymer and changes in the pore structure and morphology of the chitosan-carbon materials (CCMs) as influenced by the conditions of chitosan deposition.

EXPERIMENTAL

As electrode material we used activated carbon roving fiber Aktilen B (ACB), whose specific surface

Capacities and parameters of the electrode charging in NaCl solutions*

Sample	C_1	C_2	R, Ω	τ, s
	F g^{-1}			
0.9% NaCl				
ACF_{ini}	53.0	53.4	60.1	413.5
ACF(+900)	61.7	61.6	87.01	560
ACF-n/p	60.35	60.38	113.0	739
ACF(–900)	52.53	52.33	47.62	228
3.5% NaCl				
ACF_{ini}	53.57	53.07	40.35	209
ACF(+900)	67.6	67.55	45.44	307
ACF-n/p	60.38	60.47	47.7	288
ACF(–900)	52.33	52.18	47.7	205

* C_1 was determined from voltammetric measurements at minimal potential sweeping rate $v = 4 \times 10^{-5}$ V s^{-1}, C_2 was determined from the galvanostatic measurements.

area (determined from nitrogen adsorption by the BET procedure), pore volume, and average pore radius were 700 m^2 g^{-1}, 0.4 cm^3 g^{-1}, and 0.4 nm, respectively. We also used the modified carbon fibers prepared by deposition of chitosan on the surface of the initial fiber without polarization [ACF-n/p] and at potentials of +900 [ACF(+900)] and –900 [ACF(–900)] mV [16]. The permeability of the chitosan films and accessibility of the surface to electrolyte ions forming the electrical double layer were studied using unmodified fiberglass and that modified with chitosan at a potential of –1200 mV.

The electrochemical measurements were carried out in a standard three-electrode cell by methods of cyclic voltammetry and charging curves. Aqueous 0.9 (physiological) and 3.5% NaCl solutions were used as electrolytes. The solutions were vigorously stirred and purged with an inert gas. The electrolyte choice was governed by the further use of ACF in electrosorption processes. Samples of carbon materials in question were placed in a gold gauze (an inert current lead). A silver chloride electrode was used as a reference electrode, and the auxiliary electrode prepared from the porous carbon material was separated from the working electrode with an MB-2 membrane.

The potentiodynamic curves in the EDL area in the ±50 mV range relative to the immersion potential of the working electrode [1] were determined with a P-5848 potentiostat. The EDL capacitance C (F g^{-1}) were calculated from Eq. (1) [1, 17]:

$$C = I/mv = (I_a + I_c)/2mv, \quad (1)$$

where I_a and I_c are the anodic and cathodic polarization currents, A; m, electrode weight, g; and v, potential sweeping rate, V s^{-1}. The degree of involvement of the electrode surface in the electrochemical process, α, was calculated from Eq. (2):

$$\alpha = C/C_{max}, \quad (2)$$

where C and C_{max} are the electrode capacitances at given and minimal potential sweeping rates, respectively, F g^{-1}. Then, the potentiodynamic data were treated by the least-squares method using Eq. (3) [18]:

$$i = Cv\left\{1 - \frac{2}{\pi^2}\sum_{n=0}^{\infty}\frac{1}{(n+1/2)^2}e^{-\pi^2(n+1/2)^2\frac{t}{\tau}}\right\}, \quad (3)$$

where i is the current density, A g^{-1}; v, potential sweeping rate, V s^{-1}; t, time, s; C, capacitance, F g^{-1}; and n, summation index. Using this equation, we calculated the specific time of EDL charging τ and the ohmic resistance of electrolyte in the pores, $R = \tau/C$ (Ω).

When the galvanostatic charging curves were recorded, the polarizing current density was chosen empirically. The current at which the position of the polarization curve became constant was considered the boundary between the equilibrium and nonequilibrium current values. In all the cases, the density of the equilibrium charging current was varied within 10^{-11}–10^{-10} A cm^{-2}. From the linear portion of the charging curve, the EDL capacitances C (F g^{-1}) were calculated using Eq. (4):

$$C = I\Delta t/m\Delta E, \quad (4)$$

where I is the polarization current, A; Δt, time of electrode charging, s; m, electrode weight, g; and ΔE, shift of the electrode potential, V.

The calculated electrochemical characteristics are listed in the table.

The morphology of the fiber surface was studied with an EVO-50XVP scanning electron microscope (Germany) in the mode of recording secondary electrons at an acceleration voltage of 20 to 30 keV. Before the experiments, the materials studied were fixed with a conducting silver adhesive to an aluminum support. The microscopic experiments were also performed on a atomic-force microscope (AFM) (Zelenograd, Russia) in the contact and tapping modes.

Carbon electrodes with a developed system of internal pores filled with an electrolyte improve the efficiency of an electrochemical process, depending on the working surface area of the electrode. However, due to hindered ion supply (diffusion limitations) and to changes in the potential in the pores (ohmic limitations), certain limitations can appear in polarization of porous electrodes. As a result, various regions of the internal surface are not equally accessible to the electrochemical process. Previously published data have shown [14, 19–21] that, in the course of EDL formation, the pores whose size is larger than 0.5 nm are accessible to simple hydrated ions at low concentration-dependent rates of EDL formation. In this case, the limiting pore size providing formation of EDL is 0.4 nm [19, 22]. Modification of the surface can lead, depending on the conditions of chitosan deposition, to different changes in the pore structure of the carbon matrix and, as a result, to different conditions of its charging.

To evaluate the permeability of a chitosan film and accessibility of the carbon surface to electrolyte ions forming the EDL, we first determined the capacitance of the initial and chitosan-modified fiberglass samples. Our results showed that the capacitances of these electrodes are the same and equal to 8 $\mu F\,cm^{-2}$. This value is comparable with published data on the capacitances of the fiberglass electrodes in various solutions [1, 23]. These results suggest that the chitosan film does not hinder penetration of the electrolyte ions to the carbon surface to form EDL. As shown in [10] by various methods including cyclic voltammetry, the chitosan film deposited on the fiberglass surface exhibits high permeability and promotes rapid transfer of electrolyte ions to the surface of the carbon material.

Activated carbon fibers exhibit semiconductor properties [23], which can affect the charge redistribution at EDL formation. Changes in the structural and surface properties of the carbon material during modification can also affect the EDL formation [1, 23]. In this study, the electrode capacitances were determined by the methods of cyclic voltammetry and charging curves. The agreement of the results confirms that these methods are equivalent in determining the capacitances of the porous materials (see table). Analysis of our experimental data suggests that the capacitances of the chitosan-carbon electrodes depend on the conditions of modification of the carbon matrix. This is due to the fact that chitosan being precipitated on the carbon fiber under certain conditions changes its pore structure, which affects the EDL formation and hence the parameters of charging and the capacitance of CCM.

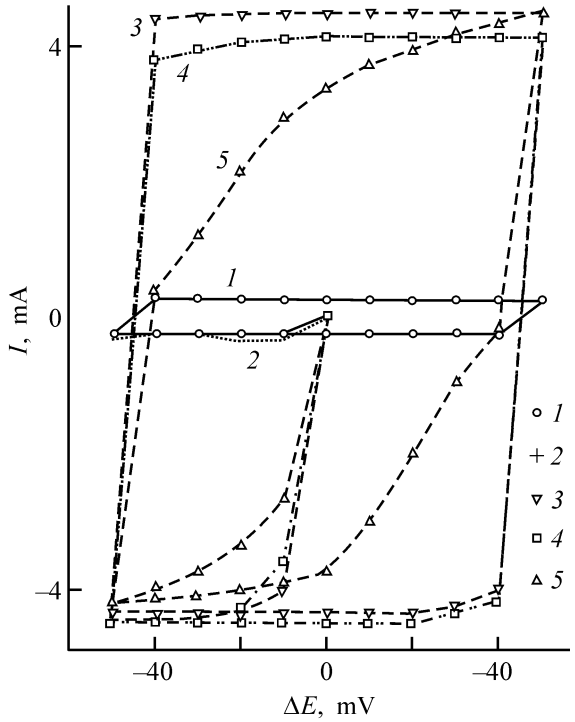


Fig. 1. Cyclic voltammograms recorded for the initial and modified fibers at different potential sweeping rates v in 0.9% NaCl solutions. (I) Current and (ΔE) potential. (*1*, *3*) ACF_{ini}, (*2*, *4*) ACF(–900), and (*5*) ACF-n/p. v, $V\,s^{-1}$: (*1*, *2*) 4×10^{-5} and (3–5) 1×10^{-4}.

The cyclic voltammograms recorded at various rates of polarization in 0.9% NaCl solution are shown as an example in Fig. 1. The shape of cyclic curves with equal areas above and below the potential axis is indicative of the absence of irreversible Faraday processes [24]. It should be noted that voltammograms recorded for the initial ACF and ACF electrochemically modified at cathodic polarization are rectangular (Fig. 1, curves *1*–*4* for ACF-n/p at $v = 4 \times 10^{-5}$ $V\,s^{-1}$ coincide with curves *1* and *2*]. This fact suggests that there is no hindrance in charging of such electrodes, in contrast to CCM prepared by chitosan deposition on the carbon surface at anodic polarization (Fig. 1, curve *5*). Hindrance of the charging processes can be due to the porous structure of the fibers, interfacial phenomena at the electrode-solution boundary, and properties of the electronic conduction band of the carbon material [25], depending on the condition of the initial fiber preparation [1, 23]. Moreover, certain changes in the inner structure and surface morphology of CCM can also occur in the course of modification. The effect of the form of precipitated chitosan and thickness of the film prepared under various deposition conditions can also affect the rate of electrolyte ion supply to the carbon matrix surface.

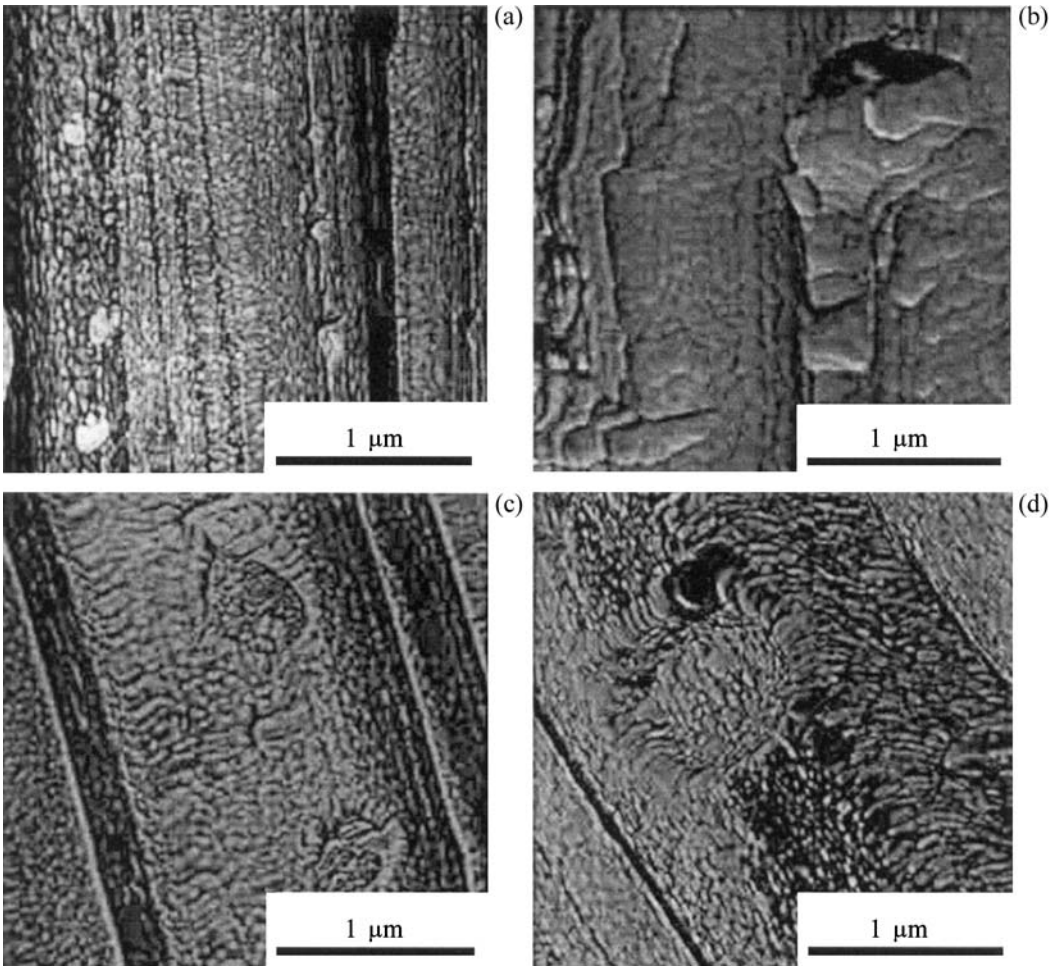


Fig. 2. AFM images of carbon fibers; 2.5 × 2.5 μm image size. (a) ACF_{ini}, (b) ACF(–900), (c) ACF(+900), and (d) ACF-n/p.

Changes in the pore structure of the fibers in the course of their modification can be evaluated using the atomic-force (AFM) and scanning electron (SEM) microscopy [26]. The AFM images of the initial and modified fibrous materials obtained are shown in Fig. 2. As seen from AFM data, the surface of the initial fiber consists of blocks (microfibrils) with cross-section diameter of about 50 nm between which micropores (~5 nm size) are distributed. Microfibrils, in turn, consist of smaller blocks (~10 nm size) between which there are supermicropores (~1 nm size). The fiber surface also has macropores (up to 1000 nm size) localized between microfibrils. Depending on the conditions of chitosan deposition on the ACF surface in the course of modification, either a film (Fig. 2b) or particle agglomerates (about 50 nm size) (Fig. 2c and 2d) are formed. Thus, by varying the conditions of the fiber modification, it is possible to prepare materials with various structural characteristics affecting the electrochemical characteristics of CCM and conditions of its charging.

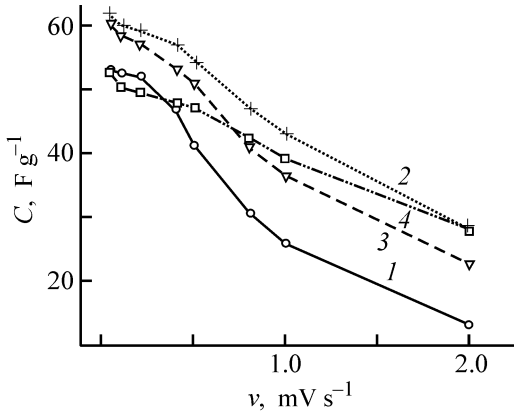


Fig. 3. Capacitance C ($F g^{-1}$) vs. the potential sweeping rate v ($mV s^{-1}$) at polarization in 0.9% NaCl solution. (*1*) ACF_{ini}, (*2*) ACF(+900), (*3*) ACF-n/p, and (*4*) ACF(–900); the same for Fig. 4.

Differences in charging and structural features of carbon materials can be judged from the dependences of the electrode capacitances in EDL areas or of

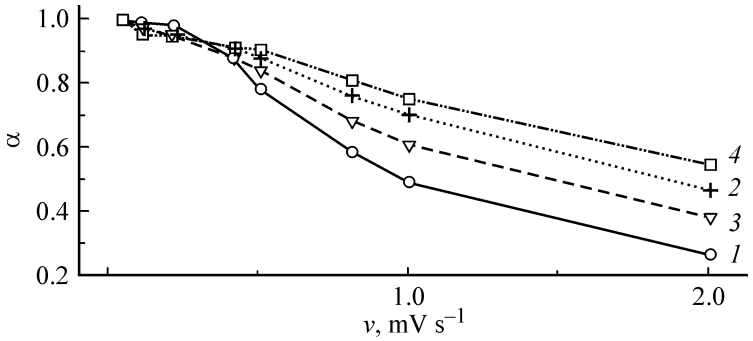


Fig. 4. Fraction α of the surface area involved in an electrochemical process vs. the potential sweeping rate v at polarization in 0.9% NaCl solution.

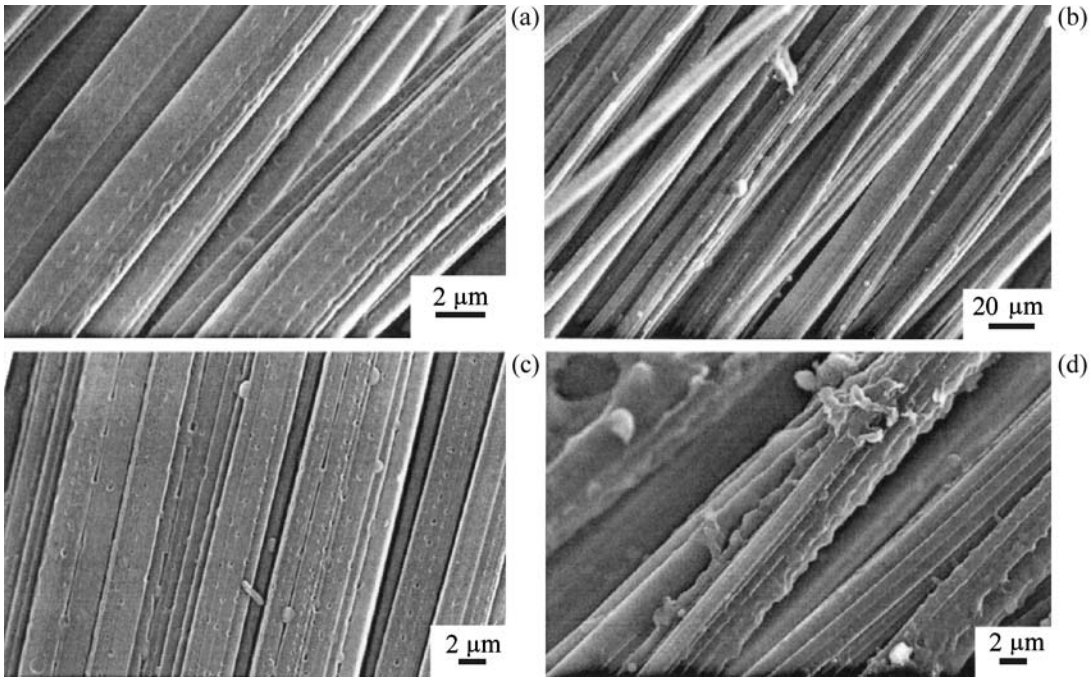


Fig. 5. SEM images of the fibers surfaces. (a) ACF_{ini}, (b) ACF-n/p, (c) ACF(+900), and (d) ACF(–900).

the degree of utilization of their surfaces on the potential sweeping rate (Figs. 3, 4). As can be seen, the electrode capacities decrease with increasing potential sweeping rate in all the cases. This is due to the fact that, at slow polarization, when the rate of applying the potential is comparable with the rate of supplying the electrolyte ions forming the EDL, the capacitance corresponds to the whole electrode surface involved in the electrochemical process. Both ohmic potential drop and diffusion limitations of the electrode process rate increase with the rate of polarization of the microporous electrode. As a result, the EDL capacitance decreases because the measured capacitance corresponds only to a certain fraction of the surface area involved in the electrochemical process.

As can be seen, a CCM prepared at anodic potentials exhibits a higher capacitance than unmodified ACF (see table). This is due to the changes in the fiber structure, in which new pores and cracks appear under the effect of anodic polarization or chitosan penetration. As a result, both the surface area and the capacitance increase. Unmodified ACF and ACF(–900) are characterized by the same capacitance. Owing to alkalization of the solution in the near-electrode layer in the course of CCM preparation under the conditions of cathodic polarization, chitosan forms an insoluble film on the fiber surface (Fig. 5d). In this case, the pore structure of the fiber remains unchanged. The chitosan film is permeable to electrolyte ions and the capacitances of ACF(–900) and the initial fiber are the same. Hence, a rather simple procedure of

cyclic voltammetry allows evaluation of differences in the pore structure of the chitosan-carbon materials, which was additionally confirmed by the AFM and SEM methods.

The SEM images of the carbon material surface are shown in Fig. 5. The surface of unmodified roving fibers is smooth and covered with a developed system of pores (Fig. 5a). It should be noted that the magnifications used in our study do not allow visualization of micropores (AFM data); however, this method provides visualization of meso- and macropores, which are probably formed on the fiber surface owing to activation in the course of its preparation [27].

Chitosan precipitated on the carbon material surface alters the morphology of the fiber surface. A SEM micrograph of the fiber modified without external polarization is shown in Fig. 5b. Chitosan occurs on the surface of carbon materials in various forms, as a film or spherical particles (500–2000 nm in diameter).

The surface image of CCM prepared by electrochemical deposition of chitosan in the range of anodic potentials is shown in Fig. 5c. With this deposition procedure, chitosan is also precipitated on the carbon material surface as a film or spherical particles localized at the macropore boundaries. In contrast to the initial material and fiberglass modified without external polarization, the CCM surface is covered with a developed system of macropores (100–600 nm size) formed under the influence of polarization. In anodic treatment of the fibers at high potentials, the pores can be formed owing to both the displacement of fibrils in the electric field and surface electrooxidation [28].

The image of the CCM surface prepared by electrochemical oxidation of chitosan in the range of cathodic potentials is shown in Fig. 5d. With this procedure of biopolymer deposition, chitosan forms an insoluble film (200–250 nm thick) or large outgrowths of irregular shape. Thus, in accordance with SEM data, the morphology of the carbon fiber strongly changes, depending on the procedure of chitosan deposition. Hence, the directed change of the surface properties of the carbon material by appropriate procedures of the fiber modification allows preparation of CCMs with various structures, which provides various conditions of charging of modified ACF.

Mathematical processing of the results of potentiodynamic charging of the porous electrode in the area of EDL potentials makes it possible to evaluate the electrolyte resistance in the pores [Eq. (3)] and the characteristic time of charging, τ (see table). Analysis of these data showed that the charging of modified electrode in 0.9% NaCl solution depends on the modification condition of carbon matrix. In contrast to the initial ACF, CCM prepared by cathodic deposition of chitosan are charged more rapidly and are characterized by lower resistance of electrolyte in the pores. This modification procedure probably yields a structure promoting formation of EDL and more uniform charging of the electrode. In contrast to initial the ACF, the composite materials prepared by anodic deposition of chitosan are charged more slowly with higher resistance of the electrolyte in the pores. These differences in the CCM charging are primarily due to changes in the pore structure and fiber morphology in the course of their modification under various conditions of chitosan deposition on the carbon material surface. It should be noted that an increase in the electrolyte concentration levels the parameters of charging of the modified materials. This effect is probably due to an increase in the number of charge carriers reducing the diffusion and ohmic limitations on the process of charging of the porous electrode.

CONCLUSIONS

(1) The conditions of biopolymer deposition on the carbon matrix affect electrochemical properties of modified fibers. As regards its electrochemical and thermal characteristics, the chitosan-carbon material prepared by electrochemical deposition of chitosan in the range of anodic potentials seems to be the most promising as an electrode material.

(2) The cyclovoltammetric data allows evaluation of changes in the pore structure of the modified fiber, which is confirmed by atomic force and scanning electron microscopy.

ACKNOWLEDGMENTS

The study was financially supported by the Far-Eastern Branch, Russian Academy of Sciences (project no. 06-1-P8-013).

REFERENCES

1. Kinoshita, K., *Carbon: Electrochemical and Physicochemical Properties*, New York: Wiley, 1988.
2. Conway, B.E., Niu, J., and Pell, W.G., *Kem. Ind.*, 2005, vol. 54, pp. 187–198.
3. Conway, B.E., *Electrochemical Supercapacitors: Scientific Principles and Technological Applications*, New York: Kluwer, 1999.
4. Zemskova, L.A. and Shepeleva, I.V., *Ross. Khim. Zh.*, 2004, vol. 48, no. 5, pp. 53–57.

5. Kaneko, K., *Carbon*, 1988, vol. 26, pp. 903–905.
6. RF Patent 2075170.
7. Beguin, F., *J. Braz. Chem. Soc.*, 2006, vol. 17, no. 6, pp. 1083–1086.
8. Shemyakina, I.V., Levchenko, L.M., Mukhin, V.V., and Yurlova, E.E., *Khim. Inter. Ustoich. Razv.*, 2005, vol. 13, pp. 111–118.
9. Muidinov, M.R., *Ros. Khim. Zh.*, 2002, vol. 46, no. 3, pp. 64–71.
10. Cruz, J., Kawasaki, M., and Gorski, W., *J. Electroanal. Chem.*, 2000, vol. 72, pp. 680–686.
11. Samonin, V.V., Amelina, I.Yu., Vedernikov, Yu.N., and Doil'nitsyn, V.A., *Zh. Fiz. Khim.*, 1999, vol. 73, no. 5, pp. 880–883.
12. Grebennikov, S.F., Udal'tsova, N.N., and Ustinov, E.A., *Zh. Prikl. Khim.*, 2005, vol. 78, no. 10, pp. 1615–1618.
13. Calas-Blanchard, C., Comtat, M., Marty, J.L., and Mauran, S., *Carbon*, 2003, vol. 41, pp. 123–130.
14. Shi, H., *Electrochim. Acta*, 1996, vol. 41, no. 10, pp. 1633–1639.
15. Sheveleva, I.V., Zemskova, L.A., Voit, A.V., et al., *Zh. Prikl. Khim.*, 2007, vol. 80, no. 5, pp. 761–766.
16. RF Patent 2281160.
17. Stromberg, A.G. and Pikula, N.P., *Elektrokhimiya*, 1981, vol. 17, no. 10, pp. 1427–1431.
18. Posey, F.A. and Morozumi, T., *J. Electrochem. Soc.*, 1966, vol. 113, no. 2, pp. 176–184.
19. Koresh, J. and Soffer, A., *J. Electrochem. Soc.*, 1977, vol. 114, no. 9, pp. 1379–1385.
20. Qu, D. and Shi, H., *J. Power Sources*, 1998, vol. 74, pp. 99–107.
21. Alvarez, S., Blanco-Lopez, M.C., Miranda-Ordieres, A.J., et al., *Carbon*, 2005, vol. 43, pp. 866–870.
22. Kim, C.-H. and Pyun, S.-I., *J. Korean Ceram. Soc.*, 2003, vol. 40, no. 9, pp. 819–826.
23. Tarasevich, M.R., *Elektrokhimiya uglerodnykh materialov* (Electrochemistry of Carbon Materials), Moscow: Nauka, 1984.
24. Koresh, J. and Soffer, A., *J. Electroanal. Chem.*, 1983, vol. 147, pp. 223–237.
25. Oren, Y. and Soffer, A., *J. Electroanal. Chem.*, 1985, vol. 186, pp. 63–67.
26. Gusev, A.I., *Nanomaterialy, nanostruktury, nanotekhnologii* (Nanomaterials, Nanostructures, and Nanotechnologies), Moscow: Fizmatlit, 2005.
27. Ermolenko, A.I., Lyubliner, I.P., and Gul'ko, N.V., *Elementosoderzhashchie ugol'nye voloknistye nateriaLy* (Element-Containing Fibrous Carbon Materials), Minsk: Nauka i Tekhnika, 1982.
28. Bondareva, G.V., Gul'ko, N.V., and Kitikova, N.V., *Zh. Prikl. Khim.*, 1997, vol. 70, no. 3, pp. 415–419.

ISSN 1070-4272, Russian Journal of Applied Chemistry, 2008, Vol. 81, No. 2, pp. 254–258. © Pleiades Publishing, Ltd., 2008.
Original Russian Text © V.P. Borovik O.P. Shkurko, 2008, published in Zhurnal Prikladnoi Khimii, 2008, Vol. 81, No. 2, pp. 265–269.

ORGANIC SYNTHESIS AND INDUSTRIAL ORGANIC CHEMISTRY

Synthesis of Isomeric Bis(aminophenyl)pyrimidines from Nitrochalcones

V. P. Borovik and O. P. Shkurko

Vorozhtsov Institute of Organic Chemistry, Siberian Branch, Russian Academy of Sciences, Novosibirsk, Russia

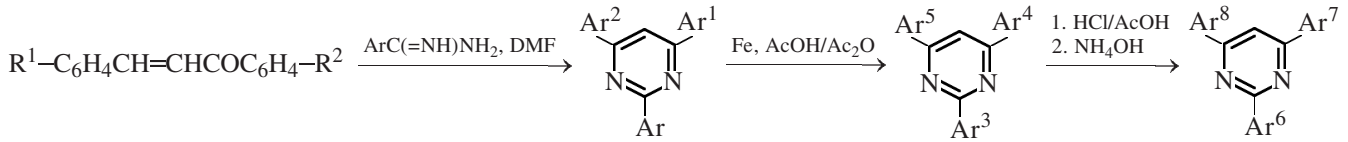
Received August 3, 2006; in final form, October 2007

Abstract—A series of isomeric bis(nitrophenyl)pyrimidines containing a phenyl substituent in the heteroring were synthesized from nitrochalcones and benzamidines. The corresponding isomeric bis(aminophenyl)-pyrimidines were prepared by reductive acetylation followed by hydrolytic elimination of the acetyl group.

DOI: 10.1134/S1070427208020171

Polyimides containing pyrimidine rings in the backbone exhibit increased heat resistance, compared to the related aromatic polyimides [1]. This is due to strong intermolecular interactions provided by pyrimidine rings in adjacent chains of polymeric molecules [2]. Polyimides exhibiting high thermomechanical characteristics have been prepared from dianhydrides of aromatic tetracarboxylic acids and such diamines as 2,5-bis(*p*-aminophenyl)pyrimidine, 2-phenyl-4,6-bis-(*p*-aminophenyl)pyrimidine, etc. [3–5]. Therefore, it has been suggested to use such diamines as starting monomers for preparing new films and fibers capable of operation at elevated temperatures [6, 7].

Here we report on the synthesis of isomeric bis-(*m*/*p*-aminophenyl)pyrimidines with an additional phenyl substituent in the pyrimidine ring, which enhances the resistance of polyimides to thermal oxidative degradation [1]. The synthesized diamines can serve as a basis for preparing other polymers, such as poly(amino imides) and poly(ester imides), and also for examining the effect of nitrogen heterocycles on the properties and structural features of the polymers [2, 8]. The most efficient route to the above-mentioned triarylpyrimidines is cyclization of substituted chalcones with arylamidines [9, 10]. The reaction is performed in a strongly alkaline solution. This procedure cannot be applied to nitro-substituted chalcones and benzamidines because of the tarring and formation of by-products (azoxy compounds) [11]. We found conditions under which the tarring of the reaction mixture is reduced to a minimum and formation of azoxy compounds is prevented. This is provided by replacing strong bases (KOH, NaOH, $NaOCH_3$, etc.) as catalysts of reactions of nitro-substituted chalcones with benzamidines with excess amidine and by performing the reaction in DMF at 120–130°C. At this temperature, the rate of dehydrogenation of the intermediate nitrophenyldihydropyrimidines [11] by atmospheric oxygen prevails over the rate of the conjugated oxidation with the nitro groups, and azoxy compounds are not formed. To attain the optimal reaction conditions, we also used zeolite as a dehydrating agent. Dry air was bubbled through the reaction mixture to ensure more efficient dehydrogenation of the dihydropyrimidine ring [11, 12]. The condensation of nitrochalcones **I**–**V** with benzamidine and with 3- and 4-nitrobenzamidines under these conditions occurs fairly smoothly and gives bis(nitrophenyl)-pyrimidines **VI**–**XII** in 50–66% yield:



I–**V** **VI**–**XII** **XIII**–**XIX** **XX**–**XXVI**

where R^1, R^2 = 4-NO_2, H (**I**); 4-NO_2, 4-NO_2 (**II**); 3-NO_2, H (**III**); 3-NO_2, 3-NO_2 (**IV**); 3-NO_2, 4-NO_2 (**V**); Ar, Ar^1, Ar^2 = 4-$NO_2C_6H_4$, 4-$NO_2C_6H_4$, Ph (**VI**); Ph, 4-$NO_2C_6H_4$, 4-$NO_2C_6H_4$ (**VII**); 3-$NO_2C_6H_4$,

Table 1. Bis(nitrophenyl)pyrimidines **VI**–**XII**

Compound	Yield, %	mp, °C	Found, %			IR spectrum, $\nu(NO_2)$, cm^{-1}
			C	H	N	
VI	52	303–308	66.17	3.58	14.35	1339, 1532
VII	6	313–318	66.54	3.65	14.05	1346, 1538
VIII	63	236–239	66.16	3.41	13.99	1350, 1530
IX	66	256–259	66.15	3.47	13.88	1352, 1528
X	40	257–261	66.43	3.69	13.81	1350, 1537
XI	50	235–240	66.36	3.69	14.49	1350, 1528
XII	55	235–240	65.90	3.70	14.31	1349, 1532

Table 2. Bis(acetylamino)pyrimidines **XIII**–**XIX** and bis(aminophenyl)pyrimidines **XX**–**XXVI**

Compound	Yield, %	mp, °C	Found,* %		
			C	H	N
XIII	93	353–356	73.73	5.55	13.56
XIV	80	>360 (>360 [18])			
XV	72	291–293	73.43	5.25	12.96
XVI	89	257–259 (246–248 [18])			
XVII	86	320–324 (320–323 [18])			
XVIII	85	311–313	74.52	5.40	13.28
XIX	85	318–321	73.69	5.69	13.17
XX	71	266–269 (266–269 [19])			
XXI	74	303–308 (302–308 [18])			
XXII	95	234–236	78.34	5.52	16.43
XXIII	94	207–209 (204–206 [18])			
XXIV	81	211–213 (205–207 [18])			
XXV	93	198–200	78.07	5.30	16.45
XXVI	95	213–216	77.91	5.35	16.31

* Calculated for **XIII**–**XIX**, $C_{26}H_{22}N_4O_2$, %: C 73.91, H 5.25, N 13.26; for **XX**–**XXVI**, $C_{26}H_{18}N_4$, %: C 78.08, H 5.36, N 16.56.

3-$NO_2C_6H_4$, Ph (**VIII**); Ph, 3-$NO_2C_6H_4$, 3-$NO_2C_6H_4$ (**IX**); Ph, 4-$NO_2C_6H_4$, 3-$NO_2C_6H_4$ (**X**); 4-$NO_2C_6H_4$, 3-$NO_2C_6H_4$, Ph (**XI**); 3-$NO_2C_6H_4$, 4-$NO_2C_6H_4$, Ph (**XII**); Ar^3, Ar^4, Ar^5 = 4-$AcNHC_6H_4$, 4-$AcNHC_6H_4$, Ph (**XIII**); Ph, 4-$AcNHC_6H_4$, 4-$AcNHC_6H_4$ (**XIV**); 3-$AcNHC_6H_4$, 3-$AcNHC_6H_4$, Ph (**XV**); Ph, 3-AcNH–C_6H_4, 3-$AcNHC_6H_4$ (**XVI**); Ph, 4-$AcNHC_6H_4$, 3-$AcNHC_6H_4$ (**XVII**); 4-$AcNHC_6H_4$, 3-$AcNHC_6H_4$, Ph (**XVIII**); 3-$AcNHC_6H_4$, 4-$AcNHC_6H_4$, Ph (**XIX**); Ar^6, Ar^7, Ar^8 = 4-$H_2NC_6H_4$, 4-$H_2NC_6H_4$, Ph (**XX**); Ph, 4-$H_2NC_6H_4$, 4-$H_2NC_6H_4$ (**XXI**); 3-$H_2NC_6H_4$, 3-H_2N–C_6H_4, Ph (**XXII**); Ph, 3-$H_2NC_6H_4$, 3-$H_2NC_6H_4$ (**XXIII**); Ph, 4-$H_2NC_6H_4$, 3-$H_2NC_6H_4$ (**XXIV**); 4-$H_2NC_6H_4$, 3-$H_2NC_6H_4$, Ph (**XXV**); 3-$H_2NC_6H_4$, 4-$H_2NC_6H_4$, Ph (**XXVI**).

An exception is the reaction of 4,4'-dinitrochalcone **II** with benzamidine, accompanied by extensive tarring (Table 1).

In the IR spectra of **VI**–**XII**, there are absorption bands of aromatic NO_2 groups in the ranges 1339–1352 and 1528–1537 cm^{-1}, and in the mass spectra there are a molecular ion peak at *m*/*z* 398 and peaks of fragment ions (*m*/*z* 352, 306) corresponding to the successive loss of two NO_2 groups.

To convert dinitro derivatives **VI**–**XII** into diamino derivatives **XX**–**XXVI**, we chose reductive acetylation with Fe powder in the presence of acetic anhydride, instead of catalytic hydrogenation. This choice is governed by the fact that the preparation of acetylamino derivatives and their subsequent hydrolysis to amino derivatives occur in high yield without formation of by-products [11]. It should be noted that catalytic hydrogenation with hydrogen, which is usually the most efficient procedure for reduction of nitro compounds, is accompanied in the case of bis(nitrophenyl)pyrimidines by formation of noticeable amounts of

Table 3. ^{1}H NMR spectra of bis(aminophenyl)pyrimidines in DMSO-d_6

Compound	Chemical shift, δ, ppm, *J*, Hz					
	NH_2 group		$-C_6H_4-$ group		$-C_6H_5$ group	5-H
	meta-	*para-*	*meta-*	*para-*		
XXIII	5.30	–	6.81 d.d (2H), *J* = 8.0, 1.8; 7.26 t (2H), *J* = 8.0; 7.55 d (2H), *J* = 8.0; 7.69 d (2H), *J* = 1.8	–	7.56–7.63 m (3H) 8.63–8.69 m (2H)	8.16
XXIV	5.23	5.72	6.79 d.d (1H), *J* = 8.0, 2.0; 7.23 t (1H), *J* = 8.0; 7.54 d (1H), *J* = 8.0; 7.68 t (1H), *J* = 2.0	6.75 d (2H), *J* = 8.8; 8.20 d (2H), *J* = 8.8	7.56–7.60 m (3H) 8.61–8.65 m (2H)	8.09
XXI	–	5.66	–	6.73 d (4H), *J* = 8.4; 8.19 d (4H), *J* = 8.4	7.51–7.58 m (3H) 8.58–8.62 m (2H)	8.04
XXII	5.24	–	6.79 d (1H), 6.81 d (1H);* 7.23 t (1H), *J* = 7.5;** 7.25 t (1H), *J* = 8.0;** 7.58 d (1H),*** 7.67 s (1H); 7.84 d (1H), *J* = 7.5; 7.92 s (1H)	–	7.58–7.64 m (3H) 8.40–8.46 m (2H)	8.27
XXVI	5.22	5.74	~6.76 m (1H); 7.21 t (1H), *J* = 7.7; 7.81 d (1H), *J* = 7.7; 7.90 t (1H), *J* = 1.8	6.74 d (2H), *J* = 8.4; 8.23 d (2H), *J* = 8.4	7.56–7.62 m (3H) 8.40–8.44 m (2H)	8.22
XXV	5.25	5.62	6.80 d.d (1H), *J* = 7.7, 2.0; 7.24 t (1H), *J* = 7.7; 7.54 d (1H), *J* = 7.7; 7.69 t (1H), *J* = 2.0	6.74 d (2H), *J* = 8.4; 8.38 d (2H), *J* = 8.4	7.55–7.62 m (3H) 8.43–8.36 m (2H)	8.12
XX	–	5.51 5.62	–	6.73 d (2H), *J* = 8.4; 6.75 d (2H), *J* = 8.1; 8.19 d (2H), *J* = 8.1; 8.36 d (2H), *J* = 8.4	7.53–7.60 m (3H) 8.36–8.42 m (2H)	8.06

* Two partly overlapping signals.

** Two partly overlapping triplet signals, forming a quartet.

*** The low-field component of the doublet is superimposed by the multiplet of the phenyl group.

difficultly removable azo compounds deteriorating the quality of the desired diamines [13]. Bis(acetylaminophenyl)pyrimidines **XIII**–**XIX** were prepared from the corresponding bis(nitrophenyl)pyrimidines **VI**–**XII** by reduction with Fe powder in a mixture of acetic acid and acetic anhydride at 130°C in 72–93% yield (Table 2). In their IR spectra, there are absorption bands at 1661–1668 and 3287–3312 cm^{-1}, characteristic of the CH_3CONH group, and in the mass spectra there are a molecular ion peak at *m*/*z* 422 and peaks of fragment ions (*m*/*z* 380, 338) corresponding to the successive loss of two CH_2CO fragments [14].

The hydrolytic deacetylation of **XIII**–**XIX** was performed by heating in a mixture of hydrochloric and acetic acids, followed by treatment of the reaction products with aqueous ammonia. The reaction occurs smoothly and gives bis(aminophenyl)pyrimidines **XX**–**XXVI** in high yield (Table 2). In their IR spectra, there are stretching vibration bands of NH_2 groups in the range 3211–3448 cm^{-1}, and in the mass spectra there is a strong peak of the molecular ion with *m*/*z* 338 (I_{rel} = 100%). The ^{1}H NMR spectra (Table 3) fully confirm the structure of these diamines. These spectra contain a singlet of the 5-H atom of the pyri-

midine ring at 8.0–8.3 ppm and show the characteristic splitting pattern of the phenylene protons. Amino group protons appear as broadened singlets whose chemical shift depends on the substitution pattern of the aminophenyl group and on its position in the heteroring. Protons of *m*-amino groups give higher-field signals (5.22–5.30 ppm) compared to *p*-amino groups (5.51–5.74 ppm), which is due to direct polar conjugation of the amino group with the electron-withdrawing pyrimidine ring in the latter case [15] and suggests a lower basicity of the *p*-aminophenyl derivatives. Approximate estimation of pK_a for diamines **XX**–**XXVI** from the $\delta(NH_2)$ values [16] gives the range pK_a 3.1–3.9, which is close to the optimum for the polycondensation of diamines with acid dianhydrides [17].

EXPERIMENTAL

The IR spectra of the compounds in KBr were recorded on a Specord M-80 spectrophotometer, and the ^1H NMR spectra, on a Bruker AM 400 spectrometer (400 MHz) in DMSO-d_6 with the residual proton signal of the solvent (2.50 ppm relative to TMS) as reference. The mass spectra were measured on a Finnigan MAT-8200 spectrometer (EI, 70 eV). The reaction progress and product purity were monitored by thinlayer chromatography (TLC) on Silufol UV-254 plates [mobile phase: benzene for nitro derivatives **VI**–**XII**, ethyl acetate for acetylamino derivatives **XIII**–**XIX**, benzene–acetone (4 : 1) for diamino derivatives **XX**–**XXVI**], with UV detection. We used 4A zeolites activated by heating for 6 h at 350°C. The starting nitroand dinitrochalcones were prepared by the procedure described in [18].

Bis(nitrophenyl)pyrimidines VI–XII were prepared by a general procedure. To a stirred suspension of 11 mmol of benzamidine hydrochloride or nitrobenzamidine hydrochloride in 40 ml of dry DMF, we added 11 mmol of sodium methylate and then, 0.5 h later, 10 mmol of appropriate chalcone **I**–**V** and 4 g of the zeolite. The mixture was heated at 120–130°C, and dry air was bubbled for 8 h. The mixture was filtered while hot and cooled to room temperature. The precipitated product was filtered off, washed with methanol, and vacuum-dried. Compound **XI** was isolated by adding 20 ml of ethanol to the hot reaction mixture; after cooling to room temperature, the precipitate was separated, washed with ethanol, and vacuum-dried. For the subsequent use, compounds **VI** and **VII** were crystallized from DMF, and compounds **VIII**–**XII** were used without additional purification. For elemental analysis, the compounds were crystallized from DMF. The yields, melting points, and analytical and IR data are listed in Table 1.

Bis(acetylaminophenyl)pyrimidines XIII–XIX. A mixture of 10 mmol of bis(nitrophenyl)pyrimidine **VI**–**XII**, 80 ml of acetic acid, 12 ml of acetic anhydride, and 7 g of Fe powder was heated with stirring for 8 h at 130°C, cooled to room temperature, and poured onto ice. The precipitate was filtered off and washed on the filter with water to remove iron salts, acetic acid, and acetic anhydride. Then the precipitate was suspended in water, the mixture was alkalized to pH 8 with a 10% NH_4OH solution, and the precipitate was filtered off, washed with water, and dried.

To purify the product of the reductive acetylation (4.22 g, 10 mmol), it was dissolved in a minimal amount of DMF at 120°C, the solution was filtered while hot through a 1–2-cm bed of Al_2O_3, and the adsorbent on the filter was washed with 2 ml of hot DMF and then with 2 ml of ethanol. The required amount of ethanol of appropriate concentration was gradually added with stirring to the combined filtrate, heated to 100–120°C. The mixture was allowed to stand at room temperature for several hours. Below are given the compound, amount of DMF (ml), and amount of aqueous ethanol (ml) and its concentration (%, in parentheses): **XIII**, 28, 140 (60%); **XIV**, 33, 70 (95%); **XV**, 12, 45 (70%); **XVI**, 10, 20 (30%); **XVII**, 36, 55 (95%); **XVIII**, 20, 6 (30%); **XIX**, 34, 76 (95%). The precipitates were filtered off, washed on the filter with two portions of ethanol of the same concentration, and dried in air at 100–120°C to constant weight. The yields, melting points, and analytical data are listed in Table 2.

Bis(aminophenyl)pyrimidines XX–XXVI. To a suspension of 4.22 g (10 mmol) of purified bis(acetylaminophenyl)pyrimidine **XIII**–**XIX** in 10 ml of acetic acid, 20 ml of concentrated HCl was added with stirring, and the resulting strongly colored solution was heated at 120°C for 1.5 h. The mixture was cooled to room temperature, the precipitate of the corresponding hydrochloride was filtered off and then suspended in 20 ml of water, and the mixture was alkalized to pH 8 with a 10% NH_4OH solution (~20 ml) with stirring. The precipitate of the diamine was filtered off, washed with water (2 × 10 ml), and dried in a vacuum over P_2O_5/KOH to constant weight.

In hydrolysis of diacetyl derivative **XV**, for more complete isolation of the dihydrochloride, 20 g of ice was added to the cooled reaction mixture, and the subsequent treatment was performed by the general procedure. The yields of the isolated compounds, their melting points, and analytical data are listed in Table 2.

CONCLUSION

A modified procedure was suggested for synthesis of triarylpyrimidines with two aminophenyl groups in even positions of the pyrimidine ring. These compounds may be of interest for preparing various polymers.

REFERENCES

1. Borovik, V.P. and Shkurko, O.P., *Khim. Geterotsikl. Soedin.*, 1997, no. 8, pp. 1011–1029.
2. Sazanov, Yu.N., Artem'eva, V.N., Mikhailov, G.M., et al., *Zh. Prikl. Khim.*, 1999, vol. 72, no. 6, pp. 975–982.
3. Koton, M.M., Mamaev, V.P., Kudryavtsev, V.V., et al., *Zh. Prikl. Khim.*, 1987, vol. 60, no. 8, pp. 1851–1855.
4. Koton, M.M., Mamaev, V.P., Dubnova, A.M., and Nekrasova, E.M., *Vysokomol. Soedin., Ser. B*, 1978, vol. 20, no. 10, pp. 792–793.
5. Mamaev, V.P., Borovik, V.P., Koton, M.M., et al., *Vysokomol. Soedin., Ser. B*, 1983, vol. 25, no. 2, pp. 102–106.
6. RF Patent 2062276.
7. RF Patent 2034862.
8. Artem'eva, V.N., Kudryavtsev, V.V., Nekrasova, E.M., et al., *Izv. Ross. Akad. Nauk, Ser. Khim.*, 1992, no. 10, pp. 2288–2296.
9. Dodson, R.M. and Seyler, J.K., *J. Org. Chem.*, 1951, vol. 16, pp. 461–465.
10. Schilt, A.A., Wu, J.F., and Case, F.H., *Talanta*, 1976, vol. 23, pp. 543–545.
11. Borovik, V.P. and Mamaev, V.P., *Izv. Sib. Otd. Akad. Nauk SSSR, Ser. Khim. Nauk*, 1990, issue 3, pp. 40–45.
12. Mamaev, V.P. and Vais, A.L., *Khim. Geterotsikl. Soedin.*, 1975, no. 11, pp. 1555–1559.
13. Borovik, V.P., Sedova, V.F., and Shkurko, O.P., *Khim. Geterotsikl. Soedin.*, 1993, no. 11, pp. 1534–1539.
14. Zaikin, V.G., Varlamov, A.V., Mikaya, A.I., and Prostakov, N.S., *Osnovy mass-spektrometrii organicheskikh soedinenii* (Fundamentals of Mass Spectrometry of Organic Compounds), Moscow: Nauka/Interperiodica, 2001, p. 157.
15. Shkurko, O.P. and Mamaev, V.P., *Zh. Org. Khim.*, 1979, vol. 25, no. 8, pp. 1737–1739.
16. USSR Inventor's Certificate, no. 1346986.
17. Bessonov, M.I., Koton, M.M., Kudryavtsev, V.V., and Laius, L.A., *Poliimidy – klass termostoikikh polimerov* (Polyimides: A Class of Heat-Resistant Polymers), Leningrad: Nauka, 1983, p. 47.
18. Borovik, V.P., Yazykov, N.A., and Mamaev, V.P., *Sib. Khim. Zh.*, 1991, issue 2, pp. 87–93.
19. Mognonov, D.M., Borovik, V.P., Radnaeva, L.D., et al., *Sib. Khim. Zh.*, 1991, issue 4, pp. 99–101.

ISSN 1070-4272, Russian Journal of Applied Chemistry, 2008, Vol. 81, No. 2, pp. 259–262. © Pleiades Publishing, Ltd., 2008.
Original Russian Text © T.S. Zhivotova, A.M. Gazaliev, O.V. Dryuk, A.Zh. Seitembetova, 2008, published in Zhurnal Prikladnoi Khimii, 2008, Vol. 81, No. 2, pp. 270–273.

ORGANIC SYNTHESIS AND INDUSTRIAL ORGANIC CHEMISTRY

Synthesis and Antioxidant Activity of Alkaloid- and Amine-containing Salts of 1,3,4-Thiadiazole-2,5-disulfonic Acid

T. S. Zhivotova, A. M. Gazaliev, O. V. Dryuk, and A. Zh. Seitembetova

Institute of Organic Synthesis and Coal Fuel Chemistry of the Republic of Kazakhstan, Karaganda, Kazakhstan
Kazakh State Medical Academy, Astana, Kazakhstan

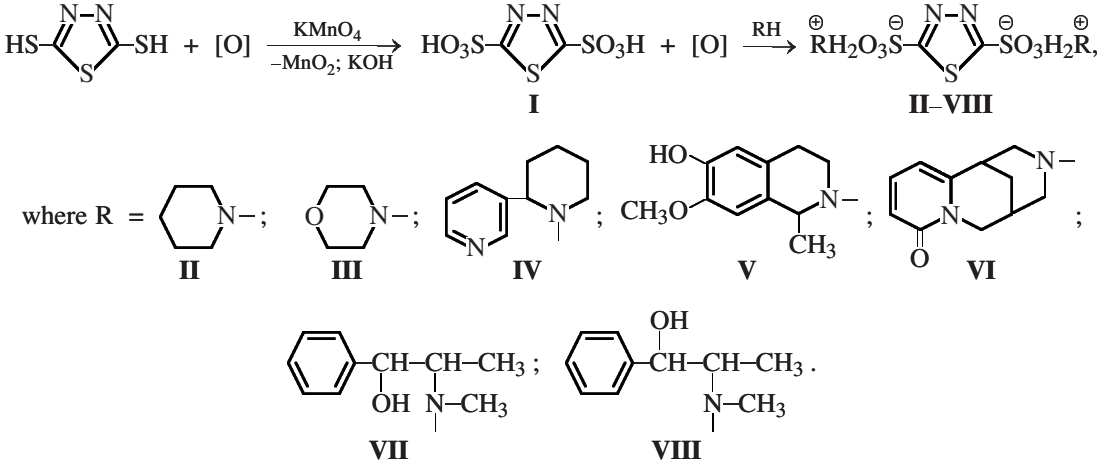
Received March 16, 2007

Abstract—1,3,4-Thiadiazole-2,5-disulfonic acid was synthesized by oxidation of 2,5-dimercapto-1,3,4-thiadiazole, and onium salts of this acid were prepared by its reactions with selected alkaloids and secondary amines. The antioxidant activity of the compounds synthesized was evaluated.

DOI: 10.1134/S1070427208020183

1,3,4-Thiadiazole derivatives exhibit various kinds of physiological activity [1–5]. However, data on alkaloid derivatives of symmetrical 2,5-disubstituted 1,3,4-thiadiazoles are lacking. Therefore, readily accessible 2,5-dimercapto-1,3,4-thiadiazole [6] is of interest as the starting compound that can be modified with the aim to prepare new potentially bioactive substances.

Oxidation of 2,5-dimercapto-1,3,4-thiadiazole with an aqueous solution of $KMnO_4$ involves exclusively the thiol groups, leaving the heterocyclic sulfur atom intact, and yields 1,3,4-thiadiazole-2,5-disulfonic acid **I**, which forms with alkaloids and their structural analogs the corresponding onium salts **II**–**VIII**:



The ratio of 2,5-dimercapto-1,3,4-thiadiazole and $KMnO_4$, required for complete oxidation of thiol groups to sulfo groups, was determined by acid–base titration to be 1 : 4. In the process, permanganate anions are reduced to manganese dioxide.

Compounds **I**–**VIII** are white crystalline substances with high melting points, readily soluble in water.

1,3,4-Thiadiazole-2,5-disulfonic acid **I** is formed in almost quantitative yield (about 98%). The yields of salts **II**–**VIII** range from 50 to 77%, depending on

Table 1. Yields, physicochemical constants, and elemental analyses of **I**–**VIII**

Compound	Yield, %	mp, °C	Found, %			Formula	Calculated, %		
			C	H	N		C	H	N
I	98.0	>350	9.67	0.90	11.30	$C_2H_2N_2O_6S_3$	9.76	0.81	11.38
II	76.9	>350	34.70	5.72	13.35	$C_{12}H_{24}N_4O_6S_3$	34.62	5.77	13.46
III	66.9	>350	28.50	4.68	13.25	$C_{10}H_{20}N_4O_8S_3$	28.57	4.76	13.33
IV	42.8	>350	46.39	5.20	14.84	$C_{22}H_{30}O_6S_3$	46.32	5.26	14.74
V	52.6	>350	50.81	5.38	9.81	$C_{24}H_{30}N_4O_6S_3$	50.88	5.30	9.89
VI	70.0	>350	46.00	4.70	13.51	$C_{24}H_{30}N_6O_8S_3$	46.01	4.79	13.42
VII	50.1	>350	45.89	5.50	9.82	$C_{22}H_{32}N_4O_8S_3$	45.83	5.56	9.72
VIII	56.1	>350	45.77	5.44	9.70	$C_{22}H_{32}N_4O_8S_3$	45.83	5.56	9.72

the electron-donor properties of the substituents and conformational rigidity of the rings in the molecules of the starting alkaloids and secondary amines. Salts **II** and **VI** were prepared in the highest yields, because in the respective bases (piperidine, cytisine), the nitrogen atom bears a higher negative charge owing to the electron-donor effect of the cycloalkyl substituent and is, therefore, more reactive. With morpholine, the yield of salt **III** is somewhat lower because of the electron-withdrawing effect of the oxygen atom. In *L*-ephedrine and *D*-pseudoephedrine, the effect of electron-donor methyl groups is weakened by the electron-withdrawing effect of the benzene ring, and this is accompanied by the steric shielding effect of methyl groups at the nitrogen atom. Therefore, the yields of **VII** and **VIII** are lower than those of **II**, **III**, and **VI**. The poor yield of **IV** is due to the steric shielding effect of the pyridyl substituent in the anabasine molecule. The presence of the electron-withdrawing benzene ring and the steric shielding effect of the methyl substituent in the salsoline molecule cause the relatively low yield of **V**.

The structure and composition of **I**–**VIII** were confirmed by IR, ^{1}H NMR, and ^{13}C NMR spectroscopy, and also by elemental analysis.

The IR spectra of all the onium salts synthesized contain characteristic absorption bands of the thiadiazole ring at 680, 730, 1400 ± 20, and 1500 ± 20 cm^{-1}, bands in the range 656–649 cm^{-1} assigned to $-SO_3^-$ vibrations, and absorption bands at 3501–3421 cm^{-1} characteristic of secondary ammonium salts [7].

In the ^{1}H NMR spectra of **II**–**VIII**, recorded in DMSO-d_6, protons of the ammonium group appear as an ill-resolved multiplet centered at 14.6 ppm. The chemical shifts of signals from protons of alkaloid and secondary amine fragments have typical values [8].

In the ^{13}C NMR spectrum of 1,3,4-thiadiazole-2,5-disulfonic acid **I**, the heterocyclic carbon atom appears as a singlet at 168.0 ppm. In the ^{13}C NMR spectrum of piperidinium salt of 1,3,4-thiadiazole-2,5-disulfonic acid **II**, the heterocyclic carbon atom appears as a singlet at 158.4 ppm, and carbon atoms of the piperidine fragment give signals at 23.1, 25.5, 26.0, 42.5, and 45.5 ppm [9].

The yields, physicochemical constants, and elemental analyses of **I**–**VIII** are listed in Table 1.

Common antioxidants are phenolic compounds [10]. At the same time, among nitrogen heterocycles containing piperidine, pyridine, pyrimidine, thiazole, and other fragments there are compounds exhibiting anti- or prooxidant effect [11].

The antioxidant activity[1] of 1,3,4-thiazole-2,5-disulfonic acid **I** and its onium salts **II**–**IV**, **VI**, and **VII** was evaluated with the aim to reveal the effect of the thiadiazole ring and sulfonic acid groups in the nitrogen-containing heterocycles on the antioxidant activity (AOA). As reference antioxidant we used Ionol. The results are listed in Table 2.

All the compounds tested, 1,3,4-thiadiazole-2,5-disulfonic acid **I** and its alkaloid- and amine-containing salts **II**–**IV**, **VI**, and **VII**, exhibited antioxidant properties, though to different extents. In view of the fact that anabasine and *L*-ephedrine exhibit no antioxidant properties and cytisine is a prooxidant [11], it can be suggested that just the introduction of the sulfo groups and thiadiazole fragment into the structure of alkaloids and secondary amines imparts to them antioxidant properties. Comparison of the antioxidant deactivities of 1,3,4-thiadiazole-2,5-disulfonic acid

[1] The antioxidant activity was evaluated at Kazakh State Medical Academy (Astana) under the guidance of A.Zh. Seitembetova.

Table 2. Antioxidant activity of compounds **I**–**IV**, **VI**, and **VII**

Compound	c_{MDA},* nM (30-min incubation)	Decrease in c_{MDA} relative to control, %
Control	30.01	–
2,6-Di-*tert*-butyl-4-methylphenol (Ionol)	9.32	68.94
1,3,4-Thiadiazole-2,5-disulfonic acid **I**	15.16	50.52
Piperidinium salt **II**	4.58	84.74
Morpholinium salt **III**	14.68	51.08
Anabasine salt **IV**	20.68	31.09
Cytisine salt **VI**	14.68	51.08
L-Ephedrine salt **VII**	14.05	53.18

* (c_{MDA}) Concentration of malonic dialdehyde.

rivatives showed that introduction of the piperidine fragment considerably enhances the antioxidant properties, the effect of the *L*-ephedrine fragment is considerably weaker, and introduction of the morpholine and cytisine fragments has virtually no effect on the AOA of the disulfonic acid. The presence of the anabasine fragment in the structure of the onium salt considerably decreases the AOA of salt **VI**, compared to 1,3,4-thiadiazole-2,5-disulfonic acid **I**.

The antioxidant activity of **II**–**IV**, **VI**, and **VII** can be attributed to the conjugation arising between substituents in positions 2 and 5 due to conductivity of the thiadiazole ring, comparable with that of the phenylene bridge [12], which is consistent with the published evidence about an increased AOA of substances with a π-excessive heterocyclic system, owing to which these substances readily undergo one-electron oxidation [13]. Introduction of electron-donor substituents and the presence of multiple bonds enhance the conjugation effect, which results in increased AOA and is also consistent with published data [11, 14, 15]. Morpholinium salt **III** shows lower AOA than does piperidinium salt **II**, because introduction of the more electron-withdrawing morpholine fragment decreases the conjugation effect. This fact is consistent with published data that introduction of the morpholinium fragment enhances the prooxidant properties [16].

EXPERIMENTAL

The IR spectra of the compounds were recorded on an Avatar-320 spectrometer in KBr pellets and mulls in mineral oil, and the ^1H and ^{13}C NMR spectra, on a Mercury-300 spectrometer with a working frequency of 300 MHz, solvent DMSO-d_6.

1,3,4-Thiadiazole-2,5-disulfonic acid I. A 2.5% aqueous solution of 6.32 g (0.04 mol) of $KMnO_4$ was added dropwise with stirring at room temperature over a period of 3 h to an aqueous solution of 1.5 g (0.01 mol) of 2,5-dimercapto-1,3,4-thiadiazole. The mixture was heated with stirring on a water bath until its complete decolorization. The precipitate of manganese dioxide was filtered off, the filtrate was evaporated, and the dry residue was washed with alcohol. 1,3,4-Thiadiazole-2,5-disulfonic acid **I** was recrystallized from ethanol–water, 10 : 1.

Alkaloid- and amine-containing salts of 1,3,4-thiadiazole-2,5-disulfonic acid, II–VIII. An aqueous solution of 0.02 mol of appropriate secondary amine or alkaloid was added dropwise with stirring over a period of 1 h to an aqueous solution of 2.46 g (0.01 mol) of 1,3,4-thiadiazole-2,5-disulfonic acid **I**. The mixture was stirred at room temperature for 12 h and left in a vacuum desiccator to remove the solvent. The solid residue was washed with alcohol, filtered off, and recrystallized from ethanol–water, 10 : 1.

The antioxidant acitivity of 1,3,4-thiadiazole-2,5-disulfonic acid **I** and its salts **II**–**IV**, **VI**, and **VII** was evaluated with oxidation of phosphatidylcholine liposomes as model reaction (test with thiobarbituric acid) [14]. The oxidation supression effect was evaluated by measuring the concentration of malonic dialdehyde (MDA) 10, 15, 20, and 30 min after the onset of the reaction.

CONCLUSIONS

(1) Oxidation of 2,5-dimercapto-1,3,4-thiadiazole with an aqueous solution of $KMnO_4$ yielded 1,3,4-thiadiazole-2,5-disulfonic acid. Its reactions with selected alkaloids and cyclic secondary amines gave the corresponding salts.

(2) The antioxidant activity of 1,3,4-thiadiazole-2,5-disulfonic acid and its alkaloid- and amine-containing salts was revealed.

REFERENCES

1. Umarov, B.B., Ishankhodzhaeva, M.M., Khusenov, K.Sh., et al., *Zh. Org. Khim.*, 1999, vol. 35, no. 4, pp. 624–627.
2. Labanauskas, L., Kalcas, V., Udrenaite, E., et al., in *1-ya Mezhdunarodnaya konferentsiya "Khimiya i biologicheskaya aktivnost' azotistykh geterotsiklov i alkaloidov"* (1st Int. Conf. "Chemistry and Biological Activity of Nitrogen Heterocycles and Alkaloids"), Moscow, October 9–12, 2001, vol. 2, p. 181.
3. Salimov, T.M., Kukaniev, M.A., Sattorov, I.T., and Osimov, D.M., *Khim.-Farm. Zh.*, 2005, vol. 39, no. 6, p. 2829.
4. Houbin, W., Shukui, J., Shufen, M., and Zhaohai, Q., *J. China Agr. Univ.*, 2004, vol. 9, no. 1, pp. 63–66.
5. Vullo, D., Franohi, M., Gallori, E., et al., *J. Med. Chem.*, 2004, vol. 47, no. 5, pp. 1272–1279.
6. Arbuzov, B.A. and Ukhvatova, E.N., *Zh. Obshch. Khim.*, 1959, vol. 29, no. 2, pp. 503–506.
7. Bellamy, L.J., *Advances in Infrared Group Frequencies*, London: Methuen, 1968.
8. Gazaliev, A.M., Zhurinov, M.Zh., and Fazylov, S.D., *Novye bioaktivnye proizvodnye alkaloidov* (New Bioactive Alkaloid Derivatives), Alma-Ata: Gylym, 1992.
9. Levy, G.C,. and Nelson, G.L., *Carbon-13 Nuclear Magnetic Resonance for Organic Chemists*, New York: Wiley, 1972.
10. Seitembetova, A.Zh. and Adekenov, S.M., *Prirodnye fenol'nye soedineniya – perspektivnyi istochnik antioksidantov* (Natural Phenolic Compounds as a Promising Source of Antioxidants), Almaty: KazgosINTI, 2001.
11. Seitembetov, T.S., Adekenov, S.M., and Dalenov, E.D., *Antioksidanty i initsiirovannaya khemilyuminestsentsiya* (Antioxidants and Initiated Chemiluminescence), Akmola: Kaz. Gos. Med. Akad., 1996.
12. Zubets, V.I., Vergizov, S.N., Yakovlev, S.I., and V'yunov, K.A., *Khim. Geterotsikl. Soedin.*, 1987, no. 2, pp. 267–270.
13. Mezheritskii, V.V., in *1-ya Mezhdunarodnaya konferentsiya "Khimiya i biologicheskaya aktivnost' azotistykh geterotsiklov i alkaloidov"* (1st Int. Conf. "Chemistry and Biological Activity of Nitrogen Heterocycles and Alkaloids"), Moscow, October 9–12, 2001, vol. 2, pp. 112–122.
14. Smirnov, L.D. and Dyumaev, K.M., *Khim.-Farm. Zh.*, 1983, no. 4, pp. 38–44.
15. Bogdashev, N.N., Tukhovskaya, N.A., and Pogrebnyak, A.V., *Khim.-Farm. Zh.*, 1998, no. 2, pp. 31–33.
16. Seitembetova, A. *Zh., Khim. Prirodn. Soedin.*, 1999, no. 6, pp. 738–742.

ISSN 1070-4272, Russian Journal of Applied Chemistry, 2008, Vol. 81, No. 2, pp. 263–267. © Pleiades Publishing, Ltd., 2008.
Original Russian Text © I.V. Kulakov, A.A. Ainabaev, O.A. Nurkenov, A.M. Gazaliev, 2008, published in Zhurnal Prikladnoi Khimii, 2008, Vol. 81, No. 2, pp. 274–277.

ORGANIC SYNTHESIS AND INDUSTRIAL ORGANIC CHEMISTRY

Synthesis of *N*-Alkaloidacyl Derivatives of Phenothiazine

I. V. Kulakov, A. A. Ainabaev, O. A. Nurkenov, and A. M. Gazaliev

Institute of Organic Synthesis and Coal Fuel Chemistry of the Republic of Kazakhstan, Karaganda, Kazakhstan

Received May 30, 2007

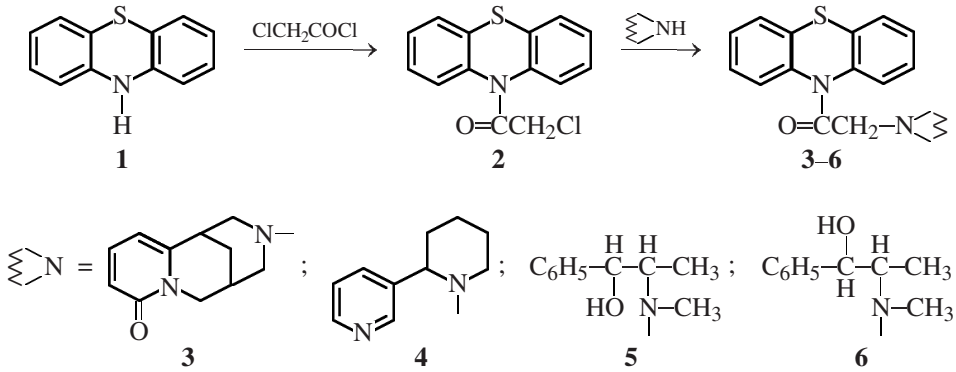
Abstract—Compounds in which cytisine, anabasine, *D*-pseudoephedrine, and *L*-ephedrine fragments are linked to the phenothiazine nitrogen atom via acyl group were synthesized. These compounds are potential drugs, and their activity was confirmed by computer prediction using PASS software.

DOI: 10.1134/S1070427208020195

Many S,N-containing heterocyclic compounds exhibit a broad spectrum of biological activity. Fused tricyclic systems occupy a particular place in this series. For example, phenothiazine **1** is very important as insecticide and helminthicide [1]. The toxicity of phenothiazine, like that of many sulfur-containing compounds, is very low.

The discovery in the 1960s of compounds with a high neuroleptic activity (aminazine, largactil) [2, 3] among 10-aminoalkyl phenothiazine derivatives stimulated their synthesis and comprehensive study. It was also found that 10-aminoacyl phenothiazine derivatives, inactive as neuroleptics, show high cholino- and adrenolytic activity and pronounced antianginal and antiarrhythmic action [4]. Among more than a thousand of new phenothiazine compounds, certain relationships were revealed between the biological activity and the structure of substituents at the N atom and in the cyclic system. 10-Aminopropionyl derivatives proved to be the most active, and lengthening or shortening of the acylalkyl chain decreased the activity [5]. However, despite a huge number of the phenothiazine derivatives synthesized, compounds combining a tricyclic phenothiazine core with certain physiologically active alkaloids as substituents have not been reported.

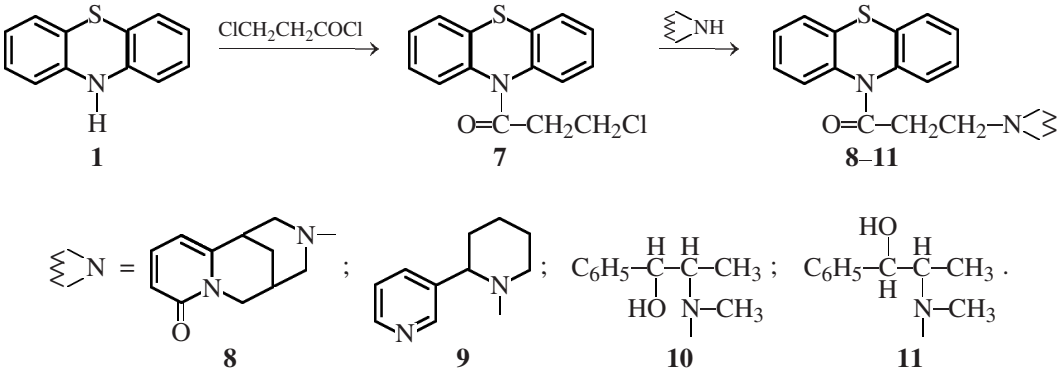
Therefore, it was interesting to prepare previously unknown phenothiazine derivatives of certain alkaloids:



The starting phenothiazine was prepared by the procedure described in [6]. The alkylation of cytisine, anabasine, *L*-ephedrine, and *D*-pseudoephedrine with 10-(2-chloroacetyl)phenothiazine was performed in refluxing toluene in the presence of triethylamine. The target products were purified by column chromatography and by conversion of the hydrochlorides into free bases that are difficultly soluble in water.

Compounds **3**–**6** are white or gray crystalline substances readily soluble in the majority of organic solvents.

To further study the structure–activity relationship, we also prepared *N*-alkaloidpropionyl phenothiazine derivatives, because specifically 10-aminopropionyl phenothiazine derivatives exhibit high cholino- and adrenolytic activity and pronounced antianginal and antiarrhythmic action:

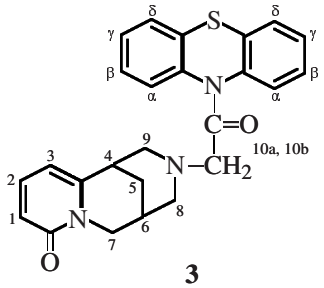


Compounds **8**–**11** are white or gray crystalline substances melting at lower temperatures than their acetyl analogs. The compounds are soluble in the majority of organic solvents. The yield, physicochemical constants, and analytical data are listed in Table 1.

The IR spectra of all the compounds prepared contain, along with bands of the functional groups of alkaloid fragments [ν(OH) at 3320–3280 cm^{-1} for ephedrine alkaloids; ν(C=O) of the cytisine core at 1647 cm^{-1}], also a strong absorption band of the carbonyl (amide) group at 1672–1650 cm^{-1}.

The mass spectra of **3**–**6** and **8**–**11** contain a peak of the molecular ion M^+ with a relative intensity of 5 to 30% and fragment peaks. Their *m*/*z* values and relative intensities I_{rel} (%) are given below for compound **4** as an example: 175 (100%), 199 (22%), 132 (24%), and 44% (58%). These peaks were assigned to the anabasine core >N–CH_2^+, phenothiazine, and other fragmentation products.

The ^1H NMR spectra of **3**–**11** contain, along with signals of phenothiazine protons (multiplets and doublets at 7.20–7.70 ppm), also signals of protons of the alkaloid fragments, having typical chemical shifts:

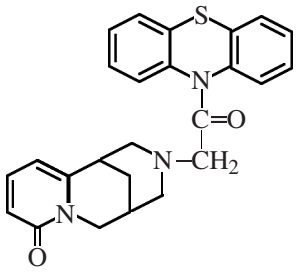
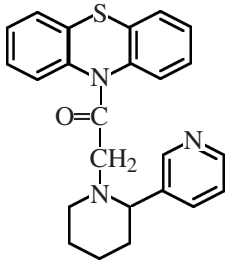
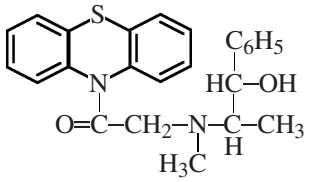
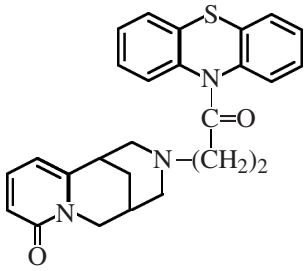
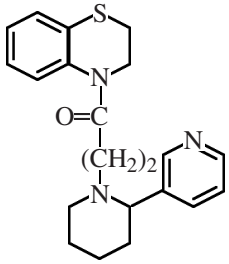
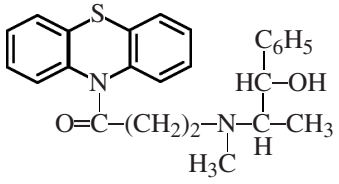


3

Table 1. Physicochemical constants and elemental analyses of the compounds prepared

Compound	Yield, %	mp, °C	Found, %			Empirical formula	Calculated, %		
			C	H	N		C	H	N
3	75.0	99–100	69.38	4.97	9.12	$C_{25}H_{23}N_3O_2S$	69.91	5.40	9.78
4	62.1	75–76	71.30	5.28	9.98	$C_{24}H_{23}N_3OS$	71.79	5.77	10.47
5	67.7	63–64	70.78	5.39	6.42	$C_{24}H_{24}N_2O_2S$	71.26	5.98	6.93
6	70.0	94–95	70.85	6.42	6.38	$C_{24}H_{24}N_2O_2S$	71.26	5.98	6.93
8	72.0	70–72	69.91	5.16	8.96	$C_{26}H_{25}N_3O_2S$	70.40	5.68	9.47
9	66.6	73–74	71.76	5.57	9.62	$C_{25}H_{25}N_3OS$	72.26	6.06	10.11
10	65.0	63–65	71.26	5.78	6.17	$C_{25}H_{26}N_2O_2S$	71.74	6.26	6.69
11	68.0	69–70	72.16	6.70	6.22	$C_{25}H_{26}N_2O_2S$	71.74	6.26	6.69

Table 2. Results of computer prediction of the bioactivity of the compounds synthesized

Compound	Structural formula	P_a	P_i	Expected kind of activity
3		0.930	0.002	Antismoking
		0.900	0.004	Analeptic
		0.867	0.003	Respiratory analeptic
		0.832	0.008	Psychotropic
		0.769	0.003	Acetylcholine nicotinic agonist
		0.767	0.007	Hypothermic
		0.755	0.007	Antiarrhythmic
4		0.843	0.011	Convulsant
		0.836	0.005	Hypothermic
		0.816	0.011	Nootropic
		0.788	0.006	Acetylcholine antagonist
		0.782	0.023	Cardiovascular analeptic
		0.756	0.007	Antiparkinsonian
		0.755	0.011	Psychotropic
6		0.924	0.006	Spasmolytic
		0.882	0.028	Hematotoxic
		0.795	0.007	Cardiodepressant
		0.792	0.007	Antitoxic
		0.788	0.007	Antiarrhythmic
		0.776	0.006	Hypertensive
		0.784	0.016	Antineurotoxic
8		0.924	0.002	Antismoking
		0.887	0.007	Psychotropic
		0.859	0.005	Analeptic
		0.856	0.004	Respiratory analeptic
		0.826	0.006	Hypothermic
		0.819	0.018	Cardioprotectant
		0.790	0.007	Antiarrhythmic
9		0.872	0.005	Hypothermic
		0.828	0.008	Psychotropic
		0.819	0.018	Cardioprotectant
		0.780	0.024	Convulsant
		0.759	0.006	Acetylcholine antagonist
		0.760	0.015	Nootropic
		0.733	0.009	Spasmolytic
11		0.920	0.006	Spasmolytic
		0.869	0.031	Hematotoxic
		0.820	0.011	Antineurotoxic
		0.810	0.007	Cardiodepressant
		0.793	0.006	Hypertensive
		0.798	0.033	Beta-adrenergic-receptor kinase inhibitor
		0.746	0.007	Antiarrhythmic

In particular, in the ^{1}H NMR spectrum of 10-(2-*N*-cytisinoacetyl)phenothiazine **3**, the phenothiazine protons give groups of overlapping multiplets and doublets centered at 7.47 ppm for H^{α} and H^{β} and at 7.25 ppm for H^{γ} and H^{δ}. The next three low-field signals belong to protons of the pyridine core. The signal at 7.35 ppm corresponds to H^2 ($J_{H^2H^3}$ ~3.2 Hz). The doublet at 6.23 ppm corresponds to H^1 ($J_{H^1H^2}$ ~3.6 Hz), and the doublet at 6.05 ppm, to H^3. The next group of lines (a complex multiplet centered at 3.66 ppm) corresponds to the axial and equatorial H^7 protons. The methylene protons of the $-NC=(O)CH_2$ group are nonequivalent and give two doublets at 3.14 and 3.20 ppm with the coupling constant $J_{H^{10a}H^{10b}}$ = 4.0 Hz. The group of lines in the range 2.67–2.85 ppm originates from the H^4 and H^6 protons. The doublets from the H^8 and H^9 protons are situated at 2.42 and 2.32 ppm. The methylene protons H^5 give a pair of doublets centered at 1.68 ppm. The integral curves are consistent with the numbers of protons.

To estimate the expected biological activity of the synthesized phenothiazine derivatives, we performed a bioprediction using the PASS software (Prediction of Activity Spectra for Substances) [7]. The results are listed in Table 2 as the expected kinds of activity and coefficients of the probability of the presence (P_a) and absence (P_i) of each kind of activity, ranging from 0 to 1. In the analysis of the predicted activity spectra, we chose the condition $P_a > 70\%$.

Analysis of the predicted bioactivity of the new alkaloid-containing phenothiazine derivatives shows that their expected activity combines the physiological activity of both the starting alkaloids and aminoacyl phenothiazine derivatives. With fairly high probability, compounds **3**–**11** may exhibit antismoking, antiarrhythmic, psychotropic, spasmolytic, analeptic, and nootropic activity. They can be suggested for tests as new effective drugs.

EXPERIMENTAL

The ^{1}H NMR spectra were recorded on a Bruker DRX500 device operating at 500 MHz from DMSO-d_6 solutions relative to internal TMS; the IR spectra, on an Avatar-320 FTIR spectrometer from KBr pellets; and the mass spectra, on a Finnigan MAT.INCOS 50 device with direct sample inlet, at an ionizing electron energy of 70 eV. The melting points were determined with a Boëtius device. The reaction progress and product purity were monitored by thin-layer chromatography on Sorbfil plates in the system benzene–acetone, 1 : 1. The plates were developed with iodine vapor.

10-(2-Cytisinoacetyl)phenothiazine 3. To a mixture of 0.97 g (0.005 mol) of cytisine and 1.38 g (0.005 mol) of 10-(2-choloroacetyl)phenothiazine in 7 ml of toluene, we added 2.02 g (0.02 mol) of triethylamine and refluxed the mixture for 3 h. The precipitate of triethylamine hydrochloride was filtered off, the solvent was removed, and the residue was crystallized from petroleum ether and purified by passing through a column packed with a 1 : 1 blend of Al_2O_3 and SiO_2 (eluent benzene). The dilution of the solution with a threefold volume of hexane resulted in the precipitation of a white crystalline product.

10-(2-*N*-Cytisinopropionyl)phenothiazine 8 was prepared similarly to **3**.

10-(2-*N*-*D*-Pseudoephedrinoacetyl)phenothiazine 6. To a mixture of 0.66 g (0.004 mol) of *D*-pseudoephedrine and 1.11 g (0.004 mol) of 10-(2-chloroacetyl)phenothiazine in 7 ml of toluene, we added 1.21 g (0.012 mol) of triethylamine and refluxed the mixture for 5 h. The precipitate of triethylamine hydrochloride was filtered off. The toluene solution was washed with distilled water and extracted with 10% HCl. The acidic solution was diluted with water, clarified with activated carbon, and alkalized with aqueous ammonia. The precipitate was filtered off and dried in air.

10-(2-*N*-Anabasinoacetyl)phenothiazine **4**, 10-(2-*N*-*L*-ephedrinoacetyl)phenothiazine **5**, 10-(3-*N*-anabasinopropionyl)phenothiazine **9**, 10-(3-*N*-*L*-ephedrinopropionyl)phenothiazine **10**, and 10-(3-*N*-*D*-pseudoephedrinopropionyl)phenothiazine **11** were prepared similarly to **6**.

CONCLUSIONS

(1) Alkylation of physiologically active alkaloids cytisine, anabasine, *D*-pseudoephedrine, and *L*-ephedrine with 10-(2-chloroacetyl)phenothiazine and 10-(3-chloropropionyl)phenothiazine was performed.

(2) The physicochemical constants of the compounds synthesized were determined, and their compositions and structures were confirmed by ^{1}H NMR, IR, and mass spectroscopy.

(3) The bioactivity of the synthesized alkaloid-containing phenothiazine derivatives was evaluated by computer prediction using the PASS program. The results obtained show that it is appropriate to further study these compounds as new effective drugs.

REFERENCES

1. *Heterocyclic Compounds*, Elderfield, R.C., Ed., New York: Chapman and Hall, 1950.
2. Burger, A., *Medicinal Chemistry*, New York: Wiley–Interscience, 1970.
3. Goodman, L.S. and Gilman, A., *The Pharmacological Basis of Therapeutics*, New York: Macmillan, 1970.
4. Gritsenko, A.N., Ermakova, Z.I., and Zhuravlev, S.V., *Khim.-Farm. Zh.*, 1971, no. 7, pp. 10–14.
5. Yakhontov, L.N. and Glushkov, R.G., *Sinteticheskie lekarstvennye sredstva* (Synthetic Drugs), Moscow: Meditsina, 1983.
6. Pozharskii, A.F., Anisimova, V.A., and Tsupak, E.B., *Prakticheskie raboty po khimii geterotsiklov* (Practical Works in Chemistry of Heterocycles), Rostov-on-Don: Rostov. Gos. Univ., 1988, p. 21.
7. Sadym, A.V., Lagunin, A.A., Filimonov, D.A., and Poroikov, V.V., *Khim.-Farm. Zh.*, 2002, vol. 36, no. 10, pp. 21–26.

ISSN 1070-4272, Russian Journal of Applied Chemistry, 2008, Vol. 81, No. 2, pp. 268–271. © Pleiades Publishing, Ltd., 2008.
Original Russian Text © A.D. Kagarlitskii, P.B. Sidoikin, L.A. Krichevskii, 2008, published in Zhurnal Prikladnoi Khimii, 2008, Vol. 81, No. 2, pp. 278–281.

ORGANIC SYNTHESIS AND INDUSTRIAL ORGANIC CHEMISTRY

Ternary Molybdenum–Antimony–Titanium Oxide Systems in Catalytic Synthesis of 2-Imidazolinecarboxamide

A. D. Kagarlitskii, P. B. Sidoikin, and L. A. Krichevskii

Fitokhimiya Research and Production Center, Joint-Stock Company, Karaganda, Kazakhstan

Received July 21, 2007

Abstract—Catalytic ammonolysis of 2-methylimidazoline (lysidine) in the presence of a number of ternary molybdenum–antimony–titanium oxide systems was studied.

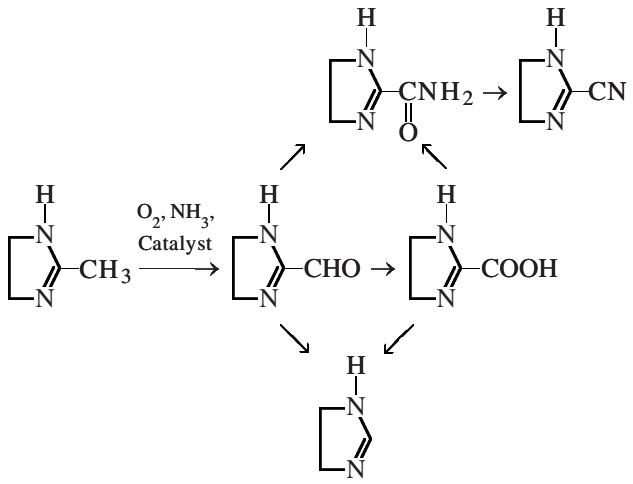
DOI: 10.1134/S1070427208020201

Imidazoline derivatives are characterized by a fairly wide spectrum of biological activity. Some of them are effective analgesics, anesthetics for central nervous system, antidiabetic and antiischemic drugs, and medicines affecting lipidic exchange [1–3]; certain imidazoline derivatives are antagonists of α-adrenergic receptors [4]. However, the chemistry of imidazolines is poorly developed and compounds of this class are relatively few [5].

To prepare functional derivatives of the imidazoline ring, it was of particular interest to study oxidative ammonolysis of the available 2-methylimidazoline (lysidine) using tertiary molybdenum–antimony–titanium oxide systems. Previously it has been found that ammonolysis of alkylpyrazines in the presence of these catalysts yields the corresponding pyrazinecarboxamides in a fairly high yield [6].

Preliminarily experiments showed that, in the presence of these compounds, 2-imidazolinecarboxamide is also the major product of lysidine ammonolysis. In addition, small amounts of compounds (namely, aldehyde, acid, and nitrile) formed by transformation of the methyl groups in the course of oxidative ammonolysis [7] were found in catalyzates. The general pattern of the process studied was complicated by the fact that it was accompanied by partial dealkylation and dehydrogenation of the initial compound to give one more product, imidazole.

Thus, the above data suggest that transformations of 2-methylimidazoline in the course of oxidative ammonolysis involve the following reactions:



We studied four samples of oxide catalysts in which the content of titanium dioxide varied from 0.00 to 0.75 mol at a constant molar ratio MoO_3 : Sb_2O_4 = 1.0 : 0.5. The results (see table) show that the selectivity with respect to 2-imidazolinecarboxamide increases with the content of TiO_2 in the catalysts.

Among the catalysts studied, the highest yield of the amide (85–90%) was provided by the catalyst with the molar ratio MoO_3 : Sb_2O_4 : TiO_2 = 1.00 : 0.50 : 0.75. The effect of temperature on the yield of the reaction products is illustrated in Fig. 1. With the temperature increasing from 320 to 360°C at a constant ratio of the starting reagents (lysidine, ammonia, water, atmospheric oxygen) and constant contact time, the lysidine conversion increases from

Yield of imidazole-2-carboxamide at various temperatures

Catalyst $MoO_3 : Sb_2O_4 : TiO_2$ (mol)	Yield, %, at indicated temperature, °C						
	320	330	340	350	360	370	380
1.00 : 0.50 : 0.00	11	13	14	14	15	16	18
1.00 : 0.50 : 0.25	35	57	64	77	75	70	65
1.00 : 0.50 : 0.50	43	61	73	82	80	78	75
1.00 : 0.50 : 0.75	74	90	89	85	82	80	78

75 to 90%. The yield of the amide increases from 70–72 to more than 80% and passes through a maximum (90%) at 330°C. Under the given experimental conditions, the yield of imidazole also increases with temperature but does not exceed 10%.

The contact time exerts a similar effect on the lysidine conversion (Fig. 2). With this time increasing from 0.6 to 1.4 s, the conversion of the initial compound grows to become virtually quantitative at a contact time of 1.2 s. Under these conditions, the yield of the amide changes insignificantly (from 80 to 90%) and reaches a maximum at 0.8–0.9 s. As for demethylation with the formation of imidazole, its yield grows with increasing contact time and reaches 16–18%.

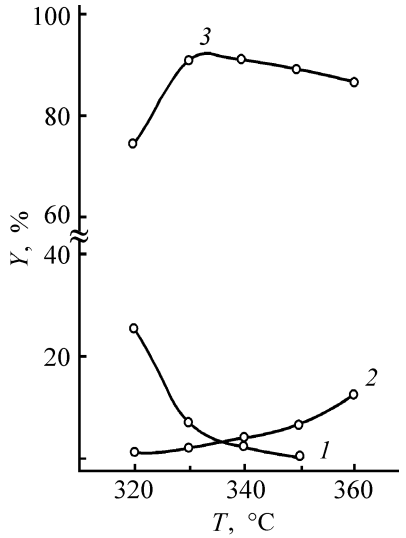


Fig. 1. Yield of the products of oxidative ammonolysis of 2-methylimidazoline vs. temperature *T*. (*Y*) Yield of the reaction products; the same for Figs. 3 and 4. Concentration of NH_3 9.1 mol/mol lysidine, τ 0.8 s. (*1*) 2-Methylimidazoline, (*2*) imidazole, and (*3*) 2-imidazolinecarboxamide; the same for Figs. 2 and 3.

Experiments in which the lysidine : NH_3 molar ratio was varied from 1 : 2.5 to 1 : 11 showed (Fig. 3) that the optimal content of ammonia to obtain the amide is 7–9 mol per mole of the initial compound. With the content of ammonia in the contact zone increasing above the optimal value, the conversion of lysidine and the yields of 2-imidazolinecarboxamide and imidazole noticeably decrease. Such an effect of ammonia on the process is probably due to the fact that, at high concentrations, it occupies the catalyst surface, hinders the adsorption of lysidine, and thus decelerates the conversion of lysidine into the amide and imidazole.

The influence of the content of titanium oxide in the catalysts studied on the conversion of the initial compound and on the yields of the main products of

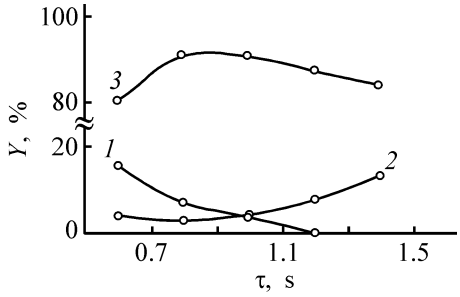


Fig. 2. Yield of the products of oxidative ammonolysis of 2-methylimidazoline vs. contact time τ. *T* 330°C, concentration of NH_3 9.1 mol/mol lysidine.

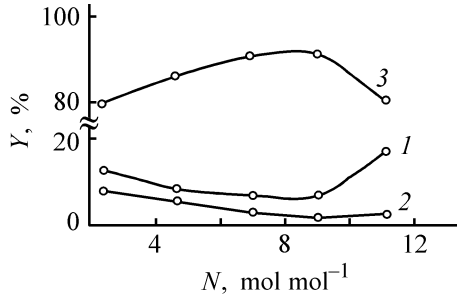


Fig. 3. Yield of the products of oxidative ammonolysis of 2-methylimidazoline vs. the NH_3/lysidine molar ratio. *T* 330°C, τ 0.8 s.

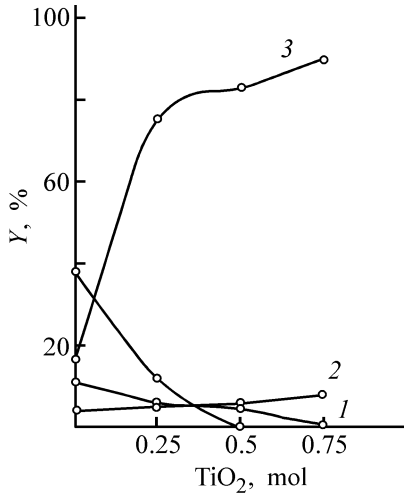


Fig. 4. Yield of the products of oxidative ammonolysis of 2-methylimidazoline vs. the content of TiO_2 in $MoO_3 : Sb_2O_4 : TiO_2$ catalysts. *T* 350°C, concentration of NH_3 9.1 mol/mol lysidine, τ 1.0 s. (*1*) 2-Methylimidazoline, (*2*) imidazole, (*3*) 2-imidazolinecarboxamide, and (*4*) 2-imidazolinecarbonitrile.

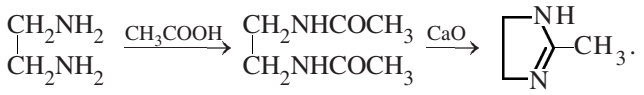
oxidative ammonolysis of lysidine is illustrated by Fig. 4. The process performed under optimal conditions determined in our previous experiments confirmed that the catalyst containing 0.75 mol of TiO_2 seems to be the most promising and provides synthesis of 2-imidazolinecarboxamide in 90% yield. However, it should be noted that the selectivity of the other two catalysts is only slightly lower.

A quite different pattern was observed with the catalysts containing no TiO_2. In this case, the main product of lysidine conversion was 2-imidazolinecarbonitrile, whose yield was a factor of 2 higher than that of the amide. These results unambiguously suggest that the formation of 2-imidazolinecarboxamide is due to a secondary process, hydrolysis of the nitrile, and the extent of this reaction is determined by the content of TiO_2 in the catalyst [8, 9].

Thus, oxidative ammonolysis of lysidine is an efficient procedure for preparing 2-imidazolinecarboxamide.

EXPERIMENTAL

2-Methylimidazoline was prepared by the procedure given in [10]:



The oxidative ammonolysis was performed in a direct-flow unit with a stainless steel tubular reactor (20 mm in diameter and 300 mm long), which was charged with a required amount (65 cm^3) of the ternary oxide catalyst with the molar ratio $MoO_3 : Sb_2O_4 : TiO_2 = 1.0 : 0.5 : (0.25 – 0.75)$, prepared by fusion of the thoroughly ground mixture of the individual oxides at 850°C.

The oxidative ammonolysis was studied under the following reaction conditions: temperature 320–370°C, ammonia concentration 0.8–11.3 mol/mol lysidine, and contact time 0.4–1.6 s.

The catalyzate was condensed in a cooled trap and the reaction products were extracted into chloroform [11]. Then, the solvent was removed on a rotary evaporator. The products were separated by column chromatography (alumina, Brockmann grade II, hexane–chloroform gradient elution).

Analysis of the reaction products was performed on a Chrom-5 gas–liquid chromatograph equipped with a flame-ionization detector. A 2.5-m glass column (0.3 cm internal diameter) was packed with Inerton AW-HMDS impregnated with 5% SE-30. Argon as carrier gas was supplied at a rate of 40 ml min^{-1}. The temperatures of the column, vaporizer, and detector were 100, 200, and 230°C, respectively. The retention times were as follows, s: imidazole 78, 2-methylimidazoline 168, 2-imidazolinecarbonitrile 230, and 2-imidazolinecarboxamide 362.

The IR spectra were recorded on a Nicolet Avatar Fourier spectrophotometer using KBr pellets. The elemental analysis was carried out on a Carlo Erba device (Italy).

Inidazole: mp 92°C; IR, ν, cm^{-1}: 3169, 3114 (NH), 1664 (C=N). Elemental analysis:

Found (%), C 53.13, H 6.01, N 41.42.
$C_3H_4N_2$.
Calculated (%): C 52.93, H 5.92, N 41.15.

2-Imidazolinecarbonitrile: mp 131–132°C; IR, ν, cm^{-1}: 3178, 3047 (NH), 2236 (C≡N), 1669 (C=N). Elemental analysis:

Found (%): C 50.89, H 5.39, N 44.52.
$C_4H_5N_3$.
Calculated (%): C 50.52, H 5.30, N 44.18.

2-Imidazolinecarboxamide: mp 148–150°C; IR, ν, cm^{-1}: 3221 ($CONH_2$), 3162, 3116 (NH), 3052 ($CONH_2$), 1650 (C=O). Elemental analysis:

Found (%): C 42.83, H 6.30, N 37.47.

$C_4H_7N_3O$.

Calculated (%): C 42.47, H 6.24, N 37.15.

The IR spectra of the catalyzates contained absorption bands at 2700–2500 and 1764 cm^{-1} corresponding to a compound with a carboxy group, i.e., to 2-imidazolinecarboxylic acid.

CONCLUSIONS

(1) 2-Methylimidazoline undergoes oxidative ammonolysis in the presence of ternary molybdenum–antimony–titanium oxide catalysts.

(2) The catalyst with the optimal composition (0.75 mol of TiO_2) provides formation of 2-imidazolecarboxamide in 85–90% yield.

(3) The formation of the amide is preceded by the stage of formation of the CN group whose hydrolysis yields the final product.

REFERENCES

1. US Patent 6884801.
2. US Patent 6175013.
3. US Patent 7064142.
4. US Patent 6294566.
5. *Heterocyclic Compounds*, Elderfield, R.C., Ed., New York: Wiley, 1957, vol. 6.
6. Balpanov, D.S., Synthesis of 2-Methylpyrazine and 2-Pyrazinecarboxamide, *Cand. Sci. Dissertation*, Karaganda, 2002.
7. Suvorov, B.V., Rafikov, S.R., and Kargalitskii, A.D., *Usp. Khim.*, 1965, vol. 35, no. 9, pp. 1526–1549.
8. Zenkovets, G.A., Paukshtis, E.A., Tarasova, D.V., and Yurchenko, E.N., *Kinet. Katal.*, 1981, vol. 22, no. 6, pp. 1584–1589.
9. Pamfilov, A.V., Bondar', P.G., and Mazurkevich, Ya.S., *Ukr. Khim. Zh.*, 1965, no. 1, pp. 48–51.
10. Rubtsov, M.V. and Baichikov, A.G., *Sinteticheskie khimiko-farmatsevticheskie preparaty* (Synthetic Pharmaceuticals), Moscow: Meditsina, 1971.
11. *Preparativnaya organicheskaya khimiya* (Preparative Organic Chemistry), Vul'fson, N.S., Ed., Moscow: Khimiya, 1964.

ISSN 1070-4272, Russian Journal of Applied Chemistry, 2008, Vol. 81, No. 2, pp. 272–275. © Pleiades Publishing, Ltd., 2008.
Original Russian Text © Sh.B. Kasenova, Zh.K. Tukhmetova, A.Zh. Abil'daeva, I.M. Oskembekov, S.M. Adekenov, B.K. Kasenov, S.D. Fazylov, A.M. Gazaliev, 2008, published in Zhurnal Prikladnoi Khimii, 2008, Vol. 81, No. 2, pp. 282–285.

ORGANIC SYNTHESIS AND INDUSTRIAL ORGANIC CHEMISTRY

Thermodynamic Properties of Solutions of Imidazolidine-2-thione and Potassium Isopropylxanthate in Ethanol and Characteristics of Individual Compounds

Sh. B. Kasenova, Zh. K. Tukhmetova, A. Zh. Abil'daeva, I. M. Oskembekov, S. M. Adekenov, B. K. Kasenov, S. D. Fazylov, and A. M. Gazaliev

Fitokhimiya Research and Production Center, Joint-Stock Company, Ministry of Education and Science of the Republic of Kazakhstan, Karaganda, Kazakhstan

Institute of Organic Synthesis and Coal Chemistry, Limited Liability Company, Karaganda, Kazakhstan

East-Kazakhstan State University, Karaganda, Kazakhstan

Received July 5, 2007

Abstract—The enthalpies of solution of imidazolidine-2-thione and potassium isopropylxanthate in ethanol and their isobaric heat capacity in the range from 173 to (T_{m-100}) K were measured by calorimetry at 298.15 K. The standard enthalpies of formation, combustion, and melting of these compounds were estimated.

DOI: 10.1134/S1070427208020213

A study of thermodynamic characteristics of biologically active substances and their derivatives is of practical and theoretical importance for their direct synthesis and establishment of relationships between their structural and energy characteristics.

EXPERIMENTAL

In this context, we performed calorimetric studies to determine the enthalpy of solution of biologically active substances, imidazolidine-2-thione $C_3H_6N_2S$ (**I**) and potassium isopropylxanthate $C_4H_7OS_2$ (**II**), in 96% ethanol, their isobaric heat capacities in the range from 173 to (T_{m-100}) K, and the thermodynamic functions ΔH^0_c, ΔH^0_m, and $\Delta_f H^0_{298.15}$.[1]

The enthalpies of solution of the above compounds in 96% ethanol were studied using a DAK-1-1A isothermal calorimeter at three dilutions [1 : 3000, 1 : 6000, and 1 : 12000 (mole of compound : mole of solvent)]. The weighed portions of **I** and **II** for calorimetric studies at the above dilutions were as follows, g: 0.0029, 0.0014, 0.0008 (**I**) and 0.0049, 0.0025, 0.0012 (**II**). The procedure used of the study was described in detail in [1–4]. At each dilution at 298.15 K, we performed five replicate measurements whose results were averaged and treated by the methods of mathematic statistics. For each averaged value of ΔH^0_{dis} we calcilated the random error using the Student test; the homogeneity of variance was estimated using the Cochran test [5]. The hypothesis of the variance homogeneity was taken with 5% significance level.

The device operation was tested by measuring the heat of solution of triply recrystallized potassium chloride at dilutions equal to 1 : 1600, 1 : 2400, and 1 : 3200 (moles of salt : moles of water). The average heat of KCl solution in water is 17640 ± 320 J mol^{-1}, which agrees well with the recommended and reference values of 17577 ± 34 [6] and 17489 ± 371 J mol^{-1} [7]. The enthalpies of solution of **I** and **II** in 96% ethanol at three dilutions are listed in Tables 1 and 2.

Table 1. Experimental enthalpies of solution of **I** (MW = 102) and **II** (MW = 174) in 96% ethanol at various dilutions

Dilution	$\Delta\bar{H}^0_{dis}$, kJ mol^{-1}, for indicated compound	
	I	**II**
1 : 3000	19.48 ± 0.48	20.37 ± 0.41
1 : 6000	23.09 ± 0.24	22.98 ± 0.20
1 : 12000	25.26 ± 0.24	25.58 ± 0.37

[1] The samples were prepared at the Institute of Organic Synthesis and Coal Chemistry (Karaganda). Their purity corresponded to the chemically pure grade.

Table 2. Experimental heat capacities of **I** and **II**

T, K	$C_p \pm \bar{\delta}$, J g^{-1} K^{-1}	$C_p \pm \mathring{\Delta}$, J mol^{-1} K^{-1}	$C_p \pm \bar{\delta}$, J g^{-1} K^{-1}	$C_p \pm \mathring{\Delta}$, J mol^{-1} K^{-1}
	I (T_m = 471 K)		**II** (T_m = 549 K)	
173	0.39 ± 0.01	40 ± 4	0.70 ± 0.02	123 ± 8
198	0.45 ± 0.01	46 ± 20	1.22 ± 0.02	213 ± 12
223	0.54 ± 0.02	55 ± 4	1.64 ± 0.04	285 ± 17
248	0.67 ± 0.02	68 ± 5	1.86 ± 0.03	325 ± 13
273	0.69 ± 0.01	70 ± 4	1.50 ± 0.03	261 ± 16
298.15	0.82 ± 0.02	84 ± 7	1.15 ± 0.04	201 ± 17
323	1.10 ± 0.02	90 ± 5	1.02 ± 0.03	177 ± 15
348	1.05 ± 0.03	107 ± 8	0.92 ± 0.03	160 ± 13
373	1.10 ± 0.02	112 ± 7	0.82 ± 0.02	143 ± 9
398			0.70 ± 0.02	122 ± 11
423			0.81 ± 0.03	141 ± 13
448			1.14 ± 0.03	198 ± 15

The experimental enthalpies of solution of **I** and **II** in 96% ethanol were extrapolated to infinite dilution using the least-squares technique. Based on the well-known relationship $\Delta H^0_{dis} \sim f\sqrt{m}$ (m is molality) [8], we derived linear equations for each compound (kJ mol^{-1}):

$$\Delta H^0_{dis}\ (\mathbf{I}) = 31.59 - 161.02\sqrt{m}, \quad (1)$$

$$\Delta H^0_{dis}\ (\mathbf{II}) = 30.53 - 136.8\sqrt{m}, \quad (2)$$

from which the standard enthalpies of solution of **I** and **II** in 96% ethanol at infinite dilution were determined to be 31.6 ± 0.5 and 30.5 ± 0.4 kJ mol^{-1}, respectively.

The isobaric heat capacities of **I** and **II** were studied by the known procedure [9] on an IT-s-400 dynamic calorimeter in the temperature range from 173 to (T_{m-100}) K. Liquid nitrogen was used as a refrigerant. The rated maximum permissible error of the device is ±10%. The delay in the attainment of the required temperature was recorded with an F-136 microvoltammeter and an SETs-100 commercial stopwatch with a step of 25 K. For each temperature, we performed five replicate runs. The results were averaged and processed by the methods of mathematic statistics with subsequent evaluation of the standard deviation $\bar{\delta}$ and random error $\mathring{\Delta}$ [5, 9]. The data obtained for the specific and molar heat capacity of the samples are listed in Table 2. The dependence $C_p^0 \sim f(T)$ is plotted in Fig. 1.

The device operation was tested by determining the heat capacity of an α-Al_2O_3 sample. The resulting value, $C_p^0(298.15)$ = 76.0 J mol^{-1} K^{-1}, agrees

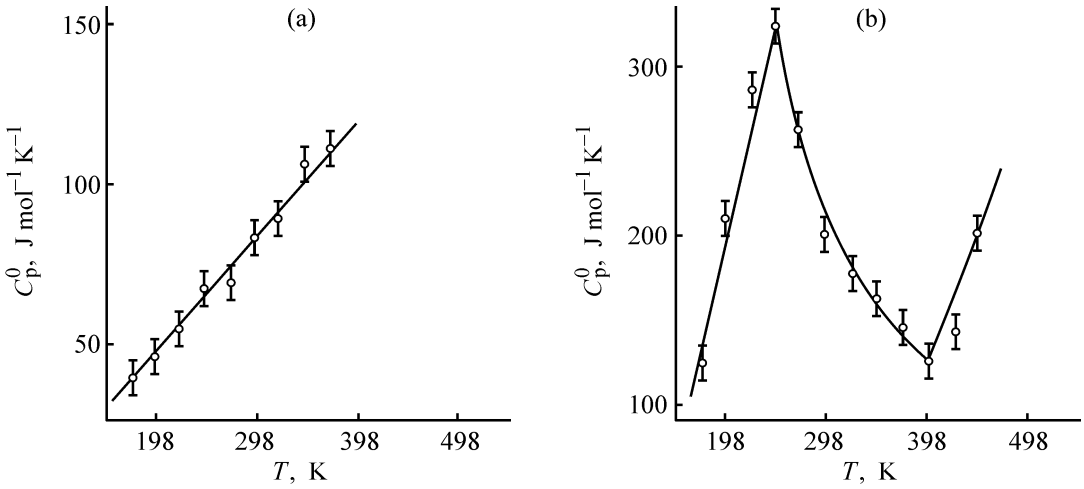


Fig. 1. Molar heat capacity C_p^0 of (a) **I** and (b) **II** vs. temperature T in the range from 173 to (T_{m-100}) K.

Table 3. Equations for the temperature dependence of the heat capacity of **I** and **II**

Compound	Coefficients of the equation $C_p^0 = a + bT + cT^{-2}$, J mol^{-1} K^{-1}			T, K
	a	$b \times 10^{-3}$	$-c \times 10^5$	
I	–(15.42 ± 1.07)	340.7 ± 23.7	1.08 ± 0.08	173–373
II	–(343.0 ± 24.4)	2692.2 ± 191.4	–	173–248
	–(422.4 ± 30.0)	841.5 ± 59.8	–(331.1 ± 23.5)	248–398
	–(480.8 ± 34.2)	1516 ± 108	–	398–448

Table 4. Enthalpy characteristics of **I** and **II**

Compound	ΔH_c^0	ΔH_m^0	$-\Delta_f H_{298.15}^0$, kJ mol^{-1}, for indicated state	
	kJ mol^{-1}		liquid	solid
I	1716	21.0	323.0	344.0
II	2507	41.8	545.2	587.2

within the limits of the device error with the value of 79.0 J mol^{-1} K^{-1} recommended in [11].

Equations for the temperature dependence of the heat capacity of the compounds, presented in Table 3 were derived by mathematical processing of the experimental data. As can be seen from Table 2 and Fig. 1, the curve for the heat capacity of potassium isopropylxanthate shows in the range 173–448 K (peak temperature 248 K), a λ-shaped effect, which is apparently caused by some variations in the molecular structure or by a second-order phase transition. In this context, we derived three equations for the dependence $C_p^0 \sim f(T)$ for the above compound (Table 3).

The enthalpy characteristics of **I** and **II**, ΔH_c^0 and ΔH_m^0 (Table 4), were calculated with the equations that were recommended in [11, 12] and used for evaluation of the thermochemical quantities of the similar compounds [13–15]. To calculate the heat of combustion (kcal mol^{-1}), we used the Karas method [11], which is the most suitable for the compounds under study:

$$\Delta H_c^0 = -26.050(4C + H - P) + \Sigma k_i \Delta_i, \qquad (3)$$

where 26.050 kcal mol^{-1} is the heat of dissociation of the C–C and C–H bonds and subsequent formation of CO_2 and H_2O; C, number of hydrogen atoms in the compound; P, number of partially displaced electrons in the compound molecule; k_i, number of identical substituents; and Δ_i, heat correction corresponding to a given substituent.

The ΔH_m^0 values of the compounds were estimated by the well-known Gambill equation recommended for organic compounds [12]:

$$\Delta H_m^0 / T_m = 20.72 \times 10^{0.00324M}, \qquad (4)$$

where M is the molecular weight of the compound.

Based on the Hess cycle, we calculated from the reactions

$$C_3H_6N_2S_{(l)} + 5.5O_{2(g)} = 3CO_{2(g)} + 3H_2O_{(l)} + N_{2(g)} + SO_{2(g)} - \Delta H_c^0, \qquad (5)$$

$$2C_4H_7OS_2K_{(l)} + 14O_{2(g)} = 8CO_{2(g)} + 7H_2O_{(l)} + 2SO_{2(g)} + K_2O_{(s)} - \Delta H_c^0 \qquad (6)$$

the standard enthalpies of formation of compounds in the liquid (molten) state (Table 4). The data required for calculation of $\Delta_f H_{298.15}^0$ [$CO_{2(g)}$, $H_2O_{(l)}$, $SO_{2(g)}$, $K_2O_{(s)}$] were taken from [16, 19].

Using the equation

$$\Delta_f H_{298.15(s)}^0 = \Delta_f H_{298.15(l)}^0 - \Delta H_m^0, \qquad (7)$$

we calculated the standard enthalpies of formation of **I** and **II** in the solid (crystalline) states (Table 4).

CONCLUSIONS

(1) The enthalpy characteristics ΔH_s^0 in 96% ethanol, ΔH_c^0, ΔH_m^0, and $\Delta_f H_{298.16}^0$ of important biolog-

ically active compounds, imidazolidine-2-thione and potassium isopropylxanthate, were determined experimentally and by calculation. The temperature dependences of the isobaric heat capacities of these compounds in the range from 173 to (T_{m-100}) K were studied and equations describing these dependences were derived.

(2) The results obtained are primary data for inclusion into databases and handbooks of thermodynamic constants. They are of interest for physicochemical simulation of reactions involving the compounds studied and their analogs.

REFERENCES

1. Skuratov, S.M., Kolesov, V.P., and Vorob'ev, A.F., *Termokhimiya* (Thermochemistry), Moscow: Mosk. Gos. Univ., 1964, vol. 1.
2. Calvet, E. and Prat, H., *Microcalorimetrie. Applications Physico-chimiques et Biologiques*, Paris: Masson, 1956.
3. Topor, N.D. and Suponitskii, Yu.L., *Usp. Khim.*, 1984, vol. 53, no. 9, pp. 1425–1462.
4. Calvet, E., *Zh. Fiz. Khim.*, 1959, vol. 33, no. 6, pp. 1161–1175.
5. Spiridonov, V.P. and Lopatkin, A.A., *Matematicheskaya obrabotka eksperimental'nykh dannykh* (Mathematical Treatment of Experimental Data), Moscow: Mosk. Gos. Univ., 1970.
6. Mishchenko, K.P. and Poltoratskii, G.M., *Termodinamika i stroenie vodnykh i nevodnykh rastvorov elektrolitov* (Thermodynamics and Structure of Aqueous and Nonaqueous Solutions of Electrolytes), Leningrad: Khimiya, 1977.
7. *Termicheskie konstanty veshchestv: Spravochnik* (Thermal Constants of Substances: Handbook), Glushko, V.P., Ed., Moscow: Nauka, 1982, issue 10, part 2.
8. Platunov, E.S., *Teplofizicheskie izmereniya v rezhime* (Thermal Measurements in a Mode), Moscow: Energiya, 1973.
9. Robie, R.A., Hewingway, B.S., and Fisher, J.K., *Thermodynamic Properties of Minerals and Related Substances at 298.15 K (and 10^5 Pa Pressure) and at Higher Temperatures*, Washington: US Government, 1978.
10. Krestov, G.A., *Termodinamika ionnykh protsessov v rastvorakh* (Thermodynamics of Ionic Processes in Solutions), Leningrad: Khimiya, 1984.
11. Kazanskaya, A.S. and Skoblo, V.A., *Raschety khimicheskikh ravnovesii* (Calculations of Chemical Equilibria), Moscow: Vysshaya Shkola, 1974.
12. Viktorov, V.V., *Metody vychisleniya fiziko-khimicheskikh velichin i prikladnye raschety* (Methods of Calculation of Physicochemical Quantities and Applied Calculations), Moscow: Khimiya, 1977.
13. Kasenov, B.K., Tukhmetova, Zh.K., Kasenova, Sh.B., et al., *Zh. Prikl. Khim.*, 2005, vol. 78, no. 12, pp. 2062–2064.
14. Kasenov, B.K., Tukhmetova, Zh.K., Kasenova, Sh.B., et al., *Zh. Prikl. Khim.*, 2006, vol. 79, no. 7, pp. 1082–1085.
15. Boldashevskii, A.V., Kasenov, B.K., Tukhmetova, Zh.K., et al., *Zh. Prikl. Khim.*, 2006, vol. 79, no. 10, pp. 1725–1727.
16. *Termicheskie konstanty veshchestv: Spravochnik* (Thermal Constants of Substances: Handbook), Glushko, V.P., Ed., Moscow: VINITI, 1970, issue 4, part 1, p. 14.
17. *Termicheskie konstanty veshchestv: Spravochnik* (Thermal Constants of Substances: Handbook), Glushko, V.P., Ed., Moscow: VINITI, 1965, issue 1, p. 24.
18. *Termicheskie konstanty veshchestv: Spravochnik* (Thermal Constants of Substances: Handbook), Glushko, V.P., Ed., Moscow: VINITI, 1966, issue 2, p. 14.
19. *Termicheskie konstanty veshchestv: Spravochnik* (Thermal Constants of Substances: Handbook), Glushko, V.P., Ed., Moscow: VINITI, 1968, issue 3, p. 66.

ISSN 1070-4272, Russian Journal of Applied Chemistry, 2008, Vol. 81, No. 2, pp. 276–280. © Pleiades Publishing, Ltd., 2008.
Original Russian Text © N.V. Bukar', S.Yu. Krasnobaeva, E.V. Ilyushenko, G.V. Avramenko, K.I. Kienskaya, 2008, published in Zhurnal Prikladnoi Khimii, 2008, Vol. 81, No. 2, pp. 286–290.

ORGANIC SYNTHESIS AND INDUSTRIAL ORGANIC CHEMISTRY

Methods for Microencapsulation of *N*-Benzylmorpholine

N. V. Bukar', S. Yu. Krasnobaeva, E. V. Ilyushenko, G. V. Avramenko, and K. I. Kienskaya

Mendeleev Russian University of Chemical Engineering, Moscow, Russia

Received February 19, 2007

Abstract—Microencapsulation of *N*-benzylmorpholine and its water-soluble derivative, *N*-benzylmorpholine hydrochloride, by simple and complex coacervation was studied, and the main steps of the processes were worked through.

DOI: 10.1134/S1070427208020225

Microencapsulation as a method for preparing disperse systems is widely used in many branches of industry, such as medicine, cosmetics, perfumery, production of dyes, etc. [1–5]. Such useful features of microencapsulated systems as the controllable and selective mass transfer across the microcapsule shell, prolonged action of the core substances, and the possibility of controlling their reactivity make the encapsulation a promising innovative technique for development of novel composite materials.

Here we present methods for microencapsulation of *N*-benzylmorpholine. The choice of this compound is caused by the wide use of morpholine derivatives in pharmaceutics. For example, derivatives of morpholine and morpholinone (3,4,5,6-tetrahydro-2*H*-1,4-oxazin-2-one) appear to be effective for treating glaucoma, prostate hyperplasia, and cardiovascular diseases (arrhythmia) [6]. One more example of the use of morpholine derivatives in pharmaceutics is the synthesis of tachykinin receptor antagonists based on *N*-substituted morpholine derivatives [7]. However, the available information on microencapsulation of such compounds is scarce. Therefore, the goal of this study was to develop methods for encapsulation of such model compounds as *N*-benzylmorpholine (BM) and its water-soluble derivative, *N*-benzylmorpholine hydrochloride (BMH).

EXPERIMENTAL

We chose a simple and a complex coacervation techniques [8] for microencapsulation of BMH and BM, respectively.

Since BM is poorly soluble in water, we chose the complex coacervation technique for its microencapsulation [1, 9]. This method is based on the interaction of two oppositely charged compounds, at least one of them being a polyelectrolyte, to give a polyelectrolyte complex. In this study, we chose for BM microencapsulation two polyelectrolytes, gelatin and chitosane succinate. A preliminary study of various polyelectrolyte pairs (gelatin–Polyquaternium-11, gum-arabic–chitosane succinate, gum-arabic–Polyquaternium-11, and gelatin–chitosane succinate) revealed that the highest efficiency of BM microencapsulation (81%) was obtained with the last pair.

The optimal polyelectrolyte weight ratio was determined spectrophotometrically. Figure 1 shows the results of titration of 0.6 wt % chitosan succinate solution with 0.6 wt % gelatin solution at pH 6.0. In this case, the solution pH is a key condition for formation of a polyelectrolyte complex, since gelatin is a polyampholyte. Chitosan succinate is a basic poly-

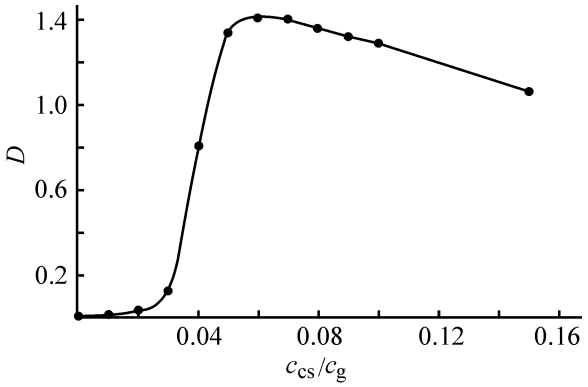


Fig. 1. Optical density D of aqueous solutions of chitosan succinate and gelatin vs. their concentration ratio c_{cs}/c_g at pH 6.0.

electrolyte, and gelatin used in our experiments demonstrates acidic properties at pH above its isoelectric point (pI 5.2). Based on the titration data, the optimal chitosan-succinate-to gelatin ratio was found to be 0.07.

The microencapsulation of BM was carried out in two stages. In the first stage, an emulsion of BM (5% of the total weight of the system) in an aqueous solution of gelatin and chitosan succinate was prepared with continuous stirring at 40°C. Aqueous solutions of the two polymers were prepared separately so that their total concentration was 0.6 wt % and the c_{cs}/c_g ratio was 0.07. The polymer solutions were heated to 40°C and then mixed just prior to preparation of the emulsion. The resulting emulsion was homogenized for 10 min by stirring at 1500 rpm, cooled to 15°C, and repeatedly homogenized for 15 min at the same stirring rate. In the second stage, the walls of the microcapsules were hardened by adding a 25 wt % aqueous solution of glutaraldehyde and aging for 3 h. A micrograph of the resulting microcapsules is shown in Fig. 2. The mean size of the BM microcapsules was 2 μm.

The most important pharmaceutical characteristics of encapsulated drug preparations are the full release time and release rate of an active component in the human body. There are different methods for studying the release of the fill of microcapsules, including in vitro methods for studying the release of an active component to a model system [10, 11]. In this study, we examined the release of BM from the microcapsules to a phosphate buffer solution (pH 6.68). The BM concentration in the aqueous phase was determined spectrophotometrically at 256 nm (UV spectrum of BM is shown in Fig. 3) using a calibration curve. The BM concentration in the phosphate buffer solution was determined at fixed intervals [dispersion of the microcapsules in the buffer solution was maintained at constant temperature (37°C) and continuous stirring throughout the sampling]. The microcapsule concentration was 1.4 wt %. The kinetic curve of BM release from the microcapsules is shown in Fig. 4.

As seen, the full release time of BM from the microcapsules was 8 h. In this case, 16.6% of BM was released in the first 0.5 h, and in the next 6 h the release rate was constant (10 wt % per hour). The initial portion of the kinetic curve is characterized by high release rate, which is possibly the case because, during encapsulation, some part of BM is adsorbed on the outer side of the polymeric coating and, therefore, is released to the solution in the first place.

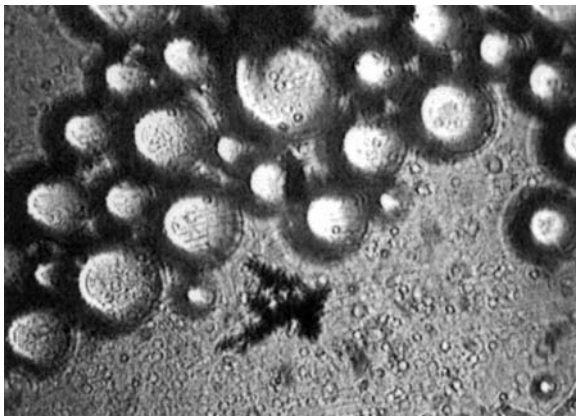


Fig. 2. Micrograph of *N*-benzylmorpholine microcapsules.

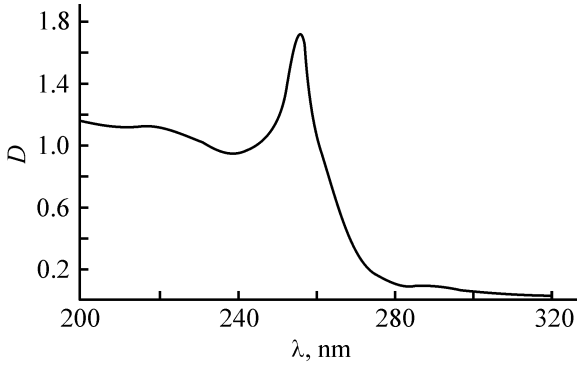


Fig. 3. UV spectrum of *N*-benzylmorpholine in a phosphate buffer solution. (*D*) Optical density and (λ) wavelength; the same for Fig. 5.

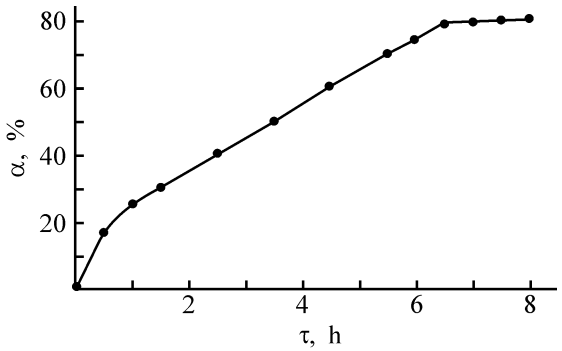
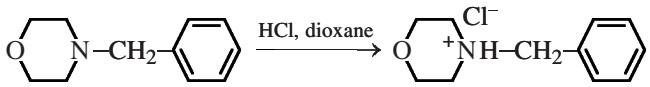


Fig. 4. Kinetic curve of BM release from the microcapsules with a shell composed of gelatin and chitosan succinate. (α) Release of BM and (τ) time; the same for Fig. 8.

In the next step of the study, we attempted to encapsulate *N*-benzylmorpholine hydrochloride, a water-soluble derivative of BM, since in some cases, it is impractical to employ oil-soluble forms of bioactive compounds. *N*-Benzylmorpholine hydrochloride was prepared by adding BM to a solution of HCl in dioxane, i.e., by the reaction



The melting point of the product twice recrystallized from an aqueous-alcoholic mixture was 239–242°C, which is well consistent with the reference data [12]. The BMH concentration in the aqueous phase was determined spectrophotometrically at 258 nm (UV spectrum of BMH is shown in Fig. 5), using a calibration curve.

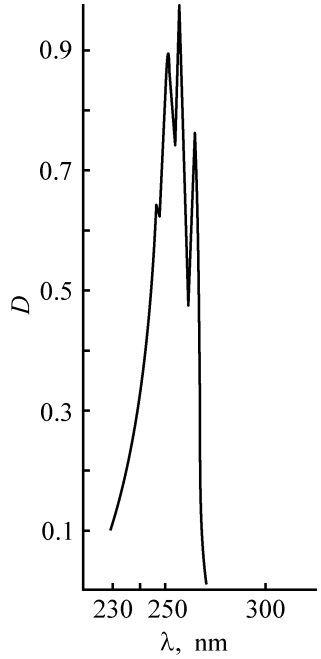


Fig. 5. UV spectrum of an aqueous solution of *N*-benzylmorpholine hydrochloride.

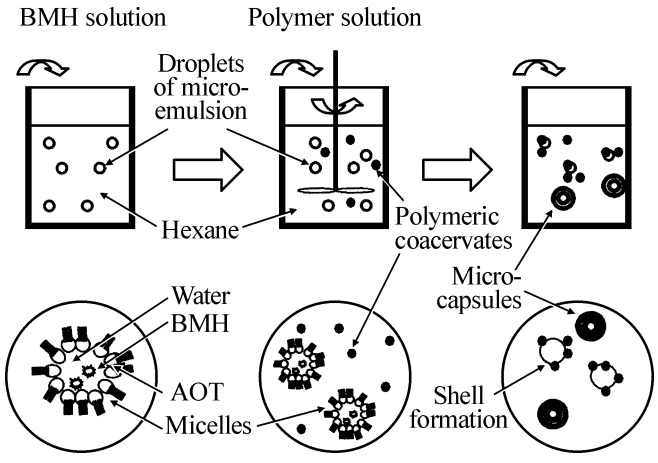


Fig. 6. Schematic of microemulsion microencapsulation of *N*-benzylmorpholine hydrochloride.

It is known that cellulose derivatives are widely used in microencapsulation of various bioactive compounds [13]. For our experiments, we chose nontoxic and biodegradable triacetyl cellulose (TAC) as a shell-forming polymer. The molecular weight of TAC was determined viscometrically, using the Kuhn–Mark–Houwink equation [14], to be 150000 g mol^{-1}.

Microencapsulation of BMH was carried out in two steps. First, an inverse microemulsion consisting of water droplets containing a certain amount of BMH in an organic solvent (hexane), stabilized with sodium di-2-ethylhexyl sulfosuccinate (AOT), was prepared. AOT was chosen as a surfactant stabilizer because of its solubility in both water and hexane, and also because it is nontoxic for human body over a wide concentration range. In the second step, a methylene chloride solution of TAC was added dropwise to the resulting microemulsion with continuous stirring. Methylene chloride was selected as a solvent because it is infinitely miscible with hexane. However, TAC is insoluble in hexane and, therefore, it precipitates in this step on the preliminarily formed droplets of the microemulsion, thus forming a shell of the microcapsules. Such microemulsion microencapsulation can be represented by the scheme shown in Fig. 6. In this case, the degree of encapsulation of water-soluble BMH approached 100%. The electronic spectra of the dispersion medium after formation of the polymeric shell revealed the absence of BMH in it. Of course, one cannot but take into account that free (nonencapsulated) BMH can be adsorbed on the outer surface of the microcapsule. However, the kinetic data on the release of BMH from the microcapsules (see below) suggests that the adsorption is insignificant.

Turning to the scheme presented in Fig. 6, let us focus on some key points of this encapsulation technique. In particular, the optimization of the AOT concentration requires data on its solubilization capacity with respect to aqueous BMH. The critical micelle concentrations (CMC) of AOT in water and hexane were determined by the solubilization of water-soluble (Thymol Blue) and oil-soluble (Sudan Yellow) dyes to be 3.7×10^{-3} and 5.0×10^{-5} M, respectively. These values are well consistent with those obtained for AOT by other methods [15].

The highest solubilization capacity of the organic (hexane) solutions of AOT for BMH was obtained at an AOT concentration of 0.05 M, which is equal to 1000 CMC. This concentration was then used for preparing microemulsions. The existence range of the microemulsion water + BMH/AOT/hexane is

shown in the phase diagram (Fig. 7). The microemulsion range *II* lies between the high-temperature T_2 (50°C) and low-temperature T_1 (5°C) solubilization phase boundaries. In outward appearance, the microemulsion is a bluish transparent opalescent fluid. The liquid–liquid interfacial tension, determined by the drop weight (volume) method, was ≤1 mN throughout range *II*, which confirms the formation of a microemulsion. The droplet size was determined by photon correlation spectroscopy to be 20–35 nm. Ranges *I* and *III* in the phase diagram correspond to binary systems. The maximal BMH concentration in the aqueous solution can amount to 0.6 wt %. Above this concentration, it becomes impossible to obtain the microemulsion at a fixed AOT concentration equal to 1000 CMC. The optimal TAC concentration in the methylene chloride solution added to the microemulsion in the second step of the process (Fig. 6) was found to be 0.25 wt %.

Finally, we experimentally optimized the microemulsion microencapsulation of BMH. At the maximal attainable 20% concentration of the microemulsion obtained in the first step of the process, the concentration of encapsulated BMH was 1.26 g l^{-1}, which is a quite reasonable concentration for practical use. The size of microcapsules in the liquid phase, i.e., before they were separated as particulate species, was determined by dynamic light scattering to be 80–150 nm.

The kinetics of BMH release from the microcapsules was also studied by the in vitro method. The microcapsules were separated from the organic medium in a vacuum using a rotary evaporator, washed three times with distilled water, filtered off, and dried to constant weight. It should be pointed out that, with such a separation method, the microcapsules could form aggregates with a size larger than 150–200 nm. To eliminate this effect, freeze drying is the best separation method. However, in this study, the kinetics of release of the active component was examined without taking into account the particle size. The electronic spectra revealed no BMH in the wash water (filtrate), suggesting that it is not adsorbed on the outer surface of the capsules, because otherwise, adsorbed BMH would have been readily washed away because of the reversibility of physisorption. Since the shell-forming material, TAC, is insoluble in water, we examined the BMH release to 0.1 N HCl at 35°C. The concentration of the filtered-off and dried microcapsules in the suspension was 7 wt %. The BMH content in the dispersion medium was determined spectrophotometrically at fixed intervals (dispersion of the microcapsules in the hydrochloric acid solution was maintained under continuous stirring throughout the sampling). It was demonstrated in the preliminary experiments that HCl has no effect on the position of the absorption maxima of BMH.

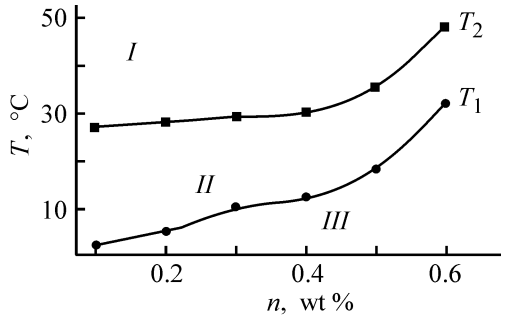


Fig. 7. Phase diagram of the system water + *N*-benzylmorpholine hydrochloride/AOT/hexane. (*T*) Temperature and (*n*) salt concentration in the solution.

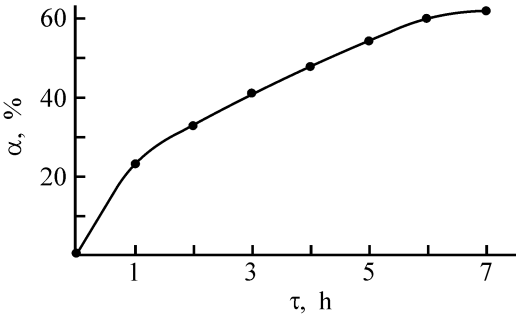


Fig. 8. Kinetic curve of *N*-benzylmorpholine hydrochloride release from the microcapsules with triacetyl cellulose shells.

Figure 8 shows the kinetics *N*-benzylmorpholine hydrochloride release from the microcapsules with triacetyl cellulose shells. As seen, about 70% of encapsulated BMH was released in 7 h, and then the kinetic curve leveled off. A virtually 100% release of BMH in the same time could be attained by raising the HCl concentration by a factor of 1.2. These data are well consistent with those presented in Fig. 4. Here, we also observe a high initial release rate of BMH, which is probably due to nonuniformity of the polymeric shell.

CONCLUSIONS

(1) A procedure for microencapsulation of *N*-benzylmorpholine by complex coacervation was developed, and the microencapsulation conditions were optimized. The best microencapsulation results were obtained with gelatin and chitosan succinate as shell-forming materials. In this case, the degree of *N*-benzylmorpholine encapsulation was 81%, and the mean size of microcapsules, 2 μm.

(2) A procedure for microemulsion microencapsulation of *N*-benzylmorpholine hydrochloride by simple coacervation was developed. The existence range of the microemulsion in the phase diagram was characterized. The droplet size of the microemulsion was found to be 20–35 nm, and the interfacial tension at the liquid/liquid interface did not exceed 1 mN m^{-1}. The method provides a virtually 100% degree of encapsulation of *N*-benzylmorpholine hydrochloride into microcapsules with triacetylcellulose shell.

(3) The release of the active compound from the microcapsules prepared by microemulsion microencapsulation was 70% in 7 h to 0.1 N HCl and 80% in 8 h to the phosphate buffer solution (pH 6.68) from the microcapsules prepared by complex coacervation.

REFERENCES

1. Solodovnik, V.D., *Mikrokapsulirovanie* (Microencapsulation), Moscow: Khimiya, 1980.
2. Coradin, T., Nassif, N., and Livage, J., *Appl. Microbiol. Biotechnol.*, 2003, vol. 61, no. 5, pp. 429–434.
3. EP Patent 1 027 147.
4. US Patent 4 686 546.
5. US Patent 4 688 060.
6. US Patent 6 362 182.
7. Layer, V., *Bioorg. Med. Chem. Lett.*, 2000, vol. 10, pp. 1665–1668.
8. Göpferich, A., Maria, J., and Langer, D., *Pharm. Res.*, 1994, vol. 11, no. 11, pp. 1568–1674.
9. US Patent 2 800 457.
10. Dubey, R.R. and Parikh, R.H., *Pharm. Sci. Tech.*, 2004, pp. 1–6.
11. Tiyaboonchai, W. and Ritthidej, G.C., *J. Sci. Technol.*, 2003, vol. 25, no. 2, pp. 245–254.
12. March, J., *Advanced Organic Chemistry: Reactions, Mechanisms, and Structure*, New York: McGraw–Hill, 1977.
13. Saleh, A., Khalil, S., and El-Gamag, E., *Pharmazie*, 1973, vol. 28, no. 11, pp. 385–388.
14. Lipatov, Yu.S., Nesterov, A.E., Gritsenko, T.M., and Veselovskii, R.A., *Spravochnik po khimii polimerov* (Handbook of Polymer Chemistry), Kiev: Naukova Dumka, 1971.
15. Egorova, E.M., *Nanotekhnologiya*, 2004, vol. 1, no. 1, pp. 15–19.

ISSN 1070-4272, Russian Journal of Applied Chemistry, 2008, Vol. 81, No. 2, pp. 281–284. © Pleiades Publishing, Ltd., 2008.
Original Russian Text © A.N. Moskvichev, A.A. Moskvichev, M.S. Fedoseev, 2008, published in Zhurnal Prikladnoi Khimii, 2008, Vol. 81, No. 2, pp. 291–294.

MACROMOLECULAR CHEMISTRY AND POLYMERIC MATERIALS

A Method of Impedance Measurements for Study of Curing of ED-20 Epoxy Resin

A. N. Moskvichev, A. A. Moskvichev, and M. S. Fedoseev

Nizhni Novgorod Branch, Blagonravov Institute of Machine Science, Russian Academy of Sciences, Nizhni Novgorod, Russia

Institute of Technical Chemistry, Ural Branch, Russian Academy of Sciences, Perm, Russia

Received July 5, 2007

Abstract—The method of impedance measurements was tested in a study of curing of ED-20 epoxy resin with 1,2,3,6-tetrahydro-3-methylphthalic anhydride (CAS 5333-84-6) in a thin layer between capacitor plates. A new equivalent electric circuit was suggested to describe the dielectric properties of the resin without using empirical equations.

DOI: 10.1134/S1070427208020237

Thermally curable adhesive and sealing compounds based on epoxy resins cured by amines and anhydrides are used to glue together and hermetically seal narrow (up to 0.5 mm) gaps between two metal surfaces. Classical optical and calorimetric methods are unsuitable for direct study of the properties of the resin, as well as the properties and formation kinetics of the resulting polymer under such conditions. It was of interest to test for this purpose the method of dielectric spectroscopy, modified by us, with the system constituted by ED-20 epoxy resin, 1,2,3,6-tetrahydro-3-methylphthalic anhydride (CAS 5333-84-6), and a catalyst as an example.

The starting epoxy resin ED-20 and the polymers formed during its curing contain hydroxy, carboxy, carbonyl, and epoxy functional groups possessing their own dipole moments. Such a structure suggests that the dipole-group, segmental, and total mobility of the molecules in a liquid oligomeric compound and in the resulting polymer vary with temperature and external electric field intensity [1, 2]. This makes the dielectric spectroscopy a suitable method for studying the properties of the oligomeric composition and the resulting polymer and the curing kinetics [3, 4]. The mobility of the dipole groups in an external alternating electric field is quantitatively characterized by the complex dielectric permittivity and dielectric loss tangent [1–4]:

$$\varepsilon^* = \varepsilon' - i\varepsilon'', \quad (1)$$

$$\tan\delta = \varepsilon''/\varepsilon'. \quad (2)$$

Variation of ε with frequency is described by the empirical equation [2]

$$[\varepsilon^*(\omega) - \varepsilon_\infty]/(\varepsilon_0 - \varepsilon_\infty) = [1 + (i\omega\tau_0)^{1-\alpha}]^{-\beta}, \quad (3)$$

where ε_0 is the static dielectric permittivity; ε_∞, high-frequency dielectric permittivity; τ, relaxation time; ω, angular frequency; α, width of the dispersion area; and β, parameter of the asymmetry of the dispersion curve.

Thus, analysis of the patterns of variation with the ac frequency for the components of the complex dielectric permittivity and dielectric loss tangent $\tan\delta$ provides information about the properties of the polymer, and analysis of the time dependences of the same parameters (at a fixed frequency), about the polymerization kinetics (kinetics of the liquid-solid phase transition of the oligomer).

EXPERIMENTAL

The impedance measurements were performed on setup consisting of a control computer with an analog-digital converter, ac generator, and a matching amplifying and measuring unit. At each preset ac frequency we recorded the active (Re) and reactive (Im) components of the impedance of the circuit consisting of two metal plates, each with an area of

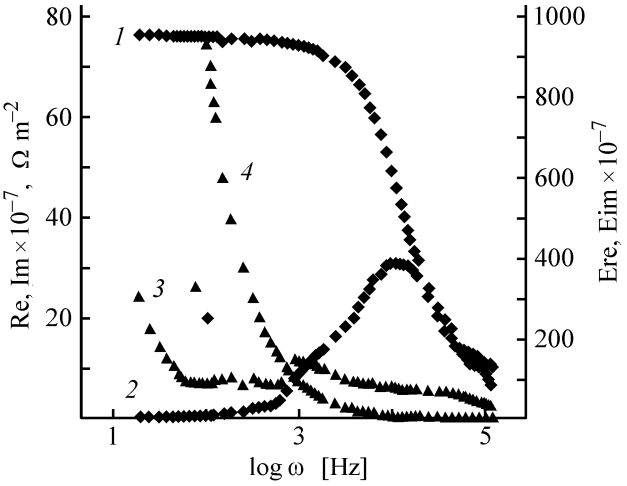


Fig. 1. Semilog plot of the components of the complex dielectric permittivity ε' and ε'' and of the impedance Re, Im of ED-20 resin vs. ω: (*1*) Re, (*2*) Im, (*3*) Eim (ε''), and (*4*) Ere (ε').

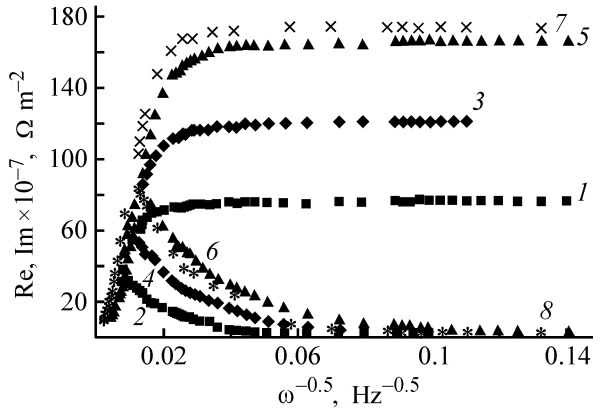


Fig. 2. Plots of the impedance components Re, Im of the ED-20 resin and the polymer vs. $\omega^{-0.5}$: (*1*) Re, 120°C; (*2*) Im, 120°C; (*3*) Re, 80°C; (*4*) Im, 80°C; (*5*) Re, 40°C; (*6*) Im, 40°C; (*7*) Re, polymer; and (*8*) Im, polymer.

4 cm^2, separated by a layer of ED-20 resin (1 mm) or, upon curing, of the polymer (a parallel-plate capacitor filled with the resin or polymer). To preclude any influence of the alternating current on the object examined, the amplitude of the signal fed into the circuit did not exceed 5–10 mV [5]. The measurements were carried out at frequencies ranging from 1 Hz to 20 kHz. The active ε' and reactive ε'' components of the complex dielectric permittivity were calculated by the formulas for a parallel-plate capacitor:

$$\varepsilon' = 1/\omega C_0 \mathrm{Re}(1 + \tan^2\delta), \quad (4)$$

$$\varepsilon'' = \tan^2\delta/\omega C_0 \mathrm{Im}(1 + \tan^2\delta), \quad (5)$$

where $C_0 = \varepsilon_0 S/d$; $\tan\delta$ = Im/Re; $\omega = 2\pi f$, $\varepsilon_0 = 8.854 \times 10^{-12}$ F m^{-1}; d is the thickness of the compound or the polymer layer, m; Re, active component of the impedance, Ω; Im, reactive component of the impedance, Ω; f, ac frequency, Hz; and S, area of the compound or polymer layer, m^2.

The formula $\tan\delta = \varepsilon''/\varepsilon'$ = Im/Re, i.e., ε'' = Im Const and ε'' = Re Const, suggests identical shapes of the frequency dependences for ε'' and Im, as well as for ε' and Re. However, actually these dependences qualitatively differ, since the impedance of the geometric vacuum capacitor relative to which the dielectric permittivity is calculated depends on frequency [i.e., Const = $f(\omega)$].

On passing from high to low frequencies, the ε'' = $f(\log\omega)$ [or ε'' = $f(\omega^{-1/2})$] plot (Fig. 1) exhibits a plateau associated with α relaxation, an extremum associated with the normal relaxation mode, and a dielectric permittivity growth area associated with the conductivity of the polymer. The active component of the dielectric permittivity increases nonlinearly as ac frequency decreases. Such a pattern of ε'' and ε' variation with frequency is also observed for other monomers and polymers [6].

The Re, Im = $f(\log\omega)$ [or Re, Im = $f(\omega^{-1/2})$] plots represent these processes in a different way (Fig. 1). With decreasing frequency, two extrema appear, which correspond to α relaxation processes and the normal relaxation mode, respectively, and a plateau is observed in the conductivity area of the polymer. The active component of the impedance initially increases with decreasing ac frequency and then levels off. An increase in the temperature of the resin (Fig. 2) causes the impedance components to decrease throughout the frequency range examined. The position of the maximum in the plot of the reactive component of the impedance is shifted to higher frequencies. A measurement of the impedance of the epoxy polymer at room temperature showed that the curing temperature (80–140°C) does not affects the impedance components but strongly affected the impedance speed. At the same time, the intensity of the bands in the IR spectra of the epoxy resins are known to be affected by the temperature changes, as revealed by Khozin [7] who attributed this phenomenon to the conformation transformations of the epoxy oligomer molecules.

An analysis of the run of the Im = f(Re) and Y_{Im} = $f(Y_{Re})$ plots for the active and reactive impedance components (by the technique from [8]) showed that the equivalent electric circuit of the system examined cannot be adequately described by an electric circuit

consisting of a limited number of interconnected resistors and capacitors. At the same time, this circuit is adequately described by the $-G_1-G_2-$ scheme, where G_1 is the frequency-sensitive Gerisher element [5] associated with α relaxation, and G_2, frequency-sensitive Gerisher element associated with the normal relaxation mode.

These frequency-sensitive elements of the equivalent electric circuit are evidently associated with transitions of the polymer macromolecules from one state to another and can be described by the corresponding chemical reactions:

$$A \rightleftarrows B^{\delta\pm} \rightleftarrows C, \qquad (6)$$

where A is the initial conformer; $B^{\delta\pm}$, intermediate conformer or a complex bearing an increased charge (governs the conductivity of the substance as a whole); and C, a new conformer.

The equilibrium volume concentration of the intermediate conformer involved in α relaxation, as calculated from the Re, Im = $f(\omega^{-1/2})$ dependence by the technique from [5] (for the degree of ionization equal to unity and diffusion coefficient of 10^{-6} m^2 s^{-1}), is temperature-dependent (Fig. 3); specifically, it increases with temperature.

Combined analysis of this dependence and the concentration of this phase in the polymer suggests that an appreciable curing of the system under consideration starts at temperatures not lower than 70°C.

We analyzed the patterns of variation of the parameters $|Z|$, $|\varepsilon^*|$, and tan δ of the epoxy resin–curing agent system in the gap between the metal plates during curing at different temperatures and found that they vary synchronously with the phase transformations and describe the curing kinetics. The range of variation of these parameters strongly depends on the ac frequency and attains a maximum in measurements of the impedance and tan δ at a frequency of 1 kHz, and in measurements of the dielectric permittivity, at a frequency of 50 Hz (in the range of the corresponding extrema in these dependences). It should be noted that, in the course of curing, the impedance increased by more than a factor of 100, and tan δ, by a factor of 10 upon the liquid-solid transition of the epoxy resin–curing agent system (Fig. 4). The dielectric loss tangent tan δ = Im/Re exhibits a more complex pattern of variation (Fig. 4).

When the system is placed in a thermostat, tan δ initially tends to increase (within the first 10 min); which is due to warming-up and conformation transformations, which cause the viscosity to change. This

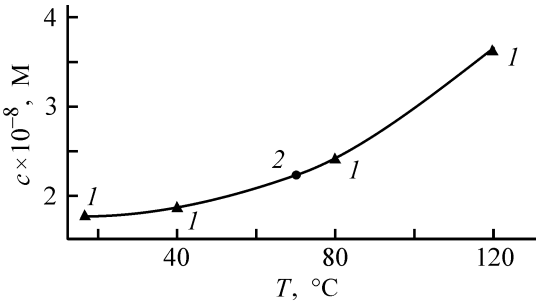


Fig. 3. Temperature dependene of the equilibrium concentration of the intermediate conformer c for (*1*) ED-20 resin and (*2*) polymer.

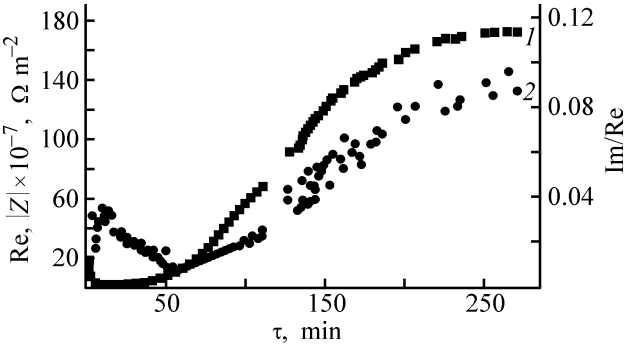
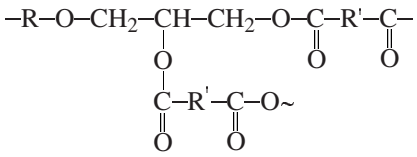


Fig. 4. Plots of (*1*) impedance $|Z|$ and (*2*) dielectric loss tangent tan δ = Im/Re vs. polymerization time τ, at a frequency of 50 Hz at 80°C.

is followed by a decrease in tan δ during 50 min, owing to the formation of the fragments of 3*D* chemical network by the condensation mechanism to the point of gelation.



In the third stage, tan δ tends to increase to a limiting value owing to the formation of a network structure of the epoxy polymer at the molecular and topological levels.

As is known, there are all the prerequisites for strong intermolecular interaction in epoxy polymers; it is of key importance for the properties of glassy polymers, as shown by numerous studies. This concerns, above all, the deformation-strength properties whose variation at temperatures below the glass transition point is determined primarily by the topological structure. Most likely, the scatter of the measured data for tan δ in the third stage is associated with this phenomenon.

We compared the kinetic data on curing of the epoxy composition, derived by the method of impedance measurements, with the corresponding DSC data. To this end, we used a DSC-111 calorimeter (SETARAM, France); the compound (weighed portion 55 ± 5 mg) was heated from room temperature to 500°C at a rate of 5 deg min^{-1}. The curing conditions were as follows: onset temperature 70°C; end temperature 144°C; activation energy of curing $E_{app} = 91.1$ kJ mol^{-1}; and reaction rate $V = 815.3 \times 10^8$ s^{-1}.

In constructing the plot of the conversion α of the liquid oligomeric fractions vs. the curing time τ we took into account the fact that, initially, the compound is a liquid ($\alpha = 0$ %), and upon curing completion, it is a solid polymer ($\alpha = 100\%$). This allows the dependence of the impedance $|Z|$ on the curing time (Fig. 4) to be easily recalculated to the $\alpha = f(\tau)$ dependence. Thus, the method of impedance measurements is suitable for studying the properties and formation kinetics of epoxy polymers in a thin layer.

CONCLUSIONS

(1) The method of impedance measurements is suitable for studying the polymerization kinetics of ED-20 epoxy resin and the physicomechanical and electrical properties of the resulting polymer.

(2) Polymerization can be adequately simulated by a homogeneous reaction of the conformation transition of the macromolecules from the stationary to a topological structure with increased energy characteristics.

REFERENCES

1. Fröhlich, H., *Theory of Dielectrics, Dielectric Constants and Dielectric Loss*, Oxford: Clarendon, 1958.
2. *Transitions and Relaxations in Polymers*, Boyer, R.F., Ed., New York: Wiley, 1966.
3. Lushcheikin, G.A., *Metody issledovaniya elektricheskikh svoistv polimerov* (Methods for Studying the Electric Properties of Polymers), Moscow: Khimiya, 1988.
4. Stetsovskii, A.P. and Zelenev, Yu.V., *Relaksatsionnaya spektroskopiya polimernykh materialov* (Relaxation Spectroscopy of Polymer Materials), Moscow: Vsesoyuzn. Nauchno-Issled. Tsentr po Materialam i Veshchestvam, 1991.
5. Damaskin, B.B. and Petrii, O.A., *Vvedenie v elektrokhimicheskuyu kinetiku* (Introduction to Electrochemical Kinetics), Moscow: Vysshaya Shkola, 1983.
6. *Novocontrol GmbH*, Product Information, 2006.
7. Khozin, V.G., *Usilenie epoksidnykh polimerov* (Reinforcement of Epoxy Polymers), Kazan: Dom Pechati, 2004.
8. Solov'eva, L.M., *Elektrodnye protsessy v galogenidnykh i okisnykh elektrolitakh* (Electrode Processes in Halide and Oxide Electrolytes), Moscow, 1981, pp. 68–82.

ISSN 1070-4272, Russian Journal of Applied Chemistry, 2008, Vol. 81, No. 2, pp. 285–289. © Pleiades Publishing, Ltd., 2008.
Original Russian Text © T.G. Ermakova, L.P. Shaulina, N.P. Kuznetsova, O.A. Burova, S.V. Amosova, G.F. Myachina, 2008, published in Zhurnal Prikladnoi Khimii, 2008, Vol. 81, No. 2, pp. 295–299.

MACROMOLECULAR CHEMISTRY AND POLYMERIC MATERIALS

New Network Copolymers of 1-Vinyl-1,2,4-Triazole as Efficient Sorbents of Mercury

T. G. Ermakova, L. P. Shaulina, N. P. Kuznetsova, O. A. Burova, S. V. Amosova, and G. F. Myachina

Favorskii Institute of Chemistry, Siberian Branch, Russian Academy of Sciences, Irkutsk, Russia
Irkutsk State University, Irkutsk, Russia

Received August 27, 2007

Abstract—The possibility of preparing copolymers by radical copolymerization of 1-vinyl-1,2,4-triazole with divinyl sulfide and divinyl diethylene glycol ether in the bulk was examined. The sorption characteristics of the new cross-linked copolymers with respect to mercury(II) ions under static conditions in acid solutions were studied.

DOI: 10.1134/S1070427208020249

Mercury is one of the most significant contaminants in the world system of environmental monitoring. The high stability of mercury compounds and their toxicity, and also the lack of efficient sorption procedures for their recovery result in that even an insignificant content of mercury in the environment presents hazard to human health and all living creatures on the Earth due to the cumulative effect [1–3]. For preconcentration and recovery of various mercury species, a large number of complexing sorbents based on various polymer matrices have been suggested [4–9]. The most efficient sorbents for preconcentration and separation of mercury are complexing copolymers with sulfur- and nitrogen-containing functional groups [10–12]. The sorption preconcentration and separation of elements, among them mercury ions, from process solutions require using sorbents resistant to corrosive media. Copolymers containing sulfur and nitrogen atoms in macromolecules are of particular interest as sorbents of mercury. Along with functional groups containing donor atoms, the performance of the sorbents is also affected by cross-linking agents, which provide a definite structure of macromolecules and their high chemical and thermal stability.

This study was aimed to prepare new cross-linked complexing copolymers with network structure by radical copolymerization of 1-vinyl-1,2,4-triazole (VT) with divinyl sulfide (DVS) and divinyl diethylene glycol ether (DVDEGE) and to examine their sorption power with respect to mercury(II) ions in acid solutions.

EXPERIMENTAL

1-Vinyl-1,2,4-triazole was synthesized by the procedure described in [13]. Before use, monomer was distilled in a vacuum: bp 48°C/3 mm Hg, n_D^{20} 1.5075, d_4^{20} 1.0857. The unique characteristics of VT such as hydrophilicity, complexing ability, chemical and thermal stability, adhesion, and nontoxicity allow preparation of copolymers with valuable characteristics for wide application in engineering, medicine, and biology [14]. Divinyl sulfide was synthesized by the procedure described in [15]; bp 86°C, n_D^{20} 1.5060. Divinyl diethylene glycol ether (synthesis procedure was described in [16]) was additionally washed with water, dried with potassium hydroxide, and distilled in a vacuum; bp 85°C/14 mm Hg, n_D^{20} 1.4430. Copolymerization of VT with DVS and VT with DVDEGE was performed in the bulk in the presence of azobis(isobutyronitrile) (AIBN, 2 wt %) at 60°C. After synthesis, the copolymers were washed with ethanol in a Soxhlet apparatus and dried in a vacuum to constant weight. The compositions of the copolymers were evaluated from the content of nitrogen and sulfur (data of elemental analysis). The degree of swelling of the copolymers, α (%), was determined gravimetrically by the formula $\alpha = (P_s - P_d/P_s) \times 100\%$, where P_s is the weight of a swollen sample and P_d is that of a sample. The softening point of the copolymers was determined on a Boëtius table. The IR spectra were recorded on a Bruker IFS-25 spectrometer from KBr pellets.

Table 1. Characteristics of copolymers of VT with DVS (**I**, **II**) and DVDEGE (**III**, **IV**) (AIBN concentration 2 wt %, 60°C)

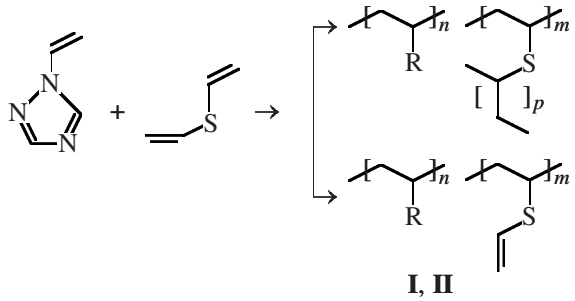
Co-polymer	Composition of starting mixture, mol %			Yield, %	Elemental analysis, wt %			Copolymer composition, mol %		
	VT	DVS	DVDEGE		N	S	O	VT	DVS	DVDEGE
I	97	3	–	71	35.83	2.72	–	80	20	–
II	70	30	–	64	25.01	10.97	–	54	46	–
III	97	–	3	30	40.01	–	3.84	99	–	1
IV	70	–	30	50	34.02	–	10.74	84	–	16

The sorption characteristics of the copolymers synthesized were studied under static conditions. A 0.01-g weighed portion of the sorbent was brought in contact for a definite time with 20 ml of a solution with a definite acidity, containing a known amount of mercury. The solid phase was separated by filtration. The mercury content of the solutions was determined by the extraction-photometric method with Dithizone [17]. The reproducibility of measurements of sorption and extraction-photometric determination of mercury is characterized by the standard deviation of 5.2%.

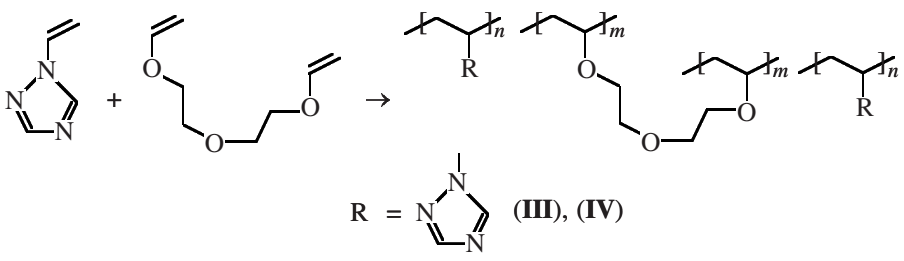
The radical copolymerization of VT with DVS and DVDEGE was performed at various molar ratios of the starting monomers: 0.97 : 0.03 and 0.70 : 0.30 (Table 1). The synthesis time depends on the nature of cross-linking agent and is 3–4 h for the system VT–DVS and 0.16–0.25 h for VT–DVDEGE. The new cross-linked copolymers, obtained in a yield of 30–71%, are colorless or light yellow glassy powders. They are insoluble in water, acids, and organic solvents and have high wettability. We found a higher reactivity of DVS in copolymerization with VT, in comparison with DVDEGE: the content of DVS in the copolymer is 20 and 46, and that of DVDEGE, 1 and 16% (Table 1). Elemental analysis shows that the copolymers are enriched in VT units whose swelling capacity is 77–100% in water and 80–120% in acid media. The compounds synthesized are thermally stable: the softening point T_{soft} is 290–330°C.

In the IR spectra of VT–DVS copolymers (**I**, **II**), there are no stretching vibration bands of the vinyl group of the VT triazole ring at 960 and 1640 cm^{-1}, but the stretching vibration bands of the triazole ring (1110, 1420, and 1500 cm^{-1}) are preserved, and an absorption band at 660 cm^{-1} assigned to stretching vibrations of the C–S bond appears. In the IR spectrum of copolymer **II**, there is a band at 1584 cm^{-1} corresponding to residual double bonds CH_2=CHS. In the IR spectra of copolymers VT–DVDEGE (**III**, **IV**), there are no absorption bands at 960 and 1650 cm^{-1} [ν(CH=CH_2)]; there are absorption bands of stretching modes of triazole heteroring at 1500 [ν(–C=N–)] and 3120 cm^{-1} [ν(CH)] and also DVDEGE units at 1100 [ν(C–O–C) of ether groups] and 1620 cm^{-1} [ν(C=C) bonds of vinyloxy groups].

The resulting swollen copolymers presumably have the following network structures:



I, **II**



R = **(III)**, **(IV)**

where n = 54–80 mol %; $m + l$ = 20–46 mol % (**I**, **II**); n = 84–99 mol %; m = 1–16 mol % (**III**, **IV**).

The synthesized copolymers have several reaction centers: pyridine nitrogen atom of VT, sulfide sulfur atoms of DVS, and oxygen atoms of ether groups of DVDEGE.

Experiments on sorption of mercury ions with new copolymers from solutions of nitric, sulfuric, and hydrochloric acids in the concentration range 1–7 M showed that mercury is recovered efficiently. As can be seen from Figs. 1a and 1b, sorption with copolymers **I**–**IV** does not noticeably depend on the anion and the concentration of nitric and sulfuric acids. The dependence appears in hydrochloric acid solutions: for sorbent **I** and **II** containing DVS units in the macromolecule, the degree of mercury recovery from hydrochloric acid solutions decreases with increasing acid concentration to a greater extent than that for sorbents **III** and **IV** containing DVDEGE fragments in the macromolecule. For sorbent **IV** at an HCl concentration of 1–3 M, the degree of mercury recovery decreases. This trend can be accounted for by the fact that the sorption from nitric and sulfuric acid solutions is due to the donor-acceptor interaction of cationic mercury species with active nitrogen and sulfur atoms in the copolymer structure. In chloride solutions, mercury is present in the form of a poorly dissociated molecular compound $HgCl_2$ and also in the form of fairly stable complexes $HgCl_3^-$ and $HgCl_4^{2-}$. The sorption is possible by the ion-exchange mechanism involving interaction of anionic mercury species with protonated nitrogen atoms, with a stronger or weaker competing effect of chloride ions. However, the ion coordination interaction of acido complexes through nitrogen and sulfur atoms is not ruled out. A larger degree of recovery is observed for cationic mercury species, in comparison with the anionic complex species $HgCl_3^-$ and $HgCl_4^{2-}$ prevailing in chloride solutions. However, an increase in the acid concentration decreases the contribution of ion-exchange interaction.

To elucidate the mechanism of interaction of mercury ions with electron-donor atoms of the sorbent, such as sulfur and oxygen, we studied the IR spectra of copolymers treated with acid and their concentrates. For copolymer **I** containing, along with vinyltriazole units, divinyl sulfide fragments, noticeable changes are observed. The absorption band of stretching vibrations of the triazole ring at 1120 cm^{-1} for the concentrate is shifted to higher frequencies by 10 cm^{-1}. There are significant changes in the range 1350–1500 cm^{-1}. This fact supports the donor-acceptor mechanism involving interaction of cationic mercury

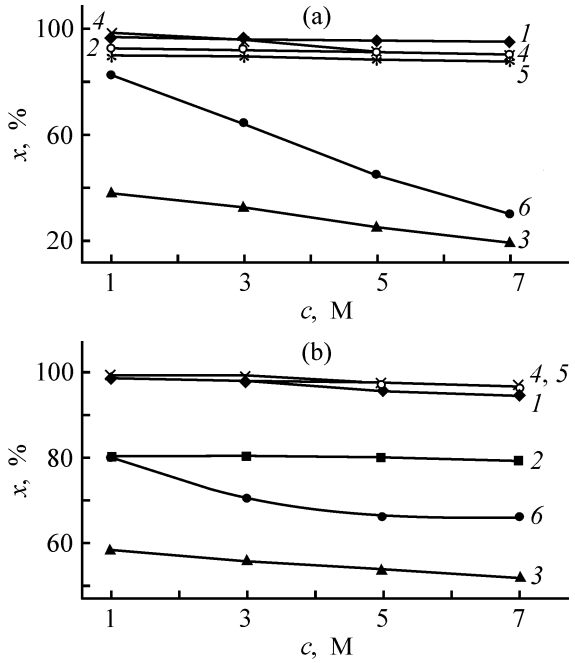


Fig. 1. Degree x of recovery of mercury(II) ions from solutions vs. concentration c of acids of varied nature. m_{sorb} = 10 mg; sorption duration 2 h. (a) Sorbents **I** and **II**: (*1*, *4*) H_2SO_4, $m(Hg^{2+})$ = 3.0 mg; (*2*, *5*) HNO_3, $m(Hg^{2+})$ = 3.0 mg; (*3*, *6*) HCl, $m(Hg^{2+})$ = 0.5 mg; (b) sorbents **III** and **IV**: (*1*, *4*) H_2SO_4, $m(Hg^{2+})$ = 4.0 mg; (*2*, *5*) HNO_3, $m(Hg^{2+})$ = 4.0 mg; (*3*, *6*) HCl, $m(Hg^{2+})$ = 1.0 mg.

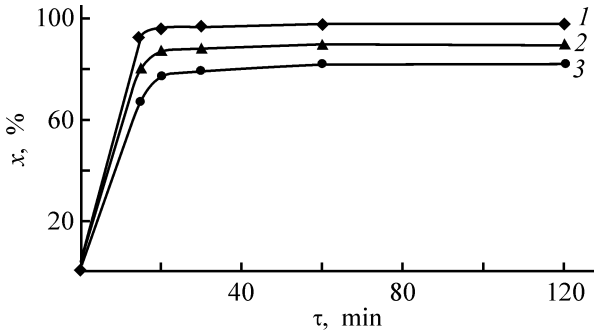


Fig. 2. Degree x of mercury(II) recovery from solutions with sorbent **II** vs. contact time τ of phases. (*1*, *2*) H_2SO_4, HNO_3, m_{sorb} = 10 mg, $m(Hg^{2+})$ = 3.0 mg; (*3*) HCl, $m(Hg^{2+})$ = 0.5 mg.

species with the nitrogen atom in position 4 of the triazole ring to form vinyltriazole-divinyl sulfide copolymer complexes of mercury(II). For copolymer of VT with DVDEGE, no significant changes in the IR spectra were observed, but a small long-wavelength shift of the band at 1490 cm^{-1} was observed in the spectrum of the concentrate.

Both cationic and anionic mercury species are recovered at a high rate. As can be seen from Fig. 2, in

Table 2. Sorption capacity SC of copolymers of VT with DVS and DVDEGE and distribution coefficients of mercury *D* in 1 M acid solutions

Copolymer	Copolymer composition, mol %			SC, mg g^{-1}	*D*, cm^3 g^{-1}	SC, mg g^{-1}	*D*, cm^3 g^{-1}	SC, mg g^{-1}	*D*, cm^3 g^{-1}
	VT	DVS	DVDEGE	HNO_3		H_2SO_4		HCl	
I	80	20	–	277	2.4×10^5	605	7.3×10^4	120	1.0×10^3
II	54	46	–	268	1.1×10^5	582	1.0×10^5	320	7.1×10^3
III	99	–	1	260	8.2×10^3	502	3.7×10^4	248	2.8×10^3
IV	84	–	16	543	4.9×10^5	846	1.8×10^5	338	3.5×10^3

sorption from 1 M acid solutions the equilibrium is established within 20–30 min; in this case, the half-sorption time is 5–10 min and the nature of cross-linking agent in copolymers does not noticeably affect the recovery kinetics.

From the equilibrium distribution curves obtained when studying the distribution of mercury ions between phases in sorption with increasing mercury concentration in 1 M acid solutions (Fig. 3), we evaluated the sorption capacity (SC) of the copolymers and the distribution coefficients *D* (Table 2).

As can be seen from the results obtained, mercury is efficiently recovered with the synthesized sorbents. The sorption capacity in 1 M sulfuric acid is approximately 2 times that in nitric acid. The decrease in sorption is apparently caused by the higher stability of mercury nitrate complexes in the solutions. In hydrochloric acid medium, sorbent **I** of the system VT–DVS with the highest content of nitrogen atoms shows a lower SC, and sorbent **II** with the lowest content of nitrogen, a higher SC. In sulfuric and nitric acid solutions, the SCs of sorbents **I** and **II** are close despite that the difference in the content of donor atoms is approximately 10%. These facts confirm

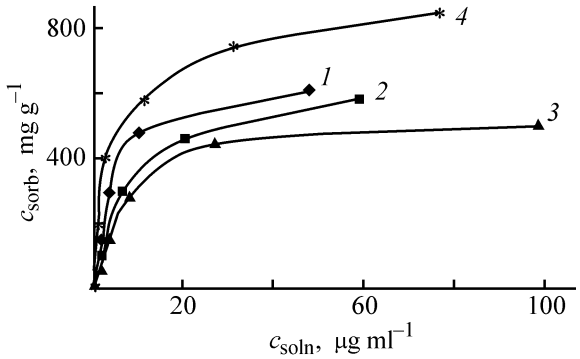


Fig. 3. Equilibrium distribution of mercury(II) for sorbents **I**–**IV** (*1*–*4*, respectively) in 1 M H_2SO_4. (c_{sorb}, c_{soln}) Concentration.

the suggestion that the coordination is affected not only by the content of active atoms, but also by the steric structure of the copolymer and packing density of its functional groups. Sorbent IV of the system VT–DVDEGE has the highest SC, which is apparently caused by more porous structure, in comparison with the other copolymers synthesized. The higher SC values of sorbents **II** and **IV** in hydrochloric acid medium, in comparison with those of sorbents **I** and **II**, are apparently caused by decease in the steric hindrance to diffusion of anionic mercury species in a sorbent particle. Apparently, the steric configuration makes nitrogen atoms of the heteroring more accessible to interaction with anionic mercury species.

The high distribution coefficients of mercury (Table 2) and the shapes of the equilibrium distribution curves (in particular, their slopes, Fig. 3) suggest the efficient operation of the sorbents at low concentrations and the possibility of mercury recovery from dilute corrosive solutions.

With the aim to recover mercury from multicomponent solutions, we studied the sorption power of sorbents **II** and **III** with respect to heavy metal ions, such as Fe^{3+}, Ni^{2+}, Co^{2+}, and Cu^{2+}. The sorption was performed from 1 M nitric acid solutions for 2 h. The sorbent weight was 10 mg, and the total solution volume, 20 ml. The solution contained solutions of 1 mg ml^{-1} Fe^{3+}, Co^{2+}, and Cu^{2+} ions, 1 ml each. The residual concentration of metals in the solution after sorption was determined by the atomic absorption method. The results showed that the polymers did not noticeably recover iron, cobalt, and nickel ions, but up to 30% of copper ions was recovered. The experimental data show that mercury can be desorbed from the sorbent phase with an ammonia solution (1 : 1), and a large elution percentage is reached with the concentrates prepared using the copolymers containing DVS units.

CONCLUSIONS

(1) New network copolymers of 1-vinyl-1,2,4-triazole with divinyl sulfide and divinyl diethyle glycol ether, containing nitrogen-, sulfur-, and oxygen-containing units, were synthesized by radical copolymerization.

(2) The effect of the nature and concentration of acids on the recovery of mercury ions was elucidated. A high sorption power of the complexing sorbents with respect to mercury ions in sulfuric and nitric acid solutions under static conditions was established. The influence of the steric structure of the polymer on its sorption capacity was shown. The sorbent containing 84 mol % 1-vinyl-1,2,4-triazole and 16 mol % divinyl diethylene glycol ether has the highest sorption capacity. The high distribution coefficients ($n \times 10^5$) suggest the possibility of mercury recovery from dilute and corrosive solutions.

(3) Along with mercury, copper ions are also recovered with the sorbents from multicomponent salt solutions.

REFERNECES

1. Ponomarenko, A.M., Environmental and Fish-Hatchery Aspects of Mercury Contamination of Water Storage Basins, *Cand. Sci. Dissertation*, Kazan, 2006.
2. Laperdina, T.G., *Opredelenie rtuti v prirodnykh vodakh* (Determination of Mercury in Natural Waters), Novosibirsk: Nauka, 2000.
3. Simonova, L.P., Bruskina, I.M., and Ivanov, V.M., *Zh. Anal. Khim.*, 1989, vol. 44, no. 4, pp. 581–596.
4. Amosova, S.V., Antsiferova, L.I., and Shaulina, L.P., *Zh. Prikl. Khim.*, 2001, vol. 74, no. 1, pp. 39–43.
5. Amosova, S.V., Shaulina, L.P., Ratovskii, G.V., et al., *Khim. Inter. Ustoich. Razv.*, 2003, vol. 11, pp. 831–835.
6. Simanova, S.A., Burmistrova, N.M., Kazakevich, Yu.A., et al., *Zh Prikl. Khim.*, 1997, vol. 70, no. 2, pp. 231–236.
7. Pozhidaev, Yu.N., Panezhda, E.V., Kirillov, A.I., et al., *Dokl. Ross. Akad. Nauk*, 2002, vol. 385, no. 5, pp. 777–779.
8. Voronkov, M.G., Vlasova, N.N., Pozhidaev, Yu.N., et al., *Nauka Proizv.*, 2003, vol. 62, no. 6, pp. 4–9.
9. Levchenko, L.M., Mit'kin, V.P., Oglezneva, I.M., et al., *Khim. Inter. Ustoich. Razv.*, 2004, vol. 12, nos. 1–6, pp. 709–724.
10. Vokina, O.G., Abramova, N.D., and Shaulina, L.P., *Zh. Prikl. Khim.*, 1991, vol. 64, no. 1, pp. 141–145.
11. Simonova, L.N., Kudryavtsev, G.V., Bruskina, I.M., et al., *Zh. Anal. Khim.*, 1987, vol. 42, no. 5, pp. 1047–1056.
12. Shaglaeva, N.S., Amosova, S.V., Shaulina, L.P., et al., *Zh. Prikl. Khim.*, 2006, vol. 78, no. 8, pp. 1296–1298.
13. Ermakova, T.G., Tatarova, L.A., and Kuznetsova, N.P., *Zh. Obshch. Khim.*, 1997, vol. 67, no. 5, pp. 859–861.
14. Ermakova, T.G. and Kuznetsova, N.P., *Nauka Proizv.*, 2003, no. 6, pp. 55–59.
15. Trofimov, B.A. and Amosova, S.V., *Divinilsul'fid i ego proizvodnye* (Divinyl Sulfide and Its Derivatives), Novosibirsk: Nauka, 1983.
16. Trofimov, B.A., Kudyakova, R.N., Oparina, L.A., et al., Zh. Prikl. Khim., 1991, vol. 64, no. 4, pp. 873–877.
17. Gladyshev, V.P., Levitskaya, S.A., and Filippova, L.M., *Analiticheskaya khimiya rtuti* (Analytical Chemistry of Mercury), Moscow: Nauka, 1974.

ISSN 1070-4272, Russian Journal of Applied Chemistry, 2008, Vol. 81, No. 2, pp. 290–293. © Pleiades Publishing, Ltd., 2008.
Original Russian Text © A.I. Vorob'eva, D.R. Sagitova, S.V. Kolesov, L.V. Spirikhin, Yu.B. Monakov, 2008, published in Zhurnal Prikladnoi Khimii, 2008, Vol. 81, No. 2, pp. 300–303.

MACROMOLECULAR CHEMISTRY AND POLYMERIC MATERIALS

Optically Active Polymeric Salts Prepared from Amino Acids and Polysulfonylpyrrolidinium Chloride

A. I. Vorob'eva, D. R. Sagitova, S. V. Kolesov, L. V. Spirikhin, and Yu. B. Monakov

Institute of Organic Chemistry, Ufa Research Center, Russian Academy of Sciences, Ufa, Bashkortostan, Russia

Ufa State Academy of Economics and Service, Ufa, Bashkortostan, Russia

Received July 16, 2007

Abstract—Possibility of preparing optically active polymers from *N*,*N*-diallyl-*N*,*N*-dimethylammonium chloride-sulfur dioxide copolymer and optically active acids was studied by the ion-exchange method.

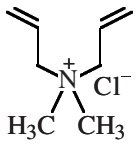
DOI: 10.1134/S1070427208020250

Optically active polymers are widely used both in studies of the mechanism of stereospecific catalysis [1–3] and in practice, e.g., as adsorbents and ion exchangers in separation of racemic mixtures, as asymmetric catalysts and modifiers in heterogeneous catalytic systems in asymmetric organic synthesis, and for preparing glass and films rotating the polarization plane of transmitted light [3–7]. In some cases, the stereoselectivity of optically active catalytic systems is higher than that of their low-molecular-weight analogs [3]. Preparation of optically active polymeric salts of amino acids with *N*,*N*-diallyl-*N*,*N*-dimethylammonium chloride (AMAC)–sulfur dioxide copolymer is of interest. This copolymer is an effective catalyst of some organic reactions [8, 9] and exhibits high physiological activity [10]. Presumably, not only chlorides, but also other polysulfonylpyrrolidinium salts may exhibit high physiological activity. In this context, preparation of polysulfonylpyrrolidinium salts of biologically active amino acids is a topical problem.

In this study, we prepared optically active salts of AMAC–SO_2 copolymer with some amino acids and tartaric acid by ion-exchange method and determined their structure.

EXPERIMENTAL

N,*N*-Diallyl-*N*,*N*-dimethylammonium chloride



was prepared from dimethylamine and allyl chloride by the procedure described in [11]. The number of AMAC units was estimated from the double bond content determined by elemental analysis and by ^{13}C NMR spectroscopy:

Found, %: C 59.38, H 10.42, N 8.48, Cl 21.51, C=C 29.61.

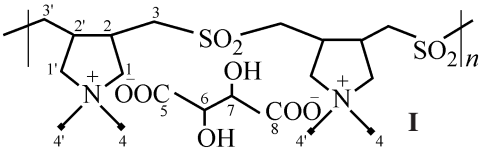
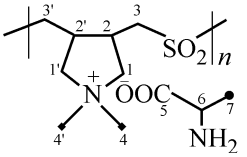
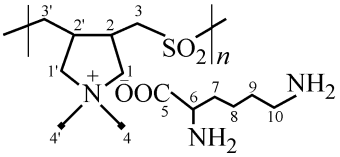
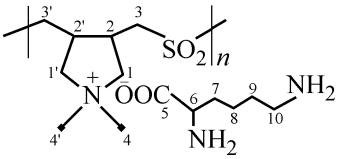
Calculated, %: C 59.44, H 9.91, N 8.67, Cl 21.98, C=C 29.72.

^{13}C NMR spectrum, ppm: C^1 68.39 t, C^2 126.62 d, C^3 131.38 t, C^4 51.75 q. No other signals were observed.

Sulfur dioxide was dried by passing through concentrated sulfuric acid and freshly calcined calcium chloride. Potassium persulfate (PP) (analytically pure grade) was doubly recrystallized from ethanol and dried in a vacuum at room temperature to constant weight.

Optically active acids (OAAs): *D*-tartaric (ultrapure grade), α-aminopropionic (*L*-α-alanine, pure grade),

Table 1. Optically active polymeric salts (OAPSs) formed by polysulfonylpyrrolidinium hydroxide and optically active acids

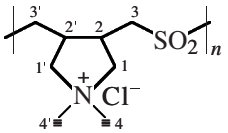
Structure of OAPS	OAA	Found, % / Calculated, %				Characteristic IR bands, cm^{-1}	$[\alpha]_D^{20}$
		C	H	N	S		
 **I**	*D*-Tartaric acid	43.82 / 45.45	6.62 / 6.82	4.22 / 5.30	10.86 / 12.12	1132, 1300 (SO_2); 1612 (COO); 964, 3536, 3400, 3160 (OH)	+8.8
 **II**	*L*-α-Alanine	45.71 / 47.48	7.18 / 7.91	9.03 / 10.07	10.62 / 11.51	1130, 1300 (SO_2); 1620 (NH_2); 1580 (COO)	+2.3
 **III**	*L*-Lysine	48.76 / 50.15	8.38 / 8.66	11.62 / 12.54	8.61 / 9.55	1132, 1300 (SO_2); 1580 (COO); 1620 (NH_2)	+4.9
 **IV**	*L*-Proline	50.12 / 51.32	7.71 / 7.89	8.98 / 9.21	9.75 / 10.53	1132, 1300 (SO_2); 1584 (COO); 1540 (NH)	–35.7

2,6-diaminocaproic (*L*-lysine, pure grade), and 2-pyrrolidinecarboxylic (*L*-proline, analytically pure grade), and also acetone (analytically pure grade) taken as a precipitant, were used without additional purification. The properties of all the chemicals used in this study were in agreement with published data.

The IR spectra of the polymers were recorded on a Specord M-80 spectrophotometer in the range 3600–600 cm^{-1}. The ^{13}C NMR spectra were recorded on a Bruker AM-300 spectrometer operating at 75.5 MHz with broad-band proton decoupling and in the JMOD mode. The spectra were recorded in D_2O and DMSO-d_6. 2,2-Dimethyl-2-silapentane-5-sulfonic acid and tetramethylsilane, respectively, were used as internal references.

The optical rotary powers $[\alpha]_D^{20}$ of the OAAs and optically active polymers were measured on a Perkin–Elmer 241 MC polarimeter (589 nm) in 20% aqueous solutions. The optical rotary powers $[\alpha]_D^{20}$ of *D*-tartaric acid, *L*-α-alanine, *L*-lysine, and *L*-proline were +12.0, +2.9, +2.9, and –86.0, respectively.

N,*N*-Diallyl-*N*,*N*-dimethylammonium chloride-sulfur dioxide copolymer, polysulfonylpyrrolidinium chloride (PSPC)



was prepared by the known procedure [12]. The purity of PSPC was determined by elemental analysis and ^{13}C NMR spectroscopy.

Found, %: C 42.28, H 7.32, N 6.12, Cl 15.51, S 14.32.
Calculated, %: C 42.57, H 7.10, N 6.21, Cl 15.74, S 14.19.

^{13}C NMR spectrum of PSPC, ppm: C^1 70.48 t, C^2 34.25 d, C^3 53.88 t, C^4 56.35 q, $C^{4'}$ 54.79 q. No signals of the initial AMAC were observed.

An attent to substitute the chloride ion in PSPC with optically active amino acid failed. Therefore, subsequent experiments on preparation of OAPSs were

Table 2. ^{13}C NMR spectra of optically active salts of polysulfonylpyrrolidinium hydroxide

Structure	Chemical shift (ppm) and multiplicity										
	C^1	C^2	C^3	C^4	$C^{4'}$	C^5	C^6	C^7	C^8	C^9	C^{10}
I	65.50 t	32.00 d	54.00 t	52.80 q	52.00 q	176.40 s	72.94 d	72.94 d	176.40 s		
II	68.34 t	32.02 d	54.30 t	52.67 q	52.50 q	177.34 s	50.66 d	17.03 q			
III	68.41 t	32.11 d	54.39 t	51.75 q	52.64 q	177.02 s	54.90 d	31.09 t	21.62 t	26.62 t	39.21 t
IV	68.38 t	32.08 d	55.24 t	53.50 q	53.03 q	176.90 s	63.36 d	34.00 t	25.02 t	47.13 t	

performed via formation of a polysulfonylpyrrolidinium hydroxide intermediate.

Polysulfonylpyrrolidinium hydroxide (PSPH) was prepared from PSPC by ion exchange on AV-17-8 strongly basic anion exchanger by the following procedure. The anion exchanger was successively washed with water and 4, 7, and 15% aqueous alkali solution until no chloride ions were detected with $AgNO_3$ in the wash water. Then the anion exchanger was washed with water to neutral reaction. An aqueous solution of PSPH was prepared by passing a 20% aqueous solution of PSPC through the anion exchanger. PSPH was precipitated from aqueous solution into acetone, reprecipitated from aqueous solution into acetone, washed with three portions of acetone, and dried in a vacuum at 50°C to constant weight. The purity of PSPH was determined by elemental analysis and ^{13}C NMR spectroscopy.

Found, %: C 46.21, H 8.52, N 6.62, S 15.34, Cl 0.24.
Calculated, %: C 46.38, H 8.21, N 6.76, S 15.46, Cl 0.

^{13}C NMR spectrum of PSPH, ppm: C^1 70.87 t, C^2 34.50 d, C^3 54.00 t, C^4 56.82 q, $C^{4'}$ 55.18 q. No other signals were observed.

OAPSs were prepared by the reaction of PSPH with optically active amino acids. To a 40% aqueous solution of PSPH, a 30% aqueous solution of OAA was added dropwise at room temperature (except for reaction with L-α-alanine). The PSPH:OAA ratio was 1.0 : 1.1. The reaction mixture was kept at the required temperature for 1 h. Since the solubility of *L*-α-alanine in water is relatively low (no more than 17.4%), the reaction with *L*-α-alanine was performed at 50°C. The reaction products were precipitated from aqueous solutions with acetone, washed with three portions of acetone, and dried in a vacuum at 50°C to constant weight. The yield was 85-87% based on the initial amount of the reactants. The elemental composition of these products is close to the calculated data (Table 1).

The IR spectra of the reaction products contain strong bands of the COO group in the range 1580–1612 cm^{-1} (depending on the acid) and the bands of NH_2 and NH groups at 1620 and 1540 cm^{-1}, respectively (Table 1). The IR spectrum of the tartaric acid salt obtained at PSPH : OAA ratio of 1.0 : 1.1 contains the band at 1705 cm^{-1} along with the band at 1612 cm^{-1}. These bands are absent in the spectrum of the product prepared at the PSPH : OAA ratio of 2 : 1 (Table 1).

All the reaction products of PSPH with OAAs are optically active. Their $[\alpha]_D^{20}$ values are listed in Table 1. The absence of the signals of the initial PSPH and other impurities in the ^{13}C NMR spectrum of OAPSs suggests complete substitution of the OH anion by OAA anions (Table 2).

CONCLUSIONS

(1) Polysulfonylpyrrolidinium hydroxide was prepared by ion exchange of chloride ions in polysulfonylpyrrolidinium chloride.

(2) It was found that polysulfonylpyrrolidinium salts with anions of *L*-α-amino acids and Dtartaric acid are optically active.

ACKNOWLEDGMENTS

This study was financially supported by the Foundation for Support of Leading Scientific Schools (project NSh-9342.2006.3).

REFERENCES

1. Klabunovskii, E.I., *Stereospetsificheskii kataliz* (Stereospecific Catalysis), Moscow: Nauka, 1968.
2. Pinot, P., *Khimiya i tekhnologiya polimerov* (Chemistry and Technology of Polymers), Rogovin, Z.A., Ed., Moscow: Mir, 1967, no. 12, pp. 54–122.

3. Klabunovskii, E.I. and Latov, V.K., *Khimiya i tekhnologiya vysokomolekulyarnykh soedinenii* (Chemistry and Technology of Macromolecular Compounds), Korshak, V.V., Ed., Moscow: VINITI, 1971, vol. 3, pp. 138–171.
4. Rogozhin, S.V. and Dovankov, V.A., *Usp. Khim.*, 1968, vol. 37, no. 7, pp. 1327–1347.
5. US Patent 4 873 301.
6. Plate, N.A., Davydova, S.L., Alieva, E.D., et al., *Vysokomol. Soedin., Ser. A*, 1973, vol. 15, no. 8, pp. 1856–1867.
7. *Entsikopediya polimerov* (Encyclopediya of Polymers), Kargin, V.A., Ed., Moscow: Sov. Entsiklopediya, 1974, vol. 2.
8. USSR Inventor's Certificate, no. 1 530 631.
9. USSR Inventor's Certificate, no. 1 495 339.
10. RF Patent 2 095 056.
11. Harada, S. and Arai, K., *Makromol. Chem.*, 1967, vol. 107, pp. 64–77.
12. Vorob'eva, A.I., Vasil'eva, E.V., Gaisina, Kh.A., et al., *Vysokomol. Soedin., Ser. A*, 1996, vol. 38, no. 10, pp. 1663–1667.

ISSN 1070-4272, Russian Journal of Applied Chemistry, 2008, Vol. 81, No. 2, pp. 294–297. © Pleiades Publishing, Ltd., 2008.
Original Russian Text © R.Z. Shakhnazarli, A.A. Alieva, Kh.G. Nazaraliev, A.M. Guliev, 2008, published in Zhurnal Prikladnoi Khimii, 2008, Vol. 81, No. 2, pp. 304–307.

MACROMOLECULAR CHEMISTRY AND POLYMERIC MATERIALS

Photosensitive Materials Based on Copolymers of Vinyl Cyclopropyl Ether with Maleic Anhydride

R. Z. Shakhnazarli, A. A. Alieva, Kh. G. Nazaraliev, and A. M. Guliev

Institute of Polymeric Materials, National Academy of Sciences of Azerbaijan, Sumgaiyt, Azerbaijan

Received October 16, 2007

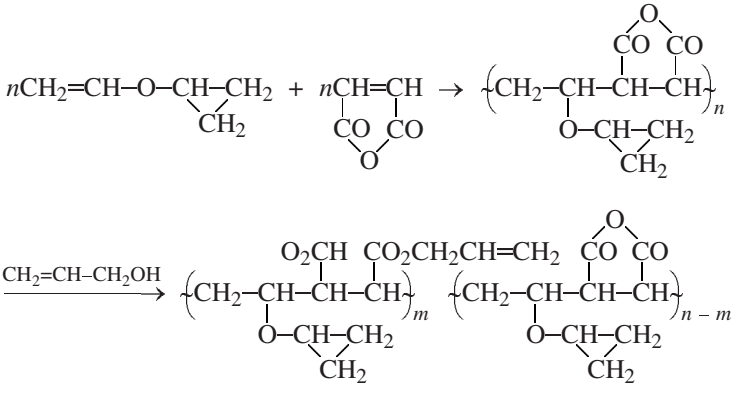
Abstract—Copolymers prepared from vinyl cyclopropyl ether and maleic anhydride were modified with allyl alcohol, and the products obtained were thermally cross-linked with styrene. Photoresists were prepared from these copolymers, and their photolithographic parameters were determined.

DOI: 10.1134/S1070427208020262

It is known that introduction of a reactive functional group into a macromolecule by chemical modification alters the structure and properties of the polymer. Films composed of such modified polymers change, after an appropriate irradiation, their physical and chemical properties. This is due to the fact that the energy of the penetrating electrons or rays considerably exceeds the energy of chemical bonds. As a result, bonds are ruptured, which is followed by cross-linking and/or degradation. This property allows such materials to be used in various photo- and electron-beam resists for microelectronics [1].

Various classes of polymers and, in particular, poly(meth)acrylates, styrene copolymers, and aliphatic polysulfones, are used today as functional polymers for preparation of photo- and electron-beam resists [2–4]. Of much interest are also copolymers of maleic anhydride (MA), which enter into various chemical reactions with opening of the anhydride ring [5]. The ease of such transformation makes these copolymers convenient as starting products for synthesis of new materials [6, 7]. At the same time, it is known that polymers whose macromolecules contain unsaturated groups in side chains readily transform into 3*D* network structures upon heat or radiation treatment. A similar pattern can also be observed in their homopolymerization of copolymerization with various vinyl monomers in the presence of both ionic catalysts and radical initiators. Such polymer-analogous transformations yield valuable products. In particular, it was suggested to use polymers containing in side chains chemically active groups, such as vinyl, epoxy, or allyl groups for fabrication of negative photo- and electron-beam resists [8, 9].

In this study, we performed esterification of previously synthesized [10] copolymers of cyclopropyl vinyl ether with MA. As a modifier we chose allyl alcohol (AA). The esterification yielded copolymers modified to different extents, depending on the reaction conditions:



The experimental results show that the copolymers are readily esterified with AA at 70–90°C without a catalyst, with a fairly high conversion of the anhydride units. With excess AA, the conversion of the anhydride units in the macromolecular chain reaches 85% in 3 h.

As the esterification is performed without catalyst and the carboxy groups formed by the anhydride ring opening appear in sterically hindered positions, their reaction with AA (in the initial steps and at a small excess of AA) becomes improbable. Hence, determination of the amount of free carboxy groups will allow estimation of the conversion of the anhydride units in the course of esterification. Since the degree of conversion of anhydride groups chiefly depends on the reaction conditions, we first examined the influence exerted by the molar ratio of the copolymer and AA and by the reaction temperature and time on the amount of carboxy groups formed by opening of the anhydride rings. The results of esterification of the copolymers with AA are listed in the table. It can be seen that, the reaction time being the same, the content of the free carboxy groups increases with the molar ratio of AA to the copolymer. For example, at a 2 : 1 ratio of AA to the copolymer, the content of carboxy groups formed in 180 min (longer reaction leads to an only insignificant increase in the content of carboxy groups) is 5.9%, whereas at a fivefold excess of AA, the content of carboxy groups at the same reaction time increases to 10.6%. The conversion of anhydride units also increases with temperature. At the reactant ratio and reaction time indicated above, the content of free carboxy groups increases from 7.8 to 12.4% as the temperature is elevated from 70 to 90°C. In other words, at 90°C the same conversion is reached in a shorter time than at 70°C.

The table shows that the copolymer synthesized is fairly readily esterified with AA without a catalyst, to a relatively high conversion of the anhydride units. Under the optimal conditions (AA : copolymer ratio 4 : 1, 80°C, 180 min), the conversion of anhydride units in the macromolecular chain of the copolymer reaches 80–87%. The modified copolymers obtained by the esterification are readily soluble in ketones and esters and insoluble in alcohols, aromatic hydrocarbons, and alkanes. The modified copolymers can be recovered from their solutions in methyl ethyl ketone by precipitation with a 3–4-fold volume of petroleum ether, followed by drying of the precipitated powders in a vacuum oven at 30–40°C.

The presence of the allyl groups in the macromolecular chains of the modified copolymers was confirmed by the IR data and by decolorization of bromine water.

Content of carboxy groups in relation to the molar ratio of the reactants and temperature

T, °C	τ, min	Content of carboxy groups at indicated allyl alcohol : copolymer ratio		
		2 : 1	4 : 1	5 : 1
70	30	1.0	1.1	1.4
	60	2.0	2.9	4.3
	90	3.1	4.5	6.7
	120	4.0	6.0	8.2
	150	4.9	7.2	9.7
	180	5.9	8.2	10.6
80	30	1.2	1.0	1.9
	60	2.4	3.1	5.7
	90	3.6	4.7	7.8
	120	4.7	6.3	9.3
	150	5.7	7.5	10.7
	180	6.8	8.7	11.6
90	30	1.1	1.3	2.2
	60	2.7	3.3	7.0
	90	4.3	5.4	9.4
	120	5.6	7.2	10.9
	150	6.7	8.6	11.8
	180	7.8	9.8	12.4

The IR spectra of the allylated copolymers contain absorption bands characteristic of the double bond (1645, 990, 915, 900 cm^{-1}). The bands at 1150–1300 and 1700–1745 cm^{-1} are indicative of the presence of ether and carbonyl groups in the macromolecular chain. Hence, the reaction of AA with the anhydride ring yields the fragments $CO_2CH_2CH{=}CH_2$. A broad absorption band centered at 3000 cm^{-1} can be assigned to out-of-plane bending vibrations of the associated OH group in the carboxyl moiety [11]. The carbonyl stretching vibration band of the carboxyl moiety is obscured by strong vibration bands of the carbonyl group in the ester moiety at 1745 cm^{-1}.

The IR and ^1H NMR data show that UV irradiation induces cross-linking of the modified copolymers, with opening of the double bond of the allyl group. Other groups and bonds are not invilved in the process. As a result of irradiation, a 3*D* cross-linked structure is formed, and the modified copolymers become insoluble.

The allylated copolymers were also converted into insoluble cross-linked products by radical copolymer-

ization with styrene in the presence of benzoyl peroxide. The reaction was performed at 70°C. The extent of gelation was the greater, and the time required for complete cross-linking the shorter, the higher the molar ratio of styrene to the copolymer.

As expected, an raising the temperature to 90°C leads to an increase in the yield of the crosslinked product and, accordingly, in the gelation rate. In particular, it was found that the yield of the cross-linked product in 40 min was 27.0% at 70°C, and 45.5% at 90°C.

Photochemical cross-linking of functional polymers is of interest in the context of their application to photo- and electron-beam lithographic processes and, in particular, to preparation of photoresists. The practice of using these resists in photolithography revealed their essential drawbacks, in particular, relatively low photosensitivity. Modified analogs of these polymers, exhibiting enhanced photosensitivity, are used today.

To assess the prospects for using the modified copolymers that we obtained, we prepared their acetone solutions with and without addition of a sensitizer (benzophenone) in an amount of about 10 wt % (relative to the dry polymer). Films of photoresists of both the straight copolymer and its modified analogs were prepared under identical conditions. After definite irradiation times, the optical density of the films was determined by UV spectroscopy and compared with that of the unirradiated films. Changes in the irradiated copolymer films were evaluated gravimetrically, by determining the amount of the soluble fraction (extraction with acetone).

Irradiation of the modified cyclopropane-containing anhydride copolymers with monochromatic light (λ = 365 nm) altered the intensity of the absorption band of the double bond at 1645 cm^{-1}. Taking as an internal reference the band of the cyclopropane group at 1045 cm^{-1}, we estimated the photosensitivity of the films of the modified copolymer to be 70–80 mJ cm^{-2}. This irradiation dose required for the exposure allows formation in the modified copolymer film of topological structures in which the component size is the minimum possible for this system. Upon irradiation of the film to a dose of 80 mJ cm^{-2}, the conversion of side double bonds is 40–45%. Irradiation to doses exceeding 120 mJ cm^{-2} raises the conversion of allyl groups to 80%. However, such an exposure is accompanied by side effects: postradiation transformations deteriorating the resolving power of the resist.

The properties of the resists obtained are consistent with the microheterogeneous model of radical polymerization of polyfunctional acrylic compounds [12]. In accordance with this model, thickly cross-linked polymeric particles (microgel) formed in the initial step of the polymerization transformation shield the yet unchanged allyl groups and thereby considerably decrease their activity. Furthermore, the 3*D* cross-linked structure hinders relaxation processes (translation and segmental motion of particles). Therefore, the hindered motion of side groups makes less probable the involvement of the allyl fragments in the photochemical cross-linking.

The photoresist we developed shows not only a high sensitivity (70–80 mJ cm^{-2}), but also increased resolving power (a structure with a component size of 1.0–1.2 μm is formed in a 1.0-μm-thick resist film).

EXPERIMENTAL

The IR spectra were recorded on a Specord M 80 spectrophotometer, and the ^1H NMR spectra, on a BS-487B spectrometer (Tesla, 80 MHz) against HMDS. The copolymers were prepared by the procedure described in [10], under the conditions of radical initiation. The esterification of the copolymers with allyl alcohol was performed in solution. The required amount of allyl alcohol was added from a dropping funnel to 0.003 mol of the copolymer in 100 ml of methyl ethyl ketone at 70°C. After a definite period, the mixture was sampled to determine the content of carboxy groups. For this purpose, the esterified copolymer was precipitated from the solution with petroleum ether, repeatedly washed, dried, and analyzed to determine the content of carboxy groups by the procedure described in [13].

The reaction of the modified copolymers with styrene was performed in sealed ampules in a dry nitrogen atmosphere. After the reaction completion, the ampules were opened and toluene (or benzene) was added. The mixture was allowed to stand for several hours to extract the forming styrene homopolymer. The insoluble fraction, cross-linked copolymer, was washed several times with toluene or benzene and dried in a vacuum oven. The process was performed at various molar ratios of the modified copolymer and styrene.

The polymeric films were irradiated under the following conditions: PRK-2 lamp as radiation source; exposure time 30–120 s (depending on the degree of esterification of the copolymers). As developer we used cyclohexanone. The development time was up

to 15 s. The photoresist layers were dried at 120°C for 30 min.

CONCLUSIONS

(1) Chemical modification of the copolymer of vinyl cyclopropyl ether and maleic anhydride with allyl alcohol was performed, and esterified copolymers with side allyloxycarbonyl and carboxy groups were prepared. The degree of esterification depends on the ratio of the reactants (copolymer and allyl alcohol) and on the reaction temperature and time.

(2) Modified copolymers readily undergo photochemical and thermal cross-linking. Introduction of allyl groups into the pendant chains of the copolymers imparts to them the capability to form 3*D* cross-linked structures under UV irradiation or in the reaction with styrene.

REFERENCES

1. Bokov, Yu.S., *Foto-, elektrono- i rentgenorezisty* (Photo-, Electon-Beam, and X-ray Resists), Radio i Svyaz', 1982.
2. Hyder Ali, A., and Srinivasan, K.S., *Polym. Int.*, 1997, vol. 43, pp. 310–316.
3. Sharma, V.K., Affrossman, S., and Pethrick, R.A., *J. Polym.*, 1983, vol. 24, pp. 387–390.
4. Ramazanov, G.A., Shakhnazarova, R.Z., and Guliev, A.M., *Zh. Prikl. Khim.*, 2005, vol. 78, no. 10, pp. 1725–1728.
5. Tsiourvas, D. and Paleos, C.M., *J. Appl. Polym. Sci.*, 1989, vol. 38, no. 2, pp. 257–264.
6. Volkova, I.F., Gorshkova, M.Yu., Izumrudov, V.A., and Stotskaya, L.L., *Vysokomol. Soedin., Ser. A*, 2004, vol. 46, no. 8, pp. 1388–1392.
7. Cole, H.S., Skelly, D.W., and Wagner, B.C., *ACS Org. Coat. Plast. Chem.*, 1975, vol. 35, no. 2, pp. 122–125.
8. Ramazanov, G.A., Gasanova, S.S., and Guliev, A.M., *Azerb. Khim. Zh.*, 2005, no. 1, pp. 36–39.
9. Akperov, O.G., Khanlarov, T.G., and Akperov, E.O., *Vysokomol. Soedin., Ser. A*, 1994, vol. 36, no. 7, pp. 1081–1085.
10. Shakhnazarova, R.Z. and Guliev, A.M., *Azerb. Khim. Zh.*, 2004, no. 2, pp. 25–30.
11. Kazitsyna, L.A. and Kupletskaya, N.B., *Primenenie UF-, IK- i YaMR-spektroskopii v organicheskoi khimii* (Applications of UV, IR, and NMR Spectroscopy to Organic Chemistry), Moscow: Vysshaya Shkola, 1971.
12. Vainer, A.Ya., Dyumaev, K.M., Likhachev, I.A., et al., *Dokl. Akad. Nauk SSSR, Fiz. Khim.*, 2004, vol. 396, no. 1, pp. 362–365.
13. Toroptseva, A.M., Belogorodskaya, K.V., and Bondarenko, V.M., *Laboratornyi praktikum po khimii i tekhnologii vysokomolekulyarnykh soedinenii* (Laboratory Course of Chemistry and Technology of Macromolecular Compounds), Leningrad: Khimiya, 1972.

ISSN 1070-4272, Russian Journal of Applied Chemistry, 2008, Vol. 81, No. 2, pp. 298–303. © Pleiades Publishing, Ltd., 2008.
Original Russian Text © B.I. Lirova, E.A. Lyutikova, N.V. Vasil'eva, B.A. Berkuta, M.I. Prusskii, 2008, published in Zhurnal Prikladnoi Khimii, 2008, Vol. 81, No. 2, pp. 308–313.

MACROMOLECULAR CHEMISTRY AND POLYMERIC MATERIALS

Influence of Filler on Migration from Plasticized Poly(vinyl chloride) Composites

B. I. Lirova, E. A. Lyutikova, N. V. Vasil'eva, B. A. Berkuta, and M. I. Prusskii

Gor'kii Ural State University, Yekaterinburg, Russia

Stroiplastpolimer Joint-Stock Company, Yekaterinburg, Russia

Received May 21, 2007

Abstract—Influence of the filler (chalk) on migration of the plasticizer into air and water from poly(vinyl chloride) films plasticized with EDOS was studied by gravimetry, thermal analysis, and IR spectroscopy.

DOI: 10.1134/S1070427208020274

Low-toxic and relatively inexpensive EDOS plasticizer prepared from high-boiling by-products of isoprene production is suggested for use instead of, or along with conventional phthalate plasticizers in production of polymers, including poly(vinyl chloride) [1–3]. EDOS is a mixture of dioxane alcohols and their high-boiling ethers [4]. However, the high volatility of EDOX can result in a significant loss of the plasticizer in production and application of PVC materials [2, 3], which deteriorates the physicomechanical properties of the composites and makes them less environmentally safe. Polymeric materials can be modified by introduction of fillers, which makes these materials less expensive. Previously we have shown [3] that introduction of chalk into PVC films plasticized with EDOS at PVC : EDOS : chalk weight ratio of 100 : 64 : 245 decreases the loss of the plasticizer. We suggested [5] that the nonmonotonic dependence of the diffusion coefficient of EDOS plasticizer in the polymer film on the filler content is caused, unlike the systems with phthalate plasticizers, by interaction of chalk with EDOS in PVC composites. The aim of this study was to examine the influence of the chalk content on the migration of EDOS from PVC films into air and water, since PVC materials can contact not only with air, but also with water. The heat resistance and physicomechanical properties of PVC films were estimated in relation to the chalk content.

EXPERIMENTAL

We studied PVC films plasticized with EDOS and filled with chalk in different amounts. The composites were prepared from the following commercial components: suspension PVC S-70 with the molecular weight determined by viscometry $M = 8.5 \times 10^4$; EDOS plasticizer; and MTD-2 chalk as the filler. All the composites were stabilized with calcium stearate and urea. The samples had the following composition (weight proportion): PVC 100, EDOS 64, chalk 0-245, Ca stearate 0.9, and urea 0.45. The samples were prepared in the form of 1-mm films by rolling on bench rollers at 140°C for 10 min. We studied samples aged for 1 month.

The weight loss Δm of the samples in air under atmospheric pressure at room temperature and 90°C was determined gravimetrically. The relative determination error of Δm at room temperature and 90°C did not exceed 10 and 5%, respectively.

The weight loss of the samples upon gradual heating from room temperature to 400°C was determined by a thermal gravimetric analysis on a TA-4000 derivatograph. The heating rate was 10 deg min^{-1}.

The qualitative composition of the substances released into air from the films and the kinetics of their liberation at 90°C in a dynamic vacuum (residual pressure ~30 Pa) were studied by the IR spectrometric procedure developed in our laboratory, with a thermal vacuum chamber (TVC) [5, 6].

The migration of low-molecular-weight compounds from PVC films into water was evaluated by their weight loss in the course of time at room temperature and by analysis of the liquid phase being in the contact with the samples [6]. The weight loss of the sam-

ples kept in water was determined gravimetrically and was calculated from the equation $\Delta m = [(m - m_0)/m_0] \times 100$ (%), where m_0 is the initial weight of the sample and m is the sample weight in a time τ. The relative weight of substances that diffused from the film into water within the experimental time was calculated by the equation $\Delta m_w = [(m_d - m_0)/m_0] \times 100$ (%), where m_0 is the initial weight of the sample and m_d is the weight of the samples kept in water for the required time and dried to constant weight at 50°C under atmospheric pressure. The swelling of the sample after the experiment completion, α, was calculated from Δm and Δm_w by the equation $\alpha = \Delta m + |\Delta m_w|$ (%).

The qualitative composition of substances that diffused from the films into water was determined as follows. The aqueous phase was evaporated to dryness at 50°C under atmospheric pressure. Tetrahydrofuran (THF) was added to the dry residue. The THF extract was applied to a KBr window. The IR spectrum of the sample was recorded after evaporation of the solvent. The absence of residual THF in the sample was determined by IR spectroscopy.

The strain curves were measured on a PT-250M2 tensile-testing machine. The stretching rate was 25 mm min^{-1}. The samples were cut in the form of trowels whose working part was 6.5 mm wide. The result was the average of two replicate experiments. The stress in the samples was calculated by the equation

$$\sigma = P/S, \quad (1)$$

where σ is the stress (MPa); P, force (kN); and S, cross section of the working part of the sample (m^2).

The tensile stress of the samples σ_t was measured. The nominal elastic modulus at elongation E, characterizing the rigidity of the material, was calculated by the equation

$$E = \sigma/\varepsilon, \quad (2)$$

where σ is the stress and ε is the strain in the initial deformation steps.

The time dependences of the relative weight loss of the samples under atmospheric pressure are shown in Fig. 1. The weight loss of all the samples at room temperature did not exceed 1.5%. The weight loss of unfilled PVC at 90°C during the experimental time was 17% (Fig. 1b). The amount of compounds released from the samples decreased with increasing filler content. The weight loss of the composite

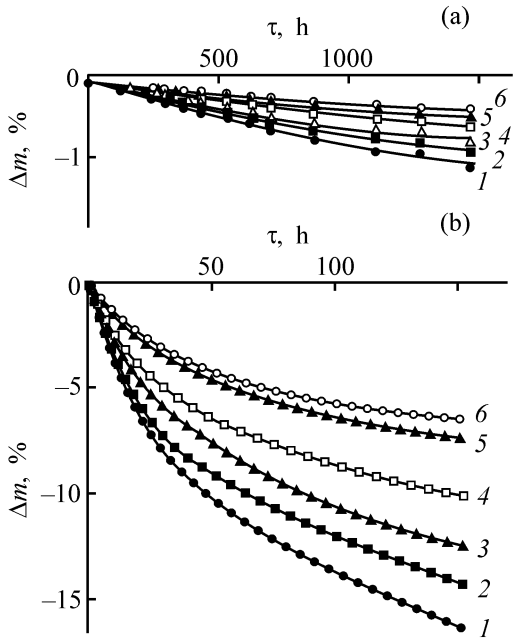


Fig. 1. Weight loss Δm of PVC films containing (*1*) 0, (*2*) 5.5, (*3*) 45, (*4*) 91, (*5*) 164, and (*6*) 245 parts by weight of chalk per 100 parts by weight of PVC (the same for Figs. 4 and 6) at (a) room temperature and (b) 90°C, vs. time τ.

containing 245 wt % chalk (relative to PVC) was approximately 6.5%. As determined by IR spectroscopy, EDOS plasticizer is released from all PVC films.

We also studied the migration of the plasticizer from the samples at 90°C. In these experiments, the released plasticizer was removed from the sample in TVC in a dynamic vacuum. The release of EDOS from the samples was monitored by IR spectroscopy. The kinetics of plasticizer liberation from the samples in the form of $A_\tau/A_\infty = f(\tau^{1/2})$ dependences was also determined by IR spectroscopy, where A_τ is the optical density of the EDOS band at ~1030 cm^{-1} in the IR spectra of the compounds liberated from the sample in time τ, and A_∞ is the optical density of this band corresponding to the initial content of the plasticizer in the sample [5]. The band at ~1030 cm^{-1} is common to all the compounds present in the plasticizer. This band can be assigned to δ_{C-OH} bending vibrations of the OH groups of primary alcohols and ν_{C-O} stretching vibrations of the C–O groups of primary alcohols and ethers [7, 8]. The kinetic curves measured in the initial desorption steps after attainment of the required temperature in TVC were linear. This fact suggests that migration of the EDOS plasticizer from PVC composites is controlled by diffusion in the polymer matrix and allows calculation of the apparent diffusion coefficient of the plasticizer D [5].

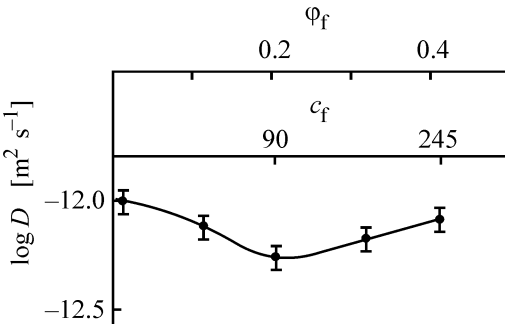


Fig. 2. Diffusion coefficient of plasticizer, D, vs. the chalk content c_f of PVC films. (φ_f) volume fraction of chalk.

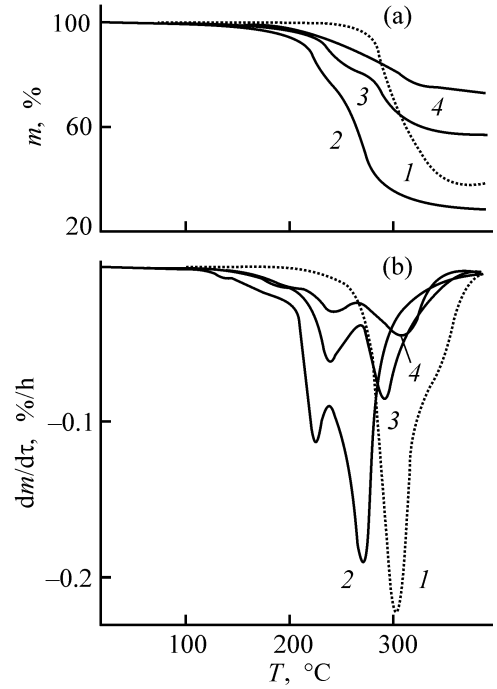


Fig. 3. (a) TG and (b) DTG curves for (*1*) nonplasiticized and (*2*–*4*) plasticized PVC films containing (*1*, *2*) 0, (*3*) 91, and (*4*) 245 parts by weight of chalk. (*m*) Weight and (*T*) temperature.

The dependence of D_{EDOS} on the chalk content of the samples is shown in Fig. 2. It can be seen that the dependence passes through a minimum. This fact confirmed our previous assumption [3] that the dependence of D of the plasticizer in the system examined can be nonmonotonic. A complex dependence of D of low-molecular-weight compounds on the filler content has been observed previously [5, 9] for some filled polymer systems. For example, the dependence of D of di-*n*-butyl-*o*-phthalate (DBP) in PVC composites on the kaolin content was nonmonotonic. The spectroscopic and thermodynamic data show that kaolin reacts with the polymer. By contrast, the dependence of D_{DBP} on the content of chalk, which does not react with PVC, is monotonic [5]. The nonmonotonic dependence of D_{EDOS} on the chalk content of the systems examined can be due to competing interaction of the components. We have shown previously [3] that PVC interacts with EDOS to form H bonds between the C–O groups of the plasticizer and CHCl groups of the polymer (C–O···CHCl) and does not interact with chalk. Under these conditions, chalk can interact with OH groups of the hydroxyl-containing component of EDOS [4], unlike phthalate plasticizers [the heats of wetting of chalk with di-(2-ethylhexyl) *o*-phthalate (DOP) and DBP are close to zero]. The decrease in the diffusion coefficient with the chalk content increasing to 90 parts by weight in PVC composite plasticized with EDOS can be due to formation of additional bonds between the plasticizer and the filler. The rize in the diffusion coefficient of EDOS with a further increase in the chalk content of the samples can be probably caused by structural features of polymer composites with a high filler content [10]. At a high chalk content, the polymer matrix can become looser, with discontinuities appearing [11, 12], which can increase the diffusion coefficient of the plasticizer into air.

The weight loss of the samples under gradual heating from room temperature to 400°C is shown in Fig. 3a. It is seen that the weight loss decreases with increasing filler content. These data are consistent with the weight loss determined under isothermal heating at 90°C (Fig. 1b). The DTG curves (first derivative of the change in the sample weight), which characterizes the thermolysis rate of the samples and removal of volatile products, is shown in Fig. 3b. The TG and DTG curves (curves *1*) for stabilized nonplasticized PVC film free of the filler are also shown in Fig. 3. The peak at ~302°C in the DTG curve of this sample is assigned to dechlorinatiion of PVC (liberation of HCl) [13]. The shoulder in the range 240–270°C in the thermal analysis curve of the plasticized samples, unlike the curve for the nonplasticized sample, is probably due to the release of the plasticizer from the PVC composite [14]. The DTG curve of the unfilled samples plasticized with EDOS (curve *2*) contains two peaks at ~270 and ~226°C and two shoulders at ~250 and ~180°C.

The thermal effect at ~270°C is probably due to dehydrochlorination of PVC. Its rate is maximal at temperatures lower (270°C) than that for the nonplasticized sample (302°C) (curve *1*). This is consistent with the data of Glazyrin et al. [2] who showed that, unlike DOP, EDOS catalyzes PVC degradation. The thermal effects observed at lower temperatures (curve *2*) can be probably assigned to liberation of dif-

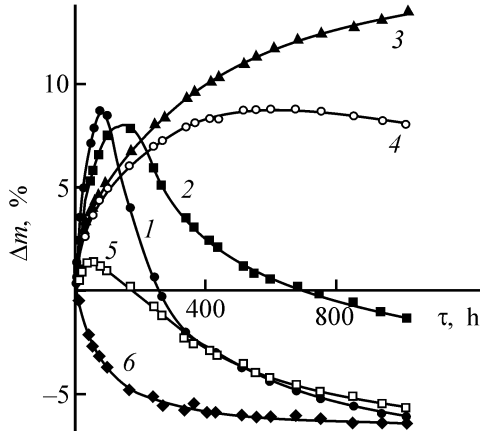


Fig. 4. Variation in the weight of PVC films, Δm, in water at room temperature with time τ.

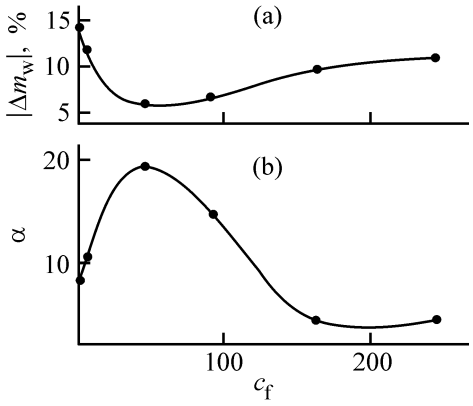


Fig. 5. (a) Wash-out of the components Δm_w and (b) swelling α of PVC films vs. the chalk content c_f (parts by weight).

ferent components of EDOS plasticizer [4]. The temperature corresponding to the maximal degradation rate increases from ~292 to ~307°C as the chalk content of the sample is raised from 91 to 245 parts by weight, respectively (Fig. 3b, curves *3* and *4*), which agrees with the rise in the heat resistance of PVC in the presence of chalk [15].

The time dependence of the weight change of PVC films in water at room temperature is shown in Fig. 4. The weight change of the samples can be due to swelling of the polymer films in the liquid and wash-out of their components. It is seen that that the unfilled samples and the samples containing 5.5 and 164 parts by weight of chalk swell first and then their components are washed out. The samples containing 45 and 91 parts by weight of chalk swell mainly in the course of the entire examined period. The main process observed throughout the experiment for the samples with the maximal filler content (245 parts by weight) is wash-out of its components.

The contributions of swelling of the films in water and wash-out of their components in the final experimental point (Fig. 4, 10^3 h) are listed in Table 1.

As can be seen from Table 1, the wash-out of the components and swelling of the samples are significant. As determined by IR spectroscopy, the EDOS plasticizer and urea are the main components washed out into water from all samples. The release of EDOS makes the major contribution to the total wash-out, since the urea concentration in the samples is 0.1–0.3%. The dependence of Δm_w and α on the chalk content of the samples is shown in Fig. 5.

The wash-out from the unfilled film is the maximal. The wash-out of EDOS can be due to its high hydrophilicity [16], in contrast to the phthalate plasticizers, and formation of solvates by interaction of polar OH and C–O groups of EDOS with water. The wash-out decreases as the chalk content increases to 90 parts by weight, which can be due to additional binding of the plasticizer via its interaction with the filler [3]. The increase in the wash-out from the samples containing 164 and 245 parts by weight of chalk can be due to loosening of the polymer matrix. The dependence of wash-out of the components (Fig. 5a) on the filler content of the PVC films correlates with the change in the apparent diffusion coefficient D_{EDOS} into air with increasing the chalk content of the composite (Fig. 2). As can be seen from Fig. 5b, the dependences of the degree of swelling of PVC films and Δm_w on the filler content pass through extrema. The wash-out of EDOS plasticizer makes lower the hydrophilicity of the polymer composite, which, in turn, changes the degree of swelling of the sample in water.

Table 1. Weight change in water at room temperature in 10^3 h of PVC films plasticized with EDOS and the contributions from swelling in water and wash-out of the components from the samples

Chalk content, parts by weight	Δm	Δm_w	α
	%		
0	–5.9	–14.1	8.2
5.5	–1.1	–11.6	10.5
45	13.5	–5.9	19.4
91	8.2	–6.5	14.7
164	–5.4	–9.6	4.2
245	–6.5	–10.9	4.3

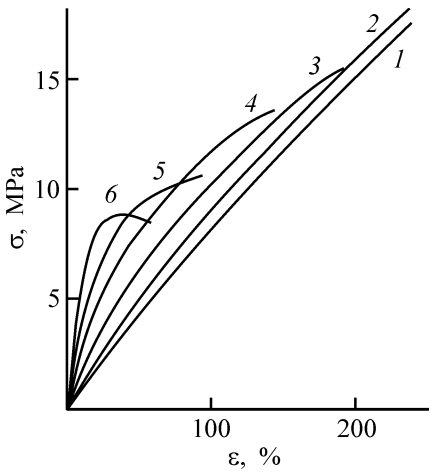


Fig. 6. Strain–stress curves of PVC films. (σ) Stress and (ε) strain.

The strain–stress curves of PVC films are shown in Fig. 6. The shape of these curves is typical of the glassy state of polymers: strong strain is observed under high stresses [17]. According to the strain–stress curves, composites containing 245 parts of chalk per 100 parts of PVC by weight are deformed with the formation of a "neck." In this case, the elongation of the sample is insignificant because of its failure. This is probably caused by structural features of highly filled polymer systems [10]. Weakly bonded structures formed by interaction of filler particles with each other also degrade during deformation of these systems. The ultimate tensile stress σ_t and elastic modulus E of PVC films are listted in Table 2.

The tensile strength of PVC films plasticized with EDOS decreases and the elastic modulus increases as the filler content becomes higher, which is consistent with changes in these parameters when powdered fillers not interacting with the polymer matrix are used [18].

Table 2. Deformation and strength properties of PVC films

Chalk content, parts by weight	σ_u	E
	MPa	
0	15.4	11.2
5.5	18.1	12.2
45	15.5	17.8
91	13.5	28.1
164	10.7	40.0
245	8.6	57.3

CONCLUSIONS

(1) The dependence of the diffusion coefficient of plasticizer into air from PVC composites plasticized with EDOS on the chalk content in the composite passes through a minimum. This can be due to competing intermolecular interaction of the components and the structural features of the polymer composites with high filler content.

(2) Large amounts of EDOS plasticizer are washed out in water. The dependence of the wash-out of the plasticizer on the filler content of the film passes through a minimum. The dependence of the swelling of the sample on the chalk content passes through a maximum. The swelling in water of poly(vinyl chloride) films plasticized with EDOS and the wash-out of the plasticizer are caused by the high hydrophilicity of EDOS.

(3) EDOS plasticizer should not be used for preparing waterproofing poly(vinyl chloride) materials since it does not provide the required stability of their performance in water.

REFERENCES

1. Sokolova A.G., Poly(vinyl chloride) and Poly(vinyl acetate) Materials Plasticized with EDOS, *Cand. Sci. Dissertation*, Penza, 1999.
2. Glazyrin, A.B., Kalganov, V.A., Abdullin, M.I., and Chuklina, N.S., *Plast. Massy*, 2001, no. 9, pp. 18–19.
3. Lirova, B.I., Lyutikova, E.A., Safronov, A.P., et al., *Zh. Prikl. Khim.*, 2006, vol. 79, pp. 1018–1024.
4. *TU* (Technical Specification) *2493-003-13 004 749–93: EDOS Plasticizer: Technical Specification*.
5. Lirova, B.I., Lyutikova, E.A., Mel'nik, A.I., and Pyzh'yanova, L.G., *Vysokomol. Soed., Ser. B*, 2002, vol. 44, no. 2, pp. 363–368.
6. Lirova, B.I., Lyutikova, E.A., Degtyareva, A.N., et al., *Zh. Prikl. Khim.*, 2004, vol. 77, no. 10, pp. 1707–1713.
7. Bellamy, L.J., *The Infra-Red Spectra of Complex Molecules*, London: Wiley, 1957.
8. *Fiziko-khimicheskie svoistva produktov proizvodstva izoprena* (Physicochemical Properties of Products of Isoprene Production), Ogorodnikov, S.K., Ed., Moscow: TsNIITEneftekhim, 1974.
9. Chalykh, A.E., *Diffuziya v polimenykh sistemakh* (Diffusion in Polymer Systems), Moscow: Khimiya, 1987.
10. Lipatov, Yu.S., *Fizicheskaya khimiya napolnennykh polimerov* (Physical Chemistry of Filled Polymers), Moscow: Khimiya, 1977.
11. Belokurova, A.P., Chalykh, T.I., Koifman, O.I., et al., *Izv. Vyssh. Uchebn. Zaved., Khim. Khim. Tekhnol.*, 1999, vol. 42, no. 4, pp. 74–76.

12. Reitlinger, S.A., *Pronitsaemost' polimernykh materialov* (Permeability of Polymer Materials), Moscow: Khimiya, 1974.
13. Minsker, K.S. and Fedoseeva, G.T., *Destruktsiya i stabilizatsiya polivinilkhlorida* (Degradation and Stabilization of Poly(vinyl chloride)), Moscow: Khimiya, 1979.
14. Wendlandt, W.Wm., *Thermal Methods of Analysis*, New York: Wiley–Interscience, 1974.
15. Asamov, M.K., Yangibaev, A.E., and Musakhanova, S.M., Abstracts of Papers, *IX Konferentsiya "Destruktsiya i stabilizatsiya polimerov"* (IX Conf. "Polymer Degradation and Stabilization"), Moscow, April 16–20, 2001, p. 19.
16. Gotlib, E.M., Koltun, E.E., and Averko-Antonovich, I.Yu., *Kauchuk Rezina*, 1999, no. 5, pp. 5–8.
17. Tager, A.A., *Fizikokhimiya polimerov* (Physical Chemistry of Polymers), Moscow: Khimiya, 1978.
18. Shtarkman, B.P., *Osnovy razrabotki termoplastichekikh polimernykh materialov* (Foundations of Development of Thermoplastic Polymer Materials), Nizhni Novgorod: Nizhegorodskii Gumanitarnyi Tsentr, 2004.

ISSN 1070-4272, Russian Journal of Applied Chemistry, 2008, Vol. 81, No. 2, pp. 304–309. © Pleiades Publishing, Ltd., 2008.
Original Russian Text © G.V. Plotnikova, S.F. Malysheva, N.K. Gusarova, A.K. Khalliulin, V.P. Udilov, K.L. Kuznetsov, 2008, published in Zhurnal Prikladnoi Khimii, 2008, Vol. 81, No. 2, pp. 314–319.

MACROMOLECULAR CHEMISTRY AND POLYMERIC MATERIALS

Triorganylphosphine Oxides as High-Performance Fire Retardants for Polyvinyl Chloride Plastisols

G. V. Plotnikova, S. F. Malysheva, N. K. Gusarova, A. K. Khalliulin, V. P. Udilov, and K. L. Kuznetsov

East-Siberian Institute, Ministry of Internal Affairs of Russia, Irkutsk, Russia

Favorskii Institute of Chemistry, Siberian Branch, Russian Academy of Sciences, Irkutsk, Russia

Received May 17, 2007

Abstract—The possibility, in principle, of using tertiary phosphine oxides with different structures as fire retardants for polyvinyl chloride plastisols was examined, and their ability to reduce the flammability of these materials was analyzed.

DOI: 10.1134/S1070427208020286

The use of polymeric materials in civil engineering provides significant economic and technical benefits by increasing the use of prefabrication technologies in construction, considerably decreasing the weight of buildings and structures, enhancing the quality of construction works and finishing, improving the exterior, and reducing the transportation volumes and labor spent for erection works. At the same time, virtually all polymeric materials suffer from an essential drawback, increased fire hazard.

The very nature of polymeric materials prevents them from being absolutely fireproof. However, their combustibility and combustion-sustaining power can be decreased. Among the state-of-the-art techniques for decreasing the combustibility of polymeric materials and, in particular, those based on polyvinyl chloride (PVC), are introduction of filling agents, application of fireproofing coatings, and use of halogenated plasticizers. However, these techniques typically impair the mechanical properties, heat resistance, and appearance of the polymeric materials [2].

Also, the combustibility of polymeric materials prepared from base polymers and, in particular, PVC can be decreased by chemical or physical modification. This typically implies the use of combustion-limiting additives, such as mineral fillers, low-combustibility plasticizers, and fire retardants. At present, significant deceleration of combustion is achieved mainly through application of fire retardants. Among them, the best performance characteristics are exhibited by phosphorus-containing fire retardants.

Most researchers believe that phosphorus compounds decrease the combustibility of polymers when added in a concentration of no less than 5% (for the base element). They attribute the decrease in combustibility to decomposition of the phosphoric acids formed, which yields P_2O_5 in the gas phase or a continuous glassy film of polyphosphoric acid on the surface [3, 4].

Wide application in preparation of polymeric materials with decreased combustibility is found by such plasticizers as esters of phosphorus acids, which replace, partially or completely, the combustible plasticizer (dioctyl phthalate) used for imparting the plasticity to PVC. Up to 80–90% of all the commercial phosphorus-containing plasticizers are triaryl phosphates. However, their commercial application is restricted by the lack of simple and efficient methods for synthesis of organophosphorus compounds (OPCs). These compounds are commonly prepared from fire- and explosion-hazardous alkali metals and highly toxic phosphorus halides, and commercial phosphorus-containing compounds are expensive.

The phosphine oxides tested in this study as fire retardants were synthesized by the Trofimov–Gusa-

rova reaction based on a new method for activation of elemental phosphorus (primarily, of its least active, though most environmentally safe red modification) in heterogeneous strongly basic media, composed of an alkali metal hydroxide and a polar aprotic solvent (DMSO, HMPA) or aqueous solution of alkali metal hydroxide, organic solvent, and a phase-transfer catalyst [5–7]. In this case, organophosphorus compounds are synthesized in a single step, and the preparation technology is very simple. This opens real prospects for commercial implementation of the synthesis procedure and wide application of these compounds, which have been previously prepared by a complex multistep procedure.

EXPERIMENTAL

We examined polyvinyl chloride based plastisols that differ from other PVC-based materials by the maximal content of the plasticizer and have the highest combustibility. The formulations were prepared from PVKh E 6250-Zh emulsion polyvinyl chloride [GOST (State Standard) 14039–78]. This is a white combustible powder consisting of 97.3 wt % main substance and 2.7 wt % monoalkyl sulfonate (an emulsifier used for preparation of PVC). Polyvinyl chloride has the following characteristics: mp 82°C, density 1430 kg m^{-3}, particle size under 0.6 μm, ignition point 335°C, and self-ignition point 530°C.

Dioctyl phthalate $C_6H_4(COOC_8H_{17})_2$ (DOP) served as plasticizer. As fire retardants we tested tertiary phosphine oxides synthesized from elemental phosphorus and alkyl bromides [8–10], benzyl chloride [11], allyl halides [12, 13], vinylpyridines [14], and phenylacetylene [5, 15, 16], as well as tris(hydroxymethyl)phosphine oxide synthesized from phosphine and formaldehyde in the presence of catalytic amounts of $PdCl_2$ [6]. Barium and cadmium stearates [TU (Technical Specifications) 6-09-17-319–96] served as stabilizers.

The necessary amounts of the components were thoroughly mixed using an electric drill with attachments until a homogeneous mass free from embedded impurities and lumps was obtained. The resulting PVC-based formulation was poured into a 30 × 20-cm metallic mold. After settling of the formulation for 2 h (to let out air bubbles), the mold containing the PVC-based formulation was placed in a desiccator for 10 min and heat-treated at 150°C.

Next, OPC, DOP, and stabilizer were introduced into the formulations in amount of 0.1–2.0, 65, and 2 parts per 100 parts of PVC by weight, respectively.

The inflammability, ignition delay time, ignition point, and self-ignition point were determined according to GOST 12.1.044–89. The ^{31}P NMR spectra were taken on a Bruker DPX 400 spectrometer with 85% H_3PO_4 as external reference and $CDCl_3$ as solvent. The flame temperature was estimated with a Promin' pyrometer, and the sample surface temperature, with a TK-505 contact thermometer.

To determine one of the major ignitability parameters, the ignition delay time, we prepared 15 samples, each shaped as a square with a side of 165 × 5 mm.

The conditioned sample to be tested was wrapped in an aluminum foil sheet (nominal thickness 0.2 mm) with a hole (140 mm in diameter) cut out in the middle. The center of the hole in the foil had to coincide with that of the exposed surface of the sample. The flame was brought in contact with the sample, and the time was noted. The time elapsed from the onset of the flame exposure till the occurrence of self-sustained combustion of the sample was taken as the ignition delay time.

To determine the flash point and the inflammation temperature we used PVC plastisol samples that were not heat-treated in an oven. The mixture examined was charged into a clean dry crucible. The latter was mounted onto the heating plate of a device for determination of the flash point and ignition point in an open crucible; a thermometer was immersed into the mixture in the crucible to the middle point between the crucible center and the wall at a distance of 6 mm from the bottom. Next, a gas burner was lit. As the flash point in the open crucible we took the temperature indicated by the thermometer at the instant of time when a flame appeared above a part of, or entire mixture surface. The flash point was measured accurately to within 1°C.

Immediately after the flash point was determined, the ignition point was measured; to this end, the crucible was further heated and exposed to an ignition source. After self-sustained combustion of the sample was established, the readings of the thermometer were taken during a period of 5 s. Specifically this temperature was taken as the ignition point of the sample.

We found that the inflammation dynamics is affected by the aliphatic phosphine oxides introduced

Table 1. Flame temperature T_{flame}, sample surface temperature T_{sur}, and self-ignition point T_{self} of plastisols with aliphatic phosphine oxide additives

Phosphine oxide	OPC content, parts per 100 parts of PVC by weight	T_{flame}	T_{sur}	T_{self}
		°C		
None	0	1270	610	400
Tris(hydroxymethyl)phosphine oxide	0.1	990	490	500
	0.5	965	475	525
	1.0	950	450	530
Triethylphosphine oxide	0.1	1200	600	410
	0.5	1200	605	415
	1.0	1150	605	418
Tripropylphosphine oxide	0.1	1180	595	420
	0.5	1160	589	430
	1.0	1160	600	438
Trioctylphosphine oxide	0.1	980	470	520
	0.5	965	440	540
	1.0	940	435	548
A mixture of tripropenylphosphine oxides	0.1	1015	570	500
	0.5	1009	545	509
	1.0	998	520	515

into the PVC-based plastisols (Table 1). The flame temperature appreciably decreases, which suggests deceleration of the oxidation reaction the occurs in the flame zone. At the same time, the ignition and self-ignition points of the samples containing these OPCs exceed those of the PVC-based plastisols free from the additives. These effects become more prominent as the length of the alkyl radical of the phosphine oxides increases, although this is paralleled by a decrease in the phosphorus content in them and, accordingly, in the formulation.

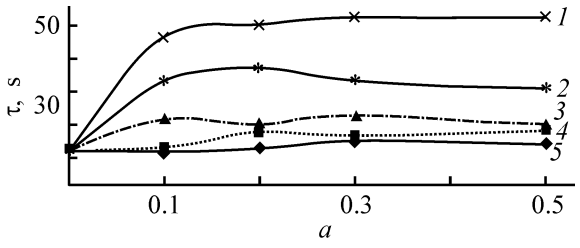


Fig. 1. Plot of the ignition delay time τ vs. the content of the phosphine oxides *a*, parts per 100 parts of PVC by weight: (*1*) tris(hydroxymethyl)phosphine oxide, (*2*) trioctylphosphine oxide, (*3*) a mixture of tripropenylphosphine oxides, (*4*) tripropylphosphine oxide, and (5) triethyphosphine oxide.

Introduction of even small amounts of trialkylphosphine oxides significantly increases the ignition delay time relative to that for the plastisols free from additives (Fig. 1).

The ignition and self-ignition points for the plastisol free from OPC additives and for DOP taken separately are very close: T_{self} was estimated at 400 and 394°C, and T_{ign}, at 205 and 200°C, respectively. Most likely, the inflammability and combustibility of the plastisols are governed by the plasticizer. Therefore, decelerated combustion of the plastisols with phosphine oxide additives is associated with the limited delivery of DOP (and its decomposition products) to the flame zone.

The high fire-retarding power of tris(hydroxymethyl)phosphine oxide can be attributed both to a high phosphorus content of its molecule and the possibility of interaction of this polyfunctional phosphine oxide with the plasticizer. For example, in the ^{31}P NMR spectrum (Fig. 2), the signal at 48 ppm characteristic of tris(hydroxymethyl)phosphine oxide disappears upon its heating with DOP, i.e., new organophosphorus compounds are formed.

The reason for the good performance characteristics of trioctylphosphine oxide as fire retardant can be

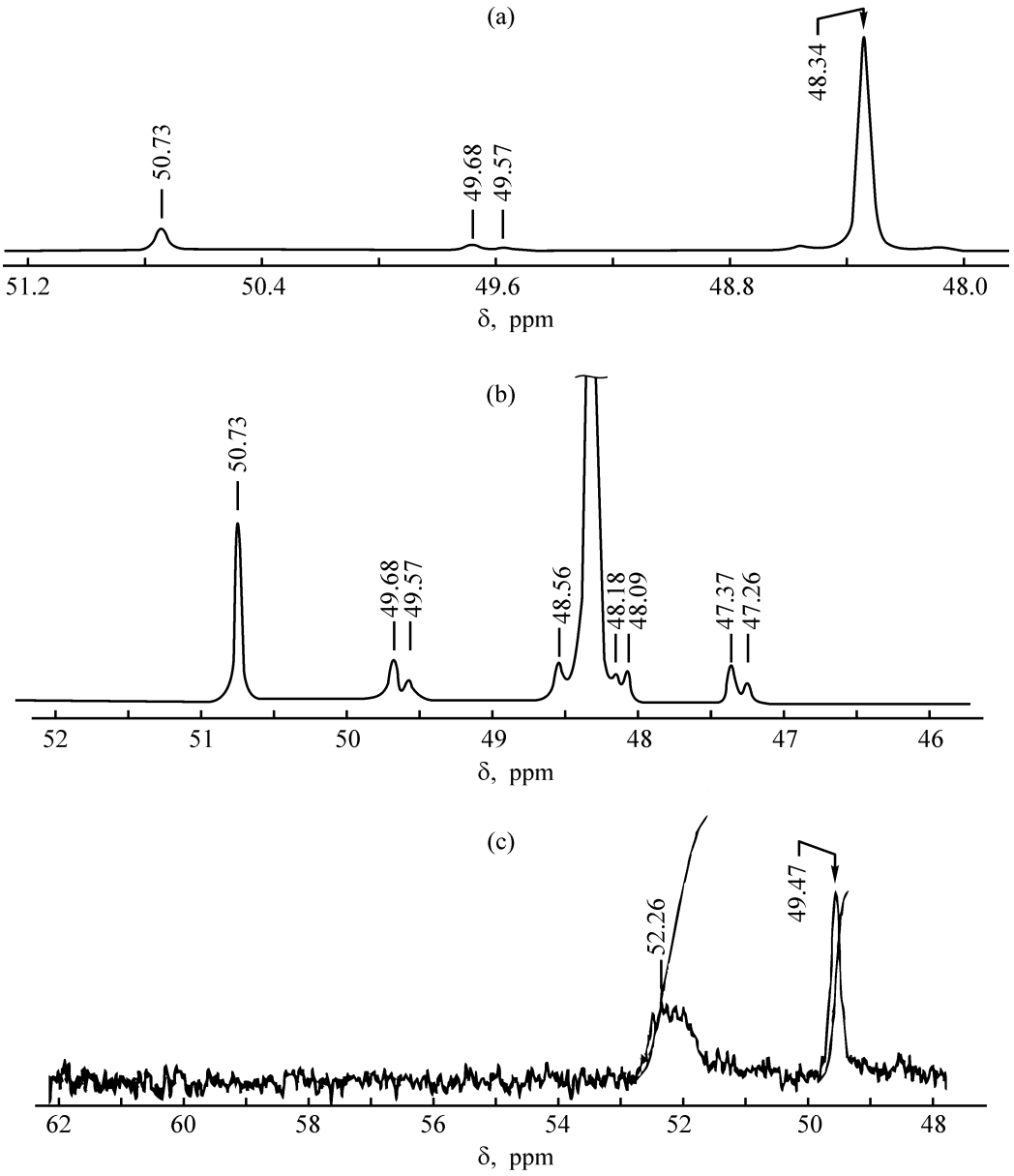


Fig. 2. ^{31}P NMR spectra of the tris(hydroxymethyl)phosphine oxide–DOP system after mixing at (a) 20, (b) 65, and (c) 80°C. (δ) Chemical shift, ppm.

found in its high complexing activity with respect to metal salts and capability to react with barium and cadmium stearates present in the plastisol formulations examined [17]. These reactions yield organometallic compounds probably incorporating DOP molecules. These compounds can catalyze the processes responsible for the formation on the burning material surface of a layer precluding both the delivery of the combustible decomposition products to the flame zone and oxygen diffusion to the surface of the burning material, as well as the heat transfer from the flame to the polymer [18].

Another factor that can be responsible for good fire-retarding characteristics of trioctylphosphine oxide is its high thermal stability: The decomposition temperature of trioctylphosphine oxide (240°C) exceeds the inflammation temperature of the PVC-based plastisol (230°C) containing a trioctylphosphine oxide addition.

The enhanced volatility of triethyl- and tripropylphosphine oxides is responsible for their faster (compared to trioctylphosphine oxide) removal from the material in the initial stage of combustion and, hence, for their enhanced inflammability.

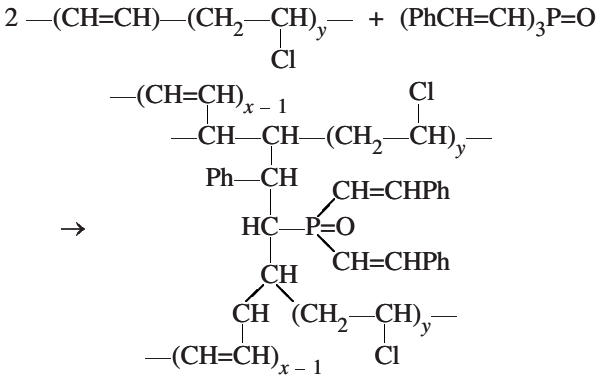
Table 2. Temperature characteristics of combustion processes for plastisols containing OPC additives with aryl(hetaryl)alkyl and styryl fragments

Phosphine oxide	OPC content, parts per 100 parts by weight of PVC	T_{flame}	T_{sur}	T_{self}
		°C		
None	0	1270	610	400
Tribenzylphosphineoxide	0.1	1105	600	500
	0.5	1095	590	500
	1.0	1020	580	510
Tris[2-(2-pyridyl)ethyl]phosphineoxide	0.1	1005	500	560
	0.5	990	485	575
	1.0	990	475	580
Tristyrylphosphineoxide	0.1	1000	545	560
	0.5	985	535	565
	1.0	980	539	570

The samples of plastisols with OPC additives comprising aromatic and heteroaromatic groups are distinguished from materials fireproofed with aliphatic phosphine oxides by higher self-ignition points (Table 2).

The self-ignition points of the samples containing tris[2-(2-pyridyl)ethyl] phosphine oxide and tristyrylphosphine oxide appreciably exceed the surface temperature of these materials. This enables self-extinguishing of fire in them, i.e., termination of combustion of a sample removed from the flame. This fact is supported by a decrease in the time of self-sustained combustion of the above-mentioned materials. The best fire-retarding characteristics were exhibited by tristyrylphosphine oxide, with which the self-sustained combustion time decreased by a factor of 6.5 relative to that for the plastisols free from additives.

A considerable fireproofing effect exerted by tristyrylphosphine oxide on the PVC-based plastisol can be associated with the possibility of interaction between this unsaturated fire retardand and the polyene blocks of decomposed PVC, in particular, by the cross-linking mechanism:



Even minor changes in the formulation of the PVC-based plastics can affect various characteristics of these materials. Hence, we must be certain that mitigation of the fire hazard posed by PVC-based plastisols does not entail deterioration of other properties. We checked this by estimating the operation and technical characteristics of PVC-based plastisols in relation to phosphorus-containing fire retardants, taking advantage of the tensile strength data from [19]. The modulus of elasticity of these formulations increases by 10–20% upon introduction of OPC additions.

Our data suggest that all the tertiary phosphine oxides we tested exert a fire-retarding effect on the plastisols examined by changing the nature of the processes occurring in the condensed phase of the combusting material. Probably, the specific influence of the phosphoryl group on this process consists in binding of HCl evolved in thermal decomposition of PVC, since phosphine oxides are known to form stable adducts with hydrogen halides [17].

At the same time, the fire-retarding effect exhibited by the examined phosphine oxides decreases in the order trioctylphosphine oxide > tris(hydroxymethyl)phosphine oxide ≈ tristyrylphosphine oxide > propenylphosphine oxides ≈ tris[2-(2-pyridyl)ethyl]phosphine oxide > tribenzylphosphine oxide ≥ tripropylphosphine oxide ≈ triethylphosphine oxide. This suggests that the fire-retarding properties of phosphine oxides are more strongly dependent on the structure of the organic radical than on the phosphorus content of their molecule.

CONCLUSIONS

(1) Tertiary phosphine oxides with different structures, containing alkyl, arylalkyl, hetarylalkyl, hy-

droxyalkyl, propenyl, and styryl substitutents are, in principle, suitable as fire retardants for polyvinyl chloride based plastisols.

(2) The fire-retarding properties of the phosphine oxides examined are more strongly dependent on their structure than on the phosphorus content of their molecule.

ACKNOWLEDGMENTS

This study was financially supported by the Russian Foundation for Basic Research (grant no. 05-03-32 859) and Siberian Branch, Russian Academy of Sciences (integration project no. 32).

REFERENCES

1. Vorob'ev, V.A., Andrianov, R.A., and Ushakov, V.A., *Goryuchest' polimernykh stroitel'nykh materialov* (Combustibility of Polymeric Construction Materials), Moscow: Khimiya, 1976.
2. Kodolov, V.I., Goryuchest' i ognestoikost' polimernykh materialov (Combustibility and Fire Resistance of Polymeric Materials), Moscow: Khimiya, 1976.
3. Aseeva, R.M. and Zaikov, G.E, *Gorenie polimernykh materialov* (Combustion of Polymeric Materials), Moscow: Khimiya, 1981.
4. Mukhin, Yu.F., Chernetskii, S.A., and Korol'chenko, A.Ya., *Pozharovzryvobezopasnost'*, 1998, no. 2, pp. 20–28.
5. Gusarova, N.K., Malysheva, S.F., Arbuzova, S.N., and Trofimov, B.A., *Izv. Ross. Akad. Nauk*, 1998, no. 9, pp. 1695–1702.
6. Trofimov, B.A., Arbuzova, S.N., and Gusarova, N.K., *Usp. Khim.*, 1999, vol. 68, no. 3, pp. 240–253.
7. Malysheva, S.F. and Arbuzova, S.N., *Sovremennyi organicheskii sintez* (Modern Organic Synthesis), Moscow: Khimiya, 2003, pp. 160–177.
8. Gusarova, N.K., Malysheva, S.F., Rakhmatullina, T.N., et al., *Zh. Obshch. Khim.*, 1990, vol. 60, no. 4, pp. 828–832.
9. RF Patent 1 680 703.
10. Malysheva, S.F., Garashchenko, Z.M., Arbuzova, S.N., et al., *Zh. Obshch. Khim.*, 1997, vol. 67, no. 11, pp. 1905–1906.
11. Trofimov, B.A., Gusarova, N.K., Malysheva, S.F., et al., *Zh. Obshch. Khim.*, 2005, vol. 75, no. 5, pp. 724–728.
12. Malysheva, S.F., Sukhov, B.G., Gusarova, N.K., et al., *Zh. Obshch. Khim.*, 2004, vol. 74, no. 7, pp. 1182–1186.
13. Sukhov, B.G., Malysheva, S.F., Kuimov, V.A., et al., *Zh. Obshch. Khim.*, 2004, vol. 74, no. 7, pp. 1219–1220.
14. Gusarova, N.K., Trofimov, B.A., Malysheva, S.F., et al., *Zh. Obshch. Khim.*, 1997, vol. 67, no. 1, pp. 70–76.
15. Gusarova, N.K., Sukhov, B.G., Malysheva, S.F., et al., *Zh. Obshch. Khim.*, 2001, vol. 71, no. 2, pp. 349–350.
16. Gusarova, N.K., Sukhov, B.G., Malysheva, S.F., et al., *Zh. Obshch. Khim.*, 2001, vol. 71, no. 5, pp. 768–770.
17. Nifant'ev, E.E., *Khimiya fosfororganicheskikh soedinenii* (Chemistry of Organophosphorus Compounds), Moscow: Mosk. Gos. Univ., 1971.
18. D'yachkov, G.A., Dzhilkibaeva, G.M., and Salikhova, M.F., *Khimiya i fizika polimerov: Sbornik statei* (Chemistry and Physics of Polymers: Coll. of Papers), Alma-Ata, 1984, pp. 127–144.
19. *Praktikum po vysokomolekulyarnym soedineniyam* (Practical Course of Macromolecular Compounds), Kabanov, V.A., Ed., Moscow: Khimiya, 1985, p. 223.

ISSN 1070-4272, Russian Journal of Applied Chemistry, 2008, Vol. 81, No. 2, pp. 310–315. © Pleiades Publishing, Ltd., 2008.
Original Russian Text © S.Ya. Inogamov, M.Yu. Mukhamedzhanova, G.I. Mukhamedov, 2008, published in Zhurnal Prikladnoi Khimii, 2008, Vol. 81, No. 2, pp. 320–326.

MACROMOLECULAR CHEMISTRY AND POLYMERIC MATERIALS

Rheological Properties of Polycomplex Gels of Carboxymethyl Cellulose with Urea-Formaldehyde Oligomers

S. Ya. Inogamov, M. Yu. Mukhamedzhanova, and G. I. Mukhamedov

Tashkent Pharmaceutical Institute, Tashkent, Uzbekistan

Institute of Bioorganic Chemistry, Academy of Sciences of the Republic of Uzbekistan, Tashkent, Uzbekistan

Received October 16, 2007

Abstract—Structural and rheological properties of polycomplex gels of sodium carboxymethyl cellulose (Na-CMC) with urea-formaldehyde oligomers were studied at various component ratios at 298–343 K. The polycomplexes were examined by IR spectroscopy. Mechanical characteristics of solutions of Na-CMC and its complexes with urea-formaldehyde oligomers and the size of structural units of these solutions were determined.

DOI: 10.1134/S1070427208020298

Studies of polymer complexation, including evaluation of the capacity of various water-soluble natural and synthetic polymers to form stable products of cooperative reactions between different polymers and between macromolecules and low-molecular-weight compounds, are of great theoretical and practical interest. Products formed in reactions between polymers and oligomers, known as polycomplexes (PCs) or polycomplex gels (PCGs), form a separate significant group. These products often demonstrate all signs of individual compounds, being characterized by a number of unique properties different from those of the starting components [1]. The topicality of a study of the polymer complexation yielding PCGs is caused by the high importance of such reactions for many natural and industrial processes, including those involving biopolymers, directed polymer modification, and technical use of polycomplexes [1].

Examination of molecular complexes of polymers allows understanding of the contribution of intermolecular interactions to special structure and properties of the complexes. In this relation, polymer–oligomer systems in which self-organization of macromolecules in the course of formation of polycomplexes leads to the formation of nanostructures are of great interest. Furthermore, polymers can be used as matrix carriers for nanoparticles, ready for synthesis of macromolecules on their surface [2, 3].

Study of the mechanism of such a matrix polymerization is important in view of directed synthesis of polymers. In this relation, intermolecular complexes based on Na-CMC and ureaformaldehyde oligomers (UFOs) show promise as models for examination of specific features of the cooperative interaction between various chemically and structurally complementary macromolecules. Such structural features of Na-CMC as the presence of reactive polar functional groups and the high degree of orientation make this rigid-chain polymer suitable for use as a matrix carrier in complexation with UFOs.

Polycomplexes and polycomplex gels find use in the following fields: as flocculants and reagents in the environmental protection practice [4]; as materials for manufacture of separating membranes and biocompatible polymers for medical use [5, 6]; as highly efficient structure-forming agents for dispersed systems and, in particular, soils in agriculture [3]; as hydrogels, for water saving in irrigation [7]; etc. In recent years, PCs and PCGs are more and more widely used in pharmacy, as base materials in preparation of ointments and other gentle drug formulations [8, 9].

Therefore, it is of interest to examine those properties of PCs and PCGs which are caused by specific interactions in the macromolecular matrices, such as mechanical properties of concentrated solutions of

Na-CMC–UFO polycomplexes and polycomplex gels, the behavior of PCs and PCGs under conditions of high shear stress, and the effect of PC and PCG composition on the viscous-flow behavior. Optimal consistency and mechanical characteristics of the matrix should provide good bioavailability of drugs and easy and painless spreading of an ointment on the skin, mucous coats, etc. [10]. Constituents of the polycomplexes and polycomplex gels should be inexpensive commercial polymers of local origin.

In this study, we examined the rheological behavior of concentrated aqueous solutions of Na-CMC–UFO-based PCs and PCGs at various component ratios. Also we monitored the variation of the size of PC and PCG nanoparticles on changing the solution composition and in the course of degradation of the concentrated solutions that form a base of ointments and other gentle drug formulations.

EXPERIMENTAL

In the study, we used purified Na-CMC produced at the Namangan Chemical Plant (degree of substitution 70; degree of polymerization 450). The second component of the polycomplex is a nitrogen-containing polymer formed in a solution of urea and formaldehyde (solution concentration 60–70%). The polycomplexes and polycomplex gels were prepared by mixing 0.1–0.4 aqueous solutions at 1 : 1 or 4 : 1 Na-CMC : UFO ratio [10].

The IR spectra over the range 400–4000 cm^{-1} were recorded on Specord-75IR and UR-20 instruments (Germany). The samples were prepared as KBr pellets, films on KRS-5 windows (prepared by removing water at 22–24°C), and 8–12-μm films.

The rheological properties of concentrated aqueous solutions of the polycomplex gels were examined on a Reotest-2 rotary viscometer with a system of coaxial cylinders. The measurements were carried out at various temperatures over the ranges of shear stress and shear rate of 2–380 Pa and 1.5–130 s^{-1}, respectively. From the rheological data, the viscous volume V^*, or the average size of kinetic units, was determined. This parameter characterizes the flexibility of structural units and their size [11]:

$$V^* = \{2K[E_a R - (\log\eta - \log A_\tau)T]\}/\tau,$$

where K is the Boltzmann constant; R, gas constant; τ, shear stress; T, absolute temperature; A_τ, preexponential factor; and E_a, apparent activation energy (determined from the slope of the $\log\eta = f(T)$ plot).

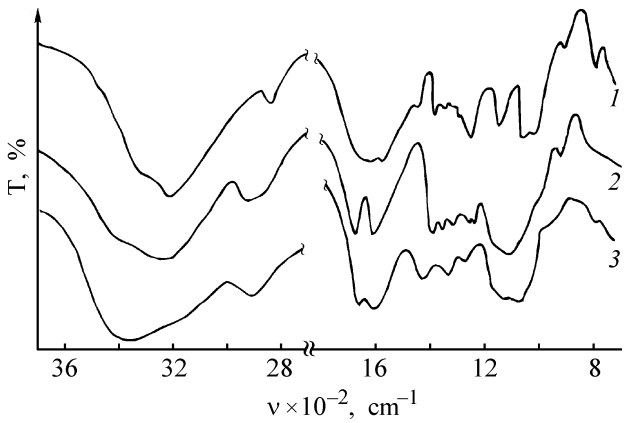


Fig. 1. IR spectra of (*1*) UFO, (*2*) Na-CMC, and (*3*) Na-CMC–UFO polycomplex gel. (T) Transmission and (ν) wavenumber.

The preexponential factor A_τ is insignificant and can be neglected.

Polymer–polymer complexes are, in fact, new polymeric materials, even though they are obtained mostly from common polymers by simply mixing solutions of components in a common solvent, i.e., by the method that can be regarded as polymer modification [12]. It is obvious that the polymer complexation alters the rheological characteristics of the resulting polymer solutions, since it is the rheological behavior that is frequently the most sensitive to changes in the polymer structure.

A detailed examination of the rheological characteristics of the concentrated systems is required to understand the interplay between the structure and properties of polycomplexes. As is known, Na-CMC is a derivative of the natural polysaccharide, cellulose. Its properties are controlled by the features of the structure of cellulose macromolecules, which are highly lyophilic rigid polymer chains. Key factors controlling the viscosity characteristics of Na-CMC are the degree of polymerization, solution concentration, temperature, solvent, and solution pH.

Note that Na-CMC is an anionic cellulose derivative. When mixed with an UFO solution, it forms polycomplex gels by virtue of electrostatic interaction, as demonstrated by the IR spectra reported in [3, 13, 14] (Fig. 1). The IR spectrum of UFO shows the bands of NH^+ and NH_2^+ at 1290 and 1580–1600 cm^{-1}, and that of Na-CMC, the COO^- at 1590–1620 and 1410 cm^{-1}. Therefore, these compounds are polyelectrolytes. Mixing of aqueous solutions of Na-CMC and UFO yields polycomplex gels stabilized by the ionic bonds between the carboxy groups of Na-CMC and amino groups of UFO (Fig. 1, spectrum *3*) [3].

Table 1. Physicochemical characteristics of Na-CMC–UFO polycomplex gels

Composition	Appearance	pH (1 : 10) (normally 6.5–7.6)	Thermal resistance		Film formation time, min	Shelf life, years
			heating (40 ± 0.2°C)	cooling (–10 ± 0.2°C)		
Na-CMC	Yellowish mass with a characteristic odor	7.2	Unstable	Unstable	8–10	0.5
Na-CMC–UFO	Yellow-white mass with a characteristic odor	6.8	Stable	Stable	5–8	2.25
Na-CMC–UFO–glycerol	The same	7.6	″	″	6–8	2.5

Physicochemical and performance characteristics of the polycomplex gels are summarized in Table 1.

Experimental results show (Table 1) that the Na-CMC–UFO polycomplex gels remain homogeneous and stable in prolonged storage. Such characteristics as the color, odor, appearance, pH, and aggregative stability at elevated and lower temperatures meet the requirements of State Pharmacopoeia XI [15].

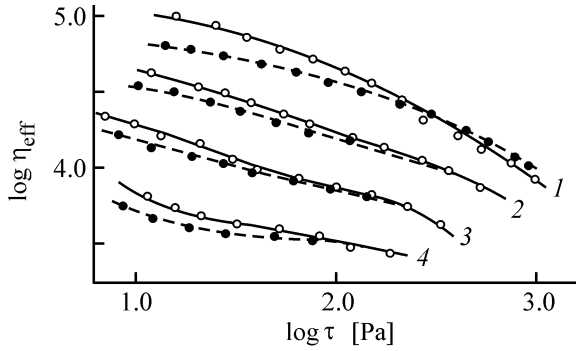


Fig. 2. Flow curves of aqueous Na-CMC solutions at various temperatures. (η_{eff}) Effective viscosity and (τ) shear stress (Pa); the same for Fig. 4. *T*, K: (*1*) 298, (*2*) 313, (*3*) 328, and (*4*) 343; the same for Fig. 4. *Dotted lines* show the viscosity hysteresis; the same for Fig. 4.

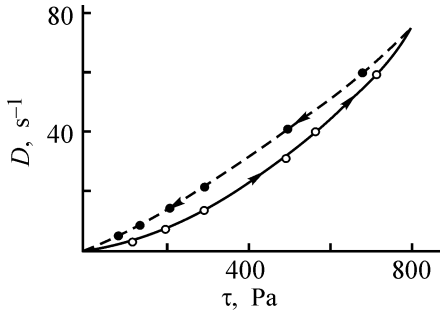


Fig. 3. Rheogram of a concentrated Na-CMC solution. (*D*) Shear rate and (τ) shear stress.

In this study, we examined the rheological behavior of polymer solutions. Experimental data were plotted as log η vs. log τ, where η is the shear viscosity and τ, shear stress. The flow curves were obtained at various temperatures ranging from 298 to 343 K and shear stresses of up to 380 Pa for aqueous solutions of Na-CMC and its polycomplex gels with urea-formaldehyde oligomers at 4 : 1 and 1 : 1 component ratios.

The mechanical properties of Na-CMC solutions were examined on a rotary viscometer initially with increasing and then with decreasing rotary speed. The resulting rheograms are shown in Figs. 2 and 3. The NaCMC solutions are thixotropic, as demonstrated by the clearly pronounced non-Newtonian type of viscous flow. It follows from the modern concepts of solutions of cellulose derivatives in various solvents that these substances form true solutions, in which the macromolecules are kinetically free. However, if cellulose ethers are inhomogeneous with respect to the degree of substitution, particular fractions of Na-CMC can be poorly soluble. The reason is that the initial cellulose consists of both amorphous and crystalline domains. The internal highly crystalline domains are less reactive in the course of preparation of alkali cellulose and its subsequent etherification [16]. As a result, the distribution of substituents along the macrochains appears to be nonuniform. Therefore, the solution contains a certain amount of dispersed Na-CMC, i.e., of aggregates of the macromolecules associated in the same manner as in the crystalline domains of the initial cellulose. As is known [16], such crystallites behave as gelation centers, i.e., they attract a relatively large amount of dissolved Na-CMC and form a 3*D* lattice stabilized by electrostatic and van der Waals interactions.

It is well known that the thixotropy of Na-CMC solutions is a result of formation of the gelation cen-

ters [17]. THe shear stress initiates partial disintegration of the gelation centers and their aggregates with the macromolecules. The effective viscosity decreases in the course of time at a constant shear stress. In this case, the structural degradation of the thixotropic solution takes a finite time. After the removal of shear stress, the thixotropic structure is formed again. When the solution is allowed to stand, the gelation centers aggregate, and the apparent viscosity of the system increases. It was demonstrated in [16] that, depending on the structure of a system in hand, the reversion time can vary from several seconds to several days. Since the thixotropic effect appeared to be time-dependent, all the experimental conditions were standardized. The rheograms presented in Figs. 2 and 3 show a clearly pronounced hysteresis, also suggesting a thixotropy. Concentrated Na-CMC solutions, like those of many other macromolecular compounds, are non-Newtonian fluids.

Complexation of the Na-CMC macromolecules with urea-formaldehyde oligomers strongly alters the structure of the polymer matrix, affecting the rheological behavior of the aqueous solutions (Figs. 4a, 4b). On passing to the equiconcentrated PCG solutions, the viscosity and critical shear stress considerably decrease, the effect being more pronounced at 1 : 1 Na-CMC/UFO ratio, compared to the 4 : 1 ratio. These systems behave essentially like ordinary pseudoplastics. The investigated interpolymer complexes were obtained by mixing the interacting components in a common solvent (water).

Mixing of Na-CMC (a rigid-chain polymer) with the oligomer yields highly oriented polymer complexes, in which the macromolecular matrix is responsible for the organization of the associating systems and their complementarity. An important characteristic of the matrix–oligomer systems is their self-organization ability [18, 19], which is manifested in a nonuniform distribution of the oligomer chains between the matrices and also in the tendency of the short chains to be arranged along the long macromolecular chain of the matrix so that to provide a maximally dense packing. As a result, some parts of the matrices will be completely filled in the limiting case. Most likely, this effect is responsible for the difference in rheological behavior between the 1 : 1 and 4 : 1 systems. Thus, in the 4 : 1 systems, the excessive content of Na-CMC causes a partial (very weak) preservation of the thixotropic effect and a slight increase in the viscosity as compared to the 1 : 1 systems. Our results show that polycomplex gels have acquired some extra properties relative to the constituent polymers (Figs. 4a, 4b).

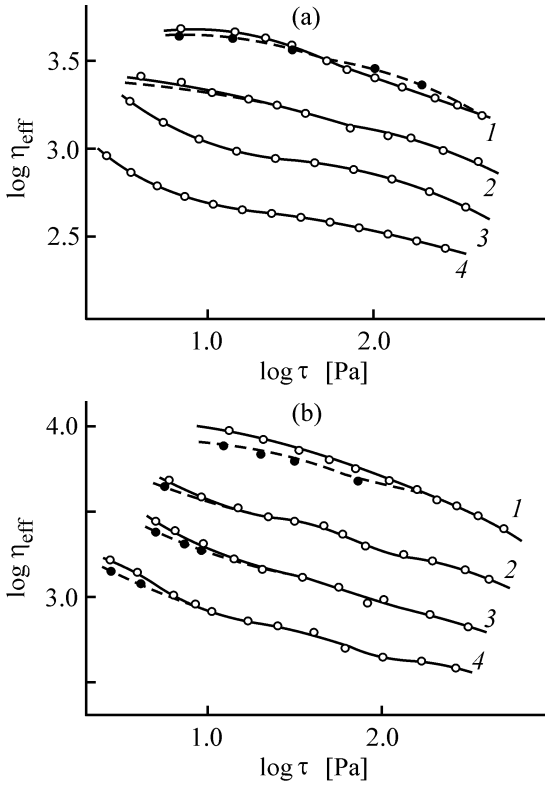


Fig. 4. Flow curves of concentrated Na-CMC–UFO polycomplex gels at various temperatures. Na-CMC : UFO ratio: (a) 1 : 1 and (b) 4 : 1.

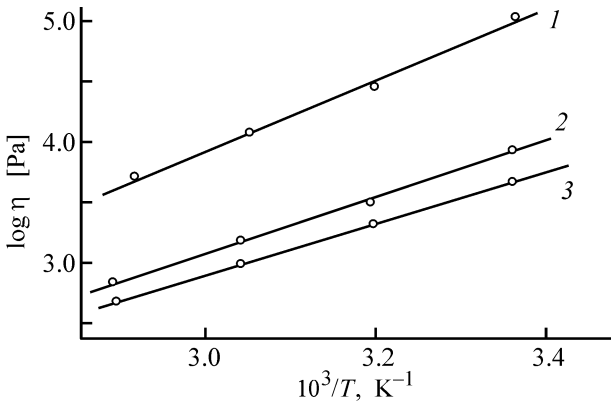


Fig. 5. log η vs. 1/*T* plot for concentrated solutions of (*1*) Na-CMC and (*2*) 4 : 1 Na-CMC–UFO and (*3*) 1 : 1 Na-CMC–UFO polycomplex gels. (η) Viscosity and (*T*) temperature.

Thus, in the PCGs studied, the thixotropic properties are virtually degenerated with a simultaneous decrease in the viscosity characteristics. The Arrhenius–Frenkel plot of the viscosity in the range 298–343 K, $\eta = Ae^{\Delta E_a/R}$, is shown in Fig. 5 for Na-CMC and PCG solutions. The Na-CMC solutions are more structured, and demonstrate higher viscosity char-

Table 2. Viscous volume V^* of Na-CMC and polycomplex gel solutions, as influenced by the temperature and shear stress

τ, Pa	T, K	Na-CMC		PCG (1 : 1)		PCG (4 : 1)	
		$V^* \times 10^{23}$, m^3	$D \times 10^9$	$V^* \times 10^{23}$, m^3	$D \times 10^9$	$V^* \times 10^{23}$, m^3	$D \times 10^9$
10	298	927.2	210	1271	233.4	1340.6	237.5
	313	971.1	213	1328	237.0	1418.9	242
	328	1013.0	216.4	1399	240.9	1474.3	245
	343	1066.6	220.1	1464	245.0	1548.1	249
158.5	298	98.3	99.4	84.1	94.4	89.1	96.3
	313	102.4	100.8	87.4	95.6	93.4	97.8
	328	106.2	102.0	90.9	96.9	96.6	99.2
	343	110.5	103.4	95.2	98.4	98.5	99.5

acteristics and critical shear stress. In these solutions, the activation energy of viscous flow, characterizing the intermolecular interaction between macromolecules and, indirectly, the strength of the polymer structure in solution, was estimated to be ΔE_a = 55.7 kJ mol^{-1}. For the 1 : 1 and 4 : 1 PCGs, the activation energies are 43.13 and 45.96 kJ mol^{-1}. Complexation of Na-CMC containing the carboxy, hydroxy, and other functional groups with UFO yields interpolymer associating systems, in which the intensity of intermolecular interaction is considerably lower than in the straight Na-CMC solutions. As a result, the structural strength and viscosity characteristics decrease. The polycomplex structure, directly related to the chemical nature of the polymer constituents, is responsible for the degeneration of the thixotropic properties in PCGs (Na-CMC macromolecules and molecular associates are shielded on the matrix surface by the UFO arrangements).

The interaction between chemically and structurally complementary macromolecules is cooperative in its nature. In this case, a linear (unidimensional) sequence of similar interchain bonds is formed, which is typical of the simplest cooperative systems. Evidently, a cooperative system can be built through formation of two or more types of bonds, e.g., ionic and hydrogen bonds. Because of the cooperative nature of bonding between different polymer chains in the complex, the formation and cleavage of the bonds occur under a definite external impact, e.g., under deformation stress. This is due to the fact that decomposition or formation of an interpolymer complex requires a simultaneous cleavage or formation of a great number of bonds, even though weak. In polymer–polymer and polymer–oligomer interactions, there typically occur equilibria of two kinds at both macromolecular and intracomplex levels, which causes a time-dependent character of the formation of polycomplexes and slow rearrangement of the intra- and supramolecular structures [20]. A high shear stress initiates fundamental changes in the initial PCG structure. To each stress corresponds a definite initial structure of the material, and the elementary event of flow consists in a chain segment hopping from a new initial state to an activated state. It is seen from the flow curves (Figs. 2–4) that the high stress significantly alters the structure and viscous properties of the polycomplex systems. From the rheological data, we estimated the viscous volume V^* [11] for Na-CMC and Na-CMC–UFO solutions (Table 2).

In the Na-CMC solutions, V^* (measure of the size and flexibility of structural units) and the lateral size of structural units D are slightly smaller than those in the PCG solutions, which gives additional evidence in favor of the complexation of the anionic derivative of cellulose with cationic MFOs. Table 2 shows that V^* increases with temperature in both Na-CMC and PCG solutions, which is due to disentangling of the macromolecules. This facilitates intermolecular interaction, resulting in an increase in the size of PCG associates.

As the shear stress increases, supramolecular structures and, therefore, PCG associates disintegrate. At a low shear stress (<10 Pa), the size of PCG associates exceeds that of Na-CMC associates, and the reverse is observed at a higher shear stress of up to 158.8 Pa, which suggest that, under high shear stress, not only PCG associates, but also the polycomplexes themselves disintegrate.

Finally, complexation of Na-CMC with synthetic oligomers allows control over the size and properties

of polymeric associates. This opens up new ways to rational use of Na-CMC, and the complexation itself can be regarded as modification and size control methods for this common polymer. Examination of molecular complexes of natural polymers allows understanding of the contribution of intermolecular interactions to the specific structure and properties of the complexes.

CONCLUSIONS

(1) Aqueous solutions of sodium carboxymethyl cellulose are thixotropic systems. Introduction of urea-formaldehyde oligomers into Na-CMC solutions results in the degeneration of the thixotropic effect.

(2) Aqueous solutions of polycomplex gels demonstrate a considerably lower structural stability as compared to Na-CMC solutions, which is due to the weaker intermolecular interactions in the polymer–oligomer complex.

(3) The structural units in the polycomplex gels are considerably larger than those in NaCMC solutions. At a high shear stress, simultaneous degradation of the polycomplex and polycomplex gel takes place through breakdown of the intermolecular associates.

REFERENCES

1. Kabanov, V.A., Zezin, A.B., Kasatkin, V.A., et al., *Usp. Khim.*, 1991, vol. 60, no. 2, pp. 595–606.
2. Kabanov, V.A. and Papisov, I.M., *Vysokomol. Soedin., Ser. A*, 1979, vol. 21, no. 2, pp. 243–281.
3. Mukhamedov, G.I., Interpolymer Complexes Based on Amine-containing Urea-Formaldehyde Oligomers and Polymers: Properties and Applications, *Doctoral Dissertation*, Moscow, 1991.
4. Zezin, A.B., El'tsefon, B.S., Rudman, A.R., et al., *Khim.-Farm. Zh.*, 1987, no. 7, pp. 788–801.
5. Kalyuzhnaya, R.N., Rudman, A.R., Vengerova, N.A., et al., *Vysokomol. Soedin., Ser. A*, 1975, vol. 17, no. 12, pp. 2786–2792.
6. Zheleznova, I.V., Rudman, A.R., Kalyuzhnaya, R.I., et al., *Khim.-Farm. Zh.*, 1988, no. 2, pp. 227–231.
7. Mukhamedov, G.I. and Akhmedzhanov, G., *Sel'sk. Khoz. Uzbek.*, 1987, no. 5, pp. 19–21.
8. Kemenova, V.A., Mustafin, R.I., Aleksina, K.V., et al., *Farmatsiya*, 1990, no. 3, pp. 80–88.
9. Inogamov, S.Ya., *Trudy Mezhdunarodnoi nauchnoi konferentsii "Khimiya i primenenie prirodnykh i sinteticheskikh biologicheski aktivnykh soedinenii" (Proc. Int. Scientific Conf.* "Chemistry and Application of Natural and Synthetic Bioactive Compounds"), Almaty, 2004, pp. 411–415.
10. Tentsova, A.I. and Gretskii, V.M., *Sovremennye aspekty issledovaniya i proizvodstva mazei* (Modern Problems of Ointment Research and Production), Moscow: Meditsina, 1980.
11. Kalantarova, T.D., Structural and Thermodynamic Characteristics of Polymer Blends Based on Polyvinylpyrrolidone and Methyl Cellulose, *Cand. Sci. Dissertation*, Tashkent, 1997.
12. Bekturov, E.A., Bimendina, L.A., and Mamytbekov, K.G., *Kompleksy vodorastvorimykh polimerov i gidrogelei* (Complexes of Water-Soluble Polymers and Hydrogels), Almaty: NITs, 2002.
13. Inogamov, S.Ya., Structure and Properties of Interpolymer Complexes Based on Carboxymethyl Cellulose and Urea–Formaldehyde Oligomers, *Cand. Sci. Dissertation*, Tashkent, 1991.
14. Inogamov, S.Ya., *Khim. Khim. Tekhnol.*, 2005, no. 2, pp. 56–60.
15. *Gosudarstvennaya Farmakopeya SSSR XI* (USSR State Pharmacopoeia XI), Moscow: Meditsina, 1987, issues 1, 2.
16. Petropavlovskii, G.A., *Gidrofil'nye i chastichno zameshchennye efiry tsellulozy i ikh modifikatsiya putem khimicheskogo sshivaniya* (Hydrophilic and Partly Substituted Cellulose Ethers and Esters and Their Modification by Chemical Cross-Linking), Leningrad: Nauka, 1988.
17. Mukhamedzhanov, M.Yu., Shirshova, N.Yu., Faizieva, R., et al., *Materialy Mezhdunarodnoi konferentsii "Tekstil'-2002"* (Proc. Int. Conf. "Textile-2002"), p. 126.
18. Papisov, I.M., Baranovskii, V.Yu., and Kabanov, V.A., *Vysokomol. Soedin., Ser. A*, 1975, vol. 17, pp. 2104–2111.
19. Birshtein, T.M., El'yashevich, A.M., and Morgenshtern, L.A., *Vysokomol. Soedin., Ser. B*, 1972, vol. 14, pp. 487–490.
20. Antipina, A.D., Baranovskii, V.Yu., Papisov, I.M., and Kabanov, I.A., *Vysokomol. Soedin., Ser. A*, 1972, vol. 14, pp. 941–949.

ISSN 1070-4272, Russian Journal of Applied Chemistry, 2008, Vol. 81, No. 2, pp. 316–319. © Pleiades Publishing, Ltd., 2008.
Original Russian Text © N.E. Kochkina, S.S. Ryabinin, V.A. Padokhin, 2008, published in Zhurnal Prikladnoi Khimii, 2008, Vol. 81, No. 2, pp. 327–331.

MACROMOLECULAR CHEMISTRY AND POLYMERIC MATERIALS

Rheological Properties of Colloid Solutions of Starch, Produced by the Mechanothermal Method

N. E. Kochkina, S. S. Ryabinin, and V. A. Padokhin

Institute of Solution Chemistry, Russian Academy of Sciences, Ivanovo, Russia

Received July 9, 2007

Abstract—Rheological method was used to study structural-mechanical properties of a solution of starch gelatinized in a two-stage rotary-pulsatory apparatus with a combined operation principle.

DOI: 10.1134/S1070427208020304

Starch is a natural annually replenishable low-cost biopolymer whose physicochemical properties can be easily modified to satisfy requirements of particular industries. Recently, it has been finding steadily increasing use in techniques for synthesis of new biodegradable materials, hybrid nanobiocomposites, and "smart" biopolymeric systems, e.g., electrorheological fluids. Synthesis of liquid-phase materials based on natural starch necessarily involves a prolonged and energy-intensive process of gelatinization of biopolymer grains. The physical treatments conventionally used for starch gelatinization (heating and pressurization) fail to provide the prescribed degree of disintegration of the crystal structure formed by amylopectin and amylose in a starch grain. Therefore, chemical compounds, environmentally hazardous splitters, are frequently additionally used when transferring starch polysaccharides into solution.

In this communication, a new alternative ecologically safe energy- and resource-saving way to obtain jellies and colloid starch solutions is suggested. The method consists in that starch suspensions are treated in a two-stage rotary-pulsatory apparatus (RPA) with a combined operation principle [1]. In the first RPA stage, the fluid flow moving along radial channels of the stator is interrupted by the rotating actuators of the rotor. This gives rise to flow pulsations at a frequency of 5 Hz. In the second stage, the fluid flow us subjected to the action of periodically changing shear deformation, whose rate gradient varies within the range $(0.5–5) \times 10^4$ s^{-1}. In the operation of the installation, quite a number of physical phenomena provoking release of a large amount of heat occur in the medium being treated. The combination of the mechanical and thermal treatments of starch dispersions in RPA provides a high degree of gelatinization of biopolymer grains.

At the same time, it is necessary to take into account that mechanical deformations of polymeric, including polysaccharide, solutions can initiate destruction and synthesis of macromolecules, and association and disintegration of structural formations [2, 4]. As a result, the structure and properties of polymer solutions are strongly changed, which is reflected in the structural-mechanical characteristics of these systems.

The aim of this study was to examine rheological properties of colloid solutions of starch, produced by mechanical-thermal treatment of its aqueous dispersions in RPA.

EXPERIMENTAL

As object of study served cornstarch [GOST (State Standard) 7697–82)] with a characteristic viscosity in water of 1.03 dl g^{-1}. To obtain colloid solutions of starch, its aqueous suspensions were heated to 90°C in two ways: on a water bath and in an RPA of original design at a rotor rotation rate of 4000 rpm [rate gradient of shear deformations $(4–4.5) \times 10^4$ s^{-1}]. The content of starch in the systems studied was varied from 3 to 6%.

The rheological studies were carried out on a Reotest-2 rotary viscometer with a set of coaxial cylinders. The shear rate was varied from 1.5 to 1312 s^{-1}. The temperature at which the viscosity was measured was in the range 30–70°C. The measure-

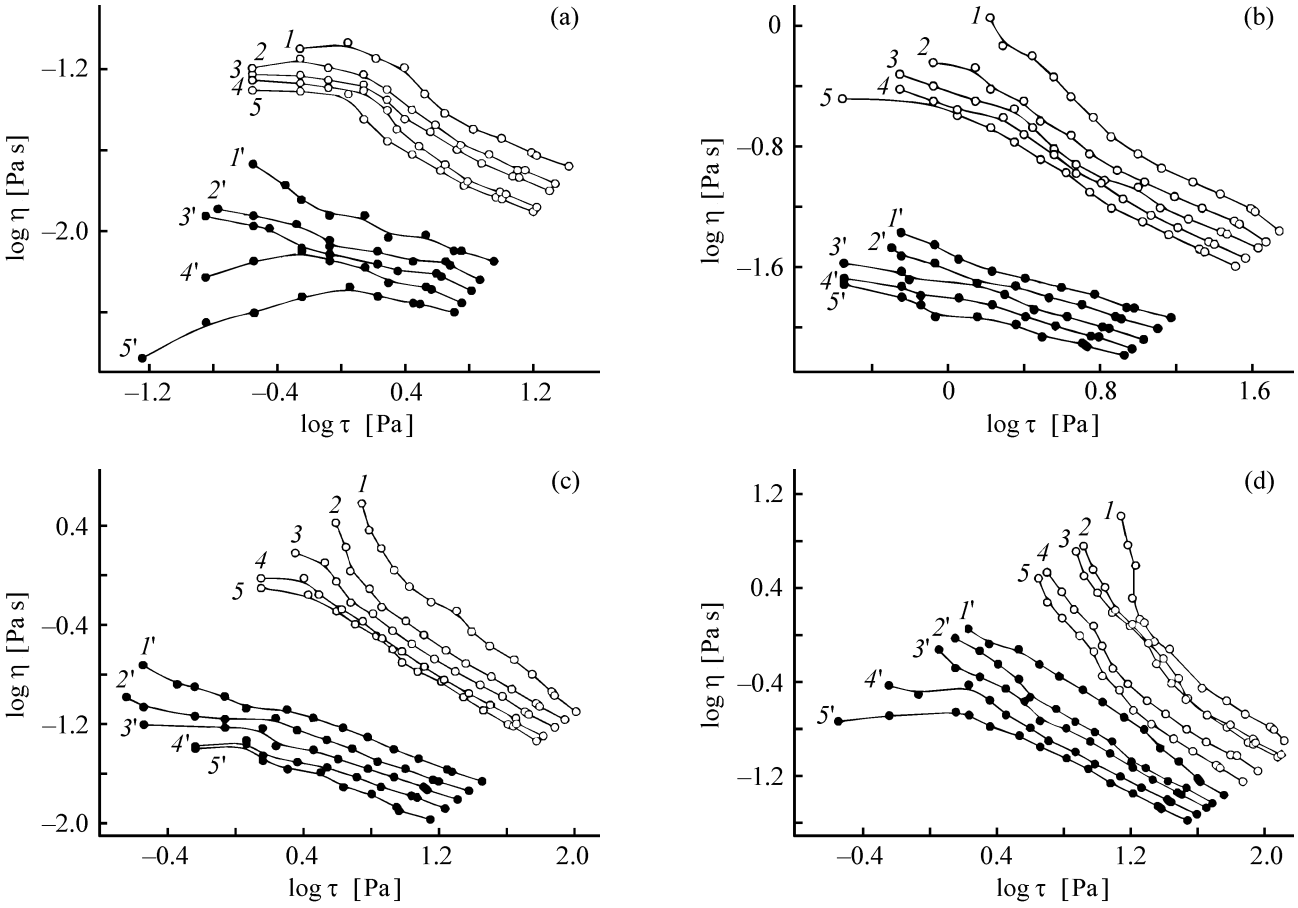


Fig. 1. Viscosity η plotted against the shear stress τ in log–log coordinates for colloid starch solutions produced by (*1*–*5*) thermal and (*1*'–*5*') mechanothermal methods. Temperature of viscosity measurements (°C): (*1*, *1*') 30, (*2*, *2*') 40, (*3*, *3*') 50, (*4*, *4*') 60, and (*5*, *5*') 70. Starch content of a solution (wt %): (a) 3, (b) 4, (c) 5, and (d) 6.

ment accuracy was ±3% according to the ratings of the viscometer.

The relative viscosity was measured at 293 K with a VPZh-2 capillary Ostwald viscometer with a capillary diameter of 1.2 mm. The rms viscosity measurement error was ±0.3%. Gelatinized starch systems were examined with a Biolam microscope.

The resulting values of the shear stress and viscosity were used to plot flow curves of gelatinized starch systems (Fig. 1). The rheograms of samples prepared by the conventional method confirm the known fact of a non-Newtonian flow of colloid starch solutions. A similar behavior in deformation is also characteristic of solutions of the biopolymer gelatinized in RPA. For both sets of the samples studied, the viscosity increases with the concentration of starch in the system.

A distinctive feature of the rheological properties of starch solutions obtained in RPA is that the shear stress and effective viscosity are low. In addition, these solutions with a starch content of 3% behave at high temperatures as dilatant fluids for which the viscosity characteristically increases with the shear stress.

The dilatant properties of colloid systems are attributed to presence in their structure of aggregates with weak interparticle interactions [5]. Aggregates of this kind can easily disintegrate to separate particles, which become closer as the shear rate increases, with the number of contacts between these particles growing to give a network of bonds that is stronger than the initial network. Such an enhancement of interparticle interactions in a colloid solution or jelly occurs to a certain limit, above which there already are no conditions for structural rearrangements. Therefore, the viscosity of colloid systems starts to decrease as the shear deformation rate increases further. It should be noted that the structural rearrangement in a colloid solution or jelly occurs markedly easier at a high temperature of rheological measurements.

Rheological parameters of the starch solutions studied (viscosity measurement temperature 30°C)

Starch content, wt %	Gelatinization method	Viscosity, Pa s		Dynamic yield point P_{k2}, Pa
		$\eta_{1.5}$	η_{1312}	
3	Thermal	–	0.020	1.1
	Mechanothermal	–	0.007	0.3
4	Thermal	1.14	0.040	19.2
	Mechanothermal	–	0.010	0.7
5	Thermal	3.79	0.070	35.8
	Mechanothermal	0.19	0.020	3.6
6	Thermal	10.24	0.100	52.0
	Mechanothermal	1.13	0.040	16.4

The conventional heating of starch suspensions to 90°C leads to formation of highly structured colloid systems in which the dispersed phase is a mixture of swollen grains, fragments of disintegrated grains, and retrograded starch [6]. A combined mechanical and thermal treatment presumably makes higher the degree of disintegration of polysaccharide aggregates of gelatinized starch. The resulting colloid solution of starch is a highly dispersed system with weak interparticle interactions. Under the conditions providing easy structural rearrangements (high temperatures and low biopolymer concentrations), a system of this kind behaves as a dilatant fluid.

The degree of structuring and strength of interparticle interactions in the samples under study can be evaluated using the rheological parameters listed in the table. It is believed that a colloid solution or jelly is the stronger, the larger the difference between the viscosity of an intact structure (η_0) and that of the structure disintegrated to the maximum extent (η_m) and the higher the dynamic yield point P_{k2} corresponding to overcoming of the elasticity of the structure and to the onset of its plastic flow [7, 8]. Because the method for evaluating the rheological properties on the Reotest-2 instrument made it possible to obtain only a limited part of the flow curve of the samples studied, the table lists the effective viscosities at the minimum and maximum shear rates $\eta_{1.5}$ and η_{1312} possible for the viscometer.

It can be seen that, as the concentration of starch in the systems under study increases, the values of the parameters listed in the table steadily grow. On

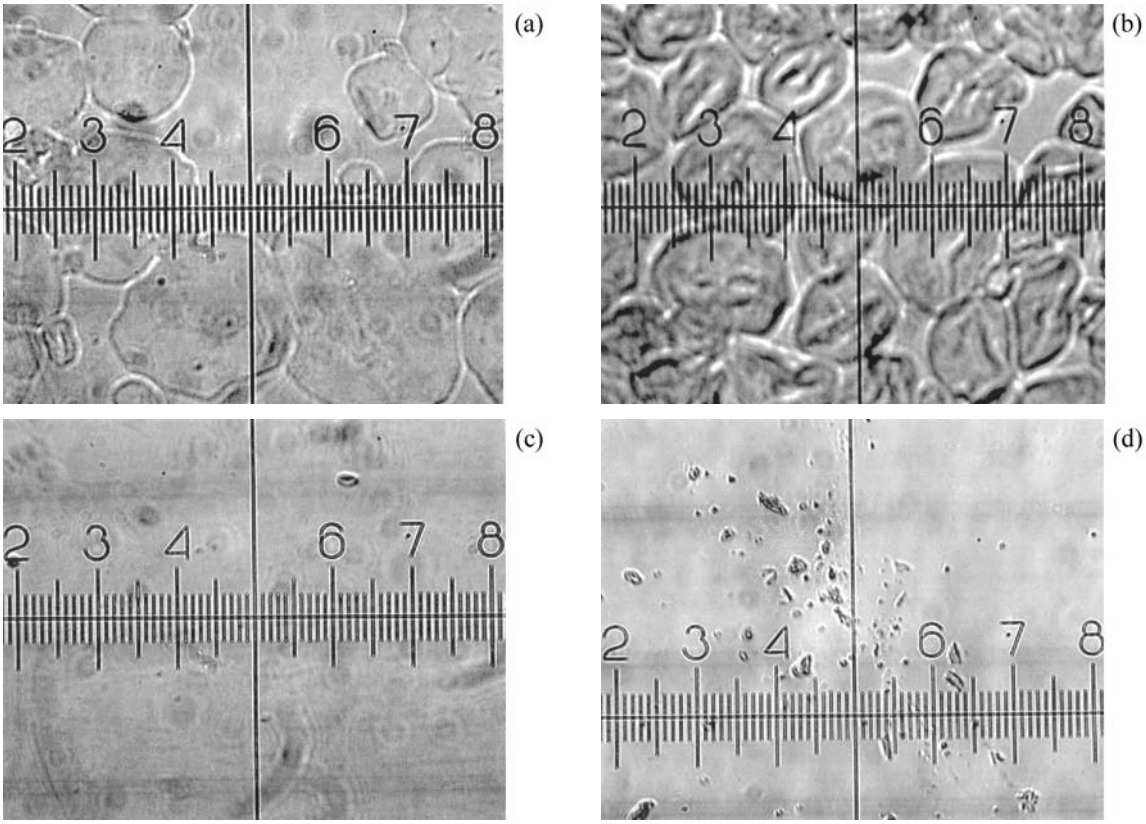


Fig. 2. Micrographs of colloid starch solutions produced by (a, b) thermal and (c, d) mechanothermal methods. Microscope scale division value 2.8 μm. Starch content of the solution (wt %): (a, c) 3 and (b, d) 6.

the whole, analysis of these data confirms the conclusion about the poor strength of the network of bonds formed by particles of starch gelatinized by the mechanothermal method. The absence of values of $\eta_{1.5}$ for 3 and 4% colloid starch solutions obtained in the RPA is an additional evidence in favor of the low degree of their structuring.

A possible reason why the structure of gelatinized starch systems becomes weaker on passing from the conventional to mechanothermal method of their synthesis is destruction of the polysaccharides of the biopolymer. Analysis of this process assumes that the degree of polymerization of macromolecules of starch subjected to gelatinization by the methods mentioned should be recorded. As is known, this is an extremely difficult experimental task. However, it has been confirmed in a number of scientific publications that determining the degree of starch destruction from changes in the viscosity of solutions containing no more than 0.5 wt % biopolymer is justified [9, 10]. This approach is based on the fact that the probability of interaction between polymer macromolecules in dilute solutions is low and, therefore, there are no supramolecular formations. Consequently, the viscosity of such systems is determined by the molecular mass of the polymer and is independent of the solution structure.

It was found that the relative viscosity of the 0.5 wt % starch solution produced by the conventional thermal method is 22, and that of a solution obtained in RPA is 17.3. These results can be regarded as evidence that, with RPA, heating of a biopolymer suspension to 90°C is accompanied by its mechanically initiated destruction, which results in that associates of macromolecules, forming the supramolecular structure of the colloid starch solution, decrease in size.

The conclusion that particles of starch gelatinized in RPA are highly dispersed is also confirmed by micrographs of colloid solutions containing 3 and 6 wt % biopolymer (Fig. 2). Swollen starch grains are clearly seen in the structure of systems obtained by heating starch suspensions on a water bath. Gelatinization of biopolymer grains by mechanochemical treatment leads to another situation, specifically, to a substantial decrease in the average size of particles of the dispersed phase. Grains of starch disintegrate upon its gelatinization in RPA in such a way that the texture of a colloid solution, observed in the light field of the microscope, virtually completely disappears. To conclude, it is important to note that the weak structuring and considerable dispersity of colloid starch solutions are necessary for obtaining functional composites with high adhesive and film-forming capacity.

CONCLUSIONS

(1) It is advisable to obtain colloid starch solutions in a rotary cavitation generator without additional supply of heat.

(2) Integrated action of mechanical deformations and heat, created in the rotary cavitation generator, provides deep disintegration of starch grains. This leads to formation of colloid biopolymer solutions with low degree of structuring.

ACKNOWLEDGMENTS

The study was financially supported by the Russian Foundation for Basic Research (project no. 06-08-01436-a).

REFERENCES

1. Ryabinin, S.S., Kochkina, N.E., Padokhin, V.A., and Anikin Ya.A., Abstracts of Papers, *III vserossiiskaya mezhdunarodnaya nauchnaya konferentsiya "Fiziko-khimiya protsessov pererabotki polimerov"* (III All-Russia Int. Sci. Conf. "Physical Chemistry of Polymer Processing"), Ivanovo, 2006, p. 82.
2. Vshivkov, S.A., Kulichikhin, S.G., and Rusinova, E.V., *Usp. Khim.*, 1998, vol. 67, no. 3, pp. 261–273.
3. Alekseeva, O.V., Rozhkova, O.V., Prusov, A.N., et al., *Zh. Prikl. Khim.*, 2004, vol. 77, no. 3, pp. 483–486.
4. Lipatova, I.M., Losev, N.V., and Yusova, A.A., *Zh. Prikl. Khim.*, 2006, vol. 79, no. 9, pp. 1548–1553.
5. Fridrikhsberg, D.A., *Kurs kolloidnoi khimii* (A Course of Colloid Chemistry), Leningrad: Khimiya, 1984.
6. Lund, D., *CRC Crit. Rev. Food Sci. Nutrition*, 1984, vol. 20, no. 4, pp. 249–273.
7. Kruglitskii, N.N., Gorovenko, G.G., and Malyushevskii, P.P., *Fiziko-khimicheskaya mekhanika dispersnykh sistem v sil'nykh impul'snykh polyakh* (Physicochemical Mechanics of Dispersed Systems in Strong Pulsed Fields), Kiev: Naukova Dumka, 1983.
8. Voyutsii, S.S., *Kurs kolloidnoi khimii* (A Course of Colloid Chemistry), Moscow: Khimiya, 1975.
9. Tager, A.A., *Fizikokhimiya polimerov* (Physical Chemistry of Polymers), Moscow: Khimiya, 1968.
10. Kadykova, E.L., Gubina, S.M., and Mel'nikov, B.N., *Izv. Vyssh. Uchebn. Zaved., Khim. Khim. Tekhnol.*, 1991, no. 11, pp. 88–93.

ISSN 1070-4272, Russian Journal of Applied Chemistry, 2008, Vol. 81, No. 2, pp. 320–322. © Pleiades Publishing, Ltd., 2008.
Original Russian Text © L.S. Postnikov, I.V. Korovina, A.D. Kagarlitskii, L.A. Krichevskii, 2008, published in Zhurnal Prikladnoi Khimii, 2008, Vol. 81, No. 2, pp. 332–334.

BRIEF COMMUNICATIONS

Oxidative Ammonolysis of 2-Methylquinoxaline on Vanadium–Titanium Oxide Catalyst

L. S. Postnikov, I. V. Korovina, A. D. Kagarlitskii, and L. A. Krichevskii

Fitokhimiya Research and Production Center, Joint-Stock Company, Karaganda, Kazakhstan

Received July 21, 2007

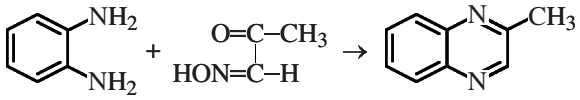
Abstract—The behavior of 2-methylquinoxaline in the course of oxidative ammonolysis on V–Ti oxide catalyst in a wide range of conditions was studied, and this reaction was examined as a route to 2-quinoxalinecarbonitrile.

DOI: 10.1134/S1070427208020316

Quinoxalines, or benzopyrazines, form an important group of heterocycles. They exhibit a broad spectrum of biological activity, including antibacterial, antitumor, fungicidal, and antiviral activity [1–3].

Interest in oxidative transformations of quinoxalines is due to the fact that the oxidation products can be used as starting compounds for preparing various drugs by more efficient procedures than multistep methods of classical organic chemistry.

As investigation object we chose readily accessible 2-methylquinoxaline synthesized by condensation of *o*-phenylenediamine with α-isonitrosoacetone [4]:



The majority of studies devoted to oxidation of quinoxalines are concerned with transformations of substituents at both benzene and pyrazine rings. Some papers deal with various procedures for preparing quinoxaline *N*-oxides showing pronounced biological activity. There are also papers reporting on oxidation of quinoxalines with the aim to obtain pyrazine derivatives, in particular, pyrazinecarboxylic acid [3, 4].

It seemed interesting to perform oxidative ammonolysis of 2-methylquinoxaline as a possible route to 2-quinoxalinecarbonitrile, a synthetic precursor of new compounds of the quinoxaline series. As catalyst we used the system $V_2O_5 : TiO_2 = 1 : 8$ [5]. The starting compound was fed as a solution in aqueous ammonia.

The process parameters were as follows: temperature 320–460°C; amounts of ammonia and water 2.5–12.5 and 35–48 mol per mole of 2-methylquinoxaline, respectively; contact time 0.3–2.0 s.

The reaction products were trapped in an airlift absorber filled with chloroform. The products were separated by column chromatography on silica gel, eluent hexane–chloroform, 6 : 1.

Gas-chromatographic and spectral studies showed that the catalyzates from oxidative ammonolysis of 2-methylquinoxaline contained unchanged starting compound, 2-quinoxalinocarbonitrile, quinoxaline,

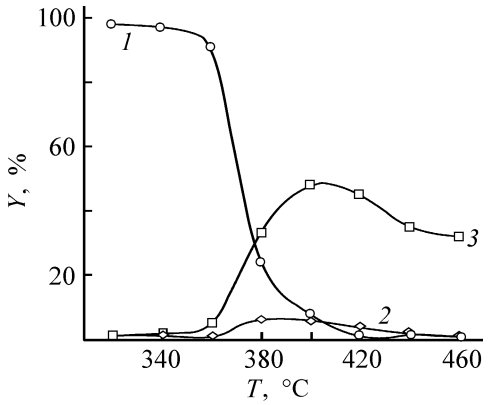


Fig. 1. Yield *Y* of products of oxidative ammonolysis of 2-methylquinoxaline in the presence of the catalyst $V_2O_5 : TiO_2$ vs. temperature *T*. Amounts of NH_3 and H_2O 12.5 and 35 mol per mole of 2-methylquinoxaline, respectively; contact time 0.7 s. (*1*) 2-Methylquinoxaline, (*2*) quinoxaline, and (*3*) 2-quinoxalinecarbonitrile; the same for Figs. 2 and 3.

and C_1 products (carbon oxides, ammonium cyanide). It should be noted that, in contrast to oxidative ammonolysis of 2-methylpyrazine [6], the reaction was not accompanied by hydrolysis of the 2-cyano derivative to the corresponding amide.

The ratio of the catalyzate components and the degree of conversion of the starting compound largely depend on the process parameters. As the reaction temperature is raised from 320 to 460°C at a constant ratio of the reactants (2-methylquinoxaline, ammonia, water) and constant contact time, the conversion of the starting compound steadily increases, becoming virtually quantitative at 420°C (Fig. 1). The yield of the major reaction product, 2-quinoxalinecarbonitrile, first considerably grows, reaching 50% at 400°C, but at higher temperatures it decreases because of the increased contribution of degradation processes yielding quinoxaline and products of deep oxidation: carbon oxides and ammonium cyanide.

As the contact time is made longer than 0.7 s, the contribution of the undesirable reactions grows, and quinoxaline becomes the major product: Its yield increases from 5 to 60% (Fig. 2).

The above specific features of the behavior of 2-methylquinoxaline in the course of oxidative ammonolysis well correlate with the data previously obtained for 2-methylpyridine [7, 8] and 2-methyl-5-ethylpyridine under similar conditions: The presence of water vapor in the contact zone favors removal of the methyl substituent in the *o*-position relative to heterocyclic nitrogen [9].

This conclusion is confirmed by experiments with a varied concentration of the aqueous ammonia solution fed to the reaction zone (Fig. 3). The lower the ammonia concentration (i.e., the larger the amount of water),

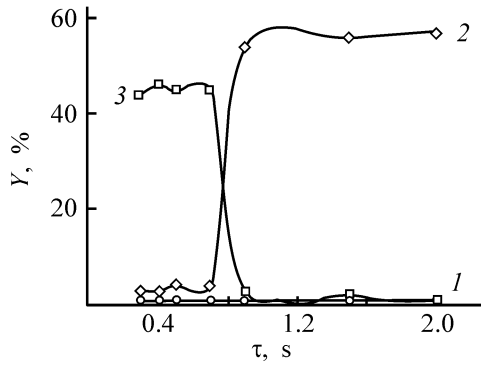


Fig. 2. Yield *Y* of products of oxidative ammonolysis of 2-methylquinoxaline in the presence of the catalyst $V_2O_5 : TiO_2$ vs. contact time τ. *T* = 420°C, amounts of NH_3 and H_2O 12.5 and 35 mol per mole of 2-methylquinoxaline, respectively.

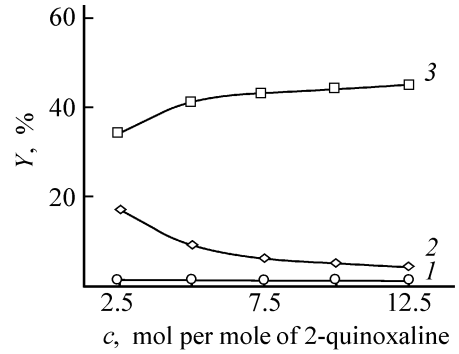
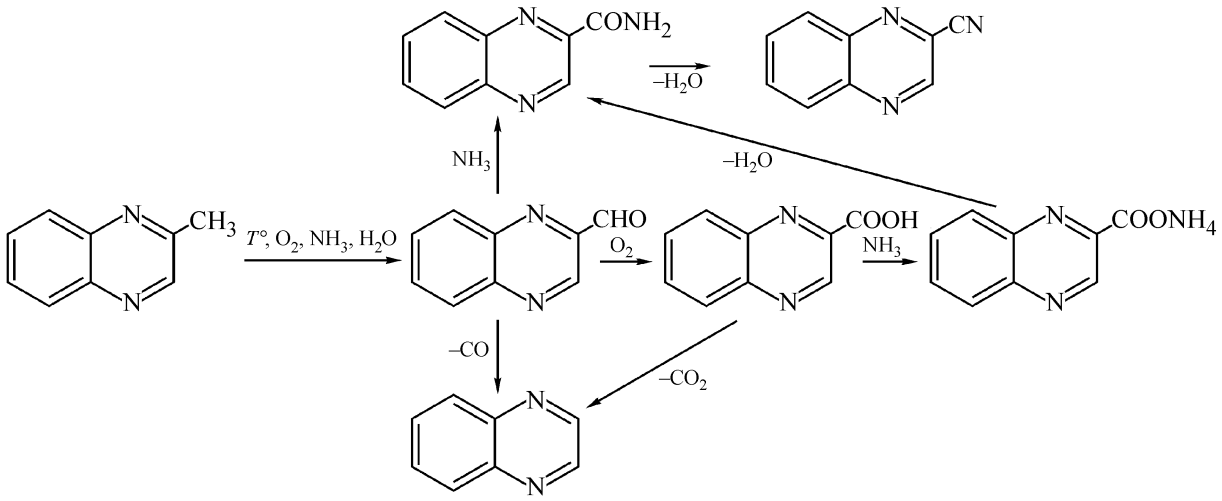


Fig. 3. Yield *Y* of products of oxidative ammonolysis of 2-methylquinoxaline in the presence of the catalyst $V_2O_5 : TiO_2$ vs. ammonia amount *c*. *T* = 420°C, τ = 0.7 s.



Scheme of transformations of 2-methylquinoxaline in the course of oxidative ammonolysis.

the higher the yield of quinoxaline. This trend is due to an increased contribution of the reaction pathways yielding aldehydes and acids, which have no time to react with ammonia under the reaction conditions and undergo decarbonylation and decarboxylation.

Based on the results obtained and conclusions made in the above-cited papers, we suggest a scheme of 2-methylquinoxaline transformations under the conditions of oxidative ammonolysis (see Scheme).

Thus, oxidative ammonolysis of 2-methylquinoxaline shows promise as a route to 2-quinoxalinecarbonitrile, taking into account the accessibility of 2-methylquinoxaline and the simplicity of the process, compared to the known procedures for preparing nitriles of the quinoxaline series, which are, as a rule, multistep and require difficultly available chemicals [3, 10].

CONCLUSION

A procedure for one-step preparation of 2-quinoxalinecarbonitrile in ~50% yield was suggested.

REFERENCES

1. Sakata, G., Makino, K., and Kurasawa, Y., *Heterocycles*, 1998, vol. 27, p. 2481.
2. Andres, J., Belen, Z., Ibnacio, A., and Antonio, M., *J. Med. Chem.*, 2005, vol. 48, p. 2019.
3. Brown, D.J., *Quinoxalines. Supplement II. Chemistry of Heterocyclic Compounds*, New York: Wiley, 2004.
4. *Heterocyclic Compounds*, Elderfield, R.C., Ed., New York: Chapman and Hall, 1950. Translated under the title *Geterotsiklicheskie soedineniya*, Moscow: Inostrannaya Literatura, 1960, vol. 6, pp. 373–403.
5. Suvorov, B.V., Kagarlitskii, A.D., Sembaev, D.Kh., and Loiko, A.I., *Kinet. Katal.*, 1974, no. 1, pp. 197–203.
6. Krichevskii, L.A. and Kagarlitskii, A.D., *Metody sinteza proizvodnykh pirazina* (Methods for Synthesis of Pyrazine Derivatives), Almaty: Gylym, 2004, pp. 98–125.
7. Kan, I.I., Kagarlitskii, A.D., and Suvorov, B.V., *Izv. Akad. Nauk Kaz. SSR, Ser. Khim.*, 1974, no. 3, pp. 57–61.
8. Suvorov, B.V., Kagarlitskii, A.D., and Kan, I.I., *Zh. Prikl. Khim.*, 1975, vol. 48, no. 9, pp. 2063–2065.
9. Suvorov, B.V., Kagarlitskii, A.D., Kan, I.I., and Kutzhanov, R.T., *Kinet. Katal.*, 1977, no. 4, pp. 957–961.
10. Nasielski, J., Heilpron, S., Nasielski-Hinkens, R., et al., *Tetrahedron*, 1989, vol. 45, pp. 7795–7804.

ISSN 1070-4272, Russian Journal of Applied Chemistry, 2008, Vol. 81, No. 2, pp. 323–325. © Pleiades Publishing, Ltd., 2008.
Original Russian Text © M.R. Bairamov, Sh.Z. Gasymova, N.N. Yusubov, E.Ch. Alieva, R.A. Gasymov, 2008, published in Zhurnal Prikladnoi Khimii, 2008, Vol. 81, No. 2, pp. 335–337.

BRIEF COMMUNICATIONS

Synthesis and Study of Cooligomers of *p*-Isopropenylphenyl γ-Chlorobutyrate with Styrene

M. R. Bairamov, Sh. Z. Gasymova, N. N. Yusubov, E. Ch. Alieva, and R. A. Gasymov

Baku State University, Baku, Azerbaijan

Received June 20, 2007

Abstract—Free-radical cooligomerization of a new polyfunctional monomer, *p*-isopropenylphenyl γ-chlorobutyrate, with styrene was studied.

DOI: 10.1134/S1070427208020328

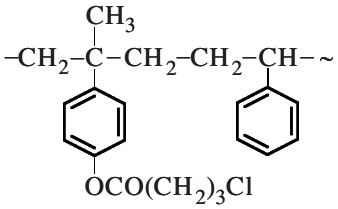
Functionalization of oligomers of α-methylstyrene and its analogs and derivatives is a promising line of the modern petrochemistry and polymer chemistry, expands possible applications of oligomers.

In view of the relative simplicity of the process for preparing *p*-isopropenylphenol and its esters and because of the lack of data on their chemical modification, it becomes topical to develop new procedures for functionalization of oligomers by copolymerization or copolycondensation with various monomers.

In this study, we examined free-radical cooligomerization of a new polyfunctional monomer, *p*-isopropenylphenyl γ-chlorobutyrate (IPCB), with styrene. We found that IPCB does not undergo homopolymerization or any other transformations when heated at 80–140°C for 30 h. In this respect, it behaves similarly to α-methylstyrene and its derivatives substituted in the aromatic ring.

The IR spectra of the cooligomers contain a strong band at 1740 cm^{-1} belonging to the carbonyl group of IPCB. The band at 1490 cm^{-1} is characteristic of a skeleton vibration of the benzene ring in the styrene unit. The bands at 1630 and 890 cm^{-1}, characteristic of the double bond, are lacking.

Comparison of the optical densities of the bands at 1250 and 1510 cm^{-1} in the spectra of the monomer and cooligomer shows that the cooligomerization occurs exclusively at the ethylene bond and the structure of the cooligomers prepared can be presented as follows:



The cooligomer is a white powder soluble in aromatic hydrocarbons, chloroform, and CCl_4, but insoluble in alcohol and hexane. All the samples of the cooligomers have amorphous structure.

With the aim to find the optimal conditions providing virtually complete conversion of the monomers, we examined the effect of temperature, amount of the initiator, cooligomerization time, and monomer ratio on the yield and properties of the cooligomers.

We found that an increase in the cooligomerization temperature to 140°C leads to acceleration of the process and favors formation of the cooligomers of lower viscosity (Fig. 1a). The accumulation rate and yield of the cooligomers are also strongly affected by the amount of the initiator, *tert*-butyl peroxide (TBP). At its concentration in the mixture equal to 0.2%, the conversion of the monomers at 120°C reaches 97% in 15 h (Fig. 1b). The influence of the monomer ratio on the cooligomerization was studied at 120°C. The ester : styrene molar ratio was varied from 1 : 2 to 1 : 10. We found that an increase in the styrene concentration in the monomer mixture accelerated the reaction, and a 97–99% conversion was reached in 15 h (Fig. 1c).

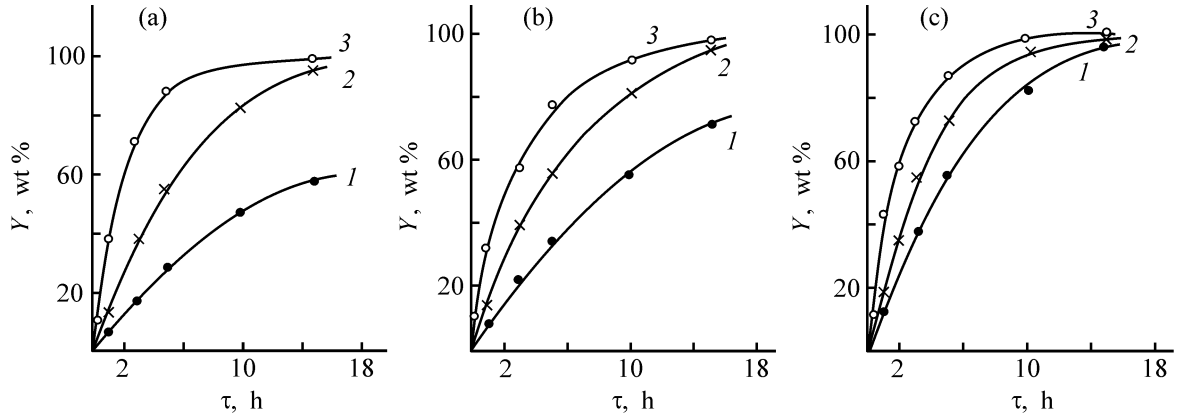


Fig. 1. Yield Y of cooligomers vs. time τ: (a) IPCB : styrene molar ratio 1 : 2, initiator (TBP) concentration 0.2 wt %; T, °C: (*1*) 100, (*2*) 120, and (*3*) 140. (b) IPCB : styrene molar ratio 1 : 2, T = 120°C; initiator (TBP) concentration, wt %: (*1*) 0.5, (*2*) 0.2, and (*3*) 0.1. (c) Initiator (TBP) concentration 0.1 wt %, T = 120°C; IPCB : styrene molar ratio: (*1*) 1 : 2, (*2*) 1 : 5, and (*3*) 1 : 10.

Experiments on fractionation and cross-linking of the cooligomers showed that the homopolymers were not formed. To determine the cooligomerization constants of IPCB (M_2) with styrene (M_1), we performed the reaction for the time providing low (~5%) conversion of the monomers. The composition of the cooligomers (Table 1) was determined from the optical densities of the absorption bands of the monosubstituted benzene ring (1490 cm^{-1}) and carbonyl group of IPCB (1740 cm^{-1}), using the previously obtained calibration curve of the ratio of the optical densities D_{1490}/D_{1740} vs. the ratio of styrene and IPCB units in the cooligomers prepared at complete conversion of the monomers. We found the following copolymerization constants: $r_1 = 2.4 \pm 0.76$, $r_2 = 0.00$ (Table 1).

The characteristics of the cooligomers with various contents of IPCB units are listed in Table 2. The characteristics of polystyrene prepared under identical conditions are given for comparison. It can be seen that, as the IPCB content of the cooligomer increases, the softening (T_s) and dropping (T_d) points and the reduced viscosity (η_r) decrease. The dielectric strength also decreases and the melt flow index increases, showing that IPCB units in the cooligomer chain exert a plasticizing effect. The strength of adhe-

Table 1. Composition of cooligomers obtained

Mole fractions of monomers in starting mixture		Mole fractions of monomeric units in cooligomer	
M_1	M_2	m_1	m_2
0.08	0.089	0.54	0.37
0.64	0.31	0.79	0.13
0.76	0.12	0.88	0.07
0.89	0.08	0.93	0.00

Table 2. Characteristics of IPCB–styrene cooligomers (120°C, initiator concentration 0.2 wt % relative to the sum of monomers, 15 h)

IPCB : styrene molar ratio	η_r (0.5% solution in benzene)	T_s, °C	T_d, °C	Dielectric strength, kV mm^{-2}	Adhesion strength, kg cm^{-2}
1 : 2	0.75	114–116	218	18.7	32
1 : 5	0.81	119–122	226	21.4	26
1 : 10	0.88	122–125	234	23.6	23
0 : 1	1.07	132–135	244	24.5	16

sion of the cooligomers to steel reaches a maximum, 32 kg cm^{-2}, at 1 : 2 molar ratio of IPCB to styrene. The dielectric strength of the cooligomers approaches that of polystyrene.

EXPERIMENTAL

p-Isopropenylphenol (IPP) was prepared by homogeneous-catalytic cracking of bisphenol [1]; IPCB was synthesized by the reaction of IPP with γ-chlorobutyric acid, following the protocol from [2]. The monomers were purified by the standard procedure and had the following constants: IPCB, bp 150°C/1 mm Hg, n_D^{20} = 1.5368, d_4^{20} = 1.0987 g cm^{-3}; styrene, bp 26.5°C/5 mm Hg, n_D^{20} = 1.5462, d_4^{20} = 0.9060 g cm^{-3}. The monomers were 99.95% pure.

The cooligomerization of IPCB with styrene was performed in sealed ampules under argon in the presence of TBP at 120 and 140°C. The monomers and initiator were placed in ampules and degassed by triple freezing–pumping–thawing, the system was purged with purified argon, and the ampules were sealed and placed in an ultrathermostat.

The products were separated from the unchanged monomers by precipitation from a benzene solution into hexane. The precipitated cooligomer was dried in a vacuum at 120°C for 2–3 h to constant weight.

The IR spectra of the cooligomers were taken from thin films on a KRS-5 plate with a UR-10 spectrophotometer in the range 4000 – 650 cm^{-1}.

The reduced viscosity of the synthesized cooligomers was measured in benzene (0.5% solutions). Also, we determined the softening and dropping points, Brinell hardness, adhesion (shear test), dielectric strength of the coating on metal, and melt flow index (at 200°C and a load of 5 kg). The samples were heated at a rate of 4 deg min^{-1}. The cooligomer compositions were determined by IR spectroscopy. The cooligomerization constants were calculated by the Fineman–Ross method.

CONCLUSIONS

(1) New cooligomers of *p*-isopropenylphenyl γ-chlorobutyrate with styrene were prepared and characterized.

(2) The optimal conditions providing complete conversion of the monomers were determined.

REFERENCES

1. Ismailov, R.I., Aliev, S.I., and Bairamov, M.R., *Azerb. Khim. Zh.*, 1967, no. 5, p. 56.
2. FRG Patent 1 193 031.

ISSN 1070-4272, Russian Journal of Applied Chemistry, 2008, Vol. 81, No. 2, pp. 326–327. © Pleiades Publishing, Ltd., 2008.
Original Russian Text © L.M. Popova, I.N. Gaidukov, 2008, published in Zhurnal Prikladnoi Khimii, 2008, Vol. 81, No. 2, pp. 338–339.

BRIEF COMMUNICATIONS

Preparation of 1,1,5-Trihydrooctafluoropentyl Dehydroabietate

L. M. Popova and I. N. Gaidukov

St. Petersburg State Technological University of Plant Polymers, St. Petersburg, Russia

Received December 25, 2007

Abstract—1,1,5-Trihydrooctafluoropentyl dehydroabietate was prepared by esterification of dehydroabietic acid with 1,1,5-trihydrooctafluoropentanol.

DOI: 10.1134/S107042720802033X

Rosin esters are widely used in the production of varnishes, paints, and adhesive composites, thanks to diversity of their properties dependent on the kind of a raw material and alcohol [1]. The use of straight rosin for this purpose is restricted by its acidity, low melting point, poor moisture resistance, and tendency toward polymerization [2].

To impart water- and oil-repellent properties to fibers and paper, these materials are treated with compounds containing long-chain fluoroalkyl groups in their molecule. This treatment is efficiently used in industry. Furthermore, fibrous materials treated with fluorinated compounds almost fully preserve their gas permeability, softness, color, strength, and other characteristics [3].

Therefore, the development of new fluorinated compounds based on esters of rosin and polyfluorinated telomeric alcohols for treatment of fibrous materials is a promising line of organic synthesis.

Various procedures for preparing esters from resin acids of rosin and various alcohols have been reported [4–7], but these do not include esterification with polyfluorinated telomeric alcohols.

The goal of this study was to synthesize of 1,1,5-trihydrooctafluoropentyl dehydroabietate, a potentially effective hydrooleophobizing agent for fibrous materials. As synthesis procedure we chose esterification of dehydroabietic acid with 1,1,5-trihydrooctafluoropentanol in the presence of catalytic amounts of concentrated sulfuric acid.

The promising source of dehydroabietic acid is tall rosin, a by-product from kraft pulp production. The ester is a noncrystallizing red-brown resinous substance.

EXPERIMENTAL

The ^{1}H and ^{19}F NMR spectra of the dehydroabietic acid ester were recorded on a Bruker WH-400 spectrometer (400.13 MHz) from 5% solutions in $CDCl_3$. The chemical shifts were determined relative to internal reference, tetramethylsilane (^{1}H) and trifluoroacetic acid (^{19}F).

The purity of the starting dehydroabietic acid and the reaction progress were monitored by TLC on Silufol UV 254 plates (eluent hexane–methylene chloride–acetone, 1 : 1 : 0.5).

Dehydroabietic acid was recovered from tall rosin (Segezha Pulp and Paper Combine, Karelia, Russia) by the procedure described in [9].

Synthesis of 1,1,5-trihydrooctafluoropentyl dehydroabietate. To a solution of 3 g (9.9×10^{-3} mol) of dehydroabietic acid in 50 ml of hexane, we added 1.6 ml (11.5×10^{-3} mol) of 1,1,5-trihydrooctafluoropentanol and a catalytic amount of concentrated sulfuric acid. The reaction mixture was stirred for 10 h at 70°C and then cooled to room temperature. The solvent was distilled off at reduced pressure (5 mm Hg), the reaction mixture was extracted with ether, and the extract was washed with water to neutral reaction and dried over $MgSO_4$. The solvent was removed on a rotary evaporator, and the product was dried in a vacuum. Yield of the ether 80–85%.

^{1}H NMR spectrum, δ, ppm: 7.2 d, 7.0 d ($-C_{ar}H=C_{ar}H-$, $^3J_{HH}$ 21 Hz); 6.89 s ($=C_{ar}H-$); 5.9 t (HCF_3-, $^2J_{HF}$ 52 Hz); 4.5 m ($-OCH_2CF_2-$, $^3J_{HF}$ 14 Hz). ^{19}F NMR spectrum, δ_F, ppm: –124.3 s, –127.2 s, –132 s ($-C^{2-4}F_2-$); –139.5 d (F_2CH-, $^2J_{HF}$ 50 Hz).

CONCLUSION

A procedure was suggested for preparing 1,1,5-trihydrooctafluoropentyl dehydroabietate by direct esterification in the presence of concentrated sulfuric acid.

REFERENCES

1. Chudinov, S.V., Trofimov, A.N., Uzlov, G.A., et al., *Spravochnik lesokhimika* (Wood Chemist's Handbook), Moscow: Lesnaya Prom–st., 1987, p. 196.
2. Gordon, L.V., Fefilov, V.V., Skvortsov, S.O., and *Atamanchukov, G.D., Tekhnologiya i oborudovanie lesokhimicheskikh proizvodstv* (Technology and Equipment of Wood-Chemical Production), Moscow: Lesnaya Prom–st., 1969, p. 343.
3. *Fluorine Compounds: Modern Technology and Applications*, Ishikawa, N., Ed., Tokyo: CMC, 1987.
4. Shulov, L.M. and Kheifits, L.A., *Dushistye veshchestva i poluprodukty parfyumerno-kosmeticheskogo proizvodstva* (Fragrance Compounds and Intermediates in Production of Perfumeries and Cosmetics), Moscow: Agropromizdat, 1990.
5. Kalninsh, A.I. and Sergeeva, V.N., *Izv. Akad. Nauk Latv. SSR*, 1994, no. 2, pp. 23–29.
6. Bardyshev, I.I. and Ferilov, V.V., *Zh. Prikl. Khim.*, 1947, vol. 20, no. 3, pp. 256–276.
7. Johnston, A.C., *Ind. Eng. Chem.*, 1929, vol. 21, no. 7, pp. 688–689.
8. Romanova, N.V., Akhmed'yanova, R.A., and Liakumovich, A.G., *Izv. Vyssh. Uchebn. Zaved., Khim. Khim. Tekhnol.*, 2005, vol. 48, no. 5, pp. 144–147.
9. Bardyshev, I.I., *Gidrolizn. Lesokhim. Prom–st.*, 1967, no. 8, pp. 10–11.

ISSN 1070-4272, Russian Journal of Applied Chemistry, 2008, Vol. 81, No. 2, pp. 328–330. © Pleiades Publishing, Ltd., 2008.
Original Russian Text © T.M. Umarova, I.N. Ganiev, 2008, published in Zhurnal Prikladnoi Khimii, 2008, Vol. 81, No. 2, pp. 340–342.

BRIEF COMMUNICATIONS

Effect of Samarium on the Corrosion-Electrochemical Properties of Aluminum in a Neutral Medium

T. M. Umarova and I. N. Ganiev

Nikitin Institute of Chemistry, Academy of Sciences of the Republic of Tajikistan, Dushanbe, Tajikistan

Received May 16, 2007

Abstract—Corrosion-electrochemical behavior of aluminum and a samarium-alloyed aluminum–manganese alloy of eutectic composition in a neutral aqueous medium was studied.

DOI: 10.1134/S1070427208020341

Owing to the positive effect on a number of most important properties of industrial alloys, rare-earth metals (REM) find use in a number of industries: metallurgy of nonferrous and ferrous metals, electronics, and nuclear power engineering. Addition of REM in an amount of 0.5% improves the strength and hardness of aluminum alloys and simultaneously raises the relative elongation by a factor of 1.5–2; at higher REM contents, aluminum alloys acquire heat-resistant properties [1]. Therefore, a study of corrosion-electrochemical properties of aluminum (and its alloys) with addition of REM is of particular scientific and practical interest.

The available published data on the corrosion resistance of aluminum and its alloys alloyed with rare-earth metals are scarce. As a rule, cerium and yttrium are used most frequently, and other REM, considerably more rarely [2–5]. That is why samarium was chosen as object of study.

It is known that light REM, from lanthanum to samarium, have a more complicated hexagonal structure, whereas heavy REM crystallize in an ordinary hexagonal close-packed lattice. Samarium is markedly distinctive in this regard: it crystallizes in a rhombohedral lattice [6].

It is known that REM (R) interact with aluminum to give a number of intermetallic compounds, of which phases of composition RAl_4 are in equilibrium with an aluminum solid solution. It has been found that no compound of the type RAl_4 exists in the system Sm–Al, in contrast to the systems Al–La, Al–Pr, Al–Ce, and Al–Nd [6]. Similarly to diagrams of most of REM, the phase diagram of Al–Sm shows formation of a eutectic $l \rightarrow Al + SmAl_3$ on the aluminum side at a temperature of 633°C and samarium content of 15%. The solubility of samarium in solid aluminum is low (< 0.10 wt %) [7].

REM-containing aluminum alloys are difficult to synthesize because the components introduced into aluminum have a high chemical activity, and the melting points of numerous binary and ternary alloys substantially exceed those of the pure components. It is known that alloying of aluminum with manganese diminishes the adverse effect of impurities, because of the formation of intermetallic compounds with a sufficiently negative electrode potential, and thereby improve the protective properties of the oxide film.

The aim of this study was to synthesize and examine the effect of samarium on the corrosion-electrochemical properties of aluminum and aluminum–manganese eutectic Al–Mn (1.9%) in a neutral aqueous medium.

EXPERIMENTAL

With account of the diagrams of state of Al–REM [7], alloys for study were obtained so as to cover the regions of solid solutions of REM in aluminum and pre-eutectic alloys whose structure is constituted by primary precipitates of the aluminum solid solution and a eutectic of composition α-Al + $SmAl_3$. The chemical-structural homogeneity, dependent on the solubility and distribution coefficient of the alloying elements (manganese and samarium) in the base metal (aluminum), predetermines the uniformity and stability of its electrochemical properties. To achieve

Corrosion-electrochemical parameters of aluminum and samarium-alloyed aluminum–manganese alloys in a 3% NaCl solution

Sm, wt %	$-E_{fc}$	$-E_{pit}$	$-E_{rp}$	$-E_{cor}$	$-E_{po}$	$-E'_{pit}$	ΔE_{pas}	i_{pit}	$i_{d.rp}$	i_{cor}
	V							A m^{-2}		
Aluminum										
–	0.90	0.68	0.74	0.910	1.02	0.66	0.34	0.10	0.10	0.006
0.01	0.78	0.57	–	0.765	1.05	0.67	0.37	0.04	0.07	0.006
0.05	0.74	0.50	–	0.750	1.00	0.62	0.36	0.04	0.08	0.005
0.10	0.72	0.59	–	0.730	0.90	0.60	0.30	0.06	0.06	0.006
0.20	0.72	0.52	–	0.725	1.02	0.59	0.41	0.07	0.06	0.007
0.50	0.72	0.48	–	0.725	1.08	0.57	0.50	0.08	0.06	0.008
Aluminum–manganese alloy										
–	0.82	0.59	–	0.730	1.10	0.62	0.50	0.06	0.10	0.008
0.01	0.74	0.57	–	0.740	1.10	0.58	0.50	0.04	0.06	0.004
0.05	0.71	0.54	0.73	0.745	1.10	0.52	0.50	0.04	0.06	0.003
0.10	0.72	0.53	0.74	0.750	1.05	0.54	0.48	0.04	0.06	0.005
0.20	0.75	0.52	0.74	0.750	1.04	0.54	0.47	0.04	0.05	0.005
0.50	0.77	0.52	0.74	0.755	1.03	0.55	0.45	0.04	0.04	0.006

homogeneity, alloys (10% aluminum–manganese and 15% Al–Sm based on A995 aluminum) were obtained in corundum crucibles at temperatures of 900–1000°C. Cylindrical rods (8 mm in diameter and 100 mm long) were cast in a heated graphite mold. Before being submerged in the electrochemical cell, the rods were ground, polished to mirror shine, washed with distilled water, and degreased with ethanol.

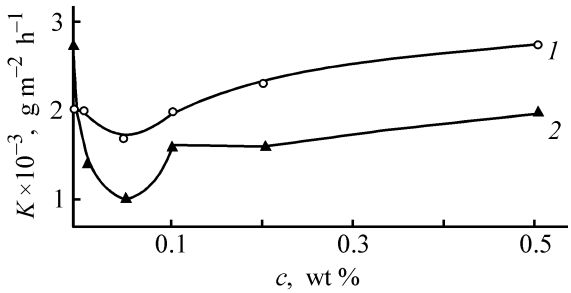
The corrosion-electrochemical studies were carried out using a PI 50-1 potentiostat with a preset program by the procedure described in [8] at a potential sweep rate of 2 mV s^{-1}. A prepared sample of an aluminum alloy was placed in the 3% NaCl solution under study. In the electrochemical cell, a silver chloride electrode served as reference, and platinum as auxiliary electrode. The potentials are given relative to the silver chloride electrode. The solution temperature of 20°C was maintained with a thermostat. The following electrochemical parameters were determined using the polarization curves obtained: free corrosion potential E_{fc} and the pitting potential and current, E_{pit} and i_{pit}, from the forward-run anodic polarization curve; repassivation potential E_{rp}, graphically from the reverse-run anodic curve; corrosion potential and current, E_{cor} and i_{cor}, corresponding to the potential at which the cathodic branch appears; passivation onset potential E_{po}; pitting potential in the absence of a natural oxide film on the surface, E'_{pit}, and the corresponding dissolution current in the repassivation region, $i_{d.rp}$, from the repeated anodic polarization curve. Then, the passivation interval ΔE_{pas} was calculated as the difference of the full passivation potential and E'_{pit}. The basic indicator of the corrosion stability, corrosion rate K (g m^{-2} h^{-1}), was calculated from the corrosion current found from the cathodic polarization curve (with a Tafel slope b_c = 0.12 V), using the formula

$$K = i_{cor}\, k,$$

where k is the electrochemical equivalent whose numerical value for aluminum is 0.335 g A^{-1} h^{-1} [9].

The results of the study are listed in the table.

The figure shows how the corrosion rate K (g m^{-2} h^{-1}) of the aluminum alloy (curve *1*) and alu-



Effect of the samarium content c on the corrosion rate K of (*1*) aluminum and (*2*) aluminum–manganese alloy of eutectic composition in 3% NaCl solution.

minum–manganese alloy of eutectic composition (curve *2*) depend on the samarium content *c* (wt %). It can be seen that the main changes in the corrosion rate are observed at samarium contents lower than 0.2%; further increase in the content of samarium has virtually no effect on the corrosion rate.

As can be seen from the figure, the runs of both the curves are identical. For example, the corrosion rate is at a minimum at a samarium content of 0.05%. However, the corrosion rate in the presence of manganese is 1.5 times lower. Further increase in the content of samarium leads only to a slight increase in the corrosion rate, with the rise beginning at 0.1% Sm for binary alloys and 0.2% Sm for alloys of the ternary system.

The facilitation of passivation processes and the improvement of the corrosion resistance of an alloy under study via amorphization may be due to a change in its microstructure. For example, a decrease in the grain size because of the modification with samarium improves the corrosion resistance of aluminum and its alloy, because the passivation process becomes more efficient.

The process of aluminum oxidation is decelerated as the potential is shifted to more negative values. The activation of the alloy is enhanced as the content of REM (samarium) in the alloy increases. Thus, the following can be noted when characterizing the effect of samarium on the corrosion-electrochemical behavior of aluminum.

(1) The free-corrosion potentials of the alloys under study (binary and ternary systems) are in the passivation region.

(2) The potentials of free corrosion, pitting, and corrosion are shifted to more positive values as a result of alloying with samarium. A similar shift occurs for the eutectic alloy Al + 1.9% Mn, with only a slight shift of the corrosion potential to more negative values.

(3) Alloying of aluminum with samarium makes lower the pitting and dissolution currents in a transition from the passive state. For the aluminum–manganese alloy, these parameters decrease by virtually a factor of 2.

(4) Introduction of samarium extends the passivation interval of the alloys and improves their corrosion resistance.

CONCLUSIONS

(1) It was shown that, similarly to other REM (Ce, Y, Pr, Nd), samarium is an effective modifier for aluminum and an aluminum–manganese alloy of eutectic composition.

(2) The optimal compositions of corrosion-resistant binary and ternary alloys of the systems Al + 0.05% Sm and Al + 1.9% Mn + 0.05% Sm in a neutral chloride-containing medium were determined

REFERENCES

1. Savitskii, E.M. and Terekhova, V.F., *Voprosy teorii i primeneniya redkozemel'nykh metallov* (Problems of the Theory and Practice of Rare-Earth Metals), Moscow: Nauka, 1964.
2. Al'tovskii, R.M. et al., *Korrozionnye svoistva ittriya* (Corrosion Propetrties of Yttrium), Moscow: Atomizdat, 1969.
3. Ganiev, I.N., Yunusov, I., and Krasnoyarskii, V.V., *Zh. Prikl. Khim.*, 1987, vol. 60, no. 9, pp. 2119–2123.
4. Ganiev, I.N., Yunusov, I., Vakhobov, A.V., and Shukroev, M.Sh., *Zh. Prikl. Khim.*, 1985, vol. 58, no. 10, pp. 2366–2368.
5. Plenkova, L.S. Bundzhe, V.G., and Zabotin, P.I., *Izv. Akad. Nauk KazSSR, Ser. Khim.*, 1985, no. 1, p. 19.
6. Gschneider, K.A. Jr., *Rare Earth Alloys*, New York: Van Nostrand, 1961.
7. Mondolfo, L.F., *Aluminium Alloys: Structure and Properties*, London: Butterworths, 1976.
8. Karimova, T.M., Ganiev, I.N., and Krasnoyarskii, V.V., *Zh. Prikl. Khim.*, 1988, vol. 61, no. 1, pp. 51–54.
9. Romanov, V.V., *Metody issledovaniya korrozii metallov* (Methods for Study of Metal Corrosion), Moscow: Metallurgiya, 1965.

ISSN 1070-4272, Russian Journal of Applied Chemistry, 2008, Vol. 81, No. 2, pp. 331–332. © Pleiades Publishing, Ltd., 2008.
Original Russian Text © E.M. Battalov, S.V. Kolesov, Yu.A. Prochukhan, A.A. Fatykhov, Yu.B. Monakov, 2008, published in Zhurnal Prikladnoi Khimii, 2008, Vol. 81, No. 2, pp. 343–344.

BRIEF COMMUNICATIONS

Postpolymerization of Oligoether Acrylate Formed by Reaction of Diethylene Glycol Diglycidyl Ether with Acrylic Acid

E. M. Battalov, S. V. Kolesov, Yu. A. Prochukhan, A. A. Fatykhov, and Yu. B. Monakov

Institute of Organic Chemistry, Ufa Scientific Center, Russian Academy of Sciences, Ufa, Bashkortostan, Russia

Received May 23, 2007

Abstract—Postpolymerization of the epoxy–acrylic oligomer derived from an aliphatic epoxy resin was studied.

DOI: 10.1134/S1070427208020353

The first report on a posteffect is apparently dated 1938 [1]; the effect was observed in photopolymerization of methyl methacrylate. By now postpolymerization effects have been reported for all vinyl monomers and oligomers. In all the cases, the point is that long-lived radicals with a lifetime of several minutes to tens of hours are formed [2–4].

Epoxy–acrylic oligomers are characterized by high photopolymerization rates, which complicates studying their curing kinetics. Therefore, examination of posteffects in photoinitiated polymerization of epoxy–acrylic oligomers makes it possible to relatively readily derive information valuable for describing the process as a whole.

EXPERIMENTAL

In our study we used epoxy–acrylic oligomer formed by esterification of an aliphatic diepoxide [DEG-1, TU (Technical Specification) 6-05-1747–76] with acrylic acid (AA). The structure of the oligoether acrylate [α,ω-bis(1-acryloyloxy-2-hydroxyprop-3-yl)-oligooxyethylene] CH_2=CHCOOCH$_2$CH(OH)–CH$_2$–[–O–CH$_2$CH$_2$OCH$_2$CH$_2$–O–CH(OH)–CH$_2$–]$_n$–OOC–CH=CH$_2$ was determined by elemental analysis and by IR and NMR spectroscopy. The polymerization initiators were benzophenone and uranyl sulfoxide complex [5]. The IR radiation source was a DRT-400 medium-pressure mercury lamp. The distance from a substrate being irradiated to the UV source was 0.14 m. The dynamic viscosity was measured with a Reotest 2.1 device. The hydrogen bonds in the oligomer were revealed by ^{1}H NMR spectroscopy. The NMR spectra were recorded on a Bruker AM-300 spectrometer with a working frequency of 300 MHz; the solvent was $CDCl_3$, and the internal reference was TMS. Analysis of the spectra and assignment of the signals were performed by 2*D* NMR correlation spectroscopy (COSY H–H, C–H).

Previously, we have described a posteffect in photosensitized (benzophenone, uranyl sulfoxide complex)

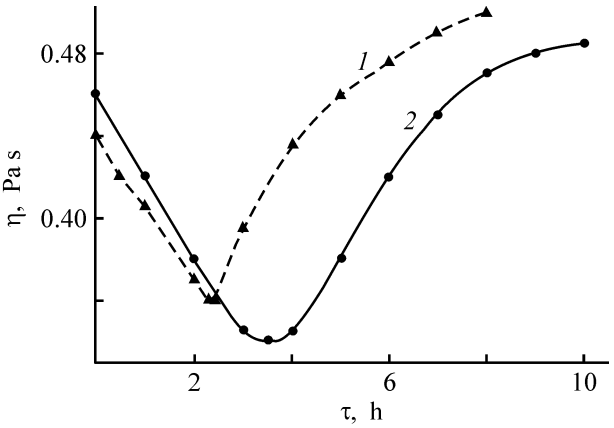


Fig. 1. Variation of the dynamic viscosity η of the epoxy–acrylic oligomer based on DEG-1 aliphatic epoxy resin after UV irradiation for 15 s. (τ) Time. Photoinitiator, M: (*1*) benzophenone, 1.0×10^{-2}; (*2*) $UO_2Cl_2 \cdot 2$DHSO (DHSO is dihexyl sulfoxide), 1.2×10^{-3}.

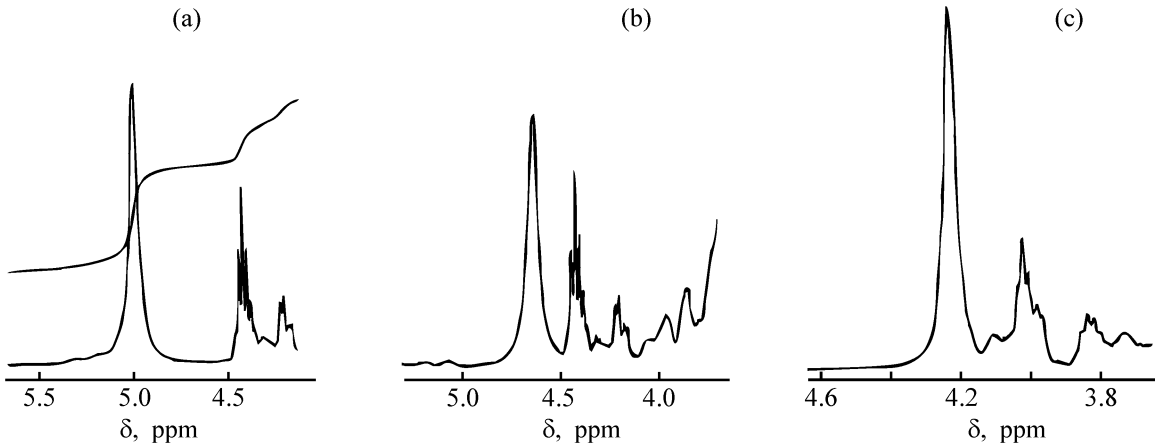


Fig. 2. ^{1}H NMR spectra of the epoxy–acrylic oligomer derived from the aliphatic epoxy resin after UV irradiation for 15 s. (δ) Chemical shift. Oligomer: (a) starting, (b) UV-irradiated, and (c) diluted by a factor of 3.

polymerization of epoxy–acrylic oligomers based on cycloaliphatic and epoxy–4,4'-isopropylidenediphenol resins. The effect consisted in a gradual increase in the dynamic viscosity of the system after a short-term UV irradiation, observed during a long period [5]. This effect was indicative of prolonged postpolymerization owing to the presence of long-lived free radicals in the viscous polymer matrix.

A different pattern is observed under similar conditions with the epoxy–acrylic oligomer, α,ω-bis(1-acryloyloxy-2-hydroxyprop-3-yl)oligooxyethylene synthesized by the reaction of diethylene glycol diglycidyl ether (DEG-1 aliphatic epoxy resin, hydroxy group content 4–5 wt %) with acrylic acid. After a short-term irradiation (15 s), the dynamic viscosity of the oligomer decreases by a factor of 1.2–1.3 over a period of 2.5–3.5 h and only later starts to increase (Fig. 1).

The viscosity increases during a long period (10 h and more), reaching the level exceeding the viscosity of the starting oligomer. In the ^{1}H NMR spectrum of the starting epoxy–acrylic oligomers, the signals of hydroxyl protons are noticeably shifted, suggesting the involvement of these protons in reversible association via hydrogen bonds (downfield shift by 4 ppm and more of hydroxyl proton signals). After UV irradiation or a therefold dilution, the signals are shifted upfield in 2.5–3.5 h, apparently owing to breakdown of the hydrogen-bonded associates of the initial oligomer molecules (Figs. 2a–2c). In the process, the major contribution to variation of the chemical shift of the hydroxyl proton signal is made by variation of the polarity of the O–H bond [6].

Thus, the absorbed of energy UV light is primarily consumed in our case for the breakdown of the supramolecular structure of the oligomer matrix and for the formation of free radicals inducing the postpolymerization. This fact indicates that intermolecular hydrogen bonds should be taken into account in studies of the postpolymerization of certain monomers and oligomers.

CONCLUSION

The postpolymerization of an epoxy–acrylic oligomer formed by the reaction of diethylene glycol diglycidyl ether with acrylic acid is accompanied by a decrease in the dynamic viscosity, due to cleavage of intermolecular hydrogen bonds.

REFERENCES

1. Bolland, J.L. and Melville, H.W., in *Proc. 1st Rubber Technology Conf.*, London, 1938, p. 239.
2. *Vinyl Polymerization*, Ham, G.E., Ed., New York: Dekker, 1969.
3. Ceresa, R.J., *Blok- i privitye sopolimery* (Block- and Graft Copolymers), Moscow: Mir, 1964.
4. Berlin, A.A., Kefeli, T.Ya., and Korolev, G.V., *Oligoefirakrilaty* (Oligoether Acrylates), Moscow: Nauka, 1967.
5. Sadykov, R.A., Gatiyatullina, G.V., Battalov, E.M., and Prochukhan, Yu.A., *Zh. Prikl. Khim.*, 2003, vol. 76, no. 4, pp. 653–657.
6. Ionin, B.I., Ershov, B.A., and Kol'tsov, A.I., *YaMR spektroskopiya v organicheskoi khimii* (NMR Spectroscopy in Organic Chemistry), Leningrad: Khimiya, 1983.

ISSN 1070-4272, Russian Journal of Applied Chemistry, 2008, Vol. 81, No. 2, pp. 333–336. © Pleiades Publishing, Ltd., 2008.
Original Russian Text © Z.V. Mamarasulova, V.V. Gromova, 2008, published in Zhurnal Prikladnoi Khimii, 2008, Vol. 81, No. 2, pp. 345–347.

BRIEF COMMUNICATIONS

Effect of *p*-Hydroxydiphenylamine and Boron-Containing Pentaerythritol Esters on Properties of an Ester Oil

Z. V. Mamarasulova and V. V. Gromova

St. Petersburg State Institute of Technology (Technical University), St. Petersburg, Russia

Received June 19, 2007

Abstract—The influence of the amount of incorporated boron on the physicochemical and service properties of a pentaerythritol ester used as a base of aviation oil was examined. The effect of an antioxidant additive, *p*-hydroxydiphenylamine, on the temperature dependence of the oil viscosity was evaluated.

DOI: 10.1134/S1070427208020365

Esters of neopentanepolyols, primarily pentaerythritol, with synthetic fatty acids C_5–C_9 are widely used as synthetic lubricating oils for aviation gas turbine engines, helicopter reduction gears, and other devices with working temperatures of oil equal to up to 200°C. The most important requirements to oils of this kind are high resistance to thermal oxidation, good lubricating, anticorrosive, and protective properties, slightly sloping temperature dependence of the viscosity, and some other standardized parameters [1].

Previously published data indicate that the resistance of pentaerythritol esters to thermal oxidation is mainly determined by the presence of readily oxidizable impurities in the raw material and by the degree of pentaerythritol esterification [2, 3]. The presence of incomplete esters considerably impairs the oil stability. At the same time, it is known that incomplete pentaerythritol esters considerably surpass their complete analogs in the lubricating properties [4].

One of possible ways to enhance simultaneously the resistance of pentaerythritol esters to thermal oxidation, their lubricating properties, and other characteristics is afteresterification of incomplete esters with boric acid. Published data show that boric acid esters exhibit high antifriction, antiwear, and anticorrosive properties, as well as high resistance to thermal oxidation [5]. At the same time, boration of the incomplete esters may alter the physicochemical properties of the oil owing to an increase in the molecular weight of the product or appearance of nonesterified OH groups of boric acid. A certain influence on the physicochemical properties of oil should also be exerted by functional groups of the commonly used antioxidant, *p*-hydroxydiphenylamine (PHDA).

Therefore, our goal was to determine the optimal concentration of boron in pentaerythritol esters and to evaluate the effect of PHDA on the physicochemical characteristics of oil.

EXPERIMENTAL

Boron was introduced into the ester molecule by esterification of free hydroxy groups of incomplete pentaerythritol esters with boric acid. The reaction was performed without a catalyst on a laboratory installation with vacuum separation of water released in the reaction. Reaction conditions: 140°C, 1 h, residual pressure 40 kPa.

The reaction products were characterized by standard methods accepted for testing Efir-2 basic oil with pentaerythritol esters as major components [6] and B-3V commercial aviation oil [1]. The viscosity of the oils was determined in accordance with GOST (State Standard) 33–2000 with a VPZh-4 Pinkevich viscometer with an accuracy of 0.2%. The tribological properties of the samples were estimated with a four-ball friction machine according to GOST 9490–75. The error in determining the wear scar diameter was ±0.1 mm. The resistance to thermal oxidation was tested according to technical specification for B-3V synthetic oil at 200°C for 10 h, at an air flow rate of 50 ml min^{-1} [1]. The oil stability was evaluated by variation of the kinematic viscosity ν at 100 and –40°C, increase in the acid number (AN), and formation of a precipitate insoluble in isooctane.

As starting materials we used pentaerythritol esters (PEEs) of individual monocarboxylic acids and their fractions: caprylic acid ester (PEE C_8), ester of C_5–

C_{10} fatty acid fraction [PEE C_5–C_{10} (lab.)], and ester of the C_5–C_9 fatty acid fraction [PEE C_5–C_9 (imp.)]. The esters PEE C_8 and PEE C_5–C_{10} (lab.) were prepared in laboratory. Their hydroxyl number was 35 (mg KOH) g^{-1}, which is close to the hydroxyl number of Efir-2 basic synthetic oil produced in Russia. The ester PEE C_5–C_9 (imp.) was a sample of imported oil similar to Efir-2, with the hydroxyl number of 5 (mg KOH) g^{-1}.

p-Hydroxyphenylenediamine was added to the cooled product after the synthesis and was dissolved at 60–80°C.

When choosing the PEE : boric acid ratio, we considered the possibility of the reaction of boric acid with one or two molecules of the incomplete pentaerythritol ester:

$$(RCOOCH_2)_3CCH_2OH + H_3BO_3 = (RCOOCH_2)_3CCH_2OB(OH)_2 + H_2O, \quad (1)$$

$$2(RCOOCH_2)_3CCH_2OH + H_3BO_3 = [(RCOOCH_2)_3CCH_2O]_2BOH + 2H_2O. \quad (2)$$

Into PEE with the incomplete ester content corresponding to a hydroxyl number of 35 (mg KOH) g^{-1}, it is possible to introduce up to 1.5 wt % boron by reaction (1) and up to 0.75 wt % boron by reaction (2). At a hydroxyl number of 5 (mg KOH) g^{-1}, up to 0.1 wt % boron can be introduced into the ester.

According to [7], introduction of 0.45 wt % boron into PEE with a hydroxyl number of 40 (mg KOH) g^{-1} decreased the hydroxyl number to 10 (mg KOH) g^{-1}. However, the viscosity of the oil at –40°C increased in this case by more than a factor of 1.5: from 10950 to 16249 $mm^2 s^{-1}$ (the limit prescribed by the standard is 10600 $mm^2 s^{-1}$).

In this study we prepared PEE C_8 with 0.2 wt % boron. The characteristics of the modified ester are compared in Table 1 with those of the initial ester.

The results obtained indicate that introduction of 0.2 wt % boron into PEE also makes the viscosity too high and deteriorates the low-temperature properties of the product.

Published data on the use of oils with boron-containing additives show that the boron content does not exceed hundredths of a percent relative to oil [8]. The effect of boron in a concentration of 0.02–0.04 wt % on the physicochemical parameters of imported PEE C_5–C_9 with a hydroxyl number of 5 (mg KOH) g^{-1} is illustrated by Table 2. Also given are data on the effect of PHDA additive taken separately or in combination with boron.

Table 1. Kinematic viscosity ν and congelation point T_c of the modified ester

Boron content, wt %	ν, $mm^2 s^{-1}$, at indicated temperature, °C		T_c, °C
	–40	100	
–	34.00	5.98	–22
0.2	39.50	7.12	–14

Table 2. Physicochemical characteristics of PEE as influenced by the boron content and addition of PHDA to the ready product

Content, wt %		ν, $mm^2 s^{-1}$, at indicated temperature, °C			Viscosity index
boron	PHDA	40	100	–40	
Sample of PEE C_5–C_9 (imp.)					
–	–	22.86	4.94	7560	146
0.02	–	23.56	5.04	7610	147
0.04	–	24.07	5.07	7650	144
–	0.5	23.68	4.92	8060	136
0.03	0.5	24.29	5.05	8030	139
Sample of PEE C_5–C_{10} (lab.)					
–	–	23.08	4.87	8610	138
0.03	–	23.61	4.98	8710	138
–	0.5	25.23	4,92	10990	120
0.03	0.5	25.03	5.00	10340	128

Table 2 shows that introduction of 0.02–0.04 wt % boron into molecules of pentaerythritol esters affects the physicochemical characteristics of the product insignificantly. The congelation point of all the samples (not given in Table 2) is virtually constant, 60 ± 2°C. Addition of PHDA in a concentration accepted for ester oils (about 0.5 wt %) considerably increases the viscosity of the oil at low temperatures and decreases the viscosity index. The observed negative effect of PHDA on the physicochemical properties of the oil is apparently due to the formation at low temperatures of hydrogen bonds between the hydroxy and amino groups of PHDA and the carbonyl oxygen atom of ester groups of the oil. At 100°C, these bonds are ruptured, and the viscosity varies insignificantly.

Table 3. Resistance of PEE to thermal oxidation, as influenced by the boron content and presence of PHDA*

Content, wt %		Increase relative to unoxidized oil			Residue insoluble in isooctane, %
boron	PHDA	AN, (mg KOH) g^{-1}	ν, %		
			100°C	–40°C	
Sample of PEE C_5–C_9 (imp.)					
–	–	3.45	23.0	142.0	0.24
0.02	–	3.25	21.0	126.0	0.12
0.04	–	3.12	19.0	109.0	0.06
–	0.5	0.20	3.0	23.0	0.01
0.03	0.5	0.06	0.0	13.0	0.01
Sample of PEE C_5–C_{10} (lab.)					
–	–	9.68	96.1	–	–
0.03	–	6.43	59.0	–	–
–	0.5	0.09	0.0	–	–
0.03	0.5	0.04	0.0	–	–

* The rate of air supply was increased relative to the standard procedure by a factor of 1.5.

The effect of boron and PHDA on PEE C_5–C_{10} (lab.) with a hydroxyl number of 35 (mg KOH) g^{-1} is qualitatively identical to the effect of these additives on imported PEE C_5–C_9 whose hydroxyl number is 5 (mg KOH) g^{-1}, but is accompanied by a somewhat stronger increase in the viscosity of the products at low temperatures (Table 2).

Table 3 shows the results of testing the resistance to thermal oxidation of products whose physicochemical characteristics are listed in Table 2.

It can be seen that modification with small amounts of boron enhances the resistance of the esters to thermal oxidation. Boron incorporated in the PEE structure affects to the greatest extent the viscosity of the oxidates at both 100 and –40°C and the formation of the precipitate insoluble in isooctane. The efficiency of modification with boron of a laboratory PEE sample containing the largest amount of unstable incomplete esters is higher, compared to the modification of the imported sample with a low content of free hydroxy groups. As expected, *p*-hydroxydiphenylamine acts as an effective antioxidant. Modification of PEE with boron, followed by addition of PHDA, further enhances the oxidation resistance of the oil.

Introduction of boron also positively affects the lubricating power of PEE. Below are the tribological characteristics of PEE C_5–C_9 (imp.), initial and modified with boron (both samples contain 0.5 wt % PHDA):

Boron content, wt %	Critical load, N	Wear scar diameter, m
–	581	0.70
0.03	697	0.67

The effect of boron is manifested to the greatest extent in the increase in the critical load.

Our results show that it is possible to enhance simultaneously the resistance of PEEs to thermal oxidation and their lubricating properties, with the low-temperature viscosity and the temperature dependence of the viscosity kept on the acceptable level, by esterification of a part of free hydroxy groups with boric acid. Modification with small amounts of boron of PEE with a low degree of esterification is the most efficient.

CONCLUSIONS

(1) Introduction of 0.02–0.04 wt % boron into the structure of incomplete pentaerythritol esters by esterification of free hydroxy groups with boric acid affects the low-temperature viscosity and the temperature dependence of the viscosity insignificantly, but noticeably enhances their resistance to thermal oxidation and improves to a certain extent the lubricating properties. Modification with boron of pentaerythritol esters with a low degree of esterification is the most efficient.

(2) *p*-Hydroxydiphenylamine, an antioxidant widely used in ester oils, appreciably increases the viscosity of pentaerythritol esters at low temperatures and makes steeper the temperature dependence of the viscosity.

REFERENCES

1. *TU* (Technical Specification) *38.101 295–85: B-2V Synthetic Oil*.
2. Itsikson, T.M., Kagan, L.Kh., Sudarikova, T.I., et al., *Khim. Tekhnol. Topl. Masel*, 1976, no. 6, pp. 33–35.
3. Kalinin, L.L., Novosartov, G.T., and Krasheninnikova, V.K., *Khim. Tekhnol. Topl. Masel*, 1975, no. 1, S. 22–24.
4. Sakurai, T., Hironaka, S., Furuta, M., and Watanabe, Y., *Bull. Jpn. Petrol. Inst.*, 1976, vol. 18, no. 1, pp. 1–8.
5. Yao, J. and Dong, J., *Lubricat. Eng.*, 1995, vol. 51, no. 6, pp. 475–479.
6. *TU* (Technical Specification) *0253-012-5 6194 358–2002: Ester no. 2: Base for Engine Oils*.
7. Nagieva, E.A., *Khim. Tekhnol. Topl. Masel*, 2004, no. 4, pp. 44–45.
8. Mikhaleva, E.V., B,N-Containing Organic Compounds as Additives to Lubricating Mineral Oils, *Cand. Sci. Dissertation*, Moscow, 1996.

ISSN 1070-4272, Russian Journal of Applied Chemistry, 2008, Vol. 81, No. 2, p. 337. © Pleiades Publishing, Ltd., 2008.
Original Russian Text © A.G. Morachevskii, M.S. Kokhatskaya, 2008, published in Zhurnal Prikladnoi Khimii, 2008, Vol. 81, No. 2, p. 348.

BOOK REVIEWS

Popova, A.A., *Anodnoe Povedenie Perekhodnykh Metallov v Vodnykh i Organicheskikh Sredakh* (Anodic Behavior of Transition Metals in Aqueous and Organic Media), Rostov-on-Don: Izd. SKNTs VSh, 2006, 184 pp.

DOI: 10.1134/S1070427208020377

The monograph by A.A. Popova summarizes and analyzes the results of numerous studies of the anodic behavior of a large group of metals, mostly in aqueous–organic and organic media. Special attention in the presentation of the material is given to the influence of complexation in solutions on the anodic behavior of metals and formation of anodic films. The book comprises an introduction, four chapters, conclusion, and a bibliographic list for the monograph as a whole.

The brief introduction (pp. 5, 6) substantiates the topicality of the issues considered in the monograph and notes the importance of the influence exerted by the type and properties of an electrolyte on anodic processes and on the formation and nature of the films formed. The first chapter (pp. 7–34) considers the fundamental aspects of the anodic behavior of metals passivated in aqueous-organic and organic media. The thermodynamic characteristics of the occurring processes, role of water in anodic reactions, and effect of anions on the anodic behavior of transition metals are discussed.

The second chapter (pp. 35–69) is devoted to the effect of complexation in solutions on the processes occurring in anodic polarization of metals. A section of the chapter contains evidence about application of chromatographic methods to determine transition metal ions in organic and mixed media. The third chapter (pp. 70–121) discusses a whole group of issues related to the nature of processes that occur on the surface of passivable metals, structure of the double layer, and formation of the metal–electrolyte interface.

The fourth chapter (pp. 122–154) includes material about the passive state of transition metals and the structure of oxide films on these metals. Also, some data obtained in studies of the semiconducting properties of anodic films are presented. In the conclusion (p. 155), the authors express hope that the monograph offered to readers' attention and based on a vast body of processed information sources will make up for the deficiency of review information about the problem discussed. The bibliographic list (pp. 156–183) is, indeed, rather spacious, with 503 references included. Unfortunately, the article titles are not presented, which somewhat reduces the information value of the list.

There is no escape from mentioning the shortcomings of the book, which are, in our opinion, due to two main reasons, lack of author's standpoint concerning the problems discussed and attempt to cover a too wide variety of issues. In fact, the monograph is a review of published information within rather uncertain limits. There are no sufficient interrelations between the chapters and between sections within the chapters. Separate publications are taken and an attempt is made to present their essence in an as brief manner as possible. What is the relationship between the phenomena of anodic dissolution, passivity, and entropy of the double layer. This is difficult to understand from the text in pp. 103–109.

There are numerous minor defects of presentation, which hinder the understanding of the material, both in the text and in the figure design. There is no such notion as "activity coefficient of the medium" (p. 7). The term "free energy" was many years ago replaced in the world literature with the term "Gibbs energy." What is the terminological difference between the heat (ΔH) of the sorption process (Figs. 2.4, 2.5) and heat of adsorption (Q) (Figs. 2.6, 2.7). In Table 2.2, the symbol ΔH already designates the "differential molar energy of sorption." The least attention is given by the book to electrochemical processes: anodic dissolution and transition to the passive state. Anodic polarization curves are shown only in a single figure (Fig. 1.3).

The author should have taken as an example of a book devoted to a similar problem the monograph by B.N. Kabakov *Elektrokhimiya metallov i adsorbtsiya* (Electrochemistry of Metals and Adsorption, Moscow: Nauka, 1966, 222 pp.). Published 40 years ago, this book still retains its scientific value.

A.G. Morachevskii and M.S. Kokhatskaya

ISSN 1070-4272, Russian Journal of Applied Chemistry, 2008, Vol. 81, No. 3, pp. 339–359. © Pleiades Publishing, Ltd., 2008.
Original Russian Text © A.G. Vitenberg, Yu.G. Dobryakov, 2008, published in Zhurnal Prikladnoi Khimii, 2008, Vol. 81, No. 3, pp. 353–373.

REVIEWS

Gas-Chromatographic Determination of the Distribution Ratios of Volatile Substances in Gas–Liquid Systems

A. G. Vitenberg and Yu. G. Dobryakov

Mendeleev All-Russian Research Institute of Metrology, Federal State Unitary Enterprise, St. Petersburg, Russia
St. Petersburg State University, St. Petersburg, Russia

Received July 12, 2007

Abstract—Methods for determining the distribution ratios of volatile substances between liquid and gas phases, based on gas–liquid chromatography or gas extraction in systems with constant or variable volume under static or dynamic conditions, are classified and described, and their application fields are indicated.

DOI: 10.1134/S1070427208030014

INTRODUCTION

The distribution ratio K, i.e., the ratio of the equilibrium concentrations of a substance in the liquid (c_L) and gas (c_G) phases

$$K = c_L/c_G, \quad (1)$$

is the most important characteristic of a heterogeneous liquid–gas system. The quantity K is dimensionless, but can be different for a given system depending on the concentration scale chosen. In analytical measurements, c_L and c_G are commonly expressed in mass concentrations (mass in volume), because these units considerably simplify the calculations, as data on the molecular masses and densities of the gas and liquid are not required. Furthermore, the distribution ratios in the mass and molar concentration scales coincide. Knowledge of the distribution ratios is necessary for the development and optimization of many industrial and laboratory chemical processes.

Formula (1) expresses the Nernst distribution law. The quantity K is constant for ideal systems and strongly diluted nonelectrolyte solutions to which the Henry law is applicable. The distribution ratio generally depends on the solution composition. The area in which the Henry law is obeyed (and K is constant) depends on particular system. For example [1], for solutions of lower alcohols in nonpolar solvents, the upper limit of this area is on the level of 0.1 mol %. Solutions of low-boiling hydrocarbons (*n*-pentane, *n*-hexane) in high-boiling hydrocarbons (squalane) obey the Henry law up to a concentration of ~1.5, and systems of polar components (water–methanol), up to a concentration of ~0.5 mol %.

In the case of dilute solutions, the distribution ratio and its temperature dependence allow calculation of the limiting activity coefficients of solutes γ^∞, which are useful for the calculation of the thermodynamic properties of dilute solutions, determination of the parameters of molecular-statistics models for simulating phase equilibria in a wide range of conditions [1], estimation of the energy of solvation of solutes [2], and evaluation of intermolecular interactions in solutions.

For solutions of limit dilution, the distribution ratio can be calculated from physicochemcial constants of the solvent and *i*th solute by the formula [1]

$$K_i = RTd_L/(\gamma_i^\infty p_i^0 M_L), \quad (2)$$

if the following quantities are known or can be measured: saturated vapor pressure p_i^0 and limiting activity coefficient γ_i^∞ (symmetrical normalization) of the solute, and the molecular weight M_L and density d_L of the solvent. In formula (2), R is the universal gas constant and T is temperature (K).

A powerful tool for determining the content of volatiles in liquid and gaseous objects is gas-chromatographic head-space analysis (HSA) [3–5]. This method is based on the principles of gas extraction [6], i.e., on the distribution of a substance in the liquid–gas system. Therefore, the key parameter determining the reliability of measurements of the content of volatiles in liquid and gas media is the distribution ratio K.

There are two ways of determining K by chromatographic and head-space analysis. The first way is gas–liquid chromatography (dynamic GLC) in which volatile substances are distributed between the mobile gas phase and stationary condensed phase. The second way is based on the gas extraction. It also involves chromatography, but the substance to be determined is distributed between the gas and liquid phases in a vessel arranged beyond the chromatographic system. In this case, the absolute or relative concentrations of a substance in one or both phases of the equilibrium system are determined by gas chromatography.

These principles underlie different procedures for gas-chromatographic determination of K, each of which has certain advantages, specific features, and limitations. For the majority of methods, such information is lacking.

In this paper, we systematize gas-chromatographic methods for measuring the distribution ratios of volatile substances between the liquid and gas phases, describe the principles and implementation of the majority of these methdos, and assess their potentialities (range of measurable values of K and attainable accuracy). In addition, we consider methods that are not yet used in experiments but deserve attention.

DETERMINATION OF DISTRIBUTION RATIOS BY GLC FROM RETENTION PARAMETERS

The distribution ratios of volatile compounds between the condensed and gas phases affect the retention of components in a chromatographic system. Measurement of K by GLC is based on the dependence of the retention volume V_R on the distribution ratio [1, 7]:

$$V_R = V_M + KV_L. \quad (3)$$

Therefore, K can be calculated from the retention parameters:

$$K = (V_R - V_M)/V_L = V'_R/V_L, \quad (4)$$

where V_M is the so-called dead volume, i.e., the volume of the gas phase of the chromatoghaphic system; V'_R, corrected retention volume; and V_L, volume of the stationary phase in the chromatographic system.

Under actual conditions of the chromatographic analysis, the gas phase of the system is under excess pressure. Because of the gradient of the carrier gas pressure, arising along the column (P_i is the inlet pressure and P_0, outlet pressure), an additional empirical parameter j, compressibility of an ideal carrier gas [8]

$$j = \frac{3(P_i/P_0)^2 - 1}{2(P_i/P_0)^3 - 1}$$

or a real carrier gas [9]

$$j = \frac{3(P_i/P_0)^4 - 1}{2(P_i/P_0)^3 - 1}$$

is introduced into Eq. (3):

$$V_R j = V_M j + KV_L,$$

whence follows

$$K = V'_R j/V_L, \quad (5)$$

This approach to the determination of the distribution ratios was developed in detail more than 50 years ago [10–12], at the outset of the development of gas–liquid distribution chromatography. Papers [10–12] are still topical. The modern viewpoint on the potentialities, limitations, and application prospects of the chromatographic method for measuring the distribution ratios is reflected in Castells' review [13].

Experimental implementation of the method is fairly simple and mainly requires only the standard chromatographic equipment. Therefore, determination of K of volatile substances from the parameters of their retention by the stationary phase is very popular and is widely used not only for analytical purposes, but also in studies of thermodynamic properties of dilute solutions. As much as 95% of data on the limiting activity coefficients of volatile substances in solutions were obtained by this dynamic method [1]. Although in most cases high-boiling liquids are used as stationary phases, there are examples of using relatively volatile liquids such as water and blood [14].

Despite simplicity of the method, to obtain accurate and reliable results it is necessary to solve certain problems. The main of them are to evaluate accurately the gas volume in the column V_G and dead volume V_M, corrected for the vaporizer and detector volumes, and to take into account an increase in the gas volume of the system upon vaporization of the sample. Furthermore, problems may arise with the accurate evaluation of C_L, which is usually calculated from the mass and density of the liquid phase. In rigorous consideration of the correlation between the retention volume and distribution ratio, it is necessary to take into

account the nonideality of the vapor phase and the solubility of the carrier gas in the stationary liquid phase [1, 7].

The sorption effects on the phase boundary in a chromatographic column can also give rise to serious problems in measurements of K from the retention parameters, because the procedure for calculating K is based on the assumption that V'_R is governed only by the dissolution of substances being chromatographed in the stationary phase in accordance with (3) or (5). At the same time, as early as the 1960s it was shown [15–21] that Eq. (5) is a particular case of the general equation

$$V_R j = KV_L + K_{G/L}S_L + K_{L/S}S_S, \quad (6)$$

taking into account not only the absorption of a substance by the liquid phase (first term), but also its adsorption on the liquid–gas phase boundary (surface area S_L, adsorption coefficient $K_{G/L}$, second term) and on the solid support surface under the layer of the liquid phase (surface area S_S, adsorption coefficient $K_{L/S}$, third term).

The contribution of adsorption on the liquid phase surface to the retention of a substance by the column packing, examined by Martin [15], may be very significant. For example, in chromatographic analysis of nonpolar substances (hydrocarbons) on polar phases, the effects of dissolution in the liquid phase and adsorption on its surface make comparable contributions. In other cases, the contrubution of the second term of Eq. (6) depends on the active surface area of the solid support and amount of the liquid phase on it.

The effect exerted on V'_R by adsorption on the solid–liquid phase boundary, revealed for the first time in [17–21], becomes considerably more pronounced with a decrease in the thickness of the liquid layer on the solid support and with an increase in the surface area of the support. Therefore, the amount of the stationary liquid phase in the column packing should be no less than 10–15%. The general case of simultaneous occurrence of the absorption and two kinds of adsorption was considered in [18, 21, 22]. Quantitative evaluation of additional adsorption interactions in the course of gas-chromatographic analysis of substances of different classes, with 1,2,3-tris(2-cyanoethoxy)propane (TCEP) as stationary phase and Chromosorb W or fire-brick as support, showed that the adsorption contribution to the retention volume of certain organic substances ranges from 40 to 70%.

The results of studying adsorption effects in chromatographic analysis of polar and nonpolar substances on a column with a polar stationary phase (TCEP), plotted in Fig. 1 [21], show that the specific retention volume V_g^0[1] of such polar substances as benzene, vinyl acetate, cyclohexene, and acetone linearly increases with the amount of the liquid phase at its content exceeding 4–8%. At a lower amount of the stationary phase, V_g^0 dramatically increases. Nonpolar hydrocarbons show anomalous behavior on this sorbent. With a decrease in the liquid phase content on the solid support (INZ-600 fire-brick), V_g^0 increases. This fact is paradoxical for gas–liquid distribution chromatography. The main cause of such behavior of nonpolar substances is their sorption on the surface of the polar phase, which makes the major contribution to the retention of substances by the column packing. Some curves in Fig. 1 intersect. This effect corresponds to the inversion of the order in which the components of the same mixture are eluted, depending on the content of the liquid phase on the solid support.

Significant and difficult-to-reveal systematic errors in measurements of the distribution ratios can be eliminated by taking into account the adsorption contribution to V'_R or by performing measurements under the conditions when this contribution is negligible. The contribution from adsorption on the solid support can be reduced by modification of the support surface with high-boiling polar substances reacting with the active surface of the support, or with substances forming protective polymeric films on the solid surface (dimethyldichlorosilane, dimethyldisilazane, etc.).

According to the existing extimates [1, 23], the error of measuring K and γ^∞ varies within 1–4% if corrections for the nonideality of the vapor phase are not required and there are no additional adsorption interactions. However, if the vapor phase is essentially nonideal and if the adsorption effects noticeably contribute to the chromatographic retention parameters, the error in measuring the distribution ratios or activity coefficients can reach tens of percents [24].

METHODS FOR MEASURING DISTRIBUTION RATIOS BY GAS EXTRACTION

Direct determination of K by measuring the absolute concentrations of a substance in the liquid and gas phases, with the calculation by Eq. (1) [25–27], is used seldom. The main reason is the necessity of calibration of the chromatograph for liquid and gas mixtures, which considerably complicates the analysis and decreases its accuracy.

[1] V_g^0 is calculated by dividing V'_R by the mass of the column packing.

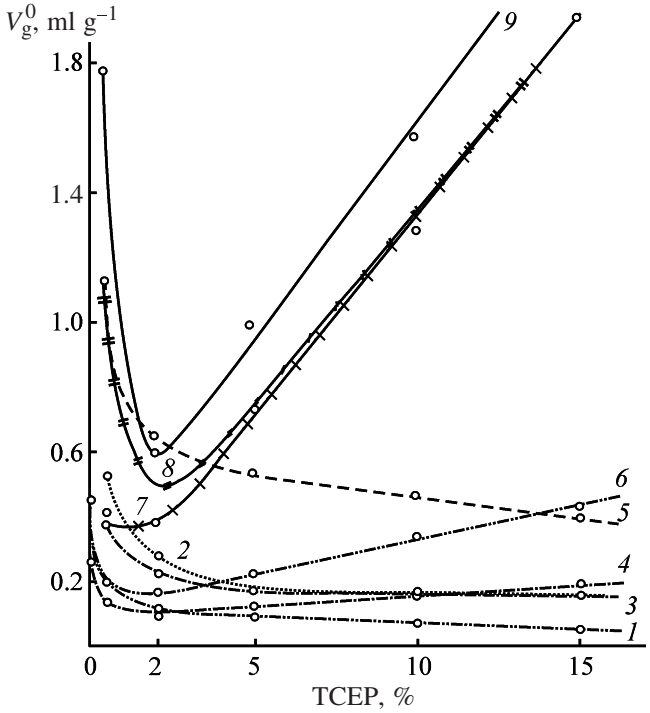


Fig. 1. Specific retention volume V_g^0 as a function of the content of TCEP liquid phase on INZ-600 solid support: (*1*) *n*-hexane, (*2*) 2,2,4-trimethylpentane, (*3*) *n*-heptane, (*4*) cyclohexane, (*5*) *n*-octane, (*6*) cyclohexene, (*7*) benzene, (*8*) vinyl acetate, and (*9*) acetone. Conditions of gas-chromatographic analysis: PAI chromatograph, model 12001, argon ionization detector; glass column 1.25 mm long, 4 mm i.d.; particle size of the solid support 0.17–0.25 mm; column temperature 50°C; carrier gas argon, flow rate 25 ml min^{-1}.

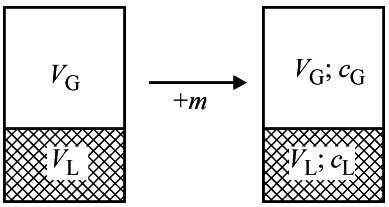


Fig. 2. Scheme of head-space determination of the distribution ratio by absolute calibration of the gas phase (Rohrschneider's method). For comments, see text.

Rohrschneider [28] suggested a procedure involving absolute calibration for the gas phase only. In that study, an automatic apparatus for head-space analysis was used for the first time, and ample data were obtained on the distribution ratios of selected reference substances (octane, toluene, ethanol, methyl ethyl ketone, dioxane, nitromethane) in 81 solvents differing in the polarity. These data are still of interest.

Rohrschneider's method consists in injecting a portion of a target substance of accurately measured volume or mass with a microsyringe into a glass vessel stoppered with an elastic plug, containing a solvent of volume V_L and a gas phase of volume V_G (Fig. 2). After the phase equilibrium is attained, the absolute concentration c_G in the gas phase is determined from the chromatographic peak height using the preliminarily obtained calibration plot. The distribution ratio is calculated in accordance with the given volume ratio of the gas and liquid phases $r = V_G/V_L$ by the formula

$$K = mV_L r/c_G. \quad (7)$$

The accuracy of the distribution ratios thus determined was not reported; according to our estimates, the error is no less than 5–10%.

A kind of absolute calibration is used for studying the thermodynamic characteristics of dilute solutions. Measurement of the limiting activity coefficients is based on relating the partial pressure of a volatile substance p_i over a solution with the known molar concentration of this substance $x_{i,L}$ to the saturated vapor pressure of the pure substance p_i^0. The equilibrium gas phase is subjected to gas-chromatographic analysis, p_i and p_i^0 are determined from the peak areas in the chromatogram (A_i^0 and A_i^0) at ultimate dilutions and in the range of the linear detector response, and γ_i^∞ is calculated by the formula [1, 29]

$$\gamma_i^\infty = \frac{p_i/p_i^0}{x_{i,L}} = \frac{A_i/A_i^0}{x_{i,L}}. \quad (8)$$

From γ_i^∞, it is possible to calculate the distribution ratio by formula (2). In contrast to Rohrschneider's method, in this case the absolute calibration is performed for solutions with the given molar concentrations of the solute $x_{i,L}$. However, this method is applicable only to systems with relatively high distribution ratios, considerably exceeding the volume ratio of the equilibrium phases in the vessel. In such cases, a change in the preset value of $x_{i,L}$ due to transfer of a part of the substance into the gas phase in the course of attainment of the phase equilibrium can be neglected. In the overwhelming majority of papers, the method is implemented under static conditions on automatic head-space analyzers [3–5, 24, 29], but a circulation pattern of head-space dosage has also been reported [30].

The progress of head-space chromatographic analysis and the development of its new versions led to the development of indirect methods for measuring *K*,

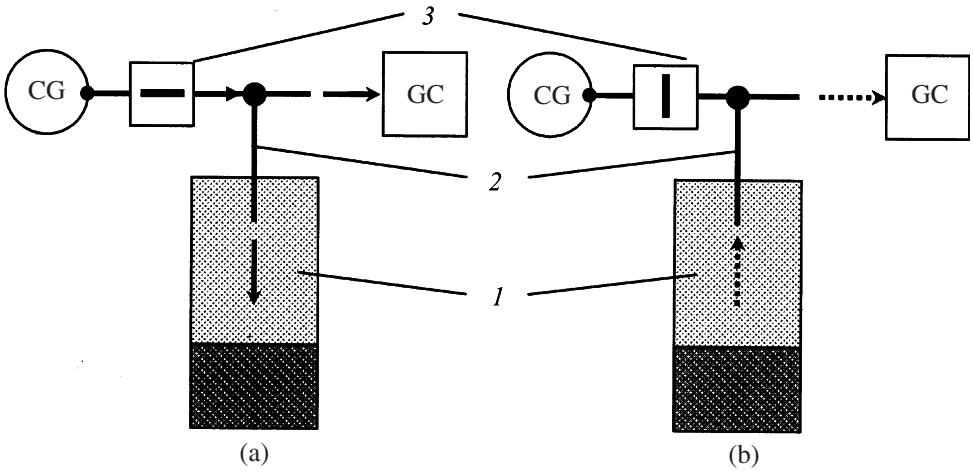


Fig. 3. Scheme of pneumatic head-space injection of equilibrium gas into a chromatograph from constant-volume vessels by providing a pressure differential at the moment of dosing (used in automatic head-space analyzers produced by Perkin–Elmer): (a) making excess pressure in the vessel with the sample and (b) dosing the equilibrium gas into a chromatograph. (CG) Source of stabilized carrier gas flow and (GC) gas chromatograph. (*1*) Vial with a sample of a solution to be analyzed, (*2*) heated needle of head-space dosing unit, and (*3*) automatically controlled electromagnetic valve.

consisting in evaluation of the change in the substance concentration in one of the phases after bringing it into a thermodynamic equilibrium with the other phase or after changing the system parameters. The main advantage of the methods developed is that K can be calculated solely from a relative change in the detector signal (peak area in the chromatogram). This procedure eliminates systematic inaccuracies associated with the determination of the absolute concentrations of a substance in the equilibrium phases and makes the results considerably more reliable. This principle was implemented in various procedures for determining K, based on single, multiple, and continuous gas extraction (CGE).

The devices used in HSA for gas extraction and subsequent dosing of the equilibrium gas into a chromatograph can be subdivided into two groups. Vessels of the first group have a constant volume, and doses[2] are taken at varied pressure. Vessels of the second group have variable volume of the gas phase, and doses are taken at a constant pressure. The constant-pressure mode is also realized in all dynamic versions of HSA. Each of these groups of devices has certain specific features which should be taken into account in choosing a procedure for sample preparation, a version of quantitative analysis, and a method for dosing gas samples into a chromatograph.

[2] By the dose is inderstood the volume of the gas phase taken from the equilibration vessel and injected into a chromatograph, and by the sample is understood the volume or mass of the solution to be analyzed (condensed phase) injected into the equilibration vessel.

Constant-volume vessels are used fairly frequently. In the standard HSA apparatus, such vessels are glass vials of the volume ranging from 10 to 25 ml. The equilibrium gas from these vials is dosed into a chromatographic column by several methods [3–5], most frequently by the pneumatic method used in automatic head-space analyzers. Pneumatic dosing is based on making a pressure differential between the vaporizer of the chromatograph and the vessel with the sample to be analyzed. This principle was implemented for the first time in the most perfect apparatus for head-space analysis, developed by Perkin–Elmer (Fig. 3). Vial *1* with a solution sample is connected via a special heated needle *2* to the carrier gas line. In the process, valve *3* of the dosing unit is open, and excess pressure equal to the gas pressure in the chromatograph vaporizer is made in the vial. The required pressure differential in this unit (Fig. 3a) is provided at the moment of dosing by automatically cutting off the carrier gas flow by valve *3*, which is followed by a decrease in the pressure in the chromatograph vaporizer (Fig. 3b).

An ingenious device for HSA with pneumatic dosing was developed in the Laboratory of Gas Chromatography of the St. Petersburg State University [31]. This device differs from the Perkin–Elmer dosing unit in that the pressure differential in it is provided in advance with an additional carrier gas line (CG_2), by setting in a vessel with a sample the pressure p' that is higher than the pressure p in the chromatograph vaporizer (Fig. 4a) [32]. The subsequent connection of the gas space of vessel *1* with the chromatograph vapor-

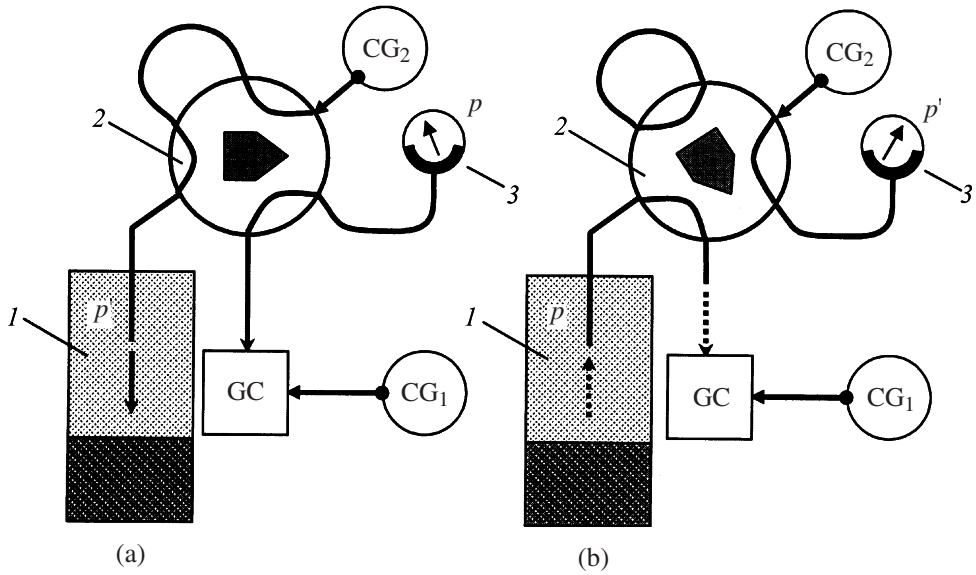


Fig. 4. Scheme of pneumatic head-space dosing of equilibrium gas into a chromatograph from constant-volume vessels with preset pressure differential: (a) making excess pressure in the vessel with the sample and (b) dosing the equilibrium gas into the chromatograph. (CG_1) Source of stabilized carrier gas flow fed to a chromatographic column, (CG_2) source of carrier gas providing the preset pressure in the vessel with the sample, and (GC) gas chromatograph. (*1*) Vial with a sample of a solution to be analyzed, (*2*) two-position gas stopcock, and (*3*) manometer.

izer via stopcock *2* provides rapid injection of the dose whose volume at atmospheric pressure v_g is determined not only by the difference between the pressures in the equilibration vessel (p') and the gas circuit of the chromatograph (p), but also by the volume of the gas phase of the heterogeneous system V_G:

$$v_g = V_G(p' - p)/p'. \quad (9)$$

This version of the pneumatic method allows accurate measurement and setting of the pressure differential and thus calculation and control of the volume of the equilibrium gas taken from the vessel.

The main advantage of the pneumatic head-space dosing is pulsed injection of the equilibrium gas directly from a vessel with a sample into a chromatographic column, without injection into intermediate units, which decreases the sorption loss and the "memory" of the dosing unit. Maintenance of a stable pressure differential provides high reproducibility of dosing of the equilibrium gas (on the level of tenth fractions of percent), and short and well heated gas tubes connecting the vial with the chromatographic column cardinally reduce the substance loss. Furthermore, pneumatic dosing can be automated more readily than other methods of injecting the equilibrium gas into a chromatograph.

"Pseudopneumatic" head-space dosing is widely used in standard gas-chromatographic apparatus produced by many companies. In this method, the equilibrium gas is injected into a chromatograph with a temperature-controlled gas stopcock whose dosing volume is filled with the gas phase from the vial by the pneumatic method (Fig. 5). To this end, excess pressure p in a vessel with a sample is provided by connecting it to an additional carrier gas line (CG_2) (Fig. 5a). The subsequent connection of vessel *1* with gas stopcock *2* occurring in the position indicated in the scheme by solid lines fills dosing loop *3* with the equilibrium gas (Fig. 3b). By turning stopcock *2* to the position indicated in the scheme by dashed lines, the equilibrium gas is dosed into a chromatograph.

A specific feature of the pseudopneumatic injection of the equilibrium gas into a chromatograph is that the concentration of the target substance in the dosing volume (loop) of the stopcock (at atmospheric pressure), as compared to its concentration in the gas phase of the vessel with the sample, decreases with an increase in the preliminarily created pressure p. As a result, the sensitivity of the analysis somewhat decreases. Furthermore, repeated pneumatic dosing of the equilibrium gas into a chromatograph from the same vial leads to a considerably greater decrease in the concentration of the target substance in the dose, which is the more pronounced, the lower the distribution ratio.

Dosing of the equilibrium gas from constant-vol-

ume vessels leads to a change in the initially set concentration of the substance in solution and in the gas phase over it. In many cases this is a drawback, because the possibility of repeated dosing of the equilibrium gas is limited by the parameters of the system being analyzed (values of K and r), volume of the dose taken, and required reproducibility of detector readings at successive injection of a gas with a constant substance concentration into a chromatograph.

With variable-volume vessels (namely, glass syringes of the volume ranging from 10 to 200 ml), the limitations of pneumatic dosing are eliminated, and doses of the equilibrium gas can be repeatedly taken from a vessel with a sample without changes in the substance concentration in the contacting phases [33]. This is due to the preservation of the initially set pressure in the system. A decrease in the pressure in the vessel after removing a certain volume of the gas is compensated by a decrease in the total volume of the system.

The equilibrium gas is dosed into a chromatographic column with a gas stopcock in accordance with the scheme shown in Fig. 6. The equilibrium gas displaced from vessel *1* fills dosing loop *3* of the gas stopcock set in the position indicated in the scheme by solid lines. By turning stopcock *2* into the position indicated by dashed lines, the dose is injected into the gas chromatograph (GC).

The major advantage of using variable-volume vessels for HSA is the possibility of taking liquid or gaseous doses from a liquid–gas heterogeneous system without disturbing the previously attained phase equilibrium. Therefore, the number of repeated measurements of the substance concentration in the gas phase is limited only by the gas phase volume.

Head-space injection of doses in this mode ensures the reproducibility of measuring the substance concentration in the gas phase on the level of no less than 1% and allows implementation of static versions of HSA, based on complete or partial replacement of the equilibrium gas by a pure extractant gas, and also of other versions involving a change in the volume of the system.

The drawback of systems with variable volume of the gas space, along with difficulty of HSA automation, consists in the necessity of using gas stopcocks for dosing the equilibrium gas into a chromatographic column. This may give rise to sorption loss and to the effect of "memory" of the dosing units in analysis of microimpurities, especially of those of polar substances.

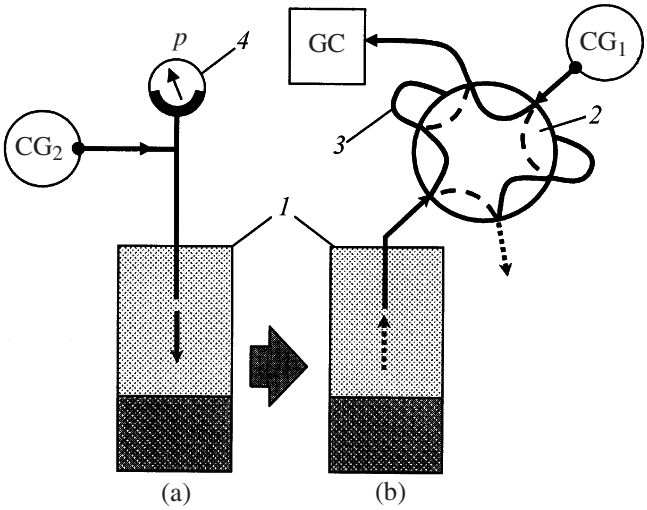


Fig. 5. Scheme of "pseudopneumatic" head-space dosing of the equilibrium gas into a chromatograph: (a) making excess pressure in a vessel with a sample; (b) filling the dosing loop with the equilibrium gas and dosing it into a chromatograph. (CG_1) Source of stabilized carrier gas flow fed to a chromatographic column, (CG_2) carier gas source providing the preset pressure in the vessel with the sample, and (GC) gas chromatograph. (*1*) Vial with a sample of a solution to be analyzed, (*2*) two-position gas stopcock, (*3*) dosing loop, and (*4*) manometer.

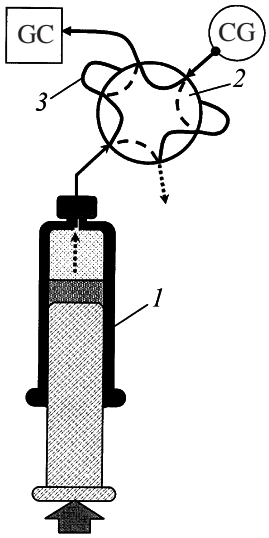


Fig. 6. Scheme of dosing of the equilibrium gas into a chromatograph from a variable-volume vessel: (CG) source of stabilized carrier gas flow and (GC) gas chromatograph. (*1*) Variable-volume vessel (syringe) with a liquid sample, (*2*) two-position gas stopcock, and (*3*) dosing loop.

In dynamic systems (CGA), substances to be determined are usually injected directly into a chromatographic column with a gas stopcock kept at an elevated temperature, whose dosing volume (loop) is

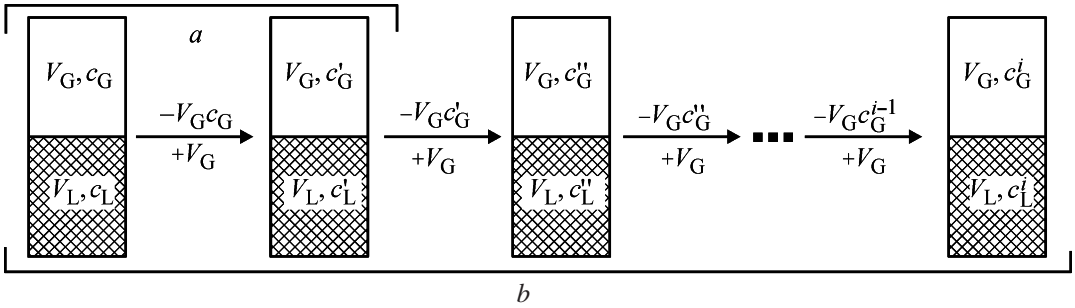


Fig. 7. Scheme of (*a*) repeated and (*b*) multiple gas extraction with complete replacement of the equilibrium gas by the pure gas. For comments, see text.

continuously flushed with a flow of a gas that has been passed through a solution being analyzed or over it.

Gas Extraction with Complete Replacement of the Equilibrium Gas by the Pure Gas

Complete replacement of the equilibrium gas by the pure gas can be realized only in variable-volume vessels, e.g., in glass syringes of the volume 10–100 ml [34, 35]. As early as the 1970s, two versions of this method, based on repeated [34–36] and multiple [37, 38] gas extraction under static conditions, were developed. These versions are still used for analytical and physicochemical measurements.

Repeated extraction. In an equilibrium liquid–gas system (Fig. 7, block *a*) with the volatile substance concentrations c_L in the liquid phase of volume V_L and c_G in the gas phase of volume V_G, after replacement of the whole volume of the equilibrium gas by the pure gas of the same volume and attainment of the phase equilibrium, new concentrations of the substance in the liquid (c'_L) and gas (c'_G) phases will be attained. According to the material balance equation

$$V_L c_L = V_L c'_L + V_G c'_G,$$

in the region of limit dilution the quantity K can be calculated by the formula

$$K = c'_G r/(c_G - c'_G).$$

In the range of linear detector response, at constant conditions of gas-chromatographic analysis, when $c_G/c'_G = A_G/A'_G$, this expression takes the form

$$K = A'_G r/(A_G - A'_G). \quad (10)$$

where A_G and A'_G are the peak areas in the chromatograms of the gas phases with the substance concentrations c_G and c'_G, respectively.

The numerical value of the distribution ratio, as well as the volume ratio of the phases in the vessel in which the equilibrium is attained and the relative error of measuring the peak areas in the chromatograms can significantly affect the accuracy of determining K. If K is large and r is small, the peak areas A_G and A'_G will differ insignificantly. As a result, the relative error of K will be large. This is well illustrated by the equation

$$\Delta K/K = [(\Delta A_G/A_G + \Delta A'_G/A'_G)A'_G]/(A_G - A'_G)$$
$$= [(\Delta A_G/A_G + \Delta A'_G/A'_G)(K + r)]/r, \quad (11)$$

obtained from Eq. (10) assuming that the error of measuring the phase volumes is negligible compared to the error of measuring the peak areas in the chromatograms. It follows from Eq. (11) that, at $r \gg K$, the relative error of measuring the distribution ratio is close to the total error of measuring the peak areas in the chromatograms. With the existing HSA technique, the gas phase volume in variable-volume vessels can exceed the liquid phas volume by a factor of no more than 100, and the accuracy of measuring the peak areas in the chromatogram reaches tenth fractions of percent. Therefore, complete replacement of the equilibrium gas by the pure gas allows measurement of K with a 10% error if $K \le 100$, but only the K values not exceeding 10 can be measured with an accuracy no worse than 1%.

Multiple extraction. This mode involves no less than two complete replacements of the equilibrium gas by a pure gas, i.e., no less than three extractions (Fig. 7, block *b*). The substance concentration in the gas phase after nth replacement or $(n + 1)$ extraction, c^i_G, is related to c_G by the equation [5]

$$c^i_G = c_G[K/(K + r)]^n, \quad (12)$$

from which it follows that, in the range of the linear distribution isotherm under the conditions of equilib-

rium distribution of a substance between two phases, the logarithm of the relative concentration of a substance in the gas phase, $\ln(c_G/c_G^i) = \ln(A_G/A_G^i)$, in the course of multiple gas extraction linearly increases with the number of replacements. The slope of this dependence, $\varphi = \ln[(K + r)/K]$ allows calculation of the distribution ratio provided that the volume ratio of the phases r is known.

The shape of the dependence $\ln(A_G/A_G^i) = f(n)$ is determined by the ratio of K and r. At $K \gg r$, the slope $\varphi \to 0$, and the peak area in the chromatogram A_G^i corresponding to the concentration c_G^i decreases insignificantly even after a large number of extraction runs. For example, at $K = 10^3$ and $r = 10$, after 11 extraction runs the concentration in the gas phase C_G^i differs from c_G by only 1.4%. In this case, it is impossible to calculate the distribution ratio with acceptable accuracy. At $K \ll r$, the concentration c_G^i drastically decreases after each extraction run. In this case, it is also difficult to calculate the distribution ratio, because the extent to which c_G^i decreases in each subsequent extraction is mainly determined by the ratio of the phase volumes in the system. The optimal conditions for measuring the distribution ratios by this method are when the values of K and r are close or comparable.

From the results of measuring A_G and A_G^i by multiple gas extraction, K can also be calculated by the formula

$$K = [(A_G/A_G^i)^{1/n}]^{-1} r. \quad (13)$$

By differentiating (13), we obtain a relationship for the relative error of measuring the distribution ratios by this method:

$$\Delta K/K = [(\Delta A_G/A_G + \Delta A'_G/A'_G)(A_G/A_G^i)^{1/n}] \times \{n[(A_G/A_G^i)^{1/n} - 1]\}^{-1}, \quad (14)$$

whence follows that an increase in the number of extraction runs decreases the relative error of measuring the distribution ratio and thus increases the upper limit of the K values accessible to determination. However, in such cases the analysis becomes more time-consuming. Therefore, it is appropriate to use multiple gas extraction with complete replacement of the equilibrium gas by the pure gas for determining large values of K (exceeding several hundreds), when single replacement of the equilibrium gas by the pure gas, even with r as large as possible, leads to only minor differences between A_G and A_G^i.

Gas Extraction with Partial Replacement of the Equilibrium Gas by the Pure Gas

This mode is used for measuring the distribution ratios of volatile substances with low K or in cases when complete replacement of the equilibrium gas by the pure gas is impossible. Partial replacement of the equilibrium gas phase by the pure gas can be performed in variable- and constant-volume vessels. However, only multiple extraction with partial replacement of the gas phase in constant-volume vessels has been realized in practice [39]; this procedure was termed multiple head-space extraction (MHE). The method is based on an exponential decrease in the concentration of a volatile substance in the gas phase of a vessel with a liquid sample in the course of successive sampling of the same fraction of the gas volume β:

$$\beta = v_g/V_G,$$

where v_g is the volume of the gas phase replaced by the pure gas.

The gas dosing and incomplete replacement of the equilibrium gas by the pure gas are performed by the pneumatic method under the conditions of excess pressure in the system, by relieving a part of the gas from the vessel (Fig. 8). In this case, excess pressure in the system first decreases from p' to p, after which the initial pressure is restored by introducing the volume of the pure gas equal to the volume of the equilibrium gas taken for the analysis.

The advantages of this version of head-space extraction are easy automation and the possibility of attaining high reproducibility of β, which at pneumatic dosing is calculated from the preset pressure differnetial by the formula

$$\beta = 1 - p/p'. \quad (15)$$

According to the equation [5, 39]

$$A_G^i = A_G e^{-q(i-1)}$$

or

$$\ln A_G^i = -q(i-1) + \ln A_G, \quad (16)$$

the slope of the dependence of $\ln c_G^i$ on $(i - 1)$, i.e., on the number of partial replacements of the equilibrium gas by the pure gas, allows calculation of the factor Q given by the relationship

$$Q = A'_G/A_G = A''_G/A'_G = ... = A_G^i/A_G^{i-1} = e^{-q},$$

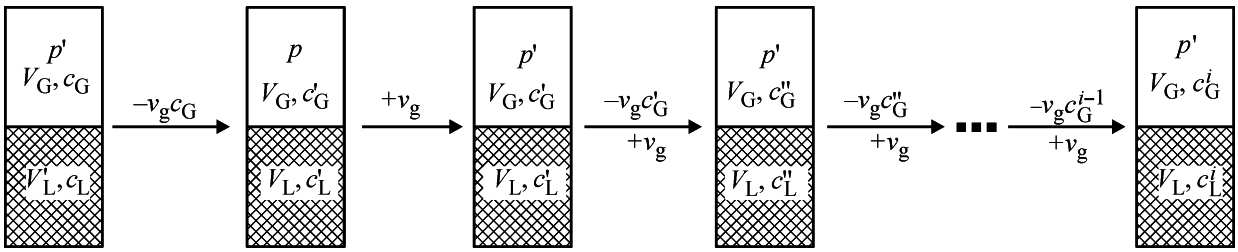


Fig. 8. Scheme of multiple head-space extraction (MHE) with partial replacement of the equilibrium gas by the pure gas in constant-volume vessels. For explanations, see text.

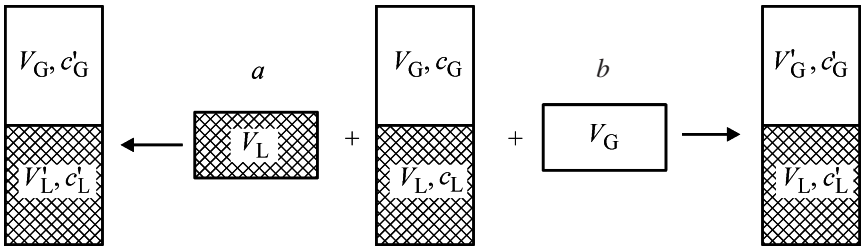


Fig. 9. Scheme of measuring the distribution ratio by the method involving variation of the phase volume ratio in variable-volume vessels by adding an additional amount of the (*a*) liquid solvent or (*b*) extractant gas.

where A_G and A_G^i are the peak areas in the chromatograms coresponding to the substance concentrations in the gas phase in the first (c_G) and *i*th (c_G^i) extraction runs; q is a constant; and i is the number of extraction runs.

The quantity Q is related to K, r, and fraction of the equilibrium gas taken for analysis β by the equation [38]

$$Q = \frac{K/r + 1 - \beta}{K/r + 1}, \quad (17)$$

whence follows

$$K = [(Q + \beta - 1)(1 - Q)]r. \quad (18)$$

Thus, the slope of dependence (16) in combination with the phase volume ratio r and the pressure differential p/p' set in the experiment allows calculation of K. The maximal values of K that can be measured by this method reach several tens.

Method of Varying the Phase Volume Ratio

The method is based on the dependence of the concentration of a volatile substance in the gas phase of a liquid–gas system, c_G, on the initial concentration of the substance in solution, c_G^0, and phase volume ratio r. This dependence is illustrated by the main relationship of quantitative head-space analysis [3, 4, 6]

$$c_G = c_L^0/(K + r), \quad (19)$$

The method can be impemented with variable- and constant-volume vessels. The principal difference between these versions is that, in variable-volume systems, the mass of the substance distributed between the liquid and gas phases is the same, whereas in constant-volume systems different portions of the same amount of the target substance are distributed. This difference changes essentially the technique and procedure of the experiment and the methods for calculating K.

Variable-volume systems. Measurements are usually performed in glass syringes of the volume larger than 50 ml and involve addition of a known amount of the pure gas or liquid (free of the substance being determined), to an equilibrium liquid–gas system containing the substance being distributed in an amount of $V_L c_L + V_G c_G$. For the case of adding the gas (Fig. 9, block *b*), the material balance equation takes the form

$$V_L c_L + V_G c_G = V'_L c'_L + V'_G c'_G. \quad (20)$$

If V'_G exceeds V_G by a factor of n_G, the distribution ratio can be calculated from the results of gas-chromatographic measurements of the concentrations c_G and c'_G (in the form of peak areas A_G and A'_G) in accordance with Eq. (20) by the formula

$$K = (n_G A'_G - A_G)r/(A_G - A'_G). \quad (21)$$

As in the previous cases, the accuracy of determin-

ing K by this method strongly depend on the experimental conditions (r and n). According to (21),

$$\Delta K/K = (\Delta A_G/A_G + \Delta A'_G/A'_G)[A_G/(A_G - A'_G)]$$
$$\times [A'_G(n - 1)]/(nA'_G - A_G)$$
$$= (\Delta A_G/A_G + \Delta A'_G/A'_G)\{[(K + rn)(K + r)]/[Kr(n - 1)]\}. \quad (22)$$

It follows from Eq. (22) that the error of determining the distribution ratio decreases with increasing n, and the quantity r should not be much greater than K. At maximal values of n and r not exceeding 20, K values as large as several hundreds can be calculated accurately to within 10%.

When a liquid solvent is added to an equilibrium liquid–gas system to a volume V'_L exceeding V_L by a factor of n_L (Fig. 9, block *a*), the distribution ratio is calculated by the formula

$$K = r(A_G - A'_G)/(n_L A'_G - A_G), \quad (23)$$

similar to (21). The experimental conditions and the maximal measurable values of K only slightly differ from those given for the case when the volume of the gas phase is increased.

Constant-volume systems. The version suggested in [7, 40] for constant-volume vessels was termed the phase ratio variation (PRV) method. If different volumes of a solution with a constant concentration of a volatile substance are introduced into several vessels of the same capacity V (Fig. 10), then, after the attainment of the phase equilibrium under isothermal conditions, different values of c_G and r will be attained in these vessels, whereas the quantity K will remain constant in the range of limit dilutions. The main relationship (19) for single extraction under static conditions can be presented in the form

$$1/c_G = r/c^0_L + K/c^0_L. \quad (24)$$

Equation (24) can be presented in the form of a linear dependence of the type $y = ax + b$, where $y = 1/c_G$, $x = r$. The experimental measurement of the concentrations c^i_G in the form of chromatographic peak areas A^i_G at different r values allows determination of the slope $a = 1/c^0_L$ and initial ordinate $b = K/c^0_L$ of this dependence. The distribution ratio is calculated from these two quantities:

$$K = b/a. \quad (25)$$

According to [5, 7, 40], it is appropriate to use the PRV method at $K \le 100$. Its main advantage is the use

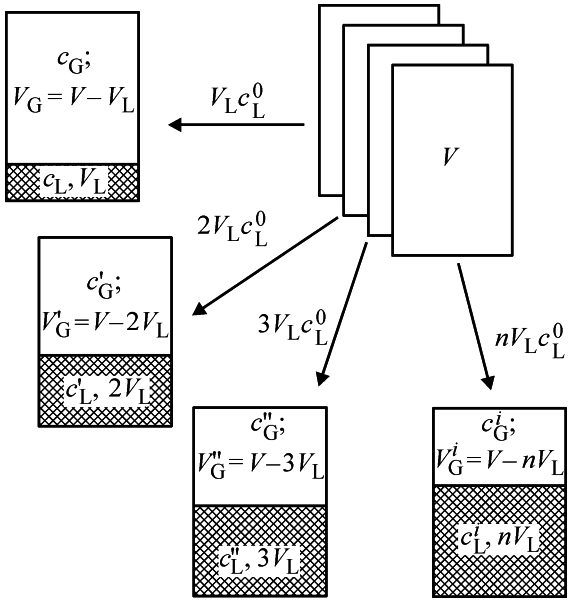


Fig. 10. Scheme of measuring the distribution ratio by varying the phase volume ratio (PRV) in constant-volume vessels. For explanations, see text.

of automatic apparatus for gas-chromatographic head-space determination of c_G. Among drawbacks are possible problems with sampling of the same dose of the gas phase from different vessels in pneumatic head-space dosing of samples into a chromatographic column.

Chai and Zhu [41] described a similar but less labor-consuming method, phase ratio calibration (PRC), which can also be implemented in constant-volume systems. It differs from the PRV method in that only two vessels of the same volume V are used. Different volumes V_L and V'_L of the same solution containing a volatile substance which is distributed between the phases are added into these vessels. After the attainment of the phase equilibrium and gas-chromatographic determination of the substance concentration in the gas phase in each vessel, c_G and c'_G, in the form of peak areas A_G and A'_G, the distribution ratio is calculated by the formula

$$K = [A_G(V - V_L) - n_L A'_G(V - V'_L)]V_L(A'_G - A_G), \quad (26)$$

where $n_L = V_L/V'_L$.

A sort of the PRV and PRC methods is the EPICS (equilibrium partitioning in closed systems) method [42] in which equal amounts of a gas mixture are introduced into two vessels hermetically stoppered with elastic rubber plugs. The vessels are of equal capacity but contain different volumes of the liquid

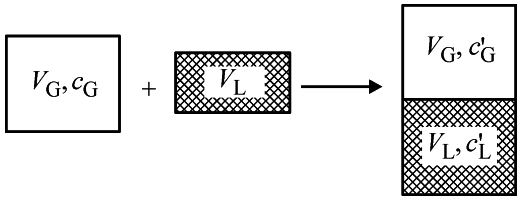


Fig. 11. Scheme of measuring the distribution ratio by introducing a liquid solvent into a gas mixture.

phase, V_L and V'_L, with concentrations c_L and c'_L, and hence different gas volumes V_G and V'_G with concentrations c_G and c'_G. Since equal amounts of a substance distributed between the phases are introduced into the vessels, the mass balance has the form similar to Eq. (20):

$$V_L c_L + V_G c_G = V'_L c'_L + V'_G c'_G.$$

and the distribution ratio, provided that $c_G/c'_G = A_G/A'_G$, is calculated by the formula

$$K = (V'_G A'_G - V_G A_G)/V_L A_G - V'_L A'_G). \quad (27)$$

The potentialities of the PRV, PRC, and EPICS methods are comparable as regards the range of measurable values of K and the accuracy actually attained (2–10%). It should be noted, however, that Eqs. (26) and (27), like (21) and (22), contain in the numerator and denominator the differences between the measured quantities A_G and A'_G. If these quantities are close, the error of determining K drastically increases [similarly, e.g., to the case of variation of the phase volume ratio in variable-volume vessels, Eq. (22)]. Therefore, to attain the best (and sometimes acceptable) accuracy in choosing the experimental conditions, it is necessary to provide the difference between the solution volumes V_L and V'_L as large as possible, and this difference should be the greater, the larger the distribution ratio. According to [41], the maximum measurable values of K can reach several hundreds; in this case, the volumes of the liquid phases in the vessels should differ by a factor (n_L) of no less than several tens.

Introduction of a Liquid into a Gas Mixture [31]

The method is based on liquid extraction, i.e., on extraction of volatile substances from a gas volume with a liquid solvent (Fig. 11). It is implemented with variable-volume vessels allowing sampling of the equilibrium gas without affecting the concentration c_G or c'_G in the gas phase. Introduction of a liquid into a gas mixture whose volume remains unchanged provides reliable information on the distribution of volatile substances between the liquid and gas phases in the range of distribution ratios from tenth fractions to several thousands. According to the material balance

$$V_G c_G = V_L c'_L + V_G c'_G.$$

the distribution ratio is calculated by the formula

$$K = r(A_G - A'_G)/A'_G. \quad (28)$$

The relative error of K

$$\Delta K/K = (\Delta A_G/A_G + \Delta A'_G/A'_G)[A_G/(A_G - A'_G)]$$

$$= (\Delta A_G/A_G + \Delta A'_G/A'_G)[(K + r)/K], \quad (29)$$

as in the methods considered above, depends on the extraction conditions. To improve the measurement accuracy, the conditions should be chosen so as to ensure significant difference between A'_G and A_G. According to Eq. (29), this condition, in contrast to repeated head-space extraction, is attained at $K > r$. Therefore, the pattern with the accuracy of measuring K is opposite to that in repeated head-space extraction: The main restrictions concern the lower, rather than higher, limit of K. At accurate measurement of the peak areas in the chromatograms (accuracy no less than 1%) and $r \approx 0.1$, introduction of a liquid into a gas mixture allows measurement of K values no lower than 1 with an error not exceeding 10%.

The uppoer limit is determined by the possibility of measuring the concentration c'_G with acceptable accuracy, i.e., by the admissible decrease in A'_G relative to A_G. According to (28), $A_G/A'_G = (K + r)/r$. If introduction of a liquid into a gas mixture provides $A_G/A'_G \leq 100$, at r close to 100 the maximum measurable values of K reach 10^4.

The vapor phase calibration (VPC) method [5, 7] is essentially similar to the method of introducing a liquid into a gas mixture, but is implemented in constant-volume vessels. Strictly equal masses m (or volumes) of a volatile substance are introduced into two different vessels of volume V, one of which is filled with a neutral gas (air) only, and the other contains a certain volume V_L of a solvent (Fig. 12). After attainment of the phase equilibrium and gas-chromatographic measurement of the substance concentrations in the head space, c_G and c'_G, in the form of chromatographic peak areas A_G and A'_G, the distribution ratio is calculated in accordance with the material balance

$Vc_G = V_G c'_G + V_L c'_L$ by the formula

$$K = [VA_G - (V - V_L)A'_G]/V_L A'_G = A_G(1 + r)/A'_G - r.$$

Although the VPC method is classed with direct methods [43], as follows from its name, it is actually an indirect method, because the absolute concentrations of a substance in the gas phase are not measured and only the peak areas in the chromatogram, along with the phase volumes, appear in the formula for calculating K.

The MHE, PRV, PRC, VPC, and EPICS methods implemented with constant-volume vessels on special chromatographic equipment for HSA are most frequently used in the analytical practice for determining the distribution ratios of volatile compounds in liquid–gas systems. Such automatic head-space analyzers considerably simplify and accelerate the experiments, providing the measurement accuracy acceptable for analytical purposes. However, specific features of pneumatic head-space dosing of the equilibrium gas in some cases may lead to significant systematic inaccuracies. In particular, the dose taken from the equilibration vessel may depend on the volume of the gas phase in it. At the same time, the above methods implemented with pneumatic dosing from constant-volume vessels are based on the compulsory condition that the dose of the equilibrium gas taken from different vessels with different volumes of the gas phase should be the same.

In cases of preliminary setting of the pressure differential (Fig. 4), the dose volume v_g is determined by Eq. (9), i.e., it varies in proportion with V_G, but in this case the fraction of the target compound taken from the gas phase, $v_g/V_G = (p' - p)/p'$, remains constant, as it depends only on the pressure differential.

When the pressure differential is created at the moment of dosing (Perkin–Elmer apparatus, Fig. 3), in Kolb and Etter's opinion [5], the volume of the equilibrium gas injected into a chromatographic column is determined only by the flow rate of the carrier gas at the inlet of the chromatographic column and by the dosing time, but is independent of the pressure. This approach is apparently suitable for rough estimation of the dose, but is absolutely unacceptable for accurate calculations. More rigorous consideration of this version of pneumatic head-space dosing showed that the volume of the equilibrium gas injected into a chromatographic column depends also on the dosing unit temperature, viscosity of the carrier gas, gas-dynamic resistance of the chromatographic column, and other factors, including V_G.

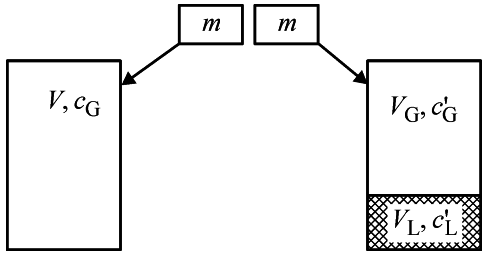


Fig. 12. Scheme of measuring the distribution ratio by vapor phase calibration (VPC) in constant-volume vessels.

The influence exerted by the volume of the gas phase in a vessel with a liquid sample on the amount of a substances pneumatically dosed into a chromatographic column was checked experimentally by the example of head-space analysis of constant-volume vessels containing different amounts of pure *n*-propyl alcohol. A neat volatile compound was chosen as the liquid phase because the saturated vapor pressure, i.e., the concentration of 1-propanol in the gas phase, under isothermal conditions is constant and independent of the volume ratio of the phases in the equilibration vessel. Therefore, if the volume V_G does not affect the dose, the peak areas in the chromatograms of the equilibrium gas taken successively from vessels with different volumes of the gas phase should be equal. If the peak areas will be different, the difference will characterize the extent to which V_G affects the dose volume.

Measurements were performed on a Perkin–Elmer chromatograph, model F-45, with pneumatic dosing of the equilibrium gas into packed and capillary columns. The results (Table 1) show that the volume V_G of the vessel with the liquid sample does affect the amount of the equilibrium gas injected into a chromatographic column.

In our case, e.g., for a packed column, with a decrease in the gas phase volume by 3 ml (from 13.5 to 10.5 mol), the amount of the introduced substance and hence the dose volume decrease by only 2.1%. However, if V_G is decreased by the same 3 ml but from 7.5 to 4.5 ml, the dose decreases by 18%. Larger changes in the volume of the vessel with the sample (very desirable in PRV, PRC, VPC, and EPICS methods) can lead to still larger changes in the dose and hence in significant errors in the determination of K.

Procedures for determining K implemented with variable-volume vessels are used more seldom, because they involve the use of special attachments and devices for HSA, which are not yet produced on the commercial scale. However, these procedures ensure

Table 1. Influence of the gas phase volume in a vessel with a liquid sample of neat 1-propanol on the amount of the substance (chromatographic peak area) injected into a chromatographic column. Analysis conditions: steel packed column 2 m long, 3 mm i.d., liquid phase 10% PEG-4000 on Chromaton N AW, carrier gas helium, 25 ml min^{-1}, dosing time 3 s; or aluminum-coated quartz capillary column 20 m long, 0.53 mm i.d., liquid phase SE-30, layer thickness 3 μm, carrier gas flow rate through the column 5 ml min^{-1}, flow splitting ratio 1 : 2, dosing time 2 s; column temperature 100°C; flame ionization detector, 150°C; injector needle temperature 100°C; column inlet pressure 1 atm

Sample no.	Phase volume, ml		Peak areas in chromatogram, μV s		Change in peak area, A_G^n/A_G^1	
	liquid, V_L	gas, V_G	packed column	capillary column	packed column	capillary column
1	1	13.5	4411	899	1	1
2	2	12.5	4478	877	1.01	0.98
3	4	10.5	4323	862	0.98	0.96
	6	8.5		818		0.91
4	7	7.5	3840		0.87	
	8	6.5		775		0.86
5	10	4.5	3145	699	0.71	0.78
6	12	2.5	2294		0.52	

higher accuracy and wider range of measurable values of K. Furthermore, with variable-volume vessels, as in the pseudopneumatic method, the equilibrium gas is injected into a chromatographic column with a gas stopcock ensuring a constant dose volume. Therefore, in such cases the volume V_G of a vessel with a sample does not affect the dose of the equilibrium gas injected into a chromatographic column.

Comparative evaluation of different methods for determining low values of K was made using 11 gaseous substances (hydrogen, oxygen, nitrogen, methane, carbon monoxide, carbon dioxide, acetylene, ethylene, ethane, propene, propane) and the system transformer oil–air [43]. The choice of this system and of the set of gases was governed by the relevance to an efficient method for monitoring the state of high-voltage electrical equipment, used throughout the world. Studies performed in the 1970s showed that flaws of high-power transformers, arising in the course of their operation, can be reliably revealed and diagnosed by the presence of traces of the above gases in the oil. The static HSA technique allows the development of a simple and reliable procedure for gas analysis in transformer oil [44], meeting the existing requirements and widely used in Russia and other countries [45]. Calculations of the initial content of the dissolved gases in the oil sample are based on Eq. (19). Therefore, the distribution ratios K of the characteristic gases in trasnformer oil at various temperatures still attract considerable researchers's attention in various countries.

Jalbert et al. [43] compared the distribution ratios K of characteristic gases in transformer oil, measured at 70°C by various methods implemented with constant-volume vessels with pneumatic dosing of the equilibrium gas into a chromatograph. The results of that study, given in Table 2, show that, in most cases, the measurement error for each method does not exceed 10%, being 2–4% on the average. The highest accuracy was attained with EPICS method, and the lowest accuracy, with MHE method. The deviations of the mean values for each component, calculated from the data of various methods, also do not exceed 10%. The exceptions are hydrogen, propene, and propane. Along with the data obtained with constant-volume vessels, the distribution ratios K measured at 25°C by other methods {repeated head-space extraction in variable-volume vessels [46], determination from gas-chromatographic (GC) retention parameters [47]} are also given in Table 2. These values are well consistent with each other and with data of the International Electrotechnical Commission (IEC) [48], but disagree with the results obtained at 70°C. The strongest inconsistency is observed with hydrogen, because at 70°C the distribution ratio is three times higher than that at 25°C, whereas actually the former value should be lower than, or at least equal to the latter value. According to [46], the distribution ratio K of hydrogen remains constant in the range 15–40°C. For the other components, with an increase in K, the extent of the inconsistency decreases. For example, the distribution ratio of propane decreases by a factor of more than 2 in going from 25 to 70°C, in agreement with the expectations. The significant differences in the results of measuring small (≤2) distribution ratios K should be attributed to systematic inaccuracies of

Table 2. Distribution ratios of gaseous substances in the system transformer oil–gas, measured by different methods at 70 and 25°C

Compound	Methods using constant-volume vessels, 70°C [39]											
	VPC		EPICS		PRV		PRC		MHE		average	
	K	S_r, %	K	S_r, %	K	S_r, %	K	S_r, %	K	S_r, %	K	S_r, %
Hydrogen	0.093	4.9	0.093	1.1	0.18	14	0.12	2.1	0.1	2.5	0.12	31.4
Oxygen	0.21	2.8	0.21	3.5	0.17	5.7	0.19	9.2	0.20	3.3	0.20	8.5
Nitrogen	0.12	9.7	0.11	7.2	0.13	10	0.13	9.3	0.13	3.3	0.12	7.2
Methane	0.45	0.7	0.46	0.1	0.50	2.0	0.49	0.9	0.45	2.0	0.47	5.0
Carbon monoxide	0.15	2.8	0.15	0.7	0.17	1.4	0.15	3.9	0.17	1.8	0.16	6.9
Carbon dioxide	0.94	1.2	0.97	0.7	1.01	3.7	1.00	2.2	0.9	5.1	0.96	4.7
Acetylene	1.98	1.5	1.11	1.2	0.98	1.6	1.01	2.4	1.03	6.3		
Ethylene	1.46	0.7	1.52	0.6	1.49	1.0	1.55	0.8	1.4	4.6	1.48	3.9
Ethane	2.07	0.8	2.18	0.5	2.07	1.0	2.16	0.6	1.9	4.6	2.08	5.3
Propene	5.1	1.3	5.7	0.9	4.9	0.9	5.16	0.7	4.1	4.4	4.95	11.6
Propane	5.8	1.9	6.7	1.9	4.9	2.5	5.2	2.3	4.2	6.8	5.36	17.6
ΣS_r, %		28.2		18.4		43.8		34.5		42.9		

Compound	Other methods, 25°C					
	repeated head-space extraction [42]		IEC data [44], K	GC retention parameters [43], K	average	
	K	S_r, %			K	S_r, %
Hydrogen	0.044	8.0	0.05	0.04	0.045	11.3
Oxygen	–	–	–	–	–	–
Nitrogen	–	–	–	–	–	–
Methane	0.40	3.7	0.43	0.37	0.40	7.5
Carbon monoxide	–	–	–	–	–	–
Carbon dioxide	1.08	4.6	1.08	1.06	1.07	1.1
Acetylene	1.1	2.8	1.20	1.24	1.18	6.1
Ethylene	1.7	3.4	1.70	1.74	1.71	1.3
Ethane	2.7	4.8	2.4	2.83	2.64	8.3
Propene	–	–	–	–	–	–
Propane	9.6	3.3	10.0	–	9.8	2.9

measurements at 70°C with constant-volume vessels, whereas at 25°C well consistent distribution ratios were obtained by methods based on different principles.

The potentialities of methods using variable-volume vessels are illustrated by Table 3 in which the distribution ratios of a number of gaseous and low-boiling substances at 37°C in the water–air system are given [49]. Many of these substances exhibit anesthetic and pronounced toxic action. Therefore, such data can be of interest for physicians and toxicologists, as the K values for water and whole blood or blood plasma differ insignificantly (within 10%). The error in measuring K, similarly to the above-considered gas–oil systems, in most cases does not exceed 10%, being about 6% on the average. On the whole, data of Table 3 (especially K and S_r for acetaldehyde and acetone) confirm the conclusion that the K values accessible to measurements by repeated head-space extraction do not exceed 100 units, but the upper limit can be increased by using multiple head-space extraction.

Continuous Gas Extraction

Dynamic HSA decreases the sorption effects in the gas circuit of a CGE installation and chromatograph,

Table 3. Distribution ratios of gaseous and low-boiling substances between aqueous and gas phases, measured in variable-volume vessels

Compound	Boiling point, °C	Distribution ratio				
		repeated head-space extraction [49], 37°C		published data		
		K	S_r, %	K	T, °C	references
Sulfur hexafluoride	–63.8	0.0037	2.7	0.0051	30	[50]
n-Heptane	98.4	0.015	9.0	–	–	–
n-Hexane	68.7	0.017	11.6	–	–	–
n-Butane	–0.5	0.021	1.9	0.026	30	[50]
Propane	–42.1	0.025	2.4	0.032	30	[50]
Methane	–161.4	0.030	2.6	0.029	40	[50]
Ethane	–88.7	0.033	2.1	0.035	40	[50]
Cyclohexane	80.7	0.087	9.4	–	–	–
Cyclopropane	–32.9	0.202	1.6	0.204	37	[51]
Halothane	50.2	0.73	2.5	0.88	37	[52]
1,1,1-Trichloroethane	74.1	0.82	4.5	–	–	–
Trichloroethylene	86.7	1.42	9.9	1.51	37	[52]
Benzene	80.1	5.06	12.9	3.4	30	[53]
Chloroform	61.3	5.50	6.2	4.6	37	[51]
Dichloromethane	39.8	8.70	5.7	–	–	–
Diethyl ether	34.6	16.4	5.6	15.5	37	[51]
1,2-Dichloroethane	84	19.7	6.9	–	–	–
Ethyl acetate	77.1	112	6.4	–	–	–
Acetaldehyde	20.2	184	16.0	–	–	–
Acetone	56.5	308	18.0	395	37	[54]

which significantly distort the analysis results. This method is used for determining the distribution ratios in a wide range, from several units to values exceeding 10^4. An important advantage is the possibility of performing the extraction in the absence of even traces of oxygen [55], which is particularly important for readily oxidizable and unstable substances, e.g., for hydrogen sulfide and mercaptans. Continuous gas extraction as a method for measuring the distribution ratios was suggested for the first time in 1963 by Burnett [56] and was tested in studying the distribution of ketones and alcohols between aqueous and gas phases in the range of limit dilutions. Considerably later, in 1977, Leroi et al. [57] used this method for determining the limiting activity coefficients of solutes in volatile and nonvolatile solvents.

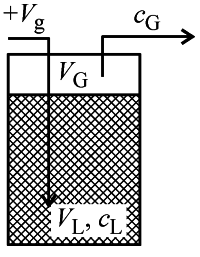


Fig. 13. Scheme of continuous gas extraction of volatile components from a solution in a nonvolatile solvent. For comments, see text.

The dynamic HSA is underlain by the equilibrium theory of continuous gas extraction, which was formulated for the first time by Vitenberg and Ioffe [58, 59] under the assumptions that the gas phase is ideal, the distribution isotherms are linear, and the solvent vapor over the pure liquid does not differ from that over the solution containing impurities of volatile substances. These assumptions are valid at limit dilutions and allow not only analytical but also physicochemical measurements [3–5].

The CGE is realized by passing a flow of a neutral extractant gas of the volume V_g through a solution of a volatile component with the initial concentration c_L^0 (Fig. 13). In the course of CGE from a nonvolatile solvent, the running concentration of the target component in solution c_L corresponding to the volume of the passed extractant gas V_g is related to the initial concentration c_L^0 by the equation [60]

$$c_L = c_L^0 \exp[-V_g/(KV_L + V_G)]. \quad (30)$$

From the results of gas-chromatographic determination of the solute concentration in the gas flow passing through a solution being analyzed, in accordance with (1) and within the range of linear detector response, the distribution ratio is calculated by the formula

$$K = \frac{V_g/V_L}{\ln(A_G^0/A_G)} - r, \quad (31)$$

where A_G^0 and A_G are the peak areas in the chromatogram corresponding to c_G^0 (initial concentration of the solute vapor in the volume V_G at $V_g = 0$) and c_G (solute concentration in the gas flow at the vessel outlet after passing the gas volume V_g), respectively.

The accuracy of the results obtained strongly depends on the volume ratio of the solution and extractant gas passed through it or, in other words, on the fraction of the target component extracted from the solution, δ_g:

$$\delta_g = 1 - \exp[-V_g/(KV_L + V_G)] = 1 - A_G/A_G^0. \quad (32)$$

The error of measuring the volumes V_G and V_L is negligible compared to the error of measuring the concentrations c_G and c_G^0 in the form of the peak areas in the chromatogram, A_G and A_G^0. In such cases, the relative error of determining the distribution ratio is related to the CGE conditions and fraction of the substance extracted from the solution by the formula

$$\Delta K/K = (\Delta A_G^0/A_G^0 + \Delta A_G/A_G)\{\ln[1/(1 - \delta_g)]\}^{-1}$$

$$= (\Delta A_G^0/A_G^0 + \Delta A_G/A_G)[\ln(\Delta A_G^0/A_G)]^{-1}$$

following from Eq. (31). It is quite evident that the relative error of measuring K by CGE decreases with an increase in the volume of the passed extractant gas, V_g, and will not exceed the total error of measuring the peak areas in the chromatogram if the fraction of the substance extracted to the gas phase will be no less than 63% and the A_G^0/A_G ratio will be no less than e (base of natural logarithm).

As an example of using dynamic HSA for determining low values of K, let us consider the results of studying the distribution of sulfur compounds (hydrogen sulfide, methyl mercaptan, ethyl mercaptan) between aqueous solutions and the gas phase [55]. The data obtained in that paper are fairly well consistent with the published values of K [61] determined by the static method. As seen from Fig. 14, in both cases the temperature dependence of the distribution ratios

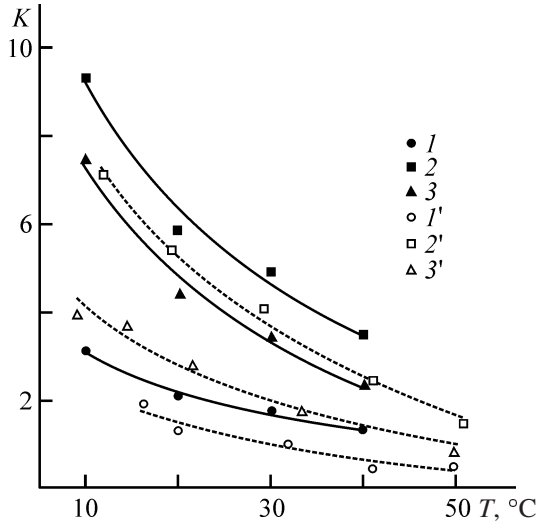


Fig. 14. Comparison of the (*1*–*3*) measured and (*1*'–*3*') published [61] distribution ratios K. (T) Temperature. (*1*) Hydrogen sulfide, (*2*) methyl mercaptan, and (*3*) ethyl mercaptan.

shows similar trend. The discrepancies are systematic, are within 10–50% for different components, and are apparently associated with the chemical composition of aqueous soltuions containing different amounts of mineral substances.

The acidity of aqueous solutions can significantly affect the fraction of the molecular form of components dissociating in the liquid phase. As the partial vapor pressure of such substances over the solution and hence their concentration in the gas phase are proportional to the fraction of the nondissociated species, the distribution ratios of hydrogen sulfide and mercaptans strongly depend on the degree of their dissociation in solution. The dissociation equilibrium is virtually totally shifted to the left at pH ≤ pK_a – 2 [3, 4, 6]. The pK_a values for hydrogen sulfide, methyl mercaptan, and ethyl mercaptan at 25°C are 7.2, 10.33, and 10.6, respectively [62]. Thus, the solution acidity should not affect the distribution ratio of hydrogen sulfide at pH ≤ 5 and those of mercaptans at pH ≤ 8. Therefore, in experiments for measuring the distribution ratios (Fig. 14), a buffer solution with pH 4.8 was chosen as the aqeuous phase. In going to a neutral solution, the distribution ratio of hydrogen sulfide becomes several times higher, whereas those of mercaptants increase insignificantly. In distilled water (Table 4), a significant fraction of hydrogen sulfide molecules occurs in the hydrated, bound form, which considerably decreases the fraction of molecular species. For mercaptans, the neutral medium is still sufficiently acidic, so that its effect on the distribution

Table 4. Distribution ratios of hydrogen sulfide, methyl mercaptan, and ethyl mercaptan in the liquid–gas system for buffer solutions and distilled water at 20°C

Compound	Distribution ratio		
	buffer solution		distilled water
	hydrosulfate, pH 0.9	phosphate, pH 4.8	
Hydrogen sulfide	2.8	2.1	7.9
Methyl mercaptan	6.2	5.8	7.9
Ethyl mercaptan	4.7	4.4	6.1

Table 5. Distribution ratios of aliphatic alcohols between water and gas phase at 25°C, measured by different methods

Component	Experimental method*					Average
	CGA	AEV**	GLC**	STAT**	TENS**	
Methanol	5200*** 4915 [63] 5580 [56]	5020 [65] 5130 [66]	4880 [68] 3830 [69] 3110 [70]	3840 [71] 5140 [72] 4970 [73]	4980 [65]	
$\bar{K} \pm S_r$, %	5233 ± 6.3	5075 ± 1.5	3940 ± 22.6	4650 ± 15.2	4980	4717 ± 15.3
Ethanol	4500*** 5260 [64] 5320 [56]	4150 [65] 5650 [27] 4630 [67] 4660 [66]	4440 [68] 3670 [69]	5060 [74] 4470 [75]	4940 [65]	
$\bar{K} \pm S_r$, %	5027 ± 9.1	4480 ± 6.4	4055 ± 13.4	4765 ± 8.8	4940	4645 ± 10.5
1-Propanol	3600*** 4090 [64] 4000 [56]	3440 [65] 3660 [66]	3650 [68] 2920 [69]	3720 [74]	3480 [65]	
$\bar{K} \pm S_r$, %	3897 ± 6.7	3550 ± 4.4	3285 ± 15.7	3720	3480	3618 ± 9.4
1-Butanol	3100*** 3600 [64] 3390 [56]	3270 [65] 3000 [66]	3310 [68]	3860 [71]	3300 [65]	
$\bar{K} \pm S_r$, %	3363 ± 7.5	3135 ± 6.1	3310	3860	3300	3354 ± 8.1

* (AEV) Analysis of equilibrium vapor under static conditions with absolute calibration for the gas phase; (GLC) gas–liquid chromatography, by retention parameters: (STAT) static method for measuring vapor pressure; (TENS) tensimetric method.
** Calculated from data on limiting activity coefficients by formula (2).
*** Our measurements.

ratios is insignificant. Certain differences in the distribution ratios of mercaptans between distilled water and buffer solutions are apparently due to the salt background.

The potentialities of continuous gas extraction for the determination of large ($>10^3$) distribution ratios are illustrated by Table 5 in which the results of measuring K of lower alcohols between aqueous and gas phases by CGE are compared with the data of traditional static methods: vapor pressure measurements, tensimetric and chromatographic analysis of equilibrium vapor (AEV), and very popular dynamic GLC method (from chromatographic retention parameters). As distribution ratios obtained by CGE we took the data from [56, 63] and the values that we measured by the procedure described in [55]. The K values given for the other methods were calculated from data on the limiting activity coefficients γ^{∞} by formula (2).

It follows from Table 5 that the best agreement of data obtained by different authors is observed in the case of static AEV: The standard deviation does not exceed 6.5%. Somewhat worse agreement (≤10%) is

observed in the case of CGE. The differences between the average values obtained by these methods do not exceed 10%. The largest scatter of K is observed in the case of GLC, which may be due to problems that arise when water is used as a stationary phase in gas chromatography.

The dynamic versions of HSA, compared to static methods, required more sophisticated equipment, and more stringent limitations are imposed on the experimental conditions. For example, to attain the equilibrium distribution, it is necessary to restrict the gas flow rate and ensure small size of gas bubbles in the liquid. Therefore, SHE should be used in cases when static measurements are inconvenient or impossible. This concerns, in particular, determination of distribution ratios of substances unstable in air or of the ratios exceeding 100.

CONCLUSION

The suggested classification of chromatographic methods for determining distribution ratios of volatile compounds in the liquid–gas system involves the use of two principally different approaches. The first approach, based on a gas-chromatographic process, involves measurement of retention parameters of substances being chromatographed. The second approach is based on gas extraction and involves gas-chromatographic measurement of the absolute or relative concentrations of substances distributed between the condensed and gas phases.

The method for determining the distribution ratios of volatile substances from their retention parameters in a chromatographic column, suggested as early as the mid-1950s, still remains very popular, as being simple and prompt [23]. However, the sorption effects at the phase boundary in a chromatographic column can lead to significant errors in measuring K, which are systematic and reach tens of percents and more.

Methods involving the use of procedures and apparatus of gas extraction are based on various versions of static and dynamic HSA. Methods involving relative measurements of chromatographic peak areas, proportional to the concentration of the target substance on one of the phases of a heterogeneous system, are the most widely used for determining K for physicochemical and analytical purposes. In such cases, the accuracy of determining K considerably increases, because errors associated with the calibration of the chromatograph and measurement of absolute concentrations of substances are eliminated.

REFERENCES

1. Morachevskii, A.G., Smirnova, N.A., Balashova, I.M., and Pukinskii, I.B., *Termodinamika razbavlennykh rastvorov neelektrolitov* (Thermodynamics of Dilute Nonelectrolyte Solutions), Leningrad: Khimiya, 1982.
2. Dobryakova, I.E. and Dobryakov, Yu.G., *Zh. Prikl. Khim.*, 2005, vol. 78, no. 2, pp. 214–218.
3. Vitenberg, A.G. and Ioffe, B.V., *Gazovaya ekstraktsiya v khromatograficheskom analize* (Gas Extraction in Chromatographic Analysis), Leningrad: Khimiya, 1982.
4. Ioffe, B.V. and Vitenberg, A.G., *Head-Space Analysis and Related Methods in Gas Chromatography*, New York: Wiley–Interscience, 1984.
5. Kolb, B. and Ettre, L.S., *Static Headspace–Gas Chromatography*, New York: Wiley, 1997.
6. Vitenberg, A.G., *Ross. Khim. Zh.*, 2003, vol. 47, no. 1, pp. 7–22.
7. Ettre, L.S., Welter, C., and Kolb, B., *Chromatographia*, 1993, vol. 35, no. 1/2, pp. 73–84.
8. James, A.T. and Martin, A.J.P., *Analyst*, 1952, vol. 77, pp. 915–932.
9. Everett, D.H., *Trans. Faraday Soc.*, 1965, vol. 61, pp. 1637–1645.
10. Bredford, B.W., Harvey, D., and Chalkey, D.E., *J. Inst. Petrol.*, 1955, vol. 41, pp. 80–91.
11. Porter, P.E., Deal, C.H., and Stross, F.H., *J. Am. Chem. Soc.*, 1956, vol. 78, pp. 2999–3006.
12. Kwantes, A. and Rijnders, G.W.A., *Gas Chromatography 1958: Amsterdam Symp., May 19–23, 1958*, Desty, D.H., Ed., London: Butterworths, 1958, pp. 125–136.
13. Castells, R.C., *J. Chromatogr. A*, 2004, vol. 1037, pp. 223–231.
14. Lowe, H.J. and Hagler, K., *Gas Chromatography in Biology and Medicine: Ciba Foundation Symp., London, February 5–6, 1969*, Porter, R., Ed., London: Churchill, 1969, pp. 86–112.
15. Martin, R.L., *Anal. Chem.*, 1961, vol. 33, no. 3, pp. 347–352.
16. Martin, R.L., *Anal. Chem.*, 1963, vol. 35, no. 1, pp. 116–117.
17. Berezkin, V.G., Pakhomov, V.P., Starobinets, L.L., et al., *Neftekhimiya*, 1965, vol. 5, no. 3, pp. 438–444.
18. Berezkin, V.G., Pakhomov, V.P., Tatarinskii, V.S., et al., *Dokl. Akad. Nauk SSSR*, 1968, vol. 180, no. 5, pp. 1135–1138.
19. Berezkin, V.G., Nikitina, N.S., Fateeva, V.M., et al., *Izv. Akad. Nauk SSSR, Ser. Khim.*, 1970, no. 1, pp. 19–21.
20. Belen'kii, B.G., Vitenberg, A.G., and D'yakonov, I.A.,

Izv. Akad. Nauk SSSR, Ser. Khim., 1964, no. 1, pp. 193–195.

21. Belen'kii, B.G., Vitenberg, A.G., Turkova, L.D., et al., *Izv. Akad. Nauk SSSR, Ser. Khim.*, 1967, no. 2, pp. 269–276.
22. Conder, J.R., Locke, D.C., and Purnell, J.H., *J. Phys. Chem.*, 1969, vol. 73, no. 3, pp. 700–708.
23. Gaile, A.A., Proskuryakov, V.A., Semenov, L.V., et al., *Predel'nye koeffitsienty aktivnosti uglevodorodov v selektivnykh rastvoritelyakh: Spravochnik* (Limiting Activity Coefficients of Hydrocarbons in Selective Solvents: Handbook), Gaile, A.A., Ed., St. Petersburg: Sankt-Peterb. Gos. Univ., 2002.
24. Dobryakov, Yu.G., Asprion, N., Hasse, G., et al., *Teor. Osn. Khim. Tekhnol.*, 1997, vol. 31, no. 6, pp. 605–612.
25. Kieckbusch, T.G. and King, C.J., *J. Chromatogr. Sci.*, 1979, vol. 17, pp. 273–279.
26. Hassam, A. and Carr, P.W., *Anal. Chem.*, 1985, vol. 57, pp. 793–797.
27. Jones, W., Egoville, M.J., Strolle, E.O., et al., *J. Chromatogr.*, 1988, vol. 455, pp. 45–52.
28. Rohrschneider, L., *Anal. Chem.*, 1973, vol. 45, no. 7, pp. 1241–1247.
29. Kolb, B., *J. Chromatogr.*, 1975, vol. 112, pp. 287–295.
30. Hovorka, S., Dohnal, V., Roux, A.H., et al., *Fluid Phase Equil.*, 2002, vol. 201, pp. 135–164.
31. Vitenberg, A.G., in *Pamyati B.V. Ioffe* (In Commemoration of B.V. Ioffe), St. Petersburg: Nauchno-Issled. Inst. Khimii Sankt-Peterb. Gos. Univ., 1998, pp. 7–69.
32. Vitenberg, A.G. and Reznik, T.L., *Zh. Anal. Khim.*, 1984, vol. 39, no. 4, pp. 683–691.
33. Vitenberg, A.G., Butaeva, I.L., and Dimitrova, Z.St., *Chromatographia*, 1975, vol. 8, no. 12, pp. 693–695.
34. Wagner, P.D., Naumann, P.F., and Laravuso, R.B., *J. Appl. Physiol.*, 1974, vol. 36, pp. 600–605.
35. Vitenberg, A.G., Ioffe, B.V., Dimitrova, Z.St., et al., *J. Chromatogr.*, 1975, vol. 112, pp. 312–327.
36. Guitart, R., Puigdemont, A., and Arboix, M., *J. Chromatogr.*, 1989, vol. 491, pp. 271–280.
37. McAuliffe, C., *Chem. Technol.*, 1971, pp. 46–51.
38. Suzuki, M., Tsuge, S., and Takeuchi, T., *Anal. Chem.*, 1970, vol. 42, pp. 1705–1708.
39. Kolb, B. and Ettre, L.S., *Chromatographia*, 1991, vol. 32, no. 11/12, pp. 505–513.
40. Robbins, G.A., Wang, S., and Stuart, J.D., *Anal. Chem.*, 1993, vol. 65, pp. 3113–3118.
41. Chai, X.S. and Zhu, J.Y., *J. Chromatogr. A*, 1998, vol. 799, pp. 207–214.
42. Gossett, J.M., *Environ. Sci. Technol.*, 1987, vol. 21, pp. 202–208.
43. Jalbert, J., Gilbert, R., and El Khakani, M.A., *Chromatographia*, 2002, vol. 56, no. 9/10, pp. 623–630.
44. Kostkina, M.I., Vitenberg, A.G., and Ioffe, B.V., *Elektr. Stantsii*, 1984, no. 4, pp. 71–74.
45. *ASTM D 3612-01: Standard Test Method for Analysis of Gases Dissolved in Electrical Insulating Oil by Gas Chromatography, Annual Book of ASTM Standards*, Philadelphia, PA: Am. Soc. for Testing and Materials, 2001, vol. 10.03.
46. Ioffe, B.V., Kostkina, M.I., and Vitenberg, A.G., *Zh. Prikl. Khim.*, 1980, vol. 53, no. 10, pp. 2280–2285.
47. Simon, F. and Lukacs, J., *Magyar Asvanyolajes Foldgazkiserleti Intezet Kozlemenyei*, 1977, vol. 18, pp. 57–62.
48. *International Electrotechnical Commission Standard*, Publication 567: *Guide for the Sampling of Gases of Oil from Oil-Filled Electrical Equipment for the Analysis of Free Dissolved Gases*, Geneva, 1977.
49. Guitart, R., Puigdemont, F., and Arboix, M., *J. Chromatogr.*, 1989, vol. 491, pp. 271–280.
50. *Gas Encyclopaedia. L'Air Liquide*, Amsterdam: Elsevier, 1976.
51. Kety, S.S., *Pharmacol. Rev.*, 1951, vol. 3, pp. 1–17.
52. Lowe, H.J. and Hagler, K., *Gas Chromatography in Biology and Medicine: A Ciba Foundation Symp.*, Porter, R., Ed., London: Churchill, 1969, p. 86.
53. Tsibul'skii, V.V., Tsibul'skaya, I.A., and Yaglitskaya, N.N., *Zh. Anal. Khim.*, 1979, vol. 34, pp. 1364–1368.
54. Sato, A. and Nakajiama, T., *Br. J. Ind. Med.*, 1979, vol. 36, pp. 231–238.
55. Dobryakov, Yu.G. and Vitenberg, A.G., *Zh. Prikl. Khim.*, 2006, vol. 79, no. 8, pp. 1259–1264.
56. Burnett, M.G., *Anal. Chem.*, 1963, vol. 35, no. 10, pp. 1567–1570.
57. Leroi, J.Cl., Masson, J.Cl., Renon, H., et al., *Ind. Eng. Chem. Process Des. Devel.*, 1977, vol. 16, no. 1, pp. 139–144.
58. Vitenberg, A.G. and Ioffe, B.V., *Dokl. Akad. Nauk SSSR*, 1977, vol. 235, no. 5, pp. 1071–1074.
59. Vitenberg, A.G. and Ioffe, B.V., *Dokl. Akad. Nauk SSSR*, 1978, vol. 238, no. 2, pp. 352–355.
60. Vitenberg, A.G. and Kostkina, M.I., *Zh. Anal. Khim.*, 1979, vol. 34, no. 9, pp. 1800–1808.
61. Vitenberg, A.G., Butaeva, I.L., Kuznetsova, L.M., et al., *Anal. Chem.*, 1977, vol. 49, no. 1, pp. 128–133.
62. Serjeant, E.P. and Dempsey, B., Ionisation Constants of Organic Acids in Aqueous Solution, *IUPAC Chem. Data Ser.*, New York: Pergamon, 1979, no. 23, p. 989.
63. Lebert, A. and Richon, D.J., *Agric. Food Chem.*, 1984, vol. 32, pp. 1156–1163.

64. Smirnova, S.A., New Possibilities of Gas-Chromatographic Determination of Volatile Organic Substances in Aqueous Solutions by Head-Space Analysis, *Cand. Sci. Dissertation*, Leningrad, 1977.

65. Vrbka, P., Fenclova, D., Lastovka, V., et al., *Fluid Phase Equil.*, 2005, vol. 237, pp. 123–129.

66. Sherman, S.R., Trampe, D.B., Bush, D.M., et al., *Ind. Eng. Chem. Res.*, 1996, vol. 35, pp. 1044–1058.

67. Park, J.H., Hussam, A., Couasnom, P., et al., *Anal. Chem.*, 1987, vol. 59, pp. 1970–1976.

68. Larkin, J.A. and Pemberton, R.C., in *Proc. Third Int. Conf. on Chemical Thermodynamics*, Baden, 1973, pp. 163–170.

69. Schaffer, D.L. and Daubert, T.E., *Anal. Chem.*, 1969, vol. 41, no. 12, pp. 1585–1589.

70. Pecsar, R. and Martin, I.I., *Anal. Chem.*, 1966, vol. 38, no. 12, pp. 1661–1669.

71. Belousov, V.P., Panov, M.Yu., and Morachevskii, A.G., *Khimiya i termodinamika rastvorov* (Chemistry and Thermodynamics of Solutions), Morachevskii, A.G. and Lilich, L.S., Eds., Leningrad: Leningr. Gos. Univ., 1977, no. 4, pp. 158–213.

72. Hoftsee, M.T., Kwantes, A., and Rijnders, C.W.A., in *Int. Symp. on Distillation*, Brighton, May 4–5, 1960, pp. 105–109.

73. Christian, S.D., Lane, E.H., and Tucker, E.E., *J. Solution Chem.*, 1981, vol. 10, pp. 181–188.

74. Panov, M.Yu., Experimental and Theoretical Study of Thermodynamic Properties of Dilute Aqueous Solutions of Alcohols, *Cand. Sci. Dissertation*, Leningrad: Leningr. Gos. Univ., 1974.

75. Nord, L., Tucker, E.E., and Christian, S.D., *J. Solution Chem.*, 1984, vol. 13, pp. 849–867.

ISSN 1070-4272, Russian Journal of Applied Chemistry, 2008, Vol. 81, No. 3, pp. 360–369. © Pleiades Publishing, Ltd., 2008.
Original Russian Text © E.A. Gurkovskaya, 2008, published in Zhurnal Prikladnoi Khimii, 2008, Vol. 81, No. 3, pp. 374–383.

REVIEWS

Thin-Layer Size-Exclusion Chromatography of Polymers

E. A. Gurkovskaya

Moscow State University of Technology and Management, Moscow, Russia

Received May 15, 2007

Abstract—Modern concepts of thin-layer chromatography of macromolecular compounds are reviewed, including the features and potentialities of thin-layer size-exclusion chromatography.

DOI: 10.1134/S1070427208030026

INTRODUCTION

The use of thin-layer chromatography (TLC) for analysis of polymers was a sign of a big success of this method. The first TLC studies of random polymers were reported in 1968 [1, 2]. Since that the primary research direction in the field of TLC of polymers was associated with the use of this method for characterization of the polydispersity of polymers (compositional and molecular heterogeneity) and identification of polymers of various classes [3, 5]. The use of TLC allowed separation of random copolymers; identification of random, block, and alternating copolymers; identification and separation of di- and triblock copolymers; separation of block and graft copolymers from homopolymers; identification and separation of stereoregular poly(methyl methacrylates) (PMMAs) and polystyrenes (PSs) of various microtacticities; separation of geometric isomers of polybutadiene (PBD) and polyisoprene (PI); and identification of linear and branched PSs as well as PSs with different terminal groups and their separation from bi- and multifunctional PSs. In polymer separations, combined TLC methods are often used, e.g., polymer separation at the origin by selective desorption, followed by fractionation using adsorption or precipitation TLC. Adsorption TLC (ATLC) was first suggested for separation of copolymers [1, 3, 6, 7] and employed for MWD analysis in homopolymers [8]. To fractionate polymers by the molecular weight, Inagaki et al. [9, 10] proposed precipitation TLC (PTLC).

All the versions of TLC of polymers can be subdivided into two groups. The first group covers the methods based on adsorption. The second group includes the methods based on phase distribution of polymer solutions: precipitation and extraction TLC. Extraction TLC (ETLC) of polymers is based on selective dissolution of polymer solution at the origin. It has been used for separation of isotactic and atactic PMMA [11] and PS [12].

THIN-LAYER SIZE-EXCLUSION CHROMATOGRAPHY

Thin-layer size-exclusion chromatography (TLSEC) of polymers is based on the molecular-sieve effect. In this technique, adsorption of polymers is suppressed, and the pore space of the sorbent is presaturated with a solvent either by virtue of capillary condensation in exposing the plate to solvent vapor [3, 8] or by using so-called preelution [13] (passing a solvent through the chromatographic layer prior to applying a sample to be analyzed). The process is schematically shown in Fig. 1.

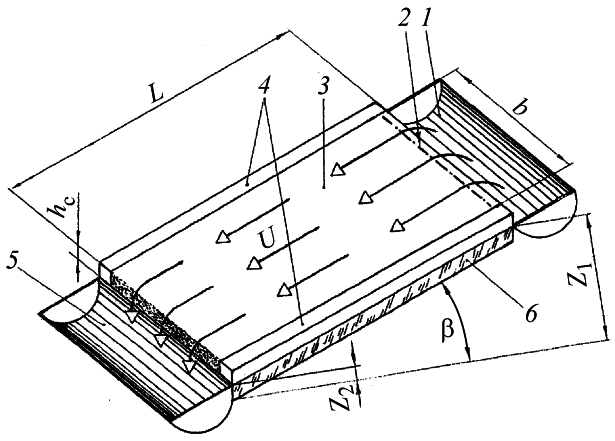


Fig. 1. Schematic of thin-layer size-exclusion chromatography. (*L*) Plate length and (*b*) plate width; (β) plate angle; (Z_1, Z_2) geometric head; and (*U*) mobile phase flow rate. (*1, 5*) Development tanks, (*2*) start line, (*3*) sorbent layer, (*4*) layer thickness control, and (*6*) glass support.

It was demonstrated that passing from size-exclusion chromatography to adsorption chromatography of polymers may be considered as a first-order phase transition. One always can accentuate one mechanism over the others by carefully controlling the chromatographic conditions. Furthermore, the molecular weight and chemical composition distributions could be analyzed separately using so-called critical chromatography. These methods were successfully used for separating oligomers, polymers, and biopolymers [14–17], and also for characterizing the compositional homogeneity of copolymers and functionality of oligomers.

The efficiency of TLSEC strongly depends on the characteristics of the adsorbent layer, particularly, its thickness [11, 17–19]. The thickness of 0.5–1 mm proved to be optimal. With decreasing adsorbent layer thickness, on the one hand, the band tailing decreases, and on the other hand, the ratio between the pore and interparticle spaces changes (interparticle space increases) as a result of decrease in the packing density of the adsorbent layer.

The effect of the packing density is particularly pronounced when comparing K_f vs. M relationships for the thin-layer mode of SEC and column gel chromatography, where the packing can be very dense (K_f is defined as the ratio of the path lengths of an analyte and a polymer completely displaced from the sorbent pores, and M is the molecular weight).

Principles of Thin-Layer Size-Exclusion Chromatography

Thin-layer size-exclusion chromatography was founded at the time when chromatographic separations on porous gels have become a routine laboratory technique of column HPLC [17–19]. Combining both techniques opened the door for the use of TLSEC for separation of macromolecular compounds, primarily proteins, as demonstrated by the experiments with various Sephadexes. In fact, a layer of a swollen Sephadex represents an "open" bed of a gel, which differs from the support in the column in only that it is amenable to manipulations, e.g., for applying samples and band development. Generally, in TLC, dry-bed plates are used [20, 21]. A solvent is moved by capillary forces after immersing the plate (most often vertically) in an eluent [22]. Johansson and Rymo [23, 24] were first who described an "open" gel bed.

As mentioned above, the use of thin-layer gel chromatography was bound to separations of proteins in aqueous buffer solutions, except a few experiments with peptides [24, 25], mucopolysaccharides [26], and ribonucleotides [27]. However, there are all reasons to believe that thin-layer gel chromatography will be widely used as a micromethod in these areas as well. The method operates with small samples, and its hardware implementation is rather simple. It allows performing a great number of determinations in a relatively short time. Therefore, thin-layer gel chromatography is particularly efficient in determination of the molecular weight of proteins. A slightly lower accuracy of this method (relative to the column mode) could be compensated by more extended statistics [14, 17, 18, 28]. Since many enzymes can be detected directly on a plate or paper strip using specific tests [28, 29], their molecular weights can be evaluated by analyzing even not very pure preparations. Moreover, this technique allows quick optimization of conditions for their further purification.

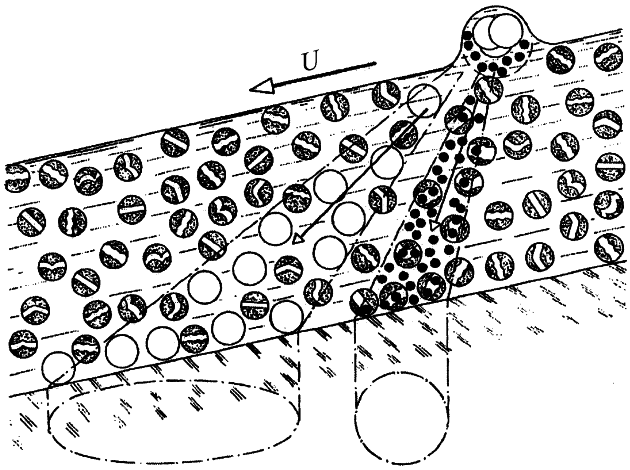


Fig. 2. Schematic of molecular-weight distribution of biopolymers and formation of chromatographic zones in TLSEC.

Thin-layer SEC can satisfactorily fractionate both macromolecular compounds (nucleic acids, polypeptides, proteins, and polysaccharides) and many oligomers such as relatively low-molecular-weight tannins and complexes. Compared to the column mode, TLSEC is simpler, more cost-efficient, much more express, and often more sensitive and precise [14, 17, 18, 30]. A schematic of molecular-weight distribution (MWD) of biopolymers in TLSEC is shown in Fig. 2.

However, the TLSEC technique is not identical to ordinary TLC. Thin-layer SEC resembles the classical TLC in that a thin layer of a sorbent is deposited onto a glass plate, a sample is spotted, and a mobile

phase is moved along the layer. The differences are as follows:

(1) In TLC, a sorbent is dried prior to sample spotting, and in TLSEC, a sample is spotted on a wet gel bed with compensation using a proper solvent.

(2) TLC is realized in the ascending mode, while TLSEC, in the descending mode; the flow rate is controlled by the plate angle; like that in TLC, the run is finished before the target compound passed into the lower tank. However, in TLSEC, continuous flow of a fluid is realized, i.e., unlike ordinary TLC, there is no solvent front here. Therefore, in TLSEC, R_f is not measured, but the position of the spots relative to appropriate references is determined.

(3) The separation efficiency should not depend on the solution concentration. The limit to which the initial solution concentration could be increased is controlled by its viscosity. High viscosity negatively affects the diffusion of the analyte, thus deteriorating the quality of separation.

The problems are in formation of a stable uniform thin layer of an adsorbent, data processing, precise determination of the molecular-weight distribution, and optimization of the development procedure.

Process and Instrumentation

Selection of sorbent. The major factor controlling the sorbent efficiency is the structure of its pore system, primarily the pore size. Following the Dubinin classification [31], the pores can be subdivided in their size into macropores ($r \sim 10^{-7}$ m), mesopores [$r = (15–1000) \times 10^{-10}$ m], and micropores ($r < 15 \times 10^{-10}$ m, specific surface area up to 10^5 $m^2\,kg^{-1}$).

Thin-layer SEC combines the experimental technique of TLC and separation mechanisms realized in gel chromatography. The same gels that are used in the column mode could be employed in TLSEC. However, in the thin-layer mode, there is a limitation in the particle size of the gel-forming material [18, 19].

The key point in gel permeation chromatography is the decision on the gel. In TLSEC, the key factor is the ability of the gel to form a stable adhesion layer on the support surface. This ability depends on the grain size, porosity, and solvation properties of the gel particles. As for widely used dextran-based Sephadex gels, superfine grades (10–40 μm) are best suited for the thin-layer mode, as providing the highest resolution [19, 28].

Dextran gels for gel-permeation chromatography are manufactured by Pharmacia Fine Chemicals AB (Uppsala, Sweden). Dextran is a polysaccharide build by glucose residues. It is obtained by fermentation of sucrose with *Leuconostoc mesenteroides*. In dextran, glucose residues are linked via α-1,6-glycoside bonds. The initial dextran is characterized by a broad molecular-weight distribution from 10^7 to 3×10^8. Purification, partial hydrolysis, and fractionation by precipitation with ethanol yield starting material for preparation of Sephadex. Alkaline solution of dextran (emulsion) is treated with epichlorohydrin to cross-link dextran chains with glyceryl bridges. As a result, an insoluble strongly hydrophilic 3D structure is formed, whose swellability depends on the degree of cross-linking.

Table 1 summarize characteristics of eight grades of Sephadex.

G-grade Sephadexes swell in DMSO, formamide, and glycol; and G-10 and G-15 gels, also in DMF. However, their swellability in organic solvents differs from that in water. These gels are stable in water, salt solutions, organic solvents, and alkaline and weakly acidic media. In strongly acidic solutions, the gels undergo hydrolysis, especially at elevated temperature. Sephadex is stable for 1–2 h in 0.1 N HCl, and for up to 6 months in 0.02 HCl.

Characteristics of Sephadex G-25 remain unchanged after keeping in 0.25 N NaOH at 60°C for 2 months. Sephadex wetted with a neutral solution is stable at 110°C, and, therefore, it can be sterilized in an autoclave. Dry Sephadex is stable up to 120°C; at higher temperature, it undergoes caramelization.

It is not allowed to expose Sephadex to long action of oxidants, since they destroy the gel matrix with the formation of free carboxy groups. The numbers marking eight grades of Sephadex gels from G-10 to G-200 correspond to their water regain W_R from 1 to 20.

Reliable MW fractionation range of Sephadex gels starts from 1500 for globular molecules and from 5000 to 10^8 for linear molecules. The grain structure of dry gels controls their water-regaining value, which, in turn, controls the possibility of formation of a stable stationary phase layer in TLSEC. Characteristics of Sephadex gels are presented in Table 2.

To apply a sorbent layer to a plate, a suspension of a swollen gel in a buffer solution is prepared first. The swelling time depends on the sorbent grade, ranging from several hours to 1 day and more. After applying a sorbent layer, a plate is arranged inside

Table 1. Characteristics of commercial dextran-based gels (according to manufacturer's data)

Gel	Dry grain size*, μm	Water regain, ml g^{-1}	Specific volume, ml g^{-1}	MW of peptides and globular proteins separated	MW of dextran fraction
G-10	4–120	1.0 ± 0.1	2–3	Up to 700	Up to 700
G-15	4–120	1.5 ± 0.1	2.5–3.5	Up to 1500	Up to 1500
G-25: coarse	100–300	2.5 ± 0.2	4–6	1000–5000	100–5000
medium	50–150	2.5 ± 0.2	4–6	1000–5000	100–5000
fine	20–80	2.5 ± 0.2	4–6	1000–5000	100–5000
G-50: coarse	100–300	5.0 ± 0.3	9–11	1000–30 000	500–10 000
medium	50–150	5.0 ± 0.3	9–11	1000–30 000	500–10 000
fine	20–80	5.0 ± 0.3	9–11	1000–30 000	500–10 000
G-75	40–120	7.5 ± 0.5	12–15	3000–70 000	1000–50 000
G-100	40–120	10.0 ± 1.0	15–20	4000–150 000	1000–100 000
G-150	40–120	15.0 ± 1.5	20–30	5000–400 000	1000–150 000
G-200	40–120	20.0 ± 2.0	30–40	5000–800 000	1000–200 000

* Gel of each grade is also produced as ultrafine fraction (grain size 10–40 μm).

a close chamber and connected to two tanks with buffer solutions via filter-paper bridges. The working chamber is arranged at an angle of 10°–20° to the horizon so that the mobile phase from the upper tank was supplied though the filter paper to the sorbent layer and passed through this layer down under gravity [18, 21, 30, 32, 33].

The plate angle, along with the sorbent type, is a key factor controlling the separation efficiency in TLSEC [18]. By changing the plate angle one can optimize the eluent flow (generally within the range from about 1 to 6 cm h^{-1}). The eluent flow depends on the sorbent type, plate angle, and molecular weight of an analyte. The eluent flow increases with increasing plate angle. The chromatographic layer should be equilibrated with the mobile phase for several hours prior to separation.

Therefore, the following conditions should be met in conducting chromatography in a thin layer of a gel: (1) the gel layer should not be dried up during several hours, (2) the plate angle and, therefore, the eluent flow should be kept constant throughout the experiment, and (3) supply and removal of the buffer solution should be continuous.

A significant advantage of TLSEC is that several samples may be spotted on a single plate, and their run could be directly compared with references. Changing the layer thickness, plate angle, and gel porosity allows optimization of the process simply by the common trial-and-error method [18, 19, 28, 33, 34].

It is not allowed to perform TLSEC separation with a dry gel layer, since a solvent from a sample, moving along the plate, causes swelling of the gel, making partitioning of a dissolved analyte impossible. The problem is eliminated in using a swollen gel in the descending flow mode [27, 35, 36].

It follows from the aforementioned that the key difference between the ordinary TLC and thin-layer gel chromatography is in that the latter is accomplished in a swollen layer of a gel suspension, and that the mobile phase is continuously moving through the gel bed.

The consistence of the gel suspension used for preparation of the chromatographic layer is the crucial

Table 2. Characteristics of Sephadex G gels

Gel	Water regain, ml g^{-1}	MW fractionation range	
		globular proteins	polysaccharides
G-25	2.5	1000–5000	100–5000
G-50	5.0	1500–30 000	500–10 000
G-75	7.5	3000–70 000	1000–50 000
G-100	10.0	4000–150 000	1000–100 000
G-150	15.0	5000–400 000	1000–150 000
G-200	20.0	5000–800 000	1000–200 000

Table 3. Optimal composition of Sephadex gel suspensions for thin-layer chromatography

Gel (superfine)	Gel concentration, g/100 ml
G-50	10.5
G-75	7.5
G-100	6.5
G-150	4.7
G-200	4.5

Table 4. Complete swelling times of Sephadex gels

Gel	Complete swelling time, h	
	at room temperature	in boiling-water bath
G-10, G-15	3	1
G-25, G-50, G-75	24	3
G-100, G-150, G-200	72	5

factor controlling the quality of the sorbent bed (Table 3). Complete swelling of gels with high W_R takes a long time. There are two methods to prepare a swollen gel. In the first method, a dry gel is soaked in an estimated volume of the buffer solution to obtain the desired consistence. In the second method, the gel is soaked in an excess of the buffer solution, and, after settling, excess solvent is removed by decantation. Occasionally, centrifugation is used to separate strongly swelling gels. Table 4 shows the complete swelling times of Sephadex gels.

The optimal layer thickness depends to a certain extent on the gel type and gel coating procedure [14, 18, 19]. The simplest tool for gel coating is a stainless steel rod or glass cylinder with a diameter no larger than 10 mm, and a length slightly above the plate width. At its edges the rod is equipped with bushings or clamps of the same thickness as the layer that is planned to apply.

An excess of the slurry is put onto the plate and drawn along it with uniform motions back and forth to obtain a layer with a thickness not above 0.5–1 mm (with layers with a thickness above 1 mm, separations were demonstrated to be unsatisfactory). The adhesion of the slurry is sufficient to eliminate the need in some additional fixing tool [17, 18, 36, 37]. After applying the layer, the plate is placed in a chamber and connected via filter bridges to reservoirs filled with the eluent, and the chamber is arranged at an angle required for the experiment. In this position, the plate is left for 3–5 h for uniform distribution of the liquid in the sorbent layer, to obtain a constant-rate flow in the course of the experiments. In applying samples, the plate (chamber) should be arranged horizontally. Otherwise, the spots appear to be expanded, resulting in distortion of the chromatogram [30, 38, 39].

After plate development, the molecular weight of an analyte is estimated from the run using a calibration curve obtained with reference compounds.

In [40–43] we reported analytical applications based on TLSEC, including those for studying biopolymers. We have optimized conditions for analysis of low- and high-molecular-weight proteins, including such factors as pH of the mobile phase [44] and protein structure [41, 44]. The features of formation of chromatographic zones in TLSEC have been considered with an example of poly(ethylene glycols) (PEGs) [45]. For total and fractionated proteins, the mechanism of formation of chromatographic zones was analyzed using data on the aspect ratio and diffusion–sorption kinetics of the process. The mechanism of conformational transformations and their effect on the globule–coil phase transitions in protein molecules in the course of TLSEC were studied [40, 46, 47].

The mass transfer and factors controlling physicochemical processes occurring in analysis of proteins by TLSEC were studied in [48]. It was demonstrated that the plate angle is the key parameter in optimization of flow modes in TLSEC as a hydraulic system.

It was demonstrated experimentally that the resolution, which can be attained in TLSEC, is well comparable with that realized in combined methods such as column gel chromatography, low voltage electrophoresis, and gel electrophoresis [49].

Features and Potentialities

The TLC features are determined by the development mechanism during elution across the open adsorbent layer. This is a simple, rapid, and relatively low-cost technique.

The adsorbent layer plays a triple role: it is a chromatographic separation substrate, a point of generation and application of capillary forces driving the eluent across the plate, and a platform for detection (visualization) of chromatographic zones (spots) formed in the chromatogram after the development. All these provide simple realization of adsorption chromatography, which is an efficient tool for analysis

of weakly polar compounds. The open adsorbent bed used in TLC allows easy application of a sample, visualization of chromatograms by spraying with some common or specific visualizing agent, or, if needed, successive treatment with several reagents, and simultaneous analysis of a great number of samples, thus providing simple visualization and preservation of thin-layer chromatograms. There are broad possibilities in selective development of chromatograms and detection of any components, including radioactive isotopes. It is also possible to detect strongly adsorbable components. These features allow easy realization of secondary (two-dimensional and multiple) chromatography, employment of gradient development techniques, programming of the activity and pH gradient for the adsorbent layer, and realization of polyzonal and multiple TLC, etc.

Advantages of TLC are simplicity, rapidity, high separation efficiency and sharpness, and clearness of results. Despite up-to-date rather complex hardware implementation of TLC, this method now, as before, remains the simplest and most available version of liquid chromatography, combining such advantages as versatility, ultrahigh sensitivity, high resolution, rapidity, and applicability to analysis of wide spectrum of compounds. In TLC, separation conditions can be varied over a wide range by changing the elution system, adsorbent nature, and development procedure (two-dimensional, gradient, isocratic, etc.). The method is best suited for analysis of low- and medium-polarity compounds. It can be used for micropreparative fractionation, preconcentration, and trace analysis. In this case, a TLC plate may be used directly for sample enrichment by compressing a chromatographic zone (spot). Multiple TLC is the most efficient technique for enrichment of strongly adsorbable compounds. In this method, a trace component migrates in the least mobile zone of the eluent. It is advisable to begin selective enrichment of a sample for TLC analysis from solid-state extraction (SSE).

Visualization. A significant advantage of TLC is the possibility of broad variation of visualizing reagents for detection of colorless compounds on the chromatogram. In TLC, detection can be performed as follows: (1) without using reagents, by registration of UV absorption or natural fluorescence and (2) with suitable detection reagents (universal and selective) to form colored, fluorescent, or UV-absorbing compounds.

The first method is realized either by UV photograph of the chromatograph, or by the use of fluorescence quenching. In the latter case, a fluorescent indicator (luminophore) is introduced into the adsorbent layer. When excited with UV light at a wavelength corresponding to the absorption of the analyte, absorbing compounds quench the uniform layer luminescence and are detected as dark spots on a bright background. In the second method, concentrated acids, primarily sulfuric acid, are used as universal reagents. After spraying with sulfuric acid, some of compounds are detected in the cold, while most compounds, after heat treatment. To detect chemically resistant compounds, some oxidants such as 5% nitric acid, $KMnO_4$, and $K_2Cr_2O_7$ are added to sulfuric acid. As universal reagents for detecting organic compounds, phosphoric, perchloric, and other acids are used, and also iodine vapor, chlorine, and sulfur dioxide. One of the most sensitive and selective detection methods is registration of the natural fluorescence of analytes or of selective fluorescent indicators added.

Selective reagents form colored or fluorescent compounds on a group- or substance-specific basis. It is possible to use several reagents successively, to detect compounds of various classes or compounds with various functional groups.

In TLC, detection may be preceded by prechromatographic derivatization. In addition to the aid of detection, derivatization could be directed to increase the separation efficiency, e.g., by virtue of changing chromatographic behavior of compounds similar in their chemical structure or chromatographic properties. Derivatization can also increase the stability of analytes against oxidation or decomposition and regulate their adsorption activity, solubility, and other characteristics. An advantage of postchromatographic derivatization is the possibility of simultaneous conversion of all components, which allows identification of compounds with close R_f values on the basis of differences in the derivatization kinetics.

Identification. The detected TLC zones are primarily identified by comparison of the characteristic R_f values of the samples and references chromatographed on the same plate. The identity of zones is confirmed further by chemical or physicochemical analysis of compounds extracted from the sorbent layer or their analysis directly on the layer.

Quantitative Analysis

Quantitative TLC analysis was developed just in very early stages of the method. The first attempts to quantify the chromatograms, based on spot size measurements, were performed in 1948 [50]. In 1962, Gagliardi and Pokorny [51] have developed a quan-

tification procedure based on an empirical relationship between the spot area and the amount of a compound contained in it. In further progress of quantitative TLC, extraction of the spot with subsequent measurement by spectroscopic or other techniques was used. Starting from 1967, passing from such elution methods to quantitative analysis in situ, i.e., to determination directly by scanning the spots on the layer, was outlined. In this case, registration by the light absorption, fluorescence, radioactivity, or some other quantities, e.g., conductivity, can be used [32, 50].

Thus, there are three approaches to quantitative TLC: (1) extraction of the material from the spot with subsequent measurement using some proper analytical method (photometry, spectrophotometry, mass spectrometry, fluorometry, gravimetry, etc.); (2) measurement of the spot area; and (3) assessment of the distribution of the compound in the spot directly on the layer (in situ) (scanning).

The scanning methods cover optical methods (reflectivity, transmission, fluorometry, and fluorescence quenching); nuclear-physical methods (autoradiography, scintillation, and ionization); electrochemical methods (polarography and conductometry); methods employing gas-chromatographic detectors (flame ionization, thermal conductivity, and electron capture detectors); and enzymatic methods (bioautography).

In ordinary TLC, semiquantitative methods are widely used. They are based on measuring parameters characterizing the geometry of the chromatographic zone. The methods employ empirical linear relationship

$$S^{1/2} = n \log q + p,$$

where S is the spot area; q, weight of the compound; and n and p are empirical constants determined from the calibration curves.

However, this relationship does not always give satisfactory results because of imperfect detection of the spot boundaries, and quantitative determination can be performed directly by comparison with a series of references spotted on the plate along with the samples.

By now, many stages of the chromatographic process are standardized, improving the reproducibility and precision of the method. This has been favored by the introduction of specially designed devices for quantitative TLC.

Optical scanning methods are based on registration of the light absorption, reflection, and their combination. Also fluorescence and fluorescence quenching can be detected. The use of glass supports limits the spectral range to >325 nm, since glass and the adsorbent layer absorb UV radiation. Detection by measuring the reflection can be used over the entire spectral range from 196 to 2500 nm, including the UV range.

A significant drawback of the quantitative methods based on light transmission is associated with the nonlinear dependence of the signal of an optical detector on the amount of a compound in the spot. This nonlinearity is caused by nonuniform thickness of the adsorbent layer and by specific features of passing light through a scattering medium (described by the Kubelka–Munk equation). The use of the two-wavelength detection technique, with the first wavelength λ_1 corresponding to the absorption by both the analyte and adsorbent and the second wavelength λ_2, to the absorption by the adsorbent only, allows determination of the analyte by the difference signal. As a result of these improvements, the accuracy of up-to-date quantitative high-performance TLC approaches 1%.

The use of two-axis scanning for elliptical spots (two-dimensional TLC) and of multistep scanning of spots of imperfect shape (TLSEC) using a densitometer with a spotlight probe improved the accuracy to about 1%.

The detection based on measuring both the reflection and fluorescence quenching is used in TLC of compounds absorbing UV radiation. The most efficient method is measurement of the fluorescence of compounds in the sorbent layer. This is a highly selective and highly sensitive technique (more so with the use of laser fluorescence detectors). Its results are independent of the spot shape. The method is characterized by a wide range of linearity of the amount vs. fluorescence intensity plot.

Many companies manufacture devices for optical scanning of TLC chromatograms, e.g., Opton universal scanning system (Zeiss, Germany–the United States). Shimadzu (Japan) produces scanning systems (c-910, 920, 930, 9000) with two-wavelength scanning over the range 200–800 nm. The systems employ single-beam scheme with variable wavelength or fixed wavelength, double-beam scheme, and fluorometer. The double-beam version allows quantitative determination of one more compound in the chromatographic

spot [52]. Camag (Switzerland) produces scanners operating in the reflectance mode for measuring the light absorption, fluorescence, and fluorescence quenching. They are used for detection in circular and anticircular TLC with macro- and microslits.

For standardization of quantitative determinations, Russian manufacturers produce automated densitometers-fluorometers Den-Skan (Lenkhrom Science and Technology Center, St. Petersburg, Russia), based on a diode matrix. Densitoscopes of two types are also produced: Sorbfil (Sorbpolimer, Krasnodar, Russia) for quantitative assessments in TLC and Sorbfil-D for quantification of chromatograms using illumination with visible light (image is registered using a flatbed scanner).

Several conditions should be met in performing analyses by elution TLC: (1) complete extraction of the sorbent material with the analyte, (2) quantitative extraction of the analyte from the sorbent, and (3) precise analysis of the resulting solutions.

In quantitative elution TLC, it is recommended to use special measures to stabilize the compounds to be separated, e.g., to perform TLC in the dark or under diminished illumination, to remove traces of heavy metals from the sorbent, etc. [21, 51].

For quantitative elution TLC, like for other quantitative TLC techniques, the sample application procedure is of great significance. Generally, a sample is applied as a continuous band or a number of spots at the start line. For quantitative elution TLC, both methods are equivalent.

The reproducibility in quantitative elution TLC is so high that, in analysis of a 50-μg sample, the method gives a standard deviation of 2.5–4% (at $N = 10$). However, it should be pointed out that such a high accuracy is attained only at optimal experimental conditions. With decreasing sample to 10 μg, the error increases to 15% [53, 54]. Therefore, the elution techniques are not employed for quantitative analysis of microgram samples.

CONCLUSION

The major trends in TLC, and TLC of polymers in particular, are instrumentalization, passing to quantitative analysis, theoretical substantiation of ways to improve the efficiency of the method, and further extension of the applications to analysis of a broad spectrum of macromolecular compounds.

Important advantages of TLC of polymers are as follows: possibility of analyzing simultaneously a large number of samples (mass screening); easy detection of any compounds by developing the plate surface; complete analysis of all components of the sample spotted on a TLC plate; analysis of samples containing insoluble particles; and possibility of analyzing compounds requiring additional exposure to visualization reagents after chromatography.

Size-exclusion TLC of biopolymers demonstrates a number of useful characteristics such as pH and temperature independence and preservation of the native composition and structure of the analyte.

Thin-layer chromatography is realized in one of two versions: (1) qualitative (semiquantitative) and (2) quantitative. It allows operation with nano- and microgram samples, providing (under optimal conditions) the detection limit at a level of 10^{-8}–10^{-7} g, i.e., at a level characteristic of such physical methods as atomic absorption, mass spectrometry, X-ray fluorescence, etc., differing advantageously from them in simplicity of hardware implementation, analysis time, sensitivity, and cost.

REFERENCES

1. Belen'kii, B.G., Gankina, E.S., and Turkova, L.D., in *Lektsii 2-i shkoly po metodam ochistki i otsenki chistoty monomerov i polimerov* (Lectures at the 2nd School on Monomer and Polymer Purification and Quality Assessment), Chernogolovka, 1968, pp. 216–267.
2. Inagaki, H., Matsuda, H., and Kamiyama, F., *Macromolecules*, 1968, vol. 1, pp. 520–525.
3. Belenkii, B.G. and Gankina, E.S., *J. Chromatogr.*, 1970, vol. 53, pp. 3–85.
4. Belenkii, B.G. and Gankina, E.S., *J. Chromatogr.*, 1976, vol. 121, pp. 13–90.
5. Otocka, E.P.M., *Adv. Chem. Ser.*, 1973, vol. 125, p. 55.
6. Belen'kii, B.G. and Gankina, E.S., *Dokl. Akad. Nauk SSSR*, 1969, vol. 186, pp. 857–859.
7. Inagaki, H. and Kamiyama, F., *Macromolecules*, 1973, vol. 6, pp. 5107–5111.
8. Belen'kii, B.G. and Gankina, E.S., *Dokl. Akad. Nauk SSSR*, 1970, vol. 194, pp. 573–576.
9. Kamiyama, F. and Inagaki, H., *Bull. Inst. Chem. Res. Kyoto Univ.*, 1971, vol. 49, pp. 53–68.
10. Inagaki, H., Miyamoto, T., and Kamiyama, F., *J. Polym. Sci., Ser. B*, 1969, vol. 7, pp. 329–333.

11. Gankina, E.S., *Cand. Sci. Dissertation*, Leningrad, 1970.
12. Donkai, N. and Inagaki, H., *J. Chromatogr*, 1972, vol. 71, pp. 473–480.
13. Belen'kii, B.G. and Vilenchik, L.Z., *Khromatografiya polimerov* (Chromatography of Polymers), Moscow: Khimiya, 1978.
14. Gurkovskaya, E.A. and Klyachko, Yu.A., *Tonkosloinaya gel'-pronikayushchaya khromatografiya biopolymerov: Nauchno-tekhnicheskaya informatsiya* (Thin-Layer Gel Permeation Chromatography of Biopolymers: Scientific and Technical Information), Moscow, 1991, issue 1, pp. 19–23.
15. Gankina, E.S., Val'chikhina, M.D., and Belen'kii, B.G., *Vysokomol. Soedin., Ser. A*, 1976, vol. 18, pp. 1170–1172.
16. Belenkii, B.G., et. al., *J. Chromatogr.*, 1976, vol. 129, pp. 115–124.
17. Palutski, G.S., Gurkovskaya, E.A., and Klyachko, Yu.A., *Agrarn. Nauka*, 1999, no. 9, pp. 79–87.
18. Gurkovskaya, E.A. and Klyachko, Yu.A., *Sorbts. Khromatogr. Prots.*, 2005, vol. 5, no. 1, pp. 32–44.
19. Determann, H., *Gel Chromatography. Gel Filtration, Gel Permeation, Molecular Sieves. A Laboratory Handbook*, Berlin: Springer, 1969.
20. Kirchner, J.G., *Thin-Layer Chromatography*, New York: Wiley, 1978.
21. Belen'kii, B.G., Gurkovskaya, E.A., Kogan, Yu.D., and Krasikov, V.D., *Tonkosloinaya khromatografiya v Rossii: "Sto let khromatografii"* (Thin-Layer Chromatography in Russia: "A Centenary of Chromatography"), Moscow: Nauka, 2003, pp. 61–99.
22. Berezkin, V.G. and Bochkov, A.S., *Kolichestvennaya tonkosloinaya khromatografiya* (Quantitative Thin-Layer Chromatography), Moscow: Nauka, 1980.
23. Johansson, B.G. and Rymo, I., *Proteides Biol. Fluids*, 1966.
24. Hanson, I.A., Johansson, B.G., and Rymo, I., *Clin. Chem. Acta*, 1966, vol. 14, p. 391.
25. Ryle, A.P., *Nature*, 1965, vol. 206, p. 1256.
26. Andrews, P., *Biochem. J.*, 1964, vol. 91, p. 222.
27. Siegel, L. M. and Monty, K.J., *Biochem. Biophys. Acta*, 1966, vol. 112, p. 396.
28. Fischer, I., *Gel Filtration Chromatography: Laboratory Techniques in Biochemistry and Molecular Biology*, Amsterdam: Elsevier, 1980.
29. Gurkovskaya, E.A. and Klyachko, Yu.A., *Sorbts. Khromatogr. Prots.*, 2005, vol. 5, no. 1, pp. 55–68.
30. Gurkovskaya, E.A., *Sorbts. Khromatogr. Prots.*, 2005, vol. 5, no. 2, pp. 202–211.
31. Dubinin, M.M., *Adsorbtsiya i poristost'* (Adsorption and Porosity), Moscow: VAKhZ, 1980, pp. 226–228.
32. *Analiticheskaya khromatografiya* (Analytical Chromatography), Sakodynskii, K.I., Ed., Moscow: Khimiya, 1993, pp. 338–334.
33. Tomasek, V., *Gel Chromatography, Laboratory Handbook of Chromatographic and Allied Methods*, Mikes, O., Ed., Chichester: Ellis Horwood, 1979.
34. Gurkovskaya, E.A., in *Issledovanie makromolekulyarnogo sostava zlakov khromatograficheskimi metodami* (Chromatographic Examination of Macromolecular Structure of Cereals), Moscow: Khlebprodinform, 2003, pp. 1–20.
35. Gurkovskaya, E.A., in *Trudy X Mezhdunarodnoi nauchno-prakticheskoi konferentsii "Strategiya razvitiya pishchevoi promyshlennosti"* (Proc. X Int. Scientific and Practical Conf. "Strategy of the Development of Food Industry"), Moscow, 2004, vol. 1, no. 1, pp. 229–230.
36. Gurkovskaya, E.A., Klyachko, Yu.A., and Londar', L.D., in *Opredelenie molekulyarnoi massy belkovykh soedinenii pishchevykh produktov: Nauchno-tekhnicheskaya informatsiya* (Determination of Molecular Weight of Proteinic Compounds of Foodstuffs: Scientific and Technical Information), Moscow, 1991, issue 5, pp. 19–22.
37. Gurkovskaya, E.A. and Klyachko, Yu.A., Abstracts of Papers, *The 2nd Int. Symp. on Chromatography and Spectroscopy in Environmental Analysis and Toxicology ISCSE'96*, St. Petersburg, June 18–21, 1996, pp. 95–96.
38. Fisher, R.B. and Parsons, P.S., *Nature*, 1948, vol. 161, pp. 764–765.
39. Gurkovskaya, E.A., *100 Years of Chromatography: 3rd Int. Symp. in Biosciences SBS'03*, Moscow, May 13–18, 2003, p. 396.
40. Gurkovskaya, E.A., *Sorbts. Khromatogr. Prots.*, 2006, vol. 6, no. 4, pp. 503–545.
41. Gurkovskaya, E.A., *Sorbts. Khromatogr. Prots.*, 2006, vol. 6, no. 4, pp. 606–611.
42. Gurkovskaya, E.A., *Sorbts. Khromatogr. Prots.*, 2006, vol. 6, no. 4, pp. 636–641.
43. Gurkovskaya, E.A., *Sorbts. Khromatogr. Prots.*, 2006, vol. 6, no. 6, part 4, pp. 1381–1392.
44. Gurkovskaya, E.A., *Sorbts. Khromatogr. Prots.*, 2006, vol. 6, no. 3, pp. 472–477.
45. Gurkovskaya, E.A. and Klyachko, Yu.A., *Sorbts. Khromatogr. Prots.*, 2005, vol. 5, no. 1, part 4, pp. 55–68.

46. Gurkovskaya, E.A., *Sorbts. Khromatogr. Prots.*, 2006, vol. 6, no. 5, pp. 712–721.
47. Gurkovskaya, E.A., *Sorbts. Khromatogr. Prots.*, 2006, vol. 6, no. 3, pp. 466–471.
48. Gurkovskaya, E.A. and Klyachko, Yu.A., *Sorbts. Khromatogr. Prots.*, 2005, vol. 5, no. 2, pp. 212–224.
49. Gurkovskaya, E.A., *Sorbts. Khromatogr. Prots.*, 2005, vol. 5, no. 5, pp. 621–640.
50. *Quantitative Paper and Thin-Layer Chromatography*, Shellard, E.J., Ed., London: Academic, 1968. Translated under the title *Kolichestvennaya bumazhnaya i tonkosloinaya khromatograhiya*, Moscow: Mir, 1971, p. 192.
51. Gagliardi, E. and Pokorny, G., *Microchim. Acta*, 1967, no. 3, pp. 550–554.
52. Krasikov, V.D., *Osnovy planarnoi khromatografii* (Fundamentals of Planar Chromatography), St. Petersburg: Khimizdat, 2005, p. 92.
53. Abbot, N.L., *Science*, 1999, vol. 283, pp. 33, 57.
54. Yager, P. et al., *Science*, 1999, vol. 283, p. 436.

ISSN 1070-4272, Russian Journal of Applied Chemistry, 2008, Vol. 81, No. 3, pp. 370–374. © Pleiades Publishing, Ltd., 2008.
Original Russian Text © L.E. Derlyukova, M.V. Vinokurova, 2008, published in Zhurnal Prikladnoi Khimii, 2008, Vol. 81, No. 3, pp. 384–388.

INORGANIC SYNTHESIS AND INDUSTRIAL INORGANIC CHEMISTRY

Effect of SO_2 on Chlorination of Zinc Ferrite $ZnFe_2O_4$ and a Mixture of ZnO and Fe_2O_3

L. E. Derlyukova and M. V. Vinokurova

Institute of Problems of Chemical Physics, Russian Academy of Sciences, Chernogolovka, Moscow oblast, Russia

Received July 21, 2007

Abstract—Results of thermodynamic calculations and kinetic studies of the reaction of zinc ferrite $ZnFe_2O_4$ and of a mixture of oxides, ZnO and Fe_2O_3, with chlorine and SO_2 are presented.

DOI: 10.1134/S1070427208030038

Chloride sublimation processes are widely used to produce anhydrous chlorides and oxychlorides in inorganic synthesis, recover rare and nonferrous metals from complex polymetallic raw materials in metallurgy, purify compounds to remove impurities, and separate metals [1–3]. In all these cases, the reacting systems are multicomponent.

Introduction of a new reagent into a heterogeneous system is, as a rule, accompanied by a change not only in the equilibrium composition of the products formed, but also in the rates of particular reactions occurring in the system [4]. It has been shown previously that results obtained in chlorination of individual metal oxides cannot be used to make definite conclusions about the chlorination kinetics of their mixtures [5, 6]. A noticeable influence on the rate of chloride sublimation is exerted by the composition of the gas phase. For example, addition of sulfur dioxide to chlorine accelerates the process even in those cases when the sulfur oxide does not react with a metal oxide in the absence of chlorine [7]. It has been found that the recovery of tungsten dioxydichloride from scheelite–wolframite concentrates into the sublimate increases in the presence of sulfur dioxide [8].

To find the optimal conditions of selective recovery of metals in the form of chlorides, it is highly important to study the reaction of double oxides or their mixtures with chlorine and the effect of the composition of the gas phase on this process.

However, published data on the behavior of double oxides in the atmosphere of chlorine are scarce. It was found in [9–11] that, in the reaction of cobalt and nickel ferrites with chlorine, the degree of chlorination of the elements contained in these compounds differs from that observed in chlorination of their individual oxides, but this fact was not explained.

Most kinds of zinc raw materials contain a large amount of iron. The basic form of zinc compounds in oxidized materials is ferrite. It has been found in a study of the reaction of ZnO with mixtures of chlorine and sulfur dioxide that formation of a stable zinc sulfate markedly diminishes the rate at which zinc chloride is formed [12]. By contrast, formation of iron sulfate in the reaction of Fe_2O_3 with chlorine in the presence of SO_2 leads to an increase in the degree of chloride sublimation of iron [13].

Here we report the results of thermodynamic calculations and kinetic studies of chlorination of zinc ferrite $ZnFe_2O_4$ and of an equimolar mixture of ZnO and Fe_2O_3 in the presence of SO_2.

EXPERIMENTAL

The equilibrium compositions of the gas and condensed phases of the system under study were calculated by the method of free energy minimization by ASTRA software [14] in the temperature range 300–800°C. The chlorination kinetics was studied at 500–700°C by the gravimetric method under isothermal conditions on an installation that automatically recorded the variation of mass with time. The sensitivity of the installation was 0.001 g per 1 mm of the scale. The weighed portion of a sample was 0.180–0.200 g. Under the experimental conditions, the $Cl_2 : SO_2$ ratio was 1 : 1. The total gas flow rate was 200 ml min^{-1} at a linear flow velocity of 0.05 m s^{-1}. Such a rate of gas supply to the surface did not impose any limitations on the chlorination process.

The reaction products formed were identified by X-ray phase analysis (XPA) on an ADP-2-01 diffractometer and by chemical analysis using standard procedures.

An equimolar mixture of oxides was produced by mechanical mixing of ZnO and α-Fe_2O_3 of ultrapure grade, and zinc ferrite, by joint decomposition of zinc and iron carbonates at 800°C [15]. According to the results of chemical and X-ray phase analyses, the sample produced by decomposition of the carbonates was composed of a single phase, $ZnFe_2O_4$, stable in air below 1590°C [16].

The specific surface area was found by the BET method from the low-temperature adsorption of krypton. The specific surface areas of ZnO, Fe_2O_3, and $ZnFe_2O_4$ were 3.4, 10.0, and 40.0 $m^2\ g^{-1}$, respectively.

The equilibrium compositions of the condensed and gas phases of the system ZnO–Fe_2O_3–Cl_2–SO_2 are shown in Figs. 1 and 2. In contrast to the system with individual zinc oxide, there is no $ZnSO_4$ in the condensed phase at 300–500°C (Fig. 1). Zinc is represented by the chloride. Iron is in the form of $Fe_2(SO_4)_3$ and Fe_2O_3. Noticeable amounts of $ZnSO_4$ appear above 550°C, when the content of $Fe_2(SO_4)_3$ and $ZnCl_2$ substantially decreases.

The main components of the gas phase (Fig. 2) are zinc and iron chlorides, SO_2, SO_3, O_2, and Cl_2. Even at 300–550°C, when the main part of $ZnCl_2$ is in the condensed phase, the partial pressure of zinc dichloride exceeds the partial pressures of iron chlorides by two orders of magnitude. At higher temperatures, the difference between the equilibrium pressures of zinc and iron becomes as large as four orders of magnitude. The partial pressures of $ZnCl_2$, SO_2, and SO_3 steadily increase with temperature, the maximum content of iron chlorides is reached at 550–600°C, when zinc is partly present in the form of a sulfate. The overall process at 300–550°C can be described by the equation

$$3ZnO + Fe_2O_3 + 3Cl_2 + 3SO_2 = 3ZnCl_2 + Fe_2(SO_4)_3.$$

At 550–650°C, part of chlorine is consumed for chlorination of Fe_2O_3 because of the parallel formation of zinc dichloride and zinc sulfate. At 650–800°C, the main part of iron is in the condensed phase in the form of an oxide. The gas phase contains considerable amounts of sulfur oxides, i.e., processes of parallel formation of $ZnCl_2$ and SO_3 may occur in the system.

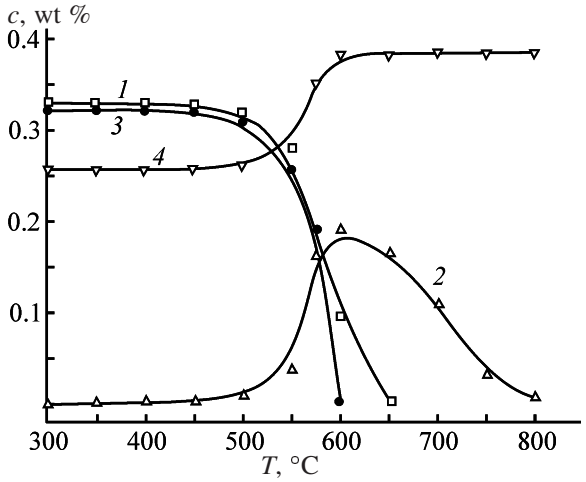


Fig. 1. Equilibrium composition c of the condensed phase of the system ZnO–Fe_2O_3–Cl_2–SO_2 vs. temperature T. (*1*) $ZnCl_2$, (*2*) $ZnSO_4$, (*3*) $Fe_2(SO_4)_3$, and (*4*) Fe_2O_3.

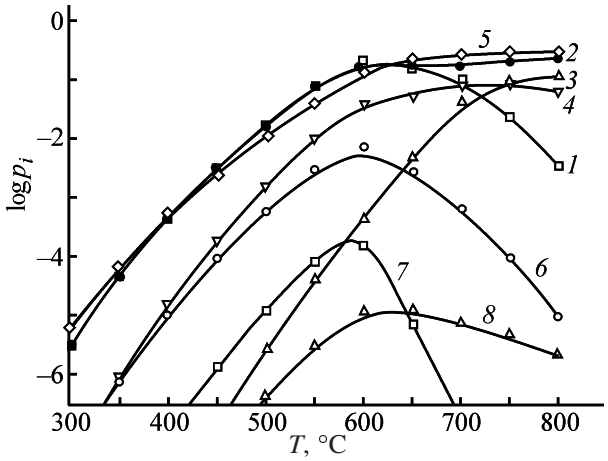


Fig. 2. Equilibrium composition of the gas phase of the system ZnO–Fe_2O_3–Cl_2–SO_2 vs. temperature T. (p_i) Partial pressure. (*1*) Cl_2, (*2*) SO_2, (*3*) O_2, (*4*) SO_3, (*5*) $ZnCl_2$, (*6*) $FeCl_3$, (*7*) Fe_2Cl_6, and (*8*) $FeCl_2$.

An increase in the content of chlorine in the starting system leads to a substantial rise in the content of iron chlorides in the gas phase and, accordingly, to a decrease in the selectivity of the process.

The pronounced difference between the partial pressures of zinc and iron chlorides in the system ZnO–Fe_2O_3–Cl_2 led the authors of [6] to conclude that selective transfer of $ZnCl_2$ to the gas phase is possible in joint chlorination of ZnO and Fe_2O_3. The thermodynamic calculations performed demonstrated that addition of SO_2 to the system under consideration must lead to a decrease in the selectivity of the process because of the increase in the concentration of iron chlorides in the gas phase.

The chlorination kinetics in the reaction of both

Table 1. Distribution of zinc and iron in the products formed in the reaction of a mixture of ZnO and Fe_2O_3 with an equimolar mixture of Cl_2 and SO_2

Reaction conditions			Content in the solid phase, % relative to initial value					Sublimation, % relative to initial content	
			Zn		Fe				
T, °C	τ, min	$\Delta m/m_0$, %	$ZnCl_2$	$ZnSO_4$	$FeCl_3$	$Fe_2(SO_4)_3$	Fe_2O_3	Zn	Fe
400	15	37.4	73.2	22.8	0	13.5	75.7	0	10.6
	60	60.4	100	0	0	44.4	43.7	0	11.2
	120	60.5	100	0	2.6	44.0	44.7	0	8.6
450	30	53.8	95.6	0	5.2	32.8	60.8	4.4	1.2
	45	35.5	87.4	0	3.3	43.3	39.4	12.6	13.9
500	15	43.8	76.9	13.8	0	37.6	44.0	9.3	18.3
	45	36.7	60.7	0	4.7	48.0	26.9	39.3	20.4
550	15	20.8	31.5	5.6	0	43.4	40.0	62.9	16.5
	30	10.8	21.3	0	0	51.4	19.3	78.7	29.4
600	10	13.3	21.9	0	0	49.4	26.8	78.1	23.8
	15	13.2	22.0	0	0	47.9	29.6	78.0	21.7
	20	–1.8	12.8	0	0	46.9	19.1	87.2	33.4
	45	–12.5	5.8	0	0	42.9	17.8	94.2	39.5

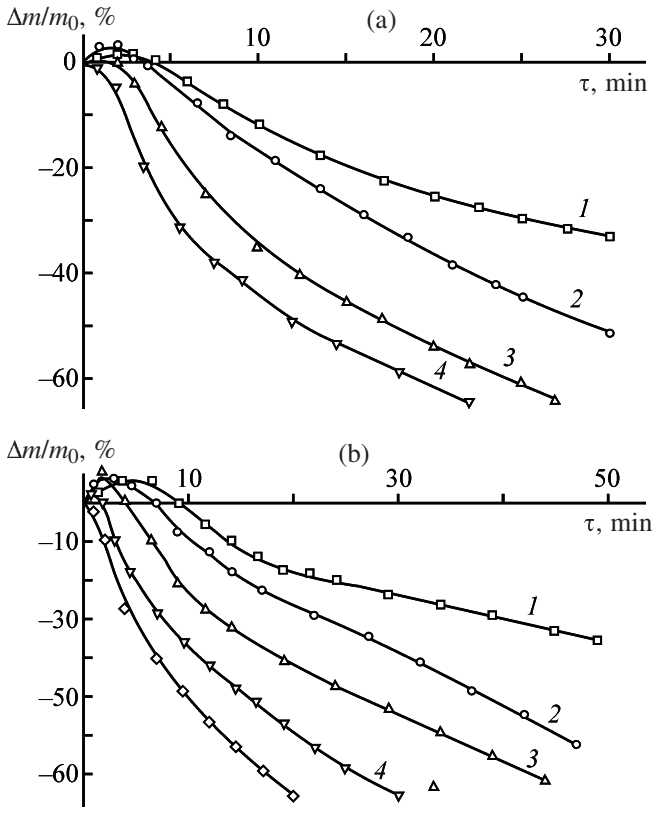


Fig. 3. Isotherms of interaction of (a) mixture of ZnO and Fe_2O_3 and (b) $ZnFe_2O_4$ with an equimolar mixture of Cl_2 and SO_2 at different temperatures. T, °C: (*1*) 500, (*2*) 550, (*3*) 600, (*4*) 650, and (*5*) 700. ($\Delta m/m_0$) Relative change in mass and (τ) time.

the equimolar mixture ZnO + Fe_2O_3 and $ZnFe_2O_4$ with chlorine in the presence of SO_2 was studied in the temperature range 500–650°C. Isotherms of chlorination of a mixture of ZnO with Fe_2O_3 are shown in Fig. 3a. At 500–600°C, the isotherms show a slight initial increase in the sample mass, which is due, according to chemical analysis data, to the formation of $Fe_2(SO_4)_3$. Making the experiment longer results in that the mass decreases because of the transfer of $ZnCl_2$ and $FeCl_3$ to the gas phase. At 500°C, the process rate markedly decreases in the course of time.

The activation energy of the process was estimated for a 15% decrease in mass. A value of 62.8 kJ mol^{-1} was obtained, which coincides with that calculated for chlorination of Fe_2O_3 in the presence of SO_2 at temperatures of 600–750°C [13].

For a more detailed examination of the composition of the chlorination products and solid-phase residue, a number of special-purpose experiments were carried out with an increased sample weight (0.600–1.000 g). The solid-phase residue was analyzed for the content of zinc, iron, and Cl^- and SO_4^{2-} ions. The distribution of zinc and iron in the chlorination products is presented in Table 1. The results obtained demonstrated that nearly the whole amount of zinc is in the form of chloride in the entire temperature range studied (400–600°C). At 400°C, $ZnCl_2$ is contained in the solid phase. As temperature is raised, the chloride sublimes. The formation of minor amounts of

Table 2. Conditions and parameters of the reaction of a mixture of ZnO and Fe_2O_3 with chlorine and an equimolar mixture of Cl_2 and SO_2. Solid phase: ZnO + Fe_2O_3

Reaction conditions			Conversion parameters				
gas phase	T, °C	τ, min	$\Delta m/m_0$, %	content in residue, %		sublimation, % relative to initial content	
				Zn	Fe	Zn	Fe
Cl_2	500	32	–33.5	0.9	67.4	97.4	0
Cl_2 + SO_2	500	31	–33.9	1.0	64.8	97.2	4.0
Cl_2	550	25	–35.1	0.9	67.9	97.4	1.3
Cl_2 + SO_2	550	25	–43.8	1.1	47.3	97.3	44.6
Cl_2	600	17	–36.1	1.9	67.1	94.6	3.9
Cl_2 + SO_2	600	13	–41.7	1.0	46.2	98.3	43.7

$ZnSO_4$ is observed only in the initial stage of chlorination at comparatively low temperatures. In contrast to $ZnSO_4$, the presence of a considerable amount of $Fe_2(SO_4)_3$ is recorded in the entire temperature range studied. As the experimental temperature increases, the content of $Fe_2(SO_4)_3$ in the solid phase grows, so that the fraction of iron in the form of sulfate approaches 50% at 500–600°C. In parallel with the accumulation of $Fe_2(SO_4)_3$, $FeCl_3$ is formed. Iron trichloride virtually completely passes into the gas phase. At 550–600°C, more than 30% of iron is in the form of $FeCl_3$.

Table 2 compares the rates at which zinc and iron chlorides pass into the gas phase under kinetic conditions in the atmosphere of chlorine or a mixture of Cl_2 with SO_2. The results obtained demonstrate that the rate at which the mass of the mixture of ZnO and Fe_2O_3 changes in the presence of SO_2 exceeds that in the atmosphere of chlorine. This is particularly noticeable at temperatures higher than 500°C. The chlorination rate of zinc is virtually unaffected by SO_2, whereas chlorination of iron occurs at a higher rate. In the atmosphere of chlorine, the appearance of iron chlorides in the gas phase was observed only upon complete chemical sublimation of zinc, whereas in the presence of SO_2, iron and zinc chlorides pass into the gas phase virtually simultaneously. As also in the atmosphere of chlorine, the rate of chemical sublimation of zinc dichloride exceeds that of iron chlorides, but the difference between the rates is not so significant.

Figure 3b shows isotherms of interaction of zinc ferrite $ZnFe_2O_4$ with an equimolar mixture of Cl_2 and SO_2. They virtually coincide with the isotherms of chlorination of a mixture of oxides. The stage of the initial increase in mass, caused by the formation of $Fe_2(SO_4)_3$, is followed by that in which the sample mass decreases because of the sublimation of both $ZnCl_2$ and $FeCl_3$. The rates of chemical sublimation of the chlorides are close for $ZnFe_2O_4$ and a mixture of oxides. As in the case of the mixture of oxides, the rate at which $FeCl_3$ passes into the gas phase from the ferrite in the presence of SO_2 exceeds that in the atmosphere of individual chlorine.

An X-ray phase analysis made after chemical sublimation of zinc chloride from the ferrite demonstrated that the solid-phase residue contains exclusively α-Fe_2O_3. The data obtained and the fact that the processes of chemical sublimation of the chlorides from the ferrite and the mixture of oxides are virtually completely identical suggest that, in the course of chlorination, the ferrite stable in air in the temperature range under consideration decomposes into ZnO and α-Fe_2O_3. The specific structural features of $ZnFe_2O_4$, which is a normal spinel, suggest that $ZnFe_2O_4$ will decompose to χ-Fe_2O_3. However, no χ-phase was found in the temperature range studied. Thus, the chlorination of $ZnFe_2O_4$ occurs simultaneously with its decomposition to ZnO and α-Fe_2O_3. The same conclusion was made by the authors of [9–11], who considered the chlorination of cobalt and nickel ferrites.

The fundamental aspects of the chemical sublimation of iron from a mixture of ZnO and Fe_2O_3 in the presence of SO_2 are similar to those observed in the chlorination of Fe_2O_3 [13]: at comparatively low temperatures (300–500°C) it predominantly occurs via the reaction of simultaneous formation of $Fe_2(SO_4)_3$ and $FeCl_3$. The accumulation of $Fe_2(SO_4)_3$, stable in the atmosphere of chlorine, in the solid phase decelerates the process. At 600–750°C, the chemical sublimation of iron is due to the parallel formation of $FeCl_3$ and SO_3.

The kinetics of the chemical sublimation of zinc from the mixture of oxides in the presence of SO_2 strongly differs from that observed in chlorination of ZnO under the same conditions [12], when $ZnCl_2$ is formed as a result of successive occurrence of the reactions of formation and chlorination of $ZnSO_4$, whose considerable amounts were recorded in a wide temperature range.

In the reaction of a mixture of oxides with Cl_2 and SO_2, the amount of $ZnSO_4$ in the solid phase is extremely low. This cannot be due to the thermal instability of the sulfate, because $ZnSO_4$ decomposes at temperatures higher than 700°C [12]. In the system under consideration, $ZnCl_2$ is formed by direct chlorination of ZnO. SO_2 is bound because of the occurrence of the most thermodynamically favorable processes of formation of $Fe_2(SO_4)_3$, which is more stable in the atmosphere of chlorine than $ZnSO_4$, and also via the reaction of simultaneous formation of $FeCl_3$ and SO_3. As a result, the rate of transfer to the gas phase changes for only a single component, iron. The rate of the chemical sublimation of $ZnCl_2$ is independent of whether SO_2 is present in the gas phase.

This process is affected by Fe_2O_3 to a considerably greater extent. As shown previously [6], the rate of the chemical sublimation of $ZnCl_2$ both from a mixture of oxides and from zinc ferrite in the atmosphere of chlorine increases nearly 10-fold in the presence of Fe_2O_3. This is due to specific features of the interaction of chlorine with the inhomogeneous surface of Fe_2O_3. Although the chlorination rate of Fe_2O_3 is lower than that of ZnO, microscopic amounts of $FeCl_3$ are formed on the most active areas of the Fe_2O_3 surface even at 350°C. The multiple involvement of $FeCl_3$ in events of reaction with ZnO results in that the concentration of chlorine near the surface of the substance being chlorinated increases and the chemical sublimation of zinc is intensified. The chemical sublimation of iron occurs only after $ZnCl_2$ completely passes into the sublimate. The presence of SO_2 in the gas phase markedly facilitates the formation of $FeCl_3$ and thereby impairs the selectivity of the chemical sublimation.

CONCLUSIONS

(1) The fundamental aspects of chlorination in the presence of SO_2 are the same for zinc ferrite $ZnFe_2O_4$ and an equimolar mixture of ZnO and Fe_2O_3, just as in the case of chlorination in the atmosphere of pure chlorine.

(2) Making the system $ZnO–Fe_2O_2–Cl_2$ more complex by introduction of an additional component, SO_2, into the gas phase does not change fundamentally the pathway of the process.

(3) Presence in the reaction mixture of a solid component, Fe_2O_3, whose reaction with chlorine changes the composition of the gas phase, affects the fundamental aspects of chlorination to a considerably greater extent.

REFERENCES

1. Kanari, N., Gaballah, I., and Allain, E., *Thermochim. Acta*, 2000, vol. 351, nos. 1–2, pp. 109–117.
2. Kanari, N., Gaballah, I., and Allain, E., *Thermochim. Acta*, 2001, vol. 371, nos. 1–2, pp. 75–86.
3. Murase, K., Nishikawa, K., Ozaki, T., et al., *J. Alloys Comp.*, 1998, vol. 264, nos. 1–2, pp. 151–156.
4. Boldyrev, V.V., Delmon, B., and Bulens, M., *The Control of the Reactivity of Solids*, Amsterdam: Elsevier, 1979.
5. Vinokurova, M.V., Derlyukova, L.E., Babievskaya, I.Z., et al., *Zh. Neorg. Khim.*, 1989, vol. 34, no. 12, pp. 2998–3003.
6. Derlyukova, L.E., Vinokurova, M.V., and Evdokimov, V.I., *Zh. Neorg. Khim.*, 1991, vol. 36, no. 5, pp. 1135–1140.
7. Vinokurova, M.V. and Derlyukova, L.E., *Zh. Neorg. Khim.*, 2004, vol. 49, no. 9, pp. 1432–1435.
8. Menendez, C.J., Tavani, E.L., and Nolasco, E.J., *Thermochim. Acta*, 1999, vol. 338, nos. 1–2, pp. 103–112.
9. Piskunov, I.N., Orlov, A.K., Smirnov, Yu.N., and Telyakov, N.M., *Izv. Vyssh. Uchebn. Zaved., Tsvetn. Met.*, 1976, no. 3, pp. 46–49.
10. Fruehan, R.J. and Martonic, I.J., *Metallurg. Trans.*, 1973, vol. 4, pp. 2793–2799.
11. Telyakov, N.M., Orlov, A.K., and Piskunov, I.N., *Izv. Vyssh. Uchebn. Zaved., Tsvetn. Met.*, 1977, no. 4, pp. 45–48.
12. Derlyukova, L.E., Vinokurova, M.V., and Evdokimov, V.I., *Zh. Neorg. Khim.*, 1986, vol. 31, no. 4, pp. 846–851.
13. Derlyukova, L.E., Eliseeva, N.A., and Evdokimov, V.I., *Zh. Neorg. Khim.*, 1987, vol. 32, no. 9, pp. 2096–2100.
14. Sinyarev, G.B., Vatolin, N.A., Trusov, B.G., and Moiseev, G.K., *Primenenie EVM dlya termodinamicheskikh raschetov metallurgicheskikh protsessov* (Use of Computers for Thermodynamic Calculations of Metallurgical Processes), Moscow: Nauka, 1982.
15. Brauer, G., *Handbuch der Präparativen anorganischen Chemie*, Stuttgart: Ferdinand Enke, 1954.
16. Goronovskii, I.T., Nazarenko, Yu.P., and Nekryach, E.F., *Spravochnik po khimii* (Handbook of Chemistry), Kiev: Naukova Dumka, 1987.

ISSN 1070-4272, Russian Journal of Applied Chemistry, 2008, Vol. 81, No. 3, pp. 375–379. © Pleiades Publishing, Ltd., 2008.
Original Russian Text © T.P. Maslennikova, E.N. Korytkova, V.V. Gusarov, 2008, published in Zhurnal Prikladnoi Khimii, 2008, Vol. 81, No. 3, pp. 389–392.

INORGANIC SYNTHESIS AND INDUSTRIAL INORGANIC CHEMISTRY

Interaction of $Mg_3Si_2O_5(OH)_4$ Nanotubes with Potassium Hydroxide

T. P. Maslennikova, E. N. Korytkova, and V. V. Gusarov

Grebenshchikov Institute of Silicate Chemistry, Russian Academy of Sciences, St. Petersburg, Russia

Received November 16, 2007

Abstract—Interaction of $Mg_3Si_2O_5(OH)_4$ nanotubes with aqueous solutions of potassium hydroxide in various temperature–time treatment modes was studied.

DOI: 10.1134/S107042720803004X

The discovery of carbon nanotubes [1], which possess a unique set of electronic, mechanical, and chemical properties and, therefore, are of particular practical interest, stimulated studies devoted to synthesis of nanotubes of various chemical compositions and analysis of their properties. It has been found that nanotubes can be formed from numerous chemical compounds [2–4]. It was shown in [5, 6] that compounds with layered structure can roll into nanotubes. By now, a large number of compounds with nanotubular structure have been synthesized, e.g., those based on boron nitride, dichalcogenides of transition metals, and oxides and hydroxides of vanadium, titanium, aluminum, silicon, etc. [2–4, 7–10]. However, the properties of such compounds are still poorly understood.

A topical issue is analysis of the mechanisms of mass transfer and chemical interaction of substances localized within inorganic nanotubes or on their surface. Studies of the behavior of fluids localized within nanotubes are primarily important because they lead to solution of a number of fundamental problems related to the structure of fluids on the nanometer scale and to the possible mutual influence of this structure on the transport of the fluid within nanochannels [11, 12] and on chemical transformations in nanoreactors [13, 14].

The applied interest in studies of the state of a substance in nanotubes is due to the potential possibility of filling the nanotubes with various substances. This makes it possible to affect their physicochemical properties [15, 18], creates conditions for immobilization and storage of substances [19], and furnishes an opportunity to improve the selectivity of separation and raise the rate of mass-transfer across membranes by using nanotubes in membrane materials [20, 21]. The large specific surface area of contact between the fluid and nanotube walls and the effect of the field of chemical interaction forces created by a nanotube on most part of the liquid medium it contains make topical an integrated study of mass transfer and chemical interaction of the fluid with nanotube walls.

Of particular interest are nanotubes based on hydrosilicates with a chrysotile structure, formed from double layers [22] via their rolling into nanorolls under the action of internal stresses in the double layer [5]. In [10, 23–26], the mechanism of nanotube formation was studied and nanotubes of chrysotile structure with varied chemical composition and morphology were obtained. The outer surface of nanotubes of this kind is mainly composed of magnesium, iron, cobalt, and nickel hydroxides, and the inner surface, of silicon dioxide.

The possibility of occurrence of chemical reactions between silicon dioxide and alkali metal hydroxides to give the corresponding salts of silicic acid makes promising an integrated study of mass-transfer processes in $Mg_3Si_2O_5(OH)_4$ nanotubes and of the chemical interaction between alkali solutions and the inner wall of a nanotube.

This study is concerned with mass-transfer processes in $Mg_3Si_2O_5(OH)_4$ nanotubes and their chemical interaction with aqueous solutions of KOH.

EXPERIMENTAL

Magnesium hydrosilicates $Mg_3Si_2O_5(OH)_4$ with a nanotubular structure were synthesized under hydrothermal conditions. As starting components served

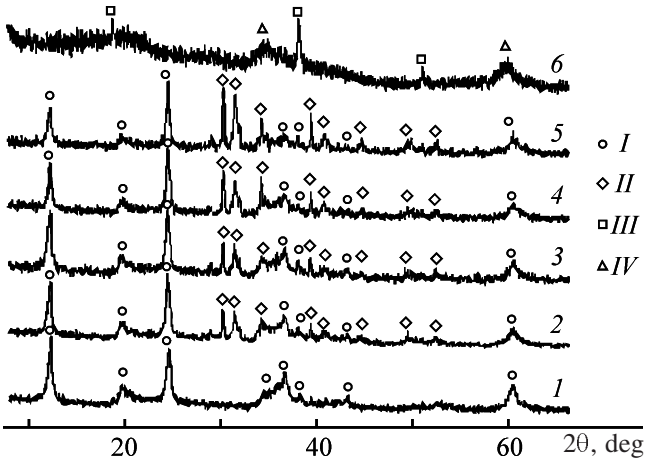


Fig. 1. X-ray diffraction patterns of (*1*) starting and (*2*–*6*) treated $Mg_3Si_2O_5(OH)_4$ nanotubes. (2θ) Bragg angle. Treatment duration, h: (*2*) 2, (*3*) 4, (*4*) 6, (*5*) 8, and (*6*) 10. (*I*) $Mg_3Si_2O_5(OH)_4$, (*II*) K_2SiO_3, (*III*) $Mg(OH)_2$, and (*IV*) $SiO_2 \cdot nH_2O$.

mixtures of magnesium oxide (analytically pure grade) and silicon oxide [KSMG silica gel, GOST (State Standard) 3956–76] with $MgO : SiO_2 = 3 : 2$. $Mg_3Si_2O_5(OH)_4$ nanotubes were synthesized, in accordance with the results of [26], at a temperature of 350°C and pressure of 70 MPa, with the starting mixture treated with a 1 wt % aqueous NaOH solution (NaOH of analytically pure grade) for 24 h. This yielded a morphologically homogeneous product, nanotubes with a chrysotile structure (Fig. 1), based on magnesium hydrosilicate. In these hydrothermal treatment modes, cylindrical nanotubes (Fig. 2) with narrowly varying inner (~4 nm) and outer (~25 nm) diameters were obtained. The products of the hydrothermal treatment were washed with distilled water to remove the alkaline components, dried, and subjected to an integrated physicochemical study.

The X-ray phase analysis of the nanotubes was performed on a DRON-3 diffractometer (CuK_α radiation). The shape and size of the nanotubes were determined by transmission electron microscopy (TEM) on an EM-125 electron microscope with an accelerating voltage of 75 kV.

The elemental composition of the samples was found by energy-dispersion X-ray fluorescence microanalysis with an Oxford Link microprobe attachment to a scanning electron microscope. The error in determining the content of elements was, on average, 0.3 wt % [27].

To study processes of filling of $Mg_3Si_2O_5(OH)_4$ nanotubes with a KOH solution and their chemical

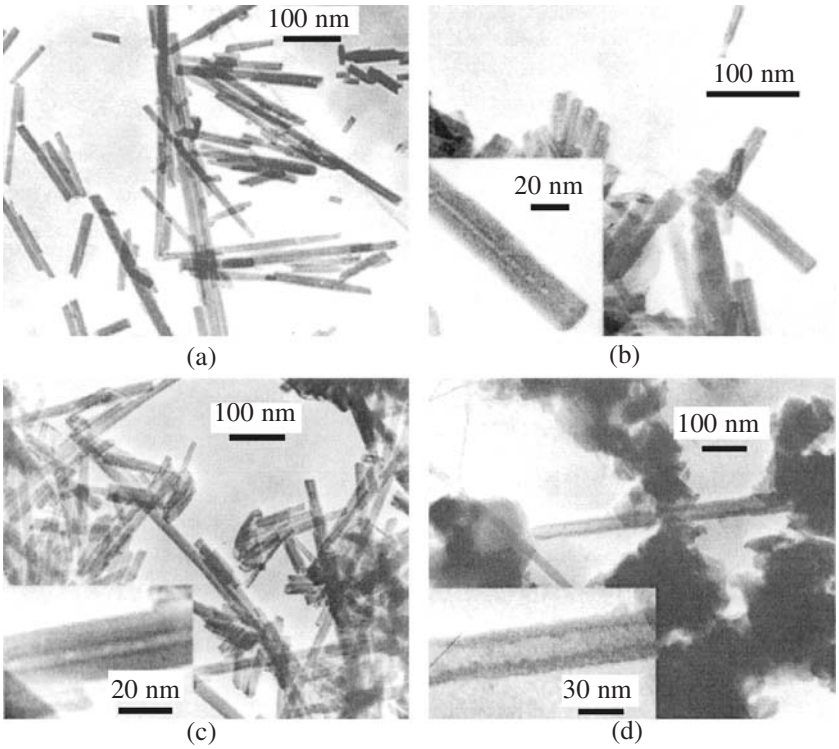


Fig. 2. TEM micrographs of (a) starting and (b–d) treated $Mg_3Si_2O_5(OH)_4$ nanotubes. Treatment duration, h: (b) 4, (c) 8, and (d) 10.

interaction at certain temperatures, weighed portions of nanotubes were placed in glass vessels with caps and poured over with a 0.5 M solution of KOH (KOH of chemically pure grade). The vessels were heated and kept in a thermostat at temperatures of 50 and 80°C for 2, 4, 6, 8, and 10 h. The thus treated nanotubes were washed with distilled water at room temperature, dried in air, and studied by the methods described above.

It was found that, in treatment of $Mg_3Si_2O_5(OH)_4$ nanotubes at 80°C for 2 and 4 h, the nanotubes are filled with the KOH solution (Fig. 3) and their inner layer, composed of SiO_2, reacts with potassium hydroxide, which is confirmed by the appearance of lines associated with K_2SiO_3 in the X-ray diffraction patterns of the samples (Fig. 1). However, the morphology and size of the nanotubes remain unchanged in this temperature–time mode of nanotube treatment with the KOH solution (Fig. 2b). If the duration of nanotube treatment with the KOH solution was extended to 6 h, and especially to 8 h, a substantial increase in the inner diameter of the nanotubes was observed (Fig. 2c).

The X-ray diffraction patterns of nanotubes treated with the KOH solution at 80°C for 8 h contain, in addition to the lines characteristic of magnesium hydrosilicate with a chrysotile structure, lines associated with K_2SiO_3, whose intensity is approximately equal to that of the $Mg_3Si_2O_5(OH)_4$ lines. A longer treatment (up to 10 h) of nanotubes with the KOH solution leads to their virtually complete disintegration (Figs. 1 and 2d). The micrograph of such a sample shows only single nanotubes with a substantially increased inner diameter (Fig. 3) and thin walls. The sample is mostly constituted by aggregates of lamellar particles, presumably composed of crystalline $Mg(OH)_2$ (Fig. 1). Thus, the chemical interaction is virtually complete after a 10-h treatment of $Mg_3Si_2O_5(OH)_4$ nanotubes with a 0.5 M KOH solution at 80°C.

In treatment of nanotubes with the KOH solution at 50°C, the chemical interaction of $Mg_3Si_2O_5(OH)_4$ nanotubes with potassium hydroxide is, presumably, considerably slower than that at 80°C, because no destruction of nanotubes was observed upon treatment of the nanotubes with the KOH solution during the whole time of the experiment, i.e., up to 10 h.

The study demonstrated that the interaction of $Mg_3Si_2O_5(OH)_4$ with an aqueous solution of KOH at 80°C can be represented as occurring in several stages at different rates. First, the nanotubes are filled with the KOH solution. KOH reacts within a nanotube

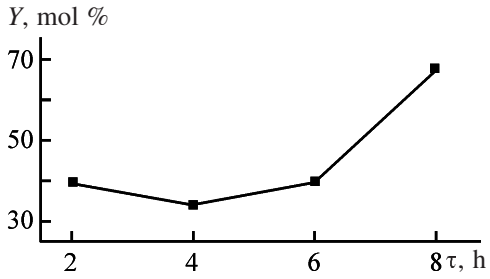


Fig. 3. Amount Y of potassium localized in a $Mg_3Si_2O_5(OH)_4$ nanotube vs. the treatment duration τ.

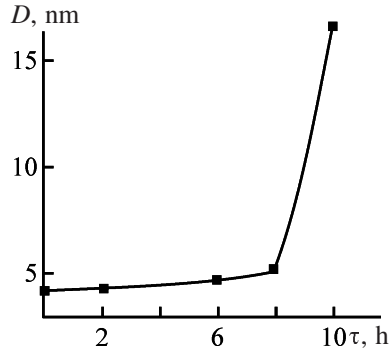


Fig. 4. Nanotube diameter D vs. the duration τ of treatment with the KOH solution. The largest of the diameters observed are presented.

with its inner silicon dioxide layer to give K_2SiO_3 and H_2O (Fig. 1). Because the potassium silicate solution has a higher viscosity, compared to water and the KOH solution [28], further supply of the reagent (KOH) and removal of the reaction product (K_2SiO_3) from the chemical interaction zone are hindered. However, the inner diameter of the nanotube increases in the course of the reaction of SiO_2 with KOH (Figs. 2 and 4), and, consequently, the transport of the components in the nanotube is facilitated, with the result that the rate of the chemical reaction increases. Thus, the chemical interaction occurs with self-acceleration after the stage in which the nanotube is filled with the KOH solution, which is manifested in the accelerating rise in the amount of the reaction product because of the increase in the inner diameter of the nanotube.

After the inner diameter of the nanotube reaches a certain critical value and the interlayer spaces increase because of the intercalation of potassium ions therein, the nanotube unrolls and the layers are split [5]. Because, as a result, the contact of the SiO_2 layer with the KOH solution becomes virtually unhindered by the transport of reagents to the surface, this stage will occur at a very high rate. This behavior of the process is confirmed both by data indicating that the reaction rate substantially increases after 8 h

of interaction and by the morphology of one of the reaction products, agglomerates of $Mg(OH)_2$ platelets (Fig. 2).

Thus, after the stage of filling of $Mg_3Si_2O_5(OH)_4$ nanotubes with a KOH solution, their interaction proceeds in two self-accelerating stages. The self-acceleration occurs because the transport of the reagent, KOH solution, into the reaction zone and the removal of the reaction products, and primarily K_2SiO_3, markedly raising the viscosity of aqueous solutions [28], from the reaction zone in the course of the chemical reaction itself are facilitated.

CONCLUSIONS

(1) Treatment of hydrosilicate nanotubes with a KOH solution at 50°C for up to 10 h does not lead to their degradation.

(2) On filling of the nanotubes with a KOH solution at 80°C, the nanotubes chemically interact with potassium hydroxide, which results in a structural-morphological transformation of nanotubes.

(3) The chemical interaction of KOH with $Mg_3Si_2O_5(OH)_4$ nanotubes and their structure mutually affect each other. As a result, the chemical interaction of KOH with nanotubes proceeds in two self-accelerating stages. The self-acceleration of the chemical reaction in the first stage occurs because the transport of components in the solution localized within the nanotube is facilitated by an increase in the nanotube diameter in the course of the chemical reaction. The self-acceleration in the second stage is due to unrolling of the nanotube.

ACKNOWLEDGMENTS

The authors are grateful to I.A. Drozdova for performing electron-microscopic studies.

REFERENCES

1. Iijima, S., *Nature*, 1991, vol. 354, pp. 56–59.
2. Tenne, R., *Endeavour*, 1996, vol. 20, no. 3, pp. 97–104.
3. Ivanovskii, A.L., *Usp. Khim.*, 2002, vol. 71, pp. 203–227.
4. Rao, C.N.R. and Nath, M., *J. Chem. Soc., Dalton Trans.*, 2003, pp. 1–24.
5. Chivilikhin, S.A., Popov, I.Yu., and Gusarov, V.V., *Dokl. Ross. Akad. Nauk*, 2007, vol. 412, no. 2, pp. 201–203.
6. Chivilikhin, S.A., Popov, I.Yu., Blinova, I.V., et al., *Fiz. Khim. Stekla*, 2007, vol. 33, no. 4, pp. 442–448.
7. Zakharova, G.S., Volkov, V.L., Ivanovskaya, I.I., and Ivanovskii, A.L., *Usp. Khim.*, 2005, vol. 74, no. 7, pp. 651–685.
8. Ivanovskaya, V.V., Enyashin, A.N., Makurin, Yu.N., and Ivanovskii, A.L., *Nanotekhnika*, 2006, no. 1, pp. 126–140.
9. Grigor'eva, A.V., Anikina, A.V., Tarasov, A.B., et al., *Dokl. Ross. Akad. Nauk*, 2006, vol. 410, no. 4, pp. 482–486.
10. Korytkova, E.N., Pivovarova, L.N., Semenova, O.E., et al., *Zh. Neorg. Khim.*, 2007, vol. 52, no. 3, pp. 388–394.
11. Maranon Di Leo, J. and Maranon, J., *J. Mol. Struct.*, 2003, vol. 623, pp. 159–166.
12. Li, T.-D., Gao, J., Szoszkiewicz, R., et al., *Phys. Rev. B*, 2007, vol. 75, pp. 115415-1–115415-6.
13. Lukashin, A.V., Kalinin, S.V., Vertegel, A.A., and Tret'yakov, Yu.D., *Dokl. Ross. Akad. Nauk*, 1999, vol. 369, no. 6, pp. 781–783.
14. Kolesnik, I.V., Eliseev, A.A., Malakho, A.P., et al., *Dokl. Ross. Akad. Nauk*, 2004, vol. 395, no. 6, pp. 776–780.
15. Zaporotskova, I.V. and Lebedev, N.G., *Khim. Fiz.*, 2006, vol. 25, no. 5, pp. 91–96.
16. Lipson, A.G., Lyakhov, B.F., Saunin, E.I., and Tsivadze, A.Yu., *Dokl. Ross. Akad. Nauk*, 2007, vol. 414, no. 5, pp. 640–644.
17. Eletskii, A.V., *Usp. Fiz. Nauk*, 2004, vol. 174, no. 11, pp. 1191–1231.
18. Rao, A. M., Eklund, P. C., Bandow, S., et al., *Nature*, 1997, vol. 388, pp. 257–259.
19. Maslennikova, T.P., Korytkova, E.N., and Gusarov, V.V., Abstracts of Papers, *VII Mezhdunarodnaya nauchnaya konferentsiya "Khimiya tverdogo tela i sovremennye mikro- i nanotekhnologii"*, (VII Int. Scientific Conf. "Solid State Chemistry and Modern Micro- and Nanotechnologies") Kislovodsk, September 17–22, 2007, pp. 186–187.
20. Kononova, S.V., Korytkova, E.N., Romashkova, K.A., et al., *Zh. Prikl. Khim.*, 2007, vol. 80, no. 12, pp. 2064–2070.
21. Che, G., Iakshmi, B.B., Fisher, E.R., and Martin, C.R., *Nature*, 1998, vol. 393, pp. 346–349.
22. Pauling, L., *Proc. Nat. Acad. Sci. USA*, 1930, vol. 16, pp. 578–582.
23. Korytkova, E.N., Maslov, A.V., Pivovarova, L.N., et al., *Neorg. Mater.*, 2005, vol. 41, no. 7, pp. 849–855.
24. Korytkova, E.N., Pivovarova, L.N., Drozdova, I.A.,

and Gusarov, V.V., *Fiz. Khim. Stekla*, 2005, vol. 31, no. 6, pp. 1099–1106.

25. Korytkova, E.N., Pivovarova, L.N., Drozdova, I.A., and Gusarov, V.V., *Zh. Obshch. Khim.*, 2007, vol. 77, no. 10, pp. 1600–1607.
26. Korytkova, E.N., Maslov, A.V., Pivovarova, L.N., et al., *Fiz. Khim. Stekla*, 2004, vol. 30, no. 1, pp. 72–78.
27. Goldstein, J.I., Newbury, D.E., Echlin, P., et al., *Scaning Electron Microscopy and X-ray Microanalysis: A Text for Biologists, Materials Scientisis, and Geologists*, New York: Plenum, 1981.
28. Mazurin, O.V., Strel'tsina, M.V., and Shvaiko-Shvaikovskaya, T.P., *Svoistva stekol i stekloobrazuyushchikh rasplavov: Spravochnik* (Properties of Glasses and Glass-Forming Melts: Reference Book), Leningrad: Nauka, 1987, vol. 5.

ISSN 1070-4272, Russian Journal of Applied Chemistry, 2008, Vol. 81, No. 3, pp. 380–385. © Pleiades Publishing, Ltd., 2008.
Original Russian Text © V.G. Minkina, S.I. Shabunya, V.I. Kalinin, V.V. Martynenko, 2008, published in Zhurnal Prikladnoi Khimii, 2008, Vol. 81, No. 3, pp. 393–398.

INORGANIC SYNTHESIS AND INDUSTRIAL INORGANIC CHEMISTRY

Stability of Aqueous-Alkaline Sodium Borohydride Formulations

V. G. Minkina, S. I. Shabunya, V. I. Kalinin, and V. V. Martynenko

Lykov Institute of Heat and Mass Exchange, National Academy of Sciences of Belarus, Minsk, Belarus

Received August 14, 2007

Abstract—Stability of sodium borohydride in the form of concentrated solutions and suspensions and solids corresponding to a crystal hydrate in composition was studied. The effects of temperature, concentrations of sodium borohydride and alkali, and nature of alkali metal cation on the rate of sodium borohydride hydrolysis were studied.

DOI: 10.1134/S1070427208030051

Hydrogen storage is an urgent problem of hydrogen power engineering. None of existing methods of hydrogen storage (under a high pressure, in the liquid state, and in the cryoadsorbed state) meet the technical and service requirements to the hydrogen content (5 wt % and 45 kg m^{-3}), working pressure, temperature, and kinetics of hydrogen absorption and liberation [1, 2]. At present, the storage of hydrogen in a bound state using hydride-forming materials with high specific surface areas, hydrides, and borohydrides is considered promising. It is expected that such approach will provide fairly compact and safety hydrogen storage.

Preparation of hydrogen by reactions of alkali metal borohydrides with water is actively studied with the aim of developing hydrogen generators for fuel cells. Sodium borohydride is the most promising in relation to hydrogen content and safety of storage [3, 4].

Sodium borohydride is known to be a hygroscopic substance actively absorbing moisture. In the literature there are some data on the stability of borohydrides of alkali metals in water and in aqueous-alkaline solutions [5–8]. However, these studies were carried out either with very dilute solutions of borohydrides or with buffer solutions.

Here we report on an experimental study of various formulations of sodium borohydride, water, and alkali with the aim of determining hydrogen loss on storage of the formulations at various temperatures.

EXPERIMENTAL

We used a sodium borohydride powder containing 98% $NaBH_4$ as the starting substance. Experiments on the stability of aqueous-alkaline solutions of sodium borohydride were carried out in sealed vessels using the following technique. A solution of an alkali of a given concentration was prepared in a beaker. A dry sodium borohydride powder was added to the cooled (to prevent $NaBH_4$ decomposition before starting the experiment) alkali solution, and the beaker was placed in an ultrasonic stirrer up to complete visual mixing and formation of a uniform formulation. Then the beaker was placed in a stainless steel reactor. The reactor was hermetically sealed and placed in a thermostat kept at a preset temperature. The increase in the hydrogen pressure in the reactor was recorded by pressure gages (PA-21SR/80520.3 Keller manometers). A signal from the manometer was recorded and processed on a computer.

Such technique records the amount of hydrogen liberated during the hydrolysis of sodium borohydride. The amount of decomposed $NaBH_4$ was calculated by Eq. (1) using the following relationships.

$$NaBH_4 + 2H_2O = NaBO_2 + 4H_2 \quad (1)$$

$$m_{H_2} = \rho_{H_2} V_{H_2} = M_{H_2} P V_{H_2}/RT,$$

$$\Delta m_{NaBH_4} = -m_{H_2} M_{NaBH_4}/4M_{H_2} = -M_{NaBH_4} P V_{H_2}/4RT,$$

where m_{H_2} is the weight of liberated hydrogen (kg); V_{H_2}; free volume of the reactor (m^3); ρ_{H_2}, hydrogen

density (kg m^{-3}); T, temperature in a reactor (K); P, hydrogen pressure in a reactor (Pa); Δm_{NaBH_4}, weight of decomposed $NaBH_4$; M, molecular weight of a component; and R, universal gas constant (J mol^{-1} K^{-1}).

The weights of the consumed water and formed sodium metaborate $NaBO_2$ were calculated similarly:

$$\Delta m_{H_2O} = -M_{H_2O} P V_{H_2}/2RT,$$

$$\Delta m_{NaBO_2} = -M_{NaBO_2} P V_{H_2}/4RT,$$

The degree of sodium borohydride decomposition (%) as a result of its hydrolysis was calculated by the relationship

$$\xi = (\Delta m_{NaBH_4}/m_{NaBH_4}) \times 100,$$

where m_{NaBH_4} is the weight of $NaBH_4$ in the starting solution (kg).

This calculation procedure assumes that the amount of intermediates in the reaction mixture is insignificant. If the amount of intermediate compounds will be noticeable, it will lead to deviations from the calculated values. This remark concerns the commonly accepted presentation of the results of hydrolysis as the degree of $NaBH_4$ decomposition, based on measuring the concentration of the BH_4^- ion by iodometric titration. From the applied point of view, it is more natural to determine the degree of hydrolysis by hydrogen liberation. In this case, the amount of liberated hydrogen is related to its amount corresponding to the complete hydrolysis. We used this approach in our study.

The experiments on the determination of the stability of concentrated sodium borohydride solutions with a content of alkali $c \geq 3$ wt % by the above-described technique take much time. Such ternary formulations are viscous solutions with a low hydrolysis rate.

In the experiments on the determination of the stability of aqueous-alkaline solutions with the molar ratio $NaBH_4 : H_2O = 1 : 5$ at room temperature (22°C) at all NaOH concentrations, kinetic curves of $NaBH_4$ hydrolysis were linear (Fig. 1). At 22°C, the average rate of $NaBH_4$ hydrolysis v (% of $NaBH_4$/h) within 50 days for $NaBH_4$–$5H_2O$ with 3, 5, and 10% NaOH was, respectively, 0.004, 0.002, and 0.0005% $NaBH_4$/h.

In the experiments, we measured either the volume of liberated hydrogen or the pressure in a sealed vessel where the hydrolysis took place. Both procedures involve difficulties associated with prolonged

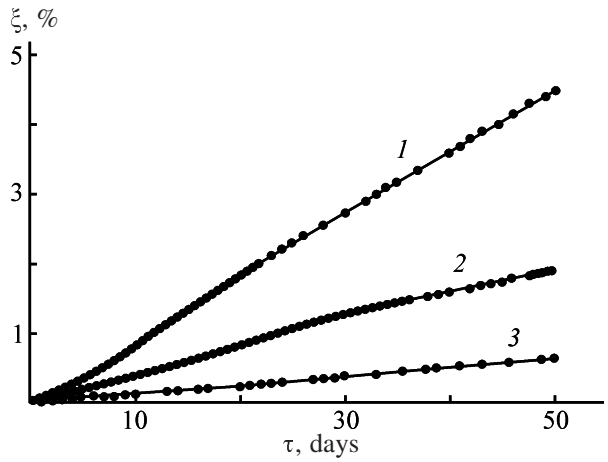


Fig. 1. Dependence of the degree of $NaBH_4$ decomposition ξ on time τ at 22°C. Molar ratio $NaBH_4 : H_2O = 1 : 5$. NaOH concentration, wt %: (*1*) 3, (*2*) 5, and (*3*) 10.

(lasting many days) measurements. When measuring volumes, it is necessary to use an instrument that provides the required accuracy both in the initial stage of the experiment (fast hydrogen liberation) and in the final stage of the hydrolysis. In measuring pressure, problems arise from high hydrogen fluidity and its leakage through joints.

To increase the accuracy of measurements at low hydrolysis rates, it is possible to use large volumes of solutions for increasing hydrogen liberation. Another step is the replacement of measurements of a time dependence of hydrogen liberation during the whole hydrolysis process from the initial state to the complete decomposition (integral procedure) by measurements of hydrolysis rates for various intermediate compositions (differential procedure).

The differential procedure requires that intermediates are absent (or present in small amounts) during the hydrolysis. Then, knowing the composition of the starting solution, it is possible to describe all the intermediate compositions of the system $NaBH_4$–$NaBO_2$–NaOH–H_2O during the hydrolysis using Eq. (1). Any composition can be prepared from $NaBH_4$, $NaBO_2$, water, and NaOH (if the alkali is added to a solution to enhance its stability). After preparing such solution of an intermediate composition, it is possible to measure the rate of its hydrolysis during a relatively short time. After carrying out measurements of hydrolysis rate for several characteristic compositions, it is possible to plot an integral time dependence of the degree of decomposition of sodium borohydride.

With such approach, several short-term experiments are carried out instead of one long-term ex-

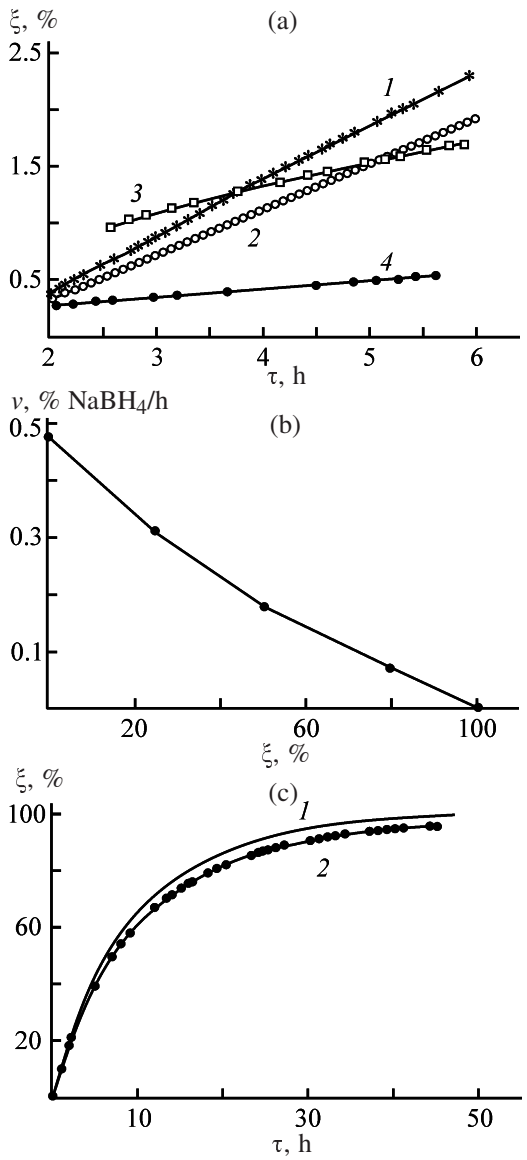


Fig. 2. Dependences of the (a) degree of $NaBH_4$ decomposition ξ on time τ for solutions of intermediate compositions, (b) rate of $NaBH_4$ hydrolysis on the degree of its decomposition ξ, and (c) degree of $NaBH_4$ decomposition ξ on time τ. (a) Degree of $NaBH_4$ decomposition, %: (*1*) 0, (*2*) 25, (*3*) 50, (*4*) 80. (c) Procedure: (*1*) differential and (*2*) integral.

periment. For slow processes, the gain in time can be appreciable, especially if it is required to obtain information on high degrees of decomposition. Advantages of such procedure consist in the possibility of carrying out simultaneous experiments with several intermediate solutions and of controlling the accuracy by varying the volumes of reactors and solutions in accordance with the hydrolysis rate.

To test the differential procedure, we used the data on the hydrolysis occurring for 45 days at 50°C up to the degree of $NaBH_4$ decomposition close to 100% (solution composition: 6.9% $NaBH_4$–90.1% H_2O–3% NaOH). The data of four experiments for the compositions corresponding to 0, 25, 50, and 80% decomposition of $NaBH_4$ are given in Fig. 2a. Points corresponding to the initial warming-up of the reactor and to attainment of the steady-stated mode are omitted from the plot. The curve of the rate of the $NaBH_4$ hydrolysis and the curve of the degree of the $NaBH_4$ decomposition obtained by integrating the former, together with the experimental data obtained by the integral procedure (a continuous experiment), are given in Figs. 2b and 2c. The maximal discrepancy between the data of the two procedures does not exceed 5% (Fig. 2c).

Stability of solutions of sodium borohydride in the system $NaBH_4$–$5H_2O$ was studied at 30 and 50°C and at concentrations of added alkali within the range 1–10% NaOH. The hydrolysis rate in the system $NaBH_4 : H_2O = 1 : 5$ was determined by a differential procedure with the following set of intermediate compositions: at 30°C, ξ_{NaBH_4} 0, 10, 20, 30, and 40%, 1% NaOH; ξ_{NaBH_4} 0, 25, and 50%, 3% NaOH; ξ_{NaBH_4} 0, 10, 30, and 40%, 5% NaOH; at 50°C, ξ_{NaBH_4} 0, 10, 20, 30, and 40%, 5% NaOH; ξ_{NaBH_4} 0, 25, and 50%, 10% NaOH.

The dependence of the rate of sodium borohydride hydrolysis and the integral dependences of the degree of its decomposition on time are given in Figs. 3 and 4. The average hydrolysis rate in the system $NaBH_4$–$5H_2O$ in a 50-day period at 30°C with 1, 3, and 5% NaOH was 0.02, 0.01, and 0.006% $NaBH_4$/h, respectively; at 50°C with 5 and 10% NaOH, 0.03 and 0.02% $NaBH_4$/h, respectively.

In going from room temperature (Fig. 1) to 50°C (Fig. 4b), the stability of sodium borohydride aqueous-alkaline solutions becomes tens times lower, and the loss of sodium borohydride becomes appreciable. At the same time, at temperatures of up to 30°C the solutions studied are sufficiently stable from the practical point of view.

The addition of alkali to a solution accelerates the aging of catalysts, which occurs the faster, the higher the alkali concentration. Weight indices of hydrogen storage also go down as the alkali concentration in the working formulation increases. The presence of alkali in the final product (sodium metaborate solution) will also make the recycling $NaBO_2 \rightarrow NaBH_4$ more difficult. We note that the experiments preformed in a thermostat allow us to estimate the kinetics and the lower boundary for the storage. Real

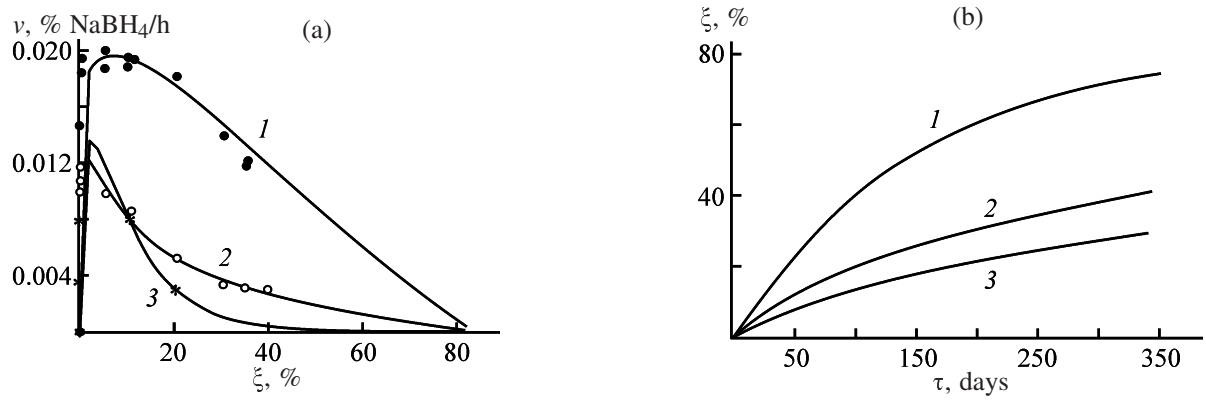


Fig. 3. Dependences of the (a) rate of $NaBH_4$ hydrolysis v on the degree of its decomposition ξ and (b) degree of $NaBH_4$ decomposition ξ on time τ at 30°C for the system $NaBH_4$–$5H_2O$. NaOH concentration, mol %: (*1*) 1, (*2*) 3, and (*3*) 5.

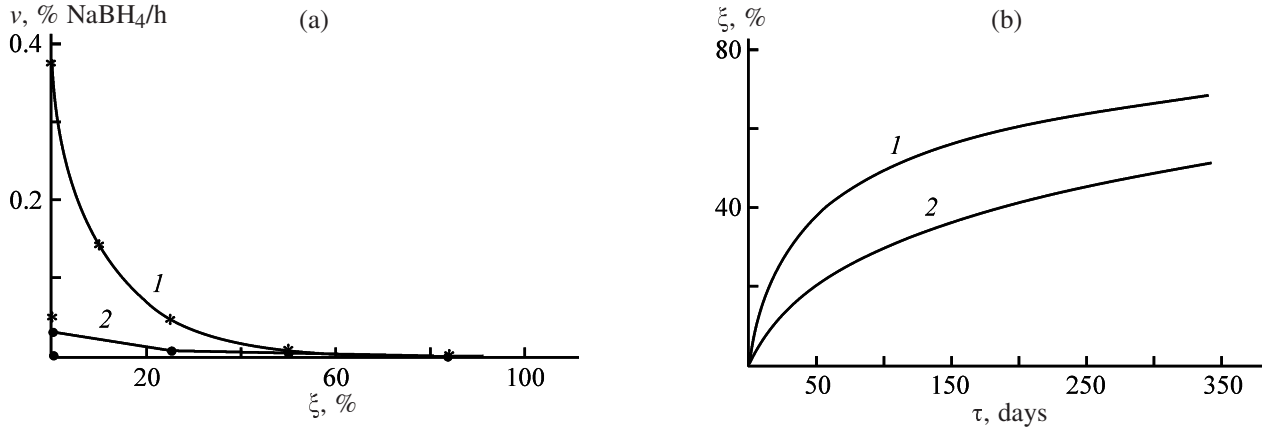


Fig. 4. Dependences of the (a) rate of $NaBH_4$ hydrolysis v on the degree of its decomposition ξ and (b) degree of $NaBH_4$ decomposition ξ on time τ at 50°C for the system $NaBH_4$–$5H_2O$. NaOH concentration, wt %: (*1*) 5 and (*2*) 10.

storage of appreciable volumes of such solutions will become complicated because of their self-heating.

The effect of the nature of alkali metal cations on the rate of hydrolysis of concentrated solutions was determined at the molar ratio $NaBH_4 : H_2O = 1 : 5$ both at equal weight concentrations of alkalis and at their equal mole fractions (see table).

The stability of $NaBH_4$–$5H_2O$ solutions at 50°C was determined by a differential procedure with the following set of intermediate compositions: 0, 10, and 20% $NaBH_4$ decomposition with 5% KOH; 0, 10, 20, 30, and 40% $NaBH_4$ decomposition with 6.85% KOH and with 5% NaOH. Curves of the rate of sodium borohydride hydrolysis and integral curves of the time dependence of the degree of its decomposition are given in Fig. 5.

At equal pH of solutions, i.e., at equal water/alkali molar ratios, the rate of the hydrolysis of BH_4^- ions is independent of the nature of alkali metal cations (Na^+ or K^+, Fig. 5, curves *1* and *2*).

The data obtained show that the hydrolysis of sodium borohydride in solutions cannot be completely suppressed by adding alkali. The addition of alkali to a solution decelerates the hydrolysis, but it is insufficiently effective at elevated temperatures. To stabilize the solutions so as to make possible their storage at temperatures above 30°C, the concentration of the added alkali should be no less than 5%.

Along with sodium borohydride solutions, we studied their suspension with a small amount of water

Gravimetric and molar composition of solutions

Concentration, wt %			Molar composition			
$NaBH_4$	KOH	NaOH	$NaBH_4$	H_2O	KOH	NaOH
28.5	5.0	–	1	5	0.12	–
27.6	6.85	–	1	5	0.17	–
28.1	–	5.0	1	5	–	0.17

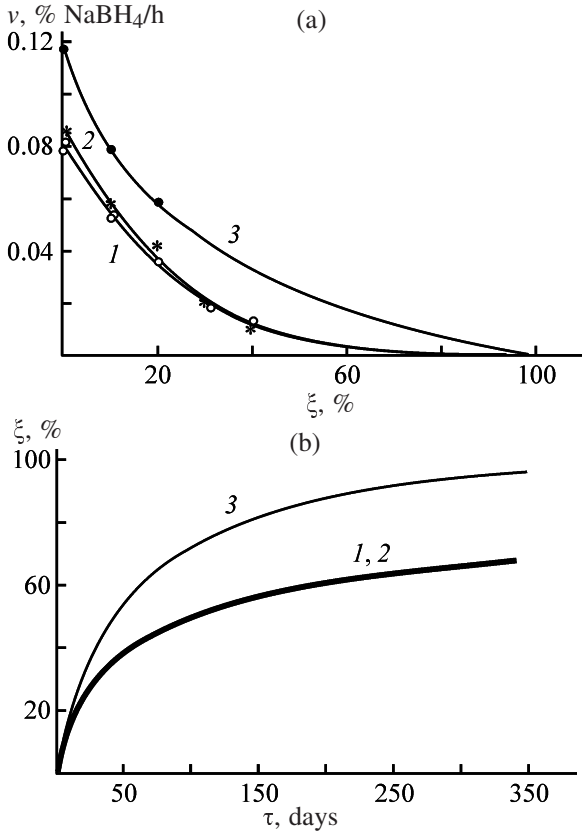


Fig. 5. Effect of the nature of the alkali metal cation on the (a) hydrolysis rate v and (b) degree of $NaBH_4$ decomposition ξ vs. time τ at 50°C for the system $NaBH_4$–$5H_2O$. Alkali concentration, wt %: (*1*) 5 NaOH, (*2*) 6.85 KOH, and (*3*) 5 KOH.

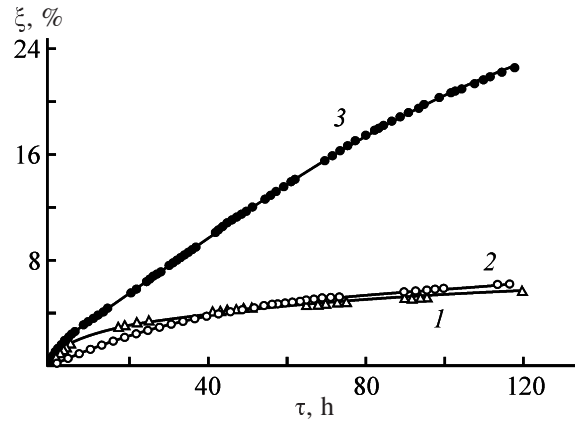


Fig. 6. Degree of decomposition ξ of pellets of the composition (*1*) $NaBH_4 \cdot 2H_2O$ and (*2*) $NaBH_4 \cdot 2H_2O$ with 0.1% NaOH, and (*3*) of suspensions of the composition $NaBH_4$–$2.67H_2O$ with 0.1% NaOH as a function of time τ at 40°C.

and solid samples with a low concentration of added alkali as a stabilizer.

Anhydrous $NaBH_4$ is a fine white hygroscopic powder with a bulk weight of 0.57 g cm^{-3}. As it absorbs water in open air at room temperature, the powder transforms into a wet foaming mass (hydrogen is liberated) and then into a vitreous mass.

It follows from the solubility polytherm of the binary system $NaBH_4$–H_2O that anhydrous $NaBH_4$ crystallizes from the aqueous solution at temperatures higher than 36.4°C, and the dihydrate $NaBH_4 \cdot 2H_2O$ crystallizes at lower temperatures. On heating, water is released from the crystal hydrate $NaBH_4 \cdot 2H_2O$, and a part of $NaBH_4$ dissolves in it, with the hydrolysis starting immediately. At $NaBH_4$ concentrations higher than 51.2 wt % and temperatures below 36.4°C, this system will be in the solid state in the form of a mixture of $NaBH_4 \cdot 2H_2O$ and $NaBH_4$. At lower concentrations, there will be mixtures of a solution and undissolved $NaBH_4 \cdot 2H_2O$. No other solid phases except for those mentioned above were found in equilibrium with a saturated aqueous solution.

It is known that alkali dehydrates sodium borohydride crystal hydrate. The concentration of alkali necessary for the dehydration is the higher, the lower the temperature. To assess the possibility of using solid formulations, we prepared pellets of dry sodium borohydride (I), sodium borohydride crystal hydrate $NaBH_4 \cdot 2H_2O$ (II), and $NaBH_4 \cdot 2H_2O$ with 0.1% NaOH (III) and studied their stability as a function of temperature. At room temperature, formulation II is in the solid state, and formulation III at the moment of its preparation looks like a dense suspension which rapidly hardens. In a closed vessel, all pellets preserve their properties and are stable up to 36.4°C for unlimited time. When stored in ~70% humid air, they "melt" within several days. Pellets of formulations II and III preserve their shape for a longer time, as they already contain water in the crystal hydrate form and absorb it more slowly than do $NaBH_4$ pellets. When stored in 30–40% humid air for 3 months, all the three types of pellets underwent no significant changes.

At temperatures exceeding 36.4°C, water of hydration is released from pellets of formulations II and III, and hydrolysis starts. The data of two experiments with pellets of formulations II and III at 40°C are presented in Fig. 6 (curves *1* and *2*). The curves practically coincide, i.e., the presence of alkali with such concentration (0.1% NaOH) under the conditions of water deficiency does not influence the hydrolysis, which occurs at a rate of approximately 0.045% $NaBH_4$/h for these formulations.

The indications [9] that sodium borohydride undergoes virtually no hydrolysis (0.01% $NaBH_4$/h) in

the course of storage in the form of a suspension in the system 44% $NaBH_4$–55.9% H_2O–0.1% NaOH at 40°C seem doubtful. The concentration of alkali suggested in [9] for the stabilization of sodium borohydride is very low, whereas water is contained in a larger amount than it is necessary for the formation of the crystal hydrate $NaBH_4 \cdot 2H_2O$ (molar composition of the suspension $NaBH_4$–$2.67H_2O$–0.002NaOH).

The experiments with this formulation (Fig. 6, curve *3*) have shown that the hydrolysis rate is approximately 20 times higher than that specified in the patent [9] and 4 times higher than the rate of the hydrolysis of sodium borohydride crystal hydrate (Fig. 6, curve *1*).

The storage in the form of suspension is an intermediate mode between the storage of solutions and solid formulations. The suspension is slightly more stable than solutions and, apparently, is more suitable for dosing than solid forms. However, it has also drawbacks inherent in both forms: like solutions, suspensions require special precautions against temperature rise; like solid forms of sodium borohydride, they are difficult to dose and require dilution with water before use.

Separate storage of water and anhydrous sodium borohydride completely eliminates stability problems. The main inconvenience of the separate storage is the necessity to prepare a working solution before its use in a reactor. Making a reliable block for feeding granules would be a natural engineering solution for a hydrogen source based on hydrolysis of sodium borohydride.

CONCLUSIONS

(1) The rate of hydrolysis in systems containing sodium borohydride, alkali, and water does not exceed 0.02% $NaBH_4$/h at temperatures of up to 30°C. An increase in temperature accelerates the hydrolysis, and even at 50°C it is impossible to store such formulations for a long time.

(2) To stabilize solutions for making possible their storage at temperatures above 30°C, it is necessary to add alkali in a concentration higher than 5 wt %.

REFERENCES

1. Schlapbach, L., *MRS Bull.*, 2002, September, p. 675.
2. Zuttel, A., *Materials Today*, 2003, September, p. 24.
3. Amendola, S.C., Sharp-Goldman, S.L., Janjua, M.S., et al., *Int. J. Hydrogen Energy*, 2000, vol. 25, no. 10, p. 969.
4. Owen, J., *Proc. Int. Hydrogen Energy Congr. and Exhibition INEC*, Istanbul, 2005, p. 1.
5. Mochalov, K.N., Shifrin, H.V., and Bogonostsev, A.S., *Zh. Fiz. Khim.*, 1963, vol. 37, no. 11, p. 2404.
6. Mochalov, K.N., Shifrin, H.V., and Bogonostsev, A.S., *Kinet. Katal.*, 1964, vol. 5, no. 1, p. 174.
7. Prokopchik, A.Yu. and Šalkauskiene, Yu.A., *Zh. Fiz. Khim.*, 1970, vol. 44, no. 11, p. 2941.
8. Khain, V.S. and Volkov, A.A., *Zh. Prikl. Khim.*, 1980, vol. 53, no. 11, p. 2404.
9. WO Patent 03/042096 A1, 2003.

ISSN 1070-4272, Russian Journal of Applied Chemistry, 2008, Vol. 81, No. 3, pp. 386–391. © Pleiades Publishing, Ltd., 2008.
Original Russian Text © N.N. Prokopchuk, V.A. Kopilevich, L.V. Voitenko, 2008, published in Zhurnal Prikladnoi Khimii, 2008, Vol. 81, No. 3, pp. 399–404.

INORGANIC SYNTHESIS AND INDUSTRIAL INORGANIC CHEMISTRY

Preparation of Double Nickel(II) Cobalt(II) Phosphates with Controlled Cationic Composition

N. N. Prokopchuk, V. A. Kopilevich, and L. V. Voitenko

National Agrarian University, Kiev, Ukraine

Received February 26, 2007

Abstract—The possibility of the heterogeneous synthesis of crystalline nickel(II) cobalt(II) aqua ammine orthophosphates with a specified ratio of cations was studied. The substances were studied by IR spectroscopy, X-ray phase analysis, and thermal analysis. Owing to a wide color spectrum, they show promise as pigments for ceramic industry.

DOI: 10.1134/S1070427208030063

Orthophosphates of the type $M_3(PO_4)_2$ are widely used in various industries. Their representatives are selective catalysts, pigments, fertilizers, active substances of corrosion-protecting materials, components of medicinal formulations, and matrices for phosphors [1–3]. Both individual phosphates and their solid solutions are of considerable practical importance. The variation of solid solution compositions allows (within the limits of the homogeneity region) adjustment of certain properties, e.g., of the color of pigments, temperature of color change for temperature-sensitive pigments, etc. [4, 5]. Therefore, the search for solid solutions based on such phosphates is promising for obtaining new materials with valuable properties. Solid neutral aqua ammine orthophosphates of certain transition metals [cobalt(II), nickel(II), copper(II), and zinc(II)] [6, 7] have been described in the literature.

The aim of this study was to prepare crystalline heterometallic nickel(II) cobalt(II) aqua ammine orthophosphates with a specified ratio of cationic contents and to examine the synthesized substances by chemical analysis, IR spectroscopy, X-ray phase analysis, and thermal analysis.

Nickel(II) cobalt(II) aqua ammine orthophosphates were prepared by heterogeneous synthesis. As starting reagents we used orthophosphates of the compositions $Ni_3(PO_4)_2 \cdot 8H_2O$ and $Co_3(PO_4)_2 \cdot 8H_2O$ synthesized by the procedure described in [8]. A mechanical mixture consisting of thoroughly ground and intermixed weighed portions of hydrated nickel(II) and cobalt(II) orthophosphates with a specified molar ratio of the metal cations was kept in a hermetically sealed chamber in the atmosphere of gaseous ammonia at room temperature up to its complete deliquescence, i.e., transformation into a transparent oily mass of bright blue color. After that, the samples were withdrawn from the chamber and left to crystallize in air at 20–25°C to constant weight. The chemical composition of the synthesized compounds is given in Table 1.

The nickel content of the samples was determined gravimetrically with dimethylglyoxime [9]; the cobalt content, photometrically with nitroso-R salt [10]; the phosphorus content, gravimetrically by the quinoline–molybdenum method [11]; the ammonia content, by distillation in a vacuum on Seren'ev's apparatus [11]; and total water and ammonia content, from the weight loss on heating to 750°C in the course of 2 h. The IR spectra were taken on a Specord 75-IR spectrophotometer. Samples of compounds to be analyzed were prepared in the form of KBr pellets in which the concentration of a substance under study was 0.2–0.3 wt %. The X-ray phase analysis was carried out on a DRON-UM1 diffractometer (CuK_α radiation). A single crystal of graphite placed in a diffracted beam was used as a monochromator. The diffraction patterns were taken by the method of step scanning in the range of angles $2\theta = 4°$–$80°$. The scanning step was 0.05°, and the exposure time in a point, 3–9 s. The measured diffraction maxima were approximated by the pseudo-Voight function, with the K_{α_1} component being separated out. Unit cell parameters were calculated by the known procedure [12].

Thermal transformations of the substances were

Table 1. Composition of heterometallic nickel(II) cobalt(II) aqua ammine orthophosphates

Compound	Found, %/Calculated, %				
	NiO	CoO	P_2O_5	NH_3	H_2O
$Ni_{0.5}Co_{2.5}(PO_4)_2 \cdot 6.17\,NH_3 \cdot 8.72\,H_2O$	6.46/5.94	30.01/29.79	22.33/22.57	16.03/16.22	25.17/25.48
$Ni_{1.5}Co_{1.5}(PO_4)_2 \cdot 3.49\,NH_3 \cdot 7.92\,H_2O$	20.05/20.10	20.40/20.16	25.33/25.46	10.08/10.06	24.14/24.22
$Ni_{2.0}Co_{1.0}(PO_4)_2 \cdot 3.14\,NH_3 \cdot 7.60\,H_2O$	27.22/27.04	13.52/13.56	25.70/25.69	8.56/8.62	25.00/25.09
$Ni_{2.5}Co_{0.5}(PO_4)_2 \cdot 3.54\,NH_3 \cdot 7.54\,H_2O$	33.52/33.58	6.85/6.74	25.45/25.53	8.28/8.25	25.90/25.90

Table 2. X-ray structural characteristics of heterometallic nickel(II) cobalt(II) aqua ammine orthophosphates (all samples belong to monoclinic system)

Compound	Unit cell parameters				Unit cell volume, nm^3
	a, nm	*b*, nm	*c*, nm	γ, deg	
$Ni_{0.5}Co_{2.5}(PO_4)_2 \cdot 6.2\,NH_3 \cdot 8.7\,H_2O$	1.0014	1.3317	0.4670	104.82	0.60199
$Ni_{1.5}Co_{1.5}(PO_4)_2 \cdot 3.5\,NH_3 \cdot 7.9\,H_2O$	1.0017	1.3323	0.4672	104.85	0.60271
$Ni_{2.0}Co_{1.0}(PO_4)_2 \cdot 3.1\,NH_3 \cdot 7.6\,H_2O$	1.0017	1.3329	0.4671	104.79	0.60303
$Ni_{2.5}Co_{0.5}(PO_4)_2 \cdot 3.5\,NH_3 \cdot 7.5\,H_2O$	0.9979	1.3304	0.4640	104.81	0.59555

studied on a Q-1500D derivatograph. Samples were heated in air up to termination of weight loss in the range 16–850°C. The experiment with the dynamic heating mode was carried out using cylindrical platinum crucibles with lids; the weighed portion of the compound was 0.450 g. The final and all intermediate decomposition products were obtained at a heating rate of the samples of 5 deg min^{-1}. Qualitative and quantitative anionic compositions of all the intermediate products and of the final heating product were determined by paper chromatography [13].

The absorption band corresponding to stretching vibrations of the N–H bonds is observed in the IR spectra of all the synthesized samples in the range 3420–3435 cm^{-1}. The bending vibrations of water and ammonia are recorded in the range 1600–1540 cm^{-1}. In the range 1470–1310 cm^{-1}, there is an absorption band corresponding to bending vibrations of metal-coordinated ammonia molecules, which form stable hydrogen bonds with the anion [14]. It should be noted that in the range 1285–1205 cm^{-1} there are only the absorption maxima corresponding to the symmetric bending vibrations of ammonia [15]. Antisymmetric and symmetric stretching vibrations of the PO_4^{3-} group are observed in the range 1050–710 cm^{-1}. Absorption bands at 680–535 cm^{-1} correspond to the vibrations of the P–O–P and O–P–O groups.

In the IR spectra of the synthesized nickel(II) cobalt(II) aqua ammine orthophosphates, there are absorption bands characteristic of coordinated ammonia molecules, which coincides with the results of chemical analysis of the substances, including the molar ratio $(NiO + CoO) : P_2O_5 = 3 : 1$ found for them.

It was found by X-ray phase analysis that all the synthesized nickel(II) cobalt(II) aqua ammine orthophosphates are crystalline and isostuctural to each other and also to hydrated cobalt orthophosphate $Co_3(PO_4)_2 \cdot 8H_2O$ [16]. The unit cell parameters of the compounds are given in Table 2.

For a detailed thermal analysis we chose nickel(II) cobalt(II) aqua ammine orthophosphate of the composition $Ni_{1.5}Co_{1.5}(PO_4)_2 \cdot 3.5NH_3 \cdot 7.9H_2O$. According to the data obtained (Fig. 1), thermolysis of the compound occurs in the range 20–830°C and is accompanied by three endothermic effects in the DTA curve with minima at 109, 174, and 208°C. At 450 and 615°C, we found two maxima of exothermic effects, which superimpose on endothermic effects and are accompanied by steps of the sample weight loss in the DTG and TG curves.

Products of thermolysis in the range 2–180°C are crystalline and isostuctural to each other and also to the starting $Co_3(PO_4)_2 \cdot 8H_2O$ [16]. On further heating, the substance becomes amorphous. The sample obtained at 505°C crystallizes again to become isostuctural to anhydrous cobalt(II) orthophosphate $Co_3(PO_4)_2$ [17]. It should be noted that, after com-

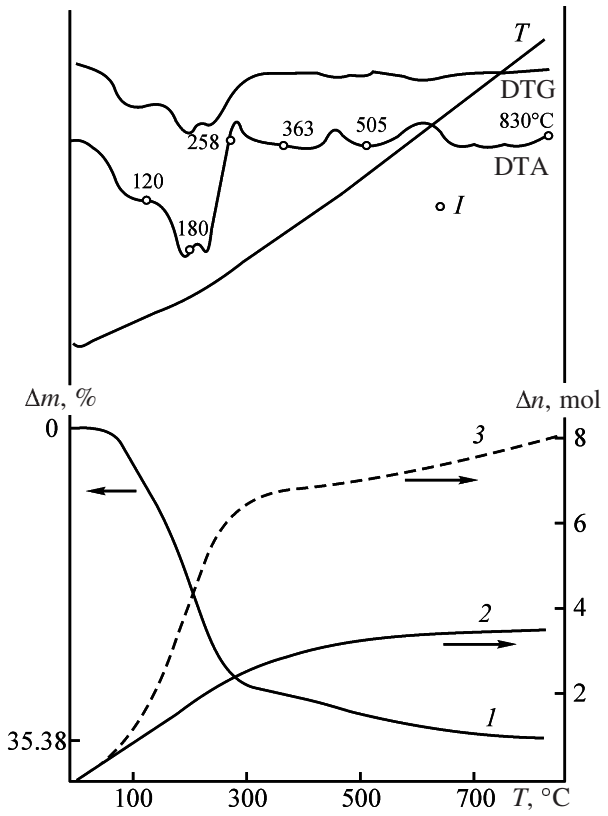


Fig. 1. DTA and TG curves of $Ni_{1.5}Co_{1.5}(PO_4)_2 \cdot 3.5NH_3 \cdot 7.9H_2O$. ($\Delta m$) Weight change, ($\Delta n$) change of the substance amount, and (T) temperature. (I) points of taking samples for analysis; (*1*) total weight loss of a sample under dynamic heating at a rate of 2.5 deg min^{-1}, (*2*) NH_3 loss, and (*3*) H_2O loss.

plete removal of water and ammonia from the starting compound, it decays to give two crystal phases, one of which is isostuctural to anhydrous cobalt orthophosphate [17] and the other, to nickel orthophosphate [18].

Absorption bands in the range 3430–1210 cm^{-1}, characteristic of vibrations of water and ammonia molecules, are observed in the IR spectra of both the initial phosphate and products of its heating to 505°C. They are absent only in the spectrum of the final sample obtained at 830°C (Table 3) from which, according to the data of chemical analysis (Table 4), H_2O and NH_3 have been completely removed. In the range 1070–730 cm^{-1}, absorption bands corresponding to asymmetric and symmetric stretching vibrations of PO_4^{3-} groups and absorption bands at 690–560 cm^{-1} corresponding to vibrations of the P–O–P and O–P–O groups are observed. Absorption maxima corresponding to bending vibrations of the phosphate tetrahedron and to vibrations of M–O bonds, which are most clearly pronounced in the spectrum of a sample taken at 830°C, are observed below 560 cm^{-1}.

The sample weight loss in the TG curve (Fig. 1) is observed in the range 60–750°C. The chemical analysis of the products of heating the compound of the composition $Ni_{1.5}Co_{1.5}(PO_4)_2 \cdot 3.5NH_3 \cdot 7.9H_2O$ (Table 4) indicates that, at 120°C, 1 mol of the sample loses 1.16 mol of ammonia and the same number of water moles, with the crystal structure remaining unchanged:

$$[Ni_{1.5}Co_{1.5}(NH_3)_{3.5}(H_2O)_{7.9}(PO_4)_2] \xrightarrow{120^\circ C} 1.16NH_3$$

$$+ 1.16H_2O + [Ni_{1.5}Co_{1.5}(NH_3)_{2.33}(H_2O)_{6.76}(PO_4)_2].$$

Upon further heating, the ammonia and water losses reach about a half of their total amount. This is accompanied by a strong endothermic effect with a minimum at 174°C:

$$[Ni_{1.5}Co_{1.5}(NH_3)_{2.33}(H_2O)_{6.76}(PO_4)_2] \xrightarrow{180^\circ C} 0.57NH_3$$

$$+ 3.25H_2O + [Ni_{1.5}Co_{1.5}(NH_3)_{1.76}(H_2O)_{3.51}(PO_4)_2].$$

In the range 180–258°C, the ammonia loss reaches approximately 70%, and the water loss, 80% of the initial content. The product of heating becomes amorphous, and, according to the data of qualitative paper chromatography, a negligible part of monophosphate anions PO_4^{3-} (less than 5 wt % of the total P_2O_5 content) transforms into the corresponding amount of the diphosphate $P_2O_7^{4-}$. This step of transformations can be described by a combination of the reactions of orthophosphate anion hydrolysis and hydrophosphate condensation to diphosphate, according to the following generalized schemes.

$$[Ni_{1.5}Co_{1.5}(NH_3)_{1.76}(H_2O)_{3.51}(PO_4)_2] \xrightarrow{258^\circ C} 0.71NH_3$$

$$+ 2.03H_2O + [Ni_{1.5}Co_{1.5}(NH_3)_{1.05}(H_2O)_{1.48}(PO_4)_2],$$

$$[M{\leftarrow}OH_2\cdots(PO_4)] \xrightarrow{180\text{–}258^\circ C} MOH^+ + HPO_4^{2-},$$

$$HPO_4^{2-} \longrightarrow P_2O_7^{4-} + H_2O.$$

Upon further heating to 363°C, the compound under study is still X-ray amorphous and contains trace amounts of diphosphate ions:

$$[Ni_{1.5}Co_{1.5}(NH_3)_{1.05}(H_2O)_{1.48}(PO_4)_2] \xrightarrow{363^\circ C} 0.45NH_3$$

$$+ 0.38H_2O + [Ni_{1.5}Co_{1.5}(NH_3)_{0.60}(H_2O)_{1.10}(PO_4)_2].$$

Table 3. IR spectroscopic analysis of $Ni_{1.5}Co_{1.5}(PO_4)_2 \cdot 3.49NH_3 \cdot 7.92H_2O$ (**I**) and products of its heating

Frequency of absorption bands,* cm^{-1}, of the calcination products obtained at indicated T, °C							Assignment
initial **I**	120	180	258	363	505	830	
3440 s	3445 s	3445 s	–	–	–	–	$\nu(H_2O)$, $\nu_{as}(NH_3)$
3400–2900 s.br	3405–3000 s.br	3405–3000 m.br	3450–3100 w.br	3345–3100 w.br	3345–3160 w.br	–	
1650 sh	1660 sh	1620 sh	1600 w	1600 w	1605 w	–	$\delta(H_2O)$, $\delta_{as}(NH_3)$
1600 m	1595 m	1600 w	–	–	–	–	
1530 sh	1525 sh	1550 sh	–	–	–	–	
1450 sh	–	–	1400 w	1400 w	1400 w	–	$\delta_s(NH_3)$
1390 w	1390 w	1420–1390 w.br	–	–	–	–	
–	1340 sh	–	–	–	–	–	
1310 w	1305 w	1290 sh	1270 sh	–	–	–	
1200 w	1210 sh	1210 sh	–	–	–	–	
1045 sh	1055 sh	1050 sh	1070 sh	–	1100 sh	1110 sh	$\nu_{as}(PO_4)$,
1010 s	1020 s	1030 s	1040 s	1015 s	1010–1050 s	1075 s	$\nu_s(PO_4)$,
						1010 s	$\nu_{as}(POH)$,
960 s	970 s	970 sh	–	990 sh	970 s	980 s	$\gamma(POH)$
						960 sh	
920 sh	930 s	935 sh	945 sh	910 sh	930 sh	900 s	
680 m	690 w	–	–	720 w	720 w	–	$\rho_r(NH_3)$, $\nu_s(POP)$
560 sh	560 sh	–	600 sh	610 sh	600 s	620 s	$\delta_{as}(PO_4)$
						590 s	
545 s	530 s	540 s	540 s	550 s	560 s	560 sh	
						520 s	
470 sh	480 sh	465 sh	–	480 sh	–	490 sh	$\delta_s(PO_4)$, ν(M–O),
410 sh	–	–	420 w	410 w	–	430 w	ν(M–N)

* (s) Strong, (m) medium, (w) weak, (br) broad, and (sh) shoulder.

Table 4. Variation of elemental and chemical compositions of nickel(II) cobalt(II) aqua ammine orthophosphate during heating

Temperature of obtaining the sample	Gross composition	P_2O_5 distribution, rel. %		H_2O and NH_3 removed from initial compound, mol	
		PO_4^{3-}	$P_2O_7^{4-}$	NH_3	H_2O
Initial	$1.5NiO \cdot 1.5CoO \cdot P_2O_5 \cdot 3.49NH_3 \cdot 7.92H_2O$	100	–	0	0
120	$1.5NiO \cdot 1.5CoO \cdot P_2O_5 \cdot 2.33NH_3 \cdot 6.76H_2O$	100	–	1.16	1.16
180	$1.5NiO \cdot 1.5CoO \cdot P_2O_5 \cdot 1.76NH_3 \cdot 3.51H_2O$	100	–	1.73	4.41
258	$1.5NiO \cdot 1.5CoO \cdot P_2O_5 \cdot 1.05NH_3 \cdot 1.48H_2O$	~100	Traces	2.44	6.44
363	$1.5NiO \cdot 1.5CoO \cdot P_2O_5 \cdot 0.60NH_3 \cdot 1.10H_2O$	~100	Traces	2.89	6.82
505	$1.5NiO \cdot 1.5CoO \cdot P_2O_5 \cdot 0.10NH_3 \cdot 0.94H_2O$	~100	Traces	3.39	6.98
830	Mixture of two components	100	–	3.49	7.92

In the range 363–505°C, a new crystal phase, isostructural to cobalt orthophosphate [17], is formed, which is accompanied by an exothermic effect and removal of almost whole amount of ammonia and 88% of the initial amount of water:

$$[Ni_{1.5}Co_{1.5}(NH_3)_{0.60}(H_2O)_{1.10}(PO_4)_2] \xrightarrow{550°C} 0.50NH_3 + 0.16H_2O + [Ni_{1.5}Co_{1.5}(NH_3)_{0.10}(H_2O)_{0.94}(PO_4)_2].$$

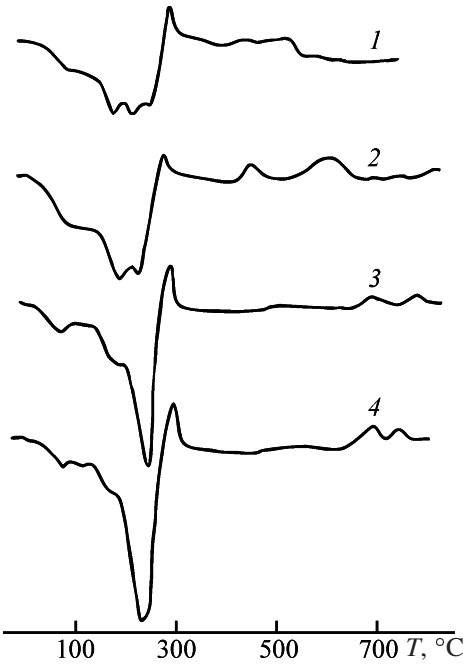


Fig. 2. DTA curves of (*1*) $Ni_{0.5}Co_{2.5}(PO_4)_2 \cdot 6.2NH_3 \cdot 8.7H_2O$, (*2*) $Ni_{1.5}Co_{1.5}(PO_4)_2 \cdot 3.5NH_3 \cdot 7.9H_2O$, (*3*) $Ni_{2.0} \cdot Co_{1.0}(PO_4)_2 \cdot 31NH_3 \cdot 7.6H_2O$, and (*4*) $Ni_{2.5}Co_{0.5}(PO_4)_2 \cdot 3.5NH_3 \cdot 7.5H_2O$. (*T*) Temperature.

With a further increase in temperature, residues of ammonia and water are removed to form two crystalline phases. This process is accompanied by a powerful exothermic effect with a maximum at 615°C:

$$[Ni_{1.5}Co_{1.5}(NH_3)_{0.10}(H_2O)_{0.94}(PO_4)_2] \xrightarrow{830°C} 0.10NH_3 + 0.94H_2O + Ni_{3.0}(PO_4)_2 + Co_{3.0}(PO_4)_2.$$

Thermal transformations of the synthesized nickel(II) cobalt(II) ammine phosphates with other ratios of cations occur similarly, as follows from the similarity of the shapes of the DTA curves shown in Fig. 2.

The X-ray analysis of final products of heating the aqua ammine phosphates $Ni_{0.5}Co_{2.5}(PO_4)_2 \cdot 6.2NH_3 \cdot 8.7H_2O$, $Ni_{2.0}Co_{1.0}(PO_4)_2 \cdot 3.1NH_3 \cdot 7.6H_2O$, and $Ni_{2.5}Co_{0.5}(PO_4)_2 \cdot 3.5NH_3 \cdot 7.5H_2O$ has shown that all of them are crystalline and are presented by a single phase, in contrast to the product of the thermolysis of the above-described sample of the composition $Ni_{1.5}Co_{1.5}(PO_4)_2 \cdot 3.5NH_3 \cdot 7.9H_2O$. It is interesting that, at the $Ni^{2+} : Co^{2+}$ molar ratio in the starting aqua ammine orthophosphate equal to 0.5 : 2.5, the final product of its thermal decomposition after complete removal of water and ammonia is isostructural to cobalt(II) orthophosphate [17]. On the contrary, in samples in which the mole fraction of Ni^{2+} is higher than 2.0 and that of Co^{2+} is lower than 1.0, the final thermolysis products are isostructural to nickel(II) orthophosphate [18].

Thus, we have determined the structure and properties of the synthesized compounds, nickel(II) cobalt(II) aqua ammine orthophosphates differing from each other in the $Ni^{2+} : Co^{2+}$ ratio.

To conclude, the synthesized substances and products of their thermolysis have various tints of lilac-violet color, which, in combination with their chemical composition, makes them promising as pigments for ceramic industry.

CONCLUSIONS

(1) Crystalline nickel(II) cobalt(II) aqua ammine orthophosphates with a specified ratio of cations have been prepared by heterogeneous synthesis.

(2) Nickel(II) cobalt(II) aqua ammine orthophosphates with the ratio NiO : CoO = 1.5 : 1.5 decompose on heating into two phases: the first phase is isostructural to nickel(II) orthophosphate, and the second, to cobalt(II) orthophosphate.

(3) At essential prevalence of one of the metals, the final thermolysis product is isostructural to the anhydrous orthophosphate of the corresponding metal.

REFERENCES

1. Tofighi, A., Rey, C., and Lee, D.D., *Proc. 7th World Biomaterials Congr.*, May 2004, p. 1444.
2. Hutchings, G.J., Lopez-Sanchez, A.J., Bartley, J.K., et al., *J. Catal.*, 2002, vol. 208, no. 1, pp. 197–210.
3. *Inorganic Phosphate Materials*, Kanazawa, T., Ed., Tokyo: Kodansha, 1989.
4. Ukrainian Patent 56492.
5. Ukrainian Patent 67078.
6. Voitenko, L.V., Kopilevich, V.A., and Shchegrov, L.N., *Zh. Neorg. Khim.*, 1992, vol. 36, no. 9, pp. 2055–2060.
7. Kopilevich, V.A., Prokopchuk, N.M., and Voitenko, L.V., *Nauk. Zap. Ternopil'sk. Nats. Ped. Univ. im. V. Gnatyuka, Khim.*, 2006, no. 10, pp. 58–61.
8. Ukrainian Patent 6826.
9. Posypaiko, V.I., Kozyreva, N.A., and Logacheva, Yu.P., *Khimicheskie metody analiza* (Chemical Methods of Analysis), Moscow: Vysshaya Shkola, 1989.

10. Pyatnitskii, I.V., *Analiticheskaya khimiya kobal'ta* (Analytical Chemistry of Cobalt), Moscow: Nauka, 1965.
11. *GOST* (State Standard) *20851.1–75 (ST SEV* (COMECON Standard) *2531–80, ST SEV 2532–80, ST SEV 3369–81), GOST 20851.2–75–GOST 20851.4–75: Mineral Fertilizers: Methods of Analysis)*, Moscow: Izd. Standartov, 1983.
12. Karpets, M.V., Milman, Y.V., Barabash, O.M., et al., *Intermetallics*, 2003, vol. 11, pp. 241–249.
13. Shchegrov, L.N., *Fosfaty dvukhvalentnykh metallov* (Phosphates of Bivalent Metals), Kiev: Naukova Dumka, 1987.
14. Shevchenko, Yu.N., Coordination Compounds of 3*d* Transition Metals with Hydroborate Anions, *Doctoral Dissertation*, Moscow, 1991.
15. Voitenko, L.V., Hydrated Ammine Phosphates of Cobalt(II), Copper(II), and Zinc, *Cand. Sci. Dissertation*, Kiev, 1994.
16. Riou, A., Cudennecy, Y., and Geraulty, Y., *Acta Crystallogr.*, 1989, vol. 45, pp. 1412–1413.
17. Anderson, J., Kostinery, E., and Millery, M., *J. Solid State Chem.*, 1975, vol. 18, pp. 372–377.
18. Calvo, C. and Faggianiy, R., *Can. J. Chem.*, 1975, vol. 53, pp. 1516–1520.

ISSN 1070-4272, Russian Journal of Applied Chemistry, 2008, Vol. 81, No. 3, pp. 392–394. © Pleiades Publishing, Ltd., 2008.
Original Russian Text © K.V. Titova, V.P. Nikol'skaya, V.V. Buyanov, O.B. Pudova, G.P. Karzhavina, Yu.G. Oboznaya, 2008, published in Zhurnal Prikladnoi Khimii, 2008, Vol. 81, No. 3, pp. 405–407.

INORGANIC SYNTHESIS AND INDUSTRIAL INORGANIC CHEMISTRY

Synthesis and Properties of Potassium Oxotriperoxovanadate(V) $K_3[VO(O–O)_3]$

K. V. Titova, V. P. Nikol'skaya, V. V. Buyanov, O. B. Pudova, G. P. Karzhavina, and Yu. G. Oboznaya

Institute for Problems of Chemical Physics, Russian Academy of Sciences, Chernogolovka, Moscow oblast, Russia

State Research Institute of Biological Instrument Making, Federal State Unitary Enterprise, Moscow, Russia

Received September 29, 2006; in final form, April 2007

Abstract—The conditions of synthesis of potassium oxotriperoxovanadate(V) $K_3[VO(O–O)_3]$ were developed, and the compound was isolated pure. Its physicochemical characteristics, including X-ray diffraction pattern, thermogravimetric data, and IR spectrum, are presented.

DOI: 10.1134/S1070427208030075

The composition and structure of various (cationic, anionic, and neutral) forms of peroxovanadates(V), determined by cryoscopic, potentiometric, spectrophotometric, X-ray structural, and NMR methods, have been reported [1–3]. In anionic forms, various ligands (chloride, fluoride, and oxalate anions, ammonia, pyridine, etc.) can also be present along with O–O groups. Among anionic forms of peroxovanadates(V), compounds containing only O–O groups are of the greatest interest. According to the ^{51}V and ^{17}O NMR data, anions of the following composition exist: $[VO_3(O–O)]^{3–}$, $[VO_2(O–O)_2]^{3–}$, $[VO(O–O)_3]^{3–}$, $[V(O–O)_4]^{3–}$, and $[\{VO_2(O–O)\}_2O]^{4–}$ [4, 5]. Peroxovanadates with the above anions are rich in oxygen in its common (oxo) and available (peroxo) form. The properties of individual salts of the above anions are poorly studied. As known, Li^+, Na^+, NH_4^+ salts of fully substituted peroxovanadates(V) do not dissolve in the reaction mixtures (V_2O_5–MOH–H_2O_2) in which they are formed, whereas the potassium salt dissolves and can be precipitated by adding ethyl alcohol [1]. Data on the compound stability are known only for several fully substituted peroxovanadates(V). These data are rather controversial. According to [6], under polythermal conditions Na_3VO_8 and K_3VO_8 decompose at 150°C. According to other data [1], K_3VO_8 is stable in storage only at 0°C and its aqueous solutions are also unstable.

In this study we developed the methods of synthesis of trisubstituted peroxovanadate(V) $K_3[VO(O–O)_3]$ (O_{av} = 17.2%), which is promising owing to high content of available oxygen. Presumably, owing to smaller size of the vanadium(V) coordination sphere, peroxovanadate of this composition is more stable than fully substituted $K_3[V(O–O)_4]$. The $[VO(O–O)_3]^{3–}$ anion in alkaline solution is stable [7]. Potassium oxotriperoxovanadate was isolated pure, and its properties were studied in the context of the problem of subsequent conversion of available oxygen into the form suitable for application in disinfection technology.

EXPERIMENTAL

To develop the synthesis of peroxovanadate(V) $K_3[VO(O–O)_3]$, we studied how the composition of the forming compounds varies with the ratio of the starting reactants (KOH, V_2O_5, and H_2O_2) and with synthesis temperature. We used the following method in the study. To a concentrated aqueous solution of KOH, dry V_2O_5 was added to complete dissolution. Then, a 30% H_2O_2 solution was added slowly. After the whole amount of hydrogen peroxide was added, a yellow-green mixture of a solid substance and a solution was formed, and then a yellow-green product was rapidly precipitated on adding ethanol. The precipitate was filtered onto a polymer filter, dried in a desiccator over sulfuric acid, and analyzed for the content of O_{av} and potassium. The potassium content was determined gravimetrically, and the O_{av} content,

Table 1. Composition of peroxovanadates synthesized under different conditions

T, °C	KOH content, g	Molar ratio		Content in products,* wt %	
		$KOH : V_2O_5$	$H_2O_2 : K_3VO_4$	O_{av}	K
20	1.07	6 : 1	10 : 1	8.15	–
20	0.99	6 : 1	10 : 1	8.65	–
20	0.29	6 : 1	20 : 1	13.70	–
20	0.92	6 : 1	20 : 1	12.76	–
20	0.91	6 : 1	20 : 1	12.46	–
20	0.90	6.2 : 1	20 : 1	16.66	40.7
20	0.92	6.4 : 1	20 : 1	16.93	41.1
20	0.90	6.4 : 1	20 : 1	16.86	40.9
0	0.90	6 : 1	20 : 1	16.12	39.4
0	0.87	6 : 1	20 : 1	16.47	40.7

* $K_3[VO(O–O)_3]$. Calculated, %: O_{av} 17.14, K 41.79.

permanganatometrically. Since peroxovanadates are analyzed for the content of available oxygen mainly by the pyrometric method [1], the permanganatometric and pyrometric methods were compared.

In the pyrometric method, a weighed portion of the substance in a porcelain crucible was placed into a muffle furnace, heated slowly from room temperature to 300°C, cooled, and then weighed again. The permanganatometric titration was performed by the standard procedure. In the course of the titration, the initially yellowish peroxovanadate solution became light brown and then, by the end of titration, transparent and colorless. The equivalence point was determined clearly. The products prepared in various syntheses contained the following amounts of O_{av}:

Method	Content, wt %			
Permanganatometric	15.91	15.52	16.17	15.51
Pyrometric	16.01	15.70	16.17	15.50

The samples with the O_{av} and potassium concentrations close to the calculated values were studied by X-ray phase and thermogravimetric analyses and by IR spectroscopy. Their stability in storage was also determined. X-ray diffraction patterns were recorded on an ADP-2-0.1 diffractometer (CuK_α radiation, Ni filter) and processed with a program developed for DRON diffractometers. The thermograms were recorded on a Q 1500 D derivatograph connected to a Pt–Pt/Rh thermocouple. Al_2O_3 was reference. The heating rate was 5 deg min^{-1}. The IR spectra of the compounds prepared (mulls in mineral oil between KBr plates) were recorded on a UR-20 spectrometer.

Table 1 shows how the composition of the peroxovanadates prepared varies with the reactant ratio and temperature.

As can be seen, peroxovanadate of the composition close to $K_3[VO(O–O)_3]$ is synthesized either at KOH excess ($KOH : V_2O_5$ = 6.2–6.4) or at a stoichiometric ratio of 6 : 1, upon cooling to 0°C. The resulting peroxovanadate $K_3[VO(O–O)_3]$ is a greenish-yellow finely crystalline substance difficultly soluble in water. It exhibits stability during storage in dry atmosphere. In storage for 50 days, peroxovanadate decomposes at an average rate of 2.6×10^{-2} (wt %) day^{-1}, whereas in storage for 85 days, at a rate of 4.6×10^{-3} (wt %) day^{-1}, i.e., in the late storage periods the decomposition rate decreases, which is characteristic of other substances containing available oxygen, for example, of peroxosolvates of salts of inorganic acids [8].

The results of X-ray phase analysis of $K_3[VO(O–O)_3]$ are given in Table 2. The X-ray characteristics of $K_3[V(O–O)_4]$ from [9] are listed for comparison.

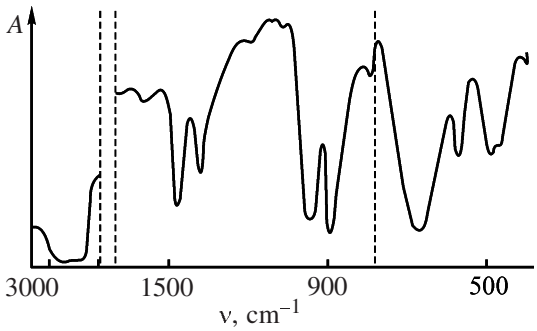
It may be suggested that, in the course of the synthesis, the asymmetric anion $[VO(O–O)_3]^{3–}$ disproportionates with the formation of more symmetric anions, $[VO_2(O–O)_2]^{3–}$ and $[V(O–O)_4]^{3–}$. The diffraction pattern of the product prepared contains no bands of fully substituted peroxovanadate. To our knowledge, no X-ray data are available from the literature on other incompletely substituted peroxovanadates, including $K_3[VO_2(O–O)_2]$. We believe that the compound synthesized is pure potassium oxotriperoxovanadate $K_3[VO(O–O)_3]$.

Thermogravimetric analysis shows that the synthesized peroxovanadate $K_3[VO(O–O)_3]$ is reasonably stable. It decomposes with the exothermic effect at 195–200°C. The mass loss in the process is 16%, which is in satisfactory agreement with the value of 16.7% found for the O_{av} content by permanganatometric titration. For all the peroxovanadates formed,

Table 2. Results of X-ray phase analysis of $K_3[VO(O–O)_3]$ and $K_3[V(O–O)_4]$

Interplanar spacing, Å	Relative intensity I_{rel}, %
$K_3[VO(O–O)_3]$	
5.735	13
5.438	15
4.611	26
3.875	19
3.170	100
2.656	16
2.315	17
2.238	25
1.841	10
$K_3[V(O–O)_4]$ [9]	
5.040	75
4.720	50
3.340	75
2.980	100
2.780	75
2.360	100
2.020	50
1.930	75
1.850	100
1.800	50
1.680	75
1.500	100
1.466	75
1.369	75
1.254	75
1.194	75

we recorded the IR spectra (Table 1). The absorption bands of water were found in none of the spectra (see figure). Evidently, under the chosen conditions of the synthesis, peroxovanadates are isolated in the anhydrous state. The observed bands (cm^{-1}) can be assigned as follows: 875 s ν(O–O), 550 s ν_{as}[V<(O–O)], 615 s ν_s[V<(O–O)], 960 vs ν(V=O). The IR spectra of potassium tetraperoxovanadate contain bands of ν(O–O) and ν[V<(O–O)] (cm^{-1}) at 850 s, 560 s, and



IR spectrum of $K_3[VO(O–O)_3]$. (*T*) Transmission and (ν) wavenumber.

605 m [10]. The absorption band ν(V=O) at 970 cm^{-1} is present in the spectra of $K_2[VO(O–O)_2Cl]$ [7] and $K_4[V_4O_4(O–O)_6F_4]$ [11]. In addition to the above bands, the spectrum contains a band at 490 cm^{-1}, which is difficult to assign in our case. In this region, the band of halooxoperoxovanadates ν(V–Hal), where Hal is F or Cl, is present [7, 12].

Evidently, application of oxoperoxovanadate $K_4[VO(O–O)_3]$ in disinfection technology will require catalysts or solvents facilitating rupture of the O–O bond and formation of ions and radicals similar to those generated in decomposition of hydrogen peroxide: H_3O^+, HO_2^-, $OH^\bullet$, and $OH_2^\bullet$. Such ions and radicals, as hydrogen peroxide itself, directly participate in suppression and killing of pathogenic microorganisms.

CONCLUSION

The conditions of synthesis of individual pure oxotriperoxovanadate $K_3[VO(O–O)_3]$ were developed. The peroxovanadate is stable: it decomposes at 150°C, the rate of loss of O_{av} in storage for 85 days is 4.6×10^{-3} (wt %) day^{-1}.

REFERENCES

1. Vol'nov, I.I., *Peroksokompleksy vanadiya, niobiya i tantala* (Peroxo Complexes of Vanadium, Niobium, and Tantalum), Moscow: Nauka, 1987.
2. Porai-Koshits, M.A. and Loginov, S.V., *Zh. Neorg. Khim.*, 1988, vol. 33, no. 6, pp. 1609–1652.
3. Sergienko, V.S., Barzunov, V.K., and Porai-Koshits, M.A., *Zh. Neorg. Khim.*, 1992, vol. 37, no. 5, pp. 1062–1679.
4. Howart, O.W., and Hunt, J.R., *J. Chem. Soc., Dalton Trans.*, 1979, no. 6, pp. 1388–1391.
5. Symons, M.C.R., *J. Chem. Soc. A*, 1970, no. 7, pp. 1889–1891.
6. Grigor'eva, N.K., and Dergacheva, K.N., *Izv. Akad. Nauk SSSR, Otd. Khim. Nauk*, 1962, no. 2, pp. 945–947.
7. Chaudhuri, M.K., and Ghosh, S.K., *Inorg. Chem.*, 1984, vol. 23, no. 2, pp. 534–537.
8. Titova, K.V., Nikol'skaya, V.P., Buyanov, V.V., et al., *Zh. Prikl. Khim.*, 2005, vol. 78, no. 2, pp. 287–291.
9. *JCPDS—International Centre for Diffraction Data*, 1995, card no. 14-0669.
10. Offner, F., and Dehard, J., *C. R. Acad. Sci. Paris*, 1971, vol. 273, no. 1, pp. 50–53.
11. Schwendt, P., and Joniakava, D., *Thermochim. Acta*, 1983, vol. 69, no. 2, pp. 297–303.
12. Chaudhuri, M.K. and Ghosh, S.K., *Polyhedron*, 1982, vol. 1, no. 2, pp. 533–535.

ISSN 1070-4272, Russian Journal of Applied Chemistry, 2008, Vol. 81, No. 3, pp. 395–398. © Pleiades Publishing, Ltd., 2008.
Original Russian Text © V.V. Siyanitsa, V.M. Kochkodan, and V.V. Goncharuk, 2008, published in Zhurnal Prikladnoi Khimii, 2008, Vol. 81, No. 3, pp. 408–411.

PHYSICOCHEMICAL STUDIES OF SYSTEMS AND PROCESSES

Nanofiltration Treatment of Aqueous Solutions to Remove Triazine Herbicides

V. V. Siyanitsa, V. M. Kochkodan, and V. V. Goncharuk

Dumanskii Institute of Colloid and Water Chemistry, National Academy of Sciences of Ukraine, Kiev, Ukraine

Received July 9, 2007

Abstract—Nanofiltration treatment of aqueous solutions to remove triazine herbicides (terbumetone, desmetrine, atrazine) with an OPMN-P membrane was studied. The effect of the molecular mass of herbicides, working pressure, and extent of permeate removal on the retention of solutes was analyzed.

DOI: 10.1134/S1070427208030087

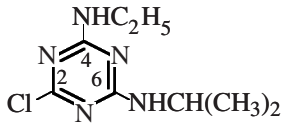
Treatment of natural water to remove herbicides is a serious environmental problem. When finding way into drainage and ground water, the herbicides used in agriculture exert a carcinogenic, mutagenic, and allergic effect on humans. Under the natural conditions, triazine herbicides are metabolized during a long time, including formation of more toxic forms [1].

Herbicides are removed from water by various physicochemical methods: ozonation, biodegradation, adsorption on activated carbons and ion-exchange resins, and coagulation [1]. However, these methods cannot always provide the necessary degree of toxicant removal from aqueous solutions, and, therefore, the problem of water treatment to remove herbicides remains topical.

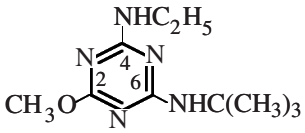
Recently, considerable attention has been given to nanofiltration treatment of underground, natural, and waste water to remove herbicides [2–4]. In this case, water is treated in a single stage, which is the most important advantage of nanofiltration over coagulation and flocculation. Moreover, this technique can replace the adsorption treatment and reagent disinfection. Other advantages of nanofiltration include no need for reagents, simple apparatus, low materials consumption, and ease of automation [5]. At the same time, the nanofiltration treatment of water to remove herbicides of various classes has been insufficiently studied.

EXPERIMENTAL

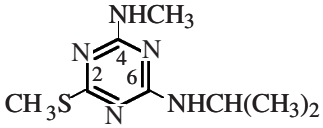
This study is concerned with the nanofiltration treatment of water to remove widely used herbicides of the triazine series: atrazine, desmetrine, and terbumetone (manufactured by Dr. Riedel de Haën, Germany):



Atrazine



Terbumetone



Desmetrine

The principal physicochemical parameters of the compounds are listed in the table. The concentration of the pesticides in solution was 10 mg dm^{-3}.

An OPMN-P nanofiltration composite membrane (manufactured by Vladipor, Russia), which is a polyamide polymeric film on a porous polypropylene substrate, was used in the study.

The nanofiltration treatment of aqueous solutions to remove herbicides was performed in the dead-end filtration mode. For this purpose, a 0.4 dm^3 stainless steel experimental membrane (membrane area 50.2 cm^2) cell equipped with a stirrer was used. The stirrer rotation rate was 300 rpm. The working pressure in the cell was created with compressed nitrogen. The solution pH was adjusted with 0.1 N NaOH or HCl. The measurements were made with an LPU-01 pH-meter.

The concentration of herbicides in the solutions

Principal physicochemical parameters of pesticides

Parameter	Atrazine	Desmetrine	Terbumetone
Molecular formula	$C_8H_{14}ClN_5$	$C_8H_{15}N_5S$	$C_{10}H_{19}N_5O$
Molecular mass	215.69	213.13	225.29
Dissociation constant pK [6]	1.68–1.85	3.1–3.93	4.2
log P*	2.61	1.82	2.09

* log P is the coefficient of substance distribution between the organic phase and water (hydrophobicity coefficient) according to [6, 7].

was determined spectrophotometrically with a Specord UV-VIS instrument (Germany) at a wavelength of 200 nm. The retention coefficient R (%) of herbicides by the membrane was calculated by the formula

$$R = 100 \times (c_0 - c_p)/c_0,$$

where c_0 and c_p are the herbicide concentrations in the starting solution and the permeate, respectively.

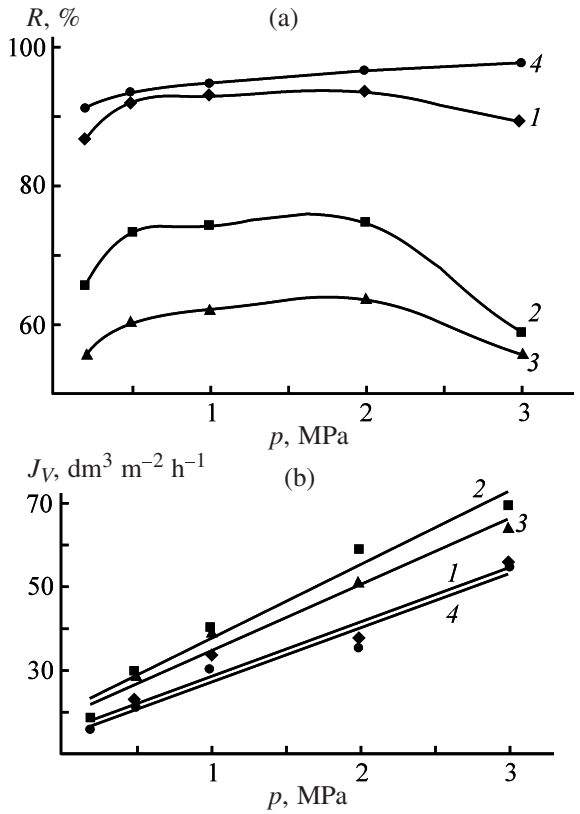


Fig. 1. (a) Retention coefficient R of herbicides and (b) membrane throughput J_V vs. the working pressure p. Herbicide concentration, mg dm^{-3}: (*1–3*) 10 and (*4*) 1; pH 6.2; extent of permeate removal 10%. (*1, 4*) Terbumetone, (*2*) desmetrine, and (*3*) atrazine.

The transmembrane flux (throughput) J_V was calculated by the equation [18]

$$J_V = \Delta V/S\Delta\tau,$$

where ΔV is the permeate volume (dm^3) that passed across a membrane of area S (m^2) in a time $\Delta\tau$ (h).

The ζ potential of the membrane was determined with an Anton Paar electrokinetic analyzer (Austria) by measuring the streaming potential along the membrane surface for a flow of a 0.001 M KCl solution. The software of the analyzer enables automatic calculation of the ζ potential by the Helmholtz–Smoluchowski equation with account of the surface conductivity of the membrane.

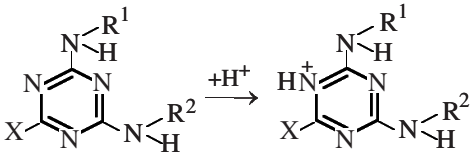
The dependences of the retention coefficient and throughput of the OPMN-P membrane on the working pressure in filtration of aqueous solutions of the herbicides under study are shown in Fig. 1. It can be seen that, as the working pressure is raised to 1.0 MPa, the retention of the herbicides becomes larger (Fig. 1a, curves *1–3*). The retention of the herbicides increases with the working pressure, as also does salt retention in reverse-osmosis water treatment, because the flux of water across the membrane is directly proportional to the working pressure, whereas the flux of the solute is virtually independent of this parameter [9]. Thus, the membrane becomes more selective as the working pressure increases. At the same time, as the working pressure is raised to above 1.0 MPa, the retention of the herbicides by the membrane somewhat decreases, which is presumably due to enhancement of the concentration polarization under these conditions [8, 9].

As can be seen in Fig. 1a, the retention of the herbicides decreases in the order terbumetone > desmetrine > atrazine, which well correlates with the decrease in their molecular mass (see table). The maximum retention of terbumetone at working pressures of 0.5–2.0 MPa is 92–94%. It should be noted that, as the herbicide concentration in the starting aqueous solution decreases to 1 mg dm^{-3}, the degree of purification with the membrane increases to 98% (Fig. 1, curve *4*), in agreement with the known data on nanofiltration of low-molecular-weight organic substances [10].

The throughput of the membrane treatment increases virtually linearly with the working pressure (Fig. 1b), which indicates that there is no shrinking of the porous structure of the membrane under the experimental conditions.

Figure 2 shows that the retention of the herbicides by the membrane strongly depends on pH of the solu-

tion being filtered. The strongest retention of the substances studied is observed in acid and alkaline media, whereas in a neutral medium it decreases. It should be noted that, at pH 3.4, the efficiency of treatment of aqueous solutions to remove terbumetone and desmetrine exceeds that for atrazine. This difference is presumably due to an electrostatic interaction of the membrane with the solutes. In an acid medium (pH < 3.4), terbumetone (pK 4.2) and desmetrine (pK 3.0) are protonated and, as a result, their molecules take on a positive charge



At the same time, at low pH values, the surface of the OPMN-P membrane is also charged positively (Fig. 3) because of the dissociation of amino groups of the selective polymeric layer [2]. Because of the appearance of electrostatic repulsion forces between the likely charged molecules of the solutes and the membrane surface, the retention of terbumetone and desmetrine exceeds that of atrazine, whose molecules are virtually not protonated under the given conditions (pK 1.7) and, consequently, cannot electrostatically interact with the membrane.

As the solution pH increases (pH ~6), the degree of protonation of terbumetone and desmetrine decreases, and so does the positive charge of the membrane (Fig. 3), which leads to weakening of the repulsion forces between the herbicide molecules and the membrane and, as a result, makes lower the retention of the solutes (Fig. 2).

It is interesting that, as pH increases further (pH > 7), the retention of the herbicides somewhat increases (Fig. 2), despite that, under these conditions, undissociated molecules of the herbicides virtually do not interact electrostatically with the membrane surface, whose negative charge is presumably due to dissociation of carboxy groups present in the aromatic polyamide layer [2, 11]. Consequently, the pH dependence of the efficiency of the nanofiltration treatment to remove herbicides with an OPMN-P membrane is governed not only by the electrostatic interaction of the membrane with the solutes, but, apparently, also by other factors.

In this context, the separating characteristics of the membrane were additionally studied at different degrees of permeate removal in filtration of an atrazine solution, which virtually does not dissociate in

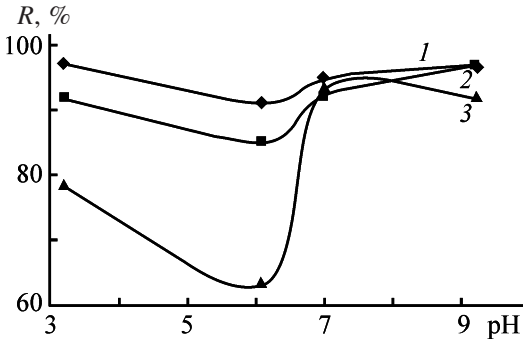


Fig. 2. Retention coefficient R of (*1*) terbumetone, (*2*) desmetrine, and (*3*) atrazine vs. pH at a working pressure of 0.5 MPa. Herbicide concentration 10 mg dm^{-3}.

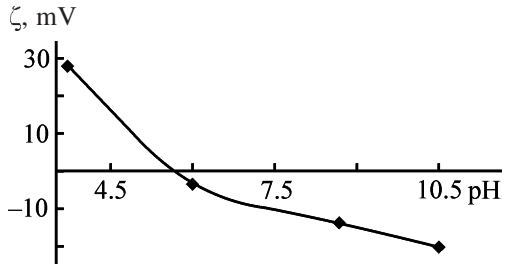


Fig. 3. ζ Potential of the OPMN-P membrane vs. pH of solution.

the pH range under study. Figure 4a shows that the retention of atrazine in acid and alkaline media markedly exceeds that at pH ~6. At the same time, the fluxes across the membrane at low and high pH are substantially lower than the throughput of the membrane at pH ~6 (Fig. 4b). It can be assumed that the effects observed are due to changes in the porous structure of the membrane upon changes in pH. For example, carboxy groups present in the active layer are completely dissociated in the alkaline region and the membrane surface acquires a negative charge [3]. Because of the mutual repulsion, negatively charged macromolecules take a more unfolded conformation, with the result that the "effective" pore size in the active layer of the membrane somewhat decreases. Similar changes apparently also occur in the active layer at low pH, when amino groups of the polymer macromolecules become positively charged [2]. Conformational transitions in the polymer macromolecules in the active layer of the membrane lead to a decrease in the flux across the membrane at low and high pH values (Fig. 4b). At the same time, it follows from Fig. 3 that the isoelectric point (IEP) of the membrane surface corresponds to pH ~6. Presumably, at this point, polymer macromolecules are more closely packed in the active layer of the membrane, so that

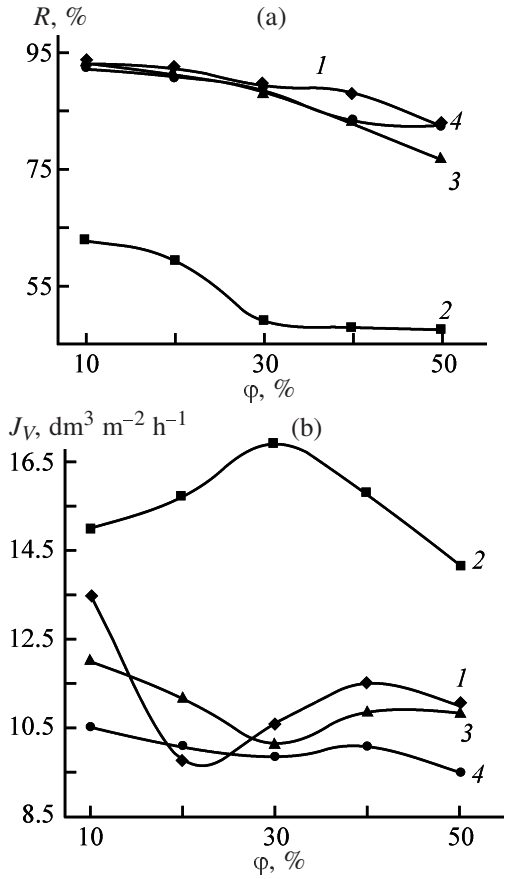


Fig. 4. (a) Retention coefficient R of atrazine and (b) membrane throughput J_V vs. the degree φ of permeate removal at different pH values. pH: (*1*) 3.2, (*2*) 6.1, (*3*) 7.0, and (*4*) 9.2.

its effective pore size somewhat increases. This assumption is confirmed both by a sharp decrease in the retention of atrazine and by an increase in the transmembrane flux in filtration of a solution with pH corresponding to the IEP of the membrane (Fig. 4).

Thus, when interpreting the dependences of the herbicide retention on pH of the medium, it is necessary to take into account the possibility of conformation transitions of charged polymer chains in the active layer of the OPMN-P membrane. Previously, similar effects associated with conformational transformations of macromolecules upon a change in pH of the solution being filtered were reported for nanofiltration separation of salts and glucose [11] and for composite membranes modified with polyelectrolytes [12].

CONCLUSIONS

(1) Nanofiltration treatment of aqueous solutions with an OPMN-P membrane can provide a high degree of removal of triazine herbicides (97–98%).

(2) The efficiency of removal of herbicides from aqueous solutions is affected by their molecular mass, working pressure, and concentration and pH of the solution being filtered.

(3) Electrostatic interactions are important in the mechanism of nanofiltration treatment of water to remove triazine herbicides with an OPMN-P membrane.

REFERENCES

1. *Ekologicheskie aspekty sovremennykh tekhnologii okhrany vodnoi sredy* (Environmental Aspects of Modern Technologies for Protection of the Aquatic Environment), Goncharuk, V.V., Ed., Kiev: Naukova Dumka, 2005.
2. Hiroaki, O. and Huafand Li, *Water Res.*, 2002, vol. 36, pp. 123–130.
3. Kiso, Y., Yosuke, S., Takane, K., and Kazuyuki, N., *J. Membr. Sci.*, 2001, vol. 192, pp. 1–10.
4. Kiso, Y., Nishimura, Y., Kitao, T., and Nishimura, K., *J. Membr. Sci.*, 2000, vol. 171, pp. 229–237.
5. Scott, K. and Huges, R., *Industrial Membrane Separation Technology*, London: Blackie, 2002.
6. Schmitt, Ph., Garrison, A.W., Freitag, D., et al., *J. Chromatogr.*, 1996, vol. 723, pp. 169–177.
7. Dauwe, S. and Sellergren, B., *J. Chromatogr.*, 1996, vol. 753, pp. 191–200.
8. Mulder, M., *Basic Principles of Membrane Technology*, Dordrecht: Kluwer, 1991.
9. Baker, R., *Membrane Technology and Application*, New York: McGraw-Hill, 2000.
10. Van der Bruggen, B., Schaep, J., Maes, W., et al., *Desalination*, 1998, vol. 117, pp. 139–147.
11. Manttari, M., Pihlajamaki, A., and Nystrom, M., *J. Membr. Sci.*, 2006, vol. 280, pp. 311–320.
12. Nigmatullin, R.R. and Bryk, M.T., *Dokl. Akad. Nauk Ukr. SSR, Ser. B*, 1989, no. 2, pp. 47–51.

ISSN 1070-4272, Russian Journal of Applied Chemistry, 2008, Vol. 81, No. 3, pp. 399–402. © Pleiades Publishing, Ltd., 2008.
Original Russian Text © E.E. Ergozhin, B.E. Begenova, T.K. Chalov, 2008, published in Zhurnal Prikladnoi Khimii, 2008, Vol. 81, No. 3, pp. 412–415.

PHYSICOCHEMICAL STUDIES OF SYSTEMS AND PROCESSES

Sorption Properties of Nitrogen-Containing Ion Exchangers

E. E. Ergozhin, B. E. Begenova, and T. K. Chalov

Bekturov Institute of Chemical Sciences, Ministry of Education and Science of Kazakhstan Republic, Almaty, Kazakhstan

Received July 25, 2007

Abstract—Sorption capacity of ion exchangers based on glycidyl derivatives of aromatic compounds and polyamines was studied in relation to pH of solution. The mechanism of sorption of polyvalent metal ions was examined.

DOI: 10.1134/S1070427208030099

High-performance ion exchangers are of particular importance in integrated processing of mineral raw materials, preservation of the environment, and development of wasteless processes. The ion-exchange processes used for treatment of potable and waste waters are environmentally safe. These processes can also be used in hydrometallurgy because modern precipitation and extraction procedures of recovery and separation of metal ions do not provide the required purification [1, 2].

EXPERIMENTAL

The ion exchangers were prepared by polycondensation of polyethylenepolyamine (PEPA), polyethylenimine (PEI), and poly-2-methyl-5-vinylpyridine (PMVP) with diglycidyl compounds, namely, diglycidylaniline (DGA) and diglycidyl phenol–aniline–formaldehyde (DGPAF) and diglycidyl toluene–phenol–formaldehyde (DGTPF) oligomers [3, 4]. The static exchange capacity (SEC) of the resulting anion exchangers for metal ions was determined using solutions of ammonium metavanadate (6 g l^{-1} V_2O_5, 3 g l^{-1} V), sodium molybdate (3 g l^{-1} Mo), sodium tungstate (3 g l^{-1} W), ammonium perrhenate (1 g l^{-1} Re), and also 0.05 M solutions of copper nitrate (1.6 g l^{-1} Cu) and nickel nitrate (1.5 g l^{-1} Ni), prepared from chemically pure grade salts. The concentrations of metal ions in solutions were determined by atomic absorption spectroscopy.

Along with chemical and thermal stability [3], the anion exchangers prepared exhibit high sorption capacity for transition metal ions (Table 1). The sorption capacity of these materials for polyvalent *d*-metal ions is higher than that of commercial AN-31 and EDE-10P resins by a factor of 2–3.

The dependence of the sorption capacity of the ion exchanger based on DGPAF and PEPA on the time of its contact with solution (Table 2) shows that the equilibrium is attained in 5 days, with 70–79% of the initial amount of polyvalent metal ions being recovered in the first 12 h, i.e., these anion exchangers exhibit high kinetic properties.

Owing to high sorption capacity for polyvalent metal ions (Table 1), the resulting anion exchangers can be used in hydrometallurgy of vanadium, molybdenum, tungsten, and rhenium, which are mainly used in various branches of industry such as metallurgy, mechanical engineering, chemistry, and electrical and radio engineering. More than 75% of molybdenum is used in alloying of cast iron and steels for aircraft and motor-car building. Heat-resistant (for jet engines) and acid-resistant (for chemical industry installations) molybdenum alloys show much promise. Vanadium, which is one of the most important alloying elements, improves such properties of steel as strength, lightness, flexibility, and heat resistance. Since vanadium compounds are highly toxic [5], its content in the environment and industrial wastes should be thoroughly controlled. It should be noted that the ion exchange is the most efficient procedure providing recovery of metal ions from aqueous solutions.

Polyvalent *d* metals occurring in solutions in the form of complex anions are sorbed on anion exchangers through anion exchange and complexation with coordination-active groups of the sorbent [6].

In the case of protonated ion exchangers, anionic

Table 1. Sorption characteristics of anion exchangers

Anion exchanger based on	SEC_M, mg g^{-1}, at optimal pH					
	Cu, 4.5	Ni, 5.0	V_2O_5, 1.9–2.2	Mo, 1.8–2.5	W, 1.6–2.8	Re, 3.0
DGA–PEPA	116.8	76.3	956.0	1190.0	1030.2	713.0
DGPAF–PEPA	128.0	70.4	832.9	955.0	708.8	540.2
DGTPF–PEPA	186.9	172.0	1200.0	1130.0	1020.0	–
DGA–PEI	166.4	85.1	733.0	501.3	502.1	519.1
DGPAF–PEI	198.4	117.4	1085.7	735.2	695.3	572.2
DGTPF–PEI	191.7	99.2	812.1	960.2	705.2	–
DGA–PMVP	74.0	60.7	835.0	520.0	503.4	–
DGPAF–PMVP	94.8	59.0	957.4	505.3	554.0	–
EDE-10P	89.6	–	400.0	384.0	–	254.0
AN-31	99.2	–	450.0	378.0	–	238.0

Table 2. Effect of sorption time on SEC_M on the ion exchanger based on DGPAF–PEPA

Recovered component	SEC_M, mg g^{-1} (%), at indicated sorption time				
	6 h	12 h	3 days	5 days	10 days
V_2O_5	335.2 (40)	583.0 (70)	791.0 (95)	832.9 (100)	832.9
Mo	525.2 (55)	754.4 (79)	927.0 (97)	955.0 (100)	955.0
W	212.6 (30)	510.8 (72)	652.1 (92)	708.8 (100)	708.8

complexes are first adsorbed by the mechanism of anion exchange:

$$(n-e)\left(\begin{matrix}\diagup\\ \diagdown\end{matrix}\!\!>\!\mathrm{NH}^+\ \mathrm{An}^-\right) + [\mathrm{MAn}_n]^{-n+e}$$
$$\rightleftarrows \left(\begin{matrix}\diagup\\ \diagdown\end{matrix}\!\!>\!\mathrm{NH}^+\right)_{n-e}[\mathrm{MAn}_n] + (n-e)\mathrm{An}^-,$$

Then, the ligands in the first coordination sphere of the metal are substituted by amino groups of the ion exchanger. On a nonprotonated ion exchanger, the sorption proceeds only by substitution of a ligand in the metal complex by ligand groups of the sorbent:

$$m\left(\begin{matrix}\diagup\\ \diagdown\end{matrix}\!\!>\!\mathrm{N}:\right) + [\mathrm{MAn}_n]^{e-n}$$
$$\rightleftarrows \left[\mathrm{M}\left(\begin{matrix}\diagup\\ \diagdown\end{matrix}\!\!>\!\mathrm{N}\right)_m \mathrm{An}_{n-m}\right]^{-n+m+e} + m\mathrm{An}^-.$$

Since the stability of complexes and their composition depends on the degree of protonation of the ionic groups in the anion exchanger [7, 8], we studied the dependence of the sorption capacity of the ion exchangers on the concentration of hydrogen ions (Fig. 1). As can be seen, the optimal pH range for sorption of vanadium is 1.9–2.2 (733–1200 mg g^{-1}); for molybdenum, 1.8–2.5 (501–1190 mg g^{-1}); for tungsten, 1.6–2.8 (502–1030 mg g^{-1}); and for rhenium, 3.0 (519–713 mg g^{-1}).

The concentration of the coordination-active (nonprotonated) ionic groups and their basicity increase with increasing solution acidity; in the process, the swelling of the ion exchangers studied also increases.

The observed increase in the sorption capacity for polyvalent metal ions with decreasing pH is probably due to the fact that the protonation enhances the hydrophilicity and, thus, the swelling of the ion exchangers, weakens the intermolecular bonds, and increases the mobility of the polymer units with ligand groups fixed on them. However, further protonation of the nitrogen atoms decreases the number of the coordination-active centers in the solid phase, increases the positive charge of the matrix and acidity inside the grain, and decreases sorption capacity of the ion exchanger [9]. As a result, with decreasing pH the sorption capacity of the ion exchangers increases to a certain limit (Fig. 1), after which the coordination activity decreases, because the concentration of the coordination-active centers and their basicity become the decisive factors.

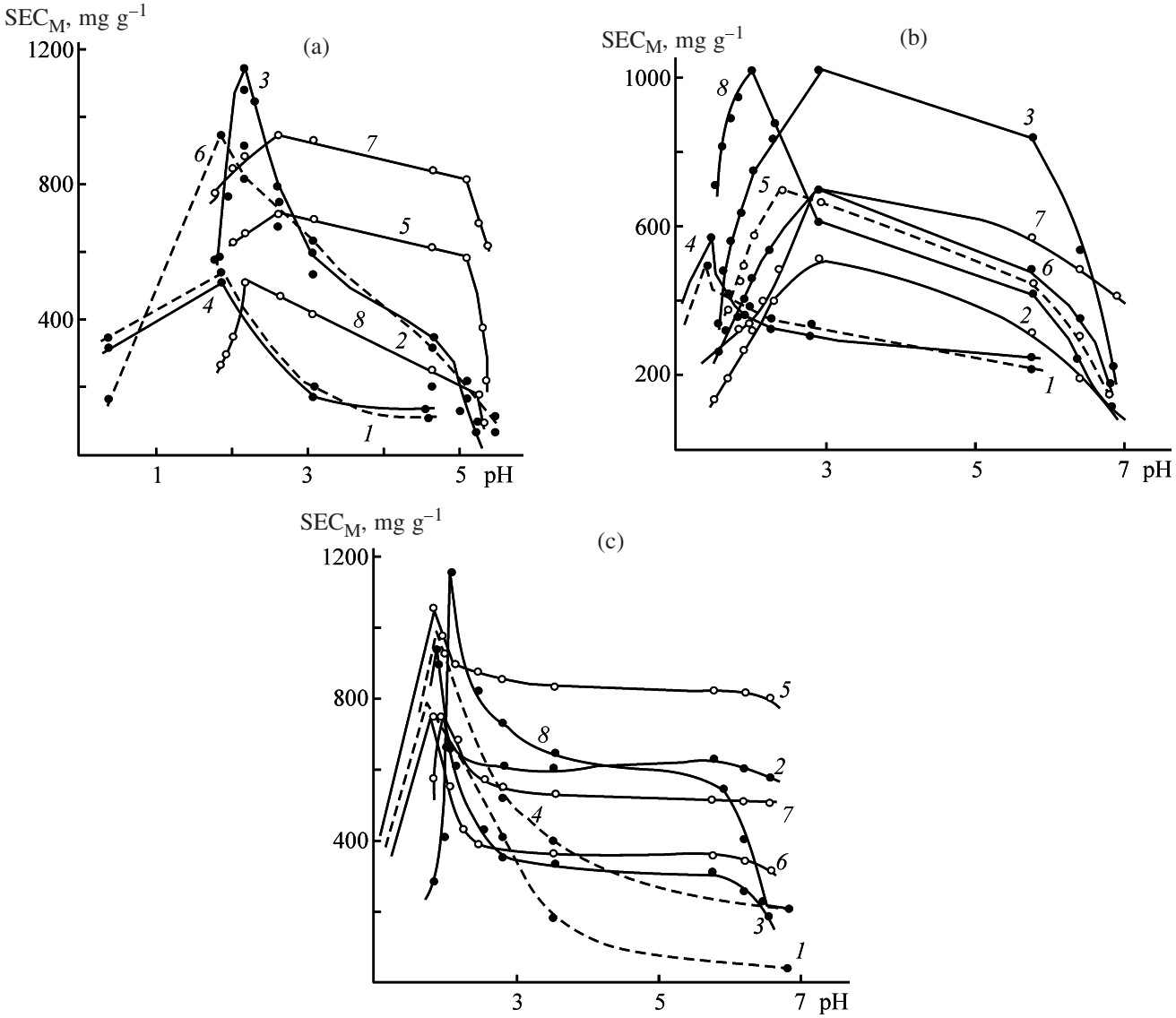


Fig. 1. Sorption of (a) Mo, (b) W, and (c) V as a function of solution pH. Ion exchangers: (*1*) DGA–PMVP, (*2*) DGA–PEI, (*3*) DGA–PEPA, (*4*) DGPAF–PMVP, (*5*) DGPAF–PEI, (*6*) DGPAF–PEPA, (*7*) DGTPF–PEI, (*8*) and DGTPF–PEPA. (SEC_M) Static exchange capacity.

The dependence of the sorption capacity of the ion exchangers on pH of the solution is also due to the ionic state of the metal. With increasing concentration of H^+ ions, MoO_4^{2-} undergoes polymerization and protonation yielding molybdenum species with various specific charges. In a weakly acidic solution, the most stable species are paramolybdate $Mo_7O_{24}^{6-}$ (pH 5–7) and tetramolybdate ions $Mo_4O_{13}^{2-}$ or $HMo_4O_{13}^{-}$ (pH 5–1.5) [10, 11].

The IR spectra of the ion exchangers after their saturation with molybdenum from solutions with optimal pH (1.8–2.5) exhibit the vibration bands of tetramolybdate ions (895–900, 906, 942 cm^{-1}). Hence, at pH 1.8–2.5 the ion exchangers studied recover molybdenum as tetramolybdate ions whose low specific charge probably also leads to an increase in the sorption capacity in the given pH range. In its physical, mechanical, and chemical properties, molybdenum is close to tungsten, which is due to similarity of their ionic radii (0.065 nm) [1]. Similarly to MoO_4^{2-}, WO_4^{2-} undergoes polymerization to form paratungstate $W_7O_{24}^{6-}$ or $W_{12}O_{41}^{10-}$ and tetratungstate ions $W_4O_{13}^{2-}$, whose small specific charge leads to an increase in the sorption capacity of the ion exchangers in the pH range 1.6–2.8.

The ionic state of vanadium also changes depending on pH of solution [13]. Sorption of decavanadate ion $V_{10}O_{28}^{6-}$ with a small specific charge on the ion

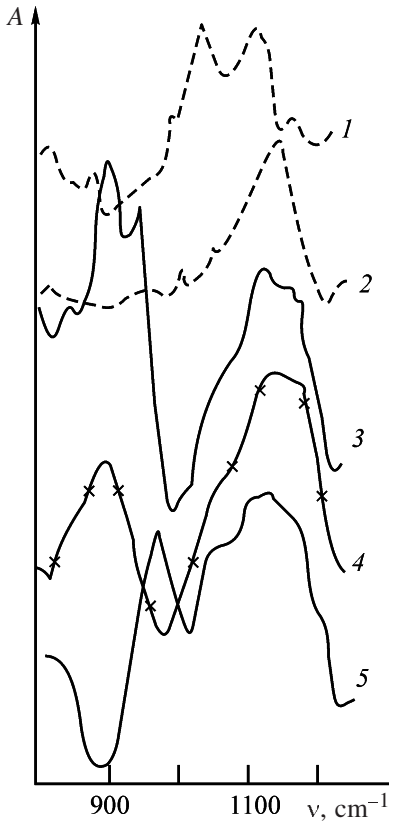


Fig. 2. IR spectra of the ion exchangers based on (*1*) DGPAF–PEPA and (*2*) DGPAF–PEI and of their complexes with (*3, 4*) molybdenum and (*5*) vanadium (DGPAF–PEPA). (*A*) Absorption and (ν) wavenumber.

exchangers studied at optimal pH 1.9–2.2 is confirmed by appearance of the absorption band at 960 cm^{-1} (Fig. 2).

CONCLUSIONS

(1) The sorption capacity of the ion exchangers studied depends on the content of coordination-active (nonprotonated) ionic groups, degree of swelling of the oligomer, and ionic state of metal in solution.

(2) The pH ranges optimal for sorption of transition metal ions were determined.

REFERENCES

1. Blokhin, A.A., Kopyrin, A.A., Mikhailenko, M.A., and Nikitin, N.V., Abstracts of Papers, *II Mezhdunarodnaya konferentsiya "Metallurgiya tsvetnykh i redkikh metallov"* (II Int. Conf. "Metallurgy of Rare and Nonferrous Metals"), Krasnoyarsk, 2003, vol. 1, pp. 95–96.
2. Zelikman, A.N. and Meerson, G.A., *Metallurgiya redkikh metallov* (Metallurgy of Rare Metals), Moscow: Metallurgiya, 1973.
3. Ergozhin, E.E., Begenova, B.E., and Chalov, T.K., *Khim. Zh. Kaz.*, 2005, no. 4 (9), pp. 104–124.
4. Ergozhin, E.E., Begenova, B.E., and Chalov, T.K., *Zh. Prikl. Khim.*, 2007, vol. 80, no. 3, pp. 473–478.
5. Muzgin, V.N., Khamzina, L.B., Zolotavin, V.L., and Bezrukov, I.Ya., *Analiticheskaya khimiya vanadiya* (Analytical Chemistry of Vanadium), Moscow: Nauka, 1981.
6. Saldadze, K.M. and Kopylova-Valova, V.D., *Kompleksoobrazuyushchie ionity (kompleksity)* (Complexing Ion Exchangers), Moscow: Khimiya, 1980.
7. Goswami, A. and Singh Ajai, K., *React. Funct. Polym.*, 2004, vol. 61, no. 2, pp. 255–263.
8. Mutalov, Sh.A., Tursunov, T., and Nazirova, R.A., *Plast. Massy*, 2005, no. 5, pp. 37–38.
9. Galitskaya, N.B., Kargman, V.B., Kozhevnikova, N.E., and Todres, I.M., in *Okhrana okruzhayushchei sredy i ratsional'noe ispol'zovanie prirodnykh resursov: Obzor informatsii* (Preservation of the Environment and Efficient Utilization of Natural Resources: Information Review), Moscow, 1980, issue 4 (29), pp. 1–41.
10. Kholmogorov, A.G., Nadol'skii, A.P., and Pilipchuk, Yu.S., *Izv. Vyssh. Uchebn. Zaved., Tsvetn. Metall.*, 1974, no. 4, pp. 109–113.
11. Kholmogorov, A.G., Nadol'skii, A.P., and Pilipchuk, Yu.S., *Tsvetn. Metall.*, 1971, no. 3, pp. 64–67.
12. Bukhtiarov, V.E., *Ionoobmennye metody v analize metallov i splavov* (Ion-Exchange Methods in Analysis of Metals and Alloys), Moscow: Metallurgiya, 1982, pp. 95–97.
13. Ptitsyn, A.N., Zolotavin, V.A., and Maletina, L.E., in *Khimiya i tekhnologiya vanadievykh soedinenii* (Chemistry and Technology of Vanadium Compounds), Perm, 1974, pp. 167–171.

ISSN 1070-4272, Russian Journal of Applied Chemistry, 2008, Vol. 81, No. 3, pp. 403–406. © Pleiades Publishing, Ltd., 2008.
Original Russian Text © O.M. Trokhimenko, V.V. Anan'eva, V.N. Zaitsev, V.I. Gerda, A.A. Golub, 2008, published in Zhurnal Prikladnoi Khimii, 2008, Vol. 81, No. 3, pp. 416–419.

PHYSICOCHEMICAL STUDIES OF SYSTEMS AND PROCESSES

Recovery of Iodide Ions from Geothermal Water with Silica with Grafted Alkylammonium Groups

O. M. Trokhimenko, V. V. Anan'eva, V. N. Zaitsev, V. I. Gerda, and A. A. Golub

Shevchenko National University, Kiev, Ukraine

Received July 15, 2007

Abstract—Effect of a number of factors (time of contact and mass ratio of phases, acidity and temperature of the medium, concentrations of macrocomponents of geothermal water) on the sorption recovery of iodide ions with 3-(octadecyldimethylammonio)propylsilica and 3-(trimethylammonio)propylsilica from aqueous solutions was studied. Sorption isotherms were discussed. The possibility of using 3-(octadecyldimethylammonio)-propylsilica for recovery of iodide ions from highly mineralized geothermal water was analyzed.

DOI: 10.1134/S1070427208030105

The main raw material for industrial manufacture of iodine is natural mineral water accompanying oil and gas in oil-and-gas fields. The content of iodine in this kind of water is 10–120 mg l^{-1}, with more than 90–95% of this amount present in the form of iodide ions [1]. I^- is recovered from water without changes in the degree of oxidation in the form of poorly soluble copper, silver, and mercury iodides or with the use of ion-exchange resins, e.g., AV-17 [2, 4]. The sorption technology of I^- recovery from underground water and brine of salt lakes occupies the leading place among the industrial techniques for manufacture of iodine.

At present, organomineral composite materials find wide use in sorption, chromatography, and catalysis [5]. Ion exchangers of this group frequently combine advantages of synthetic organic polymers with ionic functional groups and inorganic substances (silica, aluminum oxide, zeolites). The mechanical and mass-exchange properties of organomineral mass exchangers are determined by the rigid wide-porous mineral skeleton of the inorganic support, and the ion-exchange properties, by the nature of fixed functional groups.

An advantage of modified silica sorbents is the rather high rate of attainment of the sorption equilibrium, which is particularly important in the case of recovery of ions from large volumes of dilute solutions. Also important is that the quantitative desorption of ions from their surface can be provided in most cases by small volumes of eluents. As a result, the concentration coefficient in a single sorption–desorption cycle reaches 10^3–10^4, which markedly exceeds the parameters of organopolymeric analogs [6].

In this study we examined the possibility of recovering iodine in the form of iodide ions from highly mineralized geothermal water with silica gels with grafted alkylammonium groups.

EXPERIMENTAL

As object of study served anion exchangers, 3-(trimethylammonio)propylsilica (**I**) and 3-(octadecyldimethylammonio)propylsilica (**II**), which contain strongly basic quaternary ammonium groups. These functional groups were chosen for modification of the silica gel because the stability of ionic associates of tetraalkylammonium increases as the ionic radius of the counterion becomes larger. This property can favor an increased selectivity of the materials under study with respect to iodide ions, compared with other halides. In this study, we used anion exchangers with a bromide or chloride salt of a strong base, covalently fixed on the surface of the silica matrix:

$$(SiO_2)\equiv Si–C_3H_6–N^+(CH_3)_3Br^- \quad (\mathbf{I});$$

$$(SiO_2)\equiv Si–C_3H_6–N^+(CH_3)_2(C_{18}H_{37})Cl^- \quad (\mathbf{II}).$$

The procedure used to obtain samples **I** and **II** included preliminary purification and activation of silica (Merck, S_s = 500 m^2 g^{-1}, d = 60 Å) with hot (120°C) concentrated nitric acid, washing with distilled water

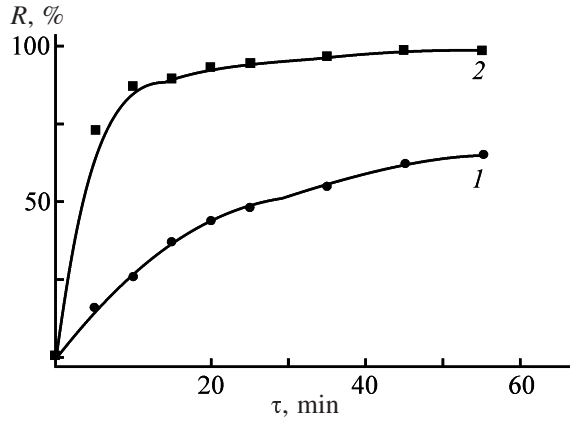


Fig. 1. Degree R of sorption of iodide ions vs. the time τ of contact between the phases. $m_{\mathbf{I,II}}$ = 0.02 g, $c_{I^-} = 8.42 \times 10^{-6}$ M, V_{aq} = 15 ml. Sorbent: (*1*) 3-(trimethylammonio)propylsilica and (*2*) 3-(octadecyldimethylammonio)-propylsilica; the same for Fig. 2.

to neutral pH, and subsequent modification of its surface with the corresponding silane in an organic solvent [5]. The concentration of grafted groups on the surface of the materials obtained was 520 ± 10 and 440 ± 10 μmol g^{-1} for **I** and **II**, respectively, as indicated by conductometric back-titration of aqueous suspensions for Cl^- and Br^- ions. The stock solutions, 1.0 M potassium chloride and 0.2 M potassium iodide, bromide, sulfate, and hydrocarbonate, were prepared by dissolving the corresponding weighed portions in distilled water. Working solutions were prepared by diluting the stock solutions.

For sorption studies, we placed a weighed portion of a sorbent in a beaker and added a solution prepared. The sorption was studied under static conditions and agitation with a magnetic stirrer at a certain temperature. The concentration of iodide ions in solutions was determined a certain time after these solutions were brought in contact with the sorbents.

The distribution of iodide ions between phases was monitored spectrophotometrically by the iodine–starch reaction [7]. For this purpose, the iodide was oxidized with bromine water to the iodate and excess bromine was removed by heating the solution and then adding phenol. After that, an excess amount of potassium iodide was added and the solution was acidified. As a result, elemental iodine was released in an amount proportional to the content of the iodate, i.e., to the initial content of I^-. When necessary, the residual concentration of microscopic amounts of iodide ions was found using the kinetic cerium(IV)–arsenite reaction [8], which is catalyzed by I^-. The light absorption of the solutions was measured with an SF-26 spectrophotometer, and their pH was monitored with an EV-74 ion meter. The electrical conductivity of the solutions was measured with an R-5058 ac bridge with a working frequency of 1 kHz.

The degree of sorption R (%) and the amount of sorbed iodide a (mol g^{-1}) were calculated by the formulas

$$R = c \times 100/c_0, \qquad a = (c_0 - c)V/m,$$

where c_0 and c are the initial and running concentrations of iodide ions in solution (M); V, solution volume (l); and m, sorbent mass (g).

The data obtained were used to plot curves describing how the amount of I^- sorption on sorbents **I** and **II** depends on various parameters of the medium and to construct the sorption isotherms.

The sorption equilibrium in the system constituted by iodide ions and a sorbent is attained in 50 min for compound **I** and 20 min for **II**, with the degree of sorption reaching 60 and 98%, respectively (Fig. 1). The difference in the behavior of the sorbents with respect to iodide ions can be attributed, first, to an increase in the stability of ionic associates of tetraalkylammonium with the molecular mass of substituents and, second, to a lower degree of dissociation of the bromide ionic associate on the surface of **I**, compared with that of the chloride associate on the surface of **II**.

The effect of the phase mass ratio $m_{aq}/m_{\mathbf{I,II}}$ on the degree of recovery of iodide ions was studied at their constant amount. A quantitative recovery of the analyte was observed at $m_{aq}/m_{\mathbf{I,II}} \leq 1300$. In this case, the concentration coefficient reaches 1.3×10^3. If the phase mass ratio increases further, the degree of recovery of iodide ions steeply falls because of the poorer contact between the sorbent and sorbate.

As the temperature of aqueous solutions increases, the degree of recovery of iodide ions steadily decreases, from 98% at 20°C to 85% at 60°C for sorbent **II** because of the rise in the entropy factor. Lowering the temperature of the solutions to 5°C has no significant effect on the degree of recovery.

In the pH range 2–8, the acidity of a solution has virtually no effect on the degree of sorption. However, raising the pH to more than 8 makes the degree of sorption of iodide ions lower, possibly because of partial disintegration of the matrix of sorbents and a decrease in the amount of ionic groups on its surface.

The sorption isotherms of iodide ions are of the Langmuir type (Fig. 2). The limiting sorption a_l (μmol g^{-1}) and sorption constant K (M^{-1}), calculated

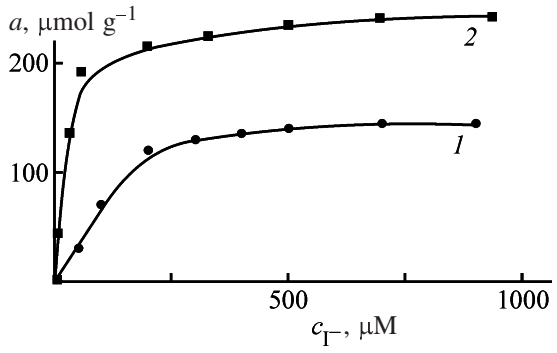


Fig. 2. Sorption isotherms of iodide ions (T = 293 ± 1 K). (*a*) Amount of sorbed iodide and (c_{I^-}) equilibrium concentration of iodide ions.

using the linear form of the Langmuir equation [9], are, respectively, 145 and $(0.21 \pm 0.08) \times 10^{-7}$ for compound **I**, and 242 and $(0.47 \pm 0.10) \times 10^{-7}$ for compound **II** at concentrations of grafted groups equal to 520 and 440 μmol g^{-1}, respectively. Thus, up to 30 and 60% of grafted groups of **I** and **II** are involved in the ion-exchange process. The sorption constant of **II** exceeds that of **I**.

Taking into account the rate at which the sorption equilibrium is attained and the capacity of the sorbents for iodide ions, we performed further experiments with compound **II**.

Geothermal water is highly mineralized and contains, mg l^{-1} (M): chlorides up to 20000 (0.56), bromides up to 100 (1.25×10^{-3}), sulfates up to 600 (6.25×10^{-3}), and hydrocarbonates up to 400 (6.55×10^{-3}) [1]. Taking into account this circumstance, we studied the effect of the concentration of these anions on the sorption of iodide ions from model solutions. As the concentration of chloride ions increases to 0.2 M, the degree of sorption of iodide ions sharply falls because of the competing effect of this anion (Fig. 3). As the concentration of chloride ions increases further, the degree of I^- sorption increases, which is possibly due to salting-out, and reaches a value of 71.3% at a Cl^- concentration of 0.6 M. In amounts commonly present in geothermal water, sulfate, hydrocarbonate, and bromide ions diminish the degree of I^- sorption at a constant sorbent mass to 56, 60, and 95%, respectively (Fig. 4).

A study of the I^- sorption by 3-(octadecyldimethylammonio)propylsilica from natural geothermal water demonstrated that the degree of sorption of iodide ions from real geothermal water is lower than that for model solutions, possibly as a result of the cooperative action of the anions present. Table 1 shows how

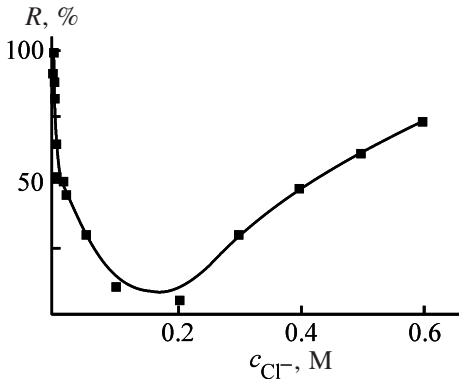


Fig. 3. Degree R of sorption of iodide ions by 3-(octadecyldimethylammonio)propylsilica vs. the concentration c_{Cl} of chloride ions. m_{II} = 0.02 g, $c_{I^-} = 8.42 \times 10^{-6}$ M, V_{aq} = 15 ml; the same for Fig. 4.

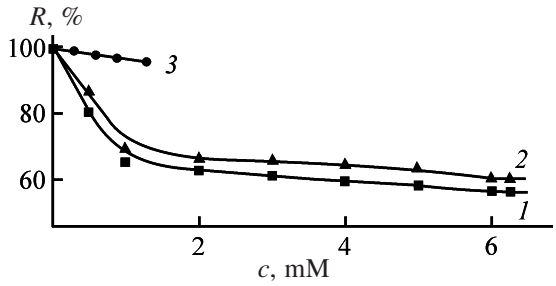


Fig. 4. Degree R of sorption of iodide ions by 3-(octadecyldimethylammonio)propylsilica vs. the concentration c of anions. Anion: (*1*) SO_4^{2-}, (*2*) HCO_3^{2-}, and (*3*) Br^-.

the degree of sorption of iodide ions from geothermal water varies with its gradual dilution, made to decrease the salt background. It can be seen that, upon a twofold dilution of a sample of geothermal water, the degree of I^- recovery exceeds 56%. An increase

Table 1. Degree R of sorption of iodide ions on 3-(octadecyldimethylammonio)propylsilica at different dilutions of a sample of geothermal water from the Medvedovka no. 4 well (Ukraine, Autonomous Republic of Crimea). T = 20°C, pH 7, sorbent mass 0.02 g, total volume 15 ml

Sample dilution, times	R, %
15	95.6
6.5	91.4
4	85.8
2.8	66.7
2	56.3
1.5	47.8
1.1	37.9
0.8	20.8
0.6	15.7
0.5	8.4

Table 2. Degree R of sorption of iodide ions from some geothermal water samples by 3-(octadecyldimethylammonio)-propylsilica (n = 3, P = 0.95). T = 20°C, pH 7, sorbent mass 0.02 g, sample volume 15 ml

Well in Autonomous Republic of Crimea (Ukraine)	Content of anions, mg l^{-1}				Content of I^-, mg l^{-1}		R, %
	Cl^-	Br^-	SO_4^{2-}	HCO_3^-	before sorption	after sorption	
Medvedovka no. 4	15366	86.6	484	268	23.9 ± 1.2	4.3 ± 0.2	82
Severno-Sivashskaya no. 36	15018	85.0	599	378	15.8 ± 0.8	3.16 ± 0.1	80
Yantarnaya no. 3	15479	82.1	11	329	7.2 ± 0.4	1.51 ± 0.1	79

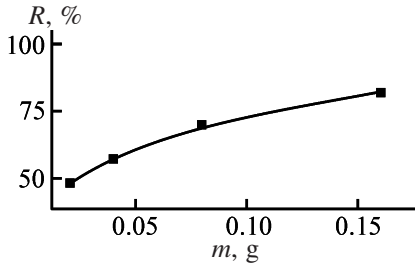


Fig. 5. Degree R of recovery of iodide ions from geothermal water vs. mass m of 3-(octadecyldimethylammonio)propylsilica. $c_{I^-} = 8.42 \times 10^{-6}$ M, V_{aq} = 15 ml. Concentration of anions (mg l^{-1}): Cl^- 15000, Br^- 85, SO_4^{2-} 400, HCO_3^{2-} 380.

in the sorbent mass from 0.02 to 0.15 g substantially improves the sorption recovery of iodide ions from geothermal water (Fig. 5). This is possible because of the increase in the number of sorption sites on the surface of the sorbent under study and the resulting decrease in the competing effect of the concomitant components. At a phase mass ratio $m_{aq}/m_{\mathbf{II}} = 100$, about 80% of iodide ions is sorbed from real geothermal water (Table 2).

CONCLUSIONS

(1) The efficiency of iodide recovery from aqueous solutions on 3-(octadecyldimethylammonio)propylsilica markedly exceeds that on 3-(trimethylammonio)-propylsilica because the stability of ionic associates of tetraalkylammonium and iodide ions increases with the molecular mass of substituents.

(2) Quantitative recovery of iodide ions on 3-(octadecyldimethylammonio)propylsilica is observed in 20 min at room temperature in the pH range 2–8, with the concentration coefficient reaching 1.3×10^3.

(3) The sorption isotherms of iodide ions are of the Langmuir type. The sorption constant of **II** exceeds that of **I**.

(4) Use of 3-(octadecyldimethylammonio)propylsilica enables recovery of about 80% of iodide ions from real geothermal water under the optimal conditions.

REFERENCES

1. Ksenzenko, V.I. and Stasinevich, D.S., *Khimiya i tekhnologiya broma, ioda i ikh soedinenii* (Chemistry and Technology of Bromine, Iodine, and Compounds of These), Moscow: Khimiya, 1995.
2. Bogacheva, L.G., Valyashko, M.G., Por'gokin, D.S., et al., *Izv. Vyssh. Uchebn. Zaved., Khim. Khim. Tekhnol.*, 1970, vol. 13, no. 3, p. 380.
3. Ksenzenko, V.I., Stasinevich, D.S, and Khodzhamamedov, A., *Ionnyi obmen* (Ion Exchange), Moscow: Nauka, 1981, pp. 201–214.
4. Puzii, A.M., Kartel', N.T., and Strelko, V.V., *Ukr. Khim. Zh.*, 1984, vol. 50, no. 4, p. 380.
5. Zaitsev, V.N., *Kompleksoobrazuyushchie kremnezemy: sintez, stroenie privitogo sloya i khimiya poverkhnosti* (Complex-Forming Silicas: Synthesis, Structure of the Grafted Layer, and Surface Chemistry), Kharkov: Folio, 1997.
6. *Khimiya privitykh poverkhnostnykh soedinenii* (Chemistry of Grafted Surface Compounds), Lisichkin, G.V., Ed., Moscow: Fizmatlit, 2003.
7. Guenther, E.A., Johnson, K.S., and Coale, K.H., *Anal. Chem.*, 2001, vol. 73, no. 1, p. 3481.
8. Trokhimenko, O.M. and Zaitsev, V.N., *Zh. Anal. Khim.*, 2004, vol. 59, no. 5, p. 491.
9. *Adsorption from Solution at the Solid/Liquid Interface*, Parfitt, G.D. and Rochester, C.H., Eds., London: Academic, 1983.

ISSN 1070-4272, Russian Journal of Applied Chemistry, 2008, Vol. 81, No. 3, pp. 407–411. © Pleiades Publishing, Ltd., 2008.
Original Russian Text © S.V. Kurbatova, O.V. Kharitonova, 2008, published in Zhurnal Prikladnoi Khimii, 2008, Vol. 81, No. 3, pp. 420–424.

PHYSICOCHEMICAL STUDIES OF SYSTEMS AND PROCESSES

Influence of Eluent Composition on the Retention Factor of Azoles in Reversed-Phase High-Performance Liquid Chromatography

S. V. Kurbatova and O. V. Kharitonova

Samara State University, Samara, Russia

Received April 18, 2007

Abstract—The linear dependence of the retention factor of indole, imidazole, triazole, and tetrazole derivatives on the acetonitrile content of the mobile phase was studied.

DOI: 10.1134/S1070427208030117

Chemistry of five-membered heterocycles and their derivatives attracts researchers' attention mainly due to their high physiological activity and their use as models in solving some problems of theoretical organic chemistry [1, 2]. It is known that many derivatives of diazoles and triazoles exhibit adrenoblocking, antimicrobial, and others kinds of pharmacological activity. In addition, many important natural compounds such as histamine, histidine, allantoin, etc. contain the imidazole group.

Azoles of various structures are relatively widely used as models in theoretical determination of the quantitative structure–property relationships (QSPR) and quantitative structure–activity relationships (QSAR) [4]. These compounds show promise in determination of the quantitative structure–retention factor relationships described in detail in [5, 6]. It should be noted that the dependence between the structure and retention factor of nitrogen-containing heterocycles was studied mainly for gas chromatography. At the same time, high-performance liquid chromatography (HPLC) is a convenient and promising tool not only for determination of structures and many physicochemical properties of compounds, but also in simulation of biochromatographic processes occurring after introduction of physiologically active compounds into a living body. In many cases, the sorption mechanism of the physiological action of a pharmaceutical or biologically active substance is suggested. Therefore, determination of sorption properties of these compounds by chromatographic methods is of interest. HPLC allows variation of the chromatographic conditions, in particular, of the type and composition of the eluent, in a wide range [7].

In this study we examined the influence of the eluent composition on the retention factor of derivatives of nitrogen-containing five-membered heterocycles under conditions of reversed-phase HPLC.

EXPERIMENTAL

The experiments were performed on a Biotronik Chromatographic system with a BT 8100 HPLC Pump and an ultraviolet detector. A 4×150 mm Separon SGX-C_{18} column was used. Elution was performed in the isocratic mode using an acetonitrile–water mixture (1 : 1, 5 : 3, and 3 : 1, v/v) as the eluent.

Prior to analysis the eluent was degassed with a UZDN-2T device and filtered. The flow rate of the eluent was 0.3 ml min^{-1}. Substrate solutions were prepared by dissolution of dry pure heterocyclic compounds in appropriate solvents. The volume of the injected sample was 20 μl. Sodium nitrite was used as nonsorbable compound.

The UV detector operated at 254 nm. The analysis was performed at 20°C.

The retention factor k was calculated by the following equation:

$$k = t'_R/t_M = (t_R - t_M)/t_M,$$

where t_R is the retention time of the examined compound and t_M is the retention time of the unsorbable compound (min) [8].

Five replicate runs were performed for each point.

It is known that chromatographic retention depends on many factors. Among them the main factors are

the type of the chromatographic system (mobile and stationary phases between which the adsorbent molecules are distributed), chromatographic conditions, and the molecular structure of the sorbate [7]. Therefore, in chromatographic studies, correlation between sorption of samples and their structure or chromatographic conditions is usually considered. In both cases the main approach is semiempirical mathematical simulaiton based on the general concept of the sorption mechanism in systems of different types.

Retention in reversed-phase HPLC is due to competing interactions of sorbate molecules with nonpolar hydrophobic surface of the sorbent and specific interactions with the polar eluent. Since, unlike gas chromatography, the mobile phase in HPLC (especially in reversed-phase HPLC) interacts with substances to be separated, its composition and properties will significantly affect the distribution of these substances in a chromatographic column, and hence will affect the retention parameters.

Correlation between the retention parameters and quantitative composition of the mobile phase was extensively studied [9, 10]. It was described by different models [7, 11] and is most frequently approximated by the following equations [7]:

$$\log k = a - bc, \quad (1)$$

$$\log k = a_1 - b_1 \log c, \quad (2)$$

$$\log k = a_2 - b_2 c + pc^2, \quad (3)$$

where k is the retention factor, c is the concentration of the organic component, and a, b, p are coefficients.

As shown in numerous studies, Eqs. (1)–(3) describe well the retention of substrates of different chemical nature. However, the use of each particular equation is determined, as a rule, by hydrophobicity of eluted compounds and the retention model. Shatts and Sakhartova [7] noted that Eq. (3) was relatively rarely used to describe and predict retention, since the influence of the pc^2 term was appreciable only in a wide concentration range of the organic component in the mobile phase.

Equation (2) is used, as a rule, in the framework of the Horvath solvophobic theory, with coefficient b_1 equal to the number of organic solvent molecules displaced from the sorbent surface by one sorbate molecule.

In this study we used acetonitrile as a modifier of the mobile phase, since it has a high affinity for the examined compounds. In general, the retention of the derivatives of five-membered nitrogen-containing heterocycles decreases with increasing acetonitrile concentration owing to strengthening of the specific interactions with the organic component of the mobile phase. Similar results were obtained for imidazole derivatives [12, 13]. The retention of all sorbates is maximal at 50% acetonitrile content.

The dependence of the retention factor of most of the examined azole derivatives on the acetonitrile content c (M) in the mobile phase is linear and can be described by equations like (1) and (2). The correlation coefficients for these equations are presented in the table. As seen from the table, Eq. (2) fits the dependence of the retention factor on the composition of the mobile phase with a higher correlation coefficient r. Coefficient a in Eq. (1) is equal to the retention factor in the absence of the organic solvent in the mobile phase. The physical meaning of term a_1 in Eq. (2) differs. This coefficient is equal to the logarithm of the retention factor at 1 M concentration of the organic modifier [7].

It is known [7] that a phenomenon similar to the compensation of the entropy and enthalpy is revealed in consideration of the dependence of the retention parameters of structurally similar compounds on the concentration of an organic modifier. If this effect takes place, extrapolated dependences of the retention factors on the concentration of the organic component should intersect in one region of the coordinate plane. As seen from the table, this is the case with some azole derivatives, i.e., the curves described by Eqs. (1) and (2) tend to an isoparametric point. It is known that the intersection point of straight lines $y = a + bx$ is described by the equation $a_1/(1 - b_1) = a_2/(1 - b_2) = K$ = constant, where a and b are equation coefficients [14]. According to the Horvath solvophobic theory, the physical meaning of a isoparametric point is determined by parameters of a chromatographic system such as molar volume, dipole moment, and polarizability. In our case, K of the sorbate in question depends on the above parameters and is in the range 0.14–1.99 and 0.34–1.04 for coefficients of Eqs. (1) and (2), respectively.

The compensation effect suggests the similar retention mechanism of the compounds in question. This fact is confirmed by the correlation between the retention factors of the examined compounds at different water : acetonitrile ratios in the eluent (Fig. 1). Usually these dependences are used to compare the retention on two sorbents [15]. For this purpose, the equation $\log k_A = a + b \log k_B$ (where k_A and k_B are the retention factors on sorbents A and B, respectively) is

Correlation coefficients in equations describing the dependences of the retention factor on the eluent composition*

Compound no.	Compound	$\log k = a + bc$			$\log k = a + b\log c$		
		a	$-b$	r	a	b	r
1	Benzene	1.667	0.110	0.9977	3.554	2.990	1.000
2	Imidazole	2.445	0.291	0.9017	7.169	7.658	0.8750
3	2-(1*H*-Imidazol-1-ylmethyl)phenol	3.000	0.195	0.9989	6.343	5.298	0.9990
4	2-Methylimidazole	0.192	0.051	0.9911	1.077	1.398	0.9970
5	4-(2-Methyl-1*H*-imidazol-1-ylmethyl)phenol	1.077	0.102	0.9997	2.819	2.77	0.9960
6	2-(1*H*-Imidazol-1-ylmethyl)benzohydrazide	1.155	0.122	0.8742	3.350	3.409	0.9010
7	4-(1*H*-Imidazol-1-ylmethyl)benzohydrazide	0.322	0.015	0.8347	–0.056	0.412	0.8660
8	*p*-Toluenesulfonic acid imidazolide	0.356	0.056	0.7175	1.225	1.441	0.6750
9	1-(2,4,6-Triisoprolylphenylsulfonyl)-1*H*-imidazole	2.094	0.135	0.9406	4.482	3.736	0.9590
10	Benzenesulfonic acid imidazolide	0.241	0.054	0.9838	1.174	1.471	0.9930
11	Benzenesulfonic acid benzimidazolide	0.067	0.037	0.9955	0.697	0.996	0.9990
12	2-Methylbenzimidazole	0.147	0.039	0.9998	0.809	1.049	0.9990
13	1-(2,4,6-Triisoprolylphenylsulfonyl)benzimidazole	0.054	0.035	0.9553	0.671	0.969	0.9710
14	Methanesulfonic acid 2-methylbenzimidazolide	1.006	0.090	0.9947	2.552	2.443	0.9990
15	Methanesulfonic acid indolide	0.883	0.083	0.9895	2.327	2.279	0.9960
16	Benzenesulfonic acid indolide	0.313	0.059	0.9920	1.314	1.580	0.9980
17	Indole	1.489	0.111	0.9983	3.390	3.011	1.000
18	4-(5-Methyl-1*H*-1,2,4-triazol-1-yl)phenol	0.141	0.044	0.7678	0.831	1.136	0.7290
19	1-(2,4,6-Triisoprolylphenylsulfonyl)-1*H*-1,2,4-triazole	2.117	0.099	0.9115	3.738	2.623	0.8860
20	Benzenesulfonic acid 1,2,4-triazolide	2.347	0.202	0.9932	5.833	5.507	0.9980
21	1-(1*H*-1,2,4-Triazol-1-ylsulfonyl)-1*H*-1,2,4-triazole	0.430	0.128	0.9824	2.578	3.437	0.9690
22	Benzotriazole	0.297	0.013	0.9841	–0.073	0.358	0.9720
23	Benzenesulfonic acid benzotriazolide	2.288	0.144	0.9998	4.741	3.897	0.9970
24	1-(2,4,6-Triisoprolylphenylsulfonyl)-1*H*-1,2,3-benzotriazole	4.381	0.359	0.9007	10.797	9.992	0.9250
25	*p*-Toluenesulfonic acid benzotriazolide	2.468	0.148	0.9996	4.982	3.996	0.9960
26	4-(1*H*-1,2,3-Benzotriazol-1-ylmethyl)phenol	0.986	0.098	0.9925	2.683	2.680	0.9980
27	5-(4-Nitrophenyl)-1*H*-tetrazole	1.252	0.119	0.9981	3.265	3.204	0.9930
28	5-Phenyl-1*H*-tetrazole	0.283	0.055	0.9613	1.191	1.458	0.9430

* The compounds were prepared at the Chairs of Organic Chemistry of Samara State University and Samara State Technical University; the structure and purity of the compounds were confirmed by elemental analysis and by IR and NMR spectroscopy.

used. Coefficient b reflects the thermodynamic similarity of the processes in these systems.

To estimate the overall effect of all interaction types in an HPLC chromatographic system, different properties of the solvents were suggested. In particular, the eluting power of the mobile phase can be characterized by the adsorption power of the solvent ε^0 which, in turn, characterizes the relative interaction energy of mobile phase molecules with the adsorbent surface [11]. Contrary to the eluting power, Snyder developed a comparison system based on different properties of the solvents. According to this approach, each solvent is characterized by the power S depending on its chromatographic properties [7]. The solubility parameter δ introduced by Hildebrand and Scott [15] is also used along with ε^0 and S to describe the mobile phase.

The solvent polarity calculated as a sum of logarithms of distribution coefficients of reference compounds between the vapor phase and the examined solvent was also introduced by Snyder [16]. The polarity of a mixture of solvents A and B can be calculated as $P'_{mixt} = V_A P'_A + V_B P'_B$, where V_A and V_B are the volume fraction of solvents A and B, and P'_A

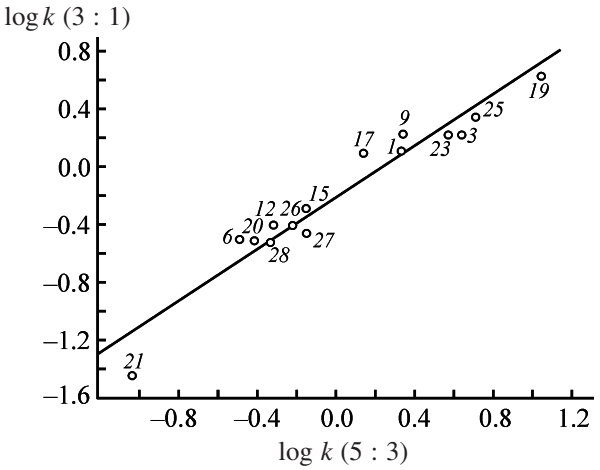


Fig. 1. Correlation between the logarithms of the retention factors of the examined compounds at acetonitrile : water ratios in the mobile phase of 3 : 1 and 5 : 3. Figures at points are compound nos. in the table; the same for Figs. 2 and 3. Regression equation: $\log k\ (3:1) = -0.229 + 0.939 \times \log k\ (5:3)$.

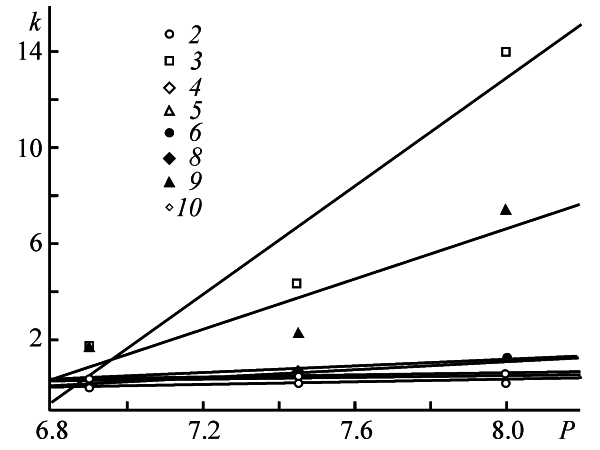


Fig. 2. Retention factor k of imidazole derivatives as a function of the eluent polarity P.

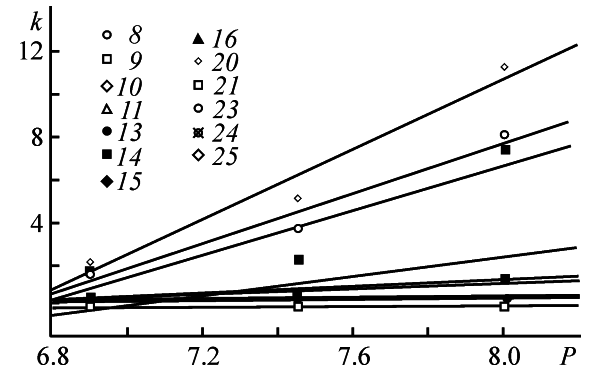


Fig. 3. Retention factor k of sulfonic acid azolides as a function of the eluent polarity P.

and P'_B are the polarities of solvents A and B, respectively. The eluting power in reversed-phase HPLC decreases and the retention on a stationary phase increases with increasing polarity. The dependence of the retention factors of the compounds in question on the eluent polarity is shown in Figs. 2 and 3. As seen from these figures, these dependences are linear. The dependence of the retention factors on the acetonitrile concentration is inverse. This is the case for all the examined compounds and eluent compositions.

Thus, the retention of azole derivatives under conditions of reversed-phase HPLC is determined by both structural features of the adsorbate and the type and composition of the eluent.

CONCLUSIONS

(1) The dependence of the retention factors of indole, imidazole, triazole, and tetrazole derivatives on the mobile phase composition is linear and can be described by Eqs. (1) and (2).

(2) The dependence of the retention parameters of the examined azoles on the concentration of the organic modifier is characterized by a phenomenon similar to the compensation effect of the entropy and enthalpy. The coordinates of the isoparametric point can be determined from the coefficients of equations of the corresponding dependences.

REFERENCES

1. Nametkin, S.S., *Geterotsiklicheskie soedineniya* (Heterocyclic Compounds), Moscow: Nauka, 1981, pp. 259–263.
2. Danaher, M., De Ruyck, H., Crooks, S.R., et al., *J. Chromatogr. B*, 2007, vol. 845, pp. 1–37.
3. Gilchrist, T.L., *Heterocyclic Chemistry*, London: Longman, 1992.
4. Baczek, T., Kaliszan, R., Novotna, K., and Jandera, P., *J. Chromatogr.*, 2005, vol. 1075, pp. 109–115.
5. Golovnya, R.V., Zhuravleva, I.L., and Sal'kova, M.A., *Zh. Anal. Khim.*, 1992, vol. 47, no. 7, pp. 1269–1274.
6. Golovnya, R.V. and Misharina, T.A., *Izv. Ross. Akad. Nauk*, 1996, no. 8, pp. 2033–2038.
7. Shatts, V.D. and Sakhartova, O.V., *Vysokoeffektivnaya zidkostnaya khromatografiya* (High-Performance Liquid Chromatography), Riga: Zinatne, 1988.
8. Sakodynskii, K.I., Brazhnikov, V.V., et al., *Analiticheskaya khromatografiya* (Analytical Chromatography), Moscow: Khimiya, 1993.
9. Espinosa, S., Bosch, E., and Roses, M., *J. Chromatogr. A.*, 2002, vol. 947, pp. 47–58.

10. Nikitas, P., Pappa-Louisi, A., and Agrafiotou, P., *J. Chromatogr. A*., 2002, vol. 946, pp. 9–32.
11. *Liquid Column Chromatography: A Survey of Modern Techniques and Applications*, Deyl, Zd., Macek, K., and Janak, J., Eds., Amsterdam: Elsevier, 1975.
12. Polyakova, Yu.L., Bulanova, A.V., Egorova, K.V., et al., *Izv. Ross. Akad. Nauk, Ser. Khim*., 2000, no. 8, pp. 1401–1404.
13. Solovova, N.V., Kurbatova, S.V., and Belousova, Z.P., *Zh. Fiz. Khim*., 2004, vol. 78, no. 1, pp. 91–95.
14. Kireev, V.A., *Metody prakticheskikh raschetov v termodinamike khimicheskikh reaktsii* (Methods of Practical Calculations in Thermodynamics of Chemical Reactions), Moscow: Khimiya, 1970.
15. Hildebrand, J.H. and Scott, R.L., *Solubility of Non-Electrolytes*, New York: Dower, 1964.
16. Snyder, L.R. and Kirkland, J.J., *Introduction to Modern Liquid Chromatography*, New York: Wiley, 1979.

ISSN 1070-4272, Russian Journal of Applied Chemistry, 2008, Vol. 81, No. 3, pp. 412–414. © Pleiades Publishing, Ltd., 2008.
Original Russian Text © V.P. Greben', I.G. Rodzik, 2008, published in Zhurnal Prikladnoi Khimii, 2008, Vol. 81, No. 3, pp. 425–427.

PHYSICOCHEMICAL STUDIES OF SYSTEMS AND PROCESSES

Difference in Transfer of Magnesium and Sodium Ions through Electrodialytic Membranes Modified with Chitosan

V. P. Greben' and I. G. Rodzik

Institute of Chemistry, Far-Eastern Branch, Russian Academy of Sciences, Vladivostok, Russia

Received April 4, 2007

Abstract—The difference in transfer of magnesium and sodium ions through electrodialytic cation-exchange membranes modified with chitosan was studied. The membranes were modified by electrodeposition of chitosan from solution on the membrane surface in the course of electrodialysis, preliminary sorption of chitosan on the membrane surface from aqueous chitosan hydrochloride, or application of a chitosan film to the dry membrane surface. The Mg^{2+}/Na^{+} selectivity of transfer through modified electrodialytic membranes was examined in relation to the current density.

DOI: 10.1134/S1070427208030129

It is known [1] that single-, double- and triple-charged cations can be separated by electrodialysis. The separation can be improved by surface modification with appropriate reagents of the electrodialytic cation-exchange membrane from the side contacting with the diluate. For example, in [2] we used poly(4-vinyl-*N*-propylpyridinium) bromide as modifier.

Chitosan, polysaccharide amino-2-deoxy-β-*D*-glucan, is prepared by deacetylation of chitin extracted from arthropoda shell. Chitosan macromolecules contain the NH_2 and OH functional groups. This compound is widely used in food and pharmaceutical industries and in medicine. Chitosan has ionic conductivity, in particular, with respect to chloride anions [4], i.e., it exhibits the properties of an anion-exchange membrane. Cross-linked strongly basic electrodialytic anion-exchange membranes for food industry can be prepared from alkylated chitosan [5].

Membranes based on chitosan have different permeability with respect to particular metal ions. It was reported in [6] that the diffusion permeability of metal ions through gel-like chitosan increases in the order $Cu^{2+} < Ni^{2+} < Zn^{2+} < Mn^{2+} < Pb^{2+} < Co^{2+} < Cd^{2+} < Ag^{+}$ [6]. For membranes based on combination of silk fibroin and chitosan, the order was as follows [7]: $Ni^{2+} < Cu^{2+} < Pb^{2+} < Cd^{2+} < Ca^{2+} < K^{+}$. Chitosan membranes can be used for treatment of aqueous solutions to remove Cr(III) [8] and Cr(VI) [9].

Presumably, in electrodialysis through a cation-exchange membrane coated with an anion-exchange chitosan layer from the diluate side, this layer as a positively charged electrostatic barrier will hinder the transmembrane transfer of single-charged cations to a lesser extent than that of double-charged cations.

In this study we examined the effect of modification of sulfonic cation-exchange heterogeneous membranes with chitosan on the selectivity of transmembrane electrodialytic transfer of Mg^{2+} relative to Na^{+}. The effect of the current density on the electrodialysis selectivity was also studied.

EXPERIMENTAL

Water-soluble chitosan hydrochloride was produced by Dal'khitosorb Limited Liability Company by treatment of chitosan with hydrochloric acid taken in an amount equivalent to the content of primary amino groups in chitosan. Chitosan was prepared by deacetylation of chitin (degree of deacetylation 85%) recovered from king crab shells. The chitosan molecular weight was 150 kDa.

The electrodialytic cell and procedures for electrodialysis and determination of chloride and magnesium ions in the diluate were identical to those reported in [10]. The separation of Mg^{2+} and Na^{+} in electrodialysis was characterized by the transference selectivity factor of Mg^{2+} relative to Na^{+} $P_{Na^+}^{Mg^{2+}}$:

$$P_{Na^+}^{Mg^{2+}} = \bar{t}^{Mg^{2+}} c_{Na^+}/(\bar{t}^{Na^+} c_{Mg^{2+}}), \quad (1)$$

where $\bar{t}^{Mg^{2+}}$ and $\bar{t}^{Na^+}$ are the transmembrane transference numbers of Mg^{2+} and Na^{+}, respectively; $c_{Mg^{2+}}$ and c_{Na^+}, magnesium and sodium concentration in the diluate.

The selectivity of transmembrane electrodialytic transfer of Mg^{2+} and Na^{+} was studied in a solution containing NaCl (0.25 N) and $MgCl_2$ (0.25 N). The

membranes tested were modified by (1) electrodeposition of chitosan from solution at the membrane surface, (2) sorption of chitosan from aqueous chitosan hydrochloride, and (3) application of chitosan film to dry cation-exchange membrane surface.

In method 1, chitosan hydrochloride was preliminarily added to the solution containing magnesium and sodium cations and then this solution was subjected to electrodialysis. Under these conditions, chitosan macromolecules are not transferred through the cation-exchange membrane and are deposited on its surface to form a film. In reference experiments, $P_{Na^+}^{Mg^{2+}}$ was determined in solutions containing no chitosan hydrochloride.

In method 2, cation-exchange membrane was kept for a certain time in aqueous chitosan hydrochloride of prescribed concentration. After this treatment, the membrane was washed with a small volume of distilled water and arranged in an electrodialytic cell, and elecrodialysis was carried out without addition of chitosan to the solution.

In method 3, a certain volume of aqueous chitosan hydrochloride (2.5%) was applied to the cation-exchange membrane surface, and the membrane was dried in air for 3–5 min and then finally dried at 50°C for 3 h. Then this membrane was kept in 1 N aqueous NaOH for 1.5 h to convert water-soluble chitosan hydrochloride into the form insoluble in alkaline and neutral media. After such treatment, the membrane was washed with distilled water to neutral reaction and arranged in an electrodialytic cell so that its modified surface contacted with the diluate.

In electrodialysis of an aqueous solution containing NaCl (0.25 N) and $MgCl_2$ (0.25 N) without chitosan, $P_{Na^+}^{Mg^{2+}}$ of sulfonic cation-exchange membrane was 1.19 at a current density of 1 A dm^{-2}. Figure 1 shows that, within the range of aqueous chitosan hydrochloride concentrations of 0–0.02 g l^{-1}, $P_{Na^+}^{Mg^{2+}}$ relatively steeply decreases with increasing chitosan hydrochloride concentration, but then the dependence becomes approximately linear. We believe that a decrease in $P_{Na^+}^{Mg^{2+}}$ and in $\bar{t}^{Mg^{2+}}$ with a simultaneous increase in $\bar{t}^{Na^+}$ with increasing chitosan hydrochloride concentration is caused by thickening of the chitosan film on the membrane surface with increasing chitosan hydrochloride concentration in the solution (Fig. 1).

Figure 2 shows that, in electrodialysis of solutions containing NaCl–$MgCl_2$ mixture and chitosan hydrochloride, an increase in the current density is accompanied by an increase in $\bar{t}^{Na^+}$ and a decrease in $\bar{t}^{Mg^{2+}}$.

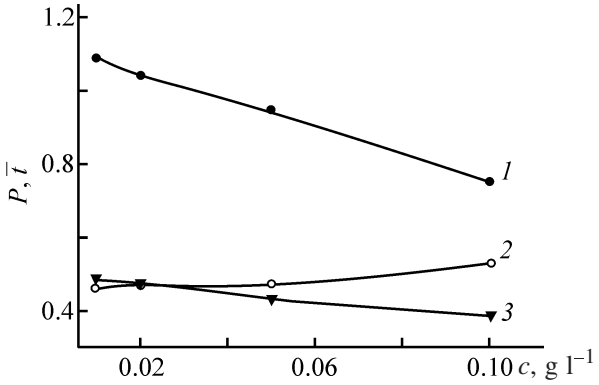


Fig. 1. Dependences of the (*1*) transference selectivity factor $P_{Na^+}^{Mg^{2+}}$ of Mg^{2+} relative to Na^+ in electrodialysis through cation-exchange membrane, (*2*) Na^+ transference number $\bar{t}^{Na^+}$, and (*3*) Mg^{2+} transference number $\bar{t}^{Mg^{2+}}$ on the chitosan hydrochloride concentration c in the diluate at a current density of 1 A dm^{-2}.

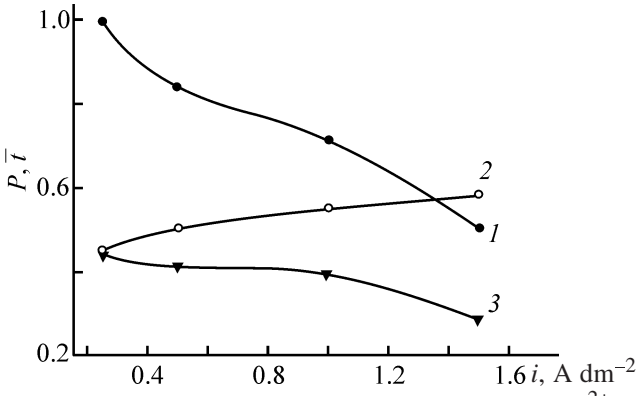


Fig. 2. Influence of the current density i on (*1*) $P_{Na^+}^{Mg^{2+}}$, (*2*) $\bar{t}^{Na^+}$, and (*3*) $\bar{t}^{Mg^{2+}}$ in electrodialysis of a solution containing NaCl (0.25 N), $MgCl_2$ (0.25 N), and chitosan hydrochloride (0.1 g l^{-1}) through cation-exchange membrane.

As a result, with increasing current density, $P_{Na^+}^{Mg^{2+}}$ decreases. We believe that these effects are caused by an increase in the chitosan flow toward the membrane surface and, therefore, by formation of thicker and denser chitosan films with an increase in the current density. Under these conditions, the separation of Mg^{2+} from Na^+ increases, whereas $P_{Na^+}^{Mg^{2+}}$ decreases.

As seen from Fig. 3, for cation-exchange membranes modified by their keeping in solution of chitosan hydrochloride the Na^+ and Mg^{2+} transference numbers change and $P_{Na^+}^{Mg^{2+}}$ decreases. These experiments show that the sorption of chitosan on the cation-exchange membrane surface is slow. For example, in keeping cation-exchange membranes in aqueous solution of chitosan hydrochloride (15 g l^{-1}) for 48 and 144 h, $P_{Na^+}^{Mg^{2+}}$ decreases from 1.19 to approximately

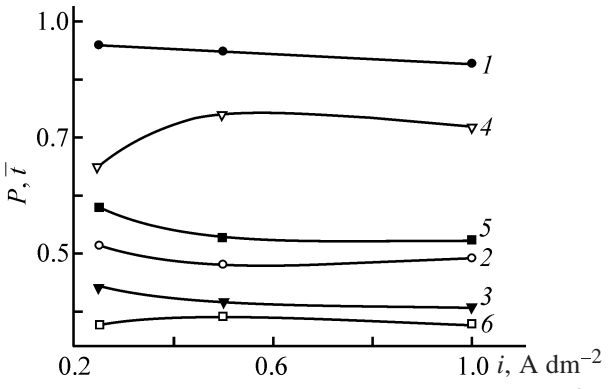


Fig. 3. Influence of the current density i on (*1, 4*) $P_{Na^+}^{Mg^{2+}}$, (*2, 5*) $\bar{t}^{Na^+}$, and (*3, 6*) $\bar{t}^{Mg^{2+}}$ in electrodialysis through a cation-exchange membrane preliminarily kept in solution of chitosan hydrochloride (15 g l^{-1}) for (*1–3*) 48 and (*4–6*) 144 h.

0.85 and 0.7, respectively (Fig. 3). As opposed to membranes modified with chitosan added to the diluate directly in the course of electrodialysis, for membranes preliminarily modified by sorption of chitosan from its solutions, $P_{Na^+}^{Mg^{2+}}$ depending on sorption time either slightly decreases (Fig. 3, curve *1*) or increases (Fig. 3, curve *4*) with increasing current density. These results are consistent with the above hypothesis that, in introduction of chitosan hydrochloride directly into the solution in the course of electrodyalysis, an increase in the current density leads to an increase in the chitosan flow toward the membrane surface; as a result, thicker and denser chitosan films are formed on the membrane surface. This factor improves the Mg^{2+}/Na^+ separation with the membrane.

For a cation-exchange membrane modified by the third method (chitosan hydrochloride film applied to membrane surface), with increasing membrane thickness, $\bar{t}^{Na^+}$ increases, whereas $\bar{t}^{Mg^{2+}}$ decreases and, as a result, $P_{Na^+}^{Mg^{2+}}$ decreases. In these experiments, the dependence of $P_{Na^+}^{Mg^{2+}}$, $\bar{t}^{Mg^{2+}}$, and $\bar{t}^{Na^+}$ on the film thickness (5–20 μm) was virtually identical to that shown in Fig. 1 for the chitosan concentration ranging from 0.01 to 0.1 g l^{-1}. These results are consistent with our hypothesis that, in electrodeposition of chitosan on the membrane surface, the chitosan film thickness increases with increasing chitosan concentration in the solution.

It should be noted in conclusion that, in analysis of the selectivity of Na^+ and Mg^{2+} transfer through membranes modified with chitosan, not only the electrostatic barrier effect of the chitosan film, but also the difference in hydration of these cations [10] should be taking into account.

CONCLUSIONS

(1) The Mg^{2+}/Na^+ selectivity factor $P_{Na^+}^{Mg^{2+}}$ of transfer through cation-exchange membranes in electrodialysis can be decreased by modification of the membrane with chitosan hydrochloride by the following techniques: electrodeposition of chitosan on the membrane surface, sorption of chitosan on the membrane surface from aqueous solution, and application of a chitosan film to the membrane surface.

(2) Increase in both the chitosan hydrochloride concentration in the diluate and the current density lead to a decrease in $P_{Na^+}^{Mg^{2+}}$ due to an increase in the chitosan film thickness. After prolonged keeping of the cation-exchange membrane in a solution of chitosan hydrochloride, $P_{Na^+}^{Mg^{2+}}$ increases with increasing current density. With a cation-exchange membrane modified by application of chitosan film to the dry membrane surface, $P_{Na^+}^{Mg^{2+}}$ decreases with increasing film thickness.

ACKNOWLEDGMENTS

The authors are grateful to D.V. Chervonetskii for submitting chitosan hydrochloride sample (flocculant Khitoflok-4).

REFERENCES

1. Sadrzadeh, M., Razmi, A., and Mohammadi, T., *Desalination*, 2007, vol. 205, nos. 1–3, pp. 53–61.
2. Greben', V.P. and Rodzik, I.G., *Zh. Prikl. Khim.*, 2006, vol. 79, no. 3, pp. 468–471.
3. Wan, Y., Greber, K.A.M., Peppley, B., and Bui, V.T., *Polymer*, 2003, vol. 44, no. 4. pp. 1057–1065.
4. Uragami, T., Yoshida, F., and Sugihara, M., *Makromol. Chem., Rapid Commun.*, 2003, vol. 4, no. 2, pp. 99–102.
5. Uragami, T., Kato, T., Nagayasu, H., and Yura I.,, *Carbohydr. Polym.*, 1993, vol. 21, no. 4, pp. 289–293.
6. Krajevska, B., *React. Funct. Polym.*, 2001, vol. 47, no. 1, pp. 37–47.
7. Chun-Hui Du, Bao-Ku Zhu, Jian-Yong Chen, and You-Yi Xu, *Polym. Int.*, 2006, vol. 55, no. 4, pp. 377–382.
8. Pietrelli, L. and Liu, X.R., *Ann. Chim.*, 2004, vol. 94, nos. 5–6, pp. 389–398.
9. Modrzejewska, Z. and Kaminski, W., *Ind. Eng. Chem. Res.*, 1999, vol. 38, no. 12, pp. 4946–4950.
10. Greben', V.P. and Rodzik, I.G., *Elektrokhimiya*, 2005, vol. 41, no. 8, pp. 997–1000.

ISSN 1070-4272, Russian Journal of Applied Chemistry, 2008, Vol. 81, No. 3, pp. 415–419. © Pleiades Publishing, Ltd., 2008.
Original Russian Text © T.E. Nikiforova, V.A. Kozlov, 2008, published in Zhurnal Prikladnoi Khimii, 2008, Vol. 81, No. 3, pp. 428–433.

PHYSICOCHEMICAL STUDIES OF SYSTEMS AND PROCESSES

Sorption of Copper(II) Ions with Soybean Crush Modified with Sodium Monochloroacetate

T. E. Nikiforova and V. A. Kozlov

Ivanovo State University of Chemical Technology, Ivanovo, Russia

Received April 9, 2007

Abstract—The effect of chemical modification on sorption properties of soybean crush with respect to copper(II) ions was examined. The optimal parameters of soybean crush treatment with sodium monochloroacetate to ensure the maximal sorption capacity of the sorbent were determined.

DOI: 10.1134/S1070427208030130

Various vegetable products can be promising sorbents for recovery of heavy metal ions from aqueous solutions, since they are cheap and renewable raw materials [1, 2]. The main drawback of such sorbents is their comparatively low sorption capacity. Therefore, modification of unconventional materials containing protein and cellulose components to increase their sorption capacity is an important step in preparation of new sorbents. Various methods of modifying cellulose-containing polymers (including mechanical, physical, chemical, mechanochemical, and physicochemical methods) were suggested [3–9]. The main goal of such modification is to increase the internal adsorption surface area and accessibility of the active groups, and also to form new sorption-active groups on the sorbent surface.

The chemical modification of secondary products from treatment of oil-bearing crop seeds (sunflower, flax, mustard, soybean, rape), formed in a large amount (>40%) in the course of vegetable oil making, shows much promise.

In spite of available data on using soybean crush [10–14], the possible presence in it of certain substances dangerous for human and animal health excludes its use as food and fodder without additional treatment. Therefore, utilization of secondary products from oil crop treatment is of interest in view of the development of resource-saving processes. One of possible directions of soybean crush and mill cake use is the sorption treatment of aqueous solutions to remove heavy metal ions. An important requirement to such sorbents is that they should not be the source of secondary pollution for media to be purified.

The goal of this study is to prepare a new efficient sorbent based on chemically modified soybean crush containing chelating sorption centers for recovery of copper(II) ions from aqueous solutions.

EXPERIMENTAL

We used soybean crush of the following composition (wt %): crude protein 43.8, moisture 11.5, ashes 6.1, crude cellulose 5.6, fat 1.6, phosphorus 0.75, calcium 0.24, total acidity 8.8, no toxicity [14], and the following chemicals: $CH_2ClCOONa$, NaOH or Na_2CO_3, HCl or H_2SO_4, and $CuSO_4 \cdot 5H_2O$ (all chemically pure grade).

Initially soybean crush was ground and bolted through sieves with mesh diameters of 1.0 mm to separate coarse particles and 0.8 mm to separate fine particles. Thus, the size of sorbent particles used in the experiment was 0.8–1.0 mm. Samples were air-dry; their moisture content did not exceed 14%.

Sorption of copper(II) ions was studied under static conditions from aqueous solutions of copper sulfate with stirring and thermostating at 293 K. The sorption kinetics was investigated by the method of limited solution volume. To obtain the kinetic curves of sorption, samples (m = 0.1 g) of the sorbent were introduced into test tubes, V = 10 ml of copper sulfate solution was added into each, and the mixtures were stored for a period from 30 min to 24 h. The initial copper ion concentration c_0 was 1.5×10^{-4} M. After definite periods of time, the solution was separated from the precipitate by filtration and the current copper concentration c_τ in it was determined by atomic absorption spectroscopy on a Saturn spectrometer.

Determination of optimal parameters of sorbent modification

Sample no.	Solvent/sorbent ratio	T, °C	τ, min	pH_{in}	pH_{fin}	Concentration, % of sorbent weight		α, %
						$ClCH_2COONa$	Na_2CO_3	
1	1	100	60	8	9	1.0	0.5	77
2	5	100	60	10	8	1.0	1.0	80
3	5	100	60	8.5	8	10	5	87
4	5	100	60	8.5	8	20	10	89
5	5	100	90	9	7	5	2.5	91
6	5	100	90	8.5	6.5	10	5	97
7	5	100	90	8.5	6	10	5	98
8	5	100	90	8.5	5.5	20	10	98
9	Unmodified soybean crush							75

The sorption capacity A_τ of the sorbent at instant of time τ was calculated by the formula

$$A_\tau = (c_0 - c_\tau)V/m.$$

When the equilibrium was attained, the metal ion concentration c_{eq} was determined and the equilibrium sorption capacity A_{eq} of the sorbent was calculated by the formula

$$A_{eq} = (c_0 - c_{eq})V/m.$$

The degree of metal ion recovery was determined as follows:

$$\alpha_{eq} = (c_0 - c_{eq}) \times 100/c_0.$$

To obtain sorption isotherms, 0.1-g portions of soybean crush were introduced into test tubes, and 10 ml of copper sulfate solutions with diffferent initial concentrations (10, 50, 100, 200, 250, and 500 mg l^{-1}) were added. The resulting mixtures were kept to attain the equilibrium. Then, the solution was separated by filtration, and the residual metal ion concentration in solution was determined.

The IR reflection spectra of the initial and modified soybean crush samples were recorded on an Avatar 360 FT-IR E.S.P. IR Fourier spectrometer within the 400–4000 cm^{-1} range. The error of determination of the sorption capacity did not exceed 10%.

Modification of soybean crush was performed in aqueous solution of sodium monochloroacetate. The following parameters were varied: time and temperature of treatment, solution/sorbent ratio, initial and final pH of the modifying solution, and concentration of the modifying agent.

As a result, eight samples of modified soybean crush were prepared. These samples were tested for sorption ability (characterized by sorption capacity and degree of recovery). The results are listed in the table. The varied parameters affect the modification of soybean crush differently. The most important factors are concentration of sodium monochloroacetate and pH. The influence of the concentration of the modifying agent is probably associated with the amount of modified sorption-active groups or polydentate sorption centers. The sorption ability of the sorbent increases with an increase in the number of such centers. The effect of pH of the resulting solution after modification is associated with the isoelectric point (IEP) of the protein component of soybean crush. It is known that the solubility of protein is minimal in IEP. Hence, the final pH value of the modifying solution should be taken so as to ensure as low amount of protein in the solution before filtration as possible. Usually pH in IEP is within the range 4–6.5 [15]. Proteins are readily precipitated at pH in IEP, because the total charge of the protein molecule is equal to zero and there is no electrostatic repulsion between the neighboring molecules.

Analysis of the experimental data shows that samples 6–8 have the best sorption properties.

Thus, modification of soybean crush was optimal when it was treated with an aqueous solution containing $CH_2ClCOONa$ (10–20% of sorbent weight) at pH 8–10, solution/sorbent ratio of 5–50 for 30–60 min on a boiling water bath. Then the acid was added to pH 5.5–6.5. The time of contact of the modified sorbent with the solution was 0.5–1.5 h at solution/sorbent ratio of 50–200.

In contrast to unprocessed soybean crush, the

modified crush does not impair the quality of the purified (to remove heavy metal ions) water. Upon modification, filtration of purified water to remove the sorbent is accelerated, and water remains transparent and preserves the initial color.

The main characteristics of the sorbent are the sorption capacity and time of attainment of the sorption equilibrium. To find the time of equilibrium attainment with aqueous solution of copper(II) sulfate, we measured the kinetic curves of sorption for the initial and modified soybean crush samples.

As seen from Fig. 1, the equilibrium is attained slowly, in 20–22 h, and the half-sorption time is 5 h irrespective of the sorbent. The equilibrium sorption capacities of the initial and modified soybean crush samples with respect to copper(II) amount to 1.8 and 15.4×10^{-3} mol kg^{-1}, respectively (degree of recovery 78 and 98%). Thus, substantial (by 23%) increase in copper(II) recovery by modified soybean crush is observed.

To determine the parameters of the sorption capacity of the initial and modified soybean crush samples, we measured isotherms of copper(II) sorption from $CuSO_4$ solutions (Fig. 2).

The data obtained can be described by Langmuir equation of absorption isotherm

$$A = A_\infty K_0 c_{eq}/(Kc_{eq} + 1),$$

where K is the concentration constant of the sorption equilibrium, which characterizes the intensity of the sorption process (l mol^{-1}).

Linearization of the sorption isotherm by the equation

$$1/A = 1/A_\infty + 1/A_\infty Kc_{eq}$$

allows graphic determination of the limiting sorption A_∞ for both the initial and modified soybean crush samples, which amounts to 0.7 and 0.8 mol kg^{-1}, respectively.

Increase in the sorption capacity of the modified sorbent as compared to the initial sorbent can be accounted for by the fact that, in the course of treatment of soybean crush with sodium monochloroacetate, polydentate sorption centers involving protein amino acids and acetate groups of the modifying agent are formed. Among amino acids composing soybean crush (valine, leucine, isoleucine, serine, threonine, cysteine, methionine, lysine, arginine, aspartic acid, glutamic acid, phenylalanine, tyrosine, histidine, proline, alanine), arginine (3%), lysine (2.5%), and cysteine (0.6%) should be noted. In addition to α-amino groups participating in formation of peptide (amide) bonds in the course of assembling peptide molecules, they contain additional functional groups:

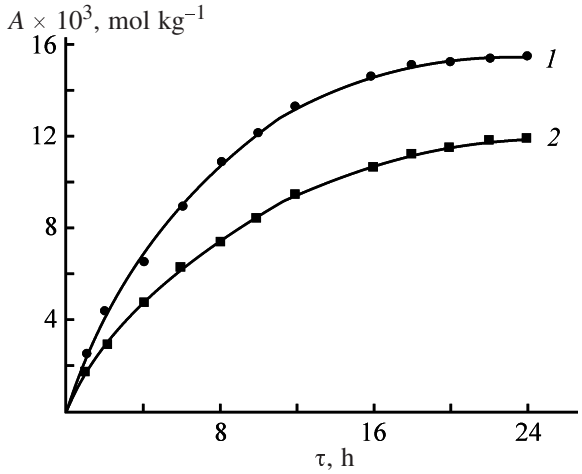


Fig. 1. Kinetic curves of sorption of copper(II) ions from $CuSO_4$ aqueous solutions with (*1*) modified and (*2*) unmodified soybean cake. (*A*) Sorption capacity and (τ) time of sorption.

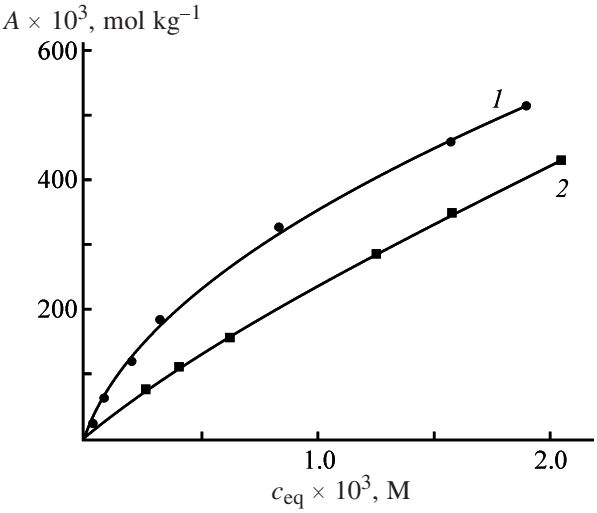
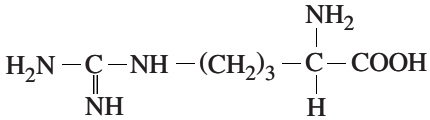
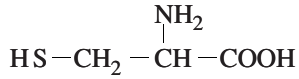


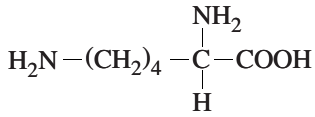
Fig. 2. Isotherms of sorption of copper(II) ions from $CuSO_4$ aqueous solutions with (*1*) modified and (*2*) unmodified soybean crush. (*A*) Sorption capacity and (c_{eq}) equilibrium copper(II) concentration.



Arginine

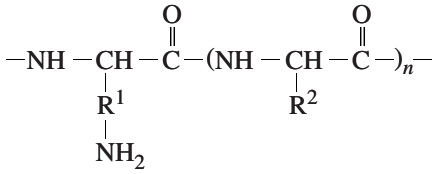


Cysteine

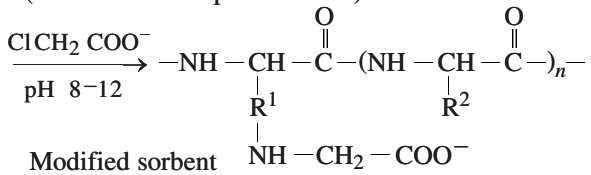


Lysine

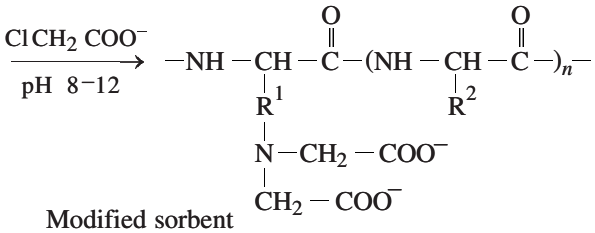
Probably, just the free functional groups of arginine, lysine, and cysteine are the first to be subjected to modification with sodium monochloroacetate. In the process, monodentate sorption centers transform into polydentate chelating centers of sorption, e.g., –NH–CH_2–COOH and –N–(CH_2–COOH)$_2$:



Initial (unmodified) sorbent
(monodentate sorption centers)

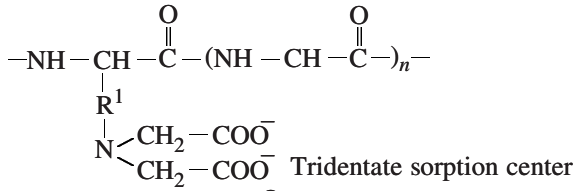


Modified sorbent
(bidentate sorption centers)

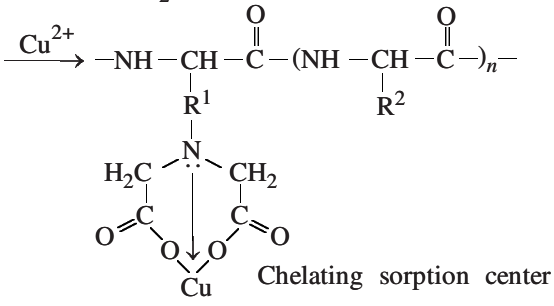


Modified sorbent
(tridentate sorption centers)

Sorption results in formation of very stable five-membered chelate rings capable to strongly retain copper(II) ions in the sorbent phase, e.g.:



Tridentate sorption center



Chelating sorption center

The strength of copper(II) binding in the complex increases with increasing number of polydentate centers in the ligand [16].

To confirm the above suggestion, we recorded the IR spectra of the initial and modified soybean crush samples (Fig. 3).

Soybean crush is a mixture of polymers (mainly proteins and cellulose) containing various functional donor groups (carboxy, hydroxy, amide, and amino groups). In the IR spectrum of unmodified soybean crush, strong absorption bands belonging to stretching vibrations of the N–H, C–N, C=O, and O–H bonds are observed. In the range 3600–3300 cm^{-1}, there are strong bands of stretching vibrations of O–H groups and N–H bonds of amino and amide groups. Bands at 3500 and 3400 cm^{-1} belong to antisymmetric and symmetric stretching vibrations of N–H group in amines, respectively. Weak bands at 3350–3310 cm^{-1} are due to N–H stretching vibrations in amides. Absorption at 1650 cm^{-1} belongs to stretching vibrations of carbonyl C=O groups in peptide bonds of proteins (amide I band). In the spectrum of modified soybean crush, splitting of this band becomes less pronounced. Bands at 1640–1560 cm^{-1} belong to bending vibrations of N–H bonds in amides. In this region, the initial soybean crush has a weak doublet, which disappears in the spectrum of the modified soybean crush. In the range 1580–1490 cm^{-1}, there are weak bands of bending vibrations of N–H groups in amides (amide II band). Splitting of the band at 1538–1539 cm^{-1} in the spectrum of the modified sorbent is less weaker than that in the spectrum of the initial cake. In the range 1300–1030 cm^{-1}, there are bending vibrations of O–H groups, bending and stretching vibrations of C–O groups in acids, and stretching vibrations of C–N groups in amines and amides (amide III band) appear. This region is characterized by bands at 1245 and 1055 cm^{-1} in the spectrum of the initial soybean crush. In the spectrum of the modified crush, these bands are shifted to 1241 and 1065 cm^{-1}, respectively. In the range 900–650 cm^{-1}, bending vibrations of N–H groups in amides appear [17]. In this range, a broad band is observed in the spectra of both initial and modified soybean crush samples. The changes observed are associated with the change of the substrate structure due to interaction of free amino groups or probably amide groups of protein molecules of soybean crush with modifying agent, sodium monochloroacetate, and formation of new functional groups that are polydentate sorption centers.

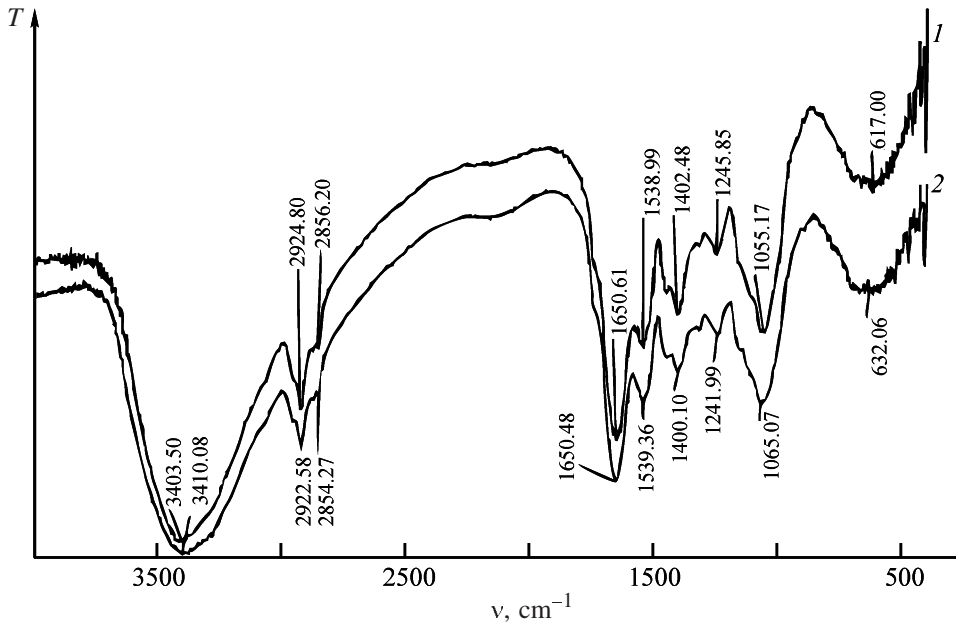


Fig. 3. IR spectra of (*1*) unmodified and (*2*) modified soybean crush. (*T*) Transmittance and (ν) wavenumber.

CONCLUSIONS

(1) Soybean crush was subjected to chemical modification by treatment with aqueous solution of sodium monochloroacetate to obtain a new efficient sorbent which recovers copper(II) from aqueous solutions through chelating sorption centers formed. The optimal parameters of modification were determined.

(2) Sorption properties of the initial and modified soybean crush with respect to copper(II) ions were studied. The treatment of soybean crush with sodium monochloroacetate increases the recovery of copper(II) ions by 23%, and the degree of recovery reaches 98%.

(3) IR spectra show that the substrate structure undergoes changes upon chemical modification, with the formation of new bonds and functional groups acting as polydentate sorption centers.

REFERENCES

1. Bagrovskaya, N.A., Nikiforova, T.E., Kozlov, V.A., and Lilin, S.A., *Izv. Vyssh. Uchebn. Zaved., Khim. Khim. Tekhnol.*, 2002, vol. 45, no. 4, pp. 131–133.
2. Michado, R., Carvalho, J.R., and Correia, M.J.N., *J. Chem. Technol. Biotechnol.*, 2002, vol. 77, no. 12, pp. 1340–1348.
3. Stavitskaya, S.S., Mironyuk, T.I., Kartel', N.T., and Strelko, V.V., *Zh. Prikl. Khim.*, 2001, vol. 74, no. 4, pp. 575–578.
4. USSR Inventor's Certificate no. 1 696 399.
5. Shukla, S.R. and Sakhardande, V.D., *J. Appl. Polym. Sci.*, 1990, vol. 41, nos. 11–12, pp. 2655–2663.
6. Toshihiko, S., Kazuhiro, K., Hiroti, K., and Yasuo, O., *J. Soc. Fiber Sci. Technol.*, 1983, vol. 39, no. 12, pp. 519–524.
7. RF Patent 2 217 231.
8. RF Patent 2 217 389.
9. RF Patent 2 258 560.
10. *Vtorichnye material'nye resursy pishchevoi promyshlennosti: obrazovanie i ispol'zovanie: Spravochnik* (Secondary Material Resources of Food Industry: Formation and Use: Handbook), Moscow: Ekonomika, 1984.
11. Tolkachev, O.N. and Zhuchenko, A.A., *Khim.-Farm. Zh.*, 2000, vol. 34, no. 7, p. 23.
12. Tsybina, T.A. et al., *Biokhimiya*, 2001, vol. 66, no. 9, pp. 1157–1164.
13. Nechaev, A.P., Traubenberg, S.E., Kochetkova, A.A., et al., *Pishchevaya khimiya* (Food Chemistry), St. Petersburg: GIORD, 2004, 3rd ed.
14. *GOST* (State Standard) *12 220–96: Soybean Crush Fodder, Toasted: Technical Specifications*.
15. Stroev, A.E., *Biologicheskaya khimiya* (Biological Chemistry), Moscow: Vysshaya Shkola, 1986.
16. Umland, F., Janssen, A., Thierig, D., and Wünsch, G., *Theorie und praktische Anwendung von Komplexbildern*, Frankfurt am Main: Akademische, 1971.
17. Gordon, A.J. and Ford, R.A., *The Chemist's Companion. A Handbook of Practical Data, Techniques, and References*, New York: Wiley 1972.

ISSN 1070-4272, Russian Journal of Applied Chemistry, 2008, Vol. 81, No. 3, pp. 420–422. © Pleiades Publishing, Ltd., 2008.
Original Russian Text © S.S. Ermakov, A.A. Sheremet, L.N. Moskvin, 2008, published in Zhurnal Prikladnoi Khimii, 2008, Vol. 81, No. 3, pp. 434–436.

APPLIED ELECTROCHEMISTRY AND CORROSION PROTECTION OF METALS

Determination of Zinc in Aqueous Solutions by a Combined No-Standard Electrochemical Method with Preliminary Electrolytic Separation of Copper

S. S. Ermakov, A. A. Sheremet, and L. N. Moskvin

St. Petersburg State University, St. Petersburg, Russia

Received September 20, 2007

Abstract—A combined method for no-standard determination of zinc in aqueous solutions (calibration of the device against standard solutions or use of standard additions is not required) is suggested. The method is based on principles of stripping voltammetry and potentiostatic coulometry.

DOI: 10.1134/S1070427208030142

Stripping voltammetry (SVA) is a commonly used method for determination of copper, cadmium, lead, and zinc in various aqueous media and food products. One of drawbacks of the method is the necessity of calibration against reference samples, i.e., it requires time-consuming construction of calibration plots.

Several versions of no-standard electrochemical methods without references, allowing determination of metals in aqueous solution, have been suggested [1–5]. Companys et al. [1, 2] used the potentiometric analytical procedure: they deposited on the surface of an electrode by pre-electrolysis an amalgam with a known concentration of a metal being determined and then used the quasi-equilibrium potential of the $M(Hg)/M_e^{n+}$ system to calculate the concentration of a substance being analyzed in solution. A stripping chronopotentiometric version of the no-standard electrochemical method has been suggested [3]. This method is based on multiple-cycle dissolution of a metal from an amalgam obtained in the pre-electrolysis stage and subsequent finding of a charge Q_∞ corresponding to complete deposition of the substance from solution. A technique termed dynamic coulometry was suggested in [4, 5]. This method is based on multiple-cycle scanning of the potential. A combined electrochemical method based on principles of SVA and potentiostatic coulometry was developed in [6–8]. The possibility of using it for the determination of lead ions [6], of copper and cadmium ions in the absence and in the presence of lead ions [7], and of mercury ions [8] was demonstrated previously. One of the main drawbacks of SVA in the case of simultaneous presence of ions of several metals is manifestation of the effects associated with formation of intermetallic compounds (IMC) in the amalgam of the working electrode. This phenomenon results in the shift of the peaks of the analyzed substances or leads to the appearance of new peaks [8].

This study is concerned with the development of a combined no-standard electrochemical method for zinc determination in the presence of copper, which includes preliminary electrolytic separation of copper to prevent formation of IMCs.

The stripping-voltammetric measurements were performed on a PU-1 polarograph (ZIP, Gomel, Belarus) with an AKV-07 sensor (Akvilon NPKF, Moscow) and on an AKV-07MK voltammetric analyzer (Akvilon) with Polar-4.1 software in the dc and ac modes. Solutions with various concentrations of zinc and copper ions were prepared from solutions of 1 g l^{-1} state reference samples (GSO 6742 and GSO 7255, respectively) using chemicals of chemically pure or analytically pure grade and double-distilled water. The measurements were carried out on a mercury–graphite film electrode rotating at a speed of 1000 rpm in the accumulation stage. A solution of composition (M) 1×10^{-4} $Hg(NO_3)_2$ + 5×10^{-2} HCl + 1×10^{-4} HNO_3 was used as supporting electrolyte. The pre-electrolysis in SVA measurements was performed at a potential of about –1.3 V, with a silver chloride reference electrode. The design of the electrochemical cell and electrodes has been described previously [6, 7]. To satisfy the conditions of complete dissolution of the metal from the amalgam, slow (2–5 mV s^{-1}) potential sweep rates were used [6].

Results of determination of zinc ions by a combined no-standard electrochemical method

Measurement no.	Introduced, M	Q_∞, μC		Found, M
		calculated	experimental	
1	1.0×10^{-7}	38.6	37.6/38.4*	$9.74 \times 10^{-8}/9.95 \times 10^{-8}$
2			39.0/36.8	$1.01 \times 10^{-7}/9.53 \times 10^{-8}$
3			41.3/36.4	$1.07 \times 10^{-7}/9.43 \times 10^{-8}$
Average			$39.9 \pm 8.0/37.2 \pm 2.3$	$(1.0 \pm 0.1) \times 10^{-7}/(9.6 \pm 0.4) \times 10^{-8}$

* After preliminary electrolytic separation of copper.

The rate at which zinc concentration varies with the electrolysis time was studied by the method used previously for lead [6] and for copper and cadmium [7]. The results of the measurements are plotted in Fig. 1. It can be seen that the $\log(c/c^0)$ vs. t plot is linear, which agrees well with the equation $\log(c/c^0) = -kt$, where c/c^0 is the ratio of current to initial concentration and k, coulometric constant. The dependence of the normalized zinc concentration on the solution volume at a constant accumulation time was determined similarly. As seen from Fig. 2, the plot in the coordinates $\log(c/c^0)$–$(-1/V)$ is linear. This agrees with the known dependence of the coulometric constant k on the solution volume V [9]:

$$k = DS/V\delta,$$

where D is the diffusion coefficient; S, electrode area; and δ, thickness of the diffusion layer.

The data obtained show that the processes occurring in an electrochemical cell in the course of successive electrolysis agree with the relationships of potentiostatic coulometry and, correspondingly, indicate that the methodic principles of the combined no-standard method can be applied to zinc determination in solution. The results of its determination at accumulation times t_1, t_2, and t_3 (240, 360, and 480 s, respectively) are presented in Table 1.

The possibility of zinc determination with preliminary electrolytic separation of copper was studied in a solution containing copper and zinc at a potential of –0.35 V (solution volume 5 ml). Under these conditions, copper is deposited at the electrode, whereas zinc remains in the solution. Then, the cathodic copper deposit was dissolved in another cell to clean the electrode.

As known, 99% of a substance is deposited within 12.5 min of electrolysis at intense agitation [9], with 70% being deposited within 8 min. Thus, simple calculation shows that, if copper is in a threefold excess with respect to zinc, then after 8 min of electrolysis a concentration ratio of less than 1 : 1 is obtained. At this ratio, IMCs practically are not formed [10]. At the same time, in natural water zinc is always present in larger amounts than copper, and the time of copper deposition can be made shorter [10].

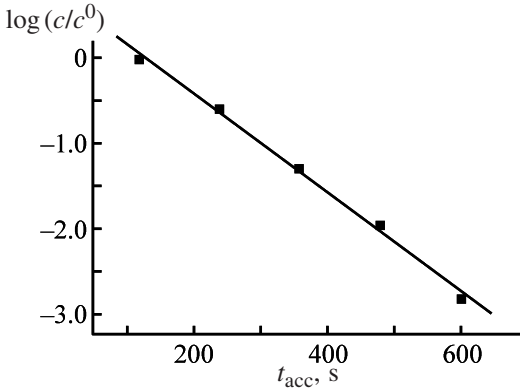


Fig. 1. Dependence of the logarithm of the normalized concentration of zinc ions, $\log(c/c^0)$, on the electrolysis duration t_{acc}.

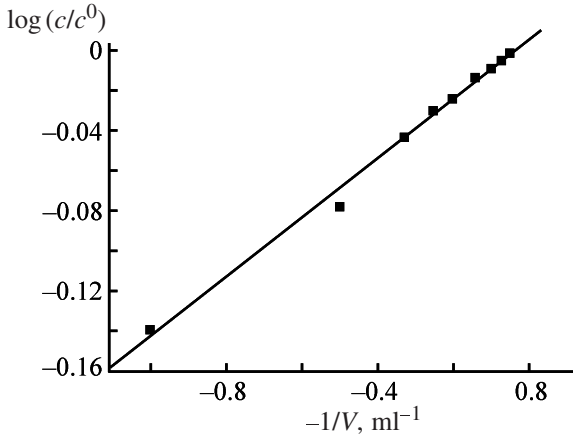


Fig. 2. Dependence of the logarithm of the normalized concentration of zinc ions, $\log(c/c^0)$, on the volume of a solution being analyzed V. Accumulation time t_{acc} = 5 min, $c^0_{Zn} = 5 \times 10^{-8}$ M.

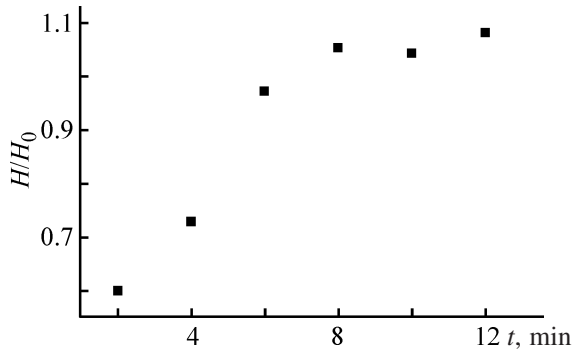


Fig. 3. Relative height of the zinc ionization peaks, H/H_0, vs. the time of electrolytical copper recovery t. Solution volume V = 5 ml, $c^0_{Cu} = c^0_{Zn} = 5 \times 10^{-8}$ M. H and H_0 the heights of the zinc ionization peaks with and without copper ions, respectively.

The effect of copper on the zinc analytical signal was studied by measuring the height of the zinc peak at various times of the electrolytic copper recovery (Fig. 3) in the solutions with equal initial concentrations of copper(II) and zinc(II). The data of Fig. 3 show that, after 8 min of electrolysis, the height of the zinc peak is a constant value equal to the analytical signal in a solution free of copper ions.

To examine the possibility of determining zinc and copper in the case of their simultaneous presence in solution by the no-standard electrochemical method, we measured solutions containing 1×10^{-7} M zinc and copper ions. The volume of the electrochemical cell was 2 ml, and the accumulation potential, –1.3 V. The total amount of electricity was calculated by the Mates formula. The electrolytic deposition of copper was performed for 8 min with subsequent dissolution in another cell (20 ml). Then, the voltammograms were recorded and the amount of electricity and the concentrations were calculated in accordance with the principles of a combined no-standard electrochemical method. The results are presented in the table. As can be seen, after electrolytic deposition of copper, the combined no-standard electrochemical method of zinc determination gives satisfactory results.

CONCLUSIONS

(1) A combined no-standard method for determination of zinc is convenient for automated analysis of process solutions and wastewater from electroplating and hydrometallurgical shops.

(2) For zinc determination in the presence of copper, it was suggested to electrolytically separate copper ions prior to analysis, to prevent formation of intermetallic compounds.

REFERENCES

1. Galceran, J., Companys, E., Puy, J., et al., *J. Electroanal. Chem.*, 2004, vol. 566, pp. 95–109.
2. Companys, E., Cecilia, J., Codina, G., et al., *J. Electroanal. Chem.*, 2005, vol. 576, pp. 21–32.
3. US Patent 5 891 322.
4. Sokolkov, S.V. and Zagorodnyuk, P.N., *Zh. Ross. Khim. O–va. im. D.I. Mendeleeva*, 2001, vol. 45, pp. 78–82.
5. RF Patent 2 199 734.
6. Ermakov, S.S., Chekmeneva, E.N., and Moskvin, L.N., *Zh. Anal. Khim.*, 2007, vol. 62, no. 1, pp. 89–94.
7. Sheremet, A.A., and Ermakov, S.S., *Zh. Prikl. Khim.*, 2006, vol. 79, no. 12, pp. 1970–1974.
8. Averyaskina, E.O, and Ermakov, S.S., *Nauchn. Priborostr.*, 2006, vol. 16, no. 4, pp. 97–101.
9. Budnikov, G.K., Maistrenko, V.N., and Vyaselov, M.P., *Osnovy sovremennogo elektrokhimicheskogo analiza* (Fundamentals of Modern Electrochemical Analysis), Moscow: Mir, 2003.
10. Brainina, Kh.Z., Neiman, E.Ya., and Slepushkin, V.V., *Inversionnye elektroanaliticheskie metody* (Stripping Electroanalytical Methods), Moscow: Khimiya, 1983.

ISSN 1070-4272, Russian Journal of Applied Chemistry, 2008, Vol. 81, No. 3, pp. 423–427. © Pleiades Publishing, Ltd., 2008.
Original Russian Text © G.A. Kolyagin, V.L. Kornienko, 2008, published in Zhurnal Prikladnoi Khimii, 2008, Vol. 81, No. 3, pp. 437–441.

APPLIED ELECTROCHEMISTRY AND CORROSION PROTECTION OF METALS

Electrochemical Reduction of Oxygen in Gas-Diffusion Electrodes Based on Expanded Natural Graphite

G. A. Kolyagin and V. L. Kornienko

Institute of Chemistry and Chemical Technology, Siberian Branch, Russian Academy of Sciences, Krasnoyarsk, Russia

Received May 17, 2007

Abstract—Electroreduction of oxygen in gas-diffusion hydrophobized porous electrodes containing 8–10 wt % fluoroplastic, made of expanded natural graphite and acetylene black, in acidic (pH 0.6) and alkaline electrolytes was studied.

DOI: 10.1134/S1070427208030154

Expanded natural graphite (ENG) has been extensively studied, in particular, with the aim of applying it to various electrochemical systems [1]. Application of ENG to manufacturing bipolar plates of fuel cells has been studied in [2, 3]. Such plates are used to supply starting components and remove reaction products from electrodes, ensure good electrical contact with the catalyst, and provide sealing of the electrochemical system. For the same purpose, composites of ENG with polymers, i.e., with aromatic polysulfides are considered in [4], and those based on ENG and high-density polyethylene, in [3, 5]. As cathode material of alkaline batteries, mixture of ENG with natural graphite was studied in [6]. Physicochemical and electrochemical properties of expanded graphite oxide and ENG are being examined [7, 8]. In [9], the electrochemical methods were used to study the structural characteristics of ENG articles; ENG electrodes are applied to determination of uric acid [10] and ethanol [11].

Since in electrochemical systems ENG can be in contact with oxygen, it is important to know the parameters of electrochemical reduction of oxygen on ENG. Because of water release in fuel cells, it is necessary to make lower the wettability of materials being used. This can be done, e.g., by introducing polytetrafluoroethylene into a composite material. Electrolytic reduction of oxygen on ENG was not studied previously; therefore, the study of electrochemical reduction of oxygen on ENG is of interest in both applied and theoretical aspects.

This study is concerned with the electrochemical reduction of oxygen in gas-diffusion hydrophobized electrodes made of ENG in aqueous alkaline and acidic solutions at atmospheric pressure. The activity of electrodes was determined, the slope of the polarization curves plotted in the Tafel coordinates was estimated, and fractions of current consumed for formation of H_2O_2 and water were determined. These studies have been started previously and reported in [1, 12]. A-437E acetylene black (AB) electrodes with a specific surface area of 100 $m^2\ g^{-1}$ were also studied for the comparison of ENG with other electrode materials.

EXPERIMENTAL

Gas-diffusion hydrophobized electrodes were made of ENG powders. To obtain them, intercalation compounds of natural graphite with inorganic acids, synthesized by electrochemical method, were heated after washing in water and drying (see table). To fabricate electrodes, a hydrophobized electrode mass constituting an aqueous suspension of F-4D fluoroplastic (analog of Teflon) as water repellant was pressed in a mold to obtain discs (thickness 0.5 mm, weight about 0.3 g, porosity 60 vol %, F-4D concentration 10 wt %), which were heated in air at 360°C for 5 min. Carbon black electrodes (thickness 1 mm, porosity 69 vol %) were fabricated from a mass containing 8 wt % F-4D. To increase their strength and electrical conductivity, a 0.1-mm-thick nickel gauze was placed inside the carbon black electrodes. Preparation of intercalation compounds, the scheme of the electrolyzer, and preparation and study of gas-diffusion ENG electrodes have been described in detail in [1, 13].

Properties of graphites used for fabricating electrodes and values of Tafel slopes

Electrode no.	Graphite brand	Concentration of intercalated acid, wt %	Amount of passed electricity in electrosynthesis of intercalation compounds, A h g^{-1}	Tafel slope, mV, for indicated electrolyte, M	
				0.2 K_2SO_4 + 0.3 H_2SO_4 (pH 0.6)	3 KOH
1	Carbon black A437E	–	–	95	40
2	GAK-3	92 H_2SO_4	0.15	130	80
3	GT-1	70 HNO_3	0.15	130	60
4	GAK-3	70 HNO_3	0.17	300	60

The electrochemical measurements were carried out in a three-chamber glass cell [13] at 20°C and atmospheric pressure. The electrolytes were 3 M KOH and 0.2 M K_2SO_4 + 0.3 M H_2SO_4 (pH 0.6). The cathodic and anodic chambers were separated with an MF-4SK-100 cation-exchange membrane. The catholyte volume was 0.023 l. As anolyte was used 1 M H_2SO_4. Oxygen was flown at atmospheric pressure through a gas chamber to enter the real side of the electrode. Polarization curves were recorded at a potential sweep rate of 1–80 mV s^{-1}. The geometric current density was calculated per unit visible frontal electrode surface (5 cm^2). The electrode potential was measured relative to a silver chloride reference electrode. The volume of the pores wetted with the electrolyte was determined by hydrostatic weighing of the electrodes in 3 M KOH after the experiments and was calculated by the formula

$$E = [1 - (P - P_s)/d_s V] \times 100,$$

where E is the electrode porosity (vol %); P, mass of dry electrode in air; P_s, mass of the wetted electrode in the solution; d_s, solution density; and V, electrode volume.

The electrolyte porosity of the samples studied was within 4–15 vol %.

According to the published data [13–15], O_2 on graphitic carbon materials is mainly reduced to H_2O_2 and then it can be reduced to H_2O. Fractions of current consumed for either reaction are determined by electrolysis conditions and by the material and structure of the electrode [16]. Therefore, we measured the fraction of current γ consumed for oxygen reduction to hydrogen peroxide or water on the electrodes studied. The time necessary for the uptake of a certain amount of oxygen was determined by the gasometric method. The quantity γ was calculated by the Faraday law

$$\gamma = Q_t/Q - 1 = (2FV_0)/(V_m I\tau) - 1,$$

where Q_t is the theoretical amount of electricity; Q, experimentally determined amount of electricity; F, Faraday constant ($2F$ is the amount of electricity required for obtaining 1 mol of H_2O_2 from O_2, 1 mol of H_2O from H_2O_2, or 1 mol of H_2 from H_2O); V_m, volume of 1 mol of oxygen (molar volume); I, current strength; τ, time of reduction of a certain volume of oxygen; V_0, volume of oxygen taken up, converted to standard conditions.

The γ value is affected by the further reduction of hydrogen peroxide to water and by repeated reduction of oxygen, which appears upon hydrogen peroxide decomposition. Naturally, γ is 1 if all oxygen is reduced to H_2O_2, or zero if all oxygen is reduced to water or to hydroxide ions. In the case when the hydrogen evolution starts simultaneously with O_2 reduction, γ becomes less than zero. If all the amount of electricity is consumed for hydrogen evolution, then $\tau = \infty$ and $\gamma = -1$. The effect exerted by the current density on γ for carbon black electrode and electrode no. 4 is shown in Fig. 1 as example (see table). In this case, it should be noted that, with increasing current density, the potential of a carbon black electrode varied from –0.25 to –0.48 V in 3 M KOH and from –0.2 to –0.55 V in an acidic solution. The potential of the ENG electrode varied from –0.64 to –1.86 V in 3 M KOH and from –0.56 to –1.24 V in an acidic solution.

As the current density increases, γ on carbon black remains virtually constant in alkaline electrolyte, whereas in acidic electrolyte it sharply increases from virtually zero to constant value, i.e., most of the obtained hydrogen peroxide is not further reduced and

is accumulated in the electrolyte. Changes in γ on gas-diffusion carbon black electrodes in acidic medium are due to the diffusion limitations with respect to hydrogen ions, which appear at higher current densities, and, consequently, due to deceleration of further reduction of H_2O_2 to H_2O [16].

In electrolysis proceeding on electrodes made of expanded natural graphite, the amount of H_2O_2 is insignificant and γ does not rise above zero. This fact indicates that virtually all H_2O_2 is reduced to water, since, evidently, owing to diffusion limitations on removal of the reaction products and high polarization, H_2O_2 has no time to leave the electrode and is reduced to water. In alkaline solution, γ starts to sharply decrease on reaching the hydrogen evolution potential (about –1.5 V), i.e., the hydrogen evolution occurs on the frontal surface of the electrode and in the region close to it, whereas, in the depth of the electrode, O_2 reduction associated with ohmic loss also occurs. In an acidic solution, hydrogen evolution starts even at small current densities and γ sharply decreases with increasing current. All these facts indicate that the boundaries of a three-phase contact are undeveloped and delivery of O_2 toward the reaction area and removal of H_2O_2 are significantly limited. Also, in acidic solution, the dissociation and reduction of O_2 to water due to strong adsorption on edge atoms of ENG cannot be ruled out. The effect of the current density on γ showed that, the lower the electrode activity in O_2 reduction, the faster the decrease in γ with increasing current density.

The Tafel slopes of the polarization curve make it possible to suggest the mechanism of O_2 reduction. Therefore, we estimated the above slopes on ENG electrodes, taking into account that, at small geometric current densities and at large inner surface area of the electrodes, the true current density will be low and the diffusion and ohmic components will be insignificant. For comparison, we determined the slopes obtained with carbon black electrode. The results are presented in Fig. 2 and Table 1. At low current densities, the values we obtained, to within probable errors associated with the effect of porous electrode structure, are mainly in qualitative agreement with the slopes of $2.3RT/2F$, $2.3RT/F$, and $2 \times 2.3RT/F$, i.e., are about 30, 60, and 120 mV, respectively. At larger polarizations, the slopes sharply increase, which, according to published data, can be caused by strong hydrogen adsorption [17, 18] or by diffusion hindrance [19]. This refers, in particular, to a slope of 300 mV obtained on electrode no. 4 in an acidic solution. Note that this value, obtained on expanded graphite, can be due to strong adsorption on edge carbon atoms whose number is considerably larger in expanded graphite than in compact graphitic carbon materials. A slope of $2.3RT/2F$ in alkaline solutions at small current densities is due to by concentration polarization with respect to removal of H_2O_2 (HO_2^-) [20], which is especially important for the porous electrode. The slopes of $2.3RT/F$ and $2 \times 2.3RT/F$ show that the stage

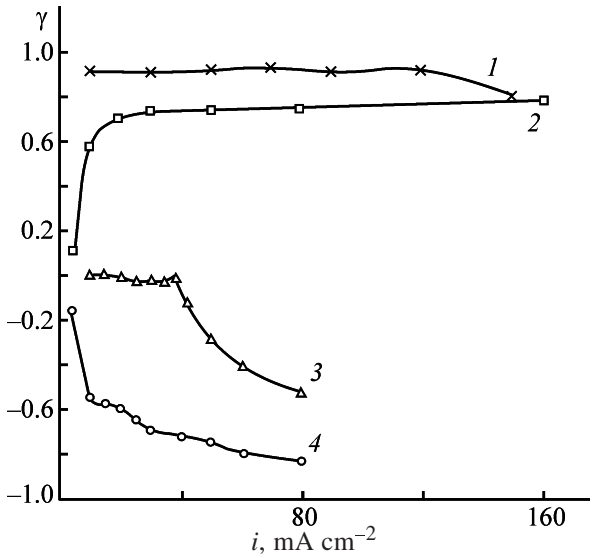


Fig. 1. Effect of current density on γ determined on (*1, 2*) carbon black electrode and (*3, 4*) electrode no. 4 (Table 1) in solutions of compositions (*1, 3*) 3 M KOH and (*2, 4*) 0.2 M K_2SO_4 + 0.3 M H_2SO_4. (*i*) Geometric current density; the same for Fig. 4.

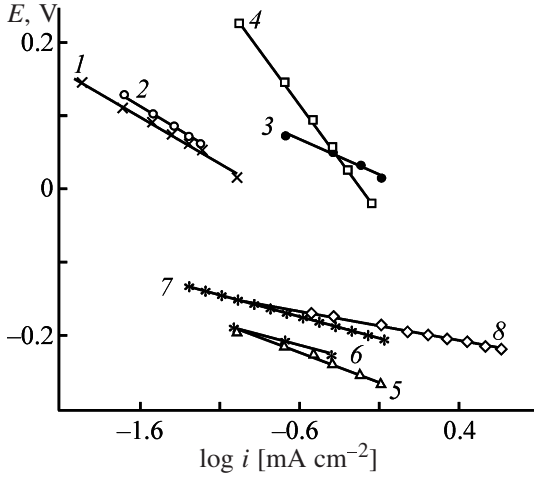


Fig. 2. Polarization curves of oxygen electroreduction, plotted in the Tafel coordinates and taken in solutions of compositions (*1–4*) 0.2 M K_2SO_4 + 0.3 M H_2SO_4 and (*5–8*) 3 M KOH at a potential sweep rate of 1 mV s^{-1}. (*E*) Electrode potential and (*i*) geometric current density. Electrode no. (see table): (*1, 5*) 2, (*2, 6*) 3, (*3, 8*) 1, and (*4, 7*) 4.

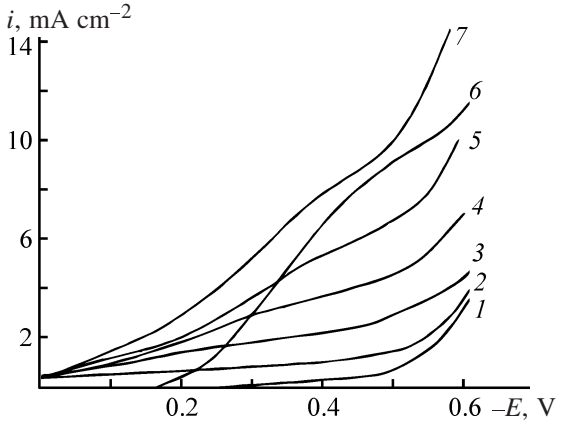


Fig. 3. Effect of potential sweep rate on polarization curves obtained on electrode no. 4. (*i*) Geometric current density, and (*E*) electrode potential. Electrolyte: (*1–5, 7*) 0.2 M K_2SO_4 + 0.3 M H_2SO_4 and (*6*) 3 M KOH. (*1*) Hydrogen evolution, (*2*) reduction of atmospheric oxygen, and (*3–7*) O_2 reduction. Potential sweep rate: (*1–3, 6*) 4, (*4*) 20, (*5*) 40, and (*7*) 80.

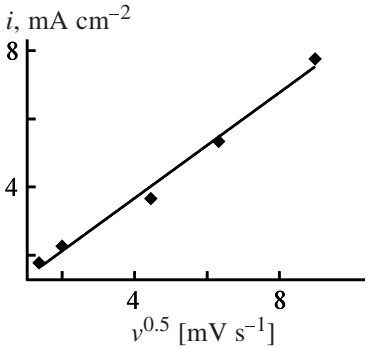


Fig. 4. Current density of the O_2 reduction vs. the square root of the potential sweep rate *v* obtained on electrode no. 4 at a potential of –0.4 V in a solution containing 0.2 M K_2SO_4 + 0.3 M H_2SO_4.

of the first electron transfer at different fillings of the surface is decelerated [17]. The slopes of the polarization curves obtained on AC electrodes qualitatively coincide with those presented in the literature: 60 mV in 2–4 M KOH on carbon black of unknown brand [15], 130 mV on AD-100 carbon black in 0.5 M H_2SO_4 [21], 35 mV in 1 M KOH, more than 120 mV in 0.5 M H_2SO_4 on acetylene black [17], and 120 mV on acetylene black in a phosphate buffer solution [19]. The slope obtained on graphite electrodes is approximately two times larger than on carbon black electrodes. Qualitatively, the slopes obtained on ENG coincided with the values obtained on pyrographite in [22]: 80 mV in 0.1 M KOH and 160 mV at pH 0.6. This fact suggests that the mechanism of O_2 electroreduction on expanded graphite is similar to that on pyrographite [14, 22]. The oxygen molecule is reduced to hydrogen peroxide without the bond cleavage, which is confirmed by the presence of H_2O_2 in an electrolyte and by its further reduction to water. The initial slope on ENG, as on other carbon materials, is larger in acidic medium than in alkaline medium. No regular trends related to the influence of the fabrication conditions of ENG on their electrochemical characteristics were found. The curves taken on electrode nos. 2 and 3 were identical. At the same time, the activity of the electrodes was lower than that of electrode no. 4, though they were made of ENG powders obtained from different graphite brands and under the different conditions.

The rate of oxygen electroreduction on ENG electrodes, as on carbon black and other graphitic carbon materials, increases as the rate of potential sweep increases [18, 23]. This dependence is presented in Fig. 3 as example. The electrode activity in alkaline electrolyte is higher than in acid electrolyte (Fig. 3, curves *3, 6*). The current peak of O_2 reduction at potential sweeping was not recorded because of gradual replacement of oxygen reduction by hydrogen evolution. Based on the voltammetry principles and owing to the fact that the experimental dependence of the current on the square root of the potential sweep rate is a straight line (Fig. 4), we may suggest that the electrode operates in the diffusion mode. On the polarization curve obtained in O_2 reduction in alkaline electrolyte, the peak or the limiting current is absent also, though active evolution of hydrogen starts only at –1.6 V. This is accounted for by the fact that the inner surface of a porous electrode is larger than that of a smooth electrode and, consequently, the true current density is low, i.e., it does not reach the limiting value in the examined range of the geometric current densities.

The replacement of oxygen by air decreases the activity of all the electrodes by a factor of approximately 2 (Fig. 3, curves *2, 3*), which indicates that the surfaces of the electrodes wetted with the electrolyte are not equally accessible. Similar results were observed on hydrophobized electrodes made of acetylene black [19]. At the same time, in [15], on an industrial gas-diffusion electrode used for H_2O_2 preparation, a five-fold decrease in the activity was observed, as in the case of equally accessible inner surface area of the electrode.

CONCLUSIONS

(1) Porous composite materials based on expanded natural graphite and F-4D fluoroplastic have low elec-

trochemical activity in oxygen reduction. In alkaline medium, the activity is higher than in acid medium.

(2) On electrodes made of expanded natural graphite, in contrast to carbon black electrodes, the main mass of oxygen is reduced to water without accumulation of H_2O_2 in the electrolyte.

(3) The obtained values of the Tafel slopes and the presence of H_2O_2 in solutions show that the O_2 electroreduction on expanded graphite electrode, as on the majority of graphitic carbon materials, occurs via formation of H_2O_2 and is limited by attachment of the first electron.

REFERENCES

1. Kolyagin, G.A., Kornienko, V.L., Kuznetsov, B.N., and Chesnokov, N.V., *Zh. Prikl. Khim*., 2005, vol. 78, no. 10, pp. 1653–1658.
2. Dobrovol'skii, Yu.A., Ukshe, A.E., Levchenko, A.V., et al., *Ross. Khim. Zh*., 2006, vol. 50, no. 6, pp. 93–94.
3. Yan, X., Hou, M., Zhang, H., et al., *J. Power Sources*, 2006, vol. 160, no. 1, pp. 252–257.
4. Song, L.N., Xiao, M., and Meng, Y.Z., *Composite Sci. Technol*., 2006, vol. 66, no. 13, pp. 2156–2162.
5. Zheng, W., Lu, X.H., and Wong, S.C., *J. Appl. Polym. Sci*., 2004, vol. 91, no. 5, pp. 2781–2788.
6. Viera, F., Cisneros, I., Sansiviero, M.T.C., et al., *J. Phys. Chem. Solids*, 2006, vol. 67, nos. 5–6, pp. 1208–1212.
7. Ramesh, P., Bhagyalakhmi, S., and Sampath, S., *J. Colloid Interface Sci*., 2004, vol. 274, no. 1, pp. 92–102.
8. Ramesh, P., and Sampath, S., *Anal. Chem*., 2003, vol. 75, no. 24, pp. 6949–6957.
9. Calas-Blanchard, C., Comtat, M., Marty, J.-L., and Mauran, S., *Carbon*, 2003, vol. 41, no. 1, pp. 123–130.
10. Ramesh, P., and Sampath, S., *Electroanalysis*, 2004, vol. 16, no. 10, pp. 866–869.
11. Ramesh, P., Sivakumar, P., and Sampath, S., *J. Electroanal. Chem*., 2002, vol. 528, nos. 1–2, pp. 82–92.
12. Kolyagin, G.A., and Kornienko, V.L., *Zh. Prikl. Khim*., 2007, vol. 80, no. 8, pp. 1302–1306.
13. Kornienko, V.L., Kolyagin, G.A., and Saltykov, Yu.V., *Zh. Prikl. Khim*., 1999, vol. 72, no. 3, pp. 353–361.
14. Sljukic, B., Banks, C.E., and Compton, R.G., *J. Iranian Chem. Soc*., 2005, vol. 2, no. 1, pp. 1–5.
15. Alcaide, F., Brillas, E., and Cabot, P.-L., *J. Electrochem. Soc*. 2002, vol. 149, no. 2, pp. E64–E70.
16. Kolyagin, G.A., and Kornienko, V.L., *Zh. Prikl. Khim*., 2003, vol. 76, no. 7, pp. 1103–1108.
17. Tarasevich, M.R., Radyushkina, K.A., and Zhutaeva, G.V., *Elektrokhimiya*, 2004, vol. 40, no. 11, pp. 1369–1383.
18. Gyenge, E.L., and Oloman, C.W., *J. Appl. Electrochem*., 2001, vol. 31, no. 2, pp. 233–243.
19. Bogdanovskaya, V.A., Tarasevich, M.R., Fridman, V.A., et al., *Elektrokhimiya*, 2000, vol. 36, no. 8, pp. 991–995.
20. Tarasevich, M.R., *Elektrokhimiya uglerodnykh materialov* (Electrochemistry of Carbon Materials), Moscow: Nauka, 1984.
21. Tarasevich, M.R., Beketaeva, L.A., Efremov, B.N., et al., *Elektrokhimiya*, 2004, vol. 40, no. 5, pp. 612–622.
22. Tarasevich, M.R., Sabirov, F.Z., and Burshtein, R.Kh., *Elektrokhimiya*, 1971, vol. 7, no. 3, pp. 404–407.
23. Wang, M., Xu, X., Gao, Zh., et al., *Elektrokhimiya*, 2006, vol. 42, no. 8, pp. 975–979.

ISSN 1070-4272, Russian Journal of Applied Chemistry, 2008, Vol. 81, No. 3, pp. 428–434. © Pleiades Publishing, Ltd., 2008.
Original Russian Text © V.N. Gorshenev, S.B. Bibikov, A.M. Kuznetsov, 2008, published in Zhurnal Prikladnoi Khimii, 2008, Vol. 81, No. 3, pp. 442–448.

APPLIED ELECTROCHEMISTRY AND CORROSION PROTECTION OF METALS

Concentration Conditions of Formation of Electrically Conducting Coatings from Colloid-Graphite Dispersions

V. N. Gorshenev, S. B. Bibikov, and A. M. Kuznetsov

Institute of Biochemical Physics, Russian Academy of Sciences, Moscow, Russia

Received September 17, 2007

Abstract—Concentration conditions under which electrically conducting graphite coatings can be formed on cardboard and polymeric dielectric substrates by deposition of graphite particles from colloid graphite dispersions were studied. It was found how the surface resistance of the samples varies, in the dc mode and in the microwave range, with the concentration and time conditions of formation of electrically conducting coatings. The transmittance and reflectance to microwave electromagnetic radiation were measured for samples coated with particles of colloid graphite from suspensions with various particle sizes.

DOI: 10.1134/S1070427208030166

Deposition of electrically conducting composites is a topical task of materials science, aimed to solve problems of science and technology, provide efficient operation of various kinds of radio equipment under the action of electromagnetic radiation, etc. There exist electrically conducting materials with a broad spectrum of physicochemical and physicomechanical properties, composed of polymers volume-filled with various conducting fillers [1–4].

Use of electrically conducting composite materials volume-filled with electrically conducting particles is not always justified as regards weight, electrical, and economical requirements. At present, there is increasing interest in studies of physicochemical properties of colloid structures of varied nature and particle size: metallic, graphite, and organosilicon [5, 6]. This specifically refers to nanostructures (<100 nm), for which it is necessary to develop technologies of production and compaction of nanoparticles, e.g., on dielectric substrates in order to form electrically conducting layers. In particular, colloid-graphite suspensions deposited onto dielectric substrates of varied nature are used to obtain electrically conducting materials [7]. Both in the case of composites with volume filling with electrically conducting particles and in treatment of dielectric materials with colloid-graphite preparation, it is necessary to determine what concentrations of graphite fillers provide a percolation transition.

In this study, we examined the concentration conditions under which dielectric materials become electrically conducting upon treatment with solutions of colloid graphites and evaluated the achievable radiophysical parameters of materials treated with colloid graphite.

EXPERIMENTAL

To obtain colloid-graphite dispersions, we used the chemical activation method [8]. Colloid graphite (CG) was produced from the thermally deashed graphite from the Taiginskoe deposit (ash content 0.2%), ground in an M-10 vibration mill. As the time of the vibration grinding was raised from 3 to 6 h, the specific surface area of graphite powders, determined by BET, increased from 250 to 450 $m^2 g^{-1}$.

To impart hydrophilic properties to graphite particles, they were oxidized with a 3 : 1 mixture of concentrated sulfuric and nitric acids. It is known [7, 8] that the redox reaction of graphite modification occurs with release of heat and nitrogen(IV) oxide to give a product close in composition to graphite disulfate. The activating agents (acids) were first removed by decantation to a density of the solution being decanted equal to 1.01–1.005 $g\ cm^{-3}$ and then by vacuum filtration to complete removal of SO_4^{2-} ions, as indicated by treating the filtrate with an aqueous solution of barium chloride in the presence of hydrochloric acid. The graphite deposit formed on the filter was mixed, depending on further use, with distilled water or isopropyl alcohol (IPA) to obtain a stable ultradisperse suspension of activated graphite. The acid modifica-

tion of graphite particles subjected to vibration grinding for 3 and 6 h yielded colloid-graphite preparations TO-3 and TO-6 with a specific surface area no less than 1300 and 1500 $m^2 g^{-1}$ for TO-3 and TO-6, respectively.

To determine the diffusion coefficients of colloid particles, we measured the average motion velocity of graphite particles in aqueous and alcoholic solutions on a photon-correlation spectrometer.

As dielectric substrates served cardboard with a density of 400 g m^{-2} and Lavsan (analog of Mylar) of thickness 52 μm. The samples were impregnated in solutions of certain concentrations during a prescribed time. The consumption of a colloid graphite solution for impregnation of dielectric materials was determined in relation to the concentration and time by the gravimetric method. The samples were dried at room temperature (20°C), with the cardboard and Lavsan samples subsequently heated to 200 and 60°C, respectively.

The conductivity of graphite coatings on dielectric materials was measured using the standard four-probe technique [4]. The volume electrical resistivity ρ_V was found using the well-known expression for the plane-parallel configuration of the samples being measured, $\rho_V = R_{av}SL^{-1}$, where R_{av} is the average measured electrical resistance of a sample; S, sample area; and L, spacing between the potential electrodes. In the case when the electrically conducting coating is homogeneous, its volume electrical resistivity ρ_V is equal (in the absence of a frequency dispersion) to the product of the surface resistance of the coating, ρ_S, by its thickness h.

The electrical parameters of the materials were also evaluated by contactless measurements of the transmittance to electromagnetic radiation with a frequency of 8–12.4 GHz. For this purpose, we used an installation based on an R2-61 panoramic scalar meter. A planar sample with a conducting surface was placed in the waveguide perpendicularly to the incident radiation (H_{01} mode) so that it completely blocked the waveguide cross section. The transmittance corresponding to the magnitude of the shielding effect of a material (by the electric field and in the far-field zone) was found as the logarithm of the power ratio between the wave incident onto, and transmitted through the sample (in decibels). The experimentally measured transmittance and reflectance to radio frequency radiation were used to calculate the surface resistance.

Table 1. Changes in the mass of cardboard samples with a graphite coating and surface resistance ρ_S (measured at 10 GHz) after treatment in aqueous colloid-graphite dispersions of TO-3

c_{CG}, g l^{-1}	t, min	Mass, g		ρ_S, Ω
		CG solution	graphite particles*	
15	1.0	11.3	0.22	290
	2.0	15.6	0.33	160
	3.0	19.7	0.44	90
30	1.0	12.5	0.52	31
	2.0	19.7	0.90	18.0
	3.0	22.1	0.94	12.5

* After drying at 20°C for four days.

A distinctive feature of oxidized graphite after washing is its ability to form colloid systems exhibiting kinetic and aggregative stability. Graphite particles are stabilized by oxygen-containing functional groups of the type –OH, –COOH, and =C=O, formed on the surface of graphite particles [9]. The suspension can be stabilized via formation of hydrogen bonds between active surface groups and molecules of a polar solvent. The size of graphite particles in the suspension is less than 2 μm, depending on the conditions of preparation and vibration grinding of the starting graphite material [10].

The following processes may occur in the course of further technological use of graphite solutions in interaction of a dielectric material with a colloid-graphite dispersion: precipitation of graphite particles on the surface, aggregation of these particles, and desorption. In this case, the mass of a sample steadily increases, with the quantitative parameters of this trend strongly dependent on the properties of the surface and on the ability of CG to be accumulated on the surface of the dielectric material.

Table 1 lists experimental data obtained in treatment of cardboard samples (with area S = 0.1 m^2) with an aqueous solution of TO-3, with the content of colloid-graphite particles equal to 15 and 30 g l^{-1}, in relation to the treatment time. The samples were dried at room temperature for 4 days.

To eliminate the errors in electrical conductivity measurements that are related to the contact resistance exhibiting a wide scatter for cardboard, the surface resistance was measured by the contactless method.

The increase in the mass of the solution absorbed by the cardboard sample and, accordingly, that in

Table 2. Changes in the surface resistance of cardboard samples after treatment in aqueous solutions of TO-3 of various concentrations

Sample no.	t, s	ρ_S, Ω, at indicated solution concentration, g l^{-1}	
		3	5
1	10	$>10^7$	7.0×10^4
2	30	5.8×10^5	1.7×10^4
3	60	1.6×10^5	5.5×10^3
4	120	1.1×10^5	3.6×10^3
5	180	7.6×10^4	5.7×10^3
6	360	2.7×10^4	1.0×10^3
7	480	1.1×10^4	2.0×10^3
8	600	1.9×10^4	1.0×10^3

the mass of graphite particles (Table 1, in the range 0.1–1.0 g) forming the electrically conducting coating naturally lead to a decrease in the surface resistance ρ_S. Presumably, the process of deposition of graphite particles on the surface of a dielectric material can be represented as a diffusion process, with the mass of graphite particles necessary for a conductivity to appear on the dielectric substrate determined using the Einstein–Smoluchowski diffusion equation [11]. Assuming that a graphite particle has the shape of a thin disk of diameter d and thickness h, we can apply the following expression for the average value of the diffusion coefficient D [12]:

$$D = kT/6\eta d, \quad (1)$$

where k is the Boltzmann constant; T, absolute temperature; and η, solvent viscosity.

The average value of the diffusion coefficient D is given by $D = 1/3(2D_{\|} + D_{\perp})$, where $D_{\|}$ and $D_{\perp}$ are the diffusion coefficients for a thin disk along (d) and across (h) its plane. To estimate the diffusion coefficients, we used the relations $D_{\|} = 3kT/16\eta d$ and $D_{\perp} = kT/8\eta d$, reported in [12]. Let colloid graphite particles diffuse from a solution with initial concentration n_0 onto a plane at $x = 0$. The particle concentration n at instant of time t is described by the known unidimensional diffusion equation. If the probability of particle adherence to the substrate is unity, the solution to the unidimensional diffusion equation [11] for the number N of particles on unit substrate surface area at instant of time t has the form

$$N(t) = n_0(4Dt/\pi)^{1/2}. \quad (2)$$

Expression (2) has a simple meaning: in a time t, a diffusing colloid particle moves to a distance equal to the diffusion length $L_d \approx (Dt)^{1/2}$ and, consequently, all the particles that are at distances shorter than L_d from the substrate will be on the substrate surface at instant of time t. Accordingly, the mass of deposited particles per unit area will be given by

$$m(t) = \gamma_g d^2 h n_0(\pi/4Dt)^{1/2}, \quad (3)$$

where γ_g is the density of graphite.

Measurements of the average motion velocity of graphite particles in aqueous and alcoholic solutions with the photon-correlation spectrometer made it possible to find the diffusion coefficients of colloid particles. The diffusion coefficients for the aqueous and alcoholic solutions of TO-3 graphite are 1.2×10^{-8} and 5.3×10^{-9} $cm^2\ s^{-1}$. Numerical estimates of the average value of the diffusion coefficient $D = 1/3(2D_{\|} + D_{\perp})$, made on the assumption that the graphite particle has the shape of a disk with a diameter $d = 5 \times 10^{-5}$ cm and thickness $h = 5 \times 10^{-6}$ cm, yielded for the aqueous and alcoholic solutions 1.35×10^{-8} and 5.6×10^{-9} $cm^2\ s^{-1}$, respectively.

Estimation by formula (3) of the mass of graphite particles deposited in 600 s from a solution of TO-3 CG with a concentration of 3 g l^{-1} onto the surface of the samples under study gives $m \approx 3 \times 10^{-3}$ g. This value is an order of magnitude smaller than that observed experimentally, which is presumably due to the strongly developed surface of cardboard and to differences in the size of colloid particles and in other factors.

The results obtained in treatment of cardboard samples with 15, 30, and 60 g l^{-1} aqueous solutions of colloid-graphite dispersions at treatment durations of 1 to 120 s demonstrated that, as the solution concentration and treatment time increase, the surface resistance of the samples decreases by two orders of magnitude, from 2.2×10^3 to 20 Ω. At a short impregnation time (up to 20 s), a wide scatter of ρ_S (by up to 20%) was observed along the surface of the samples, whereas for samples treated with concentrated solutions during a time longer than 30 s, the similar value did not exceed 10%. This may be due to a stronger influence of the solution draining from a sample during drying at lower solution concentrations.

As the concentration of the aqueous solution of TO-3 was lowered, a percolation transition was observed. The results obtained when measuring the resistance of the samples studied are listed in Table 2.

An analysis of SEM micrographs demonstrated that paper fibers of size 4–7 μm not covered with graphite

particles are seen on cardboard samples impregnated with a CG solution of concentration 3 g l^{-1}. On cardboard samples treated with TO-3 CG solutions of concentrations 3 and 5 g l^{-1}, separate graphite particles with planar structure are observed at a magnification of 10 000 (Figs. 1a–1c). The particles can be seen because of the low degree of interparticle cohesion. Because of the low degree of cohesion, scale edges differ from the lower-lying layers of the carbon coating. In this case, the electron work function decreases and a region of high intensity of secondary electrons (white fringe) appears on the electron receiver. Analysis of the electron-microscopic data shows that the average particle size is approximately 0.5–1 μm. The planar structure of the carbon coating based on TO-3 is better pronounced than that of a graphite coating based on TO-6, on which particles that are not strictly oriented in the coating plane can be seen (Figs. 1b, 1c). The increase in the mass of the cardboard sample (with a total working area of 156 cm^2) upon impregnation with a 3 g l^{-1} aqueous solution of TO-3 for 10 s and drying did not exceed 0.04 g.

The average distance L_{av} between deposited particles on the substrate surface is equal in order of magnitude to $L_{av} = N^{-1/2}$, where N is the number of particles per unit area. If we assume that percolation (a through current flow) via graphite particles occurs when $L_{av} \approx d$, where d is the characteristic size (diameter) of particles, then we obtain the following percolation condition:

$$N_{per} \sim 1/d^2. \quad (4)$$

In this case, particles cover approximately a half of the substrate surface. Consequently, the smaller the particle diameter, the greater number of particles is necessary for the percolation transition to occur.

The impregnation of cardboard samples presumably includes several stages: penetration of H_2O with graphite particles, sorption of graphite particles on the substrate surface, and formation of solid particle aggregations into a coating. A more detailed analysis shows that the number of graphite particles necessary for an electrically conducting layer to be formed depends on the structure of the substrate material, concentration of the impregnating solution, and duration of the impregnation process. It is also possible that functional groups on the surface of the dielectric material and functional groups on the surface of modified graphites may be important.

Upon impregnation of cardboard samples with a 3 g l^{-1} alcoholic solution of TO-3 for 10 to 600 s, and with a 5 g l^{-1} solution for 1 to 600 s, the surface resistance of the samples was higher than 10^7 Ω. On raising the concentration of the alcoholic solution of TO-3 to 10 g l^{-1}, an electrically conducting coating was formed on the cardboard sample surface. As the interaction time was raised from 10 to 720 s, the surface resistance of the samples changed only slightly and was in the range 5.1×10^5–4.5×10^4 Ω.

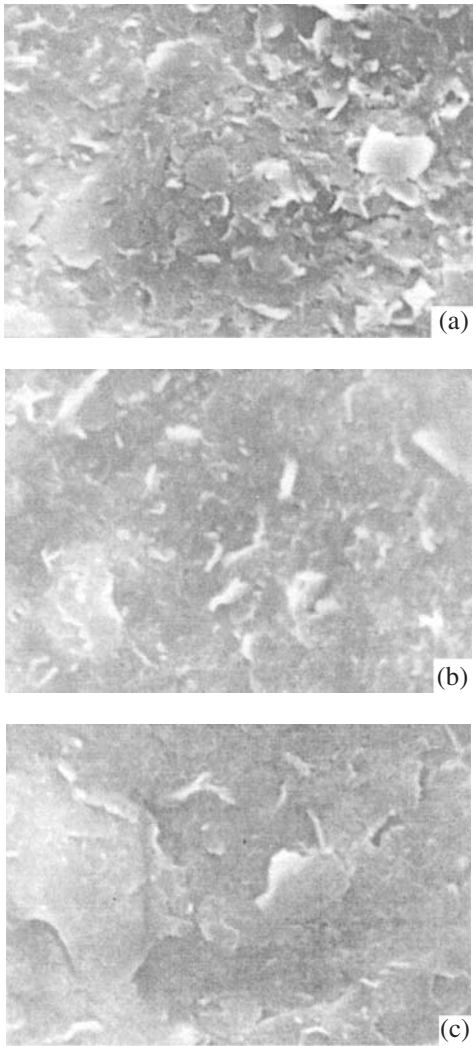


Fig. 1. SEM micrographs of the surface of carbon coatings formed on cardboard in (a, b) alcoholic and (c) aqueous CG suspensions of different concentrations. Concentration, g l^{-1}: (a) 5 (TO-3) and (b, c) 60 (TO-6).

The higher alcoholic solution concentrations necessary for overcoming the percolation transition, compared with the aqueous solutions, can be attributed to lower diffusion coefficients of colloid particles in the alcoholic solution and also, possibly, to another

Table 3. Changes in the surface resistance ρ_S of Lavsan films upon treatment in TO-3 and TO-6 (C_3H_8O) solutions of different concentrations

t, s	ρ_S, Ω, at indicated solution concentration, g l^{-1}			
	30		60	
	TO-3	TO-6	TO-3	TO-6
10	1.2×10^3	4.8×10^3	290	300
30	950	1.6×10^3	215	275
60	830	2.0×10^3	210	230
120	790	1.8×10^3	187	260
180	720	2.5×10^3	190	258

type of distribution of colloid particles on the surface of the material in their aggregation.

It is rather difficult to accurately determine the mass of graphite particles on a cardboard sample because of the difficulties in determining the amount of water in the sample. On drying a sample at 200°C, the increase in the sample mass in air at room temperature is determined by graphite particles. For a cardboard sample with a graphite coating, the surface resistance R equal to 1.4 kΩ decreased to 0.7 kΩ after drying at 160°C for 30 min. A treatment of cardboard plates with a working surface area of 2456 cm^2 with a 5 g l^{-1} aqueous solution of TO-3 for 0.5, 1.0, 2.0, 4.0, and 6.0 min led to a change in the mass of the graphite coating equal to 11, 27, 55, 88, and 120 mg, respectively. It was found that the change in the coating mass is proportional to the square root of the time of interaction between the CG solution and a dielectric cardboard sample, which corresponds to the diffusion model of formation of the graphite coating.

In contrast to cardboard samples, Lavsan films treated with a low-concentration alcoholic solution of CG were electrically conducting. In treatment of 113 cm^2 Lavsan films with a 5 g l^{-1} alcoholic colloid solution of TO-6, the mass of CG particles adsorbed on the surface was about 0.7–0.8 g; upon drying, the films were electrically conducting. In the case of exposure of Lavsan films for 5 to 180 s, their resistance decreased from 300 to 115 kΩ.

The zero current in cardboard samples upon a similar treatment can be presumably attributed to the porous, more branched surface structure of this material. The rough fibrous surface structure of cardboard requires that a larger amount of colloid graphite particles should be deposited for an electrically conducting graphite layer to be formed.

To evaluate the amount of graphite particles deposited onto the Lavsan surface, we fabricated 12.5 × 12.5 cm samples. The samples were treated with solutions of colloid graphite TO-3 and TO-6 in isopropyl alcohol, with concentrations of 60 and 30 g l^{-1}.

The results obtained in dc surface conductivity measurements are listed in Table 3. It can be seen that, as the concentration of the CG suspension is raised from 30 to 60 g l^{-1}, the conductivity of the graphite coating on Lavsan films increases, which is due to the larger number of CG particles involved in the coating formation. At the same time, the data in Table 3 show that treatment of Lavsan films with a TO-6 solution gives higher resistances, compared with the treatment with a TO-3 solution. This occurs because a decrease in the size of colloid particles makes the electrical conductivity of the coating lower under the same treatment conditions, in accordance with formula (4).

A study of electrically conducting coatings on Lavsan films demonstrated that the increase in the coating mass with the time of surface treatment with the alcoholic solution of CG is not proportional to the square root of time, in contrast to the case of treatment with aqueous solutions of CG. This may be due to absence of diffusion accumulation of CG particles on the surface of Lavsan films. Having a free affinity, the surface of the dielectric film and, specifically, the surface layer of atoms, molecules, or macromolecules interacts with CG particles upon their contact with the surface. We can assume, based on electron-microscopic data, that the adsorption layer formed on the surface of the Lavsan film and retained by attraction forces upon drying is a film composed of lamellar agglomerates of carbon particles. It was found that, as the concentration of the alcoholic suspension of TO-3 is raised from 30 to 60 g l^{-1}, the conductivity of the graphite coating grows, which is due to the larger number of CG particles involved in the formation of the coating. The dc surface resistance of the coating, measured on a sample whose width was equal to the distance between the potential electrodes, was 112 and 11 Ω at coating thicknesses of 1 and 2 μm, respectively, for two TO-3 concentrations. The shielding coefficients of the samples at a frequency of 10 GHz were 10.8 and 21.2 dB, respectively. The shielding coefficients K_{SC} are in satisfactory agreement with the values calculated by the relation derived in terms of the model of normal transmis-

Table 4. Transmittance K_{tr} and reflectance K_r of cardboard samples treated with aqueous (TO-3) and alcoholic (TO-6) colloid graphite solutions of various concentrations c. Treatment duration 10 s

Solution	T,* °C	c, g l^{-1}	K_{tr}	K_r
			dB	
TO-3	120	15	–12.2	–2.5
		20	–13.6	–2.3
		30	–14.6	–2.7
		40	–17.8	–2.0
		60	<–35	–0.3
	200	15	–12.5	–3.0
		20	–13.5	–2.3
		30	–14.7	–2.3
		40	–16.5	–2.3
		60	<–35	–0.4
TO-6	120	60	–20.8	–1.3
	200	60	–21.1	–1.3

* Drying temperature.

sion of an electromagnetic wave of THE or H_{01} mode across a thin ($d \ll \lambda$) sample:

$$K_{SC} = 20\log(1 + z_0/2\rho_S), \quad (5)$$

where ρ_S is the surface resistance of the coating and z_0 is the wave impedance of free space.

The materials with graphite coatings, obtained in this study, can be used to accomplish a number of tasks requiring materials with a prescribed surface resistance. These are, in particular, materials for shielding and absorption of electromagnetic radiation. Table 4 lists the results of measurements of the transmittance and reflectance to 10 GHz electromagnetic radiation for paper samples treated with CG solutions. At equal treatment times of the cardboard surface (~10 s), the coating conductivity increases with the concentration of the colloid-graphite dispersion. Simultaneously, the transmittance K_{tr} steadily decreases, and the reflectance K_r, increases as the concentration of the colloid-graphite dispersion becomes higher. As in the case of dc measurements, the higher transmittance for samples treated with an alcoholic solution of TO-6 is accounted for by the smaller particle size, compared to the TO-3 dispersion.

The paper- and cardboard-based electrically conducting materials obtained in this study can be successfully used in development of radio-absorbing and radio-scattering materials and structures.

CONCLUSIONS

(1) The concentration and time conditions under which electrically conducting graphite coatings can be formed on dielectric materials, cardboard and Lavsan, using aqueous and alcoholic colloid-graphite solutions were determined.

(2) A difference was revealed between the deposition conditions of colloid graphite particles from aqueous and alcoholic solutions. At the same impregnation time, conductivity appears on the surface at a concentration of 3 g l^{-1} in treatment with an aqueous solution of TO-3 and at 7.5 g l^{-1} for an alcoholic solution of TO-3. For polymeric films treated with a solution of TO-3, the conductivity of the coatings obtained exceeds that of coatings deposited from a TO-6 solution because of the larger size of colloid graphite particles in the TO-3 solution.

(3) The transmittance and reflectance to microwave electromagnetic radiation were measured for samples coated with colloid graphite particles from TO-3 and TO-6 solutions. It was shown that, in different modes of cardboard treatment with colloid graphite solutions, materials with a wide range of radiophysical properties can be obtained and, in particular, a shielding coefficient exceeding 35 dB can be provided for a planar sheet.

ACKNOWLEDGMENTS

The study was supported by the Russian Foundation for Basic Research (project no. 06-08-01590-a).

The authors thank B.Ya. Balagurov for active and fruitful discussions.

REFERENCES

1. Martyushev, K.I., in *Elektroprovodnost' kompozitsionnykh materialov: Obzor po elektronnoi tekhnike* (Electrical Conductivity of Composite Materials: Review of Electronics Engineering), Ser. 5: *Radiodetali i radiokomponenty* (Radio Components), Moscow: TsNII Elektronika, 1982, no. 8, p. 910.
2. Krikorov, V.S. and Kolmakova, L.A., *Elektroprovodyashchie polimernye materialy* (Electrically Conducting Polymeric Materials), Moscow: Energoatomizdat, 1984.
3. Shevchenko, V.G. and Ponomarenko, A.T., *Usp. Khim.*, 1983, vol. 52, no. 8, pp. 1336–1349.
4. Gorshenev, V.N., Bibikov, S.B., and Novikov, Yu.N., *Zh. Prikl. Khim.*, 2003, vol. 76, no. 4, pp. 624–628.

5. Pomogailo, A.D., *Usp. Khim.*, 1997, vol. 66, no. 8, pp. 750–790.
6. Buchachenko, A.L., *Usp. Khim.*, 2003, vol. 72, no. 5, pp. 419–437.
7. Fialkov, A.S., *Uglerodnye mezhsloevye soedineniya i kompozity na ikh osnove* (Carbon Intercalation Compounds and Composites Based on Them), Moscow: Aspekt, 1997.
8. Toporov, G.N., Semenov, M.V., Eliseeva, R.A., et al., *Kolloidn. Zh.*, 1978, no. 3, pp. 575–577.
9. Fialkov, A.S., Toporov, G.N., and Chekanova, V.D., *Zh. Fiz. Khim.*, 1963, vol. 37, no. 3, pp. 566–569.
10. Fialkov, A.S., Chuparova, L.D., Varlakov, V.P., et al., *Khim. Tverd. Topl.*, 1992, no. 6, pp. 114–119.
11. Einshtein, A. and Smoluchowski, M., *Brounovskoe dvizhenie* (Brownian Motion), Leningrad: ONTI, Glavn. Red. Obshchetekhn. Lit., 1936.
12. Landau, L.D. and Lifshits, E.M., *Gidrodinamika* (Hydrodynamics), Moscow: Nauka, 1988.

ISSN 1070-4272, Russian Journal of Applied Chemistry, 2008, Vol. 81, No. 3, pp. 435–437. © Pleiades Publishing, Ltd., 2008.
Original Russian Text © L.E. Shpilevskaya, A.M. Safonova, 2008, published in Zhurnal Prikladnoi Khimii, 2008, Vol. 81, No. 3, pp. 449–452.

APPLIED ELECTROCHEMISTRY AND CORROSION PROTECTION OF METALS

Deposition of Electrically Conducting Polymeric Coatings Using Copper-Plated Silica

L. E. Shpilevskaya and A. M. Safonova

Institute of General and Inorganic Chemistry, National Academy of Sciences of Belarus, Minsk, Belarus

Received June 18, 2007

Abstract—Silica was metallized by chemical copper plating, and the possibility of using this kind of silica as an electrically conducting filler by itself and with addition of carbon or metal–carbon fibers for preparing polymeric and paint-and-varnish electrically conducting coatings was studied.

DOI: 10.1134/S1070427208030178

Of particular interest with the development of technology (micro- and radio electronics) is a new type of polymeric and paint-and-varnish coatings, electrically conducting coatings. Preserving all the qualities of polymeric coatings, namely, low density, high strength and elasticity of films, good adhesion and anticorrosion properties, and a number of other valuable physicochemical and mechanical parameters, electrically conducting coatings, in addition, acquire one of the most important properties of a metal, ability to conduct electric current. This enables their use instead of metallic coatings in some cases.

The electrically conducting coatings are composite coatings that contain conducting fillers in a polymeric binder. As conducting fillers are used substances with high conductivity: carbon black, graphite, technical-grade carbon, carbon fibers, and powdered metals and metal alloys. The choice of a component for preparing electrically conducting coatings is governed by the set of requirements to a coating as regards its electrical, physical, chemical, and mechanical properties. The electrical conductivity of composite coatings depends on the type of a conducting filler (ability to conduct electric current), size and shape of its particles, filler concentration, chemical nature of the polymeric binder, conditions of film formation, mode of its curing and exploitation, and deposition technology [1].

The electrical conductivity is the highest for composite coatings containing a metallic filler. However, a disadvantage of such a filler is the high rate of its sedimentation in the composite, which causes segregation of the material and leads to inhomogeneity of the coatings obtained. In addition, a good conductivity of coatings can be only achieved at a high metal content (wt %) of the composite [2]. This impairs physicomechanical parameters of the coatings obtained and makes higher their density.

At present, the so-called core-pigments, combined particles with a metal-plated surface, find steadily increasing use as fillers [3, 4]. Core-pigments make it possible to diminish the density of a conducting polymeric coating and its cost, without making lower its electrical conductivity. Of particular interest are core-pigments produced by metallization of inorganic materials and, in particular, mica, glass spheres, and silica. Polymeric composites containing pigments of this kind show high spreading capacity and slower filler settling, and coatings produced on their basis have low electrical resistance and good heat-insulating properties [5]. In addition, metallized silica particles can be used as a starting stock for the subsequent sintering of ceramics, by analogy with the processes described in [6].

The electroless method for deposition of metallic coatings onto nonmetallic surfaces is well understood [7, 8], and, therefore, its application to metal plating of various insulators poses no difficulties. However, the deposition conditions should be adjusted to each particular kind of a substrate.

The aim of this study was to obtain copper-plated silica and analyze the possibility of its use as an electrically conducting filler in deposition of polymeric and paint-and-varnish coatings.

EXPERIMENTAL

Sieved silica of the OVS-15 brand from the Novoselkovskoe deposit (Ukraine) was used in the study.

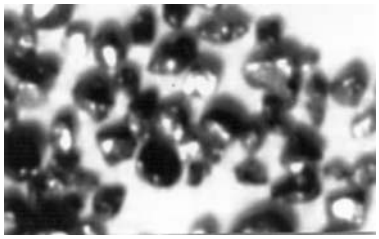


Fig. 1. Micrograph of metallized silica particles. Magnification 25.

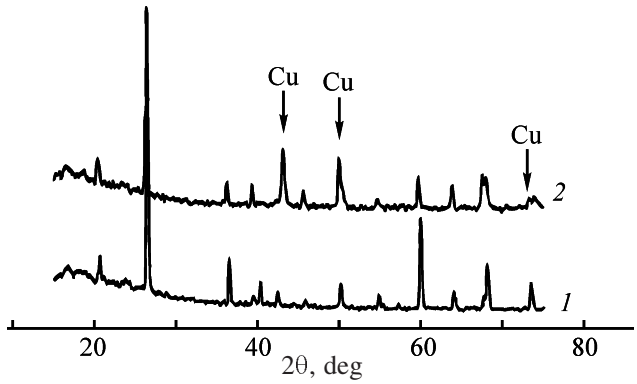


Fig. 2. X-ray diffraction pattern of (*1*) starting and (*2*) copper-plated silica. (2θ) Bragg angle.

The silica had a bulk density of 1.83 g cm^{-3} and particles with an average size of 150 μm, which enabled use of this filler without preliminary grinding. Prior to copper plating, silica was preliminarily sensitized in a 0.005 g l^{-1} palladium chloride solution. To perform metal plating, two compositions of copper-plating solutions with different component concentrations were tested. It was found that, in a solution containing an increased amount of a copper salt (35 g l^{-1} instead of 6 g l^{-1}) and, accordingly, of the other components, copper plating occurs at a substantially higher rate, so that a thicker copper layer can be obtained. That is why the copper plating was performed in all the subsequent experiments in a solution of the following composition (g l^{-1}): $CuSO_4 \cdot 5H_2O$ 35, K–Na tartrate 170, and NaOH 50; a 40% formaldehyde solution (Formalin) was added to the developer immediately before the copper plating in 1 : 10 ratio. The time of copper plating was 25 min at 20°C. Each stage was performed under permanent agitation with a magnetic stirrer. After each stage, silica was washed with water.

Table 1. Electrical resistivity ρ_v of composite films based on BS latex and zapon lacquer in relation to the content of metal-plated silica in the films

Binder	Content of components, wt %		ρ_v, Ω m
	binder	Cu-quartz	
BS latex	80	20	1.0×10^{6}
	70	30	1.0×10^{6}
	60	40	2.5×10^{1}
	50	50	7.0×10^{-1}
	40	60	7.0×10^{-2}
Zapon lacquer	80	20	1.0×10^{6}
	70	30	1.0×10^{6}
	60	40	1.0×10^{-1}
	50	50	1.0×10^{-2}
	40	60	6.0×10^{-3}

The gain in the silica mass upon the copper plating was 0.07 g g^{-1} sand, and the thickness of the copper coating was 1 μm. The silica particles obtained have a characteristic color and bright shine. The optical micrograph taken at a 25× magnification (Fig. 1) shows copper-plated silica particles. The results of an X-ray phase analysis indicate that the plated coating is composed of a single phase, metallic copper (Fig. 2).

The copper-plated silica was used as an electrically conducting filler in deposition of composite polymeric films and coatings based on a butadiene–styrene latex BS-65 of A brand and zapon lacquer [TU (Technical Specification) 2313-041-32811438–2001]. In addition, a binary filler was produced using, together with copper-plated silica, carbon fibers (CF) manufactured by Khimvolokno Production Association, Republican Unitary Enterprise (Svetlogorsk, Belarus) and Ni-containing carbon fibers (Ni-CF).[1] Ni-CF were synthesized by carbonization at 900°C of viscose rayon impregnated with an aqueous solution of nickel chloride [9]. The average length of the fibers used was 0.5 mm. Formulations of prescribed composition were deposited onto glass substrates and dried at room temperature. The coating thickness was 250–400 μm, depending on the degree of filling.

The electrical resistance of 2 × 1-cm composite coatings was measured with a V7-16A general-purpose voltmeter and related to the film thickness to find the volume electrical resistivity ρ_v. The results obtained are listed in Table 1. It can be seen that the resistivity of the coatings under study falls if the polymer contains 40 wt % metal-plated quartz or more. At the same time, it has been reported [2] that, with an ultradispersed copper powder used for polymer filling, the electrical resistance substantially decreases only at degrees of filling equal to 60–70 wt %.

[1] Method developed at the Institute of General and Inorganic Chemistry, National Academy of Sciences of Belarus.

Table 2. Resistivity ρ_v of composite films based on BS latex and containing a combined filler (metal-plated silica + carbon fibers) at various relative contents of the components

Content of components, wt %				ρ_v, Ω m
binder	Cu-quartz	CF	Ni-CF	
70	30	–	–	1.0×10^6
70	27	3	–	2.0×10^1
70	24	6	–	8.0×10^0
80	20	–	–	1.0×10^6
80	18	2	–	1.0×10^2
80	16	4	–	3.0×10^1
80	19.6	–	0.4	1.0×10^1
80	18	–	2	1.0×10^0
80	16	–	4	6.0×10^1

Thus, use of metal-plated silica makes it possible to obtain electrically conducting coatings at considerably smaller degrees of filling, which improves the physicomechanical properties of the coatings obtained.

As the degree of filling increases from 40 to 60 wt %, the resistivity of the coatings based on BS latex decreases from 2.5×10^1 to 7.0×10^{-2} Ω m. Coatings based on zapon lacquer have a lower resistivity than the composite films of the BS latex (1.0×10^{-1} and 6.0×10^{-3} Ω m at filler content of 40 and 60 wt %, respectively). To decrease the film resistance at degrees of filling with metal-plated silica equal to 20 and 30 wt %, a minor amount of carbon or Ni-carbon fibers was introduced into the formulations because these fibers (having an anisotropic shape and good electrical conductivity) combined with the main filler favor the formation of an electrically conducting cluster at smaller degrees of filling [1].

It was found that replacement of 2 and 4 wt % quartz with CF in a formulation based on BS latex and containing metal-plated quartz at a degree of filling equal to 20 wt % reduces the film resistivity by four and five orders of magnitude, respectively (Table 2). If Ni-FC is used for this purpose, ρ_v decreases by five orders of magnitude when 0.4 wt % metallized quartz sand is replaced with Ni-FC, and by six orders of magnitude (to 1.0×10^0 Ω m) upon replacement of 2 wt % metal-plated quartz with Ni-FC. Thus, addition of a minor amount of carbon fibers to metal-plated silica diminishes the threshold silica content at which the composite coating becomes electrically conducting from 40 to 18 wt %.

CONCLUSIONS

(1) Metal-plated silica can be used to obtain low-cost electrically conducting composite coatings with resistivities in the range 2.5×10^1–6.0×10^{-3} Ω m, depending on the degree of filling and type of a binder.

(2) At equal degrees of filling, coatings based on zapon lacquer have an order of magnitude lower electrical resistance than coatings based on butadiene–styrene latex.

(3) Use of a combined filler containing, together with metallized silica, a minor amount (2 wt %) of carbon or Ni-carbon fibers makes it possible to diminish the threshold content of metallized silica at which coatings become electrically conducting from 40 to 18 wt %. The decrease is more pronounced upon addition of a Ni-containing carbon fiber, compared with that upon addition of the same amount of a carbon fiber.

REFERENCES

1. Gul', V.E. and Shenfil', L.Z., *Elektroprovodyashchie polimernye kompozitsii* (Electrically Conducting Polymeric Formulations), Moscow: Khimiya, 1984.
2. Obraztsova, I.I., Simenyuk, G.Yu., and Eremenko, N.K., *Zh. Prikl. Khim.*, 2002, vol. 75, no. 11, pp. 1772–1775.
3. Gardner, E.R., *Product Eng.*, 1963, vol. 34, pp. 67–69.
4. Dunn, E.I. and Kushner, M.I., *Ind. Eng. Chem.*, 1963, no. 1, pp. 4–7.
5. Shinkareva, E.V. and Safonova, A.M., *Steklo Keram.*, 2006, no. 1, pp. 31–32.
6. Bokhan, Yu.I., Klubovich, V.V., and Saraseko, M.N., *Mater. Tekhnol. Instrum.*, 2001, vol. 6, no. 3, pp. 32–36.
7. Shalkauskas, M. and Vashkyalis, A., *Khimicheskaya metallizatsiya plastmass* (Electroless Metal Plating of Plastics), Leningrad: Khimiya, 1985.
8. *Khimicheskoe osazhdenie metallov iz vodnykh rastvorov* (Electroless Deposition of Metals from Aqueous Solutions), Sviridov, V.V., Ed., Minsk: Universitetskoe, 1987.
9. Safonova, A.M., Ermolenko, I.N., Apanasenok, V.I., et al., *Zh. Prikl. Khim.*, 1991, vol. 64, no. 11, pp. 2447–2451.

ISSN 1070-4272, Russian Journal of Applied Chemistry, 2008, Vol. 81, No. 3, pp. 438–442. © Pleiades Publishing, Ltd., 2008.
Original Russian Text © T.G. Kyazimova, E.G. Mamedov, R.S. Babaev, I.M. Mamedova, 2008, published in Zhurnal Prikladnoi Khimii, 2008, Vol. 81, No. 3, pp. 453–457.

ORGANIC SYNTHESIS AND INDUSTRIAL ORGANIC CHEMISTRY

Synthesis and Photostabilizing Properties of Hexachlorobicyclo[2.2.1]hept-5-enylmethyl Esters of Substituted Benzoic Acids

T. G. Kyazimova, E. G. Mamedov, R. S. Babaev, and I. M. Mamedova

Institute of Chemical Problems, National Academy of Sciences of Azerbaijan, Baku, Azerbaijan
Insitute of Petrochemical Processes, National Academy of Sciences of Azerbaijan, Baku, Azerbaijan

Received January 24, 2007

Abstract—Polychlorinated bicyclic esters of *p*-substituted benzoic acids were prepared by the Diels–Alder reaction of hexachlorocyclopentadiene with allyl esters of *p*-substitutted benzoic acids. Some of the adducts synthesized were tested as photostabilizers for polyethylene-based polymer formulations.

DOI: 10.1134/S107042720803018X

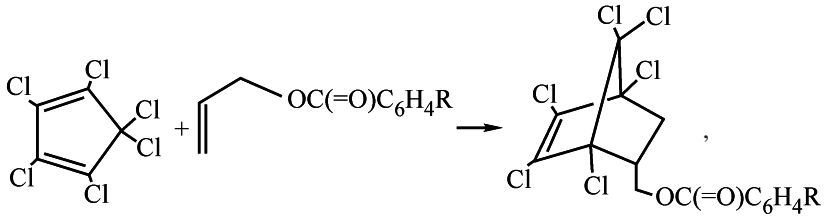
Hexachlorocyclopentadiene (HCCPD, **I**) and related compounds are among unusual objects of the modern organic chemistry. Thanks to HCCPD, the theory of X-philic reactions was developed, and the theory of pericyclic reactions was supplemented by the reversed Diels–Alder reaction. The *syn–anti* isomerism of diene condensation adducts was substantiated using data for HCCPD derivatives [1]. Simple synthesis of dihomocubane compounds from polyhalogenated cyclopentadienes attracts attention. Hexachlorocyclopentadiene and related compounds, along with practical significance, are of interest for elucidating the mechanism of the Diels–Alder reaction [2].

Halogen-containing bicyclic esters with other unique fragments are widely used for imparting flame resistance to polymeric materials, and also as modifiers and curing agents for epoxy resins and biologically active substances [3].

Synthesis of various polyhalogenated bicyclic esters from unsaturated esters of substituted benzoic acids attracts researchers' attention [4, 5].

Proceeding with studies in the field of synthesis of polyhalogenated bicyclic esters [6–9], we prepared, identified, and examined polyhalonorbornenylmethyl esters of *p*-substituted benzoic acids. First, we prepared by a common esterification procedure allyl esters of *p*-substituted benzoic acids **II**–**VIII**. Their physicochemical properties are given in Table 1.

Target products **IX**–**XV** were prepared by diene condensation of HCCPD **I** with allyl esters of *p*-substituted benzoic acids **II**–**VIII**. The reaction follows the scheme



I **II–VIII** **IX–XV**

where R = H (**II**, **IX**), CH_3 (**III**, **X**), HO (**IV**, **XI**), MeO (**V**, **XII**), Cl (**VI**, **XIII**), Br (**VII**, **XIV**), NO_2 (**VIII**, **XV**).

The reaction was performed in the temperature range 100–160°C for 4–12 h; the diene : dienophile molar ratio was from 1 : 1 to 4 : 1. The physicochemi-

Table 1. Constants of allyl esters of *p*-substituted benzoic acids

Compound	T_b, °C (1 mm Hg)	n_D^{20}	d_4^{20}	Yield, %
Allyl benzoate (**II**)	74–75	1.5156	1.056	80
Allyl *p*-methylbenzoate (**III**)	90–92	1.4940	0.8861	58
Allyl *p*-hydroxybenzoate (**IV**)	85–87	1.5040	1.0348	60
Allyl *p*-methoxybenzoate (**V**)	90–92	1.5010	1.0115	60
Allyl *p*-chlorobenzoate (**VI**)	85–89	1.6343	1.2055	78
Allyl *p*-bromobenzoate (**VII**)	95	1.5546	1.3305	82
Allyl *p*-nitrobenzoate (**VIII**)	128–132	1.5420	1.1218	58

Table 2. Properties and elemental analyses of polychloronorbornenyl esters of substituted benzoic acids

Compound	T_b, °C (P, mm Hg) or T_m, °C	n_D^{20}	d_4^{20}	Found, %			Formula	Calculated, %		
				C	H	Hlg		C	H	Hlg
IX	193–194 (1), T_m 50	1.5775	1.4625	41.38	2.30	48.97	$C_{15}H_{10}Cl_6O_2$	41.02	2.15	48.64
X	207–208 (1)	1.5750	1.6340	42.36	2.55	47.06	$C_{16}H_{12}Cl_6O_2$	42.76	2.67	47.44
XI	188–190 (1)	1.5800	1.4986	38.4	1.80	46.4	$C_{15}H_{10}Cl_6O_3$	40.0	2.2	47.2
XII	185–186 (2)	1.5820	1.5010	39.6	1.92	38.7	$C_{16}H_{12}Cl_6O_3$	41.03	2.58	45.08
XIII	97–98	–	–	38.34	1.92	52.56	$C_{15}H_9Cl_7O_2$	38.09	1.67	52.56
XIV	126	–	–	35.02	1.75	57.0	$C_{15}H_9Cl_6BrO_2$	34.86	1.46	56.74
XV	126	–	–	38.06	1.90	30.02	$C_{15}H_9Cl_6O_4$	37.64	1.58	29.88

cal properties of **IX**–**XV** are given in Table 2.

We examined the effect of reaction conditions (temperature, time, reactant ratio) on the yield of the adducts (Table 3).

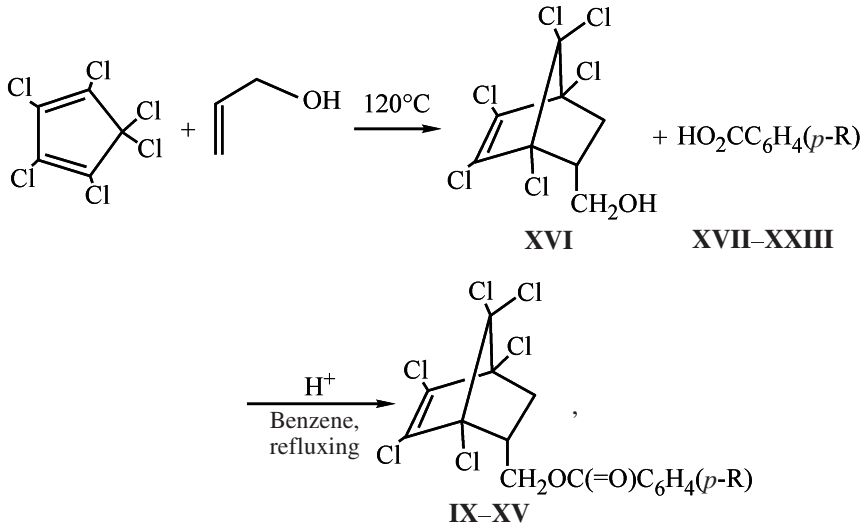
As can be seen, with an increase in the temperature from 100 to 150°C the yield of adduct **IX** increases from 58.2 to 82.4%. Further increase in the temperature (160°C) only slightly affects the yield of **IX**. The data obtained also show that the optimal conditions of adduct formation (with the reaction **I** + **II** → **IX** as example) are as follows: 150°C, 12 h, diene : dienophile ratio 2 : 1.

Under similar optimal conditions (150°C, 12 h, diene : dienophile molar ratio 2 : 1), we performed the condensation of HCCPD with allyl esters of other *p*-substituted benzoic acids **III**–**VIII**. The yields of adducts **X**–**XII** vary within 65.4–90.7%, with the lowest yield observed with allyl halobenzoates **VI** and **VII** (78.8 and 65.4%, respectively). On introducing *p*-hydroxy, *p*-methoxy, and *p*-nitro groups into the aromatic ring, the yield of the adducts increases (90.7, 88.6, and 82.7%, respectively).

The compositions and structures of **IX**–**XV** were proved by independent synthesis: preparation of 2-*endo*-hydroxymethyl-1,4,5,6,7,7-hexachlorobicyclo-[2.2.1]hept-5-ene **XVI** by the reaction of **I** with allyl alcohol according to [10], followed by esterification of alcohol **XVI** with *p*-substituted benzoic acids **XVII**–**XXIII** to obtain the corresponding bicyclic esters **IX**–**XV**:

Table 3. Influence of reaction conditions on the yield of adducts **IX**–**XV**

Dienophile	T, °C	τ, h	Diene : dienophile molar ratio	Yield of adducts **IX**–**XV**, %
II	100	12	2 : 1	58.2
II	120	12	2 : 1	65.3
II	150	12	2 : 1	82.4
II	160	12	2 : 1	84.2
II	150	12	1 : 1	64.2
II	150	12	4 : 1	69.4
II	150	4	2 : 1	43.3
II	150	8	2 : 1	49.2
II	150	16	2 : 1	85.1
III	150	12	2 : 1	64.1
IV	150	12	2 : 1	73.2
V	150	12	2 : 1	90.7
VI	150	12	2 : 1	78.8
VII	150	12	2 : 1	65.4
VIII	150	12	2 : 1	82.7



where R = H, CH_3, HO, MeO, Cl, Br, NO_2.

All the physicochemical characteristics of compounds **IX**–**XV** prepared by both procedures are identical.

The compositions and structures of **IX**–**XV** are confirmed by IR and ^{1}H NMR spectra. The purity was checked by TLC. In the IR spectra of **IX**–**XV**, there are characteristic bands of the C=O bond at 1720–1740, ester C–O bond at 1000–1200, and C–Cl bonds at 750 cm^{-1}. The C=C vibrations have somewhat decreased frequency, 1575–1685 cm^{-1}, because of the presence of chlorine atoms at the double bond. The ^{1}H NMR data for **IX**–**XV** are given in Table 4.

The ^{1}H NMR spectra of polychlorinated norbornenylmethyl derivatives show an *ABX* pattern. The lowest-field signal was assigned to the proton adjacent to the electronegative substituent, H^X. As indicated in [11], the coupling constants of H^X with protons H^A and H^B differ by a factor of approximately 2. The *endo* orientation of the substituent at C^2 is confirmed by the ^{1}H NMR spectra (Table 4) whose parameters are similar to those of the spectra of the known chlorinated analogs [12], hexabromonorbornenes [13], and 1,4,5,6-tetrabromo-7,7-dimethoxynorbornenes [14]. The *endo* orientation of the CN substituent at the C^2 atom of the hexabromonorbornene core is confirmed by comparison of the experimental and calculated dipole moments [13]. In addition, it is known that, in the case of *exo* orientation of the CN substituent at the C^2 atom of pentachloronorbornene, the parameters of the ^{1}H NMR spectrum are essentially different [15].

The *endo* configuration of 2*S*-(–)-menthyl hexachloronorborn-5-ene-2-carboxylate was confirmed by single crystal X-ray diffraction [16].

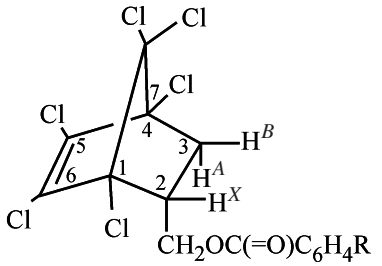
The synthesized compounds **IX**–**XV** were tested as photostabilizers for polymer formulations based on high-density polyethylene (HDPE). These compounds were added in amounts of 0.2, 0.5, and 0.8%. Compounds **IX** and **XIV** appeared to be the most active. On adding stabilizer **IX** to HDPE, the relative breaking elongation ε of the irradiated samples increased by a factor of almost 2 compared to the pure polymer, which is due to good compatibility of the stabilizer with HDPE. The results of the tests are given in Table 5.

After UV irradiation for 200 h, the stabilized formulations exhibited considerably better properties than straight high-density polyethylene. The breaking tensile stress (σ_B) of the initial polymer decreased upon irradiation by 70%, and that of the stabilized polymer, by only 10–13%. The dielectric loss tangent ($\tan\delta$) of the stabilized samples also varied significantly. The lack of degradation of the stabilized HDPE after UV irradiation is confirmed by the results of UV studies. The suggested photostabilizers are light yellow, and their performance meets the requirements of the modern standards.

EXPERIMENTAL

The IR spectra were recorded on a UR-20 spectrophotometer in the range 4000–400 cm^{-1}, and the ^{1}H NMR spectra, on a Tesla BS-48 spectrometer (80 MHz) in CCl_4, internal reference hexamethyldisiloxane. The TLC analysis was performed by the

Table 4. ^{1}H NMR spectra of **IX**–**XV**



Compound	R	Chemical shift, δ, ppm				Coupling constant, Hz		
		H^A, q	H^B, q	H^X, m	OCH_2 (2H), t	J_{AX}	J_{BX}	J_{AB}
IX	H	1.73	2.60	3.17	4.20	8.3	4.80	–11.90
X	CH_3	2.00	2.73	3.25	4.20	8.5	4.25	–12.10
XI	OH	2.15	2.80	3.40	4.30	8.4	4.15	–12.31
XII	OMe	2.10	2.86	3.30	4.50	8.1	4.29	–12.27
XIII	Cl	1.90	2.70	3.30	4.14	8.4	4.15	–12.60
XIV	Br	1.93	2.70	3.25	4.30	8.2	4.10	–12.50
XV	NO_2	2.10	2.80	3.50	4.30	8.5	4.25	–12.70

Table 5. Properties of stabilized formulations based on compounds **IX** and **XIV**

Formulation	Stabilizer content, %	Parameter value after irradiation for 200 h				
		σ_B, kgf cm^{-2}	shrinkage, %	MFI, g/10 min	$\tan\delta \times 10^{-4}$	ε, %
HDPE	–	80	–	–	–	–
HDPE + stabilizer:						
IX	0.2	120	8	0.14	8.7	2.2
IX	0.5	150	8	0.05	11.8	2.0
IX	0.8	130	12	0.08	20.0	2.1
XIV	0.2	240	16	0.11	5.6	2.0
XIV	0.5	230	16	0.21	8.8	2.0
XIV	0.8	230	14	0.46	10.9	19

procedure described in [17]. Alumina (Brockmann grade II) was used as sorbent, and heptane–acetone, as eluent. The spots were visualized by irradiation with a mercury lamp equipped with a light filter.

Hexachlorocyclopentadiene I was prepared by the procedure described in [18], bp 104°C/9 mm Hg; n_D^{20} = 1.5652, d_4^{20} = 1.719.

Allyl esters of *p*-substituted benzoic acids **II**–**VIII** were prepared by the standard procedure, esterification in benzene in the presence of an acid catalyst (sulfuric acid, 5 wt % relative to the reaction mixture). The mixture was washed with a $NaHCO_3$ solution and water, dried over $MgSO_4$, and distilled. The physicochemical parameters of the esters are given in Table 1.

Hexachloronorbornenylmethyl esters of *p*-substituted benzoic acids **IX**–**XV** were prepared by diene synthesis from HCCPD and the corresponding dienophiles **II**–**VIII**.

1,4,5,6,7,7-Hexachlorobicyclo[2.2.1]hept-2-enylmethyl benzoate IX. A mixture of 1.6 g (0.01 mol) of **II** and 5.46 g (0.02 mol) of HCCPD was heated at 150°C for 12 h. Adduct **IX** was obtained; yield 3.58 g (83%). Adducts **X**–**XV** were prepared similarly. The conditions and results are given in Tables 2 and 3.

***endo*-2-Hydroxymethyl-1,4,5,6,7,7-hexachlorobicyclo[2.2.1]hept-5-ene XVI** was prepared according to [19]. Independent synthesis of **IX**–**XV** was performed by esterification of alcohol **XVI** with the corresponding benzoic acids **XVII**–**XXIII** in the presence of an acid catalyst (5% H_2SO_4) in refluxing benzene

with azeotropic distillation of water. All the physicochemical parameters of compounds **IX**–**XV** prepared by independent synthesis are identical to those of the respective compounds prepared by the condensation of HCCPD with allyl esters **II**–**VIII**.

CONCLUSIONS

(1) The Diels–Alder reaction of allyl esters of *p*-substituted benzoic acids with hexachlorocyclopentadiene, performed at 150°C for 12 h at the diene : dienophile ratio of 2 : 1, gave in good yields (65–90%) the corresponding adducts, exclusively in the form of *endo* isomers.

(2) It was demonstrated by the example of high-density polyethylene that polychlorobicyclic esters of *p*-substituted benzoic acids are effective photostabilizers.

REFERENCES

1. Zefirov, N.S., Shestakova, T.F., and Kirpichenok, M.A., *Khimiya geksakhlortsiklopentadiena i rodstvennykh soedinenii* (Chemistry of Hexachlorocyclopentadiene and Related Compounds), Moscow: Mosk. Gos. Univ., 1965.
2. Konovalov, A.I. and Kiselev, V.D., *Izv. Ross. Akad. Nauk, Ser. Khim.*, 2003, no. 2, pp. 279–297.
3. Kyazimova, T.G., *Doctoral Dissertation*, Baku, 1992.
4. Magerramov, A.M., Mustafaev, A.M., Velieva, G.Kh., et al., *Zh. Org. Khim.*, 2004, vol. 40, no. 4, pp. 513–519.
5. Magerramov, A.M., Mustafaev, A.M., Velieva, G.Kh., et al., *Zh. Org. Khim.*, 2004, vol. 40, no. 9, pp. 1324–1328.
6. Mamedov, E.G., *Zh. Prikl. Khim.*, 2005, vol. 78, no. 9, pp. 1577–1579.
7. Mamedov, E.G., *Azerb. Khim. Zh.*, 2001, no. 2, pp. 60–64.
8. Mamedov, E.G., *Zh. Org. Khim.*, 2000, vol. 36, no. 12, pp. 1785–1787.
9. Mamedov, E.G., *Zh. Org. Khim.*, 2002, vol. 38, no. 1, pp. 25–28.
10. Fields, E.K., *J. Am. Chem. Soc.*, 1954, vol. 76, no. 27, pp. 2709–2713.
11. Laszlo, P. and Schleyer, P., *J. Am. Chem. Soc.*, 1963, vol. 85, no. 26, pp. 2709–2711.
12. Akhmedov, I.M., Peynircioglu, B., Mamedov, E.G., et al., *Tetrahedron*, 1994, vol. 50, no. 7, pp. 2099–2106.
13. Mustafaev, A.M., Alekperov, N.A., Guseinov, M.M., et al., *Zh. Org. Khim.*, 1985, vol. 21, no. 8, pp. 1691–1696.
14. Mustafaev, A.M., Imamaliev, A.B., and Guseinov, M.M., *Zh. Org. Khim.*, 1989, vol. 25, no. 9, pp. 1908–1915.
15. Williamson, K.L. and Hsu, Y., *J. Am. Chem. Soc.*, 1970, vol. 92, no. 25, pp. 7383–7389.
16. Ulku, D., Tahir, M.N., Demir, A.S., et al., *Acta Crystallogr., Sect. C*, 1997, vol. 53, pp. 899–901.
17. Akhrem, A.O. and Kuznetsova, A.N., *Tonkosloinaya khromatografiya* (Thin-Layer Chromatography), Moscow: Nauka, 1964.
18. Mamedaliev, Yu.G., Guseinov, M.M., and Mamedov, S.M., *Dokl. Akad. Nauk SSSR*, 1960, vol. 139, no. 2, pp. 379–382.
19. McBee, E.T., Rokoff H.H., and Meyers, R.J., *J. Am. Chem. Soc.*, 1955, vol. 77, no. 16, pp. 4427–4428.

ISSN 1070-4272, Russian Journal of Applied Chemistry, 2008, Vol. 81, No. 3, pp. 443–447. © Pleiades Publishing, Ltd., 2008.
Original Russian Text © R.Z. Biglova, R.F. Talipov, A.U. Galimzyanova, 2008, published in Zhurnal Prikladnoi Khimii, 2008, Vol. 81, No. 3, pp. 458–462.

ORGANIC SYNTHESIS AND INDUSTRIAL ORGANIC CHEMISTRY

Products of Reaction of the Piperylene Fraction with Elemental Sulfur as Additives to Lubricating Oils

R. Z. Biglova, R. F. Talipov, and A. U. Galimzyanova

Bashkir State University, Ufa, Bashkortostan, Russia

Received June 20, 2007

Abstract—A method for quantitative introduction of sulfur into piperylene fraction was developed. The structure of the product was examined, and the effect it exerts on the washing power of bis(oligoisobutenylsuccinimide) in model oil compositions was elucidated. The antiwear and antiscuff properties of the product were tested under pilot conditions.

DOI: 10.1134/S1070427208030191

The performance characteristics of lubricants are efficiently improved by introducing various additives. Up to now, a considerable number of compounds whose influence on the quality of lubricating oils is determined by their structure and the nature of functional groups in their molecules were synthesized and tested [1]. Among organic, above all low-molecular-weight substances, a particular place is occupied by sulfur-containing compounds which are the subject of numerous studies [2–4]. The presence of sulfur in the molecules of additives can be responsible for both antioxidant and antiwear properties they exhibit. The lubricating action of sulfur-containing substances is strongly dependent on their structural properties and character of sulfur bonding [5].

Reactions of unsaturated hydrocarbons with sulfur-containing compounds still remain to be examined more adequately. It should be noted that application of many sulfurizing agents is environmentally unsafe, which makes extremely promising the use of elemental sulfur yielded in huge amounts by hydrodesulfurization of oil products at oil refineries. However, reactions involving elemental sulfur, which is a seemingly simple object, are studied insufficiently. This is due to a complex structure of sulfur proper and to its ability to follow several reaction pathways simultaneously, as well as to possible side reactions at unsaturated bonds of piperylene. In this connection, we synthesized here sulfur-containing additives based on piperylene fraction and elemental sulfur, examined their structure and the lubrication properties of these products when introduced into various compositions, and elucidated how they affect the washing power of an alkenylsuccinimide additive.

EXPERIMENTAL

Our study was concerned with inexpensive and readily available piperylene fraction, a large-capacity by-product of isoprene dehydrogenation in isoprene rubber manufacture at synthetic rubber plants. As known [6], the performance characteristics of sulfur-containing organic compounds when used as additives to improve the lubricating properties of oils are determined by the sulfur content. The process was optimized over a wide temperature and time ranges so that the maximal possible amount of covalently bound sulfur was introduced into the final product.

The reaction of the piperylene fraction with sulfur in a temperature-controlled autoclave without stirring in the presence of cobalt phthalocyanine as catalyst [(>C=C<) : S molar ratio 1 : 4, 130°C, nonpolar solvent] gave a product containing 54.95% sulfur in 10.0% yield. When the reaction was run in a continuously rotating autoclave at the same synthesis parameters, but in a toluene medium, the content of sulfur in the product increased to 70.35%, and the yield of the product was 49.5%. The resulting samples contained a certain amount of ash because of the presence of cobalt phthalocyanine. Sulfurization of piperylene fraction was further optimized in the absence of catalyst (Table 1). The tabulated data suggest that, upon changing from toluene to kerosene, a solvent more readily available commercially, both the yield of the product and its sulfur content decreased insignificantly. At the (>C=C<) : S molar ratio of 1 : 2 in a *p*-xylene medium, sulfur reacts quantitatively. The scatter in the sulfur content of the final compound

Table 1. Reaction of the piperylene fraction with elemental sulfur in an autoclave (130°C, 3 h)

(>C=C<) : S molar ratio	Solvent	Product yield, %	Sulfur content of the product, %
1 : 2	Toluene	48.0	69.86
1 : 1	Toluene	24.9	48.23
1 : 2	Kerosene	43.0	66.11
1 : 1	Kerosene	19.5	47.01
1 : 2	*p*-Xylene	100.0	68.24
1 : 1	*p*-Xylene	78.6	50.71

is due, probably, to varying composition of the initial diene fraction.

To identify the resulting compound, we isolated *trans*-piperylene from the piperylene fraction and brought it into the reaction with sulfur. The product yield was 70%, and the mass fraction of sulfur, 64.8%. The molecular weight of the substance was estimated cryoscopically (in CCl_4) at 386 [7]. The ^1H NMR spectrum of the product exhibits signals at 6.50–7.50 ppm, characteristic of olefin protons. A signal at 1.10–1.50 ppm belongs to methyl protons, and a strong multiplet at 2.10–2.50 ppm, to methine protons. The relative integral intensities of the signals from methylene and methyl protons suggest the presence of two double bonds in the molecule of the product. The presence of double bonds is also supported by characteristic bands in the IR spectra at 1600–1660 cm^{-1}. In the ^{13}C NMR spectrum, there are signals at 38.0–39.0 ppm associated with CH_2–S groups and those at 45.0–47.0 ppm associated with –CH–S groups. Absorption at 600–450 cm^{-1} in the IR spectrum can be attributed to –S–S– vibrations.

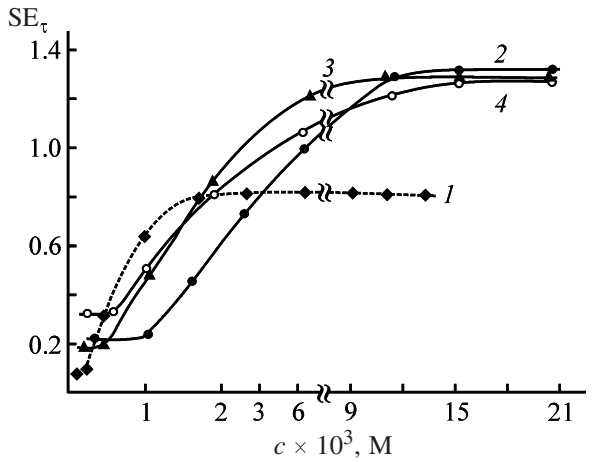


Fig. 1. Solubilizing power vs. concentration c of the additives in isooctane. (SE_τ) Solubilization effect in time τ = 15 min. Additive: (*1*) SI, (*2*) bis(piperylene tetrasulfide), (*3*) bis(piperylene tetrasulfide)–SI (0.5 wt %), and (*4*) bis(piperylene tetrasulfide)–SI (1.0 wt %).

Taken together, the results of the physicochemical analysis suggest that the reaction of *trans*-piperylene with sulfur yields bis(piperylene tetrasulfide):

$$2CH_2{=}CH{-}CH{=}CH{-}CH_3 + S_8 \longrightarrow CH_2{-}CH{=}CH{-}CH(S_4){-}CH_3$$
$$CH_2{-}CH{=}CH{-}CH(S_4){-}CH_3.$$

This scheme is in agreement with the data [2] obtained for the reaction of low-molecular-weight dienes with sulfur. The developed method of quantitative introduction of sulfur into piperylene fraction in a *p*-xylene medium was used for accumulation of an experimental batch (~2 kg) of the substance for industrial tests.

The performance characteristics of lubricating oils are typically improved by introducing formulations (packages) of several additives. Individual compounds from the packages exhibit the desired performance characteristics to a different extent; the overall result is achieved through correctly choosing, both qualitatively and quantitatively, the components, taking into account their possible interaction. In [8, 9], we elucidated the mutual influence of antioxidizing and washing and dispersing additives. Here, we attempted to optimize the composition of the additive package, to which end we elucidated how the reaction products of piperylene fraction and elemental sulfur affect the performance characteristics of a washing and dispersing additive, bis(oligoisobutenylsuccinimide) (SI).

Since the washing effect of surfactants is determined by their solubilizing power, we determined the critical micelle concentration (CMC) of bis(piperylene tetrasulfide) and SI by the dye solubilization method. The solubilizing action of the additives was examined in an isooctane medium by the technique we described in [8]. A solubilizing effect with respect to a dye in a hydrocarbon medium is observed at the surfactant content in the system lying within the CMC range. The solubilization effect (SE) is determined as the difference in the optical densities of the corresponding systems before and after introduction of the dye. The plots of the SE vs. concentration of the ingredients exhibit an exponential run up to certain ratios at which they flatten out (Fig. 1). The plots of SE vs. concentration of the additives and

Table 2 suggest that the solubilizing power of SI with respect to dyes increases when SI is combined with sulfur-containing products. This is manifested in a shift of the CMC range to low concentration and an increase in the dD/dc parameter. This effect allows not only decreased dosages of the components in an oil composition, but also significant improvement of their performance characteristics.

The antiwear and antiscuff properties of the synthesized sulfur-containing compounds based on piperylene fraction were examined on an experimental setup by known techniques [10]. These properties were characterized by the wear rate of steel rods a_m and friction coefficient K_{fr}. The antiwear properties of the composition based on cylinder oil no. 52 upon introduction of bis(piperylene tetrasulfide) were estimated on an Ekspress friction machine under stepwise increase of the specific load in the presence of 3 wt % additives (Fig. 2). We found that bis(piperylene tetrasulfide) causes the wear resistance of the rods to increase relative to a commercial analog, zinc *O,O'*-bis(octylphenyl) phosphorodithioate (VNII NP-354 additive). A sharp difference in the wear rates of rods in the presence of commercial and experimental additives, observed upon increasing the specific load, is due probably to the specific structural features of sulfur-containing moieties of the additives. The energy required for breaking the P–S bonds in the phosphorodithioate exceeds that for the S–S bond in polysulfide (260 against 218 kJ mol^{-}) [11]. A smaller energy consumed in breaking the polysulfide bonds favors more intensive tribochemical processes occurring on the metal surface, which increases the wear resistance of the surfaces under exploitation.

Comparison of the plots of the steel wear vs. the specific load at different bis(piperylene tetrasulfide) concentrations in KS-19 oil (Fig. 3) with the concentration dependence of the solubilizing power of this additive (Fig. 1) suggests the following. The antiwear properties of the oil (curves *1, 2*) are appreciably improved specifically in the CMC area [for bis(piperylene tetrasulfide), 0.05–0.45 wt %, Fig. 1]. Beyond this range, the steel wear decreases to a considerably smaller extent (curves *3, 4*). The observed effect allows the antiwear performance to be correlated with micellization. The wear resistance sharply increases at the additive concentrations approaching the micellization onset concentration. Our results agree with the data reported by Loznetsova et al. [12] and Tyul'pakov et al. [13], who examined the antiwear performance as influenced by the concentration of the fluorine- and sulfur-containing alkyl phosphates.

Table 2. Critical micelle concentration and dD/dc parameters of the additives in isooctane for the case of rhodamine solubilization

Surfactant	$c \times 10^3$, M	dD/d$c \times 10^{-3}$
SI	0.26–1.38	1.82
Bis(piperylene bistetrasulfide)	0.86–7.80	0.37
Bis(piperylene bistetrasulfide)–SI, wt %:		
0.5	0.35–8.69	0.54
1.0	0.17–8.69	0.64

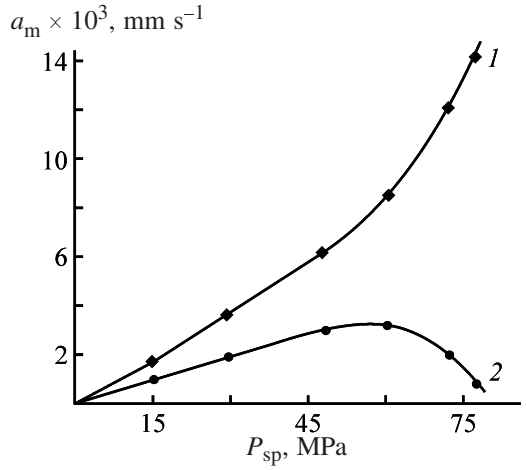


Fig. 2. Steel wear rate a_m vs. specific load P_{sp} in the presence of compositions of cylinder oil no. 52 containing various additives. Additive: (*1*) zinc *O,O'*-bis(octylphenyl) phosphorodithioate (VNII NP-354) and (*2*) bis(piperylene tetrasulfide).

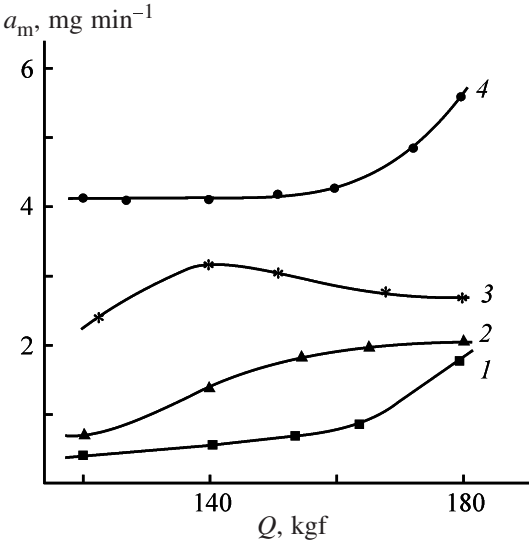


Fig. 3. Steel wear rate a_m vs. specific load Q in KS-19 oil in the presence of various concentrations of bis(piperylene bistetrasulfide). Bis(piperylene tetrasulfide) concentration, wt %: (*1*) 0.10, (*2*) 0.50, (*3*) 1.00, and (*4*) 2.00.

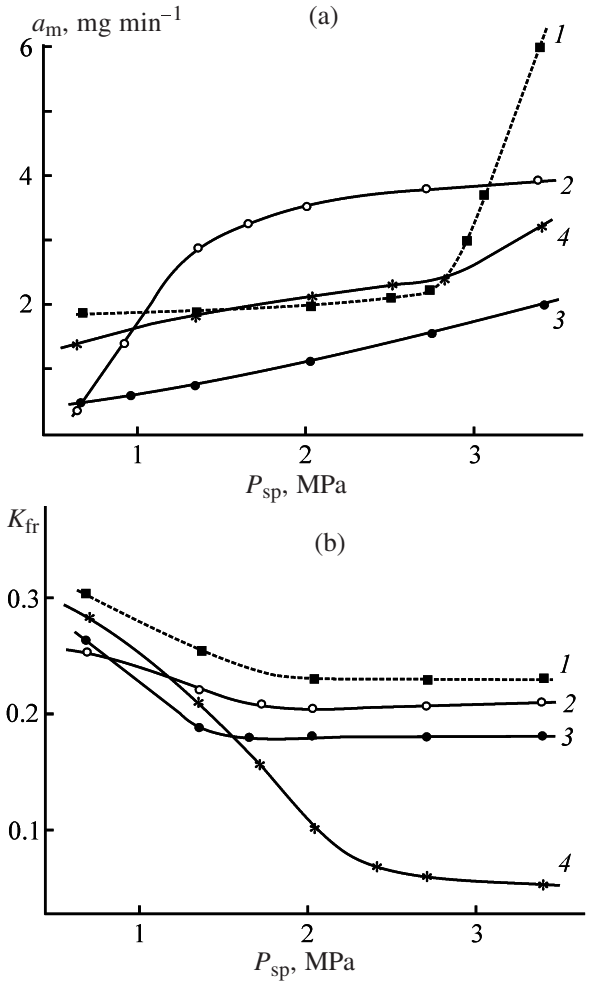


Fig. 4. (a) Steel wear rate a_m and (b) friction coefficient K_{fr} of the steel–steel couple in drilling muds containing various additives vs. the specific load P_{sp}. Additive: (*1*) none, (*2*) SDBUR (1%), (*3*) SDBUR (1%) + bis(piperylene tetrasulfide) (0.1%), and (*4*) SDBUR (1%) + bis-(piperylene tetrasulfide) (0.1%) in xylene.

We also examined here the antiwear and antifriction properties of drilling muds in the presence of minor (up to 1 wt %) amounts of bis(piperylene tetrasulfide) and up to 3 wt of SDBUR lubricant additive, a water-soluble surfactant. It was found that, in the examined range of specific loads, all the additives tend to decrease the friction coefficient of the steel–steel couple in drilling muds. The most pronounced effect was observed in the case of the SDBUR additive combined with bis(piperylene tetrasulfide) (Fig. 4b, curves *3, 4*). The same composition of the additives provides a minimal wear rate for steel (Fig. 4a, curve *3*).

Table 3. Average performance characteristics of III-215.9 MS3GV bits

Hole	Performance characteristics of base/experimental bits			
	n, number	H, m	t_d, h	V_m, m h^{-1}
3728	23/8	107/142	12.3/15.9	8.7/8.9
411	14/7	87/102	7.3/9.35	11.7/10.9
1963	19/5	114/153	9.3/12.9	12.3/11.8

We found that the performance characteristics of the compositions examined are also affected by the ingredient mixing order: The best results were obtained for SDBUR water-soluble additive preliminarily mixed with the sulfurization product of piperylene fraction.

The product of the reaction between piperylene fraction and elemental sulfur, accumulated at plants,[1] was tested under commercial conditions. Table 3 presents the results of testing a sulfur-containing additive (1%) introduced into SDP-3M lubricating grease for unsealed supports of rotary bits used in hole drilling. Table 3 shows that the headway per drill bit increased by 25.3% on the average, and the strength of the drill bit supports, by 28.6% at virtually unchanged mechanical drilling speed V_M.

Thus, the tests showed that the substances we obtained are suitable as high-performance antiwear additives to lubricants used in drilling technology.

CONCLUSIONS

(1) A method of quantitative introduction of up to 70% elemental sulfur into piperylene fraction was developed. The reaction of *trans*-piperylene with sulfur yields bis(piperylene tetrasulfide).

(2) Bis(piperylene tetrasulfide) causes the solubilizing power of succinimide additives to increase.

(3) Bis(piperylene tetrasulfide) exhibits the best antiwear performance characteristics when its concentration in oil lies within the critical micelle concentration range.

(4) Commercial tests showed that introduction of 1% sulfur-containing piperylene fraction improves the antiwear and antiscuff performance of lubricant compositions on drilling plants by 25%, on the average.

[1] The tests were carried out in Neftekamsk, Surgut, and Kogalym, as well as in Gubkino settlement (Komsomol'skoe oil and gas deposit).

REFERENCES

1. Movsumzade, M.M., Gasanova, E.T., Bilalov, S.B., et al., *Neftekhimiya*, 2002, vol. 42, no. 5, pp. 398–400.
2. *Organic Chemistry of Sulfur*, Oae, S., Ed., New York: Plenum, 1977.
3. Belinskaya, R.V., Borshchevskii, S.B., and Levinson, V.S., *Khim. Tekhnol. Topl. Masel*, 1981, no. 9, pp. 56–57.
4. Rylova, M.V. and Samuilov, Ya.D., *Materialy Tret'ei Vserossiiskoi konferentsii molodykh uchenykh "Sovremennye problemy teoreticheskoi i eksperimental'noi khimii* (Proc. 3rd Conf. of Young Scientists "Current Problems of Theoretical and Experimental Chemistry"), Saratov, June 19–20, 2001, p. 209.
5. Kirichenko, G.N., Ibragimov, A.G., Kirichenko, V.Yu., et al., *Neftekhimiya*, 2004, vol. 44, no. 4, pp. 318–320.
6. Selezneva, I.E., Levin, A.Ya., and Monin, S.V., *Khim. Tekhnol. Topl. Masel*, 1999, no. 6, pp. 39–43.
7. *Fizicheskaya khimiya: teoreticheskoe i prakticheskoe rukovodstvo. Uchebnoe posobie dlya vuzov* (Physical Chemistry: Theoretical and Practical Guide. Manual for High Schools), Nikol'skii, B.P., Ed., Leningrad: Khimiya, 1987, 2nd ed.
8. Biglova, R.Z., Galimzyanova, A.U., Konesev, G.V., et al., *Teor. Osn. Khim. Tekhnol.*, 2006, vol. 40, no. 5, pp. 572–579.
9. Biglova, R.Z., Galimzyanova, A.U., Talipov, R.F., et al., *J. Appl. Polym. Sci.*, 2007, vol. 103, no. 3, p. 1375.
10. Konesev, G.V., Mavlyutov, M.P., Spivak, A.I., and Ismagilov, R.A., *Smazochnoe deistvie sred v burovoi tekhnologii* (Lubricating Action of Media in Drilling Technology), Moscow: Nedra, 1993.
11. *Teoreticheskie osnovy khimmotologii* (Theoretical Fundamentals of Chemmotology), Bratkov, A.A., Ed., Moscow: Khimiya, 1985.
12. Loznetsova, N.N., Pavlov, K.A., Toporov, Yu.P., and Shchegolev, G.G., *Materialy II Mezhdunarodnoi konferentsii "Kolloid-2003"* (Proc. II Int. Conf. "Colloid-2003"), Minsk, October 20–24, 2003, p. 184.
13. Tyul'pakov, D.B., Bekkenev, R.Kh., Shchegolev, G.G., et al., *Materiolovedenie*, 1998, no. 8, pp. 48–50.

ISSN 1070-4272, Russian Journal of Applied Chemistry, 2008, Vol. 81, No. 3, pp. 448–451. © Pleiades Publishing, Ltd., 2008.
Original Russian Text © T.G. Dmitrienko, S.S. Popova, 2008, published in Zhurnal Prikladnoi Khimii, 2008, Vol. 81, No. 3, pp. 463–466.

ORGANIC SYNTHESIS AND INDUSTRIAL ORGANIC CHEMISTRY

A New Electrochemical Procedure for Preparing 2,4,6-Triphenylselenopyran from 1,5-Diketones under Conditions of Acid Catalysis

T. G. Dmitrienko and S. S. Popova

Technological Institute, Saratov State Technical University, Engels, Saratov oblast, Russia
Saratov Military Institute of Chemical, Biological, and Radiation Protection, Saratov, Russia

Received February 9, 2007

Abstract—A new electrochemical procedure was developed for preparing 2,4,6-triphenylselenopyran from 1,5-diketones under conditions of acid catalysis at oxidative electrochemical activation of hydrogen selenide in the presence of a one-electron oxidizing agent in a nonaqueous solution. The electrolysis products were analyzed by gas chromatography with a mass-selective detector.

DOI: 10.1134/S1070427208030208

Selenium-containing heterocyclic compounds are widely used for preparing pharmaceuticals, odorants in perfumery, photomaterials, photosensitizers, dyes, and polymer fibers [1, 2]. High biological activity of low-toxic 4H-selenopyrans was revealed recently. Therefore, development of new convenient methods for preparing these compounds becomes an urgent problem [1]. Reaction of 1,5-diketones with hydrogen sulfide in the presence of acids yields thiopyrans or their disproportionation products, thiopyrylium salts, thiacyclohexanes, or dihydrothiopyrans [3]. Selenopyrans and selenopyrylium salts can be prepared similarly by acid-catalyzed reaction with hydrogen selenide [4].

Most of methods for preparing arylaliphactic 4H-selenopyrans are based on reactions of gaseous hydrogen selenide with appropriate 1,5-diketones or reactions of selenopyrylium salts with metal hydrides [4]. The most convenient reactions of arylaliphatic 1,5-diketones with hydrogen selenide can be performed only with polysubstituted diketones. The main products of these reactions were mixtures of selenopyrylium salts and selenacyclohexanes.

Electrochemical synthesis of some organoselenium compounds and electrochemical behavior of some selenium-containing heterocyclic compounds is a relatively new field of selenium electrochemistry. Therefore, development of new procedures for preparing selenium-containing heterocyclic compounds and study of their redox properties are urgent problems.

As chemical synthesis of selenopyrans has already been developed [1], the aim of this study was to develop an electrochemical synthesis of selenopyrans and selenopyrylium salts. In this study we developed a new procedure for preparing 4H-selenopyrans and examined some features of their reactions. For this purpose, we studied reaction of 1,5-diketones with electrolytically generated hydrogen selenide under conditions of acid catalysis and oxidative activation of the reagent. Hydrogen selenide formed by electrolysis on a selenium electrode reacts with a 1,5-diketone in ethanol to give 4H-selenopyran as one of the products.

EXPERIMENTAL

Electrochemical synthesis was performed in a glass three-electrode electrochemical cell with nonseparated anode and cathode compartments in a nonaqueous solution at a fixed temperature with stirring. A platinum wire 0.25 mm in diameter was used as an auxiliary electrode (anode). Electrodes prepared by application of selenium to the surface of different metals or selenium electrodes prepared by different methods were used as working electrodes (cathodes). The first step was the development of the electrode design. Selenium was applied to nickel, copper, and platinum electrodes of different configurations. The nickel electrode was a 5 cm^2 plate cut from Ni foil; the copper electrode was a copper wire 1.5 and 2.5 mm in diameter and 5 cm long; the platinum electrode was platinum wire 0.25 mm in diameter and 10 mm long,

which was sealed in a glass tube. Selenium was applied as follows. Selenium powder in a ceramic crucible was placed in a muffle furnace and was melted at 273°C. An appropriate metallic electrode was immersed in the melt and kept there for 5 s. The electrode was taken out from the melt and cooled in air until the selenium completely solidified.

The electrolyte was prepared as follows: PCl_3 (3.1 ml) was added from a dropping funnel to ethanol (22 ml) placed in a conical flask. The flask was cooled on an ice bath, and its contents were stirred with a magnetic stirrer. Then a weighed portion of 1,3,5-triphenylpentane-1,5-dione was dissolved in the flask. The reaction course and the purity of the reaction products were monitored by thin-layer chromatography (TLC) using a hexane–ether–chloroform mixture (3 : 1 : 1) as an eluent (the chromatogram was developed with iodine vapor) and gas chromatography with mass-selective detector (GC–MSD).

The selenium electrode potential controlled with the aid of a P-5848 potentiostat was –0.4 V. The organoselenium salt was electrochemically identified by measuring its voltametric properties with a stationary platinum electrode with a surface area of 3.48 mm^2 as the working electrode and a saturated silver chloride electrode with a waterproof diaphragm as the reference electrode. A 70 mm^2 platinum plate was used as an auxiliary electrode. The supporting electrolyte was 0.20 M NBu_4ClO_4. The electrochemically prepared salt was identified on the background of 2,4,6-triphenylselenopyrylium perchlorate prepared by the chemical procedure described in [1]. Exhaustive microelectrolysis of 2,4,6-triphenylselenopyran was performed at a constant potential E_a = 1.0 V. Microelectrolysis of 2,4,6-triphenylselenopyrylium perchlorate was performed at a cathode potential E_c = –0.8 V for 3 h.

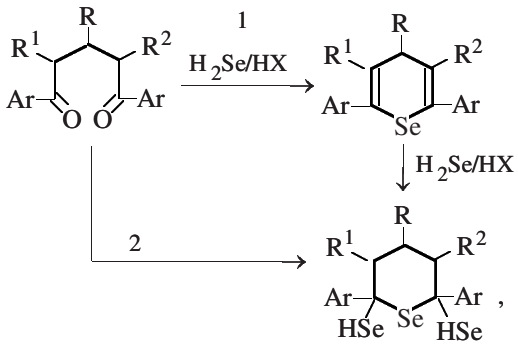
It is known [5, 6] that electrochemical preparation of different organoselenium compounds involves formation of organoelement compounds in the course of both anodic and cathodic processes. However, the electrochemical method, based on these reactions, for preparing compounds with carbon–element bonds is poorly understood.

Usually an organic compound present in an electrolyte can be reduced at the cathode during electrolysis of this solution. However, in some case another cathodic process involving dissolution of the cathode is observed. This reaction is mainly typical for electroreduction of aldehydes, ketones, some unsaturated compounds, and alkyl halides. The formation mechanism of organoelement compounds by cathodic reactions is an open question. Cathodic dissolution of an element is a paradoxical fact itself.

The majority of researchers believe [5, 6] that organoelement compounds are formed by the radical mechanism by the reaction of a radical formed at the cathode with the electrode material. However, not all the cathodic reactions of formation of organoelement compounds can be described within the framework of this concept. These facts suggest that radicals formed in the course of electrolysis are present in the form of an intermediate complex with the cathode material, rather than in the form of kinetically independent species. Under favorable conditions, this complex abstracts an atom from the crystal lattice of the cathode to form an organoelement compound. In some cases, an organoelement compound is formed by a pathway other than a direct electrochemical reaction.

Tomilov et al. [6] showed that the formation mechanism of organoelement compounds by cathodic reactions strongly depends on the type of the organic compound and cathode and should be considered separately in each particular case. The electrochemical behavior of the most widely known organoselenium compounds was examined in [7, 8]. Not only HCl but also HBr, CH_3COOH, and Lewis acids ($ZnCl_2$ and $ZnBr_2$) can be used to produce an acid media. It should be noted that chemical and electrochemical one-electron irreversible oxidation of hydrogen selenide in nonaqueous solutions yields a highly reactive radical cation which exhibits strong acid properties and can be fragmented in nonaqueous solution with proton elimination.

Electrolysis of 1,5-diketones in 4 N HCl solution in ethanol gives the following most probable products:

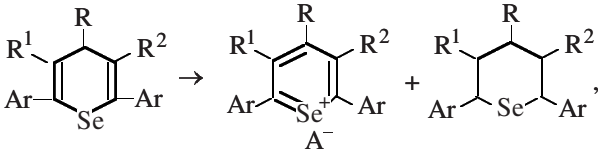


(1)

where Ar, R = Ph; R^1, R^2 = H; X = Cl, Br.

4H-Selenopyran formed at an excess of hydrogen selenide can add the HSe group to the double bonds of the selenopyran ring to form hydroselenium derivatives. The hydroselenium derivatives can be formed directly from 1,5-diketone by scheme (1.2).

The GC–MSD analysis of the electrolysis products shows that 2,4,6-triphenylselenopyran is formed even at a low current (6 mA) after electrolysis for 1 h. The amount of 2,4,6-triphenylselenopyran significantly increases and the amount of the initial 1,3,5-triphenylpentane-1,5-dione decreases after electrolysis for 1.5 h at this current. Further analysis performed at 2-h intervals showed formation and gradual accumulation of 2,4,6-triphenylselenopyran in the solution and a decrease in the amount of the initial 1,5-diketone up to its complete disappearance in 8 h after the reaction start. A flaky precipitate of 2,4,6-triphenylselenopyran was obtained after completion of the electrolysis in 4 N HCl in C_2H_5OH. However, in this case formation of selenopyrylium salts and the corresponding selenacyclohexanes by disproportionation of 4H-selenopyran is also possible:

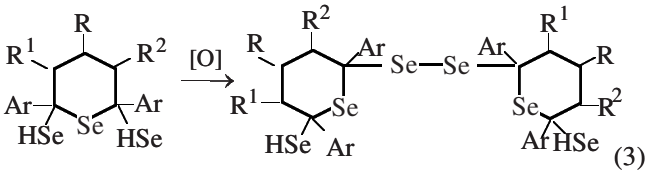

(2)

where A is anion; Ar, R = Ph; R^1, R^2 = H; X = Cl, Br.

Taking into account that fact that selenopyrylium salts are readily soluble in alcohol, we suggest that the precipitate is 2,4,6-triphenylselenacyclohexane which is poorly soluble in this solvent.

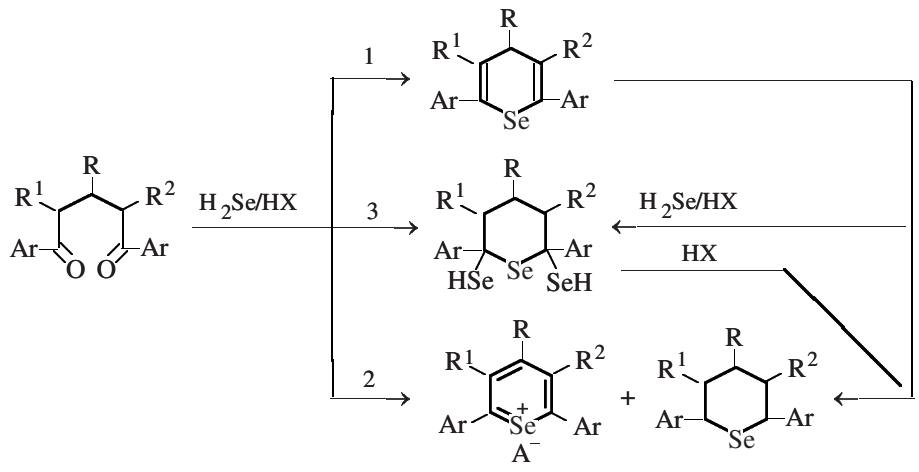
Electrolysis on a selenium-coated nickel plate as the cathode was performed for 13 h at constant current (10 mA) and voltage. Formation of 2,4,6-triphenylselenopyran was observed in 1 h after starting the electrolysis. The reaction mixture was analyzed at 2-h intervals. Hydroselenium derivatives [2,6-(dihydroseleno)-2,4,6-triphenylselenacyclohexane] and the corresponding diselenides (hydroseleno derivatives are oxidized with atmospheric oxygen to diselenides) were detected by GC–MSD in 5 h after starting the electrolysis. The fact that only a very small amount of the initial 1,5-diketone in the reaction mixture was determined by GC suggests that the reaction goes virtually to completion.

A change in the electrolysis parameters (J = 15 mA, τ = 7 h) has no effect on the quantitative composition of the system but accelerates formation of the above compounds and increases their yields. Thus, the reaction can be described by the following scheme:


(3)

where Ar, R = Ph; R^1, R^2 = H; X = Cl, Br.

Electrochemical synthesis of heterocyclic selenium-containing compounds under conditions of acid catalysis in a nonaqueous solution yields a mixture of products and can be described by the following scheme:


(4)

where A is anion; Ar, R = Ph; R^1, R^2 = H; X = Cl, Br.

Arylaliphatic 1,5-diketones react with hydrogen selenide under conditions of acid catalysis in an inert atmosphere along three pathways which differ in the extent of transformation. Reaction (4.1) yields arylaliphatic 4*H*-selenopyrans; reaction (4.2) yields disproportionation products of 4*H*-selenopyrans; and

reaction (4.3) is characterized by addition of hydrogen selenide to the double bonds of the selenopyran ring [scheme (4)].

It should be noted that the cathode material is consumed in the course of electrolysis, which is probably due to occurrence of multistep reactions and free radical formation. Two sharp waves at –0.93 and –1.19 V (I_p = 7 μA) appear in the cathodic curve after introduction of 2×10^{-5} M 2,4,6-triphenylselenopyrylium perchlorate into the cell. These waves can be probably due to oxidation and reduction of the heteroaromatic ring rather than of the substituents.

Thus, formation of organoselenium compounds in the course of electrolysis on a selenium electrode was determined by GC–MSD. 2,4,6-Triphenylselenopyran and 2,4,6-triphenylselenopyrylium perchlorate were prepared by oxidative electrochemical activation of hydrogen selenide in the presence of one-electron oxidizing agents. Solid salts of the heterocyclic aromatic cation have a layered structure typical for graphitized carbon materials. This fact suggests that electrode materials with new properties can be prepared from mixtures of the organic salt with graphitized carbon.

CONCLUSIONS

(1) An electrochemical procedure was developed for preparing 2,4,6-triphenylselenopyran and selenopyrylium salts from 1,5-diketones under conditions of acid catalysis in a nonaqueous solution on a selenium cathode. The 2,4,6-triphenylselenopyran yield was 67%.

(2) The electrolysis products were identified by gas chromatography with mass-selective detector.

(3) Procedures for preparing selenium electrodes were developed.

REFERENCES

1. Drevko, B.I., Chalcogen-Containing Heterocyclic Compounds Prepared from 1,5-Diketones: Synthesis, Properties, and Some Features of Reaction, *Doctoral Dissertation*, Saratov, 1997.
2. Tutel'yan, V.A., Knyazhev, V.A., and Khotimchenko, S.A., *Selen v organizme cheloveka: metabolizm. Antioksidantnye svoistva, rol' v kantserogeneze* (Selenium in Human Body: Metabolism. Antioxidative Properties, Role in Carcinogenesis), Moscow: Ross. Akad. Med. Nauk, 2002.
3. Kharchenko, V.G. and Kozhevnikova, N.I., in *Karbonil'nye soedineniya v sinteze geterotsiklov: Mezhvuzovskii sbornik nauchnykh statei* (Carbonyl Compounds in Synthesis of Heterocycles: Coll. of Scientific Papers of Institutes of Higher Education), Saratov: Saratov. Gos. Univ., 1989, pp. 29–31.
4. Kharchenko, V.G. and Drevko, B.I., *Khim. Geterotsikl. Soedin.*, 1984, no. 12, pp. 1634–1637.
5. Okhlobystin, O.Yu. and Berberova, N.T., *Zh. Obshch. Khim.*, 1996, vol. 66, no. 11, pp. 1796–1799.
6. Tomilov, A.P., Fioshin, M.Ya., and Smirnov, V.A., *Elektrokhimicheskii sintez organicheskikh veshchestv: Uchebnoe posobie* (Electrochemical Synthesis of Organic Compounds: Textbook), Moscow, 1976, pp. 243–278.
7. Zhuikov, V.V., Latypova, V.Z., Postnikova, M.Yu., and Kargin, Yu.M., *Zh. Obshch. Khim.*, 1987, vol. 57, no. 3, pp. 609–612.
8. Muller, R., Lamberts, L., and Evers, M., *Electrochim. Acta*, 1994, vol. 39, no. 17, pp. 2507–2516.

ISSN 1070-4272, Russian Journal of Applied Chemistry, 2008, Vol. 81, No. 3, pp. 452–454. © Pleiades Publishing, Ltd., 2008.
Original Russian Text © A.V. Babakhanyan, M.O. Manukyan, Zh.R. Babayan, R.S. Arutyunyan, 2008, published in Zhurnal Prikladnoi Khimii, 2008, Vol. 81, No. 3, pp. 467–469.

ORGANIC SYNTHESIS AND INDUSTRIAL ORGANIC CHEMISTRY

Antimicrobial Surfactants Based on *N,N'*-(5-Oxanona-2,7-diyne-1,9-diyl)bis[(alkoxycarbonylmethyl)-dimethylammonium] Chlorides

A. V. Babakhanyan, M. O. Manukyan, Zh. R. Babayan, and R. S. Arutyunyan

Institute of Organic Chemistry, National Academy of Sciences of the Republic of Armenia, Yerevan, Armenia
Abovyan Armenian State Pedagogical University, Yerevan, Armenia
Yerevan State University, Yerevan, Armenia

Received May 15, 2007

Abstract—A series of quaternary bisammonium salts containing the common 5-oxanonane-2,7-diyne-1,9-diyl fragment and different alkoxycarbonylmethyl groups was synthesized. The surfactant properties and antimicrobial activity of these compounds were studied.

DOI: 10.1134/S107042720803021X

Many practically important properties of surface-active quaternary bisammonium salts depend on the structure of the common group binding the terminal alkylammonium groups. Among these compounds, functionally substituted derivatives of mono- and bisammonium salts containing unsaturated bonds are of particular interest [1–3].

Taking into account that ammonium salts with the allyl and propargyl groups exhibit distinct antimicrobial activity, in this study we synthesized bisammonium salts containing, along with the alkoxycarbonylmethyl radicals ensuring surface activity, the common 5-oxononane-2,7-diyne-1,9-diyl group (see table).

These salts were prepared in high yields by the following reactions:

$$HC{\equiv}CCH_2Br + HOCH_2C{\equiv}CH \xrightarrow{NaOH} HC{\equiv}CCH_2OCH_2C{\equiv}CH$$

$$HC{\equiv}CCH_2OCH_2C{\equiv}CH \xrightarrow[(CH_3)_2NH,\ CH_2O]{FeCl_3,\ \text{dioxane}} (CH_3)_2NCH_2C{\equiv}CCH_2OCH_2C{\equiv}CCH_2N(CH_3)_2$$

$$(CH_3)_2NCH_2C{\equiv}CCH_2OCH_2C{\equiv}CCH_2N(CH_3)_2 \xrightarrow[ROCOCH_2Cl]{\text{Ethanol}} (CH_3)_2\overset{+}{N}(Cl^-)CH_2C{\equiv}CCH_2OCH_2C{\equiv}CCH_2\overset{+}{N}(Cl^-)(CH_3)_2,$$
$$\quad\quad\quad

Characteristics of *N,N'*-(5-oxanonane-2,7-diyne-1,9-diyl)bis[(alkoxycarbonylmethyl)dimethylammonium] chlorides **I–IV** (the salts are hygroscopic) and their antimicrobial activity*

Compound	R	Yield, %	R_f	Found/Calculated, %		Formula	CMC × 10^4, M	γ_{CMC}	G	h	Concentration, %	t_{death}, min	
				N	Cl^-							M_1	M_2
I	C_4H_9	96.7	0.43	5.1/5.5	14.35/13.95	$C_{24}H_{42}Cl_2N_2O_5$	8.91	65	6.9	0	2	10	5
											1	30	25
II	C_8H_{17}	98	0.5	4.15/4.5	11.05/11.43	$C_{32}H_{58}Cl_2N_2O_5$	4.47	54	38.4	0.3	1	5	5
											0.5	10	5
											0.1	30	25
III	$C_{10}H_{21}$	98.5	0.4	3.95/4.14	10.75/10.49	$C_{36}H_{66}Cl_2N_2O_5$	2.29	47	105.6	0.8	0.05	5	5
											0.025	25	20
IV	$C_{12}H_{25}$	96.5	0.56	3.79/3.82	9.55/9.69	$C_{40}H_{74}Cl_2N_2O_5$	2.10	44	129.4	0.9	0.1	10	5
											0.05	20	15
											0.025	>30	30

* (CMC) Critical micelle concentration; (γ_{CMC}) surface tension at CMC, mN m^{-1}; (h) froth stability; (G) surface activity, N m^2 kmol^{-1}; (t_{death}) time of death of microorganisms, where (M_1) *Escherichia coli* (strain 1257), (M_2) *Staphylococcus aureus* (strain 906).

We found that variation of G values in the series of QASs under considerations deviates from the Duclot–Traube rule, which is typical of colloidal surfactants [5].

One of practically important characteristics of surfactants is their froth stability [5]. The froth-forming ability of aqueous QASs was determined as the ratio of the initial froth column height to that after settling for 5 min [6]. We found that the froth stability increases with increasing length of radicals R. All QASs under consideration were found to be efficient froth-forming aqents.

The antimicrobial activity of QASs **I–IV** was determined by a technique based on disinfection of cambric test-objects sown with standard strains of *Staphylococcus aureus* (strain 906) and *Escherichia coli* (strain 1257) containing 2×10^9 microbial cells in 1 ml at an exposure time of 5–30 min and solution temperature of 20°C [7].

Our results show that 0.025–1% aqueous solutions of the synthesized QASs exhibit bactericidal effect with respect to the above-noted strains, and this effect is dependent on the length of hydrophobic radical R. The maximal bactericidal effect was shown by QAS **III** (R = $C_{10}H_{21}$) whose 0.05% aqueous solution eliminates *Escherichia coli* and *Staphylococcus aureus* within 5 min.

EXPERIMENTAL

The IR spectra of QASs were recorded on a Specord IR-75 spectrometer (mulls in mineral oil). The QAS purity was tested by thin-layer chromatography with Silufol UV-254 plates using *n*-butanol–ethanol–water–acidic acid mixture (10 : 7 : 6 : 4) as solvent and iodine vapor as developer.

Quaternary ammonium salts I–IV. A mixture of 1,9-dimethylamino-5-oxanonane-2,7-diyne (0.01 mol) and appropriate alkyl monochloroacetate in absolute ethanol (5 ml) was kept at room temperature for 5 days. The resulting salt was washed with absolute diethyl ether and dried in a desiccator over $CaCl_2$. The IR spectrum of the final compound contains the following absorption bands, ν, cm^{-1}: 1075, 1230, 1725 (COO), 2240 (–C≡C–).

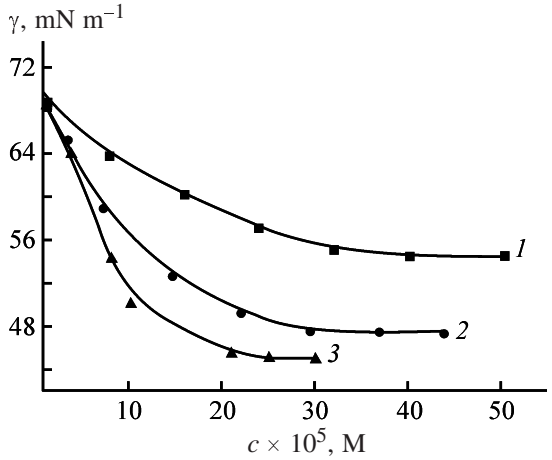


Fig. 1. Surface tension γ in the systems QAS–H_2O at T = 303 K. (c) QAS concentration. (*1*) C_8, (*2*) C_{10} and (*3*) C_{12}.

CONCLUSIONS

(1) Quaternary ammonium salts containing the common 5-oxanonane-2,7-diyne-1,9-diyl fragment and different alkoxycarbonylmethyl groups ehhibit bactericidal effect. Their antimicrobial activity depends on the length of the hydrophobic radical.

(2) With an increase in the length of the alkyl radicals in QAS molecules, both the critical micelle concentration and the surface tension decrease, whereas the surface activity increases. The strongest bactericidal effect is exhibited by *N,N*'-(5-oxanonane-2,7-diyne-1,9-diyl)bis[(decyloxycarbonylmethyl)dimethylammonium] chloride.

REFERENCES

1. Babakhanyan, A.V., Kauas, A., and Arutyunyan, R.S., *Arm. Khim. Zh.*, 1991, vol. 44, nos. 9–10, pp. 544–547.
2. Babakhanyan, A.V., Babayan, Zh.R., and Akopyan, G.S., *Biol. Zh. Arm.*, 1990, vol. 43, no. 2, pp. 150–152.
3. Ovakimyan, S.A., Babakhanyan, A.V., and Arutyunyan, R.S., *Khim. Zh. Arm.*, 2002, vol. 55, nos. 1–2, pp. 85–91.
4. *Poverkhnostno-aktivnye veshchestva: Spravochnik* (Surfactants: Handbook), Abramzon, A.A. and Gaevoi, G.M., Eds., Leningrad: Khimiya, 1979.
5. *Praktikum po kolloidnoi khimii* (Practical Course of Colloid Chemistry), Neiman, R.E., Ed., Moscow: Vysshaya Shkola, 1972.
6. Abramzon, A.A., *Poverkhnostno-aktivnye veshchestva* (Surfactants), Leningrad: Khimiya, 1981.
7. Lyarskii, P.P. and Sokolova, N.F., *Problema dezinfektsii i sterilizatsii: Sbornik nauchnykh trudov VNII dezinfektsii i sterilizatsii* (Problems of Disinfection and Sterilization: Coll. of Papers of the All-Union Research Inst. of Disinfection and Sterilization), Moscow, 1971, issue 2, vol. 2, pp. 186–199.

ISSN 1070-4272, Russian Journal of Applied Chemistry, 2008, Vol. 81, No. 3, pp. 455–458. © Pleiades Publishing, Ltd., 2008.
Original Russian Text © O.A. Garibyan, A.L. Ovanesyan, G.M. Makaryan, Zh.A. Chobanyan, 2008, published in Zhurnal Prikladnoi Khimii, 2008, Vol. 81, No. 3, pp. 470–473.

ORGANIC SYNTHESIS AND INDUSTRIAL ORGANIC CHEMISTRY

A New Synthetic Route to 1,3,5-Undecatrienes and Fucoserratene

O. A. Garibyan, A. L. Ovanesyan, G. M. Makaryan, and Zh. A. Chobanyan

Institute of Organic Chemistry, National Academy of Sciences of the Republic of Armenia, Yerevan, Armenia

Received May 15, 2007

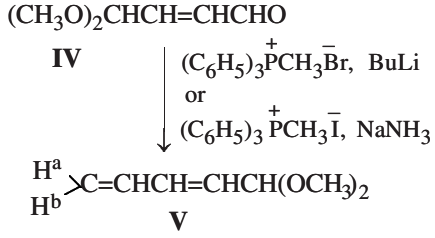
Abstract—A new procedure for preparing natural alkatrienes, fucoserratene and 1,3,5-undecatrienes, was developed. The key step of both syntheses is stereoselective formation of double bonds by the Wittig reaction starting from (*E*)-4,4-dimethoxy-2-butenal.

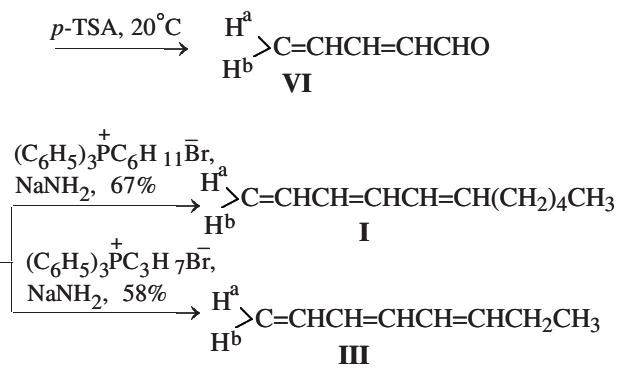
DOI: 10.1134/S1070427208030221

Conjugated trienes containing terminal vinyl group widely occur in the nature. *trans,cis*- and *trans,trans*-1,3,5-undecatrienes **I** and **II** were isolated from essential oils of *Galbanum* gum of various origins [1]. They were also found in essential oils of various algae [2, 3] and are components of various perfume compounds. In addition, triene **I** is one of the components of the odor of parsley, mandarins, apples, and pears [4]; it acts as sex pheromone on gametes of Australian kelps [5]. (3*E*,5*Z*)-1,3,5-Octatriene **III** (fucoserratene) is a pheromone isolated from fertilized ovums of some insect species [6]. These compounds are a subject of numerous studies. They are synthesized by heterolytic fragmentation of unsaturated 1,5-diols [6], stereo- and regioselective palladium-catalyzed synthesis [7], alkylation of terminal acetylene compounds [8], Wittig reation [9, 10], and also using α-haloalkylsulfonyl bromides [11], pentadienyl dithiocarbamates [12], and pyridazine *N*-oxides [13].

Here we suggest two alternative routes to the target products, (3*E*,5*Z*)-1,3,5-undecatriene **I** and fucoserratene **III**, starting from (*E*)-4,4-dimethoxy-2-butenal **IV**. The first route is the sequence of two Wittig reactions: first with triphenylmethylidenephosphorane and then with triphenylpropylidenephosphorane or triphenylhexylidenephosphorane (Scheme 1).

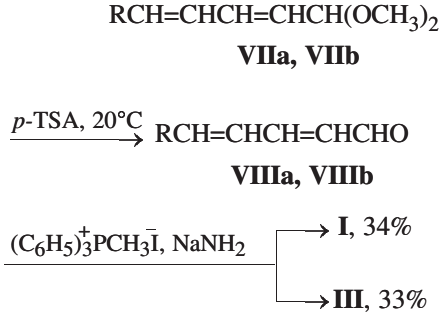
Scheme 1.





In the second route, the same reactions are performed in the reverse order (Scheme 2).

Scheme 2.



where R = Et (**VIIa**, **VIIIa**), Am (**VIIb**, **VIIIb**).

Olefination with triphenylmethylidenephosphorane (Scheme 1) was performed at 0°C in tetrahydrofuran (THF) in the presence of butyllithium. Since the yield of (3*E*)-5,5-dimethoxy-1,1-pentadiene **V** did not exceed 30%, butyllithium was replaced by sodium amide. By so doing, the yield of acetal **V** was in-

creased to 62%. After deprotection of the carbonyl group (20°C, acetone–water, 2 : 1) in the presence of catalytic amounts of *p*-toluenesulfonic acid (*p*-TSA), (2*E*)-penta-2,4-dienal **VI** was prepared in 93% yield. The second Wittig reaction with dienal **VI** was also performed in THF at 0°C. The phosphonium salts were deprotonated with sodium amide. Mixtures of stereoisomers of 1,3,5-undecatriene **I** and fucoserratene **III** were obtained in 67 and 58% yields, respectively. The content of the (3*E*,5*Z*) isomers in the isomeric mixtures exceeded 80%.

The isomer ratio was determined by ^{1}H NMR spectroscopy from the chemical shift of the H^6 atom. In the (*E*,*Z*) isomer, the H^6 signal is shifted upfield (5.50 ppm) relative to the (*E*,*E*) isomer (5.75 ppm) [8]. In the case of undecatriene **I**, the isomer ratio was also determined by GLC on a capillary column coated with SE-30.

By Wittig olefination of butenal **IV** with triphenylpropylidenephosphorane and triphenylhexylidenephosphorane, we previously prepared mixtures of isomers of acetals **VIIa** and **VIIb**, respectively, with more than 95% content of (2*E*,4*Z*) isomers. The acetal protection was removed at 0°C in acetone–water (2 : 1) in the presence of catalytic amount of *p*-toluenesulfonic acid to obtain the corresponding dienals **VIIIa** and **VIIIb**, with the configuration of (4*Z*) double bond being almost fully retained [14]. Then, by the Wittig reaction, we prepared the desired trienes: (3*E*,5*Z*)-1,3,5-undecatriene **I** and fucoserratene **III** (Scheme 2).

By choosing appropriate deprotection conditions, from acetal **VIIb** we prepared (*E*,*Z*)- and (*E*,*E*)-decadienals **IX** with the prevalence of the (*E*,*E*) isomer. For example, at 20°C in the presence of catalytic amounts of *p*-toluenesulfonic acid and equimolar amounts of water in acetone, we prepared decadienal **IX** with 81% content of the (*E*,*E*) isomer [14], which was converted by the Wittig reaction into (3*E*,5*E*)-1,3,5-undecatriene **II** with 34% yield:

$$\underset{\textbf{IX}}{CH_3(CH_2)_4CH{=}CHCH{=}CHCHO} \xrightarrow{(C_6H_5)_3^+PCH_3\bar{I},\ NaNH_2} \underset{\textbf{II}}{CH_3(CH_2)_4CH{=}CHCH{=}CHCH{=}C\begin{matrix}H^a\\H^b\end{matrix}}$$

Undecatriene **II** was also synthesized by the Schlosser reaction. (2*E*,4*E*)-1,1-Dimethoxy-2,4-decadiene **V** was prepared in 57% yield form butenal **IV** and hexyltriphenylphosphonium bromide; the product contained 90% (*E*,*E*) isomer [14]. Deacetalization of **V** followed by the Wittig reaction yielded undecatriene **II** containing 87% (*E*,*E*) isomer.

EXPERIMENTAL

The ^{1}H NMR spectra were recorded on a Varian VXR-300 spectrometer (300 MHz) in $(CD_3)_2CO$ or $CDCl_3$. The chemical shifts (δ, ppm) are given relative to TMS. The IR spectra were recorded on a UR-20 spectrophotometer from thin films. GLC analysis was performed with a Chrom-5 chromatograph (flame ionization detector, 25 m × 0.25 mm glass capillary column, liquid phase SE-30, carrier gas nitrogen, flow rate 3 ml min^{-1}). Column chromatography was performed on silica gel L 40/100. Thin-layer chromatography was performed on Silufol UV-254 plates; the chromatograms were developed by treatment with iodine vapor or $KMnO_4$ solution. Compound **IV** was prepared as described in [15], and phosphonium salts, as described in [16].

(3*E*)-5,5-Dimethoxy-1,3-pentadiene V. *a.* A 1.45 N solution of butyllithium (16.8 ml) was added dropwise at room temperature to 8.9 g of methyltriphenylphosphonium bromide in 35 ml of THF. Then the mixture was cooled to a temperature from 0 to –5°C, and a solution of 3.0 g of butenal **IV** in 5 ml of THF was added dropwise. The mixture was allowed to stand for 1 h, after which it was poured onto ice and extracted with ether. The extract was dried over sodium sulfate. The solvent was distilled off, and the residue was distilled in a vacuum to obtain 1.3 g (30%) of (3*E*)-5,5-dimethoxy-1,3-pentadiene **V**, bp 72–73°C (12 mm Hg). IR spectrum, ν, cm^{-1}: 1116 (CH_3O–C–OCH_3), 1600 (C=C). ^{1}H NMR spectrum [$(CD_3)_2CO$], δ, ppm (*J*, Hz): 3.2 s (6H, OCH_3), 4.8 d (1H, H^5, $J_{5,4}$ 5.0), 5.12 d (1H, H^{1a}, $J_{1a,2}$ 10.5), 5.28 d (1H, H^{1b}, $J_{1b,2}$ 16.0), 5.61 d.d (1H, H^4, $J_{4,3}$ 15.5, $J_{4,5}$ 5.0), 6.07 d.d.d (1H, H^2, $J_{2,1a}$ 10.5, $J_{2,1b}$ 16.0, $J_{2,3}$ 11.2), 6.67 d.d (1H, H^3, $J_{3,2}$ 11.2, $J_{3,4}$ 15.5).

Found, %: C 65.56, H 9.41.

$C_7H_{12}O_2$. Calculated, %: C 65.60, H 9.44.

b. Methyltriphenylphosphonium iodide (28.7 g) was added to 3.6 g of sodium amide in 40 ml of THF under nitrogen. The mixture was refluxed for 1 h, after which it was cooled to a temperature from 0 to –10°C, and a solution of 9.2 g of aldehyde **IV** in 10 ml of THF was added dropwise. The mixture was allowed to stand dor 1 h, after which 50 ml of water was added, and the mixture was extracted with ether. The extract was dried over sodium sulfate, the solv-

ents were removed, and the residue was distilled in a vacuum. Dimethoxy diene **V** was obtained, bp 72–73°C (12 mm Hg); yield 5.6 g (62%).

(2*E*)-2,4-Pentadienal VI. *p*-Toluenesulfonic acid (36 mg) was added to a mixture of 0.9 g of dimethoxy diene **V** in 10 ml of acetone and 5 ml of water. The mixture was stirred for 10 min at 20°C and neutralized with Na_2CO_3, after which acetone was removed and the residue was extracted with ether. The extract was dried over sodium sulfate, and the crude mixture after removing the solvent was purified on a column (silica gel, hexane : ether = 10 : 1). (2*E*)-2,4-Pentadienal **VI** was isolated; yield 534 mg (93%). IR spectrum, ν, cm^{-1}: 1620 (C=C), 1675, 2720 (C=O). ^1H NMR spectrum [$(CD_3)_2CO$], δ, ppm (*J*, Hz): 5.64 d (1H, H^{5a}, $J_{5a,4}$ 10.5), 5.81 d (1H, H^{5b}, $J_{5b,4}$ 16.0), 6.05 d.d (1H, H^2, $J_{2,1}$ 8.5, $J_{2,3}$ 15.3), 6.40 m (1H, H^4), 7.12 d.d (1H, H^3, $J_{3,2}$ 15.3, $J_{3,4}$ 10.3), 9.55 d (1H, H^1, $J_{1,2}$ 8.5) [17].

(3*E*,5*Z*)-1,3,5-Undecatriene I. *a.* Hexyltriphenylphosphonium bromide (1.6 g) was added to 0.185 g of sodium amide in 2 ml of THF. The mixture was refluxed for 1 h and cooled to a temperature from 0 to –10°C, and a solution of 0.3 g of dienal **VI** in 1 ml of THF was added dropwise. After keeping for 1 h, 3 ml of water was added, and the mixture was extracted with ether and dried over sodium sulfate. After removing the solvents, the crude mixture was purified on a column (silica gel, hexane : ether from 19 : 1 to 10 : 1) to obtain 0.37 g (67%) of (3*E*,5*Z*)-1,3,5-undecatriene **I** [relative content of the (3*E*,5*Z*) isomer 86%]. IR spectrum, ν, cm^{-1}: 840 (C=C), 935 [(*E*)-C=C], 1560 (C=C), 3100 (CH_2=CH). ^1H NMR spectrum ($CDCl_3$), δ, ppm (*J*, Hz): 0.91 t (3H, H^{11}, $J_{11,10}$ 7.0) 1.28–1.46 m (6H, H^8, H^9, H^{10}), 2.20 q (2H, H^7, $J_{7,6} = J_{7,8}$ = 7.2), 5.08 d.d (1H, H^{1a}, $J_{1a,1b}$ 1.2, $J_{1a,2}$ 10.0), 5.22 d.d (1H, H^{1b}, $J_{1b,1a}$ 1.2, $J_{1b,2}$ 16.0), 5.50 d.t (1H, H^6, $J_{6,5}$ 10.0, $J_{6,7}$ 7.0), 5.98–6.56 m (4H, H^2, H^3, H^4, H^5). Signals belonging to (3*E*,5*E*)-1,3,5-undecatriene **II** were also present: 2.14 q (2H, H^7, $J_{7,6} = J_{7,8}$ = 7.4), 5.05 d.d (1H, H^{1a}, $J_{1a,1b}$ 1.2, $J_{1a,2}$ 10.0), 5.19 d.d (1H, H^{1b}, $J_{1b,1a}$ 1.2, $J_{1b,2}$ 16.0), 5.74 d.t (1H, H^6, $J_{6,5}$ 15.0, $J_{6,7}$ 7.0) [9].

b. Methyltriphenylphosphonium iodide (0.94 g) was added to 0.13 g of sodium amide in 4 ml of THF, and the mixture was refluxed for 1 h. After cooling to a temperature from 0 to –10°C, a solution of 0.4 g of aldehyde **VIII** in 1 ml of THF was added. One hour later, 3 ml of water was added, the mixture was extracted with ether, and the extract was dried over sodium sulfate. After removing the solvent, the crude mixture was purified on a column (silica gel, hexane : ether from 19 : 1 to 10 : 1) to obtain 0.13 g (34%) of undecatriene **I** with 84% content of the (3*E*,5*Z*) isomer.

(3*E*,5*Z*)-1,3,5-Octatriene III. *a.* Propyltriphenylphosphonium bromide (1.4 g) was added to 0.185 g of sodium amide in 2 ml of THF. The mixture was refluxed for 1 h, after which it was cooled to a temperature from 0 to –10°C, and a solution of 0.3 g of aldehyde **VI** in 1 ml of THF was added dropwise. One hour later, 3 ml of water was added, and the mixture was extracted with ether. The extract was dried over sodium sulfate. After distilling off the solvents, the crude mixture was purified on a column (silica gel, hexane : ether from 19 : 1 to 10 : 1) to obtain 0.23 g (58%) of octatriene **III** with 85% content of the (3*E*, 5*Z*) isomer. IR spectrum, ν, cm^{-1}: 840 [(*Z*)-C=C], 935 [(*E*)-C=C], 1560 (C=C), 3100 (CH_2=CH). ^1H NMR spectrum ($CDCl_3$), δ, ppm (*J*, Hz): 0.9 t (3H, H^8, $J_{8,7}$ 7.0), 2.16 m (2H, H^7), 5.10 d.d (1H, H^{1a}, $J_{1a,1b}$ 1.2, $J_{1a,2}$ 10.0), 5.22 d.d (1H, H^{1b}, $J_{1b,1a}$ 1.2, $J_{1b,2}$ 16.0), 5.48 d.t (1H, H^6, $J_{6,5}$ 10.0, $J_{6,7}$ 7.0), 5.96–6.56 m (4H, H^2, H^3, H^4, H^5). Along with these signals, we found a signal at 5.78 d.t (1H, $J_{6,5}$ 15.0, $J_{6,7}$ 7.0), belonging to the H^6 atom of (3*E*,5*E*)-1,3,5-octatriene **III**.

b. Methyltriphenylphosphonium iodide (6.2 g) was added to 0.85 g of sodium amide in 6 ml of THF, and the mixture was refluxed for 1 h. After cooling to a temperature from 0 to –10°C, a solution of 1.7 g of (2*E*,4*Z*)-2,4-heptadienal **VIII** was added dropwise. The mixture was allowed to stand for 1 h, treated with water, and extracted with ether. The extract was dried over sodium sulfate. The residue after removing the solvents was chromatographed on a column (silica gel, hexane : ether = 20 : 1) to obtain 0.55 g (33%) of octatriene **III** with 89% content of the (3*E*,5*Z*) isomer.

(3*E*,5*E*)-1,3,5-Undecatriene II. Methyltriphenylphosphonium iodide was added to 0.13 g of sodium amide in 2 ml of THF. The mixture was refluxed for 1 h. After cooling to a temperature from 0 to –10°C, a solution of 0.4 g of dienal **IX** in 1 ml of THF was added dropwise. One hour later, 3 ml of water was added, and the mixture was extracted with ether. The extract was dried over sodium sulfate. The residue after removing the solvents was chromatographed on a column (silica gel, hexane : ether = 20 : 1) to obtain 0.13 g (34%) of undecatriene **II** with 87% content of the (3*E*,5*E*) isomer. IR spectrum, ν, cm^{-1}: 965 [(*E*)-C=C], 1585 (C=C), 3080 (C=C). ^1H NMR spectrum [$(CD_3)_2CO$], δ, ppm (*J*, Hz): 0.91 t (3H, H^{11}, $J_{11,10}$

7.0), 1.23–1.46 m (6H, H^8, H^9, H^{10}), 2.14 q (2H, H^7, $J_{7,8}$ 7.2), 5.05 d.d (1H, H^{1a}, $J_{1a,1b}$ 1.3, $J_{1a,2}$ 10.0), 5.19 d.d (1H, H^{1b}, $J_{1a,1b}$ 1.3, $J_{1b,2}$ 6.0), 5.74 d.t (1H, H^6, $J_{6,5}$ 14.5, $J_{6,7}$ 7.2), 5.98–6.58 m (4H, H^2, H^3, H^4, H^5).

CONCLUSION

A stereoselective procedure for preparing conjugated alkatrienes by the Wittig reaction with (*E*)-4,4-dimethoxy-2-butenal was developed.

REFERENCES

1. Naves, Y.-R., *Bull. Soc. Chim. Fr.*, 1967, no. 9, p. 3152.
2. Moore, R.E., Pettus, J.A., and Mistysyn, J., *J. Org. Chem.*, 1974, vol. 39, no. 15, p. 2201.
3. Boland, W. and Muller, D.G., *Tetrahedron Lett.*, 1987, vol. 28, no. 3, p. 307.
4. Berger, R.G., Drawert, F., Kollmannsberger, H., and Nitz, S., *J. Food Sci.*, 1985, vol. 50, p. 1655.
5. Jaenicke, L. and Seferiadis, K., *Chem. Ber.*, 1975, vol. 108, no. 1, p. 225.
6. Seferiadis, K. and Gaenicke, L., *Z. Naturforsch. (b)*, 1978, vol. 33, nos. 11–12, p. 997.
7. Teller, F., Descoins, C., and Sauvetre, R., *Tetrahedron*, 1991, vol. 47, no. 37, p. 7767.
8. Alami, A., Gueugnot, S., Domingues, S., and Linstrumelle, E., *Tetrahedron*, 1995, vol. 51, no. 9, p. 1209.
9. Naf, F., Decorzant, R., Thommen, W., et al., *Helv. Chim. Acta*, 1975, vol. 58, no. 4, p. 1016.
10. Goldbach, M., Takel, E., and Schneider, M.P., *J. Chem. Soc., Chem. Commun.*, 1987, no. 19, p. 1434.
11. Block, E., Aslam, M., Eswarakrishnan, V., et al., *J. Am. Chem. Soc.*, 1986, vol. 108, no. 18, p. 4568.
12. Hayashi, T., Yanagida, M., Matsuda, Y., and Oishi, T., *Tetrahedron Lett.*, 1983, vol. 24, no. 26, p. 2665.
13. Giraudi, E. and Teisseire, P., *Tetrahedron Lett.*, 1983, vol. 24, no. 5, p. 489.
14. Badanyan, Sh.O., Makaryan, G.M., Ovanesyan, A.L., and Panosyan, G.A., *Zh. Org. Khim.*, 2001, vol. 37, no. 5, p. 633.
15. Makin, S.M. and Telegina, N.I., *Zh. Obshch. Khim.*, 1962, vol. 32, no. 4, p. 1104.
16. Bestmann, H.J., Koschatzky, K.H., Schatzke, W., et al., *Lieb. Ann.*, 1981, no. 9, p. 1705.
17. Tufariello, J.J., Meckler, H., Pushpananda, K., and Senaratne, A., *Tetrahedron*, 1985, vol. 41, no. 17, p. 3447.

ISSN 1070-4272, Russian Journal of Applied Chemistry, 2008, Vol. 81, No. 3, pp. 459–464. © Pleiades Publishing, Ltd., 2008.
Original Russian Text © V.S. Pilyugin, Yu.E. Sapozhnikov, E.V. Klimakova, G.V. Kiseleva, S.L. Kuznetsova, T.P. Vorob'eva, G.E. Chikisheva, L.V. Yakovleva, 2008, published in Zhurnal Prikladnoi Khimii, 2008, Vol. 81, No. 3, pp. 474–479.

ORGANIC SYNTHESIS AND INDUSTRIAL ORGANIC CHEMISTRY

Development of a Procedure for Preparing 2-Nitro-4-thiocyanoaniline

V. S. Pilyugin, Yu. E. Sapozhnikov, E. V. Klimakova, G. V. Kiseleva, S. L. Kuznetsova, T. P. Vorob'eva, G. E. Chikisheva, and L. V. Yakovleva

Research and Technological Institute of Herbicides and Plant Growth Regulators, Academy of Sciences of Bashkortostan Republic, Ufa, Bashkortostan, Russia

Received April 9, 2007

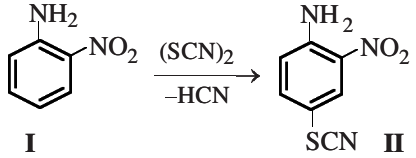
Abstract—A procedure was developed for preparing 2-nitro-4-thiocyanoaniline by thiocyanation of 2-nitroaniline with ammonium thiocyanate in acetic acid in the presence of bromine as oxidant.

DOI: 10.1134/S1070427208030233

Thiocyanation of organic compounds is most frequently performed with nascent thiocyanogen. To this end, a thiocyanic acid salt is dissolved in appropriate solvent (methanol, acetic acid, etc.), the solution is mixed with a substrate to be thiocyanated, and an oxidant (halogen or another substance capable of displacing thiocyanogen from thiocyanates) is added dropwise [1].

In thiocyanation of aromatic amines, the thiocyanato group is introduced in the *p*-position, and if this position is occupied, in the *o*-position to the amino group. In thiocyanation of chloro- and nitroanilines, the orienting effect of the amino group is preserved.

Thiocyanation of 2-nitroaniline **I** can be performed via intermediate diazo compound with the formation of 2-nitrothiocyanobenzene [1], or by the reaction with ammonium or potassium thiocyanate and bromine in acetic acid with the formation of 2-nitro-4-thiocyanoaniline **II** [2, 3]:



I **II**

Treatment of anilines or naphthylamines with ammonium thiocyanate and halogen or *N*-halo amide ($CH_3CONHBr$, $C_6H_5CONHBr$, *N*-bromosuccinimide, *N*-bromophthalimide, etc.) yields the corresponding 4-thiocyanates. The reaction is performed at 10–20°C in methanol or acetone in the presence of Chloramine T [4].

A procedure for preparing aromatic thiocyanates by treatment of the corresponding anilines with a mineral acid and alkali metal or ammonium thiocyanate is described in a patent [4]. A mixture of aniline and ammonium thiocyanate is dissolved in DMSO, concentrated sulfuric acid is added to the solution at 40–50°C, and the mixture is allowed to stand for 16 h at 20°C and poured into a 5% solution of sodium carbonate. 4-Thiocyanoaniline is thus obtained in 80% yield.

One of possible procedures for preparing organic thiocyanates (including chloro-, nitro-, and acetyl-substituted benzenes) is cleavage of organic disulfides with sodium cyanate and bromine or iodine in methanol or acetonitrile at approximately –5°C; the product yield varies from 50 to 95% [6, 7].

Under the synthesis conditions, both thiocyanogen itself and the released thiocyanic acid are unstable and can enter into side reactions. For example, thiocyanogen can partially polymerize to polythiocyanogen and react with bromine to give polybromothiocyanogen [4]:

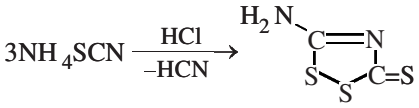
$$x(SCN)_2 \longrightarrow (SCN)_{2x}$$

$$x(SCN)_2 + Br_2 \longrightarrow 2x\text{BrSCN} \longrightarrow [\text{–S–N=C(Br)–}]_{2x}$$

It was found that, when 2-nitroaniline **I** in acetic acid is thiocyanated with ammonium (or potassium) thiocyanate using bromine as oxidant, the desired product **II** contains, along with 4-bromo-2-nitroaniline

III and minor amounts of 6-bromo-2-nitroaniline **IV** and 4,6-dibromo-2-nitroaniline **V**, also an unidentified water-insoluble organic impurity whose amount can reach 30% depending on the synthesis conditions.

Published data show that this impurity may be 1,3,5-trimercapto-*sym*-triazine or isoperthiocyanic acid **VI** (5-amino-1,2,4-dithiazole-3-thione, xanthane hydride). Acid **VI** is formed in ~25% yield by adding concentrated hydrochloric acid to an aqueous solution of ammonium thiocyanate and keeping the reaction mixture at 20–25°C for 16 h [7]:



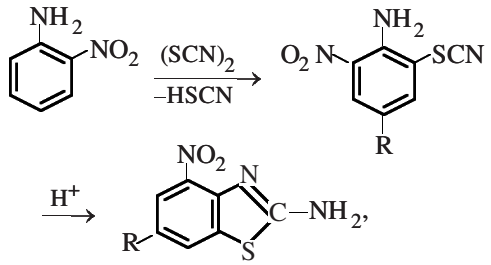
VI

Acid **VI** can also be formed directly from ammonium thiocyanate under the action of hydrogen bromide formed in the course of synthesis of thiocyanoaniline **II** [7, 8].

All these facts lead to the formation of organosulfur products insoluble in water and acetic acid. Under the conditions of preparing **II**, these substances are precipitated together with the desired products.

To prepare thiocyanoaniline **II**, we tested a procedure for direct thiocyanation of 2-nitroaniline in methanol or acetic acid. Thiocyanogen generated from potassium or ammonium thiocyanate by adding a solution of bromine reacted with aniline occurring in the same solution to give thiocyanoaniline **II**. In the process, 4-bromo-2-nitroaniline **III** (up to 1.0%) and trace amounts of 6-bromoaniline **IV** and 4,6-dibromoaniline **V** are formed as by-products.

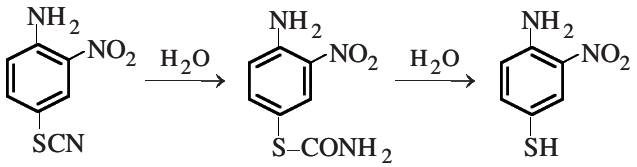
From 2-nitroaniline, 2-amino-4-nitro-1,3-benzothiazole **VII**, 2-amino-4-nitro-6-thiocyano-1,3-benzothiazole **VIII**, and 2-amino-6-bromo-4-nitro-1,3-benzothiazole **IX** can also be formed via the corresponding intermediates:



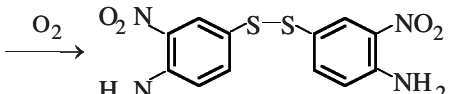
where R = H (**VII**), SCN (**VIII**), Br (**IX**).

It is known [7, 9, 10] that organic thiocyanates under the action of moisture in the presence of strong acids undergo hydrolysis with the formation of thiocarbamates, and further steps of the process yield thio compounds, disulfides, and other products.

Thiocyanation of **I** is accompanied by accumulation of hydrogen thiocyanate and hydrogen bromide in the reaction mixture, and moisture can be introduced together with the reactants and solvents. Therefore, in our case the above-mentioned processes seem to be possible. Their expected products are 4-amino-3-nitrophenyl thiocarbamate **X**, 4-amino-3-nitrothiophenol **XI**, bis(4-amino-3-nitrophenyl) disulfide **XII**, and other compounds:



X **XI**



XII

These factors were taken into account in the development of a technologically acceptable procedure for preparing 2-nitro-4-thiocyanoaniline **II** for the subsequent synthesis of anthelmintic agents based on it [11, 12].

Attempted synthesis of **II** in methanol gave unsatisfactory results: The reproducibility was poor, the main substance content of the crude product varied from 75 to 93%, and the amount of 4-bromoaniline **III** in some samples reached 4–5%. High-performance liquid chromatography of the reaction products revealed the presence of a significant amount (25–30%) of unidentified impurities. With an increase in the reaction time, the yield and quality of product **II** drastically decreased, and by-products rapidly accumulated in the reaction mixture. The use of acetic acid as solvent proved to be more efficient.

When bromine was replaced by other oxidants [Cu(II) salts, Chloramine B), thiocyanation of 2-nitroaniline proceeded more difficultly. Although copper salts were taken in excess, the reaction mixture contained a large amount of the unchanged starting compound, and other impurities were accumulated. With Chloramine B as oxidant, the desired aniline **II** was not detected in the reaction products at all. Therefore, all further studies were aimed to optimize a procedure for preparing aniline **II** in acetic acid using bromine as oxidant.

Table 1. Influence of the rate of bromine addition on the quality of crude 2-nitro-4-thiocyanoaniline. Reaction temperature 20°C; component dosage: 500 ml of acetic acid, 110.4 g (0.8 mol) of 2-nitroaniline, 250 g (2.5 mol) of potassium thiocyanate, and 176 g (1.09 mol) of bromine dissolved in 200 ml of acetic acid

Time of bromine addition, min	Product composition, wt %			
	2-nitro-4-thiocyano-aniline **II**	2-nitroaniline **I**	4-bromo-2-nitro-aniline **III**	unidentified impurities
60	94.71	0.18	0.98	4.13
60	94.66	0.09	1.08	4.17
120	95.71	0.12	0.87	3.30
120	95.89	0.11	0.96	3.04
180	97.09	0.11	0.56	2.24
180	97.21	0.07	0.37	2.35
180	96.85	0.13	0.47	2.55
210	97.59	0.09	0.37	1.95
240	98.11	Traces	0.21	1.65

Thiocyanation of aromatic amines with nascent thiocyanogen is usually performed at 0–5°C and only seldom at room temperature. Our studies showed that aniline **II** prepared at 18–20°C does not differ in the quality and yield from the product obtained at a lower temperature. Therefore, all the subsequent experiments on the development of the synthesis procedure were performed at room temperature.

It was found that removal of the residual amounts of the starting 2-nitroaniline and of by-products, bromonitroanilines, from the target products was difficult. On the one hand, to ensure more complete conversion of **I**, bromine was added in excess. At the molar ratio of **I** to bromine of 1.0 : (1.30–1.5), the resulting crude aniline **II** contained no more than 0.1% **I**.

On the other hand, to prevent formation of bromonitroanilines, thiocyanate was taken in excess. Experiments showed that the amount of ammonium or potassium thiocyanate should be 2.5–3.6 mol per mole of aniline **I**. In this case, an impurity of bromonitroanilines in the target product will be minimal. However, in the case of quick addition of bromine into the reaction mixture, the amount of thiocyanate dissolved in acetic acid can decrease considerably because of insufficient rate of its dissolution. In this case also significant amounts of bromoanilines can appear in the reaction mixture (Table 1).

We attempted to eliminate the formation of bromoanilines by preparing a solution of thiocyanogen in acetic acid in advance and adding it to the reaction mixture. For this purpose, a calculated amount of bromine was added dropwise to a suspension of potassium thiocyanate in acetic acid. The precipitate consisting of excess potassium thiocyanate and potassium bromide formed in the reaction was filtered off, and a solution of thiocyanoghen in acetic acid was used for the subsequent thiocyanation of aniline **I**. However, the resulting solution of thiocyanogen appeared to be unstable. In the course of storage and in the thiocyanation step, thiocyanogen partially polymerized with the precipitation of polymeric products.

Experiments showed that an increase in the time of bromine addition from 1 to 2–3 h led to a decrease in the content of by-product **III** in crude aniline **II** from 1.0 to 0.4%, with the content of other impurities also somewhat decreasing. Therefore, in the subsequent experiments the time of bromine addition was 3 h. An increase in the excess of potassium thiocyanate from 15 to 40% did not lead to a decrease in the amount of 4-bromoaniline **III** in the product obtained. Replacement of potassium thiocyanate by ammonium thiocyanate did not affect the yield and quality of **II**.

Becuase 4-thiocyanoaniline **II** is prone to hydrolysis under the action of moisture with the formation of the thiocarbamate and other degradation products, we examined its stability in concentrated hydrochloric and acetic acids, and also in the presence of moisture.

The stability of aniline **II** in hydrochloric acid was studied at room temperature in the course of 4 and 10 days (samples A and B, respectively). For comparison, we also obtained data on the system consisting of aniline **II** and 85% acetic acid, with the addition of the same amount of hydrochloric acid as in experiments A and B (experiment C). In this experiment, the storage time was 30 days. We found that acid hydrolysis results in accumulation in the starting compound

of an unidentified product whose content under the experimental conditions reached 4–5%. It should also be noted that the rate of accumulation of this impurity in weakly hydrated (99.5%) acetic acid was approximately two times lower than in concentrated hydrochloric acid.

Experiments performed to examine the effect of water on the product quality in the course of preparation of aniline **II** show that the use of even 95% acetic acid noticeably decreases its yield and also decreases the content of the desired compound in the crude product by 3–5%, which is mainly caused by accumulation of one of unidentified impurities whose amount in some experiments reached 8–9%. According to high-performance liquid chromatography, this impurity is identical to the product accumulating in the course of hydrolysis of thiocyanoaniline **II** in concentrated hydrochloric and 85% acetic acids.

In the course of optimization of the process for preparing aniline **II**, we examined the possibility of reusing the acetic acid filtrate for the synthesis of the crude product without preliminary regeneration of acetic acid. We found that, when acetic acid was replaced by the mother liquor from the previous experiment, the content of the desired substance in the crude product decreased from 95.8 to 78.4%, and the next reuse of this mother liquor led to a further decrease in the desired substance content to 68%, mainly owing to a sharp increase in the content of the same unidentified impurity: to 18 and 25%, respectively. Appreciable amounts (up to 2.8%) of 4-bromo-2-nitroaniline also accumulated in the crude product. The content of the other components did not change appreciably.

In the course of the studies, we tested two procedures for separating insoluble by-products in the course of the synthesis of thiocyanoaniline **II**. In the first procedure, after the reaction completion, the mixture was heated to 80°C, the insoluble precipitate was filtered off, and the filtrate was poured into a fourfold volume of cold water. The target product was isolated in 95.5% yield; it was 93.5% pure. In the second procedure, acetic acid was taken in a 2.5 times larger amount. In this case, it was unnecessary to increase the temperature. The precipitate after the reaction completion was filtered off, and thiocyanoaniline **II** containing up to 99% main substance was isolated from the filtrate in up to 60% yield with cold water.

The above-described methods for preparing pure 4-thiocyanoaniline **II** complicate the commercial process, decrease the product output from unit equipment, and make the regeneration of acetic acid more difficult. Attempts to stabilize thiocyanogen and hydrogen thiocyanate under the reaction conditions and thus to prevent formation of organosulfur by-products failed.

However, as shown previously [11, 12], the above-indicated by-products under the conditions of the synthesis of 4-amino-3,4'-dinitrodiphenyl sulfide (target product synthesized from **II**; the procedure for preparing **II** was developed with the aim of its synthesis) are either well soluble in the aqueous-alkaline reaction mixture or decompose to form water-soluble salts. Therefore, these by-products could be readily separated from 4-amino-3,4'-dinitrodiphenyl sulfide by washing.

The results of the synthesis of thiocyanoaniline **II** (Table 2) were checked on a semicommercial installation with a 160-l reactor. The data obtained (Table 3) show that the results of laboratory experiments are reproduced.

Thus, to prepare 2-nitro-4-thiocyanoaniline **II**, the water content of acetic acid used as solvent should not exceed 0.5%. Crude 2-nitroaniline whose water content may reach 25 wt % should be dried before use to a residual moisture content not exceeding 1–2%. The best results were obtained with bromine as oxidant. It was preliminarily dissolved in acetic acid on cooling. It is appropriate to perform the synthesis with slight cooling, so as to maintain the reaction temperature within 16–20°C. The molar ratio of 2-nitroaniline, bromine, and ammonium or potassium thiocyanate should be 1.0 : (1.33–1.43) : (3.4–3.6).

EXPERIMENTAL

2-Nitro-4-thiocyanoaniline **II** was prepared in a 2.0-l glass reactor equipped with a heat-exchange jacket, a thermometer, a dropping funnel, and a reflux condenser. The cooling agent cooled to the required temperature was fed to the reactor jacket from a thermostat, which allowed the preset temperature to be reliably maintained throughout the synthesis.

The thiocyanation progress was monitored by thin-layer chromatography on Silufol UV-254 plates.

The product quality was determined by high-performance liquid chromatography with a column packed with Bondapac C_{18} reversed phase. The compounds were detected with a UV detector at a wavelength of 254 nm. An Altex liquid chromatograph equipped with 25 cm × 4.6 mm stainless steel columns was used. The chromatograms were treated by the methods of internal area normalization.

Table 2. Results of the synthesis of 2-nitro-4-thiocyanoaniline on a laboratory installation.* Reaction temperature 20°C; dosage of components: 110.4 g (0.8 mol) of 2-nitroaniline, 250 g (2.5 mol) of potassium thiocyanate, and 160 g (1.0 mol) of bromine in 200 ml of acetic acid; time of adding the bromine solution 3 h

Amount of acetic acid, ml	Product composition, wt %				Yield of crude **II**, %
	2-nitro-4-thiocyano-aniline **II**	2-nitroaniline **I**	4-bromo-2-nitro-aniline **III**	unidentified impurities	
400	93.83	0.31	1.43	4.43	90.2
400	93.68	0.42	1.38	4.52	89.7
400	93.58	0.28	1.59	4.55	92.4
500	95.88	Traces	0.67	3.48	90.3
500	94.99	Traces	0.52	4.49	92.6
500	95.71	0.09	0.45	3.75	93.0
600	96.71	0.07	0.43	2.79	89.2
600	96.75	0.09	0.45	2.71	88.5
600	96.49	0.14	0.41	2.96	88.6
400**[a]	97.03	0.04	0.39	2.54	93.2
500**[b]	98.02	0.03	0.12	1.83	93.4
500**[b]	98.18	Traces	0.09	1.73	93.9

* The crude product was isolated by pouring the reaction mixture into 4000 ml of water.
** Instead of potassium thiocyanate, ammonium thiocyanate was used in an amount of (a) 2.6 and (b) 3.0 mol.

Table 3. Results of the synthesis of 2-nitro-4-thiocyanoaniline on a semicommercial installation. Dosage of components: acetic acid 50 l, 2-nitroaniline 15.5 kg, ammonium thiocyanate 25.5 kg, bromine 20.3 kg in 30 l of acetic acid; reaction temperature 18–20°C

Time, min		Product composition, wt %			Yield of crude **II**, %
of bromine addition	of additional stirring	2-nitro-4-thiocyano-aniline **II**	2-nitroaniline **I**	4-bromo-2-nitro-aniline **III**	
180	360	93.55	Traces	1.10	88.8
200	360	93.74	Traces	0.91	90.2
205	360	94.75	0.16	Traces	92.4
205	300	94.39	0.09	1.23	89.7
220	360	94.02	0.07	0.87	90.2
225	300	94.40	Traces	0.97	90.2
240	360	95.60	0.04	0.52	96.9
255	360	95.89	Traces	0.62	92.3

2-Nitro-4-thiocyanoaniline **II** was prepared as follows: To a solution of 110.4 g (0.8 mol) of 2-nitroaniline in 500 ml of acetic acid at 20°C, 250 g (2.5 mol) of potassium thiocyanate was added, after which a solution of 176 g (1.09 mol) of bromine in 200 ml of acetic acid was added with stirring from a dropping funnel over a period of 3 h. After adding the whole amount of bromine, the mixture was stirred at 20°C for an additional 3–4 h.

Thiocyanation was performed until 2-nitroaniline was detected in the reaction mixture in trace amounts. Therefore, if necessary, an additional amount of bromine was added in the course of stirring after introduction of the prescribed amount. After the residual 2-nitroaniline content decreased to the prescribed level (≤0.1%), the reaction mixture was heated to 80°C, the precipitated impurities were filtered off, and the filtrate was poured into a fourfold volume (4 l) of cold water. The precipitate formed in the process was filtered off and washed on the filter with water until the content of bromide ions in the wash water decreased to the trace level.

Semicommercial synthesis of 2-nitro-4-thiocyanoaniline **II** was performed in a 160-ml enameled react-

or equipped with a heat-exchange jacket, a bottom discharge pipe, a stirrer, a reflux condenser, and a thermocouple. The reactor with the operating stirrer was charged successively with 50 l of acetic acid, 15.5 kg of preliminarily dried 2-nitroaniline, and 25.5 g of ammonium thiocyanate. The temperature inside the reactor was maintained at 18–20°C by feeding cold water into the jacket. The mixture was stirred at this temperature for 30 min. After that, a solution of 20.3 kg of bromine in 30 l of acetic acid was added to the reactor from a dosing unit over a period of 3–4 h. In the process, the temperature in the reactor was maintained at 16–20°C. After adding the whole amount of bromine, the mixture was stirred at the same temperature for an additional 5–6 h. In the course of adding the bromine solution and subsequent stirring, the thiocyanation progress was monitored by thin-layer chromatography.

After the thiocyanation completion, the reactor contents were heated to 80°C, the precipitated impurities were filtered off, and the filtrate was diluted with cold water by a factor of 4 in a mixer. After stirring, the suspension was poured onto a nutsch filter, squeezed, and washed with water until the content of bromide ions in the wash water decreased to the trace level. The washed and well squeezed product was dried at a temperature not exceeding 60°C.

CONCLUSIONS

(1) Thiocyanation of 2-nitroaniline with ammonium or potassium thiocyanate in acetic acid in the presence of bromine as oxidant was studied as a preparative route to 2-nitro-4-thiocyanoaniline. The parameters of the thiocyanation process were optimized.

(2) The developed procedure for preparing 2-nitro-4-thiocyanoaniline was tested on a semicommercial installation.

REFERENCES

1. Mel'nikov, N.N. and Sukhareva, N.D., *Reaktsii i metody issledovaniya organicheskikh soedinenii* (Reactions and Investigation Methods of Organic Compounds), Moscow: Goskhimizdat, 1959, book 8, pp. 446–465.
2. Fridman, S.T., *Zh. Obshch. Khim.*, 1953, vol. 23, no. 1, pp. 116–118.
3. Elderfield, N. and Short, R., *J. Org. Chem.*, 1952, vol. 17, no. 3, pp. 758–763.
4. Kayzi, A., *J. Chem. Soc. Jpn., Pure Chem. Sect.*, 1960, vol. 81, no. 11, pp. 1776–1780.
5. JPN Patent 26732.
6. Pohloudek-Fabini, R., Kottke, M., and Friedrich, F., *Pharmazie*, 1971, vol. 26, no. 5, pp. 283–286.
7. Cotton, F.A. and McCleverhy, J.A., *Inorg. Chem.*, 1967, vol. 6, no. 2, pp. 229–232.
8. Gatton, G. and Gerner, R., *Z. Anorg. Allg. Chem.*, 1982, vol. 486, no. 1, pp. 102–110.
9. Asljarn, H., *Acta Chem. Scand.*, 1963, vol. 17, no. 10, pp. 2575–2592.
10. Rybin, A.G., Zil'berman, E.N., and Trachenko, V.N., *Zh. Obshch. Khim.*, 1980, vol. 50, no. 9, pp. 2102–2105.
11. Pilyugin, V.S., Sapozhnikov, Yu.E., and Shitov, G.P., *Zh. Org. Khim.*, 2003, vol. 39, no. 7, pp. 1040–1046.
12. Pilyugin, V.S., *Sintez i biologicheskaya aktivnost' proizvodnykh 2-aminobenzoimidazola* (Synthesis and Biological Activity of 2-Aminobenzimidazole Derivatives), Moscow: Khimiya, 2003.

ISSN 1070-4272, Russian Journal of Applied Chemistry, 2008, Vol. 81, No. 3, pp. 465–470. © Pleiades Publishing, Ltd., 2008.
Original Russian Text © L.G. Molokanova, P.Yu. Apel, V.V. Shirkova, A.V. Desyatov, I.A. Prokhorov, S.G. Kandykov, 2008, published in Zhurnal Prikladnoi Khimii, 2008, Vol. 81, No. 3, pp. 480–485.

MACROMOLECULAR CHEMISTRY AND POLYMERIC MATERIALS

Etching of Polyvinylidene Fluoride with an Alkaline Solution of Potassium Permanganate

L. G. Molokanova, P. Yu. Apel, V. V. Shirkova, A. V. Desyatov, I. A. Prokhorov, and S. G. Kandykov

Joint Institute for Nuclear Research, Dubna, Moscow oblast, Russia
Keldysh Center, Federal State Unitary Enterprise, Moscow, Russia

Received April 4, 2007

Abstract—Kinetics of polyvinylidene fluoride etching with a permanganate alkaline solution used in manufacture of track membranes from hydrogen-containing fluoropolymers, and also products formed in the process, were studied in relation to temperature and relative content of mixture components.

DOI: 10.1134/S1070427208030245

A particular place among the wide variety of polymeric membranes used in modern technology is occupied by track membranes (TMs). They are distinguished by narrow pore size distribution, precisely preset pore radius, and possibility of wide variation of their porosity, pore shape, and other structural parameters [1, 2]. The manufacture of TM from polycarbonate (PC) and polyethylene terephthalate (PET) films was commenced on the industrial scale in the 1970s–1980s. The membranes are produced by chemical etching with alkaline solutions of a polymeric film irradiated with accelerated ions. The PET and PC track membranes have found use in biotechnology, medicine industry, water treatment, etc. At the same time, there are promising areas in which PET and PC track membranes cannot be effectively used because of their insufficient chemical stability. By contrast, the unique chemical stability of TMs based on fluoropolymers enables their use in corrosive media, with multiple regeneration possible.

Among the industrially manufactured fluoropolymeric films, the most suitable material for fabrication of TMs is polyvinylidene fluoride (PVDF) [3].

Hydrogen-containing fluoropolymeric films irradiated with heavy ions are commonly etched with a hot alkaline solution of potassium permanganate. The etching conditions were first suggested in [4]; however, the chemical processes by which tracks are etched have not been studied in detail, primarily because of the complexity of processes occurring in this redox system. The etching of tracks in PVDF with a concentrated caustic alkali solution has also been described in the literature [5]. Under these conditions, i.e., in the absence of a strong oxidizing agent, the etching is substantially slower. The mechanism of interaction between the polymer and the alkali and the composition of the products obtained have not been determined, either.

So far, fluoropolymeric TMs have been produced only in laboratory. Development of a technology for manufacture of fluoropolymeric TM requires that the chemical processes occurring in their etching should be studied. It is necessary to know the main products formed in oxidative etching of fluoropolymers in order to, first, have at least a rough notion of the stoichiometry of the chemical reaction and, second, obtain input data for the development of appropriate procedure for waste utilization.

In the early development of the chemistry of fluoro compounds as far back as the 1950s, a number of studies concerned with oxidation of fluorinated hydrocarbons were carried out [6–11]. In the absence of modern analytical methods, the authors of these studies used procedures of preparative organic chemistry and, while working with gram amounts of substances, could identify a number of oxidation products of partly fluorinated hydrocarbons. These studies furnished valuable data on the conditions and mechanism of the dehydrofluorination occurring under the action of concentrated alkalis and on oxidation of double bonds formed in dehydrofluorination. A characteristic feature of the oxidation reactions studied is their non-

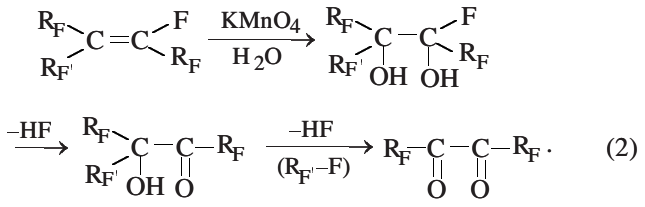
stoichiometric nature. In addition to the main product frequently formed in 70–80% yield, other products are also obtained in various proportions. This means that there occur several parallel reactions with comparable probabilities. The degree of conversion commonly depends on the time during which the reaction is carried out. The yield of the main product may markedly vary as temperature is changed by 10°C [12].

Studies carried out with low-molecular-weight organic compounds of fluorine revealed the following fundamental aspects of their reaction with NaOH and $KMnO_4$.

It was found that, if the fluorocarbon chain contains at least a single hydrogen atom, the dehydrofluorination reaction occurs in the liquid phase rather easily even at a moderate concentration of hydroxide ions [13]:

$$-CF_2-CF_2-CHF-CF_2- + OH^- \rightarrow -CF_2-CF=CF-CF_2- + F^- + H_2O. \quad (1)$$

When oxidized by potassium permanganate, fluoroolefins are converted into carbonyl compounds (α-hydroxy ketones or diketones, depending on substituents at the C=C bond) via intermediate geminal fluorocarbinols by the following scheme [14]:



(2)

Under homogeneous conditions (mixture of water and acetone as a solvent), this reaction occurs at room temperature. At high temperature, the action of potassium permanganate leads to a deeper oxidation with rupture of the C=C bond [10]. Prolonged action of $KMnO_4$ on fluoroolefins at approximately 100°C oxidizes in high yield both carbon atoms of the C=C bond to carboxy groups. For example, octafluorocyclohexa-1,4-diene oxidized with concentrated $KMnO_4$ at 95°C for 17 h gives difluoromalonic acid [15].

In [15], etching of tracks produced by heavy ions in PVDF was described and an attempt was made to determine the predominant chemical changes in the polymer under the action of a permanganate–alkaline etchant. A comparison of the IR spectra of the PVDF film, measured before and after the treatment, demonstrated that the alkali treatment leads to dehydrofluorination of PVDF and accumulation of double bonds, including conjugated bonds. Presumably, concentrated alkali can rupture the backbone of PVDF, which is identified by the appearance of terminal fluorovinyl groups $-CH=CF_2$. Acid –OH groups (contained in the carboxy group) are clearly identified. Under the action of the permanganate anion, double bonds within the chain are ruptured. The strong absorption at 1754 cm^{-1}, presumably associated with carboxylic acids of the structure $\sim CF_2-CH_2-COOH$ or $\sim CH_2-CF_2-COOH$, is preserved.

Studies by ESCA, Raman spectroscopy, and secondary-ion mass spectrometry have shown that conjugated double bonds are accumulated in PVDF under the action of an alkali [16, 17]. Because, as already noted, each double bond must be oxidized with backbone rupture, it is natural to assume that PVDF decomposes in hot alkaline permanganate solutions to complete mineralization. Complete PVDF oxidation in an alkaline permanganate solution can be represented by the equation

$$3(-CH_2CF_2-) + 8MnO_4^- + 10OH^- \longrightarrow CO_3^{2-} + 8MnO_2 + 8H_2O + 6F^-. \quad (3)$$

According to published data [6], the manganate ion MnO_4^{2-} is formed in a concentrated alkali in the presence of an excess amount of MnO_4^-:

$$4MnO_4^- + 4OH^- \longrightarrow 4MnO_4^{2-} + 2H_2O + O_2. \quad (4)$$

If reaction (4) occurs under the conditions of the experiment, the corresponding equation of the oxidation of polyvinylidene fluoride by manganate takes the form

$$(-CH_2CF_2-) + 4MnO_4^{2-} \longrightarrow 2CO_3^{2-} + 4MnO_2 + 2F^- + 2OH^-. \quad (5)$$

It can be assumed that the main part of PVDF is decomposed to complete mineralization, possibly in accordance with these equations. Presumably, other oxidation products can only be present as impurities.

Because there is no common standpoint concerning the mechanism of PVDF etching in an alkaline permanganate solution, the aim of this study was to identify the main inorganic products of PVDF oxidation and measure the stoichiometric coefficients of the presumed reaction.

EXPERIMENTAL

The study was performed with a polyvinylidene fluoride film of thickness 9 μm, manufactured by Kurecha Chemical Industries Co., Ltd. (Japan). Under the real conditions of TM production, the weight amount of the polymer per unit volume of the etching solution is commonly too small for further analysis. Therefore, the PVDF etching was studied at very high polymer concentrations in the solutions: 0.5, 1.0, and 1.5 g per 50 ml of the solution. Weighed portions (10.00 g) of $KMnO_4$ were placed in Teflon vessels, 50 ml of a 3.3 M solution of NaOH was added, and PVDF was introduced in the form of a finely cut film. The vessels were hermetically closed and placed in a thermostat heated to 115°C. The process was performed to complete dissolution of the PVDF film, which took no less than 24 h. To preclude the possible mechanical degradation of the polymer, the reaction mixture was not agitated. Because potassium permanganate decomposes at high temperatures in an alkaline medium, a blank experiment was performed under the same conditions, with the same $KMnO_4$ + NaOH solution heated without PVDF. After the dissolution process was complete, the vessels with the reaction mixture were removed from the thermostat, cooled to room temperature, and opened. The contents of the vessel were transferred to 250-ml volumetric flasks and diluted with distilled water to the mark. In the resulting solution, the expenditure of potassium permanganate and hydroxide ions and the amounts of the forming manganese dioxide and carbonate ions were determined.

The amount of the permanganate remaining in solution after the etching reaction was complete was determined by titration with oxalic acid in an acid medium. A 0.05 M solution of the titrant was prepared by dissolving a precisely weighed portion (6.303 g) of reagent-grade $H_2C_2O_4 \cdot 2H_2O$, preliminarily dried at 105–110°C, in a 1-l volumetric flask in the course of 2 h. In titration, 1 ml of the titrant solution is equivalent to a content of 0.1 mg-equiv of $KMnO_4$, or 3.161 mg, in the solution being titrated. To determine the amount of the permanganate, an aliquot of the solution (1–2 ml) was placed in a beaker flask, 10 ml of 1 M sulfuric acid was added, and the mixture was heated to 70–80°C and titrated with an oxalic acid solution. The reaction completion was judged from the disappearance of the coloration of the solution being titrated [18].

The amount of manganese dioxide in the reaction mixture was determined by weighing on an analytical balance the precipitate filtered off and dried at 165°C to constant weight. Because there was doubt concerning the possibility of determining the content of manganese dioxide gravimetrically, the precipitate formed upon etching and MnO_2 obtained by reaction of potassium permanganate with oxalic acid in a neutral medium were subjected to a differential-thermal analysis.

The precipitates were thoroughly washed to remove the solution and dried in air for several days. The analysis was made on an STA-449 Netzsch instrument in the atmosphere of argon, with heating to a temperature of 1000°C at a rate of 5 deg min^{-1}.

The heating curve of the precipitate comprises three and two portions of fast and slow loss of mass, respectively. Approximately in the range from 75 to 163°C, there occurs loss of water, which is accompanied by a rather pronounced endothermic peak. Upon further heating, two additional minor endothermic peaks, accompanied by the weight loss, appear in the curve at 544 and 772°C. The first of these presumably corresponds to decomposition of MnO_2 to Mn_2O_3 (which occurs at 506–735°C), and the second, to the onset of Mn_2O_3 decomposition to Mn_3O_4 (at 796–932°C). The thermogram of manganese dioxide, measured for comparison, was virtually identical to that of the precipitate under study, which confirms that $KMnO_4$ is reduced to manganese dioxide, stable under the given conditions, in the course of PVDF etching. These results validate the assumption that the MnO_2 precipitate is unsuitable for precise gravimetric determinations. The rather large amount of water retained by this compound and its thermolysis hinder obtaining this compound in a weighable form. However, prolonged drying of the precipitate at 165°C to constant weight and its subsequent rapid weighing on analytical balance make it possible to consider the precipitate mass reliable.

The amount of hydroxide ions remaining in solution after the etching reaction is complete was determined by titration with 0.1 M nitric acid prepared using the reference sample. The titration was performed potentiometrically with a SCHOTT-Geräte Titroline-96 instrument, with a combined glass electrode. This method also enabled differential titration of OH^- and CO_3^{2-} ions in solution.

In titration with a standard acid solution of a solution of simultaneously present alkali and carbonate, the reaction occurs in two stages:

$$OH^- + CO_3^{2-} + 2H^+ = HCO_3^- + H_2O \text{ (stage I)},$$

$$HCO_3^- + H^+ = CO_2\uparrow + H_2O \text{ (stage II)}.$$

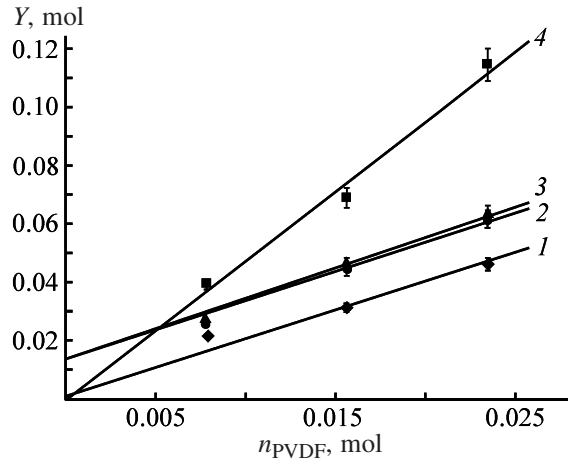


Fig. 1. Variation of the amount of the starting reactants and reaction products, *Y*, with the amount of dissolved PVDF: (*1*) accumulation of CO_3^{2-} groups, (*2*) consumption of $KMnO_4$, (*3*) accumulation of MnO_2, and (*4*) consumption of NaOH.

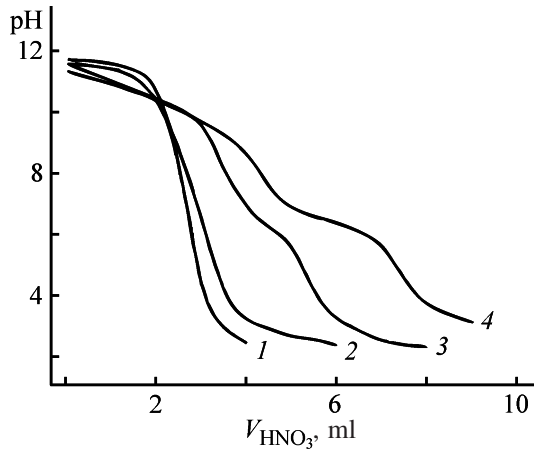


Fig. 2. Potentiometric titration curves of model solutions of a mixture of NaOH and K_2CO_3. NaOH : K_2CO_3 molar ratio: (*1*) 1 : 0, (*2*) 5 : 1, (*3*) 1 : 1, and (*4*) 0.5 : 1. (V_{HNO_3}) Volume of 0.1 M HNO_3; the same for Fig. 3.

By the end of the first stage, pH is 8.3, and by the end of the second, pH is 3.8. Potentiometric titration makes it possible to find from the titration curve, after it is differentiated and the first derivative is determined, the points of the steepest drop in the pH value, the first of which corresponds to the concentration sum $[OH^-] + [CO_3^{2-}]$, and the difference between the first and second, to the concentration of CO_3^{2-} ions [19].

The dependence of the loss of potassium permanganate on the amount of dissolved polymer is shown in Fig. 1 (curve *3*). A mathematical processing of the results obtained in three sets of experiments demonstrated that the molar expenditure *Y* of permanganate ions for PVDF dissolution can be expressed by a linear dependence of the amount *x* of the polymer (also expressed in moles):

$$Y = A + Bx,$$

where *A*, found to be 0.013 ± 0.003, is the average amount of $KMnO_4$ decomposed in a blank run (without contact with PVDF); the slope ratio $B = 2.0 \pm 0.2$ is the average amount of $KMnO_4$ spent for dissolution of a mole of PVDF.

The amount of the MnO_2 precipitate extracted from the reaction mass after the dissolution of the polymer is shown in Fig. 1 (curve *2*). It can be seen that the accumulation of manganese dioxide can also be approximated with a linear dependence on the amount of degraded PVDF. The slope of 2.0 ± 0.2 corresponds to the average amount of MnO_2 formed from potassium permanganate in etching of a mole of PVDF, and the quantity *A*, corresponding to precipitate formation in a blank experiment, is 0.013 ± 0.003 mol.

Thus, the amount of the permanganate spent in the course of etching exactly corresponds to the amount of the manganese dioxide precipitate formed from it. Such a coincidence can serve as additional evidence that the permanganate is completely reduced in the course of etching to MnO_2, which is stable under the given conditions.

The amounts of hydroxide ions spent in the course of etching and of the carbonate ions formed were calculated by differentiation of pH variation curves obtained in potentiometric titration of aliquot portions of the reaction mixtures. To analyze the capabilities of this method, we preliminarily titrated model solutions containing a mixture of a hydroxide and carbonate in various proportions (Fig. 2). It was found that, at a low content of CO_3^{2-} ions on the background of OH^-, this method fails to reveal the second step of a steep drop in pH in the titration curve. However, at comparable amounts of OH^- and CO_3^-, the run of the titration curves becomes quite suitable for processing and calculation of the amounts of these ions in the solutions being titrated.

Figure 3 shows typical potentiometric titration curves of aliquot portions of the NaOH solution used to prepare the working solution, blank NaOH + $KMnO_4$ solution warming-up under the experimental conditions, and reaction mixtures formed upon etching of various amounts of PVDF.

The amount of the acid, consumed for separate titration of CO_3^{2-} and OH^- ions, found from these

plots, made it possible to calculate their concentrations as functions of the amount of dissolved PVDF and to plot the corresponding curves (Fig. 1, curves *1* and *4*). It can be seen that, in both cases, the molar expenditure of the alkali for PVDF dissolution and the amount of carbonate ions formed in the reaction linearly depend on the amount of the polymer (also given in moles).

The formation of carbonate ions is described by a straight line with a slope of 1.9 ± 0.3, which emerges from the origin of coordinates, in good agreement with the assumption of complete oxidation of carbon contained in the polymer chain of PVDF.

The expenditure of the hydroxide for PVDF etching is described by a linear dependence with [NaOH] : [PVDF] = 4.8 ± 0.6.

To take into account the influence exerted by the reaction conditions on the decomposition of the etching solution, not associated with the dissolution of the polymer, we carried out a set of blank runs with a solution containing no PVDF film, which was heated to 115°C for various intervals of time, comparable with the etching time. The permanganate decomposition in the course of time is described by a linear dependence (Fig. 4). Even though the amount of the decomposed permanganate is small compared with its expenditure for PVDF etching, it reaches 20% upon prolonged heating for 50 h. Thus, under the TM manufacture conditions, when the mass of the polymer in the etching bath is substantially smaller than that of the solution, the loss of the oxidizing agent may be largely due to its spontaneous decomposition.

Potentiometric titration of the same solutions to determine the amount of NaOH demonstrated virtually full coincidence of the titration curves, irrespective of the heating duration. This indicates that the reaction of potassium permanganate decomposition does not involve under the given conditions the hydroxide. Also noteworthy is that the curves show total lack of the second titration step pointing to presence of carbonate ions in these solutions. This indicates that, under the experimental conditions, there was no noticeable absorption of carbon dioxide from air by the working solution.

Mass-spectrometric analyses of extracts from the reaction mixture after complete dissolution of PVDF did not reveal any fluorinated organic compounds in concentrations measurable by this technique. This confirms the assumption that PVDF decomposes in concentrated solutions of $KMnO_4$ + NaOH to complete mineralization.

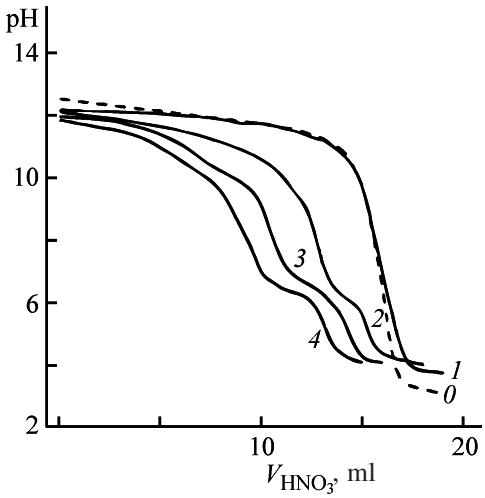


Fig. 3. Potentiometric titration curves of the starting solutions and reaction mixtures after PVDF dissolution. Solution composition, PVDF mass (g): (*0*) starting 3.3 M solution of NaOH, (*1*) blank solution, (*2*) 1.0, (*3*) 1.5, and (*4*) 2.0.

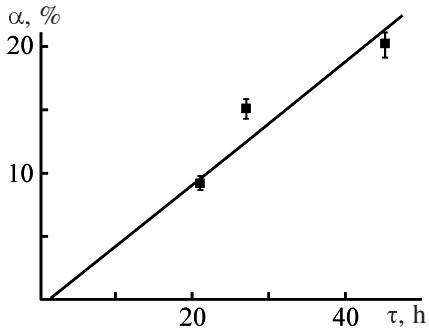


Fig. 4. Degree α of decomposition of the alkaline solution of potassium permanganate vs. the time τ of heating at 115°C.

The table lists the experimentally found ratios between the consumption of the polymer and consumption/accumulation of the etching solution components in comparison with the ratios predicted by

Consumption of the etching solution components and accumulation of reaction products (moles per mole of consumed monomeric unit of the polymer) in comparison with those corresponding to reaction equations (3) and (5)

Data	$-KMnO_4$	–NaOH	$+MnO_2$	$+CO_3^{2-}$
Experiment	2.0 ± 0.2	4.8 ± 0.6	2.0 ± 0.2	1.9 ± 0.3
Calculation by equation:				
(3)	2.7	3.3	2.7	2.0
(5)	4.0	2.0*	4.0	2.0

* The consumption of the hydroxide for the formation of manganate in accordance with Eq. (4).

reactions (3) and (5). Noteworthy is the similarity between the experimentally found ratios and the coefficients of reaction (3). Nevertheless, the expenditure of sodium hydroxide markedly exceeds the value of 3.3 corresponding to Eq. (3). On the one hand, this difference may be due to the rather large experimental errors. On the other hand, a possible reason is occurrence of other reactions leading to degradation of PVDF. For example, it was shown in [17, 18] that PVDF is partly oxidized in concentrated hydroxide solutions (even without introduction of strong oxidizing agents), which results in that hydroxy and carbonyl groups appear in the polymer chain. It was found in [5] that treatment with concentrated alkali solutions at high temperatures enables slow etching of PVDF, i.e., provides rupture of the polymer backbone. Thus, it is not improbable that, under the experimental conditions, part of the hydroxide is expended for degradation of PVDF by a reaction other than reaction (3).

CONCLUSIONS

(1) It was found that, in alkaline solutions, polyvinylidene fluoride undergoes complete oxidation to carbonate ions.

(2) The coefficients characterizing the loss of components of the working solution and accumulation of manganese oxide and carbonate ions in manufacture of track membranes from polyvinylidene fluoride films were determined.

ACKNOWLEDGMENTS

The authors thank N.D. Kagramanov (Nesmeyanov Institute of Organoelement Compounds, Russian Academy of Sciences) for gas chromatographic–mass spectrometric analyses of extracts from etching solutions and V.K. Goncharuk and E.B. Merkulov (Institute of Chemistry, Far-Eastern Branch, Russian Academy of Sciences) for an analysis by differential-scanning calorimetry of the precipitate formed.

REFERENCES

1. Flerov, G.N., Apel, P.Yu., Didyk, A.Yu., et al., *At. Energ*., 1989, vol. 67, no. 4, p. 274.
2. Apel, P., *Radiat. Meas*., 2001, vol. 34, nos. 1–6, pp. 559–566.
3. Shirkova, V.V. and Tretyakova, S.P., *Radiat. Meas*., 1997, vol. 28, nos. 1–6, pp. 791–798.
4. Tretyakova, S.P., Shirkova, V.V., Khitrova, N.B., and Borcea, C., *Nuclear Tracks*, 1986, vol. 12, nos. 1–6, pp. 75–76.
5. Komaki, Y., Ishikawa, N., Sakurai, T., et al., *Nucl. Instr. Meth. B*, 1988, vol. 34, pp. 332–336.
6. Remy, H., *Lehrbuch der anorganischen Chemie*, Leipzig: Akademische, 1961, vol. 2.
7. Tatlow, J.C., *J. Fluorine Chem*., 1995, vol. 75, pp. 7–34.
8. Smith, R.P. and Tatlow, J.C., *J. Chem. Soc*., 1957, p. 2505.
9. Tatlow, J.C. and Worthington, R.E., *J. Chem. Soc*., 1952, p. 1251.
10. Evans, D.E.M. and Tatlow, J.C., *J. Chem. Soc*., 1954, p. 3779.
11. Burdon, J. and Tatlow, J.C., *J. Appl. Chem*., 1958, no. 8 (May), p. 293.
12. *Chemistry of Organic Fluorine Compounds II. A Critical Review*, Hudlicky, M. and Pavlath, A.E., Eds., *ACS Monograph 187*, Washington DC: Am. Chem. Soc., 1995.
13. Barbour, A.K. et al., *J. Appl. Chem*., 1954, no. 4 (July), p. 341.
14. Zeifman, Yu.V., Postovoi, S.A., and Delyagina, N.I., *Izv. Akad. Nauk SSSR, Ser. Khim*., 1989, no. 3, p. 738.
15. Grasselli, M. and Betz, N., *Nucl. Instr. Meth. B*, 2005, vol. 236, p. 501.
16. Ross, G.J., Watts, J.F., Hill, M.P., and Morrissey, P., *Polymer*, 2000, no. 41, pp. 1685–1696.
17. Ross, G.J., Watts, J.F., Hill, M.P., and Morrissey, P., *Polymer*, 2001, no. 42, pp. 403–413.
18. Charlot, G., *Les methods de la chimie analytique. Analyse quantitative minerale*, Paris: Masson, 1961, 4th ed.
19. Piskareva, S.K., Barashkov, K.M., and Ol'shanova, K.M., *Analiticheskaya khimiya* (Analytical Chemistry), Moscow: Vysshaya Shkola, 1994.

ISSN 1070-4272, Russian Journal of Applied Chemistry, 2008, Vol. 81, No. 3, pp. 471–474. © Pleiades Publishing, Ltd., 2008.
Original Russian Text © V.N. Verezhnikov, A.E. Tekucheva, E.A. Grinfel'd, L.A. Korystina, 2008, published in Zhurnal Prikladnoi Khimii, 2008, Vol. 81, No. 3, pp. 486–489.

MACROMOLECULAR CHEMISTRY AND POLYMERIC MATERIALS

Chemical Agglomeration of Butadiene–Styrene Latex Using Dispersions of Carboxyl-Containing Polymers with Various Degrees of Carboxylation

V. N. Verezhnikov, A. E. Tekucheva, E. A. Grinfel'd, and L. A. Korystina

Voronezh State University, Voronezh, Russia
Voronezhsintezkauchuk Joint-Stock Company, Voronezh, Russia
Voronezh Branch, Lebedev Research Institute of Synthetic Rubber, Voronezh, Russia

Received November 27, 2007

Abstract—Agglomeration of SKS-30 ARK latex particles using dispersions of butadiene–methyl methacrylate–methacrylic acid copolymer with various contents of methacrylic acid (up to 25 wt %) was studied.

DOI: 10.1134/S1070427208030257

Synthetic latexes with elevated content of the polymer (up to 60–65 wt %) are used in such branches of industry as production of foam rubber, some types of adhesives, etc. In turn, so high latex concentrations can be only attained at a rather large size of latex particles (~200–250 nm), because, at concentrating (e.g., by evaporation) highly dispersed latexes (50–100 nm particle size) commonly formed by emulsion polymerization, the system becomes paste-like and loses fluidity even at a polymer concentration of 40–45 wt %. Although modern procedures of emulsion polymerization allow preparation of latexes with relatively large particles, this is possible only at a very low polymerization rate, which is economically unfeasible. Preparation of latexes with common dispersion and their further agglomeration up to required particle size seem more promising.

Various methods of agglomeration are known, which in all the cases are related to controlled destabilization of latex particles with their subsequent coalescence and adhesion and stabilization to prevent irreversible coagulation yielding polymer macrophase [1]. Such procedures as agglomeration under pressure (mechanical agglomeration) and frosting–defrosting method are used in industry. However, these procedures, being rather complex, not only increase particle size but also broaden the particle size distribution. Chemical agglomeration caused by small (sensitizing) additives of water-soluble polymers {e.g., poly(vinyl methyl ether) [2], polyethylenepolyamine [3], etc.} is simpler in implementation. However, this procedure has not found wide application because of a significant drawback, prolonged aftereffect (i.e., continued agglomeration up to coagulation in storage of latex after its concentration).

A peculiar procedure based on latex agglomeration using a carboxyl-containing polymer was suggested in [4]. This procedure is simple and allows elimination of the aftereffect; the particles of such latex, being agglomeration nuclei, should lose the agglomeration activity upon formation of a layer of the main latex particles on their surface. However, despite principal possibility and advantages, this procedure has not been implemented on the industrial scale.

To develop scientific principles for industrial application of chemical agglomeration, it was advisable to perform a systematic study of the relationships and mechanisms of agglomeration using carboxylated latexes and to reveal various factors affecting this process.

Previously [5, 6] we demonstrated high agglomeration performance of BMK latex, which is a copolymer of butadiene, methyl methacrylate (MMA), and methacrylic acid (MAA) containing 10 wt % MAA, in agglomeration of adsorption-unsaturated latexes with various polymer phases (butadiene–styrene, –nitrile, vinylidene chloride, polybutadiene). The average particle size of the resulting latexes was 200–250 nm (in some cases up to 300 nm); they were characterized by low surface tension and retained fluidity upon evaporation up to a polymer concentration exceeding 60 wt %.

Table 1. Characteristics of latexes

Latex brand	Copolymer composition, wt %	Weight fraction of dry compound, %	Emulsifier	σ, mN m^{-1}	pH	Average particle size, nm
SKS-30 ARK	Styrene 30, Butadiene 70	23.0	K paraffinate and resinate	67.0	10.1	78
BMK-5	Butadiene 42, MMA 53, MAA 5	34.2	Sodium alkylbenzenesulfonate (Sulfonol)	56.5	4.3	91
BMK-7	Butadiene 41, MMA 51.5, MAA 7	33.0	Sodium alkylbenzenesulfonate (Sulfonol)	54.2	4.4	110
BMK-10	Butadiene 40, MMA 50, MAA 10	36.0	Sodium alkylbenzenesulfonate (Sulfonol)	55.0	3.3	105
BMK-15	Butadiene 38, MMA 48, MAA 15	34.4	Sodium alkylbenzenesulfonate (Sulfonol)	55.3	3.7	98
BMK-20	Butadiene 36, MMA 44, MAA 20	34.0	Sodium alkylbenzenesulfonate (Sulfonol)	53.0	3.8	102
BMK-25	Butadiene 33, MMA 41.5, MAA 25	33.5	Sodium alkylbenzenesulfonate (Sulfonol)	52.6	3.6	99

In this study we examined the dependence of agglomeration using BMK latex in relation to the degree of its carboxylation.

EXPERIMENTAL

We prepared samples of BMK latex with various contents of MAA in copolymer α_m (5–25 wt % MAA recalculated to the weight of the butadiene : MMA monomer mixture at their constant ratio of 2 : 8). The synthesis was performed with increased amounts of *tert*-dodecyl mercaptan (chain-terminating agent) to obtain short copolymer chains with high mobility of the molecules. Agglomeration was studied using SKS-30 ARK commercial butadiene–styrene latex. The characteristics of latexes are listed in Table 1. The surface tension σ of latexes was measured by the anchor–ring method on a Du Nouy apparatus, and the average particle size was determined by turbidimetry from the dependences of the optical density D on the wavelength [6]. The D values were measured on an FEK-56 M photoelectrocolorimeter. The solution pH was determined with an EV-74 pH-meter.

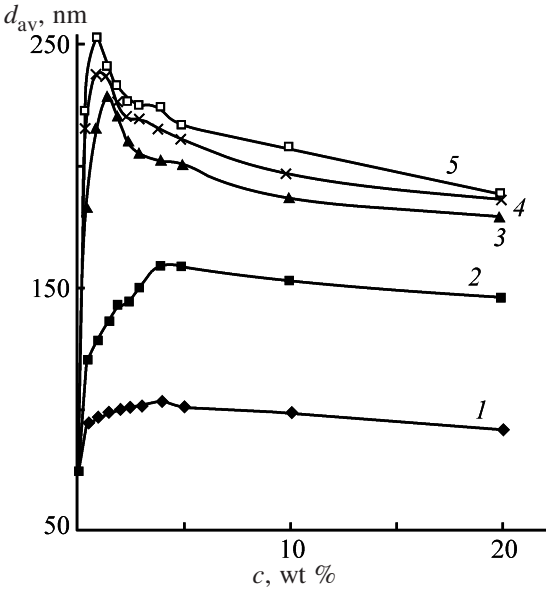


Fig. 1. Average particle size d_{av} as a function of the amount of BMK polymer c added into SKS-30 ARK latex. Degree of carboxylation n: (*1*) 5, (*2*) 7, (*3*) 10, (*4*) 15, (*5*) 20, and (*6*) 25.

A required volume of BMK latex (0.5–25.0 wt % copolymer relative to rubber) was added with stirring to a sample of SKS-30 ARK latex. After agglomeration completion (3–4 days), the optical density was measured and the average particle size d_{av} was calculated. The resulting dependences of d_{av} on the concentration of BMK are shown in Fig. 1. As can be seen, at a content of MAA in the copolymer α_m = 5 wt %, the agglomeration is inefficient and the average particle size increases insignificantly (from 80 to 105 nm). At α_m of 10, 15, 20, and 25 wt %, the dependences pass through a maximum at a concentration of agglomeration agent of 1–2 wt %, and the average particle size increases to 225–250 nm. The agglomeration performance of BMK-7 latex is intermediate between those of BMK-5 and BMK-10, and the average particle size increases to 160 nm upon addition of

4 wt % agglomeration agent. In general, the dependences shown in Fig. 1 illustrate a monotonic increase in the agglomeration effect of BMK latex with increasing degree of carboxylation (at MAA concentration of up to 25 wt %). At the same time, it should be noted that the concentration of BMK providing the maximal agglomeration effect is essentially independent of the degree of carboxylation and comprised 1–2 wt % relative to the rubber.

It was of particular importance to study the kinetics of agglomeration in relation to the degree of carboxylation of agglomeration agent. For this purpose, samples of SRS-30 ARK latex were mixed with the calculated amounts of BMK polymer with various degrees of carboxylation in amounts of 1 wt % per latex. Then samples of the reaction mixture taken in equal periods were stabilized with 1% solution of Sulfonol to prevent further particle growth, and the optical density was measured. The time dependences of the optical density are shown in Fig. 2. As seen, at MAA content of the copolymer of 5–7 wt % the optical density and, thus, the average particle size increase with time very slowly. At a higher content of MAA (10 wt % and more), D sharply increases within the first several tenths of seconds and then slowly increases up to a certain constant value in 3–4 days. The D values measured after storage for 10 days showed the absence of further increase in the optical density, i.e., the agglomeration aftereffect typical for water-soluble polymers was not observed at agglomeration of the latex dispersions using carboxylated polymers.

Sharp deceleration and subsequent termination of the particle growth suggest certain similarity of agglomeration with the first stage of coagulation of adsorption-unsaturated latexes under the action of electrolytes [7]. In both cases the absorption saturation of agglomerates increases, which is confirmed by a decrease in the surface tension of the systems observed both at coagulation [7] and agglomeration [6]. In the first case, coarsening of the particles is terminated owing to formation of a compact saturated adsorption-hydrated shell of surfactant-emulsifier on the surface of primary agglomerates and appearance of nonelectrostatic protection factor in addition to electrostatic repulsion [7]. Similar compaction of the adsorption layer should be observed in the second case. At the same time, the other mechanism of formation of the additional protection shell should be taken into account in the case of agglomeration using dispersions of the carboxylated polymer.

We assumed that, upon addition of agglomeration agent, the BMK globules become agglomeration centers at which the particles of the main latex are fixed. Further coalescence of these particles yields coarse agglomerates formed from the main and agglomerating polymers. Owing to significant molecular affinity to aqueous solutions and high molecular mobility of short polymer chains of the highly carboxylated reagent (BMK), these chains undergo spontaneous redistribution in the agglomerate bulk and become concentrated at the surface boundary. As a result, a thin layer of macromolecules of the highly carboxylated polymer is formed at the particle boundary, making the surface hydrophilic and imparting to it an additional electrical charge owing to fixed carboxylate anions. Both factors provide additional stabilization of the dispersions with coarsened particles and cause deceleration and termination of the agglomeration [5].

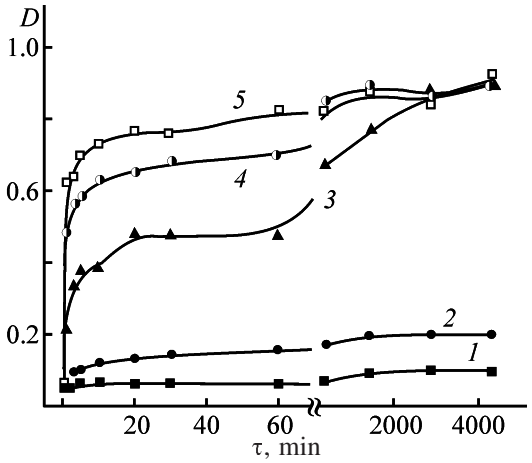


Fig. 2. Optical density D as a function of time τ in agglomeration of SKS-30 ARK latex using BMK polymer added in an amount of 1 wt % relative to rubber. Degree of carboxylation n: (*1*) 5, (*2*) 7, (*3*) 10, (*4*) 15, and (*5*) 20.

Using the data on the average particle size and composition of the initial and agglomerated latexes, we calculated their characteristics considering latexes as monodisperse systems. The degree of agglomeration was calculated as the ratio of the number of particles in the initial and agglomerated samples. The thickness of the film of highly carboxylated polymer on the agglomerate surface was calculated assuming that the BMK polymer is uniformly distributed over the particles of the agglomerated latex and is fully concentrated on their surface owing to diffusion. The results are listed in Table 2. It should be noted that the shell thicknesses given are the effective quantities which at incomplete saturation of the surface do not correspond to the actual size of macromolecules.

Our experimental data show that the highest degree

Table 2. Calculated characteristics of SKS-30 ARK latex particles agglomerated using BMK polymer with various degrees of carboxylation *n*

α_m, wt %	Degree of agglomeration at indicated *n*						Thickness of highly carboxylated shell, nm, at indicated *n*					
	5	7	10	15	20	25	5	7	10	15	20	25
0.5	3.1	3.6	12.3	20.9	23.4	16.1	0.09	0.10	0.15	0.18	0.19	0.20
1.0	3.5	4.5	21.8	28.2	34.2	22.8	0.20	0.21	0.36	0.40	0.42	0.47
1.5	3.9	5.2	24.0	27.7	29.4	37.0	0.30	0.34	0.56	0.60	0.60	0.64
2.0	4.0	6.1	22.4	24.3	26.5	44.0	0.41	0.47	0.72	0.74	0.76	0.90
2.5	4.6	6.3	19.5	22.0	24.4	47.3	0.53	0.60	0.86	0.90	0.93	1.15
3.0	5.0	7.1	18.1	20.9	23.9	43.8	0.65	0.74	1.00	1.05	1.10	1.35
4.0	4.9	8.4	17.1	19.4	23.5	37.5	0.68	1.02	1.3	1.36	1.45	1.70
5.0	5.7	8.3	16.4	17.8	21.4	37.0	1.10	1.27	1.60	1.77	1.75	2.10
10.0	7.0	7.4	12.3	16.2	18.7	33.7	2.30	2.38	2.80	3.44	3.24	3.90
20.0	6.7	7.1	11.3	15.9	13.9	32.9	4.30	4.42	5.20	5.78	5.52	7.34

of agglomeration is attained when the amount of carboxylated latex added provides formation of a monomolecular layer (0.4–0.6 nm thick) of the highly carboxylated polymer on the surface of latex particles.

CONCLUSIONS

(1) Dispersions of highly carboxylated butadiene–methyl methacrylate copolymer provide effective agglomeration of butadiene–styrene latex without agglomeration aftereffect.

(2) The average particle size of agglomerates and the rate of agglomeration increase with increasing degree of carboxylation in the range of methacrylic acid content of the copolymer from 5 to 25 wt %.

REFERENCES

1. Erkova, L.N. and Chechik, O.S., *Lateksy* (Latexes), Leningrad: Khimiya, 1983.
2. Howland, S.H. and Aleksa, L.J., *Rubber Plast. Age*, 1961, vol. 42, no. 3, pp. 868–874.
3. Kazakevich, T.S., Kuznetsov, L.D., and Lebedev, A.V., *Kauchuk Rezina*, 1967, no. 1, pp. 9–11.
4. Wesslau, H., *Makromol. Chem.*, 1963, vol. 69, no. 1, pp. 220–240.
5. Grinfel'd, E.A., Khvatova, L.K., Zhurikhina, M.A., and Korystina, L.A., Abstracts of Papers, *VII Rossiiskaya nauchno-prakticheskaya konferentsiya "Syr'e i materialy dlya rezinovoi promyshlennosti"* (Russ. Scientific and Practical Conf. "Resources and Materials for Rubber Industry), Moscow, 2000, p. 136.
6. Grinfel'd, E.A., Khvatova, L.K., Zhurikhina, M.A., et al., *Vest. Voronezh. Gos. Univ., Khim., Biol., Farm.*, 2006, no. 2, pp. 40–43.
7. Neiman, R.E., *Ocherki kolloidnoi khimii sinteticheskikh lateksov* (Sketches on Colloidal Chemistry of Synthetic Rubbers), Voronezh: Voronezh. Gos. Univ., 1980.

ISSN 1070-4272, Russian Journal of Applied Chemistry, 2008, Vol. 81, No. 3, pp. 475–477. © Pleiades Publishing, Ltd., 2008.
Original Russian Text © S.V. Kopsov, S.S. Zlotskii, 2008, published in Zhurnal Prikladnoi Khimii, 2008, Vol. 81, No. 3, pp. 490–492.

MACROMOLECULAR CHEMISTRY AND POLYMERIC MATERIALS

Acid-Catalyzed Condensation of Vinyl-*gem*-dichlorocyclopropanes with Formaldehyde in Nonaqueous Solutions

S. V. Kopsov and S. S. Zlotskii

Ufa State Petroleum Technical University, Ufa, Bashkortostan, Russia

Received January 16, 2007

Abstract—Condensation of vinyl- and vinylmethyl-1,1-dichlorocyclopropanes with formaldehyde in organic solvents of various polarities was studied.

DOI: 10.1134/S1070427208030269

Reaction of olefins with formaldehyde in the presence of acid catalysts (Prins reaction) is the main route to substituted 1,3-dioxanes [1–4]. This process is widely used in commercial synthesis of 4,4-dimethyl-1,3-dioxane whose cleavage yields isoprene [3]. The condensation is performed most frequently in an aqueous solution, but in this case it is accompanied by formation of hydroxyl-containing by-products: unsaturated alcohols, diols, hydroxyfurans, etc. [4].

To prepare dioxanes containing a *gem*-dichlorocyclopropane fragment, which can be of interest as biologically active compounds and intermediates for organic synthesis, we used the reaction of vinyl-*gem*-dichlorocyclopropanes **Ia** and **Ib** with formaldehyde in organic solvents (1,2-dichloroethane, chlorobenzene, 1,4-dioxane, diisopropyl ether) in the presence of catalytic amounds of H_2SO_4. The starting vinyl-*gem*-dichlorocyclopropanes are formed in virtually quantitative yield by the addition of dichlorocarbene to the corresponding dienes in a two-phase system [5].

We found that the reaction of **Ia** and **Ib** with formaldehyde yielded the coresponding 1,3-dioxanes (**IIa**, **IIb**) and 1,3-dioxolanes (**IIIa**, **IIIb**) in comparable amounts. Apparently, the highly reactive intermediate unsaturated alcohol reacts with formaldehyde to form a hemiacetal whose hydroxy group undergoes intramolecular adition to the double bond to form heterocycles **IIa**, **IIb**, **IIIa**, and **IIIb**:

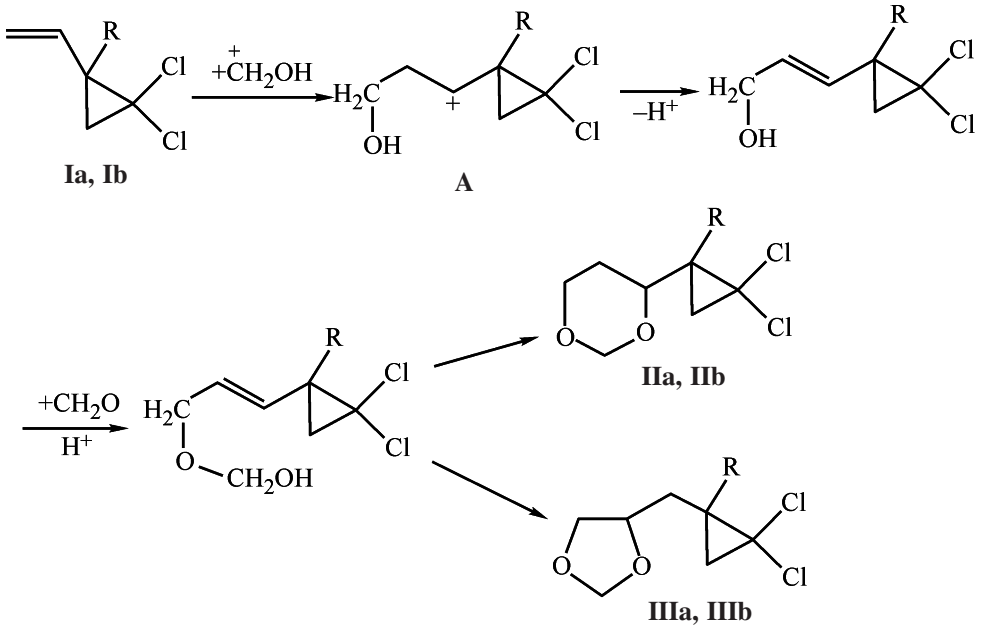


Table 1. Reaction of vinyl-*gem*-dichlorocyclopropanes **Ia** and **Ib** with formaldehyde. Molar ratio of **Ia** or **Ib** to CH_2O and H_2SO_4 1 : 2.5 : 0.5, 55°C, 3 h

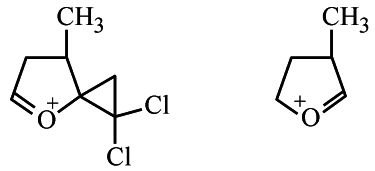
Solvent	Conversion, %		Selectivity, %			
	Ia	**Ib**	**Ia**	**Ib**	**Ia**	**Ib**
1,2-Dichloroethane	95	85*	40	50	35	35
Chlorobenzene	65	60	45	45	45	40
1,4-Dioxane	50	40**	70	50	40	20
Diisopropyl ether	95	90	75	60	35	20

* More than 20% high-boiling unidentified products.
** About 5% low-boiling components.

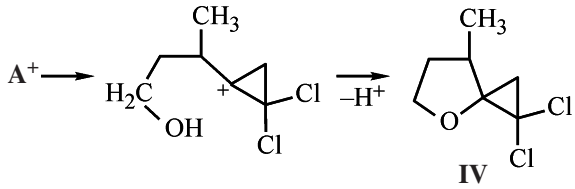
where R = H (**a**), CH_3 (**b**).

It is interesting that, in polar solvents (1,4-dioxane, diisopropyl ether), the selectivity with respect to 1,3-dioxanes **IIa** and **IIb** is somewhat higher than in chlorinated hydrocarbons (Table 1). Apparently, the ratio of the six- (**IIa**, **IIb**) and five-membered (**IIIa**, **IIIb**) products is determined by the rate of proton addition to carbon atoms of the double bond of the intermediate hemiacetal. In the isoprene derivative, the methyl group facilitates the formation of carbocations in which the positive charge is conjugated with the quasiaromatic orbitals of the three-membered carbocycle, which may be responsible for the observed prevalence the reaction pathway leading to the six-membered heterocycle.

The reaction with **Ia** in 1,2-dichloroethane yields more than 20% high-boiling unidentified products, which may be due to hindered cyclization of oligoformals and formation of noticeable amounts of polyformals. The condensation with **Ia** in 1,4-dioxane yields an impurity of low-boiling substances. The mass spectrum of one of them contains peaks of ions **B** and **C** with *m*/*z* 179 and 85, respectively. We believe that this minor component (1–1.5%) is spirocyclic compound **IV** formed by 1,2-migration of the methyl group and closure of the pyran ring in intermediate carbocation **A**:



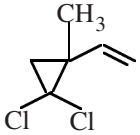
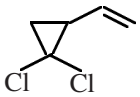
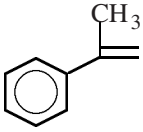
B, *m*/*z* = 179 **C**, *m*/*z* = 85



IV

Sigmatropic shifts in the course of the Prins reaction were observed previously [6].

Table 2. Relative activity of olefins in the Prins reaction. Olefin : CH_2O : H_2SO_4 molar ratio 1 : 2.5 : 0.5, 55°C, 30 min, solvent $(i\text{-Pr})_2O$

Compound	Relative activity
	1
	2.5
	0.5
	15

The activity of olefins **Ia** and **Ib** was compared with that of 1-heptene and styrene in competitive reactions. The relative activity of these unsaturated compounds was judged from the rates of formation of 1,3-dioxacyclanes **IIa**, **IIb**, **IIIa**, and **IIIb** and of 4-amyl- and 4-methyl-4-phenyl-1,3-dioxanes which are selectively formed from 1-heptene and α-methylstyrene, respectively [1]. The activity of the aromatic olefin exceeds that of **Ia** by more than an order of magnitude, and compound **IIa**, in turn, is two times more active than the terminal linear unsaturated hydrocarbon (Table 2).

Table 3. Constants and spectral characteristics of the products obtained

Compound	T_b, °C/P, mm Hg	R_f	^{1}H NMR spectrum, δ, ppm	Mass spectrum, m/z (I_{rel}, %)
4-(2,2-Dichlorocyclopropyl)-1,3-dioxane **IIa**	111/5	0.35	1.4–1.5 (m, 1H, $CHCCl_2$); 1.6–1.8 (m, 2H, CH_2CCl_2); 1.85–2.1 (m, 2H, CH_2); 3.6–3.8 (m, 2H, CH_2O); 4.0–4.15 (m, 1H, CHO); 4.6–5.0 (d.d, 2H, OCH_2O)	198, 200 (0.7) [M^+]; 109, 111 (5); 87 (100); 57 (60)
4-(2,2-Dichloro-1-methylcyclopropyl)-1,3-dioxane **IIb**	115/5	0.37	1.35 (s, 3H, CH_3); 1.4–1.6 (d.d, 2H, CH_2CCl_2); 2.4–2.6 (m, 2H, CH_2); 3.6–3.8 (m, 2H, CH_2O); 3.95–4.15 (m, 1H, CHO); 4.65–5.0 (d.d, 2H, OCH_2O)	212, 214 (1) [M^+]; 123, 125 (3); 87 (100); 57 (51); 45 (81)
4-(2,2-Dichlorocyclopropylmethyl)-1,3-dioxolane **IIIa**	105/5	0.27	1.4–1.5 (m, 1H, $CHCCl_2$); 1.6–1.8 (m, 2H, CH_2CCl_2); 1.6–2.1 (m, 2H, CH_2); 3.5–3.8 (m, 2H, CH_2O); 4.1–4.25 (m, 1H, CHO); 4.6–5.0 (d.d, 2H, OCH_2O)	198, 200 (0.1) [M^+]; 100 (45); 84 (50); 73 (100)
4-(2,2-Dichloro-1-methylcyclopropylmethyl)-1,3-dioxolane **IIIb**	108/5	0.30	1.4 (s, 3H, CH_3); 1.4–1.6 (d.d, 2H, CH_2CCl_2); 1.6–2.2 (m, 2H, CH_2); 3.4–3.7 (m, 2H, CH_2O); 4.05–4.2 (m, 1H, CHO); 4.6–5.1 (d.d, 2H, OCH_2O)	212, 214 (0.1) [M^+]; 114 (37); 84 (40); 73 (100)

EXPERIMENTAL

The ^{1}H NMR spectra were recorded on a Bruker AM-300 spectrometer (300 MHz) in acetone-d_6, $CDCl_3$, or C_6D_6 + CCl_4. GLC analyses were performed on a Tsvet-500M device (flame ionization detector, 5 × 1000-mm metal column, stationary phase 5% SE-30 on Chromaton N-AW, programmed heating from 50 to 220°C at a rate of 6 deg min^{-1}, carrier gas helium).

Vinyl-*gem*-dichlorocyclopropanes **Ia** and **Ib** were prepared by the published procedure [5]. The unsaturated compounds used in the study were no less than 99% pure.

Acid-catalyzed reaction of olefins with formaldehyde (general procedure). A solution of 0.1 mol of appropriate olefin in 10 ml of appropriate solvent was added with vigorous stirring to a mixture of 7.7 g (0.26 mol) of paraform, 3.1 ml of concentrated H_2SO_4, and 5 ml of the solvent. The mixture was heated to 50–60°C, with the stirring continued, until the paraform dissolved completely. After cooling, the mixture was neutralized with aqueous ammonia, the organic layer was separated and dried over $CaCl_2$, and the solvent was evaporated. The products were isolated by column chromatography on silica gel (eluent hexane–ethyl acetate, 6 : 1).

Some characteristics of the synthesized compounds are given in Table 3.

CONCLUSION

Condensation of vinyl- and vinylmethyl-*gem*-dichlorocyclopropanes with formaldehyde in organic solvents of various polarities was performed. The reaction occurs along two parallel pathways, yielding the corresponding 4-*gem*-dichlorocyclopropyl-1,3-dioxolanes and -1,3-dioxanes via the intermediate unsaturated alcohol.

REFERENCES

1. Shepelevich, I.S., Talipova, G.R., and Talipov, R.F., in *Novye napravleniya v khimii tsiklicheskikh atsetalei* (New Lines in Chemistry of Cyclic Acetals), Ufa: Reaktiv, 2002, p. 36.
2. Talipov, R.F. and Safarov, M.G., *Bashkir. Khim. Zh.*, 1997, vol. 4, no. 3, p. 10.
3. Rakhmankulov, D.L., Zlotskii, S.S., Kantor, E.A., et al., *Mekhanizmy reaktsii atsetalei* (Mechanisms of Reactions of Acetals), Moscow: Khimiya, 1987.
4. Talipov, R.F., Mustafin, A.M., Talipova, G.R., and Safarov, M.G., *Zh. Obshch. Khim.*, 1996, vol. 66, no. 8, p. 1382.
5. Arbuzova, T.V., Zlotskii, S.S., and Rakhmankulov, D.L., *Bashkir. Khim. Zh.*, 2005, vol. 12, no. 2, p. 19.
6. Talipov, R.F., New Approaches to Synthesis of β-Substituted Hydrogenated Furans and Role of Formaldehyde Oligomers in the Pattern of Product Formation in the Prins Reaction, *Doctoral Dissertation*, Ufa, 1998.

ISSN 1070-4272, Russian Journal of Applied Chemistry, 2008, Vol. 81, No. 3, pp. 478–481. © Pleiades Publishing, Ltd., 2008.
Original Russian Text © O.N. Novikov, L.Ya. Tsarik, A.V. Pukholenko, G.N. Koroleva, 2008, published in Zhurnal Prikladnoi Khimii, 2008, Vol. 81, No. 3, pp. 493–496.

MACROMOLECULAR CHEMISTRY AND POLYMERIC MATERIALS

Suspension Copolymerization of Divinylbenzene in a Gel Medium

O. N. Novikov, L. Ya. Tsarik, A. V. Pukholenko, and G. N. Koroleva

Irkutsk State University, Irkutsk, Russia

Received May 16, 2007

Abstract—A procedure of suspension polymerization and copolymerization in a medium of thermally reversible gels was developed.

DOI: 10.1134/S1070427208030270

Three-dimensional radical bulk copolymerization of divinylbenzene with a series of vinyl monomers was studied previously [1]. To prepare spherical particles based on these copolymers, a new procedure of polymerization in a gel medium was suggested [2, 3].

This work was aimed to prepare spherical particles of copolymers of *p*-divinylbenzene (DVB) with styrene (St) and diethyl fumarate (DEF) by suspension copolymerization in a gel medium. Since the matrices of these polymers should serve in future to produce sorbents, in the reaction we used diluents favorable for the formation of the porous structure of the copolymers (CPs).

EXPERIMENTAL

The solvents [octanol (OC), toluene (T)], monomers (St, DVB, DEF), and initiators [benzoyl peroxide (BP), azobis(isobutyronitrile) (AIBN)] were purified by the procedures described previously [1]. The linear copolymer St–DEF used as polymeric diluent for creation of the porous structure was synthesized by bulk polymerization (Table 1, run no. 1).

Copolymerization in a gel was performed as follows. To dissolve methyl cellulose (MC), it was poured over with hot distilled water; after swelling for 20 min, cold water was added and MC was dissolved with stirring over a period of 5 h at 292 K. Copolymerization of the monomer mixture in a gel was performed by dispersion of the monomer mixture in an aqueous solution of MC at 292–298 K with subsequent heating at a temperature above the gelatinization point up to the polymerization point (333–363 K). The monomer mixture was added dropwise through an extrusion nozzle into a flask filled with an aqueous solution of MC, with continuous stirring on a laboratory shaker at 293 K. A stable system of drops uniform in size is formed in the MC solution. This system does not separate into layers during a period of more than 30–60 min. Within 10 min, the MC gel is formed. The reaction vessels with the dispersion of drops were purged with argon and placed into a thermostat at 333–363 K. The gelatinization time of the MC solution was 10–15 min. Then, the polymerization proceeded in drops immobilized in the MC gel. After the reaction completion, within a certain time, the reaction mixture was cooled to 293 K; in so doing, the gel melted and granules were separated from the dispersion medium (DM) by decantation. The polymerization was carried out in an inert medium. Finer particles (from 0.1 to 1 μm) were separated by repeated decantation. The polymer was washed with cold water to remove MC, with acetone, and with diethyl ether to remove the unchanged monomer, solvent, and sol fraction. Then, the polymer was dried to constant weight. The yield of spherical particles was determined gravimetrically.

The true density of CPs was determined by the pycnometric method in hexane. The coefficient of volume swelling K_s is

$$K_s = V_s/V_0,$$

where V_s is the volume of the swollen polymer and V_0 is the polymer volume before swelling.

The molecular weight of segments between crosslinks M_c was determined by the equilibrium swelling method. The sol–gel analysis of CPs was performed

Table 1. Copolymerization in a gel medium. Content of MC 1.5%, diluent content 200 vol % relative to the mixture of monomers; ratio of monomers to the gel medium 1 : 5

Run no.	Styrene	DEF	DVB	Initiator, mol %; type of process	*T*, K	τ, h	Yield of spheres, wt %
	mol %						
1	50	50	0	AIBN, 2, in bulk	333	4	66
2	90	0	10	AIBN, 2, diluent OC : T = 1 : 1	333	4	66
3	90	0	10	AIBN, 2, diluent OC : T = 1 : 1	333	8	71
4	90	0	10	AIBN, 1, in gel	333	8	40
5	90	0	10	AIBN, 2, in gel	333	8	56
6	90	0	10	BP, 2, in suspension, 1 wt % gelatin	363	4	69
7	90	0	10	AIBN, 2, in gel	363	2	44
8	90	0	10	AIBN, 2, in gel, diluent DEF–St (5 wt %)	333	8	73
9	90	0	10	AIBN, 2, in gel, diluent DEF–St (5 wt %)	363	2	67
10	90	0	10	BP, 1, in gel	363	2	36
11	90	0	10	BP, 2, in gel	363	2	42
12	90	0	10	AIBN, 2, in gel	363	2	70
13	35	55	10	AIBN, 2, in gel (200 vol % OC)	333	8	80

by extraction with acetone in a Soxhlet apparatus. The samples obtained in run nos. 4–6 were examined by elemental analysis and IR spectroscopy (Specord 75-IR, KBr pellets).

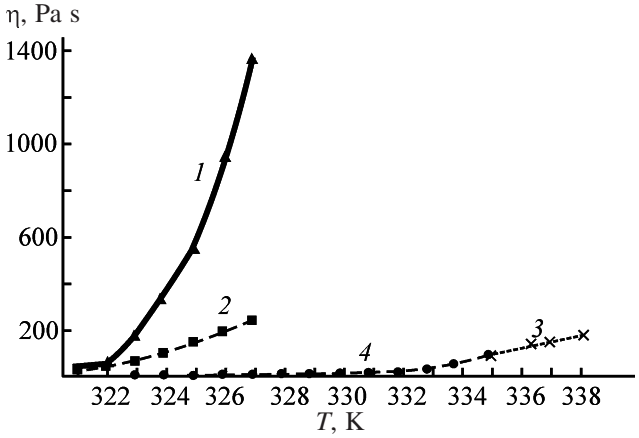
The concentration of aqueous MC solution was varied from 1 to 6 wt %. At a higher MC concentration, the solution viscosity exceeds 600 cP, which hampers the dispersion. At lower MC concentrations, the gel does not hold the drops of the monomer mixture.

The procedure of polymerization in a gel medium does not require stirring of the polymerizate during the process. In so doing, thermally reversible gels such as methyl cellulose, carboxymethyl cellulose, agar-agar, etc., are used. We performed the reaction in the methyl cellulose gel; the range of its gelatinization is shown in the figure. In the presence of sodium chloride, the gel is formed at lower temperatures. With increasing concentration of methyl cellulose, the gelatinization temperature decreases.

When the classical variant of suspension polymerization is realized below and in the gelatinization point, the dispersion system is unstable, which results in formation of coarse particles and irregular-shaped clots [4]. In the initial stage, a fairly narrow drop size distribution is reached, but coalescence results in particle consolidation and the particle size distribution becomes broad.

Polymerization in a gel implies that the dispersion of drops before polymerization and the polymerization proper are separated in time. The monomer drops having the required size are subsequently immobilized in the gel, and each drop is separated by the gel medium. During and after the gel formation, the dispersion system should not be stirred, so that the gel will not be destroyed under mechanical stress.

As a gel medium we used an aqueous solution of MC, which undergoes gelatinization under heating in the range from 308 to 329 K to form a turbid heterogeneous moderately dense gel holding drops of the monomer mixture. With decreasing temperature to 298–219 K, the gel is destroyed. The polymer structure is formed even in the stage when monomer drops dispersed in the gel are formed. There is no coales-



Viscosity η as a function of temperature *T* for solutions of MC in the course of gelatinization. Concentration, wt %: (*1*) 1.0 MC, 1.0 NaCl; (*2*) 1.5 MC, 1.0 NaCl; (*3*) 1.0 MC; and (*4*) 1.5 MC. Gelatinization temperature, K: (*1*) 325, (*2*) 323, (*3*) 333, and (*4*) 322.

Table 2. Characteristics of spherical particles

Run no. (Table 1)	Particle type	Average particle size, μm
4	White spherical	59.0±3.7
5	White spherical	46.0±1.2
6	White spherical	53.0±3.2
7	White spherical	123.0±1.1
8	Transparent spherical	112.0±3.4
9	Dull opalescent spherical	68.0±5.4
10	Dull spherical	80.0±2.3
13	White bluish spherical granules	92.0±1.34

cence of particles in the stage of polymerization. The yields of spherical polymeric particles in linear (Table 1, run no. 1) and three-dimensional (run no. 2) copolymerization in diluent are practically the same. As reaction time is increased, the yield of the polymer increases (runs nos. 2, 3).

As already mentioned, the aim of this study was to synthesize copolymers in the form of spherical particles; therefore, we first considered the influence of the reaction conditions in the gel on the yield of copolymers (Table 1, run nos. 4, 5). The experiments were performed with BP and AIBN (run nos. 4, 5, 7–9). After spherical particles of the copolymers with the size of 50 μm were obtained under conditions of traditional suspension polymerization (Table 1, run no. 6), we performed experiments on polymerization in a gel to obtain the same particle size with BP (runs nos. 10, 11). It was found that BP decreases the yield of copolymers; therefore, further experiments were performed with AIBN. Increase in the process temperature and time favors an increase in the yield. In 2 h (Table 2, run nos. 9, 12) we obtained copolymers having spherical particles in a yield of up to 70%. To form copolymers with porous structure, we performed polymerization in the MC gel medium in the presence of polymeric (Table 1, run nos. 8, 9) and low-molecular-weight (Table 1, run no. 13) diluents. The yield of spherical particles of the copolymers is from 66 to 80%. In the ternary system of monomers (Table 1, run no. 13), the yield of CPs is 80% (diluent OC).

During polymerization in a gel, the forced convection mass transfer is excluded. According to data of optical spectroscopy, the drops of the monomer mixture have a size exceeding 30 μm. The phase boundary in the system is limited in area, and the diffusion process alone cannot affect significantly the AIBN concentration in drops of the monomer mixture in 2 h. With decreasing concentration of the initiator, the yield of CPs decreases and its swellability increases.

In polymerization in gel for a longer time, the yield of spherical uniform particles with a size from 46 to 123 μm was up to 80% (Table 1, run no. 13). The yield of the gel fraction of the polymers obtained in the solution was 66 wt % (run no. 2).

Polymerization in gel a proceeds in monomer drops by the mechanism of radical polymerization in the bulk. The relative activity of DVB is 0.43, and that of St, 0.5. The relative activity of monomers in the system DVB–DEF is as follows: DVB 0.15 and DEF 0.001 [1].

Polymers obtained by polymerization in a gel have narrow particle size distribution (Table 2), whereas suspension polymerization (Table 1, run no. 6) is characterized by broad particle size distribution despite the additional stabilization of the dispersion system with gelatin.

As mentioned above, in this study polymerization in a gel was performed with the aim to obtain porous matrices. It was important to exclude mechanical action on the polymerizate at the onset of porous structure formation. In so doing, we used the copolymer of styrene with DEF as a diluent (Table 1, runs nos. 8, 9). The developed porosity can be obtained at a low concentration of the polymeric diluent. The use of various polymers of vinyl monomers as diluents is well known [5]. However, we found no studies in which polymeric and low-molecular-weight diluents were present simultaneously. Run no. 12 was performed under the same conditions in the absence of polymeric diluent. According to Table 2, the yields of CPs are governed to a greater extent by the reaction temperature and time.

The presence of a band at 990 cm^{-1} in the IR spectrum of CPs confirms the presence of DVB units in CPs. The band at 1510 cm^{-1} confirms the presence of St units. From the ratio of intensities of the absorption bands at 840 (double bonds) and 990 cm^{-1} (aromatic ring of DVB), we determined the ratio between pendant (free) double bonds (unchanged vinyl groups in DVB units) in CPs and *para*-substituted aromatic rings of DVB units. It was found that 30–40% of double bonds in DVB units were unchanged.

In the presence of a diluent, copolymers are formed in the form of white opaque particles, which is caused by their porous structure. Without blowing agent, transparent solid spherical glass-like particles were obtained. The samples obtained in a gel and in OC

Table 3. Characteristics of three-dimensional CPs synthesized in a gel

Run no.	Bulk density, g cm^{-3}	K_s (in toluene)	M_c,* g mol^{-1}
4	0.43	3.9	2242
5	0.18	2.7	473
6	0.27	1.9	342
7	0.28	2.6	858
9	0.16	2.6	694
10	0.26	2.7	774
13	0.62	1.8	1080

* Molecular weight of chain segments between cross-links.

diluent (Table 2, run no. 2) show somewhat better swelling (Table 3) than CPs synthesized by copolymerization in suspension. Under conditions of suspension copolymerization in a gel, cross-linking proceeds efficiently. In suspension polymerization in a gel, the forced convection is excluded and atmospheric oxygen does not penetrate into the gel. The samples obtained by suspension copolymerization in an argon medium (run no. 8) and in the course of copolymerization in a gel have close swelling ability with respect to M_c value (Table 3). There are ten styrene units between cross-links; the network is dense.

The diluent (a mixture of OC and T) forms pores, since under the conditions of precipitation polymerization the polymer separates out from the reaction mixture and has a dull white color. The polymer obtained in the diluent dissolving only the monomer (run no. 2) is brighter. The polymeric porophore (linear CP of styrene with DEF in an amount of 5 wt %) should favor formation of the porous structure since it promotes syneresis in the earlier stages of the copolymerization and increases the viscosity of the reaction mixture. In addition of the polymeric diluent, the swellability of CPs increased insignificantly. The regularly shaped spherical granules were formed. The particle size of CPs is governed by the reaction conditions (Table 2) and varies from 60 to 130 μm.

The density of porous copolymers St–DVB is 1.12 ± 0.19 g cm^{-3} and corresponds to fairly dense packing. The bulk density of porous samples of CPs varies from 0.11 to 0.43 g cm^{-3} and characterizes these samples as porous polymers. The pore volume is from 1.25 to 3.2 cm^3 g^{-1}, which corresponds to the developed porous structure. Under the conditions of polymerization in a gel, the densely cross-linked ternary porous copolymer DEF-St-DVB (run no. 14) was obtained.

The above data show that the molecular weight of segments of the CP chains between cross-links is the lowest in the sample prepared at the higher temperature; it is cross-linked most densely (Table 1, run no. 6). We believe that the influence of temperature is the most significant since it governs the mobility of DVB units in the structure of CP. On the whole, all CPs have densely cross-linked molecular network structure, are porous, and consist of spherical particles with a narrow size distribution. Copolymerization in a gel, due to exclusion of coalescence of polymer–monomer particles, extends the possibilities of synthesis of polymeric spherical particles from various monomers.

CONCLUSIONS

(1) Spherical particles of copolymers of *p*-divinylbenzene with styrene and diethyl fumarate were prepared by copolymerization in a medium of thermally reversible gel of methyl cellulose.

(2) The gel readily holding the drops of the monomer and reaction mixture is obtained at the concentration of methyl cellulose in water equal to 6 wt %.

(3) The polymer matrices with developed porous structure were synthesized in the presence of polymeric diluent presenting a linear analog of the cross-linked copolymer.

REFERENCES

1. Tsarik, L.Ya., Novikov, O.N., and Magdinets, V.V., *J. Polym. Sci., Ser. A*, 1998, vol. 36, pp. 371–378.
2. USSR Inventors' Certificate no. 1 551 710.
3. Novikov, O.N., Tsarik, L.Ya., Rokhin, A.V., and Tyukova, I.S., *Vysokomol. Soedin., Ser. A*, 1998, vol. 40, no. 2, pp. 228–235.
4. Ruckenstein, E. and Kong Xiang Zheng, *J. Appl. Polym. Sci*., 1999, vol. 72, no. 3, pp. 419–426.
5. Bricio, O., Coca, J., and Sastre, H., *Solvent Extr. Ion Exch*., 1997, vol. 15, no. 4, pp. 647–664.

ISSN 1070-4272, Russian Journal of Applied Chemistry, 2008, Vol. 81, No. 3, pp. 482–486. © Pleiades Publishing, Ltd., 2008.
Original Russian Text © O.O. Nikolaev, A.E. Tubolkin, V.P. Britov, G.A. Steblovskii, V.V. Bogdanov, 2008, published in Zhurnal Prikladnoi Khimii, 2008, Vol. 81, No. 3, pp. 497–501.

MACROMOLECULAR CHEMISTRY AND POLYMERIC MATERIALS

Preparation and Modification of Low-Viscous Polymeric Composites in Rotary-Pulsatory Apparatus in the Self-Oscillating Mode

O. O. Nikolaev, A. E. Tubolkin, V. P. Britov, G. A. Steblovskii, and V. V. Bogdanov

St. Petersburg State Institute of Technology (Technical University), St. Petersburg, Russia

Received May 23, 2007

Abstract—Preparation and modification of low-viscous polymeric composites in rotary-pulsatory apparatus operating in the self-oscillating mode are described. These are synthesis of antioxidant dispersions, preparation of artificial latexes from an isoprene rubber, modification of epoxy resins with low-molecular-weight carboxyl-containing rubbers, modification of *cis*-1,4-polyisoprene with a salt of *n*-nitrosodiphenylamine. The possibility of substantial intensification of these processes is analyzed.

DOI: 10.1134/S1070427208030282

Preparation and modification of polymeric composites in the course of mixing is one of the main ways to develop new materials. In recent years, new phenomenological concepts of activating mixing as a process for obtaining polymeric composite materials were put forward. According to these concepts, the energy imparted to the components not only causes homogenization and dispersion, but also either initiates chemical reactions between the components that do not occur in other conditions or accelerates the chemical transformations that otherwise are slow. These concepts have proved to be the most fruitful in the development of processes for preparation and modification of composites based on low-molecular-weight polymers [1–3].

At the same time, the already developed technologies need modification in order to raise the output capacity of the process and improve the quality of the composites obtained. One of the most effective ways to implement the activating mixing of low-viscous polymers is treatment of the mixture components in rotary-pulsatory apparatus (RPA) operating in both the laminar and turbulent modes. Under certain conditions, these apparatus can also operate in a specific self-oscillation mode, in which the power consumed is substantially lowered and the pulsating dynamic load on materials is raised. This opens up new opportunities for intensification of the processes performed in these apparatus [4].

EXPERIMENTAL

To develop a technology for synthesis and modification of formulations of various compositions in RPA under self-oscillation conditions, we used the following four groups of materials.

(A) Materials for preparing dispersions of antioxidants. We used an aqueous solution of a biodegradable and nontoxic nonionic (an oxyethylated alcohol) or anionic (a carboxylic or sulfonic acid) surfactant. The concentration of the antioxidant suspension was 1–20 wt %. As antioxidants served those commonly used for stabilization of rubbers: Neozone-D (phenyl-β-naphthylamine), DPPD (diphenyl-*p*-phenylenediamine), and Ionol (4-methyl-2,6-di-*tert*-butylphenol). Other antioxidants were also studied.

(B) Materials for preparing artificial latexes. As objects of study served aqueous emulsions of SKI-3 rubber with a concentration of 10–14 wt %.

(C) Materials for preparing composites based on epoxy resins with low-molecular-weight carboxyl-containing rubbers: composites based on an epoxy oligomer (oligoether epoxide) and liquid rubbers with terminal carboxy groups (butadiene–nitrile and butadiene); epoxy oligomer and liquid butadiene–nitrile rubber with terminal carboxy groups, diluted with furfuryl glycidyl ether.

(D) Materials for rubber modification: solutions of *cis*-1,4-polyisoprene in hexane, with various

concentrations; solutions of the sodium salt of *p*-nitrosodiphenylamine (PNDPA) in hexane, with various concentrations; and phosphoric acid of A and B grades.

The rheological characteristics of the polymers were determined on a Rheotest-2 rotational viscometer.

The physical and chemical transformations in the polymers were studied and the composites obtained were analyzed by the following methods.

The quality of the composites obtained was evaluated by the optical method, with the dynamics of antioxidant (Neozone) settling from a suspension and the number and size of particles in the microscopic field recorded, and by the oxidation rate of rubber samples with introduced antioxidant (by the decrease in the intrinsic viscosity in 1 min).

The quality of the latexes was evaluated by the optical method, with the size of rubber particles and their number in the microscopic field determined.

The structure of uncured mixtures of oligomers was studied by optical microscopy, and that of cured composites, by scanning electron microscopy (REM-100, BS-500). The chemical and physical transformations of the components were analyzed as follows: existence of chemical bonds between the functional groups of a rubber and an epoxy oligomer, by IR spectroscopy; consumption of the functional groups of the epoxy oligomer, by acid–base back-titration; and the kinetics of curing of the composites, by determining the temperature effect of curing.

The physicochemical transformations in polyisoprene in the course of its modification with PNDPA were studied with a UV spectrophotometer.

The physicomechanical and performance properties of the composites were determined in conformity with the existing GOSTs (State Standards) 270–75, 14760–91, 10722–89, 19338–90, 27109–86, etc.

The most important issue is to determine the design parameters and process operation modes of an apparatus under which there appear conditions for occurrence of a controllable oscillatory process. Self-oscillations in RPA are nonsteady hydromechanical processes and belong to complex physical phenomena that can be only described with a set of nonlinear partial differential equations. The boundary conditions necessary for solution of these equations are most frequently represented also by differential equations. For practical purposes, it is advisable to develop simple models of motion of the media being processed, which would reflect the most important features of the physical pattern of the process (criterial approach).

The main similarity criteria in fluid dynamics to which the given process belongs are Reynolds (Re), Froude, Strouhal (St), and Mach numbers. When determining the process and design parameters of RPA, required for maintaining self-oscillations in a material being processed, it is necessary to take into account at least two numbers, Re and St.

The characteristic linear size for the number Re ($\mathrm{Re} = Ul/\nu$, where U is the characteristic velocity of the fluid; l, characteristic linear size; and ν, kinematic viscosity of the fluid) will be the rotor diameter D_r, and the characteristic velocity, the average motion velocity of the fluid in the gap between the teeth of the rotor and stator. With the assumptions made, we take $U = 0.5\pi D_r n_r$. Then $\mathrm{Re} = 0.5\pi D_r^2 n_r(\rho/\mu)$. The expression obtained gives the so-called centrifugal Reynolds number.

The number St ($\mathrm{St} = VT/L$, where V is the characteristic velocity; T, characteristic interval of time, e.g., T is the period for periodic motion; and L, characteristic size) has other characteristic parameters. For the free-turbulence conditions, $V = (V_{max} - V_{min})$ and $l \approx b$, where $V_{max} - V_{min}$ is the maximum difference of averaged velocities in the cross section under consideration, and b is the agitation zone width. We take $(V_{max} - V_{min}) = 1/2\omega R$ and b equal to the width h of the gap between the rotor and stator.

Pulsations of the dynamic pressure appear when the slits in the stator are periodically closed by the teeth of the rotor. The basic frequency of these pulsations will be $F = Z_r n$, where n is the rotation rate of the rotor (rpm), and Z_r is the number of the rotor teeth.

The vortex formation is due to sharp changes in the velocity and, accordingly, in the pressure of the fluid after it leaves the gap between the teeth of the rotor and stator into the slits. In this case, there occurs separation of the boundary layer with the simultaneous formation of vortexes, which gives rise to a pressure pulse. The frequency of this process is directly proportional to the average flow velocity in the gap between the cylinders and inversely proportional to the characteristic linear size, width h of the gap between the rotor and stator.

The period of vortex formation is found from the dependence $1/T_v = f_v = æStV/h$ (æ = 1 is the harmonic number). Let us take as the characteristic period the time of vortex formation, $1/T_v = f = 1/Z_k n_r$. Then

the number St can be written, with account of $\omega = \pi n/30$, as

$$St = \pi D_r/120hZ_k.$$

Let us introduce a new parameter, ratio of the numbers Re and St, BT = Re/St, which can be written as

$$BT = [0.5\pi D_r^2 n_r(\rho/\mu)]/[\pi D_r/120hZ_k].$$

After some transformations, we obtain a dimensionless parameter, $BT = 60D_r/n_r hZ_k$.

Let us analyze the parameter obtained. It includes the following: the product of the number of revolutions, n_r, by the number of slits, Z_k, equal to the frequency f of vortex formation (or to the quantity inverse to the characteristic interval of time, $1/T$); product of the rotor diameter D_r by the width h of the minimum gap between the rotor and stator (characteristic size H); and ratio between the density ρ and viscosity μ of the fluid (quantity inverse to the kinematic viscosity ν). Thus, $BT = 60(1/T)H(1/\nu)$.

This parameter characterizes the conditions in which a self-oscillating process can occur in a viscous fluid processed in RPA. Knowing the condition in which the given process occurs in an ideal fluid, we can make a correction for the viscosity of the real medium and calculate all the necessary process and design parameters of RPA operation.

The processes occurring in the composites studied in their treatment in RPA in the self-oscillation mode can be divided into two groups: those accompanied by physical and chemical transformations.

PROCESSES FOR SYNTHESIS OF COMPOSITES WITH PHYSICAL TRANSFORMATIONS

Preparation of antioxidant dispersions. Antioxidant dispersions are used to stabilize synthetic rubbers for various purposes. Previously, RPA has been used as a mixer-disperser to improve the stability of antioxidant dispersions in the course of their preparation. It was found that the process of dispersing of antioxidant agglomerates in an aqueous solution in RPA occurs with a considerably higher efficiency when the apparatus operates in the self-oscillating mode (Table 1).

In all the cases, the power consumption decreased by 20–30%.

Preparation of artificial latexes. Let us consider a process for synthesis of the artificial latex SKI-3. This latex is widely used to replace natural latex in manufacture of foamed rubber and other articles. The most critical stage predetermining the possibility of obtaining high-quality SKI-3 latex is emulsification of the polymerizate of the SKI-3 rubber in an aqueous medium. Because the viscosity of the polymer solution is low (the content of rubber in the aqueous solution of the emulsifier is 10–14%), it is very difficult to create the required shear stresses in the system with ordinary equipment. Previously, this problem has been solved by using RPA.

Under real industrial conditions, the action of high shear stresses in the initial stages of emulsification leads to mechanical degradation of the rubber. Therefore, the process is performed in two stages: at low shear rates $\gamma = 10^4$ s^{-1} (apparatus with a stirrer, jet mixer, comb mixer), and at high shear rates $\gamma = 5 \times 10^4$ s^{-1}. The use of an RPA including a static mixture enabled a significant simplification of the process scheme and improvement of the product quality. As regards the homogenizing capacity, the static mixer with screw elements can replace the stirrer and the jet and comb mixers. At the same time, the shear stresses being developed in the material will be exceedingly low.

Processing of a material in a static mixture yields emulsions with a drop size of 20–50 μm (in the case of the conventional scheme, the drop size is 20–100 μm).

Finer emulsification occurs in the rotor part of RPA. In the conventional scheme, the required emulsification quality could only be achieved upon 5–6-fold recycling of the flow being processed.

Treatment of the material in the self-oscillating mode cannot completely exclude the recycling procedure, either. However, the number of recyclings can be reduced to two.

PROCESSES OF SYNTHESIS AND MODIFICATION OF COMPOSITES WITH PHYSICOCHEMICAL TRANSFORMATIONS

Modification of epoxy resins with low-molecular-weight carboxyl-containing rubbers. In the first stage, we examined the possibility of obtaining stable epoxy–rubber systems in RPA in the self-oscillating mode. The most stable systems were, naturally, obtained from mixtures with equal amounts of components. In a triple processing of a 1 : 1 mixture of SKN-10KTR and ED-20 in laminar and transition modes, a system that remained unsegregated for

Table 1. Advantages of the self-oscillation method over the ordinary treatment in RPA in preparation of antioxidant dispersions

Material	Advantages of self-oscillation method	Method for assessing quality of materials obtained
Dispersion of Neozone-D in 5% aqueous solution of alkylnaphthalenesulfonate (Neozone-D concentration 15%), with subsequent introduction of SKS-30 rubber into latex	Finer grinding and distribution in polymer (by 15% on average); 30% increase in output capacity of the process	By concentration of Neozone-D (shorter time of its settling from latex)
Dispersion of Ionol (1%) in 3.5% solution of sodium salt of synthetic fatty acids of C_8–C_{14} fraction, with subsequent introduction of SKS-30 ARK polymer into latex	25–30% increase in homogeneity the mixture	By concentration of Ionol in rubber
Dispersion of mixture of Neozone-D and DPPD in 5% solution of potassium stearate (DPPD : Neozone-D = 3 : 5), with subsequent introduction into SKI-3	20% increase in homogeneity of antioxidant distribution in rubber	By oxidation rate of rubber samples (by decrease in intrinsic viscosity in 1 min)
Dispersion of Neozone-D (2 wt %) in 5% solution of OS-40 surfactant (oxyethylated alcohol of C_{10} fraction)	Fivefold increase in stratification time of the mixture	Optical method
Dispersion of DPPD (20 wt %) in 8% aqueous solution of sodium oleate	Threefold increase in stratification time of the mixture	Optical method
Dispersion of Neozone-D in 5% aqueous solution of alkylnaphthalenesulfonate (Neozone-D concentration 15%), with subsequent stabilization of SKI-3 rubber obtained in solution	30% increase in homogeneity of antioxidant distribution in rubber	By concentration of Neozone-D
Dispersion of Neozone-D in 3% aqueous solution of a mixture of fractions of alkylarenesulfonates and alkanesulfonates	Twofold increase in stratification time of the mixture	Optical method

Table 2. Physicomechanical and performance parameters of composites produced by different methods

Parameter	Simple mixture (apparatus with stirrer)	Product formed upon treatment in RPA	
		six passings	with a static mixer in the self-oscillating mode
Tensile strength σ_t, MPa	4.3	14.0	16.0
Relative elongation ε, %	10.2	66.1	66.6
Adhesion strength σ_{ad}, MPa	4.0	12.2	14.8

14 days was obtained, whereas in treatment in an RPA in self-oscillation conditions, a composite that did not settle for 20 days was obtained upon single passing through the processing zone.

In the second stage of the study of the effect exerted by the mechanical treatment of epoxy–rubber composites, we identified changes introduced by the self-oscillating process into the chemical reaction between the functional groups of the oligomers being mixed. In the first stage of the study, a homogeneous system stable in the course of time was obtained and, consequently, the most favorable conditions for interaction between the groups were created. At the same time, on making the agitation conditions more "severe," the chemical interaction of the components could be achieved in a shorter time. In the case of processing in an ordinary RPA in the turbulent mode, the chemical interaction occurred only on passing the reaction mixture six times through the working zone of the mixer, whereas in the self-oscillating mode, such an interaction occurred already after the first passing. Table 2 lists the physicomechanical and performance parameters of the mixtures.

Such an improvement of the properties of the composites can be explained as follows. The processes occurring in the self-oscillating mode in an RPA with a static mixture are the same as those in an ordinary apparatus. At the same time, the dispersity of one component in the medium of the other and the homogeneity of the mixture obtained is substantially higher owing to the preliminary mixing of the components in the static mixture and to performing the process in the self-oscillating mode. This leads to narrower scatter of the physicomechanical and performance parameters being analyzed and, in the end, to their improvement upon statistical processing of the data obtained. In addition, we observed a drop in the power consumed by the mixer, compared with the conventional process in an RPA, by, on the average, 20–25%.

Modification of rubbers in solution. The self-oscillating process in RPA may be of particular importance in processes of chemical modification of rubbers in the stage of preparation of the polymer. As an example of a system of this kind can serve a solution of the SKI-3 isoprene rubber in hexane, mixed with the sodium salt of *p*-nitrosodiphenylamine. The modification process performed previously in apparatus with stirrers was distinguished by a longer duration. The use of an RPA operating in the conventional mode made it possible to reduce the process duration by a factor of 3–5.

In an experimental study, we determined the percentage content of free and bound PNDPA in solutions treated in an RPA in the conventional mode and in the mode of self-oscillations (after 1, 3, and 5 h of solution treatment in the reactor). The results obtained suggest that treatment of a system in the self-oscillating mode intensifies the chemical modification process by 25–30% on the average, which makes it possible to reduce the process duration at the same extent of the reaction.

CONCLUSIONS

(1) The processes occurring in a rotary-pulsatory apparatus can be quantitatively described using the generalizing parameter of an external energy effect, which is a combination of Reynolds and Strouhal numbers and characterizes the conditions in which a self-oscillating process may arise in a viscous fluid. This enables calculation of the operation modes and design parameters of the rotary-pulsatory apparatus.

(2) The improved technologies for synthesis and modification of composites in a rotary-pulsatory apparatus in which the mixtures undergo physical transformations yield antioxidant dispersions with a finer comminution and distribution of the antioxidant in the polymer, with the settling time of the mixture increasing, on the average, by a factor of 2–5. The preparation technology of SKI-3 artificial latexes provides finer emulsification of the polymer and reduction of the cycle duration by a factor of 2–3.

(3) The improved technologies for synthesis and modification of composites in which the mixtures undergo chemical transformations provide modification of epoxy resins with low-molecular-weight carboxyl-containing rubbers and make it possible to raise the homogeneity of the mixtures and their performance parameters by, on the average, 15%. The technology of modification of *cis*-1,4-polyisoprene with a salt of *p*-nitrosodiphenylamine reduces the process duration by, on average, 25–30% at the same extent of the reaction.

REFERENCES

1. Britov, V.P., Bogdanov, V.V., Nikolaev, O.O., et al., *Zh. Prikl. Khim.*, 2004, vol. 77, no. 1, pp. 122–127.
2. Smirnov, B.L., Tubolkin, A.E., Britov, V.P., et al., *Zh. Prikl. Khim.*, 2004, vol. 77, no. 3, pp. 499–502.
3. Britov, V.P., Bogdanov, V.V., Tubolkin, A.E., et al., *Zh. Prikl. Khim.*, 2004, vol. 77, no. 3, pp. 499–502.
4. Promtov, M.A., *Pul'satsionnye apparaty rotornogo tipa* (Pulsatory Apparatus of the Rotary Type), Moscow: Mashinostroenie, 2001.

ISSN 1070-4272, Russian Journal of Applied Chemistry, 2008, Vol. 81, No. 3, pp. 487–489. © Pleiades Publishing, Ltd., 2008.
Original Russian Text © L.P. Varlamova, V.A. Izvozchikova, A.S. Averchenko, Yu.D. Semchikov, S.A. Ryabov, 2008, published in Zhurnal Prikladnoi Khimii, 2008, Vol. 81, No. 3, pp. 502–504.

MACROMOLECULAR CHEMISTRY AND POLYMERIC MATERIALS

Effect of Aluminosilicate Microspheres on Physicomechanical and Rheological Properties of Rigid Foamed Polyurethanes

L. P. Varlamova, V. A. Izvozchikova, A. S. Averchenko, Yu. D. Semchikov, and S. A. Ryabov

Research Institute of Chemistry, Lobachevsky Nizhni Novgorod State University, Nizhni Novgorod, Russia
Lobachevsky Nizhni Novgorod State University, Nizhni Novgorod, Russia

Received July 5, 2007

Abstract—Possibility of obtaining rigid foamed polyurethanes filled with aluminosilicate microspheres was analyzed. The physicomechanical and rheological properties of these composites were studied.

DOI: 10.1134/S1070427208030294

Foamed polyurethanes (FPU) are widely used in building, transportation, and many other fields of natural economy because of their unique heat- and sound-insulating properties and simplicity of preparation and use. Numerous plants in our country and abroad manufacture on a large scale both FPU systems and finished articles for various purposes.

At the same time, purely FPU systems have exhausted their potentialities, because it is impossible to control physicomechanical and other parameters, e.g., combustibility and softening point, by only varying the FPU composition, and, therefore, use of various organic and inorganic fillers, plasticizers, and fire retardants opens up wide opportunities of modification of their properties [1].

The post promising in this context is modification of properties of FPU systems with ash aluminosilicate microspheres (AASM), which are formed as a waste, the so-called ash carryover, at thermal power plants.

The unique properties of AASM, such as the microspherical shape with diameters of 20 to 400 μm, low bulk density (0.32–0.68 g cm^{-3}), low heat conductivity, high strength, and inertness toward organic solvents, acids, and alkalis predetermined the wide applicability of this product. The low density of AASM is the most important property, which enables their use as a filler for polymeric materials and provides a low materials consumption without impairing the heat- and sound-insulating properties.

EXPERIMENTAL

As a filler were used AASM [TU (Technical Specification) 14.2-25 595 170-001–2003]. Composite FPUs were obtained by a single-stage method consisting in simultaneous mixing of all the components (A and B). Because single-stage systems are mixed at room temperature, it is necessary that all the components should be in the liquid phase and have a satisfactory degree of compatibility [2, 3]. When preparing FPU, microspheres were preliminarily mixed with component A to obtain a homogeneous mass. The samples obtained were kept at 20°C for no less than 24 h from the instant of material preparation to its study.

The kinetic parameters of foam formation (times of foaming onset, gelation, and foam rise) were monitored using a stopwatch. The apparent density was determined in conformity with GOST (State Standard) 409–77 with a determination error of ±0.5 kg m^{-3}.

The breaking compression stress was determined on an METEFEM-khr01 machine at room temperature. The dimensions of the samples for tests were 50 × 50 × 50 mm, and the compression rate was 60 mm min^{-1}. It should be particularly noted that the samples being tested are only compressed, without crumbling or brittle fracture. The measurement error was ±5%.

The heat conductivity λ (W m^{-1} K^{-1}) was determined by measuring the steady heat flux in a monotonic heating mode on an ITP-MG4 instrument in conformity with its working manual [4].

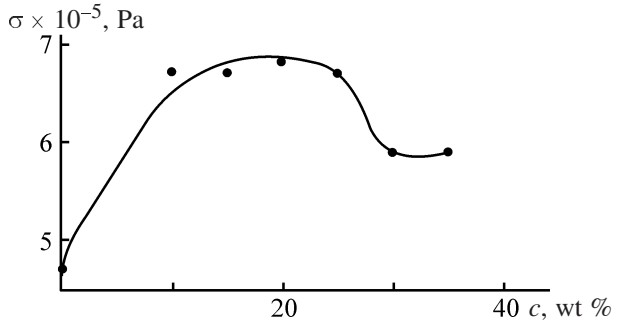


Fig. 1. Breaking compression stress σ vs. the filler content *c*.

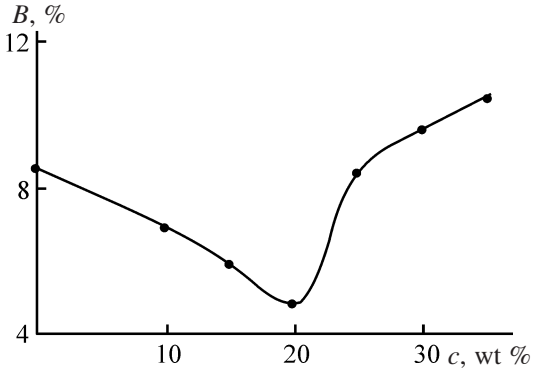


Fig. 2. Water-absorption capacity *W* vs. the filler content *c*.

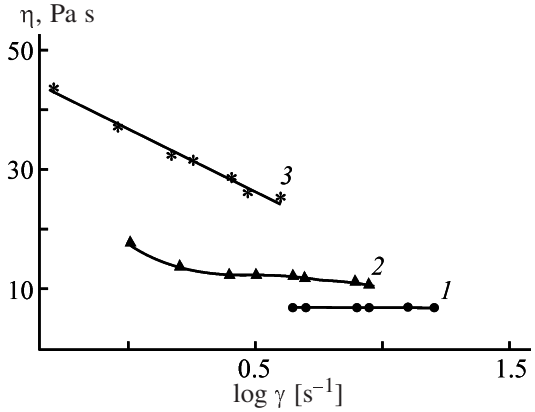


Fig. 3. Viscosity η vs. the shear rate γ in semilog coordinates. Polyol + AASM, wt %: (*1*) 34.8, (*2*) 40, and (*3*) 44.5.

The moisture-absorption capacity was measured as follows: weighed samples (d = 4.5 cm, h = 5 cm) were placed on the grid of a desiccator filled with water to a certain level and kept there for 24 h. Then the samples were again weighed and the moisture-absorption capacity W (%) was calculated by the formula

$$W = \frac{m(\tau) - m(0)}{m(0)} \times 100,$$

where $m(0)$ is the average mass of a sample before tests (g), and $m(\tau)$, that in 24 h (g).

The rheological properties were studied on a Rheotest-2 rotary viscometer in a wide range of stresses (120–3×10^3 Pa) and shear rates (0.5–437.3 s^{-1}). The operation principle of the device is based on the shear of a solution (composite) being measured in the gap between the coaxial cylinders. The device can measure the viscosity in the range 10^{-2}–10^4 Pa s. In the calculation, tabulated data on the shear rate γ (s^{-1}) were taken and the shear stress τ (Pa) and the viscosity η (Pa s) were calculated using the expressions

$$\tau = z\alpha,$$

$$\eta = (\tau/\gamma) \times 100,$$

where z is the cylinder constant (Pa) and α is the reading of the measuring instrument in scale divisions.

Different cylinders S–S_2 with constants z and z_2 were used in measurements. The rheological parameters were determined at 20°C.

It can be seen in Fig. 1 that introduction of a filler into a rigid FPU leads to an increase in the breaking compression stress σ. Introduction of ash microspheres in amounts of up to 20 wt % raises the compression strength by a factor of 1.5 because of the loss of mobility by the polymer matrix. Further increase in the content of the filler (>20 wt %) causes a decrease in σ as a result of the disruption of the integrity of the FPU matrix because of the presence of a large amount of microspheres and of the "gas phase."

Noteworthy is the fact that the catalyst concentration was chosen so that all the samples had the same apparent density (70 ± 3 kg m^{-3}), irrespective of the filler content. It should also be noted that the heat conductivity of samples with various amounts of AASM is virtually independent of the AASM content because the heat conductivity is determined by the fraction of voids in a material, the total fraction in FPU and AASM. The heat conductivity of the starting formulation is 0.028 W m^{-1} K^{-1}, and that of a composite with 25 wt % AASM, 0.029 W m^{-1} K^{-1}.

It was found that, upon introduction of 10, 15, and 25 wt % AASM into the FPU system, the water absorption somewhat decreases, compared with the starting formulation (Fig. 2), whereas introduction of a larger amount of AASM impairs the integrity of the FPU matrix via formation of contacts between ash microspheres whose surface is wetted by water.

It can be seen in Fig. 3 that both the starting systems and those containing up to 40 vol % AASM are

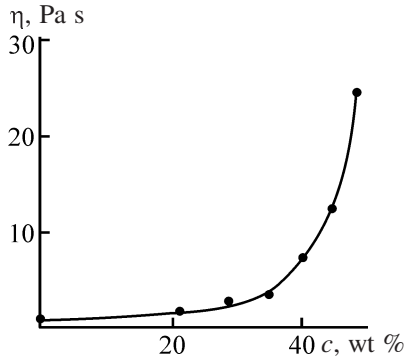


Fig. 4. Shear viscosity η vs. the AASM content c at $\log\gamma$ = 0.6.

Newtonian fluids (straight line *1*). Upon introduction of 40% AASM, the Newtonian system becomes anomalously viscous (curves *2, 3*). In this case, introduction of AASM leads to an increase in the viscosity of filled composites because of the rise in the fraction of the nonfluid component.

Introduction of a filler leads to an increase in the viscosity of the filled composite, with the most pronounced changes in viscosity observed beginning with an AASM content of about 30 wt % (Fig. 4).

Thus, FPU systems can be modified with aluminosilicate microspheres, which enables development of filled FPU composites with good physicomechanical and service properties and preserved heat-insulating characteristics and fluidity [5]. The rheological properties of filled polyol (component A) make it possible to recommend the conditions of processing of filled composites on high- and medium-pressure filling machines, which could provide a high quality of component mixing.

CONCLUSIONS

(1) Rigid foamed polyurethane systems filled with aluminosilicate microspheres were obtained.

(2) These composites enable use of standard filling machines to obtain rigid filled foamed polyurethane articles.

ACKNOWLEDGMENTS

The study was financially supported by the Foundation for Assistance to Small Innovative Enterprises (FASIE), START 05 program, project no. 3285/5703.

REFERENCES

1. *Entsiklopediya polimerov* (Encyclopedia of Polymers), Kabanov, V.A., Ed., Moscow: Sovetskaya Entsiklopediya, 1977, vol. 2, p. 54.
2. Uspenskaya, M.V., Sirotinkin, N.V., Yatsenko, S.V., and Masik, I.V., *Zh. Prikl. Khim*., 2005, vol. 78, no. 5, pp. 846–850.
3. Sirotinkin, N.V. and Yatsenko, S.V., *Prikl. Mekh*., 2002, no. 1, p. 36.
4. Platunov, I.S., *Teplofizicheskie izmereniya v monotonnom rezhime* (Thermal Measurements in Monotonic Mode), Leningrad: Energiya, 1973, p. 28.
5. RF Patent 2123013.

ISSN 1070-4272, Russian Journal of Applied Chemistry, 2008, Vol. 81, No. 3, pp. 490–493. © Pleiades Publishing, Ltd., 2008.
Original Russian Text © S.E. Shakhovets, B.L. Smirnov, V.V. Bogdanov, 2008, published in Zhurnal Prikladnoi Khimii, 2008, Vol. 81, No. 3, pp. 505–508.

MACROMOLECULAR CHEMISTRY AND POLYMERIC MATERIALS

Thermochemical Reclaiming of Vulcanized Rubbers under Exposure to Electromagnetic Field

S. E. Shakhovets, B. L. Smirnov, and V. V. Bogdanov

St. Petersburg State Institute of Technology (Technical University), St. Petersburg, Russia
ELAST-Tekhnologii Open Joint-Stock Company, St. Petersburg, Russia

Received May 23, 2007

Abstract—A method for reclaiming of vulcanized rubbers, combining the treatment with a chemical degrading agent and exposure to electromagnetic field, was described. This method considerably extends the technological potentialities of reclaiming, allowing utilization of waste based on virtually any kind of rubber, in particular, nonpolar, in the form of coarse crumb.

DOI: 10.1134/S1070427208030300

The existing methods of vulcanized rubber reclaiming are underlain by breaking the cross-links. Degrading agents (typically, chemical compounds) are selected to fit the nature of the cross-links and break them via chemical reactions. The penetration of the agent into vulcanized rubber is facilitated by its dissolution in a product that acts as rubber plasticizer and transports the degrading agent. Simultaneously, vulcanization agents are introduced into the system; they take effect at elevated temperatures and form a new vulcanization network in the reclaimed rubber.

By now, a large number of degrading formulations were developed, but their application is complicated by certain factors. First, all these formulations are selective, i.e., applicable to a certain rubber type (depending on the nature of the plasticizer solvent), which requires additional sorting of the raw material. Second, the action of the degrading and cross-linking agents is difficult to balance in time and temperature, for which reason the corresponding processes go on at room temperature, thereby affecting the properties of the reclaim. At the present time, increased interest is displayed in methods of rubber degradation under exposure to fields of different nature. They should break down the three-dimensional vulcanization network of the exposed material in such a way that the structure of the raw material used in rubber manufacture is affected to the least possible extent. The efficiency of the controlled mechanocracking can be considerably increased through exposure of the material to a combination of external fields of different nature.

We elucidated here the suitability of chemical treatment combined with electromagnetic field exposure for vulcanized rubber reclaiming. There were earlier attempts to develop reclaiming methods combining exposures to fields of different nature. In one of such methods, rubber waste was crushed and mixed with 1–15 parts by weight of the reclaiming activator comprising hydroxy and/or carboxy groups and/or quinone (in particular, organic and inorganic compounds), which was followed by 3–5-min exposure (at least once) of the resulting mixture to high-frequency currents (HFCs) with the frequency in the range 915–15 000 MHz [1].

This reclaiming process requires high temperatures and long time; otherwise, permanent irradiation for over 5 min results in overheating and degradation of the vulcanized rubber being treated. Also, analysis showed that the neat reclaim is unfit for use and can only be introduced into a new stock as addition. Satisfactorily running of this reclaiming process requires preliminary crushing of the rubber waste to a particle size under 1 mm (0.3 mm preferably); of all rubber wastes only those based on natural and styrene rubbers are suitable for utilization.

We sought here to decrease the temperature and time of the process, as well as to extend the process potentialities of reclaiming. To this end, we used the previously developed reclaiming method [2]. Essential for implementation of this method are three interconnected factors: the activator composition and

Table 1. Composition and properties of the reclaims

Characteristic	Parameter of mixture containing reclaim obtained by indicated method					
	method [1]	suggested method				
Reclaim containing rubber-based waste, wt %	NR : SKS = 20 : 80	SKI : SKS : SKD = 50 : 30 : 20		SKI-3 = 100		SKS = 100	
Reclaiming activator:							
known	1–15	–	–	–	–	–	–
Captax	–	2.13	5.18	2.13	5.18	2.13	5.18
hexamethylenetetramine	–	0.35	4.34	0.35	4.34	0.35	4.34
iron stearate	–	0.02	0.48	0.02	0.48	0.02	0.48
glycol	–	0.5	2.0	0.5	2.0	0.5	2.0
Molar ratio of components		1 : 0.2 : 0.017 : 0.37	1 : 1 : 0.017 : 0.61	1 : 0.2 : 0.0017 : 0.37	1 : 1 : 0.017 : 0.61	1 : 0.2 : 0.0017 : 0.37	1 : 1 : 0.017 : 0.61
Total dose of activator, parts by weight	15	3.0	12.0	3.0	12.0	3.0	12.0
Reclaiming temperature, °C	200–250	110	130	110	130	110	130
HFC frequency, MHz	–	13.56	50.0	13.56	27	13.56	50
Reclaiming time, min	6–10	1	3	1	3	1	3
Tensile strength of reclaim, MPa, for waste exposed to indicated factor:							
electromagnetic field	–	2.2	2.2	2.3	2.3	1.8	1.8
reclaiming activator	–	3.0	3.5	3.2	3.6	2.5	2.7
electromagnetic field + reclaiming activator	–	7.6	8.3	7.6	7.8	7.6	–
Tensile strength, MPa, of rubber containing:							
untreated crumb	18.2	12.7	12.7	13.0	13.0	12.0	12.5
reclaim	19.2	16.0	16.5	17.5	18.0	17.0	17.2
Coefficient K_0, %	5.4	26.0	29.9	34.6	38.4	36.0	37.6
Reclaim containing rubber-based waste, parts by weight	–	SKD = 100		SKN-18 = 100		Nairit = 100	
Reclaimimng activator:							
known [1]	–	–	–	–	–	–	–
Captax	–	2.13	2.59	2.13	2.59	2.13	2.59
hexamethylenetetramine	–	0.35	2.17	0.35	2.17	0.35	2.17
iron stearate	–	0.02	0.24	0.02	0.24	0.02	0.24
glycol	–	0.5	2.0	0.5	2.0	0.5	2.0
Molar ratio of components		1 : 0.2 : 0.017 : 0.37	1 : 1 : 0.017 : 0.61	1 : 0.2 : 0.0017 : 0.37	1 : 1 : 0.017 : 0.61	1 : 0.2 : 0.0017 : 0.37	1 : 1 : 0.017 : 0.61
Total dose of activator, parts by weight	–	3.0	12.0	3.0	12.0	3.0	12.0
Reclaiming temperature, °C	–	110	130	110	130	110	130
HFC frequency, MHz	–	13.6	50.0	27.0	50.0	13.6	50.0
Reclaiming time, min	–	1	3	1	3	1	3
Tensile strength of reclaim, MPa, for waste exposed to indicated factor							
electromagnetic field	–	3.0	3.0	2.5	2.5	2.1	2.1
reclaiming activator	–4.2	4.4	2.9	3.1	2.8	3.2	
electromagnetic field + reclaiming activator	–	7.9	8.1	7.8	7.8	7.7	8.0

Table 1. (Contd.)

Characteristic	Parameter of mixture containing reclaim obtained by indicated method						
	method [1]	suggested method					
Tensile strength, MPa, of rubber containing:							
untreated crumb	–	12.0	12.0	12.8	12.8	12.1	12.1
reclaim	–	15.5	16.0	13.9	14.3	15.0	15.7
Coefficient K_0, %	–	29.0	33.3	8.5	11.7	24.0	29.7

the application mode and frequency range of a high-frequency electromagnetic field.

As the reclaimimng activator served the composition including 2-mercaptobenzothiazole (Captax), hexamethylenetetramine, iron stearate, and glycol in the molar ratio of 1 : (0.2–1.0) : (0.0017– 0.017) : (0.37–0.61), respectively. This formulation was introduced in amount of 3–12 per 100 parts by weight of the waste, followed by single 1–3-min exposure of the product to a high-frequency electromagnetic field in the meter frequency range.

Thus, reclaiming of vulcanized elastomer waste consisted in the following. Vulcanized rubber waste was crushed (the method is of no significance) into crumb (with particles up to 5 mm in size) and mixed on a standard mixing equipment with a pasty reclaiming activator having the above-described composition [3]. This was followed by a single 1–3-min exposure of the resulting mixture to a high-frequency electromagnetic field in the meter frequency range, e.g., at the frequencies of 13.56, 27, or 50 MHz.

The resulting product (neat regenerate) is suitable for manufacture of various, e.g., roll articles, and also can be used as addition to new rubber stocks.

Table 1 summarizes the qualitative and quantitative compositions of the reclaims based on different wastes, as well as the properties of the reclaims and rubbers containing these reclaims. For comparison, we also presented the data for the materials obtained according to [1], which is one of the best foreign analogs.

Table 1 contains the strength characteristics of the reclaim obtained upon exposure of crumb rubber to HFCs and treatment with the reclaiming activator, both separately and in combination. Also tabulated are the properties of the rubbers containing untreated crumb and reclaims prepared by the method known from the world practice and the method we developed. The crumb rubber is comprised of wastes from various rubbers: natural (NR), styrene–butadiene (SKS), isoprene (SKI-3), and butadiene (SKD) rubber.

Also, Table 1 contains the coefficient characterizing the change of the strength properties of the rubbers, %:

$$K_0 = [(\sigma_1 - \sigma_2)/\sigma_1] \times 100,$$

where σ_1 and σ_2 are the tensile strengths of the rubbers containing untreated crumb and reclaim (crumb treated by the method we suggested), respectively.

The coefficient K_0 characterizes the extent to which the treatment method affects the quality (strength properties) of the reclaim.

Table 1 suggests that, in rubber waste reclaiming, only combined action of electromagnetic field and activator of the developed composition provides the desired properties of the reclaim.

Table 2 presents the compositions of the rubber stocks containing the reclaim obtained by the known and developed methods. For stock A, only basic components are listed. Stock B is characterized by the composition according to GOST (State Standard) 11138–89; it contains 10 parts by weight of the reclaim obtained by the procedure we suggested.

Thus, the procedure we proposed considerably extends the potentialities of the reclaiming process through creating prerequisites for continuous production of articles from "neat" reclaim (such as, e.g., roll, roofing, and waterproofing materials); utilization of rubber wastes of various compositions (based on virtually any kind of rubber); utilization of wastes comprising coarse crumb; and utilization of rubber wastes based on nonpolar rubbers and filling agents that do not contain polar groups (carbon black), since in this case the electrical conductivity of the mixtures

Table 2. Stock compositions

Composition	Content, wt %	
	mixture A (known procedure)	mixture B (suggested procedure)
Butadiene–styrene rubber:		
SBR-1500	100.0	–
SKS-30ARKM-15	–	100.0
Carbon black of indicated brand:		
HAF	50.0	–
P-324	–	50.0
Stearic acid	–	2.0
Altax (2-dibenzothiazolyl disulfide)	–	1.5
Diphenylguanidine	–	0.3
Zinc white	–	5.0
Sulfur	–	2.0
Reclaim	10.0	10.0

is preserved owing to the presence of a reclaiming activator of the above-mentioned composition and its ability to create an electrically conducting film on the crumb surface. Also, it is possible to control the reclaiming owing to the self-regulation ability of the system: The waste exposure to a high-frequency electromagnetic field solely causes combustion and decomposition of the crumb; efficient reclaiming is possible only in the presence of the reclaiming activator we suggested, i.e., under combined action of the two factors. The reason is that the activator film formed on the crumb surface prevents its contact with atmospheric oxygen, thereby decelerating the thermal oxidative degradation and preventing local overheating of the waste, responsible for its ignition.

CONCLUSIONS

(1) Combined action of a chemical agent and electromagnetic field extends the potentialities of rubber reclaiming to include continuous production of roll, roofing, and waterproofing articles from neat reclaim.

(2) Reclaim can be obtained from waste based on any kind of rubber, as well as from such waste as coarse crumb.

REFERENCES

1. JPN Accepted Application 62-21 820.
2. RF Inventor's Certificate no. 2 014 339.
3. Ahh, D., Khait, K., and Petrick, M.A., *J. Appl. Polym. Sci*., 1995, vol. 55, no. 10, pp. 1431–1440.

ISSN 1070-4272, Russian Journal of Applied Chemistry, 2008, Vol. 81, No. 3, pp. 494–496. © Pleiades Publishing, Ltd., 2008.
Original Russian Text © V.I. Samoilov, N.A. Kulenova, Z.V. Sheregeda, L.G. Gadylbekova, V.A. Agapov, L.V. Shushkevich, 2008, published in Zhurnal Prikladnoi Khimii, 2008, Vol. 81, No. 3, pp. 509–511.

BRIEF COMMUNICATIONS

Integrated Processing of Spodumene in Hydrometallurgy

V. I. Samoilov, N. A. Kulenova, Z. V. Sheregeda, L. G. Gadylbekova, V. A. Agapov, and L. V. Shushkevich

Ulba Metallurgical Plant, Joint-Stock Company, Ust-Kamenogorsk, Kazakhstan
Eastern-Kazakhstan State Technical University, Ust-Kamenogorsk, Kazakhstan

Received June 7, 2007

Abstract—Integrated processing of spodumene in hydrometallurgy in order to recover lithium, aluminum, and silica was studied.

DOI: 10.1134/S1070427208030312

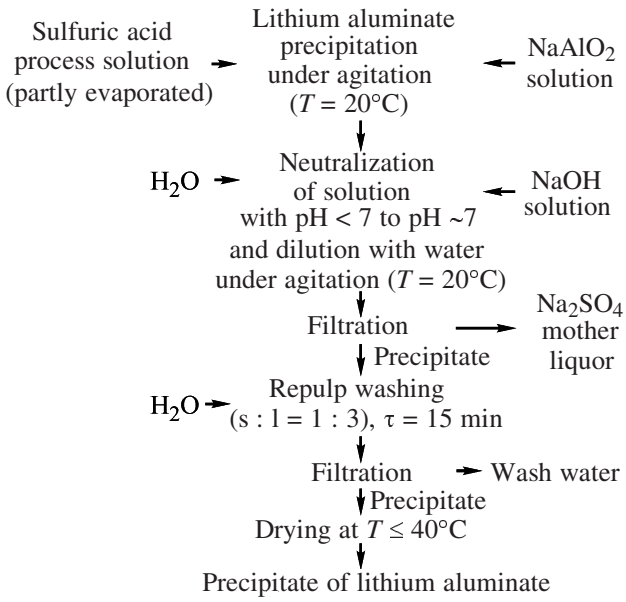
A method for alkaline decomposition of spodumene, based on its fusion with sodium carbonate and subsequent aqueous granulation of the fusion cake, is known [1, 2]. Sulfuric acid leaching of the granulate yields a sulfuric acid solution (containing about 6 g l^{-1} of lithium and aluminum, sodium, and sulfuric acid in amounts of 20–25 g l^{-1} each) and a cake (with a silica content of up to 95 wt % and more). For full use of the granulate, it can be processed to give a liquid glass by the classical technology for manufacture of glass from natural silica [2, 3]. For integrated processing of the sulfate solution produced in the granulate leaching stage, the possibility of precipitating the poorly soluble lithium aluminate was considered. In view of the fact that the technology of alkaline decomposition of spodumene [1] assumes that the obtained solution of lithium and aluminum sulfates has pH lower than the values at which $Al(OH)_3$ precipitates, it seemed appropriate to analyze the possibility of precipitating a mixture of lithium hydroxodialuminate (LHODA, $Li_2O \cdot Al_2O_3 \cdot 11H_2O$) and aluminum hydroxide by neutralization of the starting acid solution with a sodium aluminate solution (at a final pH value of mixture precipitation of about 7). For simultaneous recovery of lithium and aluminum from the sulfate solution under consideration, the scheme presented below was tested. The results obtained in a laboratory experiment are listed in the table and shown in the figure.

The results obtained (see table) show that lithium is precipitated fairly completely (83.55–99.65 wt %) at a Li : Al mass ratio in the lithium aluminate sludge equal to 1 : (11.3–16.8). In this case, 86–98 wt % of Al is recovered into the precipitate.

Thus, the method we suggest ensures simultaneously recovery of Li and Al into the precipitate from dilute solutions.

Because aluminum hydroxide decomposes at 1000°C [4], the gravimetric curve in the figure shows only a change that is characteristic of $Li_2O \cdot 2Al_2O_3 \cdot 11H_2O$ and points to dehydration of the product.

Flow chart of lithium aluminate precipitation from process solutions



Results of experiments on lithium aluminate precipitation from a sulfate solution*

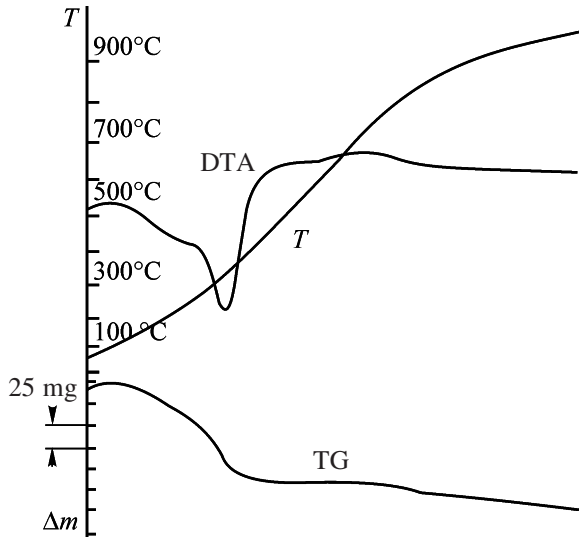
Run no.	Starting sulfate solution (partly evaporated)					Precipitation and washing of lithium aluminate						
	excess of H_2SO_4, g l^{-1}	content in solution, g l^{-1}				expenditure of $NaAlO_2$ solution, ml g^{-1} Al	Li : Al mass ratio in lithium aluminate sludge	content in mother liquor, g l^{-1}			
		Li	Al	Na	K			Li	Al	Na	K
1	109	5.4	19.8	16.5	0.52	10/2.5	1 : 10.3	0.49	0.001	31.0	0.6
2	109	5.4	19.8	16.5	0.52	15/3.75	1 : 13.6	0.009	0.0005	34.5	0.72
3	109	5.4	19.8	16.5	0.52	55/12.0	1 : 16.8	0.07	0.001	–	–
4	70	6.6	30.0	30.0	–	15/3.75	1 : 9.1	2.0	0.016	30.0	–
5	70	6.6	30.0	30.0	–	21.3/5.325	1 : 11.0	1.34	0.19	48.0	–
6	70	6.6	30.0	30.0	–	24.6/6.15	1 : 12.0	0.86	0.003	46.0	–
7	30	5.6	17.5	17.5	–	23/5.75	1 : 11.3	0.66	0.09	47.0	–
8	30	5.6	17.5	17.5	–	26/6.5	1 : 12.4	0.22	0.0064	23.5	–
9	50	5.5	19.0	20.0	–	23/5.75	1 : 11.8	0.029	0.16	31.5	–
10	50	5.5	19.0	20.0	–	23/6.5	1 : 12.9	0.2	0.003	21.5	–

Run no.	Precipitation and washing of lithium aluminate									Recovery into lithium aluminate (average for loss and finished product), wt %	
	content in wash water, g l^{-1}				dry mass of Li aluminate, g	content in lithium aluminate, wt %					
	Li	Al	Na	K		Li	Al	Na	K	Li	Al
1	0.1	0.001	11.5	0.3	19.0	1.31	18.6	3.75	0.05	75.0	95.5
2	0.0063	0.0001	12.0	0.11	20.8	1.23	19.2	3.0	<0.05	83.55	88.9
3	0.03	0.001	–	–	56.0	1.36	24.0	–	–	90.1	93.7
4	Without washing				58.8	0.96	8.43	15.8	–	78.6	83.0
5	Without washing				49.0	1.4	14.6	11.7	–	87.5	89.35
6	Without washing				57.9	1.24	14.6	10.9	–	90.85	92.7
7	Without washing				45.0	1.45	12.7	9.0	–	93.55	86.0
8	Without washing				50.0	1.41	15.5	10.0	–	99.65	94.6
9	Without washing				52.6	1.3	13.2	11.5	–	99.65	92.7
10	Without washing				50.4	1.36	16.9	9.5	–	99.4	98.0

* The initial solution was prepared by fusion of spodumene with Na_2CO_3, aqueous granulation of fusion cake, and sulfuric acid leaching of granulate. Lithium aluminate and $Al(OH)_3$ were precipitated with an alkaline solution of $NaAlO_2$ (c_{Al} = 219–250 g l^{-1}) and NaOH solution (concentration 640 g l^{-1}). For the fullest precipitation of Li and Al, the sludge obtained upon precipitation was kept at 20°C without agitation for 20 h and then filtered.

A comparative X-ray diffraction analysis of the precipitates obtained and $Li_2O \cdot 2Al_2O_3 \cdot 11H_2O$ demonstrated that these substances contain all the phases of LHODA precipitated from neutral solutions. However, the phases that were earlier characterized by weak intensity of peaks now have the maximum intensity, and, vice versa, the phases earlier exhibiting the highest intensity now show peaks with comparatively low intensity. This suggests that the mass fraction of aluminum in the LHODA precipitates obtained in this precipitation mode (pH_{con} ~7) is higher. In this case, the $Li_2O \cdot 2Al_2O_3 \cdot 11H_2O$ phase is contaminated with sodium to a greater extent than that obtained from neutral solutions. With account of the low content of lithium in the aluminate precipitates (see table), they can be recommended as starting concentrates for the classical sulfuric acid processing to give aluminum alum and, further, lithium carbonate [2].

As for the utilization of sodium discharged from the suggested process with the mother liquor from the stage of precipitation of a mixture of LHODA and aluminum hydroxide, evaporation of this mother liquor can give crystalline sodium sulfate whose



Thermogram of a lithium aluminate precipitate (see table, run no. 3). (*T*) Temperature and (Δ*m*) change in mass.

reductive smelting with breeze coke yields sodium sulfide, which is in short supply [2].

CONCLUSIONS

The technology suggested for spodumene processing enables simultaneous recovery of lithium, aluminum, and silica from this mineral and provides utilization of sodium from the dump solution.

REFERENCES

1. RF Patent 2 222 622.
2. Samoilov, V.I., *Issledovanie sovremennykh i razrabotka perspektivnykh metodov izvlecheniya litiya iz mineral'nogo syr'ya v tekhnicheskie soedineniya* (A Study of Modern Methods for Recovery of Lithium from Mineral Raw Materials into Commercial Compounds and Development of Promising Methods), Ust-Kamenogorsk: Media-Al'yans, 2005.
3. Pashchenko, A.A., Serbin, V.P., and Starchevskaya, E.A., *Vyazhushchie materialy* (Binders), Kiev: Vishcha Shkola, 1975.
4. Knorozov, B.V., Usova, L.F., Tret'yakov, A.E., et al., *Tekhnologiya metallov i materialovedenie* (Technology of Metals and Materials Science), Moscow: Metallurgiya, 1987.

ISSN 1070-4272, Russian Journal of Applied Chemistry, 2008, Vol. 81, No. 3, pp. 497–499. © Pleiades Publishing, Ltd., 2008.
Original Russian Text © L.D. Kurbatova, D.I. Kurbatov, 2008, published in Zhurnal Prikladnoi Khimii, 2008, Vol. 81, No. 3, pp. 512–514.

BRIEF COMMUNICATIONS

Joint Extraction of Vanadium(V) and Vanadium(IV) with Di(2-ethylhexyl) Hydrogen Phosphate

L. D. Kurbatova and D. I. Kurbatov

Institute of Solid State Chemistry, Ural Branch, Russian Academy of Sciences, Yekaterinburg, Russia

Received November 27, 2007

Abstract—The organic extracts formed in joint extraction of vanadium(V) and vanadium(IV) with di(2-ethylhexyl) hydrogen phosphate from weakly acidic aqueous solutions were characterized by IR and electronic spectroscopy and chemical analysis.

DOI: 10.1134/S1070427208030324

It is known that vanadium(IV) is extracted with di(2-ethylhexyl) hydrogen phosphate (HDEHP) [1]. As opposed to vanadium(IV), vanadium(V) dioxocations VO_2^+ are poorly extracted with this extractant [2]. At the same time, it was reported previously that vanadium(V) is efficiently extracted with HDEHP from weakly acidic solutions [3]. Taking into account that HDEHP is bifunctional, it was of interest to study joint extraction of vanadium(V) and vanadium(IV) with this extractant. No data have been reported previously on this matter.

EXPERIMENTAL

Vanadium(V) and vanadium(IV) were extracted with neat HDEHP at 25.0±5.0°C at the organic to aqueous phase ratio of 1 : 1 ($V_o : V_{aq} = 1 : 1$). Di(2-ethylhexyl) hydrogen phosphate was preliminarily treated to remove mono(2-ethylhexyl) dihydrogen phosphate (H_2MEHP). The working solutions were prepared from sodium metavanadate, oxovanadium(IV) sulfate, and sulfuric acid (chemically pure grade). The vanadium concentration in the aqueous and organic phases was determined by atomic-absorption and titrimetric methods [4]. The hydrogen ion concentration was determined with a pH-262 potentiometer with a glass electrode. The electronic absorption spectra of vanadium–HDEHP extracts were recorded on a Specord UV VIS spectrometer in the visible range (quartz cells, l = 0.999 and 0.199 cm). The IR spectra of these extracts were recorded on a Specord IR spectrometer in the 400–4000 cm^{-1} range (thin films of extracts between KRS-6 plates).

First the optimal conditions for extraction of vanadium(V) in the system V(V)–V(IV)–H_2SO_4–HDEHP were found at various V(V) : V(IV) ratios. The V(V) and V(IV) concentrations ranged from 5×10^{-2} to 2.5×10^{-1} M. We found that the V(V) distribution ratio increases in the presence of V(IV).

The mechanisms of joint extraction of vanadium(V) and vanadium(IV) were studied using IR and electronic spectroscopy, method of saturation of the extractant with extractable compounds, and chemical analysis. The extraction isotherms of vanadium(V) and vanadium(IV) from weakly acidic solutions were also obtained. These isotherms show that 1 mol of HDEHP extracts 10 mol of vanadium(V). Since under the extraction conditions vanadium(V) is present in the form of decavanadate anions [3], this means that in the extractable complex one decavanadate anion is bound with one HDEHP molecule. In extraction of vanadium(IV), 1 mol of HDEHP extracts 0.5 mol of vanadium. This ratio is consistent with the stoichiometry of the extraction reaction of vanadium(IV) with HDEHP reported in [1]:

$$VO^{2+} + H_2A_2 = VOA_2 + 2H^+. \quad (1)$$

We found that, in joint extraction of vanadium (V) and vanadium(IV), 1 mol of HDEHP extracts more than 10 mol of vanadium(V) and approximately 0.5 mol of vanadium(IV). Thus, the extraction of vanadium(V) sharply increases in the presence of vanadium(IV).

The IR spectra of vanadium(V, IV)–HDEHP extracts contain absorption bands at 1650, 1715, 2140, and 3410 cm^{-1} typical of the dioxonium ion [5] (Fig. 1). In accordance with [5], these absorption bands can be assigned, respectively, to the following

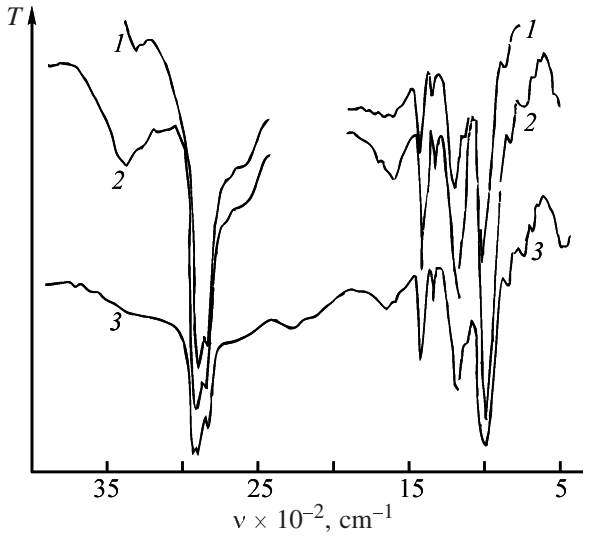


Fig. 1. IR spectra of straight HDEHP and of V(V, IV)–HDEHP and V(IV)–HDEHP extracts. (*T*) Transmission and (ν) wavenumber. (*1*) HDEHP, (*2*) V(V, IV)–HDEHP extract (C_V^{init} = 0.15 M), (*3*) V(IV)–HDEHP extract (C_V^{init} = 0.15 M).

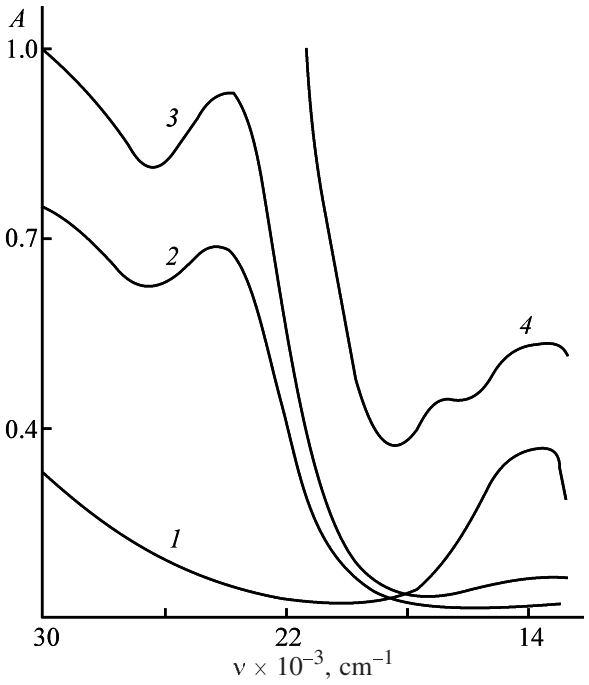


Fig. 2. Electronic absorption spectra of (*1*) vanadium(IV)–HDEPH extract, (*2*) vanadium(V)–HDEHP extract, (*3*) vanadium(V, IV)–HDEHP extract (l = 0.2 cm), and (*4*) vanadium(V, IV)–HDEHP extract (l = 1 cm). (*A*) Optical density and (ν) wavenumber.

vibrations of H_2O molecules in the organic extract (cm^{-1}): (1) bending vibrations (H_2O bound to $H_5O_2^+$), (2) bending vibrations (OH_2 groups contained in the $H_5O_2^+$ cation), (3) bending and libration vibrations (H_2O bound to $H_5O_2^+$), and (4) stretching vibrations (H_2O bound to $H_5O_2^+$). Other absorption bands belonging to $H_5O_2^+$ (1170, 1370, and 2900 cm^{-1}) partly overlapped with the stronger absorption bands of HDEHP. The IR spectra of the vanadium(IV,V)–HDEHP and vanadium(IV)–HDEHP extracts contain also the absorption bands of the P=O groups ($\nu_{P=O}^{as}$) at 1210 and 1200 cm^{-1}, respectively. In the IR spectrum of neat HDEHP, the absorption band of the phosphoryl groups occurs at 1225 cm^{-1}. Both the low-frequency shift of the absorption band of the P=O groups and the presence in the IR spectra of the absorption bands typical of dioxonium cation suggest that the hydrogen bonds are formed between the dioxonium cations and the phosphoryl group P=O. This means that, in joint extraction of vanadium(IV) and vanadium(V), vanadium(V) is extracted with HDEHP by a hydrate–solvate mechanism [3]. Along with the above-considered spectroscopic effects, the IR spectra of vanadium(IV, V)–HDEHP extracts contain no components of ν(OH) absorption bands present in the IR spectrum of the straight extractant (2660, 2260, and 1700 cm^{-1}). The disappearance of these bands shows that, in joint extraction of vanadium(V) and vanadium(IV), vanadium(IV) is extracted by the cation-exchange mechanism [6].

Thus, IR-spectra of vanadium(V)–HDEHP and vanadium(IV)–HDEHP extracts show that vanadium(V) and vanadium(IV) are bound with HDEHP molecule in the extractable complex by two different mechanisms. Whereas vanadium(V) forms hydrate–solvate complexes, vanadium(IV) is coordinated by the cation-exchange mechanism. In going from mixed vanadium(V, IV)–HDEHP extracts to vanadium(IV)–HDEHP extract, the low-frequency shift of the absorption bands of the phosphoryl group $\nu_{P=O}^{as}$ decreases. This means that, in the presence of vanadiun(V), the coordination of the phosphoryl oxygen of HDEHP with vanadium(IV) becomes weaker. It is also possible that, under these conditions, one of di(2-ethylhexyl) phosphate ligands in the inner coordination surrounding of V(V) is substituted by decavanadate anions. It should be noted that the similar low-frequency shift of the absorption band $\nu_{P=O}^{as}$ was observed in the IR spectrum of the extract of potassium chloride with copper di(2-ethylhexyl) phosphate. This shift was attributed to coordination of copper with chloride anions [7].

The formation of mixed V(V)–V(IV)–HDEHP extractable complexes was confirmed by the electronic spectra of organic extracts of vanadium(V), vanadium(IV), and their mixtures (Fig. 2).

Figure 2 shows that the electronic absorption spectrum of vanadium(IV)–HDEHP extract contains a broad asymmetric absorption band. This band can be resolved into two Gaussian components with the maxima at 13 500 and 14 500 cm^{-1}, which were assigned to *d–d* electronic transitions [8]. The electronic spectra of vanadium(V)–HDEHP extract contains a single band at 24 000 cm^{-1}. In accordance with [8], this absorption band is caused by charge transfer from occupied 2*p* orbitals of oxygen to 3*d* orbitals of vanadium(V). The electronic spectra of the vanadium(V, IV)–HDEHP extract contains four absorption bands at 24 000, 17 000, 14 500, and 13 500 cm^{-1}.

The complex electronic spectra of vanadium(V, IV)–HDEHP extracts reflect the complicated mechanism of joint extraction of vanadium(V) and vanadium(IV). The absorption band at 24 000 cm^{-1} present in the electronic spectra of the vanadium(V)–HDEHP extract and the absorption bands at 14 500 and 13 500 cm^{-1} present in the electronic spectra of the vanadium(IV)–HDEHP extract remain in the electronic spectra of the vanadium(V, IV)–HDEHP extract. This fact confirms the conclusion we made previously that, in joint extraction of vanadium(IV) and vanadium(V) with HDEHP, vanadium(V) and vanadium(IV) are extracted by hydrate–solvate and cation-exchange mechanisms, respectively. The band at 17 000 cm^{-1} is absent in the electronic spectra of the vanadium(V)–HDEHP and vanadium(IV)–HDEHP extracts but appears in the electronic spectrum of the vanadium(V, IV)–HDEHP extract. We believe that this absorption band is caused by the electronic transitions from occupied to vacant *d* orbitals and is broadened due to vanadium(V)–vanadium(IV) interactions [8].

It was reported in [9] that vanadium(V) aqua dioxo cation forms a cation–cation complex $V_2O_3^{3+}$ with vanadium(IV) aqua oxo cation. Mixed vanadium(V, IV) complexes with organic reagents were studied in [10]. The formation of mixed vanadium(V, IV) polyvanadates was also described elsewhere [10]. For example, Ostrowetsky [11] studied aqueous solutions of vanadium(V) and vanadium(IV) in the pH range 4.0–6.5 and found six polyvanadate anions with the V(IV) : V(V) ratio from 2 : 8 to 7 : 8, in particular, $[V_3^{IV}V_7O_{28}H]^{4-}$.

Thus, our results show that the vanadium(V)–vanadium(IV) mixture is extracted with HDEHP by the mixed cation-exchange and hydrate–solvate mechanisms in the form of mixed-ligand extractable complexes of vanadium(IV) with di(2-ethylhexyl) phosphate and decavanadate anions.

CONCLUSION

Infrared and electronic absorption spectra suggest that vanadium(V)–vanadium(IV) mixture is extracted with HDEHP by the mixed cation-exchange and hydrate-solvate mechanisms in the form of mixed-ligand extractable complexes of vanadium(IV) with di-(2-ethylhexyl) phosphate and decavanadate anions.

ACKNOWLEDGMENTS

This study was financially supported by the Russian Foundation for Basic Research (project no. 07-03-97 635).

REFERENCES

1. Kozlov, V.A., Kunaev, A.M., and Batrakova, L.Kh., *Kompleksn. Ispol'z. Miner. Syr'ya*, 1980, no. 12, pp. 19–21.
2. Laskorin, B.N., Ul'yanov, V.S., and Sviridov, R.A., *Zh. Prikl. Khim.*, 1965, vol. 38, no. 5, pp. 1133–1135.
3. Kurbatova, L.L., Medvedeva, N.I., and Kodess, M.I., *Zh. Neorg. Khim.*, 1997, vol. 42, no. 11, pp. 1927–1929.
4. Ul'yanov, V.S. and Sviridova, N.A., *Radiokhimiya*, 1963, vol. 5, no. 4, pp. 419–421.
5. Librovich, N.B., Skakun, V.P., and Sokolov, N.D., *Vodorodnaya svyaz'* (Hydrogen Bond), Moscow: Nauka, 1981.
6. Kurbatova, L.D. and Kurbatov, D.I., *Zh. Prikl. Khim.*, 2006, vol. 79, no. 5, pp. 862–864.
7. Mikhailov, V.A. and Stoyanov, E.S., *Dokl. Akad. Nauk SSSR*, 1983, vol. 270, no. 2, pp. 375–379.
8. Kurbatova, L.D. and Medvedeva, N.I., *Zh. Neorg. Khim.*, 2000, vol. 45, no. 1, pp. 95–97.
9. Blanc, P., Madic, C., and Launay, J.P., *Inorg. Chem.*, 1962, vol. 21, pp. 2923–2927.
10. Schulz, D., Werghermuller, T., Waghard, K., and Nuber, B., *Inorg. Chim. Acta*, 1995, vol. 240, nos. 1–2, pp. 217–221.
11. Ostrowetsky, S., *Bull. Soc. Chim. Fr.*, 1964, pp. 1012–1018.

ISSN 1070-4272, Russian Journal of Applied Chemistry, 2008, Vol. 81, No. 3, pp. 500–502. © Pleiades Publishing, Ltd., 2008.
Original Russian Text © A.I. Sokol'skii, A.A. Kotkov, E.P. Barulin, 2008, published in Zhurnal Prikladnoi Khimii, 2008, Vol. 81, No. 3, pp. 515–517.

BRIEF COMMUNICATIONS

Combined Drying of Dispersed Materials

A. I. Sokol'skii, A. A. Kotkov, and E. P. Barulin

Ivanovo State Architectural-Building University, Ivanovo, Russia

Received June 29, 2007

Abstract—Combined three-stage installation with swirling flows for drying and grinding of shungite was designed. Experimental data on drying and grinding of this mineral in the third stage of the installation are presented.

DOI: 10.1134/S1070427208030336

The advisability of using combined drying methods and apparatus has been confirmed by numerous scientific studies and by practical use [1, 2]. The development of drying apparatus has taken the way of designing apparatus that would not only provide high performance parameters, but also could satisfy high consumers' requirements, such as particle size, uniformity of the granulometric composition, and bulk density. Apparently, these requirements have also affected the design of combined dryers, in which apparatus with various hydrodynamic modes are used together with additional built-in devices for mechanical and thermal treatment of dispersed materials.

The design, improvement, and application of combined drying installations is one of the most promising areas of development of modern drying technology. These apparatus enable a considerably more rational organization of the process of thermal treatment of a material by subjecting it to fundamentally different thermal treatments with drying in various hydrodynamic modes and can combine, e.g., drying with granulation, grinding, dehydration, and cooling.

A combined whirl dryer has been suggested for drying of shungite [3, 4]. This dryer comprises three stages: cyclone, whirling chamber, and finish-dryer–grinder.

Figure 1 schematically shows a combined whirl dryer whose operation principle is as follows. A humid material is delivered into the dryer via the loading bunker *1*, after which it is preliminarily ground in the first stage of cyclone *2* with a dismembering unit *3*. The heat-transfer agent is delivered by ventilator *4* into inner chamber *2* of the cyclone via whirler *5*. In the first stage of the dryer, the material is heated and preliminarily dried in a flow of the heat-transfer agent spent in whirling chamber *6* (second stage) and finishing dryer *7* (third stage). Because of the contact of dust-like carryover particles with the product charged, the flowability of the material being processed is improved and, simultaneously, the discharged air is cleaned. The use of the heat of the dis-

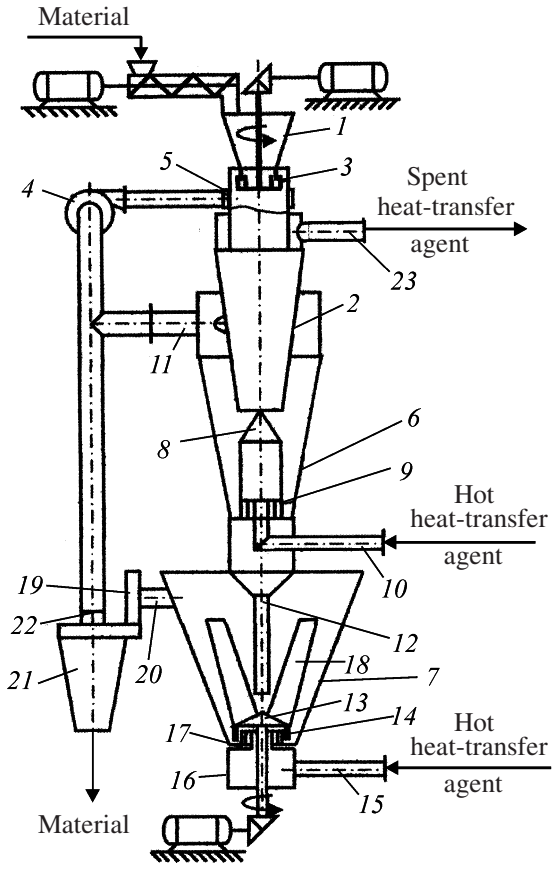


Fig. 1. Schematic of a combined whirl dryer. (*I*) Material, (*II*) spent heat-transfer agent, and (*III*) hot heat-transfer agent. For comments, see text.

charge drying agent to heat the material and subject it to preliminary drying in the cyclone makes it possible to utilize the energy of the heat-transfer agent to a fuller extent and thereby to improve the engineering and economic performance of the dryer.

The second stage of the installation is the whirling chamber intended to remove free moisture from the product being processed. Dispersed particles, delivered into the chamber from cyclone *2*, pass divider *8* and, while moving opposite to the ascending whirled flow of air heated to a high temperature, emerging from whirler *9*, form a whirled suspended bed of the product, whose mass depends on the working conditions of the dryer.

The hot heat-transfer agent is delivered into the second stage via pipe *10* and discharged via pipe *11* tangentially attached to the outer shell of the apparatus.

After the whirling chamber *6*, the material is delivered via overflow pipe *12* into the third stage *7* to grinding section *13*, where the material is subjected to finishing grinding by beaters *14*. In finishing dryer *7*, internal bound moisture is removed from the material in the ascending whirling flow.

The hot heat-transfer agent is delivered into the third stage of the apparatus via pipe *15*, arrives at gas-feeding box *16*, passes the bottom of diffuser *17*, and comes in the form of a whirling flow into bottom whirling chamber *7*. In the third stage *7*, a gas-dispersed whirling flow with a stable hydrodynamic mode is formed and maintained by blades *18*. Then, the gas-dispersed whirling flow is directed by ventilator *19* via pipe *20* into cyclone *21*, where the material is discharged. The spent heat-transfer agent is removed from the cyclone via pipe *23*.

EXPERIMENTAL

As the experimental material served shungite, a formation of unique composition, structure, and properties. This compound is a natural composite of unusual structure, a uniform distribution of highly dispersed crystalline silicate particles in an amorphous silicate matrix. The average size of the silicate particles is about 1 μm. The average composition of rocks from the deposit is 30% carbon + 70% silicates. The rock has high strength, density, chemical resistance, and electrical conductivity. The shungite carbon exhibits high activity in redox reactions. Thanks to this circumstance, the shungite rock is a valuable raw material for manufacture of foundry iron, ferrous alloys, silicon carbide and as a filler of building mixtures and paint-and-varnish coatings absorbing electromagnetic radiation.

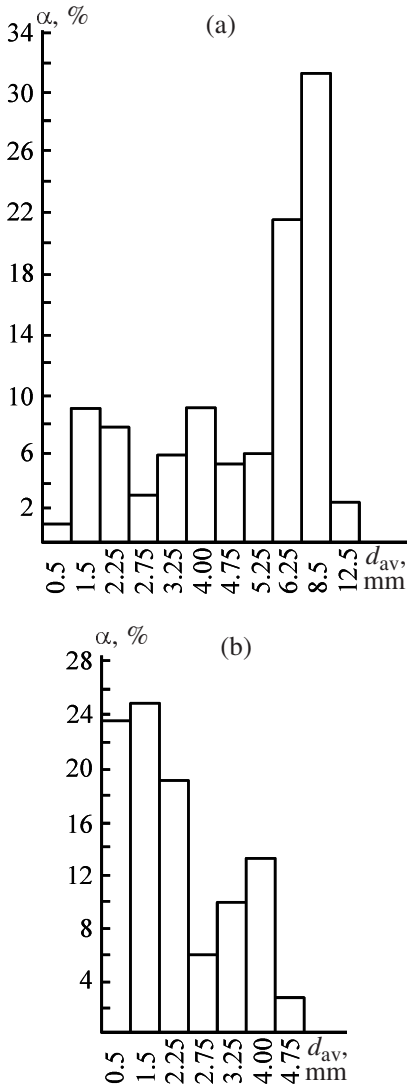


Fig. 2. Histograms of (a) starting product and (b) shungite after grinding and drying. (α) Share of fraction and (d_{av}) particle diameter.

Figures 2a and 2b show histograms of the starting and final products. It can be seen that coarse fractions (4 to 15 mm) constitute more than 70% in a shungite sample under study, and the amount of the 0.5–2.25-mm fraction in the final product at the outlet of the finishing-dryer–grinder is up to 70%, which favorably affects its subsequent grinding in a ball mill.

To determine the amount of free and bound moisture in the material, the kinetics of drying of the starting shungite at temperatures of 105 and 20°C were studied. Analysis of the curves in Fig. 3 shows that

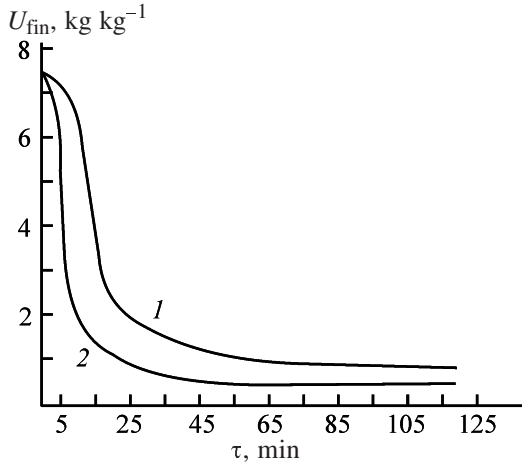


Fig. 3. Kinetics of shungite drying at (*1*) 105 and (*2*) 200°C. (U_{fin}) Final moisture content and (τ) drying duration.

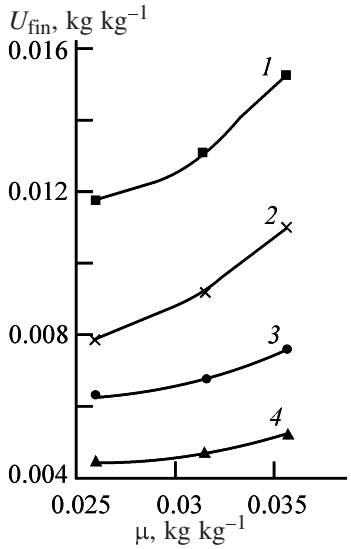


Fig. 4. Final moisture content U_{fin} vs. the consumed solid phase concentration. Drying temperature, °C: (*1*) 100, (*2*) 150, (*3*) 200, and (*4*) 250.

a considerable part of moisture is in the free state. The critical absolute moisture content is 2.3%. The prescribed final moisture content U_{fin} = 0.5% is reached in 37 min at 105°C and in 17 min at 200°C.

Figure 4 shows how the final moisture content of shungite depends on the consumed concentration of the solid phase. Analysis of the corresponding curves shows that the final moisture content of the product decreases as the temperature of the heat-transfer agent is raised and increases as the feeding rate of the solid phase becomes higher. This is accounted for by an insufficient supply of heat and too short residence time in the whirling chamber.

It should be noted, when analyzing the experimental data obtained, that the following parameters can be recommended for drying and grinding in the finish-dryer–grinder: heat-transfer agent temperature 200–250°C, consumed solid phase concentration 0.036–0.026 kg kg^{-1}.

CONCLUSIONS

(1) A combined dryer comprising a cyclone, whirling chamber, and finish-dryer–grinder was developed.

(2) The drying kinetics of the shungite mineral was studied under steady-state conditions. It was found that most part of moisture is in the free state and an effective technical and economic solution for obtaining a product with a final moisture content of 0.5% is to introduce a third stage into the installation. This can diminish the energy expenditure in subsequent grinding of the material in the ball mill.

REFERENCES

1. Romankov, P.G. and Rashkovskaya, N.B., *Sushka vo vzveshennom sostoyanii* (Drying in Suspended State), Leningrad: Khimiya, 1979, 3rd ed.
2. Sazhin, B.S., *Osnovy tekhniki sushki* (Fundamentals of the Drying Technology), Moscow: Khimiya, 1984.
3. USSR Inventor's Certificate no. 787 844.
4. RF Patent 2 245 499.

ISSN 1070-4272, Russian Journal of Applied Chemistry, 2008, Vol. 81, No. 3, pp. 503–505. © Pleiades Publishing, Ltd., 2008.
Original Russian Text © P.Yu. Andreev, E.V. Potapenko, I.P. Pogorelova, S.N. Krasil'nikov, A.N. Band, 2008, published in Zhurnal Prikladnoi Khimii, 2008, Vol. 81, No. 3, pp. 518–520.

BRIEF COMMUNICATIONS

A New Procedure for Preparing 3,4-Dinitrobenzoic Acid

P. Yu. Andreev, E. V. Potapenko, I. P. Pogorelova, S. N. Krasil'nikov, and A. N. Band

Institute of Chemical Technologies, Dal' East-Ukrainian National University, Rubezhnoe, Lugansk oblast, Ukraine

Received September 26, 2007

Abstract—A new efficient procedure of synthesis of 3,4-dinitrotoluene from 3-nitro-4-aminotoluene was developed. Oxidation of 3,4-dinitrotoluene with an ozone–oxygen mixture to 3,4-dinitrobenzoic acid in the presence of cobalt(II) acetate was studied.

DOI: 10.1134/S1070427208030348

Along with other isomeric dinitrobenzoic acids, 3,4-dinitrobenzoic acid (DNBA) is widely used as intermediate in synthesis of photosensitive materials for electrophotography [1, 2], X-ray contrast agents [3, 4], and modifying and vulcanizing agents for polyurethane plastics [5].

In common practice, DNBA is synthesized by oxidation of 3,4-dinitrotoluene (DNT) with Cr(VI) compounds or potassium permanganate. Oxidation with mineral oxidants proceeds under mild conditions; however, it is characterized by low selectivity and formation of large amounts of toxic wastes. Additional and important problem in synthesis of DNBA is the fact that the dinitrotoluenes are obtained as an isomeric mixture from which the desired 3,4 isomer (DNT) should be isolated.

With the aim to develop a new procedure of synthesis of DNBA, we studied the synthesis of DNT from 3-nitro-4-aminotoluene (NAT) and the liquid-phase oxidation of DNT with ozone–oxygen mixture in glacial acetic acid.

For the synthesis of DNT we developed a procedure based on the known procedure of synthesis of 2-dinitrobenzene from 2-nitroaniline [6]. This procedure involves diazotization of NAT with subsequent substitution of nitro group for diazo group. The yield of DNT is 92%.

Considering drawbacks of mineral oxidants, oxidation of DNT with ozone is of practical interest. At 30°C and atmospheric pressure, ozone reacts with DNT by two competing pathways, at double bonds of the aromatic ring and at the methyl group:

$$ArCH_3 + O_3 \rightarrow \begin{cases} \rightarrow Ar\dot{C}H_2 + HO^{\bullet}, & (1) \\ \rightarrow ArCH_2OH + O_2, & (2) \\ \rightarrow \text{ozonides}, & (3) \end{cases}$$

where Ar is $C_6H_3(NO_2)_2$.

Among the aromatic products, we identified 3,4-dinitrobenzaldehyde (DNBAld) and traces of 3,4-dinitrobenzyl alcohol (DNBAlc) in the initial period of the reaction and DNBA in deeper stages (Fig. 1). The yield of products formed by oxidation of the methyl group in DNT is 38%.

The selectivity of oxidation at the methyl group increases on adding variable-valence metal salts [7, 8].

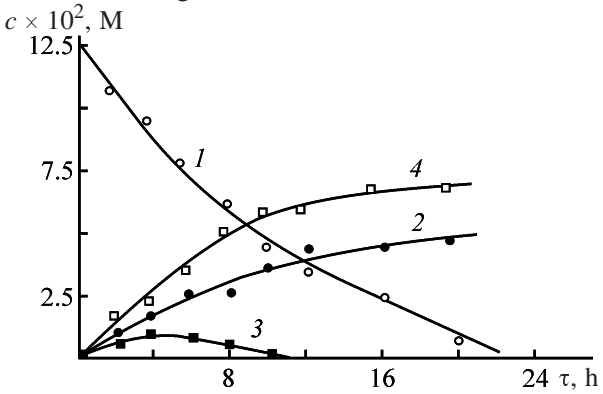


Fig. 1. Content of components of the reaction mixture as a function of time in oxidation of DNT with ozone–oxygen mixture. $W_{O_2} = 8.3 \times 10^{-3}$ l s^{-1}; $[ArCH_3]_0 = 0.125$, $[O_3]_0 = 9.5 \times 10^{-4}$ M; T = 30°C. (*c*) Concentration and (τ) time; the same for Fig. 2. (*1*) DNT, (*2*) DNBA, (*3*) DNBAld, and (*4*) peroxides.

Effect of catalyst on the selectivity of oxidation of methylbenzenes at 100°C. $[ArCH_3]_0$ = 0.50, $[M(OAc)_2]_0$ = 0.14, $[O_3]_0 = 4.0 \times 10^{-4}$ M

Catalyst	E_p^{298} M^n/M^{n+1}, V [11]	Maximum yield of acid, %		
		benzoic [12]	4-nitrobenzoic [13]	3,4-dinitrobenzoic
$Co(OAc)_2$	1.810	72.2	95.6	97.6
$Mn(OAc)_2$	1.510	31.8	36.4	62.8
$Pd(OAc)_2$	0.987	22.4	31.2	52.4
$Cr(OAc)_3$	0.740	18.6	27.9	48.2

According to published data, the selective oxidation of methylbenzenes depends on the redox potential of the catalyst [9, 10]. As seem from the table, cobalt and manganese compounds have the highest potential and these compounds are the most efficient catalysts of ozonation of methylbenzenes in acetic acid solutions.

The kinetic data for oxidation of DNT with ozone–oxygen mixture in the presence of cobalt(II) acetate at 100°C are presented in Fig. 2. The main product of oxidation at the methyl group is DNBA with a yield of 97%. DNBAld and traces of DNBAlc were also found as intermediates. In the system, the equilibrium between the oxidized and reduced cobalt species, in which cobalt occurs predominantly in the form of Co^{3+} throughout the process, is reached in the first 10–20 min.

It follows from the above facts that, in the presence of cobalt(II) acetate, DNT is oxidized in two stages: ozone predominantly reacts with Co^{2+} to form Co^{3+}:

$$Co^{2+} + O_3 + H^+ \rightarrow Co^{3+} + HO^\bullet + O_2, \qquad (4)$$

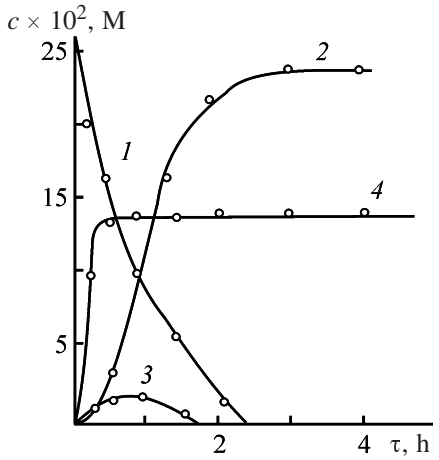


Fig. 2. Oxidation of DNT with ozone in the presence of cobalt(II) acetate in acetic acid solution. $W_{O_2} = 8.3 \times 10^{-3}$ l s^{-1}; $[ArCH_3]_0$ = 0.25, $[O_3]_0 = 6.70 \times 10^{-4}$, $[Co(AcO)_2]_0$ = 0.14 M; T = 100°C. (*1*) DNT, (*2*) DNBA, (*3*) DNBAld, and (*4*) Co^{3+}.

which further participates in initiation of selective oxidation of the substrate at the methyl group:

$$ArCH_3 + Co^{3+} \rightarrow Ar\dot{C}H_2 + Co^{2+} + H^+. \qquad (5)$$

Thus, we developed a new efficient procedure for preparing DNT from 3-nitro-4-aminotoluene. Oxidation of DNT with ozone in the presence of cobalt(II) acetate gives DNBA with an overall yield of 89%.

EXPERIMENTAL

3,4-Dinitrotoluene. 3-Nitro-4-aminotoluene of chemically pure grade (5 g) was dissolved in 30 ml of 60% sulfuric acid with heating. A 100-ml three-necked round-bottomed flask was charged with 20 ml of water and 10 g of ice, and a sulfuric acid solution of NAT was added with vigorous stirring. To the resulting mixture, 4 g of $NaNO_2$ in 15 ml of water was quickly added with vigorous stirring, and the mixture was stirred for 20 min.

The resulting solution of diazonium salt was placed into an ice bath. Then, a solution of 50 g of $NaNO_2$, 20 g of $NaHCO_3$, and 3 g of $CuNO_2$ in 500 ml of water was prepared in a 1-l three-necked round-bottomed flask. To the resulting solution, a solution of diazonium salt was added with vigorous stirring in portions through a glass tube touching the flask bottom. The solution temperature was maintained within 10–20°C. Addition of the diazonium salt was accompanied by active foaming. Ten minutes after adding the whole amount of the mixture, the precipitate was filtered off, washed with water, and dried in air.

Oxidation of DNT was performed in a reactor presenting a glass column with a finely porous membrane for dispersion of the gas mixture. The reactor was charged with 15 ml of glacial acetic acid and calculated amount of DNT; then, the reactor was thermostated and ozone–oxygen mixture was fed at a flow

rate of 8.3×10^{-1} l s^{-1}. The amount of the initial DNT and oxidation intermediates in the mixture was determined by gas–liquid chromatography on an LKhM-80 chromatograph equipped with a flame-ionization detector on a 2 m × 3 mm column packed with Chromaton N-AW support with the applied PNFS-6 stationary phase. The concentration of DNBA formed was determined by titration with 0.01 N NaOH solution on an EV-74 pH meter.

CONCLUSIONS

(1) 3,4-Dinitrotoluene was synthesized in 92% yield by diazotization of 3-amino-4-nitrotoluene with subsequent substitution of the nitro group for diazo group.

(2) In ozonation of 3,4-dinitrotoluene in acetic acid at 30°C, the yield of 3,4-dinitrobenzoic acid does not exceed 38%; the use of cobalt(II) acetate as a catalyst increases the yield of 3,4-dinitrobenzoic acid to 97%.

REFERENCES

1. Lebedev, B.A., Dolmatov, V.Yu., Zubarev, P.S., et al., *Khim.-Farm. Zh.*, 1988, no. 5, pp. 589–591.
2. US Patent 4 302 521.
3. Kunisaburo, T. and Kimie, Y., *J. Chem. Soc. Jpn.*, 1964, vol. 85, no. 1, pp. 5–6.
4. Polish Patent 233 328.
5. US Patent 4 346 014.
6. Weygand-Hilgetag, *Organisch-Chemische Experimentierkunst*, Leipzig: Johann Ambrosius Barth, 1964.
7. Yakobi, V.A., *Reaktsionnaya sposobnost' organicheskikh soedinenii* (Reactivity of Organic Compounds), Moscow: Mosk. Khim.-Tekhnol. Inst., 1978, issue 103, pp. 66–92.
8. Yakobi, V.A., Plakidin, V.L., Pokhila, S.E., et al., *Zh. Obshch. Khim.*, 1963, vol. 33, pp. 3369–3373.
9. Galstyan, T.M., Galstyan, G.A., and Yakobi, V.A., in *Trudy II Vsesoyuznoi konferentsii "Ozon, poluchenie i primenenie"* (Proc. 2nd All-Union. Conf. "Ozone, Synthesis and Applications"), Moscow: Mosk. Gos. Univ., 1991. p. 73.
10. Nakamura, A. and Tsutsui, M., *Principles and Applications of Homogeneous Catalysis*, New York: Wiley, 1980.
11. Lur'e, Yu.Yu., *Spravochnik po analiticheskoi khimii* (Handbook of Analytical Chemistry), Moscow: Khimiya, 1967.
12. Pluzhnik, I.M. and Galstyan, G.A., *Neftekhimiya*, 1999, vol. 39, no. 2, pp. 120–123.
13. Galstyan, A.G., Kudyukov, Yu.P., and Andreev, P.Yu., *Kinet. Katal.*, 2003, vol. 43, no. 1, pp. 1–4.

ISSN 1070-4272, Russian Journal of Applied Chemistry, 2008, Vol. 81, No. 3, pp. 506–508. © Pleiades Publishing, Ltd., 2008.
Original Russian Text © B.A. Zhubanov, R.F. Mukhamedova, G.I. Boiko, T.P. Maimakov, N.P. Lyubchenko, K.B. Erzhanov, 2008, published in Zhurnal Prikladnoi Khimii, 2008, Vol. 81, No. 3, pp. 521–523.

BRIEF COMMUNICATIONS

Modification of Some Mono- and Bispiperidols Exhibiting Growth-Regulating Properties

B. A. Zhubanov, R. F. Mukhamedova, G. I. Boiko, T. P. Maimakov, N. P. Lyubchenko, and K. B. Erzhanov

Bekturov Institute of Chemical Sciences, Ministry of Education and Science of the Kazakhstan Republic, Almaty, Kazakhstan
Satpaev Kazakh National University, Almaty, Kazakhstan
Unat Higher School, Almaty, Kazakhstan

Received October 11, 2007

Abstract—Procedures for esterification of biologically active mono- and bispiperidols by reactions with benzoyl and terephthaloyl chlorides were developed.

DOI: 10.1134/S107042720803035X

The development of highly effective chemical agents increasing the output of agricultural production is one of priority problems of chemical science and industry. Regulators of plant growth and development occupy an important place among such chemical agents. Numerous low-molecular-weight compounds, both natural (auxins, gibberellins, kinins, abscisic acid) and synthetic, exerting growth-regulating, stimulating, and herbicidal effect are known. At the same time, active studies aimed to develop new plant growth regulators and their derivatives are continued.

Numerous studies showed that the performance of biologically active substances (BASs) can be considerably enhanced by their chemical modification, mainly with various polymers [1, 2].

For a long period we perform comprehensive studies dealing with immobilization of low-molecular-weight BASs on a polymeric matrix with the aim to enhance and prolong their action and to ensure controlled release of the growth-regulating agent. We developed and implemented polymer-analogous transformations of copolymers of maleic anhydride with derivatives of acetylenic nitrogen- and phosphorus-containing carbo- and heterocyclic systems [3–7]. As a result, we obtained a new generation of polymeric water-soluble agents controlling the growth and development of plants and exhibiting durable action. We developed new polymeric preparations surpassing in the performance the known plant growth regulators. The laboratory, field, and commercial trials show that the polymeric preparations Zhiger, PAG, and PASA increase the productivity of crops (potatoes, sugar-beet) by 20–30% on the average, and the saccharinity of sugar-beet, by 1.5%. Polymeric plant growth regulators increase the germination energy of seeds (lucerne, goose-foot, licorice) by 12–18%, and the germinating power, by 60–80% on the average.[1]

Here we report on a new route to modified BASs. As modification substrates we chose a series of mono- and bispiperidols and their analogs: 1,2,5-trimethyl-4-(butoxypropyn-1-yl)piperid-4-ol, di(1-hydroxycyclohexyl)buta-1,3-diyne, and 1,4-bis(1,2,5-trimethyl-4-hydroxypiperid-4-yl)buta-1,3-diyne. These agents increase the productivity and improve the quality of crops such as potatoes, sugar-beet, corn, etc.

EXPERIMENTAL

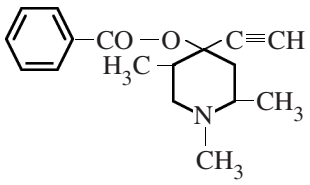
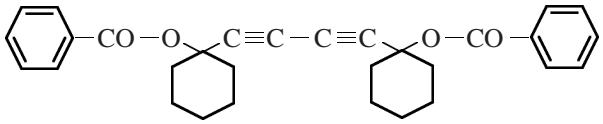
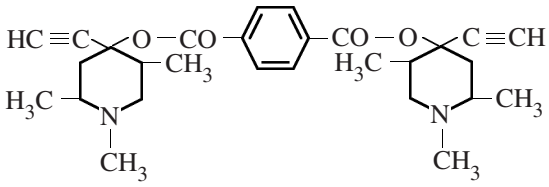
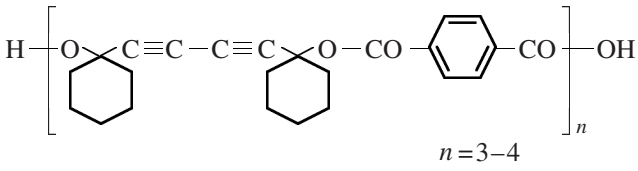
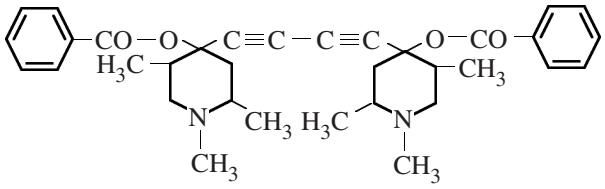
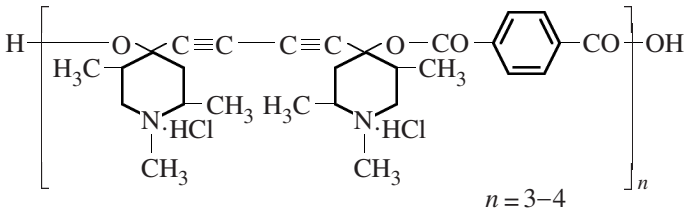
The starting compounds and solvents were purified by standard procedures. The IR spectra were measured on an IR-25 spectrophotometer (KBr pellets).

As the BASs under consideration contain hydroxy groups, one of the ways of their modification is condensation with acid chlorides. In our study we used benzoyl and terephthaloyl chlorides.

The products were identified by IR spectroscopy and elemental analysis. The main characteristics of the compounds are given in the table.

[1] Data of the Gur'ev Agricultural Station, Kazakh Research Institute of Feed Production and Pastures.

Characteristics of the esters synthesized

Compound	Structural formula	Yield, %	T_m, °C	Found, %/Calculated, %		
				C	H	N/Cl
I		28	116–118	75.27 74.86	7.74 6.92	5.16 5.15
II		14	102–104	79.29 76.80	6.60 7.02	– –
III		62	97–99	60.30 61.10	7.03 6.94	4.69 3.99
IV		30	110–114	68.81 66.97	6.06 5.62	3.13 2.84
V		18	123–125	75.27 70.14	7.71 6.59	5.16 4.63
VI		73	132–134	67.41 64.95	7.02 7.60	N 5.61 5.61 Cl 7.12 8.08

First we prepared monoesters of the above-mentioned BASs with benzoyl chloride. Monoesters **I**, **II**, and **V** (see table) were prepared at 60°C in a benzene solution in excess benzoyl chloride in the presence of triethylamine. The reaction progress was monitored by thin-layer chromatography. The synthesis was performed for 7–8 h. After removing benzene and excess benzoyl chloride, an only product was obtained, which crystallized on trituration in petroleum ether. In the IR spectrum of the products, there is an absorp-

tion band at about 1730 cm^{-1}, corresponding to vibrations of the ester group.

Diester **III** (see table) derived from 1,2,5-trimethyl-4-(3-butoxypropyn-1-yl)piperid-4-ol and terephthaloyl chloride was synthesized by the procedure for preparing activated diesters at 60°C in dioxane in the presence of pyridine. The synthesis was performed for 10 h, after which the mixture was evaporated to dryness, thoroughly washed with cold water, dried, and recrystallized from ethanol–petroleum ether. The product was identified by elemental analysis and IR spectroscopy.

Terephthalic acid esters of di(1-hydroxycyclohexyl)buta-1,3-diyne and 1,4-bis(1,2,5-trimethyl-4-hydroxypiperid-4-yl)buta-1,3-diyne (compounds **IV** and **V**, see table) were prepared by reaction of these alcohols with terephthaloyl chloride in a three-necked flask equipped with a bubbler, a stirrer, and an outlet pipe equipped with a calcium chloride tube. The reaction was performed in dichloroethane at 60–80°C in the presence of triethylamine. The synthesis time was 12 h. After the reaction completion, the product was precipitated with acetone, washed on the filter alternately with methanol and cold distilled water, and dried in a vacuum oven. The esters are readily soluble in amide solvents.

Tests performed with dicotyledonous cereals showed that the mono-, di-, and oligoesters we prepared, taken in low concentrations, exhibit a growth-stimulating effect. At the same time, esters derived from di(1-hydroxycyclohexyl)buta-1,3-diyne (see table, products **II** and **IV**) exhibit a herbicidal effect.

CONCLUSIONS

(1) New esters derived from benzoyl and terephthaloyl chlorides and biologically active mono- and bispiperidols and their analogs [1,2,5-trimethyl-4-(butoxypropyn-1-yl)piperid-4-ol, di(1-hydroxycyclohexyl)buta-1,3-diyne, and 1,4-bis(1,2,5-trimethyl-4-hydroxypiperid-4-yl)buta-1,3-diyne] were prepared and identified by IR spectroscopy and elemental analysis.

(2) The synthesized mono-, di-, and oligoesters taken in low concentrations exhibit a growth-stimulating effect.

REFERENCES

1. Shtil'man, M.I., *Soros. Obraz. Zh.*, 1998, no. 10, pp. 44–49.
2. Shtil'man, M.I., *Polimery mediko-biologicheskogo naznacheniya* (Polymers for Medicobiological Purposes), Moscow: Akademkniga, 2006.
3. RF Patent 1/88/26.
4. Kazakh Patent 1762534.
5. Kazakh Patent 1239.
6. Boiko, G.I., Lyubchenko, N.P., Maimakov, T.P., et al., in *Trudy IV Mezhdunarodnogo simpoziuma "Fizika i khimiya uglerodnykh materialov/nanoinzheneriya"* (Proc. IV Int. Symp. "Physics and Chemistry of Carbon Materials/Nanoengineering"), Almaty, 2006, pp. 140–144.
7. Boiko, G.I., Mukhamedova, R.F., Lyubchenko, N.P., et al., *Vestn. Kaz. Nats. Univ., Ser. Khim.*, 2007, no. 1 (45), pp. 207–211.

ISSN 1070-4272, Russian Journal of Applied Chemistry, 2008, Vol. 81, No. 3, pp. 509–510. © Pleiades Publishing, Ltd., 2008.
Original Russian Text © V.A. Sokolenko, N.M. Svirskaya, T.I. Kogai, M.S. Karpova, N.I. Pavlenko, 2008, published in Zhurnal Prikladnoi Khimii, 2008, Vol. 81, No. 3, pp. 524–525.

BRIEF COMMUNICATIONS

Diadamantylation of Dihydric Phenols and Their Derivatives

V. A. Sokolenko, N. M. Svirskaya, T. I. Kogai, M. S. Karpova, and N. I. Pavlenko

Institute of Chemistry and Chemical Technology, Siberian Branch, Russian Academy of Sciences, Krasnoyarsk, Russia
Siberian Federal University, Krasnoyarsk, Russia

Received July 16, 2007

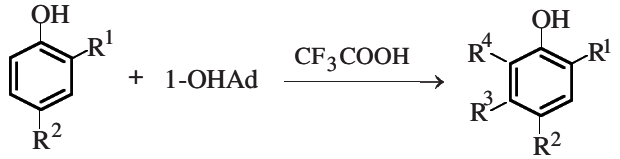
Abstract—Dihydric phenols and their monomethyl ethers were converted into diadamantyl derivatives by the reaction with 1-adamantanol in trifluoroacetic acid.

DOI: 10.1134/S1070427208030361

It is known that adamantyl derivatives of phenols, in particular, of 3,5-di(1-adamantyl)pyrocatechol, are effective antioxidants in the model reaction of cumene oxidation [1]. In addition, the antioxidant activity of 2,6-di(1-adamantyl)-4-methylphenol toward SKI-3 isoprene rubber was studied recently [3]. In this connection, it is interesting to perform diadamantylation of pyrocatechol, hydroquinone, and their monomethyl ethers.

The existing methods of diadamantylation of pyrocatechol and hydroquinone either led to poor yields of the target products [3] or required harsh reaction conditions [4]. It is known that adamantylation of *o*-methoxyphenol with 1-bromoadamantane is accompanied by elimination of the methoxy group and formation of *p*-(1-adamantyl)phenol [5]. Adamantylation of aromatic compounds with 1-adamantanol in trifluoroacetic acid was performed recently [6, 7].

Here we report on diadamantylation of pyrocatechol, hydroquinone, and their monomethyl ethers with 1-adamantanol in trifluoroacetic acid. The reaction occurs readily and with a high yield at 18–20°C:



Ia–Id **IIa–IId**

where $R^1 = OCH_3$, $R^2 = H$ (**Ia**); $R^1 = H$, $R^2 = OCH_3$ (**Ib**); $R^1 = OH$, $R^2 = H$ (**Ic**); $R^1 = H$, $R^2 = OH$ (**Id**); $R^1 = OCH_3$, $R^2 = R^4 = Ad$, $R^3 = H$ (**IIa**); $R^1 = R^3 = Ad$, $R^2 = OCH_3$, $R^4 = H$ (**IIb**); $R^1 = OH$, $R^2 = R^4 = Ad$, $R^3 = H$ (**IIc**); $R^1 = R^3 = Ad$, $R^2 = OH$, $R^4 = H$ (**IId**).

EXPERIMENTAL

The IR spectra were recorded on a Vektor-22 Fourier spectrometer in KBr, and the ^1H NMR spectra, on a Bruker-Avance DPX-200 spectrometer.

Diadamantyl derivatives IIa–IId. To a mixture of 1 mmol of **Ia–Id** and 2 mmol of 1-adamantanol, 2 ml of trifluoroacetic acid was added. The mixture was stirred and allowed to stand at 18–20°C for 16 h. The precipitate was filtered off, washed with water to neutral reaction of wash waters, and dried. The products were recrystallized from heptane–benzene, 10 : 1.

4,6-Di(1-adamantyl)-2-methoxyphenol IIa. Yield 76%, mp 201–203°C.

Found, %: C 82.96; H 9.62.
$C_{27}H_{36}O_2$. Calculated, %: C 82.61; H 9.24.

IR spectrum (KBr), ν, cm^{-1}: 3520, 3030, 2901, 2846, 1591, 1514, 1499, 1450, 1420, 1273, 1132, 1020, 793. ^1H NMR spectrum ($CDCl_3$), δ, ppm (*J*, Hz): 1.86–2.22 (30H, Ad), 3.96 s (3H, OCH_3), 5.93 s (1H, OH), 6.84 d (1H, H^3, J_{35} 1.84), 6.92 d (1H, H^5).

2,5-Di(1-adamantyl)-4-methoxyphenol IIb. Yield 86%, mp 275–276°C.

Found, %: C 82.54; H 9.32.
$C_{27}H_{36}O_2$. Calculated, %: C 82.61; H 9.24.

IR spectrum (KBr), ν, cm^{-1}: 3421, 3030, 2903, 2849, 1600, 1506, 1449, 1396, 1211, 1186, 1179, 874, 784, 756. ^1H NMR spectrum ($CDCl_3$), δ, ppm: 1.83–2.25 (30H, Ad), 3.85 s (3H, OCH_3), 4.40 (1H, OH), 6.56 s (1H, H^3), 6.80 s (1H, H^6).

3,5-Di(1-adamantyl)-2-hydroxyphenol IIc. Yield 93%. The physicochemical properties are in agreement with published data [1, 3].

2,5-Di(1-adamantyl)-4-hydroxyphenol IId. Yield 87%. The physicochemical properties are in agreement with published data [4].

CONCLUSION

A procedure was developed for preparing diadamantyl derivatives of pyrocatechol, hydroquinone, and their monomethyl ethers in 76–93% yields.

REFERENCES

1. Sokolenko, V.A., Svirskaya, N.M., Velikov, A.A., and Sizova, N.V., *Kinet. Katal.*, 2002, vol. 43, no. 2, pp. 205–208.
2. Voronchikhin, V.D., Goncharov, V.M., Vatamanyuk, O.M., et al., *Izv. Vyssh. Uchebn. Zaved., Khim. Khim. Tekhnol.*, 2005, vol. 48, pp. 144–145.
3. Miryan, N.I., Yurchenko, A.G., and Kirienko, E.I., *Ukr. Khim. Zh.*, 1990, vol. 56, no. 2, pp. 183–185.
4. Korsakova, I.Ya., Safonova, O.A., Ageeva, O.I., et al., *Khim.-Farm. Zh.*, 1982, vol. 16, no. 2, pp. 189–192.
5. Khardina, I.A. and Radchenko, S.S., Abstracts of Papers, *Nauchnaya konferentsiya po khimii organicheskikh poliedranov* (Scientific Conf. on Chemistry of Organic Polyhedranes), Volgograd, June 3–4, 1981, p. 64.
6. Sokolenko, V.A., Svirskaya, N.M., and Pavlenko, N.I., *Zh. Org. Khim.*, 2007, vol. 43, no. 5, pp. 783–784.
7. Stepankov, A.V., Molchanov, A.P., and Kostikov, P.P., *Zh. Org. Khim.*, 2007, vol. 43, no. 4, pp. 540–544.

ISSN 1070-4272, Russian Journal of Applied Chemistry, 2008, Vol. 81, No. 3, pp. 511–512. © Pleiades Publishing, Ltd., 2008.
Original Russian Text © S.A. Malin, A.S. Malin, B.M. Laskin, 2008, published in Khimicheskaya Promyshlennost', 2007, Vol. 84, No. 8, pp. 379–381.

TECHNOLOGY OF ORGANIC AND INORGANIC CHEMISTRY

Synthesis of α-Bromoisovaleric Acid in the Poliphosphoric Acid Medium

S. A. Malin, A. S. Malin, and B. M. Laskin

Russian Scientific Center "Applied Chemistry," St. Petersburg, Russia

Received March 19, 2007

Abstract—Bromination of isovaleric acid with bromine in the polyphosphoric acid mediumis was studied, regularities of the process including influence of the polyphosphoric acid composition were revealed, the process was shown technologically attractive for the organization of industrial manufacturing of α-bromoisovaleric acid.

DOI: 10.1134/S1070427208030373

As is known, α-bromoisovaleric acid is commonly obtained by the method of Gell–Folgard Zelinskii by which consists of bromination of isovaleric acid with elemental bromine in the presence of various catalysts such as red phosphorus or phosphorus halides, acyl halides, in part, isovaleroyl halides, thionyl chloride and mineral acids [1–5]. These methods are disadvantageous because of high consuming of bromine and catalyst, high temperature of the process and due to formation of isovaleric acid chlorine derivatives as side products.

An attractive method is bromination of isovaleric acid with bromine in the medium of polyphosphoric acid. This method has been considered in [6, 7], but the process features have not been published. Preparation of α-bromoisovaleric acid by his method in our opinion seems acceptable in respect of technology.

We explored bromination of isovaleric acid in the medium of polyphosphoric acid in details. We studied effects of reagents ratio, their total concentration in polyphosphoric acid, thermal and timing parameters. We found that bromination proceeds smoothly in 30–60% solutions of the reagents in polyphosphoric acid and affords α-bromoisovaleric acid in the yield up to 92–94%. For example, at the reagents content in polyphosphoric acid in the range 25–45% and isovaleric acid–bromine ratio 1 : 1.09 the bromination proceeds at 40–70°C in 4–5 h with 90–94% yield. Therewith, duration of the reaction completing increases owing probably to diffusion character of the process. The results obtained are listed in Table 1.

Yield of bromoisovaleric acid is high enough and achieves 92–94%.

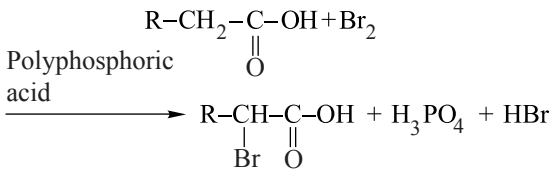
Study of isovaleric acid bromination in polyphosphoric acid of different compositions showed that at the phosphoric anhydride content in polyphosphoric acid from 20 to 40 wt% the bromination proceeds smoothly resulting in up to 92% yield of α-bromoisovaleric acid. Further increase in phosphoric anhydride content to 55% affects negatively the bromination process because the system becomes

Table 1. Bromination of isovaleric acid in the medium of polyphosphoric acid

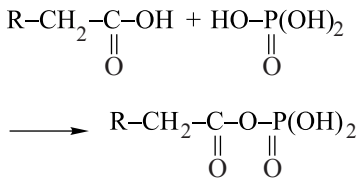
No.	Amount of polyphosphoric acid		Amount of isovalericacid		Amount of bromine		Phosphoric anhydride concentration in polyphosphoric acid		Concentration of reagents in polyphosphoric acid	Temperature of the process	Process duration	Yield
	ml	g	g	mol	g	mol	g	%	%	°C	h	%
	1	2	3	4	5	6	7	8	9	10	11	12
1	25	50	6	0.05	10.8	0.0 6	12.5	25	25	75–80	6	92–94
2	12.5	25					7.5	30	40	80	5	93–95
3	10	20					7.8	39	46	95–100	8	90–93
4	11	22					12.1	55	43	100–110	12–14	85

extremely viscous. Noteworthy that the formed α-bromoisovaleric acid is practically insoluble in polyphosphoric acid, forms a separate layer and can be isolated by separation or extraction with methylene chloride. The used polyphosphoric acid after bromination, as we established, can be further applied in bromination operations several times by refreshing with new portions of phosphoric anhydride for binding water formed in the process.

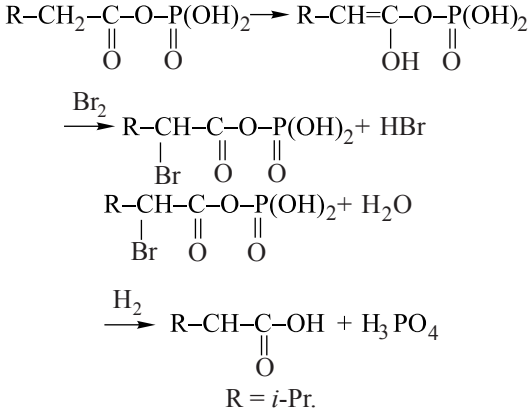
Bromination in the medium of polyphosphoric acid obviously proceeds alongside the scheme:



Probably initially isovaleroyl phosphate is formed:



The phosphate then exerts enolization and reacts with bromine to form α-bromoisovaleroyl phosphate which by controlled hydrolysis is converted into α-bromoisovaleric acid and phosphoric acid, providing high (up to 92–95%) yield of α-bromoisovaleric acid.



The studied method of α-bromoisovaleric acid formation is acceptable from the viewpoint of technology. It is advantageous because avoids application of toxic and dangerous catalysts such as phosphorus halides, thionyl chloride and others.

EXPERIMENTAL

Synthesis of α-bromoisovaleric acid. To a three-necks flask equipped with jacket, reflux condenser, dropping funnel, thermometer and magnet stirrer was loaded 20 g of polyphosphoric acid prepared alongside the procedure in [7]. For enhancing its rheological properties the acid was heated to 40–45°C, and then 6 g (0.05 mol) of isovaleric acid was added, stirring was switched on and 18.8 g (0.06 mol) of bromine was added dropwise. The mixture was heated to the temperature 95–100°C and kept at this temperature for 6–8 h. Then α-bromoisovaleric acid formed was extracted with methylene chloride, organic phase was washed and dried over magnesium sulfate. Solvent was distilled off and 9.6 g (90%) of α-bromoisovaleric acid was isolated, mp 44°C, bp 230°C.

REFERENCES

1. Ogata, Y. and Sugimoto, T., *J. Org. Chem.* 1978, vol. 43, no. 19, pp. 3684–3686.
2. Ogata, Y. and Adachi, Y., *J. Org. Chem.* 1982, vol. 47, no. 7, 1182–1184.
3. JP Patent 8226639, α-*Bromocarboxylic Acids*, 22.07.80.
4. Katsnel'son, M.M., *Prigotovlenie khomiko-farmatsevticheskikh preparatov* (Preparation of chemical-pharmaceutical substances), Leningrad, Goskhimtekhizdat, 1933.
5. RF Patent 2111954, *A Method of Preparation of Bromoisovaleric Acid Ethyl Ester*, 05.27.1998.
6. Smissman, G.J., *Am. Chem. Soc.,* 1954, vol. 76, pp. 5805–5807.
7. Ulig, F. and Snyder, G., *Uspekhi organicheskoi khimii* (Progres in Organic Chemistry), 1963, vol. 1, pp. 45–88.

ISSN 1070-4272, Russian Journal of Applied Chemistry, 2008, Vol. 81, No. 3, pp. 513–515. © Pleiades Publishing, Ltd., 2008.
Original Russian Text © O.V. Platonova, S.B. Volkova, S.A. Malin, E.A. Veretennikov, B.M. Laskin, A.S. Malin, 2008, published in Khimicheskaya Promyshlennost', 2008, Vol. 85, No. 1, pp. 1–4.

TECHNOLOGY OF ORGANIC AND INORGANIC CHEMISTRY

Synthesis of New Substituted Thiazoles Containing Aminooxadiazole Ring

O. V. Platonova, S. B. Volkova, S. A. Malin, E. A. Veretennikov, B. M. Laskin, and A. S. Malin

Russian Scientific Center "Applied Chemistry," St. Petersburg, Russia

Received February 12, 2007

Abstract—Synthesis of biheterocyclic thiazole–amonooxadiazoles, the potential biologically active compounds is developed. Regularities of transformations and physico-chemical characteristics of intermediates and final compounds are revealed.

DOI: 10.1134/S1070427208030385

The heterocycles of thiazole series are known to possess biological activity; some representatives of this class compounds are well-known medicine preparations [1, 2]. Compounds containing simultaneously thiazole and aminooxadiazole fragments merit special mentioning. Synthesis of these potentially biologically active compounds practically has not been described. We developed a few-step procedure for the synthesis of thiazole–aminooxadiazoles and studied conditions of the process and its technological parameters.

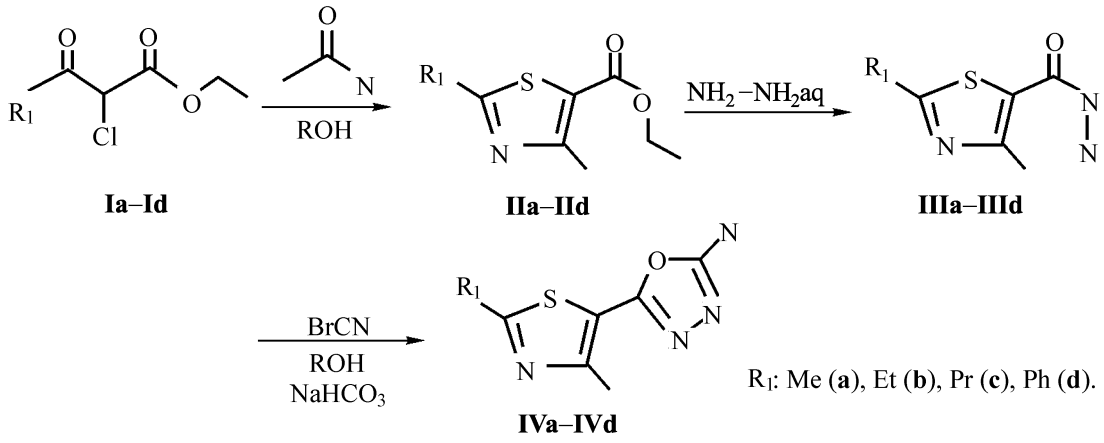
Substituted thiazoles **IIa**–**IId** were prepared by reaction of chloroacetoacetic esters prepared in correspondence with the procedure in [3] with thioacetamide in alcohol medium (like Hanch reaction [4, 5]) at 80–90°C, duration period 7–12 h, yield up to 75–80%.

Compounds **IIa**–**IId** are crystalline substances melting in the temperature range from 56 to 65°C.

Note that at the synthesis of compounds **IIa**–**IIc** the process duration increases for the series of substituents a to c, probably in connection with steric properties of these substituents. The process duration for compound **IId** increases probably due to strong electromeric effect of conjugated system that includes phenyl group. Introduction of triethylamine to the reaction zone allows accelerate the process considerably and increase yield of compound **IId** to 75%.

The process conditions for the synthesis of the thiazoles and some of their characteristics are listed in Table 1.

Synthesis of corresponding hydrazines **IIIa**–**IIId** has been poorly illuminated in literature. We prepared hydra-



Ia–Id **IIa–IId** **IIIa–IIId** **IVa–IVd**

Table 1. Process conditions for the synthesis of compounds **IIa–IId**

Compd. no.	Process duration, h	Process temperature, °C	Yield, %	mp, °C
IIa	5	80 7	8	56
IIb	7	82 7	7	65
IIc	8.5	85 7	0	61
IId	12.3 9	0	73 5	5

Table 2. Conditions of synthesis of compounds **IIIa–IIId**

Compd. no.	Process duration, h	Process temperature, °C	Yield, %	mp, °C
IIIa	10	77–83	82 1	01
IIIb	11	80–85	80 1	05
IIIc	13	84–88	77 1	14
IIId	16	90–95	74 1	58

Table 3. The process conditions for the synthesis of compounds **IVa-IVd**

Compd. no.	Process duration, h	Process temperature, °C	Yield, %	mp, °C
IVa	6	28 8	0	235
IVb	8.5	31 7	7	224
IVc	9	35 7	3	243
IVd	10	40	68 2	30

zides **IIIa–IIId** by reaction of thiazoles **IIa–IId** with 3–5-fold excess of 64% hydrazine hydrate in absolute ethnol at 90–100°C, reaction duration was 10 to 20 h, yield is as high as 95%. The compounds obtained are characterized by high melting point; they are well crystallizing from water–alcohol solutions. Results of the synthesis of compounds **IIIa–IIId** are shown in Table 2.

Aminooxadiazole derivatives **IVa–IVd** were obtained in 65–80% yield by cyclization of the prepared hydrazides [6, 7] with bromocyane in the presence of anhydrous potassium carbonate at equimolar ratio of reagents in ethanol medium at 20–40°C for 6–10h. IR spectra of the obtained compound do not contain adsorption bands of carbonyl and hydrazide groups while adsorption of aminooxadiazole NH_2 group appears in the spectra.

Structure, purity and nature of compounds **IVa–IVd** were revealed using 1H NMR spectroscopy. The NMR data obtained showed that amine fragment in compounds **IVa–IVd** is considerably less basic as compared with related unsubstituted aminooxazoles. The most probably this is defined by the presence of conjugated system thiazole–aminooxadiazole, in the case of **IVd** in particular, due to presence of phenyl group expanding conjugation. Spectral characteristics of the synthesized compounds are listed in Table 4.

CONCLUSIONS

A series of new potentially biologically active biheterocyclic compounds containing thiazole and aminooxazole rings is synthesized, optimal conditions of the synthesis are studied and revealed.

Structure of the obtained compounds is proved and they are characterized by means of ^{1}H NMR spectroscopy.

EXPERIMENTAL

The ^{1}H NMR spectra are recorded on a e Bruker AM 500 spectrometer, internal reference TMS, solvent DMSO-d_6. Melting points are measured on a PTP unit.

Synthesis of R-substituted ethyl esters of thiazolecarboxylic acids IIa–IId. Mixture of preliminary prepared R-substituted chloroacetoacetic ester **Ia–Id** (0.236 mol) and thioacetamide (0.236 mol) in 100 ml of ethanol or isopropyl alcohol was refluxed on water bath with stirring for 7–12 h. After cooling the reaction mixture was diluted with 200 ml of dichloromethane. Precipitate formed was removed by filtration and filtrate was washed with 20% solution of sodium hydrocarbonate (100 ml) to neutral reaction and then by solution (100 ml) of sodium chloride. The layers were separated, and from organic layer dicloromethane was distilled off after drying over magnesium sulfate, and then compounds **IIa–IId** were isolated in 85–90% yield.

Spectral characteristics of compounds **IIa–IId** obtained are listed in Table 4.

Synthesis of hydrazides of R-substituted thiazolecarboxylic acids IIIa–IIId. To a solution of the obtained by above procedure R-substituted ethyl ester of thiazolecarboxylic acid **IIa–IId** (0.5 mol) in 125 ml of ethanol or isopropyl alcohol was dozed at 20–30°C 100 ml of 64% hydrazine hydrate (0.236 mol) and the raction mixture obtained was refluxed with stirring for 10–20 h. Then reaction mixture was concentrated in a vacuum to 60–75%. The crystals dropped are soluble in water. They were recryctallized from ethanol, and compounds **IIIa–IIId** were obtained in 85–93% yield.

Table 4. 1H NMR spectral data of compounds **II–IV** (solutions in DMSO–*d*6)

Compound	^{1}H NMR spectra, δ, ppm
IIa	2.55 s (3H, CH_3); 2.47 s (3H, CH_3); 1.31 t (3H, CH_3); 4.27 q (2H, CH_2)
IIb	1.31 t (3H, CH_3); 1.37 t (3H, CH_3); 2.47 s (3H, CH_3); 2.9 q (2H, CH_2); 4.27 q (2H, CH_2)
IIc	0.91 t (3H, CH_3); 1.32 t (3H, CH_3); 1.6 m (2H, CH_2); 2.4 s (3H, CH_3); 2.91 t (2H, CH_2); 4.25 d (2H, CH_2)
IId	1.33 t (3H, CH_3); 2.55 s (3H, CH_3), 4.28 d (2H, CH_2); 7.72–7.8 m (5H $_{arom}$)
IIIa	2.32 s (3H, CH_3); 2.38 s (3H, CH_3); 5.68 s (3H, NH, NH_2)
IIIb	1.39 t (3H, CH_3); 2.39 s (3H, CH_3); 3.35 d (2H, CH_2); 5.68 s (3H, NH, NH_2)
IIIc	0.92 t (3H, CH_3); 1.61 m (2H, CH_2); 2.29 s (3H, CH_3); 3.35 t (2H, CH_2); 5.7 s (3H, NH, NH_2)
IIId	2.47 s (3H, CH_3); 5.4 s (3H, CH_3); 7.62–7.7 m (5H_{arom}); 5.81 s (3H, NH, NH_2)
IVa	2.37 s (3H, CH_3); 2.55 s (3H, CH_3); 7.4 s (2H, NH_2)
IVb	1.36 t (3H, CH_3); 2.38 s (3H, CH_3); 2.98 d (2H, CH_2); 7.32 s (2H, NH_2)
IVc	0.9 t (3H, CH_3); 1.64 m (2H, CH_2); 2.29 s (3H, CH_3); 2.97 t (2H, CH_2); 7.6 s (2H, NH_2)
IVd	2.46 s (3H, CH_3); 7.62–7.72 m (5H_{arom}); 7.33 7.6 s (2H, NH_2)

Spectral characteristics of compounds **IIIa–IIId** obtained are listed in Table 4.

Synthesis of R-substituted thiazoloaminooxazoles IVa–IVd. To a suspension of hydrazide **IIIa–IIId** (0.07 mol) and sodium hydrocarbonate (0.07 mol) in water (50 ml) at cooling by ice was dozed solution of brmocyane (0.07 mol) in ethanol. The reaction mixture was kept at 20–25°C for 6–12 h. Then for few hours it was cooled to 3–5°C and crystals dropped were filtered off, washed with water for removing sodium bromide, and dried. Compounds **IVa-IVd** were obtained in 65–80% yield.

Spectral characteristics of compounds **IVa–IVd** obtained are listed in Table 4.

REFERENCES

1. Plouvier, B and Bailly, C., *et al*., *Heterocycles*, 1991, vol. 32, no. 4, pp. 693–701.
2. Buchmann, E.R. and Richardson, E.M., *J. Am. Chem. Soc.,* 1939, vol. 61, no. 1-4, pp. 891–893.
3. Dey, B.B., *J. Chem. Soc.*, 1915, pp. 1645–1646.
4. Hantzsch, A., *Liebig Ann*., vol. 250, p. 269.
5. Cornwall, P., Dell, C.P., and Knight, D.W., *J. Chem. Soc., Perkin Trans. I,* 1991, pp. 2417–2428.
6. Dost, J., Heschel, M., and Stein, J., *J. Prakt. Chem.,* 1985, vol. 327 (1), p. 116.
7. Sherman, W.R., *J. Org. Chem.,* 1961, vol. 1, no. 26, pp. 88–95.

ISSN 1070-4272, Russian Journal of Applied Chemistry, 2008, Vol. 81, No. 3, pp. 516–519. © Pleiades Publishing, Ltd., 2008.
Original Russian Text © V.P. Talzi, G.V. Plaksin, V.Yu. Davydova, 2008, published in Khimicheskaya Promyshlennost', 2008, Vol. 85, No. 1, pp. 5–8.

TECHNOLOGY OF ORGANIC AND INORGANIC CHEMISTRY

Examination of Catalyst for α-Metylstyrene Oligomerization "Phosphoric Acid on Sibunit" under Conditions of Laboratory and Industrial Application

V. P. Talzi, G. V. Plaksin, and V. Yu. Davydova

Institute of the Problems of Processing Hydrocarbons, Russian Academy of Sciences, Siberian Branch, Russia

Received March 19, 2007

Abstract—A catalyst obtained by impregnation of a mesoporous carbon carrier *sibunit* with orthophosphoric acid is examined under conditions of pilot plant manufacturing for producing α-methylstyrene dimer. The produced *catalyzate* (the product obtained with catalysis, 300 ton) containing ca. 70% of targeted 2,4-diphenyl-4-methyl-1-penetene at 95% conversion was after filtration used for control of molecular mass at producing polystyrene of different sorts. Consumption of the catalyst under optimal conditions of exploitation of the installation was ca. 1.5 kg per 1 ton of dimer at temperature ca. 50°C and volume rate ~ 0.5 h^{-1}. Content of 2,4-diphenyl-4-methyl-1-pentene in the dimer can be elevated to 80% by significant decreasing conversion (~50%) and by application of solvents.

DOI: 10.1134/S1070427208030397

α-Methylstyrene dimer consisting mainly of 2,4-diphenyl-4-metyl-1-pentene (α-isomer **I**) is used for control over molecular mass at producing polystyrene and its co-polymers. After complete hydrogenation of the dimer the product obtained is the best base for high-power lubricant oil [1].

World market proposes a dimer containing up to 94% of α-isomer at the total content of linear dimers above 98%. The α-isomer serves as substance for the molecular mass control, in distinct to unwanted admixtures of 2,4-diphenyl-4-methyl-2-pentene (β-isomer **II**) and 1,1,3-trimethyl-3-phenylindane (cyclic isomer **III**). The dimer produced in Russia in correspondence with technical requirements [2] commonly contains less than 75% of α-isomer [2].

Information on the technology of α-methylstyrene oligomerization and catalysts used can be found in patent publications mainly [3]. As catalysts were applied liquid or solid acids (the latter are more useful in technology): clays, ceolites, sulfocationites, various phosphate systems, e.g., industrial catalysts used at hydrogenation of ethylene, often in the presence of a solvent. With some ceolites without a solvent was achieved high selectivity at producing α-dimer (90%) [4–6]. However, duration of application of such catalyst before regeneration has not been reported.

There is US patent on obtaining individual α-isomer in the presence of cobalt complexes as radical initiators [7]. Possibility of practical application of such process in view that domestic technologies are commonly below the high-tech range is doubtful.

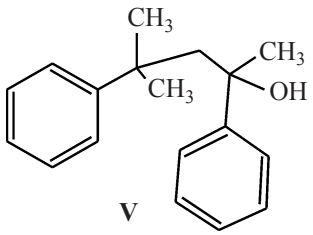
The main purpose of the present work is search of catalyst for α-methylstyrene oligomerization to provide styrene producing in Omsk with simplest technology for the synthesis of molecular mass controlling substance free of by-products, satisfactory from the viewpoint of domestic requirements, at minimal investment and producing cost.

The catalyst "phosphoric acid on sibunit" is obtained at primary screening on catalytic activity and contact selectivity of the catalysts obtained by impregnation with orthophosphoric acid of carbon material sibunit with medium diameter of mesopores of the carrier at varied acid content and regime of thermal treatment. The catalyst with appropriate catalytic activity, selectivity and life time for pilot plant manufacturing was obtained with the sibunit with average pore diameter 40 nm, phosphate

content recalculated on P_2O_5 10–15% and maximal temperature at roasting the catalyst below 250°C.

After examination of the catalyst on a laboratory installation (Fig. 1) the catalyst was tested for industrial application. Various batches of the catalyst produced in Sorbents and catalysts pilot plant department of Omsk plant were for three years used for producing dimer in low tonnage industrial circulation installation of plastic fabric of join stock company "Zavod Plastmass" on pipe type reactor for 100 kg of the catalyst constructed on the basis of ordinary heat exchanging unity which allowed maintaining the optimal reaction temperature ca. 50°C by water circulating in jacket. With fresh catalyst effective cooling was needed, at further work it should be heated to the operating temperature. The table shows data on the catalyzate content obtained under industrial conditions at two-times circulation. At exploitation of the installation was produced over 300 ton of such dimer using various batches of the catalyst. It was found that long enough (up to 30 days) pauses do not lead to significant loss in the catalyst activity. Consumption of the catalyst at optimal winter conditions of exploitation was about 1.5 kg of the catalyst per one ton of dimer. In the period from May to September the catalyst resource is affected considerably due to its hygroscopicity, therefore additional means should be applied to protect the system against moisture. Without such protection in summer time the catalyst may loss activity in a few days.

The catalyzate obtained was not purified additionally but filtered for removing catalyst particles, and used as agent for chain transfer at producing polystyrene in "Zavod Plastmass" plant. It was noted that the dimer displays inhibiting effect and decreases stability of styrene–water dispersions, like has been noted for the case of similar molecular mass controlling substance obtained with aqueous benzenesulfonic acid as catalyst [7]. The dimer obtained under optimal conditions with "phosphoric acid on sibunit" as catalyst in distinct to the dimer obtained with aqueous benzenesulfonic acid is not contaminated with 2,4-diphenyl-4-methyl-2-hydroxypentane (**V**) which suggested inherent in the mentioned negative effect on the exploitation properties of the dimeric substance [8].



V

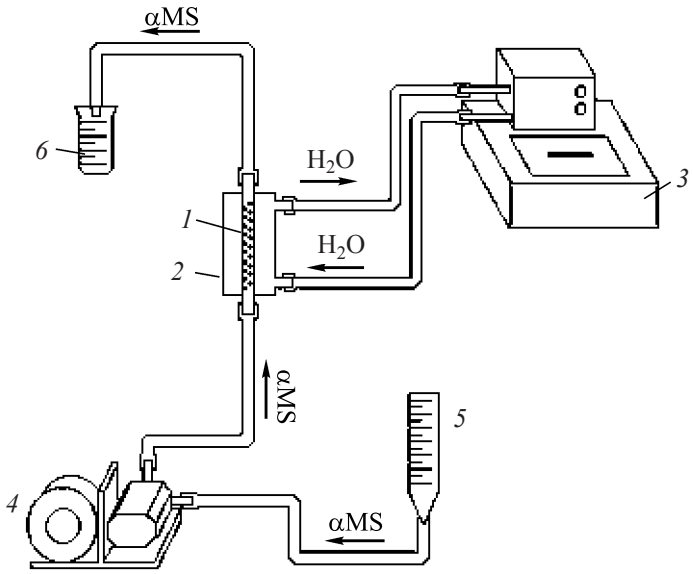
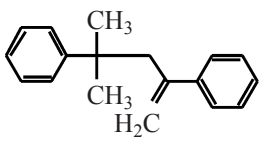
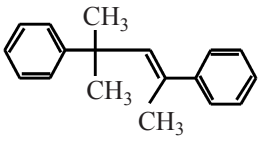


Fig. 1. Scheme of laboratory flow circulation installation for examination of catalysts for α-methylstyrene oligomerization. (*1*) reactor with catalyst loaded in it; (*2*) reactor jacket; (*3*) thermostat; (*4*) feeding mini pump; (*5*) tank for raw material ; (*6*) receiver for reaction product.

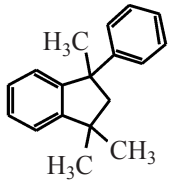
Average composition of catalyzate at α-methylstyrene oligomerization in flow-circulating installation with catalyst "phosphoric acid on sibunit"



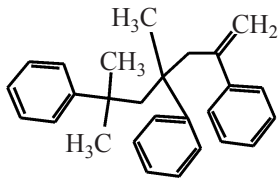
I



II



III



IV

T, °C	Volume rate, h^{-1} (two passes)	Catalyzate composition, %				
		α -methylstyrene	α-dimer **I**	β-dimer **II**	trimers (basically **IV**)	cyclic dimer **III**
50	1					
Composition of catalyzate		3	71	10	8	8

As the laboratory and industrial tests showed, the proposed catalyst does not allow achieving content of targeted isomer above 90% at high conversion (above 95%) on raw material.

We succeeded in approaching high results on the content of α-isomer like in the substance from foreign producers using "phosphoric acid on sibunit" as catalyst, without a solvent, taking a flask with stirrer as a reactor, with raw material and the catalyst in 5:1 ratio, maintaining temperature 45°C, and carrying out the process to low conversion of α-methylstyrene a (~20%). Unreacted raw material and then fraction of dimers were distilled off under reduced pressure. About 10–15% of raw material was lost therewith due to formation of trimers collected in bottom residue. Under these conditions by direct distillation was isolated dimer with content of α-isomer ca. 92%.

Use of appropriate solvent should lead to decrease in content of trimers in the catalyzate. Really, when raw material was diluted 4 – 5-fold with methylene chloride or carbon tetrachloride, we succeeded in laboratory installation (Fig. 1) at 40–50°C to increase selectivity on the targeted substance to 80% at 50% conversion.

According to published data, as the solvent can be taken also e.g., toluene or cumene and selectivity can be achieved with $HCOOH + C_6H_5OH$ system where phenol is solvent [3]. Besides, principally the selectivity can be increased at application of solvents by choosing a carrier with less size pores [6, 8], in part, with sibunit containing pores of less width. Thus, there are quite real pathways of increasing selectivity of the proposed catalyst, however, necessarily with considerable complication of technology.

EXPERIMENTAL

The catalyst "phosphoric acid on sibunit" is prepared by impregnation of spherical granules of mesoporous carbon carrier sibunit (dimeter of the granules 1.6–2.0 mm for industrial and 0.3–0.5 mm for laboratory testing) with orthophosphoric acid (10% as recalculated to P_2O_5) followed by thermal treatment at the temperature not higher than 250°C.

The catalyst samples were examined in an installation shown in Fig. 1. In some experiments the catalyzate obtained was separated in commonly used laboratory equipment by distillation at reduced pressure. α-Methylstyrene passes at ~70°C and a fraction of dimers at ~200°C, which corresponds to pressure ~30 mm Hg.

Analysis of the catalyzate was conducted on a chromato-mass spectrometer of Agilent Technologies firm (GS-MS 6890N-5973) with capillary column HP-5MS.

CONCLUSIONS

Industrial examination during three years showed that the proposed catalyst for α-methylstyrene oligomerization "phosphoric acid on sibumit" and free of by-product technology allow successfully solve the problem

of providing polystyrene production in Omsk with low tonnage molecular mass controlling substance containing targeted 2,4-diphenyl-4-methyl-1-pentene (α-isomer) approx. 70% at 95% conversion of raw material.

ACKNOWLEDGMENT

The authors grateful to Volodchenko Ludmila Ivanovna, the Principal Technologist of join stock company "Zavod Plastmass" for organization of the line for producing dimeric α-methylstyrene and testing this substance at polystyrene manufacturing.

REFERENCES

1. Isakov, Ya.I., Minachov, Kh.M., Sharf, V.Z., and Litvin, E.F., *Neftekhimiya*, 1999, vol. 39, no. 4, pp. 278–283.
2. α-*Methylstyrene Dimer. Technological Requirements*, TU 38.402-67-106-91.
3. Chaudhuri, B. and Sharma, M.M., *Ind. Eng. Chem. Res*., 1989, vol. 28, no. 12. p. 1757.
4. Grigor'eva, N.G., Dzhemilev, U.M., Kutepov, B.I., Pavlov, M.L, Rasulev, Z.G., and Zalimova, M.M., *Khim. Promyshlennost'*, 2002, no. 11, pp. 4–6.
5. Grigor'eva, N.G., Kutepov, B.I., Makhamatkhanov, R.A., Bikbaev, R.T., Khazipova, A.N., and Kovtunenko, I.A., *Zh. Prikl. Khim.,* 2002, vol.75, no. 9, pp. 1574–1575.
6. Grigor'eva, N.G., Galyautdinova, R.R., Paukshtis, E.A., Kutepov, B.I., Tselyutina, M.I., and Dzhemilev, U.M., *Neftekhimiya*, 2006, vol. 46, no. 5, pp. 360–366.
7. US Patent WO 99/41218, class PCT/US99/02768, 1999.
8. Talzi, V.P., Doronin, V.P., Sorokina, T.P., and Ignashin, S.V., *Zh. Prikl. Khim.*. 2000, vol. 73, no. 5, pp. 787–790.

ISSN 1070-4272, Russian Journal of Applied Chemistry, 2008, Vol. 81, No. 3, pp. 520–523. © Pleiades Publishing, Ltd., 2008.
Original Russian Text © V.S. Danil'chuk, N.A. Nezamaev, M.Kh. El'zhurkaev, A.N. Verigin, 2008, published in Khimicheskaya Promyshlennost', 2008, Vol. 85, No. 1, pp. 9–12.

MODELING AND CALCULATION OF TECHNOLOGICAL PROCESSES

Synthesis of New Substituted Thiazoles Containing Aminooxadiazole Ring

V. S. Danil'chuk, N. A. Nezamaev, M. Kh. El'zhurkaev, and A. N. Verigin

St. Petersburg State Technological Institute, St. Petersburg, Russia

Abstract—Heat exchangers of circulating type are used extensively in the heat exchange processes. Circulation of liquid in these devices is ensured by mechanical mixing devices, and heat exchange is enhanced by the increase of the heat exchange surface. The application of the upright heat exchange elements like double pipes providing a cross-flow regime in the device is the most effective. Calculation of the apparatus with the vertical heat-exchange elements for determination of constructive and regime parameters at maximum output of the device was presented.

DOI: 10.1134/S1070427208030403

Heat exchangers with the upright heat-exchange elements possess sufficiently high intensity of heat exchange even at the mixing of non-Newtonian fluids [1]. Rational combination of the construction of inside units and the agitator ensures intensive circulation of working media at sufficiently uniform velocity field.

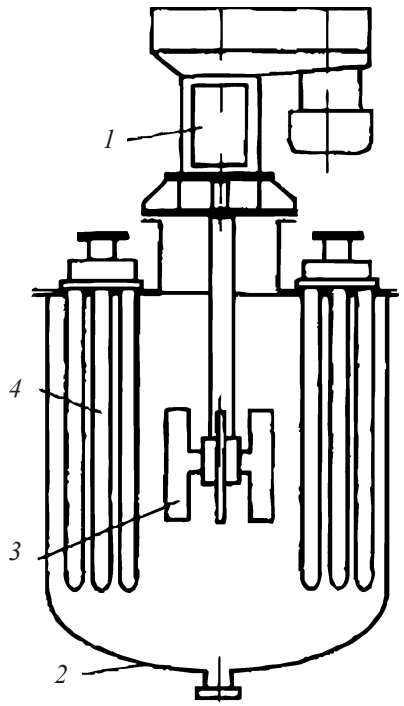


Fig. 1. Batch reactor. (*1*) Drive, (*2*) reactor body, (*3*) agitator, (*4*) upright heat exchange elements.

On the stage of calculation and development of the apparatus with upright heat-exchange elements two problems should be solved. First one is to determine constructive and regime parameters which provide maximum output of the device within conditions of the given constructions. Second problem consists in providing the given output at the minimum of costs at designing and operation of the device. A calculation and optimization of the following parameters: pipe diameter (d_t), number of pipes in the bundle (n_{tb}), number of bundles (n_b), and bundle diameter(d_b), total heat exchange surface (F), agitator diameter (d_m), drive power, characteristics of heat pump [pressure (ΔP), and cooling agent flow (V_r)] are necessary to solve the first and the second problems. The cited parameters define values of heat radiation coefficients α_1 and α_2, heat transfer coefficient (K), and heat flow through surface of heat-exchangers.

Volume of device (V_d) and heat efficiency of the processes per mass unit of heat carrier (q_u) are initial parameters to calculate maximum possible output. Required volume of the device is calculated according to equation (1):

$$V = G\tau / \rho, \quad (1)$$

where G is heat-carrier flow, kg/s; ρ is heat carrier density, kg/m^3, average duration of residence of heat carrier, s.

If the value of the volume is preset the heat carrier flow is calculated by equation (1). In such a way the found output of the apparatus G is not final. It can be limited by the possibility of heat removal. Maximum heat loads have to be provided at the non-stationary process.

$$Q \geq K_Q q_u G,$$

where Q is the required value of heat flow, Wt; K_Q is coefficients of reserve.

The optimal correlations of geometrical and technological parameters must be provided to determine heat characteristics. Some optimum relations of geometric sizes which set the most uniform hydrodynamic processes were determined earlier [2]. According to experimental data the height of cylindrical section of the apparatus body is $H_c = (0.8–1.0)D$; agitator height is $h_m = (1 + 1.2)$ d_m. The values V_d, q_u, G according to the given limits permit the calculation and optimization of the necessary designing parameters. The most compactness of heat exchangers is reached using the pipes of smaller diameter. At these conditions resistance to vibration should be provided:

$$f_t \leq 0.6 f_d \quad (2)$$

$$f_t \leq 0.6 f_v, \quad (3)$$

where f_t is the intrinsic oscillation frequency of pipes, s^{-1}; f_v is the frequency of vortex shedding in trace at rear of pipes, s^{-1}; f_d is vibration frequency caused by hydrodynamic forces originating from the flow pressure pulsation which can result from the agitator blade passing close to the pipe.

$$f_d = nz_a, \quad (4)$$

where n is agitator speed, z_a is number of the agitator blades.

The periodicity of vortex shedding is determined by dimensionless Strouhal number: relation of the frequency of vortex shedding, the characteristic size of body (d_b), and the velocity of the fluid (v) is described as:

$$\mathrm{Sh} = f_v, d_b/v.$$

According to the experimental data the maximum speed of flow is observed in the region of radial stream close to the agitator. Assuming that $w_r = w_t$ and taking into account that $w_r = 0.6\, w_{rm} / 2$ it can be written

$$w = \sqrt{w_t^2 + w_r^2} = \sqrt{2 \cdot 0.6 \omega^2 r_{rm}^2} = 0.85\, \omega r_{rm}.$$

Maximum allowable linear speed of agitator rotation $w = w_{max}$ may be used as a value of agitator diameter since the latter is not defined. If longitudinal and cross space between tubes is equal to Strouhal number for first row of staggered bundle may be obtained from the equation [2]

$$\mathrm{Sh} = 0.2 + \exp\,[-0.44\,(S_t / d_t)^{1.8}],$$

where S_t is the space between the pipes.

The intrinsic oscillation frequency of pipes is defined by equation

$$f_{tr} = \frac{\beta}{2\pi h_t} \sqrt{\frac{EI}{m}},$$

where E is the elasticity of pipe material, N/m^2, I is pipe flexural rigidity, m^4, β is the coefficient depending on the mode of pipe fixation; h_t is the pipe length, m; m is mass of the pipe and of the liquid within the pipe, kg

$$I = \frac{\pi}{64} (d_t^4 - d_{t1}^4),$$

$$m = \rho_{liq} \frac{\pi d_{t1}^2}{4} h_t + \rho_t \frac{\pi (d_{t1}^2 - d_{t1}^2) h_t}{4}, \quad (5)$$

where d_t is the inside pipe diameter, m.

Setting pipe diameter we can find values f_t, f_d, and f_v by equations (4) and (11).

When the conditions (2) and (3) are not met the diameter of pipes must be increased. The calculation is continued until the condition of resistance to vibration is met. Diameter of bundles is related to the diameters of apparatus and agitator by an equation.

$$d_B = \frac{D - d_M}{2} - \delta_{\Phi 1} - \delta_{\Phi 2}, \quad (6)$$

where $\delta_{\Phi 1}$ is the size of flange for drive installation drive, m, and $\delta_{\Phi 2}$ is the size of flange for fastening the bundles to the cover, m.

Equation defining the number of bundles is

$$n_B = \frac{2\pi}{\gamma}, \quad (7)$$

where γ (see Fig. 1) is

$$\gamma = 2\arcsin \left[\frac{\left(\frac{d_B}{2} - \delta_\Phi \right)}{\left(\frac{d_M}{2} + \frac{d_B}{2} + \delta + \delta_{\Phi 2} \right)} \right]. \quad (8)$$

With an increase of the agitator diameter the number of bundles is increased and their diameter is decreased. So an optimum value d_m/D exists corresponding to the overall maximum number of installed pipes.

Number of pipes in the bundle may change depending on a manner of their mounting. At the mounting of pipes on sides of regular triangles their number under the same conditions is greater or equal to the number of pipes placed on the sides of squares and on concentric circles with a center coinciding with the bundle center. Thus later on we use only the mounting the pipes on the sides of squares and on concentric circles with the center coinciding with the bundle center. To calculate number of pipes in a bundle the following algorithm is used. Equations of straight-lines parallel to axis x

$$(y_1 = \pm \frac{\sqrt{3}}{2} S_T i)$$

and lines inclined to the axis x at an angle of 60°

$$y_2 = x\sqrt{3} \pm iS_T \sqrt{3})$$

(Fig. 2) are solved jointly in rectangular coordinates x–y. Coordinates of points like $y_1 = y_2$ are found. Number of horizontal and inclined straight lines is chosen as the nearest to the integer number found by division

$$d_B / S_T \frac{\sqrt{3}}{2}$$

at a rounding off to the greater value. Amounts of pipes in a bundle will be equal to the number of points of crossings of straight lines for which the condition is satisfied

$$\sqrt{x^2 - y^2} \le R = \left(\frac{d_B}{2} - \frac{d_T}{2} - \delta_{\Phi 2} - \delta_n \right),$$

where δ_n – width of a gasket for installation of the bundle.

The search for the version providing the maximum output of the device is carried out by a net method which consists in calculating the criterion function for all points of the area of its existence with a certain step for arguments [2]. As target function the value of heat flow Q occurring in the apparatus is used. The area in which Q is calculated and the parameters of design are defined is set in the form of the equations

$$\alpha_1 = \alpha_{1\,max}, S_T \ge S_{T\,min}, d_T \ge d_{T\,min},$$

$$\Delta T_D \le \Delta T_{D\,max}, \quad (9)$$

$$w_b \le w_{b\,max}. \quad (10)$$

Since with increase in the agitator diameter the size of bundles decreases and their number increases the size of a heat exchange surface at the change in d_m should have an extremum. The algorithm of the search consists in the following. At increase with small step of value d_m/D in some range $d_m/D = 0.2$–0.7 the number of bundle n_B and bundle diameter d_B are calculated by equations (6)–(8). The designs are chosen where bundle are placed without a gap, and then the number of pipes in the bundle n_t is

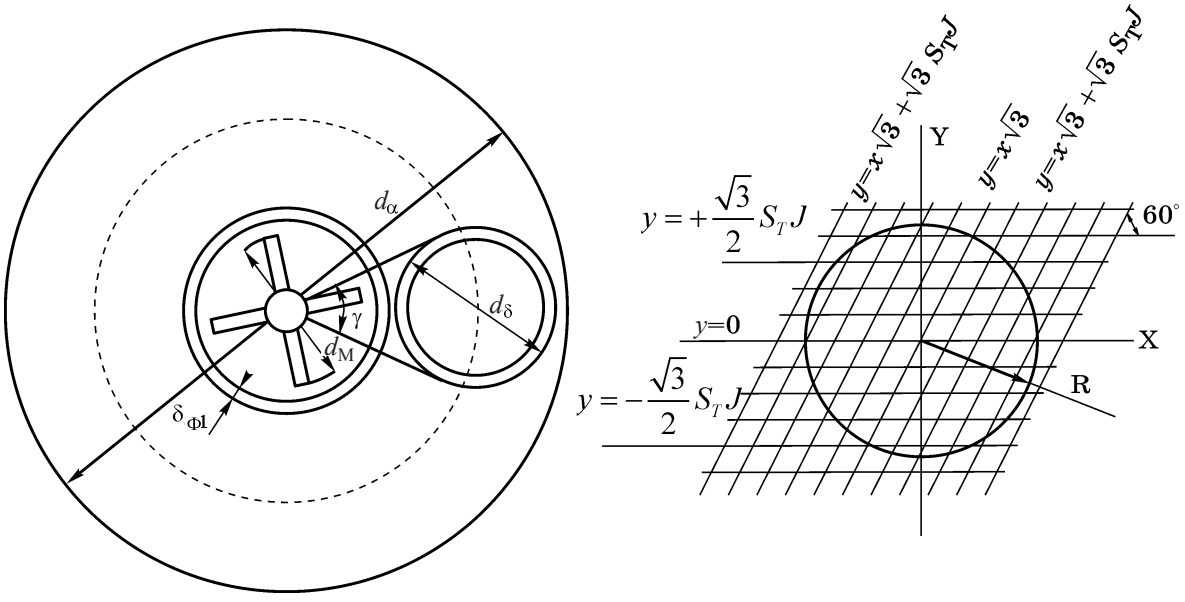


Fig. 2. Figures pertaining to the calculation of heat exchange devices.

calculated at a constriction and total number of pipes ($n_t = n_{tB}\ n_B$) is calculated. The heat exchange surface will begin as

$$F = \pi\, d_t h_t n_t$$

The constriction (10) defines for each value d_m/D the specific power which can be entered into the agitated volume

$$N_{max} = K_{N\rho}\, n^3_{max}\, d^5_m \qquad (11)$$

where n_{max} is maximum allowable frequency of rotation of an agitator, s^{-1}.

Definition for each version of size F and N_{max} allows the calculation of the heat flow.

$$Q = K_{max} F \Delta T_{Dmax},$$

$$K_{max} = \frac{1}{\frac{1}{\alpha_1} + \frac{\delta_{ST}}{\lambda_{ST}} + \frac{1}{\alpha_{2\,max}}}.$$

The equation (9) in which w_τ and w_r are estimated by an example with the greatest possible number of pipes is used. to define heat radiation coefficient α_2. Comparing Q obtained at various value d_m/D the alternative providing the maximum value of heat flow is found. Output of the apparatus is obtained from the equation

$$G_{max} = \frac{Q_{max}}{K_Q\ \ q_{ED}}.$$

If value of heat flow Q_{max} more than demanded under the conditions of the process, establishing optimum relations between α_1, α_2, F at which the minimum for designing and operation of the device is necessary. The calculations show, that the maximum heat release from the unit volume of the studied device can reach to 105 kWt/m^3.

REFERENCES

1. Verigin, A.N., Malyutin, S.A., and Shashikhin, E.Yu., *Khimiko-tekhnologicheskie agregaty. Sistemnyi analiz pri proektirovanii* (Chemico-Technological Units. System Analysis at Designing), St. Petersburg: Khimiya, 1996, 256 p.
2. Kutateladze, S.S., *Teploperedacha i gidrodinamicheskoe soprotivlenie* (Heat Transfer and Hydrodynamic Resistanse), Moscow, Energoatomizdat, 1990, 367 p.

ISSN 1070-4272, Russian Journal of Applied Chemistry, 2008, Vol. 81, No. 3, pp. 524–532. © Pleiades Publishing, Ltd., 2008.
Original Russian Text © N.A. Samoilov, I.A. Mnushkin, O.A. Mnushkina, 2008, published in Khimicheskaya Promyshlennost', 2008, Vol. 85, No. 1, pp. 19–29.

MODELING AND CALCULATION OF TECHNOLOGICAL PROCESSES

The Features of Reactive Plate Hydrodynamics of Reactive Fractionating Column for the Ethylene Glycol Manufacturing

N. A. Samoilov[a], I. A. Mnushkin[b], and O. A. Mnushkina[b]

[a]*Ufa State Oil Technical University, Ufa, Russia*
[b]*OOO "Peton," Ufa, Russia*

Received September 5, 2007

Abstract—On a fragment of a bubble-cap reactive plate in the water–air system by methods of pulse and step disturbance the features of liquid phase hydrodynamics of a reactive plate at a wide range of the liquid and gas flows were investigated. Modes of the feed input in the reaction zone and of cooling of the feed to suppress side reactions at the initial stage of ethylene oxide hydration are developed. Effect of processing modes on the chemistry of ethylene oxide hydration is considered.

DOI: 10.1134/S1070427208030415

Last years attention has grown to a development of reactive fractionating devices [1] combining executing of a chemical process with separation of reaction products that allows essential simplifying of the technological scheme of process and reduction of capital costs for design, and also optimization of process as a whole [2–8]. In [9–14] by simulation we studied in detail the features of chemical and fraction stages of the process proceeding in the reactive fractionating column for ethylene glycol manufacturing.

The most commonly used method of the ethylene glycol production is a direct hydration of ethylene oxide. Simultaneously with the target reaction side processes occur between glycols and ethylene oxide with formation of di-, tri-, and tetraethylene glycol. It was shown using simulation that for suppression of side reactions in the synthesis of ethylene glycol it should be executed at essential water excess in the reaction zone with water–ethylene oxide mole ratio of 60–90 : 1. Thus practically complete conversion of initial ethylene oxide in the reaction zone of the column where the phlegm from an overlying plate that represents practically pure water with insignificant content of organic contaminants (concentration of water in the phlegm is more than 0.9999 mol%) should mix up with the feed.

Calculating the column for the output of ethylene glycol 6.2 t/h in a wide range of the phlegm–ethylene oxide ratio and the column pressure (Table 1) it was shown that residence time of the reaction mixture on the real plate does not depend on phlegm–ethylene oxide ratio and drops with the column pressure rise owing to the decrease in the column diameter. Values of the column diameter in the field of the high pressures required for increase of temperature and acceleration of chemical process range from 2 to 4 m and that is quite feasible especially regarding the high reflux ratio ranging from 30 to 90. At temperatures 475-493 K for carrying out the reaction it is enough to have 1–3 real plates therefore the process is practically completely realized on single theoretical plate of the column.

One of the difficulties in the fractionating column operation is to set the nearby ideal mix condition for mixing the feed entered on the reactive plate with the downflowing phlegm. A good mixing of these flows should be provided otherwise on the reactive plate local streams of the feed with low water–ethylene oxide ratio will form thereby enhancing the side reactions within these streams with yield of side poly(ethylene) glycols that will move to a residuum without separation and decrease ethylene glycol concentration in the residuum. As a result the typical local feed on the plate is unsuitable.

Table 1. The phlegm : ethylene oxide ratio and pressure effects on the diameter of the reactive fractionating column

Column pressure	Specific vapor flow, kg/(m^2 h)	Column diameter (m) at the phlegm : ethylene oxide ratio				
		10:1	30:1	50:1	70:1	90:1
0.1	4345	2.30	3.98	5.13	6.07	6.89
0.5	8899	1.60	2.78	3.59	4.25	4.81
1.0	11925	1.38	2.40	3.10	3.67	4.16
1.5	14218	1.27	2.20	2.78	3.36	3.81
2.0	15962	1.20	2.07	2.68	3.17	3.59

The mixing of the feed with the phlegm should be performed stepwise putting in the feed to zones of intensive mix, e.g., in a downcomer or in an overflow section of the reaction plate (Fig. 1a, 1b), and also directly to the first row caps (Fig. 1b, 1c). In the first case the feed under the pressure may be sprayed over the surface of the phlegm downflowing through an overflow baffle (Fig. 1a) or put in through a perforated dispatch device to pressure layer of the phlegm in overflow section (Fig. 1b), also for better mixing swirlers on the dispatch devices may be used. At entering the feed directly to the plate this operation may be performed under pressure through a perforated collector over the plate width (Fig. 1c) or local feed may be provided to each cap of the first row in the zone of the vapor and liquid mixing (Fig. 1c).

Analysis of the mixing efficiency was done in the course of investigation of the process hydrodynamics on a laboratory setup simulating the first row caps operation of reactive plates in the water–air system. Ethylene glycol used as tracer has been entered either with pulse or stepped feed. Water flow was varied in the range of 0.06–0.18 m^3/h, and airflow, 0–2.4 m^3/h. In a bottom of the cap of 100 mm diameter there are openings in the form of equilateral triangle with side 10mm for uniform air bubbling. Air streams passing through the openings with equivalent diameter 5.6 mm in the liquid flow were broken to bubbles of various size which contacting with water could break further or flow together. Calculations by Todes method show that gas bubbles of diameter ranging 1–15 mm float to the water surface with speed 0.13–0.66 m/s. Time of bubble contact with water ranges from 0.34 to 0.06 s that is considerably higher than airflow speed under conditions of free skip (bypassing) across annular space around the cap of air consumption 0.42–2.4 m^3/h and airflow rate 0.021–0.093 m/s respectively. Thus on the laboratory setup air bubbling through the water is well-run without channeling effect.

The tracer was entered in the overflow device as well as in the air bubbling zone near the cap. Concentration of the tracer in the liquid flow at the outlet of bubbling zone defined with refractometry allows the displaying the functions of response of the system on the entered disturbance (tracer feeding). The obtained functions are qualitatively close to hydrodynamical model of ideal mixing (Fig. 3) and in the coordinates ln $C(\tau)$–(τ) the experimental points of these functions at presence of the bubbling well fit to a straight line, and the absence of air feeding on a plate there is a tracer delay leading to a deviation from the linearity revealing the diffusive character of the hydrodynamics (Fig. 3).

With approximation of the response functions obtained at the various regimes of operation by the method of static moments [16] we can calculate first and second static moments of the response function, its dispersion, number of cells of the ideal mixing appropriate for the examined construction, coefficient of longitudinal stirring in the liquid flow in the absence of the bubbling. The calculations showed (Table 3), that even at air flow about 1 m^3/h the liquid mixing near the cap corresponds to the cell of the ideal mixing, and at air flow 2.4 m^3/h this correspondence ranges 1.3–1.4 of the cells of the ideal mixing.

Important parameter for simulation of an industrial apparatus is water-air mole ratio in the cap examined experimentally in a wide range from tenth to hundreds (Table 3). It should be taken into account that if the number of caps in a front row of the plate is N_F, along the plate length is N_L (along the liquid flow), the vapor feed is G, mol/h, and the liquid flow is L, mol/h, then a

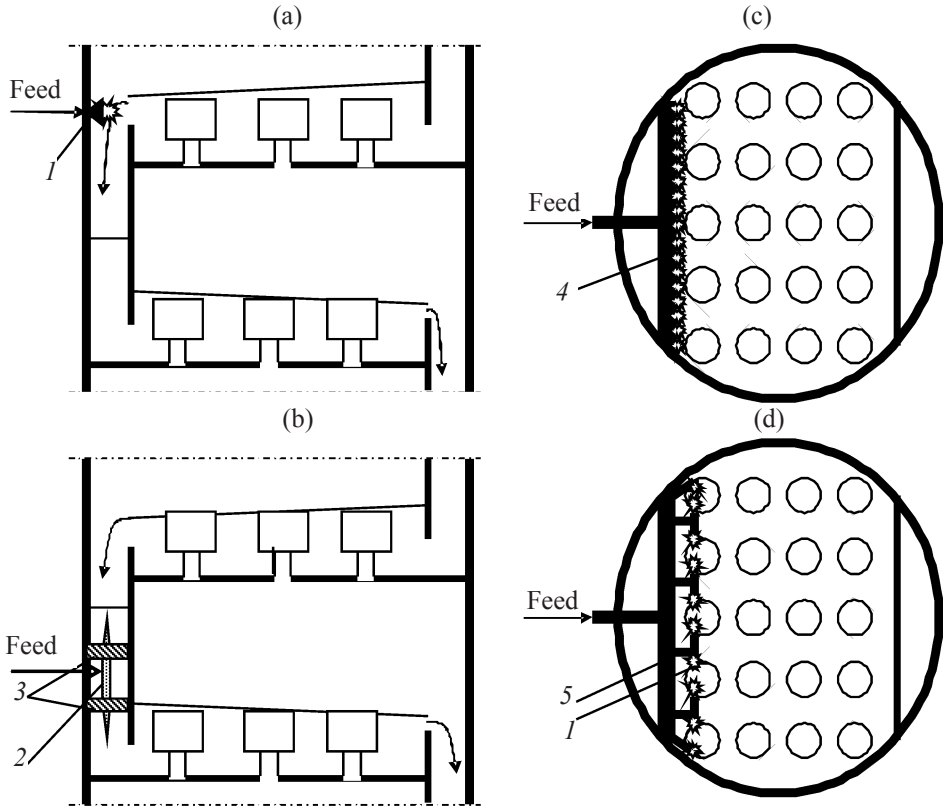


Fig. 1. Modes of the feeding on the reactive plate. (a) input of the feed over the phlegm surface; (b) input of the feed in the phlegm volume; (c) input of the feed through a perforated collector over the plate width; (d) local input of the feed directly to the caps. (*1*) Sprayer, (*2*) a distributing perforated device, (*3*) a swirler, (*4*) a pressure perforated collector, (*5*) a pressure collector.

load per a cap by vapor is $G/(N_F N_L)$, and by liquid, L/N_F. In the reactive fractionating column in the course of ethylene glycol production the vapor–liquid mole ratio is close to unity over the column section. Then the vapor–liquid mole ratio for the real plate (assuming that the caps are placed on the plate at inscribed rectangle) for a first row of the caps in a first approximation will be $(L N_L)/G$ close to N_L. Let us assume the cap diameter at 90 mm and inter-axis distance at 110 mm then for the above given data according to the column computation with output about 6.2 t/h (Table 1) we obtain, that the results of laboratory setup examined where the vapor–liquid mole ratio was in the range from 23.3 to 535.5 can be used also for estimating of the operation of

Table 2. Parameters of the air bubbling

Parameters	Diameter of the air bubbles, mm					
	15	10	5	3	2	1
Archimedes criterion	3.31×10^7	9.81×10^6	1.22×10^6	2.44×10^5	7.85×10^4	9.81×10^3
Reynolds criterion	9952.8	5393.2	1872.9	843.7	438.2	130.8
Float rate, m/s	0.663	0.539	0.374	0.281	0.219	0.131
Float time, s	6.7×10^{-2}	8.3×10^{-2}	12.0×10^{-2}	16.0×10^{-2}	20.5×10^{-2}	34.3×10^{-2}

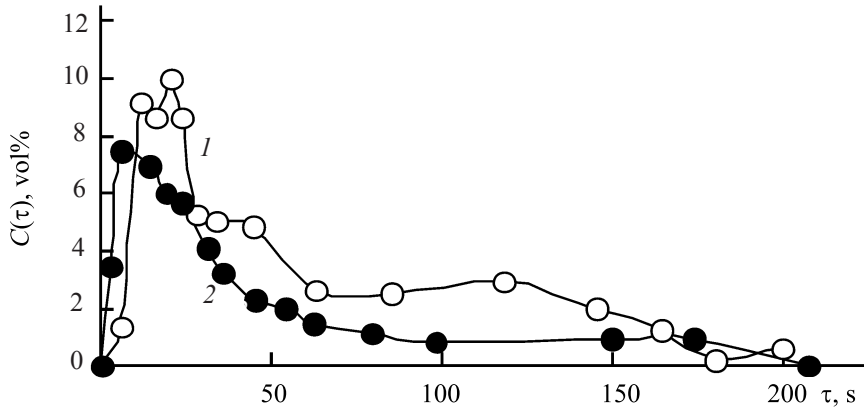


Fig. 2. The response function of the plate fragment (the change of the tracer concentration $C(\tau)$ over the time (τ) in response to the impulse disturbance put in the plate at the air flow (*1*) 0 m³/h, and (*2*) 2.4 m³/h and at the water flow 0.06 m³/h.

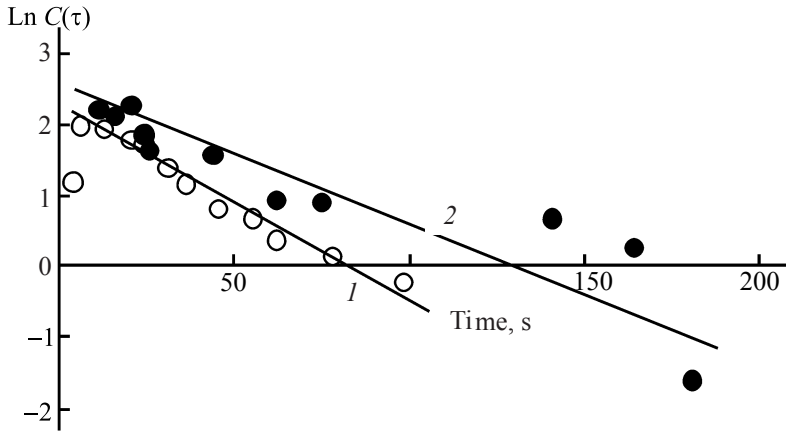


Fig. 3. The response function in the coordinates ln $C(\tau)$–(τ) in response to the impulse disturbance put in the plate at the air flow (*1*) 0 m³/h, and (*2*) 2.4 m³/h and at the water flow 0.06 m³/h.

contact device in industrial reactive fractionating column with the vapor–liquid mole ratio from 15 (columns of high pressure with low water–ethylene oxide ratio) to 90 (columns of low pressure with high water–ethylene oxide ratio) (Fig. 4). Note that the lower vapor–liquid mole ratio the higher mixing efficiency of raw material feed and the phlegm in the first row caps.

Calculation of the first static moment of the response functions of the system on an impulse disturbance appropriate for the average residence time of the tracer and respectively of the local streams in the liquid flow shows (Table 3) that the average residence time of the liquid in the mixing zone at the water flow 0.18 m³/h and the variable air flow is on average about a minute,

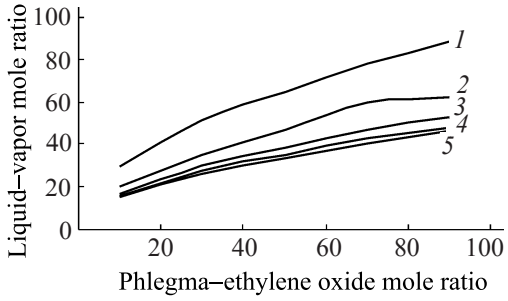


Fig. 4. Dependence of the liquid–vapor ratio of the reactive plate on the phlegm–ethylene oxide ratio for pressure (*1*) 0.1, (*2*) 0.5, (*3*) 1.0, (*4*) 1.5, and (*5*) 2.0 MPa.

Table 3. Hydrodynamic parameters of the air bubbling mixing on the bubble-cap plate

Tracer input	Flow, m^3/h		Water–air mole ratio	Static moments		Dispersion of the response function	Number of ideal mixing cells	Coefficient of longitudinal stirring, cm^2/s
	water	air		the first, s^2	the second, s^2			
In the air bubbling area near the cap	0.18	2.40	93.2	75.6	4342	0.759	1.31	
	0.18	1.80	123.9	44.9	1509	0.754	1.32	
	0.18	0.84	233.8	45.7	1897	0.908	1.10	
	0.18	0.42	535.5	63.3	5012	1.250	0.81	
	0.12	2.40	46.6	122.8	10379	0.687	1.45	
	0.06	2.40	23.8	119.5	7051	0.546	1.76	
	0.06	0	-	147.2	12269	0.566	–	12.91*
In the overflow device	0.18	2.40	93.2	63.0	3446	0.872	1.14	
	0.18	0	–	67.0	2361	0.525	–	62.20**

* The flow length from the input point of the tracer to the point of the sampling is 160 mm.
** The flow length from the input point of the tracer in the overflow device to the point of the sampling is 280 mm.

therewith main portion of the liquid passes the mixing zone in 10–15 s (Fig. 1). Testing the laboratory setup by the impulse disturbance (water flow was 0.18 m^3/h, air flow was 2.4 m^3/h) with input of the ethylene glycol tracer at 65 cm^3/min we took simultaneously 20 samples before cap of the water flow from four levels along the water flow height in five probe points of each level. The sampling was executed after 10 minutes of the tracer input to provide a steady state system. Computed mean tracer concentration in the flow at the outlet of the mixing zone should be 2.17 vol%. The experiment shows that actually at the outlet of the mixing zone averaging of concentrations does not occur (Fig. 5). Ethylene glycol concentration in water surface layer varied in the range 2.4–2.6 vol% and decreased across the water layer of the column, being 1.5–1.9 vol% near the bottom; therewith mean ethylene glycol concentration over 20 samples was 2.14 vol% and was close to the computed.

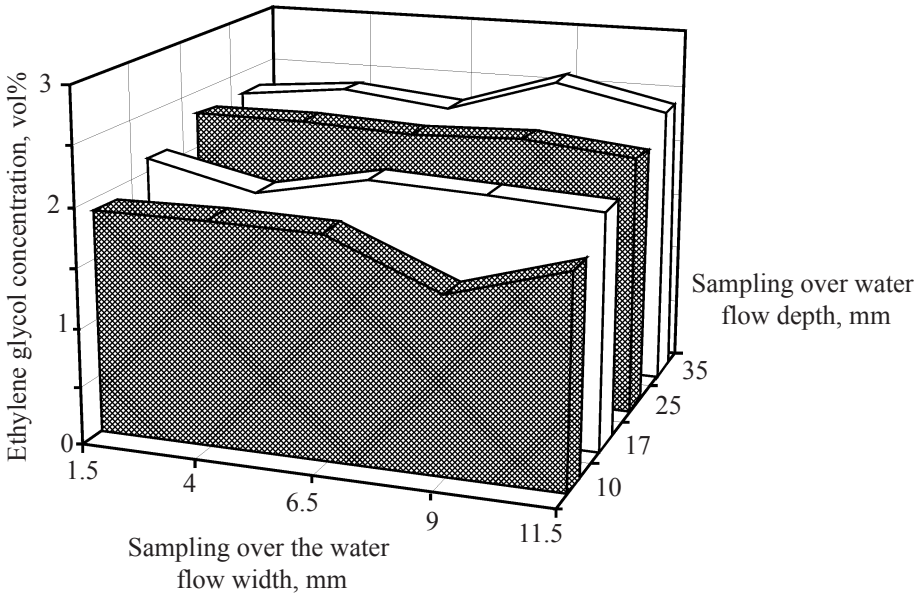


Fig. 5. Distribution of the tracer concentration over the normal section of the water flow on the laboratory setup.

With experimental data obtained we calculated kinetics of the ethylene oxide hydration taking into account the mixing of the raw material with the phlegm on the reactive plate. In the calculation we assumed that the conventional unit time of the mixing was the time of the mixing of two local streams of the equal volume therewith one of the streams contained, in part, raw components, and the second stream was phlegm. On the first unit time raw material fed as local stream of water and ethylene oxide in 1:1 ratio, at the last unit time we obtained a mixture of water and ethylene oxide in 66.5:1 ratio. For achieving such mixing of water and ethylene oxide six unit times of mixing are required. If the experimental average residence time of the flow in the mixing zone of the cap is 60 s then we set unit time of mixing equal to 10 s.

Mathematic modeling of kinetics of the hydration reaction of ethylene oxide regarding dynamics of real mixing of the feed with the phlegm shows that in initial stage ethylene oxide concentration considerably increases in comparison with the ideal mixing resulting

Table 4. The kinetic parameters of the ethylene oxide hydration on the reactive plate of the reactive fractionated column (pressure is 1.5 MPa, the phlegm–ethylene oxide ratio is 66.5 : 1)

Parameters	Theoretical plate	A plate with the mixing of the local streams		A plate with the mixing of the local streams and with cool feeding		
	Ethylene glycol concentration, mole fraction 10^2	concentration, mole fraction 10^2		temperature, K	concentration, mole fraction 10^2	
		water	ethylene glycol		water	ethylene glycol
Reaction time, min						
0.1	0.575	0.667	7.608	351.2	0.687	0.002397
0.2	0.923	0.782	9.121	393.9	0.791	0.06306
0.3	1.136	0.860	7.945	419.5	0.860	0.296
0.4	1.264	0.917	5.810	436.1	0.910	0.730
0.5	1.346	0.941	4.375	440.3	0.936	1.187
0.6	1.391	0.964	2.831	452.7	0.960	1.303
0.7	1.417	0.976	1.927	460.2	0.974	1.279
0.8	1.433	0.984	1.300	464.0	0.982	1.089
0.9	1.446	0.986	1.162	464.5	0.984	1.141
1.0	1.452	0.986	1.142	470.7	0.985	1.243
1.2	1.452	0.986	1.150	470.7	0.985	1.383
1.4	1.452	0.986	1.153	470.7	0.985	1.489
1.6	1.452	0.986	1.154	470.7	0.985	1.453
1.8	1.452	0.986	1.155	470.7	0.985	1.463
2.0	–	0.986	1.155	470.7	0.985	1.463
2.2	–	–	–	470.7	0.985	1.464
2.4	–	–	–	470.7	0.985	1.464

Table 4. (Contd.)

Feed content in the reaction start, mole fraction	Theoretic plate	Plate with the mixing of the local streams	Plate with the mixing of the local streams and with cool feeding
Ethylene glycol	0.015	0.5	0.5
Water	0.985	0.5	0.5
Feed temperature, K	470.7	470.7	300
Time for reaching the maximum output of ethylene glycol, min	1.95	1.98	2.55
Ethylene oxide concentration at the moment of the reaching maximum outout of ethylene glycol, mole fraction	1.2910"^{6}	1.49.10"^{6}	1.2610"^{6}
Time of practical reaction canceling, min	1.0	1.6	2.2
Ethylene glycol – higher glycols in the moment of reaching maximum output of ethylene glycol	80.43	6.29	50.74
Potential ethylene glycol content in the column residuum, mole fraction	0.9877	0.8629	0.9806

in a decrease in ethylene glycol output because of enhanced side reaction with giving diethylene glycol (Table 4, Fig. 6a), and adversely affects the column operation. The potential content of ethylene glycol in the residuum of reactive fractionating column falls to 0.826 mole fraction as compared with 0.9877 mole fraction expected at ideal mixing of the raw material and phlegm on the reactive plate.

For suppression of the side reaction it may be recommend feeding the raw material at low temperature (300–310 K, water–ethylene oxide mixture in 1:1 ratio) because at such temperatures ethylene oxide hydration does not occur. At mixing of the feed with the hot phlegm the feed temperature will raise with mixing and to the moment of the reaction start the water–ethylene oxide ratio will be sufficiently large to suppress the side reactions (Table 4, Fig. 6b).

One of the features of the chemistry of ethylene oxide hydration with significant water excess is maintenance of maximum concentration of ethylene glycol in the reaction mixture downflowing through the plate of the reactive fractionating column because in a point of achieving the maximum the ethylene oxide concentration is about 0.0001 of ethylene glycol concentration, and the side reactions do not practically proceed.

CONCLUSIONS

1. Structure of the flows on the laboratory fragment of the reactive plates by pulse and step disturbance was studied. The character and parameters of hydrodynamic models of the liquid phase flow were established.
2. It was shown that the regime of ideal mixing is provided in the operation zone of the first row caps.
3. The methods of feeding on the reactive plate to avoid the effects of side reactions on chemical nature of process were suggested.
4. Cold feeding on the reactive plate to suppress the ethylene oxide hydration in the local streams at the mixing the feed with phlegm on the initial stage of reactive plate operation was confirmed.

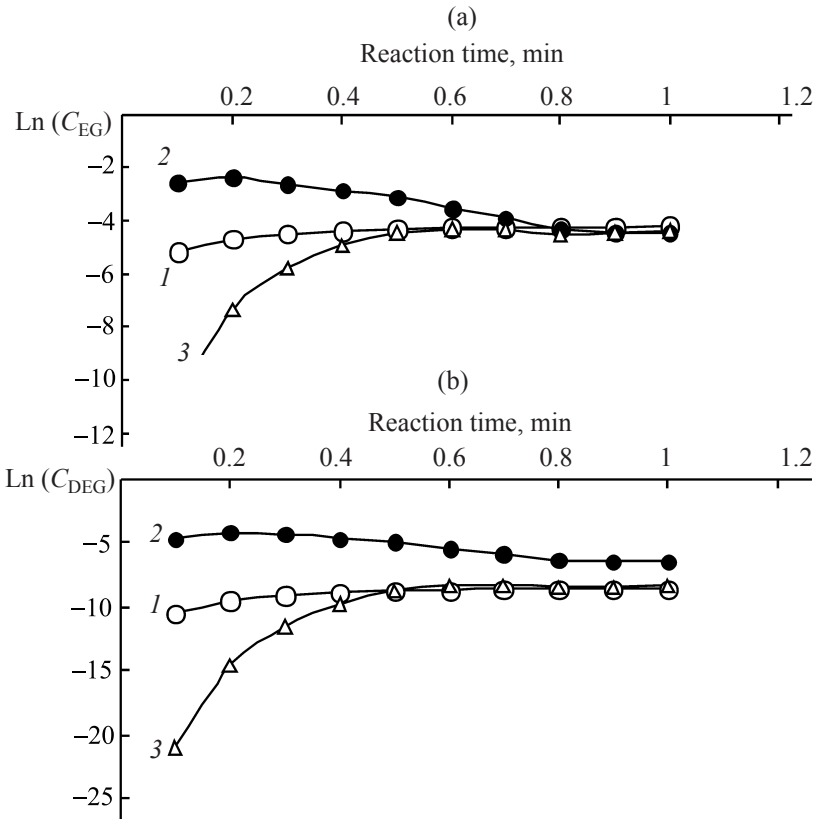


Fig. 6. Dependence of logarithm of the ethylene glycol (a) and diethylene glycol (b) concentration in the reactive mixture on the reaction time with the various flow structure of the liquid phase on the reactive plate. (*1*) The ideal mixing of the feed with the phlegm near the plate entrance at the temperature 470 K; (*2*) the real mixing of the feed with the phlegm on the plate at the feed and phlegm temperature 470 K; (*3*) the real mixing of the feed with the phlegm on the plate at the temperature of the feed near the plate entrance 300 K and of the phlegm 470.7 K.

REFERENCES

1. Astarita, Dzh., *Massoperedacha s khimicheskoi reaktsiei* (Mass Transfer with Chemical Reaction), Leningrad: Khimiya, 1978, 223 p.
2. Katalov, A.I., *Teor. Osnovy Khim. Tekhnol*., 1985, no. 3, pp. 308–310.
3. Komissarov, Yu.A., Gordeev, L.S, and Vent, D.P., *Nauchnye osnovy protsessov rektifikatsii* (Scientific Bases of Rectification), vols. 1, 2, Moscow: Khimiya, 2004.
4. Okasinski, M.J. and Doberty, M.F., *Ind. Eng. Chem. Research*, 1998, pp. 2821–2836.
5. Buzad, G. and Doherty, M.F., *Computers Chem. Eng*., 1995, pp. 395–412.
6. Venkataraman, S., Chan, W.K., and Boston, J., *Chem. Eng. Progress*, 1990, no. 8, pp. 45–53.
5. Chang, Y.A. and Seader, J.D., *Computers Chem. Eng*., 1988, no. 12, pp 1243–1257.
6. Cardoso, M.F., Salcedo, R.L., Feyo de Azevedo, S. *et al., Chem. Eng. Sci.*, 2000, vol. 55, p. 5059–5078.
7. Samoilov, N.A., Mnushkin, I. A., and Mnushkina, O.I., *Khim. Promyshlennost',* 2006, no. 1, pp. 1–7.
8. Samoilov, N.A., Mnushkin, I.A., and Mnushkina, O.I., Abstracts of Papers, *XVII International Conference on Chemical Reactors "CHEMREACTOR-17"*, 2006, Athene, pp. 694–697.
9. Samoilov, N.A., Mnushkin, I.A., and Mnushkina, O.I., Abstracts of Papers, *Konf. "Perspektivy razvitiya khimicheskoi pererabotki goryuchikh iskopaemykh (KhGPI-2006)"* (Conf. on Prospects of Chemical Treatment of the Fossil Fuel), 2006, St. Petersburg, p. 294.
10. Samoilov, N.A., Mnushkin, I.A., and Mnushkina, O.I., Abstracts of Papers, *Vserossiiskaya nauchn. konf, "Pererabotka uglevodorodnogo syr'ya. Kompleksnye, resheniya* (Levinterskie chteniya)", Russian Sci. Conf. "Treatment of Hydrocarbon Raw. Complex Desicions), 2006, Samara., 2006, pp. 136–137.
13. Samoilov, N.A., Mnushkin, I.A., and Mnushkina, O.I.,

Abstracts of Papers, *Vserossiiskaya nauchn. konf, "Pererabotka uglevodorodnogo syr'ya. Kompleksnye, resheniya* (Levinterskie chteniya)", Russian Sci. Conf. "Treatment of Hydrocarbon Raw. Complex Decisions), 2006, Samara, 2006, pp. 152–153..

14. Samoilov, N.A., Mnushkin, I.A., and Mnushkina, O.I., *III Vseross. nauchn. konf. Teoriya i praktika masoobmennykh protsessov khimicheskoi tekhnologii* (3rd Russian Conf. on Theory and Practice of Mass Change in Chemical Technology), 2006, Ufa, 2006, pp. 8–9.
15. Skoblo, A.I., Tregubova, I.A., and Molokanov, Yu.K., Protsessy i apparaty neftepererabatyvayushchei i neftekhimicheskoi promyshlennosti (Processes and Divices of Oil Processing and Oil Chemical Industry), Moscow: Gos. Toptekhizdat, 1982, 584 p.
16. Kafarov, V.V., *Metody kibernetiki v khimii i khimicheskoi tekhnologii* (Cybernetics in the Chemistry and Chemical Technology), Moscow: Khimiya, 1976, 463 p.
17. *Kolonnye apparaty. Katalog* (Column. Catalogue), Moscow: Tsintikhimneftemash, 1978, 31 p.

ISSN 1070-4272, Russian Journal of Applied Chemistry, 2008, Vol. 81, No. 3, pp. 533–541. © Pleiades Publishing, Ltd., 2008.
Original Russian Text © N.A. Gazizulin, 2008, published in Khimicheskaya Promyshlennost', 2008, Vol. 85, No. 1, pp. 30–38.

MODELING AND CALCULATION OF TECHNOLOGICAL PROCESSES

Heat Exchange in Apparatus with a Blade Agitator

N. A. Gazizulin

Kazan State Technological University, Kazan, Russia

Received June 2, 2007

Abstract—Three-dimensional model of a convective heat exchange in the apparatus with two blade agitators equipped with an outside heating device was formulated using the equations of laminar motion of viscous fluid and of energy. The Arrhenius–Frenkel–Eyring equation was used to account for the temperature dependence on the fluid viscosity. A numerical computations of the fields of velocity, pressure, and temperature were performed with algorithm Simple. The results were presented as isotherms in the meridional, and in the horizontal sections of apparatus.

DOI: 10.1134/S1070427208030427

Study of heat exchange in apparatus with an agitator is of interest both for finding theoretical dependencies describing the change of a temperature field over the volume of the apparatus and in connection with wide range of the technological application of heat exchanger. In the present work attempts on numerical computation of convective heat exchange in the apparatus with the two blade agitators under the condition of laminar motion of viscous fluid were done.

STATEMENT OF A PROBLEM

In regard to the fixed frame of reference the equations of continuity dynamics in terms of stress, energy, and continuity will read (in vector form) [1]

$$\rho \frac{\partial \bar{v}}{\partial t} + \rho(\bar{v} \quad \nabla)\bar{v} = \nabla P, \tag{1}$$

$$\frac{\partial T}{\partial t} + \bar{v} \quad \nabla T = a\nabla^2 T, \tag{2}$$

$$\nabla \bar{v} \quad = 0. \tag{3}$$

For viscous fluid taking into account general Newton's law $P = -pE + 2\mu D$ and according to rules of the actions with operator ∇ [2] equation (1) is reduced to:

$$\rho \frac{\partial \bar{v}}{\partial t} + \rho(\bar{v} \quad \nabla)\bar{v} = -\nabla p + \mu\nabla^2 \bar{v} + \quad 2D \quad \nabla\eta\,. \tag{4}$$

Assuming constant viscosity the last item in right side of the equation (4) is eliminated, and equation (4) simplifies to Navier–Stokes equation. The numerical computation by the equation (4) is connected with the feature of the viscosity change over the fluid volume. The fluid viscosity variation versus temperature is taken into account. To describe temperature dependence on the coefficient of the fluid dynamic viscosity the Arrhenius–Frenkel–Eyring equation is used [3].

$$\mu(T) = \mu(T_0)\exp\left[\frac{E_a}{R}\left(\frac{1}{T} - \frac{1}{T_0}\right)\right].$$

Introducing the cylindrical system of coordinates r, φ, z the projects of the velocity vector within the system are *u, v, w,* respectively. The fluid free surface is regarded as the surface of rotation. The basis in a space connected with a current point on the free surface and consisting of a vector of a normal is

$$\bar{n} = \left\{-\frac{dh}{dr}; 0; 1\right\}$$

and of tangents to this surface of vectors is also regarded

$$\bar{\tau}_1 = \left\{1; 0; \frac{\mathrm{d}h}{\mathrm{d}r}\right\}, \quad \bar{\tau}_2 = \{0; 1; 0\}.$$

Boundary conditions for the velocity on solid walls are reduced to the conditions of zero convective flow

and of attaching the fluid. Thus, at the bottom and at the sidewall

$$u = 0,\ v = 0,\ w = 0, \tag{5}$$

and at the surface of shaft, and of agitator, respectively

$$u = 0,\ v = wr,\ w = 0. \tag{6}$$

Boundary conditions on the free fluid surface include kinematic and dynamic conditions. The kinematic condition represents an equality to zero of a projection of a velocity vector onto a normal to the surface:

$$u\,\frac{\mathrm{d}h}{\mathrm{d}r} - w = 0 \tag{7}$$

Dynamic condition corresponds to the balance of stress tensors applied to both sides of the surface. Since curvature radius of the free surface is sufficiently large evidently the surface tension force is neglected. Therefore dynamic condition is [4]:

$$\overline{n}\quad P = -p_0\,\overline{n}\quad \mathrm{E}. \tag{8}$$

Projections of the vector equation (8) onto directions of the basis vectors represent three dynamic conditions in the coordinate form

$$(p_{zz} - p_{rr})\frac{dh}{dr} + \left[1 - \left(\frac{dh}{dr}\right)^2\right]p_{zr} = 0, \tag{9}$$

$$p_{z\varphi} - p_{\varphi r}\,\frac{dh}{dr} = 0, \tag{10}$$

$$(p_{rr} + p_0)\left(\frac{dh}{dr}\right)^2 - 2p_{zr}\,\frac{dh}{dr} + p_{zz} + p_0 = 0. \tag{11}$$

Examining the boundary condition for temperature we assume that the heat exchange in the device is steady. Let the cylindrical wall and the bottom of the apparatus are equipped with outside heating elements which maintain constant temperature T_1. Then on the cylindrical sidewall and on the bottom there boundary condition of the first type will be valid.

$$T = T_1 \tag{12}$$

Simultaneous heating and cooling of the fluid in the apparatus is not necessary to maintain the steady-state process. The fluid cooling may occur through the agitator, the shaft, and also through the fluid free surface. Boundary condition of the third type is determined by the law of heat exchange between a free surface and surroundings [5]:

$$\alpha(T - T_0) = -\lambda\,\frac{\partial T_{\mathrm{liq}}}{\partial n}, \tag{13}$$

According to this law amount of heat removed from fluid surface in the surroundings originating from the heat radiation has to be equal to the amount of heat input to the surface from the fluid by heat conductivity.

Let the boundary condition on boundary of the shaft and of the surroundings is $T = T_{\mathrm{Q}}$, and on the surface of the agitator and that of shaft there are so-called conditions of interface

$$T_{\mathrm{as}} = T_{\mathrm{liq}},\quad -\lambda_{\mathrm{as}}\,\frac{\partial T_{\mathrm{as}}}{\partial n} = -\lambda_{\mathrm{liq}}\,\frac{\partial T_{\mathrm{liq}}}{\partial n}, \tag{14}$$

that meet to physical requirements of continuity of the temperature and of the heat flow on the solid body–fluid interface (here n is a normal to a solid surface). An interface problem of two media heat exchange is solved basing on the allowed conditions. Evidently distribution of temperature inside the shaft and the agitator is described by the heat conductivity equation.

$$\nabla^2 T = 0. \tag{15}$$

If it is assumed that the rotation axis of the shaft and the agitator coincide with the rotation axis of the flow then on the rotation axis the following conditions are valid:

$$u = 0,\ v = 0,\ \frac{\partial w}{\partial z} = 0,\ \frac{\partial T}{\partial z} = 0. \tag{16}$$

BASIC RELATIONSHIPS

Since position of the free fluid surface is not known and demands definition during the solution of the problem the representation of the physical area (area of current) on the computing area with the known boundary is useful. For that overall physical area divided into bottom and top zones by a plane lying on the top of the agitator surface. Dimensionless coordinates and functions are introduced

$$t^* = \frac{Ut}{L},\quad r^* = \frac{r}{L},\quad \varphi^* = \varphi,$$

$$z^* = \begin{cases} \dfrac{z}{L}, z \le H_{\mathrm{a}} + h_{\mathrm{a}} \\ \dfrac{z - H_{\mathrm{a}} - h_{\mathrm{a}}}{h},\ z > H_{\mathrm{a}} + h_{\mathrm{a}} \end{cases},$$

$$\bar{v}^* = \frac{\bar{v}}{U}, \quad \bar{p}^* = \frac{p - p_0}{\rho U^2}, \quad \theta = \frac{T - T_0}{T_1 - T_0}. \qquad (17)$$

An agitator diameter and the agitator speed at the rim are chosen as characteristic length (L) and characteristic velocity of flow (U), respectively. A transformation (17) allows the displaying of the fluid surface in the physical area on a horizontal plane in the computing area.

As a result of transformation of coordinates the equations (2)–(4) are reduced to a dimensionless form in each of the zones of the computing area. However the continuity equation keeps the same form $\nabla\bar{V} = 0$. according to which projection U, V, W of the velocity vector in the computing area are defined in the bottom zone as follows:

$$U = u^*, \; V = v^*, \; W = w^*,$$

and in the top zone as

$$U = h^* u^*, \quad V = h^* v^*,$$
$$W = -u^* z^* \frac{dh^*}{dr^*} + w^*.$$

Here $h^* = h/L$, and u^*, v, w^* are components of the velocity vector in dimensionless physical area which is expressed by the following transformation

Three equations in the coordinate form according to the equation of motion (4) in the computing area are written as a common transport equation.

$$\frac{\partial \Phi}{\partial t^*} + \frac{1}{\gamma r^*}\frac{\partial}{\partial r^*}\left(r^* U\Phi\right) + \frac{1}{\gamma r^*}\frac{\partial}{\partial \varphi^*}(V\Phi)$$
$$+ \frac{1}{\gamma}\frac{\partial}{\partial z^*}(W\Phi) - \frac{1}{r^*}\frac{\partial}{\partial r^*}\left(\Gamma r^* \frac{\partial \Phi}{\partial r^*}\right)$$
$$- \frac{1}{r^*}\frac{\partial}{\partial \varphi^*}\left(\Gamma \frac{1}{r^*}\frac{\partial \Phi}{\partial \varphi^*}\right) - \frac{1}{\gamma^2}\frac{\partial}{\partial z^*}\left(\Gamma \frac{\partial \Phi}{\partial z^*}\right) = S_\Phi \qquad (18)$$

where $\Gamma = (\mu/(\pi\mu_0 \mathrm{Re}_c)$, $\gamma = 1$ for the bottom zone and $\gamma = h^*$ for the top zones, S_Φ is the term like source which is appropriate for the target function Φ.

The heat energy equation (2) in the dimensionless form is also reduced to Eq. (18), where $\Gamma = 1/(\pi \mathrm{Re}_c \mathrm{Pr})$.

In the bottom zone of the computed area the source items of Eq. (8) are defined by the following relations

$$S_{u^*} = -\frac{\partial p^*}{\partial r^*} + \frac{v^{*2}}{r^*} - \Gamma\frac{2}{r^{*2}}\frac{\partial v^*}{\partial \varphi^*} - \mathrm{X}_{u^*}$$
$$+ (2D \;\; \nabla\Gamma)_{r^*},$$
$$S_{r^* v^*} = -\frac{\partial p^*}{\partial \varphi^*} + \Gamma\frac{2}{r^*}\frac{\partial u^*}{\partial \varphi^*}$$
$$- \Gamma\frac{2}{r^*}\frac{\partial}{\partial r^*}\left(r^* v^*\right) - \mathrm{X}_{r^* v^*} + (2D \;\; \nabla\Gamma)_{\varphi^*},$$
$$S_{w^*} = -\frac{\partial p^*}{\partial z^*} - \mathrm{X}_{w^*} + (2D \;\; \nabla\Gamma)_{z^*}, \quad S_\theta = 0,$$

and in the top zone

$$S_{u^*} = -\frac{\partial p^*}{\partial r^*} + \frac{z^*}{h^*}\frac{dh^*}{dr^*}\frac{\partial p^*}{\partial z^*} + \frac{v^{*2}}{r^*} + \Gamma\left(\frac{1}{\mathrm{h}^*}\frac{\mathrm{dh}^*}{\mathrm{dr}^*}\right)^2 \mathrm{z}^*\frac{\partial}{\partial \mathrm{z}^*}\left(\mathrm{z}^*\frac{\partial \mathrm{u}^*}{\partial \mathrm{z}^*}\right)$$
$$- \frac{\Gamma}{r^{*2}}\left(u^* + 2\frac{\partial v^*}{\partial \varphi^*}\right) - \frac{\Gamma z^*}{r^*}\frac{\partial}{\partial r^*}\left(\frac{r^*}{h^*}\frac{dh^*}{dr^*}\frac{\partial u^*}{\partial z^*}\right) - \frac{\Gamma z^*}{h^*}\frac{dh^*}{dr^*}\frac{\partial^2 u^*}{\partial r^* \partial z^*} - -\mathrm{X}_{u^*} + (2\;D\;\nabla\Gamma)_{r^*},$$
$$S_{r^* v^*} = -\frac{\partial p^*}{\partial \varphi^*} + \frac{2\Gamma}{r^*}\frac{\partial \mathrm{u}^*}{\partial \varphi^*} + \Gamma z^*\left(\frac{1}{h^*}\frac{dh^*}{dr^*}\right)^2 \frac{\partial}{\partial z^*}\left[z^*\frac{\partial}{\partial z^*}\left(r^* v^*\right)\right]$$
$$+ \frac{2\Gamma z^*}{h^* r^*}\frac{dh^*}{dr^*}\frac{\partial}{\partial \mathrm{z}^*}\left(r^* v^*\right) - \frac{\Gamma z^*}{r^*}\frac{\partial}{\partial r^*}\left[\frac{r^*}{h^*}\frac{dh^*}{dr^*}\frac{\partial}{\partial z^*}\left(r^* v^*\right)\right]$$
$$- \frac{\Gamma z^*}{h^*}\frac{dh^*}{dr^*}\frac{\partial^2}{\partial r^* \partial z^*}\left(r^* v^*\right) - \frac{2\Gamma}{r^*}\frac{\partial}{\partial r^*}\left(r^* v^*\right) - \mathrm{X}_{r^* v^*} + (2D\;\nabla\Gamma)_{\varphi^*},$$
$$S_{w^*} = -\frac{1}{h^*}\frac{\partial p^*}{\partial z^*} + \Gamma z^*\left(\frac{1}{h^*}\frac{dh^*}{dr^*}\right)^2 \frac{\partial}{\partial z^*}\left(\mathrm{z}^*\frac{\partial w^*}{\partial z^*}\right) - \frac{\Gamma z^*}{h^*}\frac{dh^*}{dr^*}\frac{\partial^2 w^*}{\partial r^* \partial z^*}$$

$$-\frac{\Gamma z^*}{r^*}\frac{\partial}{\partial r^*}\left(\frac{r^*}{h^*}\frac{dh^*}{dr^*}\frac{\partial w^*}{\partial r^*}\right)-\mathrm{X}_{w^*}+(2D\cdot\nabla\Gamma)_{z^*},$$

$$S_\theta=\Gamma\frac{z^*}{h^{*2}}\left(\frac{dh^*}{dr^*}\right)^2\frac{\partial}{\partial z^*}\left(z^*\frac{\partial\theta}{\partial z^*}\right)-\Gamma\frac{z^*}{r^*}\frac{\partial}{\partial r^*}\left(\frac{r^*}{h^*}\frac{dh^*}{dr^*}\frac{\partial\theta}{\partial z^*}\right)-\Gamma\frac{z^*}{h^*}\frac{dh^*}{dr^*}\frac{\partial^2\theta}{\partial r^*\partial z^*},$$

where X_Φ is appropriate for the target function Φ and is described as

$$\mathrm{X}_\Phi=\frac{\partial\Phi}{\partial r^*}\frac{\partial\Gamma}{\partial r^*}+\frac{1}{r^{*2}}\frac{\partial\Phi}{\partial\varphi^*}\frac{\partial\Gamma}{\partial\varphi^*}+\frac{1}{\gamma^2}\frac{\partial\Phi}{\partial z^*}\frac{\partial\Gamma}{\partial z^*},$$

and the last items represent components of the vector 2D $\nabla\Gamma$.

The heat conductivity equation (15) in the dimensionless form is written as

$$\frac{1}{r^*}\frac{\partial}{\partial r^*}\left(r^*\frac{\partial\theta}{\partial r^*}\right)+\frac{1}{r^{*2}}\frac{\partial^2\theta}{\partial\varphi^{*2}}+\frac{1}{h_{as}^{*2}}\frac{\partial^2\theta}{\partial z^{*2}}=0, \quad (19)$$

where $h_{as}^* = h^*(r_{as}^*)$.

In the computing area the form of the boundary conditions (5), (6), and (16) is kept but the second of the conditions (6) acquires following appearance. $v^* = 2r^*$, and the boundary conditions (7), (9) – (11) respectively are reduces to

$$u^*\frac{dh^*}{dr^*}-w^*=0, \quad (20)$$

$$\frac{1}{h^*}\left[1+\left(\frac{dh^*}{dr^*}\right)^2\right]\left(\frac{\partial u^*}{\partial z^*}+\frac{dh^*}{dr^*}\frac{\partial w^*}{\partial z^*}\right)+\left[1-\left(\frac{dh^*}{dr^*}\right)^2\right]\frac{\partial w^*}{\partial r^*}-2\frac{dh^*}{dr^*}\frac{\partial u^*}{\partial r^*}=0, \quad (21)$$

$$\left[1+\left(\frac{dh^*}{dr^*}\right)^2\right]\frac{1}{h^*}\frac{\partial v^*}{\partial z^*}+\left(\frac{v^*}{r^*}-\frac{\partial v^*}{\partial r^*}-\frac{1}{r^*}\frac{\partial u^*}{\partial\varphi^*}\right)\frac{dh^*}{dr^*}+\frac{1}{r^*}\frac{\partial w^*}{\partial\varphi^*}=0, \quad (22)$$

$$\left[1+\left(\frac{dh^*}{dr^*}\right)^2\right]\left[p^*\,Re_c+\frac{2}{h^*}\left(\frac{dh^*}{dr^*}\frac{\partial u^*}{\partial z^*}+\frac{\partial w^*}{\partial z^*}\right)\right]-2\frac{dh^*}{dr^*}\left(\frac{dh^*}{dr^*}\frac{\partial u^*}{\partial r^*}-\frac{\partial w^*}{\partial r^*}\right)=0. \quad (23)$$

As regards the boundary conditions for temperature (12)–(14) in the computing area,

$$\theta=1, \quad (24)$$

$$\left(z^*\frac{dh^*}{dr^*}\cos\beta_1-\cos\beta_2\right)\frac{1}{h^*}\frac{\partial\theta}{\partial z^*}-\cos\beta_1\frac{\partial\theta}{\partial r^*}=\theta Nu, \quad (25)$$

$$\theta_{as}=\theta_{liq},\quad \lambda_{liq}\frac{\partial\theta_{as}}{\partial n}=\lambda_{liq}\frac{\partial\theta_{liq}}{\partial n}, \quad (26)$$

where $\cos\beta_1$ and $\cos\beta_2$ are directional cosines of the vector of the normal to the fluid free surface.

The theory of the central vortex formation in apparatus with an agitator according to which the vortex surface equilibrium condition expressed as [6]

$$\frac{dh}{dr}=\frac{v^2}{gr},$$

and in the dimensionless physical area looking like

$$\frac{dh^*}{dr^*}=\pi^2 Fr_c\frac{v^{*2}}{r^*}. \quad (27)$$

is used for calculation of the form of the fluid free surface.

An algorithm for solving the equation (27) is accurately described in [7] and yields

$$h^*\left(r^*\right) = \pi^2 Fr_c \int_{r_s^* + \Delta r^*}^{r^*} \frac{v^{*2}}{r} dr + h^*\left(r_a^* + \Delta r^*\right),$$

$$h^*\left(r_s^* + \Delta r^*\right) = \frac{1}{\left(r_{app}^* - \Delta r^*\right)^2 - \Delta r^{*2}} \quad (28)$$

$$\times \left[\left(h_0^* \; r_{app}^{*2} - r_a^{*2}\right) - \left(2\, r_{app}^* - \Delta r^*\right)\Delta r^* h^* \left(r_{app}^*\right)\right.$$

$$\left. -2\pi^2 \, Fr_c \int_{r_s^* + \Delta r^*}^{r_{app}^* - \Delta r^*} r^* dr^* \int_{r_s^* + \Delta r^*}^{r^*} \frac{v^{*2}}{r} dr \right]. \quad (29)$$

ALGORITHM OF CALCULATION

Numerical modeling of the flow and the heat exchange in the computing area was made by a method of control volume [8, 9] based on representation of the considered equation in integrated form. The conservatism of this method is one of its most important advantages, in other words it provides exact integrated performance of the conservation principles for overall computing area.

Let the planes divide the computing area into the control volumes (spatial meshes) and on each of the planes only one of coordinates with the constant value occurs. Let node points are placed so that each of them is in the separate mesh and the mesh sides are in the middle of the adjacent node meshes. Such arrangement of the mesh sides provides sufficiently high accuracy of the heat flow calculation through the side [9].

Placement of all node functions in the same node points leads to additional computing difficulties, namely, it results in appearance of the oscillation in a solution in particular for the pressure. Therefore the moved or so-called chess grid is chosen [10] where the node points of the velocity component are displaced on a half step in proper directions towards the main points in which the pressure and the temperature are defined. As a result the node points for velocity components are on the appropriate sides of the main control volumes for the temperature and for the pressure. Thus there are four sets of control volumes for all node functions.

Calculation of the flow and the heat exchange is done on basis of algorithm SIMPLE [9] in which the equation digitization according to the control volume method on the moved grids is used. Realization of algorithm SIMPLE originally intended just for the solution of the Navier–Stokes equation seems more effective in pseudo-non-stationary statement [11]. Hence we shall integrate the common equation (18) over the control volume ΔQ and over the time interval Δt^*. Then we shall obtain the conservation principles for Φ in the integrated form

$$\iiint_{\Delta\Omega} \int_{t^*}^{t^* + \Delta t^*} \left[\frac{\partial \Phi}{\partial t^*} + \frac{1}{\gamma r^*}\frac{\partial}{\partial r^*}\left(r^* U\Phi\right)\right.$$

$$+ \frac{1}{\gamma r^*}\frac{\partial}{\partial \varphi^*}\left(V\Phi\right) + \frac{1}{\gamma}\frac{\partial}{\partial z^*}\left(W\Phi\right)$$

$$- \frac{\Gamma}{r^*}\frac{\partial}{\partial r^*}\left(r^* \frac{\partial \Phi}{\partial r^*}\right) - \frac{\Gamma}{r^*}\frac{\partial}{\partial \varphi^*}\left(\frac{1}{r^*}\frac{\partial \Phi}{\partial \varphi^*}\right)$$

$$\left. - \frac{\Gamma}{\gamma^2}\frac{\partial}{\partial z^*}\left(\frac{\partial \Phi}{\partial z^*}\right) - S_\Phi\right] dt^* dV = 0. \quad (30)$$

Thus solution is obtained by advance over the time from some given initial distribution of the target function Φ. Since the problem is stationary the time plays role of the relaxation parameter under these conditions. An implicit scheme is used for approximation of the convective and diffusive items in the equation (30) according to which the node function Φ within the limits of the overall time step Δt^* is characterized by new value Φ^1 which is appropriate to the following time $\Delta t + \Delta t^*$. Then discrete differential analog of the equation (30) is written as

$$\frac{\Delta V}{\Delta t^*}\Phi_P^1 + \Delta\varphi^* \Delta z^* \left[r^* \left(\frac{U\Phi^1}{\gamma_P} - \Gamma\frac{\partial \Phi^1}{\partial r^*}\right)\right]_w^e$$

$$+ \Delta r^* \Delta z^* \left(\frac{V\Phi^1}{\gamma_P} - \frac{\Gamma}{r^*}\frac{\partial \Phi^1}{\partial \varphi^*}\right)_s^n$$

$$+ \frac{r_P^* \Delta r^* \Delta \varphi^*}{\gamma_P}\left(W\Phi^1 - \frac{\Gamma}{\gamma_P}\frac{\partial \Phi^1}{\partial z^*}\right)_l^u$$

$$= \Delta V\left(S_P + \frac{\Phi_P^0}{\Delta t^*}\right), \quad (31)$$

where ΔV is the mesh volume, S_p is a node value of the source item, and Φ^0 is the value of Φ at the time t^*.

The way of calculation of the target function Φ on the sides *w, e, s, n, I, u* of the cells in the equation (31) is defined by the difference scheme according to which difference approximation of the convective items of this equation occurs. The combined scheme representing a combination of the midmost difference and countercurrent schemes is used [9]. This results in the following equation

$$a_P \Phi_P^1 = a_W \Phi_W^1 + a_E \Phi_E^1 + a_S \Phi_S^1 + a_N \Phi_N^1 + a_L \Phi_L^1 + a_U \Phi_U^1 + \Delta V \left(S_P + \frac{\Phi_P^0}{\Delta t^*} \right), \quad (32)$$

connecting value of the target function in the node point *P* with its values in centers *W, E, S, N, L, U* of the next meshes.

Algorithm SIMPLE represents cyclic sequence of operations of type "guess–correction". Hence the values of the velocity components on each point of iteration are defined in two stages. At the first stage on the basis of a guess field of pressure p^{**} as a result of the solution of the equations (32) the initial guess of values u^{**}, v^{**}, w^{**} unsatisfying to the continuity equation is done. As concerns the approached solution for the velocity a correction to the pressure p^c was found from the equation (33)

$$a_P p_P^c = a_W p_W^c + a_E p_E^c + a_S p_S^c + a_N p_N^c + a_L p_L^c + a_U p_U^c + b, \quad (33)$$

which is a discrete analogue of the continuity equation. Therefore the continuity equation is fulfilled in each step of the time at the pressure field calculation

On the second stage taking into account values p^c corrected values of the velocity components satisfying to equation (33) are found by formulas

$$u_e^* = u_e^{**} + \frac{r_e^* \Delta\varphi^* \Delta z^*}{a_e} \left(p_P^c - p_E^c \right), \quad (34)$$

$$v_n^* = v_n^{**} + \frac{\Delta r^* \Delta z^*}{a_n} \left(p_P^c - p_N^c \right), \quad (35)$$

$$w_u^* = w_u^{**} + \frac{r_u^* \Delta\varphi^* \Delta r^*}{a_u} \left(p_P^c - p_U^c \right) \quad (36)$$

and the pressure

$$p^* = p^{**} + \alpha_p p^c, \quad (37)$$

where α_p is relaxation. It is assumed in the calculations that $\alpha_p = 0.8$.

Solving Eq. (32) for u^{**}, v^{**}, w^{**} on the free surface the boundary conditions (21), (22), and 23) respectively are used. Boundary values of p^c according to relationship (34) –(36) are supposed to be zero because the boundary velocity values do not require correction. Since the pressure according to Eq. (37) is defined by the correction p^c the boundary condition involving the pressure is not applied.

After calculation of fields of the velocity and of the pressure the calculation of a temperature field and refining the viscosity values $\mu(T)$ were done. The temperature was defined solving Eq. (32) in combination with the heat conductivity equation (19) whose discrete analog has the structure like Eq. (33). The boundary conditions (24) –(26) were used, and the equation (19) was solved on each step of the time.

The form of the free fluid surface according to computed flow field was defined with Eqs. (28)–(29) at the end of each iteration. A value corresponding to unperturbed surface position was considered as an initial value h^*.

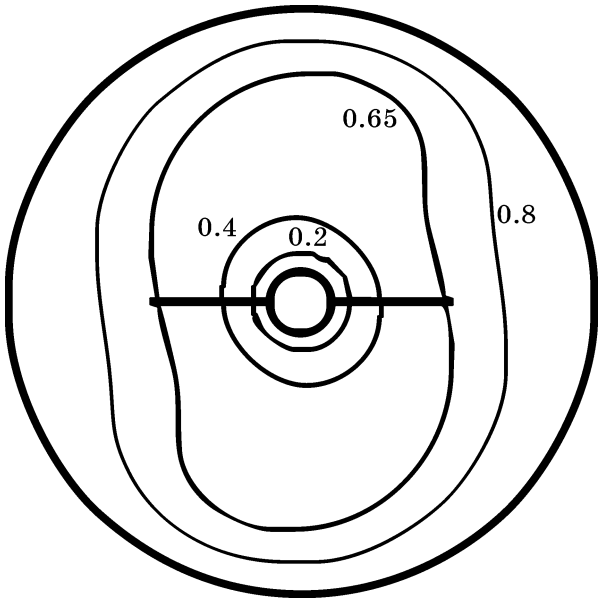


Fig. 1. The isotherm, depicted in the horisontal section of the apparatus above the agitator at $Re_c = 20$, $Fr_c = 0.1$, $Nu = 3$.

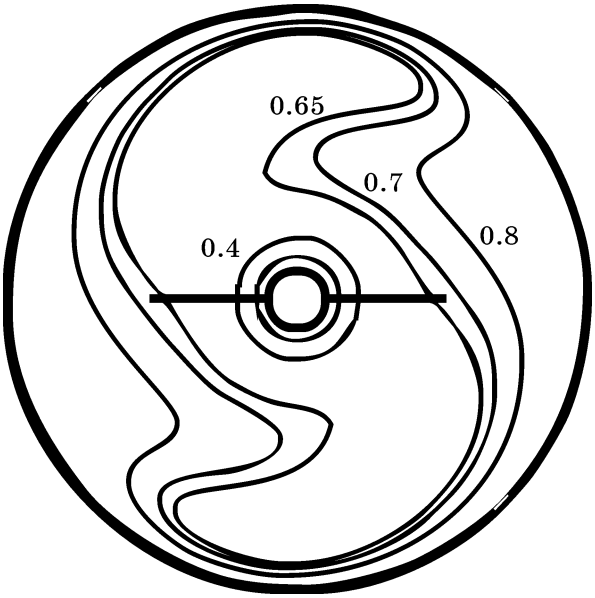


Fig. 2. The isotherm, depicted in the horisontal section of the apparatus above the agitator at $Re_c = 50$, $Fr_c = 0.1$, Nu = 3.

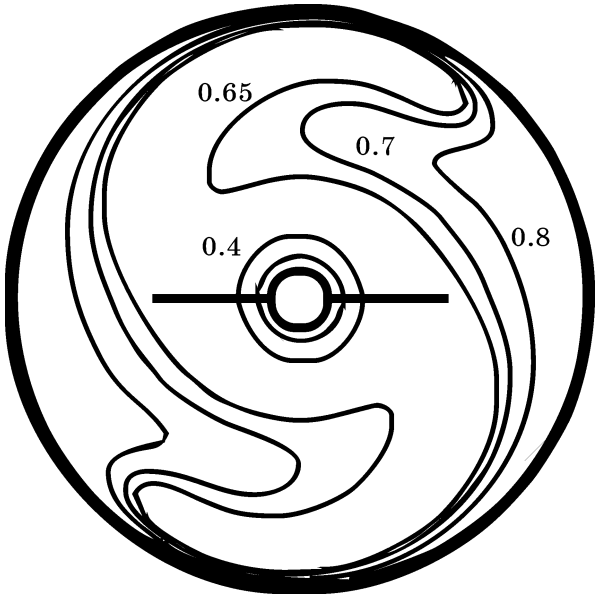


Fig. 3. The isotherm, depicted in the horisontal section of the apparatus above the agitator at $Re_c = 100$, $Fr_c = 0.1$, Nu = 3.

The Eqs. (32) and (33) were solved by the sweep method along radial direction. Ratio of sum of modules of divergences according to the continuity equation for the each mesh to the overall volume of the fluid in the computing area is considered as convergence criterion. The computation was performed according to this criterion to within 0.01%.

RESULTS OF CALCULATIONS

The calculations were executed in the grid with regular distribution of the nodes. It was assumed that $Ho = D_{app}$, $d = r_{app}$, $h_a/d = 0.2$, $H_a/H_0 = 0.3$, $\lambda_{as}/\lambda_s = 17$, Pr=2, $E_a = 22$ kJ/mol. Isotherms in horizontal and meridional sections of the apparatus present the results of calculations. The isotherms $\theta = const$ in the horizontal section located above the agitator on the distance of $0.15H_0$ are shown on the Figs. 1–3 At the small values of Reynolds number the heat convection from the heated sidewall to center of apparatus is insignificant and the formation of thermal field is mainly determined by heat conductivity (Fig. 1).

The increase of Reynolds number denotes the increase of the velocity gradients and accordingly an enhancement of the radially tangential streams. The convective component of the heat transfer increases. The tendency to increase in convective component especially appears in a tangential direction. However, close to a wall the convective heat exchange does not play an appreciable role and the heat transfer occurs due to molecular heat conductivity as a result of contact of the fluid with a heated wall (Fig. 2).

The further enhancement of tangential streams causes more evident heat transfer in the tangential direction. Quickly moving streams entrain heated liquid that results in mixing and gradual temperature smoothing (Fig. 3).

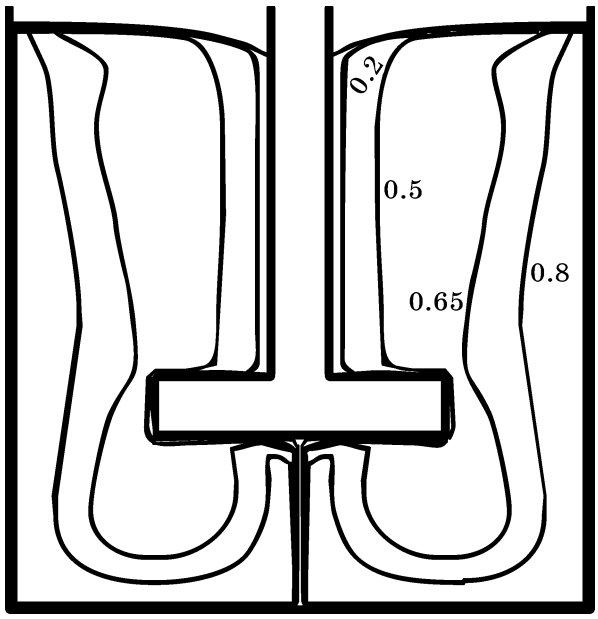


Fig. 4. Distribution of the isotherms depicted in the meridional section of the apparatus at $Re_c = 150$, $Fr_c = 0.3$, Nu = 3.

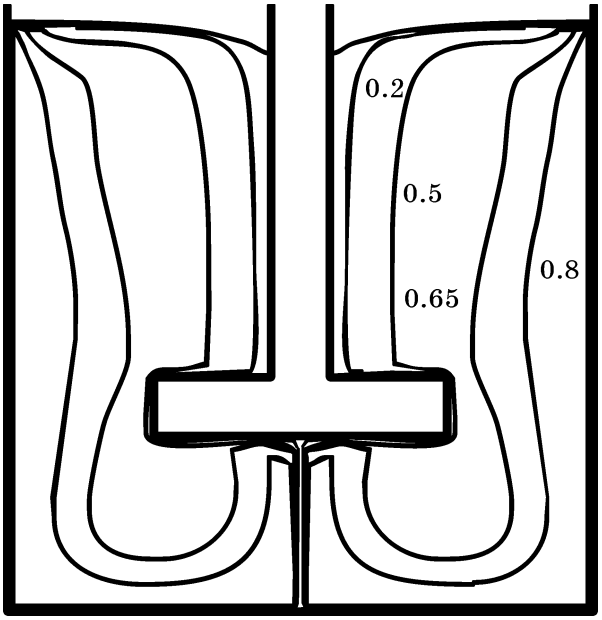


Fig. 5. Distribution of the isotherms depicted in the meridional section of the apparatus at $Re_c = 150$, $Fr_c = 0.3$, $Nu = 9$.

The further analysis of the results may be done on the basis of the isotherm in meridional section that leads through the agitator blade. Distribution of the isotherm depending on Nusselt number is presented on Figs 4, 5. At relatively small values of Nusselt number the isotherms are fairly flat near the free fluid surface and they almost closely come near the top border of the flow (Fig. 4). With increase of Nusselt number the distribution of these curves becomes more abrupt close to the free surface, namely, the heating of the top layers of a liquid decreases that quite speaks more appreciable outflow of heat in surroundings (Fig. 5).

The author expresses gratitude to Prof. Garifullin F. for the attention to this work and valuable remarks.

LEGEND

ρ is liquid density, kg/ m^3;

p is pressure, N/ m^2;

Po is atmosphere pressure, N/m^2;

p_{rr}, $p_{\varphi\varphi}$, p_{zz}, $p_{r\varphi}$, $p_{\varphi z}$, p_{zr} are components of stress tenzor, N/m^2;

g is acceleration of gravity, m/s^2;

μ is dynamic viscosity, kg/(m^2 s^2), t is time, s; T is temperature, K;

T_{env} is environment temperature, K; λ, is heat conductivity coefficient, W/(m K);

a is coefficient of thermal diffusivity, m^2/s;

α is coefficient of heat radiation, W/(m^2 K);

E_a is activation energy of viscous flow, J/mol;

R is universal gas constant, J/(mol K);

n is number of rotation of an agitator, s^{-1};

ω is agitator speed, rad/s;

d is agitator diameter, m;

h_a is height of blade, m;

h is height of free fluid surface above the agitator, m;

h_0 is height of unperturbed free fluid surface above the agitator, m;

h_Q is height of unperturbed free fluid surface above the bottom of apparatus, m;

H_a is height of location of the agitator over the bottom of apparatus, m;

P is stress tensor;

D is deformation velocity tensor;

E is unit tensor;

$Re_c = \rho n d^2/ \mu_0$ is centrifugal Reynolds number;

$Fr_c = n^2 d/g$ is centrifugal Froude number;

$Pr = \mu/(\rho a)$ is Prandtl number;

$Nu = \alpha d/\lambda$ is Nusselt number.

SUBSCRIPT INDEXES

liq is the fluid, s is the shaft, as is the agitator or the shaft of the apparatus.

REFERENCES

1. Loitsyanskii, L.G., *Mekhanika zhidkosti i gaza* (Mechanics of Fluid and Gas), Moscow: Nauka, 1978, 736 p.
2. Korn, G. and Korn, T., *Spravochnik po matematike (dlya nauch. rabotnikov i inzhenerov)* (Handbook on Mathematics: for Scientists and Engineers), Moscow: Nauka, 1973, 832 p.
3. Torner, R.V., *Teoreticheskie osnovy pererabotki polimerov* (Theoretical Bases of Treatment of Polymers), Moscow: Khimiya, 1977, 464 p.
4. Landau, L.D. and Lifshits, E.M., *Gidrodinamika* (Hydrodynamics), Moscow: Fizmatlit, 2003, 732 p.
5. Isachenko, V.P., Osipova, V.A., and Sukomel, A.S., *Teploperedacha* (Heat Transfer), Moscow: Energoizdat, 1981, 416 p.
6. Gzovskii, S.Ya., *Khim. Mashinostr.*, 1960, no. 1,

pp. 17–20.
7. Gazizullin, N.A. and Tarifullin, F.A., *Khim. Prom.*, 2004, no. 12, pp. 619–625.
8. Peire, R. and Teilor, T.D., *Vychislitel'nye metody v zadachakh mekhaniki zhidkosti* (Computational Methods in the Fluid Mechanics), Leningrad: Gidrometeoizdat, 1986, 352 p.
9. Patankar, S., *Chislennye metody resheniya zadach teploobmena i dinamiki zhidkosti* (Solution of the Problems of the Heat Exchange and of the Fluid Dynamics with Numerical Methods), Moscow: Energoatomizdat, 1984, 152 p.
10. Harlow, F.H. and Welsh, F.H., *Phys. Fluids*, 1965, vol. 8, no. 9, pp. 2182–2189.
11. Fletcher, K., *Computational Techniques for Fluid Dynamics, London:* Springer-Verlag, 1988.

ISSN 1070-4272, Russian Journal of Applied Chemistry, 2008, Vol. 81, No. 3, pp. 542–557. © Pleiades Publishing, Ltd., 2008.
Original Russian Text © A.S. Pushnov, M.G. Berngarten, A.S. Ryabushenko, 2008, published in Khimicheskaya Promyshlennost', 2007, Vol. 84, No. 8, pp. 382–402.

PROCESSES AND DEVICES OF CHEMICAL MANUFACTURES

Improving Aerodynamics of Graduating Cooling Units

A. S. Pushnov[a], M. G. Berngarten[a], and A. S. Ryabushenko[b]

[a]*Moscow State University of Engineering Ecology, Moscow, Russia*
[b]*Moscow Mendeleev Chemical Society, Moscow, Russia*

Received November 15, 2007

DOI: 10.1134/S1070427208030439

INTRODUCTION

Consideration of published data shows that most investigations concerning aerodynamics of graduating coolers denoted to tower graduators. These coolers are widely applied, e.g., in the atomic power engineering which exerted renewing in the recent years. Much less publications concern single- and poly-sectional ventilator coolers despite the fact that they cover larger part of world productivity and widely used, e.g., in chemical and petroleum processing industry.

Whole, proceeding from the published data [1–6] we resume that further development of packing* for the process of evaporation cooling is directed to their quantitative efficiency, application of novel materials and modern technology. Meanwhile, improving of aerodynamics of evaporating coolers can be ever more effective for significant increasing their performance. This publication is denoted just to development of this direction of investigations.

1. ANALYSIS OF AERODYNAMIC SITUATION IN THE INDUSTRIAL EVAPORATING COOLERS

In the recent time appeared communications on extension of reconstruction of evaporating coolers in chemical industry and other branches, including replacement of unsuitable packing blocks, eliminating sections* and sprayers* [1–6]. At the projecting reconstruction of ventilator coolers it is significant taking into account of real aerodynamic situation in the unit.

Performance of the process of evaporating cooling of circulating water in an evaporating cooler is known to depend on the uniformity of distribution of counterflow contacting gas (atmospheric air) and liquid (water) phases [1].

In a general case the aerodynamic situation in an evaporating cooler is affected by the following factors:

- Wind power;
- Size and orientation of inlet windows;
- Presence of flow separators in sectional cooler;
- Presence of flow-guiding blades in the inlet windows;
- Type of sprinkler (packing): film or drop, its construction and height;
- Uniformity of distribution of spraying density over the cooler cross-section and the whole cooler volume.

Exploitation in winter period can introduce additional negative effect on the aerodynamic situation due to partial icing of inlet windows and neighboring packing blocks.

Cooling power of counterflow tower and ventilator cooler depends significantly on the value of air flow passing through the cooler. Noteworthy that higher rate of air flow characteristic of ventilator cooler leads to more significant influence of aerodynamic situation on the process of evaporating cooling in these coolers as compared with the tower cooler with much lower flow rate.

In the recent time many experimental and theoretical investigations were denoted to the study of the features

* Concerning terminology: *Packing* is a device for increase contact surface of reacting phases in the processes of heat and mass transfer; this definition is assumed in the literature on the processes and apparatuses of chemical technology. In the literature on evaporating coolers is used term *sprinkler*. English language literature uses term *filler*. We prefer two first definitions.

Eliminator is a device, commonly of jalousie type, for trapping the drops carried away by ascending air flow. This term is used in English literature and can be defined as drop entrainment trap.

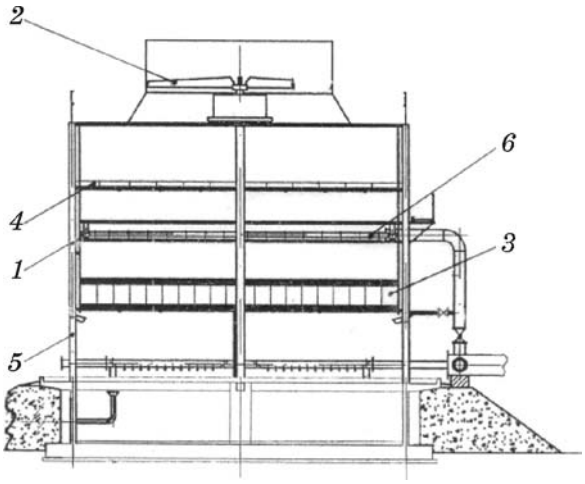


Fig. 1. Sectional ventilator cooler: (*1*) body; (*2*) ventilator; (*3*) packing blocks; (*4*) sections of water trapping lattices; (*5*) air inlet windows; (*6*) water distributing system.

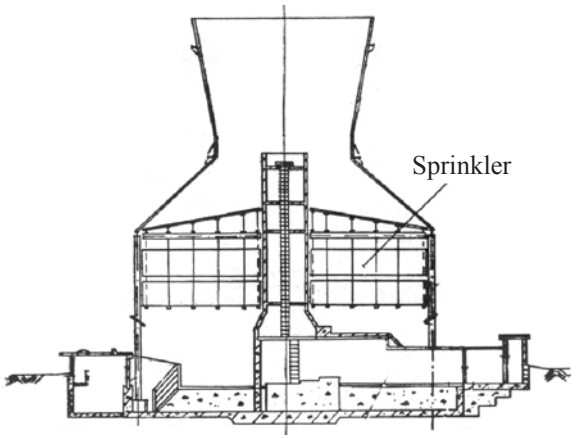


Fig. 2. Scheme of cooler SK-400.

of aerodynamic situation in evaporating coolers that take above said into account [7–14].

The schemes of most used in industry coolers of the types of multisection ventilator, single section ventilator, and tower without ventilator with natural air flow are shown in Figs. 1–3, respectively.

Distribution of the air flow vector at the inlet in the bottom region of tower cooler according to the data of [7] is shown in Fig.4. In that publication Hoffmann and Kroeger) proposed approximate solution for the air flow parameters at the inlet of the tower based on the theory of the flow potential energy. The coefficients obtained depend on the drop size, the tower size and the ratio of water and air flows.

Serous investigation by Zuciga–Gonzalez [8] is denoted to modeling the heat and mass transfer processes

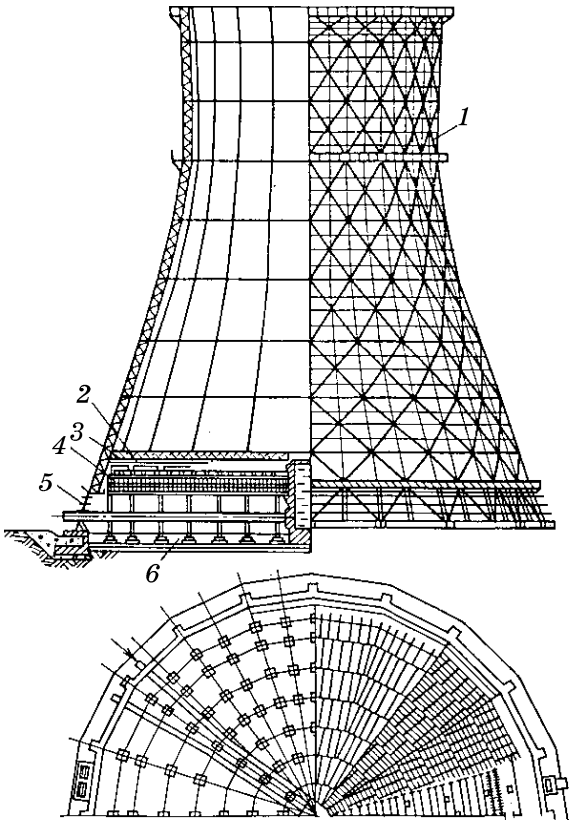


Fig. 3. Tower counterflow cooler: (*1*) air exhaust tower, (*2*) water trap, (*3*) water distributing system, (*4*) spraying device, (*5*) air control device, (*6*) water collecting receiver.

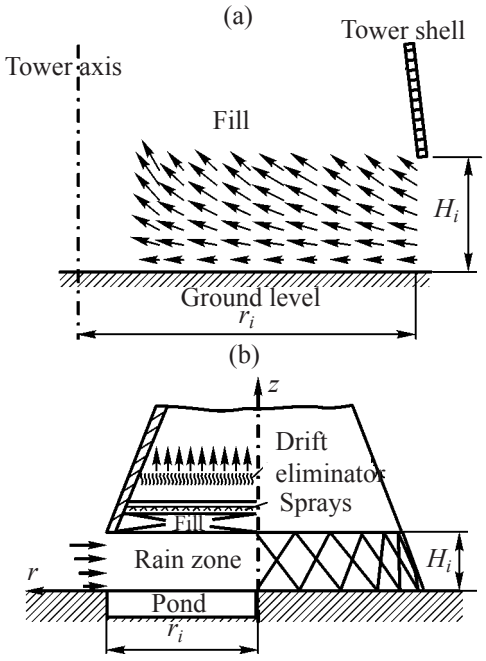


Fig. 4. (a) Air flow distribution at the inlet in the cooler bottom section by the data of [7]; (b) scheme of tower cooler.

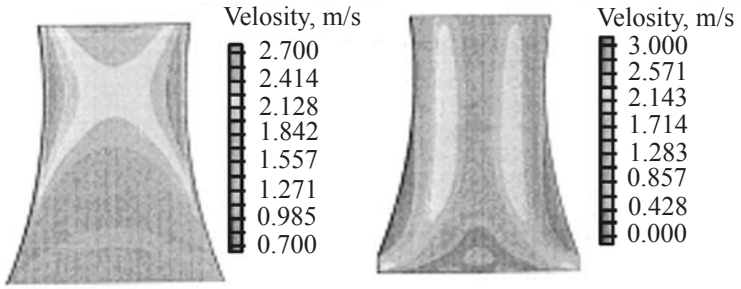


Fig. 5. Rate fields in the tower cooler by the data of theoretical calculations [8]: (a) vertical component of flow rate, (b) horizontal component of flow rate.

in tower coolers at the natural convection. Fig. 5 shows the field of rates in tower cooler obtained in [8] on the ground of developed by the author model of turbulent diffusion.

Note that in some publications, e.g. in [13], is suggested debatable assumption about uniform rate profile in the tower coolers. However, the most other authors disprove this viewpoint. Even in their early work, Bulanina, Morozov and Sukhov [14] by the investigation on the model of tower cooler with sprinkled area F = 6500 m^2 scaled to 1 : 65 showed that specific volume of air flow along the tower radius varies from 0 to 1.2 near the wall. This result was confirmed in more recent study carried out in Vedeneev Halurgy Research Institute.

Experimental data obtained in the Vadeneev Halurgy Research Institute [9] are shown in Fig. 6. The experimental research of the field of the air flow rates was carried out at the tower cooler with cross section F_{sprink} = 1520 m^2, the film sprinkler was preliminary demounted. From the plots obtained is clearly seen non-uniformity of the rate field in the tower leading, as noted by the authors [9], to non-uniform air heating from the center to periphery and to sharp, by 30–40%, decrease in efficiency as compared with typical tower coolers with film type sprinkler.

Fundamental investigation of rate field in the industrial ventilator cooler of SK-400 type operating at many fabrics of chemical industry, e.g. at the carbamide manufacturing in ACHEMA Stock Company of Achema Group Concern (Ionava, Lithuania Republic) were carried out by Gladkov, Aref'ev and Ponomarenko [10]. The results obtained are discussed in details and used by us below in the Section 3 of this article at the development of our own two-zone structural model of evaporating cooler aerodynamics. From the shown in [10] graphic representation of rates follows that maximum rate at the cooler inlet is located, like in the tower coolers, near inlet windows.

Thus, even this preliminary consideration of the published results of experimental study and theoretical investigation on the aerodynamics of industrial evaporating coolers leads to conclusion that the rate field over the cooler cross section is characterized by significant non-uniformity whose scale is comparable with the cooler size.

Whole, we can notify that a significant aerodynamic non-uniformity induced, beside others, by obvious construction features of the cooler body and in a certain extent by distribution of sprinkling density over the cross section are inherent in both tower and ventilator type coolers, the latter both of multi-section and single-section types. The construction features of the cooler body are considered as location of inlet windows in the bottom part of the body which induce sharp turning, by 90°, of air flow and its rearranging before passing to the bottom part of sprinkled volume of the cooler filled by packing.

2. INFLUENCE OF THE AIR FLOW RATE ON THE PROCESS OF EVAPORATING COOLING

The integral characteristics describing the process of evaporating cooling of circulating water in the cooler sprinkler is evaporation number K_{vap}:

$$K_{vap} = \beta_{P\sigma v} \; H / Q_L$$

Here $\beta_{P\sigma v}$ is volume coefficient of mass release assigned to the difference in partial pressure divided by barometric pressure, kg/(m^3 s).

Dependence of evaporation number K_{vap} on the relative air consumtion λ is expressed as:

$$K_{vap} = A \; \lambda^m$$

where A^m are coefficients, $\lambda = Q_G / Q_L$, Q_G =

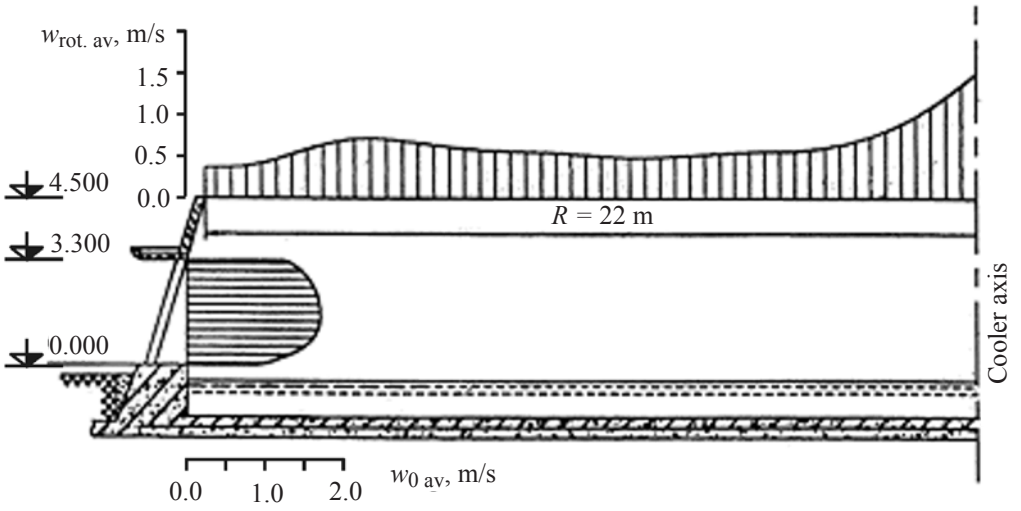


Fig. 6. Experimental investigations of the rate field of air flow in a cooler with preliminary demounted film sprinkler by the data of Vedeneev Halurgy Research Institute [9].

ρ_G (θ_1,φ_1) W_1 [kg/(m² s)], Q_G is specific mass air consuming; ρ_G is gas density; θ_1 is gas temperature; φ_1 is gas humidity; W is gas flow rate. $Q_L = \rho_L q_L/3600$ [kg/(m² s)], Q_L is specific mass water consuming; ρ_L is water density; q_L is spraying density, m³/(m² h).

In English literature is used Merkel number, the analogue of evaporation number:

$$Me = D\,\beta_{xv} H/Q_L ,$$

where β_{xv} is mass release coefficient, H is packing height, D is coefficient.

Linear dependence of Merkel number on the relative air consuming for film sprinkler in tower cooler according to the data of [8] is illustrated by the plot in Fig. 7 in logarithmic coordinates. As seen from this plot, increase in the relative air consuming λ from 1 to 2 results in growing the Merkel number from 2 to 5. Dependence of evaporation number K_{vap} on the λ parameter by the data of Gelfand [15] is given in Fig. 8.

Influencing the mass release coefficient β_{xv} by the air flow rate W_o in the cooler for net type packing of different height by the data of [16] is shown in Fig. 9. From the curves 2 and 3 follows that increase in the flow rate of gas phase leads to increase in mass release coefficient. This effect is seen better at higher packing layer.

It is clear that increase in the rate of air flow in the cooler leads to increase in pressure loss. This is well seen

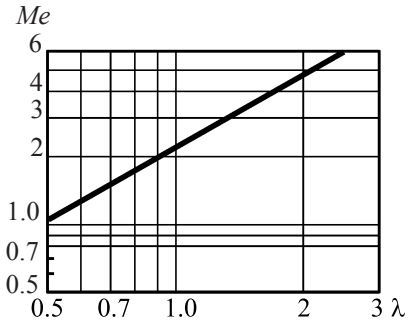


Fig. 7. Dependence of M*e* number on the ratio of the flovs gas/liquid λ by the data of [8].

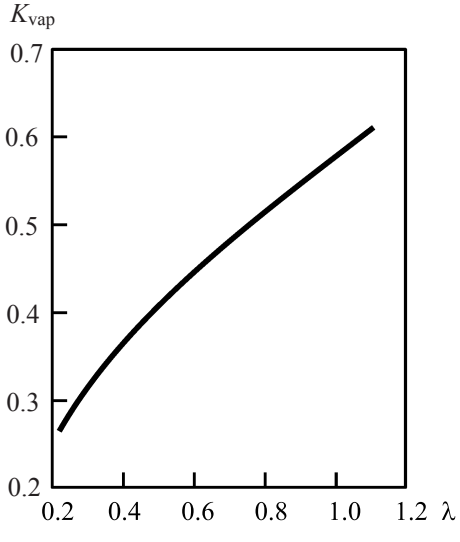


Fig. 8. Dependence of evaporation number K_{vap} on the relative air consuming λ by the data of Gelfand [15] for tower cooler with film type sprinkler.

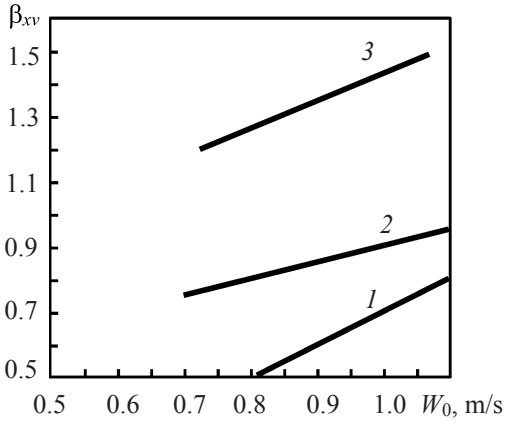


Fig. 9. Influence of air flow rate W_o on the mass release coefficient β_{xv} for the net type packing by the data of Vishnyakova [16]. (*1*) no packing; (*2*) packing layer height is 10 packing elements; (*3*) packing layer height is 18 packing elements.

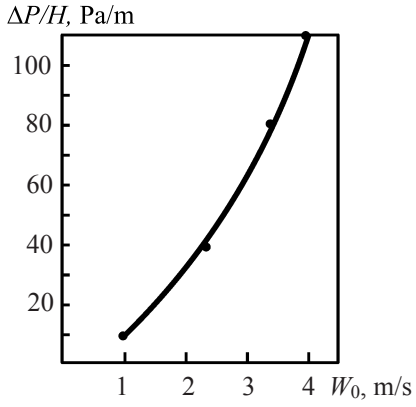


Fig. 10. Influence of air flow rate W_0 on the hydraulic resistance $\Delta P/H$ of dry regular packing from SULZER by the data of Dmitrieva [17].

from the dependence $\Delta P = f(W_0)$ for dry regular structured packing of SULZER firm (Switzerland) by the data of experiments in [17] represented as plot in Fig. 10.

Effects of height of regular film-drop type paking H of PN-2D type from TsNTU RINVO (Russia) on the value of hydraulic resistance coefficient ξ by the data of our own experiments at different productivity on liquid are shown in Fig. 11. Effect of air flow rate W_0 on the degree of cooling the water Δt in the packing layer of PN-2D type at different density of sprinkling q_L is shown in Fig. 12.

Thus, as follows from the consideration of experimental data, the value of rate of air flow in cooler affect directly orv indirectly the characteristics of the process of evaporating cooling in the graduator.

3. GENERALIZED STATISTICALLY REPRESENTATIVE PROFILE OF AIR FLOW RATE IN VENTILATOR COOLER

Analysis of published data [10] on experimental measurements of rate field in a widely distributed industrial cooler SK-400 showed a possibility of their generalization using numerical equation describing average statistical rate profile in such type coolers.

We carried out statistical treatment of experimental observations [10] using methodology of Naumov and co-authors [18–21]. This procedure has been used earlier for description of gas flow rate fields in the apparatuses of chemical technology with grain type layer. The averaging procedure was realized with the basic array of experimental data [10] on the rate fields in cooler at the air flow inlet to and outlet from the sprinkler. Normalization of current rate W_i was found convenient to carry out relatively to the rate maximum W_{max} as a dimensionless ratio W_i/W_{max}. The current coordinate is represented as dimensionless ratio Y/B, where Y is a distance from external wall of cooler [m] and B is width of the sprinkling block of cooler [m].

Initial basic array of experimental data [10], the results of its statistical treatment and of normalization on the value of maximal rate W_{max} are listed in Tables 1 and 2.

The next step is averaging rate profiles at the inlet and outlet of sprinkler followed by calculation of the value $U^* = W_{av}/W_{max}$. Final data on generalized statistically average rate profile are shown in Table 3.

Our analysis of the scope of all published [10] fragmentally represented data on the rate fields in the industrial working coolers SK-400 allowed us to describe them by one characteristic curve obeying the following equation:

$$U^* = \frac{Y/B}{a + b\left(\frac{Y}{B}\right) + c\left(\frac{Y}{B}\right)^2 + d\left(\frac{Y}{B}\right)^3 + e\left(\frac{Y}{B}\right)^4 + f\left(\frac{Y}{B}\right)^5}. \quad (1)$$

In the eq. 1 the constant coefficients are of the following values: $a = 0.053$; $b = 1.14$; $c = -0.8$; $d = 0.84$; $e = -0.22$; $f = 0.0177$. At $Y/B \geq 3$ eq. 1 looks as: $U^* \approx \approx 0.65$.

Graphically generalized statistically representative rate profile is shown in Fig. 13.

Table 1. Procedure of normalization of the experimental measurements [10] on the rate fields at the inlet into sprinkler

Y/B	1	2	3	4	5	6	7
W'_i, μ/C	1.55	1.32	1.05	0.71	0.68	0.54	0.46
W'_i/W_{max}	1.55/1.55	1.32/1.55	1.05/1.55	0.71/1.55	0.68/1.55	0.54/1.55	0.46/1.55
W''_i/W_{max}	1	0.85	0.67	0.458	0.439	0.348	0.297

Table 2. Procedure of normalization of the experimental measurements [10] on the rate fields at the outlet from sprinkler

Y/B	1	2	3	4	5	6	7
W''_i, m/s	1.16	0.92	0.96	1.01	1.06	1.22	1.25
W''_i/W_{max}	1.16/1.25	0.92/1.25	0.96/1.25	1.01/1.25	1.06/1.25	1.22/1.25	1.25/1.25
W''_i/W_{max}	0.928	0.736	0.768	0.808	0.848	0.976	1

Table 3. Averaging of experimental data over sprinkler volume in SK-400 evaporating cooler

Y/B	1	2	3	4	5	6	7
$(W'_i+W''_i)/2$, m/s	(1.16+1.55)/2	(0.92+1.32)/2	(0.96+1.05)/2	(1.01+0.71)/2	(1.06+0.68)/2	(1.22+0.54)/2	(1.25+0.46)/2
W_{Cp}, m/s	1.356	1.12	1.005	0.86	0.87	0.88	0.885
$U_*=W_{av}/W_{max}$	1.356/1.356	1.12/1.356	1.005/1.356	0.86/1.356	0.87/1.356	0.88/1.356	0.885/1.356
U_*	1.0	0.826	0.741	0.634	0.642	0.649	0.630

As seen from the $U^*=f(Y/B)$ plot in Fig. 13, this cooler contains two characteristic aerodynamic zones: peripheral near outlet windows with enhanced air consumption, and central, where specific air consumption is less deviates form the average value. The frontier between these zones is at $Y/B = 3$.

Graphical integration of generalized statistically representative rate profile in the cooler shown in Figs. 14 and 15 gives V^* value in the central zone equal to 0.66, in peripheral zone 0.88.

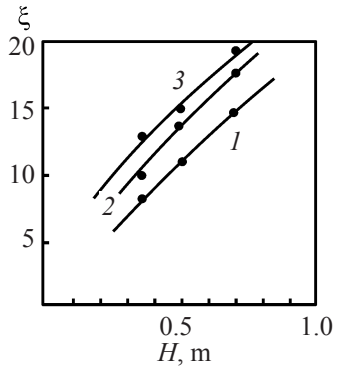


Fig. 11. Influence of packing of PN-2D type height (*H*) on the value of ξ coefficient at different efficiency by liquid (q_L = var) at $W = 2.0$ m/s (const): (1) $q_L = 0$ m³/(m² h); (2) $q_L = 7$ m³/(m² h); (3) $q_L = 11.0$ m³/(m² h).

Thus, the ratio of specific air consumptions in the two zones of the cooler is:

$$\frac{U_p^*}{U_c^*} = \frac{0.88}{0.66} = 1.333. \quad (2)$$

The numerical data on the specific air consumption thus obtained are typical for the SK-400 cooler that in the period of experimental measurements [10] contained sprinkler with the construction characterized by certain values of porosity (ε), live section (*f*) and specific surface (*s*). It can be suggested that specific consumptions in other coolers with another construction of sprinkler blocks differ by geometric characteristics can slightly differ from the U^* values in eq. (2). For example, in [22] has been shown in part that change in porosity ratio in neighboring zones by 1% only leads to change in specific consumption ratio in the same zones by 5%. However, absolute values of porosity of the layer of granules in [22] was equal or less than $\varepsilon = 0.4$, while in regular packing $\varepsilon \sim 0.8$–0.95. Therefore the qualitative regularities revealed here will

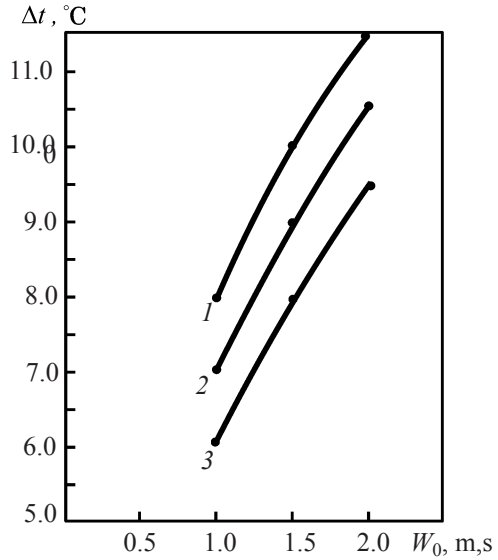


Fig. 12. Influence of air flow rate W_0 on the value of water cooling Δt in the packing layer of PN-2D type at various density of spraying: (*1*) q_L = 0 m³/(m² h); (*2*) q_L = 7 m³/(m² h); (*3*) q_L = 11.0 m³/(m² h).

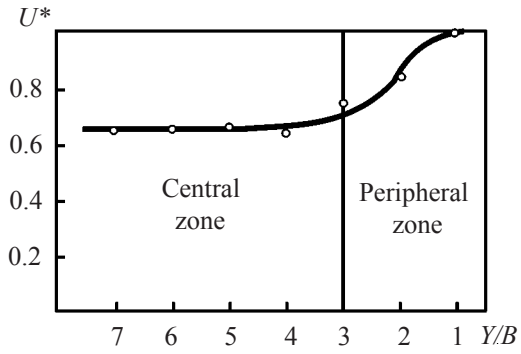


Fig. 13. Generalized average statistical rate profile in SK-400 cooler.

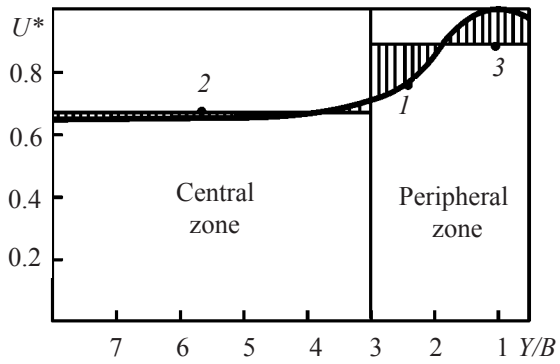


Fig. 14. Integration of generalized rate profile in cooler over two characteristic zones: (*1*) generalized average statistical rate profile in cooler according to eq. 1, (*2*) and (*3*) results of graphical integration over the corresponding zones in the cooler.

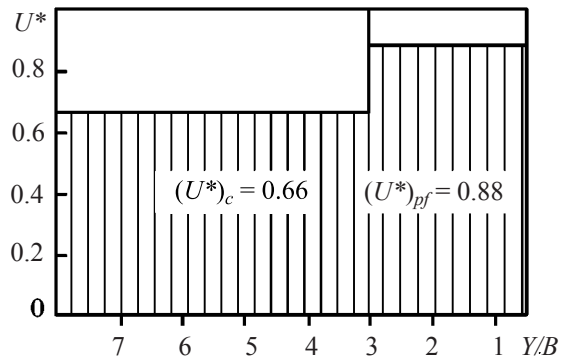


Fig. 15. Results of integration of generalized rate profile over two zones: central and peripheral.

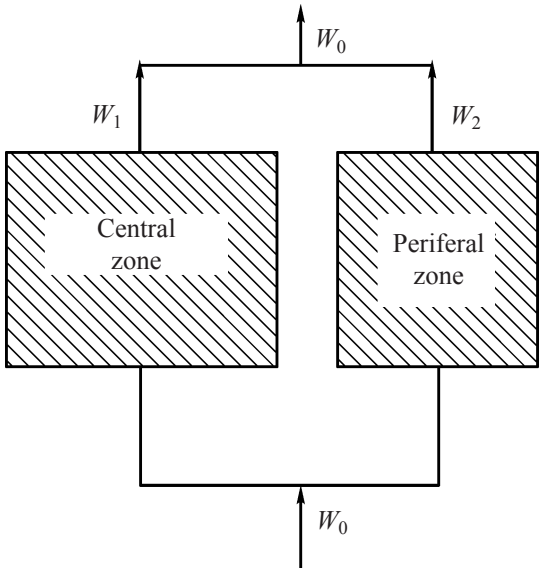


Fig. 16. Two-zone structural model of cooler aerodynamics.

be appropriate for other coolers with similar aerodynamic scheme and type of packing.

The SK-400 ventilator cooler geometry is close to cylinder. The fraction of sprinkling zone of the cooler related to peripheral region can be estimated by the following calculation. Let

$$f_2 = 1 - \left(1 - 2\frac{B}{D}\,Z\right)^2 \qquad (3)$$

where f_2 is fraction of peripheral region of cooler, D is diameter of the whole cooler.

Above in the description of generalized statistically representative rate profile was defined the frontier between peripheral and central zones of cooler Z = 3. Taking this into account we obtain:

$$f_2 = 1 - \left(1 - \frac{6}{D/B}\right)^2. \quad (4)$$

From geometry, the fraction of central zone is:

$$f_1 = 1 - f_2. \quad (5)$$

4. TWO-ZONE STRUCTURAL MODEL OF COOLER AERODYNAMICS. GEOMETRIC CHARACTERISTICS OF PACKING

The obtained statistically representative rate profile allows us to prove two-zone structural model of cooler aerodynamics. The scheme of flows in the cooler according to such model is shown in Fig. 16 where W_0 is average input-output linear rate over full section of empty cooler, W_1 and W_2 are average flow rates in central and peripheral regions of cooler, respectively.

In earlier publications by Riman [28] and Idelchik [29] has been shown principal possibility of equalization the rate field of gas flow in technological apparatuses by means of lattices. The smoothing action of lattice on the initially non-uniform gas steram in the apparatus is illustrated by plots in Fig. 17. More recently by experimental study [30] the soothing action of packing layers of different heights on the rate profile was revealed. Also, were have described [15] constructions of non-uniform sprinkler in a counterflow cooler with productivity on water 100000 m^3/h. In central region of the cooler were located the blocks with extended gape between the sprinkler sheets, that led to the difference in the coefficients of heat and mass transfer in peripheral and central regions of the cooler sprinkled zone. Constructions of coolers differ by packing type at different height are also known [16].

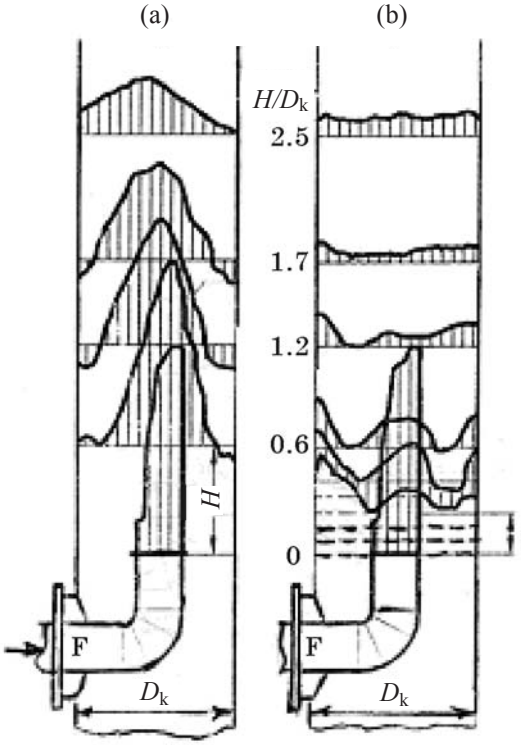


Fig. 17. Redistribution of air flow by lattice by the data of [31] (a) empty apparatus, (b) apparatus with gas redistributing lattice. D_k is diameter of the apparatus.

Meanwhile, there are no reliable methodology and recommendations in literature on the choice and calculation of aerodynamics in such complicated constructions. In earlier publication [33] has been noted than the main disadvantage of the known calculation procedure at projecting of evaporating coolers is not precise enough description of the input-output characteristics of the cooling air flow passing through the sprinkling zone of cooler.

Our two-zone structural model of cooler aerodynamics accounting for the data of investigations [28–30, 16, 18] allows programming of theoretically any possible rate profile (see Fig. 18) by placing packing blocks differ by hydraulic resistance in certain characteristic regions of the cooler sprinkling space. For this purpose we focused on the following geometric characteristics of regular packing: porosity ε [m^3/m^3], specific surface S [m^2/m^3] and equivalent diameter d [μ].

The most important integral geometric characteristics of regular and irregular packing differ by configuration and linear size is porosity. In this work, as well as in the education course “Processes and apparatuses of chemical technology” the term *porosity* is considered as empty

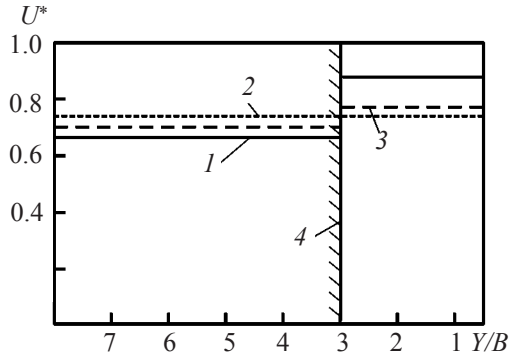


Fig. 18. Th plot $U^* = f(Y/B)$ for two-zone model. (*1*) the profile calculated with the equation; (*2*) theoretically predictable uniform rate profile in cooler; (*3*) calculated rate profile in the cooler obtained by the method of application of sprinkler blocks differ by porosity.

volume (fraction of macro cavities) in the volume unity minus the volume occupied by the packing solid phase.

For example, porosity value in a cylinder apparatus can be estimated using equation [20]:

$$\varepsilon = \left[\int_0^H \int_0^{2\pi} \varepsilon \, d\theta \, dz \right] / 2\pi H \quad [\text{m}^3/\text{m}^3], \qquad (6)$$

where θ is angular coordinate, z is axial coordinate, H is height of packing layer.

By definition, the packing porosity value depends on the geometry, size and mutual location of elements in the regular packing block. Taking this into account, we used this parameter for estimation of distribution of air flow in the cooler.

The effect of geometric characteristics of packing layer on the gas flow distribution is very significant, ever for the layer in an apparatus filled with balls. In [23] have been studied two different tetrahedral packing of balls characterized by the same value of the solid phase volume concentration $\tau = 0.74$. The difference in packing consisted only in the following: in one case there were canals through the balls layer, in the second case the packing was not "transparent" for the flow. The hydraulic resistance τ of the layer in the first case was found by 15–20% lower. The τ value is connected with the porosity value ε by the obvious relation:

$$\varepsilon = 1 - \tau. \qquad (7)$$

In [24] has been determined character of influence of the packing layer porosity on the hydraulic resistance and has been shown that this influence is different at the different values of Reynolds number. In the region of high values of Reynolds number:

$$\Delta P \approx (1 - \varepsilon)/\varepsilon^3,$$

while at small Reynolds numbers:

$$\Delta P \approx \varepsilon^3.$$

Hence, changing porosity of the blocks according to certain law allows to control distribution of rate field in cooler in a specific case of apparatus with packing.

Free volume of regular packing numerically coincides with free section and can be expressed via equivalent diameter d_{equiv}:

$$d_{\text{equiv}} = \frac{4\varepsilon}{S}, \text{ [m]} \qquad (8)$$

where S is specific surface of the packing [m²/m³].

5. PROGNOSIS OF SPECIFIC AIR CONSUMPTION IN CHARACTERISTIC ZONES OF COOLER AT DIFFERENT GEOMETRIC CHARACTERISTICS OF PACKING BLOCKS

The proposed methodology for prognosis of specific consumptions of air flows in two characteristic regions of cooler can be applied to projecting construction of new or reconstruction of currently exploited evaporating coolers for the choice optimal scheme of location and sprinkler blocks type to provide the best uniformity of the rate field. We propose to take into account not only the sprinkler type but also its principal geometric characteristic, the porosity. This is actual because industry produces now rather a wide spectrum of evaporating cooler packing differ by geometric characteristics [1, 2, 33].

Below we derive theoretical relations for calculation specific consumption of air flow based on the proposed two-zone structural model of cooler aerodynamics.

Equations for the numerical estimation of the ratio of specific consumption of air flow in characteristic regions of cooler we will deduce basing on the known equations describing hydraulic resistance of packing layer taking into account that these equations can be applied to both irregular and regular packings [27, 35]. For better statistical representation and reliability we derived relations for estimation of specific consumption of air flow in the characteristic regions of cooler using one methodology, but two different basic equations for estimation of pressure loss in grain layer, namely, Gelperin – Kagan equation [26] and widely known Ergun equation [25]. While derived the targeted relations we used the ideas developed in publications by Naumov and co-authors [18, 22] for the apparatuses of chemical technology with fixed granulated layer.

We accept the following presumptions:

– As model system (packing) we got balls with proper shape;

– Contribution of liquid phase (counter-flow) is omitted.

5.1. Deriving Expressions for Calculation of Specific Consumption of Air Flow in Two Zones of Cooler Differ by Porosity, Based on Gelperin–Kagan [26] Equation

The initial equation has form:

$$Eu_m = \frac{100}{\text{Re}_{\text{eq}}} + 0.9 \qquad (9)$$

where $Eu_m = \frac{\Delta p}{H}\frac{\varepsilon^2}{\rho\, w^2 S}$ is modified Euler criterion; $\mathrm{Re}_e = \frac{w\, d_e}{\upsilon\, \varepsilon}$ is Reynolds criterion referred to equivalent diameter of canal for granulated packing $d_{\mathrm{equiv}} = 4\varepsilon/S$; ρ is gas density, kg s^2/m^4; $S = \varphi\,(1-\varepsilon)$ is specific surface of packing, m^2/ m^3; υ is cinematic gas viscosity, m^2/s.

Let us assume that the rate field discontinuity in the two zones of cooler results from the difference in the values of packing porosity only, as shown in [22]. Therewith, the packing height in both the zones is the same. The calculation scheme is shown in Fig. 19.

After substitutions and transformations we obtain:

$$\frac{\Delta P}{H} = 100\ \frac{\rho\nu W S^2}{4\ \varepsilon^2} + 0.9\ \frac{\rho W^2 S}{\varepsilon^2}\ .$$

Finally:

$$\frac{\Delta P}{H} = 100\,\frac{\nu\ \rho\ \varphi^2\ (1-\varepsilon)^2}{4\ \varepsilon^2}\ W\left[1 + 0.036\frac{W}{\nu\ \varphi\ (1-\varepsilon)}\right]. \quad (10)$$

For a sphere:

$$\varphi = \frac{S_{1sphere}}{V_{1sphere}} = \frac{4\ \pi\ r^2}{\frac{4}{3}\ \pi\ r^3} = \frac{3}{r} = \frac{6}{d}\ .$$

In correspondence with the equation of flow continuity we accept that for both the taken zones, peripheral and central, is true:

$$\Delta P_1 = \Delta P_2 = \Delta P\ ,$$

where ΔP_1 and ΔP_2 are pressure loss in the central and peripheral zones respectively.

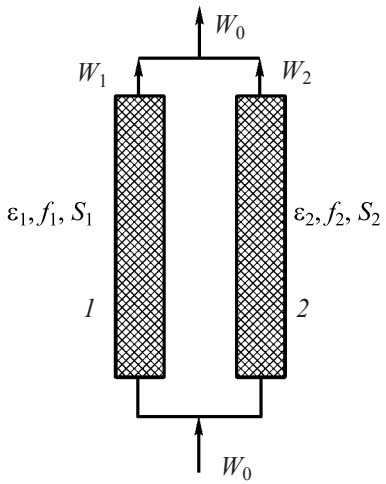


Fig. 19. Calculated scheme of cooler. (*1*) Central zone; (*2*) peripheral zone.

Then:

$$\frac{W_2}{W_1} = \left[\frac{(1-\varepsilon_1)\ \varepsilon_2}{(1-\varepsilon_2)\ \varepsilon_1}\right]^2\ \frac{1+0.006\ \frac{W_1\ d}{\nu(1-\varepsilon_1)}}{1+0.006\ \frac{W_2\ d}{\nu(1-\varepsilon_2)}},$$

And accounting for the expression for Reynolds number $\mathrm{Re}_0 = \frac{W_0\ d}{\nu}$, we obtain:

$$\frac{W_2}{W_1} = \left[\frac{(1-\varepsilon_1)\ \varepsilon_2}{(1-\varepsilon_2)\ \varepsilon_1}\right]^2\ \frac{1+0.006\ \mathrm{Re}_0\frac{1}{1-\varepsilon_1}\ \frac{W_1}{W_0}}{1+0.006\ \mathrm{Re}_0\frac{1}{1-\varepsilon_2}\ \frac{W_2}{W_0}}. \quad (11)$$

From the consumption balance in two-zone model follows:

$$\frac{W_1}{W_0} = \frac{1-\frac{W_2}{W_0}f_2}{1-f_2}\ W_1 = \frac{W_0 - W_2 f_2}{1-f_2}\ \frac{W_1}{W_2} = \frac{(W_0/W_2) - f_2}{1-f_2}$$

Or

$$\frac{W_2}{W_1} = \frac{1-f_1}{\frac{W_0}{W_2}-f_2} = \frac{\frac{W_2}{W_0}(1-f_2)}{1-f_2\ \frac{W_2}{W_0}}\ .$$

As far as $f_2 < 1$, from the last expression follows that $f_2\left(\frac{W_2}{W_0}\right) < 1$ or $\left(\frac{W_2}{W_0}\right) < \left(\frac{1}{f_2}\right)$.

In the framework of the considering model we can write:

$$\varepsilon_1 = \frac{\varepsilon_0 - \varepsilon_2\ f_2}{1-f_2},$$

$$1-\varepsilon_1 = 1 - \frac{\varepsilon_0 - \varepsilon_2\ f_2}{1-f_2} = \frac{(1-\varepsilon_0) - (1-\varepsilon_2)\ f_2}{1-f_2}\ ,$$

$$\mathrm{E} = \left[\frac{1-\varepsilon_0 - (1-\varepsilon_2)\ f_2}{\varepsilon_2 - \varepsilon_2\ f_2}\ \frac{\varepsilon_2}{1-\varepsilon_2}\right]^2 = \left[\frac{\frac{1-\varepsilon_0}{1-\varepsilon_2} - f_2}{\frac{\varepsilon_0}{\varepsilon_2} - f_2}\right]. \quad (12)$$

After algebraic transformations of expression (11) taking (12) into account we obtain:

$$\frac{\frac{W_2}{W_0}\ (1-f_2)}{1-\frac{W_2}{W_0}\ f_2} = \mathrm{E}\ \frac{1+\frac{0.006\ \mathrm{Re}_0}{1-\varepsilon_2}\ \frac{1-\frac{W_2}{W_0}\ f_2}{[(1-\varepsilon_0)/(1-\varepsilon_2)]-f_2}}{1+\frac{0.006}{1-\varepsilon_2}\ \frac{W_2}{W_0}}$$

Let us designate:

$$\frac{0.006\,\mathrm{Re}_0}{1-\varepsilon_2} = C.$$

Then:

$$\frac{\frac{W_2}{W_0}(1-f_2)}{1-\frac{W_2}{W_0}f_2} = \mathrm{E}\,\frac{\left\{1+\frac{C}{[(1-\varepsilon_0)/(1-\varepsilon_2)]-f_2}\right\}-\left\{\frac{C\,f_2}{[(1-\varepsilon_0)/(1-\varepsilon_2)]-f_2}\right\}\frac{W_2}{W_0}}{1+C\,\frac{W_2}{W_0}}.$$

After transformations from the last expression we obtain the following equation:

$$\mathrm{A}\left(\frac{W_2}{W_0}\right)^2 - \mathrm{B}\left(\frac{W_2}{W_0}\right) + Q = 0, \qquad (13)$$

where:

$$\mathrm{A} = C\left[\frac{\mathrm{E}\,f_2}{\frac{1-\varepsilon_0}{1-\varepsilon_2}-f_2}-(1-f_2)\right];$$

$$\mathrm{B} = \mathrm{E}\,f_2\left(1+\frac{C}{\frac{1-\varepsilon_0}{1-\varepsilon_2}-f_2}\right)+C\,\frac{\mathrm{E}\,f_2}{\frac{1-\varepsilon_0}{1-\varepsilon_2}-f_2}+(1-f_2);$$

$$Q = \mathrm{E}\left(1+\frac{C}{\frac{1-\varepsilon_0}{1-\varepsilon_2}-f_2}\right).$$

Following solution of eq. (13) has physical sense:

$$\mathrm{A}\left(\frac{W_2}{W_0}\right)^2 - \mathrm{B}\left(\frac{W_2}{W_0}\right) + Q = 0. \qquad (14)$$

Analysis of eq. (14) for two extreme cases gives:

for $\mathrm{Re}_0 \to 0$: $\dfrac{W_2}{W_0} = \dfrac{\mathrm{E}}{\mathrm{E}f_2 + (1-f_2)}$;

for $\mathrm{Re}_0 \to \infty$: $\dfrac{W_2}{W_0} = \dfrac{(1+\mathrm{E}\,f_2)-\hat{\mathrm{E}}}{2}$.

Here:

$$\hat{\mathrm{E}} = \sqrt{(1+f_2)^2 - 4\left[\mathrm{E}\,f_2^2 - (1-f_2)\left(\frac{1-\varepsilon_0}{1-\varepsilon_2}-f_2\right)\right]}$$

Expression for calculation W_1/W_0 value can be obtained from the consumption balance:

$$\frac{W_1}{W_0} = \frac{1-\frac{W_2}{W_0}f_2}{1-f_2}. \qquad (15)$$

Expressions (14) and (15) obviously reflect satisfactorily the process physics, because they are obtained on the basis of empirical equation [26] which in turn corresponds well to the results of ΔP calculation for, e.g., balls alongside the Sergeev's theoretical equation [36].

5.2. Deriving Expressions for Calculation of Specific Consumption of Air Flow in Two Cooler Zones Differ by Porosity, on the Basis of Ergun's Equation [25]

Initial Ergun's equation for calculation of hydraulic resistance of packing layer has the form [25]:

$$\frac{\Delta P}{H} = \mathrm{A}\,\frac{(1-\varepsilon)^2}{\varepsilon^3}\,\frac{\mu W}{d^2} + \mathrm{B}\,\frac{1-\varepsilon^2}{\varepsilon^3}\,\frac{\rho W}{d}, \qquad (16)$$

where A and B are constant coefficients. By the data [25] A = 150, B = 1.75.

Assuming that equation $\Delta P_1 = \Delta P_2 = \Delta P$ is true for both centar and peripheral zones of sprinkled region of cooler, we can writhe the Ergun's equation for the each zone:

$$\frac{\Delta P}{H} = \mathrm{A}\,\frac{(1-\varepsilon_2)^2}{\varepsilon_2^3}\,\frac{\mu W_2}{d^2} + \mathrm{B}\,\frac{1-\varepsilon^2}{\varepsilon_2^3}\,\frac{\rho W_2^2}{d}, \qquad (17)$$

$$\frac{\Delta P}{H} = \mathrm{A}\,\frac{(1-\varepsilon_1)^2}{\varepsilon_1^3}\,\frac{\mu W_1}{d^2} + \mathrm{B}\,\frac{1-\varepsilon_1}{\varepsilon_1^3}\,\frac{\rho W_1^2}{d}. \qquad (18)$$

Multiplying first and second terms in the right part of eq. (17) by (W_2/W_0) and $(W_2/W_0)^2$, respectively, we obtain:

$$\frac{\Delta P}{H} = \mathrm{A}\,\frac{(1-\varepsilon_2)^2}{\varepsilon_2^3}\,\frac{\mu W_0}{d^2}\,\frac{W_2}{W_0} + \mathrm{B}\,\frac{1-\varepsilon_2}{\varepsilon_2^3}\,\frac{\mu W_0}{d^2}\,\frac{W_0\,\rho\,d}{\mu}\left(\frac{W_2}{W_0}\right)^2. \qquad (19)$$

Index 0 in (19) and in following expressions points to the whole volume of cooler assuming that its section is empty.

As far as $\dfrac{W_0\,\rho\,d}{\mu} = \mathrm{Re}_d$, eq. (19) can be rewritten as:

$$\frac{\Delta P}{H} = \mathrm{A}\,\frac{(1-\varepsilon_2)^2}{\varepsilon_2^3}\,\frac{\mu W_0}{d^2}\,\frac{W_2}{W_0} + \mathrm{B}\,\frac{1-\varepsilon_2}{\varepsilon_2^3}\,\frac{\mu W_0}{d^2}\,\mathrm{Re}_d\left(\frac{W_2}{W_0}\right)^2.$$

After algebraic transformations of the last equation we obtain:

$$\frac{\Delta P}{H} = \mathrm{A}\ \frac{(1-\varepsilon_2)^2}{\varepsilon_2^3}\ \frac{\mu\ W_0}{d^2}\ \frac{W_2}{W_0}\left[1+\frac{\mathrm{B}}{\mathrm{A}}\ \frac{\mathrm{Re}d}{1-\varepsilon_2}\left(\frac{W_2}{W_0}\right)\right]. \quad (20)$$

Similarly, from eq. (18) we obtain expression for the cooler central zone:

$$\frac{\Delta P}{H} = \mathrm{A}\ \frac{(1-\varepsilon_1)^2}{\varepsilon_1^3}\ \frac{\mu\ W_0}{d^2}\ \frac{W_1}{W_0}\left[1+\frac{\mathrm{B}}{\mathrm{A}}\ \frac{\mathrm{Re}_d}{1-\varepsilon_1}\left(\frac{W_1}{W_0}\right)\right]. \quad (21)$$

As far as left parts of (20) and (21) are the same, we can write:

$$\frac{W_2}{W_1} = \frac{1+\frac{\mathrm{B}}{\mathrm{A}}\ \frac{\mathrm{Re}_d}{1-\varepsilon_1}\ \frac{W_1}{W_0}}{1+\frac{\mathrm{B}}{\mathrm{A}}\ \frac{\mathrm{Re}d}{1-\varepsilon_2}\ \frac{W_2}{W_0}}\left(\frac{1-\varepsilon_1}{1-\varepsilon_2}\right)^2\left(\frac{\varepsilon_2}{\varepsilon_1}\right)^3. \quad (22)$$

Expression for the balance of consumption in cooler in the framework of two-zone structural model has the form:

$$W_0 = W_2\ f_2 + W_1\ (1-f_2). \quad (23)$$

Deviding eq. (23) by W_2 we obtain:

$$\frac{W_0}{W_2} = f_2 + \frac{W_1}{W_2}\ (1-f_2), \text{ hence:}$$

$$\frac{W_2}{W_0} = \frac{\frac{W_2}{W_1}}{1-f_2+f_2\ \frac{W_2}{W_1}}. \quad (24)$$

Deviding eq. (23) by W_1 we obtain:

$$\frac{W_0}{W_1} = \left(\frac{W_2}{W_1}\right)\ f_2 + (1-f_2), \text{ hence:}$$

$$\frac{W_1}{W_0} = \frac{1}{1-f_2+f_2\left(\frac{W_2}{W_1}\right)}. \quad (25)$$

Let in (22):

$$\frac{\mathrm{B}}{\mathrm{A}}\ \frac{\mathrm{Re}_d}{1-\varepsilon_1} = Z;\ \ \frac{1-\varepsilon_1}{1-\varepsilon_2} = M;\ \ \left(\frac{1-\varepsilon_1}{1-\varepsilon_2}\right)^2\left(\frac{\varepsilon_2}{\varepsilon_1}\right)^3 = K;\ \ \frac{W_2}{W_1} = U.$$

With these assignments, eqs. (24) and (25) can be rewritten as:

$$\frac{W_2}{W_0} = \frac{U}{1-f_2+f_2\ U} \quad (26)$$

and

$$\frac{W_1}{W_0} = \frac{1}{1-f_2+f_2\ U}. \quad (27)$$

From (26) and (27) accounting for the accepted assignments, eq. (22) after simple algebraic transformations becomes:

$$(f_2 + ZM)U^2 + (1 - f_2 - K f_2)\,U - K(1-f_2+Z) = 0.$$

Only one solution of the last equation has physical sense:

$$U = \frac{-(1-f_2-Kf)}{2(f_2+ZM)} + \frac{\sqrt{(1-f_2-Kf_2)^2+4(f_2+ZM)(1-f_2+Z)K}}{2(f_2+ZM)}. \quad (28)$$

Analysis of eq. (28) for two extreme cases gives:

for $\mathrm{Re_d} \to 0$: $\frac{W_2}{W_1} = \left(\frac{1-\varepsilon_1}{1-\varepsilon_2}\right)^2\left(\frac{\varepsilon_2}{\varepsilon_1}\right)^3$;

for $\mathrm{Re_d} \to \infty$: $\frac{W_2}{W_1} = \sqrt{\frac{1-\varepsilon_1}{1-\varepsilon_2}\left(\frac{\varepsilon_2}{\varepsilon_1}\right)^3}$.

Expression for calculation of flow rate in the cooler peripheral zone becomes:

$$\frac{W_2}{W_0} = \frac{-L+\sqrt{L^2+\ 4\ F\ (1+Q\ W_0)\ W_0}}{2\ F\ W_0}, \quad (29)$$

where *L, Q, F* are defined as:

$$L = \frac{\mu_2}{\mu_0}\left(\frac{1-\varepsilon_2}{1-\varepsilon}\right)^2\left(\frac{\varepsilon}{\varepsilon_2}\right)^3; \quad (30)$$

$$Q = 1.167\cdot 10^{-2}\ \frac{\rho_0\ d}{(1-\varepsilon)\ \mu_0}; \quad (31)$$

$$F = Q\ \frac{\rho_2}{\rho_0}\left(\frac{\varepsilon}{\varepsilon_2}\right)^3\frac{1-\varepsilon_2}{1-\varepsilon}. \quad (32)$$

Expression for calculation of flow rate in the cooler central zone becomes :

$$\frac{W_1}{W_0} = \frac{-\mathrm{E}+\sqrt{\mathrm{E}^2+4\ \mathrm{X}\ (1+Q\ W_0)\ W_0}}{2\ \mathrm{X}\ W_0}, \quad (33)$$

where the constants E and X are defined as:

$$\mathrm{E} = \frac{\mu_1}{\mu_0}\left(\frac{1-\varepsilon_1}{1-\varepsilon}\right)^2\left(\frac{\varepsilon}{\varepsilon_1}\right)^3; \quad (34)$$

$$X = Q\,\frac{\rho_1}{\rho_0}\left(\frac{\varepsilon}{\varepsilon_1}\right)^3\frac{1-\varepsilon_1}{1-\varepsilon}\,. \qquad (35)$$

The set of equations (29)–(35) allows calculation of specific consuming of gas flow in the cooler peripheral and central zones in the framework of the proposed two-zone structural model of aerodynamics.

5.3. Comparing Results of Calculation by Means of the Obtained Expressions of Air Flow Specific Consumption in the Cooler Two Zones

The results of calculations of W_2/W_0 and W_1/W_0 using relations (14), (15) and (29)–(35), respectively are found differ by 5% or less at W_0 = 0.1 m/sec for the model system with ball packing d = 5 mm in the apparatus with D = 50 mm. Calculation with formulas (14), (15) leads to underestimation of W_2/W_0 values.

For practical purposes cam be recommended both relations (14), (15) and (29)–(35), the latter are obtained on the basis of Ergun's equation [25], which gas been tested within wider range of Reynolds numbers and packing types, forms and sizes as compared with Gelperin–Kagan equation [26].

6. PRACTICAL METHODS FOR AVERAGING RATE PROFILE IN THE COOLER SPRINKLING SPACE

The following method can be used for the control over distribution of specific consumption of air flow in the section of the cooler sprinkling space:

– Varying sprinkler blocks height;

– Varying the sprinkler dinsity;

– Varying the sprinkler living section.

In contrast to the method proposed in [18] based on the varying the height of the sprinkler blocks, we suggest optimal to apply the blocks with the same height but differ by living section. The advantage of the technical solution proposed by us is the absence of reasons for appearance unwanted aerodynamic non-uniformity in the upper zone of cooler near the water trapping devices.

According to the proposed methodology the problem of programming uniform rate field for the air flow in ventilator cooler is solved by means of installation in peripheral zones of sprinkling space of the packing blocks with constant height but differ by hydraulic resistance. Equalizing the flow is achieved due to the difference in living section (porosity) of packing blocks in the corresponding zones. For equalization of non-uniform initial rate profile, in the region within the cooler section characterized by lower calculated air flow rate (se Figs. 15, 18) should be installed the packing blocks with lower value of the coefficient of hydraulic resistance or, respectively, with higher living section (porosity).

Characteristics of some industrial packing made of polymer material are shown in Table 4. By the data of [2] the values of hydraulic resistance coefficient for the sprinkler packing blocks of different construction fall to the range from ξ = 7.5 to ξ = 35.4. Unfortunately, the constructions listed in the Table 4 differ by height (from 0.92 m to 2.38 m) and this retards their practical application for programmed uniform rate profile in cooler.

The optimal construction for solving the problem of programmed rate profile in the cross section of cooler is

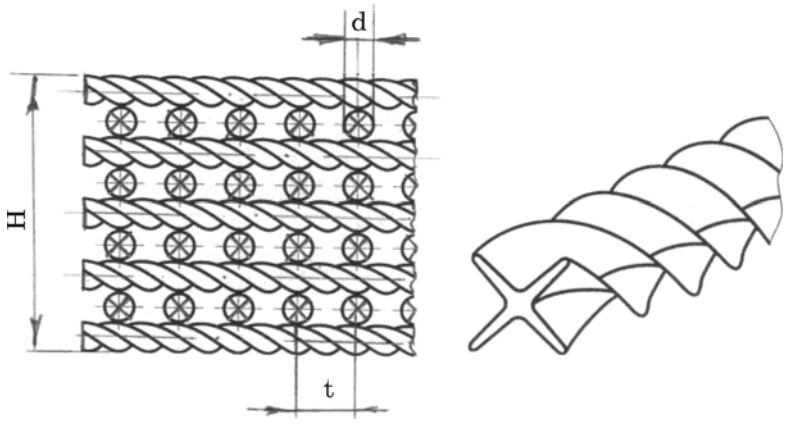


Fig. 20. General view of sprinkler block of PN-2D type and separate packing element: H is the block height; t is pitch between the central axes of neighboring helicoids in one row; d is helicoids external diameter.

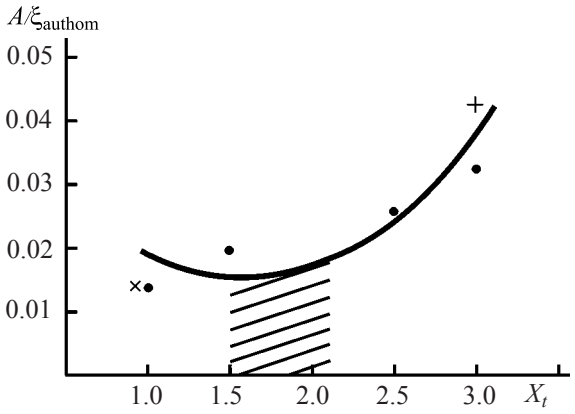


Fig. 21. Dependence of A/ξ_{authom} on geometry patameter X_t obtained in experiments with sprinkler block of PN-2D type.

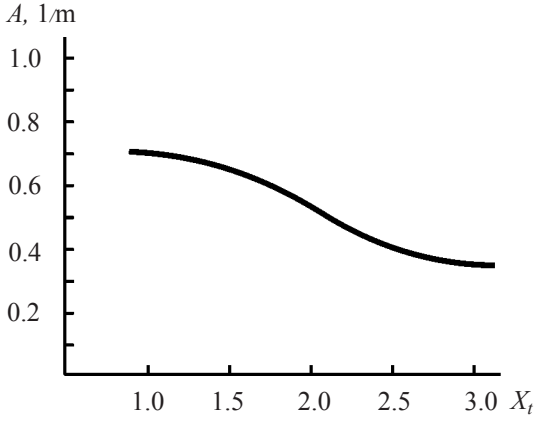


Fig. 22. Effect of geometry parameters of PN-2D packing on the value of A coefficient from the data of the experiments carried out by the authors.

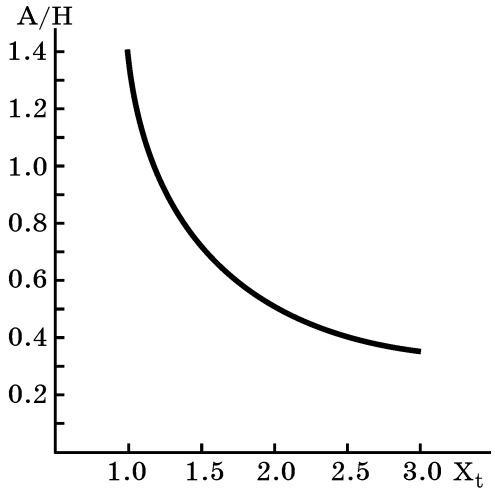


Fig. 23. Dependence of A/*H* simplex on the geometry parameter X_t from our experiments with PN-2D sprinkler block.

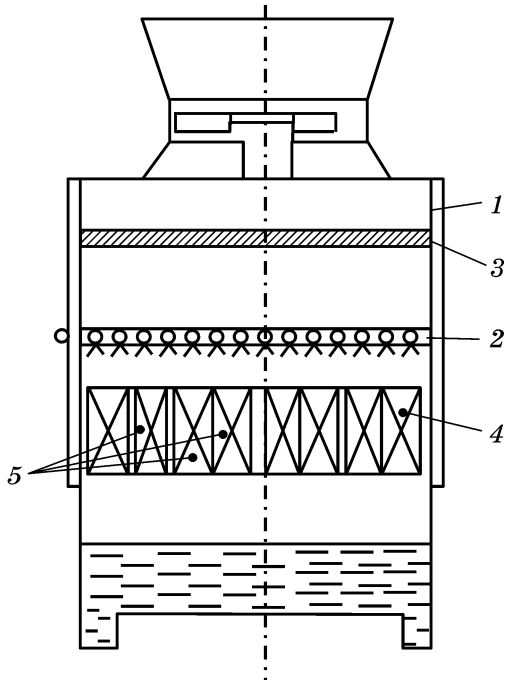


Fig. 24. Scheme of packaging sprinkler blocks in the zones of sectional ventilator cooler: (*1*) body; (*2*) water distributing system; (*3*) water trapping lattices; (*4*) sprinkler block with smaller live section in the cooler peripheral zone; (*5*) sprinkler block with larger live section in the cooler peripheral zone.

represented by the developed for this purpose a family of packing with helicoid structure and varied geometry of packing of separate helicoids in the packing block. The general view of such packing block is shown by Fig. 20. The distance between the neighboring helicoids X_t is variable value:

$$X_t = t/d,$$

where d is external diameter of a helicoid.

The dependence of A/ξ_{authom} on the geometric parameter X_t obtained in our experiments with a sprinkler block of PN-2D type is shown in Fig. 21. As seen, the optimal from the viewpoint of efficiency – energy consumption ratio are the X_t values in the range from 1.5 to 2.1.

Effect of geometry parameter X_t of packing block on the value of coefficient A charactreizing, efficiency of the process of evaporating cooling on an example of the packing of PN-2D type is shown in Fig. 22. From the plot is seen that PN-2D packing allows varying the X_t value from 1.0 to 3.0, which leads to change in A coefficient from 0.3 to 0.7. In a dimensionless form, the $A/H = f(X_t)$ dependence is shown in Fig. 23. The whole characteristics of helicoids structural packing with varied packing geometry are listed completely in [34].

To minimize losses due to hydraulic resistance, the ξ_π coefficient should be chosen according to the well known Idelchik's formula [29]:

$$\xi_\pi = \xi_{opt.i} = 2\ [1-(W_{0i})_{\min}/W_{0i}], \quad (36)$$

where:

$$\xi_\pi = \frac{2\ \Delta P_i}{\rho\ W_\pi^2}\ , \quad (37)$$

ξ_π is hydraulic resistance coefficient for *i*-th region of the flow assigned to the rate W_π ; W_π is average rate in the *i*-th region of air flow at the inlet into the sprinkler block, m/sec; W_{0i} is averaged over the section of *i*-th regionrate of air flow before the inlet into sprinkler block, m/sec.

From eq. (37) follows: $\Delta P_i = 0.5\ \xi_\pi\ \rho\ W_\pi^2$ is pressure loss in the *i*-th region of air flow, Pa.

Practically, the problem of providing uniform distribution of air flow rate profile after the sprinkler blocks in cooler is solved by selection of constructions with $\xi_p = \xi_{opt}$, that is, by solving the following equations:

$$\xi_p = \xi_{opt} = \frac{W_{01}^2 - W_{02}^2}{W_{p1}^2 - W_{p2}^2} \quad (38)$$

$$W_{p1} = \frac{W_{01}\ (W_{01}+W_{02})}{2\ W_{01}+\ W_{02}-1} \quad (39)$$

$$W_{p2} = \frac{W_{02}\ (W_{01}+\ W_{02})\ (W_{02}+1)}{2\ W_{02}^2+W_{01}\ W_{02}+W_{01}+W_{02}-1} \quad (40)$$

The scheme of packaging the sprinler blocks in certain zones of sectional ventilator cooler is shown in Fig. 24. It is seen that the proposed technical solution can be easily achieved practically at the cooler reconstruction.

In some cases when there is no data on the packing porosity but there are data on the pressure loss ΔP, for selection of two sprinklers in the framework of two-zone model can be used approximate formula:

$$\frac{W_2}{W_1} = \sqrt{\frac{\Delta P_1}{\Delta P_2}} \quad (41)$$

For example, if a cooler under project (or reconstruction) of SK-400 has: $W_2/W_1 = 1.333$.

Then from eq. (41) we have:

$$\Delta P_1 = \Delta P_2\ \ (1.333)^2 = \Delta P_2\ \ 1.7769$$

Let us assume that according to the data of producer the packing blocks $\Delta P_2 = 4$ mm water column, then:

$\Delta P_1 = 4 \cdot 1.7769 = 7.1$ mm water column.

If the packing with such hydraulic resistance is absent in the market, the nearest can be chosen and verifying calculation should be made.

CONCLUSIONS

1. An equation is proposed for the calculation the generalized statistically representative rate profile in ventilator cooler.

2. Two-zone structural model of cooler aerodynamics is proved.

3. Theoretical relations for the calculation of specific consumption of air flow in the two characteristic zones of cooler differ by live section of packing blocks is proposed.

4. A method for increasing uniformity of rate profile over the cross section of the cooler sprinkler space is proposed by means of application of helicoids-structural packing blocks with varieg packaging geometry in the blocks.

REFERENCES

1. Ponomarenko, B.S. and Aref'ev, Yu.I., *Gradirni promyshlennykh i energeticheskikh predpriyatii* (Grade coolers of industrial and energy enterprises) (Handbook). Moscow: Energoatomizdat, 1988.
2. Sverdlin, B.L., Shishov, B.I., and Pilipenko, K.B., *Khimicheskaya Tekhnika*, 2004, no. 1, pp. 5–8.
3. Sukhov, E.A. and Shishov, B.I., *Izv. BNIIG im. B.E.Bedeneeva,* 2000, vol. 236.
4. Ryabushenko, A.S., *Khimicheskaya Tekhnika*, 2004, no. 10, pp. 31–33.
5. Ryabushenko, A.S., Pushnov, A.S., and Berengarten, M.G., *Khimicheskoe Neftegazovoe Mashinostroenie*, 2006, no. 6, pp. 14–15.
6. Pushnov, A.S., Kagan, A.M. and Ryabushenko, A.S., *Khimicheskaya Tekhnika*, 2005, no. 11, p. 17.
7. Hoffmann J.E. and Kruger, J.E., Abstracts of Papers, *7th Cooling Tower and Spraying Pond Symposium*, Leningrad, USSR, May 29 – June 2, 1990, pp. A10-1–A10-8.
8. Israel Zuciga – Gonzalez, Summary of dissertation. Czech Technical University, Prague, 2005.
9. Nedviga, Yu.S. and Pilipenko, K.B., *Izv. BNIIG im. B.E.Bedeneeva*, 2000, vol. 26, pp. 248–253.
10. Gladkov, B.A., Aref'ev, Yu.I., and Ponomarenko, B.S., *Ventilyatornye gradirni* (Ventilator Coolers). Moscow: Stroiizdat, 1976.

11. Berman, L.D., *Isparitel'noe okhlazhdenie tsirkulyatsionnoi vody* (Evaporation Cooling of Water), Moscow: Gosenergoizdat, 1957.
12. Goncharov, A.B., *Izv. BNIIG im.B.E.Bedeneeva*, 2000, vol. 236, pp. 242–247.
13. Grange, J.L., Abstracts of Papers, *7th Cooling Tower and Spraying Pond Symposium*, Leningrad, 1990, pp. C28-1–C8-11.
14. Bulanina, E.B., Morozov, B.A., and Sukhov, E.A., *Izvestiya BNII Gidrotekhniki*, Leningrad, 1972, vol. 100, pp. 135–145.
15. Gel'fand, R.E., Abstracts of papers, *Konferentsiya i soveshchanie po gidrotekhnike: Gidroaerotermicheskie issledovaniya i proektirovanie okhladitelei teplovykh i atomnykh elektrostantsii* (Conference on Hydrodynamics: Hydroaerothermal Study and Projecting of Heat and Atomic Power Stations), Leningrad: Energoatomizdat, 1985, pp. 120–124.
16. Bishnyakova, I.B., *Cand. Sci. (Techn.) Dissertation*, 2008, Kazan.
17. Dmitrieva, G.B., Berengarten, M.G., Klyushenkova, M.I. and Pushnov, A.S., *Khimicheskoe Neftegazovoe Mashinostroenie*, 2005, no. 12, pp. 5–8.
18. Naumov, Yu.B., Gel'perin, I.I., Pushnov, A.S., Novikova, N.I., Novikov, E.A., and Kagan, A.M., *Khimicheskaya Promyshlennost'*, 1986, no. 8, pp. 15–17.
19. Gel'perin, I.I., Kagan, A.M., Pushnov, A.S. and Rollof, B.Yu., *Khimicheskaya Promyshlennost'*, 1983, no. 8, pp. 22–25.
20. Pushnov, A.S., Naumov, Yu.B., Kagan, A.M., Gel'perin, I.I., and Pishchik, L.Ya., *Teploenergetika*, 1986, no. 8, pp. 70–72.
21. Kagan, A.M., Sergeev, Yu.A. and Pushnov, A.S., *Teoreticheskie Osnovy Khimicheskoi Tekhnologii*, 1987, vol. 21, pp. 130–133.
22. Pushnov, A.S., *Khimicheskoe Neftegazovoe Mashinostroenie*, 2005, no. 8, pp. 9–10.
23. Borishanskii, B.M., in *Voprosy aerodinamiki i teploperedachi v kotel'no-topochnykh protsessakh* (Problems of Aerodynamics and Heat Transfer in the Boiler-Furnace Processes), Moscow: Gosenergoizdat, 1958, pp. 70–74.
24. Beskov, B.S. and Flokk, B., *Modelirovanie kataliticheskikh protsessov i reaktorov* (Modeling of Catalytic Processes and Reactors), Moscow: Khimiya, 1991 .
25. Ergun, S., *Chem. Eng. Progress*, 1952, vol. 48, no. 2, p. 89–94.
26. Gel'perin, I.I. and Kagan, A.M., *Khimicheskaya Promyshlennost'*, 1984, No. 12, p. 741–746.
27. Aerov, M.E. and Todes, O.M., *Gidravlicheskie i teplovye osnovy raboty apparatov so statsionarnym i kipyashchim zernistym sloem* (Hydraulic and Thermal Basicity of Work of Apparatuses with Stationary and Boiling Granulated Layer), Leningrad: Khimiya, 1968.
28. Riman, I.S., in *Promyshlennaya aerodinamika* (Industrial Aerodfynamics), Moscow: Oborongiz, 1960, issue 20, pp. 216–238.
29. Idel'chik, I.E., *Aerodinamika tekhnologicheskikh apparatov – podvod, otvod i raspredelenie potoka po secheniyu apparatov* (Aerodynamics of Technological Apparatuses – Inlet, Ourlet and Flow Distribution over the Apparatus Cross Section), Moscow: Mashinostroenie, 1983.
30. Pushnov, A.S., *Cand. Sci. (Techn.) Dissertation*, Moscow: GIAP, 1987.
31. Krasovickij, J.W, Baltrenas, P., Kolbeschkin, B.G., and Dobrosotskij, V.P., *Aerodynamische Verfahren zur Erhöhung der Leistungserzeugung der Entstaubung*, Vilnius Gediminas Technische Universität, Vilnius: Technika, 2006.
32. Kuraev, A.A., Larichkin, B.B. and Salenko, S.D., *Izbrannye glavy mekhaniki zhidkosti i gaza: Uchebnoe posobie* (Selected Chapters of Liquid and Gas Mechanics. Educational Tutorial), Novosibirsk: Izd. NGTU, 2004.
33. Berman, L.D., *Teploenergetika*, 1979, no. 3, pp. 71–75.
34. Pushnov, A.S., Kagan, A.M., Berengarten, M.G., Ryabushenko, A.S., and Shishov, B.I., *Khimicheskaya Promyshlennost' Segodnya*, 2007, no. 3, pp. 33–40.
35. Bespalov, A.B., Tatarinova, I.N., Prokudin, S.B., Grunskii, B.N., and Kozlov, A.I., *Khimicheskaya Promyshlennost' Segodnya*, 2007, no. 2, pp. 44–49.
36. Sergeev, S.P. and Dil'man, B.B., *Teoreticheskie Osnovy Khimicheskoi Tekhnologii*, 1986, vol. 20, no. 1, pp. 19–27.

ISSN 1070-4272, Russian Journal of Applied Chemistry, 2008, Vol. 81, No. 3, pp. 558–564. © Pleiades Publishing, Ltd., 2008.
Original Russian Text © V.L. Chechulin, V.N. Pavelkin, Yu.P. Kirin, E.F. Mazitova, V.K. Grigalashvili, A.B. Tankeev, 2008, published in Khimicheskaya Promyshlennost', 2007, Vol. 84, No. 8, pp. 408–414.

PROCESSES AND DEVICES OF CHEMICAL MANUFACTURES

About Informatization of Distillation Process for Providing Required Quality of Product

V. L. Chechulin[a], V. N. Pavelkin[a], Yu. P. Kirin[b], E. F. Mazitova[b], V. K. Grigalashvili[b], and A. B. Tankeev[b]

[a]*Perm State University, Belarus Division of Perm State Technical University and "Avisma" Subdivision, Perm, Russia*
[b]*Open Join Stock "Korporatsiya VSMPO-Avisma," Perm, Russia*

Received November 19, 2007

Abstract—General structure of informatization of the control over the process of separation of solid and gas phases is described for a class of such processes characterized by similarity of technological scheme. The informatization is realized by means of organization of observability the characteristics of energetic balance of the process. A special application is the process of vacuum separation of titanium sponge.

DOI: 10.1134/S1070427208030440

1. INTRODUCTION. DEFINITION OF A CLASS OF PROCESSES

There is a series of the processes of substances isolation by separation of phases (solid and gas) of periodical type: vacuum separation, evaporation, drying, etc., characterized by the features: (a) electric heating, (b) temperature in the technological unit is stabilized by application of controlling contour while temperature is measured by electronic gage inside the unit, (c) vacuum evacuation of internal space of the technological unit (uniformly during the process). Examples of such processes are the process of vacuum separation of titanium sponge [9], the process of crystallization [7], drying [6].

The process of vacuum separation of titanium sponge consists in distilling magnesium and magnesium chloride off from the titanium sponge block at high temperature under vacuum, practically to their complete removing. The process of crystallization consists in distilling under vacuum water off from saturated solution of a substance practically to complete crystallization. The process of drying consists in distilling off water under partial vacuuming practically to it complete removing water from wet material.

2. FORMULATING CRITERION OF PROCESS COMPLETING

For optimal control over such processes in respect of quality separation of substances of the parent non-uniform mixture at minimization of energy consuming, it is necessary in real time determine precisely enough the moment of the process ending, accounting for non-predictable process duration due to variations in the state of initial material, for, on the one hand, minimization the process duration (lower limit) and, on the other hand, maximizing the fraction of quality product, that is, minimizing contribution of the processes with insufficient separation (evaporation, drying) and determining for each process coefficient of average elongation relatively to individual for each process lower duration edge. Thermodynamic formulation of the criterion for ending such a process which has been initially made for the process of vacuum separation of titanium sponge [10] now is extended over whole class of above mentioned processes.

"As is known from the second law of thermodynamics

$$ds \geq dQ / T \quad (1)$$

where Q is heat, $dQ = E$, where E – energy flow into the system, then

$$ds \geq E/T \quad (1')$$

When the process is under equilibrium, then

$$ds = E/T \quad (1'')$$

In the system of separating furnance E and T are measured (observable) values (by means automatic means for control over technological process, AMCTP), therewith $T = const$ (is stabilized automatically). Thus, in the end of the process of separation (complete evaporation of Mg and $MgCl_2$) the system achieves equilibrium state: $ds = const$ (minimum), hence, from (1") follows that $E = const$ (energy flow is defined by energy loss only) and to the end of the process definitely observed constancy in energy flow into the system." Besides necessity, in [10] was shown also sufficiency of fulfilling this condition, which is even more important for determination of the moment of the process ending. Existence of such fundamental criterion that has not been described earlier (in [3,4,15]) allows us to formulate further practical mathematic methods for its calculation.

On the other hand, according to Aleskovskii theorem (2002) [1] on the connection between anisotropy and information, $s + I = 1$, $dI = -ds$, change in information equals to change in the entropy, correct to a sign. Informatively the end of separation process at the achieving entropy minimum ($dI = 0$) corresponds exactly to zeroing the entropy differential of the process of contaminants distilling off ($ds = 0$, heat loss omitted). When relatively constant heat loss is taken into account the process entropy becomes a sum of two terms: entropy of the process of phase transfer (evaporation) and entropy of heat flow of heat loss, $s = s_f + s_m$, thus $ds = ds_f + ds_m$, and the process end corresponds to the zeroing $ds_f = 0$, that is, informatively the process is completed when change in entropy mecomes constant, $ds_m = 0$. Further is describe a method for calculating this information criterion.

A necessary and sufficient condition of completing the process of separation at the separation of solid and gas phases (defined by difference in melting point, decomposition of first component and boiling point of second component (separated material) at not necessary vacuuming theoretically, according to the Second law of thermodynamics, is stabilization of energy flow into the system, E = *const*, but actually determination of this theoretically detectable moment consists [11], [10] in the following: "when process is completed, $E = const$, $E = 0$, and for determination the process end it is sufficient to test fulfilling the hypothesis on the equality to 0 of mathematical expectation of the value E", the first derivative of measurable, directly or indirectly, of energy flow into boilers (indirectly, at pulse type control, via calculated by computer routine using known power of heaters and results of current measurements with automatic system of control over technological process, on-off time ratio of the pulses of control over heaters)

3. DESCRIPTION OF MATHEMATIC AND ALGORITHMIC PROCEDURES FOR CALCULATION

The hypothesis about the process completing can be verified using a statistical criterion [11] [5, p. 633]: "using statistical t-criterion

$$y = \frac{\overline{E}_{(t_c)n} - 0}{S(E'(t))_{(t_c)n}/\sqrt{n}} \quad . \qquad (2)$$

Let us determine <practically> the moment of theoretical process ending ", where

$$\overline{E}_{(t_c)} = \frac{1}{t_c}\int_{t-t_c}^{t} E'(t)\,dt \qquad (3),$$

the average value of $E'(t)$ reflects change in energy flow in the interval of duration t_c from the current moment t to $t - t_c$. The expected value $E'(t)$ is known, $M(E'(t)) = 0$. Standard deviation $S(E(t))$ can be calculated within $[t - t_c, t]$ interval relatively to 0:

$$S(E'(t))_{(t_c)} = \sqrt{\frac{1}{t_c}\int_{t-t_c}^{t} (E'(t) - 0)^2\,dt}\,. \qquad (4)$$

We introduce renormalization of expressions (3), (4) relatively to E_{max}, the nominal value of heater power:

$$\overline{E}(t_c)n = \frac{1}{t_c}\int_{t-t_c}^{t} \frac{E'(t)}{E_{\max}}\,dt\,, \qquad (5)$$

$$S(E'(t))_{(t_c)n} = \sqrt{\frac{1}{t - t_c}\int_{t-t_c}^{t} \frac{(E'(t) - 0)^2}{E_{\max}}\,dt}\,. \qquad (6)$$

By means of the described statistical procedures, verifying of the hypothesis about equality of first derivative of energy flow into the unit to zero can be algorithmed. The algorithmed procedure of determination completing a given class of the process of chemical technology is general for various processes of this class and at informatization of the corresponding process can be built into information system (technology operator automatized work place).

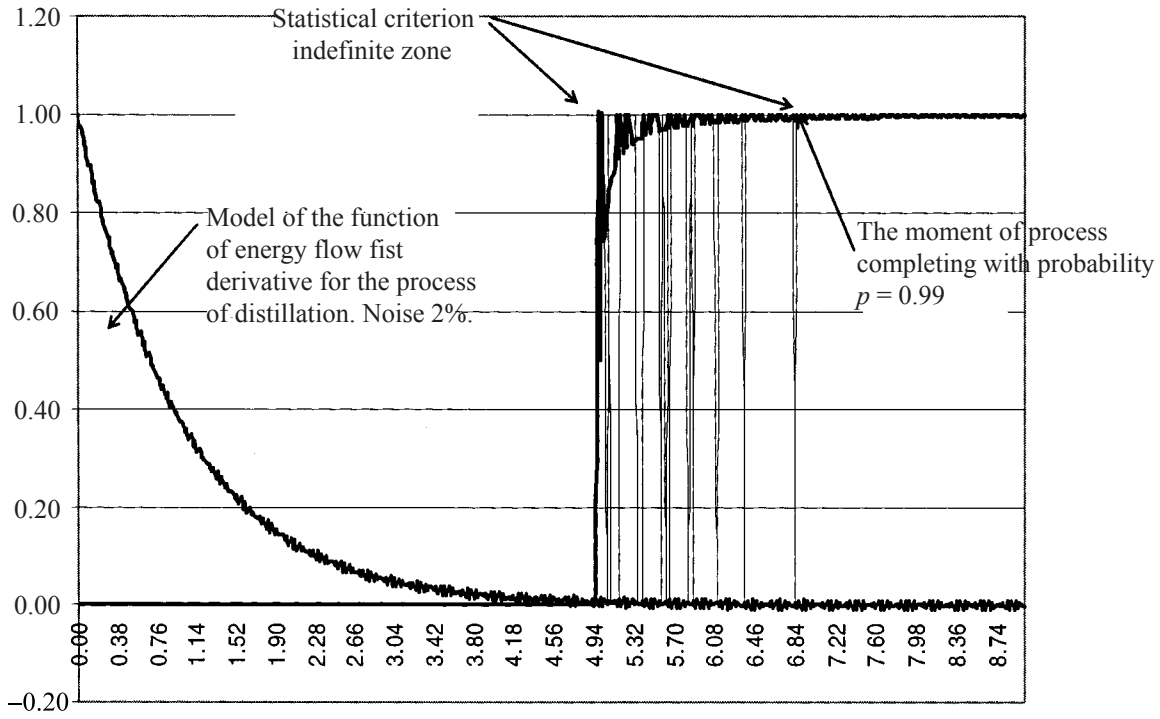


Fig. 1. The results of working of the algorithm for determination the process completing ising data of model.

These algorithms were tested on a model describing such processes. At a high noise level that corresponds to fluctuations in the function of energy flow derivative (not precise measurements) practical model determination of the process completing is enough unambiguous (see Figs. 1, 4, 5 and [14]). A system with the algorithms of less performance with quit another formulation of the criterion of process completing has been used in "Avisma" company plant since 1981 [3]. Application of statistical methods gives solution that is simoler in respect of calculations than the attempted direct analytical modeling of the system by means of integral-differential equations described in [15].

4. GENERAL TECHNOLOGICALINFORMATIONAL SCHEME OF PROCESS CONTROL

Thus, at the possibility of informational determination of completing the given class of processes using theoretical thermodynamically proven criterion of process completing, the technological and informational scheme of building this class of processes can be generalized as follows:

(1) A system of heating with measuring energy flow (system of vacuum evacuation), (2) A system of temperature stabilization inside the unit, (3) Informational measuring system (with saving data in a computer) creating data base of the process characteristics, (4) pseudoparallel in time determining the moments of processes completing (when numerous of parallel technological units are in work), (5) probability based accounting for the second sort product measure for determination on the level 4 of optimal elongation of the processes relatively to algorithmically determined moment of processes completing.

Building of the system of process control with several levels corresponds commonly used 6-level structure of Automatic system for control over technological processes (levels 1 – 3 are automatized, levels 4 – 6 are informational ones): (1) measuring (probes), 2) control over local contours (controllers), (3) data acquisition and saving (computer data base), (4) procedures of optimization in real time under monitoring by operation specialist, (5) accounting for material flows and labor consuming, solutions for supporting the process schedule, (6) prognosis and planning of commercial profit.

For example, the technological scheme of earlier studied process of crystallization (vacuum evaporation) [7] at the above considered methodology of building

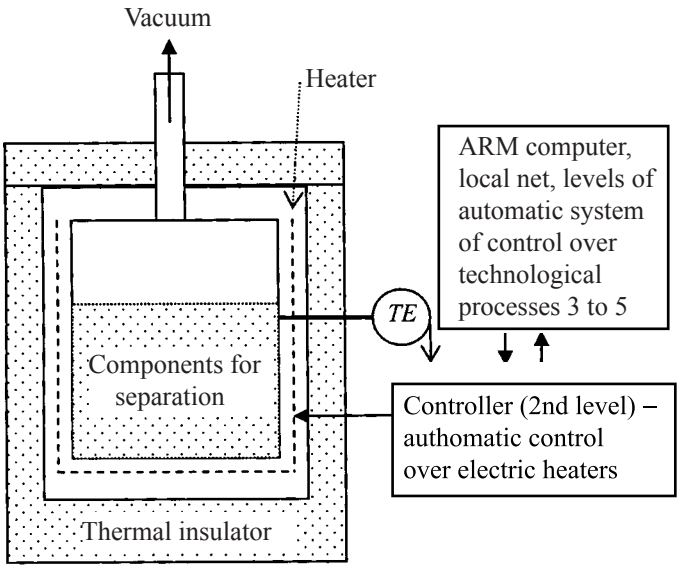


Fig. 2. The apparatuses based scheme of the process.

informational technological system for periodical process coincides (except difference in temperature regime) with the technological scheme for separation (Fig. 2).

When certain high quality of substances separation is required (minimizing the fraction of non-qualitative final product) with minimization of cost, then appears necessity of solving the problems of above mentioned real time optimization of process control which is similar for various processes owing to similarity in technological schemes. Solving the problem of optimization assumes treatment a flow of not only technological data, but also of economy data.

5. PERSPECTIVES OF OPTIMIZATION OF THE PROCESS OF DISTILLING OFF

Let us assume a number of spaces corresponding to the number of separate processes, and in each the space is defined the measuring unit of the process completing according to algorithmed criterion and can be observed actual time of the process completing and a characteristic of quality of separation substances (logarithmic, v_0 is maximum allowed concentration, v is current concentration), and let us projecting these spaces on the common coordinate system (Fig. 3). However it is impossible to determine optimal extension coefficient by a simple statistical method (like the solution of 4-th level problem of determination of the process duration). Then is remained to use knowledge on the cost and averaging over the spaces for certain preceding period to determine two functions: S_1 , the cost of the product not obtained (low quality) and S_2, the cost of extra expenditures on the process (energy consuming). The minimum of total extra expenditures, $min(S_1 + S_2)$, corresponds to optimal duration extension $k_{optim.}$, which can be recommended to the technology operator for the process control.

While optimization is possible, generally, on the characteristics of (a) material balance, (b) kinetic balance (productivity) and (c) energy balance, in this particular case the latter, energy balance, is considered for the optimization: the optimal process elongation measure relatively to the duration determined using criterion of maximal duration at the fulfilled conditions of equality

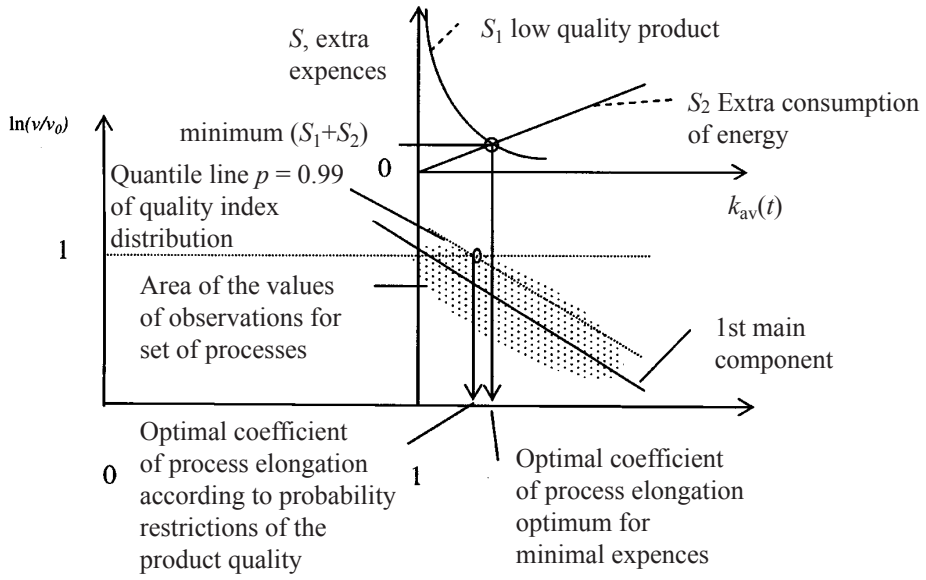


Fig. 3. Control optimization statistical diagram.

the maximum of extra expenses on electric energy to the minimum of extra expenses on electric energy due to partial formation of low quality product. A short description of the procedures is as follows: Let in first approximation that the measure of process elongation is revealed, e.g., k = 1.2, and allowed probability of obtaining quality product is defined, p = 0.995 (at the definition of the measure of quality, that means the measure of allowed fraction of not separtated product). If statistics is acquired, at the given process elongation, on the probability of obtaining quality product in a certain period (e.g., week, month, dot set 100–200), then from the revealed actual probability p_{fact} should be refined the measure of elongation k, taking into account financial estimations. If the cost of not obtained quality product S_1 (non=quality product due to non-separated substances) is higher than the cost of extra consumed energy S_2, then the measure of the process elongation k should ne increased. On the contrary, at low fraction of non-quality product and large elongation (low cost of not obtained product S_1) and substantial extra energy consuming S_2 the elongation coefficient should be decreased. Obviously, the iteration process is converged, at corrections introduced by technology operator, to equalization of the cost for the extra energy consuming and the cost of not obtained quality product, that is, to the equation minimizing total financial expenses:

$$S_1 = S_2, \; S_1 + S_2 \to min, \tag{7}$$

$$S_1 = S_0 (1 - p_{\text{observ}}), \tag{8}$$

where S_0, [Rubls] is the cost of all product (for a given period n processes), p_{observ} Is probability measure of the fraction of quality product (for the given period);

$$S_2 = C_{en} \sum_{i=1}^{n} \left(\int_{t_{init.i}}^{t_{fact.i}} \mathrm{E}_i(t)\, dt - \int_{t_{crit.i}}^{t_{fact.i}} \mathrm{E}_i(t)\, dt \right), \tag{9}$$

where C_{en} is the cost of energy (rubles per kWt/h), $t_{init.i}$, $t_{crit.i}$, $t_{fact.i}$ are the moments of beginning, ending according to criterion, and actual ending an i-th process, respectively, $\mathrm{E}_i(t)$ is the function of measure of energy flow into the system in the i-th process.

The average coefficient of the process elongation:

$$\overline{k} = \frac{1}{n} \sum_{i=1}^{n} k_i, \text{ where } k_i = \frac{t_{crit.i} - t_{init.i}}{t_{fact.i} - t_{init.i}}, \tag{10}$$

is actual and should be corrected at issuing recommendations for the cost minimization (7).

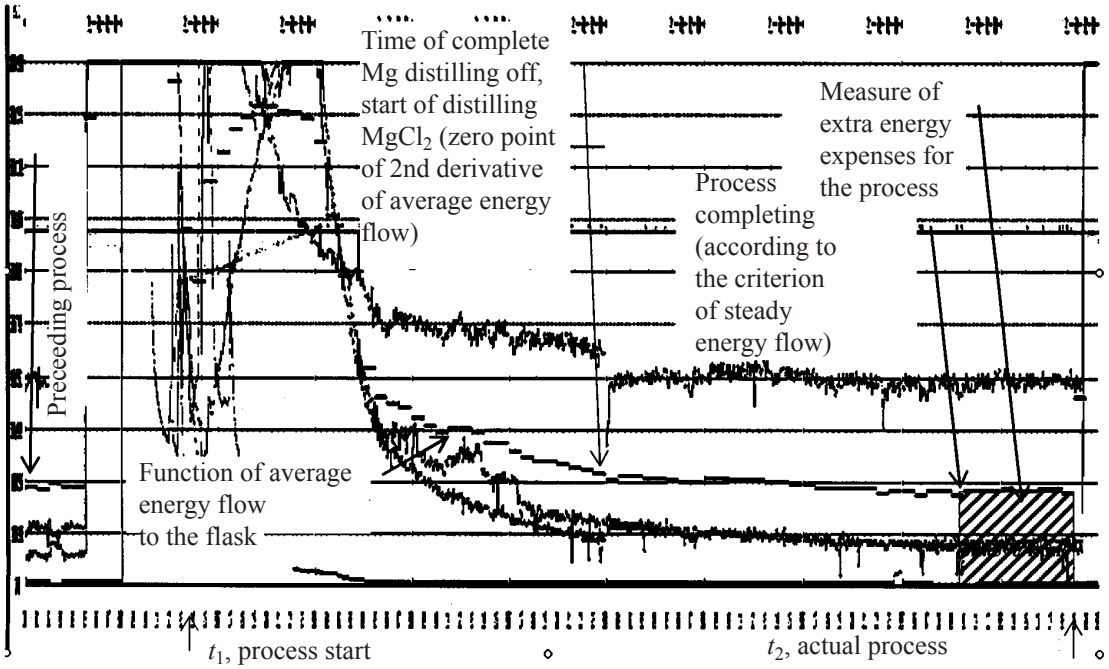


Fig. 4. Plots of the process parameters (duration ca. 80 h) with normal product quality. Photos from the computer monitor, the program product RSView (developer S.A. Evseev), time scale 20.

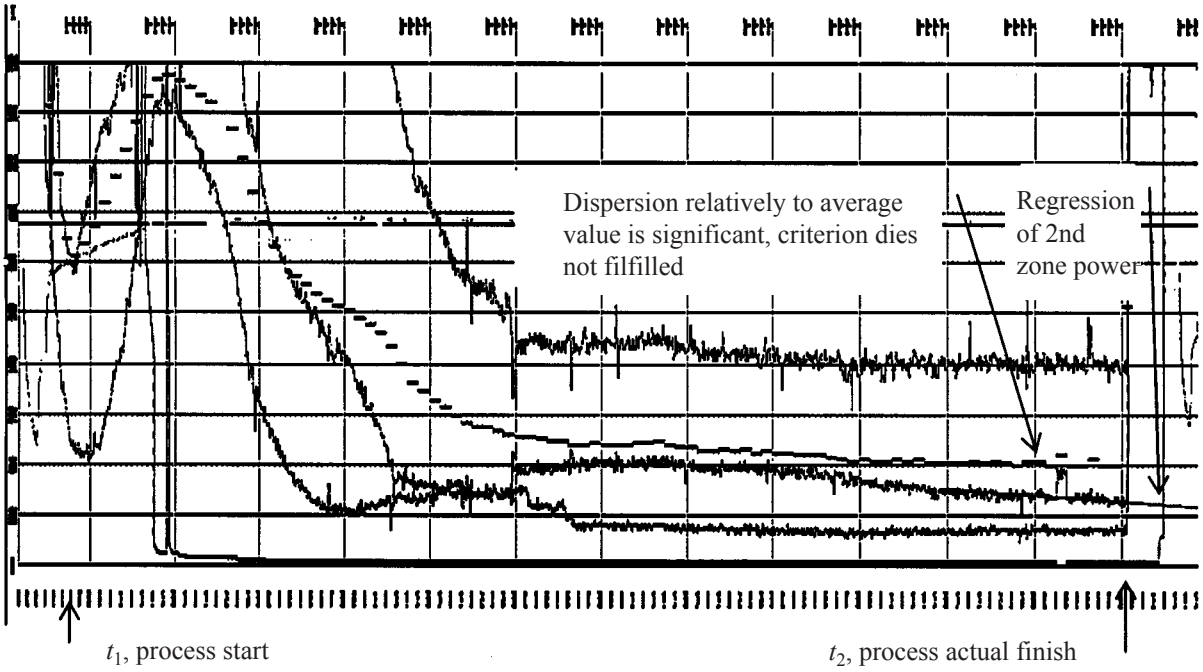


Fig. 5. Plots of the process parameters with non-quality product.

6. CONCLUSION

Information levels in the system of control over different processes of a given class of processes are fulfilled similarly, and this simplifies creation of program product capable of transfer from one information system to another. Detailed description of information system is given in [11]. At the informatization of the processes of chemical technology the methods of building technological information schemes of control over process and the methods of optimization by minimization expenses with restriction by the parameters of product quality are very similar (e.g., see [12], [13]).

REFERENCES

1. Aleskovskii, V.B., *Zh. Prikl. Khim*., 2002, vol. 75, no. 5, pp. 706–713.
2. Danilov, O.L. and Leonchik, B.I., *Ekonomiya energii pri teplovoi sushke* (Energy Economy at Heat Drying), Moscow: Energoatomizdat, 1986.
3. Kirin, Yu.P. *et al., Tsvetnaya Metallurgiya*, 1983, no. 13, pp. 31–35.
4. Kirin, Yu.P., Zatonskii, A.V., Bekker, V. F. and Bil'fel'd, N.V., *Kriterii okonchaniya protsessa vakuumnoi separatsii gubchatogo titana* (Criteria of Process Completing at the Vacuum Separation of Titanium Sponge), Berezniki: Collection of Scientific Publications of Perm State Tech. Univ., 2005, no. 4, pp. 262–267.
5. Korn, G. and Korn, T., *Handbook on Mathematic for Scientists and Engineers* (Russian translation) Moscow: Nauka. 1977..
6. Lykov, A.V., *Teoriya sushki* (Theory of Drying), Moscow: Energiya, 1968.
7. Nosov, G.A. and Bubentsov, V.Yu., *Khimicheskaya Tekhnologiya*, 2005, No. 8, p. 43–47.
8. Sergeev, V.V. and Galitskii, N.V., *Metallurgiya titana* (Titanium Metallurgy), Moscow: Metallurgia, 1971.
9. *Titan. Svoistva, syr'evaya baza* (Tiyanium: Properties, Resources), Garmata, V.A., Ed., Moscow: Metallurgiya, 1983.
10. Chechulin, V.L. and Pavelkin, V.N., *Khimicheskaya Promyshlennost'*, 2006, vol. 83, no. 12, pp. 599–600.
11. Chechulin, V.L., *Opredelenie informativnogo kriteriya okonchaniya protsessa vakuumnoi separatsii gubchatogo titana* (Determination of Information Criterion of Completing the Process of Vacuum Separation of Titanium Sponge), Perm' State Tech. Univ., 2005, unpublished manuscript.
12. Chechulin, V.L., Volchugova, E.V. and Zainullina, A.Sh., *Khimicheskaya Promyshlennost'*, 2006, vol. 83, no. 7, pp. 351–354.
13. Chechulin, V.L., *Vserossiisk. Konf. "Avtomatizirovannye*

sistemy upravleniya i informatsionnye tekhnologii" (All-Russian Conference Automatic Systems of Control and Information Technology), Perm State Tech. Univ., Perm: 2006. pp. 172-180.

14. Chechulin, V. L., Kirin, Yu. P. and Mazitova, E. F., Abstracts of Papers, *Konf. "Molodezhnaya nauka Verkhnekam'ya" pri BF PermGTU*, (Conference "Science of Young in High Kama river" at Perm State Tech. Univ.), Berezniki: 2006, pp. 45–46.
15. Shibata, K., and others, Abstracts of Papers, *Int. Congress "Titanium'95, Sciense and Tecnology"*, 1995, India, Daly: 1995, pp. 1543–1550.

ISSN 1070-4272, Russian Journal of Applied Chemistry, 2008, Vol. 81, No. 3, pp. 565–568. © Pleiades Publishing, Ltd., 2008.
Original Russian Text © B.A. Dmitrevskii, M.A. Shapkin, N.N. Terushchenko, E.B. Yarosh , 2008, published in Khimicheskaya Promyshlennost', 2007, Vol. 84, No. 8, pp. 403–407.

INDUSTRUAL ECOLOGY

Toxicology Problems at Sulfuric Acid Technology of Processing Natural Phosphates at Producing Mineral Fertilizers and Salts for Technological Application

B. A. Dmitrevskii, M. A. Shapkin, N. N. Terushchenko, and E. B. Yarosh

St. Petersburg State Technological Institute, St. Petersburg, Russia

Received August 1, 2007

Abstract—The article contains data on the content of trace contaminant of cadmium compounds in phosphate ores of volcanic and sedimentary origin. On the basis of the data of laboratory and industrial studies with participation of the authors analyzed distribution of cadmium compounds at the processing apatite concentrate of Kolskii peninsula and Maroc phosphorites. It is shown that the toxic contaminants are mostly extracted with phosphoric acid and contaminates its and products of its further processing. The most advantageous from the toxicology viewpoint is appatite concentrate of Kolskii peninsula that contaminated minimally as compared with the phosphates originated at other birthplaces.

DOI: 10.1134/S1070427208030452

The problem of contamination of mineral fertilizers with cadmium compounds harmful for human health is actual, in particular at their manufacturing from imported phosphate raw material. Ever at producing salts of food and feed quality from Kolskii peninsula apatite concentrate that contain cadmium by the order of magnitude less than foreign analogs, additional technique should be applied to provide decrease in heavy metal concentration to the allowed limit.

About 43% of world birthplaces of natural phosphates are known to afford phosphates containing 10 to 19 ppm of cadmium. 20% of resources contain 20 to 40 ppm of Cd, and in 10% of birthplaces the cadmium content is above 50 ppm. Phosphate row material of volcanic sources (apatite) contain average up to 2.5 ppm of Cd (maximal value is 5 ppm), while mass fraction of this element in phosphate ore of sedimentary origin achieves 150 ppm (Central Africa and USA) [1].

Resources of the most pure on cadmium (0.5–3 ppm) sedimentary raw material are localized in Australia (deposit Duchess), Burkina Faso (deposit Kodjari) and Iordania (deposit El Hasa). Average world content of cadmium in phosphate ore being now 21 ppm can increase in future [2].

Table 1 shows obtained by us data on the cadmium trace content in four samples of phosphate raw material: volcanic (magma) origin (Kolskii apatite flotation concentrate, Russia) and sediment origin (grinded phosphorites of birthplaces in Iordania, Maroc and Tunis).

Cadmium content was measured by the method of atomic absorption spectroscopy on inductively coupled plasma spectrophotometers "Liberty – 200" (Australia) [10] and "Unicam 939" (England) [6, 9]. For measuring mass fraction of P_2O_5 was applied chemical (photocolorimetric) method of analysis [3], which gave bone phosphate of lime (BPL) value for the natural phosphate. The data obtained are in conformity enough precisely with the data of van Kauwenburgh [1]. The cadmium trace contaminant content falls to the range from 1.5 to 51 ppm. The purest phosphate raw material in respect of the level of cadmium is apatite flotation concentrate of Kolskii birthplace related to natural phosphates of volcanic origin. Good enough material in respect of the trace contaminant content is Iordanian phosphorite. On the contrary, phosphates from North Africa and phosphorites mined in Maroc and particularly in Tunis are highly contaminated with cadmium.

The most widespread method for manufacturing extractive phosphoric acid [4–6] is dihydrate process. By this technology is produced over 80% of phosphorus-containing solutions which are processed to produce

Table 1. Content of cadmium trace contaminant in the samples of natural phosphates of volcanic (1) and sediment (2–4)

No.	Country and region of birthplace of natural phosphate	Type of natural phosphate	P_2O_5 wt. Fraction in enriched or grinded phosphate,%	BPL*	Cd concentration in phosphate, ppm
1	Rissia, Kolskii peninsula	Apatite fltation concentrate from the plant in Kirovsk town, Murmansk region	39.45	86 1	.51
2	Iordania G	rinded phosphorite 2	9.82 6	5	4.80
3	Maroc	Grinded phosphorite 3	1.60 6	9	16.2
4	Tunis	Grinded phosphorite 2	9.31 6	4	51.0

* BPL—Bone (Total) Phosphate of Lime.

Table 2. Distribution of cadmium salts at the phosphoric acid manufacturing by dihydrate method

Technological object	Consumption norm (yield) per 1 ton of P_2O_5 in acid	Cadmium content, ppm	Fraction of cadmium trace contaminant in the object (phase), %
I. Grinded Maroc phosphorite used for extraction			
Sulfuric acid (93% H_2SO_4)	3.32	0.98	5.6
Maroc phosphorite (31.6% P_2O_5, 69 BPL)	3.38	16.2	94.4
Phosphogypsum (41% H_2O total)	7.2	2.2	28.2
Extractive sulfuric acid (26% P_2O_5)	3.85	10.5	71.8
II. Apatite floated concentrate of Kolskii burthplase (Russia) is used for extraction			
Sulfuric acid (92.5 % H_2SO_4)	2.69	1.00	40.5
Floated apatite concentrate (39.4% P_2O_5, 86 BPL)	2.64	1.50	59.5
Phosphogypsum (40.0% H_2O total)	5.50	0.33	26.7
Extractive phosphoric acid (22% P_2O_5)	4.55	1.12	73.4

fertilizer, feed and technical phosphates. The acid concentration defines the methods of its further processing.

In this work we studied phase distribution of cadmium in respect of dihydrate methodology of manufacturing extractive phosphoric acid in the plant of phosphoric fertilizers in Bolgaria (town Devna) and in Polikhim company (Ukraine, town Vinnitsa). The first plant uses Maroc phosphorites (Cd content 16.2 ppm), the second producer uses flotation concentrate of Kolskii birthplace containing 1.5 ppm of cadmium compounds recalculated on Cd. The results obtained are listed in Table 2.

We established that 60 to 95% of cadmium trace contaminant incomes to the extraction process from phosphate raw material and remaining amount (2.7–3.25 ppm in 1 ton of P_2O_5 of extraction phosphoric acid) comes with "oil of vitriol". In the process of stripping natural phosphate, crystallization of gypsum and washing, 72–74% of cadmium compounds is passed into liquid phase, remaining cadmium co-crystallized with gypsum. At higher phosphoric acid concentration less cadmium is precipitated. For example, in Devna plant at manufacturing phosphoric acid containing 26% of P_2O_5 (36% H_3PO_4) which further processed into superphosphate, 71.8% of incoming cadmium is transferred into liquid phase. At the manufacturing of less strong acid (22% P_2O_5) in "Polikhim" plant (Ukraine) which is used further for producing sodium tripolyphosphate, 73.7% of cadimium incoming with raw material is passed to liquid phase. Relative error of determination of phase distribution is 3–4% that is quit acceptable. These measurements are consistent with published data [1]. According to the data

Table 3. Distribution of cadmium compounds at manufacturing superphosphate from Maroc phosphorite (31.6% P_2O_5)

Technological object	Consumption norm per 1 ton of P_2O_5 in fertilizer	Cadmium content, ppm	Cadmium fraction in the object trace contaminant, %
Extractive phosphoric acid (39% P_2O_5)	1.52 1	5.0	48.1
Maroc phosphorite (31.6% P_2O_5)	1.52 1	6.2	51.9
Double superphosphate (41.0% assimilat. P_2O_5)	2.44 1	8.0	95.8

presented by van Kauwenburgh, at processing phosphate raw material the liquid phase (extractive phosphoric acid) obtains 55 to 90% (average 68%) of the toxic metal incoming with raw material. The data obtained shows that processing of apatite flotation concentrate gives extractive phosphoric acid less contaminated with the toxic admixture.

At manufacturing double superphosphate in Devna plant alongside the return scheme of Dorr–Oliver firm [6, 7] partially evaporated phosphoric acid (39% of P_2O_5) and Maroc phosphorite are used, and the product contains 15–18 ppm of the contaminant. The process is carried out with deficiency of extracting phosphoric acid. The product contains 41–42% of phosphorus pentoxide (assimilating P_2O_5) dissolvable in 2% formic acid [2]. The balance on cadmium is achieved with error 4.2 rel%; it is shown in Table 3.

As follows from the data of Table 3, the cadmium content in the intermediates of superphosphate technology (extractive phosphoric acid and Maroc phosphorite at the second phase of separation) and in final products are closely related (15–18 ppm).

Table 4 shows distribution of toxic trace contaminants (mercury, chromium, lead, cadmium, arsenic, cobalt, nickel and copper) at manufacturing sodium tripolyphosphate ($Na_5P_3O_{10}$, STPP) from extractive phosphoric acid ob the basis of flotation concentrate of Kolskii birthplace and calcinated and caustic soda by stepwise technology [4, 8–10]. Join stock company "Metakhim" uses sodium carbonate produced from nepheline, and Open join stock "SUMS" uses sodium carbonate produced by classical Solve technology.

These data show that applied in domestuic plants two-step scheme of manufacturing sodium tripolyphosphate from apatite flotation concentrate allows removing heavy metal salts contaminants in the step of purification to obtain technical salts satisfying requirements on trace contaminants. The degree of purification from cadmium

Table 4. Content of toxic components trace contaminants in sodium tripolyphosphate (55.5–57% P_2O_5)

No.	Component	Maximal allowed level according to MDU 87 for feed phosphates, ppm	Content of component in the products, ppm, produced in plants:	
			Metakhim [8, 9]	SUMZ [10]
1	Mercury	0.1	0.01	-
2	Cadmium	0.4	0.03	0.03
3	Cromium	5.0	1.0	0.75
4	Nickel 2	0	2.0	2.1
5	Lead 5	0	1.0	1.4
6	Arsenic	50 2	.0 4	.0
7	Cobalt 5	00 0	.5 0	.4
8	Copper 5	00 3	.0 3	.5

over the technological chain that includes production of extractive phosphoric acid by extraction method with crystallization of gypsum, two-step neutralization with sodium carbonate and isolation of contaminant precipitate, drying and roasting of the salt achieves 99%.

ACKNOWLEDGMENT

This work was financially supported by the grant Contract No. INCO – CT - 2005-013359.

REFERENCES

1. Steven J. van Kauwenburgh, *Ostorozhno: kadmii. Mir Sery, N, P i K*, 2001, no. 2, pp. 5–12. Translated from: *Fertilizer International*, 2001, no. 380.
2. Kazak, V.G. and Angelov, A.I., *Khim. Promyshlennost'*, 1999, no. 11, pp. 28–35.
3. *Metody analiza fosfatnogo syr'ya, fosfornykh i kompleksnykh udobrenii* (Methods of Aalysis of Phosphate Ore, Phosphoric and Complex Fertilizers), Moscow: Khimiya, 1975.
4. Pozin, M.E., *Tekhnologiya mineral'nykh solei* (Technology

of Mineral Salts), vol. 2 , Leningrad: Khimiya, 1974.

5. Kopylev, B.A., *Tekhnologiya ekstraktsionnoi fosfornoi kisloty* (Technology of Extractive Phosphoric Acid), Leningrad: Khimiya, 1972.
6. *Tekhnologiya fosfornykh i kompleksnykh udobrenii* (Technology of Phosphoric and Complex Fertilizers), Evenchika, S.D. and Brodskogo, A.A., Eds., Moscow: Khimiya, 1987.
7. Shapkin, M.A., Zavertyaeva, T.I., Zinyuk, R.Yu., and Guller, B.D., *Dvoinoi superfosfat. Tekhnologiya i primenenie* (Double Superphosphate. Technology and Application), Leningrad: Khimiya, 1987.
8. Shapkin, M.A. and Popov, V.L., *Bytovaya Khimiya*, 2000, no. 2, pp. 5–10.
9. Shapkin, M.A., Popov, V.L., and Fedorin, P.V., *Khim. Promyshlennost*, 2000, no. 7, pp. 367–371.
10. Kozitsyn, A.A., Borisov, M.M., Sokhranov, V.A., and Gol'din, Yu.Z, *Bytovaya Khimiya*, 2001, no. 4, pp. 10–14.

ISSN 1070-4272, Russian Journal of Applied Chemistry, 2008, Vol. 81, No. 4, pp. 569–584. © Pleiades Publishing, Ltd., 2008.
Original Russian Text © S.S. Ivanchev, 2008, published in Zhurnal Prikladnoi Khimii, 2008, Vol. 81, No. 4, pp. 529–545.

REVIEWS

Fluorinated Proton-Conduction Nafion-Type Membranes, the Past and the Future

S. S. Ivanchev

St. Petersburg Branch, Boreskov Institute of Catalysis, Siberian Branch, Russian Academy of Sciences, St. Petersburg, Russia

Received February 18, 2008

DOI: 10.1134/S1070427208040010

1. INTRODUCTION

Having entered the XXI century, the humankind encountered a number of problems on which depends further normal development of the modern civilization. One of these issues is how the present level and rate of social and economic development can be provided with energy [1–3].

Most of key decisions concerning the energetic safety problems, aimed to minimize climatic changes upon an increase in the energy consumption, diminish toxic discharges into the living environment, and save energy resources were formulated in the cooperation agreement between the European Community and the United States, signed on June 25, 2003, in Washington by the EC President R. Prodi, Greek Prime Minister K. Simitis, and United States President J. Bush [4]. The energy policy of the countries that signed the agreement was based on hydrogen energetics and use of fuel cells as the most optimal variants of implementation of stable energy supply systems.

In Russia, research in hydrogen energetics and fuel cells was commenced by studies carried out in the middle of the last century. In 1947, Davtyan published a monograph [5] in which theoretical foundations and principles of direct generation of electric power with the use of chemical processes were presented. This publication served as a basis for studies in the field of hydrogen energetics and fuel cells (FC).

A fuel cell is a galvanic cell in which the energy of a chemical reaction of fuel combustion is converted into electric power. The fuel (H_2) and oxidizing agent (O_2), separately delivered to the cell electrodes, interact at electrodes to give an electric current.

The operation principles of fuel cells and fields of their efficient use are widely represented in the scientific literature [5–8]. The general operation scheme of an FC is shown in Fig. 1.

The term "fuel cell" is considered to mean a single-cell fuel cell comprising electrodes with a deposited catalytic layer and an electrolyte separating the anode and cathode spaces of FC. The fuel and the oxidizing agent are delivered into the anode and cathode spaces, respectively. The occurring physicochemical processes yield ions transported across the electrolyte. The flow of ions is compensated for by a flow electrons in the external circuit, which generates an electric current. Depending on the type of electrolyte and kind of fuel and oxidizing agent, various electrode processes may

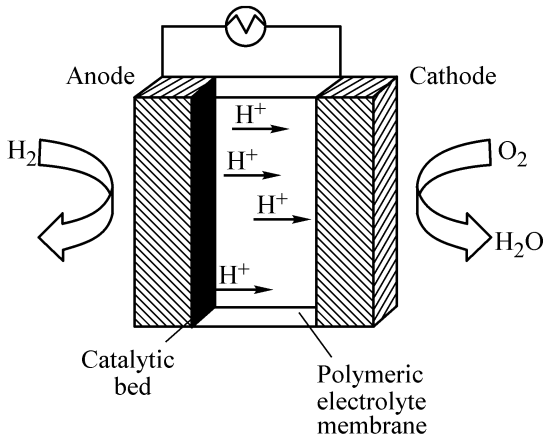


Fig. 1. Schematic of FC operation. Chemical reactions: at the anode: $H_2 \rightarrow 2H^+ + 2e$; at the cathode: $0.5O_2 + 2H^+ + 2e \rightarrow 2H_2O$; overall reaction $H_2 + 0.5O_2 \rightarrow H_2O + Q_1 + Q_2$.

Table 1. Types and selected characteristics of FC

FC type	Electrolyte	Fuel	Mobile ion	Working temperature, °C
Alkaline	Aqueous KOH	H_2	OH^-	100–250
Phosphoric acid	H_3PO_4	H_2	H^+	150–250
Carbonate-melt	$(Na, K)_2CO_3$	H_2, hydrocarbons, CO	CO_3^{2-}	500–700
Solid-oxide	$(Zr, Y)O_2$	H_2, CH_3OH	O^{2-}	700–1000
Membrane	Polymeric	H_2, CH_3OH	$H^+(H_2O)_n$	70–110

occur in FC. Table 1 lists the basic parameters of the most widely used FC [8].

Ii all these cases, atmospheric oxygen serves as the oxidizing agent. The only exception are alkaline FC, which require that pure oxygen should be used. The common advantage of all the FC is their high efficiency, resulting from the direct conversion of the chemical interaction energy into electric power, and ecological safety (with only H_2O and CO_2 as by-products). Specific difficulties are encountered in the development of each of these types of FC.

A most important condition for alkaline FC is that CO_2 should be absent in the gases supplied, in order to preclude the possible carbonization. An important problem for phosphoric acid FC is the degradation of the catalytically active layers on the electrodes and of the porous matrix used to immobilize H_3PO_4. In the case of carbonate-melt fuel cells, there appear problems associated with difficulties in retaining the carbonate melt within the porous matrix and with the stability of construction materials capable of working at temperatures of 700–1000°C. A more topical problem for membrane FC is raising their working temperature to diminish the sorption of CO contained in technical-grade hydrogen on the platinum catalyst, in order to prevent its poisoning. The fact that membrane FC cannot operate at high temperatures is presumably due to the ability of the polymeric electrolyte to retain water under this conditions, which is necessary to provide proton-conducting properties of a membrane, rather than to its thermal stability.

Despite each type of FC has its own specific features of functioning, general problems are encountered in their development, which are associated with the FC design and its improvement, enhancement of the catalyst efficiency, and functioning of the electrolyte in FC.

The electrolyte is one of the most important components of FC. On the one hand, the electrolyte provides transport of ions from one electrode to the other, and on the other hand, it precludes penetration of the fuel from the anode space into the cathode space or diffusion of the oxidizing agent in the opposite direction, both of which can result in their direct interaction. Solid electrolytes (solid oxide or polymeric) have advantages over their liquid analogues because of the wide opportunities in design and exploitation of FC.

By now, considerable advances have been made in the field of FC operating with polymeric electrolytes in the form of thin membranes. The development in this area is governed by the wide variety of application fields of membrane FC. As for solid-oxide FC, their use is presumably limited to development of high-power installations in which the loss of heat into the environment can be minimized.

Taking into account the aforesaid, we analyze in what follows the problems solely associated with polymeric electrolytes for membrane FC.

A strong stimulus to activation of research in the field of membrane FC was given by the agreement on hydrogen energetics, concluded by the Russian Academy of Sciences and Noril'skii Nikel' combine [9]. In accordance with this agreement, the research program envisaged a wide variety of studies in hydrogen energetics and fuel cells, including development of polymeric proton-conducting membranes for FC, improvement of catalytic systems on FC electrodes, improvement of the FC design, and fabrication of FC batteries. Taking into account the wide diversity of the problems associated with these tasks, we consider in more detail the development of polymeric membrane FC and analyze the synthesis and fabrication of proton-conducting polymeric (primarily fluoropolymeric) membranes for FC.

2. POLYMERIC ELECTROLYTES

Nafion. When choosing the structure of materials for polymeric electrolytes (PE), it is necessary to con-

sider the operation conditions of FC and the resulting requirements to the properties of PE.

(1) The material should have high ionic (proton) conductivity.

(2) The polymeric electrolyte should be stable in redox media, including cases of elevated temperatures.

(3) The polymeric electrolyte should be indifferent to the catalyst used, carried by the electrolyte.

(4) The polymeric electrolyte should have low permeability to the fuel used or its components (hydrogen, methanol, oxygen, etc.)

(5) The material used should possess mechanical strength, because the polymeric electrolyte is used in FC in the form of a thin membrane, and this strength should be preserved at a sufficient level in exploitation of the membrane in the hydrated state during a long time (up to 30000 h).

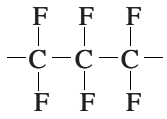
(6) With account of the fact that the proton transport occurs in the hydrated form of PE, the material should be able to retain water under the working conditions.

(7) The material should preserve its characteristics in prolonged exploitation (tens of thousands of hours).

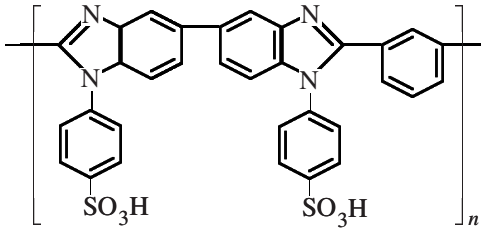
(8) The polymeric electrolyte should be comparatively inexpensive in order to provide the economic efficiency of FC.

Presumably, there is no PE fully satisfying the whole set of the above requirements now. Therefore, the development of membranes for FC is largely associated with a search for optimal variants for a particular FC.

In principle, the properties of a PE can be to a first approximation predicted on the basis of the chemical composition of the elementary unit of the polymer. For example, the proton conductivity of PE is predetermined by presence in the structure of functional groups capable of dissociation, most frequently acid groups. In practice, these may be sulfate, phosphate, or carboxy groups. If account is taken of the capacity of these groups for dissociation, sulfo groups are preferable to phosphate and, even to a greater extent, to carboxy groups. The organic radical also affects the proton conductivity of the functional groups bound to this radical. In this sense, the sulfo group bound to an aromatic ring will be more effective than that bound to an aliphatic moiety. Acid groups bound to fluorinated radicals are close in their properties to strong inorganic acids and they are more preferable, compared with structures based on aromatic compounds. The proton-conducting properties are also affected by the heat of hydration [10] and by the ability of the proton-conducting group to disintegrate (to be decarboxylated). From the standpoint of polymer chemistry, the choice of optimal solutions in this area is based on specific features of the chemical structure of the elementary unit of the polymer with account of its thermal stability and resistance to oxidative transformations. These criteria are satisfied by perfluorinated systems of the type



and by aromatic polymeric systems of the type of polybenzimidazoles (PBI)



or polymers composed of aromatic fragments of another type [poly(ester–ester)ketones etc.]

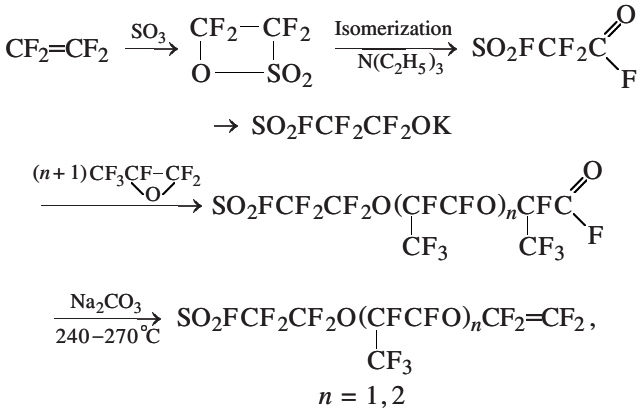
The first solution aimed to obtain a PE and fabricate FC on its basis was implemented in 1962 in the development of a power supply system for the Gemini satellite, with a PE membrane based on sulfated polystyrene [11]. The FC developed had a working life of 800 h.

The next important step in the design of a PE and fabrication of FC on its basis was made by Du Pont company in 1963 [12], which developed and patented an FC based on a copolymer of tetrafluoroethylene and perfluorinated sulfo-containing monomer of general structure



where Y = F or CF_3; R = F or C_mF_{2m-1} (m = 1–10); n = 1–3; M = F, OH, OCH_3, NH_2.

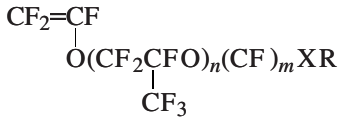
The examples in the patent [12] were mainly for structures containing Y = CF_3, R = F, n = 1, and M = F. A method used to obtain such a functionalized polymer was described in [13, 14] and consisted in a five-stage synthesis by the scheme



at n = 1—perfluoro(3,6-dioxo-4-methyl-7-octene)sulfonyl fluoride.

The know-how of each synthesis stage has not been disclosed. In Russia, the monomer received a technical name FS-141.

A sulfo-containing monomer with a close chemical structure, which was somewhat later patented by Asahi Chemical (Japan) for producing PE, had the structure [15, 16]:



where n = 0–1; m = 3–5; X = –S–, SO_2; and R = C_1–C_{10}, alkyl, perfluoroalkyl.

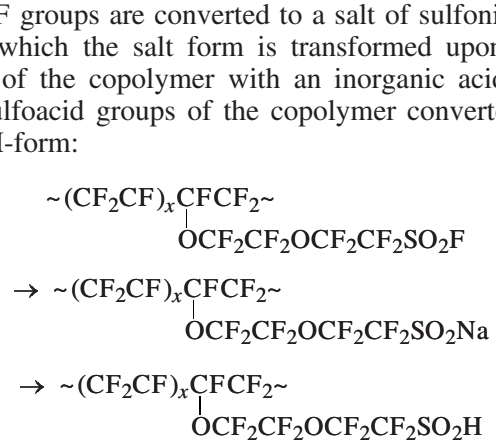
Dow Chemical developed and patented a monomer system with a sulfo group situated close to the sulfo group [17, 18]:



However further studies aimed to introduce this monomer into practice were suspended because of the lower efficiency of its use to produce a polymeric electrolyte.

The possibility of using perfluoroallyl compounds in synthesis of fluoropolymers with sulfoacid groups has been noted in the literature [19]. However, allyl derivatives of perfluorinated monomer systems failed to find real application later.

The structure of the monomer systems being synthesized shows that, both in synthesis of monomers and in their copolymerization, sulfated monomers are used as precursors containing, most frequently, sulfonyl fluoride groups, rather than sulfoacid groups. The choice of such a monomer structure makes it possible to preclude side reactions in the course of copolymerization. In this case, however, a membrane ion-exchange polymer can be obtained if the copolymerization is followed by alkaline hydrolysis and $-SO_2F$ groups are converted to a salt of sulfonic acid, after which the salt form is transformed upon treatment of the copolymer with an inorganic acid, with the sulfoacid groups of the copolymer converted into the H-form:



Copolymerization of perfluorinated sulfo-containing monomers-precursors [e.g., perfluoro(3,6-dioxa-4-methyl-7-octene)sulfonyl fluoride (FS-141)] with tetrafluoroethylene is performed, irrespective of their structural difference, mostly in a fluorocarbon solvent (Khladon 318, 350, or 113) with various initiators, peroxides of varied structure (carbon, perfluorinated, diazo compounds of N_2F_2, azo isobutyronitrile, etc.) [12, 15–21].

There is evidence, mostly in patents, that copolymerization can be performed in an aqueous medium [22–24]. These variants envisage use of water-soluble initiators (e.g., persulfates) or redox initiating systems based on persulfates or perfluorinated emulsifiers (e.g. salts of perfluoropelargic acid). The copolymer is obtained in the form of a dispersion. The process is distinguished by the possibility of performing polymerization to conversion degrees of about 50% in terms of the sulfo monomer. However, the method of emulsion polymerization have not found practical use for production of Nafion-type polyelectrolytes so far.

The copolymerization in a solution of khladons is commonly performed at temperatures of 30–80°C, depending on the initiator type. The pressure of the tetrafluoroethylene (TFE) used in the process is not a critical parameter [12] and can be chosen so as to create in the liquid phase a TFE concentration providing the necessary relative amounts of the monomers for obtaining a copolymer of the required composition. The pressure is most frequently chosen within the range 3–8 kg cm^{-2}.

The main difficulty encountered when performing copolymerization of TFE with FS-141 is in the strong difference in activity between the monomers being co-

polymerized. There are no data on the activity of TFE and the sulfo monomer in the nonclassified literature. Using information about the activity of the structurally similar analogues containing carboxy and ester groups [25], we can assume that this difference in activity is as strong as two orders of magnitude. Therefore, the whole amount of the less active sulfo-containing fluoromonomer is charged into the reactor for copolymerization, and TFE is batched in the course of the process, with its constant pressure maintained. As a rule, the process is carried out to low conversions of the monomer (~20%) in order to maintain a constant ratio between the reacting monomers and an invariable initiator concentration in the reaction medium. These conditions provide synthesis of a polymer with a comparatively narrow molecular mass distribution and functional groups uniformly arranged along the chain. The copolymerization process can be illustrated by the scheme

$$CF_2{=}CF_2 + mCF_2{=}\underset{\displaystyle OCF_2CF_2OCF_2CF_2SO_2F}{\underset{|}{CF_2}}$$

$$\xrightarrow{R^{\bullet}} R[(-CF_2CF_2)_xCF_2\underset{\displaystyle OCF_2CF_2OCF_2CF_2SO_2F}{\underset{|}{CF}}\sim]_n$$

It has been shown recently that the structure of the peroxide initiator used strongly affects the thermal stability and service characteristics of the PE obtained [26, 27]. It was experimentally confirmed that use of perfluorinated peroxide initiators in copolymerization makes it possible to obtain membranes with an improved thermal stability. A detailed study of how the service life of perfluorinated PE of the Nafion type decreases depending on the nature of terminal groups in the polymer was reported in [27].

When determining the properties of PE, the composition of copolymers is evaluated using the notion "equivalent mass" (EM), the molecular mass of a polymer chain fragment per a sulfo group. Experiments demonstrated that the EM of the polymer formed in copolymerization should fall within the interval between the limiting values, the upper of which is related to the percolation threshold, i.e., the minimum content of ionogenic groups at which an ionic (proton) conductivity appears in the membrane because of the formation of ionic clusters. The lower limit is due to deterioration of the physicomechanical properties of the polymer because of the pronounced water absorption (swelling) and even dissolution of PE in water. According to the data of [20], the EM should be in the range 800–1500. According to [29], the PE of the Nafion type have the optimal properties at EM of 1000–1100.

Table 2. Properties of membranes based on Nafion-117

Property	Value achieved
Exchange capacity, mg-equiv	~0.91 (up to 1.0)
Surface resistance Ω cm^{-2}	~0.09–0.12
Working life, h	Thousands (tens of thousands)
Proton conductivity, S cm^{-1}	~10^{-1}–10^{-2} (~0.1 at 80°C)
Current density, mA cm^{-2}, at a voltage of 0.45 V	~250–640
Methanol diffusion coefficient,	2×10^{-6}
Water absorption capacity, %	~15
Specific power mW cm^{-2}	600–800
Cost, USD/m^{-2}	~700

No information about the type of distribution of monomer links in the chain of the macromolecule is available in the literature.

After a certain extent of transformation of the monomers is reached (the corresponding amount of TFE is introduced), the polymerization process is terminated, the reactor is cooled to 15°C, the unreacted TFE is blown away, and a suspension of the copolymer in khladon is discharged. Khladon is evaporated under atmospheric pressure, and the polymer is separated, washed with khladon to remove the unreacted comonomer, and dried first in air at room temperature under agitation in the course of 24 h and then in a vacuum box at 60°C for 16 h. The polymer obtained is analyzed and processed into a film by hydrolysis and conversion of $-SO_3Na$ groups into the H-form, to give a perfluorinated ion-exchange membrane of the Nafion type.

The principles described above formed a basis of techniques used to manufacture industrially used perfluorinated membranes of the Nafion type (Flemion, Aciplex, etc.). Membranes of this type have found wide use in the development of FC. The potentialities of such materials were described in a number of reviews [7, 8, 30, 31]. To advantages of this class of membranes should be attributed their high chemical resistance, mechanical strength, and high proton conductivity in the temperature range 40–90°C.

Table 2 lists some basic parameters of membranes of the type under consideration for the example of the Nafion-117 material. Comparison of the proton conductivities of Nafion membranes and nonfluorinated

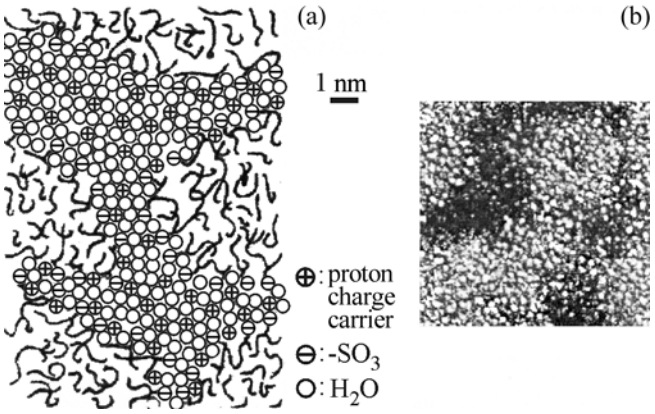


Fig. 2. Structure of perfluorinated sulfonated copolymers of the Nafion type. (a) Nanosize phase distribution according to the small-angle X-ray scattering and (b) microstructure according to the results of modeling by the molecular dynamics method.

polycondensation systems [31] clearly shows the advantage of the former.

Haile [8] analyzed the structure of the nanosize phase distribution according to the results of small-angle X-ray scattering in a membrane of the Nafion type (Fig. 2). It can be seen that the PE of the Nafion type is a submicroheterogeneous system with sulfo groups in nanosize clusters connected by channels through which the proton transport occurs.

The method of small-angle neutron scattering was first used to determine the internal structure of a polymeric electrolyte of the Nafion type and compare this structure with that of polyester ketones [32, 33]. It was shown that the maximum radius of the structural unit (cluster) is 31 Å for moistened Nafion and about 27 Å for a dry membrane. For the sulfonated polyester ketone, no structuring in the range 13–300 Å was found. An anisotropy of neutron scattering was also noted for Nafion.

Recently, the structure of perfluorinated sulfonated polymers of the Nafion type, manufactured by Du Pont, and of its domestic analogue (Plastpolimer Research and Production Association) with a technical name MF-4SK has been studied by the method of small-angle neutron scattering [34]. The new method enabled evaluation of the size characteristics of nanosize clusters and channels in the submicroheterogeneous system of the polymeric proton-conducting membranes under study.

To reveal differences in internal structure between Nafion manufactured by Du Pont and an MF-4Sk membrane, membrane samples were studied in three states: initial, that after drying at 100°C, and that after saturation of dried samples with D_2O. An analysis of the scattering intensity as a function of the momentum transferred demonstrated that, in the momentum range $q > 0.2$ nm^{-1}, the scattering intensities for Nafion and MF-4SK are close. At small momenta ($q < 0.2$ nm^{-1}), a noticeable increase in the scattering was observed for MF-4SK, whereas for Nafion, this change is small. These results indicate that small scatterers (pores) are predominant in Nafion, and the contribution of coarser pores is noticeable in MF-4SK. A processing of the experimental data demonstrated that the number of fine pores in Nafion is approximately 7 times that in MF-4SK.

The difference in the number of coarse pores is also significant. At a comparable size of about 20 nm, their number in MF-4SK is substantially larger. However, the polymeric matrix of MF-4SK is saturated with D_2O at a considerably lower rate than Nafion (in 2.5 h, 17.2% D_2O is introduced into Nafion, and only 12.3% into MF-4SK). This means that not all coarse pores in MF-4SK are connected by channels, with the result that part of the pores is not filled and, consequently, excluded from the conduction process. Thus, the MF-4SK membrane has a lower "conductivity" because of the specific features of fabrication (or storage) of this material.

A comprehensive study of the nanosize submicroheterogeneous distribution of sulfoacid groups and channels connecting these groups was found to be very important not only for a clear explanation of the mechanism of proton conduction in Nafion membranes, but also for substantiation of new approaches to modification of this kind of membranes, aimed to improve their working capacity at temperatures higher than 90°C.

It is known that the optimal working temperatures of FC based on PE of the Nafion type do not exceed 80–90°C. These conditions can only be satisfied if hydrogen used as the fuel contains no admixtures of CO, which can poison the Pt catalyst supported by the electrode at a content exceeding 10 ppm.

At temperatures higher than 130°C, the adsorption equilibrium of CO and H_2 sorption on the platinum catalyst is shifted toward H_2, which precludes catalyst poisoning. However, the proton conductivity of the membranes substantially decreases at elevated temperatures (~120–140°C) via dehydration of Nafion, because the proton conduction (or, more precisely, transport of H^+) occurs in the hydrated form (with simultaneous transfer of more than 10 molecules of water).

A recently published study by carrier out at Princeton University, was concerned with the sorption–desorption of water and the water-permeability of membranes with different thicknesses, based on Nafion-112, 115, 1110, and 1123, as a function of temperature in the range 30–90°C [35]. Emphasizing the important role of the sorption and transfer of water in PE in the control over the operation of fuel cells, the authors point to the necessity for analyzing the distribution of water in the fuel cell, which, in turn, affects the local proton conductivity. It was shown that the permeabilities of a membrane to water from the liquid aqueous phase and humidified gas are different. The membrane has a smaller swellability in the presence of a water vapor. This results in that a thin layer of the hydrophobic polytetrafluoroethylene is formed on the dry side of the membrane, and this layer makes lower its water permeability. The water permeability weakly depends on the membrane thickness. The data obtained demonstrate that the rate of water desorption from a water-saturated membrane is an order of magnitude higher than the rate of water sorption. Analysis of the data on water permeability and sorption makes it possible to determine those modes of water transfer and sorption in Nafion, which correspond to diffusion across the membrane–gas interface and swelling of the polymer in saturation with water.

Thus, despite the important advantages of proton-conducting Nafion type membranes, such as chemical resistance, mechanical strength, and high proton conductivity, it is necessary to modify the structure and properties of Nafion in order to choose the optimal mode of their exploitation with account of temperature, preservation of water content, and effect of impurities in the hydrogen-containing fuel.

In the last decade, the work on Nafion modification has acquired a decisive importance for further development of the technology of polymer-electrolyte membranes (PEM).

3. MODIFICATIONOF COMMERCIAL MEMBRANES OF THE NAFION TYPE WITH POLYMERIC SYSTEMS

Figure 2 shows specific structural features of Nafion type membranes, which are a consequence of the incompatibility of the main fluorocarbon polymeric matrix with sulfo groups grafted to the polymetric matrix. The hydrophobic nature of the fluorocarbon fragment of macromolecules and the hydrophilicity of sulfonic groups give rise to nanostructural heterogeneities composed of cluster up to 3 nm in radius, connected by 1–2-nm-wide channels. A change (e.g., decrease) in the EM of the membrane may be accompanied not only by an increase in the proton conductivity of FC, but also by deterioration of the mechanical strength of the membrane because of the increased water absorption and the resulting change in the volume of the swollen material.

In this context, intensive studies of structural transformations that alleviate these disadvantages have been performed in the last decade. In particular, methods for surface modification of Nafion membranes by radiation grafting of polystyrene [36] or by grafting of styrene in supercritical CO_2 [37], followed by sulfonation in concentrated sulfuric acid have been suggested. A study of the resulting grafted modified systems revealed an increase in the glass-transition temperature of the material of the membrane and a slight decrease in its crystallinity (because of the incorporation of amorphous fragments of polystyrene). Simultaneously, the ionic conductivity of the new modified system increases, compared with the starting material of the Nafion type [37].

In the patent [38], a variant was suggested for modification of Nafion membranes with polystyrene in a mixture with divinylbenzene or water-impermeable copolymers: polyethylene, polyhexafluoropropylene, copolymers of hexafluoropropylene with propylene or ethylene, copolymers of vinylidene fluoride with tetrafluoroethylene, etc. The grafting is initiated by irradiation with accelerated electrons. Owing to their water-impermeable properties, the resulting membranes are rather promising for use in FC employing methanol as a fuel.

A method of Nafion impregnation with polypyrrole has been suggested for surface modification of Nafion type membranes [39]. This method improves the efficiency of electron removal from the platinum layer of the electrode.

It has also been suggested to introduce polypyrrole electrochemically in situ into membrane pores [40] in order to preclude the through penetration of methanol across the membrane in the case of its use in methanol systems.

Variants of structural modification via introduction into a polymeric system of monomers containing an amino group that cross-links the monomers with two or more epoxy or isocyanate functional groups in order to raise the strength properties of Nafion membranes have been suggested [41]. The joint dissolution of these groups in Nafion and subsequent formation of a partly cross-linked or bridged polymer improves the properties of the membranes.

In the patent [42], a method was described for modification of a proton-containing membrane based on Nafion by in situ polymerization of cation monomers deposited onto the membrane surface:

$$R^1R^1C{=}CR^2\underset{\underset{O}{\|}}{C}O(CR^1R^1)_n{-}CR^1N(R^3)_3^+A^-$$

or

$$R^1C{\equiv}CR^2\underset{\underset{O}{\|}}{C}O(CR^1R^1)_n{-}CR^1N(R^3)_3^+A^-$$

where R^1 = F or H; R^2 = H, CH_3, or halogen; R^3 = CH_3, C_2H_5; A^- = SO_3^-, Cl^- anion.

Chemical or radiation initiation of the polymerization of polymers of this kind results in the formation of a protective layer that precludes partial dissolution of silicone contacts in the interaction with perfluorosulfonic acid contained in the membrane and to a substantial increase in the membrane resistance.

Methods have been patented for production of membranes with enhanced mechanical strength and increased proton conductivity at a small thickness (0.025 mm) by combining an inert highly porous polytetrafluoroethylene with impregnation with a proton-conducting Nafion [43] or by creating a three-layer proton-conducting membrane with an inner layer with EM increased by 20% and outer layers with lowered EM [44]. As shown by studies, such a three-layer design is equivalent in conductivity to a membrane with composition identical to that of the outer layer.

The patent [45] described various methods for fabrication of composite two-component membranes, based on impregnation with polymeric electrolytes of the Nafion type (or with other polymeric electrolytes) of inert polymers (perfluorinated polymers and copolymers, polyvinyl chloride, polyvinylfluorostyrene, polyester ketone, polyestersulfone, etc.) or porous inorganic materials (glass fibers, oxides, silicates). An important issue in this case is combination of an inert polymer and a polymeric electrolyte (or its precursor). If a precursor is used, it is converted into the ion-conducting form. Variants of production of polymeric membranes by this method can provide control over the physicochemical properties by varying the ratio between the components or the degree of precursor conversion into the active form.

The possibility of modifying Nafion-115 with a polymerized phenol-formaldehyde resin to improve the properties of Nafion-115 to be used in FC operating on methanol was described in [46]. After being introduced into Nafion, the resin is subjected to sulfonation. A good dispersive ability of phenol-formaldehyde resin in Nafion was demonstrated. Composite membranes of this kind are close to Nafion in proton conductivity and are more suitable for use as regards their permeability to methanol. The composite membrane substantially surpasses Nafion-115 in the maximum power density (114 and 78 mW cm^{-2}, respectively).

A research group from Uppsala University (Sweden) [47] obtained a composite membrane based on Nafion modified by diffusion of a polybenzimidazole solution at various concentrations and drying temperatures. The possibility of raising the conductivity by 50% as compared with pure Nafion, combined with a decrease in the permeability to methanol, was demonstrated.

Attention should also be given to the resumed attempts to create new types of PEM by replacing the so usual sulfo-containing polymeric systems with other industrially manufactured polymers with aryl skeleton: polystyrenes, polycarbonates, polysulfones, and other compounds subject to sulfonation by appropriate reagents [48]. The membranes synthesized were studied by various physicochemical methods in order to identify proton transport centers, determine the thermal stability of the resulting membrane systems, and their water sorption and desorption parameters. The experimentally measured ion-exchange capacities were found to be comparable with the values for industrial Nafion-type membranes. The best parameters were observed for sulfonated polycarbonates: exchange capacity as high as 0.57 meq g^{-1}, tensile strength 157 N mm^{-2}, and glass-transition temperature 120°C, at a low affinity for methanol (sorption 2.97%). The results obtained give reason to hope that new inexpensive proton-conducting membranes can be developed.

To this kind of studies can also be referred those in which ion-exchange membranes are produced by the method of graft polymerization, initiated by a preliminary irradiation, of styrene or a mixture of styrene with divinylbenzene on structured films of polytetrafluoroethylene (RX–PTFE), followed by sulfonation of the grafted polymers [49]. The achieved values of ion-exchange capacity of the membranes are within the range 1.5–2.8 meq g^{-1} and can exceed the ionic conductivity of Nafion-112.

In [50], the possibility of obtaining polystyrenes or similar polymeric systems grafted to polytetrafluoro-

ethylene with the use of ultraviolet irradiation, followed by sulfonation.

Particularly noteworthy is the recently published study [51] devoted to grafting of functionalized vinyl monomers to tetrafluoroethylene or copolymer films. The authors described a method for producing a PE membrane combining high proton conductivity and high thermal stability by grafting a vinyl monomer containing a trimethoxysilyl group (*p*-styryltrimethoxysilane) to films of a copolymer of ethylene with tetrafluoroethylene, subjected to a preliminary gamma irradiation. Films with a grafted *p*-styryltrimethoxysilane were sulfonated for groups of sulfonic acid to be added to aromatic rings of grafted chains and then were subjected to hydrolysis and condensation to give silanol cross-links between the grafted chains. In this way, a cross-linked proton-conducting polymer-electrolyte hybrid membrane was produced. The preparation conditions (grafting and sulfonation) and the properties of the polymer-electrolyte membrane obtained (ion-exchange capacity, proton conductivity, water-absorption capacity, and thermal stability) were analyzed to determine the possibility of its use in fuel cells. It was shown that the new hybrid polymer-electrolyte membrane with grafted *p*-styryltrimethoxysilane is comparable in its properties to Nafion and surpasses membranes with grafted styrene.

Recently, considerable attention has been given to modification of Nafion with various polymers in order to reduce its permeability to methanol and enable use of the polymer-electrolyte composite in fuel cells operating directly on methanol. For example, modification of Nafion-117 with organic silanes containing thiol groups was considered in [52], with the result that the permeability to methanol was reduced by 50%, but the proton conductivity also somewhat decreased.

A proton-conducting membrane operating on methanol was produced on the basis of a composite constituted by Nafion and poly(*p*-phenylenevinylene) [53]. The structure of the composite was characterized by IR spectroscopy and scanning electron microscopy. Also, the conductivity, wettability, and water-retaining capacity of the membranes obtained were determined.

In [54], production from Nafion-117 of a composite system of sulfated polystyrene and Nafion, formed on the principle of a semi-mutually penetrating network, was described. An increased proton-conductivity of the resulting membranes at temperatures higher than 110°C was noted.

A multilayer proton-conducting membrane composite has been obtained on the basis of Nafion and sulfonated polybenzimidazole by impregnation of films of sulfated polybenzimidazole with a Nafion solution [55].

In [56], synthesis of a proton-conducting membrane for methanol FC from Nafion coextruded with carbon nanotubes was reported. It was stated that the permeability of the material obtained to methanol becomes lower without any decrease in the proton conductivity.

In [57], a review of developments in the field of membranes of varied structure for fuel cells was made, with the conditions of their optimal operation and relationships between the structure and properties of the membranes, on the one hand, and their applicability in fuel cell systems, on the other, considered.

The analysis made revealed a high intensity of studies devoted to modification of properties and possibility of use of proton-conducting Nafion type membranes. Also impressive is the wide variety of polymeric systems used for modification and the diversity of methodological modification procedures. The progress made is primarily associated with the improvement of the barrier properties of membranes and strengthening of the polymer matrix. The analysis on purpose disregarded the possibility of using polymers with a clearly pronounced hydrophilicity for modification of Nafion-type systems. These systems will be considered upon analysis of membrane modification with inorganic compounds. Nevertheless, it is well seen just now that the modification of Nafion, which can improve the efficiency of its use at elevated temperatures (120–130°C), is not simple and requires further in-depth studies with the use of integrated methodological approaches.

4. MODIFICATION OF MEMBRANES OF THE NAFION TYPE WITH INORGANIC COMPONENTS

Modification with inorganic components as an approach to improvement of service characteristics of Nafion-type membranes is due to the necessity for improving the water-retaining capacity of the membranes and for precluding their dehydration because of the hydrophilicity of the inorganic component and its capacity for chemical or coordination binding of water. This variant of Nafion modification can compensate for the loss of water by membranes working at elevated temperatures and reduce or completely eliminate the deactivation of the catalytic Pt layer,

Table 3. Proton conductivity of membranes of the Nafion type, modified by repeated casting and treated with ultrasound [66]

Membrane type	Thickness, μm	Surface resistance, Ω cm^{-2}	Proton conductivity, S cm^{-1}, at a relative humidity of 70%
Nafion-115	100	1.23	8.13×10^{-3}
Nafion-115–SiO_2	100	0.92	1.07×10^{-2}
Nafion-115–SiO_2–PTA	120	0.45	2.67×10^{-2}

thereby making possible the functioning of the membrane at temperatures higher than 130°C.

In a number of studies [58–60], the possibility of improving the properties of Nafion-type membranes by introduction of silicon dioxide into their composition was considered. The modification was performed by placing a membrane in the H^+-form in a solution of tetraalkoxysilane (TEAS), with the subsequent hydrolysis of TEAS absorbed by the membrane. It was shown that modified membranes can efficiently operate at temperatures higher than 100°C (up to 140°C). The proton conductivity of the membrane increases with the SiO_2 content to reach a maximum at 10–12% and then decreases as the content of silicon dioxide introduced grows further.

Nearly simultaneously with the analysis of the influence exerted by the SiO_2 additive on the properties of Nafion-type membranes, the intrinsic proton conductivity of the class of heteropolyacids: phosphotungstic acid (PTA), silicotungstic acid, etc., was studied [61–64]. It was shown that heteropolyacids have a high room-temperature proton permeability [61] and can be immobilized in Nafion [62] to give composites with a high proton conductivity (>10 S cm^{-1}) at room temperature. However, heteropolyacids are commonly immobilized in silica gel because of their high solubility in water [61]. PTA immobilized in a silica gel, combined with polyethylene oxide, gives a hybrid proton-conducting system with a conductivity of 10^{-3}–10^{-2} S cm^{-1} in the range from room temperature to 140°C [64]. These opportunities were used in [65], whose authors replaced polyethylene oxide with Nafion and obtained a Nafion–SiO_2–PTA composite, which was successfully tested in a fuel cell operating on methanol at 145°C.

Later, the possibility of improving composite membranes of a similar composition by repeated casting with the use of a Nafion solution preliminarily subjected to ultrasonic mixing with SiO_2 and PTA was described [66]. The parameters of the material synthesized were compared with the properties of the Nafion–SiO_2 composite obtained using a similar mixing procedure. The material was studied by the following techniques: scanning electron microscopy; X-ray diffraction, thermographic, and differential-thermal analyses; and IR Fourier spectroscopy. The study revealed important advantages of the above-described method for forming a composite membrane: it provided an increase in the degree of crystallinity and in the water-absorption capacity of the membranes obtained. The crystallinity increased by 18% for a repeatedly cast starting membrane, 25% for the Nafion–SiO_2 composite, and 20% for the Nafion–SiO_2–PTA system. The increase in the water-absorption capacity for these systems after their repeated casting was 26 to 32% for the starting membrane, up to 34% for the Nafion–SiO_2 composite, and up to 38% for the Nafion–SiO_2–PTA system.

The results obtained in a study of membranes modified by the method described in [66] (Table 3) indicate that their proton conductivity substantially increased.

Thus, the suggested ultrasonic treatment of the membrane composites modified with the SiO_2–PTA system leads to a threefold increase in their proton conductivity.

The effects observed can be attributed to the hydrophilic nature of SiO_2 and PTA, changes in the degree of crystallinity of the membrane, and stronger interaction of absorbed water with the modified matrix. Previously, Zawodzinski and co-workers noted [67] that the proton conductivity of a Nafion-type membrane virtually linearly increases with its water-absorption capacity. A repeated casting of the membrane improves its properties and raises its water-absorption capacity as compared with the starting material. With composite Nafion–SiO_2 and Nafion–SiO_2–PTA membranes, higher current densities were obtained, equal to 320 and 540 mA cm^{-2}, compared with 95 mA cm^{-2} for the starting Nafion-115 membrane.

Also, the effect of various inorganic modifiers (SiO_2, SiO_2–PTA, Al_2O_3, and ZrO_2) on the proton-conductivity of Nafion-type membranes has been compared in relation to the water-retaining capacity of the modifiers and the acid-base properties of their surface [68]. The highest efficiency of the SiO_2–PTA system, resulting from its own acidity and a large amount of crystal-bound water in PTA ($H_3PW_{12}O_{40} \cdot$

$36H_2O$), was confirmed. An extremal run of the temperature dependence of the membrane resistance, with a minimum at 140–150°C, was revealed for most of the above-mentioned fillers, which is due to desorption of water contained in pores and physically sorbed on the surface. In [69], the effect of addition of highly dispersed TiO_2 powders on the properties of Nafion-type composite membranes was analyzed. In the same study, the possibility of modification of the membrane material by introduction of fluorinated montmorillonite into the Nafion structure was described. The systems obtained show improved barrier properties without any decrease in the proton conductivity.

Of particular interest is introduction into Nafion of highly dispersed SiO_2 surface-modified with $–SO_3H$ groups [70, 71]. Mixing with Nafion of modified SiO_2 produced by functionalization of the starting aerosil with 1,2,2-trifluoro-2-hydroxy-1-trifluoromethylethanesulfonic acid yields a membrane with an increased proton conductivity dependent on the concentration of the modifier introduced (the maximum value of 0.12 S cm^{-1} was achieved at a modifier content of 3%). The modified membrane also shows improved barrier properties.

The possibility of obtaining sulfonated SiO_2–SO_3H nanoparticles has been noted previously, without description of the preparation technique. For example, modification of polyesterketone-based membranes with SiO_2–SO_3H nanoparticles to give membranes with increased strength and conductivity, which can be used in methanol FC, was considered in [72].

To conclude, we note that the proton-conductivity of Nafion can be raised by the effect of physical treatments in the course of membrane casting and, in particular, that with electric field, on the formation of directionally oriented ionic channels [73].

The effect of formation of oriented nanodomain structures has also been noted for production of polyelectrolytes by plasma-initiated graft polymerization [74]. The morphology of the nanodomain structure was determined by scanning electron microscopy and IR Fourier spectroscopy. A sixfold increase in the proton conductivity, compared with the starting Nafion, was recorded.

Analysis and generalization of the data obtained and their theoretical substantiation show that a considerable progress has been made in the last decade in improvement of service characteristics of Nafion-type proton-conducting membranes by modifying their structure by introduction of polymeric and inorganic components. The possibility of extending the working temperature range of membranes to higher temperatures, raising the proton-conductivity, and improving the water-retaining capacity and barrier properties has been demonstrated. It has been shown that the structure of membranes can be modified to enable their use in fuel cells operating on methanol.

When summarizing the material being analyzed, it is necessary to take into account the data presented in some of project reports of 2003–2005 in the framework of the US Program of hydrogen energetics, which involved leading universities, national laboratories, and companies [75]. Advances in the following areas can be noted.

(1) The mechanism of the peroxide attack in the course of membrane operation has been determined.

(2) Fluorinated initiating systems providing formation of fluorinated terminal groups have been chosen.

(3) The physicomehanical properties of membranes have been improved by, in particular, the following kinds of modification: synthesis and introduction of dispersed modified silica with added sulfone groups and modification with the use of dendrite structures.

(4) Water-insoluble organic–inorganic hybrid systems mixed with Nafion, which are thermally stable up to 300°C and have a proton conductivity of 0.35 S cm^{-1} at 80°C and relative humidity of 5%, have been developed.

(5) Polyblock polymeric systems with high proton-conductivity have been created and ionic liquids have been used as proton-conducting media.

The results mentioned above presumably form an incomplete list of the achievements of the program, but demonstrate that Nafion-type polymeric membranes remain highly competitive among the so far developed proton-conducting materials and keep the leading position both in the level of their development and in the proton conductivity and service life.

5. ACHIEVEMENTS IN DEVELOPMENT OF POLYCONDENSATION PROTON-CONDUCTING MEMBRANES AND HYBRID MEMBRANE SYSTEMS [29–31]

In [30], the level (state) of the technological development and potentialities of membrane polymers of varied structure for FC operating on hydrogen and methanol and for high-temperature FC is shown graph-

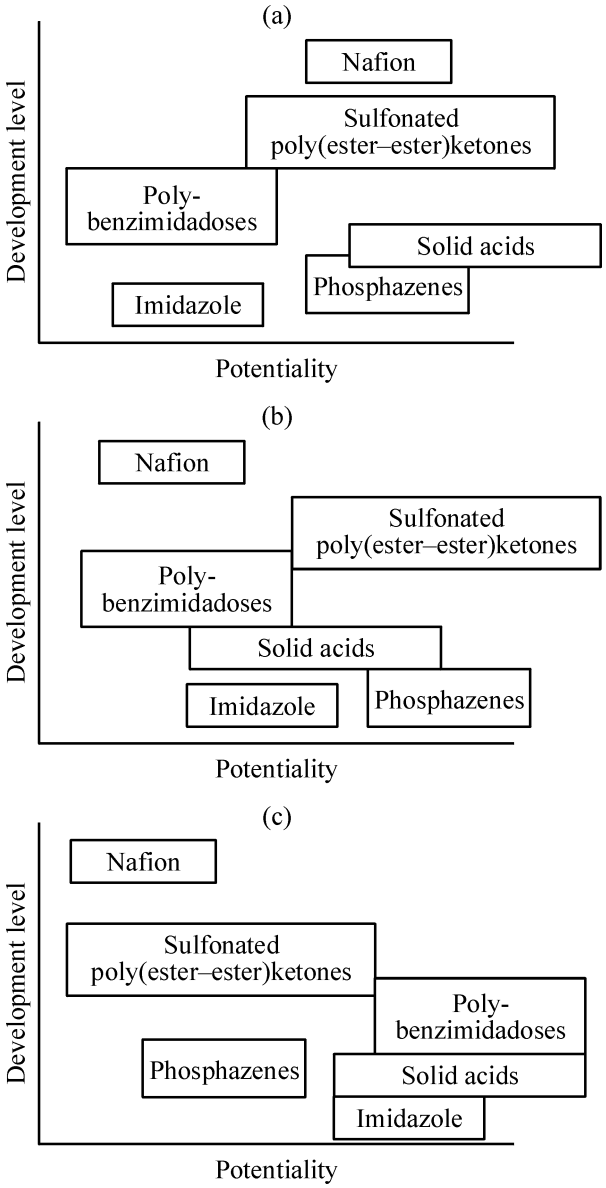


Fig. 3. Relationships between the development level and potentialities of various materials for use in (a) hydrogen, (b) methanol, and (c) high temperature FC [30].

ically (Fig. 3). It can be seen that, for methanol FC, Nafion is inferior in its potentialities to some polycondensation membranes despite the high level of development of Nafion-type membranes. For high-temperature FC, polycondensation membranes, especially those based on polybenzimidazoles, surpass Nafion-type membranes in their potentialities.

At the same time, experimental data obtained for a number of polycondensation membranes show that most of systems of this kind are inferior to Nafion in proton conductivity [31]. First industrial success in manufacture of polybenzimidazole membranes and FC operating on ethanol has been achieved and patented by Pemeas Fuel Cell Technologies with the use of a pilot installation put into operation in 2004. The Celtex-MEA membrane based on poly-2,2'-*m*-phenylene-5,5'-dibenzimidazole, developed by this company, is intended for a system composed of 35% H_2, 64.8% N_2, 2000 ppm Co, and admixtures of CO_2 and H_2O, has a service life of more than 8000, can operate in the temperature range 120–200°C, and tolerates CO in concentrations exceeding 50000 ppm. Another variety of the membrane, manufactured under the name Celtex-V, is intended for use in methanol FC.

Studies aimed to develop new improved membranes are continued. For example, sulfated poly(phthalazanone-esterketones) filled with sulfonated SiO_2–SO_3H nanoparticles have been suggested [72]. Polyblock-copolymers containing benzophenone units and methyl fragments that can be cross-linked under UV irradiation [77], cross-linkable sulfonated polyarylene esters that are soluble in organic solvents and can form flexible and transparent membranes by casting from solutions [78] have been obtained.

Another new and intensively developing area of research is associated with synthesis of hybrid polymeric membranes. Honma and co-workers [79] suggested a new class of amphiphilic organic-inorganic hybrid membranes produced by the sol–gel method from bridged polysiloxanes with acid fragments of phosphotungstic acid by the scheme

$$HO(CH_2)_nOH + 2\,(EtO)_3Si(CH_2)_3NCO \rightarrow (Et)_3Si(H_2C)_3NHCOO(CH_2)_nOCONH(CH_2)_3Si(OEt)_3$$

n = 4, 6 10, 12

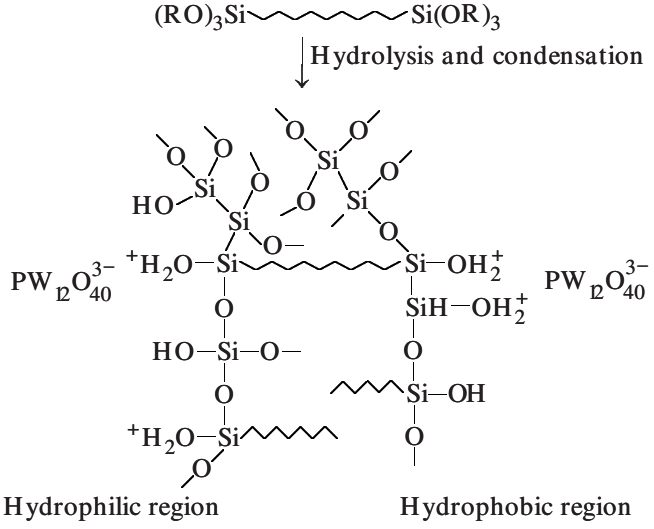
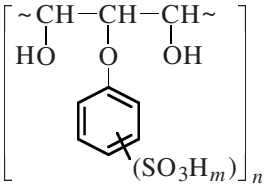


Table 4. Characteristics of biphase hybrid hydrogels*

Composition of polymer network 1, wt %				Composition of polymer network 2, wt %			Network 2 / network 1 mass ratio	EM	Proton conductivity σ_H, S cm^{-1}		Mechanical properties at 20°C		
AN	N-VP	AMSA	EGDM	AN	N-VP	EGDM			20°C	90°C	π, MPa	*E*, MPa	ε, %
41.2	41.2	16.5	1.1	49.5	49.5	1.0	0.77	2221	0.122	0.052	–	–	–
41.2	41.2	16.5	1.1	49.0	49.0	2.0	0.19	1495	0.273	0.095	2.05	3.52	183
50.0	31.6	16.5	1.9	59.1	38.9	2.0	0.29	1619	0.124	0.025	–	–	–
50.0	31.6	16.5	1.9	20.0	77.9	2.1	0.35	1694	0.314	0.019	–	–	–

* AN is acrylonitrile; N-VP, *N*-vinylpyrroidone; AMSA, 2-acrylamido-2-methyl-1-propanesulfonic acid; and EGDM, ethylene glycol dimethacrylate.

Dobrovol'skii and co-workers suggested [80] to use as high-efficiency proton-conducting membranes polymeric systems based on polyvinyl alcohol (PVA) esterificated with phenolsulfonc acids (PSA) of structure



The conductivity of PE of this kind depends on the PVA : PSA ratio (increases with the PSA content), only slightly depends on humidity, and is preserved at a high level up to 80°C.

Hybrid polymeric membranes produced by the sol–gel method at various ratios of 3-glycidyloxypropylmethoxysilane and phosphonoacetic acid are distinguished by thermal stability preserved up to 200°C, mechanical strength, high transparence, and conductivity of up to 8.7×10^{-2} S cm^{-1} [81]. A method for synthesis of organic–inorganic hybrid PE from trimethoxysilylmethylstyrene and phenylvinylphosphonic acid by radical polymerization and a study of their properties have been reported [82]. These membranes remain stable up to 180°C and their proton conductivity is as high as 3.7×10^{-2} S cm^{-1}.

A rather interesting idea of how hybrid membrane PE and electrode ensembles on their base can be produced has been implemented in a set of patents [83–87]. In this approach, a proton-conducting polymeric system is formed by copolymerization of the readily available and inexpensive hydrophilic and hydrophobic monomers containing an ionogenic group (e.g., SO_3H). The copolymers obtained on their basis can contain water and transport ions across their structure, with proton conductivity exhibited by them at moderate temperatures. The accessibility and low cost of such PE make it possible to cast an ensemble of cells and recover the expensive platinum catalysts from worked-out cells by simple burning.

We made an attempt to reproduce PE in accordance with the patents [83, 84]. The results of experiments aimed to synthesize membranes failed to give satisfactory results: the polymeric systems produced in accordance with the patents had poor strength characteristics, especially at elevated temperatures (70–90°C). Possibly, this is due to the know-how undisclosed in the patents. Therefore, another approach was used to obtain polymeric systems with improved characteristics by forming a polymeric matrix by the method of mutually penetrating networks. This technique has been employed previously in synthesis of biphase polymeric hydrogels for ophthalmologic lenses for prolonged wearing [88, 89]. The formation of mutually penetrating polymeric networks from systems constituted by polyethylene oxide and polybutadiene and by polyethylene oxide and polycarbonate was recently described in [90, 91]. Selected characteristics of the resulting hydrogel proton-conducting membranes are listed in Table 4.

As can be seen in Table 4, membrane proton-conducting systems with satisfactory strength characteristics, moisture content, and proton conductivity could be produced from the available monomers.

We attempted to analyze the basic areas of research aimed to create proton-conducting PE, with the chronology of their appearance and developments observed. In doing so, we systematized and studied the most important of the published data, which characterize the development of new approach to development of proton-conducting PE and modification of their properties.

Three structural variants of approaches to fabrication of PE for fuel cells have been revealed: (i) methods for fabrication of perfluorinated Nafion-type PE and their analogues, which have become classical in the last half-century; (ii) approaches to synthesis of nonfluorinated polycondensation aromatic systems of the type of poly(ester–ester)ketones, polybenzimidazoles, and PE on their basis; and (iii) methods for obtaining PE from the comparatively new class of hybrid polymeric systems.

Sulfoacid Nafion-type PE have been considered most fully. For these PE, methods and technology of synthesis, internal microheterogeneous phase structure with nanoclusters connected by nanosize channels, proton conduction mechanism, and various techniques for modification of their performance characteristics have been described in detail. There is no way of not mentioning here the success in wide application of Nafion-type PE in limited-power FC.

Nonfluorinated systems based on polybenzimidazoles, poly(ester–ester)ketones, polysulfones, and other polymeric systems are understood in less detail, despite being extensively studied now. Materials of this kind are believed to be promising for application in FC working at temperatures of up to 200°C; they are less sensitive to admixtures of CO in the fuel and can be used in FC operating on methanol. There have been first successful attempts of industrial manufacture of membranes of this type (Pemeas company), with a service life of about 8000 h.

Hybrid polymeric systems are being extensively studied by many research teams; however, the results accumulated by now are so far insufficient for their use in technology.

We are forced to admit the lagging behind of our studies for all the three classes of PE with respect both to the operation mechanism of membranes on their basis and to the possibility of controlling the service properties of membranes in FC.

Rather important in this context is development of a strategy of planning of actions aimed to catch up in studies and in the development of the fabrication technology of small-size fuel cells with the use of polymeric proton-conducting membranes. The principle "to overtake without catching up," previously put forward when concluding an agreement between the Presidium of the Russian Academy of Sciences and Noril'skii Nikel' Joint-Stock Company seems to be somewhat disputable.

With account of the all-inclusive nature of the problems of development of FC with the use of polymeric membrane systems, which are associated with (a) synthesis of PE and their operation in fuel cells, (b) development of catalysts and improvement of their efficiency, and (c) improvement of the FC design, it seems that coordination of R & D works is necessary, with joint discussion of their results and correction of the corresponding plans and programs.

6. CONCLUSIONS

(1) In the last decade, three groups of polymeric systems that can be used as polymeric proton-conducting membranes in fuel cells have been clearly distinguished. The first group is constituted by perfluorinated sulfo-containing polymeric systems of the Nafion type and their analogues; the second, by aromatic polycondensation systems of the type of polybenzimidazoles, polyesterketones, and polyphosphazenes; and the third, new permanently growing group, by hybrid polymeric electrolytes.

(2) The best understood and most advanced toward practical use are Nafion-type systems. Nevertheless, the potentialities of these systems are far from being exhausted and further improvement of their properties and appearance of new fields of their application would be expected. This illusory contradiction is due to the fact that the practical use of Nafion-type materials outpaced the accumulation of a critical volume of the fundamental knowledge necessary for development of substantiated technologies. At present, this knowledge continues to be accumulated, which will possibly give new effective solutions concerning the application of materials of the classes under consideration.

(3) The scientific basis for design and fabrication of optimal structures of polycondensation polymeric electrolytes is only being formed now. The potentialities of this type of polymeric proton-conducting systems are far from being exhausted. We believe that basic research should be enhanced for this group of materials, without forcing direct technological developments.

(4) Studies of hybrid polymeric systems, including hydrogels, seem to be the least developed and exceedingly promising and require a fundamental approach to their development.

(5) An analysis of the special literature demonstrated that achievements in development of polymeric membrane systems with optimal characteristics are in most cases associated with use of a specially modified Nafion.

REFERENCES

1. Antropov, P.Ya., *Toplivno-energeticheskii potentsial Zemli* (Fuel and Energy Potential of the Earth), Moscow: VINITI, 1976.
2. Fortov, V.E., *Energetika Rossii: problemy i perspektivy: Ezhegodnik* (Energetics of Russia: Problems and Prospects: Yearbook), Chernogolovka: Inst. Probl. Khim. Fiz., 2005, vol. 2, pp. 65–96.
3. Matkovskii, P.E., Aldoshin, S.M., Troitskii, V.N., et al., *Sovremennaya energetika* (Modern Energetics), Chernogolovka: ZhIPKhF, Ross. Akad. Nauk, 2007.
4. *European Commission, Eur20719 EN Hydrogen Energy and Fuel Cells: A Vision of Our Future*, Luxemburg: Office for Official Publications of the European Committees, 2003.
5. Davtyan, O.K., *Problemy neposredstvennogo prevrashcheniya khimicheskoi energii topliva v elektricheskuyu* (Problems of Direct Conversion of the Chemical Energy of a Fuel into Electric Power), Moscow: Akad. Nauk SSSR, 1947.
6. Vielstich, W., *Brennstoffelemente*, Weinheim: Chemie, 1965.
7. Bagotskii, V.S., Osetrova, A.M., and Skundin, A.M., *Elektrokhimiya*, 2003, vol. 39, no. 9, p. 1027.
8. Haile, S.M., *Acta Materialia*, 2003, vol. 51, p. 5981.
9. Mesyats, G.A. and Prokhorov, M.D., *Vestn. Ross. Akad. Nauk*, 2004, vol. 74, no. 6, p. 579.
10. Izmailov, N.A., *Elektrokhimiya rastvorov* (Electrochemistry of Solutions), Moscow: Khimiya, 1976.
11. Zawodzinski, T.A., Deronin, C., Radsinski, S., et al., *J. Electrochem. Soc.*, 1993, vol. 140, p. 1041.
12. US Patent Appl. 308650.
13. Yamabe, M., *Ionoobmennye membrany na osnove ftorsoderzhashchikh soedinenii* (Ion-Exchange Membranes Based on Fluorine-containing Compounds), Moscow: Mir, 1984, pp. 336–354.
14. Yaughan, D.J., *Du Pont Innovation*, 1973, no. 4 (3), p. 10.
15. GB Patent 1034176.
16. GB Patent 2051831.
17. US Patent 4330654.
18. US Patent 4478695.
19. US Patent 4349650.
20. US Patent 4940525.
21. Jpn Patent Appl. 53-44429.
22. US Patent 3282875.
23. US Patent 5608022.
24. Jpn Patent 62-288617.
25. Ivanchev, S.S., Barabanov, V.G., Pavlyuchenko, V.N., and Timofeev, S.V., *Trudy Mezhdunarodnogo simpoziuma po vodorodnoi energetike. Moskva, 1–2 noyabrya 2005* (Proc. Int. Symp. on Hydrogen Energetics), Moscow, 2005.
26. Ivanchev, S.S., Sokolov, L.F., and Pavlyuchenko, V.N., *2-ya Rossiiskaya konferentsiya "Fizicheskie problemy vodorodnoi energetiki", Sankt-Peterburg, 21–23 noyabrya 2005* (2nd Russian Conf. "Physical Problems of Hydrogen Energetics,") St. Petersburg, 2005, pp. 56–57.
27. Zhou, Ch., Guerra, M.A., Qiu, Z.-M., et al., *Macromolecules*, 2007, vol. 40, pp. 8695.
28. *Catalogue Handbook of Fine Chemicals*, Aldrich, 1999–2000, p. 1225.
29. Rusanov, A.L., Likhatchev, D.Yu., Kostoglodpy, P.V., et al., *Adv. Polym. Sci.*, 2005, vol. 197, p. 83.
30. Glusen, A. and Stolten, D., *Chemie Ingeneur Technik.*, 2003, vol. 75, no. 11, p. 1591.
31. Roziere, J. and Jones, D.J., *Ann. Rev. Mater. Res.*, 2003, vol. 33, p. 503.
32. Pereira, S., Willameit, R., and Haramus, V., *GKSS Rept.*, 2001, no. 5, p. 42.
33. Abetz, V., Brinkman, T., Dijkstra, M., et al., *Adv. Eng. Mater.*, 2006, vol. 8, no. 5, p. 328.
34. Trunov, V.A., Lebedev, V.T., Grushko, Yu.S., et al., *Kristallografiya*, 2007, vol. 52, no. 3, p. 536.
35. Majsztrik, P.W., Satterfield, M.B., Bocarsly, A.B., and Benzinger, J.B., *J. Membr. Sci.*, 2007, vol. 301, p. 93.
36. Nasef, M., *Eur. Polym. J.*, 2002, vol. 38, p. 87.
37. Sauk, J., Byun, J., and Kim, H., *J. Power Sources*, 2004, vol. 131, p. 188.
38. US Patent 0116546.
39. Lee, H.Y., Kim, J.Y., Park, J.H., et al., *J. Power Sources*, 2004, vol. 131, p. 188.
40. Smit, M.A., Ocampo, A.L., Espinosa-Medina, M.A., and Sebastian, P.J., *J. Power Sources*, 2003, vol. 124, p. 59.
41. US Patent 0118773.
42. US Patent 0115498.
43. US Patent 5547551.
44. US Patent 5654109.
45. US Patent 6492438.
46. Wu, Z.M., Sun, G.Q., and Jin, W., *J. Power Sources*, 2007, vol. 167, no. 2, p. 309.
47. Ainla, A. and Brandell, D., *Solid State Ionics*, 2007, vol. 178, nos. 7–10, p. 581.
48. Smitha, B., Sridhar, S., and Khan, A.A., *J. Membr. Sci.*, 2003, vol. 225, nos. 1–2, p. 63.
49. Li, J.Y., Ichizuri, S., Asano, S., et al., *J. Appl. Polym. Sci.*, 2006, vol. 101, no. 6, p. 3587.
50. Chen, J.H., Asano, M., and Mackawa, Y., *Electrochem. Solid State Lett.*, 2006, vol. 9, no. 11, p. G326.
51. Chen, J.H., Asano, M., Maekawa, Y., and Yoshida, M., *J. Membr. Sci.*, 2007, vol. 296, nos. 1–2, p. 78.
52. Ren, S.Z., Sun, G.Q., Li, C.N., et al., *J. Membr. Sci.*, 2006, vol. 282, nos. 1–2, p. 450.

53. Kim, H., Kang, M.S., Lee, D.H., et al., *J. Membr. Sci.*, 2007, vol. 304, nos. 1–2, p. 60.
54. Kundu, P.P., Kim, B.T., Ahn, J.E., et al., *J. Power Sources*, 2007, vol. 171, no. 1, p. 86.
55. Wang, L., Yi, B.L., Zhang, H.M., et al., *J. Power Sources*, 2007, vol. 164, no. 1, p. 80.
56. Tomassin, J.M., Koller, J., Caldarella, G., et al., *J. Membr. Sci.*, 2007, vol. 303, nos. 1–2, p. 252.
57. Smitha, B., Sridhar, S., and Khan, A.A., *J. Membr. Sci.*, 2005, vol. 259, nos. 1–2, p. 10.
58. Antonucci, P.L., Ario, A.S., Creti, P., et al., *Solid State Ionics*, 1997, vol. 125, p. 431.
59. Adjemian, K.T., Lee, S.J., Srinivasan, S., et al., *J. Electrochem. Soc.*, 2002, vol. 149, p. 4256.
60. Jung, D.H., Cho, S.Y., Peck, D.H., et al., *J. Power Sources*, 2002, vol. 106, p. 173.
61. Mioc, U., Davidovic, M., Tjapkin, N., et al., *Solid State Ionics*, 1991, vol. 46, p. 103.
62. Tazi, B. and Savadogo, O., *Electrochim. Acta*, 2000, vol. 45, p. 4329.
63. Tatsumisago, M., Honjo, H., Sakai, Y., and Minami, T., *Solid State Ionics*, 1994, vol. 74, p. 105.
64. Nakajima, H., Nomura, S., Sugimoto, T., et al., *J. Electrochem., Soc.*, 2002, vol. 149, p. A953.
65. Arico, A.S., Baglio, V., Lufrano, F., et al., *Solid State Ionics*, 2001, vol. 145, p. 101.
66. Shao, Z.G., Joghea, P., and Hsing, I.M., *J. Membr. Sci.*, 2004, vol. 229, no. 1–2, p. 43.
67. Zawodzinski, T.A., Deronin, J.C., Radzinski, S., et al., *J. Electrochem. Soc.*, 1993, vol. 140, p. 1041.
68. Arico, A.S., Baglio, V., Di Blasi, A., et al., *Solid State Ionics*, 2003, vol. 161, p. 251.
69. Chen, S.Y., Han, C.C., Tsai, C.H., et al., *J. Power Sources*, 2007 V. 171, no. 2, p. 363.
70. Tomassin, J.M., Pagnorelle, C., Bizzari, D., et al., *Solid State Ionics*, 2006, vol. 177, nos. 13–14, p. 1137.
71. Lin, Y.F., Yen, C.Y., Ma, C.M., et al., *J. Power Sources*, 2007, vol. 171, no. 2, p. 388.
72. Su, Y.H., Liu, Y.L. Sun, Y.M., et al., *J. Membr. Sci.*, 2007, vol. 296, nos. 1–2, p. 21.
73. Lin, H.L., Yu, T.L., and Han, F.H., *J. Polym. Res.*, 2006, vol. 13, no. 5, p. 379.
74. Chen, H., Palmese, G.R., and Elald, Y.A., *Chem. Mater.*, 2006, vol. 18, no. 20, p. 4875.
75. Doe Hydrogen Program, FY 2004, Progress Report; FY 2005, Progress Report.
76. Keres, A., Xing, D.M., and Schonberger, F., *J. Polym. Sci., Part B: Polym. Phys.*, 2006, vol. 44, no. 16, p. 2311.
77. Ishikawa, J.I., Furjiyama, S., Inone, K., et al., *J. Membr. Sci.*, 2007, vol. 98, nos. 1–2, p. 48.
78. Ding, F.C., Wang, S.J., Xiao, M., et al., *J. Power Sources*, 2007, vol. 170, no. 1, p. 20.
79. Honma, J., Nakayama, H., Nishikawa, O., et al., *Solid State Ionics*, 2003, vols. 162–163, p. 237.
80. Dobrovol'skii, Yu. A., Pisareva, A.V., Leonova, L.S., and Karelin, A.I., *Al'ternativn. Energ. Ekol.*, 2004, no. 12 (20), p. 36.
81. Kato, M., Katayama, S., Sakamoto, W., and Yogo, T., *Electrochim. Acta*, 2007, vol. 52, no. 19, p. 5924.
82. Kato, M., Sakamoto, W., and Yogo, T., *J. Membr. Sci.*, 2007, vol. 303, nos. 1–2, p. 43.
83. US Patent 0 113 603.
84. WO Patent 020 332.
85. WO Patent 124 893.
86. WO Patent 124 915.
87. WO Patent 131 758.
88. RF Patent 2 269 552.
89. Chekina, N.A., Pavlyuchenko, V.N., Danilichev, V.F., et al., *Polym. Adv. Technol.*, 2006, vols. 11–12, p. 872.
90. Plesse, C., Vidal, F., Gauthier, C., et al., *Polymer*, 2007, vol. 48, p. 696.
91. Vidal, F., Plesse, C., Popp, J.F., et al., *J. Appl. Polym. Sci.*, 2003, vol. 90, p. 3569.

ISSN 1070-4272, Russian Journal of Applied Chemistry, 2008, Vol. 81, No. 4, pp. 585–587. © Pleiades Publishing, Ltd., 2008.
Original Russian Text © Yu.I. Shtern, 2008, published in Zhurnal Prikladnoi Khimii, 2008, Vol. 81, No. 4, pp. 546–549.

INORGANIC SYNTHESIS AND INDUSTRIAL INORGANIC CHEMISTRY

Technology of Fabrication and Study of Porous Oxide Films on Aluminum Alloys

Yu. I. Shtern

Moscow State Institute of Electronics, Moscow, Russia

Received April 16, 2007

Abstract—Technology for fabrication of porous anodic oxide films on aluminum alloys is suggested. All the films have good electrical parameters in a wide temperature range. The results obtained were used to fabricate metal-insulator substrates for manufacture of electronic devices.

DOI: 10.1134/S1070427208040022

In this communication, a technology for fabrication of porous anodic oxide films (AOF) on aluminum alloys is suggested. The results obtained in studies of these films have been used to fabricate metal-insulator (MI) substrates for electronic devices, including thermoelectric units operating on the Peltier effect [1, 2]. At present, MI substrates are successfully used to fabricate microassemblies and hybrid integrated circuits [3]. It should be noted that oxide films are a promising material for nanotechnologies [4]. This circumstance also makes the study performed more topical. The optimal starting material for fabrication of MI substrates are aluminum alloys having high thermal conductivity, low density, and necessary mechanical strength. Aluminum alloys are easy to process and, when subjected to electrochemical oxidation, can form a uniform and homogeneous oxide with good dielectric properties [3, 5]. An important advantage of aluminum substrates, compared with other metallic substrates, is that the adhesion strength of a AOF–substrate system exceeds 12 kg mm^{-2}, and the strength of AOF is as high as 14 kg mm^{-2}.

The technology under consideration was tested on various aluminum alloys that, in principle, satisfy the requirements to MI substrates: AD, AV, AMTs, and AMg alloys. It should, however, be noted that, when MI substrates are used in electronics, thin metallic films are formed on their surface. This factor predetermines the necessity for subjecting the substrates to a mechanical treatment to a roughness not exceeding 0.1 μm. The most technologically convenient in this regard are AMg alloys. The physicochemical properties of AOF are largely determined by the electrolyte composition [3, 5]. The technology uses an oxalic acid electrolyte of the following composition (g l^{-1}): oxalic acid 100 and boric acid 20. This electrolyte makes it possible to form oxide films with improved dielectric properties. The presence of boric acid lowers the chemical activity of the electrolyte toward the anodic film and diminishes the surface roughness of AOF [6].

EXPERIMENTAL

In the technological process under consideration, MI substrates are fabricated in the galvanostatic mode of electrochemical oxidation at current densities of 1.5–2.0 A dm^{-2}. The study demonstrated that the current–voltage (I–V) characteristics of AOF formed at these current densities have high initial breakdown voltage and resistance. The current density in anodization was maintained constant with a current generator, with the formation voltage of the oxide layer varying from 80 to 120 V at an AOF thickness of about 60 μm. The anodization was performed at electrolyte temperatures of 291–298 K. Raising this temperature to above 300 K enhances the etching effect and makes lower the growth rate of the oxide layer, with the porosity of AOF increasing. As temperature is raised, the surface roughness of an MI substrate becomes more pronounced, the process voltage increases, and, accordingly, the thickness of the barrier layer grows.

The electrolyte temperature was stabilized in the course of anodization with water circulated within a closed circuit mounted on the outer perimeter of the electrolytic bath. The water temperature was controlled by a Lauda RC6 CP liquid thermostat. The electrolyte was agitated by bubbling of filtered

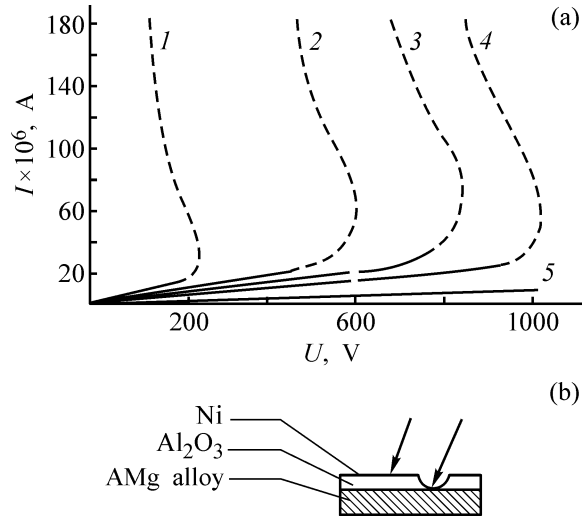


Fig. 1. (a) *I–V* characteristics of AOF with various thicknesses and (b) structure of the electrical contact. (*I*) Current strength and (*U*) voltage. h (μm): (*1*) 3.5, (*2*) 8, (*3*) 15, (*4*) 23, and (*5*) 125.

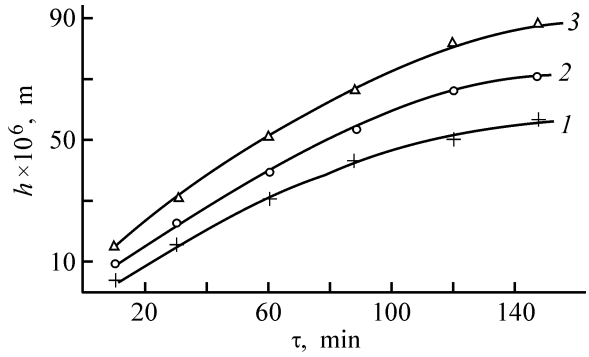


Fig. 2. AOF thickness *h* vs. the anodization duration τ at different current densities. *i* (A dm^{-2}): (*1*) 1.5, (*2*) 2.0, and (*3*) 2.5.

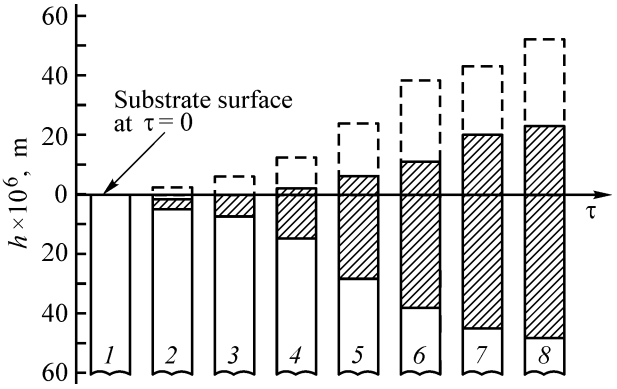


Fig. 3. Growth diagram for an AOF formed at a current density of 2 A dm^{-2} and different electrolysis durations τ. (*h*) Thickness. τ, min: (*1*) 0, (*2*) 5, (*3*) 15, (*4*) 30, (*5*) 60, (*6*) 90, (*7*) 120, and (*8*) 150.

compressed air. The AOF thickness was determined using a microscope and a Kristall-2 machine for making spherical metallographic sections. In addition, the thickness of AOF and metallic support was measured on a stand equipped with a micrometer head (scale division 1 μm). *I–V* characteristics of AOF were measured with a PNKhT-2 instrument. For this purpose, a structure constituted by a metallic contact (nickel), AOF, and metallic substrate was fabricated (see Fig. 1b). A measuring probe was attached to the metallic contact fabricated on the AOF surface by magnetron sputtering of nickel. Another probe was attached, through an opening produced in the AOF by a grinding ball, to the metallic substrate.

Figure 1 shows *I–V* characteristics of anodic oxide films of various thicknesses, produced at a current density of 2.0 A dm^{-2}. It was found that substrates with a dielectric film of thickness of about 8 μm sustain a voltage exceeding 400 V. It should be noted that the growth rate of AOF decreases in the course of anodization (Fig. 2) (as the growth rate is taken the change of the film thickness in unit time). The growth rate decreases because the supply of oxygen into the zone in which the primary oxide is formed becomes hindered as the AOF thickness increases. To control the anodization process in order to obtain MI substrate with the optimal properties, it is necessary to have data on the growth kinetics of AOF. Of particular interest is analysis of how the metal–oxide interface moves and the thickness of the MI substrate varies in the course of electrochemical oxidation.

Figure 3 shows the AOF growth diagram plotted using the results obtained by measuring the AOF and substrate thicknesses in the course of anodization. According to these data, the interface between aluminum and aluminum oxide moves into the aluminum substrate in the course of oxidation. However, the increase in volume, observed in this case, results in that the outer surface of AOF does not coincide with the original surface of the aluminum substrate. The chemical reaction in which aluminum oxide is formed is as follows:

$$4Al + 3O_2 = 2Al_2O_3.$$

Taking into account the atomic weight and the density (d = 2.7 g cm^{-3}) of aluminum and the molecular weight and the density (d = 2.55 g cm^{-3}) of the oxide film, it is possible to find the relative volumes of the AOF formed and of the metal consumed for its formation. The volume of 1 g-at Al is 10 cm^3, and that of 1 g-at Al_2O_3, 40 cm^3. Thus, it is apparent that an AOF of thickness *h* should grow at the expense of an aluminum layer of thickness 0.5 *h*. However, the results obtained by measuring how the AOF and

substrate thicknesses vary in the course of anodization show that the substrate boundary does not coincide with the calculated position represented in the diagram by a dashed line (Fig. 3). The decrease in the AOF thickness with respect to the calculated value is accounted for by the etching effect of the electrolyte on the surface of the oxide film. The calculated AOF thickness, found, taking into account the oxidation reaction, from the ratio of the specific volumes of Al and Al_2O_3, is true only at the strictly stoichiometric form of AOF and disregards the possible hydrated forms of Al_2O_3 and incorporation of electrolyte anions into AOF, which results in that the density of the oxide layer may be even lower. However, the transfer of aluminum ions into the electrolyte is disregarded too. If it is assumed that these two processes neutralize each other in anodization, then the position of the AOF boundary should correspond to the dashed line in Fig. 3.

It should be noted that, in the initial stage of anodization, the surface layer of the metal, disrupted in mechanical processing, and the oxide formed are intensely dissolved, which positively affects the properties of the AOF obtained. In the process, the substrate thickness decreases. The porosity of the oxide films strongly affects the properties of the MI substrates. According to [3], the density of pores in AOF formed in electrolytes dissolving the oxide film may reach values of 10^9–10^{10} pores/cm^2, and their volume, 36% relative to the AOF volume. The pore diameter commonly varies within the range 100–1000 Å. The presence of pores in the oxide layer is rather important for the mechanical stability of the system constituted by the oxide film and the metallic substrate. This is so because aluminum oxide has a thermal linear expansion coefficient (TLEC) $\alpha = 7 \times 10^{-6}$ K^{-1} that is strongly different from the TLEC of the metal ($\alpha = 26 \times 10^{-6}$ K^{-1}). Under a thermal treatment, the difference in TLEC gives rise to internal tensile stresses in the oxide film and compression stresses in the surface layer of the metal. The large difference in TLEC between the AOF and the metallic support should have resulted in crack formation in the oxide layer under insignificant thermal treatments. However, the presence of pores in the AOF, which serve as a kind of dampers, can neutralize the appearing mechanical stresses.

When fabricating MI substrates, particular attention was given to the state of the substrate surface, because connector elements are formed on this surface by deposition of metallic films in a vacuum [6]. Prior to anodization, AMg alloy substrate blanks are subjected to mechanical processing, including grinding with abrasive powders with particle size of 5 to 1 μm. Then, the substrates are polished with a 0.5-μm abrasive powder and diamond pastes. As a result, a 12th to 13th class of surface smoothness is obtained. After cleaning with organic solvents to remove the polishing pastes, the substrates are thermally flattened at a temperature of 650–700 K. The anodization of MI substrates ends with a thorough washing in deionized water and drying in a flow of nitrogen, after which the substrates are annealed at 730 K.

Climatic tests demonstrated that the MI fabricated by the given technology sustain temperature variations in the range 170–700 K, with the basic properties preserved, which is of key importance in fabrication of MI substrates for electronic devices, including thermoelectric units.

CONCLUSIONS

(1) The optimal aluminum alloys for fabrication of metal-insulator substrates for electronic devices were found to be AMg alloys.

(2) A study of the effect of electrochemical oxidation modes on the dielectric properties of anodic oxide films demonstrated that the optimal parameters of the galvanostatic mode are as follows: current density 1.5–2.0 A dm^{-2} and electrolyte temperature 291–298 K.

(3) It was shown the metal-insulator substrates fabricated using the technology suggested sustain temperature variations in the range 170–700 K, with their basic properties preserved.

REFERENCES

1. Shtern, Yu.I., Kozhevnikov, Ya.S., Tarasov, R.Yu., and Barabanov, D.Yu., *Izv. Vyssh. Uchebn. Zaved., Elektron.*, 2005, nos. 4–5, pp. 179–184.
2. Shtern, Yu. I., Markov, F.V., Bozhenar', D.A., and Tarasov, R.Yu., *Izv. Vyssh. Uchebn. Zaved., Elektron.*, 2000, nos. 4–5, pp. 167–169.
3. Vozhenin, I.N., Blinov, G.A., Koledov, L.A., et al., *Mikroelektronnaya apparatura na beskorpusnykh integral'nykh mikroskhemakh* (Microelectronic Apparaus Based on Unpackaged Integrated Circuits), Vozhenin, I.N., Ed., Moscow: Radio i Svyaz', 1985.
4. *Nanotekhnologii v elektronike* (Nanotechnologies in Electronics), Chaplygin, Yu.A., Ed., Moscow: Tekhnosfera, 2005.
5. *Anodnye oksidnye pokrytiya na metallakh i anodnaya zashchita* (Anodic Oxide Coatings on Metals and Anodic Protechnion), Frantsevich, I.N., Kiev: Naukova Dumka, 1985.
6. Inventor's Certificate, no. 1512433.

ISSN 1070-4272, Russian Journal of Applied Chemistry, 2008, Vol. 81, No. 4, pp. 588–591. © Pleiades Publishing, Ltd., 2008.
Original Russian Text © A.M. Aliev, R.Yu. Yusifov, A.R. Kuliev, Yu.G. Yusifov, 2008, published in Zhurnal Prikladnoi Khimii, 2008, Vol. 81, No. 4, pp. 550–553.

INORGANIC SYNTHESIS AND INDUSTRIAL INORGANIC CHEMISTRY

Method of Gas Hydrate Formation for Evaluation of Water Desalination

A. M. Aliev, R. Yu. Yusifov, A. R. Kuliev, and Yu. G. Yusifov

Institute of Chemical Problems, National Academy of Sciences of Azerbaijan, Baku, Azerbaijan

Received May 14, 2007

Abstract—Experimental technique for analysis of hydrate formation processes with an AAS-300 atomic-absorption spectrometer was developed and used to study hydrate formation in a system constituted by water and Freon R-142V.

DOI: 10.1134/S1070427208040034

The development of methods for precluding hydrate formation in natural gas pipelines [1], implementation of techniques developed for utilization of gas-hydrates formed in industry in gas storage [2, 3], separation of gas mixtures [2, 4, 5], and recovery of normal paraffin hydrocarbons from oil fractions, the drying of gases, and the intensive studies of gas-hydrate methods for desalination of salt water [5–7] presently require a detailed experimental analysis of the mechanism and kinetics of formation of gas hydrates by precision physicochemical analytical procedures.

At present, the kinetic aspects of gas hydrate formation processes are experimentally studied in batch and continuous crystallizers with gas-liquid chromatographs, automated titration apparatus, and crystallizer weighing systems. The errors of these analytical instruments fall within the range 1–2%, which is insufficient for experimental studies of the mechanisms of gas hydrate formation and development of theoretically substantiated kinetic models of the above processes. From this viewpoint, it is important, both practically and theoretically, to develop an experimental procedure for analysis of gas hydrate formation processes with a precision atomic absorption spectrometer.

In this communication, an experimental setup with a batch crystallizer and a procedure for analysis of hydrate formation processes with an AAS-300 atomic-absorption spectrometer are described and the results obtained in a study of the hydrate formation in a system constituted by water and Freon R-142V by this procedure are presented.

The experimental setup is schematically shown in Fig. 1. The setup comprises four main units. The first serves for gas preparation and delivery. The second, main unit, is a crystallizer. The third unit serves for evacuation, measurement of the vacuum and pressure, and cooling the crystallizer.

The gas preparation and delivery system comprises cylinders with nitrogen (*1*) and Freon (*2*), reducers *3* and *4*, a fine-control valve *6*, and a rotameter *7*. A three-way cock *8* serves to feed Freon into water or into the free volume over the water surface in the crystallizer.

The crystallizer *21* is made of organic glass to enable visual observation of how gas hydrates are formed. The crystallizer has two lids, *18* and *22*, having the form of flange joints with gaskets. The upper lid is made of stainless steel, and the lower lid, of organic glass. On the upper lid are mounted pipes *9* and *16* of the cooling coil *23* through which a cooling mixture circulates, feed lines for Freon delivery through water (*10*) or into the free volume over water (*12*), well *11* for a thermometer or thermocouple, stuffing box *19*, sealing rod connecting multiblade stirrer *24* to an electric motor *20*, gas outlet line *13* with a control valve *35* at its end, nipple *14* for evacuation and measurement of the vacuum and pressure in the crystallizer, and sampler *15*.

The system for evacuation and measurement of the vacuum and pressure comprises a vacuum pump *34*, vacuum gauge *27*, standard pressure gauge *28*, and four stopping valves *29–32*. Penetration of a vacuum oil into the crystallizer is prevented by a trap *33*.

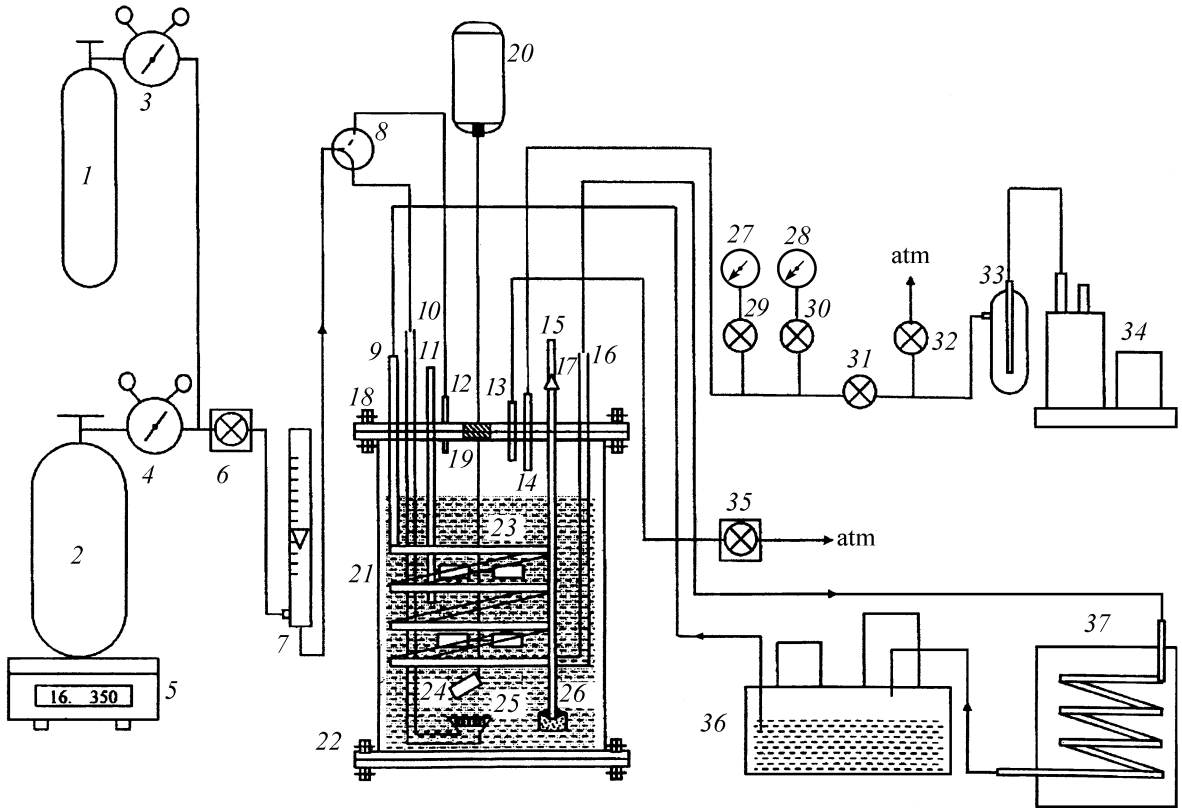


Fig. 1. Schematic of the experimental setup for studying the hydrate formation: (*1*) nitrogen cylinder, (*2*) Freon cylinder, (*3*, *4*) reducers; (*5*) electronic balance, (*6*, *35*) control valves, (*7*) rotameter, (*8*) three-way cock, (*9*, *16*) inlet and outlet a cooling mixture, (*10*, *12*) inlet for Freon through water and over water, (*11*) thermometer well, (*13*) outlet for Freon, (*14*) nipple for evacuating air and measuring pressure in the crystallizer, (*15*) sampler, (*17*) pneumatic batcher, (*18*, *22*) crystallizer lids, (*19*) stuffing box, (*20*) electric motor, (*21*) crystallizer, (*23*) cooling coil, (*24*) stirrer, (*25*) Freon distributer, (*26*) filter, (*27*) vacuum gauge, (*28*) standard pressure gauge, (*29–32*) stopping valves, (*33*) trap, (*34*) vacuum pump, (*36*) pump for cooling mixture circulation, and (*37*) refrigerator.

The system for crystallizer cooling comprises a refrigerator *37*, pump *36* for circulating the cooling mixture, and cooling coil *23* within the crystallizer.

Experiments were carried out on this installation as follows. Solutions were prepared from FIXANAL and twicedistilled water and contained a minor concentration of sodium chloride (10^{-2}–10 mg l^{-1}) to minimize the effect of ions on the hydrate formation. Into crystallizer *21*, a sodium chloride solution of certain concentration was poured. The volume of the crystallizer was 1.6 l, and that of the solution, 1.5 l. The crystallizer was closed with a lid. A multiblade (4–7 blades) stirrer *24* was connected to an electric motor *20* and all pipelines were attached to the connectors on the lid. Nitrogen from cylinder *1* was passed under a pressure of 2.0–2.5 atm through inlet pipe *12*, and the vacuum tightness of the crystallizer was checked with manometer *28*. The tightness could be also verified by evacuating the system. Valves *29* and *31* were shut when letting nitrogen into the system, and valve *30*, when evacuating the system. After that, the electric motor having eight controlled rotation rates was switched on and the stirrer was rotated. Then, air was evacuated from the crystallizer through nipple *14* in the course of approximately 30 min. The evacuation of the system was monitored with gauge *27*. After closing valve *31* and prior to beginning the experiment, the system was kept under a residual pressure of 1–2 mm Hg. Freon in cylinder *2* was weighed on electronic balance *5*. After the Freon cylinder was opened (reducer *4* and fine-control valve *6*), the gas was passed through rotameter *7* and inlet *12* and rapidly filled the volume over the water layer to a certain pressure. The pressure in the crystallizer was controlled and fixed using a standard pressure gauge *28*. A flow of Freon, controlled by valve *8*, passed through a fine-mesh distributor *25* into water at a fixed rate. This time was recorded as the beginning of an experiment. In 0.5–1.0 min, solution samples were taken from the crystallizer with a sampler

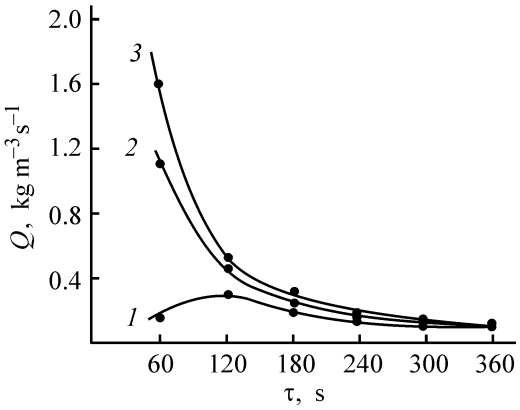


Fig. 2. Throughput Q of the reactor vs. the reaction time τ at varied stirring rate. V = 1000 ml, d_b = 0.5–1.0 mm, T = 5°C, P = 0.9 atm., c_{NaCl} = 0.01 mg l^{-1}. Stirring rate (rpm): (*1*) 200, (*2*) 950, and (*3*) 1350.

15 and a pneumatic batcher *17*, using the excess pressure over the solution layer. The samples were passed through filter *26* to inhibit penetration of gas hydrates. Up to ten samples were taken during the experiment and then analyzed on an AAS-300 atomic-absorption spectrometer. The required low temperature in the crystallizer was maintained with a cooling mixture passed through cooling coil *23* preliminary cooled in refrigerator *37* and purged with pump *36*.

After the completion of an experiment, Freon cylinder *2*, reducer *4*, and valve *6* were closed, and three-way cock *8* was brought in the neutral position. The residual Freon was weighed again and its expenditure during the experiment was determined. The excess pressure of Freon over the solution layer and the pressure of Freon produced in decomposition of gas hydrates were relieved through control valve *35*.

The amount of water involved in the clathrate formation was determined from the change in the concentration of sodium ions in the system by the formula

$$G = G^0\left(1 - \frac{\alpha^0}{\alpha}\right), \quad (1)$$

where G^0 is the amount of the initial solution (kg); α^0, salt content of the initial solution; and α, salt content of a solution after the reaction, as determined by atomic-absorption spectrometry.

The throughput of the reactor was found by the formula

$$Q = \frac{G}{\tau V}, \quad (2)$$

where τ is the reaction time (s), and V, the volume of the reaction zone [5].

The conversion X (%) was found as

$$X = \frac{\alpha - \alpha^0}{\alpha} \times 100. \quad (3)$$

The gas hydrate method for desalination of salt water is the most promising, compared with the existing methods. Hydrate-forming properties are characteristic of substances rather different in chemical nature, such as paraffin hydrocarbons and their numerous halide derivatives (Freons etc.). The properties of a hydrate-forming agent directly affect the desalination efficiency. A hydrate-forming agent should have a high temperature and low (close to atmospheric) pressure of hydrate formation, low solubility in water, high rates of hydrate formation and decomposition, low heat of formation, high chemical stability in water and be nontoxic, nonexplosive, and inexpensive. From this viewpoint, Freon R-142V is the most favorable agent for desalination of salt water. It has high temperature and low pressure at the upper invariant point, low rate of hydrolysis, and high rate of hydrate formation. In addition, Freon R-142V is noncorrosive and insoluble in water. So far, the fundamental aspects of hydrate formation in the system constituted by twice-distilled water and Freon 142-V have not been studied.

The process of hydrate formation should proceed with a high yield of crystals per unit volume and time, low energy expenditure for agitation, and small driving forces. It is reasonable to perform desalination to obtain large crystals with uniform size distribution, which depends on the hydrodynamic conditions of the process.

The influence exerted by the hydrodynamic conditions on the course of hydrate formation in the system constituted by twice-distilled water and Freon 142-V was studied on the experimental laboratory setup (Fig. 1) by the procedure suggested.

Figure 2 shows the results obtained in a study of the influence exerted by the stirring rate on the course of hydrate formation. The stirring rate was varied in the range 200–1350 rpm. As follows from Fig. 2, raising the stirring rate from 200 to 1350 rpm leads to a considerable intensification of the process of hydrate formation. This can be attributed to a decrease in the outer-diffusion resistance.

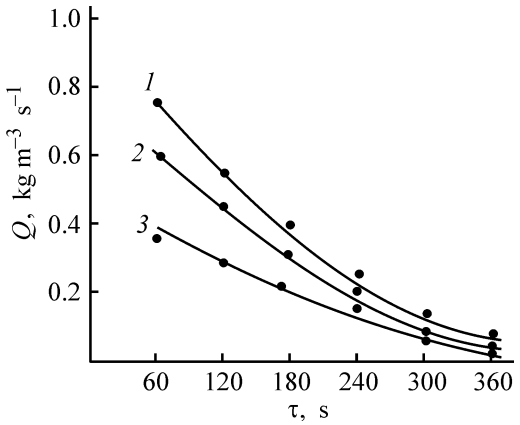


Fig. 3. Throughput Q of the reactor vs. the reaction time τ at varied diameter of gas bubbles. T = 4°C, P = 0.9 atm, c_{NaCl} = 0.01 mg l^{-1}, stirring rate 1350 rpm. Bubble diameter (mm): (*1*) 0.5–1.0, (*2*) 2.0–2.5, and (*3*) 3.0–3.5.

Figure 3 demonstrates the results obtained when studying the effect of the diameter of gas bubbles on the course of hydrate formation. The diameter of gas bubbles was varied in the range d_n = 0.5–3.5 by changing the size of apertures in the gas distributor. As follows from Fig. 3, decreasing the bubble diameter from 3.0–3.5 to 0.5–1.0 mm intensifies the hydrate formation, which can be accounted for by a decrease in the inner-diffusion resistance.

CONCLUSIONS

(1) An experimental procedure employing an AAS-300 atomic-absorption spectrometer for studying the hydrate formation was developed. The efficiency of the procedure was confirmed for the example of a system constituted by twice-distilled water and Freon 142-V.

(2) The conditions for efficient hydrate formation in the system constituted by twice-distilled water and Freon 142-V were found. Raising the stirring rate from 200 to 1350 rpm and diminishing the bubble diameter from 3.0–3.5 to 0.5–1.0 mm results in intensification of the hydrate formation.

ACKNOWLEDGMENTS

The study was financially supported by the Ukrainian Science and Technology Center (USTC) (project no. 3515).

REFERENCES

1. Mirzadzhanzade, A.Kh., Kuznetsov, O.L., Basniev, K.S., and Aliev, Z.S., *Osnovy tekhnologii dobychi gaza* (Fundamentals of Natural Gas Production Technology), Moscow: Nedra, 2003.
2. Makogon, Yu.F., *Gazovye gidraty, preduprezhdenie ikh obrazovaniya i ispol'zovanie* (Gas Hydrates, Prevention of Their Formation, and Use), Moscow: Nedra, 1985.
3. Briggs, F.A., *Advances in Chemistry, Ser. 38, Saline Water Condensation*, Washington, II, 1962, p. 150.
4. Byk, S.Sh., Makogon, Yu.F., and Fomina V.I., *Gazovye gidraty* (Gas Hydrates), Moscow: Khimiya, 1980.
5. Kul'skii, L.A., Cheptsov, A.S., Knyaz'kova, T.V., and Kucheruk, D.D., *Novye metody opresneniya vody* (New Methods of Water Desalination), Kiev: Naukova Dumka, 1974.
6. Barduhn, A.J., *First Int. Symp. on Water Desalination, Paper SWD 88*, Washington, 1965, pp. 52–54.
7. Robins, K.D. and Martin, J.C., *Oil. Gas J.*, 1962, vol. 60, no. 18, p. 85.

ISSN 1070-4272, Russian Journal of Applied Chemistry, 2008, Vol. 81, No. 4, pp. 592–596. © Pleiades Publishing, Ltd., 2008.
Original Russian Text © V.V. Rogozhin, 2008, published in Zhurnal Prikladnoi Khimii, 2008, Vol. 81, No. 4, pp. 554–558.

INORGANIC SYNTHESIS AND INDUSTRIAL INORGANIC CHEMISTRY

Comparison of the Reactivities of Main Boron-containing Additives Used in Electrodeposition of Nickel–Boron Coatings

V. V. Rogozhin

Nizhni Novgorod State Technical University, Nizhni Novgorod, Russia

Received June 29, 2007

Abstract—Reactivities of the main boron-containing additives used in electrodeposition of nickel–boron coatings were compared by measuring the rate of boron incorporation into a nickel coating and the effective activation energy.

DOI: 10.1134/S1070427208040046

Nickel–boron coatings produced by chemical deposition or electroplating possess high hardness and wear resistance, are solderable, can be ultrasonically welded, and have low electrical resistance stable in the course of time [1]. The combination of these properties of the coatings allows their use in manufacture of radio electronic articles for various purposes [2].

Electroplating with nickel–boron alloys is the most available because it can be carried out from standard electrolytes. This process implements all the conventional advantages of electrodeposition over chemical methods. Nickel–boron coatings are electrodeposited from sulfuric acid, sulfamine, ammonia citrate, and chloride electrolytes, with addition of various boron-containing compounds [3]. The composition, structure, and properties of these coatings are readily controlled by varying the electrolysis mode (current density, temperature, pH value) and the amount of a boron-containing additive in the electrolyte.

The choice of the optimal boron-containing additives for deposition of nickel–boron coatings is governed by the availability of additives, rather than by the degree of technological development of the corresponding process. Therefore, it is advisable to compare the reactivities of the boron-containing additives used and the conditions of their application in a search for new interchangeable boron-containing additives.

The results of this study make it possible to systematize the data obtained with respect to the alloy composition, electrodeposition conditions, and mechanism of boron incorporation and to relate these data to the structure and properties of the additives themselves.

EXPERIMENTAL

The experimental conditions were the same for all the additives: coatings were deposited from a sulfate electrolyte with pH 4.5 at a current density of 2 A dm^{-2} and temperature of 40°C. The content of boron was found by potentiometric titration [4]. The activation energy of nickel deposition was determined by the temperature-kinetic method, and that of boron deposition, from the dependence of the boron incorporation rate on inverse temperature. The chemical contribution in the coating deposition was evaluated by the increase in the sample mass and, theoretically, from polarization diagrams [5]. The boron incorporation rate was calculated from the resulting alloy composition. The boron-containing substances used in the study are listed in Table 1.

Table 1. Boron-containing substances under study

Additive	Formula	Initial tent, %	Working concentration, g l^{-1}	TU (Technical Specification)
Dimethylamineborane (DMAB)	$(CH_3)_2HNBH_3$	98	50	TU 2439-035-10645057–96
Sodium dicarbaundecaborate (SDCDB)	$NaC_2B_9H_{12}$	40–45	25	TU 6-02-1-453–84
Sodium decahydrodecaborate (SDHDB)	$Na_2B_{10}H_{10}$	25–27	18	TU 6-02-1-513–86
Potassium dodecaclosododecaborate (PEB)	$K_2B_{12}H_{12} \cdot 4H_2O$	99.9	12	Pilot batch

Boron is incorporated into a nickel coating in electrodeposition by the chemical-catalytic mechanism associated with decomposition of boron-containing additives on the surface of a freshly deposited nickel acting as a catalyst [6, 7]. To standardize plots for different boron-containing additives, their working concentrations were recalculated to active boron. For SDHDB and SDCDB, the initial working concentrations were taken as those of anions, and for DMAB and PEB, as those of the substances themselves.

A comparison of the effects of the chosen additives demonstrated that the DMAB additive shows the highest reactivity with respect to the boron incorporation rate and leads to the highest content of boron in a coating deposited, at the smallest amount of the additive in terms of active boron (Fig. 1). The SDHDB and SDCDB additives are similar and yield approximately the same, amounts of boron in a coating, which are smaller than that with DMAB. The boron incorporation rates are also approximately the same for these additives. Compared with the other boron-containing compounds, the PEB additive yields the smallest amount of boron in a coating, with the concentrations of PEB in the electrolyte being the highest, and the boron incorporation rate, the lowest.

The slopes of the initial portions of the curves in Fig. 1 ($\tan\alpha$) make it possible to indirectly estimate the stability of the boron-containing substances against catalytic decomposition on a growing nickel coating and, accordingly, their reactivity with respect to boron incorporation. Below are listed values of $\tan\alpha$ for various additives:

Additive	DMAB	SDHDB	SDCDB	PEB	PEB, 60°C
$\tan\alpha$	0.49	0.24	0.25	0.02	0.03

The different reactivities of the additives correlate with the activation energies of boron incorporation, obtained from characteristic dependences of the logarithm of the boron incorporation rate for each additive on the inverse temperature (Table 2). Among the additives studied, PEB has the minimum reactivity with respect to boron incorporation, but, as temperature increases, the content of boron in a coating increases, with a sharp decrease in the activation energy, which may be due to acceleration of the chemical stage of decomposition of the boron-containing anion [7]. Other comparative data on the reactivity of the additives are presented in Table 3. The differences in reactivity are apparently due to different structures of the boron-containing additives.

The SDHDB and PEB additives belong to the class of polyhedral boranes and contain $B_{10}H_{10}^{2-}$ and $B_{12}H_{12}^{2-}$ anions, respectively. The additive with $B_9C_2H_{12}^-$ belongs to the class of substances with nidocarborane anions, derivatives of $B_nH_n^{2-}$, produced from these anions by substitution of the BH^- moiety with a CH analogue [8]. The DMAB additive belongs to the class of aminoboranes with a linear molecular structure [9]. The structure of SDHDB and PEB was studied in [10], using the LCAO–MO method and that of resonant structures.

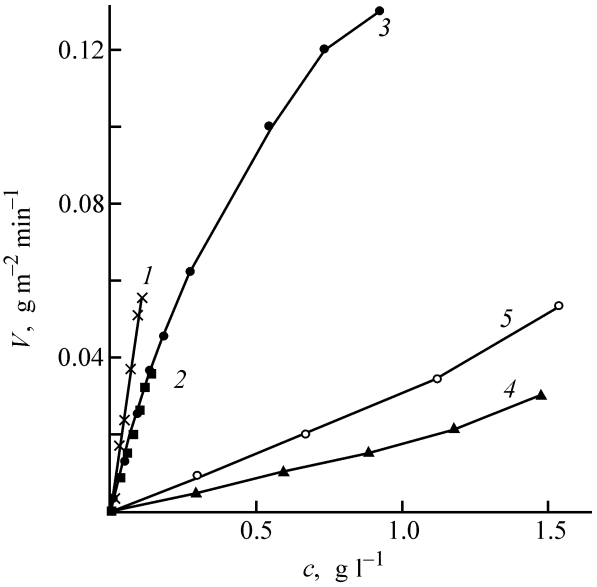


Fig. 1. Rate V of boron incorporation into a coating vs. the concentration c (in terms of boron) of various boron-containing additives (i = 2 A dm^{-2}). Additive: (*1*) DMAB, (*2*) SDHDB, (*3*) SDCDB, and (*4*, *5*) PEB. Temperature (°C): (*1*–*4*) 40 and (*5*) 60.

An equilateral rectangle on which rest equilateral triangles was taken as a basis when calculating the parameters of the $B_{10}H_{10}^{2-}$ anion. As the base of the $B_{12}H_{12}^{2-}$ anion serves an equilateral pentagon, on

Table 2. Effective activation energy E_{eff} of boron incorporation into nickel–boron coatings from electrolytes with various boron-containing additives

Additive	E_{eff}, kJ mol^{-1}, in indicated temperature range, °C	
	30–40	40–50
DMAB	25–27	–
SDHDB	25–27	25–27
SDCDB	60–70	25–35
PEB	70–90	37–40

Table 3. Comparative data on the reactivity of boron-containing additives used in electrodeposition of the nickel–boron alloy

Parameter	Determination conditions	DMAB	SDCDB	SDHDB	PEB
Boron incorporation rate, g m^{-2} min^{-1}	Optimal mode	0.035	0.04	0.04	0.038
Chemical contribution, %	95°C (45°C for DMAB)	4.2–6.4	0	33–38	0
Shift of the compromise potential, mV	Working concentrations of an additive	–350	0	–300	0…+100
Activation energy for electrodeposition of nickel, kJ mol^{-1}	E = –0.7 V, c_{max}	50–60	–	88–92	43–50
Reduced boron incorporation rate, g m^{-2} min^{-1}	Boron concentration 0.1 g l^{-1}, 2 A dm^{-2}	0.06	0.04	0.04	0.02
Limiting boron incorporation rate, g m^{-2} min^{-1}	c_{max}, 2 A dm^{-2}	0.085	–	0.120	0.05
Solution decomposition	T = 95°C, time 2 h	Yes	No	Yes	No

Table 4. Charge distribution, bond lengths, and formation energy for anions of polyhedral borates

Anion	Positions of atoms*	Length, Å	Charge		Formation energy, eV
			calculated	experimental	
$B_{10}H_{10}^{2-}$	1, 10	–	–0.33	–0.15	
	2–9	–	–0.17	–0.01	
	3, 4	1.86			181.3
	3–6	1.81	–	–	
	1–3	1.73			
$B_{12}H_{12}^{2-}$	1–12	–	–0.17	–0.02	213.68
	1–5	1.77	–	–	

* The positions of atoms correspond to Fig. 2.

which equilateral triangles also rest (Fig. 2a). The basic parameters characterizing the structure of the polyhedral anions $B_{10}H_{10}^{2-}$ and $B_{12}H_{12}^{2-}$ and some of their properties are listed in Table 4 [10].

It was found in [10] that the adsorption capacity of boron-containing additives increases in the order B_2H_6–B_5H_9–$B_{12}H_{12}^{2-}$–$B_{10}H_{10}^{2-}$–$B_{10}H_{14}$, which can be attributed to the structure and different charge distribu-

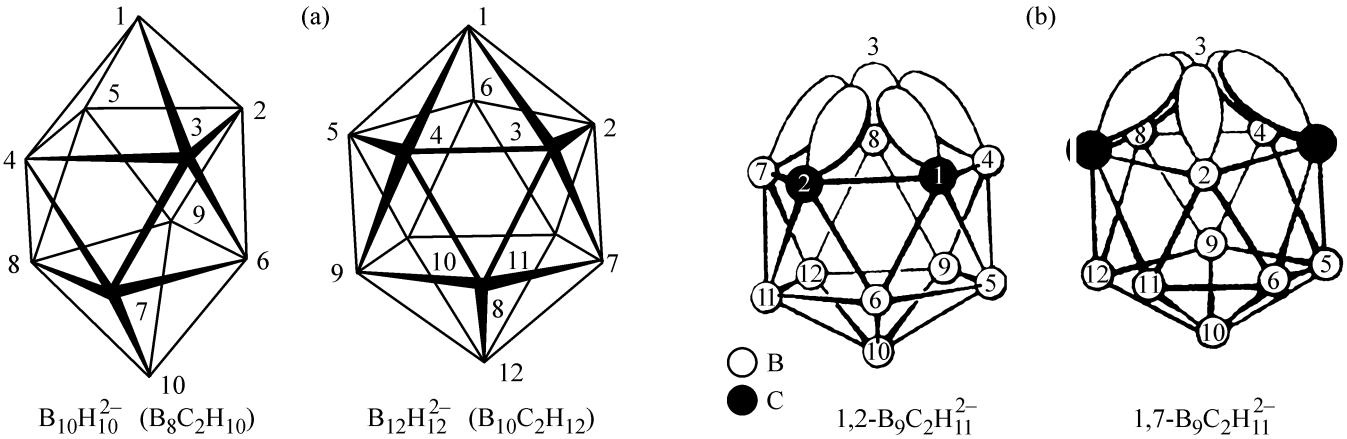


Fig. 2. Structure of (a) polyhedral anions and (b) isomeric nido-anions used in the study.

tions on boron atoms. On the negatively charged surface of the nickel cathode, the adsorption will in all probability occur at boron atoms bearing the smallest negative charge (Fig. 2, positions 2–9). The bond length for these positions is the largest, and the energy is lower than that of boron atoms in other positions. The original detachment of boron from these positions will occur with lower energy expenditure, which accounts for the rather high boron incorporation rate and for the possibility of bulk decomposition of the nickel plating solution in the absence of current at high temperatures and concentrations of the additive. Simultaneously, the high adsorption capacity of $B_{10}H_{10}^{2-}$ markedly raises the activation energy of the concurrent process of nickel electrodeposition.

A somewhat different situation is observed for nido-carborane anions (1,2-$B_9C_2H_{12}^-$ and 1,7-$B_9C_2H_{12}^-$) produced from $C_2B_{10}H_{12}$ via detachment of boron atoms in a reaction with alcoholate ions. The structure of nido anions of this kind is shown in Fig. 2b.

Calculations by the method of molecular orbitals (MO) in [8] demonstrated that carbon atoms in carboranes have high electron-acceptor properties. The most electron-deficient are borons situated near these carbons. These are positions 3 and 6 in the 1,2-$B_9C_2H_{12}^-$ anion and positions 2 and 3 in 1,7-$B_9C_2H_{12}^-$ (Fig. 2). Boron atoms of this kind will have a more positive charge and, in all probability, boron is originally incorporated into a coating from these positions.

In the $B_{12}H_{12}^{2-}$ anion, all the bonds are equivalent in length and energy. Its structure is more perfect, compared with other additives, and is believed to be hypersymmetric, with the result that the stability of the additive in the electrolyte is high, it does not undergo bulk decomposition at high temperatures, and no metal is deposited via chemical reduction.

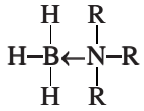
For the $B_{12}H_{12}^{2-}$ anion, boron can be detached from the borane skeleton from any position, but with high energy expenditure.

Because of its lower adsorption capacity, the anion only slightly affects the activation energy of the concurrent process of nickel electrodeposition.

The reactivity of the $B_{12}H_{12}^{2-}$ anion can be affected by the impurities it contains and by the polarizing effect of cations.

According to [11], $B_{12}H_{12}^{2-}$ readily reacts with Lewis bases. For example, an admixture of triethylamine in the $B_{12}H_{12}^{2-}$ additive may lead to formation of a substituted anion, $(Et_3NH)_2B_{12}H_{11}^-$, with the anion charge changed, and to a pronounced change in its properties, compared with the unsubstituted anion. In this case, the structure of the $B_{12}H_{12}^{2-}$ anion is also affected by the polarizing action of the cation [11]: the larger the cation charge, the more significant the distortion of the $B_{12}H_{12}^{2-}$ skeleton. According to [11], the polarizing effect of the cation in the $(Et_3NH)_2B_{12}H_{12}$ compound is at a minimum because of its large size, and the B–B bond lengths are approximately the same and equal to 1.781 Å. In the compound $CaB_{12}H_{12}$ [12], the boron skeleton is strongly distorted and the bond lengths vary from 1.72 to 1.84 Å. It is also not improbable that, under the electrodeposition conditions, the nickel cation can exert a polarizing influence on the structure of the $B_{12}H_{12}^{2-}$ anion when a surface complex is formed, as it has been reported for the $B_{10}H_{10}^{2-}$ additive [13].

In aminoboranes (borozanes), boron with three covalent bonds is connected to nitrogen by the lone electron pair of nitrogen, and their structural formula is frequently shown as



The nature of the boron–nitrogen bond formed by a shift of the electron pair of the trivalent nitrogen toward boron has not been elucidated unambiguously. The bond strength is affected by the nature of groups connected to both boron and nitrogen atoms, and, consequently, the stability of aminoboranes (borozanes) may vary very widely [9].

Aminoboranes of the R_3BH_3 type show high thermal stability only when they contain no hydrogen bonded to nitrogen. If a compound has a hydrogen bonded to nitrogen, which is the case for DMAB [$(CH_3)_2HNBH_3$], then the additive is characterized by reactions in which the boron–nitrogen bond is cleaved. This leads to the maximum reactivity of the additive in electrodeposition of nickel–boron alloys and to incorporation of boron by the known mechanism of dissociative adsorption [5, 14].

CONCLUSIONS

(1) A comparison of the reactivities of various boron-containing additives used in electrodeposition of nickel–boron coatings demonstrated that the highest activity is observed for dimethylamineborane, and the lowest, for potassium dodecaclosododecaborate, which is due to the dissimilar mechanisms of boron incorporation, different bond lengths, and

metastability of boron atoms in certain positions of the anion.

(2) Judging from the structure of the boron-containing additives used, the activation energy of boron incorporation into the nickel matrix will increase in the order $(CH_3)_2HNBH_3$–$Na_2B_{10}H_{10}$–$NaC_2B_9H_{12}$–$K_2B_{12}\cdot 4H_2O$. The reactivity of the additives decreases in the same order.

(3) Ways to raise the reactivity of the $B_{12}H_{12}^{2-}$ anion will be determined by the following parameters: working temperature of the electrolyte; charge, nature, and size of the cation; and possibility of interaction between the anion and a Lewis base. The effect of technological factors on the reactivity of the additives makes it possible to equalize their reactivities at optimal values, which makes the additives more interchangeable in practical use.

REFERENCES

1. Flerov, V.N., *Khimicheskaya tekhnologiya v proizvodstve radioelektronnykh detalei* (Chemical Technology in Manufacture of Articles for Radioelectronics), Moscow: Radio i Svyaz', 1988.
2. Rogozhin, V.V., *Materialy Mezhdunarodnoi konferentsii "Elektrokhimiya, gal'vanotekhnika i obrabotka poverkhnosti"* (Proc. Int. Conf. "Electrochemistry, Electroplating, and Surface Treatment"), Moscow, 2001, p. 95.
3. Plokhov, V.A., Flerov, V.N., and Dyagilev, V.A., *Izv. Vyssh. Uchebn. Zaved., Khim. Khim. Tekhnol.*, 1988, vol. 31, no. 1, pp. 77–80.
4. Val'syunene, Ya.I. and Norkus, P.K., *Tr. Akad. Nauk LitSSR, Ser. B*, 1972, no. 1(68), pp. 93.
5. Anan'eva, E.Yu. and Rogozhin, V.V., *Gal'vanotekhn. Obrab. Pov–sti*, 2005, vol. 13, no. 1, pp. 23–27.
6. Sadakov, G.A., Ezikyan, A.Ya., and Kukoz, F.I., *Elektrokhimiya*, 1980, vol. 16, no. 12, pp. 1837–1840.
7. Dyagilev, V.A., Rogozhin, V.V., Gribanova, Yu.N., and Flerov, V.N., *Gal'vanotekhn. Obrab. Pov–sti*, 1996, vol. 4, no. 4, pp. 22–27.
8. Cotton, F.A. and Wilkinson, G., *Basic Inorganic Chemistry*, New York: Wiley, 1976.
9. Niedenzu, K. and Dawson, J.W., *Boron Nitrogen Compounds*, New York: Academic, 1965.
10. Limpcomb, W.N. and Hoffman, R., *J. Chem. Phys.*, 1962, vol. 37, no. 12, pp. 2872–2883.
11. Agafonov, A.V., Butman, L.A., Solntsev, K.A., and Vinokurov, A.A., *Zh. Neorg. Khim.*, 1982, vol. 27, no. 1, pp. 1318–1325.
12. Solntsev, K.A., Kuznetsov, N.T., and Ponomarev, V.N., *Zh. Neorg. Mater.*, 1976, vol. 12, no. 6, p. 1366.
13. Rogozhin, V.V., Gribanova, Yu.N., and Flerov, V.N., *Gal'vanotekhn. Obrab. Pov–sti*, 2000, vol. 8, no. 3, pp. 29–34.
14. Lelental, M.J., *J. Catal.*, 1974, vol. 32, no. 3, pp. 429–431.

ISSN 1070-4272, Russian Journal of Applied Chemistry, 2008, Vol. 81, No. 4, pp. 597–602. © Pleiades Publishing, Ltd., 2008.
Original Russian Text © A.M. Ivanov, E.A. Grechushnikov, 2008, published in Zhurnal Prikladnoi Khimii, 2008, Vol. 81, No. 4, pp. 559–564.

INORGANIC SYNTHESIS AND INDUSTRIAL INORGANIC CHEMISTRY

Effect of Solvent Nature on the Reaction of Metallic Iron with Benzoic Acid in a Bead Mill

A. M. Ivanov and E. A. Grechushnikov

Kursk State Technical University, Kursk, Russia

Received February 22, 2007

Abstract—Results of an experimental study of the influence exerted by the solvent nature on the reaction rate, achieved degree of acid expenditure, selectivity with respect to salts of iron(II) and (III), and phase state of the reaction mixture in a single-stage reaction of iron with benzoic acid and atmospheric oxygen in the presence of a stimulating iodine additive are presented.

DOI: 10.1134/S1070427208040058

Iron(III) and (II) benzoates are rather widely used in various industries [1–11].

Commonly, these salts are obtained by one of the following three methods: (i) exchange interaction of iron salts and mineral acids with sodium benzoate or by a direct reaction of an iron oxide with benzoic acid in the temperature range 125–260°C in the presence of an organic dispersing agent [12]; (ii) reaction of benzoic acid with the metal nitrate in the presence of an inert organic solvent, followed by addition to the reaction mixture of ammonia and(or) amine, and(or) tetraalkylammonium hydroxide at a temperature of 20–40°C and pressure of $(1–50) \times 10^5$ N m^{-2} [13]; and (iii) direct electrosynthesis [14]. These methods require certain auxiliary substances and rather severe conditions and yield by-products that need utilization. Moreover, some of these methods cannot be performed in a single stage.

It was of interest to obtain iron benzoates in a single-stage process in accordance with the stoichiometric overall equations (HA stands for carboxylic acid)

$$2Fe + 4HA + O_2 \rightarrow 2FeA_2 + 2H_2O, \quad (1)$$

or

$$4Fe + 12HA + 3O_2 \rightarrow 4FeA_3 + 6H_2O, \quad (2)$$

i.e., with atmospheric oxygen as an oxidizing agent, crushed iron or its alloys (including those of waste origin) as a reducing agent, and also an organic solvent and iodine (the latter as a stimulating additive). By now, iron(II) and (III) formates and acetates have been synthesized by this method [15–18]. The process occurs in a single technological stage to give the target product mainly in the form of a suspension easily separated by filtration. The filtrate containing dissolved products of conversion of the stimulating additive and iron salts is recycled and thereby requires neither separation, nor repeated utilization.

The overall processes (1) and (2) are heterogeneous, complex, and multistage. Their principal stages are the following [19–22]:

$$Fe + I_2 \rightarrow FeI_2, \quad (3)$$

$$2FeI_2 + 4HA + O_2 \rightarrow 2FeA_2 + 2I_2 + 2H_2O, \quad (4)$$

and(or)

$$4FeI_2 + 12HA + 3O_2 \rightarrow 4FeA_3 + 4I_2 + 6H_2O, \quad (5)$$

and also [17, 18]

$$4FeA_2 + O_2 + 4HA \rightarrow 4FeA_3 + 2H_2O, \quad (6)$$

$$Fe + 2FeA_3 \rightarrow 3FeA_2. \quad (7)$$

Together, stages (3) + (4), (3) + (5) or (3) + (4) + (5) constitute cyclic processes of consumption and formation of iodine, and just this circumstance is the reason why it is used as a catalyst.

The main purpose of the liquid phase is the transport function. The place where the basic stages occur is the iron surface onto which the reactants are de-

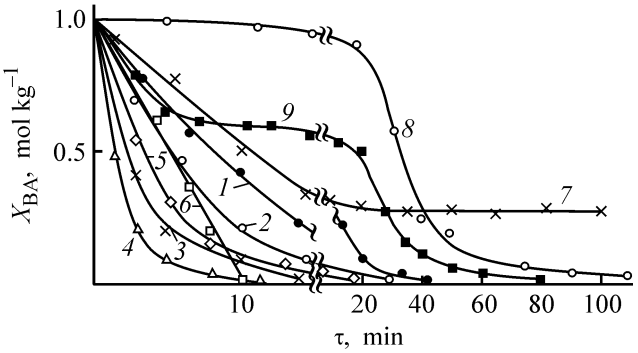


Fig. 1. Kinetic curves of benzoic acid consumption for formation of iron salts at varied nature of a solvent in the liquid phase of the charge. Reactor: vertical bead mill with a four-blade stirrer rotating at 1560 rpm; mass of beads 200 g; 1 : 1 mass ratio of beads to the liquid phase of the charge; charge: crushed cast iron 60 g, iodine 0.03 mol kg^{-1} liquid phase; temperature 60 ± 2°C. (X_{BA}) Concentration of benzoic acid and (τ) time. Solvent: (*1*) dimethylformamide, (*2*) 2 : 3 (*v*/*v*) mixture of dimethylformamide and butanol, (*3*) *n*-butanol, (*4*) chlorobenzene, (*5*) bromobenzene, (*6*) ethyl cellosolve, (*7*) toluene, (*8*) petroleum spirit, and (*9*) ethylbenzene.

livered by means of adsorption. The solid products formed on the surface should be removed into the solution bulk to preclude full passivation of the surface by their deposits. Their desorption cannot play any significant part in systems of this kind. Considerably more important is their dissolution or mechanical removal (scraping, scuffing, stripping). The role of the solvent is also important. On the whole, the solvent nature should largely determine the competitive ability of reactions (3)–(7) and, consequently, that of (1) and (2), as well as the selectivity with respect to the iron(II) and (III) salts and the heterophase state of the final reaction mixture, which may either facilitate or hinder its separation and product recovery. In this study, an attempt was made to evaluate the effect of the solvent nature on the reaction of iron with benzoic acid in a bead mill.

EXPERIMENTAL

The experiment was performed in a vertical bead mill with a high-speed (1440 and 1560 rpm) blade stirrer whose shaft was connected to that of a 0.5-kW motor. The stirrer case was made of stainless steel and had a wall thickness of about 10 mm. The blades and the shaft of the stirrer were made of st.45 or stainless steel. In both cases, their working life was rather short (1–2 months), which was predetermined by their involvement in the redox process under consideration as a source of reacting iron. To preclude rapid wear, the case and bottom of the bead mill were protected with an inserted steel shell and a well-fit false bottom with a foot bearing for the blade stirrer. As a grinding agent served glass beads 0.8–3.1 mm in diameter, both individually and together with powdered reduced iron, sieved fractions of crushed cast iron, and fragmented steel shavings with the maximum linear particle size of 5 mm. The mass ratio between the glass beads and ground iron and(or) its alloys was widely varied.

The bead mill was equipped with a reflux condenser and heat supply via a liquid bath that could be moved along the longitudinal axis of the reactor. The course of the process was monitored by sampling, with the content of carboxylic acid and its iron(II) and (III) salts determined. The monitoring results were used to plot the corresponding kinetic curves.

The reagents were charged in various orders. Most frequently, glass beads, solvent, and carboxylic acid were charged first and then agitation was switched on and thereby a solution of carboxylic acid was prepared. Occasionally, this solution was prepared preliminarily and then batched into the reactor. After that, ground iron or iron alloys and the catalyst were charged and air was fed into the reactor for bubbling. The bubbler was fabricated in an elastic version to preclude its disintegration upon contact with moving beads or heavy particles of iron or its alloys.

It was found that, without iodine, the process begins, but rapidly terminates at acid conversions not exceeding 2–3%. Therefore, if the chosen temperature mode was to be strictly maintained (in the range 15–90°C), the stimulating additive was introduced at the instant when the system reached the working temperature.

Figure 1 shows kinetic curves of benzoic acid consumption for the process performed in various solvents. The role of the solvent is manifested not only in different rates of acid consumption, but also in the existence of the period of self-accelerated development (e.g., in petroleum spirit), intermediate self-deceleration (in ethylbenzene), self-termination (in toluene), and self-resumption of the process (in ethylbenzene), in its selectivity with respect to iron(II) and (III) salts, and in the manner in which the selectivity varies in the course of the process.

In all of the solvents chosen, the amounts of iodine used for stimulation were completely soluble. Therefore, the maximum concentrations of iodine were determined only by its close. At the same time, its running concentrations were 10–20 times lower than the maximum values. This indicated that, in the course of the process, the main part of iodine

Solubility of benzoic acid and its iron salts and of iron(II) iodide in the solvents used at 17 ± 1°C

Solvent of the liquid phase	Solubility, mol kg^{-1}			
	benzoic acid	iron(III) benzoate	iron(II) benzoate	iron(II) iodide* [21]
Formamide	1.712	0.041	<0.0011	–
Dimethylformamide	4.398	0.412	0.0375	0.57
n-Butanol	2.058	0.110	0.0087	0.24
2 : 3 (*v*/*v*) mixture of dimethylformamide and *n*-butanol	3.607	0.281	0.0158	–
Ethyl cellosolve	2.724	0.183	0.0274	0.41
Petroleum spirit	0.028	0.008	<0.0003	0.0004
Toluene	0.817	0.083	<0.0003	0.0009
Ethylbenzene	0.559	0.062	<0.0003	0.0005
Chlorobenzene	0.581	0.082	<0.0003	–
Bromobenzene	0.623	0.029	<0.0003	–
Water	0.145	0.013	0.0007	>2.08

* At 29 ± 1°C.

being introduced was in the form of FeI_2, which was confirmed by direct analysis.

The acid must also be to some extent soluble in the solvent used (see table), but this extent remains unknown. The process could also be performed in dimethylformamide, in which the solubility of benzoic acid exceeds 4 mol kg^{-1}, and in petroleum spirit, in which the solubility is more than 100 times lower and the main part of the acid charged into the reactor remained in the solid phase in the course of the process. The conclusion that the solubility of the acid is not a key factor is also confirmed by the fact that the rate and time characteristics of the process depend on the initial content of the acid in the charge not only in a rather complicated way, but also not too strongly (Figs. 2, 3). In addition, clear requirements to the role played by the solubility of salt products in the liquid phase could not be formulated. At a high solubility of the metal iodide, there appears an important mass-exchange pathway to disintegration and removal of its surface deposits from iron. In this case, reactions (4) and (5) partly pass into solution, i.e., into homogeneous conditions. The FeA_2 and FeA_3 salts being accumulated are first present in solution and then, beginning at a certain instant of time, form independent solid phases. The solid phase of green FeA_2 appears first, which correlates with its poorer solubility, compared with FeA_3. As a direct experiment demonstrated, transformations of dissolved and suspended salt products into components of surface deposits on the metal are unlikely.

At the same time, at a poor solubility of iron(II) iodide in the liquid phase used (e.g., in petroleum spirit), reactions (4) and (5) will be predominantly

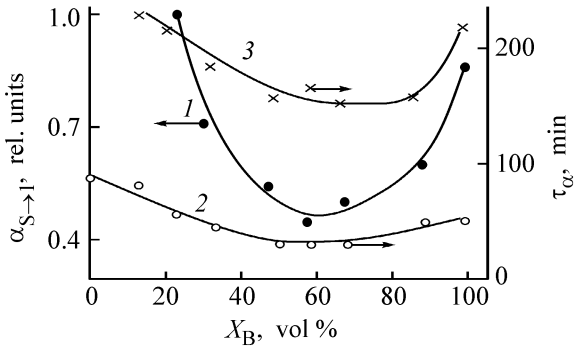


Fig. 2. Conversion α of benzoic acid in a single-stage reaction with fragmented iron in the presence of iodine vs. the content X_B of *n*-butanol mixed with dimethylformamide as a solvent of the liquid phase. Dosage: benzoic acid in accordance with its solubility at 21°C and iodine 0.125 mol kg^{-1}; 4 : 1 mass ratio of the liquid phase and reduced iron; mass of the liquid phase 200 g; temperature 60 ± 1°C; rotation rate of the blade stirrer of the vertical bead mill 1560 rpm. (*1*) ($\alpha_{S\to1}$) Conversion at the selectivity with respect to the iron(III) salt approaching 100% and remaining so till the end of the process; (*2*, *3*) (τ_α) time in which (*2*) 50% and (*3*) 100% conversion of benzoic acid is reached.

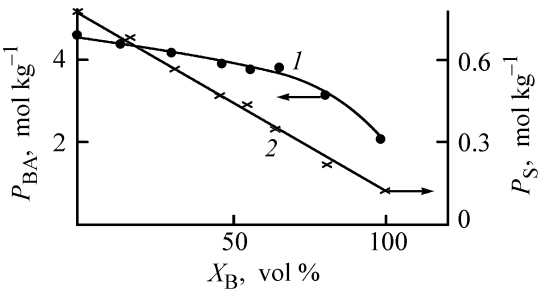


Fig. 3. Solubility of (*1*) benzoic acid (P_{BA}) and (*2*) iron(III) benzoate (P_S) vs. the content X_B of *n*-butanol in a mixture with dimethylformamide as a solvent. Temperature (°C): (*1*) 21 and (*2*) 18.

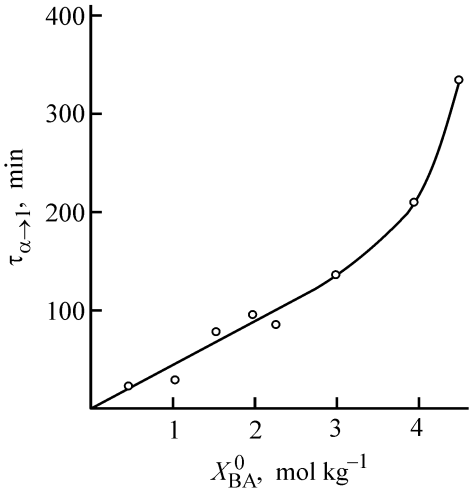


Fig. 4. Time $\tau_{\alpha\to1}$ in which a virtually quantitative conversion of benzoic acid mainly into the iron(III) salt is reached vs. the initial concentration X^0_{BA} of the acid in a 2 : 3 (*v*/*v*) mixture of dimethylformamide and butanol, taken as the liquid phase for the reaction of 30 wt % (relative to the liquid phase) crushed cast iron with benzoic acid at 60°C in the presence of 0.075 mol kg^{-1} of a stimulating iodine additive and bubbling with air. Reactor: vertical bead mill with a four-blade stirrer rotating at 1550 rpm; 1 : 1 mass ratio of beads and the liquid phase charge; air expenditure for bubbling 2.2 l min^{-1} kg^{-1} liquid phase.

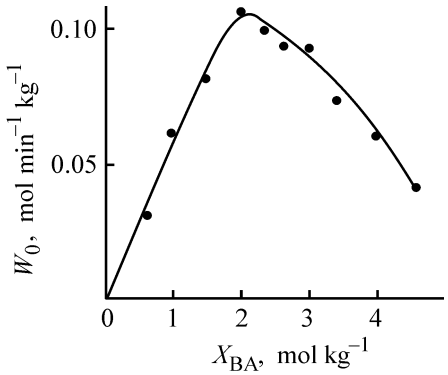


Fig. 5. Initial rate W_0 of the conversion of benzoic acid into iron salts vs. the initial content X_{BA} of benzoic acid in the liquid phase of the system. Process conditions the same as those for Fig. 4.

heterogeneous, and FeA_2 and FeA_3 remaining on the surface can well be transformed into important components of the surface deposits on iron. Mechanical methods for disintegration and removal of surface deposits become the most important in this case. Because both these variants have been implemented in practice, with the process rates and durations being comparable, there is no good reason to prefer one of them.

The following circumstance appeared to be the most important in this regard: the viscosity of the system grows as the product is accumulated both in solution and as a suspension, with the increase being self-accelerated in deep stages. This leads to a synchronous decrease in the operation efficiency of the bead mill, to the point of complete loss of its working capacity. The results obtained demonstrate that this occurs when iron salts are accumulated in a total amount of 1.2–1.5 mol kg^{-1}. Consequently, the maximum content of the acid in the charge, determined with account of the fact that its whole amount can be converted into salts, must not exceed 3.6–4.5 mol kg^{-1}. However, this does not mean that just these initial concentrations of the acid will be optimal (Figs. 2, 4, 5), because the corresponding dependences are complicated. For example, the solubilities of benzoic acid and iron(III) benzoate substantially fall as the content of *n*-butanol in the mixed solvent increases (Fig. 3), whereas the time in which a 50% or >98% conversion of benzoic acid into iron salts is reached passes through a minimum at a 60–65% content of *n*-butanol in the mixed solvent. Consequently, it is better that the solubility of the final product in the liquid phase used should not be too high, so that the product would accumulate in the form of a suspension. In this case, the viscosity grows more slowly and the product itself can be easily isolated by simple filtration.

Comparison of the data in Figs. 4 and 5 shows that the manner in which the process duration increases with the initial content of benzoic acid is associated not only with the pronounced differences in the viscosities of the reaction mixtures in deep-conversion stages, but with the fact that the initial rates pass through a maximum as functions of the content of the acid. At the beginning of the process, the viscosity of the liquid phase will also grow with the content of benzoic acid. However, this increase is incomparable with the rise in the viscosity of the reaction mixture, observed as the acid expenditure for salt formation becomes quantitative.

Experiments with different solvents revealed variants in which the reaction mixture becomes, in the course of the process, a glue-like viscous mass that entraps glass beads and solid particles of the metal. In these cases, the process is always doomed to self-termination because of the complete loss of working capacity by the bead mill. This is a rather rare phenomenon for benzoic acid (e.g., in toluene; Fig. 1, curve *7*). By contrast, this situation is one of the most frequently occurring for butyric acid.

However, not any self-termination of the process is due to a strong thickening of the reaction mixture or to its transformation into a glue-like mass. As an example can serve curve *9* in Fig. 1. Whose intermediate portion is associated with blocking of the metal surface by surface deposits of salt products, which becomes weaker in the course of time and self-resumption of the process occurs.

In some cases, self-termination of the process was observed in systems in which products were mostly accumulated as suspended solid phases, and no noticeable decrease in the operation efficiency of the bead mill was observed in the course of their accumulation. For example, self-termination occurred in water (not shown in Fig. 1, the corresponding kinetic curve is similar to curve *7*) by the 85th–90th minute, with no self-resumption observed in the following 150 min. This self-deceleration also occurred because of the blocking of the iron surface by a mixture of benzoates of iron(II) (green) and iron(III) (brown). An inspection of unreacted particles of cast iron revealed a greenish-gray deposit on their surface. The filtered-off precipitate of the salt products had the same coloration.

The nature of the solvent used strongly affects the accumulation kinetics of iron(II) and (III) salts and, consequently, the achievable selectivity with respect to the target product. This can be illustrated by the example of the mixed solvent used in this study, with varied ratio of dimethylformamide and *n*-butanol in the solvent (Fig. 2, curve *1*). The conversion on reaching and exceeding which the selectivity with respect to iron(III) salt tends to unity passes through a minimum. This minimum is observed at a content of *n*-butanol within the range 50–70% and acid conversions into the product of about 50%. It is this range of alcohol contents in the mixed solvent that should be regarded as the most interesting, although the solubility of benzoic acid in this region is substantially lower than 4 mol kg^{-1} (at 21°C).

The solubility of both the acid and iron(III) salt in dimethylformamide is considerably higher (Fig. 3). It additionally increases as temperature is raised. In dimethylformamide, the process can be brought virtually to complete expenditure of the acid for salt formation, provided that its initial concentration does not exceed 5.5 mol kg^{-1}. However, the 100% selectivity with respect to the iron(III) salt cannot be reached neither in the end, nor in the course of the process. It was found that it is impossible to obtain products in the solid phase in this medium: at so large initial contents of benzoic acid, the final reaction mixture is something intermediate between a poorly flowable paste and a glue-like mass that does not release the solid phase neither under rapid cooling, nor in the case of natural or artificially decelerated cooling. A similar pattern is observed in all the other cases when the content of *n*-butanol in the mixed solvent is smaller than 20 vol %.

The iron(III) salt can be selectively obtained at the instant of virtually quantitative consumption of the acid with such solvents as *n*-butanol, petroleum spirit, butyl acetate (not shown in Fig. 1) and the above-mentioned mixtures of dimethylformamide and *n*-butanol. The kinetic curve of iron(II) salt accumulation in these solvents passes through a weak maximum lying close to the ordinate axis and further approaches the abscissa axis and virtually runs into it. In such solvents as dimethylformamide, formamide (not shown in Fig. 1; the process is slower than that in dimethylformamide, but goes to completion and shows no self-termination), and water, iron(II) and (III) salts are always accumulated in comparable amounts.

The nature of the solvent used strongly affects, through the dynamics of variation of the phase state of the reaction mixture, the operation efficiency of the bead mill. This, in turn, is transformed to a certain extent to the apparent efficiency of the stimulating additive used and, consequently, affects its optimal amount, which is far from being the same in different solvents.

CONCLUSIONS

(1) The liquid phase predetermines the type of the kinetic curve of consumption of benzoic acid in its reaction with metallic iron in a mechanically activated process: quantitative characteristics of its separate portions, duration of the process as a whole, occurrence of autoacceleration and autodeceleration, self-termination and self-resumption, and selectivity with respect to iron(II) and (III) salts, and also the dynamics of their variation in the course of the process.

(2) At the instant of virtually quantitative consumption of benzoic acid, a selectivity for iron(III) benzoate that tends to 100% is provided by use of such solvents as white spirit, *n*-butanol, butyl acetate, and some mixtures of *n*-butanol and dimethylformamide, in which case a significant amount of the target salt is accumulated in the solid phase in the form of a suspension.

(3) The complete dissolution of the acid in the solvent for the liquid phase, used in the study, is not

a necessary condition for rapid and, a fortiori, quantitative and selective course of the redox process of the given type.

(4) The least favorable variant, as far as the rate and extent of the process, its selectivity for salts, and their isolation from the reaction mixture are concerned, was obtained with a solvent composed of dimethylformamide and its mixtures with up to 20% *n*-butanol (by volume). In this case, non of the salts is accumulated and the reaction mixture turns into a viscous glue-like system.

REFERENCES

1. GB Patent 1 184 807.
2. GB Patent 1 061 700.
3. US Patent 6 294 186.
4. GB Patent 1 414 000.
5. GB Patent 1 081 170.
6. GB Patent 390 045.
7. GB Patent 1 061 700.
8. GB Patent 804 199.
9. Jpn Patenmt Appl. 56 161 349.
10. US Patent 5 547 905.
11. GB Patent 1 446 114.
12. Canadian Patent 970 389.
13. US Patent 5 220 045.
14. US Patent 5 443 698.
15. RF Patent 2 268 874.
16. RF Patent 2 269 509.
17. RF Patent 2 291 855.
18. RF Patent 2 291 856.
19. Medvedeva, Zh.V., Oxidation of Iron and Ironcontaining Materials with Molecular Iodine in Organic Dispersion Media, *Cand. Sci. Dissertation*, Kursk, 2000.
20. Ivanov, A.M., *Nizkotemperaturnoe geterogennoe geterofaznoe okislenie metallov rastvorennym v zhidkoi faze iodom ili bromom* (Low-Temperature Heterogeneous Heterophase Oxidation of Metals by Iodine or Bromine Dissolved in Liquid Phases), Kursk: Kursk. Gos. Tekhn. Univ., 2006.
21. Altukhov, S.P., Basic, Accessory and By Processes in Oxidation of Iron by Iodine or Bromine Dissolved in Liquid Phases, *Cand. Sci. Dissertation*, Kursk, 2004.
22. Lotorev, D.S., Cyclic Processes and Stages in Synthesis of Carboxylic Acid Salts from Iron and Its Oxides in the Presence of Iodine and(or) Metal Iodide as a Stimulating Additive), *Cand. Sci. Dissertation*, Kursk, 2006.

ISSN 1070-4272, Russian Journal of Applied Chemistry, 2008, Vol. 81, No. 4, pp. 603–608. © Pleiades Publishing, Ltd., 2008.
Original Russian Text © I.I. Obraztsova, N.K. Eremenko, 2008, published in Zhurnal Prikladnoi Khimii, 2008, Vol. 81, No. 4, pp. 565–570.

PHYSICOCHEMICAL STUDIES OF SYSTEMS AND PROCESSES

Physicochemical Modification of Nanodiamonds

I. I. Obraztsova and N. K. Eremenko

Kemerovo Branch, Institute of Solid State Chemistry and Mechanochemistry, Siberian Branch, Russian Academy of Sciences, Kemerovo, Russia

Received June 18, 2007

Abstract—Thermal modification of nanodiamonds in the atmosphere of argon and hydrogen and their chemical modification with oleum and chlorine at different temperatures were studied. The effect of the modification conditions on the catalytic activity of palladium catalysts supported by nanodiamonds in the reaction of nitrobenzene hydrogenation and on the adsorption properties of nanodiamonds with respect to benzene, chloroform, and water was analysed.

DOI: 10.1134/S107042720804006X

The increased scientific and practical interest in synthesis and study of substances in the nanostate is due to the fact that they possess new functional properties because the size of nanoparticles is in the range 10^{-9}–10^{-7} m, which is comparable with that of molecules. An object of this kind are nanodiamonds (ND) produced by detonation synthesis with explosives having a negative oxygen balance in a nonoxidative medium, which yields a carbon stock containing the diamond fraction.

The recovery and purification of ND or, as they are also named, utradispersed diamonds (UDD) can be divided into the gas- and liquid-phase methods. Oxygen and air are used in the first case, and oxidizing mixtures (H_2SO_4–HNO_3, HNO_3–$HClO_4$, HNO_3–H_2SO_4–$H_2S_2O_7$, etc.), in the second [1–4]. In the process, new functional groups are added to those already present on the UDD surface, depending on the recovery technique.

The presence of functional groups with various chemical compositions on the surface of ND predetermines their widely diverse and unique properties. Therefore, methods used to modify ND may be of key importance for various applications.

At present, nanodiamonds are used in electrodeposited metal–diamond coatings, antifriction additives, various lubricants, lubricating-cooling fluids for physical modification of ferrolacquer coatings of magnetic tapes and disks, as composite materials in polymeric films and membranes, in various rubbers, and as carriers of biological and medicinal preparations [5, 6].

Development of methods for controlling the chemical composition of the nanodiamond surface by varying the amount and nature of functional groups opens the way to their modification for creating new types of ND, including those with a multifunctional surface composition.

In this study, thermal and chemical modification of nanodiamonds was carried out in order to expand the application fields of UDD.

EXPERIMENTAL

ND recovered from a detonation diamond stock by the previously developed technique [4, 7] and additionally dried in air at 150°C was used in the study.

ND were thermally treated for 4 h in a quartz reactor similar to that used for determining carbon and hydrogen in organic compounds [8]. Argon or hydrogen served as a carrier gas. Prior to an experiment, the system was purged with carrier gas for 10 min. The released water was absorbed with anhydrone and its amount was found from the increase in the mass of this drying agent. Carbon dioxide was absorbed with a $Ba(OH)_2$ solution of a known concentration (with subsequent titration with 0.2 N HCl). The amount of the released carbon monoxide was found by its absorption with an acetone solution of palladium(II), with metallic palladium recovered and the unreacted Pd^{2+} gravimetrically determined with dimethylglyoxime [9].

Table 1. Amounts of released products in relation to the thermal treatment conditions of nanodiamonds

T, °C	Concentration, mmol g^{-1} ND				
	CO_2		H_2O		CO
	Ar	H_2	Ar	H_2	Ar
200	0.19 ± 0.01	0.30 ± 0.01	1.73 ± 0.10	2.20 ± 0.12	–
400	1.85 ± 0.07	1.00 ± 0.03	2.03 ± 0.04	3.83 ± 0.25	0.38 ± 0.02
600	7.00 ± 0.16	1.23 ± 0.03	5.60 ± 0.03	5.31 ± 0.06	4.44 ± 0.12
800	4.81 ± 0.08	0.98 ± 0.04	0.86 ± 0.03	7.53 ± 0.07	6.01 ± 0.09

To study the adsorption properties of ND, a weighed portion of ND was calcined at a prescribed temperature for 4 h, cooled in a desiccator over $CaCl_2$, weighed, and placed in a desiccator with various solvents (water, benzene, and chloroform) at 21°C. The amount of an adsorbed reagent was found from the increase in the weighed portion of ND and then the procedure was repeated many times to constant weight of the sample.

The time in which equilibrium was attained was, for all the samples, 14 days in chloroform, 28 days in water, and 21 and 2 days in benzene for samples modified in argon and hydrogen, respectively.

Samples were sulfated by boiling in oleum at 180°C for 20 h. ND were chlorinated with molecular chlorine in a flow-through quartz reactor at 400 and 600°C. Chlorine and sulfur in the samples was determined by the procedure described in [8].

Nitrobenzene was hydrogenated under an atmospheric pressure of hydrogen. The method used to synthesize palladium catalysts and nitrobenzene (NB) hydrogenation conditions were the same as those in [10], but, in some cases, the catalyst was prepared without triphenylphosphine.

IR spectra were measured on a Bruker Tensor-27 IR Fourier spectrometer with a diffuse-reflection attachment.

In thermal treatment of nanodiamonds in inert (Ar) and reducing (H_2) atmospheres, the products are formed in different relative amounts (see Table 1).

The amount of carbon dioxide formed in the inert atmosphere of argon exceeds that produced in the reducing atmosphere of hydrogen. This occurs because mainly decarbonization of various carbonyl-containing groups (=C=O, –COOH, =COH) and removal of –OH groups and adsorbed water from, the ND surface occur in Ar at temperatures below 600°C. At temperatures of 600–800°C, processes in which carbon monoxide is released start to predominate, which is accompanied by a decrease in the released amounts of CO_2 and H_2O (0.89 mmol g^{-1} ND at 800°C). The formation of CO can be attributed to interaction of carbon dioxide and water with the surface carbon of nanodiamonds. The release of CO commences in the temperature range 300–400°C and its amount increases with temperature.

In the reducing atmosphere, the modifying gas interacts with the ND surface in a different way. It can be seen that the amount of released water grows and reaches the maximum value at 800°C, whereas in the argon atmosphere, it sharply decreases.

All these phenomena are accounted for by the occurrence of reducing reactions with hydrogen on the nanodiamond surface. As it is believed by the authors of [11], hydrogen is adsorbed on the ND surface at treatment temperatures below 300°C. However, this temperature is sufficient, as also in the case of thermal desorption in a flow of Ar, for the decarbonization and dehydration processes to commence. As the modification temperature is raised further (in the range 300–600°C), hydrogen reacts with oxygen-containing groups, which results in that the amount of water released in thermal treatment below 600°C exceeds that of carbon dioxide. At temperatures of 600–800°C, hydrogen continues to react with the ND surface, which results in the maximum release of water at 800°C. The decrease in the amount of CO_2 formed in H_2 at this temperature is possibly also due to the reaction of carbon dioxide with the surface, but it is impossible to determine the amount of CO released, because, in the method used, palladium acetate is reduced by the modifying hydrogen gas to metallic palladium.

The assumptions that chemical reactions occur on the ND surface in the course of modification at various temperatures are in agreement with IR spectroscopic data obtained in this study and previously [11, 12]. The modification leads to pronounced changes in the position and intensity of absorption bands associated with carbonyl groups (see figure). Treatment at 400°C in argon shifts the peak of the band at 1730 cm^{-1} to the range 1780–1790 cm^{-1}, which indicates that –C(O)–O–C(O)– structures are formed. Modification with hydrogen gives rise to an absorption band associated with isolated –OH groups (~3680 cm^{-1}) and to absorption bands at 2938 and 2867 cm^{-1}, which point to the presence of C–H bonds at the carbon atom. The changes in the IR spectra confirm that the modification of nanodiamonds change the chemical state of their surface.

After treatment with oleum, the content of sulfur in the samples modified in hydrogen and argon was 0.26 and 0.30%, respectively. A more prolonged sulfation (up to 100 h) did not lead to any increase in the content of sulfur in the samples. Probably, these conditions are insufficient for complete sulfation of nanodiamonds; however, the IR spectra obtained after treatment with oleum clearly show a new band at 620 cm^{-1}, characteristic of sulfo groups.

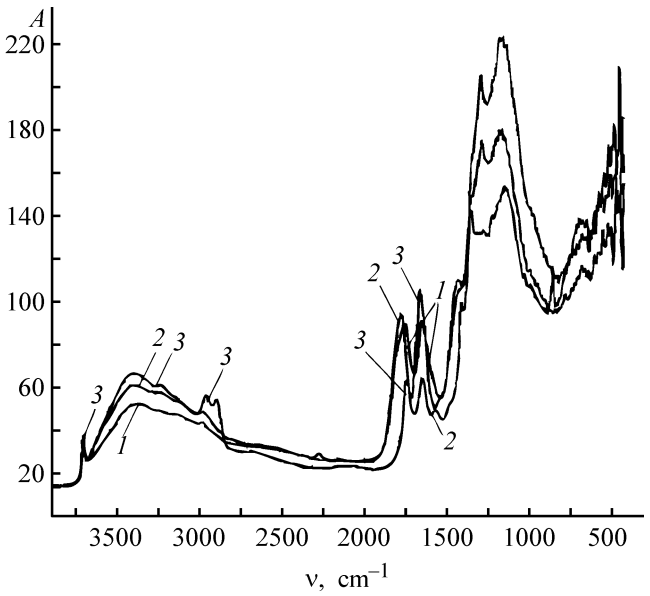
Various ND samples were chlorinated at 400 and 600°C. The results obtained are listed in Table 2.

It can be seen that chlorination of the starting sample and that modified in argon at 600°C results in that the content of chlorine increases with the chlorination temperature, whereas for samples modified in hydrogen, the content of chlorine remains constant and is independent of the ND treatment conditions and chlorination temperature.

The effect of the ND surface modification conditions on the catalytic activity of palladium catalysts supported by nanodiamonds was studied in the reaction of NB hydrogenation, chosen as the model reaction. The results obtained are listed in Table 3.

Modification of the ND surface affects the catalytic activity of nanodiamond-supported palladium catalysts in the reaction of NB hydrogenation. The relative amounts of surface groups vary with the modification conditions [13], and this circumstance is responsible for the difference in the average reaction rates. In thermal treatment, CO_2 and H_2O are removed from the surface the most easily, and phenol, ketone, and lactone groups, more difficultly [13].

As can be seen in Table 3, the highest activity is observed for the catalyst treated in a flow of argon at



IR diffuse reflection spectra of nanodiamonds. (*A*) Reflectance and (ν) wave number. (*1*) Starting sample and (*2*, *3*) that treated at 400°C with (*2*) argon and (*3*) hydrogen.

400°C (sample no. 2). As the treatment temperature is raised to 800°C, the activity of the samples modified in the atmosphere of argon somewhat falls, but remains twice that for the starting sample (sample no. 1).

Modification of nanodiamonds in the atmosphere of hydrogen (sample nos. 5–7) does not change the catalytic properties, compared with the starting ND (sample no. 1). In the case of treatment with argon, functional groups are removed and the nanodiamond surface is freed for NB adsorption, whereas in hydrogen, presumably only the chemical composition of the surface is changed (see figure).

Table 2. Effect of nanodiamond chlorination conditions on the chlorine content

ND treatment conditions	Chlorination temperature, °C	Chlorine content, %
Starting	400	11.0 ± 0.3
	600	16.0 ± 0.5
Ar, 600°C	400	8.8 ± 0.3
	600	12.0 ± 0.5
H_2, 600°C	400	10.6 ± 0.4
	600	10.6 ± 0.3
H_2, 800°C	400	10.6 ± 0.4

Table 3. Catalytic activity of catalysts produced in different support modification conditions (reaction conditions: 10 ml of ethanol, 0.3 ml of NB, weighed portion of nanodiamonds 50 mg, content of palladium 2%, temperature 40°C)

Sample no.	ND treatment conditions	W_{av},* l H_2/(g Pd min)	Sample no.	ND treatment conditions	W_{av},* l H_2/(g Pd min)
1	Starting	7.3 ± 0.2	8	600°C, oleum: Ar	13.5 ± 0.3
2	Ar: 400°C	17.5 ± 0.3	9	H_2	10.0 ± 0.2
3	600°C	16.8 ± 0.3	10	Cl_2: 400°C	13.7 ± 0.3
4	800°C	14.0 ± 0.2	11	600°C	11.0 ± 0.3
5	H_2: 400°C	4.3 ± 0.1	12	Ar, 600°C/Cl_2, 400°C	12.3 ± 0.3
6	600°C	5.3 ± 0.1	13	H_2, 600°C/Cl_2, 400°C	11.1 ± 0.2
7	800°C	6.4 ± 0.2	14	H_2, 800°C/Cl_2, 400°C	12.6 ± 0.2

* Average rate of NB hydrogenation.

Table 4. Effect of ND modification conditions on the amount of adsorption

Solvent	Adsorption, mmol g^{-1} at indicated modification temperature, °C								
	Starting ND	200	400	600	800	200	400	600	800
		Ar				H_2			
Benzene	12.3	12.6	12.7	13.2	13.6	11.4	12.1	18.7	24.9
Chloroform	13.5	14.0	14.2	14.5	14.9	14.3	14.5	14.7	15.8
Water	41.6	–	57.1	60.2	64.6	–	55.4	53.4	50.8

It can also be seen in Table 3 that modification of ND with sulfo and chloro groups makes the catalyst activity higher.

Thus, it can be concluded that the most efficient way to modify nanodiamonds is their thermal treatment in argon, which makes it possible to raise the rate of NB hydrogenation by more than a factor of 2, with ND used as a support for palladium catalysts. The nature of the support surface affects the formation of active centers in palladium catalysts and, accordingly, their catalytic activity.

A property important for various applications of nanodiamonds is their adsorption capacity. It was pointed out in [5] that UDD has a high adsorption capacity, 9 to 14 mmol g^{-1} for benzene vapor and 10.5 to 17 mmol g^{-1} for chloroform vapor, depending on a UDD brand. The adsorption properties of modified nanodiamond forms were studied. The adsorption capacity of ND for benzene, chloroform, and water vapors was determined (with an average determination error not exceeding 3 wt %). The results obtained are listed in Table 4.

It can be seen that the adsorption of chloroform is independent of the nanodiamond modification conditions and is virtually constant. Its average value is 14.55 mmol g^{-1}. The adsorption of benzene vapor on the surface of the starting nanodiamond and that modified in an inert atmosphere at various temperatures is also virtually constant, with its average value equal to 12.88 mmol g^{-1}.

Thus, the chemical composition of the ND surface (presence of functional groups of different types) weakly affects its adsorption properties. Presumably, the factor responsible for the adsorption of benzene and chloroform is the presence in a sample of sufficiently narrow pores, because nanodiamonds form stable aggregates from particles 4–5 nm in size. It should, however, be noted that the adsorption capacity for benzene vapor increases for samples modified in a flow of hydrogen, and, at the maximum thermal treatment temperature (800°C), the amount of adsorption is 24.9 mmol g^{-1}, which is more than two times the adsorption capacity of the starting ND and that modified in an inert atmosphere. Presumably, this is so because reduction reactions occur in the atmo-

sphere of hydrogen at high thermal treatment temperatures and, as a result, oxygen-containing groups are virtually absent on the nanodiamond surface and alkyl functional groups appear.

It should be noted that the maximum adsorption capacity for benzene vapor is reached in only 48 h for samples treated in a flow of hydrogen, and in 21 days for all other samples.

As can be seen in Table 4, the adsorption of water on the ND surface is two to three times that of benzene and chloroform. The adsorption capacity of samples treated in a flow of argon increases with the modification temperature and, at 800°C, exceeds that of the starting ND by a factor of 1.5. A somewhat different situation is observed for samples treated in a flow of hydrogen: the adsorption capacity slightly decreases as the sample modification temperature increases, but the amount of adsorption also exceeds that of the starting nanodiamonds. Probably, this is due to occurrence of reducing reactions in the course of thermal treatment in the atmosphere of hydrogen, with a large number of oxygen-containing groups reduced to hydrocarbon radicals at the maximum temperature (800°C). However, the adsorption capacity of samples treated in hydrogen is higher than that of the starting ND because, probably, adsorption occurs in this case at the remaining functional groups with which water forms hydrogen bonds and at active centers that appeared on the surface because of the desorption of other functional groups (amino groups, sulfo groups, etc.).

The high adsorption capacity of nanodiamonds for water can be attributed to the formation of hydrogen bonds with carboxy and hydroxy groups contained on the ND surface. Formation of strong chemical bonds between water and the ND surface is unlikely [14], which is confirmed by experiments on desorption of water from the surface with calcium chloride. Samples that absorbed water were placed in a desiccator with calcium chloride, and, after 4 days, the mass of the weighed portion of nanodiamonds took its original value. This experiment shows that a chemical interaction with the ND surface is unlikely, because chemisorption is a virtually irreversible process [15].

Thus, the higher (by a factor of 3–4.5) adsorption capacity of nanodiamonds for water, compared with chloroform and benzene, can be noted. Comparison of the amounts of adsorbed water (>100 wt %) rather unambiguously points to the physical mechanism of water adsorption in nanodiamond pores.

CONCLUSIONS

(1) Quantitative characteristics of thermal transformations of functional groups on the surface of nanodiamonds in their modification in various atmospheres were determined. It was found that a larger amount of carbon dioxide and water is released in thermal treatment of nanodiamonds in an inert atmosphere, and the maximum amount of carbon monoxide, at 800°C. In thermal treatment in a reducing atmosphere, the amount of released water exceeds that of carbon dioxide.

(2) The conditions of modification of the nanodiamond surface affect the catalytic activity of supported palladium catalysts in the reaction of nitrobenzene hydrogenation. Nanodiamonds thermally treated in the atmosphere of argon were found to be the best support for these catalysts (with the rate of nitrobenzene hydrogenation increasing by more than a factor of 2).

(3) A study of the effect of the modification conditions on the adsorption properties of nanodiamonds with respect to benzene, chloroform, and water demonstrated that the adsorption of chloroform vapor is independent of the conditions in which the nanodiamond surface is modified. The adsorption capacity for benzene vapor is independent of the modification temperature for samples treated in argon and increases with this temperature for samples treated in hydrogen. The adsorption capacity of nanodiamonds for water vapor is two to three times that for benzene and chloroform vapors.

REFERENCES

1. Vereshchagin, A.L., Ul'yanova, G.M., Novoselov, V.V., et al., *Sverkhtverd. Mater.*, 1990, no. 5, pp. 20–22.
2. RF Patent 2004491.
3. USSR Inventor's Certificate, no. 1819851.
4. Obraztsova, I.I. and Eremenko, A.N., *Zh. Prikl. Khim.*, 2003, vol. 76, no. 3, pp. 443–445.
5. Dolmatov, V.Yu., *Usp. Khim.*, 2001, vol. 70, no. 7, pp. 687–708.
6. Dolmatov, V.Yu., *Usp. Khim.*, 2007, vol. 76, no. 4, pp. 375–397.
7. RF Patent 2081821.
8. Klimova, V.A., *Osnovnye mikrometody analiza organicheskikh soedinenii* (Basic Micromethods for Analysis of Organic Compounds), Moscow: Khimiya, 1967.

9. Ginzburg, S.I., Ezerskaya, I.A., Prokof'ev, I.V., et al., *Analiticheskaya khimiya elementov: Platinovye metally: Ru, Rh, Pd, Ir, Os, Pt* (Analytical Chemistry of Elements: Platinum Metals: Ru, Rh, Pd, Ir, Os, Pt), Moscow: Nauka, 1972.
10. Obraztsova, I.I. and Efimov, O.A., *Zh. Prikl. Khim.*, 2004, vol. 77, no. 3, pp. 517–518.
11. Tapraeva, F.M., Pushkin, A.N., Epishina, N.I., et al., *Zh. Fiz. Khim.*, 1986, vol. 60, no. 7, pp. 1814–1816.
12. Kulakova, I.I., *Ross. Khim. Zh.*, 2004, vol. 48, no. 5, pp. 97–106.
13. Eremenko, A.N., Besedina, O.A., and Obraztsova, I.I., *Zh. Prikl. Khim.*, 2004, vol. 77, no. 12, pp. 1956–1959.
14. Nesmeyanov, A.N. and Nesmeyanov, N.A., *Nachala organicheskoi khimii* (Principles of Organic Chemistry), Moscow: Khimiya, 1974, book 1, p. 128, 180–181.
15. Voyutskii, S.S., *Kurs kolloidnoi khimii* (Course of Colloid Chemistry), Moscow: Khimiya, 1975.

ISSN 1070-4272, Russian Journal of Applied Chemistry, 2008, Vol. 81, No. 4, pp. 609–613. © Pleiades Publishing, Ltd., 2008.
Original Russian Text © O.V. Al'myasheva, V.L. Ugolkov, and V.V. Gusarov, 2008, published in Zhurnal Prikladnoi Khimii, 2008, Vol. 81, No. 4, pp. 571–575.

PHYSICOCHEMICAL STUDIES OF SYSTEMS AND PROCESSES

Thermochemical Analysis of Desorption and Adsorption of Water on the Surface of Zirconium Dioxide Nanoparticles

O. V. Al'myasheva, V. L. Ugolkov, and V. V. Gusarov

Grebenshchikov Institute of Silicate Chemistry, Russian Academy of Sciences, St. Petersburg, Russia

Received July 26, 2007

Abstract—Desorption and adsorption of water on the surface of ZrO_2 particles obtained under hydrothermal conditions were considered. The heat effect of desorption was determined.

DOI: 10.1134/S1070427208040071

The large specific surface area of nanopowders and the active state of functional groups on the surface of nanoparticles [1–5] make promising their use in development of highly efficient sorbents, catalysts, and catalyst supports and in syntheses of substances with a developed and active surface. ZrO_2-containing materials are known as sorbents [6–8] and are widely used as catalysts [9–13]. Because ZrO_2 particles have a hydrophilic surface and actively adsorb water [14–17], data on the adsorption and desorption of water on the surface on ZrO_2-based nanocrystalline powders are necessary for development and use of these materials. It should be noted that data on these processes for ZrO_2 nanoparticles are also exceedingly important for development of a technology for production of ceramic materials from nanopowders, because adsorption and desorption of water on the surface of nanoparticles exert a decisive influence on the densification of materials in their compaction and, particularly, sintering [18–24].

This study is devoted to a thermochemical examination of the adsorption and desorption of water on the surface of nanocrystalline ZrO_2 particles by the method of comprehensive thermal analysis.

EXPERIMENTAL

Nanocrystalline zirconium dioxide was produced by hydrothermal treatment of zirconium hydroxide precipitated from a solution of $ZrOCl_2 \cdot 8H_2O$ (chemically pure grade) with a concentrated solution of NH_4OH. The hydrothermal treatment was carried out at a temperature of 250°C and pressure of 70 MPa in the course of 4 h. The parameters of synthesis of ZrO_2 nanocrystals were chosen in accordance with [25–27] and corresponded to complete dehydration of zirconium oxyhydroxide.

The structural state of ZrO_2 nanoparticles was determined by X-ray phase analysis (XPA). X-ray diffraction patterns of samples were measured on a DRON-3 diffractometer (Cu_{K_α} radiation).

The size of crystallites (coherent-scattering regions, CSR) was found from the line broadening in X-ray diffraction patterns by the Scherrer formula. In addition, the particle size was determined by transmission electron microscopy (TEM) on an EM-125 electron microscope with U_{acc} = 75 kV and from small-angle scattering data obtained on the installation described in [28].

The specific surface area of the nanopowder was found by analyzing isotherms of butanol adsorption.

The desorption and adsorption of water on the surface of nanoparticles was studied in a flow of air containing H_2O in an amount corresponding to a 70–80% relative humidity of air and to a saturated vapor pressure at atmospheric pressure and temperature of 25°C ($P_{H_2O\,(sat)}$ = 0.0312 atm [29]) by the method of comprehensive thermal analysis on a Netzsch STA-429 installation. The heat effects accompanying these processes were found from data furnished by differential scanning calorimetry. The composition of the gas phase over a sample was monitored by mass spectrometry [QMS 403C Aecolos (Netzsch)].

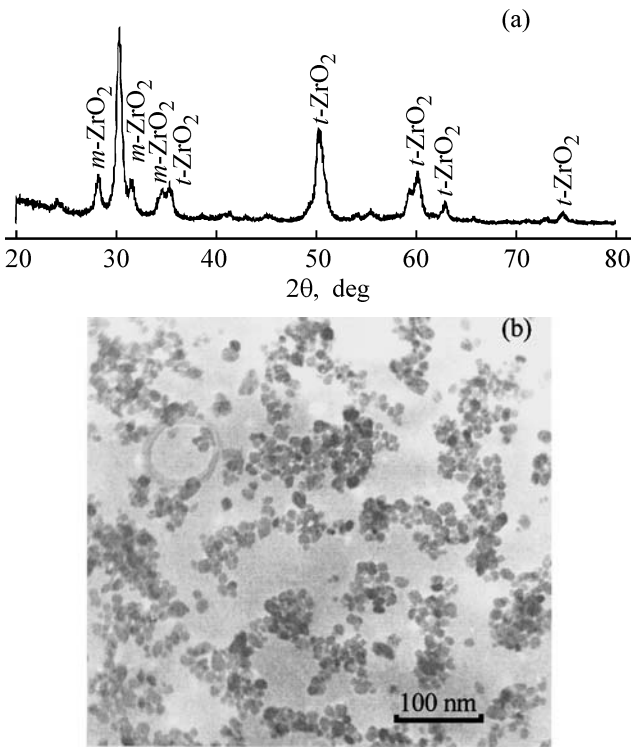


Fig. 1. (a) X-ray diffraction pattern and (b) TEM micrograph of zirconium dioxide nanocrystals produced by hydrothermal synthesis. (2θ) Bragg angle.

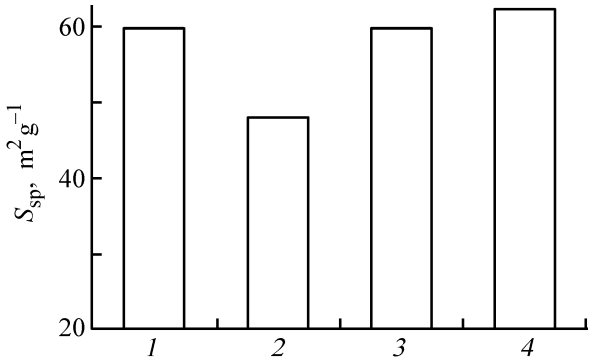


Fig. 2. Specific surface area of nanocrystalline ZrO_2, found by analyzing (*1*) small-angle X-ray scattering data, (*2*) widths of X-ray diffraction lines, (*3*) TEM data, and (*4*) data on butanol adsorption. (S_{sp}) Specific surface area of nanoparticles.

Comparison of the values obtained for the specific surface area of nanoparticles by the adsorption–desorption method and from the nanoparticle sizes found from X-ray diffraction line broadening (Fig. 1a) and by TEM (Fig. 1b) shows that these values coincide within the experimental error (Fig. 2). This coincidence is only possible if the following conditions are satisfied: nanoparticles have an isometric shape, are single crystals, the amorphous phase is virtually absent, and the nanoparticle size distribution is narrow. These characteristics of the zirconium dioxide nanoparticles under study, produced in hydrothermal conditions, is confirmed both by published data [25–27, 30] and by the results of separate experimental methods used in the study. For example, TEM data (Fig. 1b) show that the nanocrystals have an isometric shape and only slightly vary in size. It should be noted that the most pronounced, even though only falling within the experimental error, discrepancy between the specific surface areas is observed for the method in which S_{sp} is calculated from the SCR size. This, presumably, occurs because the procedure used to calculate the SCR size by the Scherrer formula for the most part takes into account coarser crystals, which results in that S_{sp} values are underestimated.

The results of a comprehensive thermal analysis of ZrO_2 nanocrystals (Fig. 3) indicate that two endothermic effects associated with the desorption of water from the surface of zirconium dioxide nanoparticles and with the transition of the monoclinic modification of ZrO_2 to *t*-ZrO_2, the equilibrium modification at the given temperature. Four exothermic effects, accompanied by a noticeable loss of mass, are presumably due to a structural rearrangement of ZrO_2 nanoparticles. A mass-spectrometric analysis of the gas phase over a sample demonstrated that mainly water is desorbed (Fig. 3b). The loss of mass by the sample, attributed to the desorption process, is virtually independent of the rate at which temperature is raised, but depends on the partial pressure of water of the sample in its isothermal keeping at 25°C. The data obtained demonstrate that the loss of mass by a nanopowder kept under saturated-vapor conditions at 25°C is about 3.7 wt %, and that by samples kept at room temperature in an atmosphere with a humidity of 70–80% is 2.2–2.7 wt %. It is noteworthy that the latter data are also confirmed by the results of other studies of ZrO_2 nanopowders obtained under similar conditions [13, 14, 30].

The area of the landing site for a water molecule is $\delta = 0.102$ nm^2 [31]. With account of the values obtained for the specific surface area of ZrO_2 nanocrystals [$S_{sp} = 61 \pm 1$ m^2 g^{-1} (Fig. 2)] and for the amount of water adsorbed on their surface [$\Delta m = (2.2–2.7) \times 10^{-2}$ or 3.7×10^{-2} g H_2O per gram of a sample], it can be concluded that, to within the error in the available data, a water layer that approaches a bimolecular layer as the air humidity increases to saturation is present in both cases on the surface of zirconium dioxide nanoparticles. This conclusion is based on the fact that the surface area that would be oc-

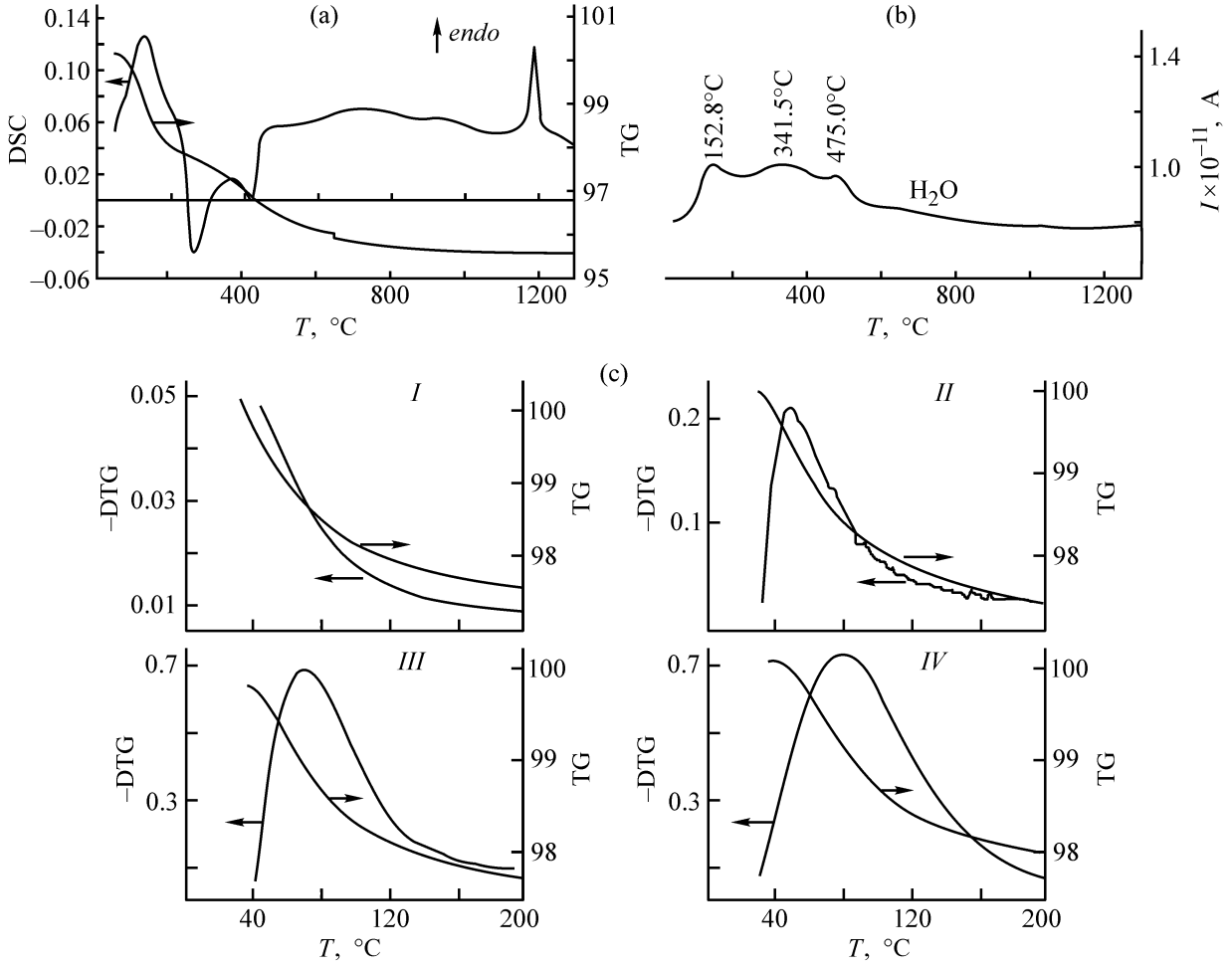


Fig. 3. Results of (a) differential-thermal, (b) mass-spectrometric, and (c) thermogravimetric analyses of nanocrystalline ZrO_2. (T) Temperature and (I) ionic current. Heating rate (deg min^{-1}): (*I*) 1, (*II*) 5, (*III*) 10, and (*IV*) 20.

cupied by a monomolecular layer of water released in desorption is $S_{sp.\ mono}$ = 75–92 or 126 m^2 (saturated vapor), which exceeds by a factor of 1.2–1.5 or nearly 2 (for the saturated vapor) the real specific surface area of ZrO_2 nanoparticles.

Analysis of the thermogravimetric data shows that, at a heating rate of 1 deg min^{-1}, the curves that describe the loss of mass (TG and –DTG) and characterize the evaporation intensity monotonically decrease as temperature becomes higher (Fig. 3c). At the same time, at heating rates of 5, 10, and 20 deg min^{-1}, the TG curves remain monotonically decreasing, whereas the –DTG curves show a maximum that is shifted, depending on the heating rate, from 60 to 80°C (Fig. 3c). The peak in the –DTG curves is presumably due, on the one hand, to a kinetic hindrance to the desorption process at low temperatures, which becomes less pronounced as temperature is raised, in accordance with the known kinetic equations [32]. On the other hand, the fall of the desorption rate, observed as temperature is raised above a certain value may be due, in accordance with the desorption equation [32], both to a decrease in the amount of the adsorbed substance in the course of desorption and to a stronger binding of water molecules, desorbed at higher temperatures, to the surface of ZrO_2 nanoparticles.

It should be noted, when analyzing the case in which a virtually bimolecular layer of adsorbed waster is present on the surface of ZrO_2 nanoparticles (Fig. 4), that the desorption rate decreases if a predominantly monomolecular layer of H_2O, known to be more strongly bound to the hydrophilic surface [33], remains on the nanoparticle surface. According to [34], a virtually monomolecular layer remains on hydrophilic surfaces when temperature is raised 65–70°C, in good agreement with the results obtained in the present study (Fig. 3). The absence of a maximum

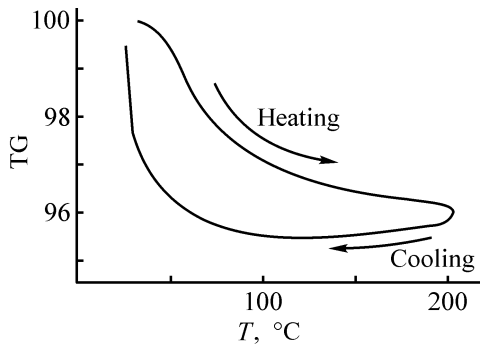


Fig. 4. Results of a thermogravimetric analysis (heating–cooling) of zirconium dioxide nanocrystals at P_{H_2O} = 0.0312 atm. (T) Temperature.

in the desorption rate at a heating rate of 1 deg min^{-1} presumably indicates that the kinetic factor is unimportant, i.e., this mode is close to the equilibrium desorption of water from the surface of ZrO_2 nanoparticles.

As follows from the results of the thermal analysis, the process of water adsorption on the surface of ZrO_2 nanoparticles is substantially slower than the desorption process and starts to occur with high intensity only at comparatively low temperatures (Fig. 4).

The DSC and DTG data were used to determine how the heat effect of desorption of 1 mol of H_2O from the surface of ZrO_2 nanoparticles depends on temperature. The results obtained indicate that, within the experimental error mostly associated with plotting of the differential curve describing the loss of mass, the heat effect can be considered constant in the whole range of desorption temperatures studied and equal to $\Delta H_{des} = 35 \pm 7$ kJ mol^{-1}. It is noteworthy that ΔH_{des} coincides within the experimental error with the enthalpy of water evaporation $\Delta H_{ev} = 40$ kJ mol^{-1} [35].

CONCLUSIONS

(1) It was shown that, upon an increase in the air humidity from 70% to a saturated vapor at room temperature, 1.2 to 2 molecular layers of water are adsorbed on the surface of nanoparticles.

(2) The heat effect of water desorption from the surface of zirconium hydroxide nanoparticles was determined ($\Delta H_{des} = 35 \pm 7$ kJ mol^{-1}) and it was demonstrated that ΔH_{des} coincides within the experimental error with the heat effect of water evaporation.

(3) It was found that, in the range of air humidities under consideration, the desorption of the monomolecular layer from the surface of zirconium dioxide nanoparticles begins at a temperature of about 74°C.

ACKNOWLEDGMENTS

The study was financially supported by the Russian Foundation for Basic Research (grant no. 07-03-00750).

REFERENCES

1. Deryagin, B.V., Churaev, N.V., and Muller, V.M., *Poverkhnostnye sily* (Surface Forces), Moscow: Nauka, 1985.
2. Aleskovskii, V.B., *Khimiya nadmolekulyarnykh soedinenii* (Chemistry of Supramolecular Compounds), St. Petersburg: SPbGU, 1996.
3. Aleskovskii, V.B. and Yuffa, A.Yu., *Zh. Vses. Khim. O–va im. D.I. Mendeleeva*, 1989, vol. 34, no. 3, pp. 317–324.
4. Karnaukhov, A.P., *Adsorbtsiya: Tekstura dispersnykh i poristykh materialov* (Adsorption: Texture of Dispersed and Porous Materials), Novosibirsk: Nauka, 1999.
5. Lisichkin, G.V., Fadeev, A.Yu., Serdan, A.A., et al., *Khimiya privitykh poverkhnostnykh soedinenii* (Chemistry of Grafted Surface Compounds), Lisichkin, G.V., Ed., Moscow: Fizmatlit, 2003.
6. Chertov, V.M., Okopnaya, N.T., and Neimark, I.E., *Dokl. Akad. Nauk SSSR*, 1973, vol. 209, no. 4, pp. 876–878.
7. Neimark, I.E., *Sinteticheskie mineral'nye adsorbenty i nositeli katalizatorov* (Synthetic Mineral Adsorbents and Catalyst Supports), Kiev: Naukova Dumka, 1982.
8. Yaroslavtsev, A.B., Nikonenko, V.V., and Zabolotskii, V.I., *Usp. Khim.*, 2003, vol. 72, no. 5, pp. 438–470.
9. Stiles, A.B., *Catalyst Supports and Supported Catalysts. Theoretical and applied concepts*, Boston: Butterworths, 1987.
10. Kohama, K., Imai, H., Hirashima, H., et al., *J. of Sol–Gel Sci. Technol.*, 1998, vol. 13, nos. 1–3, pp. 1033–1036.
11. Tomishige, K., Sakaihori, T., Ikeda, Y., and Fujimoto, K., *Catal. Lett.*, 1999, vol. 58, no. 4, pp. 225–229.
12. Yoshida, S. and Kohno, Y., *Catal. Surveys Japan*, 2001, vol. 4, no. 2, pp. 107–114.
13. Matskevich, V.V., Koryakova, O.V., Kuznetsova, O.V., et al., Abstracts of Papers, *XII Rossiiskaya studencheskaya nauchnaya konferentsiya, posvyashchennaya 100–letiyu so dnya rozhdeniya professors V.I. Esafova "Problemy teoreticheskoi i eksperimental'noi khimii"* (XII Russian Students' Sci. Conf. Devoted to 100th Birthday Anniversary of Prof. V.I. Esafov), Yekaterinburg, 2002, p. 5.
14. Podzorova, L.I., Il'icheva, A.A., Mikhailina, N.A., et al., *Ogneupory*, 1995, no. 6, pp. 2–5.

15. Pozhidaeva, O.V., Korytkova, E.N., and Gusarov, V.V., Abstracts of Papers, *I Vserossiiskaya konferentsiya "Khimiya poverkhnosti i nanotekhnologiya", 27 sentyabrya–1 oktyabrya 1999 goda* (I All-Russia Conf. "Surface Chemistry and Nanotechnology," September 27–October 1, 1999), SPb–Khilovo, 1999, p. 82.
16. Al'myasheva, O.V., Zhuravlev, N.A., Ugolkov, V.L., and Gusarov, V.V., Abstracts of Papers, *Vserossiskaya konferentsiya "Khimiya tverdogo tela i funktsional'nye materialy–2004",. Oktyabr' 2004 goda* (All-Russia Conf. "Solid-State Chemistry and Functional Materials–2004," October 2004), Yekaterinburg, 2004, p. 10.
17. Oleinikov, N.N., Pentin, I.V., Murav'eva, G.P., and Ketsko, V.A., *Zh. Neorg. Khim.*, 2001, vol. 46, no. 9, pp. 1413–1420.
18. Ivanov, V.V., Paranin, S.N., Vikhrev, A.I., and Nozdrin, A.A., *Materialovedenie*, 1997, no. 5, pp. 49–55.
19. Shevchenko, V.Ya., Glushkova, V.B., Panova, T.I., et al., *Neorg. Mater.*, 2001, vol. 37, no. 7, pp. 821–827.
20. Konstantinova, T.E., Danilenko, I.A., Gorokh, A.V., and Volkova, G.K., *Refract. Industr. Ceram.*, 2001, vol. 42, nos. 3–4, pp. 102–105.
21. Morozova, L.V., Lapshin, A.E., and Glushkova, V.B., *Ogneupory Tekhn. Keram.*, 2002, no. 5, pp. 18–19.
22. Gorelov, V.P., Zayats. S.V., Ivanov, V.V., et al., *Fiz. Khim. Stekla*, 2005, vol. 31, no. 4, pp. 635–642.
23. Glushkova, V.B., Panova, T.I., and Podzorova, L.I., *Fiz. Khim. Stekla*, 2006, vol. 32, no. 2, pp. 331–338.
24. Artamonova, O.V., Al'myasheva, O.V., Mittova, I.Ya., and Gusarov, V.V., *Neorg. Mater.*, 2006, vol. 42, no. 10, pp. 1072–1076.
25. Pozhidaeva, O.V., Korytkova, E.N., Drozdova, I.A., and Gusarov, V.V., *Zh. Obshch. Khim.*, 1999, vol. 69, no. 8, pp. 1265–1269.
26. Pozhidaeva, O.V., Korytkova, E.N., Romanov, D.P., and Gusarov, V.V., *Zh. Obshch. Khim.*, 2002, vol. 72, no. 6, pp. 910–914.
27. Sharikov, F.Yu., Al'myasheva, O.V., and Gusarov, V.V., *Zh. Neorg. Khim.*, 2006, vol. 51, no. 10, pp. 1538–1543.
28. Andreev, N.S., Mazurin, O.V., Porai-Koshits, E.A., et al., *Yavlenie likvatsii v steklakh* (Liquation in Glasses), Shul'ts, M., Ed., Leningrad: Nauka, 1974.
29. Rabinovich, V.A. and Khavin, Z.Ya., *Kratkii khimicheskii spraochnikv* (Concise Handbook of Chemistry), Leningrad: Khimiya, 1978, p. 18, 2nd ed., revised and suppl.
30. Kolen'ko, Yu.V., Burukhin, A.A., Churagulov, B.R. et al., *Zh. Neorg. Khim.*, 2002, vol. 47, no. 11, pp. 1755–1762.
31. Melas, R.N. and Lemis, F.M., *Silicones*, New York: Reinhold, 1963.
32. Dorokhov, I.N. and Kafarov, V.V., *Sistemnyi analiz protsessov khimicheskoi tekhnologii* (Systems Analysis of Processes of Chemical Technology), Moscow: Nauka, 1989.
33. Kessler, Yu.M., Petrenko, V.E., and Lyashchenko, A.K., *Voda: struktura, sostoyanie, sol'vatatsiya: Dostizheniya poslednikh let* (Water: Structure, State, and Solvation) A.M. Kutepov, Senior Ed., Moscow: Nauka, 2003.
34. Deryagin, B.V., Churaev, N.V., Ovcharenko, F.F., et al., *Voda v dispersnykh sistemakh* (Water in Dispersed Systems), Moscow: Khimiya, 1989, pp. 7–34.
35. Belov, G.V., Iorish, V.S., and Yungman, V.S., *CALPHAD*, 1999, vol. 23, no. 2, pp. 173–180.

ISSN 1070-4272, Russian Journal of Applied Chemistry, 2008, Vol. 81, No. 4, pp. 614–617. © Pleiades Publishing, Ltd., 2008.
Original Russian Text © M.B. Dergacheva, V.V. Chaikin, 2008, published in Zhurnal Prikladnoi Khimii, 2008, Vol. 81, No. 4, pp. 576–579.

PHYSICOCHEMICAL STUDIES OF SYSTEMS AND PROCESSES

Electrodeposition of Semiconducting $CuInSe_2$ Films On Glassy Carbon Electrode from Sulfuric Acid Electrolytes

M. B. Dergacheva and V. V. Chaikin

Sokol'skii Institute of Organic Catalysis and Electrochemistry, Almaty, Republic of Kazakhstan

Received July 23, 2007

Abstract—Electrochemical behavior of selenium(IV), copper(II), and indium(III) ions in joint deposition onto a glassy carbon electrode from sulfuric acid electrolytes was studied. The optimal conditions for formation of a stoichiometric compound $CuInSe_2$ were determined. The structure and composition of the compound synthesized were studied by X-ray phase, electron microscopic, and electron microprobe analyses.

DOI: 10.1134/S1070427208040083

Indium-copper diselenide $CuInSe_2$ is the most promising material for solar cells. Owing to its unique properties, such as the high absorption coefficient and band gap width (1.1 eV) that enables conversion of sunlight into photocurrent, the $CuInSe_2$ compound can find wide use in manufacture of thin-film solar cells.

Thin $CuInSe_2$ films can be formed by various methods. To these belong chemical pyrolysis sputtering, pulsed deposition, fast thermal recrystallization, and radio-frequency sputtering with oxygen batching. The electrodeposition technique is the most inexpensive and technologically convenient. It can be performed in a single stage at low temperatures not exceeding 90°C and is inexpensive.

Simultaneous electroreduction of three components to form a compound with a prescribed stoichiometric composition is a complicated task because of the considerable difference between the standard electroreduction potentials of the ions. To accomplish this task, it is necessary to study the influence exerted by the electrolysis conditions on the composition of a deposit being formed. Making studies of the electrodeposition of multicomponent semiconductor materials more extensive will enable synthesis of new materials and fabrication of new structures.

A necessary stage after a film is formed by electrodeposition is its subsequent annealing for crystallization or changing the conduction type. The effect of this stage on the characteristics of a semiconductor is not fully understood.

The aim of this study was to find the optimal conditions of electrodeposition of the $CuInSe_2$ compound of stoichiometric composition from sulfuric acid electrolytes. The structure and composition of the compound synthesized were subjected to X-ray phase (XPA), electron microscopic, and electron microprobe analyses. Characteristics of thin $CuInSe_2$ films were examined after their annealing in argon.

EXPERIMENTAL

As the working electrode we used a pyrographite disc with an apparent surface area of 0.07 cm^2. The three-electrode cell contained an electrode under study, auxiliary platinum electrode with an area of 1.5 cm^2, and a silver chloride reference electrode, relative to which all the potentials are given. Prior to each experiment, the working electrodes were trimmed with a Al_2O_3 powder and washed with ethanol and water. The following salts were used: $CuSO_4 \cdot 7H_2O$, Na_2SeO_3, and $In_2(SO_4)_3$ (all of analytically pure grade). As the supporting electrolyte served a 0.05 M H_2SO_4 + 0.45 M Na_2SO_4 solution. The voltammetric curves were recorded without agitation. The deposit was accumulated on the electrode with agitation of the electrolyte with a magnetic stirrer. The study was performed at room temperature. The films used for analysis of the structure and composition were deposited onto a glassy carbon substrate with an area of 1.5 cm^2. The working temperature in the electrodeposition was 75°C, and the deposition time, 30 to 40 min. The electrodeposited samples were washed

with distilled water and calcined at 410°C for 10 min. The X-ray phase analysis of the copper selenide deposits was made on a DRON-4 diffractometer (Co_{K_α} radiation). Simultaneously, the deposits were analyzed on an EM-125-K electron microscope by the single-stage replica technique.

The joint deposition of three components [Cu(II), In(III), Se(IV)] from sulfuric acid solutions was studied in two sets of experiments. In the first set, the concentrations of copper and selenium ions were constant [$c_{Cu(II)} = 5 \times 10^{-4}$ M and $c_{Se(IV)} = 1 \times 10^{-3}$ M], whereas the concentration of indium ions steadily increased. In the second set, the concentrations of indium and selenium ions were constant $c_{In(III)} = 1 \times 10^{-3}$ M and $c_{Se(IV)} = 5 \times 10^{-4}$ M], and the concentration of copper(II) ions was gradually raised.

Voltammetric measurements in the first set of experiments demonstrated that the cathodic branch of the voltammetric curve for reduction of Cu(II) and Se(IV) ions is in agreement with the data of [1]. It was found that, at potentials of +0.15 to –0.2 V, there occurs the main process of joint reduction of copper and selenium to give a $CuSe_x$ compound:

$$Cu^{2+} + xH_2SeO_3 + 4xH^+ + (2 + 4x)e \rightarrow CuSe_x + 3xH_2O. \quad (1)$$

The current peak associated with the formation of the Cu_2Se compound and evolution of hydrogen selenide is present in the cathodic branch at more negative potentials:

$$2CuSe_x + 2xH^+ + 2xe \rightarrow Cu_2Se + xH_2Se. \quad (2)$$

The current peak in the anodic branch of the voltammetric curve at $E_{1,A} = +0.25$ V is due to oxidation of copper ions from the two-component compound Cu_2Se

$$Cu_2Se - 2e \rightarrow 2Cu^+ + Se^0. \quad (3)$$

The current peak at $E_{2,A} = +1.1$ V corresponds to oxidation of the elementary selenium formed on the electrode to Se(IV)

$$Se(0) + 3H_2O \rightarrow H_2SeO_3 + 4e + 4H^+. \quad (4)$$

Upon addition of indium(III) ions and the subsequent increase in their concentration in the electrolyte, the cathodic branch of the voltammetric curve remains virtually unchanged. The reduction wave of indium(III) itself is not observed.

However, additional oxidation peaks, characteristic of only the ternary system and absent on the voltammogram of a copper–selenium binary system, appear on the anodic branch of the voltammetric curves. An additional oxidation peak at the potential +0.70 V, associated with the dissolution of a three-component compound, appears even at low concentrations (1×10^{-4} M) of indium(III) ions in the solution. The peak current increases with the indium(III) concentration. In a solution with an indium(III) concentration of 1×0^{-3} M and more, another two additional oxidation current peaks appear (Fig. 1). The current of the oxidation peak at –0.37 V is not characteristic of copper–selenium and indium–selenium binary systems and appears solely in joint deposition of selenium(IV), copper(II), and indium(III) at a large excess of indium(III) ions (Fig. 1). This peak can be attributed to oxidation of indium from a three-component compound

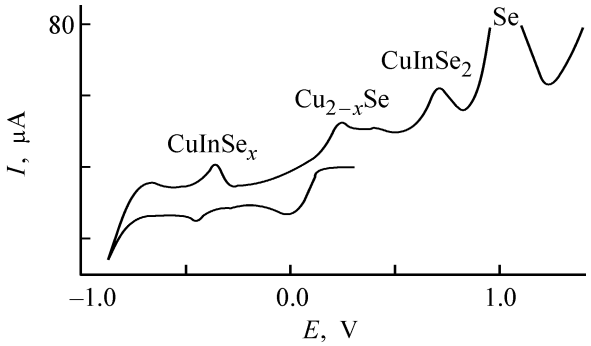


Fig. 1. Voltammetric curves obtained in a supporting electrolyte containing 0.05 M H_2SO_4 + 0.45 M Na_2SO_4. $c_{Cu(II)} = 5 \times 10^{-4}$ M, $c_{Se(IV)} = 1 \times 10^{-3}$ M, $c_{In(III)} = 2 \times 10^{-3}$ M; $v = 20$ mV s^{-1}. (I) Current and (E) potential.

$$CuInSe_2 - 3e \rightarrow In^{3+} + CuSe_x. \quad (5)$$

Comparison of the voltammograms with the data of [1, 2] for binary systems suggests that the current peak at $E_{1,A} = +0.25$ V is due to oxidation of copper from the binary compound Cu–Se.

The second set of experiments demonstrated that the joint reduction of a two-component indium(III)–selenium(IV) system is characterized by two cathodic waves ($E_{1,K} = +0.10$ V and $E_{2,K} = -0.75$ V) and two anodic waves ($E_{1,A} = +0.20$ V and $E_{2,A} = +1.10$ V). The cathodic wave appearing at a potential of +0.10 V is associated with selenium(IV) reduction, the first oxidation wave at $E_{1,A} = +0.20$ V belongs to oxidation of indium from the two-component indium–selenium system, and the oxidation wave at $E_{2,A} = +1.10$ V corresponds to reaction (4).

Addition of minor concentrations of copper(II) ions strongly changes the voltammetric curve: the limiting current of the cathodic wave beginning at the potential of +0.10 V grows. This is accounted for by the fact

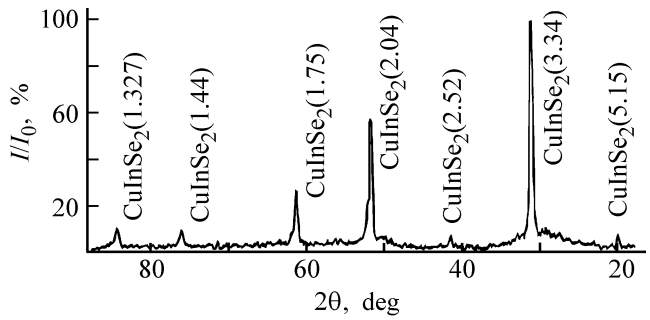


Fig. 2. X-ray diffraction pattern of the electrodeposited film. $c_{Se(IV)} = 1.3 \times 10^{-2}$ M, $c_{Cu(II)} = 5 \times 10^{-3}$ M, $c_{In(III)} = 2 \times 10^{-2}$ M; Deposition conditions: $E = -0.75$ V, $T = 75$°C, $\tau = 35$ min. (I/I_0) Relative intensity and (2θ) Bragg angle.

that the joint reduction of copper and selenium occurs at close potentials. The current peak of oxidation of the three-component compound appears in the anodic branch of the voltammetric curve at a potential of +0.70 V. The peak becomes weaker as the copper concentration in the solution increases and, at $c_{Cu(II)} > 1 \times 10^{-3}$, disappears at all by merging with the current peak of Se^0 oxidation to Se^{4+}. At the same time, the current peak of oxidation of the ternary compound, observed in the first set of experiments at a potential of –0.37 V, appears only at a concentration $c_{Cu} = 3 \times 10^{-4}$ M, and the current of the peak increases with the concentration of copper(II) ions. The increase in the current of the anodic peak of copper oxidation at the potential of 0.25 V was found to be well predictable. At a copper(II) concentration exceeding 1×10^{-3} M, an additional current peak of copper oxidation appears at a potential of 0.045 V in the anodic branch.

The effect of the concentration of indium ions in the electrolyte on the currents of the cathodic and anodic peaks was studied, with the concentration of indium ions varied in the range $(0–2.5) \times 10^{-3}$ M at a constant concentrations of copper and selenium ions in the electrolyte [($c_{Cu(II)} = 5 \times 10^{-4}$ M and $c_{Se(IV)} = 1 \times 10^{-3}$ M]. An increase in the concentration of In(III) ions results in that the current of Se(0) oxidation grows, which points to additional accumulation of selenium on the electrode via decomposition of the compounds formed on the electrode. The anodic current peak of oxidation of the ternary compound also grows. The oxidation current of the binary compound Cu_2Se decreases and then remains constant as the indium concentration is varied from 5×10^{-4} to 2×10^{-3} M. In the same concentration range, the oxidation current of the ternary compound increases. The current peak associated with In_2Se_3 oxidation remains small and depends only slightly on the concentration of indium(III) ions. Changing the concentration of indium ions has virtually no effect on the potentials of the peaks associated with the cathodic process. The cathodic current due to reduction to Se^{2-} ions sharply falls at a concentration of indium ions of 5×10^{-4} M and then gradually decreases.

In joint deposition of the three components to obtain deposits of the $CuInSe_2$ compound, the choice of the electrolyte composition was based on the results of the two sets of experiments described above. The primary goal was to choose the relative concentrations and the deposition potential at which the deposition of the ternary compound $CuInSe_2$ would prevail and that of the copper–selenium and indium–selenium binary phases would be insignificant.

It was found from the voltammetric curves obtained (Fig. 1) that two peaks of oxidation of the ternary compound at potentials of –0.37 and +0.72 V are the most pronounced at the following concentration ratio in the electrolyte: Cu : In : Se = 1 : 4 : 2.5. At other ratios, an increase in the oxidation peaks corresponding to copper-selenium or indium-selenium binary compounds is observed. In the case of a strong deviation from this ratio toward an excess of copper(II) or selenium(IV) ions in solution, excess copper(0) or selenium(0) is deposited.

The boundary regions of the deposition potentials of the $CuInSe_2$ ternary compound were chosen taking into account the previously determined deposition potentials of binary compounds [1, 2] and the chosen electrolyte composition. To accumulate a deposit on the electrode, the three components were codeposited in the potentiostatic mode at potentials of –0.4…–0.8 V (s.ch.e.). The maximum oxidation current of the corresponding peaks was used to choose the optimal deposition potential (–0.75…–0.80 V).

At the chosen potential and ratios of the component concentrations in the electrolyte, a film of the $CuInSe_2$ ternary compound was potentiostatically deposited onto glassy carbon electrodes with an area of 1.5 cm^2 at 75°C in the course of 30–40 min.

The electrodeposited samples were washed with distilled water and annealed at 410°C for 10 min in air. The phase composition of the films obtained was determined by XPA. According to the XPA data, the thus obtained films contain, in addition to the $CuInSe_2$ compound, a certain amount of the binary copper–selenium phase. The indium oxide phase also appeared. This suggested that a part of indium on the film surface is oxidized by atmospheric oxygen in the course of the annealing.

The following samples were annealed in argon under the same conditions. The X-ray diffraction pattern of the film annealed in argon is shown in Fig. 2.

The diffraction pattern contains only reflections of the ternary compound $CuInSe_2$ and, according to the ICPDS database (Table 23-209) for this phase, corresponds to the tetragonal structure.

The stoichiometric composition of this film was confirmed by electron microprobe analysis (see table). Micrographs of the surface show a rather uniform and dense coating by the film being deposited.

Thus, the compound $CuInSe_2$ with a prescribed stoichiometry can be electrodeposited from electrolytes containing copper(II), selenium(IV), and indium(III) ions, with 0.05 M sulfuric acid as the supporting electrolyte, at the chosen conditions of electrolysis and annealing.

The photoelectric properties of the obtained $CuInSe_2$ film were studied by measuring *I–E* curves under exposure to a scattered daylight. A photosensitivity was found, with the maximum short-circuit current of 6 mA and open-circuit potential of 0.4 V.

Results of an electron microprobe analysis of the surface of a $CuInSe_2$ film

Spectrum no.	Content of indicated elements, at. %			
	Si	Cu	Se	In
1	0.97	23.11	51.72	24.20
2	–	27.96	51.87	20.17
3	–	24.90	52.16	22.94
Maximum	0.97	27.96	52.16	24.20
Minimum	0.00	23.11	51.72	20.17

CONCLUSIONS

(1) The conditions of potentiostatic deposition of a stoichiometric compound $CuInSe_2$ were determined by analysis of current–voltage curves recorded in joint electrodeposition of copper(II), selenium(IV), and indium(III) ions onto a glassy carbon electrode.

(2) The composition of the compound formed was confirmed by X-ray phase and electron microprobe analyses.

REFERENCES

1. Dergacheva, M.B. and Chaikin, V.V., *Vestnik Kaz. Nats. Univ., Ser. Khim.*, 2003, no. 3, pp. 103–106.
2. Dergacheva, M.B., Chaikin, V.V., and Pantileeva, E.P., *Vestnik Kaz. Nats. Univ., Ser. Khim.*, 2004, no. 3, pp. 158–164.

ISSN 1070-4272, Russian Journal of Applied Chemistry, 2008, Vol. 81, No. 4, pp. 618–622. © Pleiades Publishing, Ltd., 2008.
Original Russian Text © B.M. Ginzburg, Sh. Tuichiev, 2008, published in Zhurnal Prikladnoi Khimii, 2008, Vol. 81, No. 4, pp. 580–584.

PHYSICOCHEMICAL STUDIES OF SYSTEMS AND PROCESSES

Structuring of Aromatic Solvents in the Presence of Small Amounts of Fullerene C_{60}

B. M. Ginzburg and Sh. Tuichiev

Institute of Problems of Engineering Science, Russian Academy of Sciences, St. Petersburg, Russia
Tajik National State University, Dushanbe, Tajikistan

Received August 10, 2007

Abstract—Changes in the structure and some properties in a series of aromatic solvents, such as *p*-xylene, toluene, and benzene, under the action small amounts of dissolved fullerene C_{60} were studied by small- and wide-angle X-ray diffractometry.

DOI: 10.1134/S1070427208040095

Because fullerenes are well soluble in aromatic solvents [1], they are widely used for recovering fullerenes from fullerene soot and for preparing and studying various fullerene-containing (e.g., fullerene-polymer) systems. However, studies of the thermal stability of systems based on fullerene C_{60} and some polymers [2] revealed some experimental facts that cannot be adequately explained without assumption that the solvent noticeably changes its properties and structure in the stage of preparation of fullerene-polymer solutions.

The high solubility itself indicates that fullerene interacts with the aromatic solvent relatively strongly. This suggests that the structure of aromatic solvent can change under the action of the dissolved fullerene C_{60}.

Previously, we have reported data on solutions of fullerene C_{60} in toluene and *p*-xylene found by small-angle X-ray scattering [3, 4]. In this paper, we analyze changes in the structure and some properties of *p*-xylene, toluene, and benzene under the effect of small amounts ($\geq 10^{-4}$%) of dissolved fullerene C_{60}, determined by small- and wide-angle X-ray diffractomertry and densitometry.

EXPERIMENTAL

The X-ray diffraction measurements were carried out using Cu_{K_α} radiation and Ni filter. The intensity of small-angle X-ray scattering was measured on a KRM-1 installation with a slit collimation of the primary radiation beam; the half-width of the beam was 2.5 min. The intensity of wide-angle X-ray scattering was measured on a DRON-2 installation with a slit collimation; the half-width of the primary beam was 36 min. Rectangular cells were made of a thin polymer film (7.5–10 μm); the thickness of the cell with a sample studied was 1.0–1.5 mm.

The solutions were studied approximately 16 h after their preparation. Before measurements, each solution was agitated and placed in a cell with a calibrated syringe; then the cell was sealed and shaken directly before the measurement to decrease the possible fullerene clustering. The scattering measurements were performed in the transmission mode as follows. First, a cell containing a sample was placed at the center of a goniometer perpendicularly to the primary beam, and the diffraction pattern (curve *1*) was recorded. Then, the sample was placed in front of the first slit and the contour of the primary beam was recorded taking into account its absorption by the sample (curve *2*). Then, by subtracting curve *2* from curve *1*, we obtained the differential curve, which represents the scattering from the cell with the sample studied, with account of the absorbed X-ray radiation and minus various kinds of parasitic scattering from slit edges, air, etc. To obtain the scattering curve of the solution, the curve of scattering from the cell should be subtracted from the differential curve. However, the scattering ability of the empty cell is very small in the angle range studied and can be neglected. As a result, the differential X-ray diffraction patterns can be represented as the $I = f(s)$ curves, where I is the intensity; $s = 4\pi \sin\theta/\lambda$; 2θ, scattering angle; and λ, wavelength of the X-ray radiation. In small-angle measurements, we took $s = 4\pi\theta/\lambda$. It should be noted

that no normalization to the intensity of the primary beam was performed, because the intensity of curves *2* at minimal angles from which we started the recording was the same (within the measurement error) for the solvent and all the fullerene solutions in the entire concentration range studied. Some small-angle X-ray diffraction patterns were processed in terms of the Guinier theory [5] by evaluating the radius of gyration of the scattering particles.

The density of the solvents and fullerene C_{60} solutions was determined pycnometrically; the measurement accuracy was ± 0.0001 g cm^{-3}, and the measurement error for a single sample was 0.01%. The main measurement errors arose upon repeated preparation of solutions and reached 4–5%. The widest data scatter was found for solutions in toluene, in which the aggregation of C_{60} is the most pronounced.

The experimental solutions were prepared using fullerene C_{60} (99.7% purity) and solvents of chemically pure grade after their double distillation.

Homogeneous liquids and glasses are characterized by a constant intensity I of small-angle X-ray scattering in the range of the scattering angles accessible to measurements [6]. In all the cases, the intensity increases with temperature. The scattering itself is due to thermal density fluctuations. The comparatively small geometric size of density fluctuations in pure glasses and their small contrast with respect to the average density of the medium are due to the solid state of the glasses.

A different situation is observed for fluctuations in liquids. The small-angle X-ray patterns of the solvents and fullerene solutions studied are shown in Fig. 1. As can be seen, in all the curves, I first monotonically decreases with increasing scattering angle (range 1) and then reaches a certain constant value I_C (range 2).

For pure benzene, *p*-xylene, and toluene (boiling point at normal pressure 80.1, 110.6, and 138.35°C, respectively [7]), the noticeable increase in I in range 1 under the ambient conditions can be only due to the relatively large number of density fluctuations acting as nuclei of a new phase. In toluene and *p*-xylene, these nuclei are characterized by approximately the same radius of gyration (1.25–1.30 nm) under the ambient conditions, whereas in benzene, the radius of gyration is an order of magnitude larger (see table).

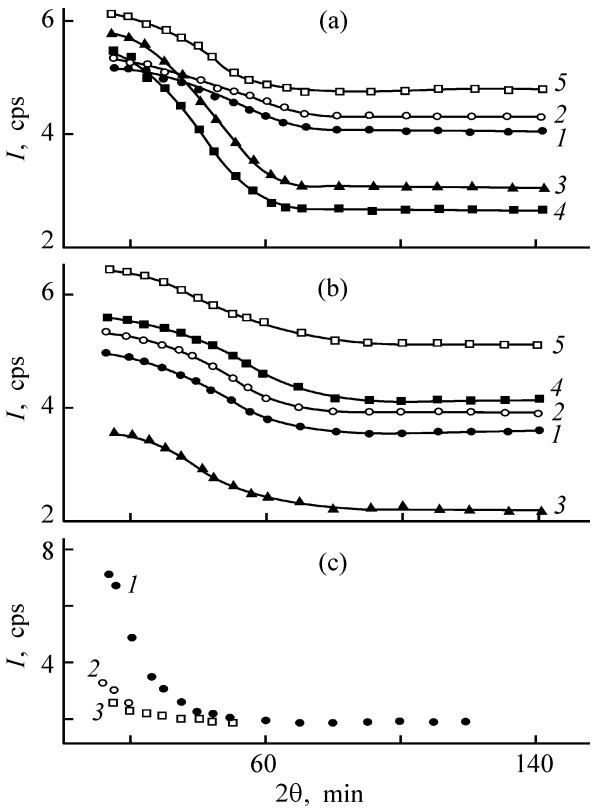


Fig. 1. Small-angle X-ray diffraction scattering curves (Cu_{K_α} radiation) of fullerene C_{60} solutions in (a) toluene, (b) *p*-xylene, and (c) benzene (T 25°C). (I) Intensity and (2θ) scattering angle; the same for Fig. 2. Fullerene concentration, %: (a) (*1*) 0 (pure toluene), (*2*) 0.001, (*3*) 0.01, (*4*) 0.1, and (*5*) 0.2; (b) (*1*) 0 (pure *p*-xylene), (*2*) 0.001, (*3*) 0.01, (*4*) 0.1, and (*5*) 0.5; and (c) (*1*) 0 (pure benzene), (*2*) 0.001, and (*3*) 0.075.

Size of heterogeneities in the samples studied*

Sample	R_g	R_e	Sample	R_g	R_e
	nm			nm	
Toluene	1.2	1.5	*p*-Xylene + 0.1% C_{60}	1.25	1.6
Toluene + 0.001% C_{60}	1.0	1.3	*p*-Xylene + 0.5% C_{60}	1.0	1.3
p-Xylene	1.25	1.6	Benzene	14	18
p-Xylene + 0.001% C_{60}	1.25	1.6	Benzene + 0.001% C_{60}	5.5	7
p-Xylene + 0.01% C_{60}	1.55	2.0			

* R_g is the radius of gyration and $R_e = R_g/(3/5)^{1/2}$ is the radius of an equivalent uniform sphere.

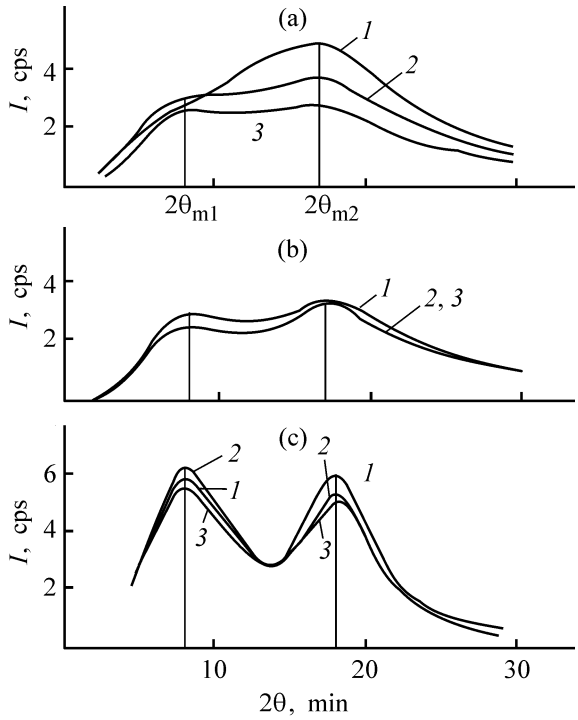


Fig. 2. Wide-angle X-ray diffraction scattering curves (Cu_{K_α} radiation) of fullerene C_{60} solutions in (a) *p*-xylene, (b) toluene, and (c) benzene. Fullerene concentration, %: (a) (*1*) 0 (pure *p*-xylene), (*2*) 0.005, and (*3*) 0.05; (b) (*1*) 0 (pure toluene), (*2*) 0.005, and (*3*) 0.05; and (c) (*1*) 0 (pure benzene), (*2*) 0.001, and (*3*) 0.075.

The most intriguing is the fact that, in the case of fullerene C_{60} solutions in toluene and *p*-xylene, the dependence of the intensity on the fullerene concentration is nonmonotonic. At a fullerene concentration of 0.001%, the scattering curves for both solvents are nearly idential (Figs. 1a and 1b, curves *2*), and their shape reproduces that of the pure solvents, but at slightly higher intensities. Sharp changes are observed as the fullerene concentration increases to 0.01% (Figs. 1a and 1b, curves *3*). Almost the whole scattering curve for toluene and the whole scattering curve for *p*-xylene lie below the scattering curves for the pure solvents. Such changes in *I* of the scattering curves can be accounted for by structuring of the solvent in the presence of fullerene (by structuring in this case is understood the suppression of the thermal density fluctuations). The structuring of a solvent is probably accompanied by an increase in its average density. In the case of toluene solutions, the observed decrease in the intensity of the small-angle X-ray scattering is accompanied by a sharp increase in the inclination of the small-angle section of the scattering curves to the abscissa (Fig. 1a, curves *3*, *4*), which can be only due to the formation of fullerene C_{60} aggregates.

At the same time, in the case of *p*-xylene (Fig. 1b), the shape of the small-angle scattering curves changes insignificantly. The X-ray diffraction patterns only shift along the intensity scale, which is due to the changes in the electron density of the scattering elements with respect to the density of the medium.

No aggregation of C_{60} molecules was observed. After the minimal intensity is reached (at some concentration c_{str} ~0.01% for *p*-xylene), the scattering intensity increases as the fullerene concentration is raised further.

In benzene (Fig. 1c), the scattering intensity in range 1 strongly decreases even at the smallest examined concentrations of fullerene. Apparently, the concentration range of fullerene in which the growth of the scattering intensity gives way to its decrease is significantly smaller than 0.001%, and concentration c_{str} is inaccessible in principle because of the relatively low solubility of fullerene in benzene. However, the structuring of benzene is confirmed by the sharp decrease in the size of density fluctuations (see table).

Among the solvents studied, the highest ordering on the molecular level is observed for *p*-xylene (Fig. 2, curve *1*): its wide-angle X-ray diffraction patterns exhibit a single amorphous halo with a small shoulder on the small-angle side. For toluene (Fig. 2, curve *1*), two poorly resolved amorphous halos are observed. As for benzene, its X-ray diffraction pattern is characterized by two pronounced amorphous halos whose half-width is comparable with that of the crystal lattice reflections (Fig. 2c, curve *1*).

The stronger the disordering of the initial system, the greater the changes in the solvent structure, observed on adding a small amount of fullerene. As a result, two amorphous halos are observed in the case of *p*-xylene (Fig. 2a, curves *2*, *3*), similarly to toluene. Addition of fullerene C_{60} to toluene decreases the width of the amorphous halos (Fig. 2b, curves *2*, *3*), but these changes are insignificant because of the fullerene aggregation. In benzene, fullerene addition does not noticeably affect the resulting scattering curves (Fig. 2c, curves *2*, *3*).

It should be noted that the angular positions of both the first ($2\theta_{m1}$) and second halos ($2\theta_{m2}$) remain essentially constant. We calculated the intermolecular distances X_m using the equation $2X_m/\sin\theta_m = K\lambda$ (where K = 1.2–1.3) [5] and found that, for all the three solvents and fullerene C_{60} solutions studied, X_{m1} = 1.3–1.4 nm and X_{m2} = 0.6–0.7 nm for the first and second halos, respectively.

Since the longitudinal sizes of the solvent molecules strongly differ (~7.8, 6.8, and 5.8 Å for *p*-xylene, toluene, and benzene, respectively), the above amorphous halos characterize the short-range order in a direction perpendicular to this size and most probably in the direction perpendicular to the plane of the benzene ring.

Methyl groups in toluene and *p*-xylene obviously break the intermolecular order as compared to benzene. In accordance with the theory of paracrystalline disturbances [8], the equation for the transition from diffraction peaks to diffuse scattering can be represented as follows: $n\Delta/X_m = 0.25$, where m is the order of the maximum and Δ is the disordering parameter (rms deviation of the distance X_m from the average value). For benzene and toluene ($n = 2$), $\Delta = 1.6–2.0$ Å, whereas for *p*-xylene, this parameter is greater by a factor of 2.

For almost all the fullerene solutions in toluene, the aggregation of fullerene molecules cannot be neglected. Thus, taking into account the cluster structure of the aggregates [1], analysis of the small-angle diffraction patterns in terms of the radii of gyration of the scattering elements becomes ambiguous. Therefore, we presented R_g in the table only for pure solvents and solutions without a pronounced fullerene aggregation.

Apparently, six-membered rings of fullerene molecules are the ordering factor. It can be assumed that benzene molecules interacting with these rings form stacks similar liquid-crystal discotics. However, the steric hindrance prevents ordering around the fullerene molecules throughout the solvent bulk and causes formation of areas with decreased density at a certain distance from C_{60} molecules.

In accordance with the data presented in [9], the fullerene molecule can be represented as a truncated icosahedron with an inner cavity with zero electron density; the radius of the inner cavity R_f is 0.2 nm and the otlet radius is 0.357 nm [10]. To a first approximation, taking into account the above sizes, we can represent the fullerene C_{60} molecule as a spherical envelope with a uniform density distribution. For such an envelope, the radius of gyration is 0.30 nm, which is significantly smaller than the radii of gyration listed in the table. This fact indicates that the fluctuations of the solvent density are the main scattering elements.

Let us compare the results of X-ray diffraction studies with published data on the densities of fullerene C_{60} solutions [11]. The density of C_{60} solutions in toluene changes nonmonotonically with increasing fullerene concentration: first it sharply decreases,

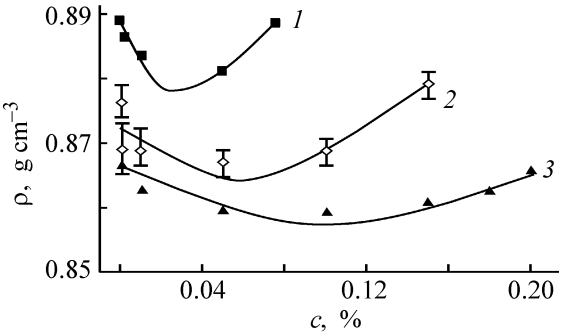


Fig. 3. Density ρ of fullerene solutions in (*1*) benzene, (*2*) toluene, and (*3*) *p*-xylene vs. fullerene C_{60} concentration c (T = 10°C).

after which it passes through a minimum and then increases. Such a dependence for solutions in *p*-xylene, toluene, and benzene is confirmed by our measurements (Fig. 3). THe nonmonotonic concentration dependences of the density of fullerene C_{60} solutions in the solvents studied are qualitatively consistent with the concentration dependence of the intensity of small-angle X-ray scattering. Probably, just this decrease in the solution density, observed at various temperatures and for various solvents, gave grounds to present in an incomplete study [11] a loose lyophobic shell around the fullerene C_{60} molecule without any additional comments.

After passing through a minimum, the solution density increases up to the density of the pure solvent and sometimes even becomes higher. Because the amounts of the denser fullerene added are very small and cannot account for the observed density increase, some compaction (structuring) of the solvent should be suggested. Thus, to account for a decrease in the intensity of small-angle scattering, we should take into account, along with the lyophobic shell around fullerene molecules, the next, lyophilic shell of the structured (compacted) solvent.

Structuring is obviously typical not of all the solvents, but only of those ("good" solvents) in which the solubility of fullerene is the highest. It should be noted that, although the density passes through a minimum in benzene solutions, the density of the pure solvent is not attained with a further increase in the fullerene concentration (Fig. 3). In the case of fullerene solutions in a "bad" solvent (e.g., CCl_4), the attainable concentrations are lower those that for aromatic solvents by an order of magnitude, and only a decrease in the solution density is observed within the possible fullerene concentrations [11].

To evaluate the number of molecules of the structured solvent per fullerene molecule, we assumed that the whole solvent is structured at c_{str} for which the in-

tensity of the small-angle X-ray scattering is minimal. Simple calculations show that there are N_S ~70000 molecules of *p*-xylene per fullerene C_{60} molecule. Let us estimate the long-range action of fullerene molecule in *p*-xylene. At such low concentrations of C_{60} studied the volume of fullerene in solution can be neglected. The density of *p*-xylene under the ambient conditions is 0.8611 g cm^{-3} [7]. Using the Avogadro number for 1 mol of C_{60}, we can determine that the volume per fullerene molecule at its critical concentration in *p*-xylene of 0.01% is about 14×10^{-18} cm^3, which corresponds to a cube with an edge of 2.5×10^{-6} cm (25 nm); and this is the distance between C_{60} molecules at their uniform distribution. Thus, the long-range action of fullerene C_{60} in *p*-xylene covers approximately 25 nm.

In conclusion, we suggest the following mechanism of changes in the intensity of small-angle X-ray scattering with increasing fullerene concentration in the case of zero aggregation. On adding fullerene to a solvent, two competing trends are observed: (1) increase in the scattering intensity with the concentration of the electron density fluctuations,which occurs because fullerene generates additional stable fluctuations with a decreased electron density, and (2) decrease in the scattering intensity owing to suppression of the thermal density fluctuations in the solution bulk.

At small concentrations (~0.001%), the first process prevails. As a result, the scattering intensities slightly increase owing to the appearance of new scattering centers, namely, fullerene macromolecules surrounded by a lyophobic shell.

With increasing fullerene concentrations, the second mechanism becomes predominant. In this case, lyophilic shells of elevated density are formed around the lyophobic centers (2.5–3.0 mm in diameter), and the size of these shells increases with the fullerene density and reaches ~25 nm at the critical concentration c_{str}. Then, the lyophilic shells merge and the intensity of X-ray scattering decreases to a minimum. The concentration c_{str} is far from the saturation concentration, and the subsequent increase in the fullerene concentration does not affect the solvent, but the heterogeneity of the system again grows, causing the intensity of the X-ray scattering to increase. It should be noted that this increase is slower than that in the case of a simultaneous structuring of the solvent.

CONCLUSIONS

(1) Changes in the structure of *p*-xylene, toluene, and benzene in the presence of small amounts ($\leq 10^{-4}$%) of fullerene C_{60} were studied by small- and wide-angle X-ray diffraction analyses under ambient conditions. These changes are attributed to the suppression of the thermal fluctuations of the solvent density and to the ordering of the solvent on the molecular level.

(2) The X-ray diffraction data agree with the nonmonotonic variation of the solution density with the fullerene concentration.

(3) Based on experimental data, the mechanism of changes in the solvent structure under the action of fullerene on the supramolecular level was suggested.

ACKNOWLEDGMENTS

The study was financially supported by the International Science and Technological Center (project no. T-1145) and by the Division of Power Engineering, Machine Building, Mechanics, and Control Processes, Russian Academy of Sciences, within the framework of Scientific Program of Basic Research no. 13 (coordinator Acad. N.F. Morozov).

REFERENCES

1. Bezmel'nitsyn, V.N., Eletskii, A.V., and Okun', M.V., *Usp. Fiz. Nauk*, 1998, vol. 168, no. 11, pp. 1195–1220.
2. Ginzburg, B.M., Shibaev, L.A., Melenevskaya, E.Yu., et al., *J. Macromol. Sci., Ser. B: Phys.*, 2004, vol. 43, no. 6, pp. 1193–1230.
3. Ginzburg, B.M., Tuichiev, Sh., Tabarov, S.Kh., et al., *Zh. Prikl. Khim.*, 2005, vol. 78, no. 6, pp. 1047–1049.
4. Ginzburg, B.M., Tuichiev, Sh., Tabarov, S.Kh., and Shepelevskii, A.A., *Kristallografiya*, 2005, vol. 50, no. 5, pp. 797–800.
5. Guinier, A., *Theorie et technique de la radiocristallographie*, Paris: Dunod, 1956.
6. Svergun, D.I. and Feigin, L.A., *Rentgenovskoe i neitronnoe malouglovoe rasseyanie* (X-ray and Neutron Small-Angle Scattering), Moscow: Fizmatgiz, 1986, p. 190.
7. *Khimicheskii entsiklopedicheskii slovar'* (Chemical Encyclopedic Dictionary), Knunyants, I.L., Ed., Moscow: Sov. Entsiklopediya, 1983.
8. Hosemann, R. and Bagchi, S.N., *Direct Analysis of Diffraction by Matter*, Amsterdam: North–Holland, 1962.
9. Kozyrev, S.V. and Rotkin, V.V., *Fiz. Tekh. Poluprovodn.*, 1993, vol. 27, no. 9, pp. 1409–1434.
10. Eletskii, A.V. and Smirnov, B.M., *Usp. Fiz. Nauk*, 1995, vol. 165, no. 9, pp. 977–979.
11. Mekalova, N.V., *Fullereny v rastvorakh* (Fullerenes in Solutions), Ufa: Gos. Neft. Tekh. Univ., 2001.

ISSN 1070-4272, Russian Journal of Applied Chemistry, 2008, Vol. 81, No. 4, pp. 623–629. © Pleiades Publishing, Ltd., 2008.
Original Russian Text © L.D. Turkova, S.V. Kononova, R.V. Kremnev, E.V. Kruchinina, Yu.P. Kuznetsov, 2008, published in Zhurnal Prikladnoi Khimii, 2008, Vol. 81, No. 4, pp. 585–592.

PHYSICOCHEMICAL STUDIES OF SYSTEMS AND PROCESSES

Prediction of Separating Characteristics of Pervaporation Membranes by Inverse Gas Chromatography

L. D. Turkova, S. V. Kononova, R. V. Kremnev, E. V. Kruchinina, and Yu. P. Kuznetsov

Institute of Macromolecular Compounds, Russian Academy of Sciences, St. Petersburg, Russia

Received November 13, 2007

Abstract—The potentiality of inverse gas chromatography to predict separating properties of pervaporation membranes is studied for the example of a membrane composed of a mixture of polyvinyl alcohol and polyacrylic acid. Correlation relationships between the retention time of substances and relative rate of their mass transfer across the membrane were derived. A comparative method for assessment of the membrane selectivity was suggested proposed, and its consistency was checked for pervaporation separation of methanol–methyl acetate–water–acetic acid, methanol–toluene, and ethanol–ethyl acetate mixtures, including those with an azeotropic composition.

DOI: 10.1134/S1070427208040101

Currently there is a steadily growing interest in energy-saving processes for separation and purification of organic mixtures. In this relation, membrane pervaporation is among the most promising processes. With highly permeable and selective membranes used, membrane processes could be well competitive with distillation, rectification, and evaporation [1–3]. Fabrication of a high-performance pervaporation membrane for a specific separation task is a very difficult problem. Even in the case of single-polymer or composite polymer membranes, prediction of the performance characteristics of the polymer material on the basis of sorption and permeation data may be inadequate and requires experimental confirmations in each particular case. Further problems arise in film formation, in determining their transport characteristics with respect to each penetrant, and in separation because of the insufficient efficiency on relatively thicker films. Making smaller the thickness of the selective layer on passing to composite or multilayer membranes even more complicates the system. In this case, decision on the membrane material and prediction of performance characteristics of the resulting membranes become very difficult, requiring development of some new approaches. Therefore, there is a need in easy and reliable methods for determination of the selectivity of membrane-forming polymers.

Inverse gas chromatography (IGC) is an old-established physicochemical method for characterization of polymers [4]. In this method, the polymer to be examined is applied to a sorbent to form a stationary phase. The method is widely used for determination of thermodynamic parameters characterizing polymer–solvent interactions [4, 5]. It has also been used to determine the glass transition temperature [6], crystallinity [7], phase transition temperatures in liquid-crystalline polymers [8], and supramolecular structure in microheterogeneous systems built by polyblock copolymers [9].

Roberts et al. [10] have employed IGC to predict thw separating characteristics of pervaporation membranes. They analyzed published data on the Kovats retention indices and McReynolds constants for several hundreds of stationary phases, chose those selective to components to be separated, examined their composition, and, finally, suggested to synthesize highly selective membrane-forming polymers with functionalities responsible for the desired specific interactions. This approach was used to solve the problem of separation of cyclohexane from cyclohexanol and cyclohexanone.

Moulay et al. [11] have employed IGC to determine the activity coefficients, Flory–Huggins parameters, and enthalpies and entropies of interaction of alcohols and their aldehydes with the membrane material (polydimethylsiloxane). Then they attempted to predict separating properties of pervaporation membranes on the basis of these data.

Park Hyun-chae et al. [12] have performed a similar study for polymer blends with various contents of polyvinyl alcohol (PVA) and polyacrylic acid (PAA), including determination of such thermodynamic characteristics as the activity coefficients and Flory–Huggins parameters.

A wide spectrum of polymers has been examined to select those promising as materials for fabrication of pervaporation membranes. The separation properties of polymers were determined by various methods, including IGC [13].

Previously, we have demonstrated the applicability of IGC to study of transport characteristics of cellulose ester membranes [14]. It was shown that the direction of selective mass transfer across the cellulose myristate (CM) membrane can be predicted from the IGC retention times corrected for the boiling points of components to be separated.

In this study, we applied the approach suggested in [14] to prediction of separation characteristics of PVA–PAA membrane. Further development of the approach was aimed at quantitative estimation of the membrane selectivity.

EXPERIMENTAL

In the experiments, we used PVA–PAA or CM to form a stationary phase of the packing in a chromatographic column and also to form a diffusion layer of the pervaporation membrane. Two kinds of the packing were prepared.

(1) An aqueous solution containing 80 wt % PVA and 20 wt % PAA was applied to Chromosorb W sorbent. The solvent was removed, and the packing was dried to constant weight at 110°C. The total polymer content of the packing was 10 wt %. With this packing, an 1-m-long chromatographic column (internal diameter 3 mm) was prepared for the subsequent use for determining the retention times of the components belonging to three homologous series (aliphatic alcohols, acetic acid esters, and aromatic hydrocarbons). The experiments were carried out at room temperature on a Tsvet chromatograph with a flame-ionization detector. The gas flow rates were as follows (ml min^{-1}): He 30, H_2 30, and air 300.

(2) Cellulose myristate was deposited from a dilute acetone solution onto Celite 22 support. The CM content of the packing was 10 wt %. With this packing, a 3-m-long chromatographic column (inner diameter 3 mm) was prepared. The experiments were carried out on an LKhM chromatograph with a thermal conductivity detector. The carrier gas (He) flow rate was 30 ml min^{-1}.

With both columns and for each component i, we obtained the concentration dependences of the retention time t_r on the peak height in the chromatogram, to determine the t_r^{15} values corresponding to the peak height of 15 cm (h_{15}) (15 cm is the half of the chart recorder scale).

Also, we prepared three kinds of pervaporation membranes with diffusion layers containing the test polymers.

(1) A composite membrane was formed by spraying 6 wt % aqueous solution of PVA–PAA (80 : 20) onto the working surface of a commercial UFM-20 ultrafiltration membrane (Vladipor), followed by drying to constant weight and heating at 110°C [this temperature corresponded to that of heat treatment of the stationary phase (column conditioning)].

(2) A homogeneous CM film (nonporous membrane) was formed by spraying a polymer solution onto the glass surface, followed by drying to constant weight.

(3) A composite membrane was prepared by applying a thin CM layer to the surface of commercial UPM-20 ultrafilter (Vladipor) according to the procedure described in [14].

The pervaporation characteristics of the membranes were determined in separation of methanol–toluene (70 wt % MeOH) and ethanol–ethyl acetate (74 wt % EtOH) mixtures at 40°C on a pervaporation unit with an effective membrane area of 12.4 cm^2. The pressure under the dry membrane (before pervaporation) was about 0.1 mbar. The pressure over the membrane was ambient. The feed solution and permeate were analyzed gas-chromatographically and refractometrically. The membrane selectivity was characterized by the partition factor $F_{i/j}$ defined as

$$F_{i/j} = (c_i/c_j)_p/(c_i/c_j)_f,$$

where $(c_i/c_j)_p$ and $(c_i/c_j)_f$ are the component concentration ratios in the permeate and feed solution, respectively.

The permeate flow across the membrane, Π (kg m^{-2} h^{-1}), was estimated from the effective surface area of the membrane and the amount of the permeate that passed across the membrane in a fixed time.

The permeates containing methanol–toluene and ethanol–ethyl acetate mixtures were analyzed on a column with 2% TCEP [1,2,3-tris(2-cyanoethoxy)-

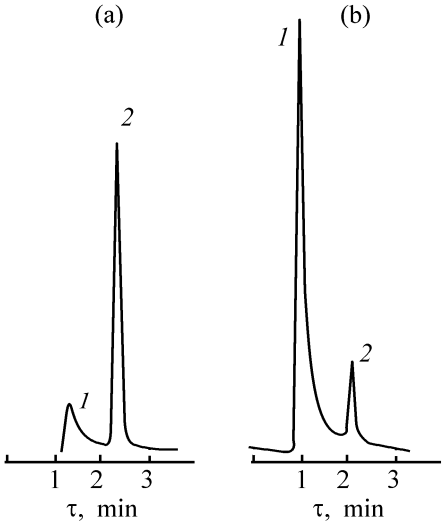


Fig. 1. Chromatograms obtained in separating methanol–toluene mixtures (column with TCEP stationary phase on Chromosorb P). (τ) Time (min); the same for Fig. 2. (a) Feed solution and (b) permeate; the same for Fig. 2. (*1*) Methanol and (*2*) toluene.

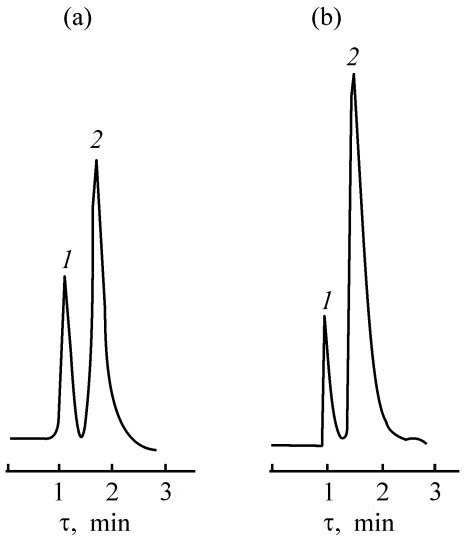


Fig. 2. Chromatograms obtained in separating ethanol–ethyl acetate mixtures (column with TCEP stationary phase on Chromosorb P). (*1*) Ethyl acetate and (*2*) ethanol.

propane] on Chromosorb P. The methanol–toluene mixtures were separated at 80°C and carrier gas (He) flow rate of 60 ml min^{-1}; and the ethanol–ethyl acetate mixtures, at 60°C and 30 ml min^{-1}.

Quantitative analysis was carried out by the internal reference method, using the relative calibration coefficients K_c, which were estimated from data obtained for reference mixtures. The K_c values were obtained for methanol–toluene mixtures, for methanol (K_m) with respect to toluene ($K_t = 1$), and for ethanol–ethyl acetate mixtures, for ethyl acetate (K_{ea}) with respect to ethanol ($K_e = 1$). Therefore, the calibration coefficients were estimated as

$$K_m = \frac{q_m}{q_t}\frac{S_t}{S_m},$$

where q_t and q_m are the toluene and MeOH concentrations in the standard mixture (%), and S_t and S_m, toluene and MeOH peak areas, calculated from the chromatogram by multiplying the peak height h by the width at half-height $\omega_{1/2}$.

The chromatograms of the mixtures are shown in Figs. 1 and 2. The estimated K_m and K_{ea} values are listed in Tables 1 and 2, respectively.

To verify the estimated K_m values, we analyzed a standard methanol–toluene mixture (70/30 w/w). The compositions of the feed solution and permeate were calculated by the following relationships:

$$q_m = \frac{S_m K_m}{S_m K_m + S_t},\ q_t = \frac{S_t}{S_m K_m + S_t}.$$

Table 1. Relative calibration coefficient of methanol K_m in methanol–toluene mixtures

Run no.	S_m, mm^2	S_t, mm^2	K_{m_i}	Averaged K_m
1	0.47	2.66	7.47	7.74
2	1.56	9.31	7.85	
3	0.63	3.94	8.10	
4	0.49	2.80	7.50	
5	0.70	4.17	7.78	

Table 2. Relative calibration coefficient of ethyl acetate K_{ea} in ethanol–ethylacetate mixtures

Run no.	S_{ea}, mm^2	S_e, mm^2	K_{ea_i}	Averaged K_{ea}
1	1.33	3.84	1.02	0.97
2	0.42	1.13	0.94	
3	1.04	2.86	0.96	

Table 3. Chromatographic analysis of the initial standard methanol–toluene mixture

Run no.	S_m	S_t	q_m	q_t	Composition, %			
					estimated		fixed*	
	mm^2		%		averaged q_m	averaged q_t	q_m	q_m
1	0.64	2.07	70.51	29.49	70.12	29.88	71.00	29.00
2	1.01	3.45	69.37	30.63				
3	1.14	3.51	71.62	28.38				
4	1.07	3.56	69.87	30.13				
5	0.54	1.85	69.21	30.79				

* The mixture was formulated according to [17].

Table 4. Chromatographic analysis of the permeate obtained in the methanol–toluene system

Run no.	S_m	S_t	q_m	q_t	Averaged q_m	Averaged q	$F^*_{m/t}$
	mm^2		%				
1	1.39	0.20	98.22	1.79	98.43	1.57	16.12
2	1.78	0.19	98.66	1.34			
3	3.03	0.432	98.19	1.81			
4	3.06	0.437	98.65	1.35			

* ($F_{m/t}$) Partition factor.

Table 5. Chromatographic analysis of the permeate obtained in the ethanol–ethyl acetate system

Run no.	S_{ea}	S_e	q_{ea}	q_e	Averaged q_{ea}	Averaged q_e	$F^*_{e/ea}$
	mm^2		%				
1	0.10	0.49	17.07	82.93	16.64	83.36	2.03
2	0.32	1.60	16.39	83.61			
3	0.45	2.22	16.46	83.59			

* ($F_{e/ea}$) Partition factor.

The results obtained in several replicate experiments and averaged are listed in Tables 3 and 4.

The permeate composition in the system ethanol–ethyl acetate was determined similarly with allowance for K_{ea} (Table 5).

In quantitative chromatographic analysis of the permeates obtained in the system methanol–methyl acetate–water–acetic acid, the separation was carried out using two columns: water, methyl acetate, and methanol were determined on a Porapak-Q column; and acetic acid, on a column with 10 wt % Reoplex-400 on Celite 545. The concentrations were estimated using the absolute calibration method.

The background of this study is based on the assumption that two processes, pervaporation and gas chromatography of fluids, can be described using interrelated parameters, if polymers of the separating diffusion layers are physicochemically identical. There is good reason to believe that this basic assumption is valid, since both processes can be described in terms of the diffusion–sorption model. Among the abovementioned parameters are primarily those characteriz-

ing the separation selectivity. Therefore, we find correlations between the partition factor of the pervaporation membrane and retention time ratio of the components to be separated with allowance for their boiling points. If found, such a correlation would open the door for optimization of the membrane structure, to solve specific separation tasks.

In so doing, we measured the t_r^{15} values for each substance, using a column with PVA/PAA supported by Chromosorb W. Then we plotted a log–log dependence of t_r^{15} on the boiling point of the component T_b (Fig. 3). Such dependences were obtained for three homologous series. Figure 3 shows that the points obtained for homologous compounds fall on a straight line, with the line for the alcohols running above that for the esters, and the line for the esters, above that for the aromatic hydrocarbons. In a GC column, the retention time is controlled by both dispersion interactions and specific interactions of the eluent with the stationary phase. For a pair of compounds with the same boiling points, the longer the retention time of a compound, the higher the contribution of specific interactions and the higher the selectivity of the column with respect to this compound. Therefore, one may suggest that the higher the line runs in the plot, the more selective is the column with respect to the corresponding homologous series.

Figure 3 shows that the selectivity of the stationary phase increases in the order aromatic hydrocarbons < acetic acid esters < aliphatic alcohols. Since the separating properties of the membrane increase with its affinity for one of components to be separated, it may be suggested that, for the test polymers, the mass transfer rate will decrease on passing from the alcohols to aromatic hydrocarbons.

Predictions made on the basis of the IGC results (Fig. 3) are consistent with data on the selectivity of the composite membrane with PVA/PAA diffusion layer (PVA : PAA = 80 : 20), obtained in the pervaporation experiments on separation of such practically significant solvent mixtures as methanol–toluene and ethanol–ethyl acetate, among them those of the azeotropic composition [15, 16]. Results of a GC analysis of the initial methanol–toluene mixtures and corresponding permeates are summarized in Tables 3 and 4. Table 3 shows that the concentrations determined by the GC analysis are well consistent with those obtained with the standard mixture. Using the estimated $K_m = 7.74$, we performed a quantitative analysis of the initial methanol–toluene mixtures and permeates sampled in the course of pervaporation. The concentrations determined by GC and the estimated partition

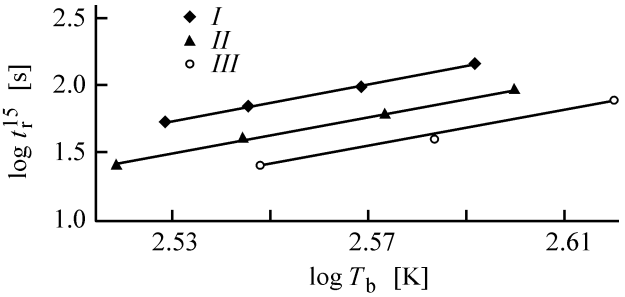


Fig. 3. t_r^{15} vs. the boiling point T_b, plotted in log–log coordinates for three homologous series: (*I*) aliphatic alcohols, (*II*) acetic acid esters, and (*III*) aromatic hydrocarbons.

factor are listed in Table 4. Similarly were determined the concentrations of the initial mixtures and permeates and the partition factor for the ethanol–ethyl acetate system (Table 5).

Tables 4 and 5 show that, indeed, the permeates are enriched in the alcohols, the effect being strongly pronounced for the mixture with the aromatic hydrocarbon, and only slightly for that with the ester. Therefore, the dependences plotted in Fig. 3 demonstrate a high prognostic power, allowing prediction of what component pairs can be separated on a given polymer membrane.

Furthermore, these plots allow comparative assessment of the selectivity of the polymeric material. With this purpose, one has to connect points corresponding to the retention times of the test components with the origin and to estimate the slope of the resulting curves (tan α). The larger the slope, the higher the selectivity of the polymeric material with respect to this compound, and the more readily it will pass across the membrane.

Table 6 shows the slopes obtained for the components of two mixtures to be separated. The slope for methanol is larger than that for toluene, and the slope for ethanol is larger than that for ethyl acetate. There-

Table 6. Slopes of the plots log t_r vs. log T_b for two mixtures to be separated*

Component	$\Delta\log t_r$	$\Delta\log T_b$	tan α
Methanol	1.71	0.02	90.83
Toluene	1.60	0.0739	21.68
Ethanol	1.85	0.04	51.40
Ethyl acetate	1.60	0.034	46.85

* (Δ) Difference between the value corresponding to a given component and that at the origin.

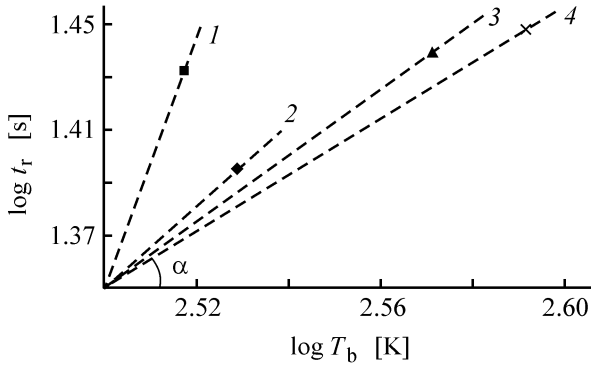


Fig. 4. Log–log dependences of t_r^{15} on the T_b for each component of the system methanol–methyl acetate–water–acetic acid: (*1*) methyl acetate, (*2*) methanol, (*3*) water, and (*4*) acetic acid.

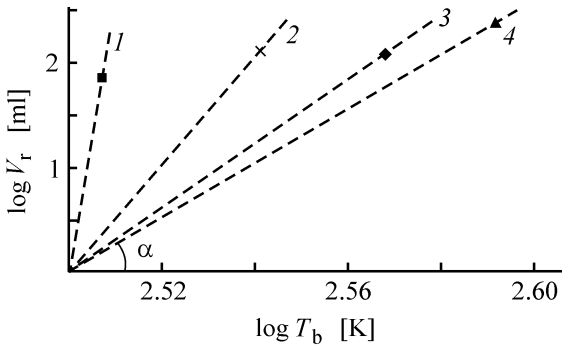


Fig. 5. Log–log dependences of the retention volume V_r of alcohols and aldehydes in PDMS column on the boiling point T_b: (*1*) propionaldehyde, (*2*) butyraldehyde, (*3*) *n*-propanol, and (*4*) *n*-butanol.

fore, methanol and ethanol will pass across the membrane more readily than toluene and ethyl acetate, respectively. In other words, our results show that the selectivity of the membrane can be judged from a comparison of the slopes of the lines connecting the origin with the points corresponding to the components to be separated.

We applied the above approach to predict the separating characteristics of CM membrane with respect to the mixture methanol–methyl acetate–water–acetic acid, which is formed in methanol esterification. The t_r^{15} values for each component of the mixture are plotted in Fig. 4 in the coordinates log t_r vs. log T_b, and the slopes tan α are listed in Table 7.

Table 7. Slopes tan α for components of the system methanol–methyl acetate–water–acetic acid

Component	T_b, K	t_r, s	tan α
Methanol	337.96	24.80	48.5
Methyl acetate	329.3	27	81.32
Water	373	27.50	20.07
Acetic acid	390.7	28	15.76

Table 8. Chromatographic analysis of the mixture methanol–methyl acetate–water–acetic acid

Sample	Membrane	Composition, wt %			
		methyl acetate	methanol	water	acetic acid
Initial mixture	–	54.1	16.7	11.6	17.6
Permeate I	Nonporous film	92.4	4.8	1.3	1.5
Permeate II	Composite	85.2	7.6	5.1	2

Based on tan α, it may be suggested that it is acetic acid that is the component most readily penetrating across the CM membrane. Results of a GC analysis of the permeates obtained in separating the indicated quaternary system on two CM membranes (homogeneous and composite) are listed in Table 8. In both cases, the permeates are enriched in methyl acetate, but strongly depleted of acetic acid. The water and methanol contents of the permeates also decrease as compared to the initial mixture, the effect being more clearly pronounced for water, which correlates with the slopes.

Therefore, to predict the separating properties of a polymeric pervaporation membrane using IGC, there is no need to obtain chromatographic data for all the members of a homologous series. It is sufficient to measure the retention time for two or more components of interest and to estimate the slopes of the straight lines connecting the origin with the points corresponding to these components in the coordinates log t_e–log T_b. The results will show whether the mixture can be separated on a given polymeric material.

To check the above procedure for consistency, we analyzed the results of [11]. The specific retention volumes of alcohols and aldehydes were obtained in [11] by IGC using PDMS (polydimethylsiloxane) as a stationary phase. We plotted these results as log V_r vs. log T_b (V_r is directly proportional to t_r) (Fig. 5) and calculated the slopes (Table 9). Table 9 also shows the activity coefficients at infinite dilu-

Table 9. Slopes tan α obtained to predict the selectivity of PDMS membrane with respect to alcohols and aldehydes

Component	T_b, K	V_r, ml	tan α	ln γ^∞	χ_i
n-Propanol	370.2	118.91	30.40	3.97	2.57
Propionaldehyde	321.8	70.60	243.60	2.05	1.05
n-Butanol	390.5	231.67	25.82	4.14	3.14
Butyraldehyde	347.7	126.18	51	2.37	1.37

tion, γ^∞, and Flory–Huggins parameters χ_i, obtained at 40°C.

It follows from Table 9 that the calculated tan α increases in the order *n*-butanol < *n*-propanol < butyraldehyde < propionaldehyde, suggesting that the column is more selective with respect to propionaldehyde, and that the permeability should decrease in the order propionaldehyde > butyraldehyde > *n*-propanol > *n*-butanol. The authors of [11] judged the membrane permeability from the thermodynamic characteristics obtained by IGC and characterizing the interaction of the alcohols and aldehydes with PDMS. The permeability decreases in the order propionaldehyde > butyraldehyde > *n*-propanol > *n*-butanol, which is consistent with the order we predicted using two different approaches.

CONCLUSIONS

(1) Method developed for predicting the separating characteristics of pervaporation membranes on the basis of inverse gas chromatographic data can be recommended for characterization of any soluble membrane-forming polymers.

(2) The method suggested for quantitative assessment of the selectivity of polymers in separation of various mixtures of liquid penetrants allows prediction of the direction of their mass transfer across the membrane.

REFERENCES

1. Mulder, M., *Basic Principles of Membrane Technology*, Dordrecht: Kluwer, 1991.
2. Volkov, V.V., *Izv. Ross. Akad. Nauk, Ser. Khim.*, 1994, no. 2, pp. 208–219.
3. Staudt-Bickel, C. and Lichtenthaler, R.N., *Vysokomol. Soedin., Ser. A*, 1994, vol. 36, no. 11, pp. 1924–1944.
4. Nesterov, A.E. and Lipatov, Yu.S., *Obrashchennaya gazovaya khromatografiya v termodinamike polimerov* (Inverse Gas Chromatography in Polymer Thermodynamics), Kiev: Naukova Dumka, 1976.
5. Tager, A.A., Kirillova, T.P., and Ikanina, T.V., *Vysokomol. Soedin., Ser. A*, 1978, vol. 20, no. 11, pp. 2543–2551.
6. Lorente, M.A., Menduina, C., and Horta, A., *J. Polym. Sci., Polym. Symp.*, 1980, vol. 68, pp. 229–237.
7. Guillet, J.E. and Stein, A.N., *Macromolecules*, 1970, vol. 3, pp. 102–105.
8. Nesterov, V.V., Turkova, L.D., Shepelevskii, A.A., and Belen'kii, B.G., *Vysokomol. Soedin., Ser. B*, 1983, vol. 25, no. 9, pp. 630–637.
9. Kalinin, A.V. and Voznyakovskii, A.P., *Zh. Prikl. Khim.*, 2006, vol. 79, no. 12, pp. 2022–2030.
10. Roberts, S.L., Koval, C.A., and Noble, R.D., *Ind. Eng. Chem. Res.*, 2000, vol. 39, no. 6, pp. 1673–1682.
11. Moulay, Saad, Benguergoura, Hassiba, and Aouak, Taieb, *J. Chromatogr. A*, 2006, vol. 1135, no. 1, pp. 78–84.
12. Park, Hyun-chae, Meertens, R.M., and Mulder, M.H.V., *Ind. Eng. Chem. Res.*, 1998, vol. 37, no. 11, pp. 4408–4417.
13. Buckley-Smith, Marion K., *The University of Waikato, Hamilton*, New Zealand, 2006.
14. Kuznetsov, Yu.P., Khripunov, A.K., Kruchinina, E.V., et al., *Zh. Prikl. Khim.*, 2004, vol. 77, no. 11, pp. 1895–1900.
15. Aptel, P., Challard, N., Cuny, J., and Neel, J., *J. Membr. Sci.*, 1976, vol. 1, pp. 271–287.
16. Chen, Wen-Jang and Martin, Charles R., *J. Membr. Sci.*, 1995, vol. 104, pp. 101–108.
17. Gordon, A.J. and Ford, R.A., *The Chemist's Companion. A Handbook of Practical Data, Techniques, and References*, New York: Wiley, 1972.

ISSN 1070-4272, Russian Journal of Applied Chemistry, 2008, Vol. 81, No. 4, pp. 630–634. © Pleiades Publishing, Ltd., 2008.
Original Russian Text © A.I. Klimuk, L.A. Obvintseva, A.D. Shepelev, V.L. Kuchaev, M.P. Dmitrieva, E.N. Ushakova, A.K. Avetisov, 2008, published in Zhurnal Prikladnoi Khimii, 2008, Vol. 81, No. 4, pp. 593–597.

PHYSICOCHEMICAL STUDIES OF SYSTEMS AND PROCESSES

A Study of Sorption and Decomposition of Ozone on Microfibrous Filtering Materials

A. I. Klimuk, L. A. Obvintseva, A. D. Shepelev, V. L. Kuchaev, M. P. Dmitrieva, E. N. Ushakova, and A. K. Avetisov

Karpov Research Physicochemical Institute, Moscow, Russia

Received October 3, 2007

Abstract—Decomposition of ozone on commercial and pilot filtering microfibrous materials based on polymers, glass fibers, and carbonized polymeric fibers was studied.

DOI: 10.1134/S1070427208040113

In view of the wide use of ozone in chemical and pulp-and-paper industries, microelectronics, water treatment, and medicine, a topical issue is development of methods for decomposition of excess ozone, including those to be used in individual and collective means for protection of the human respiratory system in those case when the maximum permissible concentration (MPC) of ozone in air is exceeded. Ozone is commonly decomposed with heterogeneous catalysts containing metals, such as Cu, Mn, Co, Fe, Ni, Ti, and Ag, and their oxides in various ratios [1]. Combined filters have also received recognition. These filters contain, in addition to catalysts, various sorbents and fibrous materials: glass fibers, carbon fibers [2, 3], and polymeric materials used both as porous supports and as active ozone-binding reagents [4–7]. Ozone is bound with various cyclic polymers: polyarene esters and sulfur-containing polymers [4], thioesters [5, 6], unsaturated polycycloolefins, and nonbornene and its higher homologues: nonbornodiene and dicyclopentadiene [5, 6]. An ozone-binding polymer can be used in a combined filter as a powder, grains, films, coatings, and finely fibrous materials. An advantage of fibrous materials is their low hydrodynamic resistance, developed surface equally accessible to ozone molecules, and room working temperatures. At present, fibrous filtering materials are efficiently used to catch aerosol particles. Industrially manufactured polymeric microfibrous materials, Petryanov filters (PF), are in common use [8, 9]. These materials are readily available and inexpensive.

A topical task is to create fibrous filtering materials for air purification to simultaneously remove aerosols and gaseous impurities. So far, several brands of materials for catching of radioactive iodine and oxidation of carbon monoxide have been developed and studies are being performed to develop new sorption-filtration materials [10–12]. It is of interest to find out whether PF and other fibrous filtering materials can be used to bind ozone. A separate issue is a search for ozone-resistant filtering materials for air purification to remove aerosol impurities in the presence of high concentrations of ozone.

The aim of this study was to examine decomposition of ozone on microfibrous filtering materials of various types in the context of the problems mentioned above. As objects of study served commercial filtering materials and pilot materials synthesized at the laboratory of aerosols at Karpov Research Physicochemical Institute.

EXPERIMENTAL

Industrial Petryanov filters [FPA-15-2.0,[1] FPP-70-0.5 (EKhMZ, Elektrostal', Moscow oblast); FPSAN-70-0.5 (Esfil, Simolaye, Estonia)], pilot materials (FPAN-10-3.0, FPF42-10-3.0, FPS-15), ultrathin glass fibers, and carbonized microfibers were studied.

All the FP samples, except glass fibers, were fabricated by electroforming [8, 9, 13]. Carbonized fibrous materials were produced by carbonization of

[1] The first figure in the designation of a filter is the average fiber diameter in tenths of a micrometer, and the second figure is the resistance to an air flow in millimeters of water at a flow velocity of 1 cm s^{-1}.

Table 1. Parameters of the microfibrous filtering materials under study

Material	Composition	Average fiber diameter, μm	Packing density, %	Specific surface area, $m^2 g^{-1}$
FPP-70-0.5	Chlorinated polyvinyl chloride	5–7	2.5	0.7
FPA-15-2.0	Cellulose diacetate	1.4	2.5–3	1.3
FPAN-10-3.0	Polyacrylonitrile	1.0	3–4	Not measured
FPF42-10-3.0	Copolymer of tetrafluoroethylene with vinylidene fluoride	1.0	3–4	″
Glass fibers	Silicon, boron, aluminum, and calcium oxides	0.2	5	″
FPSAN-70-0.5	Copolymer of styrene wit acrylonitrile	5–7	2–4	0.67
FPS-15 (pilot sample)	Polystyrene	1.5	3	1.83
Carbonized fibers	Carbon	2.0	4–5	1.56

microfibers composed of a phenol-formaldehyde resin [12]. The specific surface area of the samples was determined by the BET method on the basis of adsorption of krypton, using the standard procedure [14]. Some parameters of the materials are listed in Table 1.

The decomposition of ozone on microfibrous materials was studied using the flow-through method [15]. A gas with a known content of ozone was passed through a tube with a material under study. The change in the content of ozone after passing the gas through the tube was used to find the amount of bound ozone. The initial mass of the samples under study was 0.2 g. A tube with an inner diameter of 0.4 cm was densely packed with the material, with a 5–7-cm-long layer obtained. Ozone was produced by the electrolysis method [16]. The concentration of ozone was found by iodometric titration, with optical UV spectroscopy used in separate experiments.

The experimental setup used in the study is schematically shown in Fig. 1. Electrolyzer *1* is made of molybdenum glass. As electrolyte *2* serves a $NaClO_4$ solution. Pt-electrode *3* serves as the anode, and Ni-electrode *4*, as the cathode. Ozone-containing oxygen is liberated at the Pt-electrode, and hydrogen, at the Ni-electrode. The anode and cathode spaces are separated by ion-exchange membrane *5*. To prevent warming-up of the electrolyte, the electrolyzer is cooled with tap water (jacket *6*). Ozone-containing oxygen is delivered from the electrolyzer into fluoroplastic tube *9* packed with the material under study, passes optical cuvette *10*, and comes to a flask with a KI solution *11*. The parts of the setup are connected by fluoroplastic tubes. The loss of ozone on this ma-

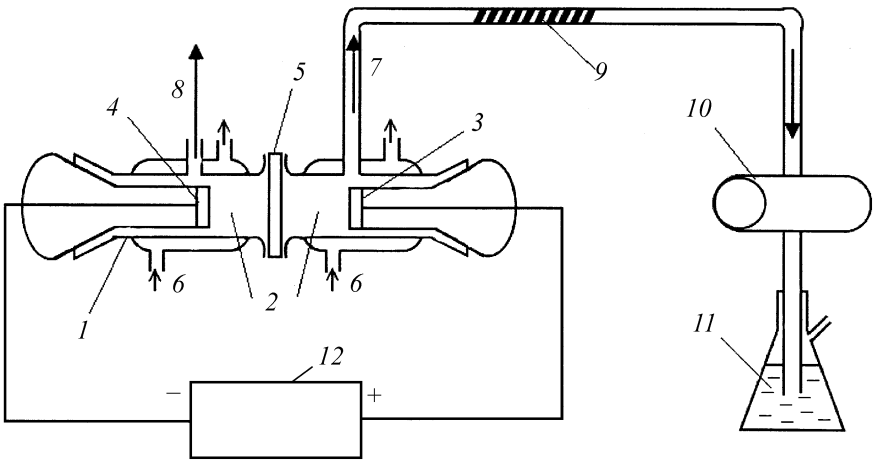


Fig. 1. Schematic of the experimental setup. (*1*) Electrolyzer, (*2*) 6 N solution of $NaClO_4$ electrolyte, (*3*) Pt-electrode, (*4*) Ni-electrode, (*5*) MF4SK (perforated ion-exchange membrane), (*6*) jacket, (*7*) $O_3 + O_2$ (gas), (*8*) H_2 (gas), (*9*) fluoroplastic tube with a material under study, (*10*) optical cuvette, (*11*) 0.05 N solution of KI, and (*12*) power unit.

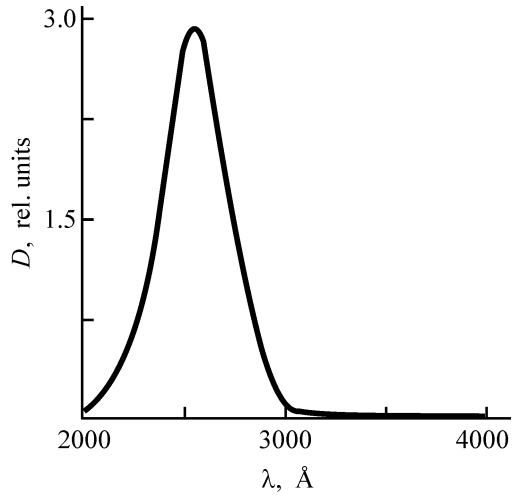


Fig. 2. UV absorption spectrum of ozone produced by electrolysis of a $NaClO_4$ solution. (*D*) Optical density and (λ) wavelength.

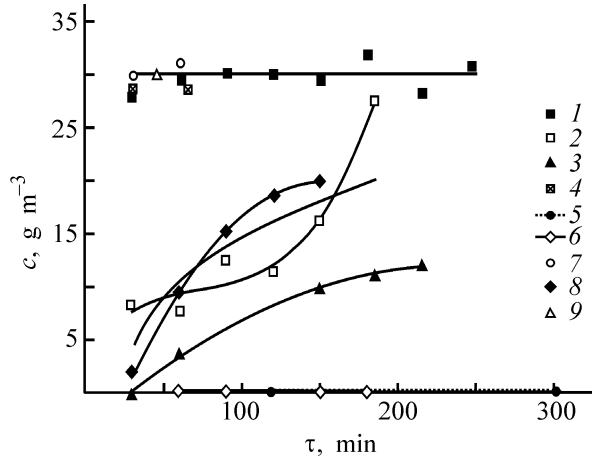


Fig. 3. Ozone concentration *c* after passing ozone-containing oxygen trough the layer of a material vs. time τ. (*1*) Empty tube, (*2*) FPP-70-0.5, (*3*) FPA-15-2.0, (*4*) FPAN-10-3.0, (*5*) FPS-15, (*6*) FPSAN-70-0.5, (*7*) glass fibers, (*8*) carbonized fibers, and (*9*) FPF42-10-3.0.

terial is insignificant because it has a small coefficient of heterogeneous decomposition of ozone [1, 17]. The tubes used in the experiments were treated with ozone for 1 h for passivation.

A UV spectrum of the ozone being formed, measured with a Perkin Elmer UV spectrometer in the range 2000–4000Å, is shown in Fig. 2. In this spectral range, only the characteristic absorption band of ozone, peaked at 2540 Å (Hartley band [18]), is present. It also follows from Fig. 2 that no chlorine dioxide (absorption band peaked at 3600 Å [18]) is formed in electrolysis of the $NaClO_4$ solution.

The content of ozone in oxygen increases with the current through the electrolyzer. The electrolyzer can produce and ozone–oxygen mixture containing 20.6 to 33.2 g m^{-3} of ozone as the current strength is varied from 296 to 550 mA. The corresponding flow rate of the ozone–oxygen mixture varies within the range 1.22–2.27 ml min^{-1}. The experiments were performed at a current strength of 510 mA. In this case, the flow rate of the ozone–oxygen mixture was 2.0 ± 0.1 ml min^{-1}. The electrolyzer was calibrated by measuring the amount of ozone absorbed by the KI solution at the outlet of an empty fluoroplastic tube of the same size as that with the material under study. The amount of ozone absorbed at this current in the course of 30 min in each of the several runs corresponded to an ozone concentration of 30 ± 2 g m^{-3} or to a content of about 1.5 vol %. The error in determining the ozone concentration is due to a minor instability in the current through the electrolyzer at a stabilized voltage across the electrodes. On absorbing ozone, the KI solution became first yellow, and then brown. In the course of the experiments, the solution was titrated, with monitoring by changes in coloration.

Figure 3 shows how the average concentration of ozone (during sampling) at the tube outlet varies with time. Straight line *1* shows the ozone concentration at the outlet of an empty tube. It can be seen in Fig. 3 that, with FPSAN-70-0.5 (points *6*) and FPS-15 (points *5*) filters, there is no ozone at the tube outlet for 6–7 h. For glass fibers (points *7*) and FPF42-10-3.0 (points *9*) and FPAN-10-3.0 (points *4*) filters, the ozone concentration at the tube outlet is the same as that in the case of an empty tube. For FPP-70-0.5 (points *2*) and FPA-15-2.0 (points *3*) filters and carbonized fibers (points *8*), a noticeable concentration of ozone is observed at the tube outlet, but this concentration is considerably lower than that observed with an empty tube.

On the basis of the data presented, all the materials studied can be divided into three groups: (i) materials inert toward ozone, on which the conversion of ozone is lower than 10% during a whole day of operation; (ii) active materials providing an ozone conversion exceeding 90%; and materials with an intermediate activity. On the materials of the third group the ozone conversion decreases during the first hours of operation.

The most active in ozone decomposition are polystyrene-containing materials: FPSAN-70-0.5 and FPS-15. These materials were used in experiments in which their activity was studied as a function of the duration of treatment with ozone. The results of seven successive runs with FPS-15 are shown in

Fig. 4. The experiments were carried out during a working day, with intervals between the runs equal to 12 to 48 h. It can be seen that, during the first three runs, the filter bound the whole amount of ozone delivered to the filter. At the end of run no. 4, a measurable ozone concentration appeared at the tube outlet (curve *4*). At the beginning of run no. 5, the ozone conversion was about 100% during 4 h and decreased to 80% by the end of the day (curve *5*). A similar behavior was also observed in the subsequent runs. By the end of run no. *7*, the conversion decreased to 50%. Similar results were obtained with FPSAN-70-0.5 filter, but its activity decreased considerably faster than that of FPS-15 filter, which may be due both to the lower specific surface area of FPSAN-70-0.5 (Table 1) and to the presence of acrylonitrile inert toward ozone in this filter. The results obtained demonstrate that the activity of the polymer with respect to ozone decomposition decreases (poisoning) both irreversibly and reversibly. The irreversible poisoning occurs via chemical reactions between a polymer and ozone, with chemical bonds in the polymer ruptured [15, 19]. The reversible poisoning may be due to formation of intermediate oxygen-containing compounds on the surface, which prevent adsorption of ozone. In a break in operation, these compounds partly decompose.

On the materials with an intermediate activity, the ozone decomposition was studied in detail on carbonized microfibers of phenol-formaldehyde resin. Four successive runs were made. Their results are shown in Fig. 5. In run nos. 1 and 2, the conversion decreased from 100 to 30% in 2 h of operation (curves *1*, *2*), but in run no. 2, the conversion gradually increased to 50% in the following 4 h. After a break of 4 days in run no. 3, a strong increase in activity was observed, so that the conversion was close to 100% during 7 h and then decreased to 80% (curve *3*). The next day, such a decrease in conversion occurred earlier (curve *4*). Thus, a complicated variation of activity was observed on carbonized fibers: under the action of ozone, the material of the filter is first deactivated and then activated. Possibly, the activation is partly due to loosening of the carbonized filter under the action of ozone and to an increase in its specific surface area.

Table 2 summarizes the results obtained in a study of the ozone treatment of microfibrous filtering materials with high and medium activity: data on the amount of ozone bound by a filter until its conversion decreases to below 90% and the corresponding duration of filter operation. A 0.2-g sample of FPS-15 filter worked for 40 h until the conversion reached

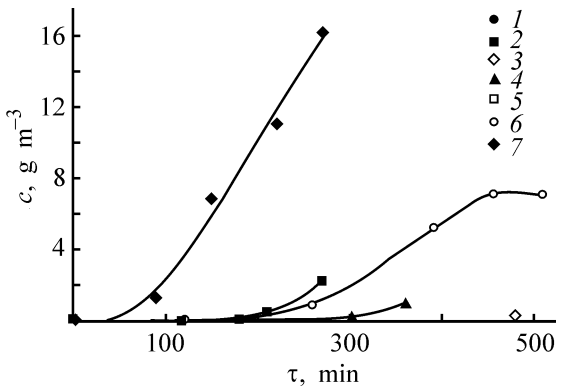


Fig. 4. Ozone concentration c after FPS-15 filter vs. time τ. *Digits at points* are run numbers.

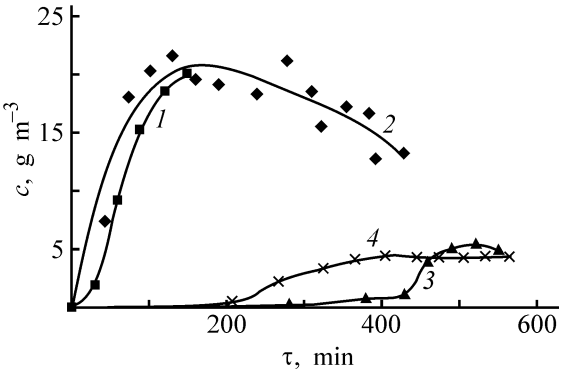


Fig. 5. Ozone concentration c after a layer of carbonized fibers vs. time τ. *Digits at points* are run numbers.

90% (inlet concentration 1.5%), with 0.15 g of ozone decomposed. The concentration of ozone in air at an MPC exceeded by an order of magnitude [19] is 4×10^{-5}%, i.e., a value four orders of magnitude lower than that in the experiments performed in this study. Under these conditions, the filter will provide a high conversion during a virtually unlimited time. This also refers to FPSAN-70-0.5 and FPA-15-2.0 filters.

Table 2. Experimentally observed efficiency of ozone catching by the materials under study

Material	Mass of ozone bound by a sample,* g	Duration of filter operation,* h
FPS-15	0.144	40
FPSAN-70-0.5	0.088	25
FPA-15-2.0	0.0066	2
Carbonized fibers	0.0018	18

* At an ozone conversion exceeding 90%.

CONCLUSIONS

(1) Analysis of the ozone decomposition on commercial and pilot filtering materials shows that filters based on polystyrene (FPS-15, FPSAN-70-0.5) exhibit a high activity in ozone binding; FPF42-10-3.0 and FPAN-10-3.0 filters and glass fibers are inert toward ozone; FPP-70-0.5 and FPA-15-2.0 filters and carbonized microfibers possess an intermediate activity.

(2) The activity of the polymeric filters decreases under the action of ozone and is partly restored in its absence. The activity of carbonized filters increases upon treatment with ozone.

(3) Carbonized fibers show a complicated variation of activity in ozone binding.

ACKNOWLEDGMENTS

The authors are grateful to E.M. Kasatkin and N.F. Potapova for the provided technique for production and titration of ozone and for detailed consultations in the course of the study and to N.V. Kozlova for measuring the UV absorption spectrum of ozone.

The study was financially supported by the International Scientific-Technological Center (grant no. 3288).

REFERENCES

1. Lunin, V.V., Popovich, M.P., and Tkachenko, S.N., *Fizicheskaya khimiya ozona* (Physical Chemistry of Ozone), Moscow: Mosk. Gos. Univ., 1998.
2. Varshavskii, V.Ya., *Uglerodnye volokna* (Carbon Fibers), Moscow: TIP VINITI, 2005.
3. US Patent 5 262 129.
4. US Patent 5 837 036.
5. US Patent 5 593 594.
6. US Patent 5 853 457.
7. US Patent 5 976 471.
8. Petryanov, I.V., Kozlov, V.I., Basmanov, P.I., and Ogorodnikov, B.I., *Voloknistye fil'truyushchie materialy FP* (FP Fibrous Filtering Materials), Moscow: Znanie, 1968.
9. Filatov, Yu.N., *Elektroformovanie voloknistykh materialov (EVF-protsess)* [Electroforming of Fibrous Materials (EVF Process), Moscow: Neft' i gaz, 1997.
10. Basmanov, P.I., Kirichenko, V.N., Filatov, Yu.N., and Yurov, F.L., *Vysokoeffektivnaya ochistka gazov ot aerozolei fil'trami Petryanova* (High-Efficiency Purification of Gases To Remove Aerosols with Petryanov Filters), Moscow: Nauka, 2003.
11. Koshcheev, A.P., Serzhantov, A.E., and Shepelev, A.D., *Tret'i Petryanovskie chteniya, 19–21 iyunya 2001 g., Trudy* (Proc. of Third Petryanov Readings, June 19–21, 2001), Moscow: RITs MGIU, pp. 148–154.
12. Budyka, A.K., Polevov, V.N., and Shepelev, A.D., Abstracts of Papers, *Mezhdunarodnaya nauchno-prakticheskaya konferentsiya "Aerozoli i bezopasnost'–2005", Obninsk, 24–28 oktyabrya 2005 g.* (Int. Sci.-Pract. Conf. "Aerosols and Safety–2005," Obninsk, October 24–28, 2005), Obninsk: FGOU GTsIPK, 2005.
13. Filatov, Yu., *Electrospinning of Micro- and Nanofibers: Fundamentals and Applications in Separation and Filtration Processes*, Budyka, A. and Kirichenko, V., Eds., New York: Begell House, 2007.
14. Braude, G.E., Semenova, T.A., and Markina, M.I., *Khimiya i tekhnologiya azotnykh udobrenii, Vypusk 12* (Chemistry and Technology of Nitrogen Fertilizers, Issue 12), Moscow: Goskhimizdat, 1961, pp. 67–75.
15. Razumovskii, S.D. and Zaikov, G.E., *Ozon i ego reaktsii s organicheskimi soedineniyami (kinetika i mekhanizm)* [Ozone and Its Reactions with Organic Compounds (Kinetics and Mechanism)], Moscow: Nauka, 1974.
16. Potapova, F. and Rakov, A.A., *Elektrokhimiya*, 1971, vol. 7, no. 4, pp. 537–540.
17. Obvintseva, L.A., Chibirova, F.Ch., Kazakov, S.A., et al., *Sensors*, 2003, vol. 3, p. 504.
18. Okabe, H., *Photochemistry of Small Molecules*, New York: John Wiley and Sons, 1978.
19. Razumovskii, S.D., *Kislorod – elementarnye formy i svoistva* (Oxygen: Elementary Forms and Properties), Moscow: Khimiya, 1979.

ISSN 1070-4272, Russian Journal of Applied Chemistry, 2008, Vol. 81, No. 4, pp. 635–638. © Pleiades Publishing, Ltd., 2008.
Original Russian Text © M.Yu. Berezkin, E.G. Polyakov, V.V. Turygin, A.P. Tomilov, 2008, published in Zhurnal Prikladnoi Khimii, 2008, Vol. 81, No. 4, pp. 598–601.

PHYSICOCHEMICAL STUDIES OF SYSTEMS AND PROCESSES

Electrochemical Synthesis of Sodium Hexamethoxyniobate

M. Yu. Berezkin, E. G. Polyakov, V. V. Turygin, and A. P. Tomilov

State Research Institute of Organic Chemistry and Technology, Federal State Unitary Enterprise, Moscow, Russia

St. Petersburg State Polytechnic University, St. Petersburg, Russia

Received February 13, 2008

Abstract—Anodic dissolution of niobium in anhydrous methanol in the presence of sodium methylate was studied. A method for recovery of niobium methylate from sodium hexamethoxyniobate by the reaction with ammonium chloride was developed.

DOI: 10.1134/S1070427208040125

The permanent need of the electronic industry in high-purity materials and, in particular, special-purity niobium used in manufacture of niobium slug capacitors enforces a search for new methods for its production and purification. Of particular interest are purification of niobium to remove admixtures of other metals and recovery of pure niobium from the raw metal and alloys. The most promising for this purpose is the electrochemical way to obtain metal alkoxides, followed by their separation. The electrochemical synthesis of niobium alkoxides has been considered previously [1, 2]. A similar method can be used to produce not only simple alkoxides, but also complex compounds, e.g., sodium hexamethoxyniobate $NaNb(OMe)_6$, whose specific properties can serve as a basis for development of a new method for recovery of pure niobium from niobium-containing alloys.

The available published data for this compound are rather scarce. This compound was first obtained by a chemical reaction of sodium and niobium methylates [3]. The principal properties of the substance were described and the electrical properties of its solutions were reported. The existence of $[Nb(OMe)_6]^-$ ions was also demonstrated in [4] by conductometric titration. No evidence about the electrochemical method for synthesis of complexes of this kind could be found in the literature.

In this study, the possibility of obtaining the sodium-niobium methoxy complex by the electrochemical method was considered and its properties and formation mechanism were analyzed.

EXPERIMENTAL

Because, according to [5], the synthesis of alkoxides is sensitive to presence of moisture, methanol of chemically pure grade used in the study was subjected to additional drying by boiling with magnesium shavings [6]. The final content of water was less than 0.01%. LiCl used in the study was also of chemically pure grade. Lithium chloride was dried by calcination at 350°C for 5 h. Sodium methylate was obtained by a direct reaction of metallic sodium (chemically pure) with methanol. The anodes were made of niobium of Nb-1 brand [GOST (State Standard) 16099–80].

Experiments were performed in a diaphragmless electrolyzer having the form of a 90-cm^3 glass cylinder equipped with a thermostating jacket and a cock at the bottom for discharging the electrolyzate. The electrolyzer was hermetically closed with a cover into which a thermometer, gas-discharge pipe with a calcium chloride packing, and current leads to the electrodes were inserted. The niobium anode was mounted below the cathode at a distance of 0.5 cm.

The working area of the anode was 8 cm^2. The cathodes were made of a platinum wire 1 mm in diameter and had a working area of 24 cm^2. Prior to each electrolysis, the electrodes were trimmed and degreased

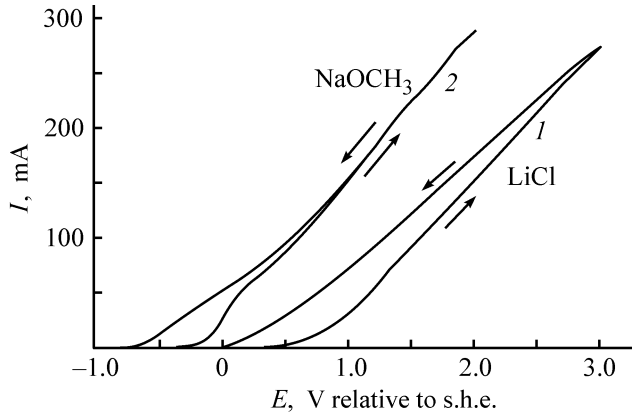


Fig. 1. Voltammetric curves obtained on Nb in 1 M solutions of (*1*) LiCl and (*2*) $NaOCH_3$ in methanol. Temperature 25°C, potential sweep rate 0.2 V s^{-1}; the same for Figs. 2, 3. (*I*) Current and (*E*) potential; the same for Figs. 2, 3.

with Vienna lime, washed with water, and weighed. After an experiment was complete, the electrolyzate was discharged into a leak-proof flask for further processing. The amount of the dissolved metal was found from the loss of mass by the anode.

To isolate niobium pentamethoxide (methylate), the alcohol was evaporated from the electrolyzate and then the product was extracted from the still bottoms with hexane. After the extractive agent was evaporated, a light yellow liquid that crystallized upon cooling remained in the flask. The resulting yellowish crystals had mp 61°C.

Sodium hexamethoxyniobate was isolated by evaporation of the alcohol from the electrolyzate and washing of the remaining white needle-like crystals with hexane.

The content of sodium methylate in the still bottoms was found by their dissolution in water and titration of the resulting solution with an alkali. The content of niobium in the still bottoms was found by their dissolution in water, addition of an acid, and gravimetric determination of the precipitated niobium pentaoxide.

Voltammetric measurements were made with an IPC computer-controlled electronic potentiostat in a 45-cm^3 cylindrical diaphragmless glass cell equipped with a thermostating jacket. Electrodes and a gas-discharge pipe were inserted into the cell cover. The electrode system comprised a niobium stationary working electrode with an area of 0.5 cm^2, platinum auxiliary electrode, and silver chloride reference electrode.

For measuring the anodic polarization curve, an electrolyte solution of a required concentration was poured into the cell and bubbled with dried argon via the gas-discharge pipe for 0.5 h. Then the required temperature was set and a trimmed electrode was placed in the cell and polarized in accordance with the preset program.

$NaNb(OMe)_6$ was synthesized as follows. Prior to electrolysis, the niobium anode was thoroughly degreased and weighed. The electrolyzer was charged with an electrolyte solution [1.1 g of $NaOCH_3$ in 90 ml of methanol (0.54 M solution)]. The content of moisture in the solution was less than 0.05 wt %. The electrolysis was performed at a constant current strength of 1 A and temperature of 18–20°C. In the course of electrolysis, the solution remained transparent, with the electrolyzer voltage equal to 10 V at the beginning of a run and increasing to 11 V by its end. In 7 h 16 min, the current was switched off and the niobium anode was weighed. The loss of mass by the anode was 4.14 g, which corresponds to a 89% current efficiency by pentavalent niobium. Methanol was evaporated from the electrolyzate under a reduced pressure (15 mm Hg). A white crystalline substance identified as $NaNb(OMe)_6$ remained in the still bottoms.

A known method for obtaining alkoxides of the aliphatic series consists in anodic dissolution of a metal in an appropriate alcohol containing a supporting electrolyte that makes the system electrically conducting [1]. Previously, a method for synthesizing niobium pentamethoxide by dissolution of a niobium anode in methanol in the presence of lithium chloride has been developed. With certain conditions satisfied, niobium pentamethoxide can be obtained with a current efficiency exceeding 95% [2].

A study of the influence exerted by the nature of a supporting electrolyte on the niobium dissolution potential in methanol solutions by cyclic voltammetry (CVA) revealed an anomalously high dissolution rate of niobium in the presence of sodium methylate. Figure 1 shows CVA curves for niobium dissolution in the presence of lithium chloride and sodium methylate. It can be seen from the CVA curve that, in the presence of $NaOCH_3$, the onset of niobium dissolution is shifted to the region of negative potentials by approximately 750 mV. Because of this circumstance, the current of anodic dissolution of niobium at a potential of 1 V in the presence of $NaOCH_3$ exceeds that in the presence of LiCl by more than a factor of 2. The so pronounced shift of the niobium dissolution potential may indicate that niobium ions formed at the anode are bound into a stable complex.

Results of a preparative synthesis of sodium hexamethoxyniobate ($NaOCH_3$ concentration 0.5 M, voltage 6–11 V, current density 0.125 A cm^{-2}, temperature 25–30°C)

Run no.	Na : Nb molar ratio	Current efficiency by Nb(V)	Yield of $NaNb(OMe)_6$	Fraction of niobium bound into sodium hexamethoxyniobate	Yield* of $Nb(OMe)_5$
		%			
1	1 : 1	99.9	99	99	0
2	1 : 2.5	98.8	97	41.6	55.3
3	1 : 5	97.2	98	18.9	79.09

* Isolated by extraction with hexane after the evaporation of methanol.

The occurrence of two anodic processes is the most clearly reflected by the voltammetric curve obtained in the presence of lithium chloride with a minor addition of lithium methylate (Fig. 2). It can be seen that, in this case, the dissolution of niobium begins at a more negative potential, a region of limiting currents appears, and the onset of the second reaction is observed when the niobium dissolution potential in the presence of lithium chloride is reached. It follows from the voltammetric curve obtained in the presence of the methoxy complex (Fig. 3) that the niobium dissolution potential lies in the intermediate region between the dissolution potentials in the presence of $NaOCH_3$ and LiCl. However, the process rate is lower.

The data obtained suggest that, in anodic polarization of the niobium electrode, the dissolution of the metal is substantially facilitated in complexation with methylate ions, whereas the reaction with chloride ions is more hindered, which leads to an increase in the potential. In the absence of ions reacting with niobium, the dissolution rate is lower.

In contrast to the process of electrosynthesis of niobium pentamethoxide in the presence of lithium chloride, in which both anodic and cathodic reaction products are involved and niobium methylate is formed in the solution bulk upon their mixing [2], the hexamethoxy complex is probably formed directly at the anode in the course of the anodic reaction

$$Nb + 6OMe^- \xrightarrow[-5e]{} [Nb(OMe)_6]^-.$$

The preparative electrolyses performed in the study with 0.1 M NaOMe as a supporting electrolyte demonstrated that niobium is converted to the pentavalent state in a nearly quantitative yield, but no free niobium pentamethoxide is formed until the concentration of Nb(V) in solution reaches a value of 0.1 M. Niobium pentamethoxide starts to appear only after the Nb : Na molar ratio in solution exceeds 1 : 1 (see table).

Sodium hexamethoxyniobate is stable in a methanol solution; however, a similar compound with the ammonium cation does not exist. On the basis of this property, the compound obtained in this study was used to isolate niobium methoxide by the exchange reaction

$$NaNb(OCH_3)_6 + NH_4Cl \rightarrow Nb(OCH_3)_5 + NaCl\downarrow + CH_3OH + NH_3\uparrow.$$

The reaction was performed in a methanol solution of the complex to give niobium pentamethoxide in 87% yield.

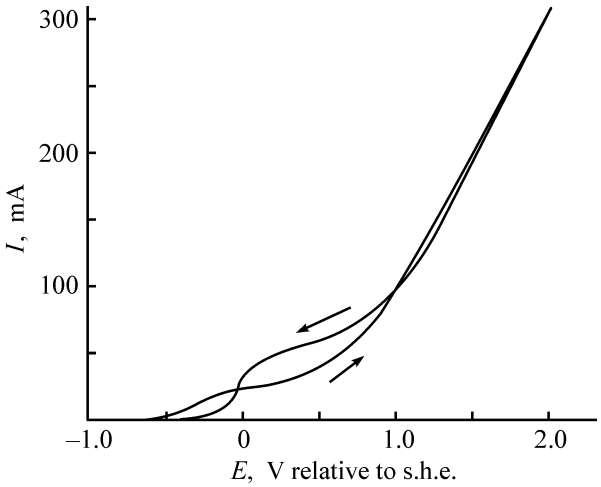


Fig. 2. Voltammetric curve obtained on Nb in a 1 M solution of LiCl in methanol containing 0.1 M $LiOCH_3$.

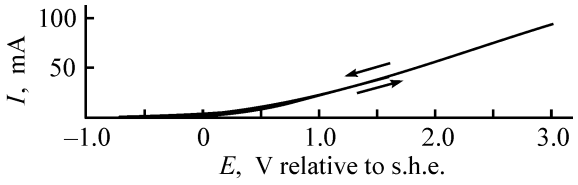


Fig. 3. Voltammetric curve obtained on Nb in a 1 M solution of $NaNb(OCH_3)_6$ in methanol.

Sodium hexamethoxyniobate is formed as white thin needle-like crystals. The substance is well soluble in methanol and insoluble in benzene and hexane. The methanol solution is electrically conducting, which indicates that this compound dissociates by the equation

$$NaNb(OMe)_6 \rightarrow Na^+ + [Nb(OMe)_6]^-.$$

An elemental analysis and calculation gave the following:

Found, %: Na 7.4, Nb 30.6.

$NaNb(OMe)_6$.

Calculated, %: Na 7.6, Nb 30.79.

Crystalline sodium hexamethoxyniobate is comparatively well soluble in water to give a weakly opalescent solution that is stable at room temperature. Evaporation of water yields coarse cubic crystals containing no carbon. Presumably, such a behavior is accounted for by instantaneous hydrolysis to give a hydroxo complex $NaNb(OH)_6$, which is well soluble in water and insoluble in a water–methanol solution.

The possibility of obtaining a compound stable in aqueous solution may be of interest for separation of niobium from admixtures of other metals.

CONCLUSIONS

(1) Sodium hexamethoxyniobate $NaNb(OMe)_6$ was electrochemically synthesized for the first time.

(2) It was demonstrated that the anodic dissolution of niobium is substantially facilitated in the presence of sodium methylate as a supporting electrolyte, compared with solutions containing lithium chloride, because of the formation of complexes with methylate ions directly in the anodic process.

(3) It was shown that pure niobium methoxide $Nb(OMe)_5$ can be obtained in the reaction of the $NaNb(OMe)_6$ formed with ammonium chloride.

(4) It was demonstrated that a water-soluble hydroxo complex $NaNb(OH)_6$ is formed in hydrolysis of $NaNb(OMe)_6$.

REFERENCES

1. Berezkin, M.Yu., Chernykh, I.N, Polyakov, E.G., and Tomilov, A.P., *Zh. Prikl. Khim.*, 2006, vol. 79, no. 5, pp. 752–756.
2. Berezkin, M.Yu., Polyakov, E.G., Turygin, V.V., and Tomilov, A.P., *Elektrokhimiya*, 2007, vol. 43, no. 10, pp. 1265–1267.
3. Mehrotra, R.C., Agrawal, M.M., and Kapoor, P.N., *J. Chem. Soc. (A)*, 1968, pp. 2673–2677.
4. Cut, R., *Helv. Chim. Acta*, 1964, vol. 47, pp. 2262–2270.
5. Turova, N.Ya., Turevskaya, E.R., Kessler, V.G., and Yanovskaya, M.I., *The Chemistry of Metal Alkoxides*, Kluwer, 2002.
6. Weissberger, A. and Proskauer, E.S., *Organic Solvents. Physical properties and methods of purification*, Riddig, J.A. and Toops, E.E., Eds., New York: Interscience, 1955.

ISSN 1070-4272, Russian Journal of Applied Chemistry, 2008, Vol. 81, No. 4, pp. 639–642. © Pleiades Publishing, Ltd., 2008.
Original Russian Text © V.Yu. Frolov, A.I. Oflidi, S.N. Bolotin, A.I. Shestavin, V.T. Panyushkin, 2008, published in Zhurnal Prikladnoi Khimii, 2008, Vol. 81, No. 4, pp. 602–605.

PHYSICOCHEMICAL STUDIES OF SYSTEMS AND PROCESSES

Effect of Amalgamation on the Passivation of Transition Metals in Their Anodic Dissolution in Tetrahydroadipic Acid Solutions

V. Yu. Frolov, A. I. Oflidi, S. N. Bolotin, A. I. Shestavin, and V. T. Panyushkin

Kuban State University, Krasnodar, Russia

Received August 2, 2007

Abstract—Effect of anode amalgamation on the degree of passivation of the electrodes and on the current efficiency in electrosynthesis of coordination compounds of copper(II), nickel(II), zinc(II), and cadmium(II) with galactaric acid was studied. An improvement of anodic synthesis characteristics was observed when amalgamated zinc, copper, and cadmium were used. Complex compounds of 1 : 1 composition were obtained and the structure of the coordination environment of the metal ion was determined by IR spectroscopy.

DOI: 10.1134/S1070427208040137

In some cases, the anodic dissolution of transition metals in solutions of various organic substances is accompanied by the formation of coordination compounds. The method of anodic synthesis [1, 2] is a rather widely used preparative technique for synthesis of coordination compounds, which can yield substances that are occasionally different in composition from those chemically synthesized. However, this method frequently encounters difficulties associated with the anode passivation by poorly soluble reaction products with low electronic conductivity. This leads to a decrease in the current density in the course of synthesis and strongly decelerates the process. Researchers' efforts in this area have been focused on solving the problem of premature passivation of electrodes. In [3], a method based on application of an asymmetric ac current with pulses with various duty factors was described. The group headed by Kharisov successfully used an ultrasonic treatment of the reaction cell for this purpose [4]. In the present study, it is suggested to use as anodes amalgamated electrodes having a semiliquid surface with a high slip coefficient, on which poorly soluble compounds are more difficultly fixed, compared with ordinary metallic anodes. Moreover, many metals used as anodes in electrosynthesis are readily amalgamated and well soluble in mercury [3–7].

The effect of amalgamation of anodes on their passivation was studied in solutions of tetrahydroxyadipic and galactaric acid (H_2Gala), which is a dibasic tetraoxyacid, a product of galactose oxidation at aldehyde and terminal alcoholic groups, used in medicinal and pharmaceutical industries. The main difficulty in obtaining salts of galactaric acid is its low solubility both in water and in organic solvents, which is due to the existence of strong intermolecular hydrogen bonds.

The aim of this study was to synthesize copper(II), nickel(II), zinc(II), and cadmium(II) galactarates and examine the effect of amalgamation of anodes made of these metals on the degree of their passivation in galactaric acid solutions.

EXPERIMENTAL

A solution of galactaric acid (Merck) was prepared by dissolving its precisely weighed portion. A solution of lithium perchlorate of chemically pure grade was used as a supporting electrolyte. The electrodes were amalgamated by keeping them in a saturated solution of $Hg_2(NO_3)_2$ under agitation.

Galactarates of *d*-metals were synthesized in an aqueous solution of galactaric acid in a two-electrode cell under permanent agitation, with metallic and amalgamated electrodes serving as soluble anodes. Prior to synthesis, the solution was bubbled with argon to remove electrically active oxygen. The electrolyzer voltage in synthesis was 10 V, and the initial concentrations of galactaric acid and the supporting electrolyte were 0.01 M. A VS-24m dc power source served as a voltage source. The areas of the metallic and corresponding amalgamated anodes submerged in the solution were the same, as also the distance between the cathode and the anode. The current density in electrosynthesis was 0.5–1.0 mA cm^{-2}.

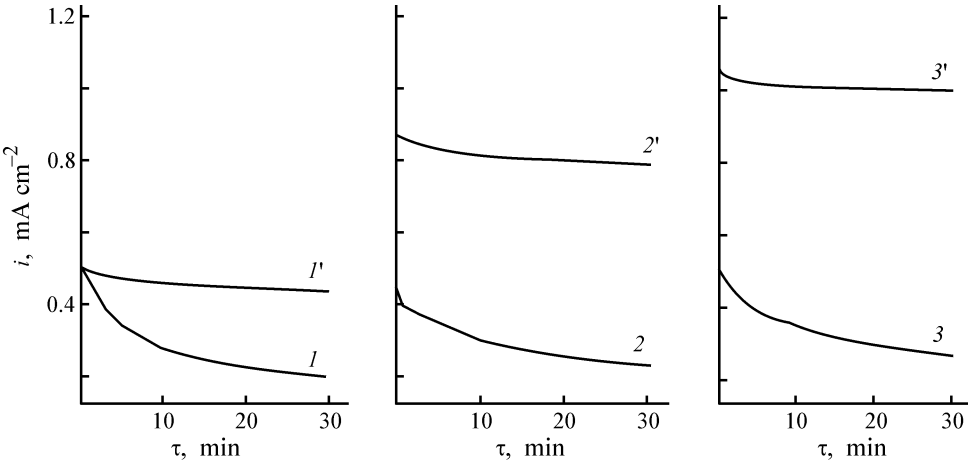


Fig. 1. Current density i vs. the electrolysis time τ with (*1'–3'*) amalgamated and (*1–3*) unamalgamated anodes. (*1*, *1'*) Cu, Cu (Hg); (*2*, *2'*) Zn, Zn (Hg); and (*3*, *3'*) Cd, Cd (Hg).

The following processes occur at the electrodes in the course of synthesis:

$$\text{A: } M - 2e \rightarrow M^{2+} \text{ or } M(Hg) - 2e \rightarrow Hg + M^{2+},$$

$$\text{K: } H_2Gala + 2e \rightarrow H_2\uparrow + Gala^{2-}.$$

The pH value was not monitored in the course of synthesis because introduction of a buffer solution into the cell would deteriorate the purity of the experiment via influence of foreign ions on the course of the process and on the composition of the compound being formed. In the course of a synthesis, the current strength was recorded and the time dependence of the current density, which reflects the degree of anode passivation, was plotted.

An anodic synthesis yielded poorly soluble solid copper(II), nickel(II), zinc(II), and cadmium(II) galactarates, which were then filtered-off under a vacuum and dried in a desiccator over phosphoric anhydride to constant weight. Near- and mid-IR spectra of the compounds synthesized were recorded on an INFRALYuM-FT-02 Fourier spectrometer at wave numbers of 4000–400 cm^{-1}. The samples for spectral measurements were prepared by compaction under a vacuum (residual pressure 5 mm Hg, pellets with 1 mg of a sample and 100 mg of KBr). The mass fraction of a metal was determined by complexonometric titration [8]. The composition was confirmed by gasvolumetric elemental analysis for C and H.

The thermal stability of the substances obtained was determined by thermogravimetric analysis on an MOM derivatograph at a heating rate of 10 deg min^{-1}, with calcined aluminum oxide as a reference and filler. The heating time was 100 min, and the final temperature, 1000°C.

The effect of amalgamation of the anodes on the degree of their passivation, which characterizes the variation of the electrosynthesis rate, was monitored by the decrease in the current density in the course of synthesis. The smaller the degree of passivation of the anode, the lesser the extent to which the current density decreases in the course of the process. It can be seen from the plots of the current density against the electrolysis duration (see figure) that, with amalgamated zinc, cadmium, and copper electrodes, the current density does not decrease significantly, compared with the corresponding metallic electrodes. This means that the degree of anode passivation decreases, and, consequently, the synthesis rate grows. This fact can be understood as follows: for the systems used in the study. amalgamated anodes have a smooth, semiliquid surface with a higher slip coefficient than that of the metallic anodes, with the result that poorly soluble reaction products are more difficultly fixed on an electrode. This was also noticeable under visual inspection: the layer of the substance formed on the amalgamated anode was thinner than that on an ordinary anode.

Use of amalgamated nickel for anodic synthesis was found to be inefficient. Nickel belongs to a group of metals for which the energy of the M–M bond exceeds that of the M–Hg bond. However, the surface nickel atoms are unsaturated and, therefore, mercury atoms enter into an electron–electron interaction with these atoms and amalgamate the surface, but further dissolution of nickel in mercury is hindered [3, 6]. Presumably, this is the reason why nickel atoms cannot be transferred, when electric current is passed, through the volume phase of the mercury coating on the amalgamated anode. After a potential difference ΔE = 10 V was reached, mercury oxidized to give

Table 1. Results of an elemental analysis and the current efficiency (CE) by the compounds synthesized

Compound	Empirical formula	Found, % / Calculated, %			CE, %, for indicated anode	
		M	C	H	M	M(Hg)
CuGala · $2H_2O$ (**I**)	$C_6H_{12}CuO_{10}$	21.00 / 20.78	23.78 / 23.37	3.99 / 3.90	57.20	80.70
NiGala · $2H_2O$ (**II**)	$C_6H_{12}NiO_{10}$	19.00 / 19.50	23.35 / 23.76	4.03 / 3.96	72.50	–
ZnGala · $4H_2O$ (**III**)	$C_6H_{16}O_{12}Zn$	19.10 / 18.80	21.16 / 20.87	4.55 / 4.64	75.20	76.70
CdGala · $4H_2O$ (**IV**)	$C_6H_{16}CdO_{12}$	28.20 / 28.60	18.02 / 18.37	4.15 / 4.08	69.50	67.90

Table 2. Absorption peaks in the IR spectra of the compounds synthesized

Compound (Table 1)	Assignment of the absorption peaks,* ν, cm^{-1}						
	ν(OH)	ν(COOH)	$\nu_{as}(COO^-)$	$\nu_s(COO^-)$	ν(C–O)		$\Delta\nu(COO^-)$
H_2Gala	3288, s	1726, s	–	–	1122, s	1061, s	–
I	3404, s	–	1616, s	1385, m	1112, m	1045, m	231
II	3392, s	–	1630, s	1384, m	1109, m	1038, w	246
III	3404, s	–	1613, s	1380, m	1110, m	1040, m	233
IV	3461, s	–	1592, s	1368, m	1107, m	1048, m	224

* s, strong; m, medium; and w, weak.

a mercury compound and the mercury layer was completely removed from the surface of the nickel electrode. The rest of the metals used in the study are easily amalgamated and well soluble in mercury [3–7], and, therefore, no undesirable effects were observed in anodic dissolution of these amalgam electrodes.

A strong increase (by a factor of 2–3) in the initial current density was observed in the case of amalgamated Zn and Cd (see figure). This indicates that the amalgamation of the electrodes markedly raises the process rate. This fact can be accounted for by the high diffusion coefficients of these metals in amalgams and by the good solubility of Zn and Cd in mercury, which makes higher the electrical conductivity of the amalgams of the metals [7]. Owing to these factors, a metal more easily passes into the amalgam and is more rapidly ionized.

The results of titrimetric and gas-volumetric elemental analyses, element composition, and presumed formulas of the substances obtained and the current efficiencies of the processes are listed in Table 1. It can be seen that a noticeable increase in the current efficiency is observed in synthesis with amalgamated copper. The possible reason is that a brick-red substance is formed in the course of electrolysis with a copper anode, and this substance partly remains on the electrode surface and is partly oxidized further to give Cu(II) galactarate. An analysis of this substance for the metal demonstrated that univalent copper oxide Cu_2O is formed. With amalgamated copper, no Cu_2O is formed and the increase in the current efficiency can be attributed to this fact. The aforesaid suggests that the anodic dissolution of copper with and without amalgamation in galactaric acid solutions occurs by different mechanisms.

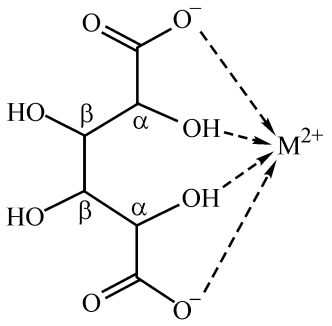
The data in Table 1 demonstrate that the synthesis yielded galactarates of *d*-metals of a 1 : 1 composition. The results of a thermographic analysis of the substances obtained show that the DTA curves of all the compounds have a peak in the temperature range 185–210°C, which points to the presence of crystallization water.

Analysis of the IR spectra of the substances obtained (Table 2) shows a complete substitution of

hydrogen in both the carboxy groups of galactaric acid in the compounds with Cu(II), Ni(II), Zn(II), and Cd(II), which is confirmed by the absence of the band associated with stretching vibrations of a free carboxy group in the IR spectra of the corresponding compounds in the range 1700–1760 cm^{-1}. At the same time, the spectra of the galactarates contain bands of asymmetric stretching vibrations of a deprotonated carboxy group at 1650–1550 cm^{-1} and symmetric stretching vibrations of the same group at 1420–1300 cm^{-1}. It is known that finding the parameter $\Delta\nu(COO^-)$, which is the difference of the wave numbers corresponding to the bands of asymmetric and symmetric stretching vibrations of the deprotonated carboxy groups, makes it possible to determine the dentate state of these groups [9]. Because $\Delta\nu(COO^-)$ exceeds 210 cm^{-1} in all cases, it can be suggested that carboxy groups are monodentate in all of the compounds synthesized [9–11].

Stretching vibrations of hydroxo groups of galactaric acid appear at around 3290 cm^{-1}. For salts of this acid, this band is shifted by approximately 100 cm^{-1} to shorter wavelengths, which may be due to a decrease in the number of hydrogen bonds in the substances obtained, caused by deprotonation of carboxy groups and coordination of oxygen atoms to the metal ion.

The bands of stretching vibrations of C–O, α- and β-OH groups are shifted in the compounds synthesized to longer wavelengths, which indicates that these groups are involved in binding to the metal ion via formation of hydrogen bonds. Comparison with data on compounds of galactaric acid with other metals (K^+, Ca^{2+}, Ba^{2+}, La^{3+}) [9] shows that only a single pair of hydroxo groups is involved in the coordination. It can be assumed that α-OH groups of galactaric acid are coordinated to the metal, which is stereochemically favorable and does not create a steric hindrance that would appear in the case of coordination of β-OH groups to the metal. The suggested structure of the coordination unit of the compounds synthesized is as follows:



CONCLUSIONS

(1) It was shown that the amalgamation method can be used in practice to improve the efficiency of the anodic electrosynthesis.

(2) A significant increase in the initial current density was observed in electrosynthesis of metal galactarates in the case of amalgamated Zn and Cd.

(3) It was demonstrated that use of amalgamated nickel in anodic synthesis is inefficient and undesirable because of the oxidation of the surface layer of mercury.

(4) It was found that the metal ion is bound to the galactarate ion at carboxy and α-hydroxo groups.

ACKNOWLEDGMENTS

The study was supported by the Russian Foundation for Basic Research (grant no. 06-0332881).

REFERENCES

1. Garnovskii, A.D., Kharisov, B.I., Gokhon-Zorrilla, G., and Garnovskii, D.A., *Usp. Khim.*, 1995, vol. 64, no. 3, pp. 215–236.
2. Frolov, V.Yu., Bolotin, S.N., and Panyushkin, V.T., *Zh. Prikl. Khim.*, 2005, vol. 78, no. 6, pp. 918–923.
3. RF Patent 2281935.
4. Kharisov, B.I., Direct Low-Temperature Synthesis of Coordination Compounds of Phthalocyanines and Azomethines, *Doctoral Dissertation*, Rostov-on-Don, 2006.
5. Kozin, L.F., Nigmetova, R.Sh., and Dergacheva, B.M., *Termodinamika binarnykh amal'gamnykh sistem* (Thermodynamics of Binary Amalgamated Systems), Alma-Ata: Nauka, 1977.
6. Smirnov, V.A., *Vosstanovlenie amal'gamami* (Reduction with Amalgams), Leningrad: Khimiya, 1970.
7. Korshunov, V.N., *Amal'gamnye sistemy* (Amalgam Systems), Moscow: Nauka, 1990.
8. Schwarzenbach, G. und Flaschka, H., *Die Komplexometrische Titration*, Stuttgart: Ferdinand Enke, 1965.
9. Wen, T., Li-Min, Y., Yi-Zhuang, X., et al., *Carbohydrate Res.*, 2000, vol. 324, no. 1, pp. 45–52.
10. Saladini, M., Ferrari, E., and Menabue, L., *Carbohydrate Res.*, 2001, vol. 336, no. 1, pp. 55–61.
11. Saladini, M., Ferrari, E., and Menabue, L., *J. Inorg. Biochem.*, 2002, vol. 92, no. 2, pp. 121–127.

ISSN 1070-4272, Russian Journal of Applied Chemistry, 2008, Vol. 81, No. 4, pp. 643–646. © Pleiades Publishing, Ltd., 2008.
Original Russian Text © E.A. Dikusar, N.A. Zhukovskaya, K.L. Moiseichuk, E.G. Zalesskaya, P.V. Kurman, O.G. Vyglazov, 2008, published in Zhurnal Prikladnoi Khimii, 2008, Vol. 81, No. 4, pp. 606–610.

ORGANIC SYNTHESIS AND INDUSTRIAL ORGANIC CHEMISTRY

Preparative Synthesis of Veratraldehyde and Citral Oxime Esters

E. A. Dikusar, N. A. Zhukovskaya, K. L. Moiseichuk, E. G. Zalesskaya, P. V. Kurman, and O. G. Vyglazov

Institute of Physicoorganic Chemistry, National Academy of Sciences of Belarus, Minsk, Belarus

Received November 10, 2006

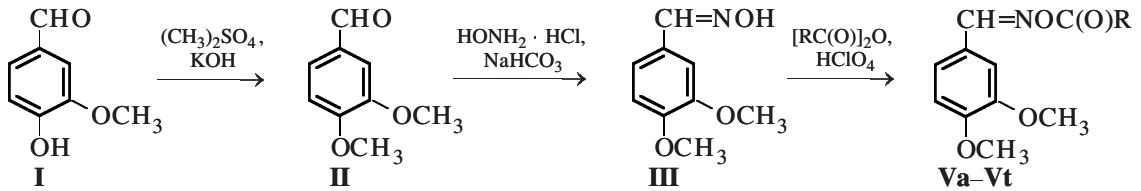
Abstract—Procedures were developed for preparing veratraldehyde, oximes of veratraldehyde and citral, and esters of these oximes, which are readily accessible fragrance compounds that can be synthesized from commercially available raw materials.

DOI: 10.1134/S1070427208040149

Veratraldehyde (3,4-dimethoxybenzaldehyde) is present in small amounts in *Cymbopogon javanensis* essential oil. It is used in relatively few perfume compounds, odorants, and food aromatizers, and also as intermediate in synthesis of certain drugs [1]. Citral (3,7-dimethyl-2,6-octadienal) is present in lemongrass, cubeb, citrus, and some other essential oils. It is a 7 : 3 mixture of *E* and *Z* isomers. Citral is widely used in many perfume compounds, odorants, and food aromatizers [1–3].

The goal of this study was to develop of procedures for preparative synthesis of veratraldehyde and citral oxime esters from commercially available raw materials: vanillin and citral. Veratraldehyde **II** was prepared by Schotten–Baumann methylation of vanillin **I** with Me_2SO_4 in the presence of KOH. We developed a synthesis procedure that is simpler and more convenient than the procedure described previously [4] and allows preparation of veratraldehyde **II** of high purity in 90% yield. Veratraldehyde oxime **III** was prepared in 92% yield by the reaction of **II** with hydroxylamine; the procedure was similar to that described in [5].

Veratraldehyde and citral oxime esters were prepared by reactions of oximes of veratraldehyde (**III**) and citral (**IV**) with alkanecarboxylic acid anhydrides in absolute benzene in the presence of catalytic amounts of $HClO_4$ or with alkane- and arenecarboxylic acid chlorides in the presence of pyridine by the procedure developed for synthesis of related compounds [6–8]. The reactants were mixed, and the mixture was allowed to stand at 20–23°C for 24–36 h. Intense cooling and stirring were not required. Oxime esters derived from veratraldehyde (**Va**–**Vs**) and citral (**VIa**–**VIt**) were prepared in 82–92% yields:



where R = Me (**Va**), Et (**Vb**), Pr (**Vc**), Me_2CH (**Vd**), Bu (**Ve**), Me_2CHCH_2 (**Vf**), $Me(CH_2)_4$ (**Vg**), $Me(CH_2)_5$ (**Vh**), **$Me(CH_2)_6$** (**Vi**), $Me(CH_2)_7$ (**Vj**), $Me(CH_2)_8$ (**Vk**), $Me(CH_2)_{11}$ (**Vl**), *cyclo*-C_6H_{11} (**Vm**), C_6H_5 (**Vn**), $C_6H_5(CH_2)_2$ (**Vo**), **$C_6H_5MeCHCH_2$** (**Vp**), *trans*-$C_6H_5CH{=}CH$ (**Vq**), MeO (**Vr**), EtO (**Vs**).

Properties of oxime esters derived from veratraldehyde (**Va–Vs**) and citral (**VIa–VIt**)

Ester	Yield, %	T_m, °C	d_{20}^{20}	n_D^{20}	Found			Formula	Calculated, %			M	
					C	H	N		C	H	N	found	calculated
Va	88	43–44			59.77	6.13	6.47	$C_{11}H_{13}NO_4$	59.19	5.87	6.27	218.6	223.2
Vb	85	61–62			61.01	6.76	5.60	$C_{12}H_{15}NO_4$	60.75	6.37	5.90	226.0	237.2
Vc	87	63–64			62.58	7.04	5.26	$C_{13}H_{17}NO_4$	62.14	6.82	5.57	240.8	251.3
Vd	86	50–51			62.37	6.97	5.41	$C_{13}H_{17}NO_4$	62.14	6.82	5.57	242.3	251.3
Ve	82	62–63			63.56	7.35	5.02	$C_{14}H_{19}NO_4$	63.38	7.22	5.28	253.7	265.3
Vf	84		1.0813	1.5480	63.51	7.25	5.10	$C_{14}H_{19}NO_4$	63.38	7.22	5.28	255.1	265.3
Vg	88	41–42			64.72	7.78	4.86	$C_{15}H_{21}NO_4$	64.50	7.58	5.01	266.2	279.3
Vh	86	44–45			65.70	8.06	4.49	$C_{16}H_{23}NO_4$	65.51	7.90	4.77	281.4	293.4
Vi	84	47–48			66.58	8.29	4.20	$C_{17}H_{25}NO_4$	66.43	8.20	4.56	290.5	307.4
Vj	85	40–41			67.45	8.52	4.12	$C_{18}H_{27}NO_4$	67.26	8.47	4.36	309.6	321.4
Vk	85	42–43			68.31	8.90	3.91	$C_{19}H_{29}NO_4$	68.03	8.71	4.18	329.4	335.4
Vl	87	56–57			70.13	9.38	3.53	$C_{22}H_{35}NO_4$	69.99	9.34	3.71	360.8	377.5
Vm	88	50–51			66.19	7.44	4.52	$C_{16}H_{21}NO_4$	65.96	7.26	4.81	283.4	291.3
Vn	86	110–111			67.90	5.72	4.55	$C_{16}H_{15}NO_4$	67.36	5.30	4.91	280.0	285.3
Vo	88	55–56			69.22	6.34	4.25	$C_{18}H_{19}NO_4$	69.00	6.11	4.47	302.7	313.4
Vp	87		1.1692	1.5795	69.94	6.58	4.06	$C_{19}H_{21}NO_4$	69.71	6.47	4.28	318.3	327.4
Vq	87		1.0484	1.6110	69.68	5.57	4.32	$C_{18}H_{17}NO_4$	69.44	5.50	4.50	303.8	311.3
Vr	84	49–50			55.61	5.60	5.53	$C_{11}H_{13}NO_5$	55.23	5.48	5.85	230.9	239.2
Vs	85	54–55			57.14	6.11	5.30	$C_{12}H_{15}NO_5$	56.91	5.97	5.53	246.2	253.3
VIa	86		1.0589	1.4968	69.62	9.17	6.67	$C_{12}H_{19}NO_2$	68.87	9.15	6.69	202.2	209.3
VIb	90		0.9758	1.4920	69.88	9.36	6.29	$C_{13}H_{21}NO_2$	69.92	9.48	6.27	211.6	223.3
VIc	83		0.9859	1.4794	70.90	9.78	6.07	$C_{14}H_{23}NO_2$	70.85	9.77	5.90	226.9	237.3
VId	85		1.0035	1.4750	70.82	9.86	5.86	$C_{14}H_{23}NO_2$	70.85	9.77	5.90	228.7	237.3
VIe	92		0.9785	1.4876	71.56	10.13	5.77	$C_{15}H_{25}NO_2$	71.67	10.03	5.57	240.1	251.4
VIf	88		0.8114	1.4798	72.36	10.51	5.06	$C_{16}H_{27}NO_2$	72.41	10.25	5.28	256.1	265.4
VIg	93		0.8901	1.4808	73.33	10.75	5.03	$C_{17}H_{29}NO_2$	73.07	10.46	5.01	269.5	279.4
VIh	84		1.9974	1.4839	73.72	10.90	4.67	$C_{18}H_{31}NO_2$	73.67	10.61	4.77	279.9	293.5
VIi	85		0.9785	1.4842	74.36	10.98	4.44	$C_{19}H_{33}NO_2$	74.22	10.82	4.55	292.8	307.5
VIj	86		0.9130	1.4798	76.40	11.55	3.81	$C_{23}H_{41}NO_2$	75.98	11.37	3.85	340.9	363.6
VIk	85		1.0580	1.4798	77.28	11.90	3.64	$C_{28}H_{51}NO_2$	77.54	11.85	3.23	415.3	433.7
VIl	80		1.0501	1.5025	74.13	10.23	4.99	$C_{17}H_{27}NO_2$	73.60	9.80	5.05	264.7	277.4
VIm	84		1.0224	1.5208	75.32	7.80	4.92	$C_{17}H_{21}NO_2$	75.25	7.80	5.16	260.3	271.4
VIn	87		0.9530	1.5268	76.58	8.48	4.70	$C_{19}H_{25}NO_2$	76.22	8.42	4.68	284.9	299.4
VIo	81		1.0752	1.5724	76.85	8.13	4.70	$C_{19}H_{23}NO_2$	76.73	7.79	4.71	287.5	297.4
VIp	80	38–39			74.70	7.34	9.12	$C_{20}H_{22}N_2O_2$	74.49	6.88	8.69	308.5	322.2
VIq	83		1.1376	1.5424	65.20	6.90	8.86	$C_{17}H_{20}N_2O_4$	64.54	6.37	8.85	306.1	316.4
VIr	82		0.9310	1.4856	63.72	8.36	6.33	$C_{12}H_{19}NO_3$	63.98	8.50	6.22	216.6	225.3
VIs	84		0.9836	1.4860	65.90	9.20	6.18	$C_{13}H_{21}NO_3$	65.25	8.85	5.85	223.0	239.3
VIt	86		0.8945	1.4848	64.49	8.75	4.82	$C_{15}H_{23}NO_4$	64.03	8.25	4.98	264.9	281.4

$$Me_2C{=}CH(CH_2)_2C(Me){=}CHCH{=}O$$

$$\rightarrow Me_2C{=}CH(CH_2)_2C(Me){=}CHCH{=}NOH$$

IV

$$\rightarrow Me_2C{=}CH(CH_2)_2C(Me){=}CHCH{=}NOC(O)R,$$

VIa–VIt

where R = Me (**VIa**), Et (**VIb**), Pr (**VIc**), Me_2CH (**VId**), Me_2CHCH_2 (**VIe**), $Me(CH_2)_4$ (**VIf**), $Me(CH_2)_5$ (**VIg**), **$Me(CH_2)_6$** (**VIh**), $Me(CH_2)_7$ (**VIi**), $Me(CH_2)_{11}$ (**VIj**), $Me(CH_2)_{16}$ (**VIk**), *cyclo*-C_6H_{11} (**VIl**), C_6H_5 (**VIm**), $C_6H_5(CH_2)_2$ (**VIn**), *cis*-$C_6H_5CH{=}CH$ (**VIo**), $C_6H_5CH{=}C(C{\equiv}N)$ (**VIp**), 3-$O_2NC_6H_4$ (**VIq**), MeO (**VIr**), EtO (**VIs**), $MeOC(O)(CH_2)_2C$ (**VIt**).

Oxime esters **Va–Vs** and **VIa–VIt** are colorless viscous liquids or crystalline compounds crystallizing from benzene–hexane (see table). The esters do not require additional purification, contain no admixtures of the starting compounds, benzene, and pyridine, and can be directly used in fragrance and food industry [3]. According to the ^{1}H NMR spectra, the compounds were 97–98% pure. Oxime esters **Va–Vs** and **VIa–VIt** can be well stored at a temperature below +5°C in the dark under anaerobic conditions. Unsaturated compounds **VI–VIt** were stabilized by adding 0.5% hydroquinone to prevent polymerization.

The compositions and structures of oxime esters **Va–Vs** and **VIa–VIt** were confirmed by elemental analysis, cryoscopic determination of the molecular weight (see table), and ^{1}H NMR and IR spectroscopy.

The IR spectra of veratraldehyde oxime esters **Va–Vs** contain the following absorption bands, cm^{-1}: CH_{Ar} in the range 3100–3000, CH_{Alk} at 3000–2800, C=O at 1770–1730, C=N at 1675–1665, Ar at 1600–1360, C–O at 1300–1000, CH_{Ar} at 880–620. In the ^{1}H NMR spectra of veratraldehyde oxime esters **Va–Vs**, the MeO protons give two singlets at 3.90–4.10 ppm. The aromatic protons appear as a multiplet at 6.70–7.50 ppm. The HC=N proton signal is a singlet at 8.20–8.30 ppm.

The IR spectra of citral oxime esters **VIa–VIt** contain the following absorption bands, cm^{-1}: CH_{Alk} in the range 3000–2800, =CH at 3050–3020, C=O at 1770–1740, C=C at 1670–1665, C=N at 1645–1635, CH_2 at 1667–1663, C–O at 1250–1180. The IR spectra of aromatic carboxylic acid esters **VIm–VIq** also contain the CH_{Ar} absorption bands at 3100–3000 and 707–690, and the Ar absorption bands at 1600–1595, 1455–1450, and 1380–1370 cm^{-1}. The C≡N group in the IR spectrum of **VIp** gives a band at 2219 cm^{-1}, and the NO_2 group in the spectrum of **VIq** gives two characteristic bands at 1535 and 1350 cm^{-1}. In the ^{1}H NMR spectra of **VIa–VIt**, the Me_2C=C protons are manifested as two broadened singlets at 1.60±0.05 and 1.66±0.04 ppm, and the MeC=C protons, as a broadened singlet at 2.05±0.05 ppm. The HC=C protons appear as signals at 4.90–6.40 ppm. The signals of aromatic protons in **VIm–VIq** are observed as a multiplet at 7.10–9.00 ppm.

The ^{1}H NMR spectra of **Va–Vs** and **VIa–VIt** also contain the characteristic signals of the ester fragments.

EXPERIMENTAL

The IR spectra were recorded on a Protege-460 IR Fourier spectrometer (Nicolet) from thin films or KBr pellets. The ^{1}H NMR spectra were measured on a BS-587A spectrometer (100 MHz, Tesla) from 5% solutions in $CDCl_3$; the chemical shifts were determined relative to internal tetramethylsilane. The molecular weight *M* was determined cryoscopically in benzene. The physicochemcial characteristics of veratraldehyde **II** and of oximes of veratraldehyde (**III**) and citral (**IV**) were in agreement with reference data [1, 9, 10].

Veratraldehyde II. A 14-g portion of 90% KOH was dissolved in 210 ml of water. The solution was cooled to 20–23°C, and 0.2 mol of vanillin was added with vigorous stirring. After vanillin fully dissolved, 22 ml of Me_2SO_4 was added in a single portion. The mixture was stirred for 6 h at 20–23°C, after which the stirring was stopped, and the mixture was cooled to 5°C and left for 10–12 h. The crystalline precipitate of veratraldehyde **II** formed in the process was filtered off on a glass frit, washed with a small amount of water, and dried in air. Yield 90%.

Veratraldehyde oxime III. A mixture of veratraldehyde **II** (0.21 mol), hydroxylamine hydrochloride (0.27 mol), sodium hydrogen carbonate (0.28 mol), and 96% ethanol (75 ml) was refluxed for 1 h. Then the mixture was poured into a beaker with 300 ml of water, cooled to 5°C, and left for 10–12 h. The crystalline precipitate of veratraldehyde oxime **III** formed in the process was filtered off on a glass frit, washed with a small amount of water, and dried in air. Yield 92%.

Veratraldehyde and citral oxime esters Va–Vd and VIa–VId (general procedure). Veratraldehyde oxime **III** or citral oxime **IV** (0.01 mol) and appropriate acid anhydride (0.011 mol) were dissolved in 20 ml of absolute benzene, and a drop of 47% $HClO_4$ was added. The mixture was shaken and allowed to stand at 20–23°C for 24–36 h. Then the mixture was

diluted with water, and the product was extracted with benzene. The organic layer was separated, washed with water and 5% aqueous $NaHCO_3$, and dried over $CaCl_2$. The solvent was removed at reduced pressure (13–20 kPa), avoiding heating above 25–30°C.

Veratraldehyde and citral oxime esters Ve–Vs and VIe–VIt (general procedure). Veratraldehyde oxime **III** or citral oxime **IV** (0.01 mol) was dissolved in 50 ml of absolute benzene, and 0.01 mol of absolute pyridine was added. Appropriate acid chloride (0.01 mol) was added to the resulting solution with cooling to 15°C and careful shaking. The mixture was allowed to stand at 20–23°C for 24–36 h, after which it was diluted with water, and the product was extracted with benzene. The organic layer was separated, washed with water and 5% $NaHCO_3$ solution, and dried over $CaCl_2$. The solvent was removed at reduced pressure (13–20 kPa), avoiding heating above 25–30°C.

CONCLUSIONS

(1) A procedure was developed for preparing veratraldehyde and citral oxime esters in high yields by reactions of the corresponding oximes with carboxylic acid anhydrides and chlorides.

(2) A series of previously unknown veratraldehyde and citral oxime esters were synthesized and characterized. The compounds are highly pure and can be directly used in fragrance and food industry.

REFERENCES

1. Voitkevich, S.A., *865 Dushistykh veshchestv dlya parfyumerii i bytovoi khimii* (865 Fragrance Compounds for Perfumery and Household Chemistry), Moscow: Pishchevaya Prom–st., 1994, pp. 140–142.
2. Kraft, P. and Swift, K.A.D., *Perspectives in Flavor and Fragrance Research*, Weinheim: Wiley–VCH, 2005.
3. Sarafanova, L.A., *Pishchevye dobavki: Entsiklopediya* (Food Additives: Encyclopedia), St. Petersburg: GIRD, 2003.
4. Johnson, S., *J. Chem. Soc.*, 1928, vol. 133, no. 12, pp. 2924–2930.
5. Beckman, T., *Chem. Ber.*, 1882, vol. 15, no. 8, pp. 2782–2790.
6. Zhukovskaya, N.A., Dikusar, E.A., Moiseichuk, K.L., et al., *Zh. Prikl. Khim.*, 2006, vol. 79, no. 4, pp. 642–644.
7. Dikusar, E.A., *Zh. Prikl. Khim.*, 2006, vol. 79, no. 6, pp. 1043–1045.
8. Dikusar, E.A., Vyglazov, O.G., Moiseichuk, K.L., et al., *Zh. Prikl. Khim.*, 2005, vol. 78, no. 1, pp. 122–126.
9. Nedel, F. and Huldschinski, I., *Chem. Ber.*, 1953, vol. 86, pp. 1005–1010.
10. *Dictionary of Organic Compounds*, New York: Eyre and Spottiswoode, 1934. Translated under the title *Slovar' organicheskikh soedinenii*, Moscow: Inostrannaya Literatura, 1949, vol. 1, pp. 555–556, 914–915.

ISSN 1070-4272, Russian Journal of Applied Chemistry, 2008, Vol. 81, No. 4, pp. 647–650. © Pleiades Publishing, Ltd., 2008.
Original Russian Text © S.I. Anson, E.V. Novikova, A.A. Iozep, 2008, published in Zhurnal Prikladnoi Khimii, 2008, Vol. 81, No. 4, pp. 611–613.

ORGANIC SYNTHESIS AND INDUSTRIAL ORGANIC CHEMISTRY

Alginic Acid Hydrazide and Its Reactions with Aromatic Aldehydes

S. I. Anson, E. V. Novikova, and A. A. Iozep

St. Petersburg State Academy of Pharmaceutical Chemistry, St. Petersburg, Russia

Received September 21, 2007

Abstract—Alginic acid hydrazide was prepared, and its reactions with aromatic aldehydes were studied. The effect of a substituent in the benzene ring of the aldehyde on the number of arylidene groups introduced into the polymer was examined.

DOI: 10.1134/S1070427208040150

Modified polysaccharides acquire growing importance in medical practice. Chemical fixation of biologically active substances on a polysaccharide allows improvement of the existing and development of new medicinal of prolonged action and low toxicity. In this context, much promise is shown by alginic acid, which is used not only in food and cosmetic industry, but also in medicine. Alginic acid salts bind and remove from a living body decay products of carbohydrates, fats, and proteins, and also heavy metal salts and radionuclides [1]. Medicinal based on alginic acid are used for treatment and prevention of diseases of gastrointestinal tract, liver, and gall bladder [2]. Unfortunately, the chemical properties of alginic acid are poorly studied, which prevents its extensive use in synthesis of physiologically active polymers.

Therefore, our goal was to prepare alginic acid hydrazide and study its reactions with aromatic aldehydes.

Chemical modification of alginic acid was performed as follows:

$$[C_6H_5O_2(OH)_2(COOH)]_n$$
I

$$\xrightarrow[2.\ NaOH]{1.\ NH_2NH_2} [C_6H_5O_2(OH)_2(COONa)_{1-k}(CONHNH_2)_k]_n$$
II

$$\xrightarrow{ArCH=O} [C_6H_5O_2(OH)_2(COONa)_{1-k}(CONHNH_2)_k]_n$$
III

where Ar = 4-$C_6H_4NO_2$, 4-C_6H_4Cl, –C_6H_5, 4-C_6H_4–CH_3, 4-$C_6H_4OC_2H_5$.

Alginic acid hydrazide **II** was synthesized by three procedures previously suggested for preparing hydrazides of carboxyalkyl polysaccharides. According to the first protocol [3], alginic acid **I** was heated in a hydrazine hydrate medium at 100°C for 2–14 h, after which a solution of an alkali was added and the polysaccharide was precipitated with alcohol. To remove ionically bound hydrazine, the product was precipitated from aqueous solutions with an acid and then from an alkaline solution with alcohol. The resulting product was washed with alcohol and ether and dried in a vacuum at 60°C. The second procedure involved treatment of alginic acid with a hydrazine hydrate–butanol–toluene mixture, preliminary dehydrated by azeotropic distillation of water, at 70–75°C for 12 h in the presence of acidic alumina. After the reaction completion, the catalyst was removed, the aqueous layer was separated, and the product was isolated as described above. Also, the hydrazide was prepared by mixing alginic acid lactone with hydrazine hydrate and keeping for 24 h at 18–20°C.

The obtained samples of alginic acid hydrazide are yellowish amorphous powders readily soluble in water but insoluble in alcohol, ether, and other organic solvents.

The IR spectra of alginic acid hydrazide samples in the H^+ form contain absorption bands at 1737 [ν(C=O), carboxy group], 1625 [ν(C=O), amide I], and 1537 cm^{-1} [δ(N–H), amide II]. The last two bands are absent in the spectrum of alginic acid [4].

The alginic acid hydrazide samples were characterized by the degree of substitution, DS (number of hydrazide groups per monomeric unit of the polysac-

Table 1. UV spectra of aqueous solutions of aldehydes and their alginoylhydrazones

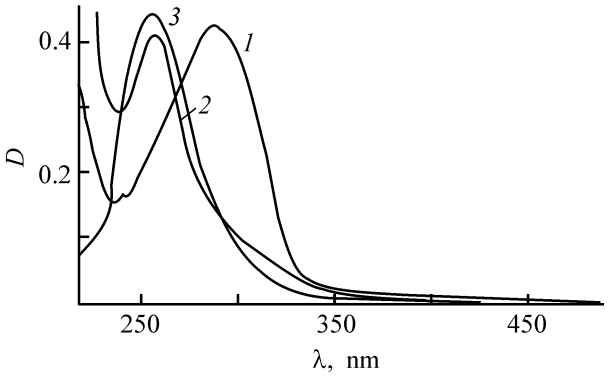
Aldehyde	λ_{max} of aqueous solutions, nm	
	aldehyde	alginoylhydrazone
4-NO_2–C_6H_4CHO	268	315
4-Cl–C_6H_4CHO	259	287
C_6H_5CHO	258	280
4-CH_3–C_6H_4CHO	260	278
4-C_2H_5O–C_6H_4CHO	283	297

charide), which was calculated from the results of iodometric titration [5].

We found that the most convenient route to alginic acid hydrazide is heating of the polysaccharide in hydrazine hydrate at 100°C, which allows preparation of samples with DS of up to 0.6. In the hydrazide samples prepared from the lactone and in the presence of alumina, DS did not exceed 0.17 and 0.13, respectively. Therefore, all the subsequent samples were prepared by the first procedure. We found that DS increased with the reaction time (at 100°C):

τ, h	DS
2	0.200 ± 0.006
4	0.347 ± 0.004
6	0.460 ± 0.004
8	0.510 ± 0.003
10	0.541 ± 0.003
12	0.572 ± 0.003
14	0.610 ± 0.002

It is known that hydrazides of carboxymethyl and carboxyethyl polysaccharides are poorly soluble in water even at low DS. This fact is accounted for by cross-linking of the polymer molecules with the formation of diacylhydrazine fragments, which was confirmed by iodometric and spectrophotometric determinations of DS [6]. All the alginic acid hydrazide samples are readily soluble in water. Therefore, it can be suggested that, with alginic acid, diacylhydrazine fragments are not formed in noticeable amounts. To confirmed this conclusion, we studied the reactions of alginic acid hydrazide with aromatic aldehydes.



UV spectrum of aqueous solutions of (*3*) 4-chlorobenzaldehyde, (*1*) its alginoylhydrazone, and (*2*) solution after completion of the hydrolysis. (*D*) Optical density and (λ) wavelength.

Aldehyde alginoylhydrazones **III** were prepared by refluxing alginic acid hydrazide **II** with benzaldehyde or its 4-nitro, 4-chloro, 4-methyl, or 4-ethoxy derivative in ethanol for 3 h in the presence of catalytic amounts of glacial acetic acid. The reaction product was filtered off and washed with hot alcohol to remove excess aldehyde.

The absence of impurities of the initial aldehydes was checked by TLC and UV spectroscopy (Table 1).

The aldehyde alginoylhydrazones are brownish amorphous powders insoluble in alcohol, ether, and other organic solvents. The solubility in water depends on the substituent in the benzene ring and decreases in going from nitro to ethoxy group.

The IR spectra of the acylhydrazones contain absorption bands at 1625 (stretching vibrations of the C=N group in the $R^1R^2C{=}NNHR^3$ fragment), 1530 (N–H bending vibrations in the amide group), 770–730 (vibrations of disubstituted benzene ring), and 1737 cm^{-1} (C=O stretching vibrations of the carboxy group).

The content of benzylidene groups in the polymer was evaluated by spectrophotometric determination of the initial aldehydes after hydrolysis of alginoylhydrazone samples in aqueous solutions of an acid in the presence of formaldehyde [7]. Replacement of sulfuric acid with acetic acid and proper choice of the reactant ratio allowed analysis under homogeneous conditions, with good reproducibility of the results.

The hydrolysis completion was checked spectrophotometrically. The UV spectra of the solution after the hydrolysis completion contain the absorption bands of the starting aldehydes only (see figure).

In addition, we performed a quantitative UV-spectrometric analysis of alginoylhydrazones without their

Table 2. Results of reactions of alginic acid hydrazide (DS = 0.259) with aldehydes (ethanol, 78°C, 1 h) and of hydrolysis of the hydrazones obtained (water, acetic acid, Formalin, 20°C)

Aldehyde	Content of converted hydrazide groups in polymer, %		Time of complete hydrolysis, h	Aldehyde	Content of converted hydrazide groups in polymer, %		Time of complete hydrolysis, h
	determined after hydrolysis	determined without hydrolysis			determined after hydrolysis	determined without hydrolysis	
4-NO_2–C_6H_4CHO	63.5	64.0	5.0	4-CH_3–C_6H_4CHO	25.4	26.2	0.6
4-Cl–C_6H_4CHO	39.5	41.0	2.5	4-C_2H_5O–C_6H_4CHO	22.0	22.4	0.3
C_6H_5CHO	43.4	44.6	1.0				

Table 3. Results of analysis of alginic acid hydrazides by iodometric and spectrophotometric methods

Run no.	DS determined by indicated method		Run no.	DS determined by indicated method		Run no.	DS determined by indicated method	
	spectrophotometry	iodometric titration		spectrophotometry	iodometric titration		spectrophotometry	iodometric titration
1	0.259 ± 0.005	0.252 ± 0.004	2	0.300 ± 0.006	0.289 ± 0.006	3	0.549 ± 0.004	0.527 ± 0.003

hydrolysis. As model compounds for constructing calibration plots were used specially prepared acetylhydrazones of the corresponding aromatic aldehydes. Their absorption peaks in aqueous solutions coincide with those of the corresponding alginoylhydrazones. This procedure allows quick and easy analysis of alginoylhydrazones. However, the calibration plots can be constructed only if the corresponding model compounds can be synthesized, which is not always the case.

The spectrophotometric methods suggested for analysis of alginoylhydrazones give comparable results (Table 2).

A study of the reactions of alginic acid hydrazide with aromatic aldehyde showed that, as with carboxyethyl dextran hydrazide [8], electron-withdrawing substituents in the benzene ring of the aldehyde accelerate the formation of alginoylhydrazones, whereas electron-donating substituents hinder it. The DS correlates with σ constants of the substituents: DS = $0.1047\sigma + 0.0839$, $R^2 = 0.999$). By contrast, 4-ethoxybenzaldehyde alginoylhydrazone is hydrolyzed considerably more readily than 4-nitrobenzaldehyde alginoylhydrazone.

By taking 4-nitrobenzaldehyde in a higher concentration and larger excess relative to alginic acid hydrazide, we achieved a quantitative conversion of the hydrazide groups of the polymer. This fact confirms the absence of diacylhydrazide fragments in the polysaccharide. In addition, the reaction can be used for a quantitative analysis of alginic acid hydrazides, because 4-nitrobenzaldehyde acylhydrazones are chromophores and become yellow in alkaline solutions [9]. The suggested conditions of spectrophotometric analysis allow quantitative analysis of alginic acid hydrazides with a relative error not exceeding 5% (Table 3).

CONCLUSIONS

(1) The degree of conversion of carboxy groups of alginic acid into hydrazide groups in hydrazine hydrate depends on the reaction time (varied from 2 to 14 h).

(2) In the reactions of alginic acid hydrazide with aromatic aldehydes, the conversion depends on the nature of the substituent in the benzene ring: electron-donating substituents reduce, and electron-with-drawing substituents raise the content of benzylidene groups in the polymer.

REFERENCES

1. Slivkin, A.I., *Vestn. Voronezh. Gos. Univ., Khim., Biol.*, 2000, pp. 30–46.
2. Mashkovskii, M.D., *Lekarstvennye sredstva* (Drugs), Moscow: Novaya Volna, 2006.
3. Bulgarian Inventor's Certificate, no. T24 119b.
4. Gordon, A.J. and Ford, R.A., *The Chemist's Companion. A Handbook of Practical Data, Techniques, and References*, New York: Wiley, 1972.
5. *Gosudarstvennaya farmakopeya SSSR* (USSR State Pharmacopeia), Moscow: Meditsina, 1987, issue 1.
6. Iozep, A.A., Kupriyanova, L.N., and Ponomarenko, M.N., *Zh. Prikl. Khim.*, 1996, vol. 69, no. 9, pp. 1537–1542.
7. Kitaev, Yu.P. and Buzykin, B.I., *Gidrazony* (Hydrazones), Moscow: Nauka, 1974.
8. Iozep, A.A., Bessonova, N.K., and Passet, B.V., *Zh. Prikl. Khim.*, 1998, vol. 71, no. 6, pp. 998–1003.
9. Siggia, S. and Hanna, J.G., *Quantitative Organic Analysis via Functional Groups*, New York: Wiley–Interscience, 1979.

ISSN 1070-4272, Russian Journal of Applied Chemistry, 2008, Vol. 81, No. 4, pp. 651–656. © Pleiades Publishing, Ltd., 2008.
Original Russian Text © S.V. Kurbatova, O.V. Parshikova, Z.P. Belousova, 2008, published in Zhurnal Prikladnoi Khimii, 2008, Vol. 81, No. 4, pp. 614–620.

ORGANIC SYNTHESIS AND INDUSTRIAL ORGANIC CHEMISTRY

Correlation between the Structure and Chromatographic Retention of Some Azole Derivatives

S. V. Kurbatova, O. V. Parshikova, and Z. P. Belousova

Samara State University, Samara, Russia

Received February 22, 2007

Abstract—The chromatographic retention of nitrogen-containing heterocycles was studied in relation to their structure. The role of the type and position of the substituents and functional groups in the chromatographic behavior of these compounds was demonstrated. THe separation in a selected chromatographic system was studied in relation to the dipole moment of the sorbates.

DOI: 10.1134/S1070427208040162

Nitrogen-containing heterocycles exhibit a wide range of biological activity [1–4]. Many of these compounds are widely used for preparing vasodilating and antispasmodic (Dibasol), antimicrobial (metronidazole), analeptic (Etimizol), adrenomimetic (naphthizin), and other pharmaceuticals. In addition, many important natural compounds such as histamine, histidine, allantoin, etc., contain an imidazole fragment. Promising in this respect are sulfonic acid imidazolides, some of which exhibit antiviral, antituberculous, antifungal, and other activities [4, 5].

An important step in preparation of biologically active compounds is identification and quality control of the pharmaceuticals prepared since they can be contaminated with intermediate products or isomers. High-performance liquid chromatography (HPLC) is one of powerful tools for analysis of heterocyclic compounds. This method is also used in physicochemical considered [6]. A study of the chromatographic behavior of nitrogen-containing heterocyclic derivatives can give insight into the retention mechanism of other heterocyclic compounds. Based on the results of such studies, the selectivity of chromatographic systems can be predicted and the conditions of chromatographic separation can be optimized.

Derivatives of five-membered heterocycles are polyfunctional compounds containing several sorption sites which can interact with the components of the chromatographic system (sorbent and eluent). The retention factors of the simplest imidazole derivates under the HPLC conditions, some physicochemical and topological properties of these compounds, and correlations between these parameters were studied in [4, 5, 7]. It should be noted that, because the range of the compounds listed was not representative, no general conclusions on how the structure of azoles and their derivatives affects their HPLC behavior were made. In this study we extended the range of azoles examined by including triazole and tetrazole derivatives and the derivatives with hydroxy, hydrazide, and nitro groups.

The aim of this study was to determine the correlation between the structure of some azole derivatives and their retention under conditions of reversed-phase HPLC (RP HPLC).

EXPERIMENTAL

The experiments were performed on a Biotronik Chromatographic system with a BT 8100 HPLC Pump. A 4×150 mm column packed with Separon SGX-C_{18} (grain size 6 μm) was used. The elution was performed in the isocratic mode using an acetonitrile–water mixture (1 : 1, 5 : 3, and 3 : 1, v/v) as the eluent.

Prior to analysis, the eluent was degassed with a UZDN-2T degasser and filtered. Substrate solutions were prepared by dissolution of dry pure heterocyclic compounds in appropriate solvents. The volume of an injected sample was 20 μl. Sodium nitrite was used as nonsorbed compound. The structural formulas and names of the compounds are listed in Table 1.[1]

[1] The compounds were prepared at the Chair of Organic Chemistry of Samara State University.

The UV detection was done at 220, 254, and 280 nm. The analysis was performed at 20°C.

The retention was characterized by the retention factor k and the relative retention r:

$$k = t'_R/t_m = (t_R - t_m)/t_m, \quad r = k_i/k_{st},$$

where t_R is the retention time of a compound examined and t_m is the retention time of unsorbed compound; k_i and k_{st} are the retention factors of the compound examined and the reference, respectively.

To evaluate the difference in retention between the nitrogen-containing heterocycles, we determined the differences between the molar Gibbs free energies of sorption of a compound examined and the reference $\delta(\Delta G)_{i,st}$:

$$\delta(\Delta G)_{i,st} = -RT\ln(k_i/k_{st}) = -RT\ln(r_{i/st}) \quad (T = 293\ \text{K}),$$

where $\delta(\Delta G)_{i,st}$ is the difference between the differential molar free energies; R, universal gas constant; and T, temperature (K).

We used benzene as the reference. Five parallel runs were performed for each point. The results are listed in Table 1.

Table 1. Relative retention r of azole derivatives under conditions of reversed-phase HPLC

Compound	Acetonitrile : water ratio					
	1 : 1		5 : 3		3 : 1	
	r	$\delta(\Delta G)_{i,st}$, kJ	r	$\delta(\Delta G)_{i,st}$, kJ	r	$\delta(\Delta G)_{i,st}$, kJ
Benzene	1	–	1	–	1	–
Imidazole	0.070	6.478	0.105	5.490	0.009	11.475
2-[(1*H*-Imidazol-1-yl)methyl]phenol	3.342	–2.939	2.052	–1.751	1.309	–0.656
2-Methylimidazole	0.785	0.589	0.169	4.331	0.233	3.549
4-[(2-Methyl-1*H*-imidazol-1-yl)methyl]phenol	0.295	2.974	0.338	2.642	0.320	2.776
2-([1*H*-Imidazol-1-yl)methyl]benzohydrazide	0.288	3.032	0.152	4.589	0.252	3.358
4-[(1*H*-Imidazol-1-yl)methyl]benzohydrazide	0.084	6.034	0.139	4.807	0.240	3.476
p-Toluenesulfonic acid imidazolide	0.130	4.969	0.317	2.799	0.235	3.528
1-(2,4,6-triisoprolylphenylsulfonyl)-1*H*-imidazole	1.763	–1.381	1.034	–0.081	1.335	–0.704
Benzenesulfonic acid imidazolide	0.130	4.969	0.174	4.259	0.242	3.456
Benzenesulfonic acid benzimidazolide	0.125	5.066	0.194	3.995	0.280	3.101
2-Methylbenzimidazole	0.143	4.738	0.225	3.634	0.313	2.830
1-(2,4,6-triisoprolylphenylsulfonyl)benzimidazole	0.128	5.008	0.187	4.084	0.292	2.999
Methanesulfonic acid 2-methylbenzimidazolide	0.345	2.592	0.378	2.370	0.430	2.056
Methanesulfonic acid indolide	0.301	2.925	0.332	2.686	0.402	2.220
Benzenesulfonic acid indolide	0.139	4.807	0.186	4.097	0.247	3.406
Indole	0.651	1.046	0.654	1.034	0.645	1.068
4-(5-methyl-1*H*-1,2,4-triazol-1-yl)phenol	0.106	5.467	0.164	4.404	0.228	3.601
1-(2,4,6-triisoprolylphenylsulfonyl)-1*H*-1,2,4-triazole	3.013	–2.687	5.252	–4.040	3.375	–2.963
Benzenesulfonic acid 1,2,4-triazolide	0.668	0.983	0.177	4.218	0.242	3.456
1-(1*H*-1,2,4-Triazol-1-yl-sulfonyl)-1*H*-1,2,4-triazole	0.035	8.166	0.043	7.665	0.029	8.625
Benzotriazole	0.088	5.920	0.166	4.374	0.256	3.319
Benzenesulfonic acid benzotriazolide	1.918	–1.033	1.750	–1.363	1.318	–0.673
1-(2,4,6-triisoprolylphenylsulfonyl)-1*H*-1,2,3-benzotriazole	3.695	5.008	0.193	4.007	0.238	3.497
p-Toluenesulfonic acid benzotriazolide	2.661	–2.384	2.413	–2.146	1.751	–1.365
4-[(1*H*-1,2,3-Benzotriazol-1-yl)methyl]phenol	0.275	3.145	0.280	3.101	0.313	2.830
5-(4-Nitrophenyl)-1*H*-tetrazole	0.303	2.909	0.332	2.686	0.275	3.145
5-Phenyl-1*H*-tetrazole	0.129	4.989	0.219	3.700	0.238	3.497

Table 2. Physicochemical properties of examined compounds

Compound	V_{VdW}, Å^3	log P	MR, cm^3 mol^{-1}	α, Å^3	μ, D
Imidazole	269	–0.04	19.95	7.60	3.599
2-[(1*H*-Imidazol-1-yl)methyl]phenol	560	1.96	50.18	19.86	2.674
2-Methylimidazole	325	–0.77	24.08	9.43	1.369
4-[(2-Methyl-1*H*-imidazol-1-yl)methyl]phenol	615	2.24	54.63	21.69	4.600
2-([1*H*-Imidazol-1-yl)methyl]benzohydrazide	666	1.06	61.56	23.84	3.857
4-[(1*H*-Imidazol-1-yl)methyl]benzohydrazide	674	1.06	61.56	23.84	3.861
p-Toluenesulfonic acid imidazolide	634	1.55	58.01	20.23	6.892
1-(2,4,6-triisoprolylphenylsulfonyl)-1*H*-imidazole	968	4.92	94.57	35.04	4.924
Benzenesulfonic acid imidazolide	592	–0.11	57.78	18.40	5.112
Benzenesulfonic acid benzimidazolide	709	0.41	73.78	24.58	4.936
2-Methylbenzimidazole	455	2.30	36.21	16.38	2.107
1-(2,4,6-triisoprolylphenylsulfonyl)benzimidazole	1044	5.62	110.56	42.31	5.454
Methanesulfonic acid 2-methylbenzimidazolide	580	–0.97	58.56	18.59	3.476
Methanesulfonic acid indolide	567	–0.33	55.46	17.46	3.729
Benzenesulfonic acid indolide	691	1.35	75.24	25.29	4.201
Indole	414	0.23	42.22	14.49	1.884
4-(5-methyl-1*H*-1,2,4-triazol-1-yl)phenol	552	1.01	49.86	19.15	4.343
1-(2,4,6-triisoprolylphenylsulfonyl)-1*H*-1,2,4-triazole	964	4.45	94.54	34.33	4.517
Benzenesulfonic acid 1,2,4-triazolide	566	0.87	51.97	17.81	4.763
1-(1*H*-1,2,4-Triazol-1-yl-sulfonyl)-1*H*-1,2,4-triazole	506	2.72	45.36	14.39	1.839
Benzotriazole	388	0.33	42.34	13.07	3.655
Benzenesulfonic acid benzotriazolide	670	1.59	75.66	23.87	3.807
1-(2,4,6-triisoprolylphenylsulfonyl)-1*H*-1,2,3-benzotriazole	1036	5.79	11.16	41.60	7.926
p-Toluenesulfonic acid benzotriazolide	739	2.68	43.63	26.92	6.124
4-[(1*H*-1,2,3-Benzotriazol-1-yl)methyl]phenol	681	2.35	66.47	26.42	4.444
5-(4-Nitrophenyl)-1*H*-tetrazole	520	3.13	51.85	17.68	3.228
5-Phenyl-1*H*-tetrazole	459	3.18	44.52	15.84	5.742

The structure of the compounds examined was confirmed by IR and NMR spectroscopy and the results of elemental analysis.

The quantum-chemical calculations were performed using the QSAR HyperChem software (version 7.0) with full optimization of the geometry of the molecules by the AM1 semiempirical method [8]. The calculated van der Waals volume V_{VdW}, molecular refraction MR, distribution log P ratio in the *n*-octanol–water system, polarizability α, and dipole moment μ of the compounds are summarized in Table 2.

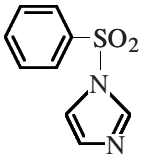
Effective methods for chromatographic analysis of complex organic compounds are, as a rule, based on the correlation between the structure of these compounds and their chromatographic retention. However, it is very difficult to take into account all the possible intermolecular interactions in a chromatographic system under conditions of liquid chromatography [6]. To study the structural influence on the chromatographic retention, different models based on the known sorption mechanism in similar chromatographic systems are used [9].

Simulation of the chromatographic retention of sorbates with a complex structure can be based on simple additive models allowing estimation of retention parameters from the set of increments. These models are frequently constructed by the method of structural similarity, based on the molecular structure–property relationship [10]. According to this method, groups of compounds with a similar substructural fragment and different substituents in a chosen position are formed. The properties of the main substructural fragments of these compounds are believed to be the same and the changes in the compound properties to be determined by the substituents [11].

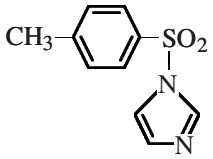
Compounds examined in this study were subdivided into structurally similar groups formed by successive introduction of one or several heteroatoms and substituents, going from azoles to sulfonic acid azolides, etc.

The main structural fragments of the compounds are imidazole, triazole, or tetrazole, which are aromatic π-deficient heterocyclic compounds. The acidity of these compounds changes owing to the redistribution of the electron density, caused by an increase in the number of nitrogen atoms in the heterocycle in going from imidazole to triazole and tetrazole. Imidazole exhibits both basic (pK_b 1.1×10^{-7}) and acidic (N–H bond) properties. The basicity of 1,2,4-triazole is significantly lower (pK_b 2×10^{-12}). Tetrazole is a weak acid in which the pyrrole hydrogen atom can migrate from one nitrogen atom to another [1].

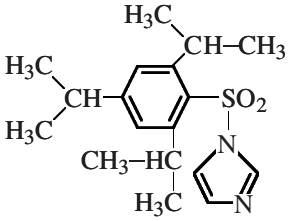
Because the interaction of sorbate molecules with the nonpolar hydrophobic surface of the stationary phase in the course of reversed-phase HPLC is mainly caused by dispersion forces, the physicochemical properties of the sorbates (such as polarizability, volume, and lipophilicity determined as the distribution ratio in the *n*-octanol–water system) significantly affect the retention [6]. As a rule, the retention of azoles increases, with the above parameters (unless other factors are important):



k = 0.373
V = 592 Å^3
log P = –0.11
α = 18.40 Å^3

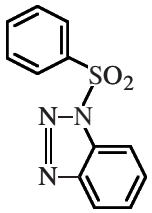


k = 0.680
V = 634 Å^3
log P = 1.55
α = 20.23 Å^3

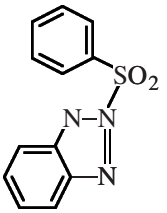


k = 2.219
V = 968 Å^3
log P = 4.92
α = 35.04 Å^3

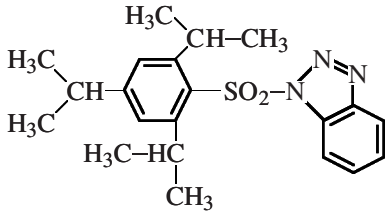
The relative retention and δ(ΔG) show similar trends. The similar dependence is observed for both sulfonic acid imidazolides and triazolides.



k = 8.086
V = 670 Å^3
log P = 1.59
α = 23.87 Å^3

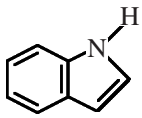


k = 11.219
V = 739 Å^3
log P = 2.68
α = 26.92 Å^3

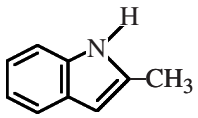


k = 15.577
V = 1036 Å^3
log P = 5.79
α = 41.60 Å^3

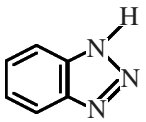
Previously we have shown [5] that introduction of the second and third nitrogen atoms into azole molecules weakens the interaction between the sorbate and the stationary phase, thus decreasing the retention. Similar dependences were observed for different compositions of the mobile phase and compounds with different substituents (Table 1). As the number of nitrogen atoms in the heterocyclic core increases, the retention factors of azole derivatives decrease, irrespective of the type of the substituent or radical bound to the heterocycle:



k = 2.746

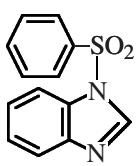


k = 0.601

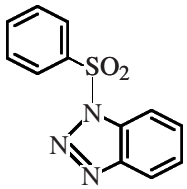


k = 0.373

Introduction of highly lipophilic phenyl substituent does not noticeably increase the retention of tetrazole derivatives, despite a significant increase in the molecular volume and liphophilicity as compared to heterocycles with a smaller number of the nitrogen atoms. At the same time, an increase in the number of heteroatoms in sulfonic acid imidazolides enhances their retention:

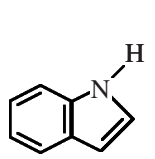


k = 0.527

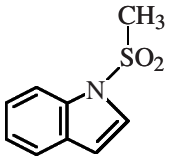


k = 8.086

A similar phenomenon is observed in going from 2,4,6-triisopropylbenzenesulfonic acid imidazolide to 2,4,6-triisopropylbenzenesulfonic acid 1,2,4-triazolide and from benzenesulfonic acid imidazolide to benzenesulfonic acid 1,2,4-triazolide. However, it should be noted that the change in the retention factors is inversely proportional to the dipole moment of these molecules. As can be seen from Table 2, the significant dipole moments of almost all of the compounds examined should noticeably affect their interaction with the components of the chromatographic system. Since the mobile phase was modified with acetonitrile whose dipole moment is 3.51 D, the orientation component should significantly contribute to the total interaction energy of the sorbates with the eluent. This fact confirms that an increase in the dipole moment decreases the retention factor of the indole derivatives, despite an increase in volume and polarizability of their molecules:

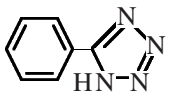


k = 2.746
μ = 1.884 D
V = 414 Å^3
α = 14.49 Å^3

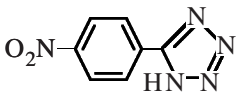


k = 1.269
μ = 3.729 D
V = 567 Å^3
α = 17.46 Å^3

The dipole moment effect can be also illustrated by the change in the retention in going from pehenyltetrazole to nitrophenyltetrazole. Introduction of the nitro group into the phenyl substituents changes the dipole moment of the sorbate molecule. As a result, the retention factors of these compounds differ, although their other properties are similar:

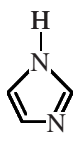


k=0.547

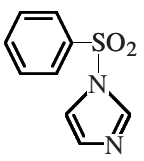


k=1.278

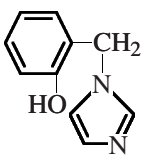
The retention of nitrogen-containing heterocycles is determined by both the type and position of a substituent in a heterocycle [8]. In particular, introduction of a substituent at the nitrogen atom of imidazole enhances the retention owing to weakening of the interaction with the eluent. This occurs irrespective of the type of the group substituting the hydrogen atom of the pyrrole nitrogen:



k=0.296



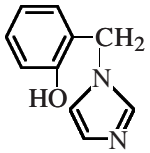
k=0.550



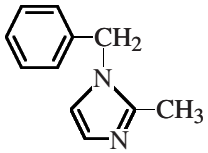
k=14.089

A significant increase in the retention of 2-[(1*H*-imidazol-1-yl)methyl]phenol is probably due to its higher lipophilicity as compared to that of imidazole and benzenesulfonic acid imidazolide (1.96, –0.04, and –0.11, respectively).

The position of the substituents at the benzene ring bound to the heterocycle significantly affects the azole retention. The data presented below show that the retention of imidazole with tolyl substituents with the *ortho*-OH group is higher than that of the compound with the *para*-OH group:

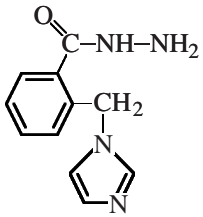


k = 14.089
μ = 2.674 D

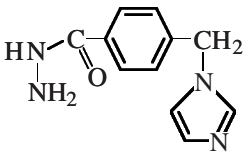


k = 1.243
μ = 4.600 D

In going from the *ortho* to *para* derivative, the dipole moment substantiality increases, with the interaction with the eluent thereby enhanced. However, in the case of para isomers the crucial factor is formation of hydrogen bonds with the eluent. For example, the retention of the corresponding hydrazine derivatives noticeably differs, although the dipole moments, lipophilicity, and molecular volume of the compounds are similar:



k = 1.213
μ = 3.857 D
V = 666 Å^3



k = 0.355
μ = 3.861 D
V = 674 Å^3

The eluent composition also affects the retention. A decrease in the content of the organic component improves separation of the compounds, but significantly raises the elution time. For example, the retention factor of 2-[(1*H*-imidazol-1-yl)methyl]phenol at the acetonitrile content in the eluent of 75 and 50% is 1.645 and 14.089, respectively. In the case of the *para* isomer, the retention factor increases to a lesser extent (from 0.402 to 1.243), which additionally confirms the significant role of hydrogen bonds in the interaction of these compounds with the mobile phase. The relative retention of these sorbates changes in a similar manner.

Thus, the retention of azole derivatives under conditions of RP HPLC is determined by a number of

factors, which are mainly associated with the sorbate structure. The presence of functional groups and substituents and their type and position in the heteroring affects the molecular properties, and mainly their volume, liphophilicity, polarizability, and dipole moment, which, in turn, enhances the interaction of the sorbate either with the stationary phase or with the eluent. Clearly, the chromatographic behavior of azoles also depends on the eluent.

CONCLUSIONS

(1) The retention factors of azole derivates under conditions of reversed-phase HPLC were determined. Analysis of the dependence of the retention factors on the molecular structure of the sorbates demonstrates significant role of the type and location of the substituents and functional groups in chromatographic behavior of the azole derivatives.

(2) Although retention of azoles is caused mainly by the dispersion forces, the dipole moment of the sorbates significantly affects their chromatographic separation by enhancement of the interaction of the polar sorbates with the components of the mobile phase.

REFERENCES

1. Nametkin, S.S., *Geterotsiklicheskie soedineniya* (Heterocyclic Compounds), Moscow: Nauka, 1981, pp. 259–263.
2. Gilchrist, T.L., *Heterocyclic Chemistry*, London: Longman, 1992.
3. Anderson, A.A., *Gazovaya khromatografiya aminosoedinenii* (Gas Chromatography of Amino Compounds), Riga: Zinatne, 1982.
4. Polyakova, Yu.L., Bulanova, A.V., Egorova, K.V., et al., *Izv. Ross. Akad. Nauk, Ser. Khim.*, 2000, no. 8, pp. 1401–1404.
5. Solovova, N.V., Kurbatova, S.V., and Belousova, Z.P., *Zh. Fiz. Khim.*, 2004, vol. 78, no. 1, pp. 91–95.
6. Shatts, V.D. and Sakhartova, O.V., *Vysokoeffektivnaya zhidkostnaya khromatografiya* (High-Performance Liquid Chromatography), Riga: Zinatne, 1988.
7. Solovova, N.V., Physicochemical Foundations of Computer Prediction of the Structure-Property Relationship for Some Carbo- and Heterocyclic Compounds under HPLC Conditions, *Cand. Sci. Dissertation*, Moscow, 2004.
8. Blatov, V.A. and Shevchenko, A.P., *Metody kom p'yuternoi khimii i kompleks program HYPERCHEM* (Methods of Computer Chemistry and HYPERCHEM Software), Samara: Samarsk. Gos. Univ., 1996.
9. Kaliszan, R. *Quantitative Structure-Chromatographic Retention Relationships*, New York: Wiley, 1987.
10. Zenkevich, I.G., *Zh. Strukt. Khim.*, 1999, vol. 40, no. 1, pp. 121–130.
11. Kurbatova, S.V., Finkel'shtein, E.E., Kolosova, E.A., et al., *Zh. Strukt. Khim.*, 2004, vol. 45, no. 1, pp. 150–157.

ISSN 1070-4272, Russian Journal of Applied Chemistry, 2008, Vol. 81, No. 4, pp. 657–662. © Pleiades Publishing, Ltd., 2008.
Original Russian Text © E.V. Fomina, Yu.A. Kurskii, G.N. Chervyakova, A.P. Sineokov, 2008, published in Zhurnal Prikladnoi Khimii, 2008, Vol. 81, No. 4, pp. 621–626.

ORGANIC SYNTHESIS AND INDUSTRIAL ORGANIC CHEMISTRY

Preparation of Dichloride of Dimerized Fatty Acid and of Oligoamides Thereof by Low-Temperature Polycondensation

E. V. Fomina, Yu. A. Kurskii, G. N. Chervyakova, and A. P. Sineokov

Kargin Research Institute of Polymers, Federal State Unitary Enterprise, Dzerzhinsk, Nizhni Novgorod oblast, Russia

Received November 1, 2007

Abstract—Dichloride of dimerized fatty acid was prepared and characterized. Conditions were developed for synthesis of oligoamides by low-temperature polycondensation of the dichloride with di- and triamines, and properties of these oligoamides were studied.

DOI: 10.1134/S1070427208040174

This study continues our research in the field of synthesis of oligo- and polyamide derivatives of dimerized fatty acid (DFA). Previously, we have reported on the preparation of these compounds by high-temperature polycondensation in a melt [1, 2].

Intramolecular plasticiziation characteristic of oligo- and polyamides of DFA, caused by the presence of bulky alkyl groups, allows wide use of these compounds as high-performance hot-melt adhesives, plasticizers and curing agents for epoxy resins, and components of paint-and-varnish materials for preparing chemically stable corrosion-resistant coatings [3–6].

Synthesis of oligo- and polyamides by equilibrium polycondensation of DFA with di(tri)amines occurs under harsh conditions (160–240°C, 5–6 h) in an inert gas and involves final evacuation of the reaction system. At the same time, similar oligoamides can be prepared from DFA dichloride and appropriate amines by irreversible polycondensation at 20°C within a few minutes [7]. In this context, it seemed topical to prepare a series of new oligomeric structures taking advantage of the milder synthesis conditions excluding amide interchange and thermal and oxidative degradation.

There are no systematic data in the literature on the formation conditions and physicochemical properties of DFA dichloride.

The goal of this study was to develop a procedure for preparing DFA dichloride, to examine its reactions with di- and triamines under the conditions of low-temperature synthesis in a stirred vessel, and to analyze how the properties of the products depend on the nature and ratio of the starting reactants.

EXPERIMENTAL

As starting compounds we used DFA of PRIPOL 1013 DIMER ACID brand (linoleic acid dimer) containing no less than 97% main substance (CAS registry no. 61788-89-4); phosphorus trichloride [GOST (State Standard) 91–73]; hexamethylenediamine, HMDA (CAS registry no. 124-09-4); diethylenetriamine, DETA (EC no. 203-865-4), fraction distilled at 65–68°C/133.33 Pa; 4,4'-diaminodiphenylmethane, 4,4'-DADPM [TU (Technical Specification) 6-09-1374–71]; preliminarily distilled triethylamine, TEA (GOST 9966–88) and toluene (GOST 5789–78); chemically pure grade acetone (GOST 2603–79); sodium hydroxide (GOST 4328–77, with revision 1); distilled water (GOST 6709).

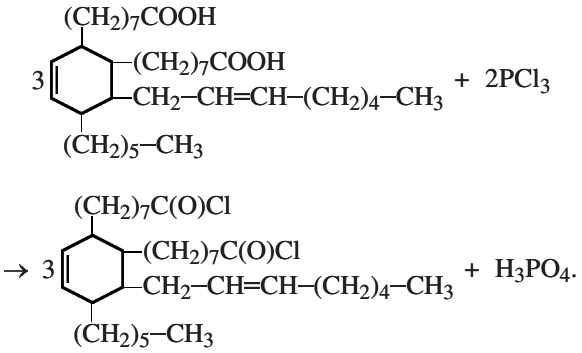
The structures of the compounds were determined by IR and NMR spectroscopy. The IR spectra were measured on a Specord M80 spectrophotometer in the range 4000–400 cm^{-1}. Liquid samples were taken as films between KBr plates, and solid samples, as KBr pellets. The NMR spectra were recorded on a Bruker

DPX-200 spectrometer operating at 200 MHz for ^1H and 50 MHz for ^{13}C. Samples were dissolved in $CDCl_3$. TMS was used as internal reference.

The amine numbers (AmNs), acid numbers (AcNs), and molecular weights evaluated chemically from the content of terminal functional groups were calculated according to the procedure described in [8]. The softening points T_s of the oligomers were determined by the ring-and-ball method (GOST 11506–73).

Attempts to prepare DFA dichloride by treatment with thionyl chloride led to the formation of a black product containing no more than 70% main substance. With PCl_3, dichloride of high quality was obtained, and the synthesis was well reproducible. Halogenation was performed according to [9–11]. The maximal conversion of carboxy groups was observed at 1.8-fold excess of PCl_3 relative to the reaction stoichiometry.

The formation of DFA dichloride is described by the scheme



I

Synthesis of the dichloride was performed in a flask equipped with a reflux condenser and a dropping funnel with $CaCl_2$ tubes. Phosphorus trichloride (82.5 g, 0.6 mol) was added dropwise over a period of 40–60 min to 280 g (0.5 mol) of DFA. The contents were heated on a water bath at 50°C for 3 h and left overnight at room temperature. Then the reaction mixture was diluted with 150 ml of toluene, stirred, and heated at 50°C for an additional 2 h. The toluene solution of dichloride **I** was separated from the precipitate of phosphorous acid by decantation, and the solvent with unchanged PCl_3 were distilled off at 50–60°C under reduced pressure (5.33–1.33 kPa). The resulting dichloride **I** was vacuum treated at 133 Pa for 1 h and was brought into subsequent transformations without additional purification. Yield 95.6%.

Dichloride of dimerized fatty acid is a mobile goldish virtually odorless liquid, n_D^{20} = 1.4895, d_4^{20} = 0.9902.

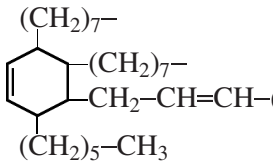
Found, %: C 77.00, H 10.81, Cl 11.72
$C_{36}H_{62}O_2Cl_2$.
Calculated, %: C 77.14, H 11.07, Cl 11.89.

In the IR spectrum of dichloride **I**, there is a pronounced absorption band of C=O stretching vibrations at ~1805 cm^{-1}. The other functional groups have no characteristic bands. In the ^1H NMR spectrum, signals at 0.85–0.88 ppm belong to CH_3 groups; a strong signal at 1.26 ppm, to CH_2 groups; and signals at 4.5–5.36 and 6.79–7.0 ppm, to the CH=CH group. It can be seen from the ^{13}C NMR spectrum that the peak at 14.2 ppm and peaks in the range 22.8–47.2 ppm belong to CH_3 and CH_2 groups, respectively. The characteristic carbon signal of the C(O)Cl group is observed at 173.6 ppm.

Dichloride **I** was used as active monomer for preparing oligoamides by low-temperature polycondensation with various amines:

$$n\mathbf{I} + n\underset{\mathbf{II–IV}}{H_2N–R–NH_2} \xrightarrow[-HCl]{\text{Acid acceptor}} \underset{\mathbf{V–VII}}{[–C(O)–R^1–C(O)–NH–R–NH–]_n},$$

where R = $(CH_2)_6$ (**II**, **V**); $C_2H_4NHC_2H_4$ (**III**, **VI**); $C_6H_4–CH_2–C_6H_4$ (**IV**, **VII**);

R^1 =  (**V–VII**);

n = 2–6.

It is known [12] that the reaction temperature, solvent, and acid acceptor strongly affect the yield and molecular weight of oligomers prepared by phase-transfer polycondensation.

Taking into account the available data, we performed the reaction at 20°C in a two-phase aqueous–organic system using toluene or toluene–acetone as organic phase. Sodium hydroxide or triethylamine was used as acid acceptor.

To obtain an oligomer of high quality by phase-transfer polycondensation in high yield, it is necessary to prevent hydrolysis of the acid dichloride. It is known [13] that the susceptibility of acid chlorides to hydrolysis is determined by their solubility in the aqueous phase. Therefore, long-chain fragments present in the dichloride make the molecule hydrophobic and hinder the hydrolysis.

Table 1. Conditions of low-temperature polycondensation of DFA dichloride with HMDA

Run no.	Dichloride	HMDA	NaOH (acid acceptor)	Solvent, ml		Yield, %
	mol			inorganic (water)	organic (toluene)	
1a	0.05	0.05	0.10	300.0	100.0	76.0
1b	0.05	0.06	0.125	600.0	200.0	82.0
1c	0.05	0.07	0.145	1500.0	300.0	80.0

Table 2. Properties and spectral characteristics of oligoamides prepared by reaction of DFA dichloride with HMDA

Compound no.	AmN	AcN	MW	T_s, °C	IR spectrum, cm^{-1}	NMR spectrum, δ, ppm
	mg KOH/g product					
Va	2.7	26.7	3820	92	1640–1670, amide I band (C=O group); 1560–1630, amide II band (NH group)	^{1}H NMR: 0.85–0.88 (CH_3, DFA); 1.26 (CH_2, DFA); 4.5–5.36 and 6.79–7.0 (CH=CH, DFA); 1.49, 2.53 and 323 (γ-CH_2, β-CH_2 and α-CH_2, HMDA); 5.5–6.5 br.s[C(O)NH]; ^{13}C NMR: 14.2, 22.8–47.2 (CH_3 and CH_2, DFA); 26.0, 36.9 and 39.1 (CH_2, HMDA); 173.5 [C(O)NH]
Vb	3.5	30.4	3310	111		
Vc	2.0	24.8	4190	99		

Table 3. Conditions of low-temperature polycondensation of DFA dichloride with DETA

Run no.	Dichloride **I**	DETA	NaOH (acid acceptor)	Solvent, ml		Yield, %
	mol			inorganic (water)	organic (toluene)	
2a	0.05	0.05	0.10	1500.0	100.0	66.0
2b	0.05	0.06	0.125	1500.0	100.0	76.0
2c	0.05	0.07	0.145	1500.0	100.0	72.0

To prepare the oligoamide from DFA dichloride and hexamethylenediamine, a beaker equipped with a stirrer was charged with a calculated amount of an aqueous solution of NaOH, HMDA was dissolved and a solution of the dichloride in toluene was added from a dropping funnel over a period of 5 min (Table 1).

In the process, a white clotted mass was formed, which partially adhered to the beaker walls. The contents were stirred for 10 min, after which 250 ml of water was added, the mixture was vigorously stirred for 30 min, and the oligoamide was separated on a glass frit. The precipitate was repeatedly washed with toluene and water to negative reaction for chloride ions. The isolated product was dried in air at 40–50°C and then in a vacuum oven at 60°C to constant weight. The dried oligoamides were pale yellow odorless powders. Their properties are listed in Table 2.

A striking fact follows from Tables 1 and 2: An increase in the HMDA concentration relative to dichloride **I** by a factor of 1.4 does not lead to significant changes in the molecular weight and softening point of the oligomers (run nos. 1a–1c), whereas in equilibrium polycondensation of DFA with HMDA, an increase in the diamine concentration by a factor of 1.4 leads to a decrease in the molecular weight by a factor of 4 [1].

The reaction of DFA dichloride with diethylenetriamine in the ratios indicated in Table 3 gave interest-

Table 4. Conditions of low-temperature polycondensation of DFA dichloride with 4,4'-DADPM

Run no.	Dichloride **I**	4,4'-DADPM	TEA (acid acceptor)	Solvent, ml		Yield, %
	mol			toluene	acetone	
3a	0.05	0.05	0.11	600.0	300.0	85.0
3b	0.05	0.06	0.145	600.0	300.0	81.0
3c	0.05	0.07	0.15	600.0	300.0	80.0

ing results. The synthesis was performed similarly to **V**, except that, after adding the dichloride to an aqueous-alkaline solution of DETA, stirring was performed for 50 min. In the process, the white milk-like reaction mixture gradually transformed into a clotty porous product. The oligoamide was squeezed through a Capron fabric and repeatedly washed with toluene and distilled water until the wash water became neutral and gave negative reaction for Cl^-. The resulting oligomer was dried in air at 60°C and then in a vacuum to constant weight.

The products obtained are soft yellow odorless lumps insoluble in isopropyl alcohol, acetone, and toluene, which did not allow determination of their amine and acid numbers and calculation of molecular weights. The compounds were infusible, and their softening points could not be determined. In the IR spectra of the oligoamides, there are well-defined bands at 1650–1680 (C=O stretching vibrations, amide I) and 1510–1570 cm^{-1} (NH bending vibrations, amide II). A distinctive feature of the spectra of these oligoamides is a weak band of C=O stretching vibrations at 1640 cm^{-1}, belonging to the tertiary amide group. The samples dissolved in $CDCl_3$ looked like a swollen gel. The ^1H NMR spectrum contained, along with signals of DFA fragments, also peaks at 2.17, 2.5, and 3.46 ppm belonging to the methylene protons of the CH_2NHCH_2 and $C(O)NHCH_2$ groups. Peaks of the broad signals of the C(O)NH groups were observed at 5.8, 6.3, and 6.8 ppm. The ^{13}C NMR spectra of compounds **VI** were of poor quality because of the low solubility of the compounds.

The observed cross-linking of oligoamides derived from FDA and DETA is apparently due to the higher reactivity of C(O)Cl groups, compared to carboxy groups (in equilibrium polycondensation), and, as a consequence, to the lower selectivity, namely, to the attack of both primary and secondary amino groups of diethylenetriamine.

Along with preparing oligoamides by low-temperature condensation of FDA dichloride with aliphatic di- and triamines, it seemed important to prepare oligoamides derived from an aromatic diamine, 4,4'-diaminodiphenylmethane.

THe particular interest in this matter is due to the fact that polycondensation in a melt is virtually inapplicable to the synthesis of oligo- and polyamides derived from aromatic diamines. The point is that, in a high-temperature process, both the starting amines themselves and the reaction products can undergo thermal degradation, because the melting points of these compounds often coincide with their decomposition points [13]. Therefore, low-temperature polycondensation can be promising for preparing a series of new oligo- and polymeric structures whose synthesis by other methods is difficult and often impossible at all.

Because 4,4'-DADPM is insoluble in water, its reaction with DFA dichloride was performed as follows: A beaker equipped with a stirrer was charged with 4,4'-DADPM, toluene, and acetone and was heated on a water bath at 50°C until the amine dissolved completely. After cooling to 20°C, we added with stirring TEA and then, dropwise, a solution of the dichloride in toluene. The reactant ratio is given in Table 4. The mixture was stirred for 3 h, after which the dark yellow precipitate was filtered off on a Büchner funnel through a Capron fabric, thoroughly washed with acetone to remove low-molecular-weight impurities and with water to negative reaction for the chloride ion, and dried to constant weight. A yellow-brown powder with a weak amine odor was obtained.

When the polycondensation is performed in solution, the hydrolysis of dichloride **I** is excluded, but some other problems arise. For example, to prevent a side reaction between 4,4'-DADPM and the released HCl, we took a certain excess of an acid acceptor, TEA. In turn, to prevent a side reaction between TEA and DFA dichloride, the latter was added to the solution of 4,4'-DADPM and TEA prepared beforehand. The possible contact of the reactants was thus excluded.

Table 5. Properties and spectral characteristics of oligoamides prepared by reaction of DFA with 4,4'-DADPM

Compound no.	AmN	AcN	MW	T_s, °C	IR spectrum, cm^{-1}	NMR spectrum, δ, ppm
	mg KOH/g product					
VIIa	7.0	39.4	2420	124	1664, amide I band (C=O group); 1540, amide II band (NHC=O); 1610, 1520, 820, bands of phenyl group; 1412, band of CH_2 group between aromatic rings	NMR spectrum, δ, ppm: 0.79–0.83 (CH_3, DFA), 1.27 (CH_2, DFA), 4.45–5.57 and 6.76–7.0 (CH=CH, DFA), 3.81 (Ar–CH_2–Ar), 7.0 and 7.4 (N–C_6H_4–CH_2–C_6H_4–N), 7.8–8.0 [C(O)NH]; ^1H NMR: 14.3 and 22.8–45.9 (CH_3 and CH_2, DFA); 120.4, 123.3, 136.3 and 137.0 (positions *3*, *5* CH, *2*, *6* CH, *1* C and *4* C–N of aromatic rings, respectively; 172.1 and 173.2 [C(O)NH]
VIIb	21.0	34.3	2030	118		
VIIc	26.0	49.2	1490	110		

Table 5 shows that the product prepared at the equimolar ratio of the reactants has the highest molecular weight; even a slight deviation from the equimolar ratio leads to a certain decrease in the molecular weight of the oligomer. The dependence we obtained confirms the higher sensitivity of the polycondensation in solution to the reactant ratio, compared to the phase-transfer polycondensation.

It should be noted that the oligoamides derived from 4,4'-DADPM show higher softening points, which is due to structural features of the oligomeric chain incorporating aromatic rings [14].

Our data allow comparison of the results of oligoamide synthesis by high-temperature [1] and low-temperature processes.

For example, the yield of compounds prepared by room-temperature acylation of the amines is relatively low. This may be due to the loss of a certain amount of low-molecular-weight fractions of the oligoamides, which are removed with the filtrate in the course of separation and washing of the solid product.

It should also be noted that the products prepared by phase-transfer polycondensation and by polycondensation in solution have, on the whole, a lower molecular weight and a higher softening point, compared to the oligomers prepared by reactions of the diamines with DFA in a melt. The observed decrease in the molecular weight may be attributed to broadening of the molecular-weight distribution, typical of these products, with an increase in the content of the low-molecular-weight fraction [13].

In turn, the revealed increase in the softening point may be due to the more ordered structure of oligoamide macromolecules formed by low-temperature polycondensation, because, as already noted, the probability of degradation processes is reduced to a minimum in this case.

CONCLUSIONS

(1) Dichloride of dimerized fatty acid was prepared and characterized (yield 95.6%).

(2) A procedure was developed for preparing oligoamides by low-temperature reaction of the dichloride of dimerized fatty acid with di- and triamines. Small deviations of the reactant ratio from the stoichiometry do not noticeably affect the molecular weight and softening point of the oligoamides obtained.

(3) The use of trifunctional diethylenetriamine leads to cross-linking of the oligomer.

REFERENCES

1. Fomina, E.V., Chervyakova, G.N., Kurskii, Yu.A., and Sineokov, A.P., *Zh. Prikl. Khim.*, 2005, vol. 78, no. 7, pp. 1142–1145.
2. Fomina, E.V., Kurskii, Yu.A., Beloded, L.N., and Chervyakova, G.N., *Zh. Prikl. Khim.*, 2006, vol. 79, no. 5, pp. 787–791.
3. RF Patent 2237697.
4. FRG Patent Appl. 4408277.
5. Kochnova, Z.A., Zhavoronok, E.S., and Chalykh, A.E., *Epoksidnye smoly i otverditeli: promyshlennye produkty* (Epoxy Resins and Hardeners: Commercial Products), Moscow: Peint-Media, 2006.
6. Popova, T.A., Zhilina, N.V., Rodivilova, L.A., et al., *Proizvodstvo oligoamidov za rubezhom: Obzornaya informatsiya* (Production of Oligomers Abroad: Review), *Ser.: Plasticheskie massy i sinteticheskie smoly* (Plastics and Synthetic Resins), Moscow: NIITEKhIM, 1979.

7. Fomina, E.V. and Sineokov, A.P., Abstracts of Papers, *XVIII Mendeleevskii s″ezd po obshchei i prikladnoi khimii* (XVIII Mendeleev Congr. on General and Applied Chemistry), Moscow, September 23–28, 2007, vol. 1, p. 489.
8. Toroptseva, A.M., Belogorodskaya, K.V., and Bondarenko, V.M., *Laboratornyi praktikum po khimii i tekhnologii vysokomolekulyarnykh soedinenii* (Practical Laboratory Course of Chemistry and Technology of Macromolecular Compounds), Leningrad: Khimiya, 1972.
9. Kushnir, S.R., Borisova, N.V., Radbil', A.B., et al., *Zh. Prikl. Khim.*, 2003, vol. 76, no. 11, pp. 1845–1847.
10. Aslanov, T.A., Salakhov, M.S., and Efendiev, A.A., *Vysokomol. Soedin., Ser. B*, 2005, vol. 47, no. 3, pp. 534–538.
11. Aslanov, T.A., Salakhov, M.S., and Efendiev, A.A., *Vysokomol. Soedin., Ser. B*, 2005, vol. 47, no. 11, pp. 2043–2044.
12. Korshak, V.V. and Frunze, T.M., *Sinteticheskie geterotsepnye poliamidy* (Synthetic Heterochain Polyamides), Moscow: Akad. Nauk SSSR, 1962.
13. Morgan, P.W., *Condensation Polymers: By Interfacial and Solution Methods*, New York: Wiley–Interscience, 1965.
14. Sokolov, L.B., Gerasimov, V.D., Savinov, V.M., and Belyakov, V.K., *Termostoikie aromaticheskie poliamidy* (Heat-Resistant Aromatic Polyamides), Moscow: Khimiya, 1975.

ISSN 1070-4272, Russian Journal of Applied Chemistry, 2008, Vol. 81, No. 4, pp. 663–667. © Pleiades Publishing, Ltd., 2008.
Original Russian Text © Yu.N. Biglova, R.Kh. Yumagulova, S.V. Kolesov, Yu.B. Monakov, 2008, published in Zhurnal Prikladnoi Khimii, 2008, Vol. 81, No. 4, pp. 627–631.

MACROMOLECULAR CHEMISTRY AND POLYMERIC MATERIALS

Effect of Fullerene C_{60} on Copolymerization Parameters of Methyl Methacrylate with Compounds Containing Allyl Bond

Yu. N. Biglova, R. Kh. Yumagulova, S. V. Kolesov, and Yu. B. Monakov

Institute of Organic Chemistry, Ufa Scientific Center, Russian Academy of Sciences, Ufa, Bashkortostan, Russia

Received August 13, 2007

Abstract—The effect of fullerene C_{60} on copolymerization of methyl methacrylate with compounds, one of which is a typical allyl monomer and the other is a vinyl monomer with a side allyl bond, was examined. The kinetic parameters of the reactions and the copolymerization constants of monomers in the absence and in the presence of fullerenes were determined. Based on the UV spectrometric data, the material balance was calculated and a variation of the molar extinction coefficient of fullerene was revealed.

DOI: 10.1134/S1070427208040186

The synthesis of practically important fullerene-containing polymers requires solving many problems. In view of the fact that these macromolecular compounds well combine the characteristics of both polymers and fullerenes, procedures for introduction of fullerenes into the composition of polymer chains are being actively developed [1–3].

Fullerene can be introduced into both the main chain and side chain by radical copolymerization of vinyl and allyl monomers of various structures. As a consequence, the resulting substances have the characteristics that strongly differ from those of the initial substances. The presence of a covalently bonded fullerene affects the size and shape of a polymer globule as a whole and fundamentally changes the optical and dielectric characteristics of macromolecules [4].

Highly symmetric fullerene molecules are also widely used as structural units of polymer chains in synthesis of macromolecular products [5, 6].

Here, we discuss the common and specific features of the influence of fullerene C_{60} on the radical copolymerization of methyl methacrylate (MMA) with allyl methacrylate (AMA) and allyl chloride (AC) on the basis of the kinetic dependences, composition of copolymers, and data of UV spectroscopy and gel chromatography.

EXPERIMENTAL

Methyl and allyl methacrylates were purified to remove the stabilizing agent with an 8% KOH solution, washed with water to neutral reaction, dried with $CaCl_2$, and twice distilled in a vacuum. For polymerization, we took a fraction of MMA with bp 48°C/70 mm Hg and AMA with bp 73°C/53 mm Hg. Allyl chloride was purified by distillation at atmospheric pressure in an inert medium, bp 44°C. Benzoyl peroxide was three times recrystallized from methanol and dried in a vacuum at room temperature to constant weight, mp 108°C (with decomposition). In all the experiments, the initiator concentration was the same: 2.0×10^{-2} M.

The copolymerization was performed in the bulk at 60 ± 0.05°C. The process kinetics was studied by the dilatometric method [7]. Fullerene C_{60} was used in the form of a saturated solution in *o*-dichlorobenzene ($[C_{60}] = 9.3 \times 10^{-3}$ M).

The content of C_{60} in the samples was measured by UV spectroscopy on a Shimadzu UV VIS NIR 3100 device, using chloroform as a solvent. The molar extinction coefficients of fullerenes at the absorption peaks, ε, were determined from the calibration dependences of the optical density on the concentration of the solutions with $[C_{60}] = 2.0 \times 10^{-4}$–$2.0 \times 10^{-5}$ M, which had the optical density of 3.6 and lower in the transparency range of chloroform, 250–750 nm. We also found the ε values of monomers at the wavelengths of the absorption peaks of C_{60}. The 7.0×10^{-4}–5.0×10^{-5} M solutions of the monomers in the range of the main absorption peak of C_{60} in chloroform λ_{350nm} had the optical density of 0.095 and lower.

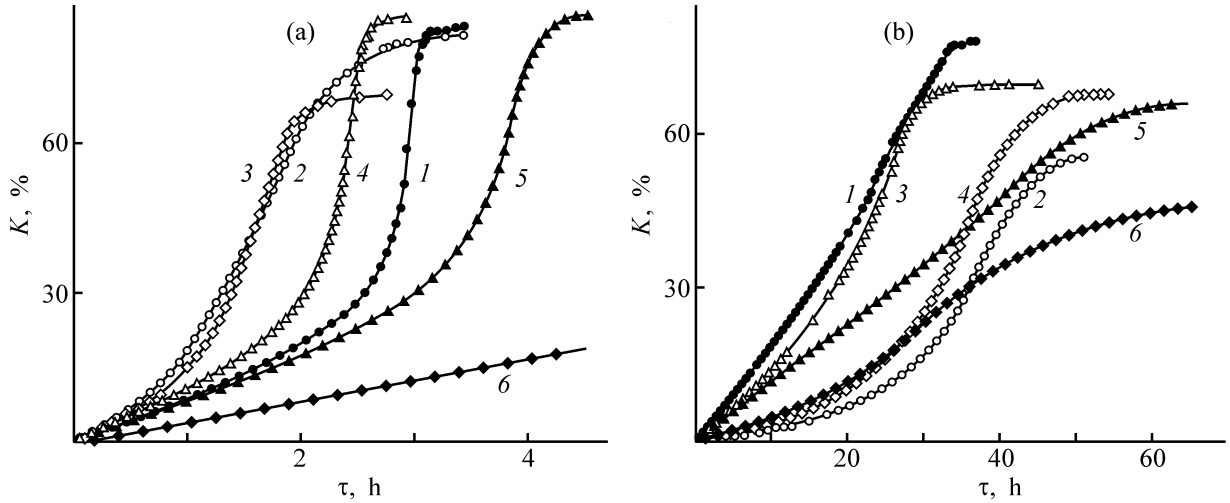


Fig. 1. Degree of conversion, K, of the monomer mixture vs. time τ in copolymerization of MMA with AC and AMA (a) in the absence and (b) in the presence of 2.25×10^{-3} M fullerene C_{60}. (*1*, *4*) AMA and (*5*, *6*) AC. Content in the initial mixture, mol %: (*1*) 0, (*2*, *5*) 10, (*3*, *6*) 50, and (*4*) 100.

The molecular-weight characteristics were determined by gel permeation chromatography. The analysis were performed on a Waters Alliance^{TM} GRC 2000 Systems liquid chromatograph at 30°C at a solvent flow rate of 1 ml min^{-1}. Tetrahydrofuran was used as an eluent. For calibration of the columns, we used close-cut polystyrene references.

In copolymerization of methyl and allyl methacrylates in the absence of fullerene, the process rate increases with the mole fraction of AMA in the initial mixture (Fig. 1a, curves *3*, *4*), which results in the onset of gel effect in earlier stages of conversion. It should be noted that the homo- and copolymerization of allyl methacrylate is accompanied by cross-linking via side allyl groups [8], contributing to an increase in the coefficient of contraction. As a result, an apparent increase in the copolymerization rate with the content of AMA in the reaction mixture is observed.

In the reaction of MMA with AC in the absence of fullerene, an increase in the amount of the allyl component in the reaction mixture leads to a decrease in the process rate (Fig. 1a, curve *6*), typical of copolymerization of allyl compounds, due to the increasing contribution of "allyl additions" [9]. The gel effect is less pronounced in this case, and at equimolar and higher content of AC it is absent at all.

At a fixed concentration of fullerene C_{60}, an increase in the mole fraction of both AMA (Fig. 1b, curves *3*, *4*) and AC (Fig. 1b, curves *5*, *6*) leads to a decrease in the copolymerization rate. However, the course of the process has its own features in each case.

In copolymerization of MMA with AMA, the degree of cross-linking of macrochains decreases owing to the reaction of allyl radicals of the side chain with fullerene and, correspondingly, the yield of the soluble polymer increases. However, steric hindrance is possible in the formation of macromolecules, which apparently results in that the process rate decreases as the content of the allyl ester increases. Just this factor is apparently responsible for the significant difference in the kinetic features of homopolymerization of allyl and methyl methacrylates in the presence of fullerene. The structure of fullerene-containing copolymers of the above compounds can be characterized as "a bracelet with pendants."

In copolymerization with the allyl monomer (Fig. 1b, curves *5*, *6*), the decrease in the rate with increasing content of AC in the reaction system is less significant than that with AMA. This is apparently caused by the high electron-acceptor power of the product formed in the reaction of the allyl monomer with fullerene and involved in the polymerization process. In copolymerization of MMA with AC, fullerene enters into the main chain of the copolymer, but formation of branched structures as a result of addition of propagating chains to C_{60} is not excluded.

The kinetic parameters of copolymerization are listed in Table 1. The results obtained suggest that the reaction orders with respect to initiator and the sum of monomers do not noticeably vary and correspond to the characteristics of the radical processes. Nevertheless, the apparent rate constant decreases and the activation energy of copolymerization increases in the presence of fullerene C_{60}. For AMA, E_a

Table 1. Kinetic parameters of radical copolymerization of methyl methacrylate with allyl chloride and allyl methacrylate*

Comonomer	C_{60}	$k_{app} \times 10^3$, $l\ mol^{-1}\ s^{-1}$	Order		E_a, kJ mol^{-1}	Copolymerization constant
			with respect to initiator	with respect to monomer		
AC	No	1.37. + 0.21	0.6	1.0	81.6. + 4.0	$r_{MMA} = 48.47 + 3.35$ $r_{AC} = 0.038 \pm 0.011$
	Yes	0.13. + 0.03	0.5	1.2	92.8. + 6.0	$r_{MMA} = 2.17 \pm 0.98$ $r_{AC} = 0.43 \pm 0.28$
AMA	No	3.21. + 0.24	0.5	1.1	69.0. + 3.5	$r_{MMA} = 1.01 + 0.46$ $r_{AMA} = 0.79 \pm 0.35$
	Yes	0.31. + 0.03	0.5	0.8	137.0. + 11.0	$r_{MMA} = 0.58 \pm 0.29$ $r_{AMA} = 1.54 \pm 0.87$

* For PMMA, $E_a = 70.4$ kJ mol^{-1}, $k_{app} = (0.45 \pm 0.05) \times 10^{-2}$ $l\ mol^{-1}\ s^{-1}$.

increases particularly strongly, which is typical of polyfunctional compounds [10].

The results of kinetic studies are in good agreement with the data obtained when studying the composition of copolymers and with experimental values of copolymerization constants (Table 1).

The behavior of AMA and AC in copolymerization is governed by their activity. According to these data, in copolymerization without fullerene, allyl and methyl methacrylates are involved to the same extent in formation of the polymer chain, and in the case of AC, the copolymers are enriched in methyl methacrylate, which is confirmed by the composition curves (Fig. 2, curves *1a*, *2a*). It is seen that, in copolymerization of two vinyl compounds with the relative activities close to 1 (Table 1), the composition of the copolymers virtually coincides with the composition of the monomer mixture.

In the presence of fullerene, the fraction of allyl (Fig. 2, curve *2a*) and vinyl (with allyl group) monomers (Fig. 2, curve *1a*) in the copolymerization products increases, which is apparently caused by the reaction of the allyl radicals with C_{60}. As a result, the relative activities of the compounds with the allyl bond grow (Table 1). In this case, the copolymerization constant of AC varies most strongly.

The presence of covalently bonded fullerene in the macromolecule composition is confirmed by the UV data.

Each event of C_{60} involvement in the radical process results in rupture of a π bond and addition of a radical to the fullerene core [11]. The total number of ruptured π bonds can be judged quantitatively from the optical densities at the π–π^* absorption peaks of fullerene ($\lambda_{max} = 330$ nm) in the electronic absorption spectra of the products isolated in the course of synthesis. In copolymerization of MMA with AMA and AC in the presence of fullerene, the optical density of the π–π^* absorption of C_{60} ($\lambda = 330$ nm) decreases with increasing degree of conversion of the initial monomer mixture.

The complete entering of fullerene into the polymer chain was confirmed on the basis of the material balance of the reaction. An increase in the mole fraction of AMA and AC in the initial mixture results in a decrease in the fullerene content in the precipitant solu-

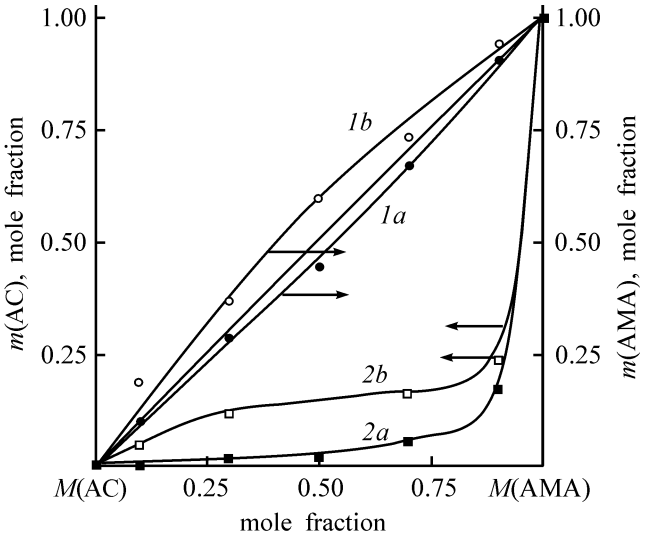


Fig. 2. Composition curves for copolymers of MMA with (*1*) AMA and (*2*) AC (*a*) in the absence and (*b*) in the presence of 2.25×10^{-3} M fullerene C_{60}.

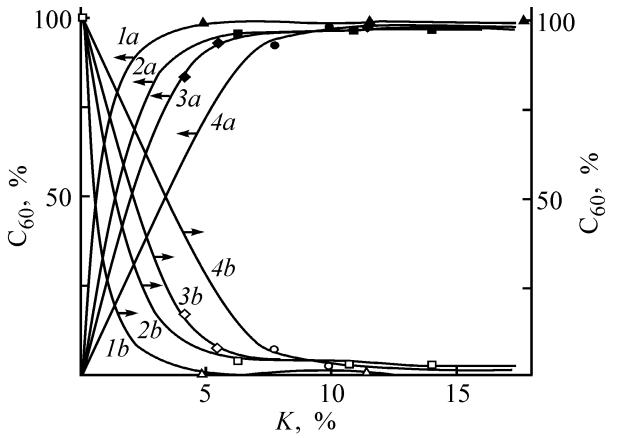


Fig. 3. Content of fullerene C_{60} (*a*) in copolymers of MMA with AMA and AC and (*b*) in the mother liquor for the samples with various degrees of conversion of the monomer mixture *K*. (*1*, *2*) AMA and (*3*, *4*) AC. Content in the initial mixture, mol %: (*1*, *4*) 10 and (*2*, *3*) 50.

tion (mother liquor) (Fig. 3, curve *2*) and a faster increase in the amount of fullerene in the reaction products (Fig. 3, curve *1*). It is important that involvement of the compounds with allyl bonds into copolymerization with MMA allows introduction of fullerene into the polymer chain in concentrations of up to 4.5×10^{-2} mol per mole of copolymer even in earlier stages of conversion of the monomer mixture (up to 10%). At the same time, the content of C_{60} in PMMA is only 3.0×10^{-3} mol per mole.

An algorithm that involves a system of equations with three unknowns and allows parallel determination of both the true extinction coefficient of fullerene and the amount of C_{60} in the resulting polymer in the mother residue was developed. An important result is that variation of the molar extinction coefficient was revealed, which decreases with increasing number of fragments joined to the C_{60} core and mole fraction of AMA and AC in the reaction mixture.

A study of the molecular-weight characteristics demonstrated that, in the absence of fullerene in the examined range of conversion, the molecular weight (MW) of copolymers of MMA with AMA does not noticeably depend on the content of their monomers in the initial mixture. The molecular weight of copolymers with AC decreases as its content in the polymerization system increases (Table 2). The dynamics of formation of macromolecules in the presence of fullerene has some features. Contrary to the stationary dependences typical of the reactions of radical homo- and copolymerization, the MW increases in the presence of C_{60} virtually during the entire process. This

Table 2. Molecular characteristics of copolymers of methyl methacrylate with allyl chloride and allyl methacrylate

Comonomer, mol %	Degree of conversion of monomer mixture, %	$M_n \times 10^{-3}$	$M_w \times 10^{-3}$	M_n / M_w
AC:				
10	5	225/75*	422/106	1.9/1.4
	10	228/77	452/109	2.0/1.4
	20	243/96	551/137	2.3/1.4
	30	256/109	568/156	2.2/1.4
	40	264/114	613/163	2.3/1.4
50	5	69/31	107/44	1.6/1.4
	10	76/35	121/47	1.6/1,4
	20	82/49	127/69	1.6/1.4
	30	84/60	132/84	1.6/1.4
	40	88/70	138/97	1.6/1.4
AMA:				
10	5	915/81	372/130	2.5/1.6
	10	1365/90	421/145	3.2/1.6
	15	c.c.**/120	c.c./140	c.c./2.0
50	5	2645/54	430/87	6.1/1.6
	10	c.c./67	c.c./122	c.c./1.8
	15	c.c./79	c.c./163	c.c./2.1

* Without fullerene/in the presence of 2.25×10^{-3} M fullerene C_{60}.

** Network structures are formed.

is apparently caused by addition of propagating chains to fullerene, which results in a decreasing concentration of radicals in the system. Therefore, the polydispersity of fullerene-containing samples is lower.

CONCLUSIONS

(1) The copolymerization reactions in the presence of fullerene C_{60} have some common and specific features. The common trend is the inhibiting influence of fullerene, which is manifested differently, depending on comonomers.

(2) For the systems studied, the reaction orders with respect to the initiator and to the sum of the monomers correspond to the parameters of radical processes. In the presence of fullerene C_{60}, the activation energy increases for both systems, but to different extents: in the case of copolymerization of vinyl monomers, E_a increases by a factor of 2, and in the reaction with allyl chloride, by only 10 kJ mol^{-1}. Hence, incorporation of fullerene bound to an allyl compound into the polymer backbone is preferable in comparison with its addition to side allyl groups of the vinyl monomer. As a consequence, the mole fraction of allyl methacrylate in the reaction products increases by only a factor of 1.5, and the fraction of allyl chloride, by an order of magnitude.

(3) The molecular weight and polydispersity of fullerene-containing copolymers of allyl methacrylate and allyl chloride decrease in both cases. The most significant change in the molecular weight was found for the system with allyl methacrylate (by a factor of 10), and in the system with allyl chloride it decreased by a factor of 3.

(4) In the case of allyl methacrylate, fullerene C_{60} enters into the polymer chain at lower degrees of conversion.

ACKNOWLEDGMENTS

This study was financially supported by the Foundation for Support of Leading Scientific Schools (project no. NSh-9342.2006.3) and by the Russian Foundation for Basic Research (project no. 0.7-03-00272-a).

REFERENCES

1. Lee, T.-W., Park, O.O., Kim, J., and Kim, Y.C., *Chem. Mater.*, 2002, vol. 14, p. 4281.
2. Armaroli, N., Marconi, G., Echegoyen, L., et al., *Chem. Eur. J.*, 2000, vol. 6, p. 1629.
3. Nierngarten, J.-F., Armaroli, N., Accorci, G., et al., *Chem. Eur. J.*, 2003, vol. 9, pp. 36–41.
4. Ryumtsev, E.I., Evlampieva, N.P., Nazarova, O.V., et al., *Dokl. Ross. Akad. Nauk*, 2003, vol. 392, no. 2, p. 212.
5. Chen, Y., Huang, Z.-E., Cai, R.-F., and Yu, B.-Ch., *Eur. Polym. J.*, 1998, vol. 34, no. 2, pp. 137–151.
6. Karpacheva, G.P., *Vysokomol. Soedin., Ser. C*, 2000, vol. 42, no. 11, pp. 1974–1999.
7. Gladyshev, G.P., *Polimerizatsiya vinilovykh polimerov* (Polymerization of Vinyl Monomers), Alma-Ata: Akad. Nauk Kaz. SSR, 1964.
8. Vorob'eva, A.I., in *Khimiya i fizicheskaya khimiya vysokomolekulyarnykh soedinenii* (Chemistry and Physical Chemistry of Macromolecular Compounds), Ufa: Bashk. Filial Akad. Nauk SSSR, 1987, pp. 32–42.
9. Gindin, L., Medvedev, S., and Fleshler, E., *Zh. Obshch. Khim.*, 1949, vol. 19, no. 9, pp. 1694–1701.
10. Nikiforenko, V.S., Zaitsev, Yu.S., Zaitseva, V.V., et al., *Dokl. Akad. Nauk SSSR*, 1988, vol. 300, no. 2, pp. 400–403.
11. Yumagulova, R.Kh., Biglova, Yu.N., Kuznetsov, S.I., et al., *Izv. Vyssh. Uchebn. Zaved., Khim. Khim. Tekhnol.*, 2007, vol. 50, no. 6, pp. 62–64.

ISSN 1070-4272, Russian Journal of Applied Chemistry, 2008, Vol. 81, No. 4, pp. 668–671. © Pleiades Publishing, Ltd., 2008.
Original Russian Text © L.B. Yakimtsova, E.L. Egorova, E.A. Murashko, Yu.I. Matusevich, A.P. Polikarpov, L.P. Krul', 2008, published in Zhurnal Prikladnoi Khimii, 2008, Vol. 81, No. 4, pp. 632–635.

MACROMOLECULAR CHEMISTRY AND POLYMERIC MATERIALS

Thermomechanical Properties and Heat Resistance of Copolymers of Methyl Methacrylate with Acrylic Acid

L. B. Yakimtsova, E. L. Egorova, E. A. Murashko, Yu. I. Matusevich, A. P. Polikarpov, and L. P. Krul'

Belarussian State University, Minsk, Belarus

Research Institute of Physicochemical Problems, Belarussian State University, Minsk, Belarus

Institute of Physical Organic Chemistry, National Academy of Sciences of Belarus, Minsk, Belarus

Received June 18, 2007

Abstract—Copolymers with a mole fraction of acrylate units of 0.20 to 0.69 were prepared by radical copolymerization of methyl methacrylate with acrylic acid. The heat resistance and thermomechanical properties of copolymer films formed from dimethylformamide solution were evaluated, and the possibilities of improving these characteristics were demonstrated.

DOI: 10.1134/S1070427208040198

Thanks to high light transmittance, polymeric compounds based on poly(methyl methacrylate) (PMMA) are widely used in optical systems for information recording, but their applicability is restricted by the relatively low glass transition and flow points of methyl methacrylate (MMA) polymers and the insufficient adhesion of the material to silicate glasses. In this context, an urgent problem is modification of PMMA properties with the aim to improve its thermomechanical properties and enhance the heat resistance and adhesion, with preservation of the optical transparency. It has been found previously [1, 2] that materials with the required characteristics can be obtained by radical copolymerization of MMA with acrylic acid (AA). However, the dependence of the properties of the copolymers (CPs) on their composition has not been studied.

In this study we examined how the composition of MMA–AA copolymers affects their thermal properties.

EXPERIMENTAL

Radical copolymerization in the bulk was performed in a nitrogen flow at 60°C for 4 h in a glass test tube equipped with a reflux condenser [3]. The AA : MMA molar ratio was varied from 1 : 4 to 4 : 1. As initiator we used 2,2'-azobis(isobutyronitrile). After the synthesis completion, the polymer sample was ground and washed at room temperature with water and ethanol to remove the unchanged monomers and a part of AA homopolymer. Then the sample was dried and dissolved in dimethylformamide (DMF). The solution was passed through a glass frit, after which the copolymerization product was precipitated from the solution into water. A small amount of PMMA, which is insoluble in DMF, remained on the filter. The AA homopolymer remained in the CP precipitant. The CP composition was determined by acid–base titration of carboxy groups in organic solvents.

Poly(methyl methacrylate) and polyacrylic acid (PAA) were prepared under the same conditions as the MMA–AA copolymer. The molecular weights (MW) of PMMA and PAA were determined viscometrically in trichloromethane at 25°C ($K = 0.48 \times 10^{-4}$, $a = 0.80$; MW $= 3.85 \times 10^5$) and in water at 30°C ($K = 7.6 \times 10^{-4}$, $a = 0.5$; MW $= 1.62 \times 10^6$), respectively. To estimate the lengths of molecular chains in CPs of various compositions at 25°C, we measured the specific viscosities of their 0.5% solutions in a common solvent, acetic acid.

The thermal properties of the CPs were studied using film samples prepared from DMF solutions. Because of the high adhesion to glass, the films could not be detached from glass supports. Therefore, when preparing film samples for studying the thermal properties of the CPs, we used as supports polypropylene

plates. After solvent evaporation, transparent polymer films were obtained. They could be readily separated from the surface of the polypropylene plates. To remove residual DMF, the films were repeatedly washed with distilled water.

The thermal properties of MMA–AA were studied by the methods of combined thermal and thermomechanical analysis. A combined thermal analysis was performed on an OD-103 derivatograph (MOM, Hungary). The TG, DTG, and DTA curves were recorded in air at a heating rate of 5 deg min^{-1}. The sample weight was 100 mg. From the TG curves, we determined the temperatures T_5 and T_{10} corresponding to 5 and 10% weight loss, respectively. From the position of the minimum in the DTG curves, we determined the temperature of the maximal degradation rate, T_m.

The thermomechanical analysis was performed with a UIP-70 device (Central Design Office with Pilot Plant, USSR Academy of Sciences) in air at the same heating rate. A pressure of 0.59 MPa was applied to the sample. The film thickness was 50–90 μm. The thermomechanical properties were evaluated from the curves of the relative punching strain ε (%) vs. temperature T (°C).

Analysis of the chemical composition of the CPs (Table 1) showed that it coincided with the composition of the monomer mixture up to AA mole fraction in the mixture equal to 0.2. With a further increase in the AA content of the monomer mixture, the CP became depleted of AA units.

Solubility tests of the CPs in various organic solvents (acetone, ethanol, 1,4-dioxane, aromatic and chlorinated hydrocarbons, acetic acid, DMF) showed that the CPs dissolve to give concentrated solutions only in DMF and glacial acetic acid. Poly(methyl methacrylate) forms in these solvents only dilute solutions.

Table 1. Resistance of MMA–AA copolymers to thermal oxidative degradation

Mole fraction		T_5	T_{10}	T_m
AA in monomer mixture	AA units in CP	°C		
0	0	161	182	283
0.2	0.20	239	267	390
0.3	0.24	240	272	380
0.4	0.28	259	280	387
0.5	0.34	240	270	380
0.6	0.40	233	261	375
0.7	0.60	161	185	380
0.8	0.69	135	168	380
1.0	1.0	131	159	255

Figure 1 shows that, as the mole fraction of AA units in the CP is raised to approximately 0.3 (monomer molar ratio AA : MMA = 1 : 1.5), the specific viscosity of the CP increases relative to PMMA. As the mole fraction of AA units is raised further, the viscosity decreases, and, at the mole fraction of AA units equal to 0.69, becomes equal to the specific viscosity of PAA. Apparently, variation of the monomer ratio in the course of the CP synthesis was accompanied by variation of not only the chemical composition but also the polymer chain length, with the maximal chain length attained at approximately equimolar ratio of the monomers.

The thermogravimetric curves of MMA and AA homopolymers and of MMA–AA copolymers of various compositions (Fig. 2) show that the weight

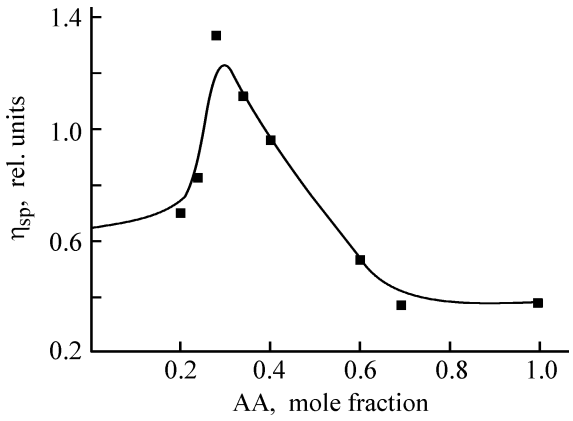


Fig. 1. Specific viscosity η_{sp} of 0.5% solutions of homo- and copolymers of MMA and AA in acetic acid vs. the mole fraction of AA units in CP.

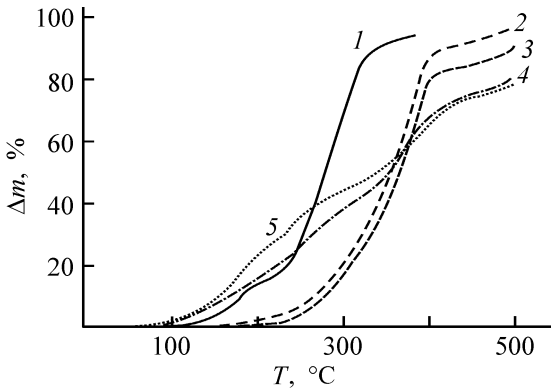


Fig. 2. Weight loss Δm vs. temperature T in thermal gravimetric analysis of (*1*) PMMA, (*2–4*) MMA–AA copolymers, and (*5*) PAA. Mole fraction of AA units in CP: (*2*) 0.20, (*3*) 0.28, and (*4*) 0.69.

Table 2. Glass transition and flow points of MMA–AA copolymers

Mole fraction of AA units in CP	T_g	T_f
	°C	
0	76	168
0.28	72	212
0.34	93	230
0.40	64	130
1.0	85	160

loss by the CPs may be either smaller or larger than the weight loss by the homopolymers, depending on the composition and temperature. For example, the weight loss by the CPs with the mole fraction of AA units equal to 0.20 and 0.28 (curves *2* and *3*, respectively) in the range from room temperature to 365–370°C is lower than the weight loss by PMMA (curve *1*) and PAA (curve *5*), and only at temperatures exceeding 370°C, the weight loss by the CPs becomes larger, compared to PAA, but remains smaller, compared to PMMA. At the mole fraction of AA units in the CP equal to 0.69, the weight loss in the range from 100 to 240–250°C (curve *4*) is smaller, compared to PAA (curve *5*), but larger, compared to PMMA (curve *1*). In the temperature range 250–500°C, the weight loss by the CP with a high content of AA units is smaller than that by PMMA and similar to that by PAA.

Thus, the CP with a relatively low content of AA units is the most resistant to thermal oxidative degradation. The observed effect is apparently associated with the decreased efficiency of cleavage of chemical bonds in the CP backbone, due to changes in the chemical nature of pendant functional groups in going from the homopolymers to CP. The low resistance to thermal oxidative degradation of the CP with a high content of AA units, compared to PMMA, in the range of up to 250°C is apparently caused by the possible decarboxylation of relatively long blocks of AA units. At temperatures exceeding 250–260°C, when the decarboxylation is complete and the observed weight loss is caused by the cleavage of chemical bonds in the CP backbone, the enhanced resistance of the copolymers to thermal oxidative degradation, compared to PMMA, is clearly manifested.

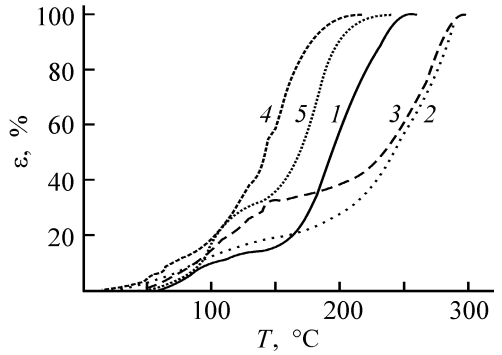


Fig. 3. Thermomechanical curves of (*1*) PMMA, (*2–4*) MAA–AA copolymers, and (*5*) PAA. (ε) Strain and (*T*) temperature. Mole fraction of AA units in CP: (*2*) 0.28, (*3*) 0.34, and (*4*) 0.40.

Data on the resistance of MMA–AA copolymers to thermal oxidative degradation (T_5, T_{10}, T_m) in relation to their composition are listed in Table 1. It can be seen that MMA and AA homopolymers show similar resistances to thermal oxidative degradation: For PMMA, T_5, T_{10}, and T_m are 161, 182, and 283°C, and for PAA, 131, 159, and 255°C, respectively. The MMA–AA copolymers with the mole fraction of AA units of 0.20 to 0.40 are more resistant to thermal oxidative degradation than PMMA and PAA. The largest values of T_5 and T_{10}, exceeding those of PMMA and PAA by almost 100°C, are attained at the mole fraction of AA units in the CP equal to 0.28, i.e., at the same copolymer composition at which the specific viscosity of 0.5% solutions of the CP in acetic acid becomes maximal. With a further increase in the mole fraction of AA units in CP to 0.60 and 0.69, T_5 and T_{10} dramatically decrease, approaching the values characteristic of PAA. It is important that the specific viscosity of 0.5% solutions of such CPs in acetic acid also becomes lower than that of the 0.5% PMMA solution. Therefore, apparently, the lower resistance to thermal oxidative degradation of the CP with a high content of AA units, observed in the initial steps of weight loss, may be due not only to possible decarboxylation of long blocks of AA units, but also to increased tendency of shorter CP chains to degrade. A certain contribution to the weight loss may also be made by removal of sorbed moisture whose amount increases with the content of AA units in the CP.

At high temperatures corresponding to active cleavage of chemical bonds in the backbone, the resistance of the CPs to thermal oxidative degradation is virtually independent of their composition. The temperature of the maximal degradation rate, T_m, of CPs fluctuates in the range 375–390°C as the mole fraction of AA units in the CP is varied from 0.20 to 0.69, whereas for PMMA, T_m is 283, and for PAA, 255°C.

The thermomechanical curves of PMMA, PAA, and MMA–AA copolymers are shown in Fig. 3, and the temperatures of transitions from one relaxation state to another are listed in Table 2. As can be seen from

Fig. 3, the thermomechanical curve of PMMA is typical of amorphous polymers. The temperature ranges corresponding to glassy, hyperelastic, and viscous-flow states can be distinguished. The temperatures of transitions from glassy to hyperelastic (glass transition point, T_g) and from hyperelastic to viscous-flow states (flow point, T_f) for PMMA are 76 and 168°C, respectively (Table 2). The thermomechanical curve of PAA is also typical of an amorphous polymer and is characterized by the temperatures T_g and T_f close to those of PMMA: 85 and 160°C, respectively.

The thermomechanical curves of MMA–AA copolymers do not differ essentially from those of PMMA and PAA. However, their position on the temperature scale relative to the curves of the homopolymers depends on the CP composition. The thermomechanical curves of CP samples with a AA mole fraction equal to 0.28 and 0.34 are shifted toward higher temperatures relative to the homopolymers. The glass transition points T_g of the CPs of these compositions are close to those of MMA and AA, whereas the flow points T_f exceed those of the homopolymers by more than 40°C. At the same time, the thermomechanical curve of the CP sample with a AA mole fraction equal to 0.40 is shifted toward lower temperatures, and T_g and T_f become lower than those of the homopolymers. Apparently, the sharp decrease in the flow point of the CP with a AA mole fraction equal to 0.40 is due to the short chain length (Fig. 1).

CONCLUSIONS

(1) Resistance to thermal oxidative degradation of methyl methacrylate–acrylic acid copolymers with the mole fraction of acrylic acid units of 0.20 to 0.40 exceeds that of the corresponding homopolymers. The heat resistance enhancement takes place for the step of cleavage of chemical bonds in the macromolecular backbone.

(2) The dependences of the glass transition and flow points of the methyl methacrylate–acrylic acid copolymers on the copolymer composition pass through a maximum at the mole fraction of acrylic acid units equal to 0.34.

REFERENCES

1. Krul, L.P., Matusevich, Yu.I., Matusevich, V.Yu., et al., *STEPI 7: 7th European Technical Symp. on Polyimides and High Perfomance Functional Polymers*, Montpellier (France), 2005, 2 S.T.L., p. 163.
2. Butovskaya, G.V., Matusevich, Yu.I., Matusevich, V.Yu., et al., *Mater. Tekhnol. Instr.*, 2006, vol. 11, no. 1, pp. 55–59.
3. *Praktikum po vysokomolekulyarnym soedineniyam* (Practical Course of Macromolecular Compounds), Kabanov, V.A., Ed., Moscow: Khimiya, 1985.

ISSN 1070-4272, Russian Journal of Applied Chemistry, 2008, Vol. 81, No. 4, pp. 672–675. © Pleiades Publishing, Ltd., 2008.
Original Russian Text © K.G. Guliev, 2008, published in Zhurnal Prikladnoi Khimii, 2008, Vol. 81, No. 4, pp. 636–639.

MACROMOLECULAR CHEMISTRY AND POLYMERIC MATERIALS

Synthesis of 2-Formyl-1-(*p*-vinylphenyl)cyclopropane and Its Polymerization and Copolymerization with Styrene

K. G. Guliev

Institute of Polymeric Materials, National Academy of Sciences of Azerbaijan, Sumgaiyt, Azerbaijan

Received July 5, 2007

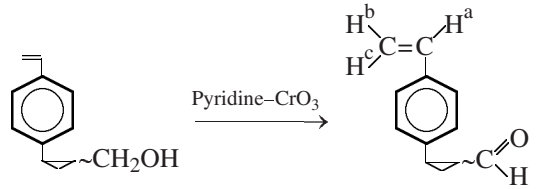
Abstract—2-Formyl-1-(*p*-vinylphenyl)cyclopropane was prepared, and its homopolymerization and copolymerization with styrene were performed. The effect of the substituent on the monomer reactivity and the photosensitivity of the copolymer obtained were examined.

DOI: 10.1134/S1070427208040204

Functional polymers find growing use in microelectronics owing to their high heat resistance, good electrical properties, and high deformation-and-strength characteristics. Such a set of properties makes some functional polymers useful for preparing protective and insulating layers in the production of microelectronic devices and circuits. A topological pattern is usually created in a polymer film by optical photolithography using a multilayer system of resists, or by appropriate modification of the polymer to make it photosensitive [1–5]. The latter alternative has a number of significant advantages, as it considerably simplifies and reduces the process of pattern formation and increases the resolving power of lithography.

The aim of this study was to prepare a new formyl-substituted cyclopropylstyrene monomer, 2-formyl-1-(*p*-vinylphenyl)cyclopropane (FVPC), and to examine its radical polymerization and copolymerization with styrene. We also intended to study systematically the influence exerted on the photosensitivity of cyclopropane-containing polymers by the substituent at the cyclopropane ring in the pendant chain of the macromolecule [6, 7].

2-Formyl-1-(*p*-vinylphenyl)cyclopropane is a new promising monomer for preparing polymers with valuable properties for microelectronics. FVPC was synthesized as follows. First, we prepared 2-ethoxycarbonyl-1-(*p*-vinylphenyl)cyclopropane. Then, this ester was reduced to 2-hydroxymethyl-1-(*p*-vinylphenyl)cyclopropane [8], which was subsequently oxidized to FVPC according to [9]:



The structure of the aldehyde prepared was determined from the IR and ^{1}H NMR spectra. The results of spectroscopic studies and GLC analysis show that FVPC is a mixture of two geometric isomers, *cis* and *trans*, in a 30 : 70 ratio.

The IR spectrum of FVPC shows absorption bands at 1635–1640, 1035–1045, 1500, and 1605 cm^{-1}, characteristic of the vinyl group in cyclopropane and benzene rings. It also contains a band at 3010 cm^{-1} characteristic of the aldehyde C–H bond and a band at 1709 cm^{-1} corresponding to the C=O group.

In the ^{1}H NMR spectrum, the vinyl proton signals are observed at 6.76 (H^a), 5.38 (H^b), and 5.80 ppm (H^c). The aromatic ring protons are manifested at 6.60–7.30 ppm. The aldehyde proton appears as a singlet at 9.1 ppm.

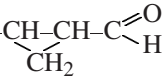
The vinyl proton signals are shifted downfield relative to unsubstituted styrene (H^a, 6.4; H^b, 5.11; H^c, 5.58 ppm). This shift is mainly caused by the mesomeric effect of substituents; specific distribution of the electron density in the cyclopropane ring also has a certain effect. The spectra suggest that all the synthesis steps leave the vinyl group and cyclopropane ring intact.

Copolymerization of FVPC (M_1) with styrene (M_2) in benzene at 333 K ($\Sigma[M] = 0.2$ M; 0.1% AIBN)

FVPC fraction in starting mixture, mol %	Yield, %	Aldehyde group, %	$[\eta]$, dl g^{-1}	Copolymer composition, mol %	
				m_1	m_2
90	12	15.5	1.19	92.19	7.81
75	8.5	13.67		81.10	18.9
50	10	10.6	1.08	63.97	37.03
25	80	7.06		41.86	58.14
10	7.5	3.79	1.05	22.48	77.52

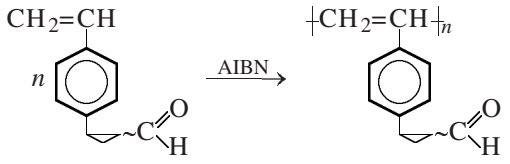
From the monomer synthesized, we prepared new homo- and copolymers. The FVPC polymerization was performed in the bulk and in benzene at 70°C in the presence of azobis(isobutyronitrile) (AIBN). Polymerization in the bulk yields 1–2 wt % of an insoluble fraction. In polymerization in solution, no insoluble fraction is formed. The polymerization occurs without induction period at a constant rate up to 85% conversion. The polymers after precipitation and drying to constant weight are white powders readily soluble in benzene, chloroform, and dimethylformamide.

The structure of the polymer was examined by IR and ^{1}H NMR spectroscopy, and the polymer composition was determined by elemental analysis.

We found that the radical polymerization occurs via vinyl groups with the formation of macromolecules containing  pendant fragments. This is confirmed by the fact that the cyclopropane ring and aldehyde group remain intact in the course of polymerization. Comparison of the IR spectra of the starting FVPC and polymer thereof shows that the positions and intensities of the absorption bands of the cyclopropane ring and aldehyde group do not change noticeably, whereas the bands of the vinyl group disappear. The same conclusion follows from the ^{1}H NMR spectra.

The ^{1}H NMR spectrum contains signals from protons of the benzene (δ 6.85–7.25 ppm) and cyclopropane (δ 0.75–1.75 ppm) rings. The aldehyde proton gives a signal at 9.1 ppm. The signals of the vinyl protons fully disappear.

The IR and ^{1}H NMR data suggest the following structure of the polymer:



To reveal specific features in the behavior of FVPC under the conditions of radical polymerization, we also studied its copolymerization with styrene.

The structures of copolymer macromolecules obtained at various conversions and containing units of both monomers in the macrochain were examined by IR spectroscopy. The IR spectra of copolymer samples prepared at various ratios of the starting monomers contain absorption bands of the aldehyde carbonyl group at 1709 cm^{-1} and bands of the cyclopropane ring at 1035–1040 cm^{-1}. Analytical data confirm the occurrence of the copolymerization. We found that the radical copolymerization of the starting monomers follows regular trends characteristic of vinyl monomers. The polymers prepared contain reactive formyl-substituted cyclopropane fragments in the pendant chains.

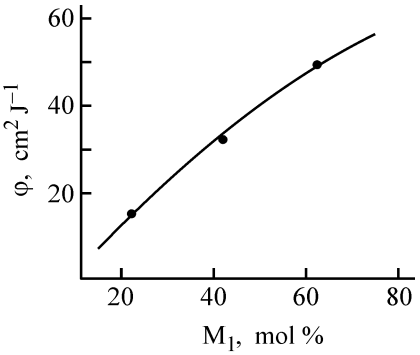
The ratio of styrene and FVPC monomer units in the copolymer macromolecule was determined by elemental analysis and titration of aldehyde groups. The results are listed in the table.

These data show that FVPC is a more active monomer than styrene.

The higher activity of FVPC, compared to styrene, also following from the calculated Fineman–Ross copolymerization constants [10] of FVPC, may be due to conjugation of the cyclopropane ring with an electron-withdrawing formyl substituent, which is consistent with the data of [11, 12]. The copolymerization constants, $r_1 = 1.25 \pm 0.025$ and $r_2 = 0.32 \pm 0.01$, demonstrate the effect of the carbonyl group in the monomer on the electronic structure of the whole molecule. This conclusion is consistent with the UV spectra in which the absorption peaks of FVPC and styrene are observed at essentially different wavelengths: 300 and 240 nm, respectively.

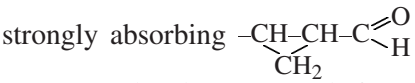
In the monomer, the vinyl group is activated and the protonating radical is stabilized by not only *–J*, but also *–M* effect of the aldehyde group.

Our results and published data suggest that this behavior of FVPC is primarily due to the effect of



Photosensitivity φ of copolymer of FVPC (M_1) with styrene vs. copolymer composition.

the cyclopropane ring directly bonded to the carbonyl group and apparently conjugated with the vinylphenyl group. Therefore, the FVPC molecule can be considered a common conjugated system.

The presence of strongly absorbing  groups in polymer macromolecules prepared from FVPC monomer makes these polymers suitable as a photosensitive base for photoresists. The two reactive groups in the pendant chains, cyclopropane and aldehyde, readily cleavable under irradiation, make the polymers highly sensitive to UV irradiation. Under UV irradiation, the polymers fairly readily transform into the insoluble form.

The decrease in the sensitivity of the absorption bands belonging to the cyclopropane and aldehyde groups in the initial steps of UV irradiation is insignificant. Upon longer UV irradiation (30 min), these absorption bands fully disappear. This fact indicates that the cyclopropane and aldehyde groups are involved in photochemical reactions apparently resulting in the photochemical cross-linking of the polymer.

Experiments showed that the presence of a three-membered ring and an aldehyde group, capable of opening and cross-linking under UV irradiation [13, 14], in the pendant chains of the polymers allows preparation of negative photoresists. The photosensitivity of the homopolymer prepared from FVPC is 56 $cm^2 J^{-1}$. As for the photosensitivity of the copolymers obtained, it depends on the copolymer composition and increases with the mole fraction of FVPC (see figure).

Also, it is possible to prepare from the polymers synthesized thin uniform coatings with low defectiveness and good adhesion to the support.

The polymers synthesized also open up wide prospects for chemical transformations of the aldehyde groups by reactions with, e.g., phenylhydrazine, hydrazine hydrochloride, or aniline with the aim to obtain polymers with required properties.

EXPERIMENTAL

2-Formyl-1-(*p*-vinylphenyl)cyclopropane was prepared by the reaction of 2-hydroxymethyl-1-(*p*-vinylphenyl)cyclopropane with a pyridine–CrO_3 complex solution (Sarett reagent) [9]; bp 88–90°C/1 mm Hg, n_D^{20} 1.5810, d_4^{20} 1.082, MR_D: calculated 52.15, found 52.98.

Found, %: C 83.52, H 6.35.

Calculated, %: C 83.72, H 6.98.

Homopolymerization of FVPC and its copolymerization with styrene were performed in the bulk and in a benzene solution at 333 K in the presence of AIBN. The molar ratios of the monomers are listed in the table. The reaction was performed in ampules under nitrogen for 3 h, after which the ampules were opened, and the product was precipitated with methanol, washed with methanol, and vacuum-dried at 40°C.

The content of aldehyde groups in the copolymer was determined by titration. A 0.2–0.3-g portion of the copolymer was dissolved in 10–15 ml of dimethylformamide. After the dissolution was complete, a 15-fold excess (by weight) of hydroxylamine hydrochloride in dimethylformamide was added. The mixture was allowed to stand for 2 h at room temperature. Then, 50 ml of distilled water was added. The precipitate was filtered off and washed once more on the filter with 50 ml of distilled water. Then, 0.8 ml of a 1% solution of Bromophenol Blue was added, and the solution was titrated with 0.1 N NaOH until the color became blue-green.

Photochemical cross-linking of the polymers was studied as described in [7].

The molecular weight of the homo- and copolymers was estimated from their intrinsic viscosity determined in benzene in an Ubbelohde viscometer at 20°C; for the homopolymer, $[\eta] = 1.03$ dl g^{-1}, and the values for the copolymer are listed in the table.

The IR spectra of the synthesized monomer and its homo- and copolymers were measured on a UR-20 spectrometer, and the ^1H NMR spectra, on a Tesla BS-487B spectrometer (80 MHz) in CCl_4. The purity of the compounds was determined by GLC on an LKhM-8MD chromatograph, model 3.

CONCLUSION

A new monomer, 2-formyl-1-(*p*-vinylphenyl)cyclopropane, its homopolymer, and copolymer with sty-

rene were prepared. The compounds show high photosensitivity due to the presence of cyclopropane and aldehyde groups in the macromolecule.

REFERENCES

1. Moreau, W.M., *Semiconductor Lithography. Principles, Practices, and Materials*, New York: Plenum, 1988.
2. Kubota, Sh., Moriwaki, T.A., and Fukami, A., *J. Appl. Polym. Sci.*, 1987, vol. 33, pp. 1763–1775.
3. Bulgakova, S.A., Mazonova, L.M., Lopatin, A.Ya., et al., *Vysokomol. Soedin., Ser. A*, 2004, vol. 46, no. 6, pp. 1052–1060.
4. USSR Inventor's Certificate, no. 622036.
5. Vannikov, A.V. and Grishina, A.D., *Vysokomol. Soedin., Ser. A*, 1990, vol. 32, no. 9, pp. 1811–1843.
6. Guliev, K.G., Ponomareva, G.Z., Nazaraliev, Kh.G., and Guliev, A.M., *Azerb. Khim. Zh.*, 2004, no. 4, pp. 168–172.
7. Guliev, K.G., Ponomareva, G.Z., and Guliev, A.M., *Zh. Prikl. Khim.*, 2006, vol. 79, no. 3, pp. 497–500.
8. Guliev, K.G., Nazaraliev, Kh.G., and Guliev, A.M., *Azerb. Khim. Zh.*, 1999, no. 1, pp. 87–90.
9. Sasaki, T., Eguchi, S., Ohno, M., and Umemura, T., *J. Org. Chem.*, 1973, vol. 38, pp. 4095–4100.
10. Toroptseva, A.M., Belogorodskaya, K.V., and Bondarenko, V.M., *Laboratornyi praktikum po khimii i tekhnologii vysokomolekulyarnykh soedinenii* (Practical Laboratory Course of Chemistry and Technology of Macromolecular Compounds), Leningrad: Khimiya, 1972.
11. Petukhov, V.A., Sein, U.I., Bolesov, I.G., and Levina, R.Ya., *Zh. Org. Khim.*, 1971, vol. 7, no. 8, p. 1626.
12. Feshin, V.P., Voronkov, M.G., Shostakovskii, S.M., et al., *Dokl. Akad. Nauk SSSR*, 1975, vol. 220, no. 6, p. 1380.
13. *Vvedenie v fotokhimiyu organicheskikh soedinenii* (Introduction to Photochemistry of Organic Compounds), Bekker, G.O. and El'tsov, A.V., Moscow: Khimiya, 1976.
14. Deboer, C.D.F., *J. Polym. Sci. Lett. Ed.*, 1973, vol. 11, no. 1, pp. 25–27.

ISSN 1070-4272, Russian Journal of Applied Chemistry, 2008, Vol. 81, No. 4, pp. 676–681. © Pleiades Publishing, Ltd., 2008.
Original Russian Text © S.E. Shakhovets, A.N. Ovechko, B.L. Smirnov, V.V. Bogdanov, 2008, published in Zhurnal Prikladnoi Khimii, 2008, Vol. 81, No. 4, pp. 640–644.

MACROMOLECULAR CHEMISTRY AND POLYMERIC MATERIALS

Influence of the Parameters of Integrated Mechanothermochemical Reclaiming on the Physicochemical Properties of Vulcanized Rubbers

S. E. Shakhovets, A. N. Ovechko, B. L. Smirnov, and V. V. Bogdanov

St. Petersburg State Institute of Technology (Technical University), St. Petersburg, Russia
ELAST-Tekhnologii Open Joint-Stock Company, St. Petersburg, Russia

Received May 23, 2007

Abstract—The influence of integrated reclaiming of vulcanized rubbers, combining the high-temperature mechanothermochemical and steam degradation methods, on the properties of reclaims was elucidated.

DOI: 10.1134/S1070427208040216

The existing methods for reclaiming of vulcanized rubber are underlain by breaking the cross-links. The available experience suggests that it is expedient to combine high-temperature mechanothermochemical and steam degradation methods in reclaiming [1, 2]. This not only provides a more extensive impact on the material being reclaimed but also excludes "harsh" modes of the process, resulting in an undesirably deep degradation.

From the economical viewpoint, the reclaiming technology is acceptable only if implemented in the continuous mode. This requirement can be satisfied with worm-gear machines. This inevitably generates a problem of intensive cooling of the equipment. At the same time, the closed design of worm-gear machines allows introduction into the processing zone of water which can, in parallel, act as a coolant and, via vaporization, as a degrading agent (the role of the latter can also be played by other substances, including those occurring in the liquid phase). Special worm-gear machines were designed for implementation of such processes [3]. They exhibit high performance characteristics with tire crumb as the raw material. The reason is twofold: This avoids emergency operation modes for the equipment in cases when foreign inclusions from vulcanized rubber pieces get into working heads, and the interface surface area between the material and the operating elements of the equipment is substantially increased, thereby providing uniform warming and uniform external impact on the material.

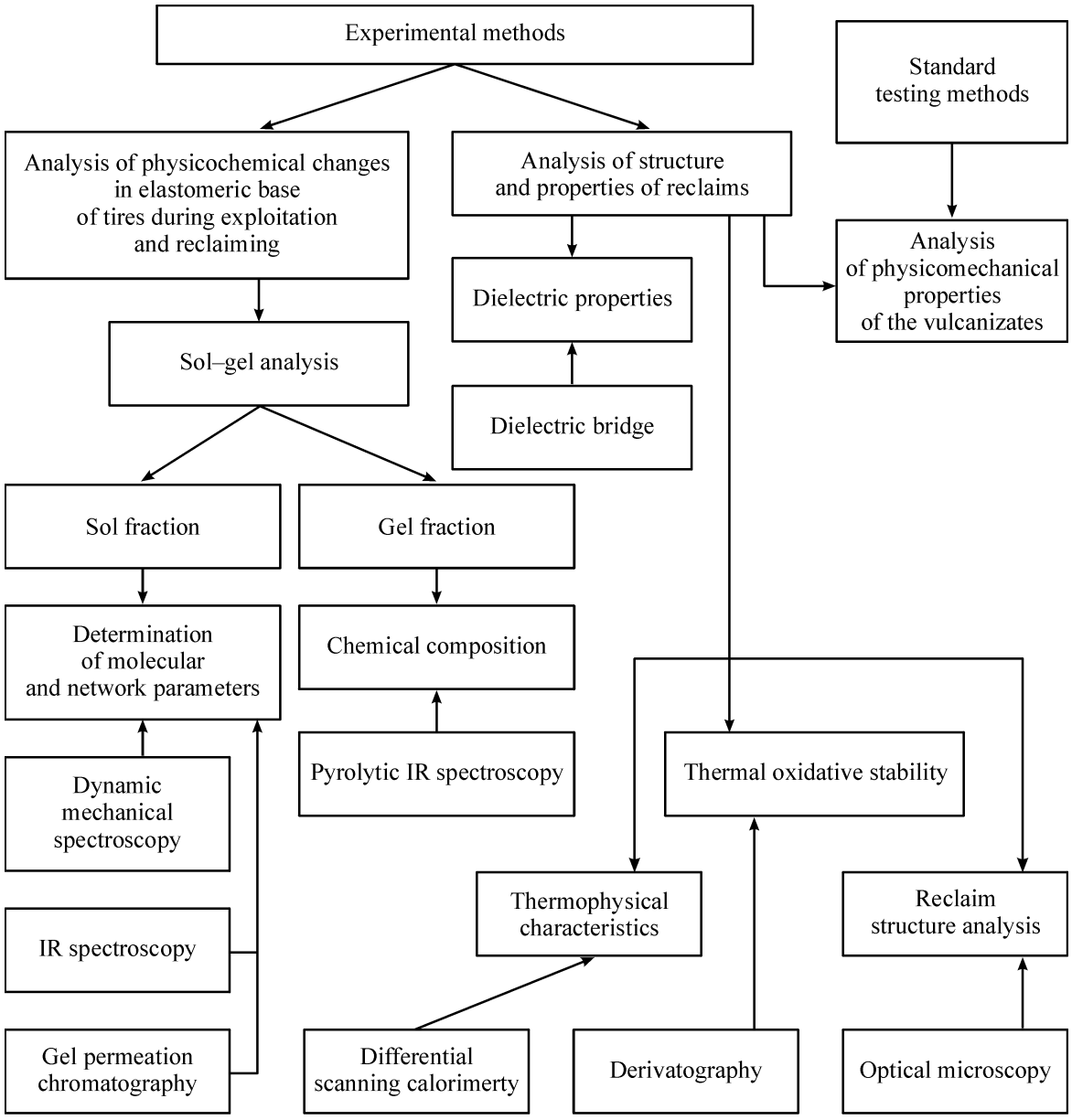
We estimated here the efficiency of the suggested procedure by analyzing how the integrated mechanothermochemical reclaiming affects the physicochemical properties of vulcanized rubbers.

EXPERIMENTAL

General information about the investigation methods we used is presented in the scheme. Below, some testing techniques and the facilities are specified.

The tire material undergoes numerous physicochemical changes during exploitation and subsequent processing. We examined here the changes in the molecular composition; micro- and macrostructures of the rubbers in the tire rubber formulation and their chemical structure; microaggregation states governed by the nature of interaction of rubbers with the filling agent; vulcanization network density; and the extent of degradation in different stages of the tire processing.

Our study was concerned with the material of the treads of automobile tires manufactured in Russia and other countries, both fresh and spent (climatic zones of the Russian Federation and the Western Europe); different size fractions of the tire rubber crumb, as well as the reclaim obtained in the com-



Scheme.

bined mechanothermochemical–steam degradation mode from a tire crumb on the worm-degradation unit we developed.

For all the objects examined, the material was separated into the gel and sol fractions in solvents convenient for subsequent analysis.

For the fresh tire samples, as well as for those spent or processed, we carried out structural analysis based on the dynamic mechanical spectroscopic data. The tests were carried out over a wide temperature range (from –100 to +150°C) at a frequency of 20 Hz on a Kuvshinskii–Sidorovich pendulum resilience tester. The measurements were carried out in the temperature scanning mode at the scanning rate of 5 deg min^{-1}.

The viscoelastic properties were estimated from two parameters, mechanical loss tangent $\tan\delta$ and dynamic modulus of elasticity E:

$$\tan\delta = \ln(A^2/B^2)/\pi, \quad E = (\pi HM)/(t^2S),$$

where A and B are the pendulum deviations before and after the impact, respectively; t, impact duration; H, height of the sample; and S, cross-sectional area of the sample.

We compared the initial and processed tire tread samples with the use of the IR data as well. The samples were extracted with tetrahydrofuran (THF); after filtration, the drops of the extract were applied to a KBr plate. The samples were dried under an IR lamp and then placed in a spectrograph.

For the soluble (sol) fraction we determined the molecular composition, chemical structure, and heterogeneity (by optical microscopy and light scattering).

The MWD parameters were determined by high-performance gel permeation chromatography on a Waters chromatograph. The samples were extracted with THF at room temperature for 24 h and then filtered. Next, we determined the amount of the polymer dissolved in THF, the number-average and weight-average molecular weights, and MWD parameters. Also, we calculated the viscosity.

The amount of the gel fraction was determined in two solvents, THF and toluene. The samples were extracted for 24 h at room temperature. The amount of the gel, %, was calculated by the formula

$$X = (m_1 \times 100)/m,$$

where m and m_1 are the weights of crushed vulcanized rubber and dried residue, g, respectively.

For the insoluble (gel) fraction we determined the chemical composition by pyrolytic IR spectroscopy and examined the heterogeneity.

The efficiencies of different reclaiming methods were compared using the optical microscopic data for the sizes of the vulcanized rubber inclusions that were preserved and remained unchanged during the treatment. To this end, we prepared dilute 1 : 10 blends of the reclaim in polyisobutylene and 1 : 10 solutions of the reclaim in toluene. The samples were applied to the object-plate of a microscope to determine the size and nature of the inclusions.

From the crumb and reclaim we prepared identically compounded vulcanizates and tested their physicomechanical properties by standard procedures.

Reclaiming substantially modifies the physicochemical properties of the material. Above all, the gel content of the material (solvent THF) sharply decreases. For example, the reclaim from imported rough material (vulcanized rubber granulate prepared using a rotary milling cutter) contains 74.8% gel; the rubber content of the sol fraction increases to 78.2% (M_w = 38000; M_n = 11000; K = 3.4; intrinsic viscosity η = 0.36 dl g^{-1}); the reclaim from the imported tire crumb contains 67.9% gel; the rubber content of the sol fraction increases to 93.3% (M_w = 46900; M_n = 13370; K = 3.5; η = 0.41). The corresponding characteristics of the reclaim from Russian crumb are as follows: gel content 67.4%; M_w = 36100; M_n = 10240; K = 3.5; η = 0.41 dl g^{-1}.

For comparison, the 0.04-mm vulcanized rubber crumb prepared by mechanical degradation combined with ultrasonication contains 77% gel (solvent toluene). In this case, the crumb preparation is accompanied by more exhaustive degradation of rubber into a wide spectrum of low-molecular-weight products. This demonstrates the high efficiency of the method we suggested.

Our data provide a fairly comprehensive information about the structural changes occurring in the spent vulcanized rubber during reclaiming. The following structural changes accompany the vulcanized rubber processing. According to data of pyrolytic IR spectroscopy, the content of the oxygen-containing groups in the reclaim obtained from the spent treads made of imported rough material decreases from 0.30 to 0.19. This can be attributed dilution of the reclaim by additives such as softeners, fillers, etc. The content of unsaturated groups remains virtually unchanged, although that of the conditionally hydroxy groups tends to increase. Hence, during preparation of the reclaim in the presence of steam, hydroxy groups are formed at the degradation sites of the macromolecules, rather than at the double bonds.

The content of oxygen-containing groups in the sol fraction from the same reclaim, estimated from the solution IR data, slightly increased, compared to the pyrolysis data (the plasticizers and stabilizer precipitated with an alcohol were removed from the sol fraction), the content of unsaturated groups decreased, and the amount of hydroxy groups slightly increased relative to the initial tread. As to the gel fraction, all the determined parameters increased. The reason is that the formation of polar groups favors interaction with the carbon black surface, and virtually all the groups having a functionality (oxygen-containing, hydroxy, and unsaturated groups) are adsorbed by the filler.

For the reclaims prepared from a crumb, the general trends in variation of the properties of the materials are preserved. At the same time, the total content (according to the data of pyrolytic IR spectroscopy) of hydroxy groups, rings, and styrene groups is increased. This is due to the change in the chemical composition of the pyrolysis products, because they are obtained from the "whole tire" crumb in which the content of the divinyl–styrene rubber is higher

than that in the tread component. However, MWD broadening in going from the rough material to the crumb can intensify the oxidation in preparation of the reclaim, especially under exposure to steam.

The characteristics of the reclaims obtained from the imported and Russian crumbs are close, which suggests that the processes occurring in different materials are identical. In particular, like in the case of the reclaim from imported tires, the gel fraction is enriched in fragments of the rubbers containing functional groups, because they are more actively sorbed by the carbon black surface.

An indirect evidence concerning the role played by the oxidation processes in preparation of the reclaim was obtained from mechanical spectroscopic data. The reclaims prepared from fresh and spent tires exhibit the tan δ maxima at identical temperatures (Fig. 1). At the same time, the position of the tan δ maximum for the imported granulate prepared by tire milling is shifted to higher temperatures (Fig. 2). For example, $T_{t\delta_{max}}$ for the reclaims from imported rough material was estimated at –30°C, and that for the Russian and imported crumb, at –35 to –40°C. It is seen that the reclaims obtained from a crumb (both Russian and imported) are characterized by virtually identical tan δ_{max} parameters; at the same time, the reclaim from imported crumb is more severely degraded, and at T ~100°C a flow area is observed for the reclaim. This reclaim exhibits a fairly extended area of a stable state of the soot-rubber gel (from 0 to 30°C).

For the reclaim obtained from the Russian tire crumb, the area of a stable state of the soot-rubber gel is narrower (from –20 to –10°C) and shifted to lower temperatures. This suggests a lower temperature stability of the reclaim. The widest area of existence of the soot-rubber gel is exhibited by the reclaim prepared from imported rough material (from –20 to +25°C), but it comprises a number of temperature steps characterizing the degradation of the soot-rubber gel in different structural formations of the reclaim. Transitions from –30 to 0…+10°C are observed for both the initial and worn tread samples. The lack of flow areas for the reclaims from the Russian crumb and imported rough material suggests that the extent of degradation of the vulcanized network is too low.

To validate this conclusion, we prepared identically compounded vulcanizates from the reclaims examined. Indeed, all the vulcanizates obtained from reclaims based on the Russian and imported crumb and rough material give close temperature dependences of

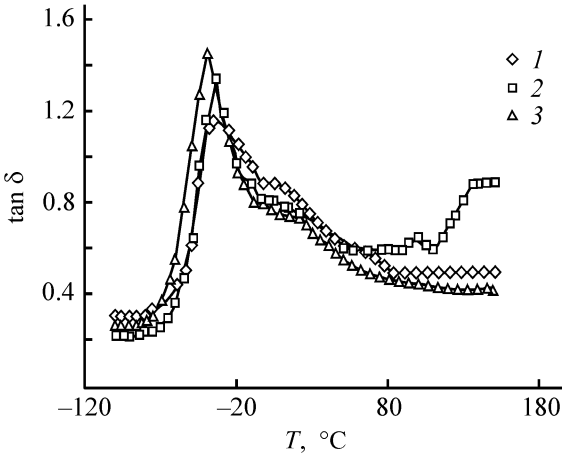


Fig. 1. Temperature dependence of the mechanical loss tangent tan δ for the samples of tread rubbers. Tread: (*1*) spent and (*2*) fresh.

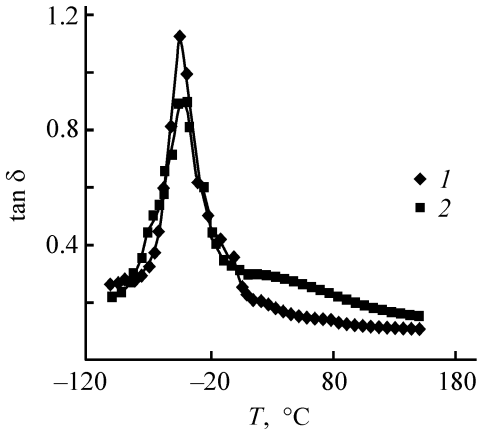


Fig. 2. Temperature dependence of the mechanical loss tangent tan δ for the reclaimed samples of tread rubbers: (*1*) imported rough material and (*2*, *3*) tire crumb: (*2*) imported and (*3*) Russian.

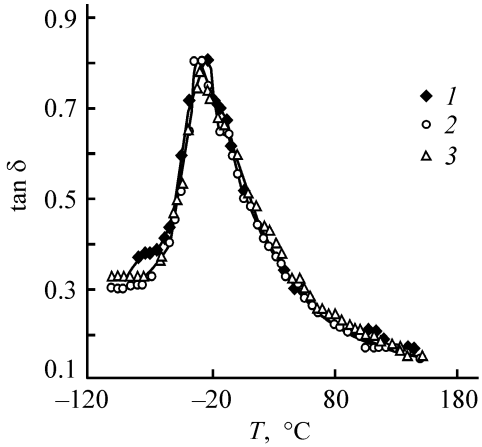


Fig. 3. Temperature dependence of the mechanical loss tangent tan δ for vulcanizates of the samples of tread rubbers: (*1*) imported crumb, (*2*) Russian tire crumb, and (*3*) imported rough material.

Table 1. Properties of vulcanizates prepared from different reclaims

Vulcanizate parameter	Reclaim from indicated material		
	imported tires	imported tire crumb	Russian tire crumb
Weight fraction of volatiles at 110°C, %	0.45	0.50	0.50
Weight fraction of ash, %	8.3 (7.0 ± 2)*	5.2 (7.0 ± 2)	3.7 (2.36–2.64)
Carbon black, %	32 (27 ± 3)	35 (27 ± 3)	36.3 (27 ± 3)
Weight fraction of softeners (acetone extract), %	15 (15 ± 3)	8.46 (15 ± 3)	12.6 (22–24)
Rubber, %, not lower than	10–11	6	6
Density, g cm^{-3}	1.2 (1.14 ± 0.02)	1.2 (1.14 ± 0.02)	1.2 (1.14 ± 0.02)
Mooney viscosity, arb. units	30 (35 ± 10)	30 (35 ± 10)	25 (17–25)
Nominal tensile strength, MPa, not lower than	4.6 (4.0)	5.0	5.0 (4.0)
Relative elongation, %, not lower than	125	160	165 (100–150)
Shore hardness A, units	52 (51 ± 3)	57 (59 ± 3)	56

* Figures in parentheses are taken from the branch standard.

Table 2. Properties of the tire reclaim obtained by different methods

Parameter	Standard for indicated brand		
	RShT	RShTN	RShTA
Weight fraction of volatiles at 110°C, %	0.5	0.6	0.8
Weight fraction of ash, %, not higher than	5.0	5.0	2.6
Weight fraction of softeners (acetone extract, %), not higher than	28.0	28.0	24.0
Mooney viscosity, arb. units	20–37	17–37	17–40
Nominal tensile strength, MPa, not lower than	4.9	3.92	4.5
Relative elongation, %, not lower than	300	250	210 (100–150)

tan δ; $\tan\delta_{max}$ is close to 0.82 (Fig. 3). The Russian crumb exhibits the tan δ maximum at –35°C, and imported crumb, at –25°C. A shoulder in the curve, a manufestation of the mobility of molecules in the soot-rubber gel, is observed at tan δ of ~0.7, and for the Russian material it is shifted to lower temperatures, –25 to –30°C, relative to the imported material (–20 to –10°C). This fact also evidences a high temperature stability of the soot-rubber gel in the imported reclaim.

To summarize, by contrast to exploitation, the processing of the material causes both the content and the average molecular weight of the soluble (sol) fraction of the material to sharply increase; a large contribution comes from the oxidation processes responsible not only for the formation of oxygen-containing groups (the α-transition temperature increases by over 10°C) but also for the increase in the aggregation stability of the soot-rubber gel; the chemical bonds of the vulcanization network for the reclaim obtained from imported crumb undergo a more exhaustive degradation, which is manifested in its flowability at 110°C.

Although the physicochemical changes in the Russian and imported materials proceed differently, the formal parameters of all the reclaims examined are close. Moreover, the recycled vulcanizates from the reclaims meet the requirements imposed by the appropriate branch standard (Table 1).

A high efficiency of the integrated mechanothermochemical reclaiming is also suggested by comparison of the properties exhibited by the tire reclaim obtained by the thermomechanical procedure (RShT, RShTN, Tchekhov Reclaim Plant) and the procedure we suggested (RShTA, Elast-Tekhnologiya) (Table 2).

Thus, the reclaiming procedure suggested affords products of the desired quality.

CONCLUSIONS

(1) The procedure suggested for integrated mechanothermochemical reclaiming of rubbers affords products of the desired quality. It compares favorably with the existing procedures in the working mode (continuous), as well as in the performance characteristics and economic efficiency, due to the use of coarser crumb as the raw material.

(2) The procedure suggested is distinguished by the possibility of fine control over the mechanothermochemical degradation.

REFERENCES

1. RF Patent 2014339.
2. Shakhovets, S.E. and Smirnov, B.L., *Kauchuk Rezina*, 2006, no. 1. pp. 34–36.
3. RF Patent 2145282.

ISSN 1070-4272, Russian Journal of Applied Chemistry, 2008, Vol. 81, No. 4, pp. 682–686. © Pleiades Publishing, Ltd., 2008.
Original Russian Text © V.N. Verezhnikov, V.A. Sedykh, N.A. Shabanova, M.N. Sergeeva, M.S. Bederkin, 2008, published in Zhurnal Prikladnoi Khimii, 2008, Vol. 81, No. 4, pp. 645–649.

MACROMOLECULAR CHEMISTRY AND POLYMERIC MATERIALS

Effect of Dispersity and Drying Mode of Silica on Deformation-Strength Properties of Latex Films

V. N. Verezhnikov, V. A. Sedykh, N. A. Shabanova, M. N. Sergeeva, and M. S. Bederkin

Voronezh State University, Voronezh, Russia
Voronezh State Technological Academy, Voronezh, Russia
Mendeleev Russian University of Chemical Engineering, Moscow, Russia

Received November 15, 2007

Abstract—Effect of dispersity, content, and nature of silica on the deformation-strength parameters of latex films obtained under various conditions was studied.

DOI: 10.1134/S1070427208040228

An effective way to modify properties of polymeric materials is to introduce various fillers (solid, liquid, or gaseous). Caoutchouc can be reinforced with solid fillers with particle sizes of 5 to 1000 nm, with fillers having particles 10 to 50 nm in size exhibiting the strongest reinforcing properties [1]. The most frequently used solid fillers are technical-grade carbon (carbon black) or silica in the form of a precipitated silicon dioxide (white carbon black, perkasil, etc.). A polymer is filled by its direct mixing with a filler or by introduction of the filler in the latex stage. Introduction of a filler into the latex yields a more uniform distribution of components, compared with introduction of fillers into a dry caoutchouc in a rolling mill of a rubber mixer, and diminishes the energy expenditure for mixing.

A promising reinforcing filler is colloid silica. Modern industry manufactures colloid silica in the form of a hydrosol that is, as a rule, stabilized with NH_4^+ or Na^+. Silica particles have a spherical shape and their size (diameter) is approximately 6 to 30 nm, depending on a brand. Both mono- and polydispersed sols are manufactured. A filler of this kind can find use in production of various rubber articles, and especially thin-walled articles fabricated by dipping (gloves, bladders, etc.)

In this communication, results obtained in a study of the influence exerted by the dispersity of silica on the deformation-strength characteristics of latex films produced by drying under various conditions are reported.

EXPERIMENTAL

The latex films were produced from an SKD-1S polybutadiene carboxylate latex manufactured by Voronezhsintezkauchuk Open Joint-Stock Company. The latex was a product of joint emulsion polymerization of butadiene with methacrylic acid (about 1 %) in the presence of sodium alkylbenzene sulfonate. As active fillers were used silica hydrosol of Sialit-30 brand (Silikat Private Company) and white carbon black of BS-100 brand. The particle size d of silica in the hydrosol was 6.3 nm (according to the results of adsorption titration by the Sears method [2]). Prior to introduction of white carbon black into the latex, an aqueous dispersion was preliminary prepared. For this purpose, a weighed portion of white carbon black (~30 g) and water (~170 ml) were introduced into a ball mill, and grinding was performed for approximately 10 h. The size of silica particles in the resulting suspension and that of polymer particles in the latex were determined by the optical method with a FEK-56 photoelectrocolorimeter to be 303 and 110 nm, respectively.

The latex films were produced by casting-and-drying on cellophane. The films were dried in two modes: at 60°C for 120 min ("mild" drying) or at 140°C for 50–60 min ("severe" drying).

To obtained filled films, a mixture of a latex and a silica hydrosol or a suspension of white carbon black was preliminarily prepared with required rela-

Table 1. Deformation-strength parameters of latex films at varied content of silica introduced in the form of a nanodispersed hydrosol

Drying mode	SiO_2, wt %	f_t, MPa	ε, %	ε_{res}, %	B, kN m^{-1}	Degree of swelling, W, wt %
Mild	0				2.96	
		0.43	451	44		5.5
	0.15				3.94	
		0.50	488	33		14.79
	1.3				3.68	
		0.38	200	9		8.87
	2.6				3.58	
		0.33	529	49		11.9
	5.0				2.56	
		0.48	271	18		–
Severe	0	0.40	138	9	1.09	4.07
	0.5	0.40	335	9	2.05	1.80
	1.0	0.51	368	7	2.06	2.26
	2.5	0.62	323	8	2.37	2.63
	5.0	0.98	239	8	2.44	9.67
Thermo-oxidative aging	0	9.83	30	0	9.81	–
	0.15	4.93	0	0	23.39	–
	1.3	15.55	0	0	30.36	–
	2.6	10.05	15	0	20.69	–
	5.0	20.40	0	0	26.29	–

Table 2. Deformation-strength parameters of latex films subjected to accelerated thermo-oxidative aging (72 h at 100°C) at varied content of the SiO_2 sol

Parameter	Content of SiO_2 sol, wt %				
	0	0.15	1.3	2.6	5.0
f_t, MPa	9.8 ± 2.0	4.9 ± 4.1	15.6 ± 13.5	10.1 ± 16.8	20.4 ± 33.3
ε_b, %	30.0 ± 19.7	0	0	15.0 ± 12.3	0
ε_{res}, %	0	0	0	0	0
B, kN m^{-1}	9.8 ± 12.5	23.4 ± 3.7	30.4 ± 14.8	20.7 ± 36.5	26.3 ± 13.5

tive amounts of silica and the polymer. The deformation-strength characteristics of the films obtained was measured on a tensile machine by the standard procedure.

In the first stage, the influence exerted by the conditions in which films of unfilled and filled polymers with varied content of SiO_2 are dried on the deformation-strength parameters (DSP) of the films was studied. It was found (Table 1) that, for the unfilled polymer, the drying mode has no effect on the relative tensile strength (conditional strength limit) f_t (0.40–0.43 MPa), but drying under severe conditions leads to a decrease in the relative tensile elongation at break (ε_b), residual relative tensile elongation after break, ε_{res}, and tear resistance B. This indicates that molecules are cross-linked at tertiary atoms of molecular chains of the polymer, with its separate DSP decreasing in the course of thermal treatment. Making the drying mode even more "severe" (thermo-oxidative aging at 100°C for 72 h) presumably leads to the maximum possible degree of cross-linking of the polymer, with the deformation parameters steeply decreasing (ε_b to 30% and ε_{res} to 0%) and strength parameters increasing (f_t by more than a factor of 20, and B by a factor of 10) (Table 2).

Table 3. Deformation-strength parameters of latex films produced by severe drying at varied content of BS-100

Parameter	Content of BS-100, wt %				
	0	0.5	1	2.5	5.0
f_t, MPa	0.4 ± 0.06	0.94 ± 0.13	1.18 ± 0.64	1.47 ± 0.1	1.71 ± 0.38
ε_b, %	138 ± 104.8	72 ± 25.3	86 ± 27.8	32 ± 19.4	51 ± 16.9
ε_{res}, %	8.8 ± 8.7	0	0.6 ± 2.4	1.5 ± 4.9	2.2 ± 4.9
B, kN m^{-1}	1.09 ± 0.8	3.54 ± 0.8	4.27 ± 0.8	4.91 ± 0.8	5.58 ± 1.7
W, wt %	4.07	7.16	6.47	5.93	6.92

In mild drying of polymer samples filled with the sol in an amount of up to 5 wt %, the content of silica has virtually no effect on the DSP of the films (Table 1). This is apparently due to the considerable residual humidity of the sol-filled polymer. The moisture bound to the surface of particles of the hydrophilic filler hinders its interaction with the polymer macromolecules. The hydrophilicity of the SiO_2 sol is confirmed by the equilibrium degree of swelling of the filled polymer in water, W = 8.9–14.8 wt % against 5.5 wt % for the unfilled polymer (Table 1).

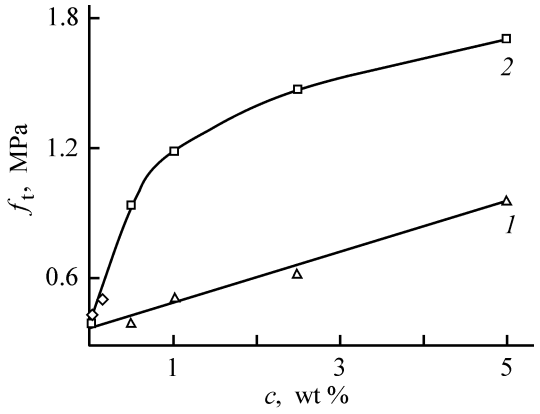


Fig. 1. Tensile strength f_t of latex films subjected to severe drying vs. content c at different sizes of filler particles. (*1*) SiO_2 sol and (*2*) white carbon black; the same for Fig. 2.

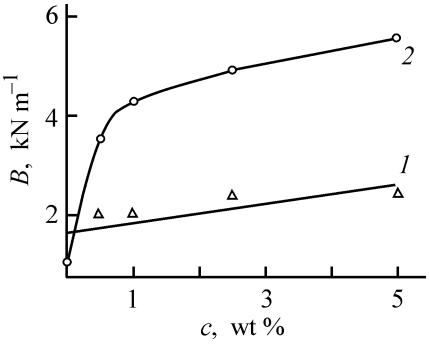


Fig. 2. Tear resistance B of latex films (severe drying) vs. content c at different sizes of filler particles.

Passing to a severe drying mode makes lower the content of the residual moisture, raises the probability of chemical cross-linking of polymer macromolecules (with ε_{res} decreasing from 18.4–49.0 to 7.0–8.75%, and W, to 1.8–9.7 wt %), and reveals the effect of SiO_2 on the DSP of filled films. As the content of silica sol increases (to 5 wt %), the tensile strength f_t and tear resistance B grow (from 0.40 to 0.98 MPa and from 2.05 to 2.44 kN m^{-1}, respectively), compared with the unfilled polymer, and the relative tensile elongation at break, ε_b, grows (by a factor of 1.7–2.7) at a residual strain ε_{res} preserved at a level of 7–9% (Table 1). Thus, the severe drying of the polymer filled with the SiO_2 sol reveals the strengthening effect of the filler (the strength of the polymer increases at unchanged deformation properties without acceleration of the chemical cross-linking of its molecules). Further studies were performed with the use of this drying mode.

In the presence of the sol, films subjected to accelerated thermo-oxidative aging exhibited an even more pronounced strength enhancement as the content of SiO_2 was raised: f_t increased to 15.6–20.4 MPa, and B, to 20.7–30.4 kN m^{-1} (at a silica content of up to 1.3–5 wt %), with ε_b and ε_{res} becoming zero (Table 2).

The results obtained upon introduction of a coarser dispersed silica in the form of a dispersion of BS-100 white carbon black are listed in Table 3. It can be seen that, compared with the case of a nanodispersed SiO_2 sol, a considerable increase in the strength parameters f_t and B of the films is observed (by a factor of 1.5 and more), but, at the same time, ε_b and ε_{res} substantially decrease. For example, f_t increased from 0.4–0.98 to 0.94–1.71 MPa, and B, from 2.05–2.44 to 3.54–5.58 kN m^{-1} (Figs. 1, 2); whereas ε_t and ε_{res}

decreased from 239–368 to 32–86% and from 7–8.8 to 0–2.2%, respectively.

Thus, on passing from the sol to white carbon black, with the filler dispersity decreasing (average particle size increasing from 6 to 303 nm), the strength of the polymer is enhanced to a greater extent but its elastic properties are strongly deteriorated.

Figure 3 shows how the stress f in polymeric latex films depends on the strain ε at a varied content and size of silica particles introduced as a hydrosol or white carbon black. The size of filler particles at the same filler content affects the slope of the f–ε straight line. Coarse particles provide a higher f at a small ε of the films. This can be attributed to acceleration of the chemical cross-linking of SKD-1S polymer in the presence of white carbon black, which leads to a decrease in ε_b and ε_{res}, i.e., to loss of elastic properties.

It should be noted that, in the presence of small amounts of BS-100, a larger degree W of equilibrium swelling of films in water is observed despite the increase in the degree of cross-linking of the polymer (Table 3).

According to the existing concepts [1], the 3D macromolecular network of an elastomer is irregular, and, therefore, deformation gives rise to considerable overstresses in its certain parts, with macromolecules ruptured there, but the most part of the network being only slightly strained. In addition, the microheterogeneity of the latex film produced by casting and drying is superimposed on the irregular 3D network of the elastomer. The residues of the emulsifier undissolved in the polymer are concentrated at places of contact between adhering globules of the elastomer and introduce additional defects into its supramolecular structure [3, 4]. The reinforcement of the elastomer with active fillers consists in that, being concentrated in the interglobular space, nanosize filler particles favor equalization of stresses in the elastomer.

The results obtained are in agreement with data on how the particle size of such a filler as chalk affects the deformation-strength properties of polyurethane elastomers [5]. Presumably, the observed effects are due to the influence exerted by the particle size on the structure and state of the network of transverse bonds of the macromolecular matrix. As the size of filler particles increases, the role of internal stresses appearing upon incorporation of particles into the 3D intermolecular network becomes more important and the fraction of the polymer volume subject to their action grows. The coarser the particles, the larger the defects in the network of transverse bonds of

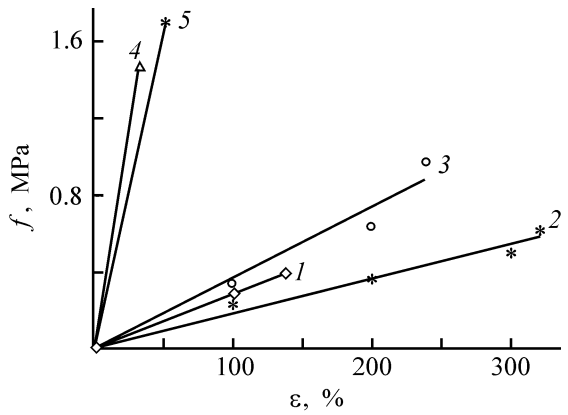


Fig. 3. Stress f vs. strain ε in latex films (severe drying). Content (wt %) of SiO_2 introduced as a sol: (*1*) 0, (*2*) 2.5, and (*3*) 5.0; and as white carbon black: (*4*) 2.5 and (*5*) 5.0.

macromolecules [6, 7]. As is known, large defects more strongly affect the DSP of the polymer, e.g., the relative tensile elongation at break, than smaller ones [7–9].

The imperfection of the network of transverse bonds in the presence of coarse particles of white carbon black also accounts for the increase in the degree of swelling in water of a polymer filled with these particles at a smaller ε_{res}, i.e., at a higher level of cross-linking of the elastomer.

CONCLUSIONS

(1) No reinforcing properties of the filler are observed in films of a sol-filled polymer, obtained in the mild drying mode (60°C for 120 min). On making the drying mode more severe (140°C for 50–60 min), f_t, B, and ε_b increase, depending on the sol content, with ε_{res} remaining unchanged.

(2) Introduction of white carbon black particles in an amount of up to 5 wt % into the polymer of latex films subjected to a similar drying improves the tensile strength, but markedly reduces the elongation and the residual strain. This is accounted for by acceleration of the cross-linking of polymer macromolecules in the presence of BS-100 particles with an average size of 303 nm.

(3) Presence of a SiO_2 sol in an amount of up to 5 wt % in polymeric latex films subjected to severe drying leads to an increase in both the strength and relative tensile elongation at break, with the residual strain preserved. The invariable level of the residual strain in polymeric latex films filled with the SiO_2 sol indicates that the cross-linking rate of polymer macromolecules in the films remains unchanged, and

the lower degree of swelling in water shows that a more ordered cross-linking structure of macromolecules is formed, compared with the unfilled polymer and that with BS-100.

(4) A linear dependence of the stress on strain is observed for films of the sol-filled polymer. The content of sol determines the strain in a wide range of strains.

REFERENCES

1. Koshelev, F.F., Kornev, A.E., and Bukanov, A.M., *Obshchaya tekhnologiya reziny* (General Technology of Rubber), Moscow: Khimiya, 1978.
2. Searsm, G.W., Jr., *Analyt. Chem.*, 1956, vol. 28, no. 12, pp. 1981–1983.
3. Eliseeva, V.I., *Polimernye dispersii* (Polymeric Dispersions), Moscow: Khimiya, 1980.
4. Voyutskii, S.S. and Shtarkh, B.V., *Fiziko-khimiya protsessov obrazovaniya plenok iz dispersii vysokopolimerov* (Physical Chemistry of Film Formation from Superpolymer Dispersions), Moscow: Gizlegprom, 1954.
5. Nielsen, L.E., *Mechanical Properties of Polymers and Composites*, New York: Marcel Dekker, 1974.
6. Gul', V.E., *Struktura i prochnost' polimerov* (Structure and Strength of Polymers), Moscow: Khimiya, 1971.
7. Bartenev, G.M., *Prochnost' i mekhanizm razrusheniya polimerov* (Strengtrh and Disintegration Mechanisms of Polymers), Moscow: Khimiya, 1984.
8. Lipatov, Yu.S., *Fizicheskaya khimiya napolnennykh polimerov* (Physical Chemistry of Filled Polymers), Moscow: Khimiya, 1977.
9. *Reinforcement of Elastomers*, Kraus, G., Ed., New York: Interscience, 1965.

ISSN 1070-4272, Russian Journal of Applied Chemistry, 2008, Vol. 81, No. 4, pp. 687–690. © Pleiades Publishing, Ltd., 2008.
Original Russian Text © S.I. Gusev, S.D. Zaitsev, Yu.D. Semchikov, 2008, published in Zhurnal Prikladnoi Khimii, 2008, Vol. 81, No. 4, pp. 650–653.

MACROMOLECULAR CHEMISTRY AND POLYMERIC MATERIALS

Preparation of Styrene-(Meth)Acrylate Copolymers in the Presence of 1-Nitroso-2-naphtholatocobalt(III)

S. I. Gusev, S. D. Zaitsev, and Yu. D. Semchikov

Lobachevsky Nizhni Novgorod State University, Nizhni Novgorod, Russia

Received October 18, 2007

Abstract—Preparation of styrene–methyl methacrylate, styrene–butyl methacrylate, and styrene–butyl methacrylate copolymers by pseudolive radical polymerization was studied.

DOI: 10.1134/S107042720804023X

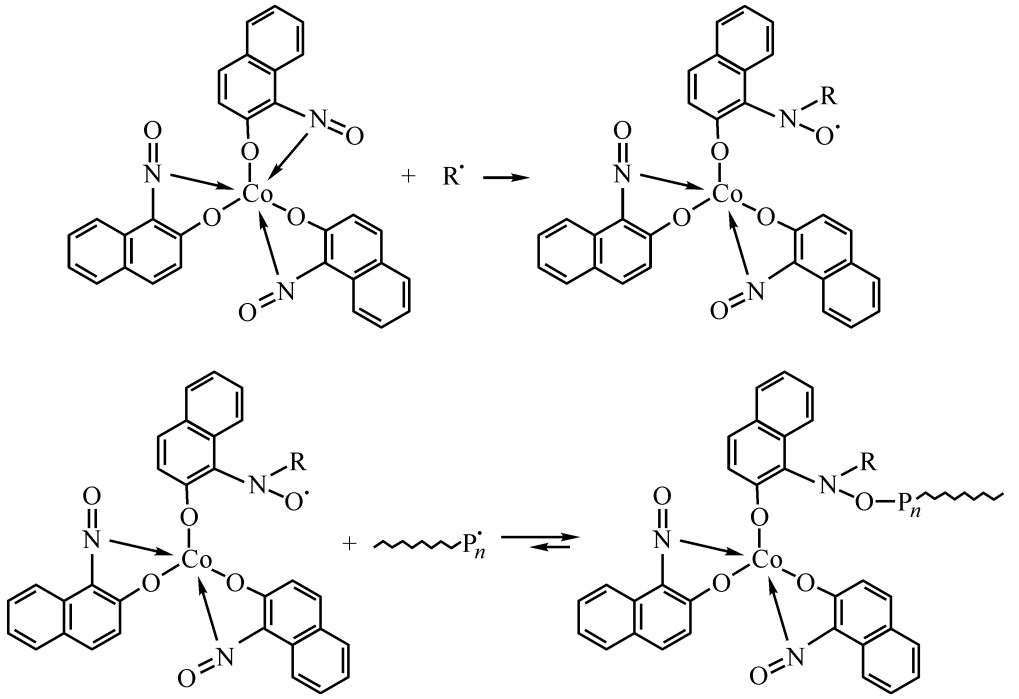
Pseudoliving radical polymerization finds growing use in preparation of new polymers. For this purpose, a wide range of sterically hindered stable nitroxyl radicals (derivatives of 2,2,6,6-tetramethylpiperidine-1-oxyl, TEMPO, di-*tert*-butylnitroxyl, etc.) can be used [1]. A significant disadvantage of TEMPO is that it provides pseudoliving polymerization of only a narrow range of monomers (mainly styrene and its derivatives). Irreversible reaction of the propagating radical with the nitroxyl radical to form hydroxylamine and a "dead" polymer prevents controlled polymerization of (meth)acrylates in the presence of alkoxyamines [2]. The range of vinyl monomers polymerizing by the pseudoliving mechanism can be extended by in situ generation of nitroxyl radicals during polymer synthesis. In this case, block copolymers of the required block length and narrow molecular-weight distribution can be prepared. These copolymers consist of blocks of varied chemical nature. Among these compounds are nitrones and nitroso compounds which are effective free-radical acceptors (spin traps) and react with free radicals to form stable spin adducts [3, 4]. We have shown [5] for the first time that 1-nitroso-2-naphtholatocobalt(III) (NNC) could be used for this purpose.

The aim of this study was to prepare block copolymers of styrene (ST) with methyl methacrylate (MMA), butyl acrylate (BA), and butyl methacrylate (BMA) in the presence of NNC generating in situ stable radicals.

EXPERIMENTAL

The block copolymers were prepared in two steps. In the first step, polystyrene (PST) blocks, in which NNC fragment is reactive at a particular temperature, were prepared at 120°C. In the second step, MMA, BA, or BMA was added to PST as a macroinitiator. The concentration of "activated" PST was 4.12 wt %. The activated PST prepared at [NNC] = 7×10^{-3} M and [AIBN] = 5×10^{-3} M and isolated at the conversion of 72 and 79 wt %, with the molecular weights of 5.4×10^4 and 4.3×10^4, was used for preparing the PST–polymethyl methacrylate (PMMA) and PST–polybutyl methacrylate (PBMA) block copolymers. PST prepared at [NNC] = 3×10^{-3} M and [AIBN] = 2×10^{-3} M and isolated at a conversion of 71 wt %, with molecular weights of 9.3×10^4, was used for preparing the PST–polybutyl methacrylate (PBMA) block copolymer. The polymerization was performed in sealed ampules after degassing by threefold freezing-pumping-thawing. The block copolymers were purified by triple reprecipitation from chloroform solutions with methanol (PST–PBA, PST–PBMA) and petroleum ether (PST–PMMA) and dried in a vacuum to constant weight at room temperature. The molecular-weight characteristics of the copolymers were studied by gel permeation chromatography at 40°C on a Prominence LC-20VP chromatograph (Shimadzu) with columns packed with polystyrene–divinylbenzene copolymer with a pore size of 1×10^6 and 1×10^5 Å. A differential refractometer was used as the detector. The eluent was tetrahydrofuran.

Previously [5] we have found that polymerization of ST and BA in the presence of NCC in the "living" chain mode was characterized by the following features: absence of the gel effect, linear dependence of the molecular weight on conversion, and linear dependence of the logarithm of conversion $\ln [M]_0/[M]$ ($[M]_0$ and [M] are the initial and current monomer concentrations) on the reaction time. Based on the kinetic features of the polymerization and analysis of the molecular-weight properties, we suggested the following polymerization mechanisms in the presence on NNC:



In the case of polymerization in the "living" chain mode, a polymer isolated at any conversion can initiate polymerization of a fresh monomer portion, i.e., can act as a macroinitiator. To test whether PST prepared in the presence of NNC is suitable as a macroinitiator, we performed the postpolymerization. To PST prepared at 120°C ([NNC] = 7×10^{-3} M and [AIBN] = 5×10^{-3} M) and isolated at a conversion of 22.3 wt % with a molecular weight of 34.8×10^5, a fresh portion of the monomer was added and polymerized at the same temperature. The dependence of the viscosity-average molecular weight of PST on the conversion for the primary polymerization of ST and ST polymerization in the presence of the macroinitiator is shown in Fig. 1. It is seen that the number of the macromolecules involved in both processes remains constant.

Synthesis of block copolymers with the use of another monomer in the second step is of practical interest. Figure 2 shows the semilog plot of $\ln [M]_0/[M]$ vs. reaction time for MMA conversion with the use of activated PST prepared in the presence of NNC.

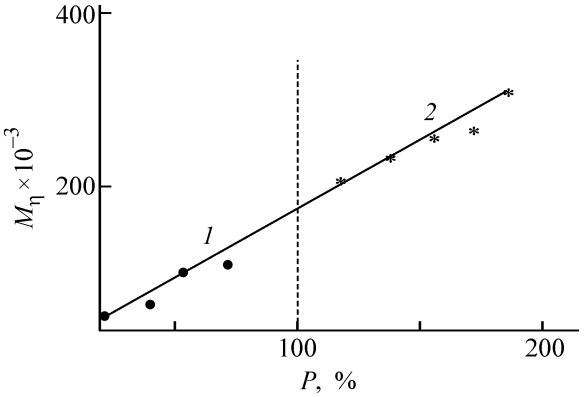


Fig. 1. Viscosity-average molecular weight of PST M_η vs. the conversion P for (*1*) primary and (*2*) secondary polymerization. T = 120°C, [AIBN] = 5×10^{-3} M, [NNC] = 7×10^{-3} M, ω_{PST} = 4.12 wt %.

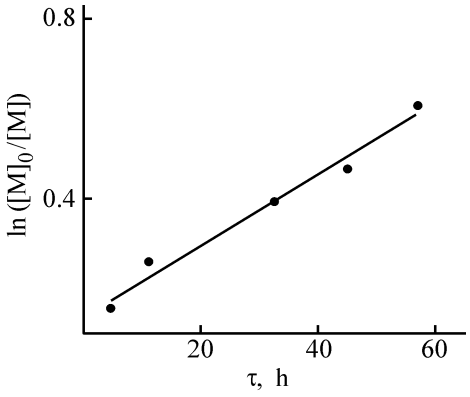


Fig. 2. $\ln [M]_0/[M]$ vs. of the time τ of MMA polymerization initiated by active PST. [AIBN] = 5×10^{-3} M, [NNC] = 7×10^{-3} M, conversion 40 wt %, $M_n = 3.1 \times 10^4$. T = 120°C, ω_{PST} = 4.12 wt %.

Molecular-weight characteristics and conversion P of activated PST and its block copolymers

Property	PST–PMMA block copolymer*			PST–PBA block copolymer**		
	Activated PST	Polymerization product		Activated PST	Polymerization product	
		mode 1 (block copolymer)	mode 2 (PMMA)		mode 1 (block copolymer)	mode 2 (PBA)
P, %	72	6.5	6.5	79	10	10
$M_n \times 10^{-4}$	5.4	7.03	99	4.3	4.8	174
M_w/M_n	1.95	1.77	1.31	1.63	1.61	1.25

* Corresponds to Fig. 3.

** Corresponds to Fig. 4.

As can be seen from Fig. 2, no gel effect typical of the conventional radical polymerization of MMA is observed. The gel permeation patterns of the initial activated PST and PST–PMMA block copolymer isolated at a conversion of 6.5 wt % are shown in Fig. 3. The presence of the high-molecular-weight peak (M_n = 8.4×10^5) in the molecular-weight distribution curve and the absence of absorption in the range of phenyl rings suggest a thermally initiated polymerization of MMA. The shift of the low-molecular-weight peak of activated PST to higher molecular weights suggests the formation of the PST–PMMA block copolymer whose molecular-weight parameters are listed in the table. The results of synthesis of PST–PBA block copolymer are presented in Fig. 4 and the table. It can be seen that, as in the preceding case, the block copolymer formation is accompanied by spontaneous polymerization of BA.

We studied block copolymerization of ST with BMA in more detail. The copolymer prepared from activated PST (molecular weight 9.4×10^4; isolated at a conversion of 7.2 wt %) was fractionated on a Soxhlet apparatus by selective extraction with isopropanol. As can be seen from the gel permeation chromatograms (Fig. 5), a significant part of PST is not converted to PST–PBMA block copolymer (curve *2*). The content of unchanged PST in the polymerization product was 75%. The unimodal curve *3* shown in

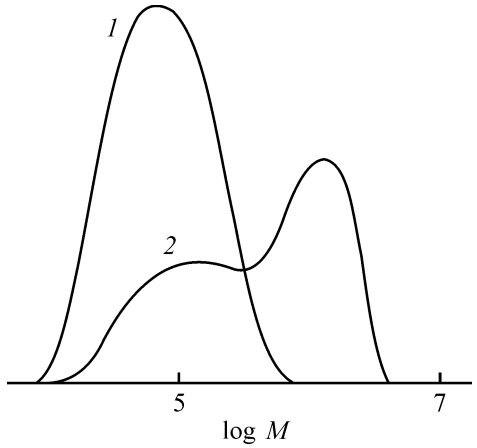


Fig. 3. Gel permeation chromatogram of (*1*) initial PST macroinitiator ([AIBN] = 5×10^{-3} M, [NNC] = 7×10^{-3} M, conversion 72 wt %, M_n = 5.4×10^4) and (*2*) PST–PMMA copolymer. T = 120°C, ε_{PST} = 4.12 wt %, conversion 6.5 wt %, refractometric detector. (M) Molecular weight of activated PST used for preparing the corresponding block copolymers; the same for Figs. 4, 5.

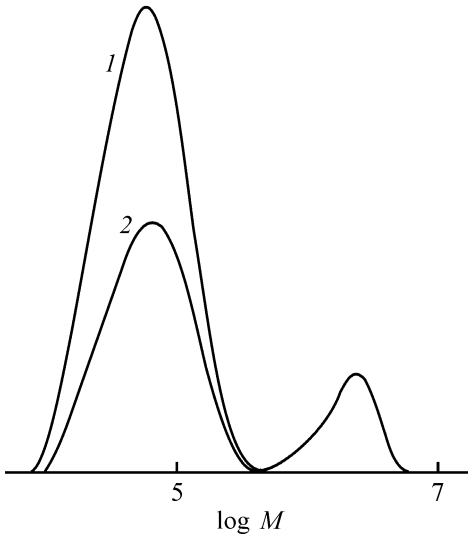


Fig. 4. Gel permeation pattern of (*1*) initial PST macroinitiator ([AIBN] = 5×10^{-3} M, [NNC] = 7×10^{-3} M, conversion 79 wt %, M_n = 4.3×10^4) and (*2*) PST–PBA copolymer. T = 120°C, ε_{PST} = 4.12 wt %, conversion 10 wt %, refractometric detector.

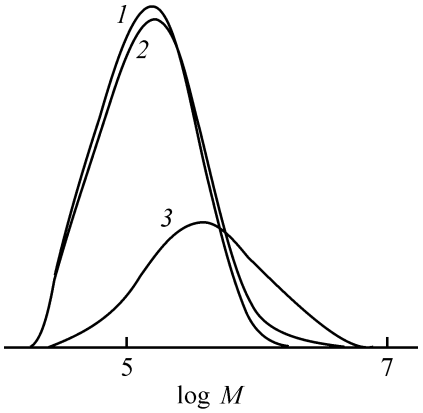


Fig. 5. Gel permeation chromatogram of (*1*) initial PST macroinitiator ([AIBN] = 2×10^{-3} M, [NNC] = 3×10^{-3} M, conversion 71 wt %, $M_n = 9.4 \times 10^4$), (*2*) unchange PST recovered from copolimerization, and (*3*) PST–PBMA copolymer. T = 120°C, ε_{PST} = 4.12 wt %, conversion 7.2 wt %, refractometric detector.

Fig. 5 is assigned to PST–PBMA copolymer ($M_n = 2.2 \times 10^4$, $M_w/M_n = 2.2$). Thus, the block (co)polymer is formed by the uncontrolled pseudoliving polymerization.

CONCLUSIONS

(1) Polystyrene prepared in the presence of 1-nitroso-2-naphtholatocobalt(III) initiates polymerization of a fresh monomer portion.

(2) Polymerization of methyl methacrylate, butyl methacrylate, and butyl acrylate in the presence of polystyrene containing the reactive fragment of 1-nitroso-2-naphtholatocobalt(III) yields the corresponding block copolymers.

ACKNOWLEDGMENTS

This study was financially supported by the Russian Foundation for Basic Research (project no. 07-03-00500), Federal Target Program "Studies and Developments in the Field of Priority Areas of Research and Technical Complex of Russia for the Years of 2007–2012" (project no. 2007-3-1.3-26-01-314), and Education National Project, Innovation Educational Program of Nizhni Novgorod State University.

REFERENCES

1. Zaremskii, M.Yu. and Golubev, V.B., *Vysokomol. Soedin., Ser. C*, 2001, vol. 43, no. 9, pp. 1689–1728.
2. Zaremskii, M.Yu., Zhaksylykov, A.B., Orlova, A.P., et al., *Vysokomol. Soedin., Ser. A*, 2005, vol. 47, no. 6, pp. 886–897.
3. Zaremskii, M.Yu., Orlova, A.P., Garina, E.S., et al., *Vysokomol. Soedin. Ser. A*, 2003, vol. 45, no. 6, pp. 871–882.
4. Grishin, D.F., Semenycheva, L.L., and Kolyakina, E.V., *Vysokomol. Soedin., Ser. A*, 1999, vol. 41, no. 4, pp. 609–614.
5. Gusev, S.I., Zaitseva, S.D., and Semchikov, Yu.D., *Vysokomol. Soedin., Ser. A*, 2008, vol. 50, no. 4, pp. 720–725.

ISSN 1070-4272, Russian Journal of Applied Chemistry, 2008, Vol. 81, No. 4, pp. 691–695. © Pleiades Publishing, Ltd., 2008.
Original Russian Text © A.M. Bochek, I.L. Shevchuk, L.M. Kalyuzhnaya, 2008, published in Zhurnal Prikladnoi Khimii, 2008, Vol. 81, No. 4, pp. 654–658.

MACROMOLECULAR CHEMISTRY AND POLYMERIC MATERIALS

Properties of Blends of Methyl Cellulose and Carboxymethyl Cellulose with Different Degrees of Ionization in Solutions and Solids

A. M. Bochek, I. L. Shevchuk, and L. M. Kalyuzhnaya

Institute of Macromolecular Compounds, Russian Academy of Sciences, St. Petersburg, Russia

Received November 12, 2007

Abstract—The rheological properties of dilute and moderately concentrated aqueous solutions of methyl cellulose with carboxymethyl cellulose having different degrees of ionization, were examined. The solvent vapor sorption method was applied to examine the compatibility of the polymers in the solid state and elucidate how the amount of nonionized carboxy groups in carboxymethyl cellulose affects its compatibility with methyl cellulose.

DOI: 10.1134/S1070427208040241

As is known, a number of cellulose compounds in aqueous solutions form physical thermoreversible gels. These compounds include methyl cellulose (MC), hydroxypropyl cellulose (HPC), hydroxypropyl methyl cellulose (HPMC), and methyl ethyl cellulose (MEC). These cellulose ethers are widely used as gelation agents, thickeners, stabilizers, and emulsifiers in food industry. The most widely used cellulose compound is MC.

The properties of aqueous solutions of MC, as well as of films and fibers thereof, can be changed by chemical or physicochemical modification of the polymer. We have shown earlier [1, 2] that introduction into the MC macromolecules of polar (cyanoethyl) and nonpolar (propyl) groups changes the thermodynamic affinity of the polymer for water and the rheological properties of the solutions of mixed cellulose ethers; the gelation onset temperature T_{gel} in solution decreases, as also does the phase segregation temperature in solutions, or the cloud point T_{cloud}. Also, the rheological properties of polymer solutions can be modified by combining in the same solvent two polymers with different chemical structures to obtain polymer blends with controlled properties. Depending on the chemical composition, rigidity of the macromolecules, degree of polymerization, and type of solvent, the blended polymers can form in solution differently organized structures with different stabilities [3–7].

Among the cellulose ethers containing ionic groups, the most widely used compound is carboxymethyl cellulose (CMC) available as the sodium salt NaCMC.

In aqueous solutions of NaCMC, solvated macromolecules undergo association. The size, shape, and mutual ordering of the associates in solutions vary, depending on the conditions. Unusual properties are displayed by films prepared from aqueous solutions of CMC in the acid form (HCMC). In concentrated aqueous solutions of HCMC, the opalescence and gelation are gradually enhanced [8, 9]. Films obtained from such solutions become water-insoluble because of the formation in them of a system of strong intra- and intermolecular H bonds [10]. The gelation in HCMC solutions reflects the change in the thermodynamic characteristics of interaction of the polymer with the solvent. The reason is the enhancement of the intermolecular interaction of solvated CMC macromolecules via hydrogen bonding because of the appearance of nonionized carboxy groups.

Modification of the rheological properties of aqueous MC solutions by adding solutions of CMC with different degrees of ionization is of scientific and practical interest. Aqueous solutions of blends of NaCMC with other cellulose ethers and synthetic polymers exhibit deviations of the viscosity from additivity [11, 12]. It is presumed that changing the number of dissociated and nondissociated carboxy groups in

the CMC macromolecules will enable varying the system of hydrogen bonds in concentrated solutions of polymer blends and the compatibility of polymers in the solid state.

We examined here the viscous properties of dilute and moderately concentrated aqueous solutions of blends of MC with CMC, having different degrees of ionization, as well the thermodynamic compatibility of the polymers in the solid state.

EXPERIMENTAL

As initial materials we used MTs-100 commercial samples of MC with the degree of substitution (DS) of 1.62 and the degree of polymerization (DP_η) of 830, as well as NaCMC with DS = 0.46 and DP_η = 460. Distilled water served as the solvent. The molecular weight and DP_η of MC were determined viscometrically, using the Mark–Kuhn–Houwink equation for MC in water [13]:

$$[\eta] = 2.8 \times 10^{-3} M^{0.63}.$$

The molecular weight of CMC was estimated viscometrically from the viscosity of the polymer in 6% aqueous NaOH solution. For calculation we used the expression $[\eta] = 7.3 \times 10^{-3} M^{0.93}$ [10]. The degree of substitution for NaCMC was estimated from its Na content by the formula

$$DS_{Na} = 162n/(2300 - 80n), \quad (1)$$

where n is the Na content of the polymer, wt %.

The Na content of CMC was determined by conductometric titration with 0.1 M HCl solution. To calculate the degree of substitution of HCMC with respect to carboxy groups DS_{COOH}, we used the expression

$$DS_{COOH} = 162m/(4500 - 58m), \quad (2)$$

where m is the content of carboxy groups, wt %.

The content of carboxy groups was determined by conductometric titration of the sample with 0.1 M NaOH solution. The degree of ionization of CMC was calculated by the expression

$$\alpha = DS_{Na}/(DS_{Na} - DS_{COOH}). \quad (3)$$

Commercial samples of NaCMC may contain low-molecular-weight impurities, chlorides of reactants used in the carboxymethylation of cellulose [10]. Therefore, the NaCMC sample was preliminarily washed to remove impurities with a hot 70% aqueous isopropanol solution in a Soxhlet apparatus. The washing was carried out for 4 h to negative reaction to Cl^- ions with an $AgNO_3$ solution. The washed sample was vacuum-dried at 50°C for 12 h. The DS_{Na}, DS_{COOH}, and DP_η parameters were determined for the samples washed to remove impurities. NaCMC was converted to the H form in an aqueous solution of the polymer (2 wt %) [8]. The 2% aqueous MC solution and dilute solutions (0.2 wt %) were prepared according to [7].

The 0.2 wt % solutions obtained by dilution of the prepared 2 wt % solutions were examined viscometrically. Films were prepared from aqueous solutions of polymer blends by casting the solution through a laboratory draw plate with a controlled slit onto Teflon plates at 20°C, which was followed by drying at 30°C. The film was detached from the support after 1 day.

The viscous characteristics of dilute 0.2 wt % solutions were determined on an Ubbelohde capillary viscometer at 20°C. The rheological properties of the concentrated solutions were examined on a Rheotest 2.1 rotary viscometer with a cylinder-cylinder working unit in the shear stress range 3–600 Pa at 20–40°C.

To evaluate the compatibility of the blended polymers, we used the solvent vapor sorption method [14]. The films prepared from aqueous solutions of polymers by the above-described procedure were vacuum-dried to constant weight. The residual content of the solvent did not exceed 0.02%. The water vapor sorption by the films was measured at 20°C in a vacuum setup with a McBain quartz-spring balance (spring sensitivity 0.5–0.7 mg mm^{-1}, accuracy within 0.01%) at the saturated solvent vapor pressure.

The polymer–solvent interaction parameters χ_1 for MC, NaCMC, CMC (α = 0.6), HCMC, and their blends were calculated from the sorption data by the Flory–Huggins equation [15]

$$\ln a_1 = \ln(P_1/P_1^0) = \ln(1 - \varphi_2) + \varphi_2 + \chi_1\varphi_2^2, \quad (4)$$

where a_1 is the solvent vapor activity, and P_1/P_1^0, relative pressure of the solvent vapor. The experiments were carried out at the saturated solvent vapor pressure, i.e., at $a_1 = P_1/P_1^0 = 1$ and, accordingly, $\ln a_1 = 0$.

The polymer–polymer interaction parameter was calculated from the sorption data by the Patterson relation [16]

$$\chi_{23} = (\chi_{12}\varphi_a + \chi_{13}\varphi_b - \chi_{1(23)})/(\varphi_a\varphi_b), \quad (5)$$

where χ_{12}, χ_{13}, and $\chi_{1(23)}$ are the respective Flory–Huggins interaction parameters for the MC, NaCMC, CMC ($\alpha = 0.6$), and HCMC polymers taken separately and for their mixtures with water, and φ_a and φ_b, respective volume fractions of the polymers in the blend.

For blends of compatible polymers, $\chi_{23} < 0$ [17].

Figures 1–3 show the flow curves of aqueous solutions of MC and CMC with different degrees of ionization and of their blends. The flow curves of the solutions are partial flow curves of non-Newtonian liquids. The structural viscosity branch for the MC solution becomes prominent at shear stresses over $\log \tau = 2.8$ ($\tau = 630$ Pa $\times 10^{-1}$). Upon conversion of NaCMC to the H form, structure formation occurs in the solution, resulting in an increase in viscosity and appreciable change in the shape of the flow curve [8]. The solution becomes more sensitive to changes in the shear stress.

The pattern of variation of the viscosity of dilute solutions of the polymer blends suggests possible interaction of different kinds of macromolecules in solution [4–7]. To test this assumption, we examined the pattern of variation of the reduced viscosity η_{red} of 0.2 wt % solutions of the blend of MC with NaCMC, CMC with the degree of ionization $\alpha = 0.6$, and HCMC ($\alpha = 0$). Figures 4a–4c demonstrate how the reduced viscosity of dilute solutions and the logarithm of viscosity of moderately concentrated solutions vary with the composition of the mixed systems.

For the dilute solutions of all the three polymer blends, η_{red} exceeds the additive value. In going from NaCMC to HCMC, the η_{red} parameters of the CMC solutions significantly decrease, which is consistent with our previous data [8].

The fact that the viscosity of the blends of the dilute solutions exceeds the additive value suggests that intermolecular interactions between the different kinds of macromolecules dominate in solution. This is responsible for the formation of structures whose hydrodynamic volume exceeds the weight-average hydrodynamic volume of the two components taken separately. The fact that the reduced viscosity of the solutions of the blends is lower than the additive value can be associated both with the compaction of the polymer macromolecules if they are incompatible and with the formation of mixed complexes whose hydrodynamic volume is smaller than those of the macromolecules of either polymer.

In going to the concentrated solutions, the shape of the curves representing log η in relation to the blend composition considerably changes, depending on the state (degree of ionization) of CMC in the blends.

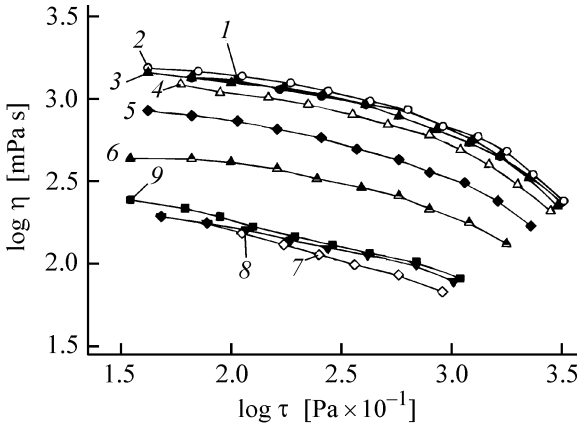


Fig. 1. Flow curves of 2 wt % solutions of (*1*) MC, (*2–8*) MC–NaCMC blends, and (*3*) NaCMC at 20°C. (η) Viscosity and (τ) shear stress; the same for Figs. 2 and 3. NaCMC content, wt %: (*2*) 5, (*3*) 10, (*4*) 23, (*5*) 50, (*6*) 70, (*7*) 90, and (*8*) 95.

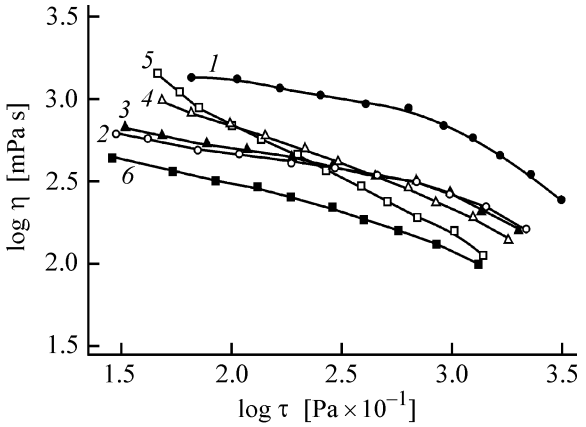


Fig. 2. Flow curves of 2 wt % solutions of (*1*) MC, (*2–5*) MC–NaCMC ($\alpha = 0.6$) blends, and (*6*) CMC at 20°C. NaCMC content, wt %: (*2*) 10, (*3*) 20, (*4*) 50, and (*5*) 70.

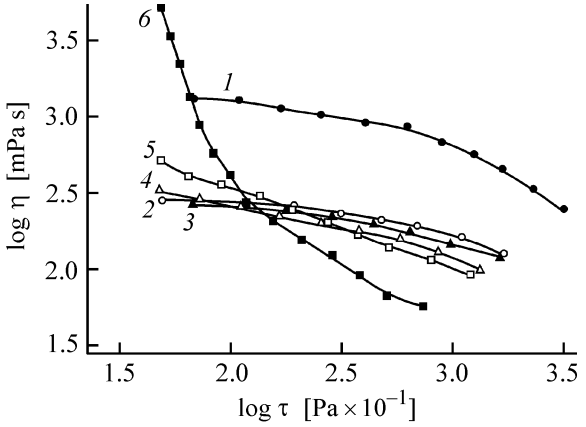


Fig. 3. Flow curves of 2 wt % solutions of (*1*) MC, (*2–5*) MC–HCMC ($\alpha = 0$) blends, and (*6*) HCMC at 20°C. HCMC content, wt %: (*2*) 10, (*3*) 20, (*4*) 50, and (*5*) 70.

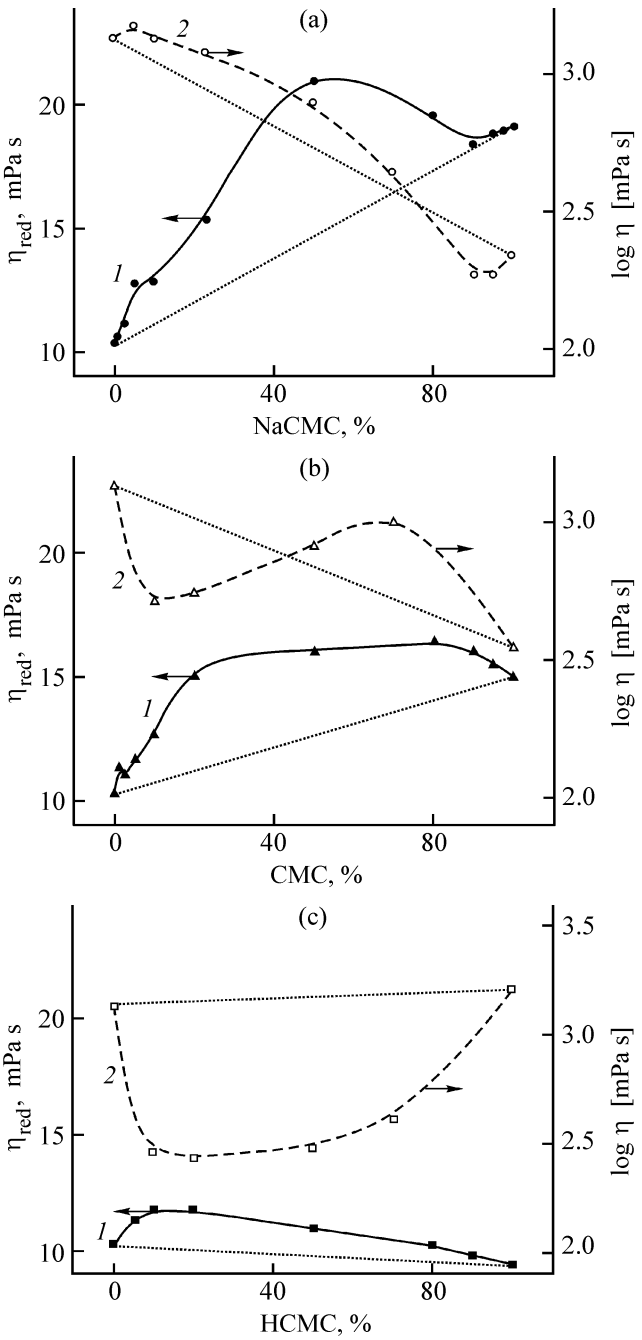


Fig. 4. (*1*) η_{red} and (*2*) log η in relation to the composition of dilute (0.2 wt %) and concentrated (2 wt %) solutions of MC–NaCMC blends at 20°C. Dotted lines denote the additive values. Blend: (a) MC–NaCMC, (b) MC–CMC, and (c) MC–HCMC.

The viscosity of the concentrated solutions of the polymer blends is affected by many factors. In blends of polymer solutions, new systems of hydrogen bonds can be formed, stronger than those in solutions of MC, NaCMC, and HCMC taken separately. It should be noted that addition to the MC solution of a different polymer can cause changes in the thermodynamic quality of the solvent (water) with respect to MC. The influence exerted on the solvent quality by a different macromolecular compound introduced into polymer solution was clearly demonstrated in [18–20]. The viscosity of concentrated solutions of polymer blends can be both higher and lower than the additive values.

At a NaCMC content of up to 80 wt %, the viscosity exceeds the additive values. For the compositions with over 80 wt % NaCMC, the viscosity is lower than the additive value (Fig. 4a). In concentrated solutions of the MC blends with a partly neutralized polyelectrolyte (CMC with $\alpha = 0.6$), the range of the compositions in which the viscosity of the solutions is lower than the additive value is wider (Fig. 4b). Finally, upon conversion of NaCMC to the H form, log η is lower than the additive value throughout the composition range examined. Major changes in the shape of the curve representing log η in relation to the composition, caused by variation of the degree of CMC ionization, can be associated with a change in the range of compositions at which the polymers are thermodynamically compatible, as well as in the hydrogen bond system in concentrated solutions of the polymers.

The table lists the results of examination of the thermodynamic compatibility of the two blended polymers in the solid state (according to solvent vapor sorption data). It is seen that MC and NaCMC are thermodynamically incompatible throughout the composition range examined. In the case of the blends of MC with partly neutralized CMC, the compatibility of polymers is observed in films containing up to 50 wt % MC. In the MC–HCMC blends, the thermodynamic compatibility of the polymers is observed at a MC content of up to 30 wt %. It can be presumed that, on passing from NaCMC to a partly neutralized polyelectrolyte, the number of carboxy groups COOH involved in the formation of a mixed system of hydrogen bonds among the functional groups of different kinds of polymers increases. With a further increase in the number of carboxy groups (passing to HCMC), the interaction of the carboxy groups is intensified so strongly that HCMC becomes virtually insoluble in water. This is responsible for the increase in the share of interactions between the macrochains of the polyelectrolyte in the blends and for the narrowing of the range of the compositions at which MC and HCMC are compatible.

Thus, by varying the amount of a different polymer introduced into an aqueous solution of MC (in particular, CMC with different degrees of ionization), it is possible to change the rheological properties of solu-

Amount of sorbed water Q and polymer–solvent (χ_1) and polymer–polymer (χ_{23}) interaction parameters

Composition, wt %		Q, g g^{-1}	χ_1	χ_{23}	Q, g g^{-1}	χ_1	χ_{23}	Q, g g^{-1}	χ_1	χ_{23}
x_1	x_2									
		MC–NaCMC (α = 1.0)			MC–CMC (α = 0.6)			MC–HCMC (α = 0)		
100	0	0.838	0.74	–	0.838	0.74	–	0.838	0.74	–
90	10	1.356	0.66	0.74	0.987	0.71	0.39	2.030	0.61	0.41
80	20	1.580	0.63	0.45	0.827	0.74	0.04	1.216	0.67	0.35
50	50	2.308	0.59	0.25	0.374	0.94	–0.77	1.080	0.69	0.10
30	70	2.641	0.58	0.21	0.762	0.75	–0.04	0.917	0.72	–0.09
0	100	2.858	0.56	–	0.690	0.76	–	1.118	0.68	–

tions and the gelation conditions in them and also to obtain films of blends in which the polymers can be thermodynamically compatible and incompatible. Solutions of MC–CMC blends are suitable as stabilizers and emulsifiers in food industry, and film materials thereof are attractive as packaging materials for foodstuff.

CONCLUSIONS

(1) The observed deviations of the viscosity from additivity in dilute and concentrated solutions of blends of methyl cellulose with carboxymethyl cellulose, having different degrees of ionization, are associated with the change in the conformation of the polymer macromolecules in the blends and structural rearrangements in solutions.

(2) Methyl cellulose is incompatible with the sodium salt of carboxymethyl cellulose. In blends of methyl cellulose with partly ionized carboxymethyl cellulose and that in the acid form, the two polymers are partially compatible. The range of the compositions in which the polymers are compatible varies with the degree of ionization of carboxymethyl cellulose.

REFERENCES

1. Bochek, A.M., Nud'ga, L.A., Petrova, V.A., and Petropavlovskii, G.A., *Zh. Prikl. Khim.*, 2000, vol. 73, no. 2, pp. 304–308.
2. Bochek, A.M., Petropavlovskii, G.A., Kutsenko, L.I., and Karetnikova, E.B., *Zh. Prikl. Khim.*, 2000, vol. 73, no 1, pp. 152–155.
3. Nikolaeva, O.V., Budtova, T.V., Kalyuzhnaya, L.M., et al., *Vysokomol. Soedin., Ser. A.*, 1999, vol. 41, no. 7, pp. 1176–1182.
4. Nud'ga, L.A., Petrova, V.A., Sergeeva, S.N., et al., *Vysokomol. Soedin., Ser. A*, 2003, vol. 45, no. 6, pp. 928–932.
5. Kutsenko, L.I., Ivanova, N.P., Karetnikova, E.B., et al., *Zh. Prikl. Khim.*, 2002, vol. 75, no. 2, pp. 314–318.
6. Kutsenko, L.I., Karetnikova, E.B., Bochek, A.M., et al., *Zh. Prikl. Khim.*, 2003, vol. 76, no. 10, pp. 1720–1724.
7. Bochek, A.M., Shevchuk, I.L., and Kalyuzhnaya, L.M., *Zh. Prikl. Khim.*, 2006, vol. 79, no. 12, pp. 2031–2036.
8. Yusupova, L.D., Bochek, A.M., and Petropavlovskii, G.A., *Zh. Prikl. Khim.*, 1994, vol. 67, no. 7, pp. 1187–1191.
9. Bochek, A.M., Petropavlovskii, G.A., Yusupova, L.D., et al. *Zh. Prikl. Khim.*, 1997, vol. 70, no. 12, pp. 2048–2052.
10. Petropavlovskii, G.A., *Gidrofil'nye chastichno zameshchennye efiry tsellyulozy i ikh modifikatsiya putem khimicheskogo sshivaniya* (Hydrophilic Partially Substituted Cellulose Ethers and Esters and Their Modification by Chemical Cross-Linking), Leningrad: Nauka, 1988.
11. Zhang, L.-M., *Colloid Polym. Sci.*, 1999, vol. 277, pp. 886–890.
12. Knyazeva, T.E., Myasnikova, I.B., Medvedeva, V.V., et al., *Vysokomol. Soedin., Ser. B.*, 2006, vol. 48, no. 5, pp. 864–868.
13. Kato, T., Yokoyama, M., and Takabashi, A., *Colloid Polym. Sci.*, 1978, vol. 256, no. 1, pp. 15–21.
14. *Eksperimental'nye metody v adsorbtsii i molekulyarnoi khromatografii* (Experimental Methods in Adsorption and Molecular Chromatography), Kiselev, A.V. and Dantsig, V.P., Eds., Moscow: Mosk. Gos. Univ., 1973.
15. Tager, A.A., *Fiziko-khimiya polimerov* (Physical Chemistry of Polymers), Moscow: Nauka, 1978, 3rd ed.
16. Su, C.S. and Patterson, D., *Macromolecules*, 1974, vol. 10, pp. 708–712.
17. Scott, R.L., *J. Polym. Sci.*, 1952, vol. 9, pp. 423–432.
18. Staszewska, D. and Bogdanecky, M., *Eur. Polym. J.*, 1981, vol. 17, no. 3, pp. 245–250.
19. Budtova, T.V., Bel'nikevich, N.G., Belyaev, V.M., et al., *Vysokomol. Soedin., Ser. B.*, 1991, vol. 33, no. 7, pp. 520–524.
20. Nud'ga, L.A., Petrova, V.A., Sergeeva, S.N., and Bochek, A.M., *Vysokomol. Soedin., Ser. A*, 2003, vol. 45, no. 6, pp. 928–932.

ISSN 1070-4272, Russian Journal of Applied Chemistry, 2008, Vol. 81, No. 4, pp. 696–703. © Pleiades Publishing, Ltd., 2008.
Original Russian Text © O.N. Bezkrovnaya, N.O. Mchedlov-Petrosyan, N.A. Vodolazkaya, V.I. Alekseeva, L.P. Savvina, A.G. Yakubovskaya, 2008, published in Zhurnal Prikladnoi Khimii, 2008, Vol. 81, No. 4, pp. 659–666.

MACROMOLECULAR CHEMISTRY AND POLYMERIC MATERIALS

Polymeric Langmuir–Blodgett Films Containing Xanthene Dyes

O. N. Bezkrovnaya, N. O. Mchedlov-Petrosyan, N. A. Vodolazkaya, V. I. Alekseeva, L. P. Savvina, and A. G. Yakubovskaya

Institute of Single Crystals, National Academy of Sciences of Ukraine, Kharkiv, Ukraine
Karazin National University, Kharkiv, Ukraine
Research Institute of Organic Intermediates and Dyes, Moscow, Russia

Received August 13, 2007

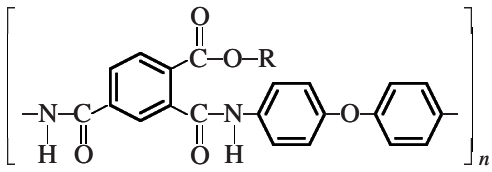
Abstract—Spectral and protolytic properties of two hydrophobic rhodamine dyes and fluorescein *n*-decyl ester were studied in Langmuir–Blodgett films based on a polyamido acid. The possibility of weakening the concentration quenching of rhodamine dye fluorescence with a polymeric matrix was demonstrated.

DOI: 10.1134/S1070427208040253

The Langmuir–Blodgett (LB) procedure allows preparation of nanosize highly ordered layers of biphilic molecules with exactly controllable thickness and directed orientation in space [1, 2]. Preparation of LB films (LBFs) containing dyes is of special interest because their optical and protolytic properties allow development various sensors in this way [3–8].

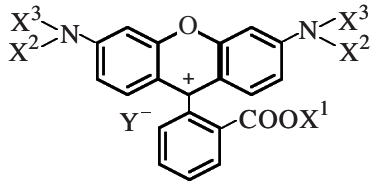
Xanthene dyes having high extinction coefficient and quantum yield of fluorescence are suitable for this purpose. Monolayers of rhodamines in stable matrices were studied in [3, 9–16]. Xanthenes are important group of dyes used in lasers [12], as photosensitizers [16], and in many other fields of photophysics and photochemistry. Both general questions of formation of mono- and *N*,*N*'-dioctadecylrhodamine B multilayers in various matrices (arachic acid and methyl arachate [9], dipalmitoylphosphatidic and dioleylphosphatidic acids [10]), and the ability of phosphors to form aggregates in films [10] have been considered. Preparation of *N*,*N*'dioctadecylrhodamine B monolayers on a subphase containing sodium lauryl sulfate was described in [11].

LBFs containing dyes in polymeric matrices have been studied to a considerably lesser extent. At the same time, films based on polymers are widely used owing to their high mechanical and chemical stability [1]. To obtain multilayer LBFs, polyamido acids (PAAs) are often used [1, 3, 4]. The structural formula of one of PAAs, poly(4,4'-diphenyl oxide)-2-carboxyisophthalamide (R = H) is shown below:



To make PAA macromolecules more hydrophobic, alkyl chains [R = $(CH_2)_{17}$–CH_3] are introduced into the PAA structure, or amines are added to form salts [17, 18]. To retain polymeric monolayers with carboxylic groups on the water surface, subphases containing metal ions are also used [1, 19, 20].

In this study, we prepared LBFs based on PAA containing immobilized xanthene dyes and examined properties of such well-ordered systems. Hydrophobic (lipoid) dyes: Rhodamine B *n*-heptadecyl ester perchlorate **1**: X^1 = *n*-$C_{17}H_{35}$, X^2 = X^3 = C_2H_5, Y^- = ClO_4^-, and *N*,*N*'-dioctadecylrhodamine chloride **2**: X^1 = X^2 = H, X^3 = *n*-$C_{18}H_{37}$, Y = Cl^-



1, **2**

and fluorescein *n*-decyl ester **3**, whose structural formulas (for the molecular and ionic form) will be presented below, were chosen as investigation objects. To prepare monolayer films, the above dyes were added to matrices that can form stable layers on the water surface. It should be taken into account that xantenes can form dimers in various matrices [21], which leads to concentration quenching of the fluorescence and to worsening of the luminophore performance. These luminophores are also used as probes; in a number of cases, they allow estimation of local electrostatic potentials [22]. Therefore, the goal of this study was not only to develop methods for preparing polymeric xantene-containing LBFs, but also to determine the optimal conditions of their probable functioning as elements of sensor devices.

EXPERIMENTAL

Dyes were synthesized by methods described in [23, 24] and identified by elemental analysis, ^{1}H NMR, and TLC. Stearic acid, *n*-octadecyl alcohol (ODA), and *n*-octadecylpyridinium bromide (ODPB), and also surfactants used in experiments with aqueous micellar solutions [cetylpyridinium chloride (CPC), cetyltrimethylammonium bromide, cetyldimethylammoniopropanesulfonate, and sodium lauryl sulfate] were purchased from Fluka (as a rule, they contained 99% main substance). Buffer mixtures were prepared from chemicals of chemically pure grade. Oligomeric PAA with a molecular weight of the chain unit of 374 g mol^{-1} was used.[1]

The initial 1×10^{-3} M PAA solutions were prepared in a 1 : 1 mixture of chemically pure dimethylformamide and chloroform, and the initial solutions of stearic acid, ODA, and ODPB of the same concentration, in chloroform. $Pb(NO_3)_2$ was of chemically pure grade. Before an experiment, a bath was successively treated with 96% aqueous ethanol and chloroform and then filled with double-distilled water or a lead nitrate solution. Double-distilled water or a 1×10^{-5} M lead salt solution was used as a subphase; a decrease in the salt concentration makes weaker the influence of lead ions on the polymer.

Measurements were performed in a Langmuir bath with two 6.5×60 cm sections. The surface pressure π was recorded with a Wilhelmy balance (measurement error ± 0.3 mN m^{-1}) at 20 ± 5°C. An organic solvent containing PAA was applied onto the water surface, and the system was allowed to stand for 5 min (time required for a monolayer to spread over the surface of the aqueous subphase, evaporation of the solvent, and accommodation of polymeric molecules). Then, the monolayer formed was compressed by an unwettable mobile barrier at a 3 cm min^{-1} velocity to a required pressure, which was then automatically kept constant.

The state of monolayers on the surface of the aqueous subphase was studied by plotting the π–A compression isotherms, where A is the surface area per recurring chain unit (Å^2). The limiting surface area S_m occupied by one chain unit was found by extrapolation of the linear portion of the isotherm to the abscissa; the determination error was $\pm$(1–3) Å^2. From the compression isotherms, we determined the optimal surface pressure of applied monolayers corresponding to the most condensed state (in the middle of the linear portion). To prepare a mixed monolayer, the dye dissolved in chloroform was added to a mixture of PAA and *n*-octadecyl alcohol (or *n*-octadecylpyridinium bromide), or stearic acid, and then the resulting mixture was applied dropwise onto the surface of the aqueous subphase.

Monolayers were deposited onto glass or quartz plates by the Scheffer method; in so doing, π was 35 mN m^{-1} in the case of **1** and 30 (25) mN m^{-1} for **2** (in stearic acid or ODPB matrix, respectively). The pressure of transfer for the PAA + ODPB + **3** mixture was 25 mN m^{-1}. Prior to monolayer deposition, supports were pretreated with a peroxide–ammonia mixture and then washed with double-distilled water, acetone, and chloroform [3].

The glass supports with deposited multilayers of ODPB + **2** and PAA + ODPB + **3** were kept for 5 and 1 min, respectively, in aqueous solutions with known pH and dried for several minutes in air. It has been shown previously that introduction of a lead salt into the subphase is the optimal method for stabilization of PAA monolayers on the water surface [20]. Pb^{2+} ions can pass into the aqueous phase because of the interaction with Br^- ions introduced with ODPB. However, special experiments showed that only a small part of lead ions pass into the aqueous phase. The Pb^{2+} content of the monolayers was monitored by analysis of LBFs by X-ray photoelectron spectroscopy (Kratos XPS-800 spectrometer; photoelectrons were excited by $Al(Mg)_{K_\alpha}$ radiation; power of X-ray tube 15 kV × 20 mA).

The pH value [$\pm$(0.01–0.04)] was monitored with a glass electrode in an electric circuit with transfer.

[1] Oligomeric polyamido acid was synthesized in the Chernigov Pedagogical University by the known procedure [25] and identified in the Kiev National University, Chair of Macromolecular Compounds.

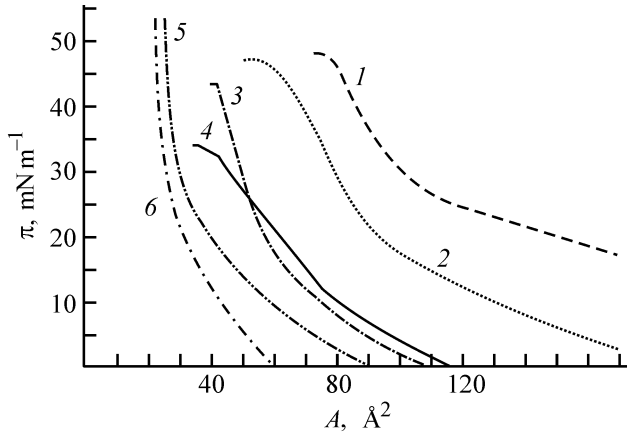


Fig. 1. Surface pressure π vs. the surface area *A* per repeating unit of polymer for different systems: (*1*) PAA : ODPB = 1 : 1 + 28 mol % **1**, (*2*) PAA : ODA = 1 : 1 + 22 mol % **1**; (*3*) PAA : ODA = 1 : 1, (*4*) PAA : ODPB = 1 : 1, (*5*) stearic acid + 3 mol % **1**, and (*6*) stearic acid + 1.5 mol % **1**. Dependences (*1–4*) were obtained with films prepared on a Pb^{2+}-containing subphase. The dye concentration is expressed in molar percent relative to the total number of moles of the components in the mixture.

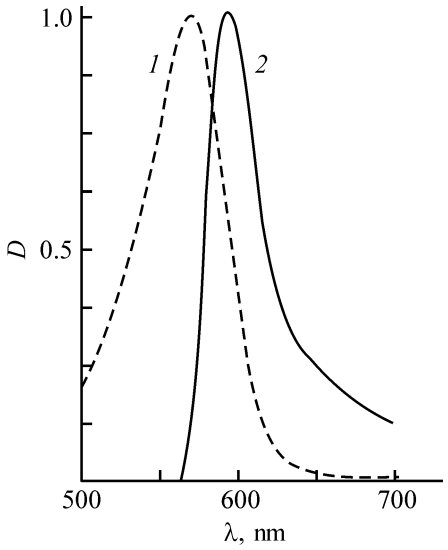


Fig. 2. (*1*) Absorption and (*2*) fluorescence spectra of dye **1** in PAA : ODPB = 1 : 1 + 6 mol % **1** film. Film was applied by the scheme ABBBABBB (n = 60, N = 240). (*D*) Optical density and (λ) wavelength; the same for Figs. 3–5.

The absorption spectra of films containing dyes were recorded on a Specord M 40 spectrophotometer, and the fluorescence spectra, on a Hitachi F-4010 spectrophotometer; the films without dyes were used as reference samples.

The fluorescence of LBFs containing dyes **1**–**3** was extremely weak. This may be due both to probable aggregation (dimerization) of dye molecules and to concentration quenching. Therefore, we recorded fluorescence using the method described in [10]. A multilayer structure was prepared by alternation of layers ABBBABBB (A is a layer of a dye-containing mixture, prepared on a Pb^{2+}-containing subphase; B is ODPB layer prepared on a pure subphase). Such a separation of layers containing a dye (their number n in all cases was 60) leads to a sharp enhancement of the fluorescence, despite that the pyridinium ring also exerts a quenching effect. The total number of layers we denoted as N.

Preliminarily, we studied the behavior of monolayers of PAA + ODA and PAA + ODPB mixtures on the surface of both pure and lead-containing water subphases. The surface areas per repeating unit of the polymer for the mixtures PAA : ODA = 1 : 1 (counting on repeating unit, S_m = 62 Å^2) and PAA : ODPB = 1 : 1 (S_m = 92 Å^2), evaluated from the compression isotherms, agree with the values published earlier for similar systems [18].

Typical compression curves for mixed layers containing dye **1** are shown in Fig. 1. Introduction of a dye into the matrix of stearic acid increases the surface area per molecule from 27.5 [content of dye **1** 1.5 mol %] to 33.4 Å^2 (3 mol %). At a dye content of 22 mol % in the PAA : ODA = 1 : 1 mixture, the maximal surface area increases to 112.7 Å^2 (in the mixture without dye, it is about 56 Å^2). The S_m value in the PAA : ODPB = 1 : 1 mixture increases from 92 to 131 Å^2 upon introduction of 28 mol % hydrophobic rhodamine **1** into the film. Figure 1 shows that mixtures without dye form a denser monolayer whose loosening becomes possible when large dye molecules are introduced.

The absorption and fluorescence spectra (wavelength of fluorescence excitation λ = 520 nm) of polymeric films containing dye **1** are shown in Fig. 2. The absorption and fluorescence peaks (±2 nm) are observed at 564 and 593 nm, respectively. For aqueous micellar solutions of both cetyltrimethylammonium bromide and sodium lauryl sulfate at a surfactant concentration of 0.01 M, these values are 555 and 579 nm, respectively, and binding of dye molecules insoluble in water with surfactant micelles is beyond any doubt. The red shift of both bands in the LBF spectra, compared to the spectra of aqueous micellar solutions, suggests a more dehydrated surrounding of the dye molecules in the multilayers.

With increasing content of dye **1** in LBF of both stearic acid and PAA + ODPB, the absorption maximum is shifted bathochromically from 564 to

Table 1. Effect of matrix on the D_2/D_1 ratio in multilayer films ($n = N = 60$) containing (**1**) Rhodamine B *n*-heptadecyl ester and (**2**) *N*,*N*'-dioctadecylrhodamine

System	Dye concentration, mol %	Method of film preparation	Absorption, λ_{max}, nm (±2)	D_1/D_2 ratio
LBF:				
PAA + ODPB + **1**	28	LB	570	0.50 ± 0.06
PAA + ODA + **1**	17.3	LB	568	0.55 ± 0.03
Stearic acid + **1**	6.5	LB	570	0.65 ± 0.03
Stearic acid + **1**	6.5	Casting	570	0.71 ± 0.03
1	100	"	572	0.80 ± 0.05
PAA + ODPB + **1**[*]	6	LB	570	0.42 ± 0.02
PAA + ODA + **1**[*]	6	LB	570	0.44 ± 0.02
Aqueous micellar solutions + **1**	10^{-5}–10^{-6} M	–	555	0.25
LBF:				
PAA + ODPB + **2**[**]	2	LB	543	0.77 ± 0.02
ODPB + **2**	2	LB	543	0.75 ± 0.05
Aqueous micellar solutions + **2**	10^{-5}–10^{-6} M	–	525–530	0.28 ± 0.33[***]

[*] Films were prepared with the introduction of sandwiching layers of ODA ($n = 60$, $N = 240$). The other films were prepared without additional ODA layers ($n = 60$).

[**] The data are related to the zwitterionic form of dye **2**, prevailing in neutral and alkaline media.

[***] For cationic form of dye **2** (measurements at HCl concentration of 0.06 M), 0.29–038.

572 nm. In going from the polymeric matrix to stearic acid and neat dye film prepared by casting, the intensity of absorption in the region of 530 nm increases and the absorption band becomes strongly broadened (Table 1, Fig. 3), which may be caused by formation of dimers and other aggregates of the dye upon an increase in its content in the film.

The main spectral maximum of monomer **1** in the LBF spectrum lies at $\lambda_1 \sim 570$ nm. The shortwave shoulder caused by the vibrational structure of the spectrum lies at $\lambda_2 \sim 530$ nm, as in the spectra of sandwich-type dimers [10]. The presence of dimers in the film studied (Fig. 3) is usually judged from the ratio of the absorption intensities at λ_2 and λ_1 (D_2/D_1). For systems with monomers, this ratio falls within 0.3–0.5 [10, 15]. Ishibashi et al. [14] reported a decrease in D_2/D_1 when the matrix with the maximal surface area at the phase boundary (dipalmitoylphosphatidylcholine as compared to dipalmitoylphosphatidic acid) was used. The decrease in D_2/D_1 was also noted [10] when dioleylphosphatidic acid characterized by a larger surface area of the molecule as compared to dipalmitoylphosphatidic acid was used.

The D_2/D_1 ratio for dye **1** is greater in stearic acid in comparison with the polymeric matrix and is considerably greater in the neat dye film prepared by casting (Table 1, Fig. 3). It is interesting that the use of both ODPB and ODA for PAA stabilization at the water–air interface shows the same effect of a decrease in the number of dimers in monolayers containing dye **1**. This can be accounted for by the fact that the polymer chain stabilized by a long-chain alcohol or amine molecule occupies larger surface area on the surface of the water subphase as compared to stearic acid molecule. As a result, in the polymeric multi-

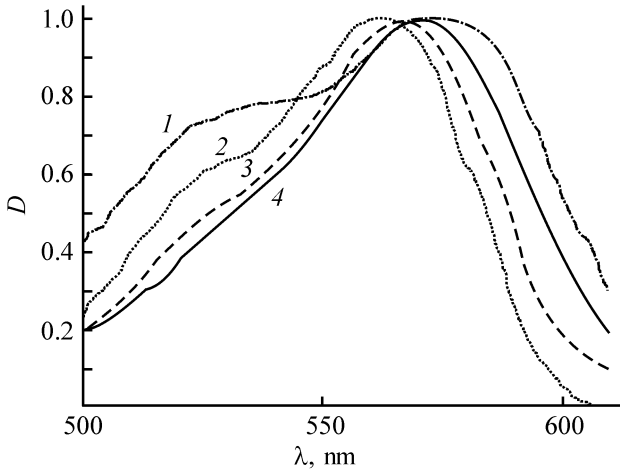


Fig. 3. Normalized absorption spectra of dye **1** in films. Film: (*1*) applied by casting of neat dye **1**; (*2*) stearic acid + 6.5 mol % **1**; (*3*) mixed PAA : ODPB = 1 : 1 + 17.3 mol % **1**; and (*4*) mixed PAA : ODPB = 1 : 1 + 28 mol % **1**. Films (*2*–*4*) are prepared on a Pb^{2+}-containing subphase ($n = N = 60$).

Table 2. Spectral properties of *N*,*N*'-dioctadecylrhodamine **2** in LBFs of various compositions

System*	pH of solution for support treatment	Sandwiching layers	Transfer pressure, mN m^{-1}	λ_{max}, nm (± 1)	
				absorption	fluorescence
PAA : ODPB = 1 : 1	6	No	30	543	590
	1.2	Yes	30	551	592
	6	"	30	543	573
	6	No	15	543	583
ODPB	6	"	25	542	–
	1.5	"	25	550–551	–

* PAA : ODPB ratio per repeating unit; the mole fraction of dye **2** is equal to 2%.

layers, the volume concentration of dye molecules becomes smaller, and they become more isolated from each other at virtually the same molar concentration in the monolayer (Fig. 3).

Introduction of intermediate ODA layers into the PAA + ODPB + **2** (2 mol % dye) film does not substantially change the D_2/D_1 ratio (0.79). At the same time, in 50 and 88 wt % aqueous ethanol, in 0.005 M solutions of cetyltrimethylammonium bromide and sodium lauryl sulfate, and in 0.001 M solution of sodium cetyldimethylammoniopropanesulfonate, the D_2/D_1 ratio for the acid and alkaline dye forms vary within 0.288–0.380 and 0.275–0.332, respectively. Since the dye concentration was 2×10^{-6} M, the monomer is the dominant form here.

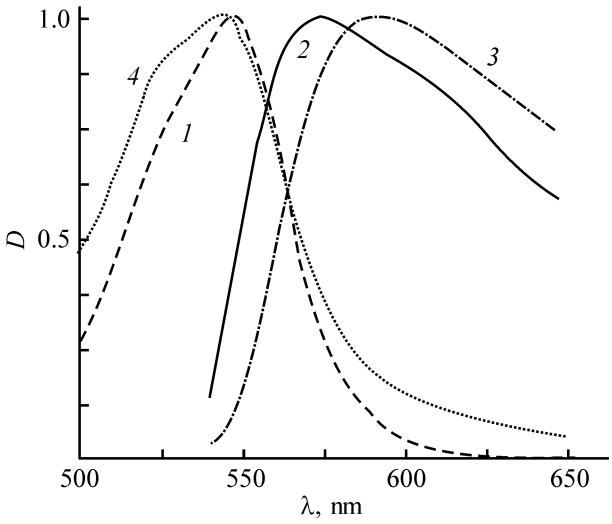


Fig. 4. (*1*) Absorption and (*2*) fluorescence spectra of PAA : ODPB = 1 : 1 + 2 mol % dye **2** films. Film was applied by the scheme ABBBABBB (n = 60, N = 240) at π = 30 mN m^{-1}; (*3*) fluorescence spectrum of the same film after treatment with a solution with pH 1.3 for 3 min; (*4*) absorption spectrum of ODPB + 2 mol % **2** ($n = N = 60$) film.

To obtain monolayers containing dye **2**, we used matrixes able to form monolayers at the water–air interface, because by applying neat dye **2** onto the surface of the water subphase (~10^{-5}–10^{-7} M) we failed to obtain a film with a sufficient surface pressure. This observation is in accordance with data for the other dyes [9].

Applying layers of ABBBABBB type causes a shift to shorter wavelengths (574 nm) as compared to alternate application of the monolayers (583 and 590 nm at a transfer pressure of 15 and 30 mN m^{-1}, respectively). Such effects are described in [10] and are associated with the dye concentration in the monolayer with increasing 2*D* compression.

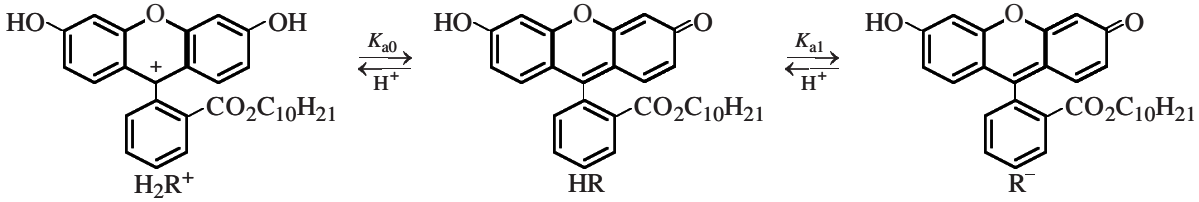
Dye **2** containing a free carboxy group can change its spectral properties with the acidity of the medium (Table 2, Fig. 4). The absorption and fluorescence peaks in the spectra of the initially prepared film lie at 543 ± 1 and 583 ± 1 nm, respectively, but after its immersion into an acid medium (aqueous HCl solution with pH 1.3) both bands are red-shifted. Similar features are observed upon introduction of dye **2** into an ODPB film. The band shift is associated with the transition of the dye molecule into the protonated form. At the same time, in micellar solutions of various surfactants, the above values of λ_{max} are lower by 20–30 nm than those for LBF, which, as in the case of dye **1**, suggests the more dehydrated surrounding of rhodamine **2** as compared to aqueous micellar solutions.

Fluorescein *n*-decyl ester **3** is one of dyes with a pH response, used for study of lyophilic dispersions [22, 26]. The possibility of preparing a Langmuir monolayer of neat dye 3 and its mixture with stearic acid was examined in [16]. In this study, we prepared

Table 3. Parameters of equilibrium for fluorescein *n*-decyl ester **3** in various systems

Parameter	LBF PAA : ODPB = 1 : 1	Aqueous solution of CPC with addition of 0.4 M NaCl	Aqueous solution of fluorescein ethyl ester as homolog of **3** [22]
λ_{max}, H_2R^+, nm	456	449	438
λ_{max}, HR, nm	470, 505	465, 490	450, 465
λ_{max}, R^-, nm	525	516	491
pK^a_{a0}	1.63 ± 0.10	1.32 ± 0.01	2.94
pK^a_{a1}	6.48 ± 0.16	5.52 ± 0.02	6.31

colored and fluorescent multilayer polymeric films based on this dye. Depending on pH of the solution, three forms of **3** exist: cationic (H_2R^+), molecular (HR), and anionic (R^-) [22, 26]:



After treatment of the support with acid solutions, dye **3** in multilayers transforms into the H_2R^+ form, which is undoubtedly confirmed by the existence of a strong absorption band at 456 nm (Fig. 5). At high pH, dye **3** in LBF transforms into anion R^- (Fig. 5, band at 525 nm). After treatment with solution with pH 2.6 (Fig. 5), a three-band spectrum characteristic of the molecular form HR is observed [22, 26]. Thus, in LBF, two steps of protolytic transformations of dye **3**, $H_2R^+ \rightleftarrows HR + H^+$ and $HR \rightleftarrows R + H^+$, are also observed. In the course of experiments, LBF was immersed into aqueous solutions whose pH was adjusted with acetate, phosphate, and borate buffer solutions and with HCl; as a rule, the ionic strength of the solution was kept constant (0.05 M) by NaCl additions.

The spectra of micellar solutions are, on the whole, similar, but all values of λ_{max} are noticeably lower (Table 3). This fact confirms the conclusion made above for rhodamines **1** and **2** about dehydration of LBF dried in air. The apparent ionization constants pK^a_{a0} and pK^a_{a1} for dye **3** in LBF and micellar CPC solution and the same parameters for a short-chain analog, fluorescein ethyl ester, found by the standard spectrophotometric method [26] are listed in Table 3.

Both values of pK^a_a for CPC in micellar solutions are lower than those in aqueous solutions, which is associated with the positive charge of the micellar surface, at which ionized groups are probably localized [22, 26]; at lower concentration of the supporting electrolyte (0.05 M instead of 0.4 M NaCl), the pK^a_a values are still lower: pK^a_{a0} 0.79 ± 0.10 and pK^a_{a1} 4.92 ± 0.07 [22]. In the case of LBF of composition PAA + ODPB at low pH values, the dye surrounding

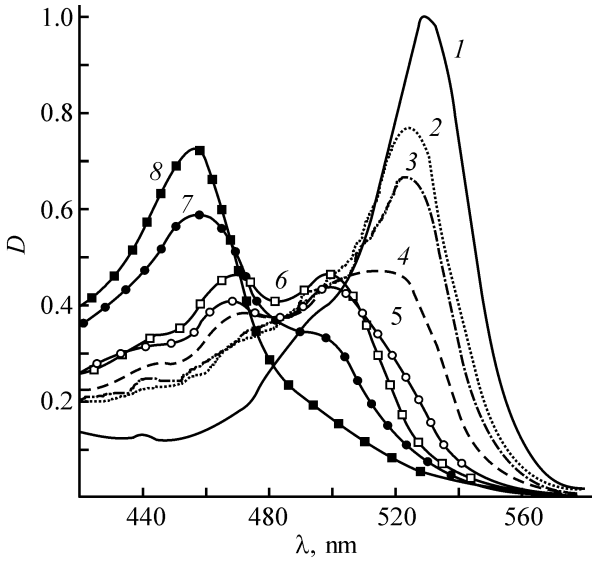


Fig. 5. Absorption spectra of fluorescein *n*-decyl ester in the PAA : ODPB = 1 : 1 ($n = N = 60$) film after its treatment for 1 min in aqueous solutions with pH (*1*) 11.2, (*2*) 8.6, (*3*) 7.0, (*4*) 6.1, (*5*) 4.26, (*6*) 2.6, (*7*) 1.4, and (*8*) ≤1.1. Films were obtained on a Pb^{2+}-containing subphase at pH 5.8; dye **3** content 13 mol %.

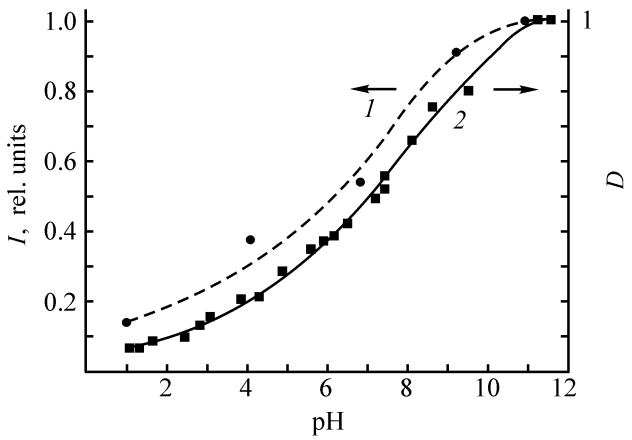


Fig. 6. pH dependence of the intensity I of (*1*) fluorescence and (*2*) absorption of LB film (PAA : ODPB = 1 : 1). Mole fraction of dye **3** in the film 13%; time of film immersion in aqueous buffer solution 1 min at 20°C; optical density was measured at 525 nm, and fluorescence, at 552 nm; Wavelength of fluorescence excitation 500 nm. Luminescence was measured for a film with $n = 60$ and $N = 240$, and absorption, for a film with $n = N = 60$.

is close to that in CPC micelles, whereas with increasing pH the carboxy groups in the polymer undergo ionization, the charges of the carboxylate and pyridinium ions are mutually neutralized, and the pK_{a1}^{a} value corresponds to a weakly charged or even neutral layer.

From the viewpoint of the practical use of such LBFs, it is important how the optical density and fluorescence intensity respond to changes in the pH of the aqueous phase in which the films are immersed. In the case of dye **3**, the transition interval covers the physiological range of pH values (Fig. 6). Unusual for acid-base indicators extension of the transition interval is of interest. Such "nonclassical" phenomena are typical of complex sensor devices [27, 28]. They may be associated with the multiplicity of localization sites of the dye in the film and with the existence of islets of the neat dye. In CPC micellar solutions (Table 3) and in other colloidal systems [22, 26], the transition intervals are quite traditional.

In general, unambiguous interpretation of the indicator behavior in sensors is a complex problem [29]. A series of fluorescent pH sensors based on derivatives of fluorescein *n*-octadecyl ester (without using LBF) was examined by Wolfbeis et al. [30, 31].

The measurements performed showed that the pH dependences of the absorption and fluorescence (Fig. 6) are well reproducible and can be used as calibrating curves in optical sensors. The films studied do not decompose and do not change their properties for two years, if kept in the dark at room temperature. The growth of the fluorescence intensity in the physiological region of pH allows use of multilayer polymeric films based on compound **3** as elements of sensor devices in biochemical studies.

CONCLUSIONS

(1) Langmuir–Blodgett multilayer films containing xanthene dyes Rhodamine B *n*-heptadecyl ester, *N*,*N*'-dioctadecylrhodamine, and fluorescein *n*-decyl ester were prepared on the basis of a polyamido acid. Their spectral-luminescence and acid–base properties were studied.

(2) The use of a polymeric matrix makes lower the possibility of formation of dimers from Rhodamine B *n*-heptadecyl ester and *N*,*N*'-dioctadecylrhodamine in Langmuir–Blodgett films.

(3) Changes in the light absorption and fluorescence of the indicator, fluorescein *n*-decyl ester, immobilized in a polymer matrix, observed in the physiological range of acidities, are well reproducible and can be used to prepare stable ultrathin nanodimensional pH-sensitive sensor films for multiple use.

ACKNOWLEDGMENTS

The authors are grateful to A.V. Tolmachev for fruitful discussion and to M.V. Dobrotvorskaya for analyses by X-ray photoelectron spectroscopy.

REFERENCES

1. Arslanov, V.V., *Usp. Khim.*, 1994, vol. 63, no. 1, pp. 3–42.
2. Blinov, L.M., *Usp. Fiz. Nauk*, 1989, vol. 155, no. 3, pp. 443–480.
3. Shtykov, S.N., Klimov, B.N., Smirnova, T.D., et al., *Zh. Fiz. Khim.*, 1997, vol. 71, no. 7, pp. 1292–1295.
4. Shtykov, S.N., Rusanova, T.Yu., Smirnova, T.D., and Gorin, D.A., *Zh. Anal. Khim.*, 2004, vol. 59, no. 2, pp. 198–201.
5. Hassan, A.K., Ray, A.K., Nabok, A.V., et al., *Sensors Actuators B: Chem.*, 2001, vol. 77, pp. 638–641.
6. Worsfold, O., Dooling, C.M., Richardson, T.H., et al., *J. Mater. Chem.*, 2001, vol. 11, pp. 399–403.
7. Jian, Y. and Xie, D., *Sensors Transducers Mag.*, 2004, vol. 39, no. 1, pp. 106–111.
8. Turshatov, A.A., Bossi, M.L., Mobius, D., et al., *Thin Solid Films*, 2005, vol. 476, pp. 336–339.
9. Yonezava, N., Ohno, M., Suga, S., et al., *J. Chem. Soc. Jpn.*, 1987, no. 1, pp. 116–118.

10. Ballet, P., Van der Auweraer, M., De Schryver, F.C., et al., *J. Phys. Chem.*, 1996, vol. 100, pp. 13 701–13 715.
11. Slyadneva, O., Harata, A., and Hatano, Y., *J. Colloid. Interface Sci.*, 2003, vol. 260, pp. 142–148.
12. Ray, K. and Nakahara, H., *J. Phys. Chem. B*, 2002, vol. 106, pp. 92–100.
13. Miura, A. and Tamai, N., *Chem. Phys. Lett.*, 2000, vol. 328, pp. 23–31.
14. Ishibashi, K.I., Sato, O., Baba, R., et al., *J. Colloid. Interface Sci.*, 2001, vol. 233, pp. 361–363.
15. Vuorimaa, E., Belovolova, L.V., and Lemmetyinen, H., *J. Luminescence*, 1997, vol. 71, pp. 57–63.
16. Alekseeva, V.I., Ibraev, N.Kh., Luk'yanets, E.A., et al., *Zh. Fiz. Khim.*, 1999, vol. 73, no. 12, pp. 2217–2222.
17. Uekita, M., Awadji, H., and Murata, M., *Thin Solid Films*, 1988, vol. 160, pp, 21–32.
18. Nishikata, Y., Kakimoto, M., Morikawa, A., et al., *Thin Solid Films*, 1988, vol. 160, pp. 15–20.
19. Kumenura, H., Kasuga, T., Watanabe, T, et al., *Thin Solid Films*, 1989, vol. 178, pp, 175–182.
20. Bezkrovnaya, O.N., Mchedlov-Petrosyan, N.O., and Savvin, Yu.N., *Zh. Fiz. Khim.*, 2003, vol. 77, no. 12, pp. 2206–2210.
21. Mchedlov-Petrosyan, N.O., and Kholin, Yu.V., *Zh. Prikl. Khim.*, 2004, vol. 77, no. 3, pp. 421–429.
22. Mchedlov-Petrosyan, N.O., *Differentsirovanie sily organicheskikh kislot v istinnykh i organizovannykh rastvorakh* (Differentiation of the Strength of Organic Acids in True and Organized Solutions), Kharkov: Khar'k. Nats. Univ., 2004.
23. Ioffe, I.S., Gofman, I.F., and Zal'manovich, M.Z., *Zh. Org. Khim.*, 1965, vol. 1, no. 3, pp. 584–587.
24. Brown, L., Halling, P.J., Johnston, G.A., et al., *J. Chem. Soc., Perkin Trans. 1*, 1990, pp. 3349–3353.
25. Adrova, N.A., Bessonov, M.I., Laius, L.A., et al., *Poliimidy – novyi klass termostoikikh polimerov* (Polyimides: A New Class of Heat-Resistant Polymers), Leningrad: Nauka, 1968.
26. Mchedlov-Petrosyan, N.O., Isaenko, Yu.V., Salamanova, N.V., et al., *Zh. Anal. Khim.*, 2003, vol. 58, no. 11, pp. 1140–1154.
27. Malis, C., Butler, T.M., and MacCraith, B.D., *Thin Solid Films*, 2000, vol. 368, pp. 105–110.
28. Bacci, M., Baldini, F., and Scheggi, A.M., *Anal. Chim. Acta*, 1988, vol. 207, pp. 343–348.
29. Janata, J., *Anal. Chem.*, 1992, vol. 64, no. 13, pp. 921A–927A.
30. Weidgans, B.M., Krause, C., Klimant, I., and Wolfbeis, O.S., *Analyst*, 2004, vol. 129, pp. 645–650.
31. Schröder, C.R., Weidgans, B.M., and Klimant, I., *Analyst*, 2005, vol. 130, pp. 907–916.

ISSN 1070-4272, Russian Journal of Applied Chemistry, 2008, Vol. 81, No. 4, pp. 704–707. © Pleiades Publishing, Ltd., 2008.
Original Russian Text © N.K. Luneva, L.I. Petrovskaya, 2008, published in Zhurnal Prikladnoi Khimii, 2008, Vol. 81, No. 4, pp. 667–671.

MACROMOLECULAR CHEMISTRY AND POLYMERIC MATERIALS

Performance of Intumescent Fire Retardant for Wood

N. K. Luneva and L. I. Petrovskaya

Institute of General and Inorganic Chemistry, National Academy of Sciences of Belarus, Minsk, Belarus

Received December 6, 2007

Abstract—Performance characteristics of new fire-retardant formulations are studied, including their water resistance and the effect of additives.

DOI: 10.1134/S1070427208040265

Wood has always been high among man's preferred building materials for many reasons. It is highly workable and has minimal environmental pollution. However, the use of wood can be restricted by safety requirements and regulations concerned with its ignitability and fire spreading characteristics. The most significant loss by fire falls at untreated wood constructions and buildings. Of course, one can raise the fire resistance only to a certain limited extent, and no building is completely fireproof. Until now, the problem of wood protection against fire remains very topical. At present, intumescent fire retardants (FRs) are mostly used for treatment of timbers. However, the mechanisms of chemical transformations in intumescent FRs under heating still remains to be understood. The reasons are their complex composition and the fact that the main reactions occur at high temperatures.

The goals of this study were to develop new green intumescent fire retardants for wood and to examine the effect of their composition and kind of binder (of various viscosities) on the protective action and water resistance. The formulations studied consisted of polyposphorous compounds, a water-organic dispersion, and fire inhibitors (organic amides and polyols providing expansion of the intumescent fire-retardant coating). Finally, thermal degradation of FR-treated wood was studied at 20–700°C.

Therefore, we report here the properties of phosphorus–nitrogen-containing fire retardants: effect of their composition on the protective action, water resistance of the formulations, and thermal decomposition and stability of phosphorus- and nitrogen-containing compounds in FR-treated wood samples.

EXPERIMENTAL

Among diverse organic amides and polyols, we selected those whose thermal decomposition occurs within the same temperature range as the thermal degradation of wood. We used as a binder water–organic dispersions of various kinds. The components were intimately ground and then mixed with a binder for 30 min to obtain a homogeneous paste. As samples served $30 \times 60 \times 150$ mm wood blocks. The FR consumption was 270–300 g m^{-2}. The fire and water-resistance tests were performed according to GOST (State Standard) 16 363–98 [1] and GOST 16 712–71 [2], respectively.

A DTA analysis of FR-treated wood samples (200 mg) was carried out on a Paulik–Paulik–Erdey derivatograph at a heating rate of 20 deg min^{-1}. For analysis, we used sawdust (3–5 mm) treated with phosphorus–nitrogen-containing formulations (wet weight increment of the fire retardant was 170% relative to dry sawdust) and then dried to constant weight at 45°C. The initial and heat-treated samples were analyzed for phosphorus and nitrogen. Phosphorus was determined photocolorimetrically [3], and nitrogen, by the method described in [4]. X-ray diffraction patterns were obtained using a DRON-3 instrument with Cu_{K_α} radiation (Ni filter) over the 2θ range 2°–60°.

Currently, phosphorus–nitrogen-containing intumescent fire retardants are most widely used for wood. We have developed high-performance green phosphorus–nitrogen-containing intumescent fire retardants consisting of Craymul 2322 vinyl acetate aqueous-organic dispersion [CRAY VALLEY (Italia)], ammonium phosphate, a polyol, an organic amide, and organometallic compounds [5]. It was demonstrated that

Table 1. Composition of phosphorus–nitrogen-containing fire retardants and their efficiency for wood (pH 5 of the FR formulation)

FR composition*	Additives to PMA, wt %	Weight loss in fire test, wt %	Rank of fire retardancy [GOST (State Standard) 16 363–98]
PMA (1 + 2 + 3 + 4)	–	22.9	Second
PMA + 5	10.0	14.0	〃
PMA + 6	10.0	7.2	First
PMA + (5 + 6)	10.0 – 5 + 10.0 – 6	5.0	〃
PMA + (5 + 6)	7.0 – 5 + 10.0 – 6	4.5	〃
PMA + (5 + 6)	5.0 – 5 + 7.0 – 6	6.4	〃

* (1) Craymul 2322, (2) ammonium phosphate, (3) aluminum hydroxide, (4) water, (5) organic amide, and (6) polyol.

Table 2. Phosphorus content in FR-treated samples after water-resistance test

Dispersion no.*	Dispersion grade	Polymer**	Viscosity, mPa s	Phosphorus content of samples, wt %	
				after test	initial
1	HW 1	VAc	12 000–20 000	7.2	9.5
2	H474 N	VAc	9000–14 000	4.4	9.4
3	H400 E8	VAc	16 000–20 000	4.4	7.5
4	A-10	St/A	200–1000	5.2	9.5
5	A-160	St/A	100–800	4.8	9.8
6	H 50	VAc	4000–7000	5.0	8.7
7	K 24	VAc/A	1500–3500	4.7	9.5
8	K 65	VAc/A	1400–4000	5.0	9.0
9	K 200	VAc/Veo	3000–7000	4.8	8.8
10	A–30	A	100–300	5.1	9.1
11	Craymul 2322 (Italia)	VAc	4800	4.1	9.1
12	Polyvinyl alcohol	PVA	–	4.7	9.2
13	B/St 65	B/St	–	3.8	8.7

* Sample nos. 1–10: FINNDISP dispersions.

** (A) Acrylate, (B) butadiene, (VAc) vinyl acetate, (Veo) vinyl versatate, and (St) styrene.

the fire retardancy is a function of the FR composition. Fire tests showed that the formulations developed are classed with the First Group in their fire-retardant efficiency, and FR-treated wood, with poorly flammable materials (Table 1) [6].

Fire tests showed (Table 1) that the phosphorus–nitrogen-containing formulation consisting of ammonium phosphate, vinyl acetate dispersion, and aluminum hydroxide (PMA formulation) is characterized by a weight loss of 22.9 wt %. Samples treated with this formulation meet the requirements for poorly flammable materials. Introduction of an organic amide (10 wt %) reduces the weight loss from 22.9 to 17.2%, whereas introduction of the same concentration of a polyol, from 22.9 to 7.2%. When both additives were introduced (10 wt % each), the weight loss decreased to the minimal value of 5.0%. The decrease in the polyol content from 10 to 7 wt % and in the amide content from 10 to 5 wt % had only a slight effect on the fire retardancy (weight loss ranged from 6.4 to 4.5%).

It is known that introduction of polyvalent organometallic compounds into some fire retardants improves the fire retardancy [7, 8]. Our previous results show that introduction of the inorganic additives into the phosphorus–nitrogen-containing formulations in amount of 2–4 wt % has practically no effect of the weight loss [6]. We also studied the effects of the nature of aqueous dispersions on the water resistance of FR-treated wood. With this purpose, we replaced Craymul 2322 vinyl acetate dispersion in the formulation providing the best fire retardancy with other aqueous-organic dispersions. Results of water-resistance tests are summarized in Table 2.

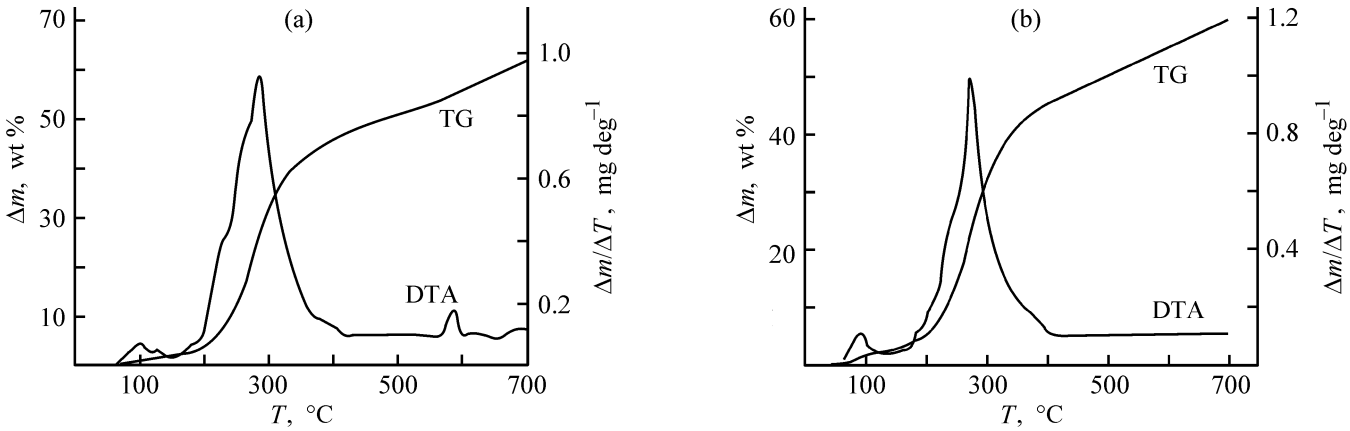


Fig. 1. TG and DTA curves. (Δm) Weight loss, ($\Delta m/\Delta T$) weight loss rate, and (T) temperature. Samples: wood treated with (a) initial fire retardant formulation and (b) that containing natural oxide additive.

Our results show that the smallest phosphorus loss is observed for HW-1 aqueous-organic dispersion (FINNDISP). With this dispersion, the phosphorus loss is lower by a factor of 1.9 as compared to Craymul 2322 (the phosphorus content increases from 18.2 to 34.4 wt %). Note that all the dispersions tested allowed keeping the phosphorus content after soaking in water or water treatment in amounts considerably exceeding (by a factor of 1.9 to 3.6) the critical value (~2%) required for providing the fire retardancy.

Table 3. Chemical analysis of pyrolysis products of wood treated with phosphorus–nitrogen-containing FR formulations

T, °C	Weight loss Δm, %	Content, wt %		Conservation of element,* wt %	
		nitrogen	phosphorus	nitrogen	phosphorus
Fire retardant (HW-1) dispersion					
20	0	8.0	4.5	100	100
200	4.8	8.4	4.7	82.5	96.4
300	22.5	8.5	5.6	55.0	88.9
400	48.0	8.5	7.7	42.5	88.9
500	56.6	7.8	9.2	16.3	80.0
Fire retardant + 1**					
20	0	7.9	4.0	100	100
200	6.1	8.3	5.0	97.5	100
300	27.9	7.8	6.7	70.0	100
400	47.4	7.8	8.9	51.3	100
500	54.7	7.6	10.5	42.5	100
Fire retardant + 2**					
20	0	7.9	4.0	100	100
200	4.2	8.1	4.3	98.7	100
300	25.2	6.9	5.3	65.8	100
400	46.9	7.3	7.6	49.4	100
500	52.7	6.9	8.7	41.8	100
Fire retardant + 3**					
20	0	6.9	4.0	100	100
200	5.0	6.8	4.2	94.2	100
300	27.2	6.5	5.5	68.1	100
400	48.5	6.9	7.8	52.2	100
500	58.6	7.6	9.7	46.4	100

* Conservation of element is defined as the ratio between the current element content at a fixed temperature (recalculated to the current weight) and its initial content (before heating).

** Additives 1, 2, and 3 differ in the natural oxide content varied within the following ranges (%): SiO_2 75–33, Al_2O_3 0.5–18, MgO 1–31, and Fe_2O_3 1–17.

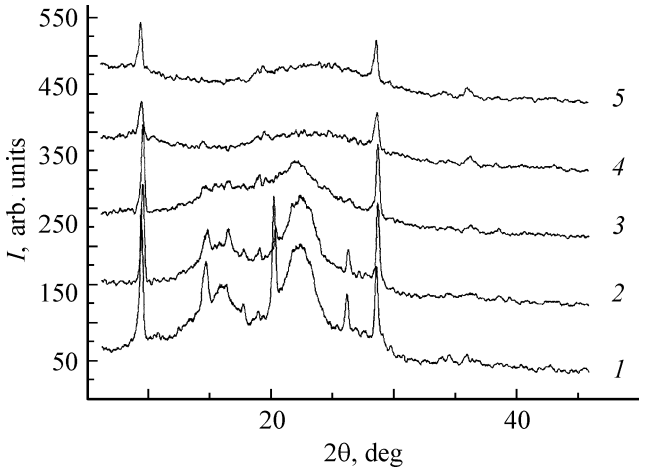


Fig. 2. X-ray diffraction patterns of pyrolysis products of wood treated with the formulation containing natural oxide additive. (*I*) Intensity and (2θ) Bragg angle. Pyrolysis temperature (°C): (*1*) 20, (*2*) 200, (*3*) 300, (*4*) 400, and (*5*) 500.

Pyrolysis products (20–700°C) of wood treated with the fire retardant formulation containing HW-1 suspension and some special inorganic additives (5 wt %) were examined by DTA, XRD, and chemical analyses. Figure 1 shows DTA curves for the initial fire retardant and that containing some natural oxides. Pyrolysis proceeds essentially within the temperature range 200–350°C, and the maximal decomposition rate is observed at 275–285°C, 0.93 to 1.02 Δm, depending on the formulation. A chemical analysis of the pyrolysis products of the FR-treated wood revealed that, on heating from 20 to 500°C, the phosphorus content in the carbonaceous residue increases, and its loss, as recalculated to the reduced mass, decreases for the formulations containing inorganic additives (Table 3). No weight loss was observed after pyrolysis (500°C) of wood treated with FR formulations containing additives, whereas without additives, the weight loss was 11.1%. It should be pointed out that the stability of the FR-treaded wood with respect to nitrogen loss is considerably lower, 41.8 to 46.4, depending on the FR formulation. Introduction of additives into the fire retardant formulation proved to have no significant effect on the TG curves (ash content is 38–41% at 700°C). An X-ray diffraction analysis revealed that, as FR-treated wood is heated, the diffraction peaks of the components constituting the FR formulation disappear, and at 500°C, only the peaks of inorganic additives are observed (Fig. 2). The residue after pyrolysis (500°C) of wood treated with the formulation containing no additives has no crystalline phases.

CONCLUSIONS

(1) Phosphorus–nitrogen-containing fire retardant developed for wood, containing ammonium phosphate, a polyol, an organic amide, organometallic compounds, and HW-1 dispersion, provides high fire retardancy and high water resistance of FR-treated wood.

(2) Introduction of natural oxide materials into the protective layer using HW-1 aqueous–organic dispersion has no significant effect on the thermal degradation of fire-retardant treated wood. Thermal degradation (weight loss) is observed essentially within the temperature range 250–350°C. The ash content is 38–41% at 700°C.

REFERENCES

1. *GOST* (State Standard) *16363–98, Protective Agents for Wood: Fire Resistance Test.*
2. *GOST* (State Standard) *16712–71, Leaching Test of Fire-Retardant Treated Wood.*
3. Prodan, E.A. and Shashkova, I.L., *Izv. Akad. Nauk BSSR, Ser. Khim. Nauk*, 1978, no. 4, pp. 79–81.
4. Losev, I.P. and Fedotova, O.Ya., *Praktikum po khimii vysokomolekulyarnykh soedinenii* (Practical Course of Macromolecular Chemistry), Moscow: Khimiya, 1962.
5. Luneva, N.K. and Petrovskaya, L.I., Abstracts of Papers, *VI Mezhdunarodnaya nauchno-tekhnicheskaya konferentsiya "Energo- i materialosberegayushchie ekologicheski chistye tekhnologii"* (6th Int. Scientific and Technical Conf. "Energy- and Materials-Saving Green Technologies"), Grodno (Belarus), November 1–2, 2005, p. 175.
6. Luneva, N.K., Petrovskaya, L.I., Vorob'ev, V.K., and Dmitrichenko, A.S., Abstracts of Papers, *III Mezhdunarodnaya nauchno-prakticheskaya konferentsiya "Chrezvychainye situatsii: preduprezhdenie i likvidatsiya"* (III Int. Scientific and Practical Conf. "Emergency Situations: Prevention and Elimination"), Minsk (Belarus), 2005, vol. 1, pp. 282–283.
7. Korol'chenko, A.Ya. and Petrova, E.I., *Zh. Ross. Khim. O–va. im D.I. Mendeleeva*, 2003, vol. 47, no. 4, pp. 49–54.
8. Seredina, M.A., Tyuganova, M.A., and Gol'braikh, L.S., *Khim. Volokna*, 2001, no. 6, pp. 21–24.

ISSN 1070-4272, Russian Journal of Applied Chemistry, 2008, Vol. 81, No. 4, pp. 708–713. © Pleiades Publishing, Ltd., 2008.
Original Russian Text © E.V. Skorobogatova, E.P. Traktina, I.I. Grinvald, A.P. Arbatskii, V.R. Kartashov, 2008, published in Zhurnal Prikladnoi Khimii, 2008, Vol. 81, No. 4, pp. 672–677.

MACROMOLECULAR CHEMISTRY AND POLYMERIC MATERIALS

Interaction of Nickel(II) and Cobalt(II) Salts with Chitosan Hydrochloride and Acetate in Aqueous Solutions

E. V. Skorobogatova, E. P. Traktina, I. I. Grinvald, A. P. Arbatskii, and V. R. Kartashov

Nizhni Novgorod State Technical University, Nizhni Novgorod, Russia

Received July 23, 2007

Abstract—Fundamental aspects of the complexation of cobalt(II) and nickel(II) ions with chitosan hydrochloride in water and chitosan in an aqueous solution of acetic acid were studied. The relation between the numbers of chitosan moles and metal ions involved in the interaction was found.. The optimal conditions for synthesis of complexes were determined and their chemical composition and spectral properties were analyzed. The possible reaction mechanisms were discussed.

DOI: 10.1134/S1070427208040277

Chitosan is an active sorbent of heavy metal ions [1]. It has been shown [2, 3] that a reason why this biopolymer exhibits sorption properties is that chelate complexes are formed between metal ions and functional groups of chitosan. However, formation of metal-containing composites in the system formed by chitosan and a solution of a metal salt is also possible via other physicochemical interactions without complexation [4].

No systematic studies of the interaction between this polymer and metal salts have been carried out under homogeneous conditions not complicated by phenomena at the phase boundary.

In aqueous solutions of acids, chitosan can be quantitatively determined by conductometric analysis [5]. It was found in [6] that, when solutions of chitosan and cobalt(II) nitrate in 0.1 M acetic acid are mixed, the content of chitosan decreases to equilibrium values. Subsequent, more detailed analysis of the titration curves of reaction mixtures revealed a portion corresponding to the formation of poorly soluble cobalt hydroxide ($L_{Co(OH)_2,\ 25°C} = (2.0–4.7) \times 10^{-16}$ in water [7, 8]) from metal cations that were unreacted with chitosan. The possibility of determining equilibrium amounts of metal ions enabled a study of this reaction and reaction with nickel nitrate ($L_{Ni(OH)_2,\ 25°C} = (1.2–2.0) \times 10^{-16}$ in water [7, 8]). In addition, the interaction of nickel(II) and cobalt(II) chlorides and nitrates with chitosan hydrochloride in aqueous solutions was examined. The aim of these studies was to analyze fundamental aspects and reveal the nature of interaction between the cations of these salts and dissolved forms of chitosan, obtained under different conditions.

EXPERIMENTAL

We used chitosan hydrochloride (CTSH) with a molecular weight of 38.2 kDa and chitosan (CTS) with a molecular weight of 120 kDa (Bioprogress Private Company, Shchelkovo, Moscow oblast). The degree of deacetylation of chitosan hydrochloride, found from the content of protonated amino groups by potentiometric and conductometric analyses of its aqueous solutions, is 81%. It should be noted that the titration curves contain no portion responsible for the HCl titration, commonly clearly manifested in analysis of chitosan dissolved in aqueous solutions of hydrochloric acid [5, 6, 9]. The data obtained suggest that the starting product contains no free HCl. Upon storage of the salt, the analytical results were reproduced.

The degree of chitosan deacetylation, determined by its conductometric and potentiometric analyses in aqueous solutions of 0.2 M acetic acid and 0.1 M hydrochloric acid, is 80%. The molecular weight of chitosan was calculated by the formula $[\eta] = KM^{\alpha}$, where $K = 3.41 \times 10^{-3}$ and $\alpha = 1.02$, from the data obtained by measuring the viscosity of chitosan solutions in a mixture of 0.33 M acetic acid and 0.3 M NaCl [10] with an Ubbelohde viscometer.

We used cobalt(II) and nickel(II) salts of analytically pure grade. Analyses for the metal cations were

made by conductometric titration with NaOH at concentrations of cobalt(II) and nickel(II) ions in the range 0.02–0.08 M in water or 2 M acetic acid. Preliminarily, we found the concentration of the cations in these solutions by titration with ethylenediaminetetraacetic acid (EDTA). The deviation from the results of analyses by titration with NaOH did not exceed 7.5% for cobalt(II) salts and 3.5% for nickel salts.

To perform the reactions, we first prepared starting solutions of the salts (0.5 M) and chitosans (0.1 M in terms of the elementary unit) and then used these solutions to obtain reaction mixtures with prescribed reagent concentrations. The experiments were carried out at initial concentration of the reagents in the range from 0.02 to 0.08 M and relative amounts of each of the reagents ranging from 1 : 1 to 1 : 4. The reaction mixtures were allowed to stand at room temperature. Their equilibration was monitored by the time variation of the content of chitosan and a metal ion, determined by conductometric titration of aliquots of the reaction mixtures.

The reaction products were isolated as follows. A 20-ml portion of acetone was poured from a pipette into 20 ml of a reaction mixture obtained at initial concentrations of the reagents equal to 0.1 M in a separating funnel without agitation. A gel-like clot was formed in the acetone layer at the phase boundary appearing because the fluid densities are different. The lower aqueous layer was separated. To remove metal ions unreacted with chitosan from the clot, and additional 20-ml portion of acetone was added, the clot was washed, and the acetone layer was separated. The treatment of the clot with acetone portions was repeated many times until the acetone layer became colorless. The completeness of removal of the ions was monitored by conductometric analysis of an aliquot part of the clot, dissolved in water. The necessary result was achieved faster if, after two or three washings with acetone, the clot was additionally washed with ethanol. Then the clot was placed in a Petri dish and dried first at 30–40°C and then to constant weight, with account of the conditions of water removal from chitosan. Chitosan is commonly dried at 105°C [5, 11]. However, according to the results of DSC studies [12], water is removed from chitosan at lower temperatures with an endothermic effect centered at 83.2°C. Therefore, samples of films composed of the reaction product were dried in two modes: at 85 and 105°C. The results of analyses of samples of dry films of the product, obtained in different conditions, coincided within the experimental error. The yield of a dry product from a single portion of the reaction mixture was 20–25% in terms of the initial amounts of the reactants. To accumulate the product, the isolation procedure was repeated.

Table 1. Results of analyses of the chemical composition of films with products formed in reactions of cobalt and nickel salts with chitosan hydrochloride in water and chitosan in a 0.2 M aqueous solution of acetic acid

Film	Content, wt %	
	metal	CTS
CTSH:		
with $Ni(NO_3)_2$	6.9	26.3
with $NiCl_2$	5.6	28.6
with $Co(NO_3)_2$	3.7	48.9
with $CoCl_2$	2.5	56.9
CTS:		
with $Ni(NO_3)_2$	2.4	21.2
with $Co(NO_3)_2$	2.5	19.9

IR spectra of film samples were measured on a Perkin-Elmer mod. 180 IR spectrophotometer. Electronic absorption spectra were obtained for aqueous solutions of the films on an SF-26 spectrophotometer. An approximately 0.5-g portion of a sample was dissolved in a 25-ml volumetric flask and analyzed by conductometry.

According to conductometric data, the isolated films contain, in addition to the reaction product, $-^{+}NH_3$ groups unreacted with the metal ion. Probably, the films are composed of polymers containing glucosamine rings with and without metal ions. The content of metal ions in the films was determined by titration with EDTA. The possibility of quantitative determination of the content of metal ions in the product by a reaction with a complexon was verified by analysis of the reaction mixtures in the simultaneous presence of the reaction product and equilibrium amounts of metal ions. In all the cases, the analysis demonstrated the initial content of the metal. This indicates that metal ions are bound to chitosan in the reaction products considerably more weakly than in the complex with EDTA. Table 1 lists data obtained chemical analyses of the films formed.

Let us consider the results of interaction of metal salts with chitosan hydrochloride in water. First, it should be noted that hydrolysis of $^{\pm}NH_3$ groups of chitosan hydrochloride is unimportant:

$$R^{+}NH_3 + H_2O \rightleftarrows RNH_2 + H_3O^{+}. \quad (1)$$

Indeed, pK_b for amino groups of chitosan is 7.7 [6, 9, 13, 14], and the dissociation of $^{\pm}NH_3$ groups,

Table 2. Results of conductometric studies of the reactions of nickel nitrate with chitosan hydrochloride in water and with chitosan in a 0.2 M aqueous solution of acetic acid*

$c_{0\,CTS} : c_{0\,Ni(NO_3)_2}$	Reaction with CTSH			Reaction with CTS		
	n	x	τ, days	n	x	τ, days
4 : 1	2.0	0.87	4	4.1	0.60	5
3.5 : 1	2.0	0.72	1	3.5	0.56	2 h
	2.0	0.73	4	3.5	0.57	5
3 : 1	2.0	0.62	4	3.1	0.58	5
2.5 : 1	2.1	0.53	2 h	2.5	0.59	5
	2.1	0.53	4			
2 : 1	2.1	0.45	4	2.0	0.54	1
				2.0	0.62	5
1.4 : 1	2.0	0.36	1	1.4	0.54	2 h
	2.0	0.39	7	1.4	0.54	1
				1.4	0.53	4
1.2 : 1	2.0	0.32	1	1.2	0.48	1
	0.2	0.38	7	1.2	0.44	3
				1.2	0.53	4
1 : 1	2.0	0.27	2 h	1	0.45	1
	1.9	0.26	1	1	0.44	2
	2.1	0.28	7	1	0.46	4
1 : 1.2	2.0	0.22	1	0.8	0.45	1
	2.0	0.21	7	0.8	0.47	4
1 : 1.4	2.0	0.21	1	0.7	0.47	1
	2.0	0.17	7	0.7	0.46	4
1 : 2	2.0	0.14	7	0.5	0.30	1
				0.5	0.29	5
1 : 4	2.0	0.11	7	0.2	0.25	1
				0.2	0.24	2

* $c_{0\,CTS}/c_{0\,Ni(NO_3)_2}$ are the initial concentrations of chitosan and nickel (M); n, number of moles of chitosan involved in the reaction with a mole of metal ions; and x, conversion of metal ions, $(c_0 - c_{eq})/c_0$.

e.g., that at a salt concentration of 0.1 M, does not exceed 0.3%. This also agrees with the IR spectra of solid films of chitosan hydrochloride, which contain two well resolved absorption bands peaked at 1645 and 1535 cm^{-1}, associated with deformation vibrations of the N–H bonds in $^{\pm}NH_3$ groups [15, 16]. Absorption bands of deformation vibrations of these bonds in $–NH_2$ groups are not observed in the spectra under study.

Table 2 lists as an example data obtained in conductometric titration of reactions with nickel nitrate. The results of conductometric analyses of the equilibrium concentrations of the reactants were used to calculate the ratio between the moles of the amino groups of chitosan and metal ions, involved in the reaction ($n = R^{\pm}NH_3/M^{2+}$).

It can be seen in Table 2 that CTSH reacts with nickel nitrate in a stoichiometric ratio of 2 : 1. A similar pattern was obtained for the reaction with nickel chloride. A somewhat different ratio is observed with cobalt salts. The stoichiometric ratio between the reactants is 1 : 1 in the reaction of chitosan hydrochloride with $CoCl_2$ and about 1.5 : 1 in the reaction with $Co(NO_3)_2$.

It can be seen in Table 2 that, for the reaction with $Ni(NO_3)_2$ the conversion of metal ions increases with the ratio $c_{0CTS}/c_{0Ni(NO_3)_2}$. Similar data were obtained for the reactions of chitosans with $Co(NO_3)_2$. In the reaction with metal chlorides, the conversion is somewhat lower and does not exceed 0.5 for the reactant concentrations used.

Under the experimental conditions, the content of protonated amino groups decreased by more than 0.01 M, but the pH value remained unchanged during a run. Despite that chitosan hydrochloride is a salt of a weak base, its aqueous solution has, at the con-

centrations used, a low buffer capacity: upon addition of hydrochloric acid to the solution to a concentration of 0.01 M, the pH value of the mixture decreased from 5.4 to 2.8.

The fact that the pH values of the reaction mixture remain invariable in the course of a run indicates that $^{+}_{-}NH_3$ groups are involved in the interaction with metal ions without loss of a proton. This means that, having no free pair of electrons, the nitrogen atom in the alkyl ammonium ion cannot enter into complexation with a metal ion by the donor-acceptor mechanism, and, consequently, there must be another mechanism of interaction between the metal and the protonated amino group of chitosan. This conclusion is in agreement with the electronic absorption spectra of the reaction mixtures and solutions of films of products formed in the reaction under study. In these spectra, the absorption bands of cobalt(II) and nickel(II) ions, peaked at 515 and 395 nm, are not shifted to any noticeable extent. It is known that cobalt(II) and nickel(II) ions exist in aqueous solutions in the form of octahedral aqua complexes $[Co(H_2O)_6]^{2+}$ and $[Ni(H_2O)_6]^{2+}$ [17]. The replacement of the ligands in the formation of amino complexes strongly affects the energy of the *d–d* electron transitions [18]. The absence of pronounced changes in the spectra of samples of the system under study suggests that the ligand in the aqua complexes of metal ions is not replaced by the amino group of chitosan.

The results observed can be accounted for by the interaction in solution of $^{+}_{-}NH_3$ groups with water molecules in metal aqua complexes by the mechanism of hydrogen bond formation. These interactions are also observed in solid films of the products. The IR spectra of the films obtained from reaction mixtures with cobalt(II) salts show a shift of the absorption band associated with deformation vibrations of the $^{+}_{-}NH_3$ group at 1645 cm^{-1} to 1635 cm^{-1} for the product formed in the reaction with cobalt chloride and to 1615 cm^{-1} for that formed with cobalt nitrate. The second absorption band associated with deformation vibrations of $^{+}_{-}NH_3$ groups is observed at 1530 cm^{-1} in films formed in both the reactions. In the spectra of the films obtained in the reaction with nickel chloride, these absorption bands are shifted to 1615 and 1510 cm^{-1}, respectively.

The IR spectra of the products isolated substantially differ from the spectra of chitosan hydrochloride in the region of stretching vibrations of –C–O groups and deformation vibrations of –O–H groups. The spectra of chitosan hydrochloride show, in the frequency range 1000–1200 cm^{-1}, strong absorption with a virtually unresolved band structure, whereas in the IR spectra of films formed of the products formed in the reaction with cobalt salts, this region is represented by three strong absorption bands peaked at 1050, 1100, and 1170 cm^{-1}. A similar spectrum was obtained for a film produced in the reaction with $NiCl_2$. Presumably, this is due to interaction of the metal ion with an oxygen atom from a hydroxy group of chitosan.

Thus, the whole set of the data presented suggests that, in solution, the metal ion is coordinated with an oxygen atom from the glucosamine ring and $^{+}_{-}NH_3$ groups form hydrogen bonds with oxygens from water molecules in the aqua complex of the metal ion.

When the product is obtained in the solid state and dried to constant mass, molecules of coordination water can be replaced with counter ions. For example, thermochemical studies with cobalt(II) complexes $[Co(NH_3)_5 \cdot H_2O]X_2$ demonstrated that the process of water replacement by a counter ion X^- is exothermic and, e.g., in the case when X = Cl, its ΔH = –19.2 kJ mol^{-1} [17]. This is due to the difference in the coordination energies of the bonds Co^{2+}–H_2O and Co^{2+}–X.

When studying reactions with cobalt salts, we obtained films that, being dried to constant mass, take on a blue color characteristic of fully or partly dehydrated salts of this metal [19]. The film produced by the reaction of CTSH with nickel(II) ions is light yellow. In this case, a salt with a complex metal cation M, $[MRN^+H_3(H_2O)_2X^-]^{2+}X^{2-}$, or a neutral complex $[MRN^+H_3(H_2O)_2X_3^-]$ can be suggested as probable structures for reaction products obtained in the solid state. Metal complexes with positively charged ligands have been more than once described in the literature [20–22].

Let us now consider the results obtained for the reaction of chitosan in an aqueous solution of acetic acid. It is noteworthy that the following equilibrium in this solvent can be suggested for the state of chitosan:

$$RNH_2 + CH_3COOH \rightleftarrows RN^+H_3 + CH_3COO^-. \quad (2)$$

To evaluate the constant of equilibrium (2), we represent this equation as an algebraic sum of the following equations:

$$(+)\ RNH_2 + H_2O \rightleftarrows RN^+H_3 + OH^-,$$

$$(+)\ CH_3COOH + H_2O \rightleftarrows CH_3COO^- + H_3O^+,$$

$$(-)\ 2H_2O \rightleftarrows H_3O^+ + OH^-.$$

Thus, the constant of equilibrium (2) can be expressed in terms of K_b of the amino group of chitosan, dissociation constant K_a of acetic acid, and ionic product for water, K_w:

$$K = K_b K_a / K_w.$$

In view of this circumstance, the content of unprotonated RNH_2 groups for a chitosan solution may be, e.g., at 0.1 M of chitosan in 0.2 M acetic acid, up to 10%. In agreement with this conclusion is the IR spectrum of a solid film produced by evaporating the solvent from a thin layer of the chitosan solution mentioned above. In addition to the absorption bands associated with deformation vibrations of $-N^+H_3$ groups (1640 and 1530 cm^{-1}), this spectrum contains absorption bands at 1670 and 1570 cm^{-1}, attributed, by analogy with [15], to deformation vibrations of $-NH_2$ groups.

This spectrum also additionally contains, compared with the spectrum of chitosan hydrochloride, absorption bands of the ionized acetate group at 1610 and 1315 cm^{-1} [15]. The presence of acetic acid residues in the film is indicated by the absorption band at 1710 cm^{-1}.

It would also be expected that, in an aqueous solution of acetic acid, metal ions interact with the unprotonated amino group of chitosan. Conductometric studies demonstrated that titration curves of reaction mixtures in this reaction have a more complex form. Particularly distinctly pronounced is a new portion in the reaction with nickel nitrate, which is presumably associated with the interaction of NaOH with the new product. It can be seen in Table 2 that, for the reaction of CTS with nickel nitrate, the number of chitosan moles reacting with a mole of metal ions varies with the ratio of the initial reactant concentrations. A similar behavior was also observed for the reaction with cobalt nitrate.

In the electronic absorption spectrum of an aqueous solution of a film produced in the reaction of cobalt nitrate with CTS, the absorption peak at 515 nm is shifted to shorter wavelengths by 10 nm. In contrast to the product formed in the reaction of this salt with CTSH, the dry film has in this case a pink color. Probably, these facts are a consequence of the interaction with the aqua complex of the cobalt(II) ion with the ligand in this complex replaced by the $-NH_2$ group. The data obtained give no way of determining the stoichiometry of the reaction of this type.

In the IR spectra of films obtained in the system CTS + $Co(NO_3)_2$, the above-mentioned absorption bands associated with deformation vibrations of $-NH_2$ groups are shifted to 1650 and 1550 cm^{-1}, respectively. The absorption band at 1640 cm^{-1}, associated with deformation vibrations of the $^{\pm}NH_3$ group, is shifted to 1630 cm^{-1}, and the second band at 1530 cm^{-1} is observed as a broad shoulder with absorption in the frequency range 1500–1550 cm^{-1}. The absorption band at 1610 cm^{-1} presumably corresponds not only to the ionized acetate group, but also to the nitrate anion [15]. In the spectrum of a film produced in the system CTS + $Ni(NO_3)_2$, one of the absorption bands associated with deformation vibrations of $-NH_2$ groups is shifted to 1660 cm^{-1}, and the region 1510–1550 cm^{-1} shows a strong absorption that can be attributed to deformation vibrations of $^{\pm}NH_3$ and $-NH_2$ groups. The film has a yellow-green color.

Thus, the data presented here indicate that metal ions are complexed with amino groups of chitosan when the reaction is performed in an aqueous solution of acetic acid. On the whole, the results of our study demonstrate that both coordination interactions and interactions by the mechanism of hydrogen bond formation occur between the metal ions and the functional groups of chitosan in the reactions under study.

CONCLUSIONS

(1) The stoichiometry of the reaction of cobalt(II) and nickel(II) salts with chitosan hydrochloride in water and chitosan in an aqueous solution of acetic acid was determined by conductometric analysis. In the number of amino groups, chitosan hydrochloride reacts with metal ions in ratios of 2 : 1 in the reactions with $NiCl_2$ and $Ni(NO_3)_2$, 1 : 1 in the reaction with $CoCl_2$, and 1.5 : 1 in that with $Co(NO_3)_2$. In the reactions with chitosan in an aqueous solution of acetic acid, the number of reacting amino groups per mole of metal ions increases with the ratio between the initial concentrations of chitosan and metal ions.

(2) Different types of interaction of soluble forms of chitosan with metal salts were revealed by pH-metry and electronic absorption and IR spectroscopies. When complexes of metal ions with chitosan hydrochloride are formed, the amino groups in the ligand remain protonated, with its oxygen atoms acting as donor centers. In the reaction of chitosan in an aqueous solution of acetic acid, complexation with $-NH_2$ groups occurs in parallel with this interaction.

REFERENCES

1. *Khitin i khitozan: Poluchenie, svoistva i primenenie* (Chitin and Chitosan: Production, Properties, and Use), Skryabin, K.G., Vikhoreva, G.A., and Varlamov, V.P., Eds., Moscow: Nauka, 2002.

2. Ershov, B.G., Seliverstov, A.F., Sukhov, I.L., and Bykov, G.L., *Izv. Akad. Nauk, Ser. Khim.*, 1992, no. 10, pp. 2305–2311.
3. Nizel'skii, Yu.N., Kozak, N.B., Ryabov, S.V., et al., *Trudy 8-oi Mezhdunarodnoi konferentsii "Sovremennye perspektivy v issledovanii khitina i khitozana", Kazan, 12–17 iyunya 2006 g.* (Proc. 8th Int. Conf. "Modern Prospects in Studies of Chitin and Chitosan," Kazan, June 12–17, 2006), Moscow: VNIRO, 2006, pp. 114–118.
4. Anpilogova, G.R. and Murinov, Yu.I., *Zh. Prikl. Khim.*, 2004, vol. 77, no. 11, pp. 1880–1886.
5. Nud'ga, L.A., Plisko, E.A., and Danilov, S.N., *Zh. Obshch. Khim.*, 1973, vol. 43, no. 12, pp. 2752–2756.
6. Arbatskii, A.P., Traktina, E.P., and Smirnova, L.A., *Zh. Prikl. Khim.*, 2006, vol. 79, no. 2, pp. 272–274.
7. Cotton, F.A. and Wilkinson, G., *Advanced Inorganic Chemistry*, New York: Interscience, 1966.
8. Lur'e, Yu.Yu., *Spravochnik po analiticheskoi khimii* (Handbook of Analytical Chemistry), Moscow: Khimiya, 1989.
9. Nud'ga, L.A., Plisko, E.A., and Danilov, S.N., *Zh. Obshch. Khim.*, 1973, vol. 43, no. 12, pp. 2756–2760.
10. Pogodina, N.V., Pavlov, G.M., Bushin, S.V., et al., *Vysokomol. Soedin., Ser. A*, 1986, vol. 28, no. 2, pp. 232–235.
11. Nud'ga, L.A., Plisko, E.A., and Danilov, S.N., *Zh. Obshch. Khim.*, 1971, vol. 41, no. 11, pp. 2555–2558.
12. Sashina, E.S., Vnuchkin, A.V., and Novoselov, N.P., *Zh. Prikl. Khim.*, 2006, vol. 79, no. 10, pp. 1664–1667.
13. Skorikova, E.E., Vikhoreva, G.A., Kalyuzhnaya, R.I., et al., *Vysokomol. Soedin., Ser. A*, 1988, vol. 30, no. 1, pp. 44–49.
14. Vikhoreva, G.A., Gal'braikh, L.S., Ovsepyan, A.M., et al., *Vysokomol. Soedin., Ser. A*, 1989, vol. 31, no. 5, pp. 1003–1007.
15. Bellamy, L.J., *The Infra-red Spectra of Complex Molecules*, London: Methuen, 1954.
16. Bol'shakov, I.N., Sizykh, A.G., Surkov, E.V., et al., *Trudy 8-oi Mezhdunarodnoi konferentsii "Sovremennye perspektivy v issledovanii khitina i khitozana", Kazan, 12–17 iyunya 2006 g.* (Proc. 8th Int. Conf. "Modern Prospects in Studies of Chitin and Chitosan," Kazan, June 12–17, 2006), Moscow: VNIRO, 2006, pp. 86–89.
17. Kukushkin, Yu.N., *Khimiya kooordinatsionnykh soedinenii* (Chemistry of Coordination Compounds), Moscow: Vysshaya Shkola, 1985.
18. Lever, A.B.P., *Inorganic Electronic Spectroscopy*, Amsterdam: Elsevier, 1984.
19. Remy, H., *Lehrbuch der anorganischen Chemie*, Leipzig: Akademische, 1961, Bd. 2.
20. Hartley, F.R., Burgess, C., and Alcock, R.M., *Solution equilibria*, Chichester: Ellis Horwood, 1980.
21. Lavrenova, L.G., Amamchan, A.R., Larionov, S.V., and Dorokhov, V.A., *Izv. Akad. Nauk, Ser. Khim.*, 1992, no. 10, pp. 2311–2314.
22. Quagliano, J.V., Banerjee, A.K., Goedken, V.L., and Vallarino, L.M., *J. Am. Chem. Soc.*, 1970, vol. 90, no. 3, pp. 482–488.

ISSN 1070-4272, Russian Journal of Applied Chemistry, 2008, Vol. 81, No. 4, pp. 714–716. © Pleiades Publishing, Ltd., 2008.
Original Russian Text © N.A. Kopylova, Yu.D. Semchikov, S.D. Zaitsev, 2008, published in Zhurnal Prikladnoi Khimii, 2008, Vol. 81, No. 4, pp. 678–680.

BRIEF COMMUNICATIONS

Thermal Oxidative Degradation of Polymethacrylates Synthesized by Pseudoliving Radical Polymerization

N. A. Kopylova, Yu. D. Semchikov, and S. D. Zaitsev

Lobachevsky Nizhni Novgorod State University, Nizhni Novgorod, Russia

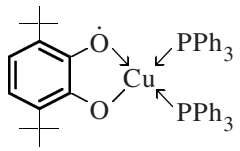
Received December 14, 2007

Abstract—The kinetics of degradation of polymethyl methacrylate, polybutyl methacrylate, and poly-2,2,3,3-tetrafluoropropyl methacrylate synthesized by pseudoliving radical polymerization at 270°C in air in the presence of bis(triphenylphosphine)(3,6-di-*tert*-butyl-1,2-semiquinolato)copper(I) was studied. The possibility of improving the thermal treatment of the resulting polymers was revealed.

DOI: 10.1134/S1070427208040289

Pseudoliving radical polymerization allows synthesis of polymers and copolymers with controlled molecular weight and narrow molecular-weight distribution, which largely affects their physicomechanical characteristics. There are several methods for implementation of this process: radical polymerization with reversible inhibition by stable free radicals (SFRP), radical polymerization with halogen atom transfer (ATRP), and polymerization by degenerate chain transfer by reversible addition-fragmentation (RAFT) [1–3]. In all these cases, the chain termination is controlled by the reversible reaction of the chain-terminating agent with the propagating radical. Macromolecules of polymers contain terminal groups bound to the chain by a labile bond that can be activated under thermal or photochemical action.

In this study, we used a copper semiquinolate complex, bis(triphenylphosphine)(3,6-di-*tert*-butyl-1,2-semiquinolato)copper(I) (CSQ) for synthesis of polymethacrylates by the SFRP method. The structure of this complex is presented below:



The process was performed at 25°C under UV irradiation. Methyl methacrylate (MMA), butyl methacrylate (BMA), and 2,2,3,3-tetrafluoropropyl methacrylate (FMA) were used as monomers. Under the above conditions, the polymerization exhibited all features of a pseudoliving radical process: linear dependences of the average molecular weight on the degree of conversion, lower values of the polydispersity parameter M_w/M_n, and initiation of secondary polymerization of monomers with polymers synthesized in the presence of CSQ [4, 5].

The kinetic curves of degradation of reprecipitated samples of polymers are shown in Figs. 1 and 2.

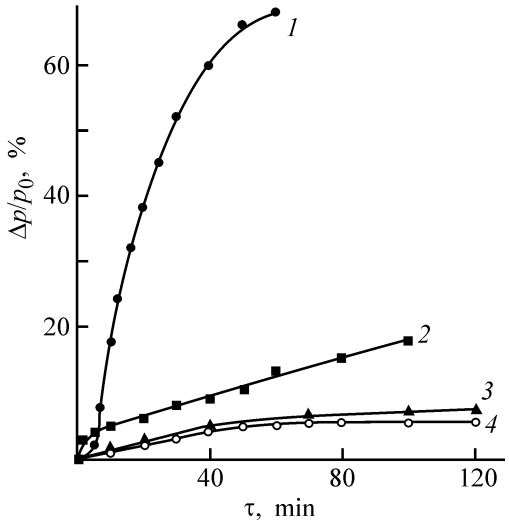


Fig. 1. Kinetic curves of degradation of polyMMA in air at 270°C. ($\Delta p/p_0$) Decomposition of volatile products, and (τ) time; the same for Fig. 2. (*1*) [CSQ] = 0, (*2*) CSQ is introduced into the prepared polymer via the solution, (*3*) polymer is synthesized by secondary polymerization of MMA initiated with polyMMA (5 wt %) from run no. 4, and (*4*) [CSQ] = 4×10^{-3} M.

The process was performed in air at 270°C. The synthesis conditions are listed in Table 1 and in the Experimental. It follows from Figs. 1 and 2 that, in the course of decomposition for 60 min, the amount of volatiles decreases by a factor of 6–12 in comparison with polymethacrylates synthesized in the absence of CSQ. Introduction of CSQ into the finished polymer (Fig. 1, curve *2*) is less efficient than its introduction in the course of the synthesis. This is apparently caused by the presence of double bonds at the ends of polymethyl methacrylate macromolecules formed in the course of the polymer synthesis in the absence of CSQ by disproportionation of macroradicals. To elucidate the role of CSQ in the enhancement of the heat resistance of the polymers, we synthesized two polystyrene samples by pseudoliving radical polymerization. One sample was prepared in the presence of CSQ by UV-induced polymerization, and the other, by thermal polymerization at 120°C in the presence of a stable radical, 2,2,6,6-tetramethylpyperidine-1-oxyl (TEMPO). The reprecipitated samples were heated at 300°C in air. It was found that, in 60 min, the first sample degraded by 10%; the second, by 29%; and polystyrene prepared by common radical polymerization, by 22%. Thus, nitroxyl radicals do not exert a stabilizing influence on the polymer degradation. The stabilization of thermal degradation of methacrylates by CSQ is apparently caused by the inhibiting effect of decomposition products of the semiquinolate complex: di-*tert*-butyl-*o*-benzoquinone, triphenylphosphine, and copper. It is well known [6, 7] that all these compounds can react with radicals and thereby can terminate the chain reaction of degradation of macromolecules.

Thus, polymethacrylates whose macromolecules contain fragments of CSQ inhibitor at the chain ends have an increased thermal stability.

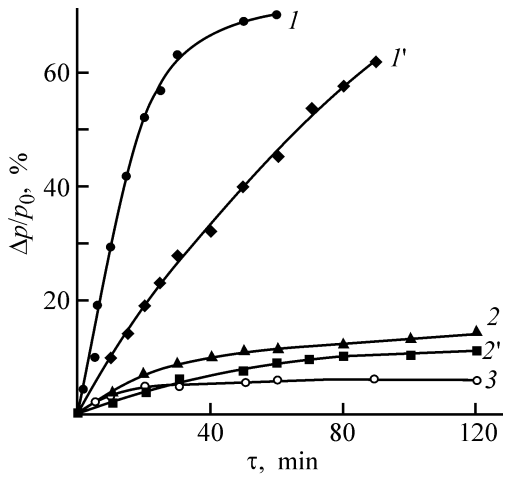


Fig. 2. Kinetic curves of degradation of (*1*, *2*) polyFMA and (*1'*, *2'*) polyBMA in air at 270°C. (*1*, *1'*) [CSQ] = 0, (*2*, *2'*) [CSQ] = 1.5×10^{-3} M, and (*3*) polyFMA synthesized by secondary polymerization of FMA initiated with polyFMA (5 wt %) from run no. 2.

EXPERIMENTAL

The procedures of purification of monomers and synthesis of polymers are described in detail in [8]. The CSQ complex was synthesized by the procedure described in [9]. The substance was a dark violet powder stable in air and readily soluble in monomers. Polymethacrylates were synthesized via formation of CSQ adduct with radicals of the initiator, azobis(isobutyronitrile) (AIBN), in the monomer medium at 70°C and then at 25°C under UV irradiation with a PRK-400 lamp. After the required conversion was reached, the ampules were opened, and the isolated polymers were purified by threefold reprecipitation, dried in a vacuum to constant weight, and then used in experiments on thermal degradation in air. The weight

Synthesis conditions of polymethacrylates (UV irradiation, 25°C, [AIBN] = 1×10^{-2} M)

Polymer	Run no.	[CSQ] × 10^2, M	Conversion, %	$M_n \times 10^{-4}$	M_w/M_n
PolyMMA	1	0	10	9.4	4.3
	2	4**	10	9.4	4.3
	3*	–	15	11.1	2.1
	4	4	10	8.2	2.0
PolyFMA	1	0	15	–	–
	2	1.5	35	12.2	1.8
	3*	–	16	330	1.4
PolyBMA	1'	0	35	8.8	2.1
	2'	1.5	15	10.1	1.6

* PolyMMA (polyFMA) synthesized under conditions of run no. 4 (no. 2) was used as an initiator.

** PolyMMA was synthesized similarly to run no. 1, but CSQ was added to the polymer solution.

loss was determined with a torsion balance. A support (metal foil) with the polymer in the form of fine chips (approximately 0.2 g) was suspeded by a metallic thread to the arms of the balance, the zero point was fixed, and then the thread was placed in a furnace heated to the required temperature for thermal decomposition. The furnace was kept in the isothermal mode.

CONCLUSION

The pseudoliving radical polymerization of methacrylates in the presence of copper semiquinolate complex allows control over the molecular weight and molecular-weight distribution of the resulting polymers and also enhancement of the heat resistance of the polymers by direct addition of the chain-terminating agent, copper semiquinolate complex, into the polymerizing system.

ACKNOWLEDGMENTS

This study was financially supported by the Russian Foundation for Basic Research (project no. 07-03-00500), Federal Target Program "Research and Development in the Priority Fields of Scientific and Technological Complex of Russia during 2007–2012" (project no. 2007-3-1.3-26-01-314), and National Project "Education" of the innovation education program of the Nizhni Novgorod State University.

REFERENCES

1. Zaremskii, M.Yu. and Golubev, V.B., *Vysokomol. Soedin., Ser. C*, 2001, vol. 43, no. 9, pp. 1689–1728.
2. Yakimanskii, A.V., *Vysokomol. Soedin., Ser. C*, 2005, vol. 47, no. 7, pp. 1241–1301.
3. Matyjaszewski, K., *Prog. Polym. Sci.*, 2005, vol. 30, no. 8, pp. 858–875.
4. Shamenkova, O.A., Kopylova, N.A., Semchikov, Yu.D., et al., *Vysokomol. Soedin., Ser. B*, 2005, vol. 47, no. 11, pp. 2045–2049.
5. Gobetskaya, O.A., Radical Photo(co)polymerization of Vinyl Monomers in the Presence of Bis(triphenylphosphino)(3,6-di-tert-butyl-1,2-semiquinolato)copper(I), *Cand. Sci. Dissertation*, Nizhni Novgorod, 2006.
6. Dolgoplosk, B.A. and Tinyakova, E.N., *Generirovanie svobodnykh radikalov i ikh reaktsii* (Generation of Free Radicals and Their Reactions), Moscow: Nauka, 1982.
7. Voigt, J., *Die Stabilisierung der Kunststoffe gegen Licht und Warme*, Berlin: Springer, 1966.
8. Shamenkova, O.A., Nekorkina, I.V., Kopylova, N.A., and Semchikov, Yu.D., *Vestn. Nizhegor. Gos. Univ.*, 2006, issue 1(5), pp. 125–131.
9. Muraev, V.A., Abakumov, G.A., Cherkasov, V.K., and Razuvaev, G.A., *Dokl. Akad. Nauk SSSR*, 1977, vol. 236, no. 3, pp. 620–623.

ISSN 1070-4272, Russian Journal of Applied Chemistry, 2008, Vol. 81, No. 4, pp. 717–719. © Pleiades Publishing, Ltd., 2008.
Original Russian Text © L.P. Varlamova, V.A. Izvozchikova, A.S. Averchenko, Yu.D. Semchikov, S.A. Ryabov, 2008, published in Zhurnal Prikladnoi Khimii, 2008, Vol. 81, No. 4, pp. 681–683.

BRIEF COMMUNICATIONS

Fireproof Polymer Compounds Based on Polyvinyl Chloride and Perchlorovinyl Resin

L. P. Varlamova, V. A. Izvozchikova, A. S. Averchenko, Yu. D. Semchikov, and S. A. Ryabov

Research Institute of Chemistry, Lobachevsky State University, Nizhni Novgorod, Russia
Lobachevsky State University, Nizhni Novgorod, Russia

Received July 5, 2007

Abstract—Preparation of fireproof polymer compounds and properties of the resulting materials were studied. The synergistic effect of mixtures of fire-retardant additives based on thermally expanding graphite was examined.

DOI: 10.1134/S1070427208040290

Most procedures for diminishing the combustibility of polymer materials are based on decreasing the burning limits and affecting the heat and mass transfer of the flame with the surface of the burning polymer. This problem is solved by changing the thermal and thermochemical characteristics of the condensed phase and by lowering the rate of release of combustible gases (products of polymer degradation), the combustion efficiency, and the rates of oxidation in the gas phase and coke formation. This can be done by chemical modification of the polymer backbone and by addition of fire-retardant additives or other fillers that are characterized by high endothermic effect and release inert reaction products or affect the degradation pathway in the condensed phase [1, 2].

Swelling fireproof coatings are of particular interest for construction industry, machine building, transport, etc. [3]. A formulation for swelling coatings containing ammonium polyphosphate as an agent for initiation of the foamed coke formation was suggested in [4].

In this study, we examined the effect of fillers, such as thermally expanding graphite (TEG), ammonium polyphosphate (APP), and pentaerythritol (PE), on the fireproof properties of polymer materials.

EXPERIMENTAL

Thermally expanding graphite [5] bloating at elevated temperatures was used as the main component of the system. In combustion, the volume of TEG considerably increases, which is accompanied by heat absorption and formation of a heat-shielding carbon foam preventing fire propagation. However, the strength of the resulting carbon foam layer is low, and it is easily broken under the conditions of real fire.

The mechanical strength of the protective carbon foam can be enhanced by modification with various fire-retardant additives.

The refractoriness of the polymer materials was studied by the UL-94 international procedure [GOST (State Standard) 28 157–89], according to which a material of group V-0 is characterized by the highest refractoriness.

The oxygen index (i.e., the minimal content of oxygen in the oxygen–nitrogen mixture at which the candle-like combustion is possible under the conditions of special tests) was determined in accordance with GOST 12.1.044–89 [6]. The physical and mechanical properties of the polymer materials were studied on an RMI-5 tensile-testing machine, and the elasticity, on an METEFEM-khr01 unit.

When exposed to high temperatures in the course of combustion, a polymer composite containing TEG is bloated, and a crust is formed on its surface.

It was found that the resulting coke layer (foam) prevents further fire propagation toward the protected surface. The intumescence coefficient K_{sw} of the polymer material was determined as follows:

$$K_{sw} = (h_b - h_n)/(h_0 - h_n),$$

Physicomechanical properties of PVC polymer compounds at various contents of the fillers

PVC : APP–PE–TEG mixture	Relative elongation at break %	Breaking tensile stress, kg cm^{-2}
No filler	350	28.1
1 : 0.5	300	29.3
1 : 1	280	33.85
1 : 1.5	150	24.45
1 : 2	120	16.8

where h_0 is the initial thickness of the sample (mm), h_b is the thickness of the sample after treatment in the furnace ($T = 650 \pm 20$°C) for 10 min (mm), and h_a is the support thickness (mm).

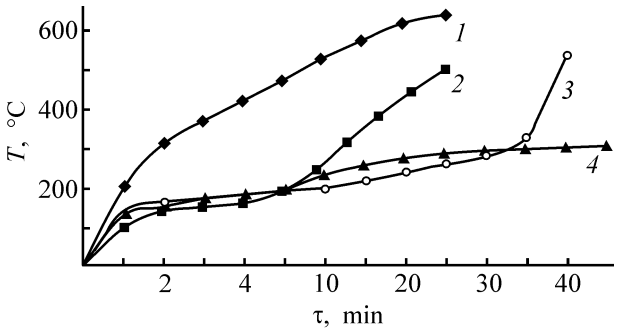
The result was averaged from the data of five and more tests.

The formulations were prepared by mechanical mixing of the components. To attain the uniformity, the mixture was ground on a three-roll mill. The 2-mm film of polyvinyl chloride (PVC) material was prepared by the plastisol procedure using dioctyl phthalate plasticizer. The coking ability was evaluated by formation of the solid layer (resistant to mechanical stresses) on the sample surface.

The refractoriness of the samples was tested by the "fire tube" procedure [6].

The formulated fireproof paint-and-varnish coatings were cast on metal supports (1 mm thick). The coating thickness was 1 mm. Wood samples were coated by partial immersion; the coating thickness was 0.6 mm.

First, we performed the blank test to determine the temperature made of the fire tests. In this case, we used the metal support (1 mm thick) without a faire-proof coating. This support was placed on top of a quartz tube, and a thermocouple was fixed at its back at the center. Then, the air-propane mixture in a gas jet was ignited and the flame temperature of 650°C was controlled with a thermocouple.



Temperature of the support T vs. time τ of fire treatment of the protective acryl coating. (*1*) Metal support without coating, (*2*) coating containing APP and PE, (*3*) coating containing TEG, and (*4*) coating containing APP, PE, and TEG.

In the second step, the metal supports with the fireproof coatings were tested using the balanced jet flame.

We attempted to enhance the strength of the foam formed after the TEG degradation, using pentaerythritol whose degradation at high temperatures yields a 3*D* network [7].

We also used a mixture of PE and APP. Under the flame treatment, this mixture degrades, yielding ammonia and forming a so-called blanket on the sample surface, protecting it from the fire.

Our tests allowed evaluation of the optimal mixture of fire-retardant additives in the blend (weight fraction): APP 2, PE 1, and TEG 1. This component ratio provides high mechanical strength of the foamed coke on the surface of the protected material. These components were added in the PVC polymer matrix, polychlorovinyl resin, and acryl dispersion.

The dependences of physicomechanical properties of the modified PVC compositions on the PVC : filler ratio are listed in the table. As can be seen, filler being added decreases the relative elongation and breaking tensile stress. It should be noted here that the physicomechanical properties of the filled composites remain relatively high.

As a result, we prepared a fireproof PVC compound exhibiting the following characteristics [8]: refractoriness corresponds to group V-0 (UL-94 procedure), bloating ratio at 650°C 20–25, oxygen index 31%, breaking tensile stress 33.85 kg cm^{-2}, and relative elongation at break 280%.

The above ratio of fire-retardant additives was also used for preparing a fireproof paint-and-varnish coating based on perchlorovinyl resin and acryl dispersion [9]. The test results are illustrated in the figure.

The sample without coating attains the critical temperature in 12 min. The samples coated with the composition containing APP and PE protect the metal for 10 min, after which the coating breaks down. Coating of the sample with the composite containing TEG strongly decreases the temperature at the back side of the support, but at prolonged high-temperature treatment the coating degrades. The best results were ob-

tained when the support was coated with the compound containing a mixture of TEG, PE, and APP. This fireproof compound provides the first protection group for timbering (film thickness 0.6 mm) and the fourth protection group for metal structures (film thickness 1 mm).

CONCLUSIONS

(1) A fireproof compound based on thermally expanding graphite, ammonium polyphosphate, and pentaerythritol was prepared.

(2) The synergistic effect increases the effectiveness of the mixture of fire-retardant additives.

(3) Fireproof polymer coatings based on polyvinyl chloride, perchlorovinyl resin, and acryl dispersion were developed.

ACKNOWLEDGMENTS

The study was financially supported within the Research Program "Foundation for Promotion of the Small-Scale Enterprises in the Scientific and Technical Sphere," Program "Start 05," project no. 3285r/5703.

REFERENCES

1. Kaziev, M.M., *Spetsializirovannyi catalog "Pozharnaya bezopastnost' 2003"* (Specialzed Catalog "Fire Safety 2003"), Moscow: Grotek, 2002.
2. Khalturinskii, N.A. and Berlin, A.A., Abstracts of Papers, *6 Vsesoyuznaya konferentsiya po goreniyu polimerov i sozdaniyu ogranichenno goryuchikh materialov* (6 All-Union Conf. on Combustion of Polymers and Development of Limitedly Combustible Materials), Suzdal, November 29–December 1, 1988, Moscow, 1988, p. 3.
3. Shuklin, S.G., Klimenko, E.N., and Kodolov, V.I., *Khim. Fiz. Mezoskop.*, 2001, vol. 3, no. 2, pp. 113–125.
4. Shuklin, S.G., Kodolov, V.I., Larionov, K.I., and Tyurin, S.A., *Fiz. Goren. Vzryva*, 1995, no. 2, pp. 73–80.
5. Fialkov, A.S., *Uglerod: mezhsloevye soedineniya i kompozity na ikh osnove* (Carbon: Intercalation Compounds and Composites Based on Them), Moscow: Aspekt, 1997.
6. *GOST* (State Standard) *12.1.044–89*.
7. *The Science of Surface Coatings*, Chatfield, H.W., Ed., London: Ernest Benn, 1962.
8. RF Patent 2229497.
9. RF Patent 2244727.

ISSN 1070-4272, Russian Journal of Applied Chemistry, 2008, Vol. 81, No. 4, pp. 720–722. © Pleiades Publishing, Ltd., 2008.
Original Russian Text © A.G. Gasanov, A.G. Azizov, L.I. Alieva, E.G. Mamedov, R.Z. Babaeva, R.A. Rustamov, I.G. Ayubov, 2008, published in Zhurnal Prikladnoi Khimii, 2008, Vol. 81, No. 4, pp. 684–686.

BRIEF COMMUNICATIONS

Ester Plasticizers Derived from 2(3)-Methylcyclohexenedicarboxylic Acid

A. G. Gasanov, A. G. Azizov, L. I. Alieva, E. G. Mamedov, R. Z. Babaeva, R. A. Rustamov, and I. G. Ayubov

Institute of Petrochemical Processes, National Academy of Sciences of Azerbaijan, Baku, Azerbaijan

Received August 14, 2007

Abstract—New plasticizers for polyvinyl chloride polymeric compounds, based on 2(3)-methylcyclohexenedicarboxylic acid diesters, were suggested. The optimal formulation was found, and its physicochemical properties were characterized.

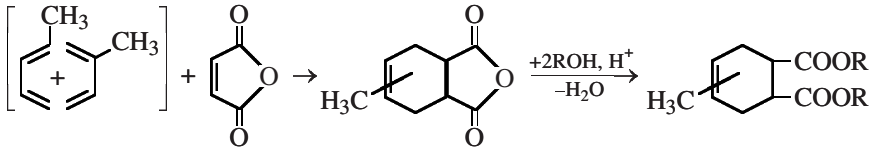
DOI: 10.1134/S1070427208040307

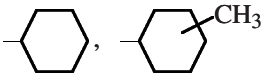
Ester plasticizers used for processing of polyvinyl chloride (PVC) compounds are large-tonnage commercial products, and the demand for them steadily increases [1–5]. Because of the wide and diverse applications of PVC compounds and large demand for ester plasticizers, a search for new promising high-quality plasticizers remains a topical issue, the more so as one of the most widely used plasticizers, dibutyl phthalate, being an aromatic compound, is very toxic.

The goal of this study was to develop PVC compounds with improved consumers properties, using high-quality environmentally clean plasticizers.

In this study, we used diesters of 2(3)-methylcyclohexenedicarboxylic acid, prepared from aliphatic 1,3-pentadienes present in the C_5 pyrolysis fraction by the scheme shown below.

The physicochemical parameters of the diesters are listed in Table 1.



R = –*i*-C_3H_7, –*n*-C_4H_9, –C_8H_{17}, 

I **II** **III** **IV** **V**

Table 1. Physicochemical properties of 2(3)-methylcyclohexenedicarboxylic acid diesters

Compound	Empirical formula	Yield, %	T_b, °C	d_4^{20}, g cm^{-3}	n_D^{20}	Acidity, mg KOH/g
I	$C_{15}H_{24}O_4$	85	300–302	1.0095	1.4630	34.7
II	$C_{17}H_{28}O_4$	87	310–312	1.0310	1.4690	32.6
III	$C_{25}H_{44}O_4$	82	338–340	1.0526	1.4735	67.3
IV	$C_{21}H_{32}O_4$	86	331–334	1.0936	1.4920	100
V	$C_{23}H_{34}O_4$	85	345–347	1.0512	1.4850	279.6

Table 2. Composition and properties of PVC compounds

Component, parameter	Compound no.									
	1	2	3	4	5	6	7	8	9	10
	Content, proportion by weight									
PVC E-7050 M	100	–	100	–	–	–	100	–	100	–
PVC S-7058 M	–	–	–	100	–	100	–	–	–	100
PVC S-7059 M	–	100	–	–	100	–	–	100	–	–
Ester **II**	60	–	–	–	10	40	–	20	30	–
Ester **I**	–	–	40	–	40	–	15	25	–	35
Ester **III**	–	–	–	20	–	10	–	–	20	–
Calcium stearate	2.0	2.5	2.8	2.5	3.0	2.8	2.6	3.0	2.8	2.5
Filler (chalk)	10	9	10	8	10	8	9	10	9	10
Pigment	0.5	0.7	0.5	1.0	0.8	0.5	1.0	0.7	0.8	1.0
	Parameter value									
Melt flow index, g min^{-1}	20–60									
Relative elongation, %	350	360	365	362	355	365	360	350	358	359
Breaking tensile stress, MPa	64.5	65.0	64.3	64.8	64.0	64.5	64.2	64.5	64.9	65.0
Frost resistance, °C	–28	–30	–32	–32	–28	–30	–29	–29	–30	–33
Shore hardness, no less than	54.5	54.2	54.8	53.8	54.2	53.5	55.0	56.0	55.0	53.0
Heat resistance at 185°C, min	157	156	158	157	154	155	157	157	158	157

Table 3. Comparison of the characteristics of dibutyl 2(3)-methylcyclohexenedicarboxylate (ester **II**), dibutyl phthalate, and dioctyl phthalate

Parameter	Ester **II**	Dibutyl phthalate	Dioctyl phthalate
Density, kg m^{-3}	932–1031	1045–4049	916–982
T_b, °C	310–312	340	386
Flash point, °C	160–165	168	205
Acid number, mg KOH/g	2.0	0.07–1.0	–
Refractive index n_D^{20}	1.4670	1.4860	–
Viscosity at 20°C, mm^2 s^{-1}	45.9	20	80–85

EXPERIMENTAL

In the experiments, we used PVC of suspension (S-7058 M, S-7059 M) or emulsion (E-7050 M) brand, a thermostabilizer (calcium stearate), and fillers (chalk and pigments). As plasticizers we used dialkyl or dicycloalkyl esters of 2(3)-methylcyclohexenedicarboxylic acid.

To prepare the polymeric compounds, the ingredients (proportion by weight), PVC resin 100, plasticizer 30–70, calcium stearate 2–5, filler 8–10, and pigment ≤0.5, were loaded into a mixer for swelling and were compounded for 10 min at 90–110°C. The swollen mixture was fed to rollers where it was homogenized at 120–130°C for 15–20 min.

From the polymeric compound obtained, we prepared samples and determined their physicochemical parameters by standard methods. The composition and properties of PVC compounds are listed in Table 2.

It can be seen that the diesters we prepared exhibit good plasticizing properties. With a decrease in the amount of the plasticizer in the compound, the plasticization and, correspondingly, the physicomechanical properties of the compound become worse.

The physicochemical characteristics of the newly synthesized dibutyl 2(3)-methylcyclohexenedicarboxylate and commercial plasticizers, dibutyl phthalate and dioctyl phthalate, are compared in Table 3.

It can be seen that dibutyl 2(3)-methylcyclohexenedicarboxylate has better properties and shows much promise as a plasticizer for PVC compounds.

The general procedure for preparing 2(3)-methylcyclohexenedicarboxylic acid diesters was as follows. A reactor was charged, using a dosing pump, with the required amounts of the starting reactants, a catalyst was added (mineral acid, 0.1–0.4% relative to the total weight), and the mixture was stirred for 1.5–2.0 h at 80–110°C. Then the reaction was continued for 4.0–4.5 h more, with slow evaporation of water released in the reaction and of excess alcohol. Water was evaporated first, as it formed a relatively low-boiling azeotrope with excess alcohol. After the reaction completion (when the water release ceased), the contents were loaded into barrels or pumped into a tank for finished products.

CONCLUSION

Dialkyl and dicycloalkyl esters of 2(3)-methylcyclohexenedicarboxylic acid were prepared and characterized. They can be used as plasticizers for PVC compounds.

REFERENCES

1. Khazova, T.N. and Cherepova, E.B., *Polim. Mater.: Izdel., Oborud., Tekhnol.*, 2006, no. 1, pp. 24–31.
2. Alieva, L.I., Gasanov, A.G., and Babaeva, R.Z., *Prots. Neftekhim. Neftepererab.*, 2004, no. 4, pp. 31–36.
3. Burturlu, E., Kilic, Y., and Kilic, M., *J. Appl. Polym. Sci.*, 2006, vol. 100, no. 6, pp. 4856–4867.
4. Balashov, S.S., Aranovich, D.A., and Khamidulova, Z.S., *Klei, Germet. Tekhnol.*, 2006, no. 8, pp. 19–23.
5. Nafikova, R.F., Afanas'ev, F.I., and Dmitriev, Yu.K., *Bashk. Khim. Zh.*, 2006, vol. 13, no. 3, pp. 63–68.

ISSN 1070-4272, Russian Journal of Applied Chemistry, 2008, Vol. 81, No. 4, pp. 723–725. © Pleiades Publishing, Ltd., 2008.
Original Russian Text © B.G. Ershov, N.M. Panich, A.F. Seliverstov, M.P. Belyaeva, 2008, published in Zhurnal Prikladnoi Khimii, 2008, Vol. 81, No. 4, pp. 687–689.

BRIEF COMMUNICATIONS

Ozone Decomposition in Concentrated Aqueous Solutions of Salts

B. G. Ershov, N. M. Panich, A. F. Seliverstov, and M. P. Belyaeva

Frumkin Institute of Physical Chemistry and Electrochemistry, Russian Academy of Sciences, Moscow, Russia

Received April 19, 2007

Abstract—Effect of high concentrations of electrolytes (Na_2SO_4, NaCl, and $NaNO_3$) on the rate of ozone decomposition in water was studied. The conversion kinetics of O_3 dissolved in these solutions was analyzed. The rate constants of ozone decomposition were determined.

DOI: 10.1134/S1070427208040319

Aqueous ozone solutions are instable in storage. The mechanism of their decomposition has already been studied for 70 years [1]. During this period, the main intermediate radical (HO_2, O_3^-, OH) and molecular (H_2O_2, O_2) products formed in the reactions of ozone and water have been identified, the rate constants of the corresponding reactions have been determined, and the chain reactions responsible for the decomposition have been elucidated [1–8].

Ozone is an exceedingly strong oxidant in water (its redox potentials are 2.07 and 1.27 V in acid and alkaline media, respectively) [9]. Ozone is widely applied for disinfection of drinking water and for oxidative decomposition of hazardous (organic and inorganic) impurities present in technological and household wastewater. In particular, ozone is used at radiochemical and nuclear power plants to decompose organic compounds in processing of a liquid radioactive waste containing high concentrations of dissolved salts (nitrates, chlorides, sulfates, etc.) [10]. Therefore, it is very important to take into account the effect of high electrolyte concentrations on the rate of ozone decomposition.

This study was aimed to determine the influence exerted by considerable concentrations of salts (Na_2SO_4, NaCl, and $NaNO_3$) on the rate of ozone decomposition in water.

EXPERIMENTAL

As objects of study served aqueous solutions (pH ~6) of Na_2SO_4, NaCl, and $NaNO_3$ (all of chemically pure grade) with concentrations of 0.35 to 3.5 M. The ozonization was performed in a temperature-controlled cell at 20°C. Ozone was obtained in a TRINITY ozonizer equipped with a capillary discharge chamber in which an ozone-oxygen mixture (OOM) with an ozone concentration of up to 180 mg l^{-1} was formed. The ozone-oxygen mixture was passed through a solution under study at a given temperature until a necessary concentration of O_3 was attained. The measurements were performed in a special quartz cell filled with a solution and in the absence of a gas phase. The concentration of ozone in the solution was continuously monitored by its absorption spectrum (λ_{max} = 258 nm, ε = 2900 l mol^{-1} cm^{-1} [11]), which made it possible to determine the time in which the limiting solubility is reached.

It has been found previously [12] that the solubility of ozone in water decreases as the salt concentration becomes higher. Ozone decomposes in water and in aqueous solutions of salts, which is manifested as a decrease in the intensity of its optical absorption in the course of time (Fig. 1). The kinetic dependences

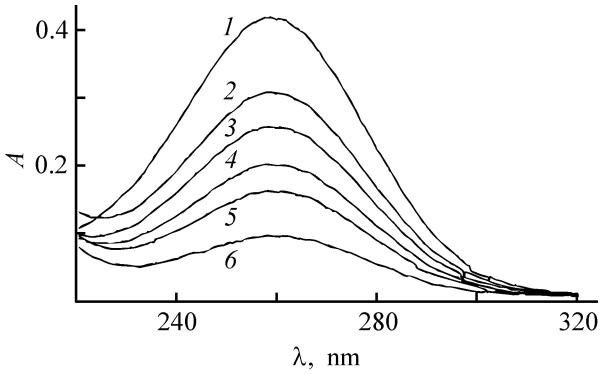


Fig. 1. Absorption spectra of ozone in a 0.35 M solution of Na_2SO_4. (*A*) Optical absorption and (λ) wavelength. Time (min): (*1*) 0.5, (*2*) 5, (*3*) 10, (*4*) 15, (*5*) 20, and (*6*) 30.

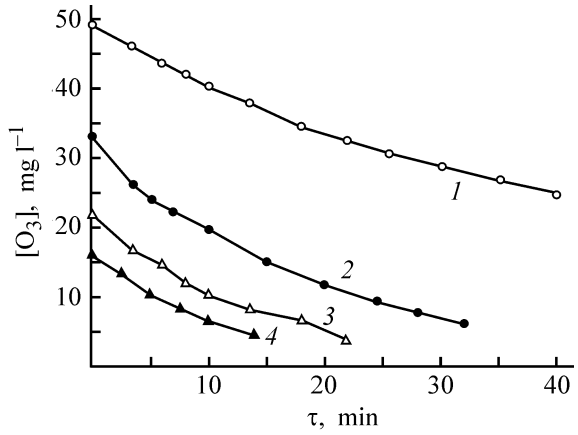


Fig. 2. Kinetic curves of ozone decomposition in Na_2SO_4 solutions of varied concentration. $[O_3]$ Ozone concentration and (t) time. Na_2SO_4 concentration (M): (*1*) 0, (*2*) 0.35, (*3*) 0.7, and (*4*) 1.06; the same for Fig. 3.

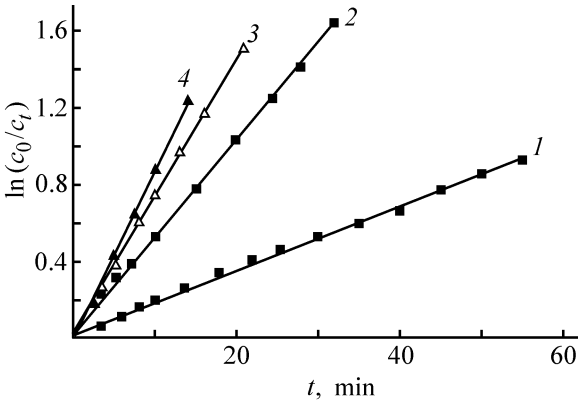


Fig. 3. Anamorphoses of the kinetic curves of ozone decomposition for the first-order reaction in Na_2SO_4 solutions of varied concentration. (c_0, c_t) Initial and current concentrations of ozone and (t) time.

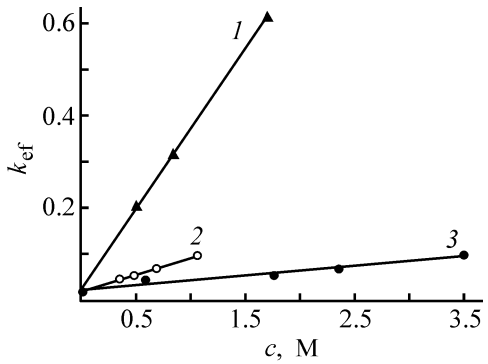


Fig. 4. k_{ef} vs. salt concentration c (M). Salt: (*1*) NaCl, (*2*) Na_2SO_4, and (*3*) $NaNO_3$.

of ozone decomposition are shown as an example for aqueous solutions of Na_2SO_4 in Fig. 2. It can be seen that the decomposition rate increases with the concentration of the dissolved salt. Similar dependences are also observed for aqueous solutions of NaCl and $NaNO_3$.

It was found that the kinetics of ozone decomposition in water and in aqueous solutions of Na_2SO_4, NaCl, and $NaNO_3$ is well described by the first-order equation. In Fig. 3, the kinetic dependences of ozone decomposition in water and in aqueous Na_2SO_4 solutions are plotted in the coordinates $\ln(c_0/c_t)$–t, where c_0 and c_t are the initial and current concentrations of ozone, respectively, and t is time. Figure 4 shows how the obtained effective rate constants k_{ef} depend on the concentration of the dissolved salt. The variation of k_{ef} with the salt concentration can be described by the equation

$$k_{ef} = k_w + k_r c_r,$$

where k_r is the true rate constant, and k_w is the rate constant of ozone decomposition in water.

It can be seen that, for all the salts, k_{ef} is virtually proportional to their molal concentration. This means that the reaction of ozone decomposition in aqueous solutions of salts is bimolecular. The slope of the dependence was used to determine the following true rate constants k_r of ozone decomposition (l mol^{-1} s^{-1}): 1.2×10^{-3} for Na_2SO_4, 5.8×10^{-3} for NaCl, and 3.5×10^{-4} for $NaNO_3$. This indicates that, at the same molar concentrations of the salts, the ozone decomposition in $NaNO_3$ solutions is a factor of 3–4 slower than that in Na_2SO_4 solutions and a factor of 17 slower than that in NaCl solutions. The intercept on the ordinate axis by the linear dependences of k_{ef} at zero salt concentration corresponds to the rate constant of ozone decomposition in pure water, k_w (2.9×10^{-4} s^{-1}). The thus calculated rate constant coincides with the experimentally measured value.

The mechanism of ozone decomposition in the presence of salts is rather complicated. The dependence of the decomposition rate on the nature of an electrolyte shows that the ionic strength of the solutions is not a predominant factor responsible for this effect. The specific effect of a salt is possibly due to decomposition of ozone in two processes involving free water and water specifically bound to the electrolyte (e.g. water from the hydrate sphere of the ion). The concentration of the hydration water, which reacts with ozone more vigorously, is proportional to the salt concentration in the solution.

CONCLUSIONS

The kinetics of ozone decomposition in aqueous solutions of salts (Na_2SO_4, NaCl, and $NaNO_3$) is described by a pseudo-first-order equation in the salt concentration. The rate increases with the concentration of the dissolved salt. Depending on the nature of a salt, the rate constants of the reactions vary in the following order: $k(NaNO_3) < k(Na_2SO_4) < k(NaCl)$.

ACKNOWLEDGMENTS

The authors are grateful to the Russian Foundation for Basic Research (project no. 06-03-32 682) for partial financial support.

REFERENCES

1. Weiss, J., *Trans. Faraday. Soc.*, 1935, vol. 31, pp. 668–681.
2. Staehelin, J. and Holgne, J., *Environ. Sci. Technol.*, 1982, vol. 16, no. 10, pp. 676–682.
3. Lin, J. and Nakajima, T., *J. Mol. Struct. (Theochem)*, 2003, vol. 625, nos. 1–3, pp. 161–167.
4. Speranza, M., *J. Phys. Chem. A.*, 1998, vol. 102, no. 38, pp. 7535–7541.
5. Sehested, K., Holcman, J., Bjergbakke, E., and Hart, E.J., *J. Phys. Chem.*, 1982, vol. 86, no. 11, pp. 2066–2069.
6. Gorbenko-Germanov, D.S. and Kozlova, I.V., *Dokl. Akad Nauk SSSR*, 1973, vol. 210, no. 4, pp. 851–854.
7. Glaze, W.H., Kang, J.-W., and Chapin, D.H., *Ozone Sci. Eng.*, 1987, vol. 9, no. 4, pp. 335–352.
8. Wallace, J.L, Vahadi, B., Fernandes, J.B., and Boyden B.H., *Ozone Sci. Eng.*, 1988, vol. 10, no. 1, pp. 103–112.
9. Razumovskii, S.D., and Zaikov, G.E., *Ozon i ego reaktsii s organicheskimi soedineniyami* (Ozone and Its Reactions with Organic Substances), Moscow: Nauka, 1974.
10. Savkin, A.E., Kobelev, A.P., Sinyakin, O.G., et al., Abstracts of Papers, *5 Rossiiskaya Konferentsiya po radiokhimii "Radiokhimiya 2006"* (5th Russian Conf. on Radiochemistry "Radiochemistry 2006"), Dubna, October 23–27, 2006, p. 203.
11. Bader, H. and Holgne, J., *Ozone Sci. Eng.*, 1982, vol. 4, no. 4, pp. 169–176.
12. Panich, N.M., Ershov, B.G., Seliverstov, A.F., and Basiev, A.G., *Zh. Prikl. Khim.*, 2007, vol. 80, no. 11, pp. 1787–1790.

ISSN 1070-4272, Russian Journal of Applied Chemistry, 2008, Vol. 81, No. 4, pp. 726–729. © Pleiades Publishing, Ltd., 2008.
Original Russian Text © E.V. Churilina, G.V. Shatalov, Ya.I. Korenman, P.T. Sukhanov, V.M. Bolotov, 2008, published in Zhurnal Prikladnoi Khimii, 2008, Vol. 81, No. 4, pp. 690–692.

BRIEF COMMUNICATIONS

Extraction and Preconcentration of Anthocyan Dye from Aqueous Solutions with Water-Soluble Poly-*N*-Vinylamides

E. V. Churilina, G. V. Shatalov, Ya. I. Korenman, P. T. Sukhanov, and V. M. Bolotov

Voronezh State Technological Academy, Voronezh, Russia

Voronezh State University, Voronezh, Russia

Received July 7, 2007

Abstract—Extraction of an anthocyan dye with poly-*N*-vinylpyrrolidone (PVP) and poly-*N*-vinylcaprolactam (PVC) under the conditions of separation of aqueous solutions of this polymer into two phases in the presence of salting-out agents (sodium chloride and sodium or ammonium sulfate) was studied.

DOI: 10.1134/S1070427208040320

Heterogeneous systems containing water-soluble polymers poly-*N*-vinylpyrrolidone (PVP) and poly-*N*-vinylcaprolactam (PVC) are used in biotechnology for separation of proteins, cells, and biologically active substances, including amino acids and vitamins [1, 2]. The main advantages of application of PVP and PVC as extractants are their nontoxicity, high hydrophilicity, and ability to form complexes with many low- and high-molecular-weight organic compounds [3].

The majority of natural red pigments are derived from anthocyans, phenolic compounds, whose structure is similar to that of plant glycosides. These compounds are readily soluble in water and form anthocyanides upon hydrolysis [4]. These dyes are used in food industry [5].

The common methods for recovery and preconcentration of anthocyan dyes from plant raw materials and aqueous solutions are based on their repeated extraction with organic solvents [5]. We believe that liquid extraction of anthocyan dyes can be improved by using two-phase aqueous systems based on water-soluble polymers containing no toxic organic solvents. Such extraction systems based on PVP and PVC have not been studied previously.

In this study, we examined the extractive preconcentration of an anthocyan dye from aqueous solutions with PVP and PVC.

EXPERIMENTAL

Anthocyan dye was extracted from black-currant berry with ethanol at 50–55°C by the procedure reported in [6]. The PVP polymer of medical grade with a molecular weight $M_\eta = 1 \times 10^4$ was used. Poly-*N*-vinylcaprolactam was prepared by radical polymerization of its monomer in isopropanol at 70°C in the presence of azobis(isobutyronitrile) initiator at various monomer concentrations. The polymer was precipitated by adding hexane to the reaction mixture and then vacuum-dried at 55–60°C. The molecular weights of the polymers were calculated from the intrinsic viscosity [η] of their solutions by the formula $[\eta] = 1.5 \times 10^{-4} M_\eta^{0.68}$ [3]. PVC samples with the molecular weights of 1×10^4, 6×10^4, and 16×10^4 were prepared.

NaCl, $(NH_4)_2SO_4$, and Na_2SO_4 (chemically pure grade) were used as salting-out agents providing separation of aqueous solutions of the polymer into two phases within a wide range of polymer and salt concentrations.

A solution of anthocyan dye (10 ml), containing a salting-out agent, was placed in a vial with a ground-glass stopper, and then 1 ml of an aqueous solution of the polymer (concentration 0.001–2 wt %) was added to obtain a two-phase extraction system. The extraction was carried out on a vibra-

tion mixer until the phase equilibrium was attained (3–5 min).

The efficiency of the extraction recovery of the dye was characterized by the degree of its recovery R (%):

$$R = [(A_0 - A)/A_0] \times 100,$$

where A_0 and A are the optical densities of aqueous anthocyan dye solutions before and after extraction (KFK-2MP spectrophotometer, λ = 490 nm, 1-cm optical cell).

The content of the red pigment in the anthocyan dye was determined with a reference solution of $CoSO_4 \cdot 7H_2O$ by the standard procedure [5].

As a rule, two-phase aqueous systems based on water-soluble polymers are prepared by their salting-out from homogeneous aqueous solutions [7]. The conditions of formation of heterogeneous systems by salting-out of PVP and PVC from their homogeneous aqueous solutions were elucidated from their phase diagrams (Fig. 1) obtained by titration of these polymers with standard salt solutions to the cloud point [8]. We found that, in all the systems under consideration, except PVP–sodium chloride–water, stable two-phase systems are formed. In phase diagrams, the fields of two-phase systems lie above binodal curves of approximately exponential shape. Irrespective of a particular poly-*N*-vinylamide, the strongest salting-out effect is reached in the presence of ammonium sulfate. It should be noted that the molecular volume and electronic structure of ammonium cations are close to those of water molecules, and ammonium cations form hydrogen bonds with surrounding water molecules. These factors favor stronger hydration of ammonium cations. To obtain the maximal amount of the aqueous phase enriched in the polymer, the salting-out is carried out at the salt concentration close to saturation.

Figure 2 shows that the extraction of anthocyan dyes is dependent on both the polymer concentration and particular dye. In salting-out with ammonium sulfate, the dye recovery is more complete. In single-step extraction, the degrees of recovery of dyes in the presence of ammonium sulfate and sodium sulfate are 95 and 79%, respectively.

In extraction of anthocyan dye with PVC, the more efficient recovery of the dye is reached with sodium chloride compared with ammonium and sodium sulfates. We believe that this difference is primarily caused by the difference in the effect of salts on the phase separation temperature T_{ps} of aqueous PVC.

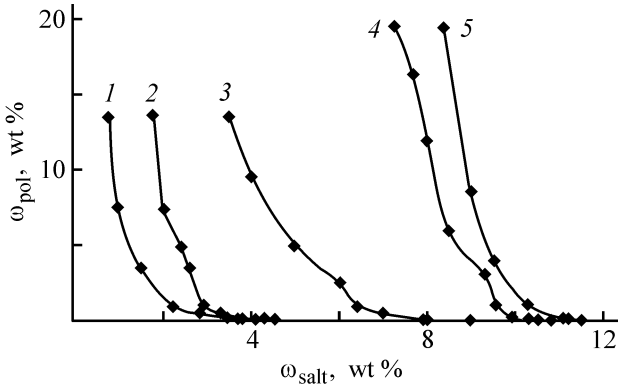


Fig. 1. Phase diagrams of the systems (*1*) PVC–ammonium sulfate, (*2*) PVC–sodium sulfate, (*3*) PVC–sodium chloride, (*4*) PVP–ammonium sulfate, and (*5*) PVP–sodium sulfate. (ω_{pol}) Weight fraction of polymer and (ω_{salt}) weight fraction of salt.

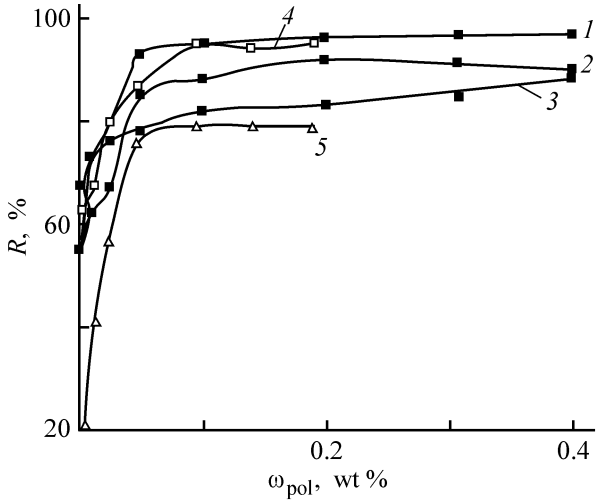


Fig. 2. Degree of extraction of anthocyan dye R from aqueous-salt solutions vs. polymer concentration ω_{pol} Polymer: (*1–3*) PVC and (*4*, *5*) PVP Salting-out agent: (*1*) sodium chloride, (*2*, *5*) sodium sulfate, and (*3*, *4*) ammonium sulfate.

It is known [9] that, in the absence of salt, the T_{ps} of this polymer is close to the temperature of warm-blooded living bodies. At the same time, on adding NaCl, the phase-separation temperature decreases to room temperature. Therefore, we suggest that the increase in efficiency of extraction of the anthocyan dye in the system poly-*N*-vinylcaprolactam–NaCl–H_2O is caused not only by salting-out of the dye and polymer but also by changes in the structure of the polymer–H_2O complex.

Figure 3 shows how the PVC molecular weight and pH affect the degree of recovery of anthocyan dye from saturated aqueous NaCl. It is seen that, irrespective of PVC concentration and its molecular weight,

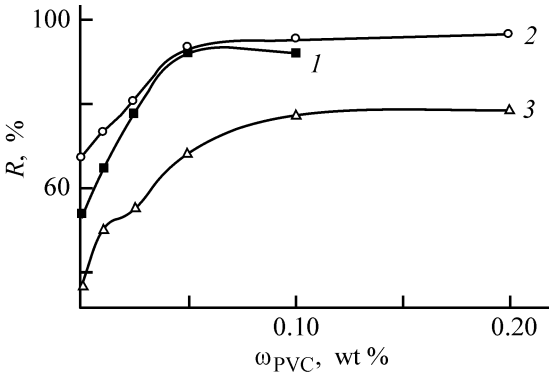


Fig. 3. Degree R of extraction of anthocyan dye from saturated aqueous NaCl vs. PVC concentration ω_{pol}. M_η: (*1*) 1×10^4 (pH 3.5), (*2*) 6×10^4 (pH 3.5), and (*3*) 6×10^4 (pH 1).

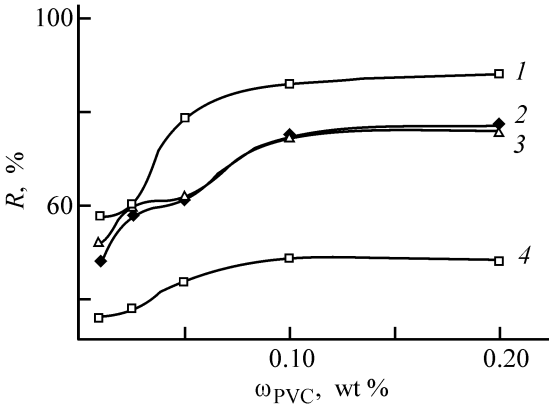


Fig. 4. Degree R of extractive recovery of anthocyan dye with aqueous PVC at phase separation induced by heating vs. the polymer concentration ω_{PVC}. M_η: (*1*) 16×10^4 (pH 3.5), (*2*) 6×10^4 (pH 3.5), (*3*) 1×10^4 (pH 3.5), and (*4*) 1×10^4 (pH 1).

the degree of recovery of the dye considerably decreases with decreasing pH. At a PVC concentration of 6×10^4 M, raising pH from 1 to 3.5 increases the degree of recovery of the anthocyan dye from 77 to 92–95%. The extraction of dyes at pH > 7 in the systems under consideration was not studied because of the chemical degradation of anthocyan dye in alkaline media [10].

Variation of the molecular weight of the polymer from 1×10^4 to 6×10^4 at pH 3.5 in the extraction systems based on PVC does not noticeably affect the degree of recovery of the anthocyan dye (Fig. 3, curves *1* and *2*). A similar behavior is exhibited by PVC in its complexation with fluorescent dyes [3].

We found that, in the extraction systems based on PVP, all factors being the same (M_η, pH, salting-out agent), the degree of recovery of the anthocyan dye was higher than in the systems based on PVC (Fig. 2, curves *3* and *4*). This difference is apparently caused by the stronger complexation of PVP with the dye. This polymer is more sterically accessible and less hydrophobic because of the smaller length of hydrocarbon chains in *N*-vinylpyrrolidone, compared to *N*-vinylcaprolactam.

The high efficiency of the extraction systems based on PVP and PVC is caused by complexation of PVP and PVC with dye molecules. This complexation is manifested in the UV absorption spectra as the absorption band at 274 nm, absent in the spectra of the aqueous solutions of particular polymers. The complexation between the polymers and anthocyan dye occurs by the mechanism of hydrogen bonding between the carbonyl groups of polymer and the hydroxy groups of the dye. Upon acidification, the complexation between the polymer and dye weakens because of the protonation of the C=O groups [11] and, as a result, the degree of recovery of the dye decreases.

In contrast to aqueous PVP, aqueous poly-*N*-vinylcaprolactams have a lower critical solution point at 32–37°C [3]. Therefore, PVC allows extraction of anthocyan dye (up to 86%) from aqueous solutions without salting-out agents at temperature exceeding the lower critical solution point (33.5°C). As can be seen from Fig. 4 (curve *4*), the extraction of the dye considerably decreases upon acidification of the extraction system based PVC to pH 1 before phase separation by heating.

CONCLUSIONS

(1) Two-phase systems based on water-soluble poly-*N*-vinylpyrrolidone and poly-*N*-vinylcaprolactam are suitable for efficient extractive recovery and preconcentration of anthocyan dyes from aqueous solutions. The highest extraction efficiency is exhibited by the two-phase extraction systems ammonium sulfate–poly-*N*-vinylpyrrolidone–water and sodium chloride–poly-*N*-vinylcaprolactam–water at pH 3.5.

(2) The anthocyan dye concentrates prepared by extraction with poly-*N*-vinylpyrrolidone and poly-*N*-vinylcaprolactam can be used for coloration of food products.

REFERENCES

1. Shlyakhina, Yu.V., Mokshina, N.Ya., Khokhlov, V.Yu., et al., *Izv. Vyssh. Uchebn. Zaved., Khim. Khim. Tekhnol.*, 2006, vol. 49, no. 6, pp. 20–22.
2. Mokshina, N.Ya., *Ekstraktsiya aminokislot i vitaminov*

(Extraction of Amino Acids and Vitamins), Voronezh: Voronezh. Gos. Tekhnol. Akad., 2007.

3. Kirsh, Yu.Ya., *Poli-N-vinilpirrolidon i drugie poli-N-vinilamidy* (Poly-*N*-vinylpyrrolidone and Other Poly-*N*-vinylamides), Moscow: Nauka, 1998.
4. Tanchev, S.S., 1Antotsiany v plodakh i ovoshchakh (Anthocyans in Fruits and Vegetables), Moscow: Pishch. Prom–st., 1980.
5. Kharlamova, O.A. and Kafka, B.V., *Natural'nye pishchevye krasiteli* (Natural Food Dyes), Moscow: Pishch. Prom–st., 1979.
6. RF patent 2 228 344.
7. Nifant'eva, T.I., Matousova, V., Adamcova, Z., and Shkinev, V.M., *Vysokomol. Soedin., Ser. A*, 1989, vol. 31, no. 8, pp. 2131–2135.
8. Molochnikova, N.P., Shkinev, V.M., and Myasoedov, B.F., *Radiokhimiya*, 1995, vol. 37, no. 5, pp. 385–397.
9. Kirsh, Yu.E., Yanul', N.A., Popkov, Yu.M., and Timashev, S.F., *Zh. Fiz. Khim.*, 1999, vol. 73, no. 2, pp. 313–319.
10. Goto, T., *Prog. Chem. Org. Nat. Prod.*, 1987, vol. 52, pp. 113–158.
11. Kirsh, Yu.E., Semina, N.V., Yanul', N.A., and Shatalov, G.V., *Zh. Fiz. Khim.*, 1994, vol. 68, no. 9, pp. 1584–1586.

ISSN 1070-4272, Russian Journal of Applied Chemistry, 2008, Vol. 81, No. 4, pp. 730–731. © Pleiades Publishing, Ltd., 2008.
Original Russian Text © K.S. Trofimova, V.G. Dronov, N.S. Shaglaeva, R.G. Sultangareev, 2008, published in Zhurnal Prikladnoi Khimii, 2008, Vol. 81, No. 4, pp. 693–694.

BRIEF COMMUNICATIONS

New Approach to Processing of Chlorine-containing Wastes: Synthesis of 2,3-Dichloropropene from 1,2,3-Trichloropropane

K. S. Trofimova, V. G. Dronov, N. S. Shaglaeva, and R. G. Sultangareev

Favorskii Institute of Chemistry, Siberian Branch, Russian Academy of Sciences, Irkutsk, Russia
Irkutsk State Technical University, Irkutsk, Russia

Received August 2, 2007

Abstract—Possibilities of utilization of by-products formed in manufacture of epichlorohydrin are considered. A promising way to utilize wastes from production of epichlorohydrin by synthesis of 2,3-dichloropropene from 1,2,3-trichloropropane is suggested.

DOI: 10.1134/S1070427208040332

Epichlorohydrin (EPI) is the main component in synthesis of glycerol, epoxy resins, and a number of other products, including chlorohydrin caoutchoucs. At present, more than 1 million tons of epichlorohydrin is manufactured by the chlorine method all over the world.

Synthesis of EPI is accompanied by a number of side reactions, which leads to formation of large amounts of organochlorine wastes: allyl chloride, 2,2-dichloropropane, 1,2-dichloropropane, 1,3-dichloropropene, 1,2,3-trichloropropane, dichloropropanols, and chloroesters. In the opinion of the authors of [1], about 400 and 100 kg of the dichloropropane and 1,2,3-trichlopropane fractions, respectively, is produced per ton of EPI.

By now, virtually no economically efficient and ecologically safe methods have been developed for utilization of organochlorine wastes. Industrial utilization of these wastes encounters severe difficulties. At the same time, all the above-mentioned kinds of by-products are promising raw materials for manufacture of valuable materials that are in steadily increasing demand.

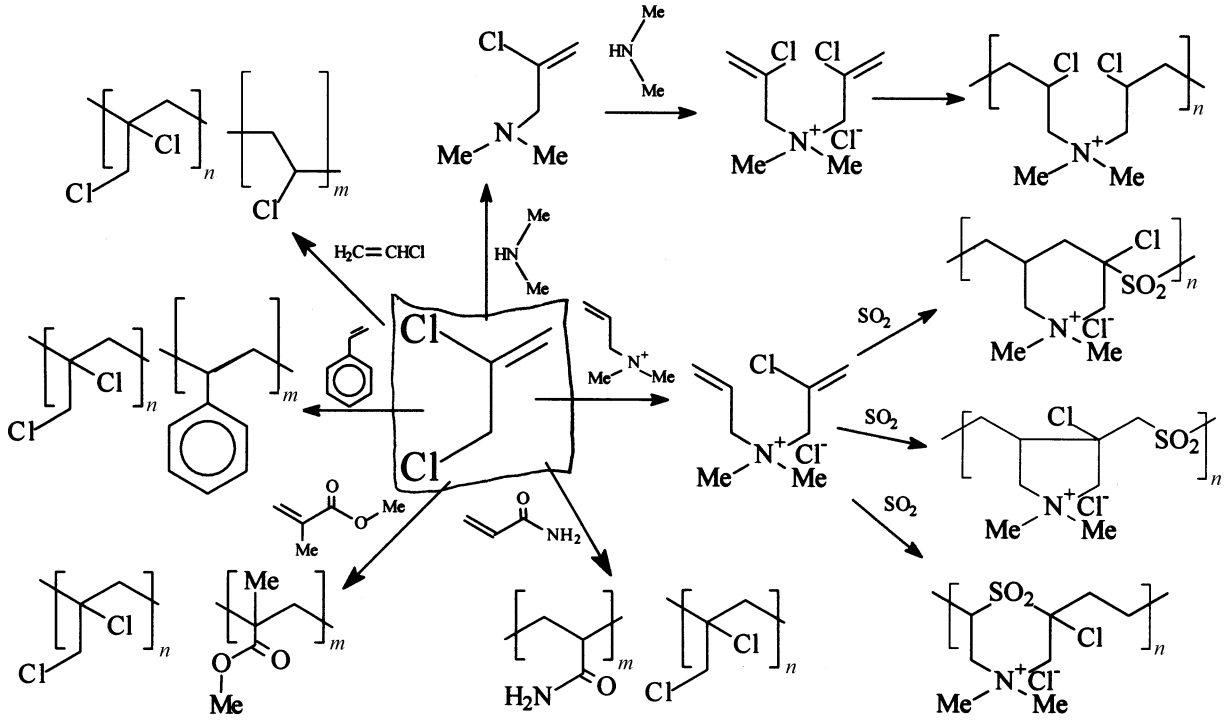
Commonly, organochlorine wastes are neutralized by the following methods: regeneration, oxidation, burning, chemical and plasmochemical processing, electrocracking, and burial [1–3]. In the present study, a method for isolation of 1,2,3-trichloropropane (TCP) from a mixture of organochlorine wastes was developed and the conditions in which 2,3-trichloropropene (DCP) is produced by dehydrochlorination of the trichloropropane fraction were analyzed.

2,3-Dichloropropene is an important and promising half-product for synthesis of a large number of polyfunctional highly reactive polymeric compounds. It has been used to find simple and convenient pathways [4] to synthesis of tertiary and quaternary polymeric salts that can be used in oil and textile industries (see scheme).

EXPERIMENTAL

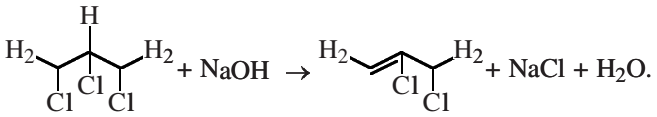
TCP was isolated from a mixture of organochlorine wastes as follows. First, all the water-soluble impurities (epichlorohydrin, dichloropropanols, chloroesters) were extracted with distilled water containing 2–3 g l^{-1} of soda ash (or an alkali for maintaining the pH of the medium at 7–8). After the water-soluble impurities were removed (with monitoring by GLC), the mixture was subjected to azeotropic dehydration, and then TCP was isolated by rectification (≥99%).

1,2,3-Trichloropropane (1 mol) was treated with a 10% alcoholic solution of NaOH at room temperature for 4 h. In the process, a white water-soluble precipitate (NaCl) is formed. After the precipitate was filtered off, the liquid phase was distilled and the fraction with bp 94°C was taken.



Scheme.

The DCP synthesized is a colorless liquid that is rather stable, does not become dark in storage under normal conditions, and is not dehydrochlorinated in prolonged storage, d_4^{20} = 1.209, n_D^{20} = 1.4609. The yield of DCP is 80%. The reaction scheme can be represented as



An elemental analysis was made on a Thermo Finniqan gas analyzer. IR spectra of the copolymers were measured in KBr pellets on a Specord IR-75 spectrophotometer, and ^{13}NMR spectra, on a Varian VXR-500S spectrometer, with HMDS as internal standard.

The physicochemical constants of the compound isolated coincide with similar values for the reference DCP.

The ^{1}H NMR spectrum of DCP contains signals of protons of the vinyl and chloromethyl groups at 5.48 and 4.19 ppm, respectively. The ^{13} NMR spectrum shows absorption signals of the chloromethyl, $=CH_2$, and =CCl groups at 47.49, 116.44, and 138.44 ppm, respectively.

The IR spectrum contains an absorption band at 1605 cm^{-1}, associated with the vinyl group. The absorption band at 680 cm^{-1} can be attributed to the C–Cl bond.

CONCLUSION

A method for isolation of 1,2,3-trichloropropane from chlorine-containing wastes formed in manufacture of epichlorohydrin and for its conversion to 2,3-dichloropropene by the dehydrochlorination reaction was developed.

ACKNOWLEDGMENTS

The study was financially supported by the Russian Foundation for Basic Research (project no. 06-08-00320).

REFERENCES

1. Khaliullin, A.K. and Salaurov, V.N., *Osnovy promyshlennoi ekologii: Uchebnoe posobie dlya vuzov* (Fundamentals of Industrial Ecology: Textbook for Higher School), Irkutsk, 2002.
2. Russavskaya, N.V., *Doctoral Dissertation*, Irkutsk, 2006.
3. Deryagina, E.N., Korchevin, N.A., and Tomin, V.P., *Nauka – proizvodstvu* (Science to the Industry), 2004, issue 1, pp. 50–58.
4. Sharifov, G.S., *Kinet. Kataliz*, 2001, vol. 42, no. 5, pp. 615–619.

ISSN 1070-4272, Russian Journal of Applied Chemistry, 2008, Vol. 81, No. 4, pp. 732–735. © Pleiades Publishing, Ltd., 2008.
Original Russian Text © M.G. Voronkov, E.N. Khimich, N.N. Khimich, 2008, published in Zhurnal Prikladnoi Khimii, 2008, Vol. 81, No. 4, pp. 695–697.

BRIEF COMMUNICATIONS

Optimization of the Conditions of Acid Hydrolysis of Tetraethoxysilane and Identification of Primary Products of Sol–Gel Synthesis

M. G. Voronkov, E. N. Khimich, and N. N. Khimich

Grebenshchikov Institute of Silicate Chemistry, Russian Academy of Sciences, St. Petersburg, Russia

Received November 30, 2007

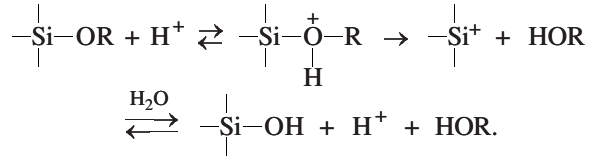
Abstract—The effect of the reactant ratio in the $Si(OEt)_4$–H_2O–EtOH–HCl system on the hydrolytic polycondensation of tetraethoxysilane and gelation rate was examined. A mass-spectrometric study showed that the primary products of the sol–gel process are linear and cyclic oligosiloxanes containing hydroxy and ethoxy groups at the silicon atoms.

DOI: 10.1134/S1070427208040344

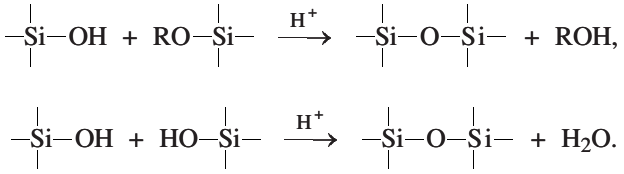
Hydrolytic polycondensation of tetraethoxysilane was historically the first studied reaction of organosilicon compounds [1, 2]. In the second half of the XX century it found wide use in many branches of industry as a sol–gel process [3]. Grebenshchikov and Suikovskaya suggested to use the sol–gel process or, more precisely, hydrolysis products of tetraethoxysilane for the so-called blooming of optics, i.e., formation on the glass surface of thin films reducing the light reflection from the surface [4]. Grebenshchikov et al. also developed a method for increasing the surface hardness of organic glasses by applying a coating based on tetraethoxysilane hydrolysis products [5].

In the subsequent period, the sol–gel method based on hydrolytic polycondensation of tetraethoxysilanes was widely used by Voronkov and numerous collaborators for hydrophobization and improvement of other service properties of building [6–9] and textile [10, 11] materials, glass [12, 13], fiber glass [14, 15], and metals [16]. They examined the influence exerted on the sol–gel synthesis by the catalyst, solvent, reactant ratio, pH of the medium, and presence of metal salts and oxides [17–22]. They also studied the formation conditions and properties of the resulting xero- and aerogels [12, 16, 17, 23].

Until recently, the mechanism of acid hydrolysis of tetraalkoxysilanes has been described by the following general schemes [20–22]:



Further hetero- and homofunctional condensation processes are described by the general equations



Owing to cyclization, cross-linking, and branching of siloxane chains, the primary products of the hydrolytic polycondensation are oligomers and polymers containing the ≡Si–O–Si≡, ≡Si–OH, and ≡Si–OR groups in various combinations and ratios in one molecule or macromolecule. Thermally stable linear peralkoxysiloxanes $(RO)_3SiO[Si(OR)_2]_nOR$ (n = 0, 1, 2, 4, 6; R = CH_3) and peralkoxycyclosiloxanes ($[(RO)_2SiO]_n$) (n = 4, 6; R = CH_3) have been isolated and identified [24].

With the aim to further study the acid hydrolysis of tetraethoxysilane in the $Si(OEt)_4$–H_2O–EtOH–HCl system, we examined the influence exerted on the process by the reactant ratio, HCl concentration, and gelation time. Our goals were, first, to elucidate the nature

Table 1. Gelation rate in the $Si(OEt)_4$–H_2O–EtOH–HCl system at various amounts of HCl solution

Oligomer mixture no.	Amount of 0.01 N HCl, g	Maximal content of SiO_2 in liquid oligomer, %	t_1^*	t_2^*	State of solidified gel
			h		
1	1.1	59.13	98	106	Monolithic
2	1.2	57.90	44	48	〃
3	1.3	55.37	32	38	Cracked
4	1.4	53.70	24	28	〃

* (t_1) Time of formation of liquid oligomer with the maximum obtained SiO_2 content; (t_2) gelation duration.

of primary labile oligomeric products by mass spectrometry and, second, to optimize the conditions of hydrolytic polycondensation of tetraethoxysilane with the aim to obtain relatively stable structures with the maximal SiO_2 content. Such highly concentrated systems are of interest from the viewpoint of their use as inorganic component in synthesis of organic–inorganic hybrids.

EXPERIMENTAL

The mass spectra were measured on an MKh-5303 device equipped with an electrospray ionization source and a time-of-flight mass analyzer [25].

The silicon content of the reaction mixture before the gelation was determined gravimetrically by decomposing the sample with a mixture of 20% oleum and concentrated nitric acid and then calcining the residue at 800°C to constant weight [26].

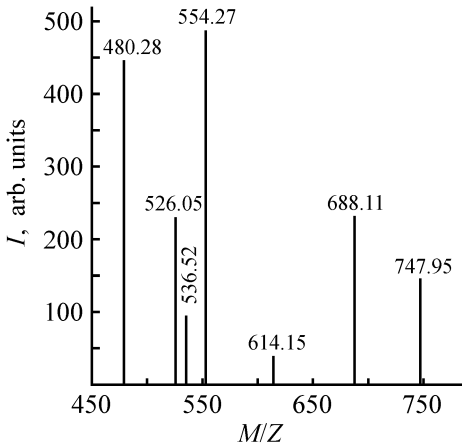
Mixtures of linear and cyclic oligoethoxysiloxanes and oligoethoxysiloxanols (which could not be separated into individual components) have been prepared by controlled hydrolytic polycondensation of tetraethoxysilane under the conditions of acid catalysis [27]. Numerous experiments have shown that the best catalyst for preparing liquid oligomer mixtures with a high SiO_2 content is 0.01 N HCl. At lower acid concentrations, the gelation time becomes several times longer, and at higher acid concentrations the reaction becomes so fast that isolation of liquid oligomers with a high SiO_2 content becomes impossible.

The $Si(OEt)_4$: EtOH molar ratio was kept constant (1 : 2.2), and the amount of a 0.01 N HCl solution was varied. To perform the process, we added 9.8 g (0.044 mol) of $Si(OEt)_4$ to a mixture of 4.8 g (0.104 mol) of EtOH and measured amount of an HCl solution. The mixture was placed in polypropylene jars with threaded caps (three vessels for each system) and kept in them for 1–4 days in a thermostat at 90°C until a gel was obtained. The hydrolytic polycondensation of alkoxysilanes accelerates as the amount of acid in the system increases. Thus, it becomes possible to control the reaction progress (gelation time) (Table 1).

The difference between t_1 and t_2 is caused by the fact that water was taken for the sol–gel process in deficiency, to ensure the relatively low rate of cross-linking in the system. In this case, after the time t_1 is elapsed, the system is no longer a classical sol and gradually loses mobility, but a continuous 3*D* structure has not yet been formed.

According to mass-spectrometric data, a mixture of oligoethoxysiloxanols of various molecular weights is formed in system nos. 1–3. The mass spectrum of oligomer mixture no. 1 is shown as an example in the figure.

It should be noted that oligomers having a higher molecular weight are formed when the acid solution is taken in a minimal amount. The major relatively stable oligomeric products of hydrolytic polycondensation of $Si(OEt)_4$ are linear octaethoxytetrasiloxanediol **I**, decaethoxypentasiloxanediol **II**, hepta-



Mass spectrum of oligoethoxysiloxanol mixture no. 1: (*I*) intensity and (*M*/*Z*) weight-to-charge ratio.

Table 2. Composition of oligosiloxanol mixture nos. 1–3

Oligomer mixture no.	Molar ratio $Si(OEt)_4 : H_2O : HCl : EtOH$	Minor components of oligomer mixtures (molecular weight)
1	$1 : 1.39 : 2.5 \times 10^{-4} : 2.36$	$(HO)_2[Si(OC_2H_5)O]_5(OEt)_3$ (614) (**V**), $[Si(OEt)O]_4$ (536) (**VI**), $(EtO)_{10}(HO)_2Si_6O_6$ (748) (**VII**)
2	$1 : 1.52 : 2.7 \times 10^{-4} : 2.36$	$HO[Si(OC_2H_5)O]_5$ (614) (**V**), $[Si(OEt)O]_4(OEt)_4$ (536) (**VI**), $HO[Si(OEt)_2O]_2Si(OEt)_3$ (448) (**VIII**)
3	$1 : 1.64 : 2.95 \times 10^{-4} : 2.36$	$[Si(OEt)O]_4(OEt)_4$ (536) (**VI**), $HO[Si(OEt)_2O]_2Si(Oet)_3$ (448) (**VIII**)

ethoxy tetrasiloxanetriol **III**, and cyclic compounds hexaethoxycyclotetrasiloxanediol **IV** and decaethoxycyclohexasiloxanediol **V**. A number of minor components were also detected and characterized (Table 2).

CONCLUSIONS

(1) A procedure was developed for hydrolytic polycondensation of tetraethoxysilane to obtain a mixture of polyalkoxysiloxanols with a high silica content.

(2) A number of organosilicon derivatives of linear (octaethoxytetrasiloxanediol **I**, decaethoxypentasiloxanediol **II**, heptaethoxytetrasiloxanetriol **III**) and cyclic (hexaethoxycyclotetrasiloxanediol **IV**) structures were identified.

REFERENCES

1. Dolgov, B.N., *Khimiya kremniiorganicheskikh soedinenii* (Chemistry of Organosilicon Compounds), Leningrad: ONTI, 1933.
2. Voronkov, M.G. and Mileshkevich, V.P., *Siloksanovaya svyaz'* (Siloxane Bond), Novosibirsk: Nauka, 1976.
3. *Sol–Gel Science and Technology: Processing, Characterization and Applications*, Sakka, S., Ed., vol. 1: *Processing*, New York: Kluwer Academic, 2005.
4. Voronkov, M.G., *Khimiya kremniiorganicheskikh soedinenii v rabotakh russkikh sovetskikh uchenykh* (Chemistry of Organosilicon Compounds in Papers by Russian and Soviet Scientists), Leningrad: Leningr. Gos. Univ., 1952.
5. *I.V. Grebenshchikov. Materialy i bibliografii uchenykh SSSR* (I.V. Grebenshchikov. Materials and Bibliographies of Soviet Scientists), Moscow: Akad. Nauk SSSR, 1947.
6. Voronkov, M.G. and Shorokhov, N.V., *Vodoottalkivayushchie pokrytiya v stroitel'stve* (Water-Repellent Coatings in Building), Leningrad: Akad. Nauk SSSR, 1963.
7. Laskaya, E.A. and Voronkov, M.G., *Kremniiorganicheskie vodoottalkivayushchie pokrytiya v stroitel'stve* (Organosilicon Water-Repellent Coatings in Building), Kiev: Budivel'nik, 1968.
8. Khrustalev, S.S. and Voronkov, M.G., *Zh. Prikl. Khim.*, 1955, vol. 28, no. 9, pp. 916–921.
9. Voronkov, M.G. and Shorokhov, N.V., *Stroit. Mater.*, 1959, no. 7, pp. 12–17.
10. Voronkov, M.G. and Makarskaya, V.M., *Appretirovanie tekstil'nykh materialov kremniiorganicheskimi monomerami i oligomerami* (Dressing of Textile Materials with Organosilicon Monomers and Oligomers), Novosibirsk: Nauka, 1978.
11. Makarskaya, V.M., Voronkov, M.G., and Kharkarov, A.A., *Zh. Prikl. Khim.*, 1978, vol. 51, no. 2, pp. 378–381.
12. Pashchenko, A.A., *Gidrofobizatsiya* (Hydrophobization), Kiev: Naukova Dumka, 1973.
13. Pashchenko, A.A. and Voronkov, M.G., *Khim. Tekhnol. (Kharkov)*, 1970, issue 16, pp. 57–65.
14. Voronkov, M.G. and Kukharskaya, E.V., *Zh. Prikl. Khim.*, 1983, vol. 56, no. 4, pp. 868–873.
15. Voronkov, M.G. and Kukharskaya, E.V., *Zh. Prikl. Khim.*, 1984, vol. 57, no. 7, pp. 1671–1672.
16. Pashchenko, A.A. and Voronkov, M.G., *Kremniiorganicheskie zashchitnye pokrytiya* (Organosilicon Protective Coatings), Kiev: Tekhnika, 1969.
17. Sviderskii, V.A. and Voronkov, M.G., *Zh. Prikl. Khim.*, 1999, vol. 72, no. 10, pp. 1600–1607.
18. Sviderskii, V.A. and Voronkov, M.G., *Zh. Prikl. Khim.*, 2001, vol. 74, no. 12, pp. 2027–2030.
19. Sviderskii, V.A. and Voronkov, M.G., *Zh. Prikl. Khim.*, 2001, vol. 74, no. 7, pp. 1137–1141.
20. Sviderskii, V.A. and Voronkov, M.G., *Zh. Prikl. Khim.*, 2003, vol. 76, no. 5, pp. 810–813.
21. Sviderskii, V.A. and Voronkov, M.G., *Zh. Prikl. Khim.*, 2004, vol. 77, no. 11, pp. 1909–1911.

22. Sviderskii, V.A. and Voronkov, M.G., Abstracts of Papers, *Mezhdunarodnaya nauchno-tekhnicheskaya konferentsiya po kompozitsionnym materialam* (Int. Scientific and Technical Conf. on Composite Materials), Kiev, 1998, pp. 10–11.
23. Voronkov, M.G., Pashchenko, A.A., and Tishchenko, V.T., *Zh. Prikl. Khim.*, 1970, vol. 43, no. 3, pp. 611–615.
24. Sviderskii, V.A. and Voronkov, M.G., *Zh. Prikl. Khim.*, 1996, vol. 69, no. 6, pp. 951–957.
25. Lebedev, A.T., *Mass-spektrometriya v organicheskoi khimii* (Mass Spectrometry in Organic Chemistry), Moscow: Binom, 2003.
26. Kreshkov, A.P. and Bork, V.A., *Prakticheskoe rukovodstvo po analizu monomernykh i polimernykh kremniiorganicheskikh soedinenii* (Manual on Analysis of Monomeric and Polymeric Organosilicon Compounds), Moscow: Goskhimizdat, 1962.
27. Lazarev, A.N. and Voronkov, M.G., *Opt. Spektrosk.*, 1960, vol. 8, no. 5, pp. 614–622.

ISSN 1070-4272, Russian Journal of Applied Chemistry, 2008, Vol. 81, No. 4, pp. 736–738. © Pleiades Publishing, Ltd., 2008.
Original Russian Text © G.A. Chiganova, N.E. Lyamkina, 2008, published in Zhurnal Prikladnoi Khimii, 2008, Vol. 81, No. 4, pp. 698–700.

BRIEF COMMUNICATIONS

Effect of Chromium(III) Oxide on Corundum Formation from Products of Shock-Wave Synthesis of Aluminum Oxide

G. A. Chiganova and N. E. Lyamkina

Polytechnic Institute, Siberian Federal University, Krasnoyarsk, Russia
Department of Physics of Nanophase Materials, Krasnoyarsk Scientific Center, Siberian Branch, Russian Academy of Sciences, Krasnoyarsk, Russia

Received October 11, 2007

Abstract—Formation of α-Al_2O_3 in thermal treatment of ultradispersed aluminum oxide powders produced by shock-wave synthesis with addition of Cr_2O_3–$(NH_4)_2Cr_2O_7$ as a precursor was studied. The acceleration of the conversion of δ-and θ-Al_2O_3 to α-Al_2O_3 upon introduction of additives in the stage of synthesis of aluminum oxide was examined.

DOI: 10.1134/S1070427208040356

Dynamic methods for synthesis of ultradispersed powders of various chemical compositions have high output capacity [1]. The synthesis parameters used in shock-wave loading of metals and free separation of explosion products in an oxygen-containing atmosphere make it possible to obtain metal oxide powders with unusual properties. The thus synthesized ultradispersed aluminum oxide has an average particle size of 75 nm and contains, according to the results of an X-ray phase analysis, only metastable δ- and θ-modifications in a ratio of approximately 7 : 1. This oxide exhibits a high phase stability under static annealing and shock-wave impact [2].

The topicality of development of methods for production of a submicrometer corundum powder used in composite construction and polishing materials makes urgent a study of the effect of various factors on the formation temperature of α-Al_2O_3 [3]. To these factors belongs introduction of additives, including chromium(III) oxide, in the course of thermal treatment of the powders, with both Cr_2O_3 itself and its precursors used [4–7]. The manner in which temperature varies and the rate of phase transformations that occur on heating the mixtures depend on the method employed to obtain aluminum oxide and on its characteristics. It has been shown [4] that introduction of Cr_2O_3 in production of aluminum oxide fibers stabilizes the transition δ- and θ-forms of Al_2O_3 and hinders formation of α-Al_2O_3. In [5], an increase in the rate of corundum formation was observed in calcination of ammonia alum with addition of minor amounts of ammonium bichromate (0.2 wt % in terms of Cr_2O_3). At a higher content of $(NH_4)_2Cr_2O_7$ in the starting mixture, the onset of α-Al_2O_3 crystallization was shifted to lower temperatures. In thermal treatment of a mixture of hydrargillite γ-$Al(OH)_3$ and $(NH_4)_2Cr_2O_7$ with steam, raising the chromium content to more than 0.3 wt % results in a slower formation of corundum [6]. In [7], a conclusion that Cr_2O_3 exerts a stabilizing influence on the δ- and θ-forms of Al_2O_3 was based on an analysis of the results of thermal treatment of a mixture of aluminum and chromium(III) oxides.

The aim of this study was to analyze the influence exerted by addition of the precursor Cr_2O_3–$(NH_4)_2Cr_2O_7$ on the formation of α-Al_2O_3 in thermal treatment of aluminum oxide produced in shock-wave synthesis.

EXPERIMENTAL

A uniform distribution of the ammonium bichromate additive in a mixture with aluminum oxide was provided by ultrasonic dispersion of an Al_2O_3 powder in an ethanol solution of $(NH_4)_2Cr_2O_7$. A differential-thermal analysis (DTA) was made on a Q-100 M derivatograph, with heating in air at a rate of 15 deg min^{-1} from 290 to 1770 K.

The average size of powder particles was found by processing of electron micrographs obtained with a JEM-100C electron microscope. The X-ray phase analysis (XPA) was made by the Debye–Scherrer

method on a DRON-4 diffractometer (copper radiation, Ni filter). The relative content of α-, δ-, and θ-Al_2O_3 in the powder was evaluated by the normalized amplitudes of the peaks at 2θ angles of 43.4 ($I_\alpha^{100\%}$), 44.8 ($I_0^{80\%}$), and 45.7 deg ($I_\delta^{50\%}$). The chemical phase analysis (CPA) of Al_2O_3 was made using the procedure developed for aluminum oxide powders produced by shock-wave synthesis [8].

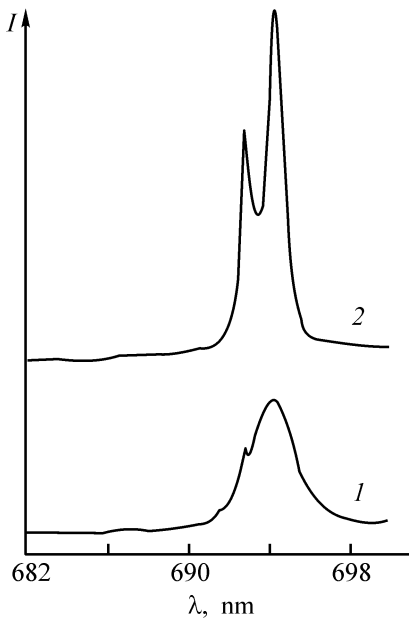
Luminescence spectra of the powders were obtained at 290 K, with excitation by quasi-CW second-harmonic emission of a Nd^{3+}:YAG laser with a wavelength λ = 530 nm.

According to DTA data, introduction of ammonium bichromate into a mixture with aluminum oxide produced by shock-wave synthesis in amounts corresponding to formation of 1.5–6 wt % Cr_2O_3 results in that the peak temperature of the exothermic effect associated with the phase transformation decreases from 1570 to 1500 K. The additive strongly affects the results of thermal treatment of Al_2O_3 under isothermal conditions: according to XPA data, upon annealing at 1470 K for 1 h, the content of corundum does not exceed 2 wt % in the absence of the additive and increases to 90% with 4 wt % $(NH_4)_2Cr_2O_7$. The average particle size in powders of this kind is 130 nm.

The luminescence spectra of powders with ammonium bichromate additive, annealed at temperatures exceeding 900°C for 1 h show luminescence of Cr^{3+} ions isomorphically incorporated into the corundum structure. The intensity of the lines at 692.8 and 694.3 nm, characteristic of ruby, increases with the powder annealing temperature (see figure). As can be seen in the figure, the luminescence spectra of the powders annealed in the temperature range studied, 870–1470 K, show no doublet lines associated with chromium(III) ions incorporated into the θ-Al_2O_3 lattice: 682 and 686 nm according to [9] or 684.5 and 688.2 nm [10]. These data are in agreement with the direct transition δ→α observed in [2], which is characteristic of Al_2O_3 produced by shock-wave synthesis and possible for the well-crystallized δ-form of aluminum oxide [11].

The phase composition of aluminum oxide and its further transformations under thermal treatment can also be affected by introduction of $(NH_4)_2Cr_2O_7$ into the aluminum powder subjected to a shock-wave treatment [12]. The table lists the XPA data on the phase composition of powders with varied content of chromium.

The experimental data indicate that introduction of ammonium bichromate in shock-wave synthesis of aluminum oxide also accelerates the corundum formation in thermal treatment of the powders.



Luminescence spectrum of chromium-containing aluminum oxide powders. (*I*) Relative intensity and (λ) wavelength. Treatment temperature (K): (*1*) 870 and (*2*) 1470.

According to the data furnished by the luminescence method (recommended for determining the phase composition of Al_2O_3 [9]), the effect of θ-Al_2O_3 stabilization is also absent at lowered annealing temperatures. The data obtained differ from those reported in [4, 7], where a clearly pronounced stabilization of δ- and θ-Al_2O_3 was observed at treatment temperatures of up to 1070 [7] and 1270 K [4], with the amount of corundum formed decreasing as the concentration of chromium in the starting mixture was raised [4]. The authors attributed this effect to a change in the oxidation number of chromium: partial oxidation of Cr^{3+} to Cr^{6+} in joint heating of Al_2O_3 and Cr_2O_3 in air [13–15] at temperatures below 1270 K [4]. The experimental fact of the partial oxidation $Cr^{3+}\rightarrow Cr^{6+}$ in the presence of Al_2O_3 [13–15], which contradicts data on thermal stability of CrO_3, is attributed

Initial phase composition of powders and content of corundum after thermal treatment at 1470 K for 1 h

Chromium content, wt %	Initial content of indicated Al_2O_3 phases, wt %			Corundum content after heating, wt %
	α	θ	δ	
–	–	13	87	–
0.01	5	35	60	15
1.20	5	65	30	85

in [15] to partial hydration of Al_2O_3 and Cr_2O_3 crystals and formation of structures close to $Al(OH)_3$ and $Cr(OH)_3$ in the surface layers. It is the oxidation of $Cr(OH)_3$ that leads to the appearance of Cr(VI) compounds in the system Al_2O_3–Cr_2O_3. Accordingly, their amount increases with the dispersity of the oxide and with the degree of hydration of their surface, which is equivalent to a rise in the number of chemically active hydroxy groups [15]. The presence of Cr(VI), which is prone to tetrahedral coordination, stimulates formation of δ- and θ-Al_2O_3. In the lattices of these modifications, aluminum cations are distributed over tetra- and octahedral positions (in θ-Al_2O_3, the role of tetrahedral positions is the most important) and hinders appearance of α-Al_2O_3 with octahedral coordination of cations [4].

Aluminum oxide Al_2O_3 produced by shock-wave synthesis is highly dispersed. However, an analysis of the surface-electrical properties of its particles demonstrated a low degree of surface hydroxylation [16]. Similarly to the enhanced phase composition stability, this is due to the decreased structural defectiveness of aluminum oxide formed by rapid cooling of liquid Al_2O_3 drops. Consequently, the main influence on the phase transformations is exerted in this case by the fact that corundum is isostructural to chromium(III) oxide with octahedral coordination of atoms, formed in decomposition of ammonium bichromate. A similar decrease in the corundum formation temperature was also observed when α-Fe_2O_3 was used as a precursor additive [3].

Incorporation of chromium(III) ions into the lattice of aluminum oxide produced by shock-wave synthesis positively affects the mechanical properties of a corundum ceramic fabricated from the flotation waste of an alumina shop and ultradispersed additives. Sintering of compacts from a mixture of Al_2O_3 micropowders and ultradispersed aluminum oxide produced by shock-wave synthesis makes it possible to preserve the finely grained structure of the material characterized by increased density, hardness, and wear resistance [17]. Use of chromium-containing ultradispersed Al_2O_3 powders provides an additional increase in the density and microhardness of sintered samples by 10–15%.

CONCLUSIONS

(1) Introduction of an ammonium bichromate additive in thermal treatment of ultradispersed aluminum oxide powders produced by shock-wave synthesis leads to a shift of the temperature range of α-Al_2O_3 formation to lower temperatures.

(2) The chromium-containing powders obtained are promising for use as an ultradispersed additive in production of a corundum ceramic with improved properties.

REFERENCES

1. Lyamkin, A.I., *Trudy VII Vserossiiskoi konferentsii "Fizikokhimiya ul'tradispersnykh (nano-) sistem", Ershovo, 22–24 noyabrya 2005 g.* (Proc. VII All-Russia Conf. "Physical Chemistry of Ultradispersed (Nano-) Systems," Ershovo, November 22–24, 2005), Moscow: MIFI, 2006, pp. 96–98.
2. Bukaemskii, A.A., Tarasova, L.S., and Fedorova, E.N., *Izv. Vyssh. Uchebn. Zaved., Tsv. Metall.*, 2000, no. 5, pp. 60–63.
3. Tolchev, A.V., Kleshchev, D.G., and Lopushan, V.I., *Zh. Prikl. Khim.*, 2002, vol. 75, no. 9, pp. 1417–1421.
4. Gavrish, A.M., Karyakin, E.L., Lysak, S.V., et al., *Ogneupory*, 1988, no. 10, pp. 15–20.
5. Ryabov, A.N., Kozhina, I.I., and Kozlov, I.L., *Zh. Neorg. Khim.*, 1970, vol. 15, no. 3, pp. 602–606.
6. Danchevskaya, M.N., Ivakin, Yu.D., and Ovchinnikova, O.G., *Vestn. Mosk. Gos. Univ., Ser. 2, Khim.*, 2003, vol. 44, no. 5, pp. 287–294.
7. Vlasova, M.V., Mamykin, E.T., Mel'nik, V.M., et al., *Poroshk. Metall.*, 1992, no. 6, pp. 44–51.
8. Chiganova, G.A., *Zh. Anal. Khim.*, 1991, vol. 46, no. 7, pp. 1439–1440.
9. Kulinkin, A.B., Feofilov, S.P., and Zakharchenya, R.I., *Fiz. Tverd. Tela*, 2000, vol. 42, no. 5, pp. 835–838.
10. Lipkin, D.M., Schaffer, N., Adar, F., and Clarke, D.R., *Appl. Phys. Lett.*, 1997, vol. 70, no. 19, pp. 2550–2552.
11. Toropov, N.A., Barzakovskii, V.P., Bondar', N.A., et al., *Diagrammy sostoyaniya silikatnykh sistem* (Phase Diagrams of Silicate Systems), Leningrad: Nauka, 1970, issue 2.
12. Lyamkina, N.E., Chiganova, G.A., Slabko, V.V., et al., *Neorg. Mater.*, 2005, vol. 41, no. 8, pp. 948–954.
13. Monsunaga, Y., *Bull. Chem. Soc. Japan*, 1957, vol. 30, no. 8, pp. 868–872.
14. *Nauchnye osnovy podbora i proizvodstva katalizatorov* (Scientific Foundations of Choice and Manufacture of Catalysts), Keier, N.P., E., Novosibirsk: Sib. Otd. Akad. Nauk SSSR, 1964.
15. Viktorov, V.V., Fotiev, A.A., Evdokimov, I.V., et al., *Neorg. Mater.*, 1988, vol. 24, no. 7, pp. 1141–1144.
16. Chiganova, G.A. and Nafikova, O.N., *Kolloid. Zh.*, 2005, vol. 67, no. 1, pp. 128–131.
17. Lefevre, S., Monsot, D., and Fedorova, E.N., *Trudy Vserossiiskoi nauchno-tekhnicheskoi konferentsii "Ul'tradispersnye poroshki, nanostruktury, materialy", Krasnoyarsk, 23–24 oktyabrya 2003 g.* (Proc. All-Russia Sci.-Techn. Conf. "Ultradispersed Powders, Nanostructures, Materials," Krasnoyarsk, October 23–24, 2003), Krasnoyarsk: IPTs KGTU, 2003, pp. 172–174.

ISSN 1070-4272, Russian Journal of Applied Chemistry, 2008, Vol. 81, No. 5, pp. 739–742. © Pleiades Publishing, Ltd., 2008.
Original Russian Text © M.V. Karpets, I.Yu. Kostiv, 2008, published in Zhurnal Prikladnoi Khimii, 2008, Vol. 81, No. 5, pp. 705–708.

INORGANIC SYNTHESIS AND INDUSTRIAL INORGANIC CHEMISTRY

Kinetics of Conversion of Langbeinite into Schoenite in Saturated Solution

M. V. Karpets and I. Yu. Kostiv

Stefanik Ciscarpathian National University, Ivano-Frankovsk, Ukraine
State Research Institute of Halurgy, Kalush, Ivano-Frankovsk oblast, Ukraine

Received December 6, 2007

Abstract—Conversion of natural langbeinite into schoenite in a suspension in a multicomponent solution, as influenced by the process time, liquid phase composition, and temperature (10–40°C), was studied.

DOI: 10.1134/S1070427208050017

Halurgical processing of polymineral potassium ores of the Ciscarpathian region is complicated by simultaneous presence in them of readily soluble potassium and potassium–magnesium minerals (sylvite KCl, kainite $K_2SO_4 \cdot MgSO_4 \cdot 3H_2O$, etc.) and difficultly soluble components (langbeinite $K_2SO_4 \cdot 2MgSO_4$, kieserite $MgSO_4 \cdot H_2O$, polyhalite $K_2SO_4 \cdot MgSO_4 \cdot 2CaSO_4 \cdot 2H_2O$). In the course of their dissolution, only 22–23% of langbeinite passes into the liquid phase, and its remaining amount and virtually the whole amount of polyhalite are dumped.

Procedures have been developed for the halurgical processing of ores with the preliminary conversion of langbeinite into readily soluble schoenite [1] or kainite [2], or with dissolution of the starting ore in water [3] to obtain a saturated solution and a langbeinite–polyhalite residue of the following composition (at 1 : 1 weight ratio of water and ore, counting on dry substance, %): K_2O 19.5–20.0, MgO 16.1–16.7, SO_4^{2-} 62.6–62.9, Cl^- less than 5.0. The sum of nutritive materials, K_2O + MgO + S, in this product is 56.5–57.7, which corresponds to a concentrated chloride-free potassium-magnesium fertilizer of prolonged action, similar in quality to a potassium–magnesium fertilizer produced from langbeinite ores in the United States [4]. The saturated solution is heated and mixed with potassium–magnesium salts from the second stage of evaporation of the schoenite solution to obtain a finely dispersed langbeinite suspension from which schoenite is crystallized after separation of coarsely crystalline NaCl. In this process, schoenite is obtained from a langbeinite suspension on cooling. Since the conversion of langbeinite into schoenite occurs in a suspension rather than in a solution, large volumes of process streams are to be heated prior to dissolution of the ore and cooled to crystallize the product. The conversion of langbeinite into schoenite is accompanied by heat release and follows the equation

$$K_2SO_4 \cdot 2MgSO_4 + 13H_2O = K_2SO_4 \cdot MgSO_4 \cdot 6H_2O + MgSO_4 \cdot 7H_2O.$$

The thermal effect of the process, calculated from the heats of solution of schoenite, epsomite, and langbeinite, is –145.2 kJ mol^{-1}. Hence, it can be expected that the conversion will increase with decreasing temperature. The conversion is accompanied by the dissolution of langbeinite from the surface, diffusion of the dissolution products into the bulk of the solution, and crystallization of the new mineral. The slowest step is the langbeinite dissolution. Its rate increases with temperature. Therefore, in this study we examined how the conversion of langbeinite into schoenite in a saturated solution in equilibrium with schoenite depends on the temperature and liquid phase composition. The formation of schoenite from langbeinite involves binding of water from the liquid phase into crystal hydrates. The process is accompanied by crystallization of NaCl contaminating the product.

EXPERIMENTAL

We examined under the laboratory conditions the effect of various factors on the conversion of langbeinite into schoenite in a schoenite solution in equilibrium with the solid phase. Langbeinite samples

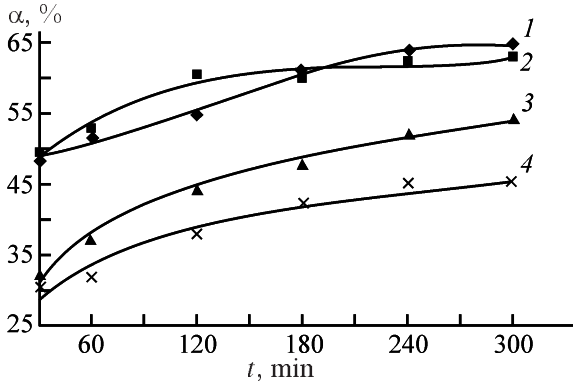


Fig. 1. Degree of langbeinite conversion α as a function of time t at various temperatures. T, °C: (*1*) 10, (*2*) 20, (*3*) 30, and (*4*) 40; the same for Fig. 2.

taken from a potassium mine were crushed to a particle size less than 0.2 mm and washed to remove impurities of soluble salts with a large amount of tap water with stirring, after which the suspension was filtered. The residual moisture was removed by washing with acetone. The washed material was dried at 50°C and sieved with wire sieves to obtain a fraction of size 0.1–0.2 mm. The langbeinite sample thus prepared had the following composition (wt %): K^+ 18.17, Mg^{2+} 11.67, Na^+ 0.11, Cl^- 0.44, SO_4^{2-} 68.07, and H_2O 1.54 (or 96.1% langbeinite, 0.5% halite, and 3.4% arcanite K_2SO_4). To perform the conversion, we used a solution with a density of 1.284 g cm^{-3}, of the following composition (wt %): K^+ 3.90, Mg^{2+} 3.40, Na^+ 4.11, Cl^- 15.99, SO_4^{2-} 5.15, and H_2O 67.45, which is formed in the course of schoenite crystallization and occurs in an equilibrium with the crystallized schoenite.

The prepared samples of langbeinite (100 g) and solution (500 ml) were kept for 24 h in an air thermostat to attain the required temperature, after which they were transferred into a temperature-controlled reactor and stirred under isothermal conditions for 300 min. Experiments were performed in the temperature range 10–40°C. After definite intervals of time, samples of the liquid and solid phases were taken for the analysis. The solid phase was additionally centrifuged on a laboratory centrifuge at 5000 rpm for better separation from the liquid phase. The samples were analyzed for K^+ and Na^+ by flame photometry, for Mg^{2+} by complexometric titration, and for SO_4^{2-} by gravimetric procedure [5]. From the results of the analysis, the material balances were constructed with a computer, and the mineral compositions of the solid phases of the suspension were calculated using a special program.

The degree of conversion α of langbeinite into schoenite was calculated by the formula

$$\alpha = m_1c_1c_2/(m_2c_3), \quad (1)$$

where m_1 is the weight of the solid phase of the suspension from the material balance; m_2, weight of the initial langbeinite; c_1, content of schoenite in the solid phase of the suspension; c_2 and c_3, content of SO_4^{2-} in schoenite (leonite) and langbeinite, respectively.

We examined the influence of temperature on the conversion. It is known [6] that the mineral composition of the solid phase depends on temperature: Schoenite is the stable phase up to 30°C, and leonite, at higher temperatures. Therefore, we substituted in formula (1) the corresponding data.

Our experiments showed (Fig. 1) that the conversion is the slowest at 40°C, and in 300 min the conversion reaches 45.7%. With decreasing temperature, the conversion increases, and at 20°C the 60.6% conversion is reached in 120 min. As the temperature is decreased to 10°C, the conversion does not change noticeably. On the other hand, performing the process at 10°C requires additional expenditures for cooling the suspension, which is unpractical. Therefore, further experiments were performed at 20°C.

As the conversion of langbeinite into schoenite involves dissolution of langbeinite, we applied to the process the Shchukarev rate equation

$$dc/dt = kS(c_s - c), \quad (2)$$

where c is the running concentration of the solute in solution (%); c_s, saturation concentration (%); t, time (min); S, surface area of langbeinite particles (dm^2); and k, dissolution rate constant.

After integration, Eq. (2) takes the form

$$\ln[c_s/(c_s - c)] = kSt. \quad (3)$$

To perform calculations by Eq. (3), it is necessary to take into account changes in the surface area of the solid phase in the course of dissolution. Therefore, we assumed that the surface area of the solid phase S in the course of conversion decreases in proportion with α:

$$S = S_{in}(1 - \alpha), \quad (4)$$

where S_{in} is the initial surface area of langbeinite.

We assumed that the solid phase is monodisperse and all the crystals have the form of a regular triangular pyramid. The mean particle size of the 0.1–0.2-mm fraction is 0.15 mm. The total surface area S_{in} of the initial langbeinite sample was calculated by determining its volume and the number of particles, with the subsequent summation of the surface areas of all the particles.

Variation of $\ln[c_s/(c_s - c)]/S$ with time is shown in Fig. 2. The kinetic curves in these coordinates are straight lines, suggesting the diffusion control of the process. At 20°C, the rate constant is maximal. To calculate the activation energy, we used the Arrhenius equation

$$\ln k = \ln A - E/(RT). \quad (5)$$

From the plots in Fig. 2, we determined the rate constants at each temperature as slopes of the straight lines, using Eq. (3). To determine the activation energy E, we plotted $\ln k$ vs. $1/T$ (Fig. 3) and found E from the slope of the straight line, $\tan\alpha = E/R$. The quantity E is as low as 14.1 kJ mol^{-1}, suggesting diffusion control of the langbeinite conversion in saturated solution.

It is known [8] that dissolution of langbeinite in water under the conditions of forced convection is not a diffusion-controlled process. Hence, the mechanism of conversion in saturated solution differs from that of dissolution in water.

We also examined how the $MgCl_2$ concentration in the liquid phase of the suspension affects the conversion at 20°C. The $MgCl_2$ concentration was 4, 6, 8, and 10 wt %. The composition of the initial solution was varied using analytically pure grade $MgCl_2$ and Na_2SO_4. The $MgCl_2$ concentration in the initial multicomponent solution was 8 wt %; it was increased by adding $MgCl_2$ and decreased by adding Na_2SO_4. Experiments were performed similarly to the previous ones. The data were treated with the Shchukarev equation. The results we obtained are plotted in Fig. 4. From these data we determined the rate constant of the process. We found that, at a $MgCl_2$ concentration in the starting solution of 4, 6, 8, and 10 wt %, the rate constant of the process is 0.0792, 0.1217, 0.11, and 0.1029 min^{-1}, respectively, i.e., it passes through a maximum at 6% $MgCl_2$.

The data we obtained will be used for developing a procedure for processing of polymineral potassium ores by conversion of langbeinite suspension into schoenite.

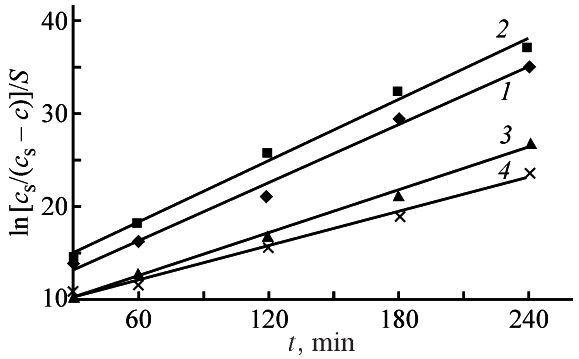


Fig. 2. Plot of $\ln[c_s/(c_s - c)]/S$ vs. time t at various temperatures. (c) Running langbeinite concentration, (c_s) saturation concentration, and (S) surface area of langbeinite particles; the same for Fig. 4.

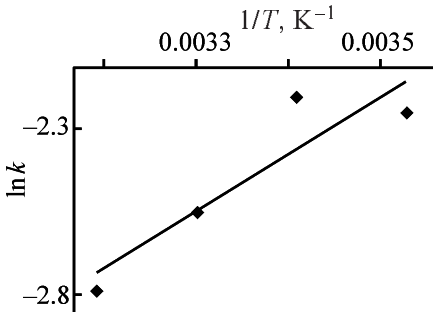


Fig. 3. Temperature dependence of the rate constant k.

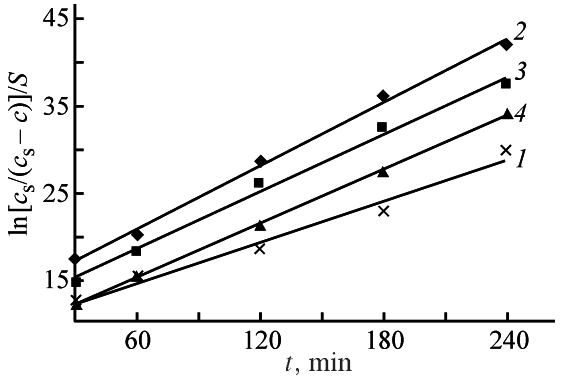


Fig. 4. Plot of $\ln[c_s/(c_s - c)]/S$ vs. time t at various concentrations of $MgCl_2$ in the initial solution. c_{MgCl_2}, wt %: (*1*) 4, (*2*) 6, (*3*) 8, and (*4*) 10.

CONCLUSIONS

(1) The highest rate of conversion of langbeinite into schoenite in a multicomponent solution is attained at 20°C.

(2) The activation energy of the conversion is 14.1 kJ mol^{-1}, suggesting the diffusion control of the process.

(3) The rate constant of the conversion is max-

imal at 6 wt % concentration of $MgCl_2$ in the liquid phase.

REFERENCES

1. Grebenyuk, D.V., Processing of Langbeinite Ores with the Aim to Obtain Chlorine-Free Potassium Fertilizers, *Cand. Sci. Dissertation*, Minsk, 1986.
2. Kostiv, I.Yu. and Khatsevich, O.M., *Zh. Prikl. Khim.*, 2004, vol. 77, no. 8, pp. 1233–1236.
3. Karpets', M.V. and Kostiv, I.Yu., *Khim. Prom–st. Ukr.*, 2007, no. 2, pp. 29–32.
4. *Pererabotka prirodnykh solei i rassolov: Spravochnik* (Processing of Natural Salts and Brines: Handbook), Sokolov, I.D., Ed., Leningrad: Khimiya, 1985.
5. Morachevskii, Yu.V. and Petrova, E.M., *Metody analiza rassolov i solei* (Methods for Analysis of Brines and Salts), Moscow: Khimiya, 1965.
6. *Spravochnik po rastvorimosti solevykh sistem* (Handbook on Solubility of Salt Systems), Leningrad, 1975, vol. 2.
7. Perekupko, T.V., *Khim. Prom–st. Ukr.*, 2005, no. 6, pp. 3–7.
8. Zdanovskii, A.B., *Kinetika rastvoreniya prirodnykh solei v usloviyakh vynuzhdennoi konvektsii: Trudy Vsesoyuznogo nauchno-issledovatel'skogo inst. galurgii* (Kinetics of Dissolution of Natural Salts under Conditions of Forced Convection: Transactions of the All-Union Research Inst. of Halurgy), Leningrad: Goskhimizdat, 1956, issue 33.

ISSN 1070-4272, Russian Journal of Applied Chemistry, 2008, Vol. 81, No. 5, pp. 743–747. © Pleiades Publishing, Ltd., 2008.
Original Russian Text © I.M. Ryshchenko, N.S. Kulatskii, A.S. Savenkov, I.N. Protiven', L.N. Ratushnaya, 2008, published in Zhurnal Prikladnoi Khimii, 2008, Vol. 81, No. 5, pp. 709–713.

INORGANIC SYNTHESIS AND INDUSTRIAL INORGANIC CHEMISTRY

Enhancing the Strength of Granules and Thermal Stability of Ammonium Nitrate

I. M. Ryshchenko, N. S. Kulatskii, A. S. Savenkov, I. N. Protiven', and L. N. Ratushnaya

Kharkov Polytechnic Institute, National Technical University, Kharkov, Ukraine

Received April 4, 2007

Abstract—The effect of sulfate ions on the physicochemical properties of ammonium nitrate with a dolomite additive was examined. Changes in the rate of the IV → III phase transition, granule strength, number of thermal cycles, and content of ammonium nitrate aerosol in air after the granulation tower were evaluated.

DOI: 10.1134/S1070427208050029

Analysis of the quality of ammonium nitrate produced by a number of enterprises showed that even a small number of thermal cycles lead to degradation of granules, increased caking, and formation of strong monoliths. Furthermore, insufficient strength of granules favors an increase in the content of ammonium nitrate dust in exhaust air from the granulation tower.

One of the most efficient ways to improve physicochemical and mechanical properties of ammonium nitrate is stabilization of the II → IV polymorphous transition when the fusion cake is cooled with minimal changes in the volume and structure. The quality of granulated ammonium nitrate is largely determined by the IV → III polymorphous transition which occurs at 32.5°C under equilibrium conditions and is accompanied by a 3.7% change in the specific volume [1]. Repeated IV → III transitions lead to a decrease in the strength, loosening of the surface, and caking of ammonium nitrate granules. Polymorphous transitions of ammonium nitrate are stabilized by conditioning additions of salts and minerals in various steps of its production. Modification transitions of ammonium nitrate were studied by DTA. The derivatograms were recorded on an OD-103 derivatograph. The phase composition of ammonium nitrate was studied by X-ray phase analysis on a DRON-1 diffractometer (Cu radiation). The moisture content of the samples was determined by Fischer titration.

The temperatures of polymorphous transitions in relation to the number of thermal cycles are given in Table 1. Sample no. 1 is ammonium nitrate with addition of nitric acid dolomite extract, without introduction of sulfuric acid; sample nos. 2–4 differ in the $CaSO_4$ content (0.65–0.75 wt %).

It follows from Table 1 that the temperatures of the IV → III and III → II polymorphous transitions are essentially independent of the number of thermal cycles. An increase in the temperature of the IV → III transition is indicative of a decrease in the the moisture content of ammonium nitrate. At a low moisture content, the dissolution and recrystallization are slow; as a result, the caking of ammonium nitrate decreases and the strength of its granules increases. A decrease in the moisture content of ammonium nitrate with an addition of sulfuric acid is due to moisture uptake by calcium sulfate with the formation of crystal hydrates [2–4]. X-ray phase analysis of ammonium nitrate samples with addition of sulfate ions revealed the presence of the $CaSO_4 \cdot 2H_2O$ and $CaSO_4 \cdot 0.5H_2O$ phases in 1.5 : 0.5 ratio. With an increase in the number of thermal cycles, the hemihydrate content increases. The formation of calcium sulfate decelerates the melting and crystallization of ammonium nitrate owing to formation of solid solutions restricting the mobility of structural elements of its lattice.

We examined the kinetics of modification transformation of ammonium nitrate with a calcium-containing additive upon addition of sulfuric acid after performing different numbers of thermal cycles, and also with different amounts of $CaSO_4$ added. To calculate the kinetic parameters of the IV → III

Table 1. Temperatures of polymorphous transitions T_{pt}

Sample no.	T_{pt}, °C, at indicated number of thermal cycles									
	1		2		3		4		5	
	IV→III	III→II	IV→III	III→II	IV→III	III→II	IV→III	III→II	IV→III	III→II
1	44	88	43	89	42	87	43	88	42	89
2	48	91	46	92	47	93	48	93	47	92
3	47	93	48	93	48	92	46	91	47	91
4	48	92	46	92	48	91	47	93	48	90

modification transition, we used the dependence of the conversion α on time τ:

$$d\alpha/d\tau = k(1 - \alpha)^n = k_0\exp[-E/(RT)](1 - \alpha)^n, \quad (1)$$

where k is the rate constant; n, kinetic parameter; k_0, preexponential factor of the Arrhenius equation; and E, activation energy of the process (kJ mol^{-1}).

The conversion α is related to the magnitudes of thermal effects in the DTA curve by

$$(1 - \alpha) = (\Delta H_i)/(\Delta H_{tot}), \quad (2)$$

where ΔH_{tot} and ΔH_i are the total and partial enthalpies of transition, respectively (J).

The quantities E, k_0, and n were calculated by the formula obtained by taking the logarithm of Eq. (1), taking into account (2):

$$\ln[(dH_i/d\tau)(1/\Delta H_{tot})] = \ln k_0 - E/(RT) + n\ln(\Delta H_i/\Delta H_{tot}), \quad (3)$$

where $dH_i/d\tau$ is the instantaneous rate of heat release in time τ (J s^{-1}).

The kinetic parameters of the IV → III transition were found by solving the system of equations of form (3). The calculation results and the rate constants k of the IV → III modification transition at 315 and 320 K, respectively, are given in Table 2.

Table 2. Kinetic parameters of the IV → III transition in ammonium nitrate with various additives

Additive	n	$k_0 \times 10^3$, s^{-1}	E, kJ mol^{-1}	Rate constant $k \times 10^9$, s^{-1}
Extract from dolomite	1	8	22	1800
Extract from dolomite, H_2SO_4	1	12	38	10

Table 2 shows that the formation of $CaSO_4$ from calcium nitrate in the dolomite extract and sulfuric acid, followed by formation of calcium sulfate crystal hydrates, considerably increases the activation energy of the IV → III modification transition and decreases the rate constant of the process by two orders of magnitude. Deceleration of the IV → III transition leads to stabilization of the physicochemical properties of ammonium nitrate: decrease in the caking and enhancement of the mechanical strength.

Data on the thermodynamic characteristics of ions in an ammonium nitrate melt are lacking. As the ammonium nitrate melt is an electrolyte, like water, the thermodynamic analysis of the reactions of precipitation with sulfate ion can be based on data on the composition and thermodynamic properties of products of similar reactions in aqueous solutions.

According to [5], at temperatures above 333 K in the $CaSO_4$–H_2O system, anhydrous $CaSO_4$ is the most thermodynamically stable solid phase, whereas in the $MgSO_4$–H_2O system at temperatures exceedintg 340.5 K kieserite $MgSO_4 \cdot H_2O$ is thermodynamically stable. The temperature dependences of the solubility products (SPs) of these compounds in the range including the reaction temperature in the industrial process, and also the related dependences for calcium sulfate hemihydrate $CaSO_4 \cdot 0.5H_2O$ and gypsum $CaSO_4 \cdot 2H_2O$ are given in a handbook [6]. These data allow us to perform a thermodynamic analysis of the reactions

$$Ca^{2+} + SO_4^{2-} \rightleftarrows CaSO_4\downarrow, \quad (4)$$

$$Ca^{2+} + SO_4^{2-} + 0.5H_2O \rightleftarrows CaSO_4 \cdot 0.5H_2O\downarrow, \quad (5)$$

$$Ca^{2+} + SO_4^{2-} + 2H_2O \rightleftarrows CaSO_4 \cdot 2H_2O\downarrow, \quad (6)$$

$$Mg^{2+} + SO_4^{2-} + H_2O \rightleftarrows MgSO_4 \cdot H_2O\downarrow. \quad (7)$$

Table 3. Thermodynamic characteristics of precipitation of calcium and magnesium sulfates

Precipitation product	log SP	Gibbs free energy, kJ (mol M^{2+})$^{-1}$	
		standard, $\Delta_r G_T^0$	of reaction, $\Delta_r G_T$
$CaSO_4$	–6.52	–56.5	–71.1
$CaSO_4 \cdot 0.5H_2O$	–6.10	–52.8	–45.8
$CaSO_4 \cdot 2H_2O$	–5.04	–43.6	28.4
$MgSO_4 \cdot H_2O$	–2.93	–25.4	–6.2
$CaSO_4 \cdot (NH_4)_2SO_4 \cdot H_2O$	–4.81	–41.6	–74.0
$5CaSO_4 \cdot (NH_4)_2SO_4 \cdot H_2O$	–22.95	–39.7	–57.9
$MgSO_4 \cdot (NH_4)_2SO_4 \cdot 6H_2O$	–4.92	–42.6	144.0

It should be taken into account that the formation of the sulfate precipitate can involve ions of the main component, NH_4NO_3 [7, 8]. Double calcium ammonium sulfates syngenite $CaSO_4 \cdot (NH_4)_2SO_4 \cdot H_2O$ and pentasulfate $5CaSO_4 \cdot (NH_4)_2SO_4 \cdot H_2O$ [9, 10] are known; in the system magnesium sulfate–ammonium sulfate–water, schoenite $MgSO_4 \cdot (NH_4)_2SO_4 \cdot 6H_2O$ is formed [9, 10]. The solubility products of these salts were estimated in [11] from data of [8, 9]. These data allow us to perform a thermodynamic analysis of the reactions

$$Ca^{2+} + 2SO_4^{2-} + 2NH_4^+ + H_2O \rightleftarrows CaSO_4 \cdot (NH_4)_2SO_4 \cdot H_2O\downarrow, \quad (8)$$

$$5Ca^{2+} + 6SO_4^{2-} + 2NH_4^+ + H_2O \rightleftarrows 5CaSO_4 \cdot (NH_4)_2SO_4 \cdot H_2O\downarrow, \quad (9)$$

$$Mg^{2+} + 2SO_4^{2-} + 2NH_4^+ + 6H_2O \rightleftarrows MgSO_4 \cdot (NH_4)_2SO_4 \cdot 6H_2O\downarrow. \quad (10)$$

The standard Gibbs energies of reactions (4)–(10) were calculated by the equation

$$\Delta_r G_T^0 = 2.3RT\log SP. \quad (11)$$

The results obtained were used for calculating the Gibbs energhies of reactions (4)–(7) and (8)–(10) under industrial conditions by Eqs. (12) and (13), respectively, for the case when the mixtures contained additions of calcium and magnium nitrates in an amount of 0.5% counting on CaO:

$$\Delta_r G_T = \Delta_r G_T^0 - 2.3RT\log a_{M^{2+}} a_{SO_4^{2-}} a_w^n = \Delta_r G_T^0 - 2.3RT\log m_{M^{2+}} m_{SO_4^{2-}} a_w^n, \quad (12)$$

$$\Delta_r G_T = \Delta_r G_T^0 - 2.3RT\log a_{M^{2+}}^k a_{SO_4^{2-}}^{k+1} a_{NH_4^+}^2 a_w^n = \Delta_r G_T^0 - 2.3RT\log m_{M^{2+}}^k m_{SO_4^{2-}}^{k+1} m_{NH_4^+}^2 m_w^n, \quad (13)$$

where M^{2+} is Ca^{2+} or Mg^{2+}; k and n are the stoichiometric coefficients at M^{2+} and H_2O, respectively; a_i is the activity of ions; and a_W is the activity of water.

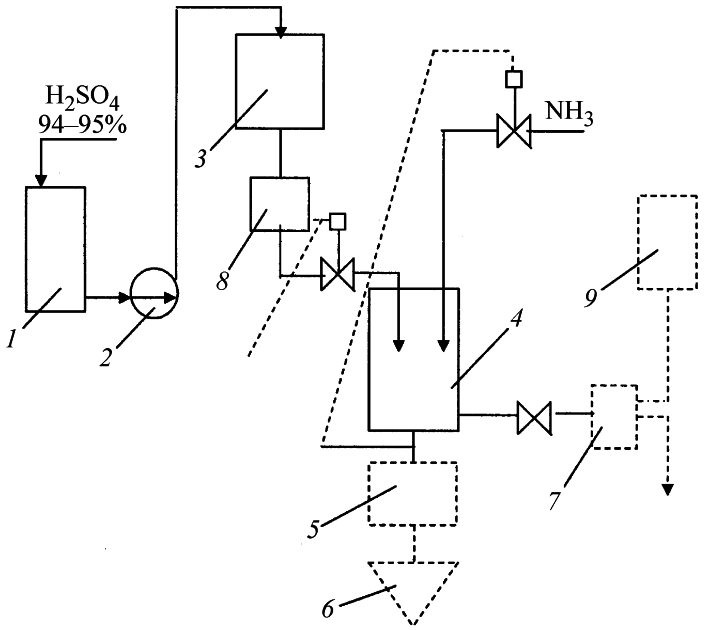
In the calculations, the activities of ions a_i were replaced by the molal concentrations of the components m_i, because the high ionic strength of the concentrated solution does not allow calculation of the activity coefficients. The calculation results are given in Table 3.

It follows from Table 3 that, among calcium sulfates, the most probable products of precipitation with sulfate ion are anhydrite $CaSO_4$ and double calcium ammonium sulfates. Precipitation of magnesium sulfates is thermodynamically impossible. Hence, sulfate ion is an efficient additive favoring the phase partitioning of calcium and magnesium ions [2].

EXPERIMENTAL

Pilot tests on introduction of sulfuric acid into a melt of ammonium nitrate containing a dolomite additive (0.4–0.55% counting on CaO) were performed on an installation shown in the figure. The installation includes a unit for the transfer of sulfuric acid from a mobile tank to a supply vessel, a unit for feeding sulfuric acid from a supply vessel to a head tank, and a unit for feeding sulfuric acid directly to an ammonium nitrate melt, with the subsequent neutralization of the reaction acid with gaseous ammonia prior to granulation. Because calcium sulfate can precipitate on internal surfaces of evaporation and afterevaporation vessels, thus impairing the heat exchange, sulfuric acid was introduced into the afterneutralizer after taking the melt from the afterevaporator.

The reaction of sulfuric acid with calcium nitrate



Scheme of introduction of sulfuric acid into ammonium nitrate melt: (*1*) receiving tank, (*2*) high-pressure pump, (*3*) supply vessel, (*4*) afterneutralizer, (*5*) filter, (*6*) granulator, (*7*) receiving tank for melt, (*8*) batcher, and (*9*) afterevaporator.

results in the evolution of free nitric acid, which should be neutralized with ammonia to pH 5.7–6.2. In the course of studies, we took samples of ammonium nitrate before and after introduction of sulfuric acid, analyzed them for the content of moisture, $CaSO_4$, and main substance, and determined the granule strength, pH of 10% aqueous solution, and content of ammonium nitrate aerosols in air after the granulation tower (Table 4). The sulfuric acid dosage was varied within 1.0–2.5 l min^{-1}. All the process parameters of the granulation tower were left unchanged.

Table 4. Influence of pH and degree of conversion of $Ca(NO_3)_2$ into $CaSO_4$ (α) on the strength of ammonium nitrate granules

pH	$CaSO_4$, wt %	Moisture, wt %	Strength, kg granule^{-1}	α, %
6.4	–	0.14	1.35	–
5.75	0.29	0.13	1.9	25.1
3.7	0.42	0.15	1.6	37.7
5.75	0.46	0.12	1.7	37.7
5.9	0.37	0.13	1.9	36.2
5.95	0.34	0.14	1.7	33.2

Table 5. Influence of pH on the strength of granules and number of thermal cycles of ammonium nitrate

pH	Strength, kg granule^{-1}		Number of thermal cycles	
	initial	with H_2SO_4	initial	with H_2SO_4
4.8	1.3	1.3	1	1
5.8	1.3	1.8	1	4
5.9	1.3	1.9	1	6
6.8	1.3	1.3	1	2

Examination of the influence exerted by pH and degree of conversion of $Ca(NO_3)_2$ into $CaSO_4$ on the strength of ammonium nitrate granules on introduction of sulfuric acid showed that pH should be kept in the range 5.6–5.8, i.e., the content of free ammonia in the melt should be 0.001–0.005%.

The results of examining the influence of pH of ammonium nitrate solution on the granule strength and number of thermal cycles are given in Table 5. It can be seen that pH of the solution should be brought to 5.9. In our experiments we managed to obtain ammonium nitrate with the strength exceeding 2.3 kg granule^{-1}, withstanding five to six thermal cycles (Table 6).

The sulfuric acid dosage was 2.0–2.4 l min^{-1} (samples with pH 5.9, 6.2). The concentration of sulfate ions was higher than 0.6 wt %, and the moisture content decreased to 0.14%. The granule strength was enhanced, suggesting the formation of $CaSO_4$ which exerts a strengthening effect. At pH > 6, the number of thermal cycles was 2–5, and at pH < 6, 5–6.

Table 6. Properties of ammonium nitrate granules

pH	$CaSO_4$, wt %	Moisture, wt %	Initial strength, kg granule^{-1}	Strength, kg granule^{-1}, after indicated number of thermal cycles					
				1	2	3	4	5	6
6.8	–	0.26	1.4	1.3	0.8	0.8	0.6	–	–
6.48	0.34	0.22	1.6	1.3	1.2	0.8	0.6	–	–
6.15	0.57	0.21	2.2	1.7	1.1	1.4	1.0	0.7	–
5.6	0.70	0.20	2.2	1.6	1.6	1.8	1.0	1.1	0.8
5.2	0.80	0.20	2.3	1.8	1.6	1.9	1.0	1.1	0.7
5.35	0.83	0.21	2.1	1.1	0.9	0.8	0.7	–	–
5.9	0.75	0.14	>2.3	2.2	1.9	1.8	1.5	1.3	1.0
6.2	0.7	0.14	>2.3	2.0	1.7	1.7	1.5	0.9	0.7

Published data on the behavior of the NH_4NO_3–$Ca(NO_3)_2$ system in the presence of sulfate ions suggest that, when the granules contain free ammonia (pH > 6), the compounds $(NH_4)_2SO_4$, $CaSO_4 \cdot (NH_4)_2SO_4 \cdot H_2O$, and $2CaSO_4 \cdot (NH_4)_2SO_4 \cdot H_2O$ can be formed along with $CaSO_4$. As a result, the number of thermal cycles decreases [12]. At pH 5.5–5.9, the amount of free ammonia is at a minimum; therefore, the number of thermal cycles is as large as 5–6. The discharge of ammonium nitrate with exhaust gases is decreased by 15%.

CONCLUSIONS

(1) Variation of the phase composition of the system based on ammonium nitrate upon introduction of sulfate ions leads to a decrease in the moisture content of the product, which, in turn, leads to deceleration of the dissolution and recrystallization processes. As a result, the caking of ammonium nitrate decreases and the strength of its granules is enhanced.

(2) The optimal degree of neutralization of the forming nitric acid with ammonia corresponds to pH 5.5–5.9 of a 10% aqueous solution of ammonium nitrate.

(3) The optimal dosage of sulfuric acid is 1.6–1.7 l min^{-1}, or 5–6 kg per ton of ammonium nitrate. In this case, the degree of conversion of calcium nitrate into calcium sulfate is 65–75%.

(4) The strength of the granules after six thermal cycles remains within the limits of the GOST (State Standard) requirements: 0.9–1.2 kg granule^{-1} (required 0.8), whereas the initial ammonium nitrate loses strength after one or two thermal cycles.

(5) The content of ammonium nitrate in the exhaust gases decreased by 15%.

REFERENCES

1. *Proizvodstvo ammiachnoi selitry v agregatakh bol'shoi edinichnoi moshchnosti* (Production of Ammonium Nitrate in Apparatus of High Unit Capacity), Olevskii, V.M., Ed., Moscow: Khimiya, 1990.
2. Ukrainian Patent 44008 A.
3. Kulatskii, N.S., Ryshchenko, I.M., Vorozhbiyan, M.I., and Savenkov, A.S., *Vestn. Nats. Tekhnol. Univ. Khar'k. Politekh. Inst.* (Kharkov), 2002, topical issue: *Khimiya, khimicheskaya tekhnologiya i ekologiya* (Chemistry, Chemical Technology, and Ecology), no. 17, pp. 45–48.
4. Miniovich, M.A., Sichkov, P.V., and Tsel'm, N.K., *Tr. Gos. Inst. Azotn. Prom–sti.*, 1959, vol. 10, pp. 285–305.
5. *Spravochnik eksperimental'nykh dannykh po rastvorimosti solevykh sistem* (Handbook of Experimental Data on the Solubility of Salt Systems), vol. 4: *Dvukhkomponentnye sistemy: Elementy II gruppy i ikh soedineniya* (Binary Systems: Group II Elements and Their Compounds), Pel'sh, A.D., Ed., Leningrad: Khimiya, 1975.
6. Marshall, W.L., *J. Inorg. Nucl. Chem.*, 1975, vol. 37, no. 10, pp. 2155–2163.
7. Valuziene, B.A., Vesiene, T.B., and Lashkova, L.I., *Zh. Neorg. Khim.*, 1968, vol. 13, no. 4, pp. 1198–1200.
8. Hill, A.E. and Yanick, N.S., *J. Am. Chem. Soc.*, 1935, vol. 57, no. 4, pp. 645–651.
9. Pilipchenko, V.N. and Shevchuk, V.G., *Zh. Neorg. Khim.*, 1969, vol. 14, no. 3, pp. 828–831.
10. Benrath, A. and Thiemann, W., *Z. Anorg. Allg. Chem.*, 1932, vol. 208, no. 2, pp. 177–193.
11. Kumok, V.N., Kuleshova, O.N., and Karabin, L.A., *Proizvedeniya rastvorimosti* (Solubility Products), Novosibirsk: Nauka, 1983.
12. Kazakova, A.A., *Granulirovanie i okhlazhdenie azotsoderzhashchikh udobrenii* (Granulation and Cooling of Nitrogen-Containing Fertilizers), Moscow: Khimiya, 1980.

ISSN 1070-4272, Russian Journal of Applied Chemistry, 2008, Vol. 81, No. 5, pp. 748–751. © Pleiades Publishing, Ltd., 2008.
Original Russian Text © G.F. Klyakin, V.A. Taranushich, 2008, published in Zhurnal Prikladnoi Khimii, 2008, Vol. 81, No. 5, pp. 714–717.

INORGANIC SYNTHESIS AND INDUSTRIAL INORGANIC CHEMISTRY

Phase Stabilization of Ammonium Nitrate with Binary Additives Consisting of Potassium Nitrate and Complexone Salts

G. F. Klyakin and V. A. Taranushich

South-Russian State Technical University, Novocherkassk, Rostov oblast, Russia

Received August 2, 2007

Abstract—The paper deals with the search for and optimization of a method for preparing phase-stabilized ammonium nitrate as oxidant for solid propellants with environmentally friendly combustion products. The effect exerted on the energy of the V → IV and IV → III polymorphous transitions of ammonium nitrate by the total content of the binary additive potassium nitrate–disodium tetrahydrogen nitrilotris-(methylenephosphonate), component ratio, and temperature and time of the cocrystallizate treatment was examined.

DOI: 10.1134/S1070427208050030

The principal possibility of prepaing phase-stabilized ammonium nitrate (PSAN) undergoing no polymorphous transitions in the temperature range from –50 to +100°C by cocrystallization of ammonium nitrate (AN) with binary additives consisting of potassium nitrate and sodium or potassium salts of complexones was demonstrated in [1]. However, the total content of the binary additive in AN (7 wt %) appreciably decreases the rated specific impulse of a solid propellant based on the suggested PSAN. Therefore, decreasing the concentration of additives introduced is a topical problem. Preliminary experiments showed that the strongest effect on the phase stability of AN is exerted by the total content of a binary additive consisting of potassium nitrate and a complexone salt and by the ratio of its components. It was also noted that, despite the measures taken to ensure maximal dehydration of the cocrystallizing components and the use of dry atmosphere for the subsequent operations, heat treatment of the finished cocrystallizates considerably decreases the height of the peaks of the V → IV and IV → III down to their full suppression. Therefore, we also examined the effect exerted by the temperature and time of the heat treatment of the cocrystallizates.

For a detailed study, as a complexone salt we chose disodium tetrahydrogen nitrilotris(methylenephosphonate), $NTPNa_2$, as a substance that shows the highest inhibiting activity toward polymorphous transitions of AN and is commercially available.

EXPERIMENTAL

A wide test tube made of heat-resistant glass was charged with analytically pure grade ammonium nitrate dried to a moisture content not exceeding 0.05% (according to Fischer titration). The test tube was placed in an oven and heated to melting. Dehydrated $NTPNa_2$ was added to the AN melt at 175–180°C and dissolved with stirring, after which the melt was cooled and the fusion cake was finely divided. All manipulations with samples after cooling the melt were performed in a box with the relative humidity of air not exceeding 50%. All the experiments were duplicated.

Differential thermal analysis of the powder (fraction <400 μm) was performed in the temperature range from –50°C to melting. The sample weight was about 0.1 g, and the heating rate, 3 deg min^{-1}. The DTA curves were recorded in the coordinates sample temperature–difference between the temperatures of the sample and reference. The energies of the polymorphous transitions J (J g^{-1}) were estimated from the areas of the corresponding peaks in the DTA curve, using a calibration chart.

With the aim to gain a general pattern of variation of the PSAN characteristics, the experimental material was presented in the form of polynomial mathematical models constructed by standard procedures [2]. When constructing the model, we excluded insignificant (with respect to the Student test) terms with the subsequent recalculation, which

allowed us to obtain adequate models with smaller numbers of terms.

We examined the effect of the above-mentioned factors on the energy of the key polymorphous transitions of ammonium nitrate, V → IV and IV → III. In the first step, two factors, the total content of the binary additive in AN and the relative content of $NTPNa_2$ in the binary additive, were set constant (3 and 44%, respectively), and the effect exerted on the energy of the V → IV and IV → III transitions by the heat treatment temperature (from 84 to 99°C, four levels of variation) and time (from 0.5 to 6 h, five levels of variation) was examined.

The dependence of the energy of the PSAN V → IV polymorphous transition on the temperature and time of the heat treatment is adequately described by the equation

$$J_{V-IV} = 174.1 - 3.974t + 0.0226t^2, \quad (1)$$

where t is the heat treatment temperature (°C).

The statistical insignificance of the coefficients at terms taking into account the time factor [Eq. (1)] indicates that the transition energy is independent of the heat treatment time varied within the examined range. The graphical interpretation of Eq. (1) is shown in Fig. 1. The curves in Fig. 1 and the subsequent figures are lines of equal energy of the corresponding polymorphous transition ($J\ g^{-1}$).

As follows from Fig. 1, degradation of the PSAN structure with the V → IV polymorphous transition starts at the heat treatment temperature exceeding 90°C practically within 30 min after the sample reaches the preset temperature, and the energy of the transition increases in proportion with the temperature squared.

The dependence of the energy of the IV → III polymorphous transition on the temperature and time of the heat treatment is more complex and is adequately described by the equation

$$J_{IV-III} = 342.5 - 7.9t - 12.07\tau + 0.137t\tau + 0.0463t^2. \quad (2)$$

Analysis of the graphical interpretation of Eq. (2) (Fig. 2, nonshaded area) shows that the energy of the IV → III transition also nonlinearly increases with an increase in the heat treatment temperature.

The dependence of J_{IV-III} on the heat treatment time is complex. The temperature of 90°C is a threshold of a sort, above which the energy of the IV → III transition nonlinearly increases, and below

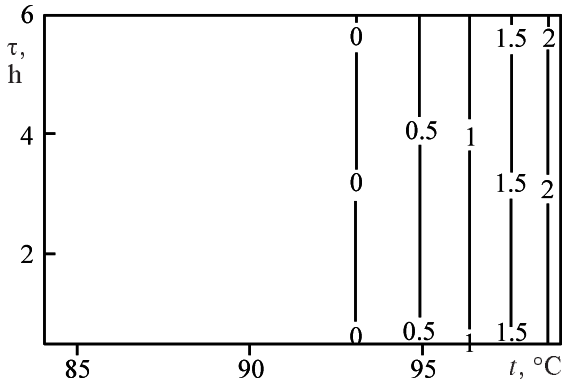


Fig. 1. Two-dimensional section of the response surface of model J_{V-IV} [Eq. (1)]. (τ) Heat treatment time and (t) temperature; the same for Fig. 2.

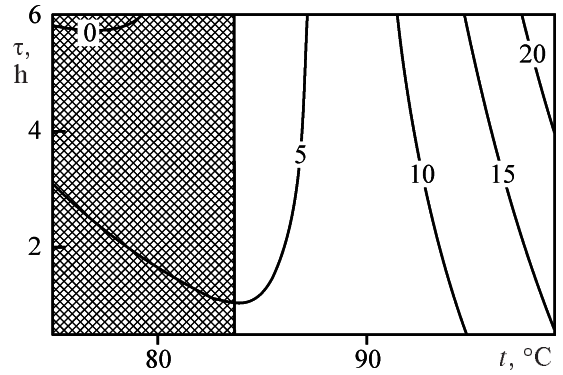


Fig. 2. Two-dimensional section of the response surface of model J_{IV-III} [Eq. (2)].

which, decreases in the entire range of heat treatment times examined. The lowest energy of the transition is attained at the lowest temperature and the longest heat treatment time. Extrapolation of the two-dimensional section toward lower heat treatment temperature (75°C; Fig. 2, shaded area) allowed us to find the area of zero energies of the transition.

At the boundary of this area (heat treatment temperature 80°C, time 6 h), we performed a series of experiments to reveal the dependence of the energy of the IV → III polymorphous transition on the total content c of the binary additive (from 2 to 4 wt %, three levels of variation) and relative content of $NTPNa_2$, c_{NTP}, in the binary additive (from 0 to 75 wt %, four levels of variation). Adequate models of the energies of the V → IV and IV → III polymorphous transitions have the form

$$J_{V-IV} = 0.83 - 0.0149c\,c_{NTP} + 0.000075c_{NTP}^2. \quad (3)$$

$$J_{IV-III} = 17.03 - 2.93c - 0.411c_{NTP} + 0.0075c_{NTP}^2. \quad (4)$$

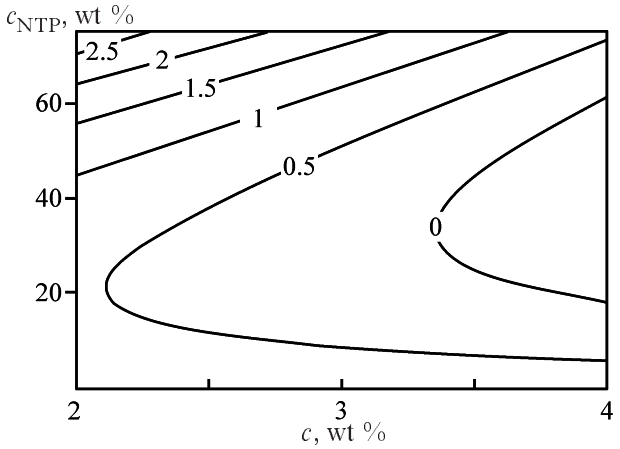


Fig. 3. Two-dimensional section of the response surface of model J_{V-IV} [Eq. (3)]. (c_{NTP}, c) Content; the same for Fig. 4.

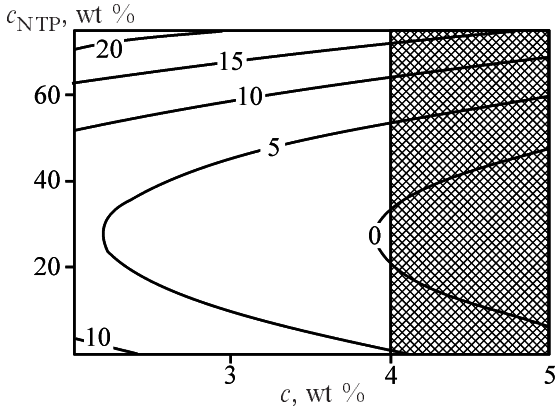


Fig. 4. Two-dimensional section of the response surface of model J_{IV-III} [Eq. (4)].

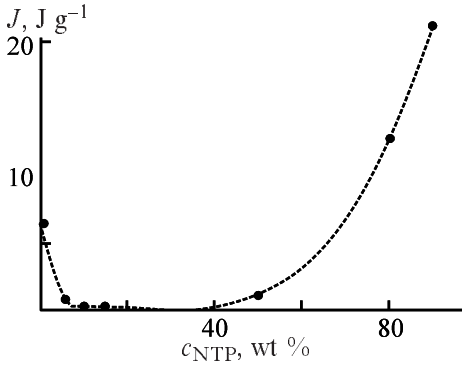


Fig. 5. Energy of the IV → III polymorphous transition as a function of the relative content of $NTPNa_2$, c_{NTP}, in the binary additive (total content 5 wt %).

Analysis of the graphical interpretation of Eqs. (3) and (4) (Figs. 3, 4) shows that, at a total content of the binary additive exceeding 3 wt %, there are areas of the zero energy of the transition, bounded by certain values of c_{NTP}.

The area of zero values of the V → IV transition energy (Fig. 3) starts at a lower total content of the bonary additive and exists in a wider range of relative amounts of $NTPNa_2$ in the additive, compared to the IV → III transition (Fig. 4, nonshaded area).

Extrapolation of the two-dimensional section (Fig. 4) toward an increase in the total content of the binary additive from 4 to 5 wt % (Fig. 4, shaded area) demonstrates the possibility of considerably expanding the area of the zero energy of the transition. The synergistic effect of the binary additive is confirmed experimentally (Fig. 5).

Figure 5 shows that, within the range of relative content of $NTPNa_2$ in the binary additive from 10 to 40 wt %, the IV → III polymorphous transition is suppressed. The V → IV transition in this series of experiments is observed only at $NTPNa_2$ concentrations of 0 and 90%. The PSAN sample with a total content of the binary additive of 5% and relative $NTPNa_2$ content of 20% stood ten cycles of heating and cooling from –50 to +50°C and thermostating at –50°C for 24 h without deterioration of the phase stability.

We performed experiments on the cocrystallization of AN with the binary additive from highly concentrated aqueous solutions of AN containing from 1 to 5 wt % water. We found that the presence of water in an amount exceeding 1 wt % fully suppresses the synergistic effect on introducing the binary additive. The pattern of polymorphous transitions of the samples obtained does not noticeably differ from that for AN without additives.

Recent studies [3] showed that the mechanism of IV $\rightleftarrows$ III polymorphous transitions of AN, including An containing a KNO_3 additive, can be considered as a chain of several successive events. Prior to the onset of the phase transition, crystallites and separate blocks are broken down. This is followed by transition of the initial phase into a certain intermediate X-ray amorphous state which subsequently transforms into the new phase. The limiting step is the transition of the initial phase into the intermediate X-ray amorphous state, rather than the nucleation and growth of centers of the new phase.

Based on this pattern, the mechanism of the synergistic effect in the system under consideration can be presented as follows. Like any topochemical reaction, the transformation of the initial phase starts on active centers located on defects of the external or internal surface of a crystal. In the salt $NTPNa_2$, the anion size is too large to form a substitution

solid solution with ammonium nitrate. Therefore, in the course of cocrystallization with ammonium nitrate, $NTPNa_2$ and products of exchange reactions with system components are adsorbed on defects of the crystal structure of AN or solid solution of KNO_3 in AN. Interaction of phosphonic acid groups of the complexone with potassium ions results in formation of a fairly strong structure suppressing the active centers and thus impeding the transition of the initial phase into the X-ray amorphous state. The same reasoning can also be applied to the V → IV polymorphous transition.

CONCLUSIONS

(1) Heat treatment of cocrystallizates of ammonium nitrate with modifying additives is the necessary step for ensuring phase stabilization of ammonium nitrate.

(2) Exceeding the threshold temperature of 90°C in the heat treatment of phase-stabilized ammonium nitrate containing the binary additive potassium nitrate–disodium tetrahydrogen nitrilotris(methylenephosphonate) is exceeded, the structure of phase-stabilized ammonium nitrate ensuring its phase stability is broken down.

(3) Phase-stabilized ammonium nitrate containing 5 wt % binary additive KNO_3–$NTPNa_2$ and undergoing no polymorphous transitions V → IV and IV → III can be obtained at a relative content of $NTPNa_2$ in the binary additive of 6–48 wt %.

(4) Analysis of the mathematical models describing the dependences of the energy of the polymorphous transition in ammonium nitrate on the concentration characteristics of the binary additive and on the temperature and time of the heat treatment allowed determination of the conditions for preparation of phase-stabilized ammonium nitrate exhibiting phase stability in the range from –50 to +100°C.

REFERENCES

1. Klyakin, G.F., *Issledovanie vliyaniya binarnykh dobavok na svoistva nitrata ammoniya* (Effect of Binary Additives on Properties of Ammonium Nitrate), Novocherkassk, 2004, Available from VINITI, January 19, 2004, no. 77-V2004.
2. Ruzinov, L.P., *Statisticheskie metody optimizatsii khimicheskikh protsessov* (Statistical Methods for Optimization of Chemical Processes), Moscow: Khimiya, 1972, p. 45.
3. Golovina, N.I., Manelis, G.B., Lempert, D.B., et al., in *Vysokoenergeticheskie materialy: Demilitarizatsiya i grazhdanskoe primenenie: Doklady Mezhdunarodnoi konferentsii "HEMs-2004"* (Highly Energetic Materials: Demilitarization and Civilian Applications: Proc. Int. Conf. "HEMs-2004"), Belokurikha (Altai krai), September 6–9, 2004, Biisk: Altai, 2004, p. 37.

ISSN 1070-4272, Russian Journal of Applied Chemistry, 2008, Vol. 81, No. 5, pp. 752–754. © Pleiades Publishing, Ltd., 2008.
Original Russian Text © Ya.I. Vakhula, M.Ya. Matsigin, K.S. Besaga, L.V. Zhuk, 2008, published in Zhurnal Prikladnoi Khimii, 2008, Vol. 81, No. 5, pp. 718–720.

INORGANIC SYNTHESIS AND INDUSTRIAL INORGANIC CHEMISTRY

Processes Occurring in Boron- and Molybdenum-Containing Glass-Forming Phosphate Solutions

Ya. I. Vakhula, M. Ya. Matsigin, K. S. Besaga, and L. V. Zhuk

L'vivs'ka Politekhnika National University, Lviv, Ukraine

Received July 25, 2007

Abstract—Phosphorus-containing formulations of low-melting glass coatings prepared from solution were developed. The chemical processes occurring in the glass-forming solution and their effect on the melting temperature of the glass coatings were examined. The optimal composition of a coating with the preset properties was determined.

DOI: 10.1134/S1070427208050042

Industrial progress places heavy demands on the service characteristics and external appearance of surfaces. The required characteristics can be attained, in particular, by applying various coatings. A special role is played by glassy coatings which can be readily formed, show good adhesion to the support, and impart required surface properties to the material [1].

In many cases glassy coatings are prepared using phosphate systems [2–4]. Thanks to the lower connectivity of the anionic framework compared to silicate glass, phosphate glass has lower hardness and lower elastic modulus. The strength of bonding between P–O groups depends on the modifier cation. A specific feature of phosphate coatings is that they have increased temperature coefficient of linear expansion, high adhesion to the support, and low formation temperature [5]. In cases when high chemical resistance is not required, these coatings can be used as connecting and priming layers, and also for decoration of articles [4, 5]. Sol–gel process is used with colloidal solutions, and solution process, with true solutions.

The aim of this study was to develop formulations of low-melting glassy coatings of phosphate system, prepared by a solution process, and also to examine processes that occur in the course of preparation and storage of boron- and molybdenum-containing phosphate glass-forming solutions.

EXPERIMENTAL

Published data [5, 6] show that, to prepare glassy coatings with the above-indicated properties, it is appropriate to use systems $Na_2O–B_2O_3–P_2O_5$ **(I)** and $Na_2O–MoO_3–P_2O_5$ **(II)**.

The procedure for forming glassy coatings involved preparation of homogeneous aqueous solutions of the required composition and their spraying onto a heated steel plate with the subsequent heat treatment. To prepare the solutions, we used H_3PO_4, $Na_2HPO_4 \cdot 12H_2O$, $Na_2B_4O_7$, $NaNO_3$, and $Na_2MoO_4 \cdot 2H_2O$ of pure grade, and H_3BO_3 of analytically pure grade. The glass formulations (see table) were chosen taking into account the data of [6] and the specific features of the solution process related to the solubility of separate components.

Compositions of glassy coatings of the systems $Na_2O–B_2O_3–P_2O_5$ and $Na_2O–MoO_3–P_2O_5$

Formulation no.	Content, wt %			
	Na_2O	P_2O_5	B_2O_3	MoO_3
System **I**				
1	31	54	15	–
2	33	54	13	–
3	35	54	11	–
4	37	54	9	–
5	39	54	7	–
System **II**				
1	33	37	–	30
2	28	37	–	35
3	23	37	–	40
4	23	32	–	45
5	23	27	–	50

When preparing coatings, it is important to understand the properties of solutions used and the processes that occur in the course of their formation. To prepare a glass-forming molybdenum-containing solution, we used H_3PO_4, $Na_2MoO_4 \cdot 2H_2O$, and $Na_2HPO_4 \cdot 12H_2O$. The salts were dissolved in water with the formation of true colorless solutions. This fact suggests that the dissolution of the molybdenum salt is not accompanied by hydrolysis, as molybdic acid formed by hydrolysis would impart to the solution a yellow color [7]. At the same time, the transparent solution obtained from system **II** is yellow, irrespective of the order of mixing the components, which suggests the occurrence of the reaction [8]

$$Na_2MoO_4 \cdot 2H_2O + H_3PO_4 = MoO_3 \cdot 2H_2O + Na_2HPO_4 + H_2O. \quad (1)$$

To confirm these assumptions, we examined the products obtained from the solution, after drying at 60°C, by X-ray phase analysis.

The results of X-ray phase analysis show that the powder contained $MoO_3 \cdot 2H_2O$ (interplanar spacings *d/n* 0.343, 0.336, 0.331, 0.325, 0.304, 0.288, 0.265, 0.245, 0.231 nm), $NaPO_3$ (*d/n* 0.507, 0.465, 0.421, 0.343, 0.298, 0.280, 0.254, 0.245, 0.226 nm), and $Na_2HPO_4 \cdot 12H_2O$ (*d/n* 0.730, 0.444, 0.384, 0.363, 0.343, 0.331, 0.325, 0.321, 0.298, 0.280 nm). The presence of molybdic acid confirms the occurrence of reaction (1). $NaPO_3$ may be formed by the reaction

$$Na_2HPO_4 \cdot 12H_2O + H_3PO_4 = 2NaPO_3 + 14H_2O. \quad (2)$$

The presence of $Na_2HPO_4 \cdot 12H_2O$ in the powder suggests that reaction (2) does not go to completion.

When preparing solutions of borate system **I**, we found no qualitative evidence for the occurrence of chemical reactions. Furthermore, we failed to dry these solutions, because in the course of storage, even at room temperature, they transformed into viscous transparent masses. This may be due to low melting points of the solution components, e.g., 42.35°C for H_3PO_4 and 34°C for $Na_2HPO_4 \cdot 12H_2O$ [7]. Therefore, X-ray phase analysis of the system was impossible.

Glassy coatings of the system Na_2O–B_2O_3–P_2O_5. To obtain coatings of this system, we prepared two series of solutions: first, from sodium phosphate, phosphoric acid, and boric acid, and second, from sodium nitrate, sodium tetraborate, and phosphoric acid. All the solutions were colorless, without visible precipitate. Aerosol spraying of the solutions onto a steel plate heated to 350°C results in deposition of a raw mixture of the preset composition as a white powder. The products were then heat-treated in a gradient furnace at the maximal temperature of 770°C.

The quality of a glassy coating (in particular, its homogeneity, continuity, adhesion strength) was evaluated visually and with a microscope. The results obtained with the first series of solutions show that, as the content of sodium oxide is increased from 31 to 39 wt %, the lower boundary of the film formation (first signs of appearance of a glassy coating) is shifted from 650 to 575°C. Comprehensive evaluation shows that, among coatings of system **I**, formulation no. 5 is the best. This coating has a low temperature of the lower boundary of the film formation (575°C). It should be particularly noted that all the coatings obtained become dull after storage for 3 weeks, i.e., their chemical resistance is poor.

Coatings prepared from the second series of solutions are not continuous and show pronounced foaming. The bubble diameter increased from 1 to 3 mm with an increase in the temperature from 575 to 750°C. This phemonenon is associated with low viscosity and high spreadability of the molten raw mixture at elevated temperatures. As in the first series, the lower boundary of the film formation decreases from 725 to 575°C with an increase in the sodium oxide content. The coatings are pale green.

Glassy coatings of the system Na_2O–MoO_3–P_2O_5. Experiments showed that in this case the lower boundary of the film formation is 250°C, and it increases to 520°C with an increase in the molybdenum oxide content from 30 to 50 wt %. The coating color varies from transparent greenish to black, which is characteristic of molybdenum-containing glasses.

In system **II**, formulation no. 1 is the best. It covers uniformly the surface of a metal plate and provides the minimal lower boundary of the film formation (250°C).

It should be noted that, with an increase in the MoO_3 content and a decrease in the Na_2O content, the surface tension of the glass coatings increases, which allows preparation of thicker coatings. This trend is due to the fact that, with a decrease in the Na_2O content, the viscosity and the amount of the liquid phase at fusion decrease. At a high tempera-

ture, the melt viscosity becomes so low that the coating transforms into separate drops because of poor wettability.

CONCLUSIONS

(1) Low-melting molybdenum-containing phosphate coatings were developed. The components of the glass-forming solution used for their preparation have relatively low melting points. Fusion results in formation of eutectics which provide melting and formation of a coating at low temperatures. In particular, formulation no. 1 of system **II**, containing the maximal amount of $Na_2HPO_4 \cdot 12H_2O$, is characterized by the minimal lower boundary of the film formation: 250°C.

(2) Because of high formation temperature and low chemical resistance of borate coatings, molybdenum-containing phosphate coatings are more efficient.

REFERENCES

1. Appen, A.A., *Temperaturoustoichivye neorganicheskie pokrytiya* (Temperature-Resistant Inorganic Coatings), Leningrad: Khimiya, 1976.
2. Borisenko, A.I., Nikolaeva, L.V., and Efimova, L.N., in *Zharostoikie pokrytiya dlya zashchity konstruktsionnykh materialov* (Refractory Coatings for Protection of Structural Materials), Leningrad, 1987, p. 28.
3. *Svoistva neorganicheskikh soedinenii: Spravochnik* (Properties of Inorganic Compounds: Handbook), Efimov, A.I., Ed., Leningrad: Khimiya, 1983.
4. US Patent 5053251.
5. Borisenko, A.I. and Nikolaeva, L.V., *Tonkosloinye stekloemalevye i steklokristallicheskie pokrytiya* (Thin Glass–Enamel and Glasse–Crystalline Coatings), Leningrad: Nauka, 1980.
6. Pavlushkin, N.M. and Zhuravlev, A.K., *Legkoplavkie stekla* (Low-Melting Glasses), Moscow: Stroiizdat, 1970.
7. *Osnovnye svoistva neorganicheskikh i organicheskikh soedinenii: Spravochnik khimika* (Main Properties of Inorganic and Organic Compounds: Chemist's Handbook), Nikol'skii, B.P., Ed., Leningrad: Khimiya, 1971.
8. *Khimicheskii entsiklopedicheskii slovar'* (Chemical Encyclopedic Dictionary), Knunyants, I.L., Ed., Moscow: Sov. Entsiklopediya, 1983.

ISSN 1070-4272, Russian Journal of Applied Chemistry, 2008, Vol. 81, No. 5, pp. 755–759. © Pleiades Publishing, Ltd., 2008.
Original Russian Text © G.I. Volkova, V.S. Sedoi, 2008, published in Zhurnal Prikladnoi Khimii, 2008, Vol. 81, No. 5, pp. 721–725.

INORGANIC SYNTHESIS AND INDUSTRIAL INORGANIC CHEMISTRY

Structure and Texture of Oxyhydroxides Formed by Oxidation of Nanodispersed Aluminum with Water

G. I. Volkova and V. S. Sedoi

Institute of Petroleum Chemistry, Siberian Branch, Russian Academy of Sciences, Tomsk, Russia
Institute of High-Current Electronics, Siberian Branch, Russian Academy of Sciences, Tomsk, Russia

Received July 23, 2007

Abstract—Aluminum oxyhydroxides were prepared by oxidation with water (55°C) of nanodispersed aluminum powders obtained by electric explosion of conductors in argon, nitrogen, carbon dioxide, and their mixtures. The structure and texture of aluminum oxyhydroxides were studied using methods of thermal desorption of nitrogen, derivatography, electron microscopy, and X-ray phase analysis.

DOI: 10.1134/S1070427208050054

Nanotechnology is today one of priority fields in developed countries. Nanomaterials are used in composites for preparing ceramics, catalysts, and sorbents, as molecular sieves, aerogels, and materials for solar batteries and fuel cells, and also in magnetic tomography, optoelectronics, photonics, microbiology, and medicine. The use of nanomaterials as sorbents is based on their high sorption ability toward various kinds of substances [1–5].

One of procedures for preparing nanomaterials is electric explosion of conductors (EEC) [6]. The first studies and semicommercial production of submicrometer aluminum powders by this method were performed in an inert gas (argon) atmosphere, with the subsequent passivation of the particles by admitting air into the explosion chamber. Aluminum nanopowders exhibit unique properties compared to submicrometer powders and, the more so, to bulk materials. For example, aluminum nanopowders react with water even at room temperature, and even slight (to 40–50°C) heating of the reaction mixture results in vigorous hydrogen evolution and self-heating of the system [7–12]. Oxidation of aluminum with water yields a mixture of finely dispersed products (aluminum oxyhydroxides) whose composition and properties strongly depend on the synthesis conditions: oxidation temperature, pH, time and temperature of aging, and time and temperature of the heat treatment of the sample [13, 14].

Today nanodispersed aluminum is produced by electric explosion process in nitrogen, carbon dioxide, and their mixtures, with nitrogen, argon, air, and carbon dioxide as passivating media [15]. In this study we examined how the media used for explosion and passivation affect the activity of nanodispersed aluminum in reactions with water and the composition of the oxidation products.

EXPERIMENTAL

In the study we used samples of nanodispersed aluminum powder (NDP) prepared by electric explosion of aluminum wire in argon, nitrogen, carbon dioxide, and their mixtures and passivated with nitrogen, air, and carbon dioxide (Table 1). We used the following notation: medium in which the wire was exploded–slash–gas used for powder passivation.

The kinetics of the oxidation of nanodispersed aluminum with water were studied with a gasometric unit provided with software for measuring the gas volume [16]. The cell with distilled water was ther-

Table 1. Main characteristics of aluminum powders prepared under various conditions

Preparation conditions	Particle diameter, nm	Al content, wt %	S_{sp}, $m^2 g^{-1}$
N_2/N_2	44.2	75	18
N_2/air	40.3	74	13
N_2/CO_2	40.4	71	21
$N_2 + CO_2/N_2$	32.4	61	34
CO_2/CO_2	30.8	16	38
Ar/air	54.6	80	17

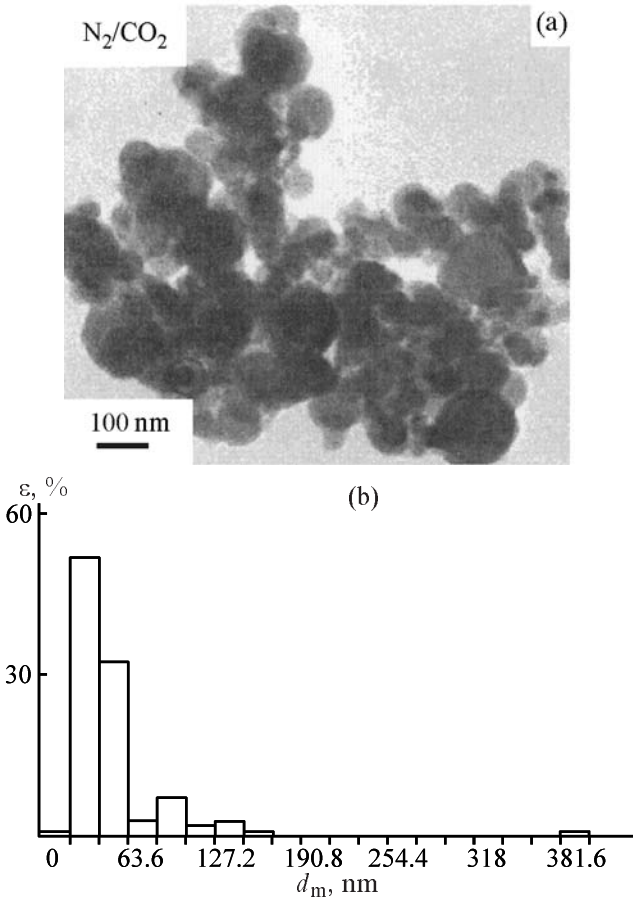


Fig. 1. (a) Electron micrograph and (b) size distribution of nanodispersed aluminum particles prepared in N_2/CO_2. (ε) Content of fraction and (d_m) mean particle diameter in fraction.

mostated at 60°C to completely remove gases dissolved in water, after which nanodispersed aluminum was added, and the volume of the released hydrogen was measured. From the kinetic curves we determined the maximal and mean rate of hydrogen evolution. We also calculated the conversion α as the ratio of the hydrogen volume actually released during the reaction to the theoretically expected volume.

The active metal content of aluminum samples was evaluated volumetrically from the hydrogen evolution in oxidation of nanodispersed aluminum with a NaOH solution [17].

Aluminum oxyhydroxides (AOHs) were prepared by the procedure described in [13]. Aluminum powders were thermostated in water (salt content 50 g l^{-1}, 55°C) with vigorous stirring of the suspension. Then the AOH powders were filtered off, washed with distilled water to neutral reaction, and dried.

The specific surface area S_{sp}, pore volume, pore size, and distribution of mesopore volume with respect to size were determined by thermal desorption of nitrogen on a Sorbtometr-M surface area analyzer (Katakon Private Company, Novosibirsk). The landing area of the adsorbate gas was taken equal to 0.162 nm^2 [18].

The content of structural water in AOHs was calculated from the results of derivatographic studies performed with a Q-1500 D deriovatograph in the dynamic mode (heating rate 10 deg min^{-1}) in the range 20–1000°C in air. The phase composition of AOHs was determined from the diffraction patterns taken with a DRON-3 diffractometer in the range of medium and large angles (2θ = 3°–60°, CuK_α radiation) with continuous scanning at a rate of 1 deg min^{-1}.

The morphology of nanodispersed aluminum particles and aluminum oxyhydroxides was studied with by transmission electron microscopy (TEM, 125 kV). A suspension of a powder in ethanol was applied onto an object-plate and dried. A carbon layer was sputtered in a vacuum onto the object-plate with the sample. The extract carbon replica was separated with an aqueous solution of gelatin. After dissolving gelatin, the carbon replica with the powder was placed on a copper grid. To determine the mean size of powder particles and their size distribution, 300–500 particles were measured.

The maximum of the size distribution of aluminum nanoparticles is at 30–55 nm, with the smallest particles formed in CO_2 (Table 1). The electron micrograph and histogram of particle distribution of one of the samples prepared in N_2/CO_2 are shown in Fig. 1. Aluminum nanoparticles prepared in Ar and passivated with air (Ar/air) contain 80%, and the N_2/N_2 and N_2/air samples, about 75% active aluminum. Introduction of CO_2 into the explosion chamber leads to aluminum oxidation. The active aluminum content decreases to 16% on complete replacement of N_2 by CO_2. Simultaneously, the specific surface area of the samples increases with increasing concentration of CO_2. A considerable increase in the specific surface area of aluminum nanopowders prepared by electric explosion may be due both to formation of smaller particles and to formation on their surface of oxides having a larger surface area than aluminum metal (Table 1).

All the aluminum NDPs studied are oxidized with water in one step (Fig. 2). The initial oxidation rate

Table 2. Main characteristics of powders of aluminum oxyhydroxides

Preparation conditions	pH_{in}/pH_{fin}*	Rate of H_2 evolution, $cm^3\ g^{-1}\ s^{-1}$		S_{sp}, $m^2\ g^{-1}$	Structural H_2O, mol mol^{-1} Al_2O_3	Pore volume, $cm^3\ g^{-1}$	Pore size,** nm
		maximal	mean				
N_2/N_2	5.2/9.6	2.22	1.59	374	1.17	0.613	6.4
N_2/air	5.0/9.7	–	–	368	1.23	–	–
N_2/CO_2	5.3/9.7	4.41	1.47	411	1.21	0.672	6.3
$N_2 + CO_2/N_2$	5.1/9.4	–	–	342	1.14	–	–
CO_2/CO_2	5.2/8.3	0.16	0.12	149	0.42	0.359	8.0
Ar/air	5.3/9.7	–	–	400	1.21	0.742	5.5

* Reaction time 2 h.
** Mean size of mesopores evaluated from the desorption isotherm.

is maximal for the N_2/CO_2 nanopowder. Oxidation of the powder prepared and passivated in CO_2 starts after the induction period and occurs slowly. The maximal rate of hydrogen evolution is 4.41, 2.22, and 0.16, and the mean rate, 1.47, 1.59, and 0.12 $cm^3\ g^{-1}\ s^{-1}$ for samples N_2/CO_2, N_2/N_2, and CO_2/CO_2, respectively (Table 2). The first sequence is apparently determined by the particle size and thickness of the protective shell. The former factor is decisive for the first two samples, and the latter factor, for the CO_2/CO_2 sample. The mean rate of hydrogen evolution is controlled exclusively by the content of active aluminum in the nanoparticles. The conversion α at 60°C in 2000 s of powders obtained in N_2/N_2, N_2/CO_2, and CO_2/CO_2 is 1.0, 0.96, and 0.38, respectively.

Oxidation of nanodispersed aluminum with water yields an ultradispersed product which is a mixture of oxyhydroxides. As shown previously for Ar/air aluminum [13, 14], the AOH phase composition is determined by oxidation conditions. Oxidized nanopowders prepared in N_2/air, N_2/N_2, and N_2/CO_2 give AOHs whose structural and texture characteristics are comparable with those of Ar/air AOHs. In the course of oxidation of these samples, pH of the reaction medium steadily increases and reaches 9.7 in 2 h. The reaction products contain virtually equal amount of structural water (Table 2). Oxidation of the CO_2/CO_2 sample ends in a less alkaline medium (pH 8.2), and the corresponding oxyhydroxide contains only 0.42 mol of structural water, i.e., three times smaller amount compared to the other samples.

The AOH samples prepared from aluminum samples of various kinds can be classed with mesoporous materials (isotherms of type IV) [19]. The capillary-condensation hysteresis loops observed with these samples correspond to type N3 characterized by slitlike pores. The maximum of the mesopore size distribution is at 4 nm for all the samples (Fig. 3). The Ar/air AOH sample has the largest mesopore volume and the smallest mean size of mesopores (Table 2). The curves of the mesopore volume distri-

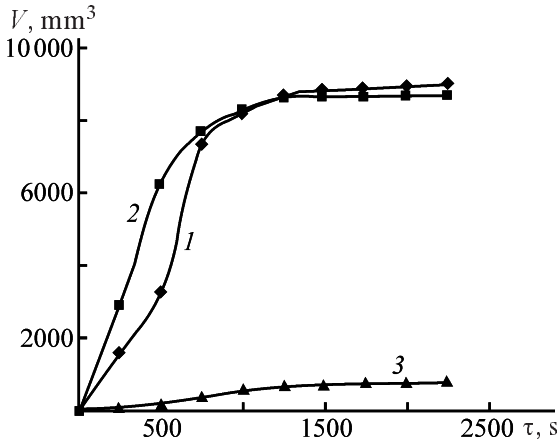


Fig. 2. Kinetic curves of hydrogen evolution in oxidation with water of aluminum particles prepared under various conditions. Reaction temperature 60°C. (V) Volume of released hydrogen and (τ) time. Conditions for preparing Al powders: (*1*) N_2/N_2, (*2*) N_2/CO_2, and (*3*) CO_2/CO_2.

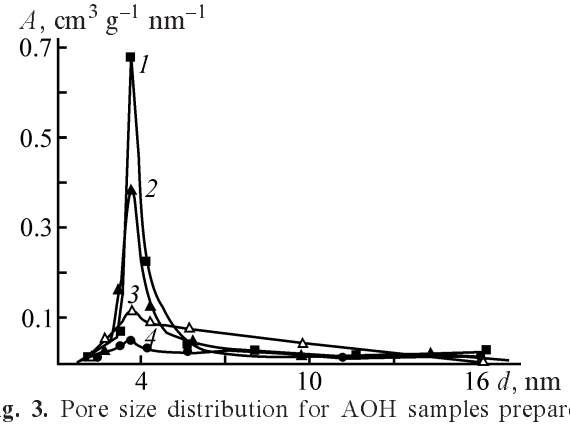


Fig. 3. Pore size distribution for AOH samples prepared from various aluminum powders. (d) Pore diameter. Conditions for preparing Al powders: (*1*) Ar/air, (*2*) N_2/N_2, (*3*) N_2/CO_2, and (*4*) CO_2/CO_2.

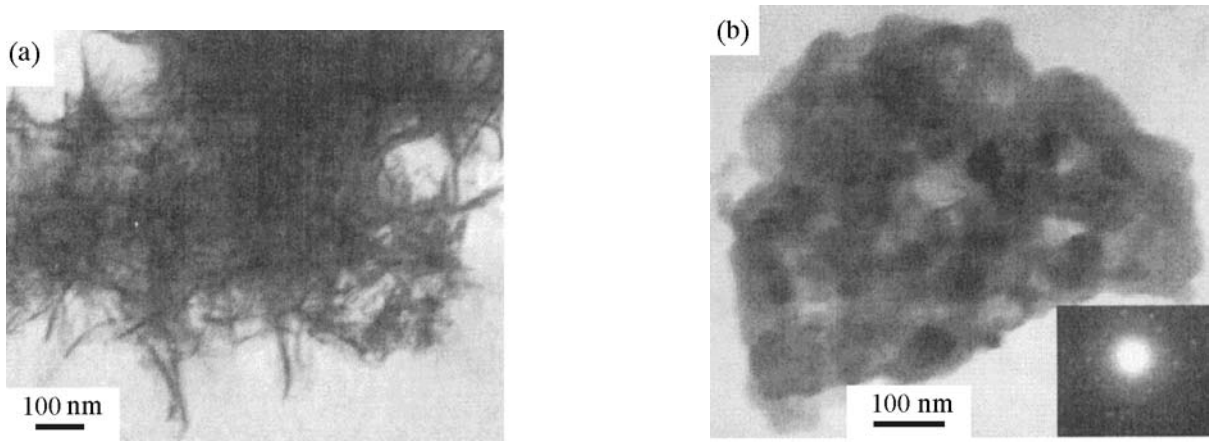


Fig. 4. Electron-microscopic image of AOH particles prepared from Al powders that were formed in (a) N_2/N_2 and (b) CO_2/CO_2.

bution with respect to the pore size for the CO_2/CO_2 AOH sample have a weakly pronounced maximum at approximately 4 nm, and the mean pore size is 8.0 nm, i.e., it is larger than in the other samples.

Electron-microscopic images of particles of the N_2/N_2 and CO_2/CO_2 AOH samples are shown in Fig. 4. The N_2/N_2 AOH sample (Fig. 4a) consists mainly of amorphous flaky formations of different shapes and sizes, characteristic of pseudoboehmite. The AOH samples prepared by oxidation of the N_2/air, N_2/CO_2, $N_2 + CO_2/N_2$, and Ar/air aluminum powders have a similar morphology. The CO_2/CO_2 AOH sample (Fig. 4c) mainly consists of round-shaped particles of size 50–250 nm, of 100–200-nm chips forming flat agglomerations, and of separate relatively coarse (1000–1500 nm) particles.

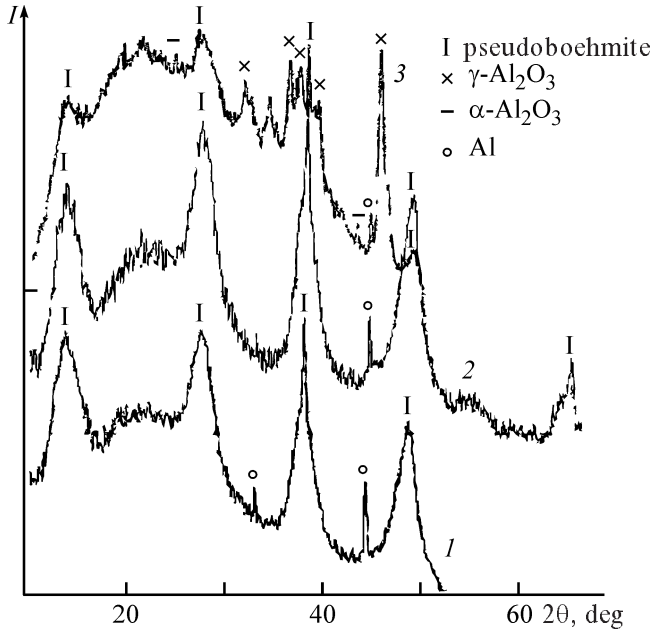


Fig. 5. Diffraction patterns of aluminum oxyhydroxides prepared from Al powders that were formed in (*1*) N_2/N_2, (*2*) N_2/CO_2, and (*3*) CO_2/CO_2. (*I*) Radiation intensity and (2θ) Bragg angle.

Oxidation of nanodispersed aluminum with water initially yields amorphous trihydroxide from which a series of oxyhydroxides are formed in the course of aging, depending on the conditions [14]. After 2 h, the dispersed phase of the reaction mixture consists of amorphous trihydroxide (halo at ~20°), pseudoboehmite (broadened reflections corresponding to interplanar spacings of 0.611, 0.316, 0.234, and 0.186 nm), and residual aluminum (d = 1.97 nm etc.) for the N_2/N_2, N_2/CO_2, N_2/air, $N_2 + CO_2/N_2$, and Ar/air samples (Fig. 5, curvese *1, 2*) [20]. Oxidation of the CO_2/CO_2 sample, complicated by aging, ends in a less alkaline medium (Table 2), which affects the product composition: The concentration of pseudoboehmite decreases and the content of α- and γ-Al_2O_3 increases (Fig. 5, curve *3*).

Thus, by varying the media of the explosion and passivation of nanodispersed aluminum powders, it is possible to vary the structural and texture characteristics of the products of aluminum oxidation with water. Complete replacement of Ar or N_2 by CO_2 leads to a decrease in the concentration of pseudoboehmite, characterized by developed surface of particles and high sorption activity, in the mixture of oxyhydroxides.

CONCLUSIONS

(1) Aluminum nanopowders prepared in Ar/air, N_2/air, and N_2/N_2 contain 75–80% active aluminum.

With an increase in the CO_2 concentration in the explosion chamber, the content of active aluminum in the samples decreases and the specific surface area increases.

(2) The rate of oxidation of nanodispersed aluminum powders depends on the particle size and active aluminum content. The N_2/CO_2 sample is characterized by the highest rate of oxidation with water.

(3) The oxyhydroxide prepared by oxidation with water of aluminum powders prepared in CO_2/CO_2 are characterized by low pseudoboehmite concentration, small specific surface area, and small mesopore volume.

ACKNOWLEDGMENTS

The authors are grateful to O.A. Kukharenko for performing X-ray phase analysis of aluminum oxyhydroxide samples.

REFERENCES

1. Sirotkina, E.E., Ivanov, V.G., Glazkov, O.V., et al., *Khim. Inter. Ustoich. Razv.*, 1997, vol. 5, no. 4, pp. 429–437.
2. Glazkov, O.V., Glazkova, E.A., Ivanov, V.G., et al., *Neftekhimiya*, 2000, vol. 40, no. 1, pp. 65–67.
3. Gerasimova, V.N., *Khim. Inter. Ustoich. Razv.*, 1999, vol. 7, pp. 135–140, 657–665.
4. Ivanov, V.G., Sirotkina, E.E., and Pirogova, I.D., Abstracts of Papers, *Mezhdunarodnaya nauchno-tekhnicheskaya konferentsiya "Tekhnika i tekhnologiya ochistki i kontrolya kachestva vody"* (Int. Scientific and Technical Conf. "Apparatus and Processes for Water Treatment and Monitoring of Its Quality"), Tomsk, September 28–30, 1999, pp. 85–86.
5. Ovsyannikova, V.S., Svarovskaya, L.I., and Volkova, G.I., Abstracts of Papers, *V Mezhdunarodnaya konferentsiya "Khimiya nefti i gaza"* (V Int. Conf. "Chemistry of Oil and Gas"), Tomsk, September 22–26, 2003, pp. 607–609.
6. Kotov, Yu.A. and Yavorskii, N.A., *Fiz. Khim. Obrab. Mater.*, 1978, no. 4, pp. 24–29.
7. Zhilinskii, V.V., Lokenbakh, A.K., and Lepin', L.K., *Izv. Akad. Nauk Latv. SSR, Ser. Khim.*, 1986, pp. 151–161.
8. Lyashko, A.P., Medvinskii, A.A., Savel'ev, G.G., et al., *Kinet. Katal.*, 1990, vol. 31, pp. 967–972.
9. RF Patent 2075345.
10. Ivanov, V.G. and Gavrilyuk, O.V., *Fiz. Goren. Vzryva*, 1999, vol. 35, no. 6, pp. 1–6.
11. Ivanov, V.G., Safronov, M.N., and Gavrilyuk, O.V., *Fiz. Goren. Vzryva*, 2001, vol. 37, no. 2, pp. 57–63.
12. Ivanov, V.G., Safronov, M.N., and Gavrilyuk, O.V., *Khim. Inter. Ustoich. Razv.*, 2000, vol. 8, no. 5, pp. 705–710.
13. Volkova, G.I., Ivanov, V.G., and Kukharenko, O.A., *Khim. Inter. Ustoich. Razv.*, 2005, vol. 13, no. 3, pp. 427–432.
14. Volkova, G.I., Ivanov, V.G., and Kukharenko, O.A., *Khim. Inter. Ustoich. Razv.*, 2006, vol. 14, no. 4, pp. 349–355.
15. Sedoi, V., Osmonaliev, M., Shemezova, L., et al., *Centr. Eur. J. Energ. Mater.*, 2007, vol. 4, nos. 1–2, pp. 17–30.
16. USSR Inventor's Certificate no. 1723445.
17. *GOST* (State Standard) *10096–76: Lump Aluminum Powder*, Moscow: Gosstandard Rossii, 1976.
18. Buyanova, N.E., Karnaukhov, A.P., and Alabuzhev, Yu.A., *Opredelenie poverkhnosti dispersnykh i poristykh materialov* (Determination of the Surface Area of Dispersed and Porous Materials), Novosibirsk: Inst. Kataliza Sib. Otd. Akad. Nauk SSSR, 1978.
19. Gregg, S.J. and Sing, K.S.W., *Adsorption, Surface Area, and Porosity*, New York: Academic, 1982, 2nd ed.
20. Tikhov, S.F., Romanenkov, V.E., Sadykov, V.A., et al., *Poristye kompozity na osnove oksid-alyuminievykh kermetov (sintez i svoistva)* (Porous Composites Based on Aluminum Oxide Cermets (Synthesis and Properties)), Novosibirsk: Sib. Otd. Ross. Akad. Nauk, 2004.

ISSN 1070-4272, Russian Journal of Applied Chemistry, 2008, Vol. 81, No. 5, pp. 760–764. © Pleiades Publishing, Ltd., 2008.
Original Russian Text © V.I. Ivanenko, E.P. Lokshin, R.I. Korneikov, S.V. Aksenova, V.T. Kalinnikov, 2008, published in Zhurnal Prikladnoi Khimii, 2008, Vol. 81, No. 5, pp. 726–729.

INORGANIC SYNTHESIS AND INDUSTRIAL INORGANIC CHEMISTRY

Compositional Dependence of the Ion-Exchange Properties of a Sorbent Based on Oxotitanium Hydrophosphate

V. I. Ivanenko, E. P. Lokshin, R. I. Korneikov, S. V. Aksenova, and V. T. Kalinnikov

Tananaev Institute of Chemistry and Technology of Rare Elements and Mineral Raw Materials, Kola Scientific Center, Russian Academy of Sciences, Apatity, Murmansk oblast, Russia

Received March 23, 2007

Abstract—Effect of the degree of hydration and the phosphorus to titanium ratio in sorbents based on hydrated oxotitanium hydrophosphate on their sorption properties: constant of heterogeneous substitution of hydrogen ions by cations of sodium, cesium, and strontium and static exchange capacity, was studied.

DOI: 10.1134/S1070427208050066

Titanium(IV) phosphates are of special interest as sorption materials. It has been shown that sorbents of this kind can absorb cations of radionuclides [1–6] and nonferrous metals and iron [7–10] from strongly diluted aqueous solutions.

Operating nuclear power plants yield liquid radioactive waste (LRW) in the form of radionuclide-contaminated seawater (possibly diluted with fresh water), in which γ- and β-emitters are mostly constituted by ^{137}Cs and ^{90}Sr [11]. Together with radionuclides, such LRW contains up to 32 g l^{-1} of salts: mostly chlorides and, to a lesser extent, sulfates and hydrocarbonates of alkali and alkaline-earth metals. Being present in substantially higher concentrations (e.g., that of sodium cations may be 10.5 g l^{-1}) and having close chemical properties, these cations can compete with radionuclides in sorption. It has been shown that a sorbent based on amorphous hydrated oxotitanium hydrophosphate can be efficient in LRW deactivation [12–14].

Depending on synthesis conditions, products of the following compositions can be obtained: $[TiO(OH)_2]_x \cdot [TiOHPO_4]_{1-x} \cdot nH_2O$, where $0 \le x < 1$ and $n \ge 1$. Despite numerous studies of sorbents belonging to this class, the sorption mechanism remains unclear, because the cations being sorbed can, in principle, replace both the proton of a hydroxy group bonded to the central titanium atom and the proton of a hydroxy group bonded to the phosphorus atom (proton of the HPO_4^{2-} anion).

The aim of this study was to analyze how the sorption properties [constant of heterogeneous substitution of hydrogen ions by cations of sodium, cesium, and strontium and static exchange capacity (SEC)] depend on the phosphorus to titanium ratio in the sorbent and on the degree of its hydration.

EXPERIMENTAL

The starting oxotitanium hydrophosphate of the composition $[TiO(OH)_2]_x \cdot [TiOHPO_4]_{1-x} \cdot nH_2O$ was synthesized directly in an aqueous medium. To a concentrated solution of ammonia taken in a 30% excess relative to the stoichiometry, we gradually added a warmed-up acid fluoride solution of titanium(IV) ($c_{Ti(IV)}$ = 1.22 M, c_{F^-} = 7.33 M or $c_{Ti(IV)}$ = 1.73 M, c_{F^-} = 10.38 M) to pH 10–11 with continuous stirring. The reaction in which the solid phase of hydrated ammonium metatitanate is formed can be represented by the equation

$$H_2TiF_6 + (6 + x)NH_4OH_{conc} \rightarrow 7(NH_4)_xH_{4-x}TiO_4 + 6NH_4F + (2 + x)H_2O. \quad (1)$$

After filtration, the precipitate formed was washed to remove fluoride ions by triple repulpation in a 5% solution of ammonia. According to the results of an analysis, the content of F^- ions did not exceed 10^{-2} wt %. The second stage consisted in substitution of ammonium cations with hydrogen ions in formation of titanium(IV) oxohydroxide and substitution of hydroxy groups in this oxohydroxide with phosphate groups. For this purpose, the synthesized hydrated ammonium titanate $(NH_4)_xH_{4-x}TiO_4$ was repulped in water and a solution of hydrochloric

acid was introduced into the resulting suspension to pH 4–5:

$$(NH_4)_xH_{4-x}TiO_4 + xHCl \rightarrow TiO(OH)_2 + xNH_4Cl + H_2O. \quad (2)$$

The content of ammonium cations was monitored using Nessler's reagent. After double treatment of the solid phase being synthesized with a hydrochloric acid solution, no ammonium cations were found in the suspension. Then, the filtered-off solid phase of the freshly precipitated titanium(IV) hydroxide was treated with an orthophosphoric acid solution under vigorous agitation. The precipitate was dried and excess orthophosphoric acid captured by the solid phase from the solution was removed by washing with water. The composition of titanium(IV) phosphate synthesized was photocolorimetrically analyzed for the content of titanium(IV) and phosphorus(V), using hydrogen peroxide and ammonium molybdate, respectively. The error in the results of the analysis did not exceed 0.5%.

Previously, the anionic substitution in the hydrated oxohydroxide matrix of titanium(IV) in synthesis of oxotitanium hydrophosphate (P : Ti = 1 : 1) was performed in suspensions with a large excess of orthophosphoric acid [12–14]. In this case, the high degree of hydration of the solid phase provided the occurrence of the process in the bulk.

In this study, the interaction of phosphoric acid with titanium(IV) hydroxide was examined at 20, 65, and 95°C in order to optimize the synthesis conditions of hydrated titanium hydroxophosphate with a prescribed P : Ti ratio. A weighed portion of titanium hydroxide was placed in a phosphoric acid solution at a preset initial molar ratio of the contents of H_3PO_4 and titanium(IV) and was kept there for 30 min under agitation. The unchanged H_3PO_4 was filtered off, with the concentration $c_{H_3PO_4}$ in the filtrate and the phosphorus to titanium(IV) molar ratio in the solid phase determined. The results obtained are listed in Table 1.

Table 1 shows that raising the temperature of the titanium(IV) oxohydroxide suspension in a phosphoric acid solution results in an increase in the phosphorus to titanium molar ratio in the solid phase. The heterogeneous anionic substitution in the oxohydroxide matrix of titanium(IV) can be represented by the equation

$$TiO(OH)_2 \cdot nH_2O + (1 - x)H_3PO_4 \rightleftarrows [TiO(OH)_2]_x[TiOHPO_4]_{1-x} \cdot nH_2O + 2(1 - x)H_2O. \quad (3)$$

Table 1. Phosphorus to titanium ratio in the suspension ($N_{P(in)}$) and in the solid phase (N_P) at different temperatures of thermal treatment of the suspension, s : l = 1 : 70

Temperatures of thermal treatment of the suspension, °C					
20		65		95	
$N_{P(in)}$	N_P	$N_{P(in)}$	N_P	$N_{P(in)}$	N_P
0.39	0.18	0.43	0.31	0.30	0.29
0.64	0.30	0.73	0.52	0.65	0.62
0.82	0.43	0.97	0.72	0.82	0.81
1.04	0.54	1.26	0.86	0.98	0.90
2.03	0.96	1.46	1.00	1.05	1.00

Table 2. Composition of the $[TiO(OH)_2]_x \cdot [TiOHPO_4]_{1-x} \cdot nH_2O$ samples synthesized

Content, wt %			Composition
TiO_2	P_2O_5	H_2O	
29.2	26.0	44.8	$TiOHPO_4 \cdot 6.30H_2O$
44.8	24.1	31.1	$[TiO(OH)_2]_{0.39} \cdot [TiOHPO_4]_{0.61} \cdot 2.38H_2O$
55.8	21.8	22.4	$[TiO(OH)_2]_{0.56} \cdot [TiOHPO_4]_{0.44} \cdot H_2O$

The influence exerted by the composition of a sorbent on its ion-exchange properties was studied with samples whose composition is presented in Table 2. The heterogeneous cationic substitution was studied potentiometrically, by analyzing the variation of pH of aqueous suspensions containing the synthesized sorbents and chloride solutions of sodium, cesium, or strontium. The studies were carried out at 20°C and constant ionic strength μ of 0.5, 1.0, and 2.0. As equilibrium values we took steady-state pH values obtained using an I130.2M.1 ion meter with an accuracy of ±0.02. In the course of a drift of pH with time τ, its steady-state value was found by extrapolation of the pH–1/τ dependence to the ordinate axis at 1/τ = 0. An ESL-43-07 electrode selective toward hydrogen ions, with the isopotential point pH_i at 7±0.3, served as indicator electrode, and an EVL-1M3 saturated silver chloride electrode whose potential at 20°C is 202±2 mV relative to the standard hydrogen electrode, as auxiliary electrode. The equilibrium concentration and activity coefficient of hydrogen ions were found from the calibration dependence pH–c_{H^+} (c_{H^+} is the total

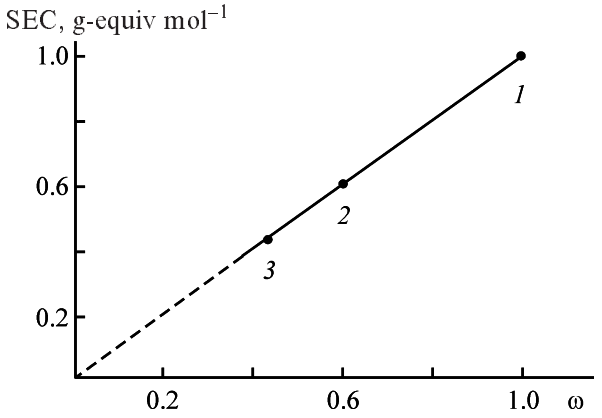


Fig. 1. SEC for cesium cations vs. the ratio ω of the specific molar content of oxotitanium hydrophosphate to the total content of titanium in various sorbents. (*1*) $TiOHPO_4 \cdot 6H_2O$, (*2*) $[TiO(OH)_2]_{0.39} \cdot [TiOHPO_4]_{0.61} \cdot 2.38H_2O$, and (*3*) $[TiO(OH)_2]_{0.56} \cdot [TiOHPO_4]_{0.44} \cdot H_2O$.

concentration of hydrogen ions in solution) at appropriate constant values of the ionic strength of the solution and from reference data. The static exchange capacity was determined with an accuracy of ±0.04 mg-equiv g^{-1}. The error in determining the logarithm of the constant of heterogeneous substitution of hydrogen ions by cations of sodium, cesium, or strontium was ±0.02. The reproducibility of the sorption parameters for sorbent samples taken from the same batch of the product synthesized confirmed that homogeneous distribution of phosphorus throughout the volume of the titanium matrix is achieved in synthesis of sorbents with a prescribed P : Ti ratio.

Figure 1 shows how the SEC of the initial samples, reduced to a mole of titanium(IV) in the sorbent, depends on the specific molar content ω of oxotitanium hydrophosphate in these samples, i.e., on the HPO_4^{2-} : Ti molar ratio. The linear dependence obtained indicates that active sorption centers are formed in the samples under study by just the hydrophosphate group, whereas protons of the hydroxy groups bonded directly to the central titanium atoms have no effect on the cation exchange. The dependences of SEC variation with the water content n of the samples was studied. For this purpose, a starting synthesized sample of the sorption matrix was gradually dehydrated by heating with an infrared lamp, with the loss of water mass determined and then SEC_{ex} found in 1 M solutions of CsCl, NaCl, and $SrCl_2$ at pH 6. The results obtained were compared with the theoretical value SEC_{theor}, calculated on the assumption that the molar concentration of the cation-exchange proton is equal to the concentration of HPO_4^{2-} groups in the sorbent.

Figure 2 shows $SEC_{ex} : SEC_{theor}$ ratios in dehydration of samples of initial compositions $TiOHPO_4 \cdot 6H_2O$ and $[TiO(OH)_2]_{0.39} \cdot [TiOHPO_4]_{0.61} \cdot 2.38H_2O$. The final compositions of the products can be described by the formulas $TiOHPO_4 \cdot 1.54H_2O$ and $[TiO(OH)_2]_{0.39} \cdot [TiOHPO_4]_{0.61} \cdot 0.30H_2O$. Figure 2 shows that the experimentally found values of SEC in dehydration of air-dry products first coincide with the theoretical values. However, as the content of crystallization water in the samples decreases further, the $SEC_{ex} : SEC_{theor}$ ratio starts to decrease and does so to dissimilar extents for different cations under study: the smallest deviation is observed for the cesium cation, and the largest, for the strontium cation. The extent to which the $SEC_{ex} : SEC_{theor}$ ratio decreases for the cations under study varies oppositely to the effective ionic potential of the cations, determined by the ratio of the cation charge to the radius of the hydrated cation.

The constants of heterogeneous substitution of the proton by cations of sodium, cesium, and strontium were found for the sorbents obtained under the conditions providing a $SEC_{ex} : SEC_{theor}$ ratio equal to unity. The constant is given by the equation

$$K_{ex} = (a_{H^+}/N_H)(N_M/a_{M^{z+}})^{1/z}, \quad (4)$$

where a_{H^+} and $a_{M^{z+}}$ are the activities of the H^+ and

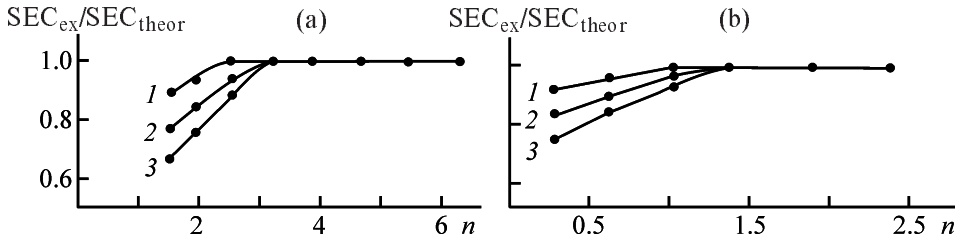


Fig. 2. $SEC_{ex} : SEC_{theor}$ ratio for (*1*) Cs^+, (*2*) Na^+, and (*3*) Sr^{2+} cations vs. the specific molar content n of water in (a) $TiOHPO_4 \cdot nH_2O$ and (b) $[TiO(OH)_2]_{0.39} \cdot [TiOHPO_4]_{0.61} \cdot nH_2O$.

Table 3. Effect of the specific molar content n of water in a sorbent of the composition $TiOHPO_4 \cdot nH_2O$ on the exchange constant $\log K_{ex}$

Composition	n	$\log K_{ex}$		
		Na^+	Cs^+	Sr^{2+}
$TiOHPO_4 \cdot 3.17H_2O$	3.17	–3.14	–1.60	–2.60
$TiOHPO_4 \cdot 4.65H_2O$	4.65	–2.99	–1.71	–2.48
$TiOHPO_4 \cdot 6.30H_2O$	6.30	–2.94	–1.80	–2.39

Table 4. Effect of the ratio between the content ω of oxotitanium hydroxophosphate and the total content of titanium in the sorption matrix on the exchange constant $\log K_{ex}$

Composition	ω	$\log K_{ex}$		
		Na^+	Cs^+	Sr^{2+}
$TiOHPO_4 \cdot 3.17H_2O$	1	–3.14	–1.60	–2.60
$[TiO(OH)_2]_{0.39} \cdot [TiOHPO_4]_{0.61} \cdot 2.38H_2O$	0.61	–2.69	–1.92	–2.42
$[TiO(OH)_2]_{0.56} \cdot [TiOHPO_4]_{0.44} \cdot H_2O$	0.44	–2.61	–1.98	–2.28

M^{z+} ions in solution; N_H and N_M, mole fractions of oxotitanium hydroxophosphate unsubstituted and substituted with metal cations; and z, charge of metal ions M^{z+}.

In the general case, this constant characterizes the substitution of hydrogen ions in a sorbent containing oxotitanium hydroxophosphate with metal cations M^{z+} present in solution, which occurs by the reaction

$$TiOHPO_4 + 1/zM^{z+} \rightarrow H^+ + 1/zM(TiOPO_4)_z. \quad (5)$$

Table 3 lists the thermodynamic constants of the cation exchange in relation to the content of water in hydrated oxotitanium hydroxophosphate. It was found that, as the degree of sorbent hydration becomes smaller, K_{ex} decreases for sodium and strontium cations and increases for cesium cations. Thus, dehydration of the sorbent leads to an increase in the selectivity of sorption of metal cations with a larger ratio of the cation charge to the radius of the hydrated cation.

The effect of the molar ratio ω between the contents of phosphorus and titanium on the exchange constant was studied (Table 4). A decrease in ω results in that the exchange constant becomes larger for sodium and strontium cations and smaller for cesium cations, i.e., it makes lower the sorption selectivity. Thus, presence of the oxohydroxide component leads to a decrease in the sorption selectivity.

The whole body of the data obtained suggests that the cation substitution processes under study are strongly affected by the number of HPO_4^{2-} cation-exchange groups and by the degree of hydration of a sorbent.

CONCLUSIONS

(1) Synthesis conditions of oxotitanium hydroxophosphate of the stoichiometric composition by reacting titanium(IV) oxohydroxide and orthophosphoric acid were substantiated.

(2) The sorption activity of the hydroxide–phosphate sorbents synthesized, $[TiO(OH)_2]_x \cdot [TiOHPO_4]_{1-x} \cdot nH_2O$, is determined by the hydrophosphate, rather than by the hydroxy group.

(3) Dehydration of the sorption matrix leads to a decrease in SEC and increase in the selectivity of recovery of cations with a higher effective ionic potential. The extent to which the SEC decreases varies oppositely to the effective ionic potential of the cations.

(4) A decrease in the phosphorus-to-titanium ratio in the hydroxide–phosphate sorbent makes lower the sorption selectivity.

ACKNOWLEDGMENTS

The study was financially supported in part by the Russian Foundation for Basic Research (project no. 06-08-00144-a).

REFERENCES

1. Sukharev, Yu.I. and Egorov, Yu.V., *Neorganicheskie ionity tipa fosfata tsirkoniya* (Inorganic Ion Exchangers of the Zirconium Phosphate Type), Moscow: Energoatomizdat, 1983.
2. Sharygin, L.M., Moiseev, V.E., Pyshkin, V.P., et al., *Neorg. Mater.*, 1983, vol. 19, no. 11, pp. 1899–1902.
3. Sharygin, L.M., Moiseev, V.E., Shtin, A.P., et al., *Radiokhimiya*, 1984, vol. 26, no. 2, pp. 156–161.
4. Sharygin, L.M., Muromskii, A.Yu., Moiseev, V.E.,

and Tsekh, A.R., *Zh. Prikl. Khim.*, 1996, vol. 69, no. 12, pp. 2009–2013.

5. US Patent 3730886.
6. RF Patent 2090944.
7. Laskorin, B.N., Goldobina, V.A., and Kopanev, A.M., *Tsvetn. Met.*, 1973, no. 1, pp. 22–24.
8. Laskorin, B.N., Goldobina, V.A., and Kopanev, A.M., *Tsvetn. Met.*, 1973, no. 2, pp. 21–22.
9. Mitchenko, T.E. and Belyakov, V.N., *Vysokochist. Veshch.*, 1989, no. 2, pp. 110–113.
10. Bortun, A.I. and Kvashenko, A.P., *Zh. Fiz. Khim.*, 1990, vol. 64, no. 7, pp. 1963–1966.
11. Vishnyakov, Yu.M., Malyshev, S.P., Pchelintsev, V.M., and Khoroshev, V.G., *Sudostroenie*, 1999, no. 3, pp. 44–48.
12. Lokshin, E.P., Ivanenko, V.I., Avsaragov, Kh.-M.B., et al., *At. Energ.*, 2002, vol. 92, no. 2, pp. 118–123.
13. RF Patent 2200994.
14. Lokshin, E.P., Ivanenko, V.I., Udalova, I.A., and Kalinnikov, V.T., *Radiokhimiya*, 2003, vol. 45, no. 4, pp. 357–361.

ISSN 1070-4272, Russian Journal of Applied Chemistry, 2008, Vol. 81, No. 5, pp. 765–770. © Pleiades Publishing, Ltd., 2008.
Original Russian Text © E.V. Shlyapunova, G.M. Sergeev, 2008, published in Zhurnal Prikladnoi Khimii, 2008, Vol. 81, No. 5, pp. 730–735.

PHYSICOCHEMICAL STUDIES OF SYSTEMS AND PROCESSES

Anion Chromatography and Redox Photometry in Potable Water Analysis

E. V. Shlyapunova and G. M. Sergeev

Lobachevsky Nizhni Novgorod State University, Nizhni Novgorod, Russia

Received December 26, 2006

Abstract—Anion chromatography with ANIEKS-N selective ion exchanger and redox photometry with an antimony(V) ionic associate as selective oxidizing agent were suggested for determination of low concentrations of toxic (F^-, Br^-, NO_2^-, NO_3^-) and biogenic (SeO_3^{2-}, I^-) ions in some potable waters available from central water supply systems and mineral water springs.

DOI: 10.1134/S1070427208050078

Anion chromatography is a versatile method for determination of the anionic composition of various potable waters [1, 2]. It should be noted that the material analysis of every water type has its specific features. Potable waters available from different water supply systems contain the analyzed components in low concentrations. In this situation, the best ion-chromatographic procedure is that with which the detection limit of, above all, toxic ions, F^-, Br^-, NO_2^-, NO_3 can be decreased [SanPiN (Sanitary Rules and Regulations) 2.1.4.1074-01]. At the same time, for mineral waters with their complex matrix composition, of primary importance is the selectivity of analysis [GOST (State Standard) 13273–88]. This makes problematic determination of the above-mentioned microcomponents in the presence of large amounts of sulfate, chloride, and hydrocarbonate ions.

These problems can be overcome using the universal conductometric detection method utilized in the available liquid chromatographs. However, this signal-recording procedure does not allow determination of nanogram amounts of biologically active selenite and iodide ions [3]. In this situation, it is expedient to apply two independent methods, ion chromatography (IC) and redox photometry. The latter enables determination of 10^{-4} mg l^{-1} of selenite and iodide ions in the presence of a large number of concomitant substances without additional preconcentration, separation, and masking procedures [4]. At the same time, under the correctly chosen chromatographic analysis conditions, the detection limits for the target analytes in the "standard" mixture comprised of F^-, Cl^-, Br^-, NO_2^-, NO_3^-, HPO_4^{2-}, and SO_4^{2-} ions can be decreased by an order of magnitude (relative to the commonly practiced methods [5, 6]), with the selectivity of analysis preserved at a sufficiently high level. The ion chromatography and redox photometry complement each other in the type of information they provide; they are characterized by good accuracy and resolution. These are reliable, easy to implement methods that do not require expensive instrumentation and reagents.

In this study we applied a combination of two methods, anion chromatography and redox photometry, to determination of some toxic and biogenic ions in potable waters available from central water supply systems and mineral water springs.

EXPERIMENTAL

We used a Tsvet-306 liquid ion chromatograph equipped with a conductometric cell. The chromatographic experiments were run in the two-column version: The separating column (100 × 6 mm) was packed with surface-grafted ANIEKS-N anion exchanger in the OH form (20-μm mesh), and the suppressing column (200 × 6 mm), with a strongly acidic KU-2 × 8 sulfonic cation exchanger in the H form (50-μm mesh). The ion-exchange resins were preliminarily freed from impurities by the known techniques. The columns and the conductometric cell were thermostated at 20.0 ± 0.2°C. At the detector outlet, a throttling column was placed to prevent carbon dioxide from entering the flow system. A

solution containing 2.8 mM $NaHCO_3$ and 2.0 mM Na_2CO_3 served as eluent; it was supplied at a rate of 3 ml min^{-1}. The solutions of the analytes were prepared in deionized water with the specific electric conductivity $\xi \leq 50$ μS m^{-1}. The content of the anions, mg l^{-1}, in the working standard solutions was varied within 0.1–50 for fluoride, 0.2–100 for chloride, 0.5–100 for hydrophosphate, bromide, and sulfate, and 1.5–100 mg dm^{-3} for nitrate and nitrite ions. The ultrapure and chemically pure grade salts utilized were freed from organic impurities and adsorbed moisture. The volume of the sample introduced was 50 μl (a loop sampler).

Sample preparation for analysis consisted in addition of an eluent "concentrate" (with $NaHCO_3$ and Na_2CO_3 concentrations by two orders of magnitude exceeding those mentioned above) in amount of 250 μl per 25 ml of the solution analyzed. If necessary, the sample was diluted with deionized water. With this sample preparation procedure, the results of processing of the chromatograms were unaffected by the "carbonate" peak. The calibration plots were constructed with the use of 5–7 solutions (five measurement runs). The content, mg l^{-1}, of the anions in the sample was calculated from the area of the chromatographic peaks (SAA-06 automatic data processing block). The correctness of the recommended ion-chromatographic technique was verified by the method of standard additions. The regular error was insignificant, since the difference between the results of analyses of the samples with and without addition falls within the confidence interval for this difference. The total relative error was estimated at 15–20% for the anion concentrations within 0.1–2 mg dm^{-3} and at 5–10% for those within 10–100 mg dm^{-3}.

In redox-photometric extraction determination of selenium(IV) and iodide ions, we used a toluene solution of the antimony(V) ionic associate. The latter is comprised of the anion of pentavalent antimony hexachloride complex and the cation of a basic dye, Crystal Violet. For preparing the ionic associate we used ultrapure grade metallic antimony, chemically pure grade sodium nitrite, ultrapure grade urea, analytically pure grade Crystal Violet purified by recrystallization, and concentrated H_2SO_4 and 6 M HCl solutions (ultrapure grade chemicals). A standard antimony(III) solution (10 ml; 1 μg l^{-1}) was poured into a separating funnel, into which 1 ml of 10% $NaNO_2$ solution was further added. The resulting mixture was stirred for 2 min to ensure Sb(III) oxidation to Sb(V). Excess oxidant was decomposed by adding 0.5 ml of saturated urea solution, after which 20 ml of double-distilled water and 3 ml of 0.2% solution of Crystal Violet were added. The colored ionic associate $[CVSbCl_6]$ was extracted with 30 ml of chemically pure grade toluene (in 10-ml portions). Along with the above-mentioned reagents, we used elemental selenium and ultrapure grade KI, whose standard solutions were prepared by known techniques. Also, we used chemically and ultrapure grade HCl, HNO_3, CH_3COOH, and NH_4OH.

The experiments in which $[CVSbCl_6]$ reacted with the analyzed reducing agents were run in test tubes (170 × 17 mm) with ground-glass stoppers. To determine Se(IV), identical volumes (3 or 4 ml) of the toluene solution of the ionic associate, the standard solution, or analyzed water, as well as of the acetate–ammonia buffer solution with pH 6 were added into the test tubes. To get reproducible results, the contents of the test tubes was mixed in a vibromixer at 20 ± 2°C and a rate of 180–200 shakings per minute for a fixed period (20 min). The optical density of the organic layer was measured on an SF-46 spectrophotometer in a 1-cm-thick cell at λ = 615 nm. The molar absorption coefficient of the toluene solution of the ionic associate ε was (8.4 ± 0.4) × 10^4 mol^{-1} cm^{-1} l. A similar system in which the solution of the analyte was replaced by a "blank sample" served as the control. To decrease the contribution of the regular error into the accuracy of the results, the experiments with the analyzed solutions were paralleled by those with the blank sample.

In analysis of iodide ions we changed to the acetate–ammonia buffer solution with pH 3 and the mixing rate of 25–30 shakings per minute to prevent alterations of the analyte species and escape of elemental iodine from the reaction system. The techniques for determining the content of selenium(IV) and iodide ions in potable waters from water supply systems and in low-mineralized waters are similar to those described above. In the case of the waters containing over 2–3 g l^{-1} mineral salts, the sample preparation for Se(IV) analysis consisted in a 5–10-fold dilution of an aliquot (20–30 ml) of the sample with double-distilled water, followed by removal of the iodide ions. If the concentration of the iodide ions exceeded 10^{-2} mg l^{-1}, the diluted sample was heated on a water bath (60–80°C) for 30–40 min with stirring to prevent the loss of the condensate.

The correctness of determination of Se(IV) and iodide ions in potable waters was verified by the

"additions" and "weighted portion variation" methods. We found that the results of analysis of the solutions containing selenium(IV) are unaffected by Se(VI), S(IV), As(III, V), Te(IV, VI), and iodide ions, whose weight proportions to Se(IV) are no greater than 50, 50, 10^6, 10^6, and 100, respectively. The iodide ions in the amount of 1×10^{-4} mg l^{-1} can be determined in the presence of a 10^6-fold excess of the carbonate, chloride, and sulfate ions, as well as of sodium, potassium, calcium, magnesium, and some other concomitant anions and cations. The relative error is within 20%. Table 1 lists the retention times, resolution of the chromatographic peaks, and metrological characteristics of the experimental results.

The nitrate ion exhibits enhanced affinity for the ANIEKS-N anion exchanger. The change in the retention time of NO_2^- in the anion mixture is due to the competing action of bromide. The NO_3^- and NO_2^- ions are separated with the resolution factor R_s of two, which is of special importance for determination of these toxic anions in a mixture; for chloride–monohydrophosphate and monohydrophosphate–bromide pairs, $R_s = 1.0$. The fluoride and chloride give sufficiently resolved signals unaffected by the "carbonate" peak. The detection limits achieved for the majority of the analyzed ions are 5–10 times lower than those in the similar IC method. It should be noted that the above-mentioned characteristics were achieved without the use of a preconcentration column whose application is not universally justified and typically leads to overlap of the chromatographic peaks for ion-exchange resins with particle size over 5–7 μm.

Thus, the correctly chosen selective sorbent and chromatographic analysis conditions can essentially expand the potentialities of the classical "basic" version of IC with conductometric detection. We found that the ratios of the maximum permissible concentrations of the analytes of interest in potable waters to the detection limits of the anions are as follows: Br^- 2, NO_2^- 6, F^- 50, NO_3^- 90, Cl^- 5000, and SO_4^{2-} 5000.

We studied the two-phase redox reactions of selenium(IV) with iodide ions, using antimony(V) hexachloride complex as the selective oxidizing agent.

Our experimental results and published data [7, 8] suggest that the ionic associate is involved in the following process occurring at the organic phase

Table 1. Retention times τ_R, chromatographic peak resolutions R_s, calibration plot slopes a,* detection limits, and range of detectable concentrations of the analyzed anions ($n = 5$; $P = 0.95$)

Anion	τ_R, min	R_s	$a \pm \Delta a$	c_{min}, mg l^{-1}	c, mg dm^{-3}
F^-	0.6		11.5 ± 0.2	0.03	0.1–50
		1.3			
Cl^-	2.4		6.71 ± 0.05	0.07	0.2–100
		1.0			
HPO_4^{2-}	3.4		5.13 ± 0.02	0.09	0.5–100
		1.0			
Br^-	8.6		4.81 ± 0.06	0.1	0.5–100
		1.5			
SO_4^{2-}	9.4		4.64 ± 0.07	0.1	0.5–100
		1.1			
NO_3^-	11.8		1.02 ± 0.06	0.5	1.5–100
		2.0			
NO_2^-	21.7		0.97 ± 0.05	0.5	1.5–100

* S, μV s = $(a \pm \Delta a)c$.

(o)|water (w) interface:

$$[CVSbCl_6]_{(o)} + 4H_2O + 2e \rightleftarrows CV^+_{(w)} + [Sb(OH)_4]^-_{(w)} + 6Cl^-_{(w)} + 4H^+_{(w)}. \quad (1)$$

The conventional redox potentials for reaction (1) vary from 0.78 (pH 2) to 1.0 V (pH 10). The optical density of the photometric organic layer decreases in proportion to the increase in the selenium(IV) concentration in the aqueous solutions analyzed. Selenium(IV) in the two-phase redox system exhibits the following specific features. The concentration of the Cl^- ions yielded by reaction (1) is sufficient for binding microamounts of Se(IV) into a chloride complex

$$HSeO_3^- + 6Cl^- + 5H^+ \rightleftarrows [SeCl_6]^{2-} + 3H_2O. \quad (2)$$

The Crystal Violet cation CV^+ acts as a phase-transfer catalyst transferring the substrate into the organic phase:

$$2CV^+_{(w)} + [SeCl_6]^{2-}_{(w)} \rightleftarrows [(CV)_2SeCl_6]_{(o)}. \quad (3)$$

Oxidation of the ion pair of the analyte proceeds as follows:

$$[(CV)_2SeCl_6]_{(o)} + 4H_2O - 2e \rightleftarrows SeO^{2-}_{4(w)} + 6Cl^-_{(w)} + 8H^+_{(w)} + 2CV^+_{(o)}. \quad (4)$$

Table 2. Parameters of the calibration dependence equations α(or β) = $(a \pm \Delta a)c + (b \pm \Delta b)$, detection limits, and ranges of detectable concentrations for the redox-photometric monitoring of the selenite and iodide ions ($n = 5$; $P = 0.95$).

Anion	Function	Parameter of equation		c_{min}, mg l^{-1}	c, mg l^{-1}
		$a \pm \Delta a$	$b \pm \Delta b$		
$HSeO_3^-$	α	48.6 ± 1.8	2.26 ± 0.13	5×10^{-5}	1×10^{-4}–1×10^{-3}
I^-	β	130 ± 6	0.012 ± 0.001	3×10^{-5}	1×10^{-4}–2×10^{-3}

The overall process can be described by the equation

$$[(CV)_2SeCl_6]_{(o)} + [CVSbCl_6]_{(o)} + 8H_2O \rightleftarrows 3CV^+_{(w)} + SeO^{2-}_{4(w)} + 12Cl^-_{(w)} + [Sb(OH)_4]^-_{(w)} + 12H^+_{(w)}. \quad (5)$$

The total concentration of Crystal Violet in the two-phase system remains unchanged. The calculations and experimental data suggest that reaction (5) goes at pH ≥ 6. This is the best pH value for selective determination of selenium(IV) in the presence of the variable-valence concomitant elements.

The measured parameter was the difference of the optical densities of the blank test A_0 and the analyzed solutions of the ionic associate A_{an}. We calculated the proportion of the ionic associate α_{as} that entered into the redox reaction, which is proportional to the selenium(IV) concentration: $\alpha_{as} = \Delta A/A_0$, where $\Delta A = A_0 - A_{an}$. The data obtained for the reaction of iodide ions with antimony(V) ionic associate suggest proceeding in the aqueous phase of the reactions yielding elemental iodine, a triiodide complex, and an ion pair of the analyte:

$$2I^- - 2e \xrightarrow[\leftarrow]{[CVSbCl_6]} I_2, \quad (6)$$

$$I_2 + I^- \rightleftarrows [I_3]^-, \quad (7)$$

$$CV^+ + [I_3]^- \rightleftarrows [CVI_3]. \quad (8)$$

In final stage (8), the Crystal Violet cation forms with the triiodide ion a product extracted with toluene.

The overall process occurring in the redox system can, apparently, be represented by the reaction

$$2[CVI_3]_{(o)} = [CVSbCl_6]_{(o)} + 4H_2O \rightleftarrows 3CV^+_{(w)} + 3I_{2(o,w)} + 6Cl^-_{(w)} + [Sb(OH)_4]^-_{(w)} + 4H^+_{(w)}. \quad (9)$$

Reactions (6)–(9) are confirmed by an increase in the optical density of the organic layer with increasing iodide concentration in the aqueous solution. Also, the calculated data proved to be identical to the experimental results for the standard solutions containing various amounts of the equimolar mixture of iodide ions and elemental iodine. To calculate the coefficients in the calibration dependence equation, we estimated the proportion β of the product of reaction (8): $\beta_{as} = \Delta A/A_0$, where $\Delta A = A_{an} - A_0$. The parameters A_0 and A_{an} designate the optical densities of the blank sample and the toluene solutions of the ionic associate subjected to photometric analysis, respectively. Table 2 lists the parameters of the calibration equations and detection limits of selenium(IV) and iodide ions. The c_{min} parameters were calculated using the tripled standard deviation of the background signal, taking into account the corresponding sensitivity coefficients.

The main advantage offered by the suggested redox-photometric techniques consists in selective determination of low concentrations of Se(IV) and iodide ions with the available instruments and reagents. The method we proposed successfully competes with state-of-the-art instrumental control methods [9–11]. Table 3 presents the results of the ion-chromatographic and redox-photometric analyses of the water available from some mineral water springs and central water supply systems, containing F^-, Cl^-, NO_3^-, SO_4^{2-}, I^-, and SeO_3^{2-} ions.

For analysis we used 5–7 samples of each mineral water brand. The Fisher's F and Student's t tests revealed no difference in the content of the analytes in different batches of the products with the same trademark or for containers made of different materials. The Vetluzhskaya mineral water contains, along with a large amount of chlorides and sulfates, increased concentrations of fluorides and nitrates compared to other mineral waters. The amount of the fluoride ions is identical to that calculated from the solubility product of the CaF_2 mineral. The Sarovo, Diveevskaya, Ya, and Borzhomi Rodniki mineral waters are characterized by low concentra-

Table 3. Results of the ion-chromatographic and redox-photometric analyses of the waters available from some mineral water springs and central water supply systems ($n = 5$, $P = 0.95$)

Sample*	Fluoride	Chloride	Nitrate	Sulfate	Iodide,** $c \times 10^4$	Selenite,** $c \times 10^4$
	mg l^{-1}					
Mineral water:						
Sarovo[1]	$<c_{min}$	1.8 ± 0.3	2.1 ± 0.4	16 ± 3	2.5 ± 0.3	5 ± 1
Vetluzhskaya[1]	6.0 ± 0.4	1230 ± 50	160 ± 10	3640 ± 220	1.0 ± 0.2	7.6 ± 0.3
Gorkovskaya-2[1]	3.0 ± 0.3	5.2 ± 0.6	25 ± 3	2200 ± 150	1.9 ± 0.3	6.4 ± 0.8
Ya[2] (Vladimir)	0.46 ± 0.07	0.9 ± 0.2	$<c_{min}$	2.4 ± 0.5	2.1 ± 0.3	3.8 ± 0.5
Borzhomi Rodniki[3]	$<c_{min}$	2.3 ± 0.5	4.3 ± 0.8	4.2 ± 0.7	2500 ± 200	17 ± 3
Water from central water supply system:						
Nizhni Novgord	$<c_{min}$–0.5	5–16	3–7	70–80	$<c_{min}$	2–4
Krasnye Baki*[4]	1.5 ± 0.2	1.0 ± 0.1	$<c_{min}$	8 ± 1	$<c_{min}$	2.7 ± 0.4
Bor*[4]	$<c_{min}$	2.7 ± 0.5	$<c_{min}$	39 ± 4	$<c_{min}$	3.2 ± 0.5

* Waters characterized by the nitrite, bromide, and hydrophosphate content under c_{min}: [1–3] mineral waters: [1] Russia, Nizhni Novgorod oblast; [2] Russia, Vladimir oblast; [3] Georgia, Borzhomi (spring no. 1, Daba deposit) and [4] waters from the centralized water supply system (artesian wells).
** Determined by the redox-photometric method.

tions of the above-mentioned analytes in comparison with Gor'kovskaya-2 and Vetluzhskaya mineral waters.

The potentialities of the technique of interest were tested in analysis of some waters available from the central water supply systems. Among the tap waters from Nizhni Novgorod, Bor, Krasnye Baki, and Nizhni Novgorod oblast, the maximal content of sulfate ions and increased concentration of chlorides and nitrates are characteristic of Nizhni Novgorod water. The lowest concentration of the analyzed anions is observed for the tap water from Krasnye Baki settlement, extracted from a 75-m-deep artesian well. Interestingly, the Vetluzhskaya mineral curative table potable water with the anionic composition essentially different from that of the above-mentioned waters is extracted from a deeper aquifer well in the same raion of the Nizhni Novgorod oblast. For all the tap waters analyzed (Table 3) the content of each of the analytes is below the maximum permissible concentration established by the valid sanitary regulations.

As to the content of the selenite and iodide ions in the water from mineral water springs and the central water supply systems, we obtained the following results. In most cases, the concentration of these biogenic anions is equal to the background level, which validates the iodine and selenium deficiencies characteristic of waters in Nizhni Novgorod and Vladimir oblasts. Increased content of selenium(IV) was revealed for the Vetluzhskaya and Borzhomi Rodniki mineral waters. The water from the Borzhomi deposit is characterized by increased content of iodide ions, which is a distinctive feature of the Caucasian region waters. Despite the difference in the salt compositions of these mineral waters, the content of the fluoride and selenite ions (along with a high mineralization) for the Vetluzhskaya water and the iodide and selenite concentrations for the Borzhomi Rodniki water are suitable as authenticity labels for traded products.

Thus, by contrast to waters available from central water supply systems, mineral waters are characterized by diversified anionic compositions. In each case, the nature and concentration of the anions are predetermined by the geochemical processes of formation of natural waters in a specific region. The impurities contained in the waters can have both anthropogenic and technogenic origins. Hence, the authenticity of mineral waters can be established only on the basis of a complete set of data on the content of the macro- and microcomponents (including toxic and biogenic species).

CONCLUSIONS

(1) An ANIEKS-N selective anion exchanger and a carbonate eluent were suggested for decreasing the detection limits and improving the resolution

of the ion-chromatographic determination of the F^-, Br^-, NO_2^-, and NO_3^- toxic ions in potable waters.

(2) The redox-photometric method utilizing the antimony(V) ionic associate as the selective oxidizing agent provides information about the content of nanogram amounts of biogenic Se(IV) and I(I) species in waters from mineral water springs and central water supply systems.

REFERENCES

1. Shpigun, O.A. and Zolotov, Yu.A., *Ionnaya khromatografiya i ee primenenie v analize vod* (Ion Chromatography and Its Application to Water Analysis), Moscow: Mosk. Gos. Univ., 1990.
2. Jackson, P.E., *TRAC: Trends Anal. Chem.*, 2001, vol. 20, nos. 6–7, pp. 320–329.
3. Pirogov, A.V., Smolenkov, A.D., and Shpigun, O.A., *Ross. Khim. Zh.*, 2005, vol. 49, no. 6, pp. 31–40.
4. Shlyapunova, E.V., Abstracts of Papers, *11-ya Nizhegorodskaya sessiya molodykh uchenykh* (11th Nizhni Novgorod Session of Young Scientists), Nizhni Novgorod, April 16–20, 2006, Nizhni Novgorod: Nizhegor. Gos. Univ., 2006, pp. 171–172.
5. Vyacheslavova, I.P., Klein, L.A., Rakhmankulov, Sh.M., et al., *Zavod. Lab.: Diagnost. Mater.*, 1998, vol. 64, no. 3, pp. 5–10.
6. Safonova, E.F., Selemenev, V.F., Chikin, G.A., and Lobanova, O.A., *Teor. Prakt. Sorbts. Prots.*, 1999, no. 24, pp. 51–53.
7. Shevchuk, I.A., *Ekstraktsiya organicheskimi osnovaniyami (ionnye assotsiaty)* (Extraction with Organic Bases (Ionic Associates)), Kiev: Vishcha Shkola, 1978.
8. Tur'yan, Ya.I., *Okislitel'no-vosstanovitel'nye reaktsii i potentsialy v analiticheskoi khimii* (Redox Reactions and Potentials in Analytical Chemistry), Moscow: Khimiya, 1989.
9. Garifzyanov, A.R., Toropova, V.F., Budnikov, G.K., and Gainutdinova, D.F., *Zavod. Lab.: Diagnost. Mater.*, 2001, vol. 67, no. 1, pp. 3–15.
10. Stozhko, N.Yu., Morosanova, E.I., Kolyadina, L.I., and Fomina, S.V., *Zh. Anal. Khim.*, 2006, vol. 61, no. 62, pp. 170–178.
11. Eickorst, T. and Seubert, A., *J. Chromatogr. A*, 2004, vol. 1050, no. 1, pp. 103–109.

ISSN 1070-4272, Russian Journal of Applied Chemistry, 2008, Vol. 81, No. 5, pp. 771–775. © Pleiades Publishing, Ltd., 2008.
Original Russian Text © M.V. Maslova, L.G. Gerasimova, N.V. Motina, 2008, published in Zhurnal Prikladnoi Khimii, 2008, Vol. 81, No. 5, pp. 736–740.

PHYSICOCHEMICAL STUDIES OF SYSTEMS AND PROCESSES

Sorption of Cs^+ and Sr^{2+} by Ion Exchanger Based on Titanium Phosphate

M. V. Maslova, L. G. Gerasimova, and N. V. Motina

Tananaev Institute of Chemistry and Technology of Rare Elements and Mineral Raw Materials, Kola Scientific Center, Russian Academy of Sciences, Apatity, Murmansk oblast, Russia

Received November 2, 2007

Abstract—Sorption capacity of a composite ion exchanger based on titanium phosphate for Cs^+ and Sr^{2+} cations was studied. The effect of pH and concentration of salts and, in particular, sodium chloride in solution on the sorption efficiency and distribution coefficient was analyzed. The diffusion coefficients were calculated for the Cs^+ and Sr^{2+} cations and the time of half-exchange of the Na^+ cation for the Cs^+ and Sr^{2+} cations was found.

DOI: 10.1134/S107042720805008X

An inevitable consequence of exploitation of any object at which radioactive substances are mined, processed, or used is that a liquid radioactive waste (LRW) is formed. The considerable decrease in the volume of the final radioactive product in selective sorption predetermines the advantage of this technique over other methods for LRW processing because of its ability to concentrate radionuclides in a small volume of a sorbent. The sorption material should exhibit selectivity and high capacity for the radionuclides being recovered, possess a certain chemical stability and mechanical strength, and be readily available and stable in prolonged storage. Ion-exchange materials based on titanium phosphates have selective properties with respect to Cs^+ and Sr^{2+} radionuclides [1–3]. Granulated titanium phosphate can be used for a long time in contact with weakly alkaline or weakly acidic aqueous media without being changed to any significant extent. The observed disintegration of the material is slow and not catastrophic [4, 5]. It is known that spent inorganic ion exchangers are well compatible with cement matrices. A heat treatment of a mixture of this kind before disposal can markedly diminish the volume of radioactive waste [6]. All these prerequisites make titanium phosphates a promising collector of radionuclides.

This study is concerned with ion-exchange properties of a new composite sorbent that contains, in addition to titanium(IV) phosphate, hydrated silica, up to 3 wt % in terms of SiO_2. The conditions in which a material of this kind can be obtained were described in detail in [7–9].

EXPERIMENTAL

The composite sorbent was studied in the Na^+ form. Cs^+ and Sr^{2+} cations were sorbed under static conditions from chloride solutions of concentration 0.01 M in terms of Cs^+ and Sr^{2+} cations. A 0.5-g portion of the sorbent was brought in contact with a solution with a prescribed pH value adjusted by addition of 1 N solutions of NaOH or HCl. The liquid to solid phase mass ratio was 1 : 200. After the equilibrium was attained, the solution was separated from the sorbent, the filtrate was analyzed, and the analytical data were used to calculate the amount of the adsorbed substance in weight percent relative to the initial value. Figure 1 shows

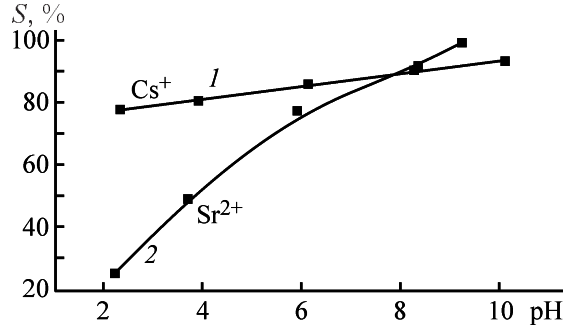


Fig. 1. Sorption of Cs^+ and Sr^{2+} cations from chloride solutions vs. pH. (*S*) Degree of sorption.

Table 1. Effect of the salt composition of the solution on the distribution coefficient

NaCl, M	K_d	
	Cs^+	Sr^{2+}
0	88 466	66 723
0.05	16 589	27 851
0.1	6133	6083
0.25	2003	1056
0.5	1067	250
0.75	606	109
1.0	465	62
2.0	235	35

data on the sorbability of Cs^+ and Sr^{2+} in the pH range 2–10.

The behavior of heavy metal cations in sorption by titanium phosphate is determined by the number and quality of functional groups and by the structure of the sorbent. As regards the composite sorbent, it can be stated that the degree of sorption increases with pH for the elements studied. The presence of strongly acidic groups in the ion exchanger enables efficient purification of solutions to remove Cs^+ ions even at low pH values. The maximum degree of sorption for this ion is 92%, or 245 mg g^{-1}. The strong affinity of phosphate sorbents for Cs^+ is accounted for by the specific interaction of phosphate groups of the ion exchanger with the low-hydrated cesium ion.

The sorption activity of titanium phosphate toward the strontium cation strongly depends on pH of the starting solution. As the basicity of the solution increases, the degree of dissociation of the functional groups of the sorbent grows and, as a result, its ion-exchange capacity becomes higher. The composite ion exchanger under study, which contains titanium(IV) phosphate, is a microporous material and, therefore, the ion exchange is sterically hindered. The capacity of such an ion exchanger for strontium ions is 80 mg g^{-1} in acid media and becomes more than two times higher at pH 9–10.

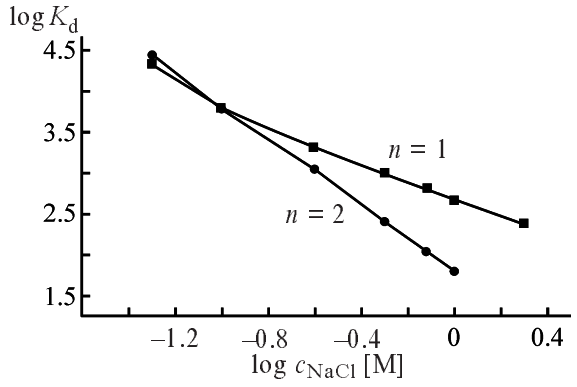


Fig. 2. Distribution coefficient K_d of cesium (n = 1) and strontium (n = 2) cations vs. the initial concentration c_{NaCl} in solution.

In a study of the sorption capacity of the ion exchanger in salt systems and, in particular, in a sodium chloride solution of concentration 0.05–2 M, the content of the microelement was 0.01 M and the l : s ratio was 1 : 200 (Table 1).

As the concentration of the electrolyte increases, the distribution coefficient K_d becomes smaller, which indicates that the sorption occurs by the ion-exchange mechanism. At up to 0.5 M of NaCl contained in the system, the distribution coefficient for Cs^+ is 10^4–10^3, and raising the NaCl concentration to 1–2 M leads to a decrease in K_d; for Sr^{2+}, K_d becomes less than 10^2. The selectivity can be regarded as a competition of cations of the solution, functional groups of the ion exchanger, and water molecules of both phases for the solvation of the ion being exchanged. Because of their dehydrating activity, the selectivity in concentrated salt solutions is higher for a larger ion (cesium), whose solvation demands are weaker than those of strontium ion.

According to the mass action law, the ion exchange in concentrated electrolyte solutions is expressed by the equation [10]

$$\log K_d = B - n\log c,$$

where c is the equilibrium electrolyte concentration; B, constant including the maximum exchange capacity of the ion exchanger and the exchange constant; and n, slope of the straight line, numerically equal to the ratio between the charges of the ion being exchanged and the ion of the macrocomponent.

This expression is valid at an insignificant intrusion of the electrolyte into the solid phase and a constant ratio between the activity coefficients. In the case of an ideal exchange, the distribution coefficient as a function of the electrolyte concentration should be expressed by a straight line with a slope n = 1 in Na^+–Cs^+ exchange and n = 2 for Na^+–Sr^{2+}. Data processing in terms of this equation suggests that the exchange of Cs^+ and Sr^{2+} ions at electrolyte concentrations in the range 0.05–2 M is nearly ideal (Fig. 2).

To analyze the statics of the interphase distribu-

tion, a set of samples with different concentrations of Cs^+ and Sr^{2+} ions in a 0.05 N solution of NaCl were prepared. The sample volume was 200 ml; weighed portion of the sorbent, 0.5 g; and time of contact between the phases, two weeks. During this time, an empirical equilibrium was attained in the system and dependences of the cesium and strontium concentrations in the sorbent on their equilibrium concentrations in solution were obtained using analytical data.

As seen from the results obtained (Fig. 3), the ion exchanger has a good sorption capacity for the metal ions under study. All the isotherms show a steep rise in the range of low equilibrium concentrations of these ions and a saturation limit from which the static capacity of the sorbent under the chosen conditions can be estimated. The amount of the cation absorbed by the ion exchanger steadily grows as its content in the starting solution increases to 400 mg l^{-1} and then remains constant, which is due to appearance of a diffusion hindrance to transport of cations across a layer of new formation on the sorbent surface. According to the degree of sorption (Fig. 4), the ion exchanger under study provides virtually complete purification to remove metal ions in solutions with initial concentrations of up to 200 mg l^{-1}.

For a more detailed analysis of the exchange of these ions, the Na^+–M^{n+} exchange constants (M^{n+} = Cs^+, Sr^{2+}) were determined by the static method at pH 7 (Table 2). The value of the ion exchange constant enables evaluation of the preferential sorption of one of the two ions being exchanged. The concentration exchange constant was calculated in accordance with the exchange reactions

$$Cs^+ + R\text{–}Na \rightleftarrows RCs + Na^+,$$

$$Sr^{2+} + 2R\text{–}Na \rightleftarrows R_2Sr + 2Na^+,$$

where R is the matrix of the ion exchanger with a bonded exchanging ion,

$$K = \bar{c}_{Cs^+} c_{Na^+}/(\bar{c}_{Na^+} c_{Cs^+}),$$

$$K = (\bar{c})^{1/2}_{Sr^{2+}} c_{Na^+}/(\bar{c}_{Na^+} c^{1/2}_{Sr^{2+}}),$$

where $\bar{c}_M$ is the concentration of the ions in the ion exchanger (mg-equiv g^{-1}), and c_M is that in solution (mg-equiv ml^{-1}).

The data obtained indicate that, in exchange of Na^+ for Cs^+, the exchange constant remains constant in the whole concentration range and independent of the ionic composition of the ion exchanger. The low-hydrated cesium ion is easily transferred into the inner zones of the ion-exchanger matrix and the ion exchange occurs without any noticeable hindrance. The average value of the exchange constant is 55.2, which is close to the data obtained previously [11] in a study of the sorbability of cesium on zirconium(IV) phosphates. In exchange of Na^+ for Sr^{2+} at solid phase compositions with an equivalent fraction $N_M < 0.3$, the exchange constant K_{ex} is virtually independent of the ionic composition of the ion exchanger and has an average value of 3.63, whereas at $N_M > 0.3$, K_{ex} sharply decreases. This fact can be accounted for by steric hindrance to incorporation of cations into the sorbent matrix and by the action of repulsion forces of likely charged counterions. The values obtained for the Na^+–Sr^{2+} exchange constant are an order of magnitude smaller than those for Na^+–Cs^+.

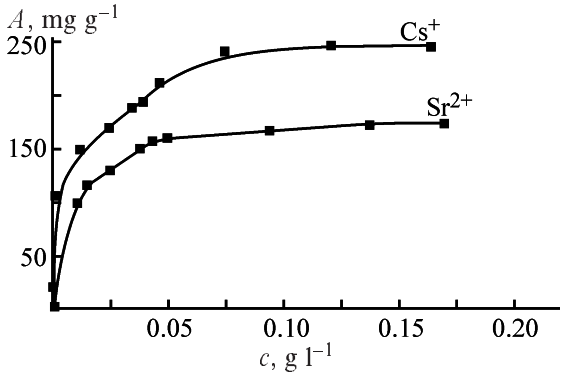


Fig. 3. Sorption isotherms of cesium and strontium cations. Temperature 25°C. (A) Static capacity of the sorbent and (c) concentration of Cs^+ and Sr^{2+}.

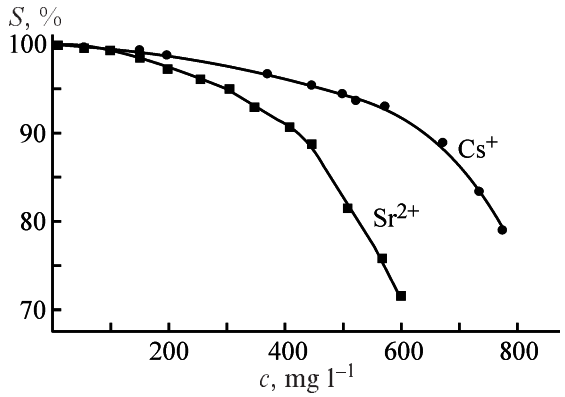


Fig. 4. Degree of sorption, S, vs. the initial concentration c of cesium and strontium cations in solution.

The sorption kinetics of cesium and strontium ions was studied at 25°C by the limited-volume method [12]. The concentration of the elements

Table 2. Concentration exchange constants of cesium and strontium ions in a 0.05 M solution of NaCl on titanium(IV) phosphate. Weighed portion of the ion exchanger 0.5 g, solution volume 200 ml

Initial concentration of metal in solution, $c \times 10^3$, mg-equiv ml^{-1}	Equilibrium concentration of M^{n+}		Concentration exchange constant
	in solid phase, mg-equiv g^{-1}	in liquid phase, mg-equiv ml^{-1}	
Cs^+:			
0.37	0.15	0.68×10^{-6}	56.3
0.75	0.3	0.62×10^{-5}	56.1
1.50	0.6	0.2×10^{-5}	55.5
3.0	1.15	0.12×10^{-3}	55.3
4.5	1.68	0.32×10^{-3}	52.7
Sr^{2+}:			
1.1	0.46	0.22×10^{-7}	3.72
2.28	0.91	1.7×10^{-7}	3.60
3.42	1.37	4.5×10^{-5}	3.58
4.56	1.82	9×10^{-5}	1.72
6.85	2.65	0.2×10^{-3}	1.22

Table 3. Kinetic parameters of the sorption of cesium and strontium cations by the composite ion exchanger based on titanium phosphate

t, min	Cs^+				Sr^{2+}			
	SEC, mg g^{-1}	F	Bt	$D \times 10^7$, cm^2 s^{-1}	SEC, mg g^{-1}	F	Bt	$D \times 10^7$, cm^2 s^{-1}
5	22.5	0.225	0.075	2.53	15.3	0.15	0.03	1.01
10	35.4	0.35	0.15	2.53	22.8	0.23	0.06	1.02
15	43.2	0.43	0.205	2.31	29.4	0.29	0.09	1.01
20	51.0	0.51	0.3	2.53	32.1	0.32	0.12	1.01
30	60.7	0.61	0.45	2.53	40.4	0.40	0.18	1.01
40	70.3	0.70	0.7	2.95	45.2	0.45	0.24	1.01

under study in solution was 100 mg g^{-1}; volume of the contact solution, 200 ml; and weighed portion of the sorbent, 1 g. The sorption was performed at pH 7.5; the starting solutions were thermostated at a prescribed temperature for 1 h and then the sorbent was introduced. The sorption was carried out with vigorous stirring at 300 rpm. By taking samples at certain intervals of time, the manner in which the concentration of the solution in contact with the ion exchanger varies until equilibration was determined.

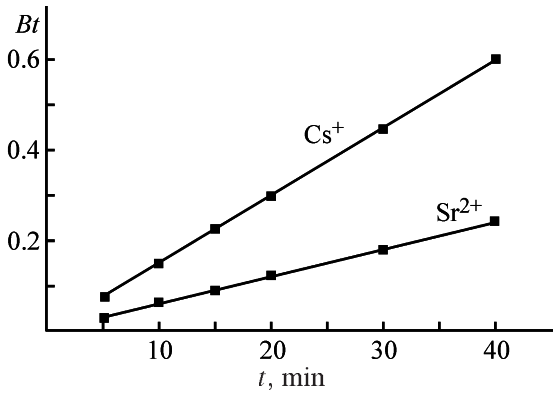


Fig. 5. Bt vs. time t.

The limiting stage of the process was determined by the interruption method. It was found that, after the process is interrupted, the absorption rate of the ions increases. Such a behavior is characteristic of the gel kinetics, in which the sorption rate depends on the diffusion of ions within the matrix of the ion exchanger.

The kinetic characteristics of the ion-exchange process whose limiting stage is the gel diffusion was approximately calculated using the rate equation of

the isotope exchange at a constant ion concentration in solution (Boyd's equation):

$$F = 1 - (6/\pi^2)\sum_{n=1}^{\infty}(1/n^2)\exp(-Dt\pi^2 n^2/R^2),$$

where $D\pi^2/R^2 = Bt$ is the kinetic coefficient; F, degree of equilibration; t, time (s); R, radius of ion exchanger particles (m); D, diffusion coefficient ($m^2\ s^{-1}$); and natural numbers n range from unity to infinity.

The degree of equilibration F was calculated by the formula $F = SEC_t/SEC_\infty$, where SEC_t and SEC_∞ ($mg\ g^{-1}$) are the amounts of ions sorbed by instant of time t and on reaching the maximum sorption. After an experimental determination of the degree of equilibration F by a prescribed time t, the dependences $Bt = f(t)$ were plotted using the reference value of Bt [13]. The plots (Fig. 5) are straight lines with a slope equal to B, which confirms the gel-diffusion control of the ion exchange on the ion exchanger under study. The diffusion coefficients were calculated by the formula $D = Btr^2/t\pi^2$ (Table 3).

The average values of the diffusion coefficient are 2.56×10^{-7} $cm^2\ s^{-1}$ for cesium ions and 1.01×10^{-7} $cm^2\ s^{-1}$ for strontium ions. The half-exchange time calculated by the formula $t_{1/2} = 0.03r^2/D$ is 1.5 min for Cs^+ and 50 min for Sr^{2+}.

CONCLUSIONS

(1) In a study of the sorption capacity of a composite ion exchanger based on titanium(IV) phosphate for Cs^+ and Sr^{2+} cations, the optimal range of pH values of solutions, in which the maximum degree of their purification is achieved, was found and substantiated.

(2) Raising the concentration of salts and, in particular, sodium chloride in solutions is accompanied by a decrease in the sorption efficiency, with a lower distribution coefficient characteristic of the more hydrated Sr^{2+} cation.

(3) The diffusion coefficients were calculated for the Cs^+ and Sr^{2+} cations and the time of half exchange of the Na^+ cation for the Cs^+ and Sr^{2+} cations was determined.

(4) The data obtained can be used for optimizing the purification of radionuclide-contaminated process wastewater.

ACKNOWLEDGMENTS

The study was financially supported by the Leading Scientific Schools grant no. NSh-4383.2006.3.

REFERENCES

1. Egorov, E.V. and Makarova, S.B., *Ionnyi obmen v radiokhimii* (Ion Exchange in Radiochemistry), Moscow: Atomizdat, 1971.
2. Amphlett, C. B., *Inorganic Ion Exchangers*, Amsterdam: Elsevier, 1964.
3. Milyutin, V.V., Gelis, V.M., and Penzin, R.A., *Radiokhimiya*, 1993, vol. 35, no. 3, pp. 76–82.
4. Mitchenko, T.E., Belyakov, V.N., Roitenberg, A.M., et al., *Zh. Prikl. Khim.*, 1986, vol. 59, no. 7, pp. 1440–1442.
5. Dolmatov, Yu.D., Bulavina, Z.N., and Pakholkov, V.S., *Ionity i ionnyi obmen* (Ion Exchangers and Ion Exchange), Leningrad: Khimiya, 1975.
6. Lokshin, E.P., Ivanenko, V.I., Avsaragov, Kh.B., et al., in *Sbornik nauchnykh dokladov VII Mezhdunarodnoi konferentsii "Ekologiya i razvitie Severo-Zapada Rossii"* (Proc. VII Int. Conf. "Ecology and Development of Northwestern Russia"), 2002, pp. 391–397.
7. Gerasimova, L.G., Matveev, V.A., Maslova, M.V., et al., *Tsvetn. Met.*, 2005, no. 3, pp. 87–91.
8. RF Patent 2207980.
9. Maslova, M.V., Gerasimova, L.G., and Chugunov, A.S., *Sorbts. Khromatogr. Prots.*, 2006, vol. 6, no. 6, part 2, pp. 1006–1011.
10. Griessbach, R., *Austauschadsorption in Theorie und Praxis*, Berlin: Akademie, 1957.
11. Bausova, N.V. and Moiseev, V.E., *Issledovanie sorbiruemosti rubidiya i tseziya iz khloridnykh sred na fosfatakh chetyrekhvalentnykh metallov* (Sorbability of Rubidium and Cesium from Chloride Media on Phosphates of Tetravalent Metals), Available from VINITI, 1978, no. 2598–78.
12. Polyanskii, N.G., Gorbunov, G.V., and Polyanskaya, N.L., *Metody issledovanii ionitov* (Methods for Studying Ion Exchangers), Moscow: Khimiya, 1976.
13. Saldadze, K.M., Pashkov, A.B., and Titov, V.S., *Ionoobmennye vysokomolekulyarnye soedineniya* (Ion-Exchange Macromolecular Compounds), Moscow, 1960.

ISSN 1070-4272, Russian Journal of Applied Chemistry, 2008, Vol. 81, No. 5, pp. 776–778. © Pleiades Publishing, Ltd., 2008.
Original Russian Text © I.B. Sladkov, M.A. Shmakova, 2008, published in Zhurnal Prikladnoi Khimii, 2008, Vol. 81, No. 5, pp. 741–743.

PHYSICOCHEMICAL STUDIES OF SYSTEMS AND PROCESSES

Critical Parameters of Tetraethyltin and Its Chlorine Derivatives

I. B. Sladkov and M. A. Shmakova

St. Petersburg State Polytechnic University, St. Petersburg, Russia

Received March 4, 2008

Abstract—Critical parameters of tetraethyltin and its chlorine derivatives were estimated by calculation methods. Reliability of the results obtained was confirmed by three independent methods.

DOI: 10.1134/S1070427208050091

Applications of organometallic compounds are steadily expanding and include such important chemical technologies as organic synthesis and fabrication of metallic coatings, plastics, semiconducting materials, etc. [1, 2]. Many organometallic compounds can be considered as derivatives of tetraethyltin $Sn(C_2H_5)_4$. The properties of tetraethyltin and its derivatives are studied poorly. For example, data on the critical parameters of these substances are lacking. At the same time, knowledge of these parameters allows many physicochemical properties to be predicted by calculation procedures based on the thermodynamic similarity theory [3, 4].

The goal of this study was to obtain data on the critical parameters of tetraethyltin and its chlorine derivatives. The choice of compounds was governed by the fact that available data on the properties of these compounds, from which the critical parameters may be predicted, are scarce.

The critical parameters (temperature T_{cr}, volume V_{cr}, and pressure P_{cr}) were calculated by formulas [5] that were already used for predicting the critical parameters of organometallic compounds.

$$T_{cr} = T_b/\theta, \quad (1)$$

$$V_{cr} = 80\Pi - 11, \quad (2)$$

where θ is the reduced temperature at the boiling point (T_b/T_{cr}), which was calculated by the relationship

$$\theta = 0.092\ln\Pi + 0.515, \quad (3)$$

where Π is parachor. Its numerical values were taken from [6, 7].

$$P_{cr} = 1.039T_{cr}/b, \quad (4)$$

where b is the van der Waals constant, which was calculated through the molar volume of a liquid at the boiling point by the equation [6]

$$b = 1.27V_b - 6. \quad (5)$$

The input data and the calculation results are listed in Table 1.

The reliability of the results obtained was assessed by three independent procedures. In the first procedure, the accuracy of the calculation formulas was checked with compounds that are thermodynamically similar to tetraethyltin, with the experimental critical parameters available from the literature. To such compounds belong tetraethylsilane and its chlorine derivatives. The input data are taken from [5], and the calculation results are listed in Table 2.

Table 1. Physicochemical properties of tetraethyltin and its chlorine derivatives [8–10]

Compound	Π, $J^{1/4}\ cm^{5/2}\ mol^{-1}$	T_b, K	V_b, $cm^3\ mol^{-1}$	T_b, K	V_{br}, $cm^3\ mol^{-1}$	P_{cr}, MPa
$Sn(C_2H_5)_4$	7.92	451.4	228.7	640	622	2.34
$Sn(C_2H_5)_3Cl$	7.13	483.0	202.6	694	559	2.87
$Sn(C_2H_5)_2Cl_2$	6.34	493.2	174.1	720	496	3.48
$Sn(C_2H_5)Cl_3$	5.55	468.0	155.8	696	433	3.77

Table 2. Error in calculating the critical parameters by Eqs. (1)–(5)

Compound	Calculation error, %		
	T_{cr}	V_{cr}	P_{cr}
$Si(C_2H_5)_4$	1.0	0.1	–8.8
$Si(C_2H_5)_3Cl$	0.7	0.5	–5.3
$Si(C_2H_5)_2Cl_2$	–0.1	1.1	0.6
$Si(C_2H_5)Cl_3$	–0.3	–1.6	–0.4
Mean absolute error	0.5	0.8	3.8

As seen from Table 2, the calculation equations used can ensure reasonably adequate prediction of the critical parameters for substances that are similar to those under consideration.

The second procedure for assessing the reliability of the results obtained consisted in the following. At present, methods based on the thermodynamic similarity theory with critical parameters of a substance as input data are used to predict with high reliability the density of molecular liquids. Experimental data on the density of liquid tetraethyltin at various temperatures are available from the literature [10]. The density was calculated from the equation based on the thermodynamic similarity theory using the T_{cr} and V_{cr} values obtained in this study. The comparison of the calculated densities with the experimental data can serve as criterion of the reliability of the critical parameters obtained. For this purpose, we calculated the density of liquid $Sn(C_2H_5)_4$ by the Matias equation [6]:

$$\rho = (M/V_{cr})[2(2 - T/T_{cr})]. \quad (6)$$

The calculation results are given in Table 3. As can be seen, they are similar to the experimental data.

Finally, the reliability of calculation of the critical parameters can be checked by a procedure of comparative calculation [6]. The procedure is based on the fact that, for similar substances, there is a linear correlation in variation of one property in two different series of the compounds (alternative 1) or of two different properties in the same series of the compounds (alternative 2).

The variation of each critical parameter in two series of similar substances was studied using alternative 1. Each series begins with tetraethyl derivative and ends with tetrachloride: EEt_4–EEt_3Cl–EEt_2Cl_2–$EEtCl_3$–ECl_4, where the E denotes element (Si or Sn) and Et, C_2H_5. The plot for the critical volume is shown in Fig. 1 as example. The scale of the critical volumes of the silicon compounds is given along the abscissa, and the scale of the critical volumes of the corresponding tin compounds, along the ordinate.

Table 3. Error in calculating the density of liquid $Sn(C_2H_5)_4$ from the critical parameters found in this study

T, K	ρ(calc.)	ρ(exp.) [10]	Deviation, %
	g cm^{-3}		
273	1.232	1.222	0.81
289	1.212	1.203	0.76
305	1.193	1.184	0.71
329	1.163	1.156	0.64
337	1.154	1.147	0.61
353	1.134	1.128	0.56
Mean error, %			0.7

The variations of the critical parameters with respect to any other property in the series of tin compounds, $SnEt_4$–$SnEt_3Cl$–$SnEt_2Cl_2$–$SnEtCl_3$–$SnCl_4$, were studied by alternative 2. The critical

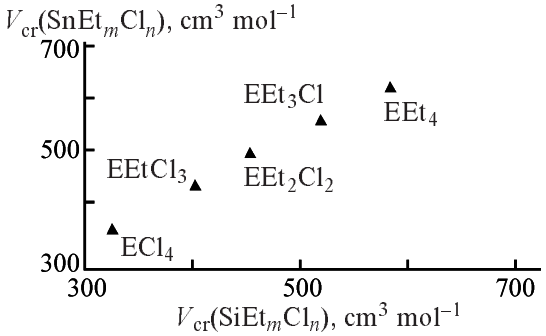


Fig. 1. Variation of the critical volume V_{cr} in the series of chlorine derivatives of tetraethyltin and tetraethylsilane.

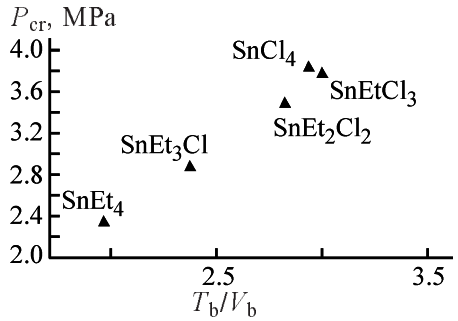


Fig. 2. Critical pressure P_{cr} vs. the T_b/V_b ratio in the series of similar tin compounds.

Table 4. Correlation coefficient r and root-mean-square error s for the dependences obtained by the comparative calculation procedure

Property	Alternative	Correlation	r	s
T_{cr}	1	Si compounds–Sn compounds	0.846	3.9
V_{cr}	1	Si compounds–Sn compounds	0.999	0.8
P_{cr}	1	Si compounds–Sn compounds	0.921	7.8
T_{cr}	2	T_{cr}–T_b	0.986	1.2
V_{cr}	2	V_{cr}–$\prod$	0.998	1.4
P_{cr}	2	P_{cr}–T_b/V_b	0.993	2.3

pressure vs. the ratio of the temperature to the molar volume at the boiling point is plotted in Fig. 2 as example.

The parameters of all the correlations considered, obtained by the comparative calculation procedure, are listed in Table 4. As can be seen, the degree of linearity is always high and the root-mean-square error is always comparatively small.

The data presented confirm reliability of the critical parameters of tetraethyltin and its chlorine derivatives obtained in this study.

REFERENCES

1. Razuvaev, G.A., Gribov, B.G., and Domrachev, G.A., *Metalloorganicheskie soedineniya v elektronike* (Organometallic Compounds in Electronics), Moscow: Nauka, 1972.
2. Efremov, E.A., Fedorov, V.A., and Grinberg, E.E., *Vysokochist. Veshch.*, 1988, no. 3, pp. 5–43.
3. Reid, R.G., Prausnitz, J.M., and Sherwood, T.K., *The Properties of Gases and Liquids*, New York: McGraw-Hill, 1977.
4. Filippov, L.P., *Podobie svoitsv veshchestv* (Similarity of Substance Properties), Moscow: Mosk. Gos. Univ., 1976.
5. Shoshkova, N.S., and Sladkov, I.B., *Zh. Prikl. Khim.*, 2006, vol. 79, no. 2, pp. 211–214.
6. Morachevskii, A.G., and Sladkov, I.B., *Fiziko-khimicheskie svoistva molekulyarnykh neorganicheskikh soedinenii* (Physicochemical Properties of Molecular Inorganic Compounds), St. Petersburg: Khimiya, 1996.
7. Sladkov, I.B., *Zh. Prikl. Khim.*, 1999, vol. 72, no. 8, pp. 1266–1272.
8. Kaufman, H.C., *Handbook of Organometallic Compounds*, New York: VNCI, 1961.
9. Sladkov, I.B., *Zh. Prikl. Khim.*, 2000, vol. 73, no. 5, pp. 727–732.
10. *Gmelin Handbook of Inorganic Chemistry. Organic Compounds of Zinc*, New York: Springer, 1975, vol. 26, part 1.

ISSN 1070-4272, Russian Journal of Applied Chemistry, 2008, Vol. 81, No. 5, pp. 779–785. © Pleiades Publishing, Ltd., 2008.
Original Russian Text © T.S. Markova, O.V. Yanush, 2008, published in Zhurnal Prikladnoi Khimii, 2008, Vol. 81, No. 5, pp. 744–750.

PHYSICOCHEMICAL STUDIES OF SYSTEMS AND PROCESSES

Correlation of Charge Transfer and *d–d* Transition Spectra of Cobalt(II) Bromide Solutions in Trimethyl Phosphate

T. S. Markova and O. V. Yanush

St. Petersburg State Technological University of Vegetable Polymers, St. Petersburg, Russia

Received June 2, 2006

Abstract—Solutions of cobalt(II) bromide in trimethyl phosphate were studied by electronic spectroscopy at 20 and 60°C.

DOI: 10.1134/S1070427208050108

The data on the charge transfer (CT) and *d–d* transition spectra of transition metal complexes in relation to the composition of an interglass polymeric matrix are necessary for developing modern light-variable and energy-saving glasses. Trimethyl phosphate (TMP) is known as a plasticizer of polymeric compounds used for this purpose. It has a high donor number and a low solvating power with respect to halide ions, which makes it possible to study properties of the entire diversity of cobalt(II) complexes and to find general relationships of their mutual transformations depending on temperature, which is necessary for optimizating the properties of chromogenic materials.

Charge transfer spectra of transition metal halide complexes originate from the excitation of electrons on σ- and π-bonding or nonbonding orbitals localized predominantly on the ligand, with the transfer of these electrons onto vacant σ- and π-antibonding orbitals mainly localized on the central metal atom [1]. The CT spectra of cobalt tetrahalide complexes $[CoHal_4]^{2-}$ (Hal is a halide ion) have been studied in detail in crystals [2–4] and solutions [3, 4]. However, the dependence of the spectral position and intensity of CT bands on the metal coordination number and on the covalence of M–L bonds [2–5] were not studied. Furthermore, actually it was not determined whether the CT and *d–d* transition spectra could be assigned to the same complexes. At the same time, these problems are of basic importance for developing light-variable materials [6–8], as CT spectra can be used for shielding undesirable short-wave solar radiation.

To study spectroscopic features and correlations of CT and *d–d* absorption bands for each type of complexes (with different symmetry and different numbers of halide ions), we have chosen solutions of cobalt(II) bromide complexes in TMP as a model system. Furthermore, this solvent is one of plasticizers of polymeric compounds suitable for fabricating light-variable devices.

The results of this study can be used for developing real thermochromic systems (solutions and films) with variable optical transmission, which should contain water as an essential component [7, 8, 11] and should be highly concentrated with respect to the content of pigments (0.1–1.0 M). Therefore, we studied in addition the relationships of the complex formation as influenced by the water content of the system.

EXPERIMENTAL

To prepare solutions of cobalt nitrate $[Co(NO_3)_2 \cdot 6H_2O]$ or bromide $(CoBr_2 \cdot 6H_2O)$ in TMP with LiBr additions, we used 0.5 M solutions of these salts (pure grade). Correspondingly, such solutions contained no less than 3 M H_2O. The content of anhydrous LiBr was varied within the limits of its solubility (0–7.5 M). In what follows, we will designate such systems as $Co(NO_3)_2 \cdot 6H_2O$–LiBr–TMP.

To reveal the role of water in the complex formation, it was added to the anhydrous system $CoBr_2$–LiBr–TMP in amounts of 0–13 M. Anhydrous cobalt bromide was prepared by calcining $CoBr_2 \cdot 6H_2O$ at 130–140°C for 8 h.

Preliminarily it was shown by IR spectroscopy of TMP–H_2O solutions (analytical frequency 3350 cm^{-1}) that 1 mol of TMP is capable of binding

up to 0.25 mol of water; at a higher water content, its state changes, as seen from a break of the plot of the optical density at $\nu = 3350$ cm^{-1} vs. water concentration. Trimethyl phosphate dried for 400 h over dehydrated (for 7 h at 200°C) $MgSO_4$ was purified by vacuum distillation. According to the IR spectral data, the solution thus obtained contained less than 0.25 M H_2O. The study of the effect of water additions was also of practical interest, as an increase in its content can enhance the performance of thermochromic materials [7, 8].

Cobalt(II) bromide solutions in TMP were prepared at 60°C, and "freshly prepared" samples were studied (*d–d* transitions and CT spectra were measured within 1–2 h after the synthesis), as the solutions are unstable. With time, especially at elevated temperatures, a solid phase is formed in the solutions. According to the IR spectra, it is a product of the reaction of lithium bromide with TMP (when lithium bromide is added to TMP, a band in the region of 3350 cm^{-1} appears in the IR spectrum of TMP, which disappears upon precipitation of the solid phase). These reactions, which proceed slowly at room temperature (in the course of days and weeks) and faster on heating, were monitored by electronic absorption spectra taken at certain intervals, in particular, every 15–20 min during heating at 100°C until a stable chemical equilibrium was attained in solutions. It was found that in the anhydrous system $CoBr_2$–LiBr–TMP the decomposition of high-halide anionic complexes and the formation of low-halide onium complexes are faster than in the system $Co(NO_3)_2 \cdot 6H_2O$–LiBr–TMP containing water.

The IR and electronic absorption spectra of solutions were recorded on computerized Specord M-80 and Specord M-40 spectrophotometers at a spectral slit width from 20 to 40 cm^{-1} at 20 and 60°C in quartz or fluorite cells temperature-controlled to within 1°C.

The spectra of individual complex species were resolved from the total electronic spectra by the Wallace–Katz method [12] consisting in the determination of the number of linearly independent rows of the optical density matrix at fixed frequencies in each experimental spectrum, which allowed the number of the complexes coexisting in solutions to be objectively estimated. To determine the structure of CT and *d–d* absorption bands more precisely, we examined even derivatives of the initial spectra.

The extinction coefficients of the strongest absorption bands of the resolved spectra belonging to individual complexes were calculated by the balance equation

$$\Sigma (D_i/\varepsilon_i) = c_{MCo^{2+}}, \quad (1)$$

where D_i is the optical density in the absorption band maximum; ε_i, peak extinction coefficient (l cm^{-1} mol^{-1}); and $c_{MCo^{2+}}$, total cobalt concentration in solution, M.

To obtain additional information on the properties of complexes,[1] we studied positions of centers of gravity λ_{cg} [Eq. (2)], integral extinction coefficient [Eq. (3)], and effective half-width of *d–d* absorption bands [Eq. (4)] as functions of the content of bromide ions in solutions.

$$\lambda_{cg} = \int_{400}^{800} D(\lambda)\lambda d\lambda / \int_{400}^{800} D(\lambda) d\lambda, \quad (2)$$

$$\varepsilon^{int} = \int \varepsilon(\lambda) d\lambda, \quad (3)$$

$$\Delta\lambda_{eff} = \left[\int D(\lambda) d\lambda / D^{max} \right] \quad (4)$$

(the integrals were taken within the limits of the band contour).

The dependence of the absorption spectra of freshly prepared $Co(NO_3)_2 \cdot 6H_2O$–LiBr–TMP solutions on the concentration of bromide ions is shown in Fig. 1. Absorption bands assignable to cobalt(II) "internal" *d–d* transitions in octahedral [$^4T_{1g}(F) \rightarrow {}^4T_{1g}(P)$] or tetrahedral [$^4A_2(F) \rightarrow T_1(P)$] complexes are observed in the visible region, in the range 460–520 nm or 550–750 nm, respectively. The CT spectra caused by "intraligand transitions" (200–250 nm) [13, 14] and by transitions in cobalt(II) complexes between molecular orbitals localized on the ligand and metal ions (250–320 nm) [2–4] are located in the UV region.

The study of even derivatives of the spectra, especially in the region of $\nu_{max} = 700$ nm (Fig. 2), and the analysis by the Wallace–Katz method [12] allowed us to reveal four types of complexes in the whole examined range of bromide ion concentrations. We found only two species, $[CoBr_4]^{2-}$ and $[Co(TMP)Br_3]^-$, in the range of ratios Br/Co = 4.5–

[1] Mathematical treatment of the spectra and their resolution into components were carried out using Matlab 6.0 and MicroCal Origin 7.1 program packages.

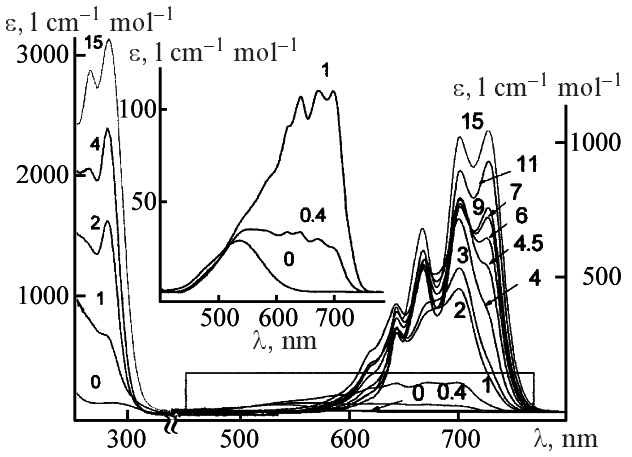


Fig. 1. Absorption spectra of "freshly prepared" $Co(NO_3)_2 \cdot 6H_2O$–LiBr–TMP solutions; insert shows the spectra at Br/Co = 0–1. T = 20°C, c_{Co} = 0.5 M. (ε) Molar extinction coefficient and (λ) wavelength; the same for Figs. 3 and 7. Figures at curves are the initial Br/Co molar ratios; the same for Fig. 2. The range 200–350 nm corresponds to the CT spectra, and the range 400–900 nm, to *d*–*d* transition spectra.

15. Examples of the resolution of spectra of the $Co(NO_3)_2 \cdot 6H_2O$–LiBr–TMP system into components are shown in Fig. 3.

As a result, in the visible region we have resolved the spectra corresponding to $[Co(TMP)_2Br_2]$, $[Co(TMP)Br_3]^-$, and $[CoBr_4]^{2-}$. Less reliably we resolved the spectra tentatively assignable to $[Co \cdot (TMP)_x(H_2O)_{6-x}]^{2+}$ and $[Co(TMP)_x(H_2O)_{5-x}Br]^+$, for which we failed to determine the TMP/H_2O ratio. We found that the resolution by the same procedure in the whole examined wavelength range (200–900 nm) automatically leads to constant (independent of solution composition) spectra for the revealed complex species in both the visible and UV ranges. The spectral forms of absorption bands found in the UV and visible ranges are shown in Fig. 3c, and the diagram of the content of complexes built using Eq. (1), in Fig. 4.

The validity of this diagram (Fig. 4) is supported by the dependences of the effective half-width $\Delta\lambda_{eff}$ and intensities of the spectra in maxima on the system composition. We found that the enrichment of a solution with one type of complexes, i.e., without overlap of absorption bands of different complexes, results in a decrease in $\Delta\lambda_{eff}$ and in the appearance of relatively narrow strong bands in accordance with the speciation diagram, for both CT and *d*–*d* bands. Spectroscopic characteristics of *d*–*d* absorption bands and CT bands (these latter are determined

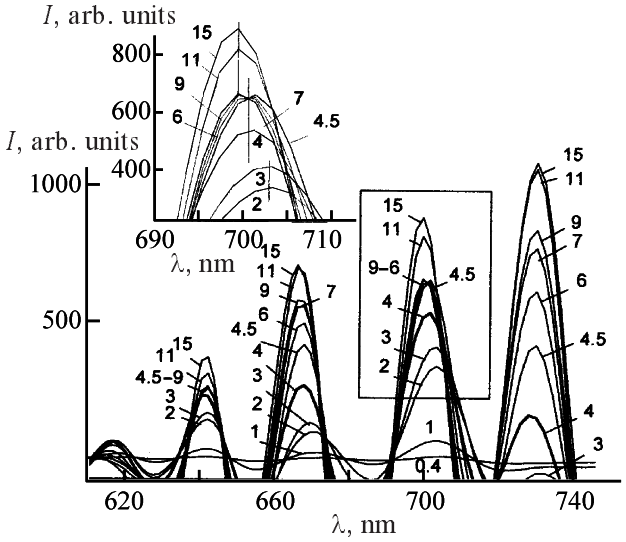


Fig. 2. Second derivatives of *d*–*d* transition spectra of $Co(NO_3)_2 \cdot 6H_2O$–LiBr–TMP solutions. (*I*) intensity and (λ) wavelength.

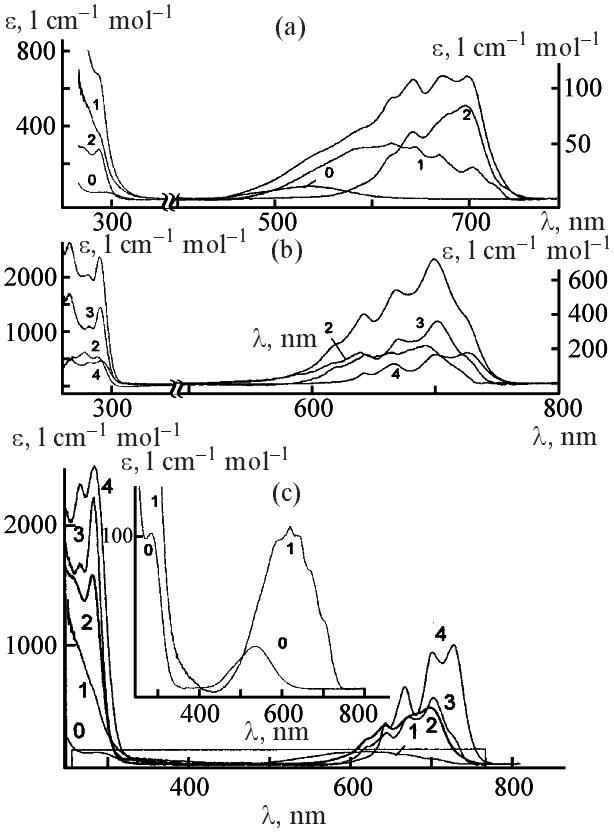


Fig. 3. Examples of the resolution of the absorption spectra of $Co(NO_3)_2 \cdot 6H_2O$–LiBr–TMP solutions into components at Br/Co (a) 1 and (b) 4 in the visible (*d*–*d* transitions) and UV (CT) ranges (c_{Co} = 0.5 M); (c) spectra of individual species. Figures at curves are numbers of bromide ions in complexes: (0) $[Co(TMP)_x(H_2O)_{6-x}]^{2+}$, (1) $[Co(TMP)_x(H_2O)_{5-x}Br]^+$, (2) $[Co(TMP)_2Br_2]$, (3) $[Co(TMP)Br_3]^-$, and (4) $[CoBr_4]^{2-}$; the same for Fig. 4.

Spectroscopic characteristics of CT and *d–d* absorption bands of the complexes revealed in the $Co(NO_3)_2 \cdot 6H_2O$–LiBr–TMP system at 20°C

Complex type	$\lambda_{max} \pm 1$, nm	$\lambda_{cg} \pm 1$, nm	ε_{max}, $l\ cm^{-1}\ mol^{-1}$	$\varepsilon^{int} \times 10^{-3}$,* $nm\ l\ cm^{-1}\ mol^{-1}$	$\Delta\lambda_{eff} \pm 1$, nm	ν_{max}, cm^{-1}	ε_{max}, $l\ cm^{-1}\ mol^{-1}$
	d–d Absorption bands					CT absorption bands	
$[Co(TMP)_x(H_2O)_{6-x}]^{2+}$	537	532	28.5 ± 0.5	2.9 ± 0.1	100	–	–
$[Co(TMP)_x(H_2O)_{5-x}Br]^{+}$	590	611	100 ± 10	16 ± 2	150	–	–
$[Co(TMP)_2Br_2]$	697	664	480 ± 50	40.1 ± 0.9	93	35600	1500 ± 80
$[Co(TMP)Br_3]^{-}$	702	678	560 ± 10	41.5 ± 0.8	61	35360	2000 ± 90
$[CoBr_4]^{2-}$	727	693	1000 ± 50	77 ± 4	82	35270	2500 ± 100

* (ε^{int}) Integral extinction coefficient determined by Eq. (3) and (ν_{max}) position of the maximum, determined for the lowest-frequency CT band.

less accurately because of overlap with intraligand bands) of the complexes revealed in the $Co(NO_3)_2 \cdot 6H_2O$–LiBr–TMP system are given in the table.

Coincidence of the data on the content of complexes (Fig. 4), found by the analysis of CT and *d–d* transitions, confirms the assignment of the spectra in the UV and visible regions to the same complexes. When the composition of complexes varies owing to variations in the ligand field strength and in the symmetry of environment, spectral properties of the *d–d* and CT bands (see table, Fig. 5) correlate with each other. Sequential replacement of trimethyl phosphate ligands by bromide ions in the inner coordination sphere of tetrahedral cobalt complexes gives rise to a gradual increase in the extinction coefficients of *d–d* and CT absorption bands (ap-

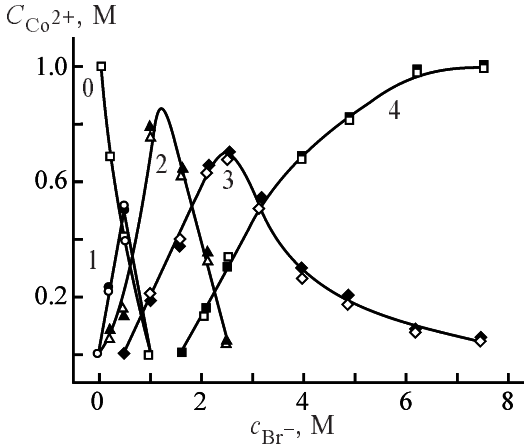


Fig. 4. Relative content of complexes in $Co(NO_3)_2 \cdot 6H_2O$–LiBr–TMP solutions at 20°C, calculated on the basis of resolution of the visible spectra (*d–d* transitions, "filled" symbols) and UV spectra (CT, empty symbols) into components. ($c_{Co^{2+}}$) Concentration of cobalt(II) ions and (c_{Br^-}) concentration of bromide ions.

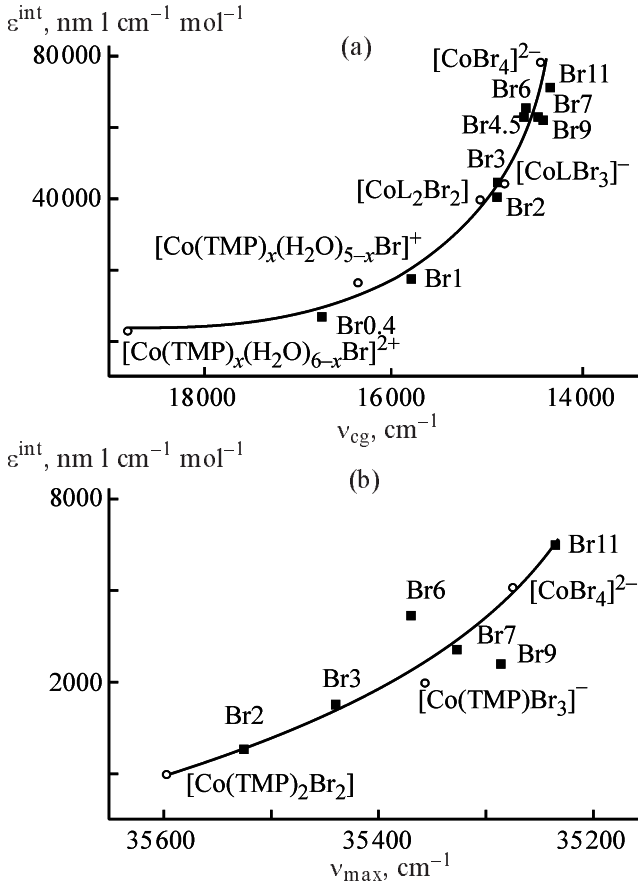


Fig. 5. Correlation of the dependences of extinction coefficients and positions of the maxima for (a) *d–d* and (b) CT bands in the resolved spectra of the indicated complexes (empty symbols) and in the total spectra of $Co(NO_3)_2 \cdot 6H_2O$–LiBr–TMP solutions (filled symbols; Br*N*, ratio of the initial molar concentrations Br/Co in solutions). (ε^{int}) Integral molar extinction coefficient, (ν_{cg}) position of the center of gravity of the absorption band, (ε_{max}) molar extinction coefficient in the maximum, and (ν_{max}) frequency of the maximum.

proximately twofold for both peak extinction coefficients of low-frequency maxima in CT spectra and integral extinction coefficients of *d–d* absorption bands), accompanied by their long-wave shift.

This correlation can be accounted for by the fact that, in the charge transfer, an electron is transferred from a ligand molecular orbital [2] to the same excited level of Co^{2+} *d* shell as in the *d–d* transition. The low-frequency shift of *d–d* absorption bands can be interpreted as a consequence of the fact that the ligand field becomes weaker as the fraction of bromide ions in the complex increases. For the examined absorption bands of *d–d* transitions, the shift ν_{cg} of the center of gravity is 1300 cm^{-1} in going from $[Co(TMP)_2Br_2]$ to $[CoBr_4]^{2-}$, and for low-frequency components of the CT spectrum, ~300 cm^{-1} (Fig. 5). This difference is attributable to the fact that *d–d* transitions occur from the $^4A_2(F)$ term and that the position of its center of gravity does not remain constant on varying composition of complexes.

As to the intensity of the spectra, according to the common reasoning [1], it can be expected that the oscillator strength of *d–d* transitions should increase as the symmetry of complexes decreases in the series $[CoBr_4]^{2-} > [Co(TMP)_2Br_2] > [Co(TMP)Br_3]^-$. This fact, together with the shift of bands toward the region of maximum sensitivity of human eye, would be attractive for developing materials with variable optical transmission. However, actually the trend is opposite (see table, Fig. 5). Similar trend was also found in the Co^{2+} (0.05 M)–LiBr (14 M)–LiCl (0–10 M)–H_2O system containing Br^- and Cl^- ligands strongly differing in the field strength. Here the extinction coefficients of the absorption bands decreased monotonously in the order $[CoBr_4]^{2-} > [CoBr_2Cl_2]^{2-} > [CoBrCl_3]^{2-} > [CoCl_4]^{2-}$ (Fig. 6).

The preservation of the high symmetry and "fine" structure of mixed tetrahalide complexes is attributable to certain delocalization of bonds and collectivization of the electron density in coordination compounds [1]. The preservation of strictly tetrahedral symmetry in the complexes $[CoBr_4]^{2-}$, $[Co(TMP)\cdot Br_3]^-$, and $[Co(TMP)_2Br_2]$ and the closeness of TMP and bromide ions in the ability for covalent bonding are manifested in the fact that, to a first approximation, even derivatives of the spectra of *d–d* transitions reveal the same maxima for different complexes (Fig. 2).

It was found that in all the examined solutions the extinction coefficients increase as ν_{max} of *d–d* and CT bands is shifted to lower frequencies (Fig. 5). The trend is described by the relationship $\ln\varepsilon^{int} \sim (-\nu_{cg})$. This common dependence can be attributed to the fact that the overlap of the wave functions increases as the energy eigenvalues approach each other, which results in an increase of the transition matrix element determining the intensity of the absorption band.

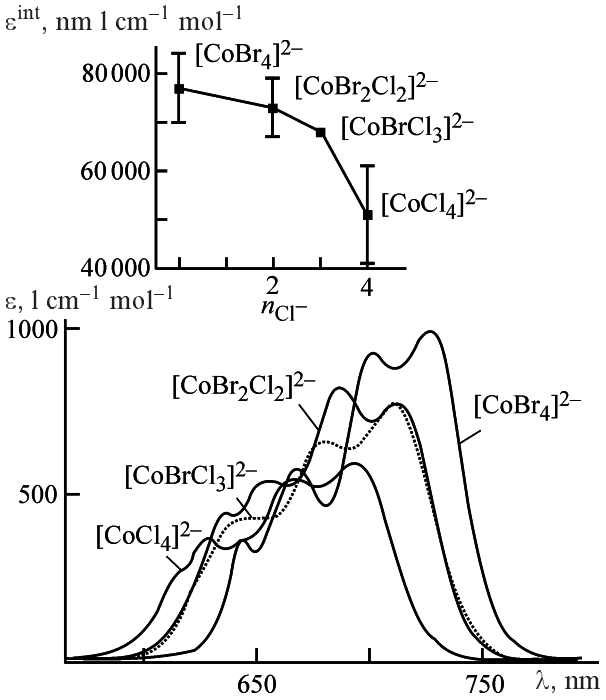


Fig. 6. Resolved components in the spectra of Co^{2+} (0.05 M)–LiBr (14 M)–LiCl (0–10 M)–H_2O solutions and a decrease in the integral extinction coefficients of *d–d* bands of these complexes in passing from $[CoBr_4]^{2-}$ to $[CoCl_4]^{2-}$ (insert). (ε^{int}) Integral molar extinction coefficient, (n_{Cl^-}) number of chloride ions in complexes, (ε) molar extinction coefficient, and (λ) wavelength.

It should be noted that the extinction coefficients of $[CoBr_4]^{2-}$ complexes for *d–d* bands (ε_{727} = 1000 ± 50 l cm^{-1} mol^{-1}) and CT bands (ε_{283} = 2500 ± 100 l cm^{-1} mol^{-1}) are characteristic and are the same in different media, e.g., in ethanol, water, and TMP. The outer-sphere effect of the solvent on the complex $[CoBr_4]^{2-}$ is manifested only in negligible (compared to the band width) shifts of the maxima, close to those observed for transition metals in nitrate melts [15]. The maximal shifts of the CT bands (about 300 cm^{-1} in the examined series of solvents) are larger by an order of magnitude than those for the *d–d* transitions (approximately 50 cm^{-1} in the same series), which is attributable to the weak effect of outer-sphere solvent molecules on the well-

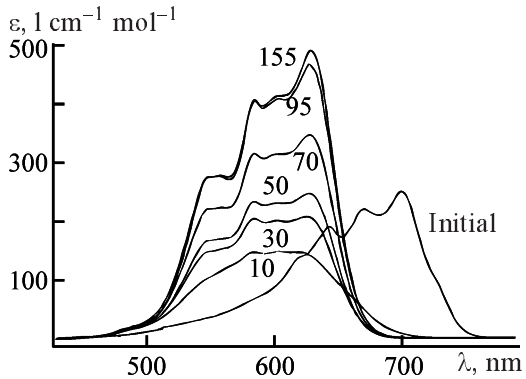


Fig. 7. Variation of the spectra of *d–d* transitions of TMP–$Co(NO_3)_2 \cdot 6H_2O$ (0.5 M)–LiBr (1 M) solution (Br/Co = 2) in the course of its heating at 100°C with the formation of an intermediate complex (10 min) and $[Co(TMP)_4]^{2+}$ (30, 50, 70, 95, and 155 min). The curve denoted as initial corresponds to the spectrum of the freshly prepared solution. Figures at curves denote heating time.

shielded levels of the *d* shell. The shifts of the CT bands are determined not only by the solvent effect on the excited state energy in the *d* shell, but also by the much stronger effect on the ligand electrons.

Unlike other high-donor solvents (e.g., H_2O), TMP has a low solvating ability toward bromide ions. Therefore, both TMP and bromide ions are equally capable to participate in the formation of the inner coordination sphere. It was found that the same spectral contour (Fig. 7, curves corresponding to 30, 50, 70, 95, and 155 min) appears in the spectra of all bromide systems under study (anhydrous and hydrated) and also of $Co(NO_3)_2 \cdot 6H_2O$–TMP and $CoI_2 \cdot 2H_2O$–TMP as a result of the ionization reactions

$$[CoBr_2(TMP)_2] + x\text{TMP} \rightarrow [CoBr_{2-x}(TMP)_{2+x}]^{x+} + x\text{Br}^-$$

occurring on heating, and also on long-term (for more than 1 month) storage of cobalt bromide solutions in TMP at room temperature. However, the complex giving this spectrum is not formed under the same conditions in cobalt chloride solutions in TMP. A high extinction coefficient (ε_{580} = 400 l cm^{-1} mol^{-1}), its weak temperature dependence, and also the structured character of the spectrum count in favor of the tetrahedral structure of this complex. Most likely, the composition of the cobalt complex with TMP containing no water, NO_3^-, Br^-, and I^- in the inner sphere can be presented as $[Co(TMP)_4]^{2+}$.

The results obtained show that the complex $[Co(TMP)_4]^{2+}$ is formed most rapidly in the system with iodide ions. In the case of bromide solutions, the formation of $[Co(TMP)_4]^{2+}$ is preceded by the formation of an additional "intermediate" complex (Fig. 7, curve for 10 min) apart from $[Co(TMP)_4]^{2+}$ and complexes in freshly prepared solutions (Fig. 3c). In the system with chloride ions, a certain low-halide complex is also formed, which is stable and is not converted to $[Co(TMP)_4]^{2+}$. These relationships are attributable to a greater strength of cobalt bonds with chlorine than with bromine and, the more so, with iodine.

The results of studying the absorption spectra show that small water additions comparable with those introduced with hydrates neither reduce the intensity, nor change the spectrum shapes within the first hours, which is accounted for by the hydration of lithium bromide in solutions. The analysis of changes in the intensities of the spectra of the systems under study in relation to the weight ratio of water and lithium bromide, analogous to that suggested in [16], allowed us to determine the average hydration number of lithium bromide equal to 4.06 ± 0.08, which agrees well with the data of other methods [17].

CONCLUSIONS

(1) The charge transfer spectra and the spectra of *d–d* transitions belong to the same complexes $[Co(TMP)_x(H_2O)_{6-x}]^{2+}$, $[Co(TMP)_2Br_2]$, $[Co(TMP)Br_3]^-$, and $[CoBr_4]^{2-}$.

(2) A correlation was found between the increase in the extinction coefficients and the long-wave shifts of charge transfer and *d–d* bands with the increase in the extent of bond covalence in the order $[Co(TMP)_2Br_2] < [Co(TMP)Br_3]^- < [CoBr_4]^{2-}$.

(3) The dependence $\ln \varepsilon^{int} \sim (-\nu_{cg})$, valid both for *d–d* bands of octahedral and tetrahedral cobalt(II) complexes and for charge transfer bands of tetrahedral cobalt(II) complexes, was obtained.

(4) The revealed relationships will be useful for developing high-performance thermochromic glasses.

ACKNOWLEDGMENTS

This study was financially supported by the Ministry of Education of the Russian Federation (project no. MO4-3.6K-352).

REFERENCES

1. Bersuker, I.B., *Elektronnoe stroenie i svoistva koordinatsionnykh soedinenii* (Electronic Structure and Properties of Coordination Compounds), Leningrad: Khimiya, 1987.
2. Bird, D.D. and Day, P., *J. Chem. Phys.*, 1968, vol. 49, no. 1, pp. 392–403.
3. Orgel, L.E., *Quart. Rev.*, 1954, vol. 8, no. 4, pp. 422–450.
4. Lever, A.B.P., *Inorganic Electronic Spectroscopy*, Amsterdam: Elsevier, 1984.
5. Kondratenko, A.V. and Neiman, K.M., *Kvantovaya khimiya i spektroskopiya vysokovozbuzhdennykh sostoyanii: Koordinatsionnye soedineniya perekhodnykh metallov* (Quantum Chemistry and Spectroscopy of Highly Excited States: Coordination Compounds of Transition Metals), Novosibirsk: Nauka, 1990.
6. Sone, K. and Fukuda, Y., *Inorganic Thermochromism*, Berlin: Springer, 1987.
7. Yanush, O., Halopenen, I., Markova, T., et al., in *Proc. GPD Conf.*, Tampere (Finland), June 18–21, 2001, pp. 815–817.
8. Arutjunjan, R.E., Markova, T., Halopenen, I., et al., in *Proc. SPIE "Advanced Optical Materials and Devices,"* Tartu, 2005, vol. 5946, pp. 346–352.
9. Gutmann, V. and Fenkart, K., *Monatsh. Chem.*, 1967, vol. 98, no. 1, pp. 1–7.
10. Gutmann, V., *Coordination Chemistry in Non-Aqueous Solutions*, Vienna: Springer, 1968.
11. Kabanov, V.O., Karapetyan, G.O., Ermolenko, N.N., et al., Abstracts of Papers, *Nauchno-tekhnicheskii progress v proizvodstve stekla: II Vsesoyuznoe soveshchanie* (Scientific and Technical Progress in Glass Production: II All-Union Meet.), 1983, p. 167.
12. Bershtein, I.Ya. and Kaminskii, Yu.L., *Spektrofotometricheskii analiz v organicheskoi khimii* (Spectrophotometric Analysis in Organic Chemistry), Leningrad, 1975.
13. Drago, R.S., *Physical Methods in Chemistry*, Philadelphia: Saunders, 1977.
14. Kryukov, A.I. and Kuchmii, S.Ya., *Fotokhimiya kompleksov perekhodnykh metallov* (Photochemistry of Complexes of Transition Metals), Kiev: Naukova Dumka, 1989.
15. Volkov, S.V. and Yatsimirskii, K.B., *Spektroskopiya rasplavlennykh solei* (Spectroscopy of Molten Salts), Kiev: Naukova Dumka, 1977.
16. Khvostova, N.O., Physicochemical Study of Solutions Activated by Cobalt(II) and Nickel(II) Salts for Obtaining Indicators on a Paper Substrate, *Cand. Sci. Dissertation*, Leningrad, 1984.
17. Ohtaki, H., *Monatsh. Chem.*, 2001, vol. 132, no. 11, pp. 1237–1268.

ISSN 1070-4272, Russian Journal of Applied Chemistry, 2008, Vol. 81, No. 5, pp. 786–791. © Pleiades Publishing, Ltd., 2008.
Original Russian Text © O.V. Popova, S.S. Popova, L.N. Ol'shanskaya, 2008, published in Zhurnal Prikladnoi Khimii, 2008, Vol. 81, No. 5, pp. 751–756.

APPLIED ELECTROCHEMISTRY AND CORROSION PROTECTION OF METALS

Prospects for Using Artificial Graphite Produced from Lignin in Electrodes of Chemical Power Cells

O. V. Popova, S. S. Popova, and L. N. Ol'shanskaya

Branch of North-Caucasian State Technical University, Kislovodsk, Stavropol krai, Russia
Saratov State Technical University, Saratov, Russia

Received June 18, 2007

Abstract—Effect of the nature of carbon–graphite materials on the kinetics of intercalation of lithium ions into the matrix of electrodes of lithium power cells, on the physicochemical characteristics of lithium intercalation–deintercalation, and discharge characteristics of compacted graphite-containing electrodes was subjected to a comparative study.

DOI: 10.1134/S107042720805011X

The improvement of lithium–ion batteries is inseparably associated with the development of effective electrode materials [1]. Lithium-intercalated carbon–graphite materials (CGM) are promising materials for negative electrodes. The kinetic features (and the mechanism) of intercalation–deintercalation in materials of this kind are governed by the nature of the carbon–graphite materials, dispersity of active paste components, methods used for pretreatment of the active paste, presence of modifying additives, and other factors [2–6].

In this study, the possibility of using artificial graphite produced by thermal modification of hydrolysis lignin (AGL) as a component of electrodes of chemical power cells was examined and this kind of graphite was compared with other graphite materials.

EXPERIMENTAL

The following materials were used to prepare the active paste of working composite electrodes: AGL; commercial powdered graphite materials GT and GT_{up} (crucible graphite and ultrapure crucible graphite); special low-ash graphite GSM-1; artificial graphite produced from oil coke and pitch (AG); and thermally expanded graphites produced from GT_{sp} (TEG) and AGL (TEGL). The thermally expanded graphites were produced from bisulfates of AGL and GT_{up} by thermal shock at 750–900°C in the course of 5–15 s. The graphite bisulfates were obtained using the method described in [7–10].

The active pastes of the composite electrodes had the following composition (wt %): composite graphite electrodes: graphite 90, PM-90V carbon black (to enhance the conductivity of the active paste) 5, and binder (F-42L fluoroplastic dissolved in acetone) 5; composite graphite electrodes in a sulfur matrix: crystalline sulfur of pure grade 10–80, graphite 80–10, and F4 fluoroplastic (Teflon) in the form of a suspension (F4D) 10.

The components were ground and then the mixture was thoroughly mixed in a magnetic mixer until a homogeneous paste was obtained. The current leads were fabricated from a 0.5×10 cm^2 nickel-plated steel or nickel grid, weighed, and degreased in acetone for 2 h. The active paste was applied onto the current leads, dried in air for 15 min, and compacted under a pressure of 1 MPa. The electrodes obtained were dried at 60–70°C. The working surface area of the electrodes was 1 cm^2, and their thickness, 100 μm.

The kinetics of intercalation–deintercalation and the effect of the nature of graphites on the electrochemical discharge characteristics of the electrodes were studied in a nonaqueous 1 M solution of $LiClO_4$ in a mixture of propylene carbonate (PC) and dimethoxyethane (DME) (1 : 1 by volume). The content of water in the electrolyte solution did not exceed 0.003–0.005%.

The intercalation of lithium into the graphite electrodes was performed in the potentiostatic mode at a potential of –3.1 V in the course of 2 h. Analysis

of the dependences $I = f(t)$ in Fig. 1 shows that, in the initial stage, lithium is intercalated into the electrodes under study at current densities in the range from 49–52 to 35–42 mA cm^{-2}; in 10 min, the current density decreases to 5±2 mA cm^{-2} and stabilizes.

To quantitatively analyze the decelerated stage in the initial phase of polarization and reveal the fundamental kinetic aspects of the process of lithium intercalation into CGM, the initial portions of the i–t curves were plotted in the coordinates i–$1/t^{1/2}$ (Fig. 2). The linear dependences obtained exhibit breaks indicating that the process occurs in two stages: in stage I, a passivating film with conduction by Li ions is formed on the graphite surface; in stage II, Li is intercalated into deep layers of graphite to give Li_xC_6 compounds.

According to the Cottrell equation [11]

$$K_i = \Delta i/\Delta(1/t^{1/2}) = zFc^0_{Li}(D_{Li})^{1/2}/\pi^{1/2},$$

where c^0_{Li} is the initial lithium concentration, and D_{Li} is the diffusion coefficient of lithium.

The intercalation constants K_i and the product $c^0_{Li}(D_{Li})^{1/2}$ were calculated for each stage of the process (Table 1).

It follows from the data in Table 1 that lithium is intercalated most easily into electrodes based on crucible graphite and AGL. It should be noted, however, that the formation rate of the surface film (portion I) is the highest for GT. This indicates that a denser film is formed, which further adversely affects the charging–discharge characteristics of the electrodes. The rates of lithium intercalation into the structure of graphite (portion II) are approximately the same for different CGMs.

Anodic chronopotentiograms were obtained in discharge of Li_xC_6 electrodes at a discharge current density of 2 mA g^{-1} (0.03 mA cm^{-2}) (Fig. 3). The chronopotentiograms were used to evaluate the output capacity of the electrodes.

The most lithium-saturated electrodes with the highest energy content are formed in a matrix of AGL graphite (Fig. 3, Table 1). This is accounted for by their homogeneous finely dispersed structure (particles smaller than 20 μm in size) and by the AGL particle structure more suitable for lithium intercalation, which has a somewhat larger interlayer spacing as compared to natural graphite (0.0336 nm) [11].

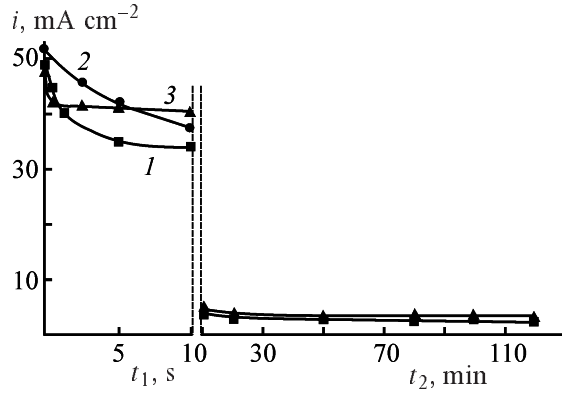


Fig. 1. Chronoamperograms of lithium intercalation into graphite electrodes. E = –3.1 V, T = 25°C. (*I*) Current density and (t_1, t_2) time; the same for Fig. 4. (*1*) AGL, (*2*) GT, and (*3*) GSM-1; the same for Figs. 2 and 3.

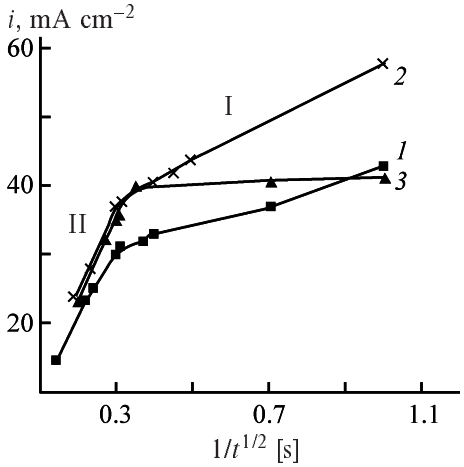


Fig. 2. i–$1/t^{1/2}$ dependences for different graphite-containing electrodes.

It is known that the lithium–sulfur system has one of the highest values of specific energy, 1675 A h kg^{-1} [12], and, therefore, use of sulfur as a cathode material in lithium power cells is of particular interest. The electrochemical reduction of sulfur is a complex multistage process. According to

Table 1. Diffusion-kinetic parameters of lithium intercalation into graphite electrodes at 25°C

Graphite	$K_i \times 10^3$, A s$^{1/2}$ cm^{-2}		$c^0_{Li}(D_{Li})^{1/2} \times 10^7$, mol cm^{-2} s$^{-1/2}$		W, W h kg^{-1}
	I	II	I	II	
AGL	16	100	2.9	18.3	720.0
GT	31	120	5.7	22.0	219.3
GSM-1	3	117	0.6	21.0	174.5

(I) Formation of a surface film and (II) formation of Li_xC_6.

Table 2. Lithium intercalation constants K_{i1}, K_{i2} and values of $c_1^0(D_1)^{1/2}$, $c_2^0(D_2)^{1/2}$ for sulfur electrodes containing various graphite matrices

–*E*, V	K_{i1}			K_{i2}			$c_1^0(D_1)^{1/2} \times 10^7$			$c_2^0(D_2)^{1/2} \times 10^7$		
	A $s^{1/2}$ cm^{-2}						mol cm^{-2} $s^{-1/2}$					
	TEG	AGL	AG	TEG	AGL	AG	TEG	AGL	AG	TEG	AGL	AG
2.8	2.50	6.55	6.00	10.20	12.03	16.13	0.229	0.601	0.551	0.936	1.101	1.469
2.7	2.28	8.20	7.20	10.00	16.71	24.12	0.209	0.753	0.661	0.918	1.538	2.203
2.6	3.37	9.20	5.60	12.40	19.02	18.05	0.309	0.845	0.514	1.138	1.744	1.653
2.5	3.23	7.44	6.40	7.10	12.11	19.25	0.296	0.683	0.588	0.651	1.101	1.744
2.4	1.33	8.70	3.60	5.50	24.25	16.37	0.122	0.798	0.330	0.504	2.260	1.469

the results of studies of the electrochemical behavior of sulfur in aprotic solvents (dimethylformamide, dimethyl sulfoxide) by the method of potentiodynamic curves, two electrochemical reactions, (1) and (3), can occur at the electrode and be accompanied by chemical reactions (2) and (4) [13]:

$$S_8 + 2e \rightarrow S_8^{2-}, \quad (1)$$

$$4S_8^{2-} \rightleftarrows 4S_6^{2-} + S_8, \quad (2)$$

$$S_6^{2-} + 2e \rightarrow 2S_3^{2-}, \quad (3)$$

$$2S_3^{2-} + S_6^{2-} \rightarrow 3S_4^{2-}. \quad (4)$$

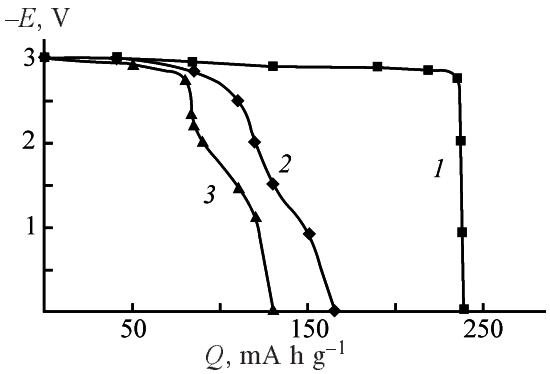


Fig. 3. Discharge curves of Li_xC_6 electrodes with matrices of different types of graphite. i_d = 0.03 mA cm^{-2}, T = 25°C. (*E*) Potential and (*Q*) discharge capacity.

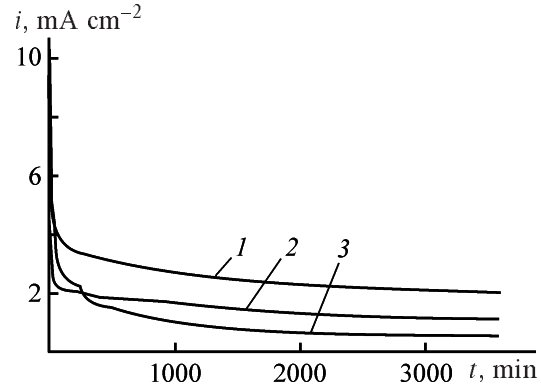


Fig. 4. Chronoamperograms of sulfur electrodes with matrices of different types of graphite at E = –2.8 V in a 1 M solution of $LiClO_4$ in PC + DME. Volume ratio 1 : 1; the same for Figs. 5 and 6. (*1*) AGL, (*2*) TEG, and (*3*) AG.

In the study, the possibility of fabricating a cycled lithium–sulfur electrode in a matrix of various carbon–graphite materials (AGL, TEG, and AG) was examined. The content of sulfur in the composite electrodes was 30%, and that of graphite, 60%. The cathodic intercalation of lithium was performed in the potentiostatic mode at potentials from –2.8 to –2.0 V in the course of 1 h. The process is the most stable for the electrodes with AGL and occurs with an insignificant decrease in the current density (Fig. 4).

An analysis of the *i*–*t* curves demonstrated that straight lines with a break are obtained in the i–$1/t^{1/2}$ coordinates, i.e., the process of intercalation of lithium ions occurs in two stages [similarly to the process of intercalation into graphite electrodes (Fig. 2)]. It can be suggested that, first, a layer of lithium polysulfides is formed on the surface via reactions (1)–(4), which is followed by the lithium intercalation proper into the structure of the electrode.

The values of the intercalation constants K_i and of the product $c_{Li}^0(D_{Li})^{1/2}$, calculated for each of the electrodes in accordance with the Cottrell equation (Table 2), indicate that films are formed on the matrix surface and lithium intercalation occurs in AG and AGL faster than in TEG.

Table 3. Concentration c^0_{Li} of lithium ions and diffusion coefficient D_{Li} for lithium–sulfur electrodes with various graphite matrices

–E, V	TEG		AGL		AG	
	$c^0_{Li}\times 10^5$, mol cm^{-2}	$D_{Li}\times 10^8$, cm^2 s^{-1}	$c^0_{Li}\times 10^5$, mol cm^{-2}	$D_{Li}\times 10^8$, cm^2 s^{-1}	$c^0_{Li}\times 10^5$, mol cm^{-2}	$D_{Li}\times 10^8$, cm^2 s^{-1}
2.6	178.7	31.0	363.0	44.3	12.7	85.7
2.5	373.0	23.3	231.6	42.4	82.9	100.3
2.4	235.7	72.9	212.2	46.7	67.3	75.0
2.3	158.0	66.7	150.5	72.9	47.9	85.7
2.2	88.3	51.7	155.1	70.0	56.9	50.2

The electrodes were discharged in the galvanostatic mode at anode current densities of 0.1, 0.3, 0.5, 0.7, and 1.0 mA cm^{-2}. The E–t dependence was used to determine the transition time τ_{tr} [14]. The results of galvanostatic measurements made it possible to find the value of $c^0_{Li}(D_{Li})^{1/2}$ by plotting the q–I dependence, where $q = i\tau$ (Fig. 5), and extrapolating the q–I straight line to the ordinate axis [15]. The intercept on the ordinate axis, q at $i = 0$, is related to the lithium ion concentration c^0_{Li} by the relationship

$$c^0_{Li} = \Delta q_\tau/(zF).$$

The diffusion coefficient of lithium was found from the slope $\Delta i/\Delta q_\tau$:

$$D_{Li} = l\Delta i/(3\Delta q_\tau),$$

where l is the electrode area.

The values of c^0_{Li} and D_{Li} are listed in Table 3. It follows from these data that the nature of graphite strongly affects characteristics of the lithium–sulfur electrode: AGL is distinguished by a higher value of c^0_{Li}, which indirectly confirms the high degree of AGL graphitization; the diffusion coefficient of lithium in AGL exceeds that in TEG; the discharge voltage of cells with AGL is lower than that of cells with TEG, which can be attributed to the more developed surface of thermally expanded graphite. At the same time, the discharge voltage of cells with AGL exceeds that for cells with AG, which is possibly due to the more "regular" graphite structure and to the higher electrical conductivity of AGL.

The good discharge characteristics of TEG-containing electrodes demonstrated that it is advisable to perform similar studies with thermally expanded graphite produced from AGL (TEGL). The kinetics of electrochemical reactions on a sulfur electrode modified with TEGL was studied at a varied content of sulfur.

It was found that varying the content of sulfur (10, 30, 50, and 80 wt %) and, accordingly, that of the TEGL carbon additive (80, 60, 40, and 10 wt %) ambiguously affects the rate of cathodic intercalation of lithium (Table 4).

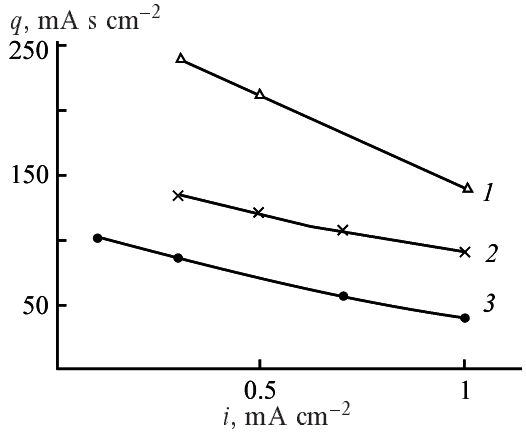


Fig. 5. q–i curves for Li–S electrodes with matrices of different graphites, measured on keeping the electrodes in a 1 M solution of $LiClO_4$ in PC + DME at E = –2.2 V for 1 h.

Table 4. Effect of the sulfur concentration on the diffusion-kinetic characteristics of the sulfur electrode with a TEGL matrix at E = –2.6 V anf t = 1 h

S content, %	K_{i1}	K_{i2}	$c^0_1(D_1)^{1/2}\times 10^7$	$c^0_2(D_2)^{1/2}\times 10^7$
	A s$^{1/2}$ cm^{-2}		mol cm^{-2} s$^{-1/2}$	
10	3.58	27.00	0.33	2.48
30	2.27	12.40	0.21	1.14
50	5.38	8.00	0.49	0.73
80	3.38	12.2	0.31	1.12

Table 5. Effect of the sulfur content on the transition time τ_{tr} (s) and product $c^0_{Li}(D_{Li})^{1/2} \times 10^7$ (mol cm^{-2} s$^{-1/2}$) for the process of anodic oxidation of a lithium-intercalated sulfur electrode with a TEGL matrix at various discharge current densities. E = –2.6 V, τ = 1 h

S content, %	τ_{tr}	$c^0_{Li}(D_{Li})^{1/2} \times 10^7$	τ_{tr}	$c^0_{Li}(D_{Li})^{1/2} \times 10^7$	τ_{tr}	$c^0_{Li}(D_{Li})^{1/2} \times 10^7$	τ_{tr}	$c^0_{Li}(D_{Li})^{1/2} \times 10^7$	τ_{tr}	$c^0_{Li}(D_{Li})^{1/2} \times 10^7$
	at indicated anode discharge current density $i \times 10^3$, A cm^{-2}									
	0.1		0.3		0.5		0.7		1.0	
10	470	0.40	3471	1.03	3075	1.62	3104	2.28	1953	2.58
30	405	0.37	2625	0.90	1360	1.08	1200	1.41	1000	1.84
50	360	0.35	3614	1.05	2103	1.00	1716	1.69	1492	2.25
80	134	0.21	993	0.55	967	0.91	794	1.13	633	1.47

The run of the potentiostatic curves plotted in the coordinates i–$1/t^{1/2}$ indicates that the lithium intercalation occurs in two stages. According to Table 4, the intercalation constants increase as the S content (%) is varied:

K_{i1}: 30 S < 80 S ≤ 10 S < 50 S,

K_{i2}: 50 S < 80 S ≤ 30 S < 10 S.

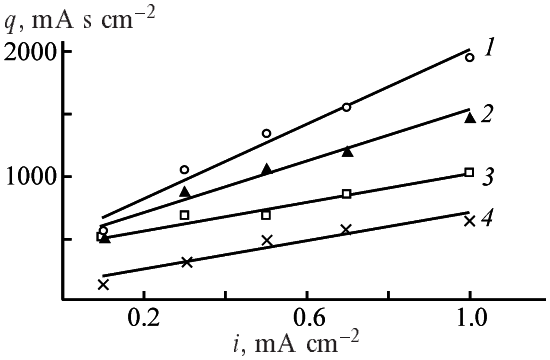


Fig. 6. q–i curves for Li–S electrodes with a TEGL matrix, measured on keeping the electrodes in a 1 M solution of $LiClO_4$ in PC + DME at E = –2.6 V for 1 h. Sulfur content, %: (*1*) 10, (*2*) 30, (*3*) 50, and (*4*) 80. (*1*) $y = 1491.7x + 509.37$, (*2*) $y = 1042.5x + 481.83$, (*3*) $y = 555.84x + 443.46$, and (*4*) $y = 557.59x + 131.04$.

Table 6. Effect of the sulfur concentration on the characteristics of the sulfur electrode with a TEGL matrix. E = –2.6 V, t = 1 h

S content, %	$q^0_\tau \times 10^3$, C cm^{-2}	$c^0_{Li} \times 10^5$, mol cm^{-2}	$D \times 10^8$, cm^2 s^{-1}
10	509	525	20.2
30	482	499	50.4
50	443	466	26.5
80	131	135	60.2

In the initial stage, the highest rate of lithium intercalation, K_{i1}, is observed on the sulfur electrode containing 50 wt % sulfur. In the case of a longer polarization, when the process rate is limited by diffusion in the solid phase, the maximum value of K_{i2} is observed for the electrode containing 10 wt % sulfur.

The longest galvanostatic discharge and the highest delay potential in the E–t curves (–2.0 to +0.15 V) correspond to a sulfur content of 10 wt %; the transition time τ_{tr} and c^0_{Li} increase as the intercalation potential is shifted in the negative direction. According to Table 5, τ_{tr} increases, as the S content (%) is varied, in the order: 80 S < 50 S < 30 S < 10 S.

The dependences q–i are shown in Fig. 6. The values of q^0_τ and of the lithium content c^0_{Li} of the electrode, found by extrapolation to the ordinate axis, and the diffusion coefficients calculated from the slope ratio $\Delta i/\Delta q_\tau$ are listed in Table 6.

Thus, the results obtained indicate that the diffusion-kinetic parameters of the lithium–sulfur electrode depend on the content of sulfur and, accordingly, of graphite in the electrode. A sulfur content of 10% (TEGL 80%) corresponds to the largest values of the specific capacity of the electrode, determined by the length of the time delay of the potential and by the lithium concentration in the electrodes (Table 6).

CONCLUSIONS

(1) The possibility and comparatively high efficiency of use of artificial graphite produced from lignin as a matrix for synthesis of graphite intercala-

tion compounds and the efficiency of thermally expanded graphite produced from lignin as a component of the active paste for electrodes of lithium power cells was confirmed.

(2) Artificial graphite produced from lignin surpasses all other graphite materials studied as a matrix for lithium intercalation and can be used to fabricate a graphite electrode for a lithium–ion battery with a high specific energy content (720 W h kg^{-1}).

(3) Sulfur electrodes with TEG and TEGL matrices have the best charging–discharge characteristics. For example, the concentration c^0_{Li} of lithium ions for sulfur electrodes containing 30% sulfur and 60% TEGL is 499×10^{-5}, which substantially exceeds the concentrations in similar electrodes with an AGL matrix ($c^0_{Li} = 363 \times 10^{-5}$ mol cm^{-2}). In turn, the electrodes with TEGL surpass those with TEG in discharge characteristics (q^0_τ = 482 and 270 mC cm^{-2}, respectively).

REFERENCES

1. Kedrinskii, I.A. and Yakovlev, V.G., *Li-Ionnye akkumulyatory* (Li–Ion Batteries), Krasnoyarsk: Platina, 2002.
2. Popova, S.S., Ol'shanskaya, L.N., and Pominova, T.V., *Elektrokhimiya*, 2002, vol. 38, no. 4, pp. 412–418.
3. Pominova, T.V., Ol'shanskaya, L.N., and Popova, S.S., *Elektrokhimiya*, 2000, vol. 36, no. 4, pp. 448–454.
4. Ol'shanskaya, L.N. and Astaf'eva, E.N., *Zh. Prikl. Khim.*, 2002, vol. 75, no. 5, pp. 759–762.
5. Ol'shanskaya, L.N., Popova, S.S., Pominova, T.V., and Astaf'eva, E.N., *Elektrokhimiya*, 2002, vol. 38, no. 4, pp. 406–411.
6. Kurbatov, A.P., Rudenko, A.B., and Krems, I.V., *Materialy VI Mezhdunarodnoi konferentsii "Fundamental'nye problemy elektrokhimicheskoi energetiki"* (Proc. VI Int. Conf. "Fundamental Problems of Electrochemical Power Enginering"), Kazarinov, I.A., Ed., Saratov, September 5–9, 2005, Saratov: Saratov. Univ., 2005, pp. 215–217.
7. Finaenov, A.I., Scientific Principles of Modification and Electrochemical Processing of Graphite for Chemical Power Cells, *Doctoral Dissertation*, Saratov, 2000.
8. Krasnov, A.V., Electrochemical Synthesis of Graphite Bisulfate from Suspensions Containing Graphite and Sulfuric Acid, *Cand. Sci. Dissertation*, Saratov, 2004.
9. Trifonov, A.I., Electrochemical Synthesis of Thermally Expanding Compounds of Graphite with Sulfuric Acid, *Cand. Sci. Dissertation*, Saratov, 2004.
10. Nastasin, V.A., Electrode Processes in Electrochemical Synthesis of Graphite Bisulfate, *Cand. Sci. Dissertation*, Saratov, 2001.
11. Popova, O.V., Scientific Foundations of Electrochemical Modification of Lignins, *Doctoral Dissertation*, Saratov, 2006.
12. Bikbaeva, G.G., Gavrilova, A.A., and Kolosnitsyn, V.S., *Elektrokhimiya*, 1993, vol. 29, no. 6, pp. 716–720.
13. Kolosnitsyn, V.S., Karaseva, E.V., Syng, D.Ya., et al., *Elektrokhimiya*, 2002, vol. 38, no. 12, pp. 1501–1504.
14. Popova, S.S., Shaposhnikova, E.A., Popova, O.V., and Serbinovskii, M.Yu., *Izv. Vyssh. Uchebn. Zaved. Sev.-Kavk. Regiona, Tekh. Nauki*, special issue: *Kompozitsionnye materialy* (Composite Materials), 2005, pp. 54–59.
15. Tysyachnyi, V.P., Ksenzhek, O.S., and Pototskaya, L.I., *Elektrokhimiya*, 1973, vol. 8, no. 11, pp. 1692–1696.

ISSN 1070-4272, Russian Journal of Applied Chemistry, 2008, Vol. 81, No. 5, pp. 792–795. © Pleiades Publishing, Ltd., 2008.
Original Russian Text © V.V. Rogozhin, 2008, published in Zhurnal Prikladnoi Khimii, 2008, Vol. 81, No. 5, pp. 757–760.

APPLIED ELECTROCHEMISTRY AND CORROSION PROTECTION OF METALS

Specific Features of Cathodic Deposition of Nickel–Boron Coatings from a Sulfuric Acid Electrolyte with Addition of Polyhedral Borates

V. V. Rogozhin

Nizhni Novgorod State Technical University, Nizhni Novgorod, Russia

Received June 8, 2007

Abstract—Specific features of the cathodic deposition of nickel–boron coatings from a sulfuric acid electrolyte with addition of polyhedral borates were considered.

DOI: 10.1134/S1070427208050121

Nickel–boron coatings with a low content of boron attract a considerable attention in manufacture of radioelectronic articles because of the possibility of imparting to these articles multifunctional characteristics by varying the formulation-and-technological modes of their deposition. Depending on the profile of articles being metal-plated, coatings of this kind can be deposited locally (chemically) or cathodically onto larger metallization surfaces [1–4]. Of interest for electrodeposition of such coatings is addition of polyhedral borate anions ($C_2B_9H_{12}^-$, $B_{10}H_{10}^{2-}$, $B_{12}H_{12}^{2-}$) [5], which can be introduced into standard nickel-plating electrolytes [6, 7]. Additives of this kind exhibit low electrochemical activity, and their parallel transformations in the course of reduction of nickel ions can be eliminated.

EXPERIMENTAL

The coatings were electrodeposited from the standard Watts electrolyte with anions of polyhedral borates at 40–45°C onto copper and nickel supports. Electrochemical studies were performed with PI-50 and P-5848 potentiostats and a standard YaSE-2 cell. The effective activation energy of the nickel deposition and boron incorporation was determined by Gorbachev's temperature-kinetic method from the effect of temperature on the rate of the electrode process at fixed potentials. X-ray diffraction analysis was made on a DRON-2 diffractometer with MoK_α radiation. The interplanar spacings were calculated by the Bragg formula. An Auger spectral analysis was carried out on a PHI-545 instrument (USA) and also on a laser mass-reflectron. As samples served Polycor plates with a vacuum-deposited copper layer, onto which coatings were deposited.

It was found that polyhedral additives do not exhibit any noticeable electrochemical activity at the cathode under polarization conditions in an electrolyte containing no nickel salt, with only hydrogen evolution observed at the cathode. Auger spectroscopy of surfaces of various metallic electrodes in the absence of polarization demonstrated that spontaneous decomposition of the additives occurs only at those electrodes which show catalytic activity with respect to this decomposition. Certain saturation of the surface with elemental boron was observed on nickel electrodes, whereas no boron was found on the surface of copper even after prolonged keeping of the electrode in a boron-containing solution without polarization (Fig. 1).

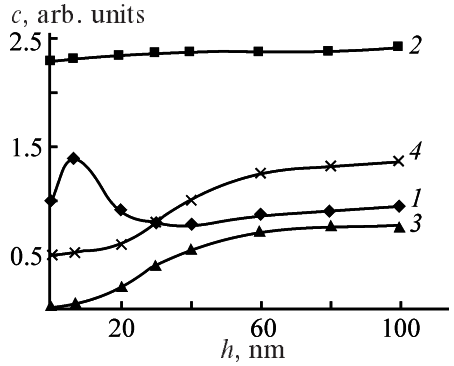


Fig. 1. Auger profiles of (*2, 4*) nickel and (*1, 3*) boron distribution on (*1, 2*) nickel and (*3, 4*) copper supports. Time of keeping the supports in a solution containing $C_2B_9H_{12}^-$ in the absence of polarization 1 h. The content of nickel is given on a 1 : 5 scale. (*c*) Content of element and (*h*) distance from the support.

The catalytic properties of the nickel surface are enhanced as its renewal in the course of cathodic deposition of the metal from the nickel-plating electrolyte is accelerated. At higher current densities, the rate of boron incorporation increases (Fig. 2) and its absolute amount in a coating becomes larger. In this case, such factors as the slow delivery of the additive to, and its adsorption on the reaction surface may be important, which is indicated by the activation energy of boron incorporation into the coating: 80–120 kJ mol^{-1} at low temperatures (kinetic control) and 25–35 kJ mol^{-1} at the working temperatures (diffusion control).

By the method of "hydrogen delay" [8] we found that a 0.8-monolayer coverage of the reaction surface is reached even at low $B_{10}H_{10}^{2-}$ concentrations of about 0.1 M, i.e., the nickel deposition and boron incorporation into the coating occur under conditions of formation of a near-cathode boron-containing film, especially at high concentrations of the additive raising the activation energy of nickel deposition at the working potentials from 40–50 to 80–90 kJ mol^{-1}.

Despite the considerable difference between the standard potentials of nickel and boron, equal to approximately 0.6 V, the cathodic curves of deposition of nickel–boron coatings are close to curves of nickel deposition and differ only by tenths and hundredths of a volt, which can only be attributed to the effects of energy release in alloying and adsorption (Fig. 3). The adsorption was confirmed by changes in the capacitance of the electrical double layer of an unpolarized nickel–boron electrode in the presence of boron-containing additives in the electrolyte.

The absence of the electrochemical mechanism of boron incorporation into a coating is clearly demonstrated by cathode balances for deposition of nickel–boron coatings, according to which the whole amount of the cathode electricity is completely expended for nickel deposition and hydrogen evolution, although the content of boron in the coating may be as high as 20–30 at %.

The results obtained make it possible to state that, in cathodic deposition of nickel–boron coatings, the coating components are deposited by different mechanisms: nickel base, by the conventional electrochemical, and boron, by chemical-catalytic under diffusion-kinetic control.

X-ray diffraction studies of the nickel–boron coatings failed to reveal any particular crystal structure characteristic of metallurgical alloys. At a comparatively low boron content of a coating, its structure is an interstitial solid solution of boron in nickel and the crystallite size decreases from 25 to 3 nm as modifying additives (sulfur, manganese) are introduced and the amount of boron in the alloy is raised (see table). The latter is achieved by making higher the concentration of boron-containing additives in

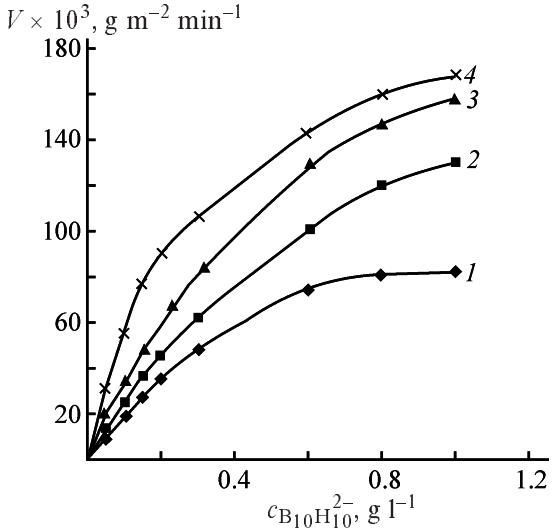


Fig. 2. Rate V of boron incorporation into a nickel coating vs. $B_{10}H_{10}^{2-}$ concentration c in a sulfate electrolyte at 45°C and different cathode current densities. Current density, A dm^{-2}: (*1*) 1.0, (*2*) 2.0, (*3*) 3.0, and (*4*) 4.0.

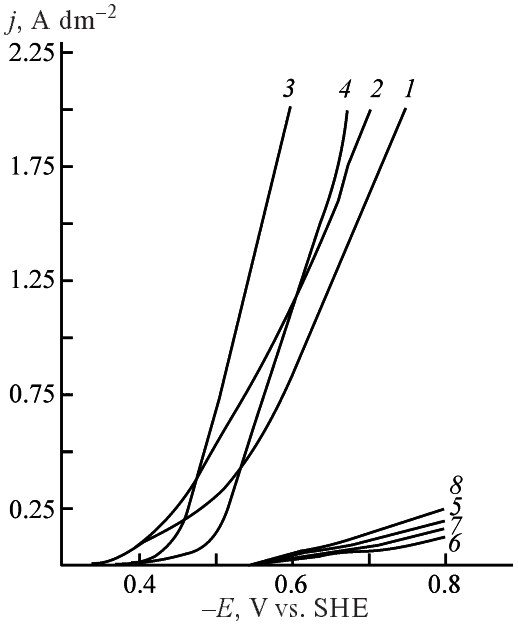


Fig. 3. Partial potentiodynamic polarization curves obtained in a sulfate electrolyte (T = 45°C) with $B_{10}H_{10}^{2-}$ additive for (*1–4*) deposition of nickel and nickel–boron coating and (*5–8*) hydrogen evolution. Additive concentration, g l^{-1}: (*1, 5*) 0, (*2, 6*) 0.05, (*3, 7*) 1.0, and (*4, 8*) 3. (j) Current density and (E) potential.

Results of an X-ray diffraction analysis of Ni–B coatings with varied content of boron, sulfur, and manganese admixtures

Admixture content, wt %			Phase composition	CSR	*d*
S	B	Mn		nm	
–	–	–	Crystalline nickel	50.0	0.3523
0.01	–	–	Solid solution	25.0	0.3501
0.01	–	0.01	Solid solution	15.0–17.0	0.3522
–	1.0	–	Polycrystalline solid solution of boron in nickel	5.0	0.3514
0.01	0.8	–	Polycrystalline solid solution of boron in nickel	3.0	0.35
0.01	0.6	0.01	Polycrystalline solid solution of boron in nickel	3.5–4.0	0.3514

* CSR is the grain size (coherent scattering region), and *d*, interplanar spacing.

the electrolyte, which results in a considerable increase in the cathodic polarization and activation energy of discharge of nickel ions. As the amount of the boron-containing additive in the electrolyte increases, the preferential crystallographic orientation of nickel–boron coatings changes from [111] to [100]. Such a change in the orientation of crystallites in the coating is probably due to predominant adsorption of ions of the boron-containing additives on faces forming the frontal growth surface of the coating.

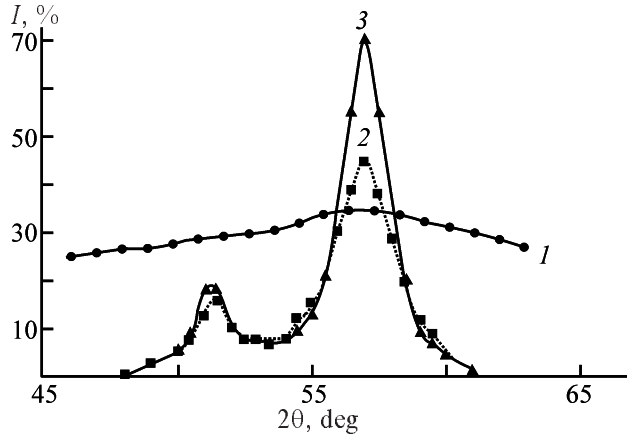


Fig. 4. X-ray diffraction pattern of nickel–boron coatings with different contents of boron. (*I*) Relative intensity and (2θ) Bragg angle.

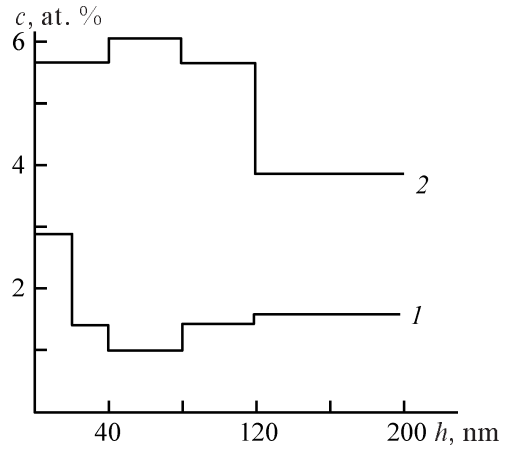


Fig. 5. Distribution of the content *c* of (*1*) boron and (*2*) oxygen in the upper layers of a nickel–boron coating after a thermal treatment at 450°C (2 min) and 380°C (8 min) in air according to the results of Auger spectroscopy. (*h*) Deposit thickness.

As the content of boron in a thermally untreated Ni–B coating is raised to 2.6%, the profile of Ni reflections (111), (200), (220), and (311) in the X-ray diffraction patterns markedly changes. The lines become broader and their intensity decreases. The coating was amorphized at a boron content of 4.3% ($B_{12}H_{12}^{2-}$ additive was used); there are no peaks characteristic of the crystalline state in the X-ray diffraction pattern of this coating (Fig. 4).

The small size of boron atoms and the absence of strong intercrystallite bonds in the alloy provide a high rate of thermal diffusion of boron atoms to the coating surface, where they are for the most part oxidized. The Gibbs energies of formation of boron and nickel oxides are –1186 and –217 kJ mol^{-1}, respectively, and, therefore, the resulting film is mainly composed of boron oxides. In the process, boron favors self-fluxing of the nickel surface by the reaction

$$3NiO + 2B = B_2O_3 + 3Ni.$$

A thermal treatment, e.g., that simulating attachment of a semiconducting crystal by means of an Au–Si eutectic and thermal-compression bonding of chip leads, results in that oxide films of thickness exceeding 200 nm are formed on the surface of nickel–boron coatings and boron diffuses toward the surface of the deposit (Fig. 5).

At high temperatures of the surface of nickel–boron coatings, boron is oxidized by the reaction

$$4B + 3O_2 = 2B_2O_3.$$

Forming a solid surface film, boron oxides mechanically hinder oxidation of nickel and simultaneously exert a self-fluxing influence. The protective film composed of boron oxides makes coatings thermally stable, and, when necessary, e.g., in high-temperature assembly of electronic devices, can be easily removed by ultrasonic treatment, with fluxes or aqueous solutions, etc.

CONCLUSIONS

(1) When nickel–boron coatings are formed from nickel-plating electrolytes with addition of polyhedral borates, the coating components are deposited by different mechanisms: nickel base by the conventional electrochemical mechanism, and boron, by the chemical-catalytic mechanism under diffusion-kinetic control.

(2) These processes mutually affect each other: acceleration of the cathodic stage of nickel deposition makes higher the rate of boron incorporation; simultaneously, as the concentration of boron-containing additives increases, the crystal structure becomes finer and the orientation of crystallites changes, with a transition from a polycrystalline solid solution of boron in the lattice of nickel to an X-ray amorphous coating.

(3) Thermal treatment of the coating causes boron diffusion to the surface, with protective oxide films formed.

REFERENCES

1. Flerov, V.N., *Khimicheskaya tekhnologiya v proizvodstve radioelektronnykh detalei* (Chemical Technology in Manufacture of Radioelectronic Articles), Moscow: Radio i Svyaz', 1988.
2. Rogozhin, V.V., *Materialy mezhdunarodnoi konferentsii "Elektrokhimiya, gal'vanotekhnika i obrabotka poverkhnosti"* (Proc. Int. Conf. "Electrochemistry, Electroplating, and Surface Treatment"), Moscow, 2001, p. 95.
3. Plokhov, V.A., Flerov, V.N., and Dyagilev, V.A., *Izv. Vyssh. Uchebn. Zaved., Khim. Khim. Tekhnol.*, 1988, vol. 31, no. 1, pp. 77–80.
4. Zvyagintseva, A.V. and Falicheva, A.I., *Gal'vanotekh. Obrab. Poverkhn.*, 1997, vol. 5, no. 2, pp. 24–31.
5. Cotton, F.A. and Wilkinson, G., *Basic Inorganic Chemistry*, New York: Wiley, 1976. Translated under the title *Osnovy neorganicheskoi khimii*, Moscow: Mir, 1979, pp. 287–291.
6. Dyagilev, V.A., Rogozhin, V.V., Gribanova, Yu.N., and Flerov, V.N., *Gal'vanotekh. Obrab. Poverkhn.*, 1996, vol. 4, no. 4, pp. 22–27.
7. Gribanova, Yu.N., Rogozhin, V.V., and Flerov, V.N., *Gal'vanotekh. Obrab. Poverkhn.*, 2000, vol. 8, no. 3, pp. 29–34.
8. Gribanova, Yu.N., Rogozhin, V.V., Galkin, A.L., et al., Abstracts of Papers, *Mezhdunarodnaya konferentsiya "Progressivnaya tekhnologiya i voprosy ekologii v gal'vanotekhnike i proizvodstve pechatnykh plat"* (Int. Conf. "Breakthrough Technology and Problems of Ecology in Electroplating and Manufacture of Printed-Circuit Boards"), Penza, 1998, pp. 21–22.

ISSN 1070-4272, Russian Journal of Applied Chemistry, 2008, Vol. 81, No. 5, pp. 796–799. © Pleiades Publishing, Ltd., 2008.
Original Russian Text © T.M. Umarova, I.N. Ganiev, 2008, published in Zhurnal Prikladnoi Khimii, 2008, Vol. 81, No. 5, pp. 761–764.

APPLIED ELECTROCHEMISTRY AND CORROSION PROTECTION OF METALS

Effect of Ytterbium on the Corrosion-Electrochemical Behavior of Aluminum in a Neutral Medium

T. M. Umarova and I. N. Ganiev

Nikitin Institute of Chemistry, Academy of Sciences of Republic of Tajikistan, Dushanbe, Tajikistan

Received June 18, 2007

Abstract—Effect of ytterbium on the corrosion-electrochemical behavior of aluminum and an aluminum–manganese alloy in a neutral 3% solution of NaCl was studied.

DOI: 10.1134/S1070427208050133

Ytterbium, one of the least widespread and worst studied rare-earth elements of the yttrium group, is a paramagnetic material that is easily mechanically processed and has high electrical conductivity, which exceeds that of other lanthanides by a factor of 3. Ytterbium is weakly oxidized in air and is one of the few rare-earth metals (REM) that have distinctive properties, compared with other metals in this series. For example, the structure of the electron shell of elements in their metallic state largely predetermines the physicochemical properties of a metal. With exception of ytterbium and europium, REMs (R) are trivalent. Ytterbium exists also in the bivalent state and, therefore, its properties in alloying can differ from those of trivalent metals.

All the REMs (except ytterbium) have at room temperature a close-packed hexagonal structure of the magnesium type (A3), whereas ytterbium crystallizes in a cubic face-centered lattice of the copper type (A1) [1]. In contrast to many REMs, ytterbium has a comparatively low melting point (816°C), which facilitates alloying [2].

The aim of this study was to examine the effect of ytterbium on the corrosion-electrochemical behavior of aluminum and an aluminum–manganese alloy containing 1.9 wt % Mn in a 3% solution of NaCl. This study continues previous investigations [3–6] of the effect of alloying elements on the corrosion behavior of aluminum and alloys based on this metal.

By now, there are no data on the corrosion behavior of aluminum alloyed with ytterbium. Therefore, the electrochemical behavior of alloys containing up to 0.5% ytterbium was examined in the study.

EXPERIMENTAL

The alloys studied were prepared from aluminum of A85 brand [GOST (State Standard) 4784–74], ytterbium of Itb M1 brand [TU (Technical Specification) 48-4-204–72), and electrolytic manganese of Mr00 brand (GOST 6008–82). To study the corrosion behavior of aluminum–manganese alloys alloyed with ytterbium, alloys of the Al–Mn–Yb system were synthesized from the corresponding addition alloys Al–Mn (10%) and Al–Yb (10%), which made it possible to obtain alloys of homogeneous chemical composition in the systems under study.

A molten aluminum alloy was poured into a steel mold in order to obtain cylindrical rods 8 mm in diameter and 100 mm long. The thus fabricated electrodes were lapped, polished to mirror shine, and washed and degreased with ethanol.

The study was performed using the experimental procedure described in [3]. A silver chloride electrode served as reference in the electrochemical cell, and a platinum electrode, as auxiliary electrode. The solution temperature of 20°C was maintained by a thermostat. The potential sweep rate was 2 mV s^{-1}, a 3% solution of sodium chloride served as a corrosion medium. The electrodes were polarized in the potentiostatic mode, with the potential shifted in the anodic direction from the free-corrosion potential (steady-state potential) to a constant current of 2 mA and then backwards to a value of –1.6 V, after which an anodic curve was measured. A full polarization curve is shown in Fig. 1.

The results of a potentiodynamic study of ytterbium-alloyed aluminum in a 3% solution of sodium chloride are listed in Table 1. All the potentials are

Table 1. Corrosion-electrochemical characteristics* of ytterbium-alloyed aluminum in a neutral medium

Yb, wt %	$-E_{fc}$	$-E_{cor}$	$-E_{rp}$	$-E_{pox}$	$-E'_{pox}$	ΔE_{pas}	i_{repass}	i_{cor}
	V						A m^{-2}	
–	0.70	0.71	0.54	0.480	0.46	0.34	0.12	0.006
0.005	0.60	0.66	0.54	0.450	0.46	0.35	0.11	0.008
0.01	0.50	0.55	–	0.420	0.46	0.37	0.10	0.011
0.05	0.53	0.56	–	0.380	0.45	0.39	0.10	0.010
0.10	0.55	0.57	0.54	0.360	0.44	0.41	0.08	0.006
0.20	0.55	0.57	0.54	0.360	0.42	0.41	0.07	0.007
0.50	0.56	0.58	0.54	0.350	0.40	0.42	0.05	0.010

* E_{fc}, E_{cor}, E_{rp}, E_{pox}, and E'_{pox} are the potentials of free corrosion, corrosion, repassivation, and pitting in the presence and absence of a natural oxide film on the surface, respectively; ΔE_{pas}, passivation interval; i_{repass} and i_{cor}, current densities of dissolution in the repassivation region and corrosion.

given relative to the standard hydrogen electrode. The corrosion current was calculated from the cathodic curve (b_c = 0.12 V) [7].

The corrosion rate as a function of the corrosion current density was found using the formula

$$K = i_{cor}k,$$

where k is the electrochemical equivalent whose numerical value is 0.335 g A^{-1} h^{-1} for aluminum [8].

As the concentration of the alloying component (Yb) increases, the passivation interval becomes wider, which indicates that the tendency of the alloys toward passivation is enhanced because of the formation of a stable protective film on the alloy surface. This behavior is also confirmed by the dissolution current densities in the repassivation region, i_{repass}, which are lower than those for pure aluminum. Comparison of the corrosion current densities of ytterbium-alloyed aluminum with those of alloys of the systems Al–R (R = Y, La, Ce, Pr, Nd, etc.) considered in [6, 9–11] shows that alloys of aluminum with ytterbium are the most corrosion-resistant.

Ternary alloys of the system Al–Mn–Yb have good castability and mold-fillability, show no shrinkage, and are outwardly characterized by strong shine and whiteness, compared with the previously studied similar alloys of the systems Al–Mn–Sc (Y, Ce, La, etc.). Table 2 lists the results of a study of the corrosion-electrochemical behavior of an aluminum–manganese alloy of a eutectic composition (1.9% Mn), alloyed with ytterbium to 0.5%, in a neutral aqueous medium. It can be seen that, as the ytterbium content increases, the free-corrosion and pitting potentials, found from the forward-run anodic polarization curve, are shifted into the region of positive values. Analysis of the full polarization curve shows that all the free-corrosion potentials of alloys of the system Al–1.9% Mn–Yb are in the passivation region.

The free-corrosion and pitting potentials are the most strongly affected by minor additions of ytterbium (0.01%). Presumably, this occurs because just these two parameters are affected to a greater extent by the initial state of the alloy surface not subjected to any treatment (cathodic polarization, etching, etc.). The alloy of composition Al–1.9% Mn–0.01% Yb is characterized by the minimum densities of the current of dissolution in the repassivation region and corrosion current. As the ytterbium content increases further, the manner in which this additive affects the characteristics under study is preserved,

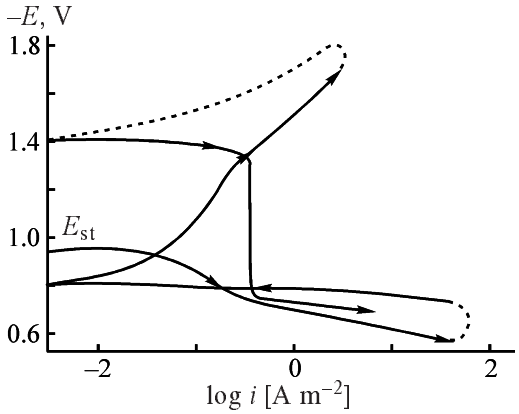


Fig. 1. Explanation of the procedure used to measure the polarization curves of the alloys under study. (E) Potential and (i) current density; the same for Fig. 2.

Table 2. Corrosion-electrochemical characteristics of ytterbium-alloyed Al–1.9% Mn alloy in a 3% NaCl solution

Yb, wt %	$-E_{fc}$	$-E_{pox}$	$-E_{rp}$	$-E_{cor}$	$-E_{np}$	$-E'_{pox}$	ΔE_{pas}	i_{repass}	i_{cor}
	V						A m^{-2}		
–	0.640	0.40	–	0.550	0.920	0.440	0.50	0.04	0.0070
0.005	0.600	0.38	–	0.55	0.920	0.450	0.45	0.03	0.0040
0.01	0.500	0.37	–	0.550	0.930	0.460	0.40	0.02	0.0025
0.05	0.535	0.40	0.54	0.555	0.980	0.430	0.50	0.04	0.0050
0.10	0.550	0.38	0.54	0.565	1.080	0.450	0.60	0.04	0.0055
0.20	0.540	0.38	–	0.565	0.950	0.450	0.550	0.05	0.0056
0.50	0.510	0.36	–	0.570	0.850	0.455	0.360	0.06	0.0060

but, even at the maximum content of ytterbium (0.5%), the corrosion resistance of the alloy exceeds that of the starting unalloyed alloy, which is only characteristic of this REM.

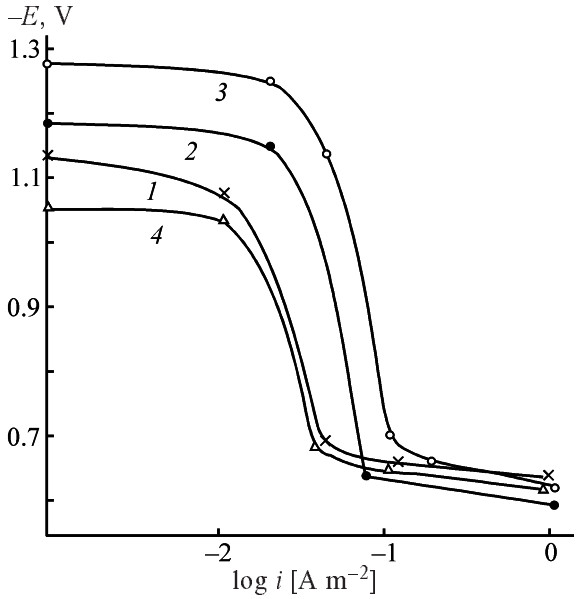


Fig. 2. Anodic polarization curves of Al–Mn–Yb alloys with a varied content of ytterbium in a 3% NaCl solution. Yb content, wt %: (*1*) 0.01, (*2*) 0.05, (*3*) 0.10, and (*4*) 0.50.

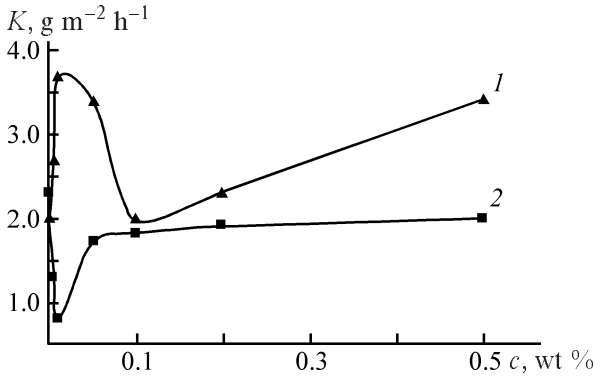


Fig. 3. Corrosion rate K of alloys of the systems (*1*) Al–Yb and (*2*) Al–Mn–Yb vs. the ytterbium content c.

Comparison of the corrosion-electrochemical parameters of alloys of the systems Al–Yb and Al–Mn–Yb (Tables 1 and 2, respectively) shows that, in the presence of manganese, the corrosion rate of the aluminum alloy is substantially lower and, consequently, alloys of the system Al–Mn–Yb are 2–3 times more corrosion-resistant than binary alloys (at ytterbium content of 0.005–0.05%). At an ytterbium content of 0.01%, the difference between the corrosion currents of the aluminum–ytterbium (0.012 A m^{-2}) and aluminum–manganese–ytterbium alloys (0.0025 A m^{-2}) is the most pronounced, which is accounted for by the stronger influence of manganese. With ytterbium added in an amount of 0.05% to aluminum and the aluminum–manganese alloy, the corrosion currents differ by a factor of 2. At an ytterbium content of 0.10%, the corrosion current densities of the binary and ternary alloys virtually coincide (0.0060 and 0.0055 A m^{-2}, respectively); the free-corrosion potentials are also equal. Thus, manganese has no effect on the corrosion behavior of aluminum at an ytterbium content of 0.10%, but at the maximum content of ytterbium (0.5 wt %), the effect of manganese again becomes noticeable.

Figure 2 shows anodic polarization curves for alloys of the system Al–Mn–Yb in a 3% NaCl solution. It can be seen that the passivation interval becomes wider at ytterbium content of 0.05–0.10% (curves *2*, *3*). To these alloy compositions correspond the highest currents of dissolution in the repassivation region. Upon addition of the maximum amount of REM (0.5% Yb), the passivation interval becomes narrower, and the dissolution currents in the repassivation region, lower.

Figure 3 shows dependences of the corrosion rate K (g m^{-2} h^{-1}) of aluminum (curve *1*) and of an aluminum–manganese alloy containing 1.9% Mn

(curve *2*) on the content of ytterbium (wt %). It can be seen that the corrosion rates of the binary and ternary alloys change to the greatest extent at ytterbium contents of 0.005 to 0.1%. In this concentration range, the ytterbium content has opposite effects (curves *1* and *2*).

Thus, addition of ytterbium in an amount of 0.01% to aluminum and the aluminum–manganese alloy (1.9% Mn) leads to an increase in the corrosion rate in the former case, and to a decrease, in the latter. Consequently, the key role in alloying of aluminum and the Al–1.9% Mn alloy with ytterbium will be played by manganese, whose presence in an alloy improves its corrosion resistance. As the ytterbium content reaches 0.10%, the corrosion rates of the binary and ternary alloys become virtually equal, and further increase in the ytterbium content leads to a steady increase in the corrosion rates of alloys of the systems Al–Yb and Al–Mn–Yb.

The optimal, with respect to corrosion, composition of the ternary alloys is that with ytterbium added in an amount of 0.005–0.10 wt %. The alloy of composition Al–1.9% Mn–0.01% Yb is the most corrosion-resistant and has a high stability against pitting corrosion in a neutral medium containing chloride ions. This is accounted for by the strong modifying effect of ytterbium.

A comparison of the effect of REM additives on the corrosion rate of aluminum and an Al–Mn alloy made it possible to arrange the metals studied in order of increasing modification efficiency as follows: La < Ce < Y < Yb.

CONCLUSIONS

(1) The free-corrosion potentials of ytterbium-containing binary alloys are in the passivation region.

(2) The optimal content of ytterbium in aluminum and the Al–1.9% Mn alloy for improving the corrosion resistance is 0.01 wt %.

REFERENCES

1. Gschneider, K.A., Jr., *Rare Earth Alloys*, New York: Van Nostrand, 1961.
2. Mondolfo, L.F., *Aluminium Alloys: Structure and Properties*, London: Butterworths, 1976.
3. Karimova, T.M., Ganiev, I.N., and Krasnoyarskii, V.V., *Zh. Prikl. Khim.*, 1988, vol. 61, no. 1, pp. 51–54.
4. Umarova, T.M., Krasnoyarskii, V.V., and Ganiev, I.N., *Zh. Prikl. Khim.*, 1991, vol. 64, no. 6, pp. 1337–1340.
5. Krasnoyarskii, V.V. and Umarova, T.M., *E.I. Ser.: Zashchita ot korrozii i okhrana okruzhayushchei sredy* (Express Information, Ser.: Corrosion Control and Environment Protection), Moscow, 1991, issue 6, p. 11.
6. Ganiev, I.N., Yunusov, I., Vakhobov, A.V., and Shukroev, M.Sh., *Zh. Prikl. Khim.*, 1985, vol. 58, no. 10, pp. 2366–2368.
7. Sinyavskii, V.S., Val'kov, V.D., and Kalinin, V.D., *Korroziya i zashchita alyuminievykh splavov* (Corrosion and Protection of Aluminum Alloys), Moscow: Metallurgiya, 1986, p. 23.
8. Romanov, V.V., *Metody issledovaniya korrozii metallov* (Methods for Studying the Metal Corrosion), Moscow: Metallurgiya, 1965.
9. Ganiev, I.N., Yunusov, I., and Krasnoyarskii, V.V., *Zh. Prikl. Khim.*, 1987, vol. 60, no. 9, pp. 2119–2123.
10. Tajik Patent Appl. 0600048.
11. Umarova, T.M., Dzhalolova, Z.S., Khakimov, A.A., and Ganiev, I.N., in *Materialy Mezhdunarodnoi konferentsii "Sovremennaya khimicheskaya nauka i ee prikladnye aspekty"* (Proc. Int. Conf. "Modern Chemical Science and Its Applied Aspects"), Dushanbe, 2006, p. 98.

ISSN 1070-4272, Russian Journal of Applied Chemistry, 2008, Vol. 81, No. 5, pp. 800–802. © Pleiades Publishing, Ltd., 2008.
Original Russian Text © M.D. Vedenyapina, Yu.N. Eremicheva, V.A. Pavlov, A.A. Vedenyapin, 2008, published in Zhurnal Prikladnoi Khimii, 2008, Vol. 81, No. 5, pp. 765–767.

APPLIED ELECTROCHEMISTRY AND CORROSION PROTECTION OF METALS

Electrochemical Degradation of Tetracycline

M. D. Vedenyapina, Yu. N. Eremicheva, V. A. Pavlov, and A. A. Vedenyapin

Zelinskii Institute of Organic Chemistry, Russian Academy of Sciences, Moscow, Russia

Received August 13, 2007

Abstract—Oxidation of tetracycline® in an electrochemical cell with separated cathodic and anodic compartments on smooth platinum was studied. The extent of electrochemical degradation of tetracycline and the energy consumption for eliminating the biological activity of its aqueous solutions were estimated.

DOI: 10.1134/S1070427208050145

Tetracycline® (TC) is a widely used antibiotic. However, in a human body it undergoes only partial metabolism. When getting into sewage, it suppresses the vital activity and growth of microorganism colonies used on water treatment plants. This results in environmental pollution with untreated wastewater [1–3] and in penetration of harmful substances into living bodies [2].

To prevent ingress of TC into water treatment plants, it is suggested to use electrochemical anodic oxidation on anodes-catalysts [4]. This method is widely used for neutralization of toxic organic substances polluting waste and natural waters. In the process, relatively small molecules such as phenol and its derivatives can be completely mineralized by electrochemical oxidation to CO_2 and H_2O with addition of 10–16 electrons [5–7]. Canizares et al. [6] suggested a method for electrochemical oxidation of phenol in a concentration of 200–400 mg l^{-1} in sewage with acceptable outlay.

According to the previous data [8], reducing the biological activity of a TC solution by an order of magnitude does not require its complete mineralization. It is sufficient to break down the initial TC molecules. However, the level of electric power consumption for electrochemical oxidation of TC, required to completely eliminate its biological activity, was not determined previously.

In this study we examined oxidation of TC on a platinum anode at various TC concentrations, determined the product yields as functions of current, and calculated from these data the amount of electricity spent for the oxidation of TC on platinum.

EXPERIMENTAL

Electrochemical oxidation of TC was performed in a glass cell with the anodic and cathodic compartments separated by an ion-exchange membrane. The anode and cathode were arranged parallel to each other at a distance of 2 cm. A platinum plate of the surface area 10 cm^2 served as a cathode. The same platinum plates served as anodes. The current density was 5 mA cm^{-2}. The anode potential vs. silver chloride electrode was 1.82–1.89 V. The TC concentration was 50–500 mg l^{-1}. As supporting electrolyte we used 0.1 N aqueous H_2SO_4. The solutions were analyzed by HPLC and polarimetry. The gas phase was analyzed by GLC.

Chromatographic analysis of the reaction mixtures from TC oxidation revealed formation of several products. The content of one of them monotonically increases in the course of the reaction, whereas the content of the other products, irrespective of the TC conversion, does not exceed 5% of the content of the major product. The TC content of the solution decreases with time (Fig. 1), and for all the concentrations studied it can be described by a first-order equation

$$c_t = ce^{-kt}, \quad (1)$$

where c and c_t are the initial and running TC concentrations in the solution (M); t, time from the reaction start (s); and k, oxidation rate constant equal to $(0.9–1.1) \times 10^{-3}$ min^{-1}.

Chromatographic analysis showed that the CO_2 release from the cell was negligible and did not exceed 0.5%. This allowed us to determine the current

efficiency of the reaction P (%) by the formula

$$P = \frac{V_0 - V_y}{V_0} \times 100, \quad (2)$$

where V_y is the oxygen volume released from the anodic compartment in the course of TC oxidation to the given conversion (ml); V_0 is the rate of oxygen evolution in the experiment with TC (ml).

Variation of the current efficiency with the TC conversion determined by HPLC is given in the table. It is seen that P does not exceed 11% and decreases in the course of the reaction. From the found values of P, we calculated the amount of electricity Q_y spent for the oxidation of TC to the preset conversion y:

$$Q_y = ItP, \quad (3)$$

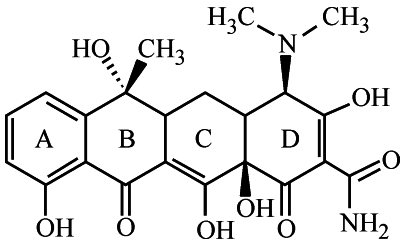
where t is the experiment time (min); I, total current passing through the cell (A); and Q_y, amount of electricity (C).

From the preset TC conversion y, we calculated the amount of electricity required for reaching this value of y, assuming that the TC oxidation is a one-electron process:

$$F_y = m/(Fmy), \quad (4)$$

where m is the TC weight (G); M, molecular weight of TC; F, Faraday number; and y, TC conversion.

The number of electrons n_e actually participating in the TC oxidation was calculated as the ratio of Q_y to F_y. Variation of all the calculated quantities in the course of the reaction is given in the table. It can be seen that decomposition of one TC molecule with the formation of the major product requires no less than 12 electrons. The quantity n_e does not appreciably vary in the course of the reaction. On the whole, this corresponds to the results of the chromatographic analysis, namely, to the fact that, irrespective of TC conversion, in the reaction mixture there is a single major product whose content exceeds the content of the other products by an order of magnitude. High value of n_e suggests that the initial molecule (see formula below) undergoes deep oxidation.



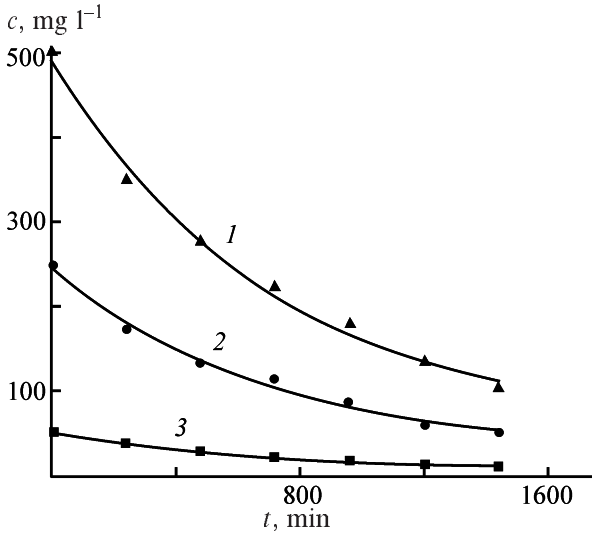


Fig. 1. Kinetic curves of electrocatalytic oxidation of tetracycline on platinum. (*c*) Tetracycline concentration and (*t*) oxidation time. Concentration of the initial tetracycline solution, mg l^{-1}: (*1*) 500, (*2*) 250, and (*3*) 50.

Oxidation of TC may occur at any ring. In each alternative, deep oxidation of TC with cleavage of C–C bonds in six-membered rings can be expected, as it is observed, e.g., in oxidation of phenol or salicylic acid [8]. In any case, cleavage of a C–C bond requires no less than 10–12 electrons. It can be seen that the charge required for the TC neutralization appears to be approximately an order of magnitude lower than the charge required for complete mineralization of TC according to the equation

$$C_{22}H_{24}O_8N_2 + 34H_2O - 92e = 22CO_2 + N_2 + 92H^+.$$

To determine what ring undergoes oxidative degradation, we used polarimetry. Figure 2 shows the dependence of the specific optical activity of the products of electrocatalytic oxidation of TC $[\alpha]_D$ on the concentration of the initial TC solution. It can be seen that this quantity linearly decreases with increasing conversion of TC. Extrapolation of the

Characteristics of electrocatalytic oxidation of tetracycline on platinum

Q_y, C	P, %	y, %	F_y, C mol^{-1}	n_e
80	11	30	6.5	12.1
115	8	45	9.8	11.7
150	6.8	56	12.1	12.1
165	5.8	65	14	11.9
180	5.1	74	16	11.5
195	4.5	79	17.2	11.3

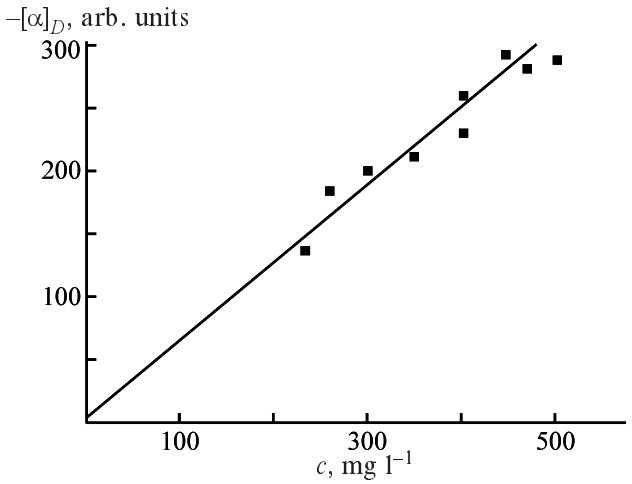


Fig. 2. Variation of the specific optical activity $[\alpha]_D$ in the course of electrocatalytic oxidation of tetracycline. (c) Tetracycline concentration.

straight line shows that, at complete conversion of the substrate, $[\alpha]_D$ is zero. The optical activity of the initial TC is caused by the presence in its molecule of four asymmetric carbon atoms in rings B and C. If only rings A and D were broken down in the course of TC oxidation, $[\alpha]_D$ would not decrease to zero. Therefore, it can be concluded that the oxidative degradation involves rings B and C and leads to disappearance of the chiral centers. Preservation of rings A and D may be responsible for the fact that the degradation of TC molecules to an extent required for the loss of the biological activity of TC aqueous solution [8] requires not 92 but only 12 electrons. The results of our study, even without identification of the major product of TC oxidation, allow a conclusion that the electricitiy consumption for neutralization of TC solutions should not appreciably exceed the electricity consumption for electrochemical degradation of phenol or salicylic acid solutions.

CONCLUSIONS

(1) Electrochemical oxidation of tetracycline on platinum involves its internal rings (two out of four).

(2) The amount of electricity required for neutralization of aqueous solutions of tetracycline was calculated from the yields of products as functions of current. This amount should not essentially exceed the electricity consumption for electrochemical degradation of phenol and salicylic acid solutions.

REFERENCES

1. Huppert, N., Elimination von Ibuprofen und NBBS in kommunalen Klaranlagen analysiert mittels Festphasenmikroextraktion, *Dissertation*, Karlsruhe, 1999.
2. *Arzneimittel in Umwelt, eine Bedrohung: Tagung*, Stuttgart, 2002, p. 7.
3. Zum Vorkommen von Arzneimitteln im Bodensee und im Baden-Württenberg Zuflüssen, *Bericht, Baden-Württenberg ISF (Institut für Seeforschung), Handesanstalt für Umweltschutz*, Baden-Württenberg, 2001, p. 27.
4. Vedenjapin, A., Baturova, M., Weichgrebe, D., et al., Abstracts of Papers, *3rd Baltic Conf. on Electrochemistry*, Gdansk, April 23–26, 2003, p. 153.
5. Rodrigo, M., Canizares, P., Carmona, M., and Lobato, J., Abstracts of Papers, *55th Meet. of the Int. Soc. of Electrochemistry*, Lausanne, 2004, p. 264.
6. Canizares, P., Saez, C., Lobato, J., and Rodrigo, M., *Electrochim. Acta*, 2004, vol. 49, no. 26, pp. 4641–4650.
7. Canizares, P., Lobato, J., Paz, R., et al., *Water Res.*, 2005, vol. 39, no. 12, pp. 2687–2703.
8. Weichgrebe, D., Danilova, E., Grube, S., et al., *Kond. Sredy Mezhfazn. Gran.*, 2003, no. 2, pp. 117–122.

ISSN 1070-4272, Russian Journal of Applied Chemistry, 2008, Vol. 81, No. 5, pp. 803–809. © Pleiades Publishing, Ltd., 2008.
Original Russian Text © N.B. Danilenko, G.G. Savel'ev, N.A. Yavorovskii, T.A. Yurmazova, 2008, published in Zhurnal Prikladnoi Khimii, 2008, Vol. 81, No. 5, pp. 768–773.

APPLIED ELECTROCHEMISTRY AND CORROSION PROTECTION OF METALS

Chemical Reactions in Electric Pulse Dispersion of Iron in Aqueous Solutions

N. B. Danilenko, G. G. Savel'ev, N. A. Yavorovskii, and T. A. Yurmazova

Research Institute of High Voltages, Tomsk, Russia
Tomsk Polytechnic University, Tomsk, Russia

Received October 11, 2007

Abstract—IR spectroscopy, X-ray phase, chemical, kinetic, and thermodynamic analyses were used to determine the nature of chemical reactions occurring in electric pulse dispersion of a metal (Fe) in aqueous solutions of inorganic substances ($MnSO_4$, NaH_2AsO_4, H_3AsO_3, $K_2Cr_2O_7$).

DOI: 10.1134/S1070427208050157

Electric discharges (ED) in solutions find practical application in water treatment to remove impurities and in synthesis of highly dispersed materials. Therefore, problems associated with determining the composition of the products formed, raising the yield, and controlling the process parameters are topical. A rather interesting area in this field is application of pulsed electric discharges (PED) in a layer of metallic grains placed in an aqueous solution [1–6]. The energy introduced acts upon the electrodes, whose part is played by metallic grains, and leads to their erosion and formation of highly dispersed particles. In a system of this kind, not only the output capacity becomes higher, but also the temperature and dispersity of the material are easily controlled. However, the composition of the products formed and chemical mechanisms of these processes remain insufficiently understood.

It has been shown [7] that, at least in the case of ED between electrodes with insulating sheaths (barrier ED) or those spaced far apart, the prevalent effect is the oxidizing action on solutes. This effect is mostly attributed [7, 8] to formation of $OH^{\cdot}$ radicals under the action of the ED plasma. The reducing effect of barrier ED in aqueous solutions is, as a rule, insignificant and is less understood [7, 9]. It may be associated with such primary products of water decomposition as hydrated electrons e_{aq} and H atoms. The oxidation by $OH^{\cdot}$ radicals is also assumed to occur under the action of ED on metallic grains (zero-barrier ED) [10]. For example, it has been shown [5] that the oxidizing action of zero-barrier ED is observed in water treatment to remove As(III), with at least part of arsenic converted to As(V). However, the metal is dispersed in this case and, if it is active, this must lead to a reducing effect of PED on a solution. This has been confirmed experimentally for the example of water treatment to remove the Cr(VI) impurity [4]. However, the role of redox reactions and the extent to which products formed in water decomposition and metal particles are involved in these processes cannot be considered well understood because the composition of the products removed from solution has been insufficiently studied.

This study was aimed to determine the composition of the products and the type of reactions occurring in PED treatment of a layer of iron grains in solutions containing oxidizing ($Cr_2O_7^{2-}$, $H_2AsO_4^-$) and reducing agents (Mn^{2+} and As^{3+}). The kinetics of water treatment to remove impurities with oxidizing and reducing properties were compared.

EXPERIMENTAL

The experimental setup comprised a 1.5-l reactor and a pulsed power source. Iron shavings ($10 \times 5 \times 2$ mm) were placed in an amount of 200 g on the bottom of the reactor fabricated from a dielectric material. A pulsed voltage (pulse amplitude 500 V, repetition frequency 300 s^{-1}, width 15 μs) was applied to two external feeding electrodes submerged into the shavings to a depth of 3 cm. The maximum discharge current was 250 A. The pulse energy was 0.5 J per pulse. St.3 served as the material of iron

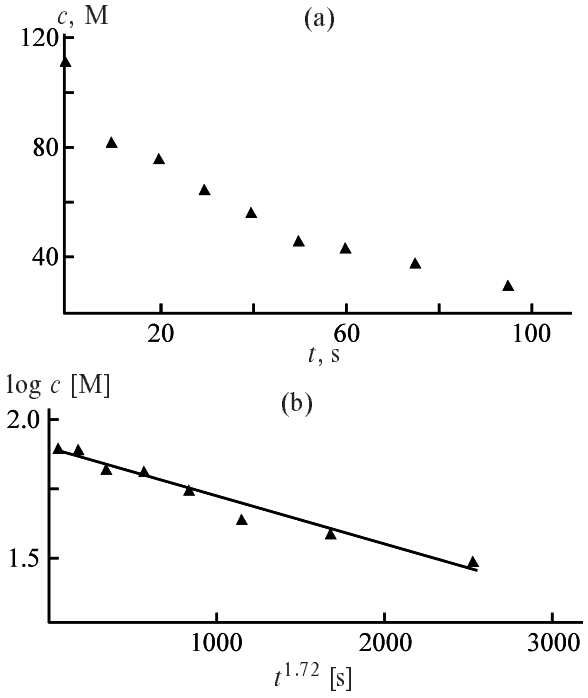


Fig. 1. (a) Concentration c of Mn^{2+} cations vs. the PED treatment time t and (b) $\log c$–$t^{1.72}$ dependence for PED treatment of iron grains in a salt solution containing Mn^{2+} cations. $c_0(Mn^{2+})$ = 110 mg l^{-1}, solution volume 100 ml.

shavings and feeding electrodes. Working solutions containing $H_2AsO_4^-$, Mn^{2+}, and $Cr_2O_7^{2-}$ ions of various concentrations were prepared from distilled water and $MnSO_4 \cdot 5H_2O$, NaH_2AsO_4, and $K_2Cr_2O_7$. Solutions containing As(III) were prepared from GSO (State Reference Sample) 7264–96 standards by dissolving As_2O_3 in HCl at pH 2.

A PED treatment of metallic grains submerged in a working solution leads to formation of a suspension composed of eroded metal particles and a solution. To obtain dry electroerosion powders, the suspension was passed through a "blue ribbon" filter and the resulting solid product was dried at room temperature. The content of Fe^{2+}, Fe^{3+}, As^{5+}, and Mn^{2+} in the filtrate was found by photocolorimetry [11]. The concentration of As^{3+} was determined by voltammetry [12].

The dry electroerosion powders were subjected to an X-ray phase analysis on a DRON-3.0 diffractometer (powder method). The X-ray diffraction patterns were interpreted using the Powder Diffraction File (PDF) compiled by Joint Committee on Powder Diffraction Standards (JCPDS). The dispersity and morphology of the particles were determined by analysis of carbon replicas with extraction on an EM-125 transmission electron microscope. The chemical composition and the structure of the compounds formed in electroerosion of metallic grains in water and aqueous solutions were found by IR spectroscopy on a Nicolet IR Fourier spectrometer in the range 4000–400 cm^{-1} with an attachment for diffuse reflection in KBr (spectral resolution 4 cm^{-1}).

It has been shown previously [6] that the electroerosion of iron grains in water and solutions under the action of PED occurs to give nano- and microparticles by the law

$$[Fe_s] = k_e t^{0.72}, \quad \text{(I)}$$

where $[Fe_s]$ is the concentration of the eroded metal in the suspension (mg l^{-1}); t, time of PED action (s); and k_e, empirical constant dependent on the PED parameters and properties of the electrodes and the medium [mg $(l\,s^{0.72})^{-1}$], with the exponent 0.72 accounting for the variation of the PED conditions in the course of electroerosion.

For dilute [$(0–5) \times 10^{-3}$ M] solutions of $H_2AsO_4^-$ and $Cr_2O_7^{2-}$ anions, the impurity is removed from the solution in accordance with the equation [4, 5]

$$\log c_i = k_i^{1+0.72} + \log c_0, \quad \text{(II)}$$

where c_0 and c_i are the initial and running concentrations of an ion in solution (mg l^{-1}), and k_i' is the effective rate constant including k_e.

Equation (II) was derived by integration of Eq. (III) with account of Eq. (I) under the condition that the concentration of the dispersed metal in the suspension changes only via erosion, i.e., increases.

$$dc_i/dt = k_i [Fe_s] c_i, \quad \text{(III)}$$

Consequently, the reaction of dispersed iron with the impurity is of partial first order with respect to both the reactants. This means that all Fe_s particles are activated and react in the discharge zone. The adequacy of the description was verified by experiments in which the PED was terminated and the initial concentration of the impurity was varied and by calculations in terms of other equations, which demonstrated a considerably poorer agreement with the experiment.

Similar experiments were carried out with a $MnSO_4$ salt solution. Figures 1a and 1b show raw data on removal of Mn^{2+} ions from water and the

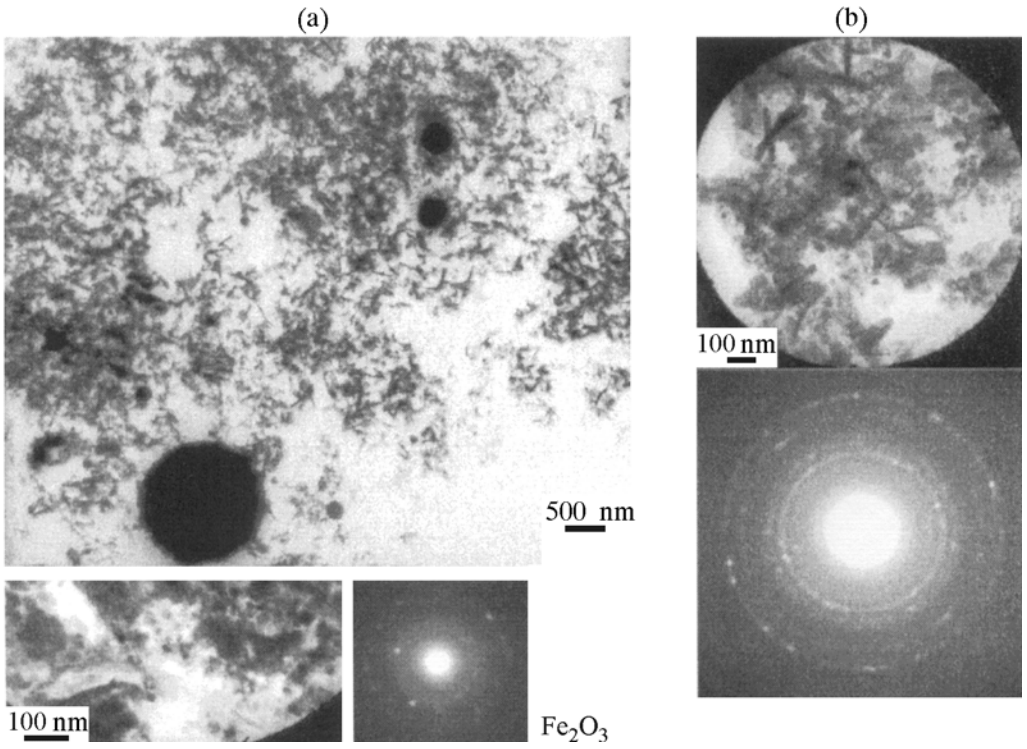


Fig. 2. Electron micrograph of (a) Fe_2O_3 and (b) Fe_3O_4 particles in a sample produced by a PED treatment of iron grains in water. PED treatment time 10 min.

same data plotted in the coordinates of Eq. (II). It can be seen that the experimental data are described by the same relations as those for $H_2AsO_4^-$ and $Cr_2O_7^{2-}$ anions [4, 5], i.e., Mn^{2+} ions are removed in accordance with the same laws, despite the possibly different chemical mechanisms.

In the next stage of the study, we determined by XPA and IR spectroscopy the composition of the products formed under the action of PED on a bed of iron grains in water and salt solutions containing $H_2AsO_4^-$, $Cr_2O_7^{2-}$, and Mn^{2+} ions and examined the occurring reactions with account of the necessary condition $\Delta G_{298} < 0$.

Fe–distilled water. A study of electroerosion powders and the suspension by transmission electron microscopy demonstrated that they contain particles with sizes ranging from several nanometers to several micrometers (largest size 5–10 μm). Two maxima are observed in the particle size distribution: at 1–30 nm and 0.2–10 μm. Particles of regular (spheres) and irregular (faceted particles, plates, rods, fibers) shapes can be found (Figs. 2a, 2b).

It can be seen from the electron micrographs that crystalline particles are observed together with those of amorphous structure, as follows from the appearance of rings constituted by point reflections. A calculation of interplanar spacings and their comparison with reference data demonstrated that, in sample produced by a PED treatment of iron grains, all fine particles (<100 nm) are composed of oxides: Fe_2O_3, Fe_3O_4, FeO. Coarse particles cannot be identified by electron diffraction analysis and are probably composed of Fe, which follows from XPA data and results of a chemical analysis, according to which the suspension produced by PED contains, immediately after the treatment, 85–90% Fe^0. This content decreases in the course of time, to become 20–40% in dry powders, which is due to oxidation of iron by atmospheric oxygen in storage, filtration, and powder drying. XPA data demonstrated that the products formed in electroerosion of iron grains mainly contain α-Fe^0, FeO, and Fe_2O_3 phases (see table). A comparison of the IR spectra obtained in this study (Figs. 3–5) with those reported in the literature [13, 14] demonstrated that the following compounds are formed in PED of a bed of iron grains in distilled water (stretching vibration frequencies are given in parentheses): Fe_2O_3 (560 and 1480 cm^{-1}), $FeFe_2O_4$ (415 cm^{-1}), FeOOH (485 cm^{-1}), and $FeOOH \cdot nH_2O$ (700, 1030, 1650 cm^{-1}). The whole body of data furnished by chemical analysis, XPA,

Diffraction angles and intensities of the main reflections for products formed in electrolysis of iron grains

Reflection no.	Experimental values				JCPDS data		Phase
	2θ, deg	H, rel. units	d, Å	I_{rel}, %	d, Å	I_{rel}, %	
1	35.318	1836	2.951	7	2.950	30	Fe_2O_3 (maghemite-Q)
2	41.766	6083	2.511	24	2.514	100	Fe_2O_3 (maghemite-Q)
3	47.079	625	2.241	2	–	–	–
4	49.274	3628	2.147	14	2.153	100	FeO (wustite)
5	50.884	1981	2.084	8	2.086	15	Fe_2O_3 (maghemite-Q)
6	52.489	25238	2.024	100	2.027	100	α-Fe
7	67.698	1417	1.607	6	1.607	24	Fe_2O_3 (maghemite-C)
8	72.245	1487	1.518	6	1.523	60	FeO (wustite)
9	74.548	2487	1.478	10	1.476	34	Fe_2O_3 (maghemite-C)
10	77.399	3980	1.432	16	1.433	20	α-Fe
11	99.892	6886	1.169	27	1.170	30	α-Fe

and IR spectroscopy shows that the main solid products formed in iron dispersion by PED in distilled water are α-Fe, α-FeO, Fe_2O_3, Fe_3O_4, FeOOH, and $FeOOH \cdot nH_2O$.

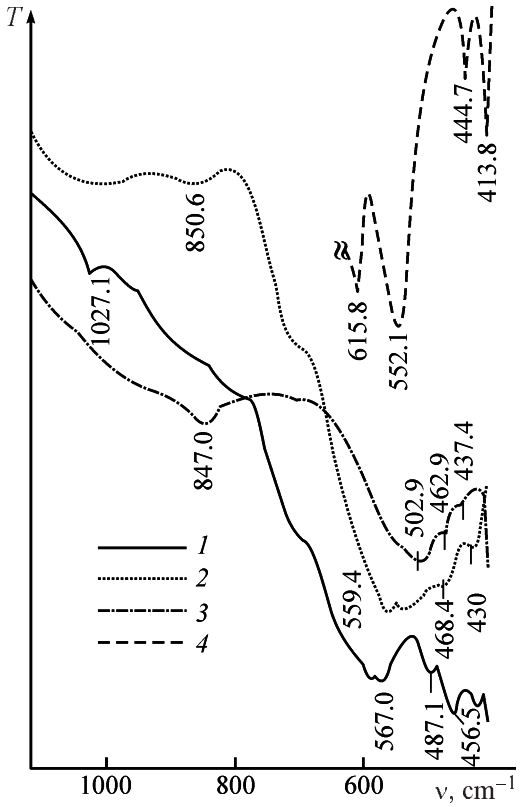


Fig. 3. IR spectra of samples produced by PED in a reactor with iron grains in (*1*) distilled water and (*2*) salt solution containing $Cr_2O_7^{2-}$ ions. (*3, 4*) Spectra of $Cr(OH)_3$ and Cr_2O_3 produced by a chemical method. (*T*) Transmission and (ν) wavenumber; the same for Figs. 4 and 5.

Thus, the results of the study suggest that, in a PED treatment of a bed of Fe grains in water, exclusively its oxidizing action is manifested. The PED energy is mostly expended for heating and dispersion of the metal, rather than for chemical reactions [1, 3, 6, 15]. Further, the dispersed iron is oxidized by water and atmospheric oxygen by the reactions

$$Fe^0 + H_2O = FeO + H_2, \quad (1)$$

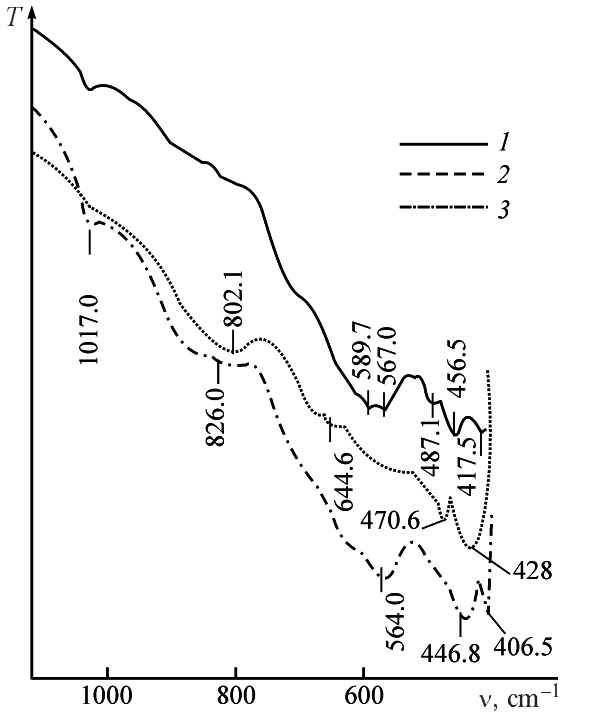


Fig. 4. IR spectra of samples produced by PED in a reactor with iron grains in (*1*) distilled water and (*2*) salt solution containing $H_2AsO_4^-$ ions. (*3*) Spectrum measured after sorption of $H_2AsO_4^-$ ions from solution on the product of electroerosion of Fe grains.

$$4FeO + O_2 + 2H_2O = 4FeOOH, \quad (2)$$

$$FeO + Fe_2O_3 = Fe_3O_4. \quad (3)$$

FeO is probably formed via $Fe(OH)_2$ decomposing because of the high local temperature in the discharge channel [15]. Also possible is oxidation of the metal by products of water decomposition. These are mainly OH radicals [8]:

$$H_2O \xrightarrow{PED} OH^{\cdot} + H^{\cdot}. \quad (4)$$

However, the steep decrease in the yield of the oxidized metal, observed as the solution temperature is lowered [1], indicates that radicals make only a small contribution to formation of the electroerosion products.

Fe–$K_2Cr_2O_7$ solution. The following vibration bands appear in the IR spectrum of a sample obtained by PED in a salt solution containing $Cr_2O_7^{2-}$ ions: band at 559 cm^{-1}, which belongs to Cr_2O_3 (552.1 cm^{-1}); bands at 430 and 850.6 cm^{-1}, which correspond to those associated with $Cr(OH)_3$ (437 and 847.0 cm^{-1}); and also a band at 846 cm^{-1}, which can be attributed to $[CrO_4]^{2-}$. Thus, it can be suggested that, as a result of PED treatment of a salt solution containing $Cr_2O_7^{2-}$ ions, the compounds Cr_2O_3, $Cr(OH)_3$, $Fe[CrO_4]$, and $Fe_2[CrO_4]_3$ are formed. Apparently, heated drops of dispersed iron reduce bichromate ions by the reactions

$$Cr_2O_7^{2-} + 3Fe + 7H_2O = 2Cr(OH)_3 + 3Fe(OH)_2 + 2OH^-, \quad (5)$$

$$Cr_2O_7^{2-} + 2Fe + 7H_2O = 2Cr(OH)_3 + 2Fe(OH)_3 + 2OH^-. \quad (6)$$

Further, Cr(III) hydroxide decomposes to give the oxide. It is also possible that insoluble chromates are formed because "superequilibrium" iron ions and an exchange interaction of $Cr_2O_7^{2-}$ with iron hydroxide occur at high temperatures:

$$2Fe^{2+} + Cr_2O_7^{2-} + H_2O = 2FeCrO_4 + 2H^+, \quad (7)$$

$$2Fe(OH)_2 + Cr_2O_7^{2-} = 2FeCrO_4 + 2OH^- + H_2O. \quad (8)$$

Fe–NaH_2AsO_4 and H_3AsO_3 solutions. The IR spectrum of a sample obtained by PED in a salt solution containing $H_2AsO_4^-$ ions shows bands associated with this ion adsorbed on erosion products (bands at 470.6 and 802 cm^{-1}) and with compounds $FeAsO_4$ or $FeAsO_3$ (band at 644.6 cm^{-1}). According to the data of [16], the presence of bands at 784–805 cm^{-1} clearly points to partial reduction of As(V) to As(III) (Fig. 4). Special-purpose experiments with an $H_3AsO_3^-$ containing solution demonstrated that, under the action of PED, the recovery of As(III) ions is incomplete and As(III) is oxidized to As(V), with the fraction of As(V) in solution constituting 7.5% relative to the initial concentration of As(III). The presence of bands associated with adsorbed anions is in agreement with published data on water treatment to remove arsenic impurities via adsorption on Fe and Al hydroxides [16]. In the case under consideration, inner-sphere complexes XH_2AsO_4 and XH_2AsO_3 (X is the goethite matrix) [16] are formed:

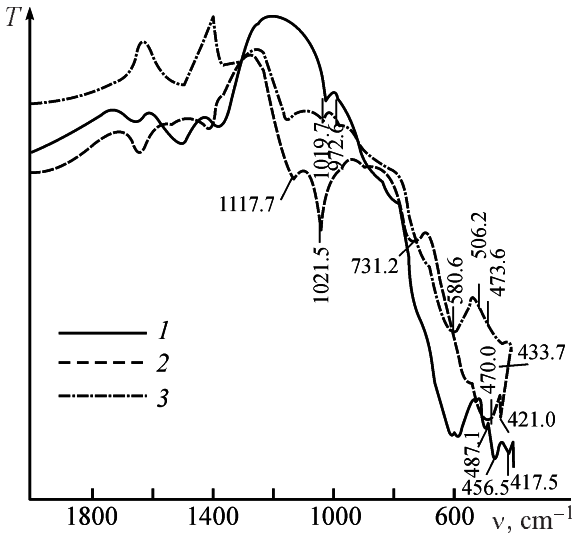


Fig. 5. IR spectra of samples produced by PED in a reactor with iron grains in (*1*) distilled water and (*2*) salt solution containing Mn^{2+} ions. (*3*) Spectrum measured after sorption of Mn^{2+} ions from solution on the product of electroerosion of Fe grains.

$$XOH + H_3AsO_4 \rightleftarrows XH_2AsO_4 + H_2O, \quad (9)$$

$$XOH + H_3AsO_3 \rightleftarrows XH_2AsO_3 + H_2O. \quad (10)$$

The transformation $As^{3+} \rightarrow As^{5+}$ in solution has been confirmed by chemical analysis [5]. This transformation virtually does not occur under the action of dissolved oxygen under ordinary conditions, even though it is thermodynamically possible. This process can occur in particular conditions because of heating or formation of $OH^{\cdot}$ radicals:

$$2H_3AsO_3 + O_2 \xrightarrow{T} 2H^+ + 2H_2AsO_4^-, \quad (11)$$

$$H_3AsO_3 + OH^{\cdot} = H^+ + H_2AsO_4^-. \quad (12)$$

As can be seen from the composition of the products, back transformation $As^{5+} \rightarrow As^{3+}$ is also possible and can occur in accordance with the equations

$$2H_2AsO_4^- + 2Fe = 2FeAsO_3 + 2OH^- + H_2O, \quad (13)$$

$$H_2AsO_4^- + 2H = H_3AsO_3 + OH^-, \quad (14)$$

$$H_2AsO_4^- + 2e_{aq} = H_3AsO_3 + 3OH^-. \quad (15)$$

However, a kinetic analysis demonstrated that both the redox reactions (11), (12) and the adsorption (9), (10) are described under PED conditions by Eq. (II), according to which the rate is proportional to the suspension concentration [Fe_s]. Hence follows that the main channel involves reactions initiated by repeated activation by the discharge of the steadily increasing number of suspension particles, i.e., reactions (11) and (13). Thus, in the case of As compounds, there may occur adsorption on erosion products [reactions (9), (10)], oxidation of As(III) by dissolved oxygen [reaction (11)], and reduction of As(V) by the discharge-dispersed metal [reaction (13)].

Fe–$MnSO_4$ solution. The IR spectrum of a sample obtained by PED in a salt solution containing Mn^{2+} ions shows absorption bands at 972.6, 731.2, 470.0, and 420.1 cm^{-1} (Fig. 5), associated with MnO_2 (characteristic bands at 970, 720, and 420 cm^{-1}) and MnOOH compounds (740, 550, and 485 cm^{-1}). The increase in the intensity of the absorption band at 1021 cm^{-1}, compared with the absorption band in the IR spectrum of a sample obtained by PED in H_2O, shows that the content of hydroxy groups in the sample increases. Thus, the following products are found experimentally: MnO_2, $Mn(OH)_4$, and MnOOH. The reduction of Mn^{2+} by iron is impossible because Mn is a more active metal than Fe. The removal of Mn^{2+} from solution may be due either to its oxidation to insoluble oxides and hydroxides of Mn^{3+} and Mn^{4+} or to precipitation of $Mn(OH)_2$. Also possible is reduction of the sulfate ion to SO_2 or to sulfide ion. Because no sulfides were found in the precipitate, the following reaction is more probable:

$$SO_4^{2-} + 2H_2O + Fe = SO_2 + Fe(OH)_2 + 2OH^-. \quad (16)$$

At the same time, oxidation of Mn^{2+} by the sulfate ion is thermodynamically impossible.

Because the removal of this ion from water is described by Eq. (II), it cannot be governed by the oxidation with the $OH^{\cdot}$ radical, which is a primary product of ED in water. The proportionality of the reaction rate to the concentration of dispersed iron may be associated with precipitation of $Mn(OH)_2$ by the hydroxide after reaction (16) and with the hydrolysis of Mn^{2+}, initiated by heated particles of the suspension and followed by oxidation of the hydroxide being formed:

$$Mn^{2+} + 2H_2O \xrightarrow{T} Mn(OH)_2 + 2H^+, \quad (17)$$

$$Mn(OH)_2 + 1/2O_2 + H_2O \xrightarrow{T} Mn(OH)_4. \quad (18)$$

Thus, the analysis of the reactions occurring under the action of PED on a bed of Fe grains in solution demonstrated that, in solutions of typical oxidizing agents (SO_4^{2-}, $Cr_2O_7^{2-}$, $H_2AsO_4^-$), these oxidants are reduced, whereas in solutions that contain reducing agents (H_3AsO_3, Mn^{2+}), these latter are oxidized. Also, to explain the results obtained, it is necessary to assume that there occur hydrolysis reactions and secondary reactions involving primary highly dispersed solid products. Such a multichannel behavior is accounted for both by the composition of the reagents and by the occurrence of the reactions under conditions of rapid temperature rises and falls.

CONCLUSIONS

(1) The products formed in chemical reactions that occur under the action of a pulsed electric discharge on a bed of iron grains in solutions of inorganic substances ($MnSO_4$, NaH_2AsO_4, H_3AsO_3, $K_2Cr_2O_7$) were identified. The composition of the products indicates that the reactions proceed in several thermodynamically possible, including opposite (oxidation and reduction), directions.

(2) The rate of recovery of a dissolved substance from water under the action of pulsed electric discharge is proportional both to the concentration of the substance and to that of dispersed iron, which points to a secondary activation of particles in subsequent discharges.

(3) The products of water decomposition in a discharge ($H^{\cdot}$ and $OH^{\cdot}$) do not contribute noticeably to the reactions with dissolved substances.

REFERENCES

1. Berkowitz, A.E. and Walter, J.L., *J. Mater Res.*, 1987, vol. 2, no. 2, pp. 277–288.

2. Khainatskii, S.A., Smal'ko, A.A., and Zubenko, A.A., *Elektron. Obrab. Mater.*, 2005, no. 4, pp. 62–65.
3. Shidlovskii, A.K., Shcherba, A.A., and Zakharchenko, S.N., *Voda Vodoochisni Tekhnol.*, 2003, no. 2, pp. 26–31.
4. Danilenko, N.B., Savel'ev, G.G., Yurmazova, T.A., and Yavorovskii, N.A., *Zh. Prikl. Khim.*, 2007, vol. 80, no. 1, pp. 88–93.
5. Danilenko, N.B., Savel'ev, G.G., Yavorovskii, N.A., et al., *Zh. Prikl. Khim.*, 2005, vol. 78, no. 10, pp. 1659–1663.
6. Danilenko, N.B., Savel'ev, G.G., Yavorovskii, N.A., et al., *Zh. Prikl. Khim.*, 2005, no. 9, vol. 78, pp. 1463–1468.
7. Zakharov, A.G., Maksimov, A.I., and Titova, Yu.V., *Usp. Khim.*, 2007, vol. 76, no. 3, pp. 260–277.
8. Kornev, Ya.I., Yavorovskii, N.A., Ivanov, G.F., et al., *Izv. Tomsk. Politekh. Univ.*, 2003, vol. 306, no. 5, pp. 78–82.
9. Piskarev, I.M., *Zh. Obshch. Khim.*, 2001, vol. 71, no. 10, pp. 1622–1627.
10. Ishibashi, V., Araki, T., Kisimoto, K., and Kuno, H., *Ceram. Jpn.*, 1971, no. 6, pp. 461–468.
11. *Unifitsirovannye metody analiza vod* (Unified Methods for Analysis of Water), Lur'e, Yu.Yu., Ed., Moscow: Khimiya, 1973.
12. Vydra, F., Štulik, K., and Julakova, E., *Rozpouštěcí polarographie a voltammetrie*, Prague: Nakl. Technicke Literatury, 1977.
13. Nakamoto, K., *Infrared and Raman Spectra of Inorganic and Coordination Compounds*, New York: Wiley, 1986.
14. Boldyrev, A.I., *IK spektry mineralov* (IR Spectra of Minerals), Moscow: Nedra, 1976.
15. Descoeudres, A., Hollenstein, Ch., Walder, G., and Perez, R., *J. Phys. D: Appl. Phys.*, 2005, vol. 38, no. 22, pp. 4066–4073.
16. Goldberg, S. and Johnston, C.T., *J. Colloid Interface Sci.*, 2001, vol. 234, pp. 204–216.

ISSN 1070-4272, Russian Journal of Applied Chemistry, 2008, Vol. 81, No. 5, pp. 810–814. © Pleiades Publishing, Ltd., 2008.
Original Russian Text © N.A. Kornilova, I.M. Lipatova, L.I. Makarova, 2008, published in Zhurnal Prikladnoi Khimii, 2008, Vol. 81, No. 5, pp. 774–777.

PROCESSES AND EQUIPMENT OF CHEMICAL INDUSTRY

Effect of Hydroacoustic Treatment on the State of Aqueous Solutions of Sodium Alginate

N. A. Kornilova, I. M. Lipatova, and L. I. Makarova

Institute of Solution Chemistry, Russian Academy of Sciences, Ivanovo, Russia

Received May 16, 2007

Abstract—Effect of a hydroacoustic treatment in a rotary-pulsed apparatus on the properties of sodium alginate solutions: dynamic viscosity, intrinsic viscosity, surface tension, and optical density, was studied. The contribution of the mechanical degradation of macromolecules to the observed decrease in the viscosity of alginate solutions was determined. The effect of the ionic strength of the solutions on their stability against hydroacoustic degradation was analyzed.

DOI: 10.1134/S1070427208050169

Sodium alginate is a polysaccharide of vegetable origin, produced from brown algae. This natural polymer is well-soluble in water and forms viscous thixotropic solutions. Owing to its unique physicochemical properties, good binding capacity, and film-forming ability, sodium alginate finds wide use in rather diverse fields: textile, paper, and food industries, as well as in cosmetology and medicine. The alginate is frequently used in mixtures with other polymers, which makes it possible to impart improved technological or consumers' properties to formulations of this kind. Highly homogeneous polymeric blends can be produced in rotary hydroacoustic apparatus. In these devices, a liquid polymeric material is subjected to an integrated action of ultrasonic vibrations and, accordingly, cavitation and also to high shear stresses created in the liquid in narrow (0.1–0.5 mm) gaps between elements of the rotor and stator [1]. Target processes of homogenization or fine dispersion under a hydroacoustic treatment (HA treatment) are, as a rule, accompanied by mechanically initiated structural and chemical transformations in polymers. Previously, data have been reported on the effect of an HA treatment on properties of solutions of certain polysaccharides: carboxymethyl cellulose [2], chitosans [3], and starch hydrogels [4]. In these studies, the primary attention was given to structural effects of the HA treatment and to its influence on the rheological properties of polysaccharide solutions. The fundamental aspects of initiation of mechanical degradation with rupture of polysaccharide molecules have been only considered for the example of starch [4]. No data on how the HA treatment affects the properties of sodium alginate solutions can be found in the literature.

The aim of this study was to examine the effect of HA treatments in a flow-through rotary-pulsed apparatus on properties of aqueous solutions of sodium alginate. A considerable attention was given to the problem of stability of sodium alginate against degradation in an HA treatment of its aqueous solutions.

EXPERIMENTAL

Aqueous solutions of sodium alginate (M = 340 000), used in the study, had concentrations in the range 0.25–8.0 wt %. The solutions were subjected to a mechanical treatment in a laboratory rotary-pulsed apparatus (RPA). The average gap between the rotating and immobile elements of the working chamber was 0.5 mm. The treatment conditions were as follows: rotor rotation rate 5000 rpm, to which corresponds a shear rate gradient of 17.7×10^4 s^{-1}; duration 4–60 s; and temperature 50°C. The choice of temperature was governed by the fact that, under an intense mechanical treatment, the solutions warm-up and heat is released into the environment. It was found experimentally that, at the chosen temperature, it can be maintained constant in the course of treatment, irrespective of the solution concentration. The only exception are solu-

tions with concentrations higher than 5 wt %, for which the treatment time did not exceed 30–40 s, which prevented an excessive warming-up.

The optical density of the solutions was measured on a Spekol-221 spectrophotometer at a wavelength $\lambda = 400$ nm. The molecular weight of sodium alginate was found using the Mark–Kuhn–Houwink equation

$$[\eta] = KM^{\alpha},$$

where K and α are empirical constants for a given polymer–solvent system; for aqueous solutions of sodium alginate, $K = 0.002$, $\alpha = 1$ [5].

The kinematic viscosity of the solutions was measured with Ubbelohde capillary viscometers (VPZh-2) with inner diameters of 0.99, 1.31, and 2.37 mm. The intrinsic viscosity was found by the viscometer with an inner diameter of 0.56 mm. The dynamic viscosity of sodium alginate solutions was measured with a Rheotest-2 rotary viscometer with a cylinder–cylinder working unit in the shear rate range 1.5–1312 s^{-1}. The surface tension of sodium alginate solutions at the interface with air was measured with a Rebinder instrument [6]. The method is based on measuring the rarefaction at which an air bubble breaks through a thermostated liquid being measured. The ratio between the diameters of the capillary and glass tube was 0.12.

The joint action of high tangential stresses and the ultrasonic field in RPA causes structural transformations in the polysaccharide solutions being treated and, accordingly, changes the structure-sensitive properties [3]. Figure 1 shows how the kinematic viscosity (a), optical density (b), and surface tension (c) of sodium alginate solutions depend on the duration of their treatment in RPA.

The viscosities of alginate solutions with different concentrations strongly differ and viscometers with different capillary diameters are to be used to measure these viscosities. Therefore, Fig. 1a presents data in the form of a ratio between the viscosity of mechanically treated solutions (η_A) and their initial viscosity (η_{in}). This approach enables comparison of the rates at which the viscosity decreases for solutions with different concentrations. Figure 1a shows that the rate of viscosity decrease increases with the solution concentration. The extent to which the viscosity decreases under mechanical treatment is determined by the degree of structuring of the solutions, which can be judged from the manner in which their dynamic viscosity depends on the shear

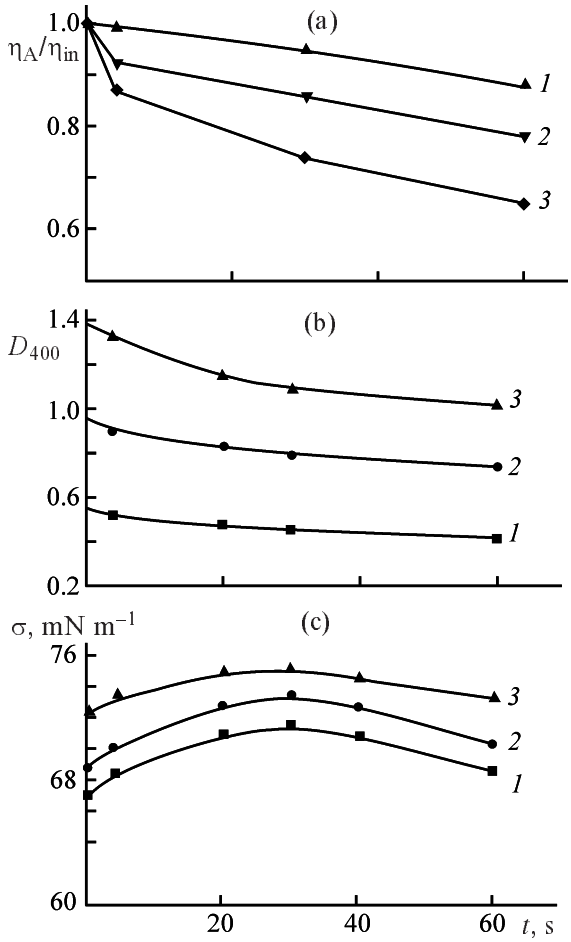


Fig. 1. Effect of the RPA treatment duration t on (a) relative viscosity η_A/η_{in}, (b) optical density D_{400}, and (c) surface tension σ of sodium alginate solutions. Content of sodium alginate, wt %: (*1*) 1, (*2*) 2, and (*3*) 3.

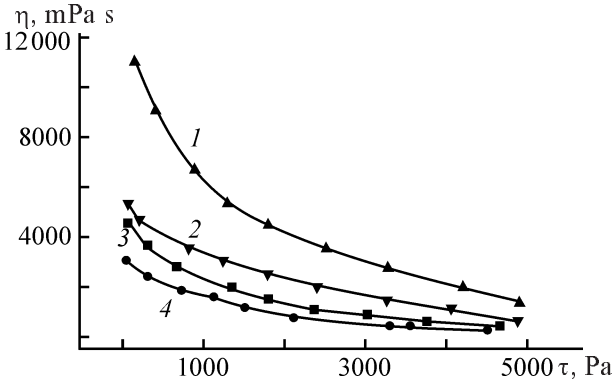


Fig. 2. Dynamic viscosity η of sodium alginate solutions vs. the shear stress τ. Treatment duration 60 s. Solution: (*1, 3*) initial and (*2, 4*) treated in RPA. Solution concentration, wt %: (*1, 2*) 5 and (*3, 4*) 4.

stress (Fig. 2). The stronger the deviation of the curves from the horizontal line, the larger the structural component of the viscosity and the greater the loss of viscosity under an intense mechanical load.

Parameters of the hydroacoustic degradation of sodium alginate

c, wt %	$M \times 10^{-5}$	$V \times 10^{-16}$, ruptures/s
0.25	2.2	0.41
0.5	2.7	0.38
1.0	3.0	0.32
2.0	2.9	1.12
3.0	2.8	1.82
4.0	2.8	2.50
5.0	2.8	3.60
6.0	2.7	4.60
7.0	3.6	–
8.0	3.7	–

Sodium alginate solutions have small structural elements [7], which do not form any strong fluctuation network at moderate concentrations. Therefore, moderately concentrated solutions of this polysaccharide show high plasticity and a weakly pronounced anomaly of viscosity. As the alginate concentration increases, the solution becomes more structured. For example, the run of the dependence under consideration for a 5% solution indicates that there exists a pronounced anomaly of viscosity (Fig. 2, curve *1*). As a result of a mechanical treatment in RPA, the fluidity and plasticity of the solutions increases, which is evidenced by a considerable decrease in the slope of the curve (Fig. 2, curve *2*). Solutions of sodium alginate used in the study, with concentrations of 6, 7, and 8 wt %, have the form of a very thick mass (at a concentration of 8% the solution has virtually zero fluidity). As a result, these solutions cannot be introduced into the apparatus in the conventional way, through a feeding pipe. In these cases, an aqueous suspension of an as yet undissolved alginate was poured into the apparatus and kept there for a time necessary for dissolution, after which the resulting solution was treated in the RPA. Already after 30 s of an HA treatment, the concentrated solutions acquired fluidity.

The decrease in the structural component of the viscosity of sodium alginate solutions under an HA treatment is due to rupture of intermolecular hydrogen bonds and disintegration of aggregates of alginate macromolecules. The latter is also confirmed by the that the optical density of the solutions steadily decreases as the time of their mechanical treatment in RPA increases (Fig. 1b).

Figure 1c shows how the surface tension of sodium alginate solutions varies under mechanical treatment. The increase in the surface tension is due to the action of strong shear stresses on the solution in narrow gaps between the rotor and stator of the apparatus. Application of shear stresses results in that the conformation of macromolecules changes via their elongation in the direction of shear forces. After the shear load is removed, the system tends to return to the equilibrium state; however, a certain structural strain is preserved because of the fixation of forced deformations at the instant of treatment. In the course of the treatment, the deformed state of macromolecules can be fixed via formation of a network of molecular entanglements, associative contacts, and cavitation-induced cross-links. The extremal nature of the dependences presented suggests that processes of formation of a strained 3D network and its mechanical disintegration simultaneously occur in the course of treatment. In storage of RPA-treated solutions, the surface tension decreases via relaxation, which is promoted by agitation and temperature rise.

To elucidate the role of the mechanical degradation of alginate macromolecules in the decrease in the viscosity of the solutions, the intrinsic viscosities of polymer samples obtained from mechanically treated solutions by drying were determined by extrapolation. The alginate films obtained were comminuted and used to prepare solutions with a concentration of 0.005 g ml^{-1}, from which solutions of lower concentrations were produced by dilution. The experimental values of the intrinsic viscosity were used to calculate the molecular weight of the samples by the Mark–Kuhn–Houwink equation presented above.

The response of polymer–solvent systems to a hydroacoustic treatment is largely determined by the polymer concentration. The table lists parameters of the hydroacoustic degradation of the alginate in relation to its concentration in the solution at the instant of treatment. After 60 s of treatment at a rotor rotation rate of 5000 rpm, the maximum decrease in the molecular weight (from 340000 to 2200000) was observed for the least concentrated solution (0.25 wt %). For other concentrations, the molecular weight that could be reached was 270000–300000. As for the degradation rate, the effect of viscosity is more pronounced in this case. The degradation rate V (ruptures/s) was calculated as the number of elementary events of rupture of macromolecules in unit time by the formula

$$V = [10c(1/P - 1/P_0)V_c N_A]/(159t),$$

where P_0 and P are the degrees of polymerization

of sodium alginate in the initial and RPA-treated solutions; c, solution concentration (wt %); V_c, volume of the working chamber (l); 159, molecular weight of the elementary unit of the alginate; and t, treatment time (s).

It can be seen from the table that, as the alginate concentration is raised, the degradation rate first somewhat decreases, reaches the minimum value at c = 1.0 wt %, and then again starts to increase as the polymer concentration in solution grows further. With account of the fact that the rate is expressed in terms of the total number of macromolecule ruptures that occurred in the working chamber of RPA, i.e., actually by the amount of the work done, the result obtained can be understood as follows. It was confirmed in [8] that, at low concentrations and, accordingly, low viscosities, the main factor affecting the polymer is the ultrasonic cavitation. As the concentration of the polymer increases, the specific, i.e., that per unit mass of the polymer, acoustic energy decreases. Accordingly decreases the number of ruptures initiated in unit time. At concentrations exceeding 2 wt % alginate, the viscosity starts to steeply increase and the contribution of the shear component of the HA treatment to initiation of the mechanical degradation of macromolecules becomes more pronounced. In this concentration range, the effect produced by the rise in the total mechanical energy because of the larger shear component exceeds the decrease in the specific energy, caused by the increase in the polymer concentration.

In an RPA treatment of solutions with the highest concentrations of sodium alginate (7 and 8 wt %), its molecular weight increased in accordance with the values obtained for the intrinsic viscosity. Such an increase in the length of macromolecular chains may be due to recombination of macroradicals formed under the hydroacoustic treatment.

Sodium alginate is a polyion whose solutions are characterized by polyelectrolyte swelling of polymer molecules. It is natural to assume that the variation of the hydrodynamic radius of particles in solution with its ionic strength causes a change in the stability of the polymer against hydroacoustic degradation. To verify this assumption, 2% sodium alginate solutions whose ionic strength was varied by introducing different amounts of NaCl were subjected to a mechanical treatment in RPA. After the treatment, the ionic strength of the solutions was brought to the same maximum value (0.05 M) in order to measure the intrinsic viscosity under identical conditions. At the given ionic strength, the viscosity of the starting sodium alginate was 558 ml g^{-1} (675 mg l^{-1} without the salt). For the alginate treated in RPA in the form of a 2% solution containing no salt, the intrinsic viscosity measured at the same ionic strength (0.05 M) was 451 ml g^{-1}. The intrinsic viscosities of the alginate after a mechanical treatment for the same time (30 s) of 2% solutions with ionic strengths of 0.01, 0.02, 0.03, and 0.05 M were 475, 492, 504, and 505 ml g^{-1}, respectively. It can be seen that the rate at which the intrinsic viscosity decreases becomes lower as the ionic strength of the solution grows. The values reached by the intrinsic viscosities of solutions treated at ionic strengths of 0.03 and 0.05 M virtually coincide. This experimental result is in agreement with the data of [8], where it was found that, as the ionic strength increases, the swelling coefficient of macromolecules in a sodium alginate solution steeply decreases until the ionic strength of the solution reaches a value of 0.02 M and then remains virtually constant as the ionic strength grows further.

CONCLUSIONS

(1) The viscosity of sodium alginate solutions decreases under hydroacoustic treatment both because of the rupture of hydrogen bonds and decrease in the size of supramolecular formations and via mechanical degradation whose rate is determined, all other conditions being the same, by the concentration of the polymer in solution.

(2) The hydroacoustic treatment gives rise to a structural strain in sodium alginate solutions, which is manifested in a reversible increase in the surface tension.

(3) The stability of sodium alginate macromolecules against hydroacoustic degradation grows as the hydrodynamic radius of the macromolecules decreases and the ionic strength of polymer solutions increases.

ACKNOWLEDGMENTS

The study was supported by the Russian Foundation for Basic Research (project no. 06-08-96 506).

REFERENCES

1. Balabyshko, A.M., Zimin, A.I., and Ruzhitskii, V.P., *Gidrodinamicheskoe dispergirovanie* (Hydrodynamic Dispersing), Moscow: Nauka, 1998.

2. Lipatova, I.M., Odintsova, O.I., Padokhin, V.A., et al., *Tekstil'n. Khim.*, 1997, no. 2(11), pp. 26–29.
3. Losev, N.V., Kornilova, N.A., Makarova, L.I., et al., *Izv. Vyssh. Uchebn. Zaved., Khim. Khim. Tekhnol.*, 2007, vol. 50, no. 3, pp. 44–48.
4. Losev, N.V., Makarova, L.I., and Lipatova, I.M., *Zh. Prikl. Khim.*, 2003, vol. 76, no. 6, pp. 1025–1029.
5. Smitsrod, O. and Haug, A., *Biopolymers*, 1971, vol. 10, pp. 1213–1227.
6. Kurilova, V.A. and Volkova, N.V., in *Novye polimernye materialy i materialovedenie v legkoi promyshlennosti* (New Polymeric Materials and Materials Science in Light Industry), Moscow: TsNIITEllegprom, 1978, vol. 1, pp. 14–17.
7. Oberyukhtina, I.A. et al., Abstracts of Papers, *II Vserossiiskaya konferentsiya "Khimiya i tekhnologiya rastitel'nykh veshchestv"* (II All-Russia Conf. "Chemistry and Technology of Plant Substances"), Kazan, June 24–27, 2002, p. 104.
8. Lipatova, I.M. and Moryganov, A.P., *Chemistry of Polysaccharides*, Zaikov, G.E., Ed., Netherlands: Brill Academic/VSP, 2005, pp. 294–343.

ISSN 1070-4272, Russian Journal of Applied Chemistry, 2008, Vol. 81, No. 5, pp. 815–819. © Pleiades Publishing, Ltd., 2008.
Original Russian Text © I.M. Lipatova, N.A. Kornilova, 2008, published in Zhurnal Prikladnoi Khimii, 2008, Vol. 81, No. 5, pp. 778–782.

PROCESSES AND EQUIPMENT OF CHEMICAL INDUSTRY

Effect of Hydroacoustic Treatment on the Rate of Hydrolytic Degradation of Chitosan in Acetic Acid Solutions

I. M. Lipatova and N. A. Kornilova

Institute of Solution Chemistry, Russian Academy of Sciences, Ivanovo, Russia

Received November 15, 2007

Abstract—Effect of a hydroacoustic treatment in a rotary-pulsatory apparatus on the rate of hydrolytic degradation of chitosan in acetic acid solutions was studied. The influence exerted on the rate of activated hydrolysis of chitosan by its molecular weight and the process temperature was considered.

DOI: 10.1134/S1070427208050170

The permanent expansion of the possible application fields of chitosan makes topical a search for new methods for production of its chemical derivatives and finely dispersed formulations based on this polymer. One of new methods of this kind consists in that the polymer is subjected to intensive mechanical treatments in the presence of chemical reagents or other modifying ingredients. The capabilities of the solid-phase mechanochemical modification of chitosan in devices creating high shear stresses in strongly compressed solid substances are being rather intensively studied [1, 2]. The liquid-phase mechanochemical modification of dissolved chitosans has not been studied. The liquid-phase mechanochemical modification of polysaccharides can be performed via hydroacoustic treatment in rotary-pulsatory apparatus (RPA) [3, 4]. In apparatus of this kind, the most important factors of the activating effect on a substance dissolved or dispersed in a liquid are ultrasonic vibrations and the resulting cavitation, as well as strong uniaxial stresses to which the liquid is subjected in the narrow (0.1–0.5 mm) gaps between elements of the rotor and stator [5, 6].

In this study, the effect of the hydroacoustic treatment on the rate of chemical transformations in dissolved chitosan was analyzed for the example of the hydrolytic degradation. It is known that chitosan, a polyglucosamine of linear structure, dissolves only in acid media, and, therefore, the acid-catalyzed hydrolysis of glycoside bonds is the most characteristic process occurring even in storage of solutions at room temperature [7].

In this study we examined the effect of hydroacoustic treatment in a rotary-pulsatory apparatus on the rate of the hydrolytic degradation of chitosan in acetic acid solutions.

EXPERIMENTAL

The study was performed with chitosan samples of domestic manufacture (Bioprogress, Shchelkovo, Moscow oblast) with molecular weights $M = 5 \times 10^5$ (Kh-500), 3.6×10^5 (Kh-360), 1.2×10^5 (Kh-120, and 0.87×10^5 (Kh-87) whose degrees of deacetylation (DD) were 0.68, 0.73, 0.78, and 0.82, respectively. Weighed portions of chitosans were dissolved in aqueous solutions of 2% acetic acid under agitation in the course of 4–5 h.

Chitosan solutions were treated in a laboratory rotary-pulsatory apparatus in the recycle mode. The thermostated working chamber of the apparatus is formed by a rotor and a stator whose cylindrical rings have rectangular channels. In rotor rotation, there occurs fast alternation of the coincidence and noncoincidence of the rotor and stator channels, which gives rise to mechanical vibrations in the liquid in a wide frequency range, including ultrasonic vibrations. The average gap between the rotating and immobile elements of the working chamber is 0.5 mm. The rotor rotation rate was 5000 rpm, to which corresponds a shear rate gradient of 17.4×10^4 s^{-1}. The treatment duration was varied in the range 4–60 s.

The relative level of the cavitation appearing in mechanically treated chitosan solutions of various concentrations was evaluated by the degree of dis-

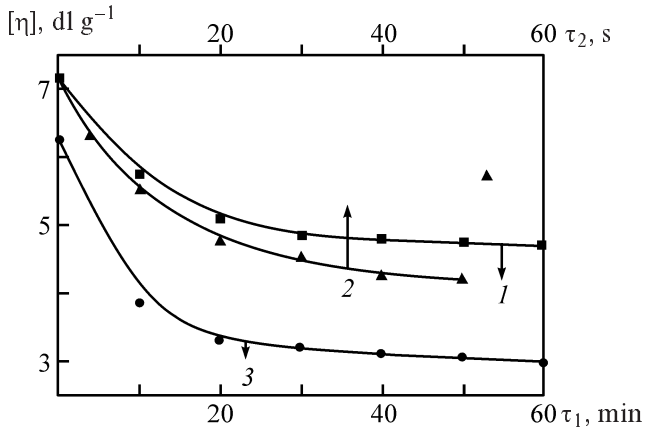


Fig. 1. Intrinsic viscosity [η] of Kh-360 chitosan vs. the duration τ_1, τ_2 of hydrolysis in a 2% acetic acid (60°C), with the process carried out in (*1*) thermostat without activation, (*3*) thermostat with activation, and (*2*) RPA.

persion of a powdered reference substance, *p*-iodonitrobenzene (initial particle size D = 50 μm). In a special-purpose experiment, this substance was introduced into chitosan solutions of various concentrations prior to mechanical treatment. The average particle size after treatment of the dispersions in RPA, d_p, was measured with an ANALYSETTE 22 COMPACT laser diffraction analyzer. The extent to which the cavitation level decreases as the viscosity of the medium becomes higher was evaluated by the ratio $(D - d_p)/(D - d_w)$ (d_w is the particle size reached in water).

The intrinsic viscosity [η] of dissolved chitosan samples was determined at 25°C in an Ubbelohde viscometer (capillary diameter 0.56 mm) by successive dissolution with 2% acetic acid. A 0.2 M solution of sodium acetate was introduced as a supporting electrolyte. The pH of the resulting buffer solution was 5.4.

The shear viscosity of the chitosan solutions was measured with a Brookfield rotation viscometer with the cylindrical rotor in the shear rate range 0.1–132 s^{-1} at 25±0.5°C.

Table 1. Parameters of a 1% solution of Kh-360 chitosan in 2% acetic acid in relation to increasing duration of treatment in RPA

τ, s	η, mPa s	DSS	$c_{RG} \times 10^4$, M	DD
0	780	9.8	0.51	0.73
4	540	16.4	0.61	0.76
20	520	17.4	0.85	0.78
30	490	18.2	0.72	0.84
40	480	16.4	0.48	0.86

The degree of deacetylation of the chitosans was found by potentiometric titration by the method described in [8].

The concentration of terminal reducing groups in chitosan was determined using the reaction with 3,5-dinitrosalycilic acid (DNSA) from the coloration intensity of the reaction product. According to the data of [9], the concentration of the reducing groups, found using this reagent, well correlates with the viscosity-average molecular weight of chitosan at its sufficiently low values, i.e., in those cases when chitosan can pass into solution at those rather high pH values of 10–12 at which DNSA dissolves. In this study, weakly colored precipitates were formed upon introduction of an alkaline solution of DNSA into solutions of the chitosans being analyzed. Upon densification in a centrifuge and separation, the precipitates were placed in planar transparent cells and, after scanning, the color differences between these precipitates and reference precipitates obtained at the same pH without DNSA were measured. The measurements were made on a colorimetric complex intended for determining the ratio of color coordinates of two similarly colored samples by the Kolorist program. The complex was calibrated against precipitates obtained from chitosan solutions into which different amounts of glucosamine sulfate were preliminarily introduced.

To study the effect of mechanical activation on the rate of hydrolytic degradation of chitosan in acetic acid solutions, the process was carried out at the same temperature (60°C) by three methods: (i) in a temperature-controlled flask with a stirrer, (ii) in a temperature-controlled vessel with a stirrer after a short (4 s) preliminary treatment in RPA, and (iii) in the working chamber of RPA. The values of [η] were found for samples taken in the course of the process. For the third method, the starting chitosan solution was subjected to several treatments, with the treatment duration increasing each time. The kinetic curves obtained for all the methods are shown in Fig. 1. It can be seen that the same decrease in the intrinsic viscosity (by 27%) is reached in 15 min without activation and in 20 s if the process is carried out in the RPA. In the case when the process is performed with a preliminary activation, the initial point of the kinetic curve lies lower, because even a short treatment of the solution in the RPA leads to a decrease in [η] of the polymer.

Treatment of chitosan solutions in RPA causes a substantial decrease in their viscosity, which is, as follows from Table 1, an overall result of the simul-

taneous occurrence of mechanically initiated structural and chemical processes. The decrease in the degree of structuring of mechanically treated solutions is evidenced by the increase in the dynamic stability of their structure (DSS), calculated from the results of rheological measurements by the formula

$$DSS = (90 - \alpha)/(\alpha - 45),$$

where α is the slope of the linear portions of the log–log dependences of the shear rate on the shear stress.

The decrease in the degree of structuring of the solutions is presumably due to mechanically initiated dispersing processes, i.e., to disintegration of stable aggregates of associated chitosan macromolecules under combined action of cavitation and shear stresses.

As follows from Table 1, the content of reducing groups in the system increases with the duration of hydroacoustic treatment. It should be noted that the molecular weights of mechanically treated chitosans, calculated from the intrinsic viscosities, were found to exceed those calculated from the concentrations of the reducing groups, whose values seem to be overestimated. The overestimation may be due to errors of calibration in the measurement procedure used. Nevertheless, the very fact of increasing content of reducing sugars confirms that the decrease in the intrinsic viscosity of chitosan after several seconds of mechanical treatment results from its mechanically activated hydrolysis by the conventional mechanism of nucleophilic substitution SN_1. As the treatment duration of the solutions in RPA increases, the concentration of the reducing groups again starts to decrease, which may be due to their activated oxidation. It is not impossible, either, that the terminal aldehyde groups can interact with the amino groups of chitosan to give a Schiff base [10]. The data in Table 1 also indicate that the depolymerization is accompanied by an increase in the degree of deacetylation of chitosan.

It is known that, the higher the content of acetylated monomer units in the polymer chain of chitosan, the faster the acid depolymerization [11]. With account of the fact that deacetylation occurs simultaneously with depolymerization in acid hydrolysis, the reaction conditions cannot be considered invariable in the course of time. Moreover, the reaction conditions additionally change with time because of the mechanically initiated structural transformations. Therefore, the reaction rates were not calculated in this study and it was considered possible to use the initial rate of the decrease in the intrinsic viscosity for comparative analysis of the kinetic curves. This rate is numerically equal to the slope of the tangent to the kinetic curve at the point corresponding to zero time. The rates V_{ah} of activated hydrolysis, calculated in this way for a reaction performed directly in the working chamber of RPA at chitosan concentrations of 0.1–1.0 wt %, were found to be, on average, two orders of magnitude higher than those for the process in a flask with a stirrer.

Table 2. Effect of the concentration of Kh-360 chitosan in 2% acetic acid on the efficiency of mechanical activation

c_{ch}, wt %	η, mPa s	V_{ah}, dl g^{-1} s^{-1}	V_A/V	CL_{rel}
0.1	6.48	0.425	–	0.96
0.25	66	0.350	1.13	0.95
0.5	180	0.290	1.54	0.92
0.8	370	0.260	1.71	0.91
1.0	780	0.175	1.92	0.82
1.5	2490	0.090	2.02	0.55
2	9720	Increase in [η]	3.22	0
3	46 200	Increase in [η]	0.72	0

The key factor of chemical activation in the hydroacoustic treatment is the ultrasonic cavitation. For polymer solutions, the acceleration of processes involving rupture of macromolecular chains results from the action of both the chemical effect of cavitation and its hydrodynamic factor (formation and collapse of cavities, appearance of shock waves). As seen from Table 2, the rate of activated hydrolysis in solution decreases as the chitosan concentration becomes higher. In this case, the effect of the concentration is manifested in two ways. As the polymer concentration increases, the energy dissipation becomes stronger and its amount per unit mass of the polymer decreases. In addition, as the polymer concentration increases, the viscosity of the solutions grows and, after it reaches a certain critical value, the cavitation starts to be suppressed. Table 2 lists relative values of the cavitation level with respect to water, CL_{rel}, for various concentrations of Kh-360 chitosan in the solutions being treated. For chitosan concentrations exceeding 2 wt %, a value at which no cavitation is observed, treatment in RPA leads to an increase in the intrinsic viscosity.

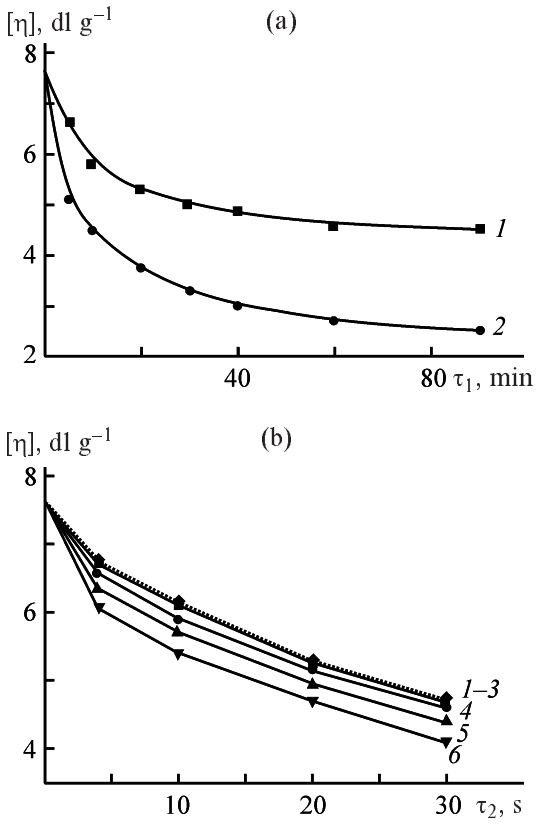


Fig. 2. Intrinsic viscosity [η] of Kh-360 chitosan vs. duration τ_1 and τ_2 of hydrolysis in 2% acetic acid at different temperatures for the process performed in (a) thermostat and (b) RPA. Temperature, °C: (a) (*1*) 60 and (*2*) 70; (b) (*1–3*) 30, 40, 50; (*4*) 60; (*5*) 70; and (*6*) 80.

The effect of the preliminary activation of solutions on the rate of the reaction performed under ordinary conditions was evaluated by the ratio of the reaction rate in an activated solution to that without activation, V_A/V. It follows from Table 2 that, as the chitosan concentration in solution increases from 0.25 to 2 wt %, the effect of preliminary activation becomes more pronounced, with V_A/V varying from 1.13 to 3.22. The increase in the process rate can be attributed to mechanical splitting of stable supramolecular formations in the solutions being treated. The degree of structuring of the solutions grows with the polymer concentration and, accordingly, the effect of activation due to the structural factor becomes more pronounced. It should be taken into account that the degradation and deacetylation processes have enough time to occur during preliminary mechanical treatment in less concentrated solutions to a greater extent, compared with more concentrated solutions. The final values of the intrinsic viscosity of chitosan, reached in the same hydrolysis time in preliminarily activated solutions of various concentrations, differ only slightly. A negative effect of preliminary activation was obtained for a 3% chitosan solution. The possible reason is that, in the absence of cavitation and high shear stresses, conditions for appearance of new stable supramolecular formations are created in sufficiently concentrated solutions. The increase in the degree of structuring of mechanically activated 3% solutions is evidenced by the decrease in the dynamic stability of their structure from 6.5 to 5.2.

When macromolecules are deformed in a mechanical field, their bond angles change and interatomic spaces increase, which leads to a decrease in the activation energy of rupture of strained bonds. It was of interest to study the effect of temperature on the rate of the mechanically activated hydrolysis of chitosan. Figure 2 shows kinetic curves for the hydrolytic degradation process performed at different temperatures in the ordinary conditions (a) and under hydroacoustic treatment (b). It can be seen that, in the latter case, the effect of temperature is considerably less pronounced, but not absent at all, which indicates that the activation of macromolecules has thermal and mechanical components. As can be seen in Fig. 2b, the initial rate of activated hydrolysis remains invariable as the temperature is changed from 30 to 50°C.

The effect of temperature on the rate of chemical reactions under a hydroacoustic treatment is due to changes in the efficiency of cavitation. As temperature increases, the water evaporation rate grows and the partial pressure of its vapor within a cavitation bubble becomes higher, which may cause a transition from gas cavitation to vapor cavitation. Thus, the appearance of cavitation is facilitated as temperature increases; however, the efficiency of bubble collapse becomes lower in this case [12]. On passing to higher temperatures (60–80°C), the temperature coefficient of the reaction increases, which may be due to a decrease in the contribution of the mechanical component to the activation of macromolecules.

The effect of the molecular weight of chitosan on the rate of mechanically activated hydrolysis depends on its concentration in solution. As follows from Table 3, the efficiency of mechanical activation at low concentrations increases with the initial molecular weight. The situation changes at higher concentrations, when the effect of viscosity on the cavitation level may be manifested. For example, the rate of hydrolysis at a polymer concentration of

Table 3. Effect of the molecular weight of chitosan on the initial rate of activated hydrolysis

c_{ch}, wt %	V_{ah}, dl g^{-1} s^{-1}			
	Kh-87	Kh-120	Kh-360	Kh-500
0.25	0.220	0.280	0.350	0.440
0.5	0.190	0.240	0.290	0.340
1.0	0.150	0.190	0.175	0.110
2.0	0.120	0.105	–	–

1.0 wt % is lower for the Kh-360 sample, compared to the Kh-120 sample. For the Kh-360 and Kh-500 samples, and increase in the intrinsic viscosity was observed at a polymer concentration of 2.0 wt % after a treatment of the solution in RPA. Naturally, the lower the molecular weight of the chitosan used, the higher will be the critical concentration of cavitation damping.

The experimental data on the influence exerted on the rate of activated hydrolysis by the concentration of a polymer, its molecular weight, and temperature confirm the decisive role of the ultrasonic cavitation in the increase in the reaction rate.

CONCLUSIONS

(1) The hydrolytic degradation under hydroacoustic treatment occurs at rate exceeding, on the average, by two orders of magnitude that under the ordinary conditions. The rate of activated hydrolysis decreases as the chitosan concentration in solution increases.

(2) Preliminary mechanical activation of solutions causes an increase in the rate of the process performed after that under ordinary conditions by a factor of 1.5–3. The efficiency of the preliminary activation grows with the chitosan concentration in solutions.

(3) The initial rate of activated hydrolysis is independent of temperature at its moderate values (30–50°C). In the range 60–80°C, the temperature coefficient of the reaction increases with temperature.

ACKNOWLEDGMENTS

The study was supported by the Russian Foundation for Basic Research (project no. 06-08-96 506).

REFERENCES

1. Rogovina, S.Z., Akopova, T.A., Vikhoreva, G.A., et al., *Vysokomol. Soedin., Ser. A*, 2000, vol. 42, no. 9, pp. 1489–1494.
2. Ivanov, A.V., Yatsenko, G.L., Bazarnova, N.G., et al., in *Materialy Shestoi mezhdunarodnoi konferentsii "Sovremennye perspektivy v issledovanii khitina i khitozana"* (Proc. Sixth Int. Conf. "Modern Prospects for Studies of Chitin and Chitosan"), Moscow: VNIRO, 2001, pp. 19–24.
3. Lipatova, I.M., Losev, N.V., and Yusova, A.A., *Zh. Prikl. Khim.*, 2006, vol. 79, no. 9, pp. 1548–1553.
4. Losev, N.V., Makarova, L.I., and Lipatova, I.M., *Zh. Prikl. Khim.*, 2003, vol. 76, no. 6, pp. 1025–1029.
5. Gershgal, D.A. and Fridman, V.M., *Ul'trazvukovaya tekhnologicheskaya apparatura* (Ultrasonic Process Apparatus), Moscow: Energiya, 1976.
6. Balabyshko, A.M., Zimin, A.I., and Ruzhitskii, V.P., *Gidrodinamicheskoe dispergirovanie* (Hydrodynamic Dispersing), Moscow: Nauka, 1998.
7. Mironov, A.V., Vikhoreva, G.A., Kil'deeva, N.R., and Uspenskii, S.A., *Vysokomol. Soedin., Ser. B*, 2007, vol. 49, no. 1, pp. 136–138.
8. Nud'ga, L.A., Plisko, E.A., and Danilov, S.N., *Zh. Obshch. Khim.*, 1973, vol. 43, no. 12, pp. 2756–2760.
9. Smirnov, V.F., Smirnova, L.A., Dormidontova, O.V., and Sergeeva, M.V., in *Materialy Shestoi mezhdunarodnoi konferentsii "Sovremennye perspektivy v issledovanii khitina i khitozana"* (Proc. Sixth Int. Conf. "Modern Prospects for Studies of Chitin and Chitosan"), Moscow: VNIRO, 2001, pp. 360–362.
10. Keelara, V.H.P. and Rudrapatham, N.T., *Carbohydr. Res.*, 2006, vol. 341, p. 169.
11. Varum, K.M., Ottoy, M.H., and Smidrod, O., *Carbohydr. Polym.*, 2001, vol. 46, no. 1, p. 89.
12. Margulis, M.A., *Osnovy zvukokhimii* (Fundamentals of Sonochemistry), Moscow: Vysshaya Shkola, 1984.

ISSN 1070-4272, Russian Journal of Applied Chemistry, 2008, Vol. 81, No. 5, pp. 820–825. © Pleiades Publishing, Ltd., 2008.
Original Russian Text © V.M. Mikhal'chuk, V.A. Beloshenko, T.E. Konstantinova, 2008, published in Zhurnal Prikladnoi Khimii, 2008, Vol. 81, No. 5, pp. 783–788.

MACROMOLECULAR CHEMISTRY AND POLYMERIC MATERIALS

Influence of Zirconium Dioxide Nanopowders on Thermal Oxidative Degradation of an Epoxy Polymer

V. M. Mikhal'chuk, V. A. Beloshenko, and T. E. Konstantinova

Donetsk National University, Donetsk, Ukraine
Galkin Physicotechnical Institute, National Academy of Sciences of Ukraine, Donetsk, Ukraine

Received August 27, 2007

Abstract—The influence of zirconium dioxide nanopowders on the thermal oxidative degradation of an amine-cured epoxy polymer was studied.

DOI: 10.1134/S1070427208050182

Introduction into polymers of nanodispersed fillers is a simple and efficient method of controlling the mechanical and thermal properties of composite materials. Zirconium dioxide nanopowders are promising fillers for composite materials based on epoxy oligomers [1]. In epoxy polymers (EPs) containing such a filler, the mechanical properties vary with the ZrO_2 content in an unusual fashion depending on both the degree of dispersion of the ZrO_2 powder and its ability to form aggregates and agglomerates with different modes of particle binding [2].

At the same time, it is known that finely dispersed transition metal oxides are catalysts of various processes that can occur at elevated temperatures in polymeric and composite materials and can affect their heat resistance [3, 4]. In particular, transition metal oxides are catalysts of decomposition of hydroperoxides [5–7], which are initial stable products of high-temperature oxidation with oxygen of organic compounds, including polymers. Catalytic decomposition of hydroperoxides with a high yield of active radicals accelerates the thermal oxidative degradation of polymers. At a low yield of active radicals, the contribution of degenerate branching of oxidation kinetic chains in thermal oxidative degradation, the steady-state concentration of hydroperoxy groups, the oxidation autoacceleration factor, and the maximal oxidation rate decrease [8–10]. All the above factors substantially enhance the heat resistance of epoxy and other polymeric materials.

The mechanism of catalytic decomposition of hydroperoxides in the presence of transition metal compounds is not fully understood. In this study, we examined how the phase composition of zirconium dioxide powder, degree of its dispersion, and ability to form aggregates and agglomerates affect the thermal oxidative degradation of amine-cured EPs.

EXPERIMENTAL

Epoxy polymers and composites filled with ZrO_2 nanopowder were prepared from a mixture of diglycidyl ether of diphenylolpropane (DGDPP) and diglycidyl camphorate (DGC) and were cured with a stoichiometric amount of cyanoethylated diethylenetriamine UP-0633M. The curing of the compounds was performed at room temperature for 20 h with the subsequent heat treatment at 60°C for 2 h. Film samples 200 ± 5 μm thick were prepared on glass plates with a polysiloxane release coating. DGDPP samples were prepared by molecular distillation of ED-22 epoxy oligomer at a residual pressure of no more than 10 Pa. The melting point of crystalline DGDPP was 36.3°C; epoxy number 25.1. DGC [TU (Technical Specification) 88 Ukr. SSR 21 533-83; epoxy number 26.0, $n_D^{20} = 1.4832$; $\eta_{25} = 0.30 \pm 0.05$ Pa s) and UP-0633M (TU 6-05-1863–78; $d_4^{20} = 1.100 \times 10^6$ g m^{-3}; $n_D^{20} = 1.4822$; $\eta_{25} = 0.18$ Pa s) were used without additional purification.

Nanopowders of zirconium dioxide were prepared by physical impacts (UHF, pulsed magnetic field, ultrasound) after precipitation of zirconium oxynitrate (to obtain the monoclinic phase) and a mix-

ture of zirconium oxynitrate and yttrium nitrate in a 0.97 : 0.03 molar ratio counting on ZrO_2 and Y_2O_3 (to obtain the tetragonal phase) with the subsequent filtration and drying.[1] Calcination of the powders provided conversion (with crystallization) of the hydroxide into oxide and growth of particles to required size controlled by the heat treatment temperature.

The calcination temperature T_c and particle size D_{CSR} found from the X-ray diffraction patterns (mean size of coherent scattering regions, CSR), considering nanoparticles as single crystals, are listed in Table 1, together with the BET specific surface area S_{BET} found from the nitrogen adsorption and the specific surface area S_{CSR} calculated assuming the powder to be a set of spherical particles of the size equal to CSR size. The fractional composition and morphology of ZrO_2 powder were studied by transmission electron microscopy. Preliminarily the powders were treated by a special procedure [11] with ultrasonic sputtering over a carbon support. The D_{CSR} value was calculated by the Selyakov–Scherrer formula from the halfwidth $B_{0.5}$ of (111) diffraction peaks.

The kinetics of oxygen uptake was studied at a pressure of 0.1 MPa and a temperature of 200°C on a laboratory gas-volumetric device with an optoelectronic sensor whose sensitivity with respect to the rate of oxygen uptake by the polymers was 10^{-6} mol kg^{-1} s^{-1}. The rate of oxygen uptake was reduced to 1 kg of the organic component of the composite. The thermal gravimetric analysis (TGA) was performed on a Q-1500 derivatograph at a heating rate of 10 deg min^{-1} and free access of atmospheric oxygen. A 200-mg sample of a polymer film cut into 2 × 2-mm pieces was introduced into ceramic crucibles. Calcined aluminum oxide was the reference.

The study of the influence of the ZrO_2 concentration on the high-temperature autooxidation of EP showed that the oxidation of unfilled EP started after a relatively short (16–18 min) induction period (Fig. 1). Usually autooxidation of EP obtained by cationic polymerization proceeds without induction period [8–10]. Its appearance for amine-cured EP may be due to the inhibiting effect of unchanged amino groups of the curing agent. As known [12], at the stoichiometric ratio of the components of epoxy–amine systems, the polyaddition does not go to completion, and unchanged epoxy and amino groups inevitably remain in the polymer phase. In turn, amines are acceptors of peroxy radicals and exhibit antioxidative effect in motor fuel and polymers [13]. The thermal oxidative stability of hydrocarbons is substantially enhanced in the presence of not only aromatic but also aliphatic amines. Among the latter, secondary amines, including those obtained by polyaddition of epoxy compounds [14], are the most effective antioxidants.

Table 1. Characteristics of ZrO_2 powders

Powder no.	T_p, °C	Lattice type	D_{CSR}, nm	S_{CSR}	S_{BET}
				$m^2 g^{-1}$	
1	500	Monoclinic	16	65	65
2	700	Monoclinic	21	52	37
3	1000	Monoclinic	48	22	8.6
4	800	Tetragonal	22	44	30

After the induction period, the dependence of the oxygen uptake on time is typical of noninitiated oxidation of polymers, with a short period of autoacceleration and a fairly long period when the oxidation proceeds at a practically constant rate (maximal oxidation rate, or rate of developed oxidation). This is followed by a relative decrease in the oxidation rate associated with decreasing "concentration" of polymeric chain fragments that are

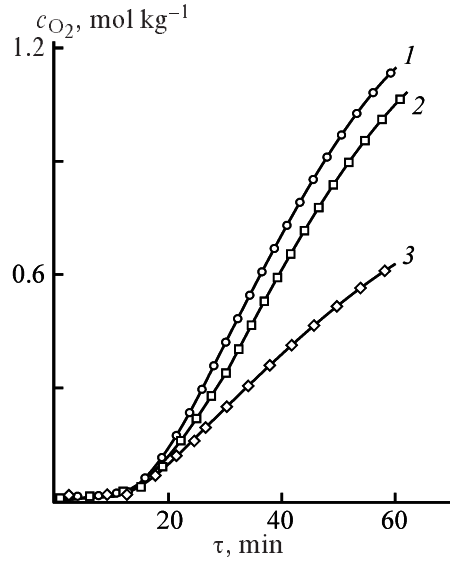


Fig. 1. Oxygen uptake c_{O_2} as a function of time τ for (*1*) EP and composites containing (*2*) 2 and (*3*) 10 wt % ZrO_2 nanopowder no. 2.

[1] Nanopowders were prepared using the technology developed at the Donetsk Physicotechnical Institute, National Academy of Sciences of Ukraine.

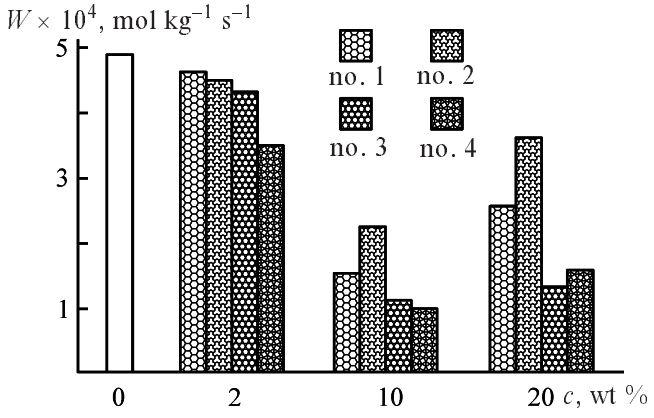


Fig. 2. Diagrams of the rate of developed oxidation W of EP and composites filled with ZrO_2 nanopowder nos. 1–4 at various filler concentrations c.

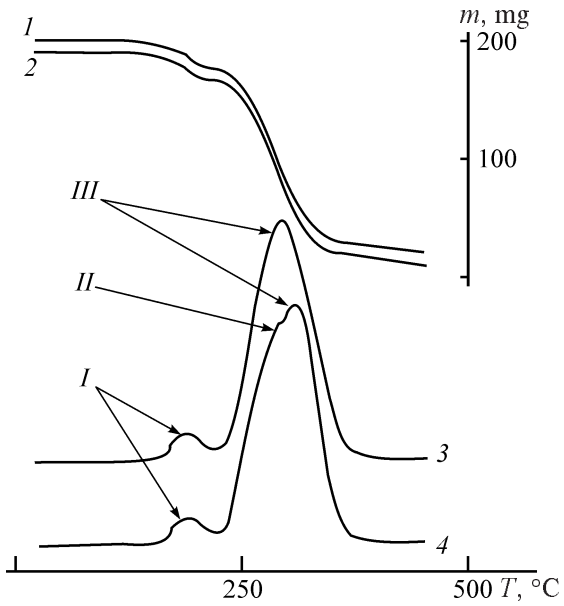


Fig. 3. Temperature dependences of the (*1, 2*) weight loss m and (*3, 4*) its temperature derivative for (*1, 3*) EP and (*2, 4*) composite filled with ZrO_2 nanopowder no. 4.

the most susceptible to oxidation. The rate of the developed oxidation for unfilled EP reaches 4.9×10^{-4} mol kg^{-1} s^{-1}.

Introduction into the polymeric matrix of ZrO_2 powder nos. 1–4 (2 wt %) does not noticeably affect the duration of the induction period (Fig. 1) and slightly decreases the rate of developed oxidation (Fig. 2). This rate decreases in the order 1 > 2 > 3 > 4 for the composites filled with powder nos. 1–4, respectively. The decrease in the maximal rate of polymer oxidation without a change in the induction period is observed, as a rule, in the case of suppression of degenerate branching of oxidation kinetic chains because of decomposition of hydroperoxides (primary stable oxidation products) by metal compounds including oxides [8–10].

In the presence of 2 wt % ZrO_2 in the polymeric matrix, the decrease in the oxidation rate is insignificant. However, at the filler content increased to 10 wt %, the rate of the polymer oxidation decreases by a factor of 1.3–3.6. The highest antioxidative activity is observed with filler nos. 3 and 4 (Fig. 2). Powder nos. 3 and 4 also decrease the maximal rate of EP oxidation, but their antioxidative power is substantially weaker. With an increase in the ZrO_2 content to 20 wt %, the stabilizing effect of the filler against thermal oxidative degradation tends to decrease, but the ratio of the rates of polymer oxidation with additives of various nanopowders remains similar: The rate of the developed oxidation for the composites filled with powder nos. 3 and 4 is lower than that for the composites filled with powder nos. 1 and 2.

The thermal gravimetric (TG) study of thermal and thermal oxidative degradation of the composite showed that introduction into the amine-cured polymer of 10 wt % ZrO_2 weakly affects the variation of its weight on heating. Typical TG and differential thermogravimetric (DTG) curves of the filled and unfilled EPs are shown in Fig. 3. The TG and DTG curves for the unfilled sample are typical of amine-cured EPs. Within the range 170–200°C, the weight loss is small and is associated with evaporation of low-molecular-weight impurities. Further heating leads to the main stage of the thermal and thermal oxidative degradation with a maximum of the weight loss rate at 300°C.

Zirconium dioxide does not noticeably affect the evaporation of low-molecular-weight impurities, and at the same time the position of maximum *I* in the DTG curves remains unchanged (Table 2). The maximum corresponding to the main stage of the degradation splits in two components: *II* and *III* (Fig. 3). The similar effect was observed in [15] for a system consisting of epoxy–novolac block copolymer and amorphous boron. This splitting is due to the effect of the filler surface on the structure of the boundary layers of the polymeric matrix. On introduction of ZrO_2 into the polymer, in most cases, the temperatures of 5% and 10% weight loss (T_5, T_{10}), temperatures of the onset of the main degradation stage T_O, and temperatures of DTG maxima T_M vary within the limits of the measurement accuracy (Table 2). Only for the composite containing ZrO_2 powder no. 4 (it exhibits the most pronounced

Table 2. Thermal characteristics* of degradation of epoxy compounds containing 10 wt % ZrO_2.

Powder no.	T_5	T_{10}	T_H	T_I	T_{II}	T_{III}	T_{50}
	°C						
Without filler	175	230	270	185	–	300	340
1	170	235	275	185	–	305	340
2	170	215	270	190	290	310	340
3	170	230	270	185	290	305	350
4	175	235	270	190	295	305	350

* T_5, T_{10}, and T_{50} are temperatures of 5, 10, and 50% weight loss, respectively; T_I, T_{II}, and T_{III}, temperatures of maxima in the DTG curve.

antioxidant properties), the temperatures characterizing thermal and thermal oxidative degradation slightly increase.

The difference in the effects exerted by ZrO_2 on the rate of oxidation of the amine-cured polymer and on its weight loss during a thermal gravimetric experiment can be attributed to the fact that the oxidation processes in thickly cross-linked EPs are accompanied by formation of additional cross-links hindering evaporation of the decomposition products [16]. Therefore, the data of derivatography and gas volumetry do not always quantitatively correlate with each other. In addition, gas-volumetric data characterize the stability of polymers with respect to thermal oxidative degradation in the initial stages of the process at relatively low temperatures, whereas derivatography gives the corresponding information for high temperatures, when pyrolytic degradation of the polymer makes a substantial contribution to the total degradation process.

It follows from the above data that the antioxidative performance of zirconium dioxide, on the whole, increases with the temperature of the ZrO_2 thermal treatment. The temperature of calcination of ZrO_2 powders substantially affects the degree of their dispersion and the ability to form aggregates. We found that, with increasing T_c from 500 to 1000°C, the mean size of the powder particles of the monoclinic modification increases from 16.5 to 48.2 nm, and their specific surface area decreases by a factor of 7 (Table 1). In the process, the particles of powder no. 1 form planar aggregates of the size exveeding 2000 nm (Fig. 4a). The fact that interparticle gaps are observed suggests that these nanoparticles are weakly bound with each other. Powder no. 2 prepared at 700°C is also characterized by relatively low degree of binding and aggregation of particles (Fig. 4b). At 1000°C, powder no. 3 is formed, which is characterized by high degree of aggregation and forms agglomerates including strongly bound particles (Fig. 4c). Such bonding is provided by diffusion processes of agglomeration type and gives polycrystalline aggregates. Powder no. 4 doped with 3 mol % Y_2O_3 has a tetragonal lattice and is characterized by small degree of particle aggregation (Fig. 4d).

The observed trends in variation of antioxidative properties of the composites, caused by the influence of ZrO_2 nanopowders, are hardly associated with differences in the specific surface area of the filler and, the more so, with the degree of their aggregation. Variation of the surface properties of the filler is apparently a more significant factor.

It is known that metal oxide nanopowders are characterized by the high degree of defectiveness of the surface, mainly associated with the oxygen nonstoichiometry. The defects give rise to excess charge and enhance the interaction with the polymeric matrix, which leads to hydroperoxide decomposition due to acceleration of the catalytic reactions. The differences in the degree of defectiveness of nanopowders are determined by conditions of their preparation, in particular, by T_p. This factor may be responsible for quantitatively different effects of powder nos. 1–3, although they all have a monoclinic lattice.

In the case of nanopowder no. 4 doped with Y_2O_3 (it has a tetragonal lattice), there is one more factor. When ZrO_2 powder is doped with Y_2O_3, replacement of one Zr(IV) atom by one Y(III) atom is accompanied by formation of two oxygen vacancies. As a result, the surface, which is neutral in monoclinic particles, becomes positively

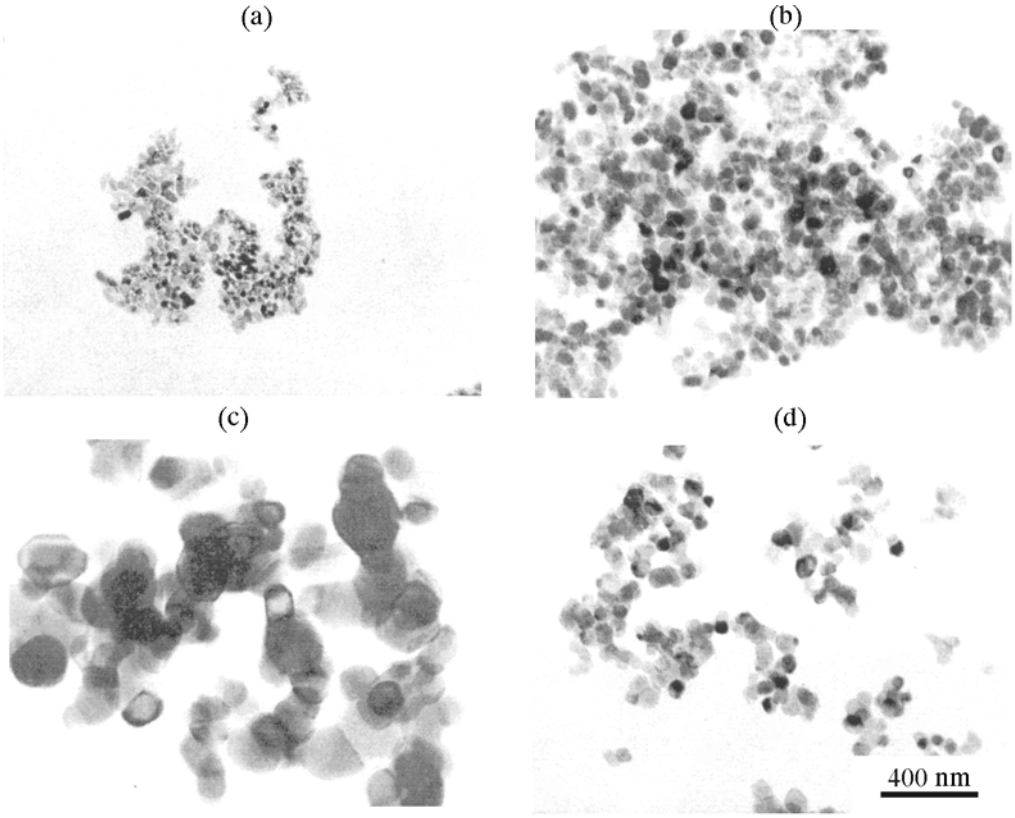


Fig. 4. Electron micrographs of ZrO_2 nanopowder nos. (a) 1, (b) 2, (c) 3, and (d) 4.

charged. This factor can favor catalysis of the hydroperoxide decomposition with a low yield of active radicals, suppression of the degenerate branching of oxidation kinetic chains, and decrease in the rate of thermal oxidative degradation.

Gas-volumetric study confirms this assumption. As seen from Fig. 2, composites containing 2 and 10 wt % powder no. 4 are characterized by the lowest oxidation rate. For such nanocomposites, the temperatures of the maxima in the DTG curves and the temperature of completion of thermal oxidative degradation are the highest.

CONCLUSIONS

(1) ZrO_2 nanopowders exhibit high antioxidative activity in amine-cured epoxy polymers, which is caused by the high defectiveness of the nanoparticle surface.

(2) The value of the antioxidant effect depends on conditions of nanopowder preparation (T_p, doping) and filler concentration.

REFERENCES

1. Konstantinova, T.E., Danilenko, I.A., Tokii, V.V., and Glazunova, V.A., *Nauka Innov.*, 2005, vol. 1, no. 3, pp. 76–87.
2. Beloshenko, V.A., Konstantinova, T.E., Borzenko, A.P., and Glazunova, V.A., *Zh. Prikl. Khim.*, 2005, vol. 78, no. 9, pp. 1533–1536.
3. Gladyshev, G.P., *Dokl. Akad. Nauk SSSR*, 1974, vol. 216, no. 3, pp. 585–587.
4. Gomez de Barros, G., Pontes, R.N.M., and Walmick, V.V., *J. Appl. Polym. Sci.*, 1992, vol. 44, no. 8, pp. 1371–1376.
5. Norikov, Yu.D., Blyumberg, E.A., Irmatov, M.D., and Bochorishvili, Sh.K., *Dokl. Akad. Nauk SSSR*, 1975, vol. 223, no. 5, pp. 1187–1190.
6. Matienko, L.I., Skibida, I.P., and Maizus, Z.K., *Izv. Akad Nauk SSSR, Ser. Khim.*, 1975, no. 6, pp. 1322–1327.
7. Labodi, I., Korablev, L.I., Tavadyan, L.A., and Blyumberg, E.A., *Kinet. Katal.*, 1982, vol. 23, no. 2, pp. 371–375.
8. Mikhal'chuk, V.M., Kryuk, T.V., and Nikolaev-

skii, A.N., *Zh. Prikl. Khim.*, 1996, vol. 69, no. 6, pp. 1008–1013.

9. Kryuk, T.V., Mikhal'chuk, V.M., Volnyanskaya, R.I., and Nikolaevskii, A.N., *Vopr. Khim. Khim. Tekhnol.*, 2002, no. 3, pp. 73–76.
10. Kryuk, T.V., Mikhal'chuk, V.M., Volnyanskaya, R.I., and Nikolaevskii, A.N., *Ukr. Khim.. Zh.*, 2002, vol. 68, no. 5, pp. 58–62.
11. Doroshkevich, A.S., Danilenko, I.A., Konstantinova, T.E., et al., *Elektron. Mikrosk. Prochn. Mater.*, 2006, no. 13, pp. 151–159.
12. Irzhak, V.I., Rozenberg, B.A., and Enikolopyan, N.S., *Setchatye polimery: Sintez, struktura, svoistva* (Network Polymers: Synthesis, Structure, and Properties), Moscow: Nauka, 1979.
13. Denisov, E.T., *Okislenie i destruktsiya karbotsepnykh polimerov* (Oxidation and Degradation of Carbon-Chain Polymers), Leningrad: Khimiya, 1990.
14. Kuliev, A.M., *Khimiya i tekhnologiya prisadok k maslam i toplivam* (Chemistry and Technology of Oil and Fuel Additives), Leningrad: Khimiya, 1985.
15. Kryzhanovskii, V.K., Panimatchenko, A.D., Abramova, N.K., and Nikitina, I.V., *Plast. Massy*, 2005, no. 4, pp. 17–19.
16. Kryuk, T.V., Mikhal'chuk, V.M., Nikolaevskii, A.N., et al., *Plast. Massy*, 2001, no. 3, pp. 12–14.

ISSN 1070-4272, Russian Journal of Applied Chemistry, 2008, Vol. 81, No. 5, pp. 826–829. © Pleiades Publishing, Ltd., 2008.
Original Russian Text © P.A. Sitnikov, A.G. Belykh, M.S. Fedoseev, I.N. Vaseneva, A.V. Kuchin, 2008, published in Zhurnal Prikladnoi Khimii, 2008, Vol. 81, No. 5, pp. 789–792.

MACROMOLECULAR CHEMISTRY AND POLYMERIC MATERIALS

Modification of Epoxy–Anhydride Polymers with Aluminum Oxide

P. A. Sitnikov, A. G. Belykh, M. S. Fedoseev, I. N. Vaseneva, and A. V. Kuchin

Institute of Chemistry, Komi Scientific Center, Ural Division, Russian Academy of Sciences, Syktyvkar, Komi Republic, Russia
Institute of Technical Chemistry, Ural Division, Russian Academy of Sciences, Perm, Russia

Received May 15, 2007

Abstract—The effect of the heat treatment of aluminum hydroxide on the heat resistance and mechanical strength of composite materials based on ED-20 epoxy oligomer cured with isomethyltetrahydrophthalic anhydride was studied.

DOI: 10.1134/S1070427208050194

Polymeric compounds based on the system ED-20 epoxy–4,4'-isopropylidenediphenol oligomer–isomethyltetrahydrophthalic anhydride (iso-MTHPA) are widely used as structural and functional materials owing to the developed production basis and long-term operation experience. ED-20–iso-MTHPA formulations have low viscosity which changes insignificantly during a period of several hours. The properties of finished materials can be controlled by using various modifiers of epoxy systems. The most widely used method is introduction into polymers of small amounts of active fillers [1]. Fillers with active surface can affect certain properties of polymeric materials, in particular, enhance the heat resistance and improve the physicomechanical characteristics [2]. Metal oxides are widely used as fillers of thermoplastics and thermosetting plastics.

In this study we chose as modifying filler aluminum oxide whose surface chemistry has been extensively and comprehensively studied [3–7]. The improvement of properties of polymeric materials on adding active fillers is due to various kinds of interaction of the filler surface with the matrix and to a change in the mobility of macromolecules on the phase boundary. The chemical composition and specific surface area of aluminum oxide are also important [8, 9].

The goal of this study was the development of anydride-curable epoxy compounds with a high level of process and service characteristics using active fillers-modifiers.

EXPERIMENTAL

As starting materials we used the following substances. Components of the polymeric compound: ED-20 epoxy–4,4'-isopropylidenediphenol oligomer [GOST (State Standard) 1587–84], iso-MTHPA [TU (Technical Specification) 6-08-3321–73]; 2,4,6-tris-(dimethylaminoethyl)phenol (Alkofen, TU 22-362–95); modifiers of the epoxy–anhydride polymer: γ-AlO(OH) (S_{sp} = 20–30 $m^2 g^{-1}$), Al_2O_3 (S_{sp} = 20–30 $m^2 g^{-1}$), and α-Al_2O_3 (S_{sp} = 15–25 $m^2 g^{-1}$).

As starting compound for preparing aluminum oxide we used aluminum hydroxide precipitated from a concentrated solution of aluminum nitrate with ammonium hydroxide. The physicochemical properties occurring in aluminum hydroxide under thermal action were studied by derivatography (Fig. 1; MOM Q-1500D derivatograph, heating rate

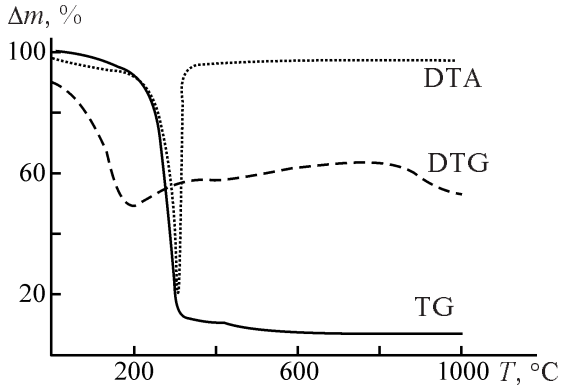


Fig. 1. Derivatograms of aluminum hydroxide powder: (Δm) weight loss and (T) temperature.

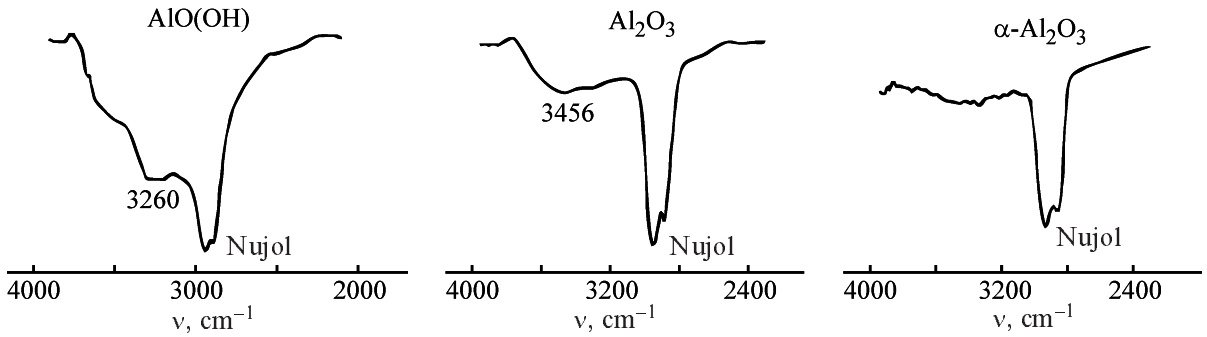


Fig. 2. Fragments of the IR spectra of products formed by thermal decomposition of aluminum hydroxide. (ν) Wavenumber.

10 deg min^{-1}). As seen from Fig. 1, the weight loss associated with the removal of adsorbed water and hydroxy groups is observed in the temperature range 150–600°C. Above 600°C, the weight does not change noticeably. Taking these data into account, to prepare modifiers with different content of surface hydroxy groups, we heated aluminum hydroxide to constant weight at 200, 600, and 1200°C. The sample of aluminum oxide prepared by isothermal heating at 200°C was identified by IR spectroscopy (IR Prestige 21) and chemical analysis as γ-AlO(OH) [10]. The sample of aluminum oxide (Al_2O_3) prepared at 600°C is X-ray amorphous. Calcination of aluminum hydroxide at 1200°C, according to X-ray phase analysis (Shimadzu XRD-6000), yields α-Al_2O_3 (corundum).

The obtained polymorphous modifications of aluminum oxide contain various amounts of hydroxy groups. An IR study showed (Fig. 2) that the intensity of the peak at 3400–3200 cm^{-1} originating from stretching vibrations of the hydroxy groups noticeably changes depending on the polymorphous modification of aluminum oxide, which indicates that different modifications contain different amounts of hydroxy groups: γ-AlO(OH) contains more OH groups and adsorbed moisture than does X-ray amorphous Al_2O_3, and α-Al_2O_3 contains no OH groups.

By differential scanning calorimetry (Shimadzu DSC-60 calorimeter) we studied the thermal effects of the polycondensation of the epoxy oligomer with the anhydride in the presence of active additives, aluminum oxides of various polymorphous modifications (Fig. 3). It can be seen that additions of γ-AlO(OH) and α-Al_2O_3 shift the exothermic peak toward higher temperatures by 15–20°C, whereas Al_2O_3 prepared at 600°C decreases the reaction onset temperature by 20°C. In the γ-AlO(OH)–oligomer–anhydride system, there is the second exothermic peak of curing at 170°C, suggesting that the oligomer/curing agent stoichiometry is disturbed by the large amount of OH groups present on the filler surface. Thus, Al_2O_3 prepared at 600°C exhibits the properties of active filler-modifier of the epoxy system: It reacts with the system components and decreases the onset temperature of the polycondensation of the epoxy oligomer with the anhydride.

The chemical reaction of the surface hydroxy groups with the epoxy groups was proved experimentally (GOST 12497–78) by the example of the model system phenyl glycidyl ether (PGE) : aluminum oxide (600°C) = 50 : 50. The results of determining the amount of epoxy groups in relation to the treatment temperature and time are given in Table 1.

It can be seen that the chemical reaction of the

Table 1. Concentration of epoxy groups X after curing in the PGE–Al_2O_3 system

T, °C	X, %, at indicated curing time, min					
	5	10	30	60	90	120
20	28.3±0.2	28.2±0.2	28.0±0.1	27.8±0.1	26.9±0.2	26.3±0.2
80	26.1±0.3	27.2±0.1	23.0±0.2	17.0±0.2	13.5±02	10.1±0.1
100	23.1±0.2	18.2±0.3	14.5±0.1	10.2±0.1	8.5±0.2	6.0±0.2
120	19.2±0.2	9.9±0.1	5.3±0.1	4.0±0.1	3.1±0.1	2.6±0.1
160	8.1±0.3	5.3±0.3	3.0±0.2	1.4±0.2	0.9±0.1	0.2±0.1

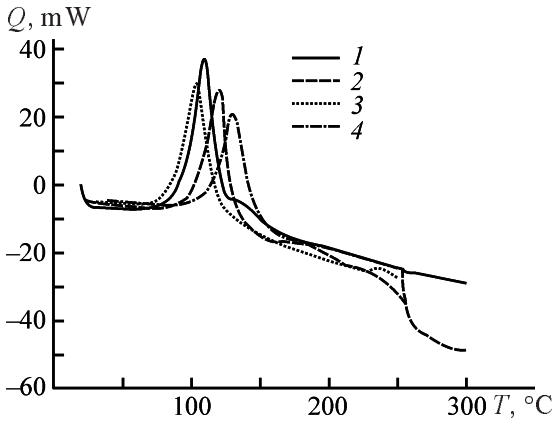


Fig. 3. Thermal effects Q of polycondensation of ED-20 with iso-MTHPA in the presence of modifiers. (T) Temperature. Modifier: (*1*) none, (*2*) γ-AlO(OH), (*3*) Al_2O_3, and (*4*) α-Al_2O_3.

hydroxy and epoxy groups with opening of the epoxy ring occus even at 20°C and becomes considerably faster at elevated temperatures; at 160°C, the epoxy groups disappeare virtually completely in 2 h.

The heat resistance after Martens for samples with various filler contents was determined according to GOST 21341. As seen from Table 2, addition of Al_2O_3 (600°C) increased the heat resistance relative to the unfilled polymer by approximately 15°C. In the polycondensation of the epoxy oligomer with the anhydride, aluminum oxide particles form additional network points and react with the epoxy matrix, which increases the adhesion of the polymer to the filler.

Table 2. Characteristics of polymeric composites prepared

Modifier, wt %	Heat resistance after Martens, °C	Strength, MPa	
		tensile	bending
–	110 ± 2	44 ± 4	110 ± 3
γ-AlO(OH):			
0.25	109 ± 3	21 ± 4	100 ± 5
0.5	106 ± 3	24 ± 2	63 ± 3
1.0	111 ± 3	20 ± 1	62 ± 3
1.5	101 ± 3	24 ± 2	63 ± 2
5.0	105 ± 1	22 ± 4	62 ± 6
Al_2O_3:			
0.25	116 ± 3	31 ± 2	105 ± 3
0.5	115 ± 2	34 ± 1	107 ± 4
1.0	123 ± 2	38 ± 2	125 ± 4
1.5	122 ± 1	35 ± 5	130 ± 4
5.0	125 ± 2	27 ± 4	82 ± 3
α-Al_2O_3:			
0.25	110 ± 2	27 ± 3	67 ± 5
0.5	114 ± 3	25 ± 1	70 ± 4
1.0	110 ± 2	25 ± 5	65 ± 4
1.5	114 ± 2	24 ± 4	60 ± 2
5.0	115 ± 3	33 ± 1	72 ± 4

Physicomechanical characteristics of the filled epoxy composites were determined with an IR 5057-50 testing machine (Table 2). The polymers modified with X-ray amorphous Al_2O_3 showed satisfactory mechanical strength. The tensile strength varied insignificantly, and the bending strength increased by approximately 15% with an increase in the modifier content by 1–1.5 wt %.

Thus, our results show that aluminum oxide prepared at 600°C exhibits properties of an active filler of epoxy–anhydride polymers. In the course of polycondensation of epoxy oligomer with the anhydride, aluminum oxide particles are incorporated in a polymeric matrix with the formation of chemical bonds between the polymer and filler, enhancing the heat resistance and mechanical strength of the material.

CONCLUSIONS

(1) The occurrence of a chemical reaction of active centers on the aluminum oxide surface with epoxy groups was proved by the example of a model system phenyl glycidyl ether–aluminum oxide.

(2) Al_2O_3 prepared at 600°C decreases the onset temperature of the polycondensation by 20°C.

(3) The highest heat resistance, increased by 15°C, is attained with X-ray amorphous Al_2O_3 used as modifier.

(4) On introducing 1–1.5 wt % X-ray amorphous Al_2O_3, the bending strength increases by approximately 15%.

ACKNOWLEDGMENTS

The study was performed within the framework of the Project of Young Scientists of the Ural Branch, Russian Academy of Sciences "Epoxy Matrix with Enhanced Thermomechanical Characteristics, Modified by Active Additives"; of the Target Program for Support of Interdisciplinary Projects Implemented by Scientists of the Siberian and Ural Branch, Russian Academy of Sciences "Basic Problems of Surface and Boundaries of Micro- and

Nanodispersed Systems"; of goalseeking research and development of scientific and technical basis for the industry of nanosystems and materials produced by critical technology "Technologies for Development and Processing of Composite and Ceramic Materials" (lot no. 2007-3-1.3-24-01; Action 1.3 of the Prorgam); and of State Contract no. 02.513.11.3105 "Structural Hibrid Organic–Inorganic Composite Materials with Enhanced Heat Resistance, Based on an Epoxy Polymer Matrix and Submicro- and Nanodispersed Particles of Modifying Components."

REFERENCES

1. Khozin, V.G., *Usilenie epoksidnykh polimerov* (Reinforcement of Epoxy Polymers), Kazan: Dom Pechati, 2004.
2. Mezhikovskii, S.M., *Fizikokhimiya reaktsionnosposobnykh oligomerov* (Physical Chemistry of Reactive Oligomers), Moscow: Nauka, 1998.
3. Ryazanov, M.A. and Dudkin, B.N., *Kolloidn. Zh.*, 2003, vol. 65, no. 6, pp. 831–836.
4. Ryazanov, M.A. and Dudkin, B.N., *Kolloidn. Zh.*, 2004, vol. 66, no. 6, pp. 807–810.
5. *Khimiya privitykh poverkhnostnykh soedinenii* (Chemistry of Grafted Surface Compounds), Lisichkin, G.V., Ed., Moscow: Fizmatlit, 2003.
6. Tsyganenko, A.A. and Mardilovich, P.P., *J. Chem. Soc., Faraday Trans.*, 1996, vol. 92, pp. 4843–4847.
7. Morterra, C. and Magnacca, G., *J. Chem. Soc., Faraday Trans.*, 1996, vol. 92, pp. 5111–5116.
8. Paukshtis, E.A. and Yurchenko, E.N., *Usp. Khim.*, 1983, vol. 52, no. 3, pp. 426–443.
9. Gregg, S.J. and Sing, K.S.W., *Adsorption, Surface Area, and Porosity*, New York: Academic, 1982, 2nd ed.
10. Lazarev, A.I., *Kolebatel'nye spektry i stroenie silikatov* (Vibration Spectra and Structure of Silicates), Leningrad: Nauka, 1968.

ISSN 1070-4272, Russian Journal of Applied Chemistry, 2008, Vol. 81, No. 5, pp. 830–835. © Pleiades Publishing, Ltd., 2008.
Original Russian Text © R.Z. Biglova, R.F. Talipov, A.U. Galimzyanova, 2008, published in Zhurnal Prikladnoi Khimii, 2008, Vol. 81, No. 5, pp. 793–798.

MACROMOLECULAR CHEMISTRY AND POLYMERIC MATERIALS

Mutual Influence of Oligoolefins, Oligodienes, and Bisoligoisobutenylsuccinimide, Modified with Sulfur and Phenols, in Model Systems

R. Z. Biglova, R. F. Talipov, and A. U. Galimzyanova

Bashkir State University, Ufa, Bashkortostan, Russia

Received February 2, 2007

Abstract—The mutual influence of olefin and diene oligomers and bisoligoisobutenylsuccinimide, functionalized with sulfur and phenols, in model oil formulations in evaluation of their solubilizing effect and antioxidant activity was examined. The solubilizing power of the synthesized water-and-oil-soluble surfactant, sodium salt of oligomeric sulfur-containing phenol, in the presence of small concentrations of water was evaluated.

DOI: 10.1134/S1070427208050200

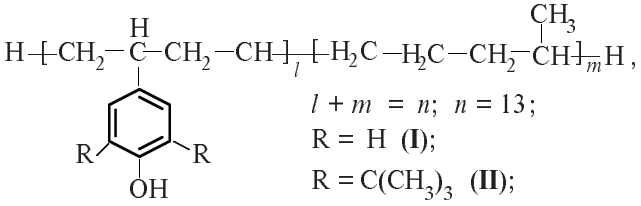
The modern level of the production of polymers and lubricants calls for the development of new additives capable to protect these materials in the course of processing, service, and storage. The problem is complicated by the fact that different kinds of actions require the presence of several additives, rather than a single additive, acting by different mechanisms. In this case, both synergistic and antagonistic effects of the components are possible. In the latter case, the consumption of ingredients reqiured to attain the desired result becomes unduly high.

It is well known that a dispersing detergent is a necessary component of additive kits. The demand for them grows annually by more than 1000 t [1]. Along with detergent, antioxidant and antiwear components are used [2]. Since separate compounds have different service properties, the required total result is attained only when the components are combined properly, taking into account the mechanism of their action [3]. The mutual influence of additives in a multicomponent system such as an oil formulation is poorly understood. At the same time, this problem is important for practice, because in going from model systems (a solution of an additive in isooctane) to real composites the mutual influence of components alters the required dosage of the ingredients.

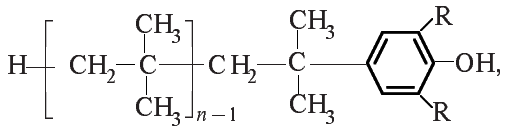
For controlling the properties of polymers and lubricating materials, additives based on oligomers with reactive groups have virtually unlimited potential. Among such oligomers, we should primarily mention oligoolefins and oligodienes. Olefin and diene oligomers functionalized with sulfur acquire antiscuff and antiwear properties, and introduction of phenolic fragments also imparts to the additives the antioxidative activity. Successive modification with introduction of sulfur and oxygen heteroatoms into oligomeric molecules expands the spectrum of their useful properties. In this study we examined the mutual influence of olefins, dienes, and bisoligoisobutenylsuccinimide, modified with sulfur and phenols, in model systems simulating oil formulations.

EXPERIMENTAL

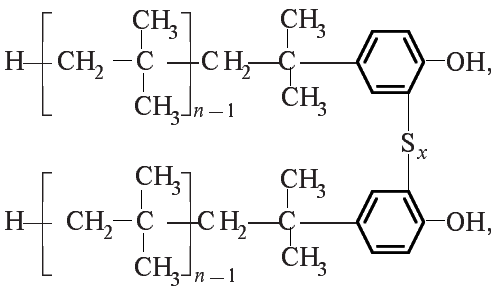
To study the mutual influence of ingredients of a model oil formulation, we prepared oligoolefinyl- and oligodienylphenols by successive modification of oligoisobutylene ($\overline{M}_n$ = 390, 880) and oligopiperylene ($\overline{M}_n$ 910) with phenols and sulfur. The synthesis of the compounds was described previously in [4]. The notations are given in Table 1, and the structural formulas are shown below.



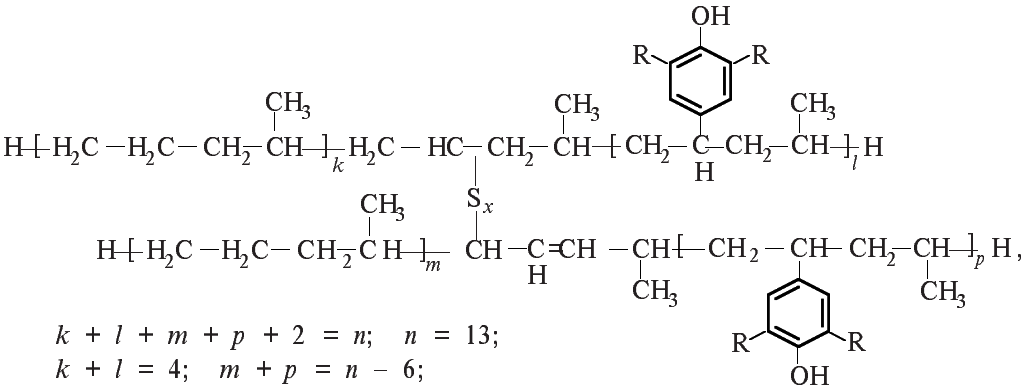
$l + m = n$; $n = 13$;
R = H (**I**);
R = C(CH$_3$)$_3$ (**II**);



R = H, n = 7 (**III**);
R = $C(CH_3)_3$, n = 7 (**IV**);
R = H, n = 16 (**V**);
R = $C(CH_3)_3$, n = 16 (**VI**);



n = 7 (**IX**); 16 (**X**);
x = 1–2.



$k + l + m + p + 2 = n$; n = 13;
$k + l$ = 4; $m + p = n - 6$;
R = H (**VII**); $C(CH_3)_3$ (**VIII**);
x = 1–2.

To optimize the concentrations of components of an oil formulation, we considered the effect of the above additives and succinimide (SI) as dispersing agent in studying their solubilizing effect and antioxidant activity (AOA). The effect of functionalized oligomers on the solubilizing effect of succinimide was evaluated on the quantitative level by calculating the critical micelle concentrations (CMCs) of products **I**–**X**. The CMC was determined spectrophotometrically at room temperature, by monitoring the variation of the optical density on varying the substance concentration in isooctane. For this purpose, we used bisoligoisobutenylsuccinimide **XI** prepared from oligoisobutylene of molecular weight 880.

Analysis of the spectrophotometric data (Fig. 1, Table 2) shows that the CMC ranges for sulfur-containing compounds are relatively narrow. A colloidal system of oligomeric alkylphenols is formed in a wider concentration interval.

The CMC values of the additives were found using the method for determining the solubilizing power of surfactants in isooctane, described in [5]. All the types of the examined compounds exhibited

Table 1. Modified oligomers

Compound	Oligomer (unit containing double bond)
I	4-Oligopiperylenylphenol
II	2,6-Di-*tert*-butyl-4-oligopiperylenylphenol
III	4-Oligoisobutenylphenol ($\overline{M}_{n_{in}}$ = 390)
IV	2,6-Di-*tert*-butyl-4-oligoisobutenylphenol ($\overline{M}_{n_{in}}$ = 390)
V	4-Oligoisobutenylphenol ($\overline{M}_{n_{in}}$ = 880)
VI	2,6-Di-*tert*-butyl-4-oligoisobutenylphenol ($\overline{M}_{n_{in}}$ = 880)
VII	Sulfur-containing 4-oligopiperylenylphenol
VIII	Sulfur-containing 2,6-di-*tert*-butyl-4-oligopiperylenylphenol
IX	Sulfur-containing bis-4-oligoisobutenylphenol ($\overline{M}_{n_{in}}$ = 390)
X	Sulfur-containing bis-4-oligoisobutenylphenol ($\overline{M}_{n_{in}}$ = 880)
XI	Bisoligoisobutenylsuccinimide

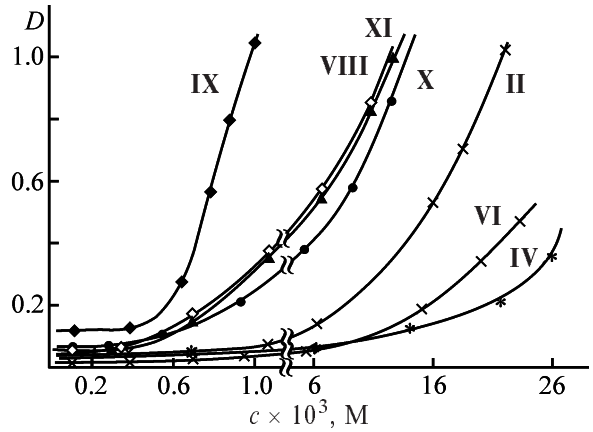


Fig. 1. Optical density D of surfactant solutions in isooctane as a function of their concentration c (for surfactant designations, see Table 1).

the capability to solubilize Rhodamine C (Figs. 2a–2c). In the experiments with Rhodamine C, two types of curves were mainly obtained, with a steep (compounds **IX**, **IX** + **XI**, **VIII**, and **VIII** + **XI**) and gradual (compounds **VI**, **IV**, **II**) increase in the optical density with increasing concentration of the additive. This is caused by the fact that the transition from the nonaggregated system to a micellar solution in the first case occurs in the narrower concentration range than in the second case. For some formulations of the synthesized compounds with SI in isooctane, the concentration dependence of the solubilizing effect (SE, difference between the optical densities of the system before and after adding the dye) has an extremum (compounds **X** + **XI**, **VI** + **XI**, **IV** + **XI**, **II** + **XI**). Apparently, in this case the ingredients interact with each other (e.g., the hydroxy group of phenol alkylated with the oligomer can form a hydrogen bond with the amino group of **XI**), and the micelle structure changes.

Table 2. Critical micelle concentrations of modified compounds in isooctane

Surfactant	$c \times 10^3$, M		
	spectrophotometric method	Rhodamine solubilization method	
II	0.98–12.16	1.24–11.36	0.49–10.08*
IV	2.04–25.05	2.33–26.12	1.16–16.48
VI	0.98–12.88	1.92–19.74	0.64–15.67
VIII	0.27–0.96	0.25–1.58	0.25–0.85
IX	0.34–0.60	0.40–0.55	0.22–0.50
X	0.32–2.00	0.28–1.79	0.06–1.70
XI	0.26–1.38	0.26–1.38	–

* CMC of additives in the presence of **XI**.

Table 3. Derivatives dD/dC for sulfur- and oxygen-containing compounds present simultaneously with bis-oligoisobutenylsuccinimide in isooctane

Surfactant	$dD/dc \times 10^{-3}$
II	0.36, 0.51*
IV	0.13, 0.23*
VI	0.21, 0.35*
VIII	0.41, 0.66*
IX	1.54, 1.90*
X	0.53, 0.86*
XI	1.82

* In the presence of **XI**.

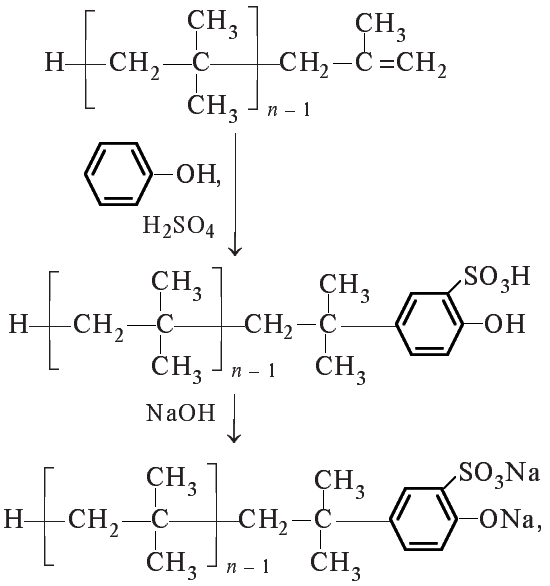
A combination of **XI** with sulfur- and oxygen-containing oligomeric additives enhances the solubilizing power with respect to the dye, which is manfested in a shift of CMC of the additives toward lower concentrations and in an increase in dD/dC (optical density increment, i.e., the slope of the dependence of the optical density on the concentration of the additive without the dye; Tables 2, 3).

Oligopiperylene functionalized with sulfur and with 2,6-di-*tert*-butylphenol and its mixture with **XI** are more effective solubilizing agents compared to the similar products of modification of oligoisobutylene. The synthesized compounds with a similar length of the hydrocarbon radical clearly demonstrate the effect of the sulfur content: CMC decreases, and its range becomes narrower. It should be noted that the CMC values of the oligomers modified with sulfur and phenols, determined by two different methods, are in good agreement (Table 2).

A study of the mutual influence of **XI** and oligomers modified with phenols and sulfur revealed that, when taken in combination, these compounds become effective solubilizing agents substantially shifting the CMC intervals toward lower values.

Effective functioning of lubricating materials implies that they should not contain even small concentration of water. Taking into account the fact that the water content of oils is subject to stringent limitations, it was interesting to examine the effect of water on the solubilizing action of oligomeric sulfur- and oxygen-containing surfactants, the more so as it was not studied previously. To examine the influence of the water concentration, we synthesized disodium salt of 4-oligoisobutenylphenolsulfonic acid by alkylation of phenol with oligoisobutylene in the

presence of sulfuric acid, followed by neutralization of the intermediate with sodium hydroxide:



where $n = 16$.

As seen from Fig. 3, introduction of a fixed amount of water (up to 0.03 wt %) leads to an increase in SE and in a shift of the CMC interval toward lower values (from 2.86×10^{-3} to 1.90×10^{-3} M). Water molecules penetrate into surfactant micelles and are bound by the functional groups, thus making the core more polar. In the process, the size and structure of micelles change and the tendency to micelle formation increases. As a result, the solubilizing power of disodium salt of 4-oligoisobutenylphenolsulfonic acid is enhanced. In so doing, the negative effect of water is eliminated. Furthermore, small concentrations of water enhance the solubilizing effect of surfactants.

Introduction of sulfur atoms into molecules of oligomeric phenolic oxidation inhibitors allows preparation of phenol (poly)sulfides that differ essentially from their low-molecular-weight analogs. In a molecule containing different inhibiting groups, e.g., a phenolic fragment and sulfide groups, intramolecular synergism is possible [6, 7]. A combination of sulfur- and oxygen-containing inhibitors in a formulation with other additives (antiwear, detergent-dispersing), can also enhance their action and give rise to a synergistic effect [8].

To examine the effect of a surfactant (we used compound **XI**) on the antioxidant activity of an inhibitor in a model oil formulation (with isopropylbenzene as substrate), we examined a combined effect of mixtures of **XI** with piperylene and isobutylene oligomers modified with phenol and sulfur, **I**–**X**. The quantitative characteristics of the antioxidative effect of individual oligomers functionalized with sulfur and phenol and of succinimide **XI** itself were determined previously [9]. The reactivity of the samples in combination with SI as antioxidants was

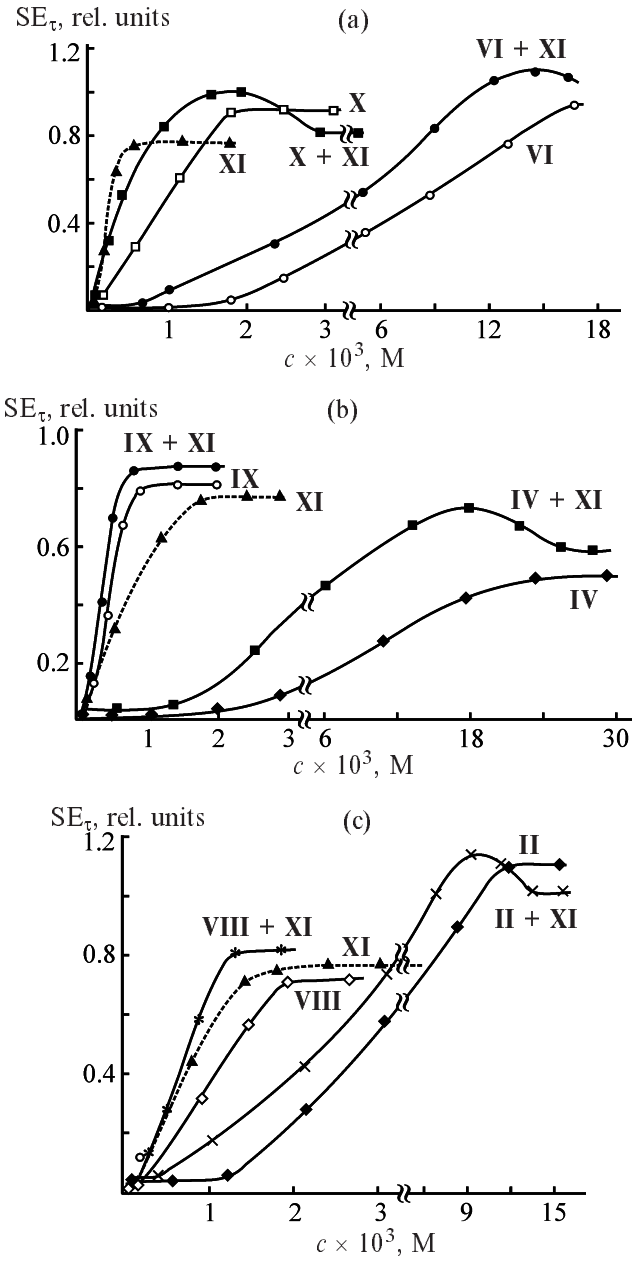


Fig. 2. Solubilizing effect SE_τ of modified oligomers as a function of their concentration c in isooctane: (a) modified oligoisobutylene (starting oligomer: $\overline{M}_n$ = 390; τ = 15 min), (b) modified oligoisobutylene (starting oligomer: $\overline{M}_n$ = 390; τ = 15 min), and (c) modified oligopiperylene (τ = 24 h). Concentration of bisoligobutenylsuccinimide in formulations with oligomeric additives 0.3 wt %.

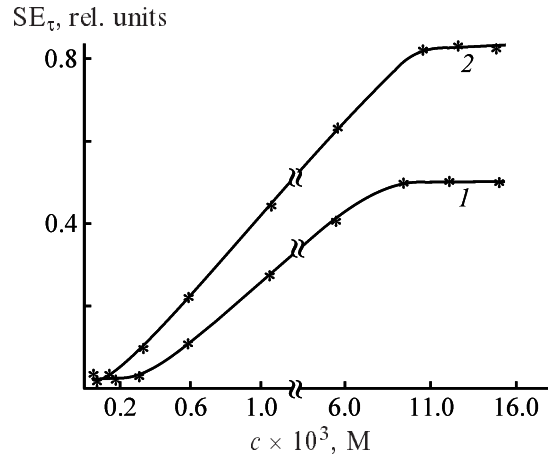


Fig. 3. Effect of water on the solubilizing effect SE_τ of disodium salt of 4-oligoisobutenylphenolsulfonic acid. (*c*) Concentration. (*1*) Without water and (*2*) in the presence of 0.03 wt % water.

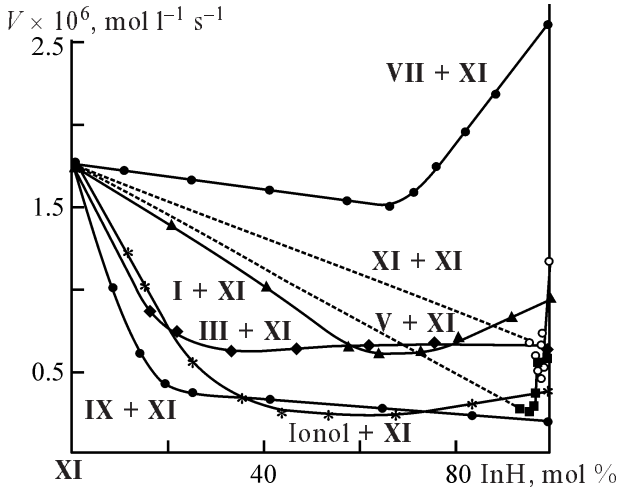


Fig. 4. Rate of cumene oxidation V as a function of the fraction of inhibitor InH in a binary mixture with bis-oligoisobutenylsuccinimide. Total concentrations, M: **III** + **XI** 1.5×10^{-4}, **IX** + **XI** 1.2×10^{-4}, **V** + **XI** 3.0×10^{-3}, **X** + **XI** = 4.5×10^{-3}, **I** + **XI** 3.0×10^{-4}, **VII** + **XI** 3.5×10^{-4}, and Ionol + **XI** 1.2×10^{-4}.

evaluated under standard conditions (T = 333 K, $V_i = 7.21 \times 10^{-8}$ mol l^{-1} s^{-1}) from the rate of the oxygen uptake (by the example of a model reaction of liquid-phase oxidation of isopropylbenzene under kinetic control, using a universal manometric unit; the relative error of the measurements does not exceed 10%). As oxidation initiator we used azobis(isobutyronitrile). The kinetic purity of cumene was estimated by comparing the specially measured oxidizability parameter $k/(2k_6)^{1/2}$ with the published data (k_2 and k_6 are the rate constants of chain propagation and termination for oxidation involving cumylperoxy radicals). The experimental value we obtained, $k_2/(2k_6)^{1/2} = (3.2 \pm 0.1) \times 10^{-3}$ (l mol^{-1} s^{-1})$^{1/2}$ (333 K, correlation coefficient r 0.9953) is in good agreement with published data [10]. The antioxidative performance of the samples was evaluated by the extent to which the initial rate of oxygen uptake in oxidation of the model substrate decreases in their presence. As reference we chose 2,6-di-*tert*-butyl-4-methylphenol (Ionol) for which we found $fk_{In} = (2.0 \pm 0.2) \times 10^4$ l mol^{-1} s^{-1}, which is also consistent with the published data [10].

The dependences of the rate of cumene oxidation on the fraction of the inhibitor in a mixture with **XI** (Fig. 4) show that, up to a certain component ratio, the inhibiting effect is stronger than the additive value. This fact is indicative of a synergistic effect. Further increase in the content of **XI** in the system leads to a decrease in the antioxidative effect. The inflection point corresponds to the concentration of the additive at which the behavior of the inhibiting system changes. A decrease in the antioxidative activity with an increase in the content of **XI** is apparently due to interaction of the system components and deactivation of the inhibiting compounds.

CONCLUSIONS

(1) The effect of oligomers modified with sulfur and phenols on the solubilizing action of bisoligoisobutenylsuccinimide was demonstrated. Introduction of the latter compound into an oil formulation makes narrower the interval of critical micelle concentrations of these compounds and shifts it toward lower values by 40% on the average.

(2) In the presence of small concentrations of water in the model colloidal system isooctane–surfactant, the solubilizing power of the synthesized surfactant, disodium salt of 4-oligoisobutenylphenolsulfonic acid, toward a dye increases.

(3) The effect of bisoligoisobutenylsuccinimide on the antioxidative activity of oligomers functionalized with sulfur and phenol was revealed. A synergistic effect in the antioxidative action is observed when products of chemical modification of oligopiperylene and oligoisobutylene are introduced into a model substrate in combination with bisoligoisobutenylsuccinimide.

(4) By taking into account the mutual influence of the synthesized oligomeric sulfur- and oxygen-containing additives and of a detergent, bisoligo-

isobutenylsuccinimide, in an oil formulation, it is possible to reduce the dosage of the additives to a minimum necessary for ensuring high service characteristics of the lubricating materials.

REFERENCES

1. Shkol'nikov, V.M., in *Materialy II Mezhdunarodnoi nauchno-prakticheskoi konferentsii "Smazochnye materialy v promyshlennosti"* (Proc. II Int. Scientific and Practical Conf. "Lubricating Materials in Industry"), Perm, October 1–4, 2001, p. 4–5.
2. Sobolev, B.A., *Mir Nefteprod.*, 2000, no. 2, pp. 1–2.
3. Selezneva, I.E., Levin, A.Ya., and Monin, S.V., *Khim. Tekhnol. Topl. Masel*, 1999, no. 6, pp. 39–43.
4. Biglova, R.Z., Galimzyanova, A.U., Dokichev, V.A., et al., *J. Appl. Polym. Sci.*, 2006, vol. 101, no. 5, pp. 3097–3105.
5. Biglova, R.Z., Galimzyanova, A.U., Konesev, G.V., et al., *Teor. Osn. Khim. Tekhnol.*, 2006, vol. 40, no. 5, pp. 572–579.
6. Bashkatova, T.V., Miryasova, F.K., Cherezova, E.N., and Bukharov, S.V., *Zh. Prikl. Khim.*, 2005, vol. 78, no. 7, pp. 1130–1134.
7. Farzaliev, V.M., Allakhverdiev, M.A., Sattarzade, R.I., and Rzaeva, I.A., *Zh. Prikl. Khim.*, 2001, vol. 74, no. 12, pp. 2023–2026.
8. Terakh, E.I., Prosenko, A.E., Nikulina, V.V., and Zaitseva, O.V., *Zh. Prikl. Khim.*, 2003, vol. 76, no. 2, pp. 261–265.
9. Galimzyanova, A.U., Biglova, R.Z., Talipov, R.F., et al., *Izv. Vyssh. Uchebn. Zaved., Khim. Khim. Tekhnol.*, 2006, vol. 49, no. 10, pp. 112–114.
10. Denisov, E.T. and Denisova, T.G., *Handbook of Antioxidants*, Boca Raton: CRC, 2000.

ISSN 1070-4272, Russian Journal of Applied Chemistry, 2008, Vol. 81, No. 5, pp. 836–839. © Pleiades Publishing, Ltd., 2008.
Original Russian Text © M.S. Fedoseev, I.V. Zvereva, 2008, published in Zhurnal Prikladnoi Khimii, 2008, Vol. 81, No. 5, pp. 799–802.

MACROMOLECULAR CHEMISTRY AND POLYMERIC MATERIALS

Imidazole and Benzotriazole Derivatives as Catalysts of Curing of Epoxy–Anhydride Binders

M. S. Fedoseev and I. V. Zvereva

Institute of Technical Chemistry, Ural Branch, Russian Academy of Sciences, Perm, Russia

Received July 14, 2007

Abstract—Derivatives of imidazole and 1,2,3-benzotriazole were prepared and studied as catalysts of curing of epoxy–anhydride binders. The physicomechanical properties and thermal endurance of the cured polymers were determined.

DOI: 10.1134/S1070427208050212

Epoxy binders for anhydride curing based on 4,4'-isopropylidenediphenol resins are widely used in production of polymer composites, in particular, organoplastics and of carbon- and glass-reinforced plastics. Curing of epoxy–anhydride binder is catalyzed by tertiary amines (triethylamine, benzyldimethylamine), Mannich bases, Lewis acids, 2,4,6-tris(dimethylaminomethyl)phenol, BF_3 complexes with aniline, α-naphthylamine, and monoethanolamine.

Imidazoles and their derivatives are also effective curing agents and catalysts of curing of epoxy compounds. The curing mechanism of epoxy oligomers in the presence of imidazole is described in detail by Jisova [1]. She showed that imidazoles containing substituents at position 2 exhibited the highest catalytic activity and could be used in practice.

Wang and Wong [2] studied properties of epoxy compounds containing 3,4-epoxycyclohexylmethyl 3,4-epoxycyclohexanecarboxylate, hexahydro-4-methylphthalic anhydride, and curing catalysts (1-cyanoethyl-2-ethyl-4-methylimidazole, imidazole, 2-ethyl-4-methylimidazole, and triphenylphosphine).

Polymers prepared by curing a mixture of epoxy oligomers containing two or three functional groups with methylendic anhydride in the presence of 2-ethyl-4-methylimidazole have relatively high glass transition point (185°C), which characterizes their thermal endurance.

Imidazole derivatives are used as latent catalysts for preparing a stable one-pot epoxy compound cured by thiols at low temperatures [4]. Imidazoles masked by reactions with toluylene, phenylene, and naphthylene diisocyanates are also used as promoters for curing epoxidized condensation products of phenol and bisphenol with formaldehyde, which, in turn, are used in production of printed-circuit boards [5].

Complexes of zinc chloride with some *N*-vinylimidazoles cure ED-6 epoxy resin in the presence of 2,4,6-tris(dimethylaminomethyl)phenol as a promoter at elevated temperatures. The Vicat softening points of the polymers cured under these conditions are higher than those of the polymers cured by anhydrides [6].

Brown et al. [7] studied the reaction products of phenyl glycidyl ether, 2-ethyl-4-methylimidazole, and Mn, Co, Ni, Cu, and Ag acetates and halides as ponetial latent curing systems for commercial epoxy resins. No data on thermal endurance of the cured polymers are reported.

The physicochemical and catalytic properties of imidazole and its substituted derivatives in curing of epoxide-containing polymer systems and in synthesis of various polymer binders used in production of composites are reviewed in [8, 9].

The aim of this study was to examine curing of epoxy resins by isomethyltetrahydrophthalic anhydride (IMTHPA) in the presence of imidazole derivatives and 1,2,3-benzotriazole (benzotriazole) and to determine elastic-deformation properties and thermal endurance of the cured polymers. As imidazole and benzotriazole derivatives we studied products of reactions of imidazole and benzotriazole with glycidol, phenyl glycidyl ether, and low-molecular-weight aliphatic epoxy resins (DEG-1 and Lap-

roksid-703), and also imidazole complex with zinc chloride.

EXPERIMENTAL

Imidazole derivatives were prepared from imidazole (99%, Johnson Mutthey Co.); 1,2,3-benzotriazole [pure grade, TU (Technical Specification) 6-09-1291–87] recrystallized from chloroform (mp 98°C), Laproksid-703 (TU 6-05-221-496–79) with 14.3% content of epoxy groups; DEG-1 (TU 6-05-1223–69) with 19.3% content of epoxy groups; phenyl glycidyl ether (PGE, TU 2225-510-00 203 521–94) with 27.0% content of epoxy groups; glycidol (TU 38.402-62-162–96) with 53.0% content of epoxy groups; and imported zinc chloride (98%).

The content of epoxy groups in all epoxy compounds was determined by back-titration [GOST (State Standard) 12497, paragraph 3]. The oligomer derivatives were prepared as follows. Imidazole or benzotriazole was dissolved in ethanol or toluene. An equivalent amount of an appropriate epoxy compound was added to the solution with stirring. The reaction mixture was stirred at 50–70°C for 1–5 h. The solvent was evaporated. The reaction of highly reactive glycidol with imidazole was performed at room temperature. In this case, glycidol was added dropwise to an ethanol solution of imidazole, and the resulting mixture was stirred for 3 h. The reaction products are viscous liquids. Their properties are given in Table 1.

The complex of imidazole with zinc chloride was prepared by mixing 1 mol of zinc chloride in diethyl ether with 2 mol of imidazole in the solvent at room temperature. The crystals precipitated in 24 h were filtered off on a Buchner funnel. The resulting crystals (mp 153–156°C) are insoluble in water, chloroform, and hexane but soluble in acetone and ethanol.

The zinc content of the complex was determined by complexometric back-titration with copper sulfate in the presence of 2-pyridylazo-2-naphthol (PAN) as an indicator [10]. The calculated and found zinc contents are 23.4 and 24.0%, respectively, which corresponds to the composition $ZnCl_2(imidazole)_2$.

Curing of ED-20 : IMTHPA = 100 : 70 compound in the presence of 1% imidazole, benzotriazole, and their reaction products was studied by differential scanning calorimetry (DSC) on a DSC-111 calorimeter (SETARAM, France) under the dynamic conditions at a heating rate of 5 deg min^{-1} in the range 20–250°C. The activation energy and enthalpy of the reaction were determined from the initial portion of the DSC curve (Piloyan's method [11]). The results are presented in Table 2.

Table 1. Properties of reaction products

Reaction product	Content of epoxy groups, %	Viscosity at 50°C, Pa s
DEG-1/imidazole	3.49	27.5
Laproksid-703/imidazole	2.78	2.5
PGE/imidazole	2.10	1.8
Glycidol/imidazole	4.47	1.8
DEG-1/benzotriazole	1.33	7.3
Laproksid-703/benzotriazole	0.30	2.5

Table 2. Kinetic parameters of curing of ED-20/IMTHPA compound in the presence of imidazole, benzotriazole, and their reaction products as catalysts

Catalyst	E_{eff}, kJ mol^{-1}	Q, J g^{-1}
DEG-1/imidazole	78.6	300
Laproksid-703/imidazole	83.1	262
PGE/imidazole	70.6	293
Glycidol/imidazole	70.6	305
DEG-1/benzotriazole	103.0	175
Laproksid-703/benzotriazole	130.0	190
1-Methylimidazole	70.6	326
Imidazole	74.6	330
Alkophen	75.6	283
$ZnCl_2$/imidazole	101.5	341.5

The viscosity of ED-20 : IMTHPA compound containing 1% $ZnCl_2(imidazole)_2$ complex was measured on a Rheotest-1 viscometer at 60°C in the course of 5 h (see figure).

The mechanical properties of epoxy polymers cured at 150°C for 2 h in the presence of the reaction products were determined according to GOST 270–75. The results are presented in Table 3.

As seen from Table 2, the reaction products of imidazole with glycidol and phenyl glycidyl ether exhibit the highest catalytic activity in curing of IMTHPA epoxy resin. The activation energy of curing in the presence of these catalysts is 70.6 kJ mol^{-1}. It should be noted that the activation energy of curing in the presence of widely used 2,4,6-tris(di-

Table 3. Physicomechanical properties and softening points of cured epoxy polymers

Epoxy resin	Catalyst	Tensile strength at 25°C, MPa	Relative elongation, ε, %	Vicat softening point, °C
ED-20	Alkophen	45	9.0	71
	DEG-imidazole	46	9.5	138
UP-610	Alkophen	65	12.0	153
	DEG-imidazole	68	10.0	190
EkhD	Alkophen	54	12.0	250
	DEG-imidazole	52	10.0	280

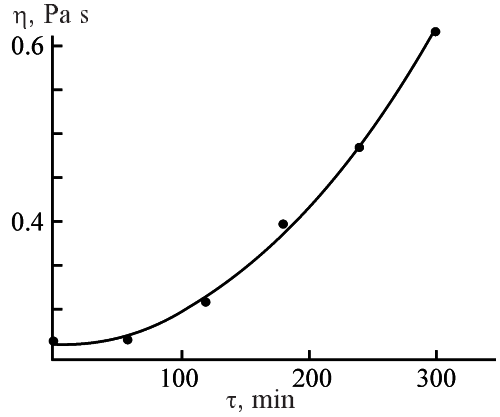
methylaminomethyl)phenol (Alkophen) and unsubstituted imidazole is 75.6 and 74.6 kJ mol^{-1}, respectively.

The reactivity of the system (activation energy 101.5 kJ mol^{-1}) in the presence of zinc chloride complex with imidazole is significantly lower, which suggests its latent catalytic activity. This is also confirmed by a small change in the viscosity of the system at 60°C in the course of 5 h.

The catalytic activity of the reaction products of benzotriazole with DEG-1 and Laproksid-703 is lower. The activation energy of the process in their presence is 103 and 130 kJ mol^{-1}, respectively. The heat release in curing is weaker.

The results of a DSC study of the curing kinetics of ED-20 epoxy resin show that the catalytic activity of the imidazole derivatives in question is comparable to that of conventional catalysts such as Alkophen.

The physicomechanical properties and softening points of epoxy resins with different functional groups cured in the presence of a conventional catalyst of anhydride curing (Alkophen) and the reaction product of imidazole with DEG-1 aliphatic resin are presented in Table 3. The softening point of the polymer cured in the presence of the imidazole derivative is higher, which is probably due to incorporation of imidazole molecules in the polymer chain, thus increasing the rigidity and density of packing of the polymer chains.



Kinetic curve of an increase in the dynamic viscosity of ED-20 : IMTHPA compound in the presence of $ZnCl_2$/imidazole at 60°C. (η) Viscosity and (τ) time.

As we expected, the tensile strength and softening point of the polymers increase in going to tri- and tetrafunctionalized UP-610 and EDX epoxy resins. Polymers with more heat-resistant and more rigid matrix formed from these resins can be used in the development of new heat-resistant polymer compounds.

CONCLUSIONS

(1) The catalytic activity of the reaction products of imidazole and 1,2,3-benzotriazole with epoxy compounds is higher than that of the reaction products of imidazole with phenyl glycidyl ether, glycidol, and DEG-1. 1,2,3- Benzotriazole derivatives exhibit a weak catalytic activity.

(2) The reaction product of imidazole and DEG-1 is an active curing catalyst. Some epoxy resins cured in the presence of this catalyst exhibit increased softening point.

(3) The complex of imidazole with zinc chloride exhibits latent catalytic activity, which allows an increase in the shelf life of the epoxy compounds at room temperature (increase in the vitality) and their rapid curing at a high temperature.

REFERENCES

1. Jisova, V., *J. Appl. Polym. Sci.*, 1987, vol. 34, pp. 2528–2547.
2. Wang, Lejun and Wong, C.P., *J. Appl. Polym. Sci.*, 2001, vol. 81, pp. 1868–1880.

3. EP Patent Appl. 1 266 919.
4. US Patent 6 232 426.
5. US Patent 6 329 474.
6. Kalmykov, V.V., Ivanov, V.A., and Kharitonov, G.V., *Zh. Prikl. Khim.*, 1979, vol. 52, no. 4, pp. 889–892.
7. Brown J., Hamerton, I., and Howlin, B.J., *J. Appl. Polym. Sci.*, 2000, vol. 75, no. 2, pp. 201–217.
8. Evtushenko, Yu.M., *Khim. Tekhnol.*, 2003, no. 1, pp. 16–20.
9. Evtushenko, Yu.M., *Khim. Tekhnol.*, 2003, no. 5, pp. 18–22.
10. Podchaikova, V.N. and Simonova, L.N., *Analiticheskaya khimiya elementov: Med'* (Analytical Chemistry of Elements: Copper), Moscow: Nauka, 1990.
11. Piloyan, G.O., Rassonskaya, I.S., and Novikova, O.S., in *Materialy vsesoyuznogo simpoziuma po metodicheskim voprosam termicheskogo analiza* (Proc. All-Union Symp. on Methodical Problems of Thermal Analysis), Kazan: Kazansk. Univ., 1968.

ISSN 1070-4272, Russian Journal of Applied Chemistry, 2008, Vol. 81, No. 5, pp. 840–844. © Pleiades Publishing, Ltd., 2008.
Original Russian Text © A.I. Vorob'eva, M.N. Gorbunova, F.A. Sataeva, R.R. Muslukhov, S.V. Kolesov, A.G. Tolstikov, Yu.B. Monakov, 2008, published in Zhurnal Prikladnoi Khimii, 2008, Vol. 81, No. 5, pp. 803–807.

MACROMOLECULAR CHEMISTRY AND POLYMERIC MATERIALS

Diallylaminophosphonium Salts in Radical Polymerization Reactions

A. I. Vorob'eva, M. N. Gorbunova, F. A. Sataeva, R. R. Muslukhov, S. V. Kolesov, A. G. Tolstikov, and Yu. B. Monakov

Institute of Organic Chemistry, Ufa Scientific Center, Russian Academy of Sciences, Ufa, Bashkortostan, Russia
Institute of Technical Chemistry, Ural Branch, Russian Academy of Sciences, Perm, Russia

Received December 14, 2007

Abstract—The activity of tris(diethylamino)diallylaminophosphonium tetrafluoroborate and chloride in radical polymerization reactions was studied. The kinetic relationships of the copolymerization with sulfur dioxide were examined.

DOI: 10.1134/S1070427208050224

Synthesis of complexing ion exchangers for selective uptake of definite ions from multicomponent solutions is an important practical problem. One of research lines in the synthesis of selective ion exchangers is preparation of phosphorus-containing complexing ion exchangers exhibiting specific features in sorption [1]. The interest in polymeric phosphorus derivatives considerably increased owing to success in the synthesis and use of organophosphorus extractants exhibiting high potential as complexing agents. An important advantage of these compounds is the possibility of widely varying substituents at the phosphorus atom and hence the electron-donor power and steric conditions of the complexing center.

Phosphorus-containing sorbents exhibit a wider range of properties compared to other known sorbents [1]. It is known that the heteroatoms N, O, and S, tending to coordinate with metals, when present in molecules of organophosphorus complexones, impart to them the specificity toward certain cations [2]. Nitrogen atoms of phosphorylated polyamine derivatives also participate in coordination with metal ions. Phosphorylated polyamines exhibiting selective action can be successfully used for fractional determination and isolation of cations occurring in difficult-to-separate combinations. The separation of transition and rare-earth metals is considerably simplified by a large difference in the strength of complexes of phosphorylated polyamines with these elements. High stability constants of complexes of some phosphorylated polyamines with Cu^{2+} and Fe^{3+} make these complexones promising in agriculture for curing of copper and iron chlorosis of plants [2]. The capability of aminopolyphosphonic compounds to form complexes with various elements (Cu, Be, U, Pb, etc.) opened prospects for their use for removing these metals from a living body [2, 3]. Thus, synthesis of novel phosphorylated polyamines is a topical problem.

In this study we examined the reactivity of diallylaminophosphonium salts in radical (co)polymerization reactions and the properties of the resulting copolymers.

EXPERIMENTAL

Tris(diethylamino)diallylaminophosphonium chloride (EAAP-Cl) was prepared as follows. To 392 g (1.5 mol) of tris(diethylamino)diallylaminophosphazohydride, we added with vigorous stirring 600 g (7.5 mol) of freshly distilled allyl chloride, and the stirring was continued until self-heating of the reaction mixture ceased. Then, with the stirring continued, 225 g (6.4 mol) of NaOH in the form of a 50% aqueous solution was added. In the process, the temperature was maintained within 38°C. After adding the whole amount of NaOH, the mixture was stirred for an additional 30–45 min and then was gently refluxed for 10–12 h with stirring. After cool-

ing, the middle layer was separated, and EAAP-Cl was extracted with dichloromethane. The extract was evaporated on a rotary evaporator at 100°C in steps: first in a water-jet-pump vacuum and then in a rough vacuum (5–7 mm Hg). Yield of EAAP-Cl 490 g (86.5%). The purity was checked by elemental analysis and ^{13}C NMR (Table 1). Elemental composition:

Found, %: C 56.82, H 11.06, N 14.55.
Calculated, %: C 57.07, H 10.57, N 14.79.

Tris(diethylamino)diallylaminophosphonium tetraphenylborate (EAAP-BF_4) was prepared as follows: 490 g (1.3 mol) of EAAP-Cl was dissolved in 2.0 l of distilled water, and 960 g of 20% aqueous solution of sodium tetrafluoroborate (1.7 mol of dry matter) was added dropwise with vigorous stirring. The mixture was stirred for 15–20 min and allowed to stand for 24 h at room temperature. Then the precipitate was filtered off, washed with distilled water, and dried in a vacuum at 80°C to constant weight. Yield of EAAP-BF_4 390 g (70.1%). The purity was checked by elemental analysis and by ^{13}C and ^{1}H NMR spectroscopy (Table 1). Elemental composition:

Found, %: C 49.72, H 10.03, N 12.83.
Calculated, %: C 50.23, H 9.30, N 13.02.

The monomers (acrylonitrile AN, methyl methacrylarte, acrylamide, *N*-vinylpyrrolidone), initiators [azobis(isobutyronitrile) AIBN, potassium persulfate, benzoyl peroxide], and solvents (dimethyl sulfoxide DMSO, methanol, tetrahydrofuran THF, dichloromethane) after purification by standard procedures had characteristics agreeing with the reference data. Sulfur dioxide was dried by passing through concentrated H_2SO_4 and freshly calcined $CaCl_2$.

Homo- and copolymerization of diallylaminophosphonium salts with vinyl monomers was performed in solution in the presence of the above initiators in evacuated ampules, and the copolymerization with SO_2, in a glass reactor as described in [4]. The polymers were purified by twofold reprecipitation from a solution in appropriate solvent into a precipitant (THF), washed with THF, and vacuum-dried to constant weight at 50°C. The composition of the copolymers was calculated from the results of elemental analysis.

The NMR spectra were recorded on a Bruker AM-300 spectrometer operating at 300 MHz for ^{1}H and 75.5 MHz for ^{13}C. The ^{13}C NMR spectra were recorded with broad-band proton decoupling and in the JMOD mode. As solvents we used DMSO-d_6 for the copolymer of EAAP-BF_4 with SO_2 and D_2O for the copolymer of EAAP-Cl with SO_2. The internal reference was tetramethylsilane and 2,2-dimethyl-2-silapentane-5-sulfonic acid, respectively.

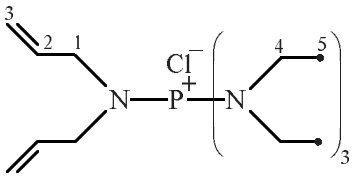
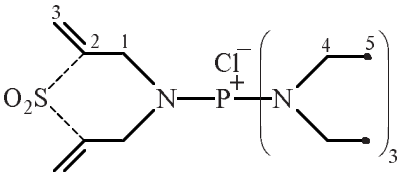
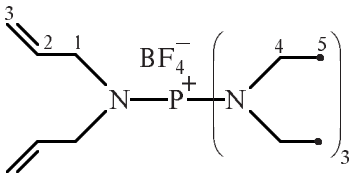
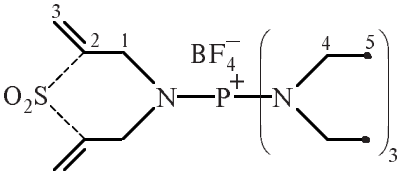
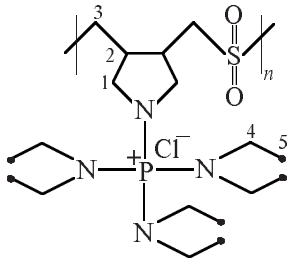
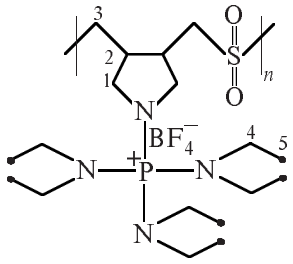
The acute toxicity parameters of copolymers of diallylaminophosphonium salts with sulfur dioxide were determined by the method described in [5]. The antimicrobial activity was studied on two strains of conditionally pathogenic cultures (*E. coli*, strain 25922; *St. aureus*, strain 906) by double serial dilutions [6]. As solvents in screening experiments we used DMSO for EAAP-BF_4–SO_2 copolymer and water for EAAP-Cl–SO_2 copolymer.

A study of the activity of the diallylaminophosphonium salts EAAP-BF_4 and EAAP-Cl showed that these compounds do not undergo substance-initiated radical homopolymerization. The diallylaminophosphonium salts exhibit also low activity in the copolymerization with vinyl monomers (AN, methyl methacrylate, acrylamide, *N*-vinylpyrrolidone, etc.): The reaction rates are low, and incorporation of the diallylaminophosphonium units into the polymer chain is insignificant. In particular, in copolymerization of EAAP-BF_4 (30 mol %) with AN (70 mol %) in DMSO solution in the presence of AIBN (3 wt %) at 80°C, a copolymer of the composition EAAP-BF_4 : AN = 2.6 : 97.4 (mol %) is formed in 27% yield in 10 h. Similar product compositions and copolymerization rates were observed in copolymerization of diallylaminophosphonium salts with the other vinyl monomers described above.

Diallylaminophosphonium salts showed considerably higher activity in copolymerization with sulfur dioxide exhibiting high electron-acceptor activity. The copolymerization occurs at high rates with the formation of alternating copolymers of equimolar composition, irrespective of the monomer ratio in the starting mixture and reaction conditions (temperature, solvent, initiator, degree of conversion).

The ^{13}C NMR spectra of mixtures of EAAP-BF_4 and EAAP-Cl with SO_2 showed that the signals of the carbon atoms of the allyl groups become noticeably shifted relative to the free monomers (Table 1). This fact suggests formation of donor–acceptor complexes of both monomers with SO_2. However, the shifts are considerably larger than those in the previously studied complexes of SO_2 with *N*-allyl

Table 1. ^{13}C NMR spectra of tris(diethylamino)diallylaminophosphonium chloride **(1)** and tetrafluoroborate **(3)** and of their complexes **(2, 4)** and copolymers **(5, 6)** with SO_2 (DMSO-d_6, TMS)

Compound		Chemical shift, ppm, and signal multiplicity					
		stereoisomer	C^1	C^2	C^3	C^4	C^5
	**(1)**		49.65 t	134.08 d	119.65 t	41.02 t	13.73 q
	**(2)**		43.01 t	136.00 d	115.48 t	39.44 t	12.75 q
	**(3)**		49.27 t	132.54 d	119.58 t	40.58 t	13.09 q
	**(4)**		43.10 t	135.67 d	115.66 t	40.25 t	13.25 q
	**(5)**	*cis* *trans*	52.60 t 53.34 t	36.71 d 38.77 d	51.98 t 54.82 t	41.27 t 40.37 t	13.94 q 13.94 q
	**(6)**	*cis* *trans*	50.57 t 51.04 t	34.90 d 36.94 d	50.42 t 52.14 t	39.40 t 39.35 t	12.93 q 12.43 q

monomers, in particular, with diallylhydrazines [7]. Apparently, in diallylaminophosphonium salts, the P and N atoms of the electron-donor $-PN(C_2H_5)_2$ groups also participate in the complexation.

A kinetic study of the copolymerization of diallylamimophosphonium salts with SO_2 at low conversions showed that the reaction rate as a function of the monomer ratio passes through a maximum at

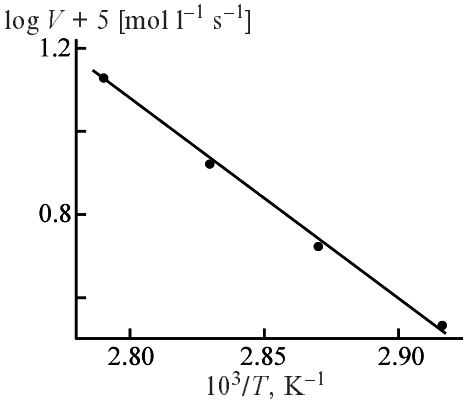


Fig. 1. Initial copolymerization rate V of EAAP-BF_4 (M_1) with SO_2 (M_2) as a function of temperature T. $[M_1 + M_2] = 1$ M; $M_1 : M_2 = 1 : 1$; 3.0×10^{-2} M AIBN.

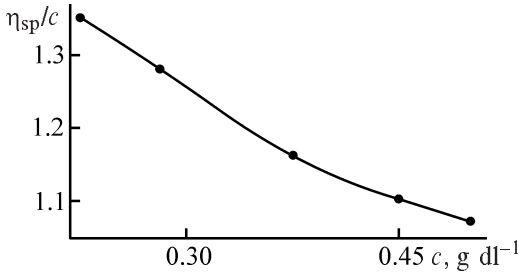


Fig. 2. Reduced viscosity η_{sp}/c of copolymer of EAAP-BF_4 (M_1) with SO_2 as a function of concentration c (DMSO, 25°C).

the equimolar ratio. Deviations from the equimolar ratio toward both sides lead to a decrease in the reaction rate due to a decrease in the concentration of the reactive complex in the system.

Kinetic studies of the copolymerization of EAAP-BF_4 with SO_2 in methanol in the initial steps of conversion showed that the reaction order is 0.75 with respect to the initiator and 1.35 with respect to the monomer (to the sum of the monomers at their equimolar ratio). Increased reaction orders with respect to the initiator and monomer (compared to those common for radical polymerization) are apparently associated with the fact that the copolymerization occurs via complexation, and also with the high viscosity of the system even at low conversions. The overall activation energy of the copolymerization of EAAP-BF_4 with SO_2 in a methanol solution at 70–90°C, calculated from the Arrhenius dependence, is 91.0 ± 2.0 kJ mol^{-1} (Fig. 1). The reaction rate and the copolymer yield depend on the medium (Table 2), with the best results obtained in methanol.

Table 2. Influence of the reaction conditions on the yield of the copolymer of tris(diethylamino)diallylaminophosphonium tetrafluoroborate with SO_2. $M_1 : M_2 = 50 : 50$, $[M_1 + M_2]$: solvent = 50 : 50 (wt %), 3 wt % AIBN, 7.0 h

Copolymerization conditions		Yield, %
T, °C	medium	
70	In bulk	39.1
80	In bulk	58.7
80	Methanol	62.9
90	In bulk	61.8
90	Methanol	70.7
90	Methanol*	76.7
90	Chloroform*	71.4

* Reaction time 10.5 h.

The ^{13}C NMR spectra (Table 1) of the copolymers contain low-field triplets from the *cis/trans*-isomeric C^1 and $C^{1'}$ atoms of the heteroring and from the C^3 and $C^{3'}$ atoms, and also doublets from the C^2 and $C^{2'}$ atoms. The content of *cis*-stereoisomeric units in the copolymers of EAAP-BF_4 and EAAP-Cl with SO_2 is four times higher than that of the *trans* units. The spectra show that the copolymerization of EAAP-Cl and EAAP-BF_4 with SO_2 involves both double bonds and occurs as intramolecular cyclization with the formation of pyrrolidine structures.

Owing to the cyclolinear structure, the copolymers obtained are soluble. The EAAP-BF_4–SO_2 copolymers are soluble in DMSO, DMF, methanol, acetone, and chloroform but insoluble in other common solvents (THF, ethyl acetate, diethyl ether, benzene, etc.). The EAAP-Cl–SO_2 copolymers are also soluble in water. Because of the polyelectrolytic effect, the reduced viscosity of the copolymer solutions increases with dilution (Fig. 2).

Experiments showed that the EAAP-Cl–SO_2 copolymer forms colored precipitates with CrO_4^{2-}, $AuCl_4^-$, and $PtCl_6^{2-}$. From a solution of $HAuCl_4$ in 0.3 M HCl (initial Au concentration 20.9 mg l^{-1}), the copolymer taken in six- and eightfold excess precipitates 92 and 98% of $AuCl_4^-$, respectively.

The copolymer of EAAP-BF_4 with SO_2 sorbs noble metal salts from solutions. We estimated the static capacity of the EAAP-BF_4–SO_2 copolymer (278 mg l^{-1}) for gold ($HAuCl_4$, 20.9 mg l^{-1} Au, 0.3 M HCl). The residual concentration of gold after keeping for 8 h, determined spectrophotometrically, was 4.4 mg l^{-1}. The static capacity of the copolymer was 59.3 mg Au/g.

Toxicological tests showed that the copolymers of

EAAP-BF_4 and EAAP-Cl with SO_2 belong to compounds of hazard class 4 and are suitable for medical applications.

Antimicrobial activity tests show that both copolymers exhibit an inhibiting effect toward *E. coli* in a concentration of 62.5 μg ml^{-1} and a bactericidal effect in a concentration of 125.0 μg ml^{-1}. The EAAP-BF_4–SO_2 and EAAP-Cl–SO_2 copolymers inhibit the growth of *St. aureus* in the concentration range 15.6–31.2 and 7.8 μg ml^{-1}, respectively. The bactericidal activity of the EAAP-BF_4–SO_2 copolymer toward gram-positive bacteria was noted at its concentration of 31.2 μg ml^{-1}, and that of the EAAP-Cl–SO_2 copolymer, at 15.6 μg ml^{-1}. Furthermore, the EAAP-BF_4–SO_2 copolymer exhibits antiulcer effect on the chosen model (indometacin), decreasing the number of ulcers by a factor of 20 relative to the control. Thus, the copolymers obtained can be used in drug production and in biotechnology.

CONCLUSIONS

(1) Diallylaminophosphonium salts in the presence of radical initiators do not undergo homopolymerization and show low activity in copolymerization with vinyl monomers.

(2) Tris(diethylamino)diallylaminophosphonium tetrafluoroborate and chloride exhibit high activity in radical copolymerization with sulfur dioxide. The copolymerization yields alternating copolymers of equimolar composition, irrespective of the monomer ratio in the starting mixture and reaction conditions. The copolymerization involves both double bonds of the monomer, which undergo intramolecular cyclization with the formation of pyrrolidine rings.

(3) Copolymers of tris(diethylamino)diallylaminophosphonium chloride with SO_2 precipitate the CrO_4^{2-}, $AuCl_4^-$, and $PtCl_6^{2-}$ ions, and copolymers of tris(diethylamino)diallylaminophosphonium tetrafluoroborate, which are insoluble in water, sorb these ions from solutions.

(4) The copolymers obtained are nontoxic (hazard class 4) and exhibit antiulcer and pronounced antimicrobial activity toward gram-positive and gram-negative bacteria.

ACKNOWLEDGMENTS

The study was financially supported by the Russian Foundation for Basic Research (project no. 05-03-32097) and by the Foundation for Support of Leading Scientific Schools (grant NSh-9342-2006.3).

REFERENCES

1. Leikin, Yu.A. and Ratajczak, V., *Khimiya i tekhnologiya vysokomolekulyarnykh soedinenii* (Chemistry and Technology of Macromolecular Compounds), Korshak, V.V., Ed., Moscow: VINITI, 1971, vol. 3, pp. 86–137.
2. Kabachnik, M.I., Medved', T.Ya., Dyatlova, N.M., et al., *Usp. Khim.*, 1968, vol. 37, no. 7, pp. 1161–1191.
3. Arkhipova, O.G., Kochetkova, T.A., Rudomino, M.V., et al., *Dokl. Akad. Nauk SSSR*, 1964, vol. 158, no. 5, pp. 1235–1237.
4. Vorob'eva, A.I., Vasil'eva, E.V., Gaisina, Kh.A., et al., *Vysokomol. Soedin., Ser. A*, 1996, vol. 38, no. 10, pp. 1663–1967.
5. Prozorovskii, V.B., Prozorovskaya, M.P., and Demchenko, V.M., *Farmakol. Toksikol.*, 1978, no. 4, pp. 497–502.
6. Pershin, G.N., *Metody eksperimental'noi khimioterapii: Prakticheskoe rukovodstvo* (Methods of Experimental Chemotherapy: Manual), Moscow: Meditsina, 1971.
7. Vorob'eva, A.I., Gorbunova, M.N., Kuznetsov, S.I., et al., *Order and Disorder in Polymer Reactivity*, Zaikov, G.E. and Howell, B.A., Eds., New York: Nova Science, 2006, ch. 9, pp. 125–135.

ISSN 1070-4272, Russian Journal of Applied Chemistry, 2008, Vol. 81, No. 5, pp. 845–849. © Pleiades Publishing, Ltd., 2008.
Original Russian Text © G.G. Balayan, S.G. Grigoryan, R.S. Martirosyan, G.M. Aivazyan, L.E. Tkachenko, 2008, published in Zhurnal Prikladnoi Khimii, 2008, Vol. 81, No. 5, pp. 808–812.

MACROMOLECULAR CHEMISTRY AND POLYMERIC MATERIALS

Modification of Ceramic Monoliths with Dimethyl(vinylethynyl)carbinol Polymers

G. G. Balayan, S. G. Grigoryan, R. S. Martirosyan, G. M. Aivazyan, and L. E. Tkachenko

Khimtekh Research Institute of Chemical Technology, Yerevan, Armenia

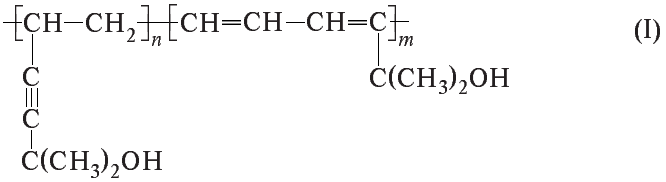
Received March 29, 2007

Abstract—Radical polymerization of dimethyl(vinylethynyl)carbinol on ceramic monolithic supports was studied with the aim to synthesize composite monolithic sorbents with applied hydrophilic–hydrophobic polymer.

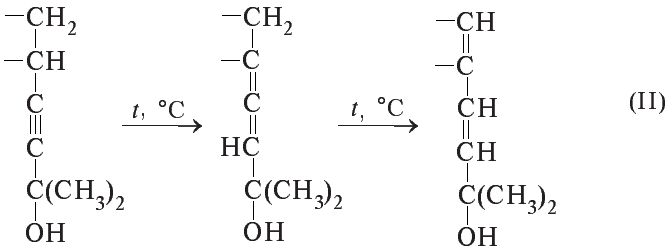
DOI: 10.1134/S1070427208050236

Dimethyl(vinylethynyl)carbinol (DMVEC) polymers, which contain a hydrophilic alcoholic group along with a hydrophobic hydrocarbon chain, are of certain interest for synthesis of organoceramic composite sorbents. Variation of hydrophilic–hydrophobic characteristics of the surface layer of the sorbents provides the possibility of controlling their selectivity in fairly wide limits. It should be noted that the initial monomer, dimethyl(vinylethynyl)carbinol (2-methylhex-5-en-3-yn-2-ol) $H_2C{=}CH{-}C{\equiv}C{-}C(CH_3)_2OH$ is a commercially available raw material used in organic synthesis and in production of adhesives.

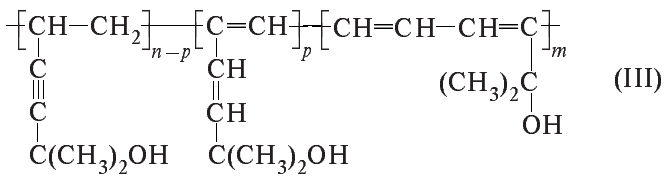
The mechanism of radical polymerization of vinylacetylene monomers, in particular, DMVEC, was studied previously [1–5]. At present, the commonly accepted mechanism of polymerization is the mechanism according to which radical polymerization of vinylacetylene monomers proceeds through the 1,2 and 1,4 positions of the vinylacetylene group ($C^1{=}C^2{-}C^3{\equiv}C^4$) [5]. This radical polymerization is a random process, and the subsequent allene–diene isomerization results in the formation of the conjugation blocks in polymers [scheme (I)]. The increase in the number of conjugation blocks upon heat treatment is caused by acetylene–allene–diene isomerization [schemes (II) and (III)]:



(I)



(II)



(III)

EXPERIMENTAL

All the chemicals used were of analytically pure or chemically pure grade. DMVEC of technical grade (Nairit Research and Production Association, Yerevan) was used after twofold distillation in a vacuum (bp 52°C/10 mm Hg, n_D^{20} 1.4750).

Permeable ceramic monoliths conventionally denoted as A and B were used as supports. Monolith A had the total porosity of 85–90% and contained macropores at practically zero specific sorption pore volume (V_s < 0.1 $cm^3\ g^{-1}$). Monolith B with a sorption pore volume of 0.38 $cm^{-3}\ g^{-1}$ and specific surface area of 101.5 $m^2\ g^{-1}$ was prepared by treating monolith A with colloidal silica [6]. The average diameter of colloidal silica particles was 22 nm. Polymerization of DMVEC on ceramic supports was performed by two procedures: (1) preim-

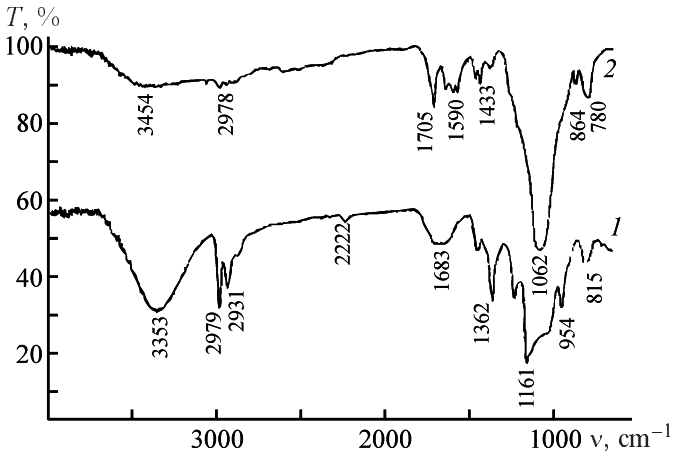


Fig. 1. IR spectra of (*1*) ceramic monolith modified with DMVEC polymer and (*2*) adduct with maleic anhydride. (*T*) Transmission and (ν) wavenumber.

pregnation of monoliths with a neat monomer or a solution of the carbinol in isopropanol in the presence of 1 wt % benzoyl peroxide, followed by polymerization in an oven at 120°C for 3 h, and (2) polymerization in a 15–50 wt % solution of isopropanol or dimethylformamide (DMF) in the presence of 1 wt % benzoyl peroxide at 80°C for 4 h in a flask equipped with a reflux condenser, followed by drying to remove the solvent and unchanged monomer in an oven at 120°C (in some experiments, at 180°C) for 2 h. After the polymerization completion, the composite monoliths modified with polymers were washed by boiling in distilled water for 2–3 h, and the samples heat-treated at 180°C were washed with isopropanol. The amount of immobilized polymer was estimated from the increase in the weight of the modified monolith, which depended on the monomer concentration in the initial solution; the higher was monomer concentration, the higher was the yield of the immobilized polymer.

The polymeric adduct of DMVEC with maleic anhydride, immobilized on a ceramic support, was synthesized by heating the ceramic monolith modified with DMVEC polymer thermally pretreated at 180°C with a twofold molar excess of maleic anhydride relative to the immobilized polymer in a methyl ethyl ketone solution for 20 h at 80°C. Then, the resulting samples were washed with distilled water and dried to constant weight at 100°C.

To determine the retention of copper ions, 0.20 ml of a 1 M solution of Cu(II) prepared from $CuSO_4 \cdot 5H_2O$ was added with a micropipet into an Eppendorf column loaded with the sorbent to be tested in the form of a cylinder 17 mm long and 5.1 mm in diameter. After 3 min, the phases were separated by centrifugation at 400*g*, and the residual content of Cu(II) ions in the liquid phase was determined spectrophotometrically at a wavelength of 650 nm using a Shimadzu 1202 spectrophotometer.

The ATR IR spectra were recorded on an Avatar Nicolet FTIR spectrometer, and the ESR spectra, on an E-3 Varian spectrometer; diphenylpicrylhydrazyl was used as a reference. The SEM images were obtained on a TESCAN 3115 scanning electron microscope. The specific surface areas of the samples and the pore volume were determined by the BET method with an Accusorb 2100E adsorption analyzer (Micrometrics Co.).

The results obtained show that the polymer is accumulated on ceramic support A considerably faster than on support B. All the resulting composite organoceramic monoliths are intensely colored from yellow to dark brown depending on treatment temperature, which is caused by the presence of segments of conjugated double bonds in the polymer structure. The materials prepared by impregnation of the ceramic support with a monomer solution with subsequent polymerization were readily washed out and contained (as judged from the optical density of the washing solution) a noticeable amount of the organic material, apparently, low-molecular-weight products of DMVEC oligomerization. This is confirmed by low values of viscosity-average molecular weight of DMVEC polymer, which was determined by the formula $[\eta] = 0.89 \times 10^{-4} M^{0.7} = 20\,000$ [7]. The polymer was isolated by extraction with methanol in a Soxhlet apparatus. The best results were obtained in polymerization of DMVEC on the surface of a ceramic support from isopropanol or DMF solution at 80°C. The wash water contained significantly smaller amount of the organic substance, which agrees well with fairly high values of the viscosity-average molecular weight of DMVEC polymer, $(120–150) \times 10^3$.

As already noted, thermal treatment of DMVEC polymers is accompanied by acetylene–diene rearrangement leading to the growth of polyconjugation blocks. This process also takes place in the case of polymers immobilized at the support surface, which is confirmed by the presence of a narrow singlet in the ESR spectrum (with *g*-factor close to that of free electron, equal to 2.0023) and an increase in the concentration of unpaired electrons from 10^{16} to 10^{18} spins per gram upon heat treatment of the polymers at 180°C for 2 h.

The IR spectra of ceramic supports modified with DMVEC polymers are shown in Fig. 1. In the IR

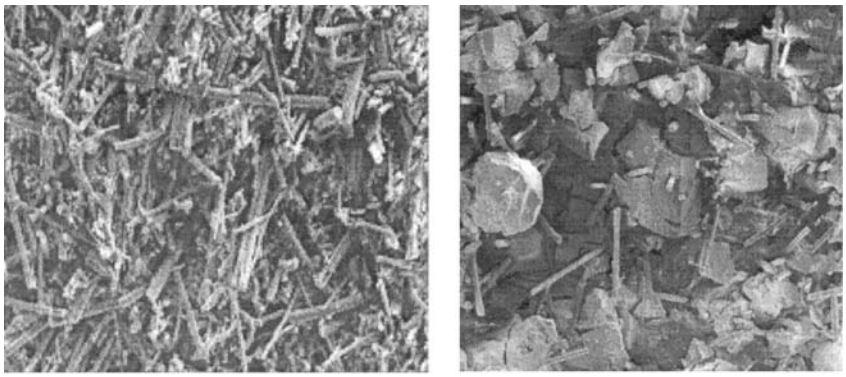
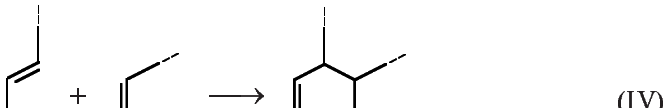


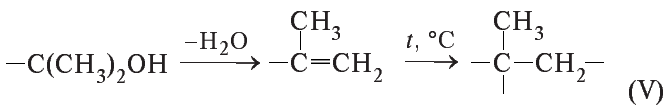
Fig. 2. SEM images of (a) unmodified ceramic monolith and (b) ceramic monolith modified with DMVEC polymer.

spectrum of the ceramic monolith modified with DMVEC polymer (Fig. 1, spectrum *1*), there are a broad absorption band of OH groups with a maximum in the region of 3350 cm^{-1}, a broad absorption band of polyconjugated C=C bonds in the range 1610–1680 cm^{-1}, and an absorption band of internal C≡C bond in the region of 2230 cm^{-1}, particularly pronounced in the case of the untreated polymer, which also suggests the growth of the blocks of polyconjugated C=C bonds by scheme (II).

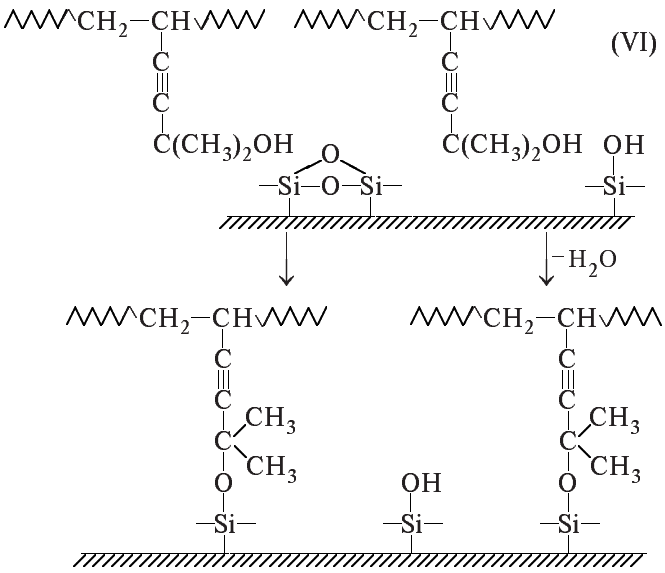
A comparison of the SEM images (Fig. 2) of (a) nonmodified ceramic monolith and (b) ceramic monolith modified with DMVEC polymer showed clearly pronounced macroporous structure of the unmodified monolith, presented by interconnected pores, and also uniform distribution of the polymer in the bulk of the modified monolith.

We revealed an interesting fact of thermal curing of DMVEC polymers applied to a ceramic support at 180°C with the transformation of the polymer into an insoluble and infusible state, which is not observed in the case of ordinary DMVEC homopolymers. In the course of heat treatment, the modified ceramic monoliths become less hydrophilic. This fact may be accounted for by the following schemes:


(IV)


(V)

Scheme (IV) suggests that thermal curing occurs as the diene synthesis involving the conjugation segments, when one fragment of conjugated double bonds of the chain acts as diene and the other, as dienophile. Apparently, only segments of conjugated double bonds with the cisoid structure can act as diene fragments in the diene synthesis. This pathway of intermolecular cross-linking of the polymer is the least probable, as it should take place in the case of (unapplied) DMVEC homopolymer also. Scheme (V) suggests that thermal curing involves dehydration of the *tert*-butanol group on the surface of dehydrated silica with formation of the isopropenyl group and subsequent cross-linking of the polymer due to cleavage of the double bond of the isopropenyl group at elevated temperatures. According to scheme (VI), transition of the polymer into the insoluble state is due to grafting of the polymer with the participation of siloxane or/and silanol groups of the silica surface [8]:


(VI)

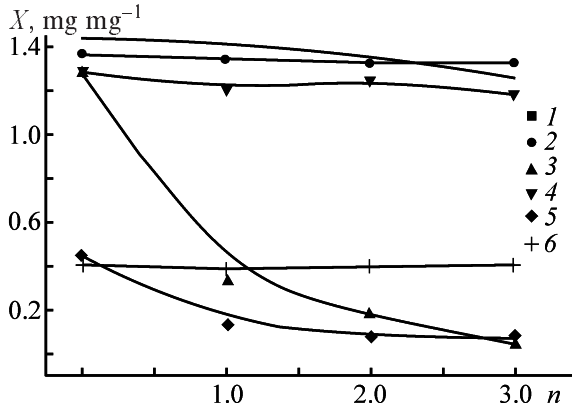


Fig. 3. Wash-out X of DMVEC polymers immobilized on ceramic supports (*1–4*) A and (*5, 6*) B. (n) Number of washing runs. Drying temperature, °C: (*1, 3*) 120 and (*2, 4*) 180. (*1, 3*) After polymerization, boiling in distilled water and drying to constant weight at 120°C; (*3, 4*) after polymerization, washing with isopropanol and drying to constant weight at 120°C; (*5*) polymerization at 80°C in solution, drying at 80°C, washing with isopropanol, and drying to constant weight at 80°C; and (*6*) polymerization at 80°C in solution, drying at 180°C, washing with isopropanol, and drying to constant weight at 180°C.

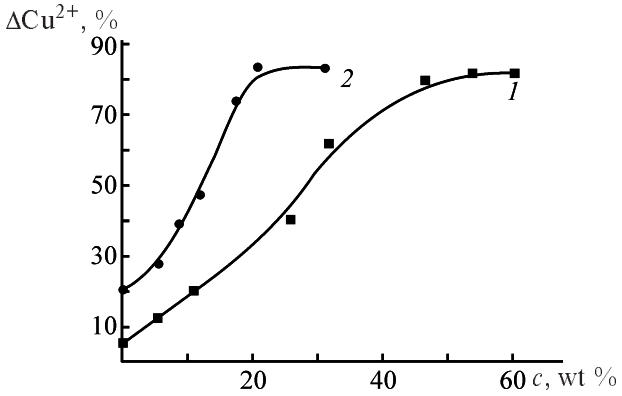


Fig. 4. Retention of copper ions ΔCu^{2+} by sorbents based on monoliths of types (*1*) A and (*2*) B as a function of the content of adduct of PDMVEC with maleic anhydride c.

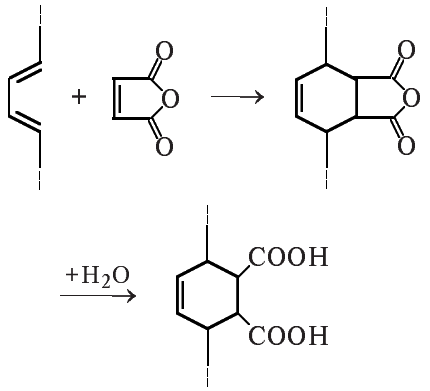
Thus, only schemes (V) and (VI) can account for the influence of the support surface on cross-linking of the polymer applied to the ceramic support. The increase in the intensity of the bands corresponding to OH vibrations in the range 3350–3365 cm^{-1} after heat treatment of immobilized DMVEC polymer at 180°C counts in favor of these schemes.

The wash-out of the applied DMVEC polymer (the amount of the residual polymer expressed in milligrams per milligram of the ceramic support) as a function of the number of washing runs for the samples washed and dried under various conditions is plotted in Fig. 3. In all cases, polymerization of DMVEC was performed from solutions at 80°C.

Curves *4* and *6* (Fig. 3) confirm the cross-linking of DMVEC polymers in thermal treatment at 180°C: the polymer is not washed out with isopropanol, DMF, and other organic solvents.

To increase the degree of hydrophilicity (control of hydrophilic–hydrophobic balance of the polymer layer) and functionalization of the polymer with the aim to synthesize cation-exchange organoceramic sorbent, we performed the diene synthesis reaction of DMVEC polymer pretreated with maleic anhydride at 180°C. The occurrence of the diene synthesis follows from the changes in the IR spectrum of the adduct (Fig. 1, spectrum *2*): appearance of absorption bands of carboxy group at 1700 cm^{-1} and of an extremely broad diffuse band in the range 2700–2500 cm^{-1}, changes in the absorption band of polyconjugated double bonds in the range 1600–1670 cm^{-1}, appearance of several narrow absorption bands instead of this band, and also from an increase in the weight and hydrophilicity of the composite ceramic monolith.

The occurrence of the diene synthesis confirms the presence of the blocks of conjugated double bonds in the polymer. However, as already mentioned, only segments of conjugated double bonds with the cisoid configuration can participate in the diene synthesis reaction as diene fragments:



The resulting sorbents based on ceramic monoliths A and B and PDMVEC adduct were tested for retention of copper ions from a 1 M copper sulfate solution. The dependence of the retention of copper ions on the amount of the applied polymer is shown in Fig. 4. It is seen that, in the case of monolith A, the retention of copper ions is 81% at 54% content of the polymer in the composite sorbent, while in the case of ceramic B 83% retention of copper ions is

reached even at significantly lower content of the polymer in the sorbent.

From the results obtained it follows that, in the case of monoliths of the type A (without additional porous silica coatings), the polymer content of these monoliths should be significant (more than 40%) for reaching sufficient sorption capacity. In the case of monoliths of type B (with applied silica coating), significantly smaller amount of the polymer (10–20%) is required.

CONCLUSIONS

(1) Polymerization of dimethyl(vinylethynyl)carbinol on ceramic monolith supports takes place at the 1,2 and 1,4 positions of the vinylacetylene groups with the formation of a polymer containing segments of conjugated double bonds. The subsequent acetylene–allene–diene rearrangement results in the growth of the polyconjugation blocks. Heat treatment of immobilized dimethyl(vinylethynyl)carbinol polymers at 180°C results in cross-linking of these polymers, making them more stable with respect to wash-out.

(2) The occurrence of the diene synthesis reaction follows from the IR spectrum of the adduct and from an increase in the hydrophilicity of the composite ceramic monolith.

REFERENCES

1. Dykstra, H., *J. Am. Chem. Soc.*, 1934, vol. 56, no. 7, pp. 1625–1629.
2. Matsoyan, S.G., *Usp. Khim.*, 1966, vol. 25, pp. 70–92.
3. Matsoyan, S.G. and Morlyan, N.M., *Vysokomol. Soedin., Ser. A*, 1964, vol. 6, no. 5, pp. 945–950.
4. Kryazhev, Yu.G., Okladnikova, Z.A., Rzhepka, A.V., et al., *Vysokomol. Soedin., Ser. A*, 1968, vol. 10, no. 12, pp. 2366–2374.
5. Matnishyan, A.A., Grigoryan, S.G., Arzumanyan, A.M., and Matsoyan, S.G., *Dokl. Akad. Nauk SSSR*, 1981, vol. 257, no. 6, pp. 1384–1387.
6. Balayan, H., Balekaev, A., Avtandilyan, S., and Grigoryan, S., Abstracts of Papers, *30th Symp. on Chromatographic Methods of Investigation of Organic Compounds*, Katovice, June 12–14, 2006, p. 66.
7. Danielyan, V.A., Barkhudaryan, V.G., Matsoyan, S.G., and Sardaryan, A.E., *Arm. Khim. Zh.*, 1969, vol. 22, pp. 774–778.
8. *Modifitsirovannye kremnezemy v sorbtsii, katalize i khromatografii* (Modified Silica in Sorption, Catalysis, and Chromatography), Lisichkin, G.V., Ed., Moscow: Khimiya, 1986.

ISSN 1070-4272, Russian Journal of Applied Chemistry, 2008, Vol. 81, No. 5, pp. 850–853. © Pleiades Publishing, Ltd., 2008.
Original Russian Text © O.G. Al'tshuler, L.A. Sapozhnikova, G.N. Al'tshuler, 2008, published in Zhurnal Prikladnoi Khimii, 2008, Vol. 81, No. 5, pp. 813–816.

MACROMOLECULAR CHEMISTRY AND POLYMERIC MATERIALS

Ion-Exchange Selectivity of a Sulfonic Cation Exchanger Based on Immobilized *cis*-Tetraphenylcalix[4]resorcinolarene

O. G. Al'tshuler, L. A. Sapozhnikova, and G. N. Al'tshuler

Kemerovo Branch, Institute of Solid State Chemistry and Mechanochemistry, Siberian Branch, Russian Academy of Sciences, Kemerovo, Russia

Received May 14, 2007

Abstract—The ion-exchange equilibrium of protons in SO_3H groups of a sulfonic cation exchanger based on immobilized *cis*-tetraphenylcalix[4]resorcinolarene with cations of Li^+, Na^+, Ag^+, Cu^{2+}, In^{3+}, and protonated 1,3,5,7-tetraazaadamantane in aqueous solutions of electrolytes at 293 K was studied. The corrected coefficients of the cation exchange selectivity were calculated.

DOI: 10.1134/S1070427208050248

Thanks to unique structure, *cis*-calix[4]resorcinolarenes attract much researchers' attention. The presence in *cis*-calix[4]resorcinolarenes of a large internal cavity and an upper hydrophilic rim containing eight hydroxy groups makes them a convenient matrix for the design of molecular ensembles realizing the complementary host–guest stereoelectronic interactions [1].

The prospects for the development of the calixarene chemistry are associated with introduction into their composition of functional groups, with the aim to obtain new types of highly organized steric structures with preset properties. Functionalized calixarenes are of interest as new complexing agents, polymer stabilizers, and extractants [2]. Immobilization of calixarenes in the polymer phase allows realization of their capability for complementary interactions with neutral molecules and multicharged ions. Previously [3–9] we prepared network polymers containing immobilized *cis*-calix[4]resorcinolarenes [3–9]. We demonstrated that these polymers are weakly acidic cation exchanges [3, 4, 7] and nanoreactors for catalytic hydrogenation processes [8, 9].

Functionalization of immobilized calixarenes by introducing carboxy [10], furylhydroxymethyl [4], and phosphoric acid [11] groups enhances the selectivity of interaction of polymers with cations. It was shown previously [12, 13] that the new sulfonated polymer based on immobilized *cis*-tetraphenylcalix[4]resorcinolarene, owing to the presence of SO_3H groups, is a strongly acidic cation exchanger surpassing in the service characteristics the known cation exchangers derived from calixarenes. In particular, this sulfonic cation exchanger exhibits cation-exchange properties in a wide range of pH, high ion-exchange capacity [12, 13], and good kinetic characteristics [14].

The elementary unit of the sulfonic cation exchanger based on immobilized *cis*-tetraphenylcalix[4]resorcinolarene, in contrast to that of the commercially available sulfonic cation exchanghers, has an ordered steric structure [13]. Figure 1 shows the simulated structure of the elementary unit of the

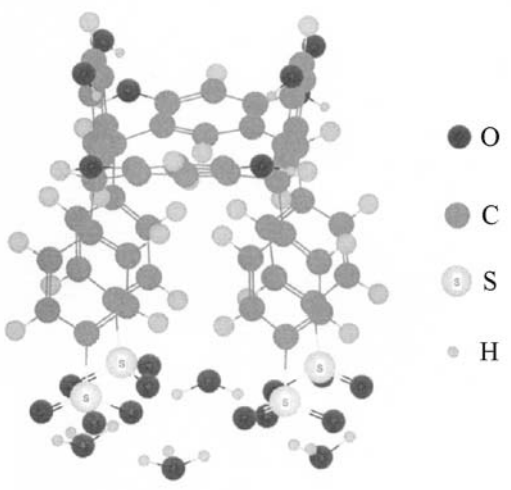


Fig. 1. Structure of a compound simulating the elementary unit of the sulfonic cation exchanger based on immobilized *cis*-tetraphenylcalix[4]resorcinolarene, minimized by the PM3 semiempirical method with respect to the enthalpy of formation.

Equilibrium compositions of phases and coefficients of the ion exchange selectivity for the sulfonic cation exchanger derived from immobilized *cis*-tetraphenylcalix[4]resorcinolarene at 293 K

Cat^{z+}	m_{Cat}	m_H	x_{Cat}	$k^a_{Cat/H}$	Function $\log k^a_{Cat/H}(x_{Cat})$	Correlation coefficient
Li^+	0.074	0.026	0.51	0.36	$\log k^a_{Li/H} = -0.75x_{Li} - 0.071$	–0.99
Na^+	0.0605	0.0395	0.51	0.67	$\log k^a_{Na/H} = -1.18x_{Na} - 0.04$	–0.95
Ag^+	0.0533	0.0450	0.54	0.99	$\log k^a_{Ag/H} = -0.61x_{Ag} - 0.35$	–0.96
Cu^{2+}	0.0102	0.0820	0.55	3.2	$\log k^a_{Cu/H} = -0.54x^2_{Cu} + 0.64x_{Cu} + 0.31$	
In^{3+}	0.0059	0.0820	0.51	1.48	$\log k^a_{In/H} = -4.75x^3_{In} + 8.3x^2_{In} - 2.8x_{In} - 0.015$	
$[C_6H_{13}N_4]^+$	0.0050	0.0046	0.29	0.37		

polymer, optimized with respect to the enthalpy of formation: The sulfur atoms occur in the vertices of a parallelogram with the side lengths of 5 and 5.5 Å. Hence, anions of the sulfo groups are distributed in the polymer matrix within structural fragments that bear four negative charges arranged near the parallelogram vertices. This steric structure may affect the cation exchange selectivity; in particular, the affinity of the polymer for multicharged cations may increase. Therefore, it is interesting to study the ion-exchange equilibria in systems consisting of a sulfonic cation exchanger based on immobilized *cis*-tetraphenylcalix[4]resorcinolarene and of binary and multicomponent electrolyte solutions.

The goal of this study was to examine the selectivity of proton exchange in ionic SO_3H groups of the polymer:

$$z\bar{H}^+ + Cat^{z+} \rightleftarrows \overline{Cat}^{z+} + zH^+, \quad (1)$$

where the overscore denotes the polymer phase; $Cat^{z+} = Li^+$, Na^+, Ag^+, Cu^{2+}, In^{3+}, or protonated 1,3,5,7-tetraazaadamantane ($C_6H_{12}N_4$) cation; and z is the cation charge.

EXPERIMENTAL

The sulfonic cation exchanger was prepared in the form of spherical granules 0.01–0.05 cm in diameter by sulfonation of a network polymer prepared by resol polycondensation of *cis*-tetraphenylcalix[4]resorcinolarene with formaldehyde [4, 5]. The sulfur content of the polymer, determined according to [15], was 7.8 wt %. The dynamic ion-exchange capacity of the polymer with respect to sulfo groups was determined in columns by passing a 0.01 M NaCl solution through a bed of the polymer in the H^+ form until the cation concentrations at the inlet and outlet of the column became equal. The exchange capacity was reduced to 1 g of the polymer in the H^+ form, dried to constant weight at 105°C. The capacity was 2.25 mg-equiv g^{-1}.

The ion exchange selectivity was studied by the dynamic method [5]. Aqueous solutions containing two electrolytes (HCl and LiCl, HNO_3 and $AgNO_3$, HCl and $C_6H_{12}N_4$, HCl and NaCl, HCl and $CuCl_2$, HCl and $InCl_3$) were passed at 293 K through a column packed with the sulfonic cation exchanger in the H^+ or Cat form until the concentrations of the electrolytes in the initial solution and several successively taken filtrate samples became equal, which was considered as the attained equilibrium. The equilibrium composition of the polymer phase was independent of the initial ionic form of the sulfonic cation exchanger. The ionic strength of the equilibrium solutions of strong electrolytes was 0.1, and for a $C_6H_{12}N_4$ solution, 0.01 M. The mean ionic molal activity coefficients of the electrolytes in solution were calculated by the Debye–Hückel equation, with the distances of the closest mutual approach of the ions assumed to be 4.5 and 6 Å [16] for $CuCl_2$ and $InCl_3$, respectiveloy. The quantum-chemical calculations were performed by the PM3 semiempirical method using the MOPAC 2000 program. The corrected coefficients of the cation exchange selectivity $k^a_{Cat/H}$ [17] were calculated by the equation

$$k^a_{Cat/H} = \frac{x_{Cat} m^z_H \gamma^{2z}_{\pm HAn}}{x^z_H m_{Cat} \gamma^{z+1}_{\pm HAn}}, \quad (2)$$

where x_i is the equivalent fraction of the cation in the polymer; m_i, molality of the cation in solution; and $\gamma_\pm$, mean ionic molal activity coefficient of the electrolyte (HAn or $CatAn_z$) in aqueous solution.

The experimental data on the equilibrium compositions of the solution and polymer phases and the

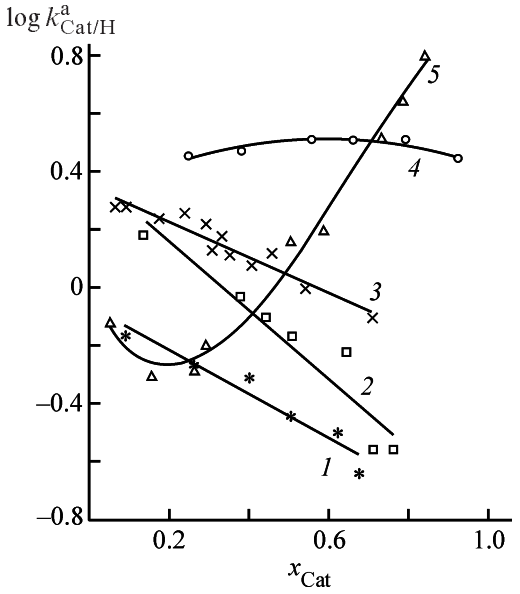


Fig. 2. Logarithm of the corrected coefficient of the ion exchange selectivity $\log k^a_{Cat/H}$ as a function of the equivalent fraction of cations x_{Cat} in the sulfonic cation exchanger derived from *cis*-tetraphenylcalix[4]resorcinolarene at 293 K. Exchange: (*1*) $H^+ \rightarrow Li^+$, (*2*) $H^+ \rightarrow Na^+$, (*3*) $H^+ \rightarrow Ag^+$, (*4*) $H^+ \rightarrow Cu^{2+}$, and (*5*) $H^+ \rightarrow In^{3+}$.

corrected coefficients of the cation exchange selectivity [reaction (1)] at the equivalent fraction of cations in the polymer close to 0.5 are given in the table.

In the systems under consideration, the counterion composition of the polymer phase strongly affects the corrected coefficient of the ion exchange selectivity. Figure 2 shows the plots of $\log k^a_{Cat/H}$ vs. equivalent fraction of cations in the sulfonic cation exchanger derived from immobilized *cis*-tetraphenylcalix[4]resorcinolarene. For single-charged cations, interactions in the polymer phase are determined by the Coulomb attraction of the sulfo group anions and exchanging cations. The exchanging sites of the cation exchanger, as a rule, are nonequivalent in energy [18]. It was shown [19] that the population of each energy level in the ion exchanger is determined by the Gibbs canonical distribution. The probability density of the exchange sites of the polymer with the energy ε is described by the equation

$$\rho = e^{(\psi - \varepsilon)/\theta}, \quad (3)$$

where ρ(ε) is the probability density of the phase with energy ε; ψ, a constant; and θ, distribution modulus.

If $\theta \gg \psi - \varepsilon$, ρ is a linear function of ε:

$$\rho = 1 + (\psi - \varepsilon)/\theta. \quad (4)$$

For an ion exchanger containing two exchanging ions, $\ln k^a_{i/j}$ is a continuous function of energy varying throughout the ion exchange isotherm from $\ln k^a_{i/j}$ at $x_i = 0$ to $\ln k^a_{i/j}$ at $x_i = 1$. In this case, the composition of the ion exchanger, determined by the mole fraction of component *i*, corresponds to the probability density of separate phases occurring in a random equilibrium. In other words, for a binary exchange the canonical energy distribution leads to a linear dependence of the logarithm of the corrected selectivity coefficient on the mole fraction of counterions in the ion exchanger phase [19]:

$$\ln k^a_{i/j} = A_{i/j} + B_{i/j}\bar{x}_i, \quad (5)$$

where $A_{i/j}$ and $B_{i/j}$ are constants.

It follows from the table that the experimental dependences of $\log k^a_{Cat/H}$ on x_{Cat} for the single-charged Li^+, Na^+, and Ag^+ cations are linear, whereas for the double-charged Cu^{2+} cations they pass through a maximum at $x_{Cu} = 0.6$. Probably, one copper cation interacts with two anions of the sulfo groups of the polymer unit. For the triple-charged In^{3+} cations, the shape of the function $\log k^a_{Cat/H}(x_{Cat})$ can be accounted for by the fact that an increase in the fraction of the triple-charged In^{3+} cations in the polymer phase leads to an increase in the probability of supramolecular interactions of the cation with the adjacent polymer chains. It is well known [20] that such interactions increase the ion exchange selectivity.

The protonated 1,3,5,7-tetraazaadamantane cation occupies a paticular place. Despite the presence of several protonation sites, this compound has a single association constant K_a [20] corresponding to the reaction $C_6H_{12}N_4 + H^+ \rightleftarrows [C_6H_{13}N_4]^+$. The coefficient of the selectivity of the $H^+/[C_6H_{13}N_4]^+$ ion exchange is given in the table. It is comparable with the corresponding quantity for Li^+. The related quantity for the ion exchange with a weakly acidic cation exchanger derived from *cis*-tetramethylcalix[4]resorcinolarene is lower by several orders of magnitude (0.2×10^{-4} [5]).

The polymer under consideration is characterized by a wider range of the selectivity coefficients of the ion exchange of inorganic cations compared to the known sulfonic cation exchangers. For the sulfonic cation exchanger based on immobilized *cis*-tetraphenylcalix[4]resorcinolarene, the corrected coefficients of the ion exchange selectivity $k^a_{Cat/H}$ at the degree of filling $x_{Cat} = 0.8$ (Fig. 2) varies from 0.25 (Na^+–H^+ exchange) to 3.2 (Cu^{2+}–H^+ exchange) and 6.3 (In^{3+}–H^+ exchange). For commercial sulfonic

cation exchangers, $k^{a}_{Cat/H}$ at x_{Cat} = 0.8 varies in a narrow range from 1.6 (Na^+–H^+ exchange on KU-2×8 [21] and Dowex-50×8 [22]) to 2.3 (Cu^{2+}–H^+ exchange on Dowex-50×8 [23]).

The wide interval of the coefficients of the ion exchange selectivity creates prerequisites for using the sulfonic cation exchanger that we prepared for separation of binary and multicomponent electrolyte mixtures. The study of the kinetics and mechanism of the interaction of metal ions with the functional groups in the elementary unit of the sulfonic cation exchanger derived from immobilized *cis*-tetraphenylcalix[4]resorcinolarene is of theoretical and applied interest.

CONCLUSIONS

(1) The ion-exchange selectivity of a strongly acidic sulfonic cation exchanger, a sulfonated network polymer based on immobilized *cis*-tetraphenylcalix[4]resorcinolarene, strongly depends on the kind of the sorbate cation and on the counterionic composition of the polymer. For the single-charged metal cations Li^+, Na^+, and Ag^+, the logarithm of the corrected coefficient of the ion exchange selectivity linearly depends on the equivalent fraction of metal cations in the ion exchanger phase. For the Cu^{2+} and In^{3+} cations, the dependence of $\log k^{a}_{Cat/H}$ on x_{Cat} suggests the occurrence of supramolecular interactions in the polymer phase.

(2) The sulfonic cation exchanger derived from immobilized *cis*-tetraphenylcalix[4]resorcinolarene is characterized by the wider range of coefficients of the ion exchange selectivity compared to the known sulfonic cation exchangers.

ACKNOWLEDGMENTS

The study was financially supported by the Russian Foundation for Basic Research (project no. 07-03-96030).

REFERENCES

1. Cram, D.J., Hye-Eyn Kim, S.K., Knoler, C.B., et al., *J. Am. Chem. Soc.*, 1988, vol. 110, pp. 2229–2237.
2. Popova, E.V., Volodina, Yu.M., Gazizov, A.S., et al., *Izv. Ross. Akad. Nauk, Ser. Khim.*, 2003, no. 10, pp. 2168–2169.
3. Al'tshuler, G.N., Fedyaeva, O.N., Sapozhnikova, L.A., and Ostapova, E.V., *Vysokomol. Soedin., Ser. B*, 2001, vol. 43, no. 4, pp. 755–759.
4. Altshuler, H., Ostapova, E., Fedyaeva, O., et al., *Macromol. Symp.*, 2002, vol. 181, pp. 1–4.
5. Al'tshuler, G.N., Sapozhnikova, L.A., and Abramova, L.P., *Izv. Ross. Akad. Nauk, Ser. Khim.*, 1998, no. 11, pp. 2214–2216.
6. Al'tshuler, G.N., Fedyaeva, O.N., and Ostapova, E.V., *Izv. Ross. Akad. Nauk, Ser. Khim.*, 2000, no. 8, pp. 1475–1477.
7. Ostapova, E.V., Al'tshuler, O.G., Sapozhnikova, L.A., and Al'tshuler, G.N., *Zh. Fiz. Khim.*, 2003, vol. 77, no. 5, pp. 909–913.
8. Al'tshuler, G.N. and Sapozhnikova, L.A., *Zh. Prikl. Khim.*, 2004, vol. 77, no. 11, pp. 1914–1916.
9. Al'tshuler, G.N. and Sapozhnikova, L.A., *Zh. Strukt. Khim.*, 2004, vol. 45, suppl., pp. 178–180.
10. Shinohara, T., Wakisaka, S., Ohto, K., and Inoue, K., *Chem. Lett.*, 2000, no. 6, pp. 640–641.
11. Alexandratos, S.D. and Natesan, S., *Macromolecules*, 2001, vol. 34, pp. 206–210.
12. RF Patent 2291171.
13. Al'tshuler, O.G., Sapozhnikova, L.A., and Al'tshuler, G.N., *Zh. Prikl. Khim.*, 2006, vol. 79, no. 8, pp. 1315–1319.
14. Al'tshuler, G.N., Malyshenko, N.V., and Shkurenko, G.Yu., *Zh. Prikl. Khim.*, 2007, vol. 80, no. 10, pp. 1708–1711.
15. Lebedeva, A.I. and Novozhilov, I.V., *Zh. Anal. Khim.*, 1961, vol. 16, pp. 223–225.
16. Robinson, R.A. and Stokes, R.H., *Electrolyte Solutions. The Measurement and Interpretation of Conductances, Chemical Potential and Diffusion in Solutions of Simple Electrolytes*, London: Butterworths, 1959, 2nd ed. Translated under the title *Rastvory elektrolitov*, Moscow: Inostrannaya Literatura, 1963, p. 277.
17. *Nomenklaturnye pravila IYuPAK po khimii* (IUPAC Rules of Chemical Nomenclature), Moscow: VINITI, 1979, vol. 1. half-vol. 2, p. 582.
18. Reichenberg, D., Ion Exchange Selectivity, *Ion Exchange. A Series of Advances*, Marinsky, J.A., Ed., New York: Dekker, 1966, vol. 1. Translated under the title *Ionnyi obmen*, Moscow: Mir, 1968, p. 151.
19. Altshuler, O.H. and Altshuler, H.N., *Comput. Mater. Sci.*, 2006, vol. 36, pp. 207–211.
20. *Stability Constants of Metal–Ion Complexes*, Sillen, L.G. and Martell, A.E., Compilers, London: Chem. Soc., 1964, p. 487.
21. Soldatov, V.S. and Bychkova, V.A., *Ionoobmennye ravnovesiya v mnogokomponentnykh sistemakh* (Ion-Exchange Equilibria in Multicomponent Systems), Minsk: Nauka i Tekhnika, 1988.
22. Bonner, O.D. and Smith, L.L., *J. Phys. Chem.*, 1957, vol. 61, no. 3, pp. 326–329.
23. Bonner, O.D. and Livingston, F.L., *J. Phys. Chem.*, 1956, vol. 60, no. 5, pp. 530–532.

ISSN 1070-4272, Russian Journal of Applied Chemistry, 2008, Vol. 81, No. 5, pp. 854–857. © Pleiades Publishing, Ltd., 2008.
Original Russian Text © Yu.V. Titova, M.I. Voronova, A.I. Maksimov, 2008, published in Zhurnal Prikladnoi Khimii, 2008, Vol. 81, No. 5, pp. 817–820.

MACROMOLECULAR CHEMISTRY AND POLYMERIC MATERIALS

Influence of Gas-Discharge Plasma Treatment in the Electrolyte Bulk on the Cellulose Properties

Yu. V. Titova, M. I. Voronova, and A. I. Maksimov

Institute of Solution Chemistry, Russian Academy of Sciences, Ivanovo, Russia

Received November, 27 2007

Abstract—The effect exerted on cellulose properties by plasma–solution treatment using the atmospheric-pressure diaphragm and end discharges was examined.

DOI: 10.1134/S10704272080502 5X

Modification of properties of polymer materials is a multi-aspect problem, topical for various industries. This typically implies modification of the surface properties of a material in the desired direction without affecting its bulk properties. However, certain applications require more profound changes of not only the surface but also the bulk properties of materials. In the former case, modification implies functionalization (creation in the surface layer of a material of new functional groups) and formation of a new surface microstructure. In the latter case, there is a need for a more profound selective chemical impact on the macromolecular compound, e.g., selective oxidation of lignin accompanied by its conversion to a water-soluble form.

The surface properties of polymers are successfully modified using low-pressure nonequilibrium plasma [1]. However, treatment of materials with a capillary porous structure within the framework of selective processes (e.g., delignification) entails major difficulties in application of low-pressure plasma. First, there are technical problems associated with relatively complex and expensive vacuum facilities and the need in combining vacuum and solution processes. The second problem consists in low selectivity and low efficiency of treatment of the inner surface of the capillaries because of a short lifetime of active species [2]. The use of plasma–solution systems which allow, in principle, a plasma-induced redox reaction to be combined with a selective process in solutions seems fairly attractive. In this context, practically convenient options are discharges with an electrolyte cathode, in which both direct-current and variable-frequency sources with a fairly low voltage of about one or several kilovolts are used. Among such discharges are glow and sliding discharges excited above the solution surface [3–6] and the so-called "underwater" discharges, in particular, the diaphragm discharge and closely related end discharge [3, 7].

In plasma–solution modification of polymer materials using a glow discharge with an electrolyte cathode, the primary active species, including H and OH radicals and solvated electrons, very rapidly (within approximately a microsecond) react in the cathode spot area, and the subsequent interaction can involve more stable secondary reactive species only [3, 4, 8]. The rate of removal of the reaction products is determined by the flows initiated by the transfer of the solution components from the cathode spot area to the plasma zone [9]. The active plasma particles exert the minimal impact on the polymer material samples placed into solution.

A slightly stronger impact of active plasma particles on polymer materials can be expected in the case of a diaphragm discharge initiated by passing current through a small hole in a dielectric diaphragm dividing the reactor with an electrolyte solution into two segments (Fig. 1). Intense warming-up of the solution in the diaphragm area leads to formation in the hole of a gas–vapor bubble disconnecting the electric circuit. At a sufficiently high emf of the source, an electric breakdown occurs in the bubble, followed by collapse of the plasma bubble and spread in the solution of a sound wave. Repetition of this process leads to a quasiperiodic discharge [3, 4, 7].

Efficient plasma treatment of polymeric materials implies that a plasma area should be formed inside

the solution and exist there for a prolonged period during which both the plasma and the thin solution layer it activates can contact the material being treated. The latter should be washed by this layer. This plasma–solution system, in which the action of solution activated by plasma is combined with direct plasma action of the discharge on the material, was developed comparatively recently; this is a so-called end discharge system [7]. The end discharge is most similar to the diaphragm discharge; it is excited in the end segments of the tubes vertically immersed in a solution together with the electrodes inside them. When current is passed through this system, a plasma zone is formed in the space separating the electrode from the tube cross section, where a gas bubble is formed by ordinary electrolysis before the breakdown (Fig. 2).

This study was concerned with cellulose extracted from a flax fiber by cooking with various oxidizing agents. In this process, the oxidation and degradation rate of the noncellulose components should be higher than that of cellulose proper. Unfortunately, chemical oxidizing agents exhibit low selectivity, and both the oxidation and removal of lignin are accompanied by intensive cellulose degradation. In this situation, plasma–solution treatment instead of oxidizing cooking, alone or combined with conventional methods, seems highly attractive.

We examined the cellulose properties as influenced by plasma–solution treatment. Specifically, we elucidated the influence of the diaphragm and end discharges on the following characteristics of flax cellulose: the content of aldehyde (HCO) and carboxy (COOH) groups, degree of polymerization, and α-cellulose content. The capillary-porous structure of various cellulose samples was characterized by the water-retaining power (WRP).

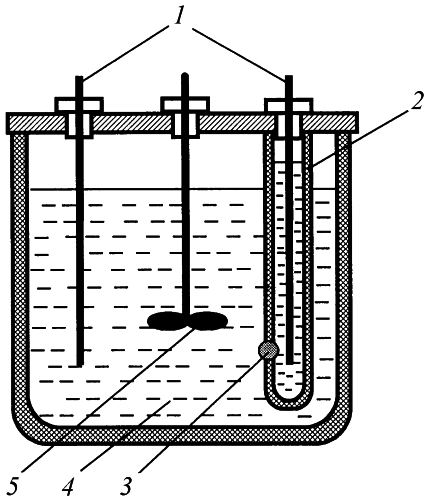


Fig. 1. Schematic of the experimental cell for diaphragm discharge: (*1*) electrodes, (*2*) quartz ampule, (*3*) plasma zone, (*4*) electrolyte solution, and (*5*) stirrer.

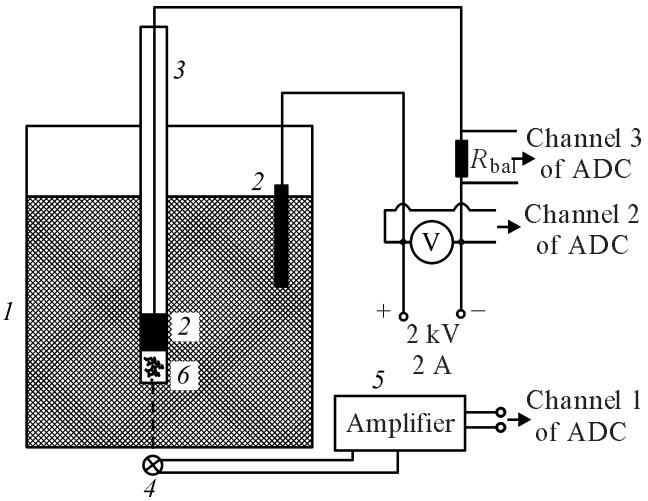


Fig. 2. Flow sheet of the end discharge setup: (*1*) electrolyte solution, (*2*) electrodes, (*3*) glass tube, (*4, 5*) radiation recording scheme, and (*6*) plasma zone.

EXPERIMENTAL

The cellulose extracted from flax fiber contained 0.8–0.95% lignin, 90.5–91.4% α-cellulose, and 7.6–8.5% hemicelluloses; the degree of polymerization (DP) was 1000–1400.

Cellulose was mechanically ground to the fiber size of 3–5 mm.

Samples of mechanically ground cellulose (fiber length 0.5–2 mm) extracted from flax fiber (3 g) were placed into a 1-l glass vessel. To elucidate the influence of the chemical composition of the electrolyte solution, we used 0.01 M NaOH, 0.01 M Na_2SO_4, and 0.05 M HNO_3 as the working solutions. At these concentrations of the solutions, the electrical conductivities of the electrolytes were virtually identical in all the cases, irrespective of pH of the medium, specifically, about 2 mS cm^{-1}. The solution volume was 600 ml.

We used an ac source for the discharges. In the cases of diaphragm discharge, the discharge current was 0.2 A. The end discharge current at the initiation time was 1 A, but after several minutes of burning it also decreased to 0.2 A, and at this current most of the treatment was carried out. In both cases we used graphite electrodes.

Changes in the cellulose properties, caused by plasma–solution treatment with discharge at a current of 200 mA

Medium	Time, min	DP	α-Cellulose	Hemicelluloses	Content of indicated groups, wt %		WRP, g g^{-1}
			%		aldehyde	carboxy	
Diaphragm discharge							
–	0	1400	91.4	7.8	5.3	3.3	0.36
HNO_3	10	835	92.3	6.9	5.94	3.54	0.41
	20	690	91.0	8.2	6.08	3.33	0.38
	30	470	88.8	10.4	6.25	3.82	0.33
Na_2SO_4	30	400	86.9	1.3	7.42	3.35	0.33
NaOH	30	825	92.1	7.1	5.11	3.62	0.38
End discharge							
–	0	1000	90.5	8.6	3.6	3.33	0.36
Na_2SO_4	10	690	92.3	6.8	2.99	3.62	0.38
	20	650	90.9	8.2	3.11	4.09	0.38
	30	630	91.3	7.8	3.92	3.95	0.37
NaOH	10	840	91.1	7.8	2.65	4.07	0.41
	20	720	90.3	8.8	2.99	4.09	0.38
	30	695	90.9	8.2	3.62	3.49	0.37

Figure 3 presents the schematic of the reactor with electrodes for end discharge excitation. The plasma zone was formed alternately on either electrode, and the discharge was burning virtually uninterruptedly. In the case of diaphragm discharge, one of the electrodes was replaced by a ceramic ampule with a 3-mm-long slot-like diaphragm (Fig. 1). During the discharge treatment, the solution and the cellulose added were mixed with a magnetic stirrer. The treatment time was 10–30 min. After treatment in the plasma–solution system was complete, cellulose was taken out of the reactor, washed, and analyzed. The content of the aldehyde and carboxy groups was determined by standard iodometric and acid–base titration techniques, respectively [10]. The degree of polymerization of cellulose was estimated from the viscosity of the solution of cellulose in Cadoxen [11], and the content of hemicelluloses and α-cellulose, by a standard technique [12]. The water-retaining power was determined according to [13].

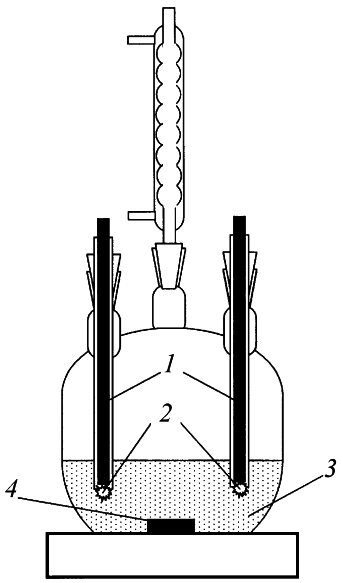


Fig. 3. Schematic of the reactor for end-discharge treatment of the polymer material: (*1*) electrodes, (*2*) plasma zone, (*3*) solution with the material being treated, and (*4*) magnetic stirrer.

The changes of the cellulose properties, caused by plasma–solution treatment (see table), correlate with the extents of degradation (change in DP) and oxidation (change in the content of aldehyde and carboxy groups). Plasma treatment causes the degree of polymerization of cellulose to decrease, depending on the type of discharge, treatment time, and electrolyte composition. In the case of diaphragm discharge, the DP decreases more profoundly, most likely because of the action of the sound wave spreading in the system when this type of discharge is burning. In the Na_2SO_4 and HNO_3 media, a decrease in the DP is accompanied by a decrease in the α-cellulose content and, despite the increase in the proportion of hemicelluloses, by weakening of the

water retention power of cellulose (WRP). The end discharge leaves the supramolecular structure of cellulose virtually unaffected. Such characteristics as WRP and the α-cellulose content are virtually unaffected by the plasma–solution treatment.

The cellulose oxidation features also depend on the discharge type. The lignin content of the resulting cellulose is under 1% (0.8–0.95%). This residual lignin content is unaffected by the plasma–solution treatment, which allows its contribution to the content of aldehyde and carboxy groups to be neglected. The resulting samples comprise basically two components, α-cellulose and hemicelluloses (noncellulose part). The change in the content of carboxy and aldehyde groups during plasma–solution treatment is associated with oxidation of both cellulose and hemicelluloses. In the case of the end discharge, their ratio remains virtually unchanged; the content of carboxy groups increases relative to the initial cellulose, and that of aldehyde groups remains virtually unchanged. Presumably, end discharge causes more profound oxidation, and the resulting aldehyde groups are oxidized to carboxy groups. In the case of diaphragm discharge, the content of the aldehyde groups increases, and that of carboxy groups remains virtually unchanged, with the composition of the medium being of minor importance.

CONCLUSIONS

(1) The α-cellulose content and water retention power of the flax cellulose samples examined are virtually unaffected by plasma-discharge treatment. The content of the aldehyde and carboxy groups increases, and the degree of polymerization of cellulose decreases, depending on the type of discharge.

(2) The plasma–solution treatment initiating the oxidizing processes in the material being treated is more efficient in the case of the frontal discharge which affords direct contact of the material with plasma zone and the activated solution layers.

(3) Application of plasma–solution systems to treating cellulose-containing materials requires careful selection of the discharge conditions and modes.

REFERENCES

1. Maksimov, A.I., *Entsiklopediya nizkotemperaturnoi plazmy* (Encyclopedia of Low-Temperature Plasma), Fortov, V.E., Ed., Moscow: Nauka, 2000, introductory vol. 4, p. 393.
2. Maksimov, A.I., *Khim. Volokna*, 2004, no. 5, pp. 22–25.
3. Kutepov, A.M., Zakharov, A.G., and Maksimov, A.I., *Vakuumno-plazmennoe i plazmenno-rastvornoe modifitsirovanie polimernykh materialov* (Vacuum Plasma and Plasma–Solution Modification of Polymer Materials), Moscow: Nauka, 2004.
4. Zakharov, A.G., Maksimov, A.I., and Titova, Yu.V., *Usp. Khim.*, 2007, vol. 76, no. 3, pp. 260–278.
5. Janca, J., Kuzmin, S., Maximov, A. et al., *Plasma Chem. Plasma Processes*, 1999, vol. 19, no. 1, pp. 53–67.
6. Maksimov, A.I. and Titova, Yu.V., *Elektron. Obrab. Mater.*, 2002, vol. 213, no. 1, pp. 64–68.
7. Maximov, A.I., *Contr. Plasma Phys.*, 2007, vol. 46, nos. 1–2, pp. 1–8.
8. Maksimov, A.I., Titova, Yu.V., and Kuz'micheva, L.A., *Goren. Plazmokhim.*, 2005, no. 3, pp. 247–250.
9. Maximov, A.I., Kuzmicheva, L.A., Kchlustova, A.V., et al., *Mendeleev Commun.*, 2007, vol. 17, no. 7, pp. 1–3
10. Sadov, F.I., Sokolova, N.M., Shikanova, I.A., et al., *Laboratornyi praktikum po kursu "Khimicheskaya tekhnologiya voloknistykh materialov"* (Laboratory Practical Guide on the "Chemical Technology of Fibrous Materials" Course), Moscow: GNTI, 1955.
11. *Analiticheskii kontrol' proizvodstva iskusstvennykh volokon: spravochnoe posobie* (Analytical Control of Manufacture of Artificial Fibers: Reference Book), Dibrov, A.K. and Matveev, V.S., Eds., Moscow: Khimiya, 1986.
12. *GOST* (State Standard) *595–79: Cotton Cellulose.*
13. Ioelovich, M.Ya., Timermanis, U.Ya., and Treimanis, A.P., *Khim. Drev.*, 1991, no. 6, pp. 20–24.

ISSN 1070-4272, Russian Journal of Applied Chemistry, 2008, Vol. 81, No. 5, pp. 858–861. © Pleiades Publishing, Ltd., 2008.
Original Russian Text © V.I. Chursin, 2008, published in Zhurnal Prikladnoi Khimii, 2008, Vol. 81, No. 5, pp. 821–824.

MACROMOLECULAR CHEMISTRY AND POLYMERIC MATERIALS

Properties of Biopolymer Compositions Based on Products of Collagen Hydrolysis and Polysaccharides

V. I. Chursin

Central Research Institute of Leather-Shoe Industry, Moscow, Russia

Received September 29, 2006

Abstract—Physicochemical properties of biopolymer compositions based on products of collagen hydrolysis and polysaccharides were studied. The effect of the component ratio on their compatibility was examined.

DOI: 10.1134/S1070427208050261

Advances in studying the structure and properties of collagen allow principally new approaches to reprocessing and efficient utilization of cheap collagen-containing raw materials [1]. Development of studies on preparing new collagen-based materials is determined, on the one hand, by availability and unique properties of this protein and, on the other hand, by appearance of new areas of its use in engineering, medicine, and light industry. Active studies are performed with the aim to prepare composite film materials based on blends of products of collagen hydrolysis (PCH) and other film-forming compounds (e.g., polyacrylates, polyvinyl alcohol, cellulose derivatives) [2]. This interest is determined by the possibility of improving some properties of the collagen films: enhancing their thermal and biological stability and strength, decreasing the extension, and increasing the sorption capacity. Application of environmentally friendly water-soluble polymers is also of particular importance.

As initial components we used polysaccharides, namely, chitosan and hydroxyethyl cellulose (HEC). The chitosan structure is close to that of cellulose, and its derivatives exhibit fiber- and film-forming properties. The use of chitosan soluble in aqueous solutions strongly simplifies preparation and decreases the environmental hazard in fabrication of finished items from these polymers [3, 4]. Hydroxyethyl cellulose, which is widely used in various branches of industry, is a cellulose ether containing nonionic hydroxyethyl groups.

In this work we prepared and studied new compositions based on PCH and polysaccharides exhibiting film-forming properties, which are of particular interest as biologically active cosmetic and pharmaceutical materials.

EXPERIMENTAL

In this study we used the 3% solutions of PCH prepared by thermal denaturation [5] of the cattle skin derma. A 3% solution of chitosan in 3% acetic acid (solution pH 4.1) was prepared from the reagent purchased from the Sonat Private Company (degree of deacetylation 0.86). Hydroxyethyl cellulose purchased from the Politsell Private Company [TU (Technical Specification) 2231-013-32957739–01] was used as a 3% aqueous solution. The molecular weights of PCH, chitosan, and HEC determined by viscometry were 34000, 120000, and 32000 Da, respectively. The formation of biopolymer compositions based on the products of collagen hydrolysis and polysaccharides was judged by the rheological characteristics (viscosity) using a Brookfield viscometer, electrical conductivity measured on a conductometer (Hanna Instruments), refractive index, and appearance of the resulting films. The size of supramolecular particles was determined by the turbidity spectrum procedure [6] at $\lambda = 300-600$ nm on a KFK-3 photocolorimeter at 20°C. The compositions were prepared from solutions of the starting reagents take in required ratios, with stirring for 1 h at 20–22°C. The films were prepared by casting of the resulting solutions onto glass or polyethylene supports, followed by drying in air for 2 days. The film quality was evaluated visually by changes in the color, transparency, and flexural strength.

Taking into account ambiguous data on the behavior of the systems containing carboxy groups

and HEC in aqueous solutions [2, 7], we studied the compatibility of PCH and HEC at various component ratios. The compatibility of the components was evaluated from the experimental data on the above characteristics and their deviation from the calculated additive values. Our studies showed that the viscous but flowable solutions are formed in the entire range of the component ratios studied.

As seen from Fig. 1, the dynamic viscosity of the compositions in question decreases with increasing PCH content and this effect is the most pronounced in the PCH–HEC system. This decrease in the system viscosity suggests formation of more compact polymer macromolecules owing to formation of mixed complexes with a smaller molecular volume. As shown in [4], the intra- and intermolecular interactions in HEC solutions are due to hydrogen bonds. Thus, we can assume that, upon addition of PCH, the hydrogen bonds formed by the functional ether groups of the polysaccharide are substituted by hydrogen bonds of these groups with the protein molecules, which weakens the intermolecular interaction and thus decreases the dynamic viscosity of the polymer composition. With increasing PCH content, deviations of the viscosity and refractive index from the additive values increase, which is probably due to the steric hindrance in interaction of relatively large macromolecules of the polymers studied. Similar changes in the viscosity upon addition of PCH were observed for chitosan (structural analog of HEC).

The experimental data on the refractive index of the PCH–HEC system (Fig. 2) show that the compatibility is the lowest at 70 : 30 component ratio. When the content of HEC in the mixture is higher than 50%, the system of hydrogen bonds in the collagen becomes weaker owing to penetration of the polysaccharide structural elements incompatible with protein, which block the active collagen centers and increase the intermolecular distances. On the contrary, free amino group in each unit of the chitosan molecule can interact with a carboxy group in collagen, which results in formation of mixed complexes at chitosan : PCH ratio of 75 : 25.

It is known that in acetic acid solutions chitosan occurs in the salt form and bears a positive charge, which leads to higher electrical conductivity. This fact suggests that, upon mixing acetic acid solution of chitosan with PCH, the polymers can interact with each other owing to the presence of carboxy groups in collagen. Indeed, as seen from the dependence shown in Fig. 3, the minimal conductivity

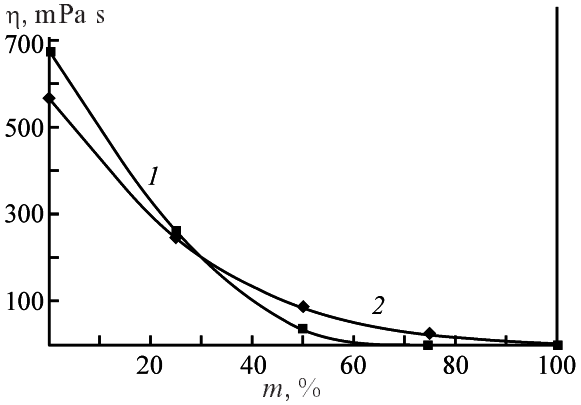


Fig. 1. Viscosity η as a function of the composition of (*1*) PCH–HEC and (*2*) PCH–chitosan systems (3% solutions). (*m*) Relative PCH content; the same for Figs. 2–4.

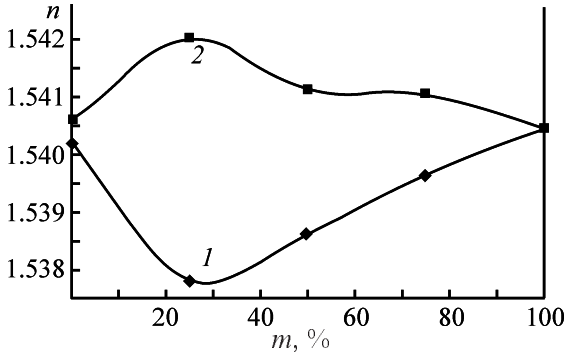


Fig. 2. Refractive index n as a function of the composition of (*1*) PCH–HEC and (*2*) PCH–chitosan systems.

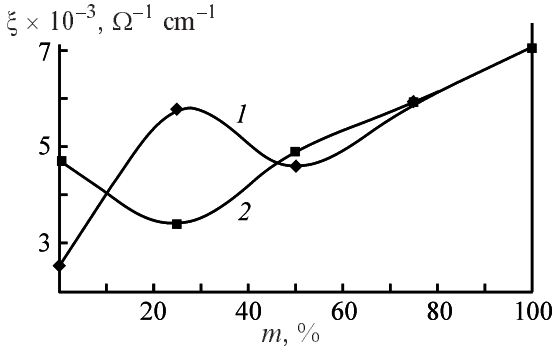


Fig. 3. Electrical conductivity ξ as a function of the composition of (*1*) PCH–HEC and (*2*) PCH–chitosan systems.

of the mixture is observed at a PCH content of 25 wt %. Such a nonmonotonic trend is apparently due to the electrostatic interaction of the protonated amino group of chitosan with the carboxy groups of protein, providing association of the macromolecules in the solution.

The electrical conductivity of the HEC solution increases with increasing content of PCH acting as weakly ionized amphoteric polyelectrolyte. In this case, a certain fraction of the functional groups

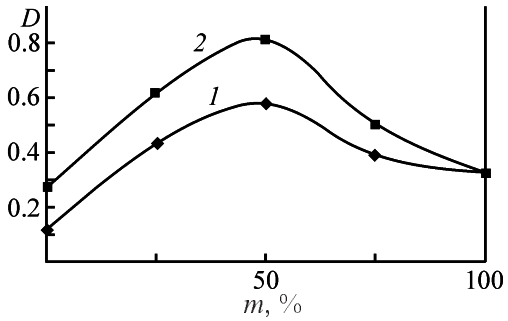


Fig. 4. Optical density D as a function of the composition of (*1*) PCH–HEC and (*2*) PCH–chitosan systems.

forms hydrogen bonds with the HEC hydroxy groups, which, in turn, promotes dissociation of oppositely charged collagen molecules.

The results of photometric studies (Fig. 4) show that, on addition of PCH into the polysaccharide solutions, the optical density of the solutions increases, reaching a maximum at the polysaccharide : PCH ratio of 50 : 50. The observed increase in the optical density upon mixing of the initial components can be probably due to the complexation (in the case of chitosan) or aggregation of macromolecules to form colloidal particles stable to sedimentation (in the case of PCH). Examination of the PCH–polysaccharide blends by the turbidity spectrum procedure allowed estimation of the average size of supramolecular particles in the solutions [6].

As seen from the table, the size of particles in the HEC–PCH blend is greater than that in the initial components and is independent of the component ratio, which confirms the absence of interaction between the components. This is probably due to the

Particle size and properties of the biopolymer films

PCH content (wt %) in composition based on polysaccharide	Particle size, nm	Film properties
HEC:		
0	100	Opaque dry elastic
25	160	Semitransparent elastic
50	165	Semitransparent brittle
75	155	Transparent brittle
100	128	No film formed
Chitosan:		
0	110	Yellow transparent semirigid
25	200	Semitransparent brittle
50	180	Opaque brittle
75	135	Opaque brittle

breakdown of intermolecular hydrogen bonds in the collagen structure as a result of penetration of polysaccharide elements incompatible with the protein, which increases the particle size. It should be noted that the size of supramolecular associates in the compositions based on two and more polymer solutions is often greater than that of the initial components [8]. However, in some cases the microheterogeneity parameters of solutions of polymer blends do not agree with visual characteristics of the films. For example, a film prepared from the HEC solutions is opaque, whereas from the HEC–PCH solutions a semitransparent film is obtained. In the chitosan–PCH system, more significant differences in the particle size depending on the PCH content are observed, as compared to the initial chitosan solution. The coarser particles are formed at a chitosan : PCH ratio of 75 : 25, their calculated size is 200 nm, whereas the particle size of the initial chitosan is 110 nm. With increasing PCH content in the solutions to 75 wt %, the particle size decreases. The observed dependences agree with experimental data on the compatibility of the polymers in the solution.

Thus, our study of the compatibility of collagen and polysaccharides in solutions, based on the analysis of deviations of the experimental data in the property–composition diagrams, show that the compatibility of the systems studied depends on the chemical structure and ratio of the initial components. In the case of chitosan, we conclude that intermolecular complexes are formed in the system, with their maximal yield at the chitosan : PCH ratio of 75 : 25. In the case of HEC, no thermodynamic compatibility is observed. Modification of polysaccharides with PCH exhibiting biological activity but incapable of film formation in the given concentration range allows utilization of these compositions in various branches of industry. Purposeful variation of the structure of biopolymer materials in combination with the unique properties of the initial components suggests that the films prepared from these materials can be used as supports for the systems with controlled release of biologically active compounds.

CONCLUSION

Data on the viscosity, electrical conductivity, refractive index, and optical density of biopolymer compositions based on polysaccharides and products of collagen hydrolysis and also on the visual characteristics of the resulting films indicate that the

compositions based on chitosan are thermodynamically compatible at the content of the protein component of 25–40 wt %, whereas the compositions based on hydroxyethyl cellulose are thermodynamically incompatible but form kinetically stable systems in the solutions studied.

REFERENCES

1. Mikhailov, A.N., *Kollagen kozhnogo pokrova i osnovy ego pererabotki* (Coverlet Collagen and Principles of Its Reprocessing), Moscow: Legkaya Industriya, 1971.
2. Anan'ev, V.N., Novikov, Yu.T., and Furin, V.L., *Novaya adresnaya immobilizirovannaya lekarstvennaya forma: Lekarstvennye zhelatinovye plenki* (New Targeted Immobilized Drug Forms: Drug Gelatin Films), Moscow, 2004.
3. Engibaryan, L.G., Preparation and Properties of Water-Soluble Derivatives of Chitosan and of Film Materials Based on Them, *Cand. Sci. Dissertation*, Moscow, 2004.
4. Vikhoreva, G.A. and Gal'braikh, L.S., *Khitin i khitozan: Poluchenie, svoistva i primenenie* (Chitin and Chitosan: Preparation, Properties, and Use), Moscow: Nauka, 2002, pp. 254–271.
5. RF Patent 2278166.
6. Kulish, E.I. and Kolesov, S.V., *Zh. Prikl. Khim.*, 2005, vol. 78, no. 9, pp. 1511–1513.
7. Antonov, S.F., Technology of Preparing Biologically Compatible Polymer Materials Based on Natural Proteins and Polysaccharides, *Cand. Sci. Dissertation*, St. Petersburg, 1999.
8. Alekseeva, O.V., Rozhkova, O.V., Prusov, A.N., et al., *Khim. Volokna*, 2006, no. 6, pp. 41–44.

ISSN 1070-4272, Russian Journal of Applied Chemistry, 2008, Vol. 81, No. 5, pp. 862–866. © Pleiades Publishing, Ltd., 2008.
Original Russian Text © S. Yu. Bratskaya, S. Schwarz, T. Liebert, T. Heinze, 2008, published in Zhurnal Prikladnoi Khimii, 2008, Vol. 81, No. 5, pp. 825–829.

MACROMOLECULAR CHEMISTRY AND POLYMERIC MATERIALS

Flocculation and Binding Properties of Highly Substituted Cationic Starches

S. Yu. Bratskaya, S. Schwarz, T. Liebert, and T. Heinze

Institute of Chemistry, Far-Eastern Branch, Russian Academy of Sciences, Vladivostok, Russia
Leibniz Institute of Polymer Research, Dresden, Germany
Center of Excellence for Polysaccharide Research, Friedrich Schiller University of Jena, Jena, Germany

Received November 16, 2007

Abstract—The flocculation properties of a series of cationic starches with the substitution degree of 0.25–1.54 in kaolin dispersions were studied, and the dependence of the kaolin retention with fiber on the surface content of starch, degree of its substitution, and amylose : amylopectin ratio was evaluated.

DOI: 10.1134/S1070427208050273

Starch (typical homopolysaccharide) is a mixture of linear polysaccharide amylose and branched amylopectin. The ratio of these components, which is determined by the source of starch, strongly affects its solubility and the gelling properties, gelation temperature, and viscosity of starch solutions. In contrast to the majority of polysaccharides, starch exhibits unique physicochemical properties in combination with a high nutritive value, which determines its extensive industrial use. Paper industry is one of the most important consumers of starch. Native starch and its derivatives (sometimes in combination with synthetic polymers) are used in paper industry to prepare chemical systems for loading, retention, and reinforcement of paper [1].

The best properties in this field are exhibited by cationic starches, whose degree of substitution (DS) can be varied in a wide range, but it is usually within 0.01–0.1 mol mol^{-1} and does not exceed 0.2–0.4 mol mol^{-1}. As compared to the native polysaccharide, cationic starches exhibit such advantages as solubility in cold water, effective adsorption on the cellulose fiber surface, and enhanced fiber–fiber interaction, which improves the strength properties of paper and increases the extent of binding of fillers (talc, kaolin, pigments) with the paper stock.

The necessity of increasing DS of cationic starches and of studying in detail their properties is determined by the following factors. First, the modern paper industry tends to increase the content of fillers in the paper. In some brands of enamel-paper the degree of filling is more than 35%. Cationic starches with low and medium DS cannot provide the required retention of fillers without additional reagents. At insufficiently high DS of starch, the retention of starch itself and of the filler on the fiber surface can be incomplete. In combination with economical expenses caused by the reagent loss, the presence of starch and fillers in recycled water strongly deteriorates its properties and requires additional treatment with flocculants.

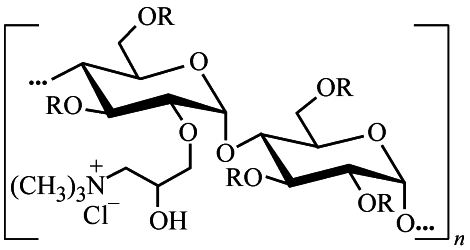
The properties of low-substituted starches were studied in detail [1–5], whereas the data on starches with medium DS (0.15–0.4) are scarce.

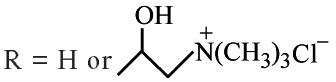
In this study we examined the flocculation properties of a series of highly substituted cationic starches (DS 0.25–1.54) in kaolin dispersions, the features of their adsorption on the cellulose fiber surface, and the effect of DS and amylose : amylopectin ratio on the performance of highly substituted cationic starches as flocculants and binders for paper industry.

EXPERIMENTAL

The kaolin dispersion in TRIS buffer system (pH 8) was prepared by ultrasonic treatment for 15 min. The cationic starches with DS from 0.25 to 1.54 mol mol^{-1} were prepared by the procedure presented elsewhere [6] using potato starch containing 28% amylose (Emsland Stärke GmbH, Germany) and corn starch containing 70% amylose (National

Starch and Chemical Ltd., the United Kingdom). The starch solutions were prepared by dissolution of weighed portions of starch with continuous stirring at 60°C and subsequent storage at room temperature for 24 h.





Bleached softwood pulp (Schopper–Riegler freeness value 22 deg) was supplied by the Institute of Paper (Heidenau, Germany).

The apparent charge density of cationic starches and the particle charge in kaolin dispersions were determined by colloidal titration. The experimental setup consisted of a precision dosing device (702 SM Titrino, Metrohm, Switzerland), a particle charge detector (PCD-03, Mütek, Germany), and a computer. The particle charge detector consists of a cylindrical Teflon cell in which a Teflon plunger moves at a constant rate and a colloidal solution being studied is placed between the cell walls and the plunger. The operation principle is as follows. The moving plunger shifts the ionic atmosphere of the colloidal particles adsorbed on the porous wall of the Teflon cell, giving rise to the electrokinetic flow potential which is detected by the electrode pair located in the top and bottom sections of the cell [7]. Although the flow potential depends on many factors and, in contrast to ζ potential, is not an absolute parameter, this procedure can be used to determine the charge sign of the polymers and colloidal particles and to evaluate the charge density in the course of colloidal titration with oppositely charged polyelectrolytes. As titration solutions we used standard (1 mg-equiv l^{-1}) solutions of sodium polyenthylenesulfonate (polyanion) and polydiallyldimethylammonium chloride (polycation).

To study the flocculation properties of starch, a 50-ml portion of an aqueous kaolin dispersion was mixed with an aliquot of the starch solution, stirred for 15 min on a magnetic stirrer, and allowed to stand for 20 min for sedimentation. The difference between the optical densities of the initial dispersion and supernatant at a wavelength of 500 nm gave the residual turbidity of the solution, which was used as a parameter of the flocculation efficiency. The minimal portion of the flocculant providing the residual turbidity of no more than 1% was taken as the effective flocculant dose.

Adsorption of cationic starches on cellulose fibers was performed using TRIS buffer system (pH 8) at 22°C for 48 h; the solid : liquid (s : l) ratio was 1 : 200 counting on cellulose dried for 4 h at 110°C. Before addition of the starch solution, the wet cellulose fibers were swollen for 4 h in the buffer solution with continuous stirring. The adsorption capacity was evaluated from the difference of the initial and equilibrium concentrations of the starch. The latter was determined by colloidal titration of the supernatant filtered through porous glass.

To a suspension of cellulose fiber with preliminarily adsorbed cationic starch, we added an aliquot of a kaolin dispersion. After stirring for 5 min, the system was allowed to stand for 5 min for sedimentation, and the optical density of the supernatant at λ = 500 nm was measured. The residual kaolin concentration was found from the calibration turbidity curve and was used for calculating the adsorption of kaolin on the modified fiber from the difference of the initial and equilibrium concentrations.

Beginning from the 1980s, there has been a tendency in the paper industry to pass from a common acidic procedure with aluminum sulfate to the more efficient alkaline technology. New operation conditions require reactants active at pH 8, which determines advantages of cationic starches with quaternary ammonium groups as compared to primary, secondary, and tertiary amines, whose positive charge decreases with increasing pH. The dependences of the apparent charge density on pH for the given series of cationic starches confirmed that, in the pH range 3–8, the charge density of starches remains constant and depends only on the degree of substitution (see table). As seen from Fig. 1, with addition of cationic starch up to a certain concentration into a kaolin dispersion (whose particle surface is charged negatively at pH 8), this dispersion becomes unstable owing to adsorption of starch on the kaolin particles. In this case, the amount of starch required for destabilization of the dispersion decreases with increasing DS.

Comparison of the system turbidity and charge density of the particles at various contents of the cationic starch (Fig. 2) shows that the efficient flocculation starts long before complete neutralization

Characteristics of cationic starches

Code	Starch source	DS	Charge density, mg-equiv g^{-1}		Molecular weight, g mol^{-1}
			pH 8	pH 3	
KT0.25	Potato	0.25	1.78	1.80	44×10^6
KT0.44	"	0.44	2.38	2.39	"
KT0.56	"	0.56	2.77	2.81	"
KT0.60	"	0.67	2.96	3.01	"
KT1.54	"	1.54	4.22	4.25	"
KK0.60	Corn	0.58	2.51	2.48	18×10^6

of the surface charge with the adsorbed polymer. Recharging of the particle surface in the area of the plateau of the adsorption isotherms [8], typical for adsorption of highly charged polyelectrolytes, is also observed with cationic starches, providing stabilization of the kaolin dispersions upon addition of excess flocculant.

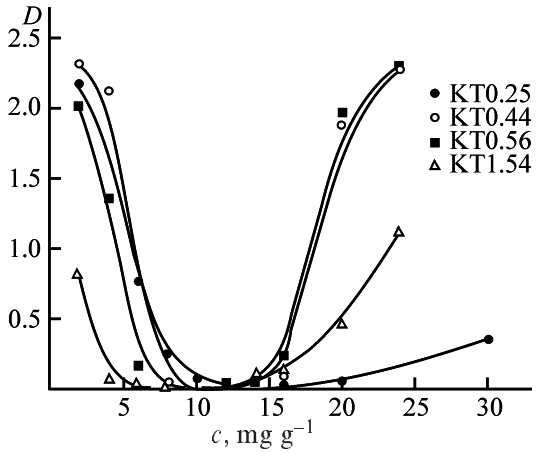


Fig. 1. Efficiency of the dispersion flocculation as a function of DS of the cationic starches. (*D*) Optical density at λ = 500 nm and (*c*) flocculant content.

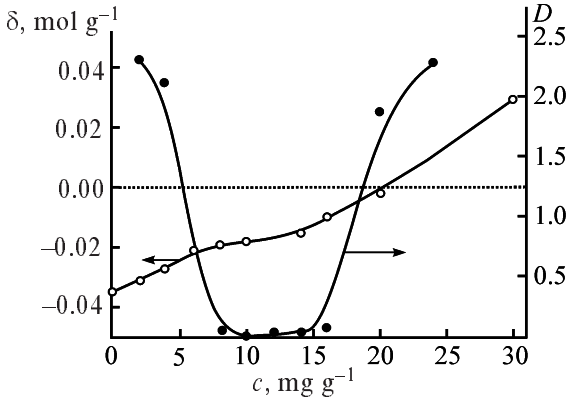


Fig. 2. Optical density and charge density on the kaolin particle surface as functions of the content of KT0.44 starch. (δ) Charge density, (*D*) optical density at λ = 500 nm, and (*c*) flocculant content.

Since the increase in the degree of cationic substitution of starch not only increases the starch cost but also affects its toxicity and biodegradability, it was of particular importance to determine the highest degree of substitution of the starch at which the increase in the starch performance as flocculant and binder in the paper production compensates the cost of its production.

Analysis of the experimental data shows that the apparent charge density of the cationic starches linearly depends on DS only in a certain concentration range. The experimental apparent charge density determined by colloidal titration at DS 1.54 is significantly smaller than the expected value (Fig. 3), which is probably due to the structural features of amylopectin. At small DS, modification proceeds predominantly through easily accessible sections of starch macromolecules, but with increasing DS certain fraction of cationic centers inevitably appears to be localized in the inner areas of the amylopectin branched fragments. Presumably, the cationic centers localized on the surface and in the bulk of amylopectin spheroids exhibit strongly different accessibility and activity.

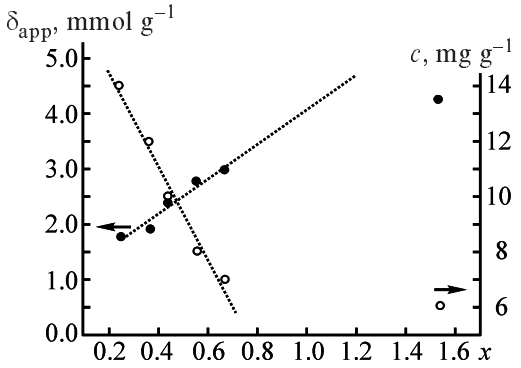


Fig. 3. Apparent charge density δ_{app} of the cationic starch in solution and their minimal effective flocculation dose *c* in dispersions as a function of the degree of cationic substitution *x*.

As seen from Fig. 3, the minimal content of the polymer required for the phase separation in the dispersion linearly decreases with increasing DS for the starch derivatives with DS < 0.7 and then slightly decreases. This fact distinguishes starch derivatives differ from linear synthetic flexible-chain polymers whose flocculation ability, as a rule, linearly depends on DS. Apparently, the steric factor acting in this case restricts the area of efficient cationic substitution of amylopectin by the upper DS level of 0.6–0.7; further increase in the starch DS is unprofitable.

To examine how DS of the cationic starches affects their performance as binding agents in adsorption of fillers on the surface of the cellulose fibers, we studied the starch adsorption on the cellulose fiber and the relationships of the kaolin retention on the fibers preliminarily modified with the starch.

We found (the data are not given in this paper) that the adsorption isotherms strongly depend on the ratio of amylopectin and amylose in the cationic starch. Irrespective of DS, for starches with the predominant content of amylopectin high-affinity adsorption isotherms were obtained. In contrast to weakly substituted starches, which are characterized by a sharp decrease of the limiting adsorption with increasing DS [1], for the starches studied (SD 0.25–1.54) the limiting adsorption only slightly depends on DS, though a certain decrease in the adsorption with increasing DS is still observed.

One of the most important functions of cationic starches in paper industry is to improve the retention of the filler and pigments by the cellulose fibber. The surface of the initial cellulose fiber is negatively charged at pH of the paper chalking. Therefore, similarly charged filler particles cannot be retained on the cellulose fiber surface without binding agents. As seen from Fig. 4, the kaolin adsorption by unmodified cellulose does not exceed 25–30 mg g^{-1}, which is smaller by an order of magnitude than the parameters required for the modern paper industry. Weakly substituted starches (DS 0.05) enhance the kaolin adsorption on the cellulose surface, but the parameters of the maximal retention of the filler are still significantly lower than the modern requirements.

With increasing DS of the cationic starch to 0.25, the degree of filling of the cellulose fibers with inorganic components increases to 50%, but this is possible only at a high surface content of the starch, close to the limiting adsorption capacity. Apparently, attainment of so high parameters involves additional problems related to possible incomplete retention of excess starch on the cellulose surface even at small fluctuations of the system composition. Thus, the performance of cationic starches with DS 0.25 only slightly exceeds that of the widely used weakly substituted derivatives.

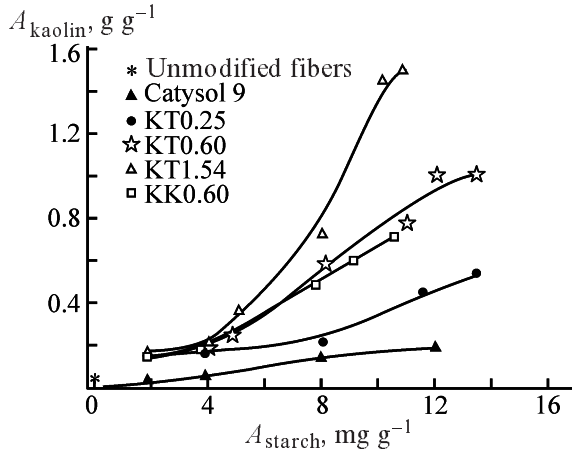


Fig. 4. Limiting adsorption of kaolin filler on the surface of cellulose fibers with various surface contents of cationic starches. (A_{kaolin}) Kaolin adsorption and (A_{starch}) starch adsorption.

As seen from Fig. 4, the behavior of cationic starches with medium (0.6) and high (1.54) DS is advantageous as compared to the weakly substituted analogs. The required degree of filling of the fiber with kaolin (up to 50%) is attained at the surface starch content of 6–8 mg g^{-1}, which is considerably lower than the limiting adsorption values. Under these experimental conditions, cationic starches are adsorbed on the surface of cellulose fiber in 30–60 s with 100% retention, which virtually completely eliminates the losses of the reagent and thus its negative effect on the quality of recycled water. It should be noted that the binding performance of the medium-substituted starch (DS 0.6) is only slightly dependent on the amylose–amylopectin ratio.

An increase in SD allows a considerable increase in the content of inorganic fillers in the paper, up to an excess of kaolin over cellulose in the system with highly substituted starch (DS 1.54), but the paper with so high content of the filler is of no practical interest because of its brittleness and too high density. However, at the kaolin content in the range 35–50%, which is of the most practical interest, more than twofold increase in DS (from 0.6 to 1.54) leads to a decrease in the content of starch required for the fiber modification by no more than 20%.

Taking into account that the production of starches with DS ≥ 1.0 is difficult [6] and their per-

formance as flocculation agents and binders increases only slightly in the DS range from 0.6 to 1.54, we concluded that the optimal DS of cationic starches is 0.6–0.7.

CONCLUSION

The optimal degree of substitution of cationic starches is 0.6–0.7, and its further increase only slightly improves their performance as flocculation agents and binders for paper production.

REFERENCES

1. Eklund, D. and Lindstrom, T., *Paper Chemistry: An Introduction*, Grankulla (Finland): DT Paper Science, 1991.
2. Jarnstrom, L., Lason, L., and Rigdahl, M., *Colloids Surf. A*, 1995, vol. 104, nos. 2–3, pp. 191–205.
3. Husband, J.C., *Colloids Surf. A*, 1998, vol. 131, nos. 1–3, pp. 145–159.
4. Hedborg, F. and Lindstrom, T., *Nord Pulp Paper Res. J.*, 1993, no. 2, pp. 258–263.
5. Nedelcheva, M.P. and Stoilkov, G.V., *J. Colloid Interface Sci.*, 1978, vol. 66, no. 3, pp. 475–482.
6. Haack, V., Heinze, T., Oelmeyer, G., and Kulicke, W.M., *Macromol. Mater. Eng.*, 2002, vol. 287, pp. 495–502.
7. Gerdes, W.F., in *Proc. 12 National ISA Analysis Instrumentation Symp.*, Houston, 1966, pp. 181–198.
8. Shin, Y.W., Roberts, J.E., and Santore, M.M., *J. Colloid Interface Sci.*, 2002, vol. 247, no. 1, pp. 220–230.

ISSN 1070-4272, Russian Journal of Applied Chemistry, 2008, Vol. 81, No. 5, pp. 867–873. © Pleiades Publishing, Ltd., 2008.
Original Russian Text © I.V. Kalashnikova, N.D. Ivanova, T.B. Tennikova, 2008, published in Zhurnal Prikladnoi Khimii, 2008, Vol. 81, No. 5, pp. 830–836.

MACROMOLECULAR CHEMISTRY AND POLYMERIC MATERIALS

The Use of Monolithic Polymeric Sorbents to Simulate Virus–Cell Interactions

I. V. Kalashnikova, N. D. Ivanova, and T. B. Tennikova

Institute of Macromolecular Compounds, Russian Academy of Sciences, St. Petersburg, Russia

Received April 2, 2008

Abstract—A simple virus–cell complementary model system can be obtained using polymer-analogous reactions of the epoxy groups of glycidyl methacrylate–ethylene glycol dimethacrylate monolithic macroporous polymeric support and of the carboxy groups of styrene–methyl methacrylate polymeric nanospheres. The effect of thus designed microenvironment on the affinity binding parameters of virus-mimicking nanoparticles with the functionalized sorbent surface is studied by high-performance monolithic disk affinity chromatography.

DOI: 10.1134/S1070427208050285

Diversity of surface properties of cells and viruses causes the occurrence of different mechanisms of their adsorption interaction via highly specific (affine) or weaker nonspecific (ionic, hydrophobic, coordination, etc.) bonding. These mechanisms can be simulated by introduction of different specific ligands into model systems.

Original macroporous monolithic sorbents [1], fabricated as thin disks (BIA Separations, Ljubljana, Slovenia) [2], as well as chromatographic processes realized with these stationary phases [high-performance monolithic disk affinity chromatography (HPMDAC) and chromatography on ultrashort monolithic columns] offer unique opportunities for studying specific complexation [3–6]. In other words, HPMDAC is an ideal method allowing adequate simulation of interactions of biocomplements and assessment of the effect of the microenvironment on these interactions. Furthermore, it was demonstrated recently that monolithic sorbent based on glycidyl methacrylate (GMA)–ethylene glycol dimethacrylate (EDMA) copolymer is well suitable to realize interfacial processes proceeding via affine binding of large particles [7] such as viruses [8, 9].

Functionality of biological macroparticles (cells, viruses) is controlled by their complex multilevel structure, which could be modeled through successive combination of different (macro)molecules. In our previous experiments, the components (phospholipids, carbohydrates, and proteins) composing cell walls were introduced into surface structure of the monolithic GMA–EDMA sorbent, while the nanoparticles with finely tuned surface structure, close in its composition to that of the membrane of the virus attacking the cell, were in the mobile phase. The virus-mimicking nanoparticles were prepared on the basis of polymeric nanospheres with a size close to that of human viruses.

Construction of such model systems adequately simulating natural ones and allowing examination of the adsorption behavior of viruses is a topical problem in studying mechanisms of their interaction with a cell. Results obtained in these studies can be used as a basis in developing procedure of affine separation of virus particles from native biological fluids. Additionally, data obtained for such model systems can be useful in selecting promising targets in developing new antiviral drugs.

EXPERIMENTAL

In the experiments we used trypsin (TR) and soybean trypsin inhibitor (SBTI) from PanEco (Russia); glucosamine hydrochloride (GA), Schiff's reagent, and ninhydrin from Sigma–Aldrich Chemie GmbH (Germany); and phosphatidylethanolamine (PTEA) from Tekhnologiya–Standart (Russia).

To activate carboxy groups of the polystyrene latex particles, we used water-soluble 1-ethyl-(3-di-

Table 1. Characteristics of polymeric nanospheres*

Particle	Surface concentration of functional groups, mg-equiv m^{-2}	Diameter, nm	Density, g cm^{-3}	S_{sp}, m^2 g^{-1}	Concentration of nanospheres in suspension, g particles/100 ml H_2O
PMMAD	0.640	63.5	1.19	79.4	4.6
PS	0.775	80.0	1.05	71.4	3.6

* (PS) Carboxylated polystyrene nanospheres and (PMMAD) carboxylated PMMA nanospheres stabilized with dextran.

methylaminopropyl)carbodiimide (EDC), 2-(*N*-morpholino)ethanesulfonic acid (Sigma–Aldrich), and 1-hydroxybenzotriazole (HBT) [Fluka AG (Switzerland)].

All buffer solutions were prepared from analytically pure grade chemicals and distilled water and were then filtered through an 0.45-μm Millipore filter [Millipore Inc. (Austria)].

As a stationary phase, we used commercial sorbents, namely, monolithic macroporous GMA–EDMA disks (CIM Epoxy Disks, BIA Separations, Ljubljana, Slovenia). The mean pore size of the sorbent was 1.5 μm; specific pore surface area, 10–15 m^2 g^{-1}; and total porosity, 0.6 ml ml^{-1}. The sorbent volume was 0.34 ml. The disks were arranged in an original cartridge from the same manufacturer.

The HPMDAC process was carried out using Gilson chromatographic system (France) consisting of two plunger pumps (models 303 and 305), a 2138 Unicord S UV detector [LKB Bromma (Sweden)], and a 2210 Recorder from the same manufacturer.

The optical density of solutions was determined with an SF-26 spectrophotometer [LOMO (Russia)].

In fabricating the virus-mimicking particles, we used polymeric nanospheres (for their characteristics, see Table 1).[1] Carboxylated PS- and PMMA-based polymeric particles were modified with ligands using the well-known two-step procedure of activation of carboxy groups with 1-hydroxybenzotriazole and a water-soluble carbodiimide [10–12].

A polystyrene latex (7.2 mg), passed through a column with G-25 using 0.1 M morpholinoethanesulfonic buffer solution (pH 5.5) as a mobile phase, was successively activated with HBT and EDC taken in equimolar amounts with respect to the amount of the surface carboxy groups. The reaction was carried out at 0°C for 15–20 min. Then the suspension was purified to remove excess reagents by gel filtration on a G-25 column buffered with 0.01 M sodium borate (pH 8.5–8.7). To obtain polymeric particles experienced to the most complex surface functionalization, 30 min after introduction of 1.6 mg of TP, we added GA and PTEA (1 mg each) to the purified suspension of the polymeric nanospheres. In all cases, surface modification of the nanospheres was carried out for 4–6 h at 20°C. After the reaction completion, excess components were removed from the suspension by dialysis or gel filtration on a column with Sephadex G-200 and 0.01 M sodium phosphate buffer (pH 7.0) containing 0.15 M sodium chloride (FSB) as a mobile phase. The other functionalized particles were prepared similarly (Table 2).

The amount of a protein required to cover the nanosphere surface was 1–3 mg per 1 m^2 of the surface area. The number of polymeric particles involved in the reaction was controlled by the volume of the latex suspension taken for the experiment. In the case of polydisperse polymeric nanospheres based on poly(methyl methacrylate) stabilized with dextran (PMMAD), fine particles were removed by gel filtration prior to modification. The PMMAD particle concentration in the eluate was determined using the calibration curve obtained for the solution optical density vs. nanosphere concentration at the UV absorption maximum (340 nm).

The amount of protein immobilized on the surface was determined by the Lowry method [13]. The amounts of GA and PTEA bound to the carboxy groups of the polymeric nanoparticles were estimated from the difference in their concentrations in the initial solution and in the solutions after dialysis.

To quantitatively determine PTEA, the mixture containing 0.5 ml of the PTEA-containing solution and 2.5 ml of 0.1% aqueous solution of Schiff's reagent was thoroughly stirred and incubated for 1 h at room temperature. It was demonstrated in the preliminary experiments that a colored complex of

[1] Polymeric nanospheres based on poly(methyl methacrylate) and polystyrene were provided by T.G. Evseeva and A.Yu. Men'shikova (Institute of Macromolecular Compounds, Russian Academy of Sciences, St. Petersburg).

Table 2. Characteristics of virus-mimicking particles

Particle	Maximal number of ligand molecules bound to the surface of nanosphere, N_{max}		Coverage of nanosphere surface with ligand, %
	theory	experiment	
PS–TP	1600	775	48.4
PS–TP/PTEA	1600/9400	690/3530	43.1/37.5
PS–TP/GA	1600/9400	390/3380	45.0/36.0
PS–TP/PTEA/GA	1600/9400/9400	670/1100/4200	41.9/11.7/44.6
PMMAD–TP	1010	675	66.8

PTEA with Schiff's reagent has an absorption maximum at 550 nm and that the detection limit is 5 μg ml^{-1}. The calibration curve of the optical density vs. PTEA concentration allowed precise determination of PTEA.

Glucosamine was determined using the reaction with ninhydrin. To 2.5 ml of the sample, 0.5 ml of 1% aqueous ninhydrin was added. The system was thoroughly mixed and heated for 30 min at 120°C in a thermostat. The calibration curve of the solution optical density vs. GA concentration was obtained at 540 nm. The detection limit was determined to be 1 μg ml^{-1}.

Immobilization of the protein or simultaneously of three NH_2-containing ligands, SBTI, PTEA, and GA, was carried out according to the previously reported procedure [14, 15]. Just prior to modification of the surface of the monolithic sorbents, the disks were successively rinsed (in a flow of the liquid phase at a rate of 5 ml min^{-1}) with ethanol, ethanol : water = 1 : 1, water, and, finally, with the corresponding reagent, to remove organic impurities from the pores of the support. After pretreatment, a monolithic disk with native epoxy groups was immersed into 2 ml of a buffer solution [0.0125 M sodium borate solution (pH 9.3) containing the protein (SBTI) or simultaneously three ligands (SBTI, PTEA, and GA)]. The ligand concentration was 5 mg ml^{-1}. The disk was allowed to stand in the solution for 16 h at 22–30°C. The amount of the ligand covalently bound to the support was estimated as the difference between the ligand concentrations before and after immobilization taking into account the ligand concentration in the washings. The Lowry test [13] was used to determine the protein concentration, and the GA and PTEA contents were determined by the above-described methods.

The chromatographic experiments were carried out in the frontal elution mode. As a result, adsorption isotherms were obtained, which were used then to estimate parameters of the affine interaction such as the maximal adsorption capacity Q_{max} and the dissociation constant of the affine complex K_d [14–17]. A solution of nanospheres modified with trypsin or with two (TP–PTEA) or three (TP–PTEA–GA) ligands simultaneously was passed through a disk with the immobilized ligand(s) until full saturation of all adsorption sites of the stationary phase. The TP concentration in solutions varied from 0.002 to 0.7 mg ml^{-1}, and the elution rate was 2.0 ml min^{-1}. In the adsorption stage, 0.01 sodium phosphate buffer solution (pH 7.0) containing 0.15 M NaCl was used as a mobile phase, and complete desorption was attained by elution with 0.01 M HCl (pH 2.0). Intermediate washing with 2 M NaCl and 2% ethanol in FSB was used to remove particles nonspecifically bound to the surface of the monolithic sorbent. Fractions thus obtained were collected in volumetric vials, and the protein concentration was determined using the Lowry test [13].

Previously [7, 18], to build simple models for viruses, we used model proteins (trypsin, ovalbumin, and soybean trypsin inhibitor), whose behavior on monoliths was well known. It was demonstrated using two variants of chromatography on monoliths that the adsorption of the resulting coarse protein-bearing particles on the outer surface is controlled by the nature and amount of the graft protein [7]. It is evident that functionalization of the surface of polymeric nanospheres with other ligands will affect the final mechanism of adsorption interactions of virus-like particles with the sorbent surface. It is well known that, in addition to proteins-antigens participating in the virus–cell interaction, the viral envelope contains also such components as lipids and carbohydrates that a virus takes over when coming away from a cell [19]. Therefore, to build more elaborated model for viruses, we made the

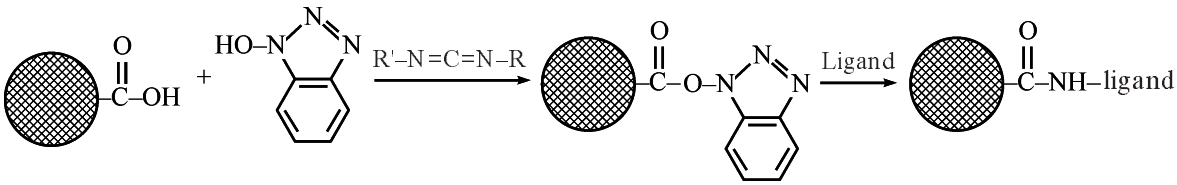


Fig. 1. Surface modification of polymeric nanospheres with amino ligands.

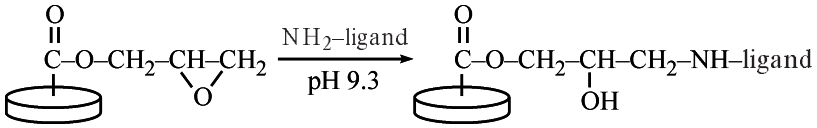


Fig. 2. Surface modification of monolithic sorbents with amino ligands.

microenvironment of a protein on the surface of polymeric nanoparticles more and more complex, thus approaching the composition of the viral envelope using low-specificity ligands of nonprotein nature.

As a basis for preparation of virus-like particles we took polymeric nanospheres of two types, namely, PS- and PMMA-based nanospheres. In the latter case, dextran arranged in the surface layer imitated the oligosaccharide component of the microenvironment to be modeled. Trypsin played the role of virus antigen on the surface of polymeric nanoparticles. Phosphatidylethanolamine and glucosamine, the most abundant components of cell membranes [20–22], were selected as ligands mimicking the lipid and carbohydrate components of the microenvironment of the protein. Covalent immobilization of amine ligands on the surface of the carboxylated nanospheres was performed by the above-described method (see scheme in Fig. 1). As a result, we obtained particles containing one or several ligands of different nature and specificity (Table 2). The coverage of the surface of nanospheres with trypsin was estimated as the ratio between the theoretical number of the protein globules that can be arranged on the smooth surface of a nanosphere to that obtained experimentally using the Lowry test [13]. The theoretical amount of molecules of the other ligands (GA and PTEA) that can be bound to a nanosphere corresponded to the amount of the carboxy groups on the surface of the particles. The experimental amount of the ligands was determined as the difference between the ligand concentrations in the solution before and after the reaction.

Table 3. Concentration of affine ligands immobilized on the surface of CIM Epoxy disks

Ligand	Ligand concentration	
	mg/ml of sorbent	$c \times 10^{16}$ SBTI globules/ml of sorbent
SBTI	3.2 ± 0.2	8.0 ± 0.5
SBTI/PTEA/GA	3.9 ± 0.3/1.2 ± 0.05/ 6.5 ± 0.4	9.8 ± 0.6

The affine partner of trypsin (soybean trypsin inhibitor), covalently bonded to the surface of the polymeric GMA–EDMA sorbent, played a role of a model cell receptor. To more adequately simulate virus–cell interaction using adsorption of virus-mimicking particles on the sorbent surface, the same phospholipid and carbohydrate were taken to build a simplified structure of a cell membrane on the surface of the monolithic sorbent. The selected amino ligands were immobilized by single-step covalent binding to the epoxy groups of the macroporous copolymer (Fig. 2, Table 3).

Thus, by modification of the surfaces of latex nanoparticles and monolithic sorbent, we obtained a simplified complementary system in which the surface of the polymeric support imitated the external shell of a cell and the combination of different ligands constructed on the nanoparticle surface imitated the shell of a virus particle attacking the cell. Schematic representation of the model system design is shown in Fig. 3. The use of the affine pair SBTI–TR as a model for the receptor–antigen interacting pair allowed control of the affinity recognition in constructing virus–cell interaction model.

Quantitative assessment of biospecific binding of virus-like particles, realized in the high-flow affinity chromatographic mode, allowed adequate estimation of the interaction of biological complements (SBTI–TR) and of the effect of the microenviron-

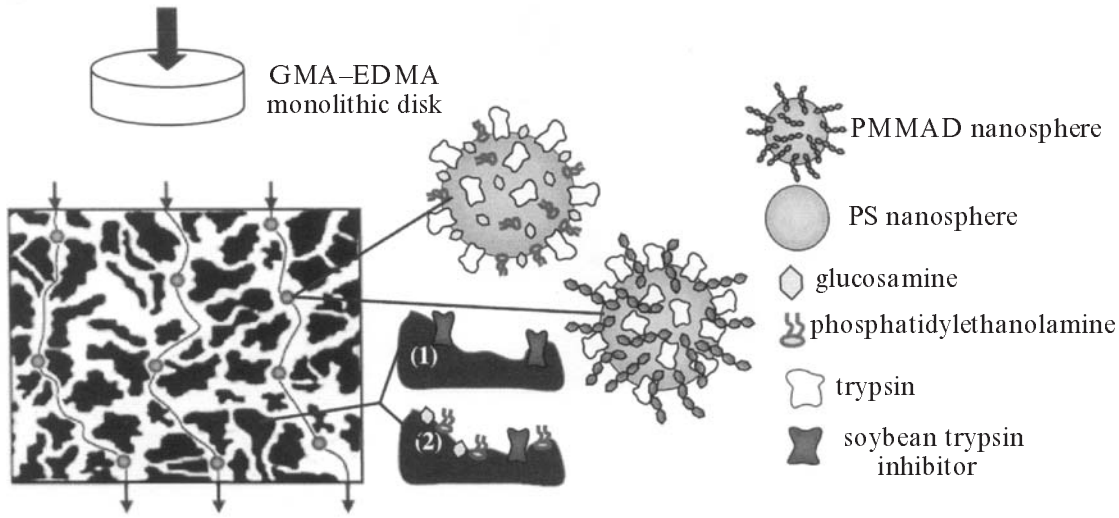


Fig. 3. Schematic representation of the model system design and biospecific binding assessment modes.

ment on the process (Table 4):

$$Q'_{max} = (Q_{max}/Q)/\rho, \quad Q = q/N; \qquad (1)$$

$$K'_d = (K/Q) \times 1/N_A, \qquad (2)$$

where Q_{max} is the maximal adsorption capacity, i.e., the amount of protein (mg) calculated from the results of frontal analysis; Q'_{max}, maximal adsorption capacity estimated by Eq. (1); N_A, Avogadro number; Q, amount of the protein (mg) bound to a nanosphere; q, total amount of the protein (mg) bound to all nanospheres in the solution; N, number of the nanospheres in the solution; ρ, concentration of the ligands immobilized in unit volume of the sorbent; K'_d, dissociation constant of the affine complex, estimated by Eq. (2); and K, constant derived from the adsorption isotherms $1/Q$ vs. $1/C$ (r 0.9895–0.9987).

Two cases were compared (Fig. 3): (1) immobilization of a single protein (SBTI) on the sorbent surface and (2) combination of two selected components (PTEA and GA) forming the microenvironment of this protein on the surface of the monolith, thus simulating the cell surface under virus attack.

Preliminarily we performed chromatographic experiments with a monolithic sorbent, SBTI covalently bount to it, PMMAD in the mobile phase, and PS particles modified with PTEA (coverage 68.2%) or GA (coverage 57.1%). The goal of these experiments was to prove or disprove the occurrence of nonspecific interactions of the lipid and saccharide ligands in hand with the surface of GMA–EDMA–SBTI sorbent.

These experiments revealed that PS–GA particles preliminarily adsorbed under physiological conditions can be totally removed from the sorbent surface only by elution with 2% ethanol in sodium phosphate salt buffer solution, suggesting the hydrophobic adsorption mechanism. As in the case of double-affinity complexation, complete desorption

Table 4. Quantitative characteristics of affine interaction, obtained by frontal analysis

Complement	SBTI		SBTI–GA–PTEA	
	$Q'_{max} \times 10^{-5}$, particles/ligand globules	$K'_d \times 10^6$, mol	$Q'_{max} \times 10^{-5}$, particles/ligand globules	$K'_d \times 10^6$, mol
PS–TR	7.2	1.0	3.3	1.9
PS–TR–GA	2.5	0.6	4.2	0.6
PS–TR–PTEA	2.1	0.6	3.1	0.2
PS–TR–GA–PTEA	1.4	1.4	1.5	0.3
PMMAD–TR	1.2	3.8	1.6	9.2

of PMMAD and PTEA-modified PS particles took place with 0.01 M HCl as an eluent (pH 2.0), suggesting stronger binding of the functionalized nanoparticles to the sorbent. This result can be attributed to the occurrence of a strong specific interaction between PTEA and graft protein in addition to the weak hydrophobic interaction.

Table 4 shows that step-by-step complication of the surface structure of the nanospheres weakened their adsorption on the sorbent surface modified with a single protein, suggesting that somewhat smaller amount of particles with a more complicated surface (compared to nanospheres modified with trypsin only) are involved in the formation of the biospecific complex SBTI–TR. Our results can be attributed to both steric factors and formation of different bonds that may compete with the specific interaction ligand–complement.

The opposite pattern was observed in adsorption of particles of different surface composition on a multicomponent surface of the sorbent (Table 4). Except for the nanospheres modified with trypsin only, for which the number of the adsorbed nanoparticles decreased by more than half as compared to adsorption on the monolith modified with a single ligand (SBTI), fine tuning of the surface microenvironment of the protein on the sorbent increased the maximal adsorption capacity (Table 4). For PS–TR particles, the increased dissociation constant of the complex (Table 4) suggests that the microenvironment of the ligand on the sorbent surface contributed to some extent to the destabilization of the affine complex.

The occurrence of an amino saccharide on the surface of PS–TR–GA particles had practically no effect on the dissociation constant of the affine complex formed from two different components in the SBTI microenvironment. Evidently, it is the lipid component of PS–TR–PTEA and PS–TR–GA–PTEA particles that imparted some extra strength to the affine complex as compared to simpler interaction mode, when only SBTI was immobilized on the sorbent surface.

In the case of PMMAD–TR particles, it may be suggested that the polysaccharide chains inhibited binding of the virus-like particles to the complicated surface of the sorbent, since the dissociation constant increased by a factor of about 2.5 (Table 4), even though this had no significant effect on the adsorption capacity, i.e., here one may say, most likely, about pseudoaffinity adsorption with lower interaction energy of the complements.

CONCLUSIONS

(1) Microenvironment of specifically interacting proteins, simulated on both the nanoparticle and sorbent surfaces, contributes significantly to the affinity binding parameters, but only slightly to the adsorption capacity of the support.

(2) The results obtained give a view of complexation of proteins surrounded by variously specific ligands. However, from the practical viewpoint, i.e., in developing high-performance biorecognition systems, designing of microenvironment can be eliminated from the procedure for preparation of stationary phases for separating viruses.

REFERENCES

1. Svec, F., Tennikova, T.B., and Deyl, Z., *Monolithic Materials: Preparation, Properties, and Applications*, New York: Elsevier, 2003.
2. Tennikova, T.B. and Reusch, J., *J. Chromatogr. A*, 2005, vol. 1065, pp. 13–17.
3. Josic, D. and Buchacher, A., *J. Biochem. Biophys. Meth.*, 2001, vol. 49, pp. 153–174.
4. Vlakh, E.G., Platonova, G.A., Vlasov, G.P., et al., *J. Chromatogr. A*, 2003, vol. 950, pp. 128–137.
5. Vlakh, E.G., Tappe, A., Kasper, C., and Tennikova, T.B., *J. Chromatogr. B*, 2004, vol. 810, pp. 15–23.
6. Ostryanina, N., Vlasov, G., and Tennikova, T., *J. Chromatogr. A*, 2002, vol. 949, pp. 163–171.
7. Kalashnikova, I., Ivanova, N., Evseeva, T., et al., *J. Chromatogr. A*, 2007, vol. 1144, pp. 40–47.
8. Branovic, K., Forcic, D., Ivancic, J., et al., *J. Virol. Meth.*, 2003, vol. 110, pp. 163–171.
9. Kramberger, P., Petrovic, N., Strancar, A., and Ravnikar, M., *J. Virol. Meth.*, 2004, vol. 120, pp. 51–58.
10. Menshikova, A., Evseeva, T., Skurkis, Yu., et al., *Polymer*, 2005, vol. 46, pp. 1417–1423.
11. Prokopov, N., Gritskova, I., Cherkasov, V., and Chalykh, A., *Usp. Khim.*, 1996, vol. 65, pp. 2–12.
12. Borgue, L., Maside, C., Rus, A., and Cura, J. del., *J. Clin. Immunoassay*, 1994, vol. 17, pp. 16–21.
13. Lowry, O., Posebrough, N., Farr, A., and Randall, P., *J. Biol. Chem.*, 1951, vol. 193, pp. 265–272.
14. Kasper, C., Meringova, L., Freitag, R., and Tenni-

kova, T., *J. Chromatogr. A*, 1998, vol. 798, pp. 65–73.

15. Platonova, G., Pankova, G., Il'ina, I.Y., et al., *J. Chromatogr. A*, 1999, vol. 852, pp. 129–135.
16. Ostryanina, N., Il'ina, O., and Tennikova, T., *J. Chromatogr. B*, 2005, vol. 770, pp. 35–42.
17. Platonova, G. and Tennikova, T., *J. Chromatogr. A*, 2005, vol. 1065, pp. 19–26.
18. Kalashnikova, I., Ivanova, N., and Tennikova, T., *Anal. Chem*., 2007, vol. 79, pp. 5173–5180.
19. Bukrinskaya, A., *Virusologiya* (Virology), Moscow: Meditsina, 1986.
20. Vas'kovskii, V., *Soros. Obraz. Zh*., 1997, vol. 3, pp. 32–40.
21. Boldyrev, A., *Soros. Obraz. Zh*., 2001, vol. 7, pp. 2–10.
22. Friedman, S. and Skehan, P., *Proc. Nat. Acad. Sci. USA*, 1980, vol. 77, pp. 1172–1178.

ISSN 1070-4272, Russian Journal of Applied Chemistry, 2008, Vol. 81, No. 5, pp. 874–879. © Pleiades Publishing, Ltd., 2008.
Original Russian Text © B.A. Radbil', S.R. Kushnir, A.B. Radbil', E.N. Shmidt, V.F. Smirnov, N.B. Mel'nikova, 2008, published in Zhurnal Prikladnoi Khimii, 2008, Vol. 81, No. 5, pp. 837–842.

MACROMOLECULAR CHEMISTRY AND POLYMERIC MATERIALS

Quaternary Ammonium Compounds Based on Resin Acids and Rosin and Their Colloidal-Chemical and Biocidal Properties

B. A. Radbil', S. R. Kushnir, A. B. Radbil', E. N. Shmidt, V. F. Smirnov, and N. B. Mel'nikova

Lesma Research and Innovation Limited Liability Company, Nizhni Novgorod, Russia
Vorozhtsov Institute of Organic Chemistry, Siberian Branch, Russian Academy of Sciences, Novosibirsk, Russia
Lobachevsky Nizhni Novgorod State University, Nizhni Novgorod, Russia
Nizhni Novgorod State Medical Academy, Nizhni Novgorod, Russia

Received November 1, 2007

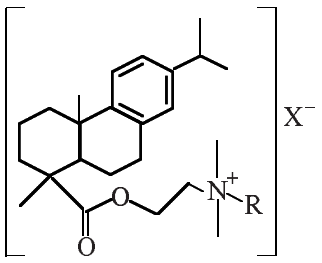
Abstract—Quaternary ammonium compounds based on resin (diterpene) acids and rosin were prepared. Their colloidal-chemical and biocidal properties were studied, and possible applications were outlined.

DOI: 10.1134/S1070427208050297

It is well known that introduction of nitrogen-containing functional groups into molecules of resin acids, the main components of rosin, is a route to very interesting environmentally friendly products finding diverse applications [1]. Of particular interest is the fact that many nitrogen derivatives of resin acids exhibit biological activity and pharmacological properties. In particular, it was shown that dehydroabietylamine is a fairly effective bactericidal and fungicidal agent [2]. Azomethines (Schiff bases) prepared from dehydroabietylamine and benzaldehyde derivatives also exhibit bactericidal properties [3].

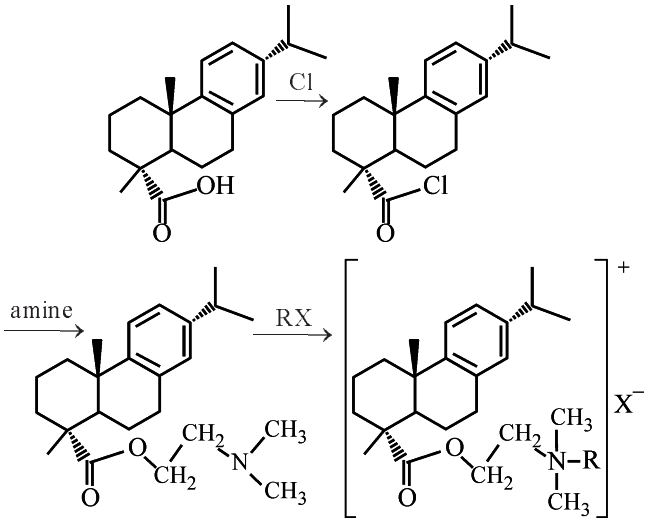
Some azomethines surpass in the bactericidal activity the starting dehydroabietic acid (DAA). Some resin acid amides are also physiologically active. In particular, they exhibit hypocholesteremic action, i.e., are capable of controlling the cholesterol level in blood of warm-blooded animals [4, 5], and also gastroprotective and cytostatic action [6].

Quaternary ammonium salts (QASs) derived from resin (diterpene) acids and rosin of the general formula



where R = ethyl or benzyl, X = Cl or Br, were developed previously [7].

The commercial name of the product is Biotsik. Here we report on the synthesis of these QASs and on their colloidal-chemical and biocidal properties. The QAS synthesis is based on the known reactions and follows the scheme



1, DAA, R = Et, X = Br; **2**, DAA, R = Bz, X = Cl; **3**, mixture of resin acids, R = Et, X = Br; **4**, disproportionated rosin, R = Et, X = Br.

As the carboxy group in resin acids is sterically hindered, many reactions characteristic of aliphatic acids occur difficultly. Therefore, the first step in-

Table 1. Compositions and properties of QASs

Compound	Empirical formula	T_m, °C	Found, %/Calculated, %					Ammonium nitrogen, %	
			C	H	N	Br	Cl	found	calculated
1	$[C_{26}H_{42}O_2N]^+Br^-$	175–178	65.05 / 64.99	8.68 / 8.81	3.40 / 3.49	15.60 / 16.63	– / –	2.73	2.91
2	$[C_{31}H_{44}O_2N]^+Cl^-$	51.5–52.5	74.93 / 74.74	8.67 / 8.90	2.98 / 2.81	– / –	7.88 / 7.12	2.89	3.02
3	$[C_{26}H_{42}O_2N]^+Br^-$	Pale yellow resin	65.30 / 65.00	9.10 / 8.80	3.65 / 3.52	15.90 / 16.60	– / –	2.69	2.91
4	Mixture of 4-(2-dimethylethylammonioethoxycarbonyl)-abieto-8,11,13-triene bromides	Pale yellow resin	65.20 / –	8.70 / –	3.20 / –	14.80 / –	– / –	2.58	–

volves synthesis of DAA chloride [8] or chlorides of a mixture of resin acids and of disproportionated rosin. In the second step, the chlorides are treated with dimethylethanolamine (DMEA) to obtain the corresponding amino esters, which are subsequently quaternized by the standard procedure with excess ethyl bromide or benzyl chloride in a solvent. The physicochemical properties of the compounds prepared and their compositions are given in Table 1. The empirical formulas of the QASs were confirmed mass-spectrometrically by the fragment peak with *m*/*z* 385.299. The IR and ^{1}H NMR spectra of all the compounds prepared are similar. In the UV spectra, there are three absorption bands at about 259, 267, and 276 nm, characteristic of the aromatic ring of DAA. In the UV spectrum of **2**, the band at 250–285 nm is somewhat broadened, which is typical of compounds with the benzyl C–H bond.

The IR spectra of all the QASs contain three characteristic absorption bands (cm^{-1}): 3400 (N–H bond), triplet at 3000–2800 (C–H), and 1727 (C=O). The bands at 1460 and 1380 cm^{-1} in the spectra of **1**, **3**, and **4** are assigned to CH_2 and CH_3 vibrations in the ethyl group.

The NMR spectrum contains characteristic signals (δ, ppm) at 6.7–7.3 (H of aromatic ring); 1.14, 1.17, and 1.22 (H of isopropyl and two CH_3 groups); a broadened signal at 4.5 (H of CH_2 group in the ester fragment C–O–CH_2–); 3.7 (4H, CH_2 groups bonded to nitrogen); and approximately 2.7 (4H, m, CH_2).

The spectral and analytical data obtained confirm the suggested structures of the quaternary ammonium salts synthesized. The compounds are soluble in water, ethanol, toluene, dioxane, acetone, acetonitrile, and carbon tetrachloride; they are stable in air at ambient temperature; they exhibit pronounced surface activity and biocidal properties. It is practically important that the colloidal-chemical and biocidal properties of the individual QASs (**1**, **2**) and of QASs derioved from rosin and a mixture of resin acids (**3**, **4**) are similar.

Figure 1 shows the surface tension isotherm characteristic of all the QASs studied, plotted in the normal and semilog coordinates. The minimal surface tension σ_{min} (mN m^{-1}) for the QASs is as follows: **1**, 35–36; **2**, 38–39; and **3** and **4**, 40–42. The critical micelle concentration (CMC) for all the QASs is 5×10^{-3} M (0.24%). From the second portion of curve *2* (Fig. 1), using the Gibbs equation, we calculated the maximal adsorption of QAS on the water–air phase boundary, $\Gamma_{max} = 4.3 \times 10^{-10}$ mol cm^{-2}. The same quantity calculated by the Shishkovskii equation for high concentrations is 3.8×10^{-10} mol cm^{-2}.

The specific electrical conductivity of the aqueous QAS solutions linearly increases with the concentration (Fig. 2). This fact demonstrates the capability

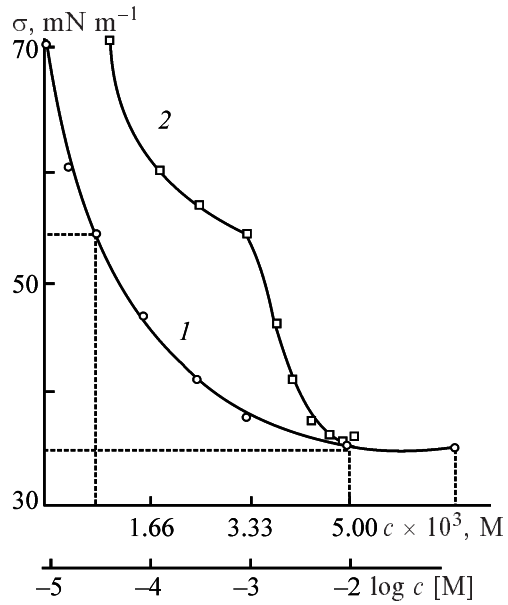


Fig. 1. Surface tension (σ) isotherm of aqueous QAS solution, plotted in (*1*) normal and (*2*) semilog coordinates. (*c*) Concentration.

of QASs for dissociation in aqueous solutions and their tendency to adsorption on negatively charged surfaces, in particular, on particles in polar media.

The dependence of the wetting angle of waxed glass on the QAS concentration in aqueous solution (Table 2) shows that the QASs studied are effective film-forming agents favoring hydrophilization of hydrophobic materials. It is well known that such surfactants are capable of chemisorption on hydrophobic surfaces and of selective wetting, which is important for using them as flotation agents and components of shampoos and conditioners.

Table 2. Wetting of the surface of waxed glass with aqueous QAS solutions

QAS concentration in water		Wetting angle	
$c \times 10^3$, M	c, g l^{-1}	θ, deg	cos θ
0	0	107	–0.29
0.04	0.02	99	–0.16
0.16	0.08	93	–0.05
0.83	0.4	82	0.14
1.66	0.8	74	0.28
3.33	1.6	60	0.5
4.16	2.0	55.5	0.57
5.00	2.4	56	0.56
6.66	3.2	54	0.59

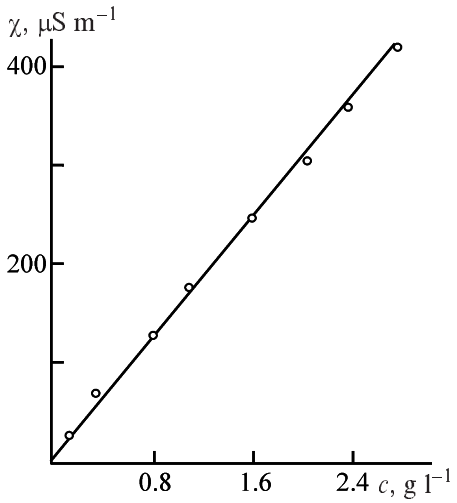


Fig. 2. Specific electrical conductivity χ of aqueous QAS solution as a function of QAS concentration *c*.

Calculation by the approximate Davies equation showed that the hydrophilic–lipophilic balance (HLB) of the QASs studied is 8.4. Calculation by the spreading coefficient (Griffiths method) gave a close HLB value, 9.

The bactericidal and fungicidal activity of QASs based on resin (diterpene) acids and rosin was studied by standard procedures, namely, by measuring the zone of microorganism growth suppression (Table 3). The characteristics of the bactericidal and fungicidal activity of some widely used biocides, determined under similar conditions, are also given for comparison. It can be seen that the QASs derived from individual resin (diterpene) acids (compounds **1** and **2**) and from a mixture of resin acids and rosin (compounds **3** and **4**) exhibit essentially similar bactericidal and fungicidal activity, although rosin, an environmentally clean, virtually inexhaustible raw material of plant origin, contains up to 10% neutral diterpenoids. Table 3 also shows that the QASs well compete in the biological activity with the known and widely used biocides, Aseptodin and Biopag-2 (the latter exhibits virtually no fungicidal properties), as well as with well-advertised biocide Triclosan (Ciba-Geigy, Switzerland), 2,4,4'-trichloro-2'-hydroxydiphenyl ether, which is environmentally hazardous as potential source of dioxins.

It is known that many QASs of various structures exhibit biocidal activity. The presence of a terpenoid fragment in the molecules of the QASs prepared undoubtedly enhances their activity.

The whole set of bactericidal-fungicidal and colloid-chemical properties of the QASs studied

Table 3. Bactericidal and fungicidal activity of QASs

QAS or agent	Concentration in water, %	Zone of bacterial growth inhibition, *R*, mm	Bactericidal activity	Zone of fungus growth inhibition, *R*, mm	Fungicidal activity
1	0.05	3	Weak	–	None
	0.1	10	Bactericide	8	Fungicide
	0.5	14	Bactericide	10	Fungicide
2	0.05	2	Weak	–	None
	0.1	5	Bactericide	–	None
	0.5	6	Bactericide	5	Fungicide
3	0.05	–	–	–	–
	0.1	6	Bactericide	4	Fungicide
	0.5	9	Bactericide	5	Fungicide
	1.0	9	Bactericide	5	Fungicide
4	0.05	–	–	–	–
	0.1	8	Bactericide	3	Weak
	0.5	9	Bactericide	5	Fungicide
	1.0	10	Bactericide	10	Fungicide
Triclosan	0.05	1	Weak	–	None
	0.1	3	Weak	1	Weak
	0.5	10	Bactericide	7	Fungicide
	1.0	14	Bactericide	10	Fungicide
Aseptodin	0.1	9	Bactericide	–	None
	0.5	12	Bactericide	–	None
	1.0	13	Bactericide	5	Fungicide
	5.0	14	Bactericide	8	Fungicide
Biopag-2	0.1	5	Bactericide	–	None
	0.5	7	Bactericide	–	None
	1.0	9	Bactericide	–	None
	4.0	11	Bactericide	2	Fungicide

suggests the following fields of their possible applications: in pulp-and-paper industry, for protection of the equipment from biological contamination, recycled wastewater treatment to remove bioformations, stabilization of the starch products used, and suppression of the development of microorganisms in them; in building, for preventing biocorrosion of building materials and structures, especially of those containing cellulose, and of buildings; for inhibiting corrosion; for enhancing the flotability of minerals; for static elimination; and in production of shampoos, conditioners, and specialty soaps (the commercial name of QAS **1** is Biotsik K, for cosmetics).

Some of these possibilities have been confirmed by practical tests.

Based on the results of our study, we developed an agent, QAS **4**, derived from a readily available and relatively cheap raw material, disproportionated rosin. This agent was termed Biotsik T [biocidal rosin for technical purpose, TU (Technical Specification) 2453-012-25588394–2005]. It exhibits fungicidal and bactericidal action (registry no. 15.245.P.002302.12.04 of December 19, 2004).

EXPERIMENTAL

For preparing **1** and **2**, we used DAA with mp 172.5°C and main substance content of 97.5 wt % (GLC). For preparing **3**, we used a crystalline mixture of resin acids isolated by the standard procedure from disproportionated oleoresin rosin, mp 169°C, acid number 184 mg KOH/g, of the following composition (GLC): DAA 70.5, dihydroabietic acid 18.1, sum of pimaric acids 10.3, and sum of acids with conjugated double bonds (of abietic type) 0.8. For preparing **4** (Biotsik T), we used disproportionated tall rosin (TU 13-00281074-265–95) with the following physicochemical characteristics: glassy, partially crystallized substance; acid number 164 mg KOH/g; weight fraction of acids with conjugated double bonds 0.8%.

The other chemicals used in the syntheses were of

chemically pure or analytically pure grade and were used without additional purification.

The UV spectra were recorded on Specord M-40 (in ethanol) and Hewlett–Packard 8453 spectrophotometers. The IR spectra were measured on a Perkin–Elmer spectrophotometer (NaCl cells, layer thickness 1.05 mm, solvent CCl_4). The ^1H and ^{13}C NMR spectra were taken on a Bruker DPX-200 spectrometer (200 and 50 MHz, respectively; $CDCl_3$). The mass spectrum was taken on a Finnigan MAT-8200 device (ion source temperature 173°C, scanning rate 1.2 scan s^{-1}, m/z range 30–350). The elemental composition of QASs was determined with a Carlo Erba automatic CHN analyzer. Ammonium nitrogen was determined as described in [9].

The melting point was determined according to GOST (State Standard) 14618.12–78 with a PTP device. The surface tension of aqueous solutions of QASs was determined by the method of maximum pressure of bubble formation and by the Wilhelmy plate method. In the first case, double-distilled water (σ = 73.05 mN m^{-1} at 18°C) was used as reference liquid. The Wilhelmy plate measurements were performed with a Waga Torsyna-WT torsion balance. The platinum plate size was 1×2 cm^2. The calibration curve of the dependence of the balance readings in the medium of the liquid surface tension was constructed on the basis of σ values of reference liquids that fully wet the platinum plate (methylene iodide, benzene, methylene chloride, toluene). All the reference liquids were of chemically pure grade.

The electrical conductivity of aqueous solutions of the QASs was measured with a DIST-3 conductometer. The device was immersed in a solution (volume 40 ml). Three replicate measurements were performed.

The wetting angles were measured on the surface of waxed glass. For this purpose, the support was kept for 1 min in a 1% solution of paraffin in hexane and then was dried in air for 30 min. A sample (1 μl) was applied with a microsyringe onto a sample stage placed in a hermetically sealed cell. The atmosphere in the cell was saturated with the vapor of the test liquid by placing this liquid on the cell bottom. The sample was applied through a hole in the cell lid. The dimensions of the drop (chord of the profile l and height h) were determined with an MPB-2 horizontal microscope, and the wetting angle θ was calculated by the formula $\theta = 2\arctan(2h/l)$.

Chlorides of resin (diterpene) acids and rosin were prepared as described in [8]. To prepare the amino esters, a reactor equipped with a stirrer, a heating jacket, and a reflux condenser was charged in succession with 85 g of dimethylethanolamine (DMEA) and 85 ml of toluene, after which 200 g of a 50% solution of appropriate acid chloride in toluene was added in portions. The mixture was heated to 95–97°C and kept at this temperature for 4 h. Then the mixture was filtered, and the filtrate was washed with water to neutral reaction of the wash waters and dried. After distilling the toluene off under reduced pressure, the corresponding dimethylaminoethyl ester was obtained in 86–88% yield.

To prepare QAS **1**, **3**, and **4**, a similar reactor was charged with 100 g of appropriate amino ester, after which 350 g of ethyl bromide was added in portions with stirring. Quaternization was performed at 30°C for 5 h. After distilling excess ethyl bromide off under reduced pressure, the corresponding QASs were obtained in virtually quantitative yields.

To prepare QAS **2**, a reactor was charged with 103 g of DAA aminoethyl ester and 15 ml of acetonitrile. The mixture was stirred at 45°C until a transparent homogeneous solution was obtained. After cooling to ambient temperature, a solution of 38.5 g of benzyl chloride in 100 ml of acetonitrile was added in portions with continuous stirring. The mixture was allowed to stand for 1 h, after which it was heated to 80°C, and the quaternization was performed for 5 h. After the reaction completion, the acetonitrile was distilled off at 50°C under reduced pressure, and 135 g of QAS **2** was obtained.

CONCLUSIONS

(1) Quaternary ammonium compounds derived from resin (diterpene) acids and rosin exhibit pronounced bactericidal and fungicidal properties and surface activity.

(2) It is appropriate to use Biotsik T agent in building industry for protection of building materials and buildings from biocorosion, and also in pulp-and-paper industry for protection of the equipment from biological contamination, recycled wastewater treatment, and stabilization of starch products used.

REFERENCES

1. Sandermann, W., *Naturharze Terpentinöl-Tallöl. Chemie und Technologie*, Berlin: Springer, 1960.

Translated under the title *Prirodnye smoly, skipidar, tallovoe maslo*, Moscow: Lesnaya Prom–st., 1964, pp. 303–310.

2. Borglin, S., *Soap Sanit. Chem.*, 1947, vol. 23, no. 12, pp. 147–149, 169.
3. Xiaoping Rao, Zhanqiang Song, Radbil' A.B., et al., *Zh. Prikl. Khim.*, 2007, vol. 80, no. 8, pp. 1334–1336.
4. Fujita, Y., Sempuku, K., Kitaguchi, K., et al., *Chem. Pharm. Bull.* (Tokyo), 1980, vol. 28, pp. 453–458.
5. Nuray Ulusu, N., Ercil, D., Koray Sakar, M., et al., *Phytother. Res.*, 2002, vol. 16, pp. 88–90.
6. Sepulveda, B., Astudillo, L., Rodriguez, J.A., et al., *Pharmacol. Res.*, 2005, vol. 52, pp. 429–437.
7. RF Patent 2256649.
8. Kushnir, S.R., Borisova, N.V., Radbil', A.B., et al., *Zh. Prikl. Khim.*, 2003, vol. 76, no. 11, pp. 1845–1847.
9. Siggia, S. and Hanna, J.G., *Quantitative Organic Analysis via Functional Groups*, New York: Wiley–Interscience, 1979. Translated under the title *Kolichestvennyi organicheskii analiz po funktsional'nym gruppam*, Moscow: Khimiya, 1983, pp. 520–522.

ISSN 1070-4272, Russian Journal of Applied Chemistry, 2008, Vol. 81, No. 5, pp. 880–882. © Pleiades Publishing, Ltd., 2008.
Original Russian Text © E.Yu. Kolosova, A.G. Morachevskii, L.B. Tsymbulov, 2008, published in Zhurnal Prikladnoi Khimii, 2008, Vol. 81, No. 5, pp. 843–845.

BRIEF COMMUNICATIONS

Description of Concentration Dependences of the Thermodynamic Functions in Liquid Alloys of the Fe–Ni, Co–Fe, and Co–Ni Systems

E. Yu. Kolosova, A. G. Morachevskii, and L. B. Tsymbulov

St. Petersburg State Polytechnic University, St. Petersburg, Russia
Gipronikel' Institute, Limited Liability Company, St. Petersburg, Russia

Received March 25, 2008

Abstract—The simplest polynomial expressions were applied to the description of the concentration dependences of integral molar excess Gibbs energy and enthalpy of mixing of the Fe–Ni, Co–Fe, and Co–Ni liquid alloys.

DOI: 10.1134/S1070427208050303

The dependences of thermodynamic properties of liquid metallic systems on the composition can be presented in the form of graphs, tables, or analytical expressions. Each form has some advantages and drawbacks in relation to accurate and clear description of the functional dependence, compactness, and convenient use of the data [1, 2].

In calculations using computer programs it is desirable to have analytical expressions for thermodynamic properties of the phases of variable composition. To create the corresponding data bank, it is appropriate to include different methods for describing the concentration dependences of thermodynamic functions, to use them depending on user's preference. In this case, one should clearly understand what characteristics are specific for each method of modeling of thermodynamic properties, depending on the character of component interaction.

In application of any mathematical model, it is rather important to assess the reliability of the input experimental data. At present, a number of criteria characterizing data reliability have been developed in practice. To them belong the author's evaluation of the measurement accuracy and the reproducibility (convergence) and self-consistency of data. Impartial assessment of data reliability in high-temperature studies is always difficult. In any specific case, the whole complex of probable errors must be taken into account and a certain experience is required. One should remember that applying the mathematical methods of averaging the set of available data for a particular system does not always give desirable result, because, in so doing, characteristic local features of the concentration dependence of the partial molar functions of components can be smoothed out.

When assessing the suitability of mathematical models used for analytical representation of the concentration dependences of the thermodynamic functions of liquid alloys, it should be taken into account whether the correct information about the thermodynamic function under consideration in the composition range studied at a given temperature can be obtained, whether the data bank is available, and whether the thermodynamic functions can be extrapolated to the composition region for which experimental data are lacking. By physical meaning, the functions of mixing in the homogeneity region must be reasonably smooth and their derivatives, continuous.

In the given study, we applied the simplest methods to the description of the dependence of the integral molar Gibbs energy ΔG^{exc} and enthalpy ΔH, which characterize the mixing in the Fe–Ni, Co–Fe, and Co–Ni liquid alloys. We choose for description the most reliable experimental data. The ΔG^{exc} values were obtained by Knudsen cell mass spectrometry [3–6], and the ΔH values, by high-temperature calorimetry [7–9]. Results of the experimental studies for binary systems under consideration are analyzed

in detail in [9]. All the three systems differ in the magnitudes and signs of deviation from the ideal behavior.

The concentration dependence of the integral functions of mixing was described by the following expressions [10]: for a regular solution we used the expression

$$\Delta\Phi = A x_1 x_2; \quad (1)$$

for a subregular solution, the expression

$$\Delta\Phi = x_1 x_2 (B x_1 + A x_2), \quad (2)$$

the Khair polynomial

$$\Delta\Phi = A x_1 x_2 \exp(B x_1), \quad (3)$$

the Redlich–Kister polynomial

$$\Phi = x_1 x_2 [b + c(2x_1 - 1) + d(2x_1 - 1)^2], \quad (4)$$

and the Wilson polynomial

$$\Phi = -RT[x_1 \ln(x_1 + A x_2) + x_2 \ln(x_2 + B x_1)], \quad (5)$$

where the symbol $\Delta\Phi$ denotes ΔG^{exc} or ΔH; x_1 and x_2 are mole fractions of components; A, B, b, c, and d are the coefficients in the equations.

The coefficients of Eqs. (1)–(5) describing the dependences of ΔG^{exc} and ΔH on composition are listed in Tables 1 and 2 along with the correlation coefficients R. The latter quantities show how adequately a given equation describes the corresponding dependence. As seen from Table 1, the regular-solution equation (1) describes well the ΔG^{exc} vs. composition dependence only for the Co–Ni system, and Eqs. (2)–(5), for all the three systems considered. The accuracy of the experimental determination of ΔH is considerably lower than that of ΔG^{exc}, which affects the correlation coefficients (Table 2). First of all, this concerns the Co–Ni liquid alloys, where ΔH is small in the absolute value (less than 0.5 kJ·mol^{-1}) and scatter of the available experimental data is considerable. It should be noted that the correlation coefficient itself cannot be considered as absolute criterion of applicability of a given equation to describing the concentration dependence of a thermodynamic function. The quality of the experimental data also plays an important role.

Table 1. Coefficients in equations for ΔG_{exc} (kJ mol^{-1})

Equation	Coefficient	System		
		Fe–Ni, 1623 K [3]	Co–Fe, 1650 K [4]	Co–Ni, 1800 K [5]
(1)	A	–9.0394	5.1468	–2.5140
	R^2	0.9341	0.7834	0.9998
(2)	A	–12.2874	8.7865	–2.5639
	B	–5.7915	1.5072	–2.4641
	R^2	0.9993	0.9999	0.9999
(3)	A	–6.3146	2.5249	–2.4645
	B	0.7005	1.3615	0.0397
	R^2	0.9979	0.9950	0.9999
(4)	b	–9.1500	5.1511	–2.5157
	c	–3.2480	3.6396	–0.0500
	d	0.7758	–0.0295	0.0120
	R^2	0.9999	0.9999	0.9999
(5)	A	2.5717	1.7865	1.0861
	B	0.5573	0.2002	1.0855
	R^2	0.9956	0.9857	0.9998

Table 2. Coefficients in equations for ΔH (kJ mol^{-1})

Equation	Coefficient	System		
		Fe–Ni, 1623 K [3]	Co–Fe, 1650 K [4]	Co–Ni, 1800 K [5]
(1)	A	–18.2246	–9.6247	1.5628
	R^2	0.7936	0.9907	0.8394
(2)	A	–7.4607	–10.8519	1.6437
	B	–26.3288	–8.3974	1.4822
	R^2	0.9885	–0.9995	0.8412
(3)	A	–28.1199	–8,4777	1.4896
	B	–1.0481	0.2516	0.9555
	R^2	–0.9819	–0.9994	0.8410
(4)	b	–17.3666	–9.7153	1.7586
	c	9.7186	–1.2273	0.0213
	d	3.4141	0.6359	–0.8799
	R^2	–0.9917	0.9999	0.8725
(5)	A	0.3479	1.6694	0.9352
	B	4.0595	1.0391	0.9603
	R^2	0.9708	0.9992	0.8388

CONCLUSION

The possibility of describing the mixing in the Fe–Ni, Co–Fe, and Co–Ni liquid alloys by using

the simplest polynomial expressions with minimal number of parameters for the concentration dependence of integral thermodynamic functions was demonstrated.

REFERENCES

1. Morachevskii, A.G. and Sladkov, I.B., *Termodinamicheskie raschety v metallurgii: Spravochnik* (Thermodynamic Calculations in Metallurgy: Reference Book), Moscow: Metallurgiya, 1993, 2nd ed.
2. Morachevskii, A.G., Voronin, G.F., Geiderikh, V.A., and Kutsenok, I.B., *Elektrokhimicheskie metody v termodinamike metallicheskikh sistem* (Electrochemical Methods in Thermodynamics of Metallic Systems), Moscow: Akademkniga, 2003.
3. Tomiska, J. and Neckel, A., *Ber. Bunsenges. Phys. Chem.*, 1985, vol. 89, no. 10, pp. 1104–1109.
4. Tomiska, J., *Z. Metallkunde*, 1986, vol. 77. no. 2, pp. 97–102.
5. Tomiska, J., Novotny, H., Erdelyi, L., and Neckel, A., *Ber. Bunsenges. Phys. Chem.*, 1979, vol. 83, pp. 1035–1042.
6. Batalin, G.I., Minenko, N.N., and Sudavtsova, V.S., *Metally*, 1974, no. 5, pp. 99–103.
7. Predel, B., and Mohs, R., *Arch. Eisenhuttenwes.*, 1970, vol. 41. no. 2, pp. 143–149.
8. Predel, B., and Mohs, R., *Arch. Eisenhuttenwes.*, 1970, vol. 41, no. 1, pp. 61–66.
9. Morachevskii, A.G., Ryabko, A.G., and Tsemekhman, L.Sh., *Termodinamika zhidkikh splavov sistemy zhelezo–nikel'–kobal't* (Thermodynamics of Liquid Alloys of the Iron–Nickel–Cobalt System), St. Petersburg: Sankt-Peterb. Gos. Politekh. Univ., 2004.
10. Choi, S.-D., and Hucke, E.E., *CALPHAD*, 1990, vol. 14, no. 4, pp. 367–376.

ISSN 1070-4272, Russian Journal of Applied Chemistry, 2008, Vol. 81, No. 5, pp. 883–885. © Pleiades Publishing, Ltd., 2008.
Original Russian Text © L.A. Gladikova, V.V. Teterin, N.B. Ovchinnikova, 2008, published in Zhurnal Prikladnoi Khimii, 2008, Vol. 81, No. 5, pp. 846–848.

BRIEF COMMUNICATIONS

Purification of Magnesium Chloride Solution Used for Carnallite Synthesis

L. A. Gladikova, V. V. Teterin, and N. B. Ovchinnikova

AVISMA Branch, VSMPO-AVISMA Corporation, Open Joint-Stock Company, Berezniki, Perm krai, Russia

Received June 20, 2007

Abstract—The neutralization of magnesium chloride solutions and their treatment to remove iron compounds was studied. The possibility of neutralization of free hydrochloric acid with brucite was determined. The effect exerted by the method of stirring of the solution in the course of neutralization was analyzed, and variations of neutralization rate with the solution temperature and with the amount and size of particles of the neutralizing agent were studied.

DOI: 10.1134/S1070427208050315

Prior to be used in production of synthetic carnallite, magnesium chloride solutions must be approximately neutral (pH ≥ 5) and the content of impurities in them must be no larger than (g dm^{-3}): 0.26 Fe, 0.08 Si, 0.003 Ni, 0.004 Cu, 0.03 Mn, 0.013 Al, 0.009 Ti, 0.004 Cr, at a $MgCl_2$ concentration of 400–450 g dm^{-3} [1, 2].

Magnesium chloride solutions obtained by leaching of oxide magnesium-containing raw material contain free hydrochloric acid and increased concentration of iron. The most suitable treatment method to remove impurities is fractional precipitation of hydroxides. The method is based on the property of metals to form hydroxides in a certain narrow range of pH [3]. Data on fractional precipitation of iron hydroxide are available from the literature [4]. From the process standpoint, the best neutralizing agent for magnesium chloride solutions is magnesium hydroxide (brucite). It is known [5] that the thermal decomposition and prolonged grinding of brucite increase the activity of magnesium hydroxide with respect to mineral acids.

In this study we determined the most active form of brucite as neutralizing agent and the conditions providing its minimal consumption and high quality of the resulting solutions.

The experiment was performed in a glass reactor which was charged with 1 l of a solution to be neutralized. The solution was obtained by leaching brucite with hydrochloric acid and contained (g l^{-1}): $MgCl_2$ 405, Fe^{n+}_{tot} 0.68, and HCl 5.5. For neutralization we used calcined and uncalcined brucite of different degrees of grinding. The solution being neutralized was stirred with a magnetic stirrer or by bubbling with compressed air. The temperature and pH of the solution were controlled in the course of the experiment. After the solution was neutralized, the contents of magnesium chloride, Fe_{tot}, and suspended substances in it were determined. The results and conditions of the experiments are presented in Figs. 1–4.

We used uncalcined brucite (d_{av} = 100 μm) to study how the amount of brucite and the method of mixing affect the neutralization rate. The data presented show that the neutralization rate is largely determined by the amount of brucite fed for neutralization (Fig. 1). For example, as the coefficient of brucite excess over stoichiometry is increased from 2 to 4, the neutralization rate increases by a factor of 5. Decreasing the solution temperature from 80 to 20°C results in a twofold decrease in the neutralization rate.

The effect exerted by the method of mixing is demonstrated in Fig. 2. The neutralization rate is shown to be independent of the method of mixing at low temperatures (20°C). At 80°C, the neutralization rate somewhat increases in the case of bubbling with compressed air. The effect of temperature on the neutralization rate is the most pronounced in the case when the brucite obtained by wet grind-

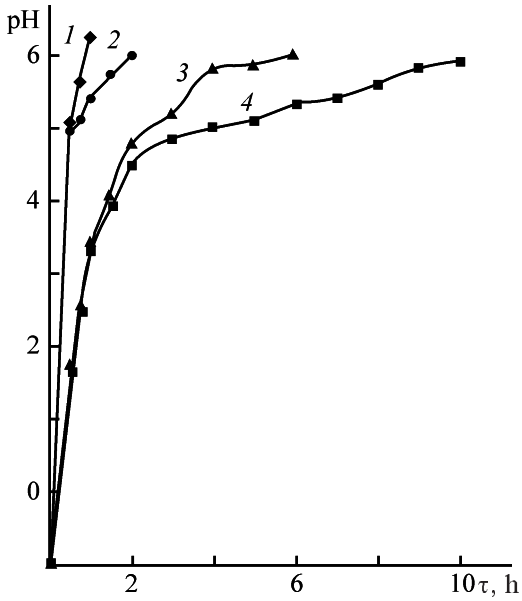


Fig. 1. Dependence of the neutralization rate on the excess of brucite. (τ) Mixing time; the same for Figs. 2–4. Coefficient of brucite excess K and T, °C: (*1*) 4.0, 80; (*2*) 3.0, 80; (*3*) 2.0, 80; and (*4*) 2.7, 20.

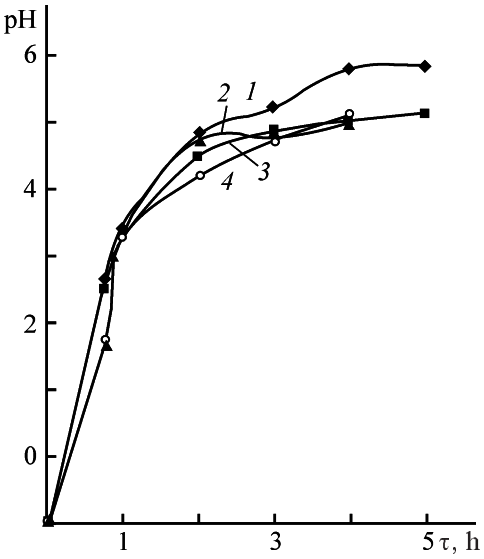


Fig. 2. Effect of mixing method on the neutralization rate: (*1*) bubbling with compressed air, T = 80°C, K = 2.0; (*2*) mechanical stirring , T = 80°C, K = 2.0; (*3*) bubbling with compressed air, T = 20°C, K = 2.7; and (*4*) mechanical stirring, T = 20°C, K = 2.7.

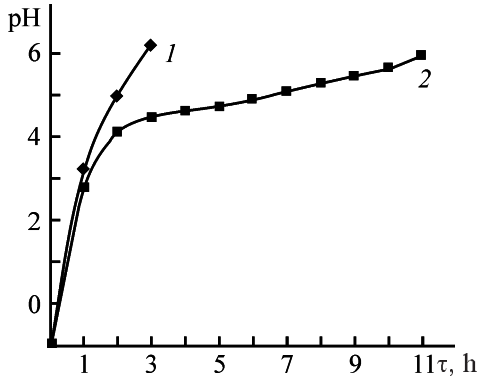


Fig. 3. Effect of temperature on the neutralization rate. Uncalcined brucite, d_{av} = 20 μm. Coefficient of brucite excess K and T, °C: (*1*) 1.5, 80 and (*2*) 2.0, 20.

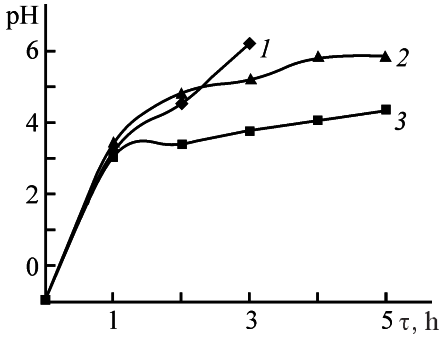


Fig. 4. Effect of particle size on the neutralization rate (T = 80°C). Brucite: (*1*) uncalcined (d_{av} = 20 μm), K = 1.5; (*2*) uncalcined (d_{av} = 100 μm), K = 2.0; and (*3*) calcined (d_{av} = 100 μm), K = 1.7.

ing on a bead mill for 30 h is used as neutralizing agent (Fig. 4).

The effect exerted by the size of particles of a neutralizing agent on the neutralization rate is demonstrated in Fig. 4. With brucite suspension obtained by wet grinding on a bead mill, the rate is maximal, which is due to the larger area of contant of brucite particle surfaces with hydrochloric acid. The lowest rate of neutralization of a brucite suspension obtained from calcined brucite can be accounted for as follows. As known, after 24 h of reaction of MgO with water, the degree of hydration is no more than 70%. This is because the hydration process is a topochemical reaction, with the reaction front at the MgO–$Mg(OH)_2$ interface. A hydroxide film on the MgO surface impedes diffusion of H_3O^+ ion toward the magnesium oxide surface. The character of the curve (Fig. 4) shows that, initially (during 1 h at pH < 3), the neutralization rate is virtually the same for all the neutralizing reagents. Evidently, till this moment, $Mg(OH)_2$ particles are formed on the surface of MgO particles. At pH 3, a film of iron(III) hydroxide is formed on brucite particles, which decreases the neutralization rate.

To evaluate the efficiency of treatment of the $MgCl_2$ solutions to remove Fe_{tot}^{n+}, we carried out a number of the experiments on the precipitation of

Solution purification with brucite

Component concentration, g l^{-1}				Degree of purification, %
before purification		after purification		
$MgCl_2$	Fe^{n+}	$MgCl_2$	Fe^{n+}	
361	0.09	389.9	0.002	97.7
108.1	0.05	115.2	0.002	96.0
157.6	0.11	161.2	0.004	96.4
246.9	0.16	250.8	0.005	96.9

iron hydroxides with milled brucite. To do this, a glass flask was charged with 200 ml of a solution containing various concentrations of iron salts and magnesium chloride. The solution having a temperature of 20°C was stirred with a magnetic stirrer, and a <100-μm fraction of natural brucite was charged to pH 0.5–7. Then the contents of the flask were heated to 100°C, kept at this temperature for 30 min, and filtered. The results of experiments on the solution purification are listed in the table. The data obtained show that the treatment of magnesium chloride solutions with natural brucite to remove iron compounds ensures high degree of its purification.

The results obtained were checked in the experiment with a solution volume of 230 l. To oxidize Fe^{2+} to Fe^{3+}, the solution was chlorinated for 1 h with a chlorine consumption of 5 kg h^{-1}. The solution obtained was poured into a tank equipped with a stirrer, and 9 kg of magnesium oxide (<1.5-mm fraction) was loaded. The mixture was stirred for 1.5 h. After that, 6 kg of MgO, preliminarily pulped with water to a volume of 15 l, was added. Stirring was performed for 20 min. Then the solution was heated to 100°C and boiled for 15 min. After cooling to 60°C, the solution was filtered. The resulting solution had a volume of 170 l. The solution contained (g l^{-1}) Fe^{3+} 21.1 and $MgCl_2$ 220 before purification, and Fe^{3+} 0.003 and $MgCl_2$ 369 after purification. The degree of purification was 99%. The precipitate contained (wt %) Fe 16.8, Mg 16.2, Si 3.3, and H_2O 19.9.

The data obtained show that the precipitation method is highly efficient for treatment of magnesium chloride solutions to remove iron compounds.

In the next stage of the study, the purified solutions were used for the production of synthetic carnallite. The carnallite obtained contained no less than 0.02 wt % Fe, which does not exceed the Fe concentration in artifical carnallite.

CONCLUSIONS

(1) The possibility of neutralizing hydrochloric acid in solutions obtained by leaching of magnesium-containing raw material with brucite was demonstrated.

(2) The neutralization rate increases as the temperature of the solution and the excess of brucite increase and as the size of particles of the neutralizing agent decreases.

(3) It is appropriate to use compressed air for stirring the solution in the course of neutralization.

(4) The most efficient method for treatment of magnesium chloride solutions to remove iron compounds is precipitation with finely ground natural brucite. The method ensures high degree of purification and, owing to neutralization of free hydrochloric acid whose concentration is 5–10 g l^{-1}, allows a 5–7% increase in the magnesium chloride concentration in the solution.

REFERENCES

1. Eidenzon, M.A., *Magnii* (Magnesium), Moscow: Metallurgiya, 1969.
2. Strelets, Kh.A., *Elektroliticheskoe poluchenie magniya* (Electrolytic Production of Magnesium), Moscow: Metallurgiya, 1972.
2. Britton, H.T.S., *Hydrogen Ions*, London: Chapman and Hall, 1932.
4. Kuz'minykh, I.N., and Babushkina, M.D., *Zh. Prikl. Khim.*, 1955, vol. 28, no. 6, pp. 565–572.
5. Teterin, V.V., Kudryavskii, Yu.P., Trudova, E.V., et al., *Khim. Tekhnol. Prom. Ekol. Neorg. Soedin.*, 2000, no. 3, pp. 75–80.

ISSN 1070-4272, Russian Journal of Applied Chemistry, 2008, Vol. 81, No. 5, pp. 886–888. © Pleiades Publishing, Ltd., 2008.
Original Russian Text © T.A. Zaporozhskikh, Ya.K. Tret'yakova, V.A. Grabel'nykh, N.V. Russavskaya, V.Yu. Vshivtsev, E.P. Levanova, E.N. Sukhomazova, I.V. Korabel', N.A. Korchevin, 2008, published in Zhurnal Prikladnoi Khimii, 2008, Vol. 81, No. 5, pp. 849–851.

BRIEF COMMUNICATIONS

Granulated Sulfur-Containing Sorbents for Recovery of Heavy Metal Ions from Aqueous Solutions

T. A. Zaporozhskikh, Ya. K. Tret'yakova, V. A. Grabel'nykh, N. V. Russavskaya, V. Yu. Vshivtsev, E. P. Levanova, E. N. Sukhomazova, I. V. Korabel', and N. A. Korchevin

Favorskii Irkutsk Institute of Chemistry, Siberian Branch, Russian Academy of Sciences, Irkutsk, Russia

Received January 31, 2007

Abstract—Granulated sorbents that can recover zinc salts from aqueous solutions were produced by polycondensation of organochlorine wastes from manufacture of epichlorohydrin with sodium polysulfide on the surface of ash-and-slag particles formed at thermal power plants in the system constituted by aqueous hydrazine and an alkali.

DOI: 10.1134/S1070427208050327

Sulfur atoms in organic molecules (sulfides, di- and polysulfides, xanthates, and other compounds) can form complexes with transition metal salts [1]. This enables use of sulfur-containing products of this kind in medicine, homogeneous catalysis, analytical chemistry, ore dressing, and extraction of metals in hydrometallurgy [2–4]. Together with the use of low-molecular-weight sulfur compounds, studies aimed to synthesize sulfur-containing polymers with sulfur atoms incorporated into the polymer matrix and to analyze their sorption properties are being performed [4, 5]. The industrially produced polysulfide polymers, thiokols, are, as a rule, highly viscous rubber-like substances [6] which cannot be used as sorbents. Polyethylene monosulfide $(–CH_2CH_2S–)_n$, which has high sorption capacity for silver(I) and mercury(II) ions, has been synthesized in the form of a powder by the reaction of dichloroethane with sodium sulfide [7]. However, the use of a finely dispersed powder as sorbent gives rise to certain technological difficulties (caking, high hydraulic resistance, easy carryover by a flow of water).

A solid sorbent was obtained by polycondensation of 1,2,3-trichloropropane (TCP) with Na_2S_n (n = 2–4), with simultaneous addition of thiourea and lignin to the reaction mixture [8]. The sorbent effectively recovers Au, Pt, Pd, and Hg ions from aqueous solutions containing these elements in low concentrations in, apparently, the most widely occurring valence states.

A solid sorbent with a fairly uniform granulometric composition was obtained from wastes formed in large-tonnage manufacture of epichlorohydrin, which is the main monomer in production of epoxy resins. Industrial synthesis of epichlorohydrin is accompanied by formation of more than 0.5 t of organochlorine wastes per ton of the commercial product [9]. At present, utilization of organochlorine wastes is a complicated environmental problem [10, 11].

Depending on the sampling place, the forming wastes are enriched in 1,2-dichloropropane, 1,2,3-trichloropropane, dichloropropanols, and epichlorohydrin. The waste composition is determined by the process mode and operation stability of the installation [9].

EXPERIMENTAL

Sulfur-containing sorbents were obtained from a fraction of organochlorine wastes that was enriched in TCP and had the following component composition (wt %): TCP 76.6, dichloropropanols 17.4, 1,2-dichloropropane 2.0, dichloropropenes 2.1, and other products 1.9.

Sodium polysulfide was prepared from elemental sulfur and sodium hydroxide in an aqueous solution in the presence of hydrazine hydrate as reducing agent [12]:

$$2nS + 4NaOH + N_2H_4 \cdot H_2O \rightarrow 2Na_2S_n + N_2 + 5H_2O.$$

Synthesis conditions and parameters of the adsorbents obtained. NaOH 10 g (0.25 mol), H_2O 50 ml, hydrazine hydrate 5 ml, organochlorine waste 11.8 g (0.08 mol counting on TCP), temperature 40–60°C

Run no.	S/NaOH molar ratio	Ash mass, g	Product yield, g	Grain color	Grain size, mm	Found, wt %	
						S	Cl
1	2	10	22	Light brown	2	60.4	3.7
2	2	5	22	Green	3	55.0	8.0
3	2	3	19	Yellow-green	3.5	62.0	8.8
4	2	1	13	Yellow	1.5–5	64.5	7.3
5	1.5	5	16	Yellow	2.5	48.9	9.6
6	1.5	3	14	Yellow-green	3.5	53.4	9.0

The value of n in the sodium polysulfide obtained is determined by the molar ratio S : NaOH: $n = 3$ at 3 : 2 and 4 at 2 : 1.

To produce polycondensation centers, an ash-and-slag material formed as a waste at thermal power plants was added into the resulting sodium polysulfide solution as a fine powder (average particle size 0.05 mm) [13]. When the resulting mixture is agitated, polysulfide anions are adsorbed on the surface of ash particles. Addition of organochlorine components (waste from manufacture of epichlorohydrin) results in the formation of polymer molecules that envelop ash particles to form grains. The synthesis of a sulfur-containing polymer can be represented by the scheme

$$3mS_n^{2-} + m\,CH_2(Cl)-CH(Cl)-CH_2(Cl) \longrightarrow \left[S_nCH_2-CH(S_n)-CH_2S_n\right]_m$$

The size of the grains formed depends on the number of polycondensation centers, which is, in turn, determined by the mass of the ash-and-slag material. As the amount of the ash material added increases, finer grains are obtained. The table lists the synthesis conditions of the adsorbents and their most important parameters.

If the amount of ash is substantially raised (10 g of ash per 10 g of NaOH used to obtain the polysulfide), a part of the ash is present in the unchanged form as an admixture to adsorbent grains. On lowering the amount of ash to 1 g per 10 g of NaOH, the grains obtained are nonuniform in size. Presumably, polymer formation without inclusion of ash occurs in this case in addition to polycondensation on the surface of ash particles.

The grains obtained have an ellipsoidal shape; the bulk density is 0.7–0.8 g cm^{-3}. If the adsorbents are heated to above 150°C, the polymer decomposes, with the grains becoming dark and cracking. For the adsorbent synthesized in run no. 2, its sorption capacity for zinc(II) ions (pH 5–6) was studied and found to be 57 mg g^{-1}. The sorption capacity for Methylene Blue was 45.8 mg g^{-1}, and that for iodine, 36.8%. The mass fraction of water was determined to be 0.89%. An excess amount of the sorbent virtually quantitatively recovers mercury(II) from an aqueous solution of $Hg(NO_3)_2$, copper(II) from a $CuSO_4$ solution, silver(I) from an $AgNO_3$ solution, and zinc(II) from a $ZnCl_2$ solution.

The sorption capacity of the material for heavy metal ions was estimated using sorption isotherms [14]. It can be seen from Fig. 1 that the sorption isotherm of Zn(II) ions corresponds to type I of isotherms in the Brunauer classification [15], characterized by a monotonic approach of the adsorption to a certain limiting value corresponding to a filled monolayer. This shape of the curves is a consequence of surface nonuniformity or corresponds to

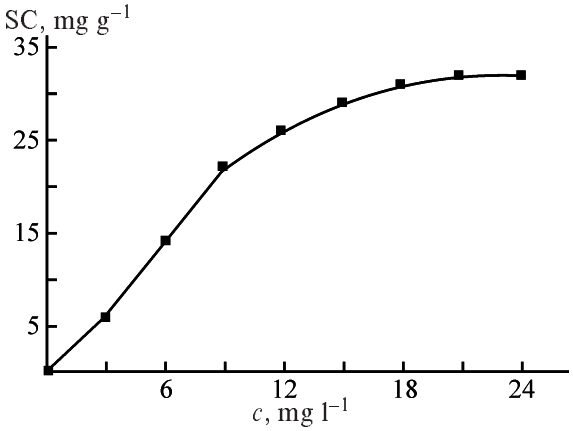


Fig. 1. Sorption isotherm of Zn(II) ions. (SC) Sorption capacity and (c) Zn(II) concentration in solution.

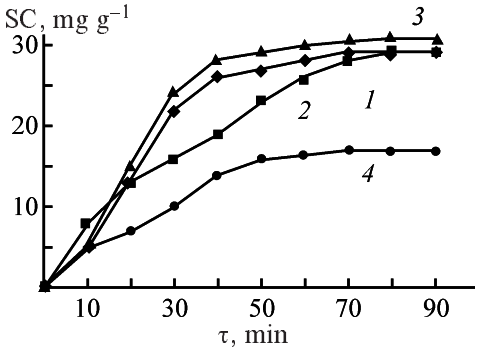


Fig. 2. Kinetic curves of sorption of Zn(II) ions. (SC) Sorption capacity and (τ) process duration. Temperature, °C: (*1*) 20, (*2*) 40, (*3*) 60, and (*4*) 80.

the case in which adsorbates may undergo phase transitions [16].

We also examined the effect of temperature on the sorbent capacity and on the sorption rate of Zn(II) ions at temperatures of 20, 40, 60, and 80°C. The kinetic curves of sorption of Zn(II) ions at different temperatures are shown in Fig. 2. It was found that the sorption interaction in the system constituted by a metal-containing solution and a sulfur-containing sorbent occurs rather intensively: the sorbent is 80–90% saturated in 30–40 min at an initial metal concentration of 23–25 mg l^{-1}.

Figure 2 shows that, as temperature is raised from 20 to 60°C, the sorption capacity of the sorbents increases, which can be attributed to an increase in the rate of diffusion processes in the sorbent matrix. The maximum capacity is observed at 60°C. At higher temperatures, the desorption rate markedly increases.

Also, the fundamental aspects of desorption of Zn(II) ions from a saturated sorbent were studied. Solutions of hydrochloric acid diluted in 1 : 1, 1 : 2, 1 : 5, and 1 : 10 ratios were used as eluents. It was found that, all other conditions being the same, the maximum desorption (>95%) occurs at a $HCl_{conc} : H_2O$ mass ratio of 1 : 1, i.e., in a strongly acidic medium.

CONCLUSIONS

(1) Solid granulated products containing 50–65% sulfur were obtained in the system constituted by sulfur, hydrazine hydrate, and alkali with the use of wastes from manufacture of epichlorohydrin and ash-and-slag wastes from thermal power plants.

(2) The granulated materials obtained can be used as sorbents in recovery of metal ions from aqueous solutions.

REFERENCES

1. Bayon, J.C., Claver, C., and Masden-Bulto, A.M., *Coord. Chem. Rev.*, 1999, vols. 193–195, pp. 73–145.
2. Garnovskii, A.D., Sadimenko, A.P., Osipov, O.A., and Tsintsadze, G.V., *Zhestko-myagkie vzaimodeistviya v koordinatsionnoi khimii* (Hard–Soft Interactions in Coordination Chemistry), Rostov-on-Don: Rostovsk. Gos. Univ., 1986.
3. Korenman, I.M., *Organicheskie reagenty v neorganicheskom analize: Spravochnik* (Organic Reagents in Inorganic Analysis: Reference Book), Moscow: Khimiya, 1990.
4. Glembotskii, V.A. and Klassen, V.I., *Flotatsionnye metody obogashcheniya* (Flotation Dressing Techniques), Moscow: Nedra, 1981.
5. Nikolaev, A.V., Fokin, A.V., Anshits, N.N., et al., *Izv. Sib. Otd. Akad. Nauk SSSR, Ser. Khim. Nauk*, 1978, issue 1, no. 2, pp. 50–58.
6. Sobolev, V.M. and Borodina, I.V., *Promyshlennye sinteticheskie kauchuki* (Industrial Synthetic Rubbers), Moscow: Khimiya, 1977, p. 392.
7. Rafikov, S.R., Nikitin, Yu.E., Bikbaeva, G.G., et al., *Dokl. Akad. Nauk SSSR*, 1980, vol. 253, no. 3, pp. 644–647.
8. Mal'kina, A.G., Sokolyanskaya, L.V., Tsykhanskii, V.D., et al., *Khim. Inter. Ustoich. Razv.*, 1996, vol. 4, no. 3, pp. 307–311.
9. Silinskaya, Ya.N., Tomin, V.P., Katul'skii, Yu.N., and Korchevin, N.A., in *Nauka, tekhnologii, obrazovanie: Sbornik nauchnykh trudov Angarskogo gosudarstvennogo tekhnologicheskogo instituta* (Science, Technologies, Education: Coll. of Scientific Works, Angarsk State Technological Inst.), Angarsk, 2000, part 2, pp. 89–93.
10. Zanaveskin, L.N., Aver'yanov, V.A., and Treger, Yu.A., *Usp. Khim.*, 1996, vol. 65, no. 7, pp. 667–675.
11. Voronkov, M.G., Tatarova, L.A., Trofimova, K.S., and Verkhozina, E.I., *Khim. Inter. Ustoich. Razv.*, 2001, vol. 9, no. 3, pp. 393–403.
12. Korchevin, N.A., Turchaninova, L.P., Deryagina, E.N., and Voronkov, M.G., *Zh. Obshch. Khim.*, 1989, vol. 59, no. 8, pp. 1785–1787.
13. Bakaev, A.Ya. and Bushueva, N.B., *Ekol. Prom–st. Ross.*, 2005, no. 3, pp. 24–26.
14. Kel'tsev, N.V., *Osnovy adsorbtsionnoi tekhniki* (Fundamentals of Adsorption Technology), Moscow: Khimiya, 1984.
15. Helfferich, F., *Ion Exchange Kinetics, Ion Exchange. A Series of Advances*, Marinsky, J.A., Ed., New York: Dekker, 1966, vol. 1.
16. Adamson, A.W., *Physical Chemistry of Surfaces*, New York: Wiley, 1976.

ISSN 1070-4272, Russian Journal of Applied Chemistry, 2008, Vol. 81, No. 5, pp. 889–891. © Pleiades Publishing, Ltd., 2008.
Original Russian Text © L.A. Gladikova, V.V. Teterin, R.G. Freidlina, 2008, published in Zhurnal Prikladnoi Khimii, 2008, Vol. 81, No. 5, pp. 852–854.

BRIEF COMMUNICATIONS

Production of Magnesium Oxide from Solutions Formed by Acid Processing of Serpentinite

L. A. Gladikova, V. V. Teterin, and R. G. Freidlina

AVISMA Branch, VSMPO–AVISMA Corporation, Open Joint-Stock Company, Berezniki, Perm krai, Russia

Received June 20, 2007

Abstract—Possibility of obtaining magnesium oxide from sulfate, nitrate, and chloride solutions from acid processing of serpentinite and producing magnesium oxide suitable for manufacture of transformer steel was studied.

DOI: 10.1134/S1070427208050339

Recently, recovery of magnesium from silicate materials, e.g., serpentinite containing up to 38–43 wt % magnesium oxide, has been extensively studied. Magnesium is recovered from serpentinite by leaching with mineral acids (H_2SO_4, HNO_3, HCl) [1–4] to obtain the corresponding salts. The salt solutions formed by leaching are contaminated with impurities present in serpentinite: Fe(II), Mn(II), Cu(II), Ni(II), Co(II), Al(III), Cr(III), etc. After a reagent purification, the resulting solutions can be used to obtain pure salts of magnesium and magnesium hydroxide or oxide.

The aim of this study was to produce from serpentinite magnesium oxide satisfying the requirements to transformer steel production. Solutions prepared by leaching of serpentinite with mineral acids at 80–90°C for 3–4 h with a stoichiometric expenditure of an acid were used in the study. The compositions of the solutions obtained upon neutralization with brucite to pH 6–7 are listed in Table 1.

The technology used to obtain magnesium oxide from solutions includes the following stages: precipitation of magnesium hydroxide, filtration, washing of the $Mg(OH)_2$ paste, drying, and calcination of $Mg(OH)_2$ to MgO. Magnesium hydroxide was precipitated with aqueous ammonia. The results obtained in precipitation of magnesium hydroxide from $MgSO_4$ solutions are listed in Table 2.

The data obtained show that the filtration throughput becomes 2.5 times lower and the degree of magnesium precipitation decreases as the concentration of the magnesium sulfate solution increases. The precipitate was washed to remove ammonium sulfate with water at s : l = 1 : 20. The filtration throughput in washing was 0.28–0.06 $m^3 m^{-2} h^{-1}$. Magnesium hydroxide was dried at 100°C and calcined at 650°C for 2 h. The resulting magnesium oxide contained 83–87% MgO and failed to satisfy the technical requirements to magnesium oxide to be used in manufacture of transformer steel. Repeated washing of magnesium oxide at s : l = 1 : 20, followed by calcination at 650°C, yielded a product of the following composition (wt %): MgO 96.5, SO_4^{2-} 0.42, Ca not found. The sample did not satisfy the requirements imposed by the technical specification, either. Use of sodium hydroxide to obtain magnesium oxide from $MgSO_4$ solutions failed to produce positive results.

From a magnesium nitrate solution, magnesium hydroxide was precipitated with aqueous ammonia to pH ~9.2. In this case, the degree of magnesium precipitation was 87.5% After separating the precipitate (paste) of magnesium hydroxide, the solution contained (g dm^{-3}): Mg 10, Ca 4.4, and NH_4NO_3 168.9. The magnesium hydroxide paste was washed with water on a filter at s : l = 1 : 25, dried, and calcined at 500°C for 2 h. The resulting magnesium oxide contained (wt %): MgO 98.1, Fe 0.016, Cl 0.12, and CaO 0.12; calcination loss 0.72 wt %; citric number 40 s. Its properties failed to satisfy the requirements of the technical specification.

From chloride solutions (350 g dm^{-3} $MgCl_2$), magnesium was precipitated with aqueous ammonia whose expenditure was 100–200% relative to the

Table 1. Composition of solutions used to obtain magnesium oxide

Solution	Component concentration, g dm^{-3}								pH
	Mg	Ca	Fe	Mn	Cu	Ni	Co	Cr	
$MgSO_4$	45–65	0.01	0.040	0.03	0.0001	0.001	0.0003	0.0004	7.5
$Mg(NO_3)_2$	80	6.50	0.001	0.10	0.0001	0.020	0.0260	0.0010	5.7
$MgCl_2$	89	2.80	0.0008	0.02	0.0006	0.0002	0.0006	<0.0001	7.1

Table 2. Effect of the $MgSO_4$ solution concentration on precipitation parameters of magnesium hydroxide

Parameter	$MgSO_4$ concentration			
	224	291	314	323
Expenditure of 100% NH_3, g	69.3	90.0	97.0	100.0
Precipitation pH	10.5	10.6	10.7	10.5
Filtration throughput, $m^3\ m^{-2}\ h^{-1}$	4.48	2.07	2.02	1.79
Filtrate composition after separation of $Mg(OH)_2$, g dm^{-3}:				
Mg^{2+}	10.7	14.1	17.7	21.2
SO_4^{2-}	168.0	170.6	173.0	175.6
Degree of magnesium precipitation, %	76.4	76.0	72.1	67.5
Washing throughput, $m^3\ m^{-2}\ s^{-1}$	0.28	0.15	0.08	0.06
Calcination temperature, °C	650	650	650	650
Product composition, wt %				
MgO	87.2	87.7	85.1	83.6
CaO	<0.01	<0.01	<0.01	<0.01
SO_4^{2-}	2.0	3.6	3.8	9.5

Table 3. $Mg(OH)_2$ precipitation from chloride solutions with ammonium hydroxide

NH_4OH expenditure, % relative to stoichiometry	pH_{pr}	Concentration in filtrate, g dm^{-3}		Degree of magnesium precipitation, %
		$MgCl_2$	$CaCl_2$	
100	9.5	76.8	4.5	76
120	9.8	47.5	4.5	85
140	9.9	37.2	4.5	88
160	10.0	33.7	3.9	89
180	10.1	35.2	3.9	89
200	10.3	33.7	3.3	89

stoichiometry. The results of these experiments are listed in Table 3.

The experimental data show that the degree of magnesium precipitation is 76% at the stoichiometric ratio between the reagents, 89% at a 60% excess of ammonia, and further remains invariable because the precipitation of magnesium hydroxide is reversible and occurs under standard conditions to an equilibrium $MgCl_2$ concentration of about 35 g dm^{-3}.

Magnesium hydroxide was washed with hot (90°C) water at various s : l ratios, with the subsequent settling, decanting, and filtration of thickened slurry. The washed precipitate was dried at 150–200°C and calcined at 800°C. It was found that washing at s : l = 1 : 40 can reduce the content

Table 4. Effect of temperature T and duration τ of calcination on the quality of magnesium oxide

T, °C	τ, h	L, s	L_{av}, s
500	1	28	30
500	2	32	
600	1	39	41
600	2	43	
700	1	58	60
700	2	62	
750	1	78	80
750	2	82	
800	1	92	94
800	2	96	
900	1	106	108
900	2	110	

Table 5. Physicochemical parameters of a pilot batch of magnesium oxide

Parameter	Value
Content, wt %:	
MgO	98.8
CaO	<0.01
chlorides	0.03
iron (FeO)	0.05
carbon	0.6
Calcination loss, %	1.0
Bulk density, g cm^{-3}	0.27
Citric number, s	80

of chloride ions to 0.12%. Washing of magnesium oxide after calcination can reduce the content of Cl^- to 0.03%. The calcination temperature strongly affects the citric number L, which is an important parameter of magnesium oxide used in manufacture of transformer steel (Table 4).

It follows from Table 4 that the optimal calcination temperature is 750°C, with the corresponding citric number (80 s) satisfying the requirements of the technical specification. The granulometric composition of magnesium oxide obtained under the optimal conditions was determined by sedimentation analysis:

Fraction, μm	Content, %	Fraction, μm	Content, %
+40	3.4	–20 ± 10	9.5
–40 ± 30	5.4	–10 ± 5	18.1
–30 ± 20	11.7	–5	51.9

This method cannot precisely determine the <1-μm fraction. The technology we suggested was used to obtain a pilot batch of magnesium oxide (Table 5). Tests performed at Verkhnyaya Iset metallurgical plant demonstrated that this magnesium oxide can be used to manufacture transformer steel. The yield of class I metal was 75.2%, which compares well with the best commercial batches.

CONCLUSIONS

The studies and tests performed demonstrated that magnesium oxide suitable for manufacture of transformer steel can be produced from chloride solutions.

REFERENCES

1. Ficara, P., Chin, E., and Walker, T., *Can. Mining Metall. Bull.*, 1998, vol. 91, no. 1019, pp. 110–115.
2. RF Inventor's Certificate no. 2097322.
3. Gaprindashvili, V.N., *Kompleksnaya pererabotka serpentinitov* (Integrated Processing of Serpentinites), Tbilisi: Metsniereba, 1970.
4. Nazharova, L.N., Hydrochloric Acid Processing of Serpentinite, *Cand. Sci. Dissertation*, Kazan, 1999.

ISSN 1070-4272, Russian Journal of Applied Chemistry, 2008, Vol. 81, No. 5, pp. 892–895. © Pleiades Publishing, Ltd., 2008.
Original Russian Text © I.G. Antropova, D.L. Khaludorov, 2008, published in Zhurnal Prikladnoi Khimii, 2008, Vol. 81, No. 5, pp. 855–858.

BRIEF COMMUNICATIONS

Kinetics of Formation of Lead and Zinc Sulfides in Sulfiding Roasting in a Superheated Steam Atmosphere

I. G. Antropova and D. L. Khaludorov

Baikal Institute of Nature Management, Siberian Branch, Russian Academy of Sciences, Ulan-Ude, Buryatia, Russia

Received July 21, 2007

Abstract—The kinetics of the formation of sulfides in reactions of oxidized lead and zinc compounds with pyrite in a superheated steam atmosphere was studied. The dependences of the rate on the roasting duration at various temperatures were found, the kinetic parameters and modes of sulfide formation were determined, and the mechanism of the process was suggested.

DOI: 10.1134/S1070427208050340

One of effective approaches to the activation of oxygen-containing minerals for the further flotation is the sulfiding of difficult-to-concentrate minerals in the course of roasting in a superheated steam atmosphere. The purpose of sulfiding roasting is the conversion of the oxidized forms entering into the composition of the initial ore to readily floatable sulfide forms for the subsequent treatment according to the traditional manufacturing scheme. Furthermore, roasting in a steam atmosphere is accompanied by selective cracking of minerals, which considerably improves the further separation of valuable ore components.

Kinetic studies are necessary for intensifying industrial processes, i.e. they are of practical interest along with theoretical importance. Therefore, it is of interest to study topochemical reactions in the system oxidized lead compounds–sulfiding agent–steam. To calculate the degree of lead and zinc conversion from the oxidized forms to sulfide forms (degree of sulfiding), we used a procedure for separate determination of different forms of lead and zinc compounds in solid products [1]. The experimental data were treated by using classical differential and integral methods of determination of kinetic parameters of sulfiding processes.

EXPERIMENTAL

Lead and zinc in oxidized lead–zinc ores are presented mainly by cerussite and smithsonite (carbonates). Therefore, we used analytically pure grade lead and zinc carbonates as starting materials and pyrite (FeS_2) as a sulfiding agent. The reaction of carbonates with pyrite in a steam atmosphere was studied on a flow-type installation. The degree and rate of sulfiding were determined in an isothermal mode in the temperature range 400–700°C. The experimental technique was as follows. A furnace was heated to a preset temperature, after which steam was passed through the working area of the furnace and a boat with a mixture of carbonate and pyrite was arranged in it. Pyrite was taken in a small excess over the stoichiometry. The charge weight was 1 g, and the water flow rate, 50 ml h^{-1}. The phase compositions of the resulting solid products were determined on DRON-3 and D8 ADVANCE (Bruker AXS) X-ray diffractometers.

The dependences of the degree of sulfiding on the duration of roasting at various temperatures and the temperature dependences of the rate constants of the reactions of lead and zinc carbonates with pyrite in a steam atmosphere are qualitatively similar, but slightly differ quantitatively. Here we report the results of the kinetic study using lead carbonate sulfiding as an example. The X-ray analysis of reaction products (Table 1) shows that the primary stage of roasting in a steam atmosphere is the lead carbonate decomposition to the oxide. Pyrite dissociation occurs in parallel to form products which react with water to liberate hydrogen sulfide and a small amount of sulfur dioxide. In the temperature range 600–700°C, reaction products present a mixture of PbS, $Fe_{1-x}S$, Fe_3O_4, and γ-Fe_2O_3, with the content of lead compounds in the nonsulfide form being no higher than 2%.

The integral kinetic curves (Fig. 1a) show that the temperature strongly affects the degree of sulfiding. For example, the degree of the conversion of products of lead carbonate decomposition to the sulfide increases from 30% at 400°C to 90% at 500°C. No induction period is observed in the kinetic curves obtained in the range 500–700°C. The curves are not sigmoidal as would be typical of topochemical reactions in which products do not appear evenly on the whole surface of grains. High reactivity of lead carbonate caused by its high specific surface area is apparently responsible for atypical kinetic curves obtained in these experiments.

Using primary experimental data, we calculated the time dependences of the reaction rates at specified temperatures. The character of time variation of the process rate at various temperatures is the same, but the curves differ quantitatively (Fig. 1b). The rate maximum is reached within 5 min of roasting. The reaction rate first sharply increases, but then it abruptly decreases, which means that the formation, rise, and fusion of nuclei occur rather rapidly and, above all, at high degrees of conversion of the initial solid substances (except for 400°C). In the initial stage, the reaction occurs under the kinetic control (up to the maximal rate), and then it becomes controlled by the hydrogen sulfide diffusion through a lead sulfide layer to the PbO–PbS boundary. The parameters of the reaction rate maximum at various temperatures are given in Table 2.

We carried out the formal-kinetic analysis using commonly applied topochemical Erofeev–Kolmogorovs equation [2]:

$$\alpha = 1 - \exp(-kr^n), \quad (1)$$

where n is a constant depending on particular substance, the presence of initial reactions centers (at $r = 0$), the shapes of nuclei, and the number of intermediate stages of the formation of the initial centers.

The constants k and n in Eq. (1) are determined by plotting the experimental data in the coordinates $Y = \log[-\log(1 - \alpha)]$, $X = \log\tau$. The values of $\log[-\log(1 - \alpha)]$ as a function of $\log\tau$ at various temperatures are presented in Table 3. On the basis of these dependences we constructed the plots in which the experimental points were fairly well fitted by straight lines. This fact suggests that the process is described by topotaxic relationships and that the choice of the equation for the kinetics description was correct.

Table 1. Results of X-ray phase analysis of reaction products

T, °C	Compounds found
Initial sample	$PbCO_3$, FeS_2
400	PbO, PbS, FeS_2, γ-Fe_2O_3
500	PbS, FeS_2, $Fe_{1-x}S$, $PbSO_4$ (traces), PbO (traces), γ-Fe_2O_3
600	PbS, $Fe_{1-x}S$, Fe_3O_4, $PbSO_4$ (traces)
700	PbS, Fe_3O_4, γ-Fe_2O_3, $PbSO_4$ (traces)

Table 2. Parameters of the maximal rate of lead carbonate sulfiding (τ_{max} = 300 s)

T, °C	$W_{max} \times 10^4 = \Delta\alpha/\Delta\tau$	α_{max}
400	2.66	0.08
500	26.0	0.78
600	28.6	0.86
700	32.0	0.96

The rate constant of the process K (Table 4) can be found from known Sakovich's equation [3]

$$K = nk^{1/n}, \quad (2)$$

where K is the reaction rate constant depending on the nature of reacting substances and process con-

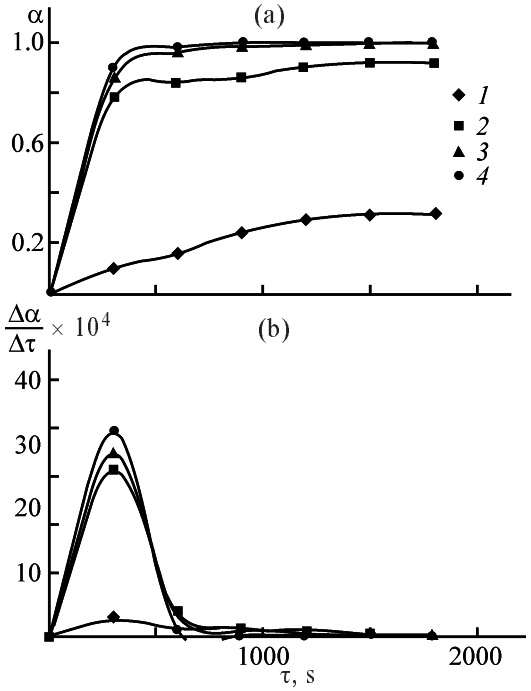


Fig. 1. Kinetic curves of the lead carbonate sulfiding by pyrite in the superheated steam atmosphere. (α) Conversion and (τ) time. Curves: (a) integral and (b) differential.

Table 3. Values of $\log[-\log(1-\alpha)]$ at various $\log\tau$ values

T, °C	$\log[-\log(1-\alpha)]$ at indicated $\log\tau$					
	2.48	2.78	2.95	3.08	3.18	3.26
400	–1.44	–1.26	–1.12	–1.06	–1.04	–1.01
500	–0.18	0	0.087	0.18	0.23	0.23
600	–0.068	0.145	0.23	0.30	0	0
700	0.145	0.30	0	0	0	0

Table 4. Results of treating kinetic data by Erofeev–Kolmogorov's equation (1)

T, °C	n	$\log k$	K
400	0.62	–2.59	0.000042
500	0.56	–1.14	0.0052
600	0.59	–1.06	0.0094
700	0.52	–0.74	0.0198

ditions; the value of the kinetic parameter $n < 1$ shows that the process under study (within the experiment boundaries) is diffusion-controlled.

Linearization of the known Eq. (3) of the activated complex theory [4] in the coordinates $y = \ln K/T$ and $x = 1/T$ gives the activation energy E of 199.89 kJ mol^{-1} in the temperature range 400–500°C and 25.45 kJ mol^{-1} at 500–700°C.

$$K = l(k_B T/h)e^{\Delta S/R}e^{-E/(RT)}. \quad (3)$$

All these facts confirm the above conclusions on the character of the sulfiding process. At the roasting temperature of 500°C and higher, the reaction is controlled by internal diffusion. The tendency to equalizing temperature in grains results in constant cracking of the initial mineral, which favors the formation of sulfides within the entire bulk of the grains. We carried out a qualitative analysis of the sulfur-containing off-gas by the standard procedures [5]. The off-gas was sequentially passed through two absorption vessels, one of which contained a $CuSO_4$ solution, and the other, an H_2O_2 solution. As a result of roasting carbonates with pyrite in a superheated steam atmosphere, the solution containing copper sulfate became black and turbid because of precipitation of copper sulfide by the reaction

$$H_2S + CuSO_4 = CuS\downarrow + H_2SO_4.$$

As a result of this reaction, owing to the formation of sulfuric acid, pH of the $CuSO_4$ solution decreased from 5 to 3. The presence of sulfur dioxide in the off-gas was determined by measuring the acidity of the solution containing H_2O_2 before and after the experiments. The pH of the medium changed from 6 to 5 owing to the occurrence of the reaction $SO_2 + H_2O_2 = H_2SO_4$. Thus, hydrogen sulfide and a small amount of sulfur dioxide are present in the gas.

Based on the above facts, we can present the following mechanism of the sulfiding of oxidized forms of lead and zinc. The thermal dissociation of iron disulfide is known to be accompanied by S^0 release according to the reaction

$$FeS_2 \rightarrow FeS + 1/2S_2.$$

Then, at temperatures higher than 400°C, the products of the iron disulfide dissociation, free sulfur and iron sulfide, react with superheated steam to form hydrogen sulfide:

$$3S + 2H_2O = 2H_2S + SO_2,$$

$$FeS + H_2O = FeO + H_2S.$$

The resulting FeO is metastable and is subsequently oxidized to Fe_3O_4. Therefore, when iron sulfide reacts with water, hydrogen sulfide in the gas phase prevails. The Gibbs energy calculations show that the sulfiding of oxidized lead and zinc compounds with hydrogen sulfide is thermodynamically the most probable in a heterogeneous process. On the whole, our experimental data on the sulfiding of oxidized lead and zinc compounds are in agreement with the thermodynamic calculations. The reactions of lead and zinc carbonates with iron sulfide in a superheated steam atmosphere with the formation of lead and zinc sulfides occur on the solid–gas, namely, MO–H_2S boundary.

CONCLUSIONS

(1) The kinetic features of the lead and zinc sulfiding in the reactions of oxidized lead and zinc compounds with iron sulfide in a steam atmosphere were determined. It was shown that lead and zinc sulfides are formed in the whole volume of particles.

(2) The reactions of oxidized lead and zinc compounds with iron sulfide in a superheated steam atmosphere to form sulfides occur on the solid–gas, namely, MO–H_2S boundary.

(3) Examination of the kinetic curves and parameters obtained shows that, at roasting temperatures lower than 500°C, the reaction is kinetically controlled, and after reaching the roasting temperature of 500°C it becomes controlled by internal diffusion.

REFERENCES

1. Fainberg, S.Yu., *Analiz rud tsevnykh metallov* (Analysis of Nonferrous Metal Ores), Moscow: Metallurgizdat, 1953, pp. 743–760.
2. Erofeev, B.V., *Dokl. Akad. Nauk SSSR*, 1946, vol. 11, no. 6, p. 515.
3. Sakovich, G.V., *Uchen. Zap. Tomsk. Univ.*, 1955, no. 26, pp. 103–107.
4. Rozovskii, A.Ya., *Kinetika topokhimicheskikh reaktsii* (Kinetics of Topochemical Reactions), Moscow: Khimiya, 1974.
5. Alekseev, V.N., *Kolichestvennyi analiz* (Quantitative Analysis), Moscow: Khimiya, 1972.

ISSN 1070-4272, Russian Journal of Applied Chemistry, 2008, Vol. 81, No. 5, pp. 896–898. © Pleiades Publishing, Ltd., 2008.
Original Russian Text © D.V. Shevelev, O.M. Vladenkova, 2008, published in Zhurnal Prikladnoi Khimii, 2008, Vol. 81, No. 5, pp. 859–861.

BRIEF COMMUNICATIONS

Effect of Catalyst Used for Chloromethylation of Styrene–Divinylbenzene Copolymer on the Service Characteristics of the Highly Basic Anion Exchanger Obtained

D. V. Shevelev and O. M. Vladenkova

Azot Kemerovo Joint-Stock Company, Kemerovo, Russia

Received October 2, 2007

Abstract—The possibility of replacing zinc chloride by a zinc-containing complex as a catalyst of chloromethylation of styrene–divinylbenzene copolymer was examined, and the effect of the catalyst on the service characteristics of the highly basic anion exchanger obtained was evaluated.

DOI: 10.1134/S1070427208050352

The main industrial procedure used today for producing anion-exchange resins is based on polymer-analogous transformations of styrene–divinylbenzene (DVB) copolymers of various modifications (gel, macroporous, isoporous), with introduction of ionogenic amino groups into the inert polymer [1].

Synthesis of an anion exchanger by this procedure involves two main steps of polymer-analogous transformations: chloromethylation and amination. The first step is decisive, because the extent of chloromethylation ultimately determines the properties of anion exchangers and, primarily, their most important characteristic, exchange capacity. Chloromethylation consists in direct replacement of a hydrogen atom by a chloromethyl group $-CH_2Cl$. In the synthesis of anion exchangers, the chloromethylation occurs at a carbon atoms of an aromatic ring of styrene–DVB copolymer [1]. In the second step, amination of chloromethylated styrene–DVB copolymer with approptiate amine, the chlorine atoms are replaced by amino groups. In the synthesis of strongly basic multifunctional anion exchanger AV-17, the amination is performed with trimethylamine, with the replacement of chlorine atoms by quaternary ammonium groups $-N^+(CH_3)_3\ Cl^-$ [1, 2].

Numerous procedures for chloromethylation of styrene–DVB copolymer under various conditions, using various catalysts and chloromethylating agents, have been reported [2–6]. The most widely used agent is monochlorodimethyl ether (MCDME) in which the styrene–DVB copolymer swells well, the catalyst dissolves, and the reaction rate is fairly high. The catalysts are aprotic Lewis acids used for performing Friedel–Crafts reactions: anhydrous $ZnCl_2$, $FeCl_3$, $AlCl_3$, $SnCl_4$, and $TiCl_4$ [3–6], with $ZnCl_2$ used most frequently.

In the production of a highly basic anion exchanger of the AV-17 type, the existing chloromethylation procedure with $ZnCl_2$ is imperfect because of high hygroscopicity of the catalyst. The use of $ZnCl_2$ containing 2–7 wt % water negatively affects quality of the desired product with respect to osmotic stability, because too vigorous reaction in some cases may lead to formation of cracks on the surface of anion exchanger granules.

We found that replacement of straight $ZnCl_2$ by a zinc-containing complex prepared from $ZnCl_2$ and MCDME provides more uniform course of the chloromethylation in time, which decreases the risk of cracking of ready anion exchanger granules:

$$CH_3OCH_2Cl + ZnCl_2 \rightarrow [CH_3OCH_2]^+ZnCl_3^-.$$

EXPERIMENTAL

With the aim to evaluate the advantages of the zinc-containing complex compared with the classical $ZnCl_2$ catalyst, we performed experiments on the synthesis of AV-17 resin with both catalysts and examined their effect on the service characteristics of AV-17 resin: osmotic stability, number of intact granules, amount of water required for washing, and mechanical strength.

To choose the optimal chloromethylation condi-

Table 1. Quality characteristics of AV-17 strongly basic anion exchanger prepared with a common catalyst and with the zinc-containing complex

Parameter	Prescribed by GOST (State Standard) 20 301–74 with revisions 1–5 for AV-17	Mean test results	
		series 1	series 2
External appearance	Pale yellow spherical granules	Meets	Meets
Grain-size distribution:			
grain size, mm	0.315–1.25	0.4–1.25	0.4–1.25
volume fraction of working fraction, %, no less than	95	98	98
effective grain size, mm, no more than	0.4–0.6	0.4–0.6	0.4–0.6
uniformity coefficient, no more than	1.7	1.4	1.4
Weight fraction of moisture, %	35–50	43.33	45.67
Total static exchange capacity, mg-equiv cm^{-3}	1.15	1.15	1.19
Equilibrium static exchange capacity, mg-equiv cm^{-3}	1.00	1.05	1.1
Dynamic exchange capacity, mg-equiv cm^{-3}	700	700	725
Filtrate oxidizability counting on oxygen, (mg O) dm^{-3}	0.55	0.15	0.15
Osmotic stability, %, no less than	92.5	98.6	100
Mechanical strength, g $granule^{-1}$	–	657	839

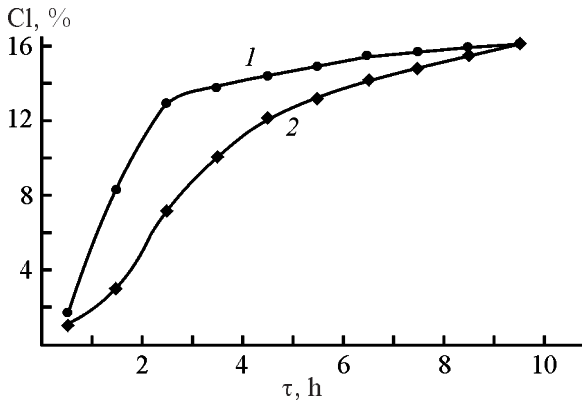
tions such as charge formulation, temperature, and process duration, the sample of the styrene–DVB copolymer was analyzed with respect to the main quality parameters: specific volume of limiting swelling in toluene (2.8 $cm^3 g^{-1}$ in 1 h 45 min) and MCDME (2.62 $cm^3 g^{-1}$ in 30 min) and content of the main fraction with the granule size of 0.25–0.8 mm (95.5%). A kinetic study of the chloromethylation of this copolymer with MCDME in the presence of $ZnCl_2$ and the zinc-containing complex showed that, in the latter case, the reaction occurred more uniformly from the first hour and up to attainment of the same final chlorine content of the chloromethylated copolymer (CMC) in both runs, 16%. This is particularly important for obtaining a strongly basic anion exchanger with high service characteristics (see figure).

On the basis of these data, we chose the optimal chloromethylation conditions and performed two series of experiments on the preparation of laboratory CMC samples: first, with $ZnCl_2$, and second, with the zinc-containing complex. Both samples were subjected to amination with the formation of AV-17 strongly basic anion exchanger. The mean quality parameters for each series of anion exchangers are given in Table 1.

We found that the technical anion exchanger prepared with the zinc-containing complex, owing to the more uniform chloromethylation course, exhibited higher levels of the mechanical strength, osmotic stability, total static exchange capacity, and dynamic exchange capacity.

To determine how the catalyst affects the specific consumption of water for washing the anion exchanger, we washed averaged samples of both series with H^+-cationized water, after their regeneration with sodium hydroxide, until the specific electrical conductivity of the filtrate reached 1.5 μS cm^{-1} (Table 2).

In washing of the anion exchanger sample of series 2, prepared with the zinc-containing complex,



Chlorine content of the chloromethylated copolymer as a function of time τ. Copolymer : MCDME weight ratio 1 : 2.4, catalyst : copolymer molar ratio 0.45 : 1.0, 45–50°C. Catalyst: (*1*) $ZnCl_2$ and (*2*) zinc-containing complex.

Table 2. Washing of AV-17 anion exchanger with H^+-cationized water after regeneration with NaOH (specific consumption of 100% NaOH 120 kg m^{-3})

Series	Specific electrical conductivity of filtrates, μS cm^{-1}, at indicated volume of H^+-cationized water, m^3 m^{-3}													
	before washing	6	7	8	9	10	11	12	13	14	15	20	30	40
1	3.40	4.18	2.62	2.46	1.95	1.91	1.75	1.61	1.60	1.35	1.41	1.40	1.4	1.4
2	3.41	2.9	2.5	2.0	1.6	1.5	1.4	1.4	1.4	1.4	1.4	1.4	1.2	1.1

the specific consumption of water for washing to the required pH value was lower than for series 1, 10 m^3 m^{-3} against 14, which is indicative of its better kinetic properties.

We prepared in the laboratory a batch of samples of AV-17 strongly basic anion exchanger from various samples of styrene–DVB copolymer, using the zinc-containing complex. All the samples met the requirements of GOST (State Standard) 20301–74 with revisions 1–5 with respect to all the quality parameters.[1]

CONCLUSIONS

(1) AV-17 anion exchanger prepared with the zinc-containing complex exhibits increased levels of the osmotic stability, mechanical strength, matrix permeability, and dynamic exchange capacity. It is better washed at the same consumption of the regenerating agent.

(2) An improved process was developed for the production of AV-17-8 highly basic anion exchanger, allowing production of the resin with improved kinetic and mechanical properties, in accordance with the more stringent requirements to the quality.

[1] With the aim to make the technical requirements to the quality of the Russian anion exchanger more stringent and to expand the assortment demanded by the market, the Azot Kemerovo Joint-Stock Company with the particilation of VTI Joint-Stock Company developed technical specification TU 2227-062-05761637–2006: Ion-Exchange Resins. AV-17-8 anion exchanger (with improved kinetic properties).

REFERENCES

1. Saldadze, K.M., Pashkov, A.B., and Titov, V.S., *Ionoobmennye vysokomolekulyarnye soedineniya* (Ion-Exchange Macromolecular Compounds), Moscow: Goskhimizdat, 1960.
2. Pokonova, Yu.V., *Galoidefiry: Sposoby polucheniya, svoistva, primenenie* (Halo Ethers: Preparation Procedures, Properties, Applications), Petrov, A.A., Ed., Moscow: Khimiya, 1966.
3. *Promyshlennye khlororganicheskie produkty: Spravochnik* (Commercial Organochlorine Products: Handbook), Oshin, L.L., Ed., Moscow: Khimiya, 1978.
4. Romanian Patent 55892, 1971.
5. GDR Patent 119799, 1975.
6. JPN Patent 56-39650, 1974.

ISSN 1070-4272, Russian Journal of Applied Chemistry, 2008, Vol. 81, No. 5, p. 899. © Pleiades Publishing, Ltd., 2008.
Original Russian Text © A.S. Lytkin, G.K. Ivakhnyuk, 2008, published in Zhurnal Prikladnoi Khimii, 2008, Vol. 81, No. 5, p. 862.

BRIEF COMMUNICATIONS

Paraffin Fractions as Additives to Diesel Fuels Increasing Their Cetane Number

A. S. Lytkin and G. K. Ivakhnyuk

St. Petersburg State University of Communications, St. Petersburg, Russia
St. Petersburg State Institute of Technology (Technical University), St. Petersburg, Russia

Received April 4, 2008

Abstract—Paraffins were purified by recrystallization. The extent to which the paraffin fractions C_{10}–C_{13}, C_{14}–C_{17}, and C_{18}–C_{23} increase the cetane numbers of summer and winter grades of Russian diesel fuel was examined. The cetane numbers of the initial diesel fuels and those with additions of paraffin fractions were determined on an IDT-69 installation by the method of flash coincidence.

DOI: 10.1134/S1070427208050364

In this study we examined the effect exerted by the C_{10}–C_{13}, C_{14}–C_{17}, and C_{18}–C_{23} paraffin fractions on the main characteristics of diesel fuel (DF). The required samples of Russian commercial diesel fuels (winter, DTZ-0.2minus35[1]; summer, DTL-0.2-62) and fractions of liquid petroleum paraffins were obtained from the Kirishi Oil Refinery. Preliminary experimental studies were performed on samples of commercial DFs purchased from St. Petersburg filling stations. Fractions of liquid petroleum paraffins were additionally purified by recrystallization to remove aromatic compounds.

To remove arenes from the C_{18}–C_{23} fraction, we used urea dewaxing, recrystallization from acetone, and acid–alkali treatment followed by urea dewaxing. The degree of arene removal from the paraffin fraction was monitored by measuring n_D^{20} [1] and by comparing its value after the purification with the tabulated value [2]. Recrystallization proved to be the most efficient purification method. The cloud and congelation points of DFs were determined by standard procedures [3]. As a cooling agent we used a mixture of acetone and solid CO_2.

The cetane numbers (CNs) of the initial DF samples and those with additions of paraffin fractions were determined in accordance with GOST (State Standard) 3122, by the method of flash coincidence on an IDT-69 installation. The CNs of the initial DF samples (both winter and summer) were 48. Samples were tested at the KINEF Limited Liability Company and in laboratories of the St. Petersburg State Institute of Technology.

[1] Congelation point below –35°C.

Cetane numbers of DF samples with paraffin additives*

Diesel fuel	Additive, wt %	CN
DTL-0.2-62	C_{10}–C_{13}, 3	50
	C_{14}–C_{17}, 3	53
DTZ-0.2minus35	C_{10}–C_{13}, 3	49
	C_{14}–C_{17}, 3	51
	C_{10}–C_{13}, 5	52
	C_{14}–C_{17}, 5	53

* CN was determined by the motor method (GOST 3122–67).

We found that the paraffin fractions studied are fairly effective CN-increasing additives to diesel fuels even in concentrations of 3.0–5.0 wt %, at which the CN number increases by 1 to 5 points (see table), in conformity with the modern requirements [4, 5].

With respect to the cloud and congelation points, the examined samples of the summer and winter DFs with paraffin-containing high-cetane additives also meet the requirements prescribed by GOST 305–82.

REFERENCES

1. Pereverzev, A.N., Bogdanov, N.F., and Roshchin, Yu.N., *Proizvodstvo parafinov* (Production of Paraffins), Moscow: Khimiya, 1973, p. 224.
2. *Khimiya nefti i gaza* (Oil and Gas Chemistry), Proskuryakov, V.A., Ed., Leningrad: Khimiya, 1995, p. 445.
3. Papok, K.K., *Khimmotologiya topliv i smazochnykh masel* (Chemmotology of Fuels and Lubricating Oils), Moscow: Voenizdat, 1987.
4. Mitusova, T.N., *Neftekhim. Neftepererab.*, 2000, no. 1, pp. 19–21.

ISSN 1070-4272, Russian Journal of Applied Chemistry, 2008, Vol. 81, No. 5, p. 900. © Pleiades Publishing, Ltd., 2008.
Original Russian Text © D.P. Khrustalev, A.A. Suleimenova, S.D. Fazylov, 2008, published in Zhurnal Prikladnoi Khimii, 2008, Vol. 81, No. 5, p. 863.

BRIEF COMMUNICATIONS

Synthesis of 2-Amino-4-phenylthiazole under Conditions of Microwave Irradiation

D. P. Khrustalev, A. A. Suleimenova, and S. D. Fazylov

Institute of Organic Synthesis and Coal Fuel Chemistry of the Kazakhstan Republic, Limited Liability Company, Karaganda, Kazakhstan

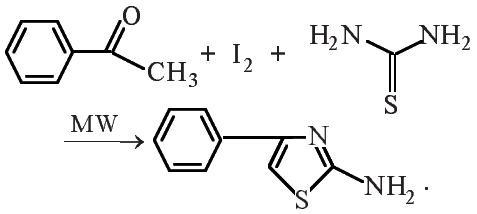
Received July 11, 2007

Abstract—The possibility of preparing 2-amino-4-phenylthiazole from acetophenone, iodine, and thiourea under the conditions of microwave irradiation was studied.

DOI: 10.1134/S1070427208050376

2-Amino-4-phenylthiazole derivatives exhibit high biological activity [1–3]. Published methods for preparing 2-amino-4-phenylthiazole are time-consuming and involve the use of highly toxic solvents [4, 5]. Therefore, the development of new synthetic routes to thiazole derivatives is of practical interest.

Here we suggest a new procedure for preparing 2-amino-4-phenylthiazole in a high yield:



We found that microwave irradiation allows the reaction time to be considerably shortened (by a factor of 280) compared to the traditional process and ensures the product yield as high as 92%.

We performed an independent synthesis of 2-amino-4-phenylthiazole (yield 94%) by the procedure described in [4]. Comparison of the melting points and IR spectra of the samples proved full identity of the substances obtained by the traditional procedure and under the conditions of microwave activation.

EXPERIMENTAL

A beaker flask made of heat-resistant glass was charged with a mixture of 7.2 g (0.06 mol) of acetophenone, 9.13 g (0.12 mol) of thiourea, and 15.23 g (0.06 mol) of iodine. The mixture was thoroughly stirred, loosely closed with a glass lid, and placed in a microwave oven at a radiator power of 70 W. The vessel was radiated for five 1-min periods with 30-s pauses. After that, 100 ml of water was added, and the mixture was heated at a power of 150 W for 5–7 min until the precipitate dissolved. Then the resulting yellow solution was decanted from a tarry liquid formed on the flask bottom and was filtered to separate a small amount of sulfur. After cooling, the filtrate was alkalized with aqueous ammonia to a weakly alkaline reaction. The precipitate formed in the process was filtered off on a glass frit, recrystallized from ethanol, and washed with diethyl ether. Yield of the crude product 92%, mp 148–149°C. IR spectrum, ν, cm^{-1}: 3420, 3240 (NH_2, two bands); 3170 (CH of C_3HNS); 3100 (CH of C_6H_5); 420, 1500, 1575 (C=C of C_6H_5); 1460 (C=N).

Found, %: C 61.45, H 4.47, N 15.55.
$C_9H_8N_2S$. Calculated, %: C 61.34, H 4.58, N 15.90.

The IR spectra were recorded on a UR-20 spectrophotometer (pellets).

CONCLUSIONS

(1) 2-Amino-4-phenylthiazole was prepared in a >90% yield by condensation of acetophenone with thiourea in the presence of iodine under the conditions of microwave irradiation.

(2) The reaction time is 280 times shorter compared to the traditional procedure.

REFERENCES

1. US Patent Appl. 20 040 077 697.
2. US Patent 7 196 104.
3. US Patent 4 847 274.
4. *Organic Reactions*, Adams, R., Ed., New York: Wiley, 1944, vol. 6.
5. Vul'fson, N.S., *Preparativnaya organicheskaya khimiya* (Preparative Organic Chemistry), Moscow: Khimiya, 1964.

ISSN 1070-4272, Russian Journal of Applied Chemistry, 2008, Vol. 81, No. 5, pp. 901–903. © Pleiades Publishing, Ltd., 2008.
Original Russian Text © V.V. Kotova, V.Z. Maslosh, T.M. Pekhtereva, A.Yu. Chervinskii, 2008, published in Zhurnal Prikladnoi Khimii, 2008, Vol. 81, No. 5, pp. 864–866.

BRIEF COMMUNICATIONS

Hantzsch Reaction in Urea–Formaldehyde Resins

V. V. Kotova, V. Z. Maslosh, T. M. Pekhtereva, and A. Yu. Chervinskii

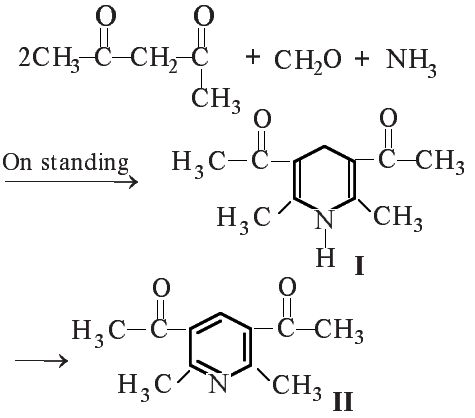
Institute of Physical Organic and Coal Fuel Chemistry, National Academy of Sciences of Ukraine, Donetsk, Ukraine
Evroplast Private Enterprise, Rubezhnoe, Lugansk oblast, Ukraine

Received August 23, 2007

Abstract—The effect of acetylacetone and ammonia in urea–formaldehyde resins on the reactions occurring in their presence was examined. The formation of 2,6-dimethyl-3,5-diacetyl-1,4-dihydropyridine in urea–formaldehyde resins was confirmed by ^{1}H NMR spectroscopy.

DOI: 10.1134/S1070427208050388

Structural studies of urea–formaldehyde (UF) resins and reduction of their free formaldehyde content are urgent problems [1–3]. Various additives and procedures decreasing the concentration of free formaldehyde have been reported. One of efficient methods is addition of β-diketones. Previously [4] we reported on a possible way to decrease the concentration of free formaldehyde in UF resin by adding acetylacetone and ammonia which enter into the Hantzsch reaction with formaldehyde:



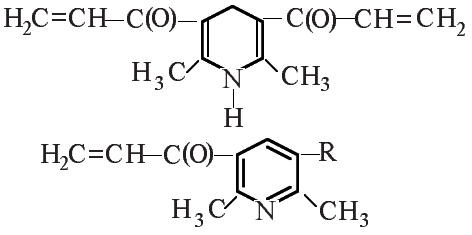
In this study we examined the mechanism of the Hantzsch reaction in UF resins by ^{1}H NMR spectroscopy.

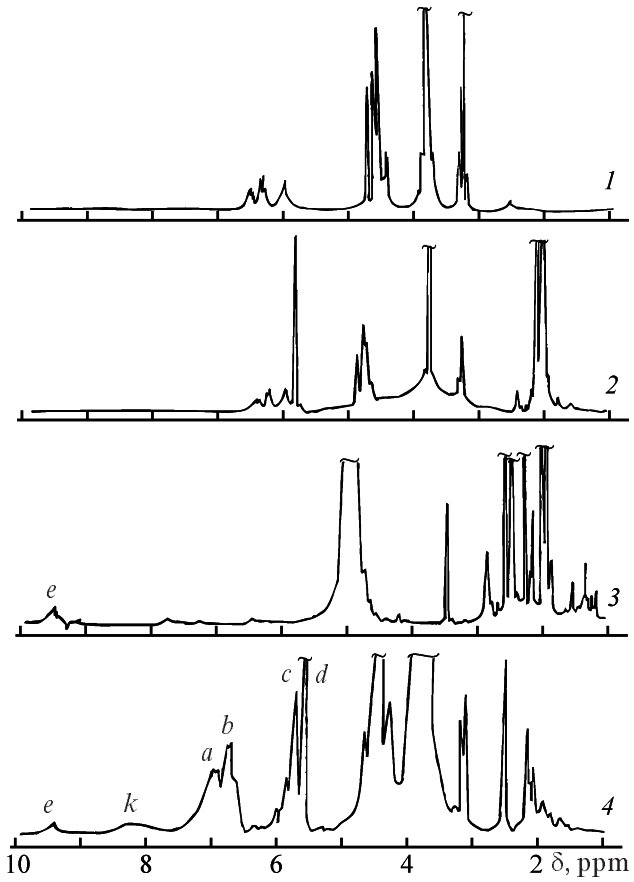
EXPERIMENTAL

Additives were introduced in amounts corresponding to the free formaldehyde content of UF resin [4]. The ^{1}H NMR spectra were recorded on a Gemini-200 spectrometer operating at 200 MHz in DMSO-d_6, reference TMS, 298 K. UF resin of the KF-MTS-15 brand [TU (Technical Specification) U-3,50-14 308 351-055–95 with revision 1] was used.

The reaction of acetylacetone and ammonia with formaldehyde, performed according to [5], yields 2,6-dimethyl-3,5-diacetyl-1,4-dihydropyridine **I**. According to published data [6, 7], in such compounds the chemical shift of the NH proton varies within 8.2–9.6 ppm depending on solvent, pH, and substituents. In the ^{1}H NMR spectrum of the reaction mixture, recorded 10 min after starting the reaction, there is a broadened NH signal at δ 9.4 ppm. Proton signals of the starting compounds (ketone, enol, formaldehyde) disappear (see figure, spectrum *2*). After 24 h, the NH proton signal disappears, and a signal appears at 7.4 ppm, which corresponds to the CH proton in the pyridine ring (compound **II**). These data show that, at pH > 7, the reaction occurs via 2,6-dimethyl-3,5-diacetyl-1,4-dihydropyridine.

As the reaction occurs in an alkaline solution, addition of formaldehyde to the OH group of the enol form of acetylacetone can be ruled out. Signals that could correspond to the CH protons at the double bond are absent. Compound **I** can subsequently react with formaldehyde to form substituted vinyl ketones [8]:





^{1}H NMR spectra. (δ) Chemical shift. (*1*) Aqueous formaldehyde solution (δ_{CH_3} 3.1–3.4, δ_{CH_2} 4.5–4.8, δ_{OH} 5.8–6.6 ppm); (*2*) mixture of acetylacetone and Formalin (acetylacetone occurs in DMSO-d_6 solution in keto and enol forms, δ_{CH_2} 3.8, δ_{CH} 5.8 ppm); (*3*) model composition (acetylacetone + Formalin + ammonia), 10 min after mixing (signal *e*, δ 9.4 ppm, corresponds to 2,6-dimethyl-3,5-diacetyl-1,4-dihydropyridine); and (*4*) UF resin with addition of acetylacetone and ammonia, 10 min after mixing (δ_{NH} 7.3–8.5 ppm, signal *k* corresponds to UF resin that has reacted with compound **I** or **II**).

In the ^{1}H NMR spectrum of the reaction mixture, we did not observe a multiplet that could correspond to CH_2=CH protons at a nonconjugated double bond (4.5–6.5 ppm) (see figure, spectrum *3*). Unfortunately, in the ^{1}H NMR spectra of the modified resin this region is obscured by the CH_2 and NH protons of the resin (see figure, spectrum *4*).

The ^{1}H NMR spectrum of the UF resin without modifying additives is fully consistent with the spectra given in [9]. In the range 4–7 ppm, it contains partially resolved signals of the NH groups in monomethylolurea, dimethylolurea, and oligomeric chains (range 6.2–7.3 ppm), and also of the NH_2 groups in oligomers and free urea (5.4–6.0 ppm).

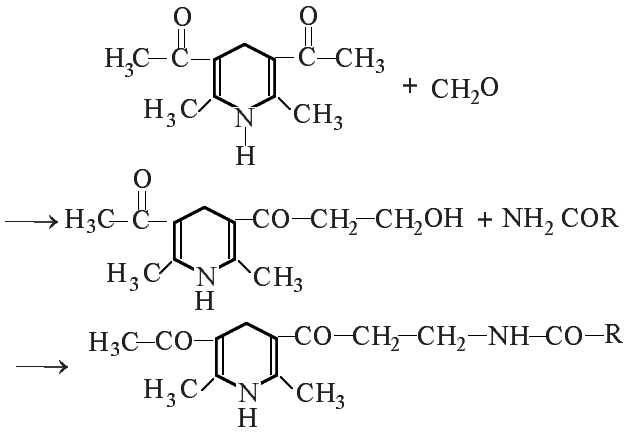
Relative content of NH_2 and NH fragments, according to ^{1}H NMR data

Range of δ, ppm	Structural fragment*	Relative content at indicated τ, min	
		10	40
5.4–6.0	NH_2 (*d*/*c*)	0.75	0.50
6.2–7.3	NH (*b*/*a*)	1.0	1.75
7.3–8.8	NH (*k*/*a* + *b*)	0.16	0.32

* (*d*) NH_2 group in free urea, (*c*) NH_2 group in oligomers, (*b*) NH group in oligomers, (*a*) NH group in monomethylolurea and dimethylolurea, and (*k*) NH group in components of the composition obtained by reaction with compound **I** or **II**. The designations are similar to those made in [9].

On introducing modifying additives (acetylacetone, ammonia) into the resin (see figure, spectrum *4*), a proton signal at δ 9.4 ppm, characteristic of the NH group of the dihydropyridine proton, and signals of methylene protons with the chemical shifts coinciding with those of the corresponding protons in the model compound (see figure, spectrum *3*) appear in the ^{1}H NMR spectrum. This fact confirms that the processes occurring in the modified resin are identical to the above-described reaction.

The table shows that the intensity of the signals from NH_2 and NH protons in oligomeric chains in the modified resin increases with time. Furthermore, chain lengthening in reactions of **I** or **II** with components of the composition is possible:



A downfield shift of the NH signal (δ_{NH} 7.3–8.8 ppm) is possible owing to a decrease in the electron density on the NH group under the influence of the electron-withdrawing C(O) group.

The signals of CH_3 groups observed in the region of methylol proton signals, as judged from the dis-

appearance of the CH_2 and CH signals of the starting formaldehyde and acetylacetone, should be assigned to products of the above reactions (see figure, spectra *3*, *4*).

CONCLUSIONS

(1) The Hantzsch reaction performed in urea–formaldehyde resin initially yields 2,6-dimethyl-3,5-diacetyl-1,4-dihydropyridine.

(2) Compounds containing vinyl fragments were not detected in the model reaction.

(3) 2,6-Dimethyl-3,5-diacetyl-1,4-dihydropyridine and pyridine derivatives, formed in urea–formaldehyde resin in the presence of additives (acetylacetone and ammonia), can undergo chain lengthening.

REFERENCES

1. Slonim, I.Ya., Alekseeva, S.G., Urman, Ya.G., et al., *Vysokomol. Soedin., Ser. A*, 1978, vol. 20, no. 7, pp. 1477–1485.
2. Slonim, I.Ya., Alekseeva, S.G., Urman, Ya.G., et al., *Vysokomol. Soedin., Ser. A*, 1978, vol. 20, no. 10, pp. 2286–2292.
3. Fedorchenko, S.V., Kurt, S.A., and Khaber, M.V., *Vopr. Khim. Khim. Tekhnol.*, 2002, no. 6, pp. 179–183.
4. Maslosh, V.Z., Kotova, V.V., and Maslosh, O.V., *Zh. Prikl. Khim.*, 2002, vol. 75, no. 8, pp. 1396–1397.
5. Surrey, A.R., *Name Reactions in Organic Chemistry*, New York: Academic, 1961.
6. Pouchert, C.J., *The Aldrich Library of NMP Spectra*, Aldrich, 1983, 1st ed., vol. 1, p. 418D.
7. Krivokolysko, S.G., D'yachenko, V.D., Chernega, A.N., and Litvinov, V.P., *Izv. Ross. Akad. Nauk, Ser. Khim.*, 2000, no. 4, pp. 733–736.
8. *Entsiklopediya polimerov* (Polymer Encyclopedia), Kargin, V.A., Ed., Moscow: Sov. Entsiklopediya, 1972, vol. 1, p. 411.
9. Slonim, I.Ya. and Urman, Ya.G., *YaMR-spektroskopiya geterogennykh polimerov* (NMR Spectroscopy of Heterogeneous Polymers), Moscow: Khimiya, 1982.

ISSN 1070-4272, Russian Journal of Applied Chemistry, 2008, Vol. 81, No. 5, pp. 904–905. © Pleiades Publishing, Ltd., 2008.
Original Russian Text © D.S. Ruzanov, A.I. Fisher, A.V. Eremin, V.G. Antonov, O.S. Fedorova, M.A. Stepanova, A.N. Belyaev, and S.A. Simanova, 2008, published in Zhurnal Prikladnoi Khimii, 2008, Vol. 81, No. 5, pp. 867–868.

BRIEF COMMUNICATIONS

Catalytic Properties of Oligonuclear Cobalt Acetate Complexes in Oxidation of Glutathione with Hydrogen Peroxide

D. S. Ruzanov, A. I. Fisher, A. V. Eremin, V. G. Antonov, O. S. Fedorova, M. A. Stepanova, A. N. Belyaev, and S. A. Simanova

St. Petersburg State Institute of Technology (Technical University), St. Petersburg, Russia
Kirov Military Medical Academy, St. Petersburg, Russia
Institute of Human Brain, Russian Academy of Sciences, St. Petersburg, Russia

Received April 8, 2008

Abstract—Catalytic activity of oligonuclear cobalt(III) and cobalt(II, III) oxoacetate complexes in homogeneous oxidation of glutathione with hydrogen peroxide was studied.

DOI: 10.1134/S107042720805039X

Commercial preparations based on oxidized glutathione (γ-glutamylcysteinylglycine, GSH), GSSG, are produced by GSH oxidation catalyzed by *cis*-$[Pt(NH_3)_2Cl_2]$ [1, 2]. High cost and potential renal toxicity of platinum compounds make urgent replacement of *cis*-$[Pt(NH_3)_2Cl_2]$ by another catalyst.

In addition, peptides with thiol groups can be oxidized not only to disulfides but also to sulfenic (R–SOH), sulfinic (R–SO_2H), and sulfonic (R–SO_3H) acids [3]. Therefore, a search for selective catalysts of mild oxidation of thiols to disulfides is of interest.

In this study we examined catalytic oxidation of GSH with hydrogen peroxide by high-performance liquid chromatography (HPLC). Oligonuclear cobalt(III) and cobalt(II, III) oxoacetate complexes $[Co_3^{III}(\mu_3\text{-}O)(\mu\text{-}O_2CCH_3)_6(H_2O)_3]NO_3 \cdot CH_3COOH$ **(I)** and $[Co_4^{II}Co_3^{III}(\mu_4\text{-}O)(\mu_3\text{-}OCH_3)_4(\mu\text{-}O_2CCH_3)_6 \cdot (H_2O)_8]F_2 \cdot 12H_2O$ **(II)** in trace amounts (10^{-9} M) were examined as catalysts of mild selective oxidation to compounds containing the –S–S group (GSSG).

The choice of these catalysts is governed by the fact that polynuclear cobalt oxoacetate complexes can effectively transfer electron and hydroperoxy radicals in oxidation of organic compounds [4].

Complexes **I** and **II** were prepared by treatment of "cobalt(III) acetate" with glacial acetic acid in the presence of nitrate ion (complex **I**) [5] or with acetone–methanol mixture in the presence of fluoride ions (complex **II**) [6].

The reaction course was monitored by high-performance liquid chromatography (HPLC) on a Gilson chromatograph (France). We used a 4.6 × 250-mm Lichrospher 100-rp-18 column (Taiwan, China), a UV-220 detector, and 0.1% trifluoroacetic acid + 2% acetonitrile as the mobile phase. The flow rate was 1.50–2.50 ml min^{-1}; the injected sample volume was 10 μl.

A model system containing 2 mg ml^{-1} GSH (1.3×10^{-4} M), equimolar amount of sodium hydroxide, and half amount of hydrogen peroxide was used to study the oxidation kinetics. The total volume of the system was brought to 20 ml with double-distilled water. The resulting solutions contained 1.7×10^{-7} M catalyst (DSH/catalyst molar ratio 1000).

The time reading started after adding an aliquot of the oxidizing agent (H_2O_2 solution) to the system. Then, the samples of the solution were taken and analyzed by HPLC. The content of oxidized GSH was determined from the chromatogram of a standard GSSG solution. The reaction systems were thermostatically controlled at 22±1°C with stirring. GSH was oxidized at pH 5.0–5.1.

According to HPLC data, the only product of catalytic oxidation of GSH is the hexapeptide with the –S–S– bridge (GSSG), with the catalytic activity of complexes **I** and **II** being similar.

Since complexes **I** and **II** are highly active catalysts of selective oxidation of GSH, these com-

pounds can be used instead of expensive catalyst, *cis*-$[Pt(NH_3)_2Cl_2]$.

ACKNOWLEDGMENTS

This study was financially supported by Departmental Target Program "Development of the Scientific Potential of Higher School" (RNP.2.1.11277).

REFERENCES

1. Krutetskaya, Z.I., Lebedev, O.E., Kurilova, L.S., et al., *Dokl. Ross. Akad. Nauk*, 2007, vol. 412, no. 5, pp. 1–4.
2. Filomeni, G., Rotilio G., and Ciriolo, M.R., *Biochem. Pharmacol.*, 2002, vol. 64, pp. 1057–1064.
3. Smirnova, G.V. and Oktyabr'skii, O.N., *Biokhimiya*, 2005, vol. 70, no. 11, p. 1459.
4. Saha, B. and Espenson, J.H., *J. Mol. Catal. A*, 2007, vol. 271, nos. 1–2, p. 1.
5. Ruzanov, D.S., Fisher, A.I., Gorlov, M.Yu., et al., Abstracts of Papers, *V Vserossiiskaya konferentsiya po khimii klasterov i poliyadernykh kompleksov* (V All-Russian Conf. on Chemistry of Clusters and Polynuclear Complexes), Astrakhan, 2006, p. P78.
6. Fisher, A.I., Ruzanov, D.S., Gorlov, M.Yu., et al., *Koord. Khim.*, 2007, vol. 33, no. 11, pp. 803–806.

ISSN 1070-4272, Russian Journal of Applied Chemistry, 2008, Vol. 81, No. 5, pp. 906–908. © Pleiades Publishing, Ltd., 2008.
Original Russian Text © O.T. Torebekov, T.K. Dzhumadilov, E.A. Bekturov, 2008, published in Zhurnal Prikladnoi Khimii, 2008, Vol. 81, No. 5, pp. 869–871.

BRIEF COMMUNICATIONS

Molecular Complexes of Polyethylene Glycol (MW 15000) with Sodium Tetraphenylborate in Aprotic Solvents

O. T. Torebekov, T. K. Dzhumadilov, and E. A. Bekturov

Bekturov Institute for Chemical Research, Ministry of Education and Science of Kazakhstan Republic, Almaty, Kazakhstan

Received March 23, 2007

Abstract—The melting point and crystallinity of molecular complexes are studied in aprotic solvents in relation to the solvent donor number.

DOI: 10.1134/S1070427208050406

It is well known that, in chemical reactions in solutions, a solvent is not only a medium, but also a reagent. The contribution of a solvent is complex. Basic parameters characterizing properties of solvents are the dielectric constant, dipole moment, donor–acceptor power, etc. However, Fialkov et al. [1] have pointed out that, in complexation, the key factor is the specific character of solvation of ions rather than the dielectric constant of a solvent.

Donor–acceptor properties of solvents characterize their chemical activity responsible for the solvent effect on reactions in solutions. In this respect, it was interesting to study the solvent effect on structure and phase formation of complexes of polyethers with low-molecular-weight salts and their properties.

Previously we examined the solvent effect on these systems for several aprotic solvents using optical microscopy and X-ray diffraction analysis.

In this work, we studied the structure and composition of complexes polyethylene glycol–sodium tetraphenylborate in one more aprotic solvent, dimethyl sulfoxide (DMSO), and discussed the results obtained for a series of aprotic solvents.

EXPERIMENTAL

Sodium tetraphenylborate $NaB(C_6H_5)_4$ (analytically pure grade) was dried prior to use. Polyethylene glycol (PEG) (MW 15000) (Schuchardt, Germany) was dried in a low vacuum. DMSO was purified using the standard procedure [2].

The complexes were synthesized by mixing solutions of individual components under ambient conditions. The solvent was removed in a vacuum at room temperature. Then, samples were vacuum-dried to constant weight at 303–308 K for several days.

The melting points of the starting components and their molecular complexes were determined on a Boetius optical microscope (Rapido, Germany) at a magnification of 16.

Large-angle X-ray diffraction patterns were obtained on a DRON-3 instrument with CuK_α radiation (35 kV, 20 mA).

Based on the X-ray diffraction data, a structural diagram for the system PEG–$NaBPh_4$ was obtained, which consists of five sections (Fig. 1). Curves *1* and *2* show the correspond to $NaBPh_4$ and PEG.

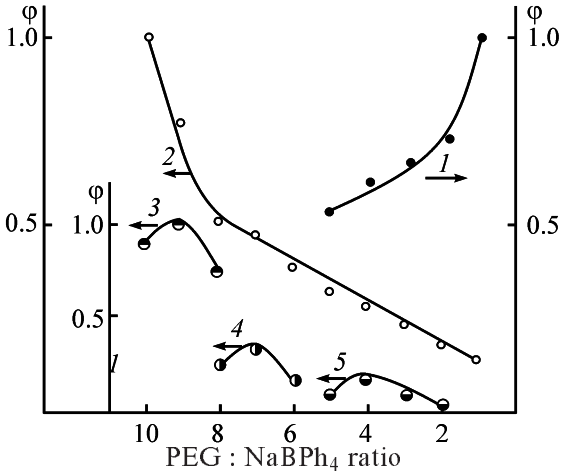


Fig. 1. Structural diagram of the system PEG–$NaBPh_4$ in DMSO: (*1*) $NaBPh_4$, (*2*) PEG, and (*3–5*) molecular complex.

The intensity of the peaks of crystalline PEG strongly decreases with increasing content of the second component, and at a component ratio of 1 : 1 these peaks disappear. The reflecitons of the crystalline salt alst decrease and at a PEG : $NaBPh_4$ ratio of 6 : 1 are not observed. Curves *3*–*5* correspond to molecular complexes. The interplanar spacings *d* (Å) of the complexes are as follows: 11.32, 7.36, 6.41, 5.60, 4.79, 4.69, 3.94, 3.70, and 3.08 (curve *3*); 6.80, 4.79, 4.69, and 3.53 (curve *4*); and 7.36, 6.41, 4.69, and 3.53 (curve *5*). As seen from Fig. 1, these curves pass through a maximum, being broken at certain component ratios. The maxima in the curves φ–(PEG : $NaBPh_4$) suggest the formation of stoichiometric molecular complexes.

The phase diagram built on the basis of the melting point data for the system PEG (MW 15000)–$NaBPh_4$ is presented in Fig. 2. The melting points of the complexes strongly differ from those of the individual components, suggesting complexation. The phase diagram contains a distectic point at a component ratio of 4 : 1 (mp 490 K) and two peritectic points at component ratios of 9 : 1 (mp 406 K) and 7 : 1 (mp 460 K). An eutectic point is observed at a component ratio of 15 : 1 (mp 328 K). For PEG, the melting point is 338 K.

The liquidus curve and the solidus lines divide the phase diagram into eight regions. Region *1* above the liquidus curve $T_{PEG}EP_1P_2M$ corresponds to a liquid phase. The other regions contain two phases (liquid and solid) each. In the region of melts from T_{PEG} to point *E*, the liquid phase coexists with PEG crystals (region *2*). The liquid phase coexists with crystals of compound MC_1 (region *3*). If a straight horizontal line is drawn from point *E* to the vertical straight line drawn through point P_1, the region of existence of PEG and MC_1 crystals is found below it (region *4*). If a horizontal line is drawn from point P_1 to the vertical line drawn through point P_2, in the region below this line (region *6*), two solid phases (MC_1 and MC_2) coexist. Along curve P_1P_2, molecular complex MC_2 crystallizes, and the crystals of MC_1 dissolve (region *5*). In this region, a liquid coexists with MC_2 crystals. If a straight horizontal line is drawn from point P_2 to a vertical line drawn through point *M*, in the region below this line, MC_2 and MC_3 crystals coexist (region *8*). In the region below curve P_2M (region *7*), a liquid coexists with a mixture of MC_2 and PEG crystals. In point *M*, a carbonized product starts to form. Then, starting from the 3 : 1 ratio to the 1 : 1 ratio, the melting point decreases. Below this curve, a liquid coexists with MC_3 crystals.

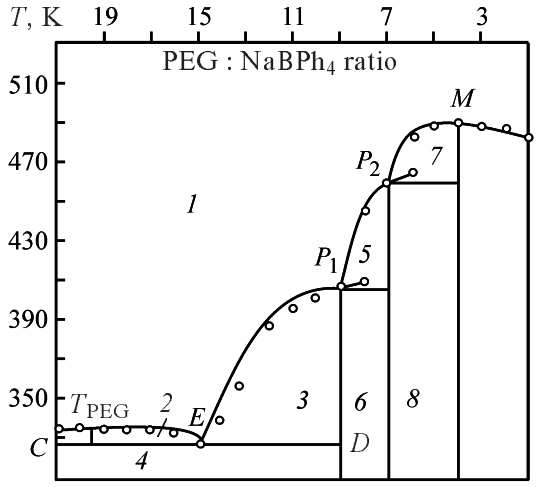


Fig. 2. Phase diagram of the system PEG (MW 15000)–$NaBPh_4$ in DMSO. (*T*) Temperature, (*M*) distectic point, (P_1, P_2) peritectic points, and (*E*) eutectic point; the same for Fig. 3.

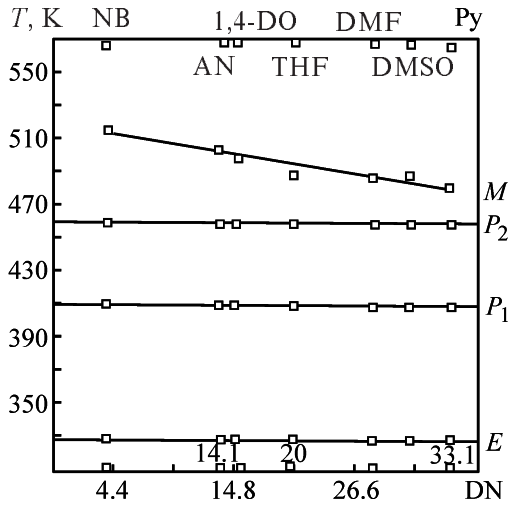


Fig. 3. Melting point *T* of molecular complexes in the system PEG (MW 15000)–$NaBPh_4$ as a function of the donor number DN of aprotic solvents.

The compositions obtained for the complexes from the structural data [9 : 1 (MC_1), 7 : 1 (MC_2), and 4 : 1 (MC_3)] are well consistent with those obtained from the phase diagram.

Complexes MC_1 (mp 406 K) and MC_2 (mp 460 K) melt incongruently. They are characterized by peritectic points P_1 and P_2. Complex MC_3 melts congruently, i.e., a distectic maximum *M* is observed.

Finally, combination of the X-ray diffraction and optical microscopic data reveals that three different molecular complexes are formed in DMSO.

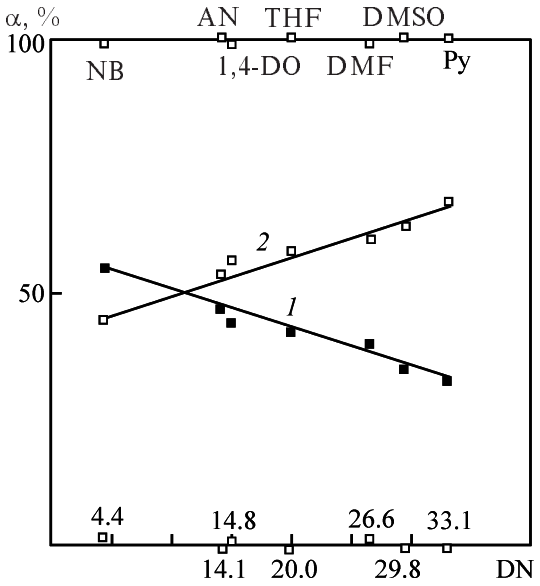


Fig. 4. Crystallinity α and degree of amorphicity (distectic point) of molecular complexes formed in the system PEG (MW 15000)–$NaBPh_4$ as functions of the donor numbers of aprotic solvents: (*1*) crystallinity and (*2*) amorphicity.

As mentioned above, the Gutmann donor number DN is among parameters characterizing the electron-donor power of solvents. We plotted the dependence of the melting points of the molecular complexes on the donor number of aprotic solvents (Fig. 3) using data from [3–5]. The peritectic and eutectic melting points are found to be independent of the donor number of the solvents. For the molecular complexes obtained in various aprotic solvents, the melting point (distectic point) is a linear function of the donor number (melting points decreases with increasing DN).

For the system $LiBF_4$–PEO (MW 5×10^6), Rayne and Wright [6] have separated a high-melting product (mp 433 K) from a chloroform–acetone mixture, and a low-melting product (mp 340 K) from methanol (solvating solvent for cations). The authors attributed the higher melting points to continuous highly ordered double-helical domains, and lower melting points, to an imperfect low-ordered structures. This interpretation is consistent with our X-ray diffraction results. Figure 4 shows linear dependences of the crystallininty and amorphicity of the complexes on the donor number of the solvents. As seen, the crystallinity is maximal and the amorphicity is minimal for complexes obtained in solvents with low DN.

CONCLUSION

More ordered high-melting complexes of polyethylene glycol (MW 15000) with $NaBPh_4$ are formed in solvents with low donor numbers, and defective disordered low-melting structures, in solvents with high donor numbers.

REFERENCES

1. Fialkov, Yu.Ya., Zhitomirskii, A.N., and Tarasenko, Yu.A., *Fizicheskaya khimiya vodnykh rastvorov* (Physical Chemistry of Aqueous Solutions), Leningrad: Khimiya, 1973.
2. Weissberger, A. and Proskauer, E.S., *Organic Solvents. Physical Properties and Methods of Purification*, Riddick, J.A., and Toops, E.E., Eds., New York: Interscience, 1955.
3. Torebekov, O.T., Dzhumadilov, T.K., and Bekturov, E.A., *Vestn. Kaz. Nats. Univ., Ser. Khim.*, 2004, vol. 35, no. 3, pp. 296–299.
4. Torebekov, O.T., Dzhumadilov, T.K., and Bekturov, E.A., *Khim. Zh. Kaz.*, 2004, no. 3(4), pp. 183–186.
5. Torebekov, O.T., Dzhumadilov, T.K., and Bekturov, E.A., *Izv. Nats. Akad. Nauk Resp. Kaz., Ser. Khim.*, 2005, no. 5, pp. 62–65.
6. Rayne, D.R. and Wright, P.V., *Polymer*, 1982, vol. 23, pp. 690–697.

ISSN 1070-4272, Russian Journal of Applied Chemistry, 2008, Vol. 81, No. 5, pp. 909–911. © Pleiades Publishing, Ltd., 2008.
Original Russian Text © Ya.I. Vakhula, I.V. Lutsyuk, I.D. Borshchishin, 2008, published in Zhurnal Prikladnoi Khimii, 2008, Vol. 81, No. 5, pp. 872–874.

BRIEF COMMUNICATIONS

Effect of pH and Reagent Concentrations on Gelation of Magnesium–Silicate Aqueous Systems

Ya. I. Vakhula, I. V. Lutsyuk, and I. D. Borshchishin

L'vivs'ka Politekhnika National University, Lviv, Ukraine

Received August 23, 2007

Abstract—The rate of gelation of the maghesium–silicate aqueous systems was studied in relation to pH and concentration of particular magnesium salts. The magnesium and silicate ions were found to interact in solutions at low temperature.

DOI: 10.1134/S1070427208050418

Forsterite ceramics are formed at low sintering temperature (normally as low as 1400 °C) and are widely used in various branches of modern engineering, primarily in electronic devices. To prepare highly homogeneous ceramics, mechanical mixing of the components is insufficient.

The sol–gel process is one of the most effective modern techniques for preparing highly dispersed powders. This technique allows preparation of ultradispersed uniform multicomponent powders suitable for preparing ceramics at reduced sintering temperature, with controlled morphology and phase composition of the product. These advantages are reached owing to uniform distribution of ceramic precursor throughout the system.

The significant contribution to study of sol–gel processes involving the effect of particular components of sol on the temperature of forsterite formation was made by researchers of the Mendeleev Russian University of Chemical Engineering [1, 2]. It was found that, in the case of precursors based on magnesium chloride, sulfate, citrate, and, particularly, nitrate, the synthesis of forsterite is decelerated and proceeds at lower temperature than for magnesium acetate. The kind of the initial magnesium salt and silicon-containing gelling agent considerably affects the course of solid-phase reactions, size distribution of crystals, their shape, and degree of dispersion of the forsterite powder.

In this study, the gelation rate in the system Mg^{2+}–SiO_3^{2-}–H_2O was examined in relation to particular magnesium salt and the initial ratio of components. The physicochemical processes accompanying the gelation were also analyzed.

EXPERIMENTAL

The initial uniform sols were prepared by adding tetraethoxysilane (TEOS) hydrolyzate (HCl) as gelling agent to aqueous magnesium salt (chloride $MgCl_2 \cdot 6H_2O$, acetate $Mg(CH_3COO)_2 \cdot 4H_2O$, and sulfate $MgSO_4 \cdot 7H_2O$) or anhydrous $MgSO_4$. The TEOS hydrolyzate is widely used for gelation of metal-containing aqueous solutions [3]. Apart from TEOS, other gelling agents, e.g., white black or silica sol, are used [1, 2]. However, we used TEOS to compare our results with other published data on this subject.

The initial magnesium salt was dissolved in distilled water at room temperature. In all the experiments the concentration of magnesium salt was 1 M.

Fifteen minutes after completion of the dissolution of the magnesium salt, pH of the mixture was measured. Table 1 shows that, except for magnesium acetate, the initial solutions were weakly acidic or neutral (pH 5.8–7.6). The aqueous magnesium acetate solution was weakly alkaline (pH 8.6).

The initial sols were prepared by adding TEOS hydrolyzate to aqueous magnesium salt in a prescribed ratio. This mixture was stirred and its pH was measured. As seen from Table 1, in all the systems pronounced acidification was observed. This effect was expected, since pH of TEOS hydrolyzate was approximately 2 by itself.

After addition of TEOS hydrolyzate, all the mix-

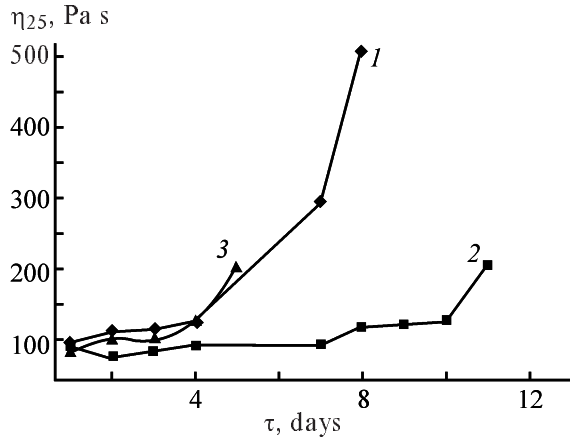
Table 1. pH of aqueous sols in systems magnesium salt–SiO_3^{2-}–H_2O–TEOS hydrolyzate

Magnesium salt	pH of aqueous system	
	initial	after adding TEOS hydrolyzate
$Mg(CH_3COO)_2 \cdot 4H_2O$	8.60	6.78
$MgSO_4 \cdot 7H_2O$	6.35	3.92
$MgCl_2 \cdot 6H_2O$	7.65	2.67
$MgSO_4$	5.87	3.90

Table 2. Gelation time τ_{gel} of systems magnesium salt–SiO_3^{2-}–H_2O–TEOS hydrolyzate

Magnesium salt	c, M	τ_{gel}, days
$Mg(CH_3COO)_2 \cdot 4H_2O$	1	10 min
	0.9	45 min
$MgSO_4 \cdot 7H_2O$	1	1
	0.7	6
$MgCl_2 \cdot 6H_2O$	1	6
	0.7	11
$MgSO_4$	1	3
	0.7	8

tures were kept at room temperature. We found that, within 10 min, the uniform stable aqueous sol based on magnesium acetate is irreversibly converted to a uniform gel for which we failed to measure the viscosity. The initial viscosity of the sol based on $MgSO_4 \cdot 7H_2O$ was 5.75 Pa s, and the gelation time was 24 h. The gelation of the system based on anhydrous $MgSO_4$ is slower. Immediately after adding TEOS, the viscosity of this system was 4.65, and in 24 h it increased to 6.4 Pa s. Within 3 days after mixing the reagents, the sol transformed into a gel.



Viscosity of sols η vs. the keeping time τ. (*1*) $MgSO_4$ (c_M = 0.7 M), (*2*) $MgCl_2 \cdot 6H_2O$ (c_M = 0.7 M) and (*3*) $MgCl_2 \cdot 6H_2O$ (c_M = 1 M).

The most long-lived sols are formed in the system based on aqueous $MgCl_2 \cdot 6H_2O$. As seen from the figure, during the first day the viscosity of this system changes insignificantly, but during the subsequent two days, and especially on the fourth day after starting the experiment, it sharply increases. The gelation was complete within 6 days after mixing the components.

The gelation of silicate-containing colloidal solutions is a complicated physicochemical process affected by numerous factors such as SiO_2 and metal concentrations, temperature, and pH.

According to Iler [4], the most stable metal silicate sols are formed at pH 2–3 and 10–12, and the plot of the gelation time vs. pH has a minimum at pH 5–6. This relationship agrees with our results, in particular, with the lifetime of sols based on magnesium acetate.

As seen from Table 2 and the figure, the gelation time τ_{gel} increases with decreasing concentration of magnesium salt. For example, with decreasing $MgCl_2 \cdot 6H_2O$ concentration from 1.0 to 0.7 M, the gelation time increases by a factor of approximately 2. The figure shows that the plots of η vs. τ consist of three portions reflecting the processes that are described in detail in the literature [4, 5].

To complete the gelation, the gel obtained by the above procedure was kept for 2–3 days at room temperature and then was dried at 115°C for 30 h. The final xerogels presented small granules, powders, or separate flakes. This material was crushed in an agate mortar to the 60–100 μm fineness suitable for X-ray phase analysis.

The powder X-ray patterns were obtained for gel samples based on $Mg(SO_4)_4 \cdot 7H_2O$ and $Mg(CH_3COO)_3 \cdot 4H_2O$ prepared at various pH values.

The X-ray phase analysis showed that the gel based on $Mg(SO_4)_4 \cdot 7H_2O$ contained the following components: $MgSiO_3$ (*d*/*n* 0.252, 0.256, 0.272, 0.290, 0.293, and 0.318 nm), $Mg(SO_4)_4 \cdot 6H_2O$ (*d*/*n* 0.268, 0.292, 0.404, 0.438, and 0.510 nm), and $Mg(OH)_2 \cdot MgSO_4 \cdot 5H_2O$ (*d*/*n* 0.229, 0.268, 0.485, and 0.545 nm).

As suggested in [6], the magnesium cations in the gel structure interact with the negatively charged

surface by the electrostatic forces. This assumption agrees with the fact that the gel prepared in our experiments contains $MgSiO_3$, which also suggests that magnesium cations interact with the SiO_3^{2-} anions already in the aqueous systems at low temperature. The thermodynamic possibility of such interaction is confirmed by the large negative value of the calculated Gibbs free energy of this reaction, $\Delta G^0_{298} = -63960$ kJ mol^{-1}.

The X-ray pattern of the gel based on $Mg(CH_3 \cdot COO)_3 \cdot 4H_2O$ shows that it is X-ray amorphous (absence of sharp reflections belonging to crystalline phases, presence of two halo at $2\theta = 10°$ and 24°).

CONCLUSIONS

(1) The chemical composition of the magnesium salt strongly affects the course of gelation in the system Mg^{2+}–SiO_3^{2-}–H_2O.

(2) The Mg^{2+} cations interact with SiO_3^{2-} anions at low temperature, and this interaction most likely occurs in the solution. The alkalization of aqueous magnesium acetate due to hydrolysis (pH > 7) hampers the gelation.

(3) With decreasing concentration of magnesium salt in the aqueous sol, the gelation time increases. For the systems based on $MgCl_2 \cdot 6H_2O$, in going from 1.0 to 0.7 M solution, the gelation time increases by a factor of 2.

REFERENCES

1. Andrianov, N.T., Strel'nikova, S.S., Dyagilets, S.M., and Fedorov, S.Yu., *Steklo Keram.*, 2002, no. 6, pp. 16–19.
2. Afonina, G.A., Leonov, V.G. and Popova, O.N., *Steklo Keram.*, 2005, no. 8, pp. 19–23.
3. Yashchishin, I.N., Vakhula, Ya.I., Romanov, A.S., and Vasiichuk, V.A., *Zh. Prikl. Khim.*, 2000, vol. 73, no. 2, pp. 187–191.
4. Iler, R.K., *The Chemistry of Silica*, New York: Wiley–Interscience, 1979.
5. Evstrop'ev, K.S. and Toropov, N.A., *Khimiya kremniya i fizicheskaya khimiya silikatov* (Silicon Chemistry and Physical Chemistry of Silicates), Moscow: Promstroiizdat, 1950.
6. Andrianov, N.T., *Steklo Keram.*, 2002, no. 10, pp. 17–22.

ISSN 1070-4272, Russian Journal of Applied Chemistry, 2008, Vol. 81, No. 5, pp. 912–913. © Pleiades Publishing, Ltd., 2008.
Original Russian Text © the Editorial Board, 2008, published in Zhurnal Prikladnoi Khimii, 2008, Vol. 81, No. 5, pp. 875–876.

ANNIVERSARIES

Professor Yu. I. Archakov (to His 80th Birthday)

DOI: 10.1134/S10704272080504 2X

On June 17, 2008, Yurii Ivanovich Archakov, doctor of technical science, professor, and honored scientist and technologist of the Russian Federation, is 80.

Yu.I. Archakov is a known scientist and researcher, prominent physical chemist, and specialist in analysis of hydrogen–metal systems and corrosion protection of metals.

Archakov was born in 1928. He graduated from the Leningrad Technological Institute in 1951, finished his postgraduate education at the same institute and received the degree of a candidate of science in 1957, and defended his doctoral dissertation in 1971 to become a professor.

Since 1957, Archakov has been working at the All-Union Research Institute of Petrochemical Processes, since 1969 he has been heading the laboratory of physicochemical studies and corrosion protection of metals at this institute. Archakov has also been conducting pedagogical work; in 1969–1975, he pluralistically organized and headed the chair of theoretical foundations of materials science at the Leningrad Technological Institute. More than 20 candidate and 5 doctoral dissertations have been defended under his supervision.

His research work combines theoretical studies with solution of practical problems.

Archakov has developed the theory of hydrogen-resistant alloying of metals and alloys and theoretical foundations of metal protection from saturation with gases.

In a series of studies concerned with the solubility and diffusion of hydrogen in metals, he for the first time established the validity of the law of gas dissolution in metals (Henry law) at high pressures, relationship between the solubility and diffusion of hydrogen in metals, on the one hand, and their electronic structure, on the other, and suggested equations for calculating the solution and diffusion constants at high pressures.

His basic research into the effect of alloying elements on the hydrogen resistance of steel has revealed that the key factors are the nature of the carbide phase and its chemical composition. He suggested a phenomenological theory of alloying of hydrogen-resistant steels, based on estimating the corrosion resistance of a steel in hydrogen by its phase composition. This theory enables development of new steels with prescribed hydrogen-resistance parameters and determination of safe application conditions of the already existing metals and alloys on the basis of their phase composition.



He has developed theoretical foundations of metal protection from gas saturation. For a steady and nonsteady gas flow through the metal, mathematical dependences have been derived, which make it possible to assess in advance the promise of new coatings.

Archakov has performed extensive studies aimed to determine fundamental kinetic and thermodynamic aspects of the hydrogen corrosion of steels, develop new original procedures to be used in analysis of corrosion processes in gas media at high pressures and temperatures. Recommendations on ap-

plication of construction steels in hydrogen-containing media have been developed.

Archakov is the author of more than 200 scientific publications and inventions, including the monographs *Vodorodnaya korroziya stali* (Hydrogen Corrosion of Steel, 1985, translated and published in Japan in 1988), *Vodorodoustoichivost' stali* (Hydrogen Resistance of Steel, 1978), *Vliyanie vodoroda na khimicheskoe i neftyanoe oborudovanie* (Effect of Hydrogen on Chemical and Petroleum Equipment, 1976, with co-authors), reference book *Korroziya i zashchita khimicheskoi apparatury* (Corrosion and Protection of Chemical Apparatus, 1974, 1990, with co-authors), and a number of reviews and sections in reference books.

Archakov is actively involved in organizing and holding Russian and international conferences and symposia on corrosion and metal protection. Archakov's scientific works are internationally acknowledged.

Dear Yurii Ivanovich! We congratulate you on your jubilee and wish you health and happiness for many years to come!

Scientific Council of VNIINeftekhim Open Joint-Stock Company and Co-workers

ISSN 1070-4272, Russian Journal of Applied Chemistry, 2008, Vol. 81, No. 5, p. 914. © Pleiades Publishing, Ltd., 2008.
Original Russian Text © the Editorial Board, 2008, published in Zhurnal Prikladnoi Khimii, 2008, Vol. 81, No. 5, p. 877.

ANNIVERSARIES

Inna Aleksandrovna Tsvetkova: 50 Years of Working Activity

DOI: 10.1134/S1070427208050431



Inna Aleksandrovna Tsvetova has been working now for 50 years at Nauka St. Petersburg Publishing House, Russian Academy of Sciences. After having graduated from the Leningrad Technological Institute, she started to work at the Publishing House of the Academy of Sciences of the USSR as an expert in the literature of the department of periodicals, and, since March 1976, she has been heading the Editorial Office of *Zhurnal Prikladnoi Khimii* (Russian Journal of Applied Chemistry). She is a specialist of very high qualification, with a broad experience of journal work, always well-wishing and attentive. Inna Aleksandrovna is invariably respected by staff members of the publishing house, numerous authors, and members of the Editorial Board of the Journal.

The staff of the Nauka Publishing House, Editorial Board and Editorial Office of *Zhurnal Prikladnoi Khimiii* heartily congratulate respected Inna Aleksandrovna on the remarkable working jubilee and wish her health and a further success in work.

ISSN 1070-4272, Russian Journal of Applied Chemistry, 2008, Vol. 81, No. 1, pp. 915–916. © Pleiades Publishing, Ltd., 2008.
Original Russian Text © A.G. Morachevskii, M.S. Kokhatskaya, 2008, published in Zhurnal Prikladnoi Khimii, 2008, Vol. 81, No. 1, p. 878.

BOOK REVIEWS

Kiiko, V.S., Makurin, Yu.N., and Ivanovskii, A.L., *Keramika na osnove oksida berilliya: poluchenie, fiziko-khimicheskie svoistva i primenenie* (Ceramics Based on Beryllium Oxide: Synthesis, Physicochemical Properties, and Use)

Yekaterinburg; Ural'skoe Otd. Ross. Akad. Nauk, 2006, 440 pp.

DOI: 10.1134/S1070427208010443

Thanks to the whole set of their unique properties, beryllium and its oxide find wide use in various fields of technology. The main consumers of beryllium in the former USSR were the nuclear and aerospace industries. At present, beryllium and beryllium-based oxide ceramics are not manufactured in Russia because of the geopolitical changes that have occurred. The previously existing two plants in Ust-Kamenogorsk now belong to the Republic of Kazakhstan. The lack of its own beryllium-manufacturing plants makes Russia dependent on the import of this important strategic commodity. Rather topical is the problem of expanding the resources of mineral raw materials and creating Russia's own beryllium industry.

The monograph by V.S. Kiiko and co-authors reflects the present-day state of studies of the physicochemical characteristics of beryllium oxide ceramics and considers its use in certain new industries and special technology. The book comprises an introduction and six chapters. References are given to each chapter separately, with the total number of references to all the chapters being very large (598 items).

The introduction (pp. 7–11) briefly characterizes the world's production of beryllium materials and lists their application fields. Chapter 1 (pp. 12–100) discusses a wide variety of issues: state of the resources of beryllium raw materials in Russia, specific features of the decomposition of beryllium-containing ores, and production of a pure beryllium oxide powder and ceramic articles thereof. Russia is one of the first in the world in the beryllium ore resources. As industrial sources of beryllium can serve both its own deposits and complex deposits in which beryllium is an associated component. Considerable attention is given in Chapter 1 to results of comprehensive studies of the structural transformations in beryllium-containing powders, which occur in technological procedures. The results presented can promote an improvement of the quality of BeO ceramics.

Chapter 2 (pp. 101–158) analyzes the electronic structure of beryllium oxide from the standpoint of modern quantum-chemical concepts. The authors make an attempt to model the most important physicochemical characteristics of beryllium oxide on the basis of quantum-chemical calculations.

Chapter 3 (pp. 159–201) considers the defective structure of the BeO powder and ceramics on its base, which largely determines the technological and service characteristics of the BeO ceramics. Particular attention is given to surface defects and to the electrical conductivity of the beryllium oxide ceramics. The electrical characteristics of the ceramics, which are its most important service characteristics, are fully governed by the defective structure of beryllium oxide.

The physicochemical properties of the BeO ceramics are strongly affected by impurities that find way into the ceramics in the course of the process or are purposefully introduced in order to modify its properties. These issues are discussed in Chapter 4 (pp. 202–281). It is noted that impurities are localized in the ceramics mostly at grain boundaries. Data on the dynamics of variation of the impurity content in the course of the process are discussed in detail. A particular attention is given to admixtures of carbon and iron, which markedly affect the service characteristics of the BeO ceramics.

Chapters 5 (pp. 282–351) and 6 (pp. 352–440) discuss the application of the beryllium oxide

ceramics in widely diverse fields of technology. Particular emphasis is placed by the authors on the use of the BeO ceramics in laser technology and the dosimetry of ionizing radiation. On the whole, the authors succeeded in generalizing, systematizing, and analyzing a large body of evidence on the synthesis technology, physicochemical properties, service characteristics, and use of the beryllium oxide ceramics in various fields of technology. The book is well written and accessible, as regards the presentation manner, to a broad audience of specialists in various fields of science and technology. It contains the results of the most recent studies.

A. G. Morachevskii and M. S. Kokhatskaya

ISSN 1070-4272, Russian Journal of Applied Chemistry, 2008, Vol. 81, No. 1, p. 917. © Pleiades Publishing, Ltd., 2008.
Original Russian Text © A.G. Morachevskii, I.N. Beloglazov, 2008, published in Zhurnal Prikladnoi Khimii, 2008, Vol. 81, No. 1, pp. 879.

BOOK REVIEWS

Meretukov, M.A., *Zoloto i prirodnoe uglerodistoe veshchestvo* (Gold and Natural Carbonaceous Substance)

Moscow: Ruda i Metally, 2007, 110 pp.

DOI: 10.1134/S1070427208010455

The book written by Prof. M.A. Meretukov, a known specialist in metallurgy of noble metals, is devoted to a rather narrow issue, nature of the scattered carbonaceous matter (SCM) contained in gold ores and deposits and its influence on the cyanidation process.

The monograph comprises an introduction and nine chapters, each with its own bibliographic list. In the brief introduction (pp. 5–8), the author gives notion of the essence of the phenomenon he describes. Small Chapter 1 (pp. 9–13) familiarizes the reader with the basic terms and concepts. Chapter 2 (pp. 14–20) characterizes various gold ore deposits. Chapter 3 (pp. 21–29) discusses the basic concepts of the origin of the carbonaceous matter in gold deposits. Chapters 4 (pp. 30–34) and 5 (pp. 35–48) are devoted to the types and structure of kerogen, the conditionally insoluble component of the organic matter scattered in sedimentary rock. Chapter 6 (pp. 49–64) discusses the genetic relationship between gold and the carbonaceous matter. Chapter 7 (pp. 65–83) contains evidence about the structure and properties of the carbonaceous matter contained in gold ores. Chapter 8 (pp. 84–95) discusses various methods for neutralizing the activity of SCM before cyanidation of gold ores. The final Chapter 9 (96–109) makes an attempt to explain specific features of the interaction between gold-containing solutions and scattered carbonaceous matter.

The monograph by Meretukov is of interest for specialists working directly with the technology of processing of gold-containing ores and methods for their cyanidation. Probably, it would be instructive to more widely use as examples the domestic deposits and technologies. The author mostly relies on the experience of the United States, Canada, and South African Republic.

A. G. Morachevskii and I. N. Beloglazov

ISSN 1070-4272, Russian Journal of Applied Chemistry, 2008, Vol. 81, No. 6, pp. 919–932. © Pleiades Publishing, Ltd., 2008.
Original Russian Text © A.V. Gribanov, Yu.N. Sazanov, 2008, published in Zhurnal Prikladnoi Khimii, 2008, Vol. 81, No. 6, pp. 881–894.

REVIEWS

Polyacrylonitrile: Carbonization Problems

A. V. Gribanov and Yu. N. Sazanov

Institute of Macromolecular Compounds, Russian Academy of Sciences, St. Petersburg, Russia

Received April 16, 2008

DOI: 10.1134/S1070427208060013

INTRODUCTION

Polyacrylonitrile (PAN) is one of widely used and industrially mastered substituted polyolefins. Its properties and applications have been described in detail in numerous monographs and reviews and form an independent field of research in chemistry, physics, and technology of synthetic macromolecular compounds, closely related to the materials science [1–10]. Much attention in these books and articles is given to PAN carbonization as a process yielding carbon materials that are indispensable for many branches of modern industry. Detailed studies of PAN carbonization give much useful information for choosing conditions required to obtain carbon articles with the best characteristics from PAN. However, specific features of thermochemical reactions leading to the formation of the carbon structure from PAN are still poorly understood. Heat treatment is the major factor determining the features of PAN carbonization. Despite enormous number of papers on PAN carbonization, there is still no generally accepted mechanism of PAN thermal transformations in a wide temperature range.

STATE OF THE ART

As in other related cases, the problem is to separate the effects of PAN heat treatment conditions on the course of two competing thermochemical reactions, degradation and cross-linking, typical of carbonization of any polymers. Already in an early book concerning thermal transformations of carbo- and heterochain polymers [11] it was noted that thermal transformations of PAN start with the reactions of nitrile groups. As a result, various cyclic (mostly six-membered) and partially cross-linked structures can be randomly formed.

Already in this step of interpretation of the cyclization process, different hypotheses related to the experimental conditions and to the structure and purity of the starting PAN samples were put forward. Comparison of the published data shows that the interpretation of the mechanism of transformation of a linear soluble PAN into an insoluble polycyclic product involves many contradictions concerning the structure of the intermediate and final compounds. The following features of the thermochemical transformation of PAN into a carbonized structure are now recognized and confirmed by the majority of researchers.

(1) When heated, linear PAN cyclizes via opening of the nitrile groups, but the number of rings in a block and their mutual arrangement in intra- and intermolecular packing are still the matter of discussion.

(2) With increasing temperature of heat treatment, the degree of polyconjugation and aromatization of PAN grows.

(3) The ambient atmosphere and the temperature conditions of the heat treatment have a decisive effect on all reactions of PAN carbonization and on the structure of the intermediate and final products.

(4) Only some of the papers consider the steric organization of the initial PAN as a factor governing the structure of the carbonizate.

The above features of the extremely complex process of polymer-analogous PAN transformations are only general criteria in the development of carbon materials with a set of unique valuable properties. The contributions of different researchers to understanding and interpretation of the results of basic and applied studies have certain specific features concerning the terminology, goals of

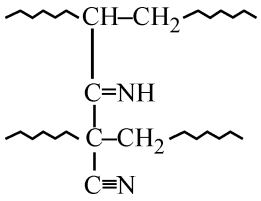
experiments, and technical, technological, economic, environmental, and other aspects. Each of these criteria is important for gaining complete information.

First, it is appropriate to discuss certain terminological issues.

The polymer name, polyacrylonitrile, means nothing other than a compound synthesized by acrylonitrile polymerization. However, without information on the chemical and physical structure formed in the course of the synthesis, numerous questions arise. Without answers to them, the results of the experiment as a whole remain obscure and open to question. There are many reasons for the scarcity of the initial information, and some of them are objective. They are associated with the lack of synthesis standardization and of the necessary minimal set of characteristics of the initial polymer. The other factor is the use of technical slang in which the term PAN is applied not only to the acrylonitrile homopolymer, but also to its copolymers. This factor is mentioned by Varshavskii [7], but even the author himself does not always follow this rule. Obviously, for PAN copolymer samples in which participation of an oxygen-containing copolymer is put on the same footing as thermal oxidative treatment of PAN, the mechanism of thermochemical transformations is strongly different from the thermochemistry of the homopolymer. Therefore, in the majority of original papers considering the mechanism of lowtemperature carbonization, which is identified with the oxidation or stabilization, the use of PAN copolymer is, as a rule, implied, but not indicated directly.

From the applied standpoint, the use of oxygen-containing compounds accelerates and simplifies preparation of carbon materials (as a rule, fibers). However, from the standpoint of elucidating the fine mechanism of cyclization involving only the initial structure of the acrylonitrile homopolymer, i.e., a macromolecule consisting of only C, H, and N atoms, introduction of oxygen further complicates the unclear pattern of thermal cyclization of PAN.

It was believed that PAN cyclization is impossible in the absence of oxygen in the reaction medium [12], but this assumption was rejected by model experiments with succinic acid dinitrile and nitriloacetic acid esters, which formed cyclic oligomers by opening of nitrile bonds via formation of dimeric complexes [13–15]. A thorough analysis of the IR spectra of the examined compounds confirmed the mechanism involving formation of cyclic structures of the naphtharidine type, suggested by Grassie and Hay [16] on the basis of experiments on isothermal heating of isolated model samples. These results disprove the scheme of intermolecular cross-linking of PAN via formation of azomethine links [17]



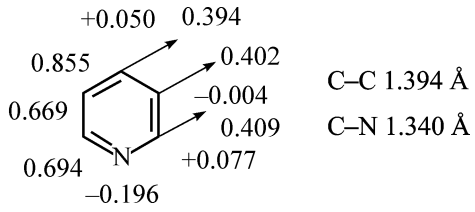
Thus, it can be considered that the first step of thermochemical transformations of PAN is the formation of six-membered naphtharidine rings. This pathway fits in the general scheme of low-temperature (100–200°C) transformations of PAN. Furthermore, the occurrence of reactions in defective areas of the molecular structure and in the comonomer unit is assumed. The last two pathways were given particular attention in view of the applied significance of PAN, and the cyclization was considered to be governed by the occurrence of thermal oxidative reactions. In addition, a question arises: Is the primary cyclization event, not complicated by oxidative reactions, the first step of PAN carbonization From the viewpoint of an increase in the carbon concentration in a sample, the PAN cyclization is not carbonization, but just a process favoring cross-linking of the substance and enhancing its heat resistance.

Only in very few studies, the PAN cyclization was not accompanied by release of volatile thermal degradation products. This pathway is possible theoretically, but actually ideal cyclization yielding long cyclic sequences does not occur. As a rule, only macrochains consisting of three to ten conjugated nitrogen-containing rings can be obtained. Some authors attribute this fact to different tacticities of PAN samples [4, 5, 18–20]. The regularity in arrangement of nitrile substituents along the PAN chain is the decisive factor in the formation of ladder naphtharidine structures, and in this respect, as indicated in [18], the isotactic PAN structure is preferable. This seeming simplicity, apparently, led to certain mistakes in schematic presentations of the cyclization mechanism in early papers on thermal degradation of PAN [21–24]. In [25], we drew attention to the importance of the steric orientation of PAN macromolecules and of geometric and energetic characteristics of all bonds participating in the formation of intermediate and final carbonization products. In this aspect, the repeatedly pres-

ented scheme of the parquet packing of carbo- and heterorings is inconsistent with the actual size of separate fragments of the cyclic structure of PAN.

When tackling with the problem of steric organization of PAN and of intermediate and final products of its carbnization by simulating structural fragments of linear and cyclic PAN [26], the model compounds 2,4-dicyano-*n*-pentane, 2,4,6-tricyano-*n*-heptane, and their higher homologs simulating linear uncyclized PAN exhibit no steric hindrance with increasing chain length. A different pattern is observed for macromolecules of cyclized PAN, in which the growth of cyclic sequences along the PAN chain is strongly restricted by a number of factors. First, the degree of tacticity of the initial PAN determines the possibilities of its cyclization. In the ideal case, the maximal length of fused cyclic units in the PAN backbone could be attained at the 100% isotactic arrangement of the nitrile groups. However, as shown in [13, 19], preparation of such PAN stereoisomers is impossible. Second, the high dipole moment of the CN group, 3.9 D, opens up wide possibilities for competing reactions, especially for an intermolecular interaction with an adjacent PAN molecule. In addition, the orbital of the lone electron pair is oriented oppositely (180°) to the C=N bond axis, which favors hydrogen bonding, donor–acceptor interaction with PAN surrounding, and, in particular, formation of molecular associates on the level of PAN monomers and oligomers.

Particular attention should be given to the poorly understood geometry of cyclic PAN structures. According to the calculations [27, 28], this is the major factor restricting the growth of cyclic sequences in PAN. Let us discuss it in more detail. The pyridine and naphtharidine structures formed by PAN cyclization and found in many papers cannot be regarded as strictly planar and, the more so, coplanar. In contrast to benzene and its fused homologs, the bond lengths and bond angles in the six-membered rings of pyridine and naphtharidine are nonequivalent. Despite the high electron delocalization energy in pyridine (33.8 kcal mol^{-1}) and pronounced aromatic properties, its geometric structure is not a regular hexagon like that of benzene:



Electronic indices of pyridine.

This gives rise to strain of the pyridine ring via its bending, and, as a result, to a decrease in the stability, compared to benzene. Furthermore, the nonuniform electron density distribution over the pyridine ring leads to its polarization and thus enhances its reactivity.

Thus, already in the step of initiation of PAN cyclization, a pyridine ring is formed, whose nitrogen atom is a certain source of strain for the whole cyclic system of PAN. The strain increases as further rings are formed along the chain. Hence it can be concluded that nitrogen (an apparently other heteroatoms, especially oxygen) plays a decisive role in the formation of rings in the early step of cyclization, i.e., it is an initiator of a polymer-analogous transformation of linear PAN. With an increase in the number of conjugated rings, the effect of steric and thermodynamic factors of pyridine and its fused derivative enhances the strain of the whole system, and the nitrogen atom starts to prevent, rather than promote, the cyclization. In this case, apparently, the number of nitrogen-containing rings in the conjugated block reaches a certain critical value dependent on many factors (both on those noted above and on purely process factors), after which the function of the nitrogen atom changes, and it ceases to participate in the further growth of the homologous series of polyheterocycles.

Without going into details of the organic chemistry of cyclization, we should note that nitriles form associates (stable dimers) via interaction of nitrile groups, with the association energy of 4–8 kcal mol^{-1}. In the PAN macromolecule, in which the mobility of nitrile groups is restricted by the hydrocarbon chain, their strong polarization at low temperatures creates conditions for the occurrence of competing intra- and intermolecular reactions. In an isolated PAN macromolecule, the adjacent CN groups repel each other, which leads to the formation of a twisted helical structure with the mean cross section not exceeding 0.6 nm [13]. In this packing, some nitrile groups protrude beyond the perimeter of the cross section of the individual PAN macromolecule, providing an intermolecular dipole–dipole interaction. Depending on the inclination angle of the CN bond relative to the axis of the PAN helix and on the angle between the CN bonds in the projection onto the plane of the cross section of the PAN molecule, the energy of intermolecular interaction of the adjacent molecules, calculated from data of [29], is close to the energy of the interaction between free macromolecules.

As for the interaction of PAN macro-molecules in a specific article (film or fiber), their steric arrangement is determined by the article forming conditions. In this case, the role of the nitrogen atom in the formation of a cyclic carbonizate structure becomes less significant, because an ordered supramolecular organization is formed under the action of external loads. It was shown in numerous papers [5–7] that, under the conditions of forced orientation, helical structures of PAN are arranged in a planar zigzag, the intermolecular interaction forces become weaker, and zones with ordered packing appear. Such zones can be formed only at a syndiotactic arrangement of the CN groups in the plane of the PAN hydrocarbon chain. This structure is the least favorable for the formation of cyclic PAN structures, but the orientation of PAN chains in the course of extension makes higher the probability of intermolecular cross-linking. In this case, the nitrogen atoms of the nitrile groups will act, owing to antiparallel orientation of the dipoles, as cross-linking agents, thus inhibiting the cyclization, the more so as the cyclization is accompanied by an additional chain strain because of the nonequivalence of the bond lengths in pyridine and naphtharidine.

Apparently, the superposition of these processes does not allow formation of conjugated cyclic sequences of lengths exceeding five to seven conjugated pyridine rings in real PAN samples [30, 31]. The results obtained show that, in an inert atmosphere, the probability of intramolecular cyclization in a nonoriented PAN macromolecule is close to zero. In an oriented isolated macromolecule, the possibility of intramolecular cyclization is determined by the steric arrangement of nitrile groups and by the molecular-weight characteristics, which depend on the PAN synthesis conditions and on conditions in which PAN-based articles are formed.

Hence, the orientation along the chain axes is the necessary condition for the intramolecular cyclization of PAN. As a rule, it is attained by using various procedures for fiber and film forming. The formation of primary PAN structures is of crucial importance for the transformation of PAN into a carbonized product in the course of its high-temperature treatment. However, because of the above-noted limitations in the geometry of nitrogen-containing heterocycles, the subsequent carbonization of PAN with the formation of a planar parquet packing of symmetrical hexagons, which was postulated by Grassie [21–24] and reproduced in numerous subsequent papers to become a certain axiom, disagrees with the calculation results.

A more rational model has been suggested by Rumynskaya et al. [32]. They convincingly confirmed the interplanar interaction of conjugated cyclic units of PAN, occurring as a donor–acceptor interaction of cyclic formations strongly polarized at the N atom with the hydrocarbon chain of an adjacent PAN macromolecule. This interaction fixes the layered macromolecule packing facilitating their subsequent carbonization and graphitization with increasing temperature.

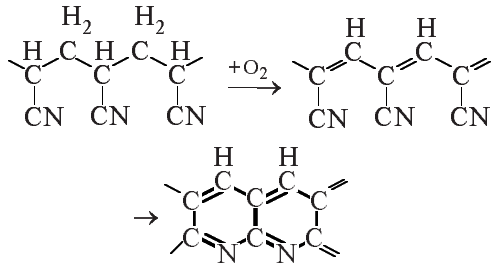
Returning to the primary step of low-temperature reactions of PAN, which initiate cyclization via nitrile groups, we should note once again that strictly speaking, this process is not carbonization, as it is not accompanied by an increase in the carbon concentration in the system. In this context, introduction of oxygen atoms into PAN is an impulse initiating carbonization. Oxygen can be introduced into the reaction system in different ways. The first way involves performing thermal transformations of PAN in an oxidizing atmosphere. The second way is introduction of oxygen-containing comonomers, mainly carboxylic acids and their esters. The third way is associated with the presence of residual catalysts and solvents used in acrylonitrile polymerization and fiber forming.

The presence of oxygen in any form substantially expands the set of thermochemical reactions in early steps of PAN heat treatment. Among these reactions are dehydrogenation, generation of free radicals, formation of hydroxy, carbonyl, carboxy, and keto imine groups. Further heating leads to activation of thermal oxidative degradation processes accompanied by the release of water, carbon oxides, hydrogen cyanide, ammonia, acrylonitrile, and other readily volatile thermal degradation products whose ratio and release sequence depend on many factors that are difficult to analyze on the quantitative level to construct the general scheme of low-temperature carbonization.

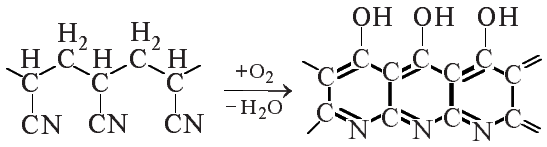
According to [33], carbonization of a PAN fiber (no characteristics of the initial sample are given) in an oxidizing atmosphere starts above 100°C with the oxidative dehydrogenation to give water, with elimination of HCN and NH_3 by disproportionation. Above 190°C, cyclization and aromatization of PAN are observed, which is followed by depolymerization at 200°C. The process ends at 250°C to give heteroaromatic units consisting of four to five naphtharidine rings. In an inert atmosphere, oxidative dehydrogenation does not occur, no carbon oxides are detcted, and the content

of nitrogen-containing volatile degradation and depolymerization products is somewhat higher. An oxidizing medium accelerates the cyclization and aromatization, but at 270–310°C causes degradation of naphtharidine rings.

This example is specific to a given PAN sample and to the experimental procedure used. There are also numerous other studies performed under other conditions and with other PAN samples (also insufficiently characterized), and the trends observed are quantitatively and qualitatively different, depending on a specific experiment. In some papers, thermochemical transformations of PAN in early steps of heat treatment were interpreted in terms of the formation of a polyene conjugation chain, competing with the cyclization via nitrile groups. It was believed that oxygen accelerates the formation of aromatic structures via generation of free radicals initiating formation of polyconjugated systems in the hydrocarbon chain [5]:



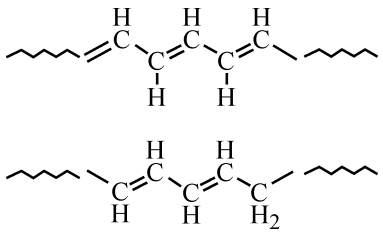
In another paper [2], it is suggested that the polyconjugated system is formed via oxidative dehydrogenation of PAN:



However, none of these schemes is provided with well-defined temperature limits from which it would be possible to determine the priority of formation of the polyconjugated system in the hydrocarbon chain. Furthermore, data on the oxygen concentration in the reaction mixture are also lacking. Therefore, the question of formation of a polyconjugated chain remains open, especially taking into account that oxygen can both initiate and inhibit the PAN cyclization [34]. Apparently, the presence of oxygen in any form in the PAN reaction system makes it impossible to distinguish the step of formation of the polyene structure against the background of cyclization via nitrile groups, also leading to the formation of a polyconjugated system. As the polyconjugation effect is a driving force of carbonization of many organic compounds [5, 6, 11], this approach is quite applicable to PAN carbonization.

The effect of separation of conjugation blocks, allowing preservation of the coplanarity of separate cyclized fragments participating in further rearrangements of the PAN structure at elevated temperature, is discussed in [35] on the basis of a hypothesis that cyclic fragments, which are conjugation blocks, catalyze further carbonization of PAN. The concept conjugation blocks catalyzing PAN carbonization have a critical size independent of the sample microtacticity and history was put forward. These conclusions were indirectly confirmed by Geidrikh et al. [36]. Based on an analysis of PAN samples heat-treated in different atmospheres in a wide temperature range (100–2800°C), they suggested preservation of the supramolecular organization and orientation of chains of the initial PAN whose carbonization yields nongraphitizing carbon forms.

The possibility of formation of carbon-chain polyconjugated systems of the type



was discussed by Artemov et al. [37]. With the reference to X-ray spectra, they demonstrated prevalence in the carbon bulk of sp^2 -hybridized carbon atoms incorporated into carbo- and heterocyclic aromatic structures. That is, the polyconjugation in the carbonizate is due to fusion of aromatic fragments into polycyclic systems.

However, the thermodynamic factor testifies against such structures. Formation of a –CH=CH– unit in a polyconjugated system $(–CH=CH–)_n$ requires an energy of +98.74 kJ mol^{-1}, i.e., the formation of such systems is strongly exothermic. The formation of cyclic structures, such as benzene and naphthalene, from short polyconjugation chains $(–CH=CH–)_3$ and $(–CH=CH–)_5$ involves the consumption of –108 and –343 kJ mol^{-1}, respectively. Therefore, the formation of long conjugation chains at low temperatures with the subsequent formation of six-membered rings and hydrogen release is improbable. To conclude the discussion of the attempts to elucidate the mechanism of low-tempera-

ture carbonization of PAN, it can be noted that all the hypotheses are associated with a process scheme for preparing materials with prescribed properties. This approach is justified in the applied aspect, because the use of oxygen in the course of production of carbon articles (fibers in most cases) by PAN carbonization is appropriate from the technological and economic viewpoints.

Attempts to elucidate the details of "oxygen-free" carbonization face the above-mentioned problems associated with the requirements of a high purity of the monomer, thorough identification of the initial polymer, and exclusion of thermal oxidation in the first step of carbonization (up to ~300°C). In so doing, it should be borne in mind that, as already noted, the terms carbonization and low-temperature cyclization are not identical as applied to PAN.

The first condition is the most difficult to meet, as it requires complex procedures of laboratory synthesis with special catalysts and reaction vessels reliably isolated from the ambient atmosphere. Furthermore, such polymers are hardly promising from the economic viewpoint. The chemical specificity of such polymers as carbon fiber precursors will be discussed below. The possibility of a more detailed examination of the mechanism of low-temperature carbonization of PAN under "sterile" conditions is of basic scientific interest, and certain attempts in this area have already been made. Unfortunately, experiments on PAN carbonization in an inert atmosphere with acrylonitrile homopolymers of insufficiently characterized structure and composition and, the more so, with acrylonitrile copolymers are of little use for this purpose.

To approach the solution of this problem, we can analyze data on PAN synthesis using anionic systems [19, 38–41] or channel complexes [18]. Such PAN samples have high high molecular weight (up to 8×10^5), narrow MWD with a polydispersity close to unity, absence of low-molecular-weight fractions and branchings, and increased stereoblock structure parameter [20]. A low-temperature treatment of these samples was not accompanied by formation and release of volatile products in the initial step of heat treatment. Structural changes occurred only as a result of intramolecular polymerization of nitrile groups. Furthermore, these polymers did not form a polymeric complex with the solvent (DMF) [42].

One could say that the onset of formation of a polyconjugated chain through naphtharidine units initiates further transformation of linear PAN into cyclic product, but the subsequent carbonization with gradual dehydrogenation and increase in the carbon concentration requires the action of oxygen in any form accepted in technology. Thus, the modeling of "sterile" conditions of the initial step of thermochemical transformations of PAN gave insight into the elementary events of carbonization on the level of a heat-driven microreactor consisting of carbon, hydrogen, and nitrogen atoms bound in a PAN macromolecule.

The interaction between carbon and nitrogen atoms participating in PAN carbonization has always attracted researchers' attention. With the development of solid-state analytical spectroscopy, there have been published papers on examination of carbonized residues of polymers containing heteroatoms.

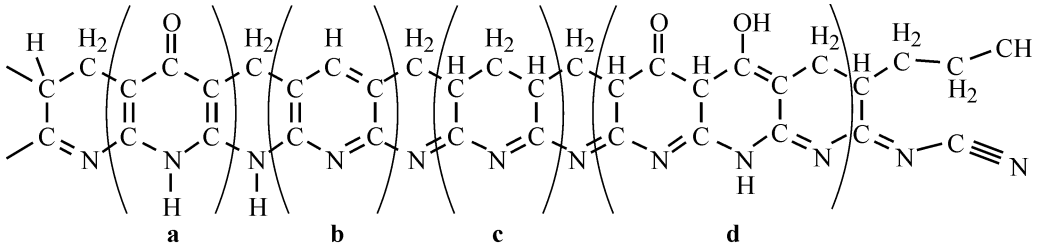
In one of early basic reviews on pyrolysis and carbonization of polymers [11], it was suggested that heteroatoms play a significant role in the formation of aromatic carbon monolayers. It was found [35, 36] that the carbon–nitrogen bond in the conjugation chain arising from PAN cyclization is very strong and determines the structural thermochemical reactions in the course of carbonization. The enhanced heat resistance of PAN heat treatment products with a conjugation system consisting of nitrogen-containing rings was substantiated from this viewpoint. This interpretation was supported [43] by the results of heating of dilute PAN solutions in an inert medium, when formation of cross-linked intermolecular structures is ruled out and formation of longer chains of conjugated C=N bonds is favored because of increased conformational mobility in solution.

Further discussion of the experimental evidences for the effect of the conjugation system on the PAN carbonization considered the effect of oxygen introduced by various methods into the PAN carbonization process. This position is based on the authors' interest related to materials science and on the principal goal of preparation of carbon fibers from PAN fibers with a set of valuable service characteristics. From this viewpoint, Varshavskii's book [7] is the most comprehensive and interesting. It summarizes the experience of a whole generation of specialists of the Khimvolokno Research and Production Association on the development of unique multiprophile carbon fibers and articles based on them. One of the main advantages of this book is the encyclopedic completeness of generalized data on carbonization of the main polymeric raw materials

used for production of carbon fibers (celluloses, pitches, PAN).

A prominent place is occupied by an ingenious hypothesis about the mechanism of high-temperature carbonization of PAN. Without going into details of this book, whose fragments have been published in periodicals [2, 6, 44], it should be noted that the majority of observations, characterizitics, and appraisals concern fibers whose specific features pose certain restrictions on the conclusions about the mechanism of PAN carbonization. As a rule, copolymer fibers are concerned, and, in almost all the cases, thermal oxidative effect on the polymer throughout the temperature range of carbonization is considered.

From the viewpoint of the mechanism of PAN carbonization, the primacy of polyconjugated systems is kept, but there are no convincing examples of the predominant formation of a polyconjugation chain by oxidative dehydrogenation or by polymerization of pendant nitrile groups. Alternative pathways of formation and lengths of systems of conjugated –C=C– and –C=N– bonds are discussed in relation to the molecular weight and steric charac-teristics of the reacting macromolecules. The results of some papers concerning the effect of PAN tacticity on the polymerization of nitrile groups are discussed very cautiously. This indirectly disproves the postulate of the infinite length of polyconjugated ladder chains of PAN. Much attention is given to specific features of the formation of the supramolecular structure on the level of PAN fibers. In one of the conclusions, the following formula is given for the macromolecule of oxidized PAN fiber:



with the ratio of units **a** : **b** : **c** : **d** = 4 : 3 : 2 : 1.

However, this is followed by a reservation that the formula is valid for the surface layer of a fiber, 4–5 nm thick. Deep layers of a fiber can have a different composition because of the effect of diffusion factors governing the degree of oxygen penetration into the fiber. This parameter depends on the heating rate in different steps of carbonization. These and many other factors related to the preparation and thermal oxidation conditions exert a significant influence on processes occurring in the course of fiber heating. It is noted that heating can lead to relaxation of internal stresses, with a decrease in the strain of bonds and angles. From the viewpoint of the maximal length of cyclic sequences, discussed above, and the role of stereoisomerism in their formation, it is unclear whether the relaxation promotes or hinders cyclization.

An interesting interpretation of the mechanism of chemical reactions occurring in the course of carbonization of oxidized PAN fibers has been suggested. The conclusions on the carbonization kinetics, based exclusively on calculations of the apparent activation energy by the laws of formal kinetics, do not give grounds to conclude that the mechanisms of chemical transformations under a catalytic effect are the same. The activation energy is of neither physical nor chemical sense for thermochemical processes in polymers. Therefore, the conclusion about the catalytic effect on the PAN carbonization process as a whole is doubtful.

An attempt to elucidate the role of polyconjugated systems in the formation of carbon structures is more interesting and ingenious. A hypothesis of the autocatalytic character of formation of aromatic conglomerates, with the forming polyconjugated systems acting as catalysts, has been put forward. The main pathways in the suggested mechanism are virtual schemes of formation of polyconjugated systems of two types: via oxidative dehydrogenation and via polymerization of nitrile groups, which is consistent with the results of experimental studies [5, 11, 33].

Further schematic construction of ladder and parquet aromatic structures somewhat resembles Grassie's schemes [21–24], without taking into ac-

count the geometry of the polyheterocycles [25]. In addition, the previously suggested empirical formula of the polystructure of oxidized PAN fiber is not reflected in the mechanism of thermal transformations at elevated temperatures. Despite the use of topochemical relationships and appeal to the complexity of solid-phase reactions on the polymeric level, regular construction of a cyclic set propagating in space like a zipper is hardly compatible with the random set of elementary structures indicated in the above formula.

The energy-related interpretation of the intermolecular interaction of propagating chains from the standpoint of adsorption–desorption and vacation of the active surface for continuing the subsequent regular cross-linking is a very fruitful, though debatable, prerequisite to the development of a theory correlating the macromolecular interactions in the polymer matrix with fine electronic rearrangements of atomic bond parameters. The application of the main postulates of catalysis on semiconductors in the suggested semiempirical virtual scheme is debatable, but, nevertheless, this is a serious step in elucidation of the extremely complex mechanism of PAN thermolysis.

Further experimental confirmation of the suggestions made, such as introduction of a boron atom as an electron-acceptor agent and counterbalance for nitrogen atoms [45], offers not only a practical proof of the autocatalytic effect of polyconjugated nitrogen-containing systems, but also a reliable tool for controlling the PAN thermolysis rate.

Unfortunately, apart from [6], there are no new studies concerning the development and confirmation of the above hypothesis. With certain admissions, there are some analogies with the concept of self-associated multiplet in the coal structure [46], but, in this case, a consistent terminological system should be developed for combining the concepts of coal chemistry and physical chemistry of macromolecular compounds.

Some papers were published later on modification of fibrous PAN precursors for improving the quality of carbon fibers. As a rule, these studies concern certain modifications of the process of low-temperature treatment of commercial copolymeric PAN fibers. For example, Ko [47] tested a four-zone scheme of heat treatment of Courtelle fiber (copolymer of PAN with 6% methyl acrylate and 1% itaconic acid) at 190, 230, 230 (275), and 230 (200, 300°C) (in parentheses are temperatures of different experiments) for 145 min. Further carbonization was performed in dry nitrogen at temperatures of 400 to 1300°C (100°C steps) on an apparatus used in the previous study [48]. As a result, carbonized fibers with the maximal modulus of almost 200 GPa, tensile strength of 3.36 GPa, and density of 1.766 $g\,cm^{-3}$ were obtained.

In another paper [49], with the aim to improve the mechanical properties of PAN fibrous precursor of carbon fibers (Courtelle copolymer), Chen and Harrison applied postplasticization extension in dimethylformamide–water (80 : 20). As a result, the elongation of the precursor increased by 18% and the tensile strength, by 12%, and for the fibers carbonized at 1000°C these parameters increased by 68 and 14%, respectively. The treatment was accompanied by an increase in the long-range order (according to X-ray diffraction analysis) and removal of surface defects. As in the paper discussed above, transformations of the chemical structure of PAN were not discussed.

One more study of the modification of PAN precursors based on carbon fabric with KOH solutions was aimed to obtain porous carbon materials [50]. The suggested process allowed preparation of inert sorbents with a specific pore area of 2500–3000 $m^2\,g^{-1}$.

Interest in the mechanism of low-temperature carbonization is expressed in [47–52]. In a recent paper [53], a copolymer of acrylonitrile with 1% itaconic acid (MW 158000) was subjected to stabilizing heat treatment using a ten-zone heating scheme at temperatures from 195 to 253°C for 1 h. After the stabilization, the low-temperature carbonization in a flow of pure nitrogen and of nitrogen with an oxygen impurity was performed using a four-zone heating scheme at fixed temperatures from 100 to 600°C. Using a set of different samples and various analytical methods (DSC, Fourier IR spectroscopy, X-ray diffraction, ESR, elemental analysis) for examining the intermediate and final products of the heat treatment, the authors postulated a three-step mechanism of the stabilization and precarbonization of the fiber. The first step (300–450°C) involves cross-linking and aromatization under the action of free radicals generated by decomposition of oxygen-containing groups. In the second step (450–550°C), generation of free radicals is continued as a result of an avalanche-like degradation of linear fragments of the fiber. The process is characterized by superposition of numerous thermal oxidative reactions and results in the aromatization of

the whole structure. However, separate aromatic fragments do not exceed in size the fragments that existed before the pyrolysis. In the third step (550–600°C), cross-linking of ladder polymers into basic planar structures starts, and the polyaromatic formations grow in size.

However, the conclusions of [53] do not differ significantly from those made in numerous previous papers by other authors. Apparently, statistical accumulation of results of polyvariant experiments will ultimately lead to fixation of the main statements and conclusions concerning the specific features of PAN carbonization. K.E. Perepelkin, a prominent specialist in the field of synthetic fibers and their materials-science characteristics, arrived at such a conclusion. In [8] he distinguishes three steps of thermal oxidative transformations of PAN fibers: (1) fast diffusion of oxygen to external zones of the fiber and oxidation in this zone; (2) relatively slow cyclization of partially oxidized polymer in the external zone of the fiber; and (3) further oxidation and cyclization in the boundary zone, gradually moving to the fiber center at a rate controlled by diffusion processes.

During this time, the oxidation in the external zone with the formation of cyclic and polyene structures imparting black color to the fibers continues and comes to the end.

As for the chemical structure of oxidized PAN, a multiplet formula reflecting fragments of nitrogen-containing heterocycles with a certain amount of oxygen functional groups is reproduced with reference to [3, 6]. The supramolecular structure of these fibers preserves, on the whole, the main features of the initial PAN. In copolymeric PAN fibers, there is no 3*D* ordering because of the nonuniform chemical and steric structure of the macromolecule. An important role is played by orientation procedures in the course of fiber formation, namely, by the degree of stretching and tension in the course of oxidation. These factors enhance the strength, increase the strain modulus, and decrease the deformability of fibers.

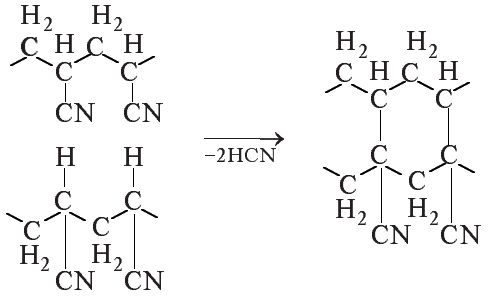
Depending on the structure of the raw material and a process used for preparing oxidized PAN fibers (Oksipan, the name suggested by Perepelkin [9]), the main physicomechanical parameters of these fibers vary within 10–30%: density, from 1.36 to 1.4 g cm^{-3}; breaking elongation, from 15 to 27%; strain modulus, from 7 to 10 GPa; strength, from 200 to 240 MPa; sorption of moisture from air (at 65% humidity and 20°C), from 8 to 9%; and oxygen index, from 45 to 50%. The bulk resistivity of the material exceeds 10^8 Ω m. Oksipan fibers are heat-resistant up to 300°C and higher temperatures. They are also resistant to acids of moderate concentrations, dilute alkalis, moderate oxidants, and all kinds of solvents.

These valuable properties of Oksipan fibers are used for high-temperature insulation in protective heat-insulating layers of clothes for hot shop workers, firemen, rescuers, and other dangerous professions, and also in interior of airplanes, trains, cars, ships, etc. The facile processing by common methods of textile industry, relatively low cost of Oksipan, low cost and availability of the precursor (PAN fibers), and relatively simple technology make the production of Oksipan fibers in Russia profitable and promising.

In these characteristics, Oksipan fibers are preferable to other heat-resistant fibers based on aromatic monomers and polymers, for which the starting monomers, multistep production process, and regeneration of production waste are incommensurably more expensive compared to the cost of production of PAN fibers. The above characteristics of PAN and the scheme of thermal oxidative transformations of PAN fibers under heat treatment at temperatures of up to 600°C refer to commercial copolymeric samples.

The apparent success in attainment of high thermomechanical characteristics of carbonized and graphitized PAN fibers at 1000–3000°C overshadowed the problem of the mechanism of the intermediate step of PAN carbonization, providing formation of regular carbon materials. In some papers concerning this problem [47, 48, 51, 52], the conclusions are based on the conclusions and schemes of early Watt's papers [54–57] on the mechanism of thermal oxidation of PAN copolymers.

In these schemes, possible combinations of carbo- and cyclochain structures are discussed in relation to the heat treatment conditions and steric arrangement of PAN macromolecules. The model of intermolecular cross-links yielding bridging pyridine rings and a ladder carbocyclochain structure deserves particular attention. In the latter process, cyano groups are partially eliminated in the form of HCN. The rest of cyano groups remain as substituents in the carbocyclic chain and do not participate in the formation of heterorings:



Because various pathways of thermochemical transformations of PAN are discussed for commercial copolymeric fibers, frequently without taking into account the effect of comonomers, studies of the thermochemistry of the homopolymers [20, 25, 58] are of particular interest. In the last study, we chose as objects three types of PAN. PAN of the first type was prepared by the anionic polymerization mechanism (A-PAN) in the presence of butyllithium. This polymer has a high molecular weight and a narrow molecular-weight distribution. It contains no low-molecular-weight fractions and branchings and is characterized by an increased parameter of the stereoblock structure. That is, it is the closest in molecular structure to the ideal polymer. PAN of the second type was prepared by the radical polymerization mechanism (R-PAN) in the presence of a widely used catalytic redox system. In contrast to A-PAN, R-PAN samples are characterized by high polydispersity, presence of branched polymer chains, noticeable content of low-molecular-weight fractions, and presence of oxygen-containing terminal groups. PAN of the third type is A-PAN partially cyclized in the course of the synthesis (C-PAN).

The samples were subjected to complex thermal analysis (TGA, DTA) in the temperature range 20–600°C. Calorimetric measurements revealed thermal effects in the range 400–600°C. Both exo- and endothermic effects were observed in thermograms of all the three PAN samples. The peak shapes suggest that these peaks reflect melting and crystallization processes.

Comparison of the peak temperatures, peak areas, and sequences of the thermal effects shows that the thermal effects are the most pronounced in A-PAN, less pronounced in C-PAN, and the least so in R-PAN. Such differences are apparently associated with the molecular-weight characteristics of the objects. It is known that thermal cyclization of R-PAN is accompanied by release of low-molecular-weight thermal degradation products [59]. This is due to the broad MWD and to the presence of branchings in R-PAN chains. Therefore, the density of packing of R-PAN macromolecules upon precipitation from solution is low, and samples are oxidized more actively, which is reflected in the temperature and area of the exothermic peak. Structural features of A-PAN samples are responsible for their higher density and for the corresponding changes in thermal effects compared to R-PAN. The 3*D* ordering of A-PAN macromolecules is an additional factor responsible for the high packing density.

In solution, A-PAN macromolecules can be represented as double helices linked by a series of weak bonds betwen the cyano groups and α-H atoms, between the cyano groups of the adjacent chains, and sometimes between the naphtharidine rings [3, 13, 32]. These structural features of A-PAN lead to the predominant occurrence of the cyclization, compared to thermal degradation, which is reflected in the TG and DTA curves. Furthermore, the stereoblock structure of A-PAN is apparently responsible for the presence of two endothermic effects in the range 400–600°C, each of which reflects the melting of the iso- or syndiotactic block. R-PAN may also contain ordered blocks, but their size and relative content are considerably smaller than in A-PAN. As for the DTA curve of the C-PAN sample, the shift of the temperature maxima of its two endothermic peaks reflects the enhanced heat resistance of the cyclic stereoblocks formed in the course of the synthesis.

The pattern of low-temperature carbonization of PAN shows that the "diffusion factor" should be taken into account for structural rearrangements to occur in the direction of formation of new condensed structure. This factor, well known in the coal chemistry, is associated with the hindered escape of low-molecular-weight thermal degradation products from the area of thermochemical reactions. As a result, the degradation $\rightleftarrows$ cross-linking balance is shifted to the right.

The simplest way to obtain effect is to raise the weighed portion and density of the substance, and also the time of heat treatment in the isothermal mode. By so doing, it becomes possible to monitor more clearly the thermal phase changes in the PAN samples. The most pronounced pattern is observed with the A-PAN sample on keeping it for 10 h at 350°C. At this temperature, the exothermic process of A-PAN cyclization with the formation of the most oriented stereoblocks of the syndiotactic structure is complete. Because this process is charac-

ter-ized by the lowest activation energy, compared to isotactic A-PAN and R-PAN, prolonged heating at 350°C leads to gradual formation of segments of a turbostratic structure, which melt at 407, 443, and 489°C and are related to different steric orientations of the cyclic blocks formed in the polymer. At lower annealing temperatures, the block structure is formed incompletely, and heating to higher temperatures leads to degradation of strained cyclic blocks and to the progress of carbonization.

The role of the diffusion factor was revealed in measurements of the packing density. Irrespective of the PAN synthesis procedure, the packing density of a sample and its isolation from the oxidizing environment strongly affect the pattern of thermal effects in the samples tested. Some of the samples exhibit not only the growth of the energy of endothermic effects associated with quantitative characteristics of ordered areas, but also exothermic effects assignable to crystallization of the labile structure of the precarbonizate. It should be noted that the sample compaction leads to an increase in the coke number, compared to small powdered samples.

An additional indirect evidence for the structural rearrangement of PAN in the temperature range 400–600°C, with the formation of ordered turbostratic fragments, is provided by data on the structural polymorphism of coals in the same temperature range. According to X-ray diffraction data [11, 37], the maximum of the internetwork ordering is observed at 450–525°C, i.e., in the range of the plastic state of coals and formation of semicoke. As the temperature is raised to 700°C, the mutual ordering of networks forming the carbon structures is disturbed, and they undergo disorientation, which is followed at temperatures exceeding 1000°C by the repeated orientation on the level of graphitizing structures. The decrease in the internetwork ordering above 700°C is attributed to the "wedging" effect of the growing carbon networks, with the preservation of strong valence bonds between them through the irregular part of the structure, which prevents mutual ordering of the networks.

Thus, even in such a complex system as coking coals, there is a temperature zone of increased molecular ordering, in which ordered carbon structures with well-defined orientation parameters are formed. The coincidence of the temperature boundaries of this zone with the region of occurrence of the endo- and exothermic effects in PAN suggests a certain analogy between these processes.

The above-noted similarity between the low-temperature carbonization of PAN and structurization of coals supports the concept of polymer cocarbonization [60] via thermochemical reactions of two polymers to give carbon structures whose thermal characteristics differ from those of the starting compounds.

An additional evidence of the low-temperature structural rearrangement on the level of formation of transition states from the polymer macromolecule to nuclei of the oriented carbon structure is obtained by comparing the results of X-ray monitoring of the carbonization of poly-*p*-phenylenebenzoxazole and PAN [61]. It was noted in that study that a combination of the high heat resistance of a polymer with a sufficient homogeneity of the supramolecular structure provides smooth transition into polyaromatic oriented compounds, precursors of graphite-like formations.

Because pyrolysis of poly-*p*-phenylenebenzoxazole occurs at approximately 500°C and aromatic structures are accumulated at the same temperature, conditions are created for combination of sixmembered rings in a plane with 2*D* ordering. This structure has a high density and is characterized by regular alternation of denser carbon areas and less dense polycondensation areas of the initial polymer structure. Hence, the turbostratic structure of carbon arises before complete breakdown of crystallites in amorphous intercrystallite areas of polyoxadiazole. Similar conclusions were made for carbonization of hydrated cellulose and PAN. All these observations and conclusions confirm the existence of ordered polymer–carbon oriented formations whose thermal effects were recorded calorimetrically [58].

An additional valuable property of PAN is that it is possible to obtain different kinds of precursors by blending with other polymers, in the form of both fibers and composites with thermosetting plastics or castable thermoplastics for production of various articles. This field is being actively developed now on the basis of the suggested principles of cocarbonization of polymers [60], whose essence consists in performing thermochemical reactions in the temperature range of the maximal thermal activity of the components. In this case, the temperature boundaries of the thermal stability of the components should be close, and the process is performed under diffusion control, with prolonged heat treatment in the isothermal mode.

These studies were initiated by reports devoted to cyclization and carbonization of polyimides and their blends with nitrogen-containing poilymers

[62–66]. These studied revealed the occurrence of thermochemical reactions of intermediates formed by degradation and cross-linking of prepolymers with components of the polymer blend. Further development of cocarbonization studies is associated with an attempt to avoid technological and economic problems in the synthesis of polyimides and their compositions. For this purpose, we chose PAN as the most mastered and the cheapest heat-resistant synthetic polymer, meeting the cocarbonization requirements in a number of parameters. As the second component we used natural polymers whose resources are renewable or which are large-tonnage wastes from various branches of process industry.

In the PAN–natural polymer combination, synthetic heat-resistant PAN can act as a modifier of a natural polymer, improving its physicochemical characteristics. These studies were started with an analysis of the thermal compatibility of PAN with chitin and chitosan [68, 69]. It was shown that PAN interacts most efficiently with chitin and chitosan in the temperature range 150–350°C. In this range, PAN undergoes thermal oxidative dehydrogenation and cyclization via nitrile groups, and the acetamido- and aminodeoxyglucopyranose rings in chitin and chitosan undergo active thermal degradation to give a wide range of low-molecular-weight oxygen- and nitrogen-containing compounds. It is difficult to follow in such reaction mixture the formation of new structures and to identify them. However, indirect evidence was obtained for certain changes in the thermochemistry of the forming composite system, relative to the initial components.

Experiments with cyanoethyl cellulose ethers as model compounds showed that the structure of the forming carbon residue is different from that of the residue formed from the initial polymers, and its amount exceeds the amount corresponding to the coke number of PAN. It was also found that, to improve the compatibility of the components, it is desirable to perform the thermochemical cocarbonization in blend films prepared from combined solutions of the components in an aprotic polar solvent. Preliminary joint solvation based on the formation of interpolymeric complexes in the temperature range of PAN cyclization (230–300°C) gives cocarbonization products in 70–80% yield at 800°C. The composite films have high strength, well comparable with that of PAN (breaking stress 48–65 MPa, breaking elongation 1.5–2.7, Young's modulus 3000–3500 MPa) [69]. As for cocarbonization with PAN of certain grafted cellulose ethers [59, 70], the role of PAN consists in an appreciable enhancement of the heat resistance of the composite and in an increase in the coke number as compared to the cellulose ethers taken separately. In turn, the products of the initial thermal degradation of cellulose derivatives make the onset temperature of PAN cyclization lower by 50–60°C. The gas medium also plays an important role in the cocarbonization of PAN with hydroxyethyl, allyloxyethyl, and allyloxycarbonylmethyl cellulose ethers, affecting the thermal cross-linking in the self-generated atmosphere. The highest coke number reaching 55–60% was obtained with graft copolymers carbonized in CO_2.

Along with cellulose derivatives, it is of interest to use another natural polymer genetically closely related to cellulose, lignin. The first attempt to perform cocarbonization of lignin with PAN was made in [71]. Already the first experiments with powdered samples revealed a catalytic effect of thermal degradation products of lignin on the kinetics of thermal stabilization of PAN. Introduction of limited amounts of PAN into lignin enhanced its heat resistance in an inert atmosphere in the range 200–300°C. Carbonizates of PAN–lignin blends differ in their characteristics from carbonizates of the polymers taken separately.

CONCLUSIONS

(1) The carbonization of polyacrylonitrile is a permanent competition of the thermal degradation the and cross-linking in all the steps of thermochemical transformations.

(2) The mechanism of carbonization of macromolecular compounds and the properties of the final carbon products depend on numerous factors governing the structure and properties of carbonizates. The main of these are the procedure for preparing the initial polymer, heat treatment conditions, presence of additional compounds in the sphere of thermochemical reactions, and, as a rule, specific features of the process for preparing carbon materials.

(3) The overwhelming majority of studies have applied purposes and do not allow unambiguous conclusions on the actual mechanism of polyacrylonitrile carbonization under "pure" experimental conditions.

REFERENCES

1. Konkin, A.A., *Uglerodnye i drugie zharostoikie vo-*

loknistye materialy (Carbon and Other Heat-Resistant Fibrous Materials), Moscow: Khimiya, 1974.
2. *Armiruyushchie khimicheskie volokna dlya kompozitsionnykh materialov* (Reinforcing Chemical Fibers for Composite Materials), Moscow: Khimiya, 1992.
3. Beevers, R.B., *Macromol. Rev.*, 1968, vol. 3, pp. 113–254.
4. Zil'berman, E.N., *Usp. Khim.*, 1968, vol. 55, no. 1, pp. 62–77.
5. Fialkov, A.S., *Uglerod, mezhsloevye soedineniya i kompozity na ego osnove* (Carbon and Intercalation Compounds and Composites Based on It), Moscow: Aspekt, 1997.
6. Varshavskii, V.Ya., *Obzornaya informatsiya* (Review), *Ser.: Promyshlennost' khimicheskikh volokon* (Chemical Fiber Industry), Moscow: NIITEKhIM, 1989, pp. 1–56.
7. Varshavskii, V.Ya., *Uglerodnye volokna* (Carbon Fibers), Moscow: Varshavskii, 2005.
8. Perepelkin, K.E., *Khim. Volokna*, 2003, no. 6, pp. 3–8.
9. Perepelkin, K.E., *Khim. Volokna*, 2002, no. 4, pp. 32–40.
10. Levit, R.M., *Elektroprovodyashchie khimicheskie volokna* (Conducting Chemical Fibers), Moscow: Khimiya, 1986.
11. *Strukturnaya khimiya ugleroda i uglei* (Structural Chemistry of Carbon and Coals), Kasatochkin, V.I., Ed., Moscow: Nauka, 1969.
12. Watt, W., *Nature*, 1959, vol. 222, no. 5190, pp. 265–266.
13. Henrici-Olive, G. and Olive, S., *Adv. Polym. Sci.*, 1979, vol. 32, pp. 125–152.
14. Takata, T., Ishii, H., Nishiyama, Y., and Taniyama, M., *Kobunshi Kogaku*, 1961, vol. 18, no. 192, pp. 236–239.
15. Takata, T., Hiroi, I., and Taniyama, M., *J. Polym. Sci. A*, 1964, vol. 2, pp. 1567–1585.
16. Grassie, N. and Hay, J.N., *J. Polym. Sci.*, 1962, vol. 56, pp. 189–193.
17. Schurz, J., *J. Polym. Sci.*, 1958, vol. 28, pp. 438–441.
18. Kubasova, N.A., Din' Suan Din', Geidrikh, M.A., and Shishkina, M.V., *Vysokomol. Soedin., Ser. A*, 1971, vol. 13, no. 1, pp. 162–167.
19. Khachaturov, A.S., Abramenko, E.L., Novoselova, A.V., et al., *Vysokomol. Soedin., Ser. A*, 1988, vol. 30, no. 6, pp. 891–896.
20. Sazanov, Yu.N., Novoselova, A.V., Amsharov, K.Yu., et al., *Zh. Prikl. Khim.*, 2005, vol. 78, no. 5, pp. 810–813.
21. Grassie, N. and McGuchan, J., *Eur. Polym. J.*, 1970, vol. 6, no. 9, pp. 1277–1291.
22. Grassie, N. and McGuchan, J., *Eur. Polym. J.*, 1971, vol. 7, no. 8, pp. 1091–1109.
23. Grassie, N. and McGuchan, J., *Eur. Polym. J.*, 1971, vol. 7, no. 10, pp. 1357–1371.
24. Grassie, N. and McGuchan, J., *Eur. Polym. J.*, 1972, vol. 8, no. 7, pp. 865–878.
25. Gribanov, A.V. and Sazanov, Yu.N., *Zh. Prikl. Khim.*, 2000, vol. 73, no. 3, pp. 465–469.
26. Sazanov, Yu.N. and Shibaev, L.A., *Acta Polym.*, 1980, vol. 31, no. 1, pp. 1–19.
27. Gribanov, A.V., Milevskaya, I.S., Lukashcheva, N.V., et al., *Vysokomol. Soedin., Ser. A*, 1989, vol. 31, no. 8, pp. 1572–1576.
28. Gribanov, A.V., Grebenkin, A.N., Elkin, A.Yu., et al., *Vysokomol. Soedin., Ser. A*, 1989, vol. 31, no. 11, pp. 2277–2281.
29. Rosenbaum, S., *J. Appl. Polym. Sci.*, 1965, vol. 9, no. 12, pp. 2071–2080.
30. Novoselova, A.V., Zgonnik, V.N., Sazanov, Yu.N., et al., *Vysokomol. Soedin., Ser. A*, 1992, vol. 34, no. 3, pp. 5963–5971.
31. Spirina, T.N., Novoselova, A.V., Sazanov, Yu.N., et al., *Vysokomol. Soedin., Ser. A*, 1992, vol. 34, no. 5, pp. 31–37.
32. Rumynskaya, I.G., Agranova, S.A., Novoselova, A.V., et al., *Vysokomol. Soedin., Ser. A*, 1999, vol. 41, no. 6, pp. 1–5.
33. Kanovich, M.M. and Rudenko, A.P., *Khim. Volokna*, 1982, no. 3, pp. 19–21.
34. Frolova, V.I., Fishberg, A.M., Samoilov, V.M., et al., *Khim. Volokna*, 1980, no. 1, pp. 225–229.
35. Davydov, B.E. and Krentsel', B.A., *Vysokomol. Soedin., Ser. A*, 1979, vol. 21, no. 5, pp. 963–978.
36. Geidrikh, M.A., Davydov, B.E., and Krentsel', B.A., *Izv. Akad. Nauk SSSR, Ser. Khim.*, 1965, no. 4, pp. 636–639.
37. Artemov, V.B., Eremin, I.V., Lisurenko, A.V., and Gagarin, S.G., *Usloviya obrazovaniya i kharakternye priznaki dinamicheski aktivnykh uglei* (Formation Conditions and Characteristic Features of Dynamically Active Coals), Moscow: Nedra, 1999.
38. Tsvetanov, Ch.B., Eizner, Yu.Ye., and Erusalimsky, B.L., *Eur. Polym. J.*, 1980, vol. 16, pp. 219–226.
39. Novoselova, A.V., Erusalimskii, B.L., Krasulina, V.N., and Zashcherinskii, E.V., *Vysokomol. Soedinen., Ser. A*, 1971, vol. 13, no. 1, pp. 87–90.
40. Novoselova, A.V., Nefedov, P.P., Frenkel', S.Ya., et al., *Vysokomol. Soedin., Ser. B*, 1974, vol. 16, no. 10, pp. 751–756.
41. Klimenko, I.B., Platonova, N.V., Novoselova, A.V., et al., *Vysokomol. Soedin., Ser. A*, 1995, vol. 37, no. 6, pp. 969–973.
42. Spirina, T.N., Sazanov, Yu.N.., Shibaev, L.A., et al., *J. Therm. Anal.*, 1990, vol. 36, pp. 2329–2338.
43. Romanova, E.P., Rumynskaya, I.G., Agranova, S.A., and Frenkel, S.Ya., *Acta Polym.*, 1989, vol. 40, no. 10, pp. 639–642.
44. Varshavskii, V.Ya., *Vysokomol. Soedin., Ser. A*, 1983, vol. 25, no. 4, pp. 823–830.
45. Kozykina, M.A., Faiberg, E.Z., Papkov, S.P., et al.,

Vysokomol. Soedin., Ser. A, 1980, vol. 22, no. 11, pp. 2598–2602.
46. Krichko, A.A., Gagarin, S.G., and Makar'ev, S.S., *Khim. Tverd. Topl.*, 1994, no. 6, pp. 27–41.
47. Ko, T., *J. Appl. Polym. Sci.*, 1991, vol. 42, pp. 1949–1957.
48. Ko, T., *J. Appl. Polym. Sci.*, 1989, vol. 37, pp. 541–547.
49. Chen, J.C. and Harrison, I.R., *Carbon*, 2002, vol. 40, no. 1, pp. 25–45.
50. Wu, M., Zha, Q., Qia, J., et al., *Carbon*, 2004, vol. 42, no. 2, pp. 205–210.
51. Ko, T., Day, T., Preng, J., and Lin, M., *Carbon*, 1993, vol. 31, no. 5, pp. 765–771.
52. Ko, T., Day, T., and Lin, M., *J. Mater. Sci. Lett.*, 1993, vol. 12, no. 3, pp. 343–345.
53. Jing, M., Wang, C.G., Wang, Q., et al., *Polym. Degrad. Stab.*, 2007, vol. 92, pp. 1737–1742.
54. Moreton, R. and Watt, W., *Nature*, 1967, vol. 213, pp. 690–692.
55. Watt, W. and Johnson, W., *Appl. Polym. Symp.*, 1969, no. 9, pp. 215–227.
56. Watt, W., *Carbon*, 1972, vol. 10, pp. 121–127.
57. Watt, W. and Johnson, W., *Nature*, 1975, vol. 257, pp. 210–212.
58. Sazanov, Yu.N., Novoselova, A.V., Fedorova, G.N., et al., *Zh. Prikl. Khim.*, 2007, vol. 80, no. 12, pp. 2046–2050.
59. Sazanov, Yu.N., Kutsenko, L.I., and Novoselova, A.V., *Zh. Prikl. Khim.*, 2005, vol. 78, no. 4, pp. 652–654.
60. Sazanov, Yu.N. and Gribanov, A.V., *Zh. Prikl. Khim.*, 2006, vol. 79, no. 3, pp. 440–445.
61. Dobrovol'skaya, I.P., Chareiskii, Z.Yu., and Stark, I.S., *Vysokomol. Soedin., Ser. A*, 1981, vol. 23, no. 6, pp. 1261–1267.
62. Mokeev, M.V., Gribanov, A.V., Sazanov, Yu.N., et al., *Zh. Prikl. Khim.*, 2005, vol. 78, no. 7, pp. 1165–1168.
63. Sazanov, Yu.N., *Zh. Prikl. Khim.*, 2001, vol. 74, no. 8, pp. 1217–1234.
64. Gribanov, A.V., Sazanov, Yu.N., Beloborodova, E.V., and Fedorova, G.N., *Zh. Prikl. Khim.*, 1999, vol. 72, no. 3, pp. 467–473.
65. Gribanov, A.V. and Sazanov, Yu.N., *Zh. Prikl. Khim.*, 2000, vol. 73, no. 6, pp. 987–991.
66. Gribanov, A.V., Mokeev, M.V., and Sazanov, Yu.N., *Zh. Prikl. Khim.*, 2002, vol. 75, no. 9, pp. 1513–1516.
67. Sazanov, Yu.N., Nud'ga, L.A., Novoselova, A.V., et al., *Zh. Prikl. Khim.*, 2004, vol. 77, no. 4, pp. 643–648.
68. Sazanov, Yu.N., Novoselova, A.V., Nud'ga, L.A., et al., *Zh. Prikl. Khim.*, 2005, vol. 78, no. 8, pp. 1344–1348.
69. Sidorovich, A.V., Sazanov, Yu.N., Prasolova, O.E., et al., *Zh. Prikl. Khim.*, 2006, vol. 79, no. 8, pp. 1341–1344.
70. Sazanov, Yu.N., Nud'ga, L.A., Petrova, V.A., et al., *Zh. Prikl. Khim.*, 2004, vol. 77, no. 8, pp. 1366–1369.
71. Sazanov, Yu.N., Fedorova, G.N., Kulikova, E.M., et al., *Zh. Prikl. Khim.*, 2007, vol. 80, no. 4, pp. 632–636.

ISSN 1070-4272, Russian Journal of Applied Chemistry, 2008, Vol. 81, No. 6, pp. 933–941. © Pleiades Publishing, Ltd., 2008.
Original Russian Text © V.I. Samoilov, A.N. Borsuk, N.A. Kulenova, B.V. Syrnev, V.A. Agapov, O.A. Utesheva, 2008, published in Zhurnal Prikladnoi Khimii, 2008, Vol. 81, No. 6, pp. 895–903.

INORGANIC SYNTHESIS AND INDUSTRIAL INORGANIC CHEMISTRY

A Study of the Chemical Stability of Beryl and of the Product of Its Mechanical Activation against Sulfuric Acid

V. I. Samoilov, A. N. Borsuk, N. A. Kulenova, B. V. Syrnev, V. A. Agapov, and O. A. Utesheva

Ul'ba Metallurgical Plant Joint-Stock Company, Ust-Kamenogorsk, Kazakhstan
Eastern-Kazakhstan State Technical University, Ust-Kamenogorsk, Kazakhstan

Received May 23, 2007

Abstract—Effect of the concentration of sulfuric acid used for beryl sulfatization, degree of beryl grinding, temperature and duration of beryl sulfatization, and other technological parameters of sulfuric acid decomposition on the extent of beryl recovery was studied. The results obtained made it possible to suggest a method for preparation of beryl concentrates for sulfatization. The method is based on a mechanochemical activation of this kind of raw materials and can serve as an alternative to the conventionally employed beryl activation techniques.

DOI: 10.1134/S1070427208060025

Of all the industrially used beryllium minerals, beryl is the most resistant to sulfuric acid and other chemical reagents. Only hydrofluoric acid reacts to a hardly noticeable extent with beryl at ordinary temperatures [1]. An X-ray diffraction analysis of beryl demonstrated that it contains discrete ring ions $Si_6O_{18}^{12-}$ symmetrically surrounded by Be^{2+} ions (coordination number 4) and Al^{3+} (coordination number 6). The metal ions are fully screened by the silicate rings [3], which accounts for the chemical inertness of the mineral.

Beryl reacts with sulfuric acid very slowly, but the reaction can be noticeably accelerated under certain conditions. For example, the reaction of beryl with concentrated sulfuric acid at 400°C in an autoclave can transfer up to 50–60 wt % of beryllium into a water-soluble form in several hours [4]. The reaction is accelerated in the presence of fluoride, which presumably occurs under the action of the forming hydrogen fluoride. Because published data on the rate of the reaction between beryl and sulfuric acid and on the extent of this process are unavailable, it is impossible to assess the advisability of direct industrial sulfatization of beryl. Therefore, the rate of the reaction between beryl from beryl concentrates and sulfuric acid taken in various concentrations was studied.

Eleven batches of beryl concentrates from Malyshevskoe and Zavitinskoe deposits were used in the study (Tables 1 and 2). Analysis of the data in Table 2 shows that, compared with the Zavitinskoe concentrates (batch nos. 5 and 7), the Malyshevskoe concentrates (batch nos. 1–4, 6, and 8) contain a substantially larger amount of calcium (by a factor of ~4); a several times larger amount of iron, manganese, and chromium; a noticeably larger amount of aluminum (by ~15 wt %), and a noticeably smaller amount of silicon (by ~30 wt %).

Decomposition of the beryl concentrate with concentrated sulfuric acid. A weighed (~105 g) portion of the concentrate from batch no. 1 (Tables 1, 2) was ground in a vibration grinder for 30 min and processed by the scheme using the following technological procedure (see scheme). Sulfatization: initial weighed portion of the concentrate 100 g, expenditure of 93% sulfuric acid 0.8 ml g^{-1} concentrate (cake), T = 250–300°C, and duration 5 h (with the reaction mass agitated with a spar every 30 min in the course of sulfatization); leaching: s : l = 1 : (4–6) (in terms of the starting concentrate), T = 95°C, and duration 20 min (with the slurry volume maintained constant in the course of leaching by permanent addition of distilled water); neutralization of the slurry to pH 3.0–3.5 (with

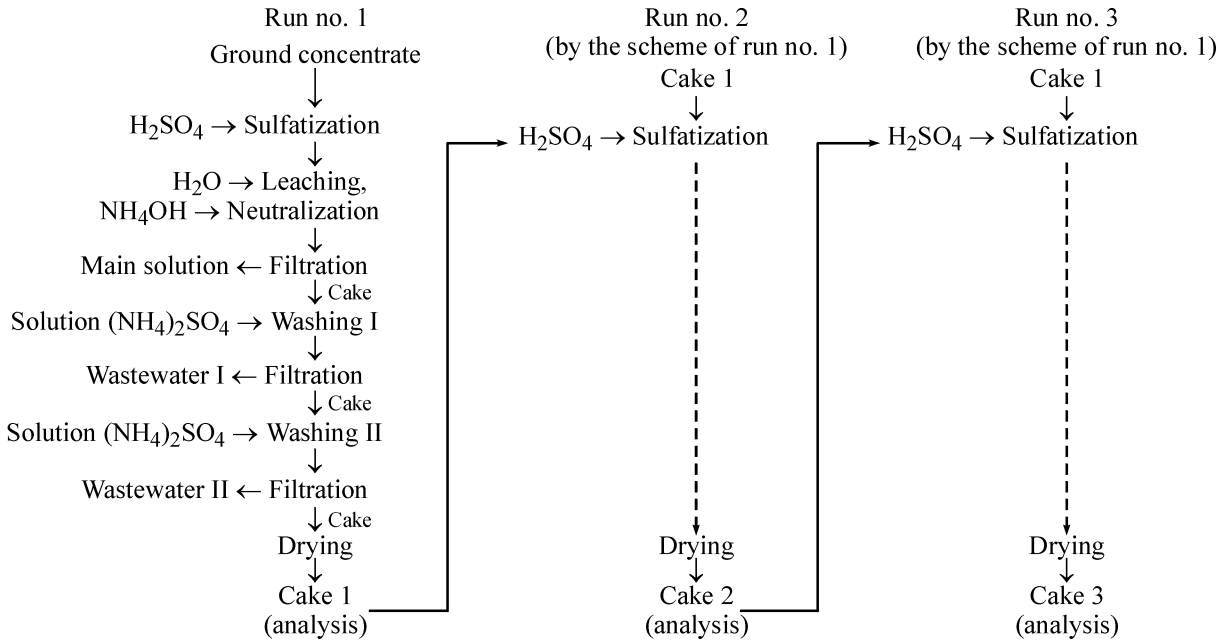
Table 1. Mineralogical composition of analyzed batches of beryl concentrates and grain size of their minerals

Mineral	Batch no. 1		Batch no. 2		Batch no. 4		Batch no. 5	
	c, wt %	grain size, mm	*c*, wt %	grain size, mm	*c*, wt %	grain size, mm	*c*, wt %	grain size, mm
Beryl	34	0.2–0.3	33	0.3	54	0.5–2.0	39	0.03–0.15
Emerald	–	–	–	–	3	0.2–0.3	–	–
Spodumene	–	–	–	–	–	–	16	0.2–0.5
Quartz, feldspars	28	0.3	38	0.3	36	0.1–1.0	30	0.2–0.3
Muscovite	20	0.5–0.7	7	0.3	3	0.3–0.4	1	0.2–0.3
Apatite	4	0.3	8	0.3	1	0.2	1	0.1–0.2
Scheelite	3	0.2	3	0.2	–	–	–	–
Biotite	3	0.5–0.7	–	–	–	–	2	0.15–0.2
Fluorite	2	0.4	2	0.3	–	–	–	–
Carbonates	2	0.2	4	0.25	1	0.3	Trace amounts	0.1–0.2
Chlorite	2	0.5–0.7	–	–	–	–	–	–
Tourmaline	1	0.1–0.4	4	0.2–0.3	1	0.25	1	0.1–0.2
Rutile	1	0.1–0.3	1	0.1–0.2	–	–	Trace amounts	0.05–0.1
Magnetite, limonite in terms of magnetite	–	–	–	–	1	0.2	2	0.2
Pyrite	–	–	Trace amounts	0.2	–	–	–	–
Carbonaceous-clayey shale	–	–	–	–	–	–	8	0.3–0.4

Table 2. Content of beryllium and impurities in beryl concentrates*

Batch no. (corresponding to Table 1)	Content, wt %							
	Be	Al	Si	Fe	Mn	Ca	F	Cr
1	1.88	8.22	19.10	1.50	0.190	4.80	2.16	–
2	1.75	12.61	21.11	1.22	0.033	7.14	1.98	–
3	1.81	9.85	21.88	3.27	0.630	5.12	–	0.0220
4	4.27	–	–	–	–	–	–	–
5	1.92	7.50	29.23	0.66	0.040	1.30	–	0.0026
6	1.90	8.06	21.91	6.21	2.970	4.80	–	0.0360
7	2.00	7.66	30.45	0.56	0.039	1.34	–	0.0030
8	1.89	11.48	20.97	1.23	0.064	8.28	2.65	0.0310
9	1.85	–	–	–	–	–	–	–
10	1.78	–	–	–	–	–	–	–
11	1.72	–	–	–	–	–	–	–

* Batch nos. 1–4, 6, 8–11, Malyshevskoe concentrate; nos. 5 and 7, Zavitinskoe concentrate; batch no. 4 is an ore-sorting concentrate with a grain size of 5 mm (analyzed upon a preliminary grinding in a mortar), and other batches, flotation concentrates.



Scheme of laboratory processing of the Malyshevskoe concentrate.

a 8–10% ammonia solution); 1st washing of the cake with a 5% ammonium sulfate solution acidified with sulfuric acid to pH 3.0–3.5, s : l = 1 : 7 (in terms of the starting concentrate), T = 95°C, and duration 15 min; 2nd washing of the cake with a 5% ammonium sulfate solution acidified with sulfuric acid to pH 3.0–3.5 in the mode used in the 1st washing.

The results of pilot studies (Table 3) show that the sulfuric acid decomposition of the beryl concentrate provides an, on average, 23% recovery of beryllium into solution in each stage of the multistage process, with the four-stage sulfatization of the concentrate resulting in a beryllium recovery into a sulfate solution of 65.4 wt % (Table 3). Extrapolation of the dependence of the extent of beryllium recovery into solution on the sulfatization time (Fig. 1a) enables prognostication of its complete transfer into solution after a 70-h multistage sulfatization of beryl.

Decomposition of the beryl concentrate with dilute sulfuric acid. In this set of experiments, sulfuric acid solutions with concentrations of 85, 77, 73, 71, 70, 69, 68, and 61 wt % were used. Prior to sulfatization, 27–105 g of the Malyshevskoe concentrate (Tables 1, 2; batch no. 1) were ground in

Table 3. Results of experiments on decomposition of the Malyshevskoe concentrate

Stage of sulfuric acid decomposition	Be content of the cake	Cake yield in a stage	Be recovery into solution in a stage (in terms of cake)	Overall Be recovery into solution (in terms of cake)
	wt %			
I*	1.84	76.8	24.8	24.8
II**	1.70	84.0	22.4	41.2
III**	2.04	65.8	21.0	54.4
IV**	2.12	73.0	24.1	65.4
Average 23.1				

* According to the results of two parallel runs.

** According to the results of a single runs.

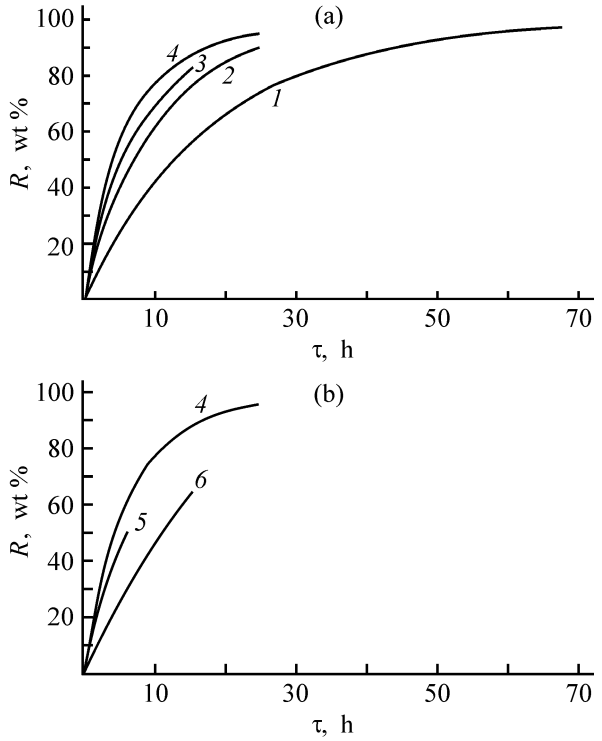


Fig. 1. Degree R of beryllium recovery from the concentrate into a sulfate solution vs. the sulfatization duration τ at initial sulfuric acid concentrations of (a) 69–93 and (b) 61–69 wt %. Sulfuric acid concentration (wt %): (*1*) 93, (*2*) 85, (*3*) 77, (*4*) 69, (*5*) 68, and (*6*) 61.

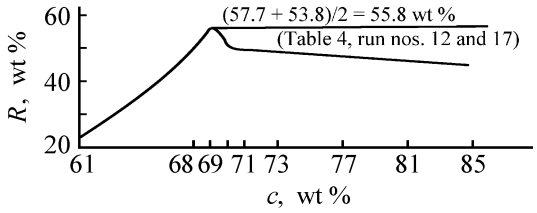


Fig. 2. Estimate of the extent R of beryllium recovery with sulfuric acid in relation to its concentration c. τ_{sulf} = 5 h.

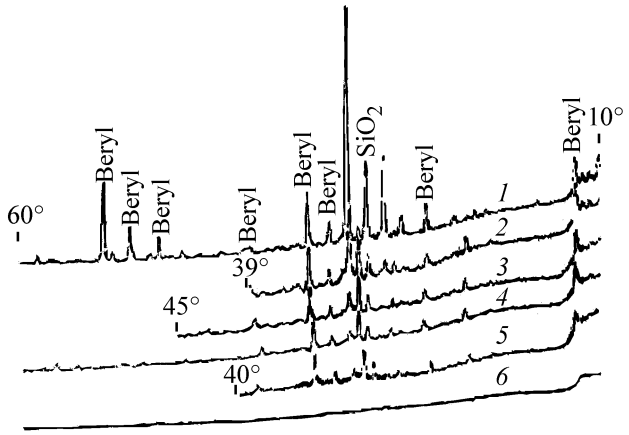


Fig. 3. X-ray diffraction patterns of a beryl concentrate (reflection angles 10°–60°) mechanically activated for varied intervals of time. (*1*) Without grinding; grinding: (*2*, *3*, *4*, *5*) in a vibration grinder for 0.5, 2.5, 5.0, and 7.5 h, respectively; (*6*) in a planetary mill for 0.5 h.

a vibration grinder for 30 min. The ground product was processed in one to five decomposition stages in the following technological mode. Sulfatization: initial weighed portion of the concentrate 20–100 g, expenditure of a sulfuric acid solution 20 ml g^{-1} concentrate (cake), and duration 5 h; further by the above scheme: leaching, slurry neutralization, 1st washing of the cake, and 2nd washing of the cake.[1] It follows from the results obtained in the experiment (Fig. 2) that the optimal sulfuric acid concentration providing the maximum decomposition rate of beryl is 69 wt % (Fig. 2). The industrially acceptable decomposition of beryl with 93% sulfuric acid requires 50–70 h (Fig. 1a), and that with 69% sulfuric acid takes only 17–25 h.

[1] The sulfatization of the concentrate (cake) was performed at the boiling point and continuous agitation of the slurry, with its initial volume maintained by addition of a sulfuric acid solution of the corresponding concentration. After the sulfatization was complete, the slurry was diluted 3-4-fold (by volume) with distilled water and filtered. The filtered-off cake was leached and processed in accordance with the technological mode.

The presently achieved extent of the sulfuric acid decomposition of beryl is 55 wt %, with the mineral sulfatized with a concentrated sulfuric acid in an autoclave during several hours. The study demonstrated that the same extent of decomposition (55.8 wt %) is reached in 5 h of sulfatization under atmospheric pressure if sulfuric acid of the optimal concentration (69 wt %) is used (Table 4, Fig. 2).

The possibility of raising the extent of beryl dissolution (Table 1, 2; batch no. 1) by preliminary mechanical activation of the beryl concentrate on a laboratory vibration grinder and a planetary mill was studied. Table 5 and Fig. 3 present results of a morphological and an X-ray structural analyses of a concentrate mechanically activated during varied time. Despite that the average particle size of the concentrate almost does not decrease after 30 min of mechanical activation on a vibration grinder, the crystal lattice of the minerals being ground progressively disintegrates during 7.5 h of mechanical activation. With the planetary mill used, the crystal lattices of the minerals in the concentrate disin-

Table 4. Results of experiments on decomposition of the Malyshevskoe concentrate with dilute sulfuric acid

Run no.	$c_{H_2SO_4}$, wt %	Stage of sulfuric acid decomposition	T_{sulf}, °C	Be content of the cake	Yield of cake in a stage	Be recovery into solution in a stage (in terms of cake)	Overall recovery of Be into solution (in terms of cake)
				wt %			
1	85	I	235	2.265	49.0	41.0	41.0
2		II		2.48	62.1	32.0	59.9
3		III		2.41	59.7	42.0	76.7
4		IV		2.39	64.2	36.4	85.2
5		V		2.53	73.0	22.8	88.6
						Average	34.84
6	77	I	195	1.93	48.0	50.7	50.7
7		II		2.08	64.8	30.2	65.6
8		III		2.20	51.1	46.0	81.4
						Average	42.3
9	73	I	180	1.98	47.7	49.8	49.8
10	71	I	175	2.06	46.6	48.9	48.9
11	70	I	170	2.12	45.8	48.4	48.4
12	69	I	165	2.06	38.6	57.7	57.7
13		II		1.97	54.8	47.6	77.8
14		III		1.87	67.03	6.4	85.9
15		IV		2.26	56.7	31.5	90.3
16		V		5.24	20.0	54.0	95.54
						Average	45.44
17	69	I	165	2.07	42.0	53.8	53.8
18	68	I	160	2.04	45.9	50.2	50.2
19	61	I	145	2.29	63.6	22.53	22.53
20		II		2.296	68.5	31.3	46.8
21		III		2.3	62.2	37.7	66.9
						Average	30.51

Table 5. Granulometric composition of the Malyshevskoe beryl flotation concentrate (analysis by the number of particles) (weighed portion of the concentrate, used for mechanical activation, 27–31 g)

Grinding duration, h	Particle size, μm		Grinding duration, h	Particle size, μm	
	maximum	average		maximum	average
No grinding	175.00	12.87	5.0	37.50	2.58
0.5	37.50	2.35	7.5	35.00	2.37
2.5	37.50	2.25	0.5*	9.38	1.90

* Grinding in a planetary mill; in the rest of the runs, in a vibration grinder.

Table 6. Results of an experiment on decomposition of a mechanically activated beryl concentrate

Run no.	T_{sulf}, °C	Be content of the cake	Yield of cake	Be recovery into solution (in terms of cake)
		wt %		
1*	165	2.13	28.4	67.8
2	165	2.06	38.6	57.7

* Weighed portion of the concentrate in the stage of its mechanical activation was 27 g.

Table 7. Results* of experiments on dissolution of a beryl concentrate mechanically activated in a vibration grinder

Duration of concentrate grinding, h	Be recovery into solution (in terms of cake), wt %
2.5	72.9
5.0	78.0
7.5	81.0

* Averaged over 3–4 runs.

tegrate to an even greater extent already after 30 min of its mechanical activation. A weighed portion (25 g) of a concentrate ground in a vibration grinder for 2.5 h was dissolved in boiling 69% sulfuric acid in accordance with the technological procedure described above. The results obtained are listed in Table 6 (run no. 1), which presents for comparison data (run no. 2) on dissolution of a concentrate ground in the vibration grinder for 0.5 h (see Table 4, run no. 12). On making longer the time of mechanical activation of the concentrate (from 0.5 to 2.5 h), the extent of beryl dissolution was raised by 10 wt % (from 57.7 to 67.8 wt %).

The positive effect of the mechanical activation of the beryl concentrate (Tables 1, 2; batch no. 1) on the extent of its dissolution in 69% sulfuric acid was also demonstrated in a set of experiments in which the expenditure of the acid was 375 ml g^{-1} concentrate, and the duration of its dissolution, about 13 h (Table 7). Raising the activation time of the concentrate from 2.5 to 5h, and further to 7.5 h provides an increase in the statistical-average extent of dissolution of the raw material from 73 to 78 wt %, and further to 81 wt %, respectively. It also follows from the data in Tables 6 and 7 that, by making the sulfuric acid dissolution of the concentrate ground for 2.5 h longer (from 5 to ~13 h) and the expenditure of sulfuric acid larger (from 20 to 375 ml g^{-1} concentrate), the extent of dissolution can be raised by 5 wt % (from 68 to 73 wt %).

The next state of the study consisted in testing the furnace variant of sulfatization of a mechanically activated beryl concentrate.

Use of dilute sulfuric acid. The dependence of the extent of decomposition with 69% sulfuric acid of a Malyshevskoe concentrate mechanically activated in a planetary mill on the duration of its activation was studied. The concentrate (Tables 1, 2; batch nos. 1–3, 6, and 8) was mechanically activated in the mill, with the crystal lattice of beryl disintegrated (Fig. 3). Weighed portions of the activated concentrate (18–37 g) were treated with sulfuric acid taken in an amount of 1.85 g per gram of the concentrate. The reaction mass was kept for 5 h at 250–300°C in a glassy graphite cup with a fluoroplastic cover, with a single agitation. After a high-temperature treatment, the reaction mass was processed in the standard mode (leaching, neutralization, twofold washing of the cake with an aqueous ammonium sulfate solution acidified with sulfuric acid).

Despite the conversion of the crystal lattice of beryl to the X-ray-amorphous state after 30 min of mechanical activation of its concentrate in the planetary mill (Fig. 3), the disintegration of the beryl crystal in such a short time is commonly not sufficiently complete for subsequent recovery from the concentrate of considerable amounts of beryllium with sulfuric acid. It was found that considerable amounts of beryllium contained in the concentrate (75–96 wt %) can be recovered with sulfuric acid from a mechanically activated concentrate if the duration of the mechanical treatment is no less than 50 min. Therefore, all the subsequent experiments were performed with the Malyshevskoe concentrate activated for 50–80 min.

Use of concentrated sulfuric acid. The mechanically activated concentrate was sulfatized with 93% acid, which makes lower the corrosion of the equipment. In some experiments, the mechanically activated material was separated into a fine and a coarse fractions (–10 and –45 μm) by air classification in a laboratory exhaust box. Weighed portions of the mechanically activated material (grain size –45 μm) and of its fine fraction (grain size –10 μm) isolated by air classification were treated with 93% sulfuric acid. The resulting reaction

Table 8. Results of experiments on sulfuric acid decomposition of a mechanically activated beryl concentrate [concentrate batch nos. 2, 3, 8, and 9–11 (as in Table 2) and mixtures of these; duration of mechanical activation 50–80 min; H_2SO_4 expenditure 1.2–1.6 ml g^{-1} concentrate]

Grain size of the concentrate taken for sulfatization, μm	Sulfatization duration, h	Be recovery into solution (in terms of cake), wt %
–10	10	88.6*
–45	10	85.7*
–45	5	85.3*
–45	0.5	53.3**

* Averaged over 8–14 runs.

** Results of a single run.

Table 9. Results of experiments on sulfuric acid decomposition of a mechanically activated beryl concentrate (two-stage decomposition) (expenditure of 93% sulfuric acid for sulfatization of the mechanically activated concentrate, 1.6 ml g^{-1} concentrate and cake)

Decomposition stage	Concentrate batch no. (as in Table 2)	Duration of mechanical activation, min	Duration of sulfatization, h	Overall Be recovery into solution (in terms of cake), wt %
1	2, 9–11 and mixtures of these	70	10	86.5
2		–	10	92.6
1	Σ 2, 9–11	70	5	85.8
2		–	5	93.9

mass was processed in the standard mode (leaching, neutralization, twofold washing of the cake).

It was found (Table 8) that the sulfatization duration strongly affects the extent of decomposition of the activated concentrate only on being raised from 0.5 to 5 h: the statistical-average Be recovery from the activated concentrate into solution increases by approximately 32 wt % (from 53 to 85 wt %). Raising the sulfatization time further, from 5 to 10 h, almost does not improve the extent of decomposition of the activated raw material at all, because the statistical-average recovery of beryllium from the concentrate into solution increases by only 0.4 wt % (from 85.3 to 85.7 wt %). Thus, the interaction of sulfuric acid with the activated concentrate nearly completely ceases after 5 h of sulfatization, which is accounted for by the formation of a layer of reaction products on the surface of particles of the activated beryl. These products are metal (beryllium, aluminum, iron, lithium, calcium, magnesium, etc.) sulfates, which hinder penetration of sulfuric acid molecules deeper into particles of the activated beryl. This conclusion is confirmed by the results of a large number of experiments on multistage decomposition of the Malyshevskoe concentrate not subjected to activation (Tables 3, 4). In these experiments, beryllium could be nearly completely recovered from cakes produced in sulfuric acid decomposition of the concentrate, because the passivating layer of sulfates was removed to a considerable extent from the reaction surface of particles of the material being decomposed.

The necessity for continuous renewal of the reaction surface of the material being decomposed in the course of its sulfatization was confirmed not only for the Malyshevskoe beryl, but also for products of its mechanical activation (Table 9). Comparison of the data in Table 9 shows that, by renewal of the reaction surface of particles of the mechanically activated beryl, the statistical-average recovery of beryllium into solution could be raised by approximately 7 wt % (from 85.8–

Table 10. Results of experiments on two-stage sulfuric acid decomposition of a mechanically activated beryl concentrate with grinding of the reaction mixture [duration of the mechanical activation of the starting concentrate (starting mixture of concentrates) 70 min; grain size of the mechanically activated material taken for sulfatization –10 μm; expenditure of 93% sulfuric acid 1.6 ml g^{-1} mechanically activated raw material (cake)]

Decomposition stage	Concentrate batch no. (as in Table 2)	Be content of the starting concentrate	Be content of the cake	Yield of cake in a stage	Be recovery into solution in a stage (in terms of cake)	Overall be recovery into solution (in terms of cake)
		wt %				
1	2	1.75	0.240	60.3	91.7	91.7
2			0.320	54.2	31.8	94.3
1	9	1.85	0.165	57.3	94.9	94.9
2			0.188	68.5	22.0	96.0
1	10	1.78	0.290	56.3	90.8	90.8
2			0.340	66.2	22.4	92.9
1	11	1.72	0.180	57.8	94.0	94.0
2			0.220	57.1	30.2	95.8
1	Σ 2, 9–11	1.78	0.435	27.2	93.4	93.4
1	Σ 2, 9–11	1.78	0.376	37.9	92.0	92.0
					Average in stage 1	92.8
					Average in stage 2	94.1

86.5 to 92.6–93.9 wt %). Almost the same efficiency of beryl decomposition was achieved by using the method of mechanical activation of the Malyshevskoe concentrate, which consists in combining the processes of mechanical activation and sulfatization of this raw material and provides the complete, to the maximum possible extent, renewal of the reaction surface of the activated beryl in the course of its sulfatization. The procedure used in this experiment included a mechanical activation of the concentrate in a planetary mill, followed by treatment with 93% sulfuric acid in a porcelain mortar and subsequent mechanochemical activation of the raw material (grinding of the concentrate with a porcelain pestle in the presence of the acid for 1.5 h at $T \approx 100$°C). In the process, the mixture, slurry-like at the beginning of grinding, became pasty by the end of the process, which indirectly points to a sufficiently high intensity of the sulfatization reaction. To complete the sulfatization of the concentrate, the thus activated material was kept at 250–300°C for 5 h, with agitation every 1–2 h. The resulting reaction mass was processed in the standard mode. After the 1st decomposition state, the dried cake was repeatedly decomposed in the mode used in the 1st stage of decomposition of the starting mechanically activated concentrate. The results of the two-stage decomposition of the mechanically activated concentrate with grinding of the reaction mixture are listed in Table 10.

The method used in the experiment for renewal of the reaction surface of particles of the mechanically activated concentrate provided a decomposition of the concentrate in the 1st stage by, on average, 93 wt %. After additional decomposition of the waste cake, the overall recovery of beryllium into solution increased to 94 wt %.

Table 11. Results of experiments on decomposition of a mechanically activated beryl concentrate

Concentrate batch no. (as in Table 2)	Mass of the concentrate taken for sulfatization, g	Be content of the cake	Yield of cake	Be recovery into solution (in terms of cake)
	wt %			
2	10.10 11.70	0.220 0.170	39.6 52.1	95.0 94.9
				Average: 95.0
9 10	8.42 12.50 10.90	0.098 0.320 0.390	46.9 49.2 45.9	97.5 91.2 90.0
				Average: 90.6
11	10.40 10.40	0.240 0.170	49.0 33.2	93.2 96.7
				Average: 95.0
Σ 2, 10, 11	9.45 9.50	0.210 0.330	43.9 51.6	94.7 90.3
				Average: 92.5
				Average over nine runs: 93.7

To further improve the extent of beryllium recovery from a mechanically activated beryl concentrate, experiments on its decomposition with a mixture of sulfuric and low-grade (as regards silicon) (waste) hydrofluoric acid were carried out. Weighed portions (30.8 g) of the concentrate were activated in a planetary mill for 70 min. The activated material (–45 μm) was treated with 93% sulfuric acid and ground with a pestle in a porcelain mortar for 1 h at $T \approx 100$°C (sulfuric acid expenditure 2.6 ml g^{-1} concentrate). Then, hydrofluoric acid was added to the reaction mass (0.2 ml g^{-1} concentrate) and the mixture was ground in a mortar at 110–120°C for 1 h. After that, the following procedure was repeated five times: the reaction mixture was kept in a porcelain mortar closed with a cover for 10 min at 200–250°C and then was ground for 10 min at 110–120°C. Further, the reaction mass was kept for 5 h at 250–300°C in a glassy graphite cup (closed with a cover), with the reaction mass ground in a porcelain mortar at 110–120°C 40 and 60 min after the beginning of the 5-h sulfatization. After 5 h of keeping, the sulfatized material was ground in a mortar for 30 min at 50–60°C, with approximately 50 ml of water added. The resulting reaction mass was processed in the normal mode. The results obtained are listed in Table 11.

CONCLUSION

The use of the mechanical activation of the beryl concentrate in the course of its sulfatization and leaching of the sulfatized material, increase in the sulfuric acid expenditure, and use of hydrofluoric acid in the sulfatization stage made it possible to raise the statistical-average recovery of beryllium into solution to 94 wt %.

REFERENCES

1. White, D.W. and Burke, J.E., *The Metal Beryllium*, Cleveland (Ohio): The American Society for Metals, 1955.
2. Everest, D.A., *The Chemistry of Beryllium*, Amsterdam: Elsevier, 1964.
3. Betekhtin, A.G., *Kurs mineralogii* (A Course of Mineralogy), Moscow: Gosgeolizdat, 1951, vol. 1.
4. Darwin, G.E. and Buddery, J.H., *Beryllium*, London: Butterworth Scientific, 1960.

ISSN 1070-4272, Russian Journal of Applied Chemistry, 2008, Vol. 81, No. 6, pp. 942–945. © Pleiades Publishing, Ltd., 2008.
Original Russian Text © M.V. Karpets, I.Yu. Kostiv, 2008, published in Zhurnal Prikladnoi Khimii, 2008, Vol. 81, No. 6, pp. 904–907.

INORGANIC SYNTHESIS AND INDUSTRIAL INORGANIC CHEMISTRY

A Study of the Conversion of a Langbeinite Suspension to Schoenite

M. V. Karpets and I. Yu. Kostiv

Carpathian Stefanik National University, Ivano-Frankivsk, Ukraine
State Research Institute of Halurgy, Kalush, Ivano-Frankivsk oblast, Ukraine

Received October 3, 2007

Abstract—Conversion of a langbeinite suspension into a schoenite suspension was studied in relation to the preparation temperature of the former, time, and amount of added water. The optimal conditions of the process for obtaining schoenite with a K_2O content exceeding 30% and chlorite content lower than 1.5% were found.

DOI: 10.1134/S1070427208060037

Halurgic processing of polymineral potassium ores involves evaporation of an excess schoenite solution and formation of a finely dispersed langbeinite, which, contained in synthetic kainite, is separated and added to a saturated solution formed in leaching of potassium-magnesium minerals in the ore [1]. Langbeinite is also formed on mixing synthetic kainite with this saturated solution at temperatures exceeding 70°C. Because of the partial dissolution of potassium chloride and kainite, a part of NaCl precipitates from the saturated solution. This part can be separated, together with sodium chloride coming with synthetic kainite, and the finely dispersed langbeinite suspension can be used to crystallize schoenite. Synthesis of a finely dispersed langbeinite suspension from the components of the synthetic kainite and the saturated solution, with separation of the coarsely crystalline sodium chloride, and conversion of this suspension, upon cooling, to a schoenite suspension can be used as an efficient way to raise the yield of schoenite and improve its quality.

EXPERIMENTAL

The effect of various factors on the conversion of langbeinite to schoenite was studied. This process occurs in accordance with the equation

$$K_2SO_4 \cdot 2MgSO_4 + 13H_2O \rightarrow K_2SO_4 \cdot MgSO_4 \cdot 6H_2O + MgSO_4 \cdot 7H_2O.$$

A mixture of a saturated solution formed in dissolution of a polymineral potassium ore in water [2] and a synthetic kainite of composition (wt %): kainite 65.6, sylvite 12.2, and halite 22.2, was heated under permanent agitation to 90–110°C for 30 min. In this case, the components of kainite are converted to give finely dispersed langbeinite by the equation

$$2[KCl \cdot MgSO_4 \cdot 3H_2O] + MgSO_4 \rightarrow K_2SO_4 \cdot 2MgSO_4 + MgCl_2 + 6H_2O.$$

The conversion results in binding of magnesium sulfate from the liquid phase into langbeinite and in an increase in the solubility of potassium chloride. Sodium chloride remains undissolved in the suspension of finely dispersed langbeinite and can be easily separated from this suspension by hydroseparation. The langbeinite suspension synthesized at 90–110°C was decanted from the NaCl precipitate and cooled to 20°C under permanent agitation, with the liquid and solid phases sampled at certain intervals of time and the samples analyzed by using the procedures accepted in halurgy [3]. The mineral composition of the solid phases was determined on a personal computer (PC) by special software. The results obtained in calculation of the mineral composition of the solid phases are shown in Fig. 1.

It can be seen in Fig. 1 that the conversion is practically complete in 30 min. At 100°C, the content of schoenite in the solid phase of the suspension is lower than that at 90°C, which is due to the transfer of a part of sulfate compounds into the precipitate separated by decantation. This precipitate contains (wt %): sylvite 0.9, kainite 27.5, and halite 71.6 at 100°C; and sylvite 1.3, kainite 22.1, and halite 76.6 at 90°C. The content of sulfate ions in the liquid phase at 100°C is lower than that at 90°C: 7.69 and 10.41%, respectively. On cooling the langbeinite suspension obtained at 90°C to 20°C, the composition of the liquid phase of the schoenite suspension in 120 min was as follows (wt %): K^+ 3.66, Mg^{2+} 3.92, Na^+ 3.21, Cl^- 15.11 and SO_4^{2-} 6.22. For the langbeinite suspension produced at 100°C, this composition was the following (wt %): K^+ 3.92, Mg^{2+} 4.06, Na^+ 2.83, Cl^- 14.9 and SO_4^{2-} 6.59. This points to a more complete recovery of K^+, Mg^{2+}, and SO_4^{2-} ions into schoenite from solution. At 90°C, a larger amount of NaCl can be separated, compared with 100°C, and the solution contains in this case a larger amount of sulfate. Consequently, the content of schoenite in the precipitate formed on cooling to 20°C will be higher.

It should be noted that, on cooling the langbeinite suspension synthesized at 110°C to 20°C, the solid phase contains no schoenite: in 120 min, the solid phase of the suspension is composed of 6.7 wt % sylvite and 93.3 wt % halite. This occurs because the langbeinite suspension formed at 110°C is rapidly clarified, langbeinite is separated together with the NaCl precipitate, NaCl and KCl dissolve in the resulting clarified solution owing to the low concentration of sulfates, and predominantly potassium chloride crystallizes from this solution upon cooling.

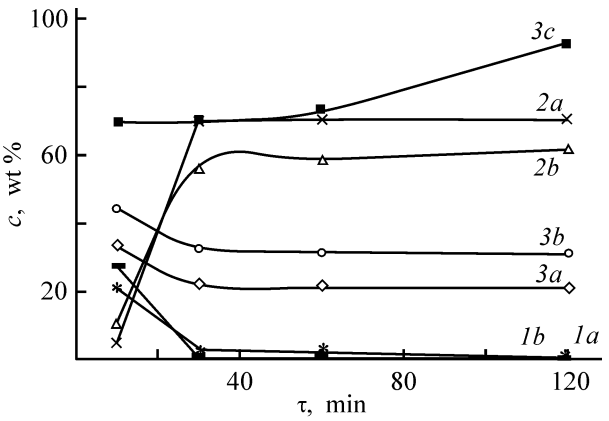


Fig. 1. Mineral composition c of the solid phase of the schoenite suspension vs. the process duration τ for different temperatures of synthesis of the langbeinite suspension. Temperature (°C): (*a*) 90, (*b*) 100, and (*c*) 110. (*1*) langbeinite, (*2*) schoenite, and (*3*) halite.

Table 1 lists the degrees of recovery of the main components of the langbeinite suspension into schoenite. The degree of recovery, α, was calculated from the material balance data obtained with a PC, using the formula

$$\alpha = \frac{m_1 c_1}{m_2 c_2 - m_3 c_3}.$$

Here m_1 is the mass of the precipitate after the precipitation and conversion; c_1, concentration of a component in question in the solid phase; m_2 and m_3, masses of the solid and liquid phases of the langbeinite suspension; and c_2 and c_3, concentrations of the component in the solid and liquid phases of the langbeinite suspension, respectively.

It can be seen from Table 1 that a higher recovery of the components into schoenite is achieved for the langbeinite suspension obtained at 100°C.

Table 1. Degree α of recovery into schoenite of the components of the langbeinite suspensions obtained at different temperatures

τ, min	α, wt %, at indicated temperature, °C					
	90			100		
	K^+	Mg^{2+}	SO_4^{2-}	K^+	Mg^{2+}	SO_4^{2-}
10	30.5	9.7	16.7	37.1	12.8	21.9
30	43.0	17.6	49.0	47.6	19.1	45.8
60	43.7	18.6	51.4	47.9	20.2	48.8
120	46.6	20.0	50.6	48.8	20.4	50.4
180	42.6	17.9	51.3	51.2	21.7	53.9

Table 2. Changes in the mineral composition of the solid phase obtained on cooling the langbeinite suspension

Composition	Content, wt %, at indicated temperature, °C					
	100	60	50	40	30	20
Langbeinite	54.7	19.2	3.1	0.2	1.8	1.1
Sylvite	–	–	–	34.5	26.2	21.6
Halite	3.7	78.9	96.5	64.0	39.6	30.3
Leonite	–	–	0.4	1.4	–	–
Schoenite	–	–	–	–	32.5	47.0
Kainite	41.6	1.9	–	–	–	–

Therefore, the langbeinite suspension for further studies was produced at this temperature.

To reduce the energy expenditure, the possibility of synthesizing langbeinite at lowered temperatures was studied. The suspension was produced by mixing a saturated solution obtained upon dissolution of the ore with synthetic kainite at 50°C, agitating the mixture for 30 min, and separating by decantation of a coarsely crystalline precipitate of the following mineral composition (wt %): kainite 14.2, halite 84.7, and sylvite 1.1. The finely dispersed solid phase obtained has the composition (wt %): kainite 37.5, leonite 1.3, and halite 61.3. This means that the temperature of 50°C is insufficient for conversion of the components of synthetic kainite to langbeinite, with leonite produced and the suspension containing a large amount of kainite separated together with sodium chloride in decantation. As a result, the separated NaCl precipitate is contaminated by impurities.

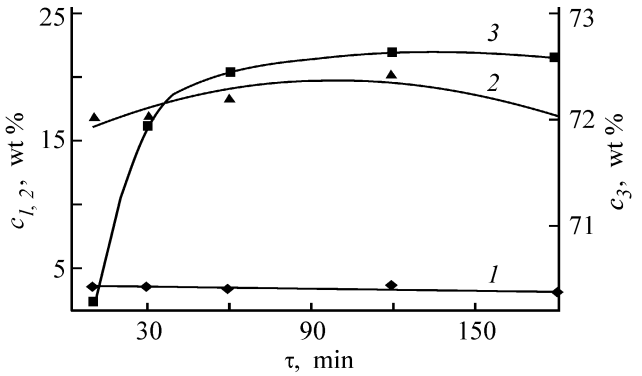


Fig. 2. Mineral composition c vs. the time τ in which the schoenite suspension is obtained after the separation of NaCl at 50°C. (*1*) Schoenite, (*2*) halite, and (*3*) langbeinite.

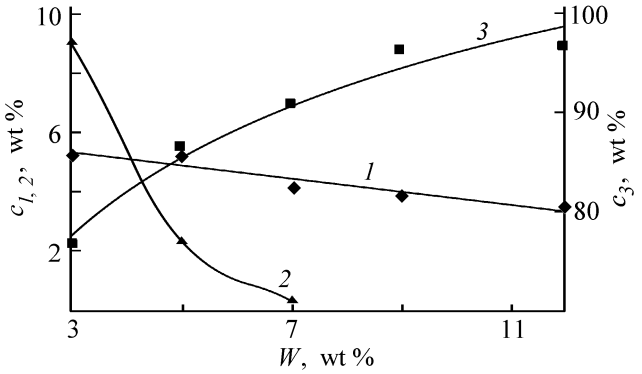


Fig. 3. Contents of langbeinite (c_1), halite (c_2), and schoenite (c_3) in the schoenite suspension vs. the amount W of water added. (*1*) Langbeinite, (*2*) halite, and (*3*) schoenite.

To find the optimal temperature for the conversion of the langbeinite suspension to a schoenite suspension and to reach the maximum yield of schoenite, the process was studied at 60–20°C, with the mineral composition determined with a PC (see Table 2).

It can be seen from the data presented that, when the suspension is cooled to 50–40°C, a small amount of leonite crystallizes, with a stable solid phase, schoenite, crystallizing at lower temperatures. At 50°C, the concentration of halite is the highest and, because it is a coarsely crystalline mineral, it is easily separated by decantation. Therefore, the langbeinite suspension synthesized at 100°C was cooled stepwise, with separation of NaCl at 50°C and subsequent cooling to 20°C. In this way, the NaCl content of the precipitate can be reduced to 16.7 wt %, with its schoenite content raised (Fig. 2).

In synthesis of schoenite, water is bound from solution into a crystal hydrate, which favors additional crystallization of NaCl. To obtain schoenite without an admixture of sodium chloride, water was added in an amount of 3 to 12 wt % to the suspension from which NaCl was separated and the mixture was agitated at 20°C for 120 min. The results obtained are shown in Fig. 3. It can be

seen that, upon addition of water, the content of halite decreases from 9.06 to 3 wt % as the content of water increases from 0.3 to 7 wt %. To obtain schoenite without admixture of chlorides, 7–9 wt % water should be added in the course of crystallization to the suspension after the separation of NaCl, with the content of K_2O, MgO, and chlorine in terms of dry substance being 30.4, 14.1, and 1.4%, respectively.

CONCLUSIONS

(1) The highest degree of conversion of the components of the langbeinite suspension to the schoenite suspension in the range 90–110°C is achieved at 100°C.

(2) On cooling the langbeinite mixture, the highest content of halite in the coarsely crystalline phase is observed at 50°C, and it can be easily separated by decanting.

(3) Addition of 9 wt % water to the langbeinite suspension after the separation of NaCl yields schoenite with 96.2 wt % main substance (or 30.4% K_2O, 14.1% MgO, and 1.4% chlorine in terms of dry substance).

REFERENCES

1. Grabovenko, V.A., *Proizvodstvo beskhlornykh kaliinykh udobrenii* (Manufacture of Chlorine-free Potassium Fertilizers), Leningrad: Khimiya, 1980.
2. Karpets', M.V. and Kostiv, I.Yu., *Khim. Prom–st. Ukrai'ni*, 2007, no. 2, pp. 29–32.
3. *Metody analiza rassolov i solei* (Methods for Analysis of Brines and Salts), Morachevskii, Yu.V. and Petrova, E.M., Eds., Moscow: Khimiya, 1964.

ISSN 1070-4272, Russian Journal of Applied Chemistry, 2008, Vol. 81, No. 6, pp. 946–951. © Pleiades Publishing, Ltd., 2008.
Original Russian Text © A.M. Zhizhaev, E.N. Merkulova, 2008, published in Zhurnal Prikladnoi Khimii, 2008, Vol. 81, No. 6, pp. 908–912.

INORGANIC SYNTHESIS AND INDUSTRIAL INORGANIC CHEMISTRY

Interaction of Sulfate Solutions of Zinc with Natural Calcium Carbonates

A. M. Zhizhaev and E. N. Merkulova

Institute of Chemistry and Chemical Technology, Siberian Branch, Russian Academy of Sciences, Krasnoyarsk, Russia

Received July 5, 2007

Abstract—Precipitation of zinc from sulfate solutions onto carbonate rock was studied. The residual concentrations of zinc and the capacity of the precipitating agent were measured, and the mineral forms of zinc in the precipitate under various process conditions were determined.

DOI: 10.1134/S1070427208060049

Precipitation of zinc from waste water poses certain difficulties because of the low formation rate of its poorly soluble compounds. As a rule, alkalization of solutions to pH ≥ 8.5 (commonly 10–12) fails to provide parameters required by water protection regulations [1]. Reagent methods, e.g., precipitation of carbonates in treatment with carbon dioxide can diminish the residual concentration of the metal to 1–5 mg l^{-1} [2]. However, these methods yield strongly hydrated amorphous precipitates difficulty separated from solutions, with their subsequent peptization and dissolution possible, similarly to the case of hydroxides [1, 2]. The expensive and toxic reagents pose the question as to whether their use, additional purification of solutions, and utilization of precipitates are complete [3]. Because of the comparatively high cost of the reagents, use of inexpensive mineral raw materials or industrial wastes for precipitation is of large interest [3, 4]. For this purpose, various materials that form, when reacting with metals, compounds with low solubility products: phosphates, silicates, carbonates, have been studied [4–12]. Nevertheless, zinc is precipitated with the lowest efficiency, compared with other heavy metals, when wastewater is purified using, e.g., natural phosphates [5–7]. Natural calcium carbonates are widely used to treat wastewater [8–12], primarily for controlling its acidity. Also, their sorption capacity for heavy nonferrous metals has been noted [4, 9–14].

The precipitation on calcite was mostly studied on compact monomineral samples (Iceland spar) from dilute solutions saturated with CO_3^{2-}, i.e., in an alkaline medium under nearly equilibrium conditions [8, 9, 12, 13, 15, 16]. It was assumed that, at low zinc concentrations in a solution, the sorption is due to a direct exchange interaction Zn^{2+}/Ca^{2+} and to incorporation of zinc ions into the crystal lattice of calcite. As the concentration increases to the solubility limit, independent zinc carbonate phases are formed on the surface: smithsonite ($ZnCO_3$) or hydrozincate [$Zn_5(OH)_6(CO_3)_2$] [4, 9, 15, 16]. However, formation of these compounds or their hydrates has not been confirmed instrumentally because of their low concentrations, high dispersity, and low ordering of new formations [4, 9, 12]. The solubility of precipitates of this kind is lower than that of hydrozincate, but higher than that of smithsonite, which is also attributed to the disorder of their crystal lattice [9, 12, 13].

The aim of this study was to examine the precipitation of zinc and the composition of precipitates formed on carbonate rock at comparatively high concentrations of starting solutions, characteristic of wastewater from galvanic shops, and at predominance of the concentration of ions of the salt balance over the equilibrium concentrations of carbonate ions.

EXPERIMENTAL

To 1 l of a zinc sulfate solution was added, under permanent agitation in a glass vessel with a magnetic stirrer, a weighed portion (4, 6, or 10 g) of limestone or marble ground to 100% of the –0.074-mm fraction. The chemical composition

of the carbonatites is presented in the table. An analysis was made on a Siemens SRS-300 X-ray spectrometer (Germany). Solutions of prescribed concentration were prepared from $ZnSO_4 \cdot 7H_2O$ of analytically pure grade. The duration of an uninterrupted experiment was as long as 30 h. Samples of the solution (5 ml) were periodically taken for analysis. The content of zinc and calcium in the liquid phase was determined using a Perkin–Elmer AAnalyst-400 atomic-absorption spectrometer. An X-ray phase analysis of the precipitates was performed on a DRON-3 X-ray diffractometer (LOMO, Russia, $Cu_{K\alpha}$ radiation, point-by-point scanning with a step of 0.02 deg, accumulation time 1 s). Reflections in the X-ray diffraction patterns obtained were identified using the JCPDS file of reference powder spectra. The starting samples of carbonate rock are mostly composed of calcite ($CaCO_3$, JCPDS, 47-1743) with a minor admixture of quartz (SiO_2, JCPDS, 5-490).

Composition of carbonate rock used to precipitate zinc from sulfate solutions

Component	Content, wt %	
	marble	limestone
CaO	50.2	52.3
MgO	1.4	0.22
SiO_2	3.97	1.62
Al_2O_3	0.4	0.7
P_2O_5	0.5	0.25
Fe_2O_3	0.17	0.2
SO_3	0.0017	0.002
K_2O	0.057	0.052
MnO	0.017	0.009
Ni	0.001	0.002
Cu	0.0018	0.0015
Zn	0.0012	0.001
Sr	0.02	0.01

Figure 1a shows kinetic curves of zinc precipitation from aqueous sulfate solutions on limestone. The residual concentration of zinc in solution reached a value of 20–22 mg l^{-1} in 20 h and did not become lower even after 30 h of agitation in contact with limestone. An increase in the fraction of the solid precipitating agent does not lead to fuller precipitation of zinc. The time in which the limiting concentration is reached becomes somewhat shorter, but its value fluctuates

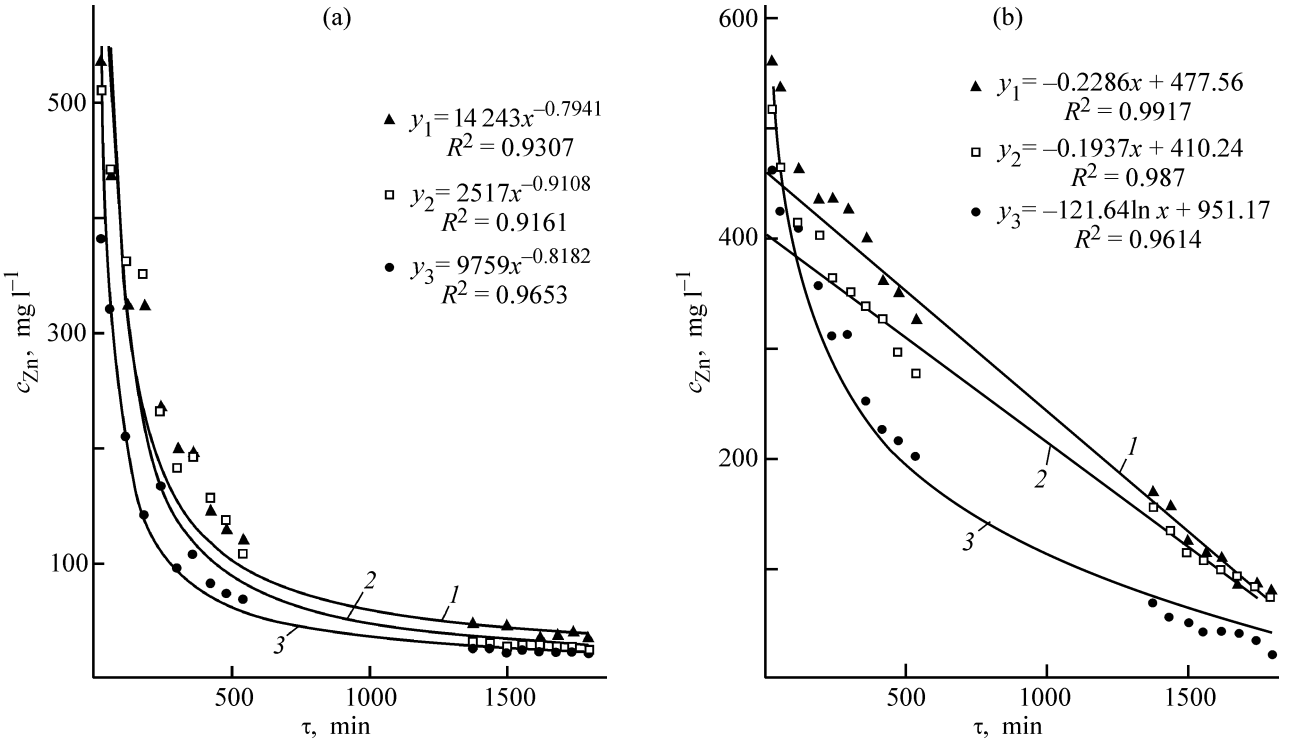


Fig. 1. Kinetic curves of zinc precipitation from a sulfate solution on (a) limestone and (b) marbled limestone. Initial concentration of zinc 1 g l^{-1}. (*c*) Metal ion concentration and (τ) time; the same for Fig. 2. Amount of the precipitating agent (g): (*1*) 4, (*2*) 6, and (*3*) 10; the same for Fig. 2.

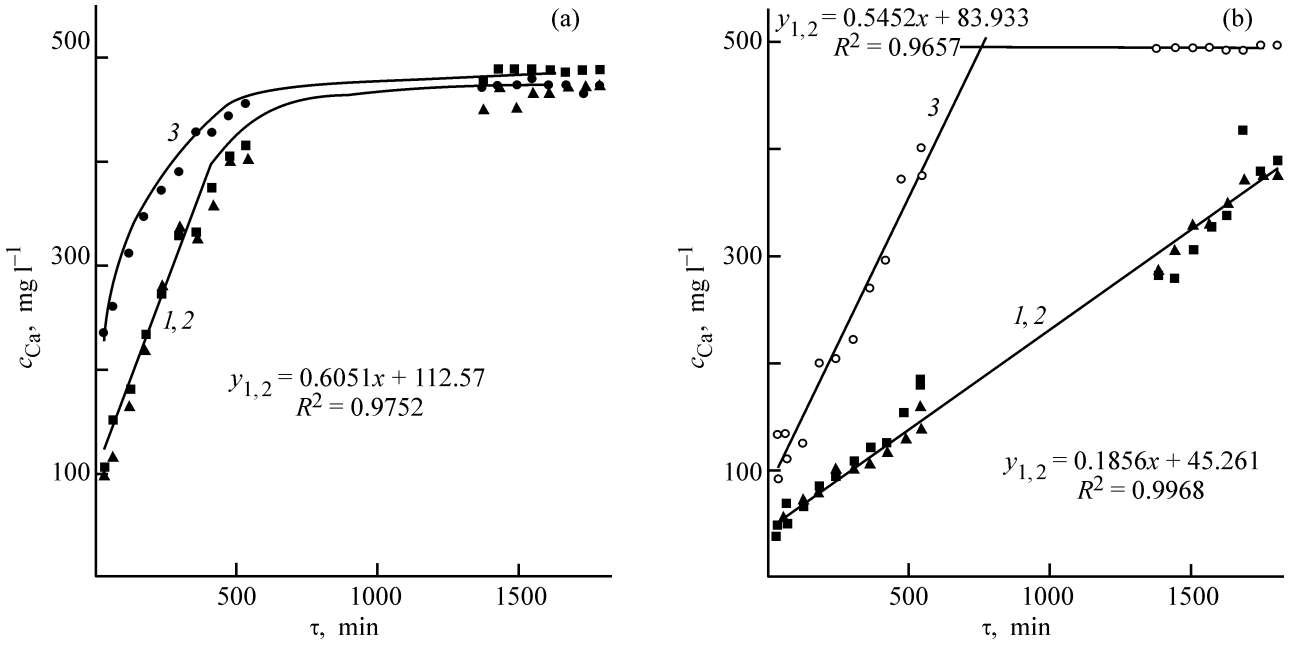


Fig. 2. Kinetic curves of calcium transfer into solution in zinc precipitation from sulfate solutions on (a) limestone and (b) marbled limestone.

within the same range, 18–20 mg l^{-1}. In the process, the concentration of calcium in solution rapidly grows to 400 mg l^{-1} during the first 10 h and then slowly increases to 450–480 mg l^{-1} and stabilizes at this level (Fig. 2a).

The precipitation on marbled limestone is substantially slower. For the weighed portions of 4 and 6 g, the process kinetics is practically linear after stabilization during the first 10 min (Fig. 1b). The residual concentration of zinc in solution is high (~100 mg l^{-1}). The concentration of calcium in solution also shows a nearly linear dependence on the keeping time and does not level out during the entire experiment (30 h) (Fig. 2b). Only when the weighed portion of the precipitating agent is raised to 10 g, a residual (after 30 h) zinc concentration of about 20 mg l^{-1} is reached. The calcium concentration in solution linearly increases during the first 10 h and reaches the limiting value of 495–498 mg l^{-1}.

The decomposition of calcite in solution neutralization or zinc precipitation in the exchange reaction yields large amounts of gypsum:

$$Zn^{2+} + SO_4^{2-} + CaCo_3 \xrightarrow{H_2O} ZnCO_3\downarrow + CaSO_4 \cdot 2H_2O\downarrow, \quad (1)$$

$$CaCO_3 + H_3O \xrightarrow{H_2O,\ SO_4^{2-}} CaSO_4 \cdot 2H_2O\downarrow + CO_2\uparrow. \quad (2)$$

The strong lines associated with gypsum are commonly recorded in X-ray diffraction patterns of precipitates (interplanar spacing d 7.56, 4.27, 2.86 Å; JCPDS, 6-46) in precipitation from solutions with sufficiently high concentrations (Fig. 3). At a more or less complete precipitation of zinc by the exchange reaction (1), the concentration of calcium in solution should, according to the salt balance conditions, approach 1 g l^{-1} or somewhat exceed this value with account of the neutralization of the acidity of the starting sulfate solution. However, the solubility of gypsum in water at room temperature (at an excess of gypsum in the solid phase) is not higher than 2 g l^{-1} [17]. It is this parameter that determines that the concentration of Ca^{2+} in solution does not exceed 0.5 g l^{-1} in a rather wide range of residual concentrations of zinc (19.4–120.7 mg l^{-1}). In this case, the acidity stabilizes at a level pH 6.75–6.8 and remains nearly unchanged till the end of the experiment, which is possibly due to formation of a gypsum carbonate buffer solution in the system during the first 10 h of tests [18].

A decrease in the initial concentration of zinc solutions to the solubility limit of gypsum results in that the line associated with gypsum disappears from X-ray diffraction patterns. However, the low concentrations of new formations and the strong lines of calcite taken in an excess hinder identification of weak, amorphous peaks of precipitation

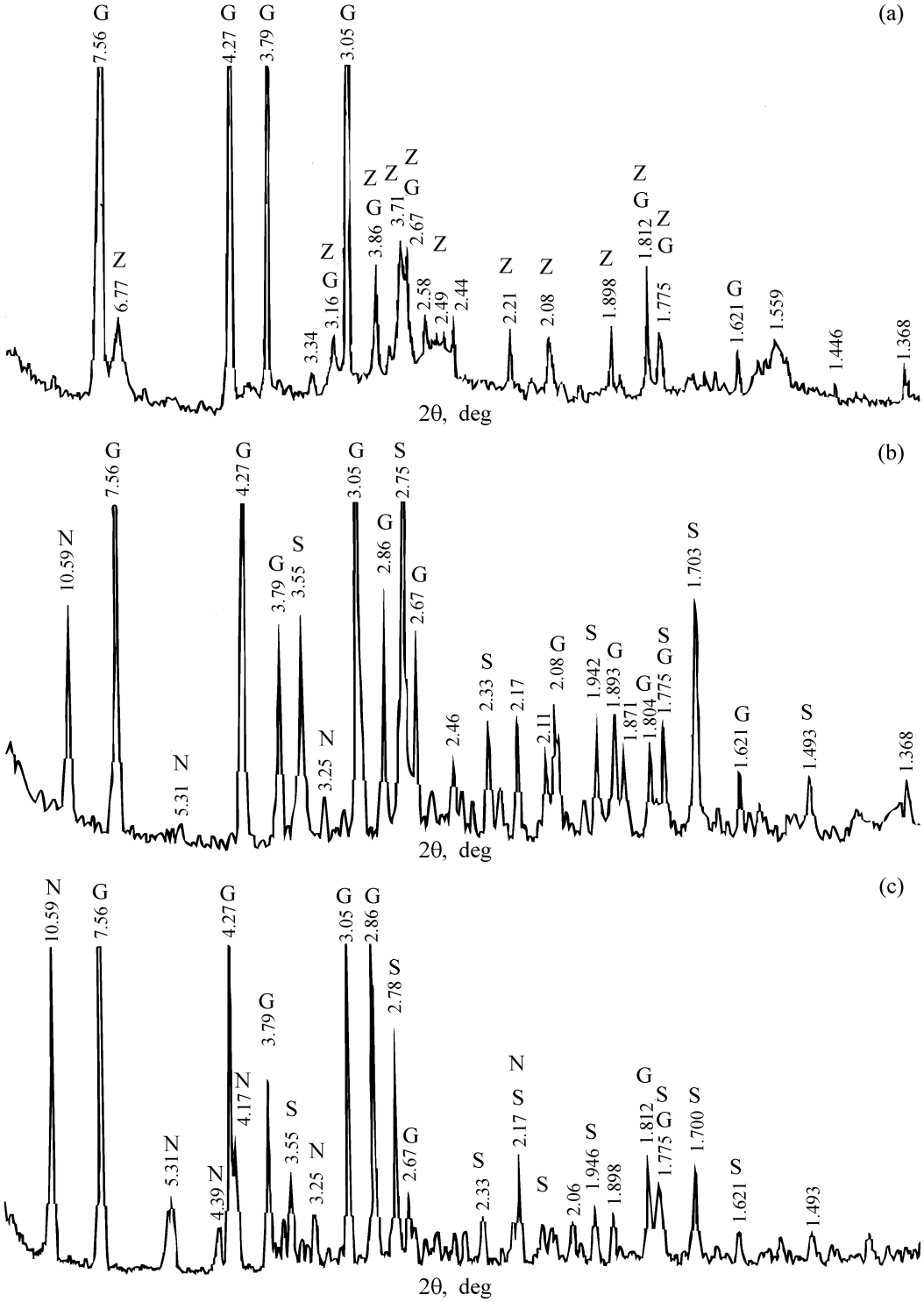


Fig. 3. X-ray diffraction patterns of products formed in precipitation of zinc from a sulfate solution on (a, c) limestome and (b) marble. Mineral phase: N, namuwite; Z, hydrozincate; G, gypsum; and S, smithsonite. (2θ) Bragg angle; interplanar spacings are given in angstroms. Initial concentration of zinc (g l^{-}): (a) 0.1 and (b, c) 1.0.

products. A detailed study of products of this kinds was performed using solutions with a comparatively high concentration of zinc (1 g l^{-1}), with an attempt to achieve a fuller use of the precipitating agent and accumulation of an as large as possible amount of new phases. The capacity of the precipi-

tating agent for zinc was as high as 0.7 g per gram of the starting calcite. However, it is more correct to speak about the coefficient of zinc fixation in the solid phase, rather than about the capacity, because calcite is nearly completely consumed in experiments aimed at the maximum degree of precipitation: its lines are not observed in the X-ray diffraction patterns of the products formed. The high value of this parameter points to the reagent mechanism of precipitation, rather than to ion exchange or simple sorption of zinc on calcite.

The X-ray diffraction patterns of the products formed in precipitation from dilute solutions or at low concentrations of the precipitating agent contain, in addition to lines of gypsum, broadened and "amorphized" lines of hydrozincite [$Zn_5(CO_3)_2(OH)_6$, *d* 6.77, 3.16, 2.71 Å; JCPDS, 19-1458] (Fig. 3a). In most cases, zinc is precipitated from dilute solutions to give just this mineral phase, in agreement with published data [4, 9, 13]. An increase in the content of the precipitating agent leads to precipitation of smithsonite ($ZnCO_3$, *d* 3.55, 2.75, 1.703 Å; JCPDS, 8-449) in a larger or smaller amount (Figs. 3b, 3c). Simultaneous presence of hydrozincate and smithsonite in noticeable amounts was not recorded in experiments. Zinc precipitates by one or the other pathway, without mixing of the mechanism of precipitate formation. Smithsonite is formed directly on calcite (topochemical reaction, large content of the latter) because of the close values of the lattice constants of these minerals (trigonal lattice with planar-axial symmetry). Hydrozincate is in all probability formed from solution similarly to gypsum, which can provide its crystals as nuclei of the new phase, because both the minerals are also crystallized in the same monoclinic crystal system. An indirect evidence that hydrozincate grows on gypsum is that the peaks common to these minerals, simultaneously present in precipitates (*d* 2.86, 2.67, 2.08 Å), are "amorphized" and their intensity decreases on the background of strong unoverlapped lines of gypsum (*d* 4.27, 3.79 Å) (compare Figs. 3a and 3b).

In addition, strong lines of a new phase with *d* 10.58, 5.31, 4.17, 3.25 appear in the X-ray diffraction patterns of precipitates. These lines best correspond to basic zinc sulfate, namuwite [$Zn_4SO_4(OH)_6 \cdot H_2O$, JCPDS, 35-528] (Figs. 3b, 3c). This phase is only formed when zinc precipitates as smithsonite and appears in amounts occasionally comparable with those of smithsonite. Not even trace amounts of this phase were found in the case of hydrozincate crystallization. The formation of basic sulfates has been observed in interaction of copper sulfate solutions with limestone [19]. Previously, formation of compounds of this kind has not been observed for zinc, and it has been disregarded in kinetic calculations [2, 9, 12, 13], although there have been reports that mineral associates of this composition are periodically found in oxidized zones of sulfide deposits of zinc. The infrequent occurrence of basic zinc sulfates is due to the lower solubility products of its carbonates [17] and, accordingly, to their predominant formation at lower CO_3^{2-} concentrations, compared with copper. Only under the conditions of rapid binding of the carbonate ion by zinc, the concentrations of the sulfate ion and the pH value become more favorable for formation of $ZnSO_4 \cdot 3Zn(OH)_2$, compared with $2Zn(CO_3)_2 \cdot 3Zn(OH)_2$. The precipitation of hydrozincate makes lower both the concentration of carbonate ions and the pH value, and, accordingly, the conditions favorable for namuwite formation are not created.

CONCLUSUIONS

(1) Calcite, the main component of natural calcium carbonates, can be successfully used to strongly diminish the concentration of zinc in wastewater. However, the residual concentrations of the contaminant after its interaction with carbonatites (18–22 mg l^{-1}) exceed the maximum permissible concentrations established by regulations for water of open water reservoirs, and additional treatment is necessary for final purification.

(2) Zinc is precipitated on calcite on the background of formation of considerable amounts of gypsum. Zinc is fixed in the solid phase as smithsonite $ZnCO_3$ or hydrozincate $2Zn(CO_3)_2 \cdot 3Zn(OH)_2$. Simultaneous presence of these minerals in noticeable amounts is not observed. In the case of smithsonite precipitation, considerable amounts of basic zinc sulfate $Zn_4SO_4(OH)_6$ are formed, which should be taken into account in calculations of the solubility of precipitates in the system constituted by a zinc sulfate solution and calcite.

REFERENCES

1. Svyatokhina, V.P., Isaeva, O.Yu., Pestrikov, S.V., and Krasnogorskaya, N.N., *Zh. Prikl. Khim.*, 2003, vol. 76, no. 2, pp. 330–332.
2. Maksin, V.I. and Standritchuk, O.Z., *Khim. Tekhnol. Vody*, 2001, vol. 23, no. 1, pp. 92–101.
3. Manvelova, N.E., Vol'f, I.V., and Sinyakova, M.A.,

Zh. Prikl. Khim., 2001, vol. 74, no. 10, pp. 1651–1654.

4. Gomez, R., Morando, P.J., and Cicerone, D.S., *J. Environ. Manage.*, 2004, vol. 71, no. 2, pp. 169–177.
5. Prasad, M., Amritphale, S.S., Saxena, S., et al., *Minerals Eng.*, 2000, vol. 13, no. 12, pp. 1301–1305.
6. Ma, Q.Y., Traina, S.J., Logan, S.J., and Ryan, J.A., *Environ. Sci. Technol.*, 1994, vol. 28, pp. 1219–1238.
7. Ford, R.G. and Sparks, D.L., *Environ. Sci. Technol.*, 2000, vol. 34, pp. 2479–3483.
8. Rimstid, J.D., Balog, A., and Webb, J., *Geochim. Cosmochim. Acta*, 1998, vol. 62, no. 11, pp. 1851–1863.
9. Zachara, J.M., Cowan, C.E., and Resch, C.T., *Geochim. Cosmochim. Acta*, 1991, vol. 55, no. 1, pp. 1549–1562.
10. Lupeiko, T.G., Ivleva, T.I., and Solov'ev, L.A., *Zh. Prikl. Khim.*, 2001, vol. 74, no. 4, pp. 567–570.
11. Lupeiko, T.G., Gorbunova, N.O., and Bayan, E.M., *Zh. Prikl. Khim.*, 2001, vol. 74, no. 10, pp. 1648–1650.
12. Zachara, J.M., Kittrick, J.A., Dake, L.S., and Harsh, J.B., *Geochim. Cosmochim. Acta*, 1989, vol. 53, no. 1, pp. 9–19.
13. Garsia-Sanchez, A. and Alvarez-Ayuso, E., *Minerals Eng.*, 2002, vol. 15, pp. 539–547.
14. Maksin, V.I., *Khim. Tekhnol. Vody*, 1999, vol. 21, no. 3, pp. 291–304.
15. Elzinga, E.J. and Reeder, R.J.X., *Geochim. Cosmochim. Acta*, 2002, vol. 66, no. 22, pp. 3943–3954.
16. Cheng, L., Shturchino, N.C., Woicik, J.C., et al., *Surf. Sci.*, 1998, vol. 415, pp. L976–L978.
17. Lur'e, Yu.Yu., *Spravochnik po analiticheskoi khimii* (Handbook of Analytical Chemistry), Moscow: Khimiya, 1979.
18. Laptev, Yu.V., Sirkis, A.L., and Kolonin, G.R., *Sera i sul'fidoobrazovanie v gidrometallurgicheskikh protsessakh* (Sulfur and Sulfide Formation in Hydrometallurgical Processes), Novosibirsk: Nauka, 1987.
19. Zhizhaev, A.M., Bragin, V.I., and Mikhailov, A.G., *Obogashch. Rud*, 2001, no. 5, pp. 13–17.

ISSN 1070-4272, Russian Journal of Applied Chemistry, 2008, Vol. 81, No. 6, pp. 952–955. © Pleiades Publishing, Ltd., 2008.
Original Russian Text © A.N. D'yachenko, R.I. Kraidenko, 2008, published in Zhurnal Prikladnoi Khimii, 2008, Vol. 81, No. 6, pp. 913–916.

INORGANIC SYNTHESIS AND INDUSTRIAL INORGANIC CHEMISTRY

Fluorination of Germanium Concentrates with Ammonium Fluorides

A. N. D'yachenko and R. I. Kraidenko

Tomsk Polytechnic University, Tomsk, Russia

Received September 20, 2007

Abstract—New method for processing of germanium-containing raw materials to obtain germanium oxide was suggested and studied. The method is based on the fluorination of germanium-containing raw materials with ammonium fluorides, followed by a sublimation isolation of ammonium hexafluorogermanate, its dissolution, and precipitation of germanium oxide from solution. The thermodynamics of the process was calculated and its thermogravimetric analysis was made. The kinetics of germanium oxide fluorination by ammonium hydrodifluoride was experimentally studied. A technological scheme for processing of germanium-containing raw materials with ammonium fluoride was suggested.

DOI: 10.1134/S1070427208060050

Proper minerals of germanium are very rare and form no commercial deposits. Germanium is obtained from the products formed in processing of zinc, copper-zinc, or lead sulfide ores, and also from coal combustion ash [1]. The technologies employed for germanium production are cost-intensive and ecologically unsafe. Pyrometallurgical processing of germanium-containing raw materials is commonly carried out at 800–1800°C in a reducing atmosphere. Germanium passes into the gas phase, from which a pure germanium product is further isolated [2]. There exists a hydrochloride acid method for processing of the germanium concentrate [3]. The resulting germanium tetrachloride is evaporated and further subjected to secondary distillation.

In this study, a new method for recovery of germanium oxide from germanium-containing raw materials with ammonium fluorides was suggested and analyzed. Previously, these have been reports [4–8] devoted to the fluoroammonium processing of certain types of mineral raw materials: zircon, ilmenite, beryl, etc. The fluoroammonium technologies for processing of mineral raw materials become increasingly topical because of the possibility of nearly complete regeneration of ammonium fluorides. It seems possible to create a completely closed cycle of fluoroammonium processing of raw materials, with recycling of the main and only reagent, ammonium fluoride or hydrodifluoride. The similarity of some physicochemical properties of germanium and silicon enables prediction of the behavior of its fluoroammonium complexes.

The thermodynamic probability of reactions between germanium dioxide and ammonium fluorides was calculated. Because of the absence of published thermodynamic data for the fluoroammonium complex of germanium, we assumed in the calculation that the fluorination of germanium dioxide by ammonium fluorides proceeds to give germanium tetrafluoride:

$$GeO_2 + 4NH_4F = GeF_4 + 4NH_3 + 2H_2O, \quad (1)$$

$$GeO_2 + 2NH_4F \cdot HF = GeF_4 + 2NH_3 + 2H_2O. \quad (2)$$

The results of the thermodynamic calculation are listed in the table.

Change in the Gibbs energy in the fluorination of germanium dioxide with ammonium fluorides

T, K	ΔG, kJ mol^{-1}, reactions	
	(1)	(2)
298	256.8	196
400	144.2	120.5
600	–75	–10.1
800	–292.8	–124.1
1000	–509.4	–225.7
1200	–725.2	–317.4

The calculated Gibbs energies suggest that the fluorination of germanium dioxide by ammonium fluorides at temperatures higher than 600 K proceeds in the forward direction. This reaction onsets already at 540 K and proceeds more completely as temperature increases further.

We carried out a thermal study of the hydrofluorination of germanium dioxide with ammonium fluorides. The experiments were performed on an SDT Q600 combined TGA/DSQ/DTA analyzer-derivatograph, with the data processed using the TA instruments Universal v4.2E software. Samples were heated at a rate of 5 deg min^{-1} in an air flow.

The thermograms of the reactions of germanium(IV) oxide with ammonium fluoride and hydrodifluoride are shown in Figs. 1a and 1b, respectively. Ammonium fluoride and hydrodifluoride were taken in a twofold excess with respect to the stoichiometry for the case in which ammonium hexafluorogermanate is formed in the reaction.

The reactions of germanium dioxide with ammonium fluoride and hydrodifluoride begin at 45°C to give a fluoroammonium complex of germanium, with gaseous ammonia and water released. In the case of the reaction with ammonium fluoride, peaks of its melting with decomposition are observed at 138°C, whereas in the case of ammonium hydrodifluoride, the peak of melting is observed at 126°C. These results completely agree with published data [8].

Upon further heating, ammonium fluoride and hydrodifluoride react with germanium dioxide. In this case, the DTA peaks coincide, with the difference in temperatures being less than 1%. All the processes occurring in the GeO_2–NH_4F and GeO_2–$NH_4F \cdot HF$ systems are identical. Heating of the mixture results in that the original fluoroammonium complex of germanium, $(NH_4)_2GeF_6 \cdot nNH_4F$, is formed and decomposes to $(NH_4)_2GeF_6 \cdot 2NH_4F$ at 170°C. Further, at 221°C, $(NH_4)_2GeF_6 \cdot 2NH_4F$ decomposes to $(NH_4)_2GeF_6$, which, in turn, decomposes to NH_4GeF_5 at 285°C. At 340°C, NH_4GeF_5 decomposes with evolution of gaseous ammonia, hydrogen fluoride, and germanium tetrafluoride. In all probability, the unsublimated part of germanium reacts with water vapor at 368°C to give germanium oxyfluoride.

The reactions of GeO_2 with NH_4F and $NH_4F \cdot HF$ are exothermic; the reactions of dissociation of germanium fluoroammonium complexes are endothermic.

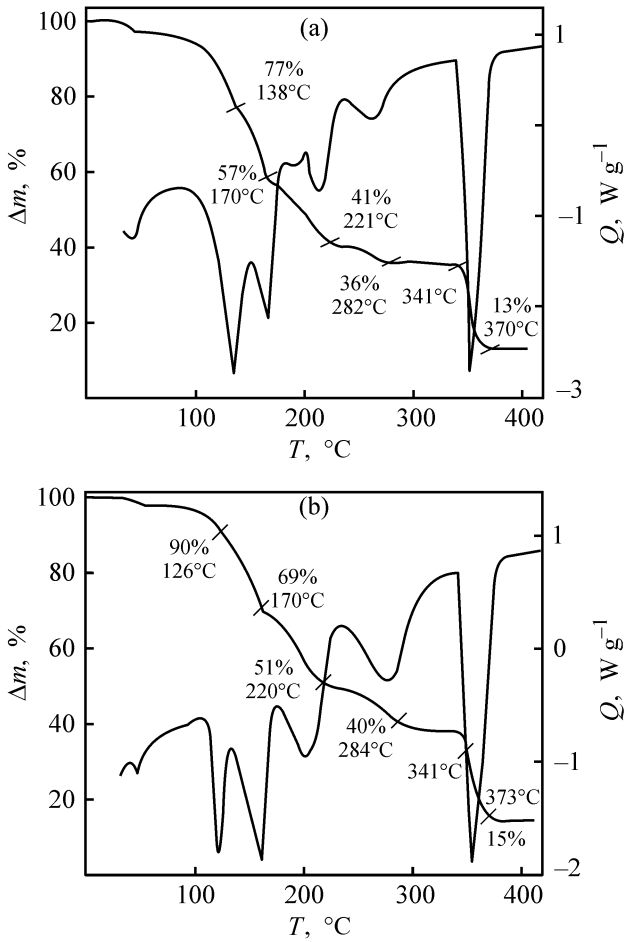


Fig. 1. TG and DTA curves for the reaction of germanium(IV) oxide with (a) ammonium fluoride and (b) ammonium hydrodifluoride. (m) Weight loss, (Q) heat flux, and (T) temperature.

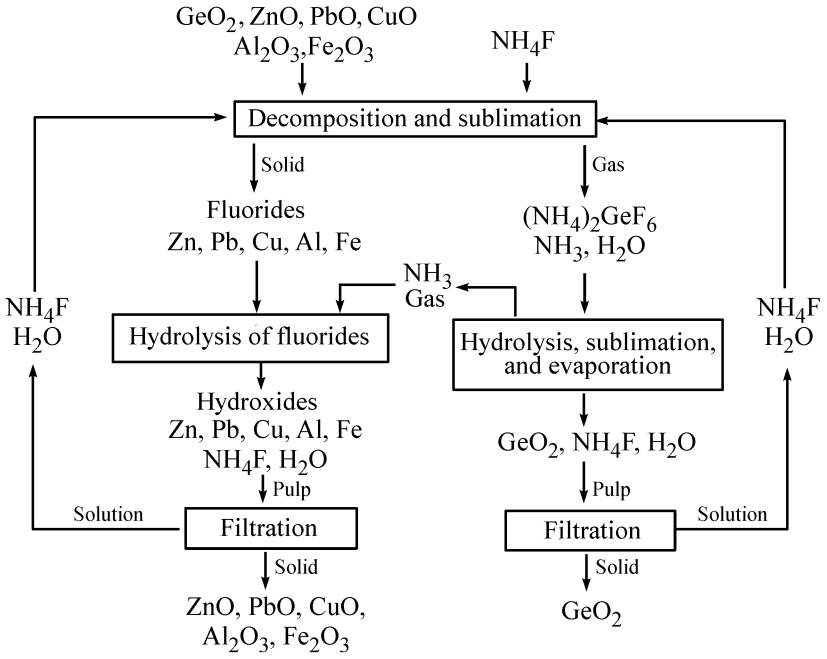
The stoichiometric composition of complex germanium fluorides was confirmed by quantitative analysis. A mixture of germanium oxide and ammonium hydrodifluoride was kept for 1 h at temperatures found by thermogravimetry, and the content of germanium in the resulting samples was determined.

The result of thermogravimetric measurements and quantitative chemical analysis suggest the following sequence of transformations:

$$GeO_2 + NH_4F \xrightarrow{126^\circ C} (NH_4)_2GeF_6 \cdot nNH_4F$$

$$\xrightarrow{170^\circ C} (NH_4)_2GeF_6 \cdot 2NH_4F \xrightarrow{220^\circ C} (NH_4)_2GeF_6$$

$$\xrightarrow{282^\circ C} NH_4GeF_5 \xrightarrow{341^\circ C} GeF_4 \xrightarrow{370^\circ C} GeF_2.$$



Scheme of the fluoroammonium cycle for processing of germanium-containing raw materials.

A kinetic study allowed us to determine the rate of germanium oxide transformation to ammonium hexafluorogermanate in a melt of ammonium fluoride. The experiment was carried out by the method of continuous weighing of the reacting mixture:

$$GeO_2 + 3NH_4F \cdot HF = (NH_4)_2GeF_6 + NH_3 + 2H_2O.$$

The conversion was determined from the weight loss caused by the formation of gaseous ammonia and water. Preliminarily, we experimentally determined the rate of ammonium fluoride decomposition at the same temperatures and the corresponding corrections were introduced into the final results.

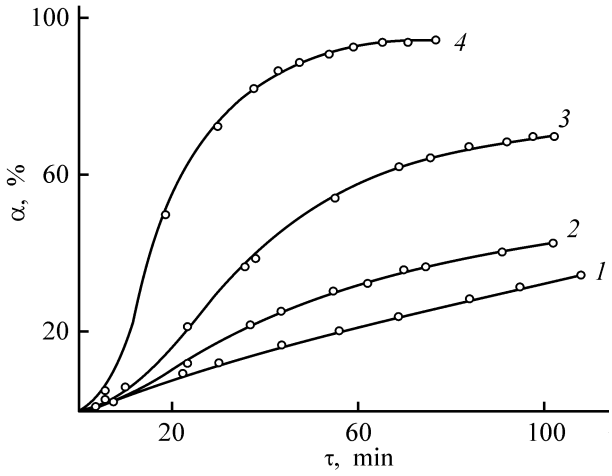


Fig. 2. Kinetic curves for the reaction of germanium dioxide with ammonium hydrodifluoride. (α) Conversion and (τ) time. Temperature (°C): (*1*) 140, (*2*) 160, (*3*) 190, (*4*) 240.

The time dependence of the degree of germanium oxide hydrofluorination by ammonium hydrodifluoride (Fig. 2) is described by the "contracting sphere" equation:

$$\alpha = 1 - \left(1 - 1.28\, e^{\frac{37\,800}{8.31T}}\tau\right)^3. \qquad (3)$$

The rate constant of the chemical reaction is 1.28 s^{-1}. The activation energy of the process is 37.8 kJ mol^{-1}. The process occurs in the transition region of reacting. The process rate is affected by temperature and stirring.

The thermodynamic, thermal, and kinetic analyses of the system under consideration, which confirmed the theoretical and laboratory possibility of performing the process, allowed us to pass to development of its technological scheme. Products formed in processing of copper-zinc ores were used as the starting germanium-containing raw material. The fluoroammonium cycle for processing of germanium-containing raw materials to germanium oxide, with recycling of ammonium fluoride, is shown in the scheme.

The starting germanium-containing ore concentrate was mixed with ammonium fluoride and

heated to 230°C. The germanium-containing concentrate entered into a reaction to give ammonium hexafluorogermanate, Cu(II), Zn(II), Pb(II), Al(III), and Fe(III) fluorides, with release of gaseous ammonia and water. When the hydrofluorination was complete, the resulting mixture of the fluorides was heated to 360°C. At this temperature, gaseous ammonium hexafluorogermanate $(NH_4)_2GeF_6$ and excess ammonium fluoride are distilled off. Thus, germanium oxide is removed from the mixture in the form of ammonium hexafluorogermanate.

The sublimated ammonium hexafluorogermanate was subjected to ammoniacal hydrolysis:

$$(NH_4)_2GeF_6 + 4NH_4OH = GeO_2 \cdot 2H_2O + 6NH_4F.$$

The resulting germanium oxide hydrate was filtered and dried. Thus, the aim of the study, specifically, GeO_2 isolation, was achieved.

The solution of ammonium fluoride can be used for fluorination of the following batch of a germanium-containing raw material. A solid residue formed upon fluorination, constituted by Cu(II), Zn(II), Pb(II), Al(III), and Fe(III) fluorides, can be subjected to ammoniacal hydrolysis for regeneration of ammonium fluoride. An important economical factor of the process is the possibility of regeneration of a larger part of ammonium fluoride.

CONCLUSIONS

(1) Thermodynamic calculations demonstrated that the reaction of hydrofluorination of germanium(IV) oxide by ammonium fluorides can be carried out at 600 K.

(2) Thermal analyses showed that germanium tetrafluoride is produced via stages of formation of fluoroammonium complexes, which successively decompose.

(3) It was demonstrated that the time dependence of the conversion for this process is described by Eq. (3).

(4) A technological sequence of the fluoroammonium cycle for processing of germanium-containing raw materials to germanium oxide was suggested.

REFERENCES

1. Korovin, S.S., Bukin, V.I., Fedorov, P.I., and Reznik, A.M., *Redkie i rasseyannye elementy; Khimiya i tekhnologiya* (Rare and Scattered Elements: Chemistry and Technology), Moscow: Mosk. Inst. Stali Splavov, 2003.
2. *Khimicheskaya entsiklopediya* (The Chemical Encyclopedia), Knunyants, I.L., Ed., Moscow: Sovetskaya Entsiklopediya, 1988, vol. 1.
3. *Rare Metals Handbook*, Hampel, C.A., Ed., New York: Reinhold, 1961.
4. Andreev, A.A., D'yachenko, A.N., and Kraidenko, R.I., *Khim. Prom–st. Segodnya*, 2007, no. 3, pp. 6–11.
5. D'yachenko, A.N., *Khim. Prom–st. Segodnya*, 2006, no. 7, pp. 22–27.
6. Mel'nichenko, E.I., *Ftoridnaya pererabotka redkometall'nykh rud Dal'nego Vostoka* (Fluoride Processing of Rare-Metal Ores of the Far East), Vladivostok: Dal'nauka, 2002.
7. Guzeev, V.V. and D'yachenko, A.N., *Zh. Prikl. Khim.*, 2006, vol. 79, no. 11, pp. 1777–1780.
8. Rakov, E.G., *Khimiya i tekhnologiya neorganicheskikh ftoridov* (Chemistry and Technology of Inorganic Fluorides), Moscow: Mosk. Khim. Tekhnol. Inst. im. D.I. Mendeleeva, 1990.

ISSN 1070-4272, Russian Journal of Applied Chemistry, 2008, Vol. 81, No. 6, pp. 956–964. © Pleiades Publishing, Ltd., 2008.
Original Russian Text © L.B. Belykh, Yu.Yu. Titova, A.V. Rokhin, L.N. Belonogova, F.K. Shmidt, 2008, published in Zhurnal Prikladnoi Khimii, 2008, Vol. 81, No. 6, pp. 917–925.

PHYSICOCHEMICAL STUDIES OF SYSTEMS AND PROCESSES

Hydrogenation Catalysts Based on Palladium Bisacetylacetonate and Lithium Tetrahydroaluminate: Formation Mechanism and Reasons for Modified Effect of Water

L. B. Belykh, Yu. Yu. Titova, A. V. Rokhin, L. N. Belonogova, and F. K. Shmidt

Irkutsk State University, Irkutsk, Russia

Institute of Petro- and Coal-Chemical Synthesis, Irkutsk State University, Irkutsk, Russia

Received January 11, 2007

Abstract—Mechanism of formation, nature of activity, and properties of species active in hydrogenation catalysis in systems based on $Pd(acac)_2$ and $LiAlH_4$ were studied. The effect consisting in activation of catalytic systems was observed and reasons for the modifying action of water were considered.

DOI: 10.1134/S1070427208060062

Catalysts of the Ziegler type [1] exhibit activity in various organic synthesis processes, among which the best known are poly-, oligo-, and dimerization of olefins and dienes [2–6], isomerization of alkenes [6–8], and hydrogenation of unsaturated compounds [6–11]. In our previous study of Ziegler-type systems based on $Pd(acac)_2$–$AlEt_3$, we revealed the microheterogeneous nature of the catalyst in hydrogenation of unsaturated compounds and demonstrated that the extremal type of the dependence of the specific activity, observed as the Al/Pd molar ratio grows, is due to a rise in the dispersity, increase in the fraction of reduced palladium, and change at the nature of the ligand shell [12]. The reason for the inhibition at large Al/Pd ratios is the adsorption of triethylaluminum on palladium nanoparticles. To obtain palladium nanoparticles exhibiting activity in hydrogenation catalysis it is necessary that, on the one hand, Pd(II) complexes should be reduced at a high rate and, on the other hand, the stabilizing ligands precluding growth and coagulation of particles should be sufficiently labile and be easily substituted by substrates in the course of the catalytic process.

Inorganic compounds, alumino- and borohydrides of alkali metals [13–15] are widely used as reducing agents, together with the conventional coreagents of Ziegler systems, organoaluminum compounds. It should be noted here that, in contrast to $NaBH_4$, lithium tetrahydroaluminate is more frequently used for selective reduction of organic compounds. Data on its use in hydrogenation catalysis and on properties of these catalysts are rather scarce [15, 16]. To find out how the nature of a reducing agent affects properties of palladium catalysts for hydrogenation, we studied here the catalytic system based on $Pd(acac)_2$ and $LiAlH_4$.

EXPERIMENTAL

We purified solvents (benzene, THF) and substrates by the standard procedures used for organometallic substances [17]. For deeper drying, benzene was subjected to an additional distillation over $LiAlH_4$ in a rectification column and stored in the atmosphere of argon in sealed ampules over 4A molecular sieves. Tetrahydrofuran was successively distilled, after removal of peroxides, over sodium, $LiAlH_4$, and benzophenone ketyl and stored in the atmosphere of argon in sealed ampules. The concentration of water, found by the Fisher method [18], was 1.1×10^{-3} M in benzene and 1.6×10^{-3} M in THF.

Palladium bisacetylacetonate was prepared by the procedure described in [19]. ^1H NMR spectrum (δ, ppm; solvent C_6D_6): 5.04 (s, 1H, CH), 1.76 (s, 6H, CH_3). IR spectrum (ν, cm^{-1}; solvent benzene): ν(C=O) + ν(C=C) 1560, 1516; UV spectrum (solvent benzene): ε_{330} = 10630 $M^{-1}\,cm^{-1}$.

Lithium tetrahydroaluminate $LiAlH_4$ (commercial) was used without preliminary recrystallization. A weighed portion of $LiAlH_4$ was dissolved in THF and the resulting solution was filtered in an inert atmosphere through a Schott filter. The $LiAlH_4$ concentration, found from the amount of hydrogen released in hydrolysis was about 95–98% of the theoretical value. ^{27}Al NMR spectrum (δ, ppm; solvent THF): 98 (quintet, $^1J_{Al-H}$ 173 Hz).

The catalytic hydrogenation was performed in a thermostated glass vessel of the "bedpan" type at 30°C and initial hydrogen pressure of 1 atm in the presence of a catalytic system formed in situ. To a solution of 0.01522 g (5×10^{-5} M) of $Pd(acac)_2$ in benzene, placed in a thermostated vessel, was added dropwise, in a flow of hydrogen, a $LiAlH_4$ solution in THF, and the reaction mixture was agitated for 5 min. The $LiAlH_4$/Pd ratio was varied from 0.5 to 30. The total volume of the solution was 10 ml. To the resulting black-brown "solution" was added a substrate hydrogenated under vigorous stirring at an initial hydrogen pressure of 1 atm, with monitoring by volumetry and GLC.

We studied the interaction of bisacetylacetonate with $LiAlH_4$ at different ratios of the starting components in dry deoxygenated argon in a thermostated vessel whose design envisages preliminary evacuation and filling with argon. The reaction was monitored by NMR (^{27}Al, ^7Li, ^1H) and UV spectroscopies, volumetry, and X-ray phase analysis.

The molecular hydrogen released in the reaction between the components of the catalytic system was quantitatively determined in a special thermostated vessel having an additional internal "pocket" for the second component. We placed a solution of 0.1522 g (5×10^{-4} M) of $Pd(acac)_2$ in 20 ml of benzene in a preliminarily evacuated, and filled with argon, thermostated vessel, and a solution of $LiAlH_4$ inTHF, in the internal "pocket" of the vessel. The vessel was closed with a Teflon stopper and the $LiAlH_4$ and $Pd(acac)_2$ solutions were mixed under vigorous agitation. The hydrogen formed was determined by volumetry. The solution was analyzed by UV spectroscopy: the amount of the reacted $Pd(acac)_2$ was calculated from the absorption band at 330 nm (ε_{330} =10630 $M^{-1}\,cm^{-1}$), and that of the forming $Al(acac)_3$, from the absorption band at 288 nm (ε_{290} = 43600 $M^{-1}\,cm^{-1}$). After the reaction was complete, the solvent was evaporated in a vacuum (two thirds of the volume) and pentane was added until a precipitate was formed. The black-brown precipitate was washed successively with THF and benzene in the atmosphere of argon and dried in a vacuum (30°C, 1 mm Hg). The samples obtained were stored in sealed ampules in argon.

We calculated the material balance of the reaction of $Pd(acac)_2$ with $LiAlH_4$ as follows. The reduction of $Pd(acac)_2$ involves two reducing agents, $LiAlH_4$ and aluminum formed in the course of the reaction. Knowing the concentration of $Al(acac)_2$ formed in the redox process

$$3Pd(acac)_2 + 2Al \rightarrow 3Pd + 2Al(acac)_2, \quad (1)$$

we can calculate the amount of Pd(0) reduced by Al(0). The difference between the total amount of reduced palladium and Pd(0) formed in the reduction by aluminum corresponds to the amount of palladium formed by the reaction

$$Pd(acac)_2 + 2LiAlH_4 \rightarrow Pd(0) + 2Li(acac) + 2/n[AlH_3]_n + H_2. \quad (2)$$

The volume of hydrogen evolved can be used to find the fraction of decomposed alane and the amount of aluminum involved in the formation of a substitutional solid solution with palladium.

The NMR spectra were recorded on a Varian VXR-500S pulse spectrometer. The chemical shifts of the ^{27}Al and ^7Li signals were measured relative to the external standards, 0.1 M solutions of $Al(NO_3)_3$ and LiCl. The chemical shifts of ^1H are given relative to tetramethylsilane. To prevent hydrolysis when recording ^{27}Al and ^7Li spectra, we sealed a solution under study in a quartz ampule 5 mm in diameter, preliminarily evacuated and filled with argon.

The X-ray phase analysis of the samples was made on a DRON-3M diffractometer with Cu_{K_α} radiation.

The reduction of $Pd(acac)_2$ by a freshly prepared solution of lithium tetrahydroaluminate at room temperature occurs in 1–2 min to give a black-brown solution exhibiting a comparatively low activity in hydrogenation catalysis. Even at the optimal reagent ratio $LiAlH_4$/Pd = 2, the catalytic activity of the system under consideration in hydrogenation of styrene does not exceed 30 moles substrate per mole of Pd per minute, which is considerably lower than that of palladium nanoclusters

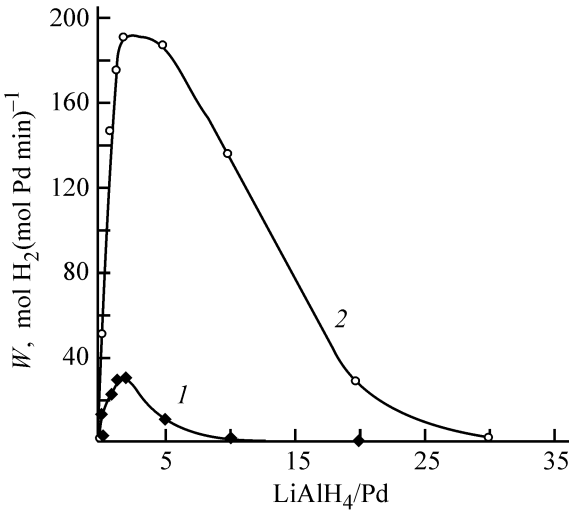


Fig. 1. Hydrogenation of styrene in the presence of the $Pd(acac)_2$–$LiAlH_4$ catalytic system (*1*) with a freshly prepared $LiAlH_4$ solution and (*2*) with that stored in an inert atmosphere for 24 h. c_{Pd} = 5 mM, [substrate]/$Pd(acac)_2$ = 170, solvent benzene, T = 30°C, P_{H_2} = 1 atm. (W) Catalytic activity.

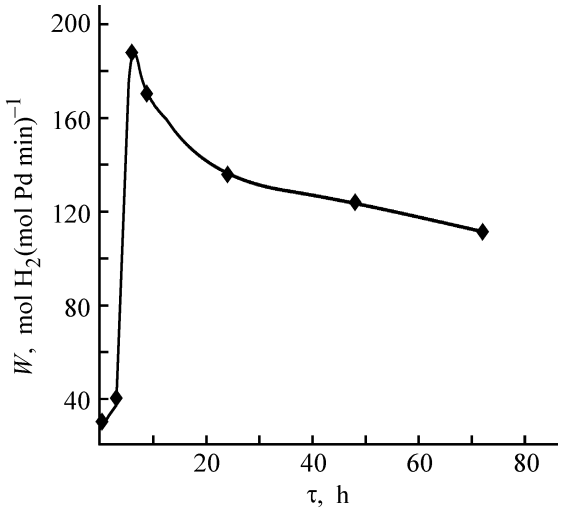


Fig. 2. Catalytic activity W of the system $Pd(acac)_2$–$LiAlH_4$ in styrene hydrogenation vs. the storage duration τ of a solution of the reducing agent. c_{Pd} = 5 mM, [substrate]/$Pd(acac)_2$ = 170, $LiAlH_4$/[Pd] = 1.5, solvent benzene, T = 30°C, P_{H_2} = 1 atm. (W) Catalytic activity.

formed in systems of the Ziegler type, including those promoted with phosphines [12] (Fig. 1).

The dependence of the specific activity on the ratio between the starting reagents is of an extremal nature, and, at $LiAlH_4/Pd \geq 10$, the hydrogenation rate falls to zero.

A study of the catalytic properties of the system $Pd(acac)_2$–$LiAlH_4$ revealed an interesting fact: the catalytic activity depends on the time during which a solution of a reducing agent is stored in the inert atmosphere in the reaction vessel (Fig. 2).

Using a $LiAlH_4$ solution 5–6 h after its preparation resulted in a steep rise in the activity of the $Pd(acac)_2$–$LiAlH_4$ catalytic system in hydrogenation of styrene (Figs. 1, 2) and other unsaturated compounds (Table 1). To find out the reason for the activation of the $Pd(acac)_2$–$LiAlH_4$ system and purposefully synthesize efficient palladium catalysts for hydrogenation, we studied the interaction between the starting components in an inert atmosphere.

In the reduction of $Pd(acac)_2$ with lithium tetrahydroaluminate, molecular hydrogen is released in an amount exceeding that calculated by Eq. (2) (Table 2).

The stoichiometric equation (2) reflects the most frequently occurring case of reduction of transition metals by $LiAlH_4$, in which the redox process comprises two stages: (i) exchange of the acido ligand for the AlH_4^- anion to give tetrahydroaluminates of transition metals and (ii) decomposition of tetrahydroaluminates of transition metals because of their instability at temperatures higher than –50°C

Table 1. Catalytic hydrogenation in the presence of the system $Pd(acac)_2$–$LiAlH_4$ (Pd concentration 5 mM, $LiAlH_4/Pd$ = 1.5, solvent benzene, T = 30°C, P_{H_2} = 1 atm)

Substrate, mmol	W,* mol H_2 (mol Pd min)$^{-1}$	Conversion, %	Yield of products, %
Styrene, 8.7	123	100	Ethylbenzene, 100
Phenyl acetylene, 9.1	106	100	The same
Nitrobenzene, 9.8	41	100	Aniline, 100
Benzaldehyde, 9.8	8	98	Benzyl alcohol, 98; toluene, 2

* $LiAlH_4$ solution was stored in an inert atmosphere for 2 days.

Table 2. Reduction of $Pd(acac)_2$ by lithium tetrahydroaluminate (concentrations: Pd 0.024 M, $LiAlH_4$ 0.54 M; solvent benzene, T = 25°C)

$\frac{LiAlH_4}{Pd(acac)_2}$	Hydrogen formation			Fraction of reduced $Pd(acac)_2$, %		$c_{Al(acac)_3}$, mM
	V, ml	mol H_2/mol Pd		experiment	calculation*	
		experiment	calculation			
Freshly prepared solution of $LiAlH_4$						
0.5	3.0	0.48	0.25	47	25	3.7
1.0	6.2	1.00	0.50	98	50	6.5
2.0	11.8	1.90	1.00	99	100	4.4
5.0	14.0	2.25	1.00	100	100	0
10.0	15.0	2.41	1.00	100	100	0
$LiAlH_4$ solution after 24 h						
0.5	3.5	0.56	0.25	38	25	4.8
1.0	6.9	1.11	0.50	81	50	7.0
2.0	12.9	2.07	1.00	98	100	5.7
5.0	13.0	2.09	1.00	100	100	0

* Calculated by Eq. (2) per mole of the starting $Pd(acac)_2$.

to give the metal, alane, and molecular hydrogen [15]:

$$MX_n + nLiAlH_4 \rightarrow M(AlH_4)_n + nLiX, \quad (3)$$

$$M(AlH_4)_n \rightarrow M + nAlH_3 + n/2H_2. \quad (4)$$

It should be noted that no significant differences were observed between the volumes of hydrogen evolved with the use of a freshly prepared $LiAlH_4$ solution and that stored in an inert atmosphere for 24–28 h (Table 2). The supraequimolar release of molecular hydrogen in the reduction of $Pd(acac)_2$ with lithium tetrahydroaluminate indicates that alane formed in reaction (2) decomposes. Alane is a comparatively unstable compound, which quntitatively decomposes into elements at temperatures exceeding 100°C [20]. This process probably occurs at room temperature because of being catalyzed by the palladium clusters (nanoparticles) formed in the reduction:

$$[AlH_3]_2 \xrightarrow{Pd} 2Al + 3H_2. \quad (5)$$

It is known that highly dispersed powders of transition metals catalyze the decomposition of alane [15]. The catalytic decomposition of boranes by nanosize particles of transition metals in reduction with tetrahydroborates of alkali metals has been studied and described in the literature in sufficient detail [13, 14].

The reaction of $Pd(acac)_2$ with $LiAlH_4$ yields Pd(0) in an amount that exceeds, at $LiAlH_4/Pd \le 1$, the value calculated by Eq. (2) by nearly a factor of 2 (Table 2). Consequently, other reducing agents are involved in the redox process, together with lithium tetrahydroaluminate.

A monitoring of the reaction of $Pd(acac)_2$ with lithium tetrahydroaluminate by UV spectroscopy demonstrated that, together with a decrease in the intensity of the absorption band at 330 nm ($\pi \rightarrow \pi^*$ electron transitions in palladium complexes with chelate-bound $acac^-$ ligands), a strong absorption band peaked at 288 nm appears in the UV spectrum (Fig. 3).

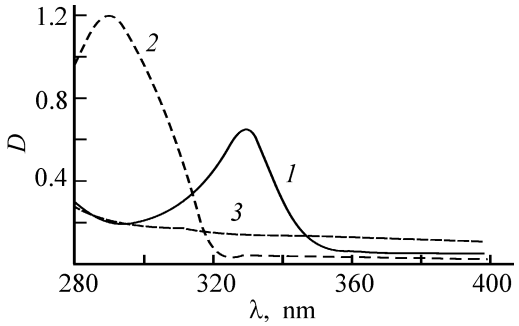


Fig. 3. UV spectra of (*1*) $Pd(acac)_2$ and (*2*) $Pd(acac)_2$–$LiAlH_4$ system at n = (*2*) 2 and (*3*) 5. c_{Pd} = 5 mM, solvent benzene, T = 30°C, l = 0.1 cm (at n = 2 the solution is 21-fold diluted). (D) Optical density and (λ) wavelength.

Table 3. Interplanar spacings *d*/*n* and relative intensities of lines in X-ray diffraction patterns of products formed in the reaction of $Pd(acac)_2$ with $LiAlH_4$

hkl	$LiAlH_4$/Pd = 0.5		$LiAlH_4$/Pd = 1		$LiAlH_4$/Pd = 2		Pd, 5-0681 [24]		Al, 4-078 [24]	
	I/I_0	*d*/*n*, Å	I/I_0	*d*/*n*, Å	I/I_0	*d*/*n*, Å	I/I_0	*d*/*n*, Å	I/I_0	*d*/*n*, Å
Freshly prepared solution of $LiAlH_4$										
111	100	2.254	100	2.254	100	2.254	100	2.246	100	2.336
200	29	1.962	30	1.968	31	1.984	42	1.945	47	2.024
220	16	1.379	15	1.378	15	1.385	25	1.376	22	1.431
	CSR 3.60 nm		CSR 3.48 nm		CSR 2.94 nm					
$LiAlH_4$ solution after 24 h										
111	100	2.248	100	2.243	100*	2.249	100	2.246	100	2.336
200	30	1.972	29	1.967			42	1.945	47	2.024
220	15	1.378	14	1.378			25	1.376	22	1.431
	CSR 3.25 nm		CSR 3.19 nm		CSR 1.12 nm					

* X-ray-amorphous substance.

It should be noted that the absorption band at 288 nm was recorded in the UV spectra of the $Pd(acac)_2$–$LiAlH_4$ reaction system at $LiAlH_4$/Pd = 0.5–2. At $LiAlH_4$/Pd = 5, 10, or 20, no absorption band at 288 nm was observed in the UV spectra. This absorption band is characteristic of acetylacetonate ligands of both lithium acetylacetonate (ε_{288} = 21 160 M^{-1} cm^{-1} in ethanol) and aluminum trisacetylacetonate (ε_{288} = 43600 M^{-1} cm^{-1} in benzene) [21]. However, assignment of the absorption band at 288 nm to lithium acetylacetonate is unlikely in the case in question, because this compound is insoluble in a benzene–THF mixture. If the given band corresponded to Li(acac), it would appear at any reagent ratio. Therefore, it was assumed that the absorption band at 288 nm belongs to acac ligands in $Al(acac)_3$. To verify this hypothesis, we subjected the white powder recovered from solution to analysis by NMR spectroscopy. The resonance signals of a solution of a sample under study in benzene-d_6 in the ^{27}Al (δ = 0 ppm) and ^1H spectra [δ = 5.38 ppm (s, 1H), 1.88 ppm (s, 6H)] correspond to $Al(acac)_3$ [22].

Thus, the reaction of $Pd(acac)_2$ with lithium tetrahydroaluminate yields $Al(acac)_3$ in addition to the products in Eq (2). The identification of $Al(acac)_3$ in the reaction system enables us to understand and explain the set of processes occurring in the reaction of palladium bisacetylacetonate with lithium tetrahydroaluminate by the following scheme: the first stage of the reaction of $Pd(acac)_2$ with lithium tetrahydroaluminate involves exchange of acac ligands for the AlH_4^- anion to give an unstable intermediate, $Pd(AlH_4)_2$ [Eq. (6), which decomposes to Pd(0), $[AlH_3]_n$, and molecular hydrogen [Eq. (7)]. The forming Pd(0) nanoparticles catalyze the decomposition of alane to give reduced aluminum [Eq. (8)]. Aluminum is, in turn, involved in a redox reaction with unreacted $Pd(acac)_2$ [Eq. (1)] at small $LiAlH_4$/Pd ratios ($LiAlH_4$/Pd ≤ 2), with the fraction of palladium in the reduced state increasing:

$$Pd(acac)_2 + 2LiAlH_4 \rightarrow Pd(AlH_4)_2 + 2Li(acac), \quad (6)$$

$$Pd(AlH_4)_2 \rightarrow Pd + 2/n[AlH_3]_n + H_2, \quad (7)$$

$$[AlH_3]_n \xrightarrow{Pd} nAl + (3n/2)H_2. \quad (8)$$

At high $LiAlH_4$ concentrations, mostly lithium tetrahydroaluminate acts a reducing agent.

Based on the above scheme and experimental data on $Pd(acac)_2$ conversion, hydrogen evolution, and $Al(acac)_3$ formation, we can calculate the degree of catalytic decomposition of alane and the fraction of aluminum involved in the redox process. The material balance data demonstrate that aluminum is not fully consumed in the redox reaction in accordance with Eq. (1), with a part of the metal remaining unreacted. For example, with a freshly prepared $LiAlH_4$ solution, the calculated amount of "free" Al(0) after the reduction of $Pd(acac)_2$ is 0.28×10^{-4}, 1.63×10^{-4}, and 2.3×10^{-4} mol of Al at $LiAlH_4$/Pd of 1, 2, and 5, respectively. The remaining aluminum can interact with Pd(0) to give palladium aluminides of various compositions [23] or solid solutions. To verify this assumption, we subjected catalyst samples produced as a result of $Pd(acac)_2$ interaction with a freshly prepared $LiAlH_4$ solution and that stored in an inert atmosphere for 24 h to an X-ray phase analysis (Table 3).

Table 4. Parameters of ^{27}Al and ^{7}Li NMR spectra of $LiAlH_4$ solutions ($LiAlH_4$ concentration 0.54 M, solvent THF, T = 25°C)

τ, h	FWHM, Hz, of lines in the NMR spectra of a $LiAlH_4$ solution				
	in a sealed ampule		in inert atmosphere in a "finger" vessel		
	$\Delta\nu_{1/2}$ ^{27}Al (δ = 98 ppm, quintet)	$\Delta\nu_{1/2}$ ^{7}Li (δ = –0.2 ppm, singlet)	$\Delta\nu_{1/2}$ ^{27}Al (δ = 98 ppm, quintet)	$\Delta\nu_{1/2}$ ^{7}Li (δ = –0.2 ppm, singlet)	$S_1 : S_2^*$
0.5	47	8	46	8	1 : 0
3.0	47	7	49	8	1 : 0
5.0	47	8	56	11	1 : 0.1
24	47	8	197	23	1 : 0.8
96	46	7	430	90	1 : 3.8

* Ratio of integral signals with δ = 98 (S_1) and 55 ppm (S_2).

The peaks in the X-ray diffraction patterns of the samples studied do not correspond to individual substances, palladium or palladium aluminides [24]. The reflections characteristic of palladium are shifted to smaller Bragg angles, toward reflections of aluminum. Because palladium and aluminum have close atomic radii (r_{Pd} = 1.37 Å, r_{Al} = 1.43 Å) and the same crystal lattice type, the increase in the interplanar spacings hkl of palladium (Table 3) may indicate that aluminum is incorporated into the palladium lattice to give a substitutional solid solution.

For catalyst samples produced by reduction of $Pd(acac)_2$ with a freshly prepared $LiAlH_4$ solution, the coherent-scattering region (CSR) calculated by the Selyakov–Scherrer formula [25] is somewhat larger that that in the case of a $LiAlH_4$ solution stored in an inert atmosphere. In both cases, an increase in the $LiAlH_4$/Pd ratio favors formation of finer catalyst particles.

It is known that addition of a second metal (Group 1B) to hydrogenation catalysts commonly improves their selectivity, but impairs the specific activity of the catalysts [26]. Probably, it is the presence of aluminum that is the main reason for the low catalytic activity in reduction of Pd(II) with a freshly prepared solution of $LiAlH_4$. It, however, remains unclear why the catalytic system is activated in storage of a solution of the reducing agent in an inert atmosphere.

To obtain additional information about the state of $LiAlH_4$ in solution and changes in this solution in the course of time, we used NMR spectroscopy on aluminum ^{27}Al and lithium ^{7}Li nuclei.

The ^{27}Al NMR spectrum of a $LiAlH_4$ solution in THF contains a single resonance signal with a chemical shift of 98 ppm, which is a quintet with a spin–spin interaction constant $^{1}J_{Al-H}$ of 173 Hz and lines with full width at half-maximum ($\Delta\nu_{1/2}$ ^{27}Al, FWHM) of 47 Hz (Fig. 4).

The region of the chemical shift observed is characteristic of the AlH_4^- anion (95–102 ppm) [27–29]. The multiplet structure of the spectrum is due to the scalar spin–spin interaction of equivalent protons with the aluminum isotope. It indicates that the tetrahedral configuration of the AlH_4^- anion is preserved in the THF solution. In the ^{7}Li spectrum, lithium tetrahydroaluminate is characterized by a singlet resonance signal with a chemical shift δ = –0.2 ppm. A ^{27}Al and ^{7}Li NMR monitoring of a solution of $LiAlH_4$ in THF in an inert atmosphere in a sealed ampule for 48 h did not reveal any changes (Table 4). At the same time, it can be seen from the ^{27}Al NMR spectra of a solution of $LiAlH_4$ in THF, stored in an inert atmosphere in

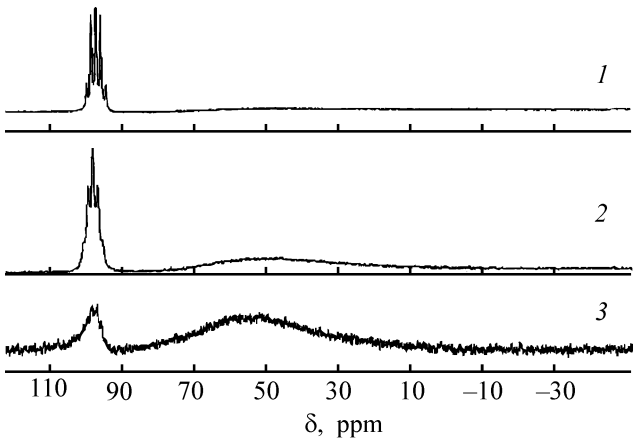


Fig. 4. ^{27}Al NMR spectra of a $LiAlH_4$ solution in THF stored in an inert atmosphere in an unsealed vessel for (*1*) 30 min, (*2*) 24h, and (*3*) 4 days. (δ) Chemical shift.

Table 5. Effect of water on the parameters of ^{27}Al NMR spectra of lithium tetrahydroaluminate solutions ($LiAlH_4$ concentration 0.54 M, solvent THF, T = 25°C, $[LiAlH_4]/[H_2O]$ = 50)

τ, h	Parameters of the ^{27}Al NMR spectrum of the $LiAlH_4$ solution upon introduction of water	
	$\Delta\nu_{1/2}$ ^{27}Al, Hz (δ = 98 ppm)	$S_1 : S_2^*$
0.1	77	1 : 0.2
0.5	108	1 : 0.3
2.0	120	1 : 0.4
24.0	291	1 : 1.6

* Ratio of the integral intensities of signals with δ = 98 (S_1) and 55 ppm (S_2).

the reaction vessel that, in the course of time, the FWHM of the lines ($\Delta\nu_{1/2}$ ^{27}Al) becomes narrower, intensity of the resonance signal with a chemical shift δ = 98 ppm decreases, and a new broad resonance signal with a chemical shift of 55 ppm appears and grows in intensity (Fig. 4, Table 4). An increase in FWHM ($\Delta\nu_{1/2}$ ^{7}Li) was also observed in the ^{7}Li spectrum. These facts indicate that the changes in the $LiAlH_4$ solution may be due to its interaction with reagents slowly diffusing from the environment, e.g., water and(or) oxygen. A contact with the $LiAlH_4$ solution with oxygen affects the spectral characteristics of the solution only slightly, whereas introduction of even small amounts of water (1/50 of the initial concentration of $LiAlH_4$) leads to observable changes in the NMR spectra (Table 5). In view of the aforesaid, we attributed the broad resonance signal with a chemical shift of 55 ppm to products of partial hydrolysis of $LiAlH_4$.

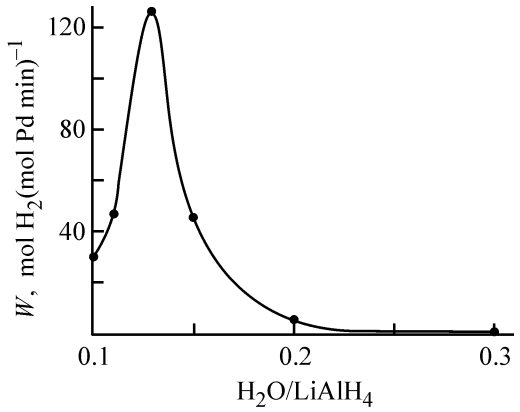
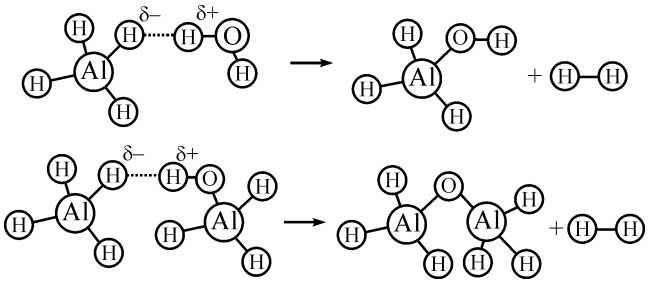


Fig. 5. Effect of water on the specific activity W of the $Pd(acac)_2$–$n$$LiAlH_4$ catalytic system in hydrogenation of styrene. c_{Pd} = 5 mM, [substrate]/$Pd(acac)_2$ = 170, $[LiAlH_4]/[Pd]$ = 2, solvent benzene, T = 30°C, P_{H_2} = 1 atm.

The width of the lines in the central component of the multiplet is affected by the following factors: distortion of the T_d symmetry of the AlH_4^- anion because of the nonequivalence of Al–H bonds in the tetrahedron in the formation of ion pairs, electric fields of the cations and dipoles of the solvent, and overlapping of the wave functions of AlH_4^- anion and other species [27]. If a ligand in the AlH_4^- anion is different in nature from the others, a multiplet structure from the EH_4^- anion will not appear in the ^{27}Al spectrum [28]. The observed increase in the FWHM ($\Delta\nu_{1/2}$ ^{27}Al) of the lines in the ^{27}Al spectrum of the $LiAlH_4$ solution is probably due to a distortion of symmetry in the environment of the aluminum atom, which may be due to its interaction with water or products of partial hydrolysis of $LiAlH_4$, followed by formation of polyoxo anions:



(the negative charge of the AlH_4^- anion and $Al_2H_6O^{2-}$ dianion is not shown in the scheme). The formation of complex compounds between the EH_4^- anion (E = Al, B, Ga) and proton-donor compounds was described in [30].

Catalytic experiments performed with preliminary addition of water to the lithium tetrahydroaluminate solution confirm the modifying effect of water on the properties of the $Pd(acac)_2$–$LiAlH_4$ system (Fig. 5).

Thus, it is the partial hydrolysis of $LiAlH_4$ that is the main reason for the observed differences in the behavior of the $Pd(acac)_2$–$LiAlH_4$ catalytic system. In the presence of small amounts of water, the reaction system simultaneously contains both $LiAlH_4$ and products of its partial hydrolysis, polyoxo anions. In this case, $LiAlH_4$, aluminum formed in decomposition of alane, and products of partial hydrolysis of $LiAlH_4$ will act as reducing agents. It is known that the reducing capacity of alkoxy

derivatives of lithium tetrahydroaluminates decreases as the number of substituted hydrogen atoms grows [31]. Therefore, on the one hand, with a partly hydrolyzed $LiAlH_4$ used, a larger part of aluminum formed in alane decomposition is consumed in the redox reaction (1). This is indicated by the increase in the $Al(acac)_3$ concentration in the case when a $LiAlH_4$ solution stored in an inert atmosphere is used (Table 2), i.e., a smaller part of reduced aluminum will be incorporated in the catalyst composition and will have an inhibiting effect. On the other hand, the redox reaction between $Pd(acac)_2$ and partly hydrolyzed $LiAlH_4$ will yield compounds of the type $[AlH_{3-x}(OH)_x]_n$:

$$Pd(acac)_2 + 2LiAlH_{4-x}(OH)_x \rightarrow Pd + 2Li(acac) + 2AlH_{3-x}(OH)_x + H_2, \quad (9)$$

rather than alane.

The catalytic decomposition of $[AlH_{3-x}(OH)_x]_n$ compounds in the presence of palladium can be represented as

$$2AlH_2(OH) \xrightarrow{Pd} H_2 + H(OH)Al{-}O{-}AlH_2. \quad (10)$$

In contrast to aluminum, the compounds being formed cannot poison the palladium catalyst because aluminum contained in these compounds is bound with oxygen.

One more reason for the promoting effect of water should be noted together with those already considered. The decrease in the particle size, observed, according to XPA, in the case when partly hydrolyzed $LiAlH_4$ is used, indicates that the polyoxo anions formed can effectively stabilize Pd particles by precluding their growth and coagulation.

CONCLUSIONS

(1) The formation and properties of the $Pd(acac)_2$–$LiAlH_4$ catalytic system in hydrogenation of unsaturated compounds was studied. It was shown that the reduction of $Pd(acac)_2$ with lithium tetrahydroaluminate is accompanied by catalytic decomposition of alane into hydrogen and aluminum. The aluminum formed reacts both with $Pd(acac)_2$, being converted to $Al(acac)_3$, and with Pd(0) particles to give a substitutional solid solution.

(2) It was demonstrated that the steep increase in the activity of the $Pd(acac)_2$–$LiAlH_4$ catalytic system in hydrogenation in storage of a solution of a reducing agent in an inert atmosphere is due to partial hydrolysis of $LiAlH_4$ and to a decrease in the fraction of the inhibitor, reduced aluminum, in the catalyst.

REFERENCES

1. Ziegler, K., Gellert, H.G., Holzkamp, E., and Wilke, G., *Brennstoff Chem.*, 1954, vol. 35, pp. 321–325.
2. Natta, G., Porri, L., Zanini, G., and Palvarini, A., *Chim. Ind.* (Milan), 1959, vol. 41, pp. 526–529.
3. Overett, M.J., Blann, K., Bollmann, A., et al., *J. Am. Chem. Soc.*, 2005, vol. 127, pp. 10 723–10 730.
4. Nekhaeva, L.A., Bondarenko, G.N., and Frolov, V.M., *Kinet. Kataliz*, 2003, vol. 44, no. 5, pp. 692–699.
5. Harlan, C.J., Bott, S.G., and Barron, A.R., *J. Am. Chem. Soc.*, 1995, vol. 117, pp. 6465–6474.
6. Shmidt, F.K., *Kataliz kompleksami metallov pervogo perekhodnogo ryada reaktsii gidrirovaniya i dimerizatsii* (Catalysis of Hydrogenation and Dimerization Reactions by Complexes of First-Row Transition Metals), Irkutsk: Irkutsk. Gos. Univ., 1986.
7. Kalechits, I.V. and Shmidt, F.K., *Kinet. Kataliz*, 1966, vol. 7, no. 4, pp. 614–617.
8. Kalechits, I.V., Lipovich, V.G., and Shmidt, F.K., *Neftekhimiya*, 1966, vol. 6, pp. 813–816.
9. Schmidt, F.K., Nindakova, L.O., Shainyan, B.A., et al., *J. Mol. Catal. A: Chem.*, 2005, vol. 235, pp. 161–172.
10. Belykh, L.B., Titova, Yu.Yu., Umanets, V.A., and Shmidt, F.K., *Zh. Prikl. Khim.*, 2006, vol. 79, no. 8, pp. 1285–1291.
11. Bonnemann, H. and Brijoux, W., *Active Metals: Preparation, Characterization, Application*, Alois Furstner, Ed., Weinheim: VCH, 1995.
12. Belykh, L.B., Goremyka, T.I., Skripov, N.I., et al., *Kinet. Kataliz*, 2006, vol. 47, no. 3, pp. 373–380.
13. Mal'tseva, N.N. and Khain, V.S., *Borogidrid natriya* (Sodium Borohydride), Moscow: Nauka, 1985.
14. Glavae, G.N., Klabunde, K.J., Sorensen, C.M., Hadjipanayis, G.S., *Inorg. Chem.*, 1993, vol. 31, pp. 474–477.
15. Soloveichik, G.L. and Bulychev, B.M., *Usp. Khim.*, 1983, vol. 52, no. 1, pp. 72–103.
16. Ishizuka, H., Tano, T., and Torigoe, K., *Colloids Surf.*, 1992, vol. 63, nos. 3–4, pp. 337–340.
17. Gordon, A.J. and Ford, R.A., *The Chemist's Companion. A Handbook of Practical Data, Techniques and References*, New York: Wiley Intersciences, 1972.
18. Mitchell, J. and Smith, D.M., *Aquametry. Part I.*

A Treatise on Methods for the Determination of Water, New York: Wiley, 1977, 2nd ed.

19. US Patent 3 474 464.
20. Nekrasov, B.V., *Osnovy obshchei khimii* (Fundamentals of General Chemistry), Moscow: Khimiya, 1973, vol. 2.
21. Schmidt, F.K., Ratovskii, G.V., Dmitrieva, T.V., et al., *J. Organometall. Chem.*, 1983, vol. 256, pp. 309–329.
22. Haraguchi, H. and Fujiwara, S., *J. Phys. Chem.*, 1969, vol. 73, no. 10, pp. 3467–3473.
23. Khoudiakov, M., Ellis, A.B., Perepezko, et al., *Chem. Mater.*, 2000, vol. 12, pp. 2008–2013.
24. Powder Diffraction F.Q., Hanawalt Search Manual, Inorganic Phases, *JCDD*, 1992, pp. 1–42.
25. Kitaigorodskii, A.I., *Rentgenostrukturnyi analiz* (X-ray Diffraction Analysis), Moscow: GITTL, 1950.
26. Molnar, A., Sarkany, A., and Vagra, M., *J. Mol. Catal. A: Chem.*, 2003, vol. 173, pp. 185–221.
27. Tarasov, V.P., Bakum, S.I., Privalov, V.I., and Buslaev, Yu.A., *Koordinats. Khim.*, 1981, vol. 7, no. 5, pp. 674–692.
28. Tarasov, V.P., Privalov, V.I., Gorbik, A.A., Bakum, S.I., *Koord. Khim.*, 1985, vol. 11, no. 12, pp. 1626–1634.
29. Tarasov, V.P., Bakum, S.I., and Kuznetsova, S.F., *Zh. Neorg. Khim.*, 1997, vol. 42, no. 5, pp. 779–786.
30. Filippov, O.A., Filin, A.M., Tsupreva, V.N., et al., *Inorg. Chem.*, 2006, vol. 46, no. 7, pp. 3086–3096.
31. Ashby, E.C., Dobbs, F.R., and Hopkins, H.P. Jr., *J. Am. Chem. Soc.*, 1975, vol. 97, pp. 3158–3162.

ISSN 1070-4272, Russian Journal of Applied Chemistry, 2008, Vol. 81, No. 6, pp. 965–969. © Pleiades Publishing, Ltd., 2008.
Original Russian Text © L.I. Bel'chinskaya, K.A. Kozlov, A.V. Bondarenko, G.A. Petukhova, M.L. Gubkina, 2008, published in Zhurnal Prikladnoi Khimii, 2008, Vol. 81, No. 6, pp. 926–930.

PHYSICOCHEMICAL STUDIES OF SYSTEMS AND PROCESSES

Effect of Salt Modification on Adsorption Properties of Acid-Activated Montmorillonite and Kaolinite

L. I. Bel'chinskaya, K. A. Kozlov, A. V. Bondarenko, G. A. Petukhova, and M. L. Gubkina

Voronezh State Forestry Academy, Voronezh, Russia
Lipetsk State Technical University, Lipetsk, Russia
Frumkin Institute of Physical Chemistry and Electrochemistry, Russian Academy of Sciences, Moscow, Russia

Received July 9, 2007

Abstract—Effect of modification of a layered aluminosilicate, montmorillonite, and rigid-structure kaolinite activated by sulfuric acid with solutions of magnesium chloride was studied in order to obtain sorbents for wastewater treatment to remove organic compounds.

DOI: 10.1134/S1070427208060074

Because of the wide use of adsorption technologies in the present-day development and modernization of various industries, it becomes an increasingly urgent task to create inexpensive and readily available sorbents. A problem that remains topical for extending the application range of sorption materials is the possibility of purposefully controlling the chemical structure of their surface layer and thereby of widely varying the adsorption-structural characteristics of adsorbents and improving their selectivity and multifunctionality.

The set of physicochemical properties of natural mineral sorbents is improved by their activation and modification. By the activation is commonly understood [1] the improvement of the sorption activity under any treatment of a material, and by modification, changes in the properties of sorbents, with their original structure preserved. In the present study, the adsorption properties of minerals were improved by activating samples with 20% sulfuric acid and modifying the activated samples with a magnesium chloride solution.

EXPERIMENTAL

As objects of study served two samples of natural silicates from a deposit in Lipetsk oblast, in which the rock-forming minerals are montmorillonite and kaolinite. Montmorillonite is a layered silicate material with an expanding structural unit. In montmorillonite, silicon in the tetrahedral layer is substituted by aluminum, and aluminum in octahedral positions is partly substituted by magnesium [2]. As a result, there appears charge deficiency compensated by interlayer ions having an exchange capacity. In natural montmorillonites, these are, as a rule, Na and Ca. The general crystallochemical formula of montmorillonite is $(Ca,Na)(Mg,Al,Fe)_2(OH)_2[Si,Al_4O_{10}] \cdot nH_2O$ [3, 4]. The montmorillonite clay used in the study contained 65 wt % rock-forming mineral, with halloysite (20 wt %) and vermiculite (15 wt %) the rest.

Kaolinite is composed of two-layered packets: one silica-oxygen tetrahedral layer of composition $[Si_{2n}O_{5n}]^{2n}$ and one aluminum–oxygen–hydroxyl octahedral layer of composition $[Al_{2n}(OH)_{4n}]^{2+}$. Both layers are combined into a packet by a hydrogen bond formed by oxygen ions of the silicon–oxygen layer and OH groups of the octahedral layer [3, 4]. The structural unit is "rigid," incapable of swelling. The composition of the sample under study was as follows (wt %): kaolinite 75, silicite 10, illite 5, and goethite 10 (with a trace amount of montmorillonite).

The acid treatment of the natural samples was performed by the following scheme: montmorillonite (kaolinite) with a grain size less than 0.5 mm was dried at a temperature of 130°C for 2 h. The dried material was mixed with 2.33 M sulfuric acid in a mass ratio of 1 : 3 and activated under permanent agitation and heating on a water bath. The resulting slurry was filtered with a vacuum pump through a filter made of synthetic fibers. The filter cake was washed with distilled water to pH 4 and dried

Table 1. Chemical composition of natural minerals

Component	Natural (native) mineral, wt %		Samples activated with 20% H_2SO_4,* wt %			
	montmorillonite	kaolinite	montmorillonite		kaolinite	
			MN_1	MN_6	MN_1	MN_6
SiO_2	56.2	49.0	60.2	69.7	55.4	59.4
Al_2O_3	19.3	20.9	19.6	15.9	21.5	22.0
Fe_2O_3	2.21	3.18	1.97	1.29	1.73	1.46
MgO	0.49	0.53	0.53	0.57	0.56	0.58
CaO	1.4	0.87	0.62	0.60	0.097	0.068
Calcination loss + unanalyzable components	20.4	25.52	17.08	11.94	20.71	16.49

* Time of treatment with sulfuric acid (h): $MN_1$and KN_1, 1; MN_6 and KN_6, 6.

to constant mass. As is known [5, 6], the duration of acid treatment is of key importance for the formation of adsorption properties and composition of the surface layer. Therefore, the samples used in the study were produced by treatment for 1 h (MN_1, KN_1), which provides an increase in the total exchange capacity, and for 6 h (MN_6, KN_6), which leads to a deeper structural transformation of the minerals and to an increase in the specific surface area and porosity of the material.

Samples subjected to the acid activation (MN_1 and KN_1) were treated with a 1 N magnesium chloride solution to obtain cation-substituted forms (MMg, KMg). The cation-substitution was performed at 55°C for 2 h, the filter cake was washed to trace amounts of Cl^- in the filtrate in terms of AgCl, with the Mg-form of the clayey mineral accordingly obtained.

The chemical composition was determined by X-ray fluorescence analysis on an SRM-25 multichannel X-ray spectrometer. The content of the exchange cations in the structure of the silicates was found using procedures described in [7, 8].

The adsorption-structural parameters of the minerals in the native and cation-substituted states were determined by the pycnometric [9, 10] and desiccator methods [9]; the capacity of the monolayer was measured using the procedure described in [9–11] and calculated by formulas reported in [9, 10].

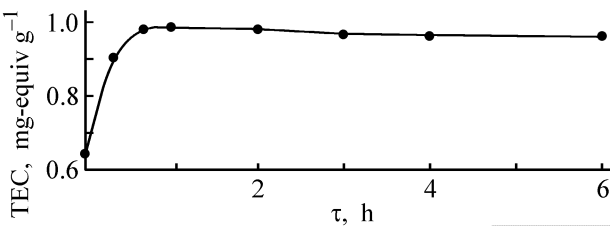


Fig. 1. Total exchange capacity of the samples, TEC, vs. the duration τ of acid activation.

The sulfuric acid treatment is a widely known method for activation of natural aluminosilicates. In numerous publications [1, 2, 5, 12], results obtained in a study of the influence exerted by the sulfuric acid concentration and treatment conditions on the surface adjustment of the minerals were reported. In the present study, the sulfuric acid activation of montmorillonite and kaolinite is only the first stage of preliminary treatment of the minerals to reach the total exchange capacity and obtain the homo-ion H-form. The modification process is the second stage, in which the unstable H-form obtained as a result of activation (for 1 h) is treated with a magnesium chloride solution to give a Mg-modified mineral (MMg, KMg). The adsorption-structural parameters of the Mg-forms of kaolinite and montmorillonite were compared with those of the minerals upon an activation for 6 h, which is the optimal duration for raising the adsorption activity of layered silicates [2, 12].

The kinetic dependence of the total exchange capacity of montmorillonite treated with a 2.33 M sulfuric acid solution is shown in Fig. 1. According to the data obtained, the optimal duration of the sulfuric acid treatment of the mineral is 1 h, in which case the TEC increases from 0.64 to 0.98 mg-equiv g^{-1}. A more prolonged treatment of the mineral with sulfuric acid leads to a slight decrease in TEC, by 0.03 mg-equiv in 6 h, which may be due to a certain instability of the H-form of aluminosilicates [5, 13]. Consequently, 1 h is the optimal time for activation of montmorillonite and synthesis of the homo-ion H-form.

The chemical composition of the minerals under study strongly changed on making longer the acid activation (Table 1). The content of free silicic

acid increases by 15–20%, and the amount of aluminum oxide decreases in montmorillonite by 17.6% as a result of ion exchange, and that of iron oxide, by 24% in montmorillonite and by 16% in kaolinite. The content of calcium oxide decreases by 55% in montmorillonite and 89% in kaolinite. The content of calcium oxide decreases more strongly in kaolinite, compared with montmorillonite, because calcium is situated in the interlayer space in montmorillonite and at the surface in kaolinite, which facilitates it reaction with the acid. The increase in the content of magnesium oxides (by 7% in MN_6) is due to the isomorphous substitution of aluminum in the octahedral network by magnesium [14].

The salt treatment of the H-forms of the minerals was performed with an excess of the magnesium chloride solution at a temperature of 40°C, with the modifier concentration varied from 0.003 to 0.5 M. The contents of the main components of the resulting forms of Mg-montmorillonite are listed in Table 2. An analysis of the results demonstrated that, at a concentration of the modifying solution equal to 0.003 M, the content of magnesium oxide in the structure of the mineral increases by 33.3%, and that of iron oxide, by 165%, with the amounts of aluminum and calcium oxides decreasing by 26 and 81%, respectively. An increase in the concentration of the $MgCl_2$ solution has nearly no effect on the content of Al_2O_3, SiO_2, and Fe_2O_3 in the mineral. The amount of CaO decreases by 58%, with the content of magnesium in the mineral increasing by 32% via ion-exchange processes whose intensity becomes lower as the concentration of the modifying solution is raised.

To study the adsorption-structural parameters, isotherms of water vapor adsorption-desorption at 25°C were experimentally obtained and the pore volume, monolayer capacity, and specific surface area were calculated (Table 3). The specific surface area increases to the maximum extent upon modification with $MgCl_2$, whereas the largest limiting sorption volume is formed upon a prolonged acid treatment of aluminosilicates. Thus, the higher sorption activity is indicated by a rise in the monolayer capacity, micropore volume, and specific surface area for Mg-samples, and by an increase in the mesopore volume for H_6-samples. Consequently, the maximum capacity is characteristic of MMg at low relative pressures, and of MN_6 at $p/p_s > 0.5$. A similar increase in the sorption activity is observed for kaolinite.

Table 2. Chemical composition of modified forms of montmorillonite

Modifier, M	Content, %				
	MgO	Al_2O_3	SiO_2	CaO	Fe_2O_3
MN_1	0.53	19.6	60.2	0.62	1.97
$MgCl_2$:					
0.003	1.77	16.47	54.65	0.12	3.25
0.03	1.92	16.61	54.09	0.08	3.71
0.1	1.97	17.07	53.39	0.09	3.71
0.3	2.05	15.92	51.72	0.07	3.03
0.5	2.07	16.13	53.74	0.07	3.23

Table 3. Adsorption-structural properties of activated (MN_1, MN_6, KN_1, KN_6) and modified (MMg, KMg) mineral*

Sample	V_s	V_{mic}	a_m, mmol g^{-1}	S_{sp}, m^2 g^{-1}
	cm^3 g^{-1}			
Montmorillonite	0.12	0.037	2.07	159
MN_1	0.16	0.036	2.00	153
MN_6	0.19	0.034	1.93	148
MMg	0.17	0.046	2.58	199
Kaolinite	0.08	0.018	1.05	80
KN_1	0.11	0.022	1.21	111
KN_6	0.12	0.017	0.94	114
KMg	0.11	0.027	1.51	114

* V_s is the limiting adsorption volume; V_{mic}, volume of micropores; a_m, monolayer capacity for water vapor at 25°C; and S_{sp}, specific surface area found from the isotherm for water vapor at 25°C by the BET method.

A characteristic feature of sorption isotherms on layered silicates (Figs. 2, 3) is their irreversibility in the whole range of relative pressures; the desorption curve does not coincide with the adsorption curve even at low p/p_s. The degree of irreversibility of the adsorption process on kaolinite is substantially lower because of the rigid structure of the rock-forming material and the smaller amount of ion-exchange cations in the structure.

The hysteresis at low pressures occurs because of the hindered desorption of water from the interpacket space, which is due to the hydration of the exchange cations and to the presence of narrow slitlike pores that hinder removal of water molecules.

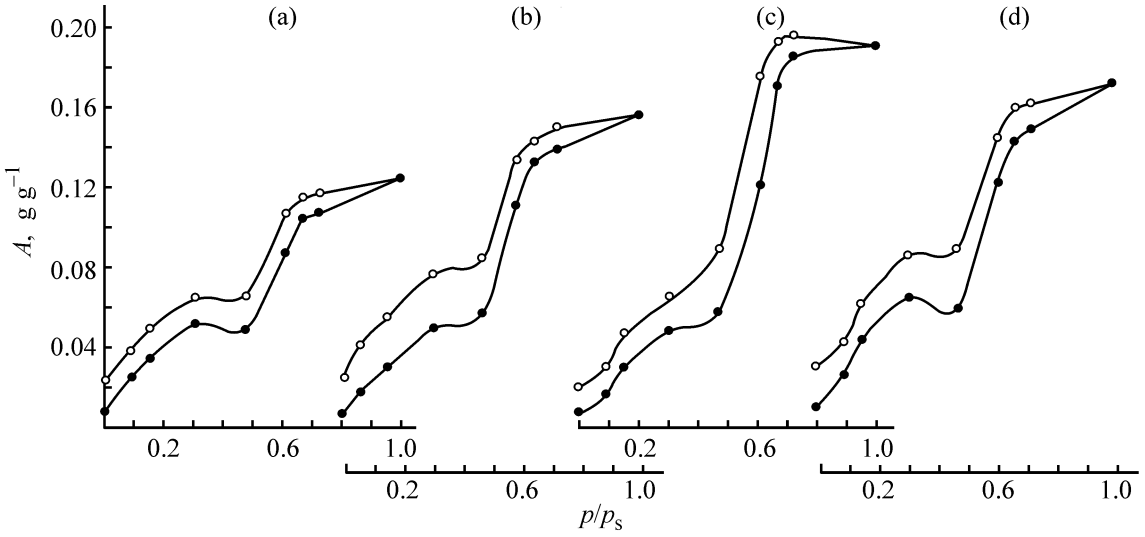


Fig. 2. Isotherms of sorption-desorption of water vapor at 25°C on natural and cation-substituted montmorillonite samples. (A) Adsorption capacity and (p/p_s) relative pressure; the same for Fig. 3. Form of montmorillonite: (a) starting M, (b) MN_1 (treatment with H_2SO_4 for 1 h), (c) MN_6 (treatment with H_2SO_4 for 6 h), and (d) MMg (treatment with a $MgCl_2$ solution).

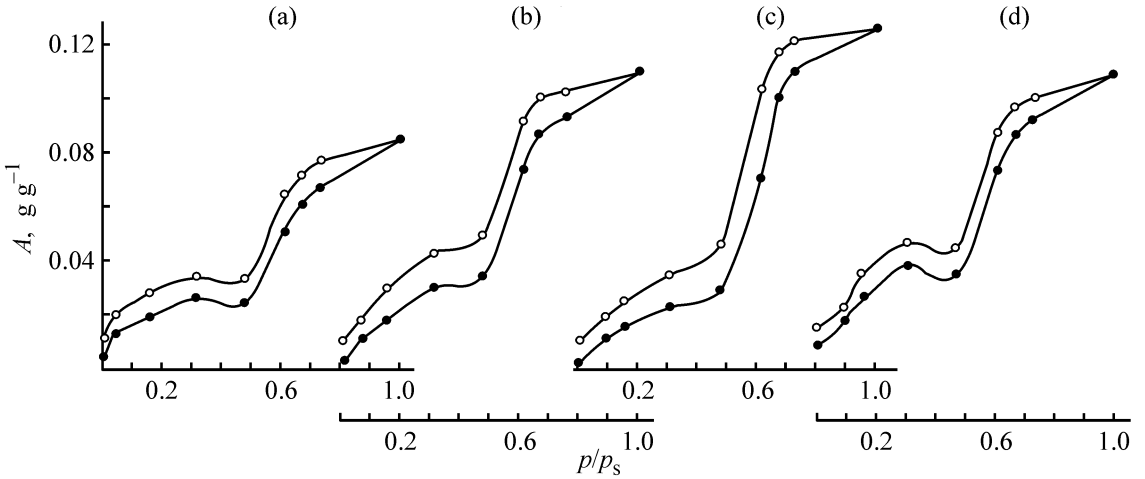


Fig. 3. Isotherms of sorption-desorption of water vapor at 25°C on natural and cation-substituted kaolinite samples. Form of kaolinite: (a) starting K, (b) KN_1 (treatment with H_2SO_4 for 1 h), (c) KN_6 (treatment with H_2SO_4 for 6 h), and (d) KMg (treatment with a $MgCl_2$ solution).

To assess the possibility of using the materials obtained in wastewater detoxication, their adsorption capacity for phenol from water was experimentally determined to be 4.8 and 6.5 mg g^{-1} adsorbent for MN_6 and MMg, respectively.

CONCLUSIONS

(1) It was found in a study of the surface properties of modified natural minerals (montmorillonite and kaolinite) that their acid activation and the subsequent salt modification improves the adsorption-structural parameters of mineral samples: V_s, by 27–39%; V_{mic}, by 20–33%; a_m, by 20–30%; and S_{sp}, by 3–20%.

(2) An analysis of the adsorption-structural parameters demonstrated that the highest sorption capacity is observed upon modification of acid-treated minerals with a 0.3 M $MgCl_2$ solution.

(3) The adsorption-structural parameters of Mg-forms of montmorillonite and kaolinite are for the most part better than those of the minerals activated for 6 h.

(4) The sorption materials obtained can be used to purify wastewater to remove phenol.

REFERENCES

1. Abdullaev, N.F., *Issledovanie adsorbtsionnykh protsessov i adsorbentov* (A Study of Adsorption Processes and Materials), Tashkent: FAN, 1979, pp. 239–254.
2. Tarasevich, Yu.I. and Ovcharenko, F.D., *Adsorbtsiya na glinistykh mineralakh* (Adsorption on Clayey Minerals), Kiev: Naukova Dumka, 1975.
3. Lazarenko, E.K., *Kurs mineralogii* (A Course of Mineralogy), Moscow: Vysshaya Shkola, 1971.
4. Bragg, W. L. and Claringbool, G.F., *Crystal Structure of Minerals*, Ithaca, N.Y.: Cornell Univ., 1965.
5. Vasil'ev, N.G. and Ovcharenko, F.D., *Usp. Khim.*, 1977, vol. 46, no. 8, pp. 1488–1511.
6. Vasil'ev, N.G. and Goncharuk, V.V., *Sintez i fiziko-khimicheskie svoistva neorganicheskikh i uglerodnykh sorbentov* (Synthesis and Physicochemical Properties of Inorganic and Carbon Sorbents), Kiev: Naukova Dumka, 1986, pp. 58–72.
7. *Osnovy analiticheskoi khimii: Uchebnoe posobie dlya vuzov* (Fundamentals of Analytical Chemistry: Textbook for Higher School), Zolotov, Yu.A., Ed., Moscow: Vysshaya Shkola, 2001.
8. Vorob'eva, L.A., *Khimicheskii analiz pochv: Uchebnik* (Chemical Analysis of Soils: Textbook), Moscow: Mosk. Gos. Univ., 1998.
9. Kel'tsev, N.V., *Osnovy adsorbtsionnoi tekhniki* (Fundamentals of Adsorption Technology), Moscow: Khimiya, 1983.
10. Gregg, S.J. and Sing, K.S.W., *Adsorption, Surface Area and Porosity*, London: Academic, 1982.
11. Dubinin, M.M., *Adsorbtsiya i poristost'* (Adsorption and Porosity), Moscow: Nauka, 1976, pp. 105–112.
12. Nadirov, N.K., *Teoreticheskie osnovy aktivatsii i mekhanizma deistviya prirodnykh sorbentov v protsesse osvetleniya rastitel'nykh masel* (Theoretical Foundations of Activation and Working Mechanism of Natural Sorbents in Clarification of Vegetable Oils), Moscow: Pishch. Prom–st., 1973.
13. Bondarenko, A.V., Bel'chinskaya, L.I., Polyakov, N.S., and Gubkina, M.L., *Fiziko-khimicheskie protsessy v kondensirovannom sostoyanii i na mezhfaznykh granitsakh ("Fagran–2004"): Sbornik nauchnykh trudov Voronezh. Gos. Univ.* [Physicochemical Processes in Condensed State and at Phase Boundaries ("Fagran–2004"): Col. of Sci. Works of Voronezh State University), Voronezh, 2004, vol. 2, pp. 528–529.
14. Millot, G., *Geologie des Argiles*, Paris: Masson, 1964.

ISSN 1070-4272, Russian Journal of Applied Chemistry, 2008, Vol. 81, No. 6, pp. 970–973. © Pleiades Publishing, Ltd., 2008.
Original Russian Text © A.N. Marinichev, 2008, published in Zhurnal Prikladnoi Khimii, 2008, Vol. 81, No. 6, pp. 931–934.

PHYSICOCHEMICAL STUDIES OF SYSTEMS AND PROCESSES

On Calculation of the Distribution Coefficient from the Results of Continuous Gas Extraction of a Volatile Component from a Liquid Mixture

A. N. Marinichev

St. Petersburg State University, St. Petersburg, Russia

Received December 24, 2007

Abstract—Distribution coefficient of a volatile component among the liquid and gas phases was calculated from equidistant data on continuous gas extraction by using an equation generalizing the relations available in the literature.

DOI: 10.1134/S1070427208060086

Gas chromatography is widely used to solve a number of analytical and physicochemical problems (preparing gas mixtures with constant, varying in a prescribed way, concentration of a volatile analyte [1]; determining the distribution coefficient [2]; vapor pressure over a solution [3]; etc.). Similar tasks are accomplished by vapor-phase gas-chromatographic analysis, a variant of which is based on continuous gas extraction (CGE) and consists in that bubbles of an extracting gas are blown through a solution containing volatiles, with their concentration subsequently recorded by gas-chromatography.

Originally, CGE was used to prepare gas mixtures of strictly defined concentration [4]. For this purpose, it was suggested to calculate the mass-volume concentration c of the volatile analyte in the gas flow emerging from the solution as a function of the volume of the gas passed, by the formula [5]

$$c = c_G^0 \exp\left(-\frac{V}{KV_L + V_G}\right). \quad (1)$$

Another model [6] of the CGE process is characterized by the relation

$$c = \frac{c_L^0/K}{1-\left(\frac{V_G}{KV_L}\right)^2}\left[\exp\left(-\frac{V}{KV_L}\right) - \frac{V_G}{KV_L}\exp\left(-\frac{V}{V_G}\right)\right]. \quad (2)$$

In these expressions, V_L and V_G are the volumes of the solution and the gas space over its surface (so-called "dead" space) in the extractor vessel; c_L^0 and c_G^0, initial concentrations of the analyte in the solution L (at $V = V_G = 0$) and in the V_G volume, respectively; and K, ratio of the mass-volume concentrations of the volatile in the solution and in the gas phase, named the distribution coefficient. This coefficient characterizes the interphase distribution and is assumed to remain unchanged during the entire extraction process.

The volume V of the gas passed can be expressed in terms of the product of the volumetric flow rate W of the extracting gas through the solution by the extraction time t. As follows from the mass balance equation [6], the concentrations c_L^0 and c_G^0 are related by

$$c_G^0 = \frac{V_L c_L^0}{KV_L + V_G}. \quad (3)$$

Equations (1)–(3) can be combined into a general formula

$$H(t) = C_1\exp(-at) + C_2\exp(-bt), \quad (4)$$

where $a = W/(KV_L + \xi V_G)$ and $b = W/V_G$ are nonnegative exponents having dimension of inverse time; $H(t) \equiv c/c_G^0$; and the pre-exponential factors C_1 and C_2 are defined by the expressions $C_1 \equiv [1 - (1 - \xi)V_G/(KV_L)]^{-1}$ and $C_2 \equiv 1 - C_1$.

Apparently, the dimensionless parameter ξ combines the above equations as follows: Eq. (4) transforms to Eq. (1) at $\xi = 1$ and to Eq. (2), with ac-

count of (3), at $\xi = 0$. In real experiments, this parameter characterizing certain specific features of the interphase mass exchange (e.g., inertia of the substance migration into the gas phase, deviation from the equilibrium distribution) may take any real (even negative) value. Because it impossible to know a priori which of the formulas, (1) or (2), describes a particular CGE process the most adequately, it seems to be optimal to process experimental data by formula (4).

The aim of our study was to analyze the potentialities of formula (4) for describing the CGE process and calculating the distribution coefficient K and parameter ξ. So far, no sufficiently detailed and systematic data on CGE, on which the validity of Eqs. (1), (2), or (4) could be verified, have been published.

In the study [7], devoted to determining the distribution coefficients of volatile sulfur-containing substances among an aqueous solution and the gas phase, an experimental procedure for CGE was described, detailed experimental data were presented in the tabulated form, and these data were used to calculate K for dimethyl disulfide by relation (1). However, the authors did not report particular values of certain quantities necessary for calculating the distribution coefficient: only $V_L = 100$ ml is known, whereas only the range 15–25 ml min^{-1} is given for the volumetric flow rate W of the extracting gas, and no data at all, for the "dead" volume V_G. This makes difficult calculation of the coefficient K.

Let us make an attempt to find W and V_G. We assume that the concentration ratio $H(t)$ can be replaced with the corresponding ratio of peak areas in the chromatogram [7]. Results of sample batching, ordered in the integer parameter n, are listed in Table 1 as $A(n)$, peak area corresponding to time $t(n)$, for the initial instant of time (at $n = 0$) and at approximately equal time intervals (~4.67 min), beginning with 32.17 min (at $n = 1$). Let us calculate the ratio $S \equiv t/\ln(A(0)/A(n))$ for each $t > 0$. The average value of S is 87.44 (standard deviation 1.33). It follows, in particular, from Eq. (1) that

$$KV_L = WS - V_G. \quad (5)$$

Table 1 lists values of S and those of the coefficient K (column K_I), calculated using formula (1). Just the coefficients of the linear regression equation for $K_I V_L$ with respect to S are the sought-for parameters W and V_G. Their estimates by the least-squares method are $W = 25.03$ (±0.05) and $V_G = 32$ (±5), with a high (0.99991) coefficient of determination (here and hereinafter, the standard deviation of a quantity is given in parentheses to the right of its estimate).

Thus, we take to be known the parameters $W = 25$ ml min^{-1}, $V_G = 30$ ml, and $V_L = 100$ ml (just these values were probably used by the authors of [7] to calculate the distribution coefficient) and find K and ξ as unknowns from CGE data by Eq. (4).

Let us consider how the behavior of the experimental data in Table 1 affects the calculation of K. It is noteworthy that the differences between the closest values of time, succeeding, $t(n + 1)$, and preceding, $t(n)$, are approximately the same, $\Delta t = 4.67$ min, with a standard deviation of 0.11 min. Thus, the areas $A(n)$ can be considered to form at $n \geq 1$ an equidistant set with close $A(n + 1)/A(n)$ ratios having an average value of 0.946 (standard deviation 0.009). If, however, we determine this ratio by the least-squares method with a single-parameter linear equation having no free term, $A(n + 1) = uA(n)$, then we obtain that $u = 0.947$ with a standard deviation of 0.002 (coefficient of determination 0.99993). This illustrates the known concept that, of all the possible estimates of the parameter u, just the least-squares estimate is effective, i.e., it has the smallest standard deviation. It can be readily shown that, in accordance with formula (1), the parameter u has the form

$$u = \exp\left(-\frac{W\Delta t}{KV_L + V_G}\right). \quad (6)$$

It follows, in particular, from relation (6) that $K = 21.0$ (±0.9), in agreement with the value 21.1, reported in [7].

We have a somewhat different situation if Eq. (4) is used. It is noteworthy that Eq. (4) is a solution to a second-order difference equation of the form

$$A(n + 2) + pA(n + 1) + qA(n) = 0, \quad (7)$$

where p and q are parameters whose least-squares estimates can be easily found by using a linear regression.

The procedure to be employed to find the parameters of (4) with the use of (7) was described in detail in [8]. We only note that, for the data from Table 1 at n in the range from 1 to 22, the parameters p and q and the roots of the characteristic equation $z^2 + pz + q = 0$ are the following: $p =$

Table 1. CGE of dimethyl disulfide from a phosphate buffer solution at 15°C

n	$t(n)$, min [7]*	$t(n+1) - t(n)$	$A(n)$ [7]*	$A(n+1)/A(n)$	K_I [7]*	S
0	0		20 852			
1	32.17	4.65	14 503	0.948	21.85	88.60
2	36.82	4.78	13 754	0.943	21.82	88.48
3	41.60	4.75	12 970	0.940	21.60	87.61
4	46.35	4.81	12 192	0.963	21.29	86.37
5	51.16	4.79	11 744	0.948	21.98	89.11
6	55.95	4.63	11 139	0.952	22.01	89.23
7	60.58	4.66	10 605	0.943	22.10	89.60
8	65.24	4.76	10 001	0.943	21.90	88.79
9	70.00	4.79	9427	0.945	21.74	88.18
10	74.79	4.80	8904	0.953	21.67	87.89
11	79.59	4.69	8482	0.935	21.82	88.48
12	84.28	4.59	7930	0.958	21.49	87.17
13	88.87	4.74	7593	0.938	21.68	87.97
14	93.61	4.85	7121	0.944	21.48	87.13
15	98.46	4.53	6720	0.960	21.44	86.95
16	102.99	4.70	6451	0.936	21.65	87.78
17	107.69	4.59	6041	0.941	21.43	86.93
18	112.28	4.50	5683	0.951	21.29	86.37
19	116.78	4.41	5405	0.952	21.32	86.50
20	121.19	4.59	5147	0.931	21.36	86.62
21	125.78	4.67	4792	0.946	21.08	85.54
22	130.45	4.56	4534	0.928	21.07	85.49
23	135.01	4.57	4208	0.951	20.79	84.36
24	139.58		4002		20.84	84.56
Average		4.67		0.946	21.56	87.44
Standard deviation		0.11		0.009	0.33	1.33

* Data from [7].

0.68567, $q = -0.24693$, $z_1 = 0.9465$, and $z_2 = -0.2609$. Therefore, for the calculated peak areas A_{calc}, equation of the type (4) with a "coded" argument $n = (t - 27.5)/\Delta t$ has the form

$$A_{calc} = 15\,380 \exp(-0.0549n) + (-1)^n 18 \exp(-1.343n). \quad (8)$$

Calculations show that, in Eq. (8), the contribution from the second alternating-sign term containing an exponential function is negligible. Therefore, the final relation can be written as

$$A_{calc} = 21\,249 \exp(-0.01176\,t). \quad (9)$$

The average value of the difference $|A_{calc} - A|$ is 80 (±50) for at $t \geq 32.17$. Because the coefficient $C_1 = 21\,249/A(0) = 21\,249/20\,852 = 1.019$ and $a = 0.01176$, we obtain from the relations

$$K = \frac{C_1(W - aV_G)}{aV_L}, \quad \xi = \frac{W(1 - C_1)}{aV_G} + C_1$$

by substituting the values of the constituent quantities that $K = 21.35$ and $\xi = -0.329$. Thus, the fact that the parameters C_1 and ξ are different from unity indicates that Eq. (1) is inadequate to the experimental data being discussed.

Table 1 lists the areas $A(n)$ for 23 instants of time, spaced by approximately equal intervals Δt. Let us consider how the basic parameters K and ξ will change if we use, e.g., different sets of peak areas. The results of the corresponding calculations are listed in Table 2, and we can conclude that there was no need at all to obtain 24 equidistant values of the peak areas $A(n)$ and 18, or even 12 values would be sufficient. The average value of

Table 2. Basic parameters of the CGE process, calculated from different sets of data in Table 1

Interval of n	z_1	C_1	a	K^*	$-\xi$
1–24	0.9465	1.019	0.01176	21.35	0.329
1–18	0.9468	1.016	0.01170	21.41	0.114
1–12	0.9469	1.016	0.01169	21.42	0.102
6–24	0.9448	1.055	0.01215	21.40	2.723
6–18	0.9452	1.049	0.01208	21.40	2.337
12–24	0.9442	1.074	0.01229	21.52	3.924
18–24	0.9422	1.141	0.01276	22.00	8.036

* Average value K = 21.50 at a standard deviation of 0.23.

the coefficient K is 21.50 (±0.23), which is somewhat overrated as compared with the value obtained earlier with Eq. (1).

A similar result can also be obtained by minimizing a nonnegative target function having the form of a sum of squared differences:

$$OF = \Sigma\{H[t(n) + \Delta t]/H[t(n)] - A(n + 1)/A(n)\}^2$$

with respect to the unknown values of the parameters K and ξ.

CONCLUSION

Application of Eq. (4) makes it possible not only to refine the sought-for value of the distribution coefficient K, but also to obtain the process parameter ξ whose numerical value validates or rejects use of formulas (1) and (2) for processing and interpretation of data on continuous gas extraction.

REFERENCES

1. Lepskii, M.V., Use of an Interphase Distribution in a Flow-through Liquid–Gas System To Obtain a Gas Flow Containing Constant Concentrations of Volatiles, *Cand. Sci. Dissertation*, Samara, 2005.
2. Castells, R.C., *J. Chromatogr. A*, 2004, vol. 1037, pp. 223–231.
3. Letcher, T.M. and Naicker, P.K., *J. Chromatogr. A*, 2004, vol. 1037, pp. 107–114.
4. Fowlis, I.A. and Scott, R.P.W., *J. Chromatogr.*, 1963, vol. 11, pp. 1–10.
5. Vitenberg, A.G. and Ioffe, B.V., *Gazovaya ekstraktsiya v khromatograficheskom analize: Parofaznyi analiz i rodstvennye metody* (Gas Extraction in Chromatographic Analysis: Vapor-Phase Analysis and Related Methods), Leningrad: Khimiya. 1982.
6. Vitenberg, A.G. and Kostkina, M.I., *Zh. Anal. Khim.*, 1979, vol. 34, no. 9, pp. 1800–1808.
7. Dobryakov, Yu.G. and Vitenberg, A.G., *Zh. Prikl. Khim.*, 2006, vol. 79, no. 8, pp. 1259–1264.
8. Marinichev, A.N., *Zh. Prikl. Khim.*, 2007, vol. 80, no. 2, pp. 209–212.

ISSN 1070-4272, Russian Journal of Applied Chemistry, 2008, Vol. 81, No. 6, pp. 974–977. © Pleiades Publishing, Ltd., 2008.
Original Russian Text © S.V. Stolyar, T.V. Antropova, D.V. Petrov, I.N. Anfimova, 2008, published in Zhurnal Prikladnoi Khimii, 2008, Vol. 81, No. 6, pp. 935–938.

PHYSICOCHEMICAL STUDIES OF SYSTEMS AND PROCESSES

Viscosity and Shrinkage of Porous and Quartzoid Glasses of the Na_2O–B_2O_3–SiO_2 System

S. V. Stolyar, T. V. Antropova, D. V. Petrov, and I. N. Anfimova

Grebenshchikov Institute of Silicate Chemistry, Russian Academy of Sciences, St. Petersburg, Russia

Received December 12, 2007

Abstract—Shrinkage of porous glasses on heating from 20 to 800°C was studied and temperature dependences of the viscosity in the range of 10^{11}–10^{13} P were determined for quartzoid (sintered) glasses based on five glasses with different compositions in the Na_2O–B_2O_3–SiO_2 system. The shrinkage of porous glasses and the viscosity of quartzoid glasses were analyzed in relation to their composition and temperature of preliminary thermal treatment.

DOI: 10.1134/S1070427208060098

A promising medium for optics and laser technology is porous glass (PG), which is a high-silica nanostructure system [1]. The advantages of PG over other materials used as solid matrices are their high thermal and chemical stability, mechanical strength, and laser resistance, combined with controllable structural characteristics. Porous glasses are used in optical technologies as a basis for composite materials produced by impregnation of PG with various substances and their subsequent sintering [2], and also for fabrication of microscopic optical elements by sintering of PG under the action of laser light [3]. Glasses based on the liquating system Na_2O–B_2O_3–SiO_2 are widely used as a starting material for production of PG of this kind.

To obtain prescribed characteristics of basic PG matrices, the information is required about the behavior of PG in a wide temperature range, depending on their composition and thermal treatment mode. The possibility of using dilatometric techniques to obtain such an information was demonstrated in [4].

The present study continues those [4, 5] devoted to changes in the size of two-phase and porous glasses based on the system Na_2O–B_2O_3–SiO_2.

EXPERIMENTAL

The compositions and porous structure parameters of PGs chosen as objects of study are listed in Table 1. The porous glasses were prepared from two-phase glasses by leaching of samples (plane-parallel polished plates of size 20 × 20 × 2 mm) in a 3 M HCl solution at 100°C.

Table 1. Compositions and pore sizes of the porous glasses studied

Starting glass	PG composition (analytical data), wt %								Pore radius, nm
	Na_2O	K_2O	B_2O_3	SiO_2	PbO	Al_2O_3	P_2O_5	F	
8B	0.25	–	4.25	95.53	–	≤0.1	–	–	1.7
NFF 40	0.41	6.11	–	93.35	–	–	0.08	0.05	5.4
NFF 140	0.30	–	5.51	94.15	–	–	0.04	–	
NK-1	0.10	0.15	6.93	92.82	–	–	–	–	7.0
NKS-1	0.37	0.30	3.87	95.14	0.07	0.25	–	–	2.9

Table 2. Compositions of the starting glasses, modes of preparation of two-phase glasses (temperature T and duration τ of thermal treatment) and glass-transition temperature T_g of the two-phase glasses prepared

Starting glass	Glass composition (analytical data), wt %								T, °C	τ, h	T_g, °C
	Na_2O	K_2O	B_2O_3	SiO_2	PbO	Al_2O_3	P_2O_5	F			
8B	7.6	–	20.4	71.9	–	0.1	–	–	550	144	505
NFF 40	6.8	–	22.1	70.4	–	–	0.19	0.52	550	40	468
NFF 140									550	142	458
NK-1	4.0	3.6	32.4	60.0	–	–	–	–	550	24	435
NKS-1	3.3	2.9	33.2	58.5	1.2	0.95	–	–	500	24	432

Table 2 lists designations, compositions, and thermal treatment modes of the starting glasses, as well as the glass-transition temperatures T_g of the two-phase glasses.[1] To be separated into two phases, the glasses under study were thermally treated at 500 or 550°C.

The following methods were selected: for a porous glass, measuring the shrinkage, i.e., the change in the linear sample size Δl, related to the initial sample size l_0 ($\Delta l/l_0$), on heating at a rate of 7 deg min^{-1}; for a quartzoid (sintered) glass, measuring the temperature dependence of the viscosity. The shrinkage and the viscosity were measured on a general-purpose quartz dilatometer–viscometer of the Chernousov–Klyuev system [6].

The measurement errors were the following: linear sample size ±1 μm, viscosity ±0.04 log η (P), temperature ±1°C, heating rate 7 ± 0.3 deg min^{-1}; the lag of the sample temperature behind the thermocouple temperature did not exceed 5–7°C.

The temperature dependences of the shrinkage $\Delta l/l_0$ of PG samples with different initial porous glass compositions and temperatures of preliminary thermal treatment are shown in Figs. 1 and 2, respectively. The temperature dependences of the vis-

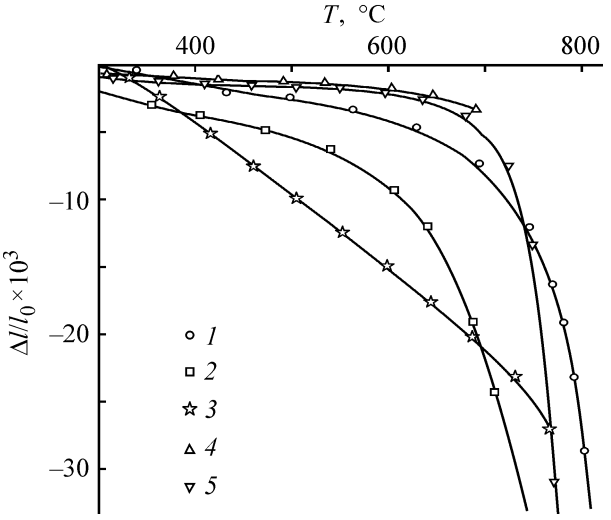


Fig. 1. $\Delta l/l_0$ of PG plates vs. temperature T at a heating rate of 7 deg min^{-1} for different compositions of the starting two-phase glass. (*1*) 8B, (*2*) NK-1, (*3*) NKS-1, (*4*) NFF-140, (*5*) NFF-40; the same for Fig. 3.

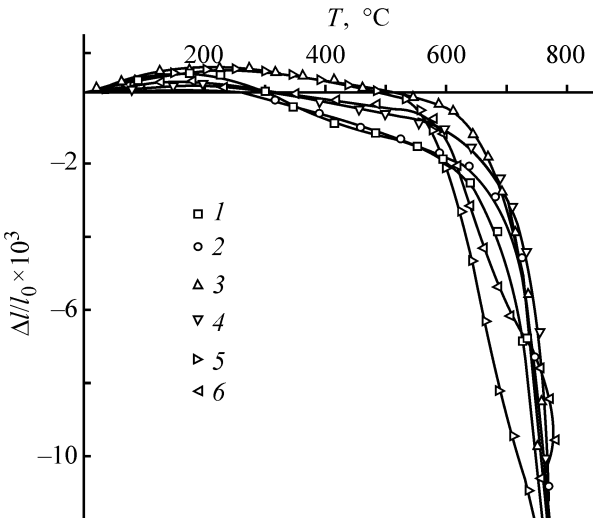


Fig. 2. $\Delta l/l_0$ of 8B PG plates vs. temperature T at a heating rate of 7 deg min^{-1} for different modes of preliminary thermal treatment of samples. Thermal treatment duration at each temperature was 1 h. Temperature of preliminary thermal treatment (°C): (*1*) 120, (*2*) 385, (*3*) 596, (*4*) 648, (*5*) 720, and (*6*) 750.

[1] The two-phase glasses were prepared from industrial glasses synthesized at the Vavilov State Optical Institute.

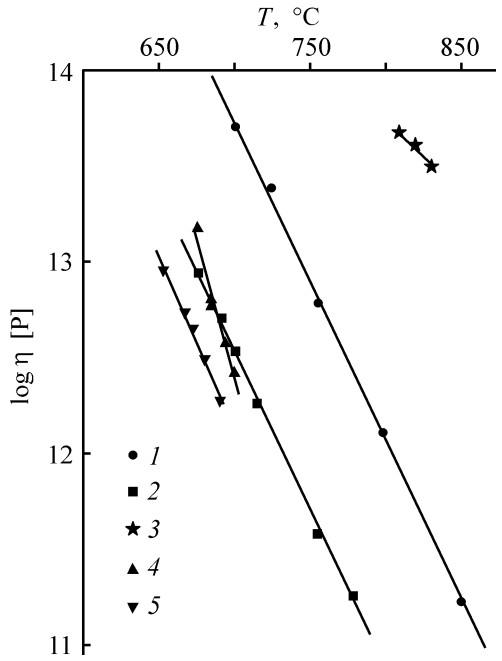


Fig. 3. Viscosity of quartzoid glasses, log η, vs. temperature T for different compositions of the starting two-phase glass.

cosity of quartzoid glasses sintered at 900–950°C are shown in Fig. 3.

Appreciable changes in the $\Delta l/l_0$ values of PG samples occur upon heating in the temperature ranges 20–250, 300–550, and 600–800°C (Figs. 1 and 2). A small expansion of the PG in the range 20–250°C results from the removal of moisture that was adsorbed in pores of the samples in storage in air before measurements. The shrinkage of the PG at higher temperatures is due to surface dehydroxylation and rearrangement (sintering) of secondary silica particles in the range 300–550°C and to softening of the skeleton of the silica phase at 600–800°C [7, 8]. In heating of PG samples at temperatures lower than the onset temperature of viscous flow in the skeleton, their linear shrinkage is the larger, the lower the Na_2O/B_2O_3 molar ratio in the starting two-phase glass and the higher the B_2O_3/SiO_2 ratio. When these quantities are equal, the PG shrinkage is the greater, the smaller the radius of the PG pores whose size is determined by the particle size of secondary SiO_2 and by the density of their packing. The weak shrinkage effect at temperatures of up to $T \le 600$°C gives no way of judging with certainty about the absolute extent to which the shrinkage of PG samples decreases as the temperature of their preliminary thermal treatment is raised (Fig. 2). However, such a tendency, presumably associated with the PG dehydration and also with the dehydroxylation resulting in stabilizations of the inner surface of pores in preliminary thermal treatment of Gs at higher temperatures, is observed. The PG shrinkage at $T > 700$°C, when skeleton softening begins, must be determined by the viscosity of the silica skeleton of PGs.

It is seen from Fig. 3 that an increase in the B_2O_3/SiO_2 molar ratio in the starting two-phase glass results in that a less viscous PG skeleton is obtained (Fig. 3). At the same B_2O_3/SiO_2, value the presence of fluoride ions in a glass considerably reduces the PG viscosity. The lower viscosity of the PG produced from FF glass (compared with the basic 8B glass) is, in all probability, due to loosening of the silicon-boron-oxygen PG skeleton upon the introduction of fluoride ions [9]. The presence of even small amounts of Al_2O_3 in the PG produced from the NKS-1 glass considerably raises its viscosity as compared with the basic NK-1 glass. The increase in the viscosity of quartzoid glasses upon introduction of Al_2O_3 into a glass is the greater, the higher the R_2O content (R = Na, Na–K) at a constant SiO_2 content of the starting two-phase glass and the larger the amount of Al_2O_3 added.

It can be assumed that it is the lower viscosity of the silica skeleton of the PG prepared from the NK-1 glass that is responsible for the onset of pore collapse in this glass at lower temperatures, compared with the PG produced from 8B glass. In a similar way can be explained the experimental data on the shrinkage of PG plates at $T \ge 700$°C (for the pair of PGs prepared from NK-1 and NKS-1 glasses) or at $T \ge 750$°C (for that prepared from 8B and NFF glasses) (Fig. 1). It is seen that the lower the viscosity of the PG skeleton (which can be judged from the viscosity of a quartzoid glass, Fig. 3), the lower the temperature (for each pair of glasses) of the onset of a sharp increase in the PG shrinkage, indicative of the onset of the viscous flow in the sample [10].

CONCLUSIONS

(1) It was found that the shrinkage of porous glasses and the viscosity of quartzoid glasses depend on the composition of the starting Na_2O–B_2O_3–SiO_2 glass and on the temperature of its thermal treatment.

(2) Three temperature regions (20–250, 300–550, and 600–800°C) of appreciable changes in

the shrinkage of porous glasses were revealed. Temperature dependences of the viscosity of quartzoid glasses were determined. These dependences can be attributed to structural transformations that occur upon sample dehydration, surface dehydroxylation, and recondensation in pores, and also as a result of thermal expansion (contraction) and viscous flow.

ACKNOWLEDGMENTS

The study was financially supported by the Russian Foundation for Basic Research (project nos. 04-03-32165, 04-02-16611a, and 08-08-00733a) and by the St. Petersburg Scientific Center of the Russian Academy of Sciences in the framework of an initiative project.

REFERENCES

1. Mazurin, O.V., Roskova, G.P., Aver'yanov, V.I., and Antropova, T.V., *Dvykhfaznye stekla: Struktura, svoistva, primenenie* (Two-Phase Glasses: Structure, Properties, Application), Leningrad: Nauka, 1991.
2. Meshkovskii, I.K., *Kompozitsionnye opticheskie materialy na osnove poristykh matrits* (Composite Optical Materials Based on Porous Matrices), St. Petersburg: SPbGITMO (Technical University), 1998.
3. Veiko, V.P., Kostyuk, G.K., Roskova, G.P., et al., *Lazernoe formirovanie opticheskikh elementov* (Laser Formation of Optical Elements), Leningrad: Znanie, 1988.
4. Antropova, T.V., Stolyar, S.V., Stolyarova, V.L., et al., *Opt. Zh.*, 2002, vol. 69, no. 3, pp. 88–90.
5. Antropova, T.V., Drozdova, I.A., Stolyar, S.V., et al., Abstracts of Papers, *Int. Conf. "Nanoparticles, Nanostructures and Nanocomposites,"* St. Petersburg, Russia, 2004, p. 79.
6. Klyuev, V.P. and Cernousov, M.A., Abstracts of Papers, *3-e Vsesoyuznoe Soveshchanie "Metody i pribory dlya tochnykh dilatometricheskikh issledovanii materialov v shirokom diapazone temperatur"* (3rd All-Union Symp. "Methods and Instruments for Accurate Dilatometric Studies of Materials in a Wide Temperature Range"), Leningrad: 1984, p. 46.
7. Antropova, T.V. and Drozdova, I.A., *Opt. Applicata*, 2003, vol. 33, no. 1, pp. 13–22.
8. Stolyar, S.V., Petrov D.V., Antropova, T.V., *Materialy 3-ego Mezhdunarodnogo seminara "Nanostructurnye materially-2004: Belarus-Rossiya"* (Proc. 3rd Int. Symp. "Nanostructural Materials-2004: Belarus-Russia"), Minsk, Belarus, 2004, pp. 273–274.
9. Antropova, T.V., Physicochemical Processes for Development of Porous Glasses and High-Silica Materials Based on Liquating Alkali-Borosilicate Systems, *Doctoral Dissertation*, St. Petersburg, 2005.
10. Elmer, T.H., *Am. Ceram. Soc. Bull.*, 1983, vol. 62, no. 4, pp. 513–516.

ISSN 1070-4272, Russian Journal of Applied Chemistry, 2008, Vol. 81, No. 6, pp. 978–982. © Pleiades Publishing, Ltd., 2008.
Original Russian Text © R.D. Apostolova, L.I. Neduzhko, E.M. Shembel', 2008, published in Zhurnal Prikladnoi Khimii, 2008, Vol. 81, No. 6, pp. 939–943.

APPLIED ELECTROCHEMISTRY AND CORROSION PROTECTION OF METALS

Electrolytic Iron Sulfides in Prototype Lithium Batteries with Gel Electrolytes Based on Poly(vinyliden fluoride) and Its Derivatives

R. D. Apostolova, L. I. Neduzhko, and E. M. Shembel'

Ukrainian State University of Chemical Engineering, Dnepropertovsk, Ukraine

Received May 16, 2007

Abstract—Electrolytic thin-film iron sulfide compounds were studied in prototype lithium batteries with gel electrolytes based on poly(vinyliden fluoride) and its derivatives by the method of galvanostatic cycling at room temperature. A discharge capacity of 200–280 mA h g^{-1} in 80–180 cycles was obtained.

DOI: 10.1134/S1070427208060104

Transition-metal sulfides (M = Mo, Ni, Fe, etc.) are widely used owing to their electrical, magnetic, optical, catalytic, and other properties. Depending on the intended use, M-sulfides are obtained as micrometer or submicrometer particles, which may be rod-like, spherical, and other amorphous or crystalline formations and films [1–3]. Films of M-sulfides are attractive because they can provide efficient electrochemical conversion in electrodes of thin-film lithium and lithium-ion batteries [4, 5]. The demand for batteries of this kind is growing because of the miniaturization of power sources necessary for portable means of communication, electronic devices, and other power consumers.

Among the numerous known film-formation methods (magnetron, laser, and RF sputtering, thermal evaporation in a vacuum, and electrodeposition), the electrolytic method was chosen for synthesis of thin-film electrode materials for lithium chemical power cells (CPC) [6].

Electrolysis has been used to obtain thin-film molybdenum sulfides [7] and Fe sulfide compounds (e-Fe,S) with a thickness of 3–20 μm [8]. Until recently, iron sulfides (FeS, FeS_2) have been used in cathodes of lithium cells and in lithium batteries of high-temperature type with a LiCl–KCl eutectic and of medium-temperature type with solid polymeric electrolytes [9, 10]. It has been shown that a reversible electrochemical transformation of natural pyrite is possible in gel electrolytes [11]. At the same time, only a minor fraction of the theoretical specific energy of natural pyrite (FeS_2) can be obtained in cycling in a lithium CPC in pair with a solar cell at room temperature [12]. At the same time, iron sulfide products of electrolysis (e-Fe, S) can be considered suitable electrode materials for low-temperature lithium batteries [4]. Their reversible capacity in electrochemical conversion in an electrolyte composed of propylene carbonate (PC), dimethoxyethane (DME), and 1 M $LiClO_4$ is 200–300 mA h g^{-1} (in 40–50th cycles). Because gel electrolytes are preferable to liquid electrolytes for thin-film lithium batteries for environmental safety reasons, studies of the thin-film e-Fe,S system were continued on prototype lithium CPC with gel-like polymeric electrolytes.

EXPERIMENTAL

The e-Fe,S compounds were deposited as compact formations with a mass of 1.5–7.0 mg cm^{-2} on 10 × 10 × 0.1-mm aluminum alloy (AMG-6) substrates by cathodic reduction of solutions containing iron sulfate, sodium thiosulfate, and stabilizing additives. The synthesis conditions have been described in detail previously [4]. The structure of the compounds synthesized was determined by an X-ray diffraction analysis (DRON-2.0 diffractometer, LiF single crystal as monochromator, Co_{K_α} radiation). The radiation intensity was measured in the range 2θ = 10°–80°.

Table 1. PE compositions and characteristics

PE	Polymer brand	Plasticizing solution		PE state	L, μm	σ, mS cm^{-1}	Solvent
		solvent	salt				
PE1(1)	PVdF-CTFE	EC : PC = 1 : 1 (vol.)	$LiClO_4$	Gel		1.08	THF, N-MPD
PE2(1)	PVdF-HFP	EC : DMC = 1 : 1 (vol.)	$LiPF_6$	″		2.04	THF
PE3(2)	PVdF-CTFE	Activating solution EC : DMC = 1 : 1(vol.), $LiPF_6$		Film	100–150	0.46	DMF
PE4(1)	PVdF	EC : DMC = 1 : 1 (vol.)	$LiN(CF_3SO_2)_2$	″	30–60		THF, acetone

The gel electrolytes were prepared from the following reagents supplied by the Solvay Group: (i) Poly(vinyliden fluoride) PVdF Solef 21 508 and its copolymers PVdF–CTFE Solef 32008/1001, PVdF–HFP Solef 20 508, (ii) lithium salts $LiClO_4$ ("Iodobrom", Saki, Ukraine), $LiPF_6$ (Merck), $LiN(CF_3SO_2)_2$ (Aldrich, USA), and (iii) solvents EC (ethylene carbonate, Merck), DMC (dimethyl carbonate, Merck), PC (polycarbonate, Angara Plant of Chemical Reagents, Russia), TGF (tetrahydrofurane, Labscan, Ireland), acetone (Merck), and N-MPD (*N*-methyl pyrrolidone, Labscan, Ireland). Polymer electrolytes (PE) were prepared by two different casting procedures. According to procedure (1), the PE constituents (solvents, lithium salts, and polymer) were mixed in a certain ratio and order, with heating when necessary. The solution obtained was poured onto a thin-layer e-Fe, S cathode to form a polymer film of thickness 30–60 μm or a gel-like mass. In this case, all the procedures were performed in a glove box in dry argon. In method (2), a solution of polymer in an organic solvent was poured onto a smooth glass surface in air. Then the microporous polymer film was activated with a lithium-containing organic electrolyte in the dry atmosphere of the box.

The electrical conductivity of the electrolytes was measured in a cell with 12Cr18Ni9Ti steel electrodes by the method of electrolytic impedance spectroscopy on a Voltalab PJZ301 analytical radiometer.

The electrochemical characteristics of the e-Fe,S system were studied in 2325 prototype lithium chemical power cells at room temperature. Lithium plates with an excess mass and a thickness of 0.3–0.5 mm served as anodes. The prototypes were assembled in a glove box in dry argon. The galvanostatic cycling of the prototypes was carried out at voltages of 2.8–1.1 V on a computerized stand at discharge current densities of 25 to 280 mA g^{-1}.

It has been shown previously [4] that mostly iron sulfides (FeS, FeS_2, Fe_3S_4, and Fe_2S_3) with admixtures of iron oxide (γ-Fe_2O_3, γ-Fe_3O_4) and sulfur are formed in the electrolytic Fe-containing deposits. The component ratio in the deposits depends on the $FeSO_4$ and $Na_2S_2O_3$ concentrations in the deposition electrolyte. Most of Fe sulfide formulations exhibit high electrochemical activity in reactions with lithium in prototype CPC with liquid electrolytes at room temperature. Some formulations were examined in this study in prototypes with gel-like polymer electrolytes. The PE compositions in the e-Fe, S/Li prototypes and their characteristics are listed in Table 1, in which the symbol *L* designates the film thickness, and σ, the electrical conductivity of the PE. The number of PE formulations actually tested in the prototypes exceeds that listed in Table 1. For example, it was shown in [13] that the use of an electrolyte composed of PVdF, TGF, dioxolane, and 1M $LiN(CF_3SO_2)_2$ is no less successful.

The open-circuit potentials of the prototype e-Fe,S/PE/Li systems vary within 2.90–3.15 V. The general feature of the discharge characteristics of prototype with both PE and a liquid electrolyte is the considerable difference between the discharge capacity Q_d in the first cycle and those in the subsequent cycles. In the first cycle, Q_{d1} exceeds 500 mA h g^{-1} and occasionally reaches values of 800 mA h g^{-1}. Q_d decreases in cycling and stabilizes after 15–20 cycles. The specific features of cycling of e-Fe, S/PE/Li prototypes in subsequent cycles are described in relation to the PE composition.

Satisfactory charging-discharge characteristics of the e-Fe,S system are obtained with PE1(1) electrolyte prepared by procedure (1). The change

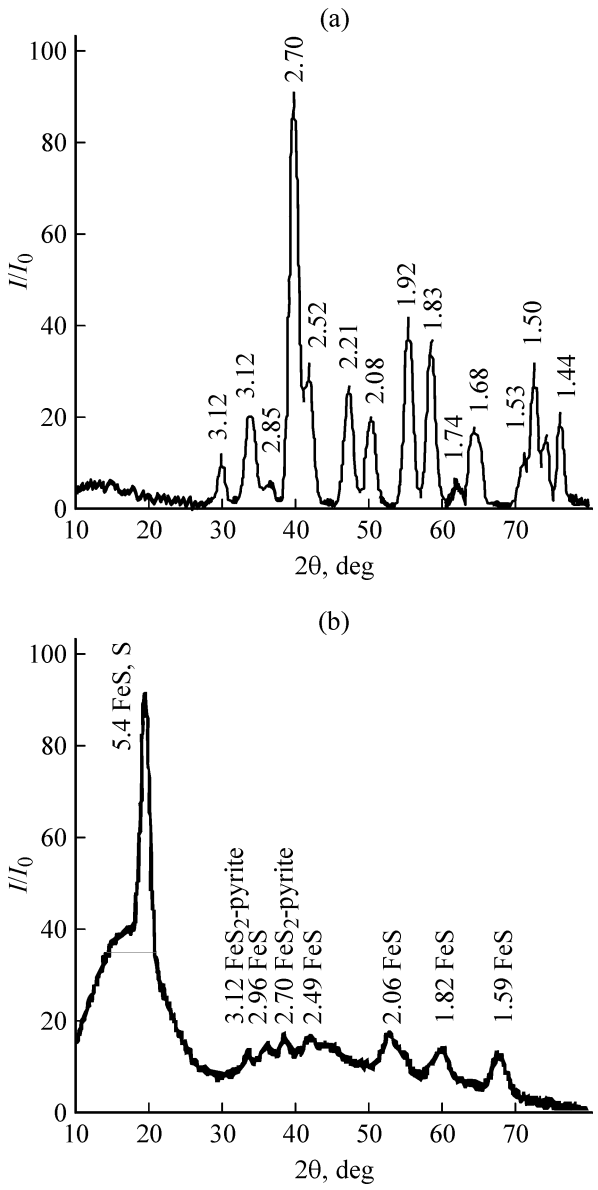


Fig. 1. X-ray diffraction patterns of e-Fe,S. (2θ) Bragg angle and (I/I_0) intensity ratio. (a) FeS_2 pyrite, FeS_2 marcasite, γ-Fe_2O_3; (b) FeS_2 pyrite, FeS, S.

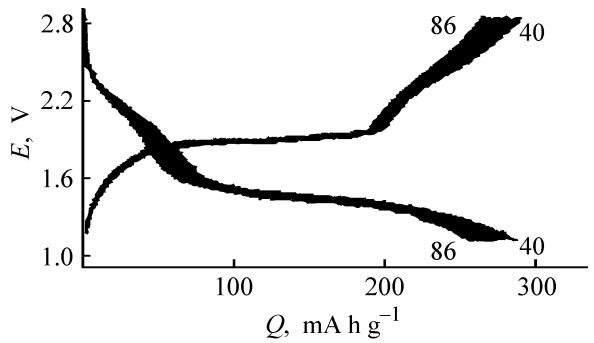


Fig. 2. Charging-discharge curves of the prototype system based on the formulation composed of FeS_2 pyrite, FeS_2 marcasite, and γ-Fe_2O_3 of mass m = 3.7 mg cm^{-2} with PE1(1). i_{dis} = 0.05, i_{char} = 0.03 mA cm^{-2}. (E) Voltage and (Q) capacity.

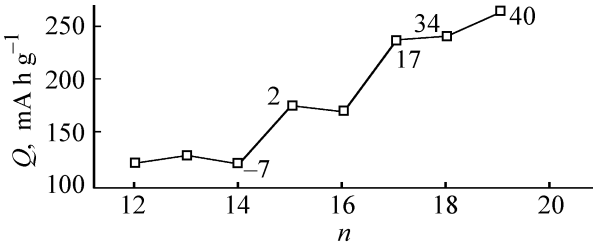


Fig. 3. Temperature dependence of the discharge capacity Q of the prototype, measured in 12th–20th cycles. The same prototype as that in Fig. 2; the same for Fig. 4. *Figures at curves* are temperatures (°C).

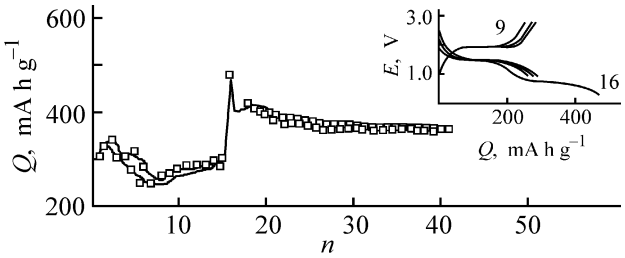


Fig. 4. Effect of prototype recharging in the 16th cycle shown in the inset on the discharge capacity Q in the subsequent cycles. (E) Voltage and (n) cycle number.

in the charging–discharge curves of a prototype in which the active cathode material (FeS_2 marcasite, FeS_2 pyrite, and γ-Fe_2O_3) is characterized by the X-ray diffraction pattern in Fig. 1a is reflected in Fig. 2. The charging–discharge profile of the prototype varies only slightly in cycling between the 40th and 86th cycles (Fig. 2). It exhibits horizontally inclined voltage plateaus at around 1.65–1.40 V in discharge and at about 1.85–1.95 V in charging. The discharge capacity decreases in cycling to reach a value of 260 mA h g^{-1} by 86th cycle. The loss of the discharge capacity is 0.2% per cycle. The temperature dependence of the discharge capacity of a prototype with PE1(1) was determined (Fig. 3). As the prototype is cooled in the temperature range 17...–7°C, the discharge capacity decreases by almost a factor of 2, which undoubtedly exceeds that upon heating from 17 to 40°C. It was found in cycling of e-Fe,S/PE1(1)/Li prototypes that the decrease in the discharge voltage to 0.35 V by the 16th cycle (inset in Fig. 4) provokes an increase in its discharge capacity in the subsequent cycles (Fig. 4). This effect should be attributed to electrochemical intercalation of Li^+ into the Al substrate of the cath-

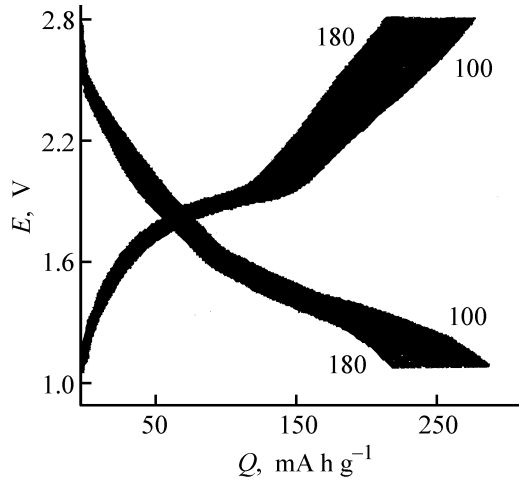


Fig. 5. Discharge-charging profile of a prototype with PE2(1) in the 100th–180th cycles. Phase composition of the cathode material: FeS, FeS_2,S; m = 1.5 mg cm^{-2}; i_{dis} = 0.05 mA cm^{-2}, i_{char} = 0.03 mA cm^{-2}. (E) Voltage and (Q) capacity; the same for Figs. 6, 7.

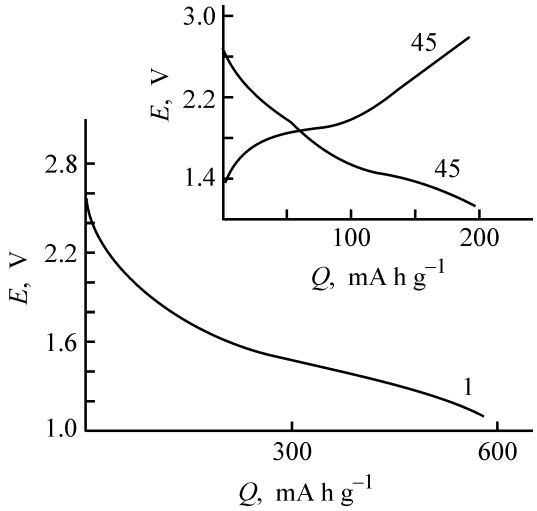


Fig. 6. Discharge curve of the prototype system constituted by FeS_2 pyrite, FeS_2 marcasite, and γ-Fe_2O_3/PE3(2)/Li in the first cycle and the discharge-charging profile in the 45th cycle (inset). m = 1.8 mg cm^{-2}, i_{dis} = 0.05 mA cm^{-2}, i_{char} = 0.03 mA cm^{-2}.

ode, in which, first, a solid α-solution $AlLi_x$ and then an intermetallic compound are formed [14, 15]. As is known, the lithiation of aluminum affects its surface and bulk properties and makes the electrode impedance lower, which exerts a positive influence on the Al/e-Fe,S interface.

The discharge characteristics of the e-Fe, S/PE2(1)/Li prototypes compare well with those of the PE1(1) prototypes. The discharge capacity of the prototypes with a PE2(1) electrolyte and a cathode material composed of FeS_2 pyrite, FeS, and S (Fig. 1b), which is 730 mA h g^{-1} in the first cycle, decreases to 280 mA h g^{-1} by the 110th cycle at a current density of 0.05 mA cm^{-2} (Fig. 5). In prolonged cycling, the loss of the discharge capacity is 0.2% per cycle in the 100th–180th cycles. The dependence of the discharge capacity on the discharge current density was determined at the end of cycling (Table 2).

Table 2. Discharge capacity at varied discharge current density in the prototype system constituted by FeS_2-pyrite, FeS, and S/PE2(1)/Li

i_{dis}, mA m^{-2}	Q_{dis}, mA h g^{-1}	Cycle no.
0.05	282	110
0.1	270	101
0.3	208	114
0.5	190	116
0.95	140	115

As follows from the data of Table 2, a discharge capacity of about 200 mA h g^{-1} can be attained at the end of prolonged cycling at a high discharge rate (300 mA g^{-1}).

In prototypes with PE3(2) electrolyte prepared by procedure (2) from the electrolytic Fe sulfide formulation (FeS_2, FeS, γ-Fe_2O_3), the discharge capacity decreases from the initial value of about 600 mA h g^{-1} (Fig. 6) to about 200 mA h g^{-1} by the end of cycling. The values of the discharge capacity for separate cycles are as follows: Q_{d20} = 201 (I_{dis} = 1.05 mA cm^{-2}), Q_{d40} = 196 mA h g^{-1} (I_{dis} = 0.2 mA cm^{-2}). The charging-discharge curves of a prototype with PE3(2) by the 45th cycle are demonstrated in Fig. 6 (inset).

Prototypes with dimensions of a flat-type lithium battery were tested in the final stage of the study. For this purpose, iron sulfides were deposited onto a 30–50-mm aluminum substrate. A PE4(1) film of thickness 30–40 μm was formed on the surface of the resulting Fe sulfide cathode and the cathode was assembled with a lithium counter electrode in a package made of laminated aluminum foil. Then, the package was sealed by hot pressing. The results obtained in cycling of the prototype battery are shown in Fig. 7. The discharge capacity of the prototype remains at a level of 200 mA h g^{-1} during 125 cycles.

The results obtained using the electrochemical impedance spectroscopy show that the conductivity of PE decreases in cycling. For example, σ of

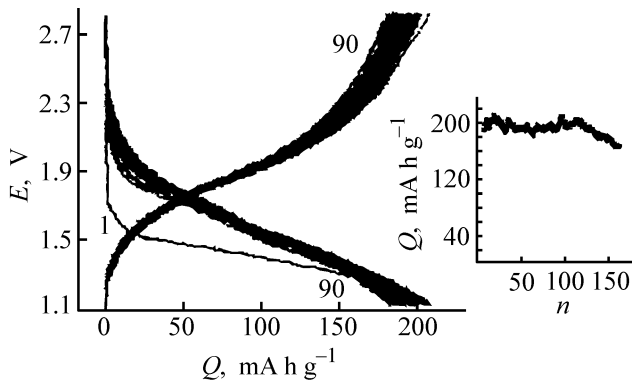


Fig. 7. Discharge-charging curves for the first 90 cycles and the variation of the discharge capacity Q with the number of cycles n (inset) of the prototype system constituted by e-FeS_2, FeS, γ-Fe_2O_3/PE4(1)/Li of size 30 × 50 mm. I_{dis} = 1.5 mA, I_{char} = 1.0 mA.

PE2(1), equal to 2.04 mCm cm^{-1} before cycling, decreases by an order of magnitude and more after the discharge capacity decreases in cycling to Q_d < 50 mA h g^{-1}. In this case, a microinjection of a liquid electrolyte into the prototype makes σ and Q_d higher. This result is accounted for by the properties of the PE composed of two macroscopic phases, a polymer and a porous space filled by the solution whose properties are close to those of the bulk solution. The polymer phase also contains ions and molecules of the solvent, but their individual properties are modified by the interaction with the polymer matrix. To factors predetermining the degradation of the e-Fe,S/PE/Li system can be attributed consumption of the liquid electrolyte in the PE pores and accumulation of electrically nonconducting products formed in interaction with the cathode material.

Thus, it was demonstrated that, as in [16–18], PVDF and its derivatives are compatible with, and swell in, liquid electrolytes and can be used together with e-Fe,S. The final result of the electrochemical conversion of the e-Fe,S/PE/Li system is determined by the nature of the cathode and the polymer materials and by the working conditions. The discharge capacity, service life, and discharge rate of the e-Fe,S/PE/Li system with PVDF electrolytes compare well with those of the system with liquid-phase electrolytes [4, 8].

CONCLUSION

Iron sulfide formulations produced by cathodic reduction of solutions containing $FeSO_4$ and $Na_2S_2O_3$ in prototype lithium chemical power cells with gel poly(vinyliden fluoride) electrolytes are capable of an electrochemical conversion in the range 2.8–1.1 V and exhibit a capacity of 200–280 mA h g^{-1} in 80–180 cycles.

ACKNOWLEDGMENTS

The study was financially supported by the Ministry of Education and Science of Ukraine (project no. 42070390).

REFERENCES

1. Wang, J., Ng, S.H., Wang, G.X., et al., *J. Power Sources*, 2006, vol. 159, no. 1, pp. 287–290.
2. Srouji, F., Afzaal, M., Waters, J., and O'Brien, P., *Chem. Vap. Deposition*, 2005, vol. 11, no. 2, pp. 91–94.
3. Yadong, Yin, Rioux, R.M., Erdonmez, C.K., et al., *Science*, 2004, vol. 304, no. 30, pp. 711–714.
4. Shembel', E.M., Apostolova, R.D., Nagirnyi, V.M., et al., *Elektrokhimiya*, 2004 vol. 40, no. 7, pp. 843–851.
5. Shembel', E.M., Apostolova, R.D., Tysyachnyi, V.P., and Kirsanova, I.V., *Elektrokhimiya*, 2005, vol. 41, no. 12, pp. 1465–1475.
6. Shembel', E.M., Nagirnyi, V.M., Apostolova, R.D., et al., *Elektrokhimicheskii sintez oksidnykh soedinenii kak osnova polucheniya vysokoeffektivnykh materialov dlya litievykh akkumulyatorov* (Electrochemical Synthesis of Oxide Compounds as Basis for Preparation of High-Efficiency Materials for Lithium Batteries), Dnepropetrovsk: Ukr. Gos. Khim. Tekhn. Univ., 2006.
7. Nagirnyi, V.M., Apostolova, R.D., Baskevich, A.S., and Shembel', E.M., *Zh. Prikl. Khim.*, 2000, vol. 73, no. 3, pp. 406–409.
8. Ukr. Patent no. 67134.
9. Strauss, E., Golodnitsky, D., and Peled, E., *Electrochim. Acta*, 2000, vol. 45, pp. 15–19.
10. Peled, E., Golodnitsky, D., Strauss, E., et al., *Electrochim. Acta*, 1998, vol. 43, pp. 1593–1599.
11. Shembel', E.M., Chervakov, O.V., Neduzko, L.I., et al., *J. Power Sources*, 2001, vol. 96, no. 1, pp. 20–28.
12. Apostolova, R.D., and Shembel', E.M., *Zh. Prikl. Khim.*, 1995, vol. 68, no. 9, pp. 1483–1487.
13. Ukr. Patent no. 60953.
14. Kabanov, B.N., Kiseleva, I.G., and Astakhov, I.I., *Elektrokhimiya*, 1972, vol. 8, no. 7, pp. 955–972.
15. Epelboin, I., Froment, M., Garreau, M., et al., *J. Electrochem. Soc.*, 1980, vol. 127, pp. 2100–2108.
16. Zhang, S.S., Ervin, M.H., Foster, D.L., et al., *J. Solid State Electrochem.*, 2005, vol. 9, no. 2, pp. 77–83.
17. Abraham, K.M., Koch, V.R., and Blacklay, T.J., *J. Electrochem. Soc.*, 2000, vol. 147, no. 4, pp. 1251–1256.
18. Prosini, P. P., Villano, P., and Carewska, M., *Electrochim. Acta*, 2002, vol. 48, no. 3, pp. 227–233.

ISSN 1070-4272, Russian Journal of Applied Chemistry, 2008, Vol. 81, No. 6, pp. 983–987. © Pleiades Publishing, Ltd., 2008.
Original Russian Text © G.A. Kolyagin, I.S. Vasil'eva, V.L. Kornienko, 2008, published in Zhurnal Prikladnoi Khimii, 2008, Vol. 81, No. 6, pp. 944–948.

APPLIED ELECTROCHEMISTRY AND CORROSION PROTECTION OF METALS

Effect of the Composition of Gas-Diffusion Carbon Black Electrodes on Electrosynthesis of Hydrogen Peroxide from Atmospheric Oxygen

G. A. Kolyagin, I. S. Vasil'eva, and V. L. Kornienko

Institute of Chemistry and Chemical Technology, Siberian Branch, Russian Academy of Sciences, Krasnoyarsk, Russia

Received December 27, 2007

Abstract—Electroreduction of oxygen to H_2O_2 on gas-diffusion air electrodes made of A 437-E acetylene black and its mixture with P 702 and P 268-E furnace blacks with various particle sizes and wettabilities by an alkaline aqueous electrolyte with 8 and 20 wt % polytetrafluoroethylene was studied.

DOI: 10.1134/S1070427208060116

Air electrodes are widely used in chemical power cells [1]. Studies are underway, intended to enable their application in new areas and, in particular, for electroextraction of oxygen from air [2] and use in hybrid power sources with simultaneous production of H_2O_2 [3].

It is known that air electrodes are less active than oxygen electrodes because the concentration of oxygen in the electrolyte becomes lower via a decrease in its partial pressure and via an increase in the resistance to diffusion of oxygen molecules across a gaseous nitrogen layer formed after atmospheric oxygen contained within electrode pores is consumed. That is inert gases create a diffusion barrier to oxygen transport to the reaction zone. However, an important advantage of air electrodes is the unlimited stock of oxygen in Earth's atmosphere at a place of its consumption without its preliminary recovery from air. This circumstance is also important for developing a process for the extensively studied electrochemical synthesis of H_2O_2 from oxygen [4–7]. In this case, it is required that the electrode structure should provide not only oxygen supply to the reaction zone across the diffusion barrier created by inert gases, but also discharge of the hydrogen peroxide obtained from the electrode volume to prevent its further reduction to water or chemical decomposition. Thus, the structure of an air electrode is even more important than that of an electrode working on pure oxygen.

Porous gas-diffusion electrodes are mostly used as air electrodes. Studies devoted to development and use of air electrodes for manufacture of H_2O_2 are only being commenced and the related published evidence is scarce. For example, an acid solution with a H_2O_2 concentration of 0.03 g l^{-1} has been obtained at a current density of 0.2 mA cm^{-2} [5], and a H_2O_2 solution with a concentration of 0.45 g l^{-1} has been produced with the use of a gas-diffusion air electrode [6].

One of methods affecting the structure of gas-diffusion electrodes is that changing their hydrophobic-hydrophilic properties by varying the content of a waterproofing agent [4, 8–11] or using carbon blacks with different wettabilities by an aqueous electrolyte [12]. For example, the use of a mixture of blacks with various properties for optimizing a gas-diffusion layer with a porosity of 70 vol % for a hydrogen-air fuel cell with a proton-exchange membrane yielded a positive effect in [13]. A mixture of acetylene black with carbon nanotubes as a carbon support for the catalytic layer of a gas-diffusion electrode for metal-air batteries was studied in [14], and the effect of a mixture of blacks on the electrosynthesis of H_2O_2 from oxygen, in [7].

The aim of the present study was to find how changes in the content of a waterproofing agent in a gas-diffusion hydrophobized electrode based on acetylene black and admixtures of a hydrophilic electrocatalyst, furnace blacks with various particle sizes, affect parameters of hydrogen peroxide synthesis from atmospheric oxygen in an aqueous electrolyte: current efficiency, electrode polarization, and kinetics of H_2O_2 accumulation. Also, the in-

Table 1. Physicochemical parameters of carbon blacks

Carbon black brand	Particle size, nm	Specific surface area, $m^2 g^{-1}$		pH of aqueous suspension	Ash content, %
		external	adsorptional		
A 473-E	30–39	101	110	9.2	0.2
P 702	60–100	37	35	8.0	0.5
P 268-E	19–35	158	265	7.8	0.1

fluence exerted by the supply rate of atmospheric oxygen to the electrode surface was analyzed. To elucidate the effect of the electrode structure on the delivery of atmospheric oxygen to the reaction zone, experiments with pure oxygen were carried out.

EXPERIMENTAL

The experimental conditions, electrolyzer design, and electrode fabrication technique are similar to those previously used in electrosynthesis of hydrogen peroxide from oxygen [4, 7, 15].

The following carbon black brands were chosen for the study: hydrophobic acetylene black of A 437-E brand and more hydrophilic furnace blacks of P 702 and P 268-E brands. The physicochemical properties of the blacks are listed in Table 1 [16]. 4D-fluoroplastic (FT-4D) served as a waterproofing agent.

The electrode material was prepared by joint coagulation of an aqueous suspension of fluoroplastic and a suspension of carbon blacks in a vessel equipped with a stirrer [17]. The mixture of carbon blacks was prepared in a 1 : 1 ratio. The material was filtered off, washed with water, dried in a drying box to constant mass at 120°C, ground in a blade mill, and screened through a sieve with 0.25-mm mesh. Further, the material was heated at 300°C for 1 h. The electrodes were formed in a mold with a piston stroke limiter as planar discs 33 mm in diameter and 0.8–0.9 mm thick, with a 0.1-mm-thick nickel grid in the middle of the electrode. The amount of the electrode material necessary for fabricating electrodes of certain porosity was calculated by the known formula [18]. The electrodes were sintered in air at 360°C for 10 min. To diminish limitations on the supply of oxygen into the electrodes, they were fabricated with a high total porosity (65 vol %). The electrolyte porosity of the electrodes was found by hydrostatic weighing [19]. Prior to experiments, the electrodes were impregnated with an electrolyte (0.5 M aqueous solution of NaOH) in the galvanostatic mode at a current density of 40 mA cm^{-2} for 1 h.

The electrolysis was performed in a three-chamber glass electrolyzer-cell [15]. A carbon black electrode (cathode) was placed between the cathode and gas chambers. The catholyte and anolyte (1 M H_2SO_4) were separated by an MF-4SK-100 cation-exchange membrane. A platinum plate served as the anode. The preparative electrolysis was performed in 0.5 M NaOH (~20 ml) at 20°C in the galvanostatic mode at an overall current density of 50 mA cm^{-2} for 5–7 h. The current density was calculated per unit apparent frontal surface area of the electrode (5 cm^2). The electrode potential was measured relative to a saturated silver chloride reference electrode (EVL-1M1). Oxygen and air were continuously fed into the electrode through its backside from the 20-ml gas chamber under atmospheric pressure. Oxygen was delivered in a small excess, discharged into the atmosphere. Air was delivered at flow rates of 0, 20, 50, and 100 ml min^{-1}. The fraction γ of current expended for synthesis of hydrogen peroxide was determined by gasometry in an electrolysis with oxygen. Potentiodynamic polarization curves were measured at a potential sweep rate of 4 mV s^{-1}. The concentration of hydrogen peroxide in solution was determined by permanganatometry. Prior to being sampled, the electrolyte was agitated by bubbling with air. The results obtained are listed in Table 2. It should be noted that by the term hydrogen peroxide are understood all forms of H_2O_2 existence in an alkaline solution, i.e., molecules and ions.

As can be seen in Table 2, a decrease in the fluoroplastic content and introduction of a hydrophilic carbon black make larger the volume of pores filled by the electrolyte. The influence exerted by replacement of oxygen with air and variation of the rate of its delivery into the gas chamber on the polarization dependence is illustrated for electrode no. 2

Table 2. Influence exerted by the electrode composition in reduction of pure oxygen, by atmospheric oxygen, and by the rate of its supply on parameters of H_2O_2 electrosynthesis (electrolysis time 7 h)

Electrode no.	Carbon black	Content of FT-4D, wt %	Electrolyte porosity, vol %	Air supply rate, ml min^{-1}	Potential,* V	Current efficiency by H_2O_2, %	H_2O_2 concentration, g l^{-1}
1	A 437-E	20	8.4	Oxygen**	0.76	70	39
				100	0.85	40	22
2	A 437-E + P 702	20	14	Oxygen**	0.46	67	38
				100	0.48	63	35
				100 + 55 cm of water	0.98	55	31
				20	0.68	55	31
3***	A 437-E + P 268-E	20	32	Oxygen**	0.66	32	13
				100	1.4	14	5.4
4	A 437-E	8	13	Oxygen**	0.52	70	39
				100	0.72	55	31
				20	0.85	40	22

* Electrode potential, current efficiency, and H_2O_2 concentration by the end of electrolysis.

** Results obtained when passing a small excess of pure O_2.

*** Electrolysis duration 5 h.

(Table 2, Figs. 1 and 2). At an air flow rate of 100 ml min^{-1}, the best results were obtained, with the dependence of the current on the air feed rate nearly leveling-off (Fig. 2). Therefore, experiments at higher rates were not performed. Figures 3 and 4 demonstrate for electrode no. 2 the effect of electrolysis duration on the H_2O_2 concentration and current efficiency. The run of these dependences is the same as that in experiments with pure oxygen [4]. The H_2O_2 accumulation curves tend to show a plateau at which the synthesis rate is equal to the decomposition rate of H_2O_2 and the differential current efficiency is zero (Figs. 3 and 4, curve *4*).

It can be seen that, as it should be, the replacement of oxygen with air makes more pronounced the electrode polarization. Varying the air feed rate has nearly no effect on the electrode polarization up to a current density of 40 mA cm^{-2}, i.e., the electrode structure manages to feed the required amount of oxygen to the reaction zone. However, at higher currents, outer-diffusion limitations become important. The electrode polarization varies in inverse proportion to the air feed rate, and, at zero rate, the polarization curve reaches the limiting current (Fig. 1). Raising the air feed rate from 20 to 100 ml min^{-1} leads to an increase in the current

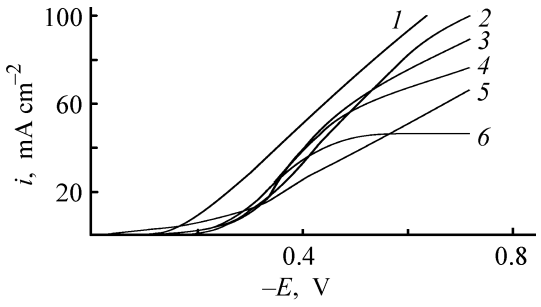


Fig. 1. Polarization curves for electroreduction of (*1*) pure and (*2–6*) atmospheric oxygen on an electrode composed of a mixture of carbon blacks: 40 wt % A 437-E + 40 wt % P 702 + 20 wt % FT-4D, in 0.5 M NaOH. (*i*) Overall current density and (E) potential. Air feed rate (ml min^{-1}): (*2*) 100, (*3*) 50, (*4*) 20, (*5*) 100 + 55 cm of water, and (*6*) 0.

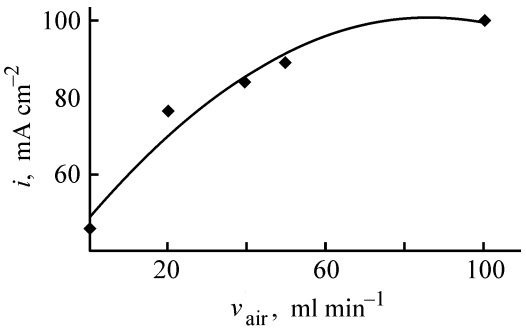


Fig. 2. Effect of the air feed rate v_{air} on the overall current density *i* in electroreduction of atmospheric oxygen at a potential of –0.72 V in 0.5 M NaOH on an electrode composed of a mixture of carbon blacks: 40 wt % A 437-E + 40 wt % P 702 + 20 wt % FT-4D.

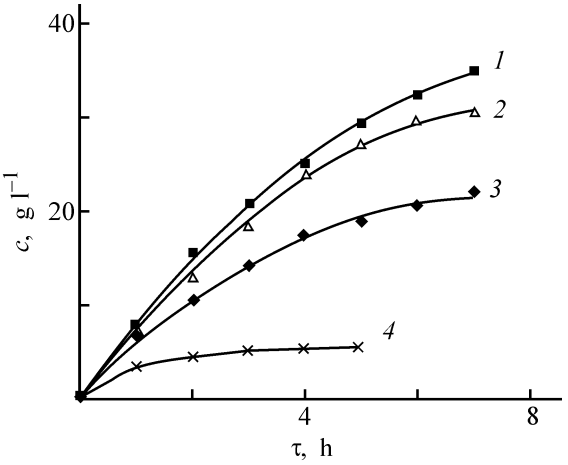


Fig. 3. H_2O_2 accumulation curves measured in electrolysis with gas-diffusion carbon black electrodes in 0.5 M NaOH. Air feed rate 100 ml min^{-1}; the same for Fig. 4. (*c*) H_2O_2 concentration in the electrolyte bulk and (τ) electrolysis duration. Electrode composition (wt %): (*1*) 40 A 437-E + 40 P 702 + 20 FT-4D, (*2*) 92 A 437-E + 8 FT-4D, (*3*) 80 A 437-E + 20 FT-4D, (*4*) 40 A 437-E + 40 P 268-E + 20 FT-4D; the same for Fig. 4.

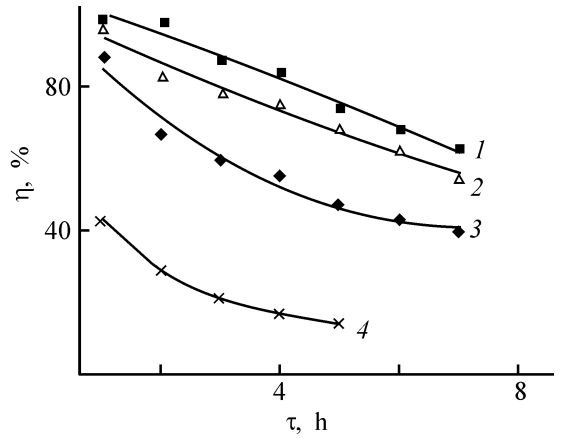


Fig. 4. Current efficiency by H_2O_2, η, vs. the electrolysis duration τ in 0.5 M NaOH for gas-diffusion carbon black electrodes.

efficiency and H_2O_2 concentration obtained by 13–41%, depending on the electrode composition. The theoretical air flow rate at a current density of 50 mA cm^{-2} and a 100% current efficiency by H_2O_2 is 8.3 ml min^{-1}. As the volume of the gas chamber, and specifically its thickness, decreases, the air flow velocity along the electrode increases, and, consequently, the air feed rate can be lowered to the corresponding extent. Raising the pressure in the gas chamber by 55 cm of water at an air feed rate of 100 ml min^{-1} results in that the electrode polarization becomes stronger and the current efficiency by H_2O_2 and its concentration decrease.

In electrolysis with oxygen, electrode nos. 1, 2, and 4 demonstrated nearly the same current efficiency by H_2O_2. The fraction of current expended for the H_2O_2 electrosynthesis is 95–98% at a concentration of 36–37 g l^{-1}, but the polarization of these electrodes is approximately inversely proportional to their electrolyte porosity and increases in order no. 2 < no.4 < no. 1. The same dependence is observed in electrolysis with air, but the current efficiency by H_2O_2 and its concentration are lower, and this decrease depends on the electrode composition, which indicates that the electrode structure affects just the delivery of atmospheric oxygen. The best results were obtained with electrodes composed of a mixture of carbon blacks A 437-E and P 702. Depending on the electrolysis duration, H_2O_2 solutions with concentrations of 8–35 g l^{-1} were obtained, with the corresponding current efficiencies of 99–63% (Figs. 3, 4). This means that changing the hydrophilic properties and the structure of an electrode by introduction of furnace black with a medium wettability is more effective than making lower the fluoroplastic content. Introduction of a hydrophilic furnace black P 268-E leads to a sharp increase in the hydrophilic porosity and to a decrease in the volume of gas pores. This results in that the inner-diffusion hindrance increases, the area of the three-phase boundary between air, carbon black, and electrolyte becomes smaller, the polarization grows, and the current efficiency by H_2O_2 decreases. The fraction γ of the current is also smaller for this electrode: 50% at a H_2O_2 concentration of 13 g l^{-1}. The size of carbon black particles is also important. Addition of larger particles (P 702) to the electrode material makes it possible to create larger pores, which facilitates oxygen delivery to the reaction zone. By contrast, introduction of a carbon black with smaller particles (P 268-E) hinders this process.

The effect of the electrode composition on the H_2O_2 electrosynthesis from atmospheric oxygen is due to the diffusion hindrance to oxygen delivery into the electrode at a comparatively low content of oxygen in air. Because of this circumstance, the diffusion component of the electrode polarization increases and the zone of H_2O_2 generation shifts to the back (gas) side of the electrode, which is in contact with air. As a result, the way to be traversed by H_2O_2 to leave the electrode volume across the front side of the electrode into the electrolyte and the residence time of H_2O_2 in the electrode become longer, which leads to an increase in its concentration and decomposition rate, with

the current efficiency decreasing. This effect becomes more pronounced as the H_2O_2 concentration in the electrolyte increases. This occurs because the rate of H_2O_2 diffusion from the electrode decreases due to the lower H_2O_2 concentration gradient between the pore volume of the electrode and the electrolyte (Fig. 4). Consequently, the farther the H_2O_2 generation zone from the front side of the electrode, the lower the H_2O_2 concentration in the electrolyte and the current efficiency. The reaction zone can also be shifted by varying the air feed rate.

Thus, in the case under consideration, the electrosynthesis parameters are affected both by the electrolyte porosity (via changes in the ohmic polarization) and by the conditions of oxygen delivery to the reaction zone (via changes in the inner- and outer-diffusion components of the electrode polarization).

CONCLUSIONS

(1) Gas-diffusion air electrodes can be successfully used for electrosynthesis of hydrogen peroxide. The best results are obtained on electrodes composed of a 1 : 1 mixture of a hydrophobic acetylene black A 437-E and a semihydrophobic furnace black P 702, with addition of 20 wt % fluoroplastic. Alkaline H_2O_2 solutions are obtained with concentrations of 8–35 g l^{-1} at the corresponding current efficiencies of 99–63%.

(2) Raising the air feed rate into the gas chamber from 20 to 100 ml min^{-1}, which corresponds to a fivefold change of the air volume in the gas chamber in 1 min, makes higher the current efficiency and the H_2O_2 concentration obtained by 13–41%, depending on the electrode composition, and lowers the electrode polarization by 0.07–0.2 V.

REFERENCES

1. *Khimicheskie istochniki toka: Spravochnik* (Chemical Power Cells: Reference Book), Korovin, V.N. and Skundin, A.M., Eds.,. Moscow: Mosk. Energet. Inst., 2003.
2. Brillas, E., Maestro, A., and Moratalla, M., *J. Appl. Electrochem.*, 1997, vol. 27, no. 1, pp. 83–92.
3. Brillas, E., Alcaide, F., and Cabot, P.-L., *Electrochim. Acta*, 2003, vol. 48, no. 4, pp. 331–340.
4. Kolyagin, G.A. and Kornienko, V.L., *Zh. Prikl. Khim.*, 2006, vol. 79, no. 5, pp. 757–761.
5. Qiang, Z., Chang, J.-H., and Huang, C.-P., *Water Res.*, 2002, vol. 36, no. 1, pp. 85–94.
6. Pozzo, A., Palma, L., Merli, C., and Petrucci, E., *J. Appl. Electrochem.*, 2005, vol. 35, no. 4, pp. 413–419.
7. Kenova, T.A., Kornienko, G.V., Vasil'eva, I.S., et al., *Zh. Prikl. Khim.*, 1997, vol. 70, no. 1, pp. 79–82.
8. Kornienko, V.L., Kolyagin, G.A., and Kornienko, G.V., *Elektrokhimiya*, 1997, vol. 33, no. 8, pp. 971–978.
9. Giorgi, L., Antolini, E., Pozio, A., and Passalacqua, E., *Electrochim. Acta*, 1998, vol. 43, no. 24, pp. 3675–3680.
10. Kolyagin, G.A. and Kornienko, V.L., *Zh. Prikl. Khim.*, 1989, vol. 62, no. 9, pp. 2082–2087.
11. Kolyagin, G.A. and Kornienko, V.L., *Zh. Prikl. Khim.*, 1990, vol. 63, no. 9, pp. 2106–2109.
12. Maja, M., Orecchia, C., Strano, M., et al., *Electrochim. Acta*, 2000, vol. 46, nos. 2–3, pp. 423–432.
13. Wang, X.L., Zhang, H.M., Zhang, J.L., et al., *Electrochim. Acta*, 2006, vol. 51, no. 23, pp. 4909–4915.
14. Huang, H., Zhang, W., Li, M., et al., *J. Colloid Interface Sci.*, 2005, vol. 284, no. 2, pp. 593–599.
15. Kolyagin, G.A. and Kornienko, V.L., *Zh. Prikl. Khim.*, 2007, vol. 80, no. 8, pp. 1302–1306.
16. Orekhov, S.V. and Rudenko, V.A., *Tekhnicheskii uglerod: Katalog* (Technical-grade Carbon: Catalogue), Moscow: TsNIITEneftekhim, 1984.
17. USSR Inventor's Certificate, no. 500557.
18. Shibryaev, B.F. and Pavlovskaya, E.I., *Metallokeramicheskie fil'try* (Metal-Ceramic Filters), Moscow: Mashinostroenie, 1972.
19. Baranov, A.P., Shteinberg, G.V., and Bagotskii, V.S., *Elektrokhimiya*, 1971, vol. 7, no. 3, pp. 387–390.

ISSN 1070-4272, Russian Journal of Applied Chemistry, 2008, Vol. 81, No. 6, pp. 988–993. © Pleiades Publishing, Ltd., 2008.
Original Russian Text © L.G. Shaidarova, A.V. Gedmina, I.A. Chelnokova, G.K. Budnikov, 2008, published in Zhurnal Prikladnoi Khimii, 2008, Vol. 81, No. 6, pp. 949–954.

APPLIED ELECTROCHEMISTRY AND CORROSION PROTECTION OF METALS

Electrocatalytic Oxidation and Flow-through Injection Determination of Cysteine with a Glassy Carbon Electrode Modified with Gold–Iridium Binary System

L. G. Shaidarova, A. V. Gedmina, I. A. Chelnokova, and G. K. Budnikov

Kazan State University, Kazan, Tatarstan, Russia
Butlerov Chemical Institute, Kazan, Tatarstan, Russia

Received August 13, 2007

Abstract—Electrocatalytic activity of gold and a gold–iridum binary system electrodeposited onto the surface of a glassy carbon in oxidation of cysteine was studied. A method for flow-through-injection determination of cysteine was developed.

DOI: 10.1134/S1070427208060128

L-Cysteine (2-amino-3-mercaptoproponic acid) is an important biomedical compound, because it is involved in numerous biochemical processes in living systems [1, 2]. This amino acid is used in pharmaceutical industry, is applied (in combination with some antibiotics) for curing of damaged skin, and can serve for protection from radio radiation. Disturbance of its normal concentration in the human body is a reason for appearance and development of nervous, mental, and other diseases. Therefore, the development of high-sensitivity methods for determination of cysteine in various objects is an important task for analytical chemistry.

Sulfur-containing amino acids are commonly determined by spectrophotometry [3], fluorimetry [4], electophoresis [5], high-performance liquid chromatography [6], and electrochemical methods [7, 8]. As disadvantages of the spectral and chromatographic methods should be mentioned the prolonged sample preparation and analysis itself, insufficient sensitivity, and use of an expensive equipment. The electrochemical methods are distinguished by simplicity, high determination sensitivity, and use of inexpensive and readily available instruments. The polarographic determination of sulfur-containing amino acids employs dropping mercury electrodes. This method is based on the formation of mercury mercaptide and its reduction at nearly zero potentials [9]. A considerably lower detection limit is demonstrated by inversion polarography with a dropping mercury electrode. In this case, the dependence of the current on the concentration is linear in the range 2×10^{-8}–5×10^{-7} M [10]. However, the toxicity of mercury hinders wide use of mercury-based electrodes in laboratory practice. Solid (metallic or carbon) electrodes cannot provide a low detection limit of cysteine and its derivatives because of the adsorption on the electrode surface of products formed in the electrochemical reaction involving amino acids.

Recently, chemically modified electrodes (CME) possessing catalytic properties have found application for voltammetric determination of sulfur-containing amino acids. For example, cysteine is determined with such CME mediators as metal oxides [11], transition-metal phthalocyanines [12–14], and inorganic films produced from hexacyanometallates [15]. The catalytic response of CME enables a considerable lowering of the detection limit of cysteine, e.g., to 5×10^{-7} M [15]. Introduction of CME into flow-through methods of analysis improves the analytical and metrological characteristics and raises the throughput of analysis.

In this study, the electrocatalytic activity of gold and the gold–iridum binary system electrodeposited onto glassy carbon (GC) electrode in oxidation of cysteine was examined and a method for flow-through injection determination of cysteine was developed.

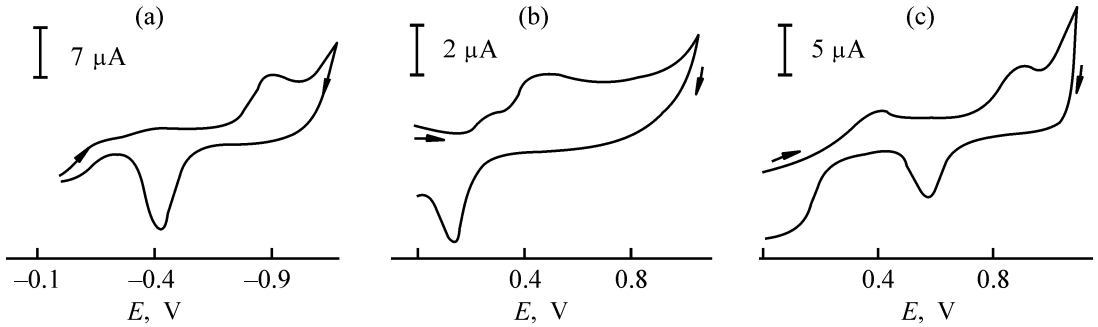
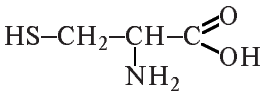


Fig. 1. Cyclic voltammograms obtained on (a) Au–GC, (b) Ir–GC, and (c) Au–Ir–GC electrodes in 1 M H_2SO_4 supporting solution. (E) Potential; the same for Figs. 2, 3c.

EXPERIMENTAL

In the experiments, dc voltammograms were recorded with a PU-1 polarograph, and cyclic voltammograms, with a PI-50-1.1 potentiostat. In a three-electrode cell, a glassy-carbon (GC) electrode with an apparent surface area of 0.1 cm^2 and Au–GC, Ir–GC, and Au–Ir–GC modified electrodes served as the working electrode. A saturated silver chloride electrode served as reference, and a platinum wire, as an auxiliary electrode. The voltammograms were recorded at a potential sweep rate of 20 mV s^{-1}.

As object of study served cysteine having the structural formula



A cysteine solution was prepared by dissolving a precisely weighed portion in an aqueous solution. Solutions of lower concentrations were prepared by successive dissolution of the initial solution immediately before the measurements. As supporting electrolyte served 0.1 M solution of H_2SO_4. The pH value was adjusted with NaOH and monitored using a pH-150 pH meter.

Measurements under the conditions of a flow-through injection analysis (FIA) were made using a setup including a peristaltic pump, injector, flow-through electrochemical cell, and recording device [16]. The solutions were delivered and discharged through pipes made of silicone tubes with an inner diameter of 2.0 mm. The injection was done with a microsyringe through the sealing membrane. Preliminarily, the electrochemical behavior of gold, iridium, and gold–iridum binary system electrodeposited on the GC electrode was studied.

The electrochemical behavior of gold electrodeposited on GC (Au–GC) is rather complex and includes formation on the CME surface of oxo and hydroxo compounds of the metal in different oxidation states: Au(OH), $Au(OH)_3$, or Au_2O_3 [17]. A cyclic voltammogram obtained on (Au–GC) electrode in 0.1 M H_2SO_4 supporting solution is shown in Fig. 1a. One pair of cathodic-anodic peaks is recorded at $E > 0.6$ V as the potential is shifted to the anodic region. The peaks can be assigned to oxidation of gold to the oxidation state +3 by the scheme [18]:

$$2Au + 3H_2O \rightleftarrows Au_2O_3 + 6H^+ + 6e. \quad (1)$$

The reverse branch of the cyclic voltammogram shows a narrow peak at $E_p \sim 0.40$ V which corresponds to formation of Au. On the subsequent anodic branch, a small current peak is recorded at $E \sim 0.40$ V, which is probably due to oxidation of Au nanoparticles. As is known [18], the electrochemical properties of single atoms of a metal and those of the atoms in the bulk are different: the absence of the crystal lattice stabilization energy in nanoparticles leads to a decrease in the oxidation overvoltage of the metal.

The cyclic voltammogram obtained on GC with an iridium deposit (Ir–GC) in a 0.1 M H_2SO_4 buffer solution is shown in Fig. 1b. The anodic branch of this voltammogram exhibits a wave at $E_{1/2} = 0.45$ V, and the cathodic branch, a peak at $E_p = 0.15$ V. Metallic iridium oxidizes to Ir(IV) via the stage of formation of the intermediate compound $Ir(OH)_3$, which immediately oxidizes to $IrO_2 \cdot H_2O$. The prewave observed at $E \sim 0.4$ V corresponds to the formation of hydrated Ir(III) oxide (hydroxide) [19]. The overall electrode process can be represented as:

$$Ir + (n + 2)H_2O \rightleftarrows IrO_2 \cdot nH_2O + 4H^+ + 4e. \quad (2)$$

Table 1. Characteristics* of voltammograms obtained on GC and CME in cysteine oxidation in a 0.1 M H_2SO_4 supporting solution (cysteine concentration 5×10^{-3} M)

Electrode	E_s, V	i_s, μA	E_{mod}, V	i_{mod}, μA	E_{cat}, V	i_{cat}, μA	i_{cat}/i_{mod}
CУ	1.05	2.5	–	–	–	–	–
Ir–GC	–	–	0.45	3.1	0.45	3.1	–
					1.05	2.5	–
Au–GC	–	–	1.0	10.0	1.0	220	22.0
Au–Ir–GC	–	–	0.45	3.1	0.45	3.1	–
			0.90	7.5	0.90	360	48.0

* E_s, i_s, E_{mod}, i_{mod}, E_{cat}, i_{cat} are potentials and peak currents of oxidation of a cysteine substratum on GC, those of oxidation of a modifier, and those of catalytic oxidation of cysteine on CME, respectively.

On passing from the deposits of individual metals to binary systems, the form of the recorded cyclic voltammograms becomes more complex. In this case, both the individual properties of metals constituting the system and the bifunctional effects can be manifested. The cyclic voltammogram obtained on GC modified with a gold–iridium binary system (Au–Ir–GC) contains two pairs of cathodic-anodic peaks, which may be due to oxidation of individual metals constituting the bimetallic system (Fig. 1c).

The good reproducibility of the cyclic voltammograms obtained in 0.1 M H_2SO_4 supporting solution confirms the high chemical and electrochemical stability of the Au–Ir binary system.

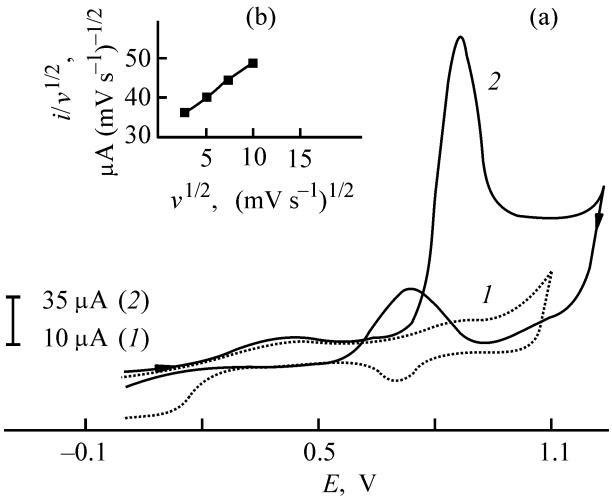


Fig. 2. (a) Cyclic voltammograms obtained on the Au–Ir–GC electrode in 0.1 M supporting solution of H_2SO_4 (*1*) without and (*2*) with cysteine and (b) dependence of the current peak of cysteine oxidation on the Au–Ir–GC electrode on the potential sweep rate *V*. Cysteine concentration 5×10^{-3} M; the same for Fig. 3. (*i*) Current strength; the same for Fig. 3.

The metrological characteristics of the electrode response remain unchanged during a month.

Cysteine oxidizes on GC irreversibly and with a large overvoltage, e.g., $E \sim 1.0$ V in an acid medium in a 0.1 M H_2SO_4 supporting electrolyte (Table 1). The oxidation wave recorded in this case is poorly reproducible because of the adsorption of products of substratum oxidation on the graphite support. Therefore, it is not appropriate to use a graphite electrode for direct voltammetric determination of cysteine.

In oxidation of cysteine on the Au–GC electrode, a manyfold increase in the current is observed at a potential of 1.0 V (Table 1), typical of the oxidation of a modifier in the absence of a substratum. On the Ir–GC electrode, two steps are recorded at potentials of 0.45 and 1.05 V (Table 1). At potentials of the first step, the modifier is oxidized, because the height of this step does not change in the presence of cysteine. The potentials of the second step correspond to oxidation of the amino acid under study, because cysteine is oxidized on unmodified GC in the same range of potentials. Thus, a change in the voltammetric characteristics of cysteine is recorded only on the Au–GC electrode. Compared with CME, the electrode with an electrodeposited Au–Ir film shows a stronger rise in the modifier oxidation current in the presence of a substratum under study (Table 1). This is due to the occurrence of the synergetic effect in cysteine oxidation on the electrode modified with a bimetallic system. Therefore, the oxidation of cysteine on Au–Ir–GC was studied in more detail.

The cyclic voltammograms obtained on the Au–Ir–GC electrode with and without cysteine are shown in Fig. 2 (curves *2* and *1*, respectively). The anodic branch of the cyclic voltammogram of

Table 2. Influence of the method of binary system deposition on the magnitude of the electrocatalytic effect in oxidation of cysteine on the Au–Ir–GC electrode

Potentiostatic deposition				Potentiodynamic deposition			
E, V	i_{cat}	i_{mod}	i_{cat}/i_{mod}	Potential cycling range, V	i_{cat}	i_{mod}	i_{cat}/i_{mod}
	μA				μA		
–0.3	10.5	380	36.2	–0.3...0.9	250	6.2	40.3
0.0	7.6	350	46.1	–0.3...0.7	280	6.8	41.2
0.3	5.2	190	37.5	–0.3...0.5	360	7.5	48
0.7	4.5	150	33.3	–0.3...0.0	370	9.4	39.4
0.9	3.6	105	29.2	0.0...0.5	210	5.5	38.2

cysteine oxidation exhibits two steps. The first step at E = 0.45 V reproduces the wave corresponding to mediator oxidation, and the second step at E = 0.90 V is preceded by a current peak whose height exceeds that of the modifier oxidation peak in this range of potentials in the absence of a substratum.

The process occurring at the Au–Ir–GC electrode can be identified as an electrocatalytic process. This is so because the modifier oxidation current i_{mod} increases manyfold in comparison with the current of cysteine oxidation on CME i_{cat} (i_{cat}/i_{mod} = 48.0), the overvoltage of substratum oxidation (E_{cat}) decreases as compared with the overvoltage of its oxidation on GC E_s ($E_{cat} - E_s$ = 150 mV), and the peak current at E_p = 0.90 V linearly depends on the cysteine concentration. The plot $i/v^{1/2}$–$v^{1/2}$ has a positive slope (Fig. 2b), which points to the adsorption contribution to the electrooxidation of cysteine at the Ir–Au–GC electrode by the scheme:

$$6RSH + Au_2O_3 \rightarrow 3RSSR + 2Au + 3H_2O. \quad (3)$$

Probably, electrogenerated oxo particles of gold in the oxidation state +3, formed by reaction (1), act as a catalyst. Noteworthy is the unusual shape of the cathodic branch of the cyclic voltammogram of cysteine oxidation, which is manifested as a rise in the anodic current at the potentials of metal reduction (Fig. 2a). This may be due to oxidation of cysteine on electrogenerated particles of the catalyst.

It was found that the electrocatalytic response of CME depends on the method used for electrochemical deposition of metals onto GC. The peak current of cysteine oxidation was studied in relation to the electrodeposition conditions of the binary system the time and potential of electrolysis in the case of potentiostatic deposition or the range and rate of cyclic variation of the potential in the case of potentiodynamic deposition. As can be seen from Table 2, a stronger catalytic effect (i_{cat}/i_{mod} = 48) is observed when the bimetal is deposited by cyclic variation of the potential in the range –0.3...–0.5 V. The rise in the current in the voltammogram of cysteine oxidation on the Au–Ir–GC electrode also depends on the time of electrodeposition of the binary system. The maximum catalytic effect is observed in the case of a potentiodynamic deposition on Au–Ir at potentials of –0.3...–0.5 V in three cycles.

The results obtained were used to develop a method for voltammetric determination of cysteine on a CME based on the Au–Ir binary system. A 10-ml volumetric flask was charged with a fixed volume of the standard solution of cysteine, 5 ml of a 0.2 M solution of H_2SO_4 was added, and the mixture was brought to the mark with distilled water. The solution was transferred into an electrochemical cell containing chemically modified, auxiliary, and silver chloride electrodes. A voltammogram was recorded in the range 0.0–1.0 V and the peak current of cysteine oxidation at E_p = 0.90 V was determined.

The peak current is proportional to the cysteine concentration over a wide concentration range 5×10^{-7}–5×10^{-3} M. This dependence is described by the equation (i_p, μA; c, M):

$$i_p = (5.4 \pm 0.3) + (7.09 \pm 0.02) \times 10^4 c, \quad (4)$$

$$r = 1.000.$$

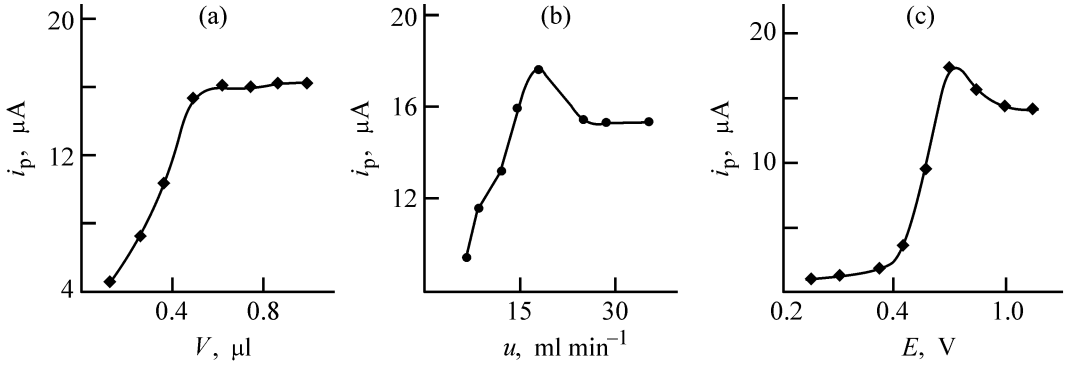


Fig. 3. FIA signal i_p obtained in cysteine oxidation on Au–Ir–GC in 0.1 M H_2SO_4 supporting electrolyte (pH 2.0) containing cysteine vs. (a) injected sample volume, (b) flow rate, and (c) applied potential. (V) Injected sample volume and (u) flow rate.

The adequacy of the procedure was assessed by the introduced–found method (Table 3).

A chemically modified electrode based on the Au–Ir binary system was used to determine cysteine under conditions of a flow-through injection analysis. The FIA signal was recorded in the potentiostatic mode. Preliminarily, the influence exerted by the hydrodynamic parameters of the system on the intensity of the analytical signal recorded under the FIA conditions was studied. The dependence of the current on the injected sample volume V and on the flow rate u was examined. The maximum FIA signal was observed at V = 0.75 ml (Fig. 3a). The i–u dependence passes through a maximum at u = 18 ml min^{-1} (Fig. 3b).

The dependence of the current on the applied potential was studied at the given hydrodynamic parameters. The maximum of this dependence was observed in cysteine oxidation on the Au–Ir–GC CME at 0.80 V (Fig. 3c). Based on the dependences obtained, the following working conditions for recording the FIA signal were chosen: V = 0.75 ml, u = 18 ml min^{-1}, and E = 0.80 V.

Table 3. Results obtained in determining cysteine on the Au–Ir–GC electrode (n = 6, P = 0.95)

Mode	Concentration, μmol l^{-1}		S_r^*
	introduced	found $x \pm \Delta x$	
Steady-state	5.0	4.8 ± 0.2	0.05
	10.0	10.1 ± 0.7	0.05
	100	101 ± 3	0.03
FIA	5.0	5.10 ± 0.09	0.02
	10.0	10.2 ± 0.3	0.03
	100	99 ± 1	0.01

* (S_r) signal reproducibility.

Cysteine was determined by the flow-through injection method on the Au–Ir–GC electrode as follows. The flow of a carrier (0.01 M H_2SO_4 solution) was passed at a rate of u = 18 ml min^{-1} through silicone pipes with an inner diameter of 2 mm. The pipes were hermetically connected to a flow-through electrochemical cell with chemically modified, auxiliary, and silver chloride electrodes. The FIA signal was recorded at 0.80 V after a sample of volume V = 0.75 ml was injected. The dependence of the FIA signal on the cysteine concentration is linear in the range 5×10^{-3}–5×10^{-8} M, which is an order of magnitude lower than that under the stationary conditions, and is described by the equation i_p, μA; c, M)

$$\log i_p = (1.22 \pm 0.09) + (0.50 \pm 0.01)\log c, \quad (5)$$
$$R = 0.9995.$$

The detection limit calculated by the 3s criterion is 2×10^{-8} M [20]. An analysis of the metrological characteristics demonstrated that the reproducibility of the analytical signals in voltammetric determination of cysteine in a flow-through system is better than that under the stationary conditions (Table 3). This occurs because the substratum and products of its oxidation are not sorbed on the CME surface.

The method suggested for voltammetric detection of cysteine with a CME based on the Au–Ir binary system under conditions of the flow-through injection analysis is characterized by simplicity, high sensitivity, and rapidity. The use of the cat-

alytic response in FIA makes it possible to achieve cysteine detection limits comparable with the values obtained for inversion voltammetry [10].

CONCLUSIONS

(1) It was shown that particles of gold and the gold–iridium binary system deposited on a glassy carbon electrode exhibit an electrocatalytic activity in cysteine oxidation. The most pronounced catalytic effect is observed for the electrode with a bimetallic system. The catalytic current is recorded in the range of oxidation potentials of Au(III) oxo particles at 0.95 V.

(2) The conditions in which an electrode based on the gold–iridium binary system is formed and the maximum catalytic current of cysteine oxidation is recorded on this electrode were determined. This modified electrode was used for voltammetric determination of cysteine under the steady-state conditions. The dependence of the catalytic current on the cysteine concentration is linear within the range 5×10^{7}–5×10^{-3} M.

(3) The possibility of using a modified electrode for amperometric detection of cysteine under the conditions of a flow-through injection analysis was demonstrated. Using the catalytic response of the modified electrode in a flow makes it possible to reduce the detection limit of cysteine by an order of magnitude to 5×10^{-8} M.

ACKNOWLEDGMENTS

The study was supported by a joint grant from CRDF (U.S. Civilian Research & Development Foundation) and Ministry of Education and Science of the Russian Federation, BRHE (Basic Research and Higher Education Program) (REC-007).

REFERENCES

1. Dévényi, T. and Gergely, J., *Amino Acids, Peptides, and Proteins*, New York: Elsevier, 1974.
2. Meister, A., *Biochemistry of Amino Acids*, New York: Academic, 1957.
3. Zaia, D.A.M., Ribas, K.C.L., and Zaia, C.T.B., *Talanta*, 1999, vol. 50, no. 5, pp. 1003–1010.
4. Wang, H., Wang, W.S., and Zhang, H.S., *Talanta*, 2001, vol. 53, no. 5, pp. 1015–1019.
5. Nakano, S., Nakano, K., Noguchi, K., and Kawashima, T., *Talanta*, 1997, vol. 44, no. 5, pp. 765–770.
6. Campanella, L., Crescentini, G., and Avino, P., *J. Chromatogr. A*, 1999, vol. 833, no. 2, pp. 137–145.
7. Vieira, I.C., and Fatibello-Filho, O., *Anal. Chim. Acta*, 1997, vol. 399, no. 3, pp. 287–293.
8. Florence, T.M., *J. Electroanal. Chem.*, 1979, vol. 97, no. 2, pp. 219–236.
9. Miskidzhyan, S.P., and Kravchenyuk, L.P., *Polyarografiya lekarstvennykh preparatov* (Polarography of Medicinal Preparations), Kiev: Vishcha Shkola, 1976.
10. Fedurco, M., Vesela, V., and Heyrovsky, M., *Electroanalysis*, 1993, vol. 5, no. 3, pp. 257–259.
11. Shaidarova, L.G., Ziganshina, S.A., and Budnikov, G.K., *Zh. Anal. Khim.*, 2003, vol. 58, no. 6, pp. 640–645.
12. Filanovsky, B., *Anal. Chim. Acta*, 1999, vol. 394, no. 1, pp. 91–100.
13. Maree, S., and Nyokong, T., *J. Electroanal. Chem.*, 2000, vol. 492, no. 2, pp. 120–127.
14. Mafatle, T.J., and Nyokong, T., *J. Electroanal. Chem.*, 1996, vol. 408, nos. 1–2, p. 213.
15. Shaidarova, L.G., Ziganshina, S.A., Tikhonova, L.N., and Budnikov, G.K., *Zh. Anal. Khim.*, 2003, vol. 58, no. 12, pp. 1277–1284.
16. Shaidarova, L.G., Zaripova, S.A., Tikhonova, L.N., et al., *Zh. Prikl. Khim.*, 2001, vol. 74, no. 5, pp. 728–732.
17. Ripan, R., and Chetyanu, I., *Neorganicheskaya khimiya* (Inorganic Chemistry), Moscow: Khimiya, 1972, vol. 2.
18. Burke, L.D., and Nugent, P.F., *Gold Bull.*, 1998, vol. 31, no. 2, pp. 39–50.
19. Juodkazyte, J., Sebeka, B., Valsiunas, I., and Juodkazis, K., *Electroanalysis*, 2005, vol. 17, no. 11, pp. 947–952.
20. Charykov, A.K., *Matematicheskaya obrabotka rezul'tatov khimicheskogo analiza: Metody obnaruzheniya i otsenki oshibok* (Mathematical Processing of Chemical Analysis Data: Methods for Error Detection and Evaluation), Leningrad: Khimiya, 1984.

ISSN 1070-4272, Russian Journal of Applied Chemistry, 2008, Vol. 81, No. 6, pp. 994–999. © Pleiades Publishing, Ltd., 2008.
Original Russian Text © A.B. Velichenko, V.A. Knysh, T.V. Luk'yanenko, D. Devilly, F.I. Danilov, 2008, published in Zhurnal Prikladnoi Khimii, 2008, Vol. 81, No. 6, pp. 955–960.

APPLIED ELECTROCHEMISTRY AND CORROSION PROTECTION OF METALS

PbO_2–TiO_2 Composites: Electrosynthesis and Physicochemical Properties

A. B. Velichenko, V. A. Knysh, T. V. Luk'yanenko, D. Devilly, and F. I. Danilov

Ukrainian State University of Chemical Engineering, Dnepropetrovsk, Ukraine
Pierre and Marie Curie University (Paris-6), Paris, France

Received November 15, 2007

Abstract—Fundamental aspects of electrodeposition of PbO_2-based composites containing titanium dioxide particles were studied. The content of the dispersed phase in the composite depends on the electrolyte composition and deposition conditions. Incorporation of titanium dioxide particles into PbO_2 leads to significant changes in the morphology and structure of the deposit.

DOI: 10.1134/S107042720806013X

Oxide composite materials find wide use in various reactions as catalysts and photo- and electrocatalysts, in electrochemical synthesis of strong oxidizing agents, and in disintegration of organic and inorganic contaminants of water and air [1–12]. Various ways to produce materials of this type are known, e.g., sol–gel techniques, plasmochemical method, etc. The electrochemical method should be distinguished as one of the most promising, which enables wide control over the composition and properties of composites because of its simple implementation and possibility of smoothly varying the technological parameters of the process [3–12].

Lead dioxide is a promising electrocatalyst widely used in practice [1–8]. Composite materials based on lead dioxide are known, which additionally contain various oxides and, in particular, Al_2O_3, Co_3O_4, RuO_2, and TiO_2 [3, 5, 8]. Despite this circumstance, the problem of directed synthesis of materials of this kind remains unsolved, because the influence exerted by the nature of the electrolyte on the composition and physicochemical properties of the resulting materials is insufficiently well understood. In this study, the fundamental aspects of electrodeposition of oxide composites PbO_2–TiO_2 and the physicochemical properties of these materials were examined.

EXPERIMENTAL

The composites were deposited in the galvanostatic mode onto pretreated platinum-plated titanium electrodes of area 4 cm^2. The deposition electrolyte contained (M): $Pb(NO_3)_2$ 0.1 and HNO_3 0.1. Additionally, TiO_2 was introduced into the electrolyte in the form of a finely dispersed powder, together with an anionic surfactant, sodium dodecyl sulfate ($C_6H_{12}SO_4Na$). Solutions were prepared from reagents of chemically pure grade and twice-distilled water. The deposition was performed in most cases at a temperature of $20 \pm 2°C$ and anode current density of 5 mA cm^{-2}; the coating deposition time was 30 min. To study the physicochemical properties of the composites, thicker coatings were deposited (at a deposition time of 2 h). It should be noted that the composite materials under study had a composition independent of the coating thickness.

The adsorption of the anionic surfactant (sodium dodecyl sulfate) on a TiO_2 powder was studied in 0.1 M HCl [13]. The content of the surfactant in the composite was determined by the procedure described in [14]. The colloid-chemical properties of the suspension electrolyte were studied by the sedimentation method with the use of a torsion balance. The electrokinetic potential was measured using the electrophoretic technique [15]. The point of zero charge (pH_0) was measured in 0.1 M KCl.

To determine the composition of the composites, the materials were dissolved in a 1 : 1 mixture of 5 M HNO_3 and 30% hydrogen peroxide. The excess of H_2O_2 in the resulting solutions was removed by boiling with a platinum catalyst. The amount of

PbO_2 was calculated from the Pb^{2+} content of the solution, found by amperometric titration with diethylthiocarbominate [16].

The surface morphology of the materials obtained was studied by scanning electron microscopy (SEM) with a LEICA S360 microscope. X-ray diffraction patterns were recorded with a PHILIPS PW3710 diffractometer (Cu_{K_α} radiation).

Accelerated resource tests of anodes with an active layer of a PbO_2–TiO_2 composite were performed in 1 M H_2SO_4.

The composition of a composite may depend on various factors, including the nature and the colloid-chemical properties of the suspension electrolyte. The main characteristics of the colloid system are the particle size of the dispersed phase, electrokinetic potential, and point of zero charge (pH_0) of the oxide. To determine the disintegration time of the suspension and the particle size of the dispersed phase, sedimentation measurements were made. It was found that the system is actually monodisperse and contains TiO_2 particles with a diameter of approximately 0.35 μm. The composite materials were deposited in the course of 30 min, during which time the suspension did not disintegrate. It should be noted that coatings for physicochemical studies of the composites should be deposited in a longer electrolysis (2 h), with the suspension partly disintegrating. Therefore, the composites were in all cases deposited under agitation in order to stabilize the electrolyte. This made it possible to obtain deposits under identical conditions, irrespective of the electrolysis duration.

When the anionic surfactant is introduced into the deposition electrolyte, the surfactant is adsorbed on TiO_2 particles, with the process satisfactorily described by the Frumkin isotherm. The adsorption parameters were calculated: limiting adsorption of 1.75×10^{-5} mol g^{-1}, reached at a sodium dodecyl sulfate concentration of 3.8×10^{-4} M; and adsorption constant of 673.81 M^{-1}. The adsorption of sodium dodecyl sulfate on the TiO_2 powder is of specific nature, which is indicated by the rather low value of the adsorption interaction energy $\Delta G = -25.6$ kJ mol^{-1} [13].

One of the factors affecting the supply rate of the inert oxide to the electrode surface is the charge of particles of the dispersed phase. According to potentiometric data, pH_0 for TiO_2 is 6.36, and, therefore, dispersed phase particles are positively charged in the suspension electrolyte. Upon the adsorption of a surfactant on TiO_2, the point of zero charge of the oxide is shifted to the alkaline region, which confirms the conclusion about the specific nature of sodium dodecyl sulfate adsorption on particles of the dispersed phase. Measurements demonstrated that the electrokinetic potential of titanium dioxide in 0.1 M HNO_3 is 0.064 V. This also points to a small positive charge on titanium dioxide particles in the suspension electrolyte. The so low value of the ζ potential is due to the high concentration of the supporting electrolyte. Upon addition of sodium dodecyl sulfate, the electrokinetic potential substantially changes to become –0.18 V. The change in the sign and magnitude of the electrokinetic potential upon addition of sodium dodecyl sulfate indicates that the electric double layer of particles of the dispersed phase is recharged because of the adsorption of the surfactant. In the presence of the anionic surfactant, particles of the dispersed phase acquire a negative charge and can move in the course of electrolysis toward the positively charged anode surface via electrophoresis.

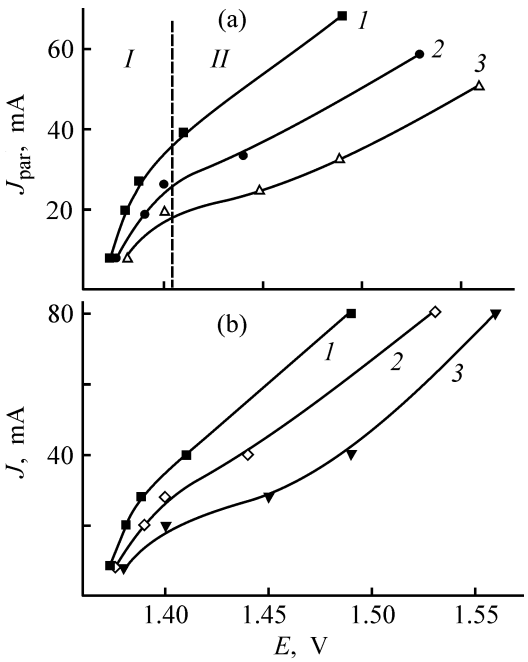


Fig. 1. (a) Partial and (b) total steady-state polarization curves obtained on a Ti/Pt electrode in electrolytes of various compositions. (J_{par}, J) Partial and total deposition currents and (E) potential. (*1*) 0.1 M $PbNO_3$ + 0.1 M HNO_3, (*2*) *1* + 2.0 g dm^{-3} TiO_2, and (*3*) *2* + 7×10^{-4} M surfactant.

To determine how particles of the dispersed phase affect the fundamental aspects of lead dioxide electrodeposition from suspension electrolytes, polar-

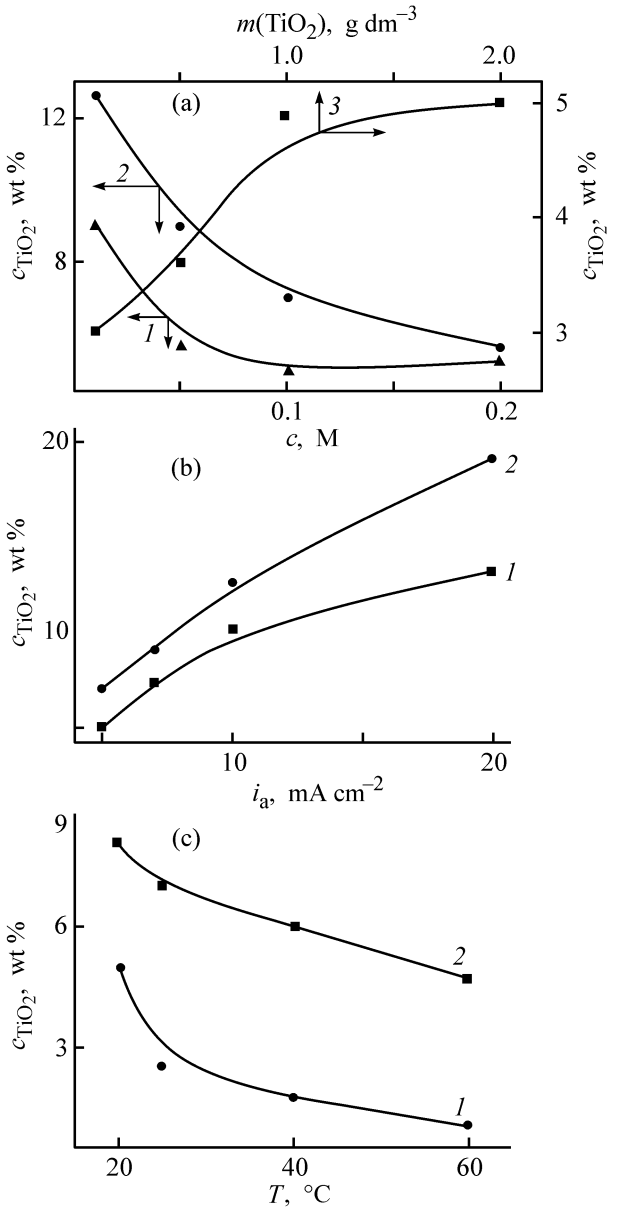


Fig. 2. TiO_2 content of the composite coating, c_{TiO_2} vs. (a) amount of the dispersed phase, $m(TiO_2)$, and HNO_3 concentration c in the deposition electrolyte, (b) anode current density i_a, and (c) temperature T. (a) (*1*) 0.1 M $Pb(NO_3)_2$ + x M HNO_3 + 2.0 g dm^{-3} TiO_2, (*2*) 1 + 7×10^{-4} M surfactant, (*3*) 0.1 M $Pb(NO_3)_2$ + 0.1 M HNO_3 + x g dm^{-3} TiO_2; (b) (*1*) 0.1 M $Pb(NO_3)_2$ + 0.1 M HNO_3 + 2.0 g dm^{-3} TiO_2 and (*2*) 1 + 7×10^{-4} M surfactant; and (c) (*1*) 0.1 M $Pb(NO_3)_2$ + 0.1 M HNO_3 + 2.0 g dm^{-3} TiO_2 and (*2*) 1 + 7×10^{-4} M surfactant.

ization measurements were performed. The polarization curve at low polarizations (Fig. 1a, region *I*), plotted in the Taffel coordinates (E–log J), is linear, which points to the kinetic control over the lead dioxide deposition [17]. At potentials more positive than 1.4 V (Fig. 1a, region *II*), the partial current starts to approach the limiting value, which indicates that the process occurs under diffusion control. Upon the introduction of TiO_2 and sodium dodecyl sulfate into the solution, the polarization somewhat increases and the current of PbO_2 electrodeposition decreases. The results obtained can be attributed to inclusion of particles of the dispersed phase into the coating and to adsorption of the surfactant on lead dioxide [18], which leads to partial blocking of the electrode surface. It should be noted that the run of the polarization curves obtained in colloid electrolytes is nearly the same as that in true solutions. Therefore, the electrodeposition of PbO_2 from suspension electrolytes can be satisfactorily described by the kinetic scheme [18].

As follows from the total polarization curves (Fig. 1b), several processes simultaneously occur at the electrode [at high anodic potentials, the total current exceeds the partial current of lead dioxide electrodeposition (Fig. 1a)]. According to published data [18], the process of PbO_2 formation occurs simultaneously with the reaction of oxygen evolution. The current efficiency (CE) by lead dioxide will be determined by the relative contributions of the two electrode processes. At the anode current density of 5 mA cm^{-2}, the CE_{PbO_2} from the true solution was 98%. Upon addition of TiO_2 to the deposition electrolyte, CE_{PbO_2} decreases to 84%, which agrees with the results of polarization measurements (Fig. 1a) and points to a certain inhibition of the electrodeposition process via partial blocking of the electrode surface by particles of TiO_2, which is a low-conductivity semiconductor.

Particles of the dispersed phase are incorporated into the growing PbO_2 deposit to give a composite material. The content of TiO_2 in the composite will, in all probability, be determined by the stages in which particles of the dispersed phase are delivered from the electrolyte bulk to the electrode surface via diffusion and(or) migration. Because the potential of zero charge of lead dioxide in 0.1 M HNO_3 is 0.91 ± 0.1 V (relative to the standard calomel electrode) [19] at the deposition potentials (>1.5 V), the electrode surface will be positively charged. Despite the positive charge on TiO_2 in the electrolyte, particles of the dispersed phase are, nevertheless, incorporated into the growing coating, which may indicate that the contribution of the migration component is insignificant.

It follows from the data in Fig. 2a that, as the content of titanium dioxide in the deposition

electrolyte decreases to 2 g dm^{-3}, the probability of particle capture by the growing deposit increases, which results in that the amount of TiO_2 in the composite material grows to 5 wt %. This effect is probably observed because the gradient of the partial concentration of the oxide in the dispersed phase grows with its content in the electrolyte. The coating composition also depends on the solution pH. For example, an increase in the HNO_3 concentration leads to a decrease in the TiO_2 content of the coating (Fig. 2a), which is, in all probability, due to a rise in the positive charge of particles of the dispersed phase and to an increase in the rate of migration of TiO_2 particles into the cathode space.

As the current density increases, the content of the inert oxide in the composite material grows (Fig. 2b). The curve describing the content of the dispersed phase in the composite as a function of the current density can be conditionally divided into two portions. In the first of these, as the deposition rate of lead dioxide grows, the probability of capture of TiO_2 particles becomes higher and the content of the inert oxide in the composite increases to 13 wt % (Fig. 2b). In the second, the content of TiO_2 in the coating remains nearly constant as soon as the deposition rate reaches its limiting value (Fig. 1a).

Introduction of a surfactant into the deposition electrolyte results in that the surface of particles of the dispersed phase is recharged. In this case, negatively charged TiO_2–surfactant particles move under the action of electrophoretic forces toward the positively charged anode, to be incorporated there into the growing coating [12]. In the presence of the surfactant, the content of particles of the inert oxide in the composite material also grows with the current density (Fig. 2b), but the concentration of titanium dioxide in the coating does not approach the limiting value. In this case, TiO_2 is delivered not only by diffusion, but also via migration whose rate steadily increases as the polarization becomes more pronounced.

As the deposition temperature is raised, the content of particles of the dispersed phase in the coating decreases (Fig. 2c). Presumably, this occurs because of a decrease in the viscosity of the electrolyte, which, in turn, results in that the partial concentration in the suspension becomes lower because of the sedimentation [20].

It should be noted that, in most cases (Fig. 2), in the presence of the surfactant in the suspension electrolyte, the content of titanium dioxide in

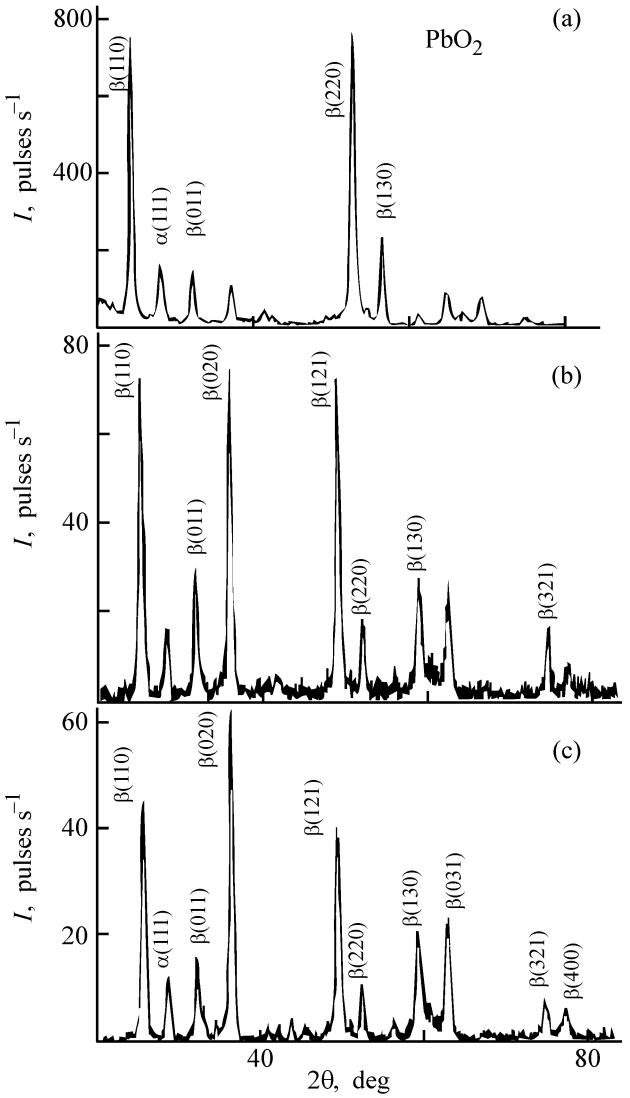


Fig. 3. X-ray diffraction patterns of composite materials deposited from different electrolytes (i_a = 5 mA cm^{-2}). (I) Intensity and (2θ) Bragg angle. (a) 0.1 M $Pb(NO_3)_2$ + 0.1 M HNO_3, (b) a + 2.0 g dm^{-3} TiO_2, and (c) b + 1 × 10^{-3} M surfactant; the same for Fig. 4.

the composite increases because of the additional supply of negatively charged particles to the electrode surface by electrophoresis. At the same time, the fact that the type of the dependence is preserved indicates that, even in the presence of the surfactant, particles are for the most part delivered to the electrode surface via diffusion.

Lead dioxide deposited from nitrate solutions is a polycrystalline formation composed of a mixture of α- and β-phases with various crystallographic orientations, with the predominance of the latter phase (Fig. 3a) [18]. As follows from the X-ray diffraction patterns in Figs. 3b and 3c, the presence of TiO_2 and a surfactant strongly affects the struc-

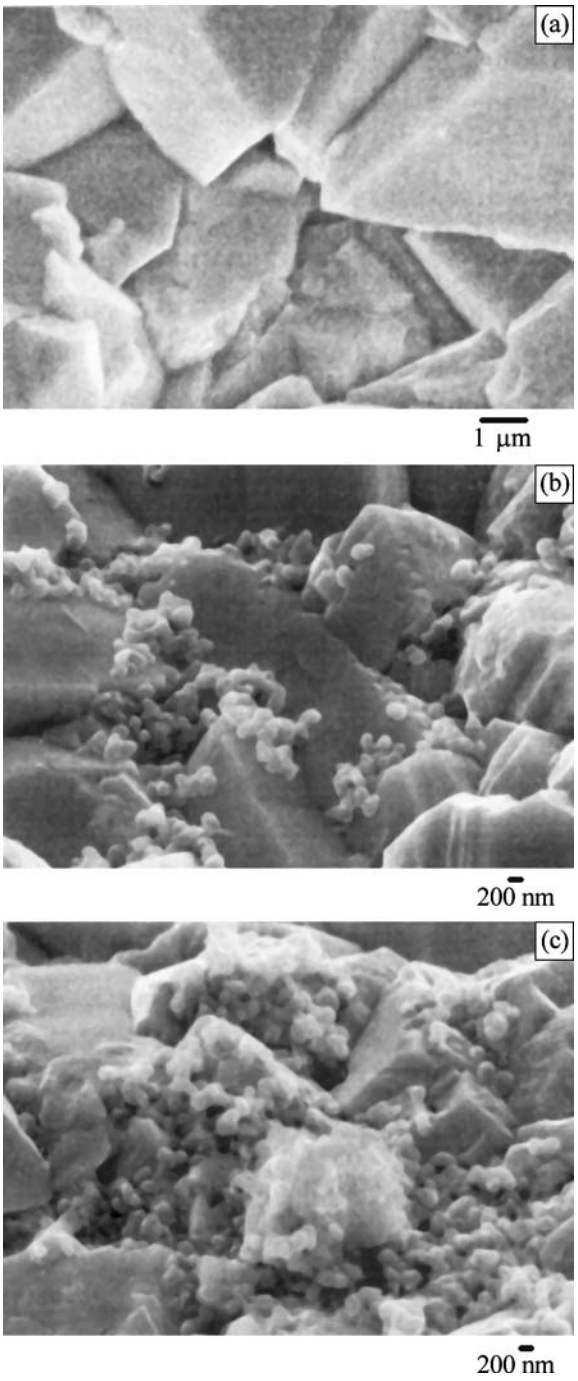


Fig. 4. SEM micrographs of materials deposited from different electrolytes (i_a = 5 mA cm^{-2}).

ture of PbO_2-based materials. The crystallographic orientation of lead dioxide in the composite material substantially changes and new faces appear: β (020), β (121), and β (031). For deposits containing particles of the inert oxide and the surfactant, the intensity of the peaks substantially decreases, which may indicate that the size of lead dioxide crystals decreases as the fraction of X-ray-amorphous phases in a sample increases. It should be noted that the X-ray diffraction patterns show no peaks of titanium dioxide. As follows from the results of sedimentation measurements, the average size of TiO_2 particles is only 0.35 μm, and, therefore, they are X-ray amorphous under the measurement conditions.

To obtain additional information, the surface morphology of the materials obtained was studied by SEM. In electrodeposition of lead dioxide from true solutions (Fig. 4a), the coatings are composed of a set of coarse polycrystalline blocks with a poorly pronounced predominant orientation of separate faces. As follows from the data obtained (Fig. 4), incorporation of titanium dioxide particles into PbO_2 results in that the morphology of the deposit significantly changes. The composite is a heterogeneous system with locally separated zones with different surface morphologies. The regions with coarse crystals are composed of lead dioxide particles, and those with fine crystals, of titanium dioxide partly or completely covered with fine crystals of lead dioxide. The disappearance of coarse crystals and polycrystalline blocks, characteristic of lead dioxide, indicates that the number of crystallization centers grows as the TiO_2 content of the composite increases and the surfactant is adsorbed on the electrode. Thus, the composite materials have the form of a PbO_2 matrix with submicrometer and nanosize crystals, into which TiO_2 crystals are incorporated.

Accelerated resource tests of anodes with an active layer of the PbO_2–TiO_2 composite were performed in 1 M H_2SO_4 at an anode current density of 200 mA cm^{-2}. The service life of the electrodes is determined by the time of uninterrupted polarization during which the potential remains nearly unchanged. A steep rise in the potential points to failure of an electrode, even though no mechanical damage to the active coating is visually observed. Such an electrode cannot be used because of the substantial increase in the electrolyzer voltage. As follows from the data obtained, electrodes containing 5 wt % titanium dioxide could operate during 207 h, and lead dioxide electrodes, during only 105 h at the same current density. Thus, the service life of the composite materials increases approximately twofold, compared with the conventional PbO_2 anodes. It should be noted that lead dioxide electrodes are commonly used at current densities of 20–50 mA cm^{-2}. In these modes, the service life of the electrodes will be 10–100 times longer than

that in the accelerated tests. As follows from a tentative comparative estimate of the electrocatalytic activities of the anodes in electrochemical disintegration of 4-chlorophenol, the composite materials are, at least, not inferior to the conventional lead dioxide electrodes. Thus, the composite materials obtained can be recommended for use as electrocatalysts with a prolonged service life in electrochemical disintegration of toxic organic substances.

CONCLUSIONS

(1) Use of suspension electrolytes makes it possible to obtain composite materials of prescribed composition, which have the form of a lead dioxide matrix into which an inert oxide is incorporated. Particles of the dispersed phase can be delivered to the electrode surface both by their diffusion and by migration. The amount of TiO_2 in the composite can be varied from 1 to 20 wt % by changing the deposition conditions and the electrolyte composition.

(2) The physicochemical properties of the composites significantly differ from those of lead dioxide and are determined by the composition of these materials. The composite has the form of a PbO_2 matrix with submicrometer and nanosize crystals, into which TiO_2 particles are incorporated. Owing to this circumstance, the composites have a large effective surface area.

REFERENCES

1. Casellato, U., Cattarin, S., and Musiani, M., *Electrochim. Acta*, 2003, vol. 48, no. 10, pp. 3991–3998.
2. Shiyun Ai, Mengnan Gao, Wen Zhang, et al., *Talanta*, 2004, vol. 62, no. 2, pp. 445–450.
3. Cattarin, S. and Musiani, M., *Electrochim. Acta*, 2006, vol. 52, no. 4, pp. 1339–1348.
4. Pei Kang Shen and Xiao Lan Wei, *Electrochim. Acta*, 2003, vol. 48, no. 5, pp. 1743–1747.
5. Casellato, U., Cattarin, S., Guerriero, P., and Musiani, M.M., *Chem. Mater.*, 1997, vol. 9, pp. 960–966.
6. Masashi Shiota, Tsuyoshi Kameda, Kazumasa Matsui, et al., *J. Power Sources*, 2005, vol. 144, pp. 358–364.
7. Quoc-Trung Vu, Martin Pavlik, Niels Hebestreit, et al., *Electrochim. Acta*, 2005, vol. 50, no. 8, pp. 1117–1124.
8. Guoting Li, Jiuhui Qu, Xiwang Zhang, and Jiantuan Ge, *Water Res.*, 2006, vol. 40, no. 4, pp. 213–220.
9. Velichenko, A.B., *Doctoral Dissertation*, Dnepropetrovsk, 2002.
10. Cattarin, S., Frateur, I., Guerriero, P., and Musiani, M., *Electrochim. Acta*, 2000, vol. 45, no. 9, pp. 2279–2288.
11. Hwang, B.J., Santhanam, R., and Chang, Y.W., *Feature Article*, June 2001, vol. 6, no. 2, pp. 432–439.
12. Velichenko, A.B., Amadelli, R., and Devilly, D., *Vestn. Kharkov Nats. Univ.*, 2005, vol. 6, p. 36.
13. *Adsorption from Solution at the Solid/Liquid Interface*, Parfitt, G.D., Rochester, C.H., Eds., London: Academic, 1983.
14. Korenman, I.M., *Fotometricheskii analiz: Metody opredeleniya organicheskikh soedinenii* (Photometric Analysis: Methods for Determining Organic Substances), Moscow: Khimiya, 1975.
15. Stender, V.V., *Prikladnaya elektrokhimiya* (Applied Electrochemistry), Kharkov: Kharkov Univ., 1961, pp. 530–533.
16. Tulyupa, F.M., *Doctoral Dissertation*, Dnepropetrovsk, 1970.
17. Trasatti, S. and Lodi, G., *Electrodes of Conductive Metallic Oxides, Part A*, Amsterdam: Elsevier, 1980, pp. 301–358.
18. Luk'yanenko, T.V., *Cand. Sci. Dissertation*, Dnepropetrovsk, 2005.
19. Campbell, S.A. and Peter, L.M., *J. Electroanal. Chem.*, 1991, vol. 306, nos. 1–2, pp. 185–194.
20. Saifullin, R.S., *Kombinirovannye elektrokhimicheskie pokrytiya i materialy* (Combined Electroplated Coatings and Materials), Moscow: Khimiya, 1972, pp. 32–46.

ISSN 1070-4272, Russian Journal of Applied Chemistry, 2008, Vol. 81, No. 6, pp. 1000–1003. © Pleiades Publishing, Ltd., 2008.
Original Russian Text © S.M. Karabanov, O.G. Lokshtanova, 2008, published in Zhurnal Prikladnoi Khimii, 2008, Vol. 81, No. 6, pp. 961–964.

APPLIED ELECTROCHEMISTRY AND CORROSION PROTECTION OF METALS

A Study of the Complex Composition of Sulfamate Ruthenium-Plating Electrolytes

S. M. Karabanov and O. G. Lokshtanova

Ryazan Plant of Metal-Ceramic Devices Open Joint-Stock Company, Ryazan, Russia

Received October 11, 2007

Abstract—Varying-with-time complex composition of a sulfamate ruthenium-plating electrolyte was studied. Recommendations are given concerning the working modes and adjustment conditions in prolonged operation of the electrolyte.

DOI: 10.1134/S1070427208060141

The sulfamate electrolyte is the most widely used industrial ruthenium-plating electrolyte [1–4]. It is prepared from a complex salt, ammonium μ-nitridobisaquatetrachlororuthenate $(NH_4)_3[Ru_2(\mu\text{-}N)(H_2O)_2Cl_8]$. In a prolonged use of the ruthenium-plating electrolyte, it is necessary to maintain its technical characteristics (e.g., the deposition rate, within the prescribed limits) and the stability of characteristics of electroplated coatings. To accomplish this task, it is necessary to know the variation dynamics of the complex composition of both the electrolyte and the adjusting solutions in prolonged storage and use during accumulation of products of chemical and electrochemical reactions.

The aim of this study was to examine the varying-with-time complex composition of ruthenium-plating electrolytes and adjusting solutions.

EXPERIMENTAL

In the study, IR spectroscopy, powder X-ray diffraction analysis, electronic absorption spectroscopy (EAS) of aqueous salt solutions, and gel-chromatography of aqueous solutions on Sefadex gels were employed.

The commonly used ruthenium-plating electrolyte has the following composition ($g\,l^{-1}$) Ru 10–20 (in terms of the metal) and ammonium sulfamate 30–80. The pH value was maintained in the range 1.5–2.0. The electrodeposition was performed at a temperature of 60–70°C and cathode current density of 1–2 A dm^{-2} with the use of Pt/Ti anodes.

Originally, the starting complex salt of ruthenium was studied. IR spectroscopy revealed the following absorption bands (cm^{-1}): 1060, vibrations of the Ru–N–Ru bond; 1450, vibrations of NH_4^+ bonds; 1543, vibrations of uncoordinated water; and 1040, vibrations of coordinated water, which is trans to the bridging nitrogen.

The complex salt was subjected to X-ray diffraction analysis. The resulting X-ray diffraction pattern is in good agreement with published data for $(NH_4)_3[Ru_2(\mu\text{-}N)(H_2O)_2Cl_8]$ [5]. It was found that the ruthenium compound used to prepare electrolytes fully corresponds to this formula, but contains hydration water: $(NH_4)_3[Ru_2(\mu\text{-}N)(H_2O)_2Cl_8]\cdot nH_2O$ (according to a calculation, $n < 1$).

It was of interest to check whether the composition of the complex changes when the electrolyte and adjusting solutions are prepared by dissolving the starting salt in water. The EAS spectra of aqueous solutions of the salt, measured immediately after the substance is dissolved, contain four absorption bands at 205, 290–292, 350, and 435 nm, in full agreement with published data [5, 6].

Solutions of the complex ruthenium salt in water and a 0.1 M solution of hydrochloric acid were subjected to chromatography on a column packed with Sefadex G-15 gel. Chromatograms of the freshly prepared aqueous and hydrochloric acid solutions are shown in Fig. 1. The chromatograms contain only a single broad brown zone containing ruthenium. The EAS spectrum of separate fractions of the zone coincides with that of the starting com-

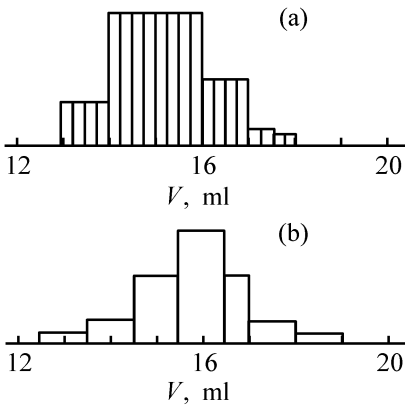


Fig. 1. Chromatograms of freshly prepared solutions of the complex salt of ruthenium in (a) water and (b) 0.1 M HCl solution. (*V*) Retained volume.

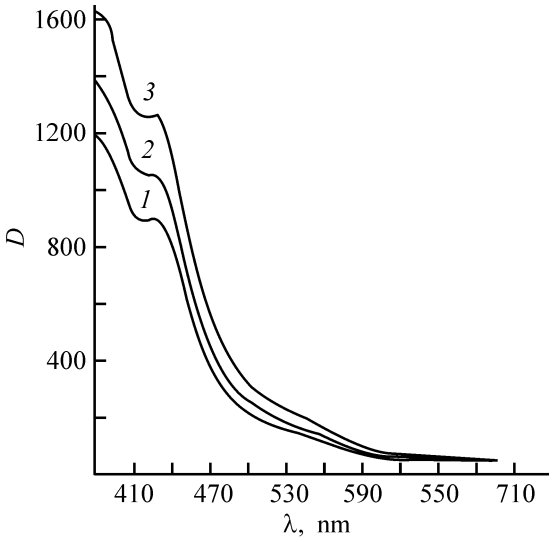


Fig. 2. EAS spectrum of a solution of the complex salt of ruthenium in (*1*) water, (*2*) 0.1 M HCl solution, and (*3*) 0.1 M HCl solution with addition of sulfaminic acid. (*D*) Optical density and (λ) wavelength; the same for Figs. 3, 4.

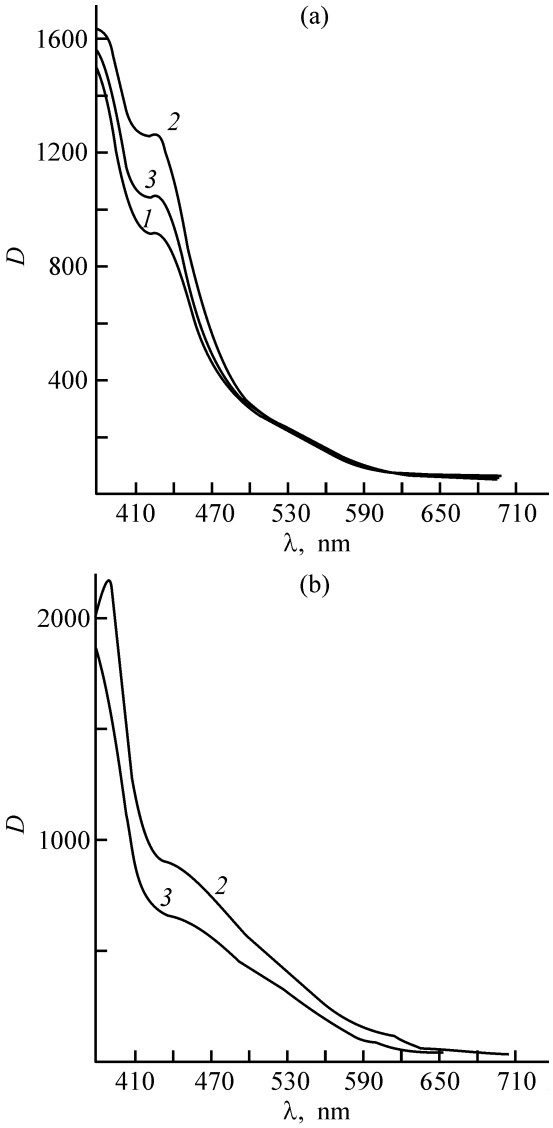


Fig. 3. EAS spectra of various fractions of (a) freshly prepared solution of the complex salt in water and (b) that after keeping for 24 h. Fraction: (*1*) 1st, (*2*) 2nd, and (*3*) 3rd.

plex (Figs. 2, 3a). The minor hypsochromic shift (up to 5–8nm) of bands of separate fractions indicates that hydrolytic processes involving the complex occur when the solution of the complex passes through the complex. In all probability, in aqueous solutions of $[Ru_2(\mu\text{-}N)(H_2O)_2Cl_8]^{3-}$, the inner-sphere chloride ions are replaced by water molecules, with the subsequent acid dissociation.

The hydrolytic process begins immediately after the salt is dissolved in water. In 24 h, the starting complex form is not found in the solution: the absorption band at λ_{max} = 435 nm, characteristic of the $[Ru_2(\mu\text{-}N)(H_2O)_2Cl_8]^{3-}$ complex, is not observed in the EAS spectra of the aqueous solution and those of separate fractions isolated by chromatography (Fig. 3b). At the same time, there appear absorption bands associated with monomeric and dimeric aqua complexes of ruthenium(III), ruthenium(IV), and ruthenium(III,IV) [7–10].

The transformations of the starting nitrido-aqua chloride complex of ruthenium(IV) in water occur rather rapidly and end in disintegration of the nitrido bridge. In 24 h, nearly only a mixture of monomeric and dimeric aqua-hydroxo chloride complexes of ruthenium(III) and ruthenium(IV) is present in the solution.

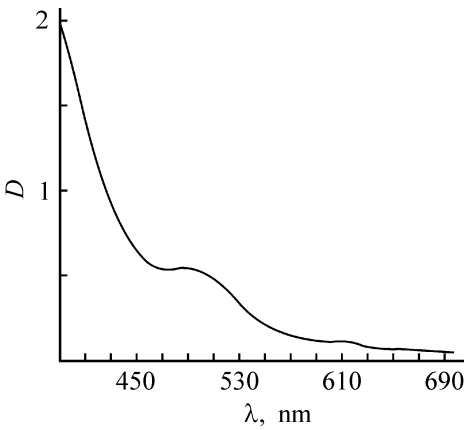


Fig. 4. EAS spectrum of an industrial adjusting solution.

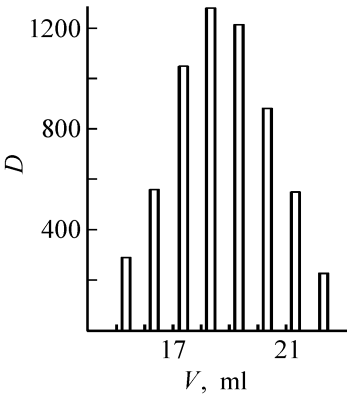


Fig. 5. Gel-chromatogram of the adjusting solution. Fourfold dilution with a 0.1 M HCl solution. (*D*) Optical density and (*V*) retained volume.

The industrially used adjusting solution with a storage life exceeding one month has an EAS spectrum shown in Fig. 4. In the spectrum, there is no absorption band at 435 nm, characteristic of the nitride complex of ruthenium, $[Ru_2(\mu\text{-}N)(H_2O)_2Cl_8]^{3-}$, whereas the band at λ_{max} = 490 nm, associated with aqua-hydroxo complexes of ruthenium(III, IV) is, by, contrast, present. This is also confirmed by the gel-chromatogram of the adjusting solution (Fig. 5). Thus, the $(NH_4)_3[Ru_2(\mu\text{-}N)(H_2O)_2Cl_8]$ salt used to prepare ruthenium-plating electrolytes and adjusting solutions is unstable in the course of time in aqueous solutions. Hydrolysis, inner-sphere dissociation of water molecules, partial reduction of the central ruthenium atom, and reactions of substitution of chloride ions result in that the starting complex is converted into a mixture of aqua and aqua-hydroxo chloride complexes of ruthenium(III,IV).

It was found that variation of the concentration of hydrochloric acid in the adjusting solution (within the technologically acceptable limits) and introduction of the sulfamate ion into this solution do not lead to any significant stabilization of the starting form of the ruthenium complex.

The behavior of a freshly prepared industrial ruthenium-plating electrolyte was studied. The composition of the electrolyte was as follows (g l^{-1}): ruthenium 18 (in terms of the metal), ammonium sulfamate 50, sulfate ions 60, and chloride ions 20.

The EAS spectra contain three absorption bands characteristic of the nitride ruthenium(IV) complex $[Ru_2(\mu\text{-}N)(H_2O)_2Cl_8]^{3-}$, peaked at 205, 290, and 435 nm. However, the intensity of the bands steeply decreased in the course of time, so that, in three days, the spectrum contained in the visible range only a weak shoulder at 430 nm (characteristic band of the nitride complex) and a new band at 490 nm [characteristic band of aqua-hydroxo chloride complexes of ruthenium(III,IV)]. This nature of the spectrum indicates that the industrial electrolyte contains a small amount of complex forms $[Ru_2(\mu\text{-}N)(OH)_m2Cl_{8-n-m}]^{k-}$, where $2 < n + m \leq 8$, and a certain amount of aqua-hydroxo complexes of retention(III,IV), whereas the main complex forms of ruthenium in solution are aqua-hydroxo complexes of ruthenium(III). Presumably, these latter predominate in the solution as a result of electrochemical and inner-sphere reduction of ruthenium(IV) to ruthenium(III) in the course of electrodeposition from the electrolyte.

Ruthenium-plating electrolytes used for a long time were studied. The following two electrolytes were examined. The first was used for two years, with fresh portions of the adjusting solution introduced at regular intervals of time, and contained (g l^{-1}): ammonium sulfamate 60, sulfate ions 250, and chloride ions 30. The second was used for about three years, exhibited an exceedingly low deposition rate, and contained (g l^{-1}): ruthenium 21, ammonium sulfamate 55, and chloride ions 35.

The EAS spectrum of electrolyte no. 1 shows a weak shoulder at 420 nm. In the EAS spectrum of electrolyte no. 2, there are no absorption bands in the visible spectral range. The nature of the EAS spectra indicates that the content of the active form of the nitrido complex $[Ru_2(\mu\text{-}N)(H_2O)_2Cl_8]^{4-}$ is nearly zero, and just this circumstance accounts for the exceedingly low rates of ruthenium deposition from this electrolyte. Apparently, adjustment of long-used electrolytes by addition of fresh portions of a solution containing the nitrido complex of ruthenium and sulfamate ions can maintain a certain content of the electrochemically active form of the ruthenium complex in electroplating baths.

An important role in the adjustment of ruthenium-plating baths is played by sulfamate ions, which form a sulfamate complex with aqua chloride complexes of ruthenium. The sulfamate complexes of ruthenium are unstable. As a result of combined internal transformations involving hydrolytic and redox reactions, the sulfamate complex is converted into a nitrido complex. A necessary condition for this reaction, in which a dimeric structure is formed, is a high concentration of ruthenium in solution. Therefore, the degree of conversion of aqua chloride complexes of ruthenium into dimeric nitrido chloride complexes in industrial electrolytes cannot be high, i.e., only a part of ruthenium is converted into the electrochemically active form of the nitrido complex in adjustment of electrolytes.

At the same time, the reaction of chloro complexes of ruthenium with the sulfamate ion is accompanied by accumulation of sulfate ions in solution. The increase in the concentration of sulfate ions in solution shifts the equilibrium of the complexation reaction toward the initial complexes of ruthenium (sulfamate and aqua-chloro complexes of ruthenium) and thereby also diminishes the concentration of the electrochemically active complex.

Thus, a stable working capacity of ruthenium-plating electrolytes is possible when the electrochemically active form of the nitrido complex of ruthenium is preserved in solution. Introduction of ammonium sulfate into the electrolyte partly solves this problem. However, the accumulation of sulfate ions as a result of multiple adjustments of the electrolyte impairs the regeneration of nitrido complexes from aqua chloride complexes of ruthenium.

Many years' practice of industrial use of ruthenium-plating electrolytes has shown that sulfate ions are accumulated to a concentration of 300–350 g l^{-1} without any deterioration of the quality of electroplated coatings. However, a substantial decrease in the ruthenium deposition rate in electroplating in the optimal modes recommended in the literature ([3, 4] j_c = 1–2.5 A dm^{-2}) was observed because of the electrolytes were depleted of the nitrido complex. In the process, other forms of ruthenium, aqua-hydroxo complexes of ruthenium(III,IV) and ruthenium(III), were accumulated in solution. The only possible way to improve the working capacity of industrial ruthenium-plating electrolytes was to perform deposition at higher cathode current densities, 3.5–4.5 A dm^{-2}. In this case, the coating quality was not impaired. Also, the ruthenium deposition rate could be raised and stabilized. In all probability, the potentials of ruthenium electrodeposition from aqua-hydroxo complexes of ruthenium, previously believed to be electrically inactive, could be reached at these current loads.

CONCLUSIONS

(1) The varying-with-time complex composition of the sulfamate ruthenium-plating electrolyte and adjusting solutions was studied. It was found that dissolution of the nitrido-aqua chloride complex of ruthenium(IV) in water is accompanied by hydrolysis, with the nitrido bridge disintegrated and a mixture of monomeric and dimeric aqua-hydroxo chloride complexes of ruthenium(III) and (IV) formed.

(2) It was shown that, to stabilize ruthenium-plating electrolytes in their prolonged use, it is necessary to perform a systematic adjustment of the electrolyte by addition of a freshly prepared adjusting solution of ammonium μ-nitridoaquachlororuthenate(IV) and ammonium sulfamate.

(3) It was demonstrated that, to maintain high performance characteristics of sulfamate ruthenium-plating electrolytes, the electrolysis should be carried out at cathode current densities of 3.5–4.5 A dm^{-2}, at which the ruthenium is electrodeposited from aqua-hydroxo chloride complexes.

ACKNOWLEDGMENTS

The authors thank staff members of the chair of inorganic chemistry at St. Petersburg State Technological Institute for assistance.

REFERENCES

1. Freunderberger, R., *Galvanotechnik*, 1999, no. 3, pp. 679–686.
2. Gones, T., *Met. Finish.*, 2001, no. 6, pp. 121–128.
3. US Patent 4082622.
4. Hydes, P.C., *Platinum Met. Rev.*, 1980, vol. 24, no. 2, pp. 50–55.
5. US Patent 3576724.
6. Cleare, M. and Griffith, W., *J. Chem. Soc., Ser. A*, 1970, pp. 1117–1123.
7. Potts, L. and Swofford, V., *Analyt. Chem.*, 1975, vol. 47, no. 1, pp. 131–135.
8. Woodhead, J.L. and Fletcher, G.M., *Atomic Energy Research Establishment*, Harwell Berkshire, Rep., 1962, pp. 4123–4137.
9. Jorgensen, C.R., *Acta Chem. Scand.*, 1956, vol. 10, no. 4, pp. 518–534.
10. Shlenskaya, V.I., Biryukov, A.A., and Kadomtseva, V.M., *Zh. Neorg. Khim.*, 1972, vol. 17, pp. 1104–1110.

ISSN 1070-4272, Russian Journal of Applied Chemistry, 2008, Vol. 81, No. 6, pp. 1004–1009. © Pleiades Publishing, Ltd., 2008.
Original Russian Text © K.K. Kalnin'sh, S.G. Semenov, 2008, published in Zhurnal Prikladnoi Khimii, 2008, Vol. 81, No. 6, pp. 965–970.

MACROMOLECULAR CHEMISTRY AND POLYMERIC MATERIALS

Mechanism of Thermal Reactions of Dimerization and Trimerization of Hexafluoro-1,3-Butadiene: A Quantum-Chemical Study

K. K. Kalnin'sh and S. G. Semenov

Institute of Macromolecular Compounds, Russian Academy of Sciences, St. Petersburg, Russia
St. Petersburg State University, St. Petersburg, Russia

Received April 2, 2008

Abstract—The mechanism of thermal oligomerization of hexafluoro-1,3-butadiene was examined using RHF, ROHF, and GVB/DH, and by B3LYP/6-31G* and /6-311G* quantum-chemical methods. The energies of highly reactive excited states of the monomer and of intermediate biradical species were estimated. Isomeric biradicals (excited monomers and dimers) with the free valences localized on two carbon atoms were shown to coexist in the reaction mixture. Recombination of such biradicals and their reactions with neutral stable molecules give rise to diverse products, depending on the reaction temperature.

DOI: 10.1134/S1070427208060153

Oligomerization of hexafluoro-1,3-butadiene (HFBD, **I**) at 130–300°C, experimentally studied in [1–3], is a convincing example of the occurrence of thermal reactions via biradical electronically excited states of the starting molecules and intermediates. The involvement of such states in thermochemical reactions has been studied previously for the examples of dimerization of perfluoroolefins [4–6] and polymerization of bicyclobutanes [7]. It was shown that the key step of these reactions is thermal excitation of a monomer molecule to a low-lying (~1 eV) electronic state, accompanied by degradation of the double bond or cleavage of a single C–C bond. The arising monomeric biradicals are highly reactive and readily recombine or undergo addition to monomer molecules to give stable dimers or biradical intermediates further yielding oligomers and polymers.

The role of thermally excited electronic states in polymerization reactions was considered in [8]. Such reactions are quite common in organic chemistry. Polymerization reactions initiated by free radicals naturally fall into a series of other polymer reactions that occur by the radical mechanism, but differ in the nature and properties of intermediates. One of the principal features of radical reactions is the full localization of an unpaired electron on a separate atom of a reaction center, in contrast to other reactions, such as, e.g., anionic polymerization in which an unpaired electron in the excited state of the reaction center is delocalized over several atoms.

Hexafluoro-1,3-butadiene has been extensively studied as a monomer in radical and anionic polymerization. It is nonreactive in the common radical polymerization, but readily polymerizes by the anionic mechanism under initiation with cesium or rubidium fluoride, cesium or rubidium *tert*-butylate, and other typical anionic initiators [9–11]. Poly-HFBD with the polyvinylene chain structure is highly crystalline and heat-resistant (360°C) [9].

The primary products of thermal reactions of HFBD in the gas phase are, depending on temperature, hexafluorocyclobutene, [2+4]-cycloadduct, and a pair of stereoisomeric [2+2]-cycloadducts [1, 2]. The reaction of [2+4]-cycloadduct with hexafluoro-1,3-butadiene yields three structurally isomeric trimers, whereas [2+2]-cycloadducts undergo thermal rearrangements with the formation of tricyclic saturated dimers or of a polymer. Kazmina et al. [1, 2] believe that the difference in the chemical behavior of 1,3-butadiene and its perfluorinated analog is due to their structural features. The planar structure of the carbon skeleton of the C_4H_6 mol-

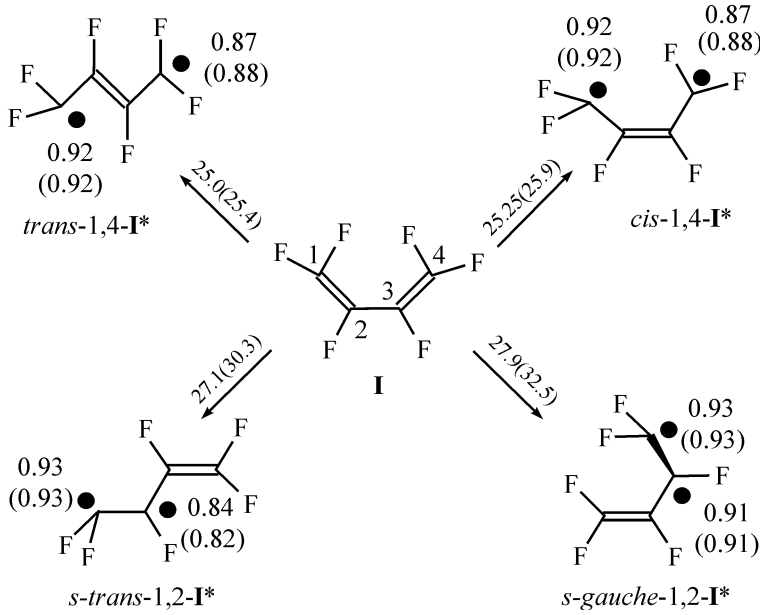


Fig. 1. Energies of triplet and singlet (in parentheses over arrows) excited states of hexafluorobutadiene, according to RHF, ROHF/DH calculations. Black circles denote reactive atoms, with the free-valence indices in the triplet and singlet (in parentheses) states indicated.

ecule favors conjugation of the double bond and imparts electron-donor properties to the molecule, whereas nonplanar HFBD exhibits electron-acceptor properties typical of fluoroolefins.

EXPERIMENTAL

Quantum-chemical calculations were performed by the RHF, ROHF, GVB, and B3LYP methods in the 6-31G*, 6-311G*, and DH basis sets, using GAMESS program [12, 13]. The methodological features of quantum-chemical calculations of molecules in the ground and excited (S_1, T_1) states are described in [6]. The calculated total energies were corrected for the zero-point vibration energies.

The hexafluoro-1,3-butadiene molecule in the ground electronic state has a nonplanar *s-cis* structure [14, 15]. The CCCC dihedral angle determined by electron diffraction is 47.4° [14]. An ab initio ROHF/DH calculation also gives preference to the *s-cis* conformation (ΔE = 0.5 kcal mol^{-1}), with the dihedral angle ∠CCCC equal to 55.8°. The same energy difference, ΔE = 0.5 kcal mol^{-1} in favor of the *s-cis* form, and similar dihedral angle ∠CCCC = 54.0° are given by B3LYP/6-311G* calculations. The nonplanarity of the carbon skeleton of the hexafluorobutadiene molecule is accounted for by the repulsion of fluorine atoms [16].

Under electronic excitation, the hexafluoro-1,3-butadiene molecule can pass into several equilibrium biradical states, which is confirmed by calculation of the indices of the free atomic valence F_A in quasidegenerate singlet and triplet states $(S \cdot T)_n$ (Fig. 1). The indices F_A, whose sum in each molecule is 2.00, are close to unity only for two carbon atoms and are negligible for the remaining atoms of the molecule. This fact, along with the closeness of the geometric parameters, energies, and indices F_A, calculated for the singlet and triplet components of the $(S \cdot T)_n$ state, confirms its biradical character.

The stereoisomeric *trans*- and *cis*-1,4-**I*** states in which the free valences are concentrated on the terminal carbon atoms C^1 and C^4 (Fig. 1) have the lowest energy. The energy of the excited state *s-trans*-1,2-**I*** in which the free valences are localized on the adjacent C^1 and C^2 atoms is only slightly higher. Due to localization of the excitation on one degraded double bond and steric proximity of the radical centers, the singlet–triplet splitting of the energy level in this case (3.2 kcal mol^{-1}) is appreciably larger than in the previous case (0.3 kcal mol^{-1}).

It is important that the above-indicated energies of the biradical states of monomer **I** molecule are sufficiently low for these states to be efficiently populated at the experimental temperatures, 130–300°C [1, 2]. The excitation energies for the other species considered below are also low. Therefore, the mech-

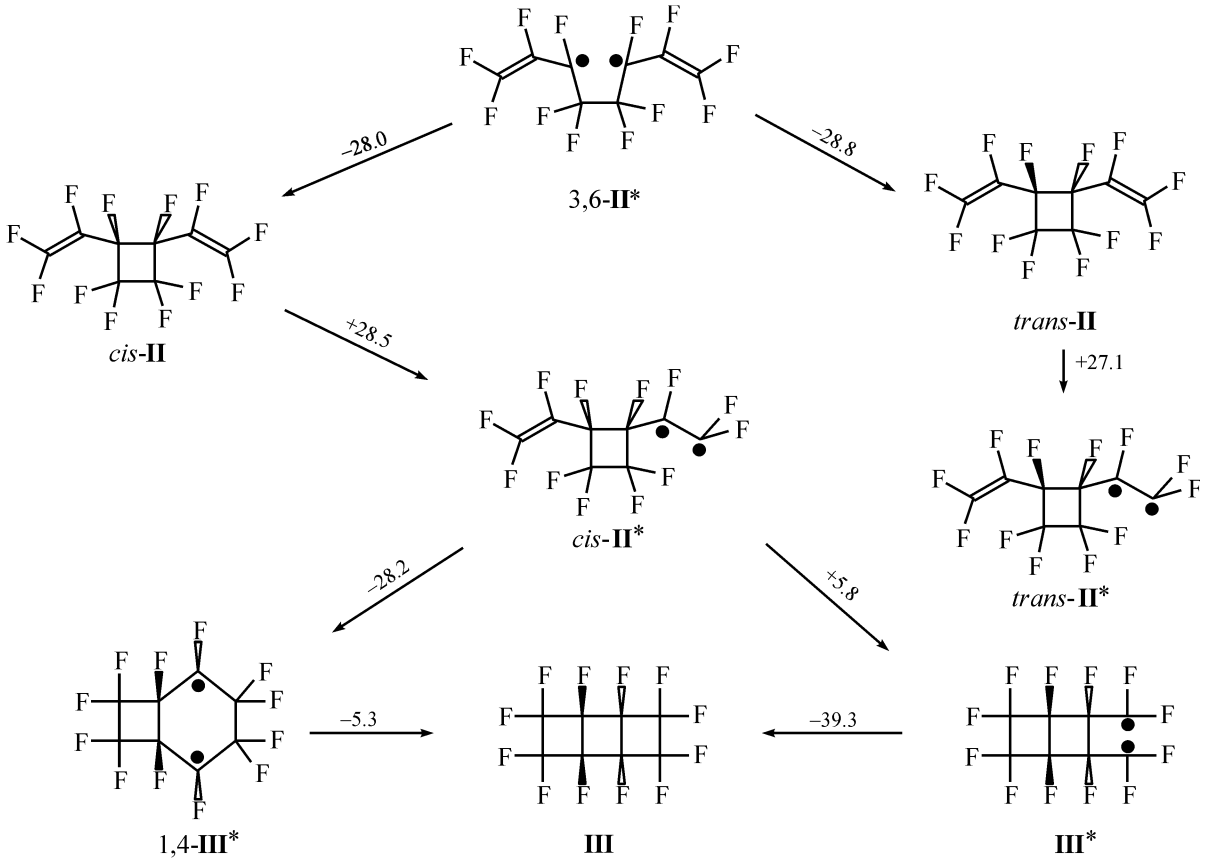


Fig. 2. Structure of hexafluorobutadiene dimers in the ground and excited triplet states. The calculated (RHF, ROFH/DH) heats of transitions with the release (–) and absorption (+) of energy are indicated over arrows.

anism of HFBD transformations on heating in the gas phase can be regarded as thermal excitation of the initial molecules and the intermediates formed to low-lying biradical states.

The excited states of hexafluoro-1,3-butadiene, discussed in this paper, have a nonplanar equilbrium structure, which is strongly different for the 1,4- and 1,2-biradicals. The presence of several excited states of HFBD with close energies, but different distributions of the free atomic valences is responsible for the occurrence of several pathways of radical reactions, involving generation of diverse structures: four-membered rings with an exocyclic vinyl group, six- and eight-membered rings, ladder-shaped molecules, etc. Some of these structures are shown in Fig. 2, with the calculated heats of transition (positive for heat absorption and negative for heat release) indicated over the arrows. The 1,4-biradical states are responsible for the formation of hexafluorocyclobutene by intramolecular recombination of free valences and of perfluorinated substituted cyclohexene as a product of the Diels–Alder-type (Lebedev) reaction. The 1,2-biradical states are involved in the formation of dimers *trans*- and *cis*-**II** with four-membered saturated rings.

The biradical states 3,6-**II*** can be populated not only by thermal excitation of these dimers, but also by the reaction of two monomer molecules, at least one of which is in the excited 1,2-biradical state. For some structures, e.g., 1,4-**III*** and **III**, the energies differ insignificantly (Fig. 2), suggesting the possibility of thermal excitation of the ladder structure to a biradical state at room temperature. Two radical structures *cis*-**II*** and **III***, differing in energy by only 5.8 kcal mol^{-1}, are also shown in Fig. 2. In the first case, the exocyclic C=C bond is excited, and in the second, the radical centers arise from cleavage of one of the single bonds of the four-membered ring.

One of the dimers, dodecafluorotricyclo[4.2.0.0^{2,5}]-octane **III** consisting of three four-membered rings in the chair conformation, is of particular interest, because it was actually isolated from the reaction mixture formed by heating of dimer *cis*-**II** (150°C)

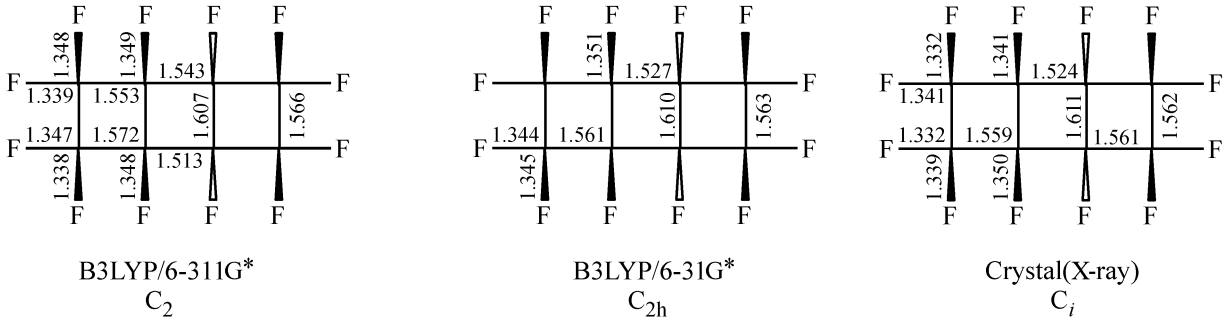


Fig. 3. Structure of hexafluorobutadiene dimer **III** in the ladder conformation, according to the results of a single-crystal X-ray diffraction analysis and to B3LYP/6-311G* and B3LYP/6-31G* calculations.

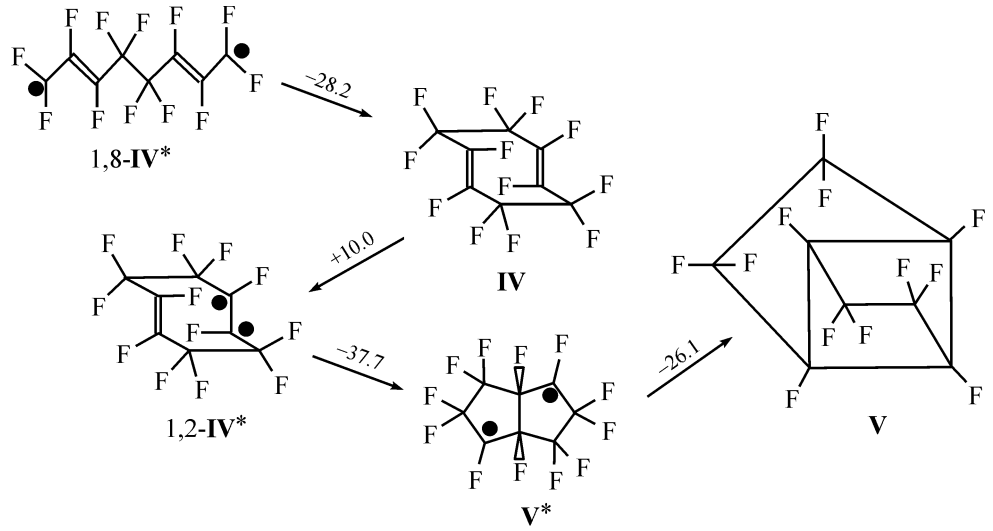


Fig. 4. Scheme of formation of a stable highly symmetric hexafluorobutadiene dimer of globular structure **V**.

and was subjected to single-crystal X-ray diffraction analysis [1]. In our calculations, the best agreement between the calculated (C_i) and experimental structural parameters is provided by the B3LYP/6-31G* method (Fig. 3). In the symmetrical (C_{2h}) molecule **III**, the presence of the symmetry center implies an ideally planar structure of the middle four-membered ring. In the extended basis set, B3LYP/6-311G*, the optimal configuration is characterized by the C_2 symmetry, but fixation of the C_{2h} symmetry leads to an increase in the energy by only 0.4 kcal mol^{-1}. The lower symmetry, C_i, of molecule **III** in the crystal, compared to the theoretically possible symmetry C_{2h}, is naturally attributable to features of molecular packing in the crystal.

Another unusual structure formed upon high-temperature heating of dimer *trans*-**II** (200°C) is dimer **V** (Fig. 4). According to [1], both dimers **III** and **V** are secondary products of thermal transformations of primary dimers *trans*-**II** and *cis*-**II** (Fig. 2). Being one of the most stable products, product **V** exists up to 300°C, in contrast to **III** which transforms at 150°C into **V** via a certain undetectable intermediate **IV**. It has been suggested [1] that intermediate **IV** is an eight-membered ring with two double bonds, namely, *trans,trans*-dodecafluoro1,5-cyclooctadiene (Fig. 4). The calculation results confirm the possibility of existence of **IV** in the chain of radical transformations of the starting hexafluorobutadiene, but the energy of excitation (**IV** → 1,2-**IV***) of this species is low (10 kcal mol^{-1}), and hence it cannot be detected at temperatures exceeding 150°C because of the fast thermochemical transformations.

Along with the above-noted products, thermal transformations of hexafluorobutadiene also yield other dimers and trimers of various structures. One of the most stable products **VI** containing a six-membered ring with an exocyclic double bond is formed from biradical 3,4-**VI*** by intramolecular recombination with a considerable heat release

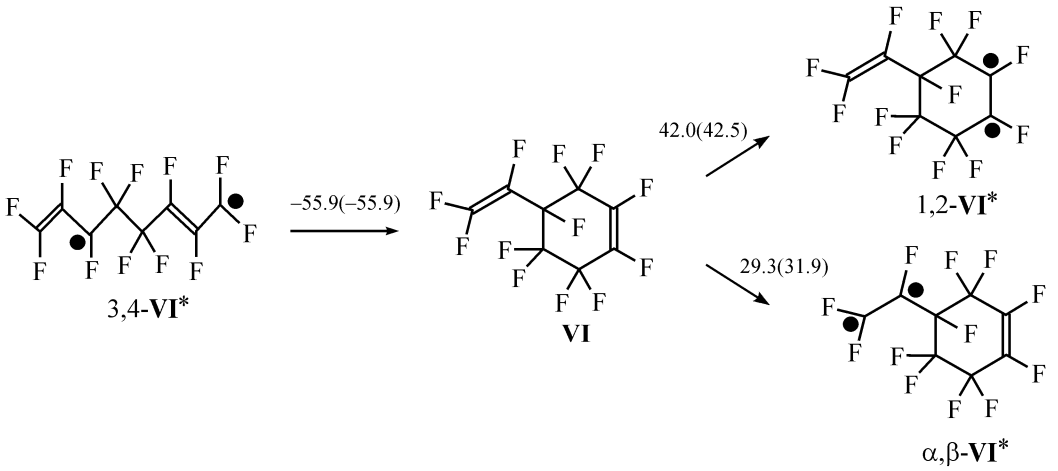


Fig. 5. Excited state of the stable dimer, 4-trifluorovinylnonafluorocyclohexene **VI** (RHF, ROHF/DH).

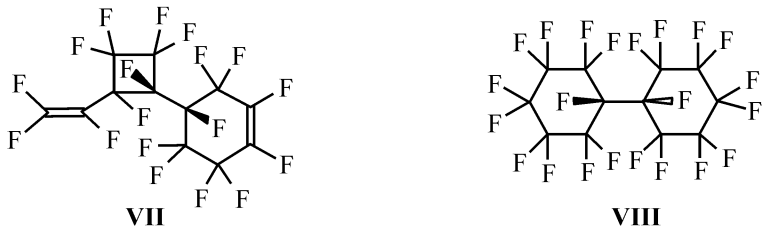


Fig. 6. Structures of hexafluorobutadiene trimers **VII** and **VIII**.

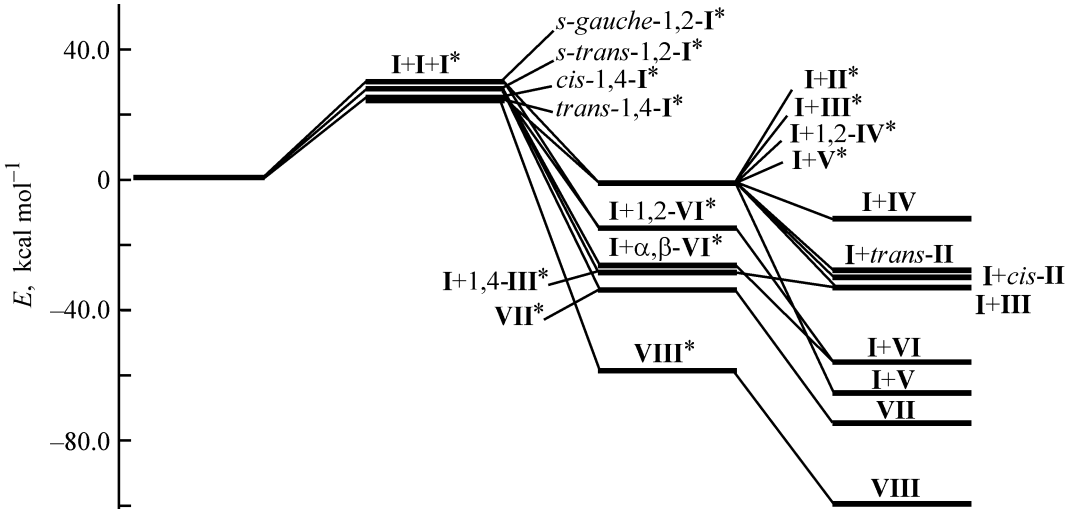
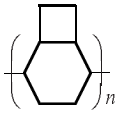


Fig. 7. Energy diagram of thermal reactions of 1,3-hexafluorobutadiene, according to RHF, ROHF/DH ab initio calculations.

(–55.9 kcal mol^{-1}, Fig. 5). Two trimers, **VII** and **VIII**, are shown in Fig. 6. Their formation by ternary collisions of C_4F_6 molecules is improbable, and the main trimerization pathway is the reaction of monomers with dimers at high temperature (>150°C).

The polymeric product formed in a small amount is the final product of thermochemical transformations of a dimer, *cis*, *trans*-dodecafluoro-1,5-cyclooctadiene **IX**, an isomeric analog of intermediate **IV**. At the same time, the polymer consisting of



units may be a product of intermolecular recombination of biradicals 1,4-**III*** [1] (Fig. 2). The latter variant of the reaction seems to be more

probable because of the low energy of excitation of dimer **III**, 5.3 kcal mol^{-1}, and full structural matching between biradical 1,4-**III*** and the elementary unit of the polymer. Dimer **IX** was not isolated pure, but its complex with (acetylacetonato)dicarbonylrhodium was prepared and studied. The excitation energy of **IX**, 9.3 kcal mol^{-1}, is close to that of the *trans*, *trans* analog, 10.0 kcal mol^{-1}.

Finally, it is appropriate to give a summary energy diagram of thermal reactions of dimerization and trimerization of hexafluorobutadiene (Fig. 7). It is of particular importance that, according to our concept, the thermal reactions in all the steps occur via electronically excited biradical states of molecules. From this standpoint, we can rationalize the main experimentally found relationships [1, 3]. In particular, structures requiring higher temperatures for their activation should have higher excitation energies. Indeed, chemically unstable dimer **III** [1] characterized by a low excitation energy (ΔE = 5.3 kcal mol^{-1}) in the biradical form involved in a number of chemical transformations, and the final product in the chain of its radical reactions is the most stable compound **V**. In contrast to **III**, dimer **V** is very stable and does not decompose up to 300°C. This compound should be characterized by high excitation energies, which is confirmed by calculations (Fig. 7).

Thus, the concept of the thermal electronic excitation is very fruitful in studying chemical transformations of unsaturated organofluoric compounds. On the whole, these data give grounds to state that, in all the steps, thermochemical reactions of hexafluorobutadiene occur via electronically excited biradical states. The molecular nature of the electronic excitation of perfluorobutadiene and related compounds consists in deformation of the carbon skeleton by a turn about the C=C bonds, with the radical centers localized on two carbon atoms. The biradical mechanism of thermal reactions of hexafluorobutadiene was suggested in experimental studies [1–3], but their authors assume the occurrence, along with the biradical mechanism, of other mechanisms (concerted, zwitterionic), impossible in our opinion.

CONCLUSIONS

(1) Thermal oligomerization of hexafluoro-1,3-butadiene in the gas phase at 130–300°C occurs via electronically excited biradical states $(S \cdot T)_n$.

(2) The existence in the reaction medium of a mixture of isomeric biradicals with close energies of $S_0 \rightarrow (S \cdot T)_n$ excitation and high free valence indices on the carbon atoms is responsible for the diversity of the reaction pathways and products: saturated polycyclic dimers with the ladder and globular structure and saturated four-membered and unsaturated six-membered rings linked by single bonds in trimers.

REFERENCES

1. Kazmina, N.B., Antipin, M.Yu., Sereda, S.V., et al., *J. Fluorine Chem.*, 1993, vol. 61, nos. 1–2, pp. 57–83.
2. Kazmina, N.B., Antipin, M.Yu., Sereda, S.V., et al., *J. Fluorine Chem.*, 1993, vol. 61, nos. 1–2, pp. 85–104.
3. Moskvin, D.I., Zharov, A.A., and Yakovleva, I.I., *Zh. Fiz. Khim.*, 2004, vol. 78, no. 5, pp. 850–853.
4. Kalnin'sh, K.K., *Zh. Prikl. Khim.*, 2002, vol. 75, no. 4, pp. 603–611.
5. Kalnin'sh, K.K., Semenov, S.G., and Panarin, E.F., *Dokl. Ross. Akad. Nauk*, 2003, vol. 390, no. 3, pp. 350–354.
6. Kalnin'sh, K.K. and Semenov, S.G., *Zh. Prikl. Khim.*, 2003, vol. 76, no. 10, pp. 1585–1600.
7. Kalnin'sh, K.K. and Semenov, S.G., *Zh. Prikl. Khim.*, 2005, vol. 78, no. 7, pp. 1157–1164.
8. Kalnin'sh, K.K. and Panarin, E.F., *Vozbuzhdennye sostoyaniya v khimii polimerov* (Excited States in Polymer Chemistry), St. Petersburg: Sankt-Peterb. Gos. Univ. Tekhnologii i Dizaina, 2007.
9. Narita, T., *J. Fluorine Chem.*, 1991, vol. 54, nos. 1–3, p. 79.
10. Nishimura, Sh., Takahashi, A., Narita, T., et al., *Macromol. Chem. Phys.*, 2003, vol. 196, no. 6, pp. 1953–1961.
11. Narita, T., *Prog. Polym. Sci.*, 1999, vol. 24, no. 8, pp. 1095–1148.
12. Schmidt, M.W., Baldridge, K.K., Boatz, J.A., et al., *J. Comput. Chem.*, 1993, vol. 14, no. 11, pp. 1347–1363.
13. Granovsky, A.A., http://classic.chem.msu.su/gran/gamess/index.html.
14. Chang, C.H., Andreassen, A.L., and Bauer, S.H., *J. Org. Chem.*, 1971, vol. 36, pp. 920–923.
15. Wurrey, C.J., Bucy, W.E., and Durig, J.R., *J. Chem. Phys.*, 1977, vol. 67, pp. 2765–2770.
16. Cho, H.-G., Kim, K.-W., and Cheong, B.-S., *Bull. Korean Chem. Soc.*, 2004, vol. 25, no. 4, pp. 452–459.

ISSN 1070-4272, Russian Journal of Applied Chemistry, 2008, Vol. 81, No. 6, pp. 1010–1014. © Pleiades Publishing, Ltd., 2008.
Original Russian Text © G.N. Gubanova, A.I. Grigor'ev, Yu.N. Sazanov, A.V. Novoselova, A.V. Gribanov, G.N. Fedorova, A.A. Kutin, T.E. Sukhanova, 2008, published in Zhurnal Prikladnoi Khimii, 2008, Vol. 81, No. 6, pp. 971–975.

MACROMOLECULAR CHEMISTRY AND POLYMERIC MATERIALS

Cyclization and Carbonization of Anionic Polyacrylonitrile in the Presence of Carbon Nanofibers

G. N. Gubanova, A. I. Grigor'ev, Yu. N. Sazanov, A. V. Novoselova, A. V. Gribanov, G. N. Fedorova, A. A. Kutin, and T. E. Sukhanova

Institute of Macromolecular Compounds, Russian Academy of Sciences, St. Petersburg, Russia

Received April 3, 2008

Abstract—Composites based on anionic polyacrylonitrile and carbon nanofibers were studied by X-ray diffraction, differential scanning calorimetry, thermal gravimetric analysis, and electron microscopy. The effect of carbon nanofibers on the specific features of cyclization and carbonization of anionic polyacrylonitrile at temperatures of to 550°C was studied.

DOI: 10.1134/S1070427208060165

Studying the cyclization and carbonization of polyacrylonitrile (PAN) in the presence of various modifiers and fillers is a topical task, because PAN-based composites and their carbonization products are widely used in many fields of engineering and industry [1, 2].

It is known that PAN carbonizates and PAN-based composites occupy a leading place among polymeric carbon materials because of the high carbon residue, reaching 60% [3]. In the initial step of carbonization of PAN and its composites in the temperature range 400–550°C, the major pathway of thermal transformations is cyclization. It is accompanied by a large heat release, frequently leading to the polymer degradation and carbon loss. The magnitude of the exothermic effect and the cyclization temperature can be decreased by using PAN copolymers or by introducing various modifying additives [4, 5].

Studies of the mechanisms of cyclization and carbonization of PAN are performed with polymer samples synthesized by both radical and anionic polymerization [6, 7]. It was shown in [8] by thermal analysis, IR spectroscopy, and mass spectrometry that PAN synthesized on anionic initiators (a-PAN) is a convenient model for studying the initial step of carbonization, as it does not contain residual amounts of the catalyst, oxidants, and other components present in PAN prepared by radical polymerization. Previous studies of a-PAN in the temperature range 20–300°C have shown the absence of impurities and volatile low-molecular-weight cyclization products [9].

Carbon nanoadditives (nanofibers, carbon nanotubes, fullerenes, shungite, etc.) find growing use for modification of polymeric materials. These additives have high specific surface area and exhibit unique mechanical and conducting properties. Introduction of carbon nanoadditives into polymers can improve their physicomechanical characteristics, enhance the heat resistance, and raise the carbon residue [10–12].

The goal of this study was to examine in more detail specific features of the cyclization and carbonization of composites of anionic polyacrylonitrile with carbon nanofibers.

EXPERIMENTAL

As object of study we used powdered a-PAN synthesized with anionic catalysts by the procedure described in [9]. For thermochemical tests we took samples with a molecular weight M_w ~20000. For the modification of a-PAN, we used carbon nanofibers (CNFs) prepared by pyrolysis of methane, using NiO as catalyst [13].[1] Composites of a-PAN with CNFs were prepared by

[1] Carbon nanofibers were prepared at a laboratory of Tambov State Technical University.

grinding in an agate mortar to obtain a uniform blend.

To assess structural changes occurring in the course of cyclization and carbonization of a-PAN, we used combined thermal analysis with simultaneous recording of the TG and DTA curves. Measurements were performed with an MOM derivatograph (Hungary) in an open crucible at a heating rate of 10 deg min^{-1}. The microstructure of carbon fibers was studied by transmission electron microscopy on a BS-500 electron microscope (Tesla, Czechia). X-ray diffraction patterns were obtained with a DRON-II device (Burevestnik Research and Production Association, Russia) using Ni-filtered Cu_{K_α} radiation (λ = 1.54 Å) in the scattering angle range $2\theta = 4°–36°$. The cyclization of a-PAN and its composites with nanofibers was monitored with a DSM-2M differential scanning calorimeter (Specialized Design Office of Instrument Making, Pushchino, Russia) at scanning rates of 8 and 16 deg min^{-1}. The temperature was calibrated using In and Sn references.

Figures 1a and 1b show, respectively, the TG and DTA curves of a-PAN, a-PAN–CNF composites (80 : 20 and 50 : 50 by weight), and CNFs. The weight loss of a-PAN (Fig. 1a, curve *1*) on heating to 270°C is 4%, which may be due to the release of adsorbed moisture. In the temperature range 270–308°C, the sample suffers a sharp weight loss (~12%) due to the release of residual low-molecular-weight polymerization products. Further heating to 330°C is not accompanied by weight loss, and at higher temperatures (up to 800°C) the TG curve reflects a typical carbonization process with gradual dehydrogenation of the formed heterochain polymer. The yield of the carbon residue at 800°C is 44%.

In contrast to a-PAN, the CNF sample (Fig. 1a, curve *4*) exhibits throughout the examined temperature range a monotonic TG curve reflecting the gradual loss of the pyrolysis products on heating. After heating the CNF sample to 800°C, the carbon residue is 66%. The TG curves of a-PAN–CNF composites reflect the superposition of thermochemical reactions characteristic of a-PAN and CNFs. Comparison of composites with various component ratios shows that a stepwise weight loss in the temperature range 160–190°C is more pronounced in curve *2* (Fig. 1a), whereas in curve *3*, the initial weight loss is complete at 260°C. The run of these curves on further heating to 350–370°C also depends on the component ratio. However, at still higher temperatures, the rates of the weight loss

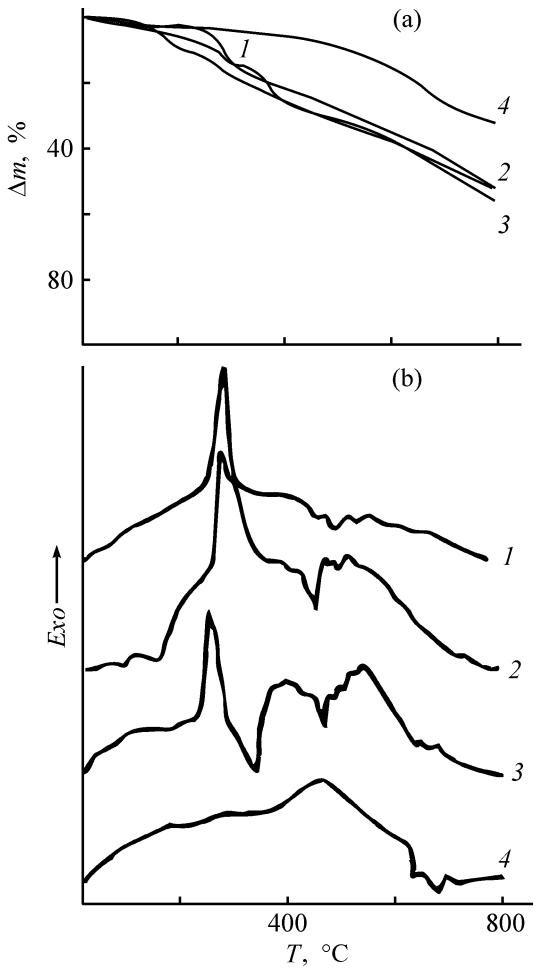


Fig. 1. (a) TG and (b) DTA curves of samples of (*1*) straight a-PAN, (*2*) 50 : 50 a-PAN–CNF composite, (*3*) 80 : 20 a-PAN–CNF composite, and (*4*) CNFs. (Δm) Weight loss and (T) temperature.

for both composites become similar. After heating to 800°C, the carbon residue for the 80 : 20 and 50 : 20 composites is 43 and 45%, respectively.

In all the DTA curves (Fig. 1b) in the temperature range 200–300°C, there are exothermic effects associated with the cyclization of a-PAN and its composites. Peaks of avalanche-like exothermic processes are observed in the range 225–250°C. The noticeable shift of the cyclization temperature, observed for the 50 : 50 a-PAN–CNF composite, may be due to the catalytic effect of CNFs on the PAN cyclization. This effect can be attributed to the presence of polyconjugated systems in CNFs, which, according to [14], accelerate condensation processes in carbonization of various compounds.

As we have found previously [15], the cyclization is followed, starting from 400°C, by carbonization

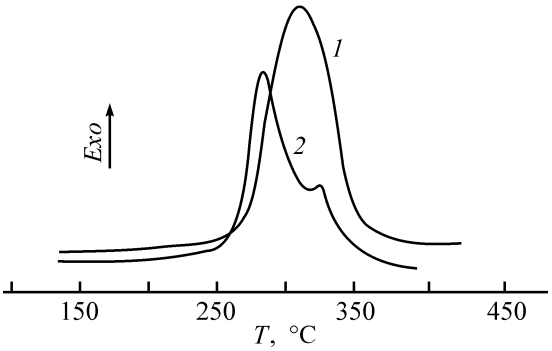


Fig. 2. DSC curves of samples of (*1*) straight a-PAN and (*2*) 50 : 50 a-PAN–CNF composite. (*T*) Temperature.

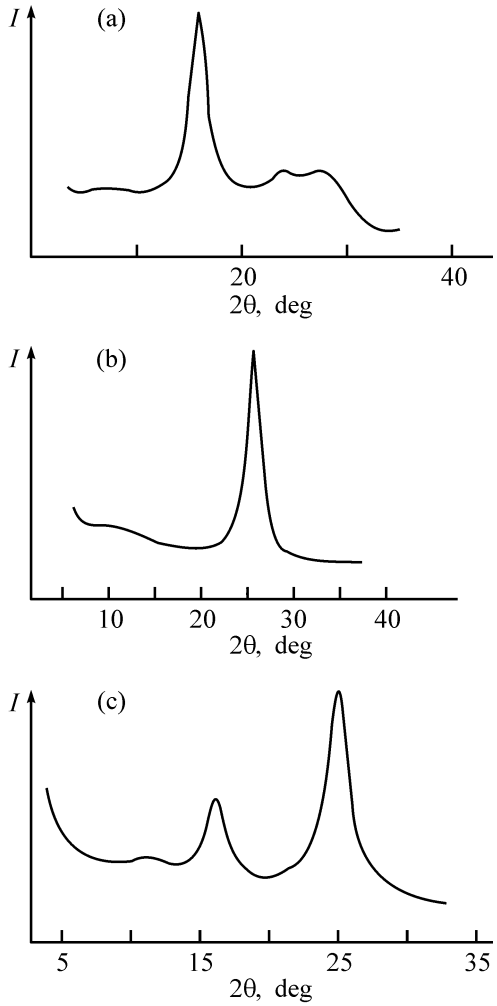


Fig. 3. X-ray diffraction patterns of samples of (a) a-PAN, (b) CNFs, and (c) 50 : 50 a-PAN–CNF composite. (*I*) Intensity and (2θ) Bragg angle; the same for Fig. 4.

of a-PAN, accompanied by slow release of volatile products. The rearrangement of the primary cyclic structure of the carbonizate in the temperature range 400–550°C is a complex process. In the DTA curve of straight a-PAN, there are ill-defined asymmetric endothermic peaks with maxima at 456, 470, and 537°C (Fig. 1b, curve *1*). In the thermograms of a-PAN–CNF composites (Fig. 1b, curves *2*, *3*), the endothermic effects in the range 400–550°C are more pronounced. As we showed in [15], the cyclization of a-PAN is accompanied by the formation of 3*D*-ordered aggregates of a-PAN macromolecules with a definite set of cyclic sequences whose fragments have a crystalline structure. These fragments were synthesized and characterized in [16]. The results of [15, 16] show that the ordering of macromolecules, in the course of a-PAN cyclization is a basis for the formation of a carbonized structure of a-PAN and a-PAN–CNF composites.

To evaluate the effect of nanofibers on the character of the occurring transformations, we examined the cyclization of the straight a-PAN powder and of the 50 : 50 a-PAN–CNF composite by DSC. Figure 2, curve *1* shows a thermogram of the cyclization of the a-PAN powder at a scanning rate of 8 deg min^{-1}. The exotherm of the cyclization of straight a-PAN is characterized by a half-width of ~50°C and a maximum at 310°C, with the onset at 250°C.

For the 50 : 50 a-PAN–CNF composite, the exotherm corresponding to the cyclization (Fig. 2b), along with the main maximum, has a high-temperature shoulder. The exothermic peaks at a scanning rate of 8 deg min^{-1} are observed at 280 and 330°C. At a higher scanning rate (16 deg min^{-1}), the peaks become better resolved. According to [15], in a-PAN prepared in DMF by the procedure described in [9], the syndiotactic configuration prevails, but the isotactic configuration is also present. The cleavage of the double bond of linear a-PAN in the course of cyclization generates active radicals capable of reacting with carbon nanofibers. The presence of two conformations in the a-PAN samples examined may be responsible for the bimodal shape of the cyclization exotherm in the presence of carbon nanofibers. It should be noted that the energy of a-PAN cyclization in the presence of CNFs is several times lower (600 J g^{-1} interms of a-PAN) than the cyclization energy of the unfilled a-PAN (2200 J g^{-1}). Furthermore, in the composite the cyclization is facilitated, as follows from the 30°C shift of the main exothermic maximum.

Figure 3 shows the X-ray diffraction patterns of (a) a-PAN, (b) CNFs, and (c) 50 : 50 a-PAN–CNF composite. In the diffraction pattern of a-PAN, there is a strong reflection at 2θ = 17°, which corre-

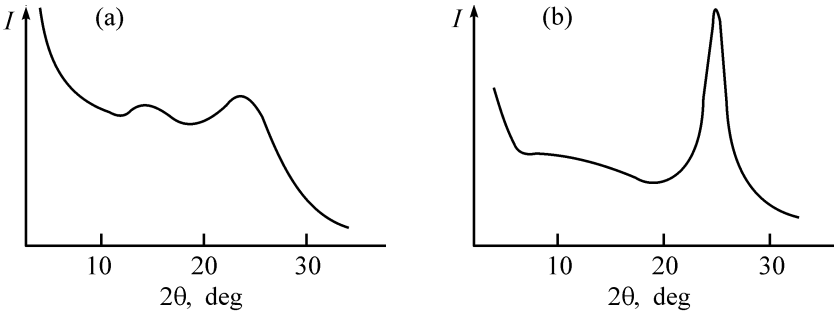


Fig. 4. Diffraction patterns of samples of (a) a-PAN and (b) 50 : 50 a-PAN–CNF composite, heated at 400°C for 3 h.

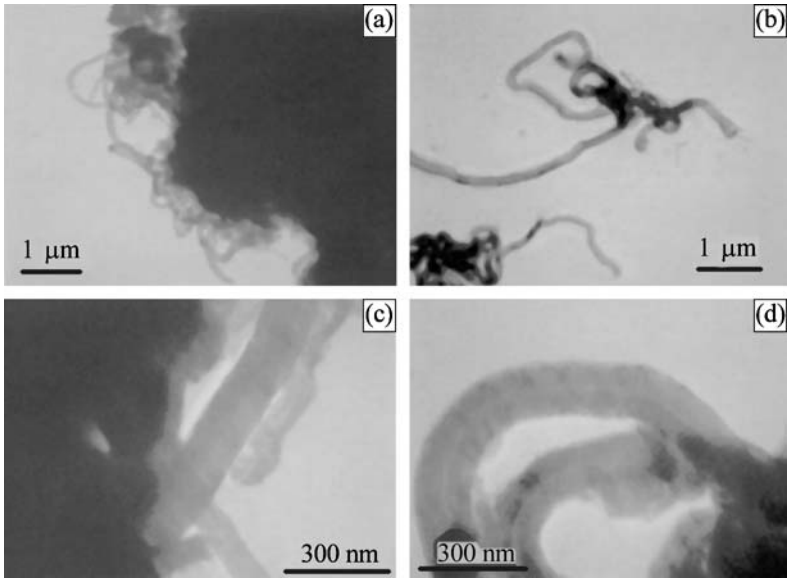


Fig. 5. Electron micrographs of CNFs at various magnifications.

sponds to the interplanar spacing d = 5.2 Å, and two weak broad reflections at 2θ = 25°30′ (d = 3.5 Å) and 29° (d = 3.1 Å), in agreement with the data reported in [17]. In the diffraction pattern of CNFs, there is a strong narrow reflection at 2θ = 26°15′ (d = 3.4 Å) corresponding to the graphite structure. In the diffraction pattern of the a-PAN–CNF blend in the initial state, there are narrow reflections at d = 5.2 Å, characteristic of a-PAN, and at d = 3.4 Å, characteristic of CNFs. That is, a superposition of the reflections of a-PAN and CNFs is observed, i.e., the composite is a mechanical blend of the components.

After heating straight a-PAN at 400°C for 3 h, the reflections characteristic of the initial a-PAN disappear (Fig. 4a), and only a weak halo at 2θ = 15° (d = 5.9 Å) is observed and a new reflection at 2θ = 25° (d = 3.55 Å) appears, which indicates that the crystal structure of the initial a-PAN is broken down and the turbostratic carbon structure is formed.

Heating of the 50 : 50 a-PAN–CNF composite at 400°C for 3 h also leads to the breakdown of the initial crystal structure of a-PAN. Only one reflection at 2θ = 26°15′ (d = 3.4 Å) remains in the X-ray diffraction pattern (Fig. 4b), and its angular width at the base is larger than that of the related CNF reflection in the unheated composite (Fig. 3c). This means that the reflection from the turbostratic carbon structure of heat-treated a-PAN overlaps with the CNF reflection.

Our results suggest the formation of ordered areas with the turbostratic carbon structure after the completion of cyclization of a-PAN and its composites, which undergo phase transitions in the range 400–550°C.

Figure 5 shows electron micrographs of carbon nanofibers used for preparing composites with a-PAN. It can be seen that the major part of the filler consists of nonfractionated nanofibers tightly linked in coarse agglomerates. A fragment of one of them is shown in Fig. 5a. Along with coarse (tens

of micrometers) agglomerates, there are also separate strongly twisted nanofibers forming submicrometer-sized globules (Fig. 5b).

An electron-microscopic examination of the agglomerates at various magnifications demonstrated that they are formed by nanofibers 60 to 150 nm thick (Figs. 5c, 5d). At larger magnifications, the fine structure of the nanofibers can be seen: a hollow channel along the nanofiber axis, 15 nm in diameter, and kinks resulting from bending [18] and suggesting high rigidity of the nanofibers (Fig. 5d). Thus, the nanofibers used in this study are hollow graphitic structures with developed surface area. It is known [19, 20] that such carbon nanofibers have high sorption capacity. Therefore, in the course of cyclization they can actively adsorb reaction products and hence shift the temperatures of cyclization peaks.

CONCLUSIONS

(1) The energy of cyclization of anionic polyacrylonitrile in a composite with carbon nanofibers is an order of magnitude lower than that of the straight polymer. Also, introduction of carbon nanofibers into anionic polyacrylonitrile decreases the cyclization temperature by 30°C.

(2) The turbostratic carbon structure is formed in anionic polyacrylonitrile and in the examined 50 : 50 composite of anionic polyacrylonitrile with carbon nanofibers in the initial step of carbonization.

REFERENCES

1. Fialkov, A.S., *Uglerod, mezhsloevye soedineniya i kompozity na ikh osnove* (Carbon and Intercalation Compounds and Composites on Its Basis), Moscow: Aspekt, 1997.
2. Perepelkin, K.E., *Khim. Volokna*, 2003, no. 6, pp. 3–8.
3. Sazanov, Yu.N. and Gribanov, A.V., *Zh. Prikl. Khim.*, 2006, vol. 79, no. 3, pp. 440–445.
4. Konkin, A.A., *Uglerodnye i drugie zharostoikie voloknistye materialy* (Carbon and Other Heat-Resistant Fibrous Materials), Moscow: Khimiya, 1974.
5. Kudryavtsev, G.I., *Armiruyushchie khimicheskie volokna dlya kompozitsionnykh materialov* (Reinforcing Chemical Fibers for Composite Materials), Moscow: Khimiya, 1992.
6. Varshavskii, V.Ya., *Vysokomol. Soedin., Ser. A*, 1983, vol. 25, no. 4, pp. 823–830.
7. Kubasova, N.A., Din' Suan Din', Geidrikh, M.A., and Shishkina, M.V., *Vysokomol. Soedin., Ser. A*, 1971, vol. 13, no. 1, pp. 162–167.
8. Spirina, T.N., Sazanov, Yu.N., Shibaev, L.A., et al., *J. Therm. Anal.*, 1990, vol. 36, pp. 2329–2338.
9. Novoselova, A.V., Zgonnik, V.N., Sazanov, Yu.N., et al., *Vysokomol. Soedin., Ser. A*, 1992, vol. 34, no. 3, pp. 59–63.
10. Jordan, J., Jacob, K., Tannenbaum, R., et al., *Mater. Sci. Eng.*, 2005, vol. 393A, pp. 1–11.
11. Rashkovan, I.A., Krasnov, A.P., Kazakov, M.E., et al., *Vopr. Materialoved.*, 2003, vol. 35, no. 3, pp. 58–64.
12. Neverov, V.M., Chvalun, S.N., Blackwell, J., et al., *Vysokomol. Soedin., Ser. A*, 2000, vol. 42, no. 3, pp. 450–461.
13. Zolotukhin, I.V., Golev, I.M., Markova, A.E., et al., *Pis'ma Zh. Tekh. Fiz.*, 2006, vol. 32, no. 5, pp. 28–32.
14. Sazanov, Yu.N., Mokeev, M.V., Novoselova, A.V., et al., *Zh. Prikl. Khim.*, 2003, vol. 76, no. 3, pp. 467–471.
15. Sazanov, Yu.N., Novoselova, A.V., Amsharov, K.Yu., et al., *Zh. Prikl. Khim.*, 2005, vol. 78, no. 5, pp. 810–813.
16. Takata, T. and Hiroi, I., *J. Polym. Sci. A*, 1964, vol. 2, pp. 1367–1385.
17. Martynov, M.A. and Vylegzhanina, K.A., *Rentgenografiya polimerov* (X-ray Diffraction Analysis of Polymers), Moscow: Khimiya. 1972.
18. Martin, D.C. and Thomas, E.L., *J. Mater. Sci.*, 1991, vol. 26, pp. 5171–5183.
19. Jae-Wook Lee, Hyun-Chul Kang, Wang-Geun Shim, et al., *J. Nanosci. Nanotechnol.*, 2006, vol. 6, no. 11, pp. 3577–3582.
20. Agrafonov, Yu.V., Petrushin, B.C., Prosekin, M.Yu., et al., *Izv. Ross. Akad. Nauk, Ser. Fiz.*, 2007, vol. 71, no. 2, pp. 186–188.

ISSN 1070-4272, Russian Journal of Applied Chemistry, 2008, Vol. 81, No. 6, pp. 1015–1018. © Pleiades Publishing, Ltd., 2008.
Original Russian Text © M.G. Veliev, M.I. Shatirova, N.Ya. Ishchenko, Z.N. Guseinova, A.I. Ibragimova, 2008, published in Zhurnal Prikladnoi Khimii, 2008, Vol. 81, No. 6, pp. 976–980.

MACROMOLECULAR CHEMISTRY AND POLYMERIC MATERIALS

Synthesis and Modification of ED-20 Epoxy–4,4'-Isopropylidenediphenol Resin with Highly Unsaturated Esters

M. G. Veliev, M. I. Shatirova, N. Ya. Ishchenko, Z. N. Guseinova, and A. I. Ibragimova

Institute of Polymeric Materials, National Academy of Sciences of Azerbaijan, Sumgaiyt, Azerbaijan

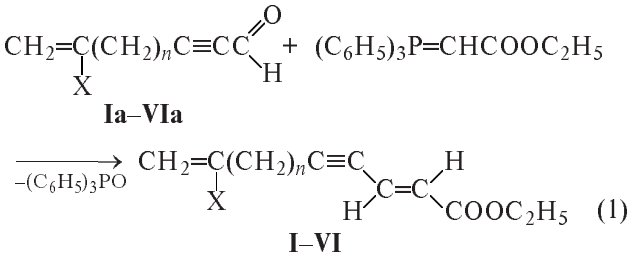
Received August 13, 2007

Abstract—Esters of the dienyne series with a *trans*-ethylene bond were prepared in 70–80% yield by reactions of enyne aldehydes with ethoxycarbonylmethylenetriphenylphosphorane. The compounds were studied by IR and ^{1}H NMR spectroscopy, and their modifying effect on ED-20 epoxy–4,4'-isopropylidenediphenol resin was revealed.

DOI: 10.1134/S1070427208060177

Highly unsaturated compounds containing double and triple bonds (enynes, diynes, enediynes, dienynes) offer vast synthetic possibilities for preparing various carbocyclic, heterocyclic, and polyunsaturated structures that are fragments of molecules many natural biologically active substances [1–7]. Diyne and dienyne derivatives isolated from plants and microorganisms exhibit strong fungicidal, antimicrobial, and insecticidal effects [8, 9]. Among highly unsaturated functional compounds, including esters, there are also modifiers of various polymeric materials [10–14].

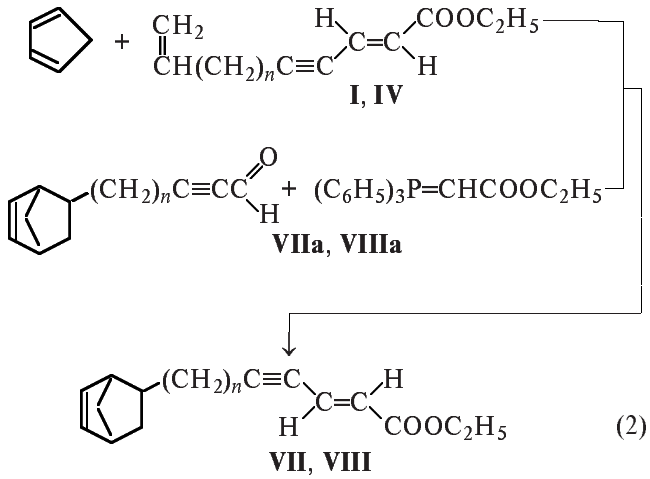
Proceeding with the search for new highly unsaturated compounds of the dienyne series as high-performance modifiers for polymers, we prepared in this study new dienyne esters and examined their modifying properties. We found that esters **I**–**VI** are formed in 65–75% yield by condensation of unsaturated aldehydes with ethoxycarbonylmethylenetriphenylphosphorane in 1 : 2 molar ratio for 6 h in benzene in a nitrogen stream [scheme (1)]:



Ia–**VIa** **I**–**VI** (1)

where n = 0, X = H (**Ia**, **I**), CH_3 (**IIa**, **II**), Cl (**IIIa**, **III**); n = 1, X = H (**IVa**, **IV**), CH_3 (**Va**, **V**), Cl (**VIa**, **VI**).

We found that the dienyne esters prepared are very reactive. In particular, they enter into the Diels–Alder reaction with cyclopentadiene (CPD) at 155–160°C through the terminal double bond to form within 8 h the corresponding norbornene esters **VII** and **VIII**. Esters **VII** and **VIII** were also prepared by an independent route, reaction of appropriate norbornene-substituted aldehydes with ethoxycarbonylmethylenetriphenylphosphorane [scheme (2)].



I, **IV**

VIIa, **VIIIa**

VII, **VIII** (2)

where n = 0 (**VII**), 1 (**VIII**).

Table 1. Characteristics of esters **I–VIII**

Ester	Yield, %	T_b, °C (P, mm Hg)	n_D^{20}	d_4^{20}	Found, %/Calculated, %			Formula
					C	H	Cl	
I	78.2	74–75 (3)	1.5074	1.0211	71.82/71.98	6.88/6.71	–/–	$C_9H_{10}O_2$
II	81.4	82–83 (2)	1.5103	1.0161	73.26/73.14	7.29/7.37	–/–	$C_{10}H_{12}O_2$
III	70.9	88–89 (2)	1.5248	1.1658	58.41/58.55	4.83/4.91	19.36/19.20	$C_9H_9ClO_2$
IV	62.0	85–86 (4)	1.4910	1.0196	73.29/73.14	7.46/7.37	–/–	$C_{10}H_{12}O_2$
V	73.4	90–91 (3)	1.4980	1.0062	74.07/74.13	7.80/7.92	–/–	$C_{11}H_{14}O_2$
VI	60.0	95–96 (2)	1.5140	1.1533	60.58/60.46	5.43/5.58	17.97/17.85	$C_{10}H_{11}ClO_2$
VII	55.1	98–99 (3)	1.5410	1.0862	77.87/77.74	7.32/7.46	–/–	$C_{14}H_{16}O_2$
VIII	63.2	106–107 (3)	1.5260	1.0710	78.39/78.23	7.75/7.88	–/–	$C_{15}H_{18}O_2$

The physicochemical characteristics of esters **I–VIII** are listed in Table 1. The compositions and structures of **I–VIII** were confirmed by GLC, TLC, and IR and ^{1}H NMR spectroscopy (Table 2) [15].

EXPERIMENTAL

The IR spectra were recorded on a UR-20 spectrophotometer in the range 400–4000 cm^{-1} from thin films. The ^{1}H NMR spectra were measured on a Tesla BS-487B spectrometer (80 MHz) from CCl_4 solutions, internal reference HMDS. The purity of the products was confirmed by TLC on Silufol UV-254 plates, using various solvent systems.

The heat resistance of epoxy compounds was examined by thermal analysis on a Q-1500D derivatograph (MOM, Hungary). All tests were performed in air with 200-mg samples at a heating rate of 5 deg min^{-1}.

The starting unsaturated aldehydes **Ia–VIIIa** were prepared by oxidation of the corresponding primary alcohols with a mixture of aqueous sulfuric acid with chromic anhydride [16–19].

Ethyl hepta-2,6-dien-4-ynoate I. A solution of 2 g (0.025 mol) of pent-4-en-2-ynal in 50 ml of benzene was added to a solution of 17.4 g (0.05 mol) of ethoxycarbonylmethylenetriphenylphosphorane in 100 ml of benzene. The mixture was refluxed in a nitrogen atmosphere for 6 h. Then, benzene was distilled off, the residue was treated with petroleum ether, the undissolved residue of triphenylphosphine oxide was filtered off, and the solvent was distilled off. The residue was distilled in a vacuum to obtain compound **I**.

Compounds **II–VI** were prepared similarly from the corresponding aldehydes.

Ethyl 5-(norborn-2-en-5-yl)pent-2-en-4-ynoate VII. A mixture of 1.7 g (0.025 mol) of cyclopentadiene and 3.7 g (0.025 mol) of **I** was heated for 8 h at 150–160°C in a sealed ampule in the presence of 0.05 g of hydroquinone. After the reaction completion, the mixture was subjected to fractional distillation in a vacuum. After distillation of the unchanged starting compounds, adduct **VII** was isolated.

Compound **VIII** was prepared similarly from **IV**.

Independent synthesis of VII and VIII. Adducts **VII** and **VIII** were prepared as described above for **I**, from 0.05 mol of ethoxycarbonylmethylenetriphenylphosphorane and 0.025 mol of the corresponding bicyclic aldehyde.

Table 2. ^{1}H NMR and IR spectra of **I–VIII**

Compound	^{1}H NMR spectrum, δ, ppm	IR spectrum, ν, cm^{-1}
I	4.80–5.38 m (2H, CH_2=C), 5.43–5.85 m (1H, C=CH), 6.30 d.d (1H, CH=C, *J* = 14.2 Hz), 5.95 d (1H, C=CH, *J* = 14.2 Hz), 3.75 d.d (2H, CH_2, *J* = 6.7 Hz); 1.27 t (3H, CH_3, *J* = 7.2 Hz)	2200, 1725, 1645, 1600, 1180, 960 730
II	4.73 c, 4.90 s (2H, CH_2=C); 1.75 s (3H, CH_3); 6.25 d.d (1H, CH=C, *J* = 6.3 Hz); 1.30 t (3H, CH_3, *J* = 7.1 Hz) *J* = 14.6 Hz); 5.85 d (1H, C=CH, *J* = 14.6 Hz); 3.68 d.d (2H, CH_2,	2215, 1720, 1640, 1605, 1175, 965, 725
III	5.20 c, 5.60 s (2H, CH_2=C); 6.23 d.d (1H, CH=C, *J* = 14.1 Hz); 5.87 d (1H, C=CH, *J* = 14.1 Hz); 3.72 d.d (2H, CH_2, *J* = 6.6 Hz); 1.32 t (3H, CH_3, *J* = 7.0 Hz)	2230, 1715, 1646, 1610, 1185, 960, 726, 650
IV	4.76–5.30 m (2H, CH_2=C), 5.45–5.86 m (1H, C=CH), 2.86–3.05 m (2H, CH_2); 6.27 d.t (1H, CH=C, *J* = 14.3 Hz), 6.00 d.t (1H, C=CH, *J* = 14.3 Hz), 3.80 d.d (2H, CH_2, *J* = 6.8 Hz), 1.30 t (3H, CH_3, *J* = 7.0 Hz)	2225, 1718, 1643, 1600, 1186, 963, 728
V	4.70 c, 4.80 s (2H, CH_2=C); 1.72 s (3H, CH_3); 2.86 s (2H, CH_2); 6.27 d.t (1H, CH=C, *J* = 14.4 Hz); 5.86 d.t (1H, C=CH, *J* = 14.4 Hz); 3.85 d.d (2H, CH2, *J* = 6.5 Hz); 1.31 t (3H, CH_3, *J* = 7.2 Hz)	2210, 1720, 1645, 1600, 1175, 960, 731
VI	5.23 c, 5.65 s (2H, CH_2=C); 3.00 s (2H, CH_2); 6.28 d.t (1H, CH=C, *J* = 14.8 Hz); 5.88 d.t (1H, C=CH, *J* = 14.8 Hz); 3.64 d.d (2H, CH_2, *J* = 6.7 Hz); 1.28 t (3H, CH_3, *J* = 7.0 Hz)	2235, 1710, 1650, 1610, 1200, 965, 730, 700
VII	2.60–2.95 m (2H, CH, CH, at the head of the bridge), 5.80–6.15 m (2H, CH=CH, ring), 2.10 m (1H, CH, ring), 0.60 m (1H, CH_{endo}), 1.80 m (1H, CH_{exo}), 1.15–1.50 m (2H, CH_2, in bridge), 6.25 d.t (1H, CH=C, *J* = 14.4 Hz), 5.80 d.t (1H, C=CH, *J* = 14.4 Hz), 3.58 d.d (2H, CH_2 *J* = 6.6 Hz), 1.30 t (3H, CH_3, *J* = 7.1 Hz)	2230, 1715, 1645, 1605, 1195, 960, 726
VIII	2.63–2.92 m (2H, CH, CH,at the head of the bridge), 5.76–6.12 m (2H, CH=CH, ring), 2.08 m (1H, CH, ring), 0.56 m (1H, CH_{endo}), 1.84 m (1H, CH_{exo}), 1.17–1.52 m (2H, CH_2, in bridge), 1.54–1.90 m (2H, CH_2), 6.30 d.t (1H, CH=C, *J* = 14.2 Hz), 5.86 d.t (1H, C=CH, *J* = 14.2 Hz), 3.45 d.d (2H, CH_2 *J* = 6.8 Hz), 1.27 t (3H, CH_3, *J* = 7.2 Hz)	2225, 1720, 1640, 1600, 1190, 963, 730

Table 3. Thermal parameters of compounds based on ED-20 resin modified with acetylenic esters **I**, **II**, and **IV–VI** (ester : resin proportion 20 : 100 by weight)

Modifier	Activation energy of thermal oxidative degradation, kJ mol^{-1}	Half-life $\tau^{1/2}$, min	Thermogravimetric index, °C
I	205	60	117
II	200.3	56.4	119
IV	194.92	62	119
V	237	64	133
VI	202.7	57.2	121
None	190.5	59.8	120

Compounds **I–VI** were tested as modifiers for ED-20 epoxy–4,4'-isopropylidenediphenol resin, and compounds **I**, **III**, and **V**, as modifiers for granulated low-density polyethylene (LDPE) of 15803-020 grade.

As investigation objects we prepared compounds from ED-20 resin, polyethylenepolyamine (PEPA) curing agent taken in a stoichiometric ratio, and modifying additives **I–VI**. The weight proportion of the modifier to ED-20 was varied from 10 : 100 to 30 : 100. Along with examining the modifying properties, we also attempted to reveal a correlation between the structure of **I–VI** and their modifying effect on the epoxy compound (Table 3).

The effect of modifier on the thermal properties of the epoxy compound can be readily monitored by variation of the activation energy of degradation

Table 4. Physicomechanical parameters of modified polyethylene

Modifier	Ultimate tensile strength σ, MPa	Relative elongation ε, %	MFI, g/10 min
I	123	615	5.8
III	135	630	6.5
V	120	610	8.0
None	115	600	4.5

and the thermogravimetric index of the compound (measurement accuracy ±2–3°C, Table 3). The modifier also appreciably affects the heat resistance of cured epoxy compounds (measurement accuracy ±2°C).

Table 3 shows that replacement of the hydrogen atom (**I**, **IV**) by the methyl group (**II**, **V**) enhances the thermal parameters of the epoxy compounds, with the highest values attained with **V**. Replacement of the hydrogen atom by chlorine in **VI** affects the heat resistance of the epoxy compound insignificantly.

It should also be noted that the modifier structure does not affect the course of curing of the epoxy compound. In all the cases, curing occurs in the range 70–120°C, as indicated by exothermic peaks of curing, manifested in the DTA curve.

The effect of modifiers on the thermal properties of cured compounds was evaluated from the thermograms.

To examine the effect of **I**, **III**, and **V** on the physicomechanical properties of polyethylene, we prepared polymer compounds. The processing was in two steps: (1) compounding (polyethylene : monomer = 100 : 3 by weight) on rollers at 120–125°C for 10–15 min and (2) compaction on a hydraulic press at 170°C. We determined the physicomechanical properties of the films obtained (1 mm thick) and the melt flow index (MFI) of the compounds, as MFI is one of the most important parameters for processing. The results are listed in Table 4.

As can be seen from Table 4, ester **III** is the most efficient as modifier: it enhances the physicomechanical parameters and improves the processability (MFI) of the PE compound.

CONCLUSIONS

(1) Esters of the dienyne series were prepared by adding a benzene solution of unsaturated aldehyde to ethoxycarbonylmethylenetriphenylphosphorane at 80–85°C in a nitrogen atmosphere. The ester molecules contain a trans-ethylene bond.

(2) It was shown that dienyne esters can act as modifiers for an epoxy resin (ED-20) and polyethylene. They enhance the physicomechanical and thermal parameters and improve the processability of polyethylene compounds.

REFERENCES

1. Kusumi, T., Ohtani, I., Nishiyama, K., and Kakisawa, H., *Tetrahedron Lett.*, 1987, vol. 28, no. 34, pp. 3981–3984.
2. Kende, A.S. and Smith, C.A., *Tetrahedron Lett.*, 1988, vol. 29, no. 34, pp. 4217–4220.
3. Veliev, M.G., Chalabiev, Ch.A., Mustafaev, A.N., and Mamedov, I.M., *Zh. Org. Khim.*, 1995, vol. 31, no. 1, pp. 58–63.
4. Falck, J.R., Manna, S., Vials, J., et al., *Tetrahedron Lett.*, 1985, vol. 26, no. 19, pp. 2287–2290.
5. Avedissian, H., Sinha, S.C., Yazbak, A., et al., *J. Org. Chem.*, 2000, vol. 65, no. 19, pp. 6035–6037.
6. Veliev, M.G. and Atakishieva, Ya.Yu., *Izv. Nats. Akad. Nauk Azerb., Biol. Nauki*, 2005, nos. 5–6, pp. 186–201.
7. Salmanov, M.A., Veliev, M.G., and Muradov, P.Z., *Izv. Nats. Akad. Nauk Azerb., Biol. Nauki*, 2004, nos. 3–4, pp. 142–149.
8. Maretina, I.A. and Trofimov, B.A., *Usp. Khim.*, 2006, vol. 75, no. 9, pp. 913–935.
9. Miftakhov, M.S., Adler, M.E., Akbutina, F.A., and Tolstikov, G.A., *Usp. Khim.*, 1994, vol. 63, no. 6, pp. 543–555.
10. Chernin, I.Z., Smekhov, F.L., and Zherdev, Yu.V., *Epoksidnye polimery i kompozitsii* (Epoxy Polymers and Compounds), Moscow: Khimiya, 1982.
11. Sokolova, Yu.A. and Gotlib, E.M., *Modifitsirovannye epoksidnye klei i pokrytiya v stroitel'stve* (Modified Epoxy Adhesives and Coatings in Building), Moscow: Stroiizdat, 1990.
12. Kardashov, D.A. and Petrova, A.P., *Polimernye klei* (Polymeric Adhesives), Moscow: Khimiya, 1983.
13. Il'chenko, A.Ya., Kolotilo, N.V., and Radchenko, O.A., *Ukr. Khim. Zh.*, 1989, vol. 55, no. 9, pp. 955–966.
14. Veliev, M.G., Chalabieva, A.Z., Ishchenko, N.Ya., and Askerov, O.V., *Plast. Massy*, 2005, no. 10, pp. 24–25.
15. Silverstein, R.M., Bassler, G.C., and Morrill, T.C., *Spectrometric Identification of Organic Compounds*, New York: Wiley, 1974.
16. USSR Inventor's Certificate, no. 666162.
17. Veliev, M.G. and Guseinov, M.M., *Synthesis*, 1980, no. 6, p. 461.
18. Shatirova, M.I., Synthesis and Properties of 2-Chloro(Bromo)-Substituted Allylacetylenic Alcohols, *Cand. Sci. Dissertation*, Baku, 1999.
19. Veliev, M.G., Shatirova, M.I., Niyazova, N.K., et al., *Azerb. Khim. Zh.*, 2002, no. 4, pp. 88–91.

ISSN 1070-4272, Russian Journal of Applied Chemistry, 2008, Vol. 81, No. 6, pp. 1019–1022. © Pleiades Publishing, Ltd., 2008.
Original Russian Text © V.V. Bestuzheva, S.A. Dushenok, F.A. Zheltikov, A.N. Lysov, 2008, published in Zhurnal Prikladnoi Khimii, 2008, Vol. 81, No. 6, pp. 981–984.

MACROMOLECULAR CHEMISTRY AND POLYMERIC MATERIALS

Plasticized Polyurethanes

V. V. Bestuzheva, S. A. Dushenok, F. A. Zheltikov, and A. N. Lysov

SKTB Tekhnolog (Special Engineering and Design Department) Federal State Unitary Enterprise, St. Petersburg, Russia

Received October 17, 2007

Abstract—Polyurethane formulations containing 10 to 75% tris(azidomethyl)nitromethane as a plasticizer were synthesized.

DOI: 10.1134/S1070427208060189

Plasticizing additives are widely used in practice of synthesis and processing of polyurethanes to improve the rheological properties of the reaction mass and raise the elasticity of the cured material. As a rule, polyurethanes have a complex 3*D* structure produced not only by chemical cross-links, but also by strong physical interactions via hydrogen bonds. To organic liquids used in the polymer technology belong compounds of three kinds: (i) comparatively indifferent substances, causing no profound changes in the polymer structure (dibutyl and dioctyl phthalate, dioctyl sebacate); (ii) those partly decross-linking the polymer matrix (toluene, cyclohexanone); and substances that can, under certain conditions, completely disintegrate the network of both hydrogen and chemical bonds (tetrahydrofuran and aprotic compounds: dimethyl sulfoxide, dimethyl formamide, and dimethyl acetamide).

However, the effect of each of the plasticizers even on polyurethanes with the same oligomeric base can be widely varied by changing the type and concentration of a diisocyanate and a cross-linking agent involved in the reaction. The ability of polyurethanes to widely vary their properties with synthesis conditions and structure and relative amounts of the starting reagents is a consequence of their pronounced tendency toward cross-linking; conformation transitions; change in the geometric, thermodynamic, and kinetic parameters; and combination of strongly ordered crystalline and disordered amorphous microscopic regions in the same macroscopic space. This opens up opportunities for their use in directed synthesis of products that are modified with a prescribed plasticizer and have required physicomechanical properties.

A particular place among the widely diverse functions of polyurethanes is occupied by their use as combustible binders for energetic condensed systems. One of the most serious problems to be solved when using polyurethanes in systems of this kind is that their efficiency should be improved [1]. This can be done by introducing placticizers with high enthalpy of formation and density, e.g., nitro, nitrato, and azido compounds [2, 3], into polyurethane binders.

The aim of our study was to examine the preparation conditions and determine the main characteristics of thermodynamically stable and mechanically strong polyurethane formulations that are placticized with the maximum possible amount of tris(azidomethyl)nitromethane, and can be used as binders in energetic condensed systems (ECS).

EXPERIMENTAL

We tested as a hydroxyl-containing component intended to form the hydrocarbon backbone of the polyurethane elastomer the P6-BA polyester, oligoethylene butylene glycol adipinate according to TU (Technical specification) 38-103-288–78, described by the formula

$$HO\left[(CH_2)_2OCO-(CH_2)_4-COO(CH_2)_4-OCO-(CH_2)_4-COO(CH_2)_2\right]_5OH.$$

Table 1. Effect of the plasticizer content on the properties of polyurethanes

Plasticizer content, %	σ_t, MPa	ε_{te}, %	γ, kg m^{-3}	ΔH, kJ kg^{-1}
0	12.00	160	1200	–4070
10	4.05	250	1215	–3310
20	2.80	290	1230	–2554
30	1.75	350	1245	–1796
40	1.10	435	1260	–1038
50	0.70	535	1280	280
60	0.40	630	1295	478
70	0.25	750	1315	1236
75	0.20	820	1320	1615

The choice of P6-BA is justified by its wide use in domestic industry and the high level of physicomechanical parameters of polymers produced on its base. The polyester we used had a molecular mass of 2000, density γ = 1200 kg m^{-3}, and enthalpy of formation ΔH = –4300 kJ kg^{-1}.

We used the following distillation-purified coreagents in urethane formation reactions: aliphatic hexamethylene diisocyanate (HMDI) $OCN(CH_2)_6NCO$, aromatic 2,4-toluylene diisocyanate (TDI) $CH_3C_6H_3(NCO)_2$, and alkyl aromatic 4,4'-methylene bisphenyl diisocyanate (MDI) $CH_2(C_6H_4NCO)_2$.

Because the starting polyester and diisocyanates are bifunctional, their interaction yields linear polymers that can be destructively affected by organic liquids, including the chosen plasticizer. To form a strong macromolecular matrix capable of retaining the maximum volume of a plasticizer, with a high level of physicomechanical properties preserved, the reaction of polyurethane synthesis was performed in the presence of trifunctional hydroxyl-containing substances providing formation of cross-links. Preliminarily dried (over phosphorus pentoxide) triols: glycerol $HOCH_2CHOHCH_2OH$ and trimethyl propane (TMP) $C_2H_5(CH_2OH)_3$, served as cross-linking substances, and tin dibutyl dilaurinate, as a catalyst (TU 6-02-818–73).

We studied as a plasticizer a compound having experimental-industrial resources of raw materials, tris(azidomethyl)nitromethane $(N_3CH_2)_3$–C–NO_2, conforming to TU 08015232–89 (SKTB Tekhnolog). The product is chemically and thermally compatible with other components, has low glass transition temperature, low viscosity, and low volatility, which predetermines its importance in assessment of this compound as a component of energy-saturated systems. We used the substance upon its chromatographic purification with activated carbon of OU A brand. The product had the following parameters: refractive index at 20°C 1.5255, density 1367 kg m^{-3}, bp 90°C at 0.04 mm Hg, flash point at a 5-s delay 240°C, onset temperature of intense decomposition 212°C (according to DTA), and calculated enthalpy of formation 3510 kJ kg^{-1} [4].

Plasticized polyurethanes were synthesized in a vacuum installation with a heated reactor and high-speed stirrer. Moisture and air inclusions, which can cause defect formation in cured samples, were removed from the polyester at 110°C and a residual pressure of 1 mm Hg. The weighed portion was cooled to 60°C and required amounts of a diisocyanate, triol, and catalyst were introduced. After the ingredients were mixed, a plasticizer was added and the mixture was kept under the same conditions for 15–20 min. The final curing was performed in hermetically sealed fluoroplastic molds at 60 ± 2°C.

The tensile strength of a cured polymer suitable as a binder for ECS should be no less than 0.1 MPa, and the relative tensile elongation, ≥700%. The enthalpy of formation and the density, which characterize the energetic efficiency of a polyurethane, grow as the concentration of tris(azidomethyl)nitromethane in the polyurethane increases. Consequently, the goal of our study was to carry out a directed synthesis of formulations that can withstand, at the maximum content of the plasticizer, an irreversible deformation at sufficiently high chemical, thermal, and mechanical loads.

To achieve such a result, we had to determine the component and concentration composition of the polymeric part of elastomers at which an as strong as possible 3*D*-cross-linked skeleton capable of retaining the maximum amount of the azide plasticizer would be formed. To assess the influence exerted by the introduced amount of tris(azidomethyl)nitromethane on the tensile strength σ_t (MPa), relative tensile elongation ε_{te} (%), enthalpy of formation ΔH (kJ kg^{-1}), and density γ (kg m^{-3}) of plasticized polyurethane, we obtained elastomers containing P6-BA polyester and hexamethylene diisocyanate at a 1.0 : 1.1 ratio between hydroxy and isocyanate groups. As a cross-linking substance was introduced trimethylol propane whose mole fraction in the reaction mixture was 0.3. As a catalyst served tin dibutyl dilaurinate , taken in an amount of 0.03% relative to the mass of the polymeric component. The physicomechanical parameters and the density were found in accordance with OST (All-Union Standard) V-84-434–71

Table 2. Influence exerted by the ratio between the reaction groups on the physicomechanical parameters of TDI-based polyurethane (plasticizer content 75%, mole fraction of trimethylol propane 0.30)

OH : NCO ratio	σ_t, MPa	ε_{te}, %
1.0 : 1.0	0.20	820
1.0 : 1.1	0.25	860
1.0 : 1.2	0.25	860
1.0 : 1.25	0.25	850
1.0 : 1.3	0.30	850

Table 3. Influence exerted by the mole fraction of glycerol on the physicomechanical parameters of TDI-based polyurethane (plasticizer content 75%, OH : NCO = 1.0 : 1.1)

Mole fraction of triol	Σ_t, MPa	ε_{te}, %
0.20	0.20	810
0.25	0.20	840
0.30	0.25	860
0.35	0.25	880
0.40	0.35	880

and GOST (State Standard) 267–73, respectively; the enthalpy of formation was calculated. The results obtained are listed in Table 1.

Combined with a diol and a triol, hexamethylene diisocyanate provides formation of chemical cross-links yielding a polymer matrix that can retain up to 75% low-viscosity fluid in the cured material without phase stratification. As can be seen from the data presented, raising the concentration of a plasticizer in the formulation of a polyurethane being synthesized results in that its strength steadily decreases as the elasticity, density, and enthalpy of formation become higher. This type of behavior is preserved when hexamethylene diisocyanate is replaced with toluylene diisocyanate or 4,4'-methylene bisphenyl diisocyanate, even though the strength parameters are somewhat higher upon such a replacement, and the elasticity is slightly lower (Figs. 1, 2). This is accounted for by the limited possible rotation of aromatic rings and the resulting increase in the rigidity of polymer chains.

Among the polyurethanes synthesized and tested, of particular interest, as regards the whole set of its energy-related (ΔH = 1625 kJ kg^{-1}, γ = 1320 kg m^{-3}) and physicomechanical parameters (σ_t = 0.25 MPa, ε_{te} = 860%), is the sample based on toluylene diisocyanate, with a plasticizer content of 75%. We studied the possibility of improving its properties by varying the content of the diisocyanate and the type and amount of the cross-linking substance. The data characterizing the role played by the ratio of the reaction groups involved in the reaction of the diisocyanate and oligoester are listed in Table 2.

It can be seen that, by lowering the amount of the diisocyanate to the stoichiometric value or raising it to a 30% excess, the strength of the polyurethane can be varied within ±20%. In this case, the elasticity remains nearly unchanged. Presumably, the increase in the diisocyanate content favors a fuller completion of the reaction. However, this does not improve the physicomechanical properties to any noticeable extent.

If we take glycerol as a cross-linking substance, instead of trimethylol propane, the parameters of polyurethane remain the same within the determination error. The effect of the ratio between the diol (P6-BA) and triol (glycerol) components in the polyurethane structure is illustrated by the data in Table 3.

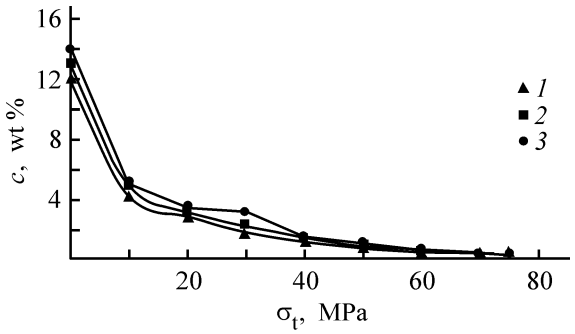


Fig. 1. Dependence of the tensile strength σ_t on the plasticizer content c for polyurethanes based on (*1*) HMDI, (*2*) TDI, and (*3*) MDI. OH : NCO = 1 : 1.1 mole fraction of TMP 0.30; the same for Fig. 2.

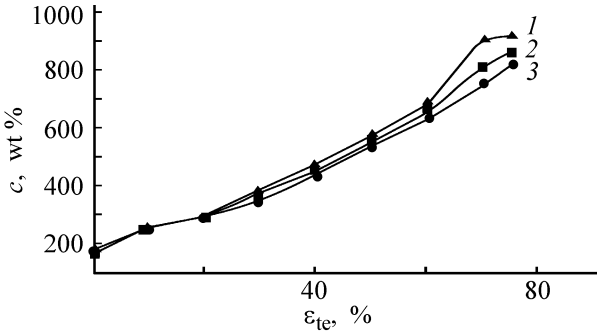


Fig. 2. Dependence of the relative tensile elongation ε_{te} on the plasticizer content c for polyurethanes based on (*1*) HMDI, (*2*) TDI, and (*3*) MDI.

As follows from the results obtained, the increased content of the trifunctional component makes higher the density of cross-linking of the material and thereby provides a certain improvement of the strength and elasticity of the polymers, all other conditions being the same.

The impact sensitivity of cured polyurethanes (according to GOST 4545–80) is 20–30%, and the friction sensitivity (GOST 50835–95), is not lower than 300 MPa. The onset temperature of intense decomposition, found by differential-thermal analysis on a Vulkan measuring-and-computing complex, is 210°C. Thus, the values of the main energy-related and performance parameters of the plasticized polymers obtained suggest that their use in energetic condensed systems is advisable.

CONCLUSIONS

(1) Polyurethanes plasticized with 10–75% tris(azidomethyl)nitromethane were obtained in a single technological cycle via directed formation of a 3*D* network (by varying the content of the plasticizer introduced and choosing the nature and concentration of a diisocyanate and a triol).

(2) It was shown that the cured elastomers have a tensile strength of 0.2–4.0 MPa, relative tensile elongation of 200–800%, and high enthalpies of formation (up to 1615 kJ kg^{-1}).

(3) It was demonstrated that the high-strength elastic polyurethane matrix provides the set of physicomechanical parameters, required for energetic condensed systems, and use of an azido-containing plasticizer leads to an increased density and enthalpy of formation, which makes the polyurethanes synthesized promising binders for energetic condensed formulations.

REFERENCES

1. Rogov, N.G. and Ishchenko, M.A., *Smesevye tverdye raketnye topliva* (Mixed Solid Rocket Propellants), St. Petersburg: Firma Kosta, 2005.
2. Tselinskii, I.V., Bestuzheva, V.V., Nalimova, N.K., and Skirdova, G.V., *Zh. Prikl. Khim.*, vol. 74, no. 11, 2000, pp. 2057–2060.
3. Tselinskii, I.V., Bestuzheva, V.V., and Nalimova, N.K., *Zh. Prikl. Khim.*, vol. 74, no. 9. 2001, pp. 1505–1507.
4. Ou Yuxiang and Chen Boren, *J. Propul. Power*, vol. 11, no. 4. 1995, pp. 838–847.

ISSN 1070-4272, Russian Journal of Applied Chemistry, 2008, Vol. 81, No. 6, pp. 1023–1026. © Pleiades Publishing, Ltd., 2008.
Original Russian Text © N.I. Kurbanova, N.Ya. Ishchenko, A.M. Kuliev, 2008, published in Zhurnal Prikladnoi Khimii, 2008, Vol. 81, No. 6, pp. 985–988.

MACROMOLECULAR CHEMISTRY AND POLYMERIC MATERIALS

Preparation of Modified Polyisoprene with a High Adhesion Strength

N. I. Kurbanova, N. Ya. Ishchenko, and A. M. Kuliev

Institute of Polymeric Materials, National Academy of Sciences of Azerbaijan, Sumgaiyt, Azerbaijan

Received November 2, 2007

Abstract—Modification of polyisoprene with trichloroacetic acid was studied, and the strength, adhesion, and thermal properties of vulcanizates obtained from the modified polyisoprene were determined.

DOI: 10.1134/S1070427208060190

One of efficient methods for preparing polymers with improved properties is chemical modification usually consisting in treatment of an already formed polymer molecule with a low-molecular-weight reagent. The most widely used modification route is introduction of functional groups into a polymer chain by addition or substitution reactions [1–4].

Introduction of functional groups into a polymer macromolecule affects its properties. This can be seen, e.g., from comparison of the properties of commercial synthetic isoprene rubber SKI-3 with those of semicommercial carboxylate isoprene rubber SKI-3K [5]. Rubber stocks based on SKI-3 exhibit decreased cohesion strength, and their vulcanizates show poor adhesion to metal surfaces, whereas SKI-3K is characterized by high strength of rubber stocks and high adhesion of vulcanizates to metals.

A known method for improving the SKI properties is modification by introduction of functional groups and, in particular, carboxy and hydroxy groups or chlorine atoms [5–7].

Previously, we have examined the modification of unsaturated elastomers with chloroacetic acids and their derivatives. Their introduction into rubber macromolecules noticeably improved the physicomechanical parameters of vulcanizates, such as the tensile, tear, and adhesion strength [8].

The goal of this study was to prepare modified SKI with improved physicomechanical properties, high adhesion, and high heat resistance by modification of rubber with trichloroacetic acid (TCAA).

EXPERIMENTAL

As object of study we used SKI-3 rubber with 96 mol % unsaturation and Mooney viscosity of 61 min (100°C); the modifier was TCAA (mp 58.7°C), and the initiator, benzoyl peroxide (BP).

To perform SKI modification, a 0.25-l flask equipped with a stirrer, reflux condenser, and dropping funnel was charged with a 2-g portion of rubber. The rubber was dissolved in 125 ml of benzene, and 5–10 wt % of the modifier (relative to rubber) was added. Then the initiator (0.1–1.0 wt % relative to rubber) was added, and the reaction was performed at 60–80°C for 1 h. In the process, 1-ml samples were taken at 5-min intervals, the rubber was precipitated with methanol, and the reaction mixture was analyzed for the residual modifier content. The precipitated rubber was washed with methanol and dried in a vacuum desiccator at room temperature.

The IR spectra were recorded on a UR-20 spectrophotometer. Samples were prepared as films on NaCl plates by complete evaporation of the solvent from 3% solutions of the rubber in benzene. The chlorine content and unsaturation were determined using the procedure described in [9].

The modification kinetics was studied at 60–80°C on a pH-673 device equipped with an electrode pair: a glass indicator electrode and an immersed silver chloride reference electrode. The content of the unchanged modifier was determined using a calibration plot.

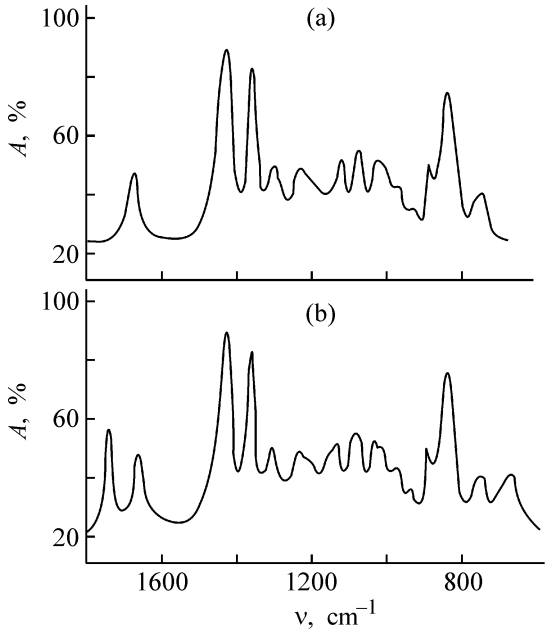


Fig. 1. IR spectra of (a) initial SKI and (b) SKI modified with trichloroacetic acid. (*A*) Absorption and (ν) wavenumber.

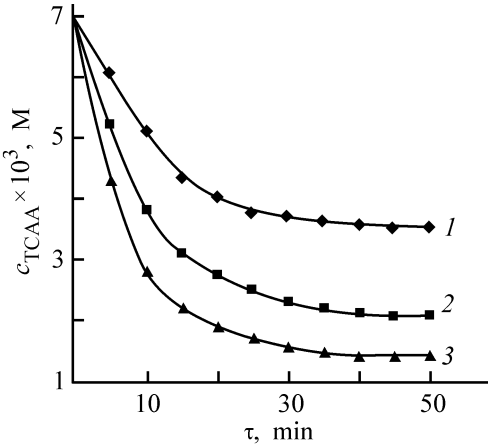


Fig. 2. Kinetic curves of trichloroacetic acid consumption in modification of polyisoprene in benzene in the presence of benzoyl peroxide at 60–80°C. Initial concentrations: $c_{BP} = 0.5 \times 10^{-4}$, $c_{TCAA} = 7 \times 10^{-3}$ M. (τ) Time. *T*, °C: (*1*) 60, (*2*) 70, and (*3*) 80.

Rubber stocks based on the modified SKI sample were prepared with standard formulations used for the straight SKI rubber. The compounding was performed on laboratory rolls whose temperature did not exceed 80°C. The vulcanization was carried out at 143°C for 25 min.

The physicomechanical tests were made on an RMI-250 tensile-testing machine at room temperature.

Derivatographic studies of vulcanizates were performed in air in the dynamic mode at a heating rate of 5 deg min^{-1} (sample weight 100 mg; sensitivities: DTA 250 μV, TG 100, DTG 1 mV) on a Q-1500D derivatograph (MOM, Hungary). The weight loss and half-life $\tau_{1/2}$ of the rubber sample on heating from 20 to 500°C were determined.

Figure 1 shows the IR spectra of the initial and modified SKI samples. Analysis of the IR spectra shows that all the absorption bands characteristic of the initial rubber are clearly pronounced in the spectrum of the modified rubber: a band of the *cis*-C=C bond at about 1130 cm^{-1}, a strong band of the methyl group at 1380 cm^{-1}, and bands of the trisubstituted double bond at 840 and 1665 cm^{-1}. In the course of modification, the intensity of the absorption band at 1665 cm^{-1} decreases, and additional bands appear at 680 (C–Cl bond) and 1160 cm^{-1} (C–O stretching vibrations). The band at 1775 cm^{-1} can be assigned to the carbonyl group of the saturated γ-lactone formed by modification.

Figure 2 shows the kinetic of the TCAA consumption in the course of SKI modification at 60–80°C. From the slope of the kinetic curves of the modifier consumption we determined the reaction rates, and from their temperature dependence we calculated the overall activation energy. The kinetic parameters of the SKI modification with TCAA are as follows: reaction rate $W \times 10^5$ = 0.378, 0.447, and 0.623 mol l^{-1} s^{-1} at 60, 70, and 80°C, respectively; apparent activation energy E_a = 27.16 kJ mol^{-1}.

The results of the kinetic study and the spectra of the modified rubber samples suggest the following scheme of the reaction of TCAA with a rubber macromolecule in the presence of BP [10]:

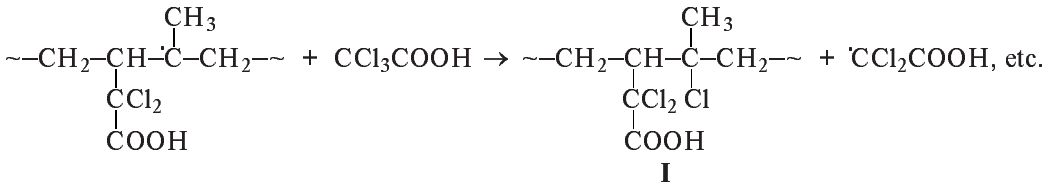
$$\mathrm{I} \xrightarrow{\Delta} 2\mathrm{R}^{\cdot},$$

$$\mathrm{R}^{\cdot} + \mathrm{CCl_3COOH} \rightarrow \mathrm{RCl} + {}^{\cdot}\mathrm{CCl_2COOH},$$

$$^{\cdot}\mathrm{CCl_2COOH} + \sim\!\!-\mathrm{CH_2}-\mathrm{CH}=\overset{\displaystyle\mathrm{CH_3}}{\overset{|}{\mathrm{C}}}-\mathrm{CH_2}-\!\!\sim$$

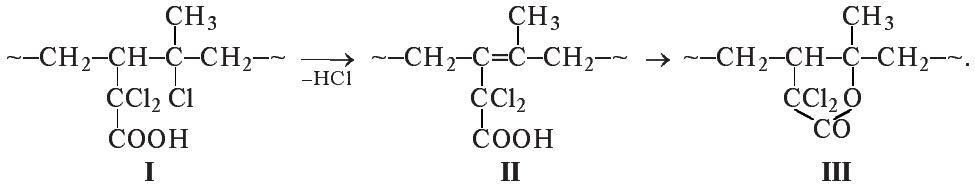
$$\rightarrow \sim\!\!-\mathrm{CH_2}-\underset{\displaystyle\mathrm{CCl_2}}{\underset{|}{\mathrm{CH}}}-\overset{\displaystyle\mathrm{CH_3}}{\overset{|}{\mathrm{C}}}-\mathrm{CH_2}-\!\!\sim,$$

$$\mathrm{COOH}$$



I

The initiator decomposes under the action of heat into radicals which, in turn, detach a chlorine atom from TCAA to form RCl. The $^{\cdot}CCl_2COOH$ radicals generated in the process undergo addition to the double bond of the rubber. This is followed by detachment of a Cl atom from TCAA by the macroradical to give product **I**. However, the reaction is accompanied by HCl evolution. Apparently, product **I** can eliminate HCl with the formation of product **II**, which subsequently undergoes lactonization under ionic conditions to give dichloro-γ-butyrolactone **III**:



I **II** **III**

To confirm this assumption, we studied the reaction of TCAA with 3-methyl-2-pentene, which is an analog of the polyisoprene unit. The reaction was performed under the conditions similar to those of SKI modification: in benzene in the presence of BP at 80°C. As a result, we isolated 2,2-dichloro-3,4-dimethyl-4-ethyl-γ-butyrolactone (bp 105–107°C/1 mm Hg) in a yield of up to 95%. The product structure was confirmed by IR and NMR spectroscopy. The IR spectrum contains the following absorption bands, cm^{-1}: 660, 710, 770 (C–Cl); 2960, 1460, 1380 (CH_3); 1250 (acetate group); 1755 (saturated γ-lactone). The following signals are observed in the NMR spectrum: 0.9 t (3H), 1.25 s (3H), 1.5 s (3H), 2.2 q (2H), and 4.9 (1H).

The addition of α-polychlorocarboxylic acids to olefins occurs similarly [11] and yields α-chloro-γ-butyrolactones.

A comparative study of the physicochemical properties of the initial and modified SKI samples revealed a change in the Mooney viscosity from 61 to 57 min and in the unsaturation from 96 to 93.2 mol %; the content of chlorine atoms in the modified SKI was 1.8%. By varying the component ratio, we found the optimal modification conditions (weight proportion): rubber : modifier : initiator = 100 : 7 : 0.5. From the modified SKI, using the standard formulation, we prepared vulcanizates and studied their physicochemical properties.

As can be seen from Table 1, the stress at 300% elongation and the tensile strength of vulcanized rubbers based on modified SKI samples are almost identical to those of the vulcanizate of the initial rubber. At the same time, the adhesion increases by a factor of 4, compared to SKI-3K.

Table 1. Physicomechanical properties of vulcanizates based on the initial and modified SKI

Elastomer	Stress at 300% elongation, MPa	Ultimate tensile strength, MPa	Elongation, %		Ultimate tear strength, kN m^{-1}	Adhesion strength to steel, MPa
			relative	residual		
SKI	14.2	28.5	490	22	70	0.05
SKI modified with TCAA	15.8	32.1	470	20	80	4.0
Carboxylate SKI-3K	15.3	30.2	460	21	72	1.0

Table 2. Weight loss of vulcanizates based on the initial and modified SKI

Elastomer	$\tau_{1/2}$, min	Weight loss, %, at indicated temperature, °C					
		150	200	250	300	350	400
SKI:							
initial	61	0	4	10	25	70	–
modified with TCAA	76	0	1	4	11	18	44

The results of a thermal analysis of the vulcanizates derived from the initial and modified SKI are listed in Table 2. It can be seen that the modification enhances the heat resistance: The weight loss of the vulcanizates derived from the initial and modified SKI is low (1–4%) up to 200°C, and at 300°C the weight loss is 25 and 11%, respectively. At still higher temperatures, the sample derived from the initial SKI rapidly degrades, whereas the weight loss of the sample derived from the modified SKI at 400°C is moderate, 44%. The half-life of the modified sample is also longer: 76 min against 61 min.

THe enhancement of the adhesion strength and thermal properties of vulcanizates prepared from modified SKI, compared to those prepared from the initial SKI, is apparently due to the fact that macromolecules of modified SKI contain butyrolactone groups and chlorine atoms, involved in the formation of the vulcanization network structure by forming labile bonds. Apparently, the best physicomechanical properties are exhibited by vulcanized rubbers with the optimal ratio of various types of cross-links [12]. Chemical cross-links of high energy provide preservation of the 3*D* network of the vulcanizate at large strains, whereas weak and readily rearranging vulcanization bonds favor relaxation of local overstrains.

CONCLUSIONS

(1) Modification of polyisoprene with trichloroacetic acid in benzene solution using a radical initiator occurs at the double bond of the polymer via an intermediate that transforms into γ-butyrolactone.

(2) The modified polyisoprene exhibits high adhesion strength and heat resistance, which allows its application fields in various branches of industry to be expanded.

REFERENCES

1. *Chemical Reactions of Polymers*, Fettes, E.M., Ed., New York: Interscience, 1964.
2. Tutorskii, I.A., Novikov, S.V., and Dogadkin, B.A., *Usp. Khim.*, 1967, vol. 36, no. 11, pp. 2026–2051.
3. Evstratov, V.A., Lykin, A.S., Shvarts, A.G., and Kavun, S.M., *Vysokomol. Soedin., Ser. A*, 1979, vol. 21, no. 11, pp. 2415–2423.
4. Arkhireev, V.P., Perukhin, Yu.V., and Kochnev, A.M., *Vestn. Kazan. Tekhnol. Univ.*, 1998, no. 1, pp. 57–70.
5. *Sinteticheskii kauchuk* (Synthetic Rubber), Garmonov, V.P., Ed., Leningrad: Khimiya, 1976.
6. Evstratov, V.F., Lykin, A.S., and Shvarts, A.G., *Kauchuk Rezina*, 1991, no. 5, pp. 22–26.
7. Kurbanova, N.I., *Zh. Prikl. Khim.*, 2005, vol. 78, no. 8, pp. 1379–1383.
8. Kurbanova, N.I., *Prots. Neftekhim. Neftepererab.*, 2004, no. 4, pp. 64–68.
9. Lazarev, S.Ya., Reikhsfel'd, V.O., and Erkova, L.N., *Laboratornyi praktikum po sinteticheskim kauchukam* (Practical Laboratory Course of Synthetic Rubbers), Leningrad: Khimiya, 1986.
10. Zamoiskaya, L.V., Denisov, V.M., Yakimanskii, A.V., and Zgonnik, V.N., *Vysokomol. Soedin., Ser. A*, 1998, vol. 40, no. 4, pp. 557–564.
11. Taichi, N., Kazuhiro, O., et al., *J. Chem. Soc. Jpn., Chem. Ind. Chem.*, 1983, no. 12, pp. 1770–1777.
12. Dogadkin, B.A., Dontsov, A.A., and Shershnev, V.A., *Khimiya elastomerov* (Elastomer Chemistry), Moscow: Khimiya, 1981.

ISSN 1070-4272, Russian Journal of Applied Chemistry, 2008, Vol. 81, No. 6, pp. 1027–1032. © Pleiades Publishing, Ltd., 2008.
Original Russian Text © R.B. Tkhakakhov, E.R. Tkhakakhov, B.S. Karamurzov, M.L. Keshtov, V.A. Vasnev, 2008, published in Zhurnal Prikladnoi Khimii, 2008, Vol. 81, No. 6, pp. 989–994.

MACROMOLECULAR CHEMISTRY AND POLYMERIC MATERIALS

Influence of the Concentrations of the Components and Preparation Procedures on the Relaxation Transitions in Blends of Polyvinyl Chloride with Butadiene–Acrylonitrile Elastomers

R. B. Tkhakakhov, E. R. Tkhakakhov, B. S. Karamurzov, M. L. Keshtov, and V. A. Vasnev

Berbekov Kabardino-Balkar State University, Nalchik, Kabardino-Balkaria, Russia
Nesmeyanov Institute of Organoelemental Compounds, Russian Academy of Sciences, Moscow, Russia

Received August 14, 2007

Abstract—The temperature dependence of the tangent of the mechanical loss angle tan δ–T and the nature of the relaxation transitions were examined for model blends of polyvinyl chloride with butadiene-acrylonitrile elastomers.

DOI: 10.1134/S1070427208060207

The phenomena occurring at the interface of components in multicomponent polymer systems are of great importance in the formation of their macroscopic properties [1–3]. The structure of the components and the transition layer in polymer blends is determined by the mode of preparation and the number of polar units in the polymer chain [4, 5]. We have shown previously [6, 7] that changing the preparation conditions (pressure, temperature) strongly modifies the morphology of polymer blends [6], which is essential for formation of their physical properties [7]. For blends of compatible elastomers SKN-18 and SKN-40, there is one maximum in the temperature dependence of the mechanical loss factor, which is intermediate between those of the starting components, and its temperature position depends on the concentrations of the components. Bartenev and Zelenev [8] reported that, in particular, it shifts to higher temperatures with increasing SKN-40 proportion. This change of the temperature position of the maximum adheres to a linear (SKN-18 + SKN-40) or nonlinear [SKN-40 + polychloroprene rubber (PCPR)] law. In blends with over 50 wt % PCPR, the glass transition point T_g sharply decreases. Bartenev and Zelenev [8] reasoned that, because of the difference in the nature of the polar nitrile and chloroprene groups, the properties of the SKN40–PCPR blends differ from those of compatible and incompatible systems.

We examined here the relaxation transitions in elastomer–rigid-chain polymer systems in relation to the component ratio, taking polyvinyl chloride (PVC) and SKN butadiene-acrylonitrile elastomers as model systems. By varying the polarity of SKN, we controlled the strength of interaction of the macromolecules of different components, and by varying the mode of preparation, the mutual diffusion of the segments of the macromolecules. This yielded polymer systems with different ratios of the volume proportions of three types of structural elements, i.e., those of the initial components and of the transition layer [9].

EXPERIMENTAL

We blended PVC with SKN containing 18, 26, and 40 mol % polar acrylonitrile groups in the polymer chain on laboratory rollers in two modes. In the first mode, the elastomer was introduced into molten PVC (T_g ~90°C) in the viscoelastic state (at 145°C) (blending at $T > T_g$ of PVC; a liquid–liquid blend). In the second mode, powdered PVC with a particle size of ca. 100 μm was introduced into the elastomer mass at 30°C (blending at $T < T_g$ of PVC; a liquid–solid blend). The standard glass transition points for SKN-18, SKN-26, and SKN-40 are –40, –30, and –20°C, respectively. The structure of the blends was fixed by subsequent cross-linking of the chains by addition of sulfur (3 wt %) at

Table 1. Average PVC particle diameter R_0 and number N_c in relation to the mode of preparation, polarity of the elastomer, and component ratio

Blend composition, wt %	Blending at $T > T_g$ of PVC		Blending at $T < T_g$ of PVC	
	R_0, μm	$N_c \times 10^3$	R_0, μm	$N_c \times 10^3$
50 PVC + 50 SKN-40	0.58	26	75	2
50 PVC + 50 SKN-26	2	4.5	83	1.8
50 PVC + 50 SKN-18	8	1.8	91	1.7
20 PVC + 80 SKN-40	–	–	60	2.5
80 PVC + 20 SKN-40	–	–	90	1.7

145°C and 100 atm on a vulcanization press. The relaxation processes were examined by the method of forced (nonresonance) oscillations at a frequency $\nu = 2.5 \times 10^{-2}$ Hz on a modified Aleksandrov–Gaev instrument [10–12]; the samples were shaped as cylinders with diameter and height of 10^{-2} m. The experiments were carried out at the relative compression strain of 10%.

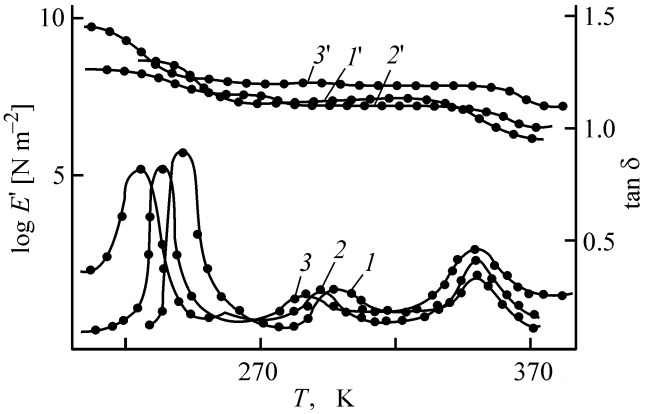


Fig. 1. Temperature dependence of (*1'–3'*) E' and (*1–3*) tan δ for blends of PVC with (*1*, *1'*) SKN-40, (*2*, *2'*) SKN-26, and (*3*, *3'*) SKN-18, obtained by blending at $T < T_g$ of PVC and 1 : 1 component ratio.

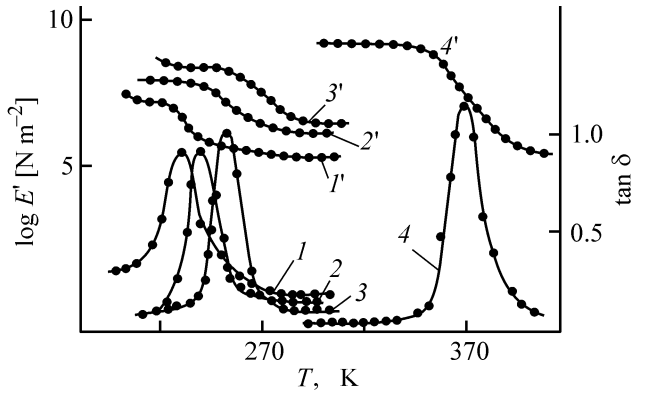


Fig. 2. Temperature dependence of (*1'–4'*) E' and (*1–4*) tan δ for (*1*, *1'*) SKN-40, (*2*, *2'*) SKN-26, (*3*, 3') SKN-18, and (*4*, *4'*) PVC.

The most important parameters of the morphology, correlated with the properties of polymer blends, are the bulk phase composition and the particle size distribution [13, 14]. We employed the Kaplan's technique [15] using the structural data, to analyze the uniformity of the morphology of the polymer blends, which is determined by the number N_c:

$$N_c = K/R_0,$$

where K = 150 Å is the characteristic dimension, the length of the segment involved in glass transition, and R_0, average diameter of the particles in the system, determining the average length corresponding to one component.

The average R_0 values were calculated using the results of an optical and electron microscopic examination of the structure of the PVC–SKN blends. At $N_c \to \infty$, the system is homogeneous, and at $N_c \to 0$, heterogeneous. The results are presented in Table 1, which suggests that an increases in the polarity of the elastomer and in the blending temperature cause the particle size to decrease.

These morphological features of the PVC–SKN blends affect their macroscopic properties, in particular, the relaxation processes.

Figure 1 shows temperature dependences of the tangent of the mechanical loss angle, tan δ, and of the dynamic modulus of elasticity, E', of the PVC–SKN-40 (curves *1*, *1'*), PVC–SKN-26 (curves *2*, *2'*), and PVC–SKN-18 (curves *3*, *3'*) blends at the 1 : 1 weight ratio of the components. There are three maxima in these dependences. The low-temperature (α_1) and high-temperature (α_2) maxima correspond to the glass transition areas of the elastomer and PVC, and the intermediate maximum α' is associated with the mobility exhibited by the kinetic segments in the transition layer [16]. Comparison of Figs. 1 and 2 shows that the high- and low-temperature maxima differ from the cor-

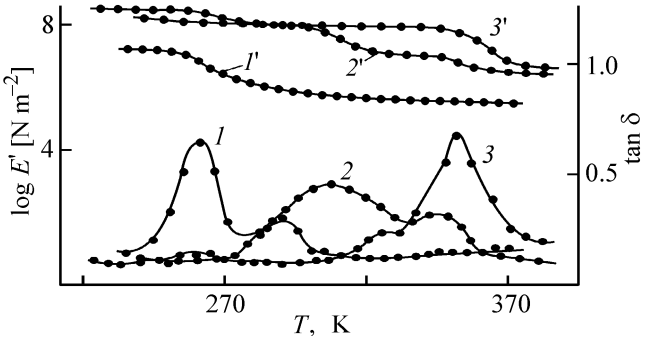


Fig. 3. Temperature dependence of (*1'–3'*) E' and (*1–3*) tan δ for the PVC–SKN-40 blends obtained by blending at $T > T_g$ of PVC. Weight ratio of the components: (*1*, *1'*) 1 : 4, (*2*, *2'*) 1 : 1, and (*3*, *3'*) 4 : 1.

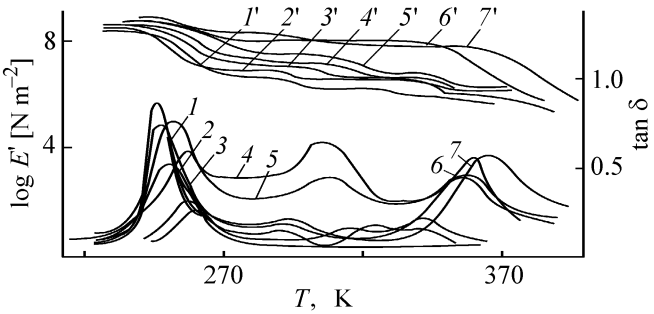


Fig. 4. Temperature dependence of (*1'–3'*) E' and (*1–3*) tan δ for the PVC–SKN-26 blends obtained by blending at $T > T_g$ of PVC. Weight ratio of the components: (*1*, *1'*) 1 : 10, (*2*, *2'*) 1 : 9, (*3*, *3'*) 1 : 4, (*4*, *4'*) 1 : 1, (*5*, *5'*) 3 : 2, (*6*, *6'*) 4 : 1, and (*7*, *7'*) 7 : 3.

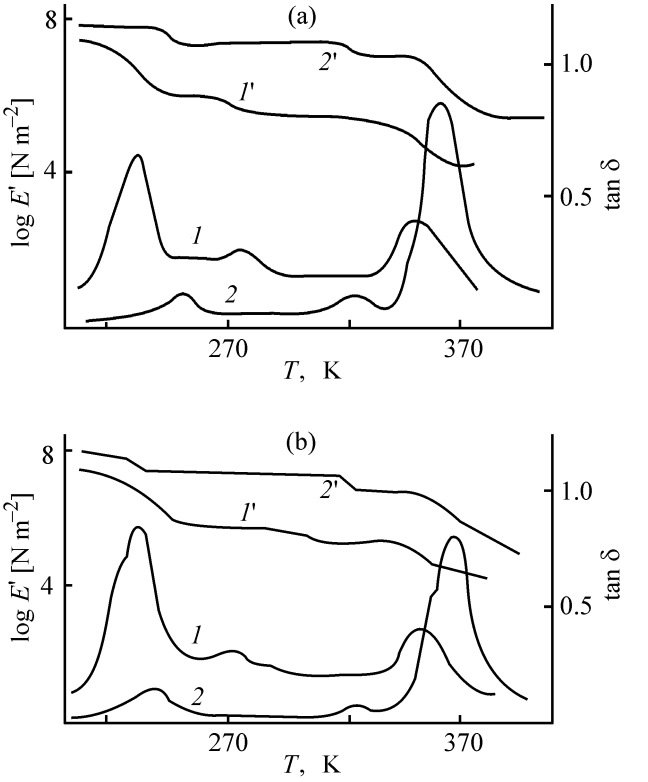


Fig. 5. Temperature dependences of (*1'–3'*) E' and (*1–3*) tan δ for PVC–SKN-18 blends obtained by blending at temperatures (a) below and (b) above T_g of PVC. Weight ratio of the components: (*1*, *1'*) 1 : 4 and (*2*, *2'*) 4 : 1.

responding α maxima of the individual components both in the height and temperature position. The low-temperature maxima are slightly shifted to higher temperatures, and the high-temperature maxima, by ca. 8 K to lower temperatures. The shift of the low-temperature maximum (α_1 process) to higher temperatures is caused by the hindrance to the segmental mobility of the elastomer molecules by the rigid-chain PVC (like in the case of carbon black filled elastomers [17]), and the shift of the high-temperature maximum, by the plasticizing action of the elastomer on PVC [18, 19]. Reznikova et al. [18] reasoned that the polar nitrile groups are responsible for the compatibility of the components in the blend, and nonpolar butadiene groups, for the plasticizing action confined to shielding of the polar groups of the polymer. The optimum effect is observed in the copolymer having two butadiene groups per nitrile group.

A decrease in the number of nitrile groups of the elastomer causes the intermediate maximum to shift to lower temperatures because of the weakening of the intermolecular interaction of different components. Simultaneously, the maximum corresponding to the glass transition range of PVC grows in height because of the change in the environment of the relaxing kinetic segments, associated with the change in the strength of interaction of the molecules of different components (a change in the number of nitrile groups in the elastomer). The difference in the conditions at which segments in the PVC–SKN blends exhibit mobility and a change in the size of the relaxing units occurs is also suggested by the changes in the height and half-width of the intermediate α' maxima in the temperature dependence of tan δ (Fig. 1, curves *1–3*).

The concentration ratio of the components strongly affects the temperature position, height, and half-width of the tan δ maxima (Figs. 3–5). A decrease in the SKN concentration causes the corresponding α_1 maximum to decrease in height and all the three (α_1, α', and α_2) maxima to shift to higher temperatures. With increasing proportion of the elastomer, the α_2 process is observed at a lower temperature, which may be due to an increase in the plasticizing influence exerted on PVC

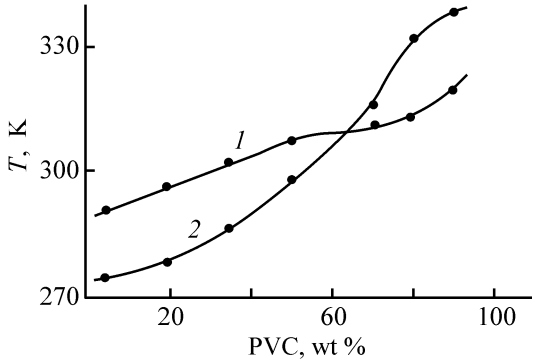


Fig. 6. Temperature position T of the intermediate maximum vs. PVC content for (*1*) PVC–SKN-26 and (*2*) PVC–SKN-18 blends. Blending at a temperature above T_g of PVC; the same for Figs. 7–9.

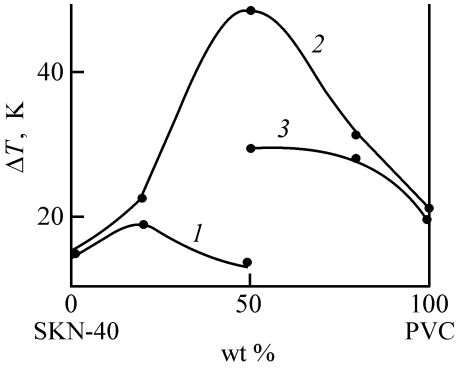


Fig. 7. Half-width ΔT for (*1*) α_1, (*2*) α', and (*3*) α_2 maxima vs. ratio of the PVC–SKN-40 blend components.

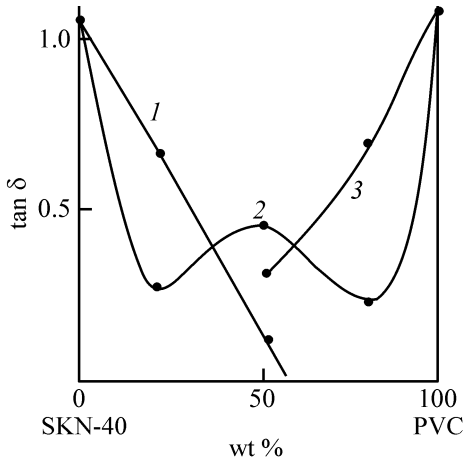


Fig. 8. Height of tan δ for (*1*) α_1, (*2*) α', and (*3*) α_2 maxima vs. ratio of the PVC–SKN-40 blend components.

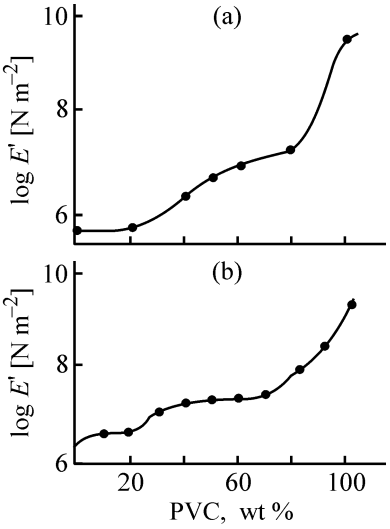


Fig. 9. Dependences of log E' on PVC content for (a) PVC–SKN-18 and (b) PVC–SKN-26 blends at 293 K.

by the elastomer [19]. The change in the temperature position of the α' process ("floating" intermediate maximum) may be associated with that in the ratio of the components in the intermediate phase. The nature of the change in the mechanical loss background in the tan δ–T plot in Figs. 3–5 still remains to be elucidated.

The parameters of the α_1, α', and α_2 maxima are strongly affected by the strength of interaction of the molecules of different components and by the composition and mode of preparation of the blend (Figs. 6–8). The variation of the maxima in the tan δ–T plot with the concentration (Fig. 7–9) are evidently associated with the change of the conditions at which the kinetic segments of the α_1, α', and α_2 processes exhibit mobility. Similar dependences were obtained for the PVC–SKN-26 and PVC–SKN-18 blends (Table 2).

The temperature position of the intermediate maximum (Fig. 6) does not vary with the PVC content by a linear law; rather, it is approximately S-shaped, which is evidently due to the difference in the nature of the polar groups of the contacting polymers.

The intermediate maxima in the tan δ–T curve for the PVC–SKN blends can be interpreted similarly to the α' process, revealed for elastomers filled with a reactive filler in [8, 20, 21] and attributed to the mobility of the kinetic segments in the polymer layer adsorbed on the filler. However, the transition layer of the macromolecules of the components in the PVC–SKN blends has a different nature. The segmental mobility of the elastomer is manifested in the environment of the PVC segments. An increase in the PVC concentration in its blends with SKN-18 and SKN-26 causes the dynamic modulus of elasticity to grow (Fig. 9).

Table 2. Temperature position T, half-width ΔT, and height tan δ of the maxima in the tan δ–T curve at different component ratios in the PVC–SKN-26 and PVC–SKN-18 blends (blending at $T > T_g$ of PVC, $\nu = 2.5 \times 10^{-2}$ Hz)

PVC : SKN weight ratio	High-temperature maximum			Intermediate maximum			Low-temperature maximum		
	T, K	ΔT	tan δ	T, K	ΔT	tan δ	T, K	ΔT	tan δ
PVC : SKN-26 blend									
100 : 0	365	20	1.12	–	–	–	–	–	–
90 : 10	363	40	0.57	320	23	0.17	252	23	0.25
80 : 20	358	35	0.56	313	25	0.19	253	25	0.3
70 : 30	355	36	0.46	312	42	0.46	254	32	0.58
50 : 50	352	40	0.45	308	42	0.64	252	30	0.75
30 : 70	348	25	0.22	303	30	0.2	250	25	0.75
10 : 90	343	23	0.11	296	25	0.19	443	23	0.76
5 : 95	–	–	–	292	23	0.15	240	20	0.89
0 : 100	–	–	–	–	–	–	238	77	0.9
PVC–SKN-18 blend									
100 : 0	365	20	1.12	–	–	–	–	–	–
80 : 20	363	20	0.85	320	27	0.12	250	20	0.13
50 : 50	361	26	0.76	298	40	0.43	234	25	0.55
20 : 80	353	35	0.42	273	38	0.3	231	25	0.67
0 : 100	–	–	–	–	–	–	228	25	0.85

The anomalies in Fig. 9 are due to phase inversion. The specific features of the relaxation transitions in the PVC–SKN blends strongly affect other macroscopic characteristics [3]. In particular, the temperature dependences of the tensile strength σ_t exhibit maxima corresponding to the absorption areas [3, 22].

Tkhakakhov et al. [23] examined the structure and the dynamic mechanical properties of the PVC–SKN blends and described their morphology in terms of a model comprising three phases (Fig. 10). Indeed, the shift of the α_1 and α_2 maxima along the temperature scale (their approximation) for the PVC–SKN blends suggests the formation of

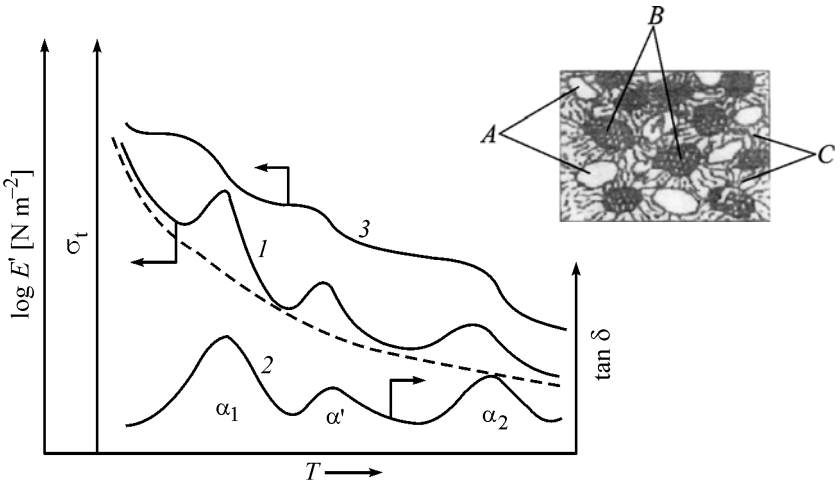


Fig. 10. Model and schematic presentation of the temperature dependences of (*1*) tensile strength, (*2*) mechanical loss, and (*3*) dynamic modulus of elasticity for a blend of two polymers with a developed diffusion layer. *Dashed line* represents the classical temperature dependence of the tensile strength. (*A*, *B*) Areas characterized by significant predominance of components A and B, respectively, and (*C*) diffusion layer.

a true solution of one component in the other, and the occurrence of an intermediate maximum, the existence of a developed transition layer.

CONCLUSIONS

(1) The system consisting of polyvinyl chloride and SKN butadiende–acrylonitrile elastomer, obtained by mechanical blending of the components, is characterized by three maxima in the temperature dependence of the tangent of the mechanical loss angle, which correspond to three relaxation transitions.

(2) Among these relaxation transitions, two α-transitions are associated with the segmental mobility of the macromolecule of the initial components, and the intermediate relaxation transition, with the segmental mobility in the transition layer.

(3) The temperature positions of all the three maxima vary with the concentration of the components, strength of interaction of the macromolecules of the contacting polymers, and mode of preparation of the blends, which is responsible for the "floating" character of the corresponding maxima.

ACKNOWLEDGMWNTS

The authors are grateful to Acad. A.R. Khokhlov for fruitful discussion of the results of this study.

This study was financially supported by the Russian Federal Education Agency and the Ministry of Education and Science of the Russian Federation (project no. RNP 2.1.2.25).

REFERENCES

1. Voyutskii, S.S., in *Geterogennye polimernye materialy* (Heterogeneous Polymer Materials), Kiev: Naukova Dumka, 1973, pp. 3–10.
2. Kuleznev, V.N., *Smesi polimerov* (Polymer Blends), Moscow: Khimiya, 1980.
3. Bartenev, G.M., Mikitaev, A.K., and Tkhakakhov, R.B., *Dokl. Akad. Nauk SSSR*, 1985, vol. 282, no. 6, pp. 1406–1412.
4. Kryszewski, M., Galeski, A., Pakula, T., and Grehowez, J., *J. Colloid Interface Sci.*, 1973, vol. 44, no. 1, pp. 85–89.
5. Tkhakakhov, R.B., Begretov, M.M., Tkhakakhov, E.R., et al., *Plast. Massy*, 2005, no. 10, pp. 7–15.
6. Tchakachow, R.B., Kardanow, Ch.K., and Zelenew, Ju.W., *Plaste Kautschuk*, 1973, vol. 20, no. 8, pp. 618–624.
7. Kardanow, Ch.K., Tchakachow, R.B., and Zelenew, Ju.W., *Plaste Kautschuk*, 1973, vol. 20, no. 8, pp. 613–619.
8. Bartenev, G.M. and Zelenev, Yu.V., *Mekh. Polim.*, 1969, no. 2, pp. 30–37.
9. Vokal', M.V., *Cand. Sci. Dissertation*, Moscow, 2004.
10. Aleksandrov, A.P. and Lazurkin, Yu.S., *Zh. Tekh. Fiz.*, 1939, vol. 9, no. 14, pp. 1249–1260.
11. Aivazov, A.B., Tkhakakhov, R.B., Dinzburg, B.N., et al., Abstracts of Papers, *Respublikanskaya konferentsiya "Polimernye materialy i ikh primenenie v narodnom khozyaistve"* (Republican Conf. "Polymer Materials and Their Application in National Economy"), Nalchik, 1976, no. 3, p. 24.
12. Tkhakakhov, R.B., Aivazov, A.B., and Zelenev, Yu.V., Abstracts of Papers, *Seminar "Instrumental'nye metody reologii"* (Workshop "Instrumental Methods of Rheology"), Moscow: Vystavka Dostizhenii Narodnogo Khozyaistva SSSR, 1977, p. 6.
13. Razinskaya, I.N., Batueva, L.N., and Shtarkman, B.P., *Kolloidn. Zh.*, 1974, vol. 36, no. 2, pp. 291–299.
14. Razinskaya, I.N., Tyves, B.S., Batueva, L.N., et al., *Vysokomol. Soedin., Ser. A*, 1974, vol. 16, no. 11, pp. 2524–2531.
15. Kaplan, D.S., *Appl. Polym. Sci.*, 1976, vol. 20, no. 10, pp. 2615–2622.
16. Tkhakakhov, R.B., Aivazov, A.B., Zelenev, Yu.V., and Dinzburg, B.N., *Vysokomol. Soedin., Ser. B*, 1980, vol. 22, no. 11, pp. 843–850.
17. Bartenew, G.M. and Lialina, N.M., *Plaste Kautschuk*, 1979, vol. 26, no. 10, pp. 556–563.
18. Reznikova, R.A., Zaionchakovskii, A.D., and Voyutskii, S.S., *Kolloidn. Zh.*, 1974, vol. 15, no. 2, pp. 108–114.
19. Teplov, B.F., Dmitrichenko, B.M., and Ovchinnikov, Yu.V., *Vysokomol. Soedin., Ser. B*, 1972, vol. 14, no. 7, pp. 487–495.
20. Bartenev, G.M. and Zelenev, Yu.V., *Kurs fiziki polimerov* (A Course of Polymer Physics), Moscow: Khimiya, 1976.
21. Bartenev, G.M. and Lyalina, N.M., *Dokl. Akad. Nauk SSSR*, 1974, vol. 201, no. 5, pp. 1130–1135.
22. Tkhakakhov, R.B. and Tkhakakhov, E.R., *Plast. Massy*, 2007, no. 9, pp. 9–13.
23. Tkhakakhov, R.B., Aivazov, A.B., and Bartenev, G.M., Abstracts of Papers, *Respublikanskaya konferentsiya "Primenenie polimernykh materialov v narodnom khozyaistve"* (Republican Conf. "Application of Polymer Materials in National Economy"), Nalchik: Kabardino-Balkar. Gos. Univ., 1982, p. 69.

ISSN 1070-4272, Russian Journal of Applied Chemistry, 2008, Vol. 81, No. 6, pp. 1033–1036. © Pleiades Publishing, Ltd., 2008.
Original Russian Text © I.S. Voloshanovskii, O.V. Shevchenko, E.V. Burenkova, 2008, published in Zhurnal Prikladnoi Khimii, 2008, Vol. 81, No. 6, pp. 995–998.

MACROMOLECULAR CHEMISTRY AND POLYMERIC MATERIALS

Benzoyl Peroxide–Cobalt(II) Vinyl-β-Diketonate Systems as Initiators of Styrene and Methyl Methacrylate Polymerization

I. S. Voloshanovskii, O. V. Shevchenko, and E. V. Burenkova

Mechnikov Odessa National University, Odessa, Ukraine

Received March 13, 2008

Abstract—New cobalt(II) vinyl-β-diketone–benzoyl peroxide [or azobis(isobutyronitrile)] binary systems were studied as initiators of polymerization of styrene and methyl methacrylate.

DOI: 10.1134/S1070427208060219

The decomposition of hydroperoxides and hydrogen peroxide in the presence of β-diketonates as activators has been extensively studied [1, 2]. However, no data on the systems containing diacyl peroxides have been reported. Previously, we have studied the degradation of benzoyl peroxide (BP) as influenced by the type of the metal and ligand in the acetylacetonate complexes and the polymerization in the presence of these initiating systems and determined the yield of the radical reaction products [3, 4]. We have also studied in detail the thermolysis of a BP-iron(III) trifluoroacetylacetonate system [5]. We found that the rate of BP thermolysis increased by three orders of magnitude. Under these conditions, the acetylacetonate complex rapidly degrades. The polymerization of styrene, vinyl acetate, and methyl methacrylate (MMA) in the presence of this system was studied. We found that the polymerization of styrene and vinyl acetate in the presence of this system is significantly faster that that initiated by its components. However, the polymerization of these compounds decelerates with an increase in the conversion owing to the inhibiting effect of the acetylacetonate [6]. This system is ineffective in the case of the MMA polymerization.

Previously, we have prepared β-diketones containing reactive double bonds [7]. Their metal complexes can initiate the radical polymerization of vinyl monomers [7]. The presence of a double bond in the ligand allows incorporation of the β-diketonate fragment into the polymeric chain. Therefore, the polymerization initiated by vinyl-β-diketonate complexes yields branched polymers and macromolecular initiators [8]. However, the polymerization in the presence of pure vinyl-β-diketonaes is not always fast. In addition, these chelates can inhibit polymerization [9]. It was of interest to study mixtures of vinyl-β-diketonates with peroxide and dinitrile initiators, since no data on these systems have been reported.

The aim of this study was to examine mixtures of BP or azobis(isobutyronitrile) (AIBN) with cobalt(II) vinyl-β-diketonate as initiators of the radical polymerization of styrene and MMA.

EXPERIMENTAL

We used cobalt(II) 3-allylpentanedionate [APD(Co)] and cobalt(II) 5-methyl-5-hexene-2,4-dionate [MHD(Co)]. In [MHD(Co)], the double bond is conjugated with the chelate ring, whereas in [APD(Co)], this conjugation is absent. A BP-cobalt(II) acetylacetonate system, in which the chelate ligand has no vinyl substituent, was studied for comparison.

Vinyl-β-diketones and their cobalt complexes were prepared by the procedures described in [7] and [10], respectively. The initiators BP and AIBN were reprecipitated from chloroform solutions with ethanol. The bulk copolymerization of styrene and MMA was performed at the equimolar ratio of the monomers. The polymerization kinetics was studied dilatometrically and gravimetrically. The initial (V_0) and average (V_{av}) polymerization rates were measured. In all cases, V_{av} was determined at a ~10% conversion. The cobalt content of the polymers, w_{Co}, was determined on a Saturn atomic absorption spectrophotometer.

Table 1. Kinetic parameters of methyl methacrylate polymerization initiated by [APD(Co)]–BP and [MHD(Co)]–BP systems ($c_{chel} = c_{BP}$)

Initiating system or initiator	$c_{in} \times 10^2$, M	T, °C	$V_0 \times 10^4$, mol l^{-1} s^{-1}	$V_{av} \times 10^4$, mol l^{-1} s^{-1}	τ, min	S, %	IP, min	w_{Co}, wt %	E_{app}, kJ mol^{-1}
APD(Co)–BP	1.0	70	24.61	22.15	42	82.6	0	0.02	54
APD(Co)	1.0		3.45	1.18	125	9.4	230	0.03	–
BP	1.0		4.43	4.43	33	9.3	0	0	75
MHD(Co)–BP	0.5		5.83	3.53	110	18.3	0	0.25	68
MHD(Co)	0.5		1.92	1.06	220	7.0	124	0.33	
BP	0.5		3.10	3.10	50	10.3	0	0	75
Co(acac)$_2$–BP	0.5		10.03	8.58	80	33.6	6	0.04	61
APD(Co)–BP	1.0	40	4.00	3.46	185	54.8	0	–	
APD(Co)	1.0		0	0	1300	0	–	–	
BP	1.0		0.36	0.36	375	9.1	0	0	
MHD(Co)–BP	0.5		0.58	0.45	650	18.0	38	0.11	
MHD(Co)	0.5		0	0	1300	0	–	–	
BP	0.5		0.25	0.25	700	13.0	0	0	
Co(acac)$_2$–BP	0.5		0.94	0.68	720	23.0	270	0.03	

We studied the MMA polymerization initiated by [APD(Co)]–BP and [MHD(Co)]–BP systems and their individual components at 70 and 40°C. The cobalt(II) acetylacetonate–BP [Co(acac)$_2$–BP] system was studied for comparison. The concentrations of the initiating systems containing APD(Co) and MHD(Co) were 1×10^{-2} and 0.5×10^{-2} M, respectively. The concentration was determined by the solubility of the cobalt complexes in the monomer. In addition, it was necessary to take into account that the dependence of V_0 on the initiator concentration is nonlinear owing to the inhibiting effect of the complexes [9].

As can be seen from Table 1, V_0 and V_{av} are higher in the presence of [APD(Co)]–BP system by a factor of more than 3 than the additive values. It should be noted that V_{av} for the system is close to V_0, whereas V_{av} for pure APD(Co) is higher by a factor of 3 than V_0. Hence, the inhibiting effect of the chelate is weak. At 40°C, the initiation efficiency by the system is higher by a factor of 10 than that by its components. It should be noted that methyl methacrylate does not polymerize at this temperature in the presence of pure [APD(Co)]. The apparent activation energy of polymerization in the presence of this system (54 kJ mol^{-1}) is significantly lower than that in the presence of BP (75 kJ mol^{-1}). It should be noted that the MMA polymerization initiated by pure [APD(Co)] is characterized by a long induction period (IP), which is also typical of other Co(II) vinyl-β-diketonates. Once the color of the polymerizing system changes from pink to green, the polymerization starts. Previously, we have shown [11] that this is due to oxidation of Co(II) to Co(III). There is no induction period in the presence of [APD(Co)]–BP system, and the color of the systems changes instantaneously after the dissolution of BP.

In the polymerization initiated by the [MHD(Co)]–BP system, the pattern is different. First, V_0 and V_{av} for this system are close to the additive values. The main difference between [APD(Co)] and [MHD(Co)] is that the double bond is not conjugated with the chelate ring in [APD(Co)]. This probably causes different types of behavior of these complexes in the course of the polymerization. Second, the cobalt content of the polymer prepared in the presence of [MHD(Co)] is higher by an order of magnitude than that of the polymer prepared in the presence of [APD(Co)]. This is probably due to the significantly higher reactivity of [MHD(Co)] in the course of polymerization, which is confirmed by the results of a study of the MHD copolymerization with vinyl monomers [12]. In addition, MHD and its metal complexes readily homopolymerize [13], whereas APD does not form homopolymers. Therefore, [MHD(Co)] copolymerizes with MMA. The apparent activation energy of the polymerization initiated by the [MHD(Co)]–BP system (E_{app} = 68 kJ mol^{-1}) is significantly higher than that for the [APD(Co)]–BP system.

Table 2. Kinetic parameters of styrene polymerization initiated by [APD(Co)]–BP and [MHD(Co)]–BP systems ($c_{chel} = c_{BP} = 1 \times 10^{-2}$ M, $T = 85°C$)

Initiating system or initiator	$V_0 \times 10^5$	$V_{av} \times 10^5$	τ, min	S, %	w_{Co}, wt %
	mol l^{-1} s^{-1}				
APD(Co)–BP	103.2	38.5	38	10.7	0.10
APD(Co)	23.1	4.3	260	8.0	0.19
BP	29.0	29.0	46	9.9	0
MHD(Co)–BP	64.5	12.4	323	29.7	0.15
MHD(Co)	38.0	12.4	110	10.1	0.47
Co(acac)$_2$–BP	24.4	17.2	240	30.5	0.04

Table 3. Kinetic parameters of MMA and styrene polymerization initiated by [APD(Co)]–BP and [MHD(Co)]–BP systems ($c_{chel} + c_{BP} = 0.5 \times 10^{-2}$ M, $T = 60°C$, 10% conversion)

Monomer	Initiating system	$V_0 \times 10^5$	$V_{av} \times 10^5$	IP, min	w_M,* wt %
		mol l^{-1} s^{-1}			
MMA	APD(Co)–AIBN	80.6	80.6	13	0
	APD(Cu)–AIBN	70.2	70.2	0	0
	AIBN	77.6	73.9	0	0
Styrene	APD(Co)–AIBN	29.7	18.4	0	0.10
	APD(Cu)–AIBN	18.6	16.7	0	0.10
	AIBN	15.3	15.3	0	0

* w_M is the weight fraction of the metal in the polymer.

The kinetic parameters of the MMA polymerization initiated by the Co(acac)$_2$–BP system, in which the cobalt complex contains no double bond, are significantly inferior to those for the [APD(Co)]–BP system. The cobalt content of the polymers prepared in the presence of the Co(acac)$_2$–BP system is low, probably due to the termination of the propagating radicals by the chelate and to the impossibility of copolymerization of Co(acac)$_2$ with the monomer.

We also studied the styrene polymerization initiated by these systems. The results are listed in Table 2. As can be seen, V_0 is significantly higher in the presence of the [APD(Co)]–BP system than that in the presence of its components. The average polymerization rate V_{av} for the system is close to the sum of the polymerization rates in the presence of [APD(Co)] and BP, taken separately. A similar deceleration of styrene polymerization was observed in the presence of pure [APD(Co)], [MHD(Co)], and Co(acac)$_2$ and various metal β-diketonate–BP systems [6]. This may be due to poisoning of the metal complex by radical reagents. Styrene polymerizes without an induction period. It should be noted that a solution of the metal chelate in the monomer instantaneously becomes greenish even in the absence of BP. The small cobalt content of the polymer prepared in the presence of a Co(acac)$_2$–BP system is caused by termination of propagating radicals by the chelate. The cobalt content of the polymer prepared in the presence of the [APD(Co)]–BP system is also low because the allyl-β-diketonate ligand does not copolymerize with styrene. Our previous ^{13}C NMR study has shown the absence of chelate fragments in the polymers prepared by initiation with the iron(III) trifluoroacetylacetonate–BP system [14]. Probably, only BP radicals initiate polymerization in this case and the metal chelate activates the BP decomposition. Metal-containing polymers can also be formed by termination of propagating radicals by the chelate to form irreversibly metal complexes that are inactive in BP degradation. The crucial role is played in this case by the polarity. It is known that propagating styrene radicals are donors (Alfrey–Price e-factor is –0.8), MMA radicals are acceptors ($e = +0.4$), and the metal in a chelate complex is always an acceptor. Therefore, the polarity factor favors the reaction of styrene radicals with the metal chelate and prevents their reaction with MMA. This is confirmed by the cobalt content of the styrene and MMA polymers.

We studied the polymerization of styrene and MMA in the presence of [APD(Co)]–AIBN and [APD(Cu)]–AIBN systems with the equimolar ratio of the components. The results are listed in Table 3. As can be seen from Table 3, the rates of the MMA polymerization initiated by the systems are similar to that provided by AIBN taken separately, i.e., the chelates do not activate the initiator decomposition and behave as inert additives. The styrene polymerization initiated by these systems is characterized by a small increase in the initial polymerization rate. However, at a 10% conversion, the rate of the styrene polymerization initiated by these systems is virtually equal to that in the case of initiatition by pure AIBN. Hence, the metal chelate–AIBN initiating systems are inefficient. This is due to the fact that the metal chelate cannot form a primary complex with AIBN.

Thus, the behavior BP and AIBN in the presence of metal β-diketonates in the course of radical polymerization varies. Metal β-diketonates form complexes with BP, which promotes the BP decomposiiton and accelerates the polymerization. Experimental results supporting the formation of these complexes were reported in our previous paper [15]. In the case of AIBN, no complexes between the metal chelate and the initiator are formed and metal β-diketonates do not accelerate the initiator decomposiiton. In this case, the polymerization is initiated by AIBN. Thus, [APD(Co)]–BP system can be used as an efficient initiator of the MMA polymerization. In the presence of this system, the polymerization is fast. The low activation energy of polymerization initiated by this system allows fast polymerization at low temperatures. We studied the thermal oxidative degradation of poly(methyl methacrylate) prepared in the presence of [APD(Co)], [APD(Co)]–BP, and BP at $c_{chel} = 1 \times 10^{-2}$ M and 70°C. The termeratures of the onset and end of the thermal oxidative degradation (T_{on} and T_{end}) were calculated by the procedure described in [16]. The values of T_{on} (numerator) and T_{end} (denominator) (T, °C) for the chelate, system, and BP are 280/405, 254/418, and 250/392, respectively. Thus, T_{on} for the system is close to that for BP, and T_{end} for the system is higher by 26°C than that for BP.

CONCLUSIONS

(1) The radical polymerization of methyl methacrylate and styrene initiated by equimolar amounts of Co(II) vinyl-β-diketonate and benzoyl peroxide involves the formation of a chelate–peroxide complex, activating the benzoyl peroxide decomposition.

(2) The [APD(Co)]–azobis(isobutyronitrile) system is an inefficient initiator, since in this case, this complex is not formed and AIBN does not decompose.

(3) The metal chelate can be incorporated in the polymer chain by copolymerization with the monomer.

REFERENCES

1. Skibida, I.P., *Usp. Khim.*, 1975, vol. 44, no. 10, pp. 1729–1747.
2. Al'masrati, S.A., Ivanchenko, P.A., and Solyanikov, V.P., *Kinet. Katal.*, 1993, vol. 34, no. 3, pp. 490–494.
3. Voloshanovskii, I.S., Mazurenko, G.A., and Krasnova, E.A., *Zh. Obshch. Khim.*, 1989, vol. 59, no. 4, pp. 755–758.
4. Voloshanovskii, I.S., Mazurenko, G.A., Ryukhin, Yu.A., and Krasnova, E.A., *Ukr. Khim. Zh.*, 1989, vol. 55, no. 1, pp. 92–95.
5. Voloshanovskii, I.S., Saeid, A.M., Revenok, L.V., et al., *Metalloorg. Khim.*, 1991, vol. 4, no. 4, pp. 916–919.
6. Voloshanovskii, I.S., *Ukr. Khim. Zh.*, 2000, vol. 66, no. 2, pp. 44–48.
7. Voloshanovskii, I.S., Butova, T.D., and Shevchenko, O.V., *Zh. Obshch. Khim.*, 1999, vol. 69, no. 9, pp. 1504–1507.
8. Shevchenko, O.V., Burenkova, E.V., and Voloshanovskii, I.S., *Vysokomol. Soedin., Ser. A*, 2006, vol. 48, no. 9, pp. 1574–1578.
9. Shevchenko, O.V., Voloshanovskii, I.S., and Berbat, T.I., *Zh. Prikl. Khim.*, 2006, vol. 79, no. 4, pp. 669–673.
10. Voloshanovskii, I.S., Shevchenko, O.V., Berezhnitskaya, A.S., and Krasnova, E.A., *Ukr. Khim. Zh.*, 2001, vol. 67, no. 5, pp. 5–10.
11. Shevchenko, O.V., Voloshanovskii, I.S., Berbat, T.I., and Zakhariya, A.I., *Vopr. Khim. Khim. Tekhnol.*, 2003, no. 6, pp. 111–115.
12. Kopeikin, V.V., Paparin, E.F., Milevskaya, I.S., and Redi, N.S., *Vysokomol. Soedin., Ser. A*, 1977, vol. 19, no. 4, pp. 861–866.
13. Movchan, T.I., Voloshanovskii, I.S., and Pomogailo, A.D., *Izv. Ross. Akad. Nauk, Ser. Khim.*, 1993, no. 12, pp. 2060–2064.
14. Saeid, A.M., Voloshanovsky, I.S., Shapiro, Yu.E., and Nizelsky, Yu.M., *Fiz. Kondens. Visokomol. Sist. (Nauk. Zap. Rivn. Derzh. Gumanitar. Univ.)*, 1999, no. 7, pp. 25–29.
15. Voloshanovskii, I.S., Saeid, A.M., and Mazurenko, G.A., *Ukr. Khim. Zh.*, 1999, vol. 65, no. 7–8, pp. 8–11.
16. Miroshnichenko, A.A., Platitsa, M.S., Volkov, V.I., and Dovbnya, V.A., *Vysokomol. Soedin., Ser. A*, 1988, vol. 30, no. 12, p. 2516.

ISSN 1070-4272, Russian Journal of Applied Chemistry, 2008, Vol. 81, No. 6, pp. 1037–1042. © Pleiades Publishing, Ltd., 2008.
Original Russian Text © G.A. Akhmedova, 2008, published in Zhurnal Prikladnoi Khimii, 2008, Vol. 81, No. 6, pp. 999–1004.

MACROMOLECULAR CHEMISTRY AND POLYMERIC MATERIALS

New Oligomeric Surfactants Based on Ethylene Glycol and Epichlorhydrin

G. A. Akhmedova

Institute of Petrochemical Processes, Azerbaijan National Academy of Sciences, Baku, Azerbaijan

Received August 14, 2007

Abstract—Oligomeric chloroxypropylates with varied contents of epoxy groups were synthesized from ethylene glycol and epichlorhydrin. The resulting oligomers were modified with phosphoric acid, diethylamine, piperidine, pyridine, and triethanolamine. The structure and composition of the products were confirmed by ^{1}H NMR and IR spectroscopy. Their physicochemical characteristics, surface activity, and ability to reduce the gasoline loss through evaporation from storage tanks are examined.

DOI: 10.1134/S1070427208060220

Environmental pollution is among the most pressing global problems. Evaporation of oil and petroleum products from reservoirs leads to their loss, quality loss, and pollution of the environment with light hydrocarbons. A lot of variously designed systems exist for reducing the evaporation of petroleum products. Even being highly efficient, these systems have some drawbacks, such as the high cost and complicated design and control system, etc. An alternative method for solving the problem consist in use of colloidal-chemical systems. The key point in this method is applying a film-forming reagent to the surface of a petroleum product. Such reagents form a stable microemulsion layer on the surface [1–10].

In this study, we synthesized and characterized oligomeric surfactants based on epichlorhydrin (ECH) and ethylene glycol (EG), having various numbers of epoxy groups, and examined their capability to retard gasoline evaporation from storage tanks.

EXPERIMENTAL

In the experiments, we used the following chemicals: 99.97–99.98% pure commercial epichlorhydrin [Orgsintez Plant (Sumgait, Azerbaijan)]; ethylene glycol (analytically pure grade, Russia); sodium hydroxide (analytically pure grade) [Chemapol (Czech Republic)]; 86.4% phosphoric acid (pure grade, Russia); diethylamine (pure grade) [Cherkassy Chemical Plant, Cherkassy (Ukraine)]; piperidines and triethanolamine (TEA) (pure grade) [Olaine Chemical Plant, Olaine (Latvia)]; pyridine (analytically pure grade) [Nizhny Tagil Metallurgical Combine, Nizhny Tagil (Russia)] distilled over KOH; $AgNO_3$ (analytically pure grade) [Urals Plant of Chemical Reagents (Russia)]; and gasoline (A-92 grade) [Aliyev Oil Refinery (formerly Azerneftyanadzhag), Baku (Azerbaijan)].

The chloroxypropylation of EG was carried out in an autoclave at 120–140°C for about 28 h, using NaOH (3 mol % relative to EG) as a catalyst. The unreacted ECH was removed by heating the product at a moderate temperature (water bath) to constant weight. The conversion of ECH and the degree of chloroxypropylation, n (ECH to EG molar ratio), were determined gravimetrically. The resulting chloroxypropylates were modified with amines in a glass reactor with a refluxer at 55–60°C (water bath) for 18–20 h. The phosphatization of the oligomers based on ECH and EG was carried out with orthophosphoric acid at 27°C.

The ^{1}H NMR spectra were recorded on a Tesla Model BS-487 instrument (Czech Republic), and IR spectra, on an UR-20 spectrometer (Germany).

The refractive index n_D was measured on a IRF-22 refractometer (Russia); extinction coefficient ε of 0.5 wt % aqueous solutions, on a AOM-102 turbidimeter (Georgia); and conductivity χ of these solutions, on an OK 102/1 conductometer (Hungary). The density ρ_4 was determined pycnometrically, and the hydroxyl and acid numbers, as in [11]. The surface activity of the aqueous solutions at the kerosene/water interface was

Table 1. Physicochemical characteristics of EG–ECH oligomers

Initial EG : ECH molar ratio	Conversion of ECH, %	n	Appearance	ρ_4 (T, °C)	n_D (T, °C)	ε, 1 mol^{-1} cm^{-1}	HLB
1 : 1	94.9	0.95	Yellow transparent oily liquid	1.214 (16)	1.4540 (15)	–	5.53
1 : 3	89.0	2.66	The same	1.276 (15)	1.4750 (15)	–	–2.25
1 : 5	90.6	4.53	Yellowish liquid	1.197 (24)	1.4580 (14)	–	–10.76
1 : 10	91.7	9.17	Reddish-brown liquid	1.298 (21)	1.4820 (21)	46.21	–31.87
1 : 15	94.2	14.13	The same	1.233 (27)	1.4570 (26)	72.98	–54.44
1 : 30	96.4	28.92	Pale yellow liquid	1.191 (22)	1.4410 (26)	144.83	–121.74
1 : 40	94.5	37.80	Yellow orange liquid	1.234 (12)	1.4570 (17)	–	–162.14
1 : 50	95.4	47.51	Pale yellow liquid	1.191 (12)	1.4420 (17)	–	–207.23
1 : 60	96.3	57.75	Yellow liquid	1.193 (11)	1.4440 (17)	–	–252.91

studied by the stalagmometric method, and that at the water/air interface, by the droplet counting method [12]. The hydrophilic–lipophilic balance (HLB) was estimated using the procedure described in [1].

The ability of the oligomers to retard the gasoline evaporation was estimated on the basis of laboratory tests [13]. Three identical volumetric beakers were filled with 100 ml of gasoline. A 5 wt % aqueous solution of additive tested and undiluted additive were introduced into the first and second beakers, respectively. No additive was introduced into the third beaker, which served as reference. The rate of gasoline evaporation was monitored by the lowering of the gasoline level in the beakers.

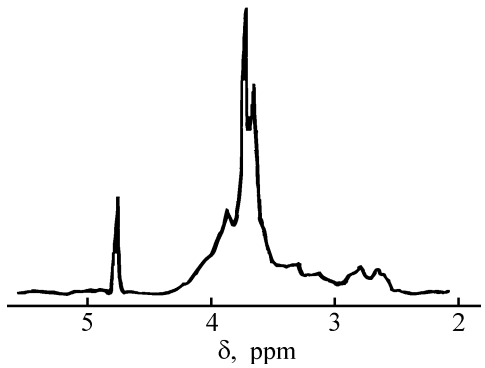


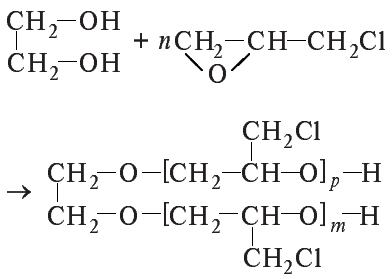
Fig. 1. ^{1}H NMR spectrum of the chloroxypropylate (n = 38.0). (δ) Chemical shift.

The retardation of evaporation E (%) was estimated as

$$E = [(V_0 - V)/V_0] \times 100,$$

where V_0 is the gasoline loss through evaporation in the blank experiment, and V, that in the experiments with the reagent.

Catalytic chloroxypropylation of EG with EPC was performed by the reaction



where $n = p + m$ is the degree of chloroxypropylation.

The reaction parameters and physicochemical characteristics of the products are summarized in Table 1.

Figure 1 shows the ^{1}H NMR spectrum of the chloroxypropylate of EG with a mean degree of chloroxypropylation of 38.0. The spectrum contains signals of the protons of the OCH_2-groups of

Table 2. Surface activity of EG–ECH oligomers

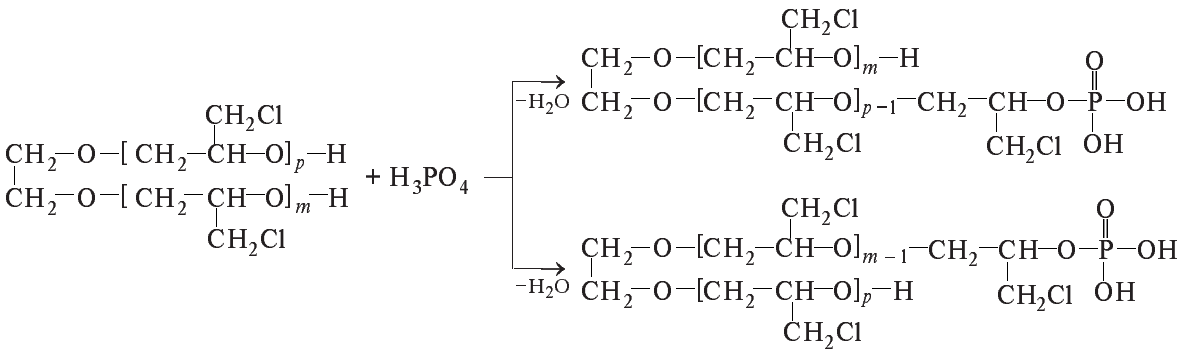
n	T, °C	Surface tension, mN m^{-1}, at indicated reagent concentration, wt %								
		0.025	0.05	0.1	0.5	1.0	3.0	5.0	7.0	10.0
Water/kerosene interface										
0.95	16	–	44.6	44.0	42.2	40.4	7.3	3.7	–	3.7
2.66	16	–	42.2	45.1	38.6	34.0	24.8	21.2	–	13.8
4.53	16	–	44.0	44.6	43.1	38.5	27.5	23.9	–	11.9
9.20	22	30.1	30.1	26.1	18.2	15.8	13.5	6.3	7.1	5.5
14.13	22	28.9	28.1	25.9	22.8	19.8	18.3	11.4	8.4	5.3
28.92	29	30.2	36.5	42.7	44.5	39.1	32.9	27.6	22.2	5.3
37.80	19	32.6	29.6	29.6	26.7	22.9	20.0	14.1	12.6	8.2
47.71	19	18.5	17.0	17.0	16.3	17.0	16.3	14.8	19.6	–
57.75	19	33.3	29.0	24.4	20.7	18.5	18.5	17.8	16.3	16.3
Water/air interface										
0.95	18	–	67.8	67.8	52.2	52.2	52.2	49.9	–	36.5
2.66	18	–	–	63.3	68.2	53.6	51.1	48.7	–	48.7
4.53	18	–	62.4	57.4	57.4	52.2	49.4	41.7	–	36.5

the initial EG at 2.80 ppm; protons of the OCH_2-, OCH-, and CH_2Cl-groups of the epoxy fragments at 3.40–4.20 ppm; and resonance signals of the OH group at 4.77 ppm.

The IR spectrum of the oligomer with a mean number of monomeric units of 4.53 shows a broad band at 3100–3700 cm^{-1} due to stretching vibrations of the hydroxy group, a band at 2840–3000 cm^{-1} due to C–H stretching vibrations in the CH_2- and CH- groups, a band at 1400–1490 cm^{-1} due to C–H bending vibrations of these groups, a band at 1090 cm^{-1} due to stretching vibrations of the C–O–C etheric group, a band at 1057 cm^{-1} due to C–O stretching vibrations of the C–OH fragment, a band at 963 cm^{-1} due to out-of-plane deformation vibrations of the C–H group of the heterochain, and a band at 760 cm^{-1} due to C–Cl vibrations.

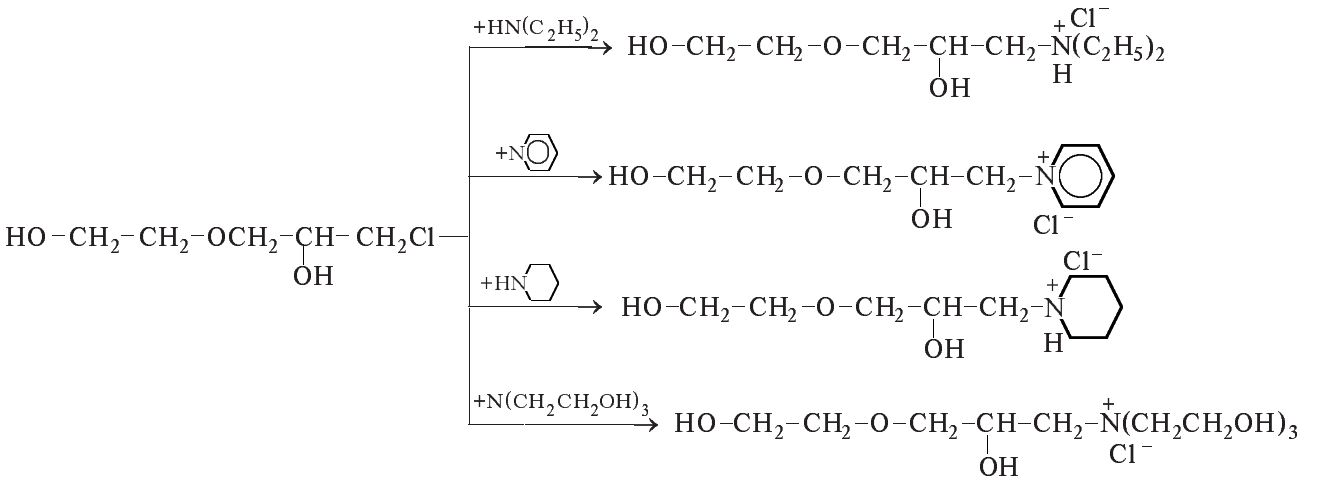
Data on the interfacial tension of variously concentrated aqueous oligomer solutions at the water/kerosene and water/air interfaces are listed in Table 2. It can be seen that these products are surfactants. The maximal surface activity at the kerosene/water interface was observed with the chloroxypropylate with a degree of chloroxypropylation of 0.95 at a concentration of 10 wt %. In this case, the surface tension decreased from 46.0–46.5 in the system without surfactant to 3.7 mN m^{-1}. The surface tension of a series of chloroxypropylates was also measured by the droplet counting method (without surfactant, the surface tension was about 72.7 mN m^{-1}).

To raise the hydrophilicity of the oligomers with the degree of chloroxypropylation of 4.53 and 37.80, we modified them with phosphoric acid:



There is a possibility of formation of diethers. The phosphatized ethers demonstrate an increased viscosity. The first phosphatized product is gold yellow. Its density at 25°C is 1.520; refractive index at 21°C, 1.4670; extinction coefficient, 49.29 $l\,mol^{-1}\,cm^{-1}$; and acid number, 709.0 mg KOH/g. The second phosphatized product is reddish brown; $\rho_4^{25} = 1.563$; $n_D^{25} = 1.4692$; and acid number, 661.6 mg KOH/g. The surface tension of 5% aqueous solution of this product at 24°C is 5.3 and 36.7 mN m^{-1} at the kerosene/water and air/water interfaces, respectively. In the case of the second phosphatized product, the phosphatization decreased the surface tension of 5 wt % aqueous solution at the water/kerosene interface from 14.1 to 5.3 mN m^{-1}.

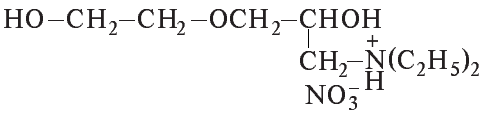
To increase the hydrophilicity of the oligomers, we also modified them with diethylamine, piperidines, pyridine, and triethanolamine. As a result, we obtained quaternary salts and protonated nitrogen salts:



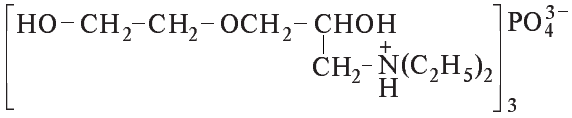
The resulting salts were liquids with refractive indices of 1.4640, 1.4555, 1.4535, and 1.5290, respectively at 20°C.

The IR spectrum of the diethylamine derivative of the oligomer ($n = 0.95$) shows a band at 3100–3700 cm^{-1} due to stretching vibrations of the hydroxy group, a band at 2860–3020 cm^{-1} due to C–H stretching vibrations in the CH_2 and CH groups, a band at 2520 cm^{-1} of the NH^+ group, a band at 1390–1510 cm^{-1} due to C–H bending vibrations in the CH_2 and CH groups, a band at 1095 cm^{-1} due to C–O stretching vibrations of the C–O–C etheric group, and a band at 1050 cm^{-1} due to C–O stretching vibrations of the C–OH group.

To confirm the formation of the salts, we performed exchange reactions of the products with $AgNO_3$ and H_3PO_4. In the case of the chloroxypropylate modified with diethylamine, the reaction with equimolar amount of aqueous $AgNO_3$ immediately afforded a white precipitate of AgCl and the salt



In this case, the chloride anion is replaced by the more bulky nitrate anion. In the exchange reaction of the same product, but with phosphoric acid (no solvent, salt : H_3PO_4 = 3 : 1), we observed liberation of HCl gas insoluble in the reaction mixture, confirming the possibility of replacement of the chloride anion for more bulky phosphate anion PO_4^{3-} to give the salt



The chloroxypropylate modified with pyridine is a yellow liquid, and that modified with piperidines, a two-phase liquid system consisting of a yellow lower layer and a pale yellow upper layer.

The IR spectrum of the chloroxypropylate (n = 47.71) modified with triethanolamine shows a broad band at 3100–3700 cm^{-1} due to stretching vibrations of the OH group, a band at 2820–3010 cm^{-1} due to C–H stretching vibrations in the CH_2 and CH groups, a band at 1350–1510 cm^{-1} due to C–H bending vibrations in the CH_2 and CH groups, bands at 1250–1260 and 1150 cm^{-1} due to antisymmetrical and symmetric stretching vibrations of the C–O–C etheric group, a band at 1060–1080 cm^{-1} due to C–O stretching vibrations in the C–OH fragment, and a band at 950–960 cm^{-1} due to C–H out-of-plane bending vibrations in the chain. The absence of the band due to C–Cl stretching vibrations confirms the formation of the salt.

The chloroxypropylate modified with triethanolamine is a homogeneous viscous yellowish brown product. The degree of conversion of triethanolamine is 90–92%. An aqueous solution of this salt demonstrates a high electrolytic conductivity (the conductivity of 0.5 wt % aqueous solution of this reagent is 0.1275 Ω^{-1} m^{-1}, while that of distilled water is 0.006 Ω^{-1} m^{-1}). The surface tension of 0.5 wt % aqueous solution at 24°C is 3.8 and 35.2 mN m^{-1} at the kerosene/water and air/water interfaces, respectively. The stalagmometric data reveal that this salt has a higher surface activity than the initial chloroxypropylate, decreasing the surface tension from 16.3 to 3.8 mN m^{-1}.

The chloroxypropylates synthesized as well as those modified with amines reduced the gasoline loss through evaporation. The reagents were tested as prepared and in the form of 5 wt % aqueous solutions.

The chloroxypropylate with one ECH unit demonstrates the effect only in the form of undiluted reagent (its efficiency was 12.5% in 11 days). The oligomer with a degree of chloroxypropylation of 2.66 is more efficient (16.3–19.2% in 11 days). For all the three chloroxypropylates (n 0.95, 2.66, and 4.53), the efficiency in the first two days was fairly high (19.0–26.5, 20.7–35.0, and 18.5–32.9%, respectively).

The chloroxypropylates with n 9.17, 14.13, and 28.92 were tested at 18–23, 25–30, and 27–30°C, respectively. The first of them demonstrate an intermediate efficiency: 13.8 and 12.4% in 26–27 days for 100% and aqueous reagents, respectively. The highest efficiency (23–43.8%) was observed in the first day. For the reagent with n = 28.92, the efficiency was 9.1 and 22.8% in 13 days for the aqueous and 100% reagents, respectively. In the undiluted form, this reagent demonstrates 48.3–57.9% efficiency in the first 5 h. The reagent with n = 14.13 has a low efficiency (3.6–4.9%).

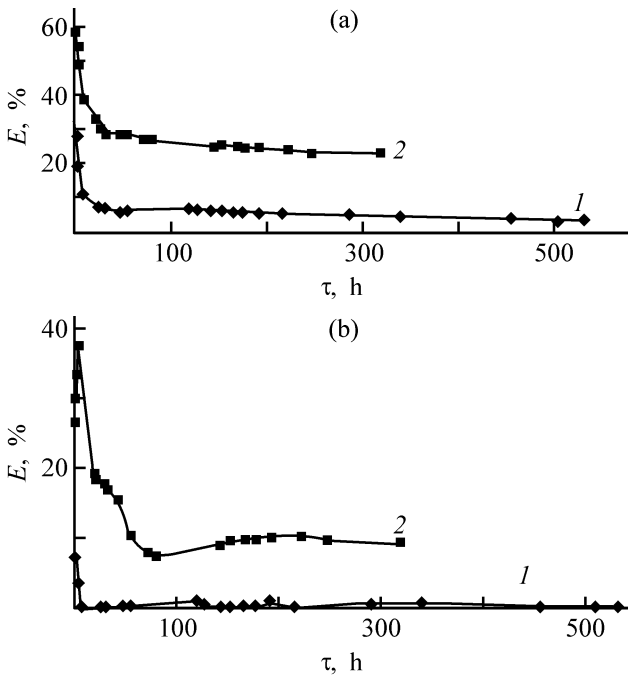


Fig. 2. Effect of chloroxypropylate (n = 28.92) on the gasoline loss through evaporation, E, vs. time τ: (a) undiluted reagent and (b) 5 wt % aqueous reagent. T (°C): (*1*) 12–15 and (*2*) 25–30.

For the chloroxypropylates with a longer heterochain (n 37.80, 47.51, and 57.75), the retardation efficiency of 5% aqueous solutions increases with n, and, vice versa, for these regents in the undiluted form, the effect decreases with increasing n.

The chloroxypropylate (n = 4.53), modified by phosphatization with phosphoric acid, taken in the undiluted form, reduces the gasoline loss by 12.6% in 18 days at 18–20°C, and, taken as 5% solution, by 13.5%. The phosphatization caused a positive effect in the first 8 days for both test forms of the reagent (compared to the unmodified chloroxypropylate): the effect increased from 11.1 to 15.3% and from 14.4 to 15.3% for 100% and 5% reagents, respectively.

The second phosphatized reagent, prepared from the chloroxypropylate with n = 37.80, also demonstrated a positive effect in both undiluted and dilute forms (gasoline loss decreased by 6.62 and 5.23%, respectively, in about 20 days). Generally, introduction of the phosphate group increased the efficiency of the reagent.

On passing from the chloroxypropylate with $n = 0.95$ to that modified with diethylamine, the efficiency of the aqueous reagent in 11 days increased by 5.1%, while that of the 100% reagent decreased from 12.5 to 8.7%.

The chloroxypropylate ($n = 47.71$) modified with triethanolamine also reduces the gasoline loss through evaporation. However, its efficiency is lower than in the unmodified product.

The effect of the temperature on the reduction of the gasoline loss through evaporation was studied for two reagents. First, we used the chloroxypropylate with $n = 28.92$ over the temperature range 12–15 and 25–30°C (Figs. 2a, 2b), and, second, the chloroxypropylate ($n = 4.53$) modified by phosphatization over the range 12–18 and 18–20°C. In both cases, the efficiency of the reagents increased with temperature.

CONCLUSIONS

(1) Oligomeric chloroxypropylates form a film on the surface of petroleum products, thus protecting them from evaporation loss.

(2) The protective efficiency could be improved through modification of the chloroxypropylates with orthophosphoric acid, diethylamine, piperidine, pyridine, and triethanolamine.

REFERENCES

1. Lange, K.R., *Poverkhnostno-aktivnye veshchestva: Sintez, svoistva, analiz, primenenie* (Surfactants: Synthesis, Properties, Analysis, and Application), St. Petersburg: Professiya, 2005.
2. Korshak, A.A., *Sovremennye sredstva sokrashcheniya poterT benzina ot ispareniya* (Modern Means To Reduce Gasoline Loss Through Evaporation), Ufa: Dizain Poligraf. Servis, 2001.
3. Dashdiev, A.R., *Azerb. Neft. Khoz–vo.*, 2004, no. 5, pp. 49–51.
4. Shalamberidze, O.V., Magaril, E.R., and Magaril, R.Z., *Izv. Vyssh. Uchebn. Zaved. Neft' Gas*, 2002, no. 1, pp. 86–89.
5. RF Patent 2 187 450.
6. RF Patent 2 256 693.
7. Shalamberidze, O.V., *Materialy nauchno-prakticheskoi konferentsii "Neftepererabotka i neftekhimiya–2003"* (Proc. Scientific and Practical Conf. "Oil Refining and Petrochemistry–2003"), Ufa, 2003, pp. 228–229.
8. Asadov, Z.H., Ahmadova, G.A., Aga-zade, A.D., and Rahimov, R.A., Abstracts of Papers, *11th Int. Conf. of Polymers and Organic Chemistry, July 18–23, 2004*, Prague (Czech Republic), 2004, p. 70.
9. Asadov, Z.H., Ahmadova, G.A., Aga-zade, A.D., and Rahimov, R.A., Abstracts of Papers, *18th Int. Conf. of Chemical Education*, 2004, Istanbul (Turkey), p. 163.
10. Asadov, Z., Ahmadova, G., Rahimov, R., and Baghirova, A., Abstracts of Papers, *Eur. Polym. Congr., 2007*, Portoroz (Slovenia), 2007, p. 190.
11. *Praktikum po khimii i fizike polimerov* (Practical Course of Polymer Chemistry and Physics), Kurenkov, V.F., Ed., Moscow: Khimiya, 1990.
12. *Praktikum po kolloidnoi khimii* (Practical Course of Colloid Chemistry), Lavrov, I.S., Ed., Moscow: Vysshaya Shkola, 1983.
13. Gumbatov, G.G. and Dashdiev, R.A., *Khimicheskie reagenty, primenyaemye pri dobyche, podgotovke nefti i gaza* (Chemical Reagents Used in Oil and Gas Production and Preparation), Baku: Elm, 1999.

ISSN 1070-4272, Russian Journal of Applied Chemistry, 2008, Vol. 81, No. 6, pp. 1043–1046. © Pleiades Publishing, Ltd., 2008.
Original Russian Text © B.M. Kudaibergenova, Sh.N. Zhumagalieva, M.K. Beisebekov, Zh.A. Abilov, M.I. Chaudkhari, 2008, published in Zhurnal Prikladnoi Khimii, 2008, Vol. 81, No. 6, pp. 1005–1008.

MACROMOLECULAR CHEMISTRY AND POLYMERIC MATERIALS

Composite Supports Based on Bentonite Clay and Polysaccharides

B. M. Kudaibergenova, Sh. N. Zhumagalieva, M. K. Beisebekov, Zh. A. Abilov, and M. I. Chaudkhari

Al-Farabi Kazakh National University, Almaty, Kazakhstan

Received August 13, 2007

Abstract—Fundamental aspects of the interaction between the bentonite clay and self-structuring polysaccharides, agar-agar and sodium salt of carboxymethyl cellulose, were studied. The possibility of using the resulting composite gels as drug carriers was examined.

DOI: 10.1134/S1070427208060232

At present, of particular interest is preparation and study of composite materials based on mineral and organic polymers. Natural self-structuring polymers, such as agar-agar, cellulose, and gelatin, used as continuous phase in composites with clays, are promising drug carriers. Introduction of the bentonite clay into composites can improve their mechanical properties. The clayey particles incorporated into the composites also acquire new valuable properties [1].

In this context, the possibility of obtaining composites based on natural polysaccharides, agar-agar and sodium salt of carboxymethyl cellulose (NaCMC), and bentonite clay from the Manrak deposit (Eastern-Kazakhstan oblast) and using these composites as drug carriers was studied. The choice of the bentonite clay and the polysaccharides was due to their ability to swell and form gels. In addition, they are nontoxic and allowed for use in medical practice.

EXPERIMENTAL

The Endo agar-agar [TU (Technical Specification) 0515088] and Na-CMC $[C_6H_7O(OH)_{3-x} \times (OCH_2COONa)_x]_n$ of pure grade (TU 2231-00250277563–00) were used without additional purification.

Alchidine, a biologically active complex produced as an extract from Kyrgyz camel's thorn (*Alhagi Kirgisorum Shrenk*) (Zhantak sirup) manufactured by Khimfarm Joint-Stock company (Shymkent). This preparation, exhibiting anti-inflammatory, styptic, wound-healing, and astringent properties, has the following composition (%, no less than): polymeric proanthocyanidins 30, amino acids 10, polysaccharides 25, flavonoids 2, microelements 10, and moisture 10; it was used without additional purification [2]. Polymeric proanthocyanidins are believed to be the active substance in alchidine.

The bentonite clay was purified by the Salo technique [3]. The sedimentation analysis was made by the Figurovskii method [4]. The degree of gel swelling was determined by the equilibrium-swelling technique [5].

Alchidine-containing composite gels based on the bentonite clay and polysaccharides were prepared as follows: a calculated amount of the bentonite clay and polymers was added to an aqueous-glycerol solution of alchidine under agitation and allowed to stay at room temperature till solidification. To determine the amount of a medicinal substance freed from the gel, a weighed portion of the gel was placed in 50 ml of distilled water and the aqueous fraction was analyzed for the content of alchidine components in the course of 24 h. The concentration of proanthocyanidins and amino acids was determined by UV spectroscopy (SF-26) at wavelengths λ = 272 and 206 nm, respectively. The amount of polysaccharides was found using the Hagedorn–Jensen microscopic method [2] based on iodometric titration.

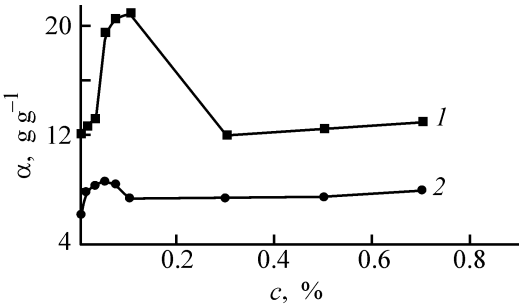


Fig. 1. Degree of swelling, α, of the bentonite clay in solutions of Na-CMC vs. its concentration *c*. (*1*) Water and (*2*) physiological solution; the same for Fig. 2.

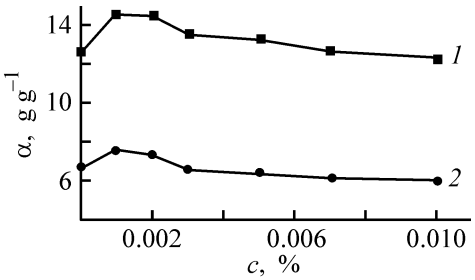


Fig. 2. Degree of swelling, α, of the bentonite clay in solutions of agar-agar vs. its concentration *c*.

The electrophoretic mobility of polymer mixtures was measured in a somewhat modified Rabinovich–Fodiman device by the mobile-boundary method [6]. The electrical conductivity of the mixtures and side liquid was measured at a constant temperature (298 K) on an R-356 installation. The electrokinetic potential ξ (V) was calculated by the Smoluchowski formula

$$\xi = \frac{4\pi\eta}{H\varepsilon} U \times 300^2,$$

where η is the viscosity of the medium (Pa s); *H*, potential gradient (V cm^{-1}); ε, dielectric constant; and *U*, electrophoretic velocity (V s^{-1}).

A study of the swelling capacity of the bentonite clay in aqueous solutions of Na-CMC and agar-agar demonstrated that the effects of polysaccharides on the swelling capacity of the bentonite clay differ both in kinetics and in nature. For example, the equilibrium swelling of the bentonite clay is attained in 20–30 min, whereas in agar solutions, the degree of swelling of the bentonite clay steadily increases. This may be due, first, to the different strengths of the polyelectrolytes: weak in the case of Na-CMC (because of the carboxy group) and strong in agar (because of the sulfo group), and, second, to the different structure-forming capacities of the polymers. In both cases, being likely charged, clayey particles and polysaccharides can interact only via hydrogen bonds. Presumably, the same circumstance can account for the different types of the concentration dependences of the swellability. For example, Na-CMC solutions show a pronounced extremal dependence of the degree of swelling of the bentonite clay on the polysaccharide concentration, whereas in agar solutions, only a slight increase is observed in the degree of swelling, irrespective of the concentration (Figs. 1, 2). At a low Na-CMC concentration (0.1%), a substantial increase in the swellability of the clay is observed. As the polysaccharide concentration increases further, the degree of swelling of the bentonite clay decreases: by almost a factor of 2 at a concentration of 0.3%.

Such a behavior of the bentonite clay in Na-CMC solutions can be understood as follows: at low concentrations, the surface of clayey particles is hydrophilized because of single contacts with polysaccharides via hydrogen bonds, which leads to an additional swelling of the bentonite clay. The tendency to form hydrogen bonds can be explained with account of the nature of the starting components. It was noted in [3] that the main mechanism by which the surface of bentonite clay particles interacts with water and other compounds is that via hydrogen bonds. At higher Na-CMC concentrations, particles of the dispersed phase aggregate and become coarser by the flocculation mechanism. In the case of agar, the strongly charged polyelectrolyte chain can exhibit an ionic strength, with the result that the swellability does not increase.

Rather interesting is the effect of polysaccharides on the stability of the bentonite clay in the presence of an electrolyte and, in particular, physiological solution (0.15 M NaCl) [7]. It can be seen in Figs. 1 and 2 (curves *2*) that the degree of swelling in the NaCl solution is almost two times lower than that in aqueous solutions. In contrast to the case of aqueous solutions, the increase in the swellability at low Na-CMC and agar concentrations in a salt solution is insignificant. This can be attributed to the high ionic strength in the NaCl solution, in good agreement with published data [3].

A characteristic feature of dispersed systems is their aggregative and sedimentation stability. It is known that the complexation processes occurring in dispersed systems are accompanied by noticeable changes in their stability [7]. It should be noted that the sodium forms of montmorillonite show high aggregative stability and can be stored in the sus-

pended state for several months to 2–3 years [3]. Therefore, a sedimentation analysis of the bentonite clay in water and Na-CMC and agar-agar solutions was performed. The results obtained agree with data on the swellability of clayey composites. Two fractions are formed in Na-CMC solutions, which correspond to the range of hydrophilization of bentonite clay particles and to the flocculation range (Fig. 3). Comparison with the swellability data shows that the range $r = 0.5 \times 10^{-5}$ m corresponds to the range of hydrophilization of clayey particles. An increase in the Na-CMC concentration leads to a decrease in the swellability of the bentonite clay, i.e., to a higher density of lyophobic parts of the dispersed phase. Similar data were obtained for composites constituted by agar and the bentonite clay. It should, however, be noted that, in the given case, there is a tendency toward a shift to a lower dispersity. Presumably, this is due to presence of bentonite clay particles bound and unbound to the polymer. This assumption is confirmed by the fact that, as the polysaccharide concentration increases, only the finely dispersed phase remains. The lyophobic parts of clayey particles act as coagulation centers and as the reason for an anomalous viscosity in dispersed systems [8, 9]. In the case in question, this leads to an insignificant coarsening of bentonite clay particles. The acceleration of the sedimentation of the clayey suspension can be favored by densification of the unit cell packing as a result of complexation.

To obtain additional information about the nature of the interaction between bentonite clay particles and polysaccharides, the variation of the electrokinetic potential in systems constituted by the bentonite clay and Na-CMC and by the bentonite clay and agar-agar was studied by means of macroelectrophoresis. The data obtained confirm to a sufficient extent the suggested mechanism of binding of Na-CMC and agar with the bentonite clay (see table).

First, the negative ξ-potential of the suspension somewhat decreases in magnitude and stabilizes at larger n. On the whole, the negative potential of the bentonite clay does not change significantly. The reason is the non-Coulomb nature of polymer binding with the bentonite clay. The observed change in the ξ-potential can be attributed to a shift of the sliding boundary of the electric double layer as a result of complexation.

To assess the possibility of using the composites as drug carriers, alchidine-containing composite gels were prepared and the release of alchidine components from these gels was studied. The kinetic curves of desorption of alchidine components into water are shown in Fig. 4. It can be seen that

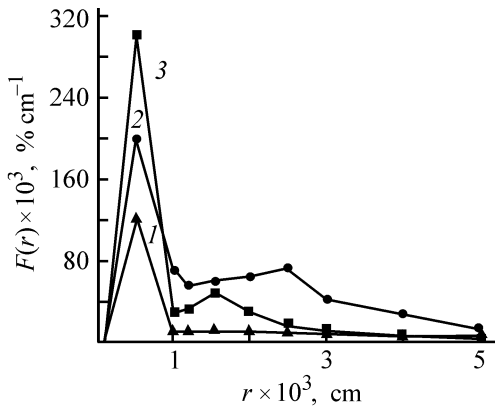


Fig. 3. Differential sedimentation curves $F(r)$–r of the bentonite clay in Na-CMC solutions. (*1*) Water; [Na-CMC] (%): (*2*) 0.05 and (*3*) 1; m_{cl} = 2.5 g.

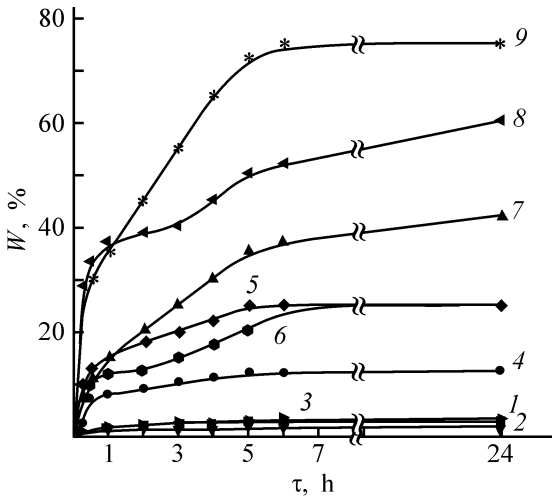


Fig. 4. Kinetic curves of desorption W of alchidine components from composite gels constituted by Na-CMC and the bentonite clay. (τ) Time. [Na-CMC] : [clay]: (*1*, *4*, *7*) 75 : 25, (*2*, *5*, *8*) 50 : 50, and (*3*, *6*, *9*) 25 : 75. (*1*–*3*) Amino acids, (*4*–*6*) proanthocyanidins, and (*7*–*9*) polysaccharides, [alcidine] = 3%.

Electrokinetic potentials of the bentonite clay and its composites with Na-CMC ([clay] = 0.25%)

$n = \frac{[\text{Na-CMC}]}{[\text{clay}]}$	ξ, V	$n = \frac{[\text{Na-CMC}]}{[\text{clay}]}$	ξ, V
0	–0.18	0.006	–0.018
0.002	–0.0083	0.007	–0.018
0.003	–0.012	0.008	–0.018
0.004	–0.014	0.01	–0.018
0.005	–0.016		

the rate and degree of release from composite gels are the highest for polysaccharides. For example, the release of polysaccharides, proanthocyanidins, and amino acids from composite gels with 75% Na-CMC in 24 h is 40, 10, and 2%, respectively. This type of release of the alchidine components is presumably associated with differences in the sizes of their molecules. In this regard, macromolecules of polysaccharides and proanthocyanidins are of approximately the same size and can be bound only with the surface of bentonite clay particles. However, the affinity of proanthocyanidins to the gels is possibly higher due to their more pronounced ability to form hydrogen bonds because of the presence of numerous hydroxy groups. The released amount of amino acids is possibly small because, owing to the small size, their molecules are sorbed, together with water molecules, by internal pores of the crystal lattice in the course of swelling of the bentonite clay, and, as a result, they are desorbed to an insignificant extent.

The release of amino acids from gels constituted by the bentonite clay and Na-CMC is 2–3%, irrespective of the composition of these gels. At the same time, the release increases for polysaccharides and proanthocyanidins as the amount of the bentonite clay in the composites grows. This indicates that the polymeric component is responsible to a greater extent for the binding of the alchidine components.

The release of polysaccharides, proanthocyanidins, and amino acids from composites constituted by the bentonite clay and agar, with the agar-agar content of 75% in 24 h is 95, 40, and 4%, respectively. Analysis of these data suggests that the content of agar-agar and the bentonite clay has nearly no effect on the release of the alchidine components.

CONCLUSIONS

(1) The polysaccharides studied interact with bentonite clay particles via hydrogen bonds. The type of interaction and the properties of the dispersed phase depend on the nature and concentration of a polysaccharide.

(2) The bentonite clay forms with polysaccharides, sodium salt of carboxymethyl cellulose and agar-agar, a homogeneous composite with good aggregative stability and component compatibility.

REFERENCES

1. Zhumagalieva, Sh.N., Beisebekov, M.K., Abilov, Zh.A., et al., *Trudy Mezhdunarodnoi nauchno-prakticheskoi konferentsii* (Proc. Int. Sci.-Pract. Conf.), Pavlodar, 2001, p. 221.
2. Burasheva, G.Sh., *Farm. Byull.*, 2004, no. 10, p. 34.
3. Salo, D.P., Ovcharenko, F.F., and Kruglitskii, N.N., *Vysokodispersnye mineraly v farmatsii i meditsine* (Highly Dispersed Minerals in Pharmacy and Medicine), Kiev: Naukova Dumka, 1963.
4. Amanzholova, E.S., *Metodika provedeniya sedimentatsionnogo analiza grubodispersnykh sistem* (Procedure for Sedimentation Analysis of Coarsely Dispersed Systems), Alma-Ata, 1980, p. 34
5. Vedenov, A.A., Levchenko, E.B., and Tret'yakova, L.I., *Priroda*, 1954, no. 4, p. 11.
6. Dukhin, S.S. and Deryagin, B.V., *Elektroforez* (Electrophoresis), Moscow: Nauka, 1976.
7. Tretinnik, V.Yu., Loktionova, L.N., Kasenko, L.V., et al., *Poluchenie i primenenie promyvochnykh i tamponazhnykh dispersii v burenii* (Production and Use of Flushing and Grouting Suspensions in Drilling), Kiev: Naukova Dumka, 1984, p. 192.
8. Musabekov, K.B., Tusupbayev, N.K., and Kudaibergenov, S.E., *Macromol. Chem. Phys.*, 1998, vol. 199, p. 401.
9. Musabekov, K.B., Tusupbaev, N.K., Muzdybaeva, Sh.A., and Aidarova, S.B., *Izv. Min. Obraz. Nauki Resp. Kazakhst., Nats. Akad. Nauk Resp. Kazakhst., Ser. Khim.*, 2003, no. 1, p. 83.

ISSN 1070-4272, Russian Journal of Applied Chemistry, 2008, Vol. 81, No. 6, pp. 1047–1051. © Pleiades Publishing, Ltd., 2008.
Original Russian Text © N.V. Sych, 2008, published in Zhurnal Prikladnoi Khimii, 2008, Vol. 81, No. 6, pp. 1009–1013.

MACROMOLECULAR CHEMISTRY AND POLYMERIC MATERIALS

Pore Structure of Activated Carbons Prepared from Polyethylene Terephthalate Waste Preliminarily Impregnated with Sulfur Compounds

N. V. Sych

Institute for Sorption and Problems of Endoecology, National Academy of Sciences of Ukraine, Kiev, Ukraine

Received October 15, 2007

Abstract—Preparation of activated carbons from a powdered polyethylene terephthalate waste preliminarily impregnated with sulfur compounds ($Na_2S_2O_3$, Na_2S) was studied. The pore structure of the resulting sorbents was examined.

DOI: 10.1134/S1070427208060244

Production of polyethylene terephthalate (PET) steadily grows. This compound is widely used for preparing fibers, press molds, films, composites, various containers for liquids, powders, and pastes, etc. In most cases, PET articles are disposable. As a result, large amounts of spent PET in solid domestic wastes are a serious environmental problem [1–3].

Depending on particular conditions and technical feasibility, various procedures are used for utilization of spent containers, and its disposal is the main procedure for waste management [4]. PET wastes are frequently incinerated or used as secondary polymer resources. Most frequently, this packaging waste is incinerated in special installations equipped with filters for absorption of hazardous exhaust gases. These filters are rather complex in production and operation, which in some cases hinders complete sorption of the hazardous gases. As a result, processing of PET waste into a secondary polymer material seems rather promising [5–9]. This problem can be probably solved by using the following processes: depolymerization to monomers and oligomers [10–12], utilization of a powdered compound as an additive to a new polymer [13–15], and mechanical reprocessing into new articles [16–18]. It should be noted, however, that reprocessing of the PET waste into new commercial products for domestic yields new solid domestic wastes in one or two years, which does not decrease the increasing volume of wastes and only simulates their utilization [19].

An alternative solution to the above problems of reprocessing of spent containers is to prepare of noval products, namely, cheap carbon adsorbents. In our previous studies [20, 21], we prepared using pretreatment of PET waste with concentrated sulfuric acid and subsequent steam activation, carbon sorbents whose porometric and service properties (S_{BET} 1030 $m^2 g^{-1}$, V_Σ 0.50 $cm^3 g^{-1}$, A^{MB} 350 mg g^{-1}) are competitive with those of activated carbons of KAU and SKN brands.

In the context of the steady growth of PET container industry, we assume that the high-temperature chemical activation with chemical modifying agents is the most appropriate procedure for PET waste reprocessing.

In this study we examined the activation of PET waste preliminarily impregnated with sulfur compounds and the formation of activated carbons as influenced by the degree of modification of the polymer matrix.

EXPERIMENTAL

As the initial material we used a crumb (2–3 mm) prepared from spent polymer containers. The composition of the initial PET is listed below:

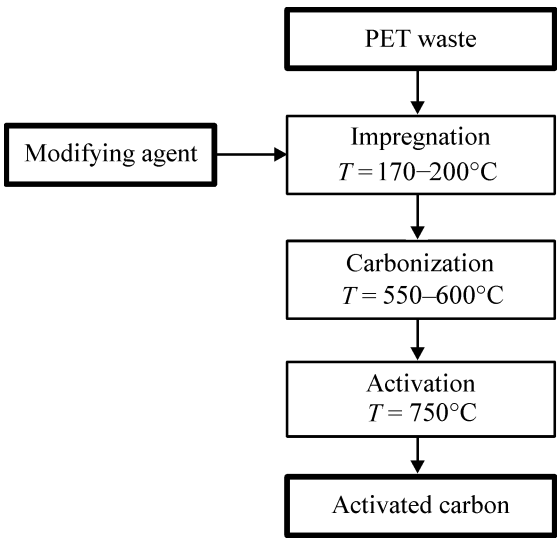
Element	O	C	H
Content, %	1.2	96.6	1.8

As can be seen, the carbon content of the material is very high, which is important for production of activated carbons.

Table 1. Development of sorption pore volume for benzene in the course of carbonization and activation of PET modified with sulfur compounds (carbonization and activation temperatures 550–600 and 750°C, respectively)

Sample	Carbonization		Activation		
	V_s, $cm^3\ g^{-1}$	yield, %	τ, min	V_s, $cm^3\ g^{-1}$	yield, %
PET–$Na_2S_2O_3$, %:					
1	0.18	15.2	15	0.24	13.8
			30	0.29	12.1
3	0.28	19.8	15	0.25	16.3
			30	0.30	14.7
5	0.26	17.2	15	0.13	14.8
			30	0.33	13.7
PET–Na_2S, %:					
1	0.18	10.0	15	0.21	7.7
			30	0.24	6.5
3	0.15	17.6	15	0.22	15.2
			30	0.30	14.4
5	0.15	19.8	15	0.20	17.4
			30	0.25	16.2
7	0.17	19.1	15	0.20	16.7
			30	0.18	15.5
PET	0.008	13.2	15	0.07	10.8
			30	0.11	9.7

The treatment of PET waste is illustrated by the scheme. Sodium thiosulfate and sulfide were used as chemical modifying agents. The modification was performed by impregnation of polymer crumb with above reagents on heating to 170–200°C. Then the modified samples were carbonized in an argon atmosphere at 550–600°C. The resulting carbons were activated with steam at 750°C. The final product is a black powder with a bulk density of 0.11–0.13 g cm^{-3}, which can be used for preparing pellets and as aerogel.



The performance of a modifying agent was preliminarily determined from the sorption pore volume for benzene [22]. A more detailed information on the development of the pore structure was derived from the isotherms of nitrogen adsorption at –196°C on a NOVA 2200 apparatus (Quantachrome, USA). The pore size distribution was calculated using the BJH method. Before measurements, the samples were degassed at 180°C for 2 h at a pressure of 1×10^{-4} torr.

Data on the porosity (sorption pore volume for benzene) and yield of products in the course of carbonization and activation of PET samples modified with sulfur compounds are listed in Table 1. As can be seen, modification improves the porosity and yield in the stage of carbonization and activation as compared to physical activation of PET. The porosity developed in the carbonization step is characterized by the sorption pore volume for benzene of 0.15–0.18 and 0.28 $cm^3\ g^{-1}$ for the samples modified with Na_2S and $Na_2S_2O_3$, respectively. In the activation step, this parameter remains nearly constant for the samples modified with $Na_2S_2O_3$, but in the case of the Na_2S modifying agent it increases from 0.15–0.17 (carbonization) to 0.33 $cm^3\ g^{-1}$ (activation). The yield of the final product is 14.7 and 14.4%, respectively. Taking into account the sorption pore volume for benzene in

Table 2. Characteristics of the pore structure of activated carbons prepared from PET waste

Sample	S_{BET}	S_{meso}	S_{micro}	V_{Σ}	V_{micro}	$V_{micro}/V_{\Sigma} \times 100\%$
	$m^2\ g^{-1}$			$cm^3\ g^{-1}$		
PET–$Na_2S_2O_3$, %:						
1	336	141	181	0.289	0.076	26.0
3	349	155	194	0.309	0.084	27.2
5	434	203	230	0.374	0.100	27.0
PET–Na_2S, %:						
1	576	178	397	0.347	0.158	45.5
3	594	174	420	0.424	0.164	38.7
5	449	113	336	0.349	0.133	38.1
7	348	85	263	0.312	0.102	32.6
PET	218	54	164	0.195	0.064	32.8

the case of $Na_2S_2O_3$ modifying agent, it is advisable to perform in this case only carbonization, which raises the yield of the final product to 19.8%. The yield of the product in reprocessing of the PET crumb without pretreatment with sulfur compounds is as low as 9–10%.

Our experimental data also show that the sorption properties of the resulting activated carbons depend on the content of sulfur compounds in the polymer matrix. With $Na_2S_2O_3$, the maximal porosity is attained upon addition of 3% sulfur, whereas with Na_2S the optimal porosity is observed at a sulfur content of 5%. With the content of impregnated sulfur increasing above these values, the yield of the final product upon carbonization decreases, which is inappropriate.

As can be seen from our data, Na_2S is a more efficient modifying agent than $Na_2S_2O_3$. This is probably due to the presence of oxygen in the $Na_2S_2O_3$ molecule, which can initiate combustion in the course of activation of the carbon matrix prepared from the PET waste.

Data on the porosity of the resulting activated carbons are listed in Table 2. The procedure of PET treatment combining a preliminary modification of the polymer matrix, heat treatment in Ar, and subsequent steam activation yields sorbents with a specific surface area ranging from 300 to 600 $m^2\ g^{-1}$. It should be noted that modification with $Na_2S_2O_3$ allows preparation of sorbents with almost constant V_{micro}/V_{Σ} ratio, whereas in the case of modification with Na_2S, this parameter varies withthe content of impregnated sulfur.

The isotherms of nitrogen sorption–desorption by the samples of activated carbons prepared by impregnation of the PET crumb with sulfur compounds, followed by carbonization and steam activation, are shown in Figs. 1a and 1b. The isotherm shape suggests that the activated carbons

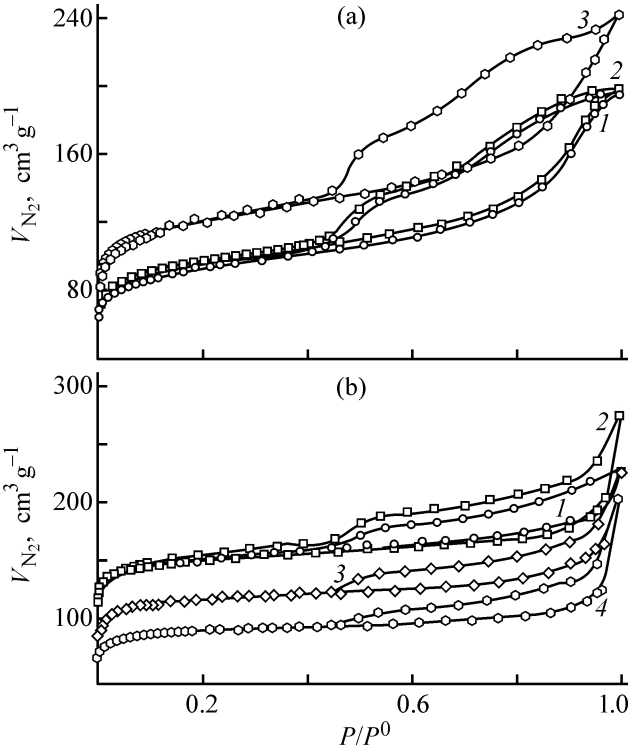


Fig. 1. Isotherms of nitrogen sorption by activated carbons prepared from the PET crumb modified with (a) $Na_2S_2O_3$ and (b) Na_2S. (V_{N_2}) Volume of adsorbed nitrogen and (P/P^0) relative pressure. Sulfur content, %: (*1*) 1, (*2*) 3, (*3*) 5, and (*4*) 7; the same for Fig. 2.

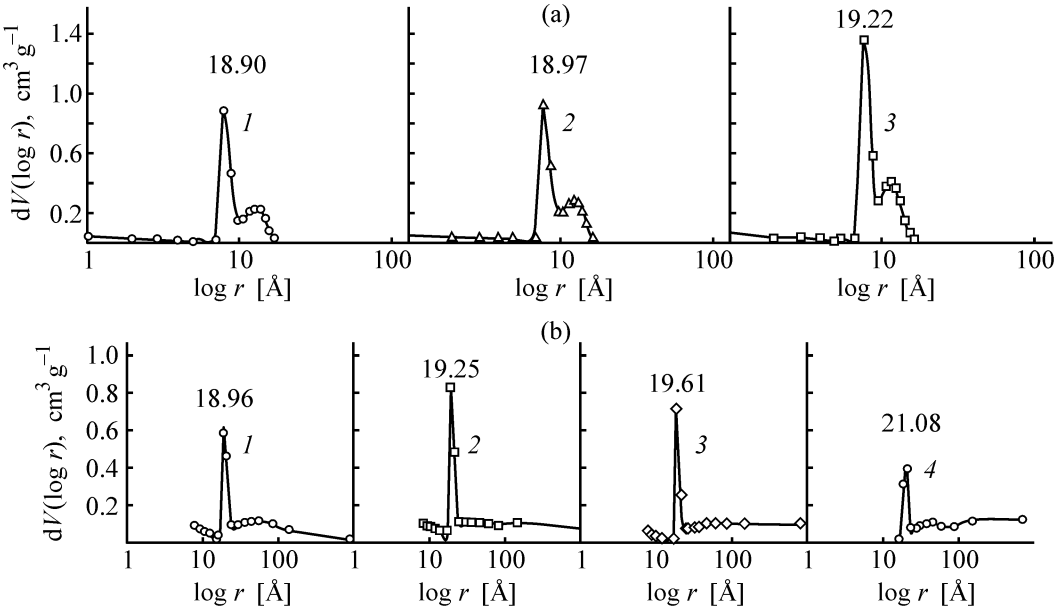


Fig. 2. Differential curves of distribution of the pore volume V with respect to the pore radius r for activated carbons prepared with (a) $Na_2S_2O_3$ and (b) Na_2S modifying agents.

prepared from PET have a polymodal pore structure, which obviously expands their application areas. The maximal volume of adsorbed nitrogen is 250 and 280 $cm^3\ g^{-1}$ for activated carbons prepared with $Na_2S_2O_3$ and Na_2S modifying agents, respectively. The $Na_2S_2O_3$ modifying agent provides formation of activated carbons with predominantly mesoporous structure, which is confirmed by the broad hysteresis loops in Fig. 1a. In the case of Na_2S modifying agent, the V_{micro}/V_{Σ} ratio can be varied depending on the content of impregnated sulfur, which allows preparation of activated carbons with controlled porosity.

Analysis of the pore size distribution (Figs. 2a, 2b) shows that the effective pore radius depends on the content of sulfur introduced into the polymer matrix and shifts toward mesoporosity. In the case of the $Na_2S_2O_3$ modifying agent, this parameter changes from 18.90 (sulfur content 1%) to 19.22 Å (sulfur content 5%). The same trend is observed with the Na_2S modifying agent. The effective pore radius shifts toward formation of mesopores from 18.96 to 21.08 Å, which suggests that the fraction of mesopores and their size increase.

Our studies are of applied importance. The alternative procedure we developed allows recycling of the valuable waste material and preparation of cheap sorbents from spent polymer containers, thus solving the problems of utilization of this type of waste. The important result of reprocessing of such waste materials into sorbents is that the environmental situation is improved, i.e., such treatment provides double positive effect. On the one hand, the problem of utilization of the large amount of PET wastes is solved and, on the other hand, the activated carbons are prepared, which, in turn, can be used to solve the problems of environmental pollution.

These results are of particular importance for the development of the resource-saving environmentally clean procedures for reprocessing of PET materials, which opens up prospects for their use in such areas of adsorption technologies as water treatment. Since the resulting sorbent is a powdered material, pelletized sorption materials can be prepared and used for gas absorption.

CONCLUSIONS

(1) Preliminary modification of the polyethylene terephthalate matrix with sulfur compounds raises the porosity and yield of the final sorbent as compared to similar treatment of unmodified polyethylene terephthalate crumb. The resulting activated carbons are characterized by the developed polymodal pore structure (S_{BET} 500–600 $m^2\ g^{-1}$ and V_{Σ} 0.37–0.42).

(2) The degree of development of the pore structure depends on the content of sulfur, and the adsorption properties of the resulting activated car-

bons depend on the amount of sulfur introduced into the polymer matrix. In the case of the $Na_2S_2O_3$ and Na_2S modifying agents, the optimal porosity is observed at 3 and 5% sulfur content, respectively.

(3) The $Na_2S_2O_3$ modifying agent provides formation of predominantly mesoporous activated carbons. The use of Na_2S modifying agent makes it possible to vary the V_{micro}/V_{Σ} ratio depending on the content of the introduced sulfur and, thus, to prepare a set of activated carbons with controlled porosity.

REFERENCES

1. Mitrofanov, R.Yu., Bochkarev, P.N., and Budaeva, V.V., Abstracts of Papers, *III Mezhdunarodnaya konferentsiya "Sotrudnichestvo dlya resheniya problem otkhodov"* (III Int. Conf. "Cooperation for Solution of the Waste Problem"), Kharkov, February 7–8, 2006, pp. 181–182.
2. Kostenko, V.F. and Timoshenko, V.V., Abstracts of Papers, *III Mezhdunarodnaya konferentsiya "Sotrudnichestvo dlya resheniya problem otkhodov"* (III Int. Conf. "Cooperation for Solution of the Waste Problem"), Kharkov, February 7–8, 2006, pp. 184–186.
3. Mishak, V.D. and Lebedev, E.V., Abstracts of Papers, *III Mezhdunarodnaya konferentsiya "Sotrudnichestvo dlya resheniya problem otkhodov"* (III Int. Conf. "Cooperation for Solution of the Waste Problem"), Kharkov, February 7–8, 2006, pp. 177–179.
4. Terekhova, A.I., Muravin, Ya.G., and Kozina, L.V., *Tara Upak.*, 1997, no. 4, pp. 38–39.
5. Klushin, V.N., Rodionov, A.I., Kasel'man, I.L., et al., *Uglerodnye sorbenty na osnove polimersoderzhashchikh otkhodov* (Carbon Sorbents Based on Polymer-Containing Waste), Moscow: Biolarus, 1993.
6. Rodionov, A.I., Klushin, V.N., and Torocheshnikov, N.S., *Teknika zashchity okruzhayushchei sredy* (Technology of Environmental Protection), Moscow: Khimiya, 1989.
7. *Handbook of Solid Waste Management*, Wilson, D.G., Ed., Van Nostrand Reinhold, 1977.
8. Mukhin, V.M. Tarasov, A.V., and Klushin, V.N., *Aktivnye ugli Rossii* (Russian Activated Carbons), Moscow: Metallurgiya, 2000.
9. Shapoval, G.S. and Kukhar', V.P., *Ekotekhn. Energosberezh.*, 1999, pp. 35–43.
10. Schut, J.H., *Plast. World*, 1996, vol. 54, no. 6, p. 25.
11. FRG Patent Appl. no. 4220473.
12. US Patent no. 5413681.
13. Artem, V., *Eur. Plast. News*, 1995, vol. 22, no. 3, p. 13.
14. Strocova, L., *Educ. Chem.*, 1996, vol. 33, no. 3, p. 1A.
15. Bourdial, J., *Sci. Vie*, 1994, no. 925, pp. 108–111.
16. Orlov, G.I., *Tara Upak.*, 1997, no. 2, pp. 4–6.
17. Gorodnichaya, O.V., Alekseev, A.A., Kirichenko, E.A., and Rybkina, G.I., in *Materialy nauchno-tekhnicheskoi konferentsii Novomoskovskogo filiala Rossiiskogo khimiko-tekhnologicheskogo universiteta* (Proc. Scientific and Technical Conf. of Novomoskovsk Branch of Russian Univ. of Chemical Engineering), Novomoskovsk, December 7–9, 1994, Novomoskovsk, 1995, vol. 1, p. 82–183.
18. Beck, E., *Plasverararbeiter*, 1996, vol. 47, no. 1, p. 45.
19. Mishak, V.D., Mamunya, E.P., Lebedev, E.V., and Seminog, V.V., in *Materialy XIII Mezhdunarodnoi nauchno-teknicheskoi kohferentsii "Ekologiya i zdorov'e cheloveka. Okhrana vodnogo, vozdushnogo basseinov. Utilizatsiya otkhodov"* (Proc. XIII Int. Scientific and Technical Conf. "Ecology and Human Health. Protection of Air and Water Basins. Waste Utilization"), Alushta, June 13–17, 2005, pp. 716–723.
20. Kartel', N.T., Gerasimenko, N.B., Tsyba, N.N., et al., *Zh. Prikl. Khim.*, 2001, vol. 74, no. 10, pp. 1711–1713.
21. Kartel', N.T., Sych, N.V., Tsyba, N.N., et al., *Ekotekhnol. Resursosber.*, 2002, no. 5, pp. 35–38.
22. Kolyshkin, D.A. and Mikhailova, K.K., *Aktivnye ugli. Spravochnik* (Activated Carbons. Handbook), Leningrad: Khimiya, 1982.

ISSN 1070-4272, Russian Journal of Applied Chemistry, 2008, Vol. 81, No. 6, pp. 1052–1056. © Pleiades Publishing, Ltd., 2008.
Original Russian Text © A.B. Shipovskaya, N.O. Gegel', G.N. Timofeeva, 2008, published in Zhurnal Prikladnoi Khimii, 2008, Vol. 81, No. 6, pp. 1014–1018.

MACROMOLECULAR CHEMISTRY AND POLYMERIC MATERIALS

Orientation Processes in Cellulose Acetate under the Action of Dimethyl Sulfoxide Vapor

A. B. Shipovskaya, N. O. Gegel', and G. N. Timofeeva

Chernyshevsky State University, Saratov, Russia
Research Institute of Natural Sciences, Saratov State University, Saratov, Russia

Received August 2, 2007

Abstract—Spontaneous variation of the linear size (elongation-contraction) of acetate fibers in a vapor of dimethyl sulfoxide, which is a mesophasogenic solvent, i.e., a solvent forming a liquid crystal phase with the polymer, is described. A mechanism of the interaction of the polymer with the solvent vapor is suggested.

DOI: 10.1134/S1070427208060256

It has been shown previously [1–8] that some solvents, such as nitromethane and trifluoroacetic acid, in the vapor state initiate orientation processes in cellulose acetates. It is well known that cellulose acetates in these mesophasogenic solvents form a liquid crystal (LC) phase [8–12]. Sorption of vapors of such solvents is accompanied by anomalous shape of the sorption kinetic curves [3, 5], suggesting that a structural rearrangement occurrs in the polymer matrix [13]. Under the action of vapor, the acetate fibers undergo a spontaneous cyclic deformation (elongation-contraction), and a spontaneous elongation of cellulose acetate films is observed [1, 7, 8], which confirms the formation of LC phase [14]. In films modified with vapor of these solvents, a persistent induced optical anisotropy arises [4], the intensities of reflections in the X-ray patterns increase [8], and the physicomechanical characteristics of the films and fibers are significantly improved [2, 6].

In this study, we examined the effect of dimethyl sulfoxide (DMSO) vapor on the structure of cellulose acetates. The choice of DMSO is caused by the fact that cellulose acetates form an anisotropic phase in this solvent [15, 16], and also by its wide use in production of cellulose acetate items for various purposes (hollow fibers, filters, membranes) [17, 18].

EXPERIMENTAL

As objects of the study served commercial acetate filaments formed by a dry procedure (Khimvolokno Joint-Stock Company, Engels) from cellulose diacetate (CDA) with 54.5% content of bound acetic acid and viscosity-average molecular weight of 8.0×10^4. The physicomechanical characteristics of the sample were as follows: linear density 6.7 tex, number of elementary single filaments n approximately 23, effective diameter 0.11 mm, strength 9.8–10.0 gf tex^{-1}, strength 8.8 cN tex^{-1}, and relative elongation at break 24.8–25.4%.

We used DMSO of analytically pure grade, ρ 1.1 g cm^{-3}, bp 189.0°C, mp 18.5°C, μ 3.96 D, and ε 48.9. DMSO is an aprotic dipolar protophilic solvent [19].

Acetate filaments were treated in a DMSO vapor medium in a hermetically sealed glass vessel filled with a liquid medium to one fifth of the volume. The fiber in the freely stretched state was horizontally fixed in a vessel at a distance of approximately 4 cm from the liquid surface. This experimental procedure allows visual observation of the sample deformation through the transparent vessel walls. The sag value in both direct and inverse processes was measured using a millimeter scale fixed on the back wall of the vessel. The experimental procedure and the algorithm used to calculate the variation of the linear size of the sample were described in detail in [7]. No less than 5–10 replicate measurements were performed under the same conditions, and the average values at the same instants of time were used for calculations. The experiments were performed at 19–60°C.

In the course of spontaneous deformation, we determined the degree of sorption of the solvent vapor by the fiber, C_s, by the gravimetric method using an E. Mettler analytical balance (Zürich, Switzerland) with a specially designed unit for sample fixation. The fiber was arranged so that it could be freely elongated. The experiments were performed with continuous weighing of the fiber in the course of swelling in the sorbate vapor. The weighing accuracy was ±0.0001 g.

For structural studies, the modified samples were removed from the vapor medium in various stages of spontaneous deformation, and the linear size in air was measured. Strain–temperature curves were obtained by linear dilatometry, by measuring the filament length on heating to 300°C. A load not exceeding 0.1% of the tensile strength was applied to the filament. The heating rate was 2–2.5 deg min^{-1}, measurement error 0.1%. X-ray diffraction patterns were recorded on a DRON-3 diffractometer with Cu_{K_α} radiation at U = 22 kV and I_a = 20 mA.

Our study showed that treatment of acetate fibers with a DMSO vapor is accompanied by their spontaneous elongation (Fig. 1). The elongation value depends on temperature. For example, in the range 20–30°C, the largest elongation L (with respect to the initial length taken as 100%) is 125–175% (curves *1*, *2*), and it is reached in 15–30 min. An increase in the temperature of the filament treatment to 35–60°C decreases the effect of self-elongation, and the process occurs in a shorter time interval (curves *3*–*5*).

This effect serves as direct experimental confirmation of the transition of the polymer system to the nematic phase [14]. Taking into account these concepts, published data [1–8, 20–22] in which spontaneous elongation of polymer bodies based on cellulose esters was observed, and also the fact of formation of an anisotropic phase in solutions of cellulose acetates in DMSO [15, 16], we conclude that the orientation processes occur in the polymer matrix under the action of vapor.

The feature of spontaneous elongation of CDA fibers in DMSO vapor is practically complete kinetic reversibility of the process. The fiber placed in the DMSO vapor after reaching the maximum elongation starts to contract, approaching the initial linear size (Fig. 1). The contraction of the acetate filament takes more time than elongation. For example, the direct process occurs at 20°C within approximately 25 min, and the reverse process, within approximately 70 min. In the reverse process, the fiber does not reach the initial linear size and remains slightly deflected; in this case, the sample subjected to cycles of elongation and partial contraction can remain slightly deflected in the DMSO vapor medium at room temperature for more than 90 days (Fig. 1, curve *1*). In addition, at some temperatures the sample swollen in vapor undergoes a slight secondary elongation and then is ruptured (Fig. 1, curves *2*–*4*).

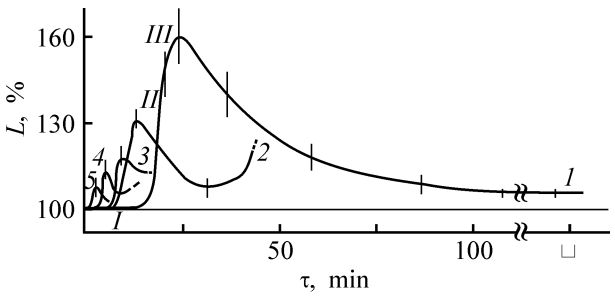


Fig. 1. Kinetic curves of spontaneous deformation (elongation-contraction) of the acetate fiber in a DMSO vapor at (*1*) 20, (*2*) 30, (*3*) 40, (*4*) 50, and (*5*) 60°C. (L) Elongation and/or contraction and (τ) time. *Dotted line*: instant of fiber rupture.

Until now, the spontaneous cyclic deformation (elongation–contraction) has been observed in only a single system, acetate filament–nitromethane vapor [1, 7, 8]. As mentioned in these papers, the term shrinkage is inadequate for describing the fiber contraction, since the initial point in variation of the linear size is not the length of the initial sample but that of the spontaneously elongated sample. Contraction of the elongated sample results from neither a temperature effect nor a relaxation response to deformation stretching when forces arising in a polymer are directed opposite to motion. Both the elongation and contraction are spontaneous processes and occur in a period of time convenient for monitoring (duration of a complete cycle is 95 min at 20°C, 30–35 min at 30°C, 15–20 min at 40°C, 10–15 min at 50°C, and less than 10 min at 60°C) and, which is the most important, under the same conditions: at the same temperature and pressure and in a hermetically sealed vessel in the presence of a sorbate vapor.

The fiber removed from the solvent vapor medium in any stage of deformation (both in the course of elongation and contraction) keeps the size in air for a long time. It should be noted that the fiber becomes thinner and more even after elongation in vapor. The elongated sample can be stretched under a load by 180–230% more.

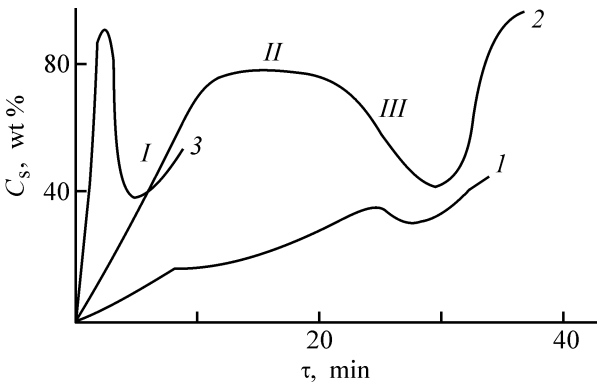


Fig. 2. Kinetic curves of sorption of the DMSO vapor by the acetate fiber in the course of spontaneous deformation at (*1*) 19, (*2*) 22, and (*3*) 60°C. (C_s) Degree of absorption of the DMSO vapor by the CDA fiber and (τ) time. (*I–III*) For comments, see text.

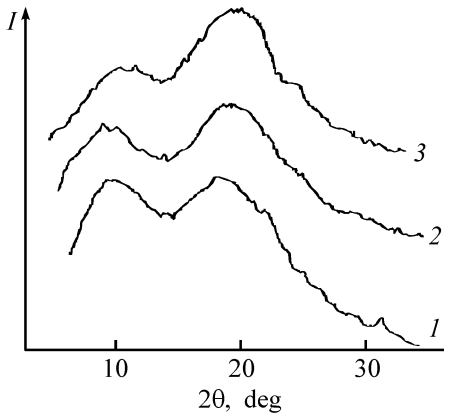


Fig. 3. X-ray diffraction pattern of acetate filaments. (*I*) diffraction intensity and (2θ) diffraction angle. Filament: (*1*) commercial (control), (*2*) elongated to the maximum extent in DMSO vapor, and (*3*) contracted after elongation and kept in this state in the sorbate vapor for 3 days.

The kinetics of sorption of the DMSO vapor by the CDA fiber in the course of spontaneous deformation is shown in Fig. 2. It can be seen that the swelling is a two-stage process. The first stage can be arbitrarily divided into several substages. For example, in the first substage of sorption at 22°C (Fig. 2, curve *2*, substage *I*) corresponding to an induction period preceding the self-elongation (Fig. 1, curve *1*, *I*), the fiber absorbs 70–75 wt % vapor within approximately 10 min (sorption rate $V \sim 7$ wt % min^{-1}). In the second substage (Fig. 2, curve *2*, *II*), the degree of sorption varies insignificantly (is practically constant); in the process, the filament length actively increases (Fig. 1, curve *1*, *II*). Then, the swollen filament desorbs 35–40 wt % of the previously absorbed vapor (Fig. 2, curve *2*, *III*; desorption rate $V \sim 5$ wt % min^{-1}) and continues to elongate (Fig. 1, curve *1*, *III*). In the second stage of swelling, a reverse effect is observed: the elongated fiber slowly contracts, approaching the initial linear size and absorbing vapor in a larger amount at a higher rate ($V \sim 15$ wt % min^{-1}). Finally, the filament ceases to absorb the sorbate vapor and, as mentioned above, remains in the deflected state in the DMSO vapor medium for a long time.

An unusual fact should be taken into account. When keeping the sample subjected to cyclic self-deformation in the DMSO vapor medium in a closed vessel, uniformly distributed small drops are formed on its surface. All drops are similar in shape and size and hang on the fiber for a long time (more than 70 days). No effect of this kind was observed in keeping an acetate filament, e.g., in a water vapor or in a vapor of other mesophasogenic (nitromethane, trifluoroacetic acid) and process (acetone, methylene chloride) solvents. This kinetic stability may be caused by various factors: surface phenomena at the phase boundary, surface energy of liquid in drop, equality of the energies of interaction of solvent vapor with polymer, and gravitational force.

The nonmonotonic sorption kinetics, squeezing of the solvent from the swollen sample, and also abrupt increase in the absorption rate (by a factor of more than 2) in the final stage of swelling are criteria of the orientation rearrangement of chains or their domains in the polymer matrix in the course of diffusion of a low-molecular-weight liquid or its vapor [5, 7, 13]. It is likely that, in this case, the DMSO vapor plays a role of a kinetic stimulant of the phase transition from the amorphous to anisotropic state [14, 22]. After removal of the kinetic hindrance, macromolecules in the swollen sample, due to their natural rigidity, are elongated to acquire the equilibrium, more straightened, conformation, become unfolded, and undergo spontaneous orientation ordering. In the macroscopic sense, this is manifested in an increase in the linear size of the fiber. In this case, the filament structure becomes compact, which results in squeezing of the solvent from the polymer matrix. It should be noted that the plateau and fall in the sorption curves (Fig. 2, curve *2*, substages *II* and *III*) correspond to the period of filament elongation (Fig. 1, curve *1*, substages *II* and *III*).

Data obtained by direct methods for studying the polymer structure suggest that the ordered state of the polymer matrix attained in the course of spontaneous deformation of the fiber in DMSO vapor. For example, X-ray diffraction patterns of the treated fiber (Fig. 3, curves *2*, *3*) have strong

reflections particularly pronounced at 2θ 18° –20° and 9°–11°. In addition, for these samples, the height and area of the peak in the range of 2θ 18°–20° increases, and those of the peak at 9°–11° decrease. In this case, the area of the peaks for the samples that underwent self-deformation in the DMSO vapor does not change noticeably in comparison with control (curve *1*). This additionally confirms that the structural rearrangements occurring in the polymer matrix under the action of the DMSO vapor are caused by orientation of macromolecules [6, 23].

The orientation ordering in the polymer matrix is confirmed by the results of a thermal deformation analysis of modified fibers (Fig. 4). For the initial sample prepared under industrial conditions by dry forming, we observed only the shrinkage (curve *1*), which suggests a weakly oriented structure of the polymer in finished acetate filaments. Contrary to the control sample, for all modified filaments, the strain–temperature curves have a different shape and are typical of preoriented polymers [3, 8, 20, 24]. The most pronounced effect of self-orientation was observed for the samples elongated in the DMSO vapor (curves *3*, *4*) and corresponding in the strain value to the middle of the strong elongation stage ($L \sim 130\%$) and to the maximum self-elongation ($L \sim 160\%$) (Fig. 1, curve *1*). The sample that sorbed the DMSO vapor before the onset of elongation (Fig. 1, curve *1*, $L \sim 101$–102%) is also characterized by orientation ordering but has a smaller peak of self-orientation (Fig. 4, curve *2*) in comparison with the more elongated samples. For the sample subjected to spontaneous cyclic deformation (i.e., the stages of elongation and subsequent partial contraction in vapor), self-ordering under the action of temperature is also observed (Fig 4, curve *5*). Contrary to the initial and other modified fibers, this sample has a higher glass transition point and, accordingly, the abrupt increase in the fiber length with linear heating occurs at higher temperatures. In addition, this sample showed virtually no contraction observed for all the other samples at $T > 230°$ and caused by the onset of thermal degradation of the polymer.

Thus, initiation of orientation processes in cellulose esters under the action of DMSO vapor takes place even in the induction period of self-elongation (Fig. 1, curve *1*, stage *I*), i.e., in the initial stage of intensive swelling of polymer in the vapor of an active medium (Fig. 2, curve *2*, stage *I*), and develops in the stages of elongation and contraction of the fiber.

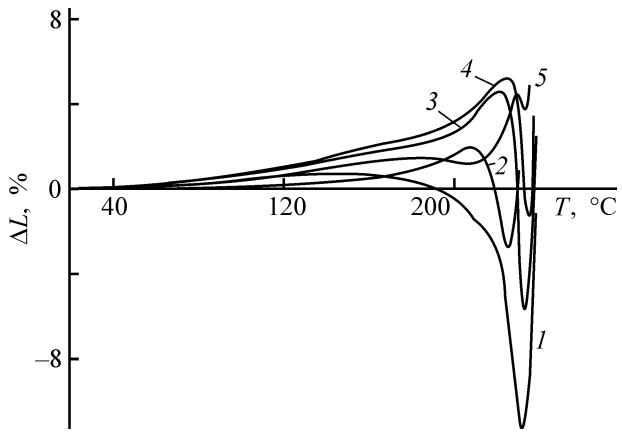


Fig. 4. Strain-temperature curves of diacetate filaments. (ΔL) Change in the sample length and (T) temperature. (*1*) Control industrial filament; samples subjected to spontaneous deformation in DMSO vapor at 20°C: (*2*) fiber swollen in vapor before beginning of self-elongation, (*3*) in the middle of the strong elongation stage, (*4*) filament elongated to the maximum, and (*5*) fiber after shortening.

It should be noted in conclusion that the ability of acetate fibers to undergo spontaneous elongation and orientation ordering under the action of DMSO vapor and also their ability to show additional stretching after removal from the sorbate vapor medium enables production of thin strong filaments with a linear density of less than 3–4 tex. It is well known that the modern industry does not produce so thin filaments by the dry forming procedure. Taking into account that DMSO is widely used in manufacture of cellulose acetate items of medical and biochemical purposes [18, 25] and also as drug [26, 27]; modified acetate filaments can be used in medicine and allied fields.

CONCLUSIONS

(1) Spontaneous variation of the linear size (elongation–contraction) of cellulose diacetate fibers in the vapor of a mesophasegenic solvent, dimethyl sulfoxide, is accompanied by initiation of orientation phenomena in the polymer matrix.

(2) The sorption of sorbate vapor with the polymer in the course of self-deformation of the fiber is described by nonmonotonic curves of swelling, rather than by Fick law , which points to the multistage mechanism of interaction of the sorbate vapor with the polymer.

(3) Treatment of acetate fibers with solvent vapor allows production of thin strong filaments for

not only textile, but also medical and biochemical purposes.

ACKNOWLEDGMENTS

This study was financially supported by the Russian Foundation for Basic Research (projects nos. 03-03-33049a, 06-08-00892a).

REFERENCES

1. Timofeeva, G.N. and Tolkunova, E.V., *Vysokomol. Soedin., Ser. A*, 1986, vol. 28, no. 4, pp. 869–872.
2. USSR Inventors' Certificate, no. 1330221.
3. Timofeeva, G.N., Protsenko, N.V., and Fedusenko, I.V., *Khim. Volokna*, 1989, no. 2, pp. 13–15.
4. Timofeeva, G.N., Fedusenko, I.V., Lashek, N.A., and Shipovskaya, A.B., *Vysokomol. Soedin., Ser. B*, 1995, vol. 37, no. 6, pp. 1093–1095.
5. Shipovskaya, A.B. and Timofeeva, G.N., *Vysokomol. Soedin., Ser. A*, 2001, vol. 43, no. 7, pp. 1237–1244.
6. Shipovskaya, A.B., Mikul'skii, G.F., and Timofeeva, G.N., *Zh. Prikl. Khim.*, 2004, vol. 77, no. 1, pp. 152–157.
7. Shipovskaya, A.B., Shmakov, S.L., and Timofeeva, G.N., *Vysokomol. Soedin., Ser. A*, 2006, vol. 48, no. 5, pp. 801–814.
8. Shipovskaya, A.B. and Timofeeva, G.N., *Inzh.-Fiz. Zh. Nats. Akad. Nauk Bel.*, 2006, vol. 79, no. 1, pp. 139–147.
9. Aharoni, S.M., *Mol. Cryst. Liquid Cryst.*, 1980, vol. 56, no. 7, pp. 237–241.
10. Yunusov, B.Yu., Khanchich, O.A., Shablygin, M.V., et al., *Vysokomol. Soedin., Ser. B*, 1983, vol. 25, no. 4, pp. 292–294.
11. Meeten, G.H. and Navard, P., *Polymer*, 1983, vol. 24, no. 7, pp. 815–819.
12. Kulichikhin, V.G. and Golova, L.K., *Khim. Drev.*, 1985, no. 3, pp. 9–27.
13. Malkin, A.Ya. and Chalykh, E.A., *Diffuziya i vyazkost' polimerov* (Diffusion and Viscosity of Polymers), Moscow: Khimiya, 1979.
14. Flory, P.J., *Proc. Royal Soc., A*, 1956, vol. 234, no. 1, pp. 60–72, 73–89.
15. Shipovskaya, A.B., Solonina, N.A., Kazmicheva, O.F., and Timofeeva, G.N., in *Struktura i dinamika molekulyarnykh sistem: Sbornik statei* (Structure and Dynamics of Molecular Systems: Coll. of Papers), Ioshkar-Ola, Mariisk. Gos. Tekh. Univ., 2005, issue 12, vol. 2, pp. 359–362.
16. Shcherbakova, Zh.S., Vinokurova, E.V., and Shipovskaya, A.B., in *Mezhvuzovskii sbornik nauchnykh trudov V Vserossiiskoi konferentsii molodykh uchenykh "Sovremennye problemy teoreticheskoi i eksperimental'noi khimii"* (Intercollegiate Coll. of Scientific Works of 5th All-Russian Conf. of Young Scientists "Modern Problems of Theoretical and Experimental Chemistry"), Saratov: Nauchnaya Kniga, 2005, pp. 237–239.
17. Kesting, R.E., *Synthetic Polymeric Membranes*, New York: Wiley, 1991.
18. Shipovskaya, A.B., Evseeva, N.V., and Timofeeva, G.N., *Zh. Prikl. Khim.*, 2003, vol. 76, no. 9, pp. 1553–1537.
19. Reichardt, Ch., *Solvents and Solvent Effects in Organic Chemistry*, Weinheim: VCH, 1988.
20. Kalashnik, A.T. and Papkov, S.P., *Vysokomol. Soedin., Ser. A*, 1981, vol. 23, no. 10, pp. 2302–2308.
21. Fridman, O.A., Naimark, N.I., Malinin, L.N., and Vladimirov, Yu.I., *Vysokomol. Soedin., Ser. A*, 1982, vol. 24, no. 3, pp. 512–516.
22. Bel'nikevich, N.G., Brestkin, Yu.V., Volosatov, V.N., and Frenkel', S.Ya., *Vysokomol. Soedin., Ser. A*, 1983, vol. 25, no. 1, pp. 119–123.
23. Vasil'ev, B.V., Ratnikov, E.N., Zhegalova, I.N., et al., *Cellulose Chem. Technol.*, 1992, vol. 26, no. 2, pp. 177–189.
24. Papkov, S.P., *Polimernye voloknistye materialy* (Polymeric Fibrous Materials), Moscow: Khimiya, 1986.
25. RF Patent 2174130.
26. *FS* (Pharmacopeia Item) *75-244-9: Dimexidum*, 1975.
27. US Patent 4565806.

ISSN 1070-4272, Russian Journal of Applied Chemistry, 2008, Vol. 81, No. 6, pp. 1057–1060. © Pleiades Publishing, Ltd., 2008.
Original Russian Text © M.V. Efanov, A.I. Galochkin, A.D. Petrakov, 2008, published in Zhurnal Prikladnoi Khimii, 2008, Vol. 81, No. 6, pp. 1019–1022.

MACROMOLECULAR CHEMISTRY AND POLYMERIC MATERIALS

Oxidative Ammolysis of Wood under the Conditions of Cavitation Treatment

M. V. Efanov, A. I. Galochkin, and A. D. Petrakov

Research Institute of Wood Thermoplastics, Federal State Scientific Institution, Barnaul, Russia
Yugra State University, Khanty-Mansiisk, Russia
TekhnoKompleks Limited Liability Company, Barnaul, Russia

Received May 15, 2007

Abstract—Effect of the composition of the lignocarbohydrate vegetable raw material, treatment duration, amount of ammonium persulfate, and concentration of free ammonia on the yield of the target product and on its content of nitrogen, carboxy groups, and lignin upon oxidative ammonolysis of vegetable waste with ammonium persulfate in aqueous ammonia under the conditions of cavitation treatment was examined. The agrochemical tests of the products as nitrogen-containing fertilizers were performed.

DOI: 10.1134/S1070427208060268

The most promising line in applied chemistry of vegetable raw materials is integrated chemical processing of the whole biomass with the aim to obtain polymeric compounds with prescribed properties. An important but poorly studied pathway of vegetable waste utilization is its use as a raw material for preparing fertilizers and sorbents [1, 2].

To obtain a nitrogen-containing fertilizer from tree bark, it was suggested to treat a vegetable raw material with oxygen in an aqueous ammonia solution (oxidative ammonolysis) [1, 3]. The drawbacks of the existing process are elevated temperature (75–200°C), high oxygen pressure (up to 8 MPa), and relatively low nitrogen content of the fertilizer obtained (1.0–3.5%).

The oxidation of lignocarbohydrate materials with ammonium persulfate in ammonia under mild conditions has yielded valuable nitrogen-containing derivatives which can be used as nitrogen-containing organic fertilizers and ion exchangers [4]. Practical use of this procedure is limited by the high cost and large consumption of ammonium persulfate.

A promising procedure of wood preactivation with the aim to enhance its reactivity in chemical modification is cavitation treatment in aqueous medium in rotary cavitation dispersers [5]. Wood subjected to cavitation treatment in various media changes its chemical composition, which leads to partial breakdown of its supramolecular structure. Cavitation treatment favors fast impregnation of lignocarbohydrate materials with solutions of modifying agents, and also leads to hydrolysis of wood polysaccharides and oxidation of lignin [5].

This treatment allows activation of lignocarbohydrate materials for chemical modification directly in the course of treatment with chemical modifiers (oxidant, alkalis, aqueous ammonia, etc.) in a reactor of a rotary cavitation disperser in the zone of intense action of hydroacoustic cavitation. For example, cavitation treatment of peat in aqueous NaOH solution increases the yield of humic substances by 50% on the average, owing to the more efficient base hydrolysis of the organic matter of the vegetable substrate [6].

There are no published data on oxidation of vegetable raw materials with ammonium persulfate in aqueous ammonia under the conditions of cavitation treatment.

In this study, we examined how the conditions of oxidative ammonolysis of lignocarbohydrate materials with ammonium persulfate in aqueous ammonia under the action of hydroacoustic cavitation affect the yield and properties of nitrogen-containing derivatives.

Table 1. Influence of the time of cavitation treatment at 60°C on the content of carboxy groups and lignin in nitrogen-containing derivatives of pine wood [$(NH_4)_2S_2O_8$ content 0.2 g g^{-1} raw material, NH_3 solution concentration 0.5%]

Treatment time, min	Product yield, %	Content, %	
		COOH groups	lignin
Initial pine wood	–	2.4	27.6
15	98	2.9	26.1
30	95	3.5	24.8
45	92	4.2	23.2
60	90	4.9	22.1

EXPERIMENTAL

As the raw material we used air-dry pine sawdust (fraction 1 mm). The raw material and treatment products were analyzed for bound nitrogen after Kjeldahl [7], for lignin after Komarov [8], and for carboxy groups by conductometric back-titration [9].

The oxidative ammonolysis was performed as follows. A 350-g portion of sawdust was placed in a 50-l temperature-controlled reactor connected to a rotary cavitation apparatus with a rotor rotation frequency of 3000 rpm. The sawdust was treated with ammonium persulfate (0.2–0.8 g g^{-1} wood) in 0.5–2.0% aqueous ammonia in an aqueous suspension at 60°C for 15–60 min. The target product was a solid residue insoluble in the reaction medium. It was filtered-off on a filter cloth, washed to negative reaction for ammonium ion with the Nessler reagent, and dried in air to constant weight, after which the yield (wt % relative to the raw material) and the content of bound nitrogen, lignin, and carboxy groups were determined. The results are given in Table 1.

Agrochemical tests of the products as nitrogen-containing organic fertilizers for pea were performed by the method of vegetation experiments, with the plant height and dry matter weight measured [10].

Table 1 and the figure show how the duration of the cavitation treatment at 60°C affect the composition of nitrogen-containing pine wood derivatives. The experiments show that a longer cavitation treatment of wood at 60°C in the presence of ammonium persulfate in aqueous ammonia results in steadily increasing content of bound nitrogen and carboxy groups, i.e., oxidative binding of nitrogen takes place.

After oxidative cavitation treatment for 60 min, up to 4.1% of bound nitrogen is introduced into the wood (see figure). With an increase in the process duration, the product yield decreases, probably because of increased oxidative base degradation of wood in aqueous ammonia. To evaluate the strength of nitrogen binding, samples of oxidized products were subjected to hydrolysis in 1 N H_2SO_4 at 100°C for 1 h (Table 2).

The acid hydrolysis under such conditions leads to active elimination of nitrogen in the form of ammonium ions from products of oxidative ammonolysis of wood. The nitrogen content of the hydrolyzed samples proportionally decreases. It is known [9] that, under such conditions, ammonia is eliminated from the $RCOONH_4$ and $RCONH_2$ groups with the formation of free carboxylic acids. Hence, if ammonia is eliminated from these functional groups, the content of carboxy groups in the hydrolyzed products should increase, which is

Table 2. Effect of hydrolyzing reagent on products of oxidative ammonolysis of pine wood

Treatment time, min	Hydrolysis conditions	Yield of solid residue, %	Characteristics of hydrolyzed product, %			
			nitrogen content	decrease in nitrogen content	content of COOH groups	gain in content of COOH groups
15	–	–	1.2	–	2.9	–
	1 N H_2SO_4, 100°C, 1 h	72.5	0.9	25	3.7	27
60	–	–	4.1	–	4.9	–
	1 N H_2SO_4, 100°C, 1 h	70.8	3.4	17	5.7	18

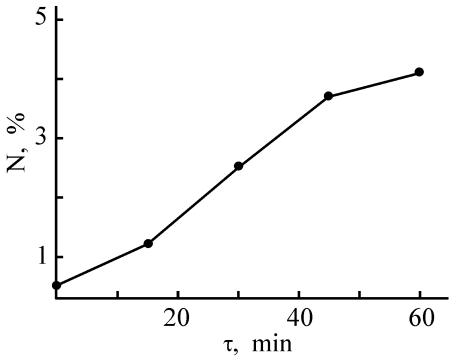
the case. The relative content of readily hydrolyzable forms of bound nitrogen in the nitrogen-containing pine wood derivatives is 17–25%, with the remaining nitrogen (75–83%) being strongly bound. A Longer oxidative ammonolysis leads to accumulation of difficultly hydrolyzable organically bound nitrogen in the wood oxidation products, whereas the content of labile nitrogen somewhat decreases.

We examined how the amount of the oxidant (ammonium persulfate) affects the functional composition of nitrogen-containing pine wood derivatives (Table 3).

The experimental results show that, with an increase in the amount of ammonium persulfate per gram of wood, the product yield decreases. This is apparently due to oxidative hydrolytic degradation of wood. With an increase in the oxidant amount from 0.2 to 0.8 g g^{-1} raw material, the content of carboxy groups and nitrogen grows from 2.9 to 6.8 and from 1.2 to 3.5%, respectively, i.e., oxidation of wood accompanied by nitrogen binding is accelerated.

We also examined the influence of the ammonia concentration on the properties of nitrogen-containing pine wood derivatives (Table 4). We found that an increase in the ammonia concentration in the aqueous suspension also leads to a certain decrease in the yield of nitrogen-containing wood derivatives, probably because of degradation (ammonolysis). An increase in the ammonia content leads to a regular increase in the content of bound nitrogen and carboxy groups in products of oxidative ammonolysis of pine wood.

The presence of various functional forms of bound nitrogen is confirmed by the IR spectra of products of oxidative ammonolysis of aspen wood. The spectra contain absorption bands characteristic of carboxylate ions in the form of ammonium salts (1595 cm^{-1}), amide groups (1625 cm^{-1}), and heterocyclic nitrogen (1680 cm^{-1}).



Bound nitrogen content in products of oxidative ammonolysis of pine wood vs. the time τ of its oxidation under the conditions of cavitation treatment.

Thus, oxidation of pine wood with ammonium persulfate in aqueous ammonia under the conditions of cavitation treatment yields macromolecular products containing up to 4.3% organic nitrogen and up to 6.8% carboxy groups. About 17–25% of the bound nitrogen is eliminated in the course of hydrolysis, and the remaining amount (75–83%) is strongly bound.

The content of lignin in products of oxidative ammonolysis of pine wood decreases with an increase in the duration of cavitation treatment and in the amounts of ammonium persulfate and ammonia (Tables 1, 3, 4), suggesting the occurrence of oxidative hydrolytic degradation of lignin in the course of oxidative ammonolysis of pine wood. That is, the process is actually delignification.

Table 3. Influence of the amount of ammonium persulfate on the properties of nitrogen-containing pine wood derivatives (duration of cavitation treatment 15 min, temperature 60°C, NH_3 concentration 0.5%)

Amount of $(NH_4)_2S_2O_8$, g g^{-1} wood	Product yield, %	Content, %		
		N	COOH groups	lignin
Initial pine wood	–	0.5	2.4	27.6
0.2	98	1.2	2.9	26.1
0.4	92	2.5	4.2	24.1
0.6	86	3.2	5.9	22.3
0.8	82	3.5	6.8	20.5

Table 4. Influence of the ammonia concentration on the properties of nitrogen-containing pine wood derivatives (duration of cavitation treatment 15 min, temperature 60°C, $(NH_4)_2S_2O_8$ amount 0.2 g g^{-1} wood)

NH_3 concentration, %	Product yield, %	Content, %		
		N	COOH groups	lignin
Initial pine wood	–	0.5	2.4	27.6
0.5	98	1.2	2.9	26.1
1.0	94	2.7	3.4	25.6
1.5	91	3.8	3.9	24.8
2.0	89	4.3	4.5	23.9

To evaluate the effect of the nitrogen-containing products obtained as growth stimulants or inhibitors for various crops, 30-day wheat acrospires of Altaiskaya-50 strain were sowed with these fertilizers. We found that the influence exerted by the products of oxidative ammonolysis of pine wood on the plant height increased with the nitrogen content of the products and the fertilizer dose. The gain in the total biomass per plant (absolutely dry weight) was 21–37%. Hence, nitrogen-containing pine wood derivatives are plant growth stimulants and can be used as nitrogen-containing organic fertilizers for crops.

CONCLUSIONS

(1) Oxidative ammonolysis of pine wood with ammonium persulfate in aqueous ammonia under the conditions of cavitation treatment yields nitrogen-containing fertilizers with a bound nitrogen content of 1.2–4.3%.

(2) Products of oxidative ammonolysis of pine wood contain, depending on the oxidation conditions, up to 4.3% organically bound nitrogen and up to 6.8% carboxy groups. The relative content of labile nitrogen is 17–25%, and the remaining 75–83% is strongly bound.

(3) With an increase in the duration of the cavitation treatment and in the amount of ammonium persulfate in aqueous ammonia, the degree of delignification of pine wood grows.

(4) The products of oxidative ammonolysis of wood stimulate the growth of the biomass of cereals and can be used as nitrogen-containing organic fertilizers.

REFERENCES

1. Deineko, I.P., Deineko, I.V., and Kornilova, L.I., *Zh. Prikl. Khim.*, 2002, vol. 75, no. 3, pp. 502–505.
2. Efanov, M.V., Dudkin, D.V., and Galochkin, A.I., *Zh. Prikl. Khim.*, 2002, vol. 75, no. 10, pp. 1745–1746.
3. USSR Inventor's Certificate, no. 545627.
4. RF Patent 2185394.
5. Katrakov, I.B., Markin, V.I., and Bazarnova, N.G., Abstracts of Papers, *3-ya Vserossiiskata konferentsiya "Khimiya i tekhnologiya rastitel'nykh veshchestv"* (3rd All-Russian Conf. "Chemistry and Technology of Vegetable Substances"), Saratov, 2004, pp. 313–314.
6. RF Patent 2296731.
7. Klimova, V.A., *Osnovnye mikrometody analiza organicheskikh soedinenii* (Main Methods for Organic Microanalysis), Moscow: Khimiya, 1975.
8. Obolenskaya, A.V., Shchegolev, V.P., Akim, G.L., et al., *Prakticheskie raboty po khimii drevesiny i tsellyulozy* (Practical Works in Chemistry of Wood and Pulp), Moscow: Lesnaya Prom–st., 1965.
9. Zakis, G.F., *Funktsional'nyi analiz ligninov i ikh proizvodnykh* (Functional Analysis of Lignins and Their Derivatives), Riga: Zinatne, 1987.
10. Dospekhov, B.A., *Metodika vegetatsionnogo opyta* (Procedure of Vegetation Experiment), Moscow: Koloss, 1985.

ISSN 1070-4272, Russian Journal of Applied Chemistry, 2008, Vol. 81, No. 6, pp. 1061–1064. © Pleiades Publishing, Ltd., 2008.
Original Russian Text © N.M. Zabivalova, A.M. Bochek, S.N. Kutuzova, 2008, published in Zhurnal Prikladnoi Khimii, 2008, Vol. 81, No. 6, pp. 1023–1026.

MACROMOLECULAR CHEMISTRY AND POLYMERIC MATERIALS

Variation of the Reactivity of Flax Fiber Cellulose in the Course of Flax Ripening

N. M. Zabivalova, A. M. Bochek, and S. N. Kutuzova

Institute of Macromolecular Compounds, Russian Academy of Sciences, St. Petersburg, Russia
Vavilov All-Russian Research Institute of Plant Cultivation, Federal Scientific Institution, Federal Scientific Center, St. Petersburg, Russia

Received December 12, 2007

Abstract—Carboxymethyl cellulose ethers were prepared from flax fibers of various degrees of ripeness. The influence exerted by the degree of ripeness of flax fibers on their reactivity in carboxymethylation was examined. The rheological properties of aqueous solutions of the synthesized carboxymethyl cellulose were studied.

DOI: 10.1134/S107042720806027X

Recently a trend has been outlined toward the use of nonwood cellulose-containing raw materials. This can be seen from papers concerning the development of procedures for production of cellulose from nontraditional sources: soybean and pea pod, ambary, jute, rice and wheat straw, cane, perennial grasses, agricultural wastes, and cotton, flax, and hemp pedicels [1].

Cellulose ethers are widely used in various fields of human activity. They are used for production of adhesives, chemical fibers, varnishes, paints, and also in other fields. For example, hydroxyethyl cellulose is used as swelling inhibitor for water-sensitive clays in well-drilling; carboxymethyl cellulose (CMC) is widely used in oil-and-gas-extracting industry as a component of viscoelastic systems in secondary treatment of oil wells. The main raw material for production of cellulose ethers is wood and cotton cellulose. A possible alternative source of cellulose for producing its derivatives is large-tonnage waste from flax production: short fibers and lignified part of flax pedicels (boon).

Flax growth and ripening are accompanied by changes in the physical and physicochemical properties of fibers, in their chemical composition, and in the molecular characteristics of cellulose and supramolecular structure of the polymer. The reactivity of flax fiber cellulose in polymer-analogous transformations depends on the above factors. The preferable period of flax collection is the early yellow-ripeness phase [2], providing collection of the maximal harvest of high-quality fibers. Before this phase, cellulose is accumulated in the fibers, and by this time fiber bundles become compact and dense, and technical ripeness of flax is attained. In this step of ripening, the lignification of shells of single fibers is insignificant [3–5]. Flax fibers in the green ripeness phase contain less lignin, so that the fibers are thinner and more flexible. After the early yellow ripeness phase is attained, lignin is accumulated up to the full ripeness phase, and the fibers become rough and rigid, losing the elasticity. As flax fibers of different degrees of ripeness are used in textile industry for different purposes, flax production wastes are formed: boon and short fibers.

It is of scientific and practical interest to compare the reactivities of cellulose from flax of various degrees of ripening in the CMC synthesis and to study the rheological properties of aqueous solutions of the ethers obtained.

EXPERIMENTAL

As starting materials we used fibers of flax of Orshanskii 2 strain, picked out in various stages of growth (budding, green ripeness, early yellow ripeness), and of Tomsk 18 strain (early yellow ripeness). Dry flax straw was soaked in distilled water for 5 days and dried in air for 24 h. From flax straw of various degrees of ripeness, fibers were picked out manually. Fiber samples were taken

Table 1. Chemical composition of flax fibers taken in various stages of ripening

Stage	Moisture content	Ash	Fats, wax	Pectins	Hemicelluloses	Lignin	Cellulose
	%						
Budding	5.66	1.13	2.67	10.07	8.97	4.80	66.70
Green ripeness	5.06	1.07	1.30	9.00	8.60	5.40	69.57
Early yellow ripeness	5.04	1.26	0.80	6.10	10.40	6.00	70.43

Table 2. Variation of DP_η and DS_{Na} of NaCMC samples in the course of carboxymethylation

Sample	Reaction time, h	Budding		Green ripeness		Early yellow ripeness	
		DP_η	DS_{Na}	DP_η	DS_{Na}	DP_η	DS_{Na}
Flax fibers*	–	3700	–	3980	–	4470	–
NaCMC	1	740	0.33	898	0.31	1080	0.39
NaCMC	2	720	0.36	810	0.35	1050	0.42
NaCMC	3.5	693	0.44	790	0.46	860	0.51
NaCMC	5	620	0.51	700	0.45	893	0.52

* After treatment with cooking solution.

from the middle part of plant pedicels. For fibers of various degrees of ripeness, we initially determined the chemical composition (Table 1). It can be seen that, with the progress of ripening, the content of cellulose and lignin in fibers increases and that of pectins and fats decreases. The concomitant substances affect the reactivity of cellulose.

Carboxymethyl cellulose samples were prepared in isopropanol [6]. First the flax fibers were pretreated with a cooking solution ($NaOH–Na_2S_2O_3–H_2O$, fiber : $NaOH$: $Na_2S_2O_3$ ratio 1 : 1.2 : 0.7) in a nitrogen flow. Such treatment allows removal of the major part of concomitant substances (hemicelluloses, pectin, lignin) with only a minor decrease in the degree of polymerization (DP_η).

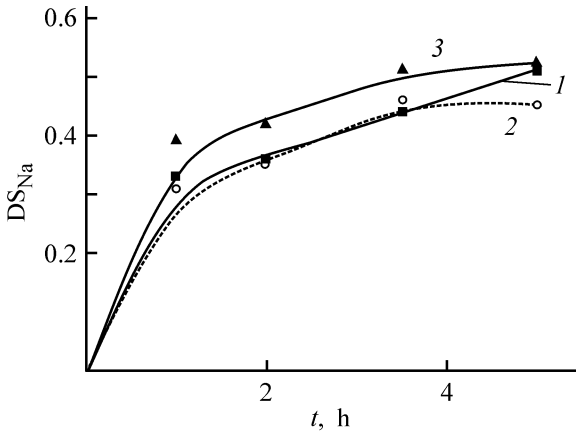


Fig. 1. Variation of DS_{Na} in the course of carboxymethylation of flax fibers of various degrees of ripeness: (*1*) budding, (*2*) green ripeness, and (*3*) early yellow ripeness; the same for Fig. 2. (t) Reaction time.

The degree of substitution with respect to carboxy groups was calculated by the formula [7]

$$DS_{Na} = \frac{162n}{2300 - 80n}, \quad (1)$$

where n is the Na content of the polymer (wt %).

The Na content of the samples was determined by conductometric titration with 0.1 N HCl. The degree of polymerization of NaCMC samples was determined viscometrically in 6% aqueous NaOH and calculated by the formula [7]

$$[\eta] = 7.3 \times 10^{-3} M^{0.93}.$$

Table 2 shows that the carboxymethylation is accompanied by a decrease in DP_η, suggesting the occurrence of oxidative degradation of the polysaccharide macromolecules. On the whole, the DP_η values of the synthesized CMC samples (based on flax fibers) are considerably higher than those of the commercial NaCMC sample (cotton linter) which was further used as a reference. For the commercial NaCMC, DP_η = 450 and DS_{Na} = 0.57. The dependences of DS_{Na} of CMC on the reaction time for fibers of flax with different degrees of ripeness are plotted in Fig. 1. Table 2 and Fig. 1 show

that the degree of ripeness of flax fibers does not appreciably affect the carboxymethylation kinetics. Apparently, pretreatment of flax fibers with the cooking solution to remove concomitant substances eliminates the effect of impurities on the cellulose reactivity. It should also be noted that preactivation of fibers with a concentrated (30%) aqueous NaOH solution before carboxymethylation also leads to partial removal of hemicelluloses, pectins, and lignin from the fibers.

Because NaCMC is widely used as aqueous solutions, we performed comparative studies of the rheological properties of moderately concentrated (wt %) aqueous solutions of NaCMC with different DS_{Na}.

Studies of the rheological properties of polymer solutions reveal specific features of the behavior of concentrated polymer solutions, gel-like systems, pastes, and suspensions, depending on the shear rate and stress, temperature, concentration, and other factors affecting the properties of these systems in the course of operation or reprocessing. Figure 2 shows the flow curves of aqueous solutions of NaCMC prepared from flax fibers of various degrees of ripeness. Similar flow curves were obtained for all the NaCMC samples represented in Table 2. The flow curves for all the systems are incomplete flow curves of non-Newtonian fluids, characteristic of strongly structured systems, such as physical thermally reversible gels [8, 9] and chemically crosslinked systems, hydrogels [10].

From the temperature dependences of the viscosity in the range 20–40°C, we calculated the activation energies of viscous flow, E_a, of the solutions. For all the solutions, the E_a values appeared to be similar, varying in the range 30.0–40.0 kJ mol^{-1}.

Table 3. Characteristics of carboxymethyl cellulose prepared by double carboxymethylation of flax fibers (Tomsk 18 strain, early yellow ripeness)

Sample	DS_{Na}	DP_η	Solubility, %
CMC (fiber):			
first etherification	0.52	950	89
second etherification	0.8	500	92
Commercial CMC	0.57	450	99

With increasing DS_{Na}, E_a tended to decrease, which is indicative of an increase in the solubility of NaCMC in water.

To raise DS_{Na}, flax fibers (Tomsk 18 strain, early yellow ripeness) were subjected to two successive carboxymethylations. The characteristics of the ethers obtained are listed in Table 3. After the first carboxymethylation of flax fibers and preparation of 1% solutions of NaCMC in water, gel particles were observed in the solution. This is caused by nonuniform carboxymethylation of flax fibers, so that fiber fragments with a low degree of substitution remain in the bulk of the material. After the repeated carboxymethylation of the same sample, DS_{Na} and the polymer solubility in water increased and the amount of gel particles decreased. The rheological properties of aqueous solutions of NaCMC samples prepared from flax fibers and of a commercial sample prepared from cotton linter are compared in Fig. 3. It is seen that aqueous solutions of NaCMC prepared from flax are more viscous than those of commercial NaCMC, which is due to the higher molecular weight of the cellulose

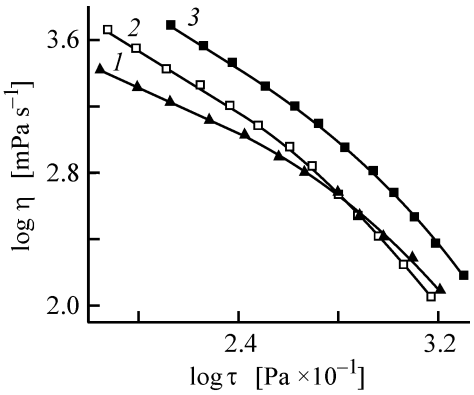


Fig. 2. Flow curves at 20°C of 1% aqueous solutions of NaCMC prepared from flax fibers of various degrees of ripeness. Reaction time 5 h. (η) Viscosity and (τ) shear stress; the same for Fig. 3.

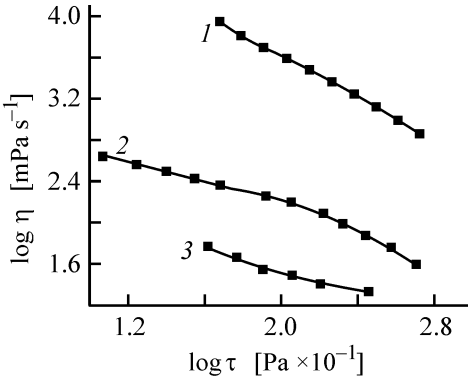


Fig. 3. Flow curves at 20°C of 1% aqueous solutions of (*1*, *2*) NaCMC prepared from flax fibers (Tomsk 18 strain, early yellow ripeness) and (*3*) commercial NaCMC (cotton). (*1*) DS_{Na} = 0.52, DP_η = 950; (*2*) DS_{Na} = 0.8, DP_η = 500; and (*3*) DS_{Na} = 0.57, DP_η = 450.

derived from flax fibers. The NaCMC prepared from flax fibers can be used as effective thickener of aqueous media in various fields of human activity.

Thus, we prepared NaCMC with various degrees of substitution from flax fibers of various degrees of ripenes.

CONCLUSIONS

(1) Pretreatment of fibers with a cooking solution to remove lignin eliminates the differences in the reactivity of flax fibers of various degrees of ripeness.

(2) Aqueous solutions (1%) of the synthesized carboxymethyl cellulose samples are more viscous than those of commercial carboxymethyl cellulose, which is caused by the considerably higher molecular weight of cellulose recovered from flax fibers.

REFERENCES

1. Barba, C., Montane, D., Rinaudo, M., and Farriol, X., *Cellulose*, 2002, no. 9, pp. 319–326.
2. *Len Belarusi* (Belarussian Flax), Golub, I.A., Ed., Minsk, 2003.
3. Kuznetsova, N.V., Biochemical Characteristics of Long-Fibered Flax of Various Geographic Origin, *Cand. Sci. Dissertation*, Leningrad, 1976.
4. Pavlencheva, N.V., Metabolism of Tissue-Specific Galactan and Development of Phloem Flax Fibers, *Cand. Sci. Dissertation*, Kazan, 2004.
5. Sal'nikov, V.V., Structural-Functional Characteristic of Formation of Cell Walls in Vegetable Tissues Specialized in Intense Synthesis of Cellulose, *Doctoral Dissertation*, St. Petersburg, 2005.
6. *Prakticheskie raboty po khimii drevesiny* (Practical Works in Wood Chemistry), Nikitin, V.M., Ed., Moscow: Lesnaya Prom–st., 1965.
7. Petropavlovskii, G.A., *Gidrofil'nye chastichno zameshchennye efiry tsellyulozy i ikh modifikatsiya putem khimicheskogo sshivaniya* (Hydrophilic Partially Substituted Cellulose Ethers and Esters and Their Modification by Chemical Cross-Linking), Leningrad: Nauka, 1988.
8. Bochek, A.M., Petropavlovskii, G.A., Kutsenko, L.I., and Karetnikova, E.B., *Zh. Prikl. Khim.*, 2000, vol. 73, no. 1, pp. 152–155.
9. Bochek, A.M., Nud'ga, L.A., Petrova, V.A., and Petropavlovskii, G.A., *Zh. Prikl. Khim.*, 2000, vol. 73, no. 2, pp. 304–308.
10. Buyanov, A.L., Revel'skaya, L.G., Petropavlovskii, G.A., and Kopytchenko, L.A., *Zh. Prikl. Khim.*, 1992, vol. 65, no. 2, pp. 679–685.

ISSN 1070-4272, Russian Journal of Applied Chemistry, 2008, Vol. 81, No. 6, pp. 1065–1067. © Pleiades Publishing, Ltd., 2008.
Original Russian Text © B.M. Ginzburg, Sh. Tuichiev, S.Kh. Tabarov, 2008, published in Zhurnal Prikladnoi Khimii, 2008, Vol. 81, No. 6, pp. 1027–1029.

BRIEF COMMUNICATIONS

Concentration Dependence of the Density of C_{70} Fullerene Solutions in Aromatic Solvents

B. M. Ginzburg, Sh. Tuichiev, and S. Kh. Tabarov

Institute of Problems in Machine Science, Russian Academy of Sciences, St. Petersburg, Russia
Tajik State National University, Dushanbe, Tajikistan

Received February 18, 2008

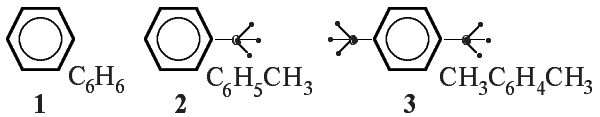
Abstract—The concentration dependences of densities of fullerene C_{70} solutions in benzene, toluene, and *p*-xylene were determined pycnometrically.

DOI: 10.1134/S1070427208060281

Previously we have determined the concentration dependences of the densities of C_{60} fullerene solutions in benzene, toluene, and *p*-xylene [1]. These dependences are nonmonotonic: The density initially decreases, passes through a minimum, and then again increases to reach values exceeding the density of the pure solvent. This trend correlates with the concentration dependences of the intensities of small-angle X-ray scattering [2–4].

It should be noted that aromatic liquids of the above type are relatively good solvents for C_{70} fullerene [5], although its solubility is lower than that of C_{60}. Nevertheless, just toluene and xylene are used for recovering C_{60} and C_{70} from the fullerene soot [6]. They are also used for preparing mixed solutions of fullerenes and polymers, or solutions of fullerenes with grafted polymer chains for subsequent construction of various fullerene–polymer systems. Thus, the behavior of fullerenes in aromatic solvents is of not only scientific, but also applied interest.

In this study, we determined the concentration dependence of the density of C_{70} fullerene solutions in benzene **(1)**, toluene **(2)**, and *p*-xylene **(3)**:



1 **2** **3**

EXPERIMENTAL

C_{70} fullerene prepared by the Kratschmer–Huffman method [6] (99.7% purity) and chemically pure grade benzene, toluene, and *p*-xylene (after their single distillation) were used. Initially a mother liquor with the known maximal fullerene concentration c_{max} (%) was prepared. Then solutions with intermediate concentrations were prepared by its dilution in appropriate volume or weight ratios. The concentration interval was varied from $c = 10^{-4}$% to concentrations close to saturation.

The error in determination of low concentrations was about 1–2%, and that for the highest concentrations, 0.1–0.2%.

The densities of solvents and solutions were determined pycnometrically. A standard Pyrex glass pycnometer (Czechia) with a ground-glass stopper and a mark corresponding to a liquid volume of 6.9 ml was used. Weight measurements were performed on a VLR-20g analytical balance with an error of 5×10^{-5} g in a temperature-controlled volume. The temperature of 24°C was maintained constant with an error of ±0.5°C. However, direct temperature measurements performed with an error of ±0.01°C showed that, during measurements of the solution density of a given concentration, the temperature does not change noticeably, and in going to other concentrations it changes by no more than 0.1°C. The error of pycnometric measurements of the density was ±0.0001 g cm^{-3}. For solutions of a given concentration, three to five measurements were performed, and the arithmetic mean was determined. The error of the density measurement for a solution of a given concentration did not exceed 0.01%.

Estimation of errors in measurements of pure solvent densities

Solvent	Density, g cm^{-3}				Relative error, %
	d, [7]	standard, corrected d_{st}^{*}	experimental, d_{exp}	$d_{exp} - d_{st}$	
Benzene	0.8790	0.8788	0.8880	+0.0092	1
Toluene	0.8669	0.8667	0.8776	+0.0099	1
p-Xylene	0.8611	0.8609	0.8665	+0.0056	0.5

* In [7], somewhat overestimated densities were reported, which were related to water density at 4°C. It is not equal to 1, but is close to 0.9998 [8]. Therefore, the d_{st} values obtained by multiplication by 0.9998 of d values presented in [7] are listed in the table. In all cases, the overestimation is 0.0002 g cm^{-3}.

The results of measurements are shown in Fig. 1. It should be noted that the accuracy in measuring the absolute values of the densities of the pure solvents was relatively high: deviations from the standard tabulated points did not exceed 1% (0.01 g cm^{-3} in absolute values, see table).

The concentration dependence of the density of C_{70} fullerene solutions in toluene and carbon disulfide has been measured previously by Tomiyama et al. [9]. In [9], the density of toluene was determined as 0.8619–0.8622 g cm^{-3}, i.e., deviation from the standard value was observed already in the third decimal place, and the minimal C_{70} concentration was 0.05 mg ml^{-1}, which corresponds to approximately 5.8%. This value substantially exceeds the concentrations we examined in this study, which explains why no density minima were observed in [9].

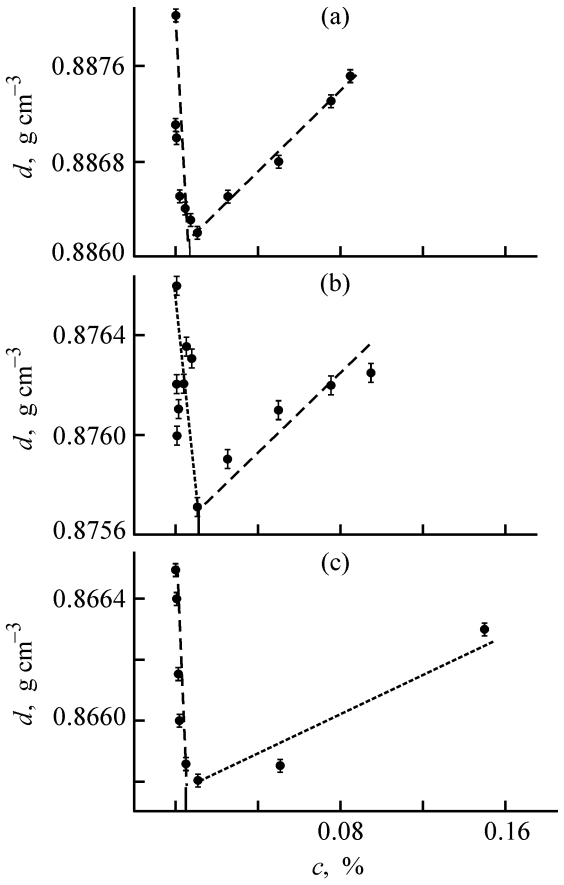


Fig. 1. Concentration dependences of densities d of C_{70} fullerene solutions in (a) benzene, (b) toluene, and (c) *p*-xylene. Temperature 24°C, pressure 697 mm Hg.

However, the main result of our study consist in revealing the specific nonmonotonic concentration dependence of the solution density, rather than in determining the absolute values of the density of C_{70} solution. For all the solvents studied, as the C_{70} concentration increases, the solution density initially sharply decreases and then, after passing through a minimum, nearly linearly grows, but does not reach the density of the pure solvent.

As can be seen from Fig. 1, each density curve is well approximated by two linear portions. Similar broken lines were observed in [10] for C_{60} solutions.

Thus, the reliability of the specific shape of the above dependences is confirmed by the following facts: (1) similarity of the dependences for three solvents, (2) similarity of the dependences for C_{60} and C_{70} solutions, and (3) correlation with data of wide-angle X-ray measurements [11].

We should note that the density, initially decreases, despite that the density of neat fullerene is approximately two times the densities of the solvents. The initial decrease in the density may be due to formation of shells with decreased density around fullerene molecules or their aggregates, and the subsequent increase in the density may be due to solvent structuring [2–4], i.e., to certain suppression of thermal fluctuations of the den-

sity and to ordering on the molecular level, which is also manifested in small- and wide-angle X-ray diffraction patterns.

It follows from Fig. 1 that the density minimum is reached at a C_{70} fullerene concentration of about 0.005–0.01% and is practically independent of the solvent, in contrast to C_{60} [1]. This is in agreement with approximately the same C_{70} solubility in the solvents examined (benzene 1.3 and toluene 1.4 mg ml^{-1} [5]). Apparently, the character of the changes in the supramolecular structure of C_{70} solutions, namely, formation of shells with decreased density and solvent structuring, should affect the solution properties.

CONCLUSION

At low C_{70} fullerene concentrations (starting from 10^{-4}%) in the aromatic solvents studied, the solution density varies nonmonotonically as the fullerene concentration increases: initially it sharply decreases and then, after passing through a minimum, sharply grows.

ACKNOWLEDGMENTS

The study was financially supported within the framework of interdisciplinary project of the St. Petersburg Scientific Center, 2008, and by ISTC (project T-1145).

REFERENCES

1. Ginzburg, B.M., Tuichiev, Sh, and Tabarov, S.Kh., *Pis'ma Zh. Tekh. Fiz.*, 2007, vol. 33, no. 15, pp. 22–26.
2. Ginzburg, B.M., Tuichiev, Sh., Tabarov, S.Kh., and Shepelevskii, A.A., *Kristallografiya*, 2005, vol. 50, no. 4, pp. 597–600.
3. Ginzburg, B.M., Tuichiev, Sh, and Tabarov, S.Kh., et al., *Zh. Prikl. Khim.*, 2005, vol. 78, no. 6, pp. 1047–1049.
4. Ginzburg, B.M. and Tuichiev, Sh., *Kristallografiya*, 2007, vol. 52, no. 1, pp. 109–112.
5. Bezmel'nitsyn, V.N., Eletskii, A.V., and Okun', M.V., *Usp. Fiz. Nauk*, 1998, vol. 168, no. 11, pp. 1195–1220.
6. Kratschmer, W. and Huffman, D.R., *Phil. Trans. Royal Soc. London, Ser. A*, 1993, vol. 1667, no. 343, pp. 33–38.
7. *Khimicheskii entsiklopedicheskii slovar'* (Chemical Encyclopedic Dictionary), Knunyants, I.L., Ed., Moscow: Sov. Entsiklopediya, 1983.
8. *Khimicheskii entsiklopedicheskii slovar'* (Chemical Encyclopedic Dictionary), Knunyants, I.L., Ed., Moscow: Sov. Entsiklopediya, 1988, p. 395.
9. Tomiyama, T., Uchiyama, S., and Shinohara, H., *Chem. Phys. Lett.*, 1997, vol. 264, pp. 143–148.
10. Mekalova, N.V., *Fullereny v rastvorakh* (Fullerenes in Solutions), Ufa: Ufimsk. Gos. Neftyanoi Tekh. Univ., 2001.
11. Ginzburg, B.M., Tuichiev, Sh., and Tabarov, S.Kh., *Kristallografiya*, 2008, vol. 53, no. 4, pp. 661–665.

ISSN 1070-4272, Russian Journal of Applied Chemistry, 2008, Vol. 81, No. 6, pp. 1068–1070. © Pleiades Publishing, Ltd., 2008.
Original Russian Text © V.P. Tolstoi, L.B. Gulina, 2008, published in Zhurnal Prikladnoi Khimii, 2008, Vol. 81, No. 6, pp. 1030–1032.

BRIEF COMMUNICATIONS

Sb_2S_3–SiO_2 Nanocomposite Layers Synthesized Using the Layer-by-Layer Technique

V. P. Tolstoi and L. B. Gulina

St. Petersburg State University, At. Petersburg, Russia

Received December 27, 2007

Abstract—Possibility of layer-by-layer synthesis by colloidal layering of Sb_2S_3–SiO_2 nanocomposite layers from colloid solutions of $\{[H_xSb_2S_5]^{m-}\}mNa^+$ and SiO_2 was studied. The composition of the layers synthesized was examined by Raman spectroscopy, transmission spectroscopy in the UV and visible spectral ranges, energy-dispersion microanalysis, and scanning electron microscopy.

DOI: 10.1134/S1070427208060293

As is known, a prominent place in preparative chemistry of nanolayers is occupied by methods of layer-by-layer synthesis. These techniques are based on performing successive acts of adsorption or adagulation of low-dimension precursors, with obligatory removal of their unreacted excess. As a result, a nanolayer of a substance being synthesized, i.e., a layer with a thickness of several nanometers or fractions of a nanometer, is formed on the surface. Upon a multiple repetition of the adsorption reactions, the thickness of this layer increases in proportion to the number of treatment cycles.

A method for synthesis of this kind is the colloidal layering (CL) technique, which consists in successively performing multiple reactions of adagulation of colloid particles at substrate surfaces in reagent solutions. Previously, two pathways have been suggested for synthesis of oxides by this method. The first [1] is based on formation of difficultly soluble compounds by performing on the substrate surface successive reactions of adagulation of $Sn(II)(OH)_xF_y^-$ colloid particles, with their subsequent oxidation to $Sn(OH)_4$. Upon the oxidation reaction, the $Sn(II) \rightarrow Sn(IV)$ transition occurs and, in the pH range of the reagent solutions used, the negative surface charge changes to positive. As a result, the reaction of adagulation of $Sn(II)(OH)_xF_y^-$ colloid particles can again proceed at the surface and a reversible cyclic growth of the layer thickness becomes possible. The second pathway [2] is based on successive treatments of a substrate with colloid solutions containing positively (ZnO) and negatively (Mg–Al-silicate) charged colloid particles yielding a layer of the nanocomposite when interacting at the surface.

The aim of this study was to examine specific features of synthesis by the CL method of Sb_2S_3–SiO_2 nanocomposite layers. As is known, Sb_2S_3 is a semiconductor and it would be expected that the quantum-confinement effect should be manifested in the electrical and optical properties of its nanoparticles. At the same time, layers of nano- and mesoporous composite can find use as inorganic membranes and ion-exchange materials.

Upon multiple successive treatments, a layer characterized by a spectrum in the UV and visible spectral ranges (Fig. 1) is formed on the surface. The intensity of the broad absorption band at

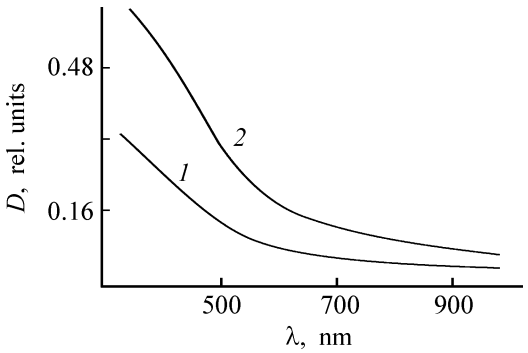


Fig. 1. Transmission spectra of Sb_2S_3–SiO_2 nanolayers synthesized on the surface of fused silica upon (*1*) 6 and (*2*) 12 CL cycles. c_{SiO_2} = 0.02 M, $c_{N_2H_4}$ = 0.01 M, $c_{Na_3SbS_4}$ = 0.01 M; the same for Figs. 2, 3. (*D*) Optical density and (λ) wavelength.

300–600 nm in this spectrum increases in proportion to the number of CL cycles. The composition of this layer was found from the Raman spectra in Fig. 2 and from results of an X-ray fluorescence microanalysis for a sample synthesized on the surface of aluminum. The Raman spectrum of this layer shows a band peaked at 300 cm^{-1}, characteristic of Sb_2S_3 [3], and, according to the X-ray data, the ratio of the element concentrations in the layer is Si : Sb : S = 1.0 : 1.0 : 1.5, which confirms the Raman data.

A SEM study of the morphology of the layers demonstrated (Fig. 3) that the layer is composed of nanoparticles 10 to 30 nm in size.

The results obtained can be accounted for by the following sequence of reactions occurring at the surface in the course of synthesis. In the first stage, after lead cations are adsorbed on the silica surface and their excess amount is removed by washing in water, ≡Si–OPbOH groups are formed on the surface and serve as centers of adsorption of $[H_xSb_2S_5]^{m-}$ colloid particles from the Na_3SbS_4 solution. Further, after a treatment in a SiO_2–$N_2H_4 \cdot HCl$ solution, the reduction $Sb^{5+} \rightarrow Sb^{3+}$ is observed and Sb_2S_3 nanoparticles are formed. These particles presumably have a positive charge on the surface and serve as adsorption centers for SiO_2 colloid particles. Thus, the subsequent cyclic treatment in solutions of the chosen reagents leads to a cyclic reproducible growth of a Sb_2S_3–SiO_2 layer.

EXPERIMENTAL

As substrates for synthesis of nanolayers were chosen polished single-crystal Si <100> wafers of KDB-40 brand (*p*-Si : B with a resistivity of 40 Ω cm), fused silica of KV brand, and electrolytic aluminum (99.99% purity). The procedure used to prepare the substrates for synthesis was described in [4].

The synthesis was performed as follows. After a standard pretreatment, the substrates were treated with a 0.01 M $Pb(NO_3)_2$ solution for 30 min, washed with water to remove the excess amount of the salt, mounted on the holder of the automated installation, and successively treated with Na_3SbS_4 solutions, water, a SiO_2–$N_2H_4 \cdot HCl$ solution, and again water. One treatment of this kind constituted a single cycle of CL, which was repeated many times. The time of treatment with each reagent was 30 s.

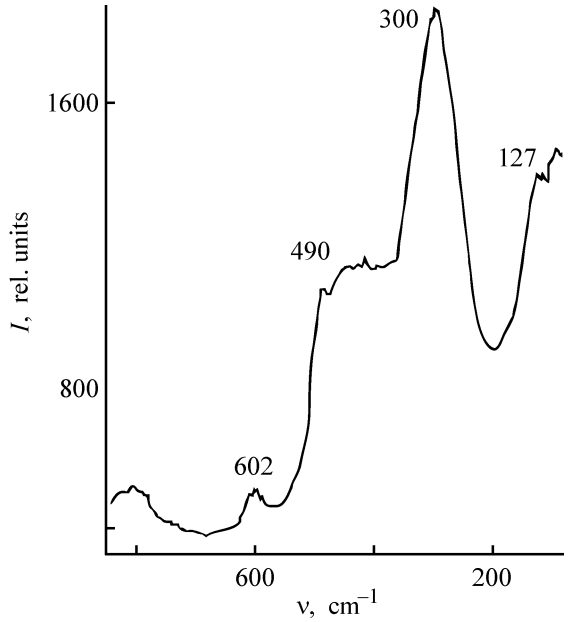


Fig. 2. Raman spectrum of a Sb_2S_3 layer synthesized on the surface of fused silica upon 10 CL cycles. (*I*) Intensity and (ν) wave number.

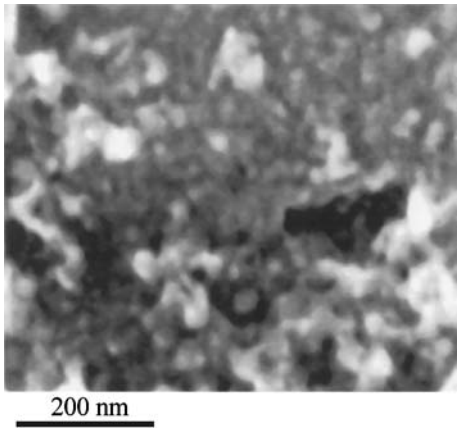


Fig. 3. SEM micrograph of the surface of a Sb_2S_3–SiO_2 layer synthesized on the surface of silicon. The layer was synthesized upon 15 CL cycles.

The colloid solution of SiO_2 was prepared by acidifying a freshly prepared 0.02 M solution of Na_2SiO_3 with HCl to pH 7. The synthesis was performed from solutions kept for 24 h at room temperature. According to the data of [5], colloid particles in a solution of this kind are 4–10 nm in size. Immediately before synthesis, $N_2H_4 \cdot HCl$ was introduced into this solution to a concentration of 0.01 M. The colloid solution of Na_3SbS_4 was prepared by dissolving the salt in water and adjusting its pH to 8.5 by addition of CH_3COOH.

It was found that, at this pH value, a light yellow colloid solution of Sb_2S_5 is formed and remains stable for 24 h.

Transmission spectra in the UV and visible spectral ranges were recorded on a Perkin–Elmer Lambda-9 spectrometer at a scanning rate of 50 nm min^{-1} and 2-nm slit program. Images of the sample surface were obtained using a Zeiss EVO40EP electron microscope with a LaB_6 cathode. An X-ray fluorescence microanalysis was performed on this microscope at an accelerating voltage of 20 kV with an Oxford Instruments INCA 350 energy-dispersion analyzer. The Raman spectra were recorded using a Bruker SENTERRA instrument, with laser excitation at a wavelength of 785 nm.

ACKNOWLEDGMENTS

The study was supported by the Russian Foundation for Basic Research (grant no. 05-03-33 207).

REFERENCES

1. Tolstoi, V.P., *Zh. Neorg. Khim.*, 1993, vol. 38, no. 7, p. 1146.
2. Szabo, T., Nemeth, J., and Dekany, I., *Coll. Surf., Ser. A: Physicochem. Eng. Asp.*, 2004, vol. 230, p. 23.
3. Mane, R.S. and Lokhande, C.D., *Mater. Chem. Phys.*, 2002, vol. 78 , p. 385.
4. Tolstoi, V.P. and Stepanenko, I.V., *Zh. Obshch. Khim.*, 2005, vol. 75, no. 1, p. 53.
5. Iler, R.K., *The Chemistry of Silica*, New York: Interscience, 1979.

ISSN 1070-4272, Russian Journal of Applied Chemistry, 2008, Vol. 81, No. 6, pp. 1071–1073. © Pleiades Publishing, Ltd., 2008.
Original Russian Text © M.V. Lyubavin, Yu.Yu. Gavronskaya, V.N. Pak, 2008, published in Zhurnal Prikladnoi Khimii, 2008, Vol. 81, No. 6, pp. 1033–1035.

BRIEF COMMUNICATIONS

Electrical Conductivity of Porous Glasses Saturated with Sulfuric Acid Solutions

M. V. Lyubavin, Yu. Yu. Gavronskaya, and V. N. Pak

Hertzen Russian State Pedagogical University, St. Petersburg, Russia

Received December 27, 2007

Abstract—Electrical conductivity of porous glasses saturated with sulfuric acid solutions was studied. At impregnating solution concentrations in the range 20–40 wt %, the glasses have high conductivities $\sigma > 0.1\ \Omega^{-1}\ cm^{-1}$. The dependences of the electrical conductivity on parameters of the porous structure of membranes are considered.

DOI: 10.1134/S107042720806030X

The current literature pays increasing attention to development of proton-conducting membranes intended for use in fuel cells and devices for detection and generation of hydrogen. A considerable part of studies in this area are devoted to sulfo polymers and polymeric media impregnated with sulfuric and phosphoric acids [1–6]. Also, potentialities of sol–gel methods are intensively studied in order to obtain composite materials with proton conductivity, including porous oxides, polymeric fillers, and inorganic acids [7–12]. In particular, it has been found recently that the electrical conductivity of mesoporous silicas impregnated with sulfuric acid reaches high values on the order of 0.1 $\Omega^{-1}\ cm^{-1}$ [12]. In this context, it seems promising to use membranes made of porous glass (PGs) as proton-conducting media. To indubitable advantages of PGs belong the widely controllable parameters of the porous structure, narrow pore size distribution, mechanical strength, and stability in acid media [13, 14]. In this study, the electrical conductivity of a number of PG membranes saturated with sulfuric acid solutions was examined.

EXPERIMENTAL

Experiments were carried out with porous glasses in the form of 10 × 10-mm square plates with a thickness of 1 mm, which had structural parameters listed in the table. The procedures used to fabricate PG membranes of the series specified have been more than once described in the literature [13–15]. In impregnation of the membranes with sulfuric acid solutions, it is necessary to provide the maximum possible and reproducible filling of the space of through channels. The actually reached content Q of encapsulated electrolyte in a PG plate of mass m_0 is linearly related to the density ρ of the impregnating solution and the pore volume V_p of the glass by the expression

Pore radius r_p, pore volume V_p, porosity ε, and degree γ of filling of the internal space of PG membranes by sulfuric acid solutions with concentrations of 20–40 wt %

r_p, nm	V_p, cm^3	ε, %	γ at indicated c, wt %				
			20	25	30	35	40
4.5	0.260	33.1	0.91	0.90	0.88	0.87	0.86
9.0	0.531	53.4	0.92	0.91	0.91	0.89	0.89
19.0	0.423	46.3	0.93	0.93	0.93	0.93	0.90
74.0	0.348	42.1	0.95	0.95	0.95	0.93	0.90

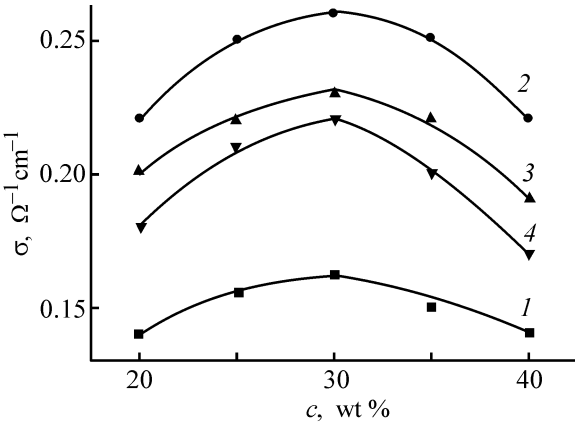


Fig. 1. Electrical conductivity σ of impregnated PGs vs. the concentration c of impregnating sulfuric acid solutions. Pore radius (nm): (*1*) 4.5, (*2*) 9, (*3*) 19, and (*4*) 74; the same for Fig. 3.

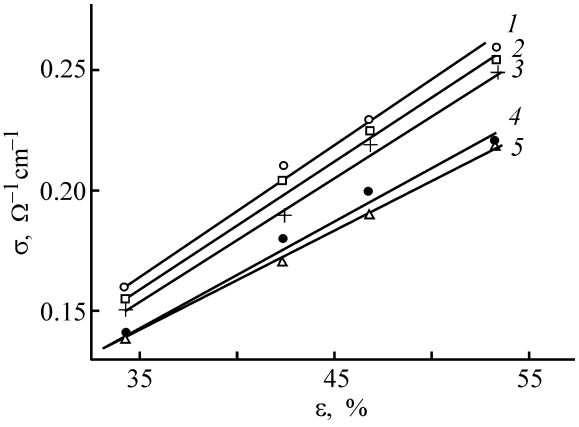


Fig. 2. Electrical conductivity σ of PG saturated with H_2SO_4 solutions vs. the volume porosity ε. H_2SO_4 concentration (wt %): (*1*) 20, (*2*) 25, (*3*) 30, (*4*) 35, and (*5*) 40.

$$Q = m_0 \rho V_p \gamma, \quad (1)$$

where $\gamma < 1$ is a dimensionless coefficient reflecting the deviation from the ideal (limiting) filling.

PGs were most fully and reproducibly impregnated via the capillary rise of the liquid in through pores. In this case, the solution was absorbed through one of the plane-parallel surfaces of a plate, with air allowed to be freely displaced through the other. As a result of impregnation in this mode, the γ defined as the ratio between the experimentally measured mass Q of the solution in PG and its limiting value was close to 0.9 in all cases, and a weak tendency was observed for γ to increase with the radius of membrane channels (see table). To reduce the contact resistance of a plate, PGs impregnated with H_2SO_4 solutions with a concentration of 20–40 wt % were coated with a layer (~1 mm thick) of graphite with an average particle size of 10–20 μm. Then, the samples were placed between planar polished graphite pressure contacts with a constant compression force of 200 g cm^{-2}. The electrical resistance was measured at 293 K in the ac mode (1 kHz) with an E7-11 multimeter. The recorded resistance was recalculated to electrical conductivity σ with account of the real dimensions of the PG plates.

Figure 1 shows how σ of impregnated PG membranes depends on the concentration of the acid introduced into the pores. In all cases, considerable values $\sigma > 0.1$ Ω^{-1} cm^{-1} are reached, with the expected maximum corresponding to an impregnating solution concentration c = 30 wt %. A strongly nonmonotonic dependence of the PG pore radius is observed on the background of pronounced differences between the electrical conductivities of different samples (Fig. 1). At the same time, it can be noted that the highest values of σ, obtained for the membrane with a channel radius of 9 nm, correspond to the maximum porosity ε = 53.3% (see table), which exceeds the volume fraction of the nonconducting silica skeleton. Comparison of the values of σ and ε for the PG membranes studied shows (Fig. 2) that an increase in the internal space filled by the acid provides a nearly linear rise in the electrical conductivity for all concentrations of the solutions used. The specific features revealed in the behavior of the PG–acid systems indicate that the pore radius itself is not an important factor affecting the electrical conductivity of impregnated glasses. Indeed, the role of a compressed electric double layer (EDL) in charge transport is at a minimum at high concentrations of acid solutions in through pores of the membranes. Thus, even at a considerable decrease in the pore radius in the set of the systems studied, the EDL is not overlapped and, as a result, the electrical conductivity is not limited.

Thus, there is reason to believe that the intrinsic electrical conductivity of strong sulfuric acid solutions remains the same in the set of the PG membranes, i.e., it is independent of their porous structure. To verify this assumption, the measured values of σ for PG–H_2SO_4 systems should be recalculated taking into account the following factors: the real free cross-section of the membranes, which provides the electrical conduction, and the degree of filling of the pore space by the electrolyte:

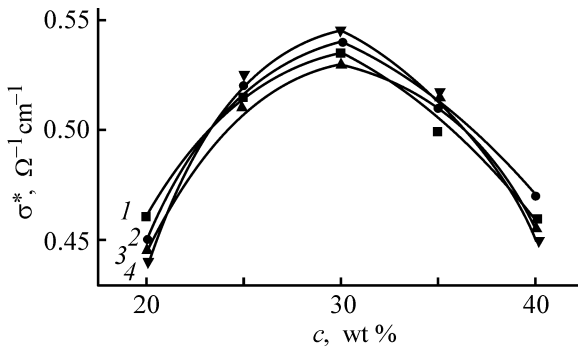


Fig. 3. Electrical conductivity σ^* of sulfuric acid in PG membranes vs. its concentration c.

$$\sigma^* = \sigma\varepsilon\gamma. \quad (2)$$

The closeness of the concentration dependences of σ^* (Fig. 3) confirms, on the whole, the assumption made: the maximum differences between the electrical conductivities of sulfuric acid for the set of membranes do not exceed 0.03 Ω^{-1} cm^{-1}, which is comparable with the measurement error. Here, it should be noted that σ^* is, on the whole, substantially lower than that of free H_2SO_4 solutions. Most likely this occurs because a contact resistance exists in the measuring system used. Nevertheless, the results obtained reliably confirm the high level of the proton electrical conductivity of the systems suggested, compared with the known published values.

CONCLUSION

Porous-glass membranes saturated with sulfuric acid solutions have a high proton electrical conductivity reaching values of 0.2 Ω^{-1} cm^{-1}. At impregnating solution concentrations in the range 20–40 wt %, the electrical conductivity of impregnated membranes is proportional to their volume porosity.

REFERENCES

1. Lin, C.W., Huang, Y.F., and Kannan, A.M., *J. Power Sources*, 2007, vol. 164, no. 2, pp. 449–456.
2. Aihara, Y. and Sonai, A., *J. Power Sources*, 2006, vol. 163, no. 1, pp. 60–65.
3. Martinelli, A., Matic, A., Jacobsson, P., et al., *Solid State Ionics*, 2006, vol. 177, Spec. Issue 26–32, pp. 2431–2435.
4. Lin, C.W., Thangamuthu, R., and Yang, C.G., J. Membr. Sci., 2005, vol. 253, nos. 1–2, pp. 23–31.
5. Asensio, J.A., Borros, S., and Gomez-Romero, P., *Electrochim. Acta*, 2004, vol. 49, no. 25, pp. 4461–4466.
6. Pu, H., Meyer, W.H., and Wegner, G., *J. Polym. Sci., Part B: Polym. Phys.*, 2002, vol. 40, no. 7, pp. 663–669.
7. Kanamura, K., Mitsui, T., and Munakata, H., *Chem. Mater.*, 2005, vol. 17, no. 19, pp. 4845–4851.
8. Honma, I., Nomura, S., and Nakajima, H., *J. Membr. Sci.*, 2001, vol. 185, no. 1, pp. 83–94.
9. Mioc, U.B., Milonjic, S.K., Malovic, D., et al., *Solid State Ionics*, 1997, vol. 97, nos. 1–4, pp. 239–246.
10. Kuraoka, K., Sato, M.A., Hamano, Y., et al., *J. Mater. Sci.*, 2007, vol. 42, no. 6, pp. 2212–2214.
11. Kalappa, P. and Lee, J.H., *Polym. Int.*, 2007, vol. 56, no. 3, pp. 371–375.
12. Lin, Y.F., Ma, C.C., Lin, Y.Y., et al., *Key Eng. Mat.*, 2007, vols. 334–335, no. 2, pp. 945–948.
13. Roskova, G.P. and Tsekhomskaya, T.S., *Fiz. Khim. Stekla*, 1981, vol. 7, no. 5, pp. 513–534.
14. Enke, D., Janovski, F., and Schwieger, W., *Micropor. Mesopor. Mater.*, 2003, vol. 60, nos. 1–3, pp. 19–30.
15. Antropova, T.V. and Drozdova, I.A., *Fiz. Khim. Stekla*, 1995, vol. 21, no. 2, pp. 199–209.

ISSN 1070-4272, Russian Journal of Applied Chemistry, 2008, Vol. 81, No. 6, pp. 1074–1077. © Pleiades Publishing, Ltd., 2008.
Original Russian Text © V.V. Patrushev, S.V. Ostanova, A.V. Chubarov, S.V. Drozdov, 2008, published in Zhurnal Prikladnoi Khimii, 2008, Vol. 81, No. 6, pp. 1036–1038.

BRIEF COMMUNICATIONS

Behavior of Silver Sulfide in the System Ag_2S–$Fe(NO_3)_3$–HNO_3–H_2O

V. V. Patrushev, S. V. Ostanova, A. V. Chubarov, and S. V. Drozdov

Institute of Chemistry and Chemical Technology, Siberian Branch, Russian Academy of Sciences, Krasnoyarsk, Russia

Received November 2, 2007

Abstract—Behavior of silver sulfide in the system Ag_2S–$Fe(NO_3)_3$–HNO_3–H_2O was studied at 25, 55, and 80°C using the method of the simplex-lattice experiment design. The quantitative dependences of Ag_2S oxidation on the concentrations of the acid and Fe^{3+} were determined. The isoconcentration diagrams were obtained.

DOI: 10.1134/S1070427208060311

The main amount of silver is extracted from complex ores and concentrates in which silver is in the form of silver sulfide, argentite, one of the most widespread minerals. Argentite is contained in gravitational and flotation concentrates produced in processing of gold- and silver-containing ores and, in particular, lead-zinc ores, and in secondary raw materials.

Hydrometallurgical procedures for recovery of silver, including that in the form of silver sulfide, employ cyanide [1, 2], thiocyanate [3], thiourea [4], and thiosulfate [5] solutions. However, it is necessary to use in such cases oxidizing agents, e.g., O_2 or Fe^{3+}, which involves additional expenditure.

A technology for processing of sulfide lead-zinc ores and concentrates and, in particular, those from the Gorevo deposit with the use of nitric acid and iron(III) nitrate solutions has been developed. The behavior of silver sulfide in systems of this kind has not been studied.

Nitric acid is a strong oxidant ($E^0_{NO_2/HNO_3}$ = 0.80 V) and, therefore, it oxidizes silver sulfide without introduction of any additional oxidizing agent into a system. However, it is of interest to study the effect of Fe^{3+} additives on the process of argentite oxidation. This is due to the composition of technological solutions, because, in most cases, the concentration of Fe^{3+} ions is appreciable when nitrate acid-salt solvents are used for processing of silver-containing ores and concentrates.

EXPERIMENTAL

To obtain information about the oxidation of silver sulfide in complex systems with various mineral forms in industrial processing of silver-containing ores and concentrates, we studied Ag_2S–$Fe(NO_3)_3$–HNO_3–H_2O systems with a high content of silver. The silver sulfide synthesized was identified by X-ray phase analysis. The behavior of Ag_2S in the systems under study was judged from the variation of the total silver concentration in solution and from the composition of insoluble precipitates. The concentration of silver in solution was determined by titration analysis and atomic-absorption spectrophotometry [6, 7], and that of HNO_3, by titration analysis [7]. The mathematical data processing was carried out by the method of simplex-lattice experiment design [8].

The experiments were performed in thermostated cells at 25 ± 0.1, 55 ± 0.1, and 80 ± 0.1°C in the course of 2 h, with mechanical stirring at s : l = 1 : 5. Preliminary experiments demonstrated that making longer the time of contact of phases does not change the silver concentration in solution. After the completion of the experiments, the solution was analyzed for the content of silver and nitric acid. The solid phase was filtered and washed with water and ethanol to remove the solution,

Design matrix for the incomplete cubic model*

Experiment no.	Volume fraction of a solution			Amounts of oxidized silver sulfide, %					
				Y_{exp}	Y_{calc}	Y_{exp}	Y_{calc}	Y_{exp}	Y_{calc}
	X_1	X_2	X_3	25°C		55°C		80°C	
1	1	0	0	ND	0	ND	0	0.922	0.922
2	0	1	0	0.618	0.618	11.538	11.538	36.896	36.896
3	0	0	1	26.815	26.815	100.000	100.000	100.000	100.000
4	0.5	0.5	0	0.249	0.249	2.769	2.769	14.989	14.989
5	0	0.5	0.5	11.885	11.885	64.846	64.846	100.000	100.000
6	0.5	0	0.5	5.192	5.192	43.154	43.154	86.474	86.474
7	0.33	0.33	0.33	4.455	4.458	35.963	35.960	66.938	66.938
8	0.15	0.15	0.7	2.538	2.539	72.040	72.041	100.000	100.951
9	0.15	0.7	0.15	11.238	11.238	24.655	24.657	52.999	53.066
10	0.7	0.15	0.15	1.568	1.569	12.882	12.883	34.755	34.753

* X_1 stands for H_2O (55.56 M); X_2, $Fe(NO_3)_3$ solution (1.8 M); X_3, HNO_3 solution (3.2 M); Y_{exp} and Y_{calc}, experimental and calculated amounts of oxidized silver sulfide; ND, not determined.

dried, and subjected to an X-ray phase analysis. The data obtained were processed by the method of simplex lattices, whose application to systems of this kind yielded good results in [9, 10]. The simplex-lattice design for an incomplete cubic model employed in the study is presented in the table.

Using the data obtained, we calculated the coefficients of polynomials of incomplete third order, which describe the dependence of the degree of silver sulfide oxidation on the reactant concentrations. The equations were used to construct composition–property diagrams (see Figs. 1a–1c).

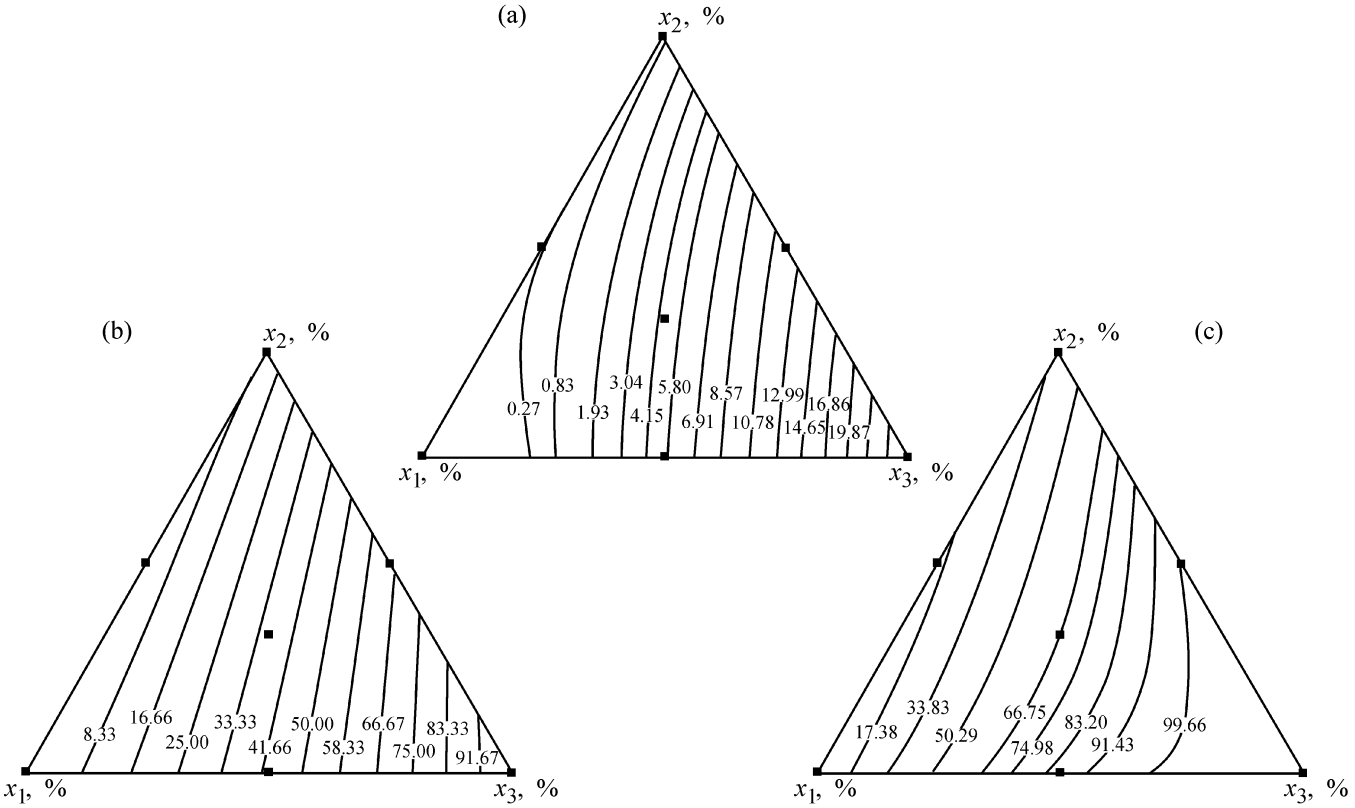


Fig. 1. Diagram of the Ag_2S oxidation (%) in the Ag_2S–$Fe(NO_3)_3$–HNO_3–H_2O system at different temperatures. Temperature (°C): (a) 25, (b) 55, (c) 80.

The oxidation of silver sulfide in the system Ag_2S–$Fe(NO_3)_3$–HNO_3–H_2O can be described by the following reaction equations:

$$Ag_2S + 4HNO_3 \rightarrow 2AgNO_3 + 2NO_2 + S^0 + 2H_2O, \quad (1)$$

$$Ag_2S + Fe(NO_3)_3 + H_2O \rightarrow 2AgNO_3 + Fe(OH)_2 + NO_2 + S^0, \quad (2)$$

$$Ag_2S + Fe(NO_3)_3 + 2HNO_3 \rightarrow 2AgNO_3 + Fe(NO_3)_2 + NO_2 + S^0 + H_2O, \quad (3)$$

$$Ag_2S + 2Fe(NO_3)_3 + 2HNO_3 \rightarrow Ag_2SO_4 + 2Fe(NO_3)_2 + 3NO_2 + NO + H_2O. \quad (4)$$

The experiments we performed demonstrated that the maximum transfer of silver into solution at 25°C (see Fig. 1a) reaches 26.8% at a HNO_3 concentration in solution of 3.0 M. Addition of iron(III) nitrate to the solution hardly affects the oxidation of silver sulfide.

The X-ray data show the presence of a significant amount of unoxidized sulfide. As the content of nitric acid in solution increases, the amount of elementary sulfur in the precipitate grows.

Based on the experimental data, we derived the regression equation relating the degree of Ag_2S oxidation to the concentrations of nitric acid and iron(III) nitrate at a temperature under consideration. A verification against the data of control run nos. 8–10 demonstrated that the equation adequately describes the process with a confidence probability of 97%. The root-mean-square error in the determination of Y values was 3%.

Raising the temperature to 55°C (see Fig. 1b) does not change the general pattern of silver sulfide oxidation in the acid–salt system under study, but only favors an increase in its transfer to solution. The maximal value (~100%) is reached at the point with the highest concentration of nitric acid. The X-ray data show the same trend toward formation of elementary sulfur in precipitates as that at 25°C. This suggests that reaction (3) predominates as the nitric acid concentration increases to 3.2 M.

For this temperature, we also derived a regression equation. To verify its adequacy, a series of control experiments were carried out. The root-mean-square deviation was 3% at a confidence probability of 97%.

At 80°C, the same behavior as that at 25 and 55°C is observed (see Fig. 1c). Only the quantitative characteristics of the process change: the whole amount of silver passes into solution even at an HNO_3 concentration of about 2.3 M.

The regression equation describing the behavior of silver sulfide in the system under consideration at 80°C was obtained. The results of control experiments show that this equation adequately describes the process with a confidence probability of 97%. The root-mean-square error in the determination of Y values was 3%.

It is necessary to note that temperature affects the possibility of occurrence of reactions (1)–(4). Reactions (1), (3), and (4) proceed in the whole temperature range under study, whereas reaction (2), only upon heating. For example, reaction (2) does not proceed at 25°C even at a Fe^{3+} concentration of 1.8 M; at 55°C, changes occur in solution beginning at a Fe^{3+} concentration of 0.744 M; and at 80°C, reaction (2) proceeds at even lower Fe^{3+} concentrations.

It was found that, in a mixture of silver and lead sulfides, produced by their coprecipitation from nitrate solutions with hydrogen sulfide, and also in mechanical mixtures of silver sulfide with elementary sulfur and lead sulfide, Ag_2S is oxidized in the same way as pure silver sulfide. An increase in HNO_3 and $Fe(NO_3)_3$ concentrations results in that the degree of silver recovery into solution becomes higher. Temperature strongly affects the process. For example, the fraction of oxidized silver sulfide was 20–30% at 25°C and 100% at 80°C. The nature of the starting solid mixtures has no effect on the degree of silver sulfide oxidation.

CONCLUSIONS

(1) A study of the effect of the concentration of nitric acid and iron(III) nitrate on the oxidation of silver sulfide in the systems Ag_2S–$Fe(NO_3)_3$–HNO_3–H_2O at various temperatures revealed that nitric acid strongly affects the oxidation of Ag_2S, which reaches the maximal value (100 %) at an HNO_3 concentration of 3.2 M.

(2) The chemical mechanism of the oxidation of Ag_2S in nitrate media to give elementary sulfur at 25 and 55°C and sulfate sulfur at 80°C was elucidated.

(3) Diagrams describing the dependence of the degree of silver sulfide oxidation on the HNO_3

and $Fe(NO_3)_3$ concentrations were constructed on the basis of the experimental data.

REFERENCES

1. Buketov, E.A. and Ugorets, M.Z., *Gidrokhimicheskoe okislenie khal'kogenov i khal'kogenidov* (Hydrochemical Oxidation of Chalcogens and Chalcogenides), Alma-Ata: Nauka, 1975.
2. Kakovskii, I.A. and Potashnikov, Yu.M., *Kinetika protsessov rastvoreniya* (Kinetics of Dissolution Processes), Moscow: Metallurgiya, 1975.
3. Chursanov, Yu.V., Potashnikov, Yu.M., and Gortsevich, S.L., *Zh. Fiz. Khim.*, 1998, vol. 72, no. 7, pp. 1181–1184.
4. Maslenitskii, I.N., Chugaev, L.V., Borbat, V.F., et al., *Metallurgiya Blagorodnykh Metallov* (Metallurgy of Noble Metals), Moscow: Metallurgiya, 1987.
5. Potashnikov, Yu.M., Chursanov, Yu.V., and Gortsevich, S.L., *Zh. Fiz. Khim.*, 2000, vol. 74, no. 9, pp. 1593–1596.
6. Fainberg, S.Yu. and Filippova, R.A., *Analiz rud tsvetnykh metallov* (Analysis of Ores of Nonferrous Metals), Moscow: Metallurgizdat, 1963.
7. Alekseev, V.I., *Kolichstvennyi analiz* (Quantitative Analysis), Moscow: Khimiya, 1972.
8. Akhnazarova, S.L. and Kafarov, V.V., *Optimizatsiya eksperimenta v khimii i khimicheskoi tekhnologii* (Optimization of the Experiment in Chemistry and Chemical Engineering), Moscow: Vysshaya Shkola, 1978.
9. Ostanova, S.V., Chubarov, A.V., Drozdov, S.V., and Patrushev, V.V., *Zh. Prikl. Khim.*, 2002, vol. 75, no. 8, pp. 1381–1383.
10. Ostanova, S.V., Chubarov A.V., Drozdov, S.V., and Patrushev, V.V., *Izv. Vyssh. Uchebn. Zaved., Khim. Khim. Tekhnol.*, 2003, vol. 46, no. 3, pp. 90–92.

ISSN 1070-4272, Russian Journal of Applied Chemistry, 2008, Vol. 81, No. 6, pp. 1078–1080. © Pleiades Publishing, Ltd., 2008.
Original Russian Text © M.D. Vedenyapina, E.D. Strel'tsova, A.K. Rakishev, A.A. Vedenyapin, 2008, published in Zhurnal Prikladnoi Khimii, 2008, Vol. 81, No. 6, pp. 1039–1041.

BRIEF COMMUNICATIONS

Hydrolysis of Acetylsalicylic Acid under the Conditions of Electrolysis

M. D. Vedenyapina, E. D. Strel'tsova, A. K. Rakishev, and A. A Vedenyapin

Zelinskii Institute of Organic Chemistry, Russian Academy of Sciences, Moscow, Russia

Received July 21, 2008

Abstract—The hydrolysis of acetylsalicylic acid in the anolyte under the conditions of electrolysis was studied.

DOI: 10.1134/S1070427208060323

Acetylsalicylic acid (ASA, Aspirin®) is one of the most popular drugs which, together with other drugs, gets into wastewater, and hampers operation of biological sewage treatment plants [1, 2]. It is known that the biological activity of ASA-containing aqueous solutions can be decreased by more than an order of magnitude by their electrooxidation [3]. However, it remains unknown whether ASA itself or its hydrolysis product, salicylic acid (SA), undergoes electrooxidation. To answer this question, we compared in this study the ASA anodic oxidation kinetics, on the one hand, and the ASA hydrolysis kinetics under electrolysis and without it, on the other hand.

EXPERIMENTAL

The ASA hydrolysis was studied in 0.1 N aqueous H_2SO_4 at room temperature. The ASA and SA anodic oxidation was carried out at 25°C in a two-electrode electrochemical cell with a membrane separating the anode and cathode chambers. A smooth platinum plate was used as anode. The current density was 10 mA cm^{-2}. The anolyte was analyzed by high-performance liquid chromatography (HPLC) and UV spectroscopy.

We found that, on keeping ASA in aqueous H_2SO_4 without electrolysis, the absorption band in its UV spectrum at 227 nm is shifted to 235 nm. This means that, under these conditions, ASA is hydrolyzed to form SA. This conclusion is consistent with Fig. 1 showing that, as the SA/ASA ratio in their mixtures increases, the absorption band at 227 cm^{-1} linearly shift to longer wavelengths. From this correlation, we determined the SA content of the ASA–SA mixtures in the course of ASA hydrolysis. We found that the ASA hydrolysis is relatively slow and a 90% degree of hydrolysis is reached only in 16 days (Fig. 2). The time dependence of the SA content of the reaction mixture

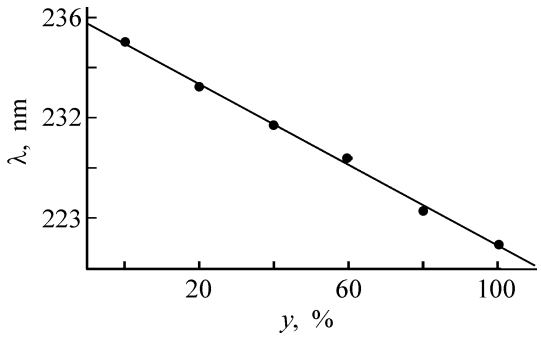


Fig. 1. Position of the maximum of the absorption band in the UV spectrum of ASA–SA solutions in 0.1 N H_2SO_4 vs. ASA content y

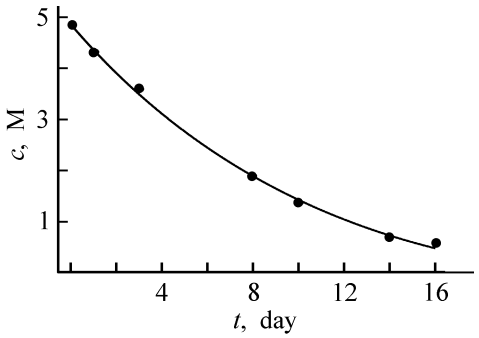
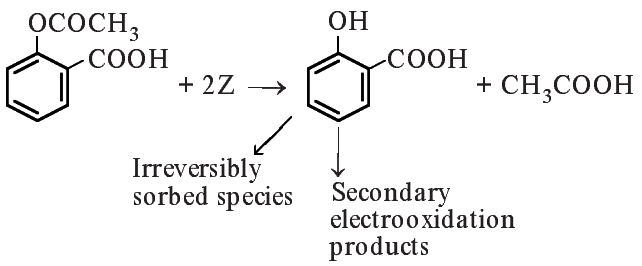


Fig. 2. Dependence of the ASA concentration c on hydrolysis time t in aqueous H_2SO_4.

showed that the ASA hydrolysis kinetics is described by a first-order rate equation with a rate constant of 0.0059 h^{-1}.

A chromatographic analysis of ASA solution subjected to electrolysis showed that the overall process of the ASA electrochemical conversion involves two successive stages. First, ASA is hydrolyzed to form SA and then, after accumulation of salicylic acid, the products of SA anodic oxidation appear in the anolyte. We found that, under the conditions of electrolysis, the rate of ASA hydrolysis is several times that under electroless conditions. Owing to the high rate of ASA hydrolysis under the conditions of electrolysis, the total ASA oxidation rate is comparable with that of the SA oxidation.

Figure 3 shows the dependence of the SA and ASA concentrations in the anolyte (M) on the electrolysis time. It is seen that the electrochemical conversion of ASA appreciably decelerates with time. It is believed [4] that this effect is caused by the fact that the SA formed by the ASA hydrolysis is irreversibly sorbed on the platinum surface and, as a result, the platinum surface becomes less accessible to ASA adsorption and its subsequent hydrolysis. Assuming that ASA hydrolysis occurs on two neighboring surface platinum atoms of the electrode, we can suggest that the ASA hydrolysis rate is proportional to the product of the ASA concentration in solution by the $(1 - \theta)^2$ factor, where θ is the fraction of platinum surface covered by irreversibly sorbed SA molecules. If the rate of the irreversible sorption of SA is proportional both to its concentration in the anolyte and to the free anode surface area $1 - \theta$, we can formulate a system of equations describing the ASA hydrolysis kinetics under the conditions of electrolysis. These equations take into account that, on the one hand, SA partially inactivates the platinum surface via its irreversible sorption, and, on the other hand, it is itself subject to anodic oxidation. The overall process of the electrochemical conversion of ASA on Pt anode can be represented by the following scheme (Z is an active center):



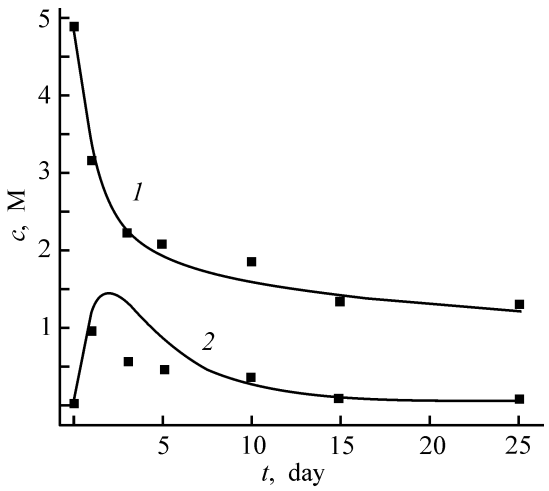


Fig. 3. Dependence of (*1*) ASA and (*2*) SA concentrations c in the anolyte (0.1 M H_2SO_4) on the electrolysis time t.

The kinetics of the processes in this scheme are described by the following equations:

$$dc_1/dt = -k_1 c_1 (1 - \theta)^2,$$

$$d\theta/dt = k_2 c_2 (1 - \theta),$$

$$dc_2/dt = k_1 c_1 (1 - \theta)^2 - k_3 c_2,$$

where c_1 and c_2 are, respectively, the ASA and SA concentrations in a time t after starting the electrolysis and k_1, k_2, and k_3 are, respectively, the rate constants of SAA hydrolysis, accumulation of irreversibly sorbed SA species, and SA oxidation.

The quantity k_3 was taken to be 0.37 h^{-1} as reported in [5]; k_1 and k_2 (0.4 and 0.17 h^{-1}, respectively) were determined from our experimental data by least-squares fitting. Figure 3 shows that the ASA hydrolysis kinetics is fairly well described by the system of the above rate equations.

Our experiments showed that the rate constant of ASA hydrolysis under the conditions of electrolysis exceeds that in the absence of current by a factor of 42. Taking into account that hydrogen peroxide promotes the ASA hydrolysis [6], we can suggest that the acceleration of ASA hydrolysis under the conditions of electrolysis is caused by adsorbed oxygen species containing O–O bonds.

In the course of ASA hydrolysis under the conditions of electrolysis, the electric current is consumed only for generation of catalytically active

oxygen adsorbed on the platinum surface. Therefore, we can suggest that, at a lower current density, the SA oxidation rate will decrease and ASA hydrolysis will become the main process. This assumption was completely confirmed by our experiments. We found that, with the current density decreasing to 0.5 mA cm^{-2}, the SA oxidation is virtually suppressed and the ASA hydrolysis becomes essentially the only process.

CONCLUSIONS

(1) Acetylsalicylic acid is not subjected to direct anodic oxidation on platinum electrode.

(2) The hydrolysis rate of acetylsalicylic acid under the conditoins of electrolysis in acidic solutions in the range of oxygen evolution potentials exceeds that in the absence of current by an order of magnitude. This phenomenon can be used to accelerate the hydrolysis of acetylsalicylic acid and other esters.

REFERENCES

1. *Arzneimittel in Umwelt, eine Bedrohung, Tagung*, Stuttgart, 2002, p. 7.
2. *Zum Vorkommen von Arzneimitteln im Bodensee und im Baden-Württenbergischen Zuflüssen, Report of Baden-Württenberg ISF (Institut für Seeforschung) handesanstalt für Umweltschutz*, Baden-Württenberg, 2001, p. 27.
3. Vedenyapin, A., Baturova, M., Rakishev, A., et al., in *Solid Products of Salicylic Acid Electrooxidation: 55th Annual Meet. of the Int. Society of Electrochemistry*, Thessaloniki (Greece), September 19–24, 2004.
4. Vedenyapin, A.A., Rakishev, A.K., Baturova, M.D., et al., *Kondens. Sredy Mezhfazn. Gran.*, 2005, vol. 2, pp. 117–122.
5. Eckert, T. and Zander, M., *Arch. Pharm.* (Weinheim), 1976, vol. 309, no. 9, pp. 689–695.
6. Vedenyapin, A.A., Rakishev, A.K., Vedenyapina, M.D., and Skundin, M.D., *Izv. Akad. Prom. Ekol.*, 2007, no. 1, pp. 61–68.

ISSN 1070-4272, Russian Journal of Applied Chemistry, 2008, Vol. 81, No. 6, pp. 1081–1083. © Pleiades Publishing, Ltd., 2008.
Original Russian Text © S.P. Peremitina, T.N. Volgina, V.T. Novikov, 2008, published in Zhurnal Prikladnoi Khimii, 2008, Vol. 81, No. 6, pp. 1042–1044.

BRIEF COMMUNICATIONS

Indirect Electrochemical Liquid-Phase Oxidation of Salicylic and Sulfosalicylic Acids

S. P. Peremitina, T. N. Volgina, and V. T. Novikov

Tomsk Polytechnic University, Tomsk, Russia

Received October 15, 2007

Abstract—Degradation of salicylic acids under the action of oxidants generated by electrolysis of sulfuric acid was studied. In the course of oxidation, salicylic acids decompose to simpler and nontoxic substances.

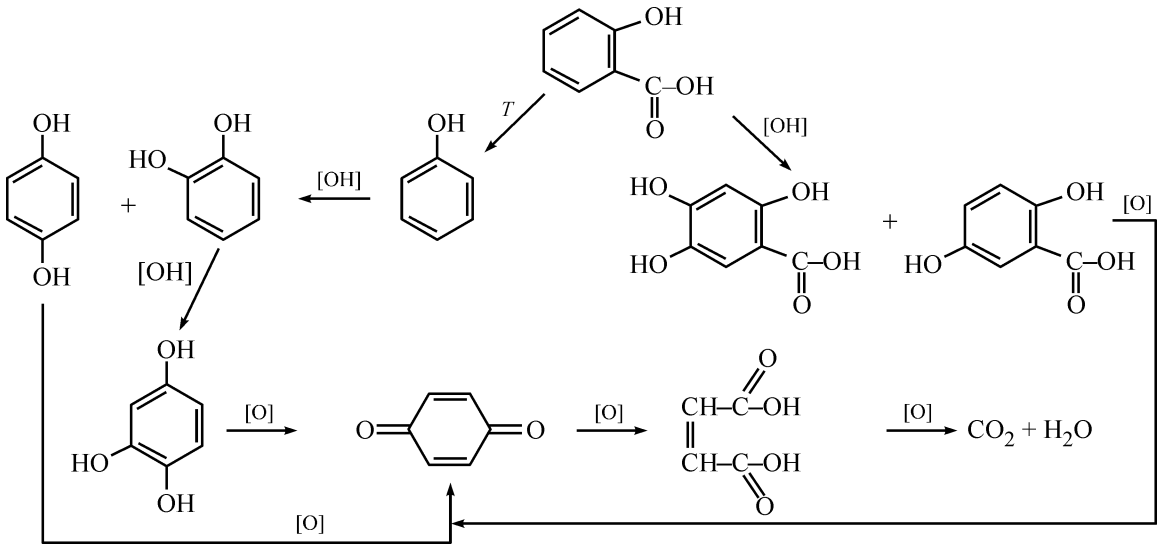
DOI: 10.1134/S1070427208060335

THe production of drugs has led to the accumulation of rejected or expired batches of pharmaceuticals, which should be eliminated for environment protection [1]. It is known [2] that pharmaceuticals are difficultly biodegradable. Therefore, the most promising ways of rendering pharmaceutical wastes harmless are thermal neutralization [3], plasma treatment [4], and liquid-phase oxidation [5]. High temperatures and the need for off-gas treatment complicate and make expensive the thermal procedure for detoxication of organic substances. Large power consumption and complexity of problems associated with plasmochemical technology restrict its applications. The main drawback of liquid-phase oxidation is the incomplete oxidation of certain substances and the high cost of the equipment.

Recently the interest in indirect oxidation of organic substances has increased. In this context, our goal was to study degradation of salicylic (SA) and sulfosalicylic (SSA) acids in the liquid phase under the action of electrolytically generated oxidants [6]. Electrolysis was performed on a laboratory installation consisting of a reactor equipped with lead electrodes, a jacket, a stirrer, a dc source, and a thermostat. Spectrophotometric measurements were performed on SF-26 and KFK-2 devices. The chemical oxygen demand (COD) was monitored throughout the process with an Ekotest-120 ion meter.

It has been found previously [7] that the current efficiency by oxidants on lead electrodes in electrolysis of aqueous solutions of sulfuric acid is the highest at 40 wt % concentration, 20–50°C, and anodic current density of 0.6–0.85 A cm^{-2}. Therefore, further experiments were performed under these conditions.

Degradation of hydroxybenzoic acids can occur both in the reaction volume and partially by an electrochemical mechanism. The composition of SA and SSA degradation products is virtually independent of the oxidation conditions. For example, deep oxidation of SA and its derivatives induced in the presence of a catalyst by ascorbic acid [8], leads, like anodic oxidation [9], to the formation of such intermediates as α- and β-resorcylic acids, gallic acid, pyrocatechol, and hydroquinone. This is followed by the formation of benzoquinone. The subsequent cleavage of the aromatic ring yields succinic, maleic, oxalic, and other acids. The common steps of the decomposition of SA and SSA are hydroxylation of the aromatic core and decarboxylation. THe hydroxylation or oxidation of side chains occurs in the *o*- and *p*-positions relative to the carboxy group with the formation of isomeric dihydroxybenzoic acids. The decarboxylation of salicylic acids occurs on their heating and yields phenols. This is followed by the formation of diketones and their subsequent oxidation via di- and monocarboxylic acids to carbon dioxide and water. Thus, the possible scheme of destructive oxidation of salicylic acids is as follows:



Scheme of oxidation of salicylic acid.

Apparently, the degradation of SA and SSA in electrochemically activated sulfuric acid solution occurs similarly. The multistep nature of these processes is confirmed by color variation in the course of oxidation of sulfuric acid solutions of hydroxybenzoic acids: colorless → yellow → orange → brown → colorless, i.e., the reaction occurs via a series of intermediates. A new absorption peak appearing at ~380 nm (Fig. 1) suggests the formation of a stable intermediate, *p*-benzoquinone [10]. The content of *p*-benzoquinone increases in the first 90 min of the reaction and, after reaching a maximum, starts to decrease as a result of further oxidation to carboxylic acids.

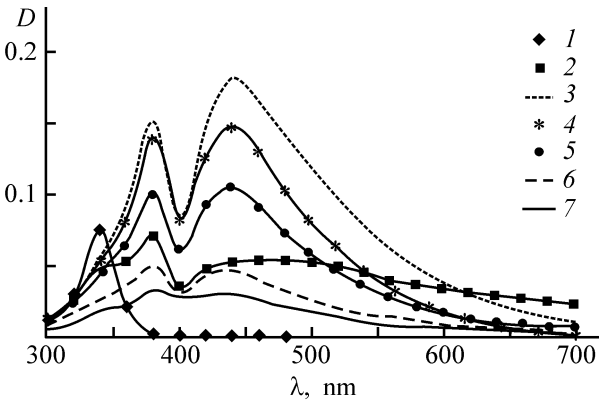


Fig. 1. Absorption spectra of a solution of sulfuric and salicylic acids, recorded after electrolysis for different times. (*D*) Optical density and (λ) wavelength; the same for Fig. 2. Electrolysis time, min: (*1*) 0, (*2*) 10, (*3*) 90, (*4*) 150, (*5*) 210, (*6*) 270, and (*7*) 330.

Salicylic acids in sulfuric acid solutions have pronounced absorption peaks at 210 and 235 nm. Therefore, variation of the optical density at these wavelengths also characterizes the oxidation of SA and SSA (Fig. 2).

In the course of electrolysis, the intensity of UV absorption of salicylic acid solutions decreases, suggesting a breakdown of the aromatic ring as a conjugated system with the formation of acetic and oxalic acids. Qualitative color reactions with Fe^{3+} showed that the initial salicylic acid fully decomposes within the first 15–20 min to give 4-hydroxysalicylic, trihydroxybenzoic, and 2,5-dihydroxybenzoic acids. The results of COD determination show that exhaustive oxidation of SSA and its degradation products at 50°C and a current density of 0.6 A cm^{-2} occurs within 80 min:

Oxidation time, min	COD_{SSA}, mg dm^{-3}
0	3500
20	2600
40	1400
60	500
80	30

Because the sulfuric acid solution after the oxidation contains no organic compounds (judging from COD) and the exit gas contains CO_2, it can be naturally assumed that the acids are oxidized to CO_2 and H_2O.

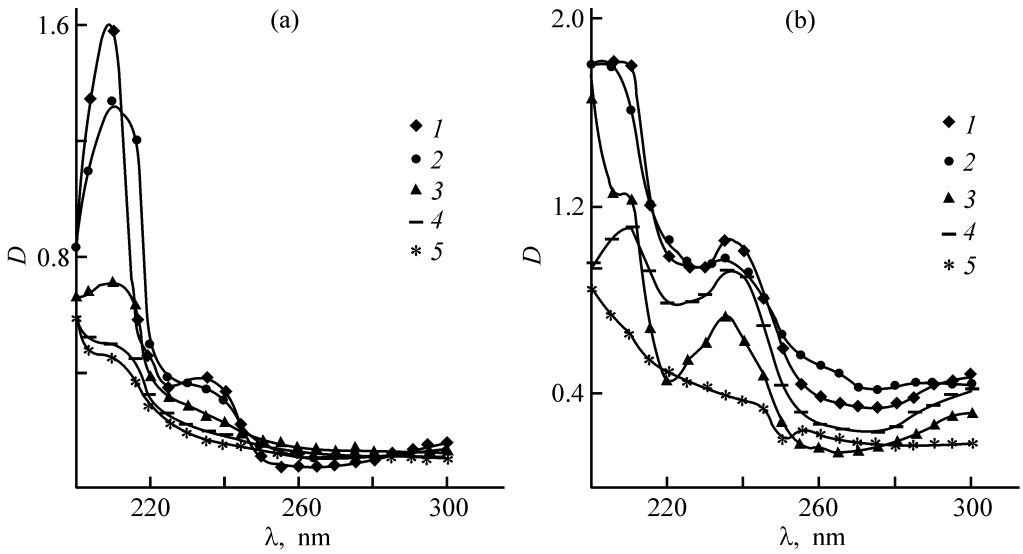


Fig. 2. Absorption spectra of sulfuric acid solutions containing (a) sulfosalicylic and (b) salicylic acids, recorded after electrolysis for different times. Electrolysis time, min: (a) (*1*) 0, (*2*) 15, (*3*) 30, (*4*) 45, and (*5*) 60; (b) (*1*) 0, (*2*) 20, (*3*) 40, (*4*) 60, and (*5*) 80.

CONCLUSIONS

(1) Indirect electrochemical oxidation is a fairly efficient method for decomposing such biologically active substances as salicylic and sulfosalicylic acids.

(2) The process yields no secondary pollutants.

REFERENCES

1. Rodionov, A.I., Kuznetsov, Yu.P., and Solov'ev, G.S., *Zashchita biosfery ot promyshlennykh vybrosov: Osnovy proektirovaniya tekhnologicheskikh protsessov* (Protection of the Biosphere from Industrial Emissions: Principles of Process Design), Moscow: Kolos, 2005.
2. Xaiang Huiqiang, Zhan Qifang, and Liu Liangjun, *Ind. Water Treat.*, 2004, no. 9, pp.55–57.
3. Bernadiner, M.N. and Shurygin, A.P., *Ognevaya pererabotka i obezvrezhivanie promyshlennykh otkhodov* (Incineration and Neutralization of Industrial Wastes), Moscow: Khimiya, 1990.
4. Paton, B.E., Chernets, A.V., Marinskii, G.S., et al., *Sovremennaya elektrometallurgiya* (Modern Electrometallurgy), 2005, part 1, no. 3, p. 54.
5. Narkevich, I.P. and Pechkovskii, V.V., *Utilizatsiya i likvidatsiya otkhodov tekhnologii organicheskikh veshchestv* (Utilization and Elimination of Organic Production Wastes), Moscow: Khimiya, 1984.
6. Kornienko, G.V., Kornienko, V.L., Maksimov, N.G., and Pavlenko, N.I., *Khim. Inter. Ustoich. Razv.*, 2001, no. 1, pp. 35–40.
7. Grishchenkova, O.V., Volgina, T.N., and Novikov, V.T., *Izv. Vyssh. Uchebn. Zaved., Khim. Khim. Tekhnol.*, 2005, vol. 48, no. 11, pp. 58–60.
8. Fieser, L.F. and Fieser, M., *Advanved Organic Chemistry*, New York: Reinhold, 1962.
9. Tomilov, A.P., Mairanovskii, M.Ya., Fioshin, M.Ya., and Smirnov, V.A., *Elektrokhimiya organicheskikh soedinenii* (Electrochemistry of Organic Compounds), Leningrad: Khimiya, 1968.
10. Silverstein, R.M., Bassler, G.C., and Morrill, T.C., *Spectrometric Identification of Organic Compounds,* New York: Wiley, 1974.

ISSN 1070-4272, Russian Journal of Applied Chemistry, 2008, Vol. 81, No. 6, pp. 1084–1086. © Pleiades Publishing, Ltd., 2008.
Original Russian Text © G.A. Mandrov, E.L. Schastlivtsev, 2008, published in Zhurnal Prikladnoi Khimii, 2008, Vol. 81, No. 6, pp. 1045–1046.

BRIEF COMMUNICATIONS

Sedimentation of Carbon-Clay Dispersions with Polyacrylamide Modified with Tetraethylene Glycol

G. A. Mandrov and E. L. Schastlivtsev

Institute of Coal and Coal Fuel Chemistry, Siberian Division, Russian Academy of Sciences, Kemerovo, Russia

Received April 24, 2007

Abstract—Sedimentation of carbon-clay dispersions with polyacrylamide modified with tetraethylene glycol was studied. The concept of the formation of a binary structure of the modified polymer in a structured ternary system was formulated.

DOI: 10.1134/S1070427208060347

Improvement of the flocculation activity of domestic flocculants is still a topical problem for clarification of recycled water at coal-cleaning plants. As shown previously [1], modification of polyacrylamide (PAA) with α-propylene chlorohydrin (polymer concentration 0.4 mg dm^{-3}) raises the rate of sedimentation of carbon-clay dispersions (mean particle size 2.25 μm) by approximately a factor of 1.7.

In this study, we examined the possibility of enhancing the flocculation activity of domestic PAA.

EXPERIMENTAL

Taking into account that the flocculation activity of a PAA increases with its molecular weight, it was of particular interest to study the flocculation activity of PAA as influenced by the monomer chain length in the course of its modification with tetraethylene glycol (TEG). For dilute solutions, it was important to estimate changes in the specific viscosity on passing from the straight polymer solution to the binary system:

$$\eta_{sp} = (\eta - \eta_0)/\eta_0,$$

where η and η_0 are the viscosities of the polymer solution and solvent, respectively.

First, the viscosities of the polymer solutions were determined from their outflow time using a capillary viscometer, and then their intrinsic viscosities [η] were graphically determined and used to calculate the viscosity-average molecular weight of the polymer from the Mark–Kuhn–Houwink equation:

$$[\eta] = KM^a,$$

where K and a are constants for a given polymer–solvent system.

For the PAA–water system, $K = 0.63 \times 10^{-4}$ and $a = 0.8$ [2]. Using known K and a, [η] was determined from the intercept on the ordinate axis (Fig. 1).

As the parameters characterizing the size and shape of macromolecules, we estimated the mean distance between the ends of the polymer molecular chain h and the polymer flexibility Γ, i.e., the h/M ratio. The quantity h characterizes the reactivity of macromolecules in the course of flocculation. The mean statistical distance between the ends of

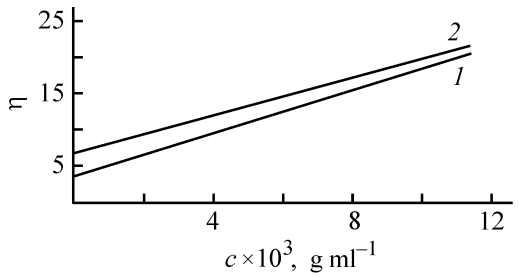


Fig. 1. Relative viscosity of flocculant solutions η vs. their concentration c. (*1*) PAA and (*2*) PAA + TEG; the same for Fig. 2. (η) Relative viscosity, $\eta = \eta_{sp}/c$.

the polymer chain, h (cm), was determined from the Flory equation:

$$[\eta] = \Phi\beta h^3/M,$$

where Φ is the Flory constant and β is the swelling coefficient equal to the ratio of [η] in the given solvent to [η] in the ideal solvent; for the majority of polymers $\Phi\beta = 2.1 \times 10^{21}$ [3]. The results of our calculations are listed in the table.

The observed difference in the molecular weights of polymers allows evaluation of their relative flocculation activity toward carbon-clay suspensions prepared from the mixture of K, KO, and KS coking coals obtained at the hydrosizer outlet. The performance of PAA modified with TEG was evaluated by analyzing the size distribution of the solid phase particles in a thickener. This distribution in the clarified recycled water was characterized by the geometric-mean diameter of 1.3 μm and weight-average geometric diameter of 4.2 μm, with standard geometric mean deviation of 1.8. The concentration of the carbon-water suspension supplied to the thickener was 5 g dm^{-3}. In the case of the PAA–TEG binary system, the concentration of the solid phase in the clarified water at the thickener outlet decreased to 0.7 g dm^{-3}. The flocculation activity of PAA at a polymer concentration of 0.4 mg dm^{-3} was lower than that of the PAA + TEG system by a factor 3. The balance of the solid phase distribution in the thickener showed that the flocculation primarily involved coarse particles of the dispersed phase, whereas fine particles, poorly captured by the PAA–TEG binary flocculant in the flow mode, remained in the clarified water.

To reveal the nature of intermolecular interactions in formation of the PAA–TEG binary structure in the ternary system (PAA + TEG + H_2O), we recorded the IR spectra of the initial and modified PAA, using a TENSOR-27 unit (Bruker). As can be seen from Fig. 2, all the spectra have a strong absorption band at 3420 cm^{-1}, which is commonly assigned to the absorption of water molecules and stretching vibrations of hydroxy groups.

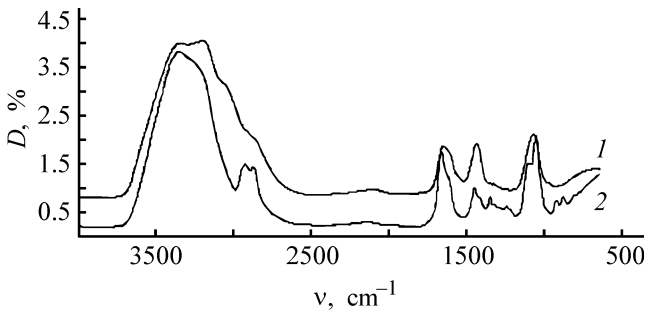
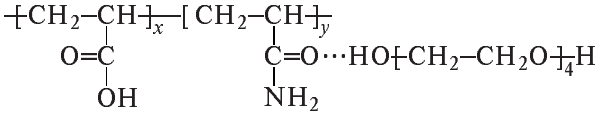


Fig. 2. IR spectra of flocculant hydrogels. (D) Optical density and (ν) wavenumber.

We also observe the absorption of the carbonyl group C=O in primary amide [4] at 1640–1650 cm^{-1}. The modified PAA has new absorption bands at 800–1350 cm^{-1}. In accordance with [5], the absorption bands in this range are typical of polyethylenimines and polyglycols and are absent in the spectrum of the initial PAA. Two bands at 800–1000 cm^{-1} belong to the C–C stretching vibrations, and the C–N and C–O stretching bands are observed at 1050–1390 and 1250 cm^{-1}, respectively.

The appearance in the PAA–TEG binary structure of absorption bands typical of polyglycols gives insight into the nature of intermolecular interactions upon the formation of the binary system in the aqueous medium. Some molecules in the structured ternary system attain the optimal energy states and occupy certain spatial positions favorable for hydrogen bonding. One of such processes is the formation of a hydrogen bond between the TEG hydroxy group and carbonyl oxygen of partially hydrolyzed PAA, which favors preservation of the open conformation of PAA, which on the whole makes higher the viscosity of the binary flocculant, its viscosityaverage molecular weight, and flocculation activity. One of the ways of hydrogen bonding between partially hydrolyzed PAA and TEG is as follows:



Polymer properties

Polymer	[η], g dl^{-1}	M	h, cm	$\Gamma = hM$
PAA	3.3	~8×10^5	1.08×10^{-5}	0.135×10^{-10}
PAA + TEG	7.0	~20×10^5	1.88×10^{-5}	0.094×10^{-10}

CONCLUSION

Modification of polyacrylamide and tetraethylene glycol makes higher the viscosity of the binary flocculant, its viscosity-average molecular weight, and the flocculation activity and can be used for clarifying the recycled water in concentration of coal slack with a hydrosizer.

REFERENCES

1. Mandrov, G.A., Klimovich, M.Yu., and Pukh, A.N., *Zh. Prikl. Khim.*, 2006, vol. 79, no. 10, pp. 1747–1748.
2. *Praktikum po khimii i fizike polimerov* (Practical Works on Chemistry and Physics of Polymers), Moscow: Khimiya, 1977.
3. Shevchenko, T.V., Osadchii, V.L., Yakovchenko, M.A., et al., *Khim. Prom–st. Segodnya*, 2004, no. 11, pp. 38–41.
4. Nakanishi, K., *Infrared Absorbtion Spectroscopy*, Tokyo: Nankido, 1962. Translated under the title *Infrakrasnye spektry i stroenie organicheskikh soedinenii*, Moscow: Mir, 1965.
5. Kuptsov, A.Kh. and Zhizhin, G.N., *Fur'e-KR i Fur'e-IK spektry polimerov* (Fourier Raman and Fourier IR Spectra of Polymers), Moscow: Fizmatlit, 2001.

ISSN 1070-4272, Russian Journal of Applied Chemistry, 2008, Vol. 81, No. 6, pp. 1087–1089. © Pleiades Publishing, Ltd., 2008.
Original Russian Text © N.V. Knyazeva, V.V. Kon'shin, N.A. Chemeris, M.M. Chemeris, 2008, published in Zhurnal Prikladnoi Khimii, 2008, Vol. 81, No. 6, pp. 1047–1049.

BRIEF COMMUNICATIONS

Synthesis of Cellulose Esters with Aliphatic Hydroxy Acids from Aspen Wood

N. V. Knyazeva, V. V. Kon'shin, N. A. Chemeris, and M. M. Chemeris

Polzunov Altai State Technical University, Barnaul, Russia

Received December 27, 2007

Abstract—Synthesis of cellulose esters with aliphatic hydroxy acids from aspen wood was studied in relation to the reaction and isolation conditions.

DOI: 10.1134/S1070427208060359

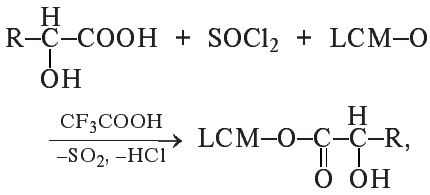
Polymers prepared from aliphatic hydroxy acids are promising materials combining various properties of plastics (thermoplasticity, capability to imitate various polymers after appropriate plasticization, etc.). At the same time, an important practical property of such polymers is the capability to degrade under definite conditions to environmentally harmless products: CO_2 and H_2O [1]. The starting materials for preparing such polymers are cellulose esters with aliphatic hydroxy acids.

In a known procedure [2], cellulose esters with aromatic carboxylic hydroxy acids are prepared by treatment of cellulose with an acylating mixture containing trifluoroacetic anhydride and aromatic hydroxy acids as acylating agents [2]. The reaction is performed with addition of dichloromethane and methanol. However, the process is multistep and involves expensive solvents.

The previously developed [3, 4] procedure for preparing cellulose esters expands the possibilities of the synthesis of practically important cellulose-based polymers containing bound carboxylic acids. In the process, it is possible to use prehydrolyzed aspen wood instead of pure cellulose.

EXPERIMENTAL

The reaction of prehydrolyzed aspen wood (lignocellulose material, LCM) containing 64.8% cellulose (Kürschner's method) and 35.2% lignin (Komarov's method [5]) with carboxylic hydroxy acids of the general formula RCHOHCOOH (R = H, CH_3) in trifluoroacetic acid (TFAA) was performed in the presence of thionyl chloride (TC), following the procedure described in [6]:



where R = H or CH_3.

After the reaction completion, the product was precipitated into a polar solvent (water, acetone, ethanol, isopropanol), washed, and dried to the air-dry state. The lignin content was determined using concentrated mineral acids [5], and the amount of bound carboxylic hydroxy acids, by potentiometric titration [6]. Qualitative tests of the products for halogens gave negative results.

One of the most important aspects of the synthesis of cellulose esters from chemically modified wood is the choice of a precipitant that would provide the optimal yield of the target product with a fairly high content of bound carboxylic acid and a low lignin content. The experiments showed that isopropyl alcohol is a suitable precipitant for isolating the cellulose ester (Table 1). Isopropyl alcohol ensures the maximal yield of cellulose hydroxyacetate with a high content of bound glycolic acid and relatively small amount of lignin. With water, ethanol, or acetone as precipitant, the product yield is considerably lower. The highest lignin content was observed with water used as precipitant.

Table 1. Characteristics of cellulose esters isolated using various precipitants (synthesis temperature 40°C, time 6 h)

Cellulose ester	Polar solvent	Yield of cellulose ester,* %	Content of bound carboxylic hydroxy acid, %	Degree of substitution with carboxylic hydroxy acid	Content of lignin in cellulose ester, %
Cellulose hydroxyacetate	Isopropyl alcohol	95	27.2	0.73	9.9
	Water	75	27.8	0.75	15.7
	Ethanol	77	27.9	0.76	7.2
	Acetone	84	28.3	0.77	6.5
Cellulose α-hydroxypropionate	Isopropyl alcohol	86	33.8	0.83	7.2
	Water	93	22.4	0.49	8.7
	Ethanol	70	23.3	0.52	8.6
	Acetone	76	35.2	0.88	8.8

* Based on the initial weighed portion of wood.

Table 2. Influence of synthesis conditions on the properties of the isolated cellulose hydroxyacetate

Conditions of LCM acylation		Characteristics of cellulose hydroxyacetate		
T, °C	τ, h	yield, %	degree of substitution with glycolic acid, %	lignin content, %
30	3	85	0.63	–
40	3	97	0.79	9.8
50	3	90	0.52	11.2
40	2	92	0.72	9.9
40	4	90	0.75	–

Table 3. Influence of synthesis conditions on the properties of the isolated cellulose α-hydroxypropionate

Conditions of LCM acylation		Characteristics of cellulose α-hydroxypropionate		
T, °C	τ, h	yield, %	degree of substitution with lactic acid, %	lignin content, %
20	3	83	1.24	–
30	3	85	1.32	7.1
40	3	75	0.32	10.6
30	2	76	1.30	7.5
30	4	75	1.30	–

In the synthesis of cellulose lactate (α-hydroxypropionate), isopropyl alcohol also appeared to be a good precipitant. It ensured the highest yield of the target product with a high content of bound lactic acid.

The other factors affecting the properties and characteristics of the cellulose esters obtained are the conditions of LCM acylation. Table 2 shows how the temperature and time of LCM acylation with a glycolic acid–TC–TFAA mixture affect the characteristics of the isolated cellulose hydroxyacetates.

The reaction temperature of 40°C and time of 3 h are optimal for preparing cellulose hydroxyacetate. At higher temperatures and shorter reaction times, the yield of cellulose hydroxyacetate decreases and the lignin content increases.

The characteristics of cellulose α-hydroxypropionates prepared by acylation of LCM with a lactic acid–TC–TFAA mixture are listed in Table 3.

The highest yield of cellulose α-hydroxypropionate containing the maximal amount of bound lactic acid is provided at the reaction temperature of 30°C and time of 3 h. Deviations from these conditions lead to an increase in the residual lignin content.

CONCLUSIONS

(1) Cellulose esters were prepared by treatment of prehydrolyzed aspen wood with the acylating mixture RCHOHCOOH (R = H or CH_3)–thionyl chloride–trifluoroacetic acid.

(2) The most appropriate precipitant providing the highest yield of the desired product, a high content of bound hydroxy acid, and a low lignin content is isopropyl alcohol.

REFERENCES

1. Fomin, V.A. and Guzeev, V.V., *Plast. Massy*, 2001, no. 2, pp. 42–46.
2. EP Patent 1215216.
3. RF Patent 2186784.
4. RF Patent 2282635.
5. Obolenskaya, A.V., El'nitskaya, Z.P., and Leonovich, A.A., *Laboratornye raboty po khimii drevesiny i tsellyulozy* (Laboratory Works on Wood and Cellulose Chemistry), Moscow: Ekologiya, 1991.
6. Protopopov, A.V., Kon'shin, V.V., and Chemeris, M.M., *Zh. Prikl. Khim.*, 2005, vol. 78, no. 10, pp. 1748–1749.

ISSN 1070-4272, Russian Journal of Applied Chemistry, 2008, Vol. 81, No. 6, pp. 1090–1092. © Pleiades Publishing, Ltd., 2008.
Original Russian Text © D.V. Onishchenko, A.K. Tsvetnikov, A.A. Popovich, V.G. Kuryavyi, 2008, published in Zhurnal Prikladnoi Khimii, 2008, Vol. 81, No. 6, pp. 1050–1052.

BRIEF COMMUNICATIONS

Production of Anode Matrices from Renewable Vegetable Raw Materials, Including Agricultural Waste

D. V. Onishchenko, A. K. Tsvetnikov, A. A. Popovich, and V. G. Kuryavyi

Institute of Chemistry, Far-Eastern Branch, Russian Academy of Sciences, Vladivostok, Russia
Kuibyshev Far-Eastern State Technical University, Vladivostok, Russia

Received September 4, 2007

Abstract—Carbon modifications (anode matrices) were produced from renewable vegetable raw materials, agricultural crop waste, by pyrolysis in a quartz reactor without access of oxygen at 900°C, as well as by mechanical synthesis, and their characteristics were examined.

DOI: 10.1134/S1070427208060360

Hydrocarbon raw materials, including oil, natural gases, coals, lignites, peat, oil shales, and natural graphite [1], are conventionally used for production of anode matrices. However, natural stocks of hydrocarbon raw materials are known to be depleted worldwide, which inevitably raises their cost. In addition, many countries suffer from shortage of hydrocarbon resources or from inefficient techniques of their extraction and processing. This stimulates researchers in a number of countries and, in particular, in China and Japan, to attempt the use of vegetable (renewable) alternatives to hydrocarbon raw materials [2–4].

We prepared here carbon materials promising for production of anodes for chemical cyclable power sources from vegetable (renewable) raw materials, agricultural waste, and examined them.

EXPERIMENTAL

As initial raw materials we used wheat, oats, and buckwheat waste, as well as rice grains, sunflower seeds, corn grains, coffee beans, tea leaves, and beet sugar.[1] The dried raw material (moisture content 1.25%) was freed from impurities with a separation sieve and ground to powder on a mechanical mill. To accelerate the heating and make it more uniform [5, 6], the purified powder was placed in a special desiccator and dried at 49°C for 43 min, which yielded a material with a 0.21–0.23% moisture content. The dried and milled raw material samples were placed successively into a quartz reactor and pyrolyzed at 900°C without access of oxygen [5]. The termination of pyrolysis was ascertained from the gas evolution cessation. The pyrolysis time of 35–72 min was chosen experimentally, depending on the weight of the initial raw material loaded into the reactor. Upon termination of the pyrolysis, the reactor was left to cool together with the furnace to 25°C, whereupon the pyrolysis products were taken out of the reactor.

The resulting carbon modifications were subjected to mechanical synthesis on an energy-intensive vibration mill[2] to prepare finely dispersed carbon particles [7]. The grinding bodies in the vibration mill were ShKh15 steel spheres 15 mm in diameter. The mechanical reactor was a hermetically sealed container with an inner diameter of 50 mm and height of 125 mm. The experimental conditions were as follows: reactor vibration frequency 12 Hz; air atmosphere; intensity (weight ratio of the initial materials and grinding spheres) 1 : 20; degree of filling of the reactor with the steel spheres 30% of its volume; and synthesis time 12 min.

[1] The experiments on production of anode matrices from renewable raw materials were carried out at the Laboratory of Fluorinated Materials, Institute of Chemistry, Far-Eastern Branch, Russian Academy of Sciences, and at the Laboratory of Synthesis of Inorganic Substances, Kuibyshev Far-Eastern State University.

[2] The energy-intensive vibration mill was designed at the Kuibyshev Far-Eastern State Technical University.

Thus, experimental carbon modifications (anode matrices) were obtained from renewable plant raw material by pyrolysis in a quartz reactor without access of oxygen at 900°C, as well as by mechanical synthesis. A scanning electron microscopic examination showed that the particle shape and size and the texture of the material depend on the nature of the plant raw material. The resulting carbon powders are mainly polydisperse; also, irregularly shaped particles and agglomerates were formed due, most likely, to the specific conditions of preparation (pyrolysis) and mechanical activation of the carbon powders. We found that the carbon particles obtained from beet sugar (see figure) are shaped as grain fragments 0.3–11 μm in size, with most of particles (about 70%) having a size of 1–3.5 μm. The 20000 × magnification reveals globular particles 12 μm in size.

According to the results of an X-ray phase analysis, the carbon modifications prepared at 900°C from wheat, oats, and buck-wheat waste, as well as from corn and rice grains, sunflower seeds, and beet sugar have an X-ray-amorphous structure with iron inclusions. The carbon modifications obtained from coffee beans and tea leaves also have an X-ray-amorphous structure with inclusions of various phases. For example, the modifications obtained from coffee beans contain Fe_2O_3, Fe_3O_4, MgO, and CaS phases, and those prepared from tea waste, $CaCO_3$ and iron impurities. The X-ray-amorphous structure is associated with the specific temperature mode of preparation of the carbon modifications. The occurrence of the Fe_2O_3, Fe_3O_4, MgO, CaS, and $CaCO_3$ phases in the carbon modifications is most likely due to specific features of organic and mineral compositions of these vegetable raw materials.

The measured bulk and physical densities of the carbon modifications synthesized (see table) are close to those of commercial anode materials: The bulk densities are within 0.90–1.10 g cm^{-3}, and physical densities, within 2.02–2.14 g cm^{-3}, depending on the type of the vegetable raw material.

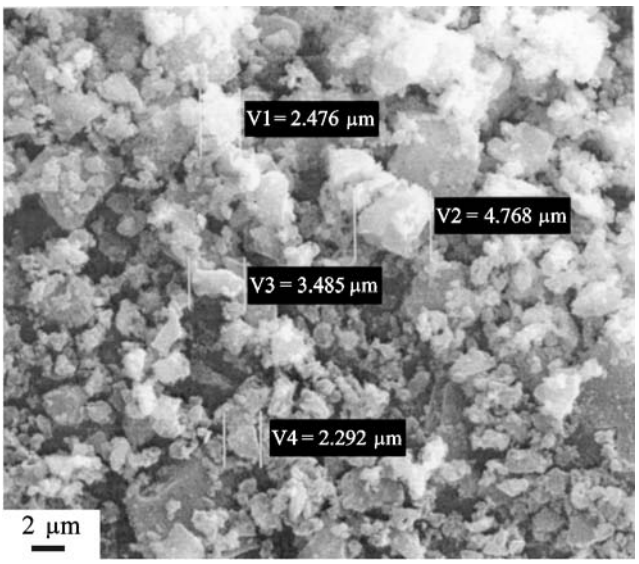
The ash content of the carbon modifications (see table) is within 0.45–0.77%. Hence, the resulting carbon materials are characterized by a high carbon yield, which is an important characteristic of anode matrices.

The specific surface area of the carbon modification obtained from beet sugar (heating to 200°C, 30 min) by pyrolysis in a quartz reactor without access of oxygen at 900°C is as follows, $m^2\ g^{-1}$: one-point BET method 217.238 and Gregg–Sing comparative method 243.133; the specific pore volume for the ultimate degree of filling is 0.103 $cm^3\ g^{-1}$, the micropore volume is 0.017×10^{-9} nm^3, and the average pore size is 1.904×10^{-9} m.

Ash content and bulk and physical density of the carbon modifications obtained from plant (renewable) raw materials by pyrolysis in a quartz reactor without access of oxygen at 900°C

Raw material	Density, g cm^{-3}		Ash content, %
	bulk	physical	
Wheat waste	0.93	2.05	0.45
Oats waste	0.90	1.99	0.41
Corn grains	1.8	2.11	0.55
Buckwheat waste	1.04	2.05	0.67
Sunflower waste	1.10	2.14	0.77
Coffee beans	1.02	2.03	0.53
Beet sugar	1.05	2.12	0.39
Tea leaves	0.97	2.02	0.48
Rice grains	1.01	2.07	0.59

Examination of the specific surface area of the powder and of the structure of the particle surface shows that the resulting carbon powders have a developed surface and are suitable as anode materials for lithium-ion (polymer) batteries.



Shape and size of particles of carbon obtained from beet sugar at 900°C by pyrolysis in a quartz reactor without oxygen access (SEM image; bar: 2 μm).

CONCLUSIONS

(1) Carbon modifications were obtained from renewable vegetable raw materials (agricultural waste, coffee beans, tea leaves) by pyrolysis in a quartz reactor at 900°C.

(2) The resulting carbon materials are finely dispersed powders with a highly developed surface.

(3) The maximal ash content (0.67%) is exhibited by the carbon samples obtained from buckwheat waste, and the minimal (0.39%), by the samples obtained from beet sugar. An X-ray phase analysis showed that the resulting structures are X-ray amorphous.

(4) A scanning electron-microscopic examination showed that the resulting carbon materials are polydisperse powders whose particles have a size of 0.1–12 μm, with most of particles (about 70%) having a size of 1–3.5 μm. The shape, size, and size distribution of the particles depend on the nature of the vegetable raw materials and preparation procedure.

(5) The resulting carbon modifications are suitable as anode materials for lithium-ion (polymer) batteries.

REFERENCES

1. Fialkov, A.S., *Uglerod, mezhsloevye soedineniya i kompozity na ego osnove* (Carbon and Carbon Interlayers and Composites), Moscow: Aspekt, 1997.
2. Xue, J.S. and Dahn, J.R., *J. Electrochem. Soc.*, 1995, vol. 142, p. 3668.
3. Zheng, T., Zhong, Q., and Dahn, J.R., *J. Electrochem. Soc.*, 1995, vol. 142, p. 211.
4. Tokumitsu, K., Mabuchi, A., Fujimoto, H., and Kasuh, T.J., *Power Sources*, 1995, vol. 54, p. 444.
5. Bock, R., *A Handbook of Decomposition Methods in Analytical Chemistry*, Glasgow: International Textbook, 1979.
6. Fuchs, P. and Szepesy, C., *Chromatographia*, 1969, vol. 1, p. 310.
7. Avakumov, E.G., Gimautdinov, Yu.V., and Boldyrev, V.V., in *Materialy V Vsesoyuznogo simpoziuma po mekhanoemissii i mekhanokhimii tverdykh tel* (Proc. X All-Union Symp. on Mechanoemission and Mechanochemistry of Solids), Tallinn, 1977, part. 2, pp. 52–55.

ISSN 1070-4272, Russian Journal of Applied Chemistry, 2008, Vol. 81, No. 6, pp. 1093–1095. © Pleiades Publishing, Ltd., 2008.
Original Russian Text © V.V. Il'ina, Yu.K. Rybak, A.V. Varlamov, 2008, published in Khimicheskaya Promyshlennost', 2008, Vol. 85, No. 2, pp. 55–57.

TECHNOLOGY OF ORGANIC AND INORGANIC CHEMISTRY

Effect of Some Components of Photosensitive Composition on the Sensitometric Characteristics of the Materials for Recording Holograms

V. V. Il'ina, Yu. K. Rybak, and A. V. Varlamov

St. Petersbutg State University of Cinema and Television, St. Petersburg, Russia

Received October 10, 2007

Abstract—Effect of ingredients of the light sensitive composition of registering layer on the photographic parameters of halosilver photographic materials for recording holograms is considered.

DOI: 10.1134/S1070427208060372

The modern materials for recording holograms are extremely diversified. They include electron-optical crystals, photoresists, photopolymerized layers, layers of chrominated gelatin, semiconductor layers, diazotype materials, systems semiconductor – metal, metallic and thermoplastic films. However, the most widespread remain halo-silver photographic materials featured by reliability, accessibility and high sensitivity.

Practically all characteristics of the quality of these materials including sensitometric ones in a great extend depend on either the mode of hologram recording, or on technology of manufacturing the registering layer photosensitive composition, or on the procedure of treatment of the material after registering exposition.

In this publication we present results of the study of influence of the photosensitive composition registering layer on the photographic parameters of the halo-silver photographic material used for recording of holograms.

EXPERIMENTAL

As is known, properties of any system are defined by essence and quantitative relation of its components.

Registering layers composed of the halo-silver photo-graphic material regardless their function are complex by composition disperse polycomponent systems on polymeric base. As the binding polymer, for the modern photographic materials the most often is used gelatin, a poymer of natural origin produced by acid or alkaline hydrolysis of collagen [1]. The binding polymer provides stability of the layer and essentially forms matrix for various active components; ratio of the latter ones defines mainly the parameters of the resulting material. Besides binding polymer, the registering layer photosensitive composition can include up to 50 ingredients varied by content in a wide enough range. Choice of the functional components is defined by the purpose of the material and always takes into account possible side effects. The main material for photosensitive compositions consists of micro crystals of silver halide formed directly in the binding polymer bulk in the process of inorganic synthesis. All other components are introduced after formation of disperse phase. They should either modify surface of photosensitive micro crystals to admit them certain photographic characteristics, or modify the matrix by chemical reaction with the binding polymer for changing physico-chemical structure of the layers to be prepared.

We studied effect of potassium bromide, 5-methyl-7-hydroxy-1,3,4-triazoindolycine (F-1) and spectral orthochromic sensitizer, the dye KR3698 on the halosilver composition including binding polymer (high viscous inert gelatin) and sensitive to light fine disperse microcrystals AgHlg.

The method of preparation of the composition includes the following steps:

– direct instant one-jet emulsifying at 40 ± 0.5°C

with silver halide at excess of silver ions pAg = 2.3 ± 0.1;

– keeping the formed dispersion under conditions identical with those of emulsifying for 10 sec (physical ripening of solid phas);

– one time freezing out the composition followed by washing – decanting with salt free water;

– introducing the modifying additive;

– coating to achieve silver content 1.6 g /m^2.

The photosensitive compositions were tested according to common sensitometric tests of the Russian standard GOST 10691.1–84, the section concerning materials with high resolution. The results are listed in Tables 1 and 2.

Comparative analysis of the obtained results (Tables 1 and 2) allows to reveal the most appropriate composition for the holography purposes.

For example, we can affirm that for the photosensitive compositions with the same filler – binding weight ratio

Table 1. Effect of photosensitive composition on sensitometric characteristics of photographic layers containing AgBr

Composition	Sensitometric characteristics			
	$S_{0.9}$, GOST units	D_0	D_{max}	γ
Gelatin // AgBr//	0.004	0.07	3.20	7.0
Gelatin // AgBr//KP3698	0.012	0.18	6.00	6.8
Gelatin // AgBr // KP3698 // F-1	0.005	0.05	3.35	5.6
Gelatin // AgBr // KP3698 // F-1 // KBr	0.020	0.04	3.20	2.5

Table 2. Effect of photosensitive composition on the sensitometric characteristics of photographic layers containing AgBrI

Composition	Sensitometric characteristics			
	$S_{0.9}$, GOST unit	D_0	D_{max}	γ
Gelatin // AgBrI //	0.008	0.08	3.58	5.2
Gelatin // AgBrI // KP3698	0.020	0.15	5.30	5.0
Gelatin // AgBrI // KP3698 // F-1	0.010	0.10	3.68	3.5
Gelatin // AgBrI // KP3698 // F-1 // KBr	0.012	0.14	2.80	3.2

polymer but differ by chemical composition of the filler, presence of microcrystals with small, ~ 3 mol %, content of iodide (≤ 6 mol % [2]) leads to substantial increase in the sensitivity of the material. Therewith, the constrastness factor γ falls significantly. The iodide most likely affects sensitometric characteristics of the material due to its presence in the disperse medium in the step of formation of solid phase. Due to lower solubility of AgBrI micro crystals as compared with AgBr, the iodide doped in a small amount is built into the lattice of conceived micro crystals and the latter become more stable than the micro crystals without iodide. Therefore the crystals are less prone to the process of ripening along the Ostwald mechanism [3]. Eventually this leads to formation of the composition with the significant scattering by sensitivity of the particles in its solid phase. High sensitivity of such compositions is stipulated by higher defectiveness of the surface of the mix based micro crystals.

As is known, sensitometric characteristics of compositions in a great extend are affected by modifying additives. As the obtained data show, their effect depends on the chemical composition of filler. For example, introducing of spectral sensitizer affects much more the sensitometric characteristics of composition with AgBr micro crystals: photosensitivity grows triple and maximal optical density is duplicated.

Introduction of potassium bromide in the step of formation of registering layer affects sensitometric characteristics only of the material containing a composition with AgBr. Potassium bromide introduced in excess behaves as a solvent of AgBr micro crystals and induces prolonged Ostwald ripping of solid phase in the process of the layer formation. This leads to not controlled grow of micro crystals resulting, on the one hand, in the increase of total sensitivity of the halosilver photographic material in account of increase in sensitivity of growing micro crystals, and, on the other hand, to decrease in the contrastness coefficient due to increase in the scattering by photosensitivity of the micro crystals differ by size. Mix based AgBrI microcrustals are less soluble than AgBr, therefore the effect of introducd potassium bromide on the compositions with AgBrI filler is much less.

Introducing to the composition the sensitizer 5-methyl-7-hydroxy-1,3,4-triazoindolycine leads to decrease in photosensitivity by a half and decreases image contrastness regardless the solid phase composition.

CONCLUSION

The optimal composition for registering layers of holographic halo-silver photographic materials from the viewpoint of sensitometric characteristics should be recognized the composition with AgBrI as a filler, containing, besides a spectral sensitizer, also a mixed stabilizer – potassium bromide with 5-methyl-7-hydroxy-1,3,4-triazoindolycine.

REFERENCES

1. D'yakonov, A.N., *Khimiya fotograficheskikh materialov* (Chemistry of Photographic Materials), Moscow: Iskusstvo, 1988.
2. Brichkin, S.B. and Razumov, V.F., *Zh. Nauchnoi Prikladnoi Fotografii*, 1999, vol. 44, no. 5, pp. 30–36.
3. Shapiro, B.I., *Teoreticheskie nachala fotograficheskogo protsessa* (Introduction to the Theory of Photographic Process), Moscow: Editorial URSS, 2000.

ISSN 1070-4272, Russian Journal of Applied Chemistry, 2008, Vol. 81, No. 6, pp. 1096–1098. © Pleiades Publishing, Ltd., 2008.
Original Russian Text © D.V. Merezhko, A.O. Grigorov, S.S. Mnatsakanov, 2008, published in Khimicheskaya Promyshlennost', 2008, Vol. 85, No. 2, pp. 58–60.

TECHNOLOGY OF ORGANIC AND INORGANIC CHEMISTRY

Appication of Ethylene–Vinyl Acetate Copolymers as a Polymeric Base of Concentrated Pigments for Coloring Polyvinyl Chloride Plastics

D. V. Merezhko, A. O. Grigorov, and S. S. Mnatsakanov

St. Petersbutg State University of Cinema and Television, St. Petersburg, Russia

Received November 2, 2007

Abstract—Physico-mechanical characteristics of compositions of polyvinyl chloride with ethylene – vinyl acetate copolymer (PVC–EVAC) are investigated. The data obtained show that these components are well compatible in the region of high content in the composition of EVAC. This result allow to conclude that EVAC can be used for producing concentrated compositions with a pigment for coloring PVC insulation of electric cables.

DOI: 10.1134/S1070427208060384

INTRODUCTION

For colorization of thermoplastic polymeric materials in bulk at the process of their transformation into a product it is reasonable from the viewpoint of economy to apply granulated concentrated pigments with polymeric base identical with the colorized polymer or technologically compatible with the latter [1, p. 50]. For colorization of plasticized polyvinyl chloride (PVC-plastic) intended for producing cables are produced granulated concentrates based on PVC only [2], which are well compatible with the cable compounds, but have certain disadvantages: low thermal stability and bad dispersing in them of organic pigments with high covering ability [3]. In recent study was shown [4] that PVC-plastic is restrictedly compatible with EVAC (ethylene and vinyl acetate copolymer), in particular, with the copolymer with high content of vinyl acetate links. It seems interesting to study a possibility of application EVAC as a polymeric base for the pigment concentrates applicable to colorization of cable PVC-plastics and displaying both colorizing and modifying action on the parent plasticized PVC.

EXPERIMENTAL

We used industrially produced PVC-plastics for cables responding to GOST 5960-72, with a sharp difference in the content of plasticizers: I40-13A (content of plasticizers 30%) and IO45-12 (content of plasticizers 70%) manufactured by Closed Join Stock Co. "Kaustik" (Sterlitamak). For modification of these PVC-plastics we used two types of EVAC with a high content of vinyl acetate (VA) links: EVAC 11507-070 (content of VA links 22%) and 12306-020 (content of VA links 18%) produces by Open Join Stock Co. "NefteKhimSevilen" in correspondence with Technical Requirments TU-6-05-1636-97. These types of EVAC as well as the types of PVC-plastics differ mutually by the viscosity of melt. As is known [5], for producing homogenous mixture of the melts of two polymers in an extruder their viscosities should differ insignificantly, therefore for the modification of rather rigid PVC-plastic I40-13A it was reasonably to apply more viscous EVAC 12306-020, while for rather soft IO45-12 more appropriate is EVAC 11507-070. We studied compositions with the content of EVAC introduced to PVC-plastic varied from 0 to 10%.

The mixtures of PVC-plastics with EVAC were prepared in a laboratory two-auger pug mill of "Thermo PRISM" firm (United Kingdom) TSE-24-TC at the temperature 130–140°C, rate of augers rotation 60 rpm, the augers configuration is for providing effective mixing.

The samples for physico-mechanical tests of PVC-plastics with EVAC varied by ratio were prepared by rolling – pressing procedure on a laboratory roller and a Scamia press (France), according to GOST 5960-72. The pressed samples had thickness 1 ± 0.1 mm.

Physico-mechaniical parameters: tensile strength and breaking relative lengthening for the samples of mixed compositions were measured on a "HOUNSFIELD" H10KT machine along the GOST 11262-80.

RESULTS AND DISCUSSION

Study of physico-mechanical characteristics in respect of the tensile strength of PVC-plastic – EVAC mixed samples for two pairs revealed that dependence of their strength on EVAC content is ambiguous.

From Figs. 1 and 2 is seen that relative elongation and tensile strength dependence of the compositions on the content of EVAC in them are differ noticeably for the different pairs of the polymers and do not obey additivity law. Physico-chemical characteristics of mixtures of PVC-plastic I40-13A with EVAC 12306-020 show an extremum in the region of 2–4 wt% of EVAC 12306-020, although tensile strength (σ_p) of individual EVAC 12306-020 is 12.5 MPa, that is, below than that of individual PVC-plastic I40-13A, and breaking elongation (ε_p) is 600%, that is, on the contratry, much higher than that of I40-13A, and then these characteristics vary insignificantly up to 10% EVAC content. Simultaneously, strength characteristics of PVC-plastic IO45-12 mixture with EVAC 11507-070 fall down monotonically and at 10% content of EVAC the sp and ε_p values of the composition fall to a half although elongation at breaking of individual EVAC 11507-070 is even higher than for EVAC 12306-020, it equals 65%. It is reasonable to assume that increase in strength and relative breaking elongation for more rigid and viscous PVC-plastic I40−13A at introducing EVAC 12306-020 in the range 2–4 wt% indicates a possibility of formation of a net of donor – acceptor type hydrogen bonds, as shown in Fig. 3.

Seems valid an assumption that dispersion of EVAC in the PVC-plastic looks in this case as follows. The particles of non-polar EVAC fragments push out polar fragments to surface, and the polar fragments on the phase interface develop donor–acceptor interaction between positively charged proton of α-methylene group and negatively charged carbonyl of vinyl acetate group. In the case PVC-plastic IO45-12 with EVAC 11507-070 the low effect of such interaction is due to high content of plasticizer (~70%) in the plastic. The plasticizer molecules surround polar groups in PVC and therefore formation of stable donor–acceptor bonds with active groups in EVAC is not

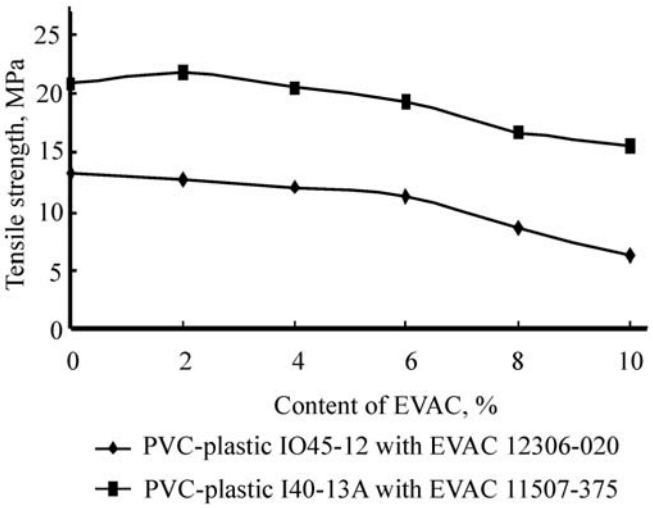


Fig. 1. Plots of tensile strength of the compositions PVC-plastic IO45-12 with EVAC 115-375 and PVC-plastic I40-13A with EVAC 12306-020 on the EVAC content.

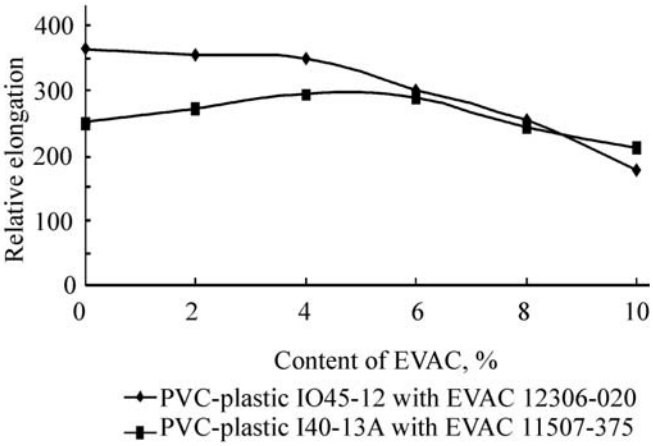


Fig. 2. Plots of relative elongation at break of the compositions PVC-plastic IO45-12 with EVAC 115-375 and PVC-plastic I40-13A with EVAC 12306-020 on the EVAC content.

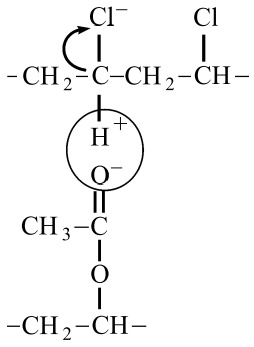


Fig. 3. Mechanism of formation of donor–acceptor bond between EVAC and PVC.

so effective due to pure sterical hindrances. Nevertheless, we can resume that at mixing EVAC with PVC-plastic can be found conditions when physico-mechanical properties of PVC-plastic are retained and even improved, at low content of EVAC in the mixture.

Taking into account that for quality colorization of cable PVC-plastics commonly the pigment concentrate is introduced to the melt in amount 1–2%, and the concentrate contains 30–80 wt% of polymeric base, it is logically to assume that creation of such concentrates based on EVAC owing to interaction of the latter with PVC can lead not only to good distribution of 1–2% of the concentrate in the colorized polymer but also can improve physico-mechanical characteristics of the colorized cable insulator.

REFERENCES

1. Myuller, A., *Okrashivanie polimernykh materialov* (Colorization of Polymeric Materials), St. Petersburg: Professiya, 2006.
2. Shtarkman, B.P., *Plastifikatsiya polivinilkhlorida* (Plasticizing of Polyvinyl Chloride), Moscow: Khimiya, 1975.
3. Lentz, H.I., Gall L.L., *et al., Colorization of Plastics*, Leningrad: Khimiya, 1980.
4. Tikhonov, N.N., Osipchik, V.S., Egorov, V.N., and Khyng, D.N., *Plasticheskie Massy*, 2003, no. 12, pp. 15–18.
5. Chang Dei Khan, *Reologiya v protsessakh pererabotki polimerov* (Reology at the Processing of Polymers), Moscow: Khimiya, 1979.

ISSN 1070-4272, Russian Journal of Applied Chemistry, 2008, Vol. 81, No. 6, pp. 1099–1102. © Pleiades Publishing, Ltd., 2008.
Original Russian Text © D.V. Merezhko, A.O. Grigorov, S.S. Mnatsakanov, 2008, published in Khimicheskaya Promyshlennost', 2008, Vol. 85, No. 2, pp. 61–64.

TECHNOLOGY OF ORGANIC AND INORGANIC CHEMISTRY

Mixing of Polyvinylchloride Plastics with Ethylene–Vinyl Acetate Copolymer

D. V. Merezhko, A. O. Grigorov, and S. S. Mnatsakanov

St. Petersbutg State University of Cinema and Television, St. Petersburg, Russia

Received November 17, 2007

Abstract—Rheological behavior of several types of polyvinyl chloride (PVC) plastics and ethylene – vinyl acetate copolymer (EVAC) is studied. The plots of flow obtained allows to conclude that principally is possible to create quality pigment concentrates based on EVAC for application at the colorization of PVC plastics.

DOI: 10.1134/S1070427208060396

INTRODUCTION

Colorization of cable PVC-plastics commonly is carried out in melt in the process of covering copper cable core by insulant. It is reasonable economically to use together pigment and modifying additive concentrate [1]. Obviously reasonable to use concentrates based on PVC: they are absolutely compatible with the colorized plastic. However, several steps of the process (at preparation of the concentrate and colorization) can be critical for such unstable polymer as PVC and can lead to its destruction, via splitting hydrogen chloride off in particular. We propose another solution: as a binder in the concentrate composition can be used stable, available and not expensive ethylene – vinyl acetate copolymer (EVAC). Application of this polymer as a base for the pigment concentrate is advantageous in several respects. First, its low cost that is comparable with that of polyethylene, much lower than the cost for PVC-plastics. Second, EVAC is thermally stable and therefore is appropriate for high shear stress defining in a great extent the pigment effective dispersing in the concentrate. Third, EVAC possess a high wettability, that is, reveals effective adsorption on the particles of pigment and filler, which, together with ability to high shear stress, provides best quality at dispersing the concentrates for cable colorization. A disadvantage of this system is relatively low compatibility of the PVC–EVAC system [2].

By recent investigations has been established [2] that PVC-plastic is well compatible with EVAC in a certain range of EVAC concentration and at the high content of vinyl acetate links (above 20%) in the copolymer. But at mixing two polymers with restricted compatibility attention should be paid to the viscosity of components. In [3] was noted that the less viscous material while is passing extruder canal will mostly wet the canal internal surface. This simple observation was well described in [4, 5] in respect of petroleum transfer through pipes. It can be concluded that, the best conditions of pigment and additive dispersion in the polymeric product will be achieved when viscosity of components at certain conditions (temperature and shifting tension) are close together. Therefore it seems interesting to compare rheological characteristics of EVAC and PVC main types at the conditions typical for a real processing.

EXPERIMENTAL

For the study were used industrially produced PVC-plastics GOST 5960-72 for cable insulation, that differ from others by the content of plasticizer: I40-13A (30% of plasticizer) and IO45-12 (70% of plasticizer) produced by Closed join stock company "Kaustik" (Sterlitamak). For modifying the chosen PVC-plastics was applied EVAC with substantial number of vinyl acetate (VA) links of two types: EVAC 11507-070 (fraction of VA links 22%) and 12306-020 (18% of VA links) produced by Open

join stock company "NefteKhimSevilen" according to technical requirements TU-6-05-1636-97. These types of EVAC as well as the types of PVC-plastics differ in pairs significantly by the melt viscosity.

High temperature and shear stress occurred in extruder lead to little changes in the properties of PVC-plastics. This results not only from thermal cross-linking, but also with possible loss of plasticizer due to sweating [8]. Therefore before rheological investigations we passed the plastics through a TSE-24-TS extruder. The procedure was intended to modeling changes in the plastic properties at processing on extruder apparatuses.

Rheological characteristics of the samples were measured in a capillary constant pressure viscosimeter.

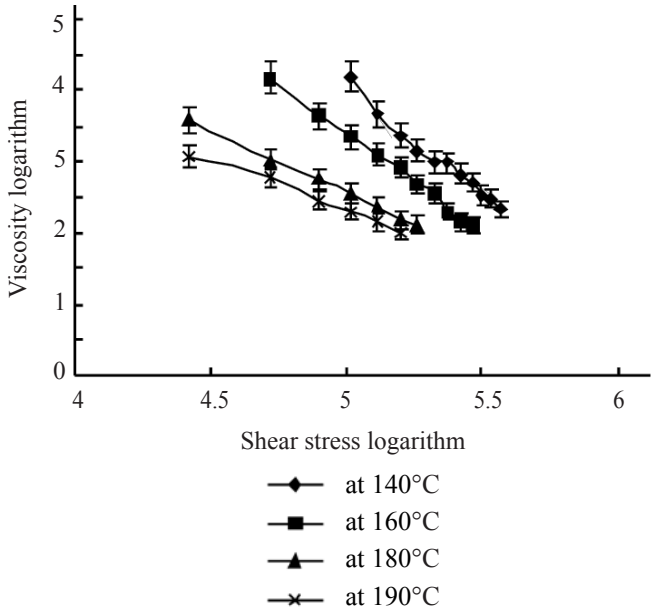


Fig. 1. PVC-plastic I40-13A.

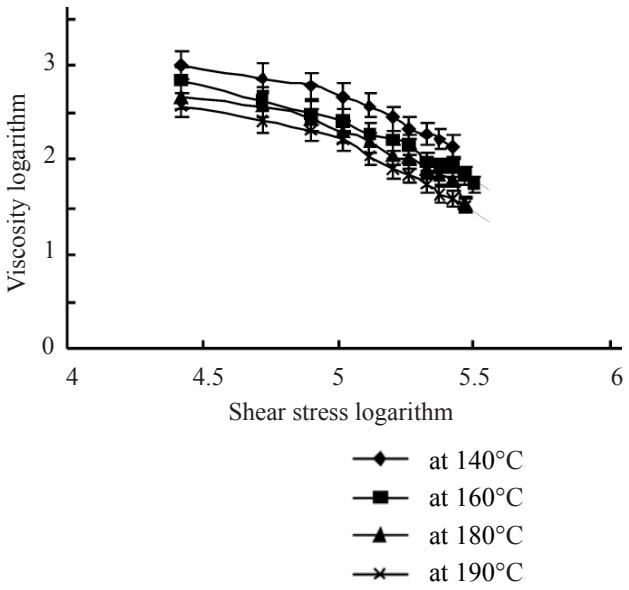


Fig. 3. Flow curves of EVAC 11507-375.

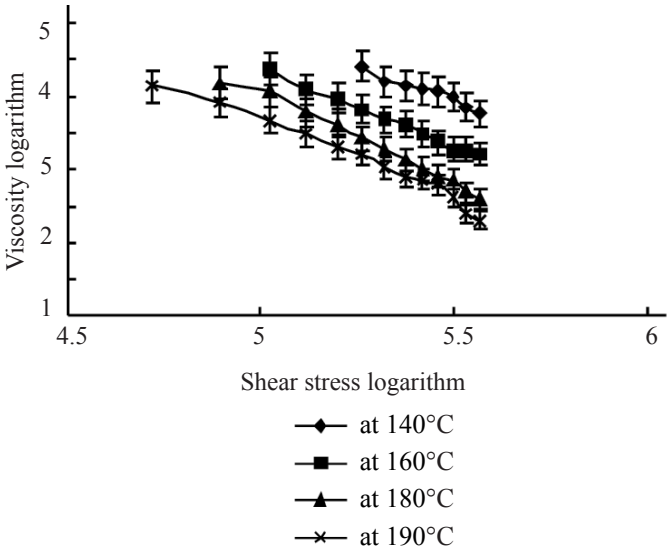


Fig. 2. Flow curves of PVC-plastic IO45-12.

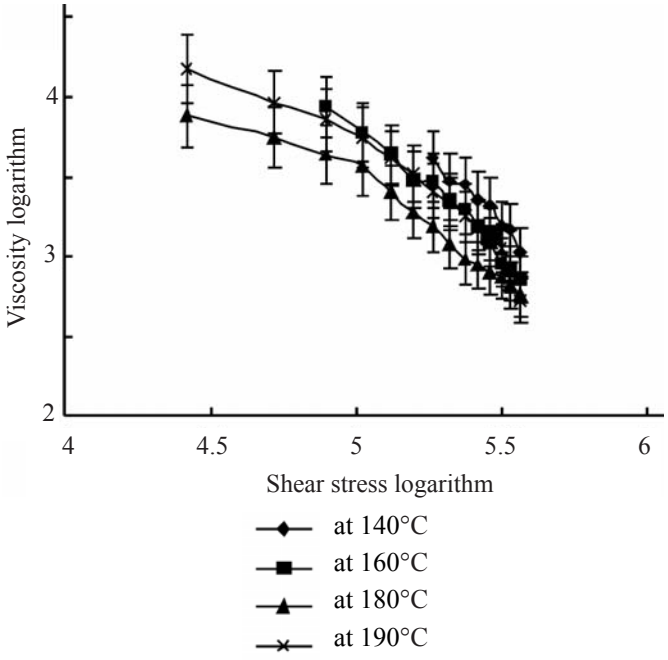


Fig. 4. Flow curves of EVAC 12306-020.

Principal scheme of the instrument and methodology of measuring viscosity are described in [6]. The measuring cycle reeated at different temperatures (160°C, 170°C, 180°C, 190°C) and shear stress (from 26 to 367 kPa). The data obtained are represented as plots [log η (log τ, T)] in Figs. 1–4.

RESULTS AND DISCUSSION

Analysis of the at 140°C shows that both EVAC 12306-020 and PVC-plastic I40-13A flow begins at high enough shear stress and therefore these data reflect the interval of shift rate not completely. For the complete description of rheoligical behavior of the material it would be logically to carry out rheological investigations at higher temperature. As seen from Figs. 3 and 4, at high enough temperatures 180 and 190°C the curves run exert change at relatively high shear stress values (clearly seen in Fig. 4). The inflection of logarithmic dependence of viscosity on the shear stress points to the possible process of destruction of the fractions with high molecular weight. Therefore we suggest that allowed temperature of the investigation is 160°C. This is even more reasonable because this value is close to the temperature of PVC processing by the cable technology [7].

Fig. 5 depicts all flow curves of samples studied at 160°C. Slope of flow curve for PVC-plastic IO45-12 differ significantly from those of the curves characterizxing PVC-plastic I40-13A and both types of EVAC, while both the EVAC samples despite the difference in content of VA links and in the melt flow index (MFI) show very similar slope in a wide range of sift tension. Therefore this investigation does not allow select universal polymeric base for the concentrate which would provide equally good mixing with any sort of PVC-plastic. Note that values of viscosity of EVAC 11507-375 and PVC-plastic IO45-12 are similar at high shear stress and flow cdurves of both EVAC12316-020 and PVC-plastic I40-13A are at near positions in the plot at wide enough range of shear stress. Seems logical to use for colorization of IO45-12 plastic the concentrate based on EVAC 11507-375 and for colorization of I40-13A plastic the concentrate based on EVAC 12316-020 or EVAC 12316-020 and EVAC 11507-375 mixture. At the development of formulation of the concentrates it is allowed to estimate rheological chatracteristics of the melts using values of their melt

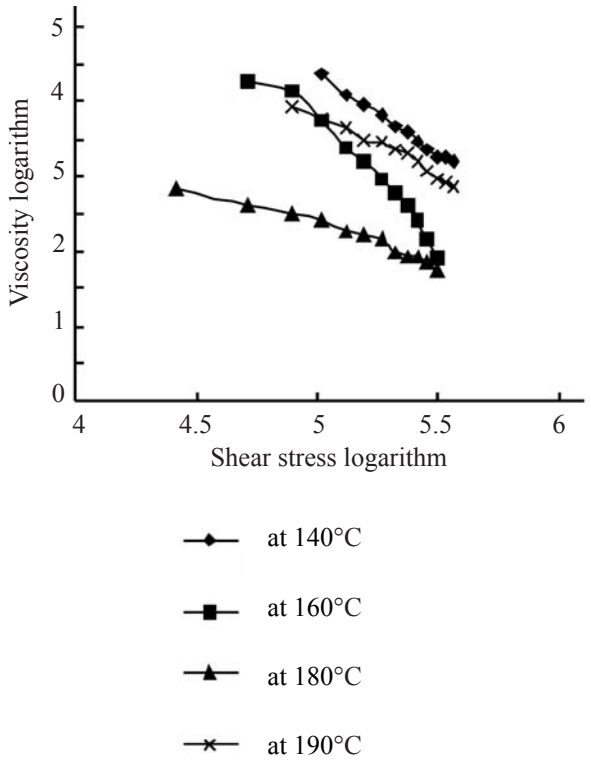


Fig. 5. Flow curves of PVC-pastics and EVAC at 160°C.

flow indices, as far as curves of flows of the EVAC sorts studied in this work are analogous in the whole range of shear stress, that is, "dot" measuring of viscosity like the melt flow index measurement defines position of flow curve of EVAC relatively to the analogous curves for the colorized PVC-plastics enough accurately.

Thus, this study showed principal possibility of creation of pigment concentrates based on EVAC with high content of vinylacetate links which by their rheological characteristics are appropriate for obtaining qualitatively colorized products using process of extrusion of PVC-plastic mixed with 1-2% of pigment based on EVAC 11507-375 and EVAC12316-020.

REFERENCES

1. Mueller, A., *Okrashivanie polimernykh materialov* (Colorrization of Polymeric Materials), St. Petersburg: Professiya, 2006.
2. *Plasticheskie massy*, 2003, no. 12, pp. 15–18.
3. Chang Dei Khan, *Reologiya v protsesse proizvodstva polimerov* (Rheology at Processing Polymers), Moscow:

Khimiya, 1979.
4. Charles, M.E.and Lilleleht, L.U., *J. Fluid Mech.*, 1965, vol. 22, p. 217.
5. Gemmel, A.R. and Epstein, N., *Can. J. Chem. Eng.*, 1962, Vol. 40, p. 215.
6. P*ererabotka plasticheskikh mass* (Processing of Polymers), Moscow: Khimiya, 1966, p. 272.
7. Grigor'yan, A.G., Dikerman, D.N., *et al., Proizvodstvo kabelei i provodov s primeneniem plastmass i rezin* (Producing of Cables and Wires using Plastics and Gums), Moscow: Energoatomizdat, 1992.
8. Shtarkman, B.P., *Plastifikatsiya polivinilkhlorida* Plastification of Polyvinylchloride), Moscow: Khimiya, 1975.

ISSN 1070-4272, Russian Journal of Applied Chemistry, 2008, Vol. 81, No. 6, pp. 1103–1106. © Pleiades Publishing, Ltd., 2008.
Original Russian Text © Sh.S. Namazov, R.K. Kurbaniyazov, A.M. Reimov, B.M. Beglov, 2008, published in Khimicheskaya Promyshlennost', 2008, Vol. 85, No. 2, pp. 65–70.

TECHNOLOGY OF ORGANIC AND INORGANIC CHEMISTRY

Hardness of the Granules of Ammonium Nitrate Doped with the Central Kyzylkum Phosphorite

Sh. S. Namazov, R. K. Kurbaniyazov, A. M. Reimov and B. M. Beglov

Institute of Inorganic Chemistry, Academy of Sciences of the Republic Uzbekistan, Tashkent, Uzbekistan

Received December 5, 2007

Abstract—The results are displayed of measuring hardness of the ammonium nitrate granules when the preceding melt is doped at 180°C either with ordinary powdered phosphorite, or with dust fraction, or with mineralized mass of the Central Kyzylkum Phosphorite in amount from 0.5 to 5.0% of P_2O_5.

DOI: 10.1134/S1070427208060402

Ammonium nitrate is the most widespread nitrogen fertilizer [1]. In Uzbekistan, three big intustrial enterprises, the Open join stock company "Electrochimprom" in Chirchik, Open join stock company "Navoiazot" and Open join stock company "Azot" in Fergana produce ammonium nitrate for agricultural application. The total productivity of these plants is above one million ton of ammonium nitrate per year. But the product is disadvantageous by two characteristics: caking at keeping and explosion hazard [2, 3]. While the caking can be diminished by introducing to the ammonium nitrate some additives, the problem of explosion hazard is not solved yet. To avoid caking, commonly are used sulfate, sulfato-phosphate or sulfato-phosphato-borate additives, caustic magnesite and other substances [4]. It is expected that the problem of explosion hazard can be solved by application of phosphorus-containing additives. In [5–7] has been described technology of manufacturing complex nitrogen-phosphate fertilizer containing 32.3% N and 5.2% P_2O_5 by adding to the ammonium nitrate melt of liquid complex fertilizer with composition 11% N and 37% P_2O_5 based on superphosphoric acid. This additive increases temperature of decomposition beginning by 22–24°C, reduces rate of its thermal decomposition, increases hardness of granules, decreases the product porosity, increasesd stability of the product to multiple phase transformations and, the most important, decreases its ability to detonation. The Open join stock company "Cherepovetskii Azot" firs applied this technology at the technological line with productivity 1000 ton per day. The plant staff noted that explosion hazard of this product is lower that that of pure ammonium nitrate, but at mixing the ammonium nitrate solution with the liquid complex fertilizer a precipitate is formed that generates problems at the steps of evaporation and granulation [7].

Russian plants "Azot" in Kemerovo, chemical mill in Kirovo-Chepetsk, Open join stock company "Minudobreniya" in Rossosh town and Open join stock company "Akron" in Novgorod decided to produce stabilized ammonium nitrate with phosphorus-containing additives. We do not know which compounds are assumed.

We decided to produce stabilized ammonium nitrate by adding to the melt the phosphorite raw material from Central Kyzylkum, namely, ordinary powdered phosphorite, or dust fraction, or mineralized mass. Two last substances are by-products at manufacturing of powdered phosphorite by the process of phosphorite ore dry enriching. Chemical and dispersion compositions of the parent ore are listed in Tables 1 and 2.

Table 1. Phosphate raw material composition

Raw material	Content of components, wt%							$\frac{P_2O_{5assim}}{P_2O_{5total}}$, %
	P_2O_5	CaO	Al_2O_3	Fe_2O_3	MgO	F	CO_2	
Ordinary powdered phosphorite	17.20	46.22	1.24	1.05	1.75	2.00	16.00	18.49
Dust fraction	18.54	44.72	0.95	0.80	0.80	2.22	14.80	20.71
Mineralized mass	14.68	40.80	1.17	1.37	0.53	1.85	12.84	16.41

Table 2. Phosphate raw material dispersion composition

Size class, mm	Fraction content, %		
	Ordinary powdered phosphorite	Dust fraction	Mineralized mass
2 ± 0.5	–	–	4.4
0.5 ± 0.315	1.5	1.5	10.2
0.315 ± 0.16	6.3	5.6	34.1
0.16 ± 0.1	20.3	5.7	14.5
0.1 ± 0.063	38.3	15.0	16.3
0.063 ± 0.05	17.2	9.8	4.7
0.05	16.4	62.4	15.8
Total	100.0	100.0	100.0

In [8] we have studied composition of the products obtained at introduction of the Central Kyzylkum phosphate raw material to the ammonium nitrate melt in amount to acieve content 0.5 to 5% of P_2O_5 in the product. The mixture was stirred for 30 min at 180°C. Analysis showed that the ammonium nitrate melt activates phosphate raw material, that is, converts P_2O_5 to assimilating form. The product with 5% content of P_2O_5 obtained by adding ordinary powdered phosphorite contains 25.24% N and contains P_2O_5 in the form that plants assimilate by 88.29% of the total P_2O_5 content. The product containing 5% of P_2O_5 obtained by adding dust fraction contains 26.01% N and 88.20% P_2O_5 of the total P_2O_5 content in the form appropriate for assimilation. The product from mineralized mass with 5% of P_2O_5 contains respectively 23.94% N and fraction of P_2O_{5assim} 55.75%. More phosphate material introduced to the ammonium nitrate melt, less fractions of assimilating forms of P_2O_5 and CaO and less degree of decarbonization are obtained. Presence of CaO (water) in the product with 5% of P_2O_5 in amounts 1.61% in the case of powdered phosphorite, 1.40% for dust fraction and 1.71% for mineralized mass indicates that at 180°C proceeds reaction between ammonium nitrate and calcium carbonate contained in the phosphate material leading to formation of calcium nitrate:

$$2NH_4NO_3 + CaCO_3 \rightarrow Ca(NO_3)_2 + 2NH_3 + CO_2 + H_2O$$

In this publication we present results of measurements of granules hardness of ammonium nitrate doped with phosphate raw material of Kyzylkum birthplace. Hardness of granules is one of the most significant characteristics of stabilized ammonium nitrate. The granulation was carried out along the following technology. Ammonium nitrate was melted at 180°C, to the melt was loaded a given amount of phosphate raw material, the mixture was stirred carefully for 30 min. The melt was then passed to granulator – a metallic receiver with perforated bottom, the holes diameter was 1 mm. In the upper part of the receiver by a pump was created a pressure, and the melt was sprinkled from 9-th flour of building on polyethylene film at ground. After that was measured the formed granules hardness.

Note that when granulatuion is carried out just after mixing the ammonium nitrate melt with phosphate material without 30 min stirring, the granules formed are unconsolidated and absolutely not hard. This probably is a result of above written reaction of ammonium nitrate with calcium catbonate at 180°C, gas phase evolved from the mixture destroys the granules.

The granules hardness of the granules 1–3 and 2–3 mm size was measured on a MIP-10-1 instrument [9]. On the instrument scale was fixed hardness (kg) at which the granules damaged. Static of granules was calculated by averaging 20 measurements:

$$X = \frac{P_1 + P_2 + P_3 + \ldots + P_{20}}{20},$$

where P_1, P_2, P_3, ····· P_{20} are the values of power for damaging the granules (kg).

Static hardness of granules Y (kg/cm^2) was calculated along the formula:

$$Y = \frac{\sum_{i=1}^{i=20} P_i}{20\,S} = \frac{\sum_{i=1}^{i=20} P_i}{20\,\frac{\pi d^2 cp}{4}} = 0.063\,\frac{\sum_{i=1}^{i=20} P_i}{d^2 cp},$$

where Pi is the power needed for damaging one granule (kg); S is area of the granule section, cm^2; d_{av} is average diameter of granules, cm.

To convert the results obtained to MPa scale the values obtained were divided by 10.2. These data are listed in Tables 3–5.

As seen from the Tables, introducing of grinded phosphorite in amount providing P_2O_5 content from 0.5 to 5.0% to the melt increases hardness of the granules with diameter 1–3 mm from 3.18 to 7.75 MPa, of those with diameter 2–3 mm from 3.2 to 7.8 MPa. Adding the same amount of dust fraction increases hardness of granules with diameter 1–3 mm from 3.15 to 7.69 MPa, and of granules with diameter 2–3 mm from 3.16 to 7.74 MPa. Effect of mineralized mass of the Central Kyzylkum phosphorites is maximal: hardness of granules

Table 3. Hardness of granules of the fertilizer obtained by adding ordinary grinded phosphorite of Central Kyzylkum into ammonium nitrate melt

No.	Amount of phosphorite, g	Amount of melt, g	Content in the mixture, %		Rigidity of granules		
			N	P_2O_5	kg/granule	kg/cm^2	MPa
Diameter of granules 1–3 mm							
1	3.0	100	33.70	0.51	1.03	32.44	3.18
2	7.0	100	32.25	1.05	1.37	43.15	4.23
3	10.0	100	31.10	1.52	1.71	53.86	5.28
4	13.0	100	30.75	2.01	1.92	60.48	5.92
5	18.0	100	29.30	2.61	2.13	67.09	6.57
6	20.0	100	29.15	3.00	2.29	72.13	7.07
7	24.0	100	28.09	3.52	2.36	74.34	7.28
8	30.0	100	27.10	4.10	2.42	76.23	7.47
9	33.4	100	26.01	4.56	2.48	78.12	7.65
10	40.0	100	25.24	5.04	2.51	79.06	7.75
Diameter of granules 2–3 mm							
1	3.0	100	33.70	0.51	1.62	32.65	3.20
2	7.0	100	32.25	1.05	2.16	43.54	4.26
3	10.0	100	31.10	1.52	2.69	54.23	5.32
4	13.0	100	30.75	2.01	3.01	60.68	5.95
5	18.0	100	29.30	2.61	3.35	67.53	6.62
6	20.0	100	29.15	3.00	3.60	72.57	7.11
7	24.0	100	28.09	3.52	3.71	74.79	7.33
8	30.0	100	27.10	4.10	3.80	76.60	7.51
9	33.4	100	26.01	4.56	3.89	78.42	7.69
10	40.0	100	25.24	5.04	3.95	79.63	7.80

Table 4. Hardness of fertilizer granules obtained at introducing into ammonium nitrate melt of the dust fraction of Central Kyzylkum

No.	Amount of phosphorite, g	Amount of melt, g	Content in the mixture, %		Rigidity of granules		
			N	P_2O_5	kg/granule	kg/cm^2	MPa
Diameter of granules 1–3 mm							
2	5.0	100	32.81	0.90	1.35	42.52	4.17
3	9.0	100	31.77	1.52	1.66	52.29	5.12
4	12.0	100	30.71	2.01	1.87	58.90	5.77
5	15.0	100	29.90	2.46	2.08	65.52	6.42
6	20.0	100	29.24	3.14	2.28	71.82	7.04
7	23.0	100	28.28	3.52	2.31	72.76	7.13
8	27.0	100	27.41	4.10	2.41	75.91	7.44
9	32.0	100	26.90	4.67	2.47	77.80	7.62
10	37.0	100	26.01	5.17	2.49	78.43	7.69
Diameter of granules 2–3 mm							
1	3.0	100	33.80	0.55	1.60	32.25	3.16
2	5.0	100	32.81	0.90	2.12	42.74	4.19
3	9.0	100	31.77	1.52	2.61	52.61	5.15
4	12.0	100	30.71	2.01	2.94	59.27	5.81
5	15.0	100	29.90	2.46	3.28	66.12	6.48
6	20.0	100	29.24	3.14	3.59	72.37	7.09
7	23.0	100	28.28	3.52	3.63	73.18	7.17
8	27.0	100	27.41	4.10	3.79	76.41	7.49
9	32.0	100	26.90	4.67	3.89	78.42	7.68
10	37.0	100	26.01	5.17	3.92	79.02	7.74

Table 5. Hardness of fertilizer granules obtained at introducing into ammonium nitrate melt of the mineralized mass of Central Kyzylkum

No.	Amount of phosphorite, g	Amount of melt, g	Content in the mixture, %		Rigidity of granules		
			N	P_2O_5	kg/granule	kg/cm^2	MPa
Diameter of granules 1–3 mm							
1	3.8	100	32.98	0.46	1.26	39.69	3.89
2	8.0	100	31.71	1.02	1.79	56.38	5.52
3	12.0	100	30.49	1.45	2.16	68.04	6.67
4	16.0	100	29.49	2.01	2.48	78.12	7.65
5	20.0	100	28.35	2.38	2.65	83.47	8.18
6	26.0	100	27.83	2.96	2.70	85.05	8.34
7	30.0	100	26.67	3.47	2.75	86.62	8.49
8	36.0	100	25.58	4.14	2.78	87.57	8.58
9	42.0	100	24.75	4.48	2.81	88.51	8.67
10	48.0	100	23.94	4.95	2.85	89.77	8.80
Diameter of granules 2–3 mm							
1	3.8	100	32.98	0.46	1.98	39.91	3.91
2	8.0	100	31.71	1.02	2.81	56.64	5.55
3	12.0	100	30.49	1.45	3.39	68.34	6.70
4	16.0	100	29.49	2.01	3.89	78.43	7.69
5	20.0	100	28.35	2.38	4.16	83.86	8.22
6	26.0	100	27.83	2.96	4.24	85.47	8.38
7	30.0	100	26.67	3.47	4.31	86.89	8.52
8	36.0	100	25.58	4.14	4.37	88.09	8.63
9	42.0	100	24.75	4.48	4.42	89.10	8.73
10	48.0	100	23.94	4.95	4.49	90.51	8.87

with diameter 1–3 mm increases from 3.89 to 8.80 MPa, that of granules with diameter 2–3 mm from 3.91 to 8.87 MPa.

Increased hardness of ammonium nitrate granules corresponds to decrease in their porosity and internal specific surface and, hence, leads to retarding penetration of the granules with diesel fuel and decreased detonation hazard.

REFERENCES

1. Zhmai, L. and Khristianova, E., *Mir Sery*, 2004, no. 2, p. 8–12.
2. Levin, B.V. and Sokolov, A.N., *Mir Sery,* 2004, no. 2, p. 13–21.
3. Lavrov, V.V. and Shvedov, K.K., *Nauchno-Tekhnicheskie Novosti*, INFOKhIM, Spetsvypusk, 2004, no. 2, p. 44–49.
4. *Tekhnologiya ammiachnoi selitry* (Technology of Ammonium Nitrate), Olevskii, V.M., Ed., Moscow: Khimiya, 1978, 312 p.
5. Il'in, V.A., *Cand. Sci. (Chem.) Dissertation,* Ivanovo, 2006.
6. Il'in, V.A., Patokhin, O.I., Glagolev, O.L., Selin, E.N., Levin, B.V., Sokolov, A.N., Sokolov, A.Yu., Samsonov, V.P., Rezen'kov, M.I., Ansheles, V.R., Simbireva, Z.P., Zhavoronkova, N.E., and Vasil'kova, O.E., RF Patent no. 2223932, Kl. SO5 V 7/00, SO5S 1/00, *Sposob polucheniya slozhnykh azotno fosfornykh udobrenii* (A Method of Preparation of Nitrogen–Phosporus Fertilizers), February 20, 2004.
7. Glagolev, O.L., *Mir Sery*, 2004, no. 2, pp. 21–23.
8. Kurbaniyazov, R.K., Reimov, A.M., Dadakhodzhaev, A.T., Namazov, Sh.S.. and Beglov, B.M., K*himicheskaya Promyshlennost*', 2007, vol. 84, no. 5, pp. 242–248.
9. *GOST 21560.2 – 82. Udobreniya mineral'nye. Metody ispytanii* (Mineral Fertilizers. Methods of Testing), Moscow: Gosstandart, 1982.

ISSN 1070-4272, Russian Journal of Applied Chemistry, 2008, Vol. 81, No. 6, pp. 1107–1111. © Pleiades Publishing, Ltd., 2008.
Original Russian Text © S.V. Usikov, Yu.I. Kartashov, L.K. Vasil'eva, V.V. Fomenko, I.M. Bogachev, N.A. Bogacheva, O.G. Petkau, L.I. Chernova, 2008, published in Khimicheskaya Promyshlennost', 2008, Vol. 85, No. 2, pp. 71–78.

TECHNOLOGY OF ORGANIC AND INORGANIC CHEMISTRY

Technology and Tools for the Rapid Quality Diagnostic and Identification of Liquids Based on the Electrophysical Method of States

S. V. Usikov[a], Yu. I. Kartashov[a], L. K. Vasil'eva[a], V. V. Fomenko[a], I. M. Bogachev[a], N. A. Bogacheva[a], O. G. Petkau[a], and L. I. Chernova[b]

[a]*State Scientific Center "Prikladnaya Khimiya", St.Peterburg, Russia*
[b]*State Eterprise "Research Institite Vector", St. Petersburg, Russia*

Received December 3, 2007

Abstract—A new electrophysical method is proposed for liquid products rapid diagnosis of quality and identification. The method is widely prospective for practical application.

DOI: 10.1134/S1070427208060414

In this publication we consider a method of revealing *state* of liquid substance for its identification or for diagnosis of its quality. Advantage of the proposed method is elucidation of earlier unknown laws for a great variety of liquid substances differ by conductivity, dielectric permeability and featured by very low magnetic susceptibility [7, 8]. The work is based on fundamental investigations [1, 2] and practical experience in the military-industrial complex.

On the basis of measurements of electrical conductivity of solutions at different affecting factors [2] we first propose generalized theoretical concept of *measuring* that includes, in conjunction, knowledge about accumulation and scattering energy in substance described by two equations of state (Maxwell equations), knowledge about mechanism of mutual influence of conductivity and mixing currents, about interface phenomenon (electrode – solution), about principles of matching parameters of cell and of measuring instrument. Owing to identity in distribution of steady current and electrostatic potentials between electrodes we succeeded in revealing conditions for measuring dielectric permeability of liquids including electrolytes and of specific electrical conductivity of liquids including dielectric ones.

This all gave a basis for creation of new methods, of reference and commonly used tools for analysis (testing) of substance composition and quality [3], and promoted revealing properties of liquids to retain independent from temperature electrical conductivity at characteristic frequency F_x of surrounding electromagnetic field.

We completed development of basic computer system of analysis (CSA) for revealing quality and for identification of liquid substances [4], which provides operations of the whole complex of devises of which each can be used separately as a basis for design lots of portable units and exploitation of the latter with various objects.

The computer system of analysis is designed as explosion-proof unit and includes following elements (Fig. 1):

– capacity probe capable of operating in chemically aggressive and dangerously explosive environment [5];

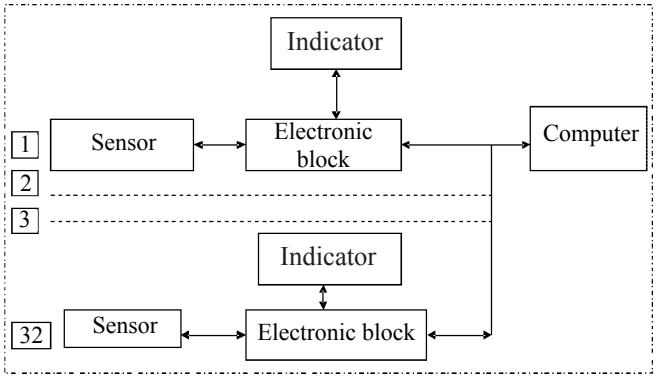


Fig. 1. CSA block-scheme.



Fig. 2. CSA general view.

– electronic block providing action of electromagnetic field with frequency from 1 kHz to 10 MHz on the substance in the operation space of the probe, obtaining responses and transformation of the latter to the form of specific electrophysical characteristics;

– indicator of the electrophysical characteristics and of their dependence on frequency;

– computer for registration and displaying frequency plots of the characteristics and for saving database.

Besides computer, the CSA includes modern portable systems based on microelectronics connected and matched with the probe at the distance up to 1.5 m by means of coaxial cables.

The system allow information acquisition and processing at the distance up to 1200 m, from 32 objects simultaneously.

Block scheme of CSA is depicted in Fig. 1, general view in Fig. 2.

The main parameters of the computer analytic system (CSA) for revealing quality and identification are:

– operating frequency: 1 kHz to 10 MHz;

– measured active conductivity: from 10 nCm to 1 mCm;

– measured capacity: 0.01 nF to 0.01 mF;

– relative error of operating frequency: 10^{-5};

– error at measuring in the frequency range from 1 kHz to 2 MHz: active conductivity from 1 S m^{-1} to 1 mS m^{-1} ± 0.5 %; capacity from 1 nF δ_O 1 000 nF ± 0.5 %;

– maximal number of points of scan frequency: 1024;

– error in measuring temperature: ± 0.05°C;

– type of interface: RS-232 and RS-422;

– power consumed by one canal: from 50 Hz electric line 85–240 W, from 5 – 12 V source 5 W.

The method used is based, first, on the Maxwell theory of electromagnetic field allowing determination of distribution and scattering of electromagnetic energy in a substance at different frequencies accounting for the fact that magnetic permeability of liquids in this field $\mu \leq 1$, and, second, on the introduction to the process of experiment a certain complex (code) of electrophysical characteristics – the new quantitative characteristics which simultaneously characterize quality of liquid and its belonging to a certain group of liquids, e.g., to a given sort of fuel and lubricant, oil from certain birthplace or mixtures of oils, to propellants, to genetic solutions, to alcohol solutions (vodka), to food, etc.

Conditions are revealed where can be commensurable the components of active conductivity stipulated by two inseparable processes of motion of "free" and bound ions and ionic associates. This is extremely needed for measuring characteristic frequency F_x at different temperatures when active conductivity remains unchanged.

In a liquid, molecules are always in the state of specific intimate collision.

Only recently were successfully realized experiments concerning the process of action of electromagnetic field at different frequency on fuel-lubricant materials and were detected characteristic frequencies F_x which are of specific value for each product depending on the chemical state (composition) of the latter. Therewith, active conductivity does not depend on the variations in temperature up to boiling point. Undoubtedly, these properties of a liquid are connected with its structure.

This situation can be adequately described as the action in the liquid of two inseparable types of the components of active current, of which one is stipulated by the motion of so-called "free" ions and another by the motion of bound ions (charges).

When molecular structure of a liquid is of multi-dimensional type (molecular associates), e.g., in the case of oil with a certain content of low boiling fractions, residual fuel oil, dark diesel fuel, nutritional vegetable oil, F_X falls to the low frequency region of spectrum (Table 1):

10 kHz –sunflower oil "Zolotoe semechko" refined;

12.6 kHz – sunflower oil "Natura", refined, GOST P524-2005;

17.4 kHz – sunflower oil "Dary Kubani", not refined,

GOST P52465-2005;

144.5 kHz – motor oil "King Oil", 5W50;

300 kHz – petroleum of West Siberian birthplace;

400 kHz – petroleum of Ukhta birthplace;

1 500 kHz – petroleum of Kaliningrad birthplace with high content of kerosene.

In the case of liquids with low electrical conductivity the F_x value is much larger. For example, a batch of propellant unsymmetrical dimethylhydrazine is characterized by F_x value 3 800 kHz, while a batch of binary mixture propellant TG-02 has F_x = 4 000 kHz [1].

At characteristic frequency of electromagnetic field F_x two types of active current have equal but of opposite signs increments. F_x belongs to the most important structural characteristics of a liquid.

The essence of electrophysical *method of states* is as follows.

At the action of electromagnetic fields differ by frequency (e.g., in the range from 1 kHz to 10 MHz or even higher) at a given temperature and pressure can be registered *responces* in the form of standard electrophysical characteristics (code of characteristics) which can be obtained experimentally and calculated theoretically:

– specific acitive conductivity ж, including that at high frequency 1 MHz, in the range from 0 to 5×10^{-6} S m^{-1} and higher and at low frequency 1 kHz in the range from 0 to 20×10^{-9} S m^{-1} and higher;

– ratio of specific active conductivities at all frequencies to specific active conductivity at 1 kHz, including ratio of specific active conductivities at the frequencies 1 MHz and 1 kHz (criterion of identity) in the range from 1 to 10 000 and higher;

– dielectric permeability ε, including measured at the frequency 1 kHz (ε_{1kHz}) and 1 MHz (ε_{1MHz}), and gain $\Delta\varepsilon_f = \varepsilon_{1kHz} - \varepsilon_{1MHz}$;

– characteristic frequency F_x in the range of few kHz to 10 MHz and higher;

– spectrum of plots of ж and ε against frequency in the range from 1 kHz to 10 MHz;

– higher specific heat of combustion Q_s^a, kJ kg^{-1} for fuels and lubricants [6].

These responses (codes) of electrophysical characteristics allow to identify belonging of a substance to certain product and to estimate its quality (composition).

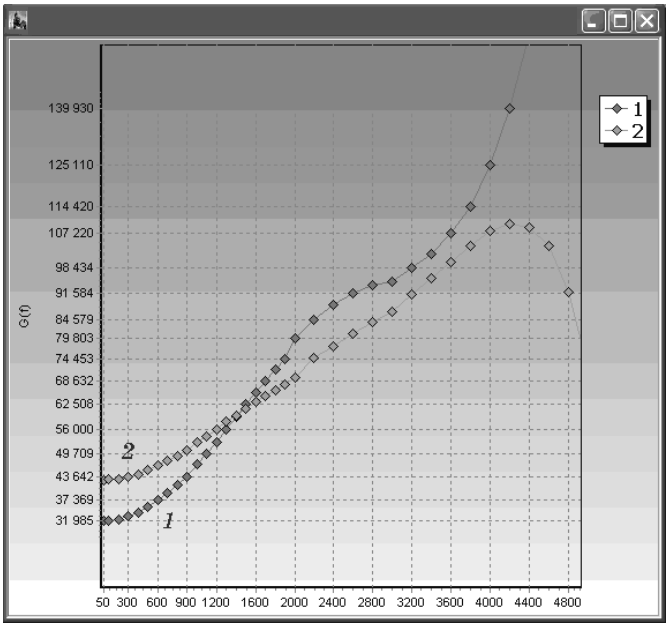


Fig. 3. Pronit (batch 1): (1) at 19.5°C; (2) at 34.0°C.

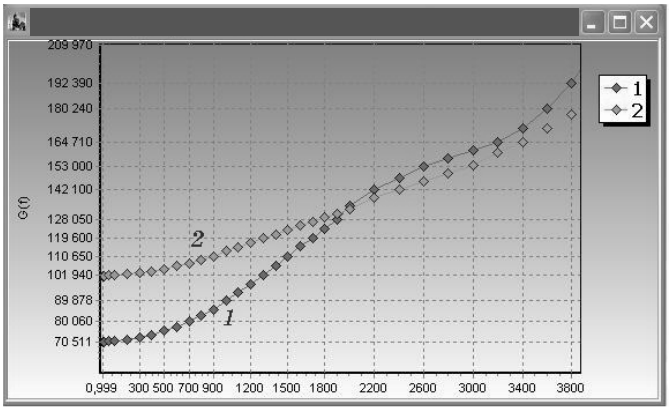


Fig. 4. Pronit (batch 2): (1) at 20.5°C; (2) at 37.0°C.

Any given product has its own values of characteristics (code). The characteristics include:

æ$_f$, æ$_{1MHz}$, , æ$_{1kHz}$, ε_f, ε_{1kHz}, ε_{1MHz}, n, Q_s^a, F_x.

They all are measured simultaneously at the same influencing factors (temperature, frequency, etc.) Applying this *computer system of quality analysis and identification* (CSA) for measuring characteristics takes 2 min or less.

Number of characteristics decreases in the cases of simple technological processes.

A significant supplement to the characteristics of products is dependence (relief) of the characteristics on frequency. This is an original spectral characteristic of electrophysical characteristics in respect of quality of

Table 1. Oil, fuel, lubricants and nutrition oil

No.	Product	Tempera-ture, °C	f_1 = 1 kHz		f_2 = 1 MHz		n = æ$_{f2}$ / æ$_{f1}$	Q_s[a] [5], kJ/kg	f_x, Hz
			ε_{f2}	æ$_{f1}$ ×10^9, S m^{-1}	ε_{f2}	æ$_{f2}$ × 10^9, S·m^{-1}			
1	2	3	4	5	6	7	8	9	10
				Oil					
1	Kaliningrad birthplace	20	2.220	81	2.190	540	6.60	45613	1500
2	Ukhta birthplace	20	2.460	80	2.360	1270	15.87	44926	400
3	West Siberia birthplace	20	2.543	67	2.425	1963	29.10	44450	300
				Diesel fuel					
1	E-4.0	24.5	2.635	5.8	2.492	3237	558	43444	
2	M-40	24.5	2.761	3.6	2.535	3900	1077	43032	
3	M-100 (fuel oil - mazut)	24.0	2.949	3.4	2.654	4200	1225	42965	
				Mineral motor lubricant oil					
1	M5-310G$_1$	20	2.364	18.46	2.303	492.9	26.70	45074.78	
2	M5$_3$-12G	20	2.378	7.17	2.319	492.9	68.79	44491.99	
3	M5$_3$-12G used (milleage 6000 km)	20	2.510	8.49	2.429	1281.7	150.96	44008.00	
4	M8	20	2.381	11.86	2.331	887.4	14.82	45437.30	
5	M8-12G used (milleage ≥ 10000 km)	20	2.509	4.23	2.415	2070.5	459.48	43322.57	
6	M14-B$_2$	22	2.409	14.56	2.322	1630	111.95	44263.18	
7	M14-B$_2$ used (milleage ≥ 10000 km)	20	2.518	3.81	–	–	–	–	
8	SAEW-30 synthetic	20	2.346	29.60	2.260	492.7	16.4	45365.97	
9	SAEW-30 used (milleage 11000 km)	20	2.436	16.90	2.260	722.6	42.76	44784.78	
10	5W 50 “King Oil”	15	2.412	3.24	2.190	510	157.4	43804	
		40	2.407	10.52	2.176	720	68.4	–	1445
1	2	3	4	5	6	7	8	9	10
				Vegetable and plant oil					
1	DTM (E1) – distilled tall oil	19.0	2.651	0.11	2.650	900	8182	41472.91	
2	DTM (E2) – distilled tall oil	19.0	2.678	0.11	2.674	1290	11727	41247.71	
3	ZhKTM (E5) – fatty acid tall oil	19.0	2.619	0.11	2.620	530	4818	41811.26	
4	“Petrocuan”– sunflower nutrition oil not refined νε	16.0	3.175	1.43	3.182	1810	1266	42475.60	
5	“Zolotoe Semechko” – sunflower nutrition oil, refined, deodorized, without cholesterol, without proofing additives	15	3.672	0.65	3.133	1880	2892.3	41877	10
		39	3.548	0.47	3.033	1470	3127.7	–	
6	“Natura” – sunflower nutrition oil, refined, first sort, without cholesterol, without proofing additives GOST P524-2005	15	3.664	0.98	3.122	1710	1744.9	42211	12.6
		39	3.482	0.64	3.019	1010	1578.1	–	
7	“Dary Kubani” – sunflower nutrition oil not refined, GOST 52465-2005	17	3.667	0.002					17.4
		39	3.535	1.26					

solutions. First in world practice appears real perspective for estimation of frequency dependence of electrophysical characteristics for solutions of any class and their connection with chemical state, hence, for creation of extra new technologies for estimation quality and identification of substances.

Whole, the complex of electrophysical characteristics obtained using CSA simultaneously and undert certain conditions and their dependence on frequency (spectrum) is specific for each product. Any deviation in the state (composition) of the substance can be registered promptly. This complex of electrophysical characteristics is imperative and adequate, a set of values of these characteristic constitute *code* of a substance. The identification and quality code is a set of normalized values of specific electrophysical characteristics measured simultaneously.

Table 2. Propellants

No.	Product	Temperature, °C	f_1 = 1 kHz		f_2 = 10 MHz		n = æ$_{f2}$/æ$_{f1}$	Q_s^a, kJ kg^{-1}	F_x, kHz
			ε $_{f1}$	æ$_{f1}$·× 10^5, S·m^{-1}	ε $_{f2}$	æ$_{f2}$·× 10^5, S·m^{-1}			
1	$Me_2N_2H_2$ nonsymmetrical	–40	13	0.08	–	0.2	2.37	–	3800
	dimethylhydrazine	40	7.5	0.6	–	0.72	1.2		
2	TG-02, 1:1	–40	5.5	0.3	–	0.6	2	–	4000
	$(C_2H_5)_3N$ (triethyl amine)	40	3.7	2.5	–	2.6	1.04		
	$Me_2C_6H_3NH_2$ (xylidine)								
3	Pronit (batch 1)	19.5	18.464	3.080	18.442	4.514	1.466	46844.2	
		34.0	17.496	4.108	17.504	5.076	1.236	46855.3	1440
4	Pronit (batch 2)	20.5	18.544	6.798	18.615	8.680	1.277	46920.3	1960
		37	17.399	9.777	17.541	10.298	1.053	46876.3	

As examples, Tables 1 and 2 and Figs. 3 and 4 display experimental data characterizing corrspondence between liquid products and their codes and quality of products in correspondence with the values of characteristics.

These technologies for diagnosis of quality and identification are protected by patents. There are perspectives of further paten application which can create a basis for technological renewing many branches of industry, chemical industry first of all, branches of agriculture and for development of analytical technologies.

Market of application of the electrophysical method of states is impressive. Any respectful business owner realizing this technology will meet a great success. The authors can represent marketing data in the process of negotiation.

To conclusion, let us note the following. The characteristic frequency F_X with high resolution corresponds to retention of initial state of a product and exerts changes at even small deviation from this state. An important factor also is identity criterion *n*. Application of the proposed method of states will result in great diminishing of failures and accidents with "Proton" rockets, airplanes, ships and other transport means that use components of propellants and fuels.

REFERENCES

1. Usikov, S. V., *Elektrometriya zhidkosti* (Electrochemistry of Liquid State), Leningrad.: Khimiya, 1974.
2. Usikov, S.V., *Opredelenie elektroprovodnosti i dielektricheskoi pronitsaemosti rastvorov* (Measuring of Electrical Conductivity and Dielectric Permeability of Solutions), St. Petersburg: Thesa, 1997.
3. Usikov, S.V., Kartashov, Yu.I., and Vasil'eva, L.K., Petkau, O.G, Bogachev, I.M., Vylegzhanin, V.V., Yakushev, V.P., Anan'ev, A.P., and Tulin, E.V., Abstracts of Papers, International Conference Denoted to 75th Anniversary of Agrophysical Institute, St. Petersburg, September 25–27, 2007.
4. RF Patent no. 2209422. Unit for Diagnosis of State of Oil and Products of Its Processing Based on Their Active Electrical Conductivity and Dielectric Permeability, 27.07.2003; Byull. no. 22.
5. Belousov, O.A., Efremov, B.M., Leonov, V.M., Litko, A.A., Ovinnikov, V.K., Solodova, M.P., and Usikov, S.V., Three-Electropde Probe, *Inventor's Certificate* no.578603, 1977, Byul. no. 40.
6. RF Patent no. 2117280. A Method for Measuring Highest Specific Heat of Combustion of Oil, 10.08.98, Byul. no. 22.
7. Khimicheskaya Entsiklopediya (Chemical Encyclopaedia), Vol. 2, p. 42; Moscow: Sovetskaya Entsiklopediya, 1980.
8. *Khimicheskaya ensiklopediya* (Chemical Encyclopaedia), vol. 3, p. 445; Moscow: Sovetskaya Entsiklopediya, 1992.

ISSN 1070-4272, Russian Journal of Applied Chemistry, 2008, Vol. 81, No. 6, pp. 1112–1116. © Pleiades Publishing, Ltd., 2008.
Original Russian Text © V.L. Chechulin, V.G. Ardavichus, O.D. Kolbasina, 2008, published in Khimicheskaya Promyshlennost', 2008, Vol. 85, No. 1, pp. 39–44.

PROCESSES AND DEVICES OF CHEMICAL MANUFACTURES

Informatization of the Process of Producing Formalin

V. L. Chechulin[a], V. G. Ardavichus[b], and O. D. Kolbasina[c]

[a]*Perm State University, Perm 614990, Russia*
e-mail: 824214962@permonline.ru
[b]*Metafaks Co., Gubakha, Perm oblast, Russia*
[c]*Perm State University, Berezniki Branch, Berezniki, Russia*

Received March 19, 2007

Abstract—Solving the problem of oxygen dozing optimization (relatively to methanol mass flow) in the process of formalin producing is achieved by maximization of the metric of final product obtaining. In the solution of the optimization problem is attention is paid to the period of catalyst renewing.

DOI: 10.1134/S1070427208060426

1. INTRODUCTION

Optimization of the process of producing formalin can be achieved at consideration the process quality determining factors: the process material balance and the criterion of the commercial product maximal yield of the possible from stoichiometry [3]. We assume common system levels structure [12]. Within the commonly used 6-level structure of the Automatic System of Technological Process Control (ASTPC) the problem is decomposed into the following automatization – information tasks over the levels:

1-st level (means for the measuring and control) should provide the technological parameters measuring: mass flows of raw materials including methanol, water (for mixing with methanol), air (air oxygen for oxidizing methanol), the mass flow of final product, technological parameters such as temperature of apparatuses, water mass flow for absorption, height of methanol – water mixture in evaporator, and others.

2-nd level (controllers, schemes of local automatics): providing control over local tuning contours, that is, maintaining the values of mass flows of raw materials (methanol, water, air) defined by 3-d and 4-th ASTPC levels, other mass flows (water for absorption), temperature regimes of apparatuses, height of methanol-water mixture in evaporator, etc.

3-d level (electronic databases): providing ability to observe the scope of technological parameters both in real time and as plots; acquisition and saving external data (digitalization of the results of analysis of raw material, mass percentage of methanol in the methanol – water mixture, content by volume of oxygen in air and fraction of commercial formalin in the final product of the process, together with registration of sampling time).

4-th level (optimization of the process in real time at partial modeling): providing the automatic calculation of methanol – water ratio at dozing to evaporator of methanol – air mixture, providing automatic calculation of the degree of air dozing on stoichiometry with certain coefficient of extension (excess depending on the probable yield of final product), providing automatic calculation of the yield of final product relatively to the yield possible from sctoichiometry, at the organization of computer-based acquisition of statistical data on calculated and measured parameters (with APM program for personal computers, see below).

5-th level (record saving and internal planning): providing saving records in real time and for the reported periods (labor shift, month, quarter, year) on the flows of raw material, final (commercial) products and side products, record of labor consuming (this is a separate problem, not within the automatization), accounting for correspondence to planes in agreement with requirements of the process uniformity and matching the planes on producing and shipping, acquisition and saving records on the data of the product net cost calculations.

6-th level (tying to external economic situation): providing accounting for external prices and prognoses for calculation of optimal releasing price (assuming 30%, 36%, …, etc. profit [13]) and determination of the metric of possible internal investment.

2. RESTRICTIONS IN APPLICATION OF MATHEMATIC METHODS

The process basic reactions are [3, 5, 6]:

1. $CH_3OH + 0.5O_2 \leftrightarrow CH_2O + H_2O + 159098.4$ J

2. $CH_3OH \leftrightarrow CH_2O + H_2 - 83738$ J

3. $H_2 + 0.5O_2 \rightarrow H_2O + 242834.4$ J

Side reactions:

4. $CH_3OH + 1{,}5\ O_2 \rightarrow CO_2 + 2H_2O$

5. $CH_3OH + O_2 \rightarrow CO + 2H_2O$

6. $CH_2O \rightarrow CO + H_2$

7. $CH_3OH + H_2 \rightarrow CH_4 + H_2O$

Another side reaction can proceed, in part:

8. $CH_4 + O_2 \rightarrow CH_2O + H_2O$

9. $CH_4 + 2O_2 \rightarrow CO_2 + 2H_2O$

Reaction (8) forms cycle with (6) and (7), therefore little possible to identify exactly the process with the model described by linear differential equations embarrassing first seven reactions. This is connected also with the fact that a system of reactions containing reaction cycles (of side products) is not describable by a system of differential equations because in such a case the continuous function argument related to the substance molar concentration is in turn a function, therefore description of processes is impossible due to natural restrictions of mathematic functional means.

This impossibility of applying a function itself as an argument of continuous (capable of differentiation in time measure parameter) function should not be mixed with the case of discrete recursive (of course appropriate for calculation) functions applied at computation programming.

In more details, the following restrictions of applying mathematic methods to the description of complex chemical processes should be accounted for. At the description of algorithmic possibility of calculation of the control parameters in real systems of process control (in the processes of chemical technology) appear additional requirements. This leads to the restrictions which do not allow algorithmic calculation of the result of (physico-chemical) process from known initial (metrics of dosing substances) and boundary (temperature, pressure) parameters of the process measured in real time scale.

Method of identification of a system and attempts of building complete model of a process (of chemical technology) are little applicable to description of real systems, as was established practically earlier in 60th of 20 century [11]. The identification was found to be partially applicable only to calculation of contours of the control parameters (2-nd level) but not for stabilization of the process quality because of omitting many factors. There is natural difference between the practice and theory in the case of complicated chemistry of the process even icluding simple inorganic reactions. (In addition, it is methodologically incorrect at the identification of a process to consider the latter as a "black box" with unknown contents despite the fact that something about the process chemistry is known).

Besides, when a system of chemical reactions includes reaction cycles, description of such system by a set of differential equation is not applicable because the function describing concentration of a component can not be taken as an argument of itself (the obvious mathematic postulate), e.g., for the cycle $A \rightarrow B \rightarrow C \rightarrow A$ the function describing concentration of substance A should be written as $v_A = v_A(v_B(v_C(v_A)))$, that is, $v_A(\ldots v_A)$, where v_A is function of concentration of substance A depends on itself and is used incorrectly. The process of producing formalin is practically of this type, and many other processes of complex chemical technology are similar (e.g., the process of reduction of titanium tetrachloride with magnesium). Therefore the only appropriate remain statistical methods of determination of the process control parameters considered below.

It is quite obvious that practically this restriction follows theoretically from the known since 20th century middle theorems about insolubility of the problem of identity of words in the semi-groups and associative systems [7, 10, 8, 2] (this restriction is also considered in [12,14]).

Let a word $a_1 \ldots a_n$ to denote left part of a chemical reaction, and $b_1 \ldots b_n$, its right part, where a_i, b_i are chars in the alphabet sequence of the names of chemical elements. Then description of chemical reaction consists in the finding identity of the words: $a_1 \ldots a_n = b_1 \ldots b_n$ for a set of reactions in a real process, the identity for a set of k words. To these words can be added sub-words F_1 (to left part) and G_1 (to right part) characterizing physico-chemical component of reaction: thermal effects,

changes in enthalpy, etc., that can be found from boundary conditions of the process. Such a set of equations forms an associative system: words are not commutative – the chars can not be replaced within alphabet – but are associative: tentative including of parentheses into the word does not changes its meaning. To such record can be applied the theorem of algebraic insolubility of the problem of words identity (A.I. Mal'tsev, see in [9, vol. 1, p. 215, line "algorithmic problem"] without evidencing), interpreted as impossibility of algorithmic calculation of results of a process of chemical technology proceeding from its initial and boundary conditions, hence, impossibility of stabilization of the process (product) quality, as has been noted by practical specialists in 60-th as absence of required mathematic methods [11]. Therefore (from practical viewpoint and due to above restrictions) control over the quality of final product is needed and appears a necessity in qualitative definition of the space of states of control system for emphasizing (besides the parameter of product quality) a parameter of control and a parameter of optimization [14], in conjunction with the known results of the theory of ability of measuring and calculating an immovable dot [4, 15].

Therefore for optimal control over the process, application of the methods of statistically optimal control described below is rather correct.

3. DESCRIPTION OF THE PROCESS MODEL

According to the main reactions of the process (1–3) at the ideal stoichiometry 1 mole of methanol affords 1 mol of formaldehyde. Practically the yield of final product is less than unity and depends (all other conditions the same) on the measure of oxygen flow into the reactor. Therefore for maximizing the final product yield should be maintained certain ratio of methanol and oxygen flows into reactor. The degree of optimality of this ratio can be judged indirectly from the data of analysis of exhaust gas that contains products of side reactions.

From the viewpoint of modeling, the process remains indefinite: the number of equations (reacting components and reaction intermediates) is greater than the number of dozed substances, and the system of linear equations at the attempted model description by the methods of linear algebra would have unknown values more than equations. Application of procedures of object identification is valuable within restricted function-space area of experiment and do not accounts for unpredictable "aging" of catalyst (decrease in activity). Therefore remains applicable only the methods of direct measuring at the co-definition of information flows and elucidation of statistical (correlation) relations of meaningful factors of the process quality (on the material balance) and control (ratio of dozing oxygen and methanol).

The more precise instrument for the determination of optimal methanol – oxygen mole ratio is providing ability of registration in the real time of the coefficient of material balance on the final product (relatively to the stoichiometric maximum). Therefore the system of the process control for the optimization toward the maximum of obtaining the product should be supplemented with revealing (in real time, during the control) the correlation between the measure of the fraction of the product obtained relatively to the maximum possible, and methanol – oxygen ratio, aimed at the optimization of the measure of air feeding into reactor. Hence, should be arranged continuous measuring of final product flow.

Similarly, from the measure of the final product as a fraction of maximally available can be determined state of catalyst, but by means of longer statistics.

Let us consider a mode. Let $m(CH_3OH)(t)$, g/s, is a measure of mass flow of methanol to the installation;

$M(CH_3OH)(t)$, mol/s, is a measure of molar flow of methanol to the installation;

$M(CH_3OH)$, g/mol, is molar mass of methanol,

$$M(CH_3OH)(t) = m(CH_3OH)(t) / M(CH_3OH). \quad (1)$$

The maximally available molar flow of the final product (according to the reactions 1–3, see above) is:

$$M_0(CH_2O)(t) = 1 \cdot M(CH_3OH)(t), \quad (2)$$

where 1 is stoichiometric coefficient in the reactions (1) and (2).

Actual flow of the final product is an object of measuring:

$m(CH_2O)(t)$, g/s, is a measure of mass flow of formaldehyde from the installation;

$M_1(CH_2O)(t)$, mol/s, is a measure of molar flow of formaldehyde from the installation;

$M(CH_2O)$, g/mol, is molar mass of formaldehyde,

$$M_1(CH_2O)(t) = m(CH_2O)(t) / M(CH_2O). \quad (3)$$

The relative measure of obtaining the product $\mu(CH_2O)$ is the ratio of real molar flow to the maximally possible from stoichiometry [ratio of the formulas (3) and (2)]:

$$\mu(CH_2O) = M_0(CH_2O)(t) / M_0(CH_2O)(t) \quad (4)$$

$$\mu(CH_2O) \in [0, 1].$$

Relative measure of dozing air oxygen relatively to methanol flow is defined by measurable relation:

$$\mu(O_2 \mid CH_3OH)(t) = M(O_2) / M(CH_3OH)(t), \quad (5)$$

where $M(O_2)$, mol/sec, is a measure of air oxygen flow determined from the results of measuring with ASTPC of the measure of air flow and calculated (with accounting for the analyses of oxygen content in air).

For the optimization of dozing air it is sufficient to arrange statistical procedure for reflecting the data on the relative dozing for determination (from sliding average values) of the measure of correlation (regression) connection between the measure of obtaining final product and the measure of the ratio of oxygen dozing:

$$regr(\ldots)(t) = regr(\mu(CH_2O); \mu(O_2 \mid CH_3OH)(t)) \quad (6)$$

with determination of oxygen dozing optimum for approaching the maximum of the final product yield (Fig. 1).

4. CONCERNING OPTIMIZATION OF THE PERIOD BEFORE RENEWING CATALYST

Measuring fraction of final product relatively to maximum available (according to stoichiometry of the process) allows determination of optimal time for renewing catalyst for the process of producing formalin and for other catalytic processes, e.g., the process of producing methanol, as described in [1], where had been noted that using the ASTPC system for the process of control of methanol manufacturing allows calculation on the 4-th level of "an estimation of the apparatuses productivity on crude methanol", and "the calculated data can be taken as a base for estimation of 'chemical activity' of the catalyst of synthesis".

As far as existing ASTPCs for producing a product (formalin or methanol) give the data for the calculation, in real time, of the fraction of practically obtained product as a part of theoretically possible, continuous statistical registration of this fraction allows solving the problem of state of catalyst and determining the time of its renewing (see Figs. 1 and 2).

Let $v_m(t)$ is a coefficient of effectiveness of transformation raw material into product (100% = 1). Obviously, the maximal period of using this catalyst is defined by the moment when the cost of not obtained product $C_i(t)$ (dashed area) becomes comparable with the cost for renewing the catalyst. With the data of the product cost it is ease to arrange calculation of the integral $C_i(t)$ in real time in the APM of ASTPC:

$$c_i(t) = \int_{t_0}^{t} \left(v_m(t_0) - v_m(t)\right) m(t)\, c(t)\, dt\,, \quad (7)$$

where $v_m(t_0) - v_m(t)$ is a difference between maximal initial (at preceding renewing) value of efficiency index and its current in time value (the measure of the product

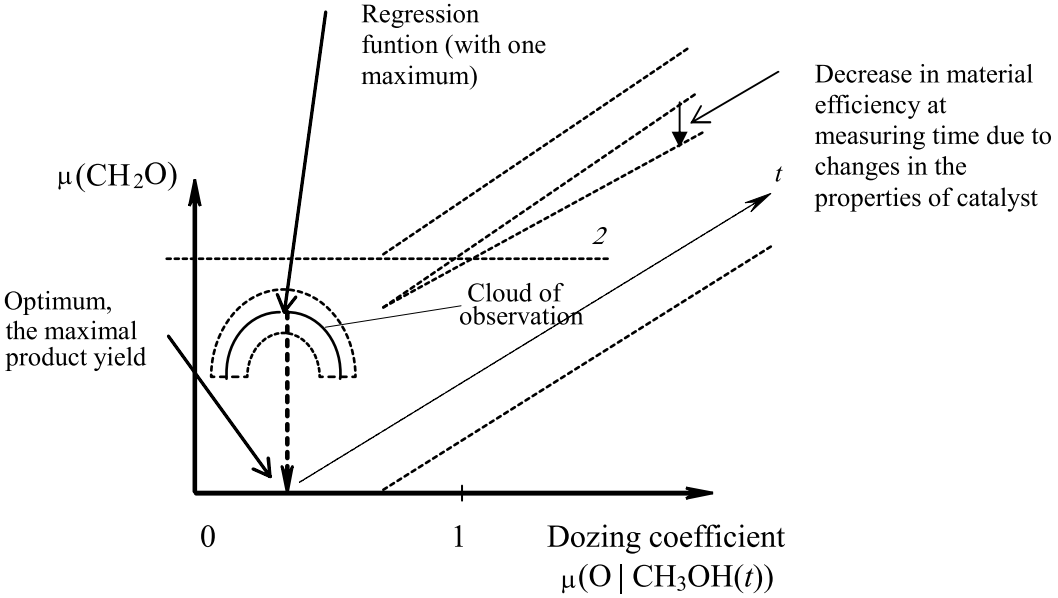


Fig. 1. Optimization diagram of the process.

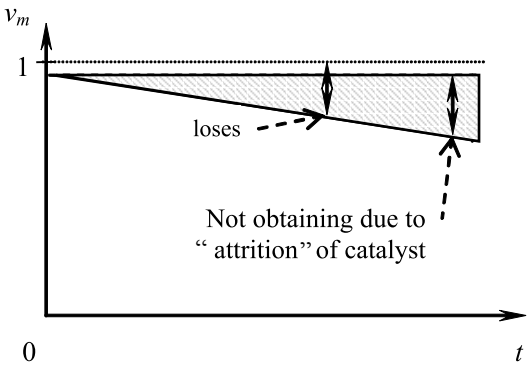


Fig. 2. Diagram of the state of catalyst.

"not obtaining"), $m(t)$ is function of measure of mass flow of final product, $c(t)$ is function of measure of the product cost (it can vary in time due to varying in prices), t_0 is the moment of beginning of use the formerly renewed catalyst.

As soon as the integral estimation of the measure of the cost of not obtained product becomes comparable with the measure of cost of the catalyst renewing (the catalyst price + cost for its mounting + product loss due to pause in the installation work), C(*catalyst renewing*),

$$C_i(t) > C(\textit{catalyst renewing}) \Rightarrow t(\textit{catalyst renewing}), \quad (8)$$

the catalyst should be renewed from the economical viewpoint (early renewing leads to extra expenses for catalyst and more product loss due to the pause for renewing; late renewing leads to increased expenses for the process due to low conversion of raw material into the product at ineffective catalyst).

Thus, calculations according to the proposed model with statistical treatment of data flows allows optimizing the process in respect of the period before renewing catalyst.

5. CONCLUSION

The problem of optimization of the process of producing formalin based on the commonly used principle of computability of unmovable point of the process control operator [14] differs from other analogous problems by complicated form of regression function, nevertheless, the method of calculation of optimal period before renewing catalyst is meaningful for this and other catalytic processes.

REFERENCES

1. Avetisov, A.K., Volin, Yu.M., Zyskin, A.G., Ostrovskii, G.M., Shub, F.S., Rodin, L.M., and Kalinichenko, F.V., *Khimicheskaya Promyshlennost'*, 2001, no. 11, pp. 16–22.
2. Adyan, S.I., *Doklady Akad. Nauk SSSR*, 1960, vol. 135, no. 6, pp. 1297–1300.
3. Ardavichus, V.G., *Avtomatizatsiya protsessa polucheniya formalina* (Automatization of the Process of Producing Formalin), Perm State Tech. Univ., 2005.
4. Barendregt, Kh., *Lambda-Calculation, its Syntaxis and Semantic*, Moscow: Mir, 1985.
5. *BSE* (Big Soviet Encyclopedia), 3d ed. ("Formalin").
6. Goronovskii, I.T., *et al., Kratkii spravochnik po khimii,* (Chemistry Brief Handbook), Kiev: Naukova Dumka, 1974.
7. Mal'tsev, A. I., *Algoritmy i rekursivnye funktsii* (Algorithms and Recursive Functions), Moscow: Nauka, 1986.
8. Markov, A. A., *Doklady Akad. Nauk SSSR*, 1947, vol. 55, no. 7, pp. 587–590; vol. 48, no. 3, pp. 353–355.
9. *Matematicheskaya entsiklopediya v 5ti t.* (Mathematic Encyclopedia in 5 Volumes), Moscow: Sovetskaya Entsiklopediya, 1977–1985.
10. Novikov, P. S., *Trudy. Mat. Inst Akad. Nauk SSSR im. Steklova*, 1955, vol. 44, pp. 1–144.
11. *Sovetskaya khimicheskaya nauka i promyshlennost' za 50 let* (Soviet Chemical Science and Industry for 50 Years), Moscow: Khimiya, 1967.
12. Chechulin, V.L., Abstracts of Papers, *International Conference Infokom-2 at North Kaukas State Tech. Univ.*, 2006, pp. 177–181.
13. Chechulin, V.L., *Proceeding of Conference "Social and Economical Statistics of Development of Region" at Perm State Univ.*, Berezniki, 2005, p. 270–281.
14. Chechulin, V.L., Abstracts of Papers, *All-Russian Conference "Automatic Systems of Control and Information Technology" at Perm State Univ.*, Perm: 2006, pp. 172–180
15. Shragin, I.V., *Doklady Akad. Nauk SSSR*, 1971, vol. 197, pp. 295–298.

ISSN 1070-4272, Russian Journal of Applied Chemistry, 2008, Vol. 81, No. 6, pp. 1117–1120. © Pleiades Publishing, Ltd., 2008.
Original Russian Text © A.M. Kagan, L.A. Yudina, A.S. Pushnov, K.V. Chizh, 2008, published in Khimicheskaya Promyshlennost', 2008, Vol. 85, No. 1, pp. 45–48.

PROCESSES AND DEVICES OF CHEMICAL MANUFACTURES

Perfecting Construction of Metallic Packing for Random Dumping

A. M. Kagan, L. A. Yudina, A. S. Pushnov and K. V. Chizh

Moscow Mendeleev Chemical Society, Moscow, Russia
Moscow State University of Engineering Ecology, Moscow, Russia

Received June 9, 2007

Abstract—Problems of further development of metallic packing for mass and heat transfer units are considered.

DOI: 10.1134/S1070427208060438

Hydraulic and mass transfer characteristics of packing affect determinately efficiency of packed columns for the processes of absorption, rectification and other.

One can resume that further development of packing design will proceed with inevitable but unbiased decrease in gaining efficiency and other characteristics of new packings. Therefore every new packing that provides gain ever in only one characteristic leaving intact others is welcome. For example, diminishing hydraulic resistance ΔP provides decrease in energy consuming and increase in carrying capacity, and therefore allows to diminish diameter of column and hence to decrease weight of metal for whole unit. The same effect would be achieved at diminishing height of packing blocks and respectively of the column. Of course, it is desirable for a new packing being of the same cost to provide enhancing of two or, more so, of three characteristics. Such situation occurred in 80-th at creation in Russia of industrial packing GIAP-N3 for random dumping which was better in all characteristics than the most widespread at that time industrial packing known as Pall's rings.

Aforesaid stimulates activity in creation of new packings.

Which direction is preferable at the development of new constructions of packung?

For providing high technological characteristics, a packing should contain as high as possible pores, that is, a fraction of free volume ε needed for achieving high hydrodynamic characteristics (low ΔP, large carrying capacity), and extended geometric surface a. The last characteristic is a mandatory condition of achieving high mass transfer characteristics. However, this is just a problem, because construction of packing should satisfy two contradicting requirements: high characteristics on mass transfer that is provided by extended surface, and high turbulization of contacting phases at or near the front of their contact that inevitably deteriorates hydrodynamic characteristics, and vice versa. Therefore at the development of new packing design one should attempt to achieve optimal ε–a ratio. The problem is confirmed by the history of development of packing constructions: the way from early industrial packing, the Raschig rings [1] invented in 1914 to the modern industrial packing, the Pall rings [2] took over 40 years, therewith the mass transfer characteristics were improved by 20% only. Therefore providing 1% gain in efficiency (not deteriorating therewith other characteristics) is undoubtedly a very complicated challenge.

Experience shows that it is reasonably to work along the following directions.

Analysis of known constructions of the packing for random dump ensures [3–5] that basic form of a packing should be ring or saddle that are the most favorable from hydrodynamics viewpoint. Therefore perfecting this form packing (some of them are depicted in Fig. 1) is the most prospective. A possibility of extension the packing surface is restricted due to unavoidable complication of their construction, therefore for achieving high mass transfer characteristics should be provided effective (close to limiting) wettability of geometric surface by contacting flows. While estimating efficiency of surface wetting of a ring packing one has to pay attention to orientation of rings in a layer. According to the data of [6], chaotic

(random) loading the packing results in vertical or aslant orientation of 45% of the rings and horizontal orientation of 55% (for the rings with height equal to diameter). At vertical orientation of ring axes the rings form a structure open for flows and thus better conditions are provided for flowing over the packing element surface and for higher carrying capacity of column. However, the flow turbulization that promotes efficiency of mass transfer capacity falls down. At horizontal orientation of ring axes the mass transfer efficiency per unit of wetted surface slightly grows, but simultaneously falls fraction of using surface a, grows ΔP and falls carrying capacity.

This analysis shows that the simplest ring packing, the Raschig rings, at random packaging principally can not provide high mass transfer characteristics with high carrying capacity and low ΔP. As is known, in a layer of Raschig rings occur screening of some of elements, low accessibility of their internal surface for liquid flowing over, significant shift of liquid flow to the column walls at moving along the packing layer regardless initial distribution.

Perforation as an instrument for perfecting packing improves many features, first of all hydrodynamic characteristics and internal flowing over the ring surface. However, perforation decreases value of specific surface. The Pall rings that known as the Raschig rings with rectangle perforation and lobes bent inside the rings, retain a value and display intense mass transfer in the packing internal cavity owing additional flow turbulization by the lobes. As a result, as was mentioned above the mass transfer characteristics increase by 20%, and ΔP exerts average two-fold decrease. Nevertheless, the last characteristic remains higher than with perforated Raschig rings not bearing the lobes.

The characteristics even higher than with Pall rings were achieved with principally new construction of ring packing, the paking GIAP-N3 [7, 8]. The elements of this packing are constructed of two half-rings joined by squire separator and mutually turned by 90°C. A gap in the middle of the half-rings and, in particular, perforation of the half-rings and separator shaped as round holes provides better than the Pall rings conditions for flowing over the packing internal surface. Due to practical coinciding of ε and a values for Pall rings and GIAP-N3 the latter show by ~ 15% higher efficiency and by 20–25% lower ΔP value.

The aforesaid can be resumed that better distribution of liquid and gas phases, more complete use of the packing geometric surface, and better renewing the front of phase contact leading eventually to enhanced efficiency in mass transfer can in a great extent be provided with perforated packing elements. At the moment knowledge concerning optimal area of perforation, size of the holes and their location is practically absent (the investigations were carried out for the GIAP-N3 packing only [9, 10]), therefore it seems that further investigations in this direction is very important.

Various swirling components, lobes, projections and other construction details promote turbulization of liquid, its dispersing, and gas flow swirl. However, they unavoidably lead to increase in hydraulic resistance and decrease in maximal efficiency. Therefore investigations should be extended to searching optimal construction solutions for maximization of intensity of the mass transfer processes and minimization of ΔP grow.

To the same direction is reasonable to extend such construction features as crimping surface of packing element or rifling it for elongation of flow route, that is, for developing the surface of phase contacts and additional turbulization of the flows.

Such practice as supplementing the packing elements with separators and other additional internal surfaces increases strength of elements and expands surface of phase contact. As a rule, this lead to increase in ΔP and decrease in carrying capacity. Increase in efficiency can be achieved only in the case of high enough coefficient of use of the internal surface. The latter should be the main task in this direction of research and development.

At the development of new forms of packing constructions a special attention should be paid to creation a possibility of the most effective flowing over the internal packing surface of both flows and the most effective using the internal surface regardless orientation of the element to the column axis. Besides perforating, other methods should be found and applied, e.g., sectioning the packing surface into separate bands and bending the latter inside the packing, like in the case of metallic saddles Inatloks (Fig. 1). The mentioned above example of the Raschig rings shows how much would be efficiency loss when effective flow over the internal surface is not provided.

We suggest also that certain attention should be paid to the problem of raising strength of the packing elements. This can lead to decrease in possibility of their damage at loading and due to hydraulic shocks and to increase their running time. For metallich packing elements this can be achieved by means of bead forming at their stamping (with possible decrease in thickness of the metal, that is,

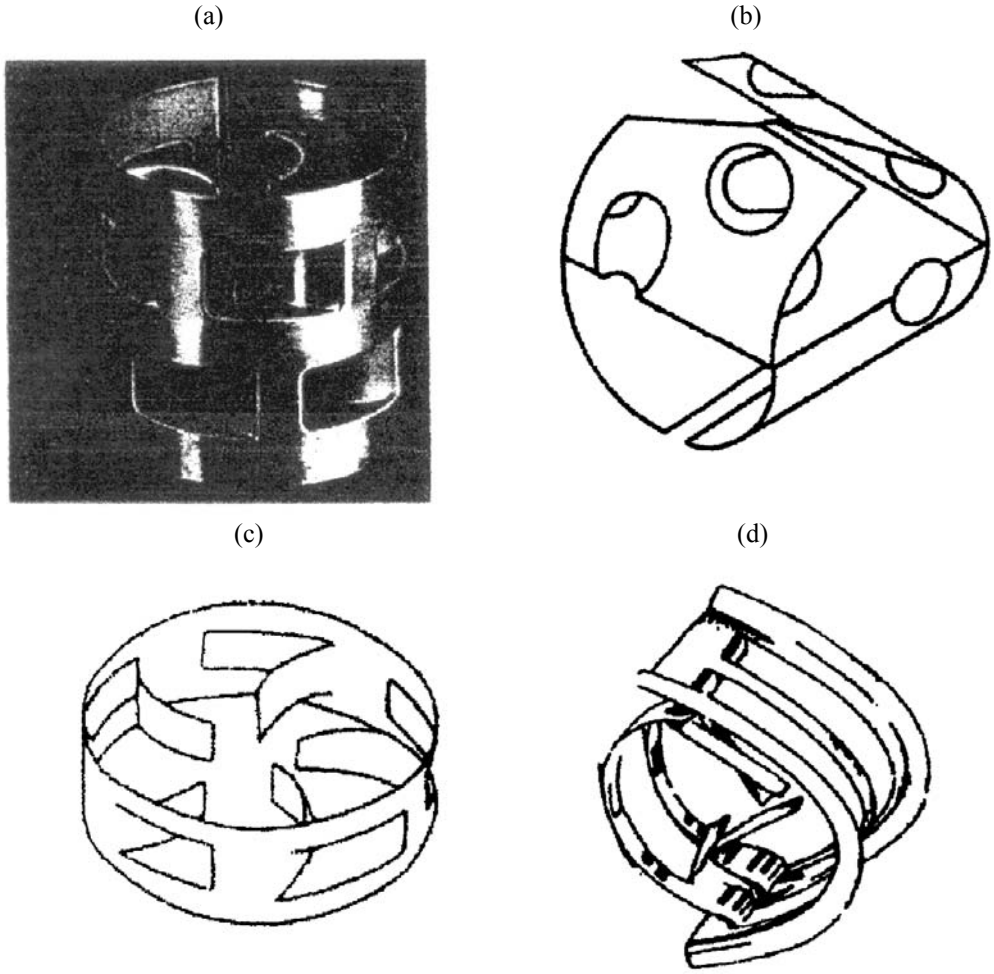


Fig. 1. Metallic packing for random dumping (a) Pall rings; (b) half-ring packing GIAP-N3; (c) miniring packing; (d) INTALOX saddles.

decrease in the packing weight per volume unit) or by means of application another technique.

An important problem for packing is increase their corrosion resistance.

For decreasing cost of metallic packing there is valuable possibility of electrochemical covering carbon steel with stainless steel [11]. Thanks to diffusion of molecules to the body bulk of a ring made of carbon steel they form cover of high strength. This excludes damage of the cover due to mutual friction of elements at their loading to column and at transportation.

Finally, an important is economical aspect, the packing cost. Therefore it seems significant now to search for new design solutions that would provide high technological efficiency and the lowest cost at the wholesale producing while retaining or enhancing main characteristics of packing. In part, metallic residues of certain profiles can be used for manufacturing.

Experience shows that expenses for consuming time and materials at the development of each new packing design or for improving an existing packing design can be reduced significantly when the fist step of investigation is blowing and study of aerodynamic characteristics of selected elements of experimental packing in a wind tunnel [12]. After introducing required corrections and achieving optimal characteristics using one element of packing can be prepared experimental batch and carried out hydrodynamic and mass transfer examination in a pilot plant installation.

REFERENCES

1. British Patent No. 6228.
2. British Patent No. 855159.
3. Kagan, A.M., Pal'mov, A.A., and Gel'perin, I.I., *Neregulyarnye metallicheskie nasadki dlya teplo-*

massoobmennykh protsessov (Irregular Metallic Packing for Heat and Mass Transfer Processes), Moscow: NIITEKhIM, 1985.
4. Gladil'shchikova, S.V., Shchelkunov, V.A., Kruglov, S.A., and Molokanov, Yu.K., *Nasadki massoobmennykh apparatov dlya neftepererabotki i neftekhimii* (Packing for Mass Transfer Units for Petroleum Processing and Petrochemistry), Moscow: TsINTIKhIMNEFTEMASh, 1983.
5. Leont'ev, V.S. and Sidorov, S.I., *Khimicheskaya Promyshlennost'*, 2005, vol. 82, no. 7, p. 347.
6. *Information's Chemic*, 1978, no. 180, p. 141.
7. Inventor's Certificate 1011207; *Otkrytiya. Izobreteniya*, 1983, no. 14.
8. Kagan, A.M., Yudina, L.A., and Pushnov, A.S., *Khimicheskaya Promyshlennost'*, 2001, no. 5, p. 43.
9. Kagan, A.M., Gel'perin, I.I., Dil'man, V.V. *et al., Khimicheskaya Promyshlennost'*, 1992, no. 8, p. 468.
10. Pal'mov, A.A. and Kagan, A.M., Abstracts of Papers, *Third All-Union Conference on the Problem: "Gas Absorption"*, Tallin, 1987.
11. Zaets, I.I., Kagan, A.M., Burtseva, I.K. *et al.*, Abstracts of Papers, *Congress "Zashchita 92"* (Protection'92), 1992, Russian Academy of Sciences, vol. 1, pt. 3, p. 193.
12. Pushnov, A.S., Abstracts of Papers, *All-Union Conference "Teplomassoobmennoe oborudovanie-88"* (Heat and Mass Transfer Equipment), Abtracts, Moscow: TsINTIKhIMNEFTEMASh, 988, p. 137–138.

ISSN 1070-4272, Russian Journal of Applied Chemistry, 2008, Vol. 81, No. 6, pp. 1121–1127. © Pleiades Publishing, Ltd., 2008.
Original Russian Text © O.V. Oshurkova, 2008, published in Khimicheskaya Promyshlennost', 2008, Vol. 85, No. 2, pp. 79–87.

PROCESSES AND DEVICES OF CHEMICAL MANUFACTURES

Separation of Various Electrolyte Mixtures by Unilateral Capillary Isotachophoresis

O. V. Oshurkova

Ioffe Physico-Technical Institute, St. Petersburg, Russia

Received October 3, 2007

Abstract—A new electrophysical method is proposed for a rapid diagnosis of liquid products relating quality and identification. The method is widely prospective for practical application.

DOI: 10.1134/S107042720806044X

Experiments on the replacement of common ion by the other ion of the same sign in the mixture of two electrolytes were realized within capillaries of a device with optic determination of boundaries by unidirectional isotachophoresis (ITP). In the work we also studied a separation on the pure electrolytes of aqueous solutions of two dyes and of several saline mixtures containing anions of organic acids. Besides we separated mixtures of the electrolytes within capillary columns using two portions of the same solution of various concentrations as catholyte and anolyte.

Acquisition of pure solutions by separation of electrolyte solutions within capillary columns in the field of direct current according to mobility of ions was first described in [1] and underlie establishment of microanalysis of complex electrolyte mixtures by ion mobility [1, 2]. The authors of [1, 2] were pioneers in developing the devices that enable the separation of electrolytes within capillaries on the zones of pure electrolytes and rendering the obtained results onto photofilm. Later the investigations in this direction were started by Martin and Everaerts [4].

Diverse solutions of electrolytes in wide range of concentrations can be studied in the capillary column can be studied. Electromigration technique for electrolyte separation within capillary developed by the authors of [1, 2] includes a quartz capillary (a separating column), high voltage power supply, electrode reservoirs for auxiliary solutions, and an arrangement for filling the capillary with sample and auxiliary solutions using at separating. It includes an optic detector to monitor the separation. Besides there is a device for recording the separation results onto a paper (shooting the obtained isotachophoregram with a photopaper). Reading the information from the photopaper is fulfilled by the measuring microscope [5].

At present large number of diverse techniques was designed for the capillary ITP with transparent and opaque capillaries of different diameters, various rearrangements for input of a sample in the capillary and plenty of sensors to record the separation of electrolyte solutions [6].

Under the influence of an electric field over the capillary length filled with solutions positively-charged particles (cationic constituents) move to cathode and negatively-charged ones (anionic constituents) move respectively to anode.

Cationic and anionic constituents of various electrolyte solutions are of different mobility. This feature of ions underlies separation of solutions. Two auxiliary solutions are used to separate the mixture of electrolytes with ITP. One of the auxiliary solutions is taken as catholyte and other, as anolyte. Since 1970 this direction has been named isotachophoresis. If the electromigration separation by the ion mobility within the capillary columns is performed with the help of one auxiliary solution possessing buffer properties then such separation is called capillary electrophoresis. Let us assume that separation of mixture of two salines containing four different ions is studied with ITP. Let it be a mixture of aqueous solutions of NaCl and $LiNO_3$. In this case it is not possible to obtain at the same time within the column two given solutions as two bordering zones of pure electrolytes NaCl and $LiNO_3$. After the separation of the mixture by ITP only

two zones can be obtained of pure electrolyte solutions with different cations and the same anion. Or on the contrary at a proper match of the auxiliary solutions the zones of pure electrolytes with different anions and the same cation can be obtained. Thus this mixture can be separated both by the difference in the mobility of cations (cationic ITP) or by the difference in the mobility of anions (anionic ITP).

For separation the studied mixture is put in the capillary column between the auxiliary solutions (between the catholyte and the anolyte). At the mixture separation according to the cation or anion mobility the different auxiliary solutions are used. At cationic separation the solution with the most mobile cation in the mixture is accepted as catholyte and then the solution with the least mobile cation in the mixture is matched as the anolyte. In the case of anionic separation the solution with the most anion mobility in the mixture is used as the anolyte and then the catholyte is the electrolyte solutions with the least anion mobility in the mixture. The matching of the auxiliary electrolytes for the solutions of the high concentrations is fulfilled according to the values of equivalent electroconductivity of solutions [8]. Suitability of the solution matching in ITP is checked experimentally. At the suitable matching the mixture of the studied ions under the electric current running through the capillary is found within capillary between the catholyte and anolyte and will be separated in the zones of the pure solutions. Each solution acquires in the column at the electrolysis one common ion coming in the solution zone from the leading solution. A place of the boundaries within capillary is defined with the detector. Correspondence of the zones to a target solution is found by comparing the primary isotachophoregram and the isotachophoregram obtained at the second separation of the mixture of the same composition by considerably increased concentration of the target constituent in the mixture. Thus the length of the single zone is largely increased. The increased zone is appropriated to the added constituent.

Cationic ITP

Before electrolysis

(catolyte) K_lA	$K_1A + K_2A$	K_tA (anolyte)
leading	mixture	terminating

After electrolysis

(catolyte) K_lA	K_1A	K_2A	K_tA (anolyte)
leading	$area_1$	$area_2$	terminating

$$u_l > u_{area1} > u_{area2} > u_t$$
$$F_l < F_{area1} < F_{area2} < F_t$$
$$\chi_l > \chi_{area1} > \chi_{area2} > \chi_t$$

Anionic ITP

Before electrolysis

(anolyte) KA_l	$KA_1 + KA_2$	KA_t (anolyte)
leading	mixture	terminating

After electrolysis

(anolyte) KA_l	KA_1	KA_2	KA_t (catolyte)
leading	$area_1$	$area_2$	terminating

$$v_l > v_{area1} > v_{area2} > v_t$$
$$E_l < E_{area1} < E_{area2} < E_t$$
$$\chi_l > \chi_{area1} > \chi_{area2} > \chi_t$$

Fig. 1. The scheme of the capillary part with the solutions before and after electrolysis at the cationic and anionic ETP, and relation of the mobility of ion constituents, the electric field strengths, and the specific electroconductivities of the pure solutions after the mixture separation on the zones of the pure solutions.

The general scheme of the location in the column of the studied mixture of two solutions, leading and terminating, before and after electrolysis in the considered types of ITP is presented on Fig. 1. A relation of the cation (u) and anion (v) mobility of the pure solutions in dependence on a solvent is denoted on the Fig. 1. Also in this figure a relation of electric field strength (E) on the parts of the pure solution and a relation of the specific electroconductivities of solutions of the pure electrolytes (χ) in the capillary in steady state [9] are appeared. A movement direction of the boundaries between electrolytes towards the walls of the separating column in the absence of electroosmotic flow and of counterflow is noted with arrows on Fig. 1. In the steady state motion velocities of the boundaries of the pure solutions acquired in result of the studied mixture separation and moving towards the column on the same direction are equal.

On Fig. 1 indexes u, v, χ, E in the bottom of the letters denote the proper solution. Index l denotes a value appropriated to leading solution. Index $area_1$ specifies a solution of the zone adjacent to the leading solution, and Index $area_2$ specifies the second solution placed between the first area and terminating solution. Letter t denotes terminating solution. The velocity of the boundary motion of the two solutions with a common ion relative to the column depends on mobility of uncommon ion, electric field strength, counterflow, and electroosomotic flow.

Counterflow, solution flow relative to the column, is the factor that allows keeping immobility of the boundaries between solutions within capillary column. Counterflow and electroosmosis, directed towards boundaries movement under the action of current promote decrease of the capillary column length. Electroosmosis as well as counterflow causes moving of the entire solution within the capillary column. Velocity of movement of the boundary between two solutions with common anion at the movement under action of current in cationic isotachophoresis is equal:

$$u_1 E_1 = u_2 E_2, \quad (1)$$

where u_1 and u_2 are different cations mobility of the solutions forming boundary ($cm^2 V^{-1} s^{-1}$); E_1 and E_2 are electric field strength in the solutions forming boundary ($V cm^{-1}$).

The boundary velocity under action of current in anionic isotachophresis respectively is

$$v_1 E_1 = v_2 E_2, \quad (2)$$

where v_1 и v_2 are uncommon anion mobility of the solutions forming boundary ($cm^2 V^{-1} s^{-1}$); E_1 and E_2 are electric field strength in the zones of pure solutions ($V cm^{-1}$).

In the steady state which is set spontaneously in isotachophoresis the solution concentrations meet to the regulating ratio of Kohlrausch [9] that is written as

$$C_l / C_{area} = T_l / T_{area}, \quad (3)$$

where C_l and C_{area} are concentration of leading solution and proper concentration of the pure electrolyte area (g.equiv/l); T_l and T_{area} are a transfer number of uncommon ionic constituents of the leading solution and the area solution within the capillary column.

The boundary between two solutions within a vertical capillary column without a filler unlike the columns of large diameters is not stirred even when solution of larger density is placed above a solution of lesser densities.

The velocity of the boundary movement between the solutions relative to the column in isotachophoresis does not coincide with velocities of boundary movement relative to the solvents of each solution.

In an experiment the transfer numbers of the ionic constituents are determined in the pure solutions relative to the solvent of this solution. Earlier such transfer numbers were called apparent.

In isotachophoresis on the solutions boundary the solvent velocity changes at solvent moving relative to the boundary from one solution into another. The solvent relative to the boundary movement moves in isotachophoresis in the strong field direction [10].

The solvent flow from leading solution to terminating solution relative to the boundary equals to [11]

$$G = g_l (W - V_l) = g_{area\,1} (W - V_{area\,1}) = g_{area\,2} (W - V_{area\,2}), \quad (4)$$

where G is the solvent flow relative to boundary ($g\ cm^{-2}\ s^{-1}$); g_l, $g_{area\,1}$, $g_{area\,2}$ are partial densities of the solvent in the leading solution and solution areas; respectively, $g\ cm^{-3}$; W is the boundary movement velocity relative to the column ($cm\ s^{-1}$); V_l, V_{area1}, V_{area2} are the solvent movement velocity of the leading first and second area solutions relative to the column.

Solvent amount coming during electrolysis from the leading solution into terminating was used for the transfer number measurement [12].

A transfer numbers sum of cationic and anionic constituents for each solution equals unity. Experimentally the transfer numbers of the ionic constituents were measured only for the leading solutions [12, 13].

It should be noted that in unidirectional isotachophoresis the common ion in the solution of all zones will be changed at replacement of this ion in the leading solution because the common ion of all the other electrolytes following the leading solution is governed by one of the leading solution ions. We use this property to form new solutions of electrolytes differing from the taken electrolyte or mixture of electrolytes by one ion.

Besides in this work the mixtures of solutions belonging to various classes of chemicals were separated to pure electrolytes. At the separation attention should be payed to the boundary between the solutions since an acquisition of the clear boundaries between the pure electrolytes and the mixture of electrolytes [14] reveals expediency of their use in electrochemical investigations as well as in works on electroseparaton and electrosynthesis.

EXPERIMENTAL

Experiments reported here were performed in U-shaped capillary column with inside diameter ranging

from 0.1 to 0.2 mm and outside diameter ranging from 0.2 to 0.4 mm. A boundary definition between the solutions was done by optical method [2, 15]. The optical method of the boundary definition is used in devices of various design and described in [2, 5, 15]. On the device [5] a capillary can be used with horizontal part of length 20–24 cm, and on the device [2] the capillary with horizontal part of length ranging from 10 to 40 cm. Length of the vertical part of U-shaped capillary used in this work was from 1 to 7 cm.

Replacement in the electrolyte solution of one ion for the other ion was carried out in the aqueous solution of $NaNO_2$ and $NaNO_3$ by anionic isotachophoresis. Mixture of $NaNO_2$ and $NaNO_3$ solutions was studied. Ion of sodium in the mixture was substituted for ion of potassium. In the study 1.0 N KCl was used as leader (anolyte) and 0.5 N $KC_7H_5O_3$ as terminator. Mixture of $NaNO_2 + NaNO_3$ solutions with chlorine concentration 1.0 g equiv/l was placed in horizontal part of U-shaped capillary between the catholyte and the anolyte (the solution column length about 6 cm) that was reached by following sample of anolyte, mixture, and catholyte in the capillary. Then we installed the capillary in the device. The ends of the U-shaped capillary put into the electrode vessels of the device. Then on the electrodes put into anolyte and catholyte voltage from a high-voltage rectifier was given. At electrolysis the boundary was kept in the horizontal part of capillary by counter flow. Theoretically the amount of electricity passed through the column should be equal to that required for deposition on the electrode of a number of gram equivalent of sodium equal to that contained in the mixture of $NaNO_2 + NaNO_3$ in the column, namely

$$It/F = CU_p, \quad (5)$$

where: I is current passing through the capillary (A); t is time (s); F is Faradey number (C/g equiv); C is concentration of the mixture (g equiv/l); U_p is the mixture volume (l).

Taking into account that at filling the capillary the solutions could mix partly with each other and also desiring in the experiment to achieve full separation of the mixture of nitrite and nitrate ions we passed through the column the larger amount of electricity than it was required for the replacement of the ions. In the experiment the current was equal to 0.5 mA and electrolysis proceeded for 2 hours. It resulted in acquisition between the catholyte and anolyte of clear zones of KNO_2 and KNO_3 solutions. Anolyte solution had a boarder with KNO_2 and catholyte, with KNO_3. Between the obtained zones of solutions of potassium nitrite and nitrate the boundary was sharp. The obtained solutions of potassium salts again were converted in solutions of sodium salts by replacement of anolyte by 2.0 N solution of NaOH. The order of passing of ions of nitrites and nitrates to an electrode at replacement of the leading solution has not changed. The zone of nitrite also concentrated ahead of a zone of nitrate.

In the work also with anionic ITP the separation of solutions of organic acid salts (formic, carbonic, acetic, propionic, salicylic, and citric acids) in the mixture onto areas of the pure solutions was studied. As leading solution (anolyte) aqueous 3.0 g equiv l^{-1} NaCl was used. A saturated borex solution was catholyte (the terminating solution). Separation results of the mixture with anions of the noted acids under 0.45 mA current during 1.5 hour electrolysis are showed on Fig. 2. On Fig. 2 a wide of a refraction picture changes in an area of the two solution interface. A dark band on the figure in the middle of the refraction picture appropriates to a parallel beam.

In this case an arrangement of the areas obtained between the leading and terminating solutions on the refraction picture corresponds to an order of the moving anions on the studied solutions when 5.0 N NaOH was used as the leading solution [16].

Beside the noted mixture we studied some solutions of dyes. At their studying with anionic ITP as leading solution an aqueous 1.0 N NaOH was used, and 0.05 N $Na_2B_4O_7$ as the terminating solution. On Fig. 3 we presented refraction picture that we observed on the device screen when only Congo red solution was in the capillary column between the leading and terminating solutions. Current run through the column was 0.025 mA. Time of the current running was about an hour. A formed dye area on the photo corresponds to a gap between two refraction pictures obtained by the beam passing through the leading and terminating solutions. The gap in the figure is caused by impenetrability of the studied dye for the beam falling on the capillary column. As shown in the Fig. 3 the dye area on the photo is clearly defined. Congo red and murexide separation is shown in Fig. 4. Two areas between anolyte and catholyte are shown on the figure: The light area of Congo red, and more dark area of the murexide solution. It is not unreasonable that light absorption by dyes can be used for defining the boundaries between the areas of solutions if their refraction pictures do not differ by size. Evidently in this case a dye flow

from one electrode solution to other is required. Then each area on the screen will have different darkening.

We like to draw attention to the width of the refraction pictures on Figs. 2–4 and to note that the width of the refraction pictures on the screen depends on a series of factors. It was shown in [17] that the width of the picture on the screen depends on solution nature and concentration. An increase in the solution concentration causes its refractive index increase that in its turn results to an extension of the refraction picture width on the device screen. In [15] the picture enlargement relative to geometric capillary parameters was studied. Both works were performed in order to increase a difference between width of the refraction pictures that reveal various areas of the pure electrolytes. However it should be noted that the most enlargement of the refraction picture it can be reached increasing the distance between the capillary column and the screen. It is shown on the figures. Figs. 2–4 were obtained when the distance between the capillary column and the screen was ranged from 5 cm to 7 cm. Fig .5 was recorded by cationic ITP separation of the mixture of cobaltous chloride and nickel chloride solutions using 7.2 N LiCl as the leading solution (catholyte and 5.0 N $CdCl_2$ as terminating solution. In this case the distance between the capillary column and the screen was increased in 2–3 times. On Fig. 5 was shown only about half of the recorded refraction picture. Entire refraction picture was not placed on the screen. If we shell observe an image obtained from the capillary column on the large screen placed on the large distance form the capillary column then on the screen the refraction picture increased would be dozens and more times in width. A factor of enlargement of the refraction picture with respect to increase of the distance between the capillary column and the screen must be studied in more detail in future. Similar investigation can widen capability of the optic boundary recording.

Except the reported experiments in the work separation of the solutions of various chlorides was studied the application of two portions of a solution of different concentrations both as catholyte and anolyte. We performed experiments according to the following method. 6.0 g equiv l^{-1} NaCl was used as catholyte, and 0.6 g equiv l^{-1} NaCl as anolyte. A solution of a mixture of lithium, copper and zinc chlorides was the separation mixture. Each salt concentration in the solution were about equal. Chlorine mixture concentration was about 6.0 g equiv l^{-1}. We put an about 1 cm of solutions mixture in the capillary column between the catholyte

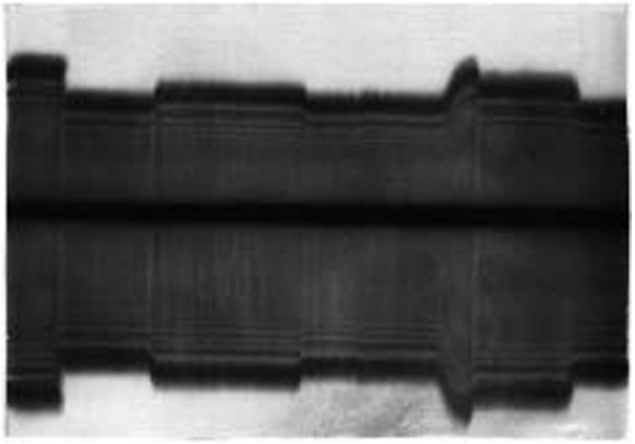


Fig. 2. The refraction picture recoded after separation of the mixture containing solutions of the organic acids salts. An order of location of the solutions in the refraction picture is from left to right: NaCl, $NaHCO_2$, Na_2CO_3, $NaC_2H_3O_2$, $NaC_3H_5O_2$, $NaC_7H_5O_3$, $Na_3C_6H_5O_7$, $Na_2B_4O_7$.

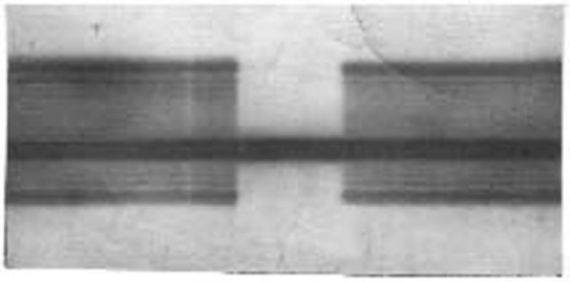


Fig. 3. Refraction picture obtained by Congo red solution study. A white bar on the figure denotes Congo red solution, on the left NaOH solution, on the right $Na_2B_4O_7$ solution.

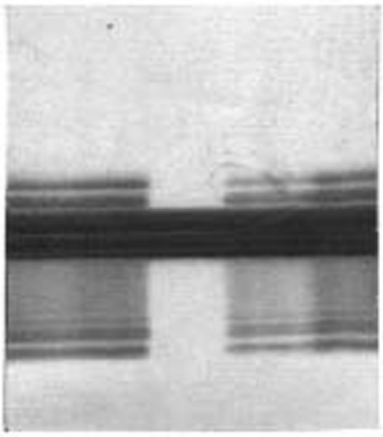


Fig. 4. Refraction picture obtained after separation of the mixture solutions of Congo red and murexide, NaOH solution is on the left, $Na_2B_4O_7$ solution is on the right, between them there are the areas of the solutions of Congo red and murexide.

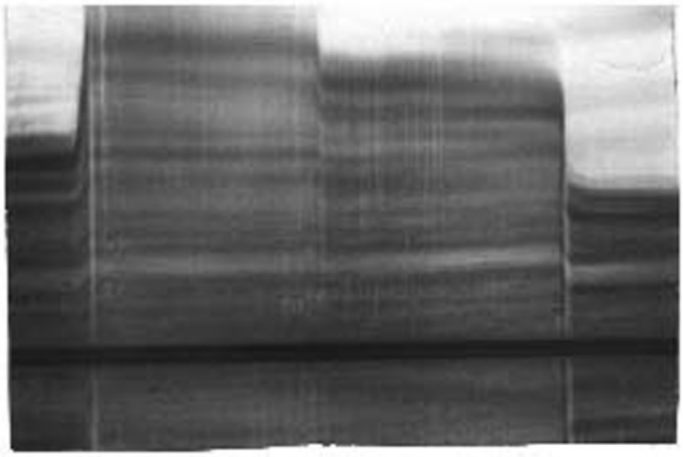


Fig. 5. The refraction picture part recorded with the separation of the cobaltous chloride and nickel chlorides solutions. LiCl solution is on the left, $CdCl_2$ is on the right, between them there are the areas of $CoCl_2$ and $NiCl_2$ solutions.

and anolyte. In the course of the electrolysis current was 0.5 mA. Time of the mixture separation was about 4 h. During this time three areas formed. A middle one was colored area of copper chloride solution, ahead of this solution was lithium chloride area, and after, was zinc chloride solution. We could not reach the steady length of the areas. In the course of the experiment the areas of solutions always changed their length. The boundaries between the solutions were not sufficiently clear. Due to decrease in the refraction picture width of areas and the unclear boundaries we assumed that the mixture constituents gradually diffuse in an anode space. Hence we carried out the following experiment. In the capillary column between the catholyte and the anolyte (6.0 N and 0.6 N HCl, respectively) we installed 4.0 N of cobaltous chloride solution. A length of the solution column in the capillary column was about 3 cm. Under running of current first we observed tuning of cobaltous chloride solution. During the experiment in course of the tuning width and length of the refraction picture from cobaltous chloride solution area ever changed. The boundary between cobaltous chloride solution and dilute HCl solution constantly moved relative to the boundary of concentrated HCl solution towards anode. Because $CoCl_2$ solution column considerably increased a device detector did not record at once both boundaries of the $CoCl_2$ solution column. Therefore in an hour of the electrolysis we removed from the capillary column HCl solution of lesser concentration and the most part of $CoCl_2$ solution. As result in the capillary column there are 6.0 N HCl and $CoCl_2$ solution column of about 1 cm of length. Then instead of removed solutions we put in the capillary column 0.6 N HCl, installed the capillary column in the device, and run current through it. First the boundaries of the small $CoCl_2$ solution column were shown sufficiently clear due to different color of the adjacent solutions. With time the area length of $CoCl_2$ solution always increased and color of $CoCl_2$ solution always turned pale. The boundaries between $CoCl_2$ solution column and 0.6 N HCl stirred. With time this results in disappearence of $CoCl_2$ solution from the capillary column. In the capillary column there was only one concentration boundary: the boundary between the catholyte (6.0 N HCl) and the anolyte (0.6 N HCl). Thus the experiments with use of two portions of different concentrations of the same solution both as catholyte and anolyte for separation of the mixture constituents revealed that at the mixture separation an amount of the mixture constituents in the capillary column constantly decreased.

CONCLUSION

The obtained results are of interest both for practical use and for development of a theory about strong solutions of electrolytes. Our experiments reveal that the study of the separation of electrolytes by electric current in the capillary columns can be carried out in a wide range of concentrations. Also the experiments prove capability of the studying substances to electrosynthesis and electroseparation, allow the recognizing of arrangement in the motion decrease of different ions of the studied solutions in comparison with the motion of different ions of the leading and terminating solutions, and the estimating of relation between the motions of ions of the mixture constituents (greater or lesser). According the experiments can be extended the recording of the boundaries on the refraction picture by the different light absorption of solutions. A considerable increase of the refraction picture width was shown at increase of the distance between the capillary column and the screen. It is not unreasonable that the increase of distance enables to improve of the recording of boundaries on refraction pictures in transparant capillary columns. However it should be noted that we did not obtain the steady state area (see [18]) using two portions on the same electrolyte of different concentrations both as catholyte and anolyte. The separation on areas conducts without reaching the steady state in these areas. Therefore application for separation of the mixture of two different solutions as catholyte and anolyte is without doubt more promising

than the use of two concentrations of the same solution. However use of two portions of the same solution of different concentrations as catholyte and anolyte allows the observation of the unsteady boundaries in the capillary columns between pure solutions of electrolytes and mixtures that expands experimental base for study of the steady and unsteady boundaries between the solutions of electrolytes and their mixtures.

REFERENCES

1. Konstantinov, B.P. and Oshurkova, O.V., *Doklady Akad. Nauk SSSR*, 1963, vol. 148, no. 5, pp. 1110–1113.
2. Konstantinov, B.P. and Oshurkova, O.V., *Zh. Teor. Fiz*, 1966, vol. 36, no. 5, pp. 942–957.
3. Martin, A.J.P. and Everaerts, F.M., *Prac. Roy. Soc. Lond*, 1970, vol. 316, pp. 493–514.
4. Lennart, Arlinger, *Journal of Chromatography*, 1974, vol. 91, pp. 785–794.
5. Bresler, P.I., Ivanova, I.A., Oshurkova, O.V., and Shtilerman, G.A., *Zh. Anal. Khim*., 1981, vol. 36, no. 3, pp. 593–599.
6. Gebauer, P., Mala, Z., and Bocek., *Electrophoresis*, 2007, vol. 18, pp.26–32
7. Haglund, H., *Science Tools*, 1970, vol.17, no. 2., pp.1–17
8. Konstantinov, B.P., Lyadov, N.S., and Oshurkova, O.V., *Elektrokhimiya*, 1970, vol. 6, no. 4, pp. 584-587.
9. Kohlrausch, F., A*nn. Phys. und Chem. (Leipzig)*, 1897, vol. 62, no. 2, pp., 209-239.
10. Donskoi, K.V. and Rozov, S.I., *Zh. Fiz. Khim.*, 1980, vol. 54, no. 8, pp., 1983–1987.
11. Milios, P. and Newmen, J., *J. Phys. Chem.*, 1969, vol. 75, pp. 298–306.
12. Konstantinov, B.P. and Kaimakov, E.A., *Zh. Fiz. Khim.*, 1962, vol. 36, no. 4, pp. 842–845.
13. Macunnec, D.A. and Longsworth, L.G., *Chemical Reviews*, 1932, vol. 9, no. 2, pp. 172–229.
14. Oshurkova, O.V., *Khimicheskaya promyshlennost'*, 2006, vol. 83, no.12, pp. 589–598.
15. Gorshkov, A.I., Oshurkova, O.V., and Konstantinov, V.B., ZhTF, 2001, vol. 71, pp. 119–123
16. Oshurkova, O. V and Nesterov, V.P., *Elektrokhimiya*, 2005, vol. 41, no. 12, pp.1485–1489.
17. Konstantinov, B.P., Lyadov, N.S., and Oshurkova, O.V., ZhTF, 1968, vol. 38, no. 12, pp. 2117–2118.
18. Stefanovskii, A.M., *Elektrokhimiya*, 1967, vol. 3, no. 4, pp. 71–75.

ISSN 1070-4272, Russian Journal of Applied Chemistry, 2008, Vol. 81, No. 6, pp. 1128–1131. © Pleiades Publishing, Ltd., 2008.
Original Russian Text © A.A. Garabazhiu, 2008, published in Khimicheskaya Promyshlennost', 2008, Vol. 85, No. 2, pp. 88–92.

MODELLING AND CALCULATION OF TECHNOLOGICAL PROCESSES

Simulation of Optimum Thickness of Acceleration Blades of a Rotary Centrifugal Grinder

A. A. Garabazhiu

Belarussian State Technological University, Minsk, Belarus

Received March 19, 2007

Abstract—We developed a method of optimum thickness simulation for the acceleration blades of the rotary centrifugal grinder. We also deduced an empirical relation that sufficiently exactly determines a minimum thickness of the acceleration blade in dependence on a currents grinder radius.

DOI: 10.1134/S1070427208060451

The energy-saving rotary centrifugal grinder with continuously flow-through classification of a product was developed in the Belarussian State Technological University ten years ago and was still in great demand in various branches of industry of Belarus. Today research workers of the university under Prof. E. I. Levdanskii developed a line of energy-saving rotary centrifugal devices of analogues operation principles and of various applications [1, 2].

Design features and principle of operation of the energy-saving rotary centrifugal grinder with continuously flow-through classification of product were set out in [2–5].

At developing the industrial sample of this grinder a simulation of the optimum thickness of the main (or the most important) design elements arouse great practical interest. An algorithm and results of a strength design of a grinder rotary disk and a bearing plate were presented in [6]. Estimation of the optimum thickness of the main design elements of the rotary centrifugal grinder allows acquisition of high reliability and wear life of the device as a whole.

A rotor of the energy-saving grinder with continuously flow-through classification of a product [2–5] has eight acceleration radial blades that are firmed to the rotary disk of the grinder at a right angle to its upper end surface

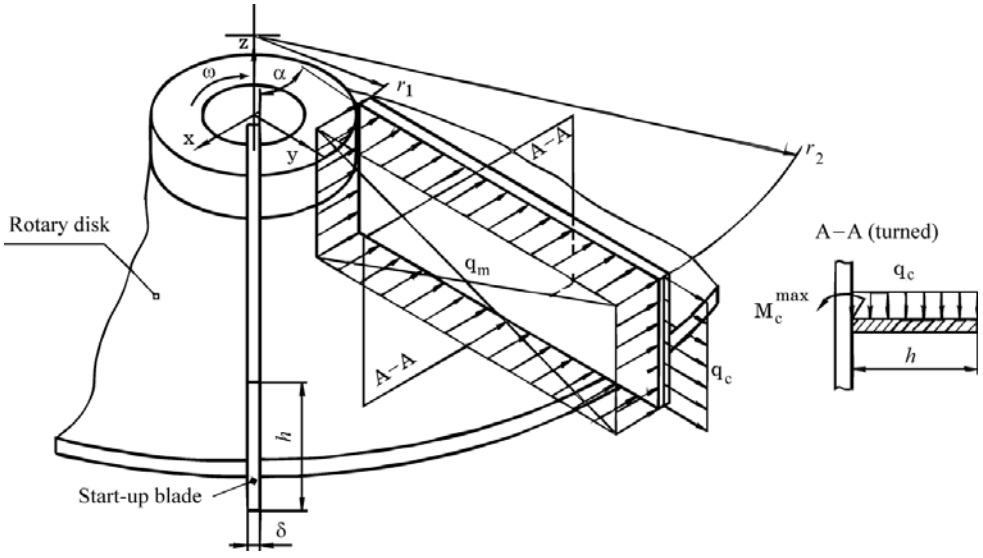


Fig. 1. A scheme for the strength design of the acceleration blade of the rotary centrifugal ginder. r_1 = 0.12 m, r_2 = 0.3 m, δ = 0.005 m, h = 0.08 m, ω = 314 rad s^{-1}, α = 45°.

(Fig. 1). The acceleration blades are made of wear-resistant steel (eg., Steel 35G2 GOST 4543-71) supplied as a sheet rolled metal.

The strength design of the grinder acceleration blade can be done according to [7] assuming the blade as an outrigger of rectangular section loaded by forces of the processed materials (P_m) in the space between the blades of the grinder rotary and by a centrifugal force (P_c).

A scheme for a computation of the acceleration blade of the rotary centrifugal grinder is presented on the Fig. 1.

For defining the maximum bending moment effected on the acceleration blade it is first required to estimate the centrifugal force values P_c and the force P_m.

The centrifugal force P_c, acting on the acceleration blade is calculated with the following equation:

$$P_c = m_b \omega^2 r_i, \quad (1)$$

where m_b is the mass of one acceleration blade, kg; ω is radial velocity of the grinder rotor, rad s^{-1} (ω = 314); r_i is the current radius of the acceleration blade, m ($r_i \in [r_1; r_2]$); r_1 is a start radius of the acceleration blade, m ($r_1 = 0.12$); r_2 is a finish radius of the acceleration blade, m ($r_2 = 0.3$).

The acceleration blade mass may be obtaines as:

$$m_b = h \delta_j r_i \rho_b, \quad (2)$$

where ρ_b is the density of the blade material, kg/m^3 (ρ_b = 7790 kg/m^3 for steel 35G2 GOST 4543-71); h is the acceleration blade height, м ($h = 0.08$); δ_j is the current blade thickness, m.

The centrifugal force P_c is evenly distributed over the whole blade height with intensity q_c (Fig. 1)

$$q_c = \frac{P_c}{h}, \quad (3)$$

The maximum bending moment (M_c^{max}) of the centrifugal force P_c in a place of the acceleration blade fixing to the rotary disk of the grinder is computed by the following equation:

$$M_c^{max} = \frac{1}{2} q_c h^2. \quad (4)$$

After appropriate substitutions the equation (4) was transformed in:

$$M_c^{max} = \frac{1}{2} \delta_j \rho_b \omega^2 r_i^2 h^2. \quad (5)$$

It is assumed that in course of the rotary centrifugal grinder operation [2–5] the processed material entirely fills the rotor space between the blades (a boundary case) and presses down with the force P_m on the flat surface of the acceleration blades. In this case the force P_m is defined according with equation (6).

$$P_m = m_m g, \quad (6)$$

where m_m is the mass of processed material (eg., gypsum) filling the rotor space between two adjacent blades, kg; g is gravitational acceleration, m s^{-2}.

The processed material mass can be computed with

$$m_m = V_m \gamma_p, \quad (7)$$

where V_m – is the processed material volume filling the rotor space between two adjacent blades, m^3; γ_p is poured density of the processed material, kg/m^3 (γ_p = 1200 kg/m^3 for gypsum).

It is assumed that the processed material fills the rotor space between two adjacent blades in a form of right trapezoidal prism of a height h and with angle between its two sides a (Fig. 1). Then after appropriate trigonometric transformations the processed material volume V_m is calculated as

$$V_m = \frac{1}{2} (r_2^2 - r_1^2) h \sin \alpha, \quad (8)$$

where α is an angle between internal longitudinal surfaces of two adjacent blades of the grinder rotor, deg (α = 45°).

The processed material force P_m is evenly distributed over the whole blade height with intensity q_m (Fig. 1)

$$q_m = \frac{P_m}{h}. \quad (9)$$

The maximum bending moment (M_m^{max}) of the force P_m in a place of the acceleration blade fixing to the rotary disk of the grinder is computed by the following equation:

$$M_m^{max} = \frac{1}{2} q_m h^2. \quad (10)$$

After appropriate substitutions the equation (10) was transformed in:

$$M_m^{max} = \frac{1}{4} (r_2^2 - r_1^2) h^2 \gamma_p g \sin \alpha. \quad (11)$$

A resultant bending moment M_{bend} from the action of the centrifugal force P_c and the force P_m will equal

$$M_{bend} = \sqrt{(M_c^{max})^2 + (M_m^{max})^2} \quad (12)$$

For the outrigger of rectangular section a bending stress is expressed by the equation:

$$\sigma_{bend} = \frac{M_{bend}}{W_r}, \quad (13)$$

where W_r is the resultant moment from a resistance of the acceleration blade cross-section area, cm^3. For our case

$$W_r = \sqrt{W_x^2 + W_y^2}, \quad (14)$$

where W_x, W_y are the resistance moments of the acceleration blade cross-section area with respect to axis x and axis y, cm^3.

For the acceleration blade of the rectangular section we have (Fig. 1) [8]:

$$W_x = \frac{\delta_j (r_2 - r_1)^2}{6}, \quad (15)$$

$$W_y = \frac{(r_2 - r_1)\delta_j^2}{6}. \quad (16)$$

After substitution and appropriate transformations an equation (13) will look as:

$$\sigma_{bend} = \frac{3h^2}{\delta_j (r_2 - r_1)} \times \sqrt{\frac{\delta_j^2 r_i^4 \rho_b^2 \omega^4 + \frac{1}{4}(r_2^2 - r_1^2)^2 \gamma_p^2 g^2 (\sin\alpha)^2}{\delta_j^2 + (r_2 - r_1)^2}}. \quad (17)$$

The largest tangential stress (a shear stress) for the outrigger of the rectangular section is calculated by the following equation [8]

$$\tau_{sh}^{max} = \frac{3}{2}\frac{Q_p}{F}. \quad (18)$$

where Q_p the resultant cross force acting on the outrigger in the considered rectangular section, N, F is an area of the outrigger cross section, m^2.

In our case

$$Q_p = \sqrt{P_c^2 + P_m^2}, \quad (19)$$

and

$$F = (r_2 - r_1)\delta_j. \quad (20)$$

Then after substitution and appropriate transformations equation (18) will look as

$$\tau_{sh}^{max} = \frac{3h}{2} \times \frac{\sqrt{\delta_j^2 r_i^4 q_b^2 \omega^4 + \frac{1}{4}(r_2^2 - r_1^2)^2 \gamma_p^2 g^2 (\sin\alpha)^2}}{(r_2 - r_1)\delta_j}. \quad (21)$$

Equivalent stresses acting on the acceleration blade of the grinder rotor can be defined according to equation (22) [9]

$$\sigma_{equiv}^{III} = \sqrt{\sigma^2 + 4 \cdot (\tau_{sh}^{max})^2} \le [\sigma]. \quad (22)$$

The comprehensive analysis of the Eqs. (17), (21), and (22) suggests that a dependence of the equivalent stresses σ_{equiv}^{III} on the acceleration blade thickness δ_j is of quadratic character. Hence a minimum permissible thickness of the acceleration blade of the grinder can obtained by equation (23) [10]

$$[\delta_j] = \sqrt{\frac{\sigma_{equiv}^{III}}{[\sigma]}}\,\delta_j, \quad (23)$$

where $[\sigma]$ is the assumed value of the blade material stress, MPa ($[\sigma] = 180$).

The main results of a simulation of the acceleration blade optimum thickness are presented on Figs. 2, 3.

Approximating the curve $[\sigma] = f(r)$ (Fig. 3) we obtained an empirical dependence $[\sigma] = -2 - 15r^3 - 7.34 / \ln r$ that quite exactly allows estimating the minimum permissible thickness of the acceleration blade in dependence in its current radius.

Methods presented in this work and in [6] of the optimum thickness computation for the rotory disk, the bearing plate, and the acceleration blades of the rotory

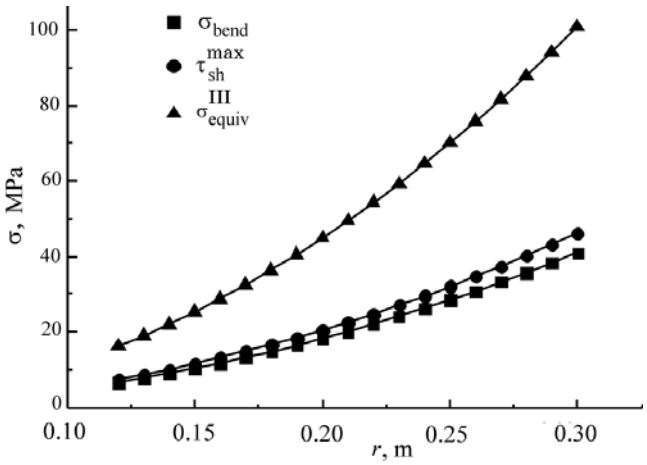


Fig. 2. The dependence of the bending stresses, the section, and equivalent stresses on the current radius of the grinder acceleration blade.

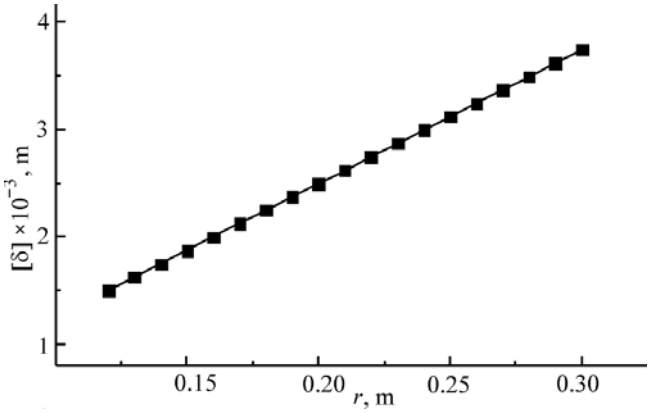


Fig. 3. The dependence of the minimum permissible thickness of the grinder acceleration blade on its current radius.

centrifugal grinder should be used for the strength design of appropriate machine elements and devices with the same operation principle.

REFERENCES

1. Levdanskii, E. I. and Levdanskii, A. E., *Energosberezhenie pri izmel'chenii* (Energy-Saving at Pounding), Minsk: Bel. Gos. Techn. Univ, 1999, 86 p.
2. Levdanskii, A. E. and Levdanskii, E. I., *Vysokoeffektivnye protochnye protsessy i apparaty* (High-Efficiency Flow-Through Processes and Devices), Minsk, Bel. Gos. Techn. Univ, 2001, 236 p.
3. Levdanskii, A.E., Garabazhiu, A.A., Levdanskii, E.I., and Levdanskii, S.E., *Mel'nitsa* (Grinder), RB Patent 4770, MPK 6–V 02S 13/14; *Izobreteniya*, 2002, no. 5.
4. Garabazhiu, A.A., Abstracts of papers, *Mezhdunarodnaya internet-konferentsiya "Arkhitekturno-stroitel'noe materialovedenie na rubezhe vekov"* (International Internet Conference on Architectural Material Science on Border of the Century), 2002, pp. 26e32.
5. Garabazhiu, A.A. and Murog, V.Yu., *Khimicheskaya promyshlennost'*, 2003. no. 5, pp. 3e11.
6. Garabazhiu, A.A., *Khimicheskaya promyshlennost'*, 2006, vol. 83, no. 9, pp. 421–426.
7. Sergeev, B.M., *Raschet na prochnost' detalei mashin pishchevykh proizvodstv* (Strength Design of Machine Elements of Food Industry) Moscow, Mashinostroenie, 1969, 143 p.
8. Feodos'ev, V.I., *Soprotivlenie materialov* (Strength of Materials), Moscow: Vysshaya Shkola, 1979, 426 p.
9. Kantorovich, Z.B., *Osnovy rascheta khimicheskikh mashin i apparatov* (The Principles of Simulation of Chemistry Machines and Devices), Moscow: Mashinostroenie, 1960, 744 p.
10. Batuner, L.M. and Pozin, M.E., *Matematicheskie metody v khimicheskoi tekhnike* (Mathematical Methods in Chemical Engineering), Leningrad: Khimiya, 1971, 824 p.

ISSN 1070-4272, Russian Journal of Applied Chemistry, 2008, Vol. 81, No. 6, pp. 1132–1134. © Pleiades Publishing, Ltd., 2008.
Original Russian Text © M.K. Abdurakhmanov, 2008, published in Khimicheskaya Promyshlennost', 2008, Vol. 85, No. 2, pp. 103–106.

INDUSTRUAL ECOLOGY

Effect of Nitrocalcuumphosphate Fertilizer on the Potato Yield and Quality

M. K. Abdurakhmanov

Samarkand State University, Samarkand, Uzbekistan

Received November 9, 2007

Abstract—This report lists results of testing a new fertilizer, nitrocalciumphosphate (NCF) produced by open join stock company "Samarkandkimye", on the grow, develop and yield of potato under conditions of Golodnaya Step' area of Uzbekistan. From the experimental results is defined year norm of the fertilizer on typical gray desert soil of low salinity: 20 ton of semi-rotten manure + $N_{220}P_{165}K_{125}$ kg per hectare. For soils of moderate salinity is recommended to apply 40 ton of semi-rotten manure + $N_{220}P_{165}K_{125}$ kg per hectare. It is confirmed that application of organic and mineral fertilizers for potato at optimal norm improves feeding regime of soil, increases yield and quality of tubers and improves significantly meliorative situation in solanized soil.

DOI: 10.1134/S1070427208060463

In correspondence with the Entrustment of Government of the Republic Uzbekistan No. 3057-xx of June 13, 2005, on the Samarkand chemical plant (open join stock company "Samarkandkimye") in 2005 started exploitation of experimental industrial installation producing nirocalcuimphosphate fertilizer with productivity 50 000 ton per year.

Technology of the nirocalcuimphosphate fertilizer is absolutely free of by-product. The fertilizer contains totally more feeding components ($N + P_2O_5 = 22–23\%$) than traditional ammonized superphosphate (13–14%). More so, while superphosphate contains 50% of gypsum as a ballast, the nirocalcuimphosphate fertilizer instead contains assimilable calcium nitrate. That is why the nirocalcuimphosphate fertilizer is very active on the soils of any type, the salinizated ones in particular. It is substantially more effective for the plants needed continuous inflow of calcium to the zone of growing stem, root and fruit elements.

By the investigation we revealed that on soddy podzolic soil with light granulometric composition it is economically profitable to apply organomineral fertilizers that promote high yield of potato with high quality and keeping ability of the product, increases biological activity of soil and affects positively further crop rotation and the soil fertility characteristics [1].

Effect has been studied of increasing dozes of potassium fertilizers on the dynamics of exchangeable potassium in the irrigated chestnut soil. Their influence on the yield, biochemical and mineral composition of potato was revealed [2]. In Uzbekistan were tested the sorts Sante, Condor and Licariya on the background of 20 ton of manure + $N_{200}P_{160}K_{100}$ at the density of the plants 71400 units. The testes showed that early yield can be obtained at least 25 ton per hectare [3]. Manure and other organic fertilizers for potato should be introduced only in autumn at fall plowing or to preceding culture [4].

Current investigations were aimed at the study of potato feeding regime under the conditions of the soil in Golodnaya Step' and revealing the fertilizer optimal year norm. We studied the following:

– Yield of potato without a fertilizer in account of precursors and the soil natural fertility;

– Yield and quality of potato tubers at growing them with mineral fertilizers;

– Effect of organic and mineral fertilizers on the potato yiels;

– Effect of organic and mineral fertilizers on the meliorative state of salinizated soils.

From the results of experiments the following optimal schedule of introducing fetrilizers is revealed. Before autumn plowing to the low salinizated soil should be introduced 20 ton per hectare, to strongly solinated 40 ton per hectare of semi-rotten manure and year norm of potassium. A half of year norm of phosphate fertilizers should be introbuced before plowing and a half at

first feeding. A half of the year norm of nitrogen fertilizers should be introduced at appearing of sprouts and the rest at abundant budding of plants..

The influence of organic and mineral fertelizers on the growing and development of potato is shown in Table 1.

From the data of Table 1 follows that increase in the fertilizers norm affects positively on the potato plant height, and this regularity is continuous.

At growing potato without fertilizers the plants height at the end of vegetation was 50.3 cm, with mineral fertilizers only it was from 65.3 to 74.8 cm.

At introducing to the soil 20 ton of semi-rotten manure the plant height was 71.7 cm. With 20 ton of semi-rotten manure + N_{220} P_{165} K_{125} kg per hectare the plant height was 78.4 cm, number of stems 3.8, number of leafs 180.4, number of axillary shoots 8.9, duration of vegetation period 87 days. At introducing 40 ton of semi-rotten manure + N_{220} P_{165} K_{125} the related values are, respectively: 81.9; 3.8; 194.7; 14. 2; 89.0.

At growing potato without fertilizers the height, development and yield depend both on te soil natural fertility and fertilizers introduced with preceding cultures.

The highest plant grow, leaf surface and biological mass of potato were achieved at introducing 20 and 40 ton per hectare of semi-rotten manure with year norm of mineral fertilizers N_{220} P_{165} K_{125}. When potato grows without fertilizers, its haulm turns yellow at 82th day after coming up; at introducing fertilizers according to year norm the vegetation period duration is 87–89 days.

At growing potato without fertilizers (Table 2) the characteristics of biochemical composition of tubers falls, but this characteristics in a great extent depends on genetic features, therefore it depends insignificantly on the agricultural technology.

Feeding regime affects significantly the potato yield. In the experiments of growing without fertilizers the yield is 5.6 ton per hectare, commercial part of tubers is 80 %. On the experimental fields the highest yield was achieved with 40 ton of semi-rotten manure + N_{220} P_{165} K_{125} kg per hectare, and with 40 ton of semi-rotten manure + N_{300} P_{224} K_{170} kg per hectare, the yield was 17.0 and 17.4 ton per hectare, respectively.

When mineral fertilizers are introduced according to higher norm, N_{300} P_{224} K_{170} kg per hectare, the tubers contain more nitrates affecting negatively the tubers, reducing their keeping and foodstuff quality. Application of fertilizers according to the high norm in Golodnaya Srep' detiorates significantly aero-ecological situation in the soil.

Table 1. Influence of organic and mineral fertilizers on the potato growing and development (2004–2006)

No.	Experiment mode	Griwing and development of plants				
		Height, cm	Number of stems, units	Number of leafs, units	Number of sprouts, units	Vegetation period duration, days
1.	Control (no fertilizer)	50.3	3.6	143.1	4.7	82
2.	N_{150} P_{112} K_{85}	65.3	3.7	162.6	7.1	84
3.	N_{220} P_{165} K_{125}	70.2	3.6	169.4	7.9	85
4.	N_{300} P_{224} K_{170}	74.8	3.7	171.8	8.2	86
5.	20 ton per hectare semi-rotten manure	76.1	3.8	173.9	8.3	86
6	20 ton per hectare semi-rotten manure + N_{150} P_{112} K_{85}	76.8	3.7	177.3	8.6	86
7	20 ton per hectare semi-rotten manure + N_{220} P_{165} K_{125}	78.4	3.8	180.4	8.9	87
8	20ton per hectare semi-rotten manure + N_{300} P_{224} K_{170}	80.5	3.7	188.2	9.2	87
9	40ton per hectare semi-rotten manure	80.1	3.7	188.9	9.2	88
10	40 ton per hectare semi-rotten manure +N_{150} P_{112} K_{85}	80.8	3.8	190.0	10.4	87
11	40 ton per hectare semi-rotten manure + N_{220} P_{165} K_{125}	81.9	3.8	194.7	14.2	89
12	40 ton per hectare semi-rotten manure + N_{300} P_{224} K_{170}	83.7	3.8	206.9	15.1	89

Table 2. Effect of organic and minerql fertilizers on the potato biochemical composition and yield (2004-2006)

No.	Experiment mode	Content in tubers			Yield of quality tubers, %	Yield, ton per hectare	Extra yield over control, ton per hectare
		Starch, %	Protein, %	Vitamine C, mg/100 g			
1.	Control (no fertilizer)	13.1	1.3	15.2	80	5.6	0.0
2.	$N_{150}\,P_{112}\,K_{85}$	13.5	1.3	15.4	84	9.1	+3.5
3.	$N_{220}\,P_{165}\,K_{125}$	13.5	1.4	15.5	85	9.4	+3.8
4.	$N_{300}\,P_{224}\,K_{170}$	13.6	1.4	15.5	85	9.5	+3.9
5.	20 ton per hectare semi-rotten manure	13.7	1.4	16.6	86	10.6	+5.0
6.	20 ton per hectare semi-rotten manure + $N_{150}\,P_{112}\,K_{85}$	13.6	1.4	15.6	87	12.2	+6.6
7.	20 ton per hectare semi-rotten manure + $N_{220}\,P_{165}\,K_{125}$	13.7	1.3	15.7	87	12.6	+7.0
8.	20ton per hectare semi-rotten manure + $N_{300}\,P_{224}\,K_{170}$	13.7	1.4	15.7	89	13.1	+7.5
9.	40ton per hectare semi-rotten manure	13.2	1.4	15.5	89	13.6	+8.0
10.	40 ton per hectare semi-rotten manure + $N_{150}\,P_{112}\,K_{85}$	13.7	1.4	15.8	90	16.2	+10.6
11.	40 ton per hectare semi-rotten manure + $N_{220}\,P_{165}\,K_{125}$	13.8	1.5	15.8	92	17.0	+11.4
12.	40 ton per hectare semi-rotten manure + $N_{300}\,P_{224}\,K_{170}$	13.8	1.5	15.9	93	17.4	+11.8

Difference in yield for the cases 11 and 12 is within the experimental error. Therefore we recommend to apply 40 ton of semi-rotten manure + $N_{220}\,P_{165}\,K_{125}$ kg per hectare at scaled growing.Then yield is 17.0 ton per hectare, by 11.4 ton per hectare higher than in the control experiments. Our experiments showed that introducing in autumn 20 and 40 ton per hectare of semi-rotten manure leads to decrease in spring of negative influence of soil salinization and improves soil melioration.

We recommend to introduce year norm of the fertilizer in the following order. 125 kg of potassium is introduced to fall-plowed field in autumn. A part of phosphoric fertilizer (80 kg) should be given to the fall plowed field and remaining 85 kg at first top dressing. Of nitrogen fertilizer, 110 kg is added before full sprouts appearing and the rest (110 kg) at second top dressing, that is, at full budding.

Thus, by our experiments we revealed year norm of the fertilizer for typical low salinizated gray desert soil: 20 ton of semi-rotten manure + $N_{220}\,P_{165}\,K_{125}$ kg per hectare. For the merely salinizated soil under the conditions of Golodnaya Step' we recommend to apply 40 ton of semi-rotten manure + $N_{220}\,P_{165}\,K_{125}$ kg per hectare. The experiments confirmed that application of these organomineral fertilizers for potato according to the optimal norm improves feeding regime of the soil, increases yield and quality of tubers and simultaneously improves considerably melioration state of the salinizated ground

REFERENCES

1. Novikov, M.A., *Cand. Sci. (Agriculture) Dissertation,* Moscow, 2005. .
2. Ubugunov, L.L., Merkusheva, M.G., and Budaev, B.Kh., *Agrokhimiya,* 2005, No. 3, p. 44-54.
3. Astanakulov, T., Otamurodov, E. and Ostanova, L., *Kartofel' Ovoshchi*, 2004, no. 5, p. 8.
4. Butov, A.V., *Kartofel' Ovoshchi*, 2006, no. 5, pp. 17–19.

ISSN 1070-4272, Russian Journal of Applied Chemistry, 2008, Vol. 81, No. 7, pp. 1135–1139. © Pleiades Publishing, Ltd., 2008.
Original Russian Text © V.E. Matyasova, N.G. Matyasov, T.L. Moroz, N.K. Kuznetsov, L.V. Bashlaeva, V.I. Samoilov, N.A. Kulenova, S.G. Strunnikov, 2008, published in Zhurnal Prikladnoi Khimii, 2008, Vol. 81, No. 7, pp. 1057–1061.

INORGANIC SYNTHESIS AND INDUSTRIAL INORGANIC CHEMISTRY

A Process for Production of Granulated Soluble Glass in Ore-Thermal Furnaces

V. E. Matyasova, N. G. Matyasov, T. L. Moroz, N. K. Kuznetsov, L. V. Bashlaeva, V. I. Samoilov, N. A. Kulenova, and S. G. Strunnikov

Ul'ba Metallurgical Plant, Joint-Stock Company, Ust-Kamenogorsk, Kazakhstan
Eastern-Kazakhstan State Technical University, Ust-Kamenogorsk, Kazakhstan

Received May 23, 2007

Abstract—A process for production of soluble sodium glass in electric-arc ore-thermal furnaces with three graphite electrodes was suggested and tested on the industrial scale. Fusion of sand with sodium carbonate, followed by rapid cooling of the fusion cake with cold water, yields finely grained sodium metasilicate with a developed network of microcracks as a result of a thermal impact in the course of aqueous granulation of the fusion cake.

DOI: 10.1134/S107042720807001X

Salts of silicic acids (silicates) are mostly insoluble in water, with the exception of sodium and potassium metasilicates (Na_2SiO_3 and K_2SiO_3). Owing to the outward similarity with glass and to their solubility in water, these two compounds are named soluble glass. Its aqueous solutions (liquid glass) are widely used in building, chemical, glassware, petroleum, petrochemical, ore-dressing, metallurgical, paper, textile, soap, and other industries.

There exist several methods for preparing soluble glass [1], of which the most widely used is the carbonate technique based on the reaction of sodium and potassium carbonates with silicon oxide at the melting point (1400–1500°C):

$$M_2CO_3 + SiO_2 = M_2SiO_3 + CO_2\uparrow, \quad (1)$$

where M stands for sodium or potassium.

The most important characteristic of a soluble glass, which predetermines its consumers' properties, is its silicate ratio M, defined as the weight ratio between silicon oxide and sodium (potassium) oxide in the glass:

$$M = [SiO_2]/[M_2O]. \quad (2)$$

The industry manufactures the soluble glass as silicate lumps, which are crushed and subjected to autoclave dissolution in a NaOH solution to give liquid glass. The process in which a liquid glass is obtained from a silicate lump has rather high cost and low output capacity, because it involves energy-intensive stages of crushing of silicate lump and its subsequent autoclave dissolution (during several hours) with expensive sodium hydroxide. To improve the economic efficiency of the process for producing sodium liquid glass from soluble glass, we suggest a process for fusion of soda with sand in an ore-thermal furnace, followed by rapid cooling of the fusion cake with water. The process we suggested and tested can produce granulated sodium metasilicate, whose processing to liquid glass is economically more attractive, compared to processing of silicate lumps.

We used natural silica containing 98.0–98.8 wt % SiO_2 (Table 1) as a silica-containing raw material for production of a silicate granulate [2]. Data on the quality of soda used to prepare a stock with sand are listed in Table 1. To obtain a silicate granulate, commercial sodium metasilicate, we mixed sand and soda to obtain a prescribed silicate ratio of the stock. The stock was charged into a graphite crucible and fused in an ShP-1 furnace for 30 min at a prescribed temperature. The fusion cake was granulated in water with an initial temperature $T \approx 20$°C at s : l ≈ 1 : 15 (no "pops," vapor discharges, or other dangerous events were observed in fusion cake granulation). The silicate granulate was separated from water and analyzed for the content of oxides of silicon, sodium, and impurities.

Table 1. Chemical composition of stock components

Component	Content, wt %						
	Na_2CO_3	SiO_2	Al_2O_3	Fe_2O_3	CaO	Ba	moisture
Silica 1 (molding sand of KO 2B brand)	–	98.8	0.32	0.36	0.14	–	2.5
Silica 2 (sand from Karasorskoe deposit)	–	98.0	0.4	0.4	0.1	–	2.4
Soda 1	99.9	–	–	<0.03	–	–	–
Soda 2	91.4	–	1.0	0.37	–	0.05	–

Table 2. Quality of the silicate granulate obtained

Starting silica-containing raw material (Table 1)	Content in silicate granulate, wt %				SiO_2/Na_2O weight ratio
	SiO_2	Na_2O	$Al_2O_3 + Fe_2O_3$	CaO + MgO	
Silica 1	67.2	28.1	<1.1	0.2	2.39
Silica 2	71.6	26.4	<0.49	<0.05	2.71
GOST 13079–73:	from 70.8 to 73.4	from 25.3 to 28.1	≤0.9	≤0.4	2.6–3.0

The results of experiments in which the silicate granulate was obtained demonstrate (Table 2) that the product nearly satisfies the requirements of GOST (State Standard) [3]. The fusion cakes become more fluidized as the silicate ratio is lowered from 3 to 2 and the fusion temperature is raised from 1350 to 1450°C. It was found that the fusion temperature of 1400–1450°C provides satisfactory fluidization of the fusion cakes if the stock used has a silicate ratio of 2–3.

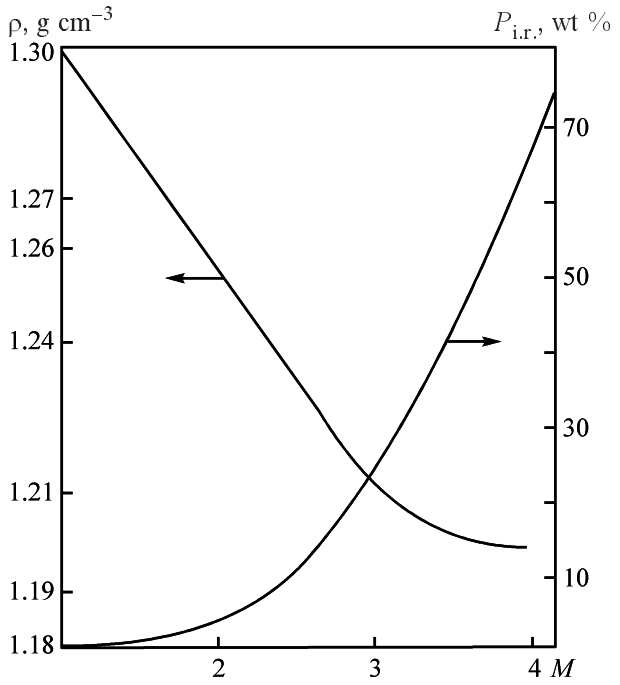


Fig. 1. Predictive estimate of how the density ρ of liquid glass and yield of the insoluble residue, $P_{i.r.}$, depend on the silicate ratio M of the silicate granulate (based on the results of 6–7 runs).

We assessed the possibility of preparing the liquid glass [2] from the silicate granulates and the silicate lump, obtained in the mode being tested (the production of silicate lump ended in cooling of the sodium metasilicate melt in air).

The solubility of sodium metasilicate, one of the most important technological properties of this compound, should provide production of solutions with a density of 1.36–1.52 g cm^{-3} [4]. To find out how the density of a liquid glass depends on the silicate ratio of the starting stock, we dissolved silicate granulate samples with different silicate ratios under the same conditions. The dissolution was performed in the course of 4 h at s : l = 1 : 2 under boiling. The results obtained are shown in Fig. 1. In the mode tested for dissolution of the silicate granulate, a decrease in the silicate ratio from 3–4 to 1 makes it possible to raise the liquid glass density from 1.18–1.21 to 1.30 g cm^{-3}, which is, however, lower than the standard value (1.36–1.52 g cm^{-3}). The required density of solutions was only achieved by their evaporation, which is economically inefficient

under industrial conditions. Positive results were obtained after preliminarily crushing the granulates to a grain size of less than 0.1 mm and raising the dissolution duration to 5 h (Table 3). However, a noticeable amount of an insoluble residue remained in this case (14 wt % relative to the initial amount of the silicate granulate), which required that the dissolution mode should be improved. Nevertheless, the experiments performed demonstrated that the liquid glass can be, in principle, obtained from a silicate granulate with a minimum expenditure for diminution of the raw material, without an autoclave and sodium hydroxide. This makes this kind of raw materials more promising than the silicate lump dissolved under industrial conditions (after its energy-intensive crushing) in autoclaves under a pressure of 5 atm in the course of 3 h with the use of sodium hydroxide. The high promise of processing of sodium metasilicate in the form of the silicate granulate, compared to the conventionally used silicate lump, was confirmed by comparative tests (Fig. 2).

The higher solubility of the silicate granulate, compared to the silicate lump, is due to the finer grain of the raw material and presence of a large number of microcracks in grains as a result of the thermal impact in the course of aqueous granulation of the molten glass. The higher dissolution rate of the silicate granulate, compared to silicate lumps, made it possible to diminish the expenditure of the alkali and steam in its autoclave dissolution under industrial conditions, which is one of the most important advantages of the silicate granulate. This was done in the course of industrial tests without grinding of the silicate granulate.

In industrial tests of the method for production of the silicate granulate, we perfected the technology of fusion of the silica–soda stock in electric-arc ore-thermal furnaces with three graphite electrodes (Fig. 3) at UMZ Joint-Stock Company [2]. In the tests, we manufactured two pilot batches of the silicate granulate (approximately 90 t each) from the raw material presented in Table 4. Both batches of the silicate granulate were industrially processed into liquid glass at Vostokmashzavod Joint-Stock Company (Ust-Kamenogorsk).

When producing the pilot batches of the silicate granulate, we used the following raw materials: stock no. 1 in the first stage of the study and stock no. 2 in the second stage (Table 4). The stock was melted at $T \approx 1400$°C. The melt was poured from the furnace into a granulator filled with water, with fine grains of the silicate granulate obtained. The product was transported in containers to Vostokmashzavod Joint-Stock Company to be processed into liquid glass.

Table 3. Effect of the duration τ of dissolution of a ground silicate granulate on the completeness of its dissolution. Silicate ratio of the starting stock 2.5

Run no.	τ, h	Solution density, g cm^{-3}	Yield of insoluble residue, wt %
1	1	1.24	–
2*	3*	1.36	25
3	5	1.41	14

* In run no. 2, the slurry formed upon 1 h of dissolution was kept for 16 h without heating and agitation, after which the product was additionally dissolved in the course of 2 h under heating and agitation.

Table 5 lists the results of analyses of the first and second pilot batches of the silicate granulate. In the first stage of the tests, the silicate granulate failed to conform to the existing regulations because of the poor quality of soda (Table 5); in the second, the product satisfied the requirements of GOST 13079–73.

It was shown in further processing of the silicate granulate batches at Vostokmashzavod Joint-Stock Company that they are suitable for manufacture of casting molds and mold cores.

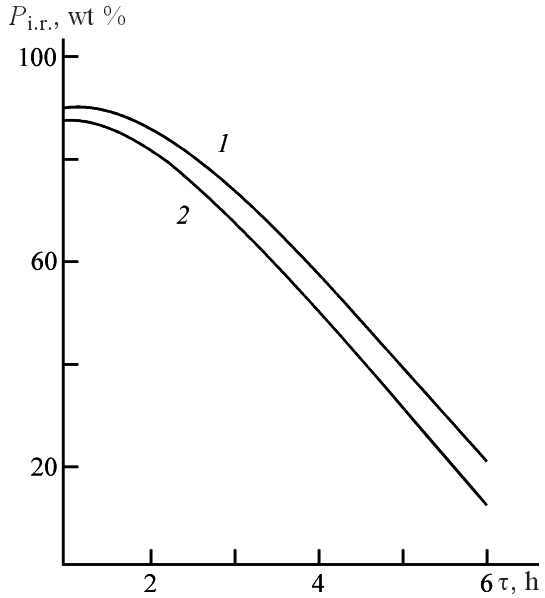


Fig. 2. Yield $P_{i.r.}$ of the insoluble residue vs. the dissolution time τ of (*1*) silicate lump and (*2*) silicate granulate.

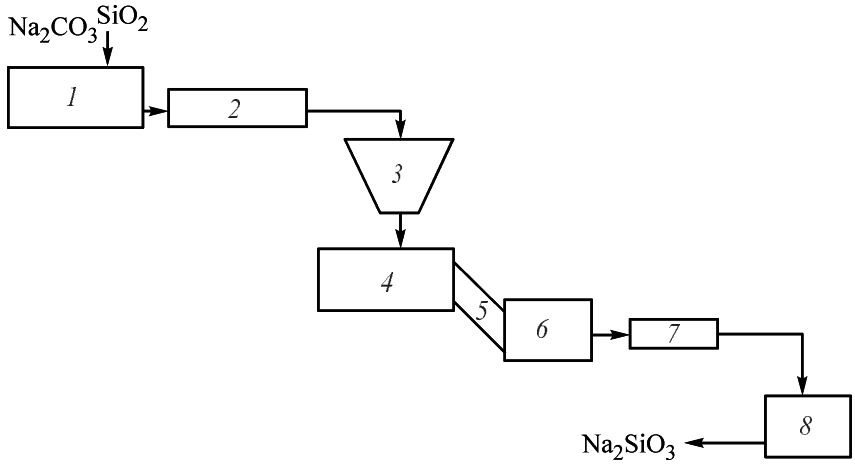


Fig. 3. Schematic of the apparatus for production of the silicate granulate: (*1*) stock scale, (*2*) belt conveyor, (*3*) furnace bunker, (*4*) ore-thermal furnace, (*5*) overflow gutter, (*6*) granulator, (*7*) vibration transporter, and (*8*) container.

The pilot batches of the silicate granulate were subjected to an autoclave treatment with addition of a sodium hydroxide solution. In contrast to the silicate lump case, this was done without preliminary crushing of the silicate granulate. The resulting liquid-glass solution was used to fabricate casting molds and mold cores. Table 6 lists data on the content of the insoluble residue in the liquid glass produced from the first and second batches of the granulate and on the chemical composition of the insoluble residue and presents the amount of the insoluble residue formed in processing of the silicate lump from Salavat-steklo plant (Bashkortostan). A considerable decrease in the content of the in-

Table 4. Silicate ratio of the starting stock and composition of its components

Stock no.	Silicate ratio	Component	Content of indicated compound in stock components, wt %					
			SiO_2	Na_2CO_3	Al_2O_3	Fe_2O_3	MgO	moisture
1	2.0–4.0	Molding sand of KO 2B brand	98.80	–	0.32	0.36	–	8.00
		Contaminated soda	11.80	81.40	0.85	0.33	1.23	0.096
2	2.6–3.0	Molding sand of KO 2B brand	98.80	–	0.32	0.36	–	8.00
		Technical-grade soda (GOST 5100-95E)	–	99.00	–	–	–	–

Table 5. Quality of pilot batches of the silicate granulate

Batch no.	Silicate granulate sample no.	Content of indicated compound in silicate granulate, wt %						Silicate ratio
		Na_2O	SiO_2	Al_2O_3	Fe_2O_3	CaO	SO_3	
1	1	29.7	77.2	<0.3	1.41	1.4	<0.01	2.6
	2	25.6	59.9	<0.3	0.37	0.07	0.01	2.3
	3	21.6	62.1	<0.3	0.87	0.66	<0.01	2.9
	4	24.1	61.4	3.02	0.54	1.62	<0.01	2.5
	5	25.9	64.9	1.4	0.51	1.46	<0.01	2.5
	6	26.6	61.5	1.4	0.76	1.15	<0.01	2.3
	7	25.58	64.50	<1.12	1.23	1.23	<0.01	2.52
2	1	27.9	71.2	0.3	–	0.3	0.1	2.63
GOST 13079–73:		25.3–28.1	70.8–73.4	$Al_2O_3 + Fe_2O_3 \le 0.9$		$CaO + MgO \le 0.4$	≤1.25	2.6–3.0

Table 6. Yield of the insoluble residue in the liquid glass and the chemical composition of the residue

Silicate granulate batch no.	Yield of insoluble residue, wt %	Content of indicated compound in insoluble residue, wt %				
		SiO_2	Na_2O	Al	Fe	Ca
1	20	68.5	12.2	0.98	1.65	0.6
2	3.5	36.1	16.4	2.1	0.06	0.25
Silicate lump	2.6	–	–	–	–	–

soluble residue was observed when processing the second batch of the granulate, which is due to the use of purer soda in stock formulation (Table 6). The insoluble residues are strongly contaminated with aluminum, iron, and calcium impurities and, therefore, cannot be completely recycled into the stage of sand fusion with soda. The mass of the insoluble residue can be reduced by using purer sand and soda, which will make it possible to lower the amount of the residue to that obtained when processing the silicate lump manufactured by Salavatsteklo Company (Table 6).

During the industrial tests aimed to obtain a liquid glass, we monitored its quality after each dissolution of the second batch of the silicate granulate (Table 7).

The data in Table 7 indicate that a liquid-glass batch satisfying the foundry requirements was obtained from the second batch of the silicate granulate. Compared to the conventional processing of the silicate lump, the processing of the silicate granulate does not require its crushing before dissolution, the dissolution rate of the material increases, and, simultaneously, the expenditure of steam noticeably decreases and the consumption of sodium hydroxide in dissolution becomes two times smaller.

Table 7. Quality of liquid glass produced at Vostokmashzavod Joint-Stock Company

Liquid-glass sample no.	Density, g cm^{-3}	Silicate ratio
1	1.49	2.41
2	1.50	2.56
3	1.52	2.56
4	1.50	2.56
5	1.53	2.56
6	1.46*	2.68*
7	1.50	2.41
8	1.50	2.56
Foundry requirements	1.48–1.52	2.20–2.50

* The quality satisfies the requirements of the chisel shop.

CONCLUSIONS

(1) The possibility of using electric-arc ore-thermal furnaces with three graphite electrodes for manufacture of a silicate granulate of sodium metasilicate was demonstrated.

(2) It was shown that such a silicate granulate has improved technological properties in manufacture of liquid glass, compared with the conventionally used silicate lump, and use of the silicate granulate in production of liquid glass creates prerequisites for raising the economic efficiency of this process.

REFERENCES

1. Appen, A.A., *Khimiya stekla* (Chemistry of Glass), Moscow: Khimiya, 2000.
2. Samoilov, V.I., *Issledovanie sovremennykh i razrabotka perspektivnykh metodov izvlecheniya litiya iz mineral'nogo syr'ya v tekhnicheskie soedineniya* (A Study of Present-Day Methods for Recovery of Lithium from Mineral Raw Materials into Technical-Grade Compounds and Development of Promising Techniques for This Purpose), Ust-Kamenogorsk: Media-Al'yans, 2005.
3. *GOST* (State Standard) *13 079–73: Soluble Sodium Silicate*.
4. *GOST* (State Standard) *13 078–81: Liquid Sodium Glass*.

ISSN 1070-4272, Russian Journal of Applied Chemistry, 2008, Vol. 81, No. 7, pp. 1140–1143. © Pleiades Publishing, Ltd., 2008.
Original Russian Text © V.V. Vol'khin, I.S. Glushankova, S.A. Kolesova, E.A. Shul'ga, 2008, published in Zhurnal Prikladnoi Khimii, 2008, Vol. 81, No. 7, pp. 1062–1065.

INORGANIC SYNTHESIS AND INDUSTRIAL INORGANIC CHEMISTRY

Sorption Recovery of Rubidium Ions from Highly Mineralized Solutions to Obtain Rubidium Chloride of Reagent Grade

V. V. Vol'khin, I. S. Glushankova, S. A. Kolesova, and E. A. Shul'ga

Perm State Technical University, Perm, Russia

Received June 7, 2007

Abstract—Recovery of Rb^+ ions from highly mineralized solutions with a granulated composite sorbent of the composition $K_{0.92-1.0}Cu_{1.50-1.54}[Fe(CN)_6]\cdot 4.9SiO_2$ in the multiple-cycle mode was studied.

DOI: 10.1134/S1070427208070021

Rubidium salts are obtained in industrial practice as a by-product in processing of potassium and magnesium salts by multiple fractionated crystallization, and metallic rubidium, by reduction of rubidium chloride with calcium at 700–800°C in a vacuum [1]. The high production cost of rubidium and its salts hinders wide use of the metal in technology.

The techniques employed to obtain rare-earth (REE) and scattered elements widely use extraction and sorption methods [2, 3]. REEs are recovered from solutions formed in processing of mineral raw materials with selective inorganic ion-exchange materials or organic polymeric resins. To isolate REEs, the sorbent is dissolved or subjected to thermal degradation (ashing) [2].

It is advisable to use sorption methods to recover rubidium from industrial brines (spent electrolytes, aqueous solutions of chlorides of alkali and alkaline-earth metals) formed in production of magnesium.

It is known that ferrocyanides [hexacyanoferrates(II)] of transition metals (copper, nickel, zinc) can selectively absorb ions of rubidium, cesium, and thallium(I) from solutions of various compositions, with high separation coefficients achieved for ion pairs Rb^+ and K^+, Rb^+ and Na^+ ($K_d = 10^2$–10^3), Cs^+ and K^+ ($K_d = 10^5$–10^6) [4, 7]. Granulated sorbents are commonly used in sorption techniques. To improve their mechanical properties, ferrocyanide sorbents are synthesized as composites, e.g., with silica gel [5].

Use of granulated composite ferrocyanide sorbents makes it possible to organize the process by the sorption–desorption–regeneration scheme, but the lack of an efficient method for Rb^+ desorption from the sorbent hinders application of the sorption technique to production of rubidium salts.

Ion-exchange and redox methods for desorption of alkali metal ions from the ferrocyanide phase are known. The ion-exchange techniques use concentrated solutions of ammonium chloride or nitrate, with ammonium ions substituting alkali metal ions in the solid phase. The desorption yields solutions of alkali metal chlorides or nitrates with a large excess of ammonium ions, which hinders their further processing.

The redox methods for desorption of alkali metal ions are based on the reaction

$$M^I_1M^{II}_{1.5}[Fe^{II}(CN)_6] + Ox = M^I + M^{II}_{1.5}[Fe^{III}(CN)_6] + Red,$$

where M^I stands for the ion of an alkali metal (Rb^+, Cs^+), and M^{II}, for Cu^{2+} or Ni^{2+}.

The oxidation of a ferrocyanide is accompanied by release of alkali metal ions from the sorbent phase. In [4, 5, 7], 12 M H_2SO_4 and 6 M HNO_3 are used as oxidizing agents for desorption of Rb^+, Cs^+, and Tl^+ ions from the ferrocyanide sorbent. The difficulty of further processing of highly concentrated acid solutions with a low content of the target component hinders application of this technique.

The goal of the study was to develop a sorption method for recovery of rubidium ions from highly mineralized solutions to obtain a rubidium salt of reagent grade.

EXPERIMENTAL

An FS-10 granulated composite sorbent, which is a mixed copper–potassium ferrocyanide (FOC Cu–K), and silica gel were used in the study. The choice of FOC Cu–K was due to its high selectivity with respect to Rb^+ ions and stability.

The Cu–K ferrocyanide was obtained by precipitation upon mixing of potassium ferrocyanide and copper sulfide solutions in the presence of sodium silicate at pH 4. The resulting paste was dried in air and granulated by decrepitation. The composition of the sorbent obtained is described by the empirical formula $K_{0.92-1.0}Cu_{1.50-1.54}[Fe(CN)_6]\cdot 4.9SiO_2$.

The concentration of alkali metal ions in solutions was determined by the atomic-absorption method with a Perkin–Elmer atomic-absorption spectrometer. Rb^+ ions were recovered from a model solution containing rubidium and potassium chlorides in a molar ratio $Rb^+ : K^+ = 1 : 150$ (the concentrations of Rb^+ and K^+ ions were 0.2–0.25 and 13.8–14.5 g l^{-1}, respectively).

The experiments were performed using ion-exchange column chromatography: column diameter 0.7 cm, sorbent bed height 20 cm, sorbent mass 5 g, column volume 7.7 ml, and filtration rate 1.0–1.2 m h^{-1} (25–30 ml h^{-1}).

The total ion-exchange capacity for the Rb^+ ion was 70–73 mg g^{-1} (0.82–0.85 mmol g^{-1}), or 0.51 mmol mol^{-1} $[Fe(CN)_6]^{4-}$, with a separation coefficient of 1.3×10^2 reached for Rb^+ and K^+ ions.

To obtain a rubidium salt of reagent grade, the problem of separate selective desorption of K^+ and Rb^+ ions from the sorbent was solved in the study. As a desorbing agent for recovery of K^+ ions we chose 1 M HCl. On passing 6–8 column volumes of the eluent (50–60 ml) through the sorbent bed, nearly complete desorption of K^+ ions (98%) was achieved, with the extraction of Rb^+ ions into solution being lower than 2.0%.

Rb^+ ions were extracted from the ferrocyanide sorbent by the redox method. It is the most appropriate to use chlorine or its compounds as an oxidizing agent because they have a high oxidizing capacity ($E^0_{Cl_2/Cl^-}$ = 1.36 V, $E^0_{OCl^-/Cl^-}$ = 1.63 V) and are readily available, being formed in the course of electrochemical processing of potassium and magnesium salts.

Rb^+ ions were desorbed from the ferrocyanide phase with an aqueous solution of Cl_2 (concentration of active chlorine 0.05 M) and a 0.1 M NaClO solution as oxidizing agents. The desorption curves of rubidium ions are shown in Fig. 1.

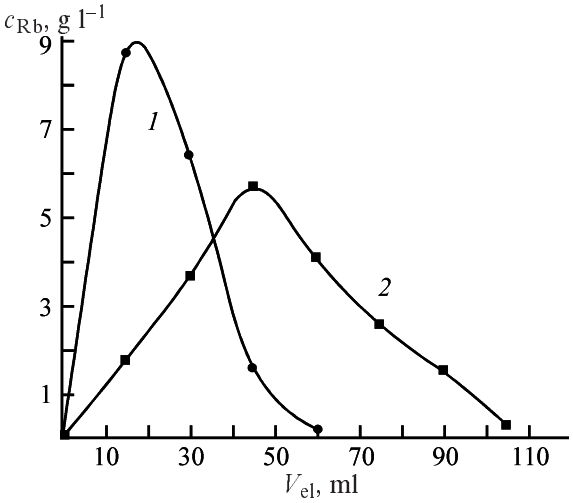


Fig. 1. Desorption curves of rubidium ions. (c_{Rb}) Concentration of rubidium ions in eluate and (V_{el}) eluent volume. Solution: (*1*) 0.1 M NaClO and (*2*) 0.05 M Cl_2 (aq).

These data show that considerable amounts of solutions with low concentration of Rb^+ ions are formed when chlorine water is used, which further leads to high energy expenditure in crystallization of rubidium chloride by evaporation of the eluates. Use of a sodium hypochlorite solution complicates further processing of eluates: a stage of purification to remove Na^+ ions is required for obtaining reagent-grade RbCl.

Raising the concentration of the oxidizing agent can considerably improve the efficiency of desorption of Rb^+ ions from the sorbent phase. Because of the low solubility of Cl_2 in water (0.1 and 0.06 M at 20 and 40°C, respectively) [8], organic liquids were chosen as solvents for chlorine. For example, it is known that gaseous chlorine is highly soluble in halogen-containing organic solvents: its solubility in carbon tetrachloride is 0.6 M at 20°C.

A solvent for chlorine should satisfy the following main requirements: low volatility, incombustibility, high chemical inertness (stability against oxidizing agents), nontoxicity, and low solubility in water. In accordance with the requirements developed, the F-13 fluorochlorocarbon liquid used in industry in lubricants and hydraulic oils was chosen for dissolution of Cl_2. The composition of F-13 is described by the chemical formula $(CF_2CFCl)_4X$, where X stands

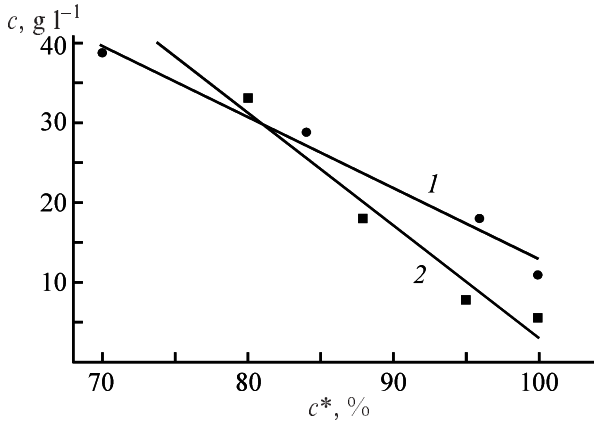


Fig. 2. Effect of the alcohol concentration c^* on the solubility of rubidium chloride in aqueous–alcoholic solutions. (c) Concentration of RbCl solution; the same for Fig. 3. (*1*) C_2H_5OH and (*2*) C_3H_7OH.

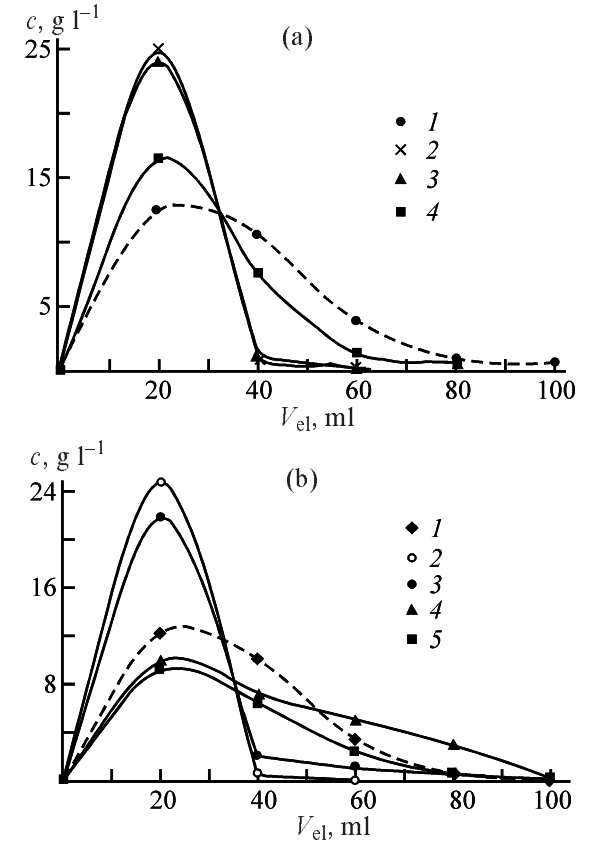


Fig. 3. Curves of elution of rubidium chlorides with water and aqueous solutions of (a) ethanol and (b) isopropanol of various concentrations. (V_{el}) Eluent volume. C_2H_5OH concentration, %: (*1*) 0, (*2*) 70, (*3*) 84, and (*4*) 96. C_3H_7OH concentration, %: (*1*) 0, (*2*) 80, (*3*) 88, (*4*) 95, and (*5*) 100.

for F or Cl. The average molar mass is 519 g mol^{-1} [9]. The equilibrium room-temperature concentration of chlorine in the organofluorine solvent is 0.5–07 M.

The expenditure of the eluent with a chlorine concentration of 0.7 M, passed through a sorbent bed at a rate of 1.0–1.5 m h^{-1}, for complete oxidation of Cu–K FOC is two column volumes. The reaction progress was monitored by the content of active chlorine in eluents at the column outlet. The spent organofluorine liquid was again saturated with chlorine and again used for oxidizing the sorbent. In the study, a single portion of the solvent was used in eight working cycles of the ion-exchange column.

In oxidation of the sorbent, rubidium chloride remains in the solid phase, because it is not dissolved in the fluorinated liquid. The study demonstrated that extraction of Rb^+ ions with distilled water yields low-concentration solutions of rubidium chloride, whose evaporation involves a gross energy expenditure.

It is known that rubidium chloride can be dissolved in monohydric alcohols. For example, its solubility in methanol (99.8%) is 1.4% or 13.2 g l^{-1} [1]. The high toxicity of methanol restricts its application areas. The possibility of using aqueous solutions of ethanol and isopropanol for desorption of Rb^+ ions was analyzed. Because of the lack of information about the solubility of RbCl in the alcohols, these values were found experimentally. The results obtained (Fig. 2) show that the solubility of RbCl in the anhydrous alcohols (ethanol and isopropanol) is 11.0 and 5.5 g l^{-1}, respectively, i.e., it decreases as the molar mass of the alcohol increases. Addition of water leads to a substantial increase in the solubility of rubidium chloride in the alcohols. Experiments on elution of RbCl from a column packed with the oxidized form of the ferrocyanide sorbent were performed in the dynamic mode. The eluate was sampled in 20-ml portions, in which the concentration of Rb^+ ions was determined. The first portions of the eluates, with the maximum concentration of rubidium ions, were processed to give RbCl.

The subsequent portions were taken separately and were repeatedly used to recover Rb^+ in a next working cycle of the column. The curves of elution of rubidium ions from the oxidized phase of the sorbent with water and aqueous–alcoholic solutions are shown in Fig. 3.

An analysis of the results obtained demonstrated that the best results in elution of RbCl are attained with an 80–85% aqueous solution of ethanol or an 80–88% aqueous solution of isopropanol, with more than 85% of Rb^+ recovered with first portions of

Content of rubidium chloride in solutions after evaporation of an alcohol

Concentration of aqueous–alcoholic solutions, vol %			RbCl concentration after evaporation of an alcohol, g l^{-1}
water	ethanol	isopropanol	
4	96	–	Salt*
16	84	–	240
30	70	–	130
0	–	100	Salt*
5	–	95	175
12	–	88	226
20	–	80	125
25	–	75	123

* Solid RbCl was obtained.

the eluate (2–3 column volumes). When distilled water is used, the salt concentration in the eluates formed is 1.5–1.8 times lower than that in aqueous–alcoholic solutions. First portions of the eluate were processed to obtain rubidium chloride, and subsequent portions were reused in the multiple-cycle process.

To enable its multiple use, the sorbent was regenerated, after desorption of K^+ and Rb^+, with a solution of a reducing agent of the following composition (g l^{-1}): Na_2SO_3 20 and KCl 20; pH 4. The pH value was adjusted using an acetic acid solution. It was shown that ferrocyanide retains its sorption activity in 8–12 sorption–desorption–regeneration cycles.

Evaporation of alcohols yielded saturated RbCl solutions (bp C_2H_5OH 78°C, C_3H_7OH 82°C) (see table). As indicated by the data in the table, use of ethanol and isopropanol solutions with concentrations lower than 70 and 80%, respectively, makes lower the content of rubidium chloride in the concentrates, which leads to an increase in the energy expenditure in their further processing. RbCl was isolated from the resulting solutions by evaporation. The finished salt was calcined at 250°C. It was found that the content of K^+ ions in the rubidium chloride obtained did not exceed 1% and the product satisfied the requirements to rubidium chloride of reagent grade.

CONCLUSIONS

(1) A sorption technique was developed for recovery of rubidium chloride from highly mineralized solutions with multiple use of a granulated ferrocyanide sorbent.

(2) Separate desorption of K^+ and Rb^+ ions was performed by the ion exchange $H^+ \rightarrow \underset{\leftarrow}{} K^+$ and oxidation of ferrocyanide with a solution of Cl_2 in an organofluorine solvent, followed by extraction of the RbCl formed with aqueous–alcoholic solutions. The process can yield RbCl of reagent grade.

REFERENCES

1. Plyushchev, V.E. and Stepin, B.D., *Khimiya i tekhnologiya soedinenii litiya, rubidiya i tseziya* (Chemistry and Technology of Lithium, Rubidium, and Cesium Compounds), Moscow: Khimiya, 1970.
2. Solodov, N.A., Balashov, L.S., and Kremenetskii, A.A., *Geokhimiya litiya, rubidiya i tseziya* (Geochemistry of Lithium, Rubidium, and Cesium), Moscow: Nedra, 1980.
3. Korovin, S.S. and Avzhieva, E.M., *Khimiya i tekhnologiya redkikh i rasseyannykh elementov* (Chemistry and Technology of Rare and Scattered Elements), Leningrad: Khimiya, 1990.
4. Betenekov, N.D., Denisov, E.I., Davydova, E.A., and Sharygin, L.M., in *Vestnik UGTU–UPI. Aktual'nye problemy fizicheskoi khimii tverdogo tela* (Gerald of the Ural State Technical Univ.–Ural Polytechnic Inst. Topical Problems of Physical Chemistry of Solids), Yekaterinburg: UGTU–UPI, 2005, p. 145.
5. Vol'khin, V.V., *Izv. Akad. Nauk SSSR, Neorg. Mater.*, 1979, vol. 15, no. 6, pp. 1086.
6. Kozlova, G.A., Vol'khin, V.V., and Zil'berman, M.V., *Khimiya i tekhnologiya neorganicheskikh sorbentov* (Chemistry and Technology of Inorganic Sorbents), Perm: Permskoe, 1979, pp. 95–97.
7. Bardov, A.I., Voroshilov, Yu.A., and Zemlina, N.P., *Radiokhimiya*, 1999, vol. 41, no. 5, pp. 451–455.
8. Ismailov, F.Kh., Glushankova, I.S., Kolesova, S.A., and Vol'khin, V.V., *Kompleksn. Ispol'z. Miner. Syr'ya* (Alma-Ata), 1991, no. 2, p. 80.
9. Sukhotin, A.M., Zotikov, V.S., Kazankina, A.F., et al., *Negoryuchie teplonositeli i gidravlicheskie zhidkosti* (Incombustible Heat Carriers and Hydraulic Liquids), Leningrad: Khimiya, 1979.

ISSN 1070-4272, Russian Journal of Applied Chemistry, 2008, Vol. 81, No. 7, pp. 1144–1146. © Pleiades Publishing, Ltd., 2008.
Original Russian Text © V.N. Viter, P.G. Nagornyi, 2008, published in Zhurnal Prikladnoi Khimii, 2008, Vol. 81, No. 7, pp. 1066–1068.

INORGANIC SYNTHESIS AND INDUSTRIAL INORGANIC CHEMISTRY

Synthesis of $(Ni_{1-x}Co_x)_2P$ ($0 \le x \le 0.65$) Substitution Solid Solution

V. N. Viter and P. G. Nagornyi

Shevchenko Kiev National University, Kiev, Ukraine

Received December 6, 2007

Abstract—The phosphides $(Ni_{1-x}Co_x)_2P$ ($0 \le x \le 0.65$) crystallizing in the hexagonal system, space group $P\bar{6}2m$, were synthesized in two steps starting from the continuous solid solution $(Ni_{1-x}Co_x)_3(PO_4)_2 \cdot 8H_2O$. The initial phosphates were first completely dehydrated at 800°C and then reduced with hydrogen at 900–1000°C for 1–2 h.

DOI: 10.1134/S1070427208070033

Nickel, cobalt, and iron phosphides and related compounds are of appreciable interest in many fields. In particular, they catalyze hydrogenolysis of C–S, C–N, and C–O bonds [1–5]. These processes are important for the removal of sulfur, nitrogen, and oxygen organic compounds from petroleum products. Coatings of nickel and cobalt phosphides exhibit good anticorrosive properties [6, 7]. In addition to individual phosphides, solid solutions on their basis are also known. In particular, $(Ni_{1-x}M_x)_2P$ (M = Co, Fe, Mn, Cr) phases were studied by neutron diffraction [8].

Nickel phosphides and related compounds can be synthesized by various methods, e.g., by direct reaction of the elements, action of phosphine on metals and oxides, and reaction of hypophosphite solutions with nickel or cobalt salts. Phosphides of some metals can also be prepared by reduction of the corresponding phosphates with hydrogen [9, 10]. In the case of the Ni_2P synthesis, the latter method is preferable. Its advantages become still more pronounced if it is necessary to obtain not pure Ni_2P, but analogous phosphides with two or more cations. In this case, it is appropriate to use phosphates containing simultaneously nickel and the corresponding metal as starting substances. For example, hydrated cobalt and nickel phosphates form with each other continuous substitution solid solutions $Ni_{1-x}Co_x(H_2PO_4)_2 \cdot 2H_2O$ (monoclinic system, space group $P2_1/n$), $Ni_{1-x}Co_xHPO_4 \cdot 1.5H_2O$ (rhombic system, space group $Pbca$), and $(Ni_{1-x} \cdot Co_x)_3(PO_4)_2 \cdot 8H_2O$ (monoclinic system, space group $P2/m$), where $0 \le x \le 1.00$ [11]. The parameters and volumes of the unit cells of these solid solutions decrease as the degree of nickel substitution for cobalt increases. In the case of $(Ni_{1-x}Co_x)_3(PO_4)_2 \cdot 8H_2O$ ($0 \le x \le 1.00$), a linear dependence is observed. The IR spectra within the limits of each of these solid solutions are very similar [11]. Taking into account the P/(Ni + Co) molar ratio in the above phosphates, it is the most appropriate to prepare the phosphides $(Ni_{1-x}Co_x)_2P$ starting from the solid solution $(Ni_{1-x}Co_x)_3(PO_4)_2 \cdot 8H_2O$ ($0 \le x \le 1.00$).

Here we report on the synthesis of cobalt–nickel phosphides $(Ni_{1-x}Co_x)_2P$ from $(Ni_{1-x}Co_x)_3(PO_4)_2 \cdot 8H_2O$ ($0 \le x \le 1.00$) by its dehydration followed by reduction with hydrogen.

EXPERIMENTAL

The starting phosphates $(Ni_{1-x}Co_x)_3(PO_4)_2 \cdot 8H_2O$ ($0 \le x \le 1.00$) were synthesized by the reaction between $CoSO_4$ and $NiSO_4$ solutions (total concentration in reaction mixture 0.1 M) and a Na_2HPO_4 solution. The P/(Ni + Co) molar ratio in the starting reactants was 0.67, and the Co/(Ni + Co) molar ratio was varied from 0 to 1.00. The reaction time was 1–5 days, and temperature, 90°C [11]. The resulting products were filtered off, washed with water, and dried. Their composition (Table 1) was determined by standard methods of chemical analysis. Then the phosphates were heated in air at 800°C up to complete dehydration. The dehydrated products were used for preparing the phosphides.

The reduction of phosphates in hydrogen was carried out in quartz boats at 900–1000°C for 1–2 h. The chemical composition of the synthesized phosphides was calculated on the basis of the composition of phosphates and the weight loss of samples during their reduction with hydrogen. Preliminarily X-ray phase and IR spectroscopic examination showed that the synthesized samples were free of

Table 1. Characteristics of the solid solution $(Ni_{1-x}Co_x)_3(PO_4)_2 \cdot 8H_2O$ $(0 \le x \le 1.00)$

Composition of phosphates, wt %				Molar ratio		Formula
P	Ni	Co	H_2O	P/(Ni + Co)	H_2O/P	
12.13	34.02	–	28.82	0.68	4.08	$Ni_3(PO_4)_2 \cdot 8H_2O$
12.18	30.60	3.45	28.80	0.68	4.06	$(Ni_{0.90}Co_{0.10})_3(PO_4)_2 \cdot 8H_2O$
12.22	26.04	8.00	28.73	0.68	4.04	$(Ni_{0.77}Co_{0.23})_3(PO_4)_2 \cdot 8H_2O$
12.20	21.06	12.89	28.69	0.68	4.04	$(Ni_{0.62}Co_{0.38})_3(PO_4)_2 \cdot 8H_2O$
12.19	15.32	18.91	28.60	0.68	4.03	$(Ni_{0.45}Co_{0.55})_3(PO_4)_2 \cdot 8H_2O$
12.20	11.89	22.23	28.50	0.68	4.02	$(Ni_{0.35}Co_{0.65})_3(PO_4)_2 \cdot 8H_2O$
12.22	5.05	29.40	28.34	0.67	3.99	$(Ni_{0.15}Co_{0.85})_3(PO_4)_2 \cdot 8H_2O$
12.14	–	34.40	28.30	0.67	4.01	$Co_3(PO_4)_2 \cdot 8H_2O$

Table 2. Chemical and phase composition of the phosphides $(Ni_{1-x}Co_x)_2P$ $(0 \le x \le 0.65)$

Initial phosphates, mole fraction		Synthesized phosphide				
		composition, wt %			P/(Ni + Co) molar ratio	formula
Ni	Co	Ni	Co	P		
1.00	0	79.14	–	20.85	0.50	Ni_2P
0.90	0.10	70.68	7.98	21.35	0.51	$(Ni_{0.90}Co_{0.10})_2P$
0.77	0.23	60.17	18.48	21.36	0.52	$(Ni_{0.77}Co_{0.23})_2P$
0.62	0.38	48.67	29.80	21.54	0.52	$(Ni_{0.62}Co_{0.38})_2P$
0.45	0.55	35,12	43.34	21.54	0.52	$(Ni_{0.45}Co_{0.55})_2P$
0.35	0.65	27.20	50.84	21.96	0.53	$(Ni_{0.35}Co_{0.65})_2P$
0.15	0.85	11.39	66.30	22.31	0.55	Mechanical mixture
0	1.00	–	74.61	25.38	0.65	"

oxygen-containing compounds (phosphates and oxides). Hence, the weight loss during the reduction of anhydrous cobalt and nickel phosphates is caused by the removal of the whole amount of oxygen and a part of phosphorus:

$$M_3(PO_4)_2 + H_2 \rightarrow M_yP_z + P_4 + H_2O$$

(M = Ni, Co).

The X-ray phase analysis was carried out with a DRON 4-07 diffractometer (CoK_α radiation, scanning step 0.01°). The IR spectra were taken in KBr pellets on a Thermo Nicolet Nexus 670 spectrophotometer in the wavenumber range 400–4000 cm^{-1}.

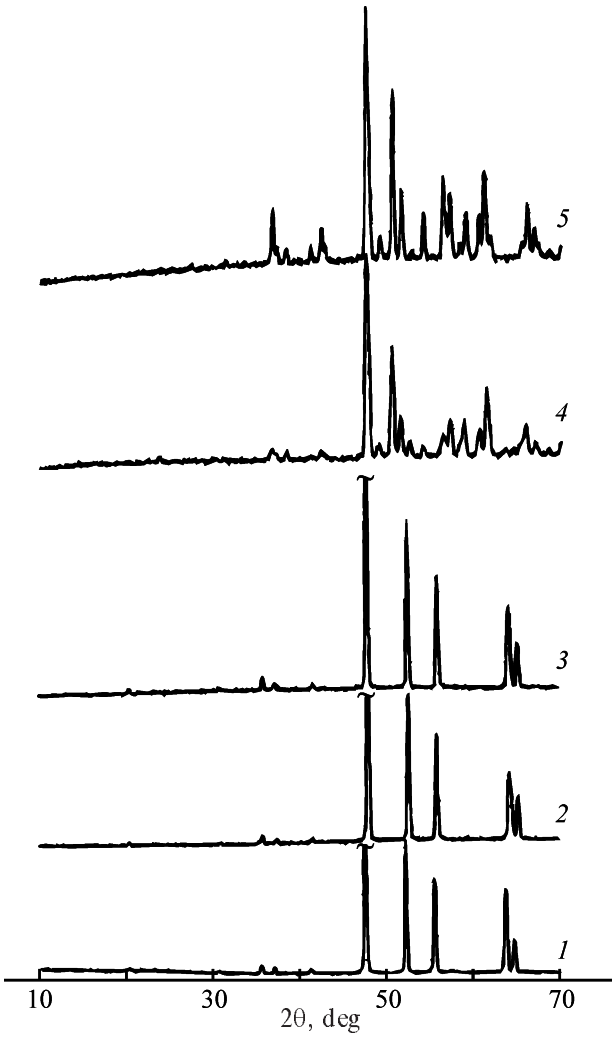
The reduction of phosphates with hydrogen yielded grey products, with appreciable weight loss. In most cases, after calcination for 1 h in a hydrogen flow, practically no further weight loss was observed with the exception of pure cobalt phosphate.

The chemical composition of the synthesized samples is given in Table 2, which shows that the P/(Ni + Co) molar ratio for phosphides with the Co/(Ni + Co) molar ratio from 0 to 0.85 is close to 0.50. This value is stoichiometric for the compounds M_2P (M = Ni, Co). In the case when pure cobalt phosphate [Co/(Ni + Co) = 1.00] was used as the starting compound, the P/Co ratio was 0.65. Thus, according to the chemical analysis, the product synthesized at Co/(Ni + Co) = 1.00 is a phase with the composition different from M_2P (or a mechanical mixture of different phases).

The X-ray phase analysis showed that the phosphides with the cobalt content Co/(Ni + Co)

Table 3. Unit cell parameters and volume of $(Ni_{1-x} \cdot Co_x)_2P$ $(0 \le x \le 0.65)$

Formula	*a*	*c*	*V*, Å^3
	Å		
Ni_2P	5.869	3.392	100.5
$(Ni_{0.90}Co_{0.10})_2P$	5.864	3.354	99.2
$(Ni_{0.77}Co_{0.23})_2P$	5.866	3.346	99.0
$(Ni_{0.45}Co_{0.55})_2P$	5.831	3.363	98.3
$(Ni_{0.35}Co_{0.65})_2P$	5.824	3.371	98.3



X-ray diffraction patterns of phosphides synthesized at various Co/(Ni + Co) ratios. (2θ) Bragg angle. Co/(Ni + Co) molar ratio: (*1*) 0, (*2*) 0.55, (*3*) 0.65, (*4*) 0.85, and (*5*) 1.00.

from 0 to 0.65 have similar X-ray diffraction patterns (see figure) and consist of one crystalline phase. The X-ray data for pure Ni_2P agree well with the data of [12]. The unit cell parameters of these phosphides are also close to each other (Table 3). Absorption bands characteristic of $Ni_3(PO_4)_2$ and $Co_3(PO_4)_2$ are absent from the IR spectra of all the synthesized samples. The above data unambiguously point to the formation of the substitution solid solution $(Ni_{1-x}Co_x)_2P$ ($0 \le x \le 0.65$), hexagonal system, space group $P\bar{6}2m$. The X-ray diffraction patterns of phosphides with the molar ratios Co/(Ni + Co) = 0.85 and 1.00 (see figure, curves *4* and *5*) differ essentially from those for the phosphides of the previous group. Some of reflections in these X-ray patterns cannot belong to a phase isostructural with Ni_2P. This fact suggests the formation of a phase (or several phases) of another type. The phosphide Co_2P, unlike Ni_2P, crystallizes in the rhombic system [13]. However, neither the composition nor the X-ray pattern of the sample synthesized at Co/(Ni + Co) = 1.00 coincide with those for Co_2P. It was noted previously that the reflections of the initial phosphates are absent from the X-ray patterns of the synthesized phosphides. The absorption bands of the initial $Co_3(PO_4)_2$ are also absent from the IR spectrum of this sample. Apparently, the sample is a mixture of cobalt phosphides (most likely, Co_2P and CoP).

CONCLUSIONS

(1) The limited solid solution $(Ni_{1-x}Co_x)_2P$ ($0 \le x \le 0.65$) was prepared by dehydration and subsequent reduction with hydrogen of the phosphates $(Ni_{1-x}Co_x)_3(PO_4)_2 \cdot 8H_2O$ ($0 \le x \le 1.00$).

(2) The phosphides synthesized at the molar ratios Co/(Ni + Co) = 0.85 and 1.00 contain other crystalline phases. In particular, the reduction of individual normal cobalt phosphate with hydrogen under the examined conditions yields not the individual phosphide, but a mechanical mixture of phosphides, most probably Co_2P and CoP.

REFERENCES

1. Abu, I.I., and Smith, K.J., *Appl. Catal. A: General*, 2007, vol. 328, no. 1, pp. 58–67.
2. Song, L., Li, W., Wang G., et al., *Catal. Today*, 2007, vol. 125, nos. 3–4, pp. 137–142.
3. Nagai, M., Fukiage, T., and Kurata, Sh., *Catal. Today*, 2005, vol. 106, nos. 1–4, pp. 201–205.
4. Oyama, S.T., Wang, X., Lee, Y.-K., and Chun W.-J., *J. Catal.*, 2004, vol. 221, no. 2, pp. 263–273.
5. Lee, Y.-K., Shu, Y., and Oyama, S.T., *Appl. Catal. A: General*, 2007, vol. 322, pp. 191–204.
6. Lo, P.-H., Tsai, W.-T., Lee, J.-T., and Hung, M.-P., *Surf. Coat. Technol.*, 1994, vol. 67, nos. 1–2, pp. 27–34.
7. Vansovskaya, K.M., *Metallicheskie pokrytiya, nanesennye khimicheskim sposobom* (Electroless-Plated Metal Coatings), Leningrad: Mashinostroenie, 1985.
8. Senateur, J.P., Rouault, A., L'Heritier, P., et al., *Mater. Res. Bull.*, 1973, vol. 8, no. 2, pp. 229–238.
9. Samsonov, G.V. and Vereikina, L.L., *Fosfidy* (Phosphides), Kiev: Akad. Nauk Ukr. SSR, 1961.
10. Gopalakrishnan, J., Pandey, S., and Rangan, K.K., *Chem. Mater.*, 1997, vol. 9, no. 10, pp. 2113–2116.
11. Nagornyi, P.G. and Viter, V.N., *Ukr. Khim. Zh.*, 2003, vol. 69, no. 4, pp. 95–98.
12. JCPDS: Powder Diffraction File 74-1385.
13. JCPDS: Powder Diffraction Files 74-0287, 32-0306.

ISSN 1070-4272, Russian Journal of Applied Chemistry, 2008, Vol. 81, No. 7, pp. 1147–1152. © Pleiades Publishing, Ltd., 2008.
Original Russian Text © A.L. Zharnyl'skaya, V.V. Vol'khin, M.G. Shcherban', H. Reuter, 2008, published in Zhurnal Prikladnoi Khimii, 2008, Vol. 81, No. 7, pp. 1069–1074.

INORGANIC SYNTHESIS AND INDUSTRIAL INORGANIC CHEMISTRY

Synthesis of a Precursor for an Alumina Ceramic Reinforced by Zirconium Dioxide from Inorganic Compounds in the Presence of Urea

A. L. Zharnyl'skaya, V. V. Vol'khin, M. G. Shcherban', and H. Reuter

Perm State Technical University, Perm, Russia
Perm State University, Perm, Russia
Forschungzentrum-Rossendorf, Dresden, Germany

Received August 27, 2007

Abstract—Samples of a precursor for an alumina ceramic reinforced by zirconium dioxide were synthesized. The samples have a uniform structure and are characterized by high ratios of the tetragonal and monoclinic modifications of ZrO_2, *t/m*, after a thermal treatment (1250°C). The structure of samples in the system Al_2O_3–ZrO_2 is formed under conditions favorable for deposition of products of hydrolysis of Al(III) ions on the surface of ZrO_2 sol particles in decomposition of urea. The coating of ZrO_2 sol particles by products of hydrolysis of Al(III) salts was confirmed by electrophoresis. The size distribution of particles of the individual ZrO_2 sol was determined by small-angle X-ray scattering. The structure of the products formed in thermal treatment of samples of mixed oxides Al_2O_3–ZrO_2 was characterized by X-ray phase analysis and scanning electron microscopy. The porosity and specific surface area of a thermally treated sample was determined by measuring nitrogen absorption isotherms.

DOI: 10.1134/S1070427208070045

The oxide system Al_2O_3–ZrO_2 is a basis for fabrication of a number of structural materials with enhanced strength and cracking resistance and, in particular, for the ZTA ceramic (alumina ceramic reinforced by zirconium dioxide). The microscopic structure of this ceramic material corresponds to that of dispersion-reinforced composites: reinforcing particles of the ZrO_2 phase (5–45%) are uniformly dispersed in the finely grained Al_2O_3 matrix [1–3]. The unique mechanical properties of the ZTA ceramic, predetermined by the phase transition t-$ZrO_2 \rightarrow m$-ZrO_2, are due to the action of a number of mechanisms of reinforcement, in particular, transformation mechanism, deviation (branching) of cracks, and modular load transfer [1, 2]. To improve the mechanical characteristics of this material, it is necessary that zirconium dioxide particles should be preserved in the form of a metastable tetragonal modification [2].

The t-ZrO_2 phase can also be stabilized by introducing modifying additives, e.g., Y_2O_3 and CeO_2 [1, 4–6], into the system of the starting components and by homogeneous mixing of highly dispersed Al_2O_3 and ZrO_2 nanocrystalline powders with a narrow particle size distribution [2]. It is known that the structure of composite materials can be controlled already in the stage of synthesis of their precursors [7]. A search for efficient technologies for obtaining a precursor for the ZTA ceramic as a basis for a ceramic material with prescribed structure and dispersity is an important task to be carried out by modern studies in the field of structural materials.

In this study, we examined the possibility of synthesis of samples in the system Al_2O_3–ZrO_2 with a t-ZrO_2 phase, stabilized by uniform distribution of zirconium dioxide in a finely dispersed α-Al_2O_3 matrix, by deposition of products formed in hydrolysis of aluminum sulfate [8] on the surface of ZrO_2 sol particles from solution, followed by drying and thermal treatment of the Al_2O_3–ZrO_2 samples synthesized at 1250°C.

EXPERIMENTAL

Al_2O_3–ZrO_2 samples were synthesized from aluminum sulfate $Al_2(SO_4)_3 \cdot 18H_2O$ of chemically pure grade and a ZrO_2 sol with a ripening time τ_{rip} of 7 days. Aluminum sulfate $Al_2(SO_4)_3 \cdot 18H_2O$ was chosen as the starting reagent in accordance with the recommendations made in [8].

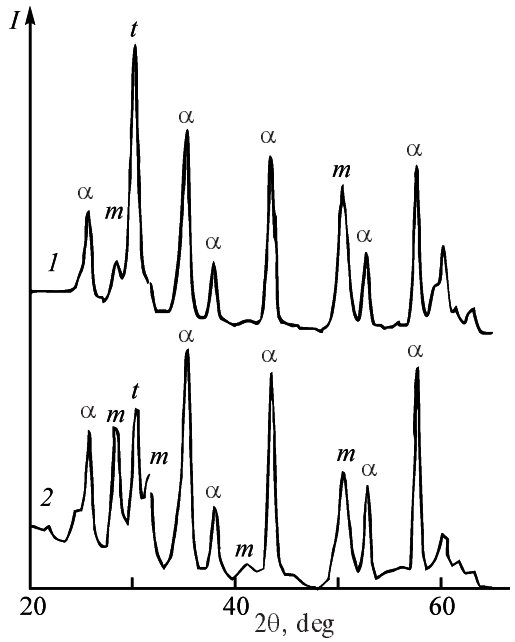


Fig. 1. X-ray diffraction pattern of Al_2O_3–ZrO_2 samples synthesized by mixing the starting components (*1*) with and (*2*) without urea. (*I*) Intensity and (2θ) Bragg angle. (α) α-Al_2O_3, (*t*) *t*-ZrO_2, and (*m*) *m*-ZrO_2.

The concentration of $Al_2(SO_4)_3 \cdot 18H_2O$ in the aqueous solution (in terms of Al_2O_3) and the ZrO_2 concentration in the liquid phase of the sol were 2.5 wt %.

The ZrO_2 and γ-AlOOH sols were synthesized by precipitation–peptization from products formed in hydrolysis of $ZrOCl_2 \cdot 8H_2O$ and $AlCl_3 \cdot 6H_2O$, respectively. Nitric acid solutions served as a peptizing agent. The molar ratios NO_3^-/Zr(IV) and NO_3^-/Al(III) were strictly fixed at 1.00 for the ZrO_2 sol and 0.33 for the boehmite sol. The concentration of the γ-AlOOH sol was also 2.5 wt % in terms of Al_2O_3.

A mixture of an aluminum sulfate solution and the ZrO_2 sol was thermostated on a water bath at 90°C for 2 h in the presence of urea $CO(NH_2)_2$ added to the solution of the starting components in a twofold excess with respect to the amount necessary for products of aluminum hydrolysis to be formed [8].

A sample was obtained in the system Al_2O_3–ZrO_2 under similar temperature conditions by mixing an aluminum sulfate solution with a zirconium dioxide sol without addition of urea. The masses of the starting components were chosen in such a way that thermally treated samples contained 75% Al_2O_3 and 25% ZrO_2. This ratio was taken in accordance with the recommendations [2].

The samples obtained were dehydrated by evaporation, dried in an SNOL-1,6.2.5.1/9-IZ chamber furnace at 105±5°C for 48 h, and calcined in a VTP low-inertia furnace at 1250°C for 2 h. The rate at which the temperature was raised to a prescribed value was 10 deg min^{-1}.

The electrophoretic behavior of mixed samples of AlOH–ZrO_2 sols, products formed in hydrolysis of aluminum sulfate in the presence of a ZrO_2 sol, and individual ZrO_2 and γ-AlOOH sols was studied by the macroelectrophoresis method with a Ken device.

An X-ray phase analysis was made on a DRON-2 diffractometer (CuK_α radiation, quartz monochromator in the primary beam path) at a counter rotation rate of 2 deg min^{-1}. The ratio between the *t*- and *m*-ZrO_2 phases in thermally treated samples was found from the ratio between the intensities of the reflections from (111) planes for *t*-ZrO_2 and (111) and ($11\bar{1}$) planes for *m*-ZrO_2 [9]. The dispersity of α-Al_2O_3 was evaluated indirectly by the half-width-to-height ratio of the peak at d = 3.48 Å [10].

The particle size distribution of ZrO_2 sols synthesized with different ripening times was analyzed by small-angle X-ray scattering.[1] A 200-μm-wide beam of CuK_α X-ray radiation was collimated by the Kratky scheme. The scattered X-ray radiation was recorded with a multiple-position detector, accumulated as a number of pulses, and processed with a computer by special software. The processed results are presented numerically and graphically in the coordinate system particle radius–volume fraction of particles.

The microscopic structure of thermally treated Al_2O_3–ZrO_2 samples was examined with a DSM 962 Leo Zeiss electron microscope (accelerating voltage 20 kV, magnification up to 20000). The grain size was evaluated using a special software of the instrument.

The porosity and specific surface area of a thermally treated Al_2O_3–ZrO_2 sample synthesized with addition of urea was found by measuring nitrogen adsorption isotherms at –176°C on a Carlo Erba Sorbtomatik 1800 installation.

The results of the X-ray phase analysis of Al_2O_3–ZrO_2 samples synthesized by mixing the starting components with and without urea $CO(NH_2)_2$ are presented in Fig. 1 in the form of X-ray diffraction patterns. Quantitative data characterizing the uni-

[1] Institute of Crystallography, Russian Academy of Sciences, Moscow.

Table 1. Starting components for synthesis of samples of the precursor for the ZTA ceramic and the phase composition of products formed by thermal treatment at 1250°C

Sample	Starting mixture	pH of mixtures		Intensity ratio of ZrO_2 phases, t/m	$b_{1/2}/h$ ratio for the line with d = 3.84 Å for α-Al_2O_3
		pH_{in}	pH, $\Delta\tau$ = 2 h		
S7	ZrO_2; $Al_2(SO_4)_3 \cdot 18H_2O$; $CO(NH_2)_2$	2.7	2.8	3.61	0.1490
S7*	ZrO_2; $Al_2(SO_4)_3 \cdot 18H_2O$	2.6	2.1	0.85	0.0810

formity of component distribution for synthesized and thermally treated Al_2O_3–ZrO_2 samples are listed in Table 1.

In the course of calcination, both the components in samples with mixed oxides undergo polymorphic transformation. It follows from the results of X-ray phase analysis that all of the samples obtained contain Al_2O_3 in the high-temperature α-form and zirconium dioxide in the tetragonal and monoclinic modifications. No chemical interaction is observed between the oxides. A criterion of uniformity of the component distribution in the Al_2O_3–ZrO_2 system is the intensity ratio between the tetragonal and monoclinic modifications of ZrO_2, t/m. The higher this ratio, the larger fraction of ZrO_2 particles uniformly distributed in the alumina matrix retain their tetragonal structure, and their size is smaller than the critical value of 0.45 μm [11]. A necessary requirement for ZrO_2 to remain in the tetragonal modification in thermally treated samples in the Al_2O_3–ZrO_2 system is that the alumina matrix should be formed from α-Al_2O_3 particles in the finely dispersed state, which is characterized by increased values of $b_{1/2}/h$ of the line with d = 3.84 Å of the α-Al_2O_3 phase.

According to the results of X-ray phase analysis of calcined Al_2O_3–ZrO_2 samples (Table 1, Fig. 1), the tetragonal phase of ZrO_2 is stabilized and α-Al_2O_3 particles are preserved in the finely dispersed state in the sample synthesized with addition of urea.

In thermal treatment of samples of mixed oxides in the Al_2O_3–ZrO_2 system, structures with different degrees of uniformity are formed, depending on the conditions in which the "aqueous" stage of synthesis occurs. To improve the structural uniformity of the synthesized samples of the precursor for the ZTA ceramic, it is necessary to restrict the size of primary particles being formed and provide the most homogeneous mixing of the components and thereby make lower the probability of recrystallization of the t-ZrO_2 phase in thermal treatment.

To hinder the phase transition t-$ZrO_2 \rightarrow m$-ZrO_2 and preserve ZrO_2 particles in the tetragonal modification in the calcined Al_2O_3–ZrO_2 material, certain requirements are imposed upon the ZrO_2 sol. A study of the electrophoretic mobility of ZrO_2 sol particles by macroelectrophoresis revealed a certain increase in positive values of the ζ-potential and a shift of the isoelectric point (IEP) to higher pH values, dependent of the sol ripening time. An indication of the aggregative stability of ZrO_2 sols with different ripening times and of the stability of the surface charge of their particles are high values of the potential ψ (~100 mV), which vary only slightly in the pH range 1.25–4. The aggregative stability of ZrO_2 sols was attributed in [12] to existence of developed boundary layers of water at the particle surface.

An analysis by small-angle X-ray scattering of the particle size distribution of the ZrO_2 sols synthesized demonstrated that the average size of ZrO_2 sol particles is 25 nm at a ripening time of 7 days.

The significant difference of the pH values used in synthesis of precursors for ZrO_2 sols from the pH of the isoelectric point and the high stability of the given colloid system are an important condition for precluding coarsening of ZrO_2 sol particles in the stage of formation of the initial structure of mixtures in the Al_2O_3–ZrO_2 system.

The hydrolysis of urea $CO(NH_2)_2$ added to the mixture of the starting components (sample S7) occurs in solution at 85–100°C and is described by the equations

$$2CO(NH_2)_2 + 5H_2O = 2NH_3 + (NH_4)_2CO_3 + CO_2,$$

$$NH_3 + H_2O = NH_4^+ + OH^-.$$

A specific feature of this process is that the precipitating agent is not poured into a solution containing ions being precipitated, but is gradually released in decomposition of urea $CO(NH_2)_2$

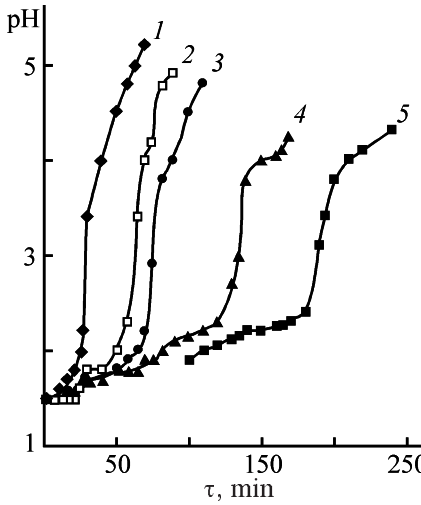


Fig. 2. Kinetic curves of joint hydrolysis of 1 M $CO(NH_2)_2$ and 0.1 M $AlCl_3$. (τ) Time. Process temperature, °C: (*1*) 98, (*2*) 95, (*3*) 90, (*4*) 85, and (*5*) 80.

because of the occurrence of its hydrolysis uniformly throughout the solution volume [13]. This favors an increase in the uniformity and a finer dispersion of the forming nuclei of the phase being precipitated in the subsequent thermal treatment of samples of mixed Al_2O_3–ZrO_2 oxides.

The hydrolysis of Al(III) salts occurs to give a number of hydrolyzed species [12, 14], of which the most typical are the following:

$$Al^{3+} \rightleftarrows Al(OH)^{2+} \rightleftarrows [Al_2(OH)_2]^{4+} \rightleftarrows [Al_7(OH)_{16}]^{5+} \rightleftarrows Al(OH)_3.$$

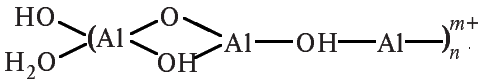
The positive charge per aluminum atom decreases in the order of the successively formed hydrolysis products.

At Al(III) concentrations in salt solutions exceeding 0.1 M, hydroxo complexes are formed at pH < 4.0 and $Al(OH)_3$ precipitates as pH values increase further [14], which is confirmed, e.g., by a description of the joint hydrolysis of a solution of $AlCl_3$ and $CO(NH_2)_2$ by kinetic curves (Fig. 2) [8].

Table 2. pH values at the isoelectric points for an Al_2O_3–ZrO_2 sample synthesized in the presence of urea and mixed and individual sols of γ-AlOOH and ZrO_2

Sample	pH at IEP
S7	8.8
γ-AlOOH freshly prepared	8.2
γ-AlOOH (τ_{life} = 15 days)	9.0
ZrO_2	6.5

Hydrolysis of Al(III) salts yields oligomeric and polymeric charged polynuclear hydroxo complexes with various structures. Their composition is described by the general formula



Aluminum is an element exhibiting a pronounced tendency to form bridging bonds –O– and –OH–, which, presumably, enables aluminum to enter into a covalent interaction with surface OH groups of particles of the zirconium dioxide sol [15].

The formation of Al(III) hydrolysis products on the surface of ZrO_2 sol particles in the aqueous stage of precursor synthesis in the presence of urea can be confirmed by studying the electrophoretic behavior of the mixed sample S7.

For comparison, the IEPs were determined for boehmite γ-AlOOH sols with various lifetimes and an individual ZrO_2 sol with a ripening time of 7 days. The experimental results obtained are listed in Table 2. The γ-AlOOH sol shows a sligt shift of the IEP to higher pH values in the course of time. The IEP of sample S7 fall within the range of the IEPs of individual γ-AlOOH sols. For all of the samples studied, positive values of the ζ-potential of the particle surface were observed at low pH values of the liquid phase.

The coincidence of the electrokinetic data for the individual γ-AlOOH boehmite sol and for sample S7 confirms that, when aluminum sulfate is hydrolyzed in the presence of urea at temperatures above 90°C, the forming Al(III) hydroxo complexes are deposited onto the surface of ZrO_2 sol particles and completely cover this surface. This occurs because OH^- ions formed in hydrolysis of urea favor (in the absence of local supersaturations with OH^- groups in solution) hydrolysis of Al(III) ions and formation of bridging bonds –O– and –OH– involving hydroxy groups localized on the surface of ZrO_2 sol particles.

Thus, a heterophase finely dispersed mixture of nanosized particles in the system Al_2O_3–ZrO_2 is synthesized, with urea $CO(NH_2)_2$ serving as a precipitating agent, via coating of ZrO_2 sol particles with products of Al(III) hydrolysis, which hinders growth of ZrO_2 particles in the aqueous stage of synthesis of precursor samples and decreases the

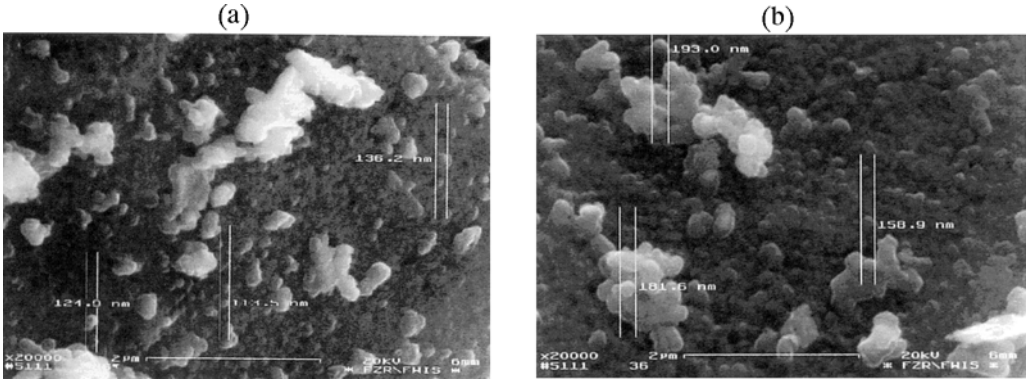


Fig. 3. SEM micrographs of surface fragments of (a) S7 and (b) S7* samples.

probability of the t-$ZrO_2 \rightarrow m$-ZrO_2 phase transition in thermal treatment of the material because of the isolation of ZrO_2 particles from each other by particles of the alumina phase.

The efficiency of using urea for synthesis of samples of a precursor for the ZTA ceramic in order to form their highly uniform finely grained structure is also confirmed by a study of the microscopic structure of thermally treated Al_2O_3–ZrO_2 samples by scanning electron microscopy (SEM). Figures 3a and 3b show micrographs of surface fragments of S7 and S7* samples, respectively. Comparison of the micrographs shows that the samples have similar structure. However, the micrograph of a surface fragment of sample S7 synthesized with addition of urea clearly shows fine individual uniformly distributed grains and medium-size regions of their agglomeration. The surface fragment of sample S7* shows larger agglomerates and coarser individual grains (their sizes are indicated in the micrograph). These facts show that the structural uniformity of S7* material synthesized without urea is considerably lower. It follows from the micrographs of the Al_2O_3–ZrO_2 samples that the average size of individual grains is 126 nm for sample S7 and 179 nm for sample S7*. Consequently, particles of the α-Al_2O_3 phase formed by thermal treatment of sample S7 stabilize the size of zirconium dioxide grains and make lower the probability of the t-$ZrO_2 \rightarrow m$-ZrO_2 phase transition.

The thermally treated Al_2O_3–ZrO_2 sample synthesized with urea (S7) has low specific surface area (S_{BET} = 4.4 $m^2\,g^{-1}$) and pore volume (W_s = 0.03 $cm^2\,g^{-1}$). Small pores (micropores) comparable in size with adsorbate molecules are not found in the sample.

CONCLUSIONS

(1) The efficiency of using urea $CO(NH_2)_2$ for hydrolysis of Al(III) on heating a solution containing aluminum sulfate and ZrO_2 sol for synthesis of Al_2O_3–ZrO_2 samples as a precursor for the ZTA ceramic was demonstrated.

(2) A study of the electrokinetic behavior of individual ZrO_2 and γ-AlOOH sols and samples of a precursor for the ZTA ceramic, obtained with the use of urea, demonstrated that, in hydrolysis of aluminum sulfate under the conditions of urea decomposition at $T \geq 90$°C, the forming products of Al(III) hydrolysis are deposited onto the surface of ZrO_2 sol particles and completely cover this surface.

(3) The results of an X-ray phase analysis and scanning electron microscopy of samples of mixed oxides Al_2O_3–ZrO_2 synthesized using urea confirm that the coating of the surface of ZrO_2 sol particles by products formed by hydrolysis of aluminum sulfate is a factor that effectively prevents coarsening of ZrO_2 particles distributed in the alumina matrix and hinders the t-$ZrO_2 \rightarrow m$-ZrO_2 phase transition in thermal treatment of Al_2O_3–ZrO_2 samples.

REFERENCES

1. Shevchenko, A.V., Ruban, A.K., and Dudnik, E.V., *Ogneupory Tekh. Keram.*, 2000, no. 9, pp. 2–8.
2. Messing, G.L. and Kumagai, M., *J. Am. Ceram. Soc.*, 1989, vol. 72, no. 1, pp. 40–44.
3. Podzorova, L.I., Il'icheva, A.A., Mikhailina, N.A., et al., *Neorg. Mater.*, 2002, vol. 38, no. 12, pp. 1455–1461.
4. Huang, X.W., Wang, S.W., and Huang, X.X., *Ceram. Int.*, 2003, vol. 29, no. 7, pp. 765–769.
5. Mangalaraja, R.V., Chandrasekhar, B.K., and

Manohar, P., *Mater. Sci. Eng. A*, 2003, vol. 343, nos. 1–2, pp. 71–75.

6. Podzorova, L.I., Il'icheva, A.A., and Pen'kova, O.I., *Ogneupory Tekh. Keram.*, 2005, no. 11, pp. 2–5.
7. Tret'yakov, Yu.D., *Usp. Khim.*, 2004, vol. 73, no. 9, pp. 899–916.
8. Kudryavtsev, P.G. and Kropacheva, M.V., *Trudy Mezhdunarodnoi nauchnoi konferentsii "Perspektivy razvitiya estestvennykh nauk v vysshei shkole"* (Proc. Int. Scientific Conf. "Prospects for Development of Natural Sciences at The Higher School"), Perm, September 18–21, 2001, vol. 2, pp. 169–174.
9. Garvie, R.S. and Nicholson, P.S., *J. Am. Ceram. Soc.*, 1972, vol. 55, no. 6, pp. 303–305.
10. *Rentgenografiya: Spetspraktikum* (X-ray Diffraction Analysis: Special Practical Course), Katsnel'son, A.A., Ed., Moscow: Mosk. Gos. Univ., 1986.
11. Srdic, V.V. and Radonjic, L., *J. Am. Ceram. Soc.*, 1997, vol. 80, no. 8, pp. 2056–2060.
12. James, I., Dony, A., and Massiot, D., *J. Am. Ceram. Soc.*, 1995, vol. 78, no. 10, pp. 2648–2654.
13. Vasserman, I.M., *Khimicheskoe osazhdenie iz rastvorov* (Chemical Precipitation from Solutions), Leningrad: Khimiya, 1980.
14. Stumm, W. and Morgan, J.J., *Aquatic Chemistry*, New York: Wiley, 1996.
15. Golikova, E.V., Burdina, N.M., and Vysokovskaya, N.A., *Kolloidn. Zh.*, 2002, vol. 64, no. 2, pp. 155–162.

ISSN 1070-4272, Russian Journal of Applied Chemistry, 2008, Vol. 81, No. 7, pp. 1153–1159. © Pleiades Publishing, Ltd., 2008.
Original Russian Text © L.B. Belykh, Yu.Yu. Titova, A.V. Rokhin, F.K. Shmidt, 2008, published in Zhurnal Prikladnoi Khimii, 2008, Vol. 81, No. 7, pp. 1075–1081.

PHYSICOCHEMICAL STUDIES OF SYSTEMS AND PROCESSES

Generation and Properties of Hydrogenation Catalysts Based on Palladium Bisacetylacetonate and Lithium Alkoxyhydroaluminates

L. B. Belykh, Yu. Yu. Titova, A. V. Rokhin, and F. K. Shmidt

Irkutsk State University, Irkutsk, Russia
Institute of Petrochemical and Coal-Chemical Synthesis, Irkutsk State University, Irkutsk, Russia

Received March 16, 2007

Abstract—Generation and properties of a catalytic system for hydrogenation, based on $Pd(acac)_2$ and $LiAlH_4$ and modified with *n*-BuOH and *t*-BuOH, were studied. The promoting and inhibiting effects of the alcohols were revealed, and their causes were discussed.

DOI: 10.1134/S1070427208070057

Palladium nanoclusters show catalytic activity in various transformations of unsaturated hydrocarbons, including hydrogenation [1]. One of the most widely used procedures for preparing metal nanoparticles is chemical condensation consisting in reduction of metal complexes in the presence of stabilizers [2]. Previously we studied how the properties of palladium hydrogenation catalysts depend on the reductant used ($AlEt_3$ [3], $LiAlH_4$ [4], NaH_2PO_2 [5], H_2 [6]) and found that the catalytic properties are influenced not only by the metal dispersity and nature of stabilizing ligands. Generation of catalytically active species is usually accompanied by a number of side reactions (degradation of phosphines taken as stabilizing ligands; catalytic decomposition of the reductant $LiAlH_4$, NaH_2PO_2, etc.), which can exert both promoting and inhibiting effect on the catalyst properties. In particular, for the system $Pd(acac)_2$–$LiAlH_4$ it was found that partial hydrolysis of lithium tetrahydroaluminate leads to a sharp (by a factor of 6) increase in the specific activity in hydrogenation of alkenes [4].

To develop efficient synthetic routes to high-performance palladium hydrogenation catalysts, in this study we examined the generation and properties of catalytic systems based on palladium bisacetylacetonate and lithium tetrahydroaluminate, modified with alcohols.

EXPERIMENTAL

Solvents (benzene, THF) and substrates were purified by standard procedures used in organometallic chemistry [7]. For more exhaustive drying, benzene was additionally distilled from $LiAlH_4$ on a distillation column and stored under argon in sealed ampules over 4A molecular sieves. Tetrahydrofuran after removal of peroxides was distilled successively from sodium, $LiAlH_4$, and benzophenone ketyl and was stored under argon in sealed ampules. The concentration of water, determined by Fischer titration [8], was 1.1×10^{-3} in benzene and 1.6×10^{-3} M in THF.

Palladium bisacetylacetonate was prepared according to [9]. ^{1}H NMR spectrum (δ, ppm, solvent C_6D_6): 5.04 (s, 1H, CH), 1.76 (s, 6H, CH_3). IR spectrum (ν, cm^{-1}, solvent benzene): ν(C=O) + ν(C=C) 1560, 1516; UV spectrum (solvent benzene): ε_{330} = 10630 l mol^{-1} cm^{-1}.

Commercial lithium tetrahydroaluminate $LiAlH_4$ was used without preliminary recrystallization. A weighed portion of $LiAlH_4$ was dissolved in THF, and the solution was filtered in an inert atmosphere through a glass frit. The $LiAlH_4$ concentration determined by the volume of hydrogen released in the course of hydrolysis was 95–98% of the theoretical value. ^{27}Al NMR spectrum (δ, ppm, solvent THF): 98 quintet ($^1J_{Al-H}$ 173 Hz).

Alcohols (*n*-butanol, *tert*-butanol) were refluxed over calcium oxide, distilled from it in an Ar atmosphere, and stored in sealed ampules under Ar.

The reactions of $LiAlH_4$ with alcohols at various component ratios were performed under dry deoxygenated argon in a temperature-controlled vessel whose design allows initial evacuation and filling with argon. The vessel connected to a volumetric system was charged with a solution of $LiAlH_4$ (2.7×10^{-3} M) in 5 ml of THF. The vessel was stoppered with a Teflon stopper, and a definite amount of an alcohol dissolved in THF (ROH : $LiAlH_4$ = 1, 2, 3) was introduced with a syringe under vigorous stirring with a magnetic stirrer. The amount of hydrogen released in the course of $LiAlH_4$ alcoholysis was determined volumetrically. The solution was transferred into a quartz ampule 5 mm in diameter, which had been preliminarily evacuated and filled with argon, and then was analyzed by ^{27}Al NMR spectroscopy. The NMR spectra were recorded on a Varian VXR-500S pulse spectrometer. The ^{27}Al chemical shifts were measured against an external reference, 0.1 M solution of $Al(NO_3)_3$. Solutions of $LiAlH_4$–ROH in THF for catalytic experiments were prepared similarly.

The reactions of palladium bisacetylacetonate with $LiAlH_4$ hydrolysis products were performed as follows. To a solution of $Pd(acac)_2$ (2.5×10^{-4} mol, 0.0761 g) in 8 ml of benzene, placed in a temperature-controlled vessel, we added dropwise with vigorous stirring under Ar a freshly prepared (as described above) solution of $LiAlH_4$–ROH in THF (ROH/$LiAlH_4$ = 1, 2, 3). The total volume of the solution was 10 ml. An aliquot of the resulting dark brown solution was transferred in an inert atmosphere into an all-sealed quartz cell and analyzed by UV spectroscopy. The palladium bisacetylacetonate concentration was calculated from the absorption band at 330 nm (ε_{330} = 10630 l mol^{-1} cm^{-1}); the concentration of acetylacetonate ligands bound to Al [$Al(acac)_3$, $Al(acac)_2$(*tert*-BuO)], from the band at 288 nm (ε_{288} = 14470 l mol^{-1} cm^{-1} per acetylacetonate group; for $Pd(acac)_2$, ε_{288} = 3090 l mol^{-1} cm^{-1}). The UV spectra were recorded on a Specord UV VIS spectrometer in the range 280–430 nm.

Catalytic hydrogenation was performed in a duck-shaped temperature-controlled glass vessel at 30°C and initial hydrogen pressure of 1 atm in the presence of the catalytic system generated in situ. A solution of $LiAlH_4$–ROH in THF was added dropwise in a hydrogen stream to a solution of 0.01522 g (5×10^{-5} mol) of $Pd(acac)_2$ in 8 ml of benzene, and the mixture was stirred for 5 min. The Red/Pd ratio was varied from 2 to 50. The total solution volume was 10 ml. To the resulting black-brown "solution," we added styrene. Its hydrogenation was performed with vigorous stirring at the initial hydrogen pressure of 1 atm. The reaction progress was monitored volumetrically and by GLC with a Chrom-5 chromatograph equipped with a packed column (3.6 m, Carbowax-20M stationary phase) and a flame ionization detector. The column temperature was 100°C, and the carrier gas was N_2.

It was shown previously that, for systems of the type $Pd(acac)_2$–Red (Red = $AlEt_3$, $LiAlH_4$), the dependence of the catalytic activity in hydrogenation of α-alkenes on the component ratio passes through a maximum [3, 4]. Studies of the formation and nature of hydrogenation-active palladium species in these reactions showed that an increase in the activity in the initial portion of the curve is due to an increase in the fraction of Pd(0) and a decrease in the size of palladium nanoparticles. The poisoning effect of excess reductant is different. Triethylaluminum acts not only as reductant, but also, when in excess, as stabilizer of palladium nanoparticles, forming surface compounds with intermediates of the catalytic cycle. Its effect as catalytic poison can be eliminated by adding alcohols which convert $AlEt_3$ into aluminum alkoxy derivatives [10]. With $LiAlH_4$, the catalytic poison is aluminum reacting with palladium to form a substitution solid solution [4]. Aluminum can arise in the reaction system $Pd(acac)_2$–$LiAlH_4$ from catalytic decomposition of alane formed by reaction of the components [4]:

$$Pd(acac)_2 + 2LiAlH_4 \rightarrow Pd(AlH_4)_2 + 2Li(acac), \quad (1)$$

$$Pd(AlH_4)_2 \rightarrow Pd + 2/n[AlH_3]_n + H_2, \quad (2)$$

$$[AlH_3]_n \xrightarrow{Pd} nAl + (3n/2)H_2. \quad (3)$$

It should be noted that, in contrast to palladium hydrogenation catalysts based on $Pd(acac)_2$ and $AlEt_3$ [3], the specific activity of the catalytic system $Pd(acac)_2$–$LiAlH_4$ is low because of the inhibiting effect of aluminum and does not exceed 30 ml of substrate per mole of Pd per minute (Fig. 1).

The above facts suggest that, to prepare high-performance palladium hydrogenation catalysts, it is appropriate to use as reductant not $LiAlH_4$ but its alkoxy derivatives. To check this hypothesis, we studied the generation and properties of catalytic

systems $Pd(acac)_2$–$LiAlH_4$–ROH (R = *n*-Bu or *tert*-Bu) in hydrogenation reactions.

The catalytic properties of the $Pd(acac)_2$–$LiAlH_4$–ROHs system in hydrogenation depend on both the Red/$Pd(acac)_2$ (Red = $LiAlH_4$–ROH) and ROH : $LiAlH_4$ molar ratios. In particular, the $Pd(acac)_2$–$LiAlH_4$–*n*-BuOH system exhibits catalytic activity in styrene hydrogenation at [*n*-BuOH]/[$LiAlH_4$] = 1 (Fig. 1). At *n*-BuOH/$LiAlH_4$ = 2 or 3, $Pd(acac)_2$ is not reduced, and the rate of styrene hydrogenation is zero. The dependence of the catalytic activity of the $Pd(acac)_2$–$LiAlH_4$–*n*-BuOH system ([*n*-BuOH] : [$LiAlH_4$] = 1) on the Red/$Pd(acac)_2$ ratio passes through a maximum (130 mol of substrate per mole of Pd per minute) at Red/Pd = 10. This activity exceeds by a factor of 4 the specific activity of the palladium catalyst prepared by reduction with lithium tetrahydroaluminate. Poisoning of the catalytic system $Pd(acac)_2$–$LiAlH_4$–*n*-BuOH ([*n*-BuOH] : [$LiAlH_4$] = 1) with excess reductant is observed at higher Red/Pd ratios compared to the $Pd(acac)_2$–$LiAlH_4$ system (Fig. 1).

With *tert*-BuOH used as modifier, the pattern somewhat changes. The catalytic system $Pd(acac)_2$–$LiAlH_4$–*tert*-BuOH ([*tert*-BuOH]/[$LiAlH_4$] = 1, 2, 3) exhibits activity in hydrogenation of styrene on adding *tert*-butyl alcohol to $LiAlH_4$ not only in 1 : 1, but also in 2 : 1 and 3 : 1 ratios (Fig. 2). The *tert*-BuOH : $LiAlH_4$ molar ratio affects the shape of the dependence of the catalytic activity on the Red/Pd ratio. At *tert*-BuOH/$LiAlH_4$ = 1, the inhibiting effect of the reductant is observed at its 50-fold excess. At *tert*-BuOH/$LiAlH_4$ ratios of 2 and 3, in the range of Red/Pd ratios from 2 to 50, no poisoning of the catalytic system $Pd(acac)_2$–$LiAlH_4$–*tert*-BuOH with excess reductant is observed.

It is well known that $LiAlH_4$ reacts with alcohols at room temperature to form lithium alkoxyalumohydrides, with the number of substituted hydride ions depending on the alcohol used [11–13]. In particular, di-, tri-, and tetraalkoxy derivatives $LiAlH_2(OR)_2$, $LiAlH(OR)_3$, and $LiAl(OR)_4$ can be readily prepared by the reaction with methanol [11]:

$$LiAlH_4 + (4 - m)ROH = LiAlH_m(OR)_{4-m} + (4 - m)H_2, \quad (4)$$

where m = 0–3.

Similar reaction occurs with *tert*-BuOH, but, because of steric hindrance, only three hydride ions are substituted with three *tert*-BuO groups. The fourth *tert*-BuO group can be introduced only upon prolonged refluxing of the solution of $LiAlH_4$ in THF [11, 12].

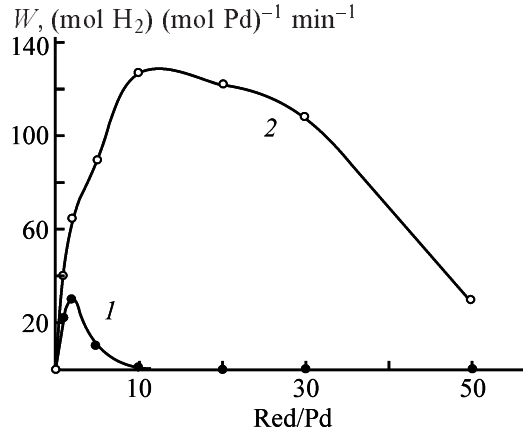


Fig. 1. Hydrogenation of styrene in the presence of the catalytic system $Pd(acac)_2$–Red. Red: (*1*) $LiAlH_4$ and (*2*) $LiAlH_4$–*n*-BuOH. c_{Pd} = 5 mM, [substrate]/$Pd(acac)_2$ ratio 170, solvent benzene, 30°C, P_{H_2} = 1 atm); the same for Fig. 2. (*W*) Catalytic activity; the same for Fig. 2.

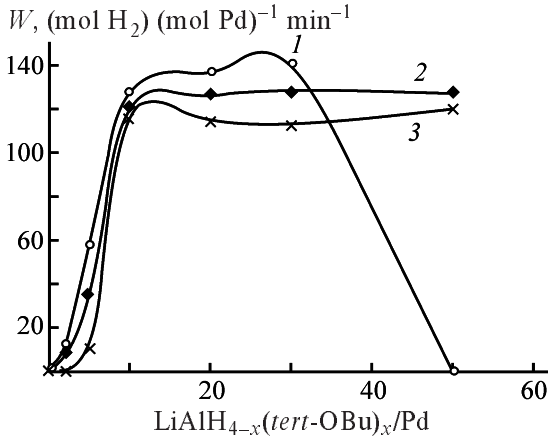


Fig. 2. Hydrogenation of styrene in the presence of the catalytic system $Pd(acac)_2$–$LiAlH_4$–*tert*-BuOH at *tert*-BuOH/$LiAlH_4$ ratios of (*1*) 1, (*2*) 2, and (*3*) 3.

With secondary alcohols, the major alcoholysis products are $LiAl(OR)_4$, apparently, owing to fast disproportionation of alkoxyhydride derivatives [12]

$$2LiAlH_2(OR)_2 \rightarrow LiAlH_4 + LiAl(OR)_4. \quad (5)$$

The formation of a mixture of $LiAlH_4$ and $LiAl(OR)_4$ (R = Et, *iso*-Pr) in partial alcoholysis of lithium tetrahydroaluminate (ROH/$LiAlH_4$ = 1–3) was also suggested by Turova et al. [13].

Since the available data on the composition of products formed by alcoholysis of lithium tetrahy-

Reaction between the components of the $Pd(acac)_2$–$LiAlH_4$–ROH systems. $c_{Pd(acac)_2} = 5 \times 10^{-3}$, $c_{LiAlH_4} = 0.54$ M, solvent benzene, 25°C

Run no.	Alcohol*	ROH/$LiAlH_4$	$H_2/LiAlH_4$,** mol/mol	$LiAlH_4/Pd(acac)_2$	Fraction of reduced $Pd(acac)_2$, %
1	*n*-BuOH	1	1.00	2	94.4
2	"	1	1.00	5	97.4
3	"	1	1.00	10	100
4	"	2	1.97	2	–
5	"	2	1.97	5	–
6	"	2	1.97	10	–
7	"	3	2.98	2	–
8	"	3	2.98	5	–
9	"	1	2.98	10	–
10	*tert*-BuOH	1	1.00	2	86.1
11	"	1	1.00	5	98.1
12	"	1	1.00	10	100
13	"	2	1.95	2	34.2
14	"	2	1.95	5	98.4
15	"	2	1.95	10	100
16	"	3	1.97	2	24.0
17	"	3	1.97	5	84.4
18	"	3	1.97	10	100

* Freshly prepared $LiAlH_4$–ROH solution was used.
** In alcoholysis of lithium tetrahydroaluminate.

droaluminate with various alcohols are ambiguous, in our study aimed to elucidate the main steps of formation of the catalytic system $Pd(acac)_2$–$LiAlH_4$–ROH we first examined the reaction of $LiAlH_4$ with *n*-BuOH and *tert*-BuOH. The results of volumetric determination of molecular hydrogen in the reaction of $LiAlH_4$ with *n*-BuOH and *tert*-BuOH are given in the table.

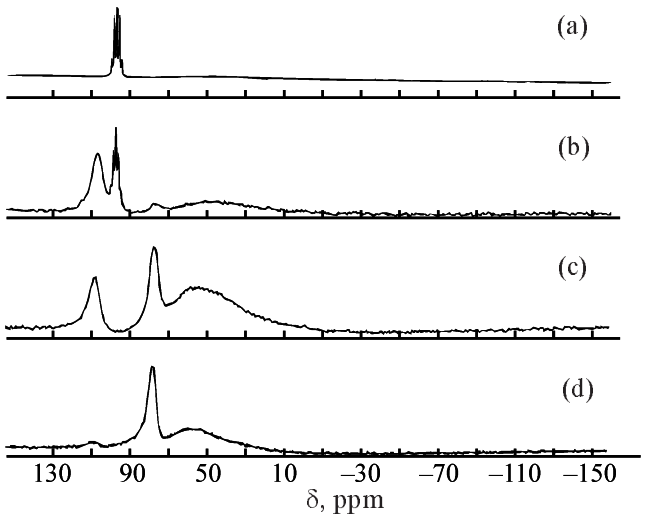


Fig. 3. ^{27}Al spectra of (a) solution of $LiAlH_4$ in THF and (b–d) products of its reaction with *tert*-BuOH at *tert*-BuOH/$LiAlH_4$ ratios of (b) 1, (c) 2, and (d) 3. c_{LiAlH_4} = 0.54 M; the same for Fig. 5. (δ) Chemical shift; the same for Figs. 4 and 5.

With *n*-butanol, alcoholysis of $LiAlH_4$ is complete in 1–2 min (c_{LiAlH_4} = 0.54 M), with an equmolar (with respect to alcohol) amount of hydrogen released. With *tert*-BuOH, the equimolar amount of hydrogen (with respect to alcohol) in alcoholysis of $LiAlH_4$ is released onlt at *tert*-BuOH/$LiAlH_4$ ratios of 1 and 2. The alcoholysis is complete in 1–2 and 60 min, respectively ($LiAlH_4$ concentration 0.54 M). At a *tert*-BuOH/$LiAlH_4$ ratio of 3 and a $LiAlH_4$ concentration of 0.54 M, even in 2 h the amount of the released hydrogen did not exceed 2 mol per mole of $LiAlH_4$, i.e., the alcoholysis did not go to completion. To gain more detailed information on the products of the reaction of $LiAlH_4$ with alcohols, we used ^{27}Al NMR spectroscopy.

The ^{27}Al NMR spectrum of a solution of $LiAlH_4$ in THF consists of one quintet at 98 ppm, with the coupling constant $^1J_{Al-H}$ = 173 Hz and line width at half maximum ($\Delta\nu_{1/2}$ ^{27}Al) of 47 Hz (Fig. 3a).

The chemical shift observed is typical of the AlH_4^- anion (95–102 ppm) [14, 15]. The multiplet structure

of the spectrum is caused by scalar spin–spin coupling of the equivalent protons with the Al isotope. It indicates that, in THF solution, the tetrahedral configuration of the AlH_4^- anion is preserved.

On adding *tert*-butanol to a $LiAlH_4$ solution ($ROH/LiAlH_4$ = 1), the spectral pattern changes. The ^{27}Al spectrum contains four signals with chemical shifts of 108.0, 98.0, 78.0, and 55.0 ppm (Fig. 3b). According to the ^1H NMR data, the reaction mixture contains no *tert*-butanol [expected signals, δ, ppm: 3.54 s (1H, OH), 1.17 s (9H, CH_3)]. The quintet at δ = 98 ppm, observed in the ^{27}Al spectrum, indicates that the $LiAlH_4$ conversion is incomplete. The relative content of unchanged $LiAlH_4$ is about 30%. In contrast to the quintet at δ = 98 ppm, the signals at 55.0, 78.0, and 108.0 ppm are broadened singlets. It is known that, if one of the ligands in the AlH_4^- anion is replaced by another ligand, the multiplet structure of the ^{27}Al signal is not manifested [15]. Hence, alcoholysis of $LiAlH_4$ with *tert*-butanol yields not one, as it could be expected from the stoichiometry of reaction (4), but three reaction products characterized in the ^{27}Al NMR spectrum by signals at 55.0, 78.0, and 108.0 ppm. Incomplete conversion of $LiAlH_4$ shows that lithium *tert*-butoxyalumohydrides are no less reactive than $LiAlH_4$ and also react with the alcohol. The products of complete alcoholysis of lithium tetrahydroaluminate with various alcohols, $LiAl(OR)_4$, are insoluble in THF, and their formation is usually judged by precipitation of a colorless product [11, 12]. The absence of the precipitate in the reaction of $LiAlH_4$ with *tert*-BuOH suggests that the reaction does not yield $LiAl(tert\text{-}BuO)_4$.

At the *tert*-$BuOH/LiAlH_4$ ratio of 2, the ^{27}Al NMR spectrum contains signals at δ 55.0, 78.0, and 108.0 ppm (Fig. 3c). At *tert*-$BuOH/LiAlH_4$ = 3, the ^{27}Al NMR spectrum consists of the same signals (δ 55.0, 78.0, and 108.0 ppm), but the ratio of their integral intensities changes (Fig. 3d). At the molar ratio *tert*-$BuOH/LiAlH_4$ = 3, the spectral pattern varied with time: In 9 days, the ^{27}Al NMR spectrum consisted of only two signals at δ 55.0 and 78.0 ppm (Fig. 4b). The relative intensity of the signal at δ 78.0 ppm decreased, and that of the signal at δ 55.0 ppm increased (Fig. 4c). In the process, the ^1H NMR signals of free *tert*-butanol decreased in the intensity.

Analysis of the NMR data allows the following assignment of signals in the ^{27}Al NMR spectrum. The signal at δ 55.0 ppm, characterizing the final

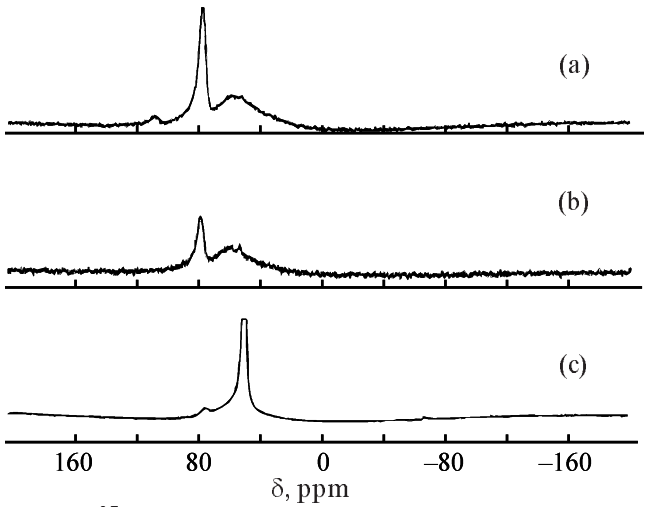


Fig. 4. ^{27}Al NMR spectra of alcoholysis products in the $LiAlH_4$–3*tert*-BuOH system in THF. Time after mixing: (a) 2 h, (b) 9 days, and (c) 3 days. c_{LiAlH_4}, M: (a, b) 0.54 and (c) 1.08.

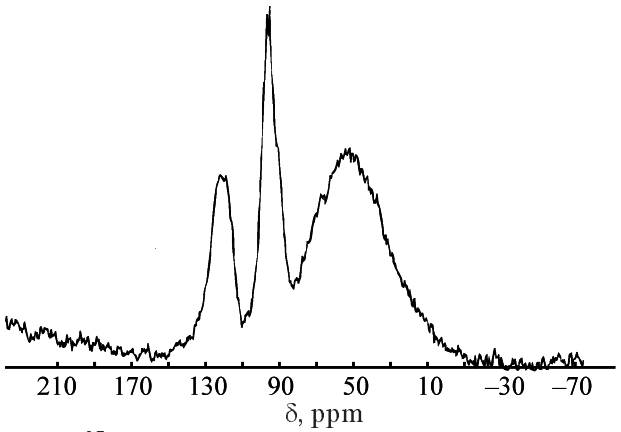


Fig. 5. ^{27}Al NMR spectrum of the $LiAlH_4$–*n*-BuOH solution in THF. $ROH/LiAlH_4$ = 1.

alcoholysis product, belongs to $LiAlH(tert\text{-}BuO)_3$; the signal at δ 78.0 ppm, to $LiAlH_2(tert\text{-}BuO)_2$; and the signal at δ 108.0 ppm, to $LiAlH_3(tert\text{-}BuO)$.

Thus, alcoholysis of $LiAlH_4$ with *tert*-butanol yields a mixture of lithium alkoxyalumohydrides $LiAlH_3(tert\text{-}BuO)$, $LiAlH_2(tert\text{-}BuO)_2$, and $LiAlH\cdot(tert\text{-}BuO)_3$ in the ratio depending on the amount of *tert*-BuOH. At *tert*-$BuOH/LiAlH_4$ = 1, about 30% of lithium tetrahydroaluminate remains unchanged.

In the reaction of $LiAlH_4$ with *n*-butanol at *n*-$BuOH/LiAlH_4$ = 1, according to the ^{27}Al NMR data, the reaction system contains both unchanged $LiAlH_4$ (δ 98.0 ppm) and products of its partial alcoholysis: $LiAlH_3(n\text{-}BuO)$ (δ 122.0 ppm), $LiAlH_2\cdot(n\text{-}BuO)_2$ (δ 71.0 ppm), and $LiAlH(n\text{-}BuO)_3$ (δ

53.0 ppm) (Fig. 5). At *n*-BuOH/$LiAlH_4$ = 3, the only transformation product is $LiAlH(n\text{-}BuO)_3$.

Hence, with $LiAlH_4$–ROH used as reductants, the system actually contains not individual compounds but a mixture of alcoholysis products and even a part of unchanged $LiAlH_4$. The composition of the reaction mixture depends not only on particular alcohol, but also on the ROH/$LiAlH_4$ ratio. Both $LiAlH_4$ and lithium alkoxyhydroaluminates $LiAlH_3(OR)$, $LiAlH_2(OR)_2$, and $LiAlH(OR)_3$ can participate in the reduction of $Pd(acac)_2$ in accordance with the equation

$$Pd(acac)_2 + 2LiAlH_{4-m}(OR)_m = Pd + 2Liacac + 2AlH_{3-m}(OR)_m + H_2, \quad (6)$$

where m = 0–3.

It should be noted that, in the $Pd(acac)_2$–$LiAlH_4$–*n*-BuOH system at *n*-BuOH/$LiAlH_4$ = 2 or 3, containing lithium alkoxyalumohydrides $LiAlH_2(OR)_2$ and $LiAlH(OR)_3$, Pd(II) is not reduced (see table, run nos. 4–9). A similar pattern was observed with the $LiAlH_4$–3*tert*-BuOH at the moment when, according to the ^{27}Al NMR data, it did not contain $LiAlH_4$ and $LiAlH_3(OR)$ (Figs. 4c, 4d), i.e., the reducing power of lithium alkoxyalumohydrides decreases in the order $LiAlH_4$ > $LiAlH_3(OR)$ > $LiAlH_2(OR)_2$ > $LiAlH(OR)_3$, so that $LiAlH_2(OR)_2$ and $LiAlH(OR)_3$ do not reduce $Pd(acac)_2$ under mild conditions. Thus, among the above reagents, only $LiAlH_4$ and $LiAlH_3(OR)$ act as reductants in the $Pd(acac)_2$–$LiAlH_4$–ROH system. At the same time, almost quantitative reduction of $Pd(acac)_2$ with a freshly prepared $LiAlH_4$–ROH solution (ROH/$LiAlH_4$ = 1, R = *n*-Bu, *tert*-Bu) at the Red : $Pd(acac)_2$ ratio of 2 (see table, run nos. 1, 10) indicates that some additional reagent, along with $LiAlH_4$ and $LiAlH_3(OR)$, participates in the Pd(II) reduction.

According to the UV data, in all the cases when $Pd(acac)_2$ was reduced, a decrease in the intensity of the absorption band at 330 nm in the UV spectrum (electronic transitions in palladium complexes with chelatingh $acac^-$ ligands) was accompanied by the appearance of a strong absorption band with a maximum at 288 nm. A previous study of the catalytic system $Pd(acac)_2$–$LiAlH_4$ by a set of spectroscopic methods (UV; ^{27}Al and ^1H NMR) showed that this band belongs to acac ligands bound to Al in $Al(acac)_3$ [4], whose formation is described by the equation

$$3Pd(acac)_2 + 2Al \longrightarrow 3Pd + 2Al(acac)_3, \quad (7)$$

or in its other derivatives, e.g., $Al(acac)(OR)_2$, $Et_2Al(acac)$ [16]. The molar extinction coefficient of this band depends on the number of chelating acac ligands at Al and is 14 470 l mol^{-1} cm^{-1} per acetylacetonate group. Hence, at the ratio *tert*-BuOH : $LiAlH_4$ > 1, when the system contains no unchanged lithium tetrahydroaluminate and hence formation of $Al(acac)_3$ is impossible, the band recorded in the UV spectrum at 288 nm can be assigned to acac ligands at Al in $Al(acac)_2$(*tert*-BuOH):

$$Pd(acac)_2 + AlH_2(OR) \rightarrow Pd + Al(acac)_2(OR) + H_2. \quad (8)$$

Thus, in generation of a hydrogenation catalyst in the $Pd(acac)_2$–$LiAlH_4$–ROH system, not only the fraction of $LiAlH_4$ unchanged in alcoholysis and lithium monoalkoxytrihydroaluminate $LiAlH_3(OR)$, but also Al and $AlH_2(OR)$ formed by redox reactions participate in the reduction of $Pd(acac)_2$. The contribution of each component will depend on the ratio of the rates of the redox processes.

The use of alcoholysis products instead of $LiAlH_4$ resulted in generation of palladium hydrogenation catalysts that were four times more active than the $Pd(acac)_2$–$LiAlH_4$ system. The promoting effect of alcohols can be caused not only by a decrease in the inhibiting effect of aluminum relative to the unmodified system. Other possible factors are the effect of the ligand surrounding and, probably, stronger ability of alkoxy anions to stabilize reduced Pd species, compared to that of AlH_4^- anions.

CONCLUSIONS

(1) A high-performance hydrogenation catalyst based on the $Pd(acac)_2$–$LiAlH_4$–ROH system was suggested.

(2) As shown by ^{27}Al NMR spectroscopy, the reaction of equimolar amounts of $LiAlH_4$ and ROH (R = *n*-Bu, *tert*-Bu) yields a mixture of lithium alkoxyalumohydrides consisting of $LiAlH_3(OR)$, $LiAlH_2(OR)_2$, and $LiAlH(OR)_3$, with a part of $LiAlH_4$ remaining unchanged.

(3) A promoting effect of alcohols on the properties of the $Pd(acac)_2$–$LiAlH_4$–ROH catalytic system in hydrogenation of unsaturated compounds was revealed. This effect is associated with two

factors: a decrease in the amount of Al acting as inhibitor owing to formation of a substitution solid solution and increased ability of alkoxy anions, compared to AlH_4^- anions, to stabilize reduced Pd species.

(4) The difference in the effects of *n*-butanol and *tert*-butanol at the ratio $ROH/LiAlH_4 > 1$ on the properties of the palladium hydrogenation catalyst is associated with the composition of the alcoholysis products and their reductive ability with respect to $Pd(acac)_2$. The inhibiting effect of *n*-butanol at $ROH/LiAlH_4 > 1$ is due to low reductive ability of lithium alkoxyalumohydrides $LiAlH_2(OR)_2$ and $LiAlH(OR)_3$.

ACKNOWLEDGMENTS

The study was financially supported by a grant of the Irkutsk State University (no. 111-02-000/7-13).

REFERENCES

1. *Catalytically Active Metal Powders and Colloids*, Furstner, A., Ed., New York: VCH, 1996, pp. 339–376.
2. Pomogailo, A.D., Rozenberg, A.S., and Uflyand, I.E., *Nanochastitsy metallov v polimerakh* (Metal Nanoparticles in Polymers), Moscow: Khimiya, 2000.
3. Belykh, L.B., Goremyka, T.V., Skripov, N.I., et al., *Kinet. Katal.*, 2006, vol. 47, no. 3, pp. 373–380.
4. Belykh, L.B., Titova, Yu.Yu., Shmidt, F.K., et al., *Zh. Prikl. Khim.*, 2008, vol. 81, no. 6, pp. 917–925.
5. Shmidt, F.K., Belykh, L.B., and Goremyka, T.V., *Kinet. Katal.*, 2003, vol. 44, no. 5, pp. 683–691.
6. Belykh, L.B., Goremyka, T.V., Belonogova, L.N., and Schmidt, F.K., *J. Mol. Catal. A: Chem.*, 2005, vol. 231, nos. 1–2, pp. 53–59.
7. Gordon, A.J. and Ford, R.A., *The Chemist's Companion. A Handbook of Practical Data, Techniques, and References*, New York: Wiley–Interscience, 1972.
8. Mitchell, J. and Smith, D.M., *Aquametry*, part I: *A Treatise on Methods for the Determination of Water*, New York: Wiley, 1977, 2nd ed.
9. US Patent 3474464.
10. Belykh, L.B., Titova, Yu.Yu., Umanets, V.A., and Shmidt, F.K., *Zh. Prikl. Khim.*, 2006, vol. 79, no. 8, pp. 1285–1291.
11. Brown, H. and Shoaf, C.J., *J. Am. Chem. Soc.*, 1964, vol. 86, pp. 1079–1085.
12. Haubenstock, H. and Mester, T., Jr., *J. Org. Chem.*, 1983, vol. 48, pp. 945–948.
13. Turova, N.Ya., Karpovskaya, M.I., and Novoselova, A.V., *Zh. Obshch. Khim.*, 1976, T. 46, no. 6, pp. 1338–1346.
14. Tarasov, V.P., Bakum, S.I., Privalov, V.I., and Buslaev, Yu.A., *Koord. Khim.*, 1981, vol. 7, no. 5, pp. 674–692.
15. Tarasov, V.P., Privalov, V.I., Gorbik, A.A., and Bakum, S.I., *Koord. Khim.*, 1985, vol. 11, no. 12, pp. 1626–1634.
16. Schmidt, F.K., Ratovskii, G.V., Dmitrieva, T.V., et al., *J. Organomet. Chem.*, 1983, vol. 256, pp. 309–329.

ISSN 1070-4272, Russian Journal of Applied Chemistry, 2008, Vol. 81, No. 7, pp. 1160–1166. © Pleiades Publishing, Ltd., 2008.
Original Russian Text © S.A. Shapovalov, 2008, published in Zhurnal Prikladnoi Khimii, 2008, Vol. 81, No. 7, pp. 1082–1087.

PHYSICOCHEMICAL STUDIES OF SYSTEMS AND PROCESSES

Effect of Surfactants on Homo- and Heteroassociation of Pinacyanol Cation in Aqueous Solution

S. A. Shapovalov

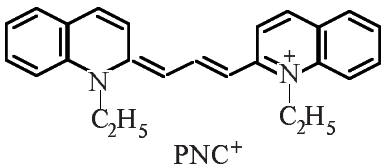
Karazin Kharkov National University, Kharkov, Ukraine

Received May 16, 2007

Abstract—The aggregative properties of pinacyanol in aqueous solution and the capability of its ionic associates to interact with surfactants were studied. The possibility of using pinacyanol associates for quantitative determination of cationic surfactants in aqueous solution and for estimation of the critical micelle concentration of anionic surfactants was examined.

DOI: 10.1134/S1070427208070069

Association between ions of various classes of dyes (heteroassociation) in solutions strongly affects the light absorption and is of both theoretical and applied interest [1, 2]. Heteroassociation in aqueous systems deserves particular attention. Water is a medium in which the interacting protolytic and aggregative species exhibit unique spectral and luminescence properties [1, 3]. Under definite conditions, a dye associate can act as analytical reagent, color marker, or bioprobe. These properties of dye associates find use in quantitative analysis, biochemistry, biomedicine, and in high technologies such as, e.g., solar power engineering and optoelectronics [4]. Cyanines exhibit particular tendency to heteroassociation. They are characterized by intense color and by capability to form stable ionic species in solutions. For a long time, much attention was given to pinacyanol {PNC, single-charged cation 2-ethyl-2-[3-(1-ethyl-1*H*-quinolin-2-ylidene)propenyl]quinolinium}:



PNC^+

Initially PNC was synthesized and tested as a standard of black-and-white photographic material in the beginning of the XX century [5, 6]. The subsequent studies concerned spectroscopic examination of PNC in liquid media of various kinds: organic solvents [7, 8], solutions with salt additions [9–11], premicellar and micellar systems [12–14], and photoemulsions [15, 16]. Pinacyanol is used, in particular, in studies of properties of biopolymers [17], steroids [18], and dendrimers [19–21], in development of metal-sensitive golographic sensors [22], and in studies of oligomeric surfactants [23] and lipopolysaccharides of complex structure [24–26].

Previously [27–30] we found that the PNC cation Ct^+ and its structural analogs interact with a series of organic anions to form in aqueous solutions ionic associates of various stoichiometric compositions. However, the dimerization and heteroassociation of PNC in solutions were studied inadequately.

In this study the aggregative properties of PNC and interaction of its heteroassociates with ionic surfactants were examined in more detail. Such studies may be useful, in particular, for the development of new procedures for determining surfactants in solutions and for estimating the critical micelle concentration (CMC) of ionic surfactants.

EXPERIMENTAL

Pinacyanol was used as chloride (Sigma). The salts and other chemicals (except dyes) were of chemically pure grade and were used without additional purification. The purity of dyes was checked spectrophotometrically from the known molar extinction coefficients at the wavelengths of the absorption maxima (λ_{max}) of the strongly colored protolytic forms. As surfactants we used anionic sodium dodecyl sulfate (SDDS) and cationic cetylpyridinium bromide (CPB), with the main substance content of no less than 98%. The solution acidity

was adjusted with phosphate, borate, and acetate buffer solutions, and also with additions of hydrochloric acid and sodium hydroxide. We found that the components of the buffer solutions in the amounts used do not noticeably affect the association processes. The pH was monitored with a glass electrode. The absorption spectra were measured at room temperature immediately after preparing the solutions on a Hitachi-U3210 or SF-46 spectrophotometer.[1] The λ_{max} values were determined with an accuracy of ±0.5 nm. From the optical densities we calculated the dimerization equilibrium constant β_{20}. The observance of the Bouguer–Beer law was checked. The measurement procedure was described elsewhere [27, 28, 30, 31]. In separate experiments[1] we found that, at the dye concentrations used, inorganic anions do not affect the molecular association of PNC.

In aqueous solutions in the pH range 3.5–9.5, PNC exists predominantly in the form of a single-charged cation appreciably protonated at pH < 2.5 and noticeably hydrolyzed at pH > 10.5. The formation of the dication, $Ct^+ + H^+ \rightleftarrows HCt^{2+}$ (for the double-charged cation, pK_a 3.5 [32]), or of the carbinol form, $Ct^+ + OH^- \rightleftarrows CtOH$, is accompanied by the break of the conjugation system of the chromophore and therefore results in decolorization of the solution. The light absorption of PNC in water depends on its concentration, because the dye shows pronounced tendency to homoassociation [33]. Figure 1 shows how the absorption spectrum changes with increasing PNC concentration. The light absorption increases throughout the examined range (curves *1–9*). However, in spectra *1–6* the major band is the α-band (ν_{max} = 16670 cm, or λ_{max} = 600 nm), and in spectra *8* and *9*, the β-band (ν_{max} = 18180 cm^{-1}, or λ_{max} = 550 nm). This redistribution of the absorption intensities is attributed to the transformation of the PNC monomer (Ct^+) into a dimer (Ct_2^{2+}) [22]. Since aggregation of a dye is of principal importance for its applications, we examined its features in more detail.

The aggregation of PNC cations can be represented by the scheme monomer → dimer → ... → H-aggregate (*n*-mer with ν_{max} = 19610 cm^{-1}, or λ_{max} = 510 nm). The dimerization of PNC is described by the equilibrium $2Ct^+ \rightleftarrows Ct_2^{2+}$ with the thermodynamic constant $\beta_{20} = a_{Ct_2}a_{Ct}^{-2}$, where a_{Ct} and a_{Ct_2} are the activities of the monomer and dimer, respectively (here and hereinafter, the charges are omitted; the dimension of the constant is l mol^{-1}). At concentrations of 5×10^{-7}–1×10^{-5} M, the ionic strength of the solutions is low, and β_{20} can be considered to be equal to $[Ct_2][Ct]^{-2}$, where the brackets denote the equilibrium concentrations (molar scale) of the species. Under these conditions, the content of higher associates Ct_n, where $n > 2$, can be neglected, then $c = [Ct] + 2[Ct_2]$, where c is the initial PNC concentration. The optical density of the solution at a given wavelength A_λ is expressed as

$$A_\lambda = \varepsilon_{Ct}[Ct]l + \varepsilon_{Ct_2}[Ct_2]l,$$

where ε_{Ct} and ε_{Ct_2} are the molar extinction coefficients of the monomer and dimer at wavelength λ; l is the layer thickness (cm).

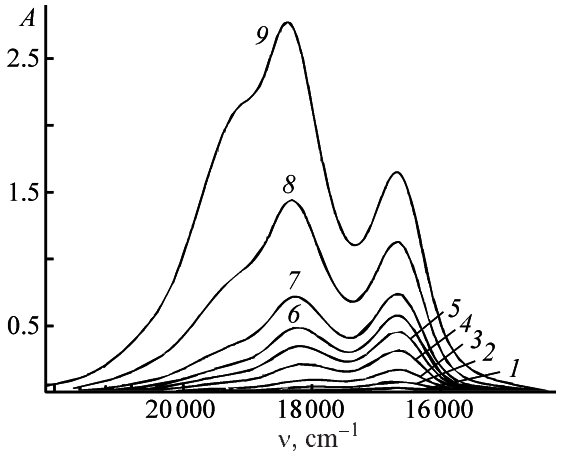


Fig. 1. Light absorption of an aqueous solution of PNC (pH 9.2). Reference solution water; the same for Figs. 3 and 4. Layer thickness 1.00 cm; the same for Figs. 3 and 5. (*A*) Optical density and (ν) wavenumber; the same for Fig. 4. c_{PNC}, M: (*1*) 5.0×10^{-7}, (*2*) 1.0×10^{-6}, (*3*) 2.0×10^{-6}, (*4*) 4.0×10^{-6}, (*5*) 6.0×10^{-6}, (*6*) 8.0×10^{-6}, (*7*) 1.0×10^{-5}, (*8*) 2.0×10^{-5}, and (*9*) 4.0×10^{-5}.

Hence, the dimerization constant $\beta_{20} = (A_\lambda - \varepsilon_{Ct}cl)(\varepsilon_{Ct_2}l - 2\varepsilon_{Ct}l)(c\varepsilon_{Ct_2}l - 2A_\lambda)^{-2}$. If l = 1 cm, we obtain $\beta_{20} = (A_\lambda - \varepsilon_{Ct}c)(\varepsilon_{Ct_2} - 2\varepsilon_{Ct})(c\varepsilon_{Ct_2} - 2A_\lambda)^{-2}$. The calculation based on solution of the system of two equations with unknown β_{20} and ε_{Ct_2} gave for two series of measurements (seven concentration points in each series) $\log\beta_{20} = 4.79 \pm 0.06$ at 297 K. Note that PNC in water shows stronger tendency to dimerization than do other cationic dyes {Rhodamine 6Zh ($\log\beta_{20} = 3.35 \pm 0.01$), Methyl Violet ($2.66 \pm 0.01$), Safranin T ($2.41 \pm 0.01$), Methylene Blue ($3.70 \pm 0.01$) [34], Rhodamine B ($2.98 \pm 0.03$) [35]}. In the series of structural analogs, in the

[1] Cand. Sci. (Chem.) T.V. Sakhno participated in the measurements and experiments.

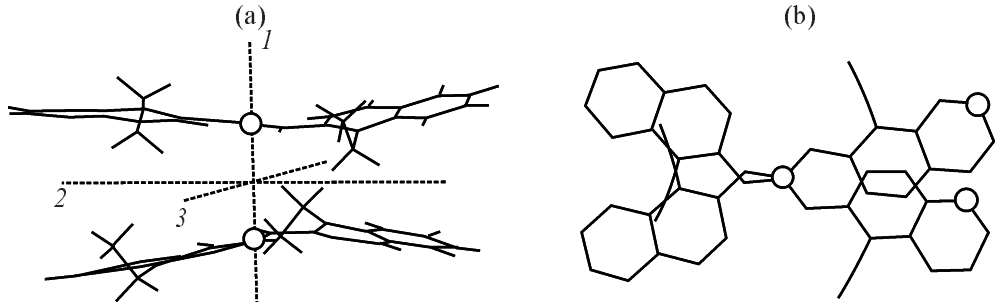


Fig. 2. Structure of PNC *trans* dimer: (a) with hydrogen atoms shown, distance between atoms denoted as circles 3.9 Å; (b) with hydrogen atoms omitted, view perlendicular to axis *1*, angle between the atoms denoted as circles (with the apex on the atom in the center of the polymethine chain) 33.9°.

tendency to dimerization PNC is inferior to some thiacarbocyanine dyes (for example, the dimerization constant of 3,3'-diethylthiatricarbocyanine is 2.4×10^5 [36]).

The dimer Ct_2^{2+} in which the ethyl radicals of the interacting cations are oriented in opposite directions (*trans* dimer, Fig. 2) appears to be more favorable energetically compared to the *cis* dimer (the ethyl radicals of the two cations are oriented in the same direction). This is indicated by the results of quantum-chemical calculations using the MOPAC 2000 software [37, 38] (AM1 semiempirical method; specific features of the calculations as applied to the dyes and their ionic associates are described in [39]). In the *trans* dimer, the cation planes are essentially coplanar. The heat of formation of this dimer is ΔH = 1325 kJ mol^{-1}, and ΔH of the Ct^+ cation is 1070 kJ mol^{-1}. For the *cis* dimer, there is no predominant mutual arrangement of the cations; ΔH of the *cis* dimer is no less than 1980 kJ mol^{-1}. Therefore, *trans* dimerization of PNC is preferable (energy gain $1070 \times 2 - 1325 = 815$ kJ mol^{-1}) over the *cis* dimerization (energy gain only $1070 \times 2 - 1980 = 160$ kJ mol^{-1}). The experimentall observed H-aggregation of PNC in solution can be represented as successive (one over another) *trans* association of the dye particles, when the π-electron interactions favoring the association are the strongest and prevail over the electrostatic repulsion of similarly charged particles.

Higher aggregates are not observed experimentally because of insufficient solubility of PNC. However, detailed analysis of the complex shape of the dye spectrum reveals their presence even at a dye concentration of 5×10^{-5} M. Deconvolution of the normalized spectrum of PNC reveals four overlapping bands [Fig. 3; the deconvolution model is equal-slope Gaussian; the maxima are sought for using the second derivative (curve *8*)]. The hypothesis of the existence of four bands is confirmed by virtual coincidence of the experimental spectrum (curve *1*) with the total calculated light absorption curve *2*: The difference between curves *1* and *2* (curve *7*) lies within a narrow corridor, from −0.039 to +0.032. The characteristics of the absorption bands of the normalized spectrum are given in the table (bands I, II, III, and IV correspond to curves *3*, *4*, *5*, and *6* in Fig. 3). The table shows that, at the indicated concentration, the PNC solution contains species more aggregated than dimers. Bands III and IV

Characteristics of the absorption bands of the normalized PNC spectrum. Concentration 5×10^{-5} M

Characteristic	Band				
	I	II	III	IV	total
λ_{max}, cm^{-1}	16680	18280	19360	20329	16660, 18360
λ_{max}, nm	599.52	547.05	516.53	492.13	600.2, 544.7
I, arb. units	0.5319	0.9532	0.6374	0.192	1.000, 0.547
Half-width, cm^{-1}	1122	1190	1008	1210	–
Band area, cm^{-1} (fraction of total, %)	635.83 (23.07)	1190.67 (43.20)	683.09 (24.78)	246.90 (8.96)	2756.49 (100.0)

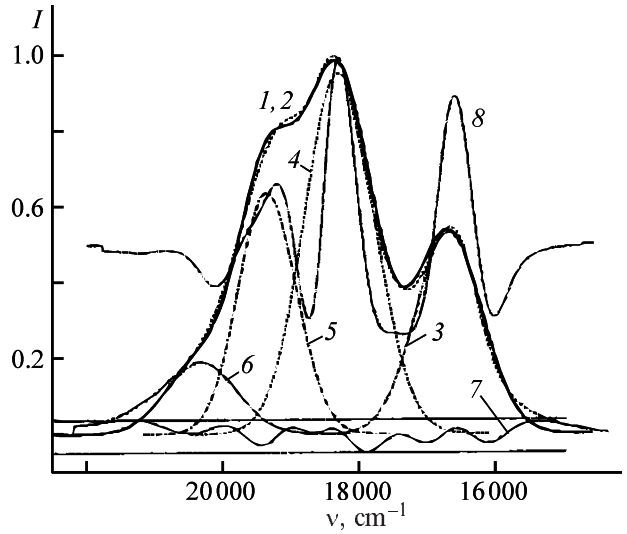


Fig. 3. Normalized absorption spectrum of the PNC solution. c_{PNC} 5.0×10^{-5} M. (*1*) Absorption intensity and (ν) wavenumber. (*1*) Experimental spectrum, (*2*) sum of absorption bands *3–6*, (*7*) difference between curves *1* and *2*, and (*8*) second derivative of band *1*.

account for approximately 1/3 of the total light absorption of PNC, whereas the relative contribution of the α-band is as low as ~23%. These data supplement the observations made in [32, 33] and allow estimation of the fraction of the PNC monomer in solution from the shape of the light absorption curve.

Cationic and anionic surfactants exert different effects on the dye. The PNC spectra at a dye concentration of 1×10^{-6}–5×10^{-5} M do not appreciably change the shape even at micellar concentrations of cationic CPB {CMC of CPB $(6.6–9.0) \times 10^{-4}$ M [40]}. This fact indicates that the dye cation forms no compounds with CPB, apparently because of electrostatic repulsion of the particles. On the contrary, interaction of PNC with SDDS is characterized by a complex pattern. At premicellar concentrations of the surfactant {CMC of SDDS is 8.5×10^{-3} M at 293 K [40]}, the dye forms with the surfactant a compound $PNC^+ + DDS^-$. This fact is consistent with data on interaction of dye ions with surfactant counterions [41]. However, at micellar (or close) concentrations of SDDS, these compounds are broken down because of solubilization of the cyanine on the surface of homomicelles. This pattern is observed irrespective of the initial concentration of PNC. Figures 4a and 4b show similar patterns of spectrum variation in PNC solutions of concentrations 2.7×10^{-6} and 1.5×10^{-5} M. In the first case, the monomeric form of PNC prevails in solution, and in the second case the fraction of the PNC

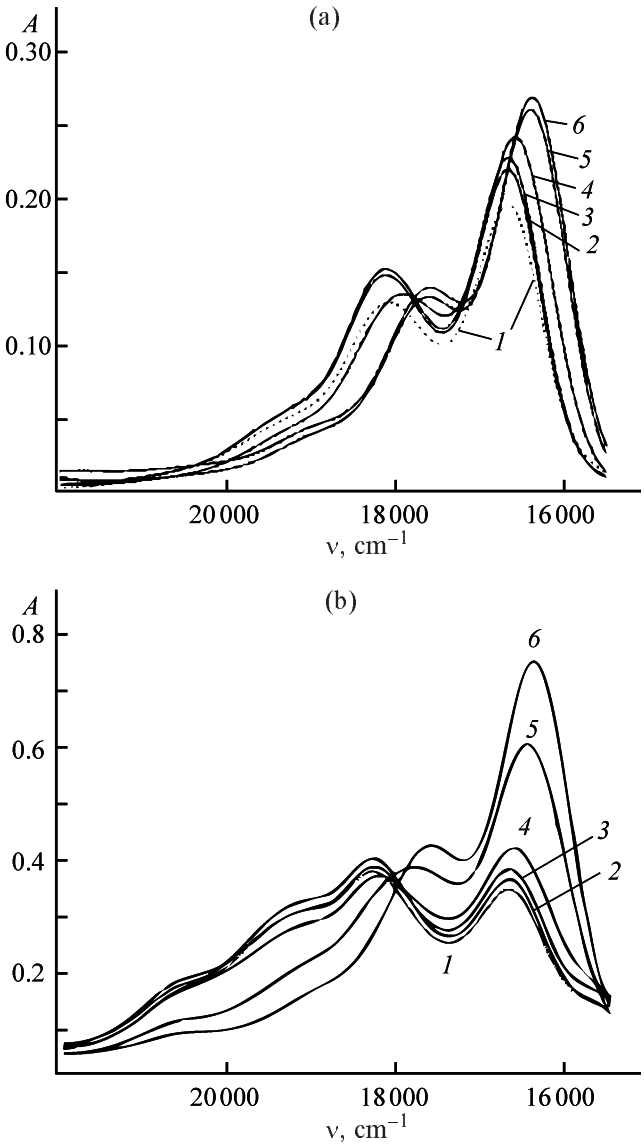


Fig. 4. Absorption spectra of the system PNC + SDDS (pH 5.9). c_{PNC}, M: (a) 2.7×10^{-6} and (b) 1.5×10^{-5}. Layer thickness, cm: (a) 1.00 and (b) 0.20. c_{SDDS}, M: (a) (*1*) 0, (*2*) 3.0×10^{-4}, (*3*) 4.0×10^{-4}, (*4*) 5.0×10^{-4}, (*5*) 6.0×10^{-4}, and (*6*) 9.5×10^{-4}; (b) (*1*) 0, (*2*) 5.0×10^{-4}, (*3*) 9.0×10^{-4}, (*4*) 2.0×10^{-3}, (*5*) 2.0×10^{-2}, and (*6*) 4.0×10^{-2}.

dimer is comparable with that of the monomer (cf. curve *1* in Fig. 4b and curves *6* and *7* in Fig. 1). However, despite different initial concentrations, the shapes of the spectra of PNC solutions at $[SDDS] \geq CMC_{SSDS}$ essentially coincide (Figs. 4a and 4b, curves *6*). The trend in the spectral changes is also similar: With a gradual increase in the SDDS content, the intensity of the long-wave α-band of PNC increases (Fig. 4b, curves *4–6*). Thus, the spectrum of PNC in micellar solutions of SDDS is similar to

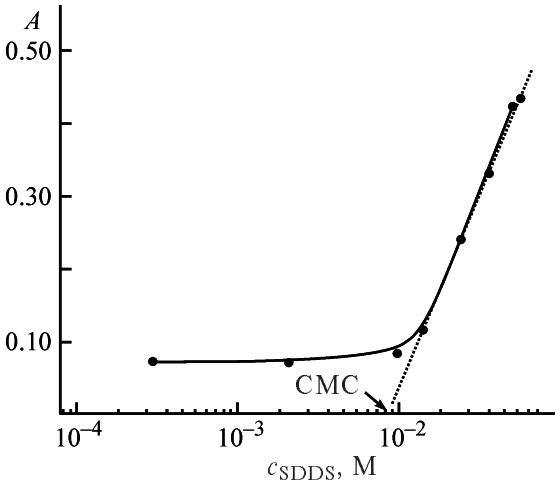
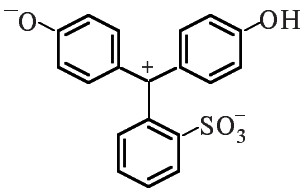


Fig. 5. Light absorption of a solution containing PNC, PR, and SDDS as a function of SDDS concentration c_{SDDS}. The reference solution contains 3.95×10^{-5} M PR and 4.86×10^{-6} M PNC; pH 9.2; λ = 608 nm. (A) Optical density.

the spectrum of the single-charged PNC cation, with a certain bathochromic shift.

It was found previously that PNC interacts with oppositely charged anions of various dyes to form ionic associates of various stoichiometries depending on the charges and concentrations of the counterions. In particular, the formation of sulfophthalein and oxyxanthene associates of the compositions $Ct^+ \cdot HAn^-$ and $(Ct^+)_2 \cdot An^{2-}$ (where HAn^- and An^{2-} are single- and double-charged dye anions), differing in the stability, has been reported [27, 29, 30]. Notably, additions of CPB of SDDS to the above associates break them down, as indicated by restoration of the shapes of absorption bands of each dye. Among sulfophthalein associates of PNC, nontrivial pattern of spectral changes is observed in the system PNC + Phenol Red (PR) + ionic surfactant:



PR^-

As this phenomenon is of practical interest, it was studied in more detail for associates of PNC^+ with single- and double-charged PR anions: $PNC^+ \cdot PR^-$ and $(PNC^+)_2 \cdot PR^{2-}$, respectively. In these experiments, the component concentrations were varied in the following ranges: cyanine, from 5×10^{-7} to 1×10^{-5} M; sulfophthalein, from 1×10^{-6} to 1×10^{-4} M; and surfactant, from 1×10^{-6} and higher. Like PNC proper, the heteroassociates show different responses on additions of cationic and anionic surfactants.

Cationic CPB breaks down the associate $PNC \cdot PR^-$ at low surfactant concentrations, from 3×10^{-6} to 2×10^{-5} M. In other words, the associate is fairly sensitive to the CPB content. The optical density at a fixed wavelength A_λ and constant concentrations of both dyes sharply increases with an increase in the surfactant concentration, c_{CPB} (M), showing a functional dependence on c_{CPB}. For example, at constant concentrations of PNC (4.9×10^{-6} M) and PR (7.1×10^{-5} M), at λ = 600 nm, the dependence is described by the equation $A_\lambda = (0.032 \pm 0.010) + (2.31 \pm 0.09) \times 10^4 c_{CPB}$. Such dependences can be used for quantitative determination of cationic surfactants in solution with a high sensitivity.

Additions of anionic SDDS break down the associate $(PNC^+)_2 \cdot PR^{2-}$ only at surfactant concentrations close to the micellar level. Figure 5 shows an example of the dependence of A_λ on the SDDS concentration. At $c_{SDDS} < CMC_{SDDS}$, variation of c_{SDDS} does not noticeably affect A_λ (linear portion virtually parallel to the abscissa). However, at $c_{SDDS} \approx CMC_{SDDS}$, A_λ at λ = 608 nm starts to sharply increase because of the release of PNC from the associate. We found that the extrapolated ascending portion (Fig. 5, dotted line) intersects the abscissa at c_{SDDS} close to CMC. Thus, it is principally possible to estimate CMC of an anionic surfactant from the experimental dependence of A_λ on c_{SDDS}.

As found previously [28], different behavior of PNC heteroassociates toward the examined surfactants can be due to different stability of the forming compounds of the cationic dye with the DDS^- anion and of the anionic dye with the CP^+ cation. Therefore, to attain the maximal effect in determination of cationic surfactants in solution and to estimate CMC of anionic surfactants, it seems important to use an associate of definite stability (in our case, associates of PNC with PR, but the use of heteroassociates of other dyes is also possible). These procedures will be characterized by high sensitivity and high contrast of the analysis. This is provided by the presence in solution of two dyes having well-resolved absorption bands in the spectrum (e.g., λ_{max} = 430 nm for PR^- and 600 nm for PNC^+). The latter fact favors not only instrumental but also visual detection of changes occurring in the solution and hence can be used in the development of test

procedures for determining cationic surfactants and/or for estimating CMC of anionic surfactants.

CONCLUSIONS

(1) The pinacyanol cation dimerizes in aqueous solution even at low concentrations. The dimerization constant was estimated from the spectroscopic data: $\log\beta_{20} = 4.79 \pm 0.06$ (at 297 K and $I \to 0$). The dimeric particle Ct_2^{2+}, most probably, has the *trans* structure.

(2) Specific features of the interaction of pinacyanol with cationic and anionic surfactants were elucidated. Ionic surfactants, when in micellar concentrations, cause solubilization of the dye, irrespective of its initial concentration and degree of dimerization.

(3) It was demonstrated by the example of heteroassociates of PNC^+ with single- and double-charged Phenol Red anions that the properties of pinacyanol associates can serve as basis of new procedures for determining the content of cationic surfactants in aqueous solutions and for estimating the critical micelle concentrations of anionic surfactants.

REFERENCES

1. Ishchenko, A.A. and Shapovalov, S.A., *Zh. Prikl. Spektrosk.*, 2004, vol. 71, no. 5, pp. 557–578.
2. Larin, V.I. and Shapovalov, S.A., *Ukr. Khim. Zh.*, 2004, vol. 70, no. 5, pp. 3–14.
3. *Voda: struktura, sostoyanie, sol'vatatsiya: Dostizheniya poslednikh let* (Water: Structure, State, Solvation: Recent Advances), Kutepov, A.M., Ed., Moscow: Nauka, 2003.
4. Ishchenko, A.A., *Polym. Adv. Technol.*, 2002, vol. 13, nos. 10–12, pp. 744–752.
5. Hitchins, A.B., *J. Franklin Inst.*, 1917, vol. 184, no. 2, pp. 179–203.
6. Wise, L.E. and Adams, E.Q., *Ind. Eng. Chem.*, 1918, vol. 10, pp. 801–802.
7. Sheppard, S.E. and Brigham, H.R., *J. Am. Chem. Soc.*, 1944, vol. 66, no. 3, pp. 380–384.
8. Sheppard, S.E. and Geddes, A.L., *J. Am. Chem. Soc.*, 1944, vol. 66, no. 12, pp. 1995–2002.
9. Klotz, I.M., *Chem. Rev.*, 1947, vol. 41, no. 2, pp. 373–399.
10. Merrill, R.C. and Spencer, R.W., *J. Am. Chem. Soc.*, 1950, vol. 72, no. 7, pp. 2894–2899.
11. Herzfeld, S.H., *J. Phys. Chem.*, 1952, vol. 56, no. 8, pp. 959–963.
12. Corrin, M.L. and Harkins, W.D., *J. Am. Chem. Soc.*, 1947, vol. 69, no. 3, pp. 679–683.
13. Mukerjee, P., *Anal. Chem.*, 1956, vol. 28, no. 5, pp. 870–873.
14. Takeda, K., Tatsumoto, N., and Yasunaga, T., *J. Colloid Interface Sci.*, 1974, vol. 47, no. 1, pp. 128–133.
15. West, W., Carroll, B.H., and Whitcomb, D.H., *J. Phys. Chem.*, 1952, vol. 56, no. 9, pp. 1054–1067.
16. Herz, A.H., *Adv. Colloid Interface Sci.*, 1977, vol. 8, no. 4, pp. 237–298.
17. Mitra, A. and Chakraborty, A.K., *Indian J. Chem., Sect. A.: Inorg., Bio-Inorg., Phys., Theor. Anal. Chem.*, 1998, vol. 37, no. 5, pp. 418–422.
18. Li, Y. and Dias, J.R., *Chem. Rev.*, 1997, vol. 97, no. 1, pp. 283–304.
19. Teobaldi, G. and Zerbetto, F., *J. Am. Chem. Soc.*, 2003, vol. 125, no. 24, pp. 7388–7393.
20. Gopidas, K.R., Whitesell, J.K., and Fox, M.A., *J. Am. Chem. Soc.*, 2003, vol. 125, no. 46, pp. 14168–14180.
21. Aulenta, F., Hayes, W., and Rannard, S., *Eur. Polym. J.*, 2003, vol. 39, no. 9, pp. 1741–1771.
22. Mayes, A.G., Blyth, J., Millington, R.B., et al., *Anal. Chem.*, 2002, vol. 74, no. 15, pp. 3649–3657.
23. Laschewsky, L., Wattebled, M., Arotcarena, J.-L., et al., *Langmuir*, 2005, vol. 21, no. 16, pp. 7170–7179.
24. Jones, G. and Jiang, H., *Bioconjugate Chem.*, 2005, vol. 16, no. 3, pp. 621–625.
25. Jana-Sur, P. and Chakraborty, A.K., *J. Photochem. Photobiol. A: Chem.*, 2005, vol. 173, no. 1, pp. 64–69.
26. Mitra, A., Nath, R.K., Biswas, S., et al., *J. Photochem. Photobiol. A: Chem.*, 2006, vol. 178, no. 1, pp. 98–105.
27. Shapovalov, S.A., Koval', V.L., Mchedlov-Petrosyan, N.O., et al., *Dokl. Nats. Akad. Nauk Ukr.*, 1999, no. 2, pp. 156–161.
28. Shapovalov, S.A. and Svishcheva, Ya.A., *Zh. Prikl. Khim.*, 2002, vol. 75, no. 3, pp. 463–467.
29. Shapovalov, S.A., *Ukr. Khim. Zh.*, 2004, vol. 70, no. 3, pp. 25–29.
30. Shapovalov, S.A., *Zh. Fiz. Khim.*, 2005, vol. 79, no. 3, pp. 565–570.
31. Ishchenko, A.A., Derevyanko, N.A., Popov, S.V., et al., *Izv. Ross. Akad. Nauk*, 1997, no. 5, pp. 950–955.
32. Herz, A.H., *Photogr. Sci. Eng.*, 1974, vol. 18, no. 2, pp. 207–215.
33. Sheppard, S.E., *Rev. Modern Phys.*, 1942, vol. 14, April–July, pp. 303–340.

34. Poluektov, N.S., Bel'tyukova, S.V., and Meshkova, S.V., *Zh. Anal. Khim.*, 1971, vol. 26, no. 6, pp. 1042–1047.

35. Adamovich, L.P., Mel'nik, V.V., and Mchedlov-Petrosyan, N.O., *Zh. Fiz. Khim.*, 1979, vol. 53, no. 2, pp. 356–359.

36. West, W. and Pearce, S., *J. Phys. Chem.*, 1965, vol. 69, no. 6, pp. 1894–1903.

37. Stewart, J.J.P., *J. Comput. Chem.*, 1989, vol. 10, no. 2, pp. 209–220.

38. Stewart, J.J.P., *MOPAC 2000. User's Manual*, New York: Fujitsu, 2000.

39. Shapovalov, S.A., Samoilov, E.A., and Ivanov, V.V., *Izv. Vyssh. Uchebn. Zaved., Khim. Khim. Tekhnol.*, 2006, vol. 49, no. 7, pp. 39–44.

40. Abramzon, A.A., Bocharov, V.V., and Gaevoi, G.M., *Poverkhnostno-aktivnye veshchestva: Spravochnik* (Surfactants: Handbook), Leningrad: Khimiya, 1979.

41. Savvin, S.B., Chernova, R.K., and Shtykov, S.N., *Poverkhnostno-aktivnye veshchestva* (Surfactants), Moscow: Nauka, 1991.

ISSN 1070-4272, Russian Journal of Applied Chemistry, 2008, Vol. 81, No. 7, pp. 1167–1170. © Pleiades Publishing, Ltd., 2008.
Original Russian Text © Yu.V. Tamarkina, L.A. Maslova, T.V. Khabarova, V.A. Kucherenko, 2008, published in Zhurnal Prikladnoi Khimii, 2008, Vol. 81, No. 7, pp. 1088–1091.

PHYSICOCHEMICAL STUDIES OF SYSTEMS AND PROCESSES

Adsorption Properties of Carbon Materials Produced by Thermolysis of Brown Coal in the Presence of Alkali Metal Hydroxides

Yu. V. Tamarkina, L. A. Maslova, T. V. Khabarova, and V. A. Kucherenko

Litvinenko Institute of Physical Organic and Coal Chemistry, National Academy of Sciences of Ukraine, Donetsk, Ukraine

Received October 15, 2007

Abstract—Activated carbons produced by thermolysis of brown coal impregnated with an alkali metal hydroxide MOH (M = Li, Na, K) at an MOH/coal ratio $R_{MOH} \le 80$ mol kg^{-1} were studied. Dependences of the adsorption capacities for iodine and Methylene Blue dye, specific surface area, and yield of activated carbons on the ratio R_{MOH} were obtained.

DOI: 10.1134/S1070427208070070

Thermolysis of fossil coal in the presence of hydroxides of alkali metals is a method for "chemical" activation [1–3] yielding activated carbons (ACs) with a large fraction of micropores, which occasionally exceeds 90% [4]. The high microporosity of materials of this kind predetermines their specific adsorption characteristics.

The chemical activation method is employed to produce ACs from fossil coals with different degrees of metamorphism, from brown coals to anthracites [2, 4–6]. Just brown coals (BCs) exhibit the highest activity in interaction with alkali metal hydroxides (MOH, where M stands for an alkali metal) because of the high content of OH-acid and other functional groups. In addition, the 3D skeleton of BC is conformationally labile, which allows MOH molecules and M^+ and OH^- ions to penetrate into the coal skeleton and form intercalation compounds of coal [7].

The mechanism by which MOH react with functional groups of coals is independent of the nature of M^+, whereas the specific surface area of ACs strongly varies depending on particular alkali metal cation [8]. It would be expected that the adsorption properties of ACs may also depend on the nature of an alkali.

The aim of the present study was to examine the adsorption characteristics of ACs produced by thermolysis of brown coal mixed with various alkali metal hydroxides and to assess the influence exerted by the nature of a cation.

EXPERIMENTAL

We used the most available alkalis (LiOH, NaOH, KOH) and brown coal from the Aleksandriiskoe deposit (particle size 0.5–1.0 mm) with the following characteristics (%): $W^a = 12.4$, $A^d = 11.7$, $V^{daf} = 57.6$, $C^{daf} = 70.4$, $H^{daf} = 6.0$, $S^{daf} = 3.8$, $N^{daf} = 2.0$, and $O^{daf}_{dif} = 17.8$.

The alkali metal hydroxide MOH was introduced into the carbon skeleton by impregnation with an aqueous–alkaline solution, followed by drying. A weighed portion of BC (20 g) was brought in contact with a 50% solution of MOH, kept there at 20 ± 2°C for 24 h, and dried. The coal impregnated with MOH was conventionally named BC–MOH compound. The thermolysis was performed in a vertical tubular stainless steel reactor. The reactor was purged with argon (~2 dm^3 h^{-1}) dried by bubbling through concentrated (≥96%) sulfuric acid. The heating of the reactor was switched on 10 min after the beginning of argon supply. The temperature mode of thermolysis was similar to that used in [9] and included a period of nonisothermal heating (4 deg min^{-1}) to 800°C, isothermal heating for 1 h, and rapid cooling in a flow of argon to $T \le 50$°C. An AC sample was washed with water to remove

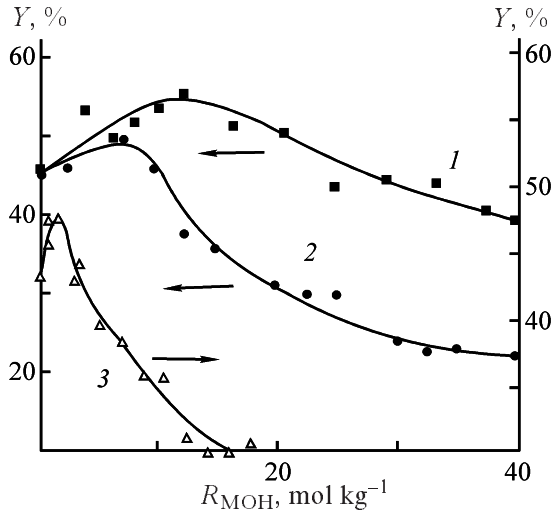


Fig. 1. Yield Y of adsorbents (based on the organic mass of coal) from BC–MOH compounds vs. the MOH/coal ratio R_{MOH}. MOH: (*1*) LiOH, (*2*) NaOH, (*3*) KOH; the same for Figs. 2–5.

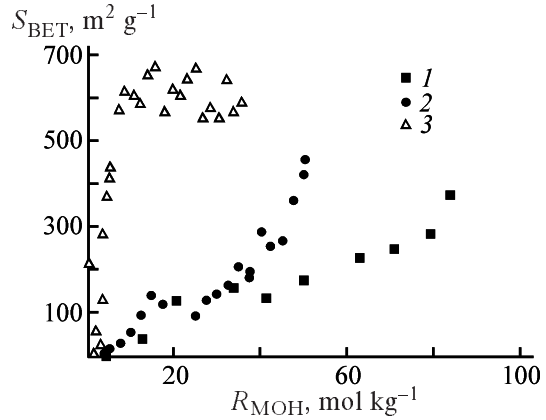


Fig. 2. Specific surface area S_{BET} of the adsorbents produced from BC–MOH compounds vs. the MOH/coal ratio R_{MOH}.

the alkali, with a 0.1 HCl solution, and again with water to negative reaction for Cl^- (with $AgNO_3$). The resulting AC sample was dried at 105±5°C to constant weight. The yield Y (%) was determined per dry coal mass, with determination errors within ±1%. The AC obtained was powder-like, with particle size of 0.05–0.25 mm and ash content A^d = 3.5–4%.

The specific surface area S_{BET} ($m^2 g^{-1}$) was found by low-temperature adsorption of argon. The determination error of S_{BET} was ±10 rel %.

As testing methods for evaluating the adsorption characteristics were chosen the adsorption capacity for Methylene Blue (MB) dye, A_{MB} (mg g^{-1}), used to evaluate the quality of clarifying carbons [10], and the adsorption capacity for iodine, A_I (mg g^{-1}) [11]. Iodine molecules are small and are adsorbed over the entire surface of AC, including the surface of micropores. On the basis of this property, a method for determining the specific surface area has been suggested [12]. The MB molecule has a considerably larger size (1.97 nm^2) and, therefore, can hardly penetrate into micropores [13]. Therefore, the quantity A_{MB} responds to changes in meso- (2–50 nm) and macropores (>50 nm) and is weakly sensitive to changes in the microporosity (≤2 nm).

For adsorbents produced by thermolysis of the chosen BC sample and BC–MOH compounds, the specific surface area and the adsorption parameters depend on the MOH/coal mass ratio and nature of an alkali.

As R_{MOH} increases, the AC yield first grows and then starts to fall (Fig. 1). The initial increase in the yield is the most pronounced for BC–LiOH compounds: from 45 to 55% at R_{LiOH} = 13 mol kg^{-1}. For BC–NaOH compounds, this effect is also well noticeable: the yield increases from 45 to 49% at R_{NaOH} = 7.5 mol kg^{-1}. In the case of KOH, the effect of an increase in yield is manifested at small alkali : coal ratios ($R_{KOH} \leq 2$ mol kg^{-1}).

On passing the maximum value, the AC yield decreases, with the yield the lower, the larger the alkali metal cation. For example, at R_{MOH} = 30 mol kg^{-1}, the AC yield is 44 (BC–LiOH), 24 (BC–NaOH), and 20% (BC–KOH).

As R_{MOH} increases, S_{BET} decreases to a minimum at R_{KOH} = 1–3 mol kg^{-1} and then increases at $R_{KOH} \rightarrow 15$ mol kg^{-1} (Fig. 2). Further increase in the amount of the alkali within the range R_{KOH} = 15–40 mol kg^{-1} does not lead to any development of the surface: it remains approximately constant within the experimental error and varies within the range S_{BET} = 550–680 $m^2 g^{-1}$.

The dependences of S_{BET} on R_{MOH} for the compounds BC–NaOH and BC–LiOH differ from that for BC–KOH. An increase in the parameter R_{NaOH} also leads to a decrease in S_{BET} to the minimum value at R_{NaOH} = 5±0.3 mol kg^{-1}. Then S_{BET} steadily increases with R_{MOH}, but the dependence does not level-off in contrast to the case of BC–KOH compounds (Fig. 2). The maximum value of S_{BET} (450 $m^2 g^{-1}$) is observed at R_{NaOH} = 50 mol kg^{-1}. A rise in the S_{BET} of solid products formed in thermolysis of BC–NaOH compounds over that of AC produced from the starting brown

coal is noticeable at $R_{NaOH} \geq 40$ mol kg^{-1}. That is, sodium hydroxide suppresses an increase in the specific surface area of brown coal under study in the range R_{NaOH} = 2.5–40 mol kg^{-1}. For ACs produced from BC–LiOH compounds, the initial decrease in the specific surface area and its subsequent increase are also observed (Fig. 2). However, on the whole, the development of the surface is less pronounced for LiOH, compared to NaOH and KOH.

The process of surface development apparently depends on the nature of an alkali metal cation. At small R_{MOH}, S_{BET} decreases for all the alkalis as the alkali/BC ratio grows, but this occurs in different ways for different alkalis (Fig. 2). As regards the development of the surface, the activity of the alkalis grows in the order LiOH < NaOH < KOH. For example, obtaining an adsorbent with S_{BET} = 400 m^2 g^{-1} requires thermolysis of a BC–MOH compound containing 80 mol kg^{-1} LiOH, or 50 mol kg^{-1} NaOH, or 5 mol kg^{-1} KOH, i.e., a 16 : 10 : 1 ratio is observed. In other words, the activity of KOH in the development of the AC surface is 10 times that of NaOH and 16 times that of LiOH. In the range R_{MOH} = 5–10 mol kg^{-1}, S_{BET} increases for LiOH and NaOH and approaches a plateau for KOH. A difference in the behavior between LiOH and NaOH is only observed at $R_{MOH} \geq 40$ mol kg^{-1}: the development of the AC surface becomes more noticeable for BC–NaOH than for BC–LiOH compounds.

The adsorption capacity for MB increases with R_{MOH} for ACs produced with all the alkalis (Fig. 3). The dependences of A_{MB} on R_{MOH} are similar for adsorbents produced from BC–LiOH and BC–NaOH compounds: the adsorption capacity steadily increases from 61 to 94 mg g^{-1} for BC–LiOH and from 58 to 157 mg g^{-1} for BC–NaOH. At the same time, the rise in A_{MB} is considerably more pronounced for ACs produced from BC–KOH compounds: A_{MB} reaches values of 300 mg g^{-1}.

The dependences of the adsorption capacity of ACs for iodine on the amount of an alkali in BC–MOH compounds are qualitatively similar (Fig. 4) to the dependences of S_{BET} on R_{MOH} (Fig. 2). For all of the alkalis, A_I decreases at small R_{MOH} and then the adsorption capacity of ACs increases and does so to a greater extent for BC–KOH compounds. For ACs obtained at R_{KOH} = 15 mol kg^{-1}, values as high as A_I = 1000–1200 mg g^{-1} are reached. For ACs produced from BC–LiOH and

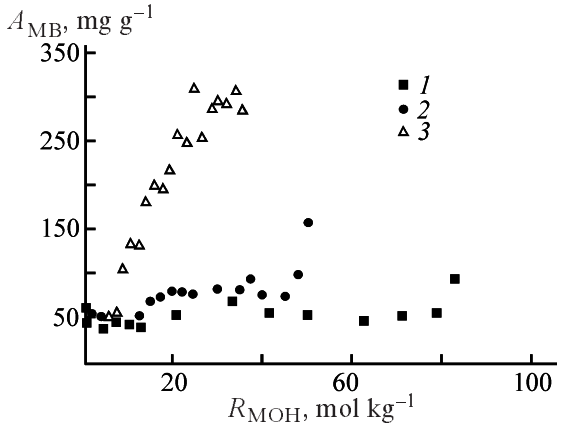


Fig. 3. Adsorption capacity for MB, A_{MB}, of adsorbents produced from BC–MOH compounds vs. the MOH/coal ratio R_{MOH}.

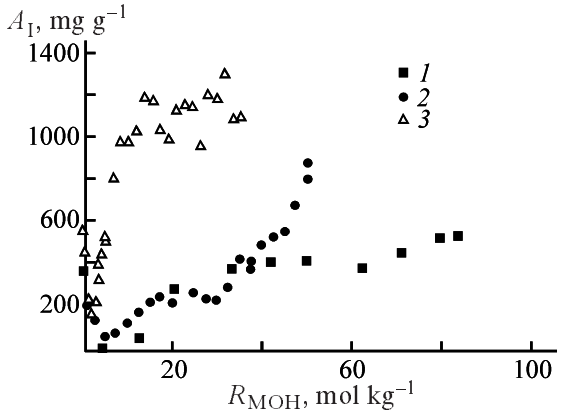


Fig. 4. Adsorption capacity for iodine, A_I, of adsorbents produced from BC–MOH compounds vs. the MOH/coal ratio R_{MOH}.

BC–NaOH, the adsorption capacities for iodine are lower (A_I = 860 mg g^{-1} for BC–NaOH and A_I = 520 mg g^{-1} for BC–LiOH), although the alkali : coal ratio is larger. For example, producing an AC with A_I = 600 mg g^{-1} requires a BC–MOH compound containing 5 mol kg^{-1} KOH, or 45 mol kg^{-1} NaOH, or no less than 100 mol kg^{-1} LiOH.

Figure 5 shows adsorption characteristics of ACs as functions of the specific surface area. As can be seen, A_{MB} changes only slightly, from 40 to 100 mg g^{-1}, as the specific surface area increases to approximately 500 m^2 g^{-1}. In the surface area range 500–800 m^2 g^{-1}, A_{MB} is independent of S_{BET}; this region is nearly entirely formed by adsorbents produced by thermolysis of BC–KOH compounds. For these adsorbents, A_{MB} increases with R_{MOH} (Fig. 3).

The adsorption capacity for iodine is directly proportional to S_{BET} (Fig. 5b), depends only slightly

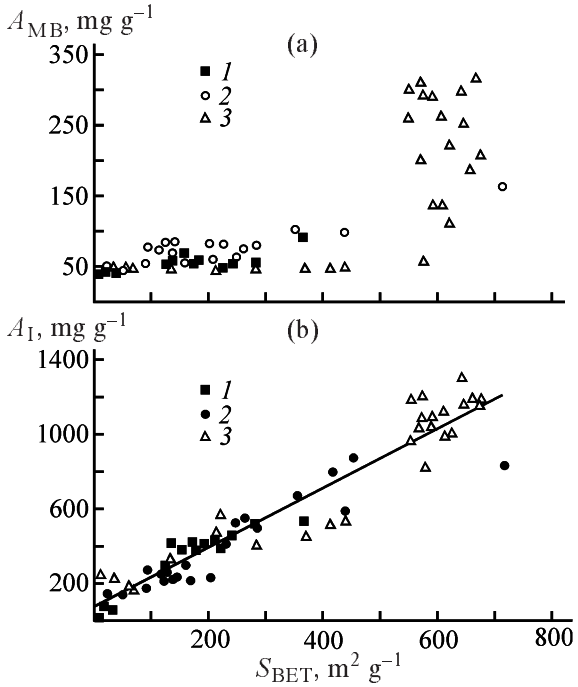


Fig. 5. Adsorption capacity for (a) MB, A_{MB}, and (b) iodine, A_I, vs. the specific surface area S_{BET} for adsorbent samples produced from BC–MOH compounds.

on the nature of a cation, and can be described by a linear dependence $A_I = 74 + 1.57S_{BET}$ ($R^2 = 0.92$). This means that only the specific surface area of the adsorbent is an important factor for the adsorption capacity for iodine, whereas the nature of an alkali is of almost no importance.

The adsorption capacity for MB ($A_{MB} \leq$ 310 mg g^{-1}) of adsorbents obtained in this study by thermolysis of BC with KOH exceeds that of carbons of OU-A and OU-B brands (A_{MB} = 210–225 mg g^{-1}), used to purify food and pharmaceutical products and process solutions [GOST (State Standard) 4453–74]. The adsorption capacity for iodine of these same adsorbents (A_I = 1000–1300 mg g^{-1}) also markedly exceeds the parameters of industrially manufactured carbons of BAU-A and BAU-MF brands (A_I = 600–700 mg g^{-1} according to GOST 6217–74).

CONCLUSIONS

(1) Thermolysis (800°C, 1 h) of brown coal impregnated with an alkali MOH (M = Li, Na, or K) yields adsorbents with high adsorbing capacities for iodine (up to 1300 mg g^{-1}) and Methylene Blue dye (up to 300 mg g^{-1}), which exceed the parameters of industrially manufactured activated carbons.

(2) The specific surface area and adsorption parameters of the adsorbents are governed by the alkali–coal ratio and increase in the order LiOH < NaOH < KOH.

(3) The dependences of the adsorption capacity for iodine on the specific surface area of the adsorbents are linear and the same for different alkalis.

REFERENCES

1. Marsh, H., Heintz, E.A., and Rodriguez-Reinoso, F., *Introduction to Carbon Technologies*, Alicante: Universidad, 1997.
2. Durie, R.A., *Fuel*, 1979, vol. 58, pp. 472–476.
3. Dubinin, M.M. and Plachenov, T.G., *Trudy III Vsesoyuznogo soveshchaniya "Adsorbenty, ikh poluchenie, svoistva i primenenie"* (Proc. III Al-Union Meet. "Adsorbents, Their Production, Properties, and Use"), Leningrad: Khimiya, 1971.
4. Lozano-Castello, D., Lillo-Rodenas, M.-A., Cazorla-Amoros, D., and Linares-Solano, A., *Carbon*, 2001, vol. 39, no. 5, pp. 741–749.
5. Yoshizawa, N., Maruyama, K., Yamada, Y., et al., *Fuel*, 2002, vol. 81, no. 15, pp. 1717–1722.
6. Tamarkina, Yu.V., Kucherenko, V.A., and Shendrik, T.G., *Zh. Prikl. Khim.*, 2004, vol. 77, no. 9, pp. 1452–1455.
7. Kucherenko, V.A. and Zubova, T.I., *Zh. Obshch. Khim.*, 1955, vol. 65, no. 8, pp. 1256–1264.
8. Addoun, A., Dentzer, J., and Ehrburger, P., *Carbon*, 2002, vol. 40, pp. 1140–1143.
9. Tamarkina, Yu.V., *Uglekhim. Zh.*, 2005, nos. 5–6, pp. 32–35.
10. *GOST* (State Standard) *4453–74: Powdered Clarifying Activated Charcoal*, Moscow: Gos. Komitet SSSR po Standartam, 1988.
11. *GOST* (State Standard) *6217–74: Crushed Activated Charcoal*, Moscow: Gos. Komitet SSSR po Standartam, 1988.
12. Marsh, H., Yan, D.S., O'Grady, T.M., and Wennerberg, A., *Carbon*, 1984, vol. 22, no. 6, pp. 603–611.
13. Pittman, C.U., Jiang, W., He, G.-R., and Gardner, S.D., *Carbon*, 1998, vol. 36, nos. 1–2, pp. 25–37.

ISSN 1070-4272, Russian Journal of Applied Chemistry, 2008, Vol. 81, No. 7, pp. 1171–1174. © Pleiades Publishing, Ltd., 2008.
Original Russian Text © I.Yu. Vashurina, A.S. Pogorelova, Yu.A. Kalinnikov, 2008, published in Zhurnal Prikladnoi Khimii, 2008, Vol. 81, No. 7, pp. 1092–1095.

PHYSICOCHEMICAL STUDIES OF SYSTEMS AND PROCESSES

Peat Humates as Alternative to Synthetic Dispersants in Leuco Acid Process of Fabric Dyeing with Vat Dyes

I. Yu. Vashurina, A. S. Pogorelova, and Yu. A. Kalinnikov

Ivanovo State University of Chemical Technology, Ivanovo, Russia
Institute of Solution Chemistry, Ivanovo, Russia

Received December 25, 2006

Abstract—The effect of humates isolated from peat on the state in solution of the leuco acid of Vat Brilliant Green C dye was examined spectrophotometrically and compared with the effect of dispersants traditionally used in textile-chemical processes: disodium methylenebis(naphthalenesulfonate) and triethanolamine.

DOI: 10.1134/S1070427208070082

Peat humates (PHs) are the salt form of humus acids, specific polymeric organic compounds synthesized in the nature from plant residues under the action of soil microorganisms and abiotic factors of the medium. Humus acids are irregular copolymers of polyhydroxycarboxylic acids, containing also diverse other fragments (both aliphatic and aromatic) and functional groups (carboxy, hydroxy, phenolic, quinone, keto, hydroxymethyl, amino, imino, etc.) [1, 2]. Therefore, PHs participate in ionic and donor–acceptor interactions, hydrogen bonding, and formation of complexes with metals and adducts with various classes of organic compounds [2–5]. For living bodies, peat humates are nontoxic and nonteratogenic. They exhibit high physiological activity, primarily as strong adaptogens [6].

Peat humates are used in plant and animal breeding [7, 8], in medicine [9–11], in technologies of soil remediation and wastewater treatment [6, 12, 13], in mining [14], in building [15], and in other branches of economy.

The environmental safety of PHs makes them very attractive for applications to any fields of human activity, especially if they can replace less environmentally friendly synthetic chemicals. The processes for recovery of humates from peat are safe and waste-free.

This work continues our studies aimed to substantiate the feasibility of using PHs in textile finishing processes. Previous studies revealed the capability of humates to modify structurally and chemically starch sizing gels [16], to catalyze the reduction of vat dyes in the course of fabric printing [17, 18], and to improve the parameters of fabric dyeing with vat dyes (intensity and uniformity of dyeing), especially in the leuco acid process [19].

In accordance with this process, a vat dye in the ionic form, reduced in an alkaline solution, is converted to a nondissociated leuco acid by weak acidification. The leuco form of the dye forms an unstable colloidal solution whose stability is provided by adding special compounds, dispersants. Interaction of the dye with the dispersant determines not only the stability of the colloidal solution, but also the course of sorption of the dye with a fiber and of the subsequent diffusion in the fiber.

The dispersants traditionally used in dyeing of fabrics with the leuco acid of a vat dye are disodium methylenebis(naphthalenesulfonate) (NF, DNF) and triethanolamine (TEA).

In this study we compared the effects of DNF, TEA, and PHs on the state in aqueous solution of the leuco acid of Vat Brilliant Green C dye (VBGC) with the aim to substantiate the dispersing effect of PHs exerted on nonionic forms of vat dyes.

EXPERIMENTAL

Colloidal solutions of VBGC leuco acid were prepared by mixing two components: alkaline solution of sodium salt of leuco compound of the vat dye and aqueous solution of acetic acid [20] into which the required amount of a dispersant (DNF, TEA, PHs) was additionally introduced. The pH of the colloidal solutions prepared was 6.0.

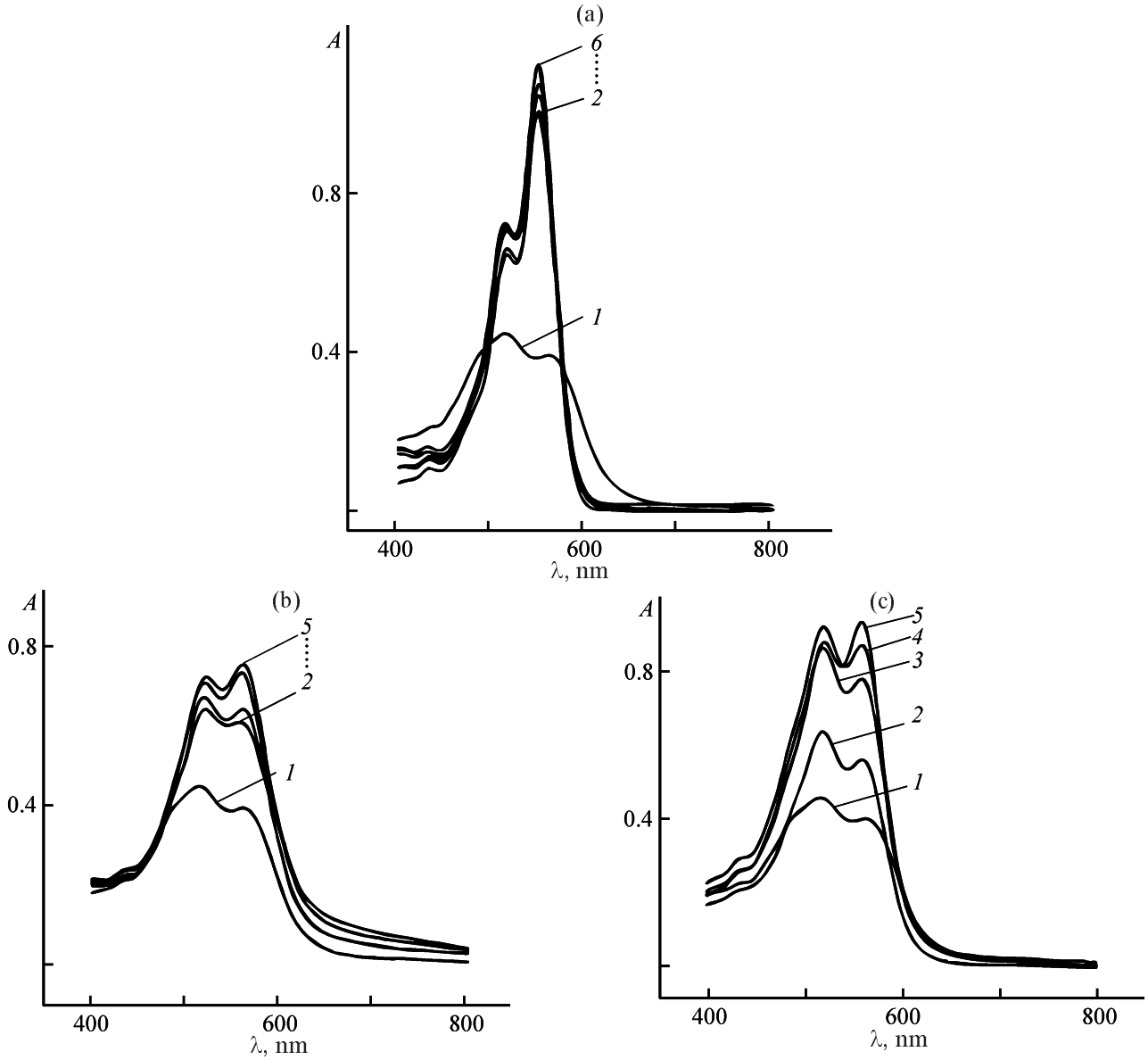


Fig. 1. Effect of the concentration of (a) DNF, (b) TEA, and (c) PHs in solution on the absorption spectra of VBGC leuco acid. (*A*) Optical density of VBGC solution and (λ) wavelength; the same for Fig. 2. [VBGC] = 8.32×10^{-5} M; 25°C. (a) [DNF], g l^{-1}: (*1*) 0, (*2*) 0.5, (*3*) 2, (*4*) 5, (*5*) 10, and (*6*) 50; (b) [TEA], g l^{-1}: (*1*) 0, (*2*) 1, (*3*) 5, (*4*) 10, and (*5*) 20; (c) [PHs], g l^{-1}: (*1*) 0, (*2*) 0.05, (*3*) 0.1, (*4*) 0.2, and (*5*) 0.5.

In the experiment we used VBGC dye as a pigment containing no additives of auxiliary textile substances.[1] The PH preparation was obtained from valley peat of the wood–sedge group by alkaline extraction [21] in the form of an aqueous solution with pH 8.2. Under these conditions, humates exhibit properties of anionic polyelectrolytes owing to dissociation of all carboxy groups and a part of phenolic groups.

[1] Submitted by Krasitel' Open Joint-Stock Company (Rubezhnoe, Ukraine).

In each series of experiments, the dye content was kept constant, and only the concentration of the additive was varied. The absorption spectra were recorded on a Specord M 400 spectrophotometer. The reference cell was filled with the solution of the dispersant of the same concentration as in the working cell and with the same pH.

The obtained series of absorption spectra of VBGC are shown in Figs. 1a–1c. As can be seen, the spectra of colloidal solutions of the leuco acid of the dye undergo noticeable changes. In all the

cases, the absorption appreciably increases (in the presence of DNF, by a factor of approximately 2.9; in the presence of TEA, by a factor of 1.6; in the presence of PHs, by a factor of 2.2). Also, DNF additions cause strong narrowing of the bands.

It is well known that, in solutions of ionic dyes, formation of disordered associates is accompanied by broadening of the absorption spectra and by a decrease in the extinction, which is the more pronounced, the larger the fraction of the dye involved in associates and the coarser the associates [22]. On the contrary, decomposition of the associates causes an increase in the optical density of the dye solution and narrowing of the spectrum. Hence, the spectral manifestations of the dispersing effect of the agents tested (DNF, TEA, PHs) toward the limitedly soluble leuco form of the vat dye coincide with the spectral manifestations of the decomposition of associates of ionic dyes into monomers.

In addition, we evaluated the effect exerted on the spectra of colloidal solutions of VBGC leuco acid by factors that a fortiori cause coagulation of the dye. In the first experiment, coagulation was induced by heating the solution, and in the second experiment, by adding an inorganic electrolyte (NaCl) acting as a salting-out agent [23]. The experimental data obtained are shown in Figs. 2a and 2b. They show that, in the course of coagulation (coarsening of dye particles in solution as a result of their aggregation, up to phase separation), the intensity of the light absorption by the dye decreases and the spectrum is broadened.

Thus, we can conclude that the dispersants tested cause disintegration of particles of the leuco acid of the vat dye in solution.

As already noted, an important feature of DNF is that even its first portions added to aqueous colloidal solutions of VBGC leuco acid cause significant narrowing of the absorption spectra of the dye. This fact indicates that the light absorption in the regions corresponding to the main electronic transition in the dye molecule becomes more efficient. From this standpoint, the observed narrowing of the spectrum can be considered as a consequence of weakening of the dye–solvent interaction on adding DNF. Hence, DNF additions cause resolvation of dye molecules, suppressing their vibrations.

This effect is not observed on adding the other two substances, TEA and PHs, to solutions of VBGC leuco acid, although the resolvation undoubtedly does take place, because the solutions are

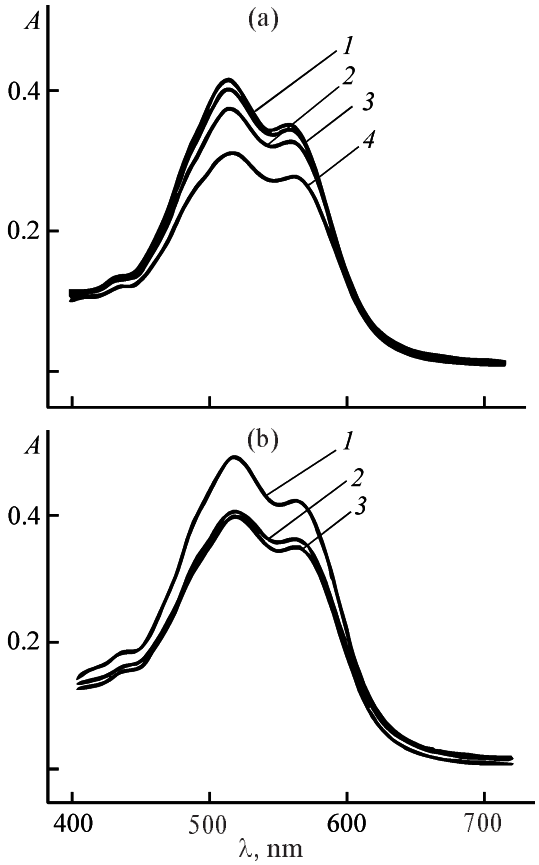


Fig. 2. Effect of (a) temperature and (b) NaCl concentration on the absorption spectra of solutions of VBGC leuco acid. [VBGC], M: (a) 6.7×10^{-5} and (b) 7.8×10^{-5}. (a) Temperature, °C: (*1*) 20, (*2*) 30, (*3*) 40, and (*4*) 50. (b) [NaCl], $g\ l^{-1}$: (*1*) 0, (*2*) 10, and (*3*) 20.

stabilized. For example, whereas without dispersants the dye coagulation starts within 30–40 min after preparing the solution, in the presence of small additions of PHs it starts in 10–12 h.

Presumably, different effects of DNF, TEA, and PHs on the absorption spectra of aqueous colloidal solutions of VBGC leuco acid are due to different nature of dye–additive interactions, which, in turn, are associated with specific features of the molecular structure of the additives. With DNF, naphthalene fragments of the dispersant molecule can interact with planar chromophores of the polycyclic vat dye molecule, which is accompanied by displacement of a part of the solvent from the solvation shell of the dye. With TEA, interaction of the dye occurs, most probably, via hydrogen bonding between hydroxy groups of the amino alcohol and functional groups of the dye. Peat humates contain in their molecules both aromatic structures and functional groups capable of hydrogen bonding.

Thus, humates recovered from peat can be recommended as adequate substitutes of synthetic dispersants. Their advantages are environmental safety, full absence of toxicity, and relatively low cost.

CONCLUSIONS

(1) In the presence of dispersants (DNF, TEA) and peat humates, the light absorption by the dye increases.

(2) In the dispersing performance, peat humates are intermediate between DNF and TEA.

ACKNOWLEDGMENTS

The study was supported by the Russian Foundation for Basic Research (project no. 06-04-08048-ofi).

REFERENCES

1. Orlov, D.S., *Gumusovye kisloty pochv i obshchaya teoriya gumifikatsii* (Humus Acids of Soils and General Theory of Humification), Moscow: Mosk. Gos. Univ., 1990.
2. Stevenson, F.J., *Humic Chemistry: Genesis, Composition, Reactions*, New York: Wiley, 1982, vol. 1.
3. Perminova, I.V., Gretschishcheva, N.Y., Kovalevskii, D.V., et al., *Environ. Sci. Technol.*, 2001, vol. 35, pp. 3841–3848.
4. Perminova, I.V., Grechishcheva, N.Yu., and Petrosyan, V.S., *Environ. Sci. Technol.*, 1999, vol. 33, pp. 3781–3787.
5. Kulikova, N.A. and Perminova, I.V., *Environ. Sci. Technol.*, 2002, vol. 36, pp. 3720–3724.
6. Perminova, I.V. et al., *Use of Humic Substances to Remediate Polluted Environments: From Theory to Practice*, Springer, 2005, pp. 285–309.
7. Chukov, S.N., Talashkina, V.D., and Nadporozhskaya, M.A., *Pochvovedenie*, 1995, no. 2, pp. 169–173.
8. Boiko, V.P., Naumova, G.V., Ovchinnikova, T.F., et al., *Prirodopol'zovanie*, 1998, no. 4, pp. 82–86.
9. Yubitskaya, N.S. and Ivanov, E.M., *Vopr. Kurortol., Fizioterap. Lech. Fizkul't.*, 1999, no. 5, pp. 22–24.
10. Avvakumova, N.P., Composition and Biological Properties of Humus Acids of Peloids (Basic and Applied Aspects), *Doctoral Dissertation*, Moscow, 2003.
11. Brzozowski, T. and Dembinski, A., *Acta Pol. Pharm.*, 1994, vol. 51, no. 1, pp. 103–107.
12. Putsykin, Yu.G. and Shapovalov, A.A., *Transport Khran. Nefteprod.*, 2003, no. 11, pp. 17–18.
13. Salem, K.M., Grechishcheva, N.Yu., Perminova, I.V., et al., *Zashch. Okruzh. Sredy Neftegaz. Kompl.*, 2004, no. 1, pp. 34–37.
14. Shishmina, L.V., Chukhareva, N.V., and Kravtsov, A.V., *Koks Khim.*, 2002, no. 2, pp. 7–9.
15. Lotov, V.A., Maslov, S.G., and Chukhareva, N.V., *Tekh. Tekhnol. Silikatov*, 2004, nos. 3–4, pp. 26–29.
16. Kochkina, N.E., Substantiation of the Use of Humic Preparations for Improving the Efficiency of Sizing of Cotton Yarn, *Cand. Sci. Dissertation*, Ivanovo, 2004.
17. Pogorelova, A.S., Development of Theoretical Principles of Applying Humic Acids to Dyeing and Printing of Fabrics with Vat Dyes, *Cand. Sci. Dissertation*, Ivanovo, 2002.
18. Vlasova, E.A., Vashurina, I.Yu., and Kalinnikov, Yu.A., *Zh. Prikl. Khim.*, 2006, vol. 79, no. 6, pp. 998–1001.
19. Vashurina, I.Yu., Pogorelova, A.S., and Kalinnikov, Yu.A., *Izv. Vyssh. Uchebn. Zaved., Tekhnol. Tekstil'n. Prom–sti.*, 2004, no. 3, pp. 63–67.
20. Yakimchuk, R.P., Mishchenko, A.V., and Bulusheva, N.E., *Primenenie kubovykh krasitelei (fiziko-khimicheskie osnovy)* (Use of Vat Dyes (Physicochemical Principles)), Moscow: Legprombytizdat, 1985.
21. Ponomareva, V.V. and Plotnikova, T.A., *Gumus i pochvoobrazovanie* (Humus and Soil Formation), Leningrad: Nauka, 1980.
22. Terenin, A.N., *Fotonika molekul krasitelei* (Photonics of Dye Molecules), Leningrad: Nauka, 1967.
23. Frolov, Yu.G., *Kurs kolloidnoi khimii: Poverkhnostnye yavleniya i dispersnye sistemy* (Course of Colloid Chemistry: Surface Phenomena and Disperse Systems), Moscow: Khimiya, 1989.

ISSN 1070-4272, Russian Journal of Applied Chemistry, 2008, Vol. 81, No. 7, pp. 1175–1179. © Pleiades Publishing, Ltd., 2008.
Original Russian Text © T.E. Nikiforova, N.A. Bagrovskaya, V.A. Kozlov, S.V. Natareev, 2008, published in Zhurnal Prikladnoi Khimii, 2008, Vol. 81, No. 7, pp. 1096–1100.

PHYSICOCHEMICAL STUDIES OF SYSTEMS AND PROCESSES

Sorption Properties of Plasma-Modified Flax Fibers

T. E. Nikiforova, N. A. Bagrovskaya, V. A. Kozlov, and S. V. Natareev

State Educational Enterprise for Higher Professional Education, Ivanovo State University of Chemical Engineering, Ivanovo, Russia
Institute of Solution Chemistry, Russian Academy of Sciences, Ivanovo, Russia

Received October 30, 2007

Abstract—Effect of plasma modification on the sorption properties of short flax fibers for Zn(II) ions was studied.

DOI: 10.1134/S1070427208070094

Of interest in development of resource-saving technologies are sorption methods for purification of various aqueous solutions to remove heavy metal ions, with natural polymeric materials of vegetable origin as sorbents. Owing to their availability and low cost [1–3], agricultural wastes are promising sorbents for recovery of heavy metal ions from aqueous media. However, sorbents of this kind, as a rule, have low sorption capacity for the target component. Therefore, an important area in the development of new sorbents is modification of natural cellulose-containing polymers to raise their sorption capacity. There have been reports [4–9] in which various methods for processing of cellulose-containing sorbents were suggested, including mechanical, physical, mechanochemical, chemical, physicochemical, and biotechnological kinds of treatment. A promising area of modification of polymeric sorbents is application of environmentally safe plasma techniques [10, 11].

The aim of this study was to examine the effect of plasma modification of a natural cellulose-containing polymer, short flax fibers, on its sorption properties with respect to Zn(II) ions.

EXPERIMENTAL

We used in the study short flax fibers, a secondary product obtained at flax mills and having the following composition (%): cellulose 75–78, hemicellulose 9.4–11.9, lignin 3.8, pectin substances 2.9–3.2, waxy substances 2.7, nitrogen-containing substances 1.9–2.1 (in terms of proteins), and mineral substances 1.3–2.8 [12]. We also used $ZnSO_4 \cdot 7H_2O$ and NaOH of chemically pure grade.

The sorbents were modified using two kinds of discharge. The laboratory installations used to treat a sorbent with an atmospheric-pressure-discharge plasma and low-pressure gas-discharge plasma were similar to those described in [13]. The short flax fibers was modified with the atmospheric-pressure-discharge plasma in a glass cell equipped with two metallic electrodes and a magnetic stirrer. One of the electrodes (cathode) was submerged in a solution, and the other (anode) was situated over the surface of the electrolyte solution at a distance of 5 mm. The sorbent was placed in the cell and poured over with a NaOH solution with a concentration of 0.5 g l^{-1} at a solution : sorbent ratio of 80. A voltage of about 1 kV was applied to the electrodes, which resulted in that an atmospheric-pressure glow gas discharge appeared between the electrode in the gas phase and the surface of the aqueous electrolyte solution. The discharge current I was varied from 15 to 30 mA, with the treatment time τ_{tr} in the range 5–30 min. After the treatment, the sorbent was extracted from the cell and dried in air at room temperature to constant mass.

Modificaiton of short flax fibers with low-pressure gas-discharge plasma was performed in a plasmochemical reactor designed as a glass tube with metallic electrodes arranged in side arms. The sorbent was placed in the reactor evacuated to a residual pressure of 1 Pa. Then air was fed at a velocity of 5 cm s^{-1} with continuous pumping. The sorbent was treated with a glow discharge under the following conditions: working pressure 100 Pa, discharge current 15 and 30 mA, electrode voltage about 1 kV, treatment time 5–30 min.

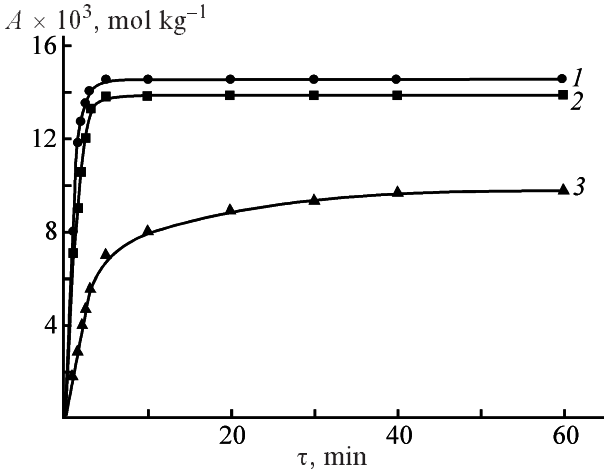


Fig. 1. Kinetics of sorption of Zn(II) ions (*1, 2*) by short flax fibers modified at I = 30 mA and τ_{tr} = 30 min with (*1*) atmospheric-pressure-discharge plasma and (*2*) low-pressure gas-discharge plasma and (*3*) by native flax fibers. (A) Sorption capacity and (τ) sorption time.

The sorption of Zn(II) ions from aqueous solutions of zinc sulfate was studied under static conditions with stirring and thermostating (293 K). The sorption kinetics was analyzed by the limited-volume method [14]. To obtain kinetic curves of sorption, weighed portions (m = 0.1 g) of native or plasma-modified flax fibers were placed in a set of test tubes, poured over with 10 ml (V) of an aqueous zinc sulfate solution with an initial concentration $c_0 = 1.5 \times 10^{-4}$ M, and kept for 30 min to 24 h. After certain intervals of time, the solution was separated from the sorbent and the current concentration of zinc ions, c_τ, in solution was determined by atomic-absorption spectroscopy on a Saturn instrument. The sorption capacity A_i of the sorbent at any given instant of time was calculated by the formula

$$A_i = \frac{c_0 - c_i}{m} V.$$

Under the conditions of an equilibrium attained by the system, we determined the equilibrium concentration of metal ions in solution, c_{eq}, and calculated the equilibrium sorption capacity of the sorbent, A_{eq}:

$$A_{eq} = \frac{c_0 - c_{eq}}{m} V.$$

The degree of recovery (%) was determined as follows:

$$\alpha = \frac{c_0 - c_{eq}}{c_0} \times 100.$$

To obtain sorption isotherms, weighed portions (0.1 g) of short flax fibers were placed in a set of test tubes, poured over with 10 ml of an aqueous zinc sulfate solution with initial concentrations of 1.5×10^{-4}–8×10^{-3} M, and kept until the equilibrium was attained. Then we separated the solution from the sorbent by filtration and determined the concentration of metal ions.

The relative experimental error was calculated using data of equilibrium and kinetic experiments in which each point is an average of the results of three parallel runs [15]. The accuracy of the Saturn instrument in determining the concentration of metal ions is 3%. The experimental error did not exceed 10%.

Important parameters of polymeric sorbents are the sorption capacity and the time in which the sorption equilibrium is attained [16]. Kinetic studies demonstrated that, in sorption of Zn(II) ions by native short flax fibers, the equilibrium in the system is attained in 40 min. The sorption capacity of the native polymer is 9.7×10^{-3} mol kg^{-1} (Fig. 1, curve *3*). The results obtained indicate that the native sorbent has good kinetic properties at a low sorption capacity.

Natural flax is composed of a set of polymers containing various functional groups exhibiting donor properties: carboxy, ether, and hydroxy groups. These groups can adsorb metal ions. Flax fibers also contain hydrophobic components, lignin and waxy substances, which hinder wetting of the natural sorbent and interfere with the sorption process. Consequently, to improve the sorption properties of flax fibers, it is necessary to remove hydrophobic substances from fibers or modify them. In addition, it is necessary to form new sorption-active groups in the sorbent. Therefore, we studied the effect of plasma treatment on the equilibrium and kinetic characteristics of short flax fibers with respect to Zn(II) ions.

The results of kinetic experiments on sorption of Zn(II) ions by short flax fibers modified by low-pressure gas-discharge and atmospheric-pressure-discharge plasmas are shown in Fig. 1 (curves *1, 2*). These data indicate that both the modification methods lead to an increase in the sorption capacity of short flax fibers by a factor of approximately 1.5. The strongest effect is obtained in activation of the sorbent by the atmospheric-pressure-discharge plasma. Simultaneously, the time of sorption of zinc ions by plasma-modified short flax fiber samples is 40 to 5 min shorter than that for the native sample.

The influence exerted by the modification time on the sorption capacity of short flax fibers is illustrated

by Fig. 2 for two kinds of discharge, with currents of 15 and 30 mA in each case. It should be noted that the duration of the modifying treatment noticeably affects the extent to which the sorption capacity of the polymer increases. Figure 2 shows that the effect of the plasma activation on the sorption properties of short flax fibers is observed already after 5 min of discharge treatment. The growth of the discharge capacity of the sorbent occurs during the entire modification process, becoming somewhat slower by its end. Upon activation for 30 min at a discharge current of 30 mA, the degree of recovery of zinc ions by modified sorbents is 1.4 and 1.5 times that of native flax fibers for low-pressure gas-discharge and atmospheric-pressure-discharge plasmas, respectively. Somewhat poorer results are observed at a discharge current of 15 mA.

To determine the optimal parameters of the plasma activation of the natural sorbent, we studied the effect of various methods and modes of modification on the kinetic and sorption characteristics of the polymer. The table presents the results obtained in modification of the short flax fibers with atmospheric-pressure-discharge and low-pressure gas-discharge plasmas in comparison with the native sorbent and short flax fibers treated with a NaOH solution with a concentration of 0.5 g l^{-1}. The treatment with such an alkali solution was chosen because, in accordance with the procedure employed, it is used for activation of the sorbent in the plasma–solution system. Therefore, it was necessary to estimate the contribution of each kind of modification to the integral effect of enhancement of the sorption capacity of short flax fibers. As seen from the table, modification of the sorbent with a NaOH solution leads to a 10% increase in the degree of recovery of zinc ions and to a decrease in the sorption time by a factor of approximately 2.5, compared to the natural fiber. This can be attributed to the following: alkaline treatment results in removal of hemicelluloses and partial removal of hydrophobic waxy substances and lignin, which hinder adsorption of aqueous solutions of reagents (zinc ions) and decelerate their penetration into the fiber. As a result, the porosity and hydrophilicity of flax fibers increases and the functional groups capable of binding heavy metal ions become more accessible.

The data in the table indicate that the plasma modification substantially improved the sorption-kinetic properties of the natural sorbent. In sorption of Zn(II) ions on sorbents modified with atmospheric-pressure-discharge and low-pressure gas-discharge plasmas, the time in which equilibrium is attained in the heterogeneous system becomes 4–8 times shorter and, depending on the treatment duration, is 5–10 min.

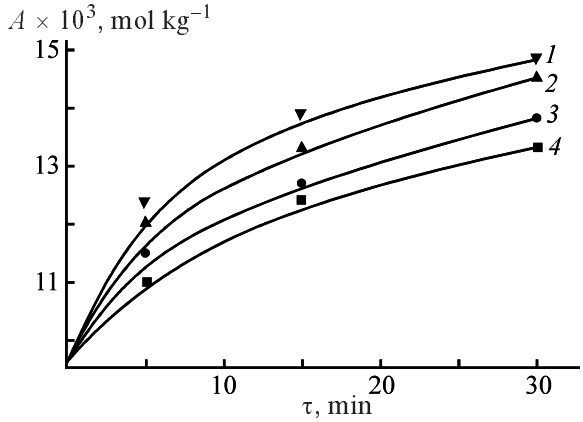


Fig. 2. Effect of the time τ of modification with (*1, 2*) atmospheric-pressure-discharge plasma and (*3, 4*) low-pressure gas-discharge plasma at I of (*1, 3*) 30 and (*2, 4*) 15 mA on the sorption capacity of short flax fibers. (*A*) Sorption capacity.

The effect observed is accounted for by simultaneous occurrence of several processes. First, these are oxidation and removal of incrusting substances:

Plasma activation parameters and characteristics of the natural sorbent in various modification conditions

Modification method	τ_{eq},* min	c_{eq}, mg l^{-1}	α, %	$A \times 10^3$, mol kg^{-1}
Unmodified sorbent	40	3.8	62	9.7
NaOH solution, 0.5 g l^{-1}	15	2.8	72	11.3
Low-pressure gas-discharge plasma				
I = 15 mA, τ_{tr}, min:				
5	10	2.2	78	12.2
15	7	1.9	81	12.7
30	5	1.5	85	13.3
I = 30 mA, τ_{tr}, min:				
5	10	2.0	80	12.5
15	7	1.7	83	13.0
30	5	1.2	88	13.8
Atmospheric-pressure-discharge plasma:				
I = 15 mA, τ_{tr}, min:				
5	8	1.6	84	13.1
15	6	1.2	88	13.8
30	5	0.7	93	14.5
I = 30 mA, τ_{tr}, min:				
5	8	1.4	86	13.4
15	6	1.0	90	14.1
30	5	0.5	95	14.8

* τ_{eq} is the equilibration time.

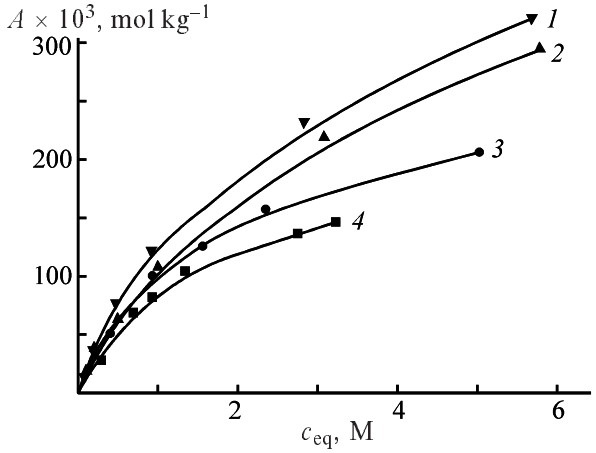


Fig. 3. Isotherm of sorption of Zn(II) ions by short flax fibers modified at I = 30 mA, τ_{tr} = 30 min with (*1*) atmospheric-pressure-discharge plasma and (*2*) low-pressure gas-discharge plasma. (*A*) Equilibrium sorption capacity and (c_{eq}) concentration of metal ions in solution. (*3*) Flax fibers treated with a NaOH solution and (*4*) native flax fibers.

hemicelluloses, waxy and pectin substances, and lignin. Second, these are partial depolymerization and oxidation of cellulose as the main component of flax.

Thus, the plasma treatment leads to chemical changes in the surface layers of flax fibers (~5 nm). Treatment in a low-pressure glow discharge makes lower the molecular weight of cellulose and oxidizes it to give mostly aldehyde groups [13]. Also noted is the formation of low-molecular-weight fractions of cellulose, which can be removed by washing in water. This accounts for the smaller increase in the degree of recovery of zinc ions by short flax fibers upon their modification with low-pressure gas-discharge plasma, compared with that upon modification of the fibers with atmospheric-pressure-discharge plasma.

Modification with the atmospheric-pressure-discharge plasma is also accompanied by depolymerization and oxidation. However, the material being processed is subjected in this case to a milder treatment, the degradation processes do not have such a deep impact on the polymer, and the resulting effect is preserved in the course of time.

The main difference between the two kinds of plasma modification of the polymer consists in the qualitative and quantitative dissimilarity of the active species being generated and of their effect on the polymer. In the atmospheric-pressure-discharge plasma, the concentration of atomic oxygen is comparable with that in the low-pressure plasma, whereas the concentration of singlet oxygen is considerably lower, and that of ozone, several orders of magnitude higher. Passing to humid air results in a substantial decrease in the concentrations of ozone and atomic oxygen, but oxidizing agents with other properties, OH and HO_2 radicals, appear instead [13].

To determine parameters characterizing the sorption capacity of unmodified and modified short flax fibers, we measured isotherms of sorption of Zn(II) ions from aqueous $ZnSO_4$ solutions (Fig. 3). The experimental data can be described by Langmuir adsorption isotherm equation:

$$A = A_\infty K c_{eq}/(1 + K c_{eq}),$$

where K is the concentration constant of the sorption equilibrium, which characterizes the intensity of the sorption process (M^{-1}).

Linearization of the sorption isotherms by the equation

$$\frac{1}{A} = \frac{1}{A_\infty} + \frac{1}{A_\infty K}\frac{1}{c_{eq}}$$

enabled graphical determination of the limiting sorption A_∞ in the Langmuir equation for native flax fibers and for flax fibers modified with an alkaline solution, low-pressure gas-discharge plasma, and atmospheric-pressure-discharge plasma: 0.15, 0.20, 0.45, and 0.53 mol kg^{-1}, respectively.

CONCLUSIONS

(1) The time τ_{eq} in which sorption equilibrium of flax fibers with respect to Zn(II) ions is attained in the system constituted by an aqueous zinc sulfate solution and plasma-modified short flax fibers is 4–8 times shorter than τ_{eq} for unmodified fibers: 5–10 min depending on the treatment duration.

(2) Plasma modification of short flax fibers leads to an increase in their limiting sorption capacity by a factor of approximately 3–3.5. The strongest effect is observed in the case of modification of flax fibers with an atmospheric-pressure-discharge plasma.

(3) The improvement of the equilibrium-kinetic characteristics of the natural polymer is accounted for by the following: occurrence of degradation and oxidation processes leading to removal of hydrophobic substances from the fibers; increase in their hydrophilicity, porosity, and internal surface area; better accessibility of the available functional groups; and formation of new sorption-active groups in the polymer being modified.

REFERENCES

1. Bagrovskaya, N.A., Nikiforova, T.E., Kozlov, V.A., and Lilin, S.A., *Izv. Vyssh. Uchebn. Zaved., Khim. Khim. Tekhnol.*, 2002, vol. 45, no. 4, pp. 131–133.
2. Michado, R., Carvalho, J.R., and Correia, M.J.N., *J. Chem. Technol. Biotechnol.*, 2002, vol. 77, no. 12, pp. 1340–1348.
3. Chamarthy, S., Seo, C.W., and Marshall, W.E., *J. Chem. Technol. Biotechnol.*, 2001, vol. 76, no. 6, pp. 593–597.
4. USSR Inventor's Certificate no. 1696399.
5. Shukla, S.R. and Sakhardande, V.D., *J. Appl. Polym. Sci.*, 1990, vol. 41, no. 11–12, pp. 2655–2663.
6. Toshihiko, S., Kazuhiro, K., Hiromi, K., and Yasuo, O., *J. Soc. Fiber Sci. Technol.*, 1983, vol. 39, no. 12, pp. 519–524.
7. Stavitskaya, S.S., Mironyuk, T.I., Kartel', N.T., and Strelko, V.V., *Zh. Prikl. Khim.*, 2001, vol. 74, no. 4, pp. 575–578.
8. RF Patent 2258560.
9. Nikiforova, T.E., Kozlov, V.A., Bagrovskaya, N.A., and Rodionova, M.V., *Zh. Prikl. Khim.*, 2007, vol. 80, no. 2, pp. 236–241.
10. RF Patent 2217231.
11. RF Patent 2217389.
12. Krichevskii, G.E., Korchagin, M.V., and Senakhov, A.V., *Khimicheskaya tekhnologiya tekstil'nykh materialov* (Chemical Technology of Textile Materials), Moscow, 1985.
13. Kutepov, A.M., *Vakuumno-plazmennoe i plazmenno-rastvornoe modifitsirovanie polimernykh materialov* (Vacuum–Plasma and Plasma–Solution Modification of Polymeric Materials), Moscow: Nauka, 2004.
14. Kokotov, Yu.A. and Pasechnik, V.A., *Ravnovesie i kinetika ionnogo obmena* (Equilibrium and Kinetics of Ion Exchange), Leningrad: Khimiya, 1970.
15. Akhnazarova, S.L. and Kafarov, V.V., *Metody optimizatsii eksperimenta v khimicheskoi tekhnologii* (Methods for Experiment Optimization in Chemical Technology), Moscow: Vysshaya Shkola, 1985.
16. Ashirov, A., *Ionoobmennaya ochistka stochnykh vod, rastvorov i gazov* (Ion-Exchange Purification of Wastewater, Solutions, and Gases), Leningrad: Khimiya, 1983.

ISSN 1070-4272, Russian Journal of Applied Chemistry, 2008, Vol. 81, No. 7, pp. 1180–1183. © Pleiades Publishing, Ltd., 2008.
Original Russian Text © N.V. Evreinova, I.A. Shoshina, V.N. Naraev, K.I. Tikhonov, 2008, published in Zhurnal Prikladnoi Khimii, 2008, Vol. 81, No. 7, pp. 1101–1105.

APPLIED ELECTROCHEMISTRY AND CORROSION PROTECTION OF METALS

Electrodeposition of Iron from Sulfate Solutions in the Presence of Aminoacetic Acid

N. V. Evreinova, I. A. Shoshina, V. N. Naraev, and K. I. Tikhonov

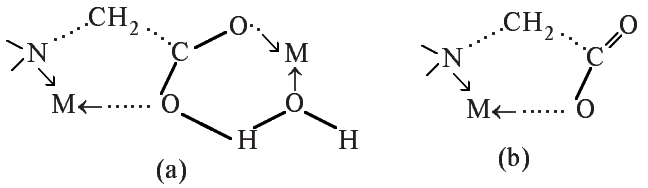
St. Petersburg State Institute of Technology (Technical University), St. Petersburg, Russia

Received December 7, 2007

Abstract—The kinetics and technology of iron electrodeposition from sulfate solutions containing various amounts of aminoacetic acid at pH 1.65, 1.95, and 2.50 in the temperature range 20–50°C were studied.

DOI: 10.1134/S1070427208070100

Amino acids are widely used in various branches of science and engineering [1–8], including electrolytic deposition of metals. Use of amino acids in electroplating is caused by the fact that electrolytes based on carboxylic acids and their derivatives can replace toxic electrolytes [2], allow preparation of alloys having preset physicochemical properties with a high current efficiency [3], and are relatively noncorrosive [6–8]. Furthermore, amino acids undergo biodegradation in sewage, which can be enhanced by adding chemical oxidants. As a result, amino acids lose the ability to bind metal ions [5]. Reactions of amino acids with metal cations result in the formation of various highly stable cyclic structures (chelates) [5]. Depending on temperature, pH of solution, ligand concentration, and some other factors, various complexes species can be formed:



It is also well known that organic acids exhibit buffer properties [4]. Their use in the deposition of electronegative metals provides the maintenance of constant pH in the cathode region. In particular, when iron group metals are electroplated, with the aim to improve the quality of the coatings, it is recommended to add certain amounts of aminoacetic acid to the electrolyte [2]. However, its role in the course of electrode reactions during the electrolysis of metal salts is poorly understood, and the choice of its optimal concentration is not substantiated.

The aim of this work was to study the kinetics of electrode reactions of iron deposition from sulfate solutions containing various amounts of aminoacetic acid (glycine) and to determine conditions for obtaining high-quality iron coatings.

EXPERIMENTAL

To prepare solutions, we used chemically pure grade $FeSO_4 \cdot 7H_2O$ and analytically pure grade NH_2CH_2COOH. The required pH was adjusted with sulfuric acid (analytically pure grade). Solutions with a constant $FeSO_4$ concentration of 0.2 M and the aminoacetic acid concentration varied within the range 0.05–0.4 M were studied. The experiments were carried out at pH 1.65, 1.95, and 2.50, at 20–50°C. The concentration of iron(II) ions and the total iron content were determined by volumetric permanganate titration [9]. The current efficiency by iron was determined gravimetrically. The electrolysis was carried out in the galvanostatic mode, using a B5-47 stabilized power source. Each experiment was repeated no less than three times on conditions that smooth deposits evenly covering the cathode working surface were obtained. Polarization curves were taken in the potentiostatic mode using a temperature-controlled three-electrode glass cell. The working electrode was a plate of electrolytic iron of 1 cm^2 area, auxiliary electrodes were made of transformer iron, and the reference electrode was a saturated silver chloride electrode. The buffer capacity was determined by potentiometric titration [10] with a 0.5 M NaOH solution. In so doing, the acidity was measured with a 150M pH-meter.

Table 1. Influence of glycine concentration and electrolyte pH on the current efficiency by iron. Temperature 20°C

Glycine concentration, M	Me : L molar ratio	pH	Current efficiency by iron, %, at indicated current density, mA cm^{-2}					
			10	15	20	25	30	50
0	1 : 0	–	–	2.4	5.6	8.9	–	
		1.95	24.7	–	28.8	29.2	30.4	–
		2.50	39.9	–	46.8	–	51.5	–
0.05	1 : 0.25	1.95	33.2	46.9	64.7	70.4	72.1	–
0.1	1 : 0.5	1.65	–	–	12.6	17.5	21.3	–
		1.95	56.9	68.7	71.9	79.4	86.2	91.1
		2.50	68.6	–	77.2	84.5	91.5	95.6
0.15	1 : 0.75	1.95	30.4	35.2	40.6	59.8	66.2	–
0.2	1 : 1	1.65	–	–	3.4	6.2	9.5	–
		1.95	–	10.4	15.3	18.7	23.6	29.3
		2.50	–	21.5	25.6	37.8	42.3	68.8
0.4	1 : 2	1.95	8.8	–	10.7	16.9	18.6	–

The current efficiency by iron in relation to the current density and pH of the solution is given in Table 1. These data show that the current efficiency increases in the whole pH range examined as the current density increases. The addition of glycine to the electrolyte first leads to an increase in the current efficiency, but at glycine concentrations higher than 0.1 M it decreases. For example, at a concentration of 0.4 M, practically only hydrogen is evolved (Table 1). In pure sulfate solutions, iron is deposited from simple iron ions, whereas, when glycine is added, iron ions partially or completely form complexes. However, the observed character of the dependence of the current efficiency by iron on the aminoacetic acid concentration cannot be attributed to the kinetics of the discharge of iron complex ions. According to the kinetics of electrode reactions, the rate of metal ion discharge from complex compounds should be less than or equal to that from simple ions, as determined by the reaction mechanism. Similar dependences were obtained at 40 and 50°C.

The addition of glycine affects not only the kinetics, but also the quality of the deposits. For example, without glycine, grey coatings with pitting are obtained; they begin to crack as the current density increases (over 30 mA cm^{-2}). Addition of glycine allows us to expand the range of working current densities to 50 mA cm^{-2} and to obtain lustrous smooth deposits. The best coatings are obtained at glycine concentrations of 0.1–0.15 M. Similar dependences were obtained at 40–50°C.

To determine the kinetics of electrode processes in the electrolytes under the above-given conditions, we recorded the cathodic and anodic polarization curves. The results obtained at 20°C and pH 1.95 are shown in Figs. 1 and 2. It can be seen that the rate of the cathode process decreases as the concentration of glycine in the electrolyte and pH decrease. The same trend is observed at 40–50°C.

We calculated the partial curves on the basis of the total polarization curves and current efficiencies by iron. The partial curves of discharge of iron ions are presented in semilog coordinates in Fig. 3. It is seen that the experimental points for all the considered variants are well fitted by straight lines with a slope corresponding to the discharge of iron ions in steps, with addition of the first electron being the slow step. Certain deviation from such

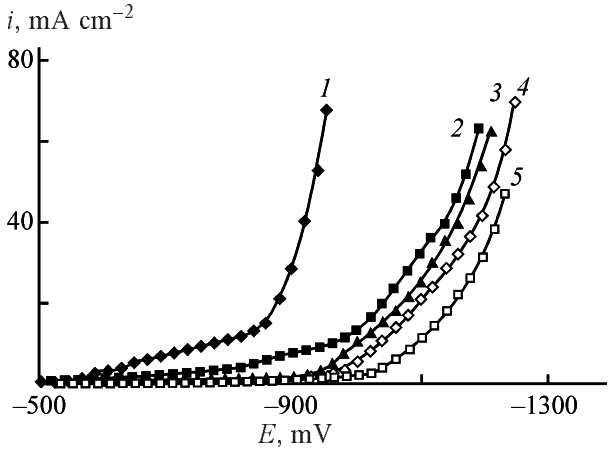


Fig. 1. Total potentiostatic polarization curves. 20°C, pH 1.95; the same for Figs. 3 and 4. (*i*) Cathode current density and (*E*) potential (vs. saturated silver chloride electrode); the same for Fig. 2. Acid concentration, M: (*1*) 0, (*2*) 0.05, (*3*) 0.1, (*4*) 0.15, and (*5*) 0.2.

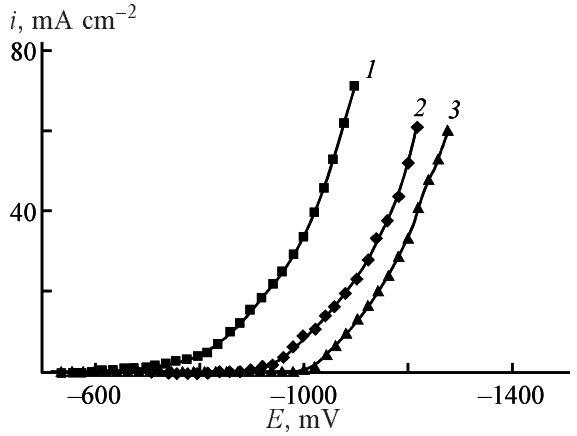


Fig. 2. Total potentiostatic polarization curves at various acidities of solution. Acid concentration 0.1 M, temperature 20°C. pH: (*1*) 1.65, (*2*) 1.95, and (*3*) 2.50.

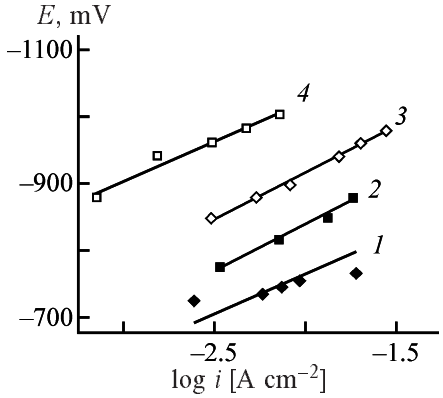


Fig. 3. Partial polarization curves for iron deposition in Tafel coordinates. (*i*) Current density and (*E*) potential (vs. saturated silver chloride electrode). Acid concentration, M: (*1*) 0, (*2*) 0.05, (*3*) 0.15, and (*4*) 0.2.

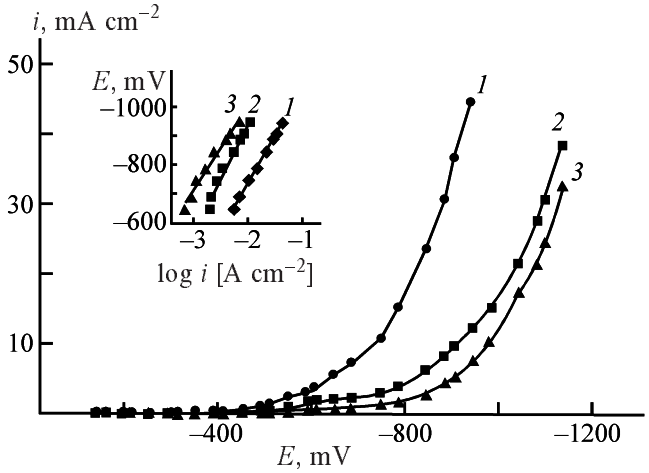


Fig. 4. Partial polarization curves for hydrogen evolution, obtained in a 0.2 M Na_2SO_4 solution, and check of the applicability of the Tafel equation. (*i*) Cathode current density and (*E*) potential (vs. saturated silver chloride electrode). Acid concentration, M: (*1*) 0, (*2*) 0.1, and (*3*) 0.2.

dependence of straight line *1* can result from the narrow range of obtaining high-quality deposits. We calculated the apparent activation energies of the discharge of iron ions, which are equal to 45.73, 32.24, and 34.30 kJ mol^{-1}, respectively, from the temperature dependence of the rate of the cathode process in solutions with different glycine concentrations of 0, 0.1, and 0.2 M. The values obtained also confirm that the electrochemical process is slow.

For the reaction of hydrogen evolution, we recorded the polarization curves in solutions similar in composition to those under study, but free of iron ions (Fig. 4). The data obtained at 20°C and pH 1.95 show that the presence of glycine in the electrolyte decreases the discharge rate of hydrogen ions, which may be due to glycine adsorption on the negatively charged electrode surface. It is known that, at the electrolyte acidity under study, glycine in solution is in the form of the $^{+}NH_3CH_2COOH$ cation [11], and the zero-charge potential of iron is −0.35 V [12]. Thus, the addition of glycine to the electrolyte affects the kinetics of both processes, but to a different extent. It is this fact that may be responsible for the observed maximum in the dependence of the current efficiency by iron on the amino acid concentration. At low glycine concentrations (up to 0.1 M), when iron is partially involved in complex formation, the current efficiency by iron grows owing to the inhibition of the parallel reaction to a greater extent. As the glycine concentration increases and iron becomes completely involved in the complex formation, the discharge rate of iron ions decreases to a greater extent than that of hydrogen ions, with the result that the current efficiency decreases.

The examination of the anode curves shows that the addition of glycine to the electrolyte does not affect the iron dissolution in the entire range of temperature and solution acidity. We found equilibrium potentials from the discharge curves of iron. For the amino acid concentrations of 0, 0.1, and 0.4 M these potentials are −0.488, −0.556, and −0.648 V, respectively. The shift of the equilibrium potential toward the negative values suggests the formation of complex species; however, these data are insufficient to make a conclusion on the structure of the complexes. The buffer capacities of the electrolyte, given in Table 2, were determined by potentiometric titration. It can be seen that the addition of glycine to the electrolyte in an amount of 0.2 M increases the buffer capacity by a factor of almost five. Furthermore, the addition of aminoacetic acid positively affects the electrolyte stability. We

Table 2. Buffer capacity of iron-plating electrolytes at various concentrations of aminoacetic acid

Electrolyte	c, M	Buffer capacity, mole of alkali per liter of electrolyte, at indicated pH			
		20°C		40°C	
		1.65–2.65	1.95–2.95	1.65–2.65	1.95–2.95
$FeSO_4 \cdot 7H_2O$	0.20	0.030	0.036	0.033	0.037
$FeSO_4 \cdot 7H_2O$, NH_2CH_2COOH	0.20, 0.10	0.075	0.090	0.096	0.102
$FeSO_4 \cdot 7H_2O$, NH_2CH_2COOH	0.20, 0.20	0.135	0.142	0.150	0.153

found that iron(III) is not accumulated in the electrolyte in the course of the six-month operation in the presence of glycine.

CONCLUSIONS

(1) Examination of the partial polarization curves of the discharge of iron and hydrogen ions during the electrolysis of sulfate solutions with various concentrations of aminoacetic acid shows that the presence of glycine in the electrolyte inhibits both processes. However, under the conditions studied, the electrochemical reaction is the limiting step of both processes.

(2) The dependence of the current efficiency by iron on the glycine concentration passes through a maximum. The influence of other factors (pH and temperature) on the coating quality was revealed. The following conditions are recommended for obtaining high-quality deposits: sulfate electrolyte containing 0.1–0.15 M glycine, pH 1.9±0.1, 20°C, and current density i_c = 20 mA cm^{-2}.

(3) The addition of glycine to the sulfate electrolyte increases its buffer capacity and also its stability in operation.

REFEWRENCES

1. Tsupak, T.E., Bek, R.Yu., Loseva, E.I., and Borodikhina, L.I., *Elektrokhimiya*, 1982, vol. 28, no. 1, pp. 86–92.
2. Yasuda Masaki, Sakaguchi Yoshikazu, Tsuji Hiromi, et al., *Metal Finish.*, 1988, vol. 39, no. 1, pp. 19–23.
3. Vinogradov, S.N., Magomedova, E.A., Mal'tseva, G.N., and Makarycheva, I.V., in *Sbornik materialov Vserossiiskoi nauchno-prakticheskoi konferentsii "Zashchitnye pokrytiya v mashinostroenii i priborostroenii"* (Proc. All-Russian Scientific and Practical Conf. "Protective Coatings in Machine Building and Instrument Making"), Penza, 2001, pp. 5–6.
4. Kurnakova, N.Yu. and Bakalai, V.I., in *Sbornik materialov Vserossiiskoi nauchno-prakticheskoi konferentsii "Zashchitnye pokrytiya v mashinostroenii i priborostroenii"* (Proc. All-Russian Scientific and Practical Conf. "Protective Coatings in Machine Building and Instrument Making"), Penza, 2005, pp. 22–25.
5. Dyatlova, N.M., Temkina, V.Ya., and Popov, K.I., *Kompleksony i kompleksonaty metallov* (Complexones and Metal Complexonates), Moscow: Khimiya, 1988.
6. Tsupak, T.E., Bek, R.Yu., Dzie Wei, and Dakhov, V.N., *Gal'vanotekh. Obrab. Poverkhn.*, 1994, vol. 3, no. 2, pp. 38–41.
7. Suravila, A. and Uksene, V., *Elektrokhimiya*, 1993, vol. 29, no. 2, pp. 225–229.
8. Voitsekhovskii, Yu.G., Voitsekhovskaya, R.N., and Galyamova, T.A., in *Prikladnaya elektrokhimiya. Teoriya, tekhnologiya i zashchitnye svoistva gal'vanicheskikh pokrytii* (Applied Electrochemistry. Theory, Technology, and Protective Properties of Electroplated Coatings), Kazan, 1989, pp. 8–16.
9. Petrov, Yu.N., Kolosov, V.P., and Stratulat, M.P., *Remont avtotraktornykh detalei gal'vanicheskimi pokrytiyami* (Repair of Automobile and Tractor Parts by Electroplating), Chisinau, 1976, pp. 27–28.
10. Peters, D.G., Hayes, J.M., and Hieftje, G.M., *Chemical Separations and Measurements; Theory and Practice of Analytical Chemistry*, Philadelphia: Saunders, 1974.
11. Butler, J.N., *Ionic Equilibrium* (A Mathematical Approach), Reading, Massachusetts: Addison-Wesley, 1964.
12. Antropov, L.I., *Teoreticheskaya elektrokhimiya: Uchebnik dlya khimiko-tekhnologicheskikh spetsial'nostei vuzov* (Theoretical Electrochemistry: Handbook for Chemical-Engineering Specialities of Institutes of Higher Education), Moscow: Vysshaya Shkola, 1984, 4th ed.

ISSN 1070-4272, Russian Journal of Applied Chemistry, 2008, Vol. 81, No. 7, pp. 1184–1186. © Pleiades Publishing, Ltd., 2008.
Original Russian Text © V.N. Tseluikin, N.D. Solov'eva, I.F. Gun'kin, 2008, published in Zhurnal Prikladnoi Khimii, 2008, Vol. 81, No. 7, pp. 1106–1108.

APPLIED ELECTROCHEMISTRY AND CORROSION PROTECTION OF METALS

Production of Composite Electroplated Nickel–Fullerene C_{60} Coatings

V. N. Tseluikin, N. D. Solov'eva, and I. F. Gun'kin

Engels Institute of Technology, Branch of Saratov State Technical University, Engels, Saratov oblast, Russia

Received June 22, 2007

Abstract—Kinetic relationships of the deposition of composite electroplated coatings based on nickel with a disperse phase of C_{60} fullerene were studied. The composition of the coatings was determined by secondary-ion mass spectrometry.

DOI: 10.1134/S1070427208070112

Composite electroplated coatings (CECs) are widely used for modifying metal surfaces. The CEC formation is affected by the nature of dispersed particles [1, 2]. Fullerenes can become a promising dispersible material for composite coatings, as they have unique chemical properties [3]. The majority of studies in the field of the electrochemistry of fullerenes are devoted to the determination of redox potentials of their derivatives [4]. However, the electrodeposition of fullerenes with metals is studied poorly.

The aim of this study was to prepare nickel–C_{60} fullerene CECs, to examine the kinetic relationships of this process, and to determine the composition of the coatings.

EXPERIMENTAL

A colloidal dispersion of C_{60} fullerene in water free of organic solvents was prepared according to [5]. By adding this dispersion to a nickel-plating electrolyte, we obtained a solution with the following concentrations of components (g l^{-1}): $NiSO_4 \cdot 7H_2O$ 220, $NiCl_2 \cdot 6H_2O$ 40, CH_3COOK 30, and C_{60} 0.05; pH 5.0. The nickel–fullerene C_{60} CEC was electrolytically deposited on a steel support (steel 45) at 25°C with continuous stirring of the electrolyte. To increase the content of the dispersed phase particles in coatings, we placed the cathode at an angle of 45° to the anode. "Pure" nickel was precipitated from the electrolyte of the same composition but without C_{60} addition.

The nickel–C_{60} fullerene CEC deposits were analyzed by secondary-ion mass spectrometry (SIMS) [6] on an MI-1305 magnetic mass spectrometer equipped with a universal unit for studying solids. The coatings intended for the analysis were deposited on a copper support.

Electrochemical measurements were carried out on a P5848 potentiostat with a KSP-4 automatic potentiometer. Potentials were set against saturated silver chloride reference electrode and recalculated to the hydrogen scale.

We have plotted the partial curves of nickel deposition (Fig. 1) on the basis of the initial currents of the deposition of nickel coatings and nickel–C_{60} CECs. In the presence of fullerene particles in the nickel-plating electrolyte, the cathode curves are shifted toward the positive potentials. The i_c–E

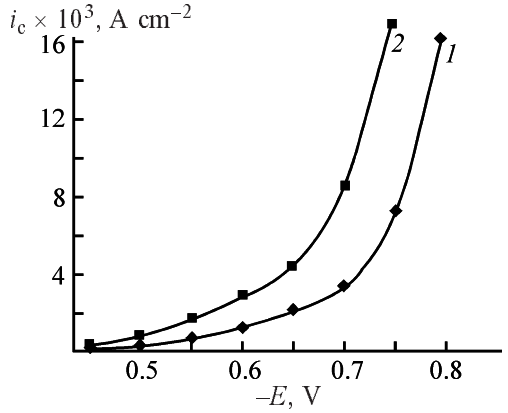


Fig. 1. Partial polarization curves of nickel deposition: (*1*) without additions and (*2*) with C_{60} fullerene addition. (i_c) Initial deposition current and (E) potential.

dependences show that the addition of C_{60} fullerene to the electrolyte makes easier the precipitation. In the presence of disperse particles, nickel is deposited at less negative potentials E in the whole examined range of potentials. The increase in currents on the CEC deposition relative to "pure" nickel coating suggests that the electrodeposition rate increases.

It is believed [7] that the transfer of dispersed phase particles to the cathode can proceed through the adsorption on their surface of cations of the metal being deposited. In the process, the particles acquire charge, are transferred to the cathode, and are discharged there, being overgrown with the metal. The ions adsorbed on particles participate in binding the dispersed phase with the cathode surface, which enhances the adhesion. Presumably, fullerene C_{60}, being an electron acceptor, gains a negative charge in the electrolyte solution on passing current and adsorbs nickel cations on its surface, which promotes the migration of dispersed particles to the cathode and their incorporation in the crystal lattice of the deposit.

In the case of the deposition in the galvanostatic mode, when fullerene is added to the nickel-plating electrolyte, the potentials are shifted toward positive values (Fig. 2). We calculated the polarization capacity of the electrical double layer from the data of the galvanostatic experiments using the expression

$$C = \frac{i}{\partial E/\partial t},$$

where i is the current density (A dm^{-2}); E; potential (V); and t, time (s).

The polarization capacity decreases on passing from nickel coatings to nickel–C_{60} fullerene coatings (see table). This is attributable to the fact that dispersed fullerene particles are relatively coarse and their incorporation in the electrical layer double increases its size.

The SIMS analysis of the composition of the nickel–C_{60} fullerene CECs revealed the presence of carbon and C–H bonds in the deposits. The content of carbon in coatings is about 1.5 wt %. The presence of C–H bonds in the structure of the deposits is caused by the fact that fullerene particles are hydrogenated before being incorporated in the coating. Probably, the hydrogenation takes place in the step of H_{ads} formation. The possibility of the electrochemical hydrogenation of C_{60} fullerene during the cathodic reduction in aqueous solutions was proved in [8]. It should be noted that the largest amount of dispersed phase particles is contained in surface layers of the composite coatings, as indicated by the fact that the intensity of secondary ions decreases when moving in depth of the deposit (Fig. 3,

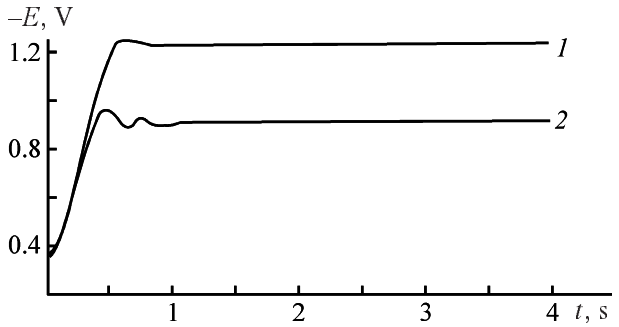


Fig. 2. Galvanostatic curves of nickel deposition at i_c = 8 A dm^{-2}: (*1*) without additions and (*2*) with addition of C_{60} fullerene. (*E*) Potential and (*t*) time.

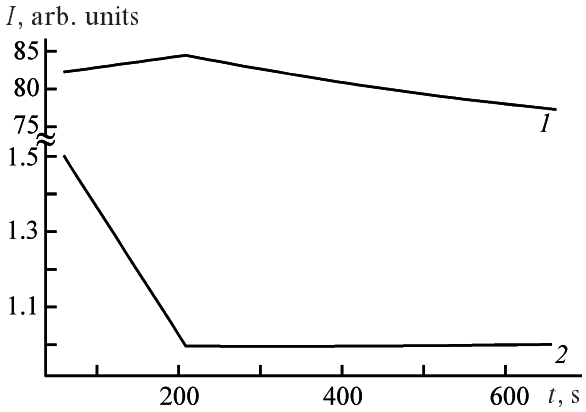


Fig. 3. (*1*) Nickel and (*2*) carbon concentration profiles in the composite nickel–C_{60} fullerene coating. (*I*) Intensity and (*t*) time.

Polarization capacity in deposition of nickel and Ni–C_{60} CECs

i_c, A dm^{-2}	$C \times 10^3$, F cm^{-1}	
	Ni	Ni–C_{60}
2	22.3	11.6
3	40.1	14.9
4	52.9	23.2
5	67.4	24.1
6	79.7	29.9
7	92.8	34.9
8	107.3	46.5
9	119.9	52.3
10	133.2	66.4

curve *2*). The content of nickel, on the contrary, increases in this direction (Fig. 3, curve *1*).

CONCLUSION

The addition of C_{60} fullerene dispersion into nickel-plating electrolyte promotes the formation of composite coatings. Fullerene particles are hydrogenated during the deposition. The largest amount of the dispersed phase is contained in surface layers of the deposits.

REFERENCES

1. Saifullin, R.S., *Neorganicheskie kompozitsionnye materialy* (Inorganic Composite Materials), Moscow: Khimiya, 1983.
2. Antropov, L.I. and Lebedinskii, Yu.N., *Kompozitsionnye elektrokhimicheskie pokrytiya i materialy* (Composite Electrochemical Coatings and Materials), Kiev: Tekhnika, 1986.
3. Sidorov, L.N., Yurovskaya, M.A., Borshchevskii, A.Ya., et al., *Fullereny* (Fullerenes), Moscow: Ekzamen, 2005.
4. Yanilkin, V.V., Gubskaya, V.P., Morozov, V.I., et al., *Elektrokhimiya*, 2003, vol. 39, no. 12, p. 1285.
5. Tseluikin, V.N., Tolstova, I.V., Gun'kin, I.F., and Pankst'yanov, A.Yu., *Kolloidn. Zh.*, 2005, vol. 67, no. 4, p. 575.
6. Bulatov, M.I. and Kalinin, I.P., *Prakticheskoe rukovodstvo po fotometricheskim metodam analiza* (Manual on Photometric Methods of Analysis), Leningrad: Khimiya, 1986.
7. Saifullin, R.S. and Abdullin, I.A., *Ross. Khim. Zh.*, 1999, vol. 63, nos. 3–4, p. 63.
8. Nozu, R. and Matsumoto, O., *J. Electrochem. Soc.*, 1996, vol. 143, p. 1919.

ISSN 1070-4272, Russian Journal of Applied Chemistry, 2008, Vol. 81, No. 7, pp. 1187–1192. © Pleiades Publishing, Ltd., 2008.
Original Russian Text © L.A. Zemskova, I.V. Sheveleva, N.N. Barinov, T.A. Kaidalova, A.V. Voit, S.V. Zheleznov, 2008, published in Zhurnal Prikladnoi Khimii, 2008, Vol. 81, No. 7, pp. 1109–1114.

APPLIED ELECTROCHEMISTRY AND CORROSION PROTECTION OF METALS

Manganese Oxide Carbon Fibrous Materials

L. A. Zemskova, I. V. Sheveleva, N. N. Barinov, T. A. Kaidalova, A. V. Voit, and S. V. Zheleznov

Institute of Chemistry, Far-Eastern Branch, Russian Academy of Sciences, Vladivostok, Russia
Far-Eastern Geological Institute, Far-Eastern Branch, Russian Academy of Sciences, Vladivostok, Russia

Received August 6, 2007

Abstract—Changes in electrochemical properties and surface morphology of carbon fibrous materials upon modification with manganese oxides under various conditions of their deposition were studied. The composition of manganese oxides was determined. The capacitances of the electrical double layer of manganese oxide carbon fibrous materials in sodium chloride solutions of various concentrations were found. Charging parameters of the modified electrodes were determined.

DOI: 10.1134/S1070427208070124

Manganese oxides and hydroxides are an object of comprehensive studies, because materials of this class are widely used as high-performance sorbents, catalysts, and materials for chemical power cells. Manganese oxide hydrate can be used as a sorbent in the form of grains produced by various methods [1–3], as a collector [4–6], or upon deposition on the developed surface of a porous support. Activated carbons [7, 8] or activated carbon fibers (ACFs) [9] are widely used as supports, which makes it possible to obtain manganese dioxide directly formed within pores of the carbon material via its interaction with the surface of the carbon support. In the last decade, much attention was given to the development of materials for electrochemical capacitors and power cells based on finely dispersed carbon powders coated with thin films of transition metal oxides, including manganese oxides [10].

The manganese oxides being deposited have a nonstoichiometric composition dependent on the synthesis methods and type of cations contained in the solution used [4, 6]. It can be assumed that finely dispersed manganese oxides are deposited as compounds that have a layered or pseudolayered structure and differ in the structure of these layers or interlayer spaces suitable for accommodation and mutual diffusion of exchange ions, similarly to natural manganese oxides [11].

As shown by the practice of studies of natural manganese oxides, determination of their structural features has been an exceedingly complicated task until recently. Reliable identification of manganese minerals requires using the whole set of modern investigation techniques (analytical electron microscopy, electron diffraction analysis, X-ray spectroscopy and diffraction analysis, X-ray photoelectron spectroscopy, etc.) [11]. Naturally, a study of surfaces on which nanosize metal oxide particles are situated within pores of the carbon matrix requires a long time and gross expenditure of material resources [12].

A large number of manganese oxide modifications differing in the composition and structure are known. Presence of these substances on the surface or within pores of the carbon matrix predetermines specific properties of a modified material. The use of manganese oxide carbon materials as sorbents or electrodes is efficient when their surface is the most accessible to molecules or ions of electrolytes. Changes in the surface properties of modified carbon materials can be analyzed by the electrochemical method [13, 14] from changes in the capacitance of the electrical double layer, whose formation depends on structural and surface properties of carbon-containing materials.

The aim of this study was to assess the possibility of using the electrochemical method for characterizing the surface changes upon modification of the carbon material and to reveal a relationship between the structure and surface composition determined by other methods.

EXPERIMENTAL

As starting matrices for study we chose Aktilen B activated carbon fiber (ACF_{st}) and the starting ACF oxidized with nitric acid at 90°C (ACF_{ox}).

ACF_{st} fibers were modified by deposition of active manganese oxide by the reaction of potassium permanganate with Mn(II) salts, following the method described in [15], in the presence of a carbon support. The resulting modified carbon fibrous material ACF–Mn(chem) was washed with water and dried in air. ACF_{ox} fibers were modified by the electrochemical method by deposition of oxygen-containing manganese compounds from a NaCl solution containing a Mn(II) salt under permanent aeration of the electrolyte [9], with an ACF_{ox} carbon support as the cathode. The resulting ACF–Mn(el.chem) composite material was also washed with water and dried.

The electrochemical measurements were made in a standard three-electrode cell by the methods of cyclic voltammetry and charging curves. As electrolytes served 0.9 and 3.5% NaCl solutions. The solutions were vigorously agitated and bubbled with inert gas. Samples of the carbon materials under study were placed in a gold basket serving as an inert current lead. A silver chloride electrode was used as reference. The auxiliary electrode fabricated from a porous carbon material was separated from the working electrode by an MB-2 bipolar membrane.

Potentiodynamic curves were measured near the electrical double layer (EDL) at the submergence potential of the working electrode within the range ±50 mV [16] with a P-5848 potentiostat. The EDL capacitance C (F g^{-1}) was calculated by the formula [16, 17]

$$C = I/(mv) = (I_a + I_c)/(2mv), \quad (1)$$

where I_a and I_c are the anode and cathode polarization currents (A); m, electrode mass (g); and v, potential sweep rate (V s^{-1}).

The degree (fraction) of utilization of the electrode surface, α, was calculated by the formula

$$\alpha = C/C_{max}, \quad (2)$$

where C and C_{max} are the electrode capacitances at the prescribed and minimum potential sweep rates (F g^{-1}).

The results of the potentiodynamic measurements were processed by the least-squares method to find the characteristic charging time of the EDL, τ, and the ohmic resistance of the electrolyte within pores ($R = \tau/C$) by the formula [18]

$$I = Cv\left[1 - 2\pi^{-2}\sum_{n=0}^{\infty}\frac{1}{(n+0.5)^2}e^{-\pi(n+0.5)^2 t\tau^{-1}}\right], \quad (3)$$

where I is the current (A); v, potential sweep rate (V s^{-1}); t, time (s); C, capacitance (F g^{-1}); and n, summation index.

When measuring galvanostatic charging curves, the polarizing current density was chosen experimentally. The current beginning from which the position of the polarization curve remained unchanged defined the boundary between the equilibrium and nonequilibrium currents. In all cases, the equilibrium charging current density was varied within the range 10^{-11}–10^{-10} A cm^{-2}. The linear portion of the charging curve was used to calculate the EDL capacitance C (F g^{-1}) by the formula

$$C = (I\Delta t)/(m\Delta E), \quad (4)$$

where I is the polarization current (A); Δt, electrode charging time (s); m, electrode mass (g); and ΔE, shift of the electrode potential (V).

All the values of the electrochemical parameters calculated are listed in the table.

Electron-microscopic studies were performed on an EVO 50 XVP scanning electron microscope equipped with an INCA 350 energy-dispersion spectrometer for determining the chemical composition of the surface. X-ray diffraction patterns of samples were measured on a Bruker D8 ADVANCE diffractometer. An X-ray phase analysis was made using an EVA search program with a PDF-2 powder database.

Depending on the deposition technique and on the composition of solutions from which manganese oxides were deposited, deposits differing in structure and nature are formed on the surface of the carbon support. This is confirmed by electron microscopy (SEM). Figure 1 shows SEM images of the surface of modified fibers. The surface of ACF–Mn(chem) is covered with a finely dispersed scaly phase (Fig. 1a), and that of ACF–Mn(el.chem), with manganese oxide crystals or aggregates of these. The results of a microprobe analysis (Figs. 1c, 1d) indicate that metal ions contained in mother liquors are incorporated into manganese oxides deposited onto the

Capacitance* and electrode charging parameters in NaCl solutions of various concentrations

Material	0.9% NaCl				3.5% NaCl			
	C_1	C	R, Ω	τ, s	C_1	C_2	R, Ω	τ, s
	F g^{-1}				F g^{-1}			
ACF_{st}	53.0	53.4	60.1	413.5	53.6	53.1	40.35	209
ACF_{ox}	56.5	56.4	12.20	723.7	61.1	61.5	7.87	492.7
ACF–Mn(chem)	53.1	53.9	80.0	5016.0	65.4	65.5	6.86	461.2
ACF–Mn(el.chem)	53.3	53.7	11.77	613.1	53.9	53.9	8.65	445.3

* C_1, C_2 are the EDL capacitances found from voltammetric measurements at the minimum potential sweep rates $v = 4 \times 10^{-5}$ V s^{-1} and from charging curves, respectively.

substrate surface. Analysis of the deposits formed on the surface in electrochemical deposition of manganese oxides reveals impurity ions, which are possibly contained in the starting salts used to prepare the electrolyte solution and are codeposited with the active manganese oxide because of the electrochemical concentration in the deposit [9].

Analysis of the X-ray diffraction patterns of the materials under study, produced by different methods, suggests that different phases are probably present in the deposited manganese oxides and hydroxides. An analysis of the X-ray diffraction patterns of the ACF–Mn(chem) sample revealed two phases belonging to synthetic K-birnessite represented by two compounds $K_{0.46}Mn_{0.54}Mn_{0.46}O_4(H_2O)_{1.4}$ [19] and $K_{0.5}Mn_2O_{4.3}(H_2O)_{0.5}$ [20] with nearly coinciding unit cell parameters (two diffuse halos with peaks corresponding to 002 and 111 reflections with interplanar spacings d 3.56 and 2.418 Å). The compound $K_{0.5}Mn_2O_{4.3}(H_2O)_{0.5}$ con-

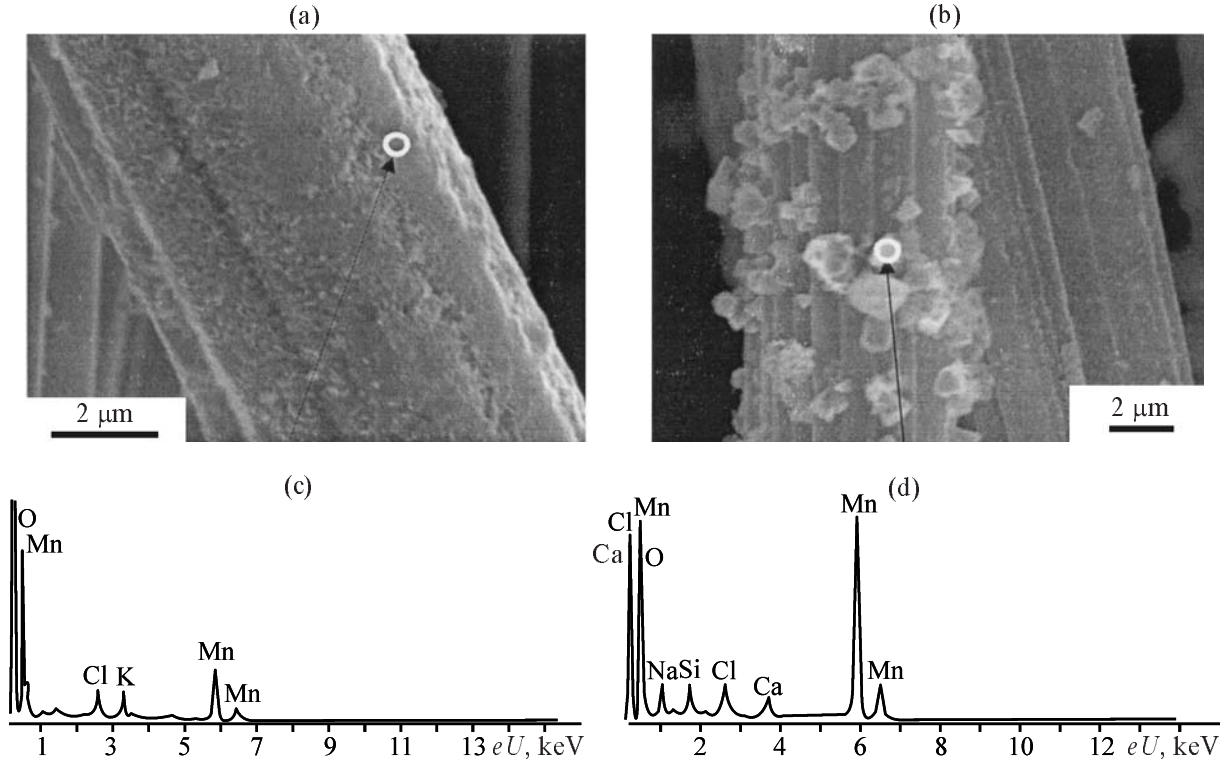


Fig. 1. SEM images of the surface of carbon fibers modified by (a) chemical [ACF–Mn(chem)] and (b) electrochemical deposition [ACF–Mn(el.chem)], and (c, d) energy-dispersion spectra of selected surface fragments. (eU) Energy. (c) ACF–Mn(chem) and (d) ACF–Mn(el.chem).

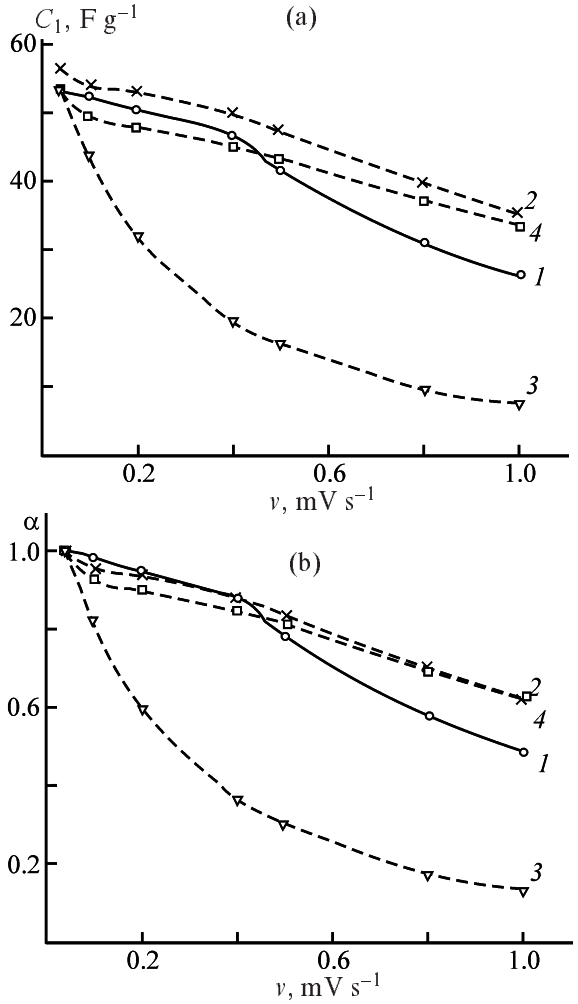


Fig. 2. (a) Capacitance C_1 and (b) surface fraction α involved in the electrochemical process vs. the potential sweep rate v in a 0.9% NaCl solution. (*1*) ACF_{st}, (*2*) ACF_{ox}, (*3*) ACF–Mn(chem), and (*4*) ACF–Mn(el.chem).

tains the exchangeable potassium ion. In addition, an α-Mn phase [21] is recorded (one diffuse halo with d = 2.09 Å), probably originating from reduction of manganese salts on the carbon matrix.

In electrochemical deposition of manganese oxides, a manganese oxide phase with a small oxygen deficiency, $MnO_2/Mn_{1.937}$ [22] (d 4.64 and 2.001 Å, 111 and 400 reflections), is formed on the surface. Also observed is synthetic ramsdellite MnO_2 (diffuse halos with maxima at d 4.01 and 2.06 Å, 110 and 410 reflections), which belongs to minerals with tunnel structure. It is known that the structure of ramsdellite is formed by identical ribbons constituted by double chains of MnO_6 octahedra [11]. The ribbons of octahedra, which form sides of the tunnels, are arranged in the structure with their wide sides approximately parallel to each other. In the tunnels in ramsdellite, there are no cations or water molecules [11]. On the whole, the powder X-ray diffraction patterns of the sample studied contain a small number of weak and diffuse reflections, which can be hardly used for reliable identification of manganese oxide compounds formed within pores of the carbon matrix. Indeed, as reported in [11], use of only such widely accepted methods as X-ray diffraction and microprobe analyses in studies of natural manganese oxides and hydroxides fails to provide reliable identification of manganese minerals. These minerals are distinguished by an exceedingly low degree of structural ordering and form finely dispersed mixtures; many of them have not been reliably identified by diffraction techniques.

The presence of manganese oxides of different compositions on the ACF surface changes the pore structure of the carbon material, which can be, in turn, evaluated by the electrochemical method of cyclic voltammetry [14] on submerging the fiber in an electrolyte solution. An electrical double layer is formed at the boundary between the solid and liquid phases, and its characteristics depend on the state of the surface and on the electrolyte concentration.

The differences in the charging and structural features of modified carbon materials can be judged from the variation of their capacitance in the EDL region with the potential sweep rate. At a slow polarization of the porous electrode, its surface is more involved in the electrochemical process because the supply rate of ions to the electrode surface is comparable with the formation rate of the EDL within which charge is transferred. As the polarization rate of the electrode is raised, the rates of ion delivery to the surface and EDL formation become strongly different because of the appearing ohmic and diffusion hindrances in the porous structure of the carbon material. As a result, the EDL capacitance decreases because the measured value of this capacitance corresponds only to that part of the working surface which is involved in the electrochemical process and has enough time to be charged during a potentiodynamic cycle. Figure 2 shows the dependences $C_1 = f(v)$ (Fig. 2a) and $\alpha = f(v)$ (Fig. 2b) obtained in a 0.9% NaCl solution for the starting and modified ACF. Analysis of these dependences suggests that the method used to deposit manganese oxides onto carbon fibers affects the extent to which the electrochemical properties of the materials obtained are changed. This is due to changes in the surface properties of the modified

ACF as a result of formation of manganese oxide phases in the carbon matrix.

If the polarization rate is raised when charging fibrous materials in a 0.9% NaCl solution, the EDL capacitance of the ACF–Mn(chem) sample steeply decreases and reaches rather small values (Fig. 2a, curve *3*). In the case of chemical deposition of manganese oxide onto the carbon matrix, the fiber surface is covered with a layer of birnessite, one of whose phases contains potassium ions in the exchangeable form. It is possible that, in charging of such an electrode, the EDL formation is accompanied by exchange of potassium for ions from the electrolyte, and the incommensurate rates of these simultaneously occurring competing processes lead to a considerable decrease in the capacitance of ACF–Mn(chem) upon an increase in the load on the electrode. It is not improbable that the birnessite film partly covering the fiber surface (Fig. 1a) diminishes its accessibility to ions from the dilute electrolyte. As seen from the table, the charging of ACF–Mn(chem) in a 0.9% NaCl solution occurs with a substantial resistance of the electrolyte in the pore space and, in contrast to other samples, requires a considerably longer time.

A less steep decrease in the EDL capacitance is observed for ACF–Mn(el.chem) (Fig. 2a, curve *4*). One of reasons why high capacitance values are retained by this electrode in the whole range of potential sweep rates used in the study is the lability of the fiber. The lability effect is manifested in that the porous structure of ACF changes upon polarization because likely charged fibrils of the fiber move apart and transport pores become larger. This makes weaker the hindering effect of the porous medium and favors preservation of high flow and mass-transfer rates in polarized carbon fibers [24]. It is known [11] that the tunnels in the ramsdellite structure are inaccessible to electrolyte cations and water molecules. Therefore, the better polarizability of ACF–Mn(el.chem) is in all probability due to changes in the porous structure of the carbon substrate as a result of deposition of manganese oxides.

It was noted in [25] that hydrated manganese oxide α-$MnO_2 \cdot nH_2O$ has low electrical conductivity and capacitance. However, use of carbon substrates with a highly porous structure, e.g., single-layer nanotubes, for deposition of α-$MnO_2 \cdot nH_2O$ yields a composite material with high capacitance, which exceeds severalfold the similar value for the starting carbon material. In this case, the texture characteristics of the composite material change in such a way that penetration of electrolyte ions into the bulk of the active material is facilitated and the resistance of an electrode fabricated from this material decreases [25]. Possibly, aggregates formed in the resulting ACF–Mn(el.chem) sample change the pore structure in such a way that the charging of this electrode occurs with a considerably lower electrolyte resistance in the pore space, compared with ACF–Mn(el.chem) (see table). It should be noted that, in the case when electrodes are polarized in a more concentrated solution (3.5% NaCl), their capacitance does not decrease substantially and the fraction of their surface involved in the electrochemical process remains rather large. This is favored by the considerable increase in the concentration of charged species causing faster formation of an EDL in the electrode in its charging.

A mathematical processing by Eq. (3) of the dependence of the electrode capacitance on the polarization rate made it possible to calculate the electrolyte resistance within pores, R, and the characteristic time of electrode charging, τ. The table lists the calculated values, which can be used to assess the efficiency with which carbon materials are used under polarization conditions. Analysis of the data obtained suggests that the method employed for deposition of manganese oxide onto a carbon matrix strongly affects the charging conditions of modified ACF. The strongest difference in the electrochemical characteristics of manganese oxide fibers is observed in polarization of these materials in a dilute electrolyte solution (0.9% NaCl). For effective charging of a porous electrode (especially in a solution with low concentration of charge carriers), it is necessary that the electrode should contain in its structure pores with a size comparable with the EDL thickness [14, 16], which provides supply of ions from the electrolyte to the surface of the solid and formation of an electrical double layer. Presumably, the electrochemical deposition of manganese onto a fibrous matrix (combined with the lability of the fiber itself) affects the surface and structural properties of the carbon material ACF–Mn(el.chem), providing rapid charging with a lower resistance of the electrolyte within pores, in contrast to ACF–Mn(chem). It should be noted that an increase in the electrolyte concentratrion eliminates differences between the charging parameters of modified ACF. This effect is probably due to an increase in the number of charge carriers weakening the diffusion and ohmic hindrances to the charging of the porous electrode.

CONCLUSIONS

(1) The composition of manganese oxides deposited under different conditions onto a carbon matrix was determined. Two phases of K-birnessite are formed in chemical deposition on the fiber surface. In electrochemical deposition of manganese oxide, ramsdellite and manganese oxide $MnO_2/MnO_{1.937}$, are deposited on the surface of an activated carbon fiber.

(2) The deposition conditions of manganese oxides affect the electrochemical properties of modified fibers. The properties of the manganese oxide material obtained by electrochemical deposition of manganese oxides make this material more suitable for use as an electrode.

(3) Cyclic voltammetry can be used to assess the structural changes in modified fibers, which was confirmed by scanning electron microscopy and X-ray phase analysis.

ACKNOWLEDGMENTS

The study was financially supported by the Far-Eastern Branch of the Russian Academy of Sciences (grant no. 06-I-P8-013).

REFERENCES

1. Leont'eva, G.V., *Zh. Prikl. Khim.*, 1997, vol. 70, no. 10, pp. 1615–1618.
2. RF Patent 2094115.
3 Leont'eva, G.V., Chirkova, L.G., and Vol'khin, V.V., *Zh. Prikl. Khim.*, 1980, vol. 53, no. 6, pp. 1229–1233.
4. Rudnev, N.A., Pustovalova, M.N., and Malofeeva, G.I., *Zh. Anal. Khim.*, 1970, vol. 25, no. 6, pp. 1085–1091.
5. Egorov, Yu.V., Pushkarev, V.V., and Tkachenko, E.V., *Radiokhimiya*, 1961, vol. 3, no. 1, pp. 87–89.
6. Krot, N.N., Bessonov, A.A., Gelis, A.V., et al., *Radiokhimiya*, 1998, vol. 40, no. 4, pp. 336–340.
7. Semushin, A.M., Belov, B.A., and Stepchenko, I.V., *Zh. Prikl. Khim.*, 1984, vol. 57, no. 11, pp. 2608–2609.
8. USSR Inventor's Certificate no. 1637867.
9. RF Patent 2218209.
10. US Patent Appl. 2006/0154071.
11. Chukhrov, F.V., Gorshkov, A.I., and Drits, V.A., *Gipergennye okisly margantsa* (Hypergenic Manganese Oxides), Moscow: Nauka, 1989.
12. Huwe, H. and Froba, M., *Carbon*, 2007, vol. 45, no. 2, pp. 304–314.
13. Conway, B.E., Niu, J., and Pell, W.G., *Kem. Ind.*, 2005, vol. 54, no. 4, pp. 187–198.
14. Calas-Blanchard, C., Comtat, M., Marty, J.-L., and Mauran, S., *Carbon*, 2003, vol. 41, pp. 123–130.
15. Karyakin, Yu.V. and Angelov, I.I., *Chistye khimicheskie veshchestva* (Pure Chemical Substances), Moscow: Khimiya, 1974.
16. Kinoshita, K., *Carbon: Electrochemical and Physicochemical Properties*, New York: Wiley, 1998.
17. Stromberg, A.G. and Pikula, N.P., *Elektrokhimiya*, 1981, vol. 17, no. 10, pp. 1427–1431.
18. Posey, F.A. and Morozumi, T., *J. Electrochem. Soc.*, 1966, vol. 113, no. 2, pp. 176–184.
19. Post, J.E. and Veblen, D.R., *Am. Mineral.*, 1990, vol. 75, nos. 5–6, pp. 477–489.
20. Holland, K.L. and Walker, J.R., *Clays Clay Miner.*, 1996, vol. 44, no. 6, pp. 744–748.
21. Hanawalt, J.D. et al., *Anal. Chem.*, 1938, vol. 10, p. 475.
22. Ohzuku, T., Kitagawa, M., Ohshita, R., et al., *Chem. Express*, 1989, vol. 4, no. 8, pp. 487–490.
23. Fong, C., Kennedy, B.J., and Elcombe, M.M., *Z. Kristallogr.*, 1994, vol. 209, no. 12, pp. 941–945.
24. Artem'yanov, A.P. and Sheveleva, I.V., *Zh. Prikl. Khim.*, 2004, vol. 77, no. 11, pp. 1811–1814.
25. Beguin, F., *J. Braz. Chem. Soc.*, 2006, vol. 17, no. 6, pp. 1083–1089.

ISSN 1070-4272, Russian Journal of Applied Chemistry, 2008, Vol. 81, No. 7, pp. 1193–1197. © Pleiades Publishing, Ltd., 2008.
Original Russian Text © V.M. Nagirnyi, R.D. Apostolova, E.M. Shembel', 2008, published in Zhurnal Prikladnoi Khimii, 2008, Vol. 81, No. 7, pp. 1115–1119.

APPLIED ELECTROCHEMISTRY AND CORROSION PROTECTION OF METALS

Effect of the Alloying Component MnO_2 on the Type of V_2O_5 Electrocrystallization

V. M. Nagirnyi, R. D. Apostolova, and E. M. Shembel'

Ukrainian State University of Chemical Engineering, Dnepropetrovsk, Ukraine

Received June 8, 2007

Abstract—The methods of polarization curves E–$\log I_a$ and atomic-force microscopy were used to study the mechanisms by which the alloying component MnO_2 affects the electrocrystallization of V_2O_5 in electrolysis from mixed solutions of salts of these metals.

DOI: 10.1134/S1070427208070136

In [1], the electrolysis conditions and nature of anodic processes in electrolytic deposition of V_2O_5 in the presence of Mn^{2+} from mixed sulfate solutions were studied. The mixed V–Mn oxides obtained exhibit better specific electrochemical characteristics and are more promising as compared to the individual components [2]. However, the possible mechanisms of anodic processes in electrolytic deposition of the V–Mn double oxide from aqueous solutions of a mixture of oxovanadium(IV) and manganese(II) sulfates remained insufficiently understood. Therefore, it seemed appropriate to continue these studies in order both to optimize and improve processes of electrolytic formation of complex multiphase systems and to extend the available concepts about their nature.

The study was performed using the procedure described in detail in [1]. Polarization curves were plotted in the coordinates E–$\log I_a$ using data on the conditional current efficiency (CE_{cond}) on the assumption that the whole amount of useful current is expended for V_2O_5 formation [1].

The possibility of performing the anodic process with quantitative deposition of the V–Mn double oxide in electrolysis of an aqueous solution of a mixture of VO^{2+} and Mn^{2+} sulfates is demonstrated by the standard potentials of the electrode reactions [3]

$$2VO^{2+} + 3H_2O - 2e \rightarrow V_2O_5 + 6H^+, \quad E^0 = 1.10 \text{ V}; \quad (1)$$

$$Mn^{2+} + 2H_2O - 2e \rightarrow MnO_2 + 4H^+, \quad E^0 = 1.23 \text{ V}; \quad (2)$$

$$2Mn^{2+} + 3H_2O - 2e \rightarrow Mn_2O_3 + 6H^+, \quad E^0 = 1.48 \text{ V}; \quad (3)$$

$$Mn_2O_3 + H_2O - 2e \rightarrow 2MnO_2 + 2H^+, \quad E^0 = 0.98 \text{ V}. \quad (4)$$

Reactions (1)–(4) can occur at the anode simultaneously with the oxygen evolution

$$2H_2O - 4e \rightarrow O_2 + 4H^+ \quad (5)$$

and with the possible redox reactions, e.g.,

$$2VO^{2+} + Mn_2O_3 + 2H_2O \rightarrow V_2O_3 + 2MnO_2. \quad (6)$$

Reaction (5) occurs in steps with the formation of a layer of chemisorbed oxygen atoms [4], which is rather important for the mechanism of anodic processes.

For energetic reasons, reactions (1)–(5) can hardly be performed at anodic polarization in aqueous solutions. It can be assumed that reactions occurring by the single-electron mechanism are preferable and thermodynamically substantiated. For example, it was noted in [5] that reaction (1) may occur in two steps in the case of the reaction with chemisorbed oxygen:

$$M + H_2O - 2e \rightarrow (M\text{–}O) + 2H^+, \quad (7)$$

$$VO^{2+} + (M\text{–}O) - e \rightarrow VO_2^+ + M, \quad (8)$$

$$VO_2 + VO_2^+ + H_2O \rightarrow V_2O_5 + 2H^+. \quad (9)$$

A similar mechanism was considered in [6]. Apparently, such a pathway is also justified for reactions (2) and (3) of anodic deposition of manganese oxides, which can be represented as a set of successive reactions

Current efficiency by V_2O_5 and MnO_2 in electrolysis from their individual solutions and CE_{cond} by V_2O_5 in its joint deposition with MnO_2 from mixed solutions of various concentrations. Average solution concentrations 0.35–0.4 M, T = 85°C, pH 2.0

I_a, mA cm^{-2}	CE, wt %		CE_{cond}, %, at indicated V : Mn ratio		
	V_2O_5	MnO_2	3 : 1	1 : 3	1 : 3 recalculated to E(MnO_2) = 1.62 g (A h)$^{-1}$
7.5	37	69	13.8	7.0	21
10	33.5	65	9.7	10.2	19.8

$$Mn^{2+} + (M–O) - e \rightarrow MnO^+ + M, \quad (10)$$

$$MnO^+ + (M–O) - e \rightarrow MnO_2 + M, \quad (11)$$

$$2MnO^+ + (M–O) \rightarrow Mn_2O_3 + M. \quad (12)$$

Apparently, the reactions of discharge of VO^{2+} and Mn^{2+} ions are the most energy-consuming. In these cases, the electron transfer is possibly facilitated via reaction with adsorbed oxygen, which can serve as a mediator. The subsequent reactions occur spontaneously and may be accompanied by release of the formation energy of V_2O_5 and MnO_2 molecules (the corresponding reactions are exothermic). The mutual influence of the above reactions in their parallel occurrence at the anode changes their relative rates in the overall process, which is characterized by a steep fall of the current efficiencies by both the main and alloying components, compared to their separate recovery from their individual solutions. This is confirmed by the current efficiencies

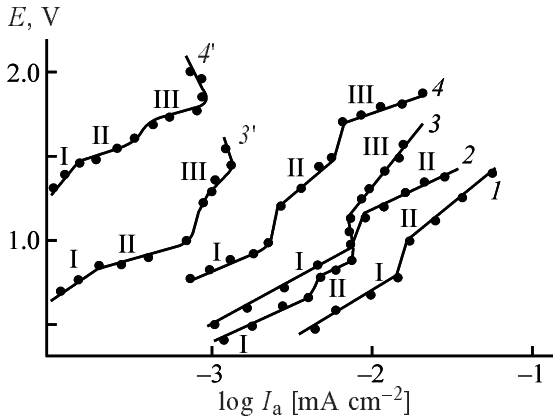


Fig. 1. (*1–4*) Overall and (*3'*, *4'*) partial anodic polarization curves obtained in sulfate solutions of (*1*) oxovanadium (0.3 M) and (2) manganese (0.4 M) and in mixed solutions with a mean concentration of 0.35–0.4 M at various V : Mn concentration ratios. Temperature 85°C, pH 2.0. (*E*) Potential and (I_a) current density. V : Mn concentration ratio: (*3*, *3'*) 3 : 1 and (*4*, *4'*) 1 : 3.

(CE) by V_2O_5 and MnO_2 in electrolysis from their individual sulfate solutions and by CE_{cond} by the V–Mn double oxide at V to Mn concentration ratios of 3 : 1 and 1 : 3 in solution (see table). It can be seen that the CE by V_2O_5 sharply decreases in the presence of Mn^{2+} even at its comparatively low concentrations in solution. The same behavior is observed for MnO_2 [in this case, CE_{cond} is formally calculated from its electrochemical equivalent E = 1.62 g (A h)$^{-1}$]. Thus, the conjugated anodic reactions are mutually decelerated, with a simultaneous increase in the rate of oxygen evolution.

Figure 1 shows the dependences E–logI_a for the overall processes of V_2O_5 and MnO_2 deposition with simultaneous evolution of oxygen from their individual solutions and for the overall and partial processes of joint deposition of V_2O_5 with MnO_2 from solutions with V : Mn concentration ratios of 3 : 1 and 1 : 3. The dependences of V_2O_5 and MnO_2 deposition from their individual solutions (curves *1*, *2*) form two ascending rectilinear branches connected by an intermediate portion. The lower branch (curve *1*) is mostly determined by the V_2O_5 deposition accompanied by discharge of oxygen. When the diffusion of VO^{2+} ions to the surface is decelerated, the anodic potential increases (intermediate portion) and reaches values corresponding to accelerated evolution of O_2. This latter becomes predominant at potentials of the upper branch of the curve [5].

Curve *2* describes the electrolytic deposition of MnO_2 from the sulfate solution [6] and reflects the step-by-step oxidation $Mn^{2+} \rightarrow Mn^{3+} \rightarrow Mn^{4+}$, with simultaneous evolution of oxygen. Comparison of curves *2* and *3* shows that curve *2* lies at higher anodic potentials. This means that manganese is oxidized at a higher anodic overvoltage.

The general shape of the overall E–logI_a dependences becomes considerably more complex in the

case of V_2O_5 deposition in the presence of Mn^{2+} (curves *3*, *4*). The dependences comprise three stepwise-arranged rectilinear portions (zones I–III) determined by the corresponding steps of the anodic process. The steps are connected by transition portions. The lower portions of curves *3* and *4* lie parallel to lower portions of curves *1* and *2* and are, apparently, mostly related to deposition of V_2O_5 under weak influence of the concomitant reactions of Mn^{2+} and oxygen discharge.

A decrease in the VO^{2+} concentration in the surface layer leads to an increase in the anodic polarization and the anodic process passes to the stage (zone II) in which joint deposition of V_2O_5, Mn_2O_3, and MnO_2 becomes possible. In this case, the rates of the competing reactions are redistributed, with a simultaneous increase in the rate of O_2 evolution (zone III). The slope of the portion of curve *3* in zone III is noticeably larger than that of the corresponding portion of curve *4*. This may be due to still higher rates of V_2O_5 and MnO_2 formation processes which hinder evolution of O_2 in the first case, and to its dominating role in the second case, which predetermines the corresponding decrease in the anodic overvoltage.

The partial E–$\log I_a$ dependences for V_2O_5 deposition in the presence of Mn^{2+} (curves *3'*, *4'*) have less pronounced transition portions. Comparison of the slopes of the corresponding steps clearly shows that the relative concentrations of the main and alloying components in solution affect the kinetics of the anodic processes. For example, steps I and II are longer at a lower Mn^{2+} concentration in solution (curve *3'*), compared to the case of its higher concentration (curve *4'*). This points to a predominant rate of V_2O_5 deposition in the first case and to a weaker influence of the reaction of manganese oxide formation, which is confirmed by the smaller slope of the corresponding portion of curve *3'*.

The smaller slope of the last branch, compared to that of the similar step in curve *4'*, is determined by processes considered above for similar portions of the overall curves *3* and *4*.

The linearity of the portions (steps) of the overall and partial E–$\log I_a$ curves under study enables analysis of the corresponding anodic processes in terms of electrochemical kinetics. However, the pronounced anomaly of the slopes of the corresponding portions of the curves in the interval 0.27–1.45 V points to their strong dependence on diffusion hindrances, which is substantiated by generalization of relationships of electrochemical and diffusion kinetics [7]. This is also indicated by the low level of limiting diffusion currents, which do not exceed 1.0–1.5 mA cm^{-2}.

Analysis of the data presented here shows that, in the anodic processes under consideration, the alloying additive hinders the efficiency of the processes in which both V_2O_5 and double V–Mn oxide are formed. It can be assumed that this is due to competition of VO^{2+} and Mn^{2+} ions in the double-layer zone. Because of the absence of electrostatic migration of the competing ions toward the anode, the electrical double layer, which is also formed by water molecules and adsorbed oxygen, is rather diffuse. Therefore, at rather close standard formation potentials of V_2O_5 and MnO_2, the smaller Mn^{2+} ions more easily penetrate to the anode and are better retained there than bulky VO^{2+} ions and thereby block the access of these latter into the reaction zone. Apparently, this leads to an increase in the overvoltage of their discharge and simultaneously stimulates the O_2 evolution. It can be seen from Fig. 1 that curve *4'* is shifted with respect to curve *3'* in the positive direction by 0.7 V. Possibly, a certain contribution to this shift is made by a change in the overvoltage of VO^{2+} discharge on changing the V : Mn concentration ratio from 3 : 1 to 1 : 3. It is difficult to determine this contribution because of the masking influence of accompanying factors and, in particular, by decelerated diffusion of ions, discharge–adsorption of oxygen, and multiple-stage nature of the main anodic processes. The contribution can be roughly estimated by the difference between the averaged shift of the potential difference upon a change in the V–Mn concentration ratio (curves *3'* and *4'*) and the difference of the onset potentials of anodic deposition of V_2O_5 and MnO_2 from their individual solutions. This difference is 0.24 V, which is a reasonable value.

The effect of the alloying MnO_2 additive in the processes under study is clearly manifested in the fundamental change in the nature of V_2O_5 electrocrystallization. Vanadium pentoxide is deposited from individual oxovanadium sulfate solution in the form of finely dispersed amorphous-crystalline conglomerates forming a pronounced relief on the surface of deposits in the form of interlacing ridges (Fig. 2a). This structure is mostly due to continuous degeneration of the nucleating crystals in the initial stages of their development. The weakened intermolecular bonding between these crystals or separate crystalline aggregates (grains), which impairs

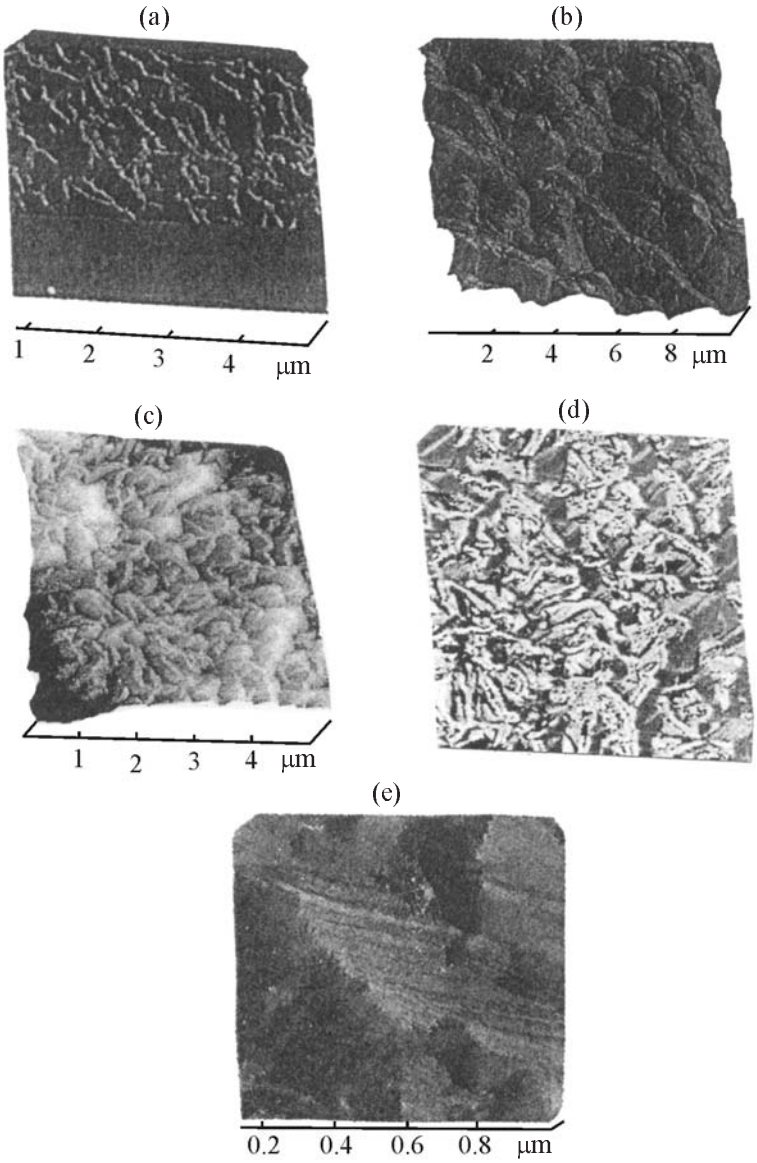


Fig. 2. Surface morphology of electrolytic deposits of (a) V_2O_5, (b) MnO_2, and (c–e) V–Mn double oxide from a mixed solution. V : Mn ratio: (c) 3 : 1, (d) the same at a height of 2500 nm from the substrate surface, and (e) 1 : 3.

the compactness of the deposit formed at the anode, may be a consequence of the high sorption activity and ability of V_2O_5 to absorb H_2O, which disrupts the intravolume intermolecular binding. A certain role can also be played in this regard by partial corrosion of the oxide, associated with the solution acidification.

The "pure" anodic MnO_2 deposit (Fig. 2a) formed from the sulfate solution is constituted by coarsened petallous grains with a rounded frontal face. The presence of crystal growth steps points to the probability of their formation by the mechanism of layer-by-layer packing of 2D crystalline aggregates (nuclei). The certain symmetry in the mutual arrangement of the grains indicates that twinned formations can exist. In the presence of Mn^{2+} (V : Mn = 3 : 1), V_2O_5 is formed at the anode as ridge-like crystalline deposits constituting a complex surface relief replicating to a certain extent the profile of pure V_2O_5 deposits (Fig. 2c). This gives reason to suggest that the forming, originally chaotically arranged, chains of amorphous-crystalline V_2O_5 deposits are covered with growing MnO_2 crystals, which is confirmed by the structure of the corresponding deposit formed at a height of 2500 nm from the substrate surface (Fig. 2d). The

deposit is a conglomerate of alternating crystalline MnO_2 deposits in the form of broken ridges (light bands) and dark areas of indefinitely crystalline V_2O_5 with a rather uniform distribution throughout the volume. Hence, the anodic deposits of the binary V–Mn oxide, obtained at concentration ratios V : Mn = 5 : 1 to 2 : 1 in solution, can apparently be regarded as sufficiently homogeneous mechanical mixtures with intravolume binding on the molecular level. Their two-phase composition is confirmed by X-ray phase analysis [1].

If the concentration of manganese in solution is substantially raised (V : Mn ≤ 1), the structure of the deposits fundamentally changes (Fig. 2e). The deposits are composed of irregularly growing coarsened MnO_2 grains of block type, with spaces between these grains filled with finely grained V_2O_5 agglomerates. This structure of the deposits is presumably due to the stimulating effect of lateral faces and separate fragments of MnO_2 crystals growing with a certain advance on the electrocrystallization of V_2O_5. This, in turn, makes higher the growth intensity of MnO_2 crystals at insignificant energy expenditure.

Thus, the electrodeposition of V_2O_5 at the anode in electrolysis from a mixed sulfate solution containing an alloying $MnSO_4$ additive yields a two-phase V–Mn oxide whose composition is determined by the V : Mn concentration ratio in the solution. Analysis of the experimental data shows that of practical importance, as regards the specific electrochemical characteristics and quality (compactness, homogeneity, adhesion), are V–Mn deposits with MnO_2 content of 5–15 wt %, formed at the ratio V : Mn = 5 : 1 to 2 : 1 and current densities of 7.5–10 mA cm^{-2}.

CONCLUSIONS

(1) The kinetics of the anodic processes occurring in electrodeposition of V_2O_5 in the presence of an alloying manganese additive from a sulfate solution at V : Mn concentration ratios of 3 : 1 to 1 : 3 was considered by analyzing the corresponding E–log I_a dependences.

(2) A stage-by-stage mechanism of the anodic processes of V_2O_5 and MnO_2 formation in their joint deposition via interaction with chemisorbed oxygen was suggested.

(3) It was shown that, in deposition of V_2O_5 in the presence of an alloying additive, the anodic polarization, including those of the concentration and chemical types, grows in proportion to the increase in the concentration of this additive in solution and to the rate of MnO_2 codeposition at the anode.

(4) An analysis of the surface morphology of anodic V_2O_5 and MnO_2 deposits produced by electrolysis from their individual solutions and by joint deposition demonstrated that, in the latter case, the structure is fundamentally different from that of the individual deposits because of the change in the nature of electrocrystallization of the components.

REFERENCES

1. Nagirnyi, V.M., Apostolova, R.D., Baskevich, A.S., et al., *Zh. Prikl. Khim.*, 2002, vol. 75, no. 4, pp. 566–571.
2. Le Gal La Salle, A., Guyomard, D., Verbaere, A., et al., *9th Int. Meet. on Lithium Batteries*, Edinburgh (Scotland), July 12–17, 1998.
3. *Spravochnik po elektrokhimii* (Handbook of Electrochemistry), Sukhotin, A.M., Ed., Leningrad: Khimiya, 1986.
4. Vetter, K.J., *Elektrochemische Kinetik*, Berlin: Springer, 1961.
5. Shembel', E.M., Nagirnyi, V.M., Apostolova, R.D., et al., *Zh. Prikl. Khim.*, 2000, vol. 73, no. 3, pp. 409–412.
6. Potiron, E., Le Gal La Salle, A., Verbaere, A., et al., *Electrochim. Acta*, 1999, vol. 45, pp. 197–214.
7. Skorchelletti, V.V., *Teoreticheskaya elektrokhimiya* (Theoretical Electrochemistry), Leningrad: Goskhimizdat, 1959.

ISSN 1070-4272, Russian Journal of Applied Chemistry, 2008, Vol. 81, No. 7, pp. 1198–1201. © Pleiades Publishing, Ltd., 2008.
Original Russian Text © A.G. Galstyan, A.S. Bushuev, R.N. Solomyannyi, 2008, published in Zhurnal Prikladnoi Khimii, 2008, Vol. 81, No. 7, pp. 1120–1123.

ORGANIC SYNTHESIS AND INDUSTRIAL ORGANIC CHEMISTRY

Oxidation of 4-Aminotoluene with Ozone in Acetic Acid Solution

A. G. Galstyan, A. S. Bushuev, and R. N. Solomyannyi

Dal' Institute of Chemical Technologies, East-Ukrainian National University, Rubezhnoe, Lugansk oblast, Ukraine

Received November 1, 2007

Abstract—The possibility of preparing 4-aminobenzoic acid by oxidation of 4-aminotoluene with ozone in acetic acid in the presence of cobalt(II) acetate and potassium bromide was examined. The optimal oxidation conditions were found.

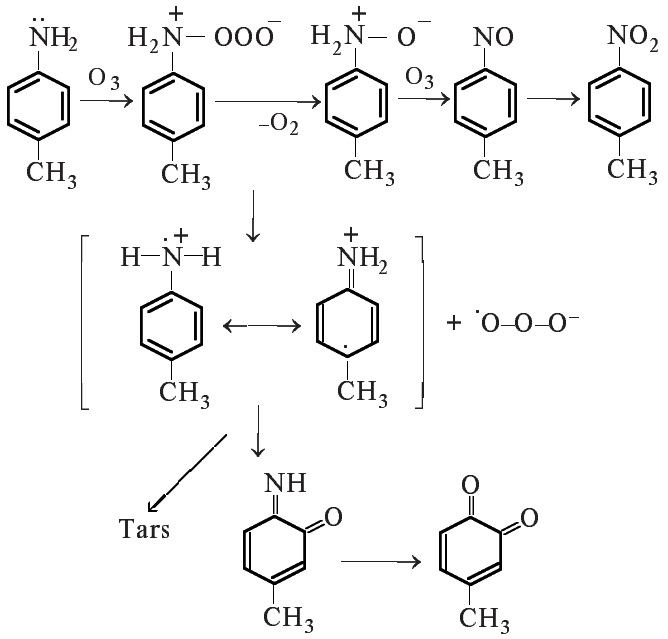
DOI: 10.1134/S1070427208070148

4-Aminobenzoic acid (4-ABA) is widely used in pharmaceutical industry, in particular, as an intermediate in production of anesthetics [1]. It is prepared by oxidation of 4-acetylaminotoluene (4-AAT) either with potassium permanganate or with atmospheric oxygen, followed by hydrolysis of the resulting 4-acetylaminobenzoic acid (4-AABAc) [1, 2]. The drawback of the first procedure is formation of large amounts of toxic, difficultly utilizable substances, and that of the second procedure is cumbersome implementation. A good choice may be the use of ozone, an environmentally friendly oxidant reacting under mild conditions with virtually all classes of organic compounds [3, 4].

The known method for oxidation of methylbenzenes with ozone in acetic acid [5] is unsuitable for preparing benzoic acids from methylbenzenes containing in the aromatic ring substituents with one or more lone electron pairs (–OH, $–NH_2$, etc.). It is known that methylanilines are oxidized with ozone at a high rate at the lone electron pair of the nitrogen atom with the formation of the molecular adduct $Ar\overset{+}{N}H_2–O_3^-$. Products of methyl group oxidation are not formed under these conditions [4, 6].

To examine the possibility of oxidative synthesis of aminobenzoic acids from methylanilines and develop low-waste processes, we studied the liquid-phase reaction of ozone with 4-aminotoluene (4-AT) in an acetic acid solution.

Preliminary studies [6] showed that ozone in an acetic acid solution reacts with 4-AT at a high rate ($k_{app} = 2.5 \times 10^3$ l mol^{-1} s^{-1}, 20°C). The major reaction products are tars. Also, 4-nitrosotoluene, 4-nitrotoluene, and traces of toluquinone are formed. The product composition is essentially similar to that described in the literature [4, 6] and corresponds to the scheme suggested for the reaction of ozone with aromatic amines [6]:

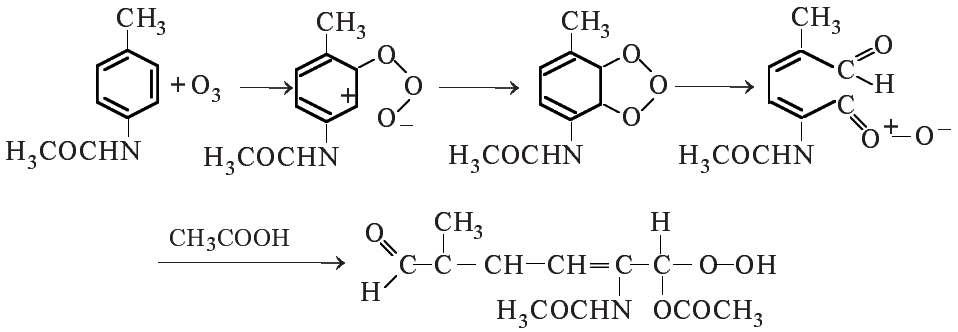


The scheme suggests fast attack of ozone at the lone electron pair of the nitrogen atom with the formation of an ion–radical pair which, depending on the structure of the amine, transforms into various products, the majority of which are unidentified polymeric tars. The absence of products of methyl group oxidation is due to the fact that the reactivity of 4-AT along this pathway is almost three orders of magnitude lower than that of the amino group [8].

To prevent the reaction of the amino group with

ozone, we protected it by acylation. 4-Acetylaminotoluene was dissolved in glacial acetic acid, and an ozone–air mixture with an ozone concentration of 4.5×10^{-4} M was passed through the solution. Kinetic studies showed that the reactivity of acylated 4-AT toward ozone decreases considerably. The rate constant of the reaction is $k_{app} = 28.7$ l mol^{-1} s^{-1} at 20°C. Drastic decrease in the rate constant of the reaction of ozone with 4-AAT suggests a change in the reaction mechanism.

Apparently, ozone under these conditions attacks not the NH group but mainly double bonds of the aromatic ring (85%) and, to a lesser extent, the methyl group (15%) (see figure). In accordance with the results of the study, 1.36 mol of ozone is consumed at 20°C per mole of 4-AAT. At such ozone consumption, the reaction with the aromatic ring, presumably, follows the scheme [9]



Among the methyl group oxidation products, 4-acetylaminobenzaldehyde (4-AABAl) prevails in the early reaction steps, and 4-AABAc, in the late steps (see figure).

The rate and selectivity of 4-AAT oxidation at the methyl group increase with temperature and on adding a catalyst, cobalt(II) acetate. The reaction becomes fast, and its major product is 4-AABAc. At 4-AAT concentration of 0.4 M, cobalt(II) acetate concentration of 0.14 M, and temperature of 95°C, the oxidation is complete in 40 min, and the selectivity with respect to the methyl group is 52%.

Addition of KBr increases the rate and selectivity of oxidation at the methyl group. The 4-AABAc yield reaches 75%. Among methyl group oxidation products, we also detected 4-acetylaminobenzyl bromide (4-AABB) and traces of 4-AABAl.

Selective oxidation at the methyl group in the presence of cobalt(II) acetate and potassium bromide becomes possible owing to two-step oxidation with ozone. Ozone predominantly reacts with Co^{2+} ($k_1 = 9.3 \times 10^2$, $k_{(AcNHArCH_3 + O_3)} = 28.7$ l mol^{-1} s^{-1}, our data) with the formation of Co^{3+} active species [reaction (1)]. The subsequent reaction (2) yields the complex $Co^{2+}Br^{\bullet}$ [10], which involves 4-AAT into fast and selective oxidation at the methyl group [reaction (5)]:

$$Co^{2+} + O_3 + H^+ \rightarrow Co^{3+} + HO^{\bullet} + O_2, \quad (1)$$

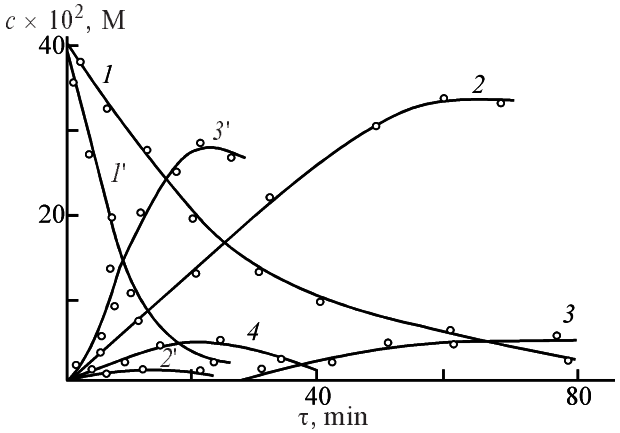
$$Co^{3+} + Br^- \rightarrow Co^{3+}Br^- \rightleftarrows Co^{2+}Br^{\bullet}, \quad (2)$$

$$Br^- + O_3 + H^+ \rightarrow Br^{\bullet} + HO_3^{\bullet}, \quad (3)$$

$$AcNHArCH_2^{\bullet} + Br^{\bullet} \rightarrow AcNHArCH_2Br, \quad (4)$$

$$AcNHArCH_3 + Co^{2+}Br^{\bullet} \rightarrow AcNHArCH_2^{\bullet} + Co^{2+} + Br^- + H^+. \quad (5)$$

To provide the occurrence of reaction (1), ozone should be continuously fed to the reaction system.



Variation of the concentrations c of components of the reaction mixture in oxidation of 4-AAT with ozone–air mixture at (*1–4*) 20 and (*1'–3'*) 95°C in the presence of cobalt(II) acetate and potassium bromide. $[4\text{-AAT}]_0 = 0.4$, $[O_3]_0 = 4.5 \times 10^{-4}$, $[Co(OAc)_2]_0 = 0.1$, $[KBr]_0 = 0.1$ M, $\nu_{air} = 8.3 \times 10^{-3}$ l s^{-1}. (τ) Time. (*1*, *1'*) 4-AAT, (*2*) peroxides, (*2'*) 4-AABB, (*3*, *3'*) 4-AABAc, and (*4*) 4-AABAl.

Interruption of the ozone supply leads to deceleration and complete termination of the process. This fact additionally confirms the formation of active catalyst species mainly by reactions (1) and (2). Under the experimental conditions, the concentration of molecular oxygen in the gas mixture is 15 times higher than that of ozone. Therefore, the acetylaminobenzyl radical formed in the system reacts predominantly with the oxygen molecule [reaction (6)] to form acetylamino peroxy radical which subsequently yields the final products [reaction (7)]:

$$AcNHArCH_2^{\bullet} + O_2 \rightarrow AcNHArCH_2O_2^{\bullet}, \quad (6)$$

$$AcNHArCH_2O_2^{\bullet} \rightarrow \text{products}. \quad (7)$$

4-AABB can appear in the system owing to the occurrence of reactions (3) and (4).

An increase in the rate and selectivity of 4-AAT oxidation in the presence of KBr is due to accumulation of the active complex $Co^{2+}Br^{\bullet}$, which involves the substrate in oxidation at a higher rate than does the oxidized form of cobalt [10].

EXPERIMENTAL

In the experiments we used analytically pure grade glacial acetic acid purified by vacuum distillation from potassium permanganate. Crystalline 4-AT was purified by repeated recrystallization from water. Cobalt(II) acetate and potassium bromide (analytically pure grade) were used without additional purification.

The calculated amount of 4-AT was dissolved in acetic anhydride in a flask at 20°C. The mixture was stirred for 15 min. After the acylation completion, the mixture was poured into ice-cold water. The 4-AAT precipitate was separated, washed with a 5% NaOH solution and water, and dried in a vacuum desiccator. Yield 94%.

A glass column equipped with a porous partition for dispersing an ozone–air mixture was loaded with 10 ml of acetic acid, 0.4 M of 4-AAT, and calculated amount of the catalyst, after which the unit was thermostated and, after attainment of the steady-state mode of ozonizer operation, an ozone–air mixture containing 4.5×10^{-4} M ozone was passed at a rate of 30 l h^{-1}. After the oxidation completion, the mixture was poured into a glass beaker filled to 2/3 with finely crushed ice, after which the mixture was diluted with cold water to a total volume of 50 ml. The precipitated 4-AABAc was filtered off, washed with cold water, and dried. Then 10 ml of concentrated HCl, 20 ml of water, and 4 ml of alcohol were added, and the mixture was refluxed for 1 h with stirring. After cooling, the precipitated 4-ABA was filtered off. Yield 68% based on the loaded 4-AAT.

The ozone concentration in the gas phase was determined spectrophotometrically from the absorption at 254–290 nm. The oxidation products were identified and quantitatively determined in solution by GLC on a chromatograph equipped with a flame ionization detector. The column, 2 m long and 4 mm in diameter, was packed with Chromaton N-AW impregnated with SE-30. Chromatographing conditions: vaporizer temperature 250°C, column temperature 180°C; flow rates, l h^{-1}: carrier gas (nitrogen) 1.8, hydrogen 1.8, and air 18. 4-Nitrochlorobenzene was used as internal reference.

The running concentration of 4-AABAc was determined by alkali titration. A 0.5-ml sample was taken from the reaction mixture, the solvent was distilled off, and the dry residue was dissolved in 30 ml of 50% ethanol. The solution was titrated with 0.05 N NaOH using phenolphthalein as indicator.

CONCLUSIONS

(1) Ozone reacts with 4-aminotoluene in acetic acid at a high rate, mainly at the nitrogen atom. Products of methyl group oxidation are not formed under these conditions. The direction of the ozone attack can be changed to the methyl group and benzene ring by amino group acylation; however, under these conditions, the yield of aromatic products does not exceed 15%.

(2) The selectivity of oxidation of 4-acetylaminotoluene increases to 52% with increasing temperature to 95°C and on adding a catalyst, cobalt(II) acetate. Addition of potassium bromide leads to a further increase in the rate and selectivity of the methyl group oxidation. The yield of 4-acetylaminobenzoic acid reaches 75%.

REFERENCES

1. Rubtsov, M.V. and Baichikov, A.G., *Sinteticheskie khimiko-farmatsevticheskie preparaty* (Synthetic Pharmaceuticals), Moscow: Meditsina, 1971.
2. Shcherbina, F.F., Tmenov, D.N., et al., *Zh. Org. Khim.*, 1980, vol. 16, no. 2, pp. 381–384.

3. Razumovs'kii, S.D., Galstyan, G.A., and Tyupalo, M.F., *Ozon ta iogo reaktsii z alifatichnimi spolukami* (Ozone and Its Reactions with Aliphatic Compounds), Lugansk: Skhidno-Ukr. Derzh. Univ., 2000.
4. Galstyan, G.A., Tyupalo, N.F., and Razumovskii, S.D., *Ozon i ego reaktsii s aromaticheskimi soedineniyami v zhidkoi faze* (Ozone and Its Reactions with Aromatic Compounds in the Liquid Phase), Lugansk: Vostochno-Ukr. Nats. Univ., 2004.
5. Galstyan, G.A., Galstyan, T.M., and Mikulenko, L.I., *Kinet. Katal.*, 1994, vol. 35, no. 2, pp. 255–260.
6. Bailey, P.S., *Ozonation in Organic Chemistry: Non-olefinic Compounds*, New York: Academic, 1982, vol. 2.
7. Galstyan, A.G., Sedykh, A.A., Bushuev, A.S., and Tarasenko, A.I., in *Materialy mezhdunarodnogo simpoziuma "Nauchnye dostizheniya v organicheskoi khimii"* (Proc. Int. Symp. "Scientific Achievements in Organic Chemistry"), Sudak, 2006, p. 147.
8. Galstyan, G.A., *Zh. Fiz. Khim.*, 1992, vol. 66, no. 4, pp. 775–778.
9. Bailey, P.S. and Ward, J.W., *J. Am. Chem. Soc.*, 1974, vol. 96, no. 14, pp. 6136–6140.
10. Zakharov, I.V., Galetii, Yu.V., and Adamyan, V.A., *Kinet. Katal.*, 1988, vol. 29, no. 5, pp. 1072–1077.

ISSN 1070-4272, Russian Journal of Applied Chemistry, 2008, Vol. 81, No. 7, pp. 1202–1207. © Pleiades Publishing, Ltd., 2008.
Original Russian Text © T.G. Dmitrienko, B.I. Drevko, 2008, published in Zhurnal Prikladnoi Khimii, 2008, Vol. 81, No. 7, pp. 1124–1129.

ORGANIC SYNTHESIS AND INDUSTRIAL ORGANIC CHEMISTRY

Photochemical Synthesis of 4*H*-Seleno(thio)pyrans and Their Salts

T. G. Dmitrienko and B. I. Drevko

Engels Institute of Technology, Branch of Saratov State Technical University, Engels, Saratov oblast, Russia
Saratov Military Institute of Chemical, Biological, and Radiation Protection, Saratov, Russia

Received February 9, 2007

Abstract—Photochemical transformations of 2,4,6-triphenylthiacyclohexane, 2,6-dimethoxyphenyl-4-phenylselenacyclohexane, 2,4,6-triphenylselenacyclohexane, 2,6-diphenyl-4-methoxyphenylselenacyclohexane, and 2,4,6-trimethoxyphenylselenacyclohexane in diisopropyl ether and ethanol under initiation with CBr_4 were studied.

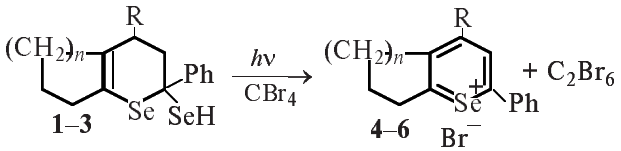
DOI: 10.1134/S107042720807015X

Selenopyrylium salts and selenopyrans are of importance as components of optical recording media, photovoltaic cells, photomaterials, photopolymerization initiators, electrophotographic materials, photoconducting materials in measuring devices, and materials for fast-relaxing passive laser gates. 4*H*-Selenopyrans and their condensed analogs show promise for medicine and veterinary.

Known methods for preparing arylaliphatic 4*H*-selenopyrans [1] are based on reactions of gaseous hydrogen selenide with 1,5-diketones. This route appeared to be applicable to polysubstituted diketones only, and the reactions yielded mixtures of selenopyrylium salts and selenacyclohexanes.

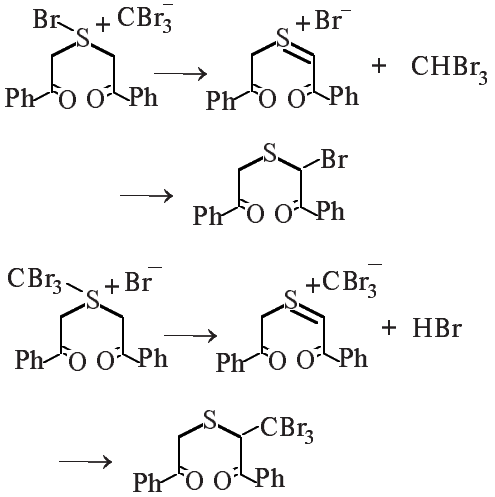
This study is aimed at search for new synthetic routes (in particular, photochemical) to selenopyrylium salts and selenopyrans and at elucidation of mechanisms of photochemical processes involving chalcogen-containing, and primarily selenium-containing heterocycles, which are used as drugs.

It is known [1] that, when irradiated with polychromatic UV light in the presence of CBr_4, hydroseleno derivatives of dihydroselenopyrans **1**–**3** transform into the corresponding selenopyrylium bromides **4**–**6** in 39–50% yield:



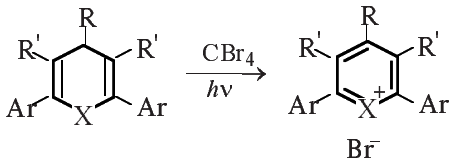
where R = Ph, n = 2 (**1**, **4**); R = $C_6H_4OCH_3$-*p*, n = 2 (**2**, **5**); R = Ph, n = 1 (**3**, **6**).

In the previous studies we prepared [2, 3] 9-phenyloximes of octahydrochalcogenoxanthenes, halogenated at the chalcogen atom, which spontaneously transformed into the corresponding heteroaromatic cations. The results of the previously performed [3] GC–MS analysis suggested that the reaction mechanism involves elimination of the hydrogen atom from the C^4 position of the heteroring, followed by aromatization and disproportionation of adducts formed by the reaction at the heteroatom. The first data on photochemical oxidation of some thiacyclohexanes are given in [4, 5]. It was found that, in chlorination of sulfur-containing 1,5-diketones, the reaction occurs at the heteroatom with the subsequent rearrangement similar in the mechanism to the Pummerer rearrangement [6]:



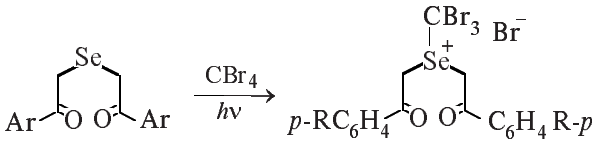
It is known that 4*H*-thio(seleno)pyrans undergo photochemical oxidation to form the corresponding

thio(seleno)pyrylium salts [7]. Therefore, a reaction scheme involving the C^4 atom of the heteroring was suggested:



where X = Se, Ar = R = Ph, R' = H; X = Se, Ar = Ph, R = R' = H; X = S, Ar = Ph, R = $C_6H_4OCH_3$-*p*; X = Se, Ar = $C_6H_4OCH_3$-*p*, R' = CH_3, R = H.

The analogous reaction with 1,5-diaryl-3-selenapentane-1,5-diones occurs by a different mechanism [8]:



In this study we examined the specific features and mechanism of photochemical oxidation of selena(thia)cyclohexanes.

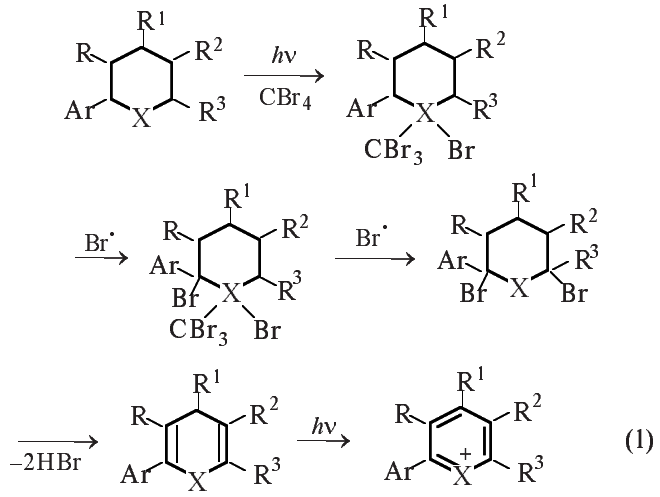
EXPERIMENTAL

Initially we prepared 1,5-diketones in accordance with [9]: 1,3,5-triphenylpentane-1,5-dione, 1,5-diphenyl-3-methoxyphenylpentane-1,5-dione, and 1,3,5-trimethoxyphenylpentane-1,5-dione, which were the starting compounds for preparing thia(selena)cyclohexanes by known procedures [1, 9].

Photochemical oxidation was performed in CCl_4 under UV initiation [10, 11]. The reaction mixture was placed in a quartz reactor, and the initiator (CBr_4) was added. The reactants were stirred with a power-driven stirred under irradiation with a polychromatic UV source (λ = 200–380 nm) arranged on the level of the reaction vessel. The irradiation was performed until the starting compound fully disappeared. The reaction progress and purity of the compounds obtained were monitored by TLC and gas chromatography with a mass-selective detector (GC–MS).

We studied the photochemical oxidation of 2,4,6-triphenylthiacyclohexane, 2,6-dimethoxyphenyl-4-phenylselenacyclohexane, 2,4,6-triphenylselenacyclohexane, 2,6-diphenyl-4-methoxyphenylselenacyclohexane, and 2,4,6-trimethoxyphenylselenacyclohexane in the presence of CBr_4.

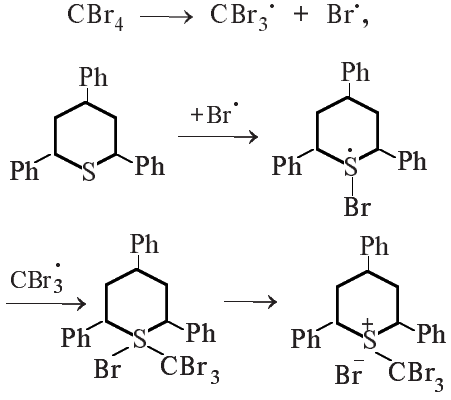
Figure 1 shows the chromatogram and mass spectrum of 2,4,6-triphenylthiacyclohexane. It can be seen that its retention time is 27 min. Figure 2 shows the chromatogram and mass spectrum of 2,4,6-triphenylselenacyclohexane. Its retention time is also 27 min. The content of the starting diketone is very low, which shows that the photochemical reaction goes virtually to completion. Analysis of the mass spectra of other components of the reaction mixture containing 2,4,6-triphenylselenacyclohexane shows that the strongest peaks belong to compounds with molecular ions with *m*/*z* 284 and 209. It could be suggested theoretically that photochemical oxidation of 2,4,6-triphenylthia(selena)cyclohexanes in the presence of CBr_4 occurs as a result of hydrogen halide elimination. In photochemical oxidation of 2,4,6-triphenylthiacyclohexane, we detected the formation of the corresponding thiopyrylium salts, which were identified as perchlorates. The mass spectra suggest the following scheme of transformations:



(1)

where X = S or Se.

The mechanism of this reaction can be described by the following scheme:



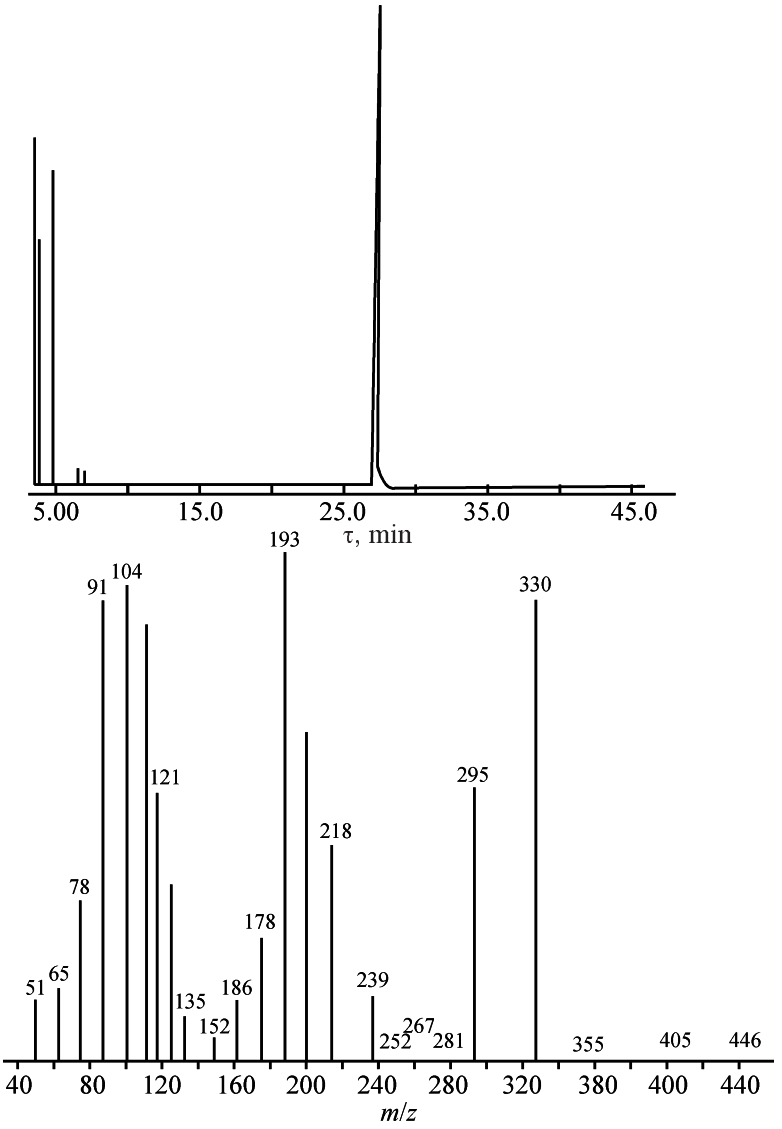
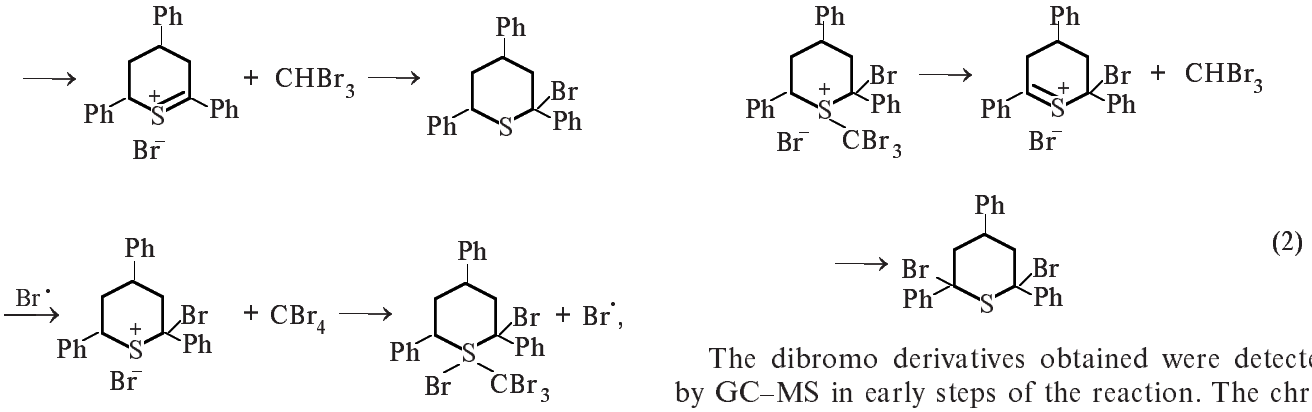


Fig. 1. Chromatogram and mass spectrum of 2,4,6-triphenylthiacyclohexane. (τ) Retention time; the same for Fig. 2.



(2)

The dibromo derivatives obtained were detected by GC–MS in early steps of the reaction. The chro-

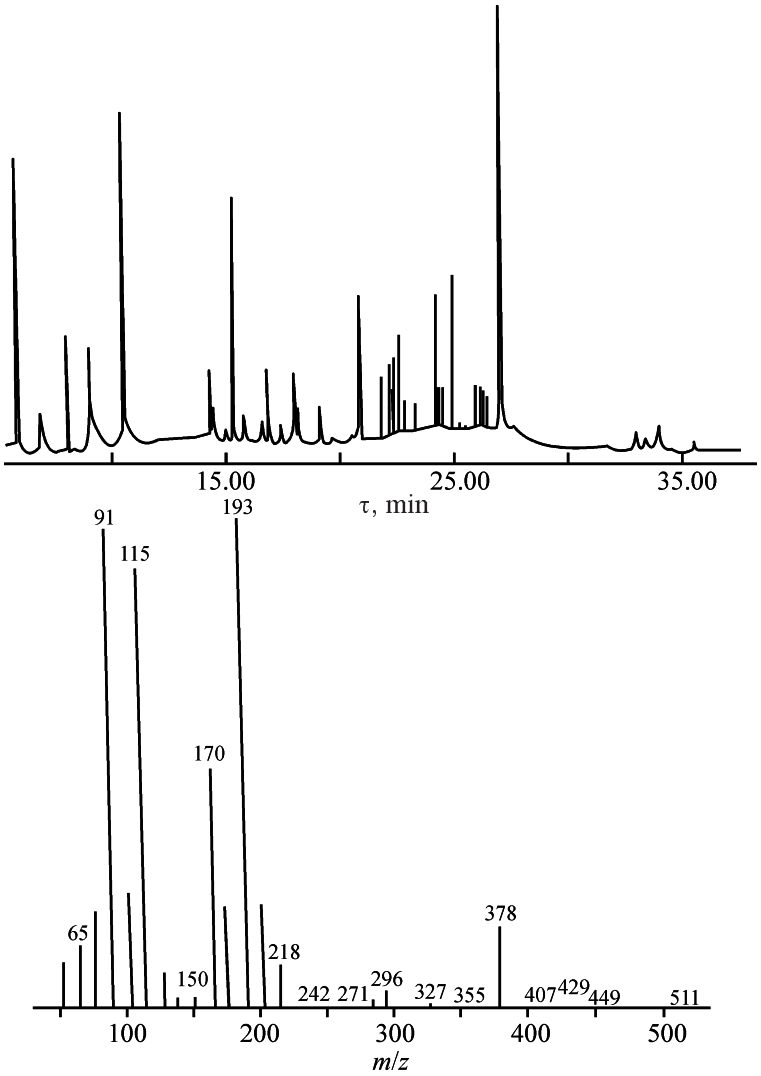
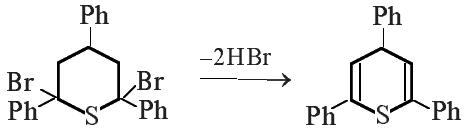
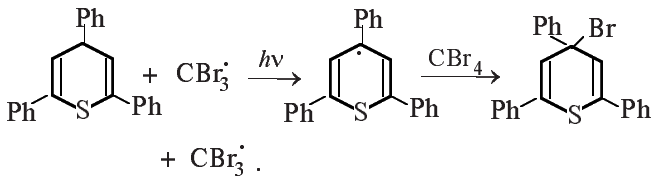


Fig. 2. Chromatogram and mass spectrum of 2,4,6-triphenylselenacyclohexane.

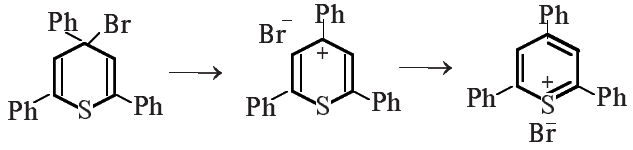
matogram of the photochemical oxidation products shows the formation of 2,4,6-triphenylthiacyclohex-2-ene. Apparently, the dibromide obtained subsequently eliminated hydrogen bromide.



The reaction product, 2,4,6-triphenyl-4*H*-thiopyran, detected by GC–MS, subsequently underwent photochemical oxidation:



The product is thermodynamically unstable and undergoes the following transformations:



The latter structure is more favorable thermodynamically. We found that 4*H*-seleno(thio)pyrans under the conditions of photochemical oxidation transform into the corresponding heteroaromatic cations. Along with the corresponding chalcogenopyrylium salts, among the reaction products we detected by GLC hexabromoethane and bromoform, which confirms the free-radical mechanism of the reaction.

Apparently, the chalcogenopyrylium salt (CP)

absorbs a visible light quantum and in the excited state transfers the energy to the complex of chalcogenopyran (HP) with CBr_4, which decomposes into chalcogenopyrylium bromide and bromoform:

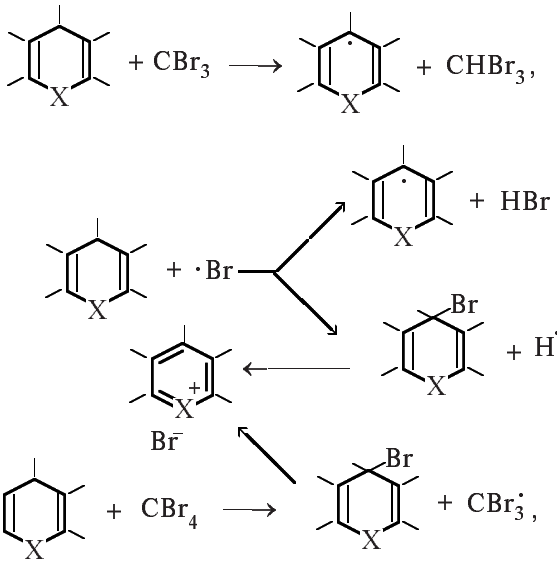
$$CP \xrightarrow{h\nu} CP^*,$$

$$CP^* + CBr_4 \cdot HP \longrightarrow CP + CBr_4 \cdot HP^*,$$

$$CBr_4 \cdot HP^* \longrightarrow CP + CHBr_3.$$

The selenopyrylium salt apparently acts as a sensitizer in this reaction, because, out of all the forming salts, only this compound exhibits strong absorption in the visible range. The following transformation scheme can be suggested:

$$CBr_4 \longrightarrow CBr_3^{\bullet} + Br^{\bullet},$$



$$CBr_4 + H^{\bullet} \longrightarrow CHBr_3 + Br^{\bullet}.$$

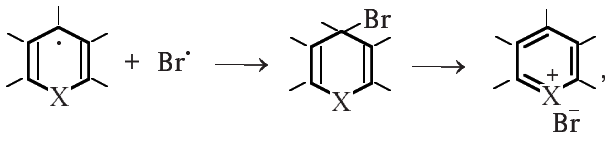
Several schemes of the chain termination in the free-radical reaction are possible:

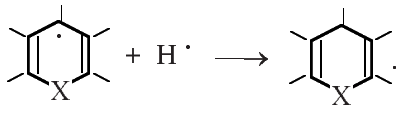
$$CBr_3^{\bullet} + CBr_3^{\bullet} \longrightarrow C_2Br_6,$$

$$CBr_3^{\bullet} + H^{\bullet} \longrightarrow CHBr_3,$$

$$CBr_3^{\bullet} + Br^{\bullet} \longrightarrow CBr_4,$$

$$Br^{\bullet} + H^{\bullet} \longrightarrow HBr,$$





Thus, the forming thio- and selenopyrans can undergo photochemical oxidation by the free-radical mechanism with the formation of the corresponding heteroaromatic cations.

Similar results were obtained in the photochemical reaction with 2,6-dimethoxyphenyl-4-phenylselenacyclohexane in CCl_4.

We attempted to perform photochemical oxidation of substituted thiacyclohexanes in CCl_4. The intrinsic absorption of CCl_4 in this range is relatively low, but it may act as sensitizer for aromatic substituted chalcogenacyclohexanes which are simultaneously the reactants. According to our experimental data, the occurrence of photochemical reactions by the free-radical chain mechanism is characteristic of all chalcogenacyclohexanes (CC):

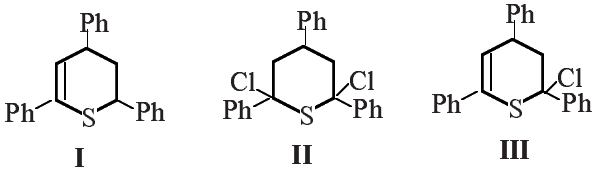
$$CC \xrightarrow{h\nu} CC^*,$$

$$CC^* + CCl_4 \longrightarrow CC + CCl_4^*,$$

$$CCl_4^* \longrightarrow CCl_3^{\bullet} + Cl^{\bullet}.$$

For the homolytic cleavage of the CCl_3–Cl bond, the light quantum with $\lambda < 330$ nm is sufficient. This wavelength correspond to absorption of the aryl substituent at $\lambda = 240–330$ nm. However, thio- and selenopyrylium salts have very high molar extinction coefficient and high quantum yield when used as sensitizers. Therefore, the reaction is autocatalytic.

In photochemical oxidation of 2,4,6-triphenylthiacyclohexane, the following products were detected in the reaction mixture by GC–MS:



I **II** **III**

The corresponding thiopyran could not exist under these conditions for a long time, because it readily transforms into the salt. In this case, the limiting step of the reaction is formation of dichloro- and dihydro derivatives of triphenylthiacyclohexanes. The major components of the reaction mixture were 2,4,6-triphenyl-2,3-dihydrothiacyclohexane **I** and 2,4,6-triphenyl-6-chlorothiacyclohex-2-ene **III**.

The latter product could be formed both in the reaction mixture and by dehydrochlorination on the adsorbent in the course of chromatographic analysis.

Thus, we developed a new procedure for preparing thio(seleno)pyrans by photochemical oxidation of thia(selena)cyclohexanes, which is of practical interest.

CONCLUSIONS

(1) Chalcogenacyclohexanes can undergo photochemical oxidation in the presence of CCl_4 and CBr_4 to form heteroaromatic cations. Chalcogenacyclohexanes can act as sensitizers in photochemical oxidation.

(2) The most thermodynamically stable products of oxidation of 4*H*-selenopyrans are the corresponding aroylselenophene derivatives.

(3) Photochemical oxidation of selenopyrans can occur both at the C^4 atom of the heteroring and at the heteroatom.

(4) The new modification of the Pummerer rearrangement is accompanied by elimination of the reagent with the formation of the corresponding unsaturated compound.

(5) Photochemical oxidation of selena(thia)cyclohexanes is a new route to seleno(thio)pyrans and seleno(thio)pyrylium salts.

REFERENCES

1. Drevko, B.I., Chalcogen-Containing Heterocyclic Compounds Based on 1,5-Diketones: Synthesis, Properties, and Some Relationships of the Reaction, *Doctoral Dissertation*, Saratov, 1997.
2. Drevko, B.I., Dmitrienko, T.G., Blinokhvatov, A.F., and Parman, I.D., in *Sbornik nauchnykh trudov SVIRKhBZ* (Coll. of Scientific Works of the Saratov Military Inst. of Radiation, Chemical, and Biological Protection), Saratov, 2002, pp. 115–118.
3. Dmitrienko, T.G., Drevko, B.I., Suchkov, M.A., and Ponomarev, A.S., in *Elektrokhimicheskie tekhnologii i kompozitsionnye pokrytiya* (Electrochemical Technologies and Composite Coatings), Saratov: Saratov. Gos. Tekh. Univ., 2000, pp. 56–60.
4. Suchkova, E.V., Egereva, Yu.V., Dmitrienko, T.G., and Drevko, B.I., Abstracts of Papers, *IV Vserossiiskaya konferentsiya molodykh uchenykh "Sovremennye problemy teoreticheskoi i eksperimental'noi khimii"* (IV All-Russian Conf. of Young Scientists "Modern Problems of Theoretical and Experimental Chemistry"), Saratov: Saratov. Gos. Univ., June 23–25, 2003, p. 84.
5. Dmitrienko, T.G. and Drevko, B.I., in *Sbornik nauchnykh trudov SVIRKhBZ* (Coll. of Scientific Works of Saratov Military Inst. of Radiation, Chemical, and Biological Protection), Saratov, 2006, p. 76.
6. Drevko, B.I., Zhukov, O.I., and Kharchenko, V.G., *Zh. Org. Khim.*, 1995, vol. 31, no. 10, pp. 1548–1552.
7. Fomenko, L.A., Selenopyrylium Salts, Selenopyrans, and Their Isoelectron Analogs: Synthesis and Transformations, *Cand. Sci. Dissertation*, Saratov, 1996.
8. USSR Inventor's Certificate no. 1703649.
9. Chalaya, S.N., Kazarinova, T.D., and Bozhenova, O.A., in *Nukleofil'nye reaktsii karbonil'nykh soedinenii* (Nucleophilic Reactions of Carbonyl Compounds), Saratov: Saratov. Gos. Univ., 1977, pp. 65–66.
10. Panov, V.B., Nekhoroshev, M.V., and Okhlobystin, O.Yu., *Dokl. Akad. Nauk SSSR*, 1979, vol. 249, no. 3, pp. 622–624.
11. Martens, J. and Pracfke, K., *J. Organomet. Chem.*, 1980, vol. 198, no. 3, pp. 321–351.

ISSN 1070-4272, Russian Journal of Applied Chemistry, 2008, Vol. 81, No. 7, pp. 1208–1212. © Pleiades Publishing, Ltd., 2008.
Original Russian Text © E.A. Vlasova, I.Yu. Vashurina, A.S. Pogorelova, Yu.A. Kalinnikov, 2008, published in Zhurnal Prikladnoi Khimii, 2008, Vol. 81, No. 7, pp. 1130–1133.

ORGANIC SYNTHESIS AND INDUSTRIAL ORGANIC CHEMISTRY

Peat Humus Acids as Catalysts of Reduction of Quinone Groups in Vat Dye Molecules

E. A. Vlasova, I. Yu. Vashurina, A. S. Pogorelova, and Yu. A. Kalinnikov

Ivanovo State University of Chemical Technology, Ivanovo, Russia
Institute of Solution Chemistry, Russian Academy of Sciences, Ivanovo, Russia

Received June 20, 2007

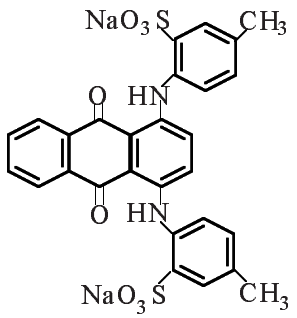
Abstract—The redox titration of peat humus acids was carried out. The effect of humic acids on the reduction kinetics of an anthraquinone dye as a model of water-soluble vat dyes with sodium hydroxymethanesulfinate was examined.

DOI: 10.1134/S1070427208070161

One of biospheric functions of natural humus acids (HA) is catalysis of redox decomposition of organic ecotoxicants, first of all, pesticides [1–4]. Currently the areas of application of catalysts based on humus acids is limited to coal fuel chemistry and such processes as purification of gaseous and solid compounds and water [3, 5–9].

It is known that many textile-chemical processes such as dyeing of textile materials with vat dyes are based on redox processes [10, 11]. For example, water-insoluble vat dyes after reduction of their quinone groups become water-soluble and acquire affinity for cellulose materials. After the subsequent reoxidation, these dyes lose solubility and are strongly fixed on the textile material. The reduction of vat dyes is accelerated in the presence of redox catalysts, e.g., anthraquinone derivatives [11]. The mechanism of functioning of these catalysts involves stepwise redox reactions. In this reaction chain, the reductant first reacts with catalyst molecules to transform them into the hydroquinone form, which reduces the dye more readily than does the reductant itself and is oxidized in the process to the initial form [11].

The accelerating effect of peat humus acids on fixation of vat dyes on cotton fabric in its printing by the rongalite–potash technique was reported in [12]. Then we further examined this effect with Chrome Green Anthraquinone dye (CGA) as analog of the vat dye [13]. This compound has the following formula:



We suggested that humus acids catalyze the reduction of the quinone groups in the dye molecules by the mechanism typical of anthraquinone compounds. In these systems, the catalytically active centers can be both the quinone (carbonyl) groups of humus acids and transition metal ions coordinated with humus acid functional groups. In this study we attempted to verify this hypothesis.

EXPERIMENTAL

The chemicals used in this study were as follows. Sodium hydroxymethanesulfinate HMS (rongalite) (standard reducing agent used in textile industry) was recrystallized two times from water by the procedure reported in [14]. Aqueous solution of humus acids in the form of sodium salt was prepared by alkaline extraction from peat by the standard technique [15]. $FeSO_4 \cdot 7H_2O$ and sodium ethylenediaminetetraacetate (Na_2EDTA) were of chemically pure and analytically pure grades, respectively. The commercial Chrome Green Anthra-

quinone acid dye CGA was purified by the method reported in [16] to attain a constant extinction coefficient.

The redox titration curves of humus acids were obtained by two-step titration. First humus acids were reduced with rongalite in alkaline medium (pH 12.7) to constant redox potential, and then the reduced form of humus acids was reoxidized with aqueous potassium ferricyanide. The redox titration involved two cycles of reduction and oxidation of humus acids. The redox titration was performed under argon at 85°C in a temperature-controlled glass cell equipped with a magnetic stirrer. The redox potentials were measured on a laboratory digital OP-211/1 pH-meter with platinum and silver chloride electrodes.

The transition metal content in HA was determined by an atomic-absorption technique [17]. The content of the quinone and carbonyl groups in HA was determined by potentiometric titration [18].

The reaction rate of CGA with excess of sodium hydroxymethanesulfinate was determined by change in the optical density of solutions of this dye at the absorption maximum of the oxidized form (λ_{max} = 612 nm, ε = 10870 l mol^{-1} cm^{-1}), which is well resolved with the absorption maximum of CGA in the reduced form. The CGA concentration in solutions was in the range of observance of the Lambert–Bouguer–Beer law. The kinetic measurements were carried out on a Specord M-400 spectrophotometer.

Taking into account that the dyeing of cotton fabric with vat dyes is commonly carried out in alkaline media, the reversibility of oxidation and reduction of HA was studied at pH 12.7, typical of industrial conditions. The redox curve of humus acids, $-E = f(V)$ (Fig 1a), has a dome-like shape. Its ascending and descending branches reflect the reduction and reoxidation of humus acid functional groups, respectively. It is seen that each of these branches has two inflection points marked with arrows. This means that both the reduction of humus acids and their subsequent reoxidation are two-step processes. We believe that this multistep character of the process is caused by successive reduction (or oxidation) of two kinds of redox-active functional groups contained in humus acids.

The reduction and oxidation potentials of these functional groups were determined by differentiating the titration curve. Figure 1b shows the differential form of the redox titration curve. In this curve, the maxima and minima correspond to the reduction and reoxidation potentials of the redox-active functional groups, respectively. These potentials are listed in Table 1.

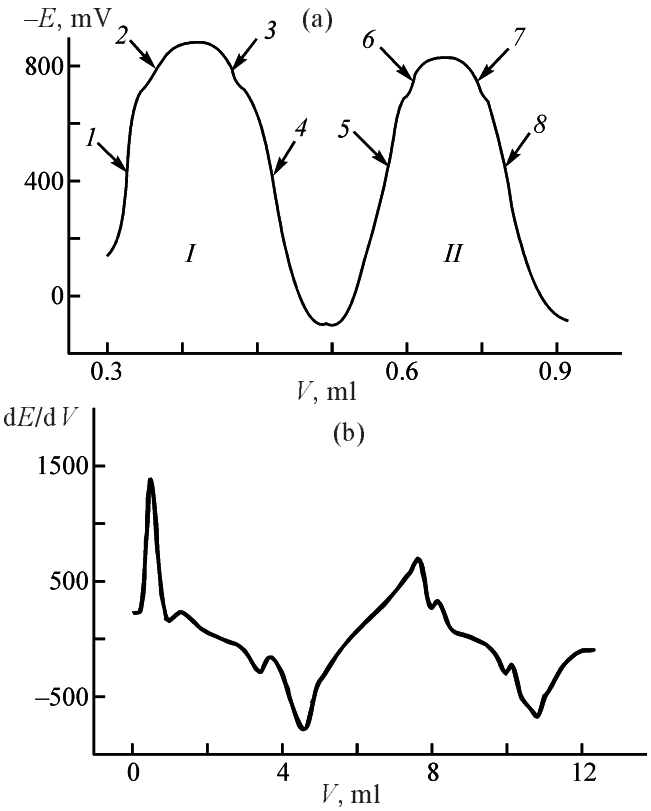


Fig. 1. (a) Redox titration curves of humus acids and (b) their differential form. c_{HA} = 0.1 g l^{-1}, c_{HMS} = 0.11 M, c_{NaOH} = 0.1 M, $c_{K_3[Fe(CN)_6]}$ = 0.24 M. 65°C. (*E*) Redox potential of HA solution, (d*E*/d*V*) first derivative of the redox potential with respect to titrant volume, and (*V*) titrant volume. Redox cycles of HA: (*I*) first and (*II*) second. (*1, 2, 5, 6*) Reduction potential of HA functional groups and (*3, 4, 7, 8*) oxidation potential of HA functional groups.

Table 1. Reduction (RP) and oxidation (OP) potentials of humus acids

Potential	Redox potential, mV	
	first redox cycle	second redox cycle
Fragments of first kind		
RP	–432	–787
OP	–420	–779
Fragments of second kind		
RP	–448	–750
OP	–441	–744

Table 2. Content of reducible functional groups in humus acids

Main fragments	Concentration, g-equiv g^{-1}
Functional groups:	
carbonyl	$(112 \pm 8.3) \times 10^{-4}$
quinone	$(10.5 \pm 0.5) \times 10^{-4}$
total	122.5×10^{-4}
Transition metals:	
Fe	$(4.25 \pm 0.758) \times 10^{-4}$
Mn	$(0.027 \pm 0.0015) \times 10^{-4}$
Cu	$(0.02 \pm 0.001) \times 10^{-4}$
total	4.297×10^{-4}

The fact that the ascending and descending branches in the titration curve are symmetrical (the oxidizing and reducing agents are consumed in equal amounts) shows that the identical functional groups of humus acids participate in the reduction and reoxidation reactions. It should be noted that the maximum height in the second redox cycle is somewhat lower than that in the first cycle. The similar trend is observed for the inflection points in the titration curves. This is apparently caused by the fact that a part of functional groups in humus acids (~10%) are reduced irreversibly in the first redox cycle.

We believe that the catalytic centers of humus acids capable of reversible reduction are, firstly, transition metal ions strongly coordinated with humus acids, whose bonds with humus acid functional groups are not broken on changing metal valence. The other redox-active centers contained in humus acids are the carbonyl and quinone groups. The concentration of these functional groups in humus acids is given in Table 2. This table shows that iron accounts for 98% of the variable-valence metals contained in humus acids. The reversible redox reactions of iron without break of its coordination bonds with humus acid functional groups were analyzed in [3, 18, 19].

The standard electrode potential of the half-reaction $Fe^{3+} + e \rightarrow Fe^{2+}$ varies in the range 360–500 mV depending on the kind of ligand and solvent [20, 21]. As seen from Fig. 1a, this potential range covers the reduction potential corresponding to the first inflection point in the redox titration curve of humus acids. The half-reaction potentials of reduction of the aldehyde, ketone, and quinone functional groups, corresponding to the second inflection point in the redox titration curve, are in the range 770–970 mV [22].

Thus, the reduction and oxidation potentials determined from the redox titration curve of humus acids allowed determination of both the kind of reducible functional groups and the order of their reduction. These results showed that the transition metal ions coordinated with humus acids are reduced first [(reaction (1)], and this is followed by the reduction of the carbonyl and quinoid groups [(reaction (2)].

$$HA(Fe^{3+}) + HOCH_2SO_2^- + 2OH^- \rightleftarrows HA(Fe^{2+}) + SO_3^{2-} + CH_2O + H_2O \quad (1)$$

$$HA(C{=}O) + SO_2^{2-} + 2OH^- \rightleftarrows HA(C{-}O)^- + SO_3^{2-} + H_2O. \quad (2)$$

We attempted also to elucidate whether both kinds of the redox-active centers in humus acids contribute to catalytic reduction of the quinone groups in CGA molecules. The contribution of particular active centers of humus acids to the total catalytic effect was also examined. Taking into account that 98% of the varible-valence metals contained in humus acids are coordinated iron ions, we chose the Fe(II)–EDTA complex as a model of the metal-containing catalytic center. The stability constants of complexes of iron cations with both EDTA and humus acids have the same order of magnitude [13, 23]. The reduction and oxidation of metals in such strong complexes is not accompanied by their breakdown.

Figure 2 shows the kinetic curves of CGA dye reduction with sodium hydroxymethanesulfinate under the following conditions: (*1*) without catalyst, (*2*) in the presence of Fe(II)–EDTA complex, and (*3*) in the presence of humus acids. The iron concentration in both Fe(II)–EDTA complex and humus acids was equal. The rate constants obtained in these experiments are listed in Table 3.

Table 3 shows that, in the presence of both the Fe(II)–EDTA complex and humus acids, the rate constant of CGA reduction with sodium hydroxymethanesulfinate increases by a factor of 1.4 and 11, respectively. The considerably higher catalytic effect of humus acids as compared to Fe(II)–EDTA complex is caused by the fact that humus acids contain two kinds of catalytic centers: metal ions and organic groups (quinone, carbonyl). Due to the catalytic

Table 3. Rate constants of reduction of CGA dye with sodium hydroxymethanesulfinate in the presence of various catalysts at 65°C

Catalyst	Concentration of catalytic centers, mg-equiv g^{-1}	Rate constant $k \times 10^3$, s^{-1}
None	–	3.7
Fe(II)–EDTA complex	0.425	5.2
Humus acids	12.68	40.8
Quinone and carbonyl functional groups in humus acids (calculated values)	12.25	29.2

activity of quinone (carbonyl) groups, the rate constant of CGA reduction increases by a factor of 7.9. The necessary condition for humus acid functioning as a catalyst is the lower activation energy E_a of reduction of its functional groups as compared to that for the quinone groups in vat dye molecules. The E_a of reduction of humus acid functional groups with sodium hydroxymethanesulfinate, determined by the Arrhenius equation, was 28.6± 1.1 kJ mol^{-1}. At the same time, the activation energy of reduction of CGA anthraquinone dye is higher by a factor of approximately 5 (E_a = 138 ± 5.9 kJ mol^{-1}) [13].

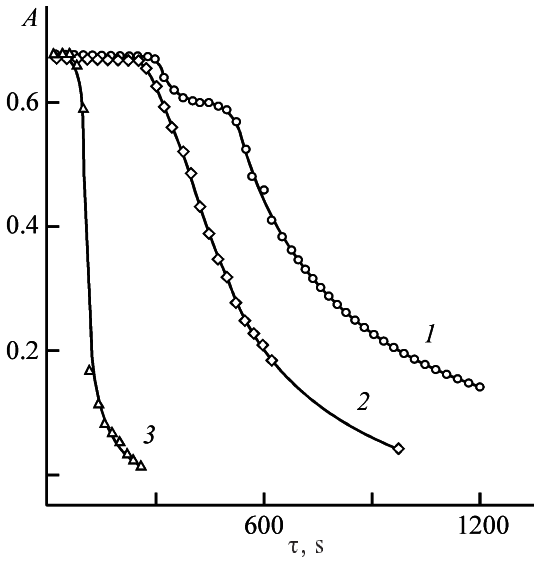


Fig. 2. Effect of humus acids and Fe(II)–EDTA complex as a model of a catalytic metal center in humus acids on the kinetics of CGA reduction with sodium hydroxymethanesulfinate at 65°C. Reagent concentration, M: c_{CGA} 5.98×10^{-5}, c_{HMS} 2.37×10^{-2}, $c_{FeSO_4 \cdot 7H_2O}$ 3×10^{-4}; c_{Na_2EDTA} 4.33×10^{-3}, c_{NaOH} 0.1; c_{HA} 0.1 g^{-1}. (*A*) Optical density of CGA solution and (τ) time. (*1*) Without catalyst, (*2*) in the presence of Fe(II)–EDTA complex, and (*3*) in the presence of humus acids.

CONCLUSIONS

(1) According to the results of redox titration, peat humus acids contain two kinds of successively reducible catalytic centers: variable-valence metal ions strongly coordinated with humus acids and organic (carbonyl, quinone) groups. The reduction potentials of these groups were determined and the reversibility of their reduction was established.

(2) In reduction of vat dyes catalyzed by humus acids, the catalytic centers are both the organic (quinone, carbonyl) groups and the coordinated variable-valence transition metal ions.

ACKNOWLEDGMENTS

This study was financially supported by the Russian Foundation for Basic Research (project no. 06-04-08048-ofi) and by the START-2006 project for support of small enterprises in scientific and technical fields (State Contract no. 4302 r/6530).

REFERENCES

1. Anisimova, M.A., Perminova, I.V., and Lebedeva, G.F., *Soil Chem.*, 1998, vol. 31, no. 9, pp. 1079–1084.
2. Perminova, I.V., Gretschishcheva, N.Y., Petrosyan, V.S., et al., *Soil Sci. Soc.*, 2001, vol. 14, pp. 275–287.
3. Perminova, I.V., Analysis and Classification of Humus Acids and Prediction of Their Properties, *Doctoral Dissertation*, Moscow, 2000.
4. Di Corcia, A., *J. Chromatogr.*, 1999, vol. 852, pp. 465–474.
5. Engebreston, R. and Wandruszka, R., *Eviron. Sci. Technol.*, 1999, vol. 33, pp, 4299–4303.
6. Wandruszka, R., *Geochem. Trans.*, 2006, vol. 7, pp. 6–10.

7. Demina, L.L., *Formy migratsii tyazhelykh metallov v okeane* (Migration Forms of Heavy Metals in Ocean), Moscow: Nauka, 1982.
8. Kholodov, V.A., Kulikova, N.A., and Perminova, I.V., *J. Ecol. Sci.*, 2003, vol. 2, nos. 3–4, pp. 50–51.
9. Perminova, I.V., Gretschishcheva, N.Y., Kovalevski, D.V., et al., *Eviron. Sci. Technol.*, 2001, vol. 35, pp. 3841–3848.
10. Totskaya, N.V., Dolmat, M.I., and Romanova, M.G., *Tekst. Prom–st.*, 1986, no. 3, pp. 43–44.
11. Yakimchuk, R.P., Mishchenko, A.V., and Bulusheva, N.E., *Primenenie kubovykh krasitelei* (Application of Vat Dyes), Moscow: Legprombytizdat, 1985.
12. Pogorelova, A.S., Vashurina, I.Yu., and Kalinnikov, Yu.A., *Izv. Vyssh. Uchebn. Zaved., Tekhnol. Tekstil'n. Prom–sti.*, 2006, no. 1, pp. 55–59.
13. Pogorelova, A.S., Development of Theoretical Fundamentals of Application of Humic Acids to Dyeing and Printing of Fabrics with Vat Dyes, *Cand. Sci. Dissertation*, Ivanovo: 2003.
14. Ponomareva, V.V. and Plotnikova, T.A., *Humus i pochvoobrazovanie* (Humus and Soil Formation), Leningrad: Nauka, 1990.
15. Makarov, S.V., *Usp. Khim.*, 2001, vol. 70, no. 10, pp. 995–1006.
16. Vashurina, I.Yu., Active Dye Association and Development of an Effective Process for Dyeing and Low-Collapsible Finishing of Cotton Fabrics, *Cand. Sci. Dissertation*, Ivanovo, 1998.
17. Ermachenko, L.A., *Atomno-absorptsionnyi analiz v sanitarno-gigienicheskikh issledovaniyakh* (Atomic-Absorption Analysis in Public Health Studies), Cheboksary: Chuvashiya, 1997.
18. Stevenson, F.J., *Humic Chemistry: Genesis, Composition, Reaction*, New York: Wiley, 1982, vol. 1.
19. Tur'yan, Ya. I., *Okislitel'no-vosstanovitel'nye potentsialy v analiticheskoi khimii* (Redox Potentials in Analytical Chemistry), Moscow: Khimiya, 1999.
20. Askarov, K.A., Berezin, B.D., and Bystritskaya, E.V., *Porfiriny: spektroskopiya, elektrokhimiya, primenenie* (Porphyrins: Spectroscopy, Electrochemistry, and Applications), Moscow: Nauka, 1987.
21. Toropova, V.F., Tur'yan, Ya.I., and Budnikov, G.K., *Elektrosintez i mekhanizm organicheskikh reaktsii* (Electrosynthesis and Mechanism of Organic Reactions), Moscow: Nauka, 1973.
22. Mann, C.K. and Barnes, K.K., *Electrochemical Reactions in Nonaqueous Solutions*, New York: Dekker, 1970.
23. Dyatlova, N.M., Temkina, V.Ya., and Popov, K.I., *Kompleksony i kompleksonaty metallov* (Complexones and Metal Complexonates), Moscow: Khimiya, 1988.

ISSN 1070-4272, Russian Journal of Applied Chemistry, 2008, Vol. 81, No. 7, pp. 1213–1219. © Pleiades Publishing, Ltd., 2008.
Original Russian Text © S.S. Ivanchev, O.N. Primachenko, V.N. Pavlyuchenko, S.Ya. Khaikin, V.A. Trunov, 2008, published in Zhurnal Prikladnoi Khimii, 2008, Vol. 81, No. 7, pp. 1134–1140.

MACROMOLECULAR CHEMISTRY AND POLYMERIC MATERIALS

Proton-Conducting Membranes Based on Multicomponent Copolymers

S. S. Ivanchev, O. N. Primachenko, V. N. Pavlyuchenko, S. Ya. Khaikin, and V. A. Trunov

St. Petersburg Branch, Boreskov Institute of Catalysis, Siberian Branch, Russian Academy of Sciences, St. Petersburg, Russia

Konstantinov Institute for Nuclear Physics, Russian Academy of Sciences, Gatchina, Leningrad oblast, Russia

Received May 12, 2007

Abstract—Preparation of proton-conducting polymeric composites via copolymerization of multicomponent monomeric systems using the interpenetrating polymer network preparation procedure is studied. The products are characterized by the protonic conductivity, water-retaining capacity, and mechanical properties. The approach used allows fabrication of membranes with a reasonable protonic conductivity over the temperature range 20–90°C. A possibility of modification of the proton-conducting materials with small additions of hydrolyzable organosilicon comonomers is analyzed. The structure of the resulting systems is examined by small-angle neutron scattering.

DOI: 10.1134/S1070427208070173

Currently one could say that the principal types or classes of proton-conducting polymeric membranes for fuel cells take a clear shape [1]. Primarily these are perfluorinated polymers of the Nafion type and composition- and structure-related polymeric composites [1–5], polycondensation membranes based on poly(benzimidazoles), polyester–ester ketones, etc. [5, 6].

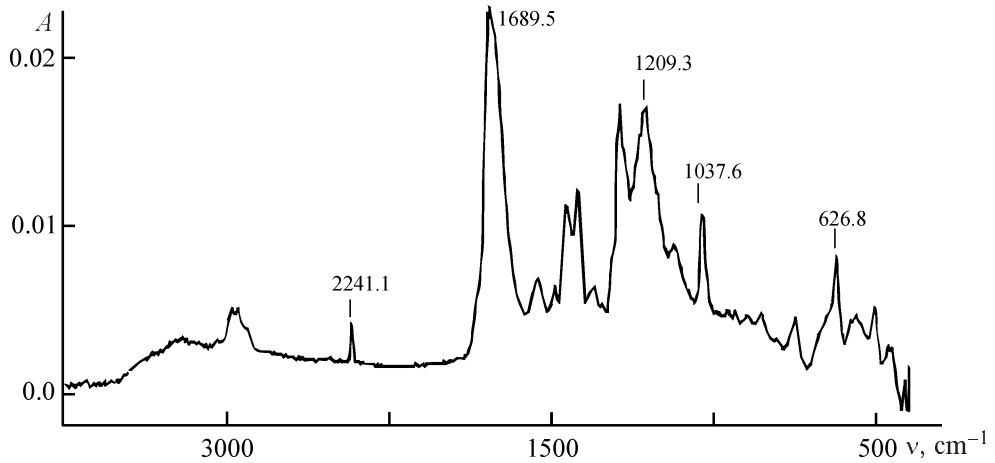
Recently data on proton-conducting polymeric membranes based on hybrid polymeric systems were reported [7–9]. In this relation, patents and developments from the recently founded ITM Power Ltd. are of particular interest [10–14]. The original development of this company proposes fabrication of not only a membrane, but also a membrane electrode assembly (MEA) consisting of electrodes and an ion-exchange polymeric membrane (PM) made of a hydrophilic polymer bearing a strong ionic group. Such an aggregate is prepared by γ-radiation-induced in situ copolymerization of a mixture of hydrophobic and hydrophilic comonomers, including a monomer containing a strong ionic group. As the authors asserted, such PMs demonstrate high protonic conductivity, controlled hydrophilicity, and capability of recycling of the platinum catalyst from MEA. Furthermore, the authors declare the possibility of reducing cost of PM and exploitation of the system by an order of magnitude as compared to Nafion membranes. They pointed out that cross-linked polymeric membranes could be prepared through not only radiation, but also chemical cross-linking. The description of the invention includes no data on the performance characteristics of the membrane materials under different exploitation conditions.

In this study, we examined the possibility of implementation of the method for fabricating polymeric membranes, proposed in [10–14], including the effect of the composition of the monomer mixture on properties of the resulting PMs and their performance characteristics as components of fuel cells (FSc).

EXPERIMENTAL

In synthesis of hydrophilic polymers containing an ionic group, we used such monomers as acrylonitrile (AN), *N*-vinylpyrrolidone (*N*-VP), vinyltrimethoxysilane (VTMS), vinyltriethoxysilane (VTES), 3-(trimethoxysilyl)propyl methacrylate (TMSPMA), 2-acrylamido-2-methyl-1-propanesulfonic acid (AMPSA), and ethylene glycol dimethacrylate (EGDM), all from Sigma Aldrich.

The hydrophilic ionic polymers were synthesized by copolymerization of three- or four-component



IR spectrum of PM (for chemical composition of PM, see Table 1, sample no. 2).

monomer mixtures in the presence of a cross-linking agent using ammonium persulfate as an initiator in an aqueous solution at room temperature for 24 h. Because of high adhesive capacity of the materials synthesized, polymeric membranes were fabricated in sealed built-up fluoroplastic molds.

The water content of PMs was determined after keeping samples in water at 25 or 90°C (equilibrium swelling conditions). From this data, we additionally determined the parameter λ defined as the amount of water in moles per $-SO_3H$ group. One more parameter used was $\Delta H_2O^{90°C}$ representing the water loss of a membrane in the equilibrium swelling state in 1 h at 90°C. Parameter λ reflects the hydrophilicity of PM, and $\Delta H_2O^{90°C}$ characterizes the stability of hydrophilic properties under heating.

Mechanical properties of hydrated PMs in the equilibrium swelling state were examined on a UTS 10 multipurpose mechanical testing machine (Germany) at 20°C. The samples represented 0.5–1.0-mm-thick spatulas with the size of the working part of 20 × 3.5 mm. The extension rate was 10 mm min^{-1}. In these tests, we determined the ultimate tensile strength σ_u, elastic modulus E, and relative elongation at break ε.

Since measurement of the elongation for highly swollen samples at 90°C is a difficult task, we determined the ultimate compression strength σ_u, elastic modulus E, and failure strain ε under uniaxial compression using the same testing machine. In this case, samples were 5-mm-high flat cylinders 12 mm in diameter. The compression rate was 1 mm min^{-1}.

The conductivity of the hydrated films at 20 and 90°C was measured in a cell with platinum electrodes using the four-probe method.

Infrared reflection spectra of dry samples were recorded on a Shimadzu FTIR-8300 instrument using Kramers–Kroning transformation.

The structure of the membranes (pore and channel distribution) was studied by small-angle neutron scattering on a Membrana-2 diffractometer at the Konstantinov Institute for Nuclear Physics using a beam of neutrons with a wavelength of 0.3 nm.

First we reproduced the procedures for preparing polymeric membranes by copolymerization of monomer mixtures of AN, *N*-VP, and AMPSA according to [10] using the chemical initiator and EGDM as a cross-linking agent.

The figure shows the IR spectrum of the polymeric membrane (Table 1, sample no. 2), suggesting that the copolymer contains the AN, *N*-VP, and AMPSA units (bands at 2240; 1690; and 625, 1040, and 1210 cm^{-1}, respectively).

The study of the films of the synthesized partially cross-linked hydrophilic ionic copolymers capable of equilibrium and reversible swelling in water showed that they are polymeric hydrogels [15]. Such hydrated materials demonstrate reasonable protonic conductivity (σ_H > 0.05 S cm^{-1} at 20°C) at an AMPSA content in PM of 16.5–23.5 wt % (Table 1, sample nos. 2–5), which is well comparable with that of Nafion membranes. Data on the effect of the chemical composition of the copolymer on the characteristics of PMs revealed that decrease in the AMPSA content in the copolymer below 15 wt % abruptly decreases the protonic conductivity of the material as a result of significant decrease in parameter λ (Table 1, sample no. 1). There is an optimal concentration of the sulfonate groups in

Table 1. Characteristics of polymeric membranes fabricated according to [10]

Sample no.	Copolymer composition, wt %				EM	Water-retaining capacity			Protonic conductivity σ_H, S cm^{-1}		Mechanical characteristics at 20°C		
	AN	*N*-VP	AMPSA	EGDM		$\lambda = nH_2O/-SO_3H$		$\Delta H_2O^{90°C}$ wt % h^{-1}	20°C	90°C	σ_u, MPa	*E*, MPa	ε, %
						25°C	90°C						
1	44.5	44.5	10.0	1.0	2070	10	16	–	0.0001	–	–	–	–
2	41.2	41.2	16.5	1.1	1255	101	1380	34.9	0.057	Degrades	1.94	2.02	170
3	40.3	40.2	18.5	1.0	1120	222	1700	–	0.083	"	–	–	–
4	39.5	39.5	20.0	1.0	1035	740	2430	–	0.064	"	0.46	0.66	110
5	37.6	37.7	23.5	1.2	880	770	3720	–	0.055	"	0.35	0.59	100
6	22.0	22.0	53.0	3.0	390	–	–	–	Degrades	"	–	–	–
7	40.3	40.2	16.5	3.0	1255	80	1010	–	–	"	–	–	–
8*	39.3	39.2	16.5	5.0	1255	61	350	–	–	–	–	–	–

* Degrades upon film formation in copolymerization.

the copolymer (15–20 wt %) at which the material exhibits a reasonable protonic conductivity. Too high AMPSA concentration (above 25 wt %) in the copolymer does not allow preparation of PMs stable under the exploitation conditions. Even at the optimal AMPSA content, the resulting PMs do not exhibit high mechanical strength. As seen from Table 1, with increasing AMPSA content, i.e., with increasing concentration of the sulfonate groups in the copolymer, from 16.5 to 23.5 wt %, λ increases from 101 to 770 (at 25°C), and σ_u decreases from 1.94 to 0.35 MPa. At elevated temperature (90°C), PMs fabricated according to the procedure described in [10] exhibit unsatisfactory mechanical characteristics, making them unsuitable for use at this temperature. The attempt to improve the mechanical strength of PMs through adding hydrophobic monomers such as methyl and *n*-butyl methacrylate failed.

Strengthening of such PMs through increasing cross-linking density in the copolymer resulted in micro- and macrocracking in formation of the membrane and in its breakdown upon hydration. It was demonstrated that the cross-linking agent content in the copolymer should be below 3 wt %. Above this critical value, cracking of PMs takes place in its formation in the course of copolymerization.

Therefore, we failed to prepare PMs with reasonable characteristics, especially at elevated temperatures, which can be attributed to the fact that the authors of [10] employed radiation copolymerization, or to some other know-how.

For polymeric hydrogels, several approaches to formation of the structure of materials can be used to impart desired properties to the polymeric system. In synthesis of polymeric hybrid hydrogels, the optimal approach is accepted to be that based on formation of interpenetrating polymer network (IPN) [16, 17].

To fabricate PMs with satisfactory characteristics, we used the IPN formation approach in which one of the networks is proton-conducting, and the other network provides reasonable mechanical strength and barrier characteristics with respect to components of the working medium of the fuel cell (oxygen, hydrogen). In the first stage, we synthesized cross-linked copolymers with ionic sulfonate groups. Their compositions and characteristics are presented in Table 1.

In the second stage, to the polymer network prepared previously, a mixture of monomers of another, more hydrophobic composition, was added, which was followed by copolymerization using the cross-linking monomer. The water-retaining and mechanical characteristics of the IPNs can be controlled over a wide range by varying the ratio of AN and *N*-VP monomers used in synthesis of the second network and the network weight ratio.

Table 2 (sample nos. 1–7) shows characteristics of IPN-based PMs. As can be seen, this method allows preparation of PMs with high protonic conductivity, exhibiting good mechanical characteristics in the hydrated state up to 90°C. It was found that, to maintain mechanical strength in IPN-based PMs at elevated temperatures, the amount of the second

Table 2. Characteristics of IPN-based polymeric membranes

Sample no.	Composition of polymer network 1, wt %						Composition of polymer network 2, wt %			Network 1 to network 2 weight ratio
	AN	*N*-VP	AMPSA	VTMS	TMSPMA	EGDM	AN	*N*-VP	EGDM	
1	41.2	41.2	16.5	–	–	1.1	49.5	49.5	1.0	0.77
2	41.2	41.2	16.5	–	–	1.1	48.6	48.9	2.5	0.27
3	41.2	41.2	16.5	–	–	1.1	49.0	49.0	2.0	0.19
4	41.3	41.3	16.5	–	–	0.9	59.6	39.0	1.4	0.24
5	50.0	31.6	16.5	–	–	1.9	59.1	38.9	2.0	0.29
6	50.0	31.6	16.5	–	–	1.9	20.0	77.9	2.1	0.35
7	39.5	39.5	20.0	–	–	1.0	56.4	41.8	1.8	0.22
8	39.8	40.7	16.4	2.0	–	1.1	49.1	49.0	1.9	0.32
9	39.7	39.8	16.5	3.0	–	1.0	49.1	49.0	1.9	0.17
10	39.8	39.7	16.5	3.0**	–	1.0	49.1	48.9	2.0	0.25
11	40.7	40.7	16.5	–	1.0	1.1	61.5	37.0	1.5	0.10
12	40.2	40.3	16.5	–	2.0	1.0	49.0	49.0	2.0	0.11
13	39.7	39.9	16.4	–	3.0	1.0	49.0	49.0	2.0	0.35
14	38.8	38.7	16.5	–	5.0	1.0	49.0	49.0	2.0	0.21

Sample no.	EM	Water-retaining characteristics			Protonic conductivity σ_H, S cm^{-1}		Mechanical characteristics at 20°C		
		$\lambda = nH_2O/-SO_3H$		$\Delta H_2O^{90°C}$ wt % h^{-1}	20°C	90°C	σ_u, MPa	*E*, MPa	ε, %
		25°C	90°C						
1	2221	120	630	61.0	0.122	0.052	2.04	–	180
2	1594	106	680	–	–	–	2.54*	1.52*	66*
3	1495	128	1175	77.1	0.273	0.095	2.05	3.52	185
4	1556	120	–	–	–	–	2.26	4.85	80
5	1619	86	420	–	0.124	0.025	–	–	–
6	1694	–	–	–	0.314	0.019	–	–	–
7	1263	225	350	–	0.174	0.061	1.16	1.50	123
8	1666	89	380	62.2	–	–	2.24	4.86	77
9	1368	71	235	83.9	0.157	0.078	–	–	–
10	1569	79	320	–	0.213	0.069	2.40	5.70	90
11	1380	89	653	–	0.130	0.025	2.59	4.50	103
12	1393	133	613	67.6	0.087	0.047	–	–	–
13	1724	95	268	53.4	0.214	0.076	2.23	8.38	69
14	1519	88	243	–	0.155	0.057	2.53	9.58	60

* Measured at 90°C (under compression stress).
** VTES.

polymer network should be at least 10–15% of the weight of the first (ionic) network. Variation of the composition and weight fraction of the second network in PM allows control of not only the water-retaining and mechanical characteristics, but also the protonic conductivity of PM. Naturally, the protonic conductivity decreases with increasing weight fraction of the second network (Table 2, sample nos. 1 and 3). Thus, it was demonstrated for PMs containing the second network with relatively high AN content (Table 2, sample nos. 5 and 6) that the resulting membranes are more rigid, having lower protonic conductivity.

Unexpectedly, IPN-based PMs appeared to have higher protonic conductivity than ionic polymer networks formed in the first stage, despite the decrease in the total concentration of the sulfonate groups in the composite material, suggesting a complex dependence of the protonic conductivity on the concentration and degree of hydration of the sulfo-

Table 3. Characteristics of polymeric membranes modified with organosilicon additives

Sample no.	Composition of polymer network, wt %							EM
	AN	*N*-VP	VTMS	VTES	TMSPMA	AMPSA	EGDM	
1	40.8	40.7	1.0	–	–	16.4	1.1	1262
2	39.8	40.7	2.0	–	–	16.4	1.1	1262
3	39.7	39.8	3.0	–	–	16.5	1.0	1255
4	38,4	39,2	5,0	–	–	16.4	1.1	1262
5	40.7	40.8	–	1.0	–	16.5	1.0	1255
6	40.2	40.3	–	2.0	–	16.5	1.0	1255
7	39.8	39.7	–	3.0	–	16.5	1.0	1255
8	40.7	40.7	–	–	1.0	16.5	1.1	1255
9	40.2	40.3	–	–	2.0	16.5	1.0	1255
10	39.7	39.9	–	–	3.0	16.4	1.0	1262
11	38.8	38.7	–	–	5.0	16.5	1.0	1255

Sample no.	Water-retaining characteristics			Protonic conductivity σ_H, S cm^{-1}		Mechanical characteristics at 20°C		
	$\lambda = nH_2O/-SO_3H$		$\Delta H_2O^{90°C}$ wt % h^{-1}	20°C	90°C	σ_u, MPa	*E*, MPa	ε, %
	25°C	90°C						
1	81	1060	43.1	0.105	0.034	2.15	3.80	85
2	77	490	53.1	0.135	0.059	–	–	–
3	73	410	48.5	0.160	0.111	2.62	6.91	79
4	75	161	33.6	0.238	0.056	–	–	–
5	230	1220	61.0	0.115	0.024	2.45	3.91	135
6	200	1180	63.1	0.129	0.028	–	–	–
7	71	650	69.3	0.177	0,030	–	–	–
8	113	1730	39.2	–	Degrades	–	–	–
9	91	550	53.5	0.100	0.059	2.03	5.08	97
10	71	355	69.2	0.292	0.044	–	–	–
11	80	307	75.7	0.317	0.068	–	–	–

nate groups, including the effects of the PM structure and transfer conditions of hydrated protons across the membrane. Many researchers [18, 19] pointed out that the membrane morphology is controlled by the nature of monomers and membrane fabrication procedure, which affect the distribution and concentration of acid groups in nanosized structural elements of PMs, limiting water-retaining properties of membranes and transport of hydrated proton across the membrane, thus controlling its protonic conductivity.

To check this hypothesis, we studied the PM structure by small-angle neutron scattering. Prior to experiment, the membranes were swollen in D_2O, which allowed examination of the system of nanosized pored filled with water. It was demonstrated that, in the initial polymer network (Table 1, sample no. 2), the clusters are nonuniform, consisting of large-sized (24–26 nm) blocks with small (about 3 nm in size) cavities inside them. Interpenetrating polymer networks (table 2, sample no. 3) prepared on the basis of the initial network have more complex structure (in this case, network 2 additionally forms water-retaining blocks up to 70 nm in size). Evidently, such an hierarchical structure favors formation of channels connecting the clusters, thus causing the increased protonic conductivity of IPN-based PMs.

It was shown that IPNs exhibit a protonic conductivity σ_H = 0.12–0.31 and 0.019–0.095 S cm^{-1} at 20 and 90°C, respectively, which is condiderably higher than in the previously fabricated structures (0.055–0.083 S cm^{-1} at 20°C). In this study, we managed to significantly improve mechanical characteristics of the hydrated IPN-based membranes

(σ_u = 2.04–2.54 MPa; elastic modulus increased to 3.52–4.85 MPa), making these membranes suitable for use at temperatures of up to 90°C. The drawback of the IPN-based PMs is in slight deterioration of the water-retaining properties, as demonstrated by the parameter $\Delta H_2O^{90°C}$.

Therefore, the way to improve performance characteristics of PMs based on ionic copolymers is the formation of interpenetrating networks in their structure.

Another possible way to improve mechanical properties of PMs is to form additional cross-linked structures in the membranes using a sol–gel process. We analyzed the effect of additions of such hydrolyzable comonomers as alkoxysilanes (VTMS, VTES, and TMSPMA) (Table 3) in the first stage of synthesis of ionic copolymers.

In hydrolytic treatment of such copolymers, the alkoxysilane groups hydrolyze into the silanol groups, which is followed by their partial condensation at elevated temperatures [20, 21]. In the case in hand, hydrolysis of the alkoxysilane groups is acid-catalyzed without adding some additional acid, since the copolymer contains the sulfonate groups, and pH of the aqueous phase in contact with the polymer hydrogel is close to 3.0.

Because of low concentration (0.3–1.7 mol %) of organosilicon fragments in the structure of PMs, the matter concerns not the formation of hydrophilic organo–inorganic clusters, but rather some additional randomly distributed cross-linked domains in the already cross-linked and swollen copolymeric system. Furthermore, after hydrolysis, cross-linking involves only a small part of the silanol groups, while the remaining silanol groups improve the water-retaining characteristics of PMs.

It was demonstrated that introduction of VTMS, VTES, or TMSPMA into the ionic copolymer allows improvement of the mechanical strength and protonic conductivity of PMs. For the ionic copolymers modified with organosilicon comonomers of VTMS and TMSPMA, parameter λ at 25°C ranges from 70 to 90, which is probably close to the optimal value (at 16.5 wt % AMPSA content in the copolymer). This causes a reasonable protonic conductivity of the material (σ_H = 0.10–0.32 S cm^{-1}, which is considerably higher than for the unmodified membranes (σ_H = 0.055 S cm^{-1}). For all the PMs studied, increase in the additive (VTMS, VTES, or TMSPMA) content at constant AMPSA concentration in the copolymer results in increasing protonic conductivity of the membranes at low temperatures, which can be attributed to both additional randomly distributed cross-links, changing the distribution of the ionic sulfonate groups in the copolymer, and also to increase in the amount of undercondensed silanol groups improving the water-retaining characteristics of the copolymer and optimizing the transport of hydrated protons across the membrane. Introduction of the modifiers also allowed fabrication of PMs mechanically stable at elevated temperatures (90°C), as in the case of IPN-based membranes, even though with slightly lower protonic conductivity.

Modification with organosilicon monomers appeared to be most effective for IPN-based PMs. The effect of hydrolyzable organosilicon fragments of networks 1 or 2 on characteristics of interpenetrating networks is ambiguous. Modification of network 1 of PM with the organosilicon additives allows preparation of IPN-based PMs with better mechanical properties (Table 2, sample nos. 8–14; σ_u = 2.24–2.59 MPa, E = 4.50–9.58 MPa) and high protonic conductivity preserved (σ_H = 0.087–0.21 S cm^{-1} at 20°C and σ_H = 0.025–0.078 S cm^{-1} at 90°C), which is caused by enhanced mechanical characteristics of the first network. The use of organosilicon additives as components of network 2 deteriorated both mechanical and proton-conducting properties of the resulting PMs.

CONCLUSIONS

(1) A novel method is developed for fabricating proton-conducting materials as a hybrid ionic hydrated copolymer, using the interpenetrating network approach.

(2) The hydrophilicity and structure of interpenetrating polymer networks can be controlled, allowing improvement of the mechanical characteristics of the polymeric membranes at ambient and elevated (90°C) temperatures, with the satisfactory protonic conductivity of the material preserved.

(3) Structural elements of the ionic copolymers proved to be nanosized; the size changes upon formation of interpenetrating networks.

REFERENCES

1. Ivanchev, S.S., *Zh. Prikl. Khim.*, 2008, vol. 81, no. 4, pp. 529–545.
2. Bagotskii, V.S., Osetrova, N.V., and Skundin, A.M., *Elektrokhimiya*, 2003, vol. 39, no. 9, pp. 1027–1045.

3. Haile, S.M., *Acta Mater.*, 2003, vol. 51, pp. 5981–6000.
4. Glüsen, A. and Stolten, D., *Chem. Ingen. Tech.*, 2003, vol. 75, no. 11, pp. 1591–1597.
5. Roziere, J. and Jones, D.J., *Ann. Rev. Mater. Res.*, 2003, vol. 33, pp. 503–555.
6. Rusanov, A.L., Likhatchev, D.Yu., Kostoglotov, P.V., et al., *Adv. Polym. Sci.*, 2005, vol. 179, p. 83.
7. Honma, I., Nakajima, H., Nishikawa, O., et al., *Solid State Ionics*, 2003, vols. 162–163, pp. 237–245.
8. Dobrovol'skii, Yu.A., Pisareva, A.V., Leonova, L.S., and Karelin, A.I., *Al'ternat. Energ. Ekol.*, 2004, no. 12 (20), pp. 36–41.
9. Kato, M., Katayama, S., Sakamoto, W., and Yogo, T., *Electrochim. Acta*, 2007, vol. 52, no. 19, pp. 5924–5931.
10. US Patent 7318972.
11. US Patent 7318888.
12. WO Patent 2005/124915.
13. WO Patent 2005/124893.
14. WO Patent 2006/131758.
15. Pepps, N.A., *Reflexive Polymers and Hydrogels: Understanding and Designing Fast-Responsive Polymeric Systems*, Boca Raton: CRC, 2004, pp. 99–113.
16. Chekina, N.A., Pavlyuchenko, V.N., Ivanchev, S.S., et al., *Polym. Adv. Technol.*, 2006, vol. 17, nos. 11–12, pp. 872–877.
17. RF Patent 2269552.
18. Dobrovol'skii, Yu.A., Jannasch, P., Lafitte, B., et al., *Elektrokhimiya*, 2007, vol. 43, no. 5, pp. 515–527.
19. Torras, C. and Garcia-Valls, R., *J. Membr. Sci.*, 2004, vol. 233, nos. 1–2, pp. 119–127.
20. Natori, S.H. and Kerita, K., *Polym. Adv. Technol.*, 2007, vol. 18, no. 4, pp. 263–267.
21. Pavlyuchenko, V.N., Sorochinskaya, O.V., Khaikin, S.Ya., et al., *Zh. Prikl. Khim.*, 2007, vol. 80, no. 1, pp. 94–102.

ISSN 1070-4272, Russian Journal of Applied Chemistry, 2008, Vol. 81, No. 7, pp. 1220–1223. © Pleiades Publishing, Ltd., 2008.
Original Russian Text © Yu.N. Sazanov, D.M. Kostycheva, G.N. Fedorova, V.L. Ugolkov, E.M. Kulikova, A.V. Gribanov, 2008, published in Zhurnal Prikladnoi Khimii, 2008, Vol. 81, No. 7, pp. 1141–1144.

MACROMOLECULAR CHEMISTRY AND POLYMERIC MATERIALS

Composites of Lignin and Polyacrylonitrile as Carbon Precursors

Yu. N. Sazanov, D. M. Kostycheva, G. N. Fedorova, V. L. Ugolkov, E. M. Kulikova, and A. V. Gribanov

Institute of Macromolecular Compounds, Russian Academy of Sciences, St. Petersburg, Russia

Received December 25, 2007

Abstract—Films of polyacrylonitrile and lignin cast from dimethylformamide were studied by dynamic thermal analysis in a self-generated atmosphere and in a vacuum. The occurrence of a thermochemical reaction of the components on heating was demonstrated. The optimal conditions of the reaction between polyacrylonitrile and lignin were determined.

DOI: 10.1134/S1070427208070185

In our previous study [1], the possibility of polyacrylonitrile (PAN) carbonization with lignin (LG) was demonstrated for powder mixtures of these compounds. It was found that, in the course of thermochemical reaction of the components, the heat resistance of LG increases owing to the reactions starting with PAN cyclization. The observed features of cocarbonization of PAN and LG suggest the necessity of closer contact of the starting reactants by their preliminary homogenization in the form of solutions or suspensions. In the case of chitin and chitosan [2], cocarbonization with PAN is strongly accelerated by thermal treatment of films prepared from solutions of these polymers. From the experimental results, the role of interpolymer complexes of PAN with chitin and chitosan in a common solvent was revealed, which allowed preparation of cocarbonized composites with properties different from that of the initial polymers.

In this study we attempted to combine polymers through interpolymer complexes using PAN to impart new properties to lignin in the course of combined thermal treatment of a mixed solution of these polymers.

EXPERIMENTAL

As starting compounds we used ND-1 PAN fibrous copolymer produced by the Khimvolokno Joint-Stock Company (Svetlogorsk, Belarus) with molecular weight of 130 000 and an LG powder recovered by base hydrolysis using the procedure given elsewhere [3], forming suspensions in dimethylformamide (DMF). The express analysis of the ND-1 fiber and films cast from its solutions in DMF on a derivatograph and on a unit for thermovolumetric analysis (TVA) showed no differences in the thermochemical behavior of this copolymer and of PAN prepared in the laboratory. A dry PAN–LG mixture was prepared by mixing finely cut ND-1 PAN fiber and LG powder sifted through a sieve (0.04 mm mesh size). The films were prepared by casting of PAN solutions and PAN–LG suspensions in DMF (5% concentration) onto glass supports with subsequent drying at room temperature in a vacuum. Based on our previous results [1], we used the weight ratio of the starting components of 1 : 1, because this ratio allows evaluation of the thermochemical parameters typical for both polymers and their changes in the course of carbonization, especially using DTA. The dynamic thermal analysis of the PAN–LG films in the self-generated atmosphere (SGA) was carried out on an MOM C derivatograph at a heating rate of 10 deg min^{-1} using ceramic crucibles (sample weight 50 mg). The dynamic analysis of the PAN–LG films in a vacuum was carried out on a TVA unit with manometric recording [4] with heating to 900°C at a rate of 7 deg min^{-1} (sample weight 50 mg). The thermal degradation kinetics was studied on a NETZSCH STA 429 device in open crucibles in air at a heating rate of 7 deg min^{-1} (sample weight 10 mg). The PAN–LG composites with a high content of LG were prepared by pouring of a PAN–LG suspension in DMF into a burnt clay mold and evaporation of the solvent on a sand bath with gradual addition of a thick suspension of LG in DMF. Then the mold was dried for 4 h in a vacuum (10^{-3} mm Hg) in the TVA device to constant weight, after which the sample was heated

to 1000°C. Similar procedure was simultaneously performed with individual PAN.

The TG curves of the weight loss on heating of the samples to 1000°C are shown in Fig. 1a, and the thermal effects accompanying thermochemical transformations of the samples in the same temperature range are illustrated by Fig. 1b (DTA curves). As seen from the TG curve (Fig. 1a, curve *4*), thermal degradation of the film samples in the oxidative atmosphere in the entire temperature range studied proceeds more smoothly than that of the initial compounds. Starting from 120°C, the rate of the weight loss is slightly smaller than in the 300–400°C range, and above 400°C the pattern of thermal degradation of the mixed films strongly differs from that of the LG degradation. Above 600°C, the rates of the weight loss of samples 1–4 are similar, although the coke number of LG is noticeably lower than that of the modified samples.

Comparison of the thermal effects of the samples studied allows certain assumptions on the mechanism of thermal reaction of LG and PAN. Curve *1* (Fig. 1b) primarily illustrates thermal cyclization of PAN with a maximum at 244°C, complicated by subsequent oxidation reactions (300–380°C). This pattern is typical for a series of various PAN samples and can be used as reference for comparison with modified samples. As for curves *3* and *4* (Fig. 1b), it should be noted that the maximum of the exothermic effect is shifted toward higher temperatures, especially for the film sample (shift by 43°C). Moreover, the DTA curve of the film sample exhibits an endothermic effect at 400°C. Comparison of these parameters with those of curves *1* and *3* suggests that the thermal treatment of the PAN–LG mixed film leads to noticeable reaction of the components. The shift of the temperature maximum of the exothermic effect toward higher temperatures and a decrease in the peak area as compared to straight PAN and mixed powder samples are indicative of a certain decrease in the rate of PAN cyclization. Changes in the shape and temperature of the maximum of the endothermic effect at 400°C suggest formation of the carbonized compound with more ordered structure as compared to samples 1 and 3. The mechanism of this phenomenon was discussed previously in a study of low-temperature PAN carbonization [5].

In contrast to our previous measurements of thermochemical parameters [1], in this work we primarily studied the kinetic parameters of cocarbonization of PAN and lignin and attempted to minimize the

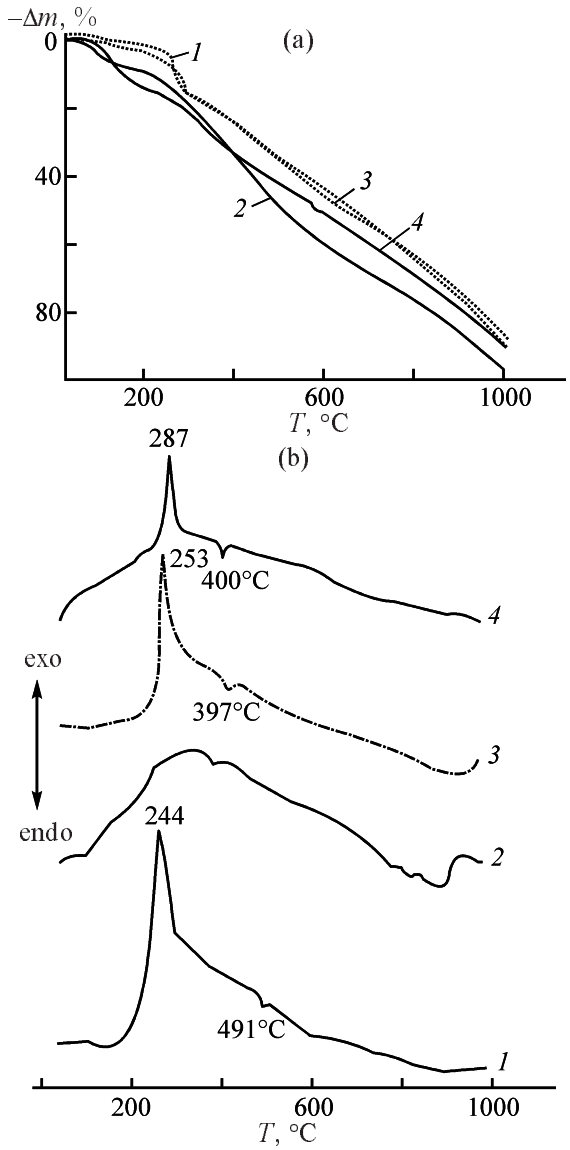


Fig. 1. (a) TG and (b) DTA curves of the LG, PAN, mixed samples, and PAN–LG (1 : 1) film, recorded in the course of dynamic heating in air at a rate of 10 deg min^{-1} (sample weight 50 mg). (Δm) Weight loss and (T) temperature. (*1*) PAN film, (*2*) LG powder, (*3*) PAN–LG (1 : 1) dry powder mixture, and (*4*) PAN–LG (1 : 1) film; the same for Fig. 2.

effect of the diffusion factors. For this purpose, the measurements were performed on a NETZSCH STA 429 device using small samples (10 mg), with a heating rate of 7 deg min^{-1}. The decrease in the sample weight to 10 mg decreases the probability of the majority of secondary reactions in the sample, which are initiated by gaseous products of thermal degradation passing through the composite layer in the case of larger samples (50–100 mg). This approach allows studying processes that are masked by the diffusion factor in large samples.

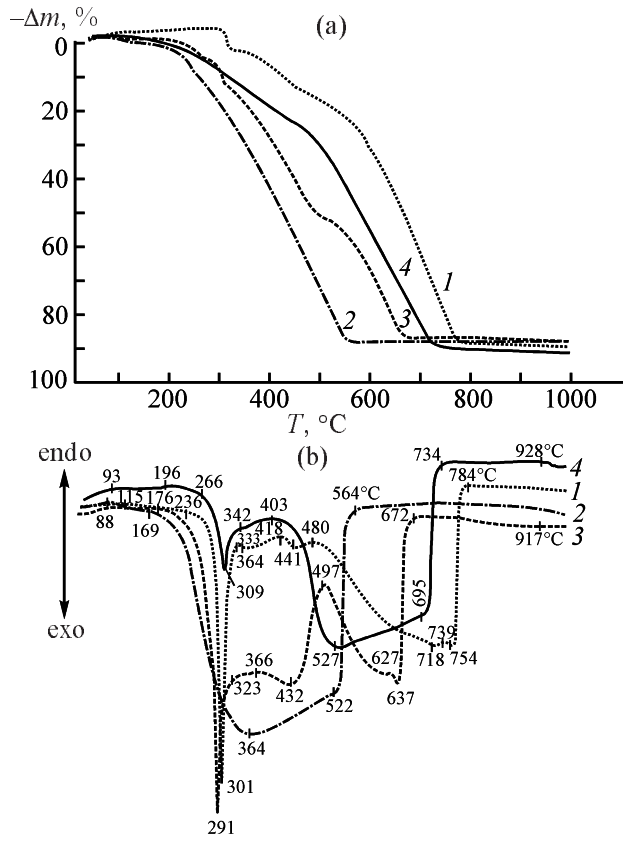


Fig. 2. (a) TG and (b) DTA curves of LG, PAN, mixed samples, and PAN–LG (1 : 1) film, recorded in the course of dynamic heating in air at a rate of 7 deg min^{-1} (sample weight 10 mg).

The TG curves shown in Fig. 2a strongly differ from those recorded on a derivatograph. As seen from the shape of these curves, oxidative atmosphere strongly affects all the process, especially in the 400–450°C range. The observed changes in the weight with temperature indicate that, in the 550–750°C range, the degradation reactions leading to complete combustion of the samples prevail. The TG curves of the initial samples correspond to the thermal degradation processes observed in the previous studies. We should note the behavior of the PAN–LG dry mixture (Fig. 2a, curve *3*). The shape of the TG curve of this sample reflects separate microreactions of the components, suggesting the absence of reaction of the components under the experimental conditions studied. As for the film sample (Fig. 2a, curve *4*), in the course of heating, after passing the range 300–350°C in which specific differences in the thermal degradation pattern are observed, the TG curve of the film becomes comparable with that of PAN. This fact suggests that more intimate and prolonged contact between the components is observed in the PAN–LG film sample as compared to the dry mixture. This assumption is confirmed by strong difference in the thermal effects at temperatures of the PAN cyclization (270–360°C, Fig. 2b). For example, the temperature peaks of cyclization of straight PAN and powdered mixed sample differ by 10°C, although the total thermal effect is proportional to the component ratio in the initial mixture.

The shape of the curve for sample 4 is quite different. The thermal effect of PAN cyclization in the mixed film is lower, compared to samples 1 and 3, by a factor of almost 5, and the peak temperature is shifted toward higher temperatures by 8°C (309°C) relative to the dry mixture. Thus, we observed changes in the thermochemical transformations of PAN whose cyclization is suppressed by LG and, probably, by its reaction with the nitrile groups in the step of their activation. This process should provide formation of new structures whose subsequent degradation is accompanied by prolonged exothermic effect in the 403–695°C range. The same specific effects are observed for dry mixed samples, for which the TG curve after 323°C exhibits the endothermic effect with a maximum at 497°C at significant heat release (Fig. 2b, curve *3*). In this sample, the cyclization of PAN proceeds completely and the exothermic effect corresponding to cyclization overlaps with an extensive exothermic effect of the LG thermal degradation.

As for the PAN–LG film prepared using DMF solution (Fig. 2b, curve *4*), the thermal peaks are smoother and shifted toward higher temperatures, and all the exothermic effects are significantly lower. The shape of the TG curve in the exothermic range 527–695°C is close to that of LG, but the effect is smaller and shifted upward in the temperature–time scale by 163 (start) and 170°C (end), as compared to LG. These facts suggest certain similarity in processes occurring in both exothermic ranges (PAN–LG film and LG), such as free-radical cleavage of bonds between the LG phenylpropane groups with the release of low-molecular-weight products of thermal degradation, followed by carbonization. This temperature range is wide and "monolithic," probably because the reaction products are diverse (low-molecular-weight aromatics, simple organic and inorganic compounds) and elimination of low-molecular-weight compounds occurs uniformly in time, which is typical for network polymers such as lignin. Whereas LG in the 180–520°C range actively degrades, the film is relatively stable in the 180–403°C range. Thus, the thermal degradation processes in the film are shifted toward higher tempera-

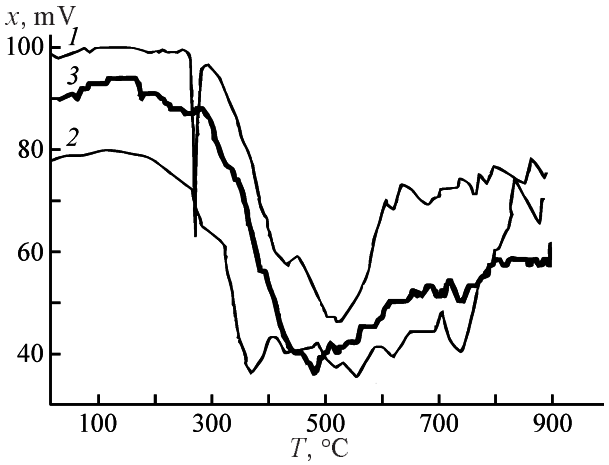


Fig. 3. TVA curves recorded in the course of dynamic heating at a rate of 7 deg min^{-1} (sample weight 50 mg). (x) Parameter of vacuum and (T) temperature. (*1*) PAN film, (*2*) LG powder, and (*3*) PAN–LG (1 : 1) film.

tures with simultaneous decrease in their intensity (inhibition of thermal degradation and deceleration of the weight loss in the course of the film pyrolysis). As a result, the thermal stability of the carbon product of thermal degradation of the mixed film increases by 60°C (as compared to the PAN–LG dry mixture) and, apparently, the carbon product of a new structure is formed.

Thermal treatment in a vacuum allows monitoring of the polymer degradation under the conditions maximally free of the effect of oxidizing atmosphere and concomitant thermal oxidative degradation of the gaseous products, which additionally complicate the pattern. As seen from the TVA data (Fig. 3), lignin in the film, apparently, hinders cyclization of the nitrile groups (absence of peak at 270°C), and the coke number of the carbonized residue formed from the PAN–LG film after its final thermal treatment is higher by 16% as compared to the theoretical value calculated assuming no thermochemical reactions of the components (Fig. 3, curve *3*). In contrast to straight LG, whose treatment at temperatures of up to 900°C yields a black powder, heating of the mixed film yields a film with a smooth lustrous surface. Thus, LG as a component of films, when heated in a vacuum, prevents cyclization of PAN and reacts with it in a wide temperature range, which decreases the carbonization onset temperature. This is confirmed by the relatively low temperature (470°C) of the end of the maximum of the gas release in the TBA curve recorded for the PAN–LG film (Fig. 3, curve *3*) and by observed stabilization of the product, which is characterized by smoother and more uniform decrease in the gas release. As for PAN film (Fig. 3, curve *1*), the maximum of the gas release is shifted by 100°C toward higher temperatures (530°C) as compared to the mixed film. In the case of LG (Fig. 3, curve *2*), the gas release decreases for a short time at 270°C, but at higher temperatures it is periodically resumed up to complete explosion-like degradation.

Thus, preparation of the LG suspensions, their mixing with PAN solutions, and subsequent film casting provide more intense interaction of the components as compared to dry mixtures. The highest possible content of LG in the PAN–LG film composites is 50–60%. Nevertheless, along with films, PAN–LG block carbon composites with a higher content of LG can be prepared from DMF solutions. The resulting PAN–LG carbonized product retains the shape and exhibits no shrinkage (in contrast to PAN carbonized in a vacuum) and is characterized by the fine-grain surface, opaque metallic luster, and strength.

CONCLUSIONS

(1) The kinetic parameters of cocarbonization of polyacrylonitrile and lignin under the conditions of minimization of the effect of the diffusion factors were studied.

(2) Thermal treatment of the film composites in a vacuum yields carbonized products without changes in the shape, which exhibit metallic luster and are characterized by the coke number higher by 16% as compared to the additive value.

(3) Cyclization of polyacrylonitrile in the film samples is partially inhibited by the products of lignin thermal degradation.

REFERENCES

1. Sazanov, Yu.N., Fedorova G.N., Kulikova, E.M., et al., *Zh. Prikl. Khim.*, 2007, vol. 80, no. 4, pp. 632–636.
2. Sazanov, Yu.N., Novoselova, A.V., Nud'ga, L.A., et al., *Zh. Prikl. Khim.*, 2005, vol. 78, no. 8, pp. 1144–1348.
3. Obolenskaya, A.V., El'nitskaya, Z.P., and Leonovich, A.A., *Laboratornye raboty po khimii drevesiny i tsellyulozy* (Laboratory Works in the Chemistry of Lignin and Cellulose), Moscow: Ekologiya, 1991.
4. Sazanov, Yu.N. and Sysoev, V.A., *Eur. Polym. J.*, 1974, vol. 10, pp. 867–869.
5. Sazanov, Yu.N., Novoselova, A.V., Fedorova, G.N., et al., *Zh. Prikl. Khim.*, 2007, vol. 80, no. 12, pp. 2046–2050.

ISSN 1070-4272, Russian Journal of Applied Chemistry, 2008, Vol. 81, No. 7, pp. 1224–1229. © Pleiades Publishing, Ltd., 2008.
Original Russian Text © G.E. Glievaya, V.A. Vilenskii, L.A. Goncharenko, 2008, published in Zhurnal Prikladnoi Khimii, 2008, Vol. 81, No. 7, pp. 1145–1149.

MACROMOLECULAR CHEMISTRY AND POLYMERIC MATERIALS

Modification of Polymeric Composites with Electric and Magnetic Fields

G. E. Glievaya, V. A. Vilenskii, and L. A. Goncharenko

Institute of Macromolecular Chemistry, National Academy of Sciences of Ukraine, Kiev, Ukraine

Received August 29, 2007

Abstract—Effect of the component composition and magnetic and electric fields on the structure and dielectric and electromechanical properties of composites constituted by incompatible polymers, cellulose acetobutyrate and segmented polyurethane, was studied.

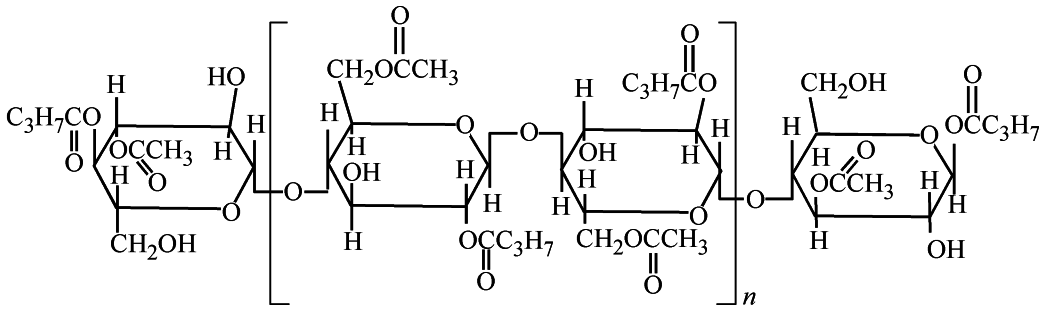
DOI: 10.1134/S1070427208070197

Use of biopolymers and their derivatives for preparing composites is a topical area of the development of the modern polymer science and technology. At present, physical methods for modification of polymeric systems are also being actively sought for. In our previous studies [1–3], we determined specific features of formation of the structure of polymers produced by a polyaddition of hydroxy groups of cellulose derivatives to diisocyanate groups of oligourethanes. It was also shown in a series of studies [4–7] devoted to the effect of magnetostatic (MSF) and electrostatic (ESF) fields on polyurethane modified by addition of cellulose acetobutyrate (CAB) that these physical fields weaken the microphase segregation in the composites and not only improve the thermal and thermomechanical properties of the starting polymers and their blends, but also impart new properties (higher conductivity and dielectric constant) to the materials, which expands their application field.

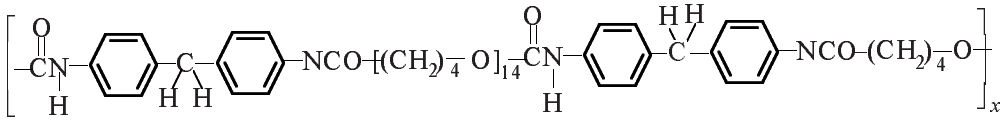
EXPERIMENTAL

In this work we continue these studies of composites in which the role of the matrix is played by a polysaccharide (CAB), and that of the modifying additive, by segmented polyurethane (PU) whose concentration was varied in the order 0.5, 1, 2, 5, 10, 15, and 25 wt % (Schemes 1, 2).

Scheme 1.
Repeating unit of CAB



Scheme 2.
Repeating unit of PU



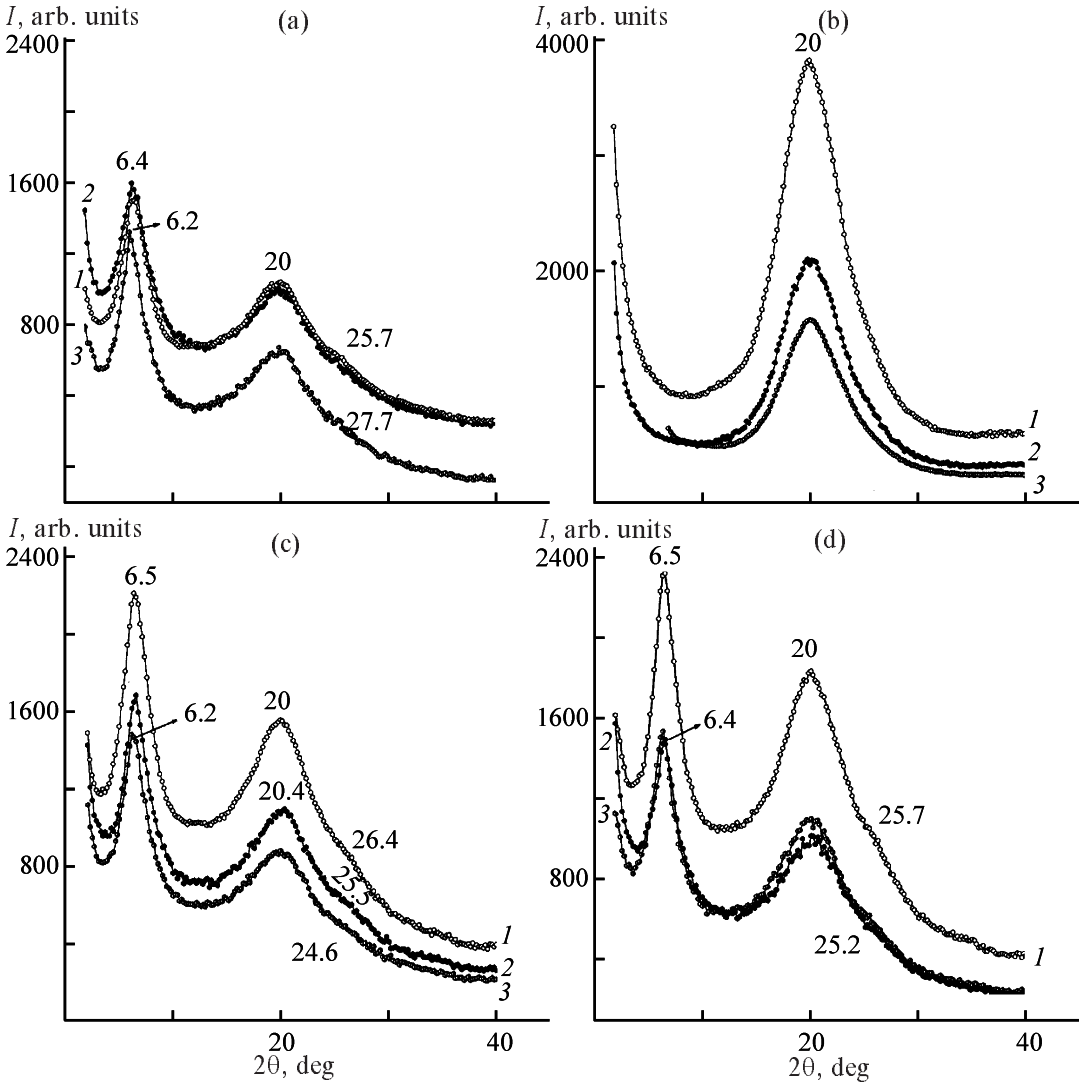


Fig. 1. X-ray diffraction patterns of (a) CAB, (b) PU, and composites (c) CAB + 0.5% PU and (d) CAB + 25% PU: (*1*) initial samples and (*2, 3*) those subjected to the action of (*2*) MSF and (*3*) ESF. (*I*) Intensity and (2θ) Bragg angle.

The procedures used to obtain the blends and treat them with physical fields were described in [2]. The effect of PU additives on the crystal structure of CAB was studied by wide-angle X-ray diffraction analysis on a DRON-4-07 installation with CuK_α radiation monochromated with a Ni filter. The diffraction patterns were normalized to the scattering volume of a sample and to the attenuation of the primary beam by the sample. The error in measuring the scattering interval did not exceed 3%.

The conductivity of the samples was studied at room temperature with a P5083 ac bridge in sandwich-type cells [8]. A pellet was placed between planar polished fluoride bronze electrodes with a pressure of 0.1 MPa applied to the sample. The time during which the dielectric characteristics were measured at each point in the frequency range 0.1–100 kHz did not exceed 4 s at a measurement error of up to 3%. The thermomechanical properties were studied on a versatile thermomechanical installation in the mode of axial compression of samples under a pressure of 2.56 MPa in the temperature range 20–250°C. Samples in the form of pellets 0.008 m in diameter and 0.005 m thick were heated at a rate of 2.5 deg min^{-1}; the error in measuring the strain ε (%) = $f(T, °C)$ was 5%.

Here we consider two extreme compound compositions: CAB + 0.5% PU and CAB + 25% PU. The choice of these composite samples is governed by the fact that they are in different thermodynamic states: the first blend is a dispersion of separate PU particles in the polysaccharide matrix; these particles

Effect of the composition of composites and physical fields on the interplanar spacings in crystal lattices and on the longitudinal size of CAB crystallites

Composite	d_1	d_2	L
	nm		
Initial sample			
CAB	1.380	0.346	3.0
CAB + 0.5% PU	1.358	0.337	2.9
CAB + 25% PU	1.358	0.346	3.6
Sample subjected to effect of MSF			
CAB	1.380	0.353	3.2
CAB + 0.5% PU	1.358	0.349	3.6
CAB + 25% PU	1.380	0.347	3.2
Sample subjected to effect of ESF			
CAB	1.423	0.323	3.8
CAB + 0.5% PU	1.423	0.361	3.5
CAB + 25% PU	1.380	0.353	4.2

serve as centers of secondary crystallization of tie CAB molecules connecting the amorphous and crystalline parts of the polymer. In the second case, it would be expected that the microphase segregation of incompatible polymers should affect the thermodynamic structure at the phase boundary between the "like" and "foreign" molecules.

It can be seen in Schemes 1 and 2 that the polymers under consideration differ in the chemical structure. It is known [10] that CAB is partly crystalline, whereas the PU structure is characterized as topological [11]. It was shown in [1, 2] that these polymers strongly differ in polarity (0.55 for the repeating unit of CAB and 0.36 for PU) and in equilibrium flexibility of macrochains. Therefore, it could be assumed that the effect of the magnetic and electric field on the packing of macromolecules of the chosen polymers would be different. It is known [12] that the ability of a substance to scatter X-rays directly depends of the packing density of the constituent molecules. Therefore, it can be stated that samples of individual polymers have different scattering capacities.

Comparison of the intensities of X-ray scattering by CAB (Fig. 1a) and PU samples (Fig. 1b) shows that the packing density of macromolecules in the topological structure of polyurethane is more sensitive to the action of physical fields than the heterophase structure of CAB. The effect of MSF as a means of orientation of the dipoles of polar groups was not observed for the crystalline CAB phase, which is indicated by the constant angular positions of the main reflections (Fig. 1a, curves *1, 2*) of the polymer and preserved intensities of X-ray scattering by CAB. At the same time, the effect of ESF, i.e., the change in the bulk polarization of the CAB insulator, affects constituents of its structure. It can be seen from Fig. 1a (curve *3*) that the scattering power of the polymer decreased and the angular positions and intensity of the reflections changed. The interplanar spacings d (nm) corresponding to the reflections at $2\theta = 6.4°$ and 25.7° of the initial CAB and that modified with physical fields were calculated using the Bragg equation [13] (see table). These changes suggest that the bulk polarization of macrochains of the polysaccharide is accompanied by spatial displacements of the crystallite planes in the crystalline phase and of kinetic segments in the intercrystallite (amorphous) regions.

It is clear that the selective action of physical fields on PU and CAB inevitably affects the structure of their composites, which is confirmed by the X-ray diffraction patterns in Figs. 1c and 1d. The scattering on blends is considerably stronger, compared to the initial CAB sample; the reflection at $2\theta = 6.4°$ is steadily shifted to larger scattering angles, and part of the reflections, e.g., those at $2\theta \approx 20°$ and 26.4°, have angular positions dependent on the composition of the composite. The decrease in the interplanar spacings in CAB, resulting from the presence of minor additions of PU, can be attributed to plasticization of the rigid heterocyclic chains of CAB by oligoether fragments of the macrochains of PU, which was demonstrated previously in [9]. Also, the polar groups of PU, which have acceptor properties (Schemes 1, 2), can interact with the donor groups of CAB. Hence follows that minor additions of PU to the mixtures make closer, by the structural plasticization mechanism [9], the packing of macromolecules of the polysaccharide in amorphous regions, with the result that the crystallites grow in size. However, the reflections at $2\theta = 20°$ and 26.4° from the CAB + 25% PU composite are sensitive to the density of the matrix polymer, as indicated by the change in their intensity. It is clear that the phase segregation of the blend is accompanied by partial removal of foreign macromolecules from the interaction regions and, accordingly, by restoration of the spatial characteristics of the crystal lattice of CAB.

It is known that the magnetostatic and electrostatic fields differ in the mechanism of interaction

with charge dipoles primarily in that the former orients the dipoles along the magnetic force lines, whereas the latter polarizes (shifts) electric charges in the directions opposite to the sign of the charges. Being polar insulators, the polymers under study were subjected to the action of MSF and ESF in a state close to that of a viscous flow, which provided relative freedom of the polar groups of hydrogen bonds, which are in fact bound dipoles. The following conclusions can be made on the basis of the X-ray diffraction patterns of the composites subjected to MSF or ESF. First, the changes in the structure of the polymer blends formed under the action of physical factors and in the intensity of X-ray scattering by these blends (Figs. 1c, 1d) demonstrate that choosing the composition of a blend and the type of a field exerting an orienting or polarizing effect on the initial structure is an effective way to create composites with the necessary set of properties. Second, on bringing the composition of a blend closer to the phase segregation range, its structure becomes incapable of orientation under the action of ESF. These conclusions are in agreement with the results of a study of how these factors affect the secondary crystallization of CAB in a blend. The longitudinal sizes L (nm) of the crystallites, calculated by the Scherrer formula [13], are listed in the table.

Analysis of the data in the table makes it possible to evaluate the influence of each factor on the secondary crystallization of CAB in the composite. The concentration component shows that the influence of small amounts of PU is within the experimental error. At the same time, the increase in the area of the surface of contact between the components in the course of their phase segregation affects the efficiency of the structural plasticization of the amorphous phase of CAB, with the result that the crystallites of the polymer matrix become longer. The situation significantly changes under the action of MSF on the dipoles of the polar groups of PU. Their orientation in the CAB medium favors secondary crystallization, with values of L increasing. An increase in the concentration of polar groups of PU in the composite also causes further development of secondary crystallization processes. However, the opposite effect is observed under the action of ESF, whose mechanism consists in the bulk polarization of polymer macrochains. It appears that the bulk polarization of heterocycles of the individual CAB is an active factor in the development of secondary polarization processes (see the value of L in relation to the nature of a field). It can

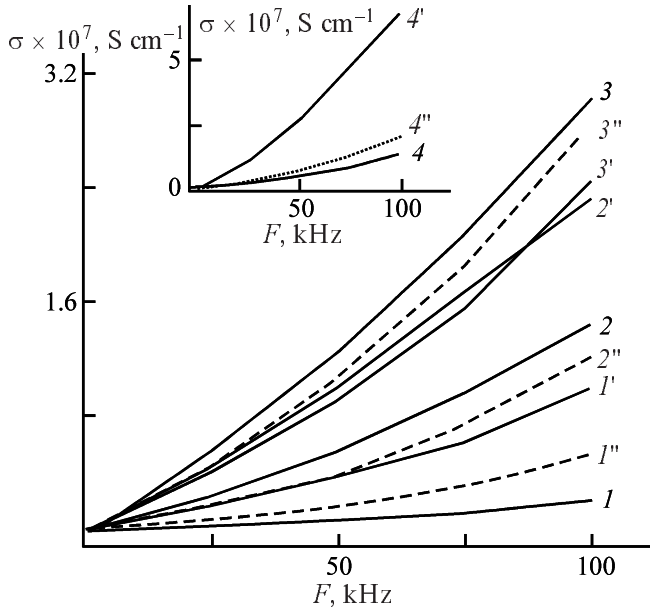


Fig. 2. Conductivity σ of the initial samples of (*1*) CAB, (*2*) CAB + 0.5% PU, (*3*) CAB + 25% PU, and (*4*) PU and those subjected to the action of (*1'–4'*) MSF and (*1"–4"*) ESF, as a function of frequency F.

be assumed that, when macrochains with different sensitivities to the action of ESF are mixed, this leads to redistribution of the front of the bulk polarization; as a result, CAB crystallization processes are inhibited (see table).

These results agree with data on the influence of physical fields on the conductivity σ of the composites. It can be seen in Fig. 2 that, under the action of MSF, the conductivity of PU dramatically increases over the entire frequency range (curves *4, 4'*). This is due to the orientation of polar groups in the specific volume of the repeating unit of the polymer and to the partial structural homogenization because of the mutual penetration of rigid and flexible segments of macrochains. Addition of PU also makes higher the conductivity of the composites; this means that the fraction of traps for free carriers becomes smaller because of the secondary crystallization of tie CAB molecules, initiated by the flexible-chain component. The effect of MSF eliminates structural differences between the composites, caused by microphase segregation processes, which is also reflected on the conductivity (Fig. 2; curves *2, 3* and *2', 3'*). The possible explanation is that the orientation of the polar groups of the elastic PU under the action of MSF induces stronger alignment of segments of the chains of unlike constituent polymers. Thus, composites with strongly different compositions and states of structural phase segrega-

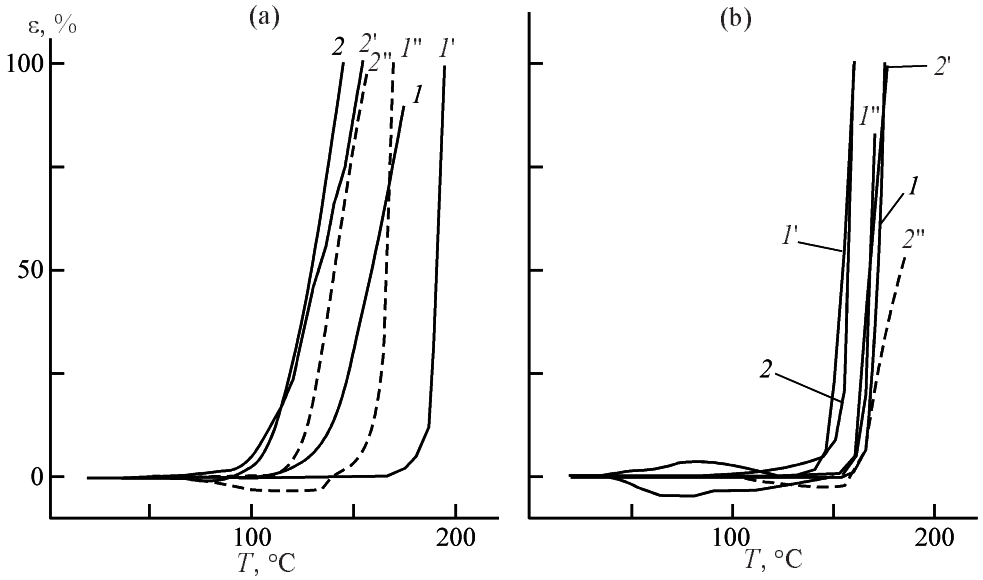


Fig. 3. Thermomechanical curves for the samples: (a) (*1*) CAB and (*2*) PU; (b) (*1*) CAB + 0.5% PU and (*2*) CAB + 25% PU. (ε) Strain and (*T*) temperature. Samples: (*1, 2*) initial and subjected to the effect of (*1'*, *2'*) MSF and (*1"*, *2"*) ESF.

tion acquire close conductivity characteristics. The effect of ESF on the conductivity of the polymers and composites is considerably weaker as compared not only with MSF, but also with the formation of a current-conducting structure under the conditions of a microphase segregation in blends.

To conclude, let us compare the effects of physical fields on the thermomechanical properties of the starting polymers and the composites. Figure 3a confirms the conclusion that physical fields strongly affect the properties of the starting polymers and, in particular, their thermomechanical properties. It can be seen that the use of these fields makes it possible to extend the range of transition to the viscous-flow state from 100 to 180°C and to change the very process of this transition from that characteristic of a partly crystalline polymer to that for the crystalline polymer. On passing to modification of the composites (Fig. 3b), it can be seen that the effect of the fields is not so pronounced as that in the case of the individual components, which is probably due to the internal compensation of the polar groups of both the components.

CONCLUSIONS

(1) The results obtained in a study of composites based on incompatible polymers, cellulose acetobutyrate and segmented polyurethane, demonstrate that integrated use of different factors (varying the concentrations of the constituents, changing the type of the physical field) affecting the structure and properties of the blends is an effective method for development of composites with predicted characteristics.

(2) Minor additions of polyurethane create a structurally plasticizing effect in the cellulose matrix, as a result of which macromolecules from amorphous regions become capable of secondary crystallization, the fraction of the crystalline phase increases, and crystallites grow in size. Samples of this kind are very sensitive to the action of physical fields.

(3) In the phase segregation region ($c_{PU} \geq 25\%$), the effect of the physical fields on the component phases is equivalent to the action on the individual polymers, polysaccharide and segmented polyurethane.

REFERENCES

1. Vilens'kii, V.O., Fainleib, A.M., Goncharenko, L.A., and Danilenko, I.Yu., *Dopov. Nats. Akad. Nauk Ukr.*, 2004, no. 1, pp. 142–148.
2. Vilenskii, V.A., Kercha, Yu.Yu., Glievaya, G.E., and Ovsyankina, V.A., *Vysokomol. Soedin., Ser. A*, 2005, vol. 47, no. 12, pp. 2130–2139.
3. Vilens'kii, V.O., Kercha, Yu.Yu., and Glieva, G.E., *Ukr. Khim. Zh.*, 2004, vol. 70, no. 2, pp. 119–124.
4. Vilens'kii, V.O., Ovsyankina, V.O., Shtompel', V.I., and Kercha, Yu.Yu., *Dopov. Nats. Akad. Nauk Ukr.*, 2004, no. 4, pp. 126–130.
5. Ukrainian Patent 75551.

6. Vilens'kii, V.O., Ovsyankina, V.O., Shtompel', V.I., and Kercha, Yu.Yu., *Dopov. Nats. Akad. Nauk Ukr.*, 2004, no. 7, pp. 131–136.
7. Vilens'kii, V.O., Ovsyankina, V.O., and Glieva, G.E., *Ukr. Khim. Zh.*, 2006, vol. 72, no. 4, pp. 113–118.
8. Ovsyankina, V.O., Vilens'kii, V.O., and Kuporev, B.O., *Fiz. Kondens. Visokomol. Sist.*, 2004, no. 10, pp. 19–23.
9. Vilens'kii, V.O., Kercha, Yu.Yu., Goncharenko, L.A., and Glieva, G.E., *Dopov. Nats. Akad. Nauk Ukr.*, 2001, no. 8, pp. 123–126.
10. *Entsiklopediya polimerov* (Encyclopedia of Polymers), Moscow: Sov. Entsiklopediya, 1974.
11. Kercha, Yu.Yu., *Fizicheskaya khimiya poliuretanov* (Physical Chemistry of Polyurethanes), Kiev: Naukova Dumka, 1979.
12. Lipatov, Yu.S., Shilov, V.V., Gomza, Yu.P., and Kruglyak, N.E., *Rentgenograficheskie metody izucheniya polimernykh sistem* (X-ray Diffraction Methods for Analysis of Polymer Systems), Kiev: Naukova Dumka, 1982.
13. Guinier, A., *Theorie et technique de la radiocristallographie*, Paris: Dunod, 1956.
14. *Fizicheskaya entsiklopediya* (Physical Encyclopedia), Moscow: Sov. Entsiklopediya. 1988.

ISSN 1070-4272, Russian Journal of Applied Chemistry, 2008, Vol. 81, No. 7, pp. 1230–1234. © Pleiades Publishing, Ltd., 2008.
Original Russian Text © T.V. Smyshlyaeva, I.A. Borisova, Yu.D. Khramtsov, 2008, published in Zhurnal Prikladnoi Khimii, 2008, Vol. 81, No. 7, pp. 1150–1154.

MACROMOLECULAR CHEMISTRY AND POLYMERIC MATERIALS

Properties of Nanoporous Carbon Powders Prepared from Phenol–Formaldehyde Resin

T. V. Smyshlyaeva, I. A. Borisova, and Yu. D. Khramtsov

Institute of Technical Chemistry, Ural Branch, Russian Academy of Sciences, Perm, Russia

Received November 28, 2007

Abstract—Formation of the pore structure of nanoporous carbon materials and their physical properties were studied in relation to the composition of stocks of phenol–formaldehyde resin and starch. The dependences of the specific surface area, resistivity, interplanar spacing d_{002}, and crystallite size on the degree of thermolysis during activation were determined.

DOI: 10.1134/S1070427208070203

Supercapacitors or electrochemical capacitors and double-layer capacitors are intermediate between batteries and common "electronic" capacitors. The main parts of supercapacitors are porous electrodes with a highly developed surface. The electrode material should meet the following requirements. Since the capacity of supercapacitors linearly depends on the surface area, the particle size of the powder electrodes should be smallest. The pore size distribution of the electrodes should provide the maximal specific surface area S_{sp} at minimal internal resistance of the electrolyte. The other requirements are chemical and electrochemical stability of the electrode material, mechanical strength, and good wettability of the electrode surface with the electrolyte [1]. These electrodes are usually prepared from activated carbon.

High capacity of supercapacitors is believed to be provided by either nanopores of the electrode [2] or interlayer spacing d_{002} of the graphite electrode [3]. Alekseeva and Amirkhanov believe [4] that the microporosity and hence the specific surface area S_{sp} are determined by the spacing between the disordered blocks of graphite-like layers of the amorphous structure.

The capacity of supercapacitors may be increased by using nanoporous powders and new carbon forms, fullerenes and nanotubes [5]. Practical application of nanotubes is restricted by their high cost. The price of 1 g of single-wall carbon nanotubes (SWCNT) ranges from \$300 to \$700 depending on their purity [6]. Therefore, development of cheap nanoporous carbon materials is an urgent problem. In this study we examined the specific surface area, density, porosity, resistivity, and structural parameters of carbon materials prepared from phenol–formaldehyde resin (PFR) in relation to the composition of the stock of phenol–formaldehyde resin and starch and to the process parameters of its thermolysis.

EXPERIMENTAL

Activated carbon powders were prepared from BZh-3 PFR containing starch as a blowing agent. The starch content in the initial stocks was 4.5, 10, 16.7, 24.5, and 45.6 wt %. The carbon powders were prepared by polymerization of the initial stock at temperatures lower than 130°C, followed by carbonization at 600°C. Under these conditions, carbon with maximal open porosity [4, 7] and maximal radical content [8] is formed. The carbonized material was ground and activated in an atmosphere of humid nitrogen at 700°C. Activation is high-temperature steam–gas or chemical treatment of carbon materials to develop their porous structure.

The specific surface area of the powders was measured on a GKh-1 gasometer from the peak area of nitrogen desorption. X-ray diffraction studies were performed on a DRON-3 diffractometer using monochromated CoK_α radiation. The X-ray diffraction patterns were recorded in the discrete scanning mode with a step of $\Delta 2\theta = 0.2°$. The interplanar spacings were determined from the center of gravity of the reflections.

Properties of carbonization products of PFR–starch stocks*

Composition, wt %		Carbon residue, %	V_{tot}	V_s	S_{sp}, $m^2 g^{-1}$	d_{002}	L_c	ρ_{min}, Ω m	γ_{pr}	γ
PFR	starch		$cm^3 g^{-1}$			nm			g cm^{-3}	
100**	0	43	–	–	39.2	0.375	3.4	270	0.980	–
100***	0	57.2	0.253	0.135	23.9	0.390	1.6	10^6	0.828	0.894
95.5	4.5	56.8	0.158	0.052	75.3	0.390	1.6	100	1.048	1.021
99.5	10.5	55.9	0.567	0.006	24.5	0.390	1.6	460	0.955	0.568
85.1	14.9	59.8	0.35	0.172	13.7	0.390	1.5	10^8	1	0.784
83.3	16.7	43.6	0.102	0.022	186	0.395	1.45	50	0.96	1.019
75.3	24.7	48.3	0.153	0.062	149.6	0.395	1.5	2.6×10^5	1.12	1.069
54	46	36.2	–	–	329.5	0.400	1.6	40	0.88	–

* (V_s) Volume of pores smaller than 100 nm, (γ_{pr}) powder density corresponding to ρ_{min}, and (γ) apparent density.
** Natural polymerization.
*** Thermal curing.

The average size of coherent scattering areas (CSAs) was calculated from the integral width of the reflections by the Selyakov–Scherrer equation for graphite [9]

$$L_c = 0.89\lambda_{Co}/\beta\cos\theta,$$

where L_c is the size of coherent layers of carbon planes parallel to the c direction of the graphite lattice and β is the reflection width (rad).

The pore size and micropore volume of carbonized materials were determined by mercury porosimetry on a Pore Sizer-9305 device (Micromeritics, USA). The resistivity of the carbon powder compositions was measured by the two-point loading scheme [10].

The properties of the carbonized materials are presented in the table. The amount of the carbon residue decreases with increasing starch content, except for the concentration range 10–15 wt %. This nonmonotonic behavior is due to formation features of the porous structure of the composites. Carbonized PFR is almost nonporous (Fig. 1a). The carbonization products of PFR–starch stocks contain mainly 10–20-μm spherical pores (Fig. 1b, 1c).

The porous structure is formed in the course of polycondensation and carbonization. The precursor is BZh-3 resol resin. PFR undergoes polycondensation in the course of curing by the reaction

$$2(\text{–}C_6H_3CH_2(OH)\text{–})_n + H_2CO$$

$$= (\text{–}C_6H_3CH_2(OH))_{n1}\text{–}CH_2\text{–}(C_6H_3CH_2(OH)\text{–})_{n2} + H_2O.$$

Cross-linking of PFR polymeric chains by this reaction increases the viscosity of the mixture and yields a branched three-dimensional polymer network. Water formed in the process is partially released into the environment and partially remains in the polymer as bubbles which form the primary pore system.

In the presence of water, starch grains are gelatinized at 55–60°C and higher temperatures, and the system consists of liquid resin and paste inclusions. At temperatures above 100°C, steam is formed and steam bubbles diffuse in the viscous medium. The final step is resin curing. The volume of the polymerized samples significantly increases owing to formation of gas cavities.

Carbonization involves pyrolysis of PFR and starch to form the carbon residue, volatile degradation products (H_2, CO, CO_2, CH_4), and unsaturated compounds [11]. The gaseous products increase the porosity and promote cracking and breakdown of the carbonization product.

Variation of the total pore volume and volume of mesopores smaller than 100 nm, determined by

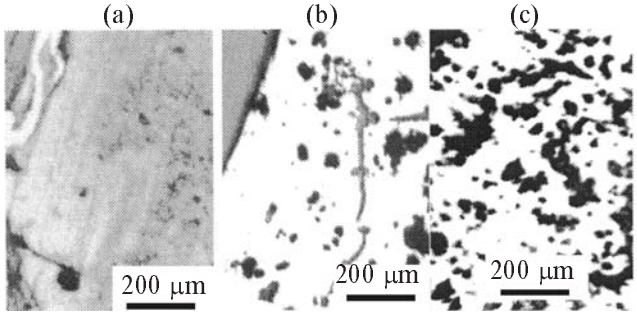


Fig. 1. Microstructure of carbonized materials: (a) PFR, (b) PFR + 10.5% starch, and (c) PFR + 17% starch.

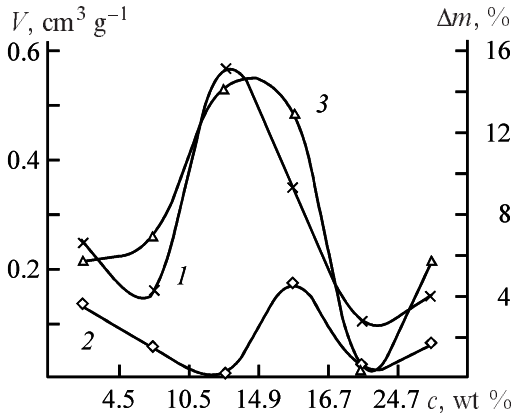


Fig. 2. Variation of the (*1*) total pore volume V and (*2*) volume of pores smaller than 100 nm and (*3*) weight loss Δm of the sample in the course of thermal curing. (c) starch content.

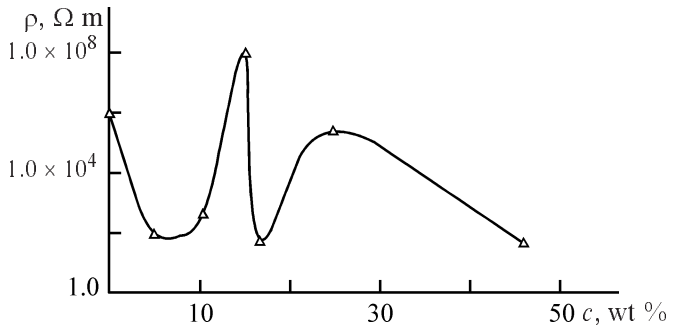


Fig. 3. Resistivity ρ of carbonized PFR–starch stocks as a function of the starch content c.

porosimetry, is shown in Fig. 2. The maximal total porosity (curve *1*) is observed in the samples containing 10% starch and is determined by relatively coarse pores (50–100 μm). The weight loss in the course of curing (Fig. 2, curve *3*) is proportional to the total volume of meso- and macropores.

The specific surface area is the parameter that is the most sensitive to the presence of micropores smaller than 6 nm, which cannot be determined by mercury porosimetry. The S_{sp} of carbonized samples shows that the number of micropores increases with increasing starch concentration. The decrease in the specific surface area of the carbonizates at a starch content of 10% is due to densification of the resin owing to vapor phase formation (Fig. 1b). In this case, the fraction of meso- and micropores sharply decreases (Fig. 2, curve *2*). Starch particles present in the resin are the sites of water vapor formation. At the starch content higher than 15%, the partially permeable porous structure is formed. These samples have a continuous contact between pores. Once the percolation threshold is reached [12], the mechanism of pore formation changes and the fraction of macropores (up to several millimeters) and mesopores (~100 nm) decreases (Fig. 2, curve *2*). Uniform contraction and water absorption by starch can result in encapsulation of the second phase, which is the case at a starch content of 16.7%. The polymerized sample with 16.7% starch content is characterized by the maximal amount of water. In the course of carbonization of these samples, additional weight loss is observed and the specific surface area increases (see table).

The dependence of the resistivity of carbonized samples on the starch content is shown in Fig. 3. The resistivity of the samples containing 15% starch is maximal. Comparison of Figs. 2 and 3 shows that the resistivity correlates with the volume of micro- and mesopores (smaller than 100 nm). The higher the content of micro- and mesopores, the higher is the resistivity. The probability of contacts of conducting clusters in nanoporous systems decreases, and the chain is disconnected. Thus, high resistivity of the carbonized material is partially caused by its nanoporosity.

The X-ray diffraction patterns of the carbonization product contain only one reflection assigned to the 002 plane of the graphite lattice.

The calculated interplanar spacings d_{002} of the carbonization products are significantly higher than that of graphite (d_{002} = 0.336 nm). The carbonization products of PFR–starch stocks meet the "large interplanar spacing" criterion [3]. The structural parameters of the carbonized material insignificantly change after introduction of starch. L_c increases or decreases depending on the degree of polymerization, and the interplanar spacing slightly increases (see table). Calculated d_{002} and L_c, as a whole, are consistent with published X-ray diffraction data for carbonization products of resins [7].

Activation of carbon materials is aimed at developing the porous structure with the maximal specific surface area. The dependence of S_{sp} of activated carbon on the weight loss (combustion loss) in the course of activation is shown in Fig. 4a. All dependences of the specific surface areas of carbonized PFR–starch stocks on the combustion loss have an inflection in the range 40–50%. In the case of the straight resin, this dependence flattens out, which is clearly due to attainment of a quasi-equilibrium between the growth of graphite crystallites and oxidation. As the activation time increases, S_{sp}

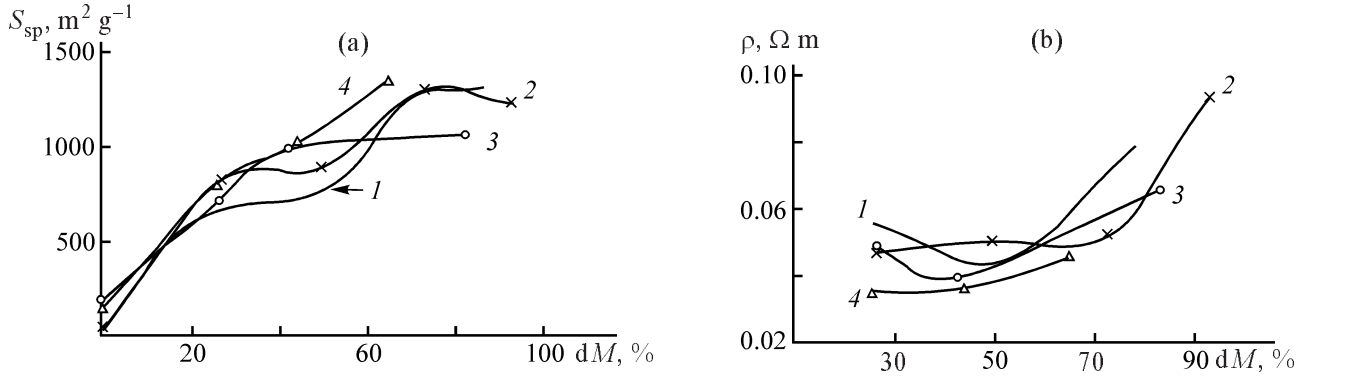


Fig. 4. Variation of the (a) specific surface area S_{sp} and (b) resistivity ρ of PFR–starch compositions containing (*1*) 0, (*2*) 10.5, (*3*) 16.7, (*4*) 24.7 wt % starch in the course of their activation. (dM) combustion loss; the same for Fig. 5.

decreases owing to burning of small particles of carbon powder. Maximal S_{sp} (1350 m^2 g^{-1}) was observed at 24.7% starch content in the stock (Fig. 4a, curve *4*).

The electrical resistivity of all compositions varies similarly in the course of their activation. In the first activation step, ρ sharply decreases. The maximal conductivity is observed at the combustion loss from 30 to 60%. The samples with high starch content are characterized by the lowest resistivity (Fig. 4b, curve *4*). The minimum in the resistivity corresponds to the inflection in the S_{sp}–dM curves (Fig. 4a).

We studied the change in the fine carbon structure during the activation with PFR–16.7% starch stock and straight phenol–formaldehyde resin as examples. The dependences of the interplanar spacing d_{002} and crystallite size L_c on the combustion loss are shown in Fig. 5.

Our experimental data show that activation of carbon powder is accompanied by the following structural transformations. At the activation temperatures, which exceed carbonization temperatures, the growth of graphene planes is accelerated (as compared to carbonization), their number in a crystallite increases (growth of L_c), and a topologically connected network within carbon particles is formed. As a rule, the interplanar spacing d_{002} decreases in this activation step. At the same time, carbon powders are activated in the presence of an oxidizing agent and less stable carbon forms (amorphous carbon etc.) burn out, thus facilitating the contact between the conducting planes. These structural transformations decrease the resistivity of the activated powder (Fig. 4b).

The activation continues owing to oxidation of graphite planes, and average L_c decreases (Fig. 5b). The shape of the 002 reflection changes simultaneously: an additional reflection with d = 0.39 nm appears and the total intensity of the reflections decreases. The changes in d_{002} of both reflections are shown in Fig. 5a. An increase in d_{002} indirectly suggests a decrease in the block size (number of layers) along crystallographic axis c [13].

The decrease in the block size in the course of combustion increases the specific surface area in the final activation step. In this step, the resistivity of the powders increases owing to changes in the morphology and the particle size of the activated powder and a sharp decrease in the apparent density, which is as low as 0.7 g cm^{-3} at 70% degree of combustion.

The properties of activated powders prepared from the straight resin significantly differ from those prepared from the starch-containing stocks: the block size L_c is larger and the interplanar spacings

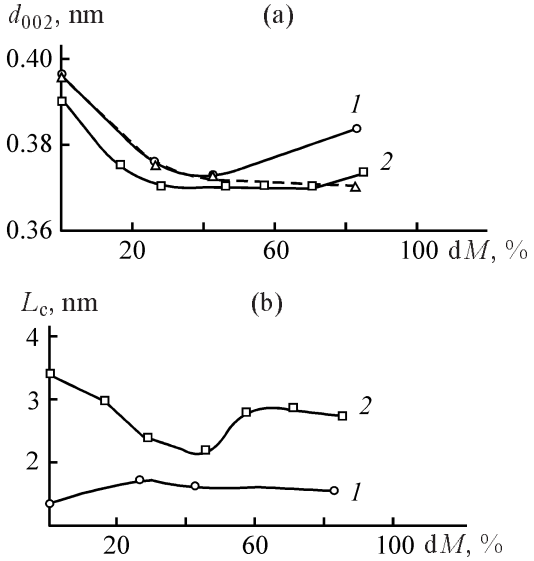


Fig. 5. Variation of the (a) interplanar spacing d_{002} and (b) size of blocks L_c of carbon powders in the course of their activation. (*1*) PFR + 16.7% starch and (*2*) PFR.

d_{002} are small in all the activation steps. Introduction of starch decreases the block size, thus increasing the density of interblock boundaries per unit length. As a result, nanopores between blocks are formed [4]. In the presence of starch, the activation time decreases by a factor of 1.5 owing to development of the porous structure.

The specific surface area S_{sp} of activated PFR–starch compositions is higher than the maximal specific surface area of activated carbons and is comparable to that of nanotubes [6]. The resulting powders have the nanoporous structure and can be used in production of supercapacitors.

CONCLUSIONS

The macro- and mesoporous structure of carbons prepared from phenol–formaldehyde resin is mainly formed in the course of polycondensation. High resistivity of the carbonization product is caused, in particular, by the presence of micropores. The block size L_c increases and the interplanar spacing d_{002} decreases in the first activation steps. In the subsequent steps, the particles are burn out and the interplanar spacing increases. The minimal resistivity observed during activation corresponds to the minimal interplanar spacing. Introduction of starch into phenol–formaldehyde resin increases the porosity of the carbonization products, decreases the block structure, increases the interplanar spacing d_{002}, and accelerates the activation. The specific surface area and resistivity of activated carbon powders prepared from phenol–formaldehyde resin in the presence of starch is 1350 $m^2 g^{-1}$ and 0.05–0.03 Ω m, respectively.

REFERENCES

1. Kravchik, A.E., *Ser. Krit. Tekhnol. Membr.*, 2003, no. 3(19), pp. 3–12.
2. US Patent 0064565.
3. US Patent 6310762.
4. Alekseeva, O.K. and Amirkhanov, D.M., *Ross. Khim. Zh.*, 2004, vol. 48, no. 5, pp. 82–88.
5. Poole, Ch.P. and Owens, F.J., *Introduction to Nanotechnology*, Wiley–Interscience, 2003.
6. Krestinin, A.V., *Ross. Nanotekhnol.*, 2007, vol. 2, nos. 5–6, pp. 18–23.
7. Pokonova, Yu.V., *Perspekt. Mater.*, 1999, no. 6, pp. 102–106.
8. Fialkov, A.S., *Uglegrafitovye materialy* (Graphitized Carbon Materials), Moscow: Energiya, 1979.
9. *Svoistva konstruktsionnykh materialov na osnove ugleroda: Spravochik* (Properties of Carbon Structural Materials: Handbook), Sosedov, V.P., Ed., Moscow: Metallurgiya, 1976.
10. Khramtsov, Yu.D. and Borisova, I.A., *Konstr. Kompoz. Mater.*, 2006, no. 4, pp. 158–163.
11. Antsiferov, V.N., Yufareva, E.G., Shchurov, V.A., et al., Specific Features of Degradation of Polymer Composites, *Preprint of the Ural Branch, USSR Acad. Sci.*, Sverdlovsk, 1989.
12. Feder, J., *Fractals*, New York: Plenum, 1988.
13. Belenkov, E.A. and Yakovlev, D.V., *Izv. Chelyab. Nauchn. Tsentra*, 2001, no. 2(11), pp. 38–45.

ISSN 1070-4272, Russian Journal of Applied Chemistry, 2008, Vol. 81, No. 7, pp. 1235–1239. © Pleiades Publishing, Ltd., 2008.
Original Russian Text © S.V. Kurmaz, I.S. Kochneva, E.O. Perepelitsina, V.V. Ozhiganov, M.L. Bubnova, 2008, published in Zhurnal Prikladnoi Khimii, 2008, Vol. 81, No. 7, pp. 1155–1159.

MACROMOLECULAR CHEMISTRY AND POLYMERIC MATERIALS

Radical Polymerization of Methyl Methacrylate in the Presence of Low-Molecular-Weight Poly(Methyl Methacrylate)

S. V. Kurmaz, I. S. Kochneva, E. O. Perepelitsina, V. V. Ozhiganov, and M. L. Bubnova

Institute of Chemical Physics Problems, Russian Academy of Sciences, Chernogolovka, Moscow oblast, Russia

Received November 1, 2007

Abstract—The kinetics of the bulk radical polymerization of methyl methacrylate and the structure and properties (physicomechanical and thermomechanical, as well as diffusion and sorption) of the polymers were examined in relation to the amount of low-molecular-weight poly(methyl methacrylate) added.

DOI: 10.1134/S1070427208070215

Published data on polymerization of monomer–polymer blends, in particular, those of methyl methacrylate (MMA) with poly(methyl methacrylate) (PMMA) additions, are scarce. They are mostly focused on the polymerization kinetics. For example, Barton et al. [1] showed that, upon introduction of PMMA into the reaction system, the initial polymerization rate decreases, and the maximal polymerization rate is not significantly affected. O'Driscoll and Capek [2] demonstrated that the stereoregularity of PMMA affects the MMA polymerization kinetics. In the presence of isotactic PMMA, the MMA polymerization is accelerated. Kandyrin et al. [3] found that, upon thickening of MMA with PMMA additions, the gel effect is observed in an earlier time.

We examined here the kinetic features of radical polymerization of MMA in the presence of the modifying additive, PMMA, as well as the structure and properties of the resulting polymers in relation to the content of the additive.

EXPERIMENTAL

We used MMA available from Lancaster without additional purification and low-molecular-weight PMMA with $M_n = 7 \times 10^3$, synthesized by radical polymerization in toluene (80 wt %) at $T = 80°C$ in the presence of 2×10^{-2} M azobis(isobutyronitrile) (AIBN) as initiator.

The MMA polymerization kinetics was examined by high-precision isothermal calorimetry on a DAK-1-1 instrument at $T = 60°C$ in the presence of 0 to 40 wt % low-molecular-weight PMMA; AIBN (1×10^{-2} M) served as initiator. The technique of sample preparation for examining the polymerization kinetics consists in the following. The necessary amount of the formulated reaction mixture was charged into glass ampules and degassed by repeated freeze–pump–thaw cycles, after which the evacuated ampules were sealed. The conversion of the C=C bonds C and the reduced polymerization rate $w/[M]$ were calculated for MMA characterized by the specific heat of polymerization of 58.82 kJ mol^{-1}.

The structure of the polymers synthesized with and without different amounts of PMMA was examined by the diffusion and sorption probing (in water and benzene vapor at atmospheric pressure and $T = 20°C$). The mechanical characteristics were measured in the uniaxial compression mode at low strain rates (1×10^{-4} s^{-1}) with a high-precision lever arm testing machine intended for examination of small samples (~0.1 g).

The thermomechanical curves for the polymers modified with additions of low-molecular-weight PMMA were obtained on a UIP-62-M setup at a heating rate of 2.5 deg min^{-1} and a constant load σ, in particular, in the dilatometric mode ($\sigma \approx 0$). The thermal expansion curves of the polymers, measured in the dilatometric mode, were used for correction of the apparent strain ε' by the formula $\varepsilon_\sigma = \varepsilon'_{\bar{\sigma}} - \varepsilon'_\sigma = 0$. For T_g we took the temperature corresponding to the maximum of the differential curves $d\varepsilon/dT$. The integrated curves $\varepsilon = f(T)$ were differentiated, and from the resulting $d\varepsilon/dT$ curves we determined for

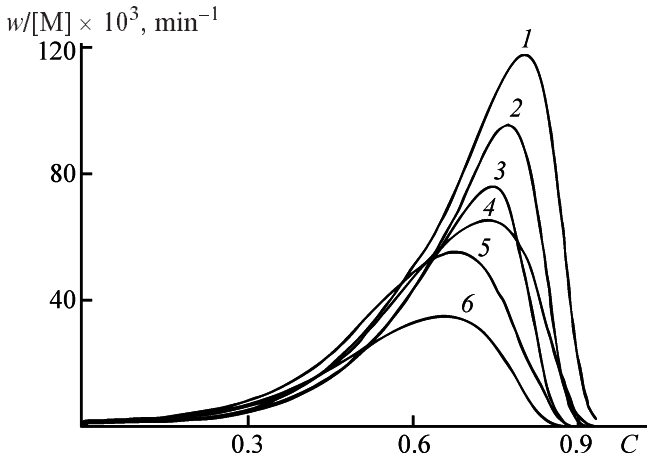


Fig. 1. Kinetic curves of MMA polymerization in the presence of low-molecular-weight PMMA. T = 60°C, [AIBN] = 0.2 wt %. (w/[M]) Reduced polymerization rate, and (C) conversion of the C=C bonds. PMMA, wt %: (*1*) 0, (*2*) 5, (*3*) 10, (*4*) 20, (*5*) 30, and (*6*) 40; the same for Figs. 2 and 3.

each load the upper (T'_{g1}) and lower (T'_{g2}) limits of the temperature range for α-transition. The temperature corresponding to the maximum of the curves was taken as T'_g at which the inflection point is observed in the integrated curves. When T'_{g1}, T'_{g2}, and T'_g depended on the load, we carried out extrapolation to the zero load to determine the T_{g1} and T_{g2} parameters and the glass transition point T_g. If such dependence was not observed, we took the average T'_{g1}, T'_{g2}, and T'_g values as T_{g1}, T_{g2}, and T_g, respectively.

For the sorption, thermomechanical, and physicomechanical measurements we used cylindrical polymer samples 5 mm high and 3 mm in diameter. The residual stress was removed by annealing of the polymers at $T \sim 120$°C. The conversion of the C=C bonds in them was determined by IR spectroscopy; the absorption band corresponding to the stretching vibrations of the C=O bond at 1725 cm^{-1} was taken as the internal reference. As analytical band served the absorption band of the bending vibrations of the H atom in the $C=CH_2$ group at 812 cm^{-1}. The conversion of the C=C bonds C was calculated by the formula

$$C = [1 - (D_{812}/D_{1725})_p/(D_{812}/D_{1725})_m] \times 100,$$

where D_{812} is the optical density of the absorption band of the bending vibrations of the H atom in the $C=CH_2$ group of the polymer (subscript p) and monomer (MMA, subscript m), and D_{1725}, optical density of the absorption band corresponding to the stretching vibrations of the C=O bond in the polymer and monomer (MMA).

The conversion of the C=C bonds in the polymers examined was 90–95%.

A gel-permeation chromatographic analysis [4] showed that the PMMA used as the modifying additive has $M_n = 7 \times 10^3$ and is characterized by a broad MWD (M_w/M_n = 2.6). This suggests that the disproportionation substantially contributes to termination of the polymer chains in MMA polymerization in toluene. This process gives rise to terminal C=C bonds in the polymer macromolecules. They were revealed by ozonolysis and IR examination. Ozonolysis showed that the content of the C=C bonds in low-molecular-weight PMMA is ca. 0.1 mol kg^{-1}. Because of a high concentration of the ends with enhanced molecular mobility, the glass transition point T_g of the low-molecular-weight PMMA is 108°C, as shown by DSC. The intrinsic viscosity measured in toluene with an Ubbelohde viscometer at T = 20°C is 0.117 dl g^{-1}.

The structure of low-molecular-weight PMMA was elucidated by spectral analysis of the conformation assumed by the ester group. Along with the band corresponding to the *cis* isomer (1192 cm^{-1}), the spectrum of PMMA contains a shoulder at 1174 cm^{-1} belonging to the *gauche* isomer. The less favorable energetically *gauche* conformation results from rotation of the $O–CH_3$ group around the C–C bond by 60° [5]. This means that PMMA is characterized by a planar conformation typical for *syndio* addition, which does not sterically hinder the *gauche* conformation of the COOR groups. The IR spectrum of the polymer of interest contains bands at 749 and 1060 cm^{-1} and does not contain bands at 1290 and 759 cm^{-1}, which also suggests *syndio* addition of methacryl groups in PMMA.

Figure 1 presents the kinetic curves of radical polymerization of MMA with and without different amounts of low-molecular-weight PMMA, plotted as the reduced polymerization rate w/[M] ([M] is the running concentration of the monomer) vs. the conversion of the C=C bonds in the monomer. Without additions, the MMA polymerization is accompanied by gel effect (Fig. 1, curve *1*) due to increase in viscosity of the reaction medium with increasing conversion of the monomer. This hinders the termination of the propagating macroradicals and causes the rate constant of the polymer chain termination to decrease. Additions of low-molecular-weight PMMA (Fig. 1, curves *2–6*) cause the

maximal reduced rate of MMA polymerization to significantly decrease via decreasing the magnitude of the gel effect and shift its onset to lower conversions. For example, with increasing PMMA content in the reaction mixture to 40 wt %, $w/[M]_{max}$ decreases approximately threefold. Low-molecular-weight PMMA, apparently, inhibits radical polymerization of MMA, which suggests formation of a polymer whose molecular weight is lower than that of the PMMA obtained without additions. In the presence of high concentrations of PMMA (≥ 20 wt %), in some cases the kinetic curves exhibited two maxima, evidently associated with microphase segregation of the reaction system.

Valuable information about the structure of the MMA polymers modified with various amounts of low-molecular-weight PMMA was derived from examination of sorption of vapors of benzene and water differing not only in the size of the molecules but also in the degree of thermodynamic affinity. Figure 2 presents the kinetic curves of water vapor sorption by the MMA polymers obtained with and without low-molecular-weight PMMA, plotted in the Fick's equation coordinates. As known, in the case of water, the diffusion and sorption properties of the polymer are determined by the structural defects like microcracks due to internal stress, as well as by possible H-bonding with ester groups. Figure 2 shows that, in the water vapor sorption, the examined polymers exhibit mostly pseudonormal kinetics, as suggested by the lack of linear portions in the $S = f(t^{1/2})$ curves. Abnormal sorption is apparently due to the relaxation phenomena accompanying the water vapor diffusion into the polymers of interest [6].

Figure 2 shows that the diffusion and sorption properties of the examined polymers depend on the content of low-molecular-weight PMMA in them. The rates of water sorption into unmodified PMMA and that obtained in the presence of 5% low-molecular-weight polymer are close (Fig. 2, curves *1*, *2*). With the content of low-molecular-weight PMMA in the polymer increasing to 10–30%, the kinetic plots of water vapor sorption are transformed into S-shaped curves (Fig. 2, curves *3*–*5*). The water diffusion rates and sorption limits decrease relative to unmodified PMMA and the polymer obtained with 5% low-molecular-weight PMMA. This suggests a decrease in the number of structural defects like microcracks due to internal stress in the polymer. A probable reason for a decrease in the internal stress level in the polymer being formed is that the rates of chemical shrinkage and the polymerization reaction get equal [7]. At the same time, Fig. 2 (curve *6*) suggests acceleration of the water vapor sorption into the polymer obtained with 40 wt % low-molecular-weight PMMA. Apparently, MMA polymerization with and without modifying addition yields a polymer characterized by a high level of internal stress responsible for numerous structural defects.

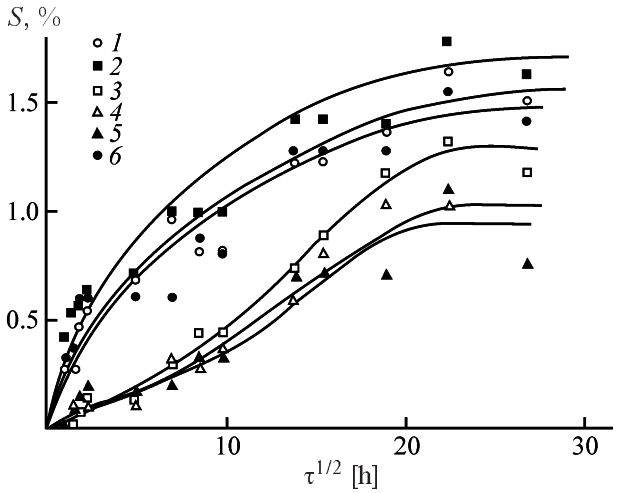


Fig. 2. Kinetic curves of water vapor sorption S by the polymers obtained from MMA in the presence of low-molecular-weight PMMA. (τ) Time; the same for Fig. 3.

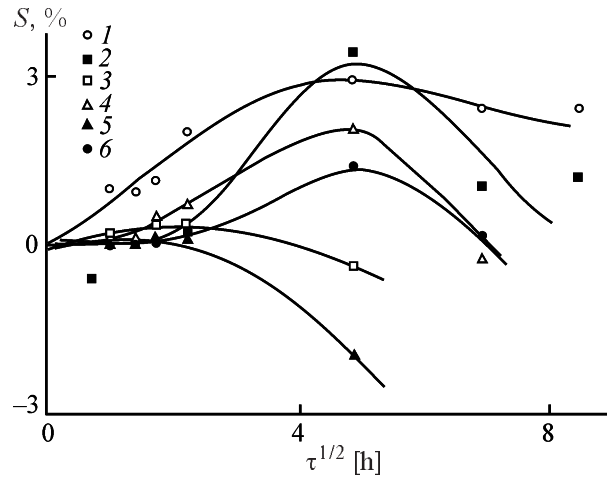


Fig. 3. Kinetic curves of benzene vapor sorption S by the polymers obtained from MMA in the presence of low-molecular-weight PMMA.

Figure 3 demonstrates the kinetics of benzene vapor sorption by the polymers obtained from MMA with and without low-molecular-weight PMMA. It is seen that benzene vapor sorption by unmodified PMMA and the polymer synthesized in the presence of various additions of low-molecular-

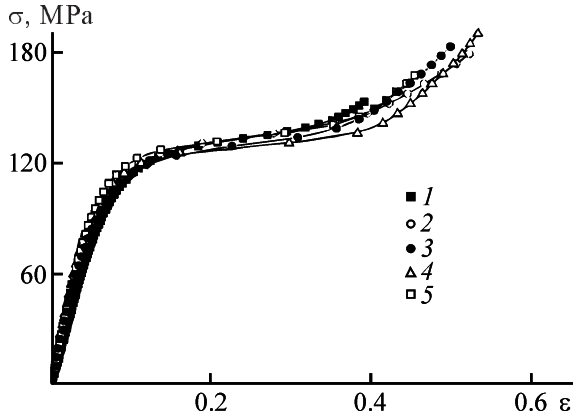


Fig. 4. σ–ε diagrams for the polymers obtained from MMA in the presence of low-molecular-weight PMMA. PMMA, wt%: (*1*) 0, (*2*) 10, (*3*) 20, (*4*) 30, and (*5*) 40.

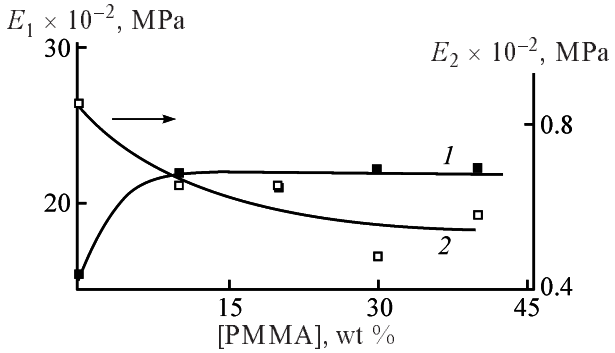


Fig. 5. Moduli of elasticity E_1 and forced elasticity E_2 of the MMA polymers vs. content of low-molecular-weight PMMA.

weight PMMA proceeds in the unlimited swelling mode with subsequent dissolution and mass loss.

The polymers obtained from MMA in the presence of low-molecular-weight PMMA exhibit a strong mutual correlation of the benzene vapor diffusion rate, sorption limit, and content of the additive in the polymer (Fig. 3). With increasing amount of the additive, the benzene vapor diffusion tends to decelerate, probably due to an increase in the molecular packing density. A decrease in the sorption limit suggests that the polymers modified with low-molecular-weight PMMA additions, compared to unmodified PMMA, have a lower molecular weight and a higher thermodynamic affinity for the solvent.

Glass transition point T_g and the transition width ΔT_g in relation to the content of low-molecular-weight PMMA in the polymer

[PMMA], wt %	T_g	ΔT_g
	°C	
0	116	23
20	118	8
40	108	8

Figure 4 shows the typical stress (σ)–strain (ε) diagrams of the polymers examined. The strain of the polymers is comprised of elastic strain and forced elasticity. At a certain stress σ the sample undergoes transition from the glassy state with the elastic modulus E_1 to the forced elasticity state characterized by the modulus $E_2 \ll E_1$. The parameter E_1 represents the contribution to the properties of the polymer, made by the physical network resulting from intermolecular interaction of the polar (ester) groups of the neighboring polymer chains [8]. The transition from the glassy state to the forced elasticity state is associated with breakdown of the physical network cross-links. The modulus E_2 in PMMA is determined by the number of the physical cross-links preserved after the transition [8]. Such stable physical cross-links originate from cooperative intermolecular interactions of the complementary segments of the chain, yielding *n*-unit *iso*- and *syndio*-regular sequences with n = 2–4 (adducts, stereo complexes formed from addition of such *iso* blocks to *syndio* blocks [9]).

Figure 5 presents the plots of the elastic moduli E_1 and forced elasticity E_2 vs. content of low-molecular-weight PMMA additive, calculated from the slopes of the first and second linear portions of the $\sigma = f(\varepsilon)$ curves. It is seen that the additions cause the elastic modulus E_1 to increase (Fig. 5, curve *1*) due to intensification of the intermolecular interactions in the polymer. For the polymers obtained in the presence of low-molecular-weight PMMA, the forced elasticity modulus E_2 is lower than that in the unmodified polymer (Fig. 5, curve *2*). In the presence of low-molecular-weight PMMA, short-lived physical cross-links are evidently formed, and they decrease in number upon transition of the polymer from the glassy state to the forced elasticity state.

Thus, low-molecular-weight PMMA introduced into the reaction mixture modifies the physicochemical properties of the resulting polymers, the magnitude of the modifying effect being dependent on the content of low-molecular-weight PMMA.

The table presents the glass transition point T_g and the transition width ΔT_g for the polymers con-

taining 0, 20, and 40 wt % low-molecular-weight PMMA, calculated from the thermomechanical curves. The experimental data suggest that T_g of the polymer with 20 wt % PMMA remains virtually unchanged relative to unmodified PMMA, while ΔT_g decreases approximately threefold. The latter fact suggests a decrease in the number of relaxants, elementary moieties of the polymer chain, whose unfreezing is necessary for transition from the glassy to hyperelastic state. Further increase in the PMMA content in the polymer to 40 wt % causes T_g to decrease by 10°C, while ΔT_g remains unchanged (see table). Thus, a high content in the polymer of the macromolecules of low-molecular-weight PMMA, characterized by enhanced molecular mobility, causes T_g of the polymer being formed to decrease. A decrease in T_g and an increase in the elastic modulus E_1 upon introduction into the polymer of 40 wt % low-molecular-weight PMMA suggests antiplasticization effect. The rigidity and brittleness of the polymers increased and T_g decreased upon introduction into the linear amorphous PMMA of phosphoric acid esters [10]. The magnitude of this effect was straightly related to the intrinsic volume of the plasticizer molecules: The larger the molecule, the larger the increase in the elastic modulus of the system.

The antiplasticization effect observed upon addition of 40 wt % low-molecular-weight PMMA can be due to heterogeneous structure of the polymer being formed and the associated heterogeneous distribution of the polymeric addition in it. The macromolecules of low-molecular-weight PMMA get into loosely packed domains in the polymer being formed, in which fairly loose chains assume a more extended conformation and get more rigid upon interaction with the plasticizer.

CONCLUSIONS

(1) Introduction of poly(methyl methacrylate) into the reaction system causes the maximal reduced rate of methyl methacrylate polymerization to substantially decrease and shifts the gel effect to lower conversions.

(2) The number of structural defects like microcracks depends on the content of the modifying addition in the polymer.

(3) Benzene vapor sorption by the polymers modified with low-molecular-weight poly(methyl methacrylate) additions proceeds in the unlimited swelling mode and is accompanied by dissolution and mass loss. The benzene vapor diffusion rate and the sorption limits vary with the content of the modifying additive in the polymer.

(4) Low-molecular-weight poly(methyl methacrylate) additions cause the rigidity of the polymer being formed to increase [the elastic modulus E_1 increases relative to unmodified poly(methyl methacrylate)]. The glass transition point T_g of the polymer containing 40% low-molecular-weight poly(methyl methacrylate) decreases by 10°C due to the antiplasticizing effect exerted by this additive.

ACKNOWLEDGMENTS

This study was financially supported by the Russian Foundation for Basic Research (project no. 06-03-33018) and the Division of Chemistry and Materials Science, Russian Academy of Sciences (program no. 8).

REFERENCES

1. Barton, J., Pastusakova, V., Vaskova, V., and Ambrovic P., *Chem. Zvesti*, 1983, vol. 37, pp. 555–560.
2. O'Driscoll, K.F. and Capek, I., *J. Polym. Sci.: Polym. Lett. Ed.*, 1981, vol. 19, pp. 401–407.
3. Kandyrin, L.B., Shcheulova, L.K., Grinberg, S.M., and Kuleznev, V.N., *Fizicheskie svoistva vyazkouprugikh polimerov* (Physical Properties of Viscoelastic Polymers), Sverdlovsk, 1981, pp. 65–68.
4. Kurmaz, S.V., Grachev, V.P., Kochneva, I.S., et al., *Vysokomol. Soedin., Ser. A*, 2007, vol. 49, no. 8, pp. 1480–1493.
5. Kuznetsov, N.A. and Smolyanskii, A.L., *Vysokomol. Soedin., Ser. A*, 1975, vol. 17, no. 6, pp. 1271–1276.
6. *Entsiklopediya polimerov* (Encyclopedia of Polymers), Moscow: Sov. Entsiklopediya, 1977, vol. 3, p. 462.
7. Kloosterboer, J.G., *Adv. Polym. Sci.*, 1988, vol. 84, pp. 1–100.
8. Berlin, A.A., Korolev, G.V., Kefeli, T.Ya., and Severgin, Yu.M., *Akrilovye oligomery i materialy na ikh osnove* (Acrylic Oligomers and Materials Based on Them), Moscow: Khimiya, 1983.
9. Korolev, G.V., Baturina, A.A., Berezin, M.P., and Kurmaz, S.V., *Vysokomol. Soedin., Ser. A*, 2004, vol. 46, no. 4, pp. 656–667.
10. Razinskaya, I.N., Shtarkman, B.P., Izvozchikova, V.A., et al., *Vysokomol. Soedin., Ser. A*, 1984, vol. 26, no. 8, pp. 1617–1622.

ISSN 1070-4272, Russian Journal of Applied Chemistry, 2008, Vol. 81, No. 7, pp. 1240–1244. © Pleiades Publishing, Ltd., 2008.
Original Russian Text © L.M. Trufakina, 2008, published in Zhurnal Prikladnoi Khimii, 2008, Vol. 81, No. 7, pp. 1160–1163.

MACROMOLECULAR CHEMISTRY AND POLYMERIC MATERIALS

Viscoelastic and Surface Properties of Polymer Complexes with Fillers of Different Nature

L. M. Trufakina

Institute of Oil Chemistry, Siberian Branch, Russian Academy of Sciences, Tomsk, Russia

Received November 29, 2007

Abstract—Rheological and surface properties of polymer blends based on aqueous solutions of polyacrylamide and polyvinyl alcohol were studied by viscometry and methods of penetration of a spherical indenter and detachment of a metal plate from a polymer body. The work of adhesion was examined in relation to the filler type and the time of formation of the polymer composites.

DOI: 10.1134/S1070427208070227

Interpolymer complexes based of polyacrylamide (PAA) and polyvinyl alcohol (PVA) have been studied in sufficient detail by now [1, 2]. Polymer matrices often need modification to acquire new properties. The advantages offered by polymer fillers include a low specific surface area which affords a high degree of filling, as well as improved rheological properties and high insulation and mechanical characteristics of the filled composites [3]. Polymer complexes with fillers in the presence of adhesion bond cause the viscosity and Young modulus of compositions to increase. Modification of the properties of polymer complexes has always been of much practical significance.

At the same time, large-scale worldwide polymer production generated another major problem: waste utilization. Scattered polymer waste under exposure to environmental factors such as microorganisms, light, water, heat energy, etc. can degrade and be assimilated by the environment. Among these processes, biodegradation of polymer waste affords the most reliable, prompt, and environmentally safe utilization of polymers. At the same time, light and water exposure, as well as other factors, often also promote their degradation. One of the ways to solve the problem of polymer waste utilization consists in the use of highly biodegradable fillers in manufacture of polymer materials.

At present, the development of this kind of materials goes along the following lines: synthesis of new polymer structures, introduction into macromolecules of photo- and hydrodegradable fragments; and use of polymer blends comprising at least one easily degradable component (natural polymer, plasticizer).

The use of polymer blends for preparing various materials with the desired set of properties is an advanced method. Biodegradable polymer blends are typically prepared by addition to a synthetic polymer of a different biopolymer (natural or synthetic). Natural substances used for this purpose are mostly represented by polysaccharides, above all starch and cellulose [4, 5].

We elucidated here the trends in variation of the rheological and surface properties of the filled complexes comprised of a polymer matrix and fillers imparting different properties to the polymer complex. For example, quartz sand is introduced to increase the efficiency of abrasion of synthetic and natural fibers; peat, to decrease the gas permeability; and sawdust and starch, to provide rapid utilization of polymer complexes.

The polymer complex for examinations was prepared by mixing aqueous solutions of PVA and PAA.

EXPERIMENTAL

We used PAA (Obninsk) samples with the molecular weight $M = 4.8 \times 10^5$, as calculated by the formula $[\eta] = 3.73 \times 10^{-4} M^{0.66}$ at 30°C [6]. The molecular weight of PVA (Nevinnomyssk), $M = 2 \times 10^5$, was calculated by the formula $[\eta] = 8.86 \times 10^{-4} M^{0.72}$ at 20°C.

From the dependence of the logarithm of the intrinsic viscosity on the volume concentration of aqueous solutions of the polymers we estimated the

critical concentrations of the crossovers c_{cr} at 1.35 and 7 wt% for PAA and PVA, respectively.

The dynamic viscosity and shear stress of the solutions of polymers were measured on a Rheotest-2 rotary viscometer with a cylinder–cylinder working unit. The measured data are summarized in Table 1.

The polymer blends were prepared by the procedure described in [7]; the dynamic viscosity and shear stress of the filled polymer complexes were measured on a cone–plate viscometer. To prepare polymer complexes with fillers, the calculated amount of the filler was introduced into an aqueous solution of PVA with stirring on a mechanical stirrer, whereupon a PAA solution was added. The resulting blend was stirred for another 10 min, and after 1 h its viscosity, elasticity, and work of adhesion were measured.

The polymer composite materials (PCMs) comprised of polymers and inorganic or organic substances of different nature are widely used in many areas. The properties of PCMs are determined by the diversified chemical and physical processes involved in interaction of the components at the interface, rather by the sum of the properties of the components [8]. We used the following materials as fillers:

(1) Poly(ethylene terephthalate) (PET) fiber with the diameter d = 0.05–0.1 mm. This is a reinforcing filler, whose main advantages are high strength and rigidity; the blends are superior in their properties to unfilled polymers.

(2) Quartz sand (QS) with the particle diameter d = 0.1 mm, imparting stability to the dispersion, having insulation properties, and exhibiting increased wear resistance and chemical stability. It does not contain hydration water and provides higher degrees of filling of the compositions.

(3) Moss, a rootless perennial sporophyte containing triterpene compounds and a phenol-like substance sphagnol preventing degradation of the structure.

(4) Cellulose (pine wood) with 4–5-mm-long fibers, the main component of cellular walls of plants. Wood exhibits high strength and elasticity combined with a low density, it is insoluble in water and organic solvents and is easily processed. The wood tissues contain 40–44% cellulose (linear polysaccharide), and lower plant tissues, 10–25%.

(5) Plant-originated peat containing both organic (carbohydrates, phenols, lipids, humic acids, and polysaccharides) and inorganic components.

Table 1. Dynamic viscosity and shear stress of the aqueous solutions of PAA and PVA at T = 20°C

c_{PAA}, wt %	η, Pa s	τ, Pa	c_{PAA}, wt %	η, Pa s	τ, Pa
0.5	0.16	26.34	4	0.14	22.76
1.0	0.27	41.45	5	0.21	34.14
2.0	0.38	66.31	6	0.31	51.21
3.0	0.47	78.12	7	0.42	68.28
			8	0.56	91.04

(6) Mechanically activated peat yielded by peat treatment in an APF-4 planetary ball mill operating in the batch mode; the acceleration of stainless steel milling balls, 10 mm in diameter, was 200 m s^{-2}; the treatment time was 2 min at 20°C.

(7) Starch, a polysaccharide of plant origin, comprised of 15–25% linear amylose and 75–86% branched amylopectin. Amylose precipitates from starch paste.

Starch is an amorphous product, insoluble in cold water, alcohol, and ether; it forms gel with hot water and undergoes biological and oxidative degradation. We used corn starch [GOST (State Standard) 7697–82)], either dry (starch 1) or as a suspension made with boiled water on a water bath at T = 90°C for 10 min (starch 2).

Figure 1 shows how the dynamic viscosity of the polymer matrix and that of the complexes with different fillers varies with the formation time. It is seen that sand, PET, and moss cause the viscosity of the polymer matrix to significantly increase with time, and peat, to increase insignificantly; with starch hydrogel, the viscosity increases substantially, which causes rapid degradation of the polymer complex (the filler concentration in all cases was 10%). Upon addition of dry starch. the viscosity remained virtually unchanged with time. The viscosity of the polymer composite with cellulose initially exceeds that of the polymer matrix, but further sharply decreases to minimal values.

The elastic modulus was measured by the method of penetration of a spherical indenter, i.e., via measuring the depth of indentation under load into an elastic body, which yields actually the modulus [9–11]. The indenter had the radius R = 7 mm. The PCM specimens were shaped as cylinders of the diameter D = 40 mm and height H = 40 mm. The

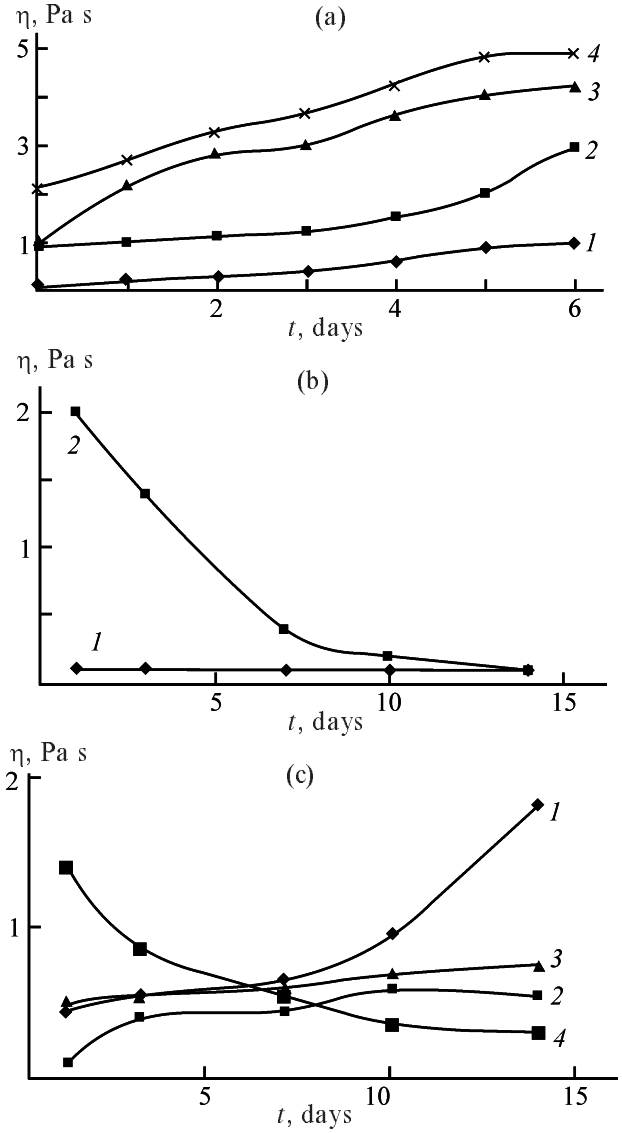


Fig. 1. Dynamic viscosity η vs. time of structure formation t of the polymer complexes. Initial concentration of PAA and PVA 1.35 and 7 wt %, respectively; temperature 20°C; the same for Figs. 2, 3. (a) (*1*) Polymer matrix, (*2*) PET, (*3*) moss, and (*4*) QS; (b) (*1*) starch 1 and (*2*) starch 2; (c): (*1*) polymer matrix, (*2*) mechanically activated peat, (*3*) plant-originated peat, and (*4*) cellulose.

elastic modulus was calculated by the formula

$$E = 3F/(16h^{3/2}R^{1/2}),$$

where F is the force acting on the indenter, and h, depth of penetration of the spherical indenter with the radius R into the flat surface of the sample.

For all the PCMs prepared we examined the elastic modulus in relation to the type of the filler.

Figure 2 shows how the elastic modulus of PCMs

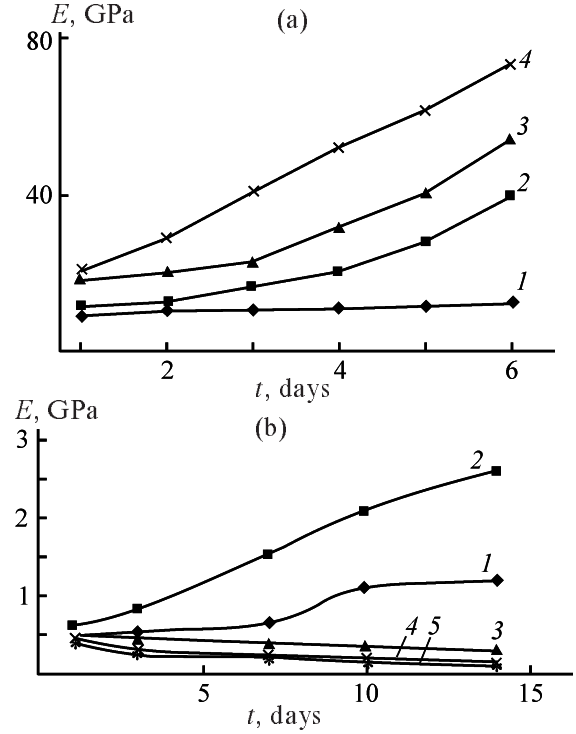


Fig. 2. Elastic modulus E vs. time of structure formation t of the polymer complexes: (a) (*1*) polymer matrix, (*2*) PET, (*3*) moss, and (*4*) QS; (b) (*1*) mechanically activated peat, (*2*) plant-originated peat, (*3*) cellulose, (*4*) starch 1, and (*5*) starch 2.

varies with the formation time at 20°C. It is seen that, among the fillers utilized, moss, sand, and PET cause the elastic modulus to significantly increase, peat affects it insignificantly, and the elastic properties of PCMs filled with starch and cellulose are negligible.

Thus, rheological examination of the PCMs with various fillers showed how the latter affect the properties of the polymer matrix based on aqueous solutions of PAA and PVA.

The method of uniform detachment of a flat metal plate from a polymer body surface, which estimates both the strength and degradation mechanism for the adhesion joint, was applied to examine the surface properties of the PCMs in relation to the type of the filler. The adhesive strength was estimated from the work of detachment of the metal plate from the polymer complex when exposed to an external force [12]:

$$W = W_{det}/S,$$

where S is the adhesive–substrate contact area.

Figure 3 demonstrates how the work of adhesion

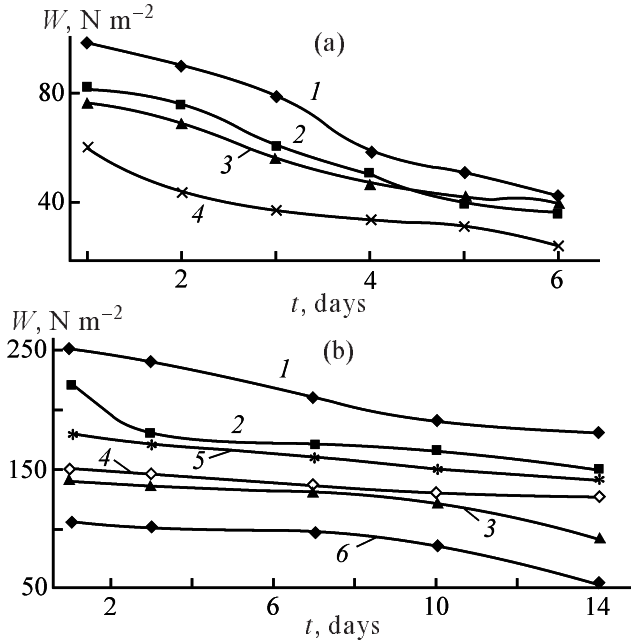


Fig. 3. Variation of the work of adhesion W with the time of structure formation t of the polymer complexes. (a) (*1*) Polymer matrix, (*2*) PET, (*3*) moss, and (*4*) QS; (b) (*1*) polymer matrix, (*2*) plant-originated peat, (*3*) mechanically activated peat, (*4*) cellulose, (*5*) starch 1, and (*6*) starch 2.

for different fillers varies with the time of formation of the polymer complex. The work of adhesion of the polymer complexes with sand, PET, and moss is lower than that of the polymer matrix. The surface layer buildup is, evidently, affected not only by formation of supramolecular structures but also by the type of filler. In the case of peats, starches, and wood, the work of adhesion is much higher. The PCMs with solid starch exhibit adhesive breakoff, in contrast to those with starch hydrogel, for which cohesive breakoff is observed. Probably, the polymer matrix degrades as a result of cleavage of swollen grains in starch hydrogels into smaller grains [13]. Also, the hydrogels exhibit enhanced concentration of the terminal reducing groups due to cleavage of the glucoside bonds in the macromolecules. The dynamic viscosity and elastic modulus of mechanically activated peat is lower than that of untreated peat. The reason is that mechanical treatment of peat causes the yield of polysaccharides, polyphenols, and humic and fulvic acids to increase [14]. Acids, most likely, cause a decrease in the number of interpolymer hydrogen bonds in the matrix.

Table 2. Initial dynamic viscosity, elastic modulus, and work of adhesion of the PVA + PAA polymer matrix and its complexes with various additives

Additive	η, Pa s	E, GPa	W, N m^{-2}
–	0.21	8.9	103
Sand	1.23	23.8	62
PET	0.87	12.2	84.1
Moss	0.29	19.8	78
Cellulose	1.34	0.42	149.6
Peat	0.46	0.63	225.3
Mechanically activated peat	0.45	0.55	144.7
Starch 1	0.11	0.41	174.2
Starch 2	2.05	0.36	250.1

Table 2 lists the measured initial dynamic viscosity, elastic modulus, and work of adhesion; it shows how the fillers modify the properties of the polymer matrix. Upon introduction of starches and cellulose, the dynamic viscosity of the polymer composites increases insignificantly, the elastic modulus decreases, and the trends in the work of adhesion suggest that supramolecular structures are not formed in the polymer composites.

CONCLUSIONS

(1) Directed modification of the polymer matrix based on polyacrylamide and polyvinyl alcohol via introduction of quartz sand, moss, and poly(ethylene terephthalate) improves its rheological and surface characteristics.

(2) Filling with starch and sawdust enables prompt utilization of the polymer matrix.

REFERENCES

1. Permyakova, N.M., Zheltonozhskaya, T.B., et al., *Ukr. Khim. Zh.*, 2002, vol. 68, no. 9, pp. 57–62.
2. Permyakova, N.M., Zheltonozhskaya, T.B., et al., *Ukr. Khim. Zh.*, 2002, vol. 68, no. 10, pp. 123–128.
3. *Napolniteli dlya polimernykh kompozitsionnykh materialov: spravochnoe posobie* (Fillers for Polymer Composite Materials: Reference Book), Moscow: Khimiya, 1981.
4. Vasnev, V.A., *Vysokomol. Soedin., Ser. B*, 1997, vol. 39, no. 12, pp. 2073–2086.
5. Suvorova, A.I., Smirnova, E.A., Tyukova, I.S., and Kochkina, T.A., *Plast. Massy*, 2006, no. 7, pp. 45–47.
6. *Entsiklopediya polimerov* (Encyclopedia of Polymers), Kargin, V.A., Ed., Moscow: Sov. Entsiklopediya, 1972.

7. Trufakina, L.M. and Kudeshova, E.G., *Inzh.-Fiz. Zh.*, 2003, vol. 76, no. 3, pp. 55–58.
8. Lipatov, Yu.S., *Fiziko-khimicheskie osnovy napolneniya polimerov* (Physicochemical Principles of Polymer Filling), Moscow: Khimiya, 1991.
9. Nielsen, L.E., *Mechanical Properties of Polymers and Composites*, New York: Dekker, 1974.
10. Lopatin, V.V., Askadskii, A.A., Vasil'ev, V.G., and Kurskaya, E.A., *Vysokomol. Soedin., Ser. A*, 2004, vol. 46, no. 7, pp. 1217–1224.
11. Medvedeva, V.V., Myasnikova, L.I., Semchikov, Yu.D., and Rogovina, L.Z., *Vysokomol. Soedin., Ser. B.*, 1998, vol. 40, no. 3, pp. 492–497.
12. Berlin, A.A. and Basin, V.E., *Osnovy adgezii polimerov* (Polymer Adhesion Fundamentals), Moscow: Khimiya, 1974.
13. Lipatova, I.M., Losev, N.V., and Yusova, A.A., *Zh. Prikl. Khim.*, 2006, vol. 79, no. 9, pp. 1548–1553.
14. Ivanov, A.A., Yudina, N.V., Mal'tseva, E.V., and Lomovskii, O.I., *Izv. Tomsk. Politekh. Univ.*, 2007, vol. 310, no. 2, pp. 159–162.

ISSN 1070-4272, Russian Journal of Applied Chemistry, 2008, Vol. 81, No. 7, pp. 1245–1251. © Pleiades Publishing, Ltd., 2008.
Original Russian Text © N.V. Shul'ga, L.A. Gomolko, N.P. Krut'ko, 2008, published in Zhurnal Prikladnoi Khimii, 2008, Vol. 81, No. 7, pp. 1164–1170.

MACROMOLECULAR CHEMISTRY AND POLYMERIC MATERIALS

Dependence of Composition and Characteristics of Lignosulfonates on the Procedures of Their Recovery and Purification

N. V. Shul'ga, L. A. Gomolko, and N. P. Krut'ko

Institute of General and Inorganic Chemistry, National Academy of Science of Belarus, Minsk, Belarus

Received December 11, 2007

Abstract—Composition and characteristics of lignosulfonic acids recovered from technical-grade lignosufonates were studied by IR spectroscopy, viscometry, and elemental and chemical analyses. The dependence of the chemical composition and characteristics of lignosulfonic acids on the procedures of their recovery and purification was examined.

DOI: 10.1134/S1070427208070239

Integrated processing of all types of raw materials, including those of plant origin, and by-products based on them is an urgent problem.

Lignosulfonates are formed in sulfite cooking of wood and are large-tonnage wastes from pulp-and-paper industry. Certain amount of these wastes is used in building and in woodworking and oil-refining industries or is chemically reprocessed for vanillin production; however, the major part of these wastes is incinerated [1–3]. At the same time, lignosulfonates as derivatives of a natural polymer, lignin, proved well as soil land-reclamation agents and also as cheap adjuvants in production of preparative forms of pesticides and nontoxic complexones in production of preparations for plant leaf treatment [4, 5]. There are extensive data on compositions and characteristics of lignins; however, data on lignosulfonic acids and their derivatives are practically lacking.

EXPERIMENTAL

Technical-grade lignosulfonates (ILSs) produced by the Sokol Pulp-and-Paper Combine according to TU (Technical Specification) 13-0281036-029 were used as raw materials for synthesis of lignosulfonic acids (LSAs). The main characteristics of ILSs were as follows: density 1235 kg m^{-3}, weight fraction of dry substances 49.1%, ash content 15.5%, pH of 20% aqueous solution 4.5, and Na base of cooking acid.

Lignosulfonates were recovered from the technical-grade product with simultaneous purification to remove concomitant impurities by two procedures.

In purification with organic salting-out agent, the initial material was dissolved in hot distilled water (60–70°C). The resulting solution with the content of dry substance of about 20–25 wt % (density 1.08–1.10 g cm^{-3}) was passed through a textile filter and cooled to room temperature. After settling for 4–5 days, the solution was separated from the precipitate and evaporated at 50–60°C to 40–45% content of dry substance. Acetone and ethanol, both of chemically pure grade, were successively added to the concentrated solution with continuous stirring. The expenditure of each organic salting-out agent was equal to the volume of the initial aqueous solution of lignosulfonates. The resulting viscous pulp was separated from the mother liquor, dried in air until it solidified, and then dried in an oven at 60°C for 1 day to completely remove residual amounts of moisture and organic solvent. The resulting product was milled, passed through a sieve, and kept in an oven at 60°C for several hours with intermittent mixing, after which the chemical composition of the purified lignosulfonates (PLSs) was determined.

In purification with an inorganic precipitant, a saturated solution of the precipitant, hexaamminecobalt(III) chloride $[Co(NH_3)_6]Cl_3$ (7.5 g of salt per 100 ml of water), was added to a solution of ILS with a concentration of 40–45%. The precipitant expenditure was approximately 4.5 g of anhydrous

Table 1. Characteristics of technical-grade lignosulfonate, intermediates prepared from it, and lignosulfonic acids*

Sample no.	Sample	Content, wt %			Atomic ratio			H^+, mg-equiv g^{-1}
		N	C	S	N	C	S	
1	ILS	0.66	37.35	7.56	2.0	132	10	–
2	PLS	0.67	38.83	8.86	1.7	117	10	–
3	LSA1 (from no. 2)	0.433	40.47	8.63	1.1	124	10	3.49
4	LSC	3.68	46.83	5.65	14.9	221	10	–
5	LSA2 (from no. 4)	1.11	52.93	6.01	4.0	235	10	1.88
6	LSA3 (from no. 2)	0.41	50.07	7.20	1.3	185	10	~1.96
7	LSA4 (from no. 3)	0.37	43.44	8.78	1.0	132	10	4.61
8	Permeate	0.79	28.35	11.00	1.6	68	10	–
9	Insoluble residue	4.43	48.30	2.94	34.4	438	10	–

* Absolute error of determination is less than 0.02 (N), 0.05 (C), and 0.08 wt % (S); 0.03 mg-equiv g^{-1} (H^+).

salt per 20 g of dry ILSs. After the precipitation completion, the mother liquor became orange. The resulting suspension was settled for 1 day, after which the precipitate was transferred onto a Buchner funnel (blue band paper filter) and thoroughly washed with distilled water. The resulting product, insoluble lignosulfonic complex (LSC), was dried in air and then in an oven at 65°C and analyzed.

The nitrogen, carbon, and sulfur content in the ILS, PLS, and LSC samples and also in the preparations obtained from them was determined on a C–H–N–O–S Vario EL-3 analyzer (Elementat, Germany).

The content of soluble sulfates in the samples was determined gravimetrically by precipitation of sulfate ions with calcium chloride solution taken in a threefold excess with respect to stoichiometry.

Lignosulfonic acid LSA1 was synthesized by the ion-exchange procedure with passing of a 20% solution of PLSs through a column packed with KU-2 cation exchanger in the H^+ form.

In synthesis of acid LSA2, the LSC complex was pretreated with concentrated NaOH solution, and the filtrate was separated and passed through an H^+ cation exchanger. In all cases, in synthesis of lignosulfonic acids the amount of lignosulfonates passed through a column did not exceed 20% of its calculated capacity. The purity of the resulting products (residual content of Na^+ ions) was monitored with an Iris Intrepid IIX DL atomic-emission spectrometer (Intertech, the United States). The sample preparation involved their mineralization.

For additional purification of the PLS sample to remove low-molecular-weight impurities of organic and inorganic origin, we used ultrafiltration. The initial product was separated into two components (permeate and concentrate) using an ultraporous membrane with a cutting limit of 100 000 amu. In subsequent experiments the concentrate was used for synthesis of lignosulfonic acid LSA3.

Lignosulfonic acid LSA4 was synthesized after preoxidation of an LSA1 sample with manganese dioxide taken in an amount of 43% of the LSA1 weight in the solution, separation of the filtrate, and passing of the filtrate through a cation exchanger in the H^+ form.

The IR spectra of the samples were recorded on a Protégé 460 IR Fourier spectrometer (Nicolette, the United States). Samples were pelletized with dried KBr powder to obtain thin discs 10 mm in diameter. The weighed portion of the sample was 1 mg. The spectrometer resolution was 4 cm^{-1}, number of scans 128.

The content of labile protons in the synthesized lignosulfonic acids was determined by potentiometric titration of aqueous solutions of LSA. In determination of the dynamic viscosity of LSA solutions we used a VPZh-3 glass capillary viscometer with a capillary diameter of 1.2 mm.

The chemical compositions of the initial ILSs and of intermediates and final products recovered from them are presented in Table 1. These results show that lignosulfonates are complicated mixtures of components having different degrees of sulfonation. In extraction with an organic solvent, the C : S ratio in the purified product is lower than that in the initial ILSs. Apparently, enrichment of the salted-out product with sulfur is caused by transfer of nonsulfonated extracted substances (resins, tanning agents, etc.) into the organic phase and coprecipitation of

sulfates with lignosulfonates under the action of an organic salting-out agent. The found content of sulfate ions is approximately 0.66 mg-equiv g^{-1} of dry ILSs and 0.67 in the salted-out product, which does not noticeably affect the position and intensity of the bands in the IR spectra of LSAs (Fig. 1).

On the contrary, treatment of an ILS solution with concentrated $[Co(NH_3)_6]Cl_3$ gives a product with noticeably increased C : S ratio. This is apparently caused by predominant precipitation of higher-molecular-weight fraction of ILS in formation of the cobalt lignosulfonate complex. In addition, lower-molecular-weight and more soluble fractions of the product can be lost in washing of the complex salt to remove excess unchanged precipitant. Similar to the products obtained from PLS by ion exchange, the sample recovered from ILS by salting-out contains nitrogen (Table 1). The largest amount of nitrogen was found in low-sulfonated poorly soluble precipitate formed by dilution and settling of ILS solution. It is likely that amino acids, precursors of lignin, are the source of nitrogen. A high content of amino acids was also found in young wood or wood that grew under unfavorable environmental conditions [6, 7].

The amorphous nature of lignin and its derivatives, complicated structure of monomeric units, and variety of bonds make impossible application of the group theory to analysis of IR spectra of these compounds. Therefore, we used an empirical approach in interpretation of the IR spectra of lignosulfonic acids and its salts (Fig. 1, Table 2).

At first glance, the IR spectra of the resulting LSA1–LSA4 samples and lignin precursor are practically identical (Table 2). In particular, this is due to the fact that the chemical reactions occurring in the course of sulfite cooking, both main (sulfonation, hydrolysis, condensation) and secondary (oxidation, reduction, dehydration, rearrangement), affect the ratio between functional groups of the initial polymer, but their main types are preserved [11].

Introduction of sulfonic group into the structural unit of lignin (nucleophilic substitution) does not give rise to new absorption bands in the IR spectra of lignosulfonates, because the frequencies of symmetric and antisymmetric vibrations of this functional group coincide with the frequencies of vibrations of lignin functional groups (Table 2). The result of this coincidence is noticeable increase in the integral intensity of absorption in the regions of

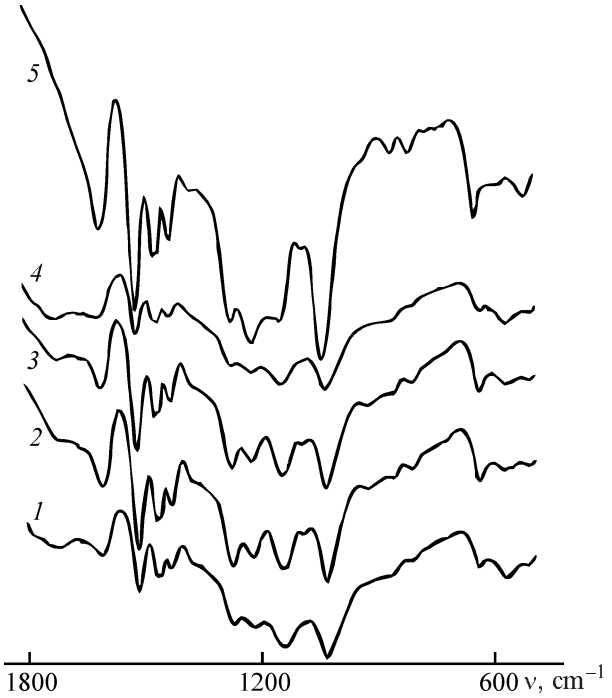


Fig. 1. IR spectra of (*1*) LSA1, (*2*) LSA2, (*3*) LSA3, (*4*) LSA4, and (*5*) LSNa. (ν) Wavenumber; the same for Figs. 2 and 3.

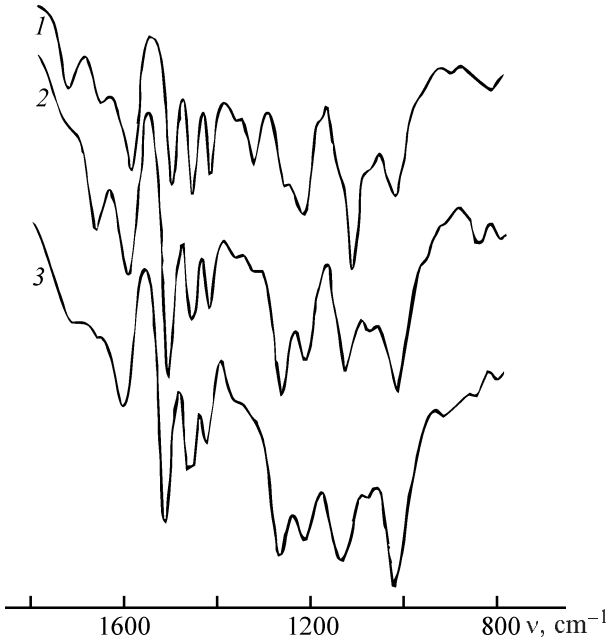


Fig. 2. IR spectra of lignins recovered form (*1*) beech and (*2*) spruce wood and (*3*) of lignosulfonic acid LSA3.

1030 and 1140 cm^{-1} in lignosulfonates in comparison with lignins (Fig. 2).

IR spectroscopy allows elucidation of the source of lignins and furnishes preliminary data on their structural features. It is well known that, in conifer-

Table 2. IR spectrum of lignosulfonic acid

Wavenumber, cm^{-1}		Assignment
coniferous lignin [8–10]	LSA	
3400	3410–3390	ν_{OH} (polymeric associates)
	~3000	ν_{CH} (Ar ring)
2930	2926	$\nu^{a}_{CH_3}$ (R–CH_3; R–OCH_3; Ar–CH_3); $\nu^{a}_{CH_2}$ (R–CH_2–R_2; R–CH_2–OR_2;)
2845	~2880	$\nu^{s}_{CH_3}$ (R–CH_3); $\nu^{s}_{CH_2}$ (R–CH_2–R')
	~2852	$\nu^{s}_{CH_3}$ (R–OCH_3; Ar–OCH_3); $\nu^{s}_{CH_2}$ (R_1–CH_2–R_2; R–CH_2–OH; R_1–CH_2–OR_2)
	~1780	$\nu_{C=O}$ (anhydrides of carboxylic acids, lactones)
1740	1750–1735	$\nu_{C=O}$ (R_1–O–CO–R_2; R–CH_2–COOH)
1720–1710	~1715	$\nu_{C=O}$ (R_1–CO–R_2; R–CHO; Ar–COOH; Ar–CO–OR; Ar–CHO)
1660–1655	~1657 (shoulder)	$\nu_{C=O}$ (R–COOH, with intramolecular hydrogen bond); $\nu_{C=C}$ (alkenes); ν_{CH} (Ar ring, overtone); $\nu_{C=O}$ (Ar–CHO in *p*-position)
1600	~1600	ν_{C-C} (Ar ring)
1510	1510	ν_{C-C} (Ar ring)
1460	1464	ν_{C-C} (Ar ring); $\delta^{a}_{CH_3}$ (R–CH_3); δ_{CH_3} (Ar–OCH_3, guaiacylpropane unit); δ_{CH_2} (R_1–CH_2–R_2)
	1453	δ_{CH_3} (R–OCH_3); δ_{CH_2} (R_1–CH_2–R_2)
1420	~1425	ν_{C-C} (Ar ring)
1365–1360	1360–1313	δ_{COH} (Ar–OH); δ_{COH} (Ar–OH; R–OH)
1325	~1335 (shoulder)	δ_{CH_3} (Ar–OCH_3, syringylpropane unit)
1270	1267	ν^{a}_{COC} (Ar–OCH_3) + ν_{COC} ~1010–1050 cm^{-1}; δ_{CH_3} (guaiacylpropane unit)
1220	1212	ν^{a}_{COC} (Ar–OR); δ_{OH} (Ar–OH); ν_{CO} (Ar–OH)
1150–1135	~1140	ν^{a}_{SO} (R–SO_3H); δ_{OH} [R_1–CH(OH)–R_2]; δ_{CH} (Ar ring)
1120	1126 (shoulder)	ν_{CO} (R_1–O–R_2); R_1CHR_2–O–R_3
1090–1080	~1085	ν_{COC} (R_1–O–R_2); δ_{OH} (R_1–CH(OH)–R_2
1030	1030	ν^{s}_{SO} (R–SO_3H); δ_{CH} (Ar ring, guaiacylpropane unit); ν_{CO} (R–OH); δ_{OH} (R–OH)
	920	δ_{OH} (R–COOH); δ_{CH} (Ar ring); ν_{S-O} (R–SO_3H)
870	880	δ_{CH} (1,2,4-substituted Ar ring); δ_{CH} (1,3-substituted Ar ring)
855	860	δ_{CH} (tetrasubstituted Ar ring)
815	813	δ_{CH} (1,2,4-substituted Ar ring) + ν~880 cm^{-1}
	643	ν_{C-S} (R–SO_3H)
	573	δ_{OSO}
	516	δ_{OSO}

ous lignins, the main structural unit is guaiacylpropane unit. For this type of lignins, the band at approximately 1600 cm^{-1} is typically weaker than the band at 1500 cm^{-1}. These bands in the IR spectrum correspond to stretching modes of the aromatic ring. The bending band of methoxyls of guaiacylpropane unit (approximately 1460 cm^{-1}) has lower intensity, and the band maxima of bending modes of the CH group of the benzene ring are observed at about 860 and 815 cm^{-1} (Fig. 2) [11, 12].

Sulfite cooking does not alter the structural type of the initial natural polymer, as it affects guaiacylpropane and syringylpropane units to a significantly lesser extent than other segments of the lignin molecule. The ratio of intensities of the absorption bands and their positions in the IR spectra of the resulting LSA samples (Figs. 1, 2) suggest that ILSs used in this study are the product of processing of coniferous wood. Coniferous lignins contain smaller amounts of methoxyls in the aromatic nucleus and are sulfonated more readily than deciduous lignins [6, 11].

Industrial lignins always contain certain amount of impurities. In their purification with organic salting-out agents there is no way to avoid coprecipitation with the main product of inorganic sulfates and

also sugars, aldonates, uronates, and sulfocarbonates having low solubility in organic solvents. Ultrafiltration is considered to be an efficient procedure allowing separation of low-molecular-weight impurities. However, it is well known that even the most narrow-porous membranes are permeable to lignins and do not fully prevent penetration of lignins of low and even intermediate molecular weight into the filtrate (permeate) [13].

In an attempt to apply this procedure to purification of not PLS sample but lignosulfonic acid LSA1 prepared from this sample, we ran into problems. Attempts to separate low-molecular-weight impurities from the main product using an ultraporous membrane failed, since a large amount of lignosulfonic acid passed into the filtrate. This can be caused by changes in the conformation of polymer molecules in an acid medium (linear form instead of globular form).

To attain more complete separation of low-molecular-weight impurities from lignosulfonates PLSs, the permeate was concentrated and subjected to repeated filtration.

The dried permeate was a hygroscopic brown mass with numerous whitish platelike inclusions, had light-beige color after grinding, and noticeably differed from the other samples in the chemical composition, having high degree of sulfonation (Table 1). This is apparently caused by passing of the most sulfonated low-molecular-weight fractions of the main substance and inorganic sulfates into the filtrate. The presence of inorganic sulfates in the filtrate is confirmed by an increase of the intensity of the bands at 1130 and 616 cm^{-1}.

Contrary to the filtrate, the membrane concentrate obtained by ultrafilration of the PLS sample did not have pronounced hydrophilic characteristics, was readily dehydrated, and after drying turned brown, which is typical for lignosulfonates. After dissolution it was used for synthesis of lignosulfonic acid LSA3. As expected, removal of the low-molecular-weight fraction of the technical-grade product resulted in a decrease in the degree of sulfonation of the residue (concentrate) and in the content of acid groups in the residue (Table 1). Chemical analysis and IR measurements show that the major organic components of the filtrate are lactones and also derivatives of uronic and sulfocarboxylic acids: after purification by ultrafiltration, the intensities of the absorption bands at 1780 and 1740 cm^{-1} noticeably decrease (Figs. 1, 3). These bands correspond to vibrations of carbonyl group in γ-lactone and open-chain forms of uronic acids [14].

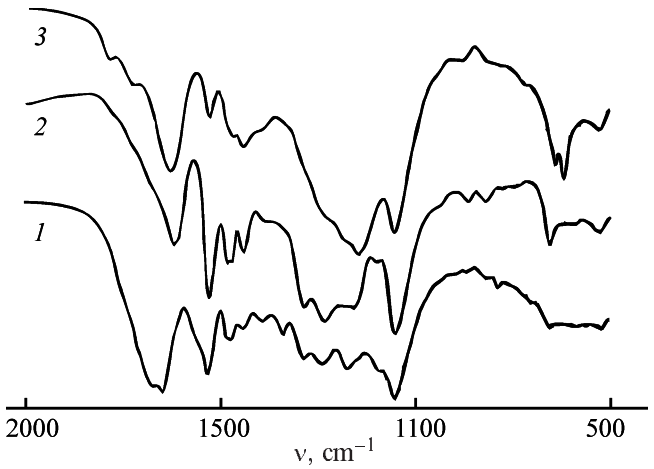


Fig. 3. IR spectra of (*1*) insoluble residue, (*2*) concentrate, and (*3*) permeate.

The band at approximately 1780 cm^{-1}, especially strong in the IR spectra of LSA1 and LSA4 (Fig. 1), can be assigned to stretching vibrations of the C=O bond in anhydrides of organic acids. Their amount can be considerable due to condensation of hydroxyls of sulfonic and carboxy groups in drying of lignosulfonic acids [15]. Dry lignosulfonic acids are practically insoluble in water, which is typical for condensed products.

A fairly strong absorption band at approximately 1717 cm^{-1} in the spectra of lignosulfonic acids (Fig. 1) can be assigned to stretching vibrations of carbonyl groups of nonconjugated keto and aldehyde groups and also of carboxy groups bonded to aromatic ring. In the spectra of salts of lignosulfonic acid, the intensity of this band noticeably decreases (Fig. 1). A weak band preserved as a shoulder at approximately 1660 cm^{-1} cannot be assigned to only carbonyls of carboxy groups. The vibrations of β-keto esters, alkenes, quinones, some aldehydes, and also nitrogen-containing functional groups also fall into this range. The presence of nitrogen-containing groups in lignosulfonates is beyond question (Table 1). The strong bands at approximately 1630 and 1660 cm^{-1} in the IR spectra of the insoluble residue presumably belong to amide functional groups (Fig. 3). It should also be noted that, under certain treatment conditions, gaseous ammonia is released from the insoluble precipitate, which is typical for hydrolytic rupture of amide bonds.

The vibrations in the range 520–650 cm^{-1} are

Table 3. C : S ratio in complex salt at various synthesis conditions

Precipitation conditions		Content, wt %		Atomic ratio	
ILS concentration in solution, wt %	precipitate treatment procedure	C	S	C	S
0.5	Settling	45.13	5.91	204	10
1.25	Washing with water	46.26	5.96	207	10
1.25	Washing with water–ethanol mixture	42.47	6.60	173	10
10.0	Without washing	44.65	6.24	191	10
10.0	Washing with water–ethanol mixture	46.44	6.14	202	10
10.0	Washing with water	46.71	5.82	214	10
40.0	Washing with water	49.74	5.80	229	10

usually assigned to sulfoxyl groups [12]. The bands at 1140–1150 and 1030–1036 cm^{-1} also belong to these groups since, according to data obtained, their positions in the above range vary depending on the nature of lignosulfonate cation or coordination of the complex cation relative to the sulfonate anion.

Purification of ILSs with complex precipitants precludes the possibility of coprecipitation of any low-molecular-weight impurities (sulfates, sugars, lactones, etc.) with the main product [16]. However, the study showed that this procedure does not allow recovery of lignosulfonates with chemical composition similar to that of lignosulfonates in the initial technical-grade product. In washing of the precipitate to remove the residual unchanged precipitant, the precipitate is peptized and the fractions enriched with strongly acidic sulfonic groups, i.e., the lowest-molecular-weight and most hydrophilic fractions (Table 3), are lost. Settling of the precipitated complex is accompanied by its progressing hydrolytic decomposition resulting in the loss of the substance. The results obtained agree well with published data showing that, with complex precipitants, no more than 60% of lignosulfonates can be recovered from a solution [8]. It is not improbable that the inorganic precipitant $[Co(NH_3)_6]Cl_3$ binds into a stable insoluble complex only less sulfonated polymer fractions having definite steric orientation.

Table 4. Dynamic characteristics of lignosulfonic acids LSA1 and LSA2

Sample	Density, g cm^{-3}	Concentration in solution, wt %	pH	Dynamic viscosity, mPa s
LSA1	1.077	23.2	0.33	1.79
LSA2	1.075	20.4	0.70	4.94

Purification of lignosulfonates to remove low-molecular-weight impurities noticeably alters not only their chemical composition but also rheological characteristics (Table 4).

It is well known that low-molecular-weight lignosulfonates enter into the composition of the solvate shell of significantly coarser molecules [6]. It can be expected that this is also true for other low-molecular-weight impurities. Participating in formation of hydrogen bonds with functional groups of macromolecular fractions of lignosulfonic acid LSA1, low-molecular-weight compounds stabilize a finely dispersed colloid. This type of structure of colloidal solution provides high mobility of individual components and, correspondingly, low viscosity.

It is likely that, in LSA2 solutions purified to remove the low-molecular-weight component, a 3D network is formed by interaction of side chains of polymer molecules, which noticeably decreases the fluidity of the colloid.

CONCLUSIONS

(1) Chemical composition and characteristics of lignosulfonates depend on the procedure of their recovery from the industrial product.

(2) The presence of the low-molecular-weight fraction in lignosulfonates significantly affects their physical characteristics.

REFERENCES

1. Okko, R., Fraktionierung und Charakterisierung von elektrochemisch behandelten Magnesium-Sulfitablaugen, *Dissertation*, Hamburg (Germany), 2006.
2. Kleinemeyer, K.H., in *1st European Workshop on*

Lignocellulosics and Pulp KONORT, Bergedorf (Germany), September 18–20, 1990, Hamburg: Wiedebusch, 1991, pp. 1–10.

3. Eck, M., KTH, The Status of Applied Lignin Research, *Report of Örnsköldsvik: Processum Technology Park AB*, August 29, 2005, no. 2.
4. *Chemistry and Technology of Agrochemical Formulation*, Knoles, D.A., Ed., Dordrecht: Kluwer Academic, 1998, pp. 158–178.
5. US Patent 3 244 505.
6. Sapotnitskii, S.A., *Ispol'zovanie sul'fitnykh shchelokov* (Use of Sulfite Liquors), Moscow: Lesnaya Prom–st., 1981.
7. Sazonova, T.A., Terebova, E.N., Osipova, I.S., and Shreders, S.M., *Lesn. Zh.*, 2001, nos. 5–6, pp. 47–51.
8. Mozheiko, L.N., Sergeeva, V.N., Grineva, L.A., et al., *Khim. Drev.*, 1972, no. 11, pp. 77–85.
9. Brauns, F.E. and Brauns, D.A., *The Chemistry of Lignin*, New York: Academic, 1960.
10. Lignins: *Occurrence, Formation, Structure, and Reactions*, Sarkanen, K.V. and Ludwig, C.H., Eds., New York: Wiley, 1971.
11. *The Chemistry of Wood*, Browning, B.L., Ed., New York: Interscience, 1963.
12. Ehara, K., Takada, D., and Saka, Sh., *J. Wood Sci.*, 2005, vol. 51, pp. 256–261.
13. Padilla, V., Rangel, M.G., Bullon, J., et al., Surface Activity of Lignin Fractions Obtained by Membrane Separation Technologies of Industrial Black Liquors, *Proc. Iberoamerican Congr. on Pulp and Paper Research*, *CIADICYP 2002*, Campinas (Brasilia), 2002, pp. 1–16.
14. Braun, D.W, Floyd, A.J., and Sainsbury, M. *Organic Spectroscopy*, New York: Wiley, 1988.
15. Chen Rubie and Wu Guoxiong, *J. Appl. Polym. Sci.*, 1991, vol. 42, no. 7, pp. 2073–2079.
16. Tsypkina, M.N. and Balashova, I.M., *Zh. Prikl. Khim.*, 1959, vol. 32, no. 1, pp. 103–108.

ISSN 1070-4272, Russian Journal of Applied Chemistry, 2008, Vol. 81, No. 7, pp. 1252–1257. © Pleiades Publishing, Ltd., 2008.
Original Russian Text © B.B. Troitskii, L.V. Khokhlova, V.N. Denisova, M.A. Novikova, A.E. Golubev, A.V. Arapova, A.A. Zaitsev, 2008, published in Zhurnal Prikladnoi Khimii, 2008, Vol. 81, No. 7, pp. 1171–1177.

MACROMOLECULAR CHEMISTRY AND POLYMERIC MATERIALS

Thermal Degradation of Composites of Poly(Methyl Methacrylate) with Alkoxysilane Hydrolyzates

B. B. Troitskii, L. V. Khokhlova, V. N. Denisova, M. A. Novikova, A. E. Golubev, A. V. Arapova, and A. A. Zaitsev

Razuvaev Institute of Organometallic Chemistry, Russian Academy of Sciences, Nizhni Novgorod, Russia

Received November 1, 2007

Abstract—Organic–inorganic composites of poly(methyl methacrylate) with alkoxysilane hydrolyzates form transparent films. Their thermal and oxidative thermal degradation were studied by differential scanning calorimetry and thermogravimetric analysis.

DOI: 10.1134/S1070427208070240

Poly(methyl methacrylate) (PMMA) is a large-tonnage commercial product. Transparent PMMA glasses are widely used in various fields of economy. However, the heat resistance of PMMA is poor. Its thermal degradation starts on heating above 150°C.

Modification of polymer properties with the aim to improve the quality and prolong the service life was and remains an urgent theoretical and applied problem. Diverse methods are used today to inhibit polymer degradation. These include choice of proper processing conditions, addition of antioxidants or oxidation inhibitors to the polymer, and control of the supramolecular structure of polymeric materials.

Active efforts have been made recently to develop polymeric nanocomposite materials. To prepare nanocomposites, an ultrafine silica sol is introduced into a polymer dispersion [1]. Nanocomposites can also be prepared by simultaneously performing polymerization of a monomer and hydrolysis of alkoxysilanes [2]. Ivanchev et al. [3] reported on preparation of a nanocomposite material based on polypropylene (PP) by hydrolysis of alkoxysilanes directly in a polymer matrix in the solid state or in a melt.

It was interesting to examine the possibility of preparing PMMA films filled with inorganic particles by introducing into a polymer solution hydrolyzates of various alkoxysilanes and to study how the hydrolysis conditions and composition of the blends affect the properties of the films obtained.

EXPERIMENTAL

PMMA(I) samples were prepared in sealed ampules by bulk polymerization of MMA with various concentrations of azobis(isobutyronitrile) (AIBN), following the standard procedure [4]. Before polymerization, MMA was purified by vacuum distillation and deoxygenated by threefold freezing–pumping–thawing. Also, PMMA(II) samples were prepared by bulk polymerization of MMA in air without initiator under UV irradiation. Emulsion PMMA was prepared as described in [5].

Tetraethoxysilane (TEOS), γ-aminopropyltriethoxysilane (APTEOS), and phenyltrimethoxysilane (PTMOS) were purified by vacuum distillation.

Hydrolysis of siloxanes was performed at room temperature in a flask. The mixture was stirred with a magnetic stirrer at a rate of 500 rpm. Water was added in an amount of 1 mol per each hydrolyzable bond in alkoxysilane. Hydrochloric acid was used as catalyst. The hydrolysis time was about 30 min. The hydrolyzate was diluted with acetone in a volume ratio of 1 : 20.

The solution of the hydrolyzate in acetone was mixed with a solution of PMMA in methylene chloride and poured onto a Petri dish. The films obtained after solvent evaporation were dried in a vacuum oven at 60–70°C to remove the solvent completely. The film thickness was about 100 μm.

IR measurements were performed with an FSM 1201 IR Fourier spectrometer, and DSC measurements, with a DSK 204 F1 Phoenix differential scan-

ning calorimeter (Netzsch, Germany) with linear heating from 20 to 450°C at a rate of 10 deg min^{-1}.

Thermogravimetric analysis of samples in the dynamic mode in a nitrogen atmosphere (thermal degradation) or in air (thermal oxidative degradation) was performed with a Perkin–Elmer Pyris 6 TGA device, with linear heating from 20 to 450°C at a rate of 10 deg min^{-1}.

The rate of thermal oxidative degradation (TOD) at a constant temperature (302°C) was evaluated by the weight loss on an installation equipped with a quartz spring balance at an oxygen pressure of 200 mm Hg.

According to published data [6], hydrolysis of alkoxysilanes occurs in several steps during which the initial two-phase liquid mixture of the reactants after stirring for a definite time transforms into a single-phase liquid. Further stirring leads to the formation of a two-phase mixture transforming into a suspension of solid silica microspheres.

In this study, the hydrolysis was stopped at the step of transformation of the two-phase system into the single-phase system by diluting the hydrolyzate with acetone. The composition of alkoxysilane hydrolysis products was examined by IR spectroscopy [7].

On mixing TEOS hydrolyzate with a PMMA solution, after removing the solvent and drying, a transparent film was obtained. Its IR spectrum contained, along with PMMA bands, also a band at 1091 cm^{-1} belonging to C–O vibrations in the Si–O–C fragment of partially hydrolyzed TEOS.

In the spectrum of the film obtained from PMMA and PTMOS hydrolyzate, a shoulder at 1030 cm^{-1} appears on the band with a maximum at 1067 cm^{-1}. These frequencies are characteristic of Si–O–Si stretching vibrations, confirming the presence of silicon compounds in PMMA films. In addition, the spectra of samples containing PTMOS hydrolysis products contain an absorption band of the phenyl group (1595 cm^{-1}).

In the spectrum of the film obtained from PMMA with APTEOS hydrolyzate, there is a strong band with a maximum at 1064 cm^{-1} and a weak band at 1030 cm^{-1}, characteristic of the Si–O–Si group in linear oligosiloxanes and in cyclic trisiloxane. A slight increase in the absorption at 1580 and 3400 cm^{-1} suggests the presence of NH groups.

The mechanism of poly(methyl methacrylate) degradation at elevated temperatures has been

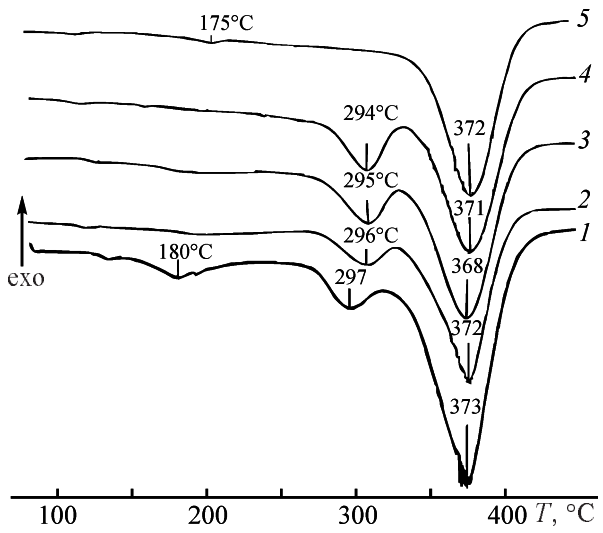


Fig. 1. DSC curves: (*1*) emulsion PMMA, (*2–4*) PMMA(I) prepared in the presence of AIBN, and (*5*) PMMA(II). (*T*) Temperature; the same for Fig. 2. AIBN concentration, wt %: (*2*) 0.1, (*3*) 0.2, and (*4*) 0.5.

studied in detail [8]. Thermal degradation of PMMA occurs by the mechanism of radical nonbranched chain reactions. The major process is depolymerization. The monomer is virtually the only product of thermal degradation of PMMA (99%) [8].

To compare the thermal properties of PMMA and organic–inorganic composites prepared by adding hydrolysis products of various alkoxysilanes into the polymer, we studied by DSC in an inert atmosphere the PMMA samples prepared in emulsion or in the bulk in the presence of an initiator and without it. The DSC curves of PMMA samples prepared by the above procedures differ in the number and positions of endothermic peaks.

The DSC curve of emulsion PMMA (Fig. 1, curve *1*) has three endothermic peaks. The total area of the peaks is proportional to the total thermal effect of processes occurring in the polymer on heating. At a heating rate of 10 deg min^{-1}, the first peak with a minimum at 180°C is observed in the temperature range 160–210°C; the second peak with a minimum at 297°C, in the range 280–315°C; and the third peak with a minimum at 373°C, in the range 315–420°C.

Kashiwagi et al. [9] studied by TG at a heating rate of 2 deg min^{-1} the thermal degradation of PMMA samples prepared by anionic (sample A) and radical (sample B) polymerization. In the DTG curve of sample A, there is only one peak at 360°C. In the DTG curve of sample B prepared in the bulk

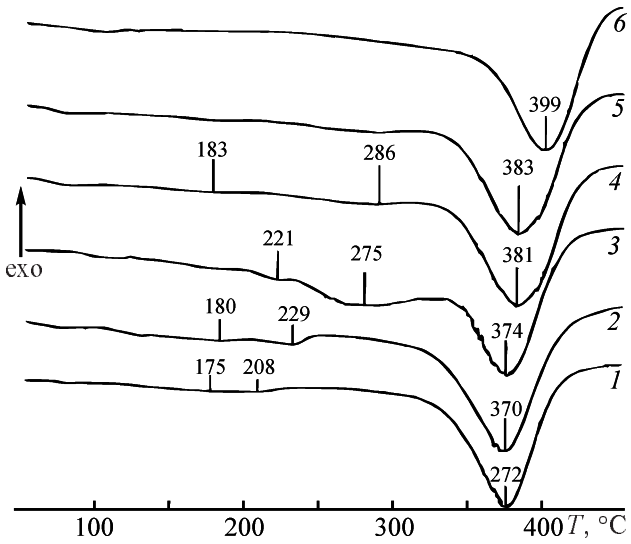


Fig. 2. DSC curves of PMMA(II) composites with hydrolyzates of various alkoxysilanes. Alkoxysilane, %: (*1*) 1 TEOS, (*2*) 10 TEOS, (*3*) 1 PTMOS, (*4*) 10 PTMOS, (*5*) 1 APTEOS, and (*6*) 7 APTEOS.

in the presence of AIBN, there are three peaks at 165, 270, and 360°C. Taking into account the data they obtained for model oligomers, Kashiwagi et al. assigned the peaks in the DTG curve of sample B to degradation initiated by unstable head-to-head grouos (165°C), unsaturated terminal bonds (270°C), and random cleavage of the macromolecular backbone (360°C). For sample A containing no unstable structures, the only peak observed in the DTG curve at 360°C is apparently due to initiation by random cleavage of the backbone. The same conclusions were made later by Shibaev et al. [10, 11].

The temperature intervals of the endothermic peaks in the DSC curves of various PMMA samples suggest that these peaks are related to the three steps of thermal degradation described in [9–11].

The first peak in the DSC curve of emulsion PMMA (Fig. 1, curve *2*) corresponds to the degradation of macromolecules initiated by cleavage of weak head-to-head bonds formed when the MMA polymerization is terminated by recombination of the macroradicals. The second peak in the DSC curve is due to initiation of the degradation by cleavage of terminal double bonds of polymer macromolecules, formed by disproportionation of the macroradicals in the course of polymerization. The largest thermal effect is associated with the last step of the degradation, initiated by random cleavage; it is proportional to the area of the third peak.

In the DSC curves of PMMA(I) samples prepared by bulk polymerization in the presence of AIBN (Fig. 1, curves *2–4*), there are only two endothermic peaks. One of the peaks (294–296°C) is apparently associated with degradation of macromolecules initiated by cleavage of terminal double bonds. Initiation by weak terminal double bonds leads to only 10–15% degradation of PMMA, as judged from the ratio of the peak areas, and it depends on the initiator concentration: The higher the initiator concentration, the larger the area of the first peak. The second peak with a minimum at about 370°C, whose relative area is 85–90%, corresponds to processes initiated by random cleavages of macromolecules.

In the DSC curve of the PMMA(II) sample prepared without initiator (Fig. 1, curve *5*), there are also two peaks, but the curve differs in shape from the previously discussed curves (Fig. 1, curves *2–4*). Namely, the first peak is observed at 174.6°C. The lower temperature of the degradation onset, apparently, suggests initiation of the degradation by cleavage of weak head-to-head bonds. As judged from the area of the first peak, the amount of such bonds is relatively low. Initiation of the degradation by cleavage of such bonds leads to only 1% degradation of the polymer. The second peak in the DSC curve of the PMMA(II) sample (about 370°C), as in the previous samples, is due to degradation initiated by random cleavages of the backbone.

The DSC curves of composites of PMMA(II) with hydrolysis products of alkoxysilanes (Fig. 2) differ from that of straight PMMA and from each other. First, in these curves the degradation processes initiated by cleavage of weak head-to-head bonds and terminal double bonds are manifested very weakly. Second, in the DSC curve of the composite with 10% TEOS, an endothermic peak appears at 229°C, absent in the PMMA(II) curve. This peak is apparently attributable to cleavage of the residual siloxane fragments in the component. In addition, the major peak is shifted toward higher temperatures. Below are given the additives to PMMA, their percentage, and the temperature of the major DSC peak: none, 372°C; 1% TEOS, 372; 10% TEOS, 375; 1% PTMOS, 374; 10% PTMOS, 385, 1% APTEOS, 383; and 7% APTEOS, 399°C, i.e., the additives enhance the heat resistance of the polymer.

In contrast to DSC, the TGA method allows not only determination of the temperature intervals of PMMA degradation, but also measurement of the weight loss rate in these intervals (see table). The

Results of TG in nitrogen and air flows

Degradation	PMMA composite*											
	no additive			1% TEOS			10% TEOS			1% PTMOS		
	(a)	(b)	(c)	(a)	(b)	(c)	(a)	(b)	(c)	(a)	(b)	(c)
In nitrogen atmosphere												
Degradation onset	110			90			110			100		
First interval	110–240	9.0		90–190	8.00		110–215	12.00		100–227	8.2	
First maximum	184		1.1	172		1.52	180		1.49	176		1.06
Second interval	240–300	19.5		190–256	18.00		215–265	21.00		227–322	32.0	
Second maximum	280		1.33	216		1.76	237		1.61	300		1.16
Third interval	300–447	100		256–455	98.80		265–465	92.7		322–455	99.1	
Third maximum	381		16.35	385		13.8	384		10.72	383		13.08
End of process	447	100		455	98.80		465	92.7		455	99.1	

Degradation	PMMA composite								
	10% PTMOS			1% APTEOS			7% APTEOS		
	(a)	(b)	(c)	(a)	(b)	(c)	(a)	(b)	(c)
In nitrogen atmosphere									
Degradation onset	105			108			120		
First interval	105–219	5.24		108–238	6.5		120–222	3.8	
First maximum	180		0.69	175		0.8	166		0.42
Second interval	219–326	19.9		238–312	13.0		222–350	15.9	
Second maximum	325		2.24	280		1.08	350		2.10
Third interval	326–480	84.1		312–485	98.7		350–487	88.7	
Third maximum	395		9.58	397		20.2	420		11.2
End of process	480	84.1		463	98.7		487	88.7	

Degradation	PMMA composite											
	no additive			1% TEOS			10% TEOS			1% PTMOS		
	(a)	(b)	(c)	(a)	(b)	(c)	(a)	(b)	(c)	(a)	(b)	(c)
In air												
Degradation onset	100			94			93			110		
First interval	110–212	5.24		94–232	7.70		93–232	9.15		110–220	5.0	
First maximum	180		0.8	175		1.0	178		1.08	170		0.60
Second interval	212–281	31.0		223–288	31.00		232–280	21.70		220–260	8.0	
Second maximum	256		6.23	260		4.8	266		4.50	242		1.60
Third interval	281–432	99.7		288–418	98.33		281–435	92.00		260–430	97.5	
Third maximum	315		8.5	324		9.5	335		7.35	320		12.00
End of process	432	99.7		418	98.33		435	92.00		430	97.5	

Table. (Contd.)

Degradation	PMMA composite								
	10% PTMOS			1% APTEOS			7% APTEOS		
	(a)	(b)	(c)	(a)	(b)	(c)	(a)	(b)	(c)
				In air					
Degradation onset	108			110			120		
First interval	108–237	4.6		110–253	4.81		120–222	2.44	
First maximum	183		0.60	185		0.54			0.36
Second interval	237–290	15.4							
Second maximum	271		3.16						
Third interval	290–482	85		253–440	98.3		222–480	92.6	
Third maximum	325		7.54	380		13.8	376		9.15
End of process	450	85		440	98.3		480	92.6	

* (a) Temperature, °C; (b) weight loss, %; (c) weight loss rate, % min^{-1}.

temperature intervals of degradation acceleration, observed in the DTG curve of the PMMA(II) sample in a nitrogen atmosphere, correspond to the endothermic peaks in the DSC curve.

In the DTG curves recorded in the course of heating in a nitrogen atmosphere the PMMA(II) samples and composites of PMMA with TEOS and PTMOS hydrolyzates (see table), steps of degradation acceleration are observed in the range 100–300°C. Additions of PTMOS and TEOS cause in this range a small additional weight loss (26.5% for PTMOS and 21–24.5% for TEOS) compared to PMMA (19.5%), apparently due to occurrence of

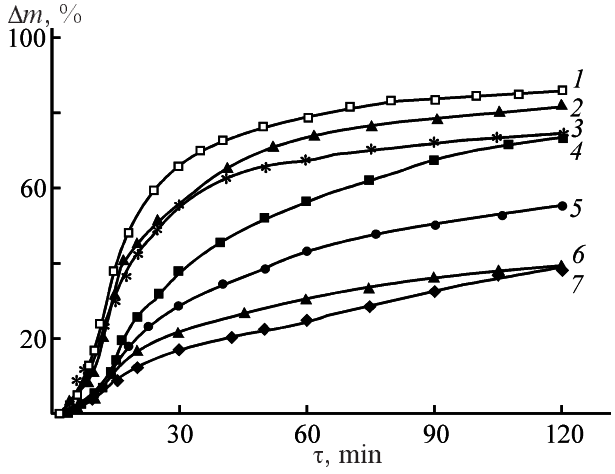
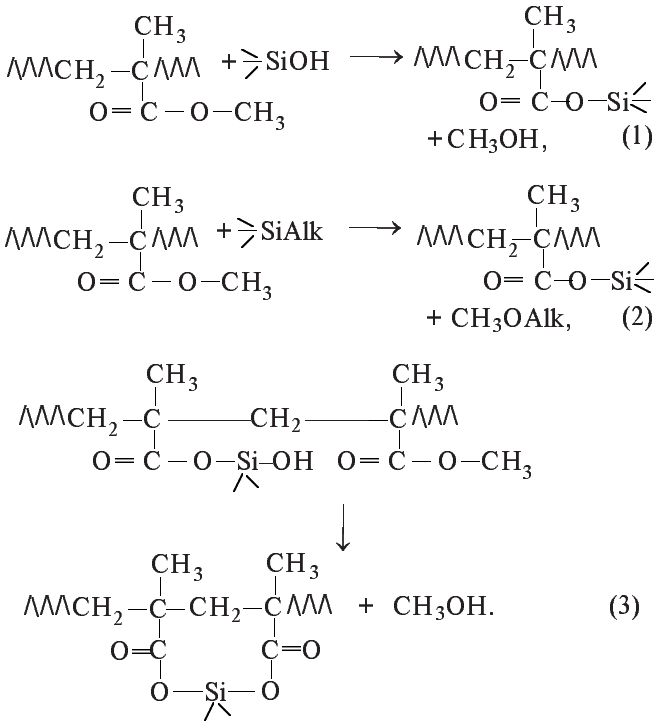


Fig. 3. Curves of the weight loss Δm in thermal oxidative degradation of (*1*) PMMA(II) and (*2–7*) composites of PMMA(II) with hydrolyzates of various alkoxysilanes. Temperature 302°C, O_2 pressure 200 mm Hg. Alkoxysilane, %: (*2*) 1 TEOS, (*3*) 10 TEOS, (*4*) 1 PTMOS, (*5*) 10 PTMOS, (*6*) 1 APTEOS, and (*7*) 7 APTEOS.

the reactions



The PMMA degradation in composites, initiated by random bond cleavage in macromolecules, in the presence of additives of alkoxysilane hydrolysis products occurs more slowly than that of straight PMMA (see table). As the rate of the chain reaction of macromolecule depolymerization is determined by the product of the initiation rate by the chain length, it can be assumed that additives do not affect the initiation rate but decrease the depolymerization

chain length by terminating it in sites of silicon addition to PMMA chain [reactions (1)–(3)].

In the degradation of PMMA in air, monitored by TG in the dynamic mode (see table), the weight loss starts at 100°C. As in thermal degradation in a nitrogen flow, three steps of the polymer degradation are observed. However, the degradation rate sharply increases already above 211°C. In the DTG curve, sharp oscillations of the weight loss rate are observed in the range from 250 to 330°C, suggesting intense release of volatiles from the sample. The polymer fully degrades below 430°C.

Additions of APTEOS hydrolysis products increase the degradation temperature and inhibit the PMMA degradation to a greater extent than do the TEOS and PTMOS hydrolyzates, both in a nitrogen flow and in air (see table). The degradation rate reaches a maximum at 400–420°C in nitrogen and 375–380°C in air, which is 60–65°C higher than the temperature of the maximal weight loss rate for straight PMMA.

Studies of the thermal oxidative degradation of blends of PMMA with alkoxysilane hydrolyzates at a constant temperature of 302°C in oxygen (Fig. 3) showed that the kinetics of their decomposition depends on the amount and kind of the additive. We found that the weight loss in them is slower than in the PMMA sample without additives. The strongest deceleration of the degradation is observed for blends of PMMA with APTEOS hydrolyzate (Fig. 3, curves *6*, *7*), as in the dynamic experiment.

Thus, it follows from the above DSC and TGA data that introduction of alkoxysilane hydrolyzates into PMMA stabilizes the polymer with respect to thermal degradation. Modification of the macromolecule with silicon-containing fragments leads to a decrease in the length of the depolymerization chain. Blends of PMMA with APTEOS hydrolysis products are the most heat-resistant. Additional stabilizing effect on the polymer in this case is exerted by the presence of the amino group in the alkoxysilane. The reaction of the amino group with the ester group of the monomer unit of PMMA, occurring on heating the polymer above 150°C, yields six-membered imide rings. This was proved by appearance of an absorption band at 1657 cm^{-1}, characteristic of imide rings, in the IR spectrum of a film of the PMMA–10% APTEOS composite after heating in a vacuum at 200°C for 30 min. Previous studies showed [12, 13] that such fragments decelerate the degradation of PMMA and its copolymers.

CONCLUSIONS

(1) Thermal and oxidative thermal degradation of poly(methyl methacrylate) is inhibited by introduction of alkoxysilane hydrolysis products into the polymer.

(2) In organic–inorganic composites of poly(methyl methacrylate), among three alkoxysilanes studied (tetraethoxysilane, γ-aminopropyltriethoxysilane, phenyltrimethoxysilane), γ-aminopropyltriethoxysilane exerts the strongest stabilizing effect.

ACKNOWLEDGMENTS

The authors are grateful to O.V. Kuznetsova for recording and discussing the IR spectra.

REFERENCES

1. Percy, M.J., Michailidou, V., Armes, S.P., et al., *Langmuir*, 2003, vol. 19, no. 6, pp. 2072–2079.
2. Hou, Z., Yu, S.H., Wang, C.U., et al., *Chem. Commun.*, 1999, no. 13, p. 1229.
3. Ivanchev, S.S., Mesh, A.M., Reichelt, N., et al., *Vysokomol. Soedin., Ser. A*, 2002, vol. 44, no. 6, pp. 996–1001.
4. Troitskii, B.B., Troitskaya, L.S., Yachnov, A.S., et al., *Eur. Polym. J.*, 1997, vol. 33, nos. 10–12, pp. 1587–1590.
5. Troitskii, B.B., Khokhlova, L.V., Denisova, V.N., et al., *Zh. Prikl. Khim.*, 2007, vol. 80, no. 8, pp. 1385–1390.
6. Karmakar, B., De, G., and Ganguli, D., *J. Non-Cryst. Solids*, 2000, vol. 272, pp. 119–126.
7. Chumaevskii, N.A., *Kolebatel'nye spektry elementoorganicheskikh soedinenii elementov IV^b i VI^b grupp* (Vibration Spectra of Organometallic Compounds of Group IV^b and VI^b Elements), Moscow: Nauka, 1971.
8. Grassie, N. and Scott, G., *Polymer Degradation and Stabilisation*, Cambridge: Cambridge Univ., 1985.
9. Kashiwagi, T., Inaba, A., Brown, J.E., et al., *Macromolecules*, 1986, vol. 19, pp. 2160–2168.
10. Shibaev, L.A., Antonova, T.A., Vinogradova, L.V., et al., *Pis'ma Zh. Tekh. Fiz.*, 1997, vol. 23, no. 18, pp. 81–85.
11. Shibaev, L.A., Ginzburg, B.M., Antonova, T.A., et al., *Vysokomol. Soedin., Ser. A*, 2002, vol. 44, no. 5, pp. 815–823.
12. Troitskii, B.B., Domrachev, G.A., Khokhlova, L.V., et al., *Zh. Obshch. Khim.*, 2003, vol. 73, no. 12, pp. 2013–2017.
13. Troitskii, B.B., Domrachev, G.A., Khokhlova, L.V., and Anikina, L.I., *Vysokomol. Soedin., Ser. A*, 2001, vol. 43, no. 9, pp. 1540–1547.

ISSN 1070-4272, Russian Journal of Applied Chemistry, 2008, Vol. 81, No. 7, pp. 1258–1261. © Pleiades Publishing, Ltd., 2008.
Original Russian Text © M.F. Galikhanov, I.A. Zhigaeva, A.K. Minnakhmetova, R.Ya. Deberdeev, 2008, published in Zhurnal Prikladnoi Khimii, 2008, Vol. 81, No. 7, pp. 1178–1181.

MACROMOLECULAR CHEMISTRY AND POLYMERIC MATERIALS

Biodegradability of Electret Polymer Materials

M. F. Galikhanov, I. A. Zhigaeva, A. K. Minnakhmetova, and R. Ya. Deberdeev

Kazan State University of Technology, Kazan, Tatarstan, Russia

Received November 1, 2007

Abstract—Corona electrets based on composites of shockproof polystyrene and starch were studied.

DOI: 10.1134/S1070427208070252

Utilization of spent polymer electrets is a topical problem because of their wide use in various converters, air filters and individual respirators, tribotechnical and sealing systems, etc. [1–3]. In Russia, polymer items are usually disposed of with solid domestic wastes. However, since polymers are extremely resistant to degradation, studies should be carried out to develop new biodegradable polymers. One of the ways to impart biodegradability to polymers is addition of fillers, which can act as a source of food for bacteria and fungi and simultaneously promote degradation of polymer chains to oligomeric fragments easily assimilated by the same microorganisms [4, 5].

Our previous studies [6–8] showed that, from polymers and dispersed fillers, it is possible to prepare electrets considerably surpassing in characteristics those based on unfilled polymers. However, as shown in [9], electric fields negatively affect the vital activity of various microorganisms. In this case, electret as a material producing an electrostatic field cannot undergo biodegradation even when modified with various fillers.

In this work we studied biodegradation of electrets based on polymers and fillers.

EXPERIMENTAL

In our studies we used shockproof polystyrene (SPPS) of 0801 brand [GOST (State Standard) 20250–89E] and potato starch (GOST 7699–78).

The polymer and filler were mixed in a Brabender blender at 190±2°C for 5 min. The composite plates with a thickness of 0.8 mm were pressed in accordance with GOST 12019–66 at 190±5°C for 5 min. Then, the resulting plates were heated at 100°C for 10 min and cooled in the field of the negative corona discharge. The corona discharge was obtained with an electrode of 196 needles uniformly distributed over the square area (7 × 7 cm). The polarization voltage and time were 35 kV and 60 s, respectively.

The electret and straight polymer plates were stored in paper envelops at ambient temperature and humidity. The electret characteristics were measured every day on an IPEP-1 meter whose operation is based on intermittent shielding of the measuring probe located at some distance from the electret surface. The measurement errors of the surface potential V_s, electric field strength E, and surface density of the electric charges σ_{sp} were no more than 3%.

To perform the biodegradation studies, the plate was placed into a Petri dish with the Saburo model culture medium containing spores of *Aspergillus niger* mycelial fungi. The biodegradation was monitored by the outward appearance and weight loss of the plates.

Shockproof polystyrene is one of the most widely used structural polymeric materials. However, its electret properties are analyzed only in a few studies [10, 11]. At the same time, corona electrets based on polystyrene, exhibiting high electret properties, were studied fairly extensively [6–8, 12, 13]. Electrets with a stable external electric field are prepared by corona discharge using specifically nonpolar polymers, which are characterized by the presence of the energy trap of charge carriers (impurity ions), free polymer volume, and specific surface defects formed in the course of oxidation. It should be noted that shockproof polystyrene has a two-phase structure typical for composites in which the matrix phase of polystyrene incorporates microgel particles

of a graft copolymer, butadiene rubber. The phase boundary also acts as an efficient trap of charge carriers. Addition of a filler into the polymer gives rise to new levels of charge carrier trapping at the polymer–filler boundary and changes the energy depth of the existing levels, which significantly alters the electret properties [6–8, 14–16].

To evaluate the effect of starch on the properties of shockproof polystyrene, we prepared composites of the polymer and filler of various compositions (Figs. 1, 2). As can be seen, as the starch content is increased, the surface potential, electric field strength, and specific surface density of the electric charges of the polystyrene composites increase. This is due to the appearance of the Maxwell–Wagner polarization at the phase boundary, which noticeably affects formation and transformation of the electret state in heterogeneous systems.

The observed increase in V_s, E, and σ_{eff} of the shockproof polystyrene with increasing filler content can probably be explained as follows. The starch dipole molecules act as traps of the injected charges, attracting and holding them owing to the Coulomb forces, i.e., starch is the source of traps of the injected charge carriers. Shockproof polystyrene, exhibiting low electrical conductivity and forming a dispersion medium, hinders depolarization and determines high stability of the electret properties of the polystyrene composites. The above mechanism is typical for blends of polar and nonpolar polymers [17].

Thus, addition of starch as a filler promoting biodegradation of polymers improves the electret properties of shockproof polystyrene. However, as shown previously, the electric fields of the polymer corona electrets can negatively affect the biodegradation processes. To study these processes, plates of the straight and electret polystyrene composites were placed in a medium simulating soil and containing spores of *Aspergillus niger* mycelial fungi. The biodegradation was monitored by the outward appearance and weight loss of the plates. For this purpose, at 1-month intervals the sample was taken from the Petri dish, washed, and examined visually with an optical microscope, and the weight changes were measured with an analytical balance (see table).

The outward appearance of shockproof polystyrene and its composites with starch noticeably changes in the course of biodegradation. Before the experiment, all the plates were smooth. After a certain time, roughness and dark small spots appeared

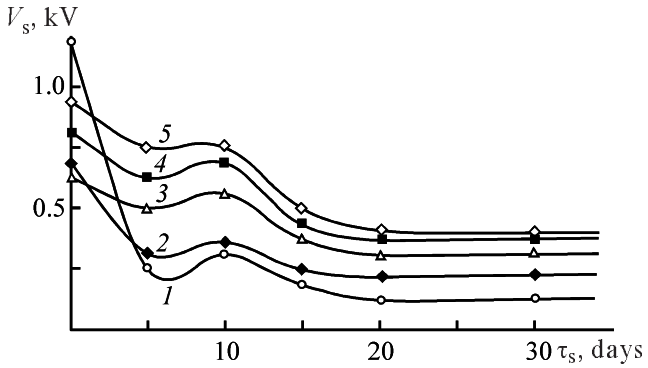


Fig. 1. Surface potential V_s of corona electrets based on (*1*) polystyrene and (*2–5*) its composites as a function of the storage time τ_s. Starch content, %: (*2*) 3, (*3*) 6, (*4*) 9, and (*5*) 12.

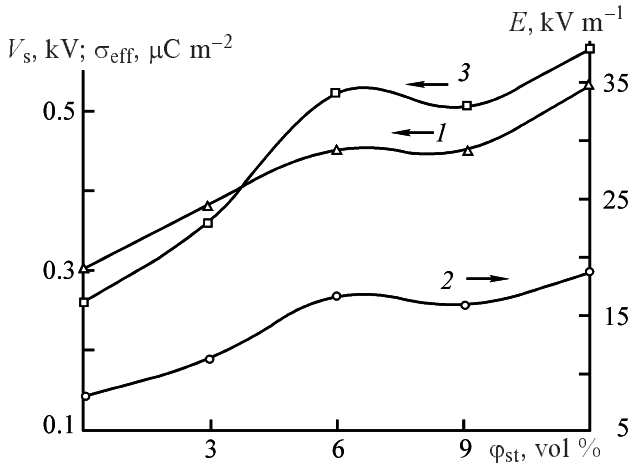


Fig. 2. (*1*) Surface potential V_s, (*2*) electric field strength E, and (*3*) effective surface density of electric charges σ_{eff} of corona electrets based on polystyrene and starch on the 20th day of storage, as functions of the filler content φ_{st}.

on the surface of the polystyrene plates with a high starch content (more than 6 vol %), and their edges became uneven. Then the plates became porous and dark and in some cases were broken on removal from the model system. However, no complete degradation of the composites in the Saburo medium was observed even after storage for 9 months.

It should be noted [18] that biodegradation of polymer composites with starch proceeds by the following mechanism. In the presence of soil moisture, starch nuclei swell. In the process, the polymer surface area increases, it is hydrolyzed and coated with glucose, which promotes formation of peroxides and hydroperoxides initiating degradation of the polymer chains. Moreover, observed increase in the volume of starch nuclei can initiate mechanical degradation of the polymer macromolecules. This is

Relative changes in the weight of polystyrene plates Δm and their outward appearance in the course of storage in the Saburo model culture medium

Composition	Straight plates				Electret plates			
	Δm, % after storage for indicated period, months							
	0	3	6	9	0	3	6	9
SPPS	100	101	101	101	100	100	99	98
SPPS + starch, %:								
3	100	100	97	95	100	99	95	92
6	100	94	86	79	100	94	82	70
9	100	91	83	70	100	91	69	60
12	100	91	71	61	100	89	74	53

especially important for polystyrene whose macromolecules are characterized by low flexibility. The bacteria and fungi feeding on starch also assimilate the resulting oligomer molecules.

As seen from the experimental data on changes in the plate weight after storage in the Saburo solution (see table), the electric field of corona electrets did not affect biodegradation. On the contrary, the rate of biodegradation of the corona electrets was significantly higher. This is probably due to the fact that certain oxidation and even slight breakdown of the polymer macromolecules occur in the course of treatment of shockproof polystyrene composites in a corona discharge. As shown previously [19], the molecular weight of polymers decreases with increasing duration of treatment in an electric field. This phenomenon can strongly facilitate assimilation of the materials studied by soil microorganisms.

The electret charge of the polystyrene composites after storage in wet media (such as the Saburo system) is rapidly relaxed, which is due to an increase in the surface electrical conductivity of the polymers and preferable relaxation of the homocharge in the surface and near-surface electret layers [12]. Hence, the effect of the electric field of the electret decreases and even disappears with time. Our studies suggest that, after storage of the electret plates in the Saburo medium for 1 month, V_s, E, and σ_{eff} decrease to zero, i.e., the electret state of the polystyrene composite does not prevent their assimilation by microorganisms.

CONCLUSIONS

(1) The surface potential, electric field strength, and specific surface density of the electric charges of the corona electrets based on composites of shockproof polystyrene with starch increase with increasing filler content, which is due to the appearance of the Maxwell–Wagner polarization at the phase boundary.

(2) Composites of shockproof polystyrene with a starch content exceeding 6 vol % are biodegradable. With increasing content of the filler, the biodegradation rate increases.

(3) Biodegradation of polystyrene corona electrets proceeds at a high rate owing to the degradation of the polymer macromolecules under treatment of the composites in a corona discharge. This phenomenon strongly facilitates assimilation of the polymer materials by soil microorganisms.

(4) The electret charge of the polystyrene composites does not affect their assimilation by microorganisms, because it is rapidly relaxed on storage of the corona electrets in a wet medium.

REFERENCES

1. *Electrets*, Sessler, G.M., Ed., Berlin: Springer, 1980.
2. Pinchuk, L.S. and Gol'dade, V.A., *Elektretnye materially v mashinostroenii* (Electret Materials in Machine Building), Gomel: Infotribo, 1998.
3. Lushcheikin, G.A., *Polimernye elektrety* (Polymeric Electrets), Moscow: Khimiya, 1984.
4. Suvorova, A.I., Tyukova, I.S., and Trufanova, E.I., *Usp. Khim.*, 2000, vol. 69, no. 5, pp. 494–503.
5. Fomin, V.A. and Guzeev, V.V., *Plast. Massy*, 2001, no. 2, pp. 42–46.
6. Galikhanov, M.F., Eremeev, D.A., and Deberdeev, R.Ya., *Zh. Prikl. Khim.*, 2003, vol. 76, no. 10, pp. 1696–1700.

7. Galikhanov, M.F., Eremeev, D.A., and Deberdeev, R.Ya., *Vopr. Materialoved.*, 2003, no. 2, pp. 32–38.
8. Galikhanov, M.F., *Mekh. Kompoz. Mater. Konstr.*, 2005, vol. 11, no. 2, pp. 199–208.
9. Makarevich, A.V., Pinchuk, L.S., and Gol'dade, V.A., *Elektricheskie polya i elektroaktivnye materially v biotekhnologii i meditsine* (Electric Fields and Electroactive Materials in Biotechnology and Medicine), Gomel: IMMS Nats. Akad. Nauk Bel., 1998.
10. Nesolenaya, L.G., Dedovets, G.S., and Kondratovich, A.A., *Khim. Tekhnol.: Nauchno-Proizv. Sb.*, 1973, no. 3 (69), pp. 15–16.
11. Galikhanov, M.F., Aitova, L.M., Borisova, A.N., et al., *Plast. Massy*, 2007, no. 4, pp. 25–27.
12. Shuvaev, V.P., Turyshev, B.I., Romanovskaya, O.S., et al., *Vysokomol. Soedin., Ser. A*, 1977, vol. 19, no. 3, pp. 603–606.
13. Singh, R. and Datt, S.C., in *Proc. 5th Int. Symp. on Electrets*, Heidelberg, 1984, pp. 191–195.
14. Vertyachikh, I.M., Pinchuk, L.S., and Tsvetkova, E.A., *Vysokomol. Soedin., Ser. B*, 1987, vol. 29, no. 6, pp. 460–463.
15. Zhang, H., Yang, Q., Wang, W., et al., in *Proc. 9th Int. Symp. on Electrets*, Shanghai (China), 1996, pp. 323–326.
16. Goldade, V.A., Kravtsov, A.G., Pinchuk, L.S., et al., in *Proc. Int. Conf. on Advances in Processing, Testing and Application of Dielectric Materials*, 2001, pp. 76–79.
17. Galikhanov, M.F., Muzibullin, M.N., and Deberdeev, R.Ya., *Plast. Massy*, 2005, no. 3, pp. 8–10.
18. Barashkov, N.N., *Polimernye kompozity: poluchenie, svoistva, primenenie* (Polymer Composites: Preparation, Properties, and Use), Moscow: Nauka, 1984.
19. Ragimov, Ya.G., Abasov, S.A., Aliguliev, R.M., et al., *Vysokomol. Soedin., Ser. B*, 1982, vol. 24, no. 6, pp. 406–409.

ISSN 1070-4272, Russian Journal of Applied Chemistry, 2008, Vol. 81, No. 7, pp. 1262–1266. © Pleiades Publishing, Ltd., 2008.
Original Russian Text © S.A. Zhil'tsov, S.A. Bulgakova, Yu.D. Semchikov, 2008, published in Zhurnal Prikladnoi Khimii, 2008, Vol. 81, No. 7, pp. 1182–1186.

MACROMOLECULAR CHEMISTRY AND POLYMERIC MATERIALS

Effect of Organosilicon Chain-Transfer Agents on the Heat Resistance of Vinyl Polymers

S. A. Zhil'tsov, S. A. Bulgakova, and Yu. D. Semchikov

Research Institute of Chemistry, Lobachevsky Nizhni Novgorod State University, Nizhni Novgorod, Russia

Received November 28, 2007

Abstract—The effect exerted on the resistance of polymers to thermal oxidation degradation by organosilicon hydrides used as chain-transfer agents in polymerization of styrene, methyl methacrylate, and vinyl acetate was examined.

DOI: 10.1134/S1070427208070264

The function of chain-transfer agents is not restricted to a decrease in the molecular weight (MW) of polymers to a level sufficient for their processing through melts. Modification of polymers at terminal functional groups can impart to them new valuable properties. For example, with such functional chain-transfer agents as organosilicon hydrides (OSHs), the radiation sensitivity of poly(methyl methacrylate) as positive radiation resist was increased by a factor of 2 [1]. OSHs also affect the physical properteis of polymers such as the glass transition point and density [2]. Furthermore, multifunctional OSHs open the possibility of preparing block and graft copolymers [3]. Assuming that OSHs can cause morphological changes in the polymer structure and thus affect their heat resistance, which is very sensitive to such changes, we examined in this study the effect of OSHs on the thermal oxidative degradation of vinyl polymes: PMMA, polystyrene (PS), and poly(vinyl acetate) (PVA).

EXPERIMENTAL

For thermal oxidative degradation experiments, we prepared samples of PMMA, PS, and PVA in the presence of OSHs indicated below.

OSH formula	Designation
(*t*-BuO)$Me_2SiSiMe_2H$	DS-1
$H_2MeSiSiMeH_2$	DS-2
$(Me_3SiO)_2SiMeH$	DS-3
$H_3SiCH_2CH_2SiH_3$	DS-5
$Me_3SiSiMe_2H$	DS-9
$(HMe_SiO)Me_2SiSiMe(OSiMe_2H)_2$	DS-11
$(Me_3Si)_3SiH$	DS-15
$(Me_3Si)_2SiMeH$	DS-18
H(*i*-Pr)$_2$SiOSi(*i*-Pr)$_2$H	DS-20
$(Me_3SiO)_3SiH$	DS-21
$MePhSiH_2$	DS-23
$PhSiH_3$	DS-24
$(Me_3SiCH_2)_3SiH$	DS-26
Ph_3SiH	DS-27

Methyl methacrylate was purified by vaporization–condensation in a vacuum. Styrene was washed with an alkali solution to remove hydroquinone, dried over calcium chloride and then over calcium hydride, and vacuum-distilled. Vinyl acetate was purified by distillation at atmospheric pressure. The initiator, azobis(isobutyronitrile) (AIBN) was recrystallized from ethanol. The OSHs used as chain-transfer agents were prepared by published procedures [4]. The polymers were prepared by radical polymerization in the bulk to high conversions at 60°C in the presence of 0.005 M AIBN in sealed deoxygenated ampules. The OSH concentration in the monomers was varied from 0 to 2.5 wt %. The polymers were purified by triple reprecipitation from acetone (PVA, PMMA) and chloroform (PS) into petroleum ether and dried in a vacuum at 30°C to constant weight.

The molecular weight of the polymers was determined with an Ubbelohde viscometer using the Mark–Kuhn–Houwink equation $[\eta] = K_\eta M_\eta^\alpha$ with the constants K_η and α taken from a reference book [5]. Thermal oxidative degradation was studied at

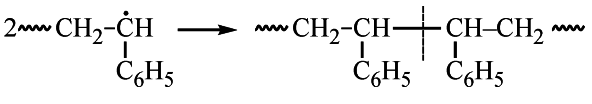
290 ± 5 (PS) and 280 ± 5°C (PMMA, PVA) by thermal gravimetric analysis in the isothermal mode on an installation consisting of a furnace, a torsion balance, and a contact thermometer. The degree of degradation was determined by graphical differentiation of the curves of weight loss vs. time in the time point of 30 min.

Pyrolysis of PS samples was performed at 290°C for 1 h in evacuated sealed glass ampules with a branch in which the decomposition products were condensed at liquid nitrogen temperature. The products were analyzed by gas chromatography–mass spectrometry (GC–MS) on a GC 8000/MD 800 device at an injector temperature of 250°C. The temperature of the chromatographic column HP 5MS, 60 m long and 0.32 mm in diameter, was raised from 70 to 250°C at a rate of 8 deg min^{-1}. The carrier gas was helium of M60 brand. The mass chromatograms were recorded in the range of *m*/*z* 33–350. The substances were identified using the NIST and Wiley databases and the MASSLAB software.

The ^1H NMR spectra of 2% solutions of PMMA in $CDCl_3$ were recorded at 50°C on a Tesla BS-567A NMR Fourier spectrometer operating at 100 MHz. The probability of *meso* addition in the course of MMA polymerization was calculated from the ratio of the areas of CH_3 signals belonging to the hetero- and syndiotactic triads in PMMA.

Figure 1 shows the dependence of MW of polystyrene samples prepared with DS-2 additive and without it on the thermal degradation time. It can be seen that, at similar shape of the curves, the extent to which the MW of the polymer decreases depends on the preparation conditions. The decrease in MW is more pronounced for the PS sample prepared without chain-transfer agent (curve *1*). For the polymer modified with the chain-transfer agent, the limiting MW is considerably higher (curve *2*).

The results obtained can be readily accounted for on the basis of concepts of the recombination mechanism of bimolecular termination of macroradicals in radical polymerization of styrene, with the formation of weak bonds in polymer macromolecules:



According to classical concepts [6], a sharp decrease in MW of the polymer in the initial step of the process, followed by stabilization, indicates that the decomposition of PS macromolecules is initiated by weak bonds. The chain transfer in polymerization

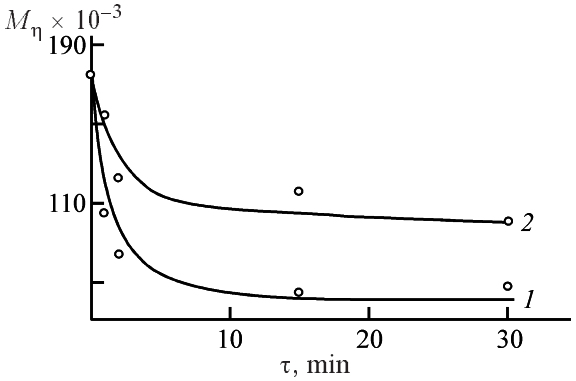


Fig. 1. M_η of polystyrene as a function of the time τ of thermal oxidative degradation at 290°C for the samples prepared by bulk polymerization in the presence of (*1*) 0.05 M AIBN and (*2*) 0.005 M AIBN + 0.4 wt % DS-2.

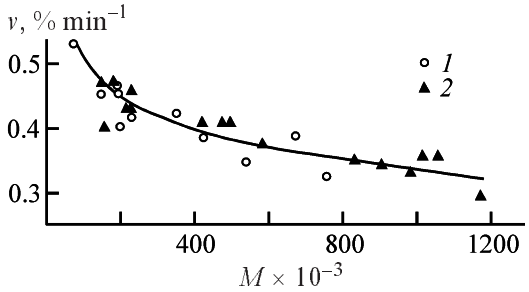


Fig. 2. Rate *v* of thermal oxidative degradation at 290°C as a function of the initial *M* of the polymer for PS samples prepared in the presence of (*1*) various concentrations of AIBN and (*2*) hydrides Et_3SiH, DS-2, DS-5, DS-11, DS-20, DS-23, DS-26, and DS-27.

leads to a decrease in the contribution of bimolecular termination involving two propagating styrene radicals and hence in the number of weak head-to-head bonds. As a result, the concentration of radicals initiating the depolymerization decreases.

Figure 2 shows how the rate of thermal oxidative degradation of PS correlates with its MW for the samples prepared at various concentrations of the initiator and chain-transfer agents. It can be seen that, in both cases, with an increase in MW of the polymer the rate of formation of volatiles decreases to an equal extent. Thus, in thermal oxidative degradation of PS, the stabilizing effect exerted by OSHs with respect to variation of MW is not noticeably manifested in the degradation rates. This is apparently due to the fact that in macromolecules modified with OSH, depending on the chemical structure of the chain-transfer agent, one more type of terminal bonds appears: Si–Si, Si–C, or Si–H. These bonds are less strong than C–C bonds [7, 8]. Therefore, the relative content of weak bonds is close in both cases, and hence the total amount of volatile

Table 1. Yield of major pyrolysis products from PS samples prepared in the presence of chain-transfer agent and without it

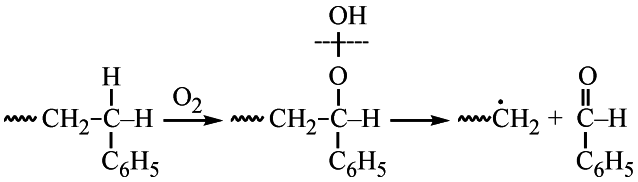
PS pyrolysis product	Yield of pyrolysis products, %	
	PS without additive	PS + Et_3SiH
Styrene	78	76
Benzaldehyde	7.5	21
Styrene dimer	2.6	0.22

Table 2. Microstructure of PMMA samples prepared in the presence of various silicon hydrides

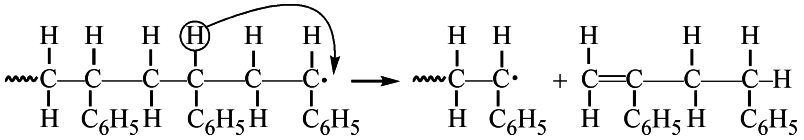
Chain-transfer agent	Probability of *meso* addition	Fraction of triads		
		syndio	*iso*	*hetero*
None	0.22	0.6084	0.0484	0.3432
DS-1	0.24	0.5776	0.0576	0.3648
DS-2	0.24	0.5576	0.0576	0.3648
DS-9	0.23	0.5881	0.0543	0.3576

degradation products is also close. However, weak bonds of the second type lead to chain cleavage at its termini, which does not appreciably affect the MW of the polymer. Therefore, as noted above, decrease in MW in the course of thermal degradation is more significant for PS prepared without OSH.

The GC–MS studies of volatile pyrolysis products of PS samples prepared without additives and in the presence of triethylsilane showed that the presence of fragments of organosilicon chain-transfer agents in the polymer chain strongly affects the composition of these products. As seen from Table 1, the yield of benzaldehyde noticeably increases in this case. This may be due to increased content on chain termini of units with secondary carbon atom, formed by chain transfer. Therefore, specifically these radicals primarily participate in oxidation leading to the formation of benzaldehyde:



High yield of benzaldehyde is also certainly favored by the chain transfer in the step of thermal degradation involving a Si–H bond of polyfunctional OSHs. Furthermore, the chain microstructure can also affect the occurring reactions, especially intramolecular reactions such as chain transfer in the course of PS degradation with the participation of the hydrogen atom bonded to the tertiary carbon atom in the backbone:



Specifically this reaction determines the yield of styrene dimers in degradation of the polymer: The yield of the dimers is the higher, the higher the probability of intramolecular chain transfer. According to Table 1, for the modified chains this reaction is less characteristic, which may be due to lesser accessibility of the hydrogen atom as a result of changes in the polymer microtacticity. The latter fact was revealed in NMR studies of PMMA samples prepared in the presence of OSHs of various structures (Table 2).

A study of the thermal degradation of PMMA revealed a similar correlation of the degradation rate with MW of the polymer as for PS samples (Fig. 3). According to [6], the thermal degradation of PMMA occurs by the mechanism similar to that of thermal degradation of PS. The reaction starts with cleavage of weak bonds, which is followed by depolymerization of the free-radical fragments. In this case, the weak bonds are terminal allyl groups formed by disproportionation of radicals in synthesis of the polymer. A decrease in the number of events of bimolecular termination due to chain transfer, on the one hand, leads to a decrease in the amount of allyl groups on the chain termini and, on the other hand, gives rise to another type of labile bonds responsible for PMMA depolymerization. As a result, the rate of PMMA degradation increases with a decrease in MW. It is interesting that data for such chain-

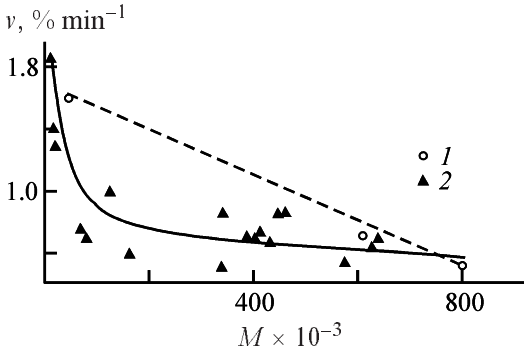


Fig. 3. Rate v of thermal oxidative degradation at 280°C as a function of the initial M of the polymer for PMMA samples prepared in the presence of (*1*) various concentrations of AIBN and (*2*) chain-transfer agents Et_3GeH, Et_3SiH, $C_{12}H_{23}SH$, DS-2, DS-3, DS-5, DS-15, DS-18, DS-20, DS-23, DS-24, and DS-26.

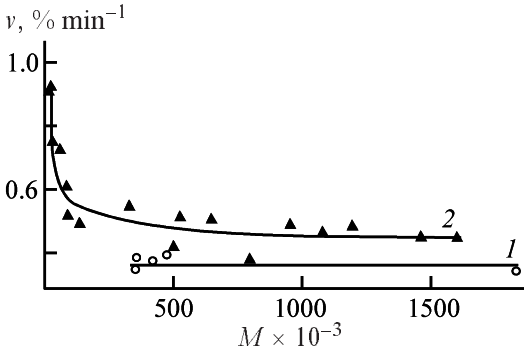
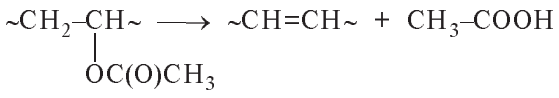


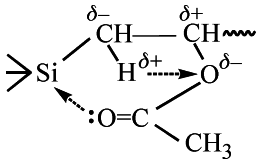
Fig. 4. Rate v of thermal oxidative degradation at 280°C as a function of the initial M of the polymer for PVA samples prepared in the presence of (*1*) various concentrations of AIBN and (*2*) chain-transfer agents Et_3SiH, DS-5, DS-9, DS-11, DS-15, and DS-21.

transfer agents as Et_3GeH and $C_{12}H_{23}SH$ also fall on the common curve. This fact can be readily accounted for, taking into account that the forming covalent bonds C–Ge and C–S are less strong than the C–C bonds in the backbone, because of longer interatomic distance. Along with the strength of terminal bonds, increased fraction of *iso* triads in PMMA samples prepared in the presence of OSHs (Table 2) can give rise to additional strain in the polymer chain and thus decrease the heat resistance.

Thermal degradation of PVA, in contrast to the cases considered above, occurs not via cleavage of the C–C bonds in the backbone but via elimination of pendant substituents by the molecular mechanism with practically 100% yield of acetic acid:



According to the known concept [6], this reaction is not random but is initiated on the macromolecule terminus and propagates along the chain toward the other terminus. Having studied in detail the kinetics of thermal degradation of PVA in a vacuum, Grassie showed [6] that all terminal groups of the polymer, both saturated and unsaturated, formed by disproportionation and chain transfer, participate in the degradation to an equal extent. Therefore, we can expect a decrease in the degradation rate with increasing MW of PVA, due to a decrease in the concentration of terminal groups initiating the degradation. As seen from Fig. 4 (curve *2*), the rate of thermal deacetylation of PVA samples modified with silicon hydrides, indeed, decreases with an increase in MW of the polymer, but only up to M ~200000, and at higher MW the degradation rate becomes essentially independent of MW. Comparison of curves *1* and *2* in Fig. 4 allows an important conclusion that, at equal MW, the polymers prepared in the presence of the chain-transfer agents are less thermostable than those prepared without modifiers. This result can be attributed only to the fact that electrophilic organosilicon fragments activate the PVA degradation via formation of complexes



with the formation of a terminal unsaturated bond and release of acetic acid. In the presence of the latter, the thermal degradation of PVA becomes autocatalytic [7, 8]. This hypothesis is well consistent with the available data [9] that thermal degradation of PVA is accelerated by electrophilic agents.

CONCLUSIONS

(1) Organosilicon chain-transfer agents introduced into polymers accelerate formation of volatile degradation products in thermal oxidative degradation of poly(vinyl acetate) and poly(methyl methacrylate) at 280°C. At the same time, modification of polystyrene chains with organosilicon hydrides does not affect the rate of formation of volatile products in thermal oxidative degradation, but noticeably increases the yields of styrene dimers and benzaldehyde.

(2) Chain-transfer agents can alter the polymer microstructure, thus affecting its heat resistance.

REFERENCES

1. Bulgakova, S.A., Semchikov, Yu.D., Semenov, V.V., et al., *Vysokomol. Soedin., Ser. B*, 1995, vol. 37, no. 4, p. 706.
2. Bulgakova, S.A., Lopatin, A.Ya., Luchin, V.I., et al., *Poverkhn. Rentgen., Sinkhrotr., Neitron. Issled.*, 2000, no. 1, p. 140.
3. Bulgakova, S.A., Mazanova, L.M., Semchikov, Yu.D., and Gribkov, B.A., *Vysokomol. Soedin., Ser. A*, 2006, vol. 48, no. 5, p. 456.
4. Basant, V., Chalovsky, V., and Rathousky, J., *Organosilicon Compounds*, Prague: Czechoslovak Acad. Sci., 1973, vol. 4.
5. Lipatov, Yu.S., Nesterov, A.E., Gritsenko, T.M., and Veselovskii, R.A., *Spravochnik po khimii polimerov* (Handbook of Polymer Chemistry), Kiev: Naukova Dumka, 1971.
6. Grassie, N., *Chemistry of High Polymer Degradation Processes*, London: Butterworths Scientific, 1956.
7. Razuvaev, G.A., Khokhlova, L.V., Troitskii, B.B., and Dubova, Z.B., *Vysokomol. Soedin., Ser. B*, 1973, vol. 15, no. 7, p. 537.
8. Troitskii, B.B., Khokhlova, L.V., and Bortnikov, G.N., *J. Polym. Sci.: Polym. Symp.*, 1973, vol. 42, part 3, p. 1363.
9. Troitskii, B.B. and Troitskaya, L.S., in *Fiziko-khimicheskie osnovy sinteza i pererabotki polimerov: Mezhvuzovskii sbornik* (Physicochemical Principles of Polymer Synthesis and Processing: Intercollegiate Coll.), Gor'kii: Gor'k. Gos. Univ., 1985, p. 3.

ISSN 1070-4272, Russian Journal of Applied Chemistry, 2008, Vol. 81, No. 7, pp. 1267–1271. © Pleiades Publishing, Ltd., 2008.
Original Russian Text © V.I. Sharypov, V.P. Kiselev, N.G. Beregovtsova, M.B. Bugaenko, B.N. Kuznetsov, 2008, published in Zhurnal Prikladnoi Khimii, 2008, Vol. 81, No. 7, pp. 1187–1191.

MACROMOLECULAR CHEMISTRY AND POLYMERIC MATERIALS

Road Asphalt Modifiers Based on Oil-Resistant Rubbers and Products of Thermal Transformations of Coals

V. I. Sharypov, V. P. Kiselev, N. G. Beregovtsova, M. B. Bugaenko, and B. N. Kuznetsov

Institute of Chemistry and Chemical Technology, Siberian Branch, Russian Academy of Sciences, Krasnoyarsk, Russia

Institute of Architecture and Building, Siberian Federal University, Krasnoyarsk, Russia

Received November 8, 2007

Abstract—The properties of asphalt binder modifiers prepared by dissolving butadiene–acrylonitrile rubbers and their production waste in liquid products of heat treatment of various brands of coal were studied.

DOI: 10.1134/S1070427208070276

The durability of asphalt pavings is mainly determined by their crack resistance. This parameter, especially in Siberia and northern Russia, depends on low-temperature properties of asphalt, i.e., on its frost resistance. The low-temperature properties can be considerably improved by modifying asphalts with additions of synthetic polymers. Synthetic rubbers are widely used as structuring modifiers of asphalts [1–3].

A specific feature of rubbers distinguishing them from other polymers used for modifying asphalts is the capability for large elastic strains. Rubbers consist of macromolecular chains in which thousands of monomeric units are linked in series by covalent bonds. High elasticity of rubbers is due to intrinsic mobility of the system, provided by weak intermolecular interaction of the chains and low crystallinity [4, 5]. Additions of rubbers improve the physicochemical properties of asphalt, making it less brittle, more crack-resistant, and more elastic [6–10].

In polymer–asphalt composites, butadiene–styrene, polyisoprene, polybutadiene, and other rubbers are widely used [1–3, 11–13]. It is well known that the group composition of asphalts determines their properties. Asphaltenes are responsible for the hardness and high softening point; resins, for elasticity and penetration; oils are a medium in which the resins are dissolved and asphaltenes swell [14]. The polymer amount in a polymer–asphalt binder should be thoroughly balanced, because certain amount of asphaltenes is required for forming an associate with the polymer, which increases the yield resistance and softening point. The aromaticity of malthenes (sum of resins and oils) is also important. Increased aromaticity predetermines decreased softening point of the polymer–asphalt binder [15].

An important aspect of modification is the way of introducing rubber into asphalt. In some procedures, synthetic rubbers or their production wastes are added directly to asphalts [4–6]. Along with advantages, such binders also have certain drawbacks: nonuniformity of the composition and low stability in the hot state. Furthermore, the use of nitrile brands of rubber for asphalt modification is limited by their practical insolubility in asphalts [16]. This fact is of particular importance when considering the problem of utilizing wastes from rubber production. In some studies, to eliminate these drawbacks, rubbers are initially dissolved in organic solvents such as kerosene, diesel fuel, black oil, shale oil, or toluene [7, 17, 18], with the subsequent addition of the resulting mixture to petroleum asphalt.

In this study we examined the properties of asphalt binder modifiers prepared from butadiene–acrylonitrile rubbers. As solvents for these rubbers we used liquid products of heat treatment of coals of various brands.

EXPERIMENTAL

To prepare the modifier, we chose a commercial sample of SKN-40 ASM-E butadiene–acrylonitrile rubber [TU (Technical Specification) 38.30313–98] and waste (coagulum) from production of BNKS-28

Table 1. Characteristics of solvents

Solvent	Elemental composition, wt %				Density, g cm^{-3}
	C	H	N	S	
Semicoking tar	87.85	8.95	0.35	0.31	1.02
Products of thermal dissolution of brown coal	87.50	9.30	0.40	0.40	1.01

Table 2. Group composition of modifiers and asphalt

Sample, composition, wt %	Content, wt %		Substances insoluble in benzene, wt %
	malthenes	asphaltenes	
M-1: coagulum 30, coal semicoking tar 70	66.3	23.7	10.0
M-2: rubber 30, high-boiling products of brown coal hydrogenation and petroleum residues 70	62.7	22.9	14.4
M-3: coagulum 30, high-boiling products of thermal dissolution of brown coal and petroleum residues 70	39.8	47.4	12.8
BND 90/130 asphalt	81.6	18.0	0.4

AMN rubber (TU 38.30313–98) from the Krasnoyarsk Plant of Synthetic Rubber. As solvents we used coal semicoking tar of D brand (TU 2453-001-22931414–96) from the Leninsk-Kuznetskii Semicoking Plant and a high-boiling (>350°C) liquid product of thermal dissolution of V2 brand brown coal from the Kansk–Achinsk coal fields. The coal was subjected to thermal dissolution in petroleum residues at 400°C in an autoclave. The experimental procedure is described elsewhere [19]. Some characteristics of solvents are given in Table 1.

Rubber samples were preliminarily crushed to a particle size of 10–20 mm and dissolved at 100–120°C with continuous stirring. The resulting rubber-containing component was used as modifier for BND-90/130 petroleum asphalt products by the Achinsk Oil Refinery, Joint-Stock Company. The physicochemical characteristics of the modifiers, initial asphalt, and asphalt–rubber binders obtained were determined by standard procedures applied to petroleum asphalts [20–23]. The aging resistance of organic binders was determined as resistance to heating at 163°C for 5 h [24], evaluated by the weight loss and changes in the penetration and softening point.

The IR spectra were recorded with a Bruker Vektor 22 spectrometer in the range 500–3500 cm^{-1} from thin films.

Studies of the solubility of the chosen rubbers in liquid products of thermal transformations of coals showed that the optimal concentration of the polymers in solution is 30 wt %. At this concentration, the process occurs within less than 1 h, and a homogeneous mixture readily miscible with petroleum asphalts at 100–120°C is formed.

The group composition of bitumen modifiers is given in Table 2. Data for BND 90/130 petroleum asphalt, obtained by averaging the results of laboratory tests of commercial batches of BND 90/130 asphalt produced during a period of 2 years, are given for comparison.

Typical IR spectra of the asphalt and three samples of the modifiers are shown in Fig. 1. The spectra of all the modifiers contain an absorption band in the range of stretching vibrations of the C≡N group at 2240 cm^{-1}, characteristic of nitrile rubbers. The spectra show that all the modifiers, in contrast to petroleum asphalt mainly consisting of paraffin hydrocarbons, are complex mixtures of organic substances with a high content of aromatic compounds. This is confirmed by high intensity of absorption bands in the range of stretching vibrations of C–H bonds in aromatic structures at 3050 cm^{-1} and of out-of-plane bending vibrations of C–C bonds in aromatic rings at 1590 cm^{-1}. The high content of aromatic compounds in the modifiers is well

consistent with the results of group analysis (Table 2) and is, apparently, the consequence of using products of heat treatment of coals and lignites as solvents in preparing the modifiers. One more significant difference of the modifiers from the asphalt is the high content of oxygen-containing compounds giving rise to strong bands in the ranges of absorption of hydroxy and carbonyl groups (3600–2100, 1700–1550 cm^{-1}) and at 1000–1300 cm^{-1} (phenolic hydroxyls, ethers, alcohols).

Comparison of the spectra of various modifiers with each other suggests considerably higher content of oxygen-containing compounds (alcohols, acids) in M-3 modifier. This is apparently associated with the procedure and temperature conditions of preparation of coal solvents for modifiers.

The results of tests of BND 90/130 asphalt with additions of modifiers are given in Tables 3 and 4. These data show that M-1 and M-2 modifiers considerably decrease the brittle point of asphalt and increase the extensibility, especially at 0°C. The use of such modifiers allows preparation of asphalt concrete resistant to cracking in the winter period. The effect of M-3 modifier on brittle point is insignificant, but this modifier increases to a greater extent the extensibility of the asphalt, making it more plastic.

Measurements of the ring-and-ball softening point (Table 4) showed that its change for the initial asphalt after heating, compared to the value before heating, is beyond the limit prescribed by GOST (State Standard), 6°C, i.e., the asphalt used in the study does not pass the aging test. Samples of the composite binder with the modifier content exceeding 5 (M-1, M-2) and 2.5 wt % (M-3) are also unstable in this test. Samples containing 5 wt % M-1 or M-2, or 2.5 wt % M-3 showed the change in the softening point by 2.5, 5.5, and 5.5°C, respectively. These data show that the modifiers inhibit oxidative aging of the organic binder. Measurements of the change in the penetration upon aging (Table 4) show that heating of composite binder samples containing no more than 5 wt % modifiers does not affect this parameter significantly.

Figure 2 shows the time dependence of the weight loss of composite binders modified with products of thermal dissolution of coal, lignite, and synthetic elastomers, monitored in the course of aging tests at 163°C. As seen from Fig. 2, additions of M-2 and especially M-3 modifiers cause larger weight loss upon heating, compared to the initial asphalt.

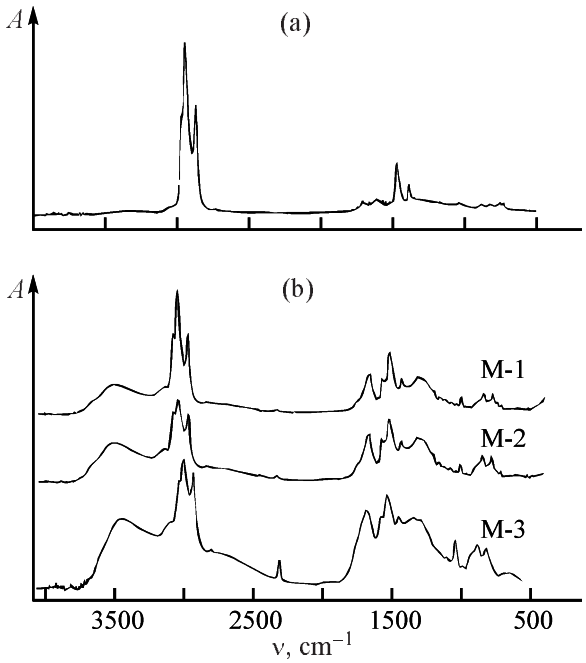


Fig. 1. IR spectra of (a) BND 90/130 asphalt and (b) M-1, M-2, and M-3 modifiers of the asphalt–rubber binder. (*A*) Absorption and (ν) wavenumber.

Apparently, addition of 7.5 wt % modifiers and more lead to thinning of asphalt, and evaporation of low-boiling fractions of both the asphalt and modifiers becomes the prevalent process. This means that the optimal content of additives in the modified asphalt should not exceed 5 wt %.

Among the modifiers obtained, M-3 is the most

Table 3. Physicomechanical properties of asphalt and a composite binder based on asphalt and products of thermal dissolution of a mixture of brown coal and synthetic polymers

Binder composition, wt %	Fraas brittle point, °C	Extensibility, mm, at indicated temperature, °C	
		25	0
Initial BND 90/130 asphalt	–20.6, no higher than –17	75	12
Asphalt + modifier:			
5 M-1	–28.5	90	24
10 M-1	–25.0	99	37
5 M-2	–26.0	90	25
10 M-2	–23.0	96	35
2.5 M-3	–21.0	>100	24
10 M-3	–19.5	>100	38

Table 4. Physicomechanical characteristics of the initial asphalt and composite binder based on asphalt and products of thermal dissolution of a mixture of brown coal and synthetic polymers*

Binder	Content of components in binder,** wt %	Before heating		After heating (163°C, 5 h)		
		P_{25}, 0.1 mm units	T_s, °C	weight loss, %	P_{25}, 0.1 mm units	T_s, °C
BND 90/130 asphalt	100	118	44.5	1.14	98	51.5
M-1	10 (asphalt 90)	148	50.5	1.46	112	54.5
M-1	7.5 (asphalt 92.5)	132	49.0	1.22	125	54.0
M-1	5 (asphalt 95)	128	46.5	1.06	120	48.5
M-1	2.5 (asphalt 97.5)	124	47.5	1.04	117	50.5
M-2	10 (asphalt 90)	156	48.5	1.56	104	53.5
M-2	7.5 (asphalt 92.5)	141	44.5	1.39	128	51.0
M-2	5 (asphalt 95)	136	46.0	0.98	98	53.5
M-2	2.5 (asphalt 97.5)	126	47.5	0.96	117	52.5
M-3	10 (asphalt 90)	178	34.9	2.82	149	44.5
M-3	2.5 (asphalt 97.5)	137	42.5	1.89	120	48.0

* (P_{25}) Penetration at 25°C; (T_s) softening point.
** Binder: asphalt + additives 100; M-1, 30 wt % coagulum; M-2, 30 wt % nitrile rubber.

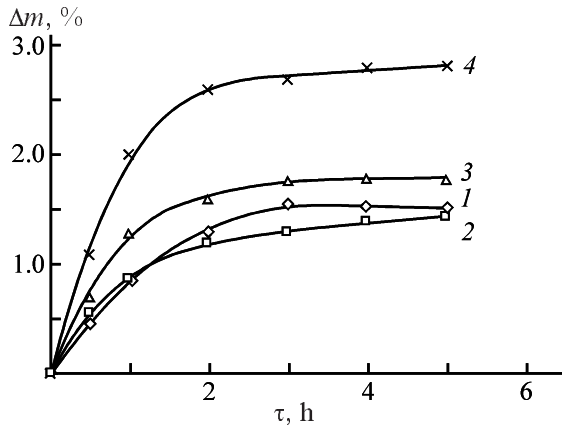


Fig. 2. Weight loss Δm (%) of composite binders modified with products of thermal dissolution of coal, lignite, and synthetic elastomers, monitored in the course of aging tests (163°C). (τ) Heating time. (*1*) Initial BND 90/130 asphalt and (*2–4*) asphalt containing 7.5 wt % modifier: (*2*) M-1, (*3*) M-2, and (*4*) M-3.

fluid (T_s <28°C, P_{25} 250). Therefore, its addition causes pronounced thinning of the asphalt, and the asphalt containing this modifier in an amount of 10% passes to the BND 130/200 grade, which is undesirable for upper layers of the pavement.

CONCLUSIONS

(1) Road asphalt modifiers were prepared by dissolving butadiene–acrylonitrile rubbers and their production waste (coagulum) in liquid products of thermal transformation of coals, characterized by increased aromaticity as compared to products of petroleum origin.

(2) Additions of 2.5–5.0 wt % modifiers obtained to BND 90/130 asphalt decrease its brittle point and enhance the aging resistance.

REFERENCES

1. Polosina-Nikitina, N.S., in *Kriterii ekologichnosti tekhnologicheskikh protsessov i materialov pri ispol'zovanii promyshlennykh otkhodov v dorozhnom stroitel'stve: Obzornaya informatsiya* (Criteria of Environmental Safety of Processes and Materials in Utilization of Industrial Wastes in Road Building: Review), Ser.: *Avtomobil'nye dorogi* (Highways), Moscow: Informavtodor, 1997, issue 4.
2. Akhmetova, R.S., *Sovremennoe sostoyanie proizvodstva i puti povysheniya kachestva bitumov razlichnogo naznacheniya* (Modern State of Production and Ways to Improve the Quality of Asphalts for Various Purposes), Moscow: TsNIITEneftekhim, 1979.
3. Rozental' D.A., Tabolina, L.S., and Fedosova, V.A., in *Modifikatsiya svoistv bitumov polimernymi dobavkami: Obzornaya informatsya* (Modification of Properties of Asphalts by Polymeric Additives: Review), Ser.: *Pererabotka nefti* (Oil Refining), Moscow: TsNIITEneftekhim, 1988.
4. *Entsiklopediya polimerov* (Polymer Encyclopedia), Kargin, V.A., Ed., Moscow: Sov. Entsiklopediya, 1974, vol. 2.

5. *Sinteticheskii kauchuk* (Synthetic Rubber), Garmonov, I.V., Ed., Leningrad: Khimiya, 1983.
6. RF Patent 2167898.
7. RF Patent 2248381.
8. USSR Inventor's Certificate no. 1671671.
9. RF Patent 2132857.
10. RF Patent 2270846.
11. Bratchikov, A.V., Shifris, G.S., and Sharafiev, Kh.F., *Stroit. Mater.*, 1983, no. 3, pp. 23–29.
12. Kisina, A.M., *Izv. Vses. Nauchno-Issled. Inst. Gal. im. B.E. Vedeneeva*, 1983. vol. 167, pp. 37–42.
13. Kutsenko, I.V., in *IX nauchnye chteniya BTISM* (IX Scientific Readings of the Belgorod Techological Inst. of Building Materials), Belgorod, 1987, part 8, pp. 60–64.
14. Rudenskaya, I.M. and Rudenskii, A.V., *Organicheskie vyazhushchie dlya dorozhnogo stroitel'stva* (Organic Binders for Road Building), Moscow: Transport, 1984.
15. Sokolov, A.B. and Levanova, S.V., *Khim. Inter. Ust. Razv.*, 2005, no. 13, pp. 859–862.
16. *Spravochnik rezinshchika: Materialy rezinovogo proizvodstva* (Handbook of Rubber Manufacturer: Materials for Rubber Production), Zakharchenko, P.I., Yashunskaya, F.I., and Evstratov, V.F., Eds., Moscow: Khimiya, 1971, p. 608.
17. RF Patent 2162476.
18. RF Patent 2190579.
19. Sharypov, V.I., Beregovtsova, N.G., Baryshnikov, S.V., and Kuznetsov, B.N., *Khim. Inter. Ust. Razv.*, 2005, no. 13, pp. 655–662.
20. *GOST* (State Standard) *11502–82: Petroleum Asphalts: Method for Determining the Depth of Needle Penetration*.
21. *GOST* (State Standard) *11506–73: Petroleum Asphalts: Method for Determining the Ring-and-Ball Softening Point*.
22. *GOST* (State Standard) *11505–75: Petroleum Asphalts. Method for Determining Extensibility*.
23. *GOST* (State Standard) *11507–78: Petroleum Asphalts: Method for Determining the Fraas Brittle Point*.
24. *GOST* (State Standard) *18180–72: Petroleum Asphalts: Method for Determining the Weight Change after Heating*.

ISSN 1070-4272, Russian Journal of Applied Chemistry, 2008, Vol. 81, No. 7, pp. 1272–1277. © Pleiades Publishing, Ltd., 2008.
Original Russian Text © O.N. Filimonova, M.V. Enyutina, 2008, published in Zhurnal Prikladnoi Khimii, 2008, Vol. 81, No. 7, pp. 1192–1197.

MACROMOLECULAR CHEMISTRY AND POLYMERIC MATERIALS

A Polymeric System Based on Wastes from Production of Butyl Alcohols and KORS Copolymer

O. N. Filimonova and M. V. Enyutina

Voronezh State Academy of Technology, Voronezh, Russia

Received May 23, 2007

Abstract—A polymer system based on KORS copolymer and RS solvent prepared from wastes from production of butyl alcohols was studied. The RS solvent can replace butyl acetate and xylene, with improvement of the physicomechanical properties of the coatings obtained.

DOI: 10.1134/S1070427208070288

Polymeric materials are multicomponent systems based, in the overwhelming majority of cases, on solutions in organic solvents. The preparation conditions and quality of polymeric coatings largely depend on propeties of the starting materials, which should meet the following requirements: possibility of distribution on the substrate surface as a thin layer, capability for film formation, and formation of coatings with the desired properties [1].

Production and use of polymeric materials involves consumption of enormous amounts of organic solvents [2]. Virtually the whole amount of them is irretrievably lost in the course of coating application, giving rise to environmental and economical problems. Powder and water-dispersible polymeric coatings used today solve these problems, but powder polymeric materials are unsuitable for domestic use because they require special equipment for application, and their decorative properties are poor. Water-dispersible polymeric formulations can be efficiently applied only in the warm period of year, and water-soluble surfactants present in them reduce the protective properties of the coatings. Therefore, one of the main avenues of the progress of the varnish-and-paint industry today is the development of polymeric formulations with decreased content of organic solvents, search for new solvents of low toxicity and for new sources of raw materials, and development of new processes for their production [3–5].

The dissolution of film-forming substances is determined by the chemical composition and structure of the film-forming agent and by the chemical nature and thermodynamic characteristics of the solvents used [6, 7].

EXPERIMENTAL

RS solvent can be prepared from wastes from production of butyl alcohols [8]. Its composition was determined by functional analysis and gas–liquid chromatography. The composition and characteristics of major components of RS solvent are given in Table 1. The main component is isobutyl acetate used in the formulations instead of butyl acetate and cyclohexanone. The content of isobutyl acetate in RS solvent reaches in some batches 75 wt %.

Formic and acetic acid esters entering into the composition of RS solvent dissolve cellulose esters, chlorinated rubber, vinyl polymers, and carbinol and other resins; they are well miscible with many solvents used in production of nitrocellulose varnish-and-paint materials (VPMs) [9].

Isomers of butyl alcohols, whose content in the solvent reaches 4.5 wt %, in a mixture with ethanol are used for dissolving urea–formaldehyde oligomers and polyvinylbutyral, and in a mixture with xylene, for dissolving polyacrylates. They are added to the majority of mixed solvents to enhance their solvency, improve the adhesion of coatings owing to a decrease in the surface tension, prevent the films from becoming turbid or white, and facilitate pouring of lacquers and enamels by decreasing their viscosity.

RS solvent contains large amounts of butyl ethers, mainly of dibutyl ether. Butyl ethers are used as solvents for certain film-forming agents [9], mainly

Table 1. Characteristics of components of RS solvent

Component	Weight fraction of component, %	Heat of vaporization, kJ mol^{-1}	Solubility parameter, $(MJ\ m^{-3})^{1/2}$
Isobutyl acetate	50.0–75.0	39.25	16.62
Butyl acetate	3.0–15.0	40.56	17.02
Isobutyl alcohol	0.5–3.0	50.83	22.97
1-Butanol	0.4–1.5	52.20	23.30
Isobutyl formate	4.7–6.8	36.05	17.98
Butyl formate	1.2–3.7	38.80	18.73
Diisobutyl ether	4.0–10.2	37.40	14.31
Butyl isobutyl ether	3.5–11.8	37.56	14.34
Dibutyl ether	8.3–15.0	38.47	14.55
Water	0.2–0.6	40.68	46.08
Unidentified components	0.1–0.5	–	–

Table 2. Physicochemical properties of RS solvent

Parameter, GOST (State Standard)	Butyl acetate, GOST 8981–78	R-5 solvent, GOST 7827–74	RS solvent
Acid number, mg KOH/g, GOST 5208–81	0.008	0.07	0.06–0.08
Ester number, mg KOH/g, GOST 8728–77	–	–	380–440
Volatility with respect to diethyl ether, GOST 7827–77	8–13	9–15	6–12
Density, kg m^{-3}, GOST 3900–85	873–875	–	780–830
Color, iodometric scale, g I_2 per 100 g [3]	–	–	0–1
Coagulation number, GOST 7827–77	–	30	38–42
Weight fraction of water after Fischer, %, GOST 14870–77	0.2	0.7	0.2–0.8

as components of mixed solvents. To evaluate the structure and properties of polymeric systems, it is necessary to study the main physicochemical properties of RS solvent as applied to (co)polymer solutions. Both individual and mixed solvents should have certain properties prescribed by state standards. According to GOST (State Standard), the following solvent parameters should be regulated: acid number, weight fraction of water after Fischer, volatility with respect to diethyl ether, and coagulation number. The physicochemical properties of RS solvent in comparison with those of butyl acetate and R-5 solvent are given in Table 2.

As follows from Table 2, RS solvent is characterized by a wider range of volatility values compared to butyl acetate and R-5 solvent. However, as RS solvent is a mixture of components, it is possible to provide, if necessary, the same volatility as that of butyl acetate or R-5 by varying the composition. This can be ensured by technological organization of the process for RS production. The coagulation number of RS solvent considerably exceeds the level prescribed for R-5, which is an advantage. The acid number and weight fraction of water after Fischer for RS solvent meet the requirements formulated for R-5 solvent.

Thus, RS solvent can replace butyl acetate as a component of R-5 solvent. It can also serve as a component of a mixed solvent or as a solvent itself. Meeting the existing requirements, RS solvent can be used for preparing solutions of (co)polymers.

According to published data [9], an efficient characteristic of the solvent and dissolved (co)polymer is the "three-dimensional" solubility parameter δ. To estimate the solubility of a film-forming agent in a solvent, their solubility parameters are compared. The closer these parameters, the higher the solvency of the given solvent with respect to the polymeric material. The parameter δ of a solvent is estimated from its heat of vaporization. In so doing, δ is deter-

Table 3. Composition of samples of RS solvent, wt %

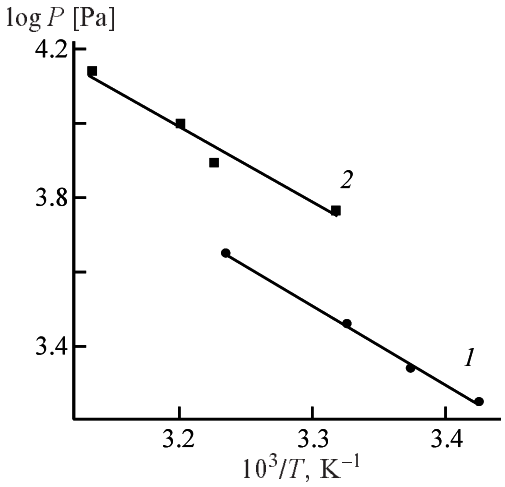
Component	Composition, wt %	
	sample 1	sample 2
Isobutyl acetate	72.3	52.1
Butyl acetate	2.6	8.8
Isobutyl alcohol	1.4	0.9
1-Butanol	0.4	2.8
Isobutyl formate	4.6	6.6
Butyl formate	1.5	1.8
Diisobutyl ether	6.4	8.8
Butyl isobutyl ether	3.2	3.8
Dibutyl ether	6.8	13.2
Water	0.5	0.7
Unidentified components	0.3	0.5

mined either by calculation from the heats of vaporization ΔH of the mixture components, taking into account their mole fractions, or from the experimentally determined ΔH. In our study we used the second approach.

Experimental determination of the heat of vaporization ΔH, required for calculating the solubility parameter δ, was performed for two RS samples (Table 3) characterized by the isobutyl acetate content close to the lower (52.1 wt %, sample no. 1) and upper (72.3 wt %, sample no. 2) limits of the range. The temperature dependence of the saturated vapor pressure P is described by the equation

$$\ln P = -\Delta H/(RT) + B \text{ or } \log P = -A/T + B, \quad (1)$$

$$A = \Delta H/(2.303R) = \Delta H/(2.303 \times 8.314) = \Delta H/19.147, \quad (2)$$



Logarithm of the saturated vapor pressure $\log P$ as a function of reciprocal temperature for RS solvent sample nos. (*1*) 1 and (*2*) 2.

where ΔH is the heat of vaporization, J mol^{-1}; P, saturated vapor pressure, Pa; T, temperature, K; and B, integration constant.

Equation (1) corresponds to the linear dependence of $\log P$ on $1/T$. The heat of vaporization can be calculated from the coefficient A determined by the least-squares method: $\Delta H = A \times 19.147$. The saturated vapor pressure was determined by the dynamic method. The installation consisted of a vessel placed in a thermostat with distilled water and connected to a vacuum system through a condenser in which the vapor of the liquid being studied was condensed. To measure the vapor pressure, the installation was evacuated until the liquid started to boil. After that, the system was connected with the atmosphere. In 5 min, the readings of the thermometer and open manometer were recorded. Measurements were performed at 4–5 K steps starting from room temperature. The experimental results for the two samples were plotted on the scale of $\log P$ vs. $1/T$ (see figure). The dependences are clearly linear and are described by the regression equations of type (1):

$$\log P_1 = 10.75 - 2189.59(1/T), \quad (3)$$

$$\log P_2 = 10.63 - 2064.30(1/T). \quad (4)$$

In both cases, the equations are characterized by the sample correlation coefficient $r \approx 1.00$.

The heat of vaporization ΔH calculated by formula (2) is 41 920 J mol^{-1} for sample no. 1 and 39 530 J mol^{-1} for sample no. 2, which may be due to higher content of more volatile ethers in sample no. 2. As the difference between the heats of vaporization of sample nos. 1 and 2 was insignificant, in what follows we used the mean value, ΔH = 40 725 J mol^{-1}. The linear character of regression equations (3) and (4) allows the experimental heat of vaporization of RS solvent to be used in the subsequent calculations by analogy with individual substances. From the experimentally determined ΔH, the solubility parameter is calculated by the formula [9]

$$\delta^2 = (\Delta H - RT)/V,$$

namely,

$$\delta = [(40\,725 - 8.3144 \times 298)/135.12]^{1/2}$$

$$= 16.82 \text{ (MJ m}^{-3})^{1/2}.$$

The results of experimental determination of the

solubility parameter of RS solvent are consistent with the results obtained by calculation [δ_m = 16.72–16.94 $(MJ\ m^{-3})^{1/2}$], so that both calculated and experimental data can be used in further studies of the properties of RS solvent.

Comparison of the solubility parameter of RS solvent with those of butyl acetate and isobutyl acetate [δ = 17.02 and 16.62 $(MJ\ m^{-3})^{1/2}$, respectively] suggests the possibility of replacing butyl acetate and isobutyl acetate in polymeric systems by RS solvent.

According to the Hildebrand–Scatchard theory, the components are infinitely mutually soluble if the molar enthalpy of mixing ΔH is low:

$$\Delta H = (\delta_1 - \delta_2)^2 V_1 \varphi_1 \varphi_2,$$

where δ_1 and δ_2 are the solubility parameters of the components $[(MJ\ m^{-3})^{1/2}]$; V_1 is the mixture volume (m^3); and φ_1, φ_2 are the volume fractions of the components.

According to the Flory–Huggins theory [6], the solute–solvent interactions and miscibility are characterized by an empirical parameter x defined as

$$x = x_s + V(\delta_1 - \delta_2)^2/RT,$$

where x_s is the parameter taking into account entropy phenomena and varying from 0.05 to 0.20; V is the molar volume of the solvent; δ_1 and δ_2 are the solubility parameters of the film-forming agent and solvent.

The maximal value of x corresponding to full miscibility of a (co)polymer and a solvent with the formation of a homogeneous solution should not exceed 0.5 at any ratios. For polymers of relatively low molecular weight, mixing is also possible at somewhat higher values of x (usually at $x \le 0.55$). Taking into account the solubility parameter of the polymers, we determined the values of x in the polymer–solvent systems for certain polymers (Table 4). It can be seen that the parameters x of RS solvent with these copolymers are close to those of butyl acetate. Hence, RS solvent can be recommended for replacement of butyl acetate in complex polymeric systems.

One of the parameters characterizing the polymer–solvent system is the intrinsic viscosity. It is related to the molecular weight of the dissolved polymer M by the formula

$$[\eta] = KM^{\alpha}, \quad (5)$$

Table 4. Solubility parameters of polymers and parameters x in various polymer–solvent systems at x_s = 0.1 and T = 298 K

Film-forming agent	Solubility parameter, $(MJ\ m^{-3})^{1/2}$	Parameter x	
		RS solvent	butyl acetate
Polystyrene	19.1	0.34	0.33
Poly(vinyl chloride)	19.2	0.36	0.35
Poly(vinyl acetate)	19.0	0.32	0.31
Cellulose nitrate	22.0	1.43	1.42
Poly(methyl methacrylate)	18.3	0.20	0.19
Fatty alkyd	19.2	0.36	0.35
Vinyl chloride (40 wt %) copolymer	18.9	0.31	0.29

where K and α are constants for the given polymer–solvent system.

The better the solvent, the higher α and the lower K [9]. Comparison of the constants α and K for the systems of a (co)polymer with various solvents allows evaluation of the solvent quality with respect to the given (co)polymer. To determine α and K, it is appropriate to take the logarithm of Eq. (5):

$$\log[\eta] = \log K + \alpha \log M. \quad (6)$$

The intrinsic viscosity [η] was measured in the systems KORS copolymer–xylene and KORS copolymer–RS solvent, with KORS copolymer samples of various average molecular weights. KORS copolymer is one of the kinds of petroleum polymeric resins widely used in formulations for preparing corrosion-protective coatings. It was prepared from styrene distillation bottoms by thermal copolymerization with maleic anhydride. KORS copolymer is a random atactic copolymer of styrene with maleic anhydride containing about 3.0 wt % maleic anhydride. The content of residual styrene monomer does not exceed 0.1 wt % [10].

The average molecular weight was calcuated from the molecular-weight distribution of the copolymer, determined on a (UONTRS-200)-POLISTIROL device. The molecular weights M_v of copolymer samples were calculated by the formula

$$M_v = \sum_{i=1}^{n} P_i M_i / \sum_{i=1}^{n} P_i,$$

where P_i is the content of the polymer with the

Table 5. Mean molecular weights of KORS copolymer

Sample no.	Molecular weight M_v	$\log M_v$
1	15 400	4.1875
2	17 500	4.2430
3	23 600	4.3729
4	34 100	4.5328

Table 6. Calculated intrinsic viscosities for the systems KORS copolymer–xylene and KORS copolymer–RS solvent

Molecular weight of KORS copolymer M_v	Intrinsic viscosity $[\eta]$	$\log[\eta]$
KORS copolymer–xylene		
M_1 = 15 400	0.2180	–0.6635
M_2 = 17 500	0.2480	–0.6055
M_3 = 23 600	0.3054	–0.5151
M_4 = 34 100	0.3988	–0.3992
KORS copolymer–RS solvent		
M_1 = 15 400	0.4589	–0.3389
M_2 = 17 500	0.4818	–0.3171
M_3 = 23 600	0.6065	–0.2172
M_4 = 34 100	0.8728	–0.0591

molecular weight within the given interval in the polymer mixture (%); n, number of intervals of molecular weights; and M_i, molecular weight M_v for the ith interval of molecular weights of the polymers.

The calculated average molecular weights of copolymer samples, calculated by formula (7), are given in Table 5. From these samples of KORS copolymer, we prepared solutions of five concentrations in xylene and RS solvents and measured, using an Ostwald–Pinkevich viscometer, the average outflow times of the pure solvent (τ_0) and polymer solutions (τ). From the experimental results, we calculated the relative viscosity $\eta_{rel} = \tau/\tau_0$, specific viscosity $\eta_{sp} = (\tau - \tau_0)/\tau_0 = \eta_{rel} - 1$, and reduced viscosity $\eta_r = \eta_{sp}/c$, where c is the concentration of the polymer solution, g (100 cm^3)$^{-1}$.

The intrinsic viscosity is determined by the formula

$$[\eta] = \lim_{c \to 0} \eta_{sp}/c$$

by extrapolation of the experimental dependence of η_{sp}/c to zero concentration (Table 6).

Having transformed Eq. (6) to the form

$$Y = a_0 + a_1 x$$

($Y = \log[\eta]$; $x = \log M_v$; $a_0 = \log K$; $a_1 = \alpha$), we determined by the least-squares method the unknown parameters a_0 and a_1 and, from these quantities, the constants K and α.

For the KORS copolymer–xylene system, $K = 1.61 \times 10^{-4}$, $\alpha = 0.75$; for the KORS copolymer–RS solvent system, $K = 1.56 \times 10^{-4}$, $\alpha = 0.83$.

The differences between the values of K for polymer solutions in xylene and RS solvent do not exceed 5% of the minimal values, i.e., the values of K for KORS copolymer in xylene and RS solvents are essentially similar. The constants α in these systems differ to a greater extent, by more than 10% of the minimal value. The constant α for the KORS copolymer–RS solvent system is higher than that for the KORS copolymer–xylene system, suggesting higher solvency and performance of RS solvent compared to xylene [9]. The use of RS solvent allows the solvent assortment to be expanded and the physicomechanical properties of coatings to be improved [11].

CONCLUSIONS

(1) RS solvent prepared from wastes from production of butyl alcohols meets the requirements to solvents for varnish-and-paint materials.

(2) A comparative estimation of the solubility of (co)polymers in RS solvent and butyl acetate, based on the solubility parameters, was made, and the possibility of replacing butyl acetate by RS solvent in polymeric systems was assessed.

(3) A polymeric system based on KORS copolymer (waste from styrene production) and RS solvent was studied, and RS solvent was shown to exhibit higher performance compared to the commonly used xylene.

REFERENCES

1. Yakovlev, A.D., *Khimiya i tekhnologiya lakokrasochnykh pokrytii* (Chemistry and Technology of Varnish-and-Paint Coatings), Leningrad: Khimiya, 1989.
2. Livshits, R.M. and Semina, R.A., *Lakokrasochnye materialy s ponizhennym soderzhaniem organicheskikh rastvoritelei* (Varnish-and-Paint Materials with Decreased Content of Organic Solvents), Moscow: Khimiya, 1989.

3. Sorokin, M.F., Kochnova, Z.A., and Shode, L.G., *Khimiya i tekhnologiya plenkoobrazuyushchikh veshchestv* Chemistry and Technology of Film-Forming Substances), Moscow: Khimiya, 1989.
4. Mitchell, M., *J. Prot. Coat. Linings*, 1994, vol. 11, no. 12, pp. 62–69.
5. Development of Solvents with the Aim to Stop the Use of Harmful Substances Polluting the Atmosphere, *Polym. Paint Colour J.*, 1995, vol. 185, no. 4374, pp. 20, 22, 23.
6. Tager, A.A., *Fizikokhimiya polimerov* (Physical Chemistry of Polymers), Moscow: Khimiya, 1978.
7. Papkov, S.P., *Fiziko-khimicheskie osnovy proizvodstva iskusstvennykh i sinteticheskikh volokon* (Physicochemical Principles of Production of Artificial and Synthetic Fibers), Moscow: Khimiya, 1972.
8. Lychkin, I.P., Petykhin, Yu.M., Enyutina, M.V., and Zartsyna, S.S., *Neftepererab. Neftekhim.*, 1994, no. 3, pp. 44–46.
9. Drinberg, S.A. and Itsko, E.F., *Rastvoriteli dlya lakokrasochnykh materialov: Spravochnoe posobie* (Solvents for Varnish-and-Paint Materials: Handbook), Leningrad: Khimiya, 1986.
10. Lychkin, I.P., Petykhin, Yu.M., and Filimonova, O.N., *Neftepererab. Neftekhim.*, 1995, no. 11, pp. 29–31.
11. USSR Inventor's Certificate no. 1781266.

ISSN 1070-4272, Russian Journal of Applied Chemistry, 2008, Vol. 81, No. 7, pp. 1278–1282. © Pleiades Publishing, Ltd., 2008.
Original Russian Text © N.V. Shul'ga, L.A. Gomolko, N.P. Krut'ko, 2008, published in Zhurnal Prikladnoi Khimii, 2008, Vol. 81, No. 7, pp. 1198–1202.

MACROMOLECULAR CHEMISTRY AND POLYMERIC MATERIALS

Potentiometric Titration of Lignosulfonic Acids

N. V. Shul'ga, L. A. Gomolko, and N. P. Krut'ko

Institute of General and Inorganic Chemistry, National Academy of Sciences of Belarus, Minsk, Belarus

Received December 11, 2007

Abstract—The conditions of potentiometric titration of lignosulfonic acids allowing quantitative determination of strongly and weakly acidic functional groups in lignosulfonates were determined.

DOI: 10.1134/S10704272080702 9X

Lignosulfonic acids (LSAs) are complex and poorly studied compounds. The analytical procedures existing today allow fairly accurate determination of the majority of functional groups in lignins, precursors of lignosulfonates [1]. Differentiation of acid groups in lignin and its derivatives is complicated because of wide range of their ionization constants and of certain specific features related to macromolecular structure of lignin, such as accessibility of acid functional groups [2, 3].

In this study we made an attempt to find potentiometric titration conditions that would furnish evidence for the existence of acid groups of different strenghths in lignosulfonates and allow their quantitative determination.

EXPERIMENTAL

As starting material for preparing LSAs we used technical-grade lignosulfonates (LSTs) from the Sokol Pulp-and-Paper Combine. Their characteristics and the conditions for their purification and synthesis of LSAs are described in detail in [4].

In potentiometric titration of LSAs, we used as solvents distilled water, mixed aqueous–organic solvent (water, ethanol, and acetone taken in 35 : 21 : 4 volume ratio), and dimethyl sulfoxide (DMSO) of chemically pure grade. As base titrant we used an aqueous or aqueous–alcoholic (1 : 19) NaOH solution (0.06–0.75 N).

When choosing the solvent, we took into account the fact that the apparent strength of acids and bases depends on the extent of their interaction with the solvent. In aqueous medium, the leveling effect of the solvent smears the inflection points in potentiometric titration curves because of close ionization constants of acids of different strengths in water and hydrolysis of the forming salt of a weak acid. However, this factor does not prevent determination of the total amount of acidic protons.

In nonaqueous titrations (in DMSO), we did not make special efforts to remove residual water (about 1 wt %) from the mixture being titrated. It is known that glass electrodes in many organic solvents give unstable data, and small amounts of H_2O stabilize the pH-meter readings [5]. Furthermore, an experiment showed that dry LSA is practically insoluble in water and DMSO. Therefore, in some cases in titration of more saturated (~2%) solutions of lignosulfonic acid in DMSO, to decrease the water content of the mixture being titrated, a sample of LSA aqueous solution containing 20–23 wt % dry matter was transferred into a titration beaker and carefully evaporated at 35–40°C to a resinous state, after which the organic solvent (60–80 ml) was added and the titration was started.

Titration was performed at room temperature wich continuous stirring in a flow of an inert gas (He or N_2) after its passing through a column packed with KOH. As indicator electrode we used an ESL 43-07 electrode. The reference electrode was an EVL-1-M3 silver chloride electrode filled with a saturated aqueous KCl solution. According to the existing experience [6], the glass electrode is preferable in titration of model lignin compounds in DMSO and DMSO–water mixtures.

The EV-74 pH meter was calibrated using standard buffer mixtures. The correctness of readings was checked every time before the measurements.

The base titrant was added to an LSA solution in

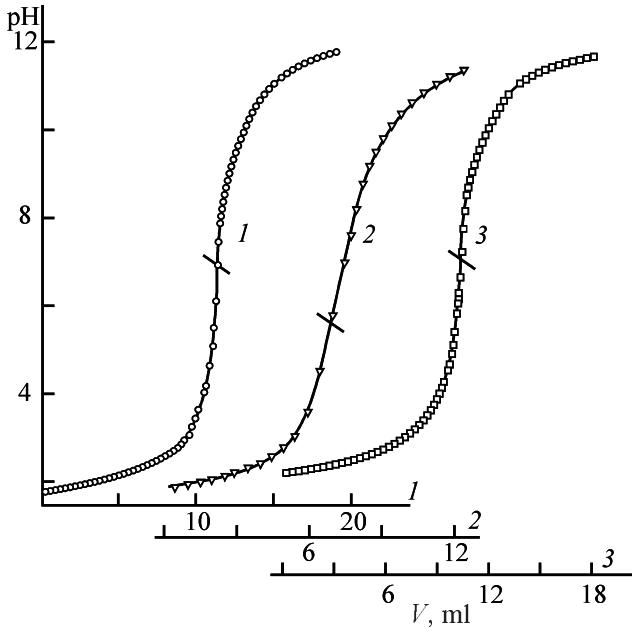


Fig. 1. Potentiometric titration curves of (*1*) LSA1, (*2*) LSA2, and (*3*) LSA4 in aqueous medium. Acid amount in solution, mg: (*1*) 200, (*2*) 223, and (*3*) 151. Titrant concentration, g-equiv l^{-1}: (*1*, *2*) 0.060 and (*3*) 0.068. (*V*) Titrant volume; the same for Figs. 2 and 3.

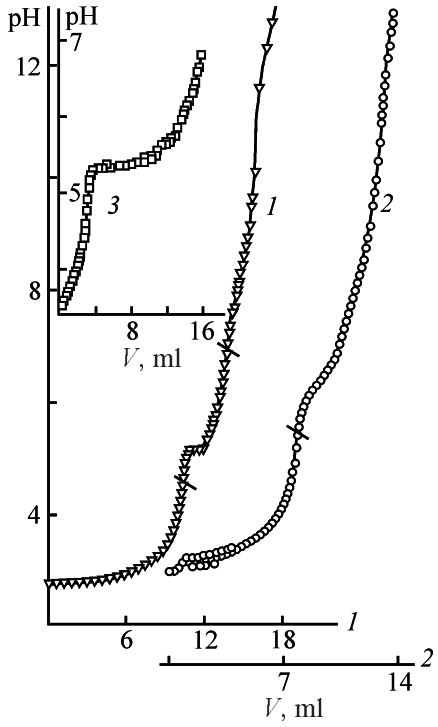


Fig. 2. Potentiometric titration curves of (*1*, *3*) LSA1 and (*2*) LSA4 in DMSO. Acid amount in solution, mg: (*1*) 248, (*2*) 192, and (*3*) 991. Titrant concentration, g-equiv l^{-1}: (*1*, *3*) 0.060 and (*2*) 0.068.

0.1-ml portions, and in the vicinity of the neutralization point, in 0.025-ml portions. Each subsequent portion of the titrant was added only after attainment of the equilibrium in the system and stabilization of the pH-meter readings. Usually this took 6–8 min.

The data obtained show that a mixed aqueous–organic solvent containing alcohol or acetone cannot be used for titration of lignosulfonic acids. Although the starting LSA readily dissolves in ethanol, the neutralization product, sodium lignosulfonate, is salted-out even in cases when the fraction of the organic component in the mixed aqueous–organic solvent does not exceed 40 vol %. The oily product deposited on the electrodes does not allow correct pH measurements.

The problem is easily solved with DMSO. This is an aprotic bipolar solvent (pK_S 18, $\varepsilon = 40$) [7]. The experimental data show that it does not enter into undesirable side reactions with lignosulfonates, and no precipitation is observed even in titration with an aqueous–alcoholic (1 : 19) NaOH solution.

It should be noted that the titration conditions chosen (electrode type, titrant, presence of small amounts of water in the mixture being titrated) do not allow determination of the concentration of phenolic hydroxyls, functional groups exhibiting weakly acidic properties.

Figures 1 and 2 show the potentiometric titration curves of samples LSA1, LSA2, and LSA4 in aqueous solution and in DMSO. In all cases, the equivalence point was found from the differential plots $\Delta pH/\Delta V–V$, where V is the spent titrant volume.

Titration in an aqueous medium (Fig. 1) allows determination of the total amount of strongly and weakly acidic functional groups in lignosulfonates (Table 1). The results obtained are well consistent with the content of metals (Zn^{2+}, Mn^{2+}, Co^{2+}, etc.) in lignosulfonic acid salts prepared by ion exchange or neutralization of LSAs with the corresponding carbonates. For example, in LSA1 salts we found (mg equiv g^{-1}) 3.44 Na^+, 3.37 Mn^{2+}, 3.41 Co^{2+}, and 3.46 Fe^{3+}, which is well consistent with the content of mobile protons (3.49 mg-equiv g^{-1}) in lignosulfonic acid sample LSA1 (Table 1).

Calculations based on data of [6] show that the activity (concentration) of H^+ ions in an aqueous–organic solution containing 90% DMSO and a weak carboxylic acid decreases by a factor of no less than 300 compared to the aqueous solution. Dissociation

Table 1. Chemical composition of lignosulfonic acids*

Sample	N	C	S	S, mg-equiv g^{-1}	H^+, mg-equiv g^{-1}		Atomic ratio			
	wt %				total	strongly acidic	N	C	S	H^+
LSA1	0.433	40.465	8.693	2.72	3.49	2.62	1.14	124.15	10.00	12.85
LSA2	1.110	52.925	6.009	1.88	1.88	1.88	4.22	234.82	10.00	10.01
LSA4	0.374	43.445	8.779	2.74	4.61	2.67	0.97	131.99	10.00	16.8

* The absolute determination error is less than 0.02 wt % for N, 0.05 wt % for C, 0.08 wt % for S, and 0.03 mg-equiv g^{-1} for H^+.

of strongly acidic groups in an organic solvent is suppressed to a considerably lesser extent. As follows from Table 2, the concentration of free protons in a 1% solution of LSA1 in DMSO decreases, compared to aqueous solution, by a factor of less than 10.

Replacement of water by DMSO affects the character of interaction of lignosulfonates with the solvent and suppresses dissociation of weakly acidic groups. As a result, no less than two inflection points corresponding to neutralization of strongly and weakly acidic functional groups become resolved in the potentiometric titration curve (Fig. 2).

In some cases, to attain clear separation of portions of the potentiometric titration curve as an indubitable evidence of the presence of weakly acidic groups in lignosulfonic acids, an LSA sample (~1 g in terms of dry matter) after preliminary evaporation was neutralized to pH ~3–4 with a concentrated alkali solution, and the mixture was kept in a hermetically sealed vessel for several days, after which it was titrated with a dilute alcoholic solution of the titrant (Fig. 2, curve *3*).

By varying the titration conditions (LSA weighed portion, LSA and titrant concentrations), it is possible to attain good separation of portions of the potentiometric titration curves and estimate the content of strongly acidic groups in lignosulfonates (Table 1, Fig. 2). It should be noted that in LSA1 and LSA4 samples about 0.67 mg-equiv g^{-1} of labile protons are bound to the sulfate anion. It was shown previously [4] that salting-out with organic solvents leads to precipitation of sulfates simultaneously with lignosulfonates.

Table 2. pH of LSA1 solutions in aqueous and organic solvents

Solvent	ω_{LSA}, wt %	pH	$c_{H^+} \times 10^3$, M
Water	1.0	1.72	19.1
Water–alcohol–acetone	1.0	2.06	8.7
DMSO	1.0	2.70	2.0
	2.4	2.47	3.4

In titration of the LSA2 sample, the shape of the potentiometric curve remained unchanged irrespective of the solvent (water or DMSO, Fig. 1, curve *2*). Titration of large LSA2 portions by the procedure described above revealed no changed in the monotonic shape of titration curves, either, and the content of acid groups found (~1.88 mg-equiv g^{-1}) strictly corresponded to the sulfur content (Table 1). The data obtained indicate that LSA2 contains no acid groups other than sulfonic acid groups. This, however, does not mean that the initial lignosulfonates could not contain carboxy groups. It was shown previously [4] that the chemical composition of lignosulfonates depends on the procedure of their recovery from the crude product.

Experiments on assessing the possibilities of potentiometric titration as applied to LSA analysis showed that titration in a mixed aqueous–organic medium gives the best results. The optimum is 10% water content in DMSO in the final steps of titration. In this case, acids of different strengths are well resolved, the pH-meter readings are stable, the titration can be performed with a fairly high accuracy, and reliable data on the nature and amount of acid groups in lignosulfonates can be obtained. The positive effect of small water additions is attributable to the following processes.

It is known that, for dissociation and neutralization processes to occur, a solvent is required. The ease of ionization of acid groups in inorganic and low-molecular-weight organic compounds is largely determined by the basic character of the solvent as proton acceptor and by its dielectric constant. The degree of ionization of an acid and its dissociation constant depend on the solvent, its chemical composition, and size and configuration of the molecules.

When macromolecular compounds of network structure, with complex mutual orientation of molecular fragments and substituents, are concerned, it is also impossible to eliminate the effect of steric factors on the results of quantitative analysis. Apparently, neutralization of acid groups in LSAs occurs in cases when they are readily accessible to solvated ions of the titrant. In this sense, water can be considered as universal solvent, but with DMSO the pattern is apparently different. Molecules of this compounds have the size comparable with that of structural units and substituents in LSA, and solvation of titrant ions with DMSO molecules gives rise to additional hindrance. As a result, steric hindrance may arise in titration of the most difficultly accessible acid groups of LSA.

Another factor that can prevent dissociation of weaker carboxy groups can be insufficiently high, compared to water, proton-acceptor power of DMSO. Furthermore, replacement of aqueous medium by an organic medium can appreciably affect the colloidal properties of LSA solutions, including the molecular conformation in solution, density of coils, and accessibility of functional groups.

Figure 3 confirms the above assumptions. The experimental results were obtained under static conditions. In the first step of titration, to a mixture containing an aliquot of DMSO and a portion of LSA1 dehydrated to a resinous state, we addded the required amount of an alcoholic solution of the titrant. The vessel was hermetically stoppered, and its contents were thoroughly mixed and kept for a long time with intermittent pH measurements. With an increase in the neutralization time, the potentiometric curve portion corresponding to titration of weakly acidic groups shifted toward lower pH values (Fig. 3, curves *1*, *2*). In the step of titration of sulfonic acid groups, the equilibrium pH value was attained considerably faster.

On adding portions of water (~12% of the liquid volume) to the mixtures being titrated, the pH-meter readings in the step of titration of sulfonic acid groups quickly stabilized (Fig. 3, curve *3*) and then remained unchanged. However, in the step of titration of weakly acidic groups, certain time was required to attain the equilibrium pH values. The ascending portion of the potentiometric curve, corresponding to the titration of a weak acid, shifted toward lower pH values. This means that addition of a more polar solvent favored "opening" of the weakest acid groups and titration completion.

Specific features of potentiometric titration in

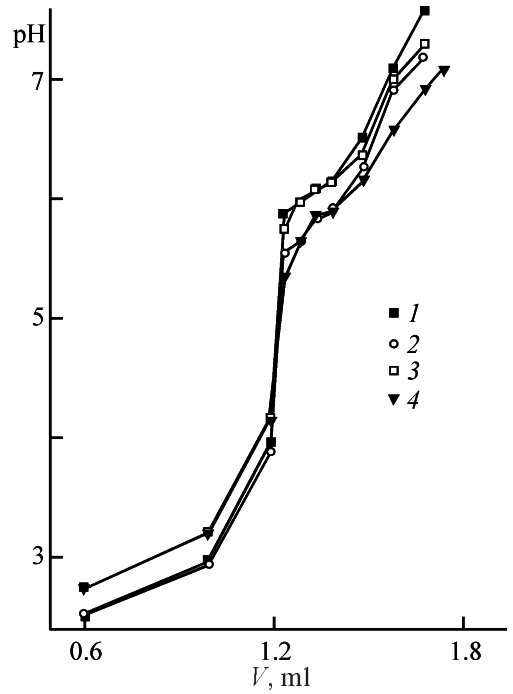


Fig. 3. Potentiometric titration curves of LSA1 in (*1*, *2*) organic and (*3*, *4*) aqueous–organic solutions. Acid amount 375 mg, titrant concentration 0.75 g-equiv l^{-1}. Storage time, days: (*1*) 2, (*2*) 20, and (*4*) 30.

DMSO (properties of electrodes and organic solvent) do not allow the titration to be performed to completion, with flattening out at pH > 11 as in titration in an aqueous medium (Figs. 1, 2), which somewhat complicates determination of the position of the equivalence point and of the total content of acids of different strengths in the sample, but does not prevent determination of strongly acidic groups (Fig. 2). Their amount corresponds to the sulfur content of the samples (Table 1). This means that practically the whole amount of sulfur in lignosulfonates (96–100%) is incorporated in strongly acidic groups.

Comparison of the results of potentiometric titration of LSA in water and DMSO shows that the content of weakly acidic (mainly carboxy) groups depends on the procedure for isolating lignosulfonates from the crude product for their further processing, ranging from 0 (LSA2) to 1.9 mg-equiv l^{-1} (LSA4).

In accordance with data of [8], lignosulfonates of high molecular weight contain no acid groups other than sulfonic acid groups. As the weight fraction of such lignosulfonates in the sulfite liquor after separating soluble inorganic impurities is about 50 wt % [8], it is difficult to imagine that the remaining part

of the liquor consists exclusively of nonlignin impurities.

Presumably, low-molecular-weight lignins as intermediates of organic transformations of amino acids are sulfonated in the course of wood cooking without breakdown of carboxy groups, which appreciably increases the solubility of their sulfonated derivatives. Furthermore, lignosulfonates of low molecular weight, in contrast to macromolecular compounds, have less branched structure and show stronger tendency to association in aqueous solutions [9]. Apparently, such properties in combination with high solubility do not favor formation of a stable organomineral complex on treatment of lignosulfonate solutions with the complex salt $[Co(NH_3)_6]Cl_3$, which leads to the loss of carboxyl-rich fractions of the main substance.

Salting-out with organic solvents, on the contrary, increases the content of carboxylated nonlignin impurities in the isolated lignosulfonate because of their low solubility in organic solvents.

We should probably agree with the opinion of Gardon and Mason [8] that there are no rigorous analytical criteria for estimating the degree of removal of concomitant nonlignin organic compounds from lignosulfonates. Also, there are apparently no ideal methods for complete separation of lignosulfonates and nonlignin impurities without loss of each component.

CONCLUSIONS

(1) Conditions were found for potentiometric titration of lignosulfonic acids in an organic solvent, dimethyl sulfoxide, allowing determination of the content of strongly acidic groups in lignosulfonic acids.

(2) The presence of small amounts of water in a mixture being titrated or in a titrant does not interfere with the separate titration of acid groups of different strengths in lignosulfonic acids and increases the neutralization rate.

(3) The amount of acid groups in lignosulfonic acids and their qualitative composition depend on the procedure for recovering lignosulfonates from the crude product.

REFERENCES

1. Zakis, G.F., Mozheiko, L.N., and Telysheva, G.M., *Metody opredeleniya funktsional'nykh grupp lignina* (Methods for Determination of Functional Groups of Lignin), Riga: Zinatne, 1975.
2. Mel'kis, A.A., Zakis, G.F., and Meksha, M.N., *Khim. Drev.*, 1983, no. 1, pp. 106–112.
3. Samylova, O.A., Aizenshtadt, A.M., Bogolitsyn, K.G., et al., *Lesn. Zh.*, 2003, no. 6, pp. 95–102.
4. Shul'ga, N.V., Gomolko, L.A., and Krut'ko, N.P., *Zh. Prikl. Khim.*, 2008, vol. 81, no. 7, pp. 1164–1170.
5. Palit, Sh.R., *Nevodnoe titrovanie* (Nonaqueous Titration), Moscow: Goskhimizdat, 1958.
6. Gorbova, N.S., Bogolitsyn, K.G., and Kosyakov, D.S., *Lesn. Zh.*, 2000, no. 4, pp. 111–117.
7. Kreshkov, A.P., Bykova, L.N., and Kazaryan, N.A., *Kislotno-osnovnoe titrovanie v nevodnykh rastvorakh* (Acid–Base Titration in Nonaqueous Solutions), Moscow: Khimiya, 1976.
8. Gardon, J.L. and Mason, S.G., *Can. J. Chem.*, 1955, vol. 33, no. 10, pp. 1477–1450.
9. Gardon, J.L. and Mason, S.G., *Can. J. Chem.*, 1955, vol. 33, no. 10, pp. 1491–1501.

ISSN 1070-4272, Russian Journal of Applied Chemistry, 2008, Vol. 81, No. 7, pp. 1283–1286. © Pleiades Publishing, Ltd., 2008.
Original Russian Text © Yu.S. Kuznetsova, O.A. Kal'ko, A.G. Morachevskii, E.V. Bakhvalova, 2008, published in Zhurnal Prikladnoi Khimii, 2008, Vol. 81, No. 7, pp. 1203–1206.

BRIEF COMMUNICATIONS

Desulfation of Active Paste from Lead Battery Scrap with Ammonium Carbonate

Yu. S. Kuznetsova, O. A. Kal'ko, A. G. Morachevskii, and E. V. Bakhvalova

Cherepovets State University, Cherepovets, Vologda oblast, Russia
St. Petersburg State Polytechnic University, St. Petersburg, Russia

Received May 13, 2008

Abstract—Results obtained in a study of the desulfation of the active paste from lead battery scrap with the use of an aqueous ammonium carbonate solution are presented.

DOI: 10.1134/S1070427208070306

In recent years, considerable attention has been paid in all the economically developed countries to utilization of worked out lead batteries. Year by year, this problem becomes increasingly economically and environmentally important [1–3]. By now, more than a half of world's output of lead is produced from secondary raw materials, mainly from lead battery scrap. In a number of leading countries, the share of secondary lead constitutes 65–85% of its total output [3].

Lead battery scrap is a specific kind of secondary raw materials whose processing must considerably differ in the apparatus and technological regards from the ore processing. The most appropriate is the technology including preliminary processing of battery scrap into the metallic (grids), oxide–sulfate (active paste of the positive and negative plates), and organic fractions. On average, after being washed with water, the oxide–sulfate fraction contains (wt %): Pb 73.5, Sb 0.3, As up to 0.04, Cu 0.1, Fe 0.05, and SO_4^{2-} 16.7 [4]. Its main components are $PbSO_4$ and PbO_2, and to a lesser extent PbO and other compounds (Fig. 1). Direct pyrometallurgical processing of the sulfate–oxide fraction in furnaces of any design leads to transfer of the whole amount of sulfur into the gas phase and necessitates its catching [5, 6]. The most appropriate in environmental and economical regards is conversion of lead sulfate to lead carbonate by a simple hydrometallurgical procedure, desulfation (desulfurization). This enables full utilization of sulfur, which passes into the aqueous phase in the form of a soluble sulfate. Physicochemical and technological studies of the desulfation process were considered in detail in the review [7]. The most appropriate reagents for desulfation are sodium or potassium carbonate and sodium hydroxide. The reaction not subject to any considerable kinetic hindrance is based on the substantially lower solubility products of lead(II) carbonate or hydroxide, compared to lead sulfate.

Previously, results of experimental studies of the desulfation with aqueous solutions of NaOH, KOH, Na_2CO_3, $NaHCO_3$, and K_2CO_3 have been presented [7–10], the possibility of using calcium hydroxide has been discussed [11], and the thermodynamics and mechanism of processes occurring in solid-phase reduction of the oxide–carbonate cake obtained upon desulfation have been studied in detail [12]. Even at 600°C, all lead compounds are converted into lead(II) oxide, which is easily reduced by carbon or any carbon-containing material at 720–740°C. Similarly to the desulfation, the reduction is relatively safe environmentally, does not require intricate apparatus, and can be performed under small-scale production conditions.

Here we report the results of studying the desulfation of the active paste from lead battery scrap with ammonium carbonate. As the starting material served active paste from batteries of various brands, including those of foreign make, after manual disassembly (total mass 25 kg). The sulfate–oxide materials were washed and dried first in air (72 h) and then in an oven at 110°C for 4 h. Further, the active paste was ground in a porcelain mortar and screened through a set of sieves with a mesh of 0.25 to 3.0 mm. The fraction with a particle size

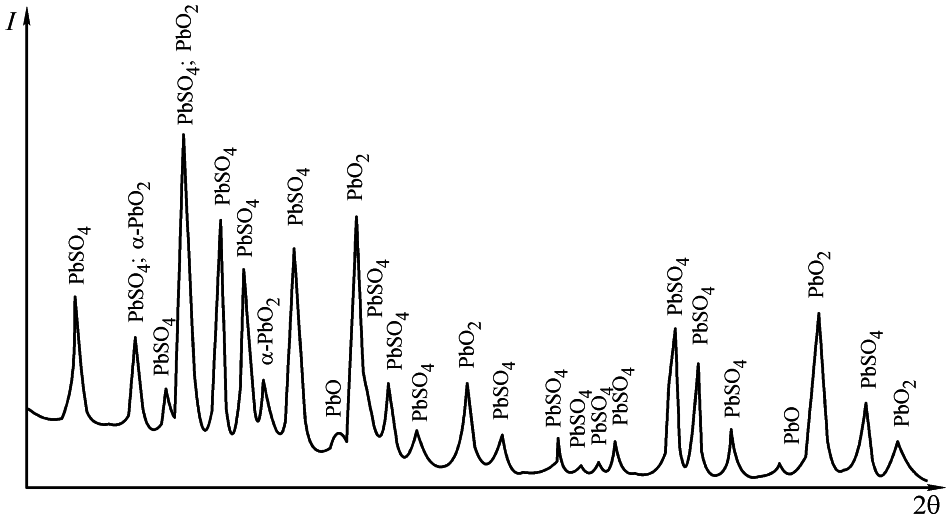


Fig. 1. X-ray diffraction pattern of the starting oxide–sulfate fractions (active paste from positive and negative plates of lead batteries). (*I*) Intensity and (2θ) Bragg angle; the same for Figs. 2 and 3.

smaller than 0.25 mm was used for desulfation (total weight of the fraction 7 kg). An analysis for the content of SO_4^{2-} was made by two methods, gravimetric and turbidimetric [13, 14], with consistent results obtained. The content of SO_4^{2-} in the sample was 16.66 wt %, which corresponds to 52.6 wt % $PbSO_4$.

The necessary theoretical amount of $(NH_4)_2CO_3$ was calculated using the reaction equation

$$PbSO_4 + (NH_4)_2CO_3 = PbCO_3 + (NH_4)_2SO_4.$$

Ammonium carbonate of analytically pure grade was used. The weighed portion of the oxide–sulfate fraction was 25 g in all the experiments, and the amount of water, 200 g. The reaction mixture was agitated with a magnetic stirrer, with the temperature and solution pH measured in the course of an experiment (duration 50 min). It was found in preliminary experiments that the extent of the desulfation process is affected by the solution pH. In the experiments, the pH value was maintained at no less than 9.5 by adding an NH_4OH solution. The temperature of the experiments was 25±2°C; raising the temperature to 45°C had no effect on the results of desulfation. The forming oxide–carbonate cake was separated by filtration, washed with a double (compared to that of the primary filtrate) volume of distilled water, and dried at 110°C. The primary filtrate and the solid phase were analyzed for the content of SO_4^{2-} ions. The results obtained are listed in the table. On the average, 94% of SO_4^{2-} contained in the starting oxide–sulfate fraction passes into the aqueous phase in the course of desulfation. The content of SO_4^{2-} in the forming oxide–carbonate cake is within 0.7–1.1 wt % (0.9 wt % SO_4^{2-} on average). As can be seen in Fig. 2, PbO_2 and $PbCO_3$ are the main components of the desulfated paste. After annealing at 600°C, virtually the only component of the oxide–carbonate cake is rhombic lead(II) oxide (Fig. 3).

Results of experiments on desulfation of the oxide–sulfate fraction with ammonium carbonate. Initial mass of the material being desulfated 25 g, water volume 200 cm^3, temperature 25°C

Run no.	Mass of solid phase after run, g	SO_4^{2-} content of solid phase, %	Volume of primary filtrate, cm^3	SO_4^{2-} concentration in filtrate, g l^{-1}	Amount of SO_4^{2-} that passed into liquid phase, %
1	22.7	0.92	210	18.84	95.1
2	22.8	0.69	207	18.90	93.9
3	22.4	0.70	210	18.90	95.3
4	22.3	1.01	210	18.10	91.2
5	22.2	0.95	200	19.80	95.1
6	22.6	1.13	206	18.92	93.6

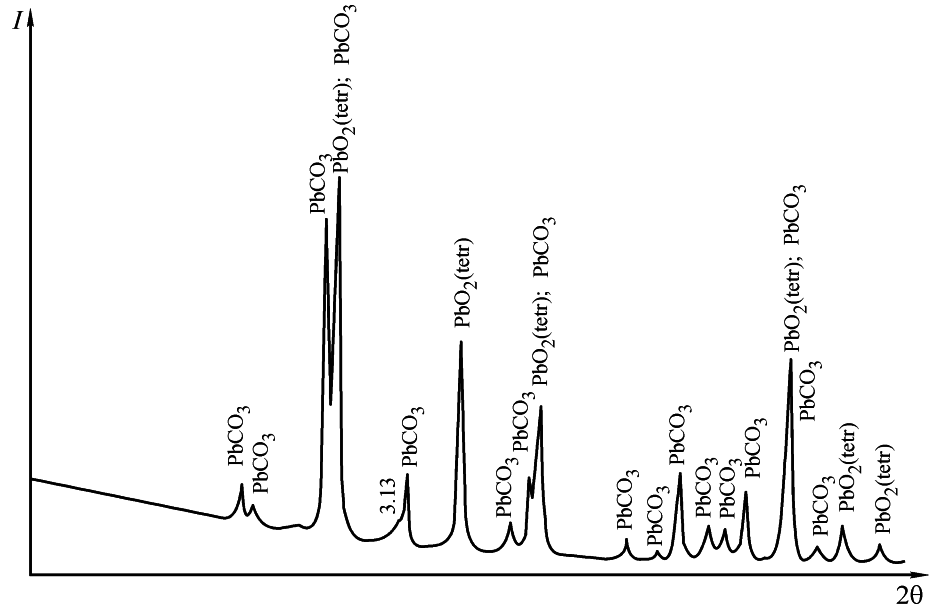


Fig. 2. X-ray diffraction pattern of the oxide–carbonate cake after desulfation with ammonium carbonate at 25°C.

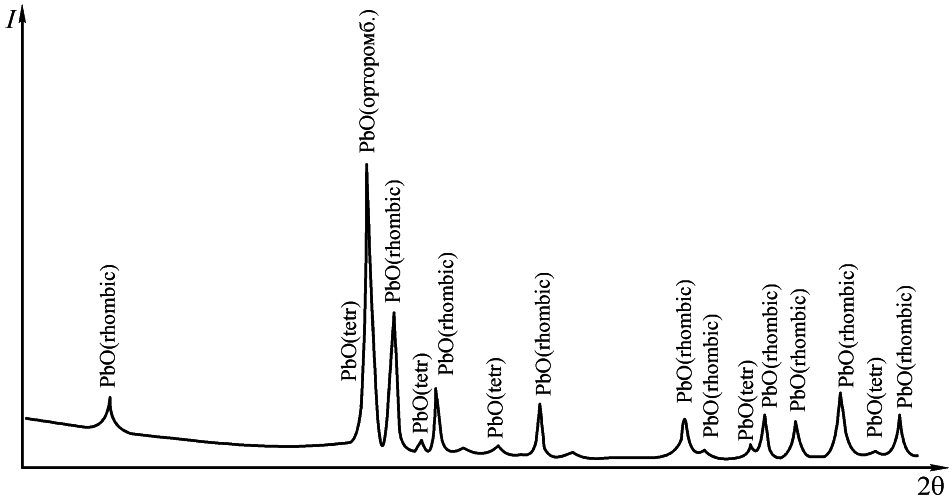


Fig. 3. X-ray diffraction pattern after annealing of the oxide–carbonate cake at 600°C.

CONCLUSIONS

(1) Ammonium carbonate can be used, together with sodium or potassium carbonate, in desulfation of the active paste from lead battery scrap.

(2) To achieve a high degree of recovery of SO_4^{2-} ions into the aqueous phase (94–95%) in desulfation, it is advisable to maintain a solution pH of no less than 9.5 by addition of NH_4OH.

(3) PbO_2 and $PbCO_3$ are the main components of the desulfated paste (oxide–carbonate cake).

(4) Upon annealing of the oxide–carbonate cake at 600°C, PbO_2 and $PbCO_3$ are converted to rhombic lead(II) oxide.

REFERENCES

1. Lamm, K.F., *Erzmetall.*, 1998, vol. 51, no. 6, pp. 438–455.
2. Morachevskii, A.G., *Zh. Prikl. Khim.*, 2003, vol. 76, no. 9, pp. 1467–1476.
3. Pogosyan, A.A., Besser, A.D., and Sorokina, V.S., *Pererabotka ispol'zovannykh akkumulyatorov – osnova retsiklinga svintsa* (Processing of Worked out Batteries as a Basic Way to Recycling of Lead), Moscow: TsNIIAtominform, 2005.
4. Morachevskii, A.G., Vaisgant, Z.I., and Korelyakov, A.V., *Zh. Prikl. Khim.*, 2000, vol. 73, no. 7, pp. 1125–1130.
5. Morachevskii, A.G., Vaisgant, Z.I., Bochagina, E.V.,

and Khabachev, M.N., *Tsvetn. Met.*, 2002, no. 8, pp. 34–37.

6. Besser, A.D., Sorokina, V.S., and Pogosyan, A.A., *Tsvetn. Met.*, 2006, no. 2, pp. 23–29.
7. Morachevskii, A.G., *Zh. Prikl. Khim.*, 1998, vol. 71, no. 6, pp. 881–890.
8. Morachevskii, A.G., Vaisgant, Z.I., Rusin, A.I., and Khabachev, M.N., *Zh. Prikl. Khim.*, 2001, vol. 74, no. 7, pp. 1075–1077.
9. Morachevskii, A.G., Bochagina, E.V., and Khabachev, M.N., *Zh. Prikl. Khim.*, 2003, vol. 76, no. 10, pp. 1748–1750.
10. Morachevskii, A.G., Kal'ko, O.A., and Kuznetsova, Yu.S., *Zh. Prikl. Khim.*, 2004, vol. 77, no. 6, pp. 1036–1037.
11. Morachevskii, A.G., Kuznetsova, Yu.S., and Kal'ko, O.A., *Zh. Prikl. Khim.*, 2005, vol. 78, no. 9, pp. 1568–1570.
12. Morachevskii, A.G., Vaisgant, Z.I., Ugolkov, V.L., et al., *Zh. Prikl. Khim.*, 2006, vol. 79, no. 2, pp. 242–250.
13. Hillebrand, W.F. and Lundell, G.E.F., *Applied Inorganic Analysis with Special Reference to the Analysis of Metals, Minerals and Rocks*, Lundell, G.E.F., Bright, H.A., and Hoffman, J.I., Eds., New York: Wiley, 1963.
14. *GOST* (State Standard) *4389–72: Potable Water. Methods for Determining the Content of Sulfates*, Moscow: Izd. Standartov, 1972.

ISSN 1070-4272, Russian Journal of Applied Chemistry, 2008, Vol. 81, No. 7, pp. 1287–1289. © Pleiades Publishing, Ltd., 2008.
Original Russian Text © E.Yu. Kolosova, A.G. Morachevskii, L.B. Tsymbulov, 2008, published in Zhurnal Prikladnoi Khimii, 2008, Vol. 81, No. 7, pp. 1207–1209.

BRIEF COMMUNICATIONS

Applicability of the Zdanovskii Rule to Sulfide Melts

E. Yu. Kolosova, A. G. Morachevskii, and L. B. Tsymbulov

St. Petersburg State Polytechnic University, St. Petersburg, Russia
Gipronikel' Institute, Limited Liability Company, St. Petersburg, Russia

Received June 6, 2008

Abstract—Applicability of the Zdanovskii rule to melts of the systems Fe–Ni–S and Cu–Ni–S was studied.

DOI: 10.1134/S1070427208070318

Zdanovskii [1] established, based on a study of a large number of aqueous solutions, a law that became known as the Zdanovskii rule: The activity of water remains unchanged on mixing isopiestic solutions of different electrolytes that do not interact chemically with each other. Later, it was demonstrated [2–4] that the above rule can also be applied to ternary systems of varied nature, in which the interaction of two of three components with each other is minimal.

In this study we considered the applicability of the Zdanovskii rule to melts of the sulfide systems iron–nickel–sulfur and copper–nickel–sulfur, which contain less than 50 mol % sulfur ($x_S \le 0.50$, x_S is the mole fraction of sulfur). Published data on the phase diagrams and thermodynamic properties of the above systems have been considered previously in detail [5, 6].

Iron–nickel–sulfur system. In the boundary binary systems iron–sulfur and nickel–sulfur, the components actively interact to form a number of compounds (FeS, FeS_2, Ni_3S_2, NiS) [7, 8]. The thermodynamic properties of melts of the metal–sulfur systems are described within the associated solution model [9, 10].

The phase diagram of the Fe–Ni system shows formation of a continuous series of solid solutions, with the interval between liquidus and solidus temperatures as small as 5–6 K. The thermodynamic properties of liquid iron–nickel alloys have been considered in detail in [11, 12]. The system exhibits slight negative deviations from the ideal behavior at 1873 K.

The applicability of the Zdanovskii rule to the ternary system Fe–Ni–S was checked along the hypothetical sulfur isoactivity lines, which were constructed from data on the sulfur activity in Ni–S and Fe–S melts (Fig. 1). The compositions of the boundary binary systems with the same values of sulfur activities and the equations of lines connecting these compositions are given in the table. This made it possible to calculate the dependence of the sulfur activity on the composition of the ternary system along secants with constant ratios of mole fractions of iron and nickel ($x_{Fe} : x_{Ni}$) and to compare the values obtained with the available experimental data for each section of the ternary system (Fig. 2). At a calculated temperature of 1573 K, all the compositions considered lie in the homogeneity region.

It should be noted that, in the previously made

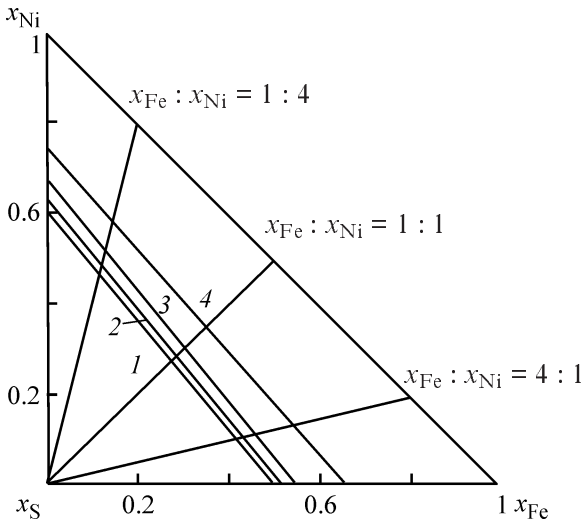


Fig. 1. Sulfur isoactivity lines in the ternary system Fe–Ni–S (mole fraction scale), based on data of sulfur activity in boundary binary systems at 1573 K. Sulfur activity: (*1*) 10^{-2}, (*2*) 10^{-3}, (*3*) 10^{-4}, and (*4*) 10^{-5}.

Compositions of boundary systems and coefficients in the equation of sulfur isoactivity lines in melts of the Fe–Ni–S and Cu–Ni–S systems

a_S	Ni–S system		$x_{Ni} = a_{Ni}x_M + b$*		M–S system	
	x_{Ni}	x_S	a	b	x_M	x_S
Fe–Ni–S system, 1573 K						
1×10^{-5}	0.74	0.26	–1.1212	0.74	0.66	0.34
1×10^{-4}	0.67	0.33	–1.2182	0.67	0.55	0.45
1×10^{-3}	0.63	0.37	–1.2115	0.63	0.52	0.48
1×10^{-2}	0.60	0.40	–1.2000	0.60	0.50	0.50
Cu–Ni–S system, 1523 K						
1×10^{-5}	0.740	0.260	–1.1061	0.74	0.669	0.331
1×10^{-4}	0.670	0.330	–1.0075	0.67	0.665	0.335
1×10^{-3}	0.630	0.370	–0.9517	0.63	0.662	0.338
1×10^{-2}	0.600	0.400	–0.9105	0.60	0.659	0.341

* M is Fe or Cu.

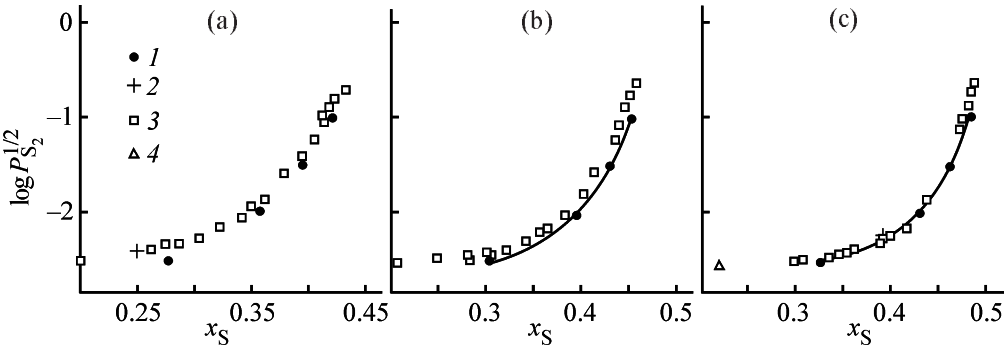


Fig. 2. Plots of $\log P_{S_2}^{1/2}$ vs. x_S for the Fe–Ni–S system along secants with varied $x_{Fe} : x_{Ni}$ ratio at 1573 K. $x_{Fe} : x_{Ni}$: (a) 1 : 4, (b) 1 : 1, and (c) 4 : 1. (*1*) calculation; data from (*2*) [13], (*3*) [14], and (*4*) [15].

experimental studies of the thermodynamic properties of melts of sulfide systems, approaches to choosing the standard state of sulfur are diverse [6]. This is due to the fact that, in metallurgical practice, copper–nickel sulfide ores are processed at relatively high temperatures. At the same time, sulfur melts at 388.36 K and its boiling point is 717.82 K. The gaseous phase has a complex composition S_n, and n varies with temperature ($1 \le n \le 8$). In [14, 15], sulfur activity is identified with a value of $P_{S_2}^{1/2}$ (P_S is the partial vapor pressure of sulfur, which is considered as ideal diatomic gas at experimental temperatures). While comparing results of the calculation with the experimental data, we used the same procedure.

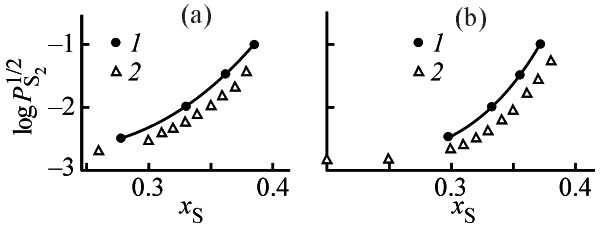


Fig. 3. Plots of $\log P_{S_2}^{1/2}$ *vs.* x_S for the Cu–Ni–S system along secants with varied $x_{Cu} : x_{Ni}$ ratio. $x_{Cu} : x_{Ni}$: (a) 1 : 3 and (b) 1 : 1. (*1*) Calculation, T = 1523 K; (*2*) data from [15], T = 1473 K.

Copper–nickel–sulfur system. In the boundary binary system copper–sulfur, the interaction of components is especially complex [16]. In the composition range considered ($x_S \le 0.50$), the phase separation region (between Cu and Cu_2S) is found, along with the compounds Cu_2S and CuS. Applicability of the associated solution model to melts of the Cu–S system has been considered in a Sharma and Chang's study [17]. In the Cu–Ni system, the component solubility in both liquid and solid state is unlimited. According to data of different authors,

the activity isotherms of the components have moderate deviations from ideality [18]. For the Cu–Ni–S system, the sulfur isoactivity lines were constructed by the same way as for the Fe–Ni–S system. The compositions of the boundary systems and the equations for the isoactivity lines are given in the table. In this system, both the sections considered lie in the homogeneity region at a calculated temperature of 1523 K. Agreement with the experimental data is satisfactory (Fig. 3).

CONCLUSION

The sulfur isoactivity lines in the Fe–Ni–S and Cu–Ni–S systems at 1573 and 1523 K, respectively, within the homogeneity region can be described by data on the boundary binary sulfide systems with the application of the Zdanovskii rule.

REFERENCES

1. Zdanovskii, A.B., *Zakonomernosti v izmenenii svoistv smeshannykh rastvorov: Trudy solyanoi laboratorii* (Fundamental Aspects of Variation of Properties of Mixed Solutions. Works of Salt Laboratory), Leningrad, 1936, issue 6.
2. Zhichang, W., *Acta Met. Sinica*, 1982, vol. 18, no. 2, pp. 141–152.
3. Morachevskii, A.G., Maiorova, E.A., and Den'-u, Ya., in *Fizikokhimicheskie issledovaniya metallurgicheskikh protsessov: Mezhvuzovskii sbornik nauchnykh trudov* (Physicochemical Study of Metallurgical Processes: Intercollegiate Coll. of Scientific Works), Sverdlovsk: Ural. Politekh. Inst., 1987, issue 15, pp. 64–69.
4. Morachevskii, A.G. and Butukhanova, T.V., *Zh. Prikl. Khim.*, 2007, vol. 80, no. 8, pp. 1261–1263.
5. Morachevskii, A.G., Ryabko, A.G., and Tsemekhman, L.Sh., *Sistema zhelezo–nikel'–sera: Fazovaya diagramma i termodinamicheskie svoista* (Iron–Nickel–Sulfur System: Phase Diagram and Thermodynamic Properties), St. Petersburg: Sankt-Peterb. Gos. Politekh. Univ., 2006.
6. Morachevskii, A.G., Tsemekhman, L.Sh., and Tsymbulov, L.B., *Sistema med'–nikel'–sera: Fazovaya diagramma i termodinamicheskie svoista* (Copper–Nickel–Sulfur System: Phase Diagram and Thermodynamic Properties), St. Petersburg: Sankt-Peterb. Gos. Politekh. Univ., 2007.
7. Morachevskii, A.G., Ryabko, A.G., and Tsemekhman, L.Sh., *Termodinamika sistemy nikel'–sera* (Thermodynamics of the Nickel–Sulfur System), St. Petersburg: Sankt-Peterb. Gos. Politekh. Univ., 2003.
8. Morachevskii, A.G., Ryabko, A.G., and Tsemekhman, L.Sh., *Termodinamika sistemy zhelezo–sera* (Thermodynamics of the Iron–Sulfur System), St. Petersburg: Sankt-Peterb. Gos. Politekh. Univ., 2005.
9. Chuang, Y.-Y., Hsiech, K.-C., and Chang, Y.A., *Met. Trans. B.*, 1985, vol. 16, pp. 277–285.
10. Sharma, R.C., and Chang, Y.A., *Met. Trans. B.*, 1980, vol. 11, pp. 139–146.
11. Lee, B.J., *CALPHAD*, 1993, vol. 17, no. 3, pp. 251–268.
12. Morachevskii, A.G., Ryabko, A.G., and Tsemekhman, L.Sh., *Termodinamika zhidkikh splavov sistemy zhelezo–nikel'–cobal't* (Thermodynamics of Liquid Alloys of the Iron–Nickel–Cobalt System), St. Petersburg: Sankt-Peterb. Gos. Politekh. Univ., 2004.
13. Hsiech, K.-C., and Chang, Y.A., *Can. Metall. Quart.*, 1987, vol. 26, no. 4, pp. 311–327.
14. Conard, B.R., Meyer, G.A., Timberg, L., et al., *Can. Metall. Quart.*, 1987, vol. 26, no. 4, pp. 299–309.
15. Kongoli, F., Dessureault, Y., and Pelton, A.D., *Metall. Mater. Trans. B*, 1998, vol. 29, pp. 591–601.
16. Morachevskii, A.G., Ryabko, A.G., and Tsemekhman, L.Sh., *Termodinamika sistemy med'–sera* (Thermodynamics of the Copper–Sulfur System), St. Petersburg: Sankt-Peterb. Gos. Politekh. Univ., 2004.
17. Sharma, R.C., and Chang, Y.A., *Met. Trans. B.*, 1980, vol. 11, pp. 575–583.
18. Morachevskii, A.G., Ryabko, A.G., and Tsemekhman, L.Sh., *Termodinamika zhidkikh splavov sistemy nikel'–med'–zhelezo* (Thermodynamics of Liquid Alloys of the Nickel–Copper–Iron System), St. Petersburg: Sankt-Peterb. Gos. Politekh. Univ., 2002.

ISSN 1070-4272, Russian Journal of Applied Chemistry, 2008, Vol. 81, No. 7, pp. 1290–1292. © Pleiades Publishing, Ltd., 2008.
Original Russian Text © T.N. Khamaganova, 2008, published in Zhurnal Prikladnoi Khimii, 2008, Vol. 81, No. 7, pp. 1210–1212.

BRIEF COMMUNICATIONS

Phases of Variable Composition in the System $Ba_{3-x}Sr_xEr(BO_3)_3$ ($0 \le x \le 3.0$)

T. N. Khamaganova

Baikal Institute of Nature Management, Siberian Branch, Russian Academy of Sciences, Ulan-Ude, Buryatia, Russia

Received December 11, 2007

Abstract—The possibility of preparing two series of solid solutions in the system $Ba_{3-x}Sr_xEr(BO_3)_3$ ($0 \le x \le 3.0$), crystallizing in different structural types, was examined. Samples of the phases of variable composition were synthesized by the method of solid-phase reactions, and their X-ray phase analysis was done. The X-ray diffraction characteristics of the phases synthesized were determined.

DOI: 10.1134/S107042720807032X

Double barium borates of the composition $Ba_3R(BO_3)_3$, where R is an yttrium-group rare-earth element (REE), are interesting objects of study, because they have noncentrosymmetrical hexagonal structure (space group $P6_3cm$) and exhibit properties making them promising for nonlinear optics and for pyro- and ferroelectrics [1, 2]. At the same time, compounds with the above structure are few. The phases of the above composition with cerium-group lanthanides (La–Dy) and isoformular strontium borates crystallize in another structural type (space group $R\bar{3}$). Structures with a center of symmetry are hardly to possess the required properties. Varying the composition of cations makes it possible to purposefully synthesize phases with the required structure and properties.

As known, crystalline substances can form solid solutions or phases of variable composition. The isomorphic substitutions can occur if cations have the same charge and close radii and polarizabilities [3, 4].

In this study, we synthesized solid solutions $Ba_{3-x}Sr_xEr(BO_3)_3$, determined their X-ray diffraction characteristics, and established the solubility regions of strontium atoms in the acentric barium structure.

EXPERIMENTAL

Samples for study were synthesized by the method of solid-phase reactions. The reaction mixtures were prepared by thorough mixing of stoichiometric amounts of the starting components, which were then annealed in platinum crucibles in air and repeatedly ground. As started components we used preliminarily calcined barium and strontium carbonates (both ultrapure grade), erbium(III) oxide (99.9% pure), and boric acid (chemically pure grade). The mixtures of the starting components taken in stoichiometric amounts (x 0, 0.1, 0.4, 0.5, 0.6, 0.8, 1.0, 1.2, 1.4, 1.6, 1.8, 2.0, 2.5, 3.0) were annealed at 500–1000°C for 70–80 h. The phase composition of powders was monitored by X-ray phase analysis [DRON UM1 diffractometer (CuK_α radiation) and D8 Advance Bruker AXS diffractometer (CuK_α radiation, graphite monochromator, $10° < 2\theta < 60°$, 0.02° interval). The unit cell parameters of the synthesized phases were refined by the least-squares method using a specially developed program. The analysis showed that in the range of $0.1 \le x \le 0.4$, rich in barium, the diffraction patterns of the samples resemble the diffraction pattern of the double borate $Ba_3Er(BO_3)_3$: both the reflection positions and relative intensities are the same. The diffraction patterns of samples of the above compositions were identified using X-ray diffraciton characteristics of double barium and erbium borate by assuming their being isostructural. The results of identification of the powder diffraction pattern of $Ba_{2.9}Sr_{0.1}Er(BO_3)_3$ are listed in Table 1.

The reflection positions in the diffraction pattern of the samples of composition $0.5 \le x \le 3.0$ are close to those of double strontium erbium borate. The diffraction patterns of the phases in this region of

Table 1. Results of indexing of the $Ba_{2.9}Sr_{0.1}Er(BO_3)_3$ (space group $P6_3cm$) and $Ba_{1.8}Sr_{1.2}Er(BO_3)_3$ (space group $R\bar{3}$) powder patterns

2θ, deg	I/I_0, %	d_e, Å	$10^4/d_e^2$	*hkl*	d_c, Å	$10^4/d_c^2$
			$Ba_{2.9}Sr_{0.1}Er(BO_3)_3$ powder			
18.898	17	4.695	453	110	4.701	452
19.555	15	4.538	485	111	4.540	485
23.175	31	3.852	679	014	3.859	675
23.947	22	3.717	724	032	3.720	723
24.353	26	3.654	749	113	3.654	749
27.787	100	3.211	969	114	3.206	973
29.368	100	3.042	1081	121	3.036	1085
29.791	29	3.000	1111	024	2.993	1116
30.401	14	2.940	1157	006	2.948	1150
31.815	84	2.814	1264	115	2.811	1265
32.619	23	2.745	1328	016	2.750	1323
32.983	40	2.716	1356	030	2.714	1358
34.025	24	2.635	1440	032	2.639	1436
36.218	22	2.480	1626	116	2.481	1626
38.240	17	2.353	1808	220	2.351	1811
38.617	13	2.331	1848	221	2/330	1844
40.061	13	2.251	1976	131	2.249	1980
43.663	24	2.073	2331	224	2.071	2335
45.178	12	2.006	2487	134	2.007	2487
46.522	13	1.952	2624	127	1.952	2624
47.258	2	1.923	2710	028	1.923	2710
48.913	40	1.862	2890	231	1.862	2890
51.156	16	1.785	3144	233	1.780	3150
53.644	29	1.708	3436	038	1.707	3436
55.741	15	1.649	3690	1110	1.649	3690
58.017	27	1.589	3968	145	1.588	3968
			$Ba_{1.8}Sr_{1.2}Er(BO_3)_3$ powder			
20.500	29	4.332	533	012	4.320	536
23.139	37	3.845	677	211	3.835	680
23.955	13	3.714	725	030	3.706	728
27.726	22	3.218	966	220	3.210	971
28.463	100	3.136	1017	122	3.129	1021
30.460	45	2.935	1161	131	2.932	1167
31.795	10	2.815	1263	113	2.810	1267
34.787	27	2.579	1504	312	2.576	1508
36.427	15	2.467	1650	321	2.461	1653
37.019	20	2.428	1698	140, 410	2.426	1701
40.213	8	2.242	1992	232	2.241	1992
44.213	13	2.048	2387	214	2.047	2387
47.398	21	1.918	2725	422	1.917	2725
48.750	13	1.867	2874	134	1.866	2874
49.574	19	1.838	2967	152	1.837	2967
51.346	19	1.779	3165	250, 520	1.780	3165
59.804	6	1.546	4184	523, 253	1.547	4184

compositions were indexed using crystallographic characteristics of $Sr_3Ho(BO_3)_3$ of the trigonal modification (space group $R\bar{3}$) [5]. The results of indexing of the $Ba_{1.8}Sr_{1.2}Er(BO_3)_3$ powder pattern are given in Table 1.

In the crystal structures of double REE borates, atoms of alkaline-earth elements (Ba, Sr) have the same surrounding (CN 9). The ionic radii of isovalent barium and strontium cations differ only slightly, by no less than 15% [6]. This fact, along

Table 2. Unit cell parameters of double borates and solid solutions based on them in the system $Ba_{3-x}Sr_xEr(BO_3)_3$ ($0 \le x \le 3.0$)

x	Space group	a, Å	c, Å	V, Å^3
0	$P6_3cm$	9.411(1)	17.541(1)	1348.8
0.1	$P6_3cm$	9.402(1)	17.531(1)	1342.0
0.4	$P6_3cm$	9.391(2)	17.480(1)	1335.0
0.5	$R\bar{3}$	12.916(2)	9.433(4)	1362.8
0.6	$R\bar{3}$	12.891(2)	9.410(3)	1354.2
0.8	$R\bar{3}$	12.884(1)	9.401(2)	1351.4
1.0	$R\bar{3}$	12.847(2)	9.385(3)	1339.8
1.2	$R\bar{3}$	12.838(2)	9.376(4)	1336.6
1.4	$R\bar{3}$	12.793(2)	9.355(2)	1324.3
1.6	$R\bar{3}$	12.745(5)	9.321(2)	1309.6
1.8	$R\bar{3}$	12.714(1)	9.311(1)	1301.8
2.0	$R\bar{3}$	12.681(1)	9.280(1)	1290.8
2.5	$R\bar{3}$	12.608(1)	9.245(0)	1271.2
3.0	$R\bar{3}$	12.501(1)	9.221(1)	1247.9

with the similar character of chemical bonds, makes possible formation of the substitution solid solutions of double borates in a wide concentration range.

According to XPA, the solubility region of strontium atoms in the acentric barium structure in the concentration range studied is narrow: $0 \le x \le 0.4$. In this concentration range, the borate $Ba_3Er(BO_3)_3$ of the hexagonal structure (space group $P6_3cm$) is stable. On the contrary, the substitution solid solutions of the $Sr_3Er(BO_3)_3$ trigonal structure (space group $R\bar{3}$) are formed in a wide range of concentrations: $0.5 \le x \le 3.0$. The unit cell parameters of double barium strontium borates and solid solutions based on them are listed in Table 2. As can be seen, the unit cell parameters of the synthesized phases within regions wherein structures of trigonal and hexagonal modifications are formed monotonically decrease as x grows. Change in the unit cell parameters and volumes confirmed formation of two series of solid solutions over the entire concentration range.

CONCLUSIONS

(1) Phases of variable composition in the system $Ba_{3-x}Sr_xEr(BO_3)_3$ ($0 \le x \le 3$) were synthesized by the method of solid-phase reactions in the range 500–1000°C.

(2) According to X-ray phase analysis, the ternary phases synthesized form two series of substitution solid solutions.

REFERENCES

1. Khamaganova, T.N., and Trunov, V.K., *Zh. Neorg. Khim.*, 1997, vol. 42, no. 1, pp. 26–28.
2. Stephanovich, S.Yu., and Khamaganova, T.N., *Neorg. Mater.*, 2002, vol. 38, no. 1, pp. 78–80.
3. Makarov, E.S., *Izomorfizm atomov v kristallakh* (Isomorphism of Atoms in Crystals), Moscow: Atomizdat, 1973.
4. Urusov, V.S., *Teoriya isomorfnoi smesimosti* (Isomorphic Miscibility Theory), Moscow: Nauka, 1977.
5. Khamaganova, T.N., Khrushcheva, N.M., and Bazarova, Zh.G., *Zh. Neorg. Khim.*, 1999, vol. 44, no. 10, pp. 1625–1626.
6. Shannon, R.D., *Acta Crystallogr., Sect. A*, 1976, vol. 32, pp. 751–767.

ISSN 1070-4272, Russian Journal of Applied Chemistry, 2008, Vol. 81, No. 7, pp. 1293–1295. © Pleiades Publishing, Ltd., 2008.
Original Russian Text © L.V. Balsanova, B.G. Bazarov, 2008, published in Zhurnal Prikladnoi Khimii, 2008, Vol. 81, No. 7, pp. 1213–1215.

BRIEF COMMUNICATIONS

Synthesis and Electrical Properties of Triple Molybdates

L. V. Balsanova and B. G. Bazarov

Buryat State University, Ulan-Ude, Buryatia, Russia
Baikal Insitute of Nature Management, Siberian Branch, Russian Academy of Sciences, Ulan-Ude, Buryatia, Russia

Received August 23, 2007

Abstract—Triple molybdates of compositions $M_5(Li_{1/3}Hf_{5/3})(MoO_4)_6$ (M is K, Rb, or Tl) and $M_3LiHf_2 \cdot (MoO_4)_6$ (M is Na, K, Rb, or Tl) were synthesized by solid-phase reaction, and their conductivity in the temperature range 200–550°C was studied.

DOI: 10.1134/S1070427208070331

Advances in the field of synthesis and study of oxygen-containing compounds are due to the development of modern materals science [1, 2]. Recent studies [3, 4] showed that some oxygen-containing molybdenum compounds exhibit ferroelastic and luminescent properties, and the majority of them are characterized by ionic conductivity. Owing to increasing production of devices and equipment that use chemical power sources (CPS), a need is evident for materials with high ionic conductivity [5]. Under the conditions of increasing demand for lithium–ion solid electrolytes [6], a search for novel functional materials with ionic conductivity becomes urgent.

In the study, we prepared triple molybdates $M_5(Li_{1/3}Hf_{5/3})(MoO_4)_6$ (M is K, Rb, or Tl) and $M_3LiHf_2(MoO_4)_6$ (M is Na, K, Rb, or Tl) and examined their conductivivty. As starting compounds we used carbonates of univalent metals (chemically pure grade) and analytically pure grade hafnium dioxide. Before syntheses, hafnium dioxide was calcined at 800–850°C for 6–8 h, and carbonates, at 400–500°C.

The molybdates were synthesized by the solid-state reaction in air. The starting carbonates in the form of a mixture of oxides and carbonates of univalent metals were thoroughly ground in an agate mortar and subjected to stepwise thermal annealing at 400–450, 450–500, and 500–550°C. The time of each step was 10–20 h. Stepwise heating of the products alternated with grinding. The reactant ratios corresponded to the given stoichiometry. The phase compositions of the starting and annealed mixtures were monitored by X-ray phase analysis. The diffraction patterns of the powders were recorded on a DRON-UM1 diffractometer in CuK_α radiation. The phase analysis of the annealed $M_5(Li_{1/3}Hf_{5/3}) \cdot (MoO_4)_6$ (M is K, Rb, or Tl) and $M_3LiHf_2(MoO_4)_6$ (M is Na, K, Rb, or Tl) samples showed that the compounds obtained were individual and contained no impurities [7, 8].

The unit cell parameters were calculated and refined by the least-squares method (LSM). To do this, we used unambiguously identified lines of the powder diffraction patterns and the POLIKRISTALL program [9]. The density in toluene was measured pycnometrically at 25°C using a 5-ml pycnometer.

Triple molybdates $M_3LiHf_2(MoO_4)_6$ (M is K or Rb) are classed with the known structural type $KAl \cdot (MoO_4)_2$ (trigonal crystal system, space group $P\bar{3}m1$, $Z = 1$) [10]. The diffraction pattern of $Tl_3LiHf_2 \cdot (MoO_4)_6$ was indexed assuming formation of a superstructure of the $KIn(MoO_4)_2$ type (rhombic crystal system, space group $Pnam$, $Z = 4$) [11], with trebling of the smallest parameter. Sodium–lithium–hafnium molybdates $Na_3LiHf_2(MoO_4)_6$ are isostructural to $NaIn(MoO_4)_2$ (triclinic crystal system, space group $P\bar{1}$, $Z = 4$) [12]. The crystallographic characteristics and the temperatures of incongruent melting of the synthesized compounds are given in Table 1. The molybdates $M_5(Li_{1/3}Hf_{5/3})(MoO_4)_6$ (M is K, Rb, or Tl) are isostructural to $K_5Mg_{0.5}Zr_{1.5}(MoO_4)_6$ (trigonal crystal system, space group $R3c$, $Z = 6$) [9] (Table 2). This is in line with the previously obtained results [8].

The differential thermal analysis (DTA) was done

Table 1. Crystallographic characteristics and melting points of the compounds synthesized

Compound	Space group	Unit cell parameters				Z	T_m, °C
		a, Å	b, Å	c, Å	α, β, γ, deg		
$Na_3iHf_2(MoO_4)_6$	$P\bar{1}$	18.288(3)	7.987(1)	7.247(1)	91.77, 84.68, 75.97	4	
$K_3LiHf_2(MoO_4)_6$	$P\bar{3}m1$	5.807(3)	–	7.169(4)	–	1	610
$Rb_3LiHf_2(MoO_4)_6$	$P\bar{3}m1$	5.801(1)	–	7.533(2)	–	1	610
$Tl_3LiHf_2(MoO_4)_6$	$Pnam$	14.970(2)	8.764(6)	17.484(2)	–	4	600

Table 2. Crystallographic characteristics and melting points of molybdates

Compound	Space group	Unit cell parameters, Å		Z	Density, g cm^{-3}		T_m, °C
		a	c		calculated	experimental	
$K_5(Li_{1/3}Hf_{5/3})(MoO_4)_6$	$R3c$	10.567(1)	37.441(9)	6	4.00	3.98	610
$Rb_5(Li_{1/3}Hf_{5/3})(MoO_4)_6$	$R3c$	10.660(2)	38.241(5)	6	4.47	4.45	600
$Tl_5(Li_{1/3}Hf_{5/3})(MoO_4)_6$	$R3c$	10.623(1)	37.961(1)	6	6.12	6.11	560

Table 3. Specific electrical conductivity σ and activation energy of conductivity E_a for triple molybdates

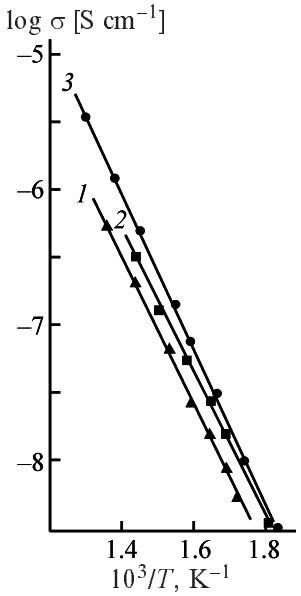
Compound	σ, S cm^{-1}, at indicated temperature T, °C			E_a, eV
	400	450	500	
$Rb_5(Li_{1/3}Hf_{2/3})(MoO_4)_6$	6.46×10^{-6}	1.23×10^{-4}	1.32×10^{-3}	0.51
$Tl_5(Li_{1/3}Hf_{2/3})(MoO_4)_6$	1.2×10^{-2}	1.0×10^{-1}	–	0.43
$Rb_3LiHf_2(MoO_4)_6$	1.5×10^{-6}	–	–	0.54
$Tl_3LiHf_2(MoO_4)_6$	2.29×10^{-3}	7.25×10^{-3}	1.95×10^{-2}	0.60
$Na_3LiHf_2(MoO_4)_6$	3.83×10^{-6}	–	–	0.59
$Na_3LiZr_2(MoO_4)_6$	1.93×10^{-6}	–	–	0.58

on an OD-103 derivatograph (MOM) and a specially designed thermal analytical installation allowing recording of heating (cooling) curves and thermal effects at temperatures of up to 1000°C. The substance weight was 0.3–0.5 g. The triple molybdates prepared melt incongruently and crystallize in four different structural modifications (Table 1).

The temperature dependence of the conductivity σ for samples of the synthesized compounds was studied by the Vest–Tallan polarization method. For this purpose, we used dense ceramic pellets 10 mm in diameter, 4–5 mm thick. The measurements were performed with an E8–4 ac bridge, to which a P5025 capacity box was connected. The frequency was 10^3 Hz. The dc current at a preset voltage of 30–60 mV was recorded wiht an E6-13A teraohmmeter. The electrodes were formed by firing a platinum paste into the surface of pellets. The experimental conductivity activation energies E_a (eV) and specific conductivities σ of the triple molybdates are given in Table 3.

The temperature vs. conductivity curves for molybdates of the compositions $Na_3LiHf_2(MoO_4)_6$ and $Rb_3LiHf_2(MoO_4)_6$ are shown in the figure. The temperature dependence for the zirconium analog $Na_3LiZr_2(MoO_4)_6$ [8] is given for comparison. The conductivity activation energies are 0.43–0.6 eV. Analysis of the conductivity values at various temperatures showed that, in the temperature range studied (400–500°C), the samples exhibit mixed conductivity (ionic and electronic), with the ionic conductivity dominating.

The conductivity values (10^{-3}–10^{-2} S cm^{-1} at 450–500°C) allow the triple molybdates to be classed with solid electrolytes.



Conductivity σ vs. temperature T curve for (*1*) $Na_3LiHf_2(MoO_4)_6$, (*2*) $Na_3LiZr_2(MoO_4)_6$, and (*3*) $Rb_3LiHf_2(MoO_4)_6$.

The electrical properties of triple molybdates are accounted for by the specific features of their structure [8]. Owing to voids and channels present in the structure, single-charged ions start to freely migrate in the corresponding direction upon the exposure of an electric filed.

CONCLUSIONS

(1) Triple molybdates $M_5(Li_{1/3}Hf_{5/3})(MoO_4)_6$ (M is K, Rb, or Tl) and $M_3LiHf_2(MoO_4)_6$ (M is Na, K, Rb, or Tl) were prepared from starting carbonates of univalent metals and hafnium dioxide by the solid-phase reaction.

(2) Molybdates of the composition $M_5(Li_{1/3}Hf_{5/3})(MoO_4)_6$ (M is K, Rb, or Tl) are isostructural and crystallize in the trigonal crystal system (space group $R3c$, $Z = 6$). Triple molybdates of the composition $M_3LiHf_2(MoO_4)_6$ (M is Na, K, Rb, or Tl) crystallize in three different structural modifications ($P\bar{1}$, $P\bar{3}m1$, and $Pnma$), depending on the nature of single-charged cations.

(3) Triple molybdates of single-charged lithium cations and zirconium exhibit mixed conductivity, with the ionic conductivity at 400–500°C dominating.

REFERENCES

1. Trunov, V.K., Efremov, V.A., and Velikodnyi, Yu.A., *Kristallokhimiya i svoistva dvoinykh molibdatov i vol'framatov* (Crystal Chemistry and Properties of Double Molybdates and Tungstates), Leningrad: Nauka, 1986.
2. Mokhosoev, M.V. and Bazarova, Zh.G., *Slozhnye oksidy molibdena i vol'frama s elementami I–IV grupp* (Complex Molybdenum and Tungsten Oxides with Group I–IV Elements), Moscow: Nauka, 1990.
3. Il'ina, A.A., Stenina, I.A., Veresov, A.G., and Yaroslavtsev, A.B., *Zh. Neorg. Khim.*, 2007, vol. 52, no. 4, pp. 525–530.
4. Il'ina, A.A., Stenina, I.A., Lysanova, G.V., et al., *Zh. Neorg. Khim.*, 2006, vol. 51, no. 6, pp. 960–965.
5. Kunshina, G.B., Gromov, O.G., Kuz'min, A.P., et al., *Zh. Prikl. Khim.*, 2004, vol. 77, no. 6, pp. 929–934.
6. Aleksandrov, P.E., Anurova, A.I., Petropavlovskii, M.E., et al., *Zh. Prikl. Khim.*, 2007, vol. 80, no. 8, pp. 1291–1294.
7. Solodovnikov, S.F., Balsanova, L.V., Bazarov, B.G., et al., *Zh. Neorg. Khim.*, 2003, vol. 48, no. 7, pp. 1197–1201.
8. Balsanova, L.V., Triple Molybdates of Lithium, Univalent Metals, and Hafnium, *Cand. Sci. Dissertation*, Irkutsk, 2004.
9. Tsybulya, S.V., Cherepanova, S.V., and Solov'eva, S.V., *Zh. Strukt. Khim.*, 1996, vol. 37, no. 2, pp. 379–382.
10. Klevtsova, R.F., and Klevtsov, P.V., *Kristallografiya*, 1970, vol. 15, no. 5, pp. 953–959.
11. Klevtsova, R.F., and Klevtsov, P.V., *Kristallografiya*, 1971, vol. 16, no. 2, pp. 292–296.
12. Klevtsova, R.F., and Klevtsov, P.V., *Kristallografiya*, 1972, vol. 17, no. 5, pp. 890–894.
13. Vest, R.W., and Tallan, N.W., *J. Appl. Phys.*, 1965, vol. 35, p. 543.

ISSN 1070-4272, Russian Journal of Applied Chemistry, 2008, Vol. 81, No. 7, pp. 1296–1298. © Pleiades Publishing, Ltd., 2008.
Original Russian Text © Yu.I. Sal'nikov, Yu.V. Sidorov, K.A. Burkov, 2008, published in Zhurnal Prikladnoi Khimii, 2008, Vol. 81, No. 7, pp. 1216–1218.

BRIEF COMMUNICATIONS

Solubility Products of Basic Salts $Cu_2(OH)_3NO_3$ and $Hg_3O_2(NO_3)_2$, Determined from Dilatometric Data

Yu. I. Sal'nikov, Yu. V. Sidorov, and K. A. Burkov

Kazan State University, Kazan, Tatarstan, Russia
St. Petersburg State University, St. Petersburg, Russia

Received May 7, 2007

Abstract—The solubility products of basic salts $Cu_2(OH)_3NO_3$ and $Hg_3O_2(NO_3)_2$ were determined using dilatometric data.

DOI: 10.1134/S1070427208070343

Difficultly soluble oxo and hydroxo compounds formed by induced hydrolysis are typical of the majority of metal ions. Data on the composition and solubility products of the above compounds are necessary for quantitative evaluation of the concentration of ions in heterogeneous systems. This is especially important for the case of metals contaminating the environment.

The dilatometric method was used previously to study the volume changes that accompany induced hydrolysis of some cations and result from the shift of the equilibrium toward formation of precipitate on adding alkali. It was shown, in particular, that chemical interactions in the systems depend on the molar ratio of alkali and a cation subject to hydrolysis (N = OH/M). The above dependence was demonstrated for the $Cu(NO_3)_2$, HNO_3–$NH_3 \cdot H_2O$–H_2O and $Cu(NO_3)_2$, HNO_3–KOH–H_2O systems in [1] and for the $Hg(NO_3)_2$, HNO_3–KOH–H_2O system in [2]. It was found that basic salts $Cu_2(OH)_3NO_3$ and $Hg_3O_2(NO_3)_2$ are formed first, which is followed by formation of $Cu(OH)_2$ and HgO (the composition of the solid phases calculated from the dilatometric data was confirmed by X-ray phase analysis). Thus, it was shown that the action of an electrolyte induces metamorphization (change in composition and structure of a solid compound) in the heterogeneous system.

Based on dilatometric data [1, 2] and potentiometric studies [3, 4], schemes of induced hydrolysis were suggested for copper(II) and mercury(II) ions, involving transformations of aqua complexes in solution into solid oxo and hydroxo compounds.

Some data on the solubility products (SPs) of oxo and hydroxo compounds of copper(II) and mercury(II) are available from the literature. According to [5], in particular, the SP for copper hydroxo nitrate

$$Cu_2(OH)_3NO_3 \rightleftarrows 2Cu^{2+} + 3OH^- + NO_3^- \qquad (1)$$

is 3.2×10^{-32} and 5.8×10^{-33} in 2 M methylammonium nitrate and 2 M diethylammonium nitrate, respectively.

For $Cu(OH)_2$, SP is 2.2×10^{-20} and for HgO, 3×10^{-26} [6]. At the same time, data on the SP of $Hg_3O_2(NO_3)_2$ are lacking.

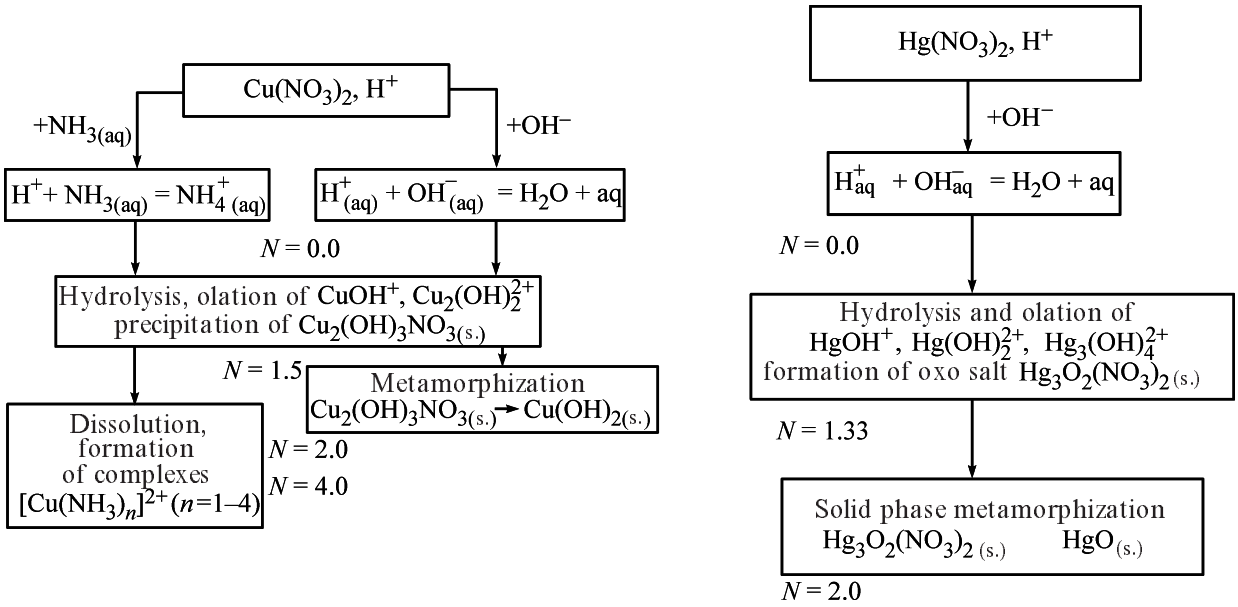
In this study, we applied the results of dilatometric measurements at 25°C in 1 M KNO_3 to obtain quantitative characteristics of the solubility products of basic salts $Cu_2(OH)_3NO_3$ and $Hg_3O_2(NO_3)_2$. The SPs of the basic salts under study were calculated by mathematical simulation (CPESSP program) [7, 8]. In calculating the equilibrium composition by Brinkley's method [9], the CPESSP program for heterogeneous systems sets limits for the solubility products of precipitate species in the form

$$\sum \nu_{ij} \ln b_j - \ln K_i \le 0, \qquad i = 1, 2, \ldots, m;\ i = 1, 2, \ldots, s;$$

or in the matrix form

$$\nu \ln b - \ln K \le \mathbf{O},$$

where K_i is the solubility product of the ith precipitate; m, number of precipitate species; s, number of



Steps of induced hydrolysis in the systems $Hg(NO_3)_2$, HNO_3–KOH–H_2O; $Cu(NO_3)_2$, HNO_3–$NH_3 \cdot H_2O$–H_2O; and $Cu(NO_3)_2$, HNO_3–KOH–H_2O at different molar ratios N.

starting reactants (basis species); v, stoichiometric matrix with respect to precipitate species; $\ln b$ and $\ln K$, vectors of equilibrium concentrations and solubility products of basis species in the logarithmic scale, respectively; and **O**, zero vector.

This procedure allows the equilibrium composition with respect to the soluble species and species separated from a liquid-phase system to be expressed in the same concentration units (in the program, in M), which makes it possible to use the additivity rule for processing results of dilatometric measurements. According to the additivity rule, the total value of the volume change ΔV_m observed in the reaction is the sum of contributions from single interactions ΔV_i:

$$\Delta V_m = \sum_{i=1}^{N} \alpha_i \Delta V_i, \qquad (2)$$

where ΔV_i is the change in the reduced volume or the volume change in formation of 1 mol of the ith species and ΔV_i is its fraction or concentration.

The matrix constructed in the course of the calculation includes a set of basis, complex, and precipitated species present in the system. To each of them, the initial value of property ΔV_i and the formation constant for soluble species or the SP value for precipitate species are ascribed.

The K_i constants were used to calculate α_i for each species at each titration point and, correspondingly, ΔV_{cal}. The convergence of the calculated and experimental points was checked by the Fisher test, which is calculated as the sum of the weighted squared deviations reduced to the number of the degrees of freedom m ($m = M$ is k, where k is the total number of the parameters being determined):

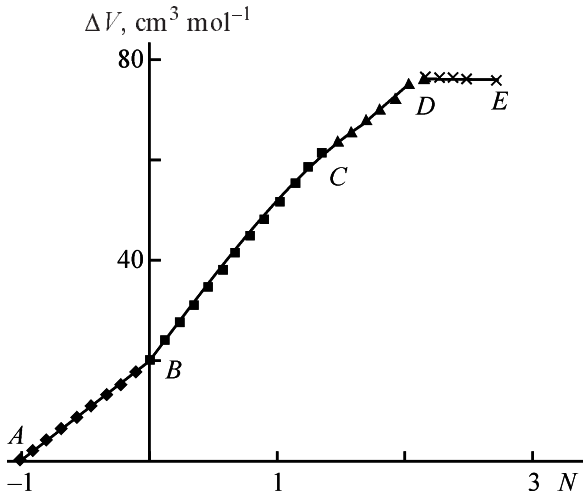
$$F_r = m^{-1} \sum_{j=1}^{M} (\Delta V_{exp} - \Delta V_{calc})^2 / [(\sigma \Delta V_{exp})^2 + (\Delta \Delta V)^2],$$

$$F_r \le 2, \quad m > 5, \qquad (3)$$

where σ is the relative (taken $\sigma = 0.05$), and $\Delta\Delta V$, absolute determination error (taken $\Delta\Delta V = 0.007$ cm^3).

The minimum was found by the iteration procedure using the dependence (2) and the target function F_r (3). We found the values of ΔV_i and of the unknown constant, SP of basic salt, corresponding to the minimum of the target function. In going to the global minimum in the program, the analysis block was used in each iteration to efficiently overcome local minima and "gullies" of the target function.

It is important that the CPESSP program for processing of the physicochemical responses [data of various methods in which the response can be described by Eq. (2)] allows simultaneous determination of the equilibrium constants and SP (solubility). Both the soluble species and the species separating out from a solution (in the form of precipitates and



Dilatometric titration curve for the $Hg(NO_3)_2$, HNO_3–KOH–H_2O system: (points) experimental data and (lines) calculation. (ΔV) change in molar volume, $N = (n_{OH} - n)/n_{Hg}$.

in the gaseous state) can be included into the stoichiometry matrix of the system in the course of simulation.

The initial model for the $Cu(NO_3)_2$, HNO_3–$NH_3 \cdot H_2O$–H_2O system included dissolved hydroxo complexes [$Cu(OH)^+$, $Cu_2(OH)_2^{2+}$, Cu_2OH^{3+}] (hydrolysis constants pK –7.4±0.1, –10.93±0.02, and –6.02±0.02, respectively [3]), ammine complexes {$Cu(NH_3)_n^{2+}$ (n = 1–4, $\log k_1$ = 4.31, $\log k_2$ = 3.67, $\log k_3$ = 3.04, $\log k_4$ = 2.30) [5]}, and solid compounds $Cu_2(OH)_3NO_3$ and $Cu(OH)_2$.

The best fit of the calculation results to the experimental SP values was achieved for $Cu_2(OH)_3 \cdot NO_3$, $(1.3 \pm 0.3) \times 10^{-31}$. This SP value correlates with the above-presented literature data. Some difference between the values is due to the effect of the medium.

The model for calculating SP of $Hg_3O_2(NO_3)_2$ included hydroxo complexes in solution {$HgOH^+$, Hg_2OH^{3+}, $Hg_3(OH)_4^{2+}$} [8]} and solid phases $Hg_3O_2(NO_3)_2$ and HgO.

The experimental results obtained in the dilatometric study of hydrolytic transformations of mercury nitrate and the theoretical curve calculated by the optimization method are presented in the figure as example. The best fit of the calculation results to the experimental data for the systems studied was achieved at SP values of basic mercury nitrate of $(5.2 \pm 0.1) \times 10^{-56}$ according to the equilibrium

$$Hg_3O_2(NO_3)_2 + 2H_2O \rightleftarrows 3Hg^{2+} + 4OH^- + 2NO_3^-. \quad (4)$$

CONCLUSIONS

(1) The applicability of dilatometric method to determination of quantitative characteristics, the solubility products of basic salts, was demonstrated.

(2) The solubility products of $Cu_2(OH)_3NO_3$ and $Hg_3O_2(NO_3)_2$ in 1 M KNO_3 at 25°C, calculated from data of the dilatometric measurements, are $(1.3 \pm 0.3) \times 10^{-31}$ and $(5.2 \pm 0.1) \times 10^{-56}$, respectively.

ACKNOWLEDGMENTS

The study was financially supported by the Russian Foundation for Basic Research (project nos. 05-03-32099 and 07-03-00991-a).

REFERENCES

1. Burkov, K.A., Sidorov, Yu.V., Sal'nikov, Yu.I., and Kryuchkova, N.A., *Zh. Prikl. Khim.*, 2002, vol. 75, no. 7, pp. 1072–1077.
2. Sidorov, Yu.V., Burkov, K.A., and Pykhteev, O.Yu., *Vestn. Sankt-Peterb. Gos. Univ., Ser. 4*, 2003, issue 1, no. 4, pp. 88–91.
3. Burkov, K.A., Bus'ko, E.A., Lilich, L.S., and Ivanova, I.N., *Zh. Neorg. Khim.*, 1982, vol. 27, no. 6, pp. 1455–1459.
4. Ahlberg, I., *Acta Chem. Scand.*, 1962, vol. 16, pp. 887–893.
5. Bjerrum, J., *Metal Ammine Formation in Aqueous Solution. Theory of Reversible Step Reactions*, Copenhagen: P. Haase, 1957.
6. Rabinovich, V.A., and Khavin, Z.Ya., *Kratkii khimicheskii spravochnik* (Concise Chemical Handbook), Leningrad: Khimiya, 1978.
7. Sal'nikov, Yu.I., Glebov, A.N., and Devyatov, F.V., *Poliyadernye kompleksy v rastvorakh* (Polynuclear Complexes in Solutions), Kazan: Kazan. Univ., 1989.
8. Sal'nikov, Yu.I. and Devyatov, F.V., *Rastvory – elektrolitnye sistemy: Mezhvuzovskii sbornik* (Solutions as Electrolyte Systems: Intercollegiate Coll.), Ivanovo, 1988, pp. 38–41.
9. Brinkley, S.R., Jr., *J. Chem. Phys.*, 1947, vol. 15, no. 2, pp. 107–110.

ISSN 1070-4272, Russian Journal of Applied Chemistry, 2008, Vol. 81, No. 7, pp. 1299–1301. © Pleiades Publishing, Ltd., 2008.
Original Russian Text © M.N. Gorbunova, A.I. Vorob'eva, D.R. Sagitova, A.G. Tolstikov, 2008, published in Zhurnal Prikladnoi Khimii, 2008, Vol. 81, No. 7, pp. 1219–1221.

BRIEF COMMUNICATIONS

Copolymerization of *N*-Vinylpyrrolidone with 2,2-Diallyl-1,1,3,3-tetraethylguanidinium Chloride

M. N. Gorbunova, A. I. Vorob'eva, D. R. Sagitova, and A. G. Tolstikov

Institute of Technical Chemistry, Ural Branch, Russian Academy of Sciences, Perm, Russia
Institute of Organic Chemistry, Ufa Research Center, Russian Academy of Sciences, Ufa, Bashkortostan, Russia

Received December 24, 2007

Abstract—Radical copolymerization of *N*-vinylpyrrolidone with 2,2-diallyl-1,1,3,3-tetraethylguanidinium chloride in the bulk and in dimethyl sulfoxide was studied. Kinetic parameters of the reaction were examined. The monomer activities were determined.

DOI: 10.1134/S1070427208070355

Directed synthesis of water-soluble polyfunctional polymers attracts growing attention. One of the promising procedures for preparing these polymers is copolymerization of monomers containing different functional groups. In this connection, *N*-vinylpyrrolidone (VP) copolymers attract much interest. These copolymers are widely used in engineering, medicine, cosmetic industry, pharmacy, and agriculture [1, 2].

Synthesis of polymers derived from diallyl compounds is also a topical problem. The study of radical polymerization of allyl monomers concerns mainly homo- and copolymerization of *N,N*-diallyl-*N,N*-dimethylammonium chloride. Copolymers of this compound are used as flocculants for wastewater treatment, catalysts of some chemical reactions, growth stimulants, aftertanning agents in leather manufacture, etc. [3–6]. A wide range of useful properties of nitrogen-containing allyl copolymers stimulates preparation and study of new copolymers of this type. In this connection, 2,2-diallyl-1,1,3,3-tetraethylguanidinium chloride (AGC) shows promise as an initial monomer for radical copolymerization. It is known that polymers containing guanidine groups exhibit biocidal activity [7] and can be used as antibacterial agents. Therefore, preparation of AGC–VP copolymers is an urgent problem.

The aim of this study was to examine radical copolymerization of VP with AGC in the bulk and in dimethyl sulfoxide (DMSO) solution and some properties of the resulting copolymers.

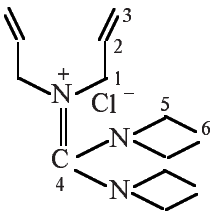
EXPERIMENTAL

N-Vinylpyrrolidone (Lancaster) was dried over KOH and distilled under reduced pressure. The fraction with bp 65°C/1.5 mm Hg and n_D^{20} = 1.5117 was collected.

2,2-Diallyl-1,1,3,3-tetraethylguanidinium chloride was prepared by the known procedure [8]. Its purity was determined by elemental analysis and ^{13}C NMR spectroscopy.

Found, %: C 62.42, H 10.67, N 14.58, Cl 12.32.
Calculated, %: C 62.61, H 10.43, N 14.61, Cl 12.35.

The chemical shifts δ (ppm) and signal multiplicities in the ^{13}C NMR spectrum are presented below



C^1	C^2	C^3	C^4	C^5	C^6
54.56	133.76	123.41	165.71	45.83	14.48
t	d	t	s	t	q

Initiator [azobis(isobutyronitrile), AIBN] and solvents were purified by standard procedures [9]. Their properties were consistent with the reference data.

Apparent copolymerization constants of VP (M_1) and AGC (AIBN, 80°C)

Medium	r_1	r_2
In bulk	0.92±0.01	1.35±0.12
DMSO	0.83±0.07	1.80±0.15

Copolymerization of VP with AGC in the bulk and in DMSO was performed under reduced pressure in the presence of AIBN in the initial steps (conversion ≤5%). The polymerization kinetics was monitored by dilatometry [10]. Once the required conversion was reached, the reaction was stopped by cooling and the copolymer was precipitated with diethyl ether. The copolymer was reprecipitated two times from a methanol solution with diethyl ether and dried in a vacuum at 40–50°C to constant weight. The copolymer composition was determined by elemental analysis.

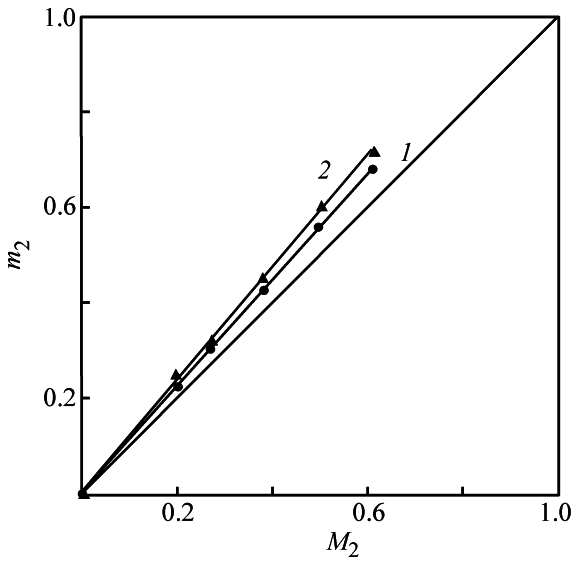


Fig. 1. Composition of VP–AGC (M_2) copolymers prepared by polymerization (*1*) in the bulk and (*2*) in DMSO solution as a function of the composition of the initial monomer mixture. [AIBN] = 1.0×10^{-2} M, T = 80°C. M_2 and m_2 are mole fractions of AGC in the initial mixture and copolymer, respectively.

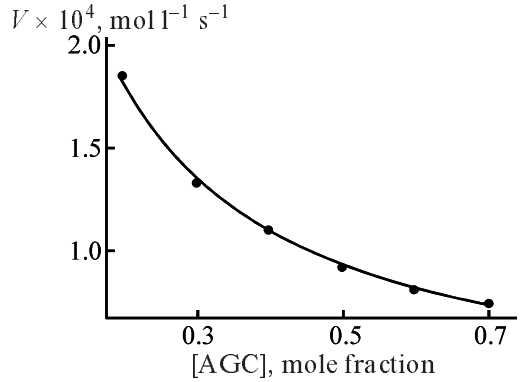


Fig. 2. Initial rate V of copolymerization of VP with AGC (M_2) as a function of the mole fraction of AGC in the initial monomer mixture. DMSO, [M_1 + M_2] = 3.2 M, [AIBN] = 1.0×10^{-2} M, T = 80°C.

The apparent copolymerization constants r_1 and r_2 were calculated by Mayo–Lewis [11], Finemann–Ross [12], and Kelen–Tudos [13] procedures.

The ^{13}C NMR spectra were recorded on Bruker AM-300 spectrometer operating at 75.5 MHz, with broad-band proton decoupling in the JMOD mode. The solvents were DMSO-d_6 and D_2O. Tetramethylsilane and 2,2-dimethyl-2-silapentane-5-sulfonic acid were used as internal references.

The intrinsic viscosity [η] was measured with an Ubbelohde viscometer.

The acute toxicity parameters of the copolymer samples were determined by the Prozorovskii express method [14].

Previously we found [8] that AGC slowly homopolymerized in the presence of radical initiators. We also showed that AGC copolymers with vinyl monomers (methyl methacrylate, acrylic acid, methacrylic acid, and VP) could be prepared. It was of interest to study copolymerization of VP with AGC in more detail. We found that VP–AGC copolymers with random distribution of monomeric units were formed. The dependence of the copolymer composition on the composition of the initial monomer mixture is show in Fig. 1. The apparent copolymerization constants of VP (M_1) with AGC (M_2) are presented in the table. It is seen that the reactivity of the allyl monomer in the system is slightly higher than that of VP. The difference is more pronounced in a DMSO solution.

Our kinetics experiments showed that the reaction order with respect to initiator was 0.5. This fact suggests bimolecular termination of the propagating chain and the absence of degradation chain transfer to the monomer, which is typical for allyl compounds. The total reaction order with respect to both monomers at their equimolar ratio in DMSO solution is 1.3. As the content of the allyl monomer (M_2) in the initial monomer mixture increases, the polymerization decelerates (Fig. 2).

The temperature dependence of the reaction rate in DMSO was studied in the range 70–90°C. The overall activation energy of copolymerization of VP with AGC is 68.3±1.5 kJ mol^{-1}.

Our previous ^{13}C NMR study [8] showed that both double bonds of AGC were involved in copolymerization to form five-membered pyrrolidinium structures. These results agree with the known data on homopolymerization of diallyl nitrogen-containing compounds, in particular, *N,N*-diallyl-*N,N*-dimethylammonium halides, and on their copolymerization with SO_2 [15].

VP–AGC copolymers are soluble in water, methanol, chloroform, dimethylformamide, and DMSO. The intrinsic viscosity of VP–AGC copolymers (80 : 20 mol %) is 0.16 dl g^{-1} (water with 0.1 N NaCl, 25°C). The molecular weight of the copolymer containing 20 mol % AGC, roughly estimated by the Levy–Frank equation for aqueous solutions of polyvinylpyrrolidone ($[\eta] = 6.76M^{0.55} \times 10^{-4}$ [16]), is 20700.

Our toxicological study shows that VP–AGC copolymers belong to the fourth hazard category.

Our study of the biocidal activity showed that the polymers exhibited pronounced antimicrobial activity with respect to gram-positive microflora (*Staphylococcus aureus*) and could be used in medicine and biotechnology.

CONCLUSIONS

(1) *N*-Vinylpyrrolidone copolymerizes with 2,2-diallyl-1,1,3,3-tetraethylguanidinium chloride to form random copolymers. The apparent copolymerization constants show that the relative reactivity of 2,2-diallyl-1,1,3,3-tetraethylguanidinium chloride is higher than that of *N*-vinylpyrrolidone.

(2) The copolymerization rate decreases with increasing fraction of the diallyl monomer in the initial monomer mixture.

(3) In the course of copolymerization, both double bonds of 2,2-diallyl-1,1,3,3-tetraethylguanidinium chloride undergo intramolecular cyclization to form pyrrolidinium rings in the macromolecule.

(4) The polymers are nontoxic in intragastric introduction, belong to the fourth hazard category, and exhibit pronounced antimicrobial activity with respect to gram-positive microflora.

ACKNOWLEDGMENTS

This study was financially supported by the Russian Foundation for Basic Research (project no. 05-03-32097).

REFERENCES

1. Sidel'kovskaya, F.P., *Khimiya N-vinylpirrolidona i ego polimerov* (Chemistry of *N*-Vinylpyrrolidone and Its Polymers), Moscow: Nauka, 1970.
2. Kirsh, Yu.E., *Poli-N-vinylpirrolidon i drugie poli-N-vinilamidy* (Poly-*N*-vinylpyrrolidone and Other Poly-*N*-vinylamides), Moscow: Nauka, 1998.
3. USSR Inventor's Certificate no. 1744797.
4. USSR Inventor's Certificate no. 910664.
5. USSR Inventor's Certificate no. 1530631.
6. USSR Inventor's Certificate no. 1495339.
7. *Khimichekaya entsiklopediya* (Chemical Encyclopedia), Knunyants, I.L., Ed., Moscow: Sov. Entsiklopediya, 1988, vol. 1.
8. Vorob'eva, A.I., Sagitova, D.R., Gorbunova, M.N., et al., *Vysokomol. Soedin., Ser. B*, 2007, vol. 49, no. 7, pp. 1293–1298.
9. Gordon, A.J. and Ford, R.A., *The Chemist's Companion. A Handbook of Practical Data, Techniques, and References*, New York: Wiley, 1972.
10. Gorbunova, M.N., Strukov, V.D., and Fedoseev, M.S., *Vysokomol. Soedin., Ser. B*, 2003, vol. 45, no. 10, pp. 1765–1768.
11. Mayo, F.R. and Lewis, F.J., *J. Am. Chem. Soc.*, 1944, vol. 66, pp. 1594–1601.
12. Finemann, M. and Ross, S.D., *J. Polym. Sci.*, 1950, vol. 5, pp. 269–284.
13. Kelne, T. and Tudos, F., *J. Macromol. Sci., Chem.*, 1975, vol. 9, no. 1, pp. 1–27.
14. Prozorovskii, V.B., Prozorovskaya, M.P., and Demchenko, V.M., *Farmokol. Toksikol.*, 1978, no. 4, pp. 497–502.
15. Vorob'eva, A.I., Vasil'eva, E.V., Gaisina, Kh.A., et al., *Vysokomol. Soedin., Ser. A*, 1996, vol. 38, no. 10, pp. 1663–1667.
16. Levy, G.B. and Frank, H.P., *J. Polym. Sci.*, 1955, vol. 17, no. 84, pp. 247–254.

ISSN 1070-4272, Russian Journal of Applied Chemistry, 2008, Vol. 81, No. 7, pp. 1302–1304. © Pleiades Publishing, Ltd., 2008.
Original Russian Text © F.E. Kalinina, D.M. Mognonov, L.D. Radnaeva, 2008, published in Zhurnal Prikladnoi Khimii, 2008, Vol. 81, No. 7, pp. 1222–1223.

BRIEF COMMUNICATIONS

Poly(Hydroxy Urethane) Coatings Prepared from Copolymers of 3-(2-Vinyloxyethoxy)-1,2-propylene Carbonate and *N*-Phenylmaleimide

F. E. Kalinina, D. M. Mognonov, and L. D. Radnaeva

Baikal Institute of Nature Management, Siberian Branch, Russian Academy of Sciences, Ulan-Ude, Buryatia, Russia

Received December 12, 2007

Abstract—Poly(hydroxy urethanes) and coatings based on them were prepared by ammonolysis of copolymers of 3-(2-vinyloxyethoxy)-1,2-propylene carbonate and *N*-phenylmaleimide.

DOI: 10.1134/S1070427208070367

Particular interest in polymers with cyclocarbonate groups is caused by the possibility of preparing from them polyurethanes without using toxic isocyanates. The isocyanate-free process is based on the reaction of cyclocarbonates with amines [1–3].

Copolymers containing five-membered carbonate rings in the pendant chain were prepared previously by radical copolymerization of 3-(2-vinyloxyethoxy)-1,2-propylene carbonate (VOPC) and *N*-phenylmaleimide (PMI) [4]. Here we report on preparation of poly(hydroxy urethane) coatings by modification of VOPC–PMI copolymers with amines at cyclocarbonate groups.

EXPERIMENTAL

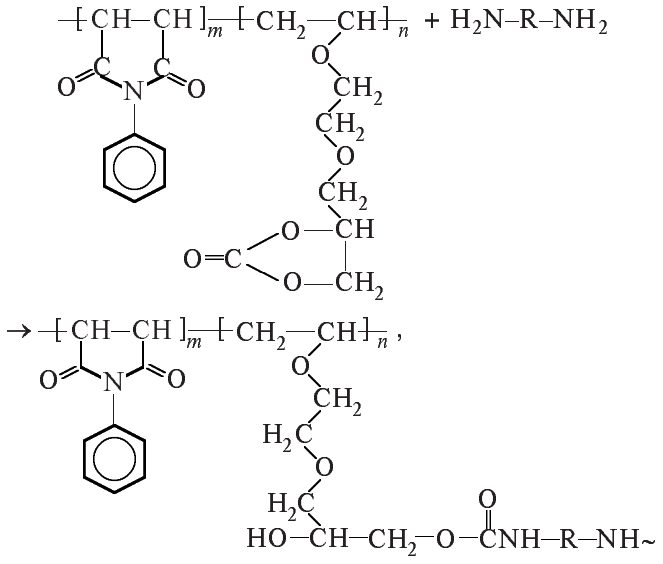
N-Phenylmaleimide was prepared by a common procedure from maleic anhydride and aniline [5]. VOPC was synthesized at the pilot plant of the Favorskii Irkutsk Institute of Chemistry, Siberian Branch, Russian Academy of Sciences [6]. VOPC–PMI copolymers were prepared by radical copolymerization in methyl ethyl ketone (MEK) in the presence of AIBN initiator [4].

Aminolysis of the copolymers was performed in DMF at room temperature for 6 h. The resulting product was precipitated with toluene and then dried in a vacuum oven at 40°C for 3 h. The copolymer has approximately equimolar composition.

Poly(hydroxy urethane) coatings were prepared as follows. VOPC–PMI copolymer was mixed with a solution of polyamine in DMF. The mixture was applied onto plates of cold-rolled 08 kp steel sheets according to GOST (State Standard) 9045–80 and dried at room temperature or at 150°C.

The IR spectra were recorded on IFS25 and UR-20 spectrophotometers in the wavenumber range 4000–400 cm^{-1}. Samples were prepared as KBr pellets. The moisture absorption was determined according to [7]. The impact strength was evaluated with a UM1 device according to GOST 4765–73. The adhesion of the coating was determined by grid notching according to GOST 15140–78.

For the modification of VOPC–PMI copolymers we used 1,2-ethylenediamine (EDA) and 1,6-hexamethylenediamine (HMDA). Aminolysis of the copolymers follows the scheme



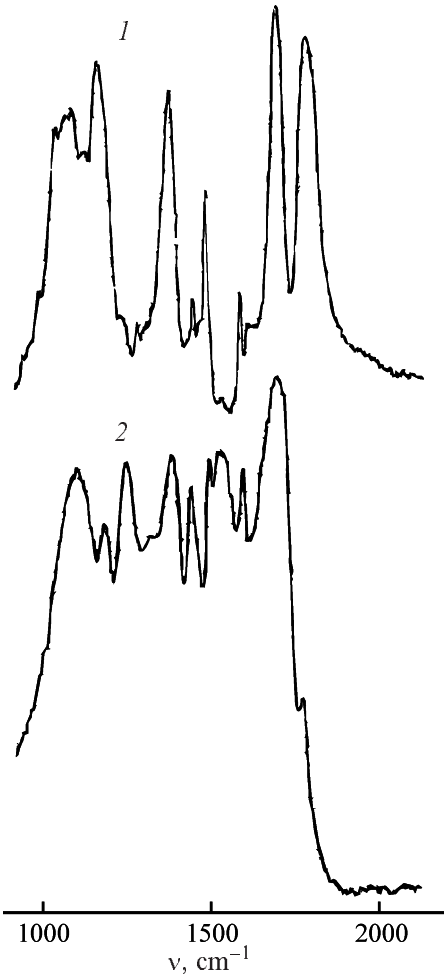
Moisture absorption and solubility of polyurethane coatings obtained (curing at 150°C for 3 h)

Composition	Moisture absorption in 24 h, %	Solubility*				
		DMF	concd. H_2SO_4	NaOH, 50% solution	petroleum ether	acetone
Copolymer–polyethylene-polyamine	17.4	Swells	S on heating	Swells	IS	IS
Copolymer–4,4'-diamino-3,3'-dimethyldiphenylmethane	0.6	IS	IS	IS	IS	IS

* (S) Soluble and (IS) insoluble.

where R = $-(CH_2)_2-$, $-(CH_2)_6-$; n = 1; m = 1.1–1.6.

The poly(hydroxy urethanes) obtained with HMDA and EDA are dark blue solid resins. The absence of the absorption band of the carbonate carbonyl group at 1830 cm^{-1} in the IR spectrum and the appearance of amide absorption bands (1252, 1538, 1675 cm^{-1}) is indicative of complete opening of the carbonate ring and formation of urethane groups (see figure).



IR spectra of (*1*) VOPC–PMI copolymer and (*2*) poly(hydroxy urethane). (ν) Wavenumber.

From the poly(hydroxy urethanes) synthesized, we prepared hot- (150°C) and cold-cured coatings. As curing agent we used EDA, HMDA, and polyethylenepolyamine at equimolar ratio of the copolymer and curing agent and at excess of the latter. The best adhesion to metal surfaces, 2 points according to GOST 15140–78 (1 point according to ISO 2409–72 standard) were obtained at equimolar ratio of the copolymer and curing agent. In impact strength tests of the coatings, signs of damage appeared at an impact height of 35–40 cm.

Coatings exhibiting high chemical resistance and low moisture absorption were prepared from the copolymer and 4,4'-diamino-3,3'-dimethyldiphenylmethane (see table). Such coatings do not dissolve in concentrated solutions of acids and alkalis, and their moisture absorption is below 1%. However, their adhesion to metal surfaces and impact strength are poor, probably because of the fact that aromatic amines react with cyclocarbonates without formation of urethane groups imparting the elasticity to the material [1].

CONCLUSION

Aminolysis of copolymers of 3-(2-vinyloxyethoxy)-1,2-propylene carbonate and *N*-phenylmaleimide, containing cyclocarbonate groups, allows preparation of poly(hydroxy urethane) coatings exhibiting good mechanical properties.

REFERENCES

1. Mikheev, V.V., Svetlakov, N.V., Garipov, R.M., et al., *Lakokras. Mater. Ikh Primen.*, 1985, no. 5, p. 27.
2. Figovsky, O.I. and Shapovalov, L.D., *Macromol. Symp.*, 2002, vol. 187, p. 325.
3. Webster, D.C., *Prog. Org. Coat.*, 2003, vol. 47, p. 77.
4. Kalinina, F.E., Radnaeva, L.D., Mognonov, D.M., et al., *Vysokomol. Soedin., Ser. B*, 2004, vol. 46, no. 6, p. 1116.
5. Landgrebe, J.A., *Theory and Practice in the Organic Laboratory*, Brooks: Cole, 2005.
6. Nedolya, N.A., Tatarova, T.F., Vyalykh, E.P., and Trofimov, B.A., *Zh. Org. Khim.*, 1988, vol. 24, no. 8, p. 1623.
7. Karyakina, M.I. and Popov, V.E., *Tekhnologiya polimernykh pokrytii* (Technology of Polymeric Coatings), Moscow: Khimiya, 1983.

ISSN 1070-4272, Russian Journal of Applied Chemistry, 2008, Vol. 81, No. 7, pp. 1305–1307. © Pleiades Publishing, Ltd., 2008.
Original Russian Text © M.V. Efanov, A.I. Galochkin, V.A. Novozhenov, 2008, published in Zhurnal Prikladnoi Khimii, 2008, Vol. 81, No. 7, pp. 1224–1226.

BRIEF COMMUNICATIONS

Synthesis of Mixed Wood Esters

M. V. Efanov, A. I. Galochkin, and V. A. Novozhenov

Research Institute of Wood Thermoplastics, Altai State University, Barnaul, Russia

Received February 5, 2008

Abstract—A new procedure was developed for preparing mixed esters of lignocarbohydrate materials. Transformations of aspen wood in the course of its acylation with a mixture of acetic anhydride with aliphatic carboxylic acid under the conditions of mechanochemical activation in the presence of ammonium sulfate as catalyst were studied.

DOI: 10.1134/S1070427208070379

Acylation of wood is a promising direction of its chemical modification. Wood acylation products are soluble in organic solvents. They exhibit hydrophobic and thermoplastic properties and are bioresistant. These physicochemical properties determine possible application fields of wood acylation products [1].

The use of acylated wood as a thermoplastic binder for preparing composite materials with a mineral or wood filler allows preparation of wood boards with good physicomechanical and hydrophobic properties. This is favored by high thermoplasticity of acylated wood and its good adhesion to mineral and especially organic substances (wood) [2].

Procedures have been developed for preparing esters from wood mechanochemically activated in the presence of catalysts by acylation with a mixture of acetic anhydride (AAn) with a carboxylic acid at 100–130°C for 4–6 h. These procedures have certain drawbacks: long synthesis time (up to 6 h), elevated temperature, and high consumption of acylating agents (up to 10 mol) [3, 4].

A more efficient mechanochemical procedure for acylation of lignocarbohydrate materials with acetic anhydride or a mixture of acetic anhydride and a carboxylic acid in the presence of ammonium sulfate as catalyst was developed previously [5, 6]. In this study we examined the composition and properties of products obtained by mechanochemical acylation of aspen wood.

EXPERIMENTAL

Mechanochemical acylation of vegetable raw materials was performed as follows: A reactor of a vibration mill (IV 98B commercial vibrator, frequency 2800 min^{-1}) with 15 steel rods (10 × 100 mm) was charged with a 2.0-g portion of air-dry sawdust of a lignocarbohydrate material, and acetic anhydride and a monobasic saturated carboxylic acid containing three to six C atoms in the molecule were added (0.3–5 mol per mole of OH groups of the raw material). The temperature in the reaction chamber was maintained at 25°C with a thermostat. The reactor was charged with 5–30% ammonium sulfate (based on the raw material), and the mixture was subjected to intense mechanical milling for 0.5–3 h. Then the products were unloaded, separated from the milling bodies, washed with water to remove the acids and catalyst, and dried to constant weight.

The content of bound acyl groups was determined by saponification of the samples of acylated lignocarbohydrate materials with a 0.5 N alcoholic solution of NaOH, followed by determination of the free carboxylic acids by GLC with an internal reference [4]. The solubility of wood acylation products in chloroform was determined by the procedure described in [7] fir cellulose acetates.

We examined how the time of the mechanochemical synthesis at an acetic anhydride amount of 1 mol per mole of OH groups of wood affects the content of bound carboxylic acids and the solubility of the acylation products in chloroform.

Experiments showed (Table 1) that, as the time of mechanochemical acylation is made longer, the content of bound acetic (AAc) and butyric (BAc) acids in the products and their solubility in chloroform regularly increase.

Table 2 shows that, with an increase in the molar

Table 1. Properties of aspen wood acetate butyrates in relation to the time of mechanochemical treatment. Molar ratio OH : AAn : BAc = 1 : 1 : 1, acylation temperature 25°C

Sample	Milling time, h	Fraction soluble in chloroform, %	Content of bound acids, %	
			acetic	butyric
1	0.5	43	12.4	6.5
2	1.0	66	18.3	7.8
3	1.5	69	23.5	8.9
4	2.0	75	27.8	10.6
5	2.5	79	32.2	11.7
6	3.0	82	32.9	12.1

Table 2. Influence of the ratio of acylating agents to OH groups of wood on properties of aspen wood acetate butyrates. Acylation time 1 h, temperature 25°C

Sample	Molar ratio of reactants and OH groups of wood	Fraction soluble in chloroform, %	Content of bound acids, %	
			acetic	butyric
2	1 : 1 : 1	66	18.3	7.8
7	0.5 : 0.5 : 1	39	10.5	4.1
8	1.5 : 1.5 : 1	72	19.8	8.7
9	2 : 2 : 1	76	21.6	9.9
10	2.5 : 2.5 : 1	79	23.2	10.7
11	3 : 3 : 1	84	24.1	11.8

Table 3. Influence of the number of carbon atoms in the carboxylic acid molecule on properties of mixed esters of aspen wood. Molar ratio OH : AAn : carboxylic acid = 1 : 1 : 1, acylation temperature 25°C

Sample	Carboxylic acid	Content of bound acids, %		Fraction soluble in chloroform, %
		acetic	other	
2	Butyric	18.3	7.8	66
12	Propionic	17.8	8.2	61
13	Valeric	19.5	7.1	73
14	Capronic	21.5	6.3	75

ratio of the acylating agents (acetic anhyride, butyric acid) to OH groups of wood from 0.5 : 0.5 : 1 to 3 : 3 : 1, the content of bound acetic and butyric acids and the solubility of the products in chloroform increase.

The chain length of the carboxylic acid also affects the properties of mixed aspen wood esters (Table 3). With an increase in the number of carbon atoms in the carboxylic acid, the solubility of the acytlated products in chloroform regularly increases. Simultaneously the content of bound higher carboxylic acid in the products somewhat decreases, probably because of a decrease in the reactivity of carboxylic acids with increasing chain length.

The amount of the catalyst (ammonium sulfate) also affects the content of the bound acids and the solubility of the wood acylation products in chloroform (Table 4).

With an increase in the amount of the catalyst (ammonium sulfate), the content of bound carboxylic acids in the products and their solubility in chloroform increase. The best properties are attained with the amount of ammonium sulfate of 20–30 wt % relative to the raw material.

For comparison, we prepared sample 19 with

Table 4. Influence of the catalyst amount on the properties of aspen wood acetate butyrates. Molar ratio of reactants 1 : 1 : 1, acylation time 1 h, temperature 25°C

Sample	Catalyst weight, % of raw material	Fraction soluble in chloroform, %	Content of bound acids, %	
			acetic	butyric
2	20	66	18.3	7.8
15	5	34	11.2	5.3
16	10	48	13.6	5.9
17	15	55	15.4	6.5
18	30	69	18.9	8.5
19*	20	60	17.2	7.2

* Magnesium perchlorate catalyst.

magnesium perchlorate [4] used as catalyst. We found that comparable results are obtained with ammonium sulfate taken in amount of 5–30 wt % relative to the raw material.

CONCLUSIONS

(1) With mechanochemical treatment, the reagent consumption in acylation of lignocarbohydrate materials can be decreased by a factor of 3–10; the process time, from 4–6 to 0.5–3 h; and the reaction temperature, from 100–130°C to 25°C, with the process as a whole made cheaper.

(2) The obtained mixed esters of lignocarbohydrate materials contain up to 32.9% bound acetic acid and up to 12.1% bound butyric acid. They are soluble in chloroform to 84%, exhibit thermoplastic properties, and can be used as binders for boards of composite materials.

REFERENCES

1. Efanov, M.V., Pershina, L.A., and Klepikov, A.G., *Plast. Massy*, 2000, no. 7, pp. 40–41.
2. Chemeris, M.M., Salin, B.N., and Mus'ko, N.P., *Izv. Vyssh. Uchebn. Zaved., Stroit.*, 1994, no. 12, pp. 80–82.
3. RF Patent 2143436.
4. Efanov, M.V., Esterification of Aspen Wood, *Cand. Sci. Dissertation*, Krasnoyarsk, 1999.
5. RF Patent 2285698.
6. RF Patent 2309960.
7. *Prakticheskie raboty po khimii drevesiny i tsellyulozy* (Practical Works in Wood and Pulp Chemistry), Moscow: Lesnaya Prom–st., 1965.

ISSN 1070-4272, Russian Journal of Applied Chemistry, 2008, Vol. 81, No. 7, pp. 1308–1309. © Pleiades Publishing, Ltd., 2008.
Original Russian Text © A.G. Morachevskii, I.N. Beloglazov, 2008, published in Zhurnal Prikladnoi Khimii, 2008, Vol. 81, No. 7, p. 1227.

BOOK REVIEWS

Meretukov, M.A., *Aktivnye ugli i tsianistyi protsess* (Activated Carbons and the Cyanide Process)

Moscow: Ruda i Metally, 2007, 288 pp.

DOI: 10.1134/S1070427208070380

At present, the carbon-sorption process is used at a number of gold-mining enterprises in the Russian Federation. In accordance with the Federal Program for Development of the Gold-Mining Industry, the share of sorption processes based on activated carbons should sharply increase. The monograph by Prof. M.A. Meretukov presents for the first time in the domestic literature the history of development of the scientific foundations and technology of carbon-sorption processes, discusses the theory of sorption of various cyanide compounds on activated carbon, and considers other processes related to the technique in question.

The book comprises an introduction, twenty-three small chapters, and a supplement. Each chapter is provided with a bibliographic list, with a total of 373 references to mostly original publications in foreign journals of last years. Chapters 11 and 19 also have lists of additional references.

The introduction (pp. 3–6) briefly presents the history of application of activated carbons in hydrometallurgical processes. Chapter 1 (pp. 7–21) considers the nature of adsorption processes and their mathematical description. Chapter 2 (pp. 22–30) discusses types of activated carbons and methods for their preparation. Chapters 3 (pp. 31–47), 4 (pp. 38–41), and 5 (pp. 42–51) are devoted to the structure and properties of activated carbons. Chapter 6 (pp. 52–60) describes in the historical aspect the development of concepts of the adsorption properties of carbons. Chapter 7 (pp. 61–77) considers the nature and composition of surface groups of both acidic and basic types on activated carbons. Chapters 8 (pp. 78–84) and 9 (pp. 85–97) are devoted to electrochemical and electrical properties of carbons. Chapter 10 (pp. 89–110) contains brief evidence about the chemistry of cyanide compounds of gold and silver.

Chapter 11 (pp. 111–127) summarizes reference data on the thermodynamic properties of cyanide compounds of gold and silver. The author is mostly based on recent publications and widely uses potential–pH diagrams in analysis of the stability regions of compounds or complex ions. Chapters 12 (pp. 128–161) and 13 (pp. 162–166) are devoted to an analysis of the existing theories of gold and silver sorption on activated carbons. Chapter 14 (pp. 167–172) presents information about the effect of oxygen on the sorption of gold and silver. Chapter 15 (pp. 173–183) describes the most informative methods for study of the sorption of gold and silver. Unfortunately, even the most recent studies fail to provide a unified concept not only about the mechanism by which carbon sorbents interact with cyanide complexes of gold, but also about the composition of compounds formed in the carbon phase. The author attributes the insufficient reproducibility of the experimental results to the heterogeneous structure of activated carbons, which depends on the starting raw material and synthesis conditions. The differences are eliminated and cease to be important only when tests are performed with large batches of activated carbon.

Chapter 16 (pp. 184–199) formulates a set of problems associated with studies of the sorption of gold from cyanide solutions and once again emphasizes the difficulty of choosing a definite mechanism of this process. Chapter 17 (pp. 200–216) presents kinetic characteristics of gold sorption by activated carbon, obtained by different authors. Most of kinetic models are based on the assumption of a local equilibrium between gold contained in solution near the carbon surface and gold already adsorbed on the surface. Very small chapter 18 (pp. 217–222) is devoted to thermodynamic and chemical properties of the cyanide ion in aqueous solutions.

Chapters 19 (pp. 223–239), 20 (pp. 240–243), 21 (pp. 244–257), 22 (pp. 258–262), and 23 (pp. 263–278) describe the technology of sorption recovery of

gold and silver from solutions and slurries and characterize the apparatus employed, mostly on the basis of the experience of foreign plants.

The very brief supplement (pp. 280–282) is devoted to calculation of the activity coefficients of separate ions in solutions on the basis of the extended Debye–Hückel equation.

The monograph by Meretukov is of indubitable interest for specialists engaged in the gold-mining industry. The book covers a wide variety of theoretical and practical issues; the manner of presentation is well understandable. The large number of references to publications and the well-prepared illustrative and tabulated material make higher the information value of the book.

A. G. Morachevskii and I. N. Beloglazov

ISSN 1070-4272, Russian Journal of Applied Chemistry, 2008, Vol. 81, No. 8, pp. 1311–1324. © Pleiades Publishing, Ltd., 2008.
Original Russian Text © A.A. Gaile, 2008, published in Zhurnal Prikladnoi Khimii, 2008, Vol. 81, No. 8, pp. 1233–1245.

REVIEWS

Development and Improvement of Extraction Processes for Separation and Purification of Petroleum Products

A. A. Gaile

St. Petersburg State Institute of Technology (Technical University), St. Petersburg, Russia

Received December 26, 2007

DOI: 10.1134/S1070427208080016

Processes of extraction, extractive and azeotropic rectification, absorption, and extractive crystallization, which use selective solvents, are widely used in petroleum processing and petrochemistry. As far back as 1950s–1960s, effective agents were suggested for separation and purification of petroleum products: sulfolane, *N*-formylmorpholine, and *N*-methylpyrrolidone.

At present, more than 150 industrial installations for extraction of aromatic hydrocarbons with sulfolane from products formed in pyrolysis and catalytic reforming of gasoline fractions are in use in the world. About 9 million tons of benzene, toluene, and xylene is annually produced by extractive rectification (Morphylane) and extraction (Morphylex) with *N*-formylmorpholine on 55 industrial installations [1]. Mixtures of *N*-formylmorpholine and *N*-acetyl-morpholine are also used in the Morphysorb process for absorption purification of natural gas and industrial gases with high content of hydrogen sulfide and carbon dioxide [2]. The Sulfinol process is widely used for absorption of hydrogen sulfide and other sulfur-bearing compounds from hydrocarbon gases and hydrogen. This process employs a mixed absorbent composed of a chemisorbent (diisopropanolamine), water, and sulfolane as a physical solvent [3].

Owing to a combination of high selectivity toward aromatic and unsaturated hydrocarbons, hydrogen sulfide, and a number of other gaseous components with an exceedingly high dissolving capacity, *N*-methylpyrrolidone is widely used in various separation processes. These are the following: recovery of arenes from mixtures with saturated hydrocarbons by extraction and extractive rectification; separation of 1,3-butadiene and isoprene by extractive rectification; selective purification of oil fractions to remove tars, polycycloarenes, and heteroatomic compounds; absorption recovery and purification of acetylene; absorption of hydrogen sulfide and other acid-type compounds from gas mixtures; removal of lubricants and technological coatings from the surface of metallic and optical articles.

In 1986, UOP company developed and put into industrial practice the Carom process intended for extraction of arenes with a mixed solvent based on tetraethylene glycol, which contains up to 20% cosolvent that raises the dissolving capacity [4]. Addition of the cosolvent, whose composition is not disclosed, makes it possible to lower the ratio between the extractive agent and the feed, diminish the specific energy expenditure, and improve the output capacity of installation. Four industrial installations operate by the Carom technology.

In the late XX century, GTC Technology Corporation developed a process for recovery of benzene, toluene, and xylenes by extractive rectification with a Tective-100 mixed selective solvent whose composition has not been disclosed, either [5]. Three industrial installations operate using this technology, and several installations are being designed and constructed.

In 2001, the first industrial extraction installation was put into operation in the United States for removal of sulfur-bearing compounds and aromatic hydrocarbons from the diesel fraction and for production of an ecologically clean diesel fuel [6]. The above-mentioned brief reports presented only a rough schematic diagram of the process, whence follows that an extractive agent of unspecified composition is regenerated from equilibrium phases by extraction with water.

The liquid–vapor and liquid–liquid equilibria are described using various empirical equations (Redlich–Kiester, Van Laar, Margules), semiempirical models

Wilson, NRTL, and UNIQUAC, developed by Renon, Prausnitz, Abrams, and others), and theoretical methods (ASOG, UNIFAC) [7, 8]. New or refined interaction parameters have been reported for 78 pairs of groups for the Dortmund model UNIFAC [9]. The effect of temperature on the mutual solubility data for 81 binary systems is better described by the extended UNIQUAC model [10] suggested in [11].

A major contribution to studies of the thermodynamics of solutions of hydrocarbons and other organic compounds in selective solvents have been made by J. Gmehling and coworkers (Oldenburg University, Germany). The following parameters have been determined: activity coefficients of hydrocarbons at infinite dilutions (by gas–liquid chromatography), selectivity of solvents toward aromatic and unsaturated hydrocarbons, and heats of mixing. The liquid–vapor and liquid–liquid equilibria have been studied. The results obtained and published data of other authors are represented in a number of reference books [12–19].

Studies of the thermodynamics of solutions of hydrocarbons in selective solvents have also been conducted under the supervision by Bittrich and are being continued by Lempe and Hradetzky (University of Halle, Germany) [20, 21].

The donor–acceptor properties of solvents, including a number of selective solvents, are characterized in the monographs [22, 23]. It is important to take these properties into account because the selectivity of polar (solvents toward aromatic and unsaturated hydrocarbons is mostly due to the formation of π-complexes [24].

In recent years, numerous studies have been reported, devoted to the selectivity of ionic fluids and their use as separating agents in extractive rectification and extraction for isolation of aromatic hydrocarbons and extractive purification of diesel fuel and oil fractions. It has been found that some ionic fluids are more selective toward the hexane–benzene system, than sulfolane, which is the most selective of the industrial extractive agents. These are, e.g., 1-ethyl and 1-butyl-3-methylimidazolium tetrafluoroborates [25] and 4-methyl-*N*-butylpyridinium tetrafluoroborate [26]. It is noted that the latter ionic fluid makes it possible to extract toluene from a mixture with heptane by using a rotary-disc extractor at a lower ratio to the feed, compared with sulfolane [27]. It is suggested to use ionic fluids for extraction of sulfur-containing compounds from diesel fractions (degree of recovery in a single stage, 10–30%) [28] and for selective purification of oil fractions [29]. However, the following disadvantages of ionic fluids can be noted.

(1) High viscosity, which must impair the efficiency of the contact members of extractors or extractive rectification columns. For example, the viscosity of the phenyl ammonium formate complex suggested for selective purification of oil lubricants at 50°C is 7.6×10^3 Pa s, and that of furfural, with which the extraction results are compared, is as low as 11.5 Pa s [29].

(2) Low dissolving capacity of highly selective ionic fluids. The solubility of benzene in 1-butyl-3-methylimidazolium tetrafluoroborate at 25.06 and 70.38°C is 2.3 and 18.73 wt %, respectively [30].

(3) The dramatic decrease in the selectivity of ionic fluids toward the cyclohexane–benzene system, compared with the hexane–benzene system, e.g., by a factor of 2.32 at 30°C for 1-butyl-3-methylimidazolium tetrafluoroborate [25]. At the same time, just the cycloalkane–arene systems are the key, most difficultly separable systems in isolation of arenes from mixtures with saturated hydrocarbons.

(4) Ionic fluids with high group selectivity also have selectivity in molecular masses. For example, the ratio between the limiting coefficients of heptane and hexane at 30°C in 1-butyl-3-methylimidazolium tetrafluoroborate is 1.614 [25]. Therefore, the ionic fluids must exhibit low selectivity toward the key, most difficultly separable components in extraction of arenes from fractions with broad boil-off limits.

Thus, with account of the set of requirements to selective solvents (high selectivity toward key components, high dissolving capacity with respect to the components being isolated, low selectivity in molecular mass, and low viscosity), the ionic fluids under study are inferior to the most efficient industrial extractive agents. However, ionic fluids may exhibit a higher efficiency, compared with sulfolane, in separation of close boiling hydrocarbons or narrow boiling fractions.

An important contribution to the development of theoretical foundations and technology of separation of mixtures of organic substances with selective solvents has been made by specialists from Russia and CIS countries. The review presented in a biobibliographic reference book [31] briefly characterizes Russia's main extraction schools; however, the biographic evidence about specialists is far from being complete.

Fundamental monographs and reference books including data on separation of mixture with the use of selective solvents and phase equilibria have been published [32–43].

Many years' studies of separation of multicomponent azeotropic mixtures have been carried out at Lomonosov State Academy of Fine Chemical Technology in Moscow under the supervision of Serafimov, Timofeev, and Frolkova [44–48].

The selectivity of separation of hydrocarbons with binary solvents are studied by E.I. Shcherbina, A.E. Shcherbina, and their pupils at Belarussian Technological Institute [49–51]. At Belarussian State University, S.M. Leshchev and co-authors study the dissolving capacity and the solvation and solvophobic effects of solvents with various polarities on various classes of nonelectrolytes. It has been suggested to use increments of the methylene and functional groups for calculating the distribution constants in extraction of organic substances [52].

R.G. Makitra has suggested to use polyparameter equations for evaluating the solvation effects in dissolution of gases and extraction of hydrocarbons and their derivatives by supplementing the Koppel–Palm equation with the Hildebrand solubility parameter [53].

S.Yu. Pavlov and co-workers have been developing the physicochemical foundations of separation of industrial mixtures of C_4–C_5 hydrocarbons by extractive rectification in order to isolate 1,3-butadiene and isoprene at Yaroslavl NIIMSK during many years [54]. At present, the work on isolation of unsaturated hydrocarbons and syntheses on their basis is being successfully continued together with O.S. Pavlov and D.S. Pavlov.

Zaretskii studies separation of products formed in thermal treatment of coals and shales at Zelinskii Institute of General Chemistry [55, 56]. Results of these studies and the author's review devoted to isolation of aromatic hydrocarbons and heterocyclic compounds are also of interest for solution of problems encountered in separation and purification of petroleum products.

At Ufa Petroleum Institute, many years' studies of extraction of aromatic hydrocarbons and selective purification of oil petroleum fractions have been performed under supervision of Bikkulov [57]. At present, technologies of selective purification and dewaxing of oil fractions by extractive crystallization are being developed by Ol'kov and coworkers [58, 59]. He also heads works on extractive dearomatization of diesel fractions with the use of, in particular, 1,4-dioxane [60]. At the same institute, Ziganshin and coworkers develop extractive agents with a regular packing, which are successsfully used industrially in installations for deasphalting and selective purification in manufacture of oil lubricants [61–63].

Studies of extractive purification of petroleum fractions and, in particular, of dearomatization of diesel fuels are being also conducted at the Institute of petrochemical processing of the Republic of Bashkortostan (State unitary enterprise INKhP RB), but the composition of the extractive agents studied has not been identified [64]. Of interest is a combined technology for production of diesel fuels by extractive and catalytic dearomatization [65].

At Gubkin Russian State University of oil and gas, studies deasphalting, selective purification, and dewaxing in manufacture of oil lubricants and deoiling of solid hydrocarbons are conducted under supervision of Fuks [66].

At VNIINP, Shkol'nikov and coworkers carry out studies aimed to improve processes of selective purification and deasphalting of oil raw materials [67, 68].

At Kazan State University, the selectivity of solvents toward aromatic hydrocarbons and organosulfur compounds have been studied by I.N. Diyarov and V.G. Kozin with coworkers [69].

The extraction of phenols and other aromatic oxy compounds from aqueous solutions is studied by Korenman and coworkers at Voronezh Technological Academy [70–72]. Works in the same area are being continued by Ermolaeva [73].

At the Institute of Organic Chemistry, Ufa Scientific Center, Russian Academy of Sciences, the extraction of phenols, organic acids, and various biologically active substances has been studied under the supervision of Yu.E. Nikitin, Yu.I. Murinov, and N.L. Egutkin [74].

In the 1960s–1970s, processes for extraction of aromatic hydrocarbons from reforming catalyzates were being developed at the laboratory of extraction at VNIINeftekhim (V.N. Pokorskii, N.F. Grishchenko with coworkers), and those for selective purification of oil fractions and deasphalting of petroleum residues, at GrozNII (A.G. Martynenko, G.L. Potashnikov with coworkers) [75].

Many years' studies of the physicochemical foundations and technology of processes of separation of hydrocarbon raw materials with selective solvents have

been carried out at St. Petersburg State Technological Institute (SPbGTI). Ya.I. Leitman and coworkers developed the first domestic process for recovery of benzene, toluene, and xylene from reforming catalyzates by extractive rectification with an LTI solvent. In 1963–1964, this process was implemented at six industrial installations. In the last 40 years, studies in this area have been conducted by A.A. Gaile and coworkers. The results obtained are represented in 3 doctoral [76–78] and 24 candidate dissertations and in 320 publications, including a number of monographs [79–85], textbooks [86–89], reviews [90–93], and topical collections of articles [94, 95]. The present review considers results of studies carried out, for the most part, in the last five years.

In the studies, the following goals were formulated [96, 97]:

(i) development and improvement of extractive and combined processes for recovery of aromatic hydrocarbons from catalyzates produced in reforming of gasoline fractions;

(ii) extractive purification of the kerosene and diesel fractions and atmospheric gas oil to obtain motor fuels satisfying the increased ecological requirements;

(iii) extractive refinement of vacuum gas oils and mazut, which are raw materials for catalytic cracking and hydrocracking.

Review [98] contains data on the selectivity of 683 solvents toward the systems hexane–benzene, cyclohexane–benzene, and 1-hexene–benzene. Of these solvents, 506 have been studied at SPbGTI. Also presented are values of the limiting activity coefficients of benzene in the solvents, which can be used to judge about their dissolving capacity, and ratios between the limiting activity coefficients of heptane and hexane, which characterize the selectivity of the solvents with respect to molecular masses. The review presents correlation equations relating the selectivity to the σ-constants of substituents in solvent molecules and to the criteria characterizing the nonuniformity of the charge distribution. The relations that can be used to choose effective extractive agents combining high selectivity and dissolving capacity toward aromatic hydrocarbons are analyzed.

Review [99] presented patent information about 230 individual extractive agents and about mixed solvents and heterogeneous extractive systems, both those used industrially and those suggested for extraction of aromatic hydrocarbons from reformates of gasoline fractions and from medium-distillate and oil fractions.

The interaction parameters of the UNIFAC method have been refined for group pairs ACH–TMS (sulfolane) and $ACCH_2$–TMS. On the basis of parameters of binary systems, liquid–liquid equilibria have been calculated using the NRTL and UNIFAC equations for 15 three-component systems constituted by sulfolane, a saturated hydrocarbon (alkanes C_5–C_{10}, cyclohexane), and an arene (benzene and its homologues C_7–C_{10}) [100].

In 2000, the extraction unit of an LG-35-8/300B installation at Kirishinefteorgsintez Production Association Ltd. was converted from triethylene glycol (TEG) to a mixed extractive agent composed of TEG and sulfolane. At a sulfolane content of 15 wt %, the ratio of the extractive agent and recycle to the feed was reduced by 20% at the same degree of recovery. In another operation mode with the same ratios of the extractive agent and recycle to the feed, as also in the case of TEG without sulfolane, the overall degree of arene recovery increased by 2.1%, and that for toluene and xylenes, by 2.4 and 10.1%, respectively [101, 102].

At the end of 2006, the content of sulfolane in the mixture with TEG was raised to 28–30 wt % in accordance with the recommendations of [103] and the mass ratio between the extractive agent and feed was lowered to 4.9. The benzene fraction isolated by rectification from the reformate of the broad gasoline fraction was used as an additional source of feed for the extraction unit. As a result, the content of benzene in motor gasoline was diminished to below 1 vol % in conformity with Euro-4 regulations, and the daily output of commercial benzene increased from 120–140 to 240 tons. The comparatively weak intermolecular interactions in the TEG–sulfolane system lead to an increase not only in the selectivity, but also in the dissolving capacity toward hydrocarbons [104]. Positive deviations from the Raoult law facilitate regeneration of the mixed extractive agent. The stripping of arenes occurs without vacuum with the use of the 10-atm steam available at the plant.

In the initial stage of operation of the installation on the mixed extractive agent, an increased loss of sulfolane with the extract was revealed. To eliminate the problem, the unit for washing with water was redesigned, which made it possible to re-extract sulfolane and TEG from the still bottoms of the toluene column,

in which xylenes and higher-boiling extractive agents are concentrated, rather than from the extract. Because the fraction of xylenes in the extract is 3–5 wt %, the expenditure of the aromatic feed delivered to water washing became 20–30 times smaller. In addition, the extraction of polar solvents with water from xylene solutions is more efficient than that from mixtures with benzene and toluene, because the systems constituted by xylenes and sulfolane (TEG) have a higher degree of nonideality [105].

After the washing scheme was changed, the loss of the extractive agent with the extract decreased by a factor of 20–25 to become about 10 g per ton of the recovered arenes.

A dramatic decrease in the required mass ratio of selective solvents to the feed to 2.8 in recovery of arenes C_6–C_8 is achieved on replacing the extraction with the combined method of extractive rectification, followed by extraction of benzene partly finding its way into the distillate [106–111]. It was suggested to use a 30/70 wt % mixture of sulfolane with *N*-methylpyrrolidone, which exhibits a synergistic effect, as a selective solvent in the stage of extractive rectification. In the stage of benzene extraction, the optimal composition of the mixed extractive agent constituted by sulfolane and *N*-methylpyrrolidone is 90/10 wt %.

The principle of combination of mutually complementary processes of extractive rectification and extraction with mixed solvents of the same qualitative, but different quantitative compositions enables regeneration of selective solvents in the same common unit. The high economic efficiency of the suggested combined method for recovery of benzene, toluene, and xylenes from reformates has been confirmed by technical-and-economic calculations [112]. The results obtained surpass the parameters of the most efficient individual processes of extraction with sulfolane or extractive rectification with *N*-formylmorpholine.

The combined method of extraction with sulfolane and the subsequent extractive-azeotropic rectification of the extract phase with sulfolane and ethanol from the reforming catalyzate of the broad gasoline fraction containing 55.6 wt % arenes C_6–C_9 was used to obtain in 65 wt % yield the gasoline component satisfying the enhanced ecological requirements. The total content of arenes in this component is 28 wt %, including about 1 wt % benzene. Simultaneously, benzene, toluene, and C_8 and C_9 arenes were recovered with degrees of recovery of 89, 77, 69, and 24 wt %, respectively.

The overall mass ratio of sulfolane to the feed in both stages of the process is 1.88, and that of ethanol, 0.032, with recycling flows being absent. Ethanol can be used in extractive-azeotropic rectification without regeneration as a high-octane component of gasoline [113, 114].

To make lower the content of benzene in motor gasoline manufactured at Kirishinefteorgsintez Production Association Ltd., it is planned to construct an installation for extractive rectification under license from GTC Technology, Inc., with the use of Tektiv-100 mixed selective solvent [115]. The solvent composition has not been reported, but, judging from its regeneration in the vacuum striping column with high-pressure steam (as in the case of recovery of arenes by extraction with sulfolane), it contains high-boiling components. For example, it has been suggested to recover arenes by extractive rectification with mixtures of sulfolane with 3-methyl sulfolane or dipropyl sulfone [116], or with alkyl derivatives of sulfolane [117]. A number of disadvantages associated with the application of mixtures of high-boiling solvents can be noted. In particular, there are difficulties in their regeneration, the elevated temperature at plates of the extractive recombination column impairs the stability of π-complexes with arenes and the selectivity of solvents. The high viscosity of the solvents leads to a decrease in the plate efficiency.

These shortcomings can be overcome by addition of a comparatively low-boiling low-viscosity solvent with an increased dissolving capacity, e.g., *N*-methylpyrrolidone, which promotes homogenization of the system with hydrocarbons being separated and makes higher the efficiency of extractive rectification [109], to the highly selective solvent (sulfolane, *N*-formylmorpholine).

Raising the content of sulfolane in the mixture with TEG to 57 wt % makes it possible to reduce the mass ratio of the mixed extractive agent to the reformate of the fraction containing arenes C_6–C_8 to 3 and the expenditure of the recycle from 80–100 to 30 wt % relative to the feed. The use of the pentane recycle instead of the C_6–C_8 hydrocarbons results in that toluene is excluded from its composition, the content of benzene in the recycle becomes substantially lower, and its expenditure additionally decreases [118, 119].

After a new installation of extractive rectification for recovery of benzene is put in operation in the extraction unit of the operating LG-35-8/300B installation, it

will become possible to extract toluene and sum of xylenes. The seven-stage counterflow extraction of arenes from the toluene–xylene fraction of the reformate with a mixed TEG–sulfolane–water extractive agent (48.1 : 48.1 : 3.8 wt %) at a mass ratio of 5 : 1 will provide a degree of recovery of toluene and xylenes exceeding 97% [120].

Another suggested way to use the extraction unit of the operating installation is to recover C_7–C_9 arenes from the reformate of the 95–190°C gasoline fraction by the combined method of extraction with a mixed TEG–sulfolane extractive agent (50 : 50 wt %), followed by removal of admixtures of saturated hydrocarbons from the extract phase by azeotropic rectification with ethanol without regeneration of the alcohol. The suggested method makes it possible to obtain a reformed component of gasoline, which satisfies the Euro-4 and Euro-5 regulations in the total content of arenes, at a small mass ratio between the extractive agent and the feed (2.5) and to recover commercial toluene and sum of xylenes with a degree of recovery equal to about 90 and 85%, respectively [121, 122].

A new principle was suggested for choosing extractive agents for recovery of aromatic hydrocarbons and heteroatomic compounds from medium-distillate petroleum fractions and vacuum gas oils. In accordance with this principle, the extractive agent must form heteroazeotropes with saturated hydrocarbons from the feed and must not yield azeotropic mixtures with the components being extracted. In this case, the rectification regeneration of the extractive agent from the extract phase is accompanied by additional removal of saturated hydrocarbons and an increase in the content of the components being extracted in the aromatic concentrate.

In extractive purification of the kerosene fraction, this requirement is satisfied by acetonitrile, which forms azeotropes with C_9–C_{10} saturated hydrocarbons and gives no azeotropes with arenes. As a result of the combined purification of the kerosene fraction with the extractive system composed of acetonitrile with 3 wt % water and pentane, the content of saturated hydrocarbons decreases from 16.4 wt % in the extract to 0.5 wt % in the aromatic concentrate in the remaining still bottoms. This method can be used to obtain a high-quality jet engine fuel with a content of arenes of 8.5 wt % from the hydropurified kerosene fraction, and aromatic Nefras solvents from the aromatic concentrate [123, 124].

The following extractability series was determined in extractive purification of the straight-run kerosene fraction with the same system: benzothiophenes > alkylnaphthalenes > biphenyls > alkylthiophenes > tetralines and indanes > alkylbenzenes > dialkyl sulfides. Thus, benzothiophenes, which are the most difficultly removed in hydropurification, is extracted the most easily [125].

A similar extractability series was determined in extractive purification of the straight-run kerosene fraction with the system constituted by methyl cellosolve and pentane [126]: dibenzothiophenes > phenanthrenes, fluorenes > benzothiophenes > naphthalenes > biphenyls > thiophenes > tetralines and indanes > alkylbenzenes > saturated organosulfur compounds.

Even more easily extracted are nitrogen-containing heterocyclic compounds of aromatic nature. The extraction of 1-methyl naphthalene, benzothiophene, and indole from model mixtures with hexadecane has been studied with *N*-methylpyrrolidone as extractive agent without a nonpolar solvent, in the presence of comparatively low-boiling alkanes: hexane, decane, and dodecane [127]. The following extractability series was established: indole > benzothiophene > 1-methyl naphthalene. It was demonstrated that extraction with a polar extractive agent in the presence of a nonpolar solvent is a more effective way to improve the selectivity of separation, compared with watering of the extractive agent.

The calculation methods UNIFAC and UNIQUAC have been used to analyze the effect of various nonpolar solvents (butane, pentane, hexane, cyclohexane, eicosane, benzene) on the results of the single-stage extraction of arenes from model mixtures containing alkanes and cycloalkanes with acetonitrile and *N*,*N*-dimethylformamide [128]. Introduction of alkanes and cyclohexane into the extractive system results in that the selectivity of the process increases: the content of arenes in the extract and the separation coefficients become higher. The extraction in the presence of benzene favors an increase in the degree of recovery of arenes; however, the selectivity of the separation process decreases. Arenes are more selectively extracted with polar extractive agents in the presence of pentane, hexane, or cyclohexane. With account of technological and technical-economic factors, it is preferable to use pentane as a nonpolar solvent limitedly miscible with a polar extractive agent.

The extraction of arenes from a hydropurified diesel fraction with acetonitrile with 2 wt % water in

the presence of pentane yielded a diesel fuel and an extract containing 15 and >90 wt % arenes, respectively [129]. The efficiency of the method has been confirmed on an installation with a rotary-disc extractor corresponding to 4.5–5 theoretical stages [130].

By using a five-stage counterflow extraction of a hydropurified diesel fraction with methyl cellosolve with 5 wt % water in the presence of pentane, the content of arenes can be reduced from 25 to 10–11 wt %, and that of sulfur, from 0.045 to 0.02 wt % [131–133].

Even more effective in extractive purification of the diesel fraction are extraction systems constituted by dimethylformamide (or *N*,*N*-dimethylacetamide) and pentane [134–135]. In contrast to acetonitrile and methyl cellosove, dimethylformamide and *N*,*N*-dimethylacetamide form azeotropic mixtures with saturated hydrocarbons contained in the extract phase. As a result, the content of saturated hydrocarbons decreases from 7 wt % in the extract to 2 wt % in the aromatic concentrate, which can be used as an aromatic Nefras solvent.

With the same dimethylformamide–pentane extractive system, ecologically clean waxy working fluids RZh-3 and RZh-8, whose arene content does not exceed 5–5.5 wt %, can be obtained from a dewaxed 200–320°C fraction [136].

The extractive purification of atmospheric gas oil with methyl cellosolve in the presence of pentane can yield a raffinate that can be used, on being subjected to hydropurification, as a component of the summer diesel fuel [137]. The high economic efficiency of the combined method for production of a diesel fuel component from the atmospheric gas oil by extraction followed by hydropurification of the raffinate under mild conditions to remove saturated organosulfur compounds was confirmed in [138].

Even more efficient is the extractive purification of atmospheric gas oil with *N*-methylpyrrolidone in the presence of undecane. In the case of a four-stage counterflow extraction at a mass ratio of *N*-methylpyrrolidone and undecane to the feed equal to 2 and 0.3, respectively, the raffinate yield was 77.6 wt %. The content of arenes in the raffinate decreased from 28.2 to 9.8 wt %, and that of sulfur, from 1.15 to 0.47 wt %. The cetane ratio increased from 50 to 59%. and the 90% point of the raffinate decreased, compared with the feed, by 17° [139, 140].

Various methods for extractive purification of motor fuels were considered in the reports [141, 142].

The five-stage counterflow extractive purification of the 225–290°C fraction of Troitsk-Anastasievsk petroleum containing about 23 wt % arenes with methyl cellosolve and 4 wt % water at a mass ratio of the extractive agent and nonpolar solvent (pentane) to the feed equal to 8 and 1, respectively, produced a raffinate in 69 wt % yield [143]. The content of arenes in the raffinate is decreased to 4.2 wt % and it satisfies requirements to the AMG-10 low cold-test hydraulic oil manufactured by the method of sulfatization with oleum, which fails to conform to modern ecological regulations.

Similarly, a five-stage counterflow extraction of arenes and heteroatomic compounds from the 300–350°C fraction of the Troitsk-Anastasievsk petroleum containing 30 vol % arenes and 0.16 wt % sulfur at a mass ratio of methyl cellosolve with 5 wt % water and pentane to the feed equal to 4 and 1, respectively, lowered the content of sulfatable compounds to 18 vol %. The raffinate yield was about 82 wt %; the content of arenes in the extract was 87 wt %, which points to a rather high selectivity of the extractive purification. The transformer oil produced from the raffinate obtained satisfies the requirements to TKp oil in all parameters with a large safety margin; in particular, the dielectric loss tangent is 0.24% at a required value of 2.2% [144].

To remove polycycloarenes, nitrogen- and sulfur-containing compounds, and heavy metals (which poison and coke hydrocracking catalysts) from heavy vacuum gas oil, a combined method of extraction followed by azeotropic rectification has been developed [145–147].

Aqueous *N*-methylpyrrolidone served as a polar solvent, and a mixture of 99 wt % heptane and 1 wt % toluene, which models the raffinate produced by the LG-35-8/300B benzene reforming installation, was used as a nonpolar solvent improving the separation selectivity. After nonpolar solvents were removed from the extract phase, ethylene glycol was added to the still bottoms in an amount of 10 wt % relative to the feed. Ethylene glycol forms heteroazeotropes with saturated hydrocarbons up to C_{28}–C_{30}, and, therefore, additional removal of saturated hydrocarbons from the extract phase leads to concentration of undesirable components in the aromatic concentrate, compared with the extract.

About half of polycycloarenes and approximately two thirds of organosulfur compounds are selectively removed from heavy vacuum gas oil. Simultaneously, most part of heavy metals are removed.

The use of the raffinate instead of the starting heavy vacuum gas oil as a raw material for the catalytic cracking made it possible to raise the yield of the gasoline and diesel fractions by 9.7 and 37%, respectively, and to diminish the coking by 31% [148].

Vacuum gas oil can also be upgraded by using extractive systems based on oxygen-containing solvents (furfural, methyl cellosolve) in the presence of heptane. In this case, the hazard of catalyst poisoning in the subsequent processing of raffinates by admixtures of the nitrogen-containing extractive agent is eliminated, but an increased ratio of the extractive agent to the feed is required, compared with purification with *N*-methylpyrrolidone [149].

Less selective is the extractive purification of vacuum gas oils by extraction with *N*-methylpyrrolidone in the presence of a low-boiling nonpolar solvent (e.g., heptane), without ethylene glycol as an azeotrope-forming component [150].

The most efficient is the extractive purification of vacuum gas oils with *N*-methylpyrrolidone in the presence of the undecane fraction recovered by vacuum distillation of C_{10}–C_{14} liquid paraffins on the Parex installation. Undecane forms with *N*-methylpyrrolidone an azeotrope boiling at 179°C and containing 36 wt % *N*-methylpyrrolidone. This makes it possible to lower by 25°C the temperature at which the extractive agent is regenerated and to reduce the degree of thermal and hydrolytic decomposition of *N*-methylpyrrolidone and the equipment corrosion rate. In addition, the selectivity of removal of undesirable components increasers in the presence of undecane. For example, the content of saturated hydrocarbons in the extract formed in purification of light vacuum gas oil decreases from 18 wt % in extraction with only *N*-methylpyrrolidone to 5–6 wt % in the presence of undecane. Owing to the more selective removal of undesirable components, the raffinate yield increases by 10–12 rel % [151, 152].

The same extractive system, *N*-methylpyrrolidone + undecane, has also been used for extractive purification of mazut [153].

The extractive purification of high-sulfur mazut with *N*-methylpyrrolidone in the presence of undecane or the undecane fraction yields a raffinate in 70–74 wt % yield. In this case, the content of sulfur decreases by more than a factor of 2; cokeability, by a factor of 1.5; and viscosity and ash content, by 30–35%. The extractive purification of mazut yields a low-sulfur fuel oil and enables use of the resulting raffinate as a feed for hydrocatalytic processes with an energy-intensive stage of vacuum rectification of mazut, with the raffinate yield substantially exceeding the output of vacuum gas oils from AVT installations. The capital expenditure for the construction of an installation for extractive purification of mazut with an annual output capacity of 2 million tons will constitute $50 million. The operating costs will be $10.9 per ton, net annual profit of the plant, $21.4 million, and the discounted payback period (without the construction time), 3.4 years [78, 154].

The main results of the research work conducted in the last decade at SPbGTI were represented in a report at the jubilee conference of the chair of technology of petrochemical and coal-chemical industries [155, 156].

The principles to be used when choosing extraction systems and combined methods for separation and purification of petroleum products in order to improve the selectivity and efficiency of separation can be formulated as follows [157]:

(i) use of mixtures of extractive agents that include an associated selective solvent and a close-boiling high-selectivity extractive agent and form azeotropic mixtures with the lowest boiling point and an endothermic effect in mixing (TEG–sulfolane, DEG–*N*-formylmorpholine);

(ii) use of extractive agents that form azeotropes with saturated hydrocarbons of a feed, but not with the components being extracted;

(iii) use of extractive systems that include a limitedly mutually soluble polar extractive agent and a nonpolar solvent (e.g., pentane);

(iv) use of extraction systems that include a polar extractive agent and a nonpolar solvent, which form an azeotropic mixture with the lowest boiling point (e.g., *N*-methylpyrrolidone–undecane);

(v) use of azeotropic rectification with high-octane components requiring no regeneration for recovery of arenes (e.g., sum of xylenes) and for removal of admixtures of saturated hydrocarbons from the extract phase and from C_6-C_8 aromatic extracts;

(vi) extractive rectification with mixtures of a high-selectivity extractive agent limitedly miscible with the feed and a comparatively low-boiling selective solvent with increased dissolving capacity toward the components being separated, with these mixtures exhibiting a synergistic effect;

(vii) combination of mutually complementary processes of extractive rectification and subsequent extraction, with mixed selective solvents of the same qualitative, but different quantitative compositions used in both stages: with predominance of the high-selectivity solvent in the extraction stage, and of the solvent with increased dissolving capacity in the stage of extractive recombination;

(viii) combination of mutually complementary processes for production of motor fuels: extraction, in which polycycloarenes (homologues of thiophene, benzothiophene, and dibenzothiophene) and nitrogen-containing compounds of aromatic type are the most easily removed; and hydropurification, in which comparatively poorly extractable saturated organosulfur compounds are easily removed;

(ix) use of extractive purification instead of vacuum distillation of mazut.

The results of studies performed in recent years and devoted to separation and purification of petroleum products were reported in [158–160].

CONCLUSION

Thus, extractive and combined processes of separation and purification of petroleum products can recover benzene and its homologues with low specific energy expenditure; these processes have been used to obtain motor gasolines and jet and diesel fuels satisfying modern ecological requirements and to produce low-sulfur mazut and high-quality raw materials for hydrocatalytic processes with vacuum gas oils and high-sulfur mazuts.

REFERENCES

1. *Spravochnik neftekhimicheskikh protsessov* (Handbook of Petrochemical Processes), *Neftegaz. Tekhnol*., 2005, no. 8, pp. 76–78.
2. Palla, N., Jamal, A., Leppin, D., et al., *Oil Gas J.*, 2004, vol. 102, no. 25, pp. 54–59.
3. Sulfinol Process, *Neftegaz. Tekhnol.*, 1977, no. 1, p. 77.
4. *Neftepererab. Neftekhim.*, 1994, no. 3, pp. 22–25.
5. *Neftegaz. Tekhnol*., 1997, no. 6, pp. 45–46.
6. *Neftegaz. Tekhnol*., 2002, no. 1, p. 100.
7. Reid, R.G., Prausnitz, J.M., and Sherwood, T.K., *The Properties of Gases and Liquids*, New York: McGraw–Hill, 1977.
8. Wales, S.M., *Phase Equilibria in Chemical Engineering*, Boston: Butterworth, 1985.
9. Gmehling, J., Lohmann, J., Jakob, A., and Joh, R., *Ind. Eng. Chem. Res.*, 1998, vol. 37, no. 12, pp. 4876–4882.
10. Nagata, I., Meyer, T., and Gmehling, J., *Fluid Phase Equil.*, 1991, vol. 65, pp. 19–39.
11. Nagata, I., *Thermochim. Acta*, 1982, vol. 56, no. 1, pp. 43–57.
12. Gmehling, J., Menke, J., and Schiller, M., *Activity Coefficients at Infinite Dilution, DECHEMA Chem. Data Series*, vol. 9, parts 3, 4, Frankfurt, 1994.
13. Gmehling, J. and Holderbaum, T., *Heats of Mixing Data Collection, DECHEMA Chem. Data Series*, vol. 3, Frankfurt, 1988.
14. Gmehling, J., Menke, J., Krafczyk, J., and Fischer, K., *Aseotropic Data*, in 3 parts, Weinheim: VCH–Verlag, 2003.
15. Gmehling, J. and Onken, U., *Vapor–Liquid Equilibrium Data Collection, DECHEMA Chem. Data Series*, Frankfurt, 1977–1978, vols. 1, 2a.
16. Gmehling, J., Onken, U., and Arlt, W., *Vapor–Liquid Equilibrium Data Collection, DECHEMA Chem. Data Series*, Frankfurt, 1978, vols. 2b, 8.
17. Gmehling, J., Onken, U., Grenzheuser, P., et al., *Vapor–Liquid Equilibrium Data Collection, DECHEMA Chem. Data Series*, Frankfurt, 1978, vols. 2d, 5, 6c.
18. Gmehling, J., Onken, U., and Rarey-Nies, J., *Vapor–Liquid Equilibrium Data Collection, DECHEMA Chem. Data Series*, Frankfurt, 1988, vols. 1b, 2e, 2f, 3a, 3b, 4a.
19. Gmehling, J. and Onken, U., *Vapor–Liquid Equilibrium Data Collection, DECHEMA Chem. Data Series*, Frankfurt, 1999, voas. 6d, 6e, 7a, 7b, 8a, 5a, 5b, 1c, 1d.
20. Bittrich, H.-J., Lempe, D., Gajle, A.A., et al., *Trennung von Kohlenwasserstoffen mit Selektivlösungsmitteln*, Leipzig: VEB Deutscher Verlag fur Grundstoffindustrie, 1987.
21. Hradetzky, G., Hammerl, I., Kisan, W., et al., *Data of Selective Solvent: DMFA – NMC – NMP*, Berlin: VEB Deutscher Verlag der Wissenschaften, 1989.
22. Gutmann, V., *The Donor–Acceptor Approach to Molecular Interactions*, New York: Plenum, 1978.
23. Reichardt, C., *Solvents and Solvent Effects in Organic Chemistry*, Weinheim: Viley–VCH, 2003, 3rd ed.
24. Andrews, L.J. and Keefer, R. *Molecular Complexes in Organic Chemistry*, San Francisco: Holden-Day, 1964.
25. Foco, G.M., Bottini, S.B., Quezada, N., et al., *J. Chem. Eng. Data*, 2006, vol. 51, no. 3, pp. 1088–1091.
26. Heintz, A., Kulikov, D.V., and Verevkin, S.P., *J. Chem. Eng. Data*, 2001, vol. 46, no. 6, pp. 1526–1529.
27. Meindersma, G.W., Vos, G.S., Klaren, M.B., and de Haan, A.B., *Int. Solvent Extraction Conf. (ISEC' 05), Beijing, 19–23 Sept., 2005*, Beijing: Chin. Acad. J. Electron. J. Publ. House, 2005, pp. 735–741.
28. *Chem. Eng. (USA)*, 2002, vol. 109, no. 10, p. 17.
29. Azizov, A.G., Samedova, F.I., Ibragimova, M.D., et al., *Mir Nefteprod*., 2007, no. 6, pp. 22–24.
30. Shang, H.-T., Wu, J.-S., Zhou, Q., and Wang, L.-S., *J. Chem. Eng. Data*, 2006, vol. 51, no. 4, pp. 1286–1288.
31. *Kto est' kto v ekstraktsii: Bibliograficheski spravochnik Ross. Akad. Nauk* (Who Is Who in Extraction: Biblio-

graphic Reference Book of the Russian Academy of Sciences), Zolotov, Yu.A., Ed., Moscow: B.i., 1995.

32. Kogan, V.B., *Azeotropnaya i ekstraktivnaya rektifikatsiya* (Azeotropic and Extractive Rectification), Leningrad: Khimiya, 1971.
33. Kogan, V.B., *Geterogennye ravnovesiya* (Heterogeneous Equilibria), Leningrad: Khimiya, 1968.
34. Kogan, V.B., Fridman, V.M., and Kafarov, V.V., *Ravnovesie mezhdu zhidkost'yu i parom: Spravochnoe posobie* (Liquid–Vapor Equilibrium: Reference Book), Moscow: Nauka, 1966, vols. 1, 2.
35. Kogan, V.B., Fridman, V.M., and Kafarov, V.V., *Spravochnik po rastvorimosti* (Reference Book of Solubilities), Moscow: Nauka, 1963–1970.
36. Ogorodnikov, S.K., Lesteva, T.M., and Kogan, V.B., *Azeotropnye smesi: Spravochnik* (Azeotropic Mixtures: Reference Book), Leningrad: Khimiya, 1971.
37. Sulimov, A.D., *Proizvodstvo aromaticheskikh uglevodorodov iz neftyanogo syr'ya* (Production of Aromatic Hydrocarbons from Petroleum Raw Materials), Moscow: Khimiya, 1975.
38. Sokolov, V.Z. and Kharlampovich, G.D., *Proizvodstvo i ispol'zovanie aromaticheskikh uglevodorodov* (Production and Use of Aromatic Hydrocarbons), Moscow: Khimiya, 1980.
39. Pavlov, S.Yu., *Vydelenie i ochistka monomerov dlya sinteticheskogo kauchuka* (Recovery and Purification of Monomers for Synthetic Caoutchouk), Leningrad: Khimiya, 1987.
40. Morachevskii, A.G., Smirnova, N.A., Balashova, I.M., and Pukinskii, I.B., *Termodinamika razbavlennykh rastvorov neelektrolitov* (Thermodynamics of Dilute Nonelectrolyte Solutions), Leningrad: Khimiya, 1982.
41. Morachevskii, A.G., Smirnova, N.A., Piotrovskaya, E.M., et al., *Termodinamika ravnovesiya zhidkost'–par* (Thermodynamics of the Liquid–Vapor Equilibrium), Morachevskii, A.G. Ed., Leningrad: Khimiya, 1989.
42. Chernozhukov, N.I., *Tekhnologiya pererabotki nefti i gaza, Ch. 3, Ochistka i razdelenie neftyanogo syr'ya, proizvodstvo tovarnykh nefteproduktov* (Technology of Processing of Petroleum and Natural Gas, part 3, Purification and Separation of Petroleum Raw Materials, Manufacture of Commercial Petroleum Products), Moscow: Khimiya, 1978.
43. Kazakova, L.P. and Krein, S.E., *Fiziko-khimicheskie osnovy proizvodstva neftyanykh masel* (Physicochemical Foundation of Production of Petroleum Oils), Moscow: Khimiya, 1978.
44. Zharov, V.T. and Serafimov, L.A., *Fiziko-khimicheskie osnovy distillyatsii i rektifikatsii* (Physicochemical Foundations of Distillation and Rectification), Leningrad: Khimiya, 1975.
45. Petlyuk, F.B. and Serafimov, L.A., *Mnogokomponentnaya rektifikatsiya. Teoriya i raschet* (Multicomponent Rectification: Theory and Calculation), Moscow: Khimiya, 1983.
46. Serafimov, L.A., Timofeev, V.S., and Babich, S.V., *Fizikokhimicheskie osnovy rektifikatsionnykh protsessov razdeleniya: Uchebnoe posobie* (Physicochemical Foundations of Rectification Separation Processes: Textbook),. Moscow: MITKhT, 1982.
47. Frolkova, A.K., Theoretical Foundations of Separation of Multicomponent Multiple-Phase Systems with the Use of Functional Complexes, *Doctoral Dissertation*, Moscow, 2000
48. Frolkova, A.K. and Serafimov, L.A., *Vestn. MITKhT*, 2007, vol. 2, no. 1, pp. 3–14.
49. Shcherbina, E.I., Intermolecular Interactions and Fundamental Aspects of Selective Separation of Hydrocarbons with Binary Solvents, *Doctoral Dissertation*, Moscow, 1979.
50. Shcherbina, A.E., Selectivity of Separation of Hydrocarbons with Binary Solvents, *Doctoral Dissertation*, Leningrad, 1987.
51. Grushova, E.I. and Yusevich, A.I., *Primenenie dobavok khimicheskikh soedinenii dlya intensifikatsii protsessov ekstraktsii, flotatsii, adsorbtsii* (Addition of Chemical Compounds for Intensification of Extraction, Flotation, and Adsorption Processes), Minsk: BGTU, 2006.
52. Leshchev, S.M., Novik, N.P., Sin'kevich, A.V., and Novik, T.P., *Sovremennye problemy khimii i tekhnologii ekstraktsii* (Modern Problems of Extraction Chemistry and Technology), Moscow, 1999, vol. 1, pp. 173–185.
53. Makitra, R.G., Evaluation of Solvation Effects in Gas Dissolution, Extraction, and Complexation, *Doctoral Dissertation*, L'vov, 1990.
54. Pavlov, S.Yu., A Study of Separation of Industrial Mixtures of Hydrocarbons C_4–C_5, *Doctoral Dissertation*, Moscow: MITKhT, 1974.
55. Zaretskii, M.I., Development of Scientific Foundations of a New Technology for Selective Separation of Mixtures of Organic Compounds with Close Physicochemical Properties, *Doctoral Dissertation*, Moscow, 1990.
56. Blokhin, A.I., Zaretskii, M.I., Stel'makh, G.P., and Eivazov, T.S., *Novye tekhnologii pererabotki vysokosernistykh slantsev* (New Technologies for Processing of High-Sulfur Shales), Moscow: Svetlyi STAN, 2001.
57. Bikkulov, A.Z., *Neftekhimicheskie protsessy i produkty (Voprosy zhidkostnoi ekstraktsii uglevodorodov): Trudy Ufimskogo neftyanogo instituta* [Petrochemical Processes and Products (Problems of Liquid Extraction of Hydrocarbons): Trans. Ufa Petroleum Institute)], Ufa, 1973, issue 14, pp. 5–24.
58. Ol'kov, P.L., Van Litszyun', Aznabaev, Sh.T., and Safarov, D.O., *Bashkir. Khim. Zh.*, 2001, vol. 8, no. 5, pp. 22–24.
59. Cadulaeva, A.S., Ol'kov, P.L., and Syrkin, A.M., *Khim. Tekhnol. Topl. Masel*, 2007, no. 3, pp. 19–21.
60. Khalikov, D.E., Extractive Dearomatization of Diesel eractions To Give a Component of Ecologicall Clean Diesel Fuel, Cand. Sci. Dissertation, 2004.
61. Ziganshin, G.K., Improvement of Liquid Extraction Technology in Production of Petroleum Oils with the Use of New Catalytic Devices, *Doctoral Dissertation*, Ufa, 1999.

62. Osintsev, A.A., Ziganshin, K.G., Ziganshin, G.K., et al., *Neftepererabotka i neftekhimiya – 2005: Materialy Mezhdunarodnoi nauchno-prakticheskoi konferentsii, Ufa, 25 maya, 2005 g.* (Petroleum Processing and Petrochemistry 2005: Proc. Int. Sci.-Pract. Conf., Ufa, May 25, 2005), Ufa: GUP INKhP RB, 2005, pp. 67–68.

63. Osintsev, A.A., Ziganshin, K.G., Ziganshin, G.K., et al., *Neftepererabotka i neftekhimiya – 2005: Materialy Mezhdunarodnoi nauchno-prakticheskoi konferentsii, Ufa, 25 maya, 2005 g.* (Petroleum Processing and Petrochemistry 2005: Proc. Int. Sci.-Pract. Conf., Ufa, May 25, 2005), Ufa: GUP INKhP RB, 2005, , pp. 202–203.

64. Khalikov, D.E., Obukhova, S.A., and Vezirov, R.R., *Neftepererab. Neftekhim.*, 2000, no. 1, pp. 46–48.

65. Obukhova, S.A., Khalikov, D.E., Kulik, A.A., and Telyashev, E.G., *Neftepererabotka i neftekhimiya – problemy i perspektivy: Materialy Mezhdunarodnoi nauchno-prakticheskoi konferentsii, Ufa, 23 maya 2001 g.* (Petroleum Processing and Petrochemistry, Problems and Prospects: Proc. Int. Sci.-Pract. Conf., Ufa, May 23, 2001), Ufa: IP NKhP Akad. Nauk RB, 2001, pp. 105–108.

66. Fuks, I.G. and Sochevko, T.I., *Neft', Gaz Biznes*, 2005, nos. 2–3, pp. 73–80.

67. Shkol'nikov, V.M. and Kolesnik, I.O., *Sovershenstvovanie protsessov selektivnoi ochistki i deasfal'tizatsii maslyanogo syr'ya na osnove primeneniya novykh rastvoritelei* (Improvement of Processes for Selective Purification and Deasphalting of Oil Raw Materials by Using New Solvents), Moscow: TsNIITEneftekhim, 1986.

68. Kolesnik, I.O., Vavanov, V.V., and Shkol'nikov, V.M., *Proizvodstvo bazovykh masel uluchshenogo kachestva – osnov perspektivnogo assortimenta motornykh masel* (Production of Base Oils with Improved Properties as a Basis for a Promising Assortment of Motor Oils), Moscow: TsNIITEneftekhim, 1989.

69. Kozin, V.G., Physicochemical Foundations of Extractive Recovery of Organosulfur Compounds from Diesel Fractions, *Doctoral Dissertation*, Ufa, 1988.

70. Korenman, Ya.I., *Ekstraktsiya fenolov* (Extraction of Phenols), Gorky: Volgo-Vyat. Knizhn. Izd., 1973.

71. Korenman, Ya.I., Extraction in Analytical Chemistry of Aromatic Compounds, *Doctoral Dissertation*, Kiev, 1978.

72. Korenman, Ya.I., *Koeffitsienty raspredeleniya organicheskikh soedinenii: Spravochnik* (Distribution Coefficients of Organic Compounds: Reference Book), Voronezh: Voronezh. Univ., 1992.

73. Ermolaeva, T.N., *Ekstraktsiya mono- i polifunktsional'nykh aromaticheskikh soedinenii gidrofil'nymi rastvoritelyami – obshchie zakonomernosti i elektrokhimicheskii analiz nevodnykh kontsentratov* (Extraction of Mono- and Polyfunctional Aromatic Compounds with Hydrophilic Solvents: Fundamental Aspects and Electrochemical Analysis of Nonaqueous Concentrates), Moscow: Mosk. Gos. Univ. im. M.V. Lomonosova, 1999.

74. Egutkin, N.L., Chemistry of Extraction of a Number of Mono- and Polyfunctional Organic Compounds, *Doctoral Dissertation*, Ufa, 1993.

75. Potashnikov, G.L., Development of a Process for Selective Purification of Petroleum Residue with Furfural-Propane with Addition of Cresol, *Cand. Sci. Dissertation*, Groznyi, 1983.

76. Gaile, A.A., A Study of the Selectivity of Solvents toward Hydrocarbon Systems, *Doctoral Dissertation*, Leningrad, 1975.

77. Semenov, L.V., Intermolecular Interactions and Separation of Hydrocarbons with Selective Solvents, *Doctoral Dissertation*, Leningrad, 1986.

78. Zalishchevskii, G.D., Development and Improvement of Extraction Technology for Separation of Petroleum Products, *Doctoral Dissertation*, St. Petersburg: SPbGTI, 2006.

79. Bittrich, H.-J., Gaile, A.A., Lempe, D., et al., *Razdelenie uglevodorodov s ispol'zovaniem selektivnykh rastvoritelei* (Separation of Hydrocarbons with the Use of Selective Solvents), Leningrad: Khimiya, 1987.

80. Pokonova, Yu.V., Gaile, A.A., Spirkin, V.G., et al., *Khimiya nefti* (Chemistry of Petroleum), Leningrad: Khimiya, 1984.

81. Gaile, A.A., Somov, V.E., Varshavskii, O.M., and Semenov, L.V., *Sul'folan: Svoistva i primenenie v kachestve selektivnogo rastvoritelya* (Sulfolane: Properties and Use as a Selective Solvent), St. Petersburg: Khimizdat, 1998.

82. Gaile, A.A., Somov, V.E., and Varshavskii, O.M., *Aromaticheskie uglevodorody: Vydelenie, primenenie, rynok: Spravochnik* (Aromatic Hydrocarbons: Recovery, Use, and Marketing), St. Petersburg: Khimizdat, 2000.

83. Gaile, A.A., Proskuryakov, V.A., Semenov, L.V., et al., *Predel'nye koeffitsienty aktivnosti uglevodorodov v selektivnykh rastvoritelyakh: Spravochnik* (Limiting Activity Coefficients of Hydrocarbons in Selective Solvents: Reference Book), Gaile, A.A., Ed., St. Petersburg: SPb Gos. Univ., 2002.

84. Gaile, A.A. and Zalishchevskii, G.D., *N-Metilpirrolidon: Poluchenie, svoistva i primenenie v kachestve selektivnogo rastvoritelya* (*N*-Methylpyrrolidone: Production, Properties, and Use as a Selective Solvent), St. Petersburg: Khimizdat, 2005.

85. Gaile, A.A., Somov, V.E., and Zalishchevskii, G.D., *Morfolin i ego proizvodnye: Poluchenie, svoistva i primenenie v kachestve selektivnykh rastvoritelei* (Morpholine and Its Derivatives: Production, Properties, and Use as Selective Solvents), St. Petersburg: Khimizdat, 2007.

86. Gaile, A.A., *Khimiya nefti i ee khimicheskaya pererabotka.* Ch. I. *Metody razdeleniya uglevodorodov nefti: Uchebnoe posobie* (Chemistry of Petroleum and Its Chemical Processing, part I, Methods for Separation of Petroleum Hydrocarbons: Textbook), Leningrad: Leningr. Tekhnol. Inst. im. Lensoveta, 1972.

87. Gaile, A.A., *Fiziko-khimicheskie osnovy protsessov razdeleniya uglevodorodov s ispol'zovaniem izbiratel'nykh rastvoritelei* (Physicochemical Foundations of Processes for Separation of Hydrocarbons with the Use of Selective Solvents), Leningrad: Leningr. Tekhnol. Inst. im. Lensoveta, 1978.

88. Gaile, A.A., *Oborudovanie neftekhimicheskikh zavodov i osnovy proektirovaniya: Protsessy i apparaty dlya razdeleniya uglevodorodov i neftekhimicheskikh produktov: Uchebnoe posobie* (Equipment of Petrochemical Plants and Fundamentals of Designing: Processes and Apparatus for Separation of Hydrocarbons and Petrochemical Products), Leningrad: Leningr. Tekhnol. Inst. im. Lensoveta, 1986.

89. Bogomolov, A.I., Gaile, A.A., Gromova, V.V., et al., *Khimiya nefti i gaza: Uchebnoe posobie* (Chemistry of Petroleum and Natural Gas: Textbook), St. Petersburg: Khimiya, 1995, 3rd ed.

90. Gaile, A.A., *Issledovaniya v oblasti khimii i tekhnologii produktov pererabotki goryuchikh iskopaemykh: Mezhvuzovskii sbornik nauchnykh trudov* (Research in Chemistry and Technology of Products Formed in Processing of Fossil Fuels: Intercollegiate Coll. of Sci. Works), Leningrad: Leningr. Tekhnol. Inst. im. Lensoveta, 1979, pp. 54–67.

91. Gaile, A.A. and Semenov, L.V., *Neftekhimiya* (Petrochemistry), Leningrad: Nauka, 1985, pp. 163–169.

92. Gaile, A.A. and Semenov, L.V., *Zh. Prikl. Khim.*, 1993, vol. 66, no. 11, pp. 2425–2438.

93. Gaile, A.A., Somov, V.E., Semenov, L.V., et al., *Sbornik nauchnykh trudov OOO PO "KINEF" za 1998–2000 gg.* (Coll. of Sci. Works of PO KINEF Ltd. in 1998–2000), Moscow: TsNIITEneftekhim, 2001, pp. 49–57.

94. *Ekstraktsiya i primenenie arenov srednedistillyatnykh neftyanykh fraktsii: sbornik trudov OOO "KINEF"* (Extraction and Use of Arenes of Medium-Distillate Petroleum Fractions: Coll. of Works of KINEF Ltd.), Gaile, A.A. and Somov, V.E., Eds., St. Petersburg: IK Sintez, 1998.

95. *Ekstraktsionnaya dearomatizatsiya neftyanykh fraktsii: Sbornik trudov OOO "KINEF"* (Extractive Dearomatization of Petroleum Fractions: Coll. of Works of KINEF Ltd.), Gaile, A.A. and Somov, V.E., Eds., St. Petersburg: SPb Gos. Univ., 2002.

96. Gaile, A.A., Zalishchevskii, G.D., and Somov, V.E., *4-i Mezhdunarodnyi forum "TEK Rossii: regional'nye aspekty". Sbornik trudov, St. Petersburg, 6–9 aprelya 2004 g.* (4th Int. Symp. "Fuel-Energy Complex of Russia: Regional Aspects," Coll. of Works, St. Petersburg, April 6–9, 2004), St. Petersburg, 2004, pp. 122–123.

97. Gaile, A.A. and Somov, V.E., *Neftepererabotka i neftekhimiya* (Petroleum Processing and Petrochemistry), Moscow: TsNIITEneftekhim, 2004, no. 10, pp. 14–16.

98. Gaile, A.A., Semenov, L.V., Zalishchevskii, G.D., and Varshavskii, O.M., *Ekstraktsionnaya dearomatizatsiya neftyanykh fraktsii: Sbornik trudov OOO "KINEF"* (Extractive Dearomatization of Petroleum Fractions: Coll. of Works of KINEF Ltd.), Gaile, A.A. and Somov, V.E., Eds., St. Petersburg: SPb Gos. Univ., 2002, pp. 5–34, 164–285.

99. Gaile, A.A., Semenov, L.V., Zalishchevskii, G.D., and Varshavskii, O.M., in *Ekstraktsionnaya dearomatizatsiya neftyanykh fraktsii: Sbornik trudov OOO "KINEF"* (Extractive Dearomatization of Petroleum Fractions: Coll. of Works of KINEF Ltd.), Gaile, A.A. and Somov, V.E., Eds., St. Petersburg: SPb Gos. Univ., 2002, pp. 35–51, 286–318.

100. Erzhenkov, A.S., Gaile, A.A., Somov, V.E., and Semenov, L.V., *Ekstraktsionnaya dearomatizatsiya neftyanykh fraktsii: Sbornik trudov OOO "KINEF"* (Extractive Dearomatization of Petroleum Fractions: Coll. of Works of KINEF Ltd.), Gaile, A.A. and Somov, V.E., Eds., St. Petersburg: SPb Gos. Univ., 2002, pp. 52–93.

101. Gaile, A.A., Erzhenkov, A.S., Semenov, L.V., et al., *Zh. Prikl. Khim.*, 2001, vol. 74, no. 10, pp. 1618–1621.

102. Gaile, A.A., Erzhenkov, A.S., Somov, V.E., et al., *Mezhdunarodnyi forum "TEK Rossii: regional'nye aspekty". Sbornik trudov, St. Petersburg, 2–5 aprelya 2002 g.* (Int. Symp. "Fuel-Energy Complex of Russia: Regional Aspects," Coll. of Works, St. Petersburg, April 2–5, 2002), St. Petersburg., 2002, pp. 145–146.

103. Marusina, N.B., Gaile, A.A., and Semenov, L.V., *Zh. Prikl. Khim.*, 1994, vol. 67, no. 8, pp. 1311–1315.

104. Marusina, N.B., Gaile, A.A., and Semenov, L.V., *Zh. Prikl. Khim.*, 1996, vol. 69, no. 7, pp. 1163–1169.

105. RF Patent 2 177 023.

106. Gaile, A.A., Zalishchevskii, G.D., Semenov, L.V., et al., *Mezhdunarodnyi forum "TEK Rossii: regional'nye aspekty". Sbornik trudov, St. Petersburg, 8–11 aprelya 2003 g.* (Int. Symp. "Fuel-Energy Complex of Russia: Regional Aspects," Coll. of Works, St. Petersburg, April 8–11, 2003), St. Petersburg, 2003, p. 164.

107. Gaile, A.A., Zalishchevskii, G.D., Semenov, L.V., et al., *Neftepererabotka i neftekhimiya* (Petroleum Processing and Petrochemistry), Moscow: TsNIITEneftekhim, 2003, no. 12, pp. 18–21.

108. Gaile, A.A., Semenov, L.V., Zalishchevskii, G.D., and Gafur, N.N., *Toplivo–dvigatel' – ekologicheski chistaya sistema: Sbornik materialov nauchno-tekhnicheskogo seminara, St. Petersburg, 13–14 marta 2003 g.* (Fuel–Engine, an Ecologically Clean System: Proc. Sci.-Pract. Symp., St. Petersburg, March 13–14, 2003), St. Petersburg: SPb. Nauch. Tsentr Ross. Akad. Nauk, 2006, pp. 84–85.

109. Gaile, A.A., Zalishchevskii, G.D., Gafur, N.N., et al., *Khim. Tekhnol. Topl. Masel*, 2004, no. 3, pp. 10–13.

110. Gaile, A.A., Zalishchevskii, G.D., Semenov, L.V., and Gafur, N.N., Abstracts of Papers, *X Mezhdunarodnaya nauchno-tekhnicheskaya konferentsiya "Naukoemkie khimicheskie tekhnologii – 2004", Volgograd, 7–10 sentyabrya 2004 g.* (X Int. Sci.-Pract. Conf. "High-End Chemical Technologies 2004," Volgograd, September 7–10, 2004), Volgograd: RKP "Politekhnik", 2004, vol. 1, pp. 65–67.

111. RF Patent 2 254 317.

112. Zalishchevskii, G.D., Gaile, A.A., Yakovlev, A.A., et al., *Neftepererabotka i neftekhimiya* (Petroleum Processing and Petrochemistry), Moscow: TsNIITEneftekhim, 2004, no. 9, pp. 31–34.

113. Gaile, A.A., Zalishchevskii, G.D., Gafur, N.N., et al., *Khim. Tekhnol. Topl. Masel*, 2004, no. 4, pp. 11–14.

114. RF Patent 2 256 691.

115. Jentry, J.C., Cumar, K.S., Lee, H.M., Lee, I.H., *Khim. Tekhnol. Topl. Masel*, 2003, nos. 1–2, pp. 12–17.

116. Lee, F.-M., *Ind. Eng. Chem. Process Des. Dev.*, 1986, vol. 25, no. 4, pp. 949–957.

117. PCT Int. Appl. WO 01 83 642.

118. Gaile, A.A., Zalishchevskii, G.D., Erzhenkov, A.S., et al., *Zh. Prikl. Khim.,* 2007, vol. 80, no. 4, pp. 605–607.

119. Gaile, A.A., Zalishchevskii, G.D., Erzhenkov, A.S., et al., *Neftepererabotka i neftekhimiya 2006: Materialy Mezhdunarodnoi nauchno-prakticheskoi konferentsii, Ufa, 24 maya 2006 g.* (Petroleum Processing and Petrochemistry 2006: Proc. Int. Sci.-Pract. Conf., Ufa, May 24, 2006), Ufa: GUP INKhP RB, 2006, pp. 126–127.

120. Gaile, A.A., Erzhenkov, A.S., Koldobskaya, L.L., and Kaifadzhyan, E.A., *Zh. Prikl. Khim.,* 2007, vol. 80, no. 4, pp. 608–611.

121. Gaile, A.A., Erzhenkov, A.S., Kaifadzhyan, E.A., and Koldobskaya, L.L., *Zh. Prikl. Khim.*, 2007, vol. 80, no. 4, pp. 612–613.

122. Gaile, A.A., Zalishchevskii, G.D., Kaifadzhyan, E.A., et al., *7-i Mezhdunarodnyi forum "TEK Rossii: regional'nye aspekty". Sbornik trudov, St. Petersburg, 10–12 aprelya 2007 g.* (7th Int. Symp. "Fuel-Energy Complex of Russia: Regional Aspects," Coll. of Works, St. Petersburg, April 10–12, 2007), St. Petersburg, 2007, pp. 46–49.

123. Gaile, A.A., Semenov, L.V., Zalishchevskii, G.D., and Varshavskii, O.M., *Toplivo–dvigatel' – ekologicheski chistaya sistema: Sbornik materialov nauchno-tekhnicheskogo seminara, St. Petersburg, 13–14 marta 2003 g.* (Fuel–Engine, an Ecologically Clean System: Proc. Sci.-Pract. Symp., St. Petersburg, March 13–14, 2003), St. Petersburg: SPb nauch. tsentr Ross. Akad. Nauk, 2006, pp. 43–47.

124. RF Patent 2 177 024.

125. Gaile, A.A., Zalishchevskii, G.D., Semenov, L.V., et al., *Neftepererabotka i neftekhimiya* (Petroleum Processing and Petrochemistry), Moscow: TsNIITEneftekhim, 2003, no. 11, pp. 26–29.

126. Gaile, A.A., Zalishchevskii, G.D., Semenov, L.V., et al., *Neftepererabotka i neftekhimiya* (Petroleum Processing and Petrochemistry), Moscow: TsNIITEneftekhim, 2004, no. 1, pp. 23–27.

127. Gaile, A.A., Kostenko, A.V., Semenov, L.V., and Koldobskaya, L.L., *Zh. Prikl. Khim*., 2005, vol. 78, no. 9, pp. 1428–1432.

128. Erzhenkov, A.S., Gaile, A.A., Somov, V.E., and Semenov, L.V., in *Ekstraktsionnaya dearomatizatsiya neftyanykh fraktsii: Sbornik trudov OOO "KINEF"* (Extractive Dearomatization of Petroleum Fractions: Coll. of Works of KINEF Ltd.), Gaile, A.A. and Somov, V.E., Eds., St. Petersburg: SPb Gos. Univ., 2002, pp. 94–101.

129. Gaile, A.A., Zalishchevskii, G.D., Varshavskii, O.M., et al., in *Ekstraktsionnaya dearomatizatsiya neftyanykh fraktsii: Sbornik trudov OOO "KINEF"* (Extractive Dearomatization of Petroleum Fractions: Coll. of Works of KINEF Ltd.), Gaile, A.A. and Somov, V.E., Eds., St. Petersburg: SPb Gos. Univ., 2002, pp. 102–107.

130. Gaile, A.A., Flisyuk, O.M., Semenov, L.V., et al., in *Ekstraktsionnaya dearomatizatsiya neftyanykh fraktsii: Sbornik trudov OOO "KINEF"* (Extractive Dearomatization of Petroleum Fractions: Coll. of Works of KINEF Ltd.), Gaile, A.A. and Somov, V.E., Eds., St. Petersburg: SPb Gos. Univ., 2002, pp. 114–127.

131. Gaile, A.A., Zalishchevskii, G.D., and Semenov, L.V., *Mezhdunarodnyi forum "TEK Rossii: regional'nye aspekty". Sbornik trudov, St. Petersburg, 8–11 aprelya 2003 g.* (Int. Symp. "Fuel-Energy Complex of Russia: Regional Aspects," Coll. of Works, St. Petersburg, April 8–11, 2003), St. Petersburg, 2003, p. 202.

132. Gaile, A.A., Zalishchevskii, G.D., Semenov, L.V., et al., *Neftepererabotka i neftekhimiya* (Petroleum Processing and Petrochemistry), Moscow: TsNIITEneftekhim, 2004, no. 2, pp. 21–23.

133. Gaile, A.A., Zalishchevskii, G.D., Semenov, L.V., et al., *Zh. Prikl. Khim*., 2004, vol. 77, no. 4, pp. 571–575.

134. Gaile, A.A., Zalishchevskii, G.D., Varshavskii, O.M., et al., in *Ekstraktsionnaya dearomatizatsiya neftyanykh fraktsii: Sbornik trudov OOO "KINEF"* (Extractive Dearomatization of Petroleum Fractions: Coll. of Works of KINEF Ltd.), Gaile, A.A. and Somov, V.E., Eds., St. Petersburg: SPb Gos. Univ., 2002, pp. 108–113.

135. RF Patent 2 185 416.

136. *Ekstraktsionnaya dearomatizatsiya neftyanykh fraktsii: Sbornik trudov OOO "KINEF"* (Extractive Dearomatization of Petroleum Fractions: Coll. of Works of KINEF Ltd.), Gaile, A.A. and Somov, V.E.,Eds., St. Petersburg: SPb Gos. Univ., 2002, pp. 128–136.

137. Gaile, A.A., Zalishchevskii, G.D., Semenov, L.V., et al., *Neftepererabotka i neftekhimiya* (Petroleum Processing and Petrochemistry), Moscow: TsNIITEneftekhim, 2004, no. 5, pp. 29–32.

138. Zalishchevskii, G.D., Gaile, A.A., Yakovlev, A.A., et al., *Neftepererabotka i neftekhimiya* (Petroleum Processing and Petrochemistry), Moscow: TsNIITEneftekhim, 2004, no. 10, pp. 26–30.

139. Gaile, A.A., Zalishchevskii, G.D., Kostenko, A.V., et al., *6-i Mezhdunarodnyi forum "TEK Rossii: regional'nye aspekty". Sbornik trudov, St. Petersburg, 11–13 aprelya 2006 g.* (6th Int. Symp. "Fuel-Energy Complex of Russia: Regional Aspects," Coll. of Works, St. Petersburg, April 11–13, 2006), St. Petersburg, 2006, pp. 65–69.

140. Gaile, A.A., Somov, V.E., Zalishchevskii, G.D., et al., *Zh. Prikl. Khim*., 2006, vol. 79, no. 4, pp. 599–604.

141. Gaile, A.A., Zalishchevskii, G.D., Koldobskaya, L.L., and Kaifadzhyan, E.A., *Neftepererabotka i neftekhimiya 2005: Materialy Mezhdunarodnoi nauchno-prakticheskoi konferentsii, Ufa, 24–27 maya 2005 g.* (Petroleum Processing and Petrochemistry 2005: Proc. Int. Sci.-Pract. Conf., Ufa, May 24–27, 2006), Ufa: GUP INKhP RB, 2005, pp. 170–171.

142. Gaile, A.A. and Flisuyuk, O.M., *2nd Int. Symp. on Hydrocarbons and Chemistry*, Ghardaia–Algeria, March 21–23, 2004, p. 161.

143. Gaile, A.A., Dyurik, N.M., Semenov, L.V., et al., *Zh. Prikl. Khim*., 2003, vol. 76, no. 1, pp. 150–153.

144. Gaile, A.A., Dyurik, N.M., Semenov, L.V., et al., *Zh. Prikl. Khim*., 2003, vol. 76, no. 1, pp. 146–149.

145. Gaile, A.A., Zalishchevskii, G.D., Varshavskii, O.M., et al., in *Ekstraktsionnaya dearomatizatsiya neftyanykh fraktsii: Sbornik trudov OOO "KINEF"* (Extractive Dearomatization of Petroleum Fractions: Coll. of Works of KINEF Ltd.), Gaile, A.A. and Somov, V.E., Eds., St. Petersburg: SPb Gos. Univ., 2002, pp. 137–152.

146. Gaile, A.A., Zalishchevskii, G.D., Varshavskii, O.M., et al., in *Ekstraktsionnaya dearomatizatsiya neftyanykh fraktsii: Sbornik trudov OOO "KINEF"* (Extractive Dearomatization of Petroleum Fractions: Coll. of Works of KINEF Ltd.), Gaile, A.A. and Somov, V.E., Eds., St. Petersburg: SPb Gos. Univ., 2002, pp. 153–163.

147. RF Patent 2 221 836.

148. Gaile, A.A., Khvorov, A.P., Zalishchevskii, G.D., et al., *Khim. Tekhnol. Topl. Masel*, 2005, no. 1, pp. 19–21.

149. Gaile, A.A., Zalishchevskii, G.D., Varshavskii, O.M., et al., *Neftepererabotka i neftekhimiya (platinum),* Moscow: TsNIITEneftekhim, 2004, no. 6, pp. 16–20.

150. RF Patent 2 203 306.

151. Gaile, A.A., Kaifadzhyan, E.A., Koldobskaya, L.L., et al., *5-i Mezhdunarodnyi forum "TEK Rossii: regional'nye aspekty". Sbornik trudov, St. Petersburg, 4–7 aprelya 2005 g.* (5th Int. Symp. "Fuel-Energy Complex of Russia: Regional Aspects," Coll. of Works, St. Petersburg, April 4-7, 2005), St. Petersburg., 2005, pp. 173–177.

152. RF Patent 2 275 413.

153. Gaile, A.A., Zalishchevskii, G.D., Kostenko, A.V., et al., *Khim. Tekhnol. Topl. Masel*, 2005, no. 4, pp. 3–9.

154. Gaile, A.A., Zalishchevskii, G.D., Kostenko, A.V., et al., *Neftepererabotka i neftekhimiya 2005: Materialy Mezhdunarodnoi nauchno-prakticheskoi konferentsii, Ufa, 24–27 maya 2005 g.* (Petroleum Processing and Petrochemistry 2005: Proc. Int. Sci.-Pract. Conf., Ufa, May 24–27, 2006), Ufa: GUP INKhP RB, 2005, pp. 201–202.

155. Gaile, A.A., Kaifadzhyan, E.A., Koldobskaya, L.L., et al., *Perspektivy razvitiya khimicheskoi pererabotki goryuchikh iskopaemykh (KhPGI – 2006): Mezhdunarodnaya konferentsiya k 135-letiyu kafedry tekhnologii neftekhimicheskikh i uglekhimicheskikh proizvodstv SPbGTI (TU). St. Petersburg, 12–15 sentyabrya 2006 g.* [Prospects of Development of Chemical Processing of Fossil Fuel (KhPGI 2006): Int. Conf. timed with the 135th foundation anniversary of the chair of technology of petrochemical and coal-chemical industries at SPbGTI (TU), St. Petersburg, September 12–15, 2006], Petersburg: Khimizdat, 2006, pp. 46–47.

156. Gaile, A.A., Somov, V.E., Zalishchevskii, G.D., et al., *Neftekhimiya*, 2007, vol. 47, no. 4, pp. 314–317.

157. Gaile, A.A., Zalishchevskii, G.D., Somov, V.E., et al., *Khim. Tekhnol. Topl. Masel*, 2007, no. 3, pp. 12–14.

158. Erzhenkov, A.S., Development and Improvement of Extraction Processes for Recovery of Aromatic Hydrocarbons from Medium-Distillate Petroleum Fractions and Benzene Reforming Catalyzate, *Cand. Sci. Dissertation*, St. Petersburg, 2003.

159. Khadartsev, A.Ch., Recovery of Aromatic Extracts from Petroleum Fractions and Their Use, *Cand. Sci. Dissertation*, St. Petersburg, 2003.

160. Gafur, N.N., Recovery of Arenes from Reformates of Gasoline Fractions by Combined Methods of Extraction and extractive and azeotropic Rectification, *Cand. Sci. Dissertation*, St. Petersburg, 2004.

ISSN 1070-4272, Russian Journal of Applied Chemistry, 2008, Vol. 81, No. 8, pp. 1325–1331. © Pleiades Publishing, Ltd., 2008.
Original Russian Text © V.V. Sidorchuk, J. Skubiszewska-Zięba, S.V. Khalameida, V.A. Zazhigalov, R. Leboda, 2008, published in Zhurnal Prikladnoi Khimii, 2008, Vol. 81, No. 8, pp. 1246–1252.

INORGANIC SYNTHESIS AND INDUSTRIAL INORGANIC CHEMISTRY

Synthesis of Vanadium-Phosphorus Oxide Catalysts Deposited onto Silica-Carbon Supports

V. V. Sidorchuk, J. Skubiszewska-Zięba, S. V. Khalameida, V. A. Zazhigalov, and R. Leboda

Institute of Sorption and Endoecology Problems, National Academy of Sciences of Ukraine, Kiev, Ukraine

Received November 27, 2007

Abstract—Effect of conditions of hydrothermal and microwave synthesis of supported vanadium-phosphorus oxide catalysts in an aqueous medium on the physicochemical properties of the vanadyl hydrophosphate obtained was studied. The transformations occurring in the system were examined using X-ray phase and differential-thermal analyses, adsorption-structural method, and scanning electron microscopy.

DOI: 10.1134/S1070427208080028

The problem of development of physicochemically and technologically efficient heterogeneous catalysts for numerous processes remains topical. In particular, it is necessary to improve vanadium-phosphorus oxide (VPO) catalysts for oxidation of *n*-butane into maleic anhydride [1]. It seems that one of ways to solve this problem is to develop methods for deposition of the active phase, vanadyl diphosphate $(VO)_2P_2O_7$ (VDP) or its precursor, vanadyl hydrophosphate semihydrate $VOHPO_4 \cdot 0.5H_2O$ (VHP), onto an appropriate support [1, 2]. It should be noted that substances of varied nature and different physicochemical characteristics have been used as supports of this kind: silica gel, aerosil, silicas with regular porosity (MCM-41, SBA-15), zeolites, titanium and aluminum oxides, metal phosphates, silicon carbide, and silicon and boron nitrides [2, 3–8]. However, the methods reported in the scientific and patent literature have failed to raise the yield of the target product, compared with the bulk analogues.

It should be emphasized that most of the supported VPO catalysts described in the literature have been synthesized, similarly to their bulk analogues, in organic media (butanol, isobutanol, benzyl alcohol) with the use of organic reducing agents [1–9]. Therefore, it is a topical ecological task to prepare catalysts of this kind in an aqueous medium [1].

A possibly interesting class of supports for VPO systems are carbosils, which, on the one hand, combine numerous advantages of both carbon and silica materials [10] and, on the other, enable synthesis of VDP or VHP in an aqueous medium, because the carbon surface of carbosils acts as a substrate for the active phase, and surface carbon atoms, as a reducing agent for vanadium.

The aim of this study was to examine the effect of conditions of hydrothermal (HTS) and microwave (MWS) syntheses on the formation of VPO phases, and VHP in the first place, on the surface of carbosils with varied content of carbon and to analyze the physicochemical properties of the supported composites obtained. It should be added that the hydrothermal method has already been used to prepare VPO catalysts [1, 9, 11, 12], whereas use of the microwave synthesis for this purpose has not been reported.

EXPERIMENTAL

As VPO supports served carbosils produced from porous silicon dioxide, silica gel Sipernat-50, and nonporous pyrogenic silicon dioxide Aerosil-200 (both silicas manufactured by Degussa, Germany) by carbonization of potato starch in a flow of nitrogen at 500°C for 5 h in a flow-through rotating laboratory reactor [13]. Starch was deposited on the surface of the silicas from aqueous dispersions of the com-ponents. Selected characteristics of the starting silicas and carbosils prepared from these silicas are listed in Table 1.

Table 1. Selected characteristics of starting supports

Support	c, wt %	S_{BET}, $m^2 g^{-1}$	V_{N_2}	V_{mi}	d, nm	ΔT, °C
			$cm^3 g^{-1}$			
Supernat-50	0	503	1.190	0.0034	9.5	–
Carbosil 1	18.7	361	0.971	0.0357	10.8	340–585
Carbosil 2	26.4	338	0.722	0.0536	8.6	350–590
Carbosil 3	33.8	356	0.568	0.0699	6.4	340–590
Aerosil 200	0	236	–	–	–	–
Carbosil 4	8.5	245	0.030	0.024	–	350–580
Carbosil 5	31.2	265	0.025	0.021	–	345–600

* ΔT is the combustion temperature range of pyrolytic carbon (according to DTA in air), and $d = 4V_{N_2}/S_{BET} \times 10^3$, average pore diameter.

It is noteworthy that carbosils 1–3 were synthesized from porous silica, and carbosils 4 and 5, from nonporous silica. As a source of vanadium(V) served vanadium pentoxide of chemically pure grade, which is the most frequently used for this purpose [1, 2, 9, 12]. A 85% aqueous solution of orthophosphoric acid (chemically pure) was used as a source of phosphorus. The *P*/*V* ratio in the reaction mixture was 1.15 [2, 3, 9]. The amount of a support introduced into the reaction mixture was chosen in such a way that the concentration of the supported VPO phase was 10–35 wt % in terms of VHP. Supported VPO were synthesized at 175–240°C by two methods: (i) in a 45-ml stainless steel laboratory autoclave, with the reaction mixture (carbosil, V_2O_5, and 85% H_3PO_4) introduced into a Teflon test tube and 5 ml of water placed at the autoclave bottom (to create pressure), duration 6 h; and (ii) in a NANO-2000 laboratory microwave reactor (Plazmotronica, Poland), with the reagents charged in a similar way, duration 0.5–1 h.

When synthesizing supported samples based on purely silica supports, citric acid was added as a mild reducing agent.

After the hydrothermal or microwave treatment, the reaction products were washed with distilled water and dried at 110°C for 3 h.

The X-ray phase analysis (XPA) was performed with a Philips PW 1830 diffractometer (Cu_{K_α} radiation). The size of crystallites was found from the line broadening in X-ray diffraction patterns by using the Debye–Scherrer formula. The thermogravimetric analysis (DTA–TGA) was made on an MOM C derivatograph (Hungary) in the temperature range 20–700°C at a heating rate of 10 deg min^{-1} in air and in the atmosphere of argon (sensitivity 10 mg, weighed portion 20 mg). The content of the supported VPO phase was calculated from the decrease in the fraction of pyrolytic carbon in supported samples, compared with the starting carbosils.

The content of the supported VPO phase was calculated from gravimetric data on the assumption that neither carbon, nor silica from the support pass into the acid medium in the course of deposition and, consequently, their mass ratio c_C/c_{SiO_2} in the solid phase (in carbosil) remains unchanged after the reaction:

$$c_C^0/c_{SiO_2}^0 = c_C/c_{SiO_2},$$

where the concentration c^0 is related to the starting carbosil.

Thus, the mass content c_{VPO} of the supported phase can be calculated by the formula

$$c_{VPO} = 100 - c_C - c_C(100 - c_C^0)/c_C^0.$$

The concentrations of carbon in the starting carbosil (c_C^0) and in the supported sample (c_C) were found from TG curves for the corresponding samples.

The porous structure parameters were calculated for all samples from isotherms of low-temperature adsorption–desorption of nitrogen, measured with a Micromeritics ASAP 2405N analyzer as follows: specific surface area S_{BET}, by the BET method; limiting sorption volume of pores, V_{N_2}, from the amount of adsorption at a relative pressure close to unity; surface area and volume of micropores, S_{mi} and V_{mi}, by the *t*-method; and the pore size distribution, by the Barrett–Joiner–Halenda method (BJH) [14]. The total pore volume V_Σ was found by impregnation with water from the liquid phase.

The surface morphology of the deposited samples was studied by scanning electron microscopy (SEM) with a TESLA BS 301 instrument.

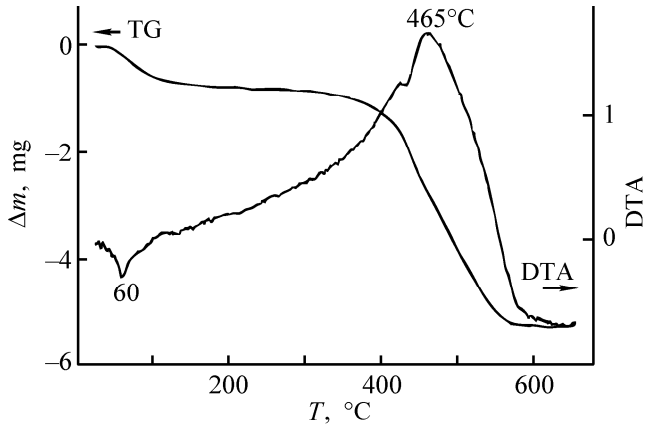


Fig. 1. DTA and TG curves for a VPO sample produced from carbosil 3 by MWS at 190°C. (Δ*m*) Change in mass and (*T*) Temperature.

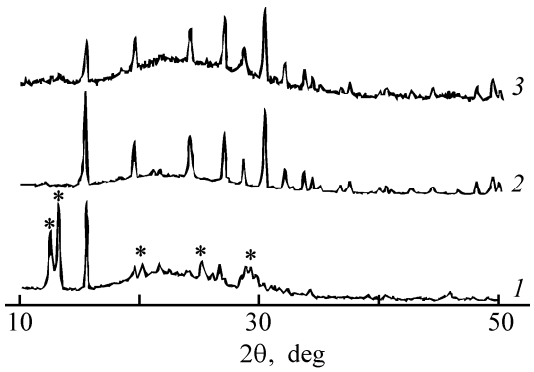


Fig. 2. X-ray diffraction patterns of supported VPO samples prepared (*1*) from the starting Sipernat-50 by MWS at 175°C and from carbosil 3 at 190°C by (*2*) MWS and (*3*) HTS.

Figure 1 shows as an example DTA–TG curves for a supported VPO sample produced from porous carbosil 3. It can be seen that the run of these curves is the same as that for the corresponding pure carbosil [13]: the loss of mass at 50–150°C, accompanied by an endothermic effect, is due to removal of adsorbed water from the surface and pore volume, and the loss of mass in the temperature range 350–650°C and the corresponding exothermic effect are due to combustion of pyrolytic carbon [10].

The results obtained in thermogravimetric measurements of supported samples are summarized in Table 2. It can be seen that, irrespective of the content of carbon in the starting carbosil, the amount of the supported VPO phase is in good agreement with the content of vanadium and phosphorus in the reaction mixture. Because VPO catalysts for oxidation of *n*-butane into maleic anhydride are active in the range 300–400°C [9, 15], an important factor is the thermal stability of carbon-containing supported composites. Table 1 lists combustion temperature ranges of pyrolytic carbon, found from DTA data obtained in air: for most of the supported samples, the combustion onset is at 360–390°C (which exceeds by at least 20–30°C that for similar starting carbosils). The highest thermal stability is observed for supported samples produced from a car-bosil with the lowest carbon content: the onset of carbon combustion for these samples is at 400–410°C. Apparently, in these samples, the minimum layer of car-bon is screened by the supported VPO phase to the max-imum extent. When estimating the thermal stability, it is necessary to take into account that VPO catalysts work in a reaction mixture containing 1.5–3 vol % *n*-butane in air [1, 3, 7–9], i.e., in the presence of a reducing agent, which may shift the combustion of carbon to higher temperatures. For example, thermographic experiments in the atmosphere of argon demonstrated that the combustion onset temperature of carbon increases by 20–30°C for supported samples, compared with the data in Table 2 for heating of these samples in air.

Table 2. Synthesis conditions and selected properties of supported VPO samples

Support	Synthesis conditions	Content, %		c_C/c_{SiO_2}	T*	ΔT*
		carbon	VPO phase		°C	
Carbosil 1	MWS, 240	14.1	24.6 (25.0)**	0.23	385	385–600
	HTS, 240	16.1	13.8 (15.0)	0.23	360	360–590
Carbosil 2	MWS, 240	18.5	30.2 (30.0)	0.36	380	380–600
Carbosil 3	MWS, 190	21.7	35.7 (35.0)	0.51	390	390–600
	MWS, 215	22.1	34.6 (35.0)		385	385–595
	HTS, 190	24.3	28.1 (30.0)		360	360–585
Carbosil 4	MWS, 200	6.5	23.5 (25.0)	0.09	410	410–600
	HTS, 200	7.5	11.9 (10.0)		400	400–560
Carbosil 5	MWS, 175	26.4	15.5 (15.0)	0.45	360	360–620
	HTS, 175	26.5	14.6 (15.0)		370	370–630

* T and ΔT are the onset temperature and temperature range of combustion of pyrolytic carbon.

** The contents of vanadium and phosphorus in the reaction mixture are given in parentheses.

Table 3. X-ray diffraction data for supported VPO samples

Support	Synthesis conditions, T, °C	Main phase	VHP parameters		Impurity phase
			I_{001}/I_{220}	D_{001}, nm	
Supernat 50	MWS, 175	VHP, V/P-micas	11.50	28.8	γ-$VOPO_4$
	HTS, 175	V/P-micas	–	–	VHP, γ-$VOPO_4$, $VO(H_2PO_4)_2$
Carbosil 1	MWS, 240	VHP	1.25	26.0	–
	HTS, 240	VHP	9.56	33.8	$VO(H_2PO_4)_2$
Carbosil 2	MWS, 240	VHP	1.08	29.2	–
Carbosil 3	MWS, 190	VHP	1.19	22.2	–
	MWS, 215	VHP	0.71	27.5	V/P-micas
	HTS, 190	VHP	0.60	27.6	–
Aerosil 200	MWS, 175	VHP, V/P-micas	1.19	30.9	–
		VHP	3.44	24.5	V/P-micas
Carbosil 4	MWS, 200	VHP	0.86	22.5	$VO(H_2PO_4)_2$
	HTS 200	VHP	2.19	24.3	–
Carbosil 5	MWS, 175	VHP	1.07	22.1	–
	HTS, 175	VHP	0.72	18.9	V/P-micas

Table 3 and Fig. 2 present results of XPA for supported composites prepared on starting silicas and on carbosils. The X-ray data were interpreted in accordance with the data of [16, 17]. It should be noted that synthesis from the starting silica yields, even in the presence of citric acid, not only VHP, but also other VPO phases in which the degree of vanadium oxidation exceeds 4+. For example, X-ray diffraction pattern *1* in Fig. 2 contains strong reflections belonging to the impurity phase of V/P-micas (denoted by asterisks). At the same time, a single-phase layer of VHP is formed on the surface of all carbosils. It should be noted that 0.5–1.0 h is sufficient for this to occur in the case of MWS, and no less than 6 h for HTS. The last experimental fact is in agreement with published data indicating that chemical and physicochemical transformations are strongly accelerated by microwave heating of other oxide systems [18, 19]. In addition, control over the synthesis conditions enables formation of the VHP phase with a varying intensity ratio of two principal reflections in the X-ray diffraction patterns, I_{001}/I_{220}, which correspond to different crystallographic planes: basal (001) and lateral (220). This ratio widely varies, from 0.60 to 9.56 (Table 3). The following tendency is observed in this case: in HTS, I_{001}/I_{220} markedly exceed unity in some cases (even by an order of magnitude), which points to the preferential surface orientation of the basal surface of VHP , responsible for selective oxidation of *n*-butane [9]. At the same time, MWS yields VHP with comparable surface concentrations of the basal and lateral phases. The data in Fig. 3 indicate that the VHP crystallites formed on the surface of carbosils are in the nanodispersed state and have sizes in the range 20–30 nm.

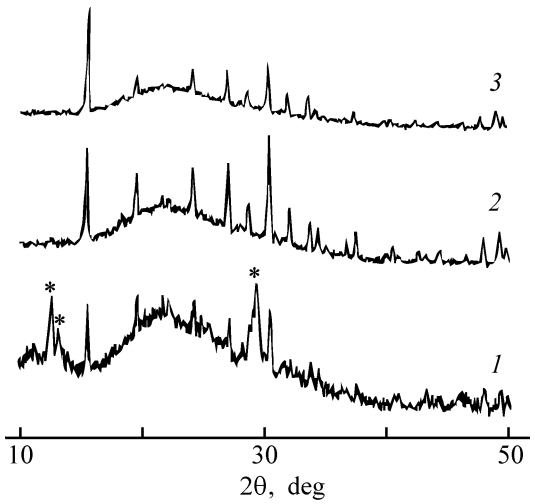


Fig. 3. X-ray diffraction patterns of supported VPO samples synthesized (*1*) from the starting Aerosil-200 by MWS at 175°C and from carbosil 4 at 200°C by (*2*) MWS and (*3*) HTS.

Table 4. Porous structure parameters of VPO samples

Support	Synthesis conditions, T, °C	S_{BET}	S_{mi}	V_{N_2}	V_{mi}	V_Σ	d_{me},* nm
		$m^2 g^{-1}$		$cm^3 g^{-1}$			
Supernat 50	MWS, 175	184	12	0.71	0.005	0.70	35.6
	HTS, 175	250	14	0.84	0.005	0.86	28.2
Carbosil 1	MWS, 240	198	16	0.40	0.005	0.40	32.6
	HTS, 240	235	53	0.48	0.020	0.49	22.6
Carbosil 2	MWS, 240	126	–	0.40	–	0.40	29.0
Carbosil 3	MWS, 190	82	6	0.28	–	0.28	33.8
	MWS, 215	132	39	0.32	0.015	0.33	31.4
	HTS, 190	212	80	0.38	0.035	0.36	21.0
Aerosil 200	MWS, 175	104	–	0.39	–	1.56	49.2
	HTS, 175	154	20	0.51	0.010	1.48	42.6
Carbosil 4	MWS, 200	112	1	0.43	–	1.35	52.4
	HTS 200	147	12	0.45	0.005	1.26	47.8
Carbosil 5	MWS, 175	59	1	0.26	–	0.78	59.4
	HTS, 175	108	15	0.29	0.005	1.41	34.8

* d_{me} is the diameter of mesopores, found from curves of pore volume distribution over pore size by using the BJH method.

Table 4 lists porous structure parameters of the supported samples obtained. For composites prepared on porous supports (starting Sipernat-50 and carbosils 1–3), the specific surface area and the pore volume typically steadily decrease as the degree of VPO deposition increases, in agreement with the previously established fundamental aspects of their behavior [20]. The decrease in S_{BET} and V_{N_2}, observed in the case of MWS, always exceeds that for samples produced by HTS. In addition, all samples prepared on the basis of silica gel and carbosils 1–3, i.e., on porous supports, contain nearly only mesopores, with the share of micropores being as low as 1–10% of the total volume of pores. There are no macropores in these samples, which is indicated by the coincidence of V_{N_2} and V_Σ.

In synthesis of supported samples from carbosils 4 and 5, which are, as already mentioned, nearly nonporous, the crystalline VHP phase is formed (Fig. 3) simultaneously with the porous structure of the whole composite. This has been reported previously for the case of deposition of VPO phases onto a pure nonporous silica, aerosil [21]. An interesting specific feature of these samples is that the total pore volume V_Σ, found by impregnation with water from the liquid phase, substantially exceeds the limiting-sorption pore volume V_{N_2}, which confirms that the samples contain macropores unfilled in the course of capillary condensation of the adsorbate (nitrogen). At the same time, the amount of micropores in the samples is close to zero (Table 4). Thus, the supported VPO samples prepared from nonporous carbosils have a meso-macroporous structure (the macroporous component is 0.5–1.1 ml g^{-1}, or 65–85% of the total pore volume). This makes samples of this kind especially promising as catalysts, for which transport pores are necessary, because the role of these pores can be played by macropores [15].

The results obtained in an analysis of the structure of a supported VPO layer and of the morphology of its constituent particles are shown in the SEM micrographs in Figs. 4 and 5. Because a mixture of several

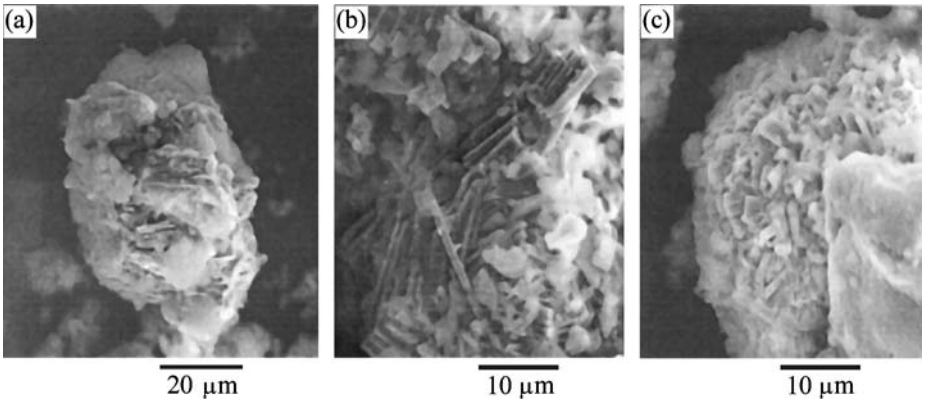


Fig. 4. SEM micrographs of supported VPO samples prepared from (a) Sipernat-50 by MWS and from carbosil 3 by (b) MWS and (c) HTS.

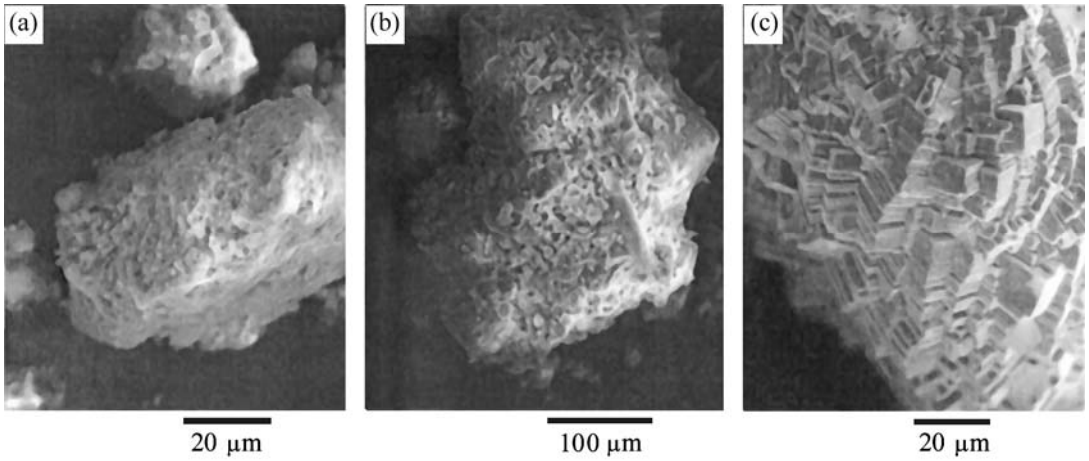


Fig. 5. SEM micrographs of supported VPO samples prepared from (a) Aerosil-200 by MWS and from carbosil 4 by (b) MWS and (c) HTS.

VPO phases is formed on pure silica supports, it is rather difficult to determine the shape of their crystals (Figs. 4a and 5a). At the same time it can well be seen that VHP crystallites are formed on the surface of porous carbosils in the form of rods 1–2 μm in diameter and 10–20 μm long after MWS (Fig. 4b) or 2–4 μm long after HTS (Fig. 4c). It can also be seen in the micrographs that not the entire surface of carbosils is covered by the VPO phase. Comparison of the pore diameters of the starting supports (6.5–11 nm, Table 1) with the crystallite size suggests that the supported phase is on the external surface of the support, rather than within its pores. The observed decrease in S_{BET} and V_{Σ} is presumably due to blocking of a part of pores by the VPO crystallites formed.

Deposition of VPO onto nonporous supports, during which the porous and crystalline structures are simultaneously formed, yields are more uniform, nearly continuous coating (including that within pores). This is indicated by the micrographs in Fig. 5. Particularly characteristic in this regard is the sample synthesized by HTS from carbosil 4 (Fig. 5c). VHP crystalites, which are nearly regular parallelepipeds with edge lengths of 5–15 μm, are aggregated on its surface into a kind of solid brickwork. The shape of VHP crystallites on the surface of carbosils strongly differs from that for bulk samples prepared by other methods. For example, the crystallites formed in organic media frequently have the shape of rosettes [1].

CONCLUSIONS

(1) A supported vanadyl hydrophosphate semihydrate, precursor of the active phase of vanadium-phosphorus oxide catalysts, was obtained on silica-carbon (carbosil) supports by hydrothermal or microwave treatment in an aqueous medium.

(2) It was shown that supported samples have an acceptable thermal stability, widely controllable parameters of the crystal and porous structure, and variable morphology of particles of the supported phase.

REFERENCES

1. Hutchings, G.J., *J. Mater. Chem.,* 2004, vol. 14, pp. 3385–3395.
2. Guliants, V.V., *Catal. Today*, 1999, vol. 51, pp. 255–268.
3. Zazhigalov, V.A., Belousov, V.M., Bacherikova, I.V., and Zaitsev, Yu.P., *Teor. Eksp. Khim*., 1991, vol. 27, no. 3, pp. 370–375.
4. Holmes, S., Sartoni, L., Durrows, A., et al., *Stud. Surf. Sci. Catal.*, 2000, vol. 130, pp. 1700–1714.
5. Ruitenbeck, M., Van Dillen, A.J., Koningsberger, D.C., and Geus, J.W., *Stud. Surf. Sci. Catal*., 1998, vol. 118, pp. 549–555.
6. Ledoux, M.J., Turines, V., Crouzet, C., et al., *Stud. Surf. Sci. Catal.*, 2000, vol. 130, pp. 821–826.
7. Xiao, C.Y, Chen, X., Wang, Z.Y., et al., *Catal. Today*, 2004, vols. 93–95, pp. 223–228.
8. Li, X.-K., Ji, W.-J., Zhao, J., et al., J. Catal., 2006, vol. 238, pp. 232–241.
9. Zazhigalov, V.A., Yaremenko, V.E., and Il'in, V.G., *Kinet. Kataliz*, 1999, vol. 40, no. 1, pp. 141–144.
10. Leboda, R., Skubiszewska-Zięba, J., Sidorchuk, V.V., et al., *J. Non-Cryst. Solids*, 1995, vol. 189, pp. 265–269.
11. Sidorchuk, V.V., *Neorg. Mater*., 1993, vol. 29, no. 2, pp. 274–277.
12. Sidorchuk, V.V., Diyuk, E.A., and Zazhigalov, V.A., *Neorg. Mater*., 2007, vol. 43, no. 4, pp. 471–476.

13. Gun'ko, V.M., Skubiszewska-Zięba, J., Leboda, R., et al., *Appl. Surf. Sci*., 2004, vol. 227, pp. 219–243.

14. Gregg, S.J. and Sing, K.S.W., *Adsorption, Surface Area and Porosity*, London: Academic, 1982.

15. Zazhigalov, V.A., Belousov, V.M., Pyatnitskaya, A.I. et al., *Zh. Prikl. Khim*., 1988, vol. 61, no. 1, pp. 101–105.

16. Bordes, E., *Catal. Today*, 1987, vol. 1, no. 5, pp. 499–526.

17. Zazhigalov, V.A., *Kataliz Katalizatory*, 1992, no. 28, pp. 3–19.

18. Berlan, J., *Radiat. Phys. Chem*., 1995, vol. 45, no. 4, pp. 581–589.

19. Vanetsev, A.S., Makshina, E.V., Oleinikov, N.N., et al., *Dokl. Ross. Akad. Nauk*, 2005, vol. 405, no. 2, pp. 204–207.

20. Sidorchuk, V.V., *Zh. Prikl. Khim*., 2006, vol. 79, no. 1, pp. 66–70.

21. Sydorchuk, V.V., Diyuk, E.A., and Zazhigalov, V.A., *IX Ukr.-Pol. Symp. "Theoretical and Experimental Studies of Interfacial Phenomena and Their Technological Applications,"* 2005, pp. 280–281.

ISSN 1070-4272, Russian Journal of Applied Chemistry, 2008, Vol. 81, No. 8, pp. 1332–1336. © Pleiades Publishing, Ltd., 2008.
Original Russian Text © V.A. Matveev, 2008, published in Zhurnal Prikladnoi Khimii, 2008, Vol. 81, No. 8, pp. 1253–1257.

INORGANIC SYNTHESIS AND INDUSTRIAL INORGANIC CHEMISTRY

Specific Features of Phase Transformations of Amorphous Aluminum Hydroxide Produced by Ammoniation of Potassium Alum

V. A. Matveev

Institute of Chemistry and Technology of Rare Elements and Mineral Resources, Kola Scientific Center, Russian Academy of Sciences, Apatity, Murmansk oblast, Russia

Received December 10, 2007

Abstract—A novel method for neutralization of aluminum salts was suggested for the example of treatment of crystalline potassium alum with gaseous ammonia. An assumption was made that the structure of the forming primary particles is specific. The process of formation of a pseudoboehmite structure was studied in relation to the aging conditions of the aluminum hydroxide precipitate.

DOI: 10.1134/S107042720808003X

Amorphous aluminum hydroxide (AH) can be obtained by precipitation from an aluminum salt solution treated with an alkaline reagent, e.g., an ammonia hydrate solution. There is no common opinion about the phase composition of AH and factors affecting the formation and stability of various forms of AH [1–5]. The reason is that the decisive influence on the chemical and phase composition, morphology, and specific surface area of particles of the AH being formed is exerted by a set of its synthesis conditions: pH value and temperature of neutralization and aging, preliminary keeping of aluminum salt solutions, order and duration of solution mixing, agitation intensity, etc.

This communication reports results obtained in a study of the phase transformations that occur in amorphous AH produced from potassium alum (PA) in the course of aging of the precipitate and its thermal treatment.

EXPERIMENTAL

PA was chosen as a source for obtaining AH because it can be rather easily isolated in a sufficiently pure form in sulfuric acid treatment of the widely available nepheline-containing raw materials [6]. In the study, potassium alum isolated from the a sulfuric acid extract from a nepheline concentrate was used. It had the following composition (wt %): Al_2O_3 10.4, K_2O 9.9, Fe_2O_3 0.006. The specificity of obtaining amorphous AH consisted in that the salt was neutralized by direct treatment of crystalline PA with gaseous ammonia produced by slow heating of concentrated (25–27% NH_3) of an ammonia hydrate solution [7]. Melting of the alum (mp ≥ 92.5°C) leads to its balling and to an incomplete reaction. To prevent melting, the temperature was maintained in the range 50–80°C.

The neutralization process was monitored as follows: a sample of the ammoniation product was suspended in water and the pH of the suspension was measured. After a pH ≥ 7 was reached, the neutralization process was considered to be complete. The ammoniation product was treated with warm water for 5–10 min and the precipitated amorphous AH was separated by filtration from the solution containing ammonium and potassium sulfates. The AH precipitate was subjected to aging in an ammonia hydrate solution under various conditions. The treatment was carried out in hermetically sealed vessels to prevent loss of NH_3. After the process was complete, the precipitate was filtered off and washed with water to complete disappearance of the SO_4^{2-} ion from the washing water, as indicated by the absence of turbidization upon addition of a drop of a barium chloride solution. The precipitate was dried at 105°C to constant weight and examined by various physicochemical analytical techniques. The table shows how the phase composition of the samples [according to the results of an X-ray phase analysis (XPA)] and their specific surface area, determined by the BET method from low-temperature adsorption of nitrogen, depend on the aging conditions.

Effect of the aging conditions of the aluminum hydroxide precipitate on the phase composition and specific surface area of the product obtained

Aging conditions			S, $m^2 g^{-1}$	Phase composition*	Aging conditions			S, $m^2 g^{-1}$	Phase composition*
pH	τ, h	T, °C			pH	τ, h	T, °C		
7.0	0.5	75	2.1	A	11.0	0.5	75	246.6	PB
	2.0	75	3.0	A		2.0	75	285.9	PB
	4.0	75	9.4	A		4.0	75	303.9	PB
	6.0	75	10.9	A		6.0	75	336.1	PB
9.0	0.5	75	76.4	A + PB	10.0	0.5	60	203.1	A + PB
	2.0	75	94.8	A + PB		2.0	60	218.5	A + PB
	4.0	75	165.0	A + PB		4.0	60	238.8	PB
	6.0	75	202.4	A + PB		6.0	60	267.9	PB
10.0	0.5	75	215.6	A + PB	9.0	0.5	105	82.9	A + PB
	2.0	75	276.0	PB		2.0	105	119.6	A + PB
	4.0	75	293.7	PB		4.0	105	181.8	A + PB
	6.0	75	321.3	PB		6.0	105	244.3	PB

* (A) stands for amorphous aluminum hydroxide, and (PB), for pseudoboehmite.

As can be seen from these data, only a single crystalline phase, pseudoboehmite (PB), is formed, irrespective of the aging conditions of amorphous AH. It is known [1] that the direction of phase transformation of AH is "programmed" as early as the very first stage of neutralization. Hence follows that, in neutralization of crystalline PA with gaseous ammonia, the composition and structure of the forming primary particles are such that the subsequent phase transformations of AH occur solely via formation of the pseudoboehmite structure. In the process, the decisive influence is exerted on the crystallization process by the pH of the medium: as pH increases, the content of the pseudoboehmite phase and the specific surface area of its particles steadily grow. PB is formed the most rapidly and to the fullest extent at pH > 10, i.e., under conditions believed to be typically of the bayerite kind [1].

This fact confirms that the composition and structure of primary particles formed in neutralization of crystalline PA with gaseous ammonia are specific. Probably, this is due to the absence of a liquid phase at the instant of formation of the primary particles.

The effect of the aging temperature is substantially weaker and is manifested in that raising this temperature leads to a certain increase in the specific surface area of particles and favors earlier appearance of only a single phase, pseudobelite. The aging duration of the hydrate precipitate is mainly determined by the pH value: at pH 11, the crystallization process is almost complete already in 30 min, whereas at pH 10, is duration should be raised to 2 h.

For a more detailed study of the influence exerted by the aging pH on the course of the crystallization, the products obtained were examined by XPA, DTA, IR spectroscopy, and electron-microscopic and crystal-loptical analyses.

The X-ray diffraction patterns of the samples under study (Fig. 1) were obtained on a DRON-3 instru-

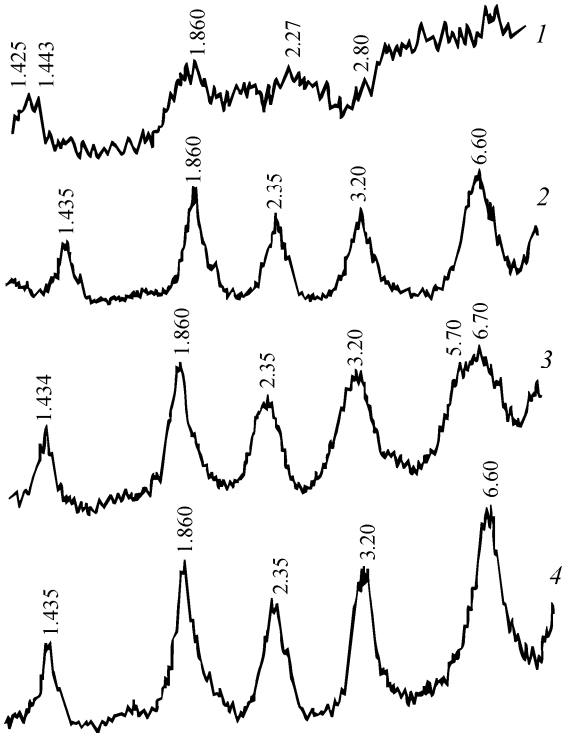


Fig. 1. X-ray diffraction patterns of aging products 1–4. Aging conditions: (*1*) pH 7, T = 75°C, τ = 4 h; (*2*) pH 9, T = 75°C, τ = 4 h; (*3*) pH 10, T = 75°C, τ = 2 h; and (*4*) pH 11, T = 75°C, τ = 1 h; the same for Figs. 2–4.

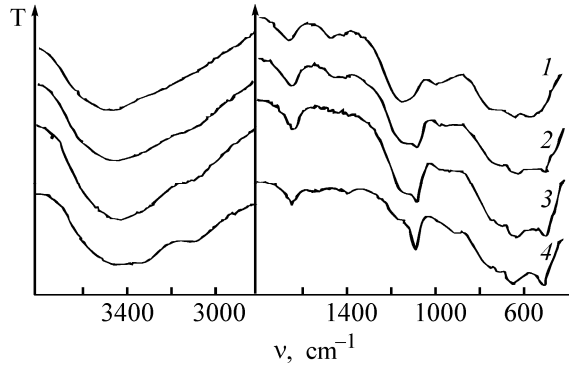


Fig. 2. IR spectra of aging products *1–4*. (T) Transmittance and (ν) wave number.

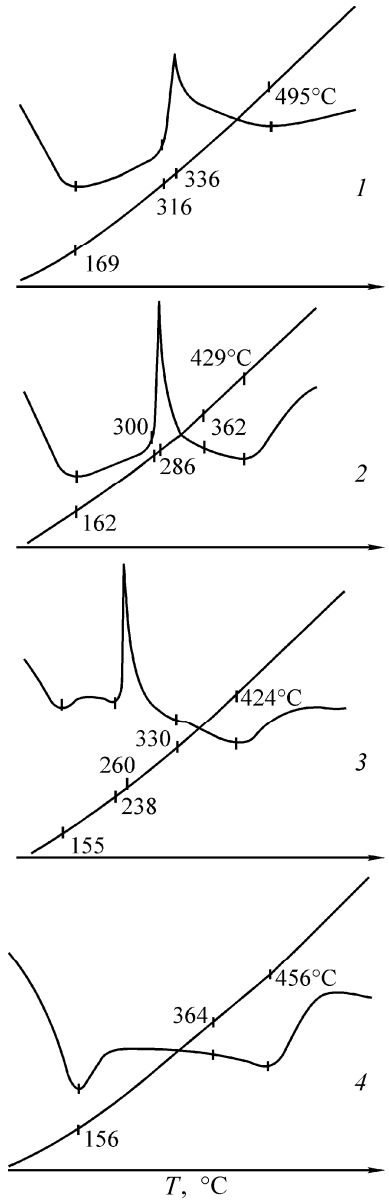


Fig. 3. Thermograms of aging products *1–4*. (*T*) Temperature.

ment with Cu_{K_α} radiation.[1] The X-ray diffraction pattern of the sample formed at pH 7 shows separate weak peaks, which gives no way of identifying any particular crystal structure of AH. The samples is mostly X-ray amorphous. As the pH is raised, increasingly intense lines belonging to the crystalline phase identified as pseudoboehmite appear in the X-ray diffraction patterns. The product obtained at aging pH 11 (sample 4) is nearly fully composed of the pseudoboehmite phase.

The IR spectra of the samples are shown in Fig. 2.[2] The absorption peaks at 3060 and 1080 cm^{-1}, associated with pseudoboehmite, are clearly seen in the spectrum of sample 4. The spectra of the samples obtained at lower pH values show a steadily decreasing intensity of the corresponding absorption bands, to the point of their complete disappearance, which suggests the total absence of pseudoboehmite in sample 1.

The XPA and IR spectral data are in good agreement with the results of a differential-thermal analysis carried out at a heating rate of 9 deg min^{-1} in air. The mass of the samples was 0.12 g. Their thermograms are shown in Fig. 3.[3] A feature common to all of the samples studied is that the differential curves of their thermograms exhibit a low-temperature endothermic effect at 155–169°C, which corresponds to removal of unbound water. As temperature is raised, a strong exothermic effect associated with crystallization of the pseudoboehmite phase appears in the DTA curves of samples 1–3. As the pH at which the samples are prepared increases, the exothermic effect is noticeably shifted to lower temperatures, from 316–336°C for sample 1 to 238–260°C for sample 3. This indicates that the "degree of readiness" to transition to the crystalline state increases as the pH of aging of the AH precipitate becomes higher. The reason for the absence of an exothermic effect in the curve for sample 4 is that the sample is originally composed of AH with a pseudoboehmite structure. Each of the differential DTA curves for samples 2–4 also shows two endothermic effects: a weak effect at 330–364°C and a more pronounced one at 424–456°C. The first of these is probably due to dehydration of pseudoboehmite.

To determine the nature of the occurring transformations, sample 4 was kept at a temperature of 365°C for 1 h and then subjected to XPA. The X-ray diffraction pattern obtained in this case is similar to that of

[1] The X-ray diffraction patterns were measured by T.I. Makarova.

[2] The IR spectra were measured by N.L. Mikhailova.

[3] The thermograms were measured by O.A. Zalkind.

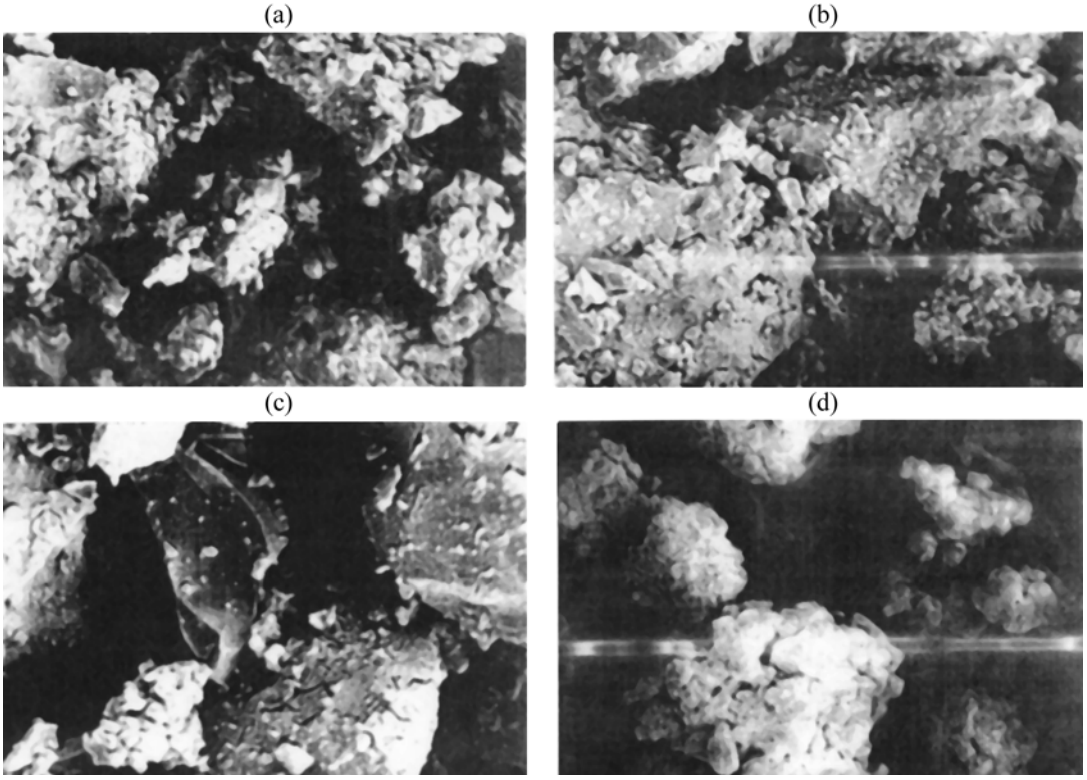


Fig. 4. (a–d) SEM micrographs of aging products 1–4.

sample 4, but has three additional low-intensity peaks with *d*/*I* 7.70, 3.64, and 1.70 Å, which indicates that a somewhat different pseudoboehmite structure is formed. These results are in full agreement with published data [1, 2, 4], according to which there exist two morphological pseudoboehmite structures with different contents of interlayer water. The second endothermic effect is due to pseudoboehmite dehydration to give γ-Al_2O_3. The first endothermic effect is not observed in the DTA curve of sample 1. This is so because, as a result of the crystallization occurring at higher temperatures as compared with samples 2 and 3, the pseudoboehmite phase with lower content of structural water is formed from the very beginning.

The morphology of the aging products was studied with a SEM LEO-420 digital scanning electron microscope. SEM micrographs of the constituent particles (5000 magnification) are shown in Fig. 4.[4] The outward appearance of particles of sample 1 is nearly the same as that of particles of amorphous AH. As the aging pH is raised, crystalline formations appear in an increasing amount and sample 4 is fully composed of conglomerates of crystallites mostly having a rounded shape.

According to the results of a crystal-optical analysis,[5] sample 1 is for the most part optically isotropic, with only a minor part of its substance exhibiting birefringence. These two phases are either cocrystallized or individual. The refractive index of one of these phases is $N \approx 1.508 \pm 0.005$, and that of the other is within the range 1.46 ± 0.01. Sample 2 is also composed of no less than two phases. A part of its substance exhibits weak birefringence (in separate areas). A characteristic feature is cocrystallization of phases in the form of both simple and more complex configurations. The refractive index of one of the phases is within the range 1.442–1.480, and that of the other is about 1.510. Sample 3 is for the most part optically isotropic and is formed by complex cocrystallization of two phases.? One of these has $N \approx 1.460$, and the other, $N \approx 1.555 \pm 0.005$. The vast majority of the substance in sample 4 is optically isotropic and has a refractive index within the range 1.556–1.564.

CONCLUSIONS

(1) A novel method for neutralization of aluminum salts was suggested for the example of potassium alum. The method consists in direct treatment of the crystalline salt with gaseous ammonia.

[4] Studied by A.T. Belyavskii.

[5] Analyzed by M.P. Rys'kin.

(2) It was suggested that neutralization by this method yields primary particles of specific structure, which is due to the absence of a liquid phase at the instant of their nucleation.

(3) It was found that, irrespective of the aging conditions of precipitated amorphous aluminum hydroxide, the crystallization proceeds exclusively via formation of the pseudoboehmite structure.

(4) It was demonstrated that pseudoboehmite is formed the most rapidly and fully under the conditions believed to be of the typically bayerite kind.

(5) The existence of two morphological pseudoboehmite structures was confirmed.

ACKNOWLEDGMENTS

The study was financially supported by a grant "Leading Scientific Schools" no. NSh-4383.2006.3.

REFERENCES

1. Krivoruchko, O.P., Buyanov, R.A., Fedotov, M.A., and Plyasova, L.M., *Zh. Neorg. Khim.*, 1978, vol. 23, no. 7, pp. 1798–1803.
2. Ivanova, A.S., Pugach, M.M., Moroz, M.M., et al., *Izv. Akad. Nauk SSSR, Ser. Khim.*, 1989, no. 10, pp. 2169–2176.
3. Aptikasheva, A.G., Lamberov, A.A., Egorova, S.R., et al., *Zh. Fiz. Khim.*, 2005, vol. 79, no. 9. 1633.
4. Lamberov, A.A., Aptikasheva, A.G., Egorova, S.R., et al., *Zh. Prikl. Khim.*, 2005, vol. 78, no. 2, pp. 177–184.
5. Aptikasheva, A.G., Lamberov, A.A., Egorova, S.R., et al., *Khim. Tekhnol.*, 2007, vol. 8, no. 9, pp. 396–401.
6. Pozin, M.E., *Tekhnologiya mineral'nykh solei* (Technology of Mineral Salts), Leningrad: Khimiya, 1970, part 1, pp. 653–658.
7. Karyakin, Yu.V. and Angelov, I.I., *Chistye khimicheskie veshchestva* (Pure Chemical Substances), Moscow: Khimiya, 1974.

ISSN 1070-4272, Russian Journal of Applied Chemistry, 2008, Vol. 81, No. 8, pp. 1337–1341. © Pleiades Publishing, Ltd., 2008.
Original Russian Text © B.A. Sechkarev, F.V. Titov, O.V. Salishcheva, D.V. Dyagilev, K.A. Bodak, A.A. Vladimirov, U.V. Sharaeva, 2008, published in Zhurnal Prikladnoi Khimii, 2008, Vol. 81, No. 8, pp. 1258–1262.

INORGANIC SYNTHESIS
AND INDUSTRIAL INORGANIC CHEMISTRY

Photoprocess in AgBr Microcrystals in the Presence of Pt(II) and Pd(II) Complex Ions

B. A. Sechkarev, F. V. Titov, O. V. Salishcheva, D. V. Dyagilev, K. A. Bodak, A. A. Vladimirov, and U. V. Sharaeva

Kemerovo State University, Kemerovo, Russia
Kemerovo Technological Institute of Food-Processing Industry, Kemerovo, Russia

Received June 29, 2007

Abstract—Results of a systematic study of the chemical sensitization of cubic-faceted AgBr emulsion microcrystals with complex compounds $K_2[XY_4]$ and $Na_6[XZ_4]$ [X = Pd, Pt; Y = Br^-, Cl^-, SCN^-; Z = $(SO_3)^{2-}$] were considered. The role of secondary dissociation of complex ions during the chemical sensitizing was established. Conditions were determined in which the compounds specified can be used as chemical sensitizers of AgBr. The effect of these complexes on the basic photographic characteristics was demonstrated.

DOI: 10.1134/S1070427208080041

The efficiency of the photoprocess in silver-halide photographic materials can be raised by more intensive utilization of the energy of light, localization of the latent image (LI), and use of AgHlg microcrystals with impurity ions in chemical-photographic processing of the materials. The use of doping ions makes it possible to create centers on the surface or in the bulk of AgHlg. Most frequently, ions of heavy metals are introduced into AgHlg microcrystals for controlling their photographic properties [1].

The formation of a latent image in silver halide microcrystals has been repeatedly and comprehensively studied. The main goal has been to develop emulsion AgHlg microcrystals with prescribed properties. A large number of studies in this field have been devoted to controlled introduction of impurities into the AgHlg matrix to change the kinetics of the photochemical reaction kinetics and, specifically, to inhibit the carrier recombination. The processes occurring on the surface of microcrystals in chemical sensitization (CS) have been given less attention and, for the most part, the empirical approach has been used. The conventional methods for chemical sensitization of AgHlg microcrystals fail to always provide the required photographic characteristics. Therefore, a purposeful search for new CS methods is a topical task.

It is known that Pt(II) and Pd(II) ions introduced into AgHlg form deep electron traps [2–4]. It has been shown [5] that introduction of Pd(II) ions into the bulk of microcrystals results in that the layer desensitization, which becomes more pronounced as the concentration of these ions increases and the depth of the related trap levels decreases. Complex ions $[PdBr_4]^{2-}$ used as chemical sensitizers makethe photosensitivity higher. It becomes apparent that these ions have a positive effect because sensitivity centers become coarser in their presence. Thus, the photographic effect of these ions must depend on their state (localization) on the microcrystal surface. Therefore, it is necessary to choose conditions of chemical sensitization and compositions of Pt(II) and Pd(II) complex ions to be introduced into the surface sensitivity centers being formed during sensitization. Possibly, Pd(II) and Pt(II) ions introduced into surface clusters perform several functions, such as intensification of the catalytic activity of latent image centers (LIC) and increase in their stability during formation and further in the dark stage [6].

This study is devoted to the influence of $K_2[XY_4]$ and $Na_6[XZ_4]$ complex compounds [X = Pd, Pt; Y = Br^-, Cl^-, SCN^-; Z = $(SO_3)^{2-}$] on AgHlg microcrystals in the stage of chemical sensitization of isometric AgBr microcrystals.

The aim of the study was to raise the CS efficiency by finding conditions in which palladium(II) or platinum(II) complex ions can be introduced into LIC of isometric AgBr microcrystals and to examine the photographic properties of emulsion layers based on such microcrystals.

EXPERIMENTAL

Complex compounds $K_2[XY_4]$ (X = Pt, Pd; Y = Cl^-, SCN^-) were synthesized by the known procedures [7]. $K_2[PtBr_4]$ was obtained using the procedure described in [8], and $K_2[PdBr_4]$ was prepared similarly to $K_2[PtBr_4]$ by reacting potassium bromide with $K_2[PdCl_4]$. The complexes $Na_6[X(SO_3)_4]$ (X = Pt, Pd) were synthesized by treating the corresponding tetracido compounds $K_2[XCl_4]$ with a Na_2SO_3 solution.

The photographic emulsion containing AgBr {100} microcrystals with an average equivalent diameter d = 0.5 μm and the size variation factor C_v = 10–15% was produced by controlled two-jet crystallization. A reactor containing a required amount of a water-gelatinous solution was charged with KBr and $AgNO_3$ solutions under permanent stirring. During the synthesis, the temperature, concentration of [Br^-] ions, and feed rate of reagent solutions were controlled. After the synthesis process was complete, soluble salts were removed from the emulsion by washing and pBr 3.0 and pH 6.9 were set. During the sul-fur-gold sensitization of the resulting emulsion at 50°C, solutions of Pt (II) and Pd(II) complex compounds were added after the main sensitizers ($Na_2S_2O_3$ and $HAuCl_4$) in concentrations of 10^{-6} to 10^{-3} mol mol^{-1} Ag. The volume of the solution of the complex being added was 0.3% of the total emulsion volume, and the CS time, 60–90 min. The sensitized emulsions were poured onto a triacetate support, dried, and subjected to sensitometric tests. The samples were exposed in a UKEP-1M universal contact exposition instrument with a color temperature of the radiation source equal to 2850 K and exposure time of 0.05 s. Then, the standard photochemical processing of sensitograms at 20 ± 0.5°C was carried out using a methylhydroquinone developer and an acid fixer. The optical density of darkening in the developed sensitograms was measured on a DP-1M densitometer. The characteristic curves obtained were used to determine the photosensitivity according to the criterial density of 0.2 and 0.85 units over the fog level.

Table 1. Effect of ligands on sensitometric characteristics of emulsion layers*

Chemically sensitizing additives		Sensitometric characteristics			
complex	c, mol mol^{-1} Ag	$S_{0.2}$	$S_{0.85}$	D_{max}	D_0
–	–	2.8	11	3.5	0.04
$K_2[PdCl_4]/K_2[PtCl_4]$	10^{-3}	2.1/0.0	10/0	3.7/0.1	0.04/0.01
	10^{-4}	2.0/1.6	7/6	2.8/2.3	0.02/0.03
	10^{-5}	1.5/2.6	4/11	2.5/3.3	0.03/0.04
	10^{-6}	2.6/2.6	10/11	3.2/3.4	0.03/0.04
$K_2[PdBr_4]/K_2[PtBr_4]$	10^{-3}	1.5/0.5	9/0	3.5/0.7	0.03/0/01
	10^{-4}	2.3/0.7	15/3	3.6/1.4	0.04/0.02
	10^{-5}	3.0/29	13/11	3.8/3.4	0.01/0.04
	10^{-6}	2.6/2.9	11/11	3.6/3.4	0.03/0.04
$K_2[Pd(SCN)_4]/K_2[Pt(SCN)_4]$	10^{-3}	3.0/0.4	12/0	4.2/0.6	1.02/0.03
	10^{-4}	4.0/1.1	15/5	3.8/2.3	0.70/0.03
	10^{-5}	4.0/4.5	18/23	3.3/5.1	0.40/0.16
	10^{-6}	4.0/4.5	17/18	3.3/4.2	0.35/0.10
$Na_6[Pd(SO_3)_4]/Na_6[Pt(SO_3)_4]$	10^{-3}	1.6/0.5	9/2	3.4/0.9	0.01/0.03
	10^{-4}	5.0/22.0	23/60	4.5/4.0	0.01/0.80
	10^{-5}	1.3/13.0	7/19	3.4/4.4	0.05/0.28
	10^{-6}	2.4/13.0	10/19	3.6/4.4	0.04/0.28

* Sensitometric characteristics after addition of Pd(II) or Pt(II) complex compounds are given in the numerator and denominator, respectively.

The nucleation of AgAuS clusters (sensitivity centers) on the surface of AgHlg microcrystals is a complex process dependent on many factors. One of these is the algorithm of sensitizer introduction. Solutions of sensitizers were introduced in the following order: sodium isobutylbenzene thiosulfate (KF-4026), $Na_2S_2O_3$, and $HAuCl_4$. During thermostating, hydrochloroauric(III) acid is reduced to metallic gold and makes coarser silver sulfide centers. It was found in a set of preliminary experiments that Pt(II) and Pd(II) complex compounds should be added after the main sensitizers, which apparently raises the probability of their incorporation into sensitivity centers.

The sensitometric characteristics of layers containing AgBr microcrystals sensitized with Pt(II) and Pd(II) complex compounds with various ligands are listed in Table 1. It can be seen that Pt(II) compounds with Cl^- and Br^- ligands cause desensitization at any concentrations, and the extent of this desensitization increases with the concentration. It is possible that, because of the lower stability of the complexes and a lower ligand-exchange rate, these compounds are the most predisposed to incorporation into the AgBr surface in the form of ions with partial or full preservation of coordinated ions, which results in the formation of deep electron traps that can irreversibly capture electrons [2, 3]. Being incorporated into the lattice, the activated ions create even deeper electron traps [3]. At a Pt (II) concentration of 10^{-3} mol mol^{-1} Ag, the sensitivity $S_{0.2}$ decreases to 0 and 0.5 units for complexes with Cl^- and Br^- ligands, respectively.

For Pd(II) complex ions with halide ligands (Cl^- and Br^-), the dependences of the sensitometric characteristics show extrema, with the sensitivity passing through a minimum in the case of Cl^- of ligands and through a maximum for Br^- ligands (Fig. 1). The depth of the electron trap created by the Pd(II) ion is 0.61 eV [4], which also results in a prolonged capture of a photoelectron in the temperature range under study.

It can be suggested that the dependences observed are determined by two competing processes. The first of these is incorporation of Pd(II) ions into the surface layer of microcrystals, which results in the formation of deep electron traps making lower the probability of LIC formation. The second is reduction of Pd(II) ions to metallic palladium, which probably occurs the impurity centers and intensifies the catalytic activity of these centers. In the end, the sensitometric characteristics are governed by the kinetics of these parallel processes. It is possible that the differences in the kinetics of the competitive processes are determined by in the cases of Cl^- and Br^- ligands differences in their chemical properties: instability constants ($pK_4([PdCl_4]^{2-})$ 12.2 and $pK_4([PdBr_4]^{2-})$ 16.1) and redox potentials ($E^0_{[PdCl_4]^{2-}}$/Pd = 0.623 and $E^0_{[PdBr_4]^{2-}}$/Pd = 0.60). The stability of the bromide complex is higher and its redox potential is lower than the corresponding parameters for the chloride complex, which promotes incorporation of Pd(II) ions into sensitivity centers and thereby makes higher the photosensitivity.

An increase in the sensitivity is also observed for thiocyanate and sulfite complexes, which is attributable to the additive sensitization by thiocyanate and sulfite ions in parallel with the processes considered above. Thiocyanate ions formed upon the secondary dissociation of complex ions interact with the surface of microcrystals and thereby accelerate the sensitization process. However, the optical density of the fog considerably increases (D_0 0.7 and 0.4 for concentrations of 10^{-4} and 10^{-5} mol mol^{-1} Ag, respectively) in this case.

Thus, we can assume that the coordination sphere affects the interaction of Pt(II) and Pd(II) complex ions with the AgBr surface. This results in qualitative and quantitative changes in LIC formation processes. Probably, it can be concluded that the coordination sphere changes the topography of platinum and palladium centers on the surface of microcrystals.

Therefore, if the secondary dissociation of complex ions is eliminated or minimized, approaches based on use of palladium and platinum complex compounds as chemical sensitizers become possible.

It is known that $[XY_4]^{2-}$ complex ions easily undergo secondary dissociation in an aqueous solution, which decreases the ion charge. The secondary disso-

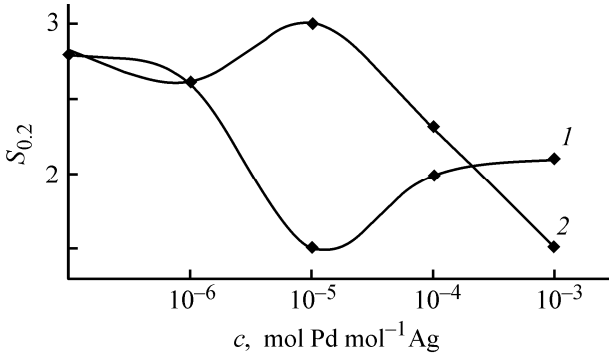


Fig. 1. Photosensitivity $S_{0.2}$ vs. the concentration c of complex ions. (*1*) $[PdCl_4]^{2-}$ and (*2*) $[PdBr_4]^{2-}$.

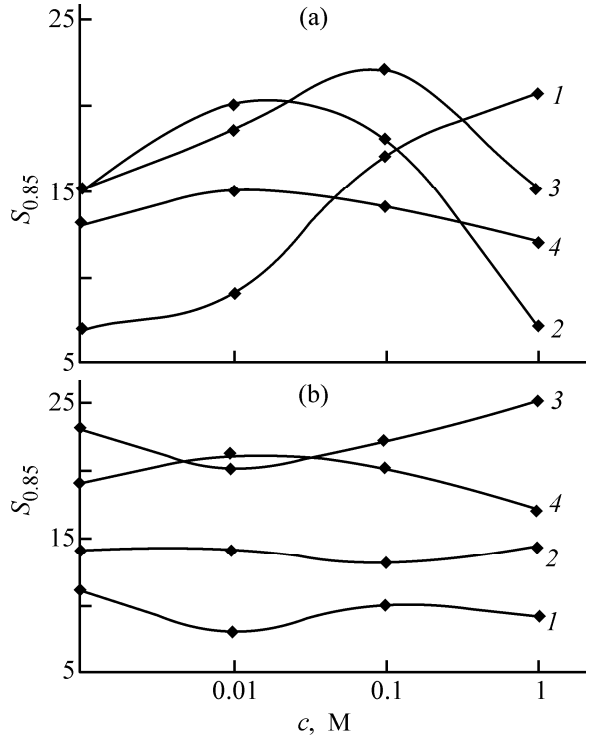


Fig. 2. Photosensitivity $S_{0.85}$ vs. the concentration c of the supporting electrolyte for compounds containing complex ions (a) Pd(II) and (b) Pt(II). Concentration of ions (mol mol^{-1} Ag): Pd(II), 10^{-4}; and Pt(II), 10^{-5}. (*1*) $K_2[XCl_4]$, (*2*) $K_2[XBr_4]$, (*3*) $K_2[X(SCN)_4]$, and (*4*) $Na_6[X(SO_3)_4]$, where X = Pt, Pd.

ciation of complex ions can be diminished by adding to the solution an electrolyte containing ligand ions[9]. Therefore, we added an electrolyte containing ligand ions (supporting electrolyte) to a solution of a complex compound used in the chemical sensitization. The effect of the supporting electrolyte is shown in Fig. 2 in the form of dependences of the photosensitivity on the concentration of the supporting electrolyte.

In the case of the palladium complex compound with chloride ligands, an increase in the sensitivity is observed when the concentration of the supporting electrolyte concentration is higher than 0.1 M. Because the stability of this complex against secondary dissociation is at a minimum, we can assume that, at concentrations lower than 0.1 M, the secondary dissociation, nevertheless, takes place. We can also assume that the driving force of the catalytic action of Pd(II) ions in this compound is the substitution of bromide ligands for chloride ligands at the surface of AgHlg microcrystals. This makes higher the probability of incorporation of Pd(II) ions into impurity sensitivity centers.

In the case of Br^- ligands, the optimal concentration of the supporting electrolyte is in the range from 0.01 to 0.1 M. A higher concentrations leads to desensitization, apparently, because of the excess of Br^- ions, which are adsorbed on the AgBr surface and hinder formation of sensitivity centers.

It follows from the results obtained that it is most appropriate to use palladium complex ions with Cl^- ligands in chemical sensitization. In this case, the solution of the complex ions should be added with no less than 1 M of the supporting KCl electrolyte.

When the concentration of the supporting electrolyte concentration is changed, compounds with SCN^- ligands make lower the sensitivity of microcrystals because of the increasing minimum optical density level. In this case, a certain rise in the sensitivity may result from an increase in the amount of SCN^- ions introduced into the reaction vessel, because this ion is known to be an AgHlg sensitizer. In this context, we performed experiments in which an equivalent amount of SCN^- ions was introduced into the emulsion under study in the course of its sensitization. The results obtained are listed in Table 2.

Table 2. Sensitometric characteristics of samples containing AgBr microcrystals sensitized with $K_2[Pd(SCN_4)]$, with various concentrations of the supporting electrolyte and equivalent amounts of KSCN

Sample no.	Chemically sensitizing additives, mol mol^{-1} Ag		Sensitometric characteristics			
	$K_2[Pd(SCN)_4]$	KSCN	$S_{0.2}$	$S_{0.85}$	D_{max}	D_0
1	–	–	2.8	11	3.5	0.04
2	10^{-5}	–	4.0	18	3.3	0.03
		5×10^{-6}	4.0	17	3.7	0.03
		5×10^{-5}	3.0	15	3.7	0.02
		5×10^{-4}	4.5	20	3.9	0.03
3	–	5×10^{-6}	2.0	10	3.5	0.02
		5×10^{-5}	1.5	12	2.0	0.02
		5×10^{-4}	1.5	10	1.8	0.02

It follows from Table 2 that addition of thiocyanate ions in the amount equivalent to their content in the complex compound $K_2[Pd(SCN_4)]$ does not increase the sensitivity. At the same time, addition of the complex compound both with and without a supporting electrolyte results in a substantial increase in the photosensitivity. Apparently, the sensitizing effect is due to palladium complex ions.

CONCLUSIONS

(1) It was found that the chemical sensitization of AgHlg microcrystals is hindered by the secondary dissociation of $[XY_4]^{2-}$ (X = Pt, Pd; Y = Cl^-, Br^-), which makes lower the charge of complex ions. The secondary dissociation of complex ions can be diminished by addition of an electrolyte containing ligand ions to the solution.

(2) It is the most appropriate to use platinum(II) and palladium(II) thiocyanate complexes as sensitizers of AgBr microcrystals. In this case, solutions of palladium complexes should be used with supporting electrolytes taken in a concentration of no less than 0.01 M. When platinum(II) compounds are used as chemical sensitizers of AgBr, the supporting electrolyte has the minimum effect.

REFERENCES

1. Roewer, G., Gahler, S., and Berndt, E., *Z. Signalaufzeichn. Mater.*, 1986, vol. 14, no. 6, pp. 433–444.
2. Olm, M.T., Eachus, R.S., and Graves, R.E., *Int. Cong. of Photographic Science*, 1978, p. 39.
3. Echus, R.S. and Graves, R.E., *J. Chem. Phys.*, 1975, vol. 63, no. 1, pp. 83–88.
4. Echus, R.S. and Graves, R.E., *J. Chem. Phys.*, 1976, vol. 65, no. 12, pp. 5445–5452.
5. Dyagilev, D.V., *Cand. Sci. Dissertation*, Kemerovo, 2003.
6. Friese, M., Roever, G. and Rittmier, K.E., *J. Inf. Rec. Mater.*, 1987, vol. 15, pp. 153–162.
7. Chernyaev, I.I., *Sintez kompleksnykh soedinenii metallov platinovoi gruppy: Spravochnik* (Synthesis of Complex Compounds of Platinum Metals: Handbook), Moscow: Nauka, 1964.
8. Gil'dengershel', Kh.I. and Gel'fman, M.I., *Zh. Prikl. Khim.*, 1960, vol. 33, pp. 2773–2779.
9. Pobelov, I.V., Borzenko, M.I., Tsirlina, G.A., and Petrii, O.A., *Elektrokhimiya*, 2001, vol. 37, no. 3, pp. 233–243.

ISSN 1070-4272, Russian Journal of Applied Chemistry, 2008, Vol. 81, No. 8, pp. 1342–1347. © Pleiades Publishing, Ltd., 2008.
Original Russian Text © S.A. Kulichenko, V.A. Doroshchuk, V.S. Starova, 2008, published in Zhurnal Prikladnoi Khimii, 2008, Vol. 81, No. 8, pp. 1263–1268.

PHYSICOCHEMICAL STUDIES OF SYSTEMS AND PROCESSES

Micellar Phases Based on Sodium Dodecyl Sulfate for Preconcentration

S. A. Kulichenko, V. A. Doroshchuk, and V. S. Starova

Shevchenko National University, Kiev, Ukraine

Received April 3, 2007

Abstract—Features of phase formation from solutions of sodium dodecyl sulfate on cooling were examined. The effect of electrolyte and phenol additions on the parameters of phase formation and distribution of model substrates was examined. Conditions were found for albumin preconcentration with phases in the system sodium dodecyl sulfate–phenol–NaCl.

DOI: 10.1134/S1070427208080053

Micellar extraction of microcomponents with phases of nonionic surfactants (NSAs) at the cloud point is considered today as an efficient alternative to common liquid–liquid extraction with organic solvents [1, 2]. The method is based on the phenomenon of phase separation of NSA aqueous solutions on heating, with the microcomponent concentrated in the forming micellar phase. The prospects for using micellar extraction in analysis are determined by high preconcentration factors with small sample volume, ability of the surfactant phase to extract hydrophobic, hydrophilic, and ionic compounds, and good compatibility with physicochemical determination methods [3–5]. An additional advantage of micellar extraction is the improved environmental safety of the analysis.

The need for heating the system is a basic limitation of the common micellar extraction, complicating preconcentration of readily hydrolyzable and volatile components [6]. This drawback can be overcome by using low-temperature versions of micellar extraction with NSAs having low cloud point, or by adding hydrotropes. In addition, the phase transition temperature in surfactant solutions is decreased on adding electrolytes, oxygen-containing block copolymers, and hydrotropic additives (urea, organic solvents, phenol) [7–9].

Phenol has proved to be the most effective hydrotrope lowering the phase transition temperature in NSA solutions owing to its breaking effect on the system of hydrogen bonds between the oxygen atoms of the polyoxyethylene chain and water molecules [9].

Heterophase transitions occurring with temperature variations are also characteristic of ionic surfactant (ISA) solutions. The formation of ISA phases can be predicted from the temperature diagram of the solubility and the Kraft point [10, 11]. Ionic surfactant phases have been used for preconcentration of metal ions [12–14], cyclic aromatic hydrocarbons [15], and microorganisms [16]. The use of ionic phases in analysis can open new possibilitites for preconcentration of diverse substrates: from highly hydrophobic electrically neutral organic compounds to charged forms of inorganic toxicants.

The efficient use of ISA phases for preconcentration and separation of microcomponents, as well as the phenomenon of phase separation in ionic surfactant solutions in the presence of hydrotropes itself, requires a systematic study. Therefore, the goal of this study was to examine the fundamental aspect of in recovery of various organic compounds with phases of an anionic surfactant (ASA), sodium dodecyl sulfate (SDDS), and to assess the possibilities of using these systems for preconcentration. To this end, we examined the conditions of formation of low-temperature phases in SDDS solutions and the effect of hydrotropic additives on the phase formation in the system.

EXPERIMENTAL

The choice of SDDS (Merck, main substance content >98.5%) was governed by its wide use in analytical practice, good knowledge of its colloid-chemical

properties, and combination of low CMC and low Kraft point with high solubilizing power. Working SDDS solutions were prepared by dissolving the corresponding accurately weighed portions in distilled water.

In the study, we used as hydrotropic additives phenol and electrolytes, which proved to be efficient in many systems based on surfactants. The chemicals were of analytically pure grade.

Aliphatic carboxylic acids are convenient objects for studying the effect of the overall hydrophobicity of a substrate on the efficiency of its recovery into the SDDS phase. We used acids of the general formula $C_nH_{2n+1}COOH$ with n = 1–15. The liquid acids were of analytically pure grade, and the solid acids were of the pure grade and were additionally purified by recrystallization from acetone–alcohol [17]. Solutions of the acids were prepared by dissolving their accurately weighed portions in SDDS solutions.

In our study, we used basic triphenylmethane dyes: Methyl Violet (MV), Crystalline Violet (CV), Methyl Green, and Malachite Green; zwitterionic dyes: Methyl Orange and reagents of the tropeolin series; sulfophthaleins: Phenol Red (PR), Bromophenol Red (BPR), Bromophenol Blue (BPB), Bromocresol Purple (BCP), and Bromothymol Blue (BTB), all of analytically pure grade. Solutions of dyes were prepared by dissolving their weighed portions in distilled water.

The absorption spectra of the solutions were measured on SF-46 and KFK-3 spectrophotometers. The solution acidity was monitored with a pH-340 pH-meter equipped with an ESL-43-07 glass electrode.

Aqueous SDDS solutions containing all the required components were placed to 10-ml volumetric cylinders, which were fastened in a stand and immersed in a water bath with ice. The temperature was monitored with thermometers immersed in the cylinders and in the water bath. The solutions were cooled at a rate of about 1 deg min^{-1}. The phase formation temperature was recorded when the solutions became opalescent. The forming ASA phase precipitated on the cylinder bottom. If necessary, the mixture was centrifuged before decanting the aqueous phase.

The distribution of carboxylic acids was monitored by pH-metric titration of their micellar solutions before and after the phase separation and by titration of the micellar phase after its dilution [18]. The distribution of organic dyes was monitored spectrophotometrically by measuring the absorption at the peak absorption wavelength of the corresponding form of the dye. The albumin distribution was monitored by the biuret reaction [19].

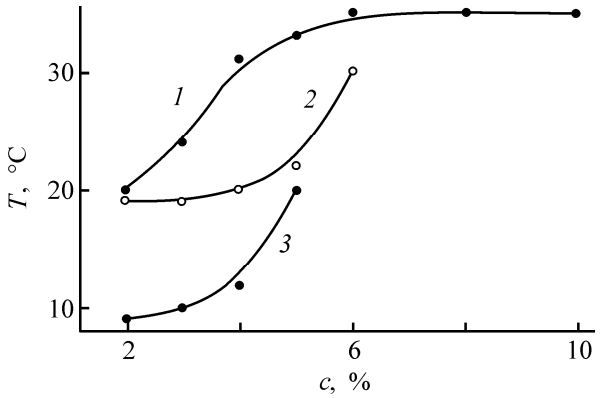


Fig. 1. Phase formation temperature T in (*1*) SDDS and (*2*, *3*) SDDS–phenol solutions vs. NaCl concentration c. c_{SDDS} = 0.1 M; c_{phenol}, %: (*2*) 1 and (*3*) 2.

The SDDS phase formation on cooling is due to the disappearance of the micellar constituent of the solubility below the Kraft point [10]. In the process, excess SDDS forms a crystallie precipitate. With an increase in the concentration, the volume of the SDDS phase linearly grows. However, the precipitation is slow, and the decantation of the precipitate is complicated by its rapid dissolution upon a small rise in the temperature. Therefore, the forming SDDS phase is unsuitable for preconcentration of microimpurities.

Upon introduction of adding electrolytes, the phase formation temperature increases and precipitates are formed already at room temperature. For example, at [NaCl] ≤ 2%, the crystalline phase of SDDS is formed at 20°C. An in-crease in the NaCl concentration in the system to $c \geq 6\%$ leads to a rise in the phase formation temperature to 35°C (Fig. 1, curve *1*). Owing to the salting-out effect, the volume of the forming phase also increases. The phase being formed in the SDDS–NaCl system is stable at room temperature, can be readily separated by centrifugation, and is convenient for preconcentration of microcomponents.

Addition of phenol to SDDS solutions raises the solubility of the ASA phase and appreciably lowers the phase formation temperature. However, the crystalline precipitate formed in the SDDS–phenol system is poorly decantable. Therefore, with an increase in the phenol concentration, the volume of the forming phase decreases, and, at a fourfold molar excess of phenol, cooling to 3°C no longer leads to formation of precipitates.

Comparative characteristics of the efficiency of recovery of various substrates with SDDS-based phases ($c_R = 4\times10^{-5}$, c_{SDDS} = 0.1 M; $c_{NaCl} = 6$, $c_{phenol} = 1\%$; $V_0 = 10$ ml)

Dye, MW	Dye form	*R*, %			
		SDDS*	SDDS–NaCl	SDDS–phenol	SDDS–phenol–NaCl
Malachite Green, 329	R^+	30	28	91	98
Methyl Violet, 346	R^+	13	11	95	99
Crystalline Violet, 372	R^+	11	0.7	99	99
Methyl Orange, 327	R^+	3.5	49	39	59
	R^-	0.7	3.4	3.4	27
Bromophenol Blue, 670	R^-	14	44	16	91
	R^{2-}	0	31	9.5	84

* $c_{SDDS} = 0.01$ M.

Joint addition of phenol and NaCl to SDDS solutions leads to formation in the system of two types of phases: a liquid phase and a solid amorphous phase. Phenol and NaCl affect the phase formation temperature in SDDS solutions differently: phenol lowers it and NaCl, by contrast, raises (Fig. 1). Owing to the opposite and mutually compensating effect of the additives, precipitates in the SDDS–NaCl–phenol system are formed at 15°C, which is lower than the phase formation temperature in the SDDS–NaCl system and higher than that in individual SDDS solutions and in the SDDS–phenol system. With an increase in the temperature to 25°C, the initially formed solid phase transforms into a gel. Such transitions are reversible, and, upon cooling, an amorphous precipitate is again formed in the system. The phases formed in the three-component system are stable at room temperature, are readily decanted, and are convenient for preconcentration of microimpurities.

We found that, for two- and three-component systems, the volume of the forming phase increases with the SDDS concentration, and decreases with an increase in the phenol and electrolyte concentrations. The phase volume determines the preconcentration efficiency, and the volume ratio of the aqueous and "micellar" phases corresponds to the maximal absolute preconcentration factor for microimpurities, attainable under the experimental conditions. By properly choosing the ratio and the absolute concentrations of components in the SDDS–NaCl–phenol system ($c_{SDDS} = 0.1$ M, $c_{phenol} = 1\%$, $c_{NaCl} = 6\%$), we obtained a phase convenient for processing with acceptable preconcentration parameters.

With cationic, anionic, and zwitterionic dyes and carboxylic acids as examples, we assessed the possibility of using SDDS-based phases for recovering various forms of organic substrates.

Phases formed from SDDS and SDDS–phenol solutions poorly recover basic triphenylmethane dyes. At the same time, dyes are efficiently extracted in the SDDS–NaCl and SDDS–phenol–NaCl systems (see table). However, because of the virtually complete extraction of basic reagents with these phases, we could not trace the effect of the hydrophobicity and structure of the dyes on their distribution parameters. For example, the molecular weight of the dyes affects their recovery insignificantly. For the SDDS and SDDS–phenol phases, the efficiency of the dye extraction decreases with an increase in their hydrophobicity, which suggests the predominantly hydrophilic character of the takeup phase.

We found that the zwitterionic form of the substrate (pH 1) is recovered by SDDS phases better than does the corresponding monoanion (pH 10) (see table). Under the experimental conditions, the zwitterionsic form of tropeolins is recovered virtually completely ($R > 97\%$). Notably, the degree of recovery of the R^- and R^+ forms into SDDS-based phases increases with the molecular weight of dyes.

The degree of recovery of sulfophthaleins with SDDS phases increases with the hydrophobicity. The dye monoanion (pH 2) is recovered into the collector phase better than the corresponding dianion (pH 10) (Fig. 2). Although the ability of anionic surfactants to solubilize anionic reagents is known from the literature [10], the high efficiency of binding of anionic forms of sulfophthaleins with SDDS phases appeared to be somewhat unexpected. The high hydrophobicity of the substrate eliminates the mutual repulsion of similarly

charged particles of the substrate and SDDS-based phase. With an increase in the hydrophobicity of the indicators, the dependences $R = f(M_R)$ obtained for the mono- and dianions converge (Fig. 2). However, for all the dyes studied, the HR^- form is recovered better than the R^{2-} form.

The influence of the hydrophobicity of a substrate on its recovery with SDDS phases was analyzed for the example of monocarboxylic aliphatic acids. The data obtained show that the molecular uncharged forms of the substrates (pH 2) are recovered by SDDS phases more completely than the corresponding anionic forms (pH 9). A similar trend was also observed in recovery of carboxylic acids with classical micellar phases of nonionic surfactants at the cloud point [20]. For example, the degree of recovery of the molecular form of caproic acod in the SDDS–NaCl system is approximately 40% higher than that of the anionic form and reaches 74%. However, the recovery of caproic acid into the phase formed from SDDS–NaCl–phenol solutions is virtually independent of pH, with $R = 80\%$.

We found that the degree of recovery of aliphatic carboxylic acids with SDDS phases increases with the length of their hydrocarbon radical (Fig. 3). However, for moderately hydrophobic acids with $n = 3$–4 the trend is the opposite and the degree of recovery of the acids somewhat decreases. The break of the monotonic trend in the recovery of the homologs may be due to the appearance of certain "organization" of the takeup surfactant phase [1, 6]. Notably, for carboxylic acids, the shape of the $R = f(n)$ plots does not appreciably change in going from SSDS–phenol–NaCl to SSDS–NaCl phases.

The data we obtained allow ranking of the organic substrates in the following order with respect to the solubilization efficiency: cationic substrate > uncharged or zwitterionic substrate > anionic substrate. In particular, SDDS phases provide optimal parameters for the recovery of cationic substrates owing to the solubilization enhancement by the electrostatic attraction of oppositely charged particles of the substrate and takeup phase. Elimination of the electrostatic constituent leads to a decrease in the efficiency of the extraction of uncharged or zwitterionic substrates. The electrostatic repulsion of similarly charged particles leads to the weakest binding of anionic forms of the reagents. An increase in the charge of a cationic substrate enhances its recovery into the SDDS phase, whereas an increase in the charge of the anionic substrate has an opposite effect. It is important that an increase in the overall hydrophobicity within a given series of substrates enhances their extraction with the phases examined. Thus, SDDS-based phases are the most suitable for pre-concentration of highly hydrophobic positively charged substrates.

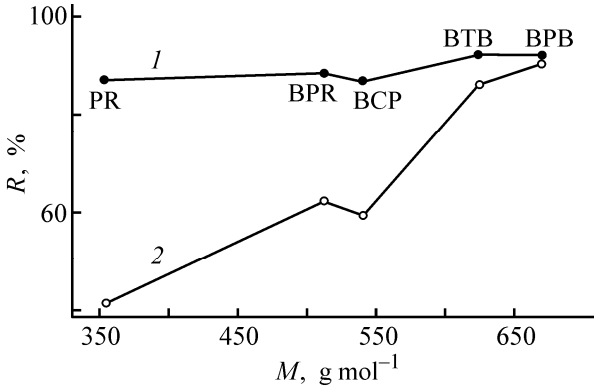


Fig. 2. Degree of recovery R of (*1*) HR^- and (*2*) R^{2-} forms of sulfophthalein indicators with the SDDS-based phase in the SDDS–phenol–NaCl system, plotted against the dye molecular weight M. $c_R = 4\times10^{-5}$ M, $c_{SDDS} = 0.1$ M, $c_{NaCl} = 6\%$, $c_{phenol} = 1\%$; $V_0 = 10$ ml. pH: (*1*) 2 and (*2*) 10.

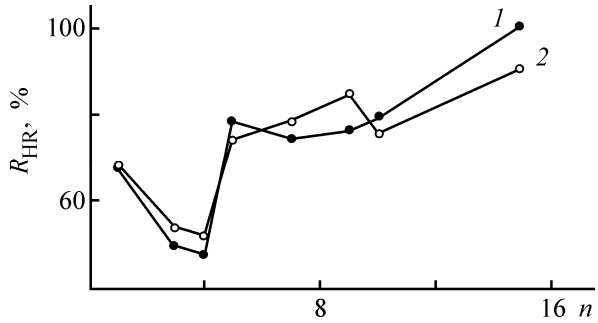


Fig. 3. Degree of recovery RHR of carboxylic acids with (*1*) NaCl–SDDS and (*2*) SDDS–phenol–NaCl phases, plotted against the number n of carbon atoms in the hydrocarbon radical of the acid. $c_{SDDS} = 0.1$ M, $c_{HR} = 1\times10^{-2}$ M, $c_{NaCl} = 6\%$, $c_{phenol} = 1\%$, pH 2, $V_0 = 10$ ml.

Analysis and comparison of our data on the recovery of various substrates allowed us to rank the SDDS-based phases in the following order with respect to the solubilization activity: SDDS–phenol–NaCl > SDDS–NaCl > SDDS–phenol > SDDS. Thus, hydrotropes favoring the phase formation proved to be efficient additives enhancing the recovery of organic substrates into the SDDS phases. The phases obtained in the SDDS–phenol–NaCl and SDDS–NaCl systems are stable at room temperatures; they are readily separated and are convenient for preconcentration of microcomponents.

By the example of albumin, we demonstrated the efficiency of low-temperature SDDS phases for pre-

concentration of cationic hydrophobic microimpurities. Development of efficient methods for preconcentration of biomolecules remains a topical task in screening of biological objects [21–24]. The micellar extraction with surfactant phases is considered to be one of the most efficient methods for preconcentration and separation of hydrophobic and hydrophilic biomaterials. Preliminary experiments showed that albumin is not recovered by nonionic surfactant phases because of the prevalence of hydrophilic properties. Therefore, micellar NSA phases are used for separating other, more hydrophobic proteins from albumin [25, 26]. In protein preconcentration with anion-active phases, the hydrophobic binding is supplemented by the attraction of oppositely charged particles. Therefore, it could be expected that albumin would be bound more efficiently by SDDS phases from acidic solutions at pH below the isoelectric point. However, such phases recover albumin to only 14% (c_{SDDS} = 0.01 M, pH 4, c_{Alb} = 10 mg ml^{-1}). Use of an electrolyte and phenol-modified phases enhances the albumin recovery. At c_{SDDS} = 0.1 M, c_{NaCl} = 6%, c_{phenol} = 1%, pH 4, and c_{Alb} = 10 mg ml^{-1}, albumin passed into the collector phase almost completely (~99%). The SDDS–phenol–NaCl is more convenient from the technological standpoint.

Based on the data obtained, we suggested a new approach to detection and determination of proteins. In the process, the solubilizing power of SDDS is used for efficient washout of protein molecules from the surface of a solid specimen (sample preparation), and the subsequent precipitation of a low-temperature anionic phase is used for the preconcentration. The procedure was tested as applied to determination of albumin on a fabric.

A sample of cotton fabric (10 × 10 cm) with preliminarily applied albumin was placed in 50 ml of a 0.1 M SDDS solution and rinsed for 20 min with a magnetic stirrer. The fabric was removed, and 0.5 g of phenol and 3 g of NaCl were successively added to the resulting solution, pH 4 was adjusted, and the mixture was cooled to 3°C. After complete phase separation and removal of the aqueous phase by decantation, the precipitate was transferred into a 25-ml volumetric flask, 5 ml of the biuret reagent (1.5 g of $CuSO_4 \times 5H_2O$ + 6.0 g of sodium potassium tartrate + 30 g of NaOH per liter) was added, and the solution was brought to the mark with distilled water. The contents were mixed and allowed to stand for 30 min, after which the optical density of the solution was measured at λ = 540 nm, l = 2 cm, against a solution from a blank experiment (without protein). The protein concentration in the sample was determined using a calibration plot.

After applying 5.0 mg of albumin to the fabric, we found 4.9 ± 0.1 mg (S_r = 0.02, n = 5, P = 0.95). These data show that the procedure is adequate and fairly accurate. The conditions suggested for the recovery and determination of protein compounds can be implemented in forensic examinations and also in analyses of solid samples for the presence of protein molecules (after washing with a surfactant solution).

CONCLUSIONS

(1) Studies of the effect of additions of electrolytes and phenol on the parameters of phase formation and distribution of model substrates allowed the phases based on sodium dodecyl sulfate to be ranked in the following order with respect to the solubilizing activity: sodium dodecyl sulfate–phenol–NaCl > sodium dodecyl sulfate–NaCl > sodium dodecyl sulfate–phenol > sodium dodecyl sulfate.

(2) Analysis of the parameters of phase distribution of various organic reagents allowed the substrate forms to be ranked in the following order with respect to the efficiency of solubilization by anion-active phases: cationic substrate > uncharged or zwitterionic substrate > anionic substrate.

(3) An increase in the charge of a cationic substrate enhances its recovery into the sodium dodecyl sulfate phase, whereas an increase in the charge of an anionic substrate has an opposite effect. An increase in the overall hydrophobicity within particular substrate groups enhances their extraction with the phases examined.

REFERENCES

1. Shtykov, S.N., *Zh. Anal. Khim.*, 2000, vol. 55, no. 7, pp. 679–686.
2. Quina, F.H. and Hinze, W.L., *Ind. Eng. Chem. Res.*, 1999, vol. 38, no. 11, pp. 4150–4168.
3. Hinze, W.L. and Pramauro, E., *CRC Crit. Rev. Anal. Chem.*, 1993, vol. 24, no. 2, pp. 133–177.
4. Kulichenko, S.A., Doroschuk, V.O., and Lelyushok, S.O., *Talanta*, 2003, vol. 59, no. 4, pp. 767–773.
5. Kulichenko, S.A. and Doroshchuk, V.A., *Zh. Anal. Khim.*, 2003, vol. 58, no. 6, pp. 586–590.
6. Shtykov, S.N., *Zh. Anal. Khim.*, 2002, vol. 57, no. 10, pp. 1018–1028.
7. Briganti, G., Puvvada, S., and Blankschtein, D., *J. Phys. Chem.*, 1991, vol. 95, no. 22, p. 8989.

8. Zhao, G. and Chen, S.B., *Langmuir*, 2006, vol. 22, p. 9129.
9. Wang, Z., Zhao, F., and Li, D., *Colloids Surf.*, 2003, vol. 216, nos. 1–3, p. 207.
10. Savvin, S.B., Chernova, R.K., and Shtykov, S.N., *Poverkhnostno-aktivnye veshchestva* (Surfactants), Moscow: Nauka, 1991.
11. Rusanov, A.I., *Mitseloobrazovanie v rastvorakh PAV* (Micelle Formation in Surfactant Solutions), St. Petersburg: Khimiya, 1992.
12. Tagashira, S., Murakami, Y., and Yano, M., *Bull. Chem. Soc. Jpn.*, 1998, vol. 71, pp. 2137–2140.
13. Tagashira, S., Murakami, Y., and Otobe, S., *Anal. Sci.*, 1998, vol. 13, pp. 857–858.
14. Nakai, T., Murakami, Y., Sasaki, Y., et al., *Talanta*, 2005, vol. 66, no. 1, pp. 45–50.
15. Goryacheva, I.Y., Shtykov, S.N., Loginov, A.S., et al., *Anal. Bioanal. Chem.*, 2005, vol. 382, pp. 1413–1418.
16. Man, B.K.-W., Lam, M.H.-W., Lam, P.K.S., et al., *Environ. Sci. Technol.*, 2002, vol. 36, no. 18, pp. 3985–3990.
17. *Beilsteins Handbuch der Organischen Chemie*, Berlin: Springer, 1920, vol. 2.
18. Kulichenko, S.A., *Visn. Kiivs'k. Univ., Khim.*, 2000, no. 36, pp. 37–40.
19. *Praktikum po biokhimii* (Practical Course of Biochemistry), Severin, S.E. and Solov'eva, G.A., Eds., Moscow, 1989.
20. Kulichenko, S.A. and Doroshchuk, V.A., *Zh. Obshch. Khim.*, 2003, vol. 73, no. 6, pp. 909–913.
21. Saitoh, T. and Hinze, W.L., *Anal. Chem.*, 1991, vol. 63, no. 21, pp. 2520–2525.
22. Saitoh, T. and Hinze, W.L., *Talanta*, 1995, vol. 42, no. 1, pp. 119–127.
23. Saitoh, T., Tani, H., Kamidate, T., and Watanabe, H., *Trends Anal. Chem.*, 1995, vol. 14, no. 5, pp. 213–217.
24. Tang Huang Yang and Mei Gang Yet, *J. Biosci. Bioeng.*, 2001, vol. 92, no. 3, pp. 214–220.
25. Bordier, C., *J. Biol. Chem.*, 1981, vol. 256, no. 10, pp. 1604–1607.
26. Liu, S., Tobias, R., McClure, S., et al., *Clin. Biochem.*, 1997, vol. 30, no. 6, pp. 455–463.

ISSN 1070-4272, Russian Journal of Applied Chemistry, 2008, Vol. 81, No. 8, pp. 1348–1355. © Pleiades Publishing, Ltd., 2008.
Original Russian Text © L.P. Tikhonova, V.E. Goba, M.F. Kovtun, Yu.A. Tarasenko, V.D. Khavryuchenko, S.B. Lyubchik, A.N. Boiko, 2008, published in Zhurnal Prikladnoi Khimii, 2008, Vol. 81, No. 8, pp. 1269–1276.

PHYSICOCHEMICAL STUDIES OF SYSTEMS AND PROCESSES

Sorption of Metal Ions from Multicomponent Aqueous Solutions by Activated Carbons Produced from Waste

L. P. Tikhonova, V. E. Goba, M. F. Kovtun, Yu. A. Tarasenko, V. D. Khavryuchenko, S. B. Lyubchik, and A. N. Boiko

Institute of Sorption and Endoecology Problems, National Academy of Sciences of Ukraine, Kiev, Ukraine

Litvinenko Institute of Physicoorganic Chemistry and Coal Chemistry, National Academy of Sciences of Ukraine, Donetsk, Ukraine

Shevchenko National University, Kiev, Ukraine

Received August 2, 2007

Abstract—Activated carbons produced by thermal treatment of a mixture of sunflower husks, low-grade coal, and refinery waste were studied as adsorbents of transition ion metals from aqueous solutions of various compositions. The optimal conditions and the mechanism of sorption, as well as the structure of the sorbents, were studied.

DOI: 10.1134/S1070427208080065

The possible waste processing to obtain activated carbons (AC) is aimed to solve two important ecological problems: utilization of wastes and production of carbon adsorbents for purification of aqueous solutions to remove toxic impurities. For example, it has been suggested to recover heavy metals with inexpensive ACs synthesized by processing of rice husks [1], coconuts [2, 3], bituminous carbon [4], bog moss [5], saw dust [6], and solid industrial waste [7]. It has been found that low-temperature carbonization and the subsequent high-temperature coactivation of a mixture of wastes can yield ACs whose adsorption capacity for Cr(III) and Cr(VI) substantially exceeds the values obtained for commercial ACs manufactured by Norit and Merck [8]. It has also been shown that adsorbents of this kind can recover copper and other heavy metals from multicomponent aqueous solutions, including technological mixtures [9].

The present communication reports on a study of the sorption properties of these carbons with respect to recovery of Cu(II), Fe(II), Co(II), Ni(II), Mn(II), and Pd(II) from various solutions, including washing and waste water formed in processing of palladium-containing raw materials.

EXPERIMENTAL

Carbon adsorbents were prepared from a mixture of secondary natural materials: sunflower husks (25%), refinery waste (50%), and low-grade coal (25%) from the Donetsk region by the previously described method [8, 9]. The composition of ACs and their physicochemical properties [specific surface area, pore volume, pore size distribution, presence and nature of surface functional groups (SFG)] of the adsorbents under study were determined by elemental analysis, ?Behm titration, and nitrogen adsorption at 77 K.

The structure of the ACs obtained was modeled by the PM3 quantum-chemical method [10–12]. As input structures served $C_{96}H_{24}$ carbon clusters as a model of coal, low-molecular-weight alkyl phenanthrene as a model of the refinery waste, and two fragments of a cellulose chain as a model of vegetable wastes. Successively, step by step, these clusters were stripped of hydroxy groups and hydrogen atoms, which appear in hydrolysis of organic substances and form water and hydrogen molecules as a result of the reaction. Then, the spatial structure was optimized for the system obtained. The number of steps for the dehydrogenation-dehydroxylation process was chosen so that the result-

Table 1. Texture and surface characteristics of AC samples

Sample	S_{BET}, $m^2 g^{-1}$	V_{tot}	V_{micro}	S_{meso}	S_{micro}	pH_{PZC}
		$cm^3 g^{-1}$		$m^2 g^{-1}$		
AC-1	638	0.32	0.23	267	371	5.02
AC-1 oxidized with HNO_3	537	0.26	0.19	324	213	3.37

Table 2. Surface functional groups of AC samples

Sample	S_{sp}, $m^2 g^{-1}$	Functional groups, mg-equiv g^{-1}		
		carboxy		phenol
		hydrate	nonhydrate	
AC-1 (starting) aliphatic	638	0.05	0.13	2.18
AC-1(ox) oxidized with HNO_3	537	0.39	0.93	2.50
AC-2 (starting) aromatic	296.4	0	0.6	0
AC-2(ox) oxidized with HNO_3		0.24	1.88	0.64
AC-3 (starting) mixture	375.3	0	0	0.36
AC-3(ox) oxidized with HNO_3		0.4	1	0.4

ing carbon cluster was sufficiently close in composition to the experimentally obtained carbon materials.

Single- and multicomponent model solutions were prepared using weighed portions of commercial salts of Cu(II), Fe(II), Co(II), Ni(II), Mn(II), and Pd(II), acids of chemically pure and analytically pure grades, and distilled water. Technological solutions obtained in final stages of processing of secondary platinum-containing raw materials (washing and waste water) were provided by the near-Dnieper Plant of Nonferrous Metals State Enterprise.

The adsorption of Cu(II), Fe(II), Co(II), Ni(II), and Mn(II) ions on AC from the model and technological solutions was studied in static and dynamic modes: (i) by the method of separate weighed portions under the standard conditions at the same s : l ratio at a temperature of 21 ± 4°C (The time of contact of the solutions and the adsorbent was 24 h in most experiments, which corresponded to the time in which the adsorption equilibrium was attained.) and (ii) by the method of dynamic sorption at different solution flow rates at a temperature of 21 ± 4°C (sorption columns with a diameter d = 9 mm, bed height h = 9.5 mm, weighed portion of AC m = 1 g).

For evaluation of the adsorption equilibrium in the systems under study, the static and dynamic sorption capacities of a carbon (SEC and DEC, respectively) and the degrees of metal recovery were used.

The concentration of the metals in the starting solutions and their residual concentration in filtrates after separation of the solid phase were determined by the atomic-absorption method [13]; the concentration of palladium(II) was also found by the selective catalytic method [14].

When studying the sorption properties of ACs, it is necessary to take into account that, in each particular case, wastes with widely varying composition were used to produce the carbons. In a set of experiments, carbons differing in the nature of a single component were used, which enabled certain general assumptions and conclusions. Carbon samples produced under identical conditions from mixtures in which the agricultural waste (sunflower husks) and low-grade coal served as components with fixed nature and amount. The refinery wastes differed in the nature of hydrocarbons: AC-1, AC-2, and AC-3 were produced from predominantly aliphatic hydrocarbons, mainly aromatic hydrocarbons, and a mixture of both kinds of hydrocarbons, respectively. The sorption properties of starting samples and those oxidized with nitric acid were studied. The characteristics of different carbon samples are rather close, the structural parameters and surface group compositions are listed for some of the samples in Tables 1 and 2. As follows from these data, the ACs produced from aliphatic hydrocarbons have a larger specific surface area, and oxidation of the activated carbons leads to an increase in the number of oxygen-containing functional

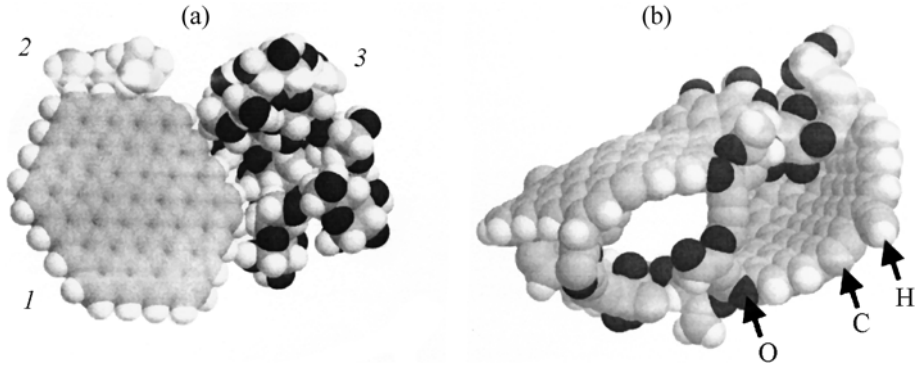


Fig. 1. Results of a quantum-chemical simulation of carbon formation from a mixture of organic materials. (a) Starting molecules: (*1*) $C_{96}H_{24}$ carbon cluster modeling the structure of a graphene plane, (*2*) low-molecular-weight alkyl phenanthrene as a model of refinery wastes, and (*3*) two fragments of a cellulose chain as a model of vegetable wastes. (b) Structure of the carbon material formed (the arrows show different types of atoms constituting the cluster).

groups on the surface, with the total surface area changing only slightly.

As follows from the model obtained in a quantum-chemical analysis, the structure of unoxidized carbon (Fig. 1) includes surface areas that differ to a certain extent in chemical nature. For example, the porous structure of the carbon is constituted by fragments of graphene planes, which are preserved in a sufficiently large size and bear no functional groups. The edges of these fragments contain doubly coordinated carbon atoms, which are the most active in oxidation are converted in this case to phenol and quinoid groups. The same atoms are possible sites of reductive sorption of noble metals.

Because of the presence of oxygen atoms in cellulose molecules in the starting mixture, the carbon material obtained contains oxygen in the form of various functional groups differing in the coordination activity and ability to undergo further transformations. Most part of oxygen is in ester groups included in the rings, so that their chemical and coordination activity must be low, and their stability against oxidation and hydrolysis, high. Also present is a rather large amount of aldehyde residues that can be coordinated and oxidized to carboxy groups providing the ion exchange properties of the oxidized carbon. Complexation processes may involve α-diketone groups in the aliphatic chain, which are preserved in a small amount, as well as ketone groups and esteric (heterocyclic) oxygen atoms whose mutual position will favor manifestation of the chelate-formation effect. Thus, the structure of the carbon material can provide both physical sorption within graphene planes and chemisorption on active groups, including the complexation and reductive sorption of noble metals.

Sorption of heavy metal ions from model solutions. To determine the time in which the adsorption equilibrium is attained under static conditions, a set of sorption measurements of the recovery of copper and compounds of other metals from solutions with a concentration of each ion in the mixture in the range 1–10 mg l^{-1}, i.e., in solutions modeling natural water whose contamination with heavy metals exceeds the maximum permissible concentrations and wastewater in technologies for processing of various metal-contain-ing secondary raw materials. The measurements were made during 1 to 72 h.

When the concentration of metals in solutions is about 1 mg l^{-1}, the mixture of ions of all metals is completely recovered on all AC samples, irrespective of the solution pH, in already less than1 h of contact in the solution–adsorbent system: the content of metal ions in the filtrate after the sorption is below the sensitivity limit of the atomic-absorption method. In multicomponent solutions with pH ≥ 3 and a concentration of each ion approximately equal to 10 mg l^{-1}, a period of time slightly longer than 1 h is required for a nearly equilibrium adsorption of Cu(II) on the starting carbon and its oxidized sample (Table 3). Similar results were obtained in sorption of Fe(II), which suggests that the sorption mechanisms of these ions are close.

Further studies of the static sorption of metal ions were based on results obtained in 24 h, i.e., under the conditions of complete attainment of the sorption equilibrium. The influence exerted by the acidity and by the nature of an acid on the sorption properties of ACs in recovery of metal ions (~10 mg l^{-1}) from single-component solutions and the role of ammonium ions commonly present in technological solutions formed in

Table 3. Recovery of metal ions from multicomponent hydrochloric acid aqueous solutions on AC-1 activated carbon and its oxidized sample AC-1(ox) (V = 20 ml, m = 0.1 g, T = 22°C)

M, mg l^{-1}	Sorption A, mg g^{-1}, in indicated time, h					
	1	3	6	24	48	72
AC-1 carbon						
Cu(II), 11.4	1.06	1.14	1.156	1.232	1.232	1.232
Fe(II), 11.07	1.478	1.69	1.75	1.942	1.954	1.974
Co(II), 9.4	0.28	0.28	0.28	0.4	0.4	0.44
Ni(II), 9.8	0.32	0.32	0.32	0.38	0.44	0.56
Mn(II), 9.5	0.18	0.22	0.26	0.3	0.38	0.38
AC-1(ox) carbon						
Cu(II), 9.8	1.74	1.85	1.85	1.85	1.89	1.89
Fe(II), 9.2	1.68	1.74	1.74	1.78	1.78	1.79
Co(II), 9.3	0.54	0.65	0.74	0.74	0.74	0.74
Ni(II), 10	0.76	0.76	0.96	1.18	1.18	1.08
Mn(II), 10	0.26	0.3	0.34	0.34	0.32	0.29

processing of platinum-containing raw materials were examined. It was found that, as the acidity increases, the sorption decreases even in single-component solutions (Table 4), and ammonium ions additionally diminish the degree of recovery. From solutions with pH > 3.5, ions of all the metals studied are recovered completely. In acid (pH ≤ 0.1) single- and multicomponent solutions with a concentration of each of the present metal ions equal to 10 mg l^{-1}, no more than 20% of Cu(II) and Fe(II) ions and less than 10% of other metal ions is recovered in 72 h of sorption.

The decrease in the adsorption of metal ions, observed as the solution acidity increases, may be due to a shift of the reaction equilibrium in complexation of metal ions with the SFG of adsorbents via the protonation of these latter. In addition, the comparatively low capacity of ACs produced from secondary raw materials in sorption of metal ions from acid solutions can be also well understood in terms of competition in the systems for metal ions: between a ligand in the corresponding aqueous acid solution and a ligand fixed on the adsorbent surface. This is the more so because of the complex structure of ACs, which is not always accessible for approach of metal ions to the surface ligand. Ammonium ions can play a twofold role: this is competition in the formation of sufficiently stable ammonia complexes of metals in solution and the interaction of these complexes with the SFG, on the one hand, and the ion exchange of protons between the SFG and ammonium ions. In the case of multicomponent solutions with pH ≥ 3.5, the sorption capacity for each of the metal ions decreases, compared with single-com-

Table 4. Effect of pH on the sorption of metals from single-component hydrochloric acid solutions (AC-3, m = 0.1 g, V = 20 ml, t = 24 h)

M	Initial concentration, mg l^{-1}	pH	A, mg g^{-1}	Degree of recovery, %
Cu(II)	10.8	1.98	0.46	21
	8.8*	1.82	0.08	4.5
	10.5	3.75	2.1	100
Fe(II)	10.3	2.03	2.02	99
	10.8*	1.77	0.36	16.6
	8.7	3.6	1.74	100
Co(II)	9.9	1.97	0.06	3
	8.7*	1.7	0.1	57
	9.7	3.7	1.96	100
Ni(II)	8.5	2.02	0.02	1.1
	8.7*	1.62	0.1	5.7
	8.7	3.56	1.7	97
Mn(II)	10.9	2.02	2.16	99
	10.1*	1.79	0.02	1
	11.06	3.56	2.06	88

* NH_4OH (10 g l^{-1}) is present in the hydrochloric acid solutions.

Table 5. Comparison of the amounts of metal ion sorption from single- and multicomponent solutions under static conditions (m = 0.1 g, V = 20 ml, pH ~3.6 + 0.2, metal concentration 10 ± 0.3 mg l^{-1}, t = 24 h)

M	Sorption capacity, mg g^{-1}				
	hydrochloric acid solution			sulfuric acid solution, AC-3	
	single-component AC-3	multicomponent		single-component	multicomponent
		AC-3	AC-3(ox)		
Cu(II)	1.82	1.08	1.232	1.81	0.68
Fe(II)	1.86	1.3	1.954	2.1	0.22
Co(II)	2.14	0.46	0.4	1.88	0.06
Ni(II)	1.64	0.49	0.44	1.06	0.06
Mn(II)	1.82	0.52	0.38	2.1	0.04

ponent solutions (Table 5), which is especially noticeable in sulfuric acid solutions. Here, the main explanation may consist both in the low sorption capacity of the carbon itself and in the competitive complexation of each of the metal ions with SFG, whose amount is rather limited (Table 1). Under the optimal conditions (pH ~ 4), the degree of copper(II) and iron(II) recovery in 24 h of sorption is 54 and 87%, respectively, for AC-1 and 82 and 97% for AC-1(ox); the sorption of Cu(II) from single-component solution on AC-2 and AC-2(ox) is 47.7 and 94%, respectively; and that from multicomponent solutions of the same acidity, 60.3 and 89.6%.

Similar results were obtained for all the AC samples, irrespective of the nature of refinery wastes used in their production. Thus, it can be assumed that the key role is in sorption of copper(II) and, presumably, iron(II) is the possible presence and amount of SFG. In all of the systems, the sorption capacity for the metal ions studied increases in the following order: Fe(II) > Cu(II) > Co(II) > Ni(II) > Mn(II), which almost coincides with the series of stability constants of complexes of these metals with organic acids (acetate, tartrate, malonate, etc.) [15]. On the whole, it should be noted that the ACs studied are the best suitable as adsorbents for purification of aqueous solutions to remove metal impurities with concentrations not exceeding 10 mg l^{-1}, i.e., for purification of contaminated natural and certain technological washing waters.

The sorption of metal ions was studied under dynamic conditions on AC-3 produced from a mixture of refinery wastes of aliphatic and aromatic nature and solutions with a varied content of the main component, copper(II). It was shown that copper(II) and iron(II) ions are completely recovered from a model multicomponent solution containing a mixture of chlorides of divalent metals at a concentration of each of these ions close to 10 mg l^{-1} and solution flow rate through the column of 25 ml h^{-1} (Fig. 2). The degree of recovery

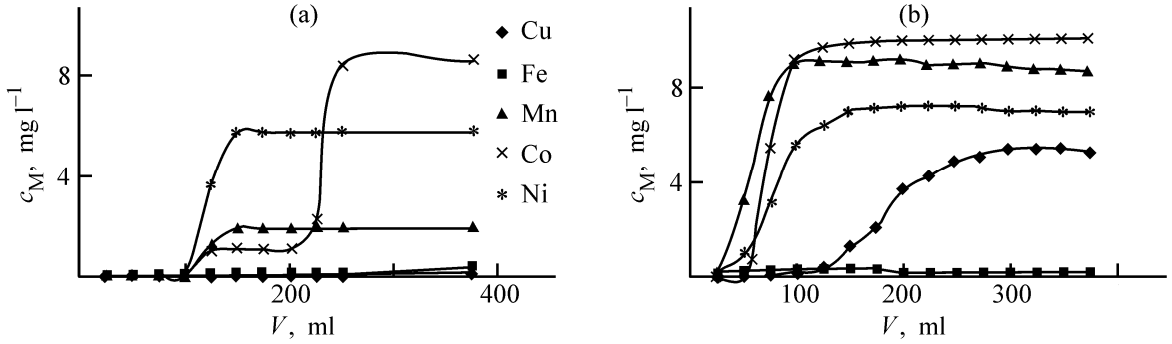


Fig. 2. Sorption of heavy metal ions from model hydrochloric acid solutions under dynamic conditions. m = 1 g, V = 25 ml, bed height h = 95 mm, diameter d = 9 mm. (c_M) Concentration of the M^{2+} cation in a sample and (V) volume of solution passed through the sorbent. Initial concentration of metals (mg l^{-1}): (a) Cu 8.1, Fe 8.9, Co 8.9, Ni 8.9, Mn 11.3; (b) Cu 8.9, Fe 10.9, Co 9.8, Ni 7.5, Mn 10.4. v (ml h^{-1}): (a) 25 and (b) 100. pH: (a) 3.66 and (b) 3.36.

Table 6. Recovery of metal ions from multicomponent model solutions under dynamic conditions on passing 200 ml of a solution at a flow rate of 25 ml h^{-1} (AC-3, m = 1 g, V = 25 ml, bed height h = 9.5 mm, diameter d = 9 mm)

Parameter	Cu(II)	Fe(II)	Co(II)	Mn(II)	Ni(II)	Parameter	Cu(II)	Fe(II)	Co(II)	Mn(II)	Ni(II)
In the absence of NH_4OH, pH 3.66						In the presence of 10 g l^{-1} of NH_4OH, pH 3.54					
Initial concentration in the mixture, mg l^{-1}	8.1	8.9	8.9	8.9	11.3	Initial concentration in the mixture, mg l^{-1}	8.7	9	9.8	9	11.5
Degree of recovery, %	100	100	61	64	79	Degree of recovery, %	96.8	100	43	45	43

Table 7. Compositions of industrial washing water under study* and results of adsorption recovery of Cu(II), Fe(II), Co(II), Ni(II), and Mn(II) from this water under static conditions (adsorbent AC-2(ox), V = 20 ml, m = 0.1 g, T = 22°C, sorption time 24 h)

M^{2+} in solution	Solution 1, pH 3.63			Solution 2, pH 4.25		
	in solution, mg l^{-1}	recovered, %	A, mg g^{-1}	in solution, mg l^{-1}	recovered, %	A, mg g^{-1}
Cu(II)	74	23	3.42	57	63	7.16
Fe(II)	7.2	85	1.232	9.4	100	1.88
Co(II)	0.58	0	0	0.77	40	0.06
Mn(II)	0.23	13	0.006	0.28	64	0.04
Ni(II)	13.2	5.3	0.14	13.3	6.7	0.18

* Washing water contains an excess amount of alkali metals; chloride, sulfate, and nitrate ions; and an admixture of ammonium salts.

of other metal ions corresponds to the order of their sorption under static conditions. An increase in the solution flow rate through the column does not change the type of the dependence in Fig. 2a, but makes the time to breakthrough shorter and the amount of a metal absorbed by a certain instant of time smaller (Fig. 2b), which can improve the selectivity of iron(II) recovery, compared with copper(II).

It was found in recovery of copper(II) from a model single-component solution with pH 3.56 and rather high concentration of the ion that, as the concentration of copper(II) increases, its sorption to breakthrough changes only slightly (DEC for solutions with initial copper concentrations of 48.2 and 97 mg l^{-1} is 7.21 and 6.84 mg l^{-1}, respectively) and is presumably determined primarily by the adsorbent properties. The presence of ammonium ions in multicomponent solutions with pH 3.56 has no effect on the absorption of copper(II) and iron(II) and somewhat reduces that of cobalt(II),nickel(II), and manganese(II) (Table 6).

Sorption of Cu(II), Fe(II), Co(II), Ni(II), Mn(II), and Pd(II) ions from technological solutions. The possibility of using ACs produced from wastes for recovery of ions of copper(II) and other metals from technological solutions was assessed using high-salt acid (up to 1 M in terms of an acid) solutions (washing water) with a copper concentration of up to 100 mg l^{-1}. The solutions contained alkali metals, ammonium, and carbonate, sulfate, and nitrate ions in a manyfold excess and admixtures (up to 5–10 mg l^{-1}) of iron(II), lead(II), and other metals. As follows from the results obtained (Table 7), copper(II) is recovered under static conditions from washing water with complex composition in accordance with the sorption capacities of the carbons, and raising the solution pH enables a pronounced increase in copper(II) recovery. Iron is completely sorbed at its concentration of about 10 mg l^{-1}.

In sorption purification of technological solutions formed in processing of platinum-containing raw materials, the possibility of selective separation of residual amounts of target products, platinum metals, was taken into account. Previously, data on selective sorption of small amounts of platinum metals and, in particular palladium(II) from acid aqueous solutions on the activated carbons, irrespective of their nature and origin, have been obtained [16–18]. It was assumed on the basis of these data that residual amounts of palladium(II) can be recovered with a sufficient selectivity by sorption

Table 8. Sorption of metal ions from an industrial solution* on passing 175 ml of the solution at a rate of 25 ml h^{-1} (m = 1 g, V = 25 ml, bed height h = 9.5 mm, diameter d = 9 mm)

Parameter	Pd(II)	Cu(II)	Fe(II)	Co(II)	Ni(II)	Mn(II)
Without treatment, pH 1.86						
Initial concentration in the mixture, mg l^{-1}	2	23.4	25.4	16.3	25.4	18.5
Pd : M ratio in solution		1 : 11.7	1 : 12.7	1 : 8.15	1 : 12.7	1 : 9.25
Degree of recovery, %	100	39	68	38	23	28
Pd : M ratio on the sorbent		1 : 4.5	1 : 4.6	1 : 3	1 : 1.8	1 : 3
After separation of Pd and alkalization, pH 3.54						
Initial concentration in the mixture, mg l^{-1}		19	8	14	14.4	14.4
Degree of recovery, %		95	69	38.6	35	45

* In addition to the metal ions specified, the solution contains a 1000-fold excess of potassium and sodium salts, up to 10 g l^{-1} of ammonium ions, about 1 M of hydrochloric acid, and up to 0.1% nitric acid.

from acid technological solutions, and then, on changing the acidity of the medium, ions of other accessory metals. It was found that palladium(II) is completely recovered on passing a high-acidity (pH < 2) multicomponent technological solution containing an excess of ammonium salts through a column packed with an AC. It was also found that the Pd(II) : M(II) ratio on the adsorbent substantially exceeds that in the starting solution: already after passing the solution for 1 h, the Pd(II) : M(II) ratio becomes at least two times larger; after 7 h of purification, the Pd(II) : M(II) ratio is approximately 1 : 5 for iron and copper and no less than 1 : 3 for the other metals. The degree of recovery of the other metal ions is within the range 20–40% (Table 8). Alkalization of the solution after the separation of palladium enables subsequent purification of the solution: on raising the solution pH after separating palladium ions, the remaining copper and iron are completely removed and the amount of the other metal ions substantially decreases in the solution volume being purified.

CONCLUSIONS

(1) Activated carbons produced by thermal processing of a mixture of sunflower husks, low-grade coal, and refinery wastes are adsorbents for ions of copper(II), iron(II), and other metals from multicomponent solutions, including those of technological origin, irrespective of the nature of a refinery waste.

(2) A decisive stage in the interaction of metal ions with activated carbons is the ion exchange and complexation with oxygen-containing surface functional groups; additional oxidation of the carbons makes it possible to raise the content of surface functional groups and the sorption of metal ions.

(3) Activated carbons produced from waste selectively absorb palladium(II) from acid multicomponent technological solutions; dynamic adsorption makes it possible to diminish the excess amount of the accessory metals from a 20-fold in solution to a 3-fold on the adsorbent.

ACKNOWLEDGMENTS

The authors thank for the financial support of the study the NATO program (project SfP 977 984) and a program of the Ukrainian Scientific and Technological Center (project 3004).

REFERENCES

1. Srinivasan, K., Balasubramanian, N., and Ramakrishnan, T.V., *Ind. J. Environ. Health*, 1998, vol. 30, no. 40, pp. 376–387.
2. Alaerts, G.J., Jitjaturant, V., and Kelderman, P., *Water Sci. Technol.*, 1989, vol. 21, pp. 1701–1704.
3. Chand, S., Agarwal, V.K., and Pavankumar, C., *Ind. J. Environ. Health*, 1994, vol. 36, no. 3, pp. 151–158.
4. Rawat, N.S. and Singh, D., *Asian Environ.,* 1992, vol. 14, pp. 30–41.
5. Sharma, D.C. and Forster, C.F., *Water Res.*, 1993, vol. 27, no. 7, pp. 1201–1208.
6. Raji, C. and Anirudhan, T.S., *Ind. J. Chem. Technol.*, 1996, vol. 3, pp. 345–350.
7. Bhatnagar, A. and Jain, A.K., *J. Coll. Interface Sci.*, 2005, vol. 281, no. 1. 2005, pp. 49–55.
8. Lyubchik, S.I., Lyubchik, A.I., Galushko, O.L., et al., *Colloids Surfaces A: Physicochem. Eng. Aspects*, 2004, vol. 242, nos. 1–3, 151–158.

9. Tikhonova, L,P., Kopyl, S.A., Goba, V.E., et al., *Ekotekhnol. Resursosberezh.*, 2005, no. 5, pp. 39–44.

10. Stewart, J.J.P., *J. Comp. Chem.*, 1989, vol. 10, no. 2, p. 209.

11. James, J.P. and Stewart, J.J.P., *J. Comp. Chem.*, 1989, vol. 10, no. 2, p. 221.

12. Khavryutchenko, V., *Eurasian Chem. Tech. J.*, 2004, vol. 6, no. 3, p. 157.

13. *Standard Methods for the Examination of Water and Wastewater*, Washington, DC: Am. Publ. Health Association, 1992, 18th ed.

14. Tikhonova, L,P., Goncharik, V. P., Kozhara, L.I., and Svarkovskaya, I.P., *Zh. Anal. Khim.*, 1991, vol. 46, no. 10, pp. 2009–2013.

15. Tarkovskaya, I.A., *Okislennyi ugol'* (Oxidized Carbon), Kiev: Naukova Dumka, 1981.

16. Tikhonova, L.P., Tarkovskaya, I.A., Rosokha, S.V., et al., *Zh. Prikl. Khim.*, 1998, vol. 71, no. 10, p. 1632.

17. Tarkovskaya, I.A., Kulik, N.V., Rosokha, S.V., et al., *Zh. Fiz. Khim.*, 2000, vol. 74, no. 5, pp. 899–903.

18. Tikhonova, L.P., Lyubchik, S.B., Tarasenko, Yu.A., et al., *Zh. Prikl. Khim.*, 2006, vol. 79, no. 5, pp. 737–743.

ISSN 1070-4272, Russian Journal of Applied Chemistry, 2008, Vol. 81, No. 8, pp. 1356–1359. © Pleiades Publishing, Ltd., 2008.
Original Russian Text © E.E. Ergozhin, G.K. Kabulova, A.I. Nikitina, N.A. Bektenov, 2008, published in Zhurnal Prikladnoi Khimii, 2008, Vol. 81, No. 8, pp. 1277–1280.

PHYSICOCHEMICAL STUDIES OF SYSTEMS AND PROCESSES

Sorption Capacity of New Cation Exchangers Based on Oil Residue and Epoxy Resin for Chromium(III) Ions

E. E. Ergozhin, G. K. Kabulova, A. I. Nikitina, and N. A. Bektenov

Bekturov Institute of Chemical Sciences, Ministry of Education and Science of the Republic of Kazakhstan, Almaty, Kazakhstan

Received December 6, 2007

Abstract—Sorption of chromium(III) ions by cation exchangers based on oil residue and ED-20 epoxy resin was studied in comparison with that of KU-2 × 8 industrial cation exchanger.

DOI: 10.1134/S1070427208080077

Chromium compounds are among the most toxic contaminants of natural water [1, 2]. The find their way into the environment as a result of technological activities and can migrate in the aqueous medium during a long time. In addition to having a generally toxic effect, chromium compounds exert a mutagenic and teratogenic influence and, therefore, their penetration into water reservoirs is hazardous for people's health. Removal from wastewater and concentration of chromium ions is a topical task for environment protection services, especially for Eastern Kazakhstan, where richest deposits of chromite ores are being developed [3]. From slime stores of Aktobinsk chemical plants, which contain millions of tons of highly toxic water-soluble chromium compounds, they penetrate via underground and surface water into the Ilek and Ural rivers and further into the Caspian Sea. For water reservoirs used for sanitary and household purposes, the maximum permissible concentration (MPC) is 0.5 mgl^{-1} for Cr(III) and 0.1 mgl^{-1} for Cr(VI); near the town of Aktobe, the chromium concentration exceeds the MPC by a factor of 20.

Compared with chemical reagent purification methods, sorption techniques for recovery of chromium are more promising and ecologically and energetically favorable. However, choosing ion-exchange materials and sorbents for recovery of chromium compounds from technical, natural, and potable water is a complicated task, because removal of chromium salts from these kinds of water is difficult due to the wide variety of oxidation states of this element and to the large number of its complexes with natural compounds.

The aim of this study was to examine the sorption capacity of new cation exchangers based on oil residue and ED-20 epoxy resin for chromium(III) ions.

EXPERIMENTAL

Cation exchangers based on oil residue and ED-20 epoxy resin were synthesized by the procedure described in [4, 5] as follows: sulfo cation exchangers: K-SM, from mazut (ED-20 : mazut : H_2SO_4 = 3.0 : 1.0 : 0.5, heating at 110°C for 30 h); K-SG, from goudron (ED-20 : goudron : H_2SO_4 = 2.0 : 1.0 : 3.0, heating at 110°C for 24 h); K-SB, from bitumen (ED-20 : bitumen : H_2SO_4 = 1.0 : 1.0 : 2.5, heating at 140°C for 24 h); phosphoric acid cation exchanger K-FB, from bitumen (ED-20 : bitumen : H_3PO_4 = 1.0 : 1.0 : 2.5, heating at 140°C for 24 h). The yield of the cation exchangers synthesized was 68–88%; SEC for 0.1 N NaOH solution, 2.75–5.50 mg-equiv g^{-1}; specific volume, 1.6–3.8 $mg\,l^{-1}$; pK 2.0–3.8. In all the cases, the cation exchangers are have irregularly shaped grains with sizes of 1.0–2.5 mm (~35%) and 0.25–0.5 mm (>55%), with dust the rest (particles less than 0.25 mm in size). KU-2 × 8 industrial cation exchanger [GOST (State Standard) 20 298–74] in the H^+ form was also used for sorption.

The recovery of chromium ions from a $Cr_2(SO_4)_3$ solution was studied by the static method at a 1 : 400 ratio between a cation exchanger and solution. The contact duration was varied from 10 min to 7 days. The concentration of chromium ions in the starting and equilibrium solutions was found polarographically, because chromium can be determined from the Cr^{3+}

Sorption capacity of various cation exchangers in Cr^{3+} recovery from acodic and alkaline $Cr_2(SO_4)_3$ solutions (contact durtion 7 days)

Cation exchanger	pH 3.1 (0.316 g l^{-1} Cr^{3+})			pH 12.1 (0.199 g l^{-1} Cr^{3+})		
	Cr^{3+} concentration after sorption, g l^{-1}	Degree of recovery, %	SC, mg g^{-1}	Cr^{3+} concentration after sorption, g l^{-1}	Degree of recovery, %	SC, mg g^{-1}
K-SM	0.151	52.22	66.30	0.143	28.14	21.79
K-SG	0.173	45.25	55.86	0.113	43.22	33.73
K-SB	0.151	52.22	65.75	0.173	13.06	10.09
K-FB	0.143	54.75	68.11	0.143	28.14	22.40
KU-2 × 8	0.226	28.48	35.26	0.143	28.14	22.27

reduction wave [6]. The polarograms were measured with a PU-1 polarograph in a thermostated cell at 25 ± 0.5°C, with a dropping mercury electrode. Oxygen was removed from the solutions being analyzed by bubbling with argon for 5 min. A saturated calomel electrode served as reference. The content of Cr^{3+} ions was determined on the background of 0.5 M $CaCl_2$ ($E_{1/2}$ = –0.92 V). The amount of the sorbed metal was calculated from the difference of its concentrations in the starting solution and in the filtrate.

The purification of wastewater to remove chromium ions has been extensively studied [7–9], with a considerable attention paid to development of ion-exchange and sorption methods. Data on recovery of various chromium ions by anion and cation exchangers have been reported. The recovery of chromium from wastewater is difficult because, depending on a purification method, chromium is either reduced to the trivalent state or oxidized to become hexavalent. Of particular importance in this case is the pH value or wastewater or technological water and the chromium concentration. This study is devoted just to the influence of these factors on the sorption properties of new cation exchangers.

Cation exchangers based on oil residue (K-SM, K-SG, K-SB, and K-FB) were used for sorption of chromium ions. An industrial sample of KU-2 × 8 cation exchanger was taken for comparison, because KU-2 × 8 and KU-2 × 20 cation exchangers are the best for absorption of trivalent chromium [7].

The PH value of the starting solution is one of the most important parameters affecting the sorption and ion-exchange processes, because the pH value of the medium affects the chemical form of both the ion exchanger and the metal ion. Figure 1 shows how the sorption capacity (SC) for Cr^{3+} ions of various cation exchangers based on oil residue depends on the pH of the medium in the range 2–4. The upper limit to pH is due to the decrease in the stability of the chromium salt in the alkaline medium, and the lower, to inexpediency of performing sorption processes from strongly acidic media.

As can be seen in Fig. 1, the maximum recovery of Cr^{3+} ions is observed for all samples at pH 3.5. The sorption capacity of K-SM cation exchanger for Cr^{3+} ions from the given solution at pH 2–4 is lower than that of other resins.

It has been reported [10] that Cr(III) and Cr(VI) ions are strongly absorbed not only in the acid region at pH 2–5, but also in the alkaline region: anion exchangers adsorb Cr(III) and Cr(VI) ions to the greatest extent at pH 9.0 and 4.0, respectively. Therefore, the sorption of Cr^{3+} ions was studied not only from acid solutions, but also from an alkaline solution (pH 12.1) in which no precipitation of chromium hydroxide or a basic salt of chromium is observed (see table).

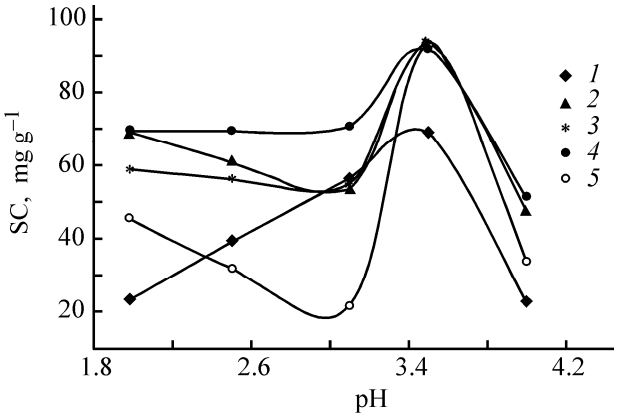


Fig. 1. Sorption capacity SC of (*1*) K-SM, (*2*) K-SG, (*3*) K-SB, (*4*) K-FB, and (*5*) KU-2 × 8 for Cr^{3+} ions vs. the pH of the medium. 0.025 N $Cr_2(SO_4)_3$ solution, 7 days.

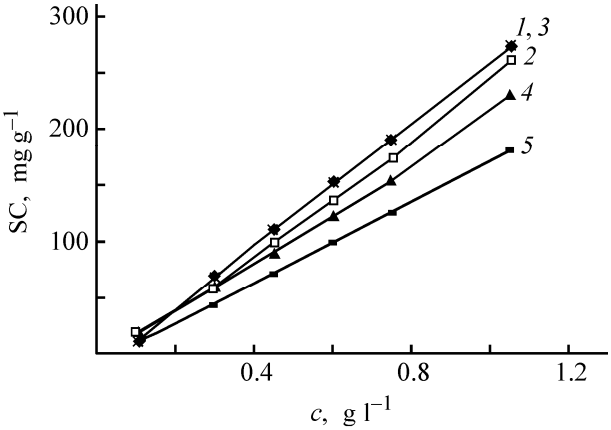


Fig. 2. Sorption isotherms of Cr^{3+} ions on (*1*) K-SM, (*2*) K-SG, (*3*) K-SB, (*4*) K-FB, and (*5*) KU-2 × 8 cation exchangers. Contact duration 7 days. (SC) Sorption capacity and (*c*) initial Cr^{3+} concentration.

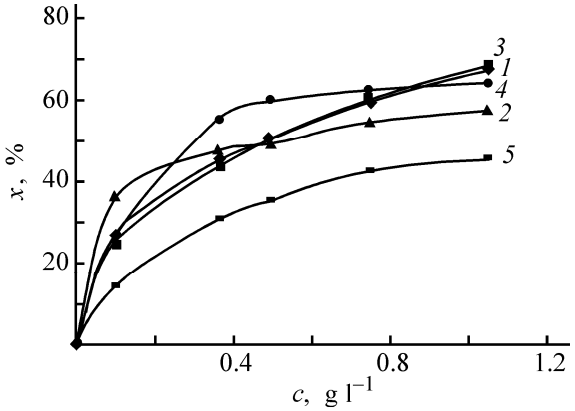


Fig. 3. Degree of recovery of Cr^{3+} ions, *x*, vs. their initial concentration *c* in a solution of $Cr_2(SO_4)_3$ on (*1*) K-SM, (*2*) K-SG, (*3*) K-SB, (*4*) K-FB, and (*5*) KU-2 × 8 cation exchangers.

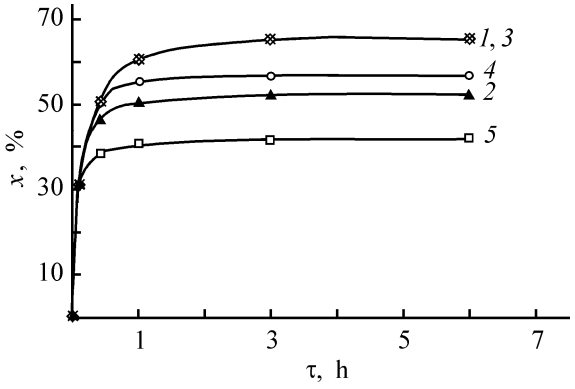


Fig. 4. Degree of recovery of Cr^{3+} ions, *x*, by (*1*) K-SM, (*2*) K-SG, (*3*) K-SB, (*4*) K-FB, and (*5*) KU-2 × 8 cation exchangers vs. the contact duration τ.

As can be seen in the table, the degree of Cr^{3+} recoery from the alkaline solution is substantially lower than that from the acid solution. Cr^{3+} ions are absorbed to the minimum extent by K-SB cation exchanger. All the ion exchangers synthesized adsorb chromium(III) ions from a solution with pH 3.1 better than the industrial sorbent KU-2 × 8 does. The highest sorption capacity for Cr^{3+} (68.11 mg g^{-1}) is observed for the phosphoric acid cation exchanger based on bitumen, K-FB. The sulfo cation exchanger K-SG is inferior to other ion exchangers based on oil residue in absorption of chromium(III) ions from acid media, and surpasses them in absorption from alkaline media.

The sorption capacity of the cation exchangers synthesized strongly depends on the concentration of $Cr_2(SO_4)_3$ solutions. At a content of chromium(III) cations in the starting solution equal to 1.04 g l^{-1}, the SC for these cations is 273 mg g^{-1} for K-SM and K-SB resins, 229 mg g^{-1} for K-SG and K-FB, and 181 mg g^{-1} for KU-2 × 8 (Fig. 2). At initial Cr^{3+} concentrations below 0.5 g l^{-1} Cr^{3+}, sulfo cation exchangers K-SM and K-SB recover chromium ions to the same extent as does phosphoric acid ion exchanger K-FB, and in solutions with higher content of chromium ions, the sorption capacity of the latter is higher.

As is known [7], the sorption isotherm provides information about the selectivity of an ion exchanger, and it follows from the slope of the dependences obtained that these cation exchangers have a rather high selectivity with respect to Cr^{3+} ions.

The solution concentration also affects the degree of recovery of Cr^{3+} cations (Fig. 3). The higher the content of Cr^{3+} ions in the starting solution, the larger the amount of ions absorbed by the cation exchangers. In the concentration range studied, the degree of recovery for K-FB resin reaches 55% for the solution with the Cr3+ ion concentration of 0.31 g l^{-1} and remains nearly unchanged as the concentration increases further. The best sorption properties are observed for K-SM and K-SB cation exchangers in absorption of Cr^{3+} ions from solutions with their concentration of 1.04 g l^{-1}. In this case, the degree of recovery is 67.5%.

At higher concentrations of Cr^{3+} ions, their recovery from solutions was not studied because it is believed [8] that the ion exchange or sorption is economically sound only for solutions containing the metal ion being recovered in a concentration not exceeding 1.0 g l^{-1}.

A no less important for development of the technology of sorption processes is analysis of the kinetic properties of ion exchangers. Figures 4 and 5 show how the degree of recovery of Cr^{3+} ions and the sorption capacity of various cation exchangers depend on

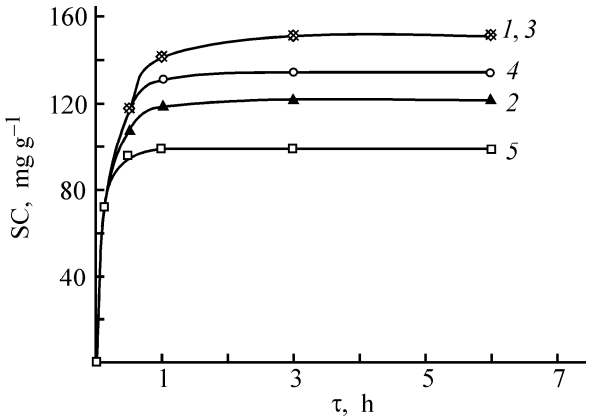


Fig. 5. Sorption capacity SC of (*1*) K-SM, (*2*) K-SG, (*3*) K-SB, (*4*) K-FB, and (5) KU-2 × 8 exchangers for Cr^{3+} ions vs. the contact duration τ.

time. The variation of these parameters with the duration of contact between the resins and the $Cr_2(SO_4)_3$ solution containing 0.6 g l^{-1} shows that the equilibrium is attained for the cation exchangers synthesized from oil residue in nearly 1 h. The industrial cation exchanger KU-2 × 8 exhibits better kinetic properties (the equilibrium state is attained in 0.5 h), although the degree of recovery by this cation exchanger and its sorption capacity for Cr^{3+} ions are lower.

CONCLUSIONS

(1) The static sorption of chromium ions by synthetic cation exchangers based on oil residue and ED-20 epoxy resin are better in the conditions studied than those of the industrial KU-2 × 8.

(2) Owing to their high sorption and kinetic parameters, it promising to use new cation exchangers for wastewater purification to remove chromium(III) ions.

REFERENCES

1. Tsygankov, A.P., Balatskii, O.F., and Senin, V.N., *Tekhnicheskii progress–khimiya–okruzhayushchaya sreda* (Technological Advance, Chemistry, and Environment), Moscow: Khimiya, 1979.

2. Alekseeva, S.L., Bolotin, S.N., and Tsypko, T.G., *Zh. Prikl. Khim.*, 2007, vol. 80, no. 3, pp. 378–380.

3. *Sarsenov, A., Ekologicheskaya bezopasnost' i resursosberezhenie pri pererabotke khromitovykh i boratovykh rud* (Ecological Safety and Resource Saving in Processing of Chromite and Borate Ores), Almaty: Vysshaya Shkola Kazakhstana, 2000.

4. Bektenov, N.A., Chopabaeva, N.N., and Kabulova, G.K., *Trudy Respublikanskoi nauchnoi konferentsii "Molodye uchenye – budushchee nauki," Almaty, 12–13 marta 2004 g.* (Proc. Rp. Sci. Conf. "Young Scientists as Future of the Science," Almaty, March 12–13, 2004), Almaty: KazNTU, 2004, part 1, pp. 318–321.

5. Ergozhin, E.E., Bektenov, N.A., Chopabaeva, N.N., and Kabulova, G.K., *Materialy Vserossiskoi nauchnoi konferentsii s mezhdunarodnym uchastiem "Sorbenty kak faktor kachestva zhizni i zdorov'ya," Belgorod, 11–14 oktyabrya 2004 g.* (Proc. All-Russia Sci. Conf. with Foreign Participants "Sorbents as a Factor Important for the Quality of Life and Health," Belgorod, October 11–14, 2004), Moscow–Belgorod, 2004, pp. 53–56.

6. Kryukova, T.A., Sinyakova, S.I., and Aref'eva, T.V., *Polyarograficheskii analiz* (Polarographic Analysis), Moscow: Goskhimizdat, 1959.

7. Lebedev, K.B., Kazantsev, E.I., Rozmanov, V.M., et al., *Ionity v tsvetnoi metallurgii* (Ion Exchangers in Nonferrous Metallurgy), Moscow: Metallurgiya, 1975.

8. Shirshina, L.G., Shvarts, Z., and Taubert, D., *Zh. Prikl. Khim.*, 1985, vol. 58, no. 8, pp. 1734–1739.

9. Kunaev, A.M., Dadabaev, A.Yu., and Tarasova, E.G., *Ionoobmennye protsessy v gidrometallurgii tsvetnykh metallov* (Ion-Exchange Processes in Hydrometallurgy of Nonferrous Metals), Alma-Ata: Nauka, 1986.

10. *Ionnyi obmen i ionity* (Ion Exchange and Ion Exchangers), Samsonov, G.V. and Nikitin, N.I., Eds., Leningrad: Nauka, 1970.

ISSN 1070-4272, Russian Journal of Applied Chemistry, 2008, Vol. 81, No. 8, pp. 1360–1363. © Pleiades Publishing, Ltd., 2008.
Original Russian Text © M.Yu. Berezkin, E.G. Polyakov, V.V. Turygin, L.V. Kaabak, A.V. Khudenko, A.P. Tomilov, 2008, published in Zhurnal Prikladnoi Khimii, 2008, Vol. 81, No. 8, pp. 1281–1284.

APPLIED ELECTROCHEMISTRY AND CORROSION PROTECTION OF METALS

Electrochemical Synthesis of Niobium Compounds in Anodic Dissolution of Ferroniobium in Methanol

M. Yu. Berezkin, E. G. Polyakov, V. V. Turygin, L. V. Kaabak, A. V. Khudenko, and A. P. Tomilov

State Research Institute of Organic Chemistry and Technology, Federal State Unitary Enterprise, Moscow, Russia

St. Petersburg State Polytechnic University, St. Petersburg, Russia

Received May 4, 2008

Abstract—Anodic dissolution of ferroniobium in anhydrous methanol in the presence of sodium methylate was studied. The possibility of recovering pure hexamethoxyniobate from the electrolyzate and its conversion into niobium methylate with an iron content not exceeding 0.01% was analyzed.

DOI: 10.1134/S1070427208080089

The permanent need of the electronic industry in high-purity materials and, in particular, in special-purity niobium used in manufacture of bulk-porous niobium capacitors enforces a search for new methods for its production and purification. Of particular interest is recovery of niobium from the inexpensive and industrially produced ferroniobium and other alloys. Rather promising for this purpose is the electrochemical method for obtaining metal alkoxides by anodic dissolution of a metal in an aliphatic alcohol [1]. Published data on the anodic dissolution of alloys in alcohols are virtually lacking. The only exception are data on formation of tetraethoxysilane by anodic dissolution of ferrosilicon in ethanol on the background of ammonium chloride [2].

The anodic dissolution of technical-grade niobium in anhydrous methyl alcohol has been described previously [3, 4]. It was established that the mechanism of the process largely depends on the nature of a supporting electrolyte. Niobium(V) methylate was obtained in high yield by using lithium chloride as a supporting electrolyte. In this process, niobium methoxychlorides are first formed at the anode and readily interact in the solution bulk with methoxyl ions generated at the cathode. In the case of a sodium methylate supporting electrolyte, niobium cations generated at the anode are bound into a stable complex compound $NaNb(OCH_3)_6$, which is not subject to any transformation in the course of electrolysis and can be easily isolated from the electrolyzate in a nearly quantitative yield. It can serve as the starting material for preparing niobium(V) methylate by the reaction with ammonium chloride:

$$NaNb(OMe)_6 + NH_4Cl \rightarrow Nb(OMe)_5 + NaCl\downarrow + CH_3OH + NH_3\uparrow.$$

In this study, the possibility of obtaining niobium methylate and sodium hexamethoxyniobate from ferroniobium by the electrochemical method was considered and it was demonstrated that sodium hexamethoxyniobate can be converted to other niobium-containing compounds.

EXPERIMENTAL

Because the synthesis of alkoxides is sensitive to presence of moisture, methanol of chemically pure grade used in the study was subjected to additional drying by boiling with magnesium shavings [5]. The final content of water was less than 0.01%.

Sodium methylate was obtained by a direct reaction of metallic sodium (chemically puregrade) with methanol. Ferroniobium anodes were made of technical-grade ferroniobium containing (wt %): Nb 67.5, Al 0.45, Si 0.45, Ti 0.47, Ta 0.109, P 0.144, S 0.094, C 0.105, and Fe the remainder. The other reagents (lithium chloride, hydrochloric acid, and toluene) used in the study were of chemically pure grade.

Experiments were performed in a diaphragmless electrolyzer having the form of a 90-cm^3 glass cylinder with a thermostating jacket and a cock at the bottom for discharging the electrolyzate. The electrolyzer was hermetically closed with a cover into which a thermometer, gas-discharge pipe with a calcium chloride packing, and current leads to the electrodes were inserted. The ferroniobium anode was mounted below the cathode at a distance of 0.5 cm.

The working area of the anode was 10 cm^2. The cathode was made of a coiled iron wire 1 mm in diameter and had a working area of 24 cm^2. Prior to each electrolysis, the electrodes were trimmed and degreased with Vienna lime, washed with distilled water, dried, and weighed. After an experiment was complete, the electrolyzate was discharged for further processing into a flask preliminarily purged with argon. The amount of the dissolved metal was found from the loss of mass by the anode.

The residual iron(II) methylate was filtered from the electrolyzate without access of air.

To isolate niobium pentamethoxide (methylate), methanol was evaporated from the electrolyzate under a reduced pressure and then the product was extracted from the still bottoms with hexane. After the extractive agent was evaporated, a light yellow liquid that crystallized upon cooling remained in the flask. The resulting yellowish crystals had mp 61°C, in agreement with published data for niobium methylate [1].

Sodium hexamethoxyniobate was isolated from the filtrate, after the precipitated iron methylate was separated, by distilling off methanol until the onset of precipitation of crystals. After that, a fivefold amount of toluene or benzene was added to the solution and the mixture was kept at a lowered temperature until the crystallization was complete. The precipitated white needle-like crystals were filtered off and washed with toluene.

The content of sodium methylate in the still bottoms was found by their dissolution in water and titration of the resulting solution with an alkali. The content of niobium in the still bottoms was found by their dissolution in water, addition of hydrochloric acid, and gravimetric determination of the precipitated niobium pentoxide.

Dissolution of ferroniobium on the background of LiCl. Prior to electrolysis, the ferroniobium anode was thoroughly degreased and weighed. The electrolyzer was charged with an electrolyte solution [2.12 g of LiCl in 90 ml of methanol (0.5 M solution)]. The electrolysis was performed in the galvanostatic mode at a current density of 0.1 A cm^{-2} and temperature of 30–35°C. In the course of electrolysis, the solution remained transparent and the voltage was constant (9 V). The time of the experiment was 5 h, and the quantity of passed electricity, 5.0 A h^{-1}. The loss of mass by the electrode was 3.48 g, which corresponds to a 99.8% current efficiency by pentavalent niobium and trivalent iron. The precipitated iron methylate was filtered off, and methanol was evaporated from the electrolyzate under a reduced pressure (15 mm Hg). $Nb(OCH_3)_5$ was extracted (3.42 g) from the still bottoms with hexane, which corresponds to a 55% substance yield by a dissolved niobium. The content of the iron impurity in the product obtained was 0.54 wt %.

Dissolution of ferroniobium on the background of $NaOCH_3$. Prior to electrolysis, the ferro-niobium anode was thoroughly degreased and weighed. The electrolyzer was charged with an electrolyte solution [0.57 g of Na in 50 ml of methanol (0.5 M solution)]. The content of moisture in the solution was less than 0.05 wt %. The electrolysis was performed in the gal-vanostatic mode at a current density of 0.025 A cm^{-2} and temperature of 30–35°C. In the course of electrolysis, the solution remained transparent, with the electrolyzer voltage equal to 4 V at the beginning of a run and increasing to 9 V by its end. The experiment duration was 19 h 50 min, and the amount of passed electricity, 4.96 A h. The loss of mass by the electrode was 3.46 g, which corresponds to a 99.5% current efficiency by pentavalent niobium and trivalent iron. The precipitated iron methylate was filtered off and methanol was evaporated from the filtrate under a reduced pressure (15 mm Hg) before a crystalline pecipitate started to be formed. A five-fold volume of toluene was added to the resulting solution and the remaining methanol was evaporated under a reduced pressure until the precipitation of sodium hexamethoxyniobate crystals. The crystals obtained were filtered off and washed with toluene. The mass of the crystals was 7.26 g. The yield of sodium hexamethoxyniobate was 96.5% in terms of dissolved niobium. The obtained complex compound was dissolved in methanol and then a methanol solution of ammonium chloride (equimolar amount) was added to it. After the evaporation of methanol, 5.23 g of niobium methylate was isolated from the resulting residue with hexane. The substance yield was 87.5%.

Voltammetric measurements were made with an IPC-2000 computer-controlled electronic potentiostat

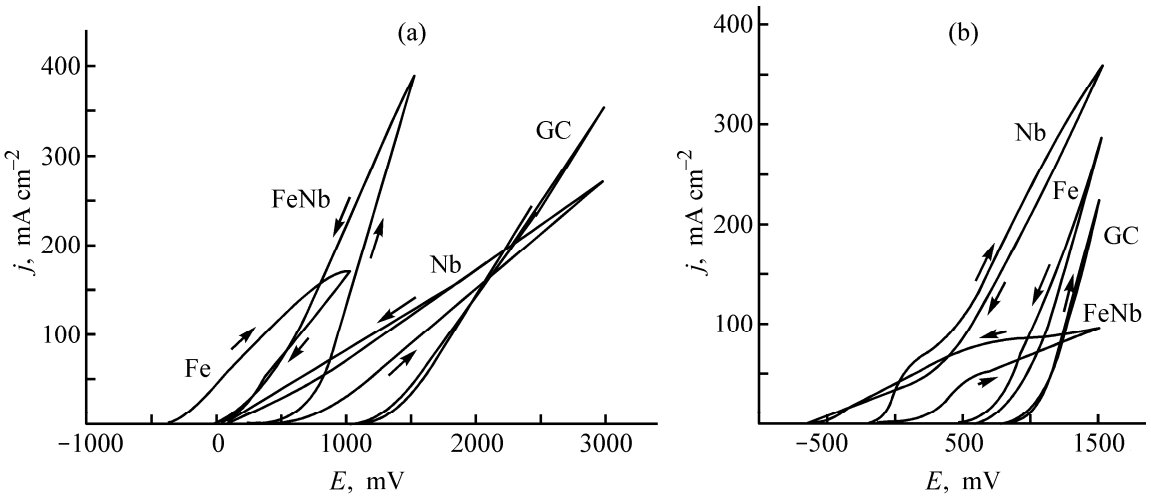


Fig. 1. Voltammetric curves obtained on iron, niobium, ferroniobium and glassy carbon (GC) in 1 M solutions of (a) LiCl and (b) NaOMe in anhydrous methanol. The potential is given relative to a silver chloride reference electrode. Temperature 25°C, potential sweep rate 0.2 V s^{-1}. (j) Current density and (E) potential.

in a 20-cm^3 cylindrical diaphragmless glass cell with a thermostating jacket. Electrodes and a gas-discharge pipe were inserted into the cell cover. The electrode system comprised a stationary working electrode with an area of 0.5 cm^2 [made of a material under study (niobium, iron, ferroniobium, or glassy carbon)], platinum auxiliary electrode, and silver chloride reference electrode. The last electrode was brought in close vicinity of the working electrode with a capillary.

To measure a voltammetric curve, the cell was charged with an electrolyte solution of the required concentration and bubbled with dry argon through the outlet tube for 0.5 h. Then, the trimmed electrode was introduced into the cell preheated to the required temperature and was polarized following the preset program.

To have a notion of the anodic behavior of ferroniobium under the above-described conditions of synthesis of niobium methylate and hexamethoxyniobate, voltammetric measurements were performed with lithium chloride and sodium methylate as supporting electrolytes. Figures 1a and 1b show sets of voltammograms obtained in anodic dissolution of iron, niobium, and ferroniobium and anodic polarization curves for glassy carbon. It can be seen that the onset potential of niobium dissolution on the background of sodium methylate is shifted to the negative region by approximately 750 mV in comparison with the corresponding potential in a lithium chloride solution. This indicates that niobium ions are bound into complexes in the presence of methylate ions. At the same time, the onset potential of iron dissolution on the background of sodium methylate is, by contrast, shifted to the positive region by 700 mV. This suggests that iron forms no complexes with methylate ions in the course of anodic dissolution and, in addition, the potential barrier of the electrode reaction for iron is higher in a solution with sodium methylate, compared with the solution with lithium chloride. In both cases, the onset potential of ferroniobium dissolution lies between the dissolution potentials of pure iron and niobium, which points to their joint dissolution.

Comparison of the slopes of the polarization curves in Fig. 1a shows that the dissolution of ferroniobium in the presence of lithium chloride is more intense than that of its individual components. It is easier than that in the case of niobium and, as the current density increases, occurs in approximately the same region of potentials as the dissolution of iron. In the presence of sodium methylate, the opposite situation is observed (Fig. 1b). Ferroniobium dissolves at the same potential as niobium. In all probability, hexamethoxyniobate is formed in both cases. Raising the potential results in the passivation of a surface.

It is seen from the results of voltammetric measurements that ferroniobium easily dissolves in methanol on the background of lithium chloride. In this case, electrolysis yields a mixture of iron and niobium methylates. It was difficult to recover niobium methylate free of iron compounds from the mixture obtained. A treatment of the electrolyzate by a verified extraction scheme

with hexane gave in low yield (≤55 %) a product rather strongly contaminated with iron.

As is known [1], niobium methylate itself exists in the form of a dimer including a four-member cycle $Nb_2(OMe_2)$. Probably, joint dissolution of niobium and iron yields a binuclear complex of Nb with Fe. The complex is poorly extracted with hexane and remains in the residue. Passing into the extractant, the compound contaminates the recovered niobium methylate with iron. Special experiments devoted to mixing of preliminarily obtained niobium and iron methylates in methanol showed that niobium methylate can be separated from the above mixtures in a considerably higher yield (up to 70%).

The situation changes profoundly when sodium methylate is used as a supporting electrolyte. In this case, niobium methylate being formed at the anode is bound into a stable complex hexamethoxiniobate anion, which forms no compounds with iron methylate. Sodium hexamethoxiniobate is easily recovered by crystallization from the mixture obtained upon electrolysis. The yield of sodium hexamethoxiniobate in terms of the dissolved metal exceeds 90 %. It was demonstrated by the spectral analysis that the con-tent of the iron impurity does not exceed 0.01 %. The thus obtained hexamethoxiniobate can be used as a starting material for preparation of pure niobium compounds. For example, niobium oxide was produced by hydrolysis of the isolated crystals with water, followed by addition of hydrochloric acid, and niobium methylate was obtained by the reaction with ammonium chloride. The results of the preparative electrolyses are listed in the table.

Thus, the attempts to separate the electrolysis products obtained in anodic dissolution of ferroniobium in a methanol solution of lithium chloride were unsuccessful. It was shown that, by contrast, the electrolysis with sodium methylate as a supporting electrolyte makes it possible to obtain a complex easily separable from iron compounds and can be considered a promising way of niobium purification.

Anodic dissolution of ferroniobium in methanol

Electrolyte	Yield, %		Substance yield, %	Fe content of final product, %
	Fe^{2+}	Fe^{3+}		
LiCl	90	10	Nb(OMe), 55	0.54
$NaOCH_3$	63	37	NaNb(OMe), 96	0.01

CONCLUSIONS

(1) A new direct way was found for separation of niobium from iron. The method involves anodic dissolution of ferroniobium in a methanol solution of sodium methylate, followed by separation of sodium hexamethoxyniobate from the electrolyzate.

(2) Sodium hexamethoxyniobate can be easily converted to niobium methylate by the reaction with ammonium chloride. In turn, the methylate can serve as a starting material for preparation of other niobium compounds.

(3) In contrast to the processes used in industry, the process of niobium separation from a ferroalloy occurs under mild conditions, with no aggressive media required.

REFERENCES

1. Turova, N.Ya., Turevskaya, E.R., Kessler, V.G., and Yanovskaya, M.I., The Chemistry of Metal Alkoxides, *Springer*, 2002.
2. FRG Patent no. 2 121 732.
3. Berezkin, M.Yu., Chernykh, I.N, Polyakov, E.G., and Tomilov, A.P., *Zh. Prikl. Khim*., 2006, vol. 79, no. 5, pp. 752–756.
4. Berezkin, M.Yu., Polyakov, E.G., Turygin, V.V., and Tomilov, A.P., *Elektrokhimiya*, 2007, vol. 43, no. 10, pp. 1265–1267.
5. Weissberger, A., and Proskauer, E.S., *Organic Solvents. Physical Properties and Methods of Purification*, Riddig, J.A. and Toops, E.E., Eds., New York: Interscience, 1955.

ISSN 1070-4272, Russian Journal of Applied Chemistry, 2008, Vol. 81, No. 8, pp. 1364–1368. © Pleiades Publishing, Ltd., 2008.
Original Russian Text © G.V. Kornienko, N.V. Chaenko, V.L. Kornienko, 2008, published in Zhurnal Prikladnoi Khimii, 2008, Vol. 81, No. 8, pp. 1285–1289.

APPLIED ELECTROCHEMISTRY AND CORROSION PROTECTION OF METALS

Indirect Electrochemical Oxidation of *N*-Methyl-*n*-aminophenol by Active Oxygen Species Generated in Situ from O_2, H_2O, and H_2O_2

G. V. Kornienko, N. V. Chaenko, and V. L. Kornienko

Institute of Chemistry and Chemical Engineering, Siberian Branch, Russian Academy of Sciences, Krasnoyarsk, Russia

Received December 27, 2007

Abstract—Indirect electrochemical oxidation of *N*-methyl-*n*-aminophenol by active oxygen species was studied. The active species were in situ generated from O_2, H_2O_2, and H_2O in aqueous solutions with various pH values by using a gas-diffusion cathode in a diaphragmless electrolyzer with anodes made of platinum, lead dioxide, and ruthenium-titanium oxide (RTO).

DOI: 10.1134/S1070427208080090

In recent years, technologies for purification of industrial wastewater by ecologically safe reagents, such as chemically bound active oxygen species, have aroused increasing interest. It is known [1–3] that electrochemical methods enable comparatively simple in situ generation of active oxygen species by conjugated processes from O_2, H_2O_2, and H_2O in the form of intermediates $HO^{\bullet}$, HO_2^-, and $HO_2^{\bullet}$ differing in oxidizing ability by 5–6 orders of magnitude.

Aromatic amines, which are typical hydrosphere contaminants [4], are widely used in industry, e.g., as starting and intermediate products in production of dyes and medicinal preparations.

Presently, the electrochemical technique of sewage treatment with highly reactive intermediates, active oxygen species in situ generated from O_2, H_2O, and H_2O_2, becomes increasingly attractive because of the ease of control, high efficiency, and ecological safety. Processes of indirect oxidation consist in the electrochemical generation at the cathode or anode (possibly, at the cathode and anode simultaneously) of intermediates of oxygen reduction and water oxidation (hetero-geneous stage) and in their subsequent in situ chemical reactions with organic substrates in an electrolyte solution (homogeneous stage).

At present, carbon-graphite gas-diffusion electrodes (GDE) are widely used in experimental practice, because these electrodes make it possible to raise the current density of O_2 reduction to H_2O_2 by 2–3 orders of magnitude, compared with smooth electrodes, which is important for practical application of such processes [5, 6].

Depending on the pH value, oxygen is reduced to hydrogen peroxide by one of the following reactions:

$$O_2 + 2H_2O + 2e = H_2O_2 + 2OH^-, \text{ pH} \geq 7; \quad (1)$$

$$O_2 + 2H^+ + 2e = H_2O_2, \text{ pH} < 7. \quad (2)$$

The oxidation reactions occur at metal-oxide anodes in diaphragmless cells:

$$H_2O \rightarrow 2HO^{\bullet} + 2H^+ + 2e, \quad (3)$$

$$H_2O_2 \rightarrow HO_2^{\bullet} + H^+ + e, \quad (4)$$

$$HO_2^{\bullet} \rightarrow O_2 + H^+ + e. \quad (5)$$

Studies of the oxidation of *N*-methyl-*n*-aminophenol by the Fenton photoreaction, UV/H_2O_2, at 60°C and its photocatalytic oxidation with TiO_2/H_2O_2 have shown [7–9] that, under these conditions, *N*-methyl-*n*-aminophenol is oxidized via formation of several intermediates: various cyclic carbonyl compounds and carboxylic acids, which are further oxidized to CO_2 and water.

The aim of this study was to examine the indirect electrochemical oxidation of *N*-methyl-*n*-aminophenol

by active oxygen species in situ generated from O_2, H_2O, and H_2O_2 in alkaline and acid electrolytes in a diaphragmless electrolyzer with carbon-black and graphite gas-diffusion cathodes and Pt, PbO_2, and RTO anodes.

EXPERIMENTAL

To obtain H_2O_2 and carry out in situ electrolyses involving hydrogen peroxide, we used temperature-controlled cells with unseparated cathode and anode spaces (two-chamber cells). The gas-diffusion cathode had the form of a planar disk with a total porosity of 65–70% and thickness of 0.8–0.9 mm, composed of a mixture of A 437-E carbon black (60 wt %) and FP-4D (40 wt %). The design of a cell of this kind was described in [10]. A platinum plate served as the anode. The volume of the electrolyte cell was 50 ml. The electrode potential was monitored on the front side of the gas-diffusion cathode relative to a silver chloride reference electrode.

N-methyl-*n*-aminophenol was oxidized at current densities of 20, 50, and 70 mA cm^{-2} at pH 2–3 and 9–10. The initial solution concentration was 1000 mg l^{-1}.

In electrolyses with a graphite cathode, we used a standard electrochemical cell with a cathode area S = 3 cm^2 and Pt, Pb/PbO_2, and RTO anodes. The PbO_2 anode was fabricated by anodic oxidation of a $2 \times 10 \times$ 25-mm lead plate in a 0.7 M solution of sulfuric acid at a current strength of 1 A within 1 h [11]. An X-ray phase analysis demonstrated that the coating formed in this way consisted of PbO–α-PbO_2 (3 : 1). Model solutions of *N*-methyl-*n*-aminophenol were oxidized at a current density of 150 mA cm^{-2}. The initial solution concentration was 500 and 1000 mg l^{-1}.

The variation of contents of *N*-methyl-*n*-aminophenol and other organic intermediates during the electrolysis was monitored by changes in the chemical oxygen demand (COD) [12]. The composition of the oxidation products was analyzed by UV spectroscopy. We used solutions of 0.1 and 0.2 M NaOH as an alkaline electrolyte, and 1 M Na_2SO_4 with addition of iron(II) sulfate ($c_{Fe^{2+}} = 0.4 \times 10^{-3}$ mg l^{-1}), acidified with 10% H_2SO_4 to pH 2–3, as the acid electrolyte; the electrolyte temperature was 30 ± 2°C.

When discussing the results obtained, we used the dependence of the Faraday efficiency on the quantity of passed electricity [13–15]:

$$\eta = \Delta \mathrm{COD} VF/(8I\Delta t).$$

Here COD is the chemical oxygen demand (mg l^{-1}); V, electrolyte volume (l); F, Faraday constant; I, current strength (A); and Δt, electrolysis duration (s).

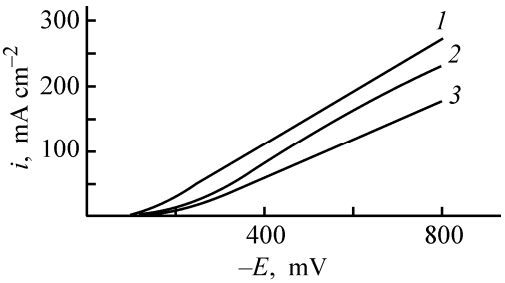


Fig. 1. Polarization curves for oxygen reduction at a gas-diffusion cathode. (*i*) Current and (*E*) potential. (*1*) 0.1 M NaOH, (*2*) 0.1 M NaOH + *N*-methyl-*n*-aminophenol (500 mg l^{-1}), (*3*) after electrolysis (5 h).

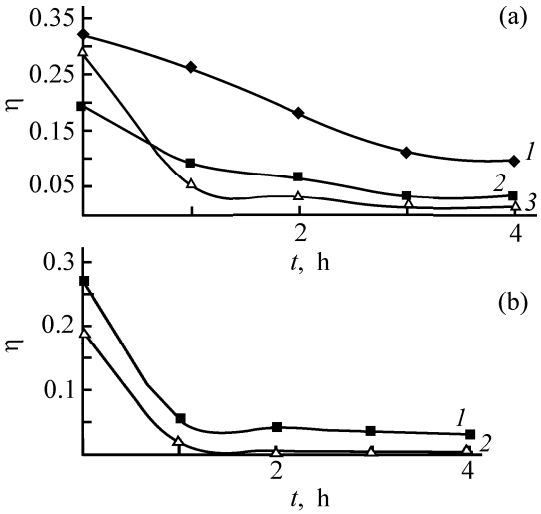


Fig. 2. Faraday efficiency η of *N*-methyl-*n*-aminophenol oxidation at pH (a) 9–10 and (b) 2–3 vs. the electrolysis duration t at various current densities at GDE. Metol concentration 1000 mg l^{-1}, Pt anode. (*i*) (mA cm^{-2}): (*1*) 20, (*2*) 50, and (*3*) 70.

To study the activity of gas-diffusion electrodes and the stability of the cathodic generation of hydrogen peroxide from oxygen, we recorded polarization curves. Figure 1 shows polarization curves of oxygen reduction at GDE in 0.1 M NaOH. Curve *1* indicates that the electroreduction of O_2 to H_2O_2 proceeds smoothly with a slight polarization. When, e.g., the current density increases from 100 to 150 mA cm^{-2}, the electrode potential shifts to the cathodic region by 100 mV. In the presence of *N*-methyl-*n*-aminophenol, the GDE potential slightly shifts to the cathodic region at all current densities, probably, due to the adsorption of the organic substrate. After performing electrolysis in the presence of Metol for 5 h, the polarization also increases further because of the adsorption of oxidation products on the cathode surface.

Figures 2a and 2b show how the Faraday efficiency of *N*-methyl-*n*-aminophenol oxidation at GDE

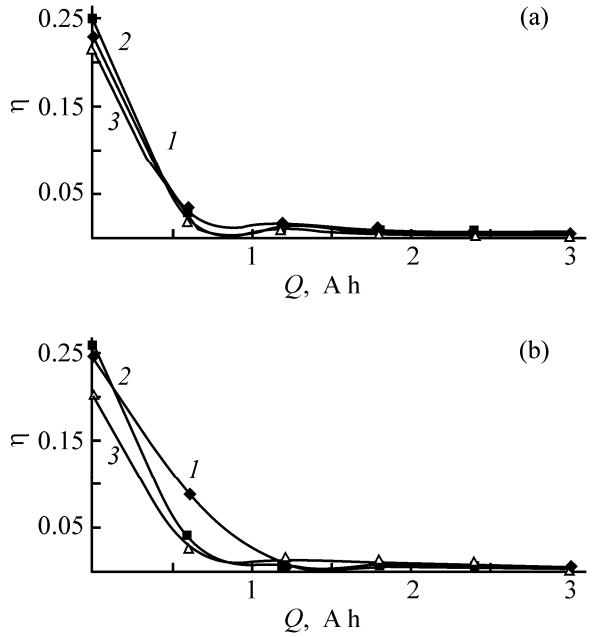


Fig. 3. Faraday efficiency η of *N*-methyl-*n*-aminophenol oxidation by oxygen vs. the quantity *Q* of passed electricity at pH (a) 2–3 and (b) 9–10. Current strength 600 mA, Metol concentration 1000 mg l^{-1}. (*1*) RTO, (*2*) Pb/PbO_2, (*3*) Pt.

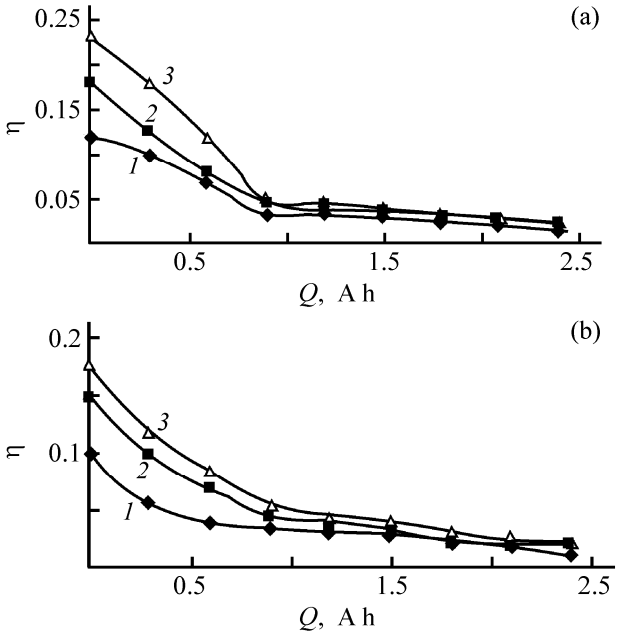


Fig. 4. Faraday efficiency η of the *N*-methyl-*n*-aminophenol oxidation by hydrogen peroxide vs. the quantity *Q* of passed electricity in (*1*) 0.1 M and (*2*) 0.2 M NaOH solutions. Current strength 600 mA, Metol concentration 500 mg l^{-1}, Pt anode. Peroxide concentration (M): (*1*) 0, (*2*) 0.1, and (*3*) 0.2.

depends on the current density at an initial Metol concentration of 1000 mg l^{-1} and pH 9–10 and 2–3. It can be seen that the Faraday efficiency increases with the current density. For example, η = 0.2 at i = 20 mA cm^{-2} and η = 0.33 at i = 70 mA cm^{-2} for the alkaline electrolyte. The oxidation is more effective in 0.1 M NaOH, compared with the acid electrolyte. This presumably occurs because hydrogen peroxide being formed is more stable in the acid electrolyte, compared with the alkaline electrolyte. Similar dependences were obtained in oxidation of phenol, with the calculated kinetic constants k found to be 1.8 h^{-1} and 1.4 h^{-1} for alkaline and acid electrolytes, respectively [10, 16].

Figures 3a and 3b show how the Faraday efficiency of *N*-methyl-*n*-aminophenol oxidation by molecular oxygen on various anode materials, with oxygen bubbled through a solution in which reactions (1)–(3) occur in this case, depends on the quantity of passed electricity. Oxygen is reduced at the graphite cathode to hydrogen peroxide, whose concentration was 0.002 M at pH 2–3 and 0.006 M at pH 9–10. The initial concentration c_{met} of *N*-methyl-*n*-aminophenol was 1000 mg l^{-1}, and the current strength, 600 mA. These dependences show that the oxidation better proceeds at pH 9–10 at Pb/PbO_2 (η = 0.27), RTO (η = 0.25), and Pt (η = 0.2) anodes, and at pH 2–3 at Pb/PbO_2 (η = 0.26), RTO (η = 0.23), and Pt (η = 0.22) anodes. Under these conditions, it is preferable to use Pb/PbO_2 and RTO anodes.

Figures 4a and 4b show how the Faraday efficiency depends on the quantity of passed electricity in direct anodic oxidation of *N*-methyl-*n*-aminophenol and in its indirect oxidation with addition of hydrogen peroxide ($c_{H_2O_2}$ 0.1 and 0.2 M) in a cell with a graphite cathode and a platinum anode in 0.1 and 0.2 M NaOH. The initial concentration of *N*-methyl-*n*-aminophenol was 500 mg l^{-1}.

In is seen from Fig. 4 that the efficiency of direct anodic oxidation is comparatively low: η = 0.12 for 0.1 M NaOH and η = 0.1 for 0.2 M NaOH, which is probably due to a low $HO_2^{\bullet}$ concentration. Addition of hydrogen peroxide leads to a rise in the oxidation efficiency due to an increase in the $HO_2^{\bullet}$ concentration via reaction (4). The Faraday efficiency is 0.23 for 0.1 M NaOH and 0.18 for 0.2 M NaOH. These data show that the oxidation in a 0.2 M alkali solution is less efficient than that in 0.1 M NaOH. Similar dependences were obtained in [16] for the phenol oxidation. The results of mineralization of *N*-methyl-*n*-aminophenol under various electrolysis conditions are listed in the table.

Results of *N*-methyl-*n*-aminophenol mineralization under various electrolysis conditions

c_{met}, mg l^{-1}; electrolysis conditions	i, mA cm^{-2}	Anode	Electrolyte, M	Mineralization efficiency, %
1000; GDE + O_2	70	Pt	0.1NaOH	98–99
	20	Pt	0.1NaOH	60–65
	20	Pt	1 Na_2SO_4 + 2H_2SO_4	25–30
1000; graphite + O_2	150	Pb/PbO_2		95–96
	150	OPTA	1 Na_2SO_4 + 2H_2SO_4	98–99
	150	Pt		89–90
1000; graphite + O_2	150	Pb/PbO_2		95–96
	150	OPTA	0.1NaOH	98–99
	150	Pt		91–92
500; graphite	150	Pt	0.1NaOH	72–73
500; graphite + H_2O_2	150	Pt	0.1NaOH + 0.1H_2O_2	95–96
	150	Pt	0.1NaOH +0.2H_2O_2	98–99
500; graphite	150	Pt	0.2NaOH	54–55
500; graphite + H_2O_2	150	Pt	0.2NaOH + 0.1H_2O_2	61–62
	150	Pt	0.2NaOH + 0.2H_2O_2	64–65

It is seen from the table that the indirect oxidation of *N*-methyl-*n*-aminophenol in a diaphragmless cell with GDE is more efficient in alkaline electrolytes, compared with acid electrolytes, and depends on the current density. In the oxidation by oxygen with the use of a graph-ite cathode at various pH, the best anode material is Pb/PbO_2: the efficiency of Metol mineralization is 99%. The indirect oxidation of *N*-methyl-*n*-aminophenol by hydrogen peroxide occurs with a 98% mineralization to CO_2 and H_2O in 0.1 M NaOH, whereas in 0.2 M NaOH, the efficiency is 65%.

The UV spectroscopic data show that the *N*-methyl-*n*-aminophenol oxidation via oxidative polymerization of the starting compounds is not predominating. The oxidation of *N*-methyl-*n*-aminophenol at various pH values proceeds by various successive oxidation pathways: at pH 2–3, intermediates of the carboxylale type are mainly formed, and at pH 9–10, products of *N*-methyl-*n*-aminophenol hydroxylation, with the subsequent conversion to aliphatic acids, which are further oxidized to CO_2 and water. A similar scheme of the *N*-methyl-*n*-aminophenol oxidation has been described in the literature [9, 17]. It is necessary to note that, when Fe^{2+} cations are present in the initial solution, the oxidation of the organic substrate is accompanied by the appearance of Fe^{3+} cations which have their own absorption bands in UV spectra. These bands are superimposed on the absorption bands of organic products and surpass these latter in intensity. Under these conditions, analysis of organic products is difficult.

CONCLUSIONS

(1) *N*-Methyl-*n*-aminophenol can be oxidized by active oxygen species generated in situ from oxygen, hydrogen peroxide, and water with the use of gas-diffusion electrodes, graphite cathodes, and various anode materials at various pH values.

(2) The indirect oxidation of *N*-methyl-*n*-aminophenol in a diaphragmless cell with gas-diffusion electrodes is more efficient in an alkaline electrolyte and depends on the current density.

(3) When oxygen is bubbled through a solution at various pH in a cell with a graphite cathode, the best anode material is Pb/PbO_2: the efficiency of *N*-methyl-*n*-aminophenol mineralization is 99%.

(4) The indirect oxidation of *N*-methyl-*n*-aminophenol by hydrogen peroxide in 0.1 M NaOH proceeds with a 98% mineralization to CO_2 and H_2O.

(5) According to UV spectroscopic data, the intermediate products of *N*-methyl-*n*-aminophenol oxidation in an acid electrolyte are various organic compounds of the carboxylate type, whereas upon addition of iron ions, mainly oxalate complexes are formed. In the case of electrochemical oxidation in an alkaline

electrolyte, the intermediate products are quinone, hydroquinone, and organic acids.

REFERENCES

1. Pletcher, D., *Acta Chem. Scand.*, 1999, vol. 53, pp. 745–750.
2. Oturan, M.A., *J. Appl. Electrochem.*, 2000, vol. 30, pp. 475–482
3. Brillas, E., Mur, E., and Casado, J., *J. Electrochem. Soc.*, 1996, vol. 143, pp. 49–53.
4. Maksimov, V.F., Vol'f, V., Vinokurov, T.A., et al., *Ochistka i rekuperatsiya promyshlennykh vybros*ov (Purification and Recuperation of Industrial Discharges), Moscow: Lesnaya promyshlennost', 1989.
5. Chaenko, N.V., Kornienko, V.L., Turenko, L.G., et al., *Zh. Prikl. Khim.*, 1989, vol. 62, no. 1, pp. 57–60.
6. Kolyagin, G.A. and Kornienko, V.L., *Khim. Interesakh Ustoich. Razv.*, 2000, vol. 8, pp. 803–807.
7. Andreozzi, R., Caprio, V., Insola, A., and Marotta, R., *Water Res.*, 2000, vol. 34, pp. 463–472.
8. Lunar, L., Sicilia, D., Rubio, S., and Perez-Bendito, D., *Water Res.*, 2000, vol. 34, pp. 1791–1802.
9. Aceituno, M, Stalikas, C.D., Lunar, L. et al., *Water Res.*, 2002, vol. 36, pp. 3582–3592.
10. Kornienko, G.V., Maksimov, N.G., Kornienko, V.L., and Pavlenko, N.I., *Khim. Interesakh Ustoich. Razv.*, 2002, vol. 10, pp. 321–324.
11. Dzhafarov, E.A., *Elektroosazhdenie, svoistva i primenenie dvuokisi svintsa* (Electrodeposition, Properties and Application of Lead Dioxide), Moscow: Nauka, 1967.
12. *Unifitsirovannye metody analiza vod* (Unified Methods of Water Analysis), Lur'e, Yu., Ed., Moscow: Khimiya, 1971.
13. Panizza, M., Bocca, C., and Cerisola, G., *Water Res.*, 2000, vol. 34, pp. 2601–2605.
14. Iniesta, J., Michaud, P.A., Panizza, M., et al., *Electrochim. Acta.*, 2001, vol. 46, pp. 3573–3578.
15. Montilla, F., Michaud, P.A., Morallon, E., et al., *Electrochim. Acta.*, 2002, vol. 47, pp. 3509–3513.
16. Kornienko, G.V., Chaenko, N.V., and Kornienko, V.L., *Khim. Interesakh Ustoich. Razv.*, 2006, vol. 14, pp. 23– 26.
17. Lunar, L., Sicilia, D., Rubio, S., et al., *Water Res.*, 2000, vol. 34, pp. 3400–3412.

ISSN 1070-4272, Russian Journal of Applied Chemistry, 2008, Vol. 81, No. 8, pp. 1369–1374. © Pleiades Publishing, Ltd., 2008.
Original Russian Text © I.M. Lipatova, N.V. Losev, 2008, published in Zhurnal Prikladnoi Khimii, 2008, Vol. 81, No. 8, pp. 1290–1295.

PROCESSES AND EQUIPMENT OF CHEMICAL INDUSTRY

Chemical Effects of Hydroacoustic Treatment in Starch Hydrogels

I. M. Lipatova and N. V. Losev

Institute of Solution Chemistry, Russian Academy of Sciences, Ivanovo, Russia

Received December 27, 2007

Abstract—Energetic efficiency of application of a hydroacoustic treatment in a rotary-pulsatory apparatus in initiation or acceleration of chemical processes in starch hydrogels was studied. The contribution of the acoustic and shear components of this treatment to the activation of systems under study was evaluated for the example of destruction, acid hydrolysis, and oxidation of gelatinized starch.

DOI: 10.1134/S1070427208080107

The most efficient and, at the same time, less studied among the physical methods used to intensify technological processes in liquid media is the hydroacoustic treatment (HA treatment) in rotary apparatus with a pulsating flow. The main distinctive design feature of apparatus of this kind is the existence of alternating immobile and rotating revolution bodies with a common axis, which are perforated on their periphery to produce slits and openings. The most important factors affecting the structure of liquid polymeric materials being treated in hydroacoustic apparatus are ultrasonic pulsations and, accordingly, cavitation, as well as the high shear stresses to which the fluid is subjected in narrow (0.1–0.5 mm) gaps between the rotor and stator members [1, 2].

The scientific and special literature reflects the most extensively the applied and theoretical aspects of the liquid-phase hydroacoustic dispersion and homogenization [2, 3]. Comparatively recently there appeared reports devoted to application of HA apparatus for acceleration of homogeneous and heterogeneous chemical processes in systems with low-molecular-weight reagents and a low-viscosity medium [4, 5]. In the opinion of the authors of these studies, the main activating factor for systems of this kind is ultrasonic cavitation. In our previous studies, we demonstrated for the first time the possibility of using the HA treatment for initiation or acceleration of chemical processes in starch hydrogels and suggested that, in the case of viscous polymeric systems, an important contribution to the activation is made by high shear stresses [6–8].

The aim of this study was to find an approach to prognostication of the chemical effects of the HA treatment in starch hydrogels on the basis of the imparted mechanical energy, with account of the viscosity of the medium, and to evaluate the contribution of the acoustic and shear components of this treatment to the activation of the systems under study. The problem was to be solved using experimental data previously obtained in studies of the effect of the HA treatment on the dissolution [6], destruction [7], and acid hydrolysis [8] of gelatinized starch, as well as new data on mechanically activated oxidation of starch by various oxidizing agents.

EXPERIMENTAL

Corn starch served as the object of study. Starch hydrogels were prepared by thermal treatment of starch suspensions on a water bath at $T = 90°C$ for 15 min.

The starch hydrogels were treated in a laboratory rotary-pulsatory apparatus (RPA) with a set of replaceable rotors. The average gap between the rotating and immobile members of the working chamber was 0.3 mm. The rotor rotation rate was varied within the range 1000–5000 rpm, to which corresponded the shear rate gradient range $(0.5–17.4)\times10^4$ s^{-1}.

The ultrasonic treatment of the starch hydrogels was performed in a UZDN-2T disintegrator at a frequency of 22 kHz. The exposure time was varied from

Table 1. Effect of the concentration of starch in hydrogels on the rate of its oxidation by various oxidizing agents under a hydroacoustic treatment ($\gamma = 1.1\times10^5$ s^{-1}, $T = 40$°C)

c, wt %	$S_2O_8^{2-}$			MnO_4^-			$Cr_2O_7^{2-}$		
	$k\times10^4$	$k_A\times10^2$	k/k_A	k	k_A	k/k_A	$k\times10^5$	$k_A\times10^3$	k/k_A
	s^{-1}			M^{-1} s^{-1}			s^{-1}		
0.3	–	–	–	0.04	12.81	320	5.20	9.98	192
1	0.83	2.36	284	0.45	106.2	236	6.29	7.05	112
2	1.33	1.50	113	0.89	101.1	113	12.50	5.25	42
3	2.30	1.65	72	1.44	93.64	65	12.06	3.16	38
4	2.97	1.84	62	1.96	98.45	50	11.81	3.66	31
5	4.26	2.90	68	2.71	94.73	35	11.46	2.26	26
6	2.36	1.72	73	3.05	94.55	31	11.29	1.86	21
7	1.26	1.32	105	3.78	94.5	25	–	–	–
8	1.30	1.60	124	–	–	–	–	–	–

5 to 60 s. The volume density of the acoustic power was 1.34 W cm^{-3}.

The amount of acoustic energy imparted to a liquid medium in its treatment in RPA or UZDN in unit time, characterized by the acoustic power, was determined by chemical dosimetry with the standard test systems [9].

The procedures for measuring the rates of mechanically initiated destruction of starch and mechanically activated acid hydrolysis were described in [7, 8]. The rate of starch oxidation reactions was measured by determining the loss of the oxidant concentration by the iodometric technique. To measure the rate of mechanically activated reactions, the reaction mixtures were prepared in number equal to that of points in the kinetic curve to be obtained. Each mixture was activated for a different time, after which a sample was immediately taken for analysis. The kinetic order of the reactions was determined graphically.

By the chemical effect of the HA treatment on polymer–solvent or polymer–solvent–reagent systems is understood either initiation of chemical processes that do not occur under ordinary conditions (mechanically initiated processes) or a change in the reaction rate, caused by mechanical activation (mechanically activated processes). As a measure of the chemical effect in the first case commonly serves the rate of the mechanically initiated process. For processes of the second group, i.e., those accelerated by the HA treatment, we use in this study the acceleration coefficients equal to the factor by which the reaction rate constant increases under mechanical activation (k_A/k).

We consider in this study reactions of oxidation of gelatinized starch as an example of mechanically activated processes. These reactions were performed in parallel in a thermostated working chamber of RPA and under ordinary conditions at the same temperature. We used potassium permanganate (6×10^{-4} M) and potassium bichromate (6×10^{-4} M) as oxidizing agents with the ionic mechanism of action, and ammonium persulfate (0.02 M) as an oxidizing agent with a radical mechanism of action.

In the oxidation of polysaccharides by the oxidizing agents used, the hydroxy groups of the glucopyranose units (mostly primary ones) are oxidized to carbonyl and carboxy groups, whose relative amounts depend on the process condition [10]. It should be noted that the oxidation of polysaccharides may also be accompanied by oxidative destruction of polymers. To estimate the extent of oxidative destruction, we measured the viscosity of hydrogels in parallel with measurements of the concentration of the oxidizing agent. In the case of potassium permanganate and bichromate, the viscosity data we obtained suggested that, under the chosen rather mild conditions (low oxidant concentrations and moderate temperatures), the oxidation occurs predominantly at hydroxy groups.

Table 1 lists values of k, k_A, and k_A/k at various starch concentrations in the hydrogels for the oxidation reactions under study. It is noteworthy that the nature of the dependence of the acceleration coefficients on the starch concentration in the hydrogels varies with the type of the oxidizing agent.

As can be seen in Table 1, the oxidation rate increases with the concentration of starch in hydrogels

under ordinary conditions when oxidizing agents with an ionic mechanism of action (potassium permanganate and bichromate) are used. However, the effect of reaction acceleration under mechanical activation, characterized by the ratio k_A/k, steadily decreases in this case.

When ammonium persulfate is used as a radical-forming oxidizing agent and the concentration of starch in hydrogels becomes higher, the reaction acceleration coefficient first decreases because of the mechanical treatment and then again starts to increase. A parallel viscometric monitoring demonstrated a substantial decrease in the viscosity of starch hydrogels in the course of the oxidation reaction. This indicates that the process occurs with predominance of oxidative destruction. The oxidative destruction is a process occurring with rupture of polymer backbones, and the probability of rupture increases under the action of deforming loads. Therefore, similarly to the case of the reaction of acid hydrolysis [8], the role of shear stresses in the chemical activation of starch increases as the polymer concentration and, accordingly, the viscosity of the hydrogels become higher.

The activation energy of the reactions under study decreased under mechanical treatment within an order of magnitude. For example, the activation energy of the reaction of interaction of starch in a 5% paste with ammonium persulfate was 86.9 kJ mol^{-1} under ordinary conditions and 17 kJ mol^{-1} under a hydroacoustic treatment.

The energy-related approach to the problem of prognostication of the chemical effects produced by HA treatment presumes that the following tasks should be accomplished. It is necessary reveal the decisive factors of the chemical activation of the system, determine the total amount of mechanical energy imparted to the reaction mixture, and, finally, to find how the chemical effect obtained depends on the amount of imparted mechanical energy.

To assess the role of the acoustic component of the HA treatment, it was appropriate to compare the mechanoacoustic yields of ultrasonic and hydroacoustic initiation of the same processes. The mechanoacoustic yield, equal to the number of initiated elementary events per 100 eV of absorbed acoustic energy, was calculated using the quantitative characteristics of processes of dissolution [6], depolymerization [7], and acid hydrolysis [8] and experimental values of the acoustic power W_{ac} (J s^{-1}) of ultrasonic and HA treatments. It was shown in [8] that, at a temperatures below 45°C and sulfuric acid concentrations in the range 0.03–0.15 M, the hydrolysis reaction does not occur under ordinary conditions, but proceeds at a measurable rate in the working chamber of RPA. Therefore, the process can be considered to be mechanically activated under the conditions specified and, consequently, its mechanoacoustic yield can be calculated by the formula

$$G = \frac{\Delta c_{RG} V N_A \times 100}{W_{ac} t \times 6.25 \times 10^{18}}, \quad (1)$$

where Δc_{RG} is the change in the concentration of terminal reducing groups in starch (M); V, volume of the working chamber of RPA (l); and t, treatment duration (s).

At higher temperatures, the process occurs even under ordinary conditions and can be regarded as mechanically activated in this case.

For a mechanically activated physicochemical dissolution process, we used the number of elementary starch units in the polymer that passed into solution, with the amount of this polymer found from the increase in the concentration of the water-soluble fraction in activated hydrogels, ΔA (wt %) [6]:

$$G = \frac{\Delta A c V N_A \times 100}{10 \times 159 W_{ac} t \times 6.25 \times 10^{18}}, \quad (2)$$

where c is the concentration of starch in the hydrogels (wt %), and 159 is the molecular mass of the elementary unit of starch.

The mechanoacoustic yield of the destruction of gelatinized starch was calculated using the experimental data of [7] by the formula

$$G = \frac{10c\left(\frac{1}{P} - \frac{1}{P_0}\right) V N_A \times 100}{159 W_{ac} t \times 6.25 \times 10^{18}}, \quad (3)$$

where P_0 and P are the degrees of starch polymerization in the starting and activated hydrogels.

The data in Table 2 show that, at starch concentrations not exceeding the critical gelation concentration c_{cr}, the mechanoacoustic yields for the ultrasonic and HA treatments are close. At higher concentrations, the effect of the HA treatment starts to substantially exceed that of the ultrasonic field. This increase begins at a concentration corresponding to c_{cr} for the starting hydrogels (c_{cr} = 23 wt %) for processes involving destruction of the primary gel structure and at a concentration corresponding to c_{cr} of mechanically disintegrated starch hydrogels (c_{cr} = 5 wt %) for the chem-ical process (hydrolysis) [11]. Thus, it was found that, at c

Table 2. Effect of the starch concentration in hydrogels on the mechanoacoustic yield of varius processes under ultrasonic and hydroacoustic treatmets

c, wt %	Dissolution, number of units per 100 eV		Destruction		Acid hydrolysis	
			number of ruptures per 100 eV			
	UZDN	RPA	?UZDN	RPA	UZDN	RPA
1	1.79	1.85	0.020	0.018	0.270	0.279
2	2.35	2.52	0.030	0.028	0.252	0.311
3	2.70	2.75	0.033	0.032	0.204	0.212
4	2.46	3.20	0.030	0.045	0.075	0.075
5	2.12	3.48	0.021	0.057	0.070	0.123
6	1.98	3.81	0.015	0.062	0.061	0.187
7	–	4.22	–	0.065	–	0.220
8	–	4.60	–	0.075	–	0.252

$< c_{cr}$, ultrasonic cavitation is the main factor initiating and accelerating chemical and physicochemical processes. At concentrations exceeding c_{cr}, the contribution of noncavitational mechanical factors becomes noticeable, and the most important among these factors is the unidirectional shear in radial gaps between the rotor and stator members.

The experimental data in Table 2 can be used to prognosticate the extent of the processes in question under ultrasonic or hydroacoustic treatment at low concentrations of starch hydrogels on the basis of the calculated or measured amount of imparted acoustic energy. As for the range of hydrogel concentrations corresponding to a joint treatment by cavitation and shear stresses, the data in Table 2 are only valid for the RPA design used in the apparatus. Of particular interest in this context was to find a correlation between the known or easily determinable characteristics of an arbitrary apparatus and a medium being treated, on the one hand, and the chemical effect produced by the treatment, on the other.

The energy-related approach to prognostication of treatment results, used in this study, is based on the assumption that the chemical effect in the case of a combined action of two basic factors, namely, ultrasonic cavitation and shear stresses in the radial gaps of the apparatus, are additively related to the total amount of mechanical energy imparted to the liquid medium in unit time. The intensity of supply of the acoustic energy in HA treatment, W_{ac}, was found in this study experimentally by the method of chemical dosimetry. The intensity of supply of the mechanical energy under shear stresses, W_τ, which is calculated as a product of the average shear stress by the shear rate, can be expressed in terms of the known RPA parameters, rotor rotation rate n (rpm), and dynamic viscosity of the medium being treated, μ (Pa s):

$$W_\tau = \frac{\pi^3 n^2 R_r^2 h(R_r + R_s)}{900\delta}\mu, \quad (4)$$

where R_r and R_s are the rotor and stator radii, respectively (m); δ, radial gap (m); and h, height of the rotor and stator slits (m).

An analysis of the experimental data demonstrated a strong dependence of the chemical effect of the HA treatment on the polymer concentration. Therefore, we studied how the magnitude of the chemical effect, g factor, depends on the intensity of supply of the total mechanical energy E_m (J) related to the starch concentration c (wt %) in a unit volume V of the hydrogel being treated (l):

$$g = \frac{E_m}{V \times 10c}. \quad (5)$$

It can be assumed that the product $V \times 10c$ is the mass of the polymer in the volume of the medium being treated, because, as the concentration of starch in the hydrogels varies from 1 to 8 wt %, the density of hydrogels varies from 1.005 to 1.036 g cm^{-3} (density of dry starch is 1.45 g cm^{-3}). Thus, the g factor describes the amount of mechanical energy supplied to unit mass of the polymer. Using expressions (1) and (2), we obtain

$$g = \frac{1}{V \times 10c}\left[W_{ac} + \frac{\pi^3 n^2 R_r^2 h(R_r + R_s)}{900\delta}\right]. \quad (6)$$

Figure 1a shows how the overall g factor calculated by Eq. (6) for the hydroacoustic treatment in RPA depends on the concentration of starch in the hydrogels being treated. At comparatively low concentra-

tions, the *g* factor decreases as the concentration increases, but at concentrations characterized by the formation of a 3*D* physical network of the starch hydrogel and a steep increase in viscosity, the situation changes. In this concentration range, the increase in the g factor because of the rapid rise in viscosity and, accordingly, in the intensity of energy supply exceeds its decrease caused by the increasing concentration of the polymer in solution. Curve *2* in Fig. 1a is the dependence of the *g* factor on the starch concentration for a hypothetic case in which only the acoustic (cavitational) component of the HA treatment is effective [here, the term "acoustic *g* factor" (g_{ac}) is used].

The concentration dependences of the chemical effects of the HA treatment of starch hydrogels, i.e., of the acceleration coefficients for the reactions of mechanically activated oxidation, are shown in Fig. 1b, and the rates of mechanically initiated destruction of starch and rate constants of the reaction of mechanically activated acid hydrolysis, in Fig. 1c.

It is noteworthy that the run of the concentration dependences for the processes occurring with rupture of skeletal bonds in starch macromolecules (mechanical destruction, acid hydrolysis, oxidative destruction) is symbate to that of the dependence of the same type for the overall *g* factor. For the concentration dependence of the rate of mechanically initiated destruction at low starch concentration, the symbasis to the concentration dependence of the *g* factor is disturbed. At concentrations of about 2 wt %, an extremal variation of the rate of mechanical destruction is observed. This can be understood as follows. In the starting hydrogel, the main part of starch is contained in swollen grains. At low starch concentrations, the efficiency of grain disintegration via collapse of cavitation bubbles decreases because of the probability factor. It is known that, for dispersions with low content of dispersed phase particles, the rate of their cavitation-induced diminution becomes lower as the concentration of these dispersions decreases [12]. The splitting of the swollen grains in starch hydrogels into finer fragments also favors the simultaneously occurring destructive processes. Possibly, it is this circumstance that is responsible for the lack of correlation between the rate of mechanical destruction and values of the *g* factor in low-concentration starch hydrogels.

A fundamentally different run is observed for the dependences corresponding to reactions between gelatinized starch and oxidizing agents with ionic mechanism of action. The conditions in which such reactions were performed were specially chosen so that the oxidation occurred at hydroxy groups. The acceleration coefficients for these reactions steadily decrease as the starch concentration grows, and the increase in viscosity with the concentration and the corresponding rise in the shear loads hardly affect the magnitude of the chemical effect. A comparative analysis of the curves in the figure demonstrated that the dependences of the chemical effects for the reactions involving pendant bonds are symbate to a similar dependence for the acoustic *g* factor.

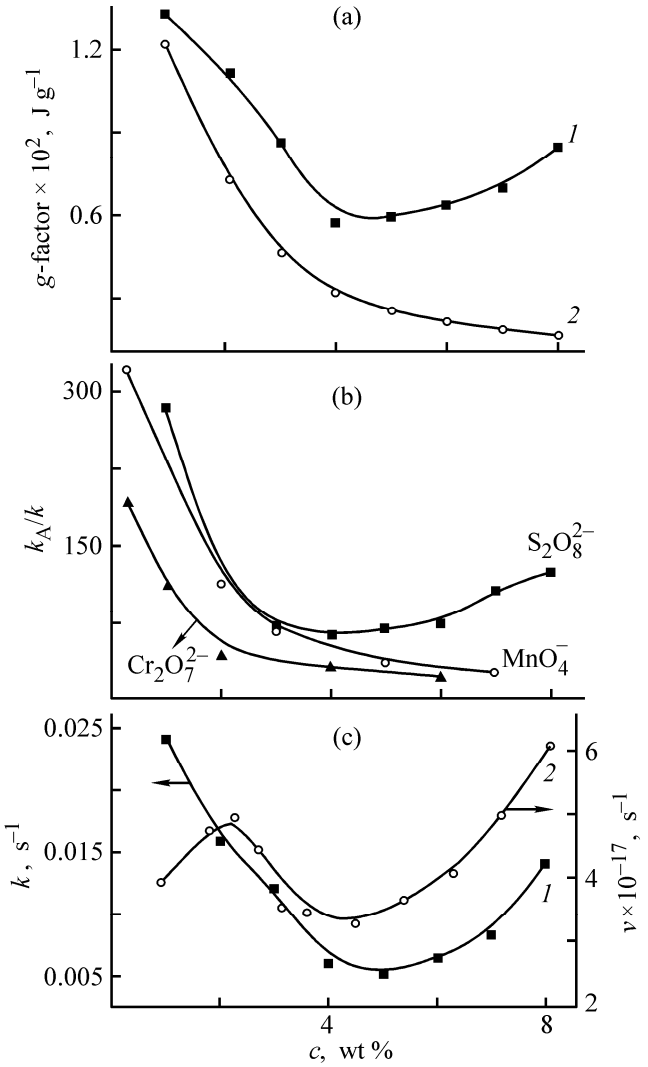


Fig. 1. (a) (*1*) Overall and (*2*) acoustic *g* factors, (b) acceleration coefficients k_A/k for reactions of oxidation by various oxidizing agents, and (c) (*1*) rate constants *k* of mechanically activated acid hydrolysis and (*2*) rate *v* of mechanically initiated destruction of gelatinized starch vs. its concentration *c* in hydrogels under a hydroacoustic treatment.

Thus, it was shown that prognostication of the chemical effects of an HA treatment in starch hydrogels is, in principle, possible. In the present stage of studies, the results obtained enable qualitative prognostication of changes in the chemical effects of an HA treatment, caused by changes in the polymer concentration or in the viscosity of the medium at a constant polymer concentration.

CONCLUSION

In the case of a hydroacoustic treatment of starch hydrogels, the rate of mechanically activated processes involving rupture of main-valence (skeletal) bonds is determined by the overall g factor (amount of total mechanical energy per unit mass of a polymer), and that of processes involving pendant groups, by the acoustic *g* factor.

REFERENCES

1. Gershgal, D.A and Fridman, V.M., *Ul'trazvukovaya tekhnologicheskaya apparatura* (Ultrasonic Technological Apparatus), Moscow: Energiya, 1976.
2. Balabyshko, A.M., Zimin, A.I., and Ruzhitskii, V.P., *Gidrodinamicheskoe dispergirovanie* (Hydrodynamic Dispersion), Moscow: Nauka, 1998.
3. Balabudkin, M.A., *Rotorno-pul'satsionnye apparaty v khimiko-farmatsevticheskoi promyshlennosti* (Rotary-Pulsatory Apparatus in Chemical-Pharmaceutical Industry), Moscow: Meditsina, 1983.
4. Badikov, Yu.V., Pilyugin, V.S., and Valitov, R.B., *Ispol'zovanie apparatov gidroakusticheskogo vozdeistviya v geterofaznykh protsessakh* (Use of Apparatus for Hydroacoustic Treatment in Heterophase Processes), Moscow: Khimiya, 2004.
5. Kurochkin, A.K., Smorodov, E.A., Margulis, M.A., and Badikov, Yu.V., *Zh. Fiz. Khim*., 1986, no. 4, pp. 893–897.
6. Lipatova, I.M., Yusova, A.A., and Moryganov, A.P., *Zh. Prikl. Khim*., 2000, vol. 73, no. 8, pp. 1372–1376.
7. Lipatova, I.M., Losev, N.V., and Yusova, A.A., *Zh. Prikl. Khim.*, 2006, vol. 79, no. 9, pp. 1548–1553.
8. Losev, N.V., Makarova, L.I., and Lipatova, I.M., *Zh. Prikl. Khim.*, 2003, vol. 76, no. 6, pp. 1025–1029.
9. Margulis, M.A., *Zvukokhimicheskie reaktsii i sonolyuministsentsiya* (Sound-Chemical Reactions and Sonoluminescence), Moscow: Khimiya, 1986.
10. Hasmon, R.E., *Starke*, 1971, no. 6, pp. 197–199.
11. Lipatova, I.M., Yusova, A.A., Blokhina, S.V., and Moryganov, A.P., *Zh. Prikl. Khim*., 2001, vol. 74, no. 9, pp. 1517–1521.
12. Matsievich, E.B. and Butyagin, P.Yu., *Kolloid. Zh*., 1958, vol. 20, no. 5, pp. 665–673.

ISSN 1070-4272, Russian Journal of Applied Chemistry, 2008, Vol. 81, No. 8, pp. 1375–1381. © Pleiades Publishing, Ltd., 2008.
Original Russian Text © A.A. Gaile, G.D. Zalishchevskii, A.S. Erzhenkov, L.L. Koldobskaya, 2008, published in Zhurnal Prikladnoi Khimii, 2008, Vol. 81, No. 8, pp. 1296–1302.

PROCESSES AND EQUIPMENT OF CHEMICAL INDUSTRY

Benzene Separation from the Benzene Fraction of Reformer Naphtha by Extractive Rectification with *N*-Methylpyrrolidone–Sulfolane Mixtures

A. A. Gaile, G. D. Zalishchevskii, A. S. Erzhenkov, and L. L. Koldobskaya

St. Petersburg State Institute of Technology (Technical University), St. Petersburg, Russia
Kirishinefteorgsintez Production Association, Limited Liability Company, Kirishi, Leningrad oblast, Russia

Received December 28, 2007

Abstract—Extractive rectification of the benzene fraction of reformer naphtha with *N*-methylpyrrolidone–sulfolane mixtures exhibiting synergistic effect was studied. After benzene separation, the distillate contains less than 1 vol % benzene and can be used as component of automobile gasolines.

DOI: 10.1134/S1070427208080119

In accordance with Euro-4 European specification for automobile gasolines, valid since 2005, the benzene content should not exceed 1 vol % [1]. At the same time, the major component of Russian automobile gasolines is reformer naphtha distilled in the range from the start of boiling to 180°C and containing 3–5 vol % benzene.

For large oil refineries producing more than 1.5 million tons of reformer naphthas annually, the most efficient way to reduce the benzene content of automobile gasolines is postfractionation of reformer naphtha, followed by benzene separation from the benzene fraction by extractive rectification [2]. The following selective solvents are used in industry for extractive rectification: *N*-methylpyrrolidone (N-MP) [3], *N*-formyl-morpholine (N-FM) [4], and Tektiv-100 mixed solvent [5].

The main drawback of highly selective solvents (sulfolane, N-FM, etc.) is their insufficiently high solvency toward hydrocarbons, leading to phase separation on trays of extractive rectification tower and to decreased efficiency of benzene separation.

To prevent phase separation of the system hydrocarbon feed–selective solvent, a method has been patented for arene separation from hydrocarbon mixtures by extractive rectification with N-FM, differing in that the process is performed at elevated pressures (up to 0.5 MPa) [6]. Elevated pressures lead to an increase in the temperature in the tower and in the solubility of saturated hydrocarbons in N-FM. However, the drawback of the method suggested is that the separation selectivity decreases due to the lower stability of π complexes of arenes with polar solvents at elevated temperatures.

The solvency of *N*-methylpyrrolidone is very high, so that the system on trays of the extractive rectification tower is homogeneous. This solvent, however, is less selective to arenes than sulfolane and N-FM.

The composition of Tektiv-100 mixed solvent has not been reported. However, as judged from the use of vacuum and high-pressure steam in the stripping tower for arene distillation, it contains high-boiling selective solvents like sulfolane regenerated by a similar procedure [7].

For example, a method has been patented for separation of arenes from hydrocarbon fractions by extractive rectification using a mixture of sulfolane with a cosolvent, alkylsulfolanes containing up to eight carbon atoms in the molecules [8]. This procedure has certain drawbacks: Use of high-boiling selective solvents (the boiling point of sulfolane is 285°C, and that of alkylsulfolanes is still higher) results in a high temperature in the extractive rectification tower and in the boiler and leads to a decrease in the separation selectivity; the high viscosity of the mixed solvent impairs the efficiency of trays and make smaller the number of theoretical plates of the extractive rectification tower; problems arise in solvent regeneration (need for high-

Table 1. Physicochemical and selective properties of solvents in benzene separation from mixtures with saturated hydrocarbons

Parameter	Sulfolane [7]	N-FM [4]	N-MP [3]
Boiling point,°C	285	244	202–204
Congealing point,°C	28.4	20–23	–24
Density at 30°C, g cm^{-3}	1.262	1.142	1.0217
Dynamic viscosity, cP:			
at 30°C	10.286	6.68	1.54
at 75°C	3.85	2.4	0.88
Heat capacity, J g^{-1} $(°C)^{-1}$:			
at 30°C	1.34	1.64	1.80
at 100°C	1.46	2.01	2.03
Enthalpy of vaporization at normal boiling point, kJ mol^{-1}	54.5	46.1	44
Limiting activity coefficients in solvents at 30°C:			
γ_h^0	71.9	42.0	14.1
γ_b^0	2.43	2.28	1.08
Selectivity γ_h^0/γ_b^0	29.6	18.4	13.1
Solvency $1/\gamma_b^0$	0.412	0.439	0.926
Performance criterion $(\gamma_h^0/\gamma_b^0)(1/\gamma_b^0)$	12.2	8.08	12.1

pressure steam generator and for a vacuum in the stripping tower); need for using a vacuum-producing system and a vacuum tower of increased diameter, compared to an atmospheric-ressure stripping tower, leads to larger capital outlays.

The above drawbacks can be eliminated by adding to a highly selective solvent a relatively low-boiling solvent with low viscosity and increased solvency toward hydrocarbons. As such solvent we chose N-MP, and as highly selective solvent, sulfolane.

The physicochemical and selective properties of these solvents are listed in Table 1. These data show that sulfolane is considerably more selective than N-MP toward the hexane–benzene model system, as indicated by the ratio of the limiting activity coefficients of these hydrocarbons in solvents, γ_h^0/γ_b^0. At the same time, N-MP shows higher solvency characterized by the quantity reciprocal to the limiting activity coefficient of benzene, $1/\gamma_b^0$. With respect to a combined performance criterion taking into account both the selectivity and solvency, sulfolane and N-MP differ insignificantly. The advantages of N-MP are the lower values of viscosity, enthalpy of vaporization, and congealing point.

EXPERIMENTAL

As feed we used the commercial benzene fraction 55–85°C recovered by distillation from reformer naphtha (boiling range from start of boiling to 180°C). The composition of the initial benzene fraction, determined by capillary gas–liquid chromatography, is given in Table 2.

Extractive rectification experiments were performed on a laboratory packed column operating in the batch mode, with a 15 TP efficiency. A definite amount of feed was charged into a boiler equipped with a thermometer and heated on an oil bath. In the upper part of the column we arranged a heated dropping funnel with the selective solvent. By heating the boiler and jacket, the column, was brought to the flooding state, after which the column operated for 10–15 min in the normal mode without distillate takeoff. Then we started to add dropwise the selective solvent preheated to 70–75°C and to take off distillate fractions. The rates of solvent feeding and distillate takeoff were determined by the preset solvent : feed ratio. For example, at a solvent : feed weight ratio of 2 : 1, with into account of the total con-

Table 2. Individual hydrocarbon composition of the benzene fraction, distillate, and aromatic concentrate

Hydrocarbon	T,°C	Benzene fraction	Distillate	Aromatic concentrate
		wt %		
Isobutane	–11.7	0.11	0.13	–
n-Butane	–0.5	0.25	0.35	–
Isopentane	27.9	1.30	1.80	–
n-Pentane	36.1	1.23	1.75	–
2,2-Dimethylbutane	49.7	0.34	0.50	–
Cyclopentane	49.3	0.08	0.13	–
2,3-Dimethylbutane	58.0	0.84	1.23	–
2-Methylpentane	60.3	7.27	10.45	–
3-Methylpentane	63.3	9.52	13.72	–
n-Hexane	68.7	17.57	25.56	–
Methylcyclopentane	71.8	8.88	12.83	–
Unidentified unsaturated hydrocabons	–	0.45	0.66	–
2,4-Dimethylpentane	79.2	6.64	9.60	–
Benzene	80.1	30.48	0.53	98.42
2,2,3-Trimethylbutane	80.9	0.06	0.10	–
3,3-Dimethylpentane	86.1	1.30	2.82	–
Cyclohexane	80.7	0.20	0.29	–
3-Methylhexane	90.1	5.69	8.10	0.01
2,3-Dimethylpentane	89.8	1.99	2.82	0.01
3-Methylhexane	91.9	4.20	6.02	0.01
cis-1,3-Dimethylcyclopentane	90.8	0.11	0.15	–
trans-1,3-Dimethylcyclopentane	91.7	0.33	0.48	–
trans-1,2-Dimethylcyclopentane	91.9	0.10	0.10	–
n-Heptane	98.4	0.60	0.85	0.05
Toluene	110.6	0.46	–	1.50

tent of arenes in the benzene fraction (about 31 wt%), the solvent : distillate weight ratio should be about 2.9 : 1.

In each experiment, we took several fractions of the distillate, determined their yield, and analyzed by GLC for the benzene content (the distillate fractions contained no toluene). The distillate takeoff was stopped when nearly the whole amount of nonaromatic hydrocarbons passed into the distillate (at calculated concentration of arenes in the aromatic concentrate of the bottom residue of 99.9 wt %). The aromatic concentrate was distilled-off from the bottoms with live steam.

Preliminary experiments for determining the possible synergistic effect and optimal composition of the mixed solvent were performed with technical-grade sulfolane containing 2.6 wt % water, anhydrous N-MP, and mixed selective solvents of various compositions, prepared by adding M-MP to technical-grade sulfolane. The water content of the initial sulfolane sample was determined from the congealing point, +8°C, corresponding to a water content of about 2.5 wt % [7], and then was refined by azeotropic distillation of water with benzene, using a Dean–Stark trap.

All the preliminary experiments on selective rectification were performed at the same weight ratio of the selective solvents and feed, 2 : 1 (Table 3).

The dependence of the degree of arene separation on the N-MP content of the mixed solvent, plotted according to data of Table 3, is shown in Fig. 1 (curve *1*).

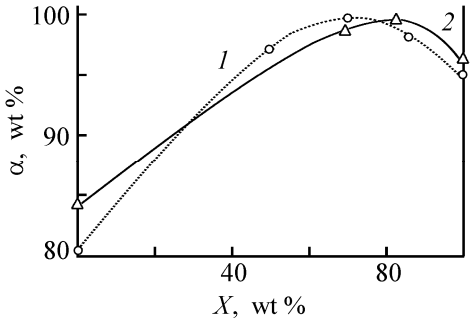


Fig. 1. Degree of arene separation α vs. N-MP content X of the mixed selective extractant, according to data of (*1*) Table 3 and (*2*) Table 4, run nos. 2–5.

Table 3. Results of benzene separation from the benzene fraction of reformer naphtha by extractive rectification with sulfolane containing 2.6 wt % water, *N*-methylpyrrolidone, and mixed solvents

Solvent composition, wt %			Boiler temperature,°C	Distillate yield, wt %	Takeoff of nonaromatic hydrocarbons with distillate, wt %	Arene content, wt %		Degree of separation, wt %	
Sulfolane	N-MP	water				distillate	bottoms	sum of arenes	benzene
97.4	–	2.6	190	84.98	99.97	8.05	99.92	80.5	80.18
–	100	–	170	70.59	99.97	2.18	99.91	95.0	94.95
48.7	50.0	1.3	145	69.94	99.97	1.28	99.93	97.1	97.07
29.22	70.0	0.78	140	69.1	99.97	0.07	99.93	99.9	99.9
14.61	85.0	0.39	150	69.6	99.97	0.80	99.93	98.2	98.17

Table 4. Results of benzene separation from the benzene fraction of reformer naphtha by extractive rectification with sulfolane, *N*-methylpyrrolidone, and mixed solvents

Run no.	Solvent composition, wt %			Solvent : feed weight ratio	Boiler temperature,°C	Distillate yield, wt %	Takeoff of nonaromatic hydrocarbons with distillate, wt %	Arene content, wt %		Degree of separation, wt %	
	sulfolane	N-MP	water					distillate	bottoms	sum of arenes	benzene
1	29.25	68.25	2.5	2:1	150	70.23	99.94	1.76	99.87	96.0	95.94
2	29.4	68.6	2.0	2:1	148	69.57	99.94	0.77	99.87	98.25	98.23
3	14.7	83.3	2.0	2:1	150	69.40	99.96	0.53	99.92	98.82	98.80
4	–	98.0	2.0	2:1	145	70.05	99.97	1.44	99.9	95.25	95.2
5	98.0	–	2.0	2:1	170	73.99	99.97	6.67	99.9	83.99	83.64
6	14.7	83.3	2.0	1.5:1	140	69.65	99.94	0.89	99.87	98.0	97.97
7	14.7	83.3	2.0	1:1	145	70.25	99.94	1.82	99.87	95.87	95.81

As follows from Table 3 and Fig. 1, the worst results in extractive rectification are obtained with technical-grade sulfolane, despite its highest selectivity to arenes. This may be due to the insufficient solvency of sulfolane, which leads to phase separation of the liquid in the extractive rectification column. With N-MP, which provides the homogeneity of the system with the hydrocarbons being separated, the process is more efficient. The best results are obtained on adding sulfolane enhancing the separation selectivity to N-MP in an amount with which the system is still homogeneous, namely, up to 30 wt % content of technical-grade sulfolane in the mixed solvent. At this composition, a synergistic effect is observed: The degree of arene separation, equal to 99.9 wt %, is considerably higher than with individual N-MP or with technical-grade sulfolane.

Previously, when developing a combined procedure for separating C_6–C_8 arenes from the 62–105°C fraction of reformer naphtha by extractive rectification followed by extraction of the benzene that partially gets to the distillate, we suggested to use in both steps mixtures of sulfolane with N-MP [9, 10]. In the extractive rectification step, we used a mixture of these solvents containing 30 wt % sulfolane, which showed a synergistic effect.

A change in the fractional composition of the feed could lead to a change in the optimal composition of the mixed solvent. However, it actually remained the same. This may be due to the effect of two factors acting in opposite directions. On the one hand, the major components of the benzene fraction of reformer naphtha are C_6 saturated hydrocarbons, which are better soluble in polar solvents than C_7–C_8 hydrocarbons, and, for homogenization of the system, it is sufficient to add smaller amounts of N-MP to ensure the system homogeneity (provided that the process temperature is the same). However, on the other hand, in separation of relatively low-boiling C_6 hydrocarbons, the temperature in the extractive rectification tower decreases, which leads to a decrease in the solubility of saturated hydrocarbons in polar solvents.

The optimal composition of mixed selective solvents also depends on their water content. Water is added to decrease the temperature in the low sections of the extractive rectification tower and in the stripping tower. This is necessary to make lower the probability of thermal and hydrolytic decomposition of the solvent and to perform the process at a moderate (about 10 atm) steam pressure.

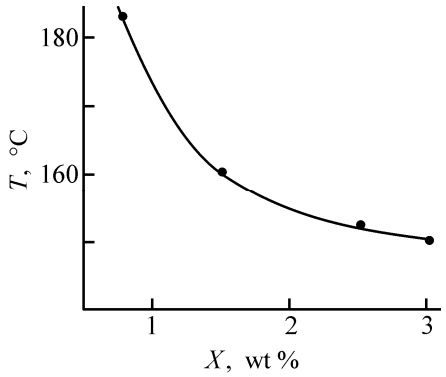


Fig. 2. Boiling point T of the mixed selective solvent sulfolane : N-MP = 30 : 70 (w/w) vs. its water content X.

The water content of the selective solvent should be chosen on the level at which the boiler temperature in the stripping tower does not exceed 165–170 °C, which corresponds to the normal boiling point of about 155 °C. To determine this level, we examined how the water content affects the boiling point of sulfolane–N-MP mixtures of the composition (30 : 70 wt %) providing a synergistic effect in extractive rectification (Fig. 2). The above condition is met at a water content as low as 2 wt %.

An increase in the water content of the mixed solvent to 2.5 wt % leads to a decrease in the degree of arene separation in extractive rectification to 96% against 98.25% at a water content of 2.0 wt % (Table 4, run nos. 1, 2). In the process, the benzene concentration in the distillate increases to 1.76 wt %, which exceeds the permissible level of 1 vol %. Thus, an increase in the water content of the mixed solvent to 2.5 wt % is undesirable, as it would require an increase in the solvent-to-feed ratio.

The synergistic effect was revealed for the mixed solvent sulfolane : N-MP = 30 : 70 wt % containing 0.78 wt % water. An increase in the water content to 2.0 wt % may somewhat alter the optimal composition of the solvent. To refine this composition, we performed experiments with solvents containing 2 wt % water, both individual and mixed with various sulfolane : N-MP ratios (Table 4, run nos. 2–5).

Figure 1 shows that the optimal composition of the mixed solvent containing 2 wt % water shifts toward a higher N-MP content (85 wt % N-MP–15 wt % sulfolane). In this case, the synergistic effect in extractive rectification is manifested to the greatest extent.

Table 5. Relative fugacity coefficients of the heptane–benzene system in the presence of selective solvents (solvent : hydrocarbons weight ratio 2 : 1)

Solvent composition, wt %			T, °C	Heptane content, mol %		Phase equilibrium constants		$\alpha = K_{hp}/K_b$
sulfolane	N-MP	water		in liquid phase, X_{hp}	in vapor phase, Y_{hp}	K_{hp}	K_b	
98.0	–	2.0	98	55.20	70.8	1.28	0.65	1.97
83.3	14.7	2.0	103	54.32	73.3	1.35	0.58	2.33
63.7	34.3	2.0	105	60.00	74.69	1.24	0.63	1.96

Experiments aimed to determine the minimal ratio of the mixed selective solvent to the feed, providing recovery of commercial benzene and its content in the distillate not exceeding 1 vol %, were performed with the solvent of the optimal composition, sulfolane : N-MP : water = 14.7 : 83.3 : 2.0 wt % (Table 4, run nos. 3, 6, 7).

At the solvent-to-feed ratio decreased to 1.5 : 1, fairly pure arenes can be obtained at the benzene content of the distillate less than 1 vol %. Further decrease in the solvent-to-feed ratio to 1 : 1 by weight (0.7 : 1 by volume) leads to a considerable decrease in the degree of benzene separation and to an increase in its content in the distillate over 1 vol %.

The individual hydrocarbon composition of the distillate and aromatic concentrate obtained by extractive rectification with the mixed selective solvent N-MP–sulfolane of the optimal composition (Table 4, conditions of run no. 3) is given in Table 2.

The total content of saturated hydrocarbons in the aromatic concentrate is as low as 0.08 wt %, and all these impurities are C_7 alkanes with boiling points higher than that of benzene. By fractional distillation of the aromatic concentrate, 99.9 wt % pure benzene and ~99 wt % pure toluene were obtained. The aliphatic distillate formed meets the modern requirements to gasolines with respect to the benzene content.

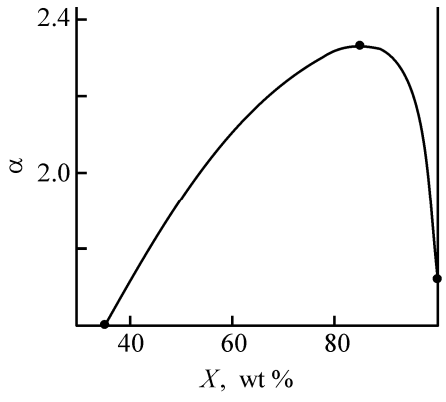


Fig. 3. Relative fugacity coefficient α of the heptane–benzene system vs. the N-MP content X of the mixed selective extractant sulfolane–N-MP–water.

The synergistic effect for the mixed selective solvent sulfolane–N-MP containing 2 wt % water was confirmed by studying the liquid–vapor equilibrium by the circulation method with a modified Othmer device [11]. At 2 : 1 weight ratio of the selective solvent and heptane–benzene model system, we determined the phase equilibrium constants for heptane (K_{hp}) and benzene (K_b) and calculated the relative fugacity coefficients (Table 5). As follows from Table 5 and Fig. 3, the relative fugacity coefficient of the heptane–benzene system is at maximum in the presence of the mixed solvent sulfolane–N-MP–water of the composition 14.7 : 83.3 : 2.0 wt%, which showed the best performance in benzene separation by extractive rectification.

CONCLUSIONS

(1) The mixed selective solvent sulfolane–*N*-methylpyrrolidone–water containing about 15–30 wt % sulfolane and 0.8–2.0 wt % water shows a synergistic effect in benzene separation from the benzene fraction of reformer naphtha by extractive rectification, which provides a higher degree of benzene separation, compared to sulfolane and *N*-methylpyrrolidone taken separately.

(2) The maximal relative fugacity coefficient of the heptane–benzene system, $\alpha = 2.33$, at the solvent to hydrocarbons weight ratio of 2 : 1 corresponds to the optimal composition sulfolane : *N*-methylpyrrolidone : water = 14.7 : 83.3 : 2.0 wt %.

(3) A decrease in the benzene content from 30–31 wt % in the benzene fraction of the reformer naphtha to the level below 1 wt % is provided at the weight ratio of the mixed selective solvent to the feed of 1.5 : 1 and 15 TP performance of the extractive rectification tower.

REFERENCES

1. Kaminskii, E.F. and Khavkin, V.A., *Glubokaya pererabotka nefti: tekhnologicheskii i ekonomicheskii aspekty* (Deep Oil Refining: Technolgical and Economic Aspects), Moscow: Tekhnika, 2001.
2. Mirimanyan, A.A., Vikhman, A.G., Maryshev, I.B., et al., *Mir Nefteprod.*, 2006, no. 5, pp. 26–27.
3. Gaile, A.A. and Zalishchevskii, G.D., *N-Metilpirrolidon: Poluchenie, svoistva i primenenie v kachestve selektivnogo rastvoritelya* (*N*-Methylpyrrolidone: Production, Properties, and Use as Selective Solvent), St. Petersburg: Khimizdat, 2005.
4. Gaile, A.A., Somov, V.E., and Zalishchevskii, G.D., *Mor-folin i ego proizvodnye. Poluchenie, svoistva i primenenie v kachestve selektivnykh rastvoritelei* (Morpholine and Its Derivatives. Production, Properties, and Use as Selective Solvents), St. Petersburg: Khimizdat, 2007.
5. Gentry, J.K., Kumar, K.S., Li, H.M., and Li, I.H., *Khim. Tekhnol. Topl. Masel*, 2003, nos. 1–2, pp. 12–17.
6. FRG Patent 2 005 648.
7. Gaile, A.A., Somov, V.E., Varshavskii, O.M., and Semenov, L.V., *Sul'folan: Svoistva i primenenie v kachestve selektivnogo rastvoritelya* (Sulfolane: Properties and Use as Selective Solvent), St. Petersburg: Khimizdat, 1998.
8. Int. Patent 0 183 642.
9. Gaile, A.A., Zalishchevskii, G.D., Gafur, N.N., et al., *Khim. Tekhnol. Topl. Masel*, 2004, no. 3, pp. 10–13.
10. Zalishchevskii, G.D., Gaile, A.A., Yakovlev, A.A., et al., *Neftepererab. Neftekhim.*, 2004, no. 9, pp. 31–34.
11. Hala, E., Pick, I., Fried, V., and Vilm, O., *Vapour–Liquid Equilibrium*, London: Pergamon, 1958.

ISSN 1070-4272, Russian Journal of Applied Chemistry, 2008, Vol. 81, No. 8, pp. 1382–1385. © Pleiades Publishing, Ltd., 2008.
Original Russian Text © S.V. Chichkanov, A.I. Shamsullin, V.A. Myagchenkov, 2008, published in Zhurnal Prikladnoi Khimii, 2008, Vol. 81, No. 8, pp. 1303–1306.

PROCESSES AND EQUIPMENT OF CHEMICAL INDUSTRY

Effect of Water-Soluble Polymeric Additives on Energy Expenditure in Transportation of Water–Oil Systems in Turbulent Mode

S. V. Chichkanov, A. I. Shamsullin, and V. A. Myagchenkov

Kazan State Technological University, Kazan, Tatarstan, Russia

Received September 26, 2007

Abstract—New installation of the circulation type was used to perform a joint analysis of rheological and energy parameters of turbulent flows of water and water–oil media in the presence of polymeric additives of anionic copolymers of acrylamide. Copolymers with varied molecular mass were produced by ultrasonic destruction of a starting high-molecular-weight sample of the polymer under mild conditions. The effect of the molecular mass of the polymer additive on the specific energy expenditure in the case of circulation of water–oil media in the turbulent mode was analyzed.

DOI: 10.1134/S1070427208080120

The effect of a decrease in the hydraulic resistance of a turbulent flow of a fluid in the presence of small doses of polymer additives (<0.001%) has been known for a rather long time. The first results of experiments of this kind were reported as far back as 1948 by Toms [1]. Since that time the interest of numerous researchers has been concentrated on this unusual and, in a sense, paradoxical phenomenon. The paradoxicality consists in that, upon introduction of minor concentrations of a polymer into a turbulent flow, its velocity increases, rather than decreases (as is the case in a laminar flow). This occurs because the hydraulic resistance becomes lower, which leads to an increase in the flow velocity and fluid flow rate, decrease in the pressure difference at pipeline ends, etc. Naturally, this effect has found wide use in various industries associated with high-speed pipeline transportation of large volumes of fluids and, in particular, in the oil industry in pipeline transportation of water, oil, oil products, and oil emulsions [2].

When attempting to practically use the Toms effect in real pipeline transport objects, it is necessary to take into account a number of specific technological features. This is primarily due to the fact that, upon introduction of a polymeric additive into a turbulent flow of a fluid in real systems, the effect can be manifested in several ways [3, 4]: (i) an increase in the fluid flow rate at a constant pressure in the pipeline and constant load on the drives of transfer pumps, (ii) a decrease in the pipeline pressure at a constant fluid flow rate, and (iii) a decrease in the load on the drives of transport pumps.

In view of the fact that, in most cases, the fluid flow rate and the pumping pressure remain invariable, the expected positive effect of introduction of a polymeric additive is that the energy consumption by the transport pumps per unit volume of the fluid being transported could decrease. Now, this circumstance becomes increasingly important because of the deficiency of electric power and a steady increase in its cost and 24/7 operation of pumping stations consuming an enormous amount of electric power in oil-producing regions of Russia. Therefore, even a minor decrease in the electric power consumed in high-speed transportation of water–oil media could become an important energy-saving factor making lower the cost of products transported by pipelines.

Analysis of published data shows that, in most cases, classical studies of the Toms effect are based on considering only the rheological aspects of the process (e.g., in motion of solutions in capillaries and pipes) [5, 6] or examining the structure of various zones of

turbulent flows of polymer solutions (laser Doppler anemometry) [7]. Owing to the vast experience of application of the Toms effect in oil industry and to the topicality of the problem, of particular interest are experimental studies in which the most important technological parameters of the pipeline transportation of fluids (e.g., fluid flow rate and electric power consumed for transportation of a unit volume of a fluid) serve as the main estimation characteristics.

In this study, we evaluated the efficiency of anionic copolymers of acrylamide as additives that can be used to raise the fluid flow rate and diminish the electric power consumed in a turbulent flow of water and water–oil media.

EXPERIMENTAL

To perform the experiment, we developed an installation of the circulation type, schematically shown in Fig. 1. A distinctive feature of this installation is its bifunctionality. First, the installation makes it possible to obtain dispersed systems of ?direct and inverse? types, using unit I. Second, this system can be used to perform extended tests of polymeric additives as agents reducing the hydraulic resistance ?of turbulent flows and energy expenditure for transportation of the fluids under study (in unit II).

As already noted, a topical issue are studies of the influence exerted by polymeric additives on the hydrodynamic and energy parameters of the processes of pipeline transportation of fluids. Therefore, a double monitoring of the fluid circulation in the limiting circuit was used in unit II: the fluid flow rate and the electric power consumed by the pump were simultaneously recorded.

The experimental procedure consisted in the following. To obtain 10 vol % direct emulsions of oil, calculated amounts of water, oil, and stabilizer (nonionogenic surfactant, Neonol AF9-10 in an amount of 1 vol % relative to the volume of oil) were charged into vessel *8*. Then the mixture was circulated by pump *1* over the small circuit through grid membrane unit *2* intended for additional disintegration of particles of the dispersed phase (oil). This way to obtain direct emulsions of oil guaranteed their high aggregative and sedimentation stability in the course of further experiments. After a certain interval of time, pump *1* was switched off. To study the rheological properties of fluids and energy parameters of turbulent flows, unit II was put to use. For this purpose, pump *4* was switched on and the fluid was circulated

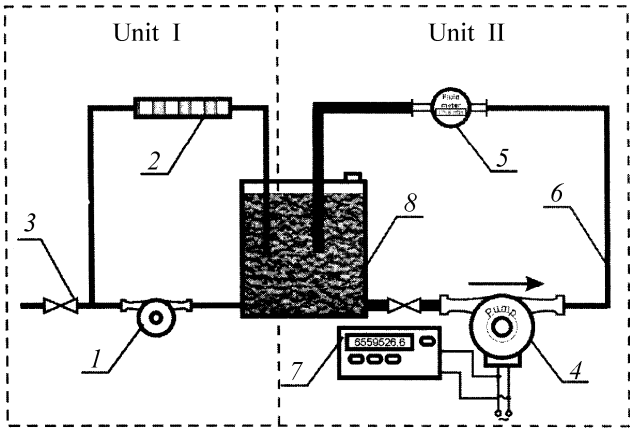


Fig. 1. Schematic of the installation used to prepare emulsions and to study the hydrodynamic and energy parameters of turbulent water and water–oil flows: (*1*) pump serving to produce emulsions, (*2*) grid membrane unit, (*3*) valve for dis-charging a spent emulsion, (*4*) centrifugal pump, (*5*) flow meter, (*6*) control pipeline (diameter 12 mm, length 15 m), (*7*) electricity supply meter, (*8*) working vessel with a fluid being analyzed.

through control pipeline *6* (inner diameter 12 mm, length 15 mm) made of reinforced polyethylene. In the course of circulation, the fluid flow rate was monitored with flow meter *5*, and the amount of electricity consumed by the pump in the course of circulation, with electricity supply meter *7*. It should be noted that the power of the pump provided a developed turbulent mode of fluid flow in the pipeline (Reynolds number for water was about 3×10^4).

It was appropriate to use as an indicator of the efficiency of a polymeric additive not simply a change in the fluid flow rate or in the electric power consumed by the pump, but a combined parameter: relative energy consumption by the pumping unit, ε, defined by

$$\varepsilon = E/E_0,$$

where E and E_0 are the specific energy consumptions by the pump [electric power consumption (kW h) in transportation of 1 m^3 of the fluid] in circulation of the fluid in the limiting circuit with and without a polymer additive, respectively.

To obtain samples of anionic copolymers of acrylamide with different values of M, we used the method of ultrasonic destruction (USD) of a starting sample of a statistical copolymer of acrylamide with sodium acrylate, with $M = 1.6 \times 10^6$ and content of ionogenic (acrylate) groups, $\alpha = 17.5$ mol%. By analogy with [8, 9], the USD of the copolymers was performed with a UZDN-1 device at a frequency of 22 kHz in

Modes of ultrasonic treatment of solutions and molecular masses of the copolymer samples being analyzed

Sample no.	Treatment duration, min	Ultrasonic power, W cm^{-2}	$[\eta p]$, cm g^{-1}	$M \times 10^{-6}$
1	–	–	662.2	1.61
2	5	1.0	561.1	1.32
3	5	4.0	504.6	1.15
4	6.5	7.9	303.9	0.62
5	7	11.8	223.3	0.42
6	8	15.2	96.7	0.15

the mild mode in a 0.2% aqueous solution, with varied power of the ultrasonic field and exposure time. The developed USD mode made it possible to obtain six copolymer samples with widely different molecular masses.

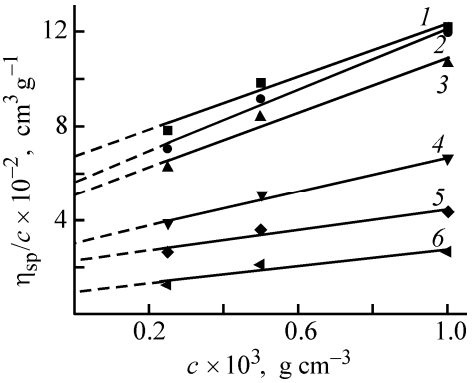


Fig. 2. Viscosity numbers η_{sp}/c in a 0.5 N NaCl solution vs. the concentration c of anionic copolymers of acrylamide (sample nos. 1–6), produced by ultrasonic destruction (see table).

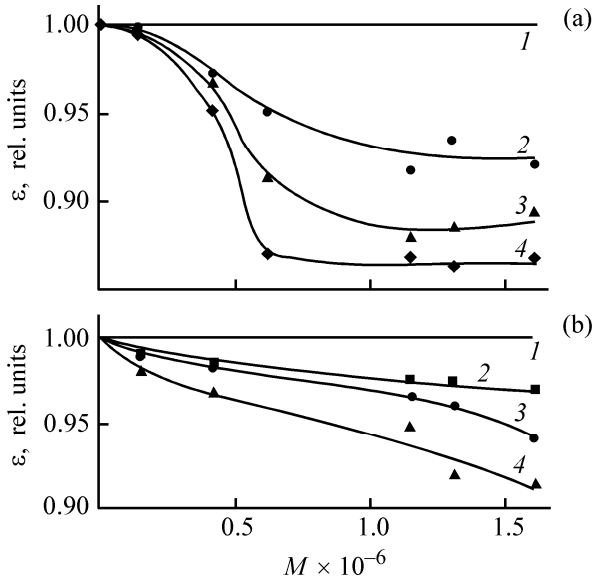


Fig. 3. Relative energy consumption ε vs. the molecular mass M of anionic copolymers in (a) water medium and (b) 10% direct emulsion of oil. Copolymer concentration c (kg m^{-3}): (*1*) 0, (*2*) 0.01, (*3*) 0.025, and (*4*) 0.05.

It should be particularly noted that the method chosen for obtaining samples with different molecular masses provided identity of all copolymer fractions in composition α and polydispersity [10, 11].

Values of the limiting viscosity numbers [η] were found by extrapolating the dependences $\eta_{sp}/c = f(c)$ in a 0.5 N NaCl solution to $c = 0$ (Fig. 2). The molecular masses M of the samples obtained were calculated using the Staudinger–Mark–Houwink equation:

$$[\eta] = KM^a,$$

where K and a are constants ($K = 0.0062$, $a = 0.81$) [12].

Generalized data on the USD process parameters and molecular masses of copolymer samples are listed in the table.

In the preliminary stage, experiments aimed to evaluate the rheological and energy parameters of turbulent flows in purely water flows were performed.

According to the data in Fig. 3a, the relative energy consumption by the pumping unit, ε, is lower than unity for all concentrations and molecular masses of the copolymers. This indicates that, in all of the experiments carried out, introduction of a polymeric additive leads to an increase in the fluid flow rate and this is not due to a rise in the electric power consumed by the pump (i.e., to an increase in the load on the pump). This circumstance is a very important argument indicating that the increase in the pipeline throughput is not due to any additional energy expenditure for maintaining the accelerated mode of fluid transportation.

It can also be seen in Fig. 3a that the parameter ε decreases as the molecular mass of the copolymer and its concentration in solution increase. In this case, the dependence $\varepsilon = f(c)$ is quite understandable [13, 14], whereas the run of the experimental dependence $\varepsilon = f(M)$ is less predictable [15] and, with account of difficulties in performing the experiments and interpreting their results, it required an additional elucidation. The point is that, with the commonly accepted procedure used to process the experimental data (effect evaluated by the gain in the fluid flow rate), the magnitude of the Toms effect gradually grows with the molecular mass [11]. At the same time, the dependences $\varepsilon = f(M)$ exhibit certain threshold values of the molecular masses of the polymers [~$(0.6–0.7) \times 10^6$], below which the polymer becomes inefficient as an agent reducing the relative energy consumption. This behav-

ior of the empirical dependences $\varepsilon = f(M)$ can be attributed to two circumstances. First, the dynamic viscosity of the solutions grows with M both in the flow core and in its near-wall zone, which leads to an increase in the energy consumption in transportation of the fluid. Second, macromolecules are subjected in the working zone of the pump and in the turbulent fluid flow in the pipeline to strong local stresses. In this mode of the fluid flow, a quite probable process is mechanical destruction of macromolecules, which is characteristic to a greater extent of polymer fractions with high molecular masses [16].

Let us now analyze the dependences $\varepsilon = f(M)$ for direct emulsions of oil (Fig. 3b). An important result can be noted for these emulsions (as also for water media): the rise in the fluid flow rate in the turbulent mode is not accompanied by any increase in the energy expenditure for circulation of the fluid.

Comparative analysis of the data in Figs. 3a and 3b suggests that, in turbulent flows and fixed values of c and M, the parameter ε for direct emulsions of oil exceeds that for purely water media. As regards the energy expenditure, these results indicate that the efficiency of the polymeric additive is lower in the oil emulsion, compared with the water medium. This is, in all probability, due to adsorption of polymer macromolecules on particles of the dispersed phase, which leads to a decrease in the real ("working") concentration of the polymer in the dispersion medium [17].

CONCLUSIONS

(1) A new experimental installation was suggested and tested. This installation makes it possible to use the volumetric flow rate of the fluid and the electric power consumed by the pump as complex estimation parameters.

(2) The method of ultrasonic destruction was used to obtain samples of anionic copolymers of acrylamide, with different molecular masses and identical composition and polydispersity characteristics.

(3) The dependence of the relative energy consumption by the pumping unit on the concentration and molecular mass of the polymer additive in both water and oil-containing media (direct emulsions of oil) was analyzed.

REFERENCES

1. Toms, B.A., *Proc. 1st Int. Congr. Rheol.*, vol. 2, Amsterdam, 1948, pp. 135–141.
2. Poraiko, I.N., *Primenenie poliakrilamida v technologicheskikh protsessakh, svyazannykh s dobychei nefti: Tematicheskii nauchno-tekhnicheskii obzor* (Use of Polyacryalamide in Technological Processes Employed in Oil Production: Topical Sci.-Techn. Review), Moscow: VNIIOENG. 1974.
3. Ivanenkov, V.V. and Pimenov, O.V., *Transp. Khran. Nefteprod.*, 2006, no. 2, pp. 3–7.
4. Akhmadullin, K.R., Khazhnev, R.Kh., Matchin, V.K., and Galleev, I.M., *Transp. Khran. Nefteprod.*, 2006, no. 4, pp. 3–7.
5. Escudier, M.P., Presti, F., and Smith, S., J. *Non-Newton Fluid Mech.*, 1999, vol. 81, no. 3, pp. 197–213.
6. De Guzman Manuel, R., Takashi, S., Hiromoto, U., and Tatsuo, N., *J. Chem. Eng. Japan*, 1999, vol. 32, no. 4, pp. 402–408.
7. Donohue, G.L., Tiederman, W.G., and Reischman, M.M., *J. Fluid Mech.*, 1972, vol. 56, pp. 559–575.
8. Myagchenkov, V.A. and Krikunenko, O.V., *Vysokomol. Soedin., Ser. A*, 1995, vol. 37, no. 1, pp. 44–49.
9. Myagchenkov, V.A., Panarin, E.F., Yunusov, O.A., et al., *Dokl. Akad. Nauk SSSR*, 1992, vol. 324, no. 4, pp. 826–829.
10. Myagchenkov, V.A. and Frenkel', S.Ya., *Kompozitsionnaya neodnorodnost' sopolimerov* (Compositional Inhomogeneity of Copolymers), Leningrad: Khimiya, 1988,
11. Myagchenkov, V.A., Chichkanov, S.V., Proskurina, V.E., and Myagchenkov, A.V., *Zh. Prikl. Khim.*, 2002, vol. 75, no. 9, pp. 1517–1520.
12. Myagchenkov, V.A., Krikunenko, O.V., and Churikov, F.I., *Ul'trazvukovaya destruktsiya vodorastvorimykh (so) polimerov* [Ultrasonic Destruction of Water-Soluble (Co)polymers], Kazan: Kazan. Khim.-Tekhnol. Inst., 1998.
13. Povkh, I.L. and Stupin, A.B., *Inzh.-Fiz. Zh.*, 1972, vol. 22, no. 1, pp. 59–65.
14. Manzhai, V.N., Echevskaya, L.G., Ilyushnikov, A.V., et al., *Zh. Prikl. Khim.*, 2004, vol. 77, no. 3, pp. 456–460.
15. Martischius, F. and Heide, W., *Drag Reduct. 3rd Int. Conf., Bristol, July 2–5, 1984*, Bristol, 1984, D9/1–D9/3.
16. Baramboim, N.K., *Mekhanokhimiya vysokomolekulyarnykh soedinenii* (Mechanochemistry of Macromolecular Compounds), Moscow: Khimiya, 1971.
17. Chichkanov, S.V., Shamsullin, A.I., and Myagchenkov, V.A., *Inzh.-Fiz. Zh.*, 2007, vol. 80, no. 3, pp. 155–163.

ISSN 1070-4272, Russian Journal of Applied Chemistry, 2008, Vol. 81, No. 8, pp. 1386–1389. © Pleiades Publishing, Ltd., 2008.
Original Russian Text © E.R. Guseinov, 2008, published in Zhurnal Prikladnoi Khimii, 2008, Vol. 81, No. 8, pp. 1307–1310.

PROCESSES AND EQUIPMENT OF CHEMICAL INDUSTRY

Extraction Method for Purification of Industrial Aluminate-Alkaline Solutions To Remove Iron Impurities

E. R. Guseinov

Institute of Chemical Problems, National Academy of Sciences of Azerbaijan, Baku, Azerbaijan

Received July 25, 2007

Abstract—Extraction of iron from aluminate-alkaline solutions was studied in relation to the concentration of the extracting reagent, 2-hydroxy-5-alkyl(C_8–C_9)benzyldiethanolamine and the volume ratio between the aqueous and organic phases. The re-extraction conditions were determined.

DOI: 10.1134/S1070427208080132

At present, extraction is the most important among the best known methods used to concentrate and separate metals from various complex compositions. The intensive manufacturing application of the extraction technique and the rather effective use of extraction processes in a number industries recovery of precious metals from industrial raw materials make profitable and cost-efficient and enable development of rational technological schemes for separation of metals with close physicochemical properties, which is now a rather topical issue for modern hydrometallurgy.

A promising field of hydrometallurgy is recovery of metals from alkaline solutions. However, concentration of metals from solutions of this kind and their further processing is rather labor-consuming and inefficient, which leads to loss of valuable components. In addition, the lack of effective and available extractants that could recover metals from strongly alkaline solutions hinders wide use of the extraction technique for recovery and concentration of metals from products with a complex salt composition and, in particular, from aluminate-alkaline solutions. This technique could simultaneously solve a no less important problem of purification of the final product (alumina) to remove iron impurities.

Thus, a search for, and synthesis of the most accessible extraction reagents and development on this basis of sufficiently efficient and selective methods for recovery and separation of metals from alkaline solutions with a complex composition constitute a rather topical task of extraction chemistry.

This communication reports results obtained in studies of extraction purification of industrial aluminate-alkaline solutions, formed in manufacture of alumina to remove iron impurities present in these solutions, to give a gallium concentrate and pure alumina. A technological scheme that provides integrated processing of solutions with complex salt composition for hydrometallurgical purposes was developed and suggested.

One of the main impurities in gallium-containing technological solutions is iron [1, 2], which is present in oxidation states II and III, or in a mixture of these. In most cases, the concentration of iron is many times that of gallium [3, 4]. In the alkaline technique for production of alumina from alunites or bauxites, there is a special technological unit for purification of aluminate-alkaline solutions to remove iron impurities. Therefore, it is necessary to briefly analyze the level of understanding of methods for purification of these solutions, produced by alkaline treatment of basic ores in manufacture of alumina.

At present, this process is performed using classical methods, which have a rather low efficiency and fail to provide the required degree of purification of

Purification of aluminate-alkaline solutions to remove iron impurities with 2-hydroxy-5-alkyl(C_8–C_9)benzyldiethanolamine in kerosene in relation to its concentration and volume ratio between the aqueous and organic phases

$V_{aq} : V_{org}$	Degree of purification* (%) at indicated concentration of the extraction reagent, M									
	0.2		0.3		0.4		0.5		0.6	
	I	II	I	II	I	II	I	II	I	II
0.5 : 1	70.0	81.0	80.0	88.0	83.0	93.0	83.0	94.0	83.0	95.0
1 : 1	82.0	92.0	95.0	100	96.0	100	97.0	100	96.5	100
1.5 : 1	80.0	91.0	94.0	100	95.0	100	95.5	100	95.0	100
2 : 1	79.0	89.0	93.0	100	93.5	100	94.0	100	94.0	100
4 : 1	74.0	85.0	90.0	95.5	91.0	98.5	91.0	99.0	90.0	99.0
10 : 1	70.5	80.0	84.7	94.0	86.0	97.0	86.0	97.2	85.5	96.0

* In stages I and II of the extraction process.

aluminate-alkaline solutions, and, therefore, the quality of the final product obtained is low. One of methods for purification of aluminate-alkaline solutions to remove iron impurities is that by treatment with gas–air mixtures, e.g., by ozone, air, or ozonized air [5]. The treatment time is 3–8 h. As a result the Fe_2O_3 concentration decreases from 0.018 to 0.0018 g l^{-1}, with the degree of purification equal to 90%. A disadvantage of this method is the long duration of the process itself and the low degree of purification. In a method used to purify aluminate-alkaline solutions to remove ion impurities [6], chromium-containing materials and, in particular, chromium(III) oxide Cr_2O_3 are used as reagents. The starting aluminate-alkaline solution containing 0.018 g l^{-1} is mixed with chromium(III) oxide, taken in an amount of 1 mol per 2/3 mol Fe_2O_3, at 95°C for 20 min. After a prolonged settling, 0.002 g l^{-1} of iron remains in solution, i.e., the degree of purification is 89%.

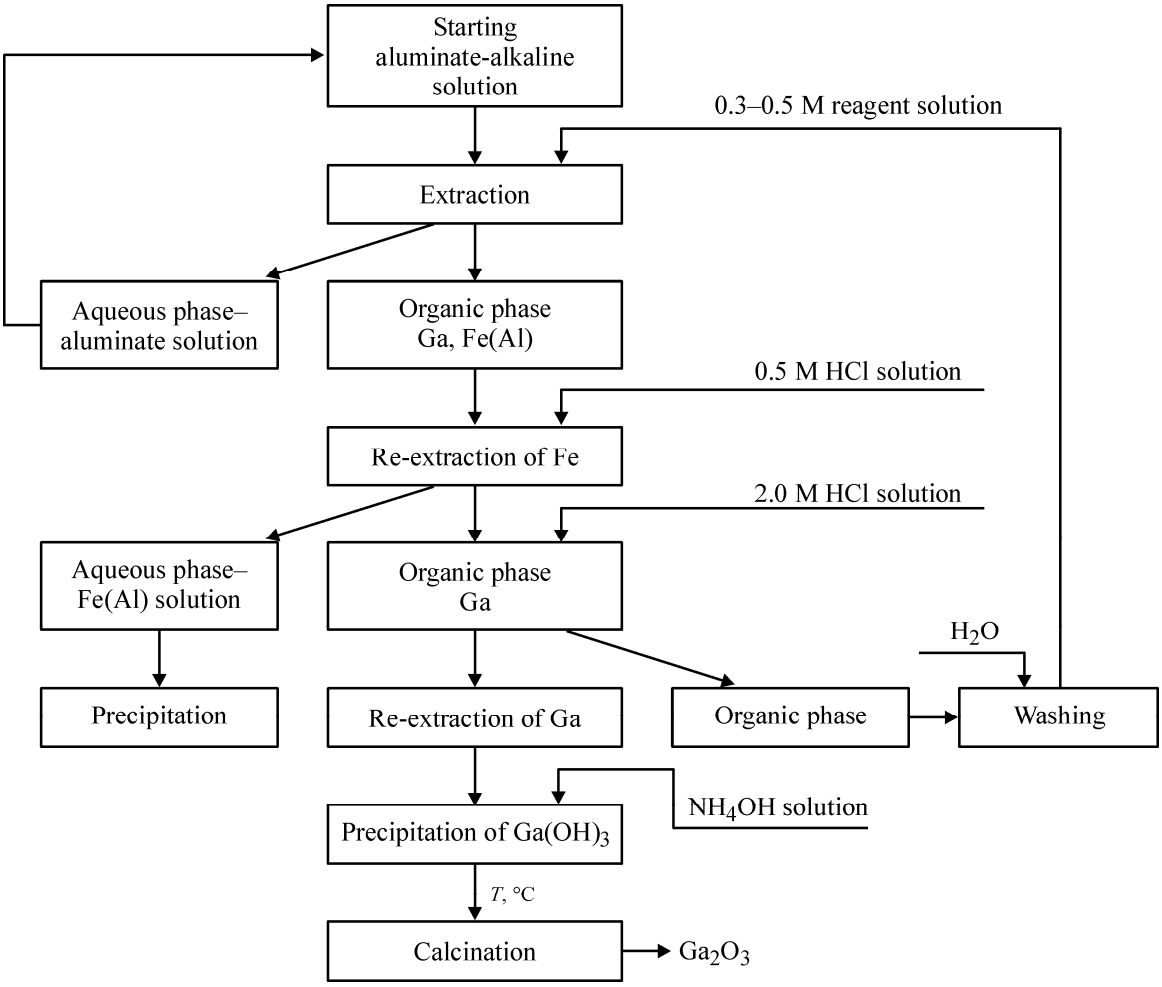
The most widely used method for purification of aluminate-alkaline solutions to remove iron impurities is treatment with calcium oxide CaO with addition of sodium sulfite [7]. This method consists in that 2.5 g l^{-1} calcium oxide and 0.5–10.0 g l^{-1} sodium sulfite are introduced into a solution containing (g l^{-1}): Na_2O 150, Al_2O_3 0.75, and iron in the form of Fe_2O_3 0.24. As a result, the Fe_2O_3 concentration in solution decreases to 0.003 g l^{-1}, which constitutes a 94% degree of purification of the starting solution. However, this method fails to provide solutions with a required purity, and, in addition, sodium sulfite contaminates aluminate-alkaline solutions with sulfur.

Because there is no published evidence about purification of aluminate-alkaline solutions to remove iron impurities by the extraction method, the previously studied extraction systems with aminomethylene derivatives of substituted phenols, used to remove iron from alkaline solutions [8], and the revealed optimal conditions of the extraction process make it possible, in principle, to solve a number of practical tasks.

In this communication, a technological scheme for purification of aluminate-alkaline solutions, formed in alumina production, to remove iron impurities by the extraction method, with 2-hydroxy-5-alkyl(C_8–C_9) benzyldiethanolamine in a kerosene diluent as the extraction agent. As object of study served industrial aluminate-alkaline solutions produced at Gyanja aluminum plant and having, prior to a purification cycle, the following composition (g l^{-1}): Na_2O 180–210, Al_2O_3 80–105, Fe_2O_3 0.45–0.50, Ga_2O_3 0.095–0.125. The solution under study was brought in contact with a 0.3–0.5 M solution of 2-hydroxy-5-alkyl(C_8–C_9) benzyldiethanolamine in kerosene at a (1–4) : 1 volume ratio between the aqueous and organic phases for 10–20 min. The phase separation in the settler was rather distinct and occured rather rapidly in the course of no more than 10–15 min. After the distinct phase separation, the residual content of iron in the aqueous solution was monitored.

Depending on the number of stages of the extraction process, the concentration of iron in the aluminate-alkaline solution decreases to a minimum, with a full purification reached (95–100% after two treatment stages). The spent extraction agent is easily regenerated by washing with a 0.1–0.5 M solution of hydrochloric acid and can be reused for purification of aluminate-alkaline solutions to remove iron impurities. The results obtained in purification of aluminate-alkaline solutions, formed in alumina production, to remove iron impurities are listed in the table.

As can be seen in the table, use of the extraction method for purification of aluminate-alkaline solutions to remove iron impurities makes it possible to raise



Technological scheme for purification of aluminate-alkaline solutions to remove iron impurities by the extraction method.

the degree of purification of solutions of this kind to 95–100%.

It should be noted that the conditions and aqueous medium of the extraction purification of aluminate-alkaline solutions with a representative of aminomethylene derivatives of substituted phenols, 2-hydroxy-5-alkyl(C_8–C_9)benzyldiethanolamine, in kerosene correspond to recovery of gallium from these solutions. Therefore, purification of aluminate-alkaline solutions to remove iron impurities under these conditions results in that gallium contained in these solutions is extracted into the organic phase together with iron. However, differences in the stability of the iron and gallium compounds being extracted in the organic phase enable their separation in the re-extraction stage. Therefore, iron and galium are re-extracted in the organic phase in stages. First, iron is completely re-extracted by treatment of the extract with a 0.5 M solution of hydrochloric acid, and then gallium readily passes from the organic phase into the aqueous stage in the subsequent cycle of re-extraction with a more concentrated 2.0 HCl solution. Further, gallium is precipitated from the re-extract with ammonium hydroxide and, after drying, the precipitated $Ga(OH)_3$ is calcined at 20–30°C to obtain the final product, gallium oxide.

The conditions of iron re-extraction with a 0.5 M HCl solutions are almost identical to those of aluminum re-extraction, which enables separation of gallium and these metals, iron and aluminum, in the re-extraction stage. Above is presented a technological scheme of the extraction recovery of gallium and purification of aluminate-alkaline solutions to remove iron impurities with 2-hydroxy-5-alkyl(C_8–C_9)benzyldiethanolamine in kerosene. The suggested method en-

ables a steep rise in the degree of purification of the aluminate-alkaline solutions under study to 100%. The technique was tested on real industrial solutions from the alumina shop of Gyanja aluminum plant.

CONCLUSIONS

(1) The extraction purification of industrial aluminate-alkaline solutions, formed in manufacture of alumina, to remove the iron impurities they contain, with a gallium concentrate further obtained with the use of 2-hydroxy-5-alkyl(C_8–C_9)benzyldiethanolamine in a kerosene diluent, was studied.

(2) It was found that iron is extracted from aluminate-alkaline solutions at a concentration of the extraction agent equal to 0.3–0.5 M and a (1–4) : 1 volume ratio of the aqueous and organic phases, with the degree of purification of solutions of this kind to remove impurities being as high as 95–100%.

(3) The conditions of the stage-by-stage re-extraction of iron and gallium were determined and it was found that iron is completely re-extracted from the organic phase with a 0.5 M solution of hydrochloric acid, and gallium, with 2.0 M HCl.

(4) A technological scheme for purification of aluminate-alkaline solutions to remove iron impurities by the extraction method was suggested.

REFERENCES

1. Bol'shakov, K.A., *Khimiya i tekhnologiya redkikh i rasseyannykh elementov* (Chemistry and Technology of Rare and Scattered Elements), Moscow: Vysshaya Shkola, 1976.
2. Lishchenko, T.T., Vdovina, L.V., and Korobko, G.P., *Trudy GIREDMET*, 1981, no. 104, pp. 43–49.
3. *Data of Inorganic Solvent Extraction*, Japan Atomic Energy Research Institute, 1963, no. 1047, p. 36.
4. Nagumo, T. and Murakoshi, M., *Kogyo Kagaku Zasshi*, 1963, vol. 66, pp. 757–759.
5. USSR Inventor's Certificate, no. 335 920.
6. USSR Inventor's Certificate, no. 345 095.
7. USSR Inventor's Certificate, no. 468 888.
8. Babaev, V.A., Guseinov, E.R., Soltanova, S.M., and Dzhabbarova, Z.A., *Materialy nauchnoi konferentsii* (Proc. Sci. Conf.), Baku, 2007, p. 127.

ISSN 1070-4272, Russian Journal of Applied Chemistry, 2008, Vol. 81, No. 8, pp. 1390–1397. © Pleiades Publishing, Ltd., 2008.
Original Russian Text © V.A. Korzhikov, A.P. Filippov, E.N. Vlasova, E.F. Panarin, T.B. Tennikova, 2008, published in Zhurnal Prikladnoi Khimii, 2008, Vol. 81, No. 8, pp. 1311–1319.

MACROMOLECULAR CHEMISTRY AND POLYMERIC MATERIALS

A Physicochemical Study of the Structure of Polymers Derived from 2-Deoxy-*N*-methacryloylamido-*D*-glucose and Their Conjugates with Ligands of Various Molecular Sizes

V. A. Korzhikov, A. P. Filippov, E. N. Vlasova, E. F. Panarin, and T. B. Tennikova

Institute of Macromolecular Compounds, Russian Academy of Sciences, St. Petersburg, Russia

Received May 14, 2008

Abstract—Conjugates of polymers of 2-deoxy-*N*-methacryloylamido-*D*-glucose with ligands of various molecular sizes were synthesized. The structures and compositions of the starting polymers and conjugates were examined, and their structure in aqueous solutions was studied by viscometry .

DOI: 10.1134/S1070427208080144

Water-soluble biocompatible polymers attract enormous interest today because of the possibility of using them in various biomedical technologies [1]. For example, the recently developed approach to preparation of biofunctional polymer–inorganic composites (scaffolds) for repairing bone tissues involves adsorption coating of the surface of a 3*D* mineral matrix with a polyfunctional biocompatible nonbiodegradable polymer [2]. The inorganic constituent should ensure the mechanical stability of the scaffold, and the biological polyfunctionality is provided by the covalent binding of special signal molecules with the polymer. It seems most promising to use for this purpose ligands of both low (e.g., poly-*L*-lysine) and high specificity (a peptide containing the arginine–glycine–aspartic acid sequence, i.e., an RGD peptide [3, 4] and a special protein, cell growth factor [5, 6]). Creation of such a polyfunctional polymeric vector on the surface of a mineral matrix should intensify the adhesion and 3*D* cell growth and, ultimately, the formation of a tissue structure.

Much promise for the development of polymer–mineral scaffolds is shown by synthetic polyvinyl saccharides [7–10], carbon-chain polymers containing saccharide residues as pendant groups. For covalent linking of bioligands to polymers, it seems most appropriate to use aldehyde groups providing binding of amine-containing ligands (peptides, proteins) under mild conditions without release of toxic by-products.

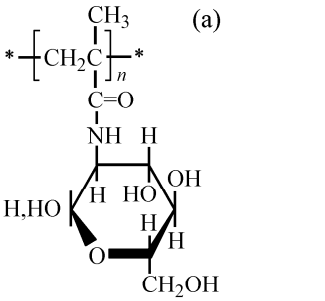
In previous studies, we developed procedures for preparing new hydrophilic aldehyde-containing polymers based on vinyl saccharides and differing in the chemical structure, composition, and molecular weight [11]. With the aim to introduce a controllable amount of aldehyde groups, we examined periodate oxidation of poly(2-deoxy-*N*-methacryloylamido-*D*-glucose) (pMAG). Aldehyde-containing polymers were also prepared by terpolymerization of MAG with *N*-vinylpyrrolidone (VP) and acrolein diethyl acetal (AcDA), followed by aldehyde deprotection. Simultaneously, procedures were developed for controllable introduction of aldehyde groups, followed by modification with the above bioligands [12]. It was also shown that the polymers and conjugates obtained exhibit high adsorption affinity for the chosen mineral materix (Sponceram®). Furthermore, the first experiments on cells showed that the composites developed do intensify the adhesion and cell growth [12].

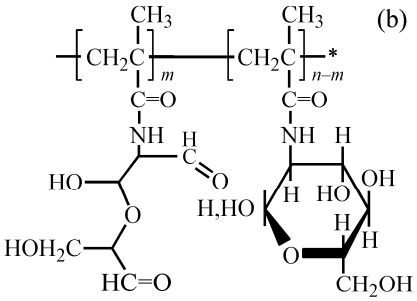
Nevertheless, further optimization of the process for preparing the above-described polymer–inorganic composites should involve studies of physicochemical characteristics of the polymers and conjugates. In this study we made the first attempt to determine their hydrodynamic parameters from viscometric data. To this end, we measured the viscosities of solutions of both the initial polymers and those modified with low- (glycine) and high-molecular-weight (ribonuclease A-RNAase) model ligands.

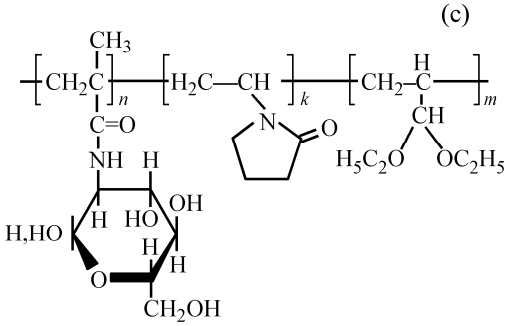
EXPERIMENTAL

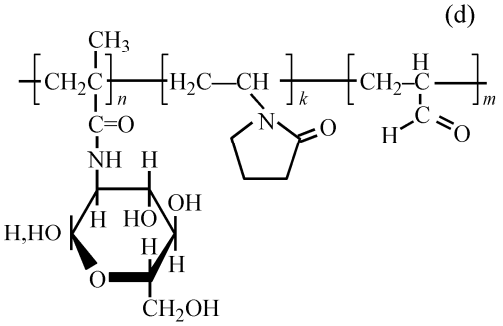
All the salts for preparing buffer solutions (Fluka Chemie AG, Switzerland), glycine, and RNAase (Sigma AG, Germany) were of analytically pure grade and were used without additional purification. For desalination of solutions of polymers and conjugates and removal of low-molecular-weight impurities from them, we used dialysis bags (Spectra/Pore®, USA; MWCO: 1000).

Samples of pMAG, MAG–VP–AcDA copolymer {p(MAG–VP–AcDA), [MAG] : [VP] : [AcDA] = 77 : 15 : 8 mol %}, and their activated forms, i.e., oxidized pMAG and p(MAG–VP–Ac) containing 32 and 8 mol % aldehyde groups, respectively, were synthesized as described previously [11]. The covalent binding of glycine and RNAase was performed by the previously developed procedures [12]. Samples of all the polymers and conjugates were purified by dialysis against water and stored at –20°C. The structures of the initial and activated polymers pMAG (a), oxidized pMAG (b), p(MAG–VP–AcDA) (c), and p(MAG–VP–Ac) (d) are given below:









The ^{1}H COSY NMR spectra of the polymers were recorded with a Bruker AV400 NMR spectrometer, and the IR spectra, with a Bruker IFS 88 spectrophotometer (Germany). The UV spectra were measured with an ND-1000 spectrophotometer (peQLab Biotechnologie GmbH, Germany).

The molar amount of aldehyde groups in the polymers was determined by a highly specific reaction with the Schiff reagent (fuchsinsulfurous acid) using a calibration plot preliminarily constructed with a model (glutaric) aldehyde. For this purpose, to 0.5 ml of a solution of an aldehyde-containing polymer we added 2.5 ml of a Schiff reagent solution and, on Keeping the mixture for 40 min, measured the absorption of the colored complex at λ= 550 nm. This method was also used for determining the amount of bound glycine from the amount of residual aldehyde groups.

The molar content of VP in the p(MAG–VP–Ac) copolymer was determined using the so-called "iodine test." To 0.5 ml of a sample of a polymer solution, we added 3 ml of a 0.003 M solution of iodine in 0.2 M sodium acetate buffer solution (pH 4.6). The formation of a colored complex was recorded immediately after adding the reagent. To calculate the amount of VP, we used a calibration curve constructed with poly(*N*-vinylpyrrolidone) (pVP) as reference.

The amount of RNAase bound with polymers was determined by the well-known Lowry–Folin method [13]. The intrinsic viscosity [η] of samples was measured with an Ubbelohde viscometer (chamber volume 2 ml) at 25°C. We used the following solvents: 0.1 M Na_2SO_4; 0.01 M sodium borate buffer solution, pH 9.5; borate solution, pH 7.0 (0.01 M sodium borate solution, pH 9.5, acidified to pH 7.0 by adding boric acid).

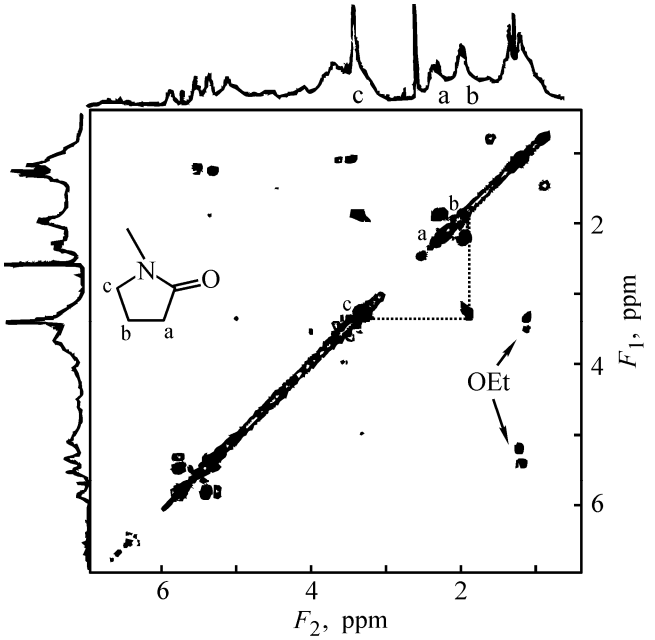


Fig. 1. ^{1}H COSY NMR spectrum of p(MAG–VP–AcDA) copolymer. (F_1, F_2) 1H NMR chemical shifts.

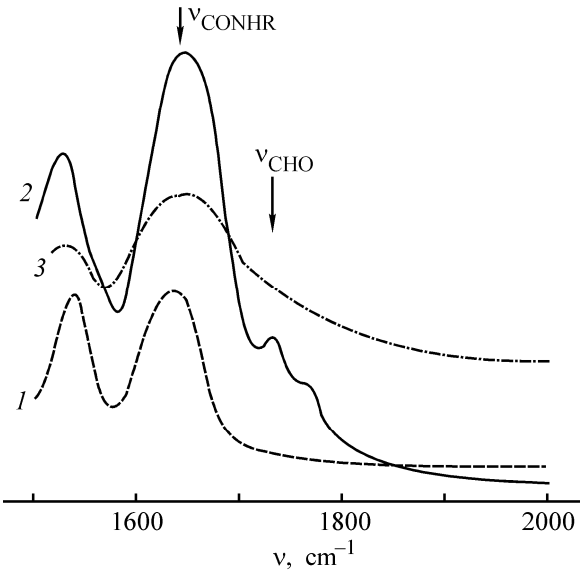


Fig. 2. IR spectra of (*1*) pMAG and (*1–3*) aldehyde-containing polymers: (*2*) oxidized pMAG and (*3*) p(MAG–VP–Ac). (ν) Wavenumber; the same for Fig. 3.

To calculate the molecular weights of pMAG and p(MAG–VP–AcDA), we used the previously derived Mark–Kuhn–Houwink equation for solutions of pMAG in 0.1 M Na_2SO_4 [7]:

$$[\eta]^{25^\circ C} = 8.29 \times 10^{-4} M^{0.49}.$$

To calculate the root-mean-square distance between the chain ends $\langle h^2 \rangle^{1/2}$ and the radius of inertia R_G, we used the well-known relationship [14]

$$[\eta] = \Phi \frac{\langle h^2 \rangle^{3/2}}{M} = \Phi \frac{\langle 6R_G^2 \rangle^{3/2}}{M}.$$

In these calculations, with the aim to compare the above parameters of the polymers and conjugates under consideration, we used for all the samples the common experimental value of the Flory parameter, $\Phi = 2.1 \times 10^{21}$ mol^{-1}.

To estimate the hydrodynamic radius R_H of macromolecules of the initial polymers and their conjugates with glycine and RNAase, we used the Einstein relationship for impermeable spheres:

$$[\eta] = \left(\frac{10\pi}{3}\right) N_A \frac{\left(R_H^{[\eta]}\right)^3}{M}.$$

where $R_H^{[\eta]}$ is the viscometric hydrodynamic radius of the equivalent sphere.

The formation of the p(MAG–VP–AcDA) terpolymer was confirmed by COSY NMR spectroscopy (Fig. 1). In the spectrum of the copolymer, we found cross signals corresponding to interaction of protons of the EtO groups in AcDA and of the lactam ring in VP.

The aldehyde groups are qualitatively detected by IR spectroscopy (Fig. 2). In the spectrum of oxidized pMAG, on the short-wave wing of the strong band of amide carbonyl groups, there are two minor peaks at 1755 and 1735 cm^{-1}, assigned to two aldehyde groups formed by oxidation of the *vic*-glycol group of glucose. In the spectrum of the activated terpolymer p(MAG–VP–Ac), on the short-wave wing of the band of the amide carbonyl group in the range corresponding to the absorption of aldehyde groups, there is a shoulder suggesting the presence of a small amount of an aldehyde.

For the synthesized activated polymers, we determined the composition, M_η, and content of aldehyde groups. The copolymer composition was determined from the results of the iodine test and the Schiff reaction (determination of the VP and Ac content, respectively; the Ac content was determined after AcDA deprotection). The MAG content was determined by subtraction of the percentage mole fractions of VP and AcDA from 100%.

The results are listed in Table 1. It can be seen that the molecular weight of the copolymers is relatively low. This is important from the standpoint of excretion of polymers from a living body in the case of their desorption from the mineral support. It is also evident that the polymers contain aldehyde groups in an amount sufficient both for ligand binding and for formation of mixed polyfunctional conjugates.

The covalent binding of glycine and RNAase to aldehyde-containing polymers was qualitatively confirmed by comparison of the IR spectra of oxidized pMAG, gly-cine, and RNAase with those of the pMAG–glycine and pMAG–RNAase conjugates (Figs. 3a, 3b). The spectrum of oxidized pMAG contains a fairly pronounced absorption band of aldehyde groups, whereas in the spectra of the conjugates, it is considerably less intense. Also, despite the prolonged (150 h) purification of the polymeric derivatives by dialysis against water, the spectra of pMAG–glycine and pMAG–RNAase contain absorption bands of carboxylate groups, ν_{COO^-}. Both these facts, i.e., the considerable decrease in the intensity of the aldehyde band and the appearance of absorption bands untypical of the initial polymer and corresponding to symmetric vibrations of carboxylate anion, along with a noticeable change in the shape of the amide carbonyl absorption band, confirm the formation of the conjugates.

A quantitative estimation of the ligand binding with the polymers was performed by chemical analytical methods. For conjugates with glycine, the degree of substitution of aldehyde groups of the polymer with the amino acid was determined from the results of quantitative determination of the residual CHO groups by the Schiff reaction. To estimate the molar amount of immobilized RNAase, we used the Lowry method. To examine the hydrodynamic parameters of mixed polyfunctional conjugates of both polymers, we synthesized samples containing both RNAase and glycine, namely, pMAG–(RNAase–glycine) and p(MAG–VP–Ac)–(RNAase–glycine). These conjugates were prepared in two steps. First we performed covalent binding of RNAase, using the same [CHO] : [RNAase] ratio as that in conjugates with a single ligand, after which we added to the reaction mixture excess glycine to substitute the residual aldehyde groups. The results are listed in Table 2.

Prior to discussing data on the viscosity of solutions of the polymers and conjugates, it is necessary to consider a procedure for preparing 3*D* polymer–inorganic composite supports of bone tissue cells, because the solvent choice was governed specifically by the strategy used. In accordance with our approach, in the first step, the aldehyde-containing polymers syn-

Table 1. Molecular weights M_η and compositions of the polymers

Sample no.	Polymer	$M_\eta \times 10^{-3}$	$[M_1]:[M_2]:[M_3]$, mol %	Content of CHO groups, mol %
1	pMAG	25.0	–	–
2	Oxidized pMAG	25.0	–	32
3	p(MAG–VP–AcDA)	17.5	77 : 15 : 8	–
4	p(MAG–VP–Ac)	17.5	77 : 15 : 8	8

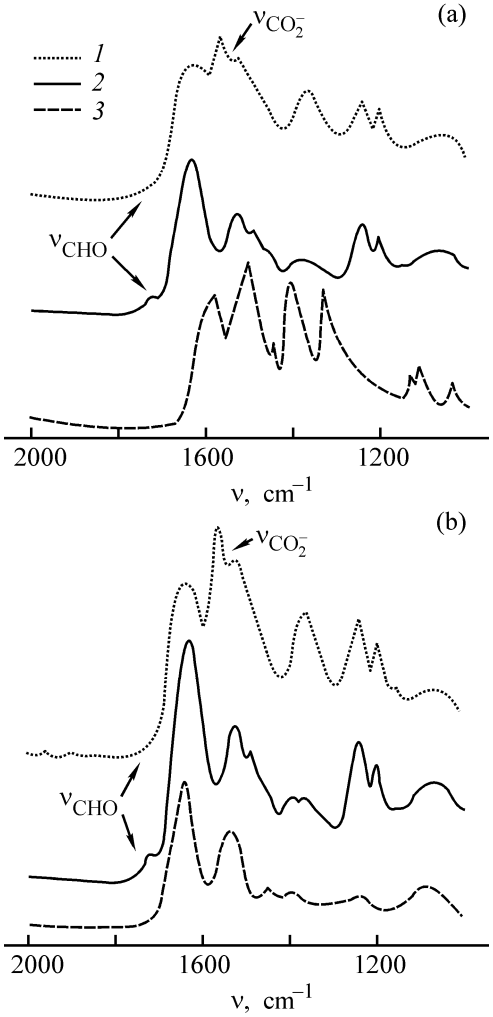


Fig. 3. Comparison of the IR spectra of conjugates with those of the initial reactants: (a) (*1*) glycine, (*2*) oxidized pMAG, and (*3*) pMAG–glycine; (b) (*1*) RNAase, (*2*) oxidized pMAG, and (*3*) pMAG–RNAase.

Table 2. Degree of conversion of aldehyde groups and RNAase in formation of conjugates

Sample no.	Conjugate	Conversion, mol %	
		CHO groups	RNAase
pMAG (32 mol % [CHO]			
5	pMAG–glycine	20	–
6	The same	~100	–
7	pMAG–RNAase	Not determined	29
8	pMAG–(RNAase–glycine)	~100	27
p(MAG–VP–Ac) (8 mol % [CHO]			
9	p(MAG–VP–Ac)–glycine	15	–
10	The same	~100	–
11	p(MAG–VP–Ac)–RNAase	Not determined	33
12	p(MAG–VP–Ac)–(RNAase–glycine)	~100	35

thesized are modified with low- and high-molecular-weight ligands. The reaction is performed in a 0.01 M sodium borate buffer solution, pH 9.5 (b/b 9.5). Therefore, the viscosities of pMAG and p(MAG–VP–AcDA) were measured specifically in this buffer solution. The second step of formation of the composite support involves adsorption of the conjugates obtained on the surface of a mineral support at physiological pH values. For this purpose, we used the same 0.01 M sodium borate buffer solution, pH 9.5, and acidified it to pH 7.0 with boric acid (borate solution, pH 7.0: b/s 7.0). In this solution, we measured the intrinsic viscosities of the conjugates and initial polymers with the aim to determine their hydrodynamic parameters in the course of adsorption.

The intrinsic viscosities of pMAG and p(MAG–VP–AcDA) were measured in 0.1 M Na_2SO_4. To calculate M_η, we used the Mark–Kuhn–Houwink (MKH) equation derived for pMAG by Klein [7]. It should be noted that, previously, Pavlov has examined in detail the hy-drodynamic characteristics of pMAG, using water as sol-vent [15]. The MKH equation obtained is as follows:

$$[\eta]^{25^\circ C} = 2.18 \times 10^{-5} M^{0.76}.$$

The choice of 0.1 M Na_2SO_4 as solvent is governed by the fact that, in this solvent, the contribution of polyelectrolytic swelling, caused by the possible presence of methacrylic acid units in the copolymer, is avoided. Furthermore, as shown by Klein [7], 0.1 M Na_2SO_4 is nearly a θ-solvent for MAG polymers ($[\eta] \sim M^{0.49}$). Thus, the hydrodynamic characteristics of the starting polymers, obtained in this solvent [Table 3, sample nos. 1 (0.1 M Na_2SO_4), 3], were taken as unperturbed values for comparison with the values for the initial polymers and their conjugates in other solvents.

Comparison of the mean contour lengths of the polymers, determined from viscometric data [pMAG ~31, p(MAG–VP–AcDA) ~25 nm], with the RH values [Table 3, sample nos. 1 (0.1 M Na_2SO_4), 3] suggests a comparatively coiled conformation of the macromolecules, despite bulky glucose pendant groups. The approximate lengths of the Kuhn segment, calculated from the general relationship $A = \langle h^2 \rangle L^{-1}$, appeared to be 4 nm for pMAG and 3.5 nm for p(MAG–VP–AcDA), in agreement with Pavlov's data [15].

As the polymers under consideration contain saccharide residues of *D*-aminoglucose, it can be presumed that their size in dilute solutions should be determined by the energy of intramolecular hydrogen bonds [16] in the chosen solvent.

In addition, introduction of aldehyde groups that are able to form intramolecular hemiacetals should give rise to additional intramolecular interactions.

Measurement of the intrinsic viscosity of pMAG in b/b 9.5 showed that [η], R_G, and R_H [Table 3, sam-

Table 3. Intrinsic viscosities and calculated hydrodynamic parameters of the initial and activated polymers and of their conjugates with glycine and RNAase

Sample no.	Polymer/conjugate	Solvent	$[\eta]$, dl g^{-1}	$R_G^{[\eta]}$	$\langle h^2 \rangle^{1/2}$	$R_H^{[\eta]}$
				nm		
			pMAG			
1	pMAG	0.1 M Na_2SO_4	0.12	4.5	11.3	3.6
1	pMAG	b/b, pH 9.5	0.15	4.9	12.1	3.9
2	Oxidized pMAG	b/s, pH 7.0	0.11	4.4	10.9	3.5
5	pMAG–glycine	b/s, pH 7.0	0.28	6.0	14.9	4.8
6	pMAG–glycine	b/s, pH 7.0	0.40	6.7	16.8	5.4
7	pMAG–RNAase	b/s, pH 7.0	0.24	5.8	14.5	4.7
8	pMAG–RNAase–glycine	b/s, pH 7.0	0.22	5.6	14.1	4.5
			p(MAG–VP–AcDA)			
3	p(MAG–VP–AcDA)	0.1 M Na_2SO_4	0.10	3.8	9.4	3.0
4	p(MAG–VP–Ac)	b/s, pH 7.0	0.10	3.8	9.4	3.0
9	p(MAG–VP–Ac)–glycine	b/s, pH 7.0	0.12	4.0	10.0	3.2
10	p(MAG–VP–Ac)–glycine	b/s, pH 7.0	0.18	4.6	11.4	3.7
11	p(MAG–VP–Ac)–RNAase	b/s, pH 7.0	0.21	5.0	12.4	4.0
12	p(MAG–VP–Ac)–RNAase–glycine	b/s, pH 7.0	0.23	5.1	12.8	4.1

ple no. 1 (in 0.1 M Na_2SO_4 and b/b 9.5); Fig. 4a, curves *1*, *2*] increase relative to those in 0.1 M Na_2SO_4. Therefore, b/b 9.5 can be considered a good solvent for pMAG. The hydrodynamic radius determined for pMAG and b/b 9.5 from the viscometric data (Table 3, sample no. 1, b/b 9.5) coincided with that determined from light scattering, R_H^{DLC} = 3.9 nm).

A study of the concentration dependences of η_{sp}/c for activated polymers, oxidized pMAG and p(MAG–VP–Ac), in b/b 9.5 revealed a polyelectrolytic effect (Figs. 4a, 5a, curves 3). This may be due to the presence of a small amount of carboxy groups formed by partial oxidation of aldehyde groups. For oxidized pMAG, with an increase in the solution concentration,

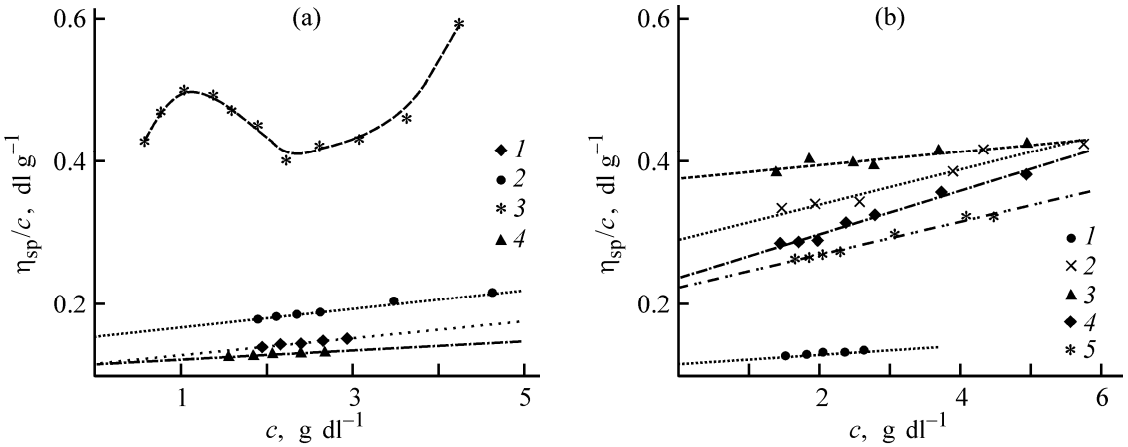


Fig. 4. Reduced specific viscosity η_{sp}/c vs. concentration c for pMAG, oxidized pMAG, and conjugates with glycine and RNAase. (a) (*1*) pMAG (sample no. 1) in 0.1 M Na_2SO_4, (*2*) pMAG (sample no. 1) in b/b 9.5, (*3*) oxidized pMAG (sample no. 2) in b/b 9.5, and (*4*) oxidized pMAG (sample no. 2) in b/s 7/0; (b) (*1*) oxidized pMAG (sample no. 2), (*2*) pMAG–glycine (sample no. 5), (*3*) pMAG–glycine (sample no. 6), (*4*) pMAG–RNAase (sample no. 7), and (*5*) pMAG–(RNAase–glycine) (sample no. 8), all in b/s 7.0.

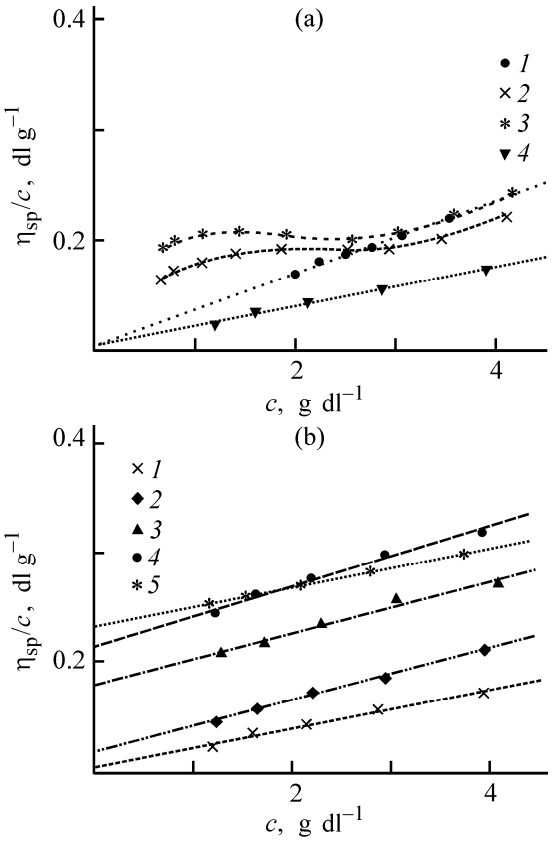


Fig. 5. Reduced specific viscosity η_{sp}/c vs. concentration c for p(MAG–VP–AcDA), p(MAG–VP–Ac), and conjugates with glycine and RNAase. (a) (*1*) p(MAG–VP–AcDA) (sample no. 3) in 0.1 M Na_2SO_4, (*2*) p(MAG–VP–AcDA) (sample no. 3) in b/b 9.5, (*3*) p(MAG–VP–Ac) (sample no. 4) in b/b 9.5, and (*4*) p(MAG–VP–Ac) (sample no. 4) in b/s 7.0; (b) (*1*) p(MAG–VP–Ac) (sample no. 4), (*2*) p(MAG–VP–Ac)–glycine (sample no. 9), (*3*) p(MAG–VP–Ac)–glycine (sample no. 10), (*4*) p(MAG–VP–Ac)–RNAase (sample no. 11), and (*5*) p(MAG–VP–Ac)–(RNAase–glycine) (sample no. 12), all in b/s 7.0.

the specific viscosity sharply grows (Fig. 4a, curve *3*) owing to the formation of associates via hydrogen bonding and possible formation of intramolecular hemiacetals. The polyelectrolytic effect is also observed with the nonactivated terpolymer p(MAG–VP–AcDA) (Fig. 5a, curve *2*), apparently due to partial removal of diethyl acetal protecting groups in the course of polymer synthesis and purification to give aldehyde groups, followed by their partial oxidation to carboxy groups. The occurrence of the polyelectrolytic effect indicates that, in these cases, conformations of the polymer macromolecules in an alkaline borate buffer solution are more unfolded, compared to their solutions in the standard solvent, 0.1 M Na_2SO_4. Along with the polyelectrolytic interaction causing an increase in the size of the macromolecules, a small contribution to the increase in the hydrodynamic size of the aldehyde-containing polymers can be made by the reversible interaction of aldehyde groups with hydroxide anions, which makes lower the degree of formation of intramolecular hemiacetals. Apparently, the hydrodynamic swelling of polymes should increase their reactivity due to an increase in the steric accessibility of aldehyde groups to ligands of different molecular sizes (amino acids, peptides, proteins). The concentration dependences of the specific viscosity of solutions of oxidized pMAG and p(MAG–VP–Ac) in b/s 7.0 (Figs. 4a, 5a, curves *4*) showed no polyelectrolytic effect.

As noted above, it was very interesting to examine the hydrodynamic parameters of oxidized pMAG, p(MAG–VP–Ac), and their conjugates with low- and high-molecular-weight ligands in the same solvent as that used for performing adsorption on the macroporous mineral matrix in the course of preparation of polymer–inorganic composites, namely, in b/s 7.0.

The concentration dependence of η_{sp}/c for solutions of pMAG and p(MAG–VP–Ac) in b/s 7.0 showed no polyelectrolytic effect (Figs. 4a, 5a, curves *4*). This result may be due to suppression of the formation of carboxylate anions by protons of boric acid added to adjust pH 7.0. It is interesting that the quantities [η], R_G, and R_H, determined for the polymers under consideration in b/s 7.0 and in 0.1 M Na_2SO_4, nearly coincide. Hence, presumably, the pH adjustment for pMAG and p(MAG–VP–Ac) solutions by the above-described procedure makes their properties close to the θ-conditions [Table 3, sample nos. 1 (0.1 M Na_2SO_4), 2–4]. This assumption, in turn, may be one more explanation for the previously found high adsorption rate and considerable amount of the adsorbed substance [11].

To determine the size of the polymer macromolecules upon modification with glycine and RNAase, we measured the viscositites and calculated the hydrodynamic parameters of the above-described conjugates (Table 2). The data obtained are listed in Table 3. The dependences of η_{sp}/c on c for conjugates with one and two ligands are shown in Figs. 4b and 5b (curves *2–5*) in comparison with the dependences for the initial aldehyde-containing polymers (Fig. 4b and 5b, curves *1*).

It can be seen that binding of glycine with oxidized pMAG leads to an increase in the hydrodynamic size of its macromolecules. This is due to the fact that modification with glycine involves introduction of a large amount of pendant carboxy groups, which leads to polyelectrolytic repulsion of the macromolecular units even at pH 7.0. Furthermore, blocking of alde-

hyde groups with the amino acid makes impossible formation of intramolecular hemiacetals, which also should lead to an increase in the hydrodynamic size of the macromolecules. We found that the swelling noticeably increases with the degree of substitution of aldehyde groups with glycine (Table 3, sample nos. 5, 6). This effect is considerably less pronounced for the terpolymer (Table 3, sample nos. 9, 10), in which the amount of aldehyde groups is smaller, and their distance from the backbone, shorter.

Covalent binding of RNAase, as expected, leads to an increase in the size R_G and R_H of the forming conjugate, compared to the initial polymer. In view of the possible cross-linking between the activated polymer as polyaldehyde and the protein as polyamine, we used strongly dilute solutions of both reactants and took the polymer in a large excess. The conditions we chose [12] allowed us to obtain water-soluble polymer–protein conjugates.

The hydrodynamic size of the pMAG–RNAase conjugate (Table 3, sample no. 7) appeared to be smaller than that of the pMAG–glycine conjugate, whereas with the terpolymer (Table 3, sample no. 11), the pattern was the opposite. This difference may be due to a different distribution of aldehyde groups in the polymers examined. Aldehyde groups formed by oxidation of pMAG are randomly distributed over the polymer chain, whereas in the course of terpolymer formation, AcDA, being an allyl-type monomer, causes degradation chain transfer accompanying the chain propagation. Hence, the aldehyde groups in p(MAG–VP–Ac) should be arranged in the copolymer structure loosely, at a long distance from each other. Thus, presumably, the binding may be multipoint with oxidized pMAG, whereas with the terpolymer, the binding with RNAase if effected by separate Ac units.

As noted above, synthesis of mixed conjugates (different ligands on one polymer chain) starts with the addition of RNAase. This fact explains why the hydrodynamic parameters of pMAG–(RNAase–glycine) (Table 3, sample no. 8) and p(MAG–VP–Ac)–(RNAase–glycine) (Table 3, sample no. 12) are close to those of the conjugates of the same polymers with RNAase.

CONCLUSIONS

(1) Macromolecules of two types of new aldehyde-containing polymers derived from 2-deoxy-*N*-methacryloylamido-*D*-glucose and of their conjugates with glycine and ribonuclease A (low- and high-molecular-weight model ligands, respectively) have a comparatively coiled conformation.

(2) The concentration dependences of η_{sp}/c of aldehyde-containing forms of both types of polymers demonstrate a polyelectrolytic effect, and oxidized poly(2-deoxy-*N*-methacryloylamido-*D*-glucose) forms associates as the concentration increases.

(3) The behavior and structure of polymer–glycine and polymer–ribonuclease conjugates in aqueous solutions depend on the chemical structure of the polymres, distribution of aldehyde groups in the polymer chain, and amount of the bound ligand.

ACKNOWLEDGMENTS

The study was financially supported by the Russian Foundation for Basic Research (project no. 05-03-32 310) and German Scientific Society (DFG, KA 1784/4-1).

REFERENCES

1. Yaszemski, J., Hasirci, V., and Lewandrowski, K.-U., *Tissue Engineering and Novel Delivery Systems*, New York: Dekker, 2004.
2. Vlakh, E., Panarin, E., Tennikova, T., et al., *J. Biomed. Mater. Res.*, 2005, vol. 75, pp. 333–341.
3. Massia, S.P. and Hubbell, J.A., *Anal. Biochem.*, 1990, vol. 187, pp. 292–301.
4. Lin, H.-B., Sun, W., Mosher, D.F., et al., *J. Biomed. Mater. Res.*, 1994, vol. 28, pp. 329–342.
5. Xu, X.L., Lou, J., Tang, T., et al., *J. Biomed. Mater. Res.*, 2006, vol. 75B, pp. 289–303.
6. Park, M.S., Kim, S.-S., Cho, S.-W., et al., *J. Biomed. Mater. Res.*, 2006, vol. 79B, pp. 353–359.
7. Klein, J. and Herzog, D., *Macromol. Ch*em., 1987, vol. 188, pp. 1217–1232.
8. Spain, S., Gibson, M., and Cameron, N., *J. Polym. Sci., Part A: Polym. Chem.*, 2007, vol. 45, pp. 2059–2072.
9. Ladmiral, V., Melia, E., and Haddelton, D., *Eur. Polym. J.*, 2004, vol. 40, pp. 431–449.
10. Miura, Y., *J. Polym. Sci., Part A: Polym. Chem.*, 2007, vol. 45, pp. 5031–5036.
11. Korzhikov, V.A., Diederichs, S., Nazarova, O.V., et al., *J. Appl. Polym. Sci.*, 2008, vol. 108, pp. 2386–2397.
12. Korzhikov, V., Roeker, S., Vlakh, E., et al., *Bioconj. Chem.*, 2008, vol. 19, pp. 617–625.
13. Dawson, R.M.C., Elliot, D.C., Elliot, W.H., and Jones, K.M., *Data for Biochemical Research*, Oxford: Clarendon, 1986.
14. Tsvetkov, V., Eskin, V., and Frenkel, S., *Structure of Macromolecules in Solution*, London: Butterworths, 1970.
15. Pavlov, G., Ivanova, N., Korneeva, E., et al., *J. Carbohydr. Chem.*, 1996, vol. 15, pp. 419–433.
16. Brinke, G., Ruokolainen, J., and Ikkala, O., *Adv. Polym. Sci.*, 2007, vol. 207, pp. 113–177.

ISSN 1070-4272, Russian Journal of Applied Chemistry, 2008, Vol. 81, No. 8, pp. 1398–1402. © Pleiades Publishing, Ltd., 2008.
Original Russian Text © N.M. Geller, A.G. Ivanov, L.B. Nadezhdina, V.V. Shamanin, L.A. Shibaev, A.V. Gribanov, 2008, published in Zhurnal Prikladnoi Khimii, 2008, Vol. 81, No. 8, pp. 1320–1325.

MACROMOLECULAR CHEMISTRY AND POLYMERIC MATERIALS

Synthesis and Spectral Characteristics of Silicon-containing Poly(Salicylidene Azomethines) Derived from Aromatic Di- and Tetraamines

N. M. Geller, A. G. Ivanov, L. B. Nadezhdina, V. V. Shamanin, L. A. Shibaev, and A. V. Gribanov

Institute of Macromolecular Compounds, Russian Academy of Sciences, St. Petersburg, Russia

Received March 25, 2007

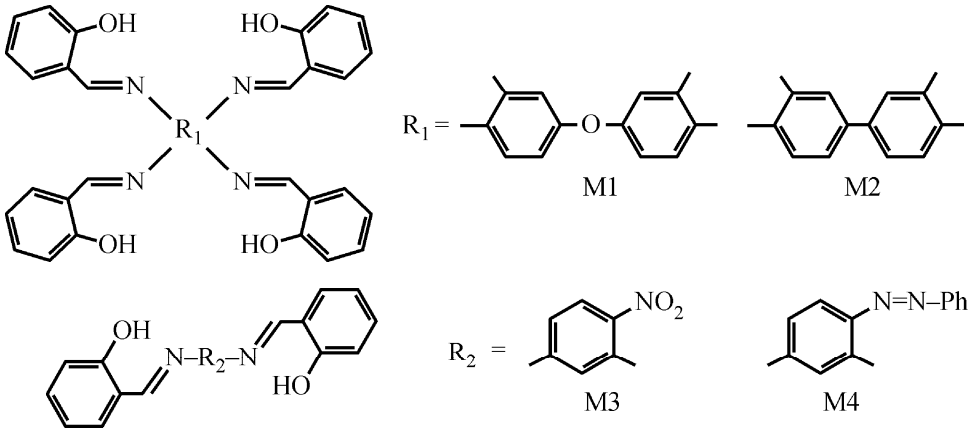
Abstract—New silicon-containing poly(salicylidene azomethines) were prepared by polycondensation of di- or tetrasalicylidene derivatives of aromatic di- or tetraamines. The spectral data suggest the occurrence of noncovalent transannular donor–acceptor interaction N→Si providing "nonclassical" conjugation.

DOI: 10.1134/S1070427208080156

The goal of this study was to develop a procedure for preparing a new class of polymers, Si-containing poly(salicylidene azomethines) containing donor nitrogen atoms and acceptor silicon atoms in the chain, which creates prerequisites for the formation of intramolecular donor–acceptor charge-transfer complexes (CTCs) in the polymer chain. Such kind of complexation should be accompanied by effective charge transfer, which will polarize the polymers and hence impart to them specific electro- and photophysical properties.

EXPERIMENTAL

As comonomers we used *N*,*N*',*N*'',*N*'''-tetra-salicylidene-3,3',4,4'-tetraaminodiphenyl ether (M1), *N*,*N*',*N*'',*N*'''-tetrasalicylidene-3,3',4,4'-tetraaminodiphenyl (M2), 1,3-bis(salicylidenimino)-4-nitrobenzene (M3), and 2,4-bis(salicylidenimino)azobenzene (M4):



The monomers were prepared by reactions of salicylaldehyde with 3,3',4,4'-tetraaminodiphenyl and 3,3',4,4'-tetraaminodiphenyl ether in 4 : 1 molar ratio or with 4-nitro-1,3-diaminobenzene and 2,4-diaminoazobenzene in 2 : 1 ratio.

The polymers were prepared in a DMF solution by polycondensation of the corresponding salicylidene derivatives of tetraamines and diamines with tetrachlorosilane or tetraethoxysilane (Vekton, bp 57 and 168°C, respectively). Polycondensation of disalicylidene de-

Characteristics of the polymers obtained

Polymer	UV, λ, nm	IR, ν, cm^{-1}	NMR, δ, ppm	M_n
P1	236, 289, 314, 444, 461	1610 (C=N), 1597 (C_{ar}–C_{ar}), 1110 (Si–O)	9.3 (C=N), 6.9–7.6 (C_{ar}–H)	11 000
P2	230, 295, 315, 430, 455	1606 (C=N), 1596 (C_{ar}–C_{ar}), 1110 (Si–O)	9.4 (C=N), 6.9–7.6 (C_{ar}–H)	8000
P3	230, 323, 349, 421	1613 (C=N), 1595 (C_{ar}–C_{ar}), 1112 (Si–O)	9.0 (C=N), 6.9–7.5 (C_{ar}–H)	12 000
P4	242, 270, 347, 428	1603 (C=N), 1582 (C_{ar}–C_{ar}), 1100 (Si–O)	9.3 (C=N), 6.8–7.5 (C_{ar}–H)	9000

rivatives of aromatic diamines was performed with dimethyldiethoxysilane prepared from dimethyldichlorosilane and sodium ethylate. The polymers were isolated by precipitation into diethyl ether. The characteristics of the polymers are listed in the table.

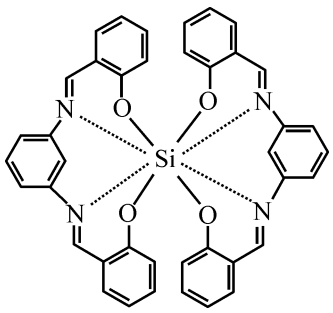
Polymers P1 and P2. To a solution of 0.006 mol of M1 in 15 ml of DMF, 0.006 mol of tetrachlorosilane was added dropwise under agitation. The reaction was performed at room temperature in an inert atmosphere (dry Ar) for 8 h, after which the reaction mixture was concentrated on a rotary evaporator and the dry residue was dissolved in methanol. Polymer P1 was isolated by precipitation from methanol solution into diethyl ether. Yield 94%.

Polymer P2 was prepared similarly.

Polymers P3 and P4. To a solution of 0.011 mol of M3 in 20 ml of DMF, we added 0.011 ml of dimethyldiethoxysilane under agitation. The reaction was performed in an inert medium (dry Ar) for 6 h at 80°C, after which the mixture was concentrated on a rotary evaporator and the dry residue was dissolved in methanol. Polymer P3 was isolated by precipitation from methanol solution into diethyl ether. Yield 89%.

Polymer P4 was prepared similarly.

The model compound necessary for identifying the spectra of the synthesized polymers was prepared by condensation of 1,3-bis(salicylidenimino)benzene with tetraethoxysilane in 2 : 1 molar ratio:



An elemental analysis of the monomers was performed on a LECO CHNS(O)-932 dewvice, and consistent results were obtained.

The ^1H NMR spectra of 4–5 wt% solutions of the monomers and polymers in DMF-*d*–7 were recorded on a Bruker Avance 200 NMR spectrometer operating at 200 MHz; the UV spectra, on an SF-2000 spectrophotometer in methanol or isopropanol in the wavelength range 200–700 nm; and the IR spectra, on a Vertex IR Fourier spectrometer (Bruker) from KBr pellets in the 400–4000 cm^{-1} range. The bands were assigned taking into account published data [1–3] and data obtained for the model compound.

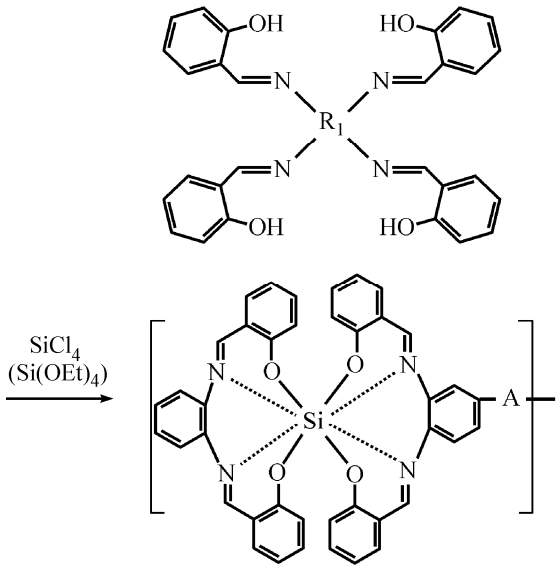
The ESR spectra were measured at 35 GHz with the magnetic field varied in a wide range.

The number-average molecular weights and degrees of polymerization of the polymers were estimated by NMR spectroscopy from the ratio of the integral intensity of the signal of terminal hydroxy groups to the total integral intensity of the signals of aromatic protons or to the integral intensity of the signal of the azomethine proton.

Donor–acceptor interactions are well understood for "low-molecular-weight" reactions of silanes with various organic polydentate ligands. In particular, reactions of dialkyldichlorosilanes with salen-type ligands [salen stands for *N*,*N*'-ethylenebis(salicylidenimine)] have been reported [4–9]. These data on the synthesis of low-molecular-weight CTCs give grounds to expect that replacement of mono- with di- and tetrasalicylidene derivatives will allow synthesis of polymeric CTCs. In our case, the polycondensation should involve, firstly, nucleophilic substitution at the silicon atom and, secondly, N→Si donor–acceptor interaction with the formation of a stable six-membered ring, which should significantly stabilize the corresponding segment of the forming polymer chain.

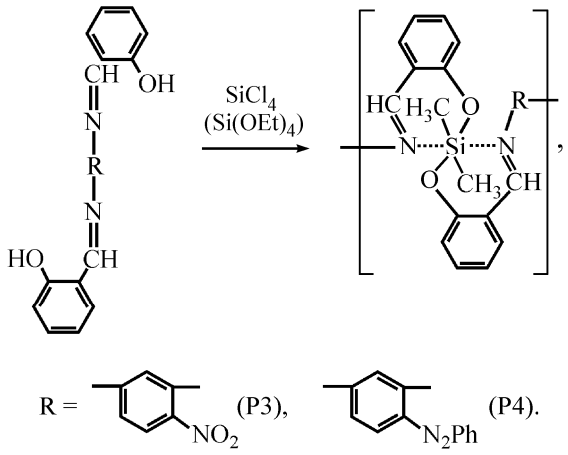
Polymers P1 and P2 were prepared by polycondensation of salicylidene derivatives of tetraamines M1

and M2 with tetrachloro- or tetraethoxysilane in a 1 : 1 molar ratio by the following scheme:



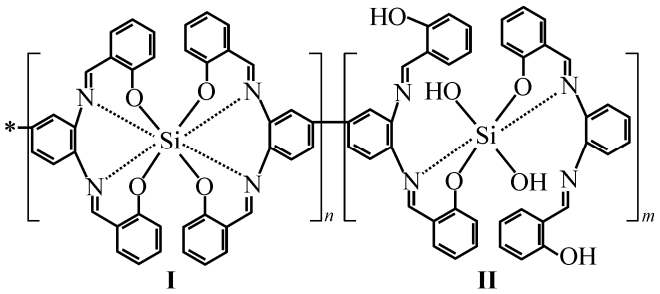
A = –O– (P1), – (P2).

Polymers P3 and P4 were prepared from bis(salicylidenimino) derivatives and dimethyldiethoxysilane, also in a 1 : 1 molar ratio:



R = (P3), (P4).

The major factor determining the yield and molecular weight of the product is the strict observance of the equimolar ratio of the reactants. It is also important to properly choose the solvent, monomer concentration, and temperature. As solvent we chose DMF, which well dissolves the starting monomers and the forming polymer and can also serve as acceptor for the hydrogen chloride released in the reation. To prepare poly-[tetra(salicylidene azomethines)], it is appropriate to take the starting monomers as dilute (5–10%) solutions, because the probability of formation of disubstituted fragments **II,** along with the desired tetrasalicylidene fragments **I,** increases at high concentrations :



I **II**

Because chlorosilanes are highly reactive, to suppress side reactions (hydrolysis of chlorosilanes, followed by tetracyclization) and raise the probability of more complete substitution at silicon (i.e., to raise the relative content of tetrasalicylidene units **I**), the polycondensation should be performed at low temperature (20–25°C). Another way to suppress the contribution of undesirable processes, such as hydrolysis of chlorosilanes, is their replacement with ethoxysilanes, which are less reactive and less susceptible to hydrolysis. However, in the latter case, the leaving group in the polycondensation is the ethoxy group, and therefore, to ensure its complete removal, the reaction should be performed at 85–90°C.

The main spectral problem in analysis of the polymers obtained is to confirm the structure of the monomeric unit, i.e., to confirm the presence in polymer chians of a six-membered ring formed by N→Si coordination interaction. This interaction results in a shift of the electron density from the donor to the acceptor, which, in turn, should affect the spectral characteristics of the substance.

According to published data, the formation of low-molecular-weight complexes is accompanied by pronounced changes in the IR spectra of both donor and acceptor molecules [10]. The vibration frequencies of the donor are shifted toward higher frequencies, and those of the acceptor, toward lower frequencies. The intensities of the absorption bands also change. In the NMR spectra, the signals of the donor are shifted downfield [11]. In our cases, the strongest changes should be expected for the azomethine group, because this group is directly involved in the coordination bonding. Indeed, the intensity ratio of the stretching vibration bands of the azomethine groups (C=N) and aromatic rings (C_{ar} –C_{ar}) in the IR spectra of the samples examined changes upon complexation. Comparison of the intensities of the bands at 1610 and 1597 cm^{-1} shows that,

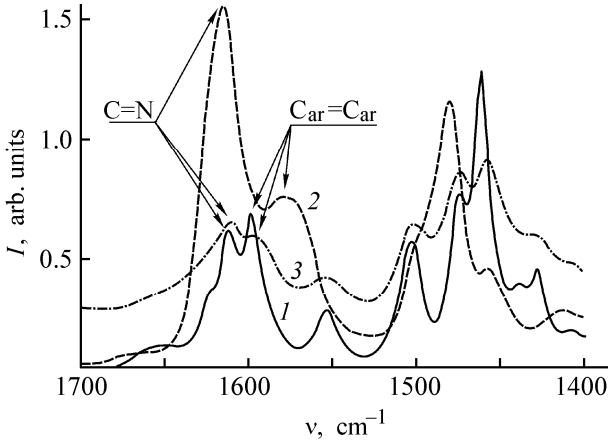


Fig. 1. IR spectra of (*1*) model low-molecular-weight compound, (*2*) M1, and (*3*) P1 (1700–1400 cm^{-1}). (*I*) Intensity and (ν) wavenumber; the same for Fig. 2.

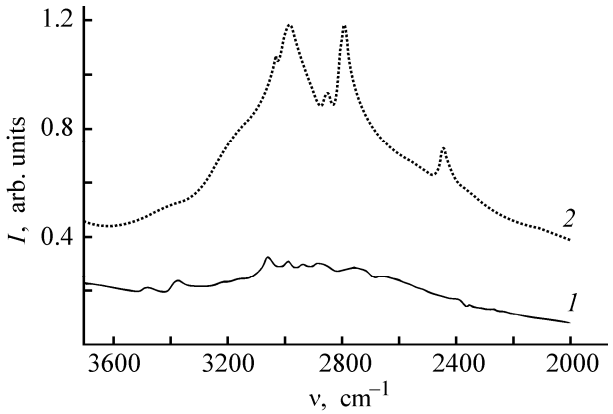


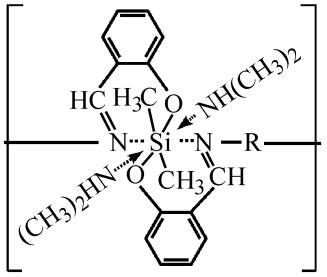
Fig. 2. IR spectra of (*1*) M2 and (*2*) P2 (3600–2000 cm^{-1}).

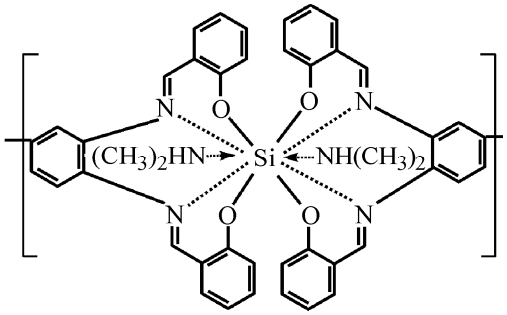
in the spectrum of the monomer, the intensity of the first band (C=N groups) is considerably higher than that of the second band (stretching vibrations of the ring), whereas in the polymer, the intensity of the first band decreases and for the model compound, it becomes even lower than that of the C_{ar}–C_{ar} band (Fig. 1).

These differences may be due to a decrease in the extinction coefficient of azomethine groups as a result of donor–acceptor interactions. Thus, the intensity ratio of these bands can serve as a criterion of the efficiency of N→Si donor–acceptor bonding.

Along with the above features, strong absorption in the range from 2000 to 4000 cm^{-1} engages attention (Fig. 2). According to the previously described polymerization scheme, the amount of OH groups directly is involved in the formation of the polymer chain should decrease in the course of the synthesis. Thus, a decrease in the absorption in the range of stretching vibrations of hydroxy groups whould be expected. However, by contrast, a series of strong bands at 2978, 2780, and 2439 cm^{-1} appear in the spectrum. These bands cannot be assigned to absorption of the polymer and suggest that DMF is involved in side processes accompanying the polymerization. In polycondensation of salicylidene derivatives and chlorosilanes, the release of hydrogen chloride favors decomposition of the solvent. The decomposition products, primarily dimethylamine, are capable of binding with the polymer by donor–acceptor interaction with vacant *d* orbitals of the Si atoms.

In the process, the N atom of the amine competes with the N atoms of azomethine groups, thereby decreasing the effective conjugation length. The forming complex is apparently so stable that the amine cannot be removed by simple reprecipitation. To eliminate the above-described side processes, eses we replaced DMF with a more inert dioxane in further synth.





Figures 3a and 3b show the absorption spectra of the monomers and the synthesized polymers. A considerable bathochromic shift (50–70 nm) accompanied by a hyperchromic effect and the appearance of additional long-wave bands in going from the monomers to the polymer suggest that multiple CTCs are formed in the polymer structure and the conjugation length increases.

The absorption spectra of 1,3-bis(salicylidenimino)-4-phenylazobenzene (M4) and its silicon-containing polymer P4 are markedly different. The strong

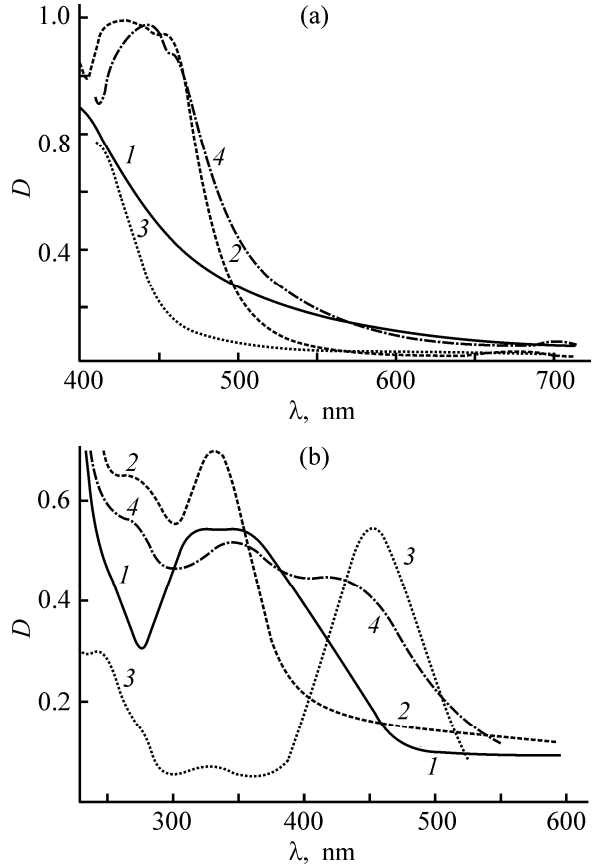


Fig. 3. UV spectra of monomers and polymers derived from (a) tetra- and (b) di(salicylidene azomethines). (*D*) Optical density and (λ) wavelength. (a) (*1*) M2, (*2*) P2, (*3*) M1, and (*4*) P1; (b) (*1*) P3, (*2*) M3, (*3*) M4, and (*4*) P4.

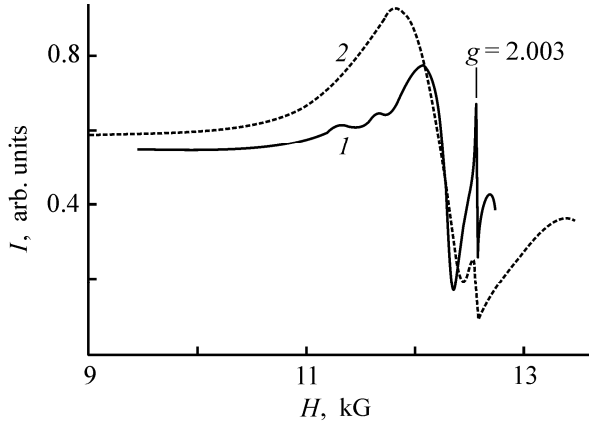


Fig. 4. ESR spectra of polymers (*1*) P1 and (*2*) P3. (*I*) Intensity and (*H*) magnetic field intensity.

absorption band of the azo group present in the spectrum of the monomer (λ = 470 nm, Fig. 3b, curve *3*) disappears in the spectrum of the polymer (Fig. 3b, curve *4*), suggesting this group is involved either in specific donor–acceptor interaction, or in a polymer-analogous transformation in the reaction with the released hydrogen chloride.

The position of the azomethine proton signal in the ^{1}H NMR spectrum also suggests a strong coordination interaction of the lone electron pair of nitrogen with the *d* orbitals of the Si atom.

Interesting information is furnished by ESR spectra. In the ESR spectra of polysalicylidene derivatives (Fig. 4), there is a narrow singlet with the *g*-factor close to that of the free electron, which suggests conjugation in the polymer chain.

CONCLUSION

In the silicon-containing poly(salicylidene azomethines) prepared, there is intramolecular donor–acceptor interaction resulting in the formation of charge-transfer complexes in the polymer backbone.

ACKNOWLEDGMENTS

The study was financially supported by the Division of Chemistry and Materials Science, Russian Academy of Sciences, program "Development of Efficient Methods for Chemical Analysis and Structural Study of Substances and Materials" (coordinator Acad. Yu.A. Zolotov).

REFERENCES

1. Archer, R.D., *Inorganic and Organometallic Polymers*, New York: Wiley, 2001.
2. Chen, H. and Archer, R.D., *Macromolecules*, 1995, vol. 28, no. 5, pp. 1609 –1617.
3. Chen, H. and Archer, R.D., *Macromolecules*, 1996, vol. 29, no. 6, pp. 1957 –1964.
4. Much, F., Haberecht, J., Bochme, U., and Roewer, G., *Monatsh. Chem.,* 1999, vol. 130, no. 1, pp. 117 –132.
5. Kalikhman, I., Krivonos, S., Ellern, A., and Kost, D., *Organometallics*, 1996, vol. 15, no. 24, pp. 5073–5076.
6. Agustin, D., Rima, G., Gornitzka, H., and Barrau, J., J. *Organomet. Chem.*, 1999, vol. 592, no. 1, pp. 1–10.
7. Kost, D. and Kalikhman, I., *Adv. Organomet. Chem.*, 2004, vol. 50, pp. 1–106.
8. Kost, D., Kalikhman, I., and Raban, M., *J. Am. Chem. Soc.*, 1995, vol. 117, no. 46, pp. 11 512–11 522.
9. Kalikhman, I., Gostevskii, B., Sivaramakrishna, A., et al., *J. Organomet. Chem.*, 2003, vol. 686, no. 1, pp. 202–214.
10. Gur'yanova, E.N., Gol'dshtein, I.P., and Romm, I.P., *Donorno-aktseptornaya svyaz'* (Donor–Acceptor Bond), Moscow: Khimiya, 1973.
11. Andrews, L.J. and Keefer, R.M., *Molecular Complexes in Organic Chemistry*, San Francisco: Holden-Day, 1964.

ISSN 1070-4272, Russian Journal of Applied Chemistry, 2008, Vol. 81, No. 8, pp. 1403–1409. © Pleiades Publishing, Ltd., 2008.
Original Russian Text © E.S. Sinitsyna, E.N. Vlasova, E.G. Vlakh, T.B. Tennikova, 2008, published in Zhurnal Prikladnoi Khimii, 2008, Vol. 81, No. 8, pp. 1326–1332.

MACROMOLECULAR CHEMISTRY AND POLYMERIC MATERIALS

Monolithic Methacrylate Polymeric Sorbents: Development of Methods for Chemical Modification of the Surface for the Subsequent Bioaffine Functionalization

E. S. Sinitsyna, E. N. Vlasova, E. G. Vlakh, and T. B. Tennikova

Institute of Macromolecular Compounds, Russian Academy of Sciences, St. Petersburg, Russia

Received January 16, 2008

Abstract—Copolymers containing aldehyde, succinimidyl carbonate, and imidazolecarbamate groups were prepared by polymer-analogous transformations of epoxy groups of a macroporous monolithic polymeric support derived from glycidyl methacrylate and ethylene glycol dimethacyrlate. The effect of certain parameters on the course of the copolymer modification and immobilization of a protein on the surface of the polymeric support was studied. The possibility of using the matrices obtained for development of biorecognizing systems was examined.

DOI: 10.1134/S1070427208080168

In the late 1980s–early 1990s, novel polymeric sorbents were developed: solid macroporous polymers prepared as monoliths of various designs (continuous macroporous phases) [1, 2]. These materials are characterized by a constant pore structure which is formed and controlled directly in the synthesis step and is preserved in the dry state. The morphological and hydrodynamic properties of continuous macroporous phases allow separation processes to be performed with very high, anomalous for liquid chromatography, flow rates of the mobile phase [3]. Performing high-speed separations becomes possible owing to the nearly full absence of diffusion hindrance to the normal phase transfer of a substance.

Continuous macroporous phases are prepared by in situ polymerization directly inside an empty column or another mold of the required shape and design. The necessary condition for the pore structure formation is the presence in the polymerization mixture of an inert solvent acting as a porophore. The main criterion of a possible use of a substance as a porophore is its thermodynamic compatibility with the forming polymer [4].

Since the second half of the 1990s, the interest in continuous macroporous phases showed avalanche-like growth. Monolithic materials based on a wide range of synthetic polymers, such as polystyrene, polyacrylates, polymethacrylates, polyacrylamide, etc., have been developed and are used in practice.

The development of the ideology of modern affine separations is closely associated with the development of new support materials and new approaches to the preparation of affine sorbents. Among monolithic polymeric sorbents used to prepare affine supports are copolymers of 2,3-epoxypropyl methacrylate (glycidyl methacrylate, GMA) with ethylene glycol dimethacrylate (EDMA) [3, 5, 6]. An advantage of GMA–EDMA matrices is their mechanical strength and chemical stability. An extremely important property of these materials is that the cross-linked copolymer contains reactive epoxy groups with which diverse polymer-analogous transformations can be performed for functionalization of the sorbent surface. It is known that the procedure for covalent immobilization of a ligand on the surface strongly affects the ligand immobilization capacity and the immobilization rate. Therefore, it was interesting to use different chemical reactions for introducing a bioadsorption site into the structure of a polymer matrix.

Thus, the goal of this study was to prepare modified macroporous supports based on GMA–EDMA

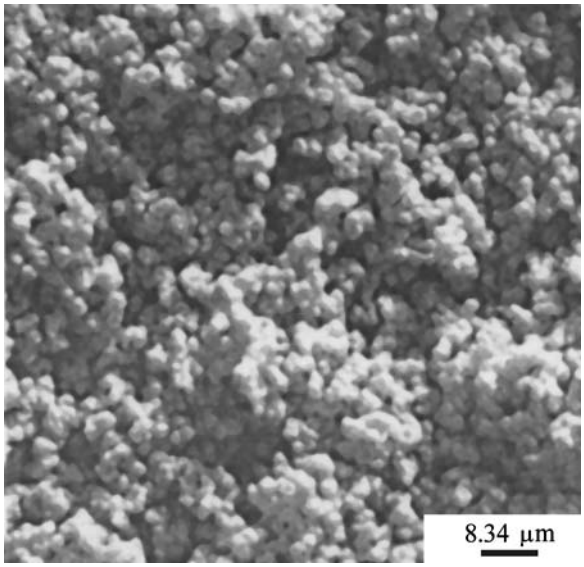


Fig. 1. Electron micrograph of the surface of GMA–EDMA continuous macroporous support prepared by radical photoinitiated copolymerization.

copolymer, examine the effect of various parameters on the covalent immobilization of proteins on the surface of modified matrices, and test the performance of the supports obtained with respect to a model affine pair.

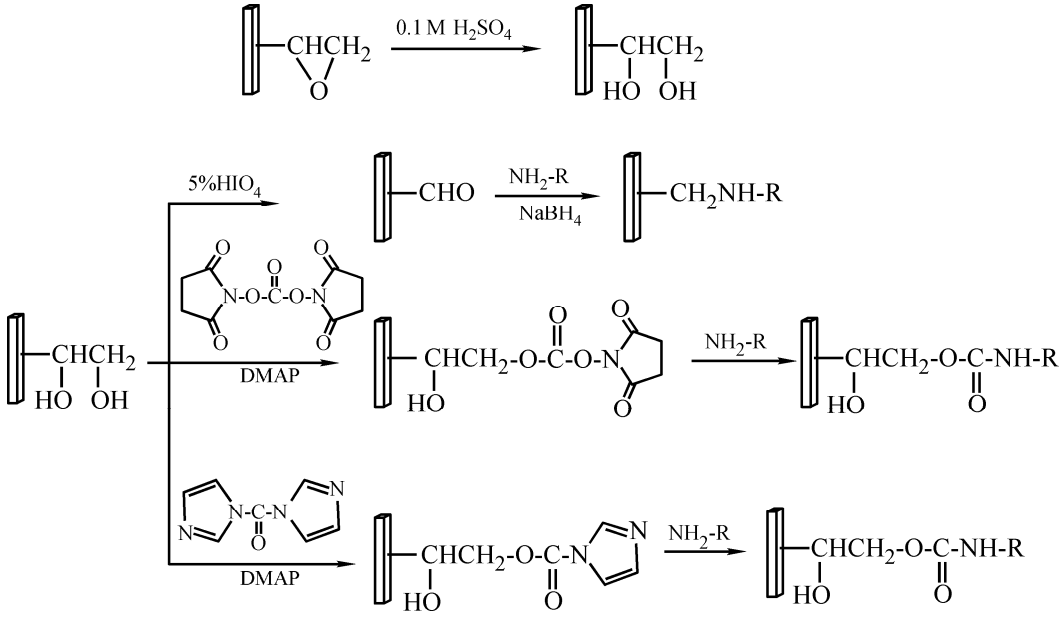
EXPERIMENTAL

The most widely used procedure for preparing continuous macroporous stationary phases based on GMA–EMDA copolymer is thermally initiated radical polymerization of the corresponding monomers in the presence of porophores. However, to prepare monolithic columns with a diameter exceeding the height, or thin layers (planar analytical test systems), it is preferable to use photoinitiation, which not only requires no elevated temperatures, but also is less time-consuming. The photoinitiated free-radical polymerization of GMA and EDMA has been studied previously [7], with the suitable initiator found and optimal synthesis conditions determined. The monomers, solvent-porophore (cyclohexanol), and initiator, 2-hydroxy-2,2-dimethylacetophenone (Darocure-1173) were purchased from Merck–Schuchard (Germany). The following volume ratios of the reactants were used: GMA : EDMA = 60 : 40, porophore : monomers = 60 : 40; the initiator concentration was 1 wt % relative to the monomers. The irradiation time was 20 min, and the copolymer yield, 93%.

To perform photoinitiated copolymerization of GMA and EDMA, we used as a UV source a 125 W mercury lamp with a wide radiation spectrum and constant intensity (Philips, the Netherlands). For quantitative determination of the mean pore size and pore-size distribution, we used a Thermoquest Pascal 440, mercury porosimeter (Rodano, Italy). The weight of the sample taken for the analysis was about 100 mg. According to the data of intrusion mercury porosimetry, the mean pore radius of the sorbent obtained was 0.8 μm at a surface area of 28 $m^2 g^{-1}$ and 55% porosity. The pore characteristics obtained provide free penetration of protein molecules inside the 3*D* pore space in the course of immobilization and subsequent affine interaction of the complements, and also a high adsorption capacity of the support. According to theoretical calculations, the content of epoxy groups in the copolymer is within 3.9–4.2 mmol g^{-1} sorbent.

The morphology of the polymer samples obtained was studied with a JSM-35 CF scanning electron microscope (Japan). The thickness of the sputtered gold layer was 50–100 Å. An electron micrograph of the surface of the continuous macroporous polymeric material obtained is shown in Fig. 1. In addition, we used for this purpose the qualitative "ink test" which was performed by immersing the samples into an alcoholic solution of Methylene Blue for 1 min. The homogeneity of the pore structure was estimated from the extent of penetration of the dye into the sorbent pores. The results of our experiments show that the chosen synthesis conditions allow preparation of a polymeric support with a homogeneous structure of the pore space and a narrow pore-size distribution.

To introduce highly reactive groups into the macroporous polymeric support for the subsequent reaction with a biospecific ligand (protein), we used polymer-analogous transformations. An advantage of this approach to introduction of highly reactive groups is that of the pore structure of the starting copolymer is preserved, which is certainly very important for the subsequent analysis based on affine interactions. As such highly reactive groups we chose aldehyde, succinimidyl carbonate, and imidazolecarbamate groups. The scheme of reactions involved in the modification and immobilization of a bioligand on the surface of the GMA–EDMA copolymer is given below:



In the first step, we performed hydrolysis of native epoxy groups of GMA–EDMA copolymer to vicinal diol. The hydrolysis was performed in an excess of 0.1 M sulfuric acid at 80°C for 6 h. The degree of hydrolysis of the epoxy groups was estimated by IR spectroscopy. For qualitative and quantitative analysis, IR spectra were measured using equal weighed portions of the starting epoxy sorbent and the hydroxy sorbent obtained. Samples for IR spectroscopy were prepared by compacting a uniform mixture of 5 mg of finely ground GMA–EDMA copolymer and 600 mg of KBr. The spectra were measured in the range 200–4000 cm^{-1} with a Specord M 80 automatic spectrometer (Carl Zeiss, Germany).

The disappearance of all the characteristic absorption bands of the epoxy ring (1250, 950–810, and 840–750 cm^{-1}) and the appearance of a broad band in the range 3200–3600 cm^{-1}, corresponding to stretching vibrations of the OH groups, and a band at about 1100 cm^{-1}, corresponding to stretching vibrations of secondary hydroxy groups, are indicative of the occurrence of hydrolysis (Fig. 2a). The degree of hydrolysis was estimated quantitatively using the so-called method of internal reference [8]. We found that the conversion of epoxy groups into hydroxy groups was 80%.

An intrusion mercury porosimetric analysis of the samples obtained after hydrolysis showed that the hydrolysis somewhat affected the mean pore size. In particular, we found that the mean pore radius increased by 50 nm and the total content of pores coarser than 500 nm increased from 87 to 90%. It is also important that samples of the macroporous polymeric support obtained after hydrolysis of the epoxy groups of GMA–EDMA preserved the external appearance and mechanical properties of the monolithic matrix.

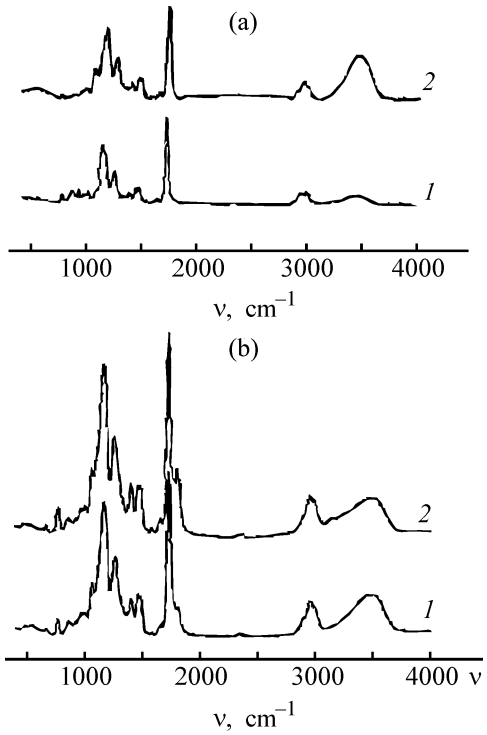


Fig. 2. IR spectra of (a) (*1*) initial GMA–EDMA copolymer, (*2*) copolymer formed upon hydrolysis of epoxy groups, and (b) copolymer modified with 1,1'-carbonyldiimidazole. (ν) Wavenumber. (b) Amount of modifying agent, % of the total amount of hydroxy groups: (*1*) 8 and (*2*) 180.

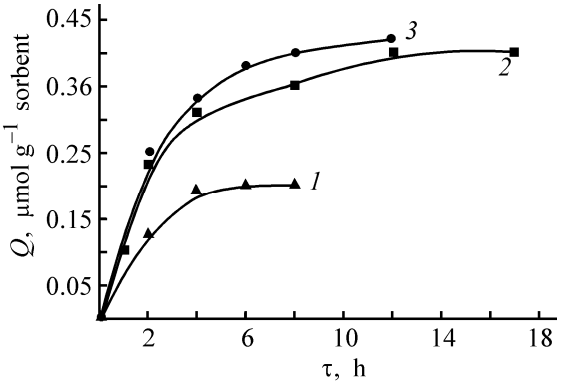


Fig. 3. Amount Q of the protein covalently bound to the surface of modified materials as a function of the time t of copolymer modification: (*1*) oxidation, (*2*) modification with 1,1'-carbonyldiimidazole, and (*3*) modification with bis(*N*-succinimidyl) carbonate; the same for Fig. 4.

With the aim to generate aldehyde groups on the surface of 2,3-dihydroxypropyl methacrylate–ethylene glycol dimethacrylate (DHPMA–EDMA) copolymer prepared by hydrolysis of epoxy groups of GMA–EDMA copolymer, we oxidized the hydroxy groups with an excess of a 5% solution of periodic acid in 90% acetic acid. The amount of periodic acid taken per 150 mg of the copolymer was 110 mg (0.48 mmol). The reaction was performed by keeping the polymeric support in the oxidant at 22°C. After the reaction completion, the sorbent was washed with distilled water for 3 h, with 2 N NaCl for 1 h, and again with distilled water for 3 h. The presence of aldehyde groups in the oxidized samples was qualitatively confirmed by the specific reaction with fuchsinsulfurous acid (Schiff reagent) [9]. The uniform lilac coloration of the polymeric support confirmed the presence of aldehyde groups in the modified copolymer. An IR analysis, however, appeared to be inefficient because the absorption bands of the aldehyde groups (1724 cm^{-1}) were obscured by bands of ester groups (1730 cm^{-1}) present in a large excess.

The modification of DHPMA–EDMA copolymer with bis(*N*-succinimidyl) carbonate (Aldrich, Germany) was performed in acetonitrile in the presence of 4-(dimethylamino)pyridine (DMAP) (Merck, Germany). Per 150 mg of the polymer, we took 44 mg of bis(*N*-succinimidyl) carbonate (0.17 mmol) and 33 mg of DMAP (0.27 mmol). The amount of the taken modifying agent corresponded to an 18% theoretical conversion of hydroxyl groups. The reaction was performed at 22°C by immersing the polymer matrix into a solution of the modifying agent. After the modification was complete, the copolymer was washed using a laboratory shaker with acetonitrile for 2 h and then with distilled water for 1 h.

The introduction of succinimidyl carbonate groups was confirmed by IR spectroscopy. A shoulder appearing at about 1790 cm^{-1} was indicative of the presence of the five-membered imide ring in the copolymer and hence of the occurrence of the modification.

The modification of DHPMA–EDMA copolymer with carbonyldiimidazole was performed in two modes. In the first mode, the amount of the modifying agent was 18% relative to hydroxy groups, and in the second mode it was 180%. For this purpose, the hydroxyl-containing sample of the copolymer was placed in a solution containing 1,1-carbonyldiimidazole (Aldrich, Germany) and DMAP. Acetonitrile was used as a solvent. The amount of 1,1-carbonyldiimidazole taken for modification of 150 mg of the copolymer was 31 and 310 mg (0.19 and 1.90 mmol), and that of DMAP, 33 and 330 mg (0.27 and 2.70 mmol). The reaction and washing conditions were the same as in the modification with bis(*N*-succinimidyl) carbonate.

The conversion of hydroxy groups was judged from the IR data. For the sample obtained at a deficiency of the modifying agent (i.e., with an excess of hydroxy groups of the polymer), a small shoulder appeared in the IR spectrum at 1804 cm^{-1}. With an excess of the mod-ifying agent, the band in the same region became more pronounced (Fig. 2b). In both cases, the characteristic bands appearing in this range correspond to the absorption of imidazolecarbamate groups.

The amount of imidazolecarbonate groups introduced into the structure of the methacrylate copolymer was estimated by elemental analysis. With the modifying agent taken in an amount of 18%, the content of imidazolecarbamate groups introduced into the copolymer structure was 5–7.5%, which corresponds to 300–450 μmol of reactive groups per gram of the sorbent. With a 180% excess of the modifying agent, the solid-phase reaction occurs with 30% conversion and the amount of imidazolecarbamate groups introduced into the copolymer structure is 15%, or approximately 900 μmol g^{-1} sorbent.

The progress of the covalent binding of proteins in time is illustrated by Fig. 3. For the aldehyde-containing copolymer, the maximal binding capacity is attained within 4 h, and for the copolymers modified with the other two agents, within 8 h. The immobilization capacities obtained were compared with the amount of the protein introduced into the structure of the GMA–EDMA copolymer by the reaction between the epoxy groups of the sorbent and the amino groups of the protein. We found that, in the latter case, the maximal capacity was 0.2 μmol of protein per gram of

the sorbent, and it was attained within 16–18 h at 35°C. At the same time, for the aldehyde-containing sample, the same immobilization capacity was attained in 4 h at 22°C. With the other two modification procedures, the same amount of the protein was bound within 1.5–2 h at 22°C.

The schemes of the reactions of covalent immobilization of proteins on the surface of supports containing aldehyde, succinimidyl carbonate, and imidazolecarbamate groups are given above. To develop and optimize a procedure for covalent binding of a proten on the surface of modified polymeric supports, we examined the effect of certain experimental parameters on the capacity of the matrices obtained. In particular, we examined the dependences of the amount of the immobilized ligand on the reaction time, initial protein concentration, pH of solution, and temperature.

The procedure of protein immobilization on the surface of a monolithic macroporous support was performed by incubation in a protein solution. In experiments on optimizing the immobilization conditions, we used bovine serum albumin (BSA) and soyben trypsin inhibitor (STRI), both purchased from Sigma–Aldrich, Germany. After the reaction completion, the polymeric support was washed with the reaction buffer solution for 40 min, with 2 M NaCl (three portions, for 15 min with each portion), and with a 0.01 M sodium phosphate buffer solution (pH 7.0) containing 0.15 M NaCl for 40 min. The amount of the immobilized ligand (mg) was determined from the difference between the ligand amounts in the initial solution (mg) and in the solution after immobilization plus wash solutions (mg). The protein content was determined by the Lowry –Folin method [10]. The optical density of solutions was determined with an SF-26 spectrophotometer (LOMO, Russia). After the immobilization, the azomethine bonds were reduced with sodium borohydride. The residual imidazolecarbamate and succinimidyl carbonate groups were blocked with ethanolamine.

The dependence of the amount of the ligand covalently linked to the surface of the polymeric matrix on the protein concentration in solution shows that, with all the modified supports, the maximum capacity is attained at a protein concentration in solution of 4.5–5.0 mg ml^{-1}. Furthermore, the ligand binding in biofunctionalization of the starting GMA–EDMA copolymer also reaches a maximum at this concentration .

The influence of pH on the covalent binding of the protein with aldehyde, succinimidyl carbonate, and imidazolecarbamate groups was studied with STRI as an example. The maximal binding of the protein with

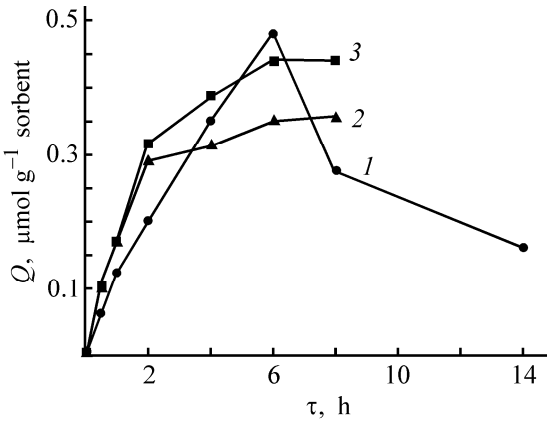


Fig. 4. Amount Q of the protein covalently bound to the surface of modified materials as a function of the reaction time τ. Initial protein concentration 5 mg ml^{-1}, pH 8.1 for the aldehyde-containing support and 7.6 for the supports containing succinimidyl carbonate and imidazolecarbamate groups.

the sorbent (15 mg g^{-1}, or 0.63 μmol g^{-1}) for the aldehyde-containing copolymer was observed at pH 8.1–9.4. For the other two reaction groups, the immobilization capacity (12 mg g^{-1}, or 0.5 μmol g^{-1}) was maximal at pH 7.6–9.4, varying in this range insignificantly.

The immobilization data allowed us to calculate the surface area occupied by the covalently bound protein macromolecules, using the equation

$$S_{surf} = \pi R^2 Q N_A,$$

where S_{surf} is the surface area occupied by the protein (m^2 g^{-1}); N_A, Avogadro number (mol^{-1}); R, radius of the protein molecule (m); and Q, amount of the substance (mol g^{-1}).

In the case of STRI immobilization, the surface area occupied by the protein was 3.5–5.0 m^2 g^{-1} for the aldehyde-containing support, which corresponds to 13–18% of the total surface area of the pores. For the supports containing succinimidyl carbonate and imidazolecarbamate groups, these values decreased to 3.5–4.0 m^2 g^{-1}, which corresponded to a 13–14% coverage of the pore surface. In the case of immobilization on the initial epoxy-containing polymeric support, the related quantity obtained for covalent binding of STRI was 2 m^2 g^{-1}, which corresponded to a 7% coverage of the surface area of the pore space of the sorbent.

To determine the optimal time of biofunctionalization of the polymeric materials obtained, we examined the dependence of the amount of the immobilized model protein, BSA, on the reaction time. As can be seen from Fig. 4, the maximal BSA binding is attained in 6 h for all the three modified forms of the polymeric

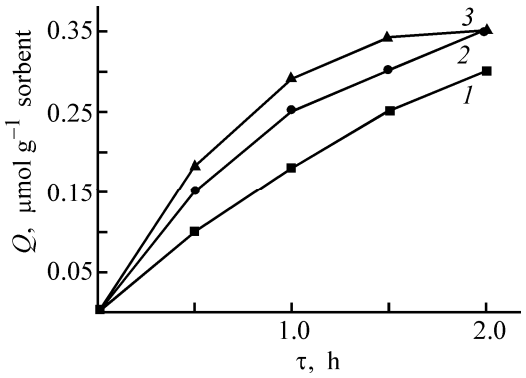


Fig. 5. Amount Q of BSA immobilized on the surface of the imidazolecarbamate-containing support vs. the reaction time τ. Temperature, °C: (*1*) 22, (*2*) 30, and (*3*) 37. Initial protein concentration 5 mg ml^{-1}, pH 7.6.

materials. In the case of aldehyde-containing supports, this is followed by a sharp decrtease in the amount of the bound protein, apparently due to instability of the azomethine bonds formed. For succinimidyl carbonate and imidazolylcarbamate supports, the maximal binding capacities were attained in 6 h and then remained virtually unchanged. As noted above, the maximal protein binding, equal to 0.2 μmol g^{-1} in the reaction of BSA amino groups with epoxy groups of the GMA–EDMA sorbent, was attained in 16 h, and in the case of aldehyde groups, it was attained in 2 h. At the same time, in the case of succinimodyl carbonate groups, the immobilization capacity of the sorbent in reached 0.3 μmol g^{-1} 2 h, and in the case of imidazolecarbamate groups, 0.28 μmol g^{-1}. Furthermore, the use of epoxy groups for the immobilization, along with the slow kinetics, does not allow the sorbent capacity to be raised, whereas for the modified copolymers, the capacity can be raised by more than a factor of 2.

With the aim to examine the effect of temperature on the ligand immobilization, with the supports containing imidazolecarbamate groups as examples, we performed experiments at 22, 30, and 37°C, with the reaction time varied from 0.5 to 2 h. The data we obtained (Fig. 5) show that, with increasing temperature, the amount of the protein bound in a given time noticeably grows. In particular, the amount of the protein bound in 2 h at 22°C is bound in 1 h at 37°C.

To confirm the possibility of using the modified supports for the development of biorecognizing systems, we used two approaches:

(1) frontal method of affinity high-performance monolithic disc chromatography (HPMDC) and (2) analysis using test systems (planar 3*D* biochips).

As HPMDC sorbent we used commercial macroporous discs based on GMA–EDMA copolymer (CIM® Epoxy Disks, BIA Separations d.o.o., Ljubljana, Slovenia, of size 12×3 mm, mean pore size 1 μm, porosity 60%. As a model affine pair we used the trypsin (TR)–STRI pair. To determine the apparent dissociation constants of the affine complex we passed trypsin solutions across a disc containing immobilized STRI as ligand, to complete adsorption saturation of the affine sorbent surface, following the procedure described in [3]. The results of our dynamic (chromatoghraphic) experiments show that all the affine matrices prepared by intermediate modification of CIM discs with aldehyde, succinimidyl carbonate, and imidazolecarbamate groups are capable of specific binding of trypsin. For all the sorbents prepared, the dissociation constants for the TR–STRI pair were commensurable, on the order of 10^{-5} mol l^{-1}, which confirms that the materials we obtained are suitable for the development of biorecognizing systems.

In parallel with the dynamic experiments, we examined the possibility of using the sorbents based on the modified polymers as static test systems. As a model of a planar biochip we used a thin layer of modified GMA–EDMA copolymer bound to a glass support [11]. Analysis on the surface of polymer layers functionalized with trypsin inhibitor was performed by the method of fluorescence densitometry. Spots were detected at λ = 365 nm. Trypsin solutions were prepared by dissolving trypsin marked with fluorescamin in 0.01 M sodium phosphate buffer solution containing 0.15 M NaCl, pH 7.0. The resulting solutions containing 0.002–2.0 mg ml^{-1} protein were applied in 0.3-μl portions onto the surface of a polymer layer containing immobilized STRI. Correspondingly, the trypsin content in the adsorption spots was in the range 0.0006–0.6 μg/spot (spot is the formed analytical zone 1.5 mm in diameter). The biochip with the applied protein spots was kept in the dark for 10 min and then successively washed with a 0.01 M sodium phosphate buffer solution containing 0.15 M NaCl for 40 min and with a 2 N NaCl solution also for 40 min. After that, the biochip was washed with distilled water for 10 min. After the washing was completie, solutions of marked trypsin of known concentration were applied onto the polymer layer surface to construct the calibration plot. We found that the sensitivity limit of the bioassay performed using aldehyde affine matrices was 0.5 ng of trypsin per spot, or 20 fmol/spot, i.e., the procedure is four times more sensitive than with the other two modified forms of the polymer.

CONCLUSIONS

(1) Macroporous methacrylate supports containing aldehyde, succinimidyl carbonate, and imidazolecarbamate groups were prepared by chemical transformations of epoxy groups of the glycidyl methacrylate–ethylene glycol dimethacrylate copolymer.

(2) It was demonstrated that the modification methods chosen do not alter significantly the pore size of macroporous supports, which is important for their subsequent applications.

(3) It was shown that affine sorbents based on modified continuous macroporous phases are capable of fast and sterically unhindered specific binding of biological partners one of which is covalently bonded to the sorbent surface.

ACKNOWLEDGMENTS

The authors are grateful to M.Yu. Slabospitskaya for assistance in the experiments and participation in the discussion of the results.

The study was supported by grants of the St. Petersburg Government (PD06-1.3-67) and Russian Foundation for Basic Research (project no. 06-03- 32 363).

REFERENCES

1. Tennikova, T.B., Bleha, M., Svec, F., et al., *J. Chromatogr.*, 1991, vol. 555, pp. 97–107.
2. Tennikova, T.B. and Svec, F., *J. Chromatogr.*, 1993, vol. 646, pp. 279–288.
3. Ostryanina, N.D., Il'ina, O.V., and Tennikova, T.B., *J. Chromatogr. B*, 2002, vol. 770, pp. 35–43.
4. Svec, F. and Frechet, J.M.J., *Monolithic Materials: Preparation, Properties and Applications*, Svec, F., Tennikova, T.B., and Deyl, Z., Eds., Amsterdam: Elsevier, 2003, pp. 19–50.
5. Vlakh, E. and Tennikova, T., *J. Sep. Sci.*, 2007, vol. 30, pp. 2801–2813.
6. Meringova, L.F., Leont'eva, G.F., Gupalova, T.V., et al., *Biotekhnologiya*, 2000, vol. 4, pp. 45–53.
7. Khimich, G.N., Rakhmatullina E.N., Slabospitskaya, M.Yu., and Tennikova, T.B., *Zh. Prikl. Khim.*, 2005, vol. 78, no. 4, pp. 623–628.
8. Dechant, J., Danz, R., Kimmer, W., et al., *Ultrarotspektroskopische Untersuchungen an Polymeren*, Berlin: Akademie, 1972.
9. Shriner, R.L., Fuson, R.C., Curtin, D.Y., and Morrill, T.C., *The Systematic Identification of Organic Compounds. A Laboratory Manual*, New York: Wiley, 1980, 6th ed.
10. Dawson, R.M.C., Elliot, D.C., Elliot, W.H., and Jones, K.M., *Data for Biochemical Research*, Oxford: Clarendon, 1986.
11. Slabospitskaya, M.Yu., Vlakh, E.G., Razdol'skaya, N.V., et al., in *Sbornik trudov konferentsii "Izmeritel'nye i informatsionnye tekhnologii v okhrane zdorov'ya "Metromed-2007""* (Proc. Conf. "Measurement and Information Technologies in Health Protection "Metromed-2007""), St. Petersburg, April 17–19, 2007, pp. 191–196.

ISSN 1070-4272, Russian Journal of Applied Chemistry, 2008, Vol. 81, No. 8, pp. 1410–1413. © Pleiades Publishing, Ltd., 2008.
Original Russian Text © E.N. Khimich, G.S. Buslaev, A.V. Zdravkov, N.N. Khimich, M.G. Voronkov 2008, published in Zhurnal Prikladnoi Khimii, 2008, Vol. 81, No. 8, pp. 1333–1336.

MACROMOLECULAR CHEMISTRY AND POLYMERIC MATERIALS

Polysiloxane Structures Cross-Linked with Hydroquinone and Phloroglucinol

E. N. Khimich, G. S. Buslaev, A. V. Zdravkov, N. N. Khimich, and M. G. Voronkov

Grebenshchikov Institute of Silicate Chemistry, Russian Academy of Sciences, St. Petersburg, Russia

Received November 30, 2007

Abstract—Organic–inorganic hybrids in the system polyhydric phenols–silica were prepared by hydrolytic polycondensation of tetraethoxysilane in the presence of di- and trihydroxy derivatives of benzene. From these materials, film coatings were prepared, and their physical properties were studied

DOI: 10.1134/S107042720808017X

One of interesting and promising fields of polysiloxane chemistry is the development of methods for constructing polymeric composites exhibiting valuable properties. Such composites surpass unmodified polysiloxanes in many technical characteristics [1].

Composites prepared as organic–inorganic hybrids combine the elasticity and flexibility of organic components with high heat resistance, mechanical strength, and chemical stability of inorganic materials [2], which expands the fields and possibilities of their application [3].

The widely used way to prepare hybrid coatings is incorporation into a polysiloxane matrix of film-forming organic polymers that form thermoplastic coatings with a set of valuable physicochemical properties (high elasticity, mechanical strength, abrasion resistance, etc.) [4, 5]. Of particular interest for designing hybrid coatings for various purposes is the use of ogranosilicon monomers and oligomers, as they are readily soluble in the majority of organic solvents. This allows preparation of solutions with a relatively high content of the main substance (>40%) [6]. The technology of forming polymeric coatings from such solutions is particularly promising because of their lower viscosity and lower surface tension (better wettability), compared to solutions of the corresponding polymers. Owing to the increased covering capacity of such solutions, they can penetrate into pores and defects of the surfaces being treated. With hybrid composites based on organosilicon monomers and oligomers, the polymeric coating is formed not only on the surface but also in pores of a material.

One of the simplest and promising methods for preparing a polysiloxane matrix is the sol–gel procedure of hydrolytic polycondensation of tetraalkoxysilanes [7]. The sol–gel process performed in the presence of organic compounds yields organic–inorganic hybrids [8].

With polyphenols, the stability and uniformity of structures formed in the process should be provided by chemical binding of the system components:

$$-\overset{|}{\underset{|}{Si}}-H + HO-Ar \rightarrow -\overset{|}{\underset{|}{Si}}-O-Ar + HX,$$

where X = OR, OH, Cl, $-C\begin{matrix}O\\ \diagdown\\ OR\end{matrix}$.

In this study, we examined the possibility of performing heterofunctional polycondensation of oligoethoxysilanes with 1,4-dihydroxybenzene (hydroquinone) or 1,3,5-trihydroxybenzene (phloroglucinol).

EXPERIMENTAL

The silicon content of the samples was determined gravimetrically by decomposition of a weighed portion of a substance with a mixture of 20% oleum with concentrated nitric acid, followed by calcination of the residue to constant weight at 800°C [9].

The density ρ (g cm^{-3}) of the solid materials obtained was measured by the Archimedean method (toluene–water system). The porosity W (%) was determined from the ethanol adsorption–desorption with a McBain vacuum spring balance [10]. The microhardness (MH) was measured with a PMT-3 microhardness meter.

All the above parameters were determined for samples that did not crack in the course of drying and measurements. The gel point was characterized by the time after which the system lost mobility.

Thermal analysis was performed with a Q-1500D derivatograph (Hungary). The samples were heated to 1000°C at a rate of 20 deg min^{-1}.

Electron-microscopic examination of xerogels was performed with an EM-125 device at an accelerating voltage of 75 kV.

To prepare hybrid coatings by the sol–gel procedure, to tetraethoxysilane hydrolyzate we added organic components: hydroquinone **I** (Vekton) or phloroglucinol **II** (Merck). We also used 1,4-bis(triethoxysilyloxy)benzene **III** and 1,3,5-tris(triethoxysilyloxy)benzene **IV** prepared by the reactions of $Si(OEt)_4$ with hydroquinone and phloroglucinol in 2 : 1 and 3 : 1 molar ratios, respectively, in the presence of CF_3COOH as catalyst, according to the general equation

$$n\mathrm{Si(OEt)_4} + (\mathrm{HO})_n\mathrm{C_6H_{6-n}} \xrightarrow{\mathrm{H^+}} [(\mathrm{EtO})_3\mathrm{SiO}]_n\mathrm{C_{6-n}H_2} + n\mathrm{EtOH},\ \ n = 2, 3.$$

1,4-Bis(triethoxysilyloxy)benzene III. A mixture of 10.0 g (0.048 mol) of tetraethoxysilane (TEOS), 1.32 g (0.012 mol) of hydroquinone, and 0.2 g of CF_3COOH was refluxed for 4 h, after which the released ethanol was distilled off. The residue was distilled in a vacuum to obtain 2.5 g (yield 48%) of **III**, bp 180–190°C (0.01 mm Hg). ^{1}H NMR spectrum ($CDCl_3$): 6.88 s (4H, H_{ar}), 3.89 q (12H, –Si–O–CH_2–), 1.23 t (18H, CH_3).

1,3,5-Tris(triethoxysilyloxy)benzene IV was prepared similarly from 10.0 g (0.048 mol) of TEOS, 1.0 g (0.008 mol) of phloroglucinol, and 0.2 ml of CF_3COOH. Yield 1.2 g (25%), bp 210–220°C (0.01 mm Hg). ^{1}H NMR spectrum ($CDCl_3$): 6.64 s (3H, H_{ar}), 3.85 q (18H, –Si–O–CH_2–), 1.24 t (27H, CH_3). Compounds **III** and **IV** are readily hydrolyzable colorless liquids with a weak odor.

To prepare a polysiloxane matrix, we used a mixture of polyethoxysiloxanes **V** and **VI** prepared by controllable hydrolytic polycondensation of tetraethoxysilane under the conditions of acid catalysis.

To prepare oligomers **V** and **VI**, we took 9.8 g (0.044 mol) of TEOS, 4.8 g (0.104 mol) of ethanol, and 1.1 and 1.2 g of 0.01 N HCl, respectively. The components were mixed in the following order: ethanol, HCl solution, TEOS. The resulting mixture was placed in polypropylene jars with screwed caps (three samples for each system) and kept for 2–4 days in a thermostat at 90°C to obtain a xerogel (Table 1).

Table 1. Gelation rate in the $Si(OEt)_4$–H_2O–EtOH–HCl system at various amounts of HCl solution

Oligomer	Amount of 0.01 N HCl, g	SiO_2 content of liquid oligomer, %	t_1*	t_2*	State of solidified gel
			h		
V	1.1	59.13	98	106	Monolithic
IV	1.2	57.90	44	48	″

* (t_1) Time of formation of the liquid oligomer with the maximum attained SiO_2 content at which the mixture remained mobile; (t_2) gelation time.

Table 2. Physicochemical properties of polymer film samples **VII–XI***

Composite	Oligomer	Phenol content, g	t,** h	ρ, g cm^{-3}	W, %	MH, kg mm^{-2}
VII	**V**	0.03	18	1.45	37	90
VIII	**V**	0.045	18	1.46	35	90
IX	**VI**	0.045	18	1.44	37	88
X	**VI**	0.03	21	1.48	35	96
XI	**VI**	0.03	23	1.53	32	101

* Films prepared with (**VII–IX**) hydroquinone and (**X**, **XI**) phloroglucinol.

** (t) Time of film drying at 80°C.

The formation of polymeric composites based on products of the condensation of a mixture of oligoethoxysiloxanols **V** and **VI** with hydroquinone and phloroglucinol involves the following main reactions (with hydroquinone as example):

$$2\text{–}\overset{|}{\underset{|}{\mathrm{Si}}}\text{–OH} + \mathrm{HO–C_6H_4OH} \rightarrow \text{–}\overset{|}{\underset{|}{\mathrm{Si}}}\text{–O–C}_6\mathrm{H_4}\text{–O–}\overset{|}{\underset{|}{\mathrm{Si}}}\text{–} + 2\mathrm{H_2O},$$

$$2\text{–}\overset{|}{\underset{|}{\mathrm{Si}}}\text{–OEt} + \mathrm{HO–C_6H_4OH} \rightarrow \text{–}\overset{|}{\underset{|}{\mathrm{Si}}}\text{–O–C}_6\mathrm{H_4}\text{–O–}\overset{|}{\underset{|}{\mathrm{Si}}}\text{–} + 2\mathrm{EtOH}.$$

To perform these reactions, to 0.5 g of a mixture of polyethoxysiloxanols **V** or **VI** in dimethylacetamide (DMAA) heated to 70–80°C we added a solution of hydroquinone **I** or phloroglucinol **II** in DMAA and 0.2 ml of CF_3COOH. The amount of hydroquinone was varied from 0.015 to 0.075, and that of phloroglucinol, from 0.01 to 0.04 g. The hot mixture was cast onto a glass plate and dried at 80°C in a DMAA vapor for 1–2 days. In the process, polymer films formed on the glass surface. The physicochemical parameters of some film samples are listed in Table 2.

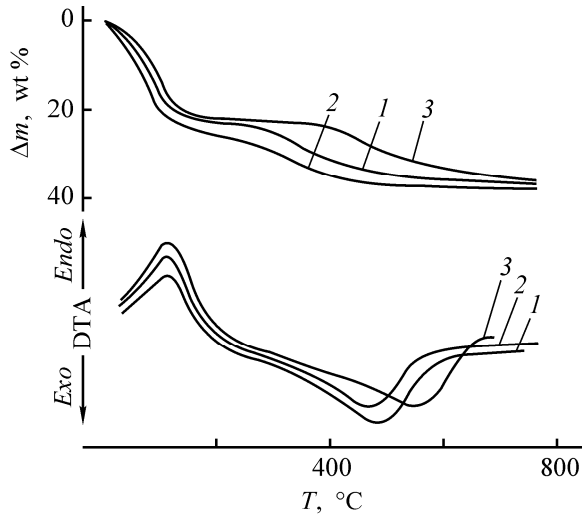


Fig. 1. DTA and TG curves of composites **VII**, **VIII**, and **X**. Film prepared with (*1*, *2*) hydroquinone (samples **VII** and **VIII**, respectively) and (*3*) phloroglucinol (sample **X**). (Δm) Weight loss and (T) temperature; the same for Fig. 2.

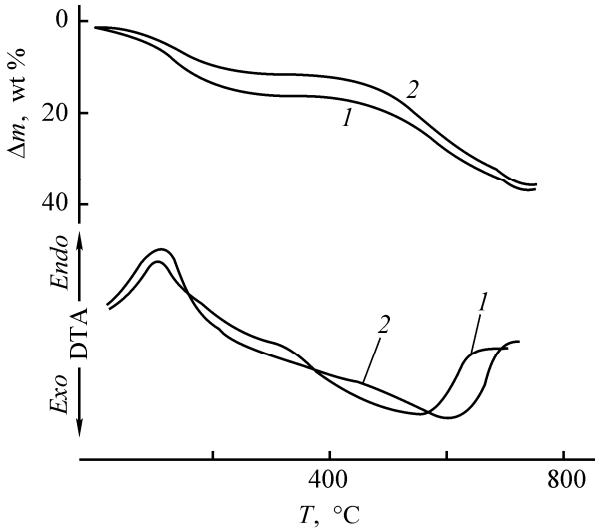


Fig. 2. DTA and TG curves of film samples **XVI** and **XVII**. Film prepared from (*1*) 1,4-bis(triethoxysilyloxy)-benzene **III** and oligomer **V** and (*2*) 1,3,5-tris(triethoxysilyloxy)benzene **IV** and oligomer **VI**.

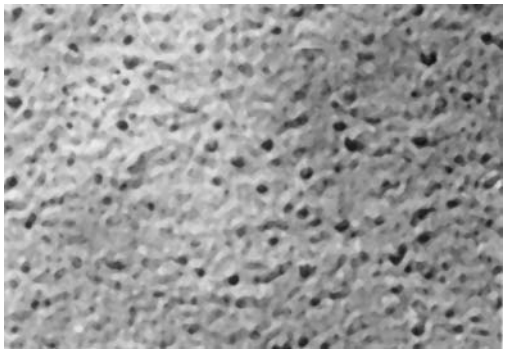


Fig. 3. Electron micrograph of a film of composite **VIII**. Magnification 80 000.

Table 2 shows that film samples **X** and **XI**, with phloroglucinol as cross-linking agent, have a somewhat higher density and microhardness, despite lower concentration of phloroglucinol in the coating, compared to systems with hydroquinone. This may be due to the fact that trifunctional hydroquinone, in contrast to bifunctional hydroquinone, binds the siloxane structures in a three-dimensional network.

In the DTA curves (Fig. 1) of composites **VII**, **VIII**, and **X**, there are two peaks. The endothermic peak at 150–180°C corresponds to the removal of sorbed ethanol and water from the composite. The exothermic peak in the range 400–600°C is due to burnout of organic components (ethoxy groups, benzene rings). The high-temperature shift of the exothermic maximum in the DTA curves of composite **X,** compared to **VII** and **VIII,** indicates that composite **X** is more resistant to thermal oxidation, which is due to its cross-linked 3*D* structure.

Replacement of hydroxy groups in hydroquinone and phloroglucinol with triethoxysilyloxy groups allows the initial content of ethoxy groups in the composites formed by reactions with $Si(OEt)_4$ hydrolyzates **V** and **VI** to be increased. Compounds **III** and **IV** are liquids that form liquid mixtures with oligomers **V** and **VI** homogeneous. The formation of composites from these mixtures is due to the occurrence of parallel-consecutive condensation (ether interchange) reactions:

$$\begin{aligned} &\text{–Si(–)–OH} + (C_2H_5O)_3SiO–C_6H_4–OSi(OC_2H_5)_3 \\ &\rightarrow \text{–Si(–)–O–Si(OEt)}_2–O–C_6H_4–OSi(OEt)_3 + C_2H_5OH. \end{aligned}$$

From triethoxysilyl ethers of hydroquinone and phloroglucinol and oligomers **V** and **VI**, the composites were prepared as follows. To 0.7 g of oligomer mixture **V** or **VI** in 0.5 g of ethanol, we added 1,4-bis(triethoxysilyloxy)benzene (from 0.05 to 0.5 g) or 1,3,5-tris(triethoxysilyloxy)benzene (from 0.2 to 0.5 g) and 0.03 g of a 0.01 N HCl solution. The resulting mixture was cast onto a glass plate, which was dried at 80°C for 1–2 days. The physicochemical parameters of some of the films are listed in Table 3.

Figure 2 shows the TG and DTA curves for film samples **XVI** and **XVII**. As in the case of composites derived from phenols (Fig. 1), there are two peaks in the DTA curve. The endothermic peak (140–180°C) corresponds to the removal of sorbed ethanol and water from the system. The exothermic peaks in the range 450–630°C for composites **XVI** and **XVII** are some-

Table 3. Physicochemical properties of polymer film samples **XII–XV***

Composite	Oligomer	Content of alkoxysilyl phenol, g	t,** h	ρ, g cm^{-3}	W, %	MH, kg mm^{-2}
XII	**V**	0.25	23	1.54	33	104
XIII	**VI**	0.25	18	1.47	35	98
XIV	**V**	0.4	23	1.59	29	112
XV	**VI**	0.4	18	1.47	32	105

* Films prepared with (**XII**, **XIII**) 1,4-bis(triethoxysilyloxy)-benzene and (**XIV**, **XV**) 1,3,5-tris(triethoxysilyloxy)benzene.

what shifted toward higher temperatures relative to samples **VII** and **X**.

The structures of all the synthesized composites are similar. Figure 3 shows as an example an electron micrograph of composite **VIII**. The structure is fairly uniform, with a mean pore size of 15–20 nm.

CONCLUSION

Polyethoxysiloxanes cross-linked with hydroquinone or phloroglucinol were prepared for the first time. The structures cross-linked with phloroglucinol are more resistant to thermal oxidation than those cross-linked with hydroquinone.

REFERENCES

1. Kharitonov, N.M., Krotikov, V.A., and Khudoblin, Yu.I., *Organosilikatnye materialy – svoistva i tekhnologiya primeneniya* (Organosilicate Materials: Properties and Application Technology), Leningrad: Nauka, 1979.
2. *Handbook of Sol–Gel Science and Technology, vol. 1: Sol–Gel Processing*, Sakka, S., Ed., New York: Kluwer Academic, 2005.
3. US Patent 7 166 661.
4. Sorokin, M.F. and Shode, L.G., *Khimiya i tekhnologiya plenkoobrazuyushchikh veshchestv* (Chemistry and Technology of Film-Forming Substances), Leningrad: Khimiya, 1981.
5. Tomita, R. and Urano, S., *J. Polym. Sci. A: Polym. Chem.*, 2002, vol. 40, pp. 2917–2926.
6. US Patent 6 291 697.
7. Brinker, C.J. and Scherer, G.W., *Sol–Gel Science: The Physics and Chemistry of Sol–Gel Processing*, San Diego: Academic, 1990.
8. Khimich, N.N., *Fiz. Khim. Stekla*, 2004, vol. 30, no. 5, p. 586–603.
9. Kreshkov, A.P. and Bork, V.A., *Prakticheskoe rukovodstvo po analizu monomernykh i polimernykh kremnii-organicheskikh soedinenii* (Practical Guide to Analysis of Monomeric and Polymeric Organosilicon Compounds), Moscow: 1962.
10. Venzel', B.I. and Svatovskaya, L.G., *Fiz. Khim. Stekla*, 1994, vol. 20, no. 4, pp. 523–528.

ISSN 1070-4272, Russian Journal of Applied Chemistry, 2008, Vol. 81, No. 8, pp. 1414–1418. © Pleiades Publishing, Ltd., 2008.
Original Russian Text © V.F. Kurenkov, T.A. Gubanova, A.V. Kurenkov, F.I. Lobanov, 2008, published in Zhurnal Prikladnoi Khimii, 2008, Vol. 81, No. 8, pp. 1337–1341.

MACROMOLECULAR CHEMISTRY AND POLYMERIC MATERIALS

Copolymerization of Acrylamide with Sodium Acrylate in Aqueous Salt Solutions

V. F. Kurenkov, T. A. Gubanova, A. V. Kurenkov, and F. I. Lobanov

Kazan State Technological University, Kazan, Tatarstan, Russia
Ashland Eurasia Limited Liability Company, Moscow, Russia

Received December 11, 2007

Abstract—Kinetic relationships in homogeneous radical copolymerization of acrylamide with sodium acrylate, initiated by potassium peroxosulfate in concentrated aqueous solutions at 60°C, were examined in relation to the ionic strength of the solution and pH of the medium.

DOI: 10.1134/S1070427208080181

Water-soluble copolymers of acrylamide (AA) with acrylates having specific molecular characteristics find application as flocculants and stabilizers of dispersed systems, thickeners, and cross-linking agents [1, 2]. Considering the high practical value of the copolymers, of much importance is the most efficient, though inadequately understood, method of their preparation: copolymerization in concentrated aqueous solutions. Our previous studies have been focused on the copolymerization of AA with sodium acrylate (SA) at pH 7 [3] and pH 8 [4] and with ammonium acrylate at pH 8 [5], as well as on the binary copolymerization of AA with SA and ammonium acrylate in relation to the nature of the cation [4].

As is known [6, 7], the radical copolymerization of ionic monomers in aqueous solutions can be substantially affected by the ionic strength of the solution, μ, and the pH of the medium. We elucidated here how these factors affect the kinetic relationships in preparation of water-soluble AA–SA copolymers with different intrinsic viscosities, molecular weights, and chemical compositions by homogeneous radical copolymerization initiated by potassium peroxosulfate in concentrated aqueous solutions at 60°C. We took into account that pH in alkaline media and the ionic strength μ of the solution affect the polymerization of acrylic acid [6, 8] and do not affect that of AA [8].

EXPERIMENTAL

We used biocatalytically prepared aqueous solutions of monomers (40% AA and 18% SA) available from Ashland Eurasia MSP Private Company, Perm, as well as pure-grade potassium peroxosulfate (PP), analytically pure grade sodium hydroxide and acetone, and high-purity helium. In all the experiments, we used distilled water.

The initial copolymerization rate v_0 was estimated at low conversions ($x < 3\%$) from the dilatometrically recorded kinetic curves. For the copolymerization technique, as well as for the technique and devices used for dilatometric, viscometric, and potentiometric analyses, see [5]. When the reaction was complete, the copolymer was precipitated from the aqueous solution into an acetone excess, after which it was washed with acetone and vacuum-dried in a desiccator at 50°C to constant weight.

The intrinsic viscosity [η] of the copolymers was determined viscometrically in 0.5 M NaCl at 30°C and used for calculating the viscosity-average molecular weight M of the AA–SA copolymers by the Mark–Houwink–Kuhn equation:

$$[\eta] = KM^{\alpha}.$$

The parameters K and α, dependent on the content of the SA units in the copolymer, were taken from [9].

The content of the SA units in the AA–SA copolymer was estimated from potentiometric data by the technique described in [10].

Copolymerization of AA (M_1) with SA (M_2) was carried out in 18% aqueous solutions at 60°C with PP as initiator ([PP] = 7.4×10^{-4} M). Maintaining pH at 10

and 12 afforded efficient initiation by PP [11] and a constant initiation rate at varied concentrations of SA and NaOH and NaCl additions, since the PP decomposition rate in alkaline media is independent of μ [12]. Under the actual experimental conditions, the copolymerization did not go without initiator, and in the presence of PP it proceeded under homogeneous conditions.

Let us analyze the AA–SA copolymerization in relation to the composition of the initial monomer mixture. The experiments were run at $M_1 + M_2 = \text{const}$, with all other conditions remaining unchanged as well; the results are shown in Fig. 1. It is seen that, with increasing SA content in the initial monomer mixture, v_0 tends to decrease at pH 10 and 12, both with and without NaCl. Comparative analysis of the data in Fig. 1 at $[M_2] = \text{const}$ (cf. curves *3*, *4* and *1*, *2*) shows that, at pH 10 and 12 over a wide range of compositions of the initial monomer mixture, v_0 increases on passing from aqueous solutions to 1% NaCl, owing to the change in μ.

Figure 1 also demonstrates a decrease in v_0 with increasing pH in the absence of NaCl, which reasonably agrees with the data on homopolymerization of acrylic acid in alkaline media [6, 8]. This decrease in v_0 is due to a decrease in the local concentration of the charged SA monomer near the macroradicals, associated with contraction of macromolecular coils in alkaline solutions.

Figure 2 shows how [η] and $\bar{M}_\eta$ of the resulting AA–SA copolymers vary with the composition of the initial monomer mixture during copolymerization. It is seen that, with increasing M_2 concentration, [η] (Fig. 2a) and $\bar{M}_\eta$ (Fig. 2b) of the copolymers tend to decrease. Similar trends in variation of v_0 (Fig. 1) and $\bar{M}_\eta$ (Fig. 2) with M_2 are characteristic of polymerization of ionic monomers [6, 7]. Figure 2 also shows that copolymerization in the monomer mixtures enriched in AA yields AA–SA copolymers with the highest molecular weights. It is also seen from Fig. 2 that both [η] (Fig. 2a) and $\bar{M}_\eta$ (Fig. 2b) tend to slightly decrease upon addition of NaCl at pH 12.

Figure 3 plots the yield of the resulting AA–SA copolymer vs. the M_2 content in the initial monomer mixture. For the copolymerization in alkaline media without NaCl, the plot exhibits a maximum at $[M_1]/[M_2] \approx 1$ (curves *1*, *2*). Comparative analysis of the data in Fig. 3 (at $[M_2] = \text{const}$) shows that the yield

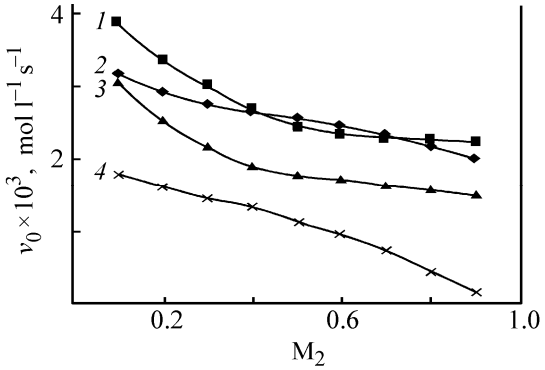


Fig. 1. Initial rate of AA–SA copolymerization, v_0, vs. the mole fraction of the ionic monomer in the initial monomer mixture, M_2, at (*2*, *3*) pH 10 and (*1*, *4*) pH 12 (*3*, *4*) without and (*1*, *2*) with 1% NaCl.

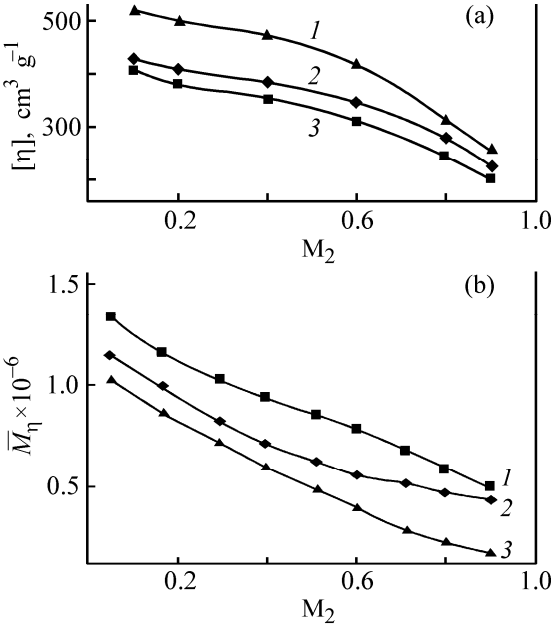


Fig. 2. (a) [η] and (b) $\bar{M}_\eta$ vs. SA mole fraction in the initial monomer mixture, M_2, for AA–SA copolymerization at (*1*) pH 10 and (*2*, *3*) 12 (*2*) without and (*3*) with NaCl (1%).

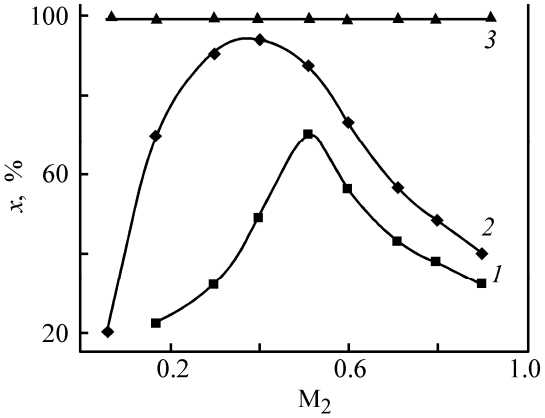


Fig. 3. Copolymer yield x vs. SA mole fraction in the initial monomer mixture, M_2, for AA–SA copolymerization at pH (*1*) 10 and (*2*, *3*) 12 without (*1*, *2*) and (*3*) with 1% NaCl.

Table 1. Parameters r_1 and r_2, determined by different methods for the AA–SA copolymerization in aqueous solutions

Copolymerization conditions	Method of determination	$r_1 \pm 0.03$ (AA)	$r_2 \pm 0.03$ (SA)
pH 10	Fineman–Ross	2.00	0.60
	Kelen–Tüdös	2.00	0.60
pH 10 + 1% NaCl	Fineman–Ross	1.40	0.90
	Kelen–Tüdös	1.50	0.80

Table 2. AA–SA copolymerization in relation to the NaCl concentration*

[NaCl], M	Yield, %	$[m_2]$, mol %	$[\eta]$, $cm^3 g^{-1}$
0.034	–	12.8	–
0.085	88	13.4	–
0.171	91	16.9	450
0.513	95	22.9	250
0.855	99	24.7	230

* The copolymerization conditions are identical to those for Fig. 5.

grows as pH increases from 10 to 12 (curves *1*, *2*) and upon addition of NaCl (at pH 12) (curves *2*, *3*).

Figure 4 shows how the running composition of the AA–SA copolymers (at conversions $x < 3\%$) varies with the M_2 mole fraction in the initial monomer mixture during copolymerization. It is seen that, over a wide range of compositions of the initial monomer mixture without (curve *1*) and with (curve *2*) NaCl, the copolymerization yields copolymers enriched in AA units. Using the data from Fig. 4, the apparent relative activities of the monomers $r_1 = k_{11}/k_{12}$ (AA) and $r_2 = k_{22}/k_{21}$ (SA) were calculated by the Fineman–Ross and Kelen–Tüdös methods (Table 1). The r_1 and r_2 values determined by these different methods reasonably agree. As can be seen from Table 1, $r_1 > r_2$, which indicates that AA is more reactive in copolymerization than SA. Figure 4 shows that addition of NaCl at pH 10 causes the mole fraction of the SA units in the copolymer to increase (curve *1* against curve *2*). This is associated with an increase in μ, which accelerates the reaction of SA with the macroradical of the terminal SA unit and favors enrichment of the copolymer with the SA units, thereby raising r_2 and lowering r_1 (Table 1).

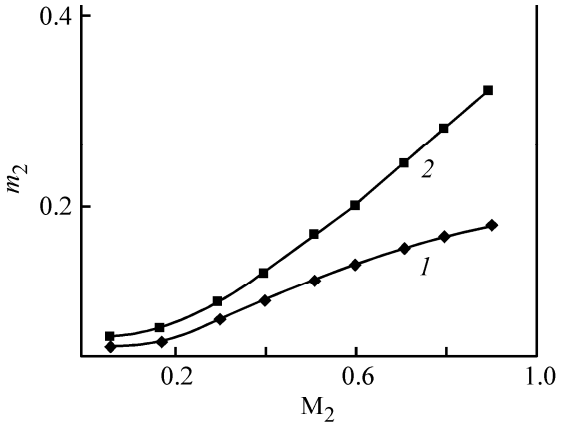


Fig. 4. Mole fraction of the SA units, m_2, in the copolymer vs. SA mole fraction in the initial monomer mixture, M_2, for AA–SA copolymerization at pH 10 (*1*) without and (*2*) with 1% NaCl. Fig. 5. Initial AA–SA copolymerization rate v_0, mol l^{-1} s^{-1}, at pH 10 vs. NaCl concentration.

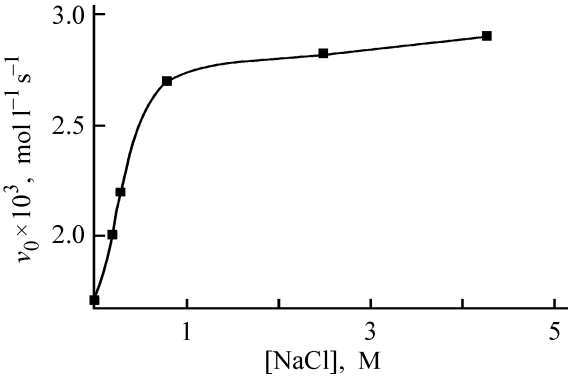


Fig. 5. Initial AA–SA copolymerization rate v_0 at pH 10 vs. the NaCl concentration. $[M_1]:[M_2] = 4:6$, $[PP] = 7.4 \times 10^{-4}$ M.

Figure 5 shows how the NaCl concentration (at pH 10) affects v_0, and Table 2 lists the characteristics of the resulting copolymers. With increasing electrolyte concentration, v_0 tends to grow and reaches a limiting value (Fig. 5); also, the yield of the copolymer and the content of the SA units in its macromolecules tend to increase, and $[\eta]$, to decrease (Table 2).

To interpret the kinetic data obtained, we will consider the ionization balance of the ionic groups in the salt solutions:

$$\underset{\text{I}}{A^+Na^-} \rightleftarrows \underset{\text{II}}{A^-} \,||\, Na^+ \rightleftarrows \underset{\text{III}}{A^- + Na^+},$$

where A^- is the anion of the monomer and macroradical; I, II, and III are contact and solvent-separated ion pairs and free ions in solution, respectively.

As is known [6], in alkaline solutions, the ionic groups of SA and its units in the copolymer macromolecules are ionized. With increasing μ (upon addition of NaCl), the ionization balance shifts to the left. This favors weakening of the electrostatic repulsion between the acrylate anions along the chain and diminishes the size of the macromolecular coils, as indirectly confirmed by a decrease in the reduced viscosity of the copolymer solution η_{sp}/c_p with increasing NaCl concen-

tration (Fig. 6). Under the copolymerization conditions, an increase in μ weakens the electrostatic repulsion between the identically charged SA monomer and macroradical with the terminal SA unit, thereby raising both the chain propagation rate constant k_{11} and v_0.

To derive an equation for the AA–SA copolymerization rate at pH 10, we carried out experiments at variable concentrations of the comonomers and the initiator, with the concentrations of the other components of the system and the reaction conditions remaining unchanged. The AA, SA, and PP concen-trations were varied within 2.2–9.5, 7.4–8.8, and $(3.9–14.8)\times 10^{-4}$ M, respectively. Figure 7a presents the experimental results. It is seen that v_0 tends to increase with increasing AA and PP concentrations and to decrease with increasing SA concentration, which agrees well with Fig. 1. From the slope of the straight lines in Fig. 7, we determined the reaction orders with respect to the components of the reaction mixture and derived the following empirical equation for the AA–SA copolymerization in aqueous solutions at pH 10:

$$v_c = k_c[AA]^{0.8}[SA]^{-1.0}[PP]^{0.5}.$$

Table 3. Intrinsic viscosity [η] of the AA–SA copolymers at different concentrations of the comonomers and the initiator

[AA]	[SA]	[PP]	[η], $cm^3 g^{-1}$
M			
2.2	7.4	7.4	125
2.8	–	–	145
4.0	–	–	150
6.5	–	–	160
8.5	–	–	185
6.5	7.4	7.4	160
–	7.9	–	330
–	8.5	–	370
6.5	7.4	3.7	440
–	–	4.9	410
–	–	7.4	160

In this equation, the reaction order with respect to the initiator suggests the bimolecular termination of the kinetic chains. The dependence of the polymerization rate on the total concentration of the monomers in the mixture was estimated at $[M_1]/[M_2] = 4:6$ (Fig. 7b); the reaction order with respect to the total concentra-

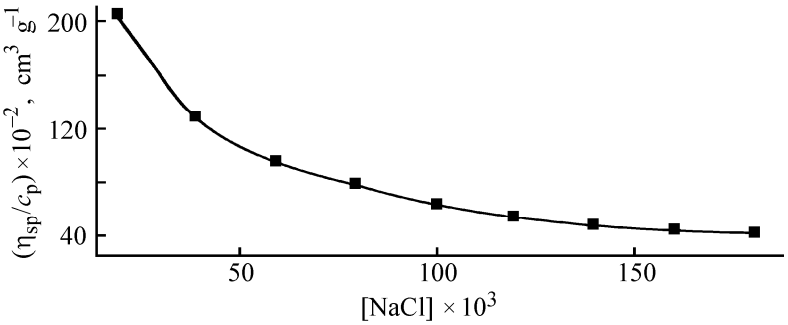


Fig. 6. Reduced viscosity of solutions, η_{sp}/c_p, of the AA–SA copolymer ($\bar{M}_\eta = 7.7\times 10^6$, content of SA units 51 mol %) vs. NaCl concentration at 25°C.

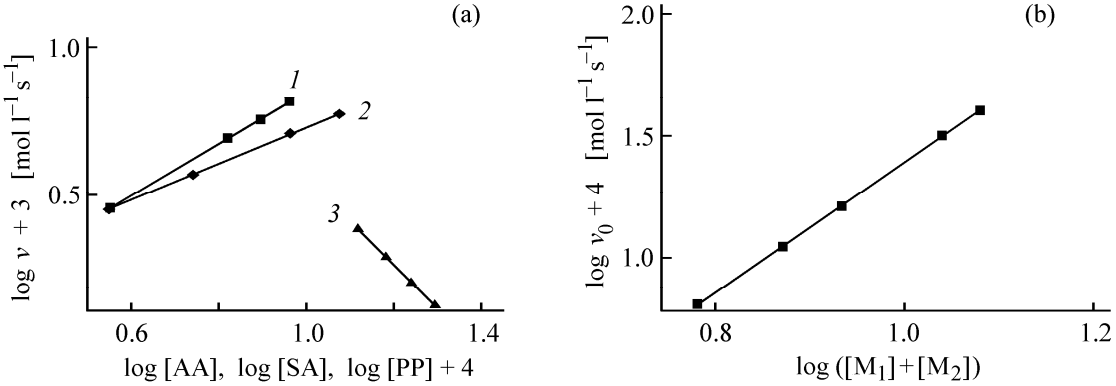


Fig. 7. Initial rate of AA–SA copolymerization, v_0, in aqueous solutions vs. concentrations of (a) (*1*) AA, (*2*) PP, and (*3*) SA and (b) $M_1 + M_2$ mixture in the log–log coordinates. (a) Concentration, M: (*1*) [SA] = 7.4, [PP] = 7.4×10^{-4}; (*2*) [AA] = 6.5, [SA] = 7.4; (*3*) [AA] = 6.5, [PP] = 7.4×10^{-4} and (b) $[M_1] : [M_2] = 4 : 6$, [PP] = 7.4×10^{-4}.

tion of the monomer mixture is 2.5. This yields the following copolymerization equation:

$$v_c = k_c([M_1] + [M_2])^{2.5}[PP]^{0.5}.$$

Table 3 lists the intrinsic viscosities [η] of the resulting copolymers in relation to the concentration of the reaction mixture components. It is seen that [η] tends to increase with increasing concentration of the AA and SA comonomers and with decreasing initiator concentration, in agreement with the general relationships in radical copolymerization.

CONCLUSION

Homogeneous radical copolymerization of acrylamide with sodium acrylate in concentrated aqueous solutions at 60°C, initiated by potassium peroxosulfate, can yield water-soluble high-molecular-weight copolymers, for which the initial rate of copolymerization, as well as the intrinsic viscosity, molecular weight, composition, and yield can be controlled by varying the pH and ionic strength.

REFERENCES

1. Abramova, L.I., Baiburdov, T.A., Grigoryan, E.P., et al., *Poliakrilamid* (Polyacrylamide), Kurenkov, V.F., Ed., Moscow: Khimiya, 1992.
2. Kurenkov, V.F., *Soros. Obraz. Zh.*, 1997, no. 5, pp. 48–53.
3. Kurenkov, V.F., Bulgakova, G.I., Filippova, A.N., and Aleeva, Yu.V., *Zh. Prikl. Khim.*, 1994, vol. 67, no. 7, pp. 1157–1161.
4. Kurenkov, V.F., Kurenkov, A.V., and Lobanov, F.I., *Khim. Tekhnol.*, 2007, vol. 8, no. 11, pp. 501–506.
5. Kurenkov, V.F., Grigor'eva, S.S., Kurenkov, A.V., and Lobanov, F.I., *Zh. Prikl. Khim.*, 2007, vol. 80, no. 2, pp. 291–294.
6. Kabanov, V.A. and Topchiev, D.A., *Polimerizatsiya ionizuyushchikhsya monomerov* (Polymerization of Ionizable Monomers), Moscow: Nauka, 1975.
7. Kurenkov, V.F. and Myagchenkov, V.A., *Zh. Prikl. Khim.*, 1999, vol. 72, no. 6, pp. 881–890.
8. Topchiev, D.A., Shakirov, R.Z., Kalinina, L.P., et al., *Vysokomol. Soedin., Ser. A*, 1972, vol. 14, no. 3, pp. 581–586.
9. Klein, J. and Conrad, K.-D., *Makromol. Chem.*, 1980, vol. 181, no. 1, pp. 227–229.
10. Kurenkov, V.F., Baiburdov, T.A., and Stupen'kova, L.L., *Fiziko-khimicheskie osnovy sinteza i pererabotki polimerov* (Physicochemical Principles of Synthesis and Processing of Polymers), Gorky: Gork. Gos. Univ., 1985, pp. 79–86.
11. Kholodnova, L.V., Pavlyuchenko, V.M., Alekseeva, Z.M., and Andreeva, A.I., *Kataliticheskie i initsiiruyushchie sistemy dlya sinteza i modifikatsii polimerov* (Catalytic and Initiating Systems for Synthesis and Modification of Polymers), Leningrad: Plastpolimer, 1984, pp. 90–104.
12. Kolthoff, I.M. and Miller, I.K., *J. Am. Chem. Soc.*, 1951, vol. 73, pp. 3055–3059.

ISSN 1070-4272, Russian Journal of Applied Chemistry, 2008, Vol. 81, No. 8, pp. 1419–1422. © Pleiades Publishing, Ltd., 2008.
Original Russian Text © A.Ya. Samuilov, L.A. Zenitova, I.N. Bakirova, Ya.D. Samuilov, 2008, published in Zhurnal Prikladnoi Khimii, 2008, Vol. 81, No. 8, pp. 1342–1345.

MACROMOLECULAR CHEMISTRY AND POLYMERIC MATERIALS

Thermodynamic Parameters of Urethane Formation Reactions and Concomitant Processes

A. Ya. Samuilov, L. A. Zenitova, I. N. Bakirova, and Ya. D. Samuilov

Kazan State University of Technology, Kazan, Tatarstan, Russia

Received September 17, 2007

Abstract–Thermodynamic parameters of reactions of methyl and phenyl isocyanates with a series of compounds were determined by quantum-chemical calculations. The products of these reactions model for various functional groups present in commercial polyurethanes. The thermodynamic stability series for compounds formed from aliphatic and aromatic isocyanates were constructed.

DOI: 10.1134/S1070427208080193

Production of polyurethanes based on reactions of isocyanates with polyols grows year by year [1, 2]. The main reaction of isocyanates with alcoholsto give urethanes is accompanied by side processes: formation of allophanates and isocyanurates [1–3]. When bisamines are used in synthesis of polyurethanes or when amino groups are purposefully generated from isocyanate groups, urea and biuret fragments arise in the polymer structure. The properties of the polyurethanes obtained largely depend on the ratio of these groups. Purposeful variation of the functional composition of polyurethanes is the most important way to control their physicomechanical properties. Both that urethane formation and concomitant processes are reversible [4–10]. Therefore, knowledge of the thermodynamic parameters of these reactions would allow their efficient control. In the available literature, there are only scarce data on thermochemical characteristics of particular reactions involved, and complete thermodynamic data are lacking. Experimental determination of the thermodynamic characteristics of particular reactions is complicated by the fact that the main reaction, urethane formation, is accompanied to one or another extent by side reactions [11]. To estimate the thermodynamic parameters of urethane formation and concomitant reactions, we examined quantum-chemically a series of model reactions simulating certain processes that occurr in real systems in the course of polyurethane formation:

$$\underset{\mathbf{I}}{CH_3NCO} + \underset{\mathbf{II}}{CH_3OH} \rightarrow \underset{\mathbf{III}}{CH_3NHCOOCH_3}, \quad (1)$$

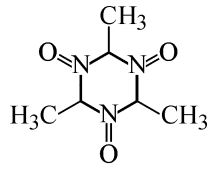
$$\underset{\mathbf{IV}}{C_6H_5NCO} + \mathbf{II} \rightarrow \underset{\mathbf{V}}{CH_3NCOOCH_3}, \quad (2)$$

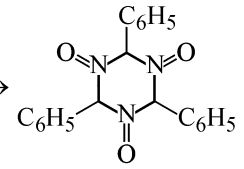
$$\mathbf{I} + \mathbf{III} \rightarrow \underset{\mathbf{VI}}{CH_3N(COOCH_3)CONHCH_3}, \quad (3)$$

$$\mathbf{V} + \mathbf{IV} \rightarrow \underset{\mathbf{VII}}{C_6H_5N(COOCH_3)CONHC_6H_5}, \quad (4)$$

$$\mathbf{I} + \mathbf{VI} \rightarrow \underset{\mathbf{VIII}}{CH_3N(COOCH_3)CON(CH_3)CONHCH_3}, \quad (5)$$

$$\mathbf{IV} + \mathbf{VII} \rightarrow \underset{\mathbf{IX}}{C_6H_5N(COOCH_3)CON(C_6H_5)CONHC_6H_5}, \quad (6)$$

$3\mathbf{I} \rightarrow$  **X** (7)

$3\mathbf{IV} \rightarrow$  **XI** (8)

$$\mathbf{I} + CH_3NH_2 \rightarrow \underset{\mathbf{XII}}{CH_3NHCONHCH_3}, \quad (9)$$

$$\mathbf{IV} + C_6H_5NH_2 \rightarrow \underset{\mathbf{XIII}}{C_6H_5NHCONHC_6H_5}, \quad (10)$$

Enthalpies ΔH, entropies ΔS, Gibbs free energies ΔG, and equilibrium constants K_{eq} of reactions (1)–(12) at 298 K and limiting decomposition temperatures T_{lim} in the gas phase

Reaction	ΔH, kJ mol^{-1}	ΔS, J mol^{-1} K^{-1}	ΔG_{298}, kJ mol^{-1}	$K_{eq\,298}$	T_{lim}, K
1	–132	–188	–76	2.1×10^{13}	702
2	–127	–178	–74	9.4×10^{12}	713
3	–102	–180	–48	2.6×10^{8}	567
4	–69	–188	–13	1.9×10^{2}	367
5	–40	–191	18	7×10^{-4}	209
6	–4	–175	48	3.9×10^{-9}	23
7	–310	–415	–187	6×10^{32}	747
8	–198	–401	–78	4.7×10^{13}	494
9	–110	–176	–89	2.2×10^{7}	630
10	–90	–178	–37	3.1×10^{6}	506
11	–118	–202	–58	1.5×10^{10}	584
12	–90	–185	–35	9.1×10^{5}	486

$$\mathbf{I} + \mathbf{XII} \rightarrow \underset{\mathbf{XIV}}{CH_3NHCON(CH_3)CONHCH_3}, \quad (11)$$

$$\mathbf{IV} + \mathbf{VIII} \rightarrow C_6H_5NHCONC_6H_5CONHC_6H_5. \quad (12)$$

EXPERIMENTAL

Quantum-chemical calculations were performed using the Gaussian 03 software package [12] with full geometry optimization involving determination of the most energetically favorable conformations of the compounds. Initially the molecular geometry was optimized by the PM3 semiempirical method, after which the results obtained were used in DFT calculations using the PBE1PBE/6-31G(d) hybrid method. This method was recommended for calculating thermodynamic characteristics of organic compounds [13, 14]. Initially, we calculated the Gibbs energies, enthalpies, and entropies of formation of the compounds appearing in Eqs. (1)–(12). The thermodynamic characteristics of reactions were determined as differences between the corresponding quantities for the reaction products and reactants. The entropies were calculated taking into account the translation, rotation, and vibration degrees of freedom.

Pre-isocyanate from polyethylene glycol adipate (PEA) and 2,4-toluene diisocyanate (2,4-TDI). A thoroughly dried PEA sample (M = 1874 amu, 1.79 wt % OH groups) was mixed with freshly distilled 2,4-TDI. The NCO : OH molar ratio was 2 : 1 and 1.6 : 1 in preparation of pre-isocyanates for SKU-6 and SKU-7, respectively. The reaction mixture was heated in a flow of dry nitrogen at 80°C with stirring to attain a constant concentration of NCO groups.

Castable polyurethane elastomer SKU-6. The pre-isocyanate was mixed with trimethylolpropane (TMP) and 1,4-butanediol (BD) to obtain the molar ratio PE : 2,4-TDI : TMP : BD = 1 : 2 : 0.32 : 0.24. The resulting mixture was cast into molds and kept first at 120°C for 24 h and then at room temperature for no less than 2 weeks.

Castable polyurethane elastomer SKU-7. The pre-isocyanate was mixed with MOKA melt to obtain the molar ratio PEA : 2,4-TDI : MOKA = 1 : 1.6 : 0.4. The subsequent work-up was the same as for SKU-6.

Castable polyurethane elastomer SKU-OM. The pre-isocyanate was mixed with 2,4-TDI to obtain the molar ratio PEA : 2,4-TDI = 1 : 1.25. Then 2,4,6-tris(dimethyl-aminomethyl)phenol (0.25 wt %) was added as catalyst of trimerization of isocyanate groups. The resulting mixture was cast into molds, which were kept at 80°C for 25 h and then at room temperature for no less than 2 weeks.

The tensile strength was determined with a TR-3 kN tensile-testing machine equipped with a temperature-controlled chamber. The clamp velocity was 500 mm min^{-1}.

We compared the thermodynamic functions of the model reactions involving an aliphatic isocyanate (methyl isocyanate **I**) and an aromatic isocyanate (phenyl isocyanate **IV**) to find how the π–π conjugation of the isocyanate group with the aromatic ring affects the thermodynamic functions of the transformations. The results are listed in the table.

As for the correctness of these data, the following can be noted. The enthalpy of the reaction of isocyanic acid with compound II, calculated from the enthalpies of formation in the gas phase (kJ mol^{-1}) of isocyanic acid (–104 [15]), methanol (–201 [16]), and methyl carbamate (–425 [17]), is –120 kJ mol^{-1}.

This is a reaction of a nonconjugated isocyanate with a primary alcohol. The enthalpy of the liquid-phase reaction of isocyanate **IV** with 1-butanol is –84 [18] or –105 kJ mol^{-1} [19], according to data of differ-

ent authors. The enthalpy of reaction (10) in 1,4-dioxane is –82 kJ mol^{-1} [20]. The heat of trimerization of isocyanate **I** in the gas phase is estimated in [21] at –278 kJ mol^{-1} [21]. All these values are close to the results of our calculations, which supports their reliability. Bonetskaya et al. [22] reported for the enthalpy of reaction (8) in diglyme the value of –52 kJ mol^{-1}. This value is apparently overestimated, as it suggests a low thermal stability of isocyanurate rings, which is in-consistent with the available experimental data [1–3].

The data we obtained show that all the reactions with methyl isocyanate **I** are more exothermic than those with phenyl isocyanate **IV**. This is primarily due to the fact that the reactions with **IV** involve break of the conjugation between the isocyanate group and aromatic ring, with a significant energy loss. The Gibbs energies of reactions involving the aliphatic isocyanate are also more negative, compared to the related reactions with the aromatic isocyanate. Therefore, urethanes derived from aliphatic isocyanates should be more thermostable than those derived from aromatic isocyanates. This is indeed the case. Urethanes derived from aliphatic isocyanates and alcohols start to dissociate at 250°C, and those derived from aromatic isocyanates, at 200°C [23]. The stronger exothermicity of reactions of alcohols with aliphatic isocyanates, compared to aromatic isocyanates, was shown in [24]. These data suggest that, to obtain polyurethanes with a higher temperature limit of operation, it is necessary to choose di- and polyisocyanates in which the isocyanate group is not conjugated with the aromatic ring.

Synthesis of polyurethanes can be accompanied by formation of *N*-alkoxycarbonylbiurets [reactions (5) and (6)]. These compounds show low stability. Therefore, involvement of these functional groups in the formation of the structure of polyurethanes is questionable. Among the products under consideration, isocyanurates **X** and **XI** are highly stable. The stability of these heterocycles is primarily due to the fact that their formation is characterized by high negative enthalpies of reactions (7) and (8).

To quantitatively characterize the thermal stability of particular functional groups in polyurethanes on the basis of thermodynamics of the model compounds, we calculated the limiting temperatures T_{lim} of their stability, i.e., the temperatures at which the Gibbs energies of the reactions of their formation become zero. The limiting temperatures were calculated as follows:

$$T_{lim} = \Delta H/\Delta S.$$

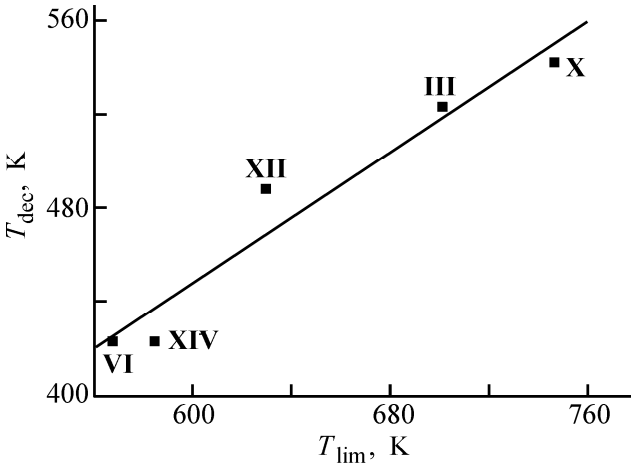
Based on the limiting temperatures (see table), we can rank structural fragments of polyurethanes in the following orders of thermodynamic stability: for reactions with aliphatic isocyanates: isocyanurates > urethanes > ureas > biurets > allophanates > *N*-alkoxycarbonylbiurets; for reactions with aromatic isocyanates: urethanes > ureas > isocyanurates > biurets > allophanates > *N*-alkoxycarbonylbiurets.

The thermodynamic functions of the reactions, given in the table, show that the transformations leading to allophanates and biurets become essentially reversible with increasing temperature. If the data obtained for model reactions adequately reflect the thermodynamic stability of various functional groups in polyurethanes, polyurethanes containing large amounts of these groups should exhibit a relatively low thermal stability. The experimental data are consistent with this conclusion. It is believed that long-term service of polyurethane items is possible only at temperatures not exceeding 80°C [25].

We supplemented the quantum-chemical calculations by experimental determination of the tensile strength in relation to temperature for a series of castable polyurethane elastomers: SKU-6, SKU-7, and SKU-OM. All these rubbers contain ester groups as main structural fragments. In addition, SKU-6 rubber contains urethane and allophanate groups; SKU-7, urethane, urea, and biuret fragments; and SKU-OM, urethane and isocyanurate groups. At 25°C, the breaking tensile stress for SKU-6, SKU-7, and SKU-OM rubbers is 38.6, 43.4, and 42.2 MPa, respectively. At 100°C, the breaking stress is 5.0, 3.0, and 13.5 MPa, respectively. As can be seen, only SKU-OM rubber exhibits an acceptable strength at elevated temperatures. These data show that the thermodynamic functions of model reactions do correlate with those of reactions yielding definite functional groups in polyurethanes. Furthermore, there is satisfactory correlation between T_{lim} in model reactions and the decomposition temperatures of separate functional groups in polyurethanes (see figure). The decomposition temperatures are characterized by a definite interval of values [26]. When plotting the diagram, we took the mean values. The correlation is described by the equation

$$T_{lim} = 27.480 + 0.70T_{dec} \quad (R = 0.973).$$

The existance of this correlation indicates that the differences in thermal stability between functional groups in polyurethanes are primarily due to differences in the thermodynamic parameters of their forma-



Decomposition temperature T_{dec} of various functional groups in polyurethanes [25] vs. the limiting temperature of stability of model compounds, T_{lim}.

tions. The thermodynamic parameters of the intermolecular interaction between polyurethane macromolecules make a contrast contribution accounted for by the free term in the equation.

The thermodynamics of dimerization of isocyanate **IV** in toluene was studied in [27]. It follows from these data that, even at low temperatures, the equilibrium of this reaction is strongly shifted toward the isocyanate. These results indicate that uretidinedione groups cannot determine the functional composition of polyurethanes to a significant extent, because their synthesis, as a rule, involves high temperatures.

All the reactions (1)–(12) are characterized by large negative entropies. The transformations we considered are models for the formation of particular functional fragments in polyurethanes. The large negative entropies of the reactions account for the low heat resistance of polyurethane items, because they lead to an increase in the Gibbs free energy with temperature. As a result, the reaction equilibria become shifted toward the reactants.

CONCLUSIONS

(1) All reactions with methyl isocyanate are more exothermic than the analogous reactions with phenyl isocyanate. All the reactions are characterized by large negative entropies.

(2) The presence of allophanate and biuret fragments in the structure of polyurethanes decreases their heat resistance.

REFERENCES

1. Szycher, M., *Szycher's Handbook of Polyurethanes*, Boca Raton: CRC, 1999.
2. Randall, D. and Lee, S., *The Polyurethanes Book*, New York: Wiley, 2003.
3. Saunders, J.H. and Frish, K.C., *Polyurethanes. Chemistry and Technology*, part 1: *Chemistry*, New York: Interscience, 1962.
4. Shaw, W.H.R. and Gvushkin, B., *J. Am. Chem. Soc.*, 1960, vol. 82, no. 5, pp. 1022–1024.
5. Chiba, M. and Cherniak, E.A., *J. Agric. Food Chem.*, 1978, vol. 26, no. 3, pp. 573–576.
6. Yang, W.P., Marcosco Ch.W., and Wellinghoff, S.T., *Polymer*, 1986, vol. 27, no. 8, pp. 1235–1240.
7. Joel, D. and Hauser, A., *Angew. Macromol. Chem.*, 1994, no. 217, pp. 191–199.
8. Valli, V.L.K. and Alper, H., *J. Org. Chem.*, 1995, vol. 60, no. 1, pp. 257–258.
9. Steinlein, Ch., Harnandez, L., and Eisenbach, C.D., *Macromol. Chem. Phys.*, 1996, vol. 197, no. 10, pp. 3365–3382.
10. Lu, Q., Huye, T.R., and Marcosco, Ch.W., *J. Polym. Sci., part A: Polym. Chem.*, 2002, vol. 40, no. 14, pp. 2310–2328.
11. Schwettick, K. and Noack, R., *J. Chem. Soc., Perkin Trans. 2*, 1995, no. 2, pp. 395–402.
12. Frisch, M.J., Trucks, G.W., Schlegel, H.B., et al., *Gaussian 03, Revision B.04*, Pittsburgh, PA: Gaussian, 2003.
13. Keal, T.W. and Tozer, D.J., *J. Chem. Phys.*, 2005, vol. 123, no. 12, pp. 121103-1–121103-4.
14. Vydrov, O.A. and Scuseria, E.G., *J. Chem. Phys.*, 2006, vol. 125, no. 23, pp. 234109-1–234109-9.
15. Spiglanin, T.A., Perry, R.A., and Chandlez, D.W., *J. Phys. Chem.*, 1986, vol. 90, no. 23, pp. 6184–6189.
16. Hine, J. and Arata, K., *Bull. Chem. Soc. Jpn.*, 1976, vol. 49, no. 11, pp. 3089–3092.
17. Bernard, M.A., Boukari, Y., and Busnot, F., *Thermochim. Acta*, 1976, vol. 16, no. 3, pp. 267–275.
18. Pannone, M.C. and Marcosco, Ch.W., *J. Appl. Polym. Sci.*, 1987, vol. 34, no. 7, pp. 2409–2432.
19. Lovering, E.G. and Laider, K.J., *Can. J. Chem.*, 1962, vol. 40, no. 1, pp. 26–30.
20. Kiselev, V.D., Malkov, V.B., Murzin, D.G., et al., *Dokl. Akad. Nauk SSSR*, 1989, vol. 308, no. 1, pp. 111–113.
21. Imamura, A., Takahashi, K., Murata, S., et al., *J. Chem. Thermodyn.*, 1989, vol. 21, no. 3, pp. 237–246.
22. Bonetskaya, A.K., Kravchenko, M.D., Frenkel', T.M., et al., *Vysokomol. Soedin., Ser. A*, 1985, vol. 27, no. 6, pp. 1269–1273.
23. Gedan-Smolka, M., Haübler, L., and Fischer, D., *Thermochim. Acta*, 2000, vol. 351, nos. 1–2, pp. 95–105.
24. Sultan, W. and Busnel, J.-P., *J. Therm. Anal. Calorim.*, 2006, vol. 83, no. 2, pp. 355–359.
25. Wright, P. and Cumming, A.P.C., *Solid Polyurethane Elastomers*, London: Maclaren, 1969.
26. Simon, J., Barla, F., Kelemen–Haller, A., et al., *Chromotographia*, 1988, vol. 25, no. 2, pp. 99–106.
27. Buckles, R.E. and McGrew, L.A., *J. Am. Chem. Soc.*, 1966, vol. 88, no. 15, pp. 3582–3586.

ISSN 1070-4272, Russian Journal of Applied Chemistry, 2008, Vol. 81, No. 8, pp. 1423–1426. © Pleiades Publishing, Ltd., 2008.
Original Russian Text © A.P. Rossinskii, A.A. Alalykin, S.V. Talantov, S.V. Chagaev, 2008, published in Zhurnal Prikladnoi Khimii, 2008, Vol. 81, No. 8, pp. 1346–1349.

MACROMOLECULAR CHEMISTRY AND POLYMERIC MATERIALS

Acid-Catalyzed Alkenylation of Aromatic Compounds with 1,3-Pentadiene as a Route to New Modifying Additives for Polymer Compounds

A. P. Rossinskii, A. A. Alalykin, S. V. Talantov, and S. V. Chagaev

Vyatka State University, Kirov, Russia

Received March 4, 2008

Abstract—Alkenylation of a series of aromatic compounds with 1,3-pentadiene was studied. The oligomeric alkenylation products cured with hexamethylenetetramine were used for modifying elastic-strength properties of elastomeric compounds and improving the compatibility of the elastomers with silicic acid fillers.

DOI: 10.1134/S107042720808020X

The growing requirements to consumers' properties, service characteristics, and environmental safety of modern tires and general mechanical rubber goods call for development and application of new high-performance auxiliary ingredients, modifiers of polymer compounds considerably enhancing their strength. Phenolic compounds (resorcinol, 5-methylresorcinol) in combination with hexamethylenetetramine, widely used as modifying additives in formulations of rubber stocks and showing fairly high performance, have certain drawbacks [1].

As a continuation of previous studies [2–4] of acid-catalyzed alkenylation of shale resorcinols with 1,3-pentadiene (piperylene), it was interesting to further expand the range of aromatic compounds subject to alkylation with the aim to find new, more effective modifying additives to skimming rubber stocks based on general-purpose rubbers. Alkenylated derivatives introduced into an elastomeric matrix with the aim to improve the physicomechanical parameters of ready rubber items enhance the adhesion strength of rubber–metal cord systems under the conditions of steam and salt aging and positively affect the compatibility of rubbers with silicic acid fillers.

In this study, we examined the composition of alkylates formed by some aromatic compounds with 1,3-pentadiene under the conditions of phosphoric acid catalysis and evaluated the character and efficiency of the modifying action of the alkenylation products in polymer compounds.

EXPERIMENTAL

The following compounds were subjected to alkenylation with 1,3-pentadiene. Aromatic compounds with hydroxy group directly bonded to the aromatic ring: phenol, *p*-cresol, *p*-nonylphenol (Agidol 21, distilled, T grade), salicylic acid, a-naphthol, resorcinol, 5-methylresorcinol, and Alkirez-1 (a technical mixture of dihydric phenols mainly consisting of 5-methylresorcinol, 2,5-dimethyl-resorcinol, and their closest homologs); aromatic compounds containing no phenolic hydroxyls: styrene, a-methylstyrene, and benzoic acid.

The alkenylation was performed in the melt at 140°C. The molar ratio aromatic compound : 1,3-pentadiene : orthophosphoric acid was 1 : 2 : 0.1. The reaction was performed in two modes: (a) in the course of 5 h in a 30-cm^3 steel autoclave without forced stirring; (b) for 2–2.5 h in a 250 cm^3 glass vessel equipped with a power-driven stirrer, a dosing unit, and a reflux condenser. In the latter case, 1,3-pentadiene was added to the reaction mixture gradually in small portions.

The components were separated on a 30-m quartz capillary column coated with a nonpolar stationary phase, poly(methyl–5% phenyl)siloxane. In identification of the chromatographic peaks, we used along with the mass spectra the estimated boiling points and retention indices of the suggested compounds, obtained using the ACD Labs 4.0 and NIST MS Search 2.0 soft-

Products of alkenylation of aromatic compounds with 1,3-pentadiene

Substrate	Conditions	Conversion, %	Content of products with indicated degree of alkenylation, mol %			
			mono-	di-	tri-	other
Phenol	Autoclave	88	57	31	–	–
	Reactor	96	45	51	Traces	–
p-Cresol	″	98	75	23	Traces	–
p-Nonylphenol*	Autoclave	74	51	23	–	–
α-Naphthol	″	80	47	33	–	–
	Reactor	100	32	68	–	–
Resorcinol	″	100	68	32	–	–
2-Methylresorcinol	Autoclave	70	53	17	Traces	–
	Reactor	100	15	85	–	–
Alkirez-1	″	100	46	54	–	–
α-Methylstyrene	″	100	58	–	–	42**

* Reaction duration 20 h.

** Compounds corresponding in composition to α-methylstyrene dimers.

ware.The reaction products were identified by gas chromatography–mass spectrometry (GC–MS) on a Shimadzu GCMS-QP 2010 quadrupole device.

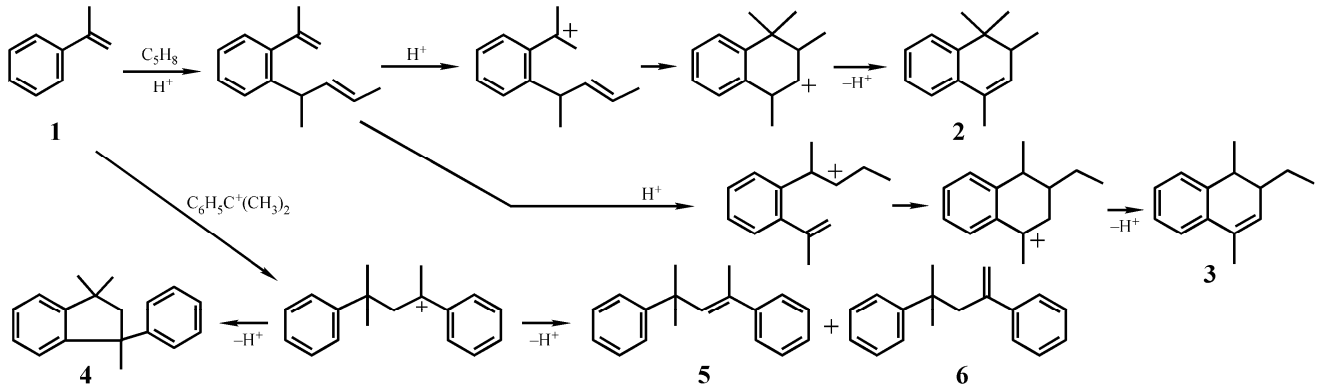
The quantitative composition of reaction mixtures was determined using a Kristall-2000M gas chromatograph equipped with a thermal conductivity detector. A 1-m steel column, 3 mm i.d., was packed with Chromaton N-AW-HMDS (0.25–0.315 mm) + 15% Apiezon L. The column was heated from 90 to 300°C at a rate of 16 deg min^{-1}. The flow rate of the carrier gas (He) was 20 $cm^3 min^{-1}$.

A TLC analysis was performed on Silufol UV-254 plates, using toluene as eluent. The component spots were developed with iodine vapor.

To convert the alkenylation products to the commercial form convenient for further use in rubber stock formulations, they were treated with hexamethylenetetramine. Transformation of the alkylate into the oligomeric form (“curing”) was monitored by the dropping point measured by the ring-and-ball method according to GOST (State Standard) 11 506. The iodine number of the products was determined in accordance with GOST 17 823.2–72.

Data on the composition of reaction mixtures obtained by alkenylation of aromatic compounds with 1,3-pentadiene are listed in the table.

A GC–MS analysis showed that the reaction of α-methylstyrene **1** with 1,3-pentadiene yields four monoalkenylation products whose structure cannot be unambiguously determined from the mass spectra because of their similarity for the suggested isomers. However, the major product of a-methylstyrene monoalkenylation (>60% of the total amount) is, presumably, compound **2** (1,1,2,4-tetramethyl-1,2-dihydronaphthalene) or **3** (1,4-dimethyl-2-ethyl-1,2-dihydronaphthalene).



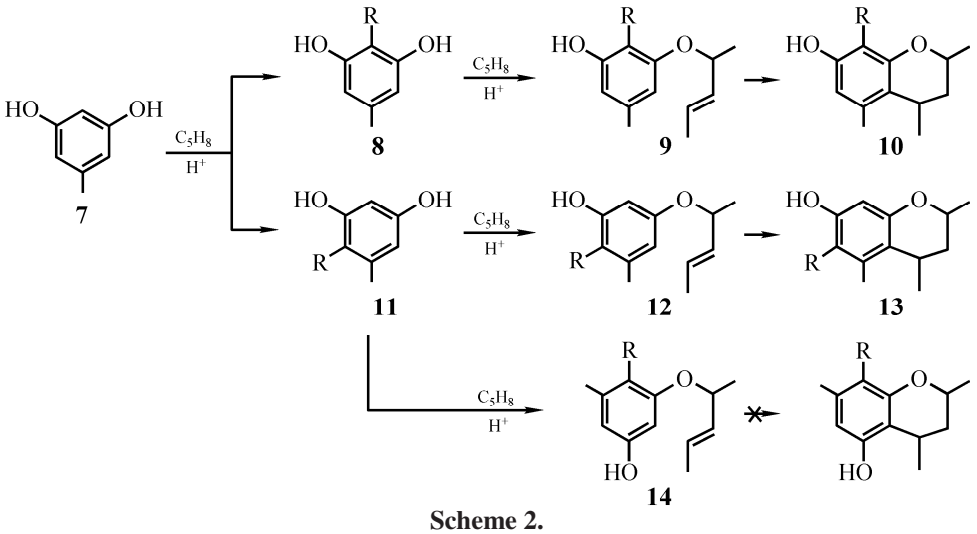
Scheme 1.

The reaction mixture obtained from α-methyl-styrene contains no dialkenylation products but contains dimers of the starting α-methylstyrene: 1,1,3-trimethyl-3-phenyl-2,3-dihydro-1*H*-indene **4**, (2-methyl-4-phen-ylpent-3-en-2-yl)benzene **5**, and (2-methyl-4-phenylpent-4-en-2-yl)benzene **6** in 75 : 10 : 15 molar ratio. This composiiton of the α-methylstyrene alken-ylation products agrees with the measured iodine nu-ber, 78.0 (value of 76.7, calculated on the assumption that the major monoalkenylkation products contain no more than one olefinic or cycloolefinic double bond in the molecule).

Transformations similar to those shown in Scheme 1 are also observed in alkenylation of styrene with piperylene.

A TLC analysis showed that the alkenylation of salicylic and benzoic acids with 1,3-pentadiene occurrs at the carboxy group and yields the corresponding pent-3-en-2-yl esters. With salicylic acid, the alkenylation also partially occurrs in the benzene ring owing to the activating effect of the phenolic hydroxyl.

Specifically the alkenylation of compounds containing phenolic hydroxy groups is of most interest from the standpoint of using the products as modifiers for polymer compounds. A detailed GC–MS analysis of the alkylate obtained from 5-methylresorcinol **7** allowed us to suggest the following scheme of its alkenylation with 1,3-pentadiene.



Scheme 2.

We found that the monoalkenylated fraction is composed of approximately equal amounts of 1,3-dihydroxy-5-methyl-2-(pent-3-en-2-yl)benzene **8** and 1,3-dihydroxy-5-methyl-4-(pent-3-en-2-yl)benzene **11**, formed by introduction of the alkenyl group into position 2 or 4 of the aromatic ring of 5-methylresorcinol, respectively. Further reaction of these monoalkenylation products with 1,3-pentadiene involves phenolic hydroxyls and yields mixed C,O-dialkenylation products: 5-methyl-2-(pent-3-en-2-yl)-3-(pent-3-en-2-yloxy)phenol **9**, 5-methyl-6-(pent-3-en-2-yl)-3-(pent-3-en-2-yloxy)phenol **12**, and 5-methyl-4-(pent-3-en-2-yl)-3-(pent-3-en-2-yloxy)phenol **14**, which are present in the reaction mixture in comparable amounts.

Under the reaction conditions, the dialkenylation products undergo partial cyclization. Compounds **9** and **12** form 2,4,5-trimethyl-8-(pent-3-en-2-yl)-3,4-dihydro-2*H*-benzo[*b*]pyran-7-ol 10 and 2,4,5-trimethyl-6-(pent-3-en-2-yl)-3,4-dihydro-2H-benzo[*b*]-pyran-7-ol **13**, respectively. Compounds **10** and **13** can be considered to be products of intramolecular electrophilic substitution in the aromatic ring with alkenyloxy groups as electrophilic agents. On the whole, the fraction of dialkenylated compounds contains about 70% C,O-dialkenylation products **9**, **12**, and **14**, with the remaining 30% being chroman derivatives **10** and **13**. It should be noted that we did not detect the expected cyclization product of compound **14** in the reaction mixture in noticeable amounts.

Bringing the alkylate obtained by the reaction of 1,3-pentadiene with 5-methylresorcinol or Alkirez-1 into the subsequent reaction with hexamethylenetetramine gives an oligomeric (so-called "cured") product with a softening point of about 75°C. A special study showed that nearly the whole available amount of the monoalkenylated dihydric phenol **8** or **11** undergoes condensation to give Resorcinol–amino aldehyde resin, whereas dialkenylated compounds **9**, **10**, and **12–14** remain unchanged and control the melting point of the resulting oligomer. The cured product with a higher

degree of oligomerization would have an unacceptably high melting point, which would make impossible its further use as a modifier of elastomeric compounds because of the insufficiently uniform distribution in the rubber stock.

The piperylene alkylate of Alkirez-1 condensed with hexamethylenetetramine (AP-U resin) was tested as modifier for improving the elastic-strength properties of thermoplastic elastomers (TPEs) of the composition SKEPT Elastokam 6305–PVD 10 803-020 (50:50 ratio), filled with BS-100 white black. The TPE modification with AP-U resin enhanced the strength (by up to 75%) and raised the relative elongation (by up to 20%) relative to the unmodified formulations.

The use of a silicic acid filler in the polymer compounds without addition of a phenolic modifier, as well as the modification without silicic acid filler, has nearly no effect on the TPE strength. The use of the reinforcing filler and oligomeric phenolic modifier in a combination affords a very significant improvement of the properties, i.e., a synergistic effect is observed.

Apparently, the alkenylresorcinol oligomer interacts, on the one hand, with the surface of BS-100 filler via phenolic hydroxyls and, on the other hand, with the rubber phase of TPE via alkenyl fragments, which strongly enhances the reinforcing effect of the filler [5].

In 2007, two batches of AP-U resin (25 kg) were produced on a pilot installation at the Central Plant Laboratory of the Kauchuk Joint-Stock Company (Sterli-tamak, Bashkortostan, Russia).

CONCLUSIONS

(1) Alkenylation of 5-methylresorcinol with 1,3-pentadiene yields complex mixtures of mono- and dialkenylated products. Monoalkenylation mainly occurs at the aromatic ring, whereas introduction of the second alkenyl group yields C,O-dialkenylated derivatives subsequently undergoing partial cyclization.

(2) Introduction of AP-U resin into polymer compounds based on thermoplastic elastomers is accompanied by a considerable enhancement of the strength characteristics of the ready items owing to the synergistic effect of interaction of the hydroxylcontaining moiety of the resin with the filler and of alkenyl substituents with the elastomer matrix.

ACKNOWLEDGMENTS

The authors are grateful for the assistance to staff members of the demonstration center of Analit Limited Liability Company, General Distributer of Shimadzu in St. Petersburg.

REFERENCES

1. Tutorskii, I.A., Potapov, E.E., and Shvarts, A.G., *Khimicheskaya modifikatsiya elastomerov* (Chemical Modification of Elastomers), Moscow: Khimiya, 1993.

2. Talantov, S.V. and Rossinskii, A.P., *Kauchuk Rezina*, 2000, no. 3, pp. 21–24.

3. Talantov, S.V., Rossinskii, A.P., and Derevkova, N.G., *Kauchuk Rezina*, 2001, no. 3, pp. 13–14.

4. Khitrin, S.V. and Alalykin, A.A., *Kauchuk Rezina*, 2001, no. 3, pp. 10–12.

5. Musin, I.N., Volkov, I.V., Kimel'blat, V.I., and Vol'fson, S.I., in *Kompozitsionnye materialy v aviastroenii i narodnom khozyaistve: Sbornik nauchykh trudov Vserossiiskoi nauchno-tekhnicheskoi konferentsii* (Composite Materials in Aircraft Building and National Economy: Proc. All-Russia Scientific and Technical Conf.), Kazan, October 5–8, 2000, pp. 35–40.

ISSN 1070-4272, Russian Journal of Applied Chemistry, 2008, Vol. 81, No. 8, pp. 1427–1433. © Pleiades Publishing, Ltd., 2008.
Original Russian Text © V.E. Proskurina, V.A. Myagchenkov, 2008, published in Zhurnal Prikladnoi Khimii, 2008, Vol. 81, No. 8, pp. 1350–1357.

MACROMOLECULAR CHEMISTRY AND POLYMERIC MATERIALS

Effect of Selective Interactions of Ionic Acrylamide Copolymers on Flocculation Properties with Respect to Titanium Oxide in Aqueous Salt Solutions

V. E. Proskurina and V. A. Myagchenkov

Kazan State Technological University, Kazan, Tatarstan, Russia

Received December 28, 2007

Abstract—The kinetics of unhindered sedimentation of a titanium dioxide suspension (as model dispersed system) was studied, and the effect of the concentration and mode of addition of various formulations based on anionic and cationic acrylamide copolymers on their flocculation properties in aqueous salt (NaCl) solutions was evaluated.

DOI: 10.1134/S1070427208080211

The effect of macromolecular compounds [in particular, polyacrylamide flocculants (PAAFs)] and their mixtures on various physicochemical processes such as adsorption, flocculation, flotation, and filtration are still of particular importance in both theoretical and practical aspects [1–3]. As compared to individual polymer components, their mixtures provide more direct and efficient control over the properties of various model and real dispersed systems (DSs) and, thus, of the aggregation and sedimentation processes occurring in these systems. The above differences are primarily due to the specific interactions of the functional groups in various macromolecules, which change their conformation state and, as a result, make stronger or weaker the effect of copolymer mixtures with respect to certain fixed parameters of dispersed systems [4, 5].

Therefore, the kinetic studies using a relatively poorly studied model DS (titanium dioxide TiO_2 suspension) are a promising way to evaluate the effect of selective interactions in mixtures of ionic PAAFs on flocculation processes in multicomponent systems. As compared to common DSs used in Russia (such as kaolin, ocher, copper oxide), the given system exhibits more stable surface characteristics and higher surface charge density ($\zeta = -55$ mV) [6, 7]. Previously, we have studied [8] the kinetic features of hindered sedimentation of an ocher suspension in the presence of binary mixtures of ionic (anionic and cationic) PAAFs with a high content of ionic groups. It is of particular interest to study the flocculation kinetics of a TiO_2 suspension in the mode of unhindered sedimentation, using ionic [anionic (A) and cationic (C)] random polymers of acrylamide (AA) with a high molecular weight ($M > 2 \times 10^6$) and lower or similar concentrations of ionic groups β.

We emphasize that the positively and negatively charged fragments in both anionic and cationic AA copolymers are identical in chemical nature and have similar lengths of the flexible nonionic acrylamide fragments. This fact makes it a priori unnecessary to take into account various difficultly controllable specific interactions of nonionic fragments in mixtures of oppositely charged ionic copolymers, which is of particular importance for polymer mixtures in passing from aqueous to aqueous salt solutions.

EXPERIMENTAL

In our study, we examined the flocculation power of various AA copolymers, using a rutile (TiO_2) suspension [TU (Technical Specification) 24.1-05 762 329-001–2003] with an average particle radius $R = 8.7 \times 10^6$ m and density $\rho = 3.9 \times 10^3$ kg m^{-3}. The following ionic PAAFs were used: anionic (A) random copolymer of acrylamide and sodium acrylate (molecular weight $M = 6.7 \times 10^6$, content of ionic groups $\beta = 17.5\%$) and cationic (C) random copolymer of acrylamide and dimethylaminoethyl methacrylate hydrochloride ($M = 2.3 \times 10^6$, $\beta = 16.3\%$).

The flocculation kinetics of the TiO_2 suspension in the mode of free (unhindered) sedimentation in the presence of various AA copolymers was evaluated by sedimentometric analysis in a 400-ml cylinder, using a VT-500 torsion balance. In all the tests, the initial con-

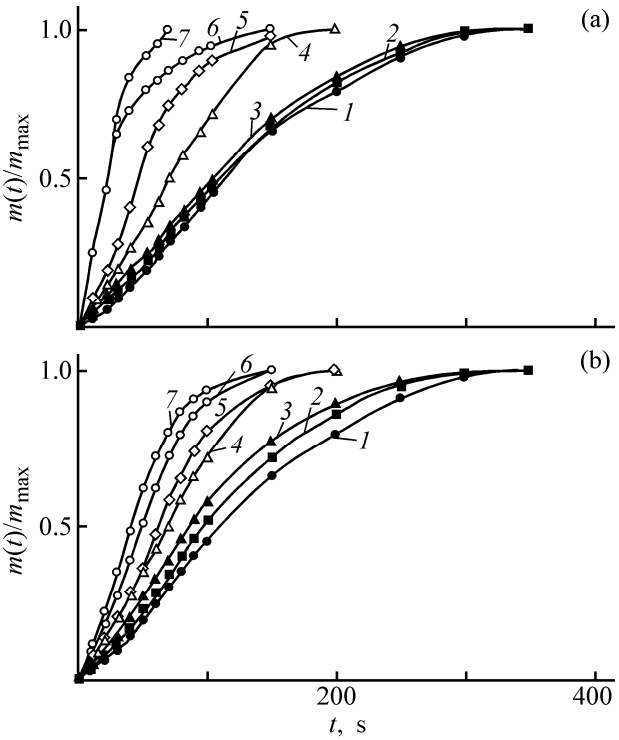


Fig. 1. Kinetic curves of sedimentation of a TiO_2 suspension in the presence of various concentrations of copolymers (a) A and (b) C. $m(t)/m_{max}$. (t) Time and [$m(t)$, m_{max}] current and maximal weights of precipitates on the cup of the torsion balance; the same for Figs. 2, 3, and 6. [A] = [C] $\times 10^6$, %: (*1*) 0, (*2*) 1.0, (*3*) 2.5, (*4*) 4.5, (*5*) 8.46, (*6*) 16.4, and (*7*) 31.9.

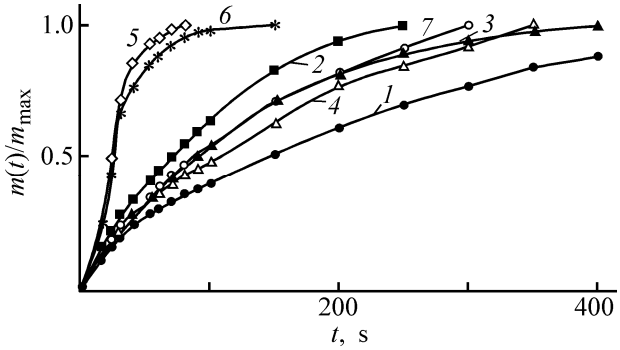


Fig. 2. Kinetic curves of sedimentation of a TiO_2 suspension at dosed charging of mixtures of copolymers A and C copolymer. (*1*) No additives; with addition of copolymer mixtures, binary: (*2*) AC, (*3*) CA, and (*4*) 2(1/2A + 1/2C); quaternary: (*5*) ACAC, (*6*) CACA, and (*7*) 4(1/2A + 1/2C); the same for Fig. 3.

centration of the dispersed phase was constant, c_d = 0.3%. The TiO_2 suspensions were clarified for 1 day before adding polymer mixtures to aqueous salt solutions with various ionic strengths (adjusted by adding various amounts of NaCl). The rutile suspension was mixed with a perforated disk stirrer (12 holes), which was slowly shifted in the cylinder 10 times in the vertical direction.

The viscometric analysis of the PAAF solutions was performed on an Ostwald viscometer (capillary diameter 0.54 mm). The correction for the kinetic energy of the flow was less than 1.5% and, thus, was neglected in the calculations of the reduced viscosity η_{sp}/c of copolymers and their mixtures by the following expression:

$$\eta_{sp}/c = (\tau - \tau_0)/\tau_0 c, \quad (1)$$

where τ and τ_0 are the flow times of the polymer solution of concentration c and the solvent, respectively.

To prepare the mixture of the ionic copolymers A and C of volume $V_A + V_C$ with fixed concentration $c = c_0$ and the ratio of the polymer components w_A =[A]/([A] + [C]), we mixed solutions of A and C (at [A] = [C] = c_0) in the following volume ratio: $V_A = w_A(V_A + V_C)$ and $V_C = (1 - w_A)(V_A + V_C)$. With this approach, the contraction in the aqueous and aqueous salt solutions of mixtures of copolymers A and C is less than 0.01%, and thus we can neglect it in treat-ment of the flocculation, viscometric, conductometric, and optical density data. The optical densities Q of the solutions of PAAFs and their mixtures were de-termined on a UNICO-1200 spectrophotometer.

The electrical conductivity of PAAF solutions was measured with an ANION-4100 conductometer with a working cell volume of 10 cm^3.

First, to evaluate the optimal charge of the flocculants in the mixtures, we studied the flocculation kinetics of a TiO_2 suspension in the presence of various concentrations of ionic polymer flocculants A and C (Fig. 1). Based on these data, we determined the optimal (standard) concentration $c = 4.98 \times 10^6$ % for all the further flocculation tests with various mixtures of copolymers A and C.

As shown in a series of papers [1, 8–10], on passing from water-soluble copolymers to binary mixtures, their effect on flocculation processes increases. Therefore, it was of interest to study the flocculation kinetics of the given model system (TiO_2), using not only binary (AC and CA), but also more complex systems of copolymers A and C (ACA, CAC, ACAC, and CACA).

Some kinetic curves of TiO_2 sedimentation with binary and quaternary systems of copolymers A and C in aqueous solution are shown as examples in Fig. 2. As can be seen, binary and quaternary systems of copolymers A and C have similar overall compositions and, thus, comparison of their flocculation properties would allow certain conclusions about the specific in-

teractions of the polymer components in various modes of their addition. Our experimental data suggest a strong dependence of the flocculation properties on the mode of addition of the polymer components to the disperse system. As can be seen, the flocculation performance decreases in the case of a simultaneous addition of the copolymers (1/2A+1/2C, Fig. 2, curves *4* and *7*) as compared to successive addition of these components (Fig. 2, curves *2*, *3* and *5*, *6*). This result unambiguously indicates that copolymers A and C, when added simultaneously as DS flocculants, show an antagonistic effect. In this paper, we show that this is due to sharp changes in the conformation state of the A and C macroions already in the stage of formation of the binary mixture (1/2A + 1/2C).

Comparison of the kinetic curves for binary (AC, CA, Fig. 2, curves *2*, *3*) and quaternary (ACAC, CACA, Fig. 2, curves *5*, *6*) systems with similar total compositions indicates that the AC and ACAC systems (when copolymer C is added second and fourth) exhibit higher flocculation properties as compared to the CA and CACA systems. On the one hand, this effect is probably due to the irreversible adsorption of macromolecules and, on the other hand, to different conformation states of macromolecules of copolymers A and C on the TiO_2 surface upon addition of a new copolymer additive.

As can be seen from published data, flocculation in the presence of macromolecular compounds may be due either to the adsorption of a macromolecule on the surface of the dispersed phase (DP) particles, or to their intermolecular binding with the previously adsorbed macromolecules to form links, interweavings, secondary structures, and aggregates [11]. It should be noted that the molecular binding is possible not only in the stage of interaction of DP particles with the already formed adsorption layer, but also in the stage of formation of the surface layer in the course of interaction of macromolecule aggregates with the TiO_2 surface [12]. Taking into account the high negative charge of TiO_2 particles ($\zeta = -55$ mV) and the kinetic data (Fig. 2), we suggested that formation of bridges in the AC and ACAC systems is more probable than that in CA and CACA systems [13]. Obviously, in such an approach the probability of formation of anchor bonds (inefficient in flocculation) changes in the opposite direction.

In treatment of the experimental kinetic data we used the procedure described previously in [14], which allows evaluation of the integral and differential characteristics of the flocculation in the presence of copolymers A and C. The integral parameters of the flocculation effect D and flocculation activity λ were calculated by the following equations:

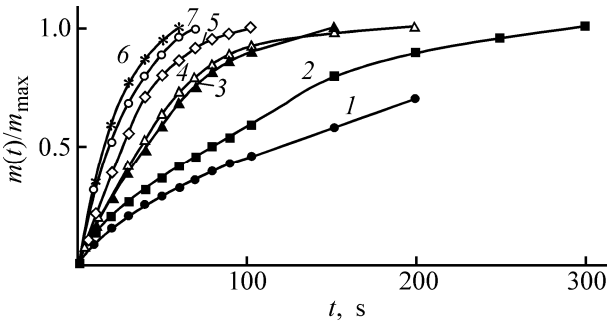


Fig. 3. Kinetic curves of sedimentation of the TiO_2 suspension at dosed charging of the A + C copolymer systems at $I = 0.05$ N.

$$D = \frac{\bar{u}_i}{\bar{u}_0} - 1, \quad (2)$$

$$\lambda = \left(\frac{\bar{u}_i}{\bar{u}_0} - 1\right)\frac{1}{c} = \frac{D}{c}, \quad (3)$$

where $\bar{u}_i$ and $\bar{u}_0$ are the average rates of the rutile sedimentation [at fixed $m(t)/m_{max}$ 0.7] in the presence of AA copolymer mixtures (concentration c) and without them, respectively.

The differential parameters of the flocculation effect D_i^* and flocculation activity λ_i^* were calculated by the equations reported in [8]:

$$D_i^* = \frac{\bar{u}_i}{\bar{u}_{i-1}} - 1,$$

$$\lambda_i^* = \frac{\bar{u}_i}{\bar{c}_i^*},$$

where $\bar{u}_i$ and $\bar{u}_{i-1}$ are the average rates of the rutile sedimentation at dosed addition of $(i - 1)$th and ith polymer doses, and $\bar{c}_i^*$ is the concentration of ith polymer dose.

It should be noted that, at dosed addition of the polymer components, the differential quantitative parameters of the flocculation D_i and λ_i allow evaluation of the contribution of each successively added polymer dose to the total flocculation effect.

In the second stage of our studies, to illustrate the potential of the kinetic analysis for finding efficient ways to control the sedimentation stability of the disperse system, we studied the flocculation of the TiO_2 suspension in aqueous salt (NaCl) solutions with various ionic strengths, using binary, ternary, and quaternary systems of copolymers A and C. Figure 3 shows as an example the kinetic curves of TiO_2 sedimentation in the presence of mixtures of copolymers A and C in the solution with $I = 0.01$ N. As can be seen from

Table 1. Parameters of flocculation of the TiO_2 suspension in aqueous salt solutions

Copolymer system	$c\times10^6$, %	D	D_{calc}	D^*	$\lambda^*\times10^{-4}$, $m^3\ kg^{-1}$
		$I = 0$			
A	4.98	0.223	0.223	0.223	0.448
AC	9.95	1.25	0.516	0.839	1.69
ACA	14.9	5.30	0.855	1.80	3.62
ACAC	19.8	7.69	2.03	0.379	0.766
C	4.98	0.240	0.240	0.240	0.482
CA	9.95	0.850	0.516	0.486	0.978
CAC	14.9	3.03	0.880	1.18	2.37
CACA	19.8	7.06	2.03	1.0	2.02
(1/2A + 1/2C)	4.98	0.200	–	0.200	0.402
2(1/2A + 1/2C)	9.95	0.270	–	0.056	0.113
3(1/2A + 1/2C)	14.9	0.310	–	0.035	0.071
4(1/2A + 1/2C)	19.8	0.520	–	0.160	0.323
		$I = 0.0025$ N			
A	4.98	0.065	0.065	0.065	0.131
AC	9.95	0.438	0.212	0.350	0.704
ACA	14.9	2.96	0.291	1.76	3.54
ACAC	19.8	6.67	0.469	0.933	1.88
C	4.98	0.138	0.138	0.138	0.277
CA	9.95	0.229	0.212	0.081	0.163
CAC	14.9	0.820	0.379	0.480	0.968
CACA	19.8	1.53	0.469	0.389	0.786
(1/2A + 1/2C)	4.98	0.076	–	0.076	0.153
2(1/2A + 1/2C}	9.95	0.105	–	0.026	0.052
3(1/2A + 1/2C)	14.9	0.050	–	–0.050	–0.101
4(1/2A + 1/2C)	19.8	0.024	–	–0.02	–0.04
		$I = 0.01$ N			
A	4.98	0.053	0.053	0.053	0.106
AC	9.95	0.587	0.079	0.508	1.02
ACA	14.9	2.77	0.137	1.38	2.78
ACAC	19.8	4.00	0.165	0.325	0.657
C	4.98	0.025	0.025	0.025	0.050
CA	9.95	0.323	0.079	0.290	0.584
CAC	14.9	1.73	0.106	1.07	2.16
CACA	19.8	2.15	0.165	0.154	0.311
(1/2A + 1/2C)	4.98	0.014	–	0.014	0.028
2(1/2A + 1/2C}	9.95	0.321	–	0.304	0.612
3(1/2A + 1/2C)	14.9	0.762	–	0.333	0.671
4(1/2A + 1/2C)	19.8	1.21	–	0.313	0.632
		$I = 0.05$ N			
A	4.98	0.071	0.071	0.071	0.143
AC	9.95	0.364	0.259	0.273	0.549
ACA	14.9	0.875	0.349	0.375	0.756
ACAC	19.8	2.00	0.586	0.600	1.21
C	4.98	0.176	0.176	0.176	0.353
CA	9.95	0.404	0.259	0.192	0.386
CAC	14.9	1.35	0.481	0.676	1.36
CACA	19.8	2.33	0.586	0.417	0.84
(1/2A + 1/2C)	4.98	0.122	–	0.122	0.245
2(1/2A + 1/2C}	9.95	0.703	–	0.519	1.04
3(1/2A + 1/2C)	14.9	1.0	–	0.174	0.351
4(1/2A + 1/2C)	19.8	1.71	–	0.353	0.178

the comparison of Figs. 2 and 3, passing from aqueous (I = 0) to aqueous-salt (I = 0.01 N) solutions causes strong changes in the flocculation parameters for similar polymer systems. The flocculation par-ameters in aqueous-salt solutions are summarized in Table 1. The values of the flocculation effect D_{calc} for the systems of copolymers A and C were calculated from the following equations:

$$D_{calc}(AC) = D_{calc}(CA) = (1 + D_A)(1 + D_C) - 1, \quad (4)$$

$$D_{calc}(ACA) = (1 + D_A)^2(1 + D_C) - 1, \quad (5)$$

$$D_{calc}(CAC) = (1 + D_A)(1 + D_C)^2 - 1, \quad (6)$$

$$D_{calc}(ACAC) = D_{calc}(CACA) = (1 + D_A)^2(1 + D_C)^2 - 1. \quad (7)$$

As can be seen from the experimental data (Table 1), the experimental D values are noticeably higher than the calculated values, which is probably due to the occurrence of selective interactions of the charged fragments of macromolecules A and C on the DP particle surface, and heterocontacts of macroions A and C appearing in the course of adsorption promote coarsening of the floccules and formation of bridges between the DP particles. This conclusion is confirmed by comparison of the experimental data on the ratio of the differential parameters λ^*_{CA}, λ^*_A and λ^*_{AC}, λ^*_C in aqueous salt solutions with systems CA, AC and CACA, ACAC, namely, $\lambda^*_{CA} \geq \lambda^*_A$ and $\lambda^*_{AC} \geq \lambda^*_C$. At dosed addition of the polymer mixture (1/2A + 1/2C) as a binary or quaternary additive, the flocculation effect D is significantly smaller as compared to the flocculation effect of the binary or quaternary systems of components A and C added to the rutile suspension successively.

Our experimental data listed in Table 1 indicate that the mode of addition of the polymer components affects the formation of floccules and, thus, such their important properties as the average size of the floccules, their size distribution, density, and shape asymmetry [15]. The observed effect of the modes of copolymers addition and differences in the structures of the resulting floccules are primarily due to the differences in the parameters of the electrical double layers at the DP particles. Since the adsorption of macromolecules on the DP particles in mainly irreversible [11], with complication of the polymer mixture, the forming more complex (e.g., ternary) floccules retain certain elements of the simpler aggregates (in our case, binary) in their modified structure [4].

Data on interactions of polymer components are necessary to understand dependences of the macroscopic sedimentation process in complex multicompo-

nent systems in the presence of copolymers A and C. Such interactions can be judged from the data of viscometric analysis [16]. To evaluate the conformational changes, we use the well-known Flory equation:

$$\eta M = \Phi(\bar{R}^2)^{0.5}, \quad (8)$$

where $[\eta] = \lim_{c\to 0}(\eta_{sp}/c)$ is the intrinsic viscosity; $(\bar{R}^2)^{0.5}$, root-mean-square radius of inertia of the macromolecule; and Φ, Flory constant.

Severe problems appear even in the step of evaluation of $[\eta]$ for electrolytes A and C and especially for their mixtures, because the dilution at concentrations $c \to 0$ is nonisoionic [16]. To overcome this problem, we used the De Gennes principle of invariance [17]. With the reduced viscosity $[\eta_{sp}/c]$ used instead of $[\eta]$ at final relatively low polymer concentrations c, the Flory equation can be transformed as follows:

$$[h_{sp}/c]^{1/3}M = \Phi'(\bar{R}^2)^{0.5}, \quad (9)$$

where Φ' is a constant.

It is not improbable that the constant Φ' is not identical to the Flory constant Φ, but this is not critical for further analysis, because the most important fact is that $\Phi' = \text{const}$ at fixed molecular weights of the (co)polymers.

Based on expression (9) for quantitative evaluation of the selective interactions between macromolecules of varied nature at a certain fixed concentration of the binary copolymer mixture (c = const), we can use the dimensionless parameter F [8, 18]:

$$F = (h_{sp}/c)^{1/3}_{exp}\,(h_{sp}/c)^{-1/3}_{calc} - 1. \quad (10)$$

On applying the rule of additivity of the contributions of copolymers A and C to the viscosity of the binary mixture, the calculated values $(h_{sp}/c)_{calc}$ can be determined as follows:

$$(h_{sp}/c)_{calc} = w_A(h_{sp}/c)_A + (1 - w_A)(h_{sp}/c)_C\,. \quad (11)$$

where w_A is the weight fraction of copolymer A in the mixture.

It is obvious that the parameter F determined by the above procedure is a reliable and convenient characteristic of the intermolecular interactions of the polymer components upon their mixing. Actually, the condition $F = 0$ [and thus $(h_{sp}/c)^{1/3}_{exp} = (h_{sp}/c)^{1/3}_{calc}$] suggests the absence of specific interactions between copolymers A and C. The other limiting case ($F = -1$) is typical of systems in which copolymers A and C form very compact interpolymer complexes (of globule type) [19]. When $F > 0$ [i.e., $(h_{sp}/c)^{1/3}_{exp} > (h_{sp}/c)^{1/3}_{calc}$], the heterocontacts being formed between the AC molecules lead to an increase in the effective size of macromolecular aggregates $(\bar{R}^2)^{0.5}_A$ and $(\bar{R}^2)^{0.5}_C$. At $F < 0$ [i.e., $(h_{sp}/c)^{1/3}_{exp} < (h_{sp}/c)^{1/3}_{calc}$], macromolecules are compacted in the presence of macromolecules of another kind, so that $(\bar{R}^2)^{0.5}_A$ and $(\bar{R}^2)^{0.5}_C$ decrease. Specifically this type of the selective interactions was observed for all the compositions of the binary mixture (A + C) because the following conditions were satisfied: $F < 0$ (Fig. 4) and $(h_{sp}/c)^{1/3}_{exp}\,(h_{sp}/c)^{1/3}_{calc} < 1$.

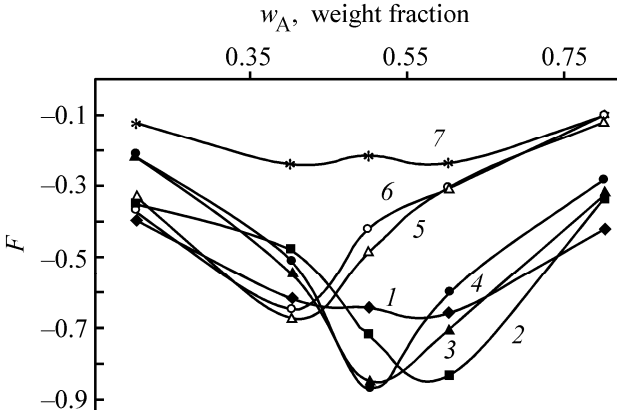


Fig. 4. Parameter F vs. the composition of A + C copolymer mixture. ([A] + [C]) × 10^2, kg m^{-3}: (*1*) 2, (*2*) 4, (*3*, *5*) 6, and (*4*, *6*, *7*) 10. I, N: (*1*–*4*) 0, (*5*, *6*) 0.01, and (*7*) 0.05.

The dependences $F = f(w_A)$ are characterized by a clearly pronounced extremum (minimum) for $w_A \sim 0.5$, which directly confirms the occurrence of strong selective interactions of the ionic fragments of macromolecules of the anionic and cationic AA copolymer. With account taken of the low density of the ionic units in copolymers A and C ($\beta < 20\%$), relatively small values of parameter $F < -0.7$ at $w_A \sim 0.5$–0.6 seem unexpected. This fact suggests that strongly compressed, close to globular, macromolecular aggregates are formed in the above range of the polymer mixture compositions.

In this context, evaluation of the effect of low-molecular-weight electrolytes on the intensity of inter- and intramolecular interactions in polyelectrolytes A and C is of particular importance [18]. We studied the dependences of parameter F on w_A for aqueous-salt solutions (I = 0.01 N) (Fig. 4, curves *5*, *6*). The dependences $F = f(w_A)$ pass through a minimum, which is shifted for curves *5* and *6* (Fig. 4) toward smaller w_A (0.4). Certain increase in parameter F for aqueous-salt solutions with I = 0.01 M, compared to the aqueous solutions, suggests weakening of the selective interactions of macroions A and C. More pronounced changes in the dependences $F = f(w_A)$ are observed as the ionic strength of the solutions increases to 0.05 N (Fig. 4, curve *7*). In this case, the probability of selective electrostatic interactions of the charged macromolecular

Table 2. Results of a conductometric analysis of aqueous solutions of copolymers A and C and their 1 : 1 mixtures

Parameter	Copolymer concentration c, %	
	0.002	0.1
χ_A, S cm^{-1}	6.13	11.7
$\chi_C \times 10^6$, S cm^{-1}	4.85	19.4
χ_{mix}, S cm^{-1}	26.02	36.9
χ_{ad}, S cm^{-1}	2.38	12.4
Y	9.63	2.73

fragments A and C sharply falls, the parameters η_{sp}/c and $(R^2)^{0.5}$ decrease simultaneously, and the parameter F strongly increases, with the minimum in the dependence $F = f(w_A)$ becoming less pronounced.

Along with the viscometric parameter F, the conductometric parameter Y is an additional sensitive characteristic of the selective interactions of the ionic PAAFs:

$$Y = \frac{\chi_{exp}}{\chi_{calc}} = \frac{\chi_{mix} - \chi_0}{\bar{\chi}_{ad}}, \qquad (12)$$

where χ_0 is the electrical conductivity of the solution (water, $\chi_0 = 3.109 \times 10^{-6}$ S cm^{-1}); χ_C and χ_A are the electrical conductivities of the solutions of copolymers A and C; and $\bar{\chi}_{ad}$ is the average electrical conductivity calculated on the assumption of additivity.

The values of Y for two fixed concentrations of the copolymers are given in Table 2. These values indicate that the interaction of macroanion A with macrocation C is accompanied by the formation of NaCl. In the process, the counterions Na^+ and Cl^- escape from "microreactors" (macroions) into the dispersion medium. As a result, χ_{exp} increases, and Y becomes greater than 1. The relationship between the parameters Y for two copolymer concentrations, Y (c = 0.002%) > Y (c = 0.01%), is also quite understandable, because at lower concentrations of A and C the macroion coils have more open conformations, and hence the charged fragments of macroions A and C interact with each other more strongly.

The intense intermolecular interactions of macroions A and C in aqueous salt solutions with the formation of compact structural elements are additionally confirmed by the optical method. The dependences of the optical density Q on the wavelength of incident light at fixed concentration of copolymers [A] = [C] = 0.006% and their 1 : 1 mixture are shown in Fig. 5. In this series of experiments, we used 1 : 1 polymer complex (1/2A + 1/2C) (Fig. 5, curve *3*) to which the calculated amounts of NaCl were added to prepare solutions with the ionic strength I of 0.002, 0.01, and 0.05 N. At low and intermediate ionic strengths, the dependence $Q = f(\lambda)$ lies slightly higher than the basis line, whereas at higher ionic strength (I = 0.05 N) a sharp decrease in the optical density is observed in the entire special range, which is due to partial degradation of compact globular aggregates formed by macromolecules of copolymers A and C. Thus, the dependences $Q = f(\lambda)$ shown in Fig. 5 qualitatively characterize the decrease in the intensity of selective interactions of macroions A and C in passing from aqueous to aqueous-salt solutions with I = 0.05 N.

To evaluate the influence exerted by the mode of addition of the active components (electrolyte and flocculants) on the flocculation properties with respect to TiO_2 suspension in aqueous-salt solutions, we performed a series of experiments at a fixed ionic strength I = 0.0025 N. The kinetic curves for the first (electrolyte and then the mixture of copolymers A and C, curves *2–4*) and second addition mode (mixture of copolymers A and C and then electrolyte, curves *2'–4'*) are shown in Fig. 6. As can be seen, changes in the addition mode significantly affect the flocculation pa-

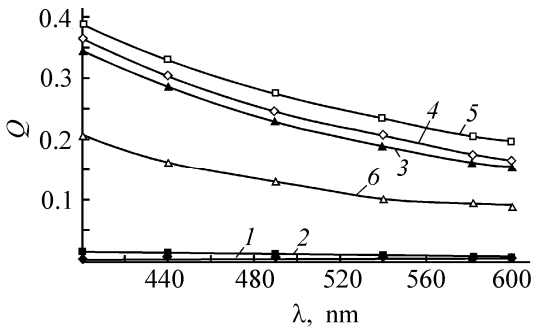


Fig. 5. Optical density Q vs. the wavelength λ of incident light for copolymers (*1*) A, (*2*) C, and (*3–6*) their 1 : 1 mixtures [1/2A + 1/2C]. I, N: (*3*) 0, (*4*) 0.002, (*5*) 0.01, and (*6*) 0.05.

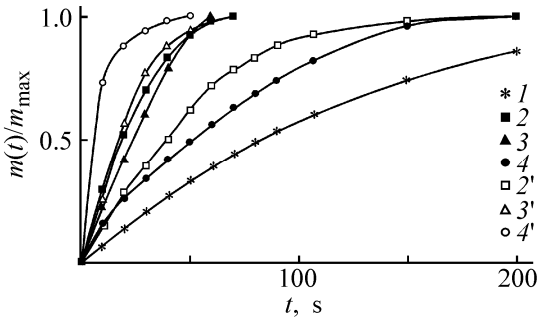


Fig. 6. Kinetic curves of sedimentation of the TiO_2 suspension (*1*) in the absence of flocculants and at dosed charging of copolymers A and C: (*2*, *2'*) ACAC, (*3*, *3'*) CACA, (*4*, *4'*) 4[1/2A + 1/2C]; I = 0.0025 N and c = 19.8 × 10^{-6}%. (*2–4*, *2'–4'*) First and second mode of addition of the copolymers and electrolyte, respectively.

rameters of the system and, thus, the resulting flocculation effect in the aqueous-salt solutions of PAAFs strongly depends on technological parameters.

The observed differences in the flocculation parameters may be due to the irreversibility of the adsorption of copolymers and to the effect of electrolyte ions Na^+ and Cl^- on the electrical properties of the surface of TiO_2 particles and, primarily, on the ζ-potential and physicochemical properties of the localized and nonlocalized adsorption centers and on the length and structure of the adsorption layers. Initial addition of the electrolyte causes strong changes in the parameters of the electrical double layer near the TiO_2 particle and makes the diffusion layer thinner and the electrokinetic potential lower. As a result, the aggregation and sedimentation stability of the disperse system decreases. With successive addition of various mixtures of the ionic PAAFs into the aqueous salt solution, the size of macromolecular globules of the A and C macroions strongly decreases and, thus, the probability of formation of bridges between the dispersed particles also falls.

Thus, the main reason for differences in the kinetics of flocculation of the TiO_2 suspension for the first and second addition modes of addition of the polymer mixtures and electrolyte is due to the differences in the structure and thickness of the electrical double layer, in the conformation of A and C macroions on the surface of dispersed phase particles, and in the size and structure of the resulting floccules.

CONCLUSIONS

(1) in the case of dosed addition of binary, ternary, and quaternary systems of acrylamide copolymers into a rutile suspension, the resulting flocculation effect strongly depends on the selective interactions of the ionic fragments of macromolecules of the anionic and cationic polyacrylamide flocculants on the surface of the dispersed phase. With increasing ionic strength of the solution, the intensity of the selective interaction between the macroions of the anionic and cationic copolymers decreases, and degradation of the polymer aggregates is observed at a higher ionic strength (I = 0.05 N).

(2) The flocculation parameters of polyacrylamide flocculants with respect to the rutile depend on the mode of addition of the polymer flocculants (simultaneously or successively) and on the mode of addition of the polymer flocculants and the electrolyte.

REFERENCES

1. Myagchenkov, V.A., Baran, A.A., Bekturov, V.A., and Bulidorova, G.V., *Poliakrilamidnye flokulyanty* (Polyacrylamide Flocculants), Kazan: Tekhnol. Univ., 1998.
2. Myagchenkov, V.A., Proskurina, V.E., and Bulidorova, G.V., *Khim. Tekhnol. Vody*, 2001, vol. 23, no. 5, pp. 453–492.
3. Kurenkov, V.F., Nagel', M.A., Baiburdov, T.A., and Myagchenkov, V.A., in *Khimiya i tekhnologiya elementoorganicheskikh soedinenii i polimerov* (Chemistry and Technology of Organoelement Compounds and Polymers), Kazan: Kazan. Khim.-Tekhnol. Inst., 1987, pp. 90–95.
4. Proskurina, V.E., Churikov, F.I., and Myagchenkov, V.A., *Izv. Vyssh. Uchebn. Zaved., Khim. Khim. Tekhnol.*, 2002, vol. 45, no. 2, pp. 23–26.
5. Vorob'ev, P.D., Krut'ko, N.P., Vorob'eva, E.V., et al., *Kolloidn. Zh.*, 2007, vol. 69, no. 5, pp. 592–596.
6. Li, D., Zha, S., Pelton, R.H., and Spafford, M., *Colloid Polym. Sci.*, 1999, vol. 277, pp. 108–114.
7. Ma, M. and Zha, S., *Colloid Polym. Sci.*, 1999, vol. 277, pp. 115–122.
8. Myagchenkov, V.A., Proskurina, V.E., and Bulidorova, G.V., *Kolloidn. Zh.*, 2000, vol. 62, no. 2, pp. 223–227.
9. Myagchenkov, V.A. and Proskurina, V.E., *Kolloidn. Zh.*, 2000, vol. 62, no. 5, pp. 654–659.
10. Myagchenkov, V.A. and Proskurina, V.E., *Zh. Prikl. Khim.*, 2000, vol. 73, no. 12, pp. 2030–2035.
11. Lipatov, Yu.S., *Kolloidnaya khimiya polimerov* (Colloidal Chemistry of Copolymers), Kiev: Naukova Dumka, 1984.
12. Lipatov, Yu.S. and Sergeeva, L.M., *Adsorbtsiya polimerov* (Adsorption of Polymers), Kiev: Naukova Dumka, 1972.
13. Baran, A.A., *Polimersoderzhashchie dispersnye sistemy* (Polymer-Containing Disperse Systems), Kiev: Naukova Dumka, 1986.
14. Myagchenkov, V.A. and Proskurina, V.E., *Kinetika sedimentatsii okhry v rezhime svobodnogo osedaniya v prisutstvii poliakrilamidnykh flokulyantov. Metodicheskie ukazaniya k laboratornoi rabote* (Kinetics of Ocher Sedimentation in the Unhindered Mode in the Presence of Polyacrylamide Flocculants. Methodical Guide to Laboratory Work), Kazan: Tekhnol. Univ., 2004.
15. Zapol'skii, A.G. and Baran, A.A., *Koagulyanty i flokulyanty v protsessakh ochistki vody: Svoistva. Poluchenie. Primenenie* (Coagulants and Flocculants in Water Treatment. Properties. Preparation. Use), Leningrad: Khimiya, 1987.
16. Tsvetkov, V.N., Eskin, V.E., and Frenkel', S.Ya., *Struktura makromolekul v rastvore* (Structure of Macromolecules in Solutions), Moscow: Nauka, 1964.
17. De Gennes, P.-G., *Scaling Concepts In Polymer Physics*, Ithaca and London: Cornell Univ., 1979.
18. Tanford, Ch., *Physical Chemistry of Macromolecules*, New York: Wiley, 1963.
19. Bekturov, E.A. and Bimendina, L.A., *Interpolimernye kompleksy* (Interpolymer Complexes), Alma-Ata: Nauka, 1977.

ISSN 1070-4272, Russian Journal of Applied Chemistry, 2008, Vol. 81, No. 8, pp. 1434–1440. © Pleiades Publishing, Ltd., 2008.
Original Russian Text © Yu.P. Ioshchenko, V.F. Kablov, G.E. Zaikov, 2008, published in Zhurnal Prikladnoi Khimii, 2008, Vol. 81, No. 8, pp. 1358–1364.

MACROMOLECULAR CHEMISTRY AND POLYMERIC MATERIALS

Polymeric Complexes of Chitosan with Proteins and Hydroxyl-containing Polymers

Yu. P. Ioshchenko, V. F. Kablov, and G. E. Zaikov

Volzhskii Polytechnic Institute, Branch of the Volgograd State Technical University, Volzhskii, Volgograd oblast, Russia

Emanuel' Institute of Biochemical Physics, Russian Academy of Sciences, Moscow, Russia

Received May 23, 2007

Abstract—The structures of polymeric complexes of chitosan with methyl cellulose, lactoserum protein, gelatin, and polyvinyl alcohol were simulated on a computer. The mechanism of metal captures in cavities of these complexes was analyzed. The conformational and geometric characteristics of polymeric complexes of chitosan were obtained. The properties and structure of complexes in solutions and in the bulk were examined.

DOI: 10.1134/S1070427208080223

Chitosan, a promising biopolymeric material of the XXI century, is characterized by a number of valuable properties, such as biocompatibility, biodegradability, biological activity without toxicity, and availability of raw materials. One of specific features of chitosan as compared to other polymers is its pronounced capacity for intermolecular interactions with other compounds [1–4]. In particular, chitosan forms polymolecular and interpolyelectrolytic complexes and associates with other biopolymers and polar synthetic polymers via hydrogen bonds [5–9]. Such modification of chitosan allows improvement of its characteristics. In this respect, complexes of chitosan with proteins, cellulose derivatives, and water-soluble synthetic polymers, e.g., polyvinyl alcohol are of particulat interest [10, 11]. The search for fields of application of these complexes and development of methods for their production are urgent problems. At present, polymeric complexes of chitosan (PCCs) are poorly studied, especially in the solid state.

EXPERIMENTAL

Chitosan (CS) with a degree of deacetylation of 0.97 was isolated from fresh-water *Branchipus Stagnalis* anthropoda branchiopodas and was used as solutions (5 wt %) in 2% acetic acid. The other chemicals were as follows: food gelatin (G) of P-11 brand [TU (Technical Specification) 9219-017-179 102 261–01); lactoserum protein (LCP) isolated as a by-product in production of pot cheese; 5% aqueous solutions of commercial methyl cellulose (MC, TU 6-9-2344–78) and polyvinyl alcohol (PVA) [GOST (State Standard) 10 779–64].

The molecular weights (MW) of polymers were determined viscometrically: that of chitosan, on an Ubbelohde viscometer in the mixed solvent 2% CH_3COOH + 0.2 M CH_3COONa under standard conditions; those of gelatin, PVA, and lactoserum protein, on a BPZh-2 viscometer in distilled water under standard conditions [12]. The molecular weights of chitosan, gelatin, PVA, and lactoserum protein were 86.9×10^3, 14.4×10^3, 36.0×10^3, 56×10^3, and 83.2×10^3, respectively.

At present, for polymers of complicated structure, some physical characteristics whose experimental determination is difficult or impossible can be determined by calculation. In this study, the physicochemical characteristics of polymers were calculated by computer simulation methods using reference structural characteristics of polymeric chains and functional groups [13–15].

The initial chitosan and its complexes with other polymers were characterized by IR spectra recorded on a Bio-Rad Win-IR spectrometer (NaBr pellets) [16].

The complexes of chitosan with polymers were prepared as follows. A solution of chitosan in aqueous acetic acid was added to a solution of a polymer (methyl cellulose, lactoserum protein, gelatin, or polyvinyl alcohol) in distilled water at a prescribed chitosan-to-polymer ratio, and the resulting mixture was stirred with a magnetic stirrer for 30 min.

The polymeric films were prepared by casting of polymer solutions onto a glass support surface, followed by evaporation of the solvent in a vacuum at 25°C.

The structural characteristics of chitosan-containing complexes were determined by thin-layer chromatography, using Silufol UV-254 plates and various solvents [17].

The particle size of complexes was determined from the "turbidity spectra." The optical density was measured on a KFK-2 photocolorimeter (TU 3-3.1766–82) [18, 19].

The concentrations of phenol and petroleum products (PPs) in wastewater samples were determined by the fluorescence technique on a Flyuorat-02 analyzer of liquids (TU 4321-001-20 506 233–94) [20].

The amounts of metals bound by polymeric complexes were determined by compexometric titration [21]. The water content of the films was determined in accordance with GOST 11 736–78 [22].

The deformation-strength characteristics of films cast from solution of polymeric complexes (tensile strength, relative elongation at break) were determined on an RT-250M-2 tensile-testing mashine (GOST 14236–81) [23].

The swelling kinetics of chitosan films in various solvents (water, acetone, oil) was studied in accordance with GOST 4650–80 [24].

The oxygen index of the polymolecular materials was determined in accordance with GOST 21 793–76 [25]. The coke number was determined thermogravimetrically on heating a weighed sample (0.05–0.5 g) at a prescribed rate in an inert atmosphere to 800–900°C [26]. The flame propagation velocity on ignition of horizontally placed films of the polymolecular complexes was determined in accordance with GOST 28 157–89 [27].

The thermal behavior of the polymeric complexes was studied by thermomechanical analysis [26, 28].

The electrical characteristics of films prepared from solutions of polymeric complexes (electrical resistance, electrical conductivity, permittivity) were measured on an Immitans E7-14 digital device (TU 2.724.013) [29].

Table 1. Calculated physicochemical parameters of chitin and chitosan structural units

Parameter	Chitin	Chitosan
van der Waals volume $\sum_i \Delta V_i$, Å	168.1	132.4
Density, ρ, g cm^{-3}	1.35	1.40
Cohesion energy, $\Sigma \Delta E_i$, J mol^{-1}	78 294	56 272
Cohesion energy density δ, (J cm^{-3})$^{1/2}$	27.8	26.6
Surface tension γ_s, dyne cm^{-1}	40.5	36.6
Permittivity ε	4.5	3.3
Temperature, K:		
glass transition T_g	289	183
degradation of polymer T_d	570	615

Table 2. Calculated characteristics of macromolecules

Macromolecule	$M \times 10^{-3}$	$V_M^h \times 10^3$, cm^3	$h \times 10^6$, cm
Chitosan	86.9	6.5	4.5
Methyl cellulose	56.0	11.5	4.2
LSP	36.0	0.2	2.0
Gelatin	14.4	2.3	2.1
PVA	83.2	1.3	3.5

Table 1 lists physicochemical characteristics of chitin and chitosan fragments, determined in this study by the computer simulation technique.

The following volume parameters of polymeric complexes were calculated: the mean statistical distance between the ends of the macromolecules h, responsible for their flocculation and sorption ability, and the hydrodynamic volume V_M^h occupied in solution by unit weight of macromolecules and determining the overall size of the macromolecule [30]. These characteristics are listed in Table 2.

The volume characteristics of macromolecules under consideration show that the distance between the terminal groups of chitosan, methyl cellulose, and polyvinyl alcohol macromolecules exceeds that for gelatin and lactoserum protein by a factor of 2–4. This fact indicates that the terminal groups of the first series of macromolecules are more active in flocculation and sorption processes.

The hydrodynamic volumes of chitosan and methyl cellulose macromolecules are considerably larger

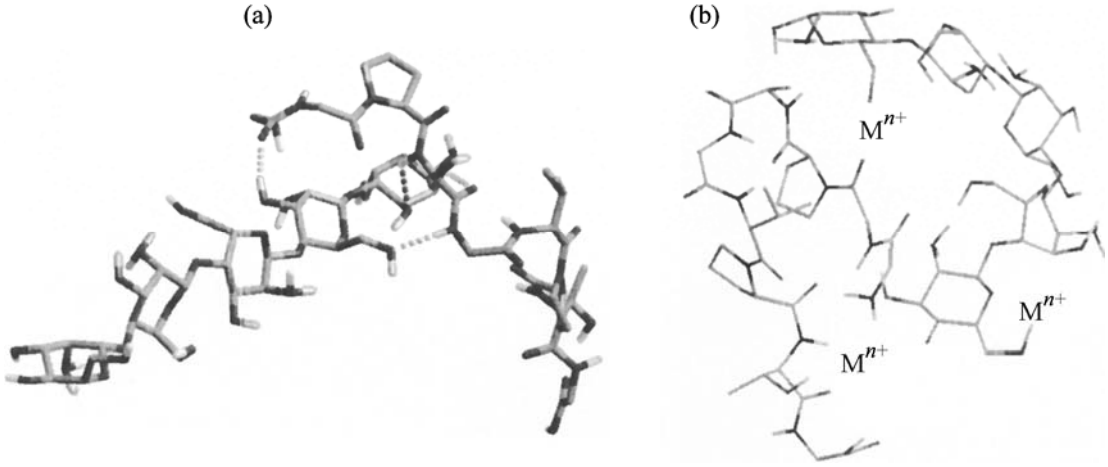


Fig. 1. Structure of (a) chitosan-gelatin and (b) chitosan-gelatin-metal complexes.

than those of the other macromolecules under consideration, i.e., their structures are bulkier and less coiled. Therefore, the functional groups of chitosan and methyl cellose are more accessible to intermolecular interactions.

Figure 1 shows the hypothetical structures of chitosan-gelatin complexes with a coordinated metal and without it. In these schemes, the intermolecular contacts are indicated by dotted lines. The calculated geometric characteristics of complexes are listed in Table 3. The number of intermolecular contacts in these structures reflects the stability of the complex.

Table 3 shows that the metal-capturing cavities are considerably larger than the metal ion size [31]. Owing to chemisorption, metal ions are strongly retained in macromolecular cativities, and the large weight of these macromolecular complexes can promote their sedimentation.

The features of structure formation in the systems under consideration can be elucidated by a computer technique allowing steric visualization of macromolecular complexes (Fig. 1) [14].

Table 3. Calculated geometric characteristics of polymeric complexes

Parameter	Parameter value
Particle size of complex, nm	80–130
Metal-capturing cavity size, nm	5–9
Metal ion size, nm	Cu^{2+} = 0.071, Fe^{3+} = 0.063, Zn^{2+} = 0.083, Cd^{2+} = 0.092, Ni^{2+} = 0.069

The size of polymeric complexes in aqueous medium was measured by turbidimetric spectroscopy. It was found that macromolecules in aqueous solutions form associates approximately 130 nm in size (macromolecular nanostructures).

We found that the macromolecular complexes are so stable that they are not separated into two components when subjected to thin-layer chromatography.

The physicomechanical and physicochemical characteristics of polymeric complexes under consideration and their constituents are poorly understood. In this study, we examined the deformation-strength, sorption, thermal, dielectric, thermomechanical, relaxation, and combustion characteristics of these polymers.

Table 4 show that treatment of water with polymeric complexes ensures a higher efficiency of its decontamination from petroleum products as compared to treatment with individual polymers (methyl cellulose, lactoserum protein, gelatin, and polyvinyl alcohol). The degree of decontamination of water with these individual polymers is as follows (%). Decontamination to remove petroleum products: gelatin 65.8, lactoserum protein 63.2, methyl cellulose 42.1, and polyvinyl alcohol 39.3. Decontamination to remove phenol: gelatin 40.3, lactoserum protein 39.2, methyl cellulose 23.6, and polyvinyl alcohol 21.6.

It has been reported previously that the sorption of metals with chitosan-containing sorbents (Fig. 2) is controlled by diffusion of metal ions into the sorbent [32]. Among polymeric complexes under consideration, a somewhat higher sorption ability toward metals is exhibited by chitosan–protein complexes containing a larger number complexing sites. These complexes also exceed straight chitosan in sorption ability.

Table 4. Degree of decontamination of wastewater to remove petroleum products and phenol by treatment with chitosan and polymeric complexes (initial content of petroleum products X_{init} PP and phenol in water 1.450 and 0.736 mg dm^{-3}, respectively; weight ratio between chitosan and a second polymer in binary polymeric complexes 1 : 1)

Composition	PP concentration in water sample, X_{PP}, mg dm^{-3}	Degree of decontamination of water to remove PP, Q_{PP}, %	Phenol concentration in water, X_{ph}, mg dm^{-3}	Degree of decontamination of water to remove phenol, Q_{ph}, %
Chitosan	0.147	98.9	0.101	86.3
CS–MC	0.155	98.7	0.130	82.3
CS–G	0.162	98.5	0.116	84.2
CS–LSP	0.163	98.3	0.105	85.7
CS–PVA	0.153	98.4	0.169	77.0

Table 5. Deformation-strength parameters of films

Film	Tensile strength σ_t, MPa	Relative elongation at break ε_b, %
Chitosan	112	31
CS–MC	102	29
CS–G	98	27
CS–LSP	96	25
CS–PVA	107	25

The increased stability of polymeric complexes is due to their polynuclear structure with multicenter bridging bonds between functional groups of neighboring macromolecules. The polymeric complexes are characterized by increased capacity for capturing not only cations, but also anions. The resulting heavy cation-anionic complexes lose solubility and undergo sedimentation from aqueous media in 30 min.

As can be seen from Table 5, the best deformation-strength properties among the complexes studied are exhibited by the CS–PVA complex. The strength of films of this complex is approximately equal to that of chitosan films. Owing to the low production cost, this complex is a commercially promising material. The hydrogen-bound water molecules present in the structure of this polymeric complex provide the elasticity of films [33].

We found that, on prolonged heating of chitosan-containing films at temperatures of up to 80°C, these materials retain water (up to 80–85%) and, therefore, do not lose their strength properties. Since water is the fireproofing agent, it imparts flame resistance to polymers and also allows introduction into the polymer and retention of additional appropriate hydrophilic fireproofing compounds, e.g., crystal hydrates.

Figure 3 shows the time dependence of swelling of chitosan-containing films in water. The first portion of this curve reflects fast swelling caused by chemical

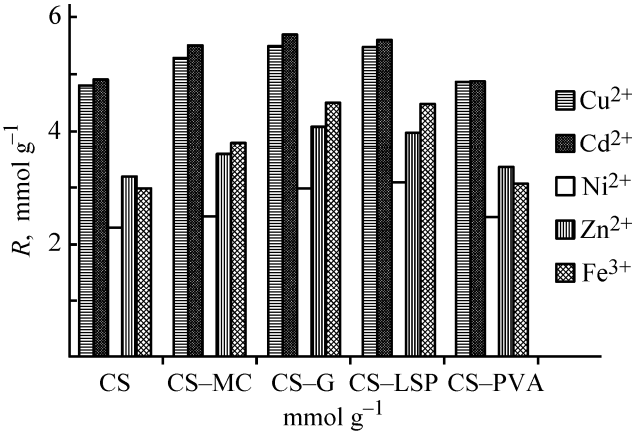


Fig. 2. Retention R of metal ions by chitosan and chitosan-containing polymeric complexes.

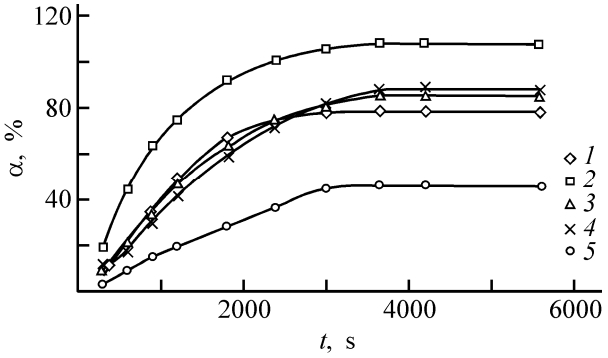


Fig. 3. Degree of swelling of chitosan-containing films in water, α, vs. time t. (*1*) CS, (*2*) CS–MC, (*3*) CS–LSP, (*4*) CS–G, and (*5*) CS–PVA.

Table 6. Combustion characteristics of chitosan and chitosan-containing polymeric complexes

Film	OI	CN	Combustion rate, mm s^{-1}
	%		
Chitosan	30	40	6.7
CS–MC	26	58	6.3
CS–G	31	43	5.7
CS–LSP	29	52	5.6
CS–PVA	28	44	5.3

binding of water with the polymer. In going from water to acetone and oil, the degree of swelling of all the films becomes less than 3 and 0.01%, respectively. Figure 3 shows that the largest swelling is shown by the CS–MC film, which is due to the high hydrophilicity of methyl cellulose.

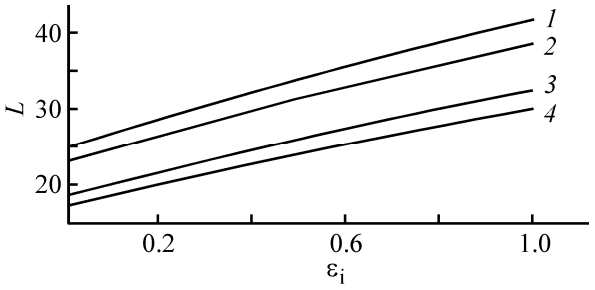


Fig. 4. Performance parameter L of (*1*, *2*) hydrated and (*3*, *4*) anhydrous CS–PVA complexes vs. the intumescence deformation ε_i at various thermal effects of pyrolysis Q and material densities ρ. (*1*) Q = 1300 kJ kg^{-1}, ρ = 1.22 kg m^{-3}; (*2*) Q = 1000 kJ kg^{-1}, ρ = 1.22 kg m^{-3}; (*3*) Q = 1300 kJ kg^{-1}, ρ = 1.32 kg m^{-3}; and (*4*) Q = 1000 kJ kg^{-1}, ρ = 1.32 kg m^{-3}.

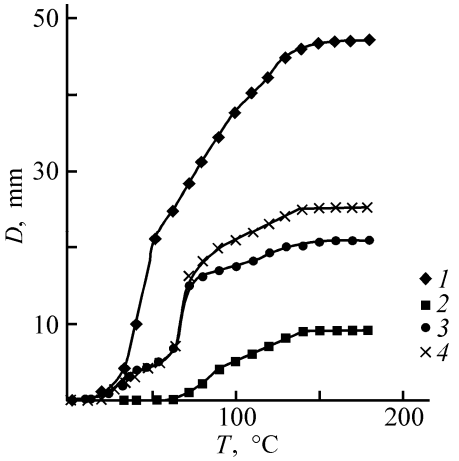


Fig. 5. Results of thermomechanical analysis of films of chitosan-containing complexes: deformation D vs. temperature T. (*1*) CS–MC, (*2*) CS–PVA, (*3*) CS–G, and (*4*) CS–LSP; the same for Fig. 6.

Table 6 lists the combustion characteristics of chitosan and chitosan-containing polymeric complexes. The oxygen index (OI), coke number (CN), and combustion rate of chitosan and chitosan-containing polymeric films show that these polymers belong to the group of self-extinquishing materials with reduced flammability and are suitable for preparing fireproofing coatings.

We believe that enhanced flame resistance of the chitosan complexes is due to the high content of bound water and to the presence of cyclic groups and nitrogen atoms.

Using a multifactorial model of heating of fireproofing and heat-shielding materials and Teplo 1 software [34], we simulated the fireproofing and heat-shielding characteristics of chitosan-containing coatings in relation to their thermolphysical parameters and heating mode, taking into account the physicochemical transformations of coatings (pyrolysis, intumescence, pore formation).

We found that the intumescence, coking, and amount of retained water determine to the greatest extent the performance characteristics of polymers. For example, the retention of 20% water in a coating increases the total endothermic effect by more than 30%. Figure 4 shows the dependence of the performance parameter L of CS–PVA complex on the intumescence strain ε_i at various thermal effects of pyrolysis Q and material densities.

After thermal treatment of coatings, the following characteristics were determined: thickness of degraded layer, δ_d; thickness of heated layer, δ_h; total thickness of heated layer, $\delta = \delta_d + \delta_h$; performance parameter L taking into account the degradation rate V_d and material density ρ, where $L = 1/(V_d\rho)$, $V_d = \xi_z/\sqrt{t}$; ξ_z, param-eter related to the temperature conductivity, intumescence deformation, and heat of pyrolysis; and t, heating time (s).

Figure 5 shows that heating causes a considerable deformation of polymeric materials. It is seen that the most deformable is CS–MC polymeric complex, and the least deformable, CS–PVA. The reinforcement of the latter polymer can be caused both by the cross-linking effect of PVA and by the formation of interpenetrating networks of PVA and chitosan.

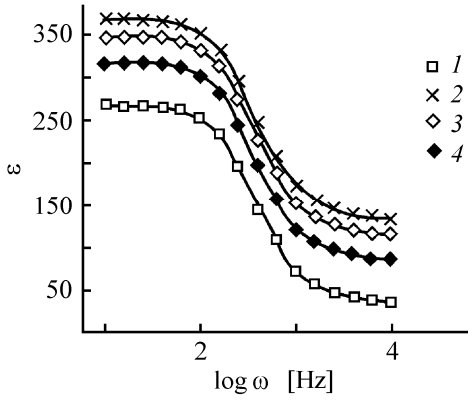


Fig. 6. Permittivity ε of chitosan-containing films vs. frequency ω.

The relaxation characteristics of polymeric complexes were obtained from the frequency dependence of their permittivity. Figure 6 shows that, for all the polymeric complexes under consideration, the mobility of macromolecules decreases with increasing frequency. A particularly sharp decrease in the permittivity is observed in the 100–1000 Hz frequency range. This behavior indicates that the polymeric complexes consist of mobile kinetic units. Among the materials tested, the CS–PVA complex has the highest permittivity and the longest relaxation time.

CONCLUSIONS

(1) Complexes of chitosan with synthetic polymers and biopolymers are characterized by increased flame resistance and high sorption ability toward metal ions and organic compounds.

(2) Accordingly to the results of a computer simulation, the sorption of metal ions and organic compounds by chitosan-containing polymers occurs by the mechanism of their capture in polymer cavities.

(3) Upon prolonged heating of chitosan-containing films at temperatures of up to 80°C, these materials retain water (80–85%). Their strength properties are not inferior to those of chitosan, and the flammability is lower than that of chitosan by a factor of 1.3.

(4) The chitosan-containing materials can be used for sorption of phenols, petroleum products, and toxic metal ions from aqueous solutions and for preparation of fireproofing and heat-shielding coatings, membranes, and films, especially in the case of stringent toxicity restrictions. These materials are characterized by such advantages as availability of raw materials, nontoxicity, and environmental safety.

REFERENCES

1. Vikhoreva, G.A., Gorbacheva, I.N., and Gal'braikh, L.S., *Khim. Volokna*, 1994, no. 5, pp. 36–45.
2. *Khitin i khitozan. Poluchenie, svoistva i primenenie* (Chitin and Chitosan. Preparation, Properties, and Applications), Skryabin, K.G., Vikhoreva, G.A., and Varlamova, V.P., Eds., Moscow: Nauka, 2002.
3. Plisko, E.A., Nud'ga, L.N., and Danilov, S.N., *Usp. Khim.*, 1977, vol. 46, no. 8, pp. 1470–1487.
4. Gal'braikh, L.S., *Soros. Obraz. Zh.*, 2001, vol. 7, no. 1, pp. 51–56.
5. Kasatkin, V.A., Kharenko, O.A. and Kharenko, A.V., *Vysokomol. Soedin., Ser. B*, 1979, vol. 21, no.1, pp. 84–85.
6. Kabanov, V.A., *Usp. Khim.*, 2005, vol. 74, no. 1, pp. 5–23.
7. Kovaleva, O.Yu., Hydrophobic Complexes of Cationic Polyelectrolytes and Amphiphilic Anions: Relationships of Formation and Properties, *Cand. Sci. Dissertation*, Volgograd, 2005.
8. Mukhina, V.R., Pastukhova, I.N., Semchikov, Yu.D., et al., *Vysokomol. Soedin., Ser. A*, 2001, vol. 43, no. 10, pp. 1797–1804.
9. Nud'ga, L.A., Petrova, V.A., Bochek, A.M., et al., *Vysokomol. Soedin.*, 1999, vol. 41, no. 11, pp. 1786–1792.
10. Zezin, A.B. and Rogacheva, V.B., in *Uspekhi khimii i fiziki polimerov* (Advances in Chemistry and Physics of Polymers), Moscow: Khimiya, 1973.
11. Tager, A.A., *Fizikokhimiya polimerov* (Physical Chemistry of Polymers), Moscow: Khimiya, 1983.
12. Vasil'ev, V.P., *Analiticheskaya khimiya: Fiziko-khimicheskie metody analiza* (Analytical Chemistry. Physicochemical Methods of Analysis), Moscow: Drofa, 2004.
13. Askadskii, A.A. and Kondrashchenko, V.I., *Komp'yuternoe materialovedenie polimerov* (Computer-Aided Materials Science of Polymers), vol. 1: *Atomno-molekulyarnyi uroven'* (Atomic-Molecular Level), Moscow: Nauchnyi Mir, 1999.
14. Solov'ev, O.V and Solov'ev, M.M., *Komp'yuternaya khimiya* (Computer Chemistry), Moscow: Solon, 2005.
15. Vershinin, V.I., Derendyaev, B.G., and Lebedev, K.S., *Komp'yuternaya identifikatsiya organicheskikh soedinenii* (Computer Identification of Organic Compounds), Moscow: Akademkniga, 2002.
16. Sannan, T., Kurita, K., and Iwakura, I., *Polymer*, 1978, vol. 19, no. 3, pp. 458–459.
17. Akhrem, A.A. and Kuznetsova, A.I., *Tonkosloinaya khromatografiya* (Thin-Layer Chromatography), Moscow: Nauka, 1984.
18. *GOST* (State Standard) *15 875–80: Plastics. Methods for Determination of Transmittance and Turbidity Factors*.

19. Babko, A.K. and Pilipenko, A.G., *Fotometricheskii analiz* (Photometric Analysis), Moscow: Khimiya, 1978.

20. *TU* (Technical Specification) *4321-001-20506233: Methods for Measurement of Mass Concentration of Phenol and Petroleum Products in Samples of Wastewater on a Fluorat-02 Analyzer of Liquids.*

21. Korostylev, P.P., *Fotometricheskii i kompleksonometricheskii analiz v metallurgii* (Photomertic and Complexometric Analysis in Metallurgy), Moscow: Metallurgiya, 1984.

22. *GOST* (State Standard) *11 736–78: Plastics: Procedure for Determination of Water Content*.

23. *GOST* (State Standard) *14 236–81: Polymeric Films: Procedure for Tensile Test.*

24. *GOST* (State Standard) *4650–80: Plastics. Procedures for Determination of Water Absorption*.

25. *GOST* (State Standard) *21 793–76: Plastics: Procedure for Determination of Oxygen Index.*

26. Averko-Antonovich, I.Yu. and Bikmullin, R.T., *Metody issledovaniya struktury i svoistv polimerov* (Methods for Studying the Structure and Properties of Polymers), Kazan: Kazansk. Gos. Tekh. Univ., 2002.

27. *GOST* (State Standard) *28 157–89: Plastics: Procedures for Determination of Resistance to Combustion*.

28. Shur, A.M., *Vysokomolekulyarnye soedineniya: Uchebnoe posobie dlya universitetov* (Macromolecular Compounds: Textbook for Universities), Moscow: Vysshaya Shkola, 1971, 2nd ed.

29. *TU* (Technical Specification) *2.724.013: Procedure for Measurement of Complex Quantities (Impedance, Conductivity, Permittivity, and Other Electrical Characteristics) on an Immitans E7-14 Digital Device.*

30. Shevchenko, T.V., Osadchii, V.L., Yakovchenko, M.A., and Ul'rikh, E.V., *Khim. Prom–st. Segodnya*, 2004, no. 11, pp. 38–41.

31. *Khimicheskaya entsiklopediya* (Chemical Encyclopedia), Knunyants, I.L. Ed., Moscow: Sov. Entsiklopediya, 1988.

32. Kablov, V.F., Ioshchenko, Yu.P., and Kondrutskii, D.A., *Vestn. Mosk. Inst. Tonk. Khim. Tekhnol*., 2006, no. 5, pp. 49–53.

33. Kablov, V.F., Ioshchenko, Yu.P., and Kondrutskii, D.A., *Sovrem. Naukoemk. Tekhnol*., 2004, vol. 4, pp. 87–88.

34. Kablov, V.F., *Kauchuk Rezina*, 1997, no. 1, pp. 8–10.

ISSN 1070-4272, Russian Journal of Applied Chemistry, 2008, Vol. 81, No. 8, pp. 1441–1445. © Pleiades Publishing, Ltd., 2008.
Original Russian Text © B.B. Troitskii, V.N. Denisova, M.A. Novikova, M.A. Lopatin, L.V. Khokhlova, A.E. Golubev, 2008, published in Zhurnal Prikladnoi Khimii, 2008, Vol. 81, No. 8, pp. 1365–1369.

MACROMOLECULAR CHEMISTRY AND POLYMERIC MATERIALS

Deposition of Thin Antireflection Coatings Based on Mesoporous Silicon Dioxide by the Sol–Gel Method in the Presence of Carbochain Polymers and Statistical Copolymers

B. B. Troitskii, V. N. Denisova, M. A. Novikova, M. A. Lopatin, L. V. Khokhlova, and A. E. Golubev

Razuvaev Institute of Organometallic Chemistry, Russian Academy of Sciences, Nizhni Novgorod, Russia

Received February 13, 2008

Abstract—Antireflection coatings with a low refractive index (1.25–1.34) were prepared from mesoporous silicon dioxide by using carbochain polymers and statistical copolymers, instead of ionogenic and noionogenic surfactants and amphiphilic block-copolymers in a sol–gel process. The optimal concentration of the organic additive in the sol, at which a transparent film with the maximum antireflection effect is formed in the sol–gel process followed by heating of a sample, was determined.

DOI: 10.1134/S1070427208080235

Thin-film antireflection interference coatings of optical articles are widely used in optical and commercial industries (antireflection coatings of display screens, photodetectors, fiber-optic waveguides, etc.). The principal limitation of thin-film antireflection coatings is the impossibility of their deposition in a vacuum onto large-size optical articles (large-aperture optics based on optical articles fabricated from fused silica and optical glass of various brands, nonlinear water-soluble crystals, etc.).

In the general case, light is reflected at the interface between two materials, e.g., silicate glass and air. At a refractive index of glass $n \approx 1.51$, about 8.6% of light incident at a zero angle is reflected at two glass–air interfaces. Theoretically, to minimize (to 0.0% in the limiting case) the reflection of light with a wavelength λ, glass should be coated with a transparent film with a refractive index $n_t = \sqrt{n} \approx 1.23$ and optical thickness $\lambda/4$.

However, film-forming materials with such a low refractive index are nonexistent in the nature. For example, low refractive indices are observed for fluorinated compounds: magnesium difluoride (refractive index 1.38) and Teflon (1.33), but the refractive indices of these substances substantially exceed the theoretical value of 1.23.

Therefore, multilayer coatings are widely used in practice as antireflection coatings of optical articles: two-layer, three-layer, four-layer, etc. [1]. Various types of multilayer antireflection coatings on silicate glass are well known and have been considered in detail, e.g., in US patents [2–5].

The practice of deposition of thin-film antireflection coatings onto optical articles employs vacuum technologies [1] and the sol–gel method [6–10]. The vacuum technologies use expensive equipment whose cost increases with the size of optical articles. The dimensions of optical articles are limited by the size of the vacuum chamber of deposition installations. The sol–gel process is simpler experimentally and can be used for deposition of coating onto large optical articles.

In 1992, scientists of Mobil Oil Corp. (USA) made an important discovery in synthesis of new nanomaterials [11–13], they developed matrix synthesis of mesoporous silicates and aluminosilicates. A group of mesoporous materials, M41S (MCM-4, hexagonal mesophase; MCM-48, cubic mesophase; MCM-50, lamellar mesophase), with a regular, well-pronounced system of nanosize structures was synthesized for the first time by a sol–gel process in the presence of a cationic surfactant. Owing to the comparatively simple synthesis of new mesoporous materials and wide op-

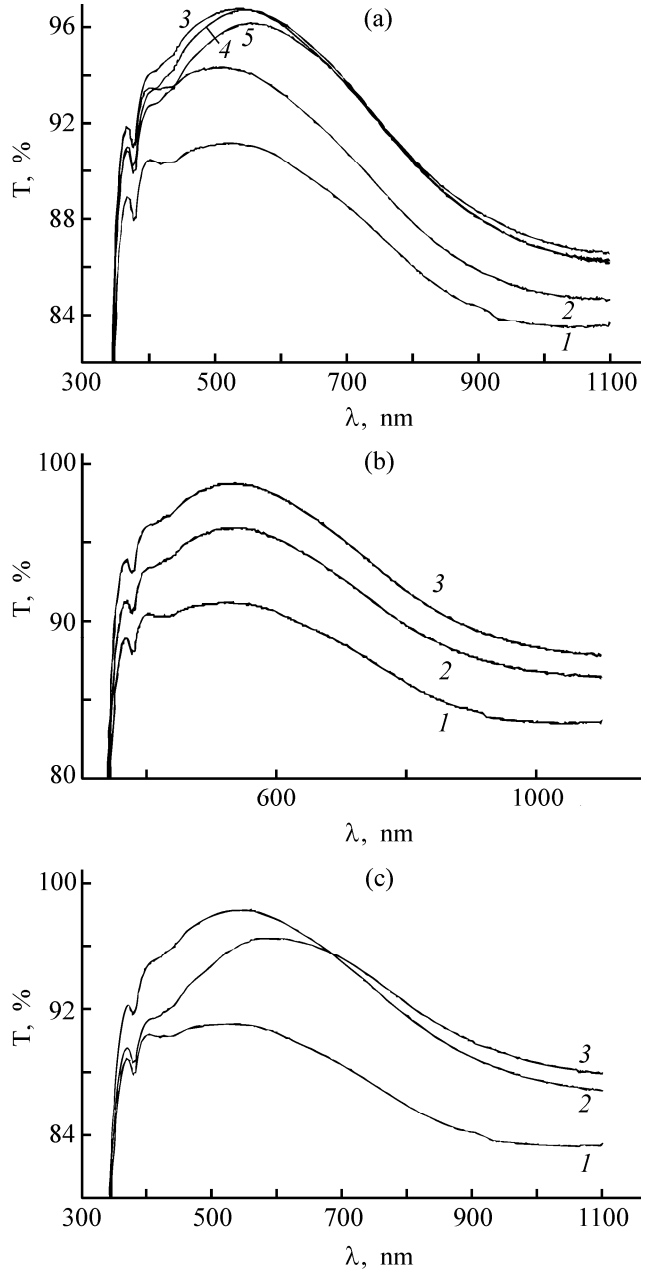


Fig. 1. Influence of additives on the antireflection capacity of single-layer two-side coatings on glass. (T) Transmission and (λ) wavelength; the same for Figs. 2, 3. Additive: (a) polyvinyl butyral, (b) polyvinyl acetate, and (c) polyvinyl methacrylate. (*1*) Coating-free glass; additive content (wt %): (a) (*2*) 0.35, (*3*) 1.0, (*4*) 1.5, and (*5*) 2.0; (b) (*2*) 1.0 and (*3*) 1.5; (c) (*2*) 1.0 and (*3*) 2.0.

portunities for their practical use in catalysis, microelectronics, optics, and sensor fabrication, this area of research has been vigorously developing since that time [14].

It should be noted that, in early studies [11–13], mesoporous silicates and aluminosilicates were produced only in the form of powders. In 1997, the EISA (evaporation-induced self-assembly) technique for deposition of nanoporous silicon dioxide films onto substrates was developed and a way was opened-up to obtain single-layer transparent coatings having a low refractive index and exhibiting a nearly theoretical antireflection effect [15]. This was done using cationactive surfactants (cetyltrimethylammonium bromide an others) as a matrix, an organic compound that predetermines self-organization of inorganic-organic nanosize structures in a forming film.

The aim of the present study was to examine the possibility of obtaining antireflection coatings with a low refractive index (1.25–1.34) on the basis of mesoporous silicon dioxide with the use of carbochain polymers and statistical copolymers, instead of ionogenic and nonionogenic surfactants and amphiphilic block copolymers [14], in the sol–gel process.

EXPERIMENTAL

A 1.0-ml portion of tetraethoxysilane (TEOS) and 5.0 ml of isopropanol were placed in a 50-ml glass flask and then water was added in a stoichiometric ratio to TEOS (4 : 1 mol/mol) [9], and hydrochloric acid, in a concentration of 3.0×10^{-3} mol per mole of TEOS. The contents of the flask were agitated at room temperature with a magnetic rabble for 1–4 h. A solution of polyvinyl butyral or polyvinyl acetate in isopropanol was introduced into the flask and the mixture was agitated for 1.0 h at room temperature. Then the mixture was diluted with isopropanol to a concentration of 1.0 wt % in terms of SiO_2.

When synthesizing sols with addition of polymethyl methacrylate (PMMA) and statistical copolymers of methyl methacrylate (MMA), tetrahydrofuran was used as organic solvent. Tetraethoxysilane and organic solvents were purified prior to use by the known procedures. Twice-distilled water was used.

Silicate glass slides (thickness 2.0 mm, length 20 mm, width 10 mm, refractive index 1.506) were used as substrates. The slides were cleaned to remove contaminations from the glass surface by submersion in a solution of an alkali with hydrogen peroxide, washed with water and distilled water, and dried in a thermostat at 150°C for 6–8 h.

Coatings were deposited onto the glass by the method of spinning at 500–2000 rpm for several minutes at room temperature. Then the glasses were kept at room temperature for 12 h. Further, the coated glasses were

placed in a thermostat at 150°C and were heated at a rate of 5 deg min^{-1} to 500°C. The samples were kept at this temperature for 5–6 h. After a slow cooling, the samples were removed from the thermostat and their optical transmission was determined in the wavelength range 200–1100 nm on a Perkin–Elmer Lambda 25 spectrometer with an accuracy of ±0.1%.

The optical thickness of the films and their refractive index were measured with an LEF-3M1 ellipsometer.

Figure 1 shows optical transmission curves for coating-free glasses and those with two-side single-layer coatings based on mesoporous silicon dioxide, deposited by the sol–gel method in the presence of various concentrations of polyvinyl butyral (Fig. 1a), polyvinyl acetate (Fig. 1b), and polymethyl methacrylate (Fig. 1c).

The optical transmission of the coating-free glass is the highest (91.1%) at wavelengths of 515–520 nm (curve *1*) and steadily decreases to 83.3% into the near-IR region. The glass is nontransparent for UV light with wavelengths shorter than 325 nm.

Transparent coatings of mesoporous silicon dioxide, deposited with polyvinyl butyral as an additive, make the optical transmission of the glass higher (antireflection effect) at wavelengths in the range 350–1100 nm (Fig. 1a, curves *2–5*). The antireflection effect depends on the concentration of polyvinyl butyral in the sol: its magnitude first increases, passes through a maximum, and further decreases as the concentration of the additive grows (Fig. 1a, curves *2–5*). The maximum transmission (97.0%; degree of antireflection, 5.9%) is observed at wavelengths of 530–540 nm at the optical concentration of polyvinyl butyral of 1.0 wt % (Fig. 1a, curve *3*). The optical thickness of the film is 120 nm, and the refractive index, 1.34.

Transparent coatings of mesoporous silicon dioxide, deposited with addition of polyvinyl acetate to the sol, also make higher the optical transmission of the glass (Fig. 1b, curves *2* and *3*). The maximum transmission (98.6%; degree of antireflection, 7.5%) is observed at a wavelength of 530 nm at a polymer concentration of 1.5 wt % (curve *3*). The optical thickness of the film is 136 nm, and the refractive index, 1.25.

The same effect is observed for coatings based on mesoporous silicon dioxide, deposited by the sol–gel method in the presence of various concentrations of polymethyl methacrylate (Fig. 1c, curves *2* and *3*). The maximum transmission (98.4%; degree of antireflection, 7.3%) is observed at wavelengths of 540–550 nm at the optimal concentration of the polymer of 1.0 wt % (curve *2*). The optical thickness of the film is 137 nm, and the refractive index, 1.26.

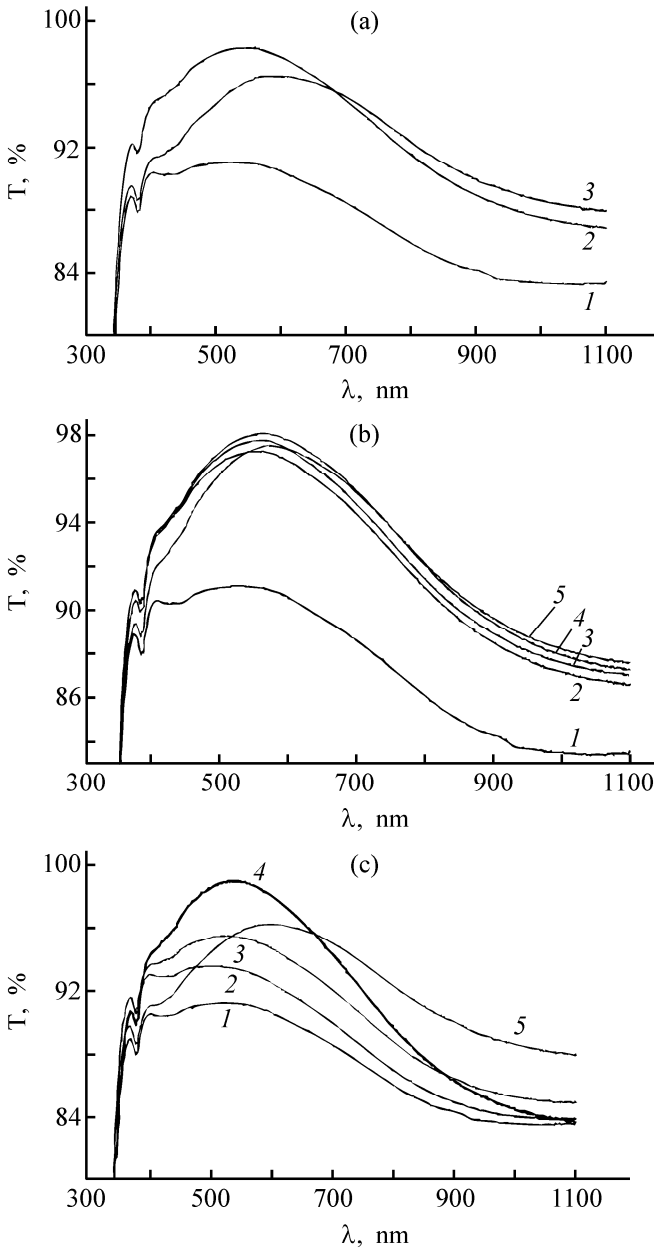


Fig. 2. Influence exerted on the antireflection capacity of single-layer two-side coatings on glass by addition of (a) copolymers of methyl methacrylate with 5.0 mol % hydroxyethyl methacrylate, (b) 20.0 mol % merhacrylic acid, and (c) 10 mol % vinylpyrrolidone. (*1*) Coating-free glass; additive content (wt %): (a) (*2*) 0.5, (*3*) 0.7, and (*4*) 1.0; (b) (*2*) 0.5, (*3*) 1.0, (*4*) 1.2, and (*5*) 1.5; (c) (*2*) 0.5, (*3*) 0.7, (*4*) 1.0, and (*5*) 1.5.

Figure 2 shows optical transmission curves for a coating-free glass (curve *1*) and glasses with two-side

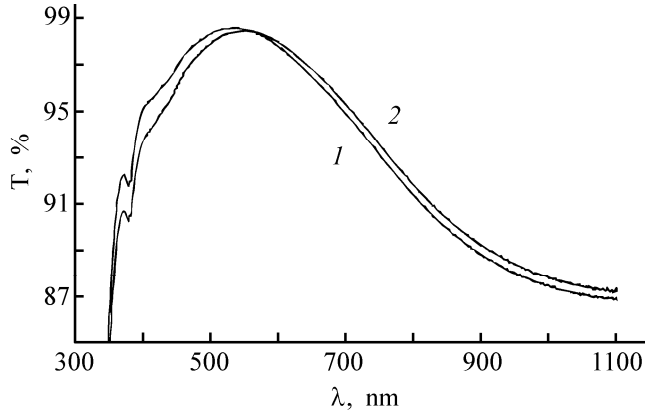


Fig. 3. Change in the antireflection capacity of single-layer two-side coatings on glass in the presence of 1.0 wt % copolymers of methyl methacrylate with (*1*) acrylamide (5 wt %) and (*2*) maleic anhydride in the sol.

single-layer coatings based on mesoporous silicon dioxide, deposited by the sol–gel method in the presence of various concentrations of methyl methacrylate copolymers with 5 mol % hydroxyethyl methacrylate (Fig. 2a, curves *2–4*), with 20.0 mol % methacrylic acid (Fig. 2b, curves *2–5*), and with 10 mol % vinylpyrrolidone in the sol (Fig. 2c, curves *2–5*).

The magnitude of the antireflection effect depends on the concentration of a copolymer in the sol: it first increases, passes through a maximum, and further decreases as the concentration of an additive increases (Figs. 2a–2c).

For films with addition of a copolymer of methyl methacrylate with hydroxyethyl methacrylate in the sol (Fig. 2a, curves *2–4*), the maximum transmission of 98.0% (degree of antireflection, 6.9%) is observed at wavelengths of 580–590 nm at the optimal concentration of the copolymer equal to 0.7 wt % (Fig. 2a, curve *3*). The optical thickness of the film is 150 nm, and the refractive index, 1.285.

For films with addition of a copolymer of methyl methacrylate with methacrylic acid (Fig. 2b, curves *2–5*), the maximum transmission of 98.1% (degree of antireflection, 7.0%) is observed at wavelengths of 580–590 nm at the optimal concentration of 1.0 wt % (Fig. 2b, curve *3*). The optical thickness of the film is 140 nm, and the refractive index, 1.28.

For films with addition of a copolymer of methyl methacrylate with vinylpyrrolidone (Fig. 2c, curves *2–5*), the maximum transmission of 98.4% (degree of antireflection, 7.3%) is observed at wavelengths of 530–540 nm at the optimal concentration of the copolymer of 1.0 wt % (curve *4*). The optical thickness of the film is 130 nm, and the refractive index, 1.26.

Antireflection effects are also observed in experiments with addition to the sol of a statistical copolymer of methyl methacrylate with 5 mol % acrylamide (Fig. 3, curve *1*) and a statistical copolymer of methyl methacrylate with 10 mol % maleic anhydride (Fig. 3, curve *2*). The maximum transmissions of 98.4% (degree of antireflection, 7.3%) and 98.5% (degree of antireflection, 7.4%) are observed at wavelengths of 540–550 nm at the copolymer concentrations of 1.0 wt %. The optical thicknesses of the films are 130 and 132 nm, and the refractive index, 1.26.

The examples presented in Figs. 1–3 indicate that the previously developed EISA technique [15] for matrix synthesis of transparent coatings based on mesoporous silicon dioxide can be modified by replacement of surfactants and amphiphilic block polymers with well-known carbochain polymers and statistical copolymers easily produced by radical polymerization. The EISA method can be conditionally divided into three stages [15]. During the first, the most important stage, after the deposition of a solution of hydrolyzed TEOS with a surfactant (starting sol) onto a substrate by its dipping or spinning, the easily volatile solvent and most part of water evaporate in the course of several seconds from the substrate and the inorganic and organic phases undergo spontaneous microseparation to give an inorganic-organic film on the substrate. The role of various classes of surfactants and amphiphilic block copolymers in the self-organization of inorganic-organic structures has been studied in detail [14] and attributed to joint formation of liquid–crystalline mesophases by a surfactant and oligosiloxanes. A mesophase serves as a matrix for synthesis of inorganic cross-linked networks. In the second stage of the EISA technique, the sample with a coating is kept at room temperature for 12 h and more. In the third stage, the sample is slowly heated in air to 500–700°C. In the process, organic nanostructures "burn-out" and a transparent film of mesoporous silicon dioxide is formed. The mesoporous structure of the film spatially reproduces the structure of the corresponding mesophase formed in the first two stages.

It should be noted that the mechanism of spontaneous microseparation of the inorganic and organic phases in sol–gel processes performed with addition of carbochain polymers and statistical copolymers that are not surfactants or amphiphilic block copolymers remains unknown. The architecture of nanopores has

not been studied, either. Probably, the microseparation of phases is due to supramolecular interactions of growing inorganic chains with fragments of macromolecules of organic polymers and statistical copolymers. This is indicated by the following experimental fact. If polystyrene is used as an additive in the sol–gel process, then only macroseparation of phases is always observed and the films obtained already in the first stage of the EISA method are turbid. The starting sol is transparent because products of partial hydrolysis of TEOS and polystyrene are well dissolved in tetrahydrofuran. Polystyrene is an aromatic hydrocarbon in which there are no functional groups. The interaction of fragments of polymer macromolecules with growing inorganic chains is weaker than that between inorganic macromolecules, and, therefore, macroseparation of inorganic and organic phases occurs in the stage of film formation.

As can be seen from the experimental data in Figs. 1 and 2, the antireflection effect of deposition of a film coating onto glass depends on the concentration of the carbochain polymer (copolymer) in the sol and is the strongest (with the minimum refractive index observed for the film) at the optimal additive concentration of 0.7–1.5 wt %. As follows from the Lorentz–Lorenz formula, the decrease in the refractive index of meso-porous silicon dioxide films is due to an increase in the volume content of air (whose refractive index is 1.0). Air can be contained only within nanopores of the material, and, consequently, introduction of a polymer additive into the sol may affect both the number of nanopores and their size in the course of formation of a mesoporous silicon dioxide film. The minimum refractive index is observed at the optimal relationship between these parameters.

CONCLUSIONS

(1) Carbochain polymers and statistical copolymers can be used as an organic additive to a silicon dioxide sol. The additive predetermines spontaneous microseparation of inorganic and organic phases in the formation of a gel in the form of a transparent thin film on the surface of a silicate glass.

(2) In "burning-out" of the organic phase at 500°C in the atmosphere of oxygen from the gel formed, a transparent film of mesoporous silicon dioxide is obtained on the glass surface. The film has a low refractive index (1.25–1.34) and produces an antireflection effect.

(3) The optimal concentration of the organic additive in the sol is 0.7–1.5 wt %. At this concentration, a transparent film of mesoporous silicon dioxide, with the maximum antireflection effect, is formed in the sol–gel process followed by heating of a sample with a coating.

REFERENCES

1. Macleod, H.A., *Thin Film Optical Filters*, Bristol: Adam Hilger, 1985.
2. US Patent 5 147 125.
3. US Patent 6 238 781.
4. US Patent 6 436 541.
5. US Patent 7 005 188.
6. Suikovskaya, N.V., *Khimicheskie metody polucheniya tonkikh prozrachnykh plenok* (Chemical Methods for Deposition of Thin Transparent Films), Moscow: Khimiya, 1971.
7. Nikolaeva, L.V. and Borisenko, A.I., *Tonkosloinye steklоemalevye i steklokeramicheskie pokrytiy*a (Thin-Film Glass-Enamel and Glass-Ceramic Coatings), Leningrad: Nauka, 1980.
8. Shilova, O.A., Hashkovsky, S.V., and Kuznetsova, L.A., *J. Sol–gel Sci. Tech.*, 2003, vol. 26, pp. 687–691.
9. Movchan, T.G., Ur'ev, N.B., Khamova, T.V., et al., *Fiz. Khim. Stekla*, 2005, vol. 31, pp. 294–308.
10. Movchan, T.G., Khamova, T.V., Shilova, O.A., et al., *Fiz. Khim. Stekla*, 2006, vol. 32, pp. 916–925.
11. US Patent 5 057 296.
12. US Patent 5 145 816.
13. Kresge, C.T., Leonowicz, M.E., Roth, W.J., et al., *Nature*, 1992, vol. 359, pp. 710–712.
14. Wan, Y. and Zhao, D., *Chem. Rev.*, 2007, vol. 107, no. 7, pp. 2821–2860.
15. Lu, Y., Ganguli, R., Drewien, C.A., et al., *Nature*, 1997, vol. 389, pp. 364–368.

ISSN 1070-4272, Russian Journal of Applied Chemistry, 2008, Vol. 81, No. 8, pp. 1446–1451. © Pleiades Publishing, Ltd., 2008.
Original Russian Text © S.A. Bulgakova, A.I. Mashin, I.A. Kazantseva, D.E. Kashtanov, M.M. Jones, G.S. Tsepkov, A.V. Korobkov, A.V. Nezhdanov, 2008, published in Zhurnal Prikladnoi Khimii, 2008, Vol. 81, No. 8, pp. 1370–1375.

MACROMOLECULAR CHEMISTRY AND POLYMERIC MATERIALS

Influence of the Composition of the Polymer Matrix on the Electrooptical Properties of Films with a Dispersed Liquid Crystal

S. A. Bulgakova, A. I. Mashin, I. A. Kazantseva, D. E. Kashtanov, M. M. Jones, G. S. Tsepkov, A. V. Korobkov, and A. V. Nezhdanov

Research Institute of Chemistry, Lobachevsky Nizhni Novgorod State University, Nizhni Novgorod, Russia

Lobachevsky State University, Nizhni Novgorod, Russia

Received November 2, 2007

Abstract–Polymer films with a dispersed liquid crystal were prepared by photopolymerization of (meth)acrylic monomers. The electrooptical properties of these films were studied. The influence exerted by the composition of the monomer mixture, cross-linking agents, and chain-transfer agent on the liquid crystal drop size and on the transmission of the polymer–liquid crystal films was examined.

DOI: 10.1134/S1070427208080247

Polymer films with a liquid crystal (LC) dispersed in them [polymer-dispersed liquid crystal (PDLC) films] are promising composite materials for use in display devices, in glasses with controllable transparency, in TV projection systems, in optical fibers, and in other electrooptical devices [1]. The use of PDLC films in these systems is based on their ability to transmit light under the action of an external electric field and to become nontransparent in the common state. As compared to liquid crystal twist cells, PDLC films have a number of advantages: higher contrast and brightness (as the use of polarizers is not required), mechanical strength and flexibility due to the polymer matrix, and simpler fabrication. Despite that PDLC films have been extensively studied by now [1–10], they have not found wide use yet because of the high control voltages.

The electrooptical properties of PDLC films depend on numerous parameters: optical constants of the LC and polymer; size, shape, concentration, polydispersity, and degree of alignment of LC groups; drop director and orientation of optical axes of the drops [2]. The major factor controlling the electrooptical properties of PDLC systems is the drop size. It has been shown [3, 4] that the best results can be obtained with the submicrometer drop size.

The strong dependence of the electrooptical properties on the drop size and geometry is due to the fact that the operation of a PDLC cell is based on the effect of electric-field-controlled light scattering, consisting in reorientation of LC drops in an external electric field. The major problem in the development and optimization of electrooptical properties of PDLC films is that these properties depend on the LC drop size oppositely. For example, it is known [5] that reorientation of coarser drops requires weaker threshold fields, but in this case, the switch-off time becomes longer and the film contrast becomes worse. When the LC drop size is decreased to the wavelength of light (e.g., visible), the light scattering by the film increases and the contrast becomes better. The electrooptical properties of polymer composites with a drop size $d \approx \lambda$ have been studied poorly. Extensive data are available only for PDLC films with a drop size $d >> \lambda$ (1–10 mm) [6–8]. In turn, the particle size, shape, and size distribution will be determined by the conditions of phase separation in curing of a polymer matrix, its composition, and component concentrations.

In this study, we examined how the composition of the polymer matrix prepared by photopolymerization of (meth)acrylic monomers affects the electrooptical properties of PDLC films.

EXPERIMENTAL

The monomers (methacrylic acid, MAA; 2-ethylexyl acrylate, EHA; acrylic acid, AA; ethylene glycol diacrylate, EGDA; ethylene glycol dimethacrylate, EGDM) and chain-transfer agent (dodecyl mercaptan, DDM) were purified in a vacuum. MAA and AA were dehydrated by triple freezing–thawing. The copolymerization of MAA and AA with EHA to construct the composition curves was performed in the bulk in the presence of 0.005 M azobis(isobutyronitrile) at 60°C. To this end, the prepared monomer mixtures were placed in glass ampules, deoxygenated by triple freezing–pump-ing–thawing, sealed, and placed in a thermostat. The polymerization was performed to 5–10% conversion. The copolymers obtained were purified by triple reprecipitation from a solution in acetone–methanol with acetonitrile–diethyl ether for EHA–AA or with hexane–diethyl ether for EHA–MAA. The acid content of the copolymer was determined by potentiometric titration of solutions of copolymers in dimethylformamide with a 0.1 N methanolic solution of KOH on TV-6L 1 device in the presence of phenolphthalein indicator with an accuracy of ±(0.3–0.7) mol %.

PDLC films were prepared by photopolymerization of monomer mixtures containing 2 wt % photoinitiator and various concentrations of a liquid crystal on an ST-301 photolithographic installation at irradiation wavelength λ = 365 nm and irradiation power of 0.3–0.5 mW cm^{-2}. For this purpose, the reaction mixture formed after mixing the starting components was placed between two glass plates. The distance between these plates was controlled with spacers (SiO_2 particles) 25–35 μm in diameter. To study the electrooptical properties of the films, the inner sides of the glass plates were preliminarily coated with an ITO layer, and indium con-tacts were soldered-on. The irradiation time was about 10 min in all the experiments. As photoinitiator we used 2,2-dimethoxy-2-phenylacetophenone (Irgacure 651 brand name). The E7 liquid crystal (Merck) was a mixture of nematic liquid crystals (4'-pentyl-4-cyanobiphenyl : 4'-heptyl-4-cyanobiphenyl : 4'-octyl-4-cyanobiphenyl : 4'-pentyl-4-[4-cyanobenzyl]-biphenyl = 51 : 25 : 16 : 8) with the refractive indices for ordinary and extraordinary beams, n_o = 1.5258 and n_e = 1.7366, respectively.

The size and polydispersity of LC particles were determined from photomicrographs obtained with an Axioscop 40 Pol optical polarization microscope (Carl Zeiss), with computer processing of the images. The microstructure of EHA–MAA films was examined by confocal Raman spectroscopy with a Ntegra Spectra NT-MDT device. To obtain a confocal image, we used the Raman line of E7 at 1600 cm^{-1} as the base line and a line at 1283 cm^{-1} as additional line to confirm the reliability of the information obtained. The excitation wavelength was 488 nm, at a power of no more than 1 mW. The dependence of the transmission factor of PDLC films on the applied voltage was determined with a spectrometer based on MDR-204 monochromator (LOMO-fotonika). To measure the response time, square pulses were modulated with an ac voltage (5 kHz).

To impart elastic properties to PDLC films, we introduced polymers with a low glass transition point into the polymer matrix. One of such polymers is poly (ethylhexyl) acrylate (PEHA), which has been studied by Roussel and Buisine as a polymer matrix for PDLC [11]. They noted that the PDLC microstructure was unstable, which was manifested in an increase in the LC drop size in time. The results of that study were confirmed in analysis the stability of PDLC films prepared by photopolymerization of a mixture of EHA with E7 liquid crystal. First, we found that, because of the high solubility of E7 in the polymer–monomer mixture, the phase separation in the system upon photocuring is observed only at LC concentrations no less than 30 wt %. Immediately after the sample preparation, the drop size showed scatter from 1 to 5 μm, and after 3 h the drop size increased to 10 μm, but the polydispersity appreciably decreased. The drop texture in crossed polarizers was typical of radial distribution of molecules, suggesting the homeotropic alignment of molecules on the drop|matrix boundary.

The instability of the LC drop size is most likely due to the fact that, owing to its low glass transition point T_g = –50ºC [12], PEHA does not prevent the mobility and coalescence of drops. One of possible ways to solve the problem is copolymerization of EHA with monomers that raise the glass transition point of the polymer. As such monomers we examined unsaturated acids AA and MAA, whose homopolymers have glass transition points of 105 and 228ºC, respectively [13].

A study of the systems EHA–MAA and EHA–AA with a liquid crystal showed that even minor concentrations of acids in copolymers not only stabilized the PDLC structure, but also decreased the LC drop size. It was found that the drops formed in the presence of MAA were coarser than those in the system with AA. In particular, in films of EHA–AA and EHA–MAA copolymers of similar composition, we detected LC

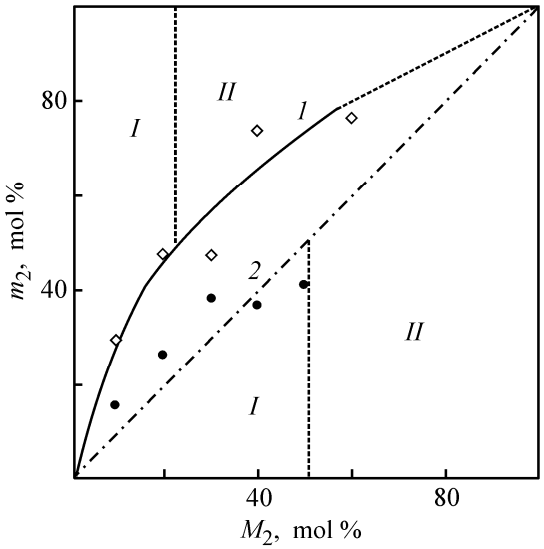


Fig. 1. Initial composition of copolymers (*1*) EHA–MAA and (*2*) EHA–AA vs. the composition of the monomer mixture. (m_2, M_2) Content of unsaturated acid units in the copolymer and of unsaturated acid in the monomer mixture, respectively. Area of copolymerization: *I* homogeneous and *II* heterophase.

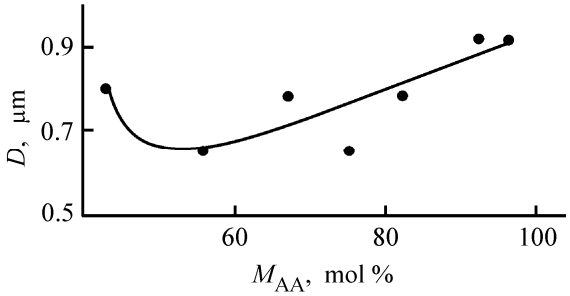


Fig. 2. The most probable LC drop size D at a concentration of 23 wt % vs. the composition of the EHA–AA monomer mixture. (M_{AA}) Acid content.

drops of size $d \le 0.8$ and 1 μm, respectively, and in the EHA–MAA copolymer, conglomerates of the size exceeding 1 μm were also formed. To account for the trends observed, it was interesting to compare these systems in substance-initiated copolymerization to low conversions.

Figure 1 shows the composition curves for the copolymers prepared by bulk polymerization in the presence of a radical initiator. It is seen that the EHA–AA copolymerization is approximately azeotropic, whereas the EHA–MAA is appreciably enriched in MAA units copolymer in the entire composition range of monomer mixtures. This fact is indicative of its high composition nonuniformity in polymerization to high conversions. Apparently, specifically the composition nonuniformity of macromolecules, arising in the course of the copolymer synthesis, is responsible for the formation of drops coarser than those in the EHA–AA system. It should be noted that the heterophase area in this system (area *II* in the diagram) is appreciably wider than that in EHA–AA copolymerization, which restricts the applicability of this systems to preparation of PDLC films.

Therefore, systematic examination of the influence exerted by the composition of the photopolymerizing mixture on the properties of PDLC films was performed with the EHA–AA system. As can be seen from Fig. 2, the phase separation in this system is primarily determined by the composition of the monomer mixture: The dependence of the LC drop size on the acid content of the reaction mixture passes through a minimum at approximately 50 mol % content of AA. Presumably, an increase in the drop size at AA content lower than 50 mol % is associated with low T_g^1 of the copolymer (lower than 27°C), when the mobility of the macromolecules is fairly high and does not prevent coalescence of the liquid crystal drops. In addition, previous data [14] suggest that, with a decrease in the AA concentration, the LC solubility in the polymer–monomer mixture increaes, and on reaching the gel point, coarser drops are formed. At AA content higher than 50 mol %, the system becomes heterophase, as can be seen from Fig. 1, and the copolymer itself forms a separate phase, preventing coalescence of the LC drops in the course of phase separation. Simultaneously, with an increase in the AA content, the LC solubility in the polymer–monomer mixture decreases, which leads to formation of coarser drops.

The properties of a copolymer are determined not only by the composition, but also by its molecular-weight characteristics. To control them, we used a chain-transfer agent (dodecyl mercaptan $C_{12}H_{27}SH$) and two kinds of cross-linking agents: EGDA and EGDM. Chain-transfer agents decrease the molecular weight (MW) of a copolymer, and cross-linking agents cause formation of a 3*D* polymer network. The effect of the additives on the formation of LC drops was examined in photopolymerization of EHA–AA mixture (25 : 75 mol %) containing 2 wt % photoinitiator and 23 wt % LC. The results obtained in studying the effect of the chain-transfer and cross-linking agents are shown in Fig. 3 as size-distribution curves for LC drops.

[1] The glass transition point of the copolymer was calculated by the additive scheme from T_g of the homopolymers.

As can be seen from Fig. 3, both a decrease in MW of the copolymer in the presence of DDM (curve *3*) and cross-linking of the chains with EGDA–EGDM (curve *2*) lead to a decrease in the size of LC drops and in the particle polysidpersity, compared to the system with-out additives (curve *1*). Proceeding from the common standpoint [15, 16] that thiols not only decrease MW of a copolymer but also make narrower its molecular-weight distribution and make the copolymer composition more uniform, we can conclude that specifically these changes are responsible for a decrease in the LC drop size. In 3*D*-cross-linked systems obtained in the presence of EGDM and EGDA, the polymer chains are less mobile, restricting the coalescence of LC drops and correspondingly their size.

It is well known [17–21] that simultaneous addition of a chain-transfer agent and a cross-linking agent leads, depending on their molar ratio, to formation of either a branched polymer or a cross-linked 3*D* network. The presence of a chain-transfer agent allows control over either the length of branchings or the length of segments between the network junctions. Therefore, we examined in this study the effect of jointly introduced additives on the LC drop size in the course of curing of the polymer matrix.

Figure 4 shows the dependence of the LC drop size on the concentration of one of MW regulators at a fixed concentration of another regulator. It can be seen (curve *1*) that, with an increase in the concentration of the chain-transfer agent, when the length of branchings (in the case of formation of a branched structure) or the length of the segment between the network junctions (in the case of formation of a 3*D* network) decreases, the LC particle size decreases. A similar trend in the LC particle size is observed at a fixed

concentration of DDM with an increase in the amount of cross-linking agents (curve *2*). In both cases, a decrease in the size of LC drops can be accounted for by strengthening of the structure of the polymer matrix due to formation of either branched or 3*D*-cross-linked structure.

Thus, our studies show that introduction of modifiers (chain-transfer and cross-linking agents) into a photocurable compound leads to a decrease in the LC drop size. This, in turn, should affect the electrooptical properties of PDLC films.

The electrooptical characteristics of PDLC films are the switching-on voltage V_{on}, switching-off voltage V_{of}, contrast ratio K, and response times: switching-on

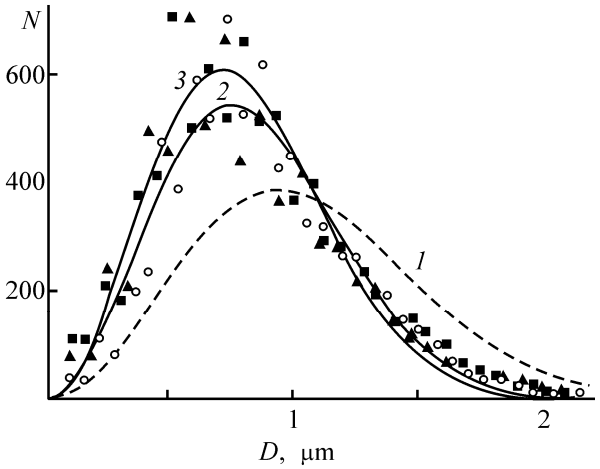


Fig. 3. Size distribution of LC drops formed in the course of polymerization of EHA : AA = 25 : 75 mol % mixture (*1*) without additives and with addition of (*2*) 0.58 mol % EGDA or 0.52 mol % EGDM and (*3*) DDM. (*N*) Number of particles and (*D*) particle size.

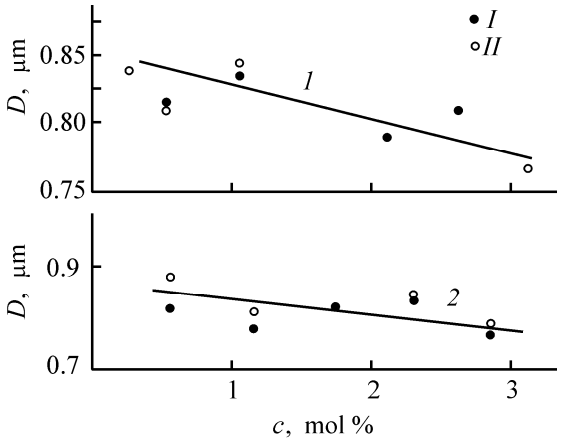


Fig. 4. Particle size *D* of LC drops formed in the EHA : AA = 25 : 75 mol % mixture vs. the concentration *c* (*1*) of chain-transfer agent DDM in the presence of *I* 0.58 mol % EGDA and *II* 0.52 mol % EGDM, and (*2*) of cross-linking agents *I* EGDA and *II* EGDM in the presence of 1.5 mol % DDM.

time t_{on} and switching-off time t_{of}. The first three parameters are determined by the formulas

$$V_{on} = 0.9(T_{max} - T_{min}),$$

$$V_{of} = 0.1(T_{max} - T_{min}),$$

$$K = (T_{max} - T_{min})/(T_{max} + T_{min}),$$

from the dependence of the transmission factor on the applied electric voltage, where T_{max} and T_{min} are the maximal transmission in the switched-on state and the minimal transmission in the switched-off state, respectively. The switching-on and switching-off times are measured by applying to a PDLC film a square

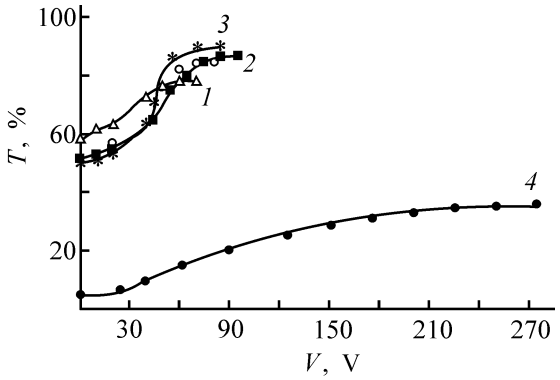


Fig. 5. Transmission factor T vs. the applied electric voltage V for 25-mm-thick PDLC films prepared by photopolymerization of the system EHA : AA = 25 : 75 mol % + 0.5 mol % EGDM + 23 wt % LC at DDM concentrations of (*1*) 0.25, (*2*) 0.5 and 1, and (*3*) 3 mol %, and (*4*) for films of EHA : MAA = 65 : 35 mol % copolymer containing 30 wt % E7 liquid crystal.

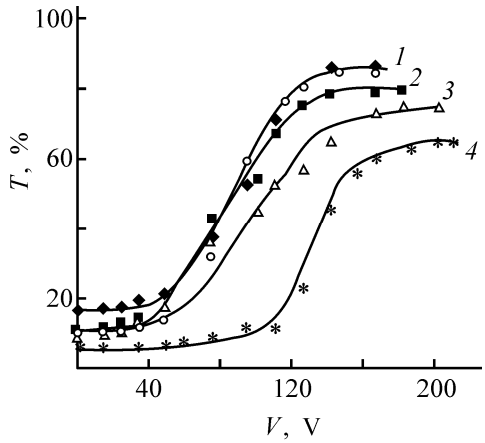


Fig. 6. Transmission factor T vs. the applied electric voltage V for 35-mm-thick PDLC films prepared by photopolymerization of the system EHA : AA = 25 : 75 mol % + 1.5 mol % DDM + 23 wt % LC at EGDM concentrations of (*1*) 0.5 and 1, (*2*) 2, (*3*) 2.5, and (*4*) 3 mol %.

voltage pulse and measuring the dependence of the transmission on time. The theoretical values of the switching-on voltage and switching-off time can be calculated through the elastic distortion energy and electric field energy by the equations [9, 11]

$$V_{on} \sim \frac{d}{R}\left[L^2 - 1\right]\left[\frac{4\pi K}{\Delta\varepsilon}\right]^{1/2},$$

$$\tau_{of} = \sim\frac{\gamma R^2}{K(L^2 - 1)},$$

where R is the mean radius of an LC drop; $L = R_1/R_2$, drop ellipticity; R_1 and R_2, major and minor radii of the elliptic drop; d, PDLC film thickness; g, viscosity; K and $\Delta\varepsilon$, elastic constant and dielectric anisotropy of the liquid crystal, respectively.

As follows from Eqs. (1) and (2), with a decrease in the drop size, the switching-on voltage increases and the switching-off time decreases. This fact indicates that, to obtain PDLC films with high electrooptical characteristics, conditions should be found for the formation of LC drops of the optimal size.

The results obtained in studying the electrooptical properties of PDLC films with polymer matrices of different compositions are shown in Figs. 5 and 6 in the form of curves of the film transmission vs. applied voltage. Comparison of the results obtained with EHA–AA and EHA–MAA copolymers shows that films of the former copolymers exhibit a considerably higher transmission in the switched-on state. As both systems are heterophase, the differences are associated with the particle size of the dispersed phase of the copolymer proper, rather than with that of LC. Apparently, EHA–MAA polymer particles coalesce in the course of the synthesis to a size exceeding the wavelength of visible light, which results in a low transmission of the PDLC films both in the switched-off and switched-on states. It is significant that the threshold voltages V_{on} in films based on EHA–AA copolymer are considerably lower than those for the EHA–MAA copolymer: 1.6–4.5 and 8 V μm^{-1}, respectively. This fact is, at first glance, unexpected, as drops formed in EHA–MAA films are coarser than those formed in the EHA–AA films and, therefore, require a lower threshold voltage for reorientation. The observed inconsistency with the theoretical expectations can be accounted for only by the higher polarity of the EHA–AA copolymer, which contains 75 mol % acid, against 35 mol % MAA in EHA–MAA copolymer. Therefore, the dielectric constant of the films in the first case will be higher, which favors a decrease in the threshold voltage.

Thus, the EHA–AA polymer matrix is more promising also from the standpoint of electrooptical properties. We optimized the composition of this matrix with respect to the content of molecular weight regulators: EGDM and DDM. Figure 5 shows that, with an increase in the DDM concentration, the transmission of samples in the switched-off state decreases and that in the switched-on state increases. With an increase in the concentration of the cross-linking agent EGDM (Fig. 6), both the lower and upper boundaries of the film transmission decrease. The film contrast grows in both cases, which is associated with an increase in the number of scattering centers due to a decrease in the LC drop size, observed as the concentrations of the chain-transfer agent DDM and cross-linking agent EGDM are raised. It was concluded from the threshold voltages

Threshold voltages V_{on} of PDLC films prepared by photopolymerization of EGA : AA = 25 : 75 mol % + 23 wt % LC mixture at various kinds and concentrations of MW regulator

c, mol %	V_{on}, V μm^{-1}	
	EGDM	DDM
0.25	–	1.6
0.5	3	2
1.0	3	2.4
2	3.4	3.2
2.5	4.2	–
3	4.5	2.1

(see table) and transmission of the films that the optimal concentrations of MW regulators in the composition of the EHA–AA polymeriz-ing mixture are 1–2 mol % DDM and 1 mol % EGDM. This corresponds to the minimal values of the threshold voltage and transmission in the switched-off state and to the maximal transmission in the switched-on state.

Along with the threshold voltage, an important characteristic of PDLC films is the switching-off time. According to formula (2), the switching-off time depends on the LC drop size. Namely, it decreases with a decrease in the particle size. The results obtained in studying the PDLC response on a square voltage pulse show that the switching-off time of films modified with additions of a cross-linking agent and a chain-transfer agent is shorter, which is consistent with the theoretical concepts. For example, for the films without additives, the switching-off time was 3–6 ms, and for the films modified with EGDM and DDM, 1–3 ms at a switching-on time t_{on} of about 0.7 ms, which opens prospects for the use of these films in electrooptical devices.

CONCLUSIONS

(1) In preparation of PDLC films by photopolymerization of the 2-ethylhexyl acrylate–acrylic acid–liquid crystal system, the size of the forming liquid crystal drops does not exceed 0.8 μm, whereas in copolymerization of 2-ethylhexyl acrylate with methacrylic acid, the liquid crystal particle size exceeds 1 μm.

(2) Analysis of the dependence of the liquid crystal particle size on the composition of the monomer mixture 2-ethylhexyl acrylate–acrylic acid shows that the smallest drops are formed at acrylic acid content of about 50 mol %.

(3) PDLC films based on 2-ethylhexyl acrylate–acrylic acid copolymer show a higher transmission in the switched-on state with a lower threshold voltage, compared to 2-ethylhexyl acrylate–methacrylic acid films.

(4) Introduction of molecular weight regulators, a chain-transfer agent and a cross-linking agent, into the photocurable compound 2-ethylhexyl acrylate–acrylic acid leads to a decrease in the liquid crystal drop size and to improvement of the electrooptical properties of PDLC films.

(5) The threshold voltage for films based on 2-ethylhexyl acrylate–acrylic acid copolymer modified with molecular weight regulators is 1.6–4.5 V μm^{-1}, the switching-off time is 1–3 ms, and the switching-on time is about 0.7 ms.

REFERENCES

1. Crawford, G.P. and Zumer, S., *Liquid Crystals in Complex Geometries*, London: Taylor and Francis, 1996.
2. Amundson, K., Blaaderen, A. van, and Wiltzius, P., *Phys. Rev. E*, 1997, vol. 55, no. 2, p. 1646.
3. Chidichimo, G., Arabia, G., Golemme, A., and Doane, J.W., *Liq. Cryst.*, 1989, vol. 5, no. 5, p. 1443.
4. Peng, S.-C., Yu, L.-W., and Lee, S.-N., *J. Polym. Sci.: Polym. Phys.*, 1997, vol. 35, no. 9, p. 1373.
5. Bouchaour, T., Benmouna, M., Coqueret, X., et al., *Mol. Cryst. Liq. Cryst.*, 2004, vol. 413, no. 1, p. 29.
6. Montgomery, G.P. and Vaz, N.A., *Appl. Opt.*, 1987, vol. 26, no. 4, p. 738.
7. Seeboth, A., *Thin Solid Films*, 1993, vol. 223, no. 1, p. 140.
8. Park, N.H., Park, S.-I., and Shun, K.-D., *Colloid Polym. Sci.*, 2001, vol. 279, no. 11, p. 1082.
9. Carter, S.A., LeGrange, J.D., White, W., et al., *J. Appl. Phys.*, 1997, vol. 81, no. 9, p. 5992.
10. Lin, Y.H., Ren, H., and Wu, S.T., *Appl. Phys. Lett.*, 2004, vol. 84, no. 20, p. 4083.
11. Roussel, F. and Buisine, J.M., *Phys. Rev. E.*, 2000, vol. 62, no. 2, p. 2310.
12. Lipatov, Yu.S., Nesterov, A.E., Gritsenko, T.M., et al., *Spravochnik po khimii polimerov* (Handbook of Polymer Chemistry), Kiev: Naukova Dumka, 1971.
13. *Khimicheskaya entsiklopediya* (Chemical Encyclopedia), Moscow: Sov. Entsiklopediya, 1992, vol. 3.
14. Mashin, A.I., Bulgakova, S.A., Chidichimo, G., et al., *Vestn. Nizhegorod. Univ., Fiz.*, 2006, issue 1 (9), p. 191.
15. Sorokina, L.I., Radbil', T.I., Sorokina, G.N., and Shtarkman, B.P., *Vysokomol. Soedin., Ser. A*, 1983, vol. 25, no. 10, p. 2081.
16. Semchikov, Yu.D., Knyazeva, T.E., Smirnova, L.A., et al., *Vysokomol. Soedin., Ser. A*, 1987, vol. 29, no. 12, p. 2625.
17. O'Briep, N., MsKee, A., Sherripgtop, D.C., et al., *Polymer*, 2000, vol. 41, no. 15, p. 6027.
18. Costello, R.A., Martip, L.K., Slark, A.T., et al., *Polymer*, 2002, vol. 43, no. 2, p. 245.
19. Isaure, F., Cormack, R.A.O., and Sherripgtop, D.C., *J. Mater. Chem.*, 2003, vol. 13, no. 11, p. 2701.
20. Isaure, R., Cormack, R.A.O., and Sherripgtop, D.C., *Macromolecules*, 2004, vol. 37, no. 6, p. 2096.
21. Graham, S., Cormack, R.A.O., and Sherripgtop, D.C., *Macromolecules*, 2005, vol. 38, no. 1, p. 86.

ISSN 1070-4272, Russian Journal of Applied Chemistry, 2008, Vol. 81, No. 8, pp. 1452–1457. © Pleiades Publishing, Ltd., 2008.
Original Russian Text © L.E. Shpilevskaya, A.M. Safonova, 2008, published in Zhurnal Prikladnoi Khimii, 2008, Vol. 81, No. 8, pp. 1376–1381.

MACROMOLECULAR CHEMISTRY AND POLYMERIC MATERIALS

Electrically Conducting Composite Films Based on Polymers and Ni-Carbon Fibers

L. E. Shpilevskaya and A. M. Safonova

Institute of General and Inorganic Chemistry, State Scientific Institution, Belarussian National Academy of Sciences, Minsk, Belarus

Received November 15, 2007

Abstract—The volume electrical resistivity of composite films based on polystyrene, polyvinyl chloride, polymethyl methacrylate, and butadiene-styrene latex containing Ni-carbon fibers was studied in relation to the degree of filling, fiber length, and temperature.

DOI: 10.1134/S1070427208080259

Raising in the electrical conductivity of polymers is of particular importance for preparing conducting materials for various purposes: low-temperature heating elements, electrodes of chemical power cells, antistatic coatings, etc. One of ways to improve the conductivity of polymers is to conducting fillers, including carbon fillers, which, are known to be characterized by fairly high conductivity, chemical inertness, and sedimentation stability [1, 2]. The electrical conductivity of carbon-containing polymer composites strongly depends on the physical form of the fillers used [3]. It is known that fibrous carbon fillers are more efficient in decreasing the polymer conductivity as compared to powder materials [4, 5]. Appropriate carbon fibers containing various metals heve been developed at the Institute of General and Inorganic Chemistry (Belarussian National Academy of Sciences) [6].

In this study, composite polymer films based on Ni-containing carbon fibers (Ni-CF), polystyrene (PS), polyvinyl chloride (PVC), polymethyl methacrylate (PMMA), and butadiene-styrene (BS) latex were prepared and their conducting properties were examined in relation to the degree of filling, fiber length, and temperature. In some cases, Ni-free carbon fibers (CFs) and highly dispersed powder carbon (HDC) were used as fillers for comparison.

EXPERIMENTAL

The Ni-carbon fibers were prepared by carbonization of hydrated cellulose fibers (preliminarily treated with a nickel chloride solution) in an inert gas flow at 900°C [7, 8] in accordance with TU RB (Technical Specifications of the Belarus Republic) 100 029 049.020–2003.The carbonized fibers were finely divided and the fractions with an average length (l_{av}) of 0.1, 0.5, and 3 mm were taken. The nickel-free carbon fibers were prepared under the same conditions, excluding impregnation of the initial fibers with $NiCl_2$ solution. As the polymer we used the following polymers: polystyrene (PS-S), polyvinyl chloride (S 63 Zh brand), polymehyl methacrylate [GOST (State Standard) 24 234–80], and butadiene-styrene latex (BS-65 A brand). The composites were prepared by dispersion of the carbon fibers of a certain size in benzene containing PS (15%), in cyclohexanone–pentane mixture (9 : 1) containing PVC (10%), in cyclohexanone–benzene mixture (9 : 1) containing PMMA (5%), and in 50% aqueous dispersion of butadiene-styrene latex. The concentrations of the polymer solutions were determined in our preliminarily tests so as to obtain the solutions with an optimal viscosity, acceptable for preparation of films. The content of the carbon filler was varied from 5 to 33% to the composite weight. The larger amount of the filler was not added because of a strong increase in the viscosity, which hinders mixing and casting of the films. The liquid compositions were poured onto degreased glass supports (7.5 × 2.7 cm) in amounts of 0.1 ml cm^{-2} and dried at room temperature. The thickness of the films prepared from PS, PVC, and BS latex at medium degrees of filling was 120–170, and that of the PMMA films, 90–100 μm.

Changes in the volume electrical resistivity of the composite films were measured by the two–contact

Volume electrical resistivity of the composite films based on PS, PVC, PMMa, and BS latex containing various carbon fillers

Filler content, wt %	ρ_V				
	HDC	CF	Ni-CF with indicated fiber length, mm		
			0.1	0.5	3
			Polystyrene		
5	1.0×10^8	1.7×10^1	1.0×10^8	1.6×10^{-1}	3.8×10^{-2}
10	1.0×10^8	4.0×10^0	8.4×10^{-1}	2.2×10^{-2}	2.0×10^{-2}
17	1.0×10^6	9.2×10^{-1}	5.0×10^{-2}	7.5×10^{-3}	7.5×10^{-3}
23	2.0×10^2	2.3×10^{-1}	1.0×10^{-2}	7.5×10^{-3}	7.5×10^{-3}
28	Break*	1.0×10^{-1}	1.0×10^{-2}	7.5×10^{-3}	7.5×10^{-3}
33	″	1.0×10^{-1}	1.0×10^{-2}	7.5×10^{-3}	Break
			Polyvinyl chloride		
5	1.0×10^8	–	1.0×10^8	1.0×10^6	1.0×10^{-1}
10	1.0×10^8	3.0×10^1	1.0×10^8	5.0×10^{-1}	4.0×10^{-2}
17	2.0×10^6	3.0	1.0×10^6	4.0×10^{-2}	3.0×10^{-2}
23	2.0×10^2	2.5	5.0×10^{-1}	1.0×10^{-2}	1.0×10^{-2}
28	Break	2.0×10^{-1}	5.0×10^{-1}	1.0×10^{-2}	1.0×10^{-2}
33	″	Break	5.0×10^{-1}	7.5×10^{-3}	Break
			Polymehyl methacrylate		
5	1.0×10^8	–	1.0×10^8	1.0×10^8	1.0×10^8
10	1.0×10^8	2.3×10^1	1.0×10^6	4.0	3.5×10^{-1}
17	3.0×10^6	2.0×10^{-1}	2.0×10^2	2.6×10^{-1}	7.5×10^{-3}
23	2.0×10^2	2.0×10^{-1}	2.0×10^2	2.0×10^{-2}	5.5×10^{-3}
28	Break	2.0×10^{-1}	8.0×10^{-2}	1.0×10^{-2}	5.5×10^{-3}
33	″	Break	4.0×10^{-2}	5.5×10^{-3}	Break
			Butadiene–styrene latex		
5	1.0×10^8	3.2×10^0	6.5×100	4.5×10^{-2}	6.6×10^{-2}
10	1.0×10^8	4.0×10^{-1}	2.0×10^{-1}	1.4×10^{-2}	4.5×10^{-2}
17	3.0×10^6	3.0×10^{-1}	3.5×10^{-2}	8.0×10^{-3}	3.8×10^{-2}
23	2.0×10^2	2.0×10^{-1}	1.7×10^{-2}	8.0×10^{-3}	1.5×10^{-1}
28	Break	2.0×10^{-1}	1.2×10^{-2}	8.0×10^{-3}	Break
33	″	Break	Break	Break	Break

* Break of the continuous film.

method in a cell equipped with two brass clamps, using a V7-16A universal voltmeter and an E6-13A teraohmeter. The volume electrical resistivity of the films, ρ_V (Ω m) was calculated from the expression $\rho_V = (RS)/l$, where R is the measured resistivity; S, film sectional area; and l, film length. To study the temperature dependence of the electrical resistivity, the cell with a sam-ple was placed in a temperature–controlled chamber, and the electrical resistivity of the sample was measured in the course of heating to 130°C (in the case of BS latex, to 240°C) at 10°C steps.

The confidence interval of the experimental error was evaluated from the measurements of at least five samples. The relative rms measurement error increased with the length of the filler fibers and amounted to 15–20%.

The electrical resistivities of the composite films based on PS, PVC, PMMA, and BS latex filled with HDC (30–50 nm particle size), CF (l_{av} 0.5 mm), and Ni-CF of various sizes are listed in the table. These data show that all the films containing powdered fil-ler HDC exhibit relatively high electrical resistivity (2.0×10^2 Ω m) even at a 23 wt % degree of filling,

whereas ρ_V of the films containing fibrous filler CF (even at the same degrees of filling) is smaller by 2–3 orders of magnitude and amounts to 0.2–2.5 Ω m, depending on the polymeric binder. It should be noted that, in the case of the HDC filler, we failed to prepare films with a degree of filling higher than 23 wt % because of the cracking and disturbance of the film continuity.

Filling of the polymers with Ni-carbon fibers decreases ρ_V of the films studied still more strongly. For example, ρ_V of the films containing 23 wt % Ni-CF (l_{av} 0.5 mm) is 7.5×10^{-3}–2.0×10^{-2} Ω m, depending on the polymer type, which is probably due to the effect of metal contained in the fibers on the structure of carbon in the course of pyrolysis.

With increasing Ni-CF length, the resistance of the composite films decreases, and, in this case, ρ_V depends on the type of the polymer and degree of its filling. At small degrees of filling, the dependence of ρ_V of the composite films on the Ni-CF length is the most pronounced. As can be seen from the table, ρ_V of the PS films at 5% degree of filling varies from 1.0×10^8 to 3.8×10^{-2} Ω m as the length of the filler fibers increases from 0.1 to 3.0 mm. In this cases, the strongest decrease in ρ_V (by 7 orders of magnitude) is observed as the fiber length increases from 0.1 to 0.5 mm, whereas with l_{av} increasing from 0.5 to 3.0 mm, ρ_V changes by less than an order of magnitude. With increasing degree of filling, the effect of the fiber length on ρ_V decreases. At 10–17 wt % degree of filling, ρ_V decreases by less than an order of magnitude as the l_{av} increases from 0.1 to 0.5 mm, and further increase in l_{av} to 3.0 mm does not noticeably decrease the film resistivity ($\rho_V \approx$ const). At higher degrees of filling (>23 wt %), ρ_V is at all independent of the fiber filler length.

These results show that the resistivity of the polymer films can be varied in a wide range by varying the length of Ni-CFs used for filling of the polymer films. The fibrous structure of the filler provides formation of conducting chains even at small degrees of filling, which well agrees with the percolation conductivity theory [3]. In accordance with this theory, the dielectric state of composite materials containing both a low-conducting polymer phase and a highly conducting filler phase shaprly changes to the conducting state on attainment of a certain degree of filling (so-called percolation threshold, c_p). This process occurs owing to the fact that, at c_p, the filler particles form a continuous conducting cluster, which provides a sharp increase in the electrical conductivity of the system.

It was found that the percolation threshold in the composites containing needle-like filler particles is attained at lower concentrations than those in composites with spherical filler particles [3, 5]. This is due to the fact the lengthy particles (in particular, fibers) have a larger number of contacts with the neighboring particles, which facilitates formation of conducting chains. For such filler type, the percolation threshold is directly proportional to the radius of the needle-like particles and inversely proportional to their length. For the fillers studied, the ratios of the fiber radius to their length were 0.1, 0.02, and 0.003 for l_{av} of 0.1, 0.5, and 3.0 mm, respectively. In accordance with these data, the percolation threshold of the films studied decreased in the same order. In particular, c_p of the films based on PS decreased from 10 to less than 5 wt % (see table).

In the case of PVC films at 5 wt % content of Ni-CF, the percolation threshold is observed only for the filler with the fiber length of 3.0 mm. Probably, in the case of shorter fibers (l_{av} 0.1 and 0.5 mm), no continuous conducting cluster was formed, i.e., the concentration of the filler in these composite films is lower than the percolation threshold. As in the case of PS films, the strongest changes in ρ_V (by eight orders of magnitude) are observed at a 10% degree of filling as the fiber length increases from 0.1 to 0.5 mm, whereas with l_{av} increasing from 0.5 to 3.0 mm, it decreases by only an order of magnitude. With increasing degree of filling, the dependence of ρ_V on l_{av} becomes less pronounced, and, at degrees of filling greater than 17 wt %, the resistivity of the films filled with fibers with l_{av} 0.5 and 3.0 mm is essentially the same. In the case of a short-fiber filler (l_{av} 0.1 mm), the percolation threshold of the composite films based on PVC is observed at higher degrees of filling (23 wt %) as compared to the PS films.

The dependences of ρ_V of the films based on PMMA filled with Ni-CF of various lengths are similar to those for PVC films, with only difference that the films based on PMMA with a 5 wt % degree of filling did not attain the percolation threshold even at l_{av} 3 mm. With the shortest fibers (l_{av} 0.1 mm), the percolation in this polymer was attained at c_p of 17 wt %. With increasing fiber length, it decreased and, for Ni-CF with l_{av} 0.5 and 3.0 mm, c_p was 10 wt % (see table).

The composite films based on BS latex with a 5 wt % degree of filling and fiber length of 0.1–3.0 mm are conducting, i.e., their c_p is smaller than 5 wt %. Our additional experiments showed that, at l_{av} of 0.1 and 0.5–3.0 mm, the percolation threshold of the films was

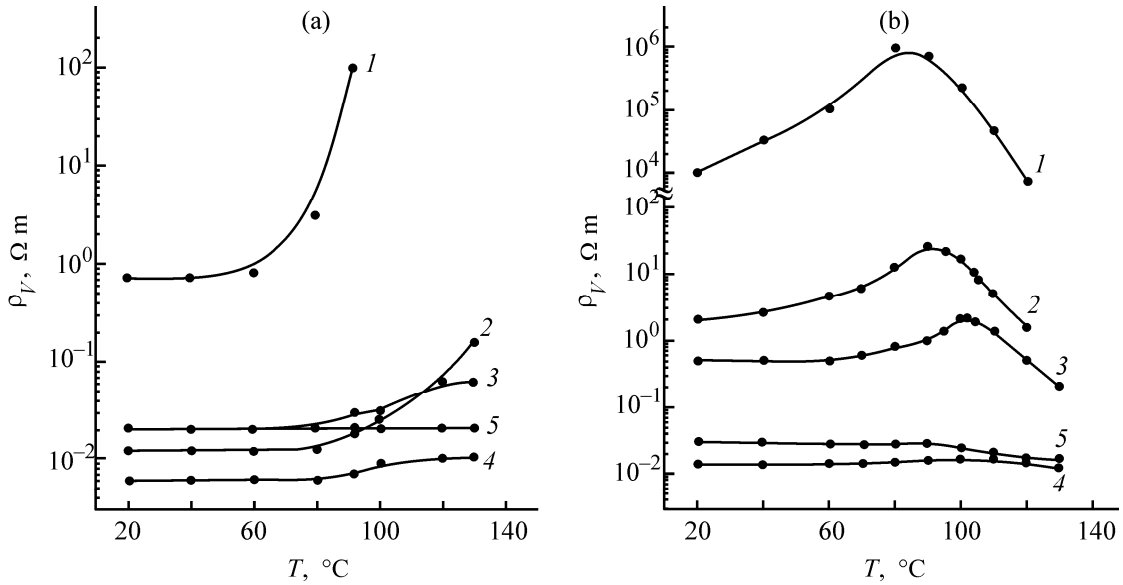


Fig. 1. Temperature dependence of the volume electrical resistivity ρ_V of the composite films based on (a) PS and (b) PVC filled with Ni-CF of various lengths. Length, mm: (*1*, *2*) 0.1, (*3*, *4*) 0.5, and (*5*) 3.0. Degree of filling, wt %: (*1*, *3*, *5*) 10 and (*2*, *4*) 23.

3 and 2 wt %, respectively. As in the case of PS films, the strongest change in ρ_V was observed at small degrees of filling with l_{av} increasing from 0.1 to 0.5 mm. A specific feature of the composite films based on BS latex is that the resistivity of the films containing fibers with l_{av} = 3.0 mm is higher at all the examined degrees of filling than that of the films filled with shorter fibers (l_{av} = 0.5 mm). This is probably due to the irregular distribution of the long fibers in the BS latex. Hence, the use of fibers with l_{av} = 0.5 mm seems to be preferable in this case.

As can be seen from our experimental data, the composite films based on PS exhibit the lowest electrical resistivity, $(7.5 \pm 1.5) \times 10^{-3}$ Ω m, at a 17 wt % degree of filling (Ni-CF, l_{av} = 0.5–3.0 mm). At the same degree of filling, the electrical resistivity of the PVC films is higher by a factor of 4, and only at a 33 wt % degree of filling their electrical resistivity reaches 7.5×10^{-3} Ω m. The composite films based on PMMA at a 17 wt % degree of filling (l_{av} = 3.0 mm) are characterized by the electrical resistivity similar to that of PS films, and at a 28 wt % degree of filling ρ_V is still lower [$(5.5 \pm 1.5) \times 10^{-3}$ Ω m]. The higher degree of filling of the PMMA films with the long fibers (l_{av} = 3.0 mm) was not attained because of the break of the continuous films due to the binder deficiency. The lowest electrical resistivities of the composite films based on PS and BS latex are attained at a 17 wt % degree of filling and l_{av} = 0.5 mm. At this relatively low degree of filling, the composite films retained their rather high physicomechanical properties.

Since data on the electrical resistivity at elevated temperatures are of particular importance in working with composite films [9], we studied the temperature dependence of the electrical resistivity of the composite films in the ranges 20–130°C for PS- and PVC-based films and 20–240°C for BS latex films. It was found that the temperature dependence of the electrical resistivity of these films strongly depends on the polymer type, degree of its filling, and length of the filler fibers.

For example, ρ_V of the PS films containing 10 wt % Ni-CF (l_{av} = 0.1 mm) remains almost constant on heating to 60°C. With a further increase to 90°C, ρ_V changes insignificantly, whereas at temperatures above 90°C ρ_V increases by several orders of magnitude (Fig. 1a, curve *1*). With the degree of filling increasing to 23 wt %, the temperature range in which ρ_V of the PS films is stable extends to 90°C, and with further heating the increase in ρ_V is less pronounced than that at a 10 wt % degree of filling (Fig. 1a, curve *2*). With increasing Ni-CF length (l_{av} 0.5 mm), the temperature dependence of ρ_V becomes smoother (Fig. 1a, curves *3*, *4*). The electrical resistivity of the films filled with the longest fibers (l_{av} 3.0 mm) remains constant in the entire temperature range studied (Fig. 1a, curve *5*).

The trends observed can be accounted for as follows. It is known that the glass–transition point of polystyrene is 93°C [10]. With the temperature increasing above this value, PS passes into the hyperelastic state, and the mobility of its molecular chains increases. Since the linear expansion coefficient of PS is

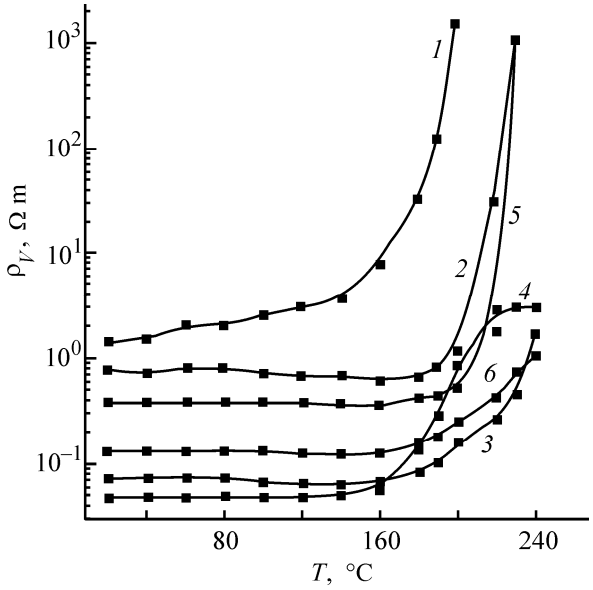


Fig. 2. Temperature dependence of the volume electrical resistance ρ_V of the composite films based on (a) PS and (b) PVC filled with Ni-CF of various lengths. Length, mm: (*1*) 0.1, (*2–4*) 0.5, and (*5*, *6*) 3.0. Degtee of filling, wt %: (*5*) 3, (*2*, *6*) 5, (*3*) 10, and (*1*, *4*) 23.

higher than that of the carbon fibers [6] by a factor of 15–20 [11], the volume fraction of the polymer in the composite film increases with temperature as compared to the Ni-CF fraction. As a result, the contact area of the fiber filler particles decreases, causing an increase in the electrical resistivity of the composite film. This factor is the most important at small degrees of filling and small particle size. With increasing fiber particle length and degree of filling, the effect of the polymer on the contact area between the filler fibers decreases and the temperature dependence of the electrical resistivity of the composite films becomes insignificant.

The temperature dependence of ρ_V of the films based on PVC is more complex. The strongest temperature dependence is observed for the films filled with the shortest fibers (l_{av} = 0.1 mm) (Fig. 1b, curves *1*, *2*). For these films, ρ_V increases as the temperature is raised from 40 to 90°C. On further heating, the electrical resistivity of the films decreases and at 120°C it becomes lower than that at room temperature. As in the case of the PS films, with the Ni-CF length increasing from 0.1 to 0.5 mm, the temperature dependence of ρ_V becomes smoother even at relatively low degrees of filling (10 wt %; Fig. 1b, curve *3*). With the degree of filling increasing to 23 wt %, changes in ρ_V become smaller than 25% in the 20–130°C range (Fig. 1b, curve *4*). A similar relatively high temperature stability of the electrical resistivity is observed for PVC films containing 10 wt % Ni-CF (l_{av} = 3.0 mm) (Fig. 1b, curve *5*).

As in the case of PS films, the electrical resistivity of PVC films filled with finely dispersed fibers increases as the temperature is raised from 40 to 90°C. This trend may be due to the difference in the linear thermal expansion coefficients of the polymer and fiber, which deteriorates the contact between the filler particles in the course of heating. This effect is strongly enhanced when the polymer passes into the hyperelastic state. The temperature of this transition in PVC is 80°C [12]. Further decrease in the electrical resistivity as the temperature is raised above 110°C may be due to transformations of the polymer itself, giving rise to conductivity of another type. It is known that, at temperatures higher than 100°C, PVC undergoes slow degradation with elimination of hydrogen chloride and formation of a system of conjugated double bonds [13–15]. As a result, the conductivity mechanism in the PVC polymer may change, with a decrease in the resistivity with increasing temperature. As in the case of PS films, the electrical resistivity of the composite films based on PVC becomes more independent of temperature with an increase in the degree of filling and in the length of the filler fibers (Fig. 1b, curves *4*, *5*).

In contrast to the composite PS- and PVC-based films, the films based on BS latex are characterized by significantly broader (20–160°C) temperature range in which ρ_V is either independent of temperature or only slightly changes with temperature (Fig. 2). At temperatures above 160–180°C, the electrical resistivity sharply increases. The onset temperature of this step and the character of ρ_V variation depend on the length of the Ni-containing fibers. The temperature dependence of ρ_V of BS latex films filled with Ni-CF (l_{av} = 0.1 mm) only slightly depends on the degree of filling within the range 10–20 wt % (Fig. 2, curve *1*). A sharp increase in ρ_V of these films is observed only on heating to temperatures higher than 160°C. At the fiber length of 0.5 and 3.0 mm, the observed increase in ρ_V depends on the content of Ni-CF in the polymer, namely, the shape of the temperature dependences of the electrical resistivity becomes smoother with increasing degree of filling. A sharp increase in ρ_V of the BS latex films containing Ni-CF (l_{av} = 0.5 mm) starts at temperatures higher than 200°C (Fig. 2, curve *2*), which is probably due to the degradation of the latex matrix.

The observed sharp increase in the electrical resistivity of the films with temperature can be of particular interest in the design of posistors (devices used to con-

trol the temperature parameters of the medium). To examine the possibility of using BS latex films for this purpose, we studied changes in the electrical resistivity of these films in the heating–cooling cycles. We found that, after cooling of the initially heated films, their resistivity increased by more than an order of magnitude as compared to the initial films. In the course of repeated heating, the onset of the sharp change in the electrical resistivity shifted toward lower temperatures, which may be due to the latex degradation at high temperatures. Therefore, these films can be used as disposable thermal sensors and indicators preventing heating of system to temperatures higher than 220°C.

Thus, by varying the degree of filling and length of the Ni-containing fibers used to prepare filled films based on PS, PVC, and BS latex, we can prepare both composite films with different temperature coefficients of resistivity (TCR) and films with stable electrical resistivity. The composite films based on PS and PVC, exhibiting constant electrical resistivity in the 20–120°C range, and the BS latex films with ρ_V stable at 20–180°C can be used as conducting elements in systems operating at elevated temperatures.

Our results show that, by using various polymers and Ni-containing fibers, it is possible to prepare conducting polymer coatings with ρ_V of 10^{-1}–10^{-2} Ω m at small degrees of filling, which would allow strength properties of the initial polymers to be preserved and the disadvantages of metallic fillers (sedimentation and oxidation) to be avoided. Moreover, the presence of a ferromagnetic metal in the Ni-containing filler provides a high specific magnetization of the resulting fibers [8, 16], which would allow direct orientation of the fibrous conducting filler in the magnetic field [17] and, thus, preparation of composites with anisotropic magnetic and conducting properties. It should also be noted that the commercial production of Ni-containing carbon fibers is mastered at the Khimvolokno Production Association (Svetlogorsk, Belarus).

CONCLUSIONS

(1) The composite films based on polystyrene, polyvinyl chloride, polymehyl meth-acrylate, and butadiene-styrene latex containing Ni-carbon fibers are characterized by the volume resistivity of $(5.5–8.0) \times 10^{-3}$ Ω m at small degrees of filling.

(2) The temperature dependence of the electrical resistivity decreases with an increase in the degree of filling of the film and in the average length of the Ni-containing carbon fibers.

REFERENCES

1. Gul', V.E. and Shenfil', L.Z., *Elektroprovodya-shchie polimernye kompozitsii* (Electrically Conducting Polymer Composites), Moscow: Khimiya, 1984.
2. Mironov, V.S., *Elektroprovodyashchie polimernye kompozity* (Electrically Conducting Polymer Composites), Minsk: BelNIINTI, 1991.
3. Chmutin, I.A., Letyagin, S.V., Shevchenko, V.G., et al., *Vysokomol. Soedin., Ser. A*, 1994, vol. 36, no. 4, pp. 699–713.
4. *Carbon Fibers and Their Applications*, Shimamura, S., Ed., New York: VCH, 1990.
5. *Elektroprovodyashchie volokha, ikh svoistva i primenenie. Obzor informatsii* (Electrically Conducting Fibers, Their Properties, and Use. Information Review), *Ser.: Promyshlennost' khimicheskikh volokon* (Chemical Fiber Industry), Moscow: NIITEKhIM, 1997, vol. 14.
6. Ermolenko, I.N., Lyubliner, I.P., and Gul'ko, N.V., *Elementosoderzhashchie ugol'nye voloknistye materially* (Element-containing Fibrous Carbon Materials), Minsk: Nauka i Tekhnika, 1982.
7. Ermolenko, I.N., Safonova, A.M., and Malashevich, Zh.V., *Vestsi Akad. Navuk Bel. SSR, Ser. Khim. Navuk*, 1977, no. 2, pp. 96–99.
8. Safonova, A.M., Ermolenko, I.N., Apanasenok, V.I., et al., *Zh. Prikl. Khim.*, 1991, vol. 64, no. 11, pp. 2447–2451.
9. Kashevich, I.F., Shut, V.N., and Syrtsov, S.R., *Mater. Tekhnol. Instr.*, 2001, vol. 6, no. 2, pp. 35–38.
10. *Entsiklopediya polimerov* (Encyclopedia of Polymers), Kabanov, V.A., Ed., Moscow: Sov. Entsiklopediya, 1977.
11. *Kompozitsionnye materially. Spravochnik* (Composite Materials. Handbook), Karpinos, D.M., Ed., Kiev: Naukova Dumka, 1985.
12. Manson, J.A. and Sperling. L.H., *Polymer Blends and Composites*, New York: Plenum, 1976.
13. Voigt, J., *Die Stabilisierung der Kunststoffe gegen Licht und Warme*, Berlin: Springer, 1966.
14. Minsker, K.S. and Fedoseeva, G.T., *Detruktsiya i stabilizatsiya PVKh* (Degradation and Stabilization of PVC), Moscow: Khimiya, 1979.
15. *Elektricheskie svoistva polimerov* (Electrical Properties of Polymers), Sazhin, B.I., Ed., Leningrad: Khimiya, 1979.
16. Safonova, A.M., Titova, L.V., Shchurevich, O.A., et al., *Zh. Prikl. Khim.*, 1997, vol. 70, no. 2, pp. 237–241.
17. Shpilevskaya, L.E. and Safonova, A.M., *Mater. Tekhnol. Instr.*, 2004, vol. 9, no. 3, pp. 56–58.

ISSN 1070-4272, Russian Journal of Applied Chemistry, 2008, Vol. 81, No. 8, pp. 1458–1464. © Pleiades Publishing, Ltd., 2008.
Original Russian Text © S.S. Nikulin, T.N. Poyarkova, V.M. Misin, 2008, published in Zhurnal Prikladnoi Khimii, 2008, Vol. 81, No. 8, pp. 1382–1388.

MACROMOLECULAR CHEMISTRY AND POLYMERIC MATERIALS

Use of *N*,*N*-Dimethyl-*N*,*N*-diallylammonium Chloride–Maleic Acid Copolymer for Recovery of Butadiene–Styrene Rubber from a Latex

S. S. Nikulin, T. N. Poyarkova, and V. M. Misin

Voronezh State Academy of Forestry Engineering, Voronezh, Russia

Voronezh State University, Voronezh, Russia

Institute of Biochemical Physics, Russian Academy of Sciences, Moscow, Russia

Received December 14, 2007

Abstract—The flocculating effect of a cationic polyelectrolyte, *N*,*N*-dimethyl-*N*,*N*-diallylammonium chloride–maleic acid copolymer, in the recovery of rubber from SKS-30 ARK butadiene–styrene latex at various concentrations of the dispersed phase and H_2SO_4 and at various temperatures was studied.

DOI: 10.1134/S1070427208080260

Recovery of rubbers from latexes is one of the most labor-, material-, and power-consuming process operations. It should be noted, however, that this problem is not given due attention today. It is well known that shops for rubber recovery from latexes discharge tens and hundreds of thousand tons of mineral salts and other compounds, which are not removed at wastewater treatment facilities and pollute natural water basins.

Traditional procedures for rubber recovery from latexes are based on using sodium chloride, which shows high performance and is inexpensive, as the main coagulant. However, a significant disadvantage of NaCl is its relatively high consumption for rubber recovery from a latex (up to 250 kg per ton of rubber). Furthermore, NaCl is not trapped on wastewater treatment facilities, and virtually the whole its amount is discharged with wastewater into natural basins.

Therefore, a search for new coagulants and for ingenious process designs with lower consumption of chemicals and water and the water discharge by shops for rubber recovery from latexes is an urgent problem. Alternative coagulants (proteins, Mannich base, salts of polyvalent metals, such as Ca, Mg, Al, etc.) suggested [1–4] for recovering rubbers from latexes find yet very limited use on the industrial scale and are mainly used for production of only pilot batches.

Published data show that there are numerous and diverse organic coagulants, both synthetic and natural, that can either fully replace inorganic salts or considerably reduce their consumption. Of particular interest in this respect are polymeric quaternary ammonium salts which have a set of interesting properties and can find various industrial applications [5]. As shown in a review [6], complete recovery of rubbers from latexes is attained at relatively low consumption of these agents (3–6 kg per ton of rubber). However, data on the possibility of using them in production of emulsion rubbers are fragmentary, and the influence exerted by these agents on the rubber recovery from latexes and on the properties of the rubbers obtained and of articles thereof is poorly understood. Furthermore, data on the extent of contamination and amount of wastewater discharged by shops for rubber recovery from latexes are lacking.

The available data on the use of polymeric quaternary ammonium salts for rubber recovery show that the consumption of coagulants decreases by a factor of 50–100. One more significant fact is that, with these salts, the process becomes only slightly sensitive to pH fluctuations (polymeric quaternary ammonium salts can well be used in the pH 2–5 range). An important positive factor is that polymeric quaternary ammonium

salts, being cation-active products, actively interact with soaps of carboxylic and sulfonic acids to form insoluble salts and are captured by the forming rubber crumb. This leads to a decrease in the amount of organic salt–acid fractions discharged from rubber recovery shops and provides, to some extent, solution of environmental problems. However, the presence in the rubber of polymeric quaternary ammonium salts and products of their interaction with components of the emulsion system leads to acceleration of the rubber vulcanization [7] and requires correction of the rubber stock formulation.

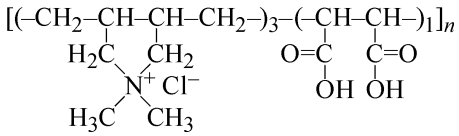
The above-noted advantages of quaternary ammonium salts make appropriate further studies of application of the known, and synthesis of new quaternary ammonium salts with the aim to evaluate their coagulating effect and prospects for their use for rubber recovery from latexes.

Here, we consider the possibility of using *N*,*N*-dimethyl-*N*,*N*-diallylammonium chloride–maleic acid copolymer for rubber recovery from latexes.

A possible advantage of the suggested copolymer is that its component, maleic acid, is a by-product from production of phthalic and maleic anhydrides [8], which may reduce the cost of the polymeric coagulant and make it more competitive. This may open up new prospects for utilization of wastes from chemical industry and thus for a decrease in the environmental pollution. Furthermore, introduction into a polymer chain of units containing different functional groups will provide a tool for controlling their flocculating power by varying the chemical composition, steric structure, and charge of the chains.

EXPERIMENTAL

N,*N*-Dimethyl-*N*,*N*-diallylammonium chloride–maleic acid (DDACMA) copolymer is readily soluble in water and infinitely miscible with it. The concentration of the initial aqueous solution was about 51 wt %, pH ~2, average molecular weight $(3–8)\times 10^3$. The structure of the copolymer is as follows:



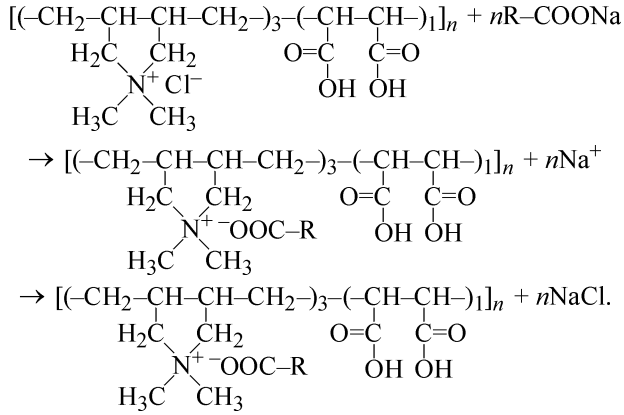
Experiments were performed with a commercial sample of SKS-30 ARK butadiene–styrene latex. As emulsifiers we used soaps derived from disproportionated rosin and tall oil resin acids. The colloid-chemical characteristics of the latex were as follows: dry residue 21.1%, pH 9.3, mean particle radius 50.8 nm, surface tension 63.7 mN m^{-1}.

The coagulation was performed as follows. A vessel placed in a thermostat was charged with butadiene–styrene rubber latex and kept at the prescribed temperature for 10–15 min, after which definite amounts of an aqueous solution of DDACMA copolymer were added. The coagulated system was acidified with a 2.0% aqueous solution of sulfuric acid in an amount of 15 kg per ton of rubber. The coagulum was separated from the serum, washed with water, and dried at 75–80°C.

The efficiency of the coagulating (flocculating) effect of DDACMA copolymer was evaluated gravimetrically (by the relative amount of the coagulum formed) and visually (from the serum transparency).

The concentration of the dispersed phase and temperature play an important role in the rubber recovery from latex, especially with organic cationic coagulants [9, 10]. Therefore, in the first step of our study we examined the effect of these factors on the completeness of rubber recovery. The experiment showed (Fig. 1) that the weight of the coagulum formed steadily increases with the amount of the coagulant added, and complete coagulation is attained at a coagulant consumption of 2.5–3.0 kg per ton of rubber (the amount of sulfuric acid added was constant, about 15 kg per ton of rubber).

In the course of coagulation of SKS-30 ARK latex, the particle charge is neutralized owing to a chemical reaction of the coagulant cation with anions of surfactants present on the surface of latex globules and entering into the composition of the adsorption layer [11]. As a result, an insoluble nondissociating complex is formed:



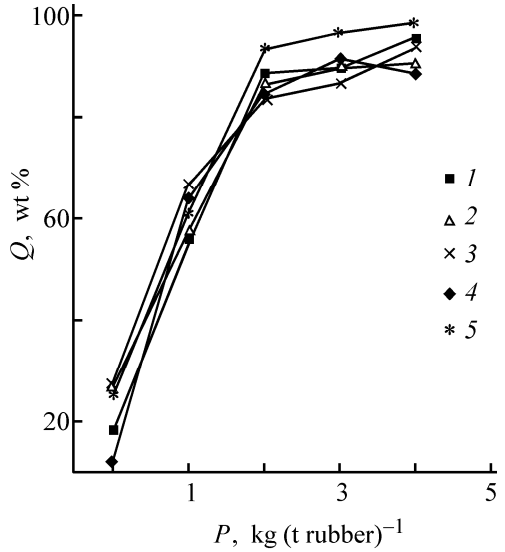


Fig. 1. Fraction Q of the polymer recovered from SKS-30 ARK latex vs. the concentration of DDACMA copolymer P at various temperatures. Dispersed phase concentration $c_{d.p}$ = 211 g l^{-1}, H_2SO_4 consumption 15 kg per ton of rubber. T, °C: (*1*) 1, (*2*) 20, (*3*) 40, (*4*) 60, and (*5*) 80.

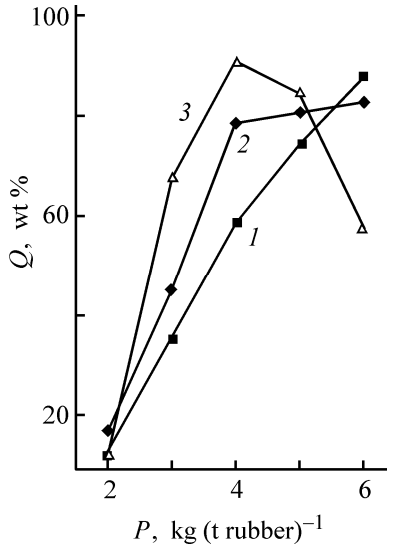


Fig. 2. Influence of the DDACMA copolymer concentration P on the degree Q of coagulation of SKS-30 ARK latex. Dispersed phase concentration $c_{d.p}$ = 52.7 g l^{-1}, H_2SO_4 consumption 15 kg (t rubber)$^{-1}$. T, °C: (*1*) 20, (*2*) 60, and (*3*) 80.

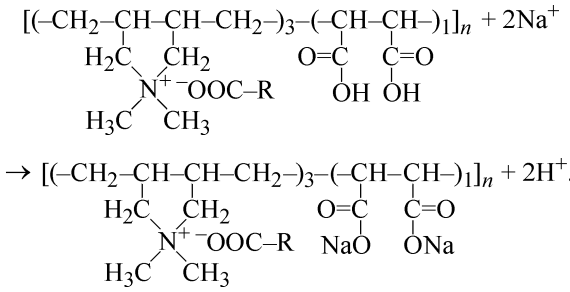
It should be noted that sodium chloride formed by this exchange reaction can also be involved in the coagulation as a salt coagulant, which is an advantage of DDACMA copolymer. It is extremely difficult to evaluate the contribution of the noticeably different components to the total coagulating effect. However, most probably, the coagulating effect is due to a combination of two factors: neutralization and bridge formation [12]. In addition, it should be emphasized that acid groups of maleic acid should cause acidification of the system and thus additionally promote its destabilization. This also positively affects the coagulation and allows its completion at a lower coagulant consumption (2.5–3.0 kg per ton of rubber, which is two orders of magnitude less than that with NaCl).

An additional advantage of the suggested coagulant is that the presence of acid groups makes the coagulating system considerably less sensitive to fluctuations of the content of the acidifying agent, which should inevitably lead to stabilization of the coagulation process. Thus, our study revealed a number of advantages of DDACMA copolymer as coagulant for rubber recovery from latex.

Our experiments show (Fig. 1) that the temperature affects the consumption of DDACMA copolymer required for complete recovery of the rubber from the latex, with the highest coagulum yield observed at low temperatures (1–20°C). An increase in the coagulation temperature led to a slight decrease in the coagulum eight, which may be due to several factors. First, the solubility of the coagulant and products of its interaction with surfactants decreases at low temperatures, and they are less readily washed out from the rubber crumb. Second, a denser coagulum is formed at low temperatures, whereas the coagulum formed at elevated temperatures is "looser," which, in turn, is accompanied by accumulation of a certain amount of finely dispersed rubber crumb in the serum. On the one hand, the presence of loose coagulum and finely dispersed rubber crumb favor a more efficient washing-out of impurities from the rubber. On the other hand, this factor increases the rubber loss with wash waters, which negatively affects the process efficiency and leads to environmental pollution. The denser coagulum is free of these drawbacks, its weight is higher because components of the emulsion system are captured by the coagulum, but its washing becomes inefficient, which may exert a negative effect on the properties of rubber stocks and vulcanizates. These trends were revealed in experiments on coagulation of the concentrated latex (21.1 wt %). A decrease in the dispersed phase concentration at 20°C (1 : 1, 1 : 2, 1 : 3 dilutions) leads to an increase in the coagulant consumption to 3–4 kg per ton of rubber (Figs. 2, 3), against starting 2 kg t^{-1} for the initial latex.

Figures 1 and 2 show that, with a decrease in the dispersed phase concentration, not only the coagulant

consumption increases (Fig. 3), but also the shape of the curves changes, especially at the maximal dilution. Namely, at a dispersed phase concentration of about 5.3 wt % (1 : 3 dilution) and temperature of 80°C, a flocculation optimum is observed, and deviation from it toward an increase in the consumption of DDACMA copolymer leads to a decrease in the coagulum weight. This may be due to adsorption of charged copolymer macromolecules on the particle surface, which makes possible both neutralization by the interaction of surfactant anions with cationic groups of the polyelectrolyte to give an insoluble complex, and formation of an oppositely charged (with excess flocculant) protective adsorption layer. The recharging phenomena have been repeatedly observed in experiments on coagulation of SKS-30 ARK latexes with poly(*N*,*N*-dimethyl-*N*,*N*-diallylammonium chloride) [13]. In addition, it is possible that, after the interaction of quaternary ammonium groups of DDACMA copolymer with surfactant anions is complete, free carboxy groups of maleic acid interact with sodium cations to form the corresponding salt, which can act as a surfactant of a new protective layer:



As noted by Pelssers et al. [14], it is also necessary to take into account the occurrence of relaxation processes in layers of adsorbing macromolecules. As a result of these processes, the number of segments contacting with the particle surface increases with time. In the process, the length of "tails" and "loops" remaining in the aqueous phase and responsible for capture of adjacent particles (bridging flocculation mechanism) decreases. The relaxation processes lead to "smoothening" of the polymer molecules and their "deactivation" (loss of the capacity for bridge formation) and favor formation of a dense adsorption layer exerting a protective effect, which is particularly manifested at low latex concentrations. As the dispersed phase concentration is raised, the frequency of particle collision increases and the time of the relaxation of the adsorption layers becomes shorter. At a certain concentration of the dispersed phase, the time intervals between the collisions become too short for the smoothening of the adsorbed molecules to occur to a significant extent, and the capacity for bridge formation is preserved. Then, even despite the recharging and the arising electrostatic repulsion, the flocculation activity of a cationic polyelectrolyte is preserved owing to the bridging mechanism.

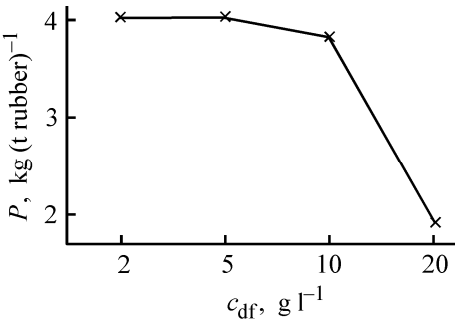


Fig. 3. Consumption of DDACMA copolymer P vs. the dispersed phase concentration $c_{d.p}$ H_2SO_4 consumption 15 kg per ton of rubber, $T = 20$°C.

Thus, at a definite concentration of the dispersed phase (latex concentration), the restabilization effect is suppressed and the degree of flocculation reaches the limiting value corresponding to complete breakdown of the dispersed phase (complete recovery of the rubber from the latex).

It is significant that, at decreased concentrations of the dispersed phase (Figs. 1, 2), an increase in the temperature leads to a decrease in the consumption of DDACMA copolymer for complete recovery of the rubber. Hence follows that dilute latexes should be coagulated at higher temperatures. This may be due to the fact that the latex particles separated from each other by a large distance due to dilution interact with each other at elevated temperatures more actively.

It is well known [1] that, in industry, rubber is recovered from a latex by adding NaCl in the presence of ~15.0 kg t^{-1} of sulfuric acid. Therefore, evaluation of the effect of sulfuric acid additions on the rubber recovery from latex is extremely important. As shown by an experiment (dispersed phase concentration 21.1 wt %, Figs. 4a, 4b), with the amount of the polyelectrolyte added of 1.0 kg per ton of rubber and the acidifying agent consumption varied from 5.0 to 30.0 kg per ton of rubber, the coagulation was incomplete. The maximal yield of the coagulum was observed at coagulation temperatures of 1–20°C and reached 80 wt % at best.

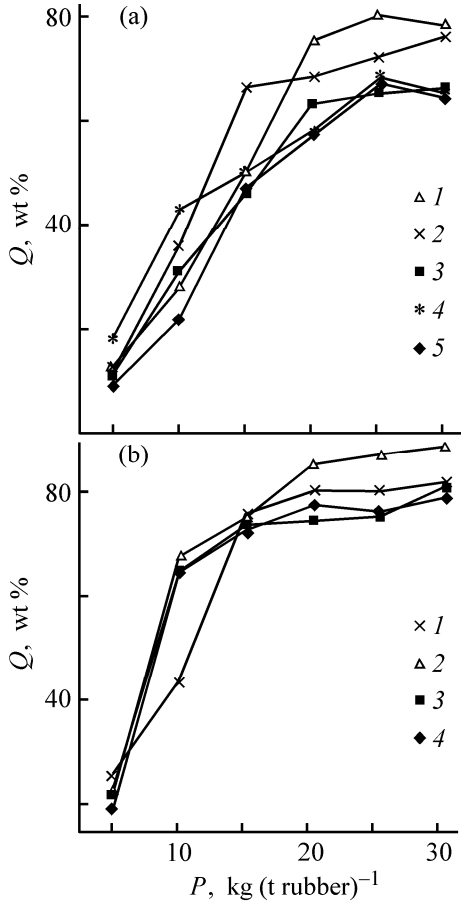


Fig. 4. Coagulum yield Q from SKS-30 ARK latex vs. the sulfuric acid consumption P at various temperatures. Dispersed phase concentration $c_{d.p}$ = 211 g l^{-1}, consumption of DDACMA copolymer (a) 1 and (b) 1.5 kg per ton of rubber. T, °C: (a) (*1*) 1, (*2*) 20, (*3*) 40, (*4*) 60, and (*5*) 80; (b) (*1*) 1, (*2*) 20, (*3*) 40, and (*4*) 80.

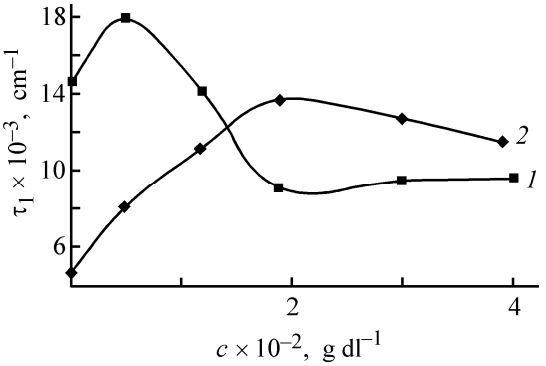


Fig. 5. Influence of the concentration of DDACMA copolymer, $c \times 10^{-2}$, on the 1-min turbidity $\tau_1 \times 10^{-3}$ of SKS-30 ARK latex at pH (*1*) 3 and (*2*) 9.

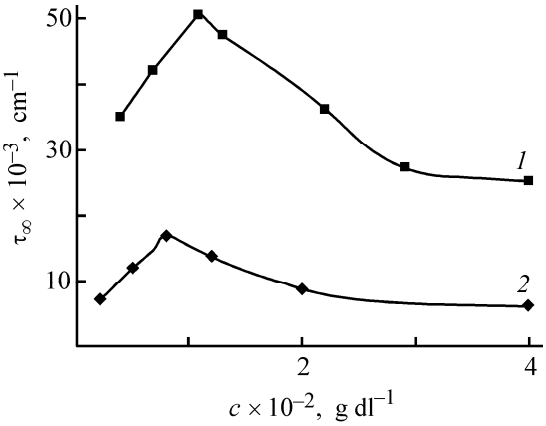


Fig. 6. Limiting turbidity $\tau_\infty \times 10^{-3}$ of SKS-30 ARK latex vs. DDACMA copolymer concentration $c \times 10^{-2}$. pH: (*1*) 3 and (*2*) 9.

Raising the coagulation temperature to 80°C led to a decrease in the coagulum weight, which can be attributed to the two factors discussed above.

With an increase in the DDACMA copolymer consumption to 1.5 kg per ton of rubber (Fig. 4b), the coagulation was the most complete (91 wt %) at the acidifying agent consumption of 30 kg per ton of rubber. An increase in the temperature led to a decrease in the coagulum yield to 70–80 wt %.

The coagulating performance of electrolytes is commonly assessed, along with the influence of their consumption on the degree of coagulation, by the initial coagulation rate. This quantity is usually evaluated nephelometrically, by measuring the 1-min turbidity [15].

To a latex diluted by a factor of 10^4, we added various amounts of the coagulant at pH 3 and 9 (adjusted with aqueous sulfuric acid). The turbidity was measured 1 min after introducing DDACMA copolymer into SKS-30 ARK latex.

Figure 5 shows the dependences of the 1-min latex turbidity τ_1 on the concentration of the polyelectrolyte added. As can be seen, both curves pass through a maximum. An increase in the initial rate of the latex flocculation in the ascending portions of curves *1* and *2* may be due to binding of emulsifier anions into an insoluble and virtually nondissociating complex. The optimum point corresponds to complete neutralization of the surface electric charge of the particles. Further decrease in the 1-min turbidity characterizes an increase in the stability of the disperse system, apparently due to recharging of the latex globules [13].

Notably, acidification of the system to pH 3 leads to a considerable enhancement of the flocculating effect of the polyelectrolyte (Fig. 5, curve *2*). The floccu-

lation optimum at pH 3 is observed at a polyelectrolyte concentration approximately five times lower than at pH 9. This fact has been noted previously in the literature [16] and is due to the pronounced coagulating effect of sulfuric acid itself, which is an efficient electrolyte-coagulant causing contraction of the electrical double layer on the surface of latex globules.

Another quantitative characteristic of the flocculating effect of the polyelectrolyte is the maximal turbidity τ_∞, which is determined from the kinetic data and characterizes the size of floccules that are not broken down in storage. The effect of polyelectrolyte additions on τ_∞ is shown in Fig. 6. As can be seen, at small additions of the polyelectrolyte, τ_∞ (and, accordingly, the mean floccule size) increases. Acidification of the system (Fig. 6, curve *1*) leads to considerable coarsening of the aggregates formed, which would be expected. Further increase in the amount of the polyelectrolyte added leads to a decrease in τ_∞, which confirms the previously found increase in the system stability. Similar results have been obtained previously [17] on polystyrene latexes coagulated with poly(*N*,*N*-dimethyl-*N*,*N*-diallylammonium chloride). The data obtained are consistent with the data on the degree of the rubber recovery from concentrated SKS-30 ARK latex at various pH values.

The final stage of this study was to determine the physicomechanical parameters of rubber stocks and vulcanizates based on SKS-30 ARK butadiene–styrene rubber recovered from the latex with DDACMA copolymer. As control sample we used a rubber sample recovered from SKS-30 ARK latex with the traditional coagulant, NaCl. Rubber stocks were prepared on laboratory rollers, using standard ingredients, and subjected to vulcanization at 143°C for 60 min. The results are listed in the table.

The data obtained show that rubber stocks prepared from the experimental sample undergo vulcanization faster than does the control stock. The vulcanization is accelerated by DDACMA copolymer and products of its interaction with the emulsion system components remaining in the rubber after its recovery from the latex. This leads to a slight decrease in the strength characteristics. Hence, for commercial use of DDACMA copolymer for recovering butadiene–styrene rubbers from latexes, it is necessary to additionally correct the composition of rubber stocks. We also found that the experimental sample surpass the control samples in the resistance to thermal aging and to crack propagation. The other characteristics of the experimental and control samples coincided within the experimental error.

Properties of rubber stocks and vulcanizates based on SKS-30 ARK rubber

Parameter	Sample	
	experimental	control
Mooney viscosity of rubber stocks MB 1+4 (100°C)	60.5	63.0
Nominal stress at 300% elongation, MPa	6.3	6.7
Nominal tensile strength, MPa	21.9	25.1
Relative breaking elongation, %	650	690
Relative remanent strain	16	20
Rebound elasticity, %:		
at 20°C	48	46
at 60°C	50	50
Shore hardness A	51	48
Tear resistance, kN m^{-1}	61.0	58.0
Resistance to crack propagation with ≤12-mm puncture, thousand cycles	112.7	98.6
Thermal aging resistance factor (72 h, 100°C):		
for nominal strength	0.71	0.63
for relative elongation	0.43	0.38

CONCLUSIONS

(1) A decrease in the concentration of the dispersed phase from 21 to 5.3 wt % leads to an increase in the coagulant consumption to 3.0–4.0 kg per ton of rubber.

(2) An increase in the acidifying agent consumption from 15 to 30 kg per ton of rubber ensures complete rubber recovery from the latex at a consumption of *N*,*N*-dimethyl-*N*,*N*-diallylammonium chloride–maleic acid copolymer as low as 1.5 kg per ton of rubber.

(3) The dependences of the 1-min and maximal turbidity of the dilute latex on the amount of *N*,*N*-dimethyl-*N*,*N*-diallylammonium chloride–maleic acid copolymer added pass through a maximum, which points to enhancement of the flocculating performance of the polyelectrolyte at its small additions and to an increase in the latex stability at the polyelectrolyte overdose.

(4) The *N*,*N*-dimethyl-*N*,*N*-diallylammonium chloride–maleic acid copolymer can be used in the industrial process of rubber recovery from latexes. The complete recovery is attained at its consumption of 2.5–3.0 kg per ton of rubber. Its use as coagulating agent does not significantly alter the properties of the rubber

obtained, rubber stocks, and vulcanizates. The vulcanizate strength slightly decreases, whereas the resistance to thermal aging and crack propagation increases.

REFERENCES

1. Kirpichnikov, P.A., Averko-Antonovich, L.A., and Averko-Antonovich, Yu.O., *Khimiya i tekhnologiya sinteticheskogo kauchuka* (Chemistry and Technology of Synthetic Rubber), Leningrad: Khimiya, 1987.
2. Moiseev, V.V., Popova, O.K., Kosovtsev, V.V., and Evdokimova, O.V., *Primenenie belkov pri poluchenii elastomerov* (Use of Proteins in Production of Elastomers), Moscow: TsNIITEneftekhim, 1985.
3. USSR Inventor's Certificate, no. 1 131 883.
4. JPN Patent Appl. 59-98 101.
5. Topchiev, D.A. and Malkanduev, Yu.A., *Kationnye polielektrolity ryada poli-N,N-dialkil-N,N-diallilammonii galogenidov: osobennosti protsessov obrazovaniya, svoistva i primenenie* (Cationic Polyelectrolytes of the Poly-*N*,*N*-dialkyl-*N*,*N*-diallylammonium Halide Series: Formation Features, Properties, and Applications), Nalchik, 1997.
6. Nikulin, S.S. and Verezhnikov, V.N., *Khim. Prom–st. Segodnya*, 2004, no. 11, pp. 26–37.
7. Garshin, A.P., Nikulin, S.S., Slukina, Z.D., et al., *Proizv. Ispol'z. Elastom.*, 1996, no. 9, pp. 14–19.
8. Moldavskii, B.L. and Kernos, Yu.D., *Maleinovyi angidridi maleinovaya kislota* (Maleic Anhydride and Maleic Acid), Leningrad: Khimiya, 1976.
9. Verezhnikov, V.N., Nikulin, S.S., Poyarkova, T.N., and Misin, V.M., *Zh. Prikl. Khim.*, 2000, vol. 73, no. 10, pp. 1720–1724.
10. Nikulin, S.S., Verezhnikov, V.N., Poyarkova, T.N., and Dankovtsev, V.A., *Kauchuk Rezina*, 2000, no. 5, pp. 2–4.
11. Garshin, A.P., Nikulin, S.S., Ryl'kov, A.A., et al., *Proizv. Ispol'z. Elastom.*, 1996, no. 5, pp. 8–10.
12. Baran, A.A. and Solomentseva, I.M., *Khim. Tekhnol. Vody*, 1983, vol. 5, no. 2, pp. 120–137.
13. Verezhnikov, V.N., Nikulin, S.S., Poyarkova, T.N., and Misin, V.M., *Zh. Prikl. Khim.*, 2001, vol. 74, no. 7, pp. 1191–1194.
14. Pelssers, E., Cohen, M., and Fleer, G., *J. Chem. Soc., Faraday Trans.*, 1990, vol. 86, no. 9, pp. 1355–1361.
15. *Kolloidnaya khimiya sinteticheskikh lateksov* (Colloid Chemistry of Synthetic Latexes), Neiman, R.E., Ed., Voronezh: Voronezh. Gos. Univ., 1984.
16. Nikulin, S.S., Poyarkova, T.N., and Misin, V.M., *Zh. Prikl. Khim.*, 2004, vol. 77, no. 6, pp. 996–1000.
17. Verezhnikov, V.N., Nikulin, S.S., Krutikov, M.Yu., and Poyarkova, T.N., *Kolloidn. Zh.*, 1999, vol. 61, no. 1, pp. 37–40.

ISSN 1070-4272, Russian Journal of Applied Chemistry, 2008, Vol. 81, No. 8, pp. 1465–1468. © Pleiades Publishing, Ltd., 2008.
Original Russian Text © I.A. Novakov, S.S. Radchenko, F.S. Radchenko, A.S. Ozerin, A.V. Karaulov, 2008, published in Zhurnal Prikladnoi Khimii, 2008, Vol. 81, No. 8, pp. 1389–1393.

MACROMOLECULAR CHEMISTRY AND POLYMERIC MATERIALS

Polyacrylamide–Aluminum Pentahydroxochloride–Urea Formulations as Waterproofing Agents for Oil Pool

I. A. Novakov, S. S. Radchenko, F. S. Radchenko, A. S. Ozerin, and A. V. Karaulov

Volgograd State Technical University, Volgograd, Russia

Lukoil-Volgograd NIPImorneft' Limited Liability Company, Volgograd, Russia

Received November 1, 2007

Abstract—Gel-forming polyacrylamide (PAA)–aluminum pentahydroxochloride (APHC) formulaitons were studied as waterproofing agents for an oil pool. The optimal formula and the gelation rate were determined.

DOI: 10.1134/S1070427208080272

The majority of methods for raising the oil recovery from oil strata are based on flooding. Breakthrough of injected and stratal waters through areas with high filtration properties results in the formation of flooded-out regions. Water is filtered through these regions, bypassing low-permeable oil-bearing areas of a pay. The oil production decreases and water content of oil increases.

To raise the oil recovery from oil pools, chemicals that form a waterproofing shield in highly watered interlayer, which prevents water penetration in producing oil wells, are pumped in [1].

However, most of these chemicals have significant disadvantages. Among them is the high cost, contamination of underground and surface waters, poor technological properties, and short life of the protecting shields. To selectively protect strata from water, gel-forming formulations of organic, inorganic, or organomineral compounds are used and, in particular, a mixture of a polyacrylamide (PAA) solution, aluminum salt, and urea (U) [2, 3]. The resulting aluminum hydroxide gel is a polydisperse system with poor and nonuniform adhesion to the stratum rock. Although an introduction of polyacrylamide improves the adhesion, the resulting system is freely disperse and is gradually washed out from the collector by injected or stratal water.

A gel-forming formulation containing aluminum pentahydroxochloride (APHC) yields a more stable and longer-lived gel. Colloidal polymer complex (CPC) [4] is almost instantaneously formed by the reaction of APHC with polyacrylamide in the starting solution. Urea introduced in the course of preparation of the starting solution decomposes in a stratum. The hydrolysis product initiates hydrolysis of the aluminum salt [5]. As a result, a stable strong gel-in-gel (combined gel) dispersion resistant to washout is formed.

The aim of this study was to develop a gel-forming PAA-APHC formulation for water-shutoff of oil pools, to find the best formula, to determine the gelation rate, and to estimate waterproof properties of this gel toward oil pools.

EXPERIMENTAL

Aluminum pentahydroxochloride prepared by the patented procedure [6] had the following properties: Al^{3+} content 12.8 wt %, Cl^-/Al^{3+} atomic ratio 0.48, pH 4.5, $\rho = 1330$ kg m^{-3}, dry residue 46.5 wt %. PAA with molecular weight of 6×10^6 was purchased from ACROS Company (USA), and urea, from Ekros Company (Russia). The formulations were prepared by mixing an aqueous PAA solution (1 wt %) with an aqueous APHC solution and urea at room temperature.

The instant of gelation was visually determined by the absence of fluidity of the liquid and more precisely by the solution viscosity measured with a Reokinetika-M vibration viscometer with a temperature-controlled cell. The vibration frequency was 750 Hz, and amplitude, 0.02 mm.

Table 1. Dependence of the gelation time on the APHC : U ratio (temperature 75°C)

APHC : U weight ratio	Gelation	Gelation time, h*
1 : 0.25	–	–
1 : 0.50	–	–
1 : 1	–	–
1 : 2	+	13
1 : 4	+	8.5
1 : 6	+	6
1 : 8	+	5
1 : 10	–	–

* In the case of negative results, the mixture was heated for 22 h.

Table 2. Dependence of the gelation time on the concentration of APHC–U mixture in the solution (APHC : U weight ratio = 1 : 6, T = 75°C)

Concentration, %	Gelation	Gelation time, h*
5	–	–
10	+	6.0
15	+	4.2
20	+	4.0

* In the case of negative results, the mixture was heated for 34 h.

The waterproofing properties were studied in a glass column with a heated jacket in which the required temperature was maintained with the aid of a thermostat.

The bench experiments were performed on a UIPK unit. Water and oil prepared in accordance with OST (Branch Standard) 39-235–89 were used as stratal liquids. The experiments were performed under the model thermobaric conditions (stratal pressure 31 MPa, temperature 75°C).

To analyze the ability of the gel to be confined in the rock (resistance of the gel to washout), pressure differences were produced taking into account the technical possibilities of the equipment (discreteness of the filtration rate) and the fluid properties. The pressure difference during washing of oil- and water-saturated samples was 18.8–21.9 and 1.1–3.2 MPa, respectively. The waterproofing power G (%) was calculated by the equation

$$G = \frac{k_0 - k}{k_0} \times 100,$$

where k_0 the penetrability of the rock before gel injection and k is that,

$$k = \frac{Q f \mu}{ps},$$

Q is the flow rate of water passed through the bulk model ($m^3 s^{-1}$); L, height of the rock bed (m); μ, water viscosity (Pa s); p, pressure (Pa); and s, cross-section area of the bulk model (m^2).

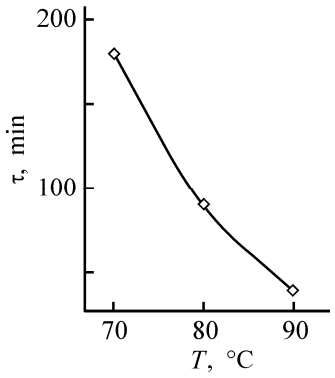


Fig. 1. Gelation time τ of APHC–U mixture vs. temperature T.

The main gelation parameters are the gelation time and the dependence of this time on the reagent ratio and temperature. To study the gelation, formulations with different component ratios and different component concentrations were placed in test tubes and heated in a thermostat at different temperatures until a gel was formed. The gel state and gelation time were determined. The results of the experiments on the influence of the component ratio on gelation in the examined system and gelation time are presented in Table 1.

As can be seen from Table 1, the gel is formed in a definite range of component ratios. No gelation was observed within the examined time at both decreased (less than 1 : 2) and significantly increased (more than 1 : 8) APHC amount. It should be noted the gel could also be formed at low APHC : U ratios in a longer time, but this possibility was not examined.

The dependence of the gelation time on the total component concentration in an aqueous solution is presented in Table 2. It is seen that no gel is formed at a total component concentration decreased to 5%. The gelation time somewhat decreases with increasing urea concentration.

The temperature is an important parameter which determines the hydrolysis rate of urea and hence the increase in the pH of the solutions to the values providing hydrolysis of the aluminum salt to form an amorphous gel of aluminum hydroxide. As can be seen from Fig. 1, the temperature is a key factor for gelation.

Table 3. Water permeability of quartz sand upon formation of an aluminum hydroxide gel in the presence of PAA in the bulk of the bed

Gel-forming system, weight proportion	Time of water drainage before treatment, min	Gelation time at 75°C, h	Time of water drainage after treatment, h	Waterproofing factor, %
APHC : U = 1 : 6	0.6	1	1.2	90
PAA : APHC : U = 0.07 : 1 : 6	3.1	6	1.3	93

To determine the gelation time and other rheological parameters of the gels more precisely, we studied the gelation kinetics of APHC–U formulations with different component ratios at 75°C. The kinetic curves (Fig. 2) show a significant dependence of gelation on the component ratio.

All the curves are characterized by a sharp increase in the viscosity due to transformation of the disperse system into gel. The shape of the curve corresponding to gelation depends on local changes of viscosity in the gel body and features of propagation of mechanical vibrations in the structurally nonuniform media. As the APHC : U ratio increases, the gelation time and the gel viscosity decrease since the amount of the reagent initiating gelation under these conditions grows and the weight of the gel-forming component (APHC) becomes lower.

These results confirm our previous assumption that the required gelation time and rheological properties of gel-forming formulations can be attained by varying the component ratio.

To study the waterproofing properties of aluminum hydroxide gels in the presence of polyacrylamide, we modeled a stratum by a bulk bed of quartz sand, since quartz is one of the natural strata of terrigenous sedimentary rocks contained in oil-saturated collectors. The main parameter used to estimate the influence exerted on the waterproofing properties of the gels was the waterproofing factor.

The time of water drainage through a bed of quartz sand at room and gelation temperature is presented in Table 3. It is seen that the time of water drainage through the sand bed sharply increases after gelation in the bed. Introduction of PAA improves the waterproofing effect.

Gel-forming formulation containing polyacrylamide, urea, and an aqueous solution of the aluminum salt was prepared by mixing a 0.1–1.0% aqueous polyacrylamide solution with a aqueous colloidal solution of aluminum pentahydroxochloride to form a colloidal polymer complex by intermolecular interaction of flexible polyacrylamide chains with the surface of colloidal APHC particles. Urea undergoes thermolysis on heating by the equation

$$CO(NH_2)_2 + H_2O \xrightarrow{T,\ ^\circ C} CO_2 + NH_3$$

and the pH solution gradually increases, reaching the threshold value (pH > 6.8) at which aluminum hydroxide gel is instantaneously formed in the bulk of the solution.

Apparently the gel–polyacrylamide system is structured with time. The formulation containing APHC was kept for a long time in a fixed bed. Water was passed through the quartz sand bed at regular intervals and the rate of water drainage was measured. The results are presented below:

Day after gelation	3	6	9	12	22	26	35	37	40	45
Time of water drainage, $V = 100$ cm^3, h	1.5	2.5	6.3	7.2	7.5	7.7	8.1	8.2	8.4	8.5

The results show that the gel strength increases and its waterproofing properties are improved with time.

We studied the influence of the gel-forming formulation containing polyacrylaamide, aluminum pentahydroxochloride, and hydrolyzing agent (urea) on

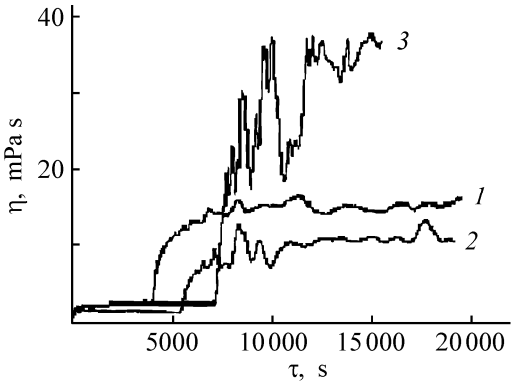


Fig. 2. Viscosity η of the formulation with APHC : U weight ratio of (*1*) 1 : 4, (*2*) 1 : 6, and (*3*) 1 : 8 vs. time τ.

Table 4. Influence of gel-forming formulation on filtration properties of deposit rocks

Sample no.	Porosity, %	Modeled saturation zone	Permeability coefficient, $K_{pm} \times 10^{-3}$, μm^2		
			initial	after injection of gel	after washout of gel
1	13.1	Water-saturated	33.6	0.034	0.084
2	10.22	Oil-saturated	0.06	0.014	0.045

the permeability of the rock saturated with stratal liquids (oil, stratal water). In these experiments, we studied core materials of oil wells. The rheological properties of collectors before and the treatment with the developed formulation were determined. The results of the bench experiments are presented in Table 4.

The permeation of water through the water-saturated samples decreased by a factor of 10^3 after treatment with the gel-forming formulation.

Analysis of gel retention in the rock (resistance of the gel to washout) showed that the permeability increased by a factor of 1.5–2.5. Thus, the gel is fairly resistant to washout.

Treatment of the water-saturated zone with the formulation developed decreases the permeability by a factor of 400 owing to plugging of the collector pores with gel particles (mudding).

The influence of the gel-forming formulation on the oil-saturated zone of the stratum was weaker. The penetrability of oil after injection of gel decreased by a factor of 4.3. The final permeability after washing (determination of the gel resistance to washout) decreased by a factor of 1.3 relative to the initial value.

CONCLUSION

Gel prepared from a polyacrylamide–aluminum pentaoxochloride-urea mixture of the optimal composition decreases the rock permeability by a factor of 400 and hardly affects the permeability of the oil-saturated zone. The gel is resistant to washout from the water-saturated zone of a stratum.

REFERENCES

1. Manyrin, V.N. and Shevtsov, I.A., *Fiziko-khimicheskie metody pri zavodnenii* (Physicochemical Methods in Flooding), Samara: ROING, 2002.
2. Surguchev, M.L. et al., *Metody iszvlecheniya ostatochnoi nefti* (Methods for Recovering Residual Oil), Moscow: Nedra, 1993.
3. RF Patent 2 076 202.
4. Novakov, I.A., Radchenko, F.S., and Papisov, I.M., *Vysokomolek. Soedin.*, 2003, vol. 45, no. 8, pp. 1340–1344.
5. Altunina, L.K. and Kuvshinov V.A., *Neft. Khoz.*, 1995, no. 4, pp. 36–38.
6. RF Patent 2 280 615.

ISSN 1070-4272, Russian Journal of Applied Chemistry, 2008, Vol. 81, No. 8, pp. 1469–1472. © Pleiades Publishing, Ltd., 2008.
Original Russian Text © T.N. Teryaeva, O.V. Kas'yanova, G.M. Rotova, O.V. Kostenko, 2008, published in Zhurnal Prikladnoi Khimii, 2008, Vol. 81, No. 8, pp. 1394–1397.

MACROMOLECULAR CHEMISTRY AND POLYMERIC MATERIALS

Physicochemical Properties of Ocher Used as Polymer Filler

T. N. Teryaeva, O. V. Kas'yanova, G. M. Rotova, and O. V. Kostenko

Kuzbass State Technical University, Kemerovo, Russia

Received December 27, 2007

Abstract—Principal physicochemical properties of ocher were studied in order to use it as a mineral filler for polymers.

DOI: 10.1134/S1070427208080284

Fillers produced by crushing and processing of natural minerals, such as, e.g., talc, chalk, kaolin, and mica, find wide use in manufacture of polymeric composite materials (PCM). Introduction of mineral fillers into a polymer makes it possible to solve a number of problems related to materials science (extending the raw materials base, improving the strength, rigidity, heat resistance, etc.), technology (controlling the viscosity and thermal stability of melts), and economics (lowering the production cost of PCM) [1, 2]. However, the available commercial assortment of domestically manufactured fillers used on the industrial scale for synthesis of PCM is limited and cannot satisfy the diverse and steadily growing requirements of consumers. Therefore, a search for effective fillers of natural origin, large raw material resources, and low cost is a topical task.

Rather promising in this regard for polymer filling is use of ocher, a readily available and ecologically safe mineral raw material, whose deposits are present in sufficient number on the territory of Russia, including those in Kuzbass.

Ocher is mostly used as a pigment in production of paint-and-varnish materials and its properties reported in the technical literature are the spreading capacity, light resistance, oil capacity, density, particle size, and elemental composition, which is insufficient for characterizing a mineral powder as a polymer filler [3].

There is published evidence about the possible use of ocher for polymer filling [4–6], but neither recommendations about the composition of formulations and necessity for preparation procedures, nor parameters commonly determined for dispersed mineral polymer fillers can be found in the literature.

This communication reports the results of a study of the physicochemical properties of ocher, which make it possible to assess its applicability as a polymer filler.

EXPERIMENTAL

As object of study served ocher of O2 brand [TU (Technical Specification) 301-10-019–90] from the Gavrilovskoe deposit (town of Salair, Kemerovo oblast). It had the following composition (%): Fe_2O_3 17.6, Al_2O_3 29.1, SiO_2 44.8, SO_4 0.05, K 0.26, Cu 0.03, PO_4 0.57, Cr 0.9, Ca 1.4, Ni 0.003, Mn 0.64, Mg 0.64, and Cl 0.001.

Standard procedures were employed to find the density ρ [in accordance with GOST (State Standard) 15 139], content W of water and volatiles (GOST 19 728.19), and bulk density ρ_b (GOST 11 035). The pH of a water extract, granulometric composition, particle size d, and specific surface area S_{sp} were determined using the methods described in [7].

The thermochemical properties of ocher were studied on a Q-1500D derivatograph in air.

The thermal properties of ocher (heat conductivity λ, specific heat c_p) were found using the integrated thermographic method [8].

The experimental results were processed in accordance with GOST (MI 2336–2002.GSI) [10, 11].

Ocher is a finely ground goldish yellow powder. As regards the content of iron oxide hydrate, the ocher under study is classed as ordinary clayey, with Fe_2O_3 content of about 17.6%. The outward appearance of ocher is shown in Fig. 1.

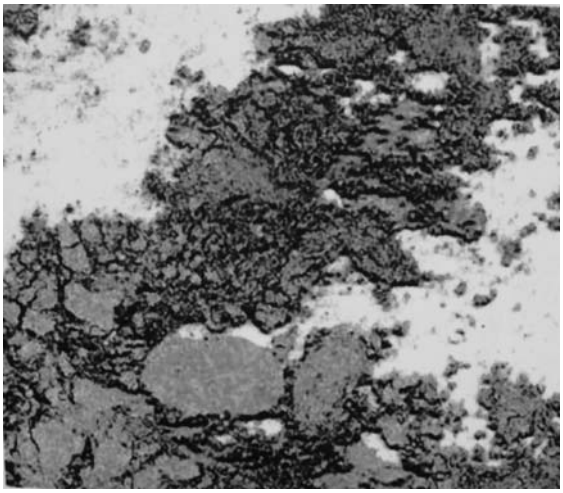


Fig. 1. Outward appearance of ocher.

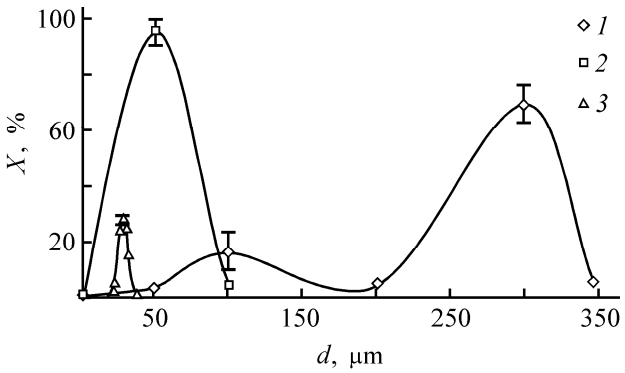


Fig. 2. Granulometric composition of ocher. (*X*) Content of a fraction and (*d*) particle size. Sieving: (*1*) dry and (*2*) wet; (*3*) sedimentation analysis.

Ocher particles have a lamellar shape, which is indicated by their form factor, found using a rheological method (Einsten coefficient k_e is 16.5), and by the accordingly stronger effect of the filler on the viscosity of, and the stress concentration in filled polymers.

The particle size and the granulometric composition of a filler largely affect the PCM properties. In the industry, the granulometric composition of powders is most frequently determined by dry or wet sieving analysis. The particle size distribution curves found for ocher by dry or wet sieving are shown in Fig. 2. In addition, the same figure presents results of a sedimentation analysis. This dependence was obtained in five parallel runs, with the plots constructed using the average values. The deviation in the content of particles of a certain size does not exceed 5% (the error is shown in the plots).

As can be seen from the curves in Fig. 2, in the case of dry sieving, the size distribution of ocher particles has two peaks, at 100 and 300 μm. In the case of wet sieving, most part of particles are 50 μm in size. The results obtained can be attributed to the tendency of ocher particles to form agglomerates, which is characteristic of the majority of dispersed fillers. This is also confirmed by the outward appearance of ocher particles (Fig. 1). Upon wetting with a liquid, coarse agglomerates disintegrate.

The particle size of ocher was found by sedimentation analysis to be 20–40 μm. This means that ocher belongs to the group of medium-dispersity fillers ($10 \le d \le 40$ μm) [1]. The results of sedimentation analysis were used to calculate the specific surface area of ocher ($S_{sp} = 0.08 \pm 0.05$ m^2 g^{-1}) and the degree of polydispersity $\delta = 1.6$.

It is rather difficult to determine the chemical composition and the nature of the surface of mineral fillers. Therefore, the common way is to evaluate the overall chemical nature and the degree of contamination by the pH of an aqueous extract of the filler. For ocher, pH 6, i.e., the particle surface of ocher under study are weakly acidic.

The true and bulk density of ocher was measured to be 2630 ± 60 kg m^{-3} and 680 ± 90 kg m^{-3}, respectively, which made it possible to find the maximum volume degree of filling, φ_{max}, to be 26 ± 2 vol %. The quantity φ_{max} is the upper limit on the filler content of the two-phase material. In the end, it determines the properties of PCM, technological parameters of the forming process, and the service characteristics of articles. The larger φ_{max}, the greater amount of the filler can be introduced without substantially impairing the technological properties, including the melt viscosity [1, 8].

The abrasiveness, or abrasion capacity, is a negative characteristic of mineral powders. In grinding, dispersion, transportation, and other technological procedures, the equipment undergoes a strong wear [4]. To preclude this phenomenon, it is recommended to use PCM fillers with low hardness (Mohs hardness ≤ 2). For ocher, the Mohs hardness (MH) is 1–2 and is approximately equal to that of kaolin, which enables processing of formulations with ocher in standard apparatus.

The thermal properties of ocher were as follows: $c_p = 0.6 \pm 0.02$ kJ kg^{-1} K^{-1} and $\lambda = 0.26 \pm 0.03$ W m^{-1} K^{-1}, which corresponds to similar characteristics of natural minerals.

The moisture content of ocher is 1.91 wt %, which necessitates drying of ocher in the case of its introduction into polymers in amounts exceeding 1 wt %. The increased moisture content of the filler will primarily affect the type of interaction between the polymeric matrix and the filler. An excessive content of moisture and volatiles (> 0.02%) leads to formation of pores and voids at the polymer–filler interface and, as a result, can impair the service characteristics of PCM (hardness, strength) and adversely affect their outward appearance (porosity, bulging). An increased moisture content of the filler may lead to arching of the material in the bunker of a processing apparatus, which disturbs the even feeding of the machine.

Moisture is commonly removed by thermal treatment at the minimum possible temperature.

To study the behavior of ocher under heating, the derivatogram shown in Fig. 3 was measured. The DTA curve obtained shows endothermic peaks at 105, 275, 502, and 700°C, accompanied by loss of mass by the sample under study. For example, ocher loses 1.91 to 5.4% of its mass at 105–300°C, and 8.17 to 12.43% at 490–740°C.

Moisture is removed via evaporation (at 100–105°C) of water adsorbed by the ocher surface and via chemical reactions at higher temperatures:

$$2FeO(OH) \rightarrow Fe_2O_3 + H_2O,$$

$$Al_2O_3 \cdot 2SiO_2 \cdot 2H_2O \rightarrow Al_2O_3 \cdot 2SiO_2 + 2H_2O.$$

It should be noted that the color of ocher changes from goldish yellow to red-brown at temperatures higher than 150°C. At 250–300°C, ocher is nearly completely dehydrated and transformed to red-brown iron oxide. At temperatures of 490–700°C, there occurs dehydration and disintegration of the kaolin lattice [4].

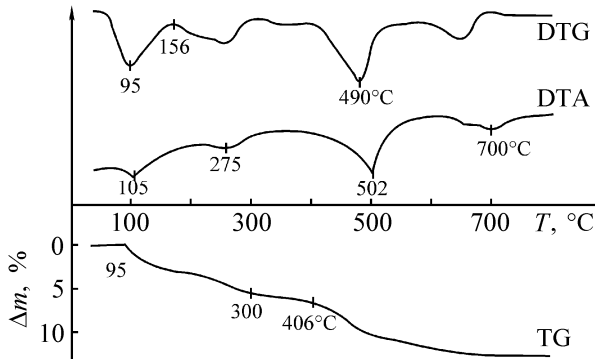


Fig. 3. Derivatogram of ocher (sample mass 402 mg). (Δm) Loss of mass and (T) temperature.

The results of the thermal analysis suggest that ocher should be treated at 300°C to remove moisture. The duration of such a thermal treatment for an ocher layer with a thickness of up to 10 mm is 90 min.

For a thermally treated ocher, the same characteristics as those for the starting ocher were determined. The results obtained are listed in the table, together with the parameters of the presently most widely used mineral polymer fillers.

Analysis of the data in the table shows that thermal treatment of ocher leads to an increase in the density, heat conductivity, specific heat, and specific geometric surface area and to a decrease in agglomeration because of the moisture removal.

Physicochemical properties of ocher and mineral fillers

Parameter	Filler				
	ocher*	talc	kaolin	chalk	mica
ρ, kg m^{-3}	2830	2800	2600	2600–2900	2830
d, μm	16–28	5–40	0.5–10	2–50	35–40
pH	4–5	9.2	4.5	8.1–9.6	7.5
j_{max}, vol %	30	31	15	34	–
λ, W m^{-1} K^{-1}	0.3	2.1	0.18	2.4	0.6–2.5
c_p, kJ kg^{-1} K^{-1}	0.75	0.87	0.89	0.82	0.87
MH, arb. units	2	1	1–2	3	2.5–3.5
W, %	0	–	–	–	–
ρ_b, kg m^{-3}	810	–	–	–	–
S_{sp}, m^2	0.1	–	–	–	–

* Thermally treated.

Comparison of the properties of the starting and thermally treated ocher with those of the conventional dispersed mineral polymer fillers shows that they are on the same order of magnitude or slightly differ, and, consequently, ocher can be used to obtain polymeric composite materials. Kaolin has parameters the closest to those of ocher.

CONCLUSIONS

(1) Preparation of ocher as a polymer filler should include thermal treatment at 300°C to remove moisture and obtain high-quality articles.

(2) As a result of thermal treatment of ocher, its density, specific heat, heat conductivity, and specific geometric surface area increase by 5–15%, the degree of its agglomeration decreases, and its color changes because of the moisture removal.

REFERENCES

1. Vlasov, S.V., Kandyrin, L.B., Kuleznev, V.N., et al., *Osnovy tekhnologii pererabotki plasticheskikh mass* (Foundations of the Processing Technology of Plastic Masses), Moscow: Khimiya, 2004.
2. *Composite Polymer Materials*, Katz, G. and Milevsky, J., Eds., Translated under the title *Napolniteli dlya polimernykh kompozitsionnykh materialov*, Babaevskii, P.G., Ed., Moscow: Khimiya, 1981.
3. Belen'kii, E.F. and Riskin, I.V., *Khimiya i tekhnologiya pigmentov* (Chemistry and Technology of Pigments), Leningrad: Goskhimizdat, 1960.
4. Ermilov, P.I., Indeikin, E.A., and Tolmachev, I.A., *Pigmenty i pigmentirovannye lakokrasochnye materialy* (Pigments and Pigmented Paint-and-Varnish Materials), Leningrad: Khimiya, 1987.
5. Kas'yanova, O.V. and Teryaeva, T.N., *Vestn. Kuzb. Gos. Tekh. Univ.*, 2003, no. 1, p. 60.
6. RF Patent 2 078 104.
7. Aristovskaya, L.V., Babaevskii, P.G., Vlasov, S.N., et al., *Praktikum po polimernomu materialovedeniyu* (Laboratory Course of Polymer Materials Science), Moscow: Khimiya, 1980.
8. Piven', A.N., Grechanaya, N.A., and Chernobyl'skii, I.I., *Teplofizicheskie svoistva polimernykh materialov* (Thermal Properties of Polymeric Materials), Kiev: Vysshaya Shkola, 1976.
9. Kryzhanovskii, V.K. and Burlov, V.V., *Prikladnaya fizika polimernykh materialov* (Applied Physics of Polymeric Materials), St. Petersburg: SPb Gos. Tekhnol. Inst. (Tekhnol. Univ.), 2001.
10. *GOST* (State Standard) *R.ISO 5725-2–2002. Accuracy (Adequacy and Precision of Measurement Methods and Results), Part 2, Main Method for Determining the Reproducibility of the Standard Measurement Technique.*
11. *GOST* (State Standard) *8.207–76. State System for Provision of the Uni-fication of Measurements, Direct Measurements with Multiple Observations, Methods for Processing of Observation Results, Principal Concepts.*

ISSN 1070-4272, Russian Journal of Applied Chemistry, 2008, Vol. 81, No. 8, pp. 1473–1475. © Pleiades Publishing, Ltd., 2008.
Original Russian Text © S.S. Smirnov, V.A. Zhorin, 2008, published in Zhurnal Prikladnoi Khimii, 2008, Vol. 81, No. 8, pp. 1398–1400.

BRIEF COMMUNICATION

Effect of Mechanical Activation on the Synthesis and Electrochemical Properties of Lithium-Vanadium Bronze

S. S. Smirnov and V. A. Zhorin

Moscow Institute of Power Engineering, Moscow, Russia

Received December 11, 2007

Abstract—An original technique for production of a lithium-vanadium bronze was developed. It includes mechanical activation of a mixture of vanadium oxide with lithium hydroxide in the course of plastic flow under twisting.

DOI: 10.1134/S1070427208080296

In presently manufactured lithium-ion batteries, the positive electrodes are as a rule fabricated from lithiated cobalt, nickel, and manganese oxides [1–3]. In recent years, the technology of these conventional electrodes has been refined and novel materials have been sought for. The main way to refine the conventional materials is doping, i.e., synthesis of mixed cobaltates, nickelates, spinels and development of two-phase composites containing particles of an active material enveloped with thin films of a foreign substance.

Recently, interest has been revived in vanadium oxides, a promising material for positive electrode of secondary lithium power cells. Materials based on vanadium oxides were intensively studied in the 1980s**.** After that, however, researchers' attention has been mostly concentrated on cobalt and nickel oxides and manganese spinels, which have a more positive potential. Among vanadium compounds, the most promising materials for positive electrodes are lithium-vanadium bronzes (LiV_3O_8) [3]. A large number of both high- and low-temperature methods for their preparation have been suggested: solid-phase thermochemical method, sol-gel procedure, melt technique, and hydrothermal method [4–8].

However, lithium-vanadium bronzes obtained by the sol-gel procedure contain a large amount of water, which is then extracted into the electrolyte. In addition, such vanadium oxides absorb a considerable amount of organic solvents. The high-temperature solid-phase method has the shortcomings of multistage nature, prolonged process duration, and low dispersity of LiV_3O_8 powders, which affects the capacity and service life of the electrodes fabricated from this compound and of a battery as a whole.

At present, a considerable attention is given to preliminary treatment of precursors. The authors of [9] used the mechanical activation to synthesize cathode materials for lithium batteries. A mixture of precursors was mechanically activated in planetary centrifugal mills. The method made it possible to prepare dispersions with a required structural disordering and thus to improve the quality of the cathode material.

An effective way to affect the structure of solids is their treatment in high-pressure apparatus of the type of Bridgman anvils**.** This treatment of mixtures of powdered substances makes sizes of the heterophases considerably lower. A large number of defects are formed in the structure of single components. Owing to a sharp acceleration of mass-transfer processes, the components can be mixed at nearly a molecular level, with various chemical processes also activated in this case [10].

The previously performed studies have shown that use of high pressure and shear deformations in manufacture of cathodes for lithium power cells considerably improves their electrochemical characteristics [11, 12].

A lithium-vanadium bronze is obtained by mixing of vanadium oxide with lithium salts or hydroxide, followed by heat treatment of the mixture. Therefore, it was suggested in this study to perform mixing in high-pressure apparatus.

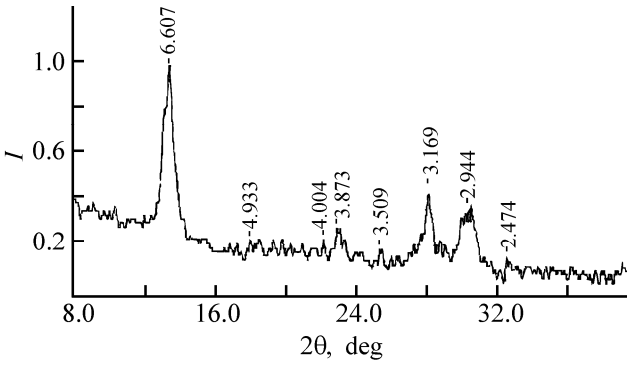


Fig. 1. X-ray diffraction pattern of a V_2O_3 + 15% LiOH sample plastically deformed under a pressure of 1.7 GPa (anvil rotation angle 500°) and then heat-treated at 200°C for 5 h. (*I*) Radiation intensity and (2θ) Bragg angle.

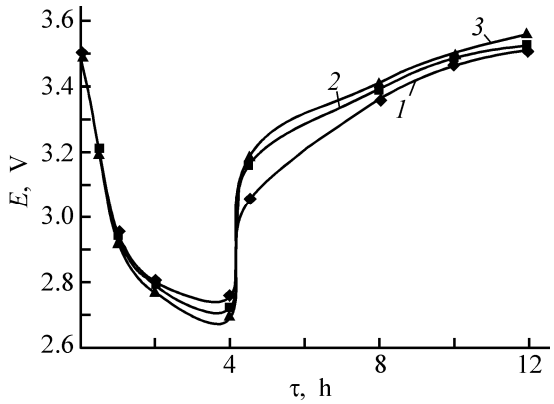


Fig. 2. Discharge-charging curves of the battery cathode. $I_d = I_{ch} = 0.5$ mA cm^{-2}. (*E*) Potential and (τ) time. Cycle: (*1*) 5th, (*2*) 70th, and (*3*) 150th.

EXPERIMENTAL

A mixture of V_2O_3 and LiOH was poured in a ceramic bowl, gently agitated in dry state with a glassy rod for 10–15 s, and subjected to plastic deformation on a Bridgman anvil type high-pressure apparatus. Anvils made of a VK-6 hard alloy (working diameter 20 mm) were used. The treatment was performed at room temperature under a pressure of 1–2 GPa (anvil rotation angle 500°). As starting reagents served vanadium oxide V_2O_3 and lithium hydroxide (chemically pure grade). The resulting discs (2 cm in diameter) were wrapped in aluminum foil and heat-treated in a muffle furnace at temperatures of 100, 200, 300, and 400°C for 0.5–10 h.

Then, the substance obtained was washed in distilled water to remove excess OH^- ions and dried at 80–100°C to constant mass.

X-ray diffraction patterns of the electrode samples studied, fabricated from a lithium–vanadium bronze were obtained on a DRON-3 diffractometer in $Cu_{K\alpha}$ monochromatic radiation in the range 2θ 8°–40°, using automated recording programs.

To prepare the cathodes, a powdered lithium–vanadium bronze, to which an electrically conducting additive was introduced in a ratio of 85 : 10, was agitated in a mortar. Then, the mass obtained was impregnated with a solution of lithium perchlorate and polysulfone in dimethylacetamide and dried at 100°C in a vacuum. The resulting mass was ground, poured onto a current lead made of aluminum foil, and compacted in a special press mold under a pressure of 100 kg cm^{-2}. Before a model battery was assembled, the electrodes were kept in a desiccator at 100°C for 1–1.5 h.

The cathode was mounted at the bottom of a three-electrode measuring cell made of polypropylene. From above, the cell was covered with a polymer electrolyte and lithium foil. The working surface of the electrodes was 1 cm^2; their active mass, 0.07 g; and thickness, about 0.1 mm. The Li/Li^+ electrode was used as reference. The electrodes were uniformly spring-loaded. The current was collected by means of stainless steel rods pressed against tabs of the current leads. Electrochemical studies were performed with a Solartron SI 1287 Electrochemical interface potentiostat.

A high-pressure apparatus made it possible to subject the substances studied to uniaxial compression and shear forces, whose value did not exceed the yield stress of a material under a given pressure. On the apparatus of this kind, the plastic flow is observed in the case when the skin-friction force is large or equal to the yield stress of the material being processed. For the mixtures of vanadium oxide V_2O_3 and lithium hydroxide LiOH, this ratio occurs at pressures of about 1.7 GPa. At lower compression pressures, the anvil and the punch slip through the surface of a substance and the starting powdered materials remain powdered. At pressures above 1.7 GPa, the powdered materials are compacted, i.e., their constituents are subjected to plastic deformation.

The standard method for production of lithium–vanadium bronzes consists in sintering of powdered mixtures of vanadium oxide and lithium salts or hydroxide at a temperature of 700°C or higher for 24 h. It has been shown previously [13] that, if the starting mixtures of V_2O_5 and LiOH are preliminarily treated under a high pressure, then a LiV_3O_8 phase is formed even at 400°C in the course of 10 h. In this study, mixtures of V_2O_3 with LiOH were subjected to plastic deformation under a pressure of 1–2 GPa and then sintered at high temperatures.

According to the results of an X-ray diffraction analysis, the diffraction patterns of the samples treated under pressure contain reflections belonging to the LiV_3O_8 phase, for which the sizes of coherent scattering regions (CSRs), calculated from the reflections' width, were 20 nm. This means that the substance is in a highly dispersed state. Heating of such samples at 200°C for 5 h considerably raises the intensity of the LiV_3O_8 lines in the X-ray spectrum. At the same time, the width of the lines, i.e., the sizes of the CSRs do not virtually change, which confirms the high thermal stability of the ultradispersed structure formed upon the treatment under a pressure (Fig. 1). Annealing of samples at higher temperatures did not lead to any noticeable changes in the LiV_3O_8 structure obtained by annealing at 200°C.

Thus, owing to the mechanical activation of the mixture of V_2O_3 and LiOH on the Bridgman anvils, the annealing temperature at which a highly dispersed state of the substance was attained was lowered by 500°C (from 700 to 200°C). This result can be accounted for by the following processes**.** The action of pressure and a shear force results in that nanostructures are formed. In this case, a large number of structural defects (dislocations) appear in the structure of individual solids. In the course of a plastic deformation, there occurs intense mass-transfer leading to homogenization of the starting heterogeneous mixtures at a nearly molecular level. The annealing of such a system raises the solubility of lithium atoms in vanadium oxide and causes their concentration diffusion.

The study demonstrated that cathodes fabricated from a lithium-vanadium bronze can be reversibly cycled at a current density of 0.5–1.0 mA cm^{-2}. The specific capacity of the cathodes in the potential range 3.5–2.5 V is 150 mA h g^{-1}, which exceeds the capacity of high-temperature samples (120 mA h g^{-1}) by approximately 20%. The discharge-charging characteristics of the LiV_3O_8 cathodes demonstrate a high stability during 150 cycles: the loss of capacity does not exceed 5.5% (Fig. 2). A comparison of the results obtained with published data showed that the electrodes fabricated from the LiV_3O_8 prepared surpass the analogs known from the literature [4–9] in stability by, on average, 25%.

CONCLUSION

An original technique for fabrication of cathodes for lithium power cells by using a Bridgman anvil type high-pressure apparatus was developed. The technique made it possible to raise the electrode capacity by 20% and improve the electrode stability by 25%, as well as to reduce severalfold the duration of the technological cycle of their fabrication.

REFERENCES

1. Kedrinskii, I.A. and Yakovlev, V.G., *Li-ionnye akkumulyatory* (Lithium-Ion Batteries), Krasnoyarsk: IPK Platina, 2002.
2. *Khimicheskie istochniki toka. Spravochnik* (Chemical Power Cells. Reference Book), Korovin, N.V., and Skundin, A.M., Eds.**,** Moscow: Mosk. Energ. Inst., 2003.
3. Skundin, A.M., *Elektrokhim. Energ*., 2005, vol. 5, no. 2, pp. 65–73.
4. Volkov, V.L., Lazarev, V.F., and Zakharova, G.S., *Elektrokhim. Energ.*, 2001, vol. 1, no. 3, pp. 3–8.
5. Manthiram, A., and Kannan, A. M., *Solid State Ionics*, 2003, vol. 159, nos. 3–4, pp. 265–268.
6. Apostolova, R.D., Shembel', E.M., and Nagirnyi, V.M., *Materialy VI Mezhdunarodnoi konferentsii "Litievye istochniki toka"* (Proc. VI Intern. Conf. "Lithium Power Cells"), Novocherkassk, 2000, p. 62.
7. Dai, Jinxiang, Li, Sam F.Y., Gao, Zhiqiang, and Siow, Siong, *J. Electrochem. Soc*., 1998, vol. 145, no. 9, pp. 3057–3060.
8. Manthiram A. and Kannan, A.M., *Solid State Ionics*, 2003, vol. 159, no. 3–4, pp. 265–268.
9. Kosova, N.V., *Elektrokhim. Energ*., 2005, vol. 1, no. 2, pp. 123–126.
10. Zhorin, V.A., and Andreeva, G.V., *Dokl. Akad. Nauk SSSR*, 1988, vol. 298, no. 2, pp. 388–391.
11. Zhorin, V.A., and Smirnov, S.E., *Elektrokhimiya*, 2001, vol. 37, no. 9, pp. 1093–1095.
12. Smirnov, S.E., Zhorin, V.A., and Sivtsov, A.V., *Elektrokhimiya*, 2003, vol. 39, no. 3, pp. 276–279.
13. Smirnov, S.S., Zhorinn, V.A., and Adamson, B.I., *Naukoemk. Tekhnol*., 2006, vol. 7, no. 9, pp. 19–23.

ISSN 1070-4272, Russian Journal of Applied Chemistry, 2008, Vol. 81, No. 8, pp. 1476–1478. © Pleiades Publishing, Ltd., 2008.
Original Russian Text © D.M. Mognonov, Zh.P. Mazurevskaya, V.V. Khakhinov, O.V. Il'ina, 2008, published in Zhurnal Prikladnoi Khimii, 2008, Vol. 81, No. 8, pp. 1401–1403.

BRIEF COMMUNICATION

Manifestations of Crystallinity in Polyamidobenzimidazoles

D. M. Mognonov, Zh. P. Mazurevskaya, V. V. Khakhinov, and O. V. Il'ina

Baikal Institute of Nature Management, Siberian Branch, Russian Academy of Sciences, Ulan-Ude, Buryatia, Russia

Received December 27, 2007

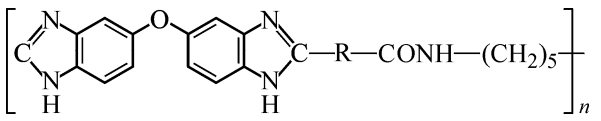
Abstract—Polyamidobenzimidazoles derived from 3,3',4,4'-tetraaminodiphenyl ether, diphenyl esters of aliphatic and aromatic dicarboxylic acids, and ε-caprolactam were prepared by solid-phase polycondensation. The relative degree of crystallinity, imparting the plasticity to the polymers as compared to the corresponding polybenzimidazoles, was determined by X-ray phase analysis.

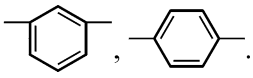
DOI: 10.1134/S1070427208080302

In this study, we examined the physicochemical-properties of polyamidobenzimidazoles (PABIs) prepared at various molar ratios of the starting monomers.

EXPERIMENTAL

Polyamidobenzimidazoles were prepared by solid-phase polycondensation from 3,3'4,4'-tetraaminodiphenyl ether (TADPE), diphenyl esters of adipic (DPA), sebacic (DPS), isophthalic, and terephthalic (DPT) acids, and ε-caprolactam (CL) [1]. The substances are copolymers of polybenzimidazole (PBI) and polycaproamide (PCA), containing benzimidazole rings and amide groups. The unit composition depends on the starting monomers and their molar ratio in the reaction mixture and, at equimolar ratio of the comonomers, can be represented by the following formula:



where R = $-(CH_2)_4-$, $-(CH_2)_8-$,  .

The polymers were purified by reprecipitation from a solution in concentrated formic acid by dilution with a small amount of water, avoiding turbidity, followed by addition of a 0.5% solution of ammonium carbonate. The product was filtered off on a Büchner funnel, repeatedly washed with distilled water to neutral reaction, and dried in a vacuum oven at 60–70°C. The X-ray phase analysis was performed on a DRON-UM1 diffractometer using Ni-filtered Cu_{K_α} radiation. The thermal and chemical characteristics of PABIs are given in [2], and some properties of the copolymers are listed in the table.

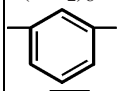
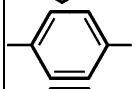
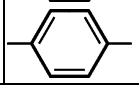
The majority of PABIs are amorphous, but show high resistance to acid and base agents and relatively high strength preserved at elevated and low temperatures [3]. Such properties of the copolymers are due to the presence of thermally stable benzimidazole rings, and amide groups in PABI macromolecules make the copolymers soluble in amide and other available organic solvents.

The relatively high structural regularity of the PABIs containing aliphatic (sebacic acid) fragments can be judged from the swellability in organic solvents (dioxane, MEK). Experimental data show that this copolymer considerably swells (to up to 100%) and partially dissolves upon heating. The Koenig hardness of the polymer is 0.54, i.e., it has a high surface strength and increased brittleness.

An increase in the length of aliphatic fragments in the polymer (sebacic acid residues) leads to a rise in its elasticity, as judged from the low hardness (0.045); the polymer is in the hyper-elastic state. Swelling in a solvent suggests its denser regular structure. After heating, the polymer loses solubility.

In PABI, there are elements of crystallinity, particularly clearly manifested at the equimolar ratio of

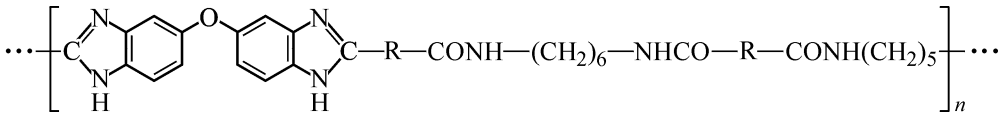
Properties of polyamidobenzimidazoles prepared at equimolar ratio of the starting monomers *

Polymer	–R–	η_r,** [η], d lg^{-1}	T_{soft}	T_{dec}	Solubility in indicated solvent					
			°C		H_2SO_4	HCOOH	tricresol	DMF	$C_6H_5CH_2OH$	glacial CH_3COOH
PBI	$-(CH_2)_4-$	6.36	250–260		S	S	PSH	SH	PS	PS
PCA	$-[NH(CH_2)_5CO]-$		210–230		S	S	S	–	SH	SH
PABI	$-(CH_2)_4-$	3.63, 3.48	205–215		S	S	SH	S	SH	SH
	$-(CH_2)_8-$	3.60, 3.30	190–200		S	S	SH	S	S	PS
		0.98, 0.93	265–275		S	S	SH	S	PS	PSH
		1.36, 1.31	325–335		S	S	PS	SH	IS	IS
PBI		1.18, 1.12	390–400		S	S	IS	SH	IS	IS

* (S) Fully soluble in the cold, (PS) partially soluble in the cold, (SH) fully soluble on heating, (PSH) partially soluble on heating, and (IS) insoluble.

** (η_r) Reduced viscosity of 0.5% solution of the polymer in HCOOH, 20°C.

the comonomers (Fig. 1). The degree of crystallinity increases upon replacement of adipic acid by sebacic acid, which is due to an increase in the chain length or, in the case of a terpolymer prepared using hexamethylenediamine along with CL as the amine-containing component, to the specific structure of the monomeric unit:



Whereas the polymer derived from 3,3',4,4'-tetraaminodiphenyl ether and diphenyl terephthalate has an amorphous structure, the copolymer prepared from the same monomers with the addition of ε-caprolactam at its mole fraction of 0.2 and above preserves, according to X-ray phase analysis, a highly organized fibrillar-crystalline structure. Moreover, in going from polycrystalline poly-ε-caproamide (degree of crystallinity ~40%) to PABI with a smaller content of lactam units, up to homopolybenzimidazole, the crystal lattice of the copolymers rearranges with the appearance of new crystalline formations (Fig. 2). The highest intensity is attained at the equimolar ratio of the starting monomers (degree of crystallinity 10–20%). Copolymers derived from diphenyl isophthalate and diphenyl phthalate are amorphous, and the degree of ordering of their molecules decreases as the mole fraction of CL units in the chain becomes smaller, as in the case of PABIs derived from aliphatic acids.

It is known that PBIs have high melting points, and some of them decompose without melting. This fact severely complicates their processing into items [4]. The appearance of crystalline areas in PABIs makes them more plastic and convenient for process-

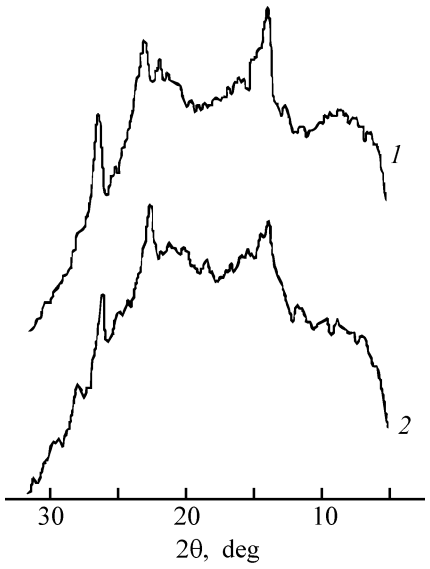


Fig. 1. X-ray diffraction patterns of PABI pre-pared at equimolar ratio of the monomers. (2θ) Bragg angle; the same for Fig. 2. (*1*) TADPE : DPS : CL and (*2*) TADPE : DPA : CL.

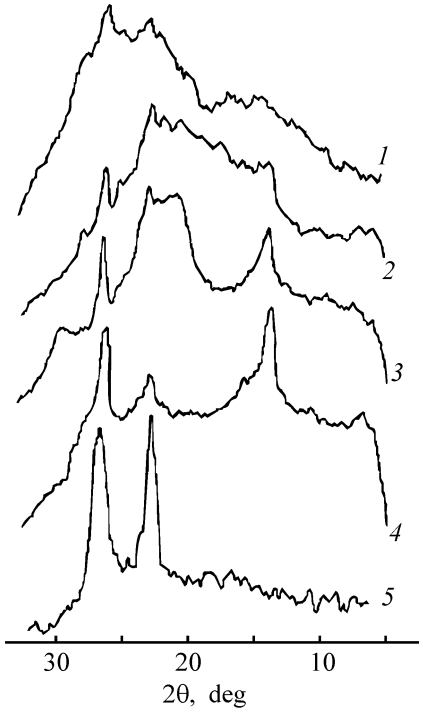


Fig. 2. X-ray diffraction patterns of (*1*) PBI TADPE : DPT, (*2–4*) PABIs TADPE : DPT : CL [molar ratios of comonomers: (*2*) 0.8 : 0.8 : 0.2, (*3*) 0.5 : 0.5 : 0.5, and (*4*) 0.2 : 0.2 : 0.8], and (*5*) PCA.

ing, compared to the corresponding PBIs. Polyamidobenzimidazoles have lower and more distinct melting points, especially the terpolymers whose macromolecule additionally contains six methylene groups. At the same time, they have relatively high decomposition points. The fabrication conditions and physicomechanical properties of compression samples based on PABI are described in [5].

CONCLUSIONS

(1) Polyamidobenzimidazoles with terephthalic acid residues in the macrochain show the highest crystallinity. They have a highly organized fibrillar-crystalline structure.

(2) In contrast to the corresponding commercial polybenzimidazoles, polyamidobenzimidazoles are more plastic and convenient in processing. At the same time, they preserve high decomposition points.

REFERENCES

1. Izyneev, A.A., Korshak, V.V., and Mazurevskaya, Zh.P., *Dokl. Akad. Nauk SSSR*, 1974, vol. 217, no. 3, pp. 585–588.
2. Khakhinov, V.V., Mazurevskaya, Zh.P., Mognonov, D.M., and Il'ina, O.V., *Zh. Prikl. Khim.*, 2001, vol. 74, no. 4, pp. 649–652.
3. Mognonov, D.M., Mazurevskaya, Zh.P., and Volodarskii, L.B., *Zh. Prikl. Khim.*, 2002, vol. 75, no. 3, pp. 481–484.
4. Vinogradov, S.V. and Vasnev, V.A., *Polikondensatsionnye protsessy i polimery* (Polycondensation Processes and Polymers), Moscow: Nauka/Interperiodica, 2000.
5. RF Patent 2022984, *Byull. Izobret.*, 1994, no. 21.

ISSN 1070-4272, Russian Journal of Applied Chemistry, 2008, Vol. 81, No. 8, pp. 1479–1481. © Pleiades Publishing, Ltd., 2008.
Original Russian Text © M.S. Salakhov, B.T. Bagmanov, V.S. Umaeva, M.I. Bagmanova, 2008, published in Zhurnal Prikladnoi Khimii, 2008, Vol. 81, No. 8, pp. 1404–1406.

BRIEF COMMUNICATION

Oxidative Bromination of Aniline and Its Derivatives

M. S. Salakhov, B. T. Bagmanov, V. S. Umaeva, and M. I. Bagmanova

Institute of Polymeric Materials, National Academy of Sciences of Azerbaijan, Sumgait, Azerbaijan

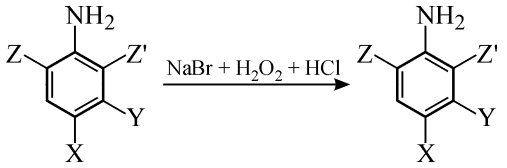
Received December 12, 2007

Abstract—Oxidative bromination of aniline and its derivatives containing various substituents (CH_3, Cl, NO_2, COOH) in *ortho*, *meta*, and *para* positions with a brominating mixture of NaBr (KBr) and 20–22% hydrogen peroxide in 6–8% hydrochloric acid at the molar ratio aniline : NaBr (KBr) : H_2O_2 : HCl = 1 : 3.5 : 3.2 : 4.5 is described.

DOI: 10.1134/S1070427208080314

Compounds containing nitrogen and bromine are effective antipyrenes used to prepare noncombustible polymeric materials [1, 2]. To compounds of this class belongs 2,4,6-tribromoaniline (TBA), which also finds use as a constituent of biologically active preparations, pharmaceuticals [3], and herbicides [4]. A variety of methods for preparing TBA have been described [4–8]. However, all these methods [2, 5] provide only a 15–50% yield of a product that requires additional purification.

This study is concerned with the development of a wasteless method for preparation of TBA and its derivatives by oxidative bromination of aniline with a mixture containing a brominating agent (potassium or sodium bromide) and 20–22% hydrogen peroxide in 6–8% hydrochloric acid at 15 ± 5°C for 2 h [8] by the scheme:



I–V, **XI–XIV** **II–X**, **XV–XVIII**

Z = Z' = X = Y = H (**I**), Z = Z' = X = Br, Y = H (**VI**); Z = Z' = X = H, Y = CH_3 (**II**), Z = Z' = X = Br, Y = CH_3 (**VII**); Z = Z' = X = H, Y = Cl (**III**), Z = Z' = X = Br, Y = Cl (**VIII**); Z = Z' = X = H, Y = NO_2 (**IV**), Z = Z' = X = Br, Y = NO_2 (**IX**); Z = Z' = X = H, Y = COOH (**V**), Z = Z' = X = Br, Y = COOH (**X**); Z = Z' = Y = H, X = NO_2 (**XI**), Z = Z' = X = Br, X = NO_2 (**XV**); Z = Z' = Y = H, X = COOH (**XII**), Z = Z' = X = Br, X = COOH (**XVI**); Z = Y = X = H, Z' = NO_2 (**XIII**), Z = Z' = X = Br, Z' = NO_2 (**XVII**); Z = Y = X = H, Z' = COOH (**XIV**), Z = Z' = X = Br, Z' = COOH (**XVIII**).

The reaction involved aniline and its *ortho*-, *meta*-, and *para*-substituted analogues containing various substituents (CH_3, Cl, NO_2, COOH). To determine the optimal conditions of oxidative bromination**,** we studied how the concentrations of hydrogen peroxide and hydrochloric acid and the molar ratio of the reagents affect the yield of tribromoaniline (TBA) for the example of aniline and its *m*-substituted derivatives.

The reaction was performed in hydrochloric acid at 15 ± 5°C in the course of 2 h.

In studying the influence exerted by the hydrogen peroxide concentration, a 20–22% aqueous solution at the molar ratio NaBr (KBr) : H_2O_2 : HCl = 1 : 3.5 : 3.2 : 4.5 was found to be the optimal.

Under these conditions, the yield of TBA reaches 99.9%. With concentration of the H_2O_2 aqueous solution raised to 25% or lowered to 16–18%, the TBA yield decreases to 86 and 90.2%, respectively.

The yield of TBA is the highest (99.9%0) at a hydrochloric acid concentration of 6–8%. Lowering the HCl concentration to 4% or raising it to 10% leads to a decrease in the TBA yield to 86 and 90.9%, respectively.

The influence exerted by the molar ratio of the reagents on the TBA yield in oxidative bromination of aniline was studied at NaBr(KBr) : 20–22% H_2O_2 : 6–8% HCl = 1 : 3 : 3 : 3, temperature of 15 ± 5°C, and reaction time of 2 h.

It was shown that, under the above conditions, the yield of TBA is 98%, whereas at a NaBr(KBr) : H_2O_2 : HCl molar ratio equal to 1 : 4.5 : 6.5 : 8.0, the TBA yield reaches 99.9%. At the same time, to use the latter ratio is unreasonable, because the same yield of TBA is

Characteristics of the compounds synthesized

Compound	Yield, %	mp, °C	R_f	Found / Calculation				
				C	H	Hal	N	Empirical formula
2,4,6-Tribromoaniline (**VI**)	99.9	122	0.56	21.80 / 21.75	1.35 / 1.30	72.60 / 72.72	4.28 / 4.28	$C_6H_4Br_3N$
3-Methyl-2,4,6-tribromoaniline (**VII**)	99.6	101	0.62	24.31 / 24.42	1.72 / 1.74	69.80 / 70.00	4.01 / 4.07	$C_7H_6Br_3N$
3-Chloro-2,4,6-tribromoaniline (**VIII**)	99.8	124	0.78	19.60 / 19.75	0.81 / 0.82	75.74 / 75.75	3.79 / 3.84	$C_6H_3Br_3ClN$
3-Nitro-2,4,6-tribromoaniline (**IX**)	95.0	102	0.69	18.98 / 19.20	0.61 / 0.80	63.88 / 64.00	7.12 / 7.47	$C_6H_3Br_3N_2O_2$
3-Carboxy-2,4,6-tribromoaniline (**X**)	98.0	170	0.71	22.30 / 22.46	1.00 / 1.07	64.07 / 64.17	3.67 / 3.74	$C_7H_4Br_3NO_2$
4-Nitro-2,6-dibromoaniline (**XV**)	93.0	195	0.70	24.00 / 24.32	1.11 / 1.35	53.78 / 54.05	9.05 / 9.45	$C_6H_4Br_2N_2O_2$
4-Carboxy-2,6-dibromoaniline (**XVI**)	95.0	330	0.72	28.12 / 28.47	1.51 / 1.69	54.00 / 54.24	4.48 / 4.74	$C_7H_5Br_2NO_2$
2-Nitro-4,6-dibromoaniline (**XVII**)	94.0	128	0.68	24.19 / 24.32	1.27 / 1.35	53.79 / 54.05	9.16 / 9.46	$C_6H_4Br_2N_2O_2$
2-Carboxy-4,6-dibromoaniline (**XVIII**)	95.0	76	0.76	28.10 / 28.48	1.53 / 1.70	53.87 / 54.10	4.51 / 4.74	$C_7H_5Br_2NO_2$

reached at a ratio NaBr(KBr) : H_2O_2 : HCl = 1 : 3.3 : 3.2 : 4.5.

m-Substituted TBAs containing electron-donating and electron-accepting substituents in the aromatic ring were obtained similarly. In all cases, *m*-substituted TBAs were isolated in quantitative yield and no additional purification was required. The characteristics of compounds **VI–X** are listed in the table.

The oxidative bromination of *o*- and *p*-substituted anilines differs from the bromination of *m*-substituted derivatives and depends on the electronic nature of substituents in the phenyl ring. It was found that, in *o*- and *p*-substituted anilines, substituents of the first kind (CH_3, –Cl) lead to black solid products. This shows that, in the course of oxidative bromination, molecules of *o*- and *p*-substituted anilines can take on a quinoid structure, which is facilitated by electron-donating substituents. The target products were not isolated.

With substituents of the second kind (COOH, NO_2), *o*- and *p*-substituted anilines undergo oxidative bromination under the optimal conditions without blackening of the reaction mass, with 2,4- and 2,6-dibromoanilines isolated as a target product. This confirms the decisive role of the electronic nature of the substituents in the stabilization of the aromatic nucleus in the course of oxidative bromination.

The structure of compounds **VI–X** and **XV–XVIII** was found from IR spectra, in which bands associated with stretching vibrations of the C–Br bond at 540–680 cm^{-1} were observed, and from a comparison of their physical parameters (melting point, elemental composition) with the known data [2, 3, 6, 8].

EXPERIMENTAL

The IR spectra of the compounds (suspensions in Vaseline oil) were recorded on an UR-20 spectrophotometer.

The purity R_f of the compounds was monitored by TLC on Silufol plates with spot development by UV light [9]. A mixture of benzene, dichloroethane, and acetic acid [benzene : dichloroethane : acetic acid = 4 : 1.5 : 1 (by volume)] served as eluent.

2,4,6-Tribromaniline VI. A flask was charged with 0.1 M of aniline and 0.45 M of 6% hydrochloric acid. To the reaction mixture was added dropwise under agitation 0.35 M of NaBr or KBr dissolved in 0.32 M of 20% hydrogen peroxide. The temperature was main-

tained within 15±5°C. Molar ratio aniline : NaBr(KBr) : H_2O_2 : HCl = 1 : 3.5 : 3.2 : 4.5**.** After addition of the brominating mixture was terminated, the flask was charged with 100 ml of water and the agitation was continued for another 1 h. The precipitated crystals were filtered off, washed with water to neutral reaction, and dried. The yield of TBA VI was 99.9%.

The oxidative bromination of *m*-substituted anilines **II–V** was performed similarly. *m*-Substituted tribromoanilines **VII–X** were isolated. Their characteristics are listed in the table.

Dibromo-substituted anilines XV–XVIII. The reaction was similar to that employed to obtain tribromoaniline**,** but with *p*-substituted anilines **XI**, **XII** and *m*-sub-stituted anilines **XII**, **XIV** used. The characteristics of dibromo derivatives **XV–XVIII** are listed in the table.

CONCLUSIONS

(1) Irrespective of the nature of a substituent in the phenyl ring, *m*-substituted anilines result in the formation of 2,4,6-tribromoanilines in high yield.

(2) Use of *o*- and *p*-substituted anilines with substituents of the second kind results in the formation of 2,4- or 2,6-dibromoanilines.

REFERENCES

1. Aseeva, R.M. and Zaikov, G.E., *Snizhenie goryuchesti polimernykh materialov* (Reducing the Combustibility of Polymeric Materials), Moscow: Znanie, 1981.
2. Gaevskii, B.D., Dorofeev, V.T., Matveeva, A.P., and Rilo, R.P., *Chemistry of 2,4,6-tribromoaniline*, VNIIiodobrom, Available from VINITI, Saki, no. 962.
3. Badische Anilin und Soda Fabrik, *Chem. Industrie J*., 1954, vol. 72, no. 5, pp. 965–968.
4. JPN patent 7521.
5. Golodnikov, G.V., and Mandel'shtam, T.V., Praktikum po organicheskomu sintezu (Practical Course of Organic Synthesis), Ogloblin, K.A., Ed., Leningrad: Len. Gos. Univ., 1976.
6. FRG Patent Appl. 2 723 137.
7. Snyder, H.R. and Geller, H.C., *J. Amer. Chem. Soc*., 1952, vol. 74, p. 2006.
8. USSR Inventor's Certificate, no. 1 398 346.
9. Akhrem, R.M. and Kuznetsova, A.I., *Tonkosloinaya khromatographiya* (Thin-Film Chromatography), Moscow: Nauka, 1964.

ISSN 1070-4272, Russian Journal of Applied Chemistry, 2008, Vol. 81, No. 9, pp. 1483–1486. © Pleiades Publishing, Ltd., 2008.
Original Russian Text © V.N. Lebedev, 2008, published in Zhurnal Prikladnoi Khimii, 2008, Vol. 81, No. 9, pp. 1409–1412.

INORGANIC SYNTHESIS AND INDUSTRIAL INORGANIC CHEMISTRY

Extraction of Oxalic Acid from Solutions of Electrolyte Mixtures

V. N. Lebedev

Tananaev Institute of Chemistry and Technology of Rare Elements and Mineral Raw Materials, Kola Scientific Center, Russian Academy of Sciences, Apatity, Murmansk oblast, Russia

Received November 8, 2007

Abstract—Extraction of oxalic acid with tributyl phosphate and triisoamyl phosphate from solutions of its mixtures with nitric, phosphoric, sulfuric, and hydrochloric acid and with ammonium nitrate and chloride was studied. In the extractability series, oxalic acid occupies the position between nitric and phosphoric acids, with sulfuric and hydrochloric acids acting as strong salting-out agents. Nitric acid salts drastically decrease the distribution ratios of oxalic acid.

DOI: 10.1134/S1070427208090012

Khibiny apatite concentrate remains the most important potential source of rare-earth elements (REE) in Russia [1]. Their concomitant recovery is possible in the nitric acid procedure for apatite processing into phosphorus fertilizers. However, involvement of this kind of raw materials into production is hampered, among other factors, by certain problems arising in processing of the recovered rare-earth phosphate concentrate. Primary purification to remove phosphorus is mainly performed by oxalate precipitation or extraction [2, 3]. The simplest variant of purification via oxalates is direct conversion into oxalates [4].

Because of high cost of oxalic acid, purification via oxalates should involve the regeneration of oxalic acid incorporated in REE oxalates by their treatment with an alkali [5]. The recovery of excess oxalic acid from mother liquors is not provided, although, along with economic aspects, one should take into account the environmental and economic consequences of the ingress of oxalate ions into production or waste solutions (MPC 2 mg g^{-1}).

In this study we examined the extraction of oxalic acid from solutions of electrolyte mixtures with the aim to evaluate the possibility of its utilization by extraction. For the extraction we used tributyl phosphate (TBP) and triisoamyl phosphate (TiAP), with dodecane as diluent. Preliminary experiments showed that oxalic acid is not noticeably extracted with higher alkanols. Extraction of oxalic acid from its straight aqueous solutions with TBP was studied by Allamuratov et al. [6]. We found no data on extraction in systems containing in the aqueous phase, along with oxalic acid, also mineral acids and their salts. Extraction of oxalic acid with triisoamyl phosphate was not studied either.

EXPERIMENTAL

Extraction was performed in a beaker at room temperature for 3 min with stirring. The phase separation in all the systems was good. Samples were taken after settling for 10 min. The salt composition of the aqueous solution was varied within the limits determined by the conditions of the conversion of phosphates into oxalates. The oxalic acid concentration was determined by titration with potassium permanganate, and the total acidity, by titration with alkali.

Experimental data on the extraction of oxalic acid with TBP and TiAP are given in Figs. 1 and 2. These data show that oxalic acid can be fully recovered with both neat and diluted extractants. The log–log plots of the distribution ratios D on the extractant concentration S (M) are straight lines with a slope close to 2, which suggests formation of the stable extractable complex $H_2C_2O_4 \cdot 2L$ (L = TiAP, TBP). The apparent extraction constant of oxalic acid is

$$K = D/([HC_2O_4^-]_{aq} S_{free}^2),$$

where $[HC_2O_4^-]_{aq}$ is the oxalic acid concentration in the equilibrium aqueous phase (M), and S_{free} is the free extractant concentration (M), which was 2–3 M in our experiments, i.e., it was by an order of mag-

Table 1. Distribution of oxalic acid in extraction of tributyl phosphate containing 20 vol % dodecane

Run no.	Initial solution concentration, M		Equilibrium concentration, M				D
	acid (salt)	$H_2C_2O_4$	$[H^+]_o$	$[H^+]_{aq}$	$[H_2C_2O_4]_o$	$[H_2C_2O_4]_{aq}$	
	HNO_3:						
1	–	0.33	0.31	0.15	0.23	0.1	2.3
2	0.5	0.24	0.41	0.56	0.18	0.06	3.0
3	1.0	0.33	0.61	0.82	0.23	0.1	2.3
4	2.0	0.33	0.97	1.53	0.17	0.16	1.1
5	3.0	0.33	1.37	2.35	0.12	0.22	0.54
	H_3PO_4:						
6*	0.5	0.33	0.76	1.43	0.22	0.11	2.0
7*	1.0	0.33	0.82	1.84	0.22	0.11	2.0
8	2.0	0.38	0.41	1.16	0.27	0.12	2.3
	H_2SO_4:						
9	1.07	0.24	0.41	2.24	0.18	0.06	3.0
10	2.0	0.26	0.46	4.08	0.22	0.04	5.5
	HCl:						
11	1.0	0.24	0.36	1.12	0.18	0.06	3.0
12	1.9	0.24	0.41	2.24	0.2	0.04	5.0
	NH_4NO_3:						
13	1.0	0.38	0.26	0.23	0.19	0.20	0.95
14	2.0	0.38	0.26	0.22	0.15	0.24	0.62
	NH_4Cl:						
15	1	0.38	0.25	0.22	0.25	0.14	1.7
16	2	0.38	0.24	0.21	0.25	0.14	1.7

* In run nos. 6 and 7, the aqueous phase also contained 1 M HNO_3.

nitude higher than that of nitric acid and by several orders of magnitude higher than those of sulfuric, hydrochloric, and phosphoric acids.

Data on extraction of oxalic acid with diluted TBP and TiAP from mixtures of electrolytes are given in Tables 1 and 2. To an oxalic acid solution we added nitric and phosphoric acids, whose presence is predetermined by the conditions of the conversion of REE phosphates into oxalates, and also, for comparison, sulfuric and hydrochloric acids and

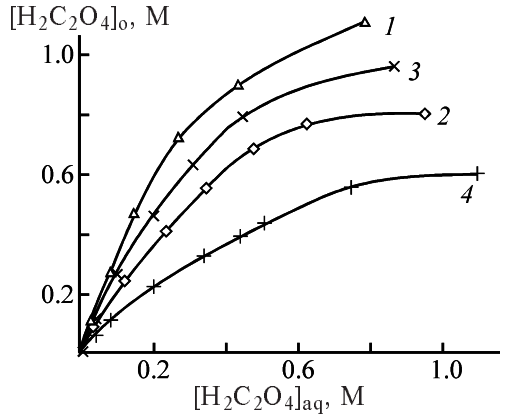


Fig. 1. Isotherms of oxalic acid extraction with (*1*, *2*) tributyl phosphate and (*3*, *4*) triisolamyl phosphate. Extractant content, vol %: (*1*, *3*) 100, (*2*) 80, and (*4*) 70. ($[H_2C_2O_4^-]_o$, $[H_2C_2O_4^-]_{aq}$) $H_2C_2O_4$ concentration in the organic and aqueous phases, respectively.

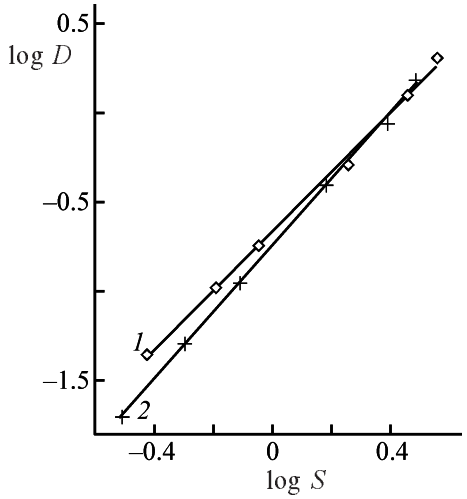


Fig. 2. log–log plot of the distribution ratio of oxalic acid D vs. extractant concentration S. (*1*) TBP and (*2*) TiAP.

Table 2. Distribution of oxalic acid in extraction with triisoamyl phosphate containing 30 vol % dodecane

Run no.	Initial solution concentration, M		Equilibrium concentration, M				D
	acid (salt)	$H_2C_2O_4$	$[H^+]_o$	$[H^+]_{aq}$	$[H_2C_2O_4]_o$	$[H_2C_2O_4]_{aq}$	
	HNO_3:						
1	–	0.33	0.2	0.2	0.19	0.14	1.3
2	0.5	0.33	0.35	0.56	0.19	0.14	1.3
3	1.0	0.33	0.46	0.92	0.20	0.13	1.5
4	2.0	0.33	0.71	1.73	0.13	0.2	0.64
5	3.0	0.33	0.97	2.45	0.08	0.25	0.3
	H_3PO_4:						
6*	0.5	0.33	0.48	1.43	0.19	0.14	1.4
7*	1.0	0.33	0.51	1.84	0.19	0.14	1.4
8	2.0	0.38	0.31	1.15	0.25	0.14	1.7
	H_2SO_4:						
9	0.5	0.24	0.20	1.38	0.18	0.06	3.0
10	1.0	0.24	0.2	2.14	0.2	0.04	5.0
	HCl:						
11	1.0	0.24	0.25	1.12	0.16	0.08	2.0
12	2.0	0.24	0.25	2.14	0.18	0.06	3.0
	NH_4NO_3:						
13	1.0	0.59	0.46	0.66	0.16	0.43	0.37
14	2.0	0.59	0.46	0.66	0.14	0.45	0.31
	NH_4Cl:						
15	1	0.38	0.25	0.2	0.19	0.19	1.0
16	2	0.38	0.25	0.2	0.2	0.18	1.2

* In run nos. 6 and 7, the aqueous phase also contained 1 M HNO_3.

ammonium nitrate and chloride. The distribution data are given for the binary mixtures with oxalic acid, except a ternary mixture containing phosphoric acid in a mixture with nitric acid. The extraction was performed at 1 : 1 ratio of the organic and aqueous phases.

As seen from Tables 1 and 2, relationships in the oxalic acid distribution in extraction with TBP and TiAP in the presence of electrolytes are similar. Nitric acid at its concentration of up to 1 M affects the extraction of oxalic acid insignificantly and even acts, to a small extent, as a salting-out agent. However, as the nitric acid concentration is increased, its distribution ratio increases also, and nitric acid starts to displace oxalic acid from the organic phase. Introduction of up to 3 M HNO_3 into the aqueous phase decreases the distribution ratios of oxalic acid by a factor of more than 4. Oxalic acid, on the contrary, exerted no salting-out effect on nitric acid.

Phosphoric acid only slightly affects the extraction, and in the ternary system containing 1 M H_3PO_4 and 1 M HNO_3 the distribution ratios of oxalic acid are relatively high.

Sulfuric and hydrochloric acids are poorly extracted with neutral extractants and therefore act as salting-out agents increasing the activity of oxalic acid. The distribution ratio of oxalic acid in the presence of these acids increases by a factor of more than 2.

Introduction of ammonium nitrate drastically decreases the extraction of oxalic acid because of the exchange decreasing the oxalic acid concentration:

$$2NH_4NO_3 + H_2C_2O_4 \rightleftarrows 2HNO_3 + (NH_4)_2C_2O_4,$$

with simultaneous extraction of the released nitric acid. In the presence of ammonium nitrate, the distribution ratio of nitric acid increases.

In the presence of ammonium chloride, the exchange occurs also and the concentration of oxalic acid decreases. However, the released hydrochloric acid exerts a salting-out effect, and as a result the oxalic acid extraction decreases only slightly.

Thus, oxalic acid recovery from electrolyte solutions by extraction with TBP and TiAP is quite feasible. The extracted oxalic acid can be readily

backwashed with an equivalent amount of aqueous ammonia, as ammonium oxalate is only slightly soluble in the extractant.

CONCLUSIONS

(1) The extraction of oxalic acid from a mixture of electrolytes with tributyl phosphate and triisoamyl phosphate was studied. Nitric acid at its concentration in the initial aqueous solution of up to 1 M exerts a weak salting-out effect on the extraction of oxalic acid, and at its higher concentrations nitric acid starts to displace oxalic acid from the organic phase. Phosphoric acid does not noticeably affect the extraction, whereas sulfuric and hydrochloric acids act as strong salting-out agents, increasing the distribution ratios of oxalic acid by a factor of more than 2. Nitric acid salts suppress the extraction of oxalic acid, and hydrochloric acid salts decrease its extraction slightly.

(2) The data on the oxalic acid distribution demonstrate the feasibility of oxalic acid utilization by extraction.

REFERENCES

1. Kosynkin, V.D., Shatalov, V.V., and Makarov, V.I., *Metally*, 2001, no. 1, pp. 35–41.
2. Kogan, B.I. and Skripka, I.P., in *Redkie elementy* (Rare Elements), Moscow: IMGRE, 1973, issue 8, pp. 3–58.
3. Kosynkin, V.D., Shatalov, V.V., Selivanovskii, A.K., et al., *Khim. Tekhnol.*, 2001, no. 1, pp. 27–36.
4. Lebedev, V.N. and Sergeeva, S.D., *Khim. Tekhnol.*, 2002, no. 11, pp. 29–33.
5. Yagodin, G.A., Sinegribova, O.A., and Chekmarev, A.M., *Tekhnologiya redkikh metallov v atomnoi tekhnike* (Rare Metal Technology in Atomic Engineering), Moscow: Atomizdat, 1974.
6. Allamuratov, D., Rakhimov, Kh.R., and Bogdanova, G.V., *Vestn. Kara-Kalpak. Filiala Akad. Nauk Uzb. SSR*, 1967, no. 2(28), pp. 24–27.

ISSN 1070-4272, Russian Journal of Applied Chemistry, 2008, Vol. 81, No. 9, pp. 1487–1491. © Pleiades Publishing, Ltd., 2008.
Original Russian Text © T.I. Markovich, 2008, published in Zhurnal Prikladnoi Khimii, 2008, Vol. 81, No. 9, pp. 1413–1417.

INORGANIC SYNTHESIS AND INDUSTRIAL INORGANIC CHEMISTRY

Kinetics of Iron(II) Oxidation in Pyrrhotine Leaching with Acid Sulfate Solutions in the Presence of Nitrous Acid

T. I. Markovich

Institute of Geology and Mineralogy, Siberian Branch, Russian Academy of Sciences, Novosibirsk, Russia

Received September 10, 2008

Abstract—Variation of the ratio between the concentrations of Fe^{2+} and Fe^{3+} ions in leaching of pyrrhotine with acid sulfate solutions containing HNO_2 was studied for the example of the oxidation of iron(II) with molecular oxygen, which widely occurs in the nature and is widely used in hydrometallurgy.

DOI: 10.1134/S1070427208090024

According to modern concepts, oxidative leaching of iron sulfides in acid media is not limited to only a topochemical reaction, but may also include multistep reaction between molecular oxygen and solutions of iron(II) salts [1, 2].

One of methods for raising the rate of this process is to use activating agents, nitrogen compounds (oxides, nitrates, nitrites, etc.) [3–6]. The mechanism of catalysis is rather complex and has not been elucidated so far. In the course of oxidation, quite a number of species (NO, N_2O_3, NO_2, N_2O_4, HNO_2, NO_2^-, HNO_3, NO_3^-, NO^+, NO_2^+) with widely different activating capacities can be formed in various amounts and disappear. According to numerous experimental studies, nitrous acid and products of its dissociation are the most kinetically reactive species. As shown in [4, 6], the activating effect of HNO_2 at low concentrations (<1 M) exceeds severalfold the catalytic activity of all other oxygen compounds of nitrogen.

Another way to accelerate the oxidation of Fe^{2+} is based on passing from the homogeneous mechanism of activation of molecular O_2 to a heterogeneous mechanism based on the capacity of a number of solid substances to absorb dissolved oxygen on active centers of their surface [7].

This study is concerned with the behavior of iron(II) in the system $Fe_{0.88}S + H_2O + H_2SO_4 + O_2 + HNO_2$ in decomposition of the solid sulfide phase that can chemisorb dissolved oxygen [8].

EXPERIMENTAL

We studied the kinetics of Fe^{2+} oxidation in sulfuric acid solutions containing nitrous acid in parallel with an analysis of the process of pyrrhotine breakdown. For this purpose, we used polydisperse samples (53–74-μm fraction) of the selective pyrrhotine concentrate from the Norilsk deposit, which contained, according to the results of an X-ray phase analysis, 93.2% $Fe_{0.88}S$, 1.5% $CuFeS_2$, and 4.5% SiO_2.

A weighed portion of the sulfide was leached under temperature control and continuous agitation with an upper drive in a closed reaction vessel equipped with a sampler with a finely porous filter, a batcher for an activating solution, and a system for delivery and discharge of gases, which provided oxygen supply to the reaction zone at a pressure of 1 atm. Nitrous acid was produced by the reaction

$$2NaNO_2 + H_2SO_4 = 2HNO_2 + Na_2SO_4, \quad (1)$$

by batching a sodium nitrite solution directly into the reaction pulp at prescribed intervals of time. The catalyst supply mode was developed with account of the occurrence of concurrent processes in the oxidizing system and made it possible to maintain the concentration of nitrous acid at a level as close as possible to the prescribed value of 0.001 M.

The initial concentration of sulfuric acid in the solution, $c^0_{H_2SO_4}$, was varied from 0.25 to 1.02 M, and the temperature of the experiment, in the range 293–333 K. The concentration of nitric acid (0.001 M), angular velocity of stirrer rotation (ω = 168 s^{-1}), and oxygen pressure ($P_{O_2} = 1.01 \times 10^5$ Pa) were maintained constant in all the experiments. The s : l ratio was 1 : 100 (2 g of the sulfide per 200 ml of the solution).

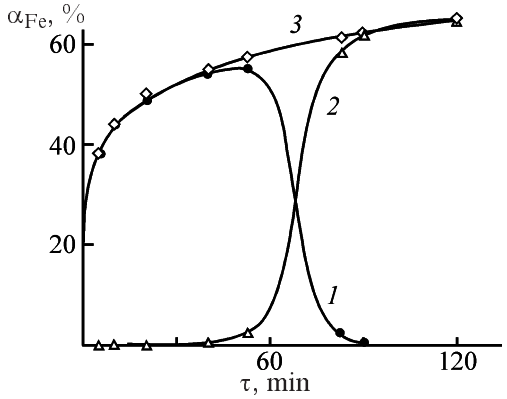


Fig. 1. Kinetic curves describing the degree of recovery, α_{Fe}, of (*1*) Fe^{2+} and (*2*) Fe^{3+} ions and (*3*) total iron (Fe^{2+} + Fe^{3+}) into solution in pyrrhotine leaching at $c_{H_2SO_4}$ = 0.51 M. T = 298 K, ω = 168 s^{-1}, P_{O_2} = 1.01 × 10^5 Pa, c_{HNO_2} = 0.001 M; the same for Fig. 2. (τ) Time.

We analyzed the solutions for the content of iron ions by complexometric titration [9]. We used standard methods for calculating the main process parameters (activation energy, reaction orders with respect to reagents) [10].

It has been shown previously [11] that pyrrhotine leaching in an acid sulfate–nitrite medium occurs in two successive steps with rapid (first step, up to 10 min) and slow (second step, from 10 to 120 min) dissolution. The observed nature of the process is possibly due to a change of the leaching mechanism from nonoxidative to give hydrogen sulfide to oxidative:

$$FeS + H_2SO_4 = FeSO_4 + H_2S, \quad (2)$$

$$FeS + 2HNO_2 + H_2SO_4 + O_2 = FeSO_4 + 2NO_2 + S^0 + 2H_2O. \quad (3)$$

The decrease in the process rate is probably due to formation of a film of difficultly soluble compounds (iron oxides, elementary sulfur) on the reaction surface [11].

The manner in which the content of Fe^{2+} and Fe^{3+} ions in solution varies in the course of pyrrhotine decomposition is shown in Fig. 1. A similar shape of kinetic curves was observed for all the experimental conditions. It should be noted that, in all the experiments, iron(III) ions appeared only in the second, slow step of sulfide leaching, after the degree of breakdown of the solid phase reached nearly 80% of its maximum value for the given conditions.

The absence of iron(III) in the system in the initial, rapid step is probably due to occurrence of competing processes

$$2FeSO_4 + 2HNO_2 + H_2SO_4 + O_2 = Fe_2(SO_4)_3 + 2NO_2 + 2H_2O, \quad (4)$$

$$H_2S + Fe_2(SO_4)_3 = 2FeSO_4 + S^0 + H_2SO_4. \quad (5)$$

Apparently, reaction (5) predominates over (4) until the main part of hydrogen sulfide is oxidized to elemental sulfur or sulfuric acid:

$$2H_2S + O_2 = 2S^0 + 2H_2O, \quad (6)$$

$$H_2S + 2HNO_2 = 2NO + S^0 + 2H_2O, \quad (7)$$

$$H_2S + 2O_2 = H_2SO_4, \quad (8)$$

$$2H_2S + 4HNO_2 + 3O_2 = 4NO + 2H_2SO_4 + 2H_2O. \quad (9)$$

According to Blyumberg and co-workers [12], the liquid-phase oxidation of hydrogen sulfide with molecular oxygen is substantially accelerated in the presence of nitric acid. A new ion–radical mechanism of catalysis is suggested, in which the nitrosonium ion NO^+ generated in the system in secondary oxidation of products formed in HNO_3 decomposition is the process-activating agent. The probability of occurrence of reactions (6)–(9) in the oxidizing system under study, which contains nitrous acid, a stronger source of NO^+ ($HNO_2 \rightleftarrows NO^+ + OH^-$), is very high.

We took as a factor characterizing the rate of Fe^{2+} conversion into Fe^{3+} the quantity inverse to the time τ_{eq} in which the concentrations of the oxidized and reduced forms of iron reached the same value: $1/\tau_{eq}$. When determining the kinetic parameters of the process (reaction order with respect to sulfuric acid and activation energy), we took into account that the following changes occur in the system during the first stage: the solution acidity decreases by reaction (1) and the Fe^{2+} concentration unevenly increases by the beginning of the second stage.

We calculated the content of sulfuric acid in the system (at τ = 10 min) for each experiment by the kinetic equation of pyrrhotine leaching, according to which the process rate linearly increases with the acidity of the medium [11] (Table 1).

Based on published data on oxidation of iron(II) salts with molecular oxygen in acid sulfate solutions

[13, 14] (including that involving nitrous acid [6] and that in the presence of a solid phase, activated carbon [7]), we suggested that, in experiments at a substantial, 2–14-fold excess of H_2SO_4, the rate of the reaction under study linearly depends on the initial content of Fe^{2+} ions in solution.

In this case, the rate equation describing the oxidation of iron(II) ions takes the form

$$1/\tau_{eq} = kc_{Fe^{2+}}c^n_{H_2SO_4}, \quad (10)$$

where $c_{Fe^{2+}}$ and $c_{H_2SO_4}$ are the concentrations of iron(II) ions and sulfuric acid, respectively, at the beginning of the second stage (τ = 10 min) (M); n, reaction order with respect to sulfuric acid; and k, an empirical constant.

The experimental results of a study of how the solution acidity affects the variation of the concentrations of oxidized (Fe^{3+}) and reduced (Fe^{2+}) forms of iron in the course of pyrrhotine decomposition are listed in Table 1. An increase in the H_2SO_4 concentration from 0.22 to 0.95 M makes the oxidation process slower and the time τ_{eq} in which equal concentrations are reached by a factor of 2.4 longer.

In the log–log coordinates, the resulting dependence (Fig. 2) has the form

$$\log(1/\tau_{eq}) - \log c_{Fe^{2+}} = -1.09\log c_{H_2SO_4} - 0.92. \quad (11)$$

Thus, the reaction order n with respect to sulfuric acid is, with account of the corrections described above, -1.1 ± 0.1.

A similar result was described in [6, 13, 14]. An analysis of a rather complex kinetic equation describing a vast body of experimental data [14] demonstrated that a higher acid concentration hinders oxidation of iron(II) in sulfate media and accelerates it in chloride media, which is due to the increased reactivity of $FeSO_4^+$ complexes.

It should be noted that the presence of activated carbon strongly changes the kinetics and mechanism of the process [7]. The decelerating effect of sulfuric acid is only manifested starting from a certain instant of time (under conditions of blocking of centers at the reaction surface by hydroxonium and hydrosulfite ions), when liquid-phase oxidation of iron(II) predominates in the heterogeneous system. At H_2SO_4 concentrations in the range from the initial concentration to 1.5–2 M (value dependent on the state of the surface of the solid phase), the topochemical reaction predominates and the process rate linearly grows with the solution acidity.

Table 1. Effect of the initial concentration of sulfuric acid, $c^0_{H_2SO_4}$, on the pyrrhotine leaching in acid sulfate–nitrite solutions* (c_{HNO_2} = 0.001 M, T = 293 K, P_{O_2} = 1.01×10^5 Pa)

$c^0_{H_2SO_4}$, M	$c_{H_2SO_4}$, M	α_{Fe}, %	$c_{Fe^{2+}}$, M	τ_{eq}, min	$1/\tau_{eq}$, min^{-1}
0.25	0.22	29	0.034	47	0.021
0.51	0.46	44	0.050	68	0.015
0.75	0.67	50	0.056	96	0.010
1.02	0.95	60	0.067	113	0.009

* $c_{H_2SO_4}$, $c_{Fe^{2+}}$, and α_{Fe} are, respectively, the concentrations of H_2SO_4 and Fe^{2+} ions and degree of recovery of total iron (Fe^{2+} + Fe^{3+}) into solution at the beginning of the second stage (τ = 10 min); τ_{eq} is the time in which equal concentrations of Fe^{2+} and Fe^{3+} are reached.

We studied the effect of temperature on the rate of Fe^{2+} conversion to Fe^{3+} in two modes at different initial H_2SO_4 concentrations of 0.25 and 1.02 M. The results obtained are listed in Table 2. Raising the temperature from 293 to 333 K accelerates the oxidation process and makes shorter the time τ_{eq} in which equal concentrations are reached by factors of 4.7 and 5.6 at the minimum and maximum solution acidities, respectively.

In the temperature range under study, the increase in the oxidation rate of iron(II) ions is described in the general form in the Arrhenius coordinates at the sulfuric acid concentrations specified

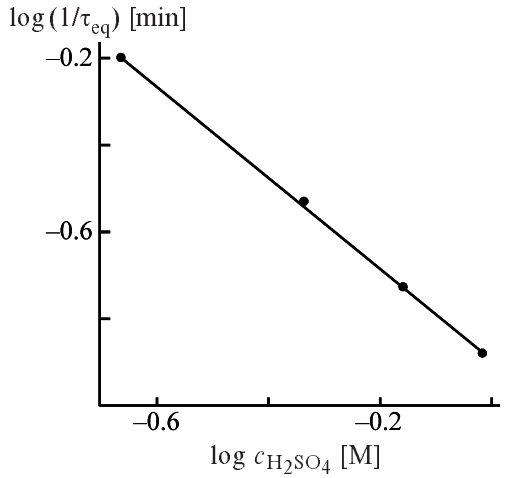


Fig. 2. Logarithm $\log(1/\tau_{eq})$ of the oxidation rate of Fe^{2+} ions (for explanations, see text) vs. the sulfuric acid concentration $c_{H_2SO_4}$. (τ_{eq}) Time in which equal concentrations of Fe^{2+} and Fe^{3+} are reached; the same for Fig. 3.

Table 2. Effect of temperature on the pyrrhotine leaching at different initial concentrations of sulfuric acid H_2SO_4 (c_{HNO_2} = 0.001 M, T = 293 K, P_{O_2} = 1.01×10^5 Pa)

T, K	$c_{H_2SO_4}$,* M	τ_{eq}, min	$1/\tau_{eq}$, min^{-1}	α_{Fe}, %	$c_{Fe^{2+}}$, M	s : l**
293	0.219/0.940	47/113	0.021/0.009	27/70	0.031/0.080	1.46 : 200/0.60 : 200
303	0.207/0.936	28/68	0.036/0.015	38/74	0.043/0.084	1.24 : 200/0.52 : 200
318	0.189/0.929	16/36	0.062/0.028	54/80	0.061/0.091	0.92 : 200/0.40 : 200
333	0.171/0.923	10/20	0.010/0.050	70/85	0.079/0.097	0.60 : 200/0.30 : 200

* Numerator, $c^0_{H_2SO_4}$ = 0.25 M; denominator, $c^0_{H_2SO_4}$ = 1.02 M.
** The s : l ratio by the beginning of the second step of leaching.

above by the equation

$$1/\tau_{eq} = k_1 c_{Fe^{2+}} (c_{H_2SO_4})^{-1.1} \exp(-E_a/RT), \quad (12)$$

where E_a is the activation energy (kJ mol^{-1}); R, gas constant (J mol^{-1} K^{-1}); T, temperature (K); and $k_1 = k/[\exp(-E/RT)]$.

Having transformed Eq. (12) to the logarithmic form, we obtained for different initial H_2SO_4 concentrations the following expressions:

$$\ln(1/\tau_{eq}) - \ln c_{Fe^{2+}} + 1.1 \ln c_{H_2SO_4} = -801.8/T + 0.7 \quad (13)$$

at $c^0_{H_2SO_4}$ = 0.25 M, and

$$\ln(1/\tau_{eq}) - \ln c_{Fe^{2+}} + 1.1 \ln c_{H_2SO_4} = -3679.0/T + 10.3 \quad (14)$$

at $c^0_{H_2SO_4}$ = 1.02 M.

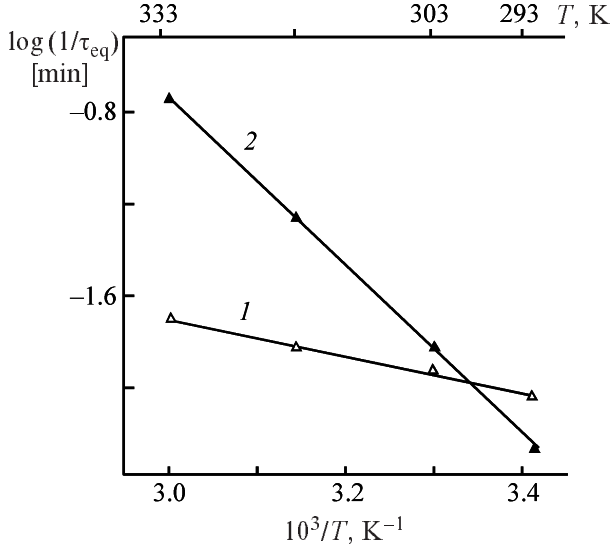


Fig. 3. Logarithm $\log(1/\tau_{eq})$ of the oxidation rate of Fe^{2+} ions vs. temperature T at different initial H_2SO_4 concentrations. ω = 168 s^{-1}, c_{HNO_2} = 0.001 M, P_{O_2} = 1.01×10^5 Pa; $c^0_{H_2SO_4}$, M: (*1*) 0.25 and (*2*) 1.02.

The thus determined effective activation energies of the process under study are 7±5 [Eq. (13)] and 31±5 [Eq. (14)] kJ mol^{-1}.

The strong differences between the E_a values obtained are possibly due to different contents of the solid phase of pyrrhotine in the system at the beginning of the second step of leaching (Table 2) (provided that the assumption of a linear dependence of the process rate on $c_{Fe^{2+}}$ is correct). The s : l ratio at $c^0_{H_2SO_4}$ = 0.25 M exceeds the corresponding value at $c^0_{H_2SO_4}$ = 1.02 M by a factor of 2.

It should be emphasized that, in the case of homogeneous oxidation of iron(II) ions under similar conditions (in acid sulfate solutions in the presence of nitrous acid), the effective activation energy of the process is even higher, 59 kJ mol^{-1} [6].

The considerable changes in the kinetics of Fe^{2+} to Fe^{3+} conversion in the presence of activated carbon in the system confirm the possibility of oxidation of iron(II) ions with molecular oxygen in sulfate media not only in solution, but also at the surface of the solid phase [7].

Thus, our experimental data indicate that the surface of the sulfide phase affects the kinetics of Fe^{2+} oxidation.

CONCLUSIONS

(1) Iron(II) ions are oxidized with molecular oxygen in pyrrhotine leaching in acid sulfate solutions in the presence of nitrous acid only in the second, slow step of the process, after the degree of decomposition of the solid phase reaches nearly 80% of the maximum value for the given conditions.

(2) The absence of Fe^{3+} ions in the system in the first step results from their reduction to the initial state with hydrogen sulfide, a product of nonoxidative leaching of pyrrhotine.

(3) In the presence of the solid sulfide phase, Fe^{2+} ions are oxidized to Fe^{3+} in the system under study with a substantially lower energy expenditure.

REFERENCES

1. Tyutyunova, F.I., *Gidrogeokhimiya tekhnogeneza* (Hydrogeochemistry of Technogenesis), Moscow: Nauka, 1987.
2. Klushin, D.N., Reznik, I.D., and Sobol', S.I., *Primenenie kisloroda v metallurgii* (Use of Oxygen in Metallurgy), Moscow: Metallurgiya, 1983.
3. Zyatkovskii, V.M., Filippov, A.P., Belousov, V.M., et al., *Ukr. Khim. Zh.*, 1977, no. 9, pp. 989–991.
4. Baldwin, S.A. and Van Weert, G., *Hydrometallurgy*, 1996, vol. 42, pp. 209–219.
5. Filippov, A.P., Nesterov, Yu.V., Smyshlyaev, V.Yu., et al., *Khim. Tekhnol.*, 2002, no. 6, pp. 30–33.
6. Shivrin, G.N., Kolmakov, A.A., and Polyakov, M.L., *Izv. Vyssh. Uchebn. Zaved., Tsvetn. Metall.*, 1980, no. 6, pp. 42–45.
7. Thomas, G. and Ingraham, T.R., in *Int. Symp. on Hydrometallurgy*, Chicago (USA): AIMME, 1973, pp. 67–69.
8. Ioffe, P.A. and Shneerson, Ya.M., *Dokl. Akad. Nauk SSSR*, 1981, vol. 258, no. 2, pp. 397–399.
9. Umland, F., Janssen, A., Thierig, D., and Wünsch, G., *Theorie und praktische Anwendung von Komplexbildnern*, Frankfurt am Main: Akademische, 1971.
10. Kakovskii, I.A. and Naboichenko, S.S., *Termodinamika i kinetika gidrometallurgicheskikh protsessov* (Thermodynamics and Kinetics of Hydrometallurgical Processes), Alma-Ata: Nauka, 1986.
11. Markovich, T.I., *Khim. Inter. Ustoich. Razv.*, 2005, vol. 13, pp. 541–550.
12. Blyumberg, E.A., Bulygin, M.G., and Son, S.B., *Khim. Fiz.*, 1995, vol. 14, no. 10, pp. 9–14.
13. Sysoeva, V.V. and Nikishova, N.I., *Zh. Prikl. Khim.*, 1971, vol. 44, no. 11, pp. 2436–2441.
14. Nikishova, N.I., Rotinyan, A.L., and Sysoeva, V.V., *Zh. Prikl. Khim.*, 1974, vol. 47, no. 10, pp. 2228–2232.

ISSN 1070-4272, Russian Journal of Applied Chemistry, 2008, Vol. 81, No. 9, pp. 1492–1496. © Pleiades Publishing, Ltd., 2008.
Original Russian Text © D.A. Savchenko, V.A. Kopilevich, L.V. Voitenko, 2008, published in Zhurnal Prikladnoi Khimii, 2008, Vol. 81, No. 9, pp. 1418–1422.

INORGANIC SYNTHESIS AND INDUSTRIAL INORGANIC CHEMISTRY

Zinc Cadmium Ammine Aqua Monophosphate and Its Thermal Transformations

D. A. Savchenko, V. A. Kopilevich, and L. V. Voitenko

National Agrarian University, Kiev, Ukraine

Received January 30, 2008

Abstract—Synthesis of amorphous zinc cadmium ammine aqua monophosphates $Zn_{3-x}Cd_x(PO_4)\cdot 2n(NH_3)\cdot m(H_2O)$ (x = 0.6–2.4, n = 1.3–3.1, m = 2.3–3.4) with variable molar ratio of the cations is described. The sequence of thermal transformations of compound $[Zn_{1.5}Cd_{1.5}(NH_3)_{1.4}(H_2O)_{3.2}(PO_4)_2]$ with equimolar ratio of cations is studied, and schemes of its transformation into the crystalline zinc cadmium monophosphate $Zn_{1.5}Cd_{1.5}(PO_4)_2$ are suggested.

DOI: 10.1134/S1070427208090036

Phosphates of divalent metals find expanding application as materials for modern engineering [1]. It is known that cadmium phosphates $CdHPO_4$, $Cd_3(PO_4)_2$, $Cd_2P_2O_7$, and $Cd(PO_3)_2$ and zinc phosphates $Zn_3(PO_4)_2$, $Zn_2P_2O_7$, $Zn(PO_3)_2$, $Zn(PO_3)_2\cdot Cd(PO_3)_2$, $Zn(PO_3)_2\cdot Mg(PO_3)_2$, $Zn_3(PO_4)_2\cdot 4H_2O$, and $Zn(H_2PO_4)_2$ are used for preparing phosphors, special glass, and catalysts for organic synthesis [1–14]. Their performance is frequently determined by the composition and thermal stability. Scientific statistics in the field of chemistry of phosphates [1] shows that the number of new phosphate engineering materials has noticeably increased as the nomenclature of phosphor compounds was expanded and the technology of their preparation was improved. In this connection, of special interest are crystalline and amorphous heterometallic [5] and mixed-anion phosphates which seem to have a wider spectrum of useful technological properties.

EXPERIMENTAL

Zinc cadmium ammine aqua monophosphate was isolated from an aqueous ammonia solution by precipitation with acetone [15], using as starting reactants $Zn_3(PO_4)_2\cdot 4H_2O$ synthesized according to [16] and $Cd_3(PO_4)_2\cdot 5H_2O$ synthesized according to [2].

The content of zinc and cadmium in the compounds synthesized was determined by stripping chronopotentiometry [17], that of phosphorus, by gravimetry [18], and that of ammonia, by distillation on a Seren'ev's apparatus [18]. The total content of water and ammonia was determined by the weight loss on heating to 750°C for 2 h [18].

The IR spectra were taken on a Specord 75-IR spectrophotometer. Samples of compounds to be analyzed were prepared in the form of KBr pellets in which the concentration of the substance under study was 0.2–0.3 wt %. The X-ray phase analysis was carried out on a DRON-UM1 diffractometer (CuK_α radiation). A single crystal of graphite placed in the diffracted beam was used as a monochromator. The diffraction patterns were taken in the step scanning mode in the range of angles 2θ = 4°–80°. The scanning step was 0.05°, and the exposure time in a point, 3–9 s. The measured diffraction maxima were approximated by a pseudo-Voight function, with the K_{α_1} component singled out. The unit cell parameters were calculated by the known procedure [19]. Qualitative and quantitative anionic composition of all intermediate and final products of heating was determined by paper chromatography [20].

Thermal transformations of zinc cadmium ammine aqua monophosphates were studied by thermal analysis on a Q-1500D derivatograh. Samples were heated in air in the range 15–900°C up to termination of weight loss. The experiment with the dynamic heating mode was carried out using platinum cylindrical crucibles with lids; the weighed portion of a compound was 0.500 g. Final and all intermediate heating products were obtained at a heating rate of 5 deg min^{-1}.

Table 1. Composition of zinc cadmium ammine aqua monophosphates

ZnO : CdO molar ratio in starting mixture	Content in products, %					Product composition
	ZnO	CdO	P_2O_5	NH_3	H_2O	
0.6 : 2.4	8.38	52.92	24.41	3.88	10.44	$Zn_{0.6}Cd_{2.4}(PO_4)_2 \cdot 1.3NH_3 \cdot 3.4H_2O$
1.2 : 1.8	17.46	41.31	25.37	5.76	10.15	$Zn_{1.2}Cd_{1.8}(PO_4)_2 \cdot 1.9NH_3 \cdot 3.2H_2O$
1.5 : 1.5	22.72	35.79	26.38	4.52	10.68	$Zn_{1.5}Cd_{1.5}(PO_4)_2 \cdot 1.4NH_3 \cdot 3.2H_2O$
1.8 : 1.2	27.28	28.68	26.43	8.54	9.05	$Zn_{1.8}Cd_{1.2}(PO_4)_2 \cdot 2.7NH_3 \cdot 2.7H_2O$
2.4 : 0.6	38.47	15.25	27.93	10.19	8.19	$Zn_{2.4}Cd_{0.6}(PO_4)_2 \cdot 3.1NH_3 \cdot 2.3H_2O$

To obtain zinc cadmium ammine aqua monophosphates, we took weighed portions of $Zn_3(PO_4)_2 \cdot 4H_2O$ and $Cd_3(PO_4)_2 \cdot 5H_2O$ corresponding to a specified ZnO:CdO molar ratio in the starting mixture and dissolved them in concentrated aqueous ammonia. The resulting solution was poured into acetone. In so doing, two liquid phases formed. Then the upper phase was decanted, and the bottom phase looking like a transparent oily film was left to crystallize in air at 20–25°C to constant weight.

The compositions of thus isolated compounds are given in Table 1. We found that the ZnO : CdO molar ratio in the starting mixtures of monophosphates was identical to that of the components in the synthesized products.

X-ray phase analysis shows that the initial zinc and cadmium monophosphates are crystalline, whereas zinc cadmium ammine aqua monophosphates synthesized on their basis are X-ray amorphous irrespective of their composition (Table 1).

The IR spectra of the zinc cadmium ammine aqua monophosphates under study are practically identical to each other and contain several groups of absorption bands. For example, a strong broad absorption band corresponding to stretching vibrations of water and coordinated ammonia molecules in the range 3435–2485 cm^{-1} is observed in the IR spectra of $Zn_{1.5}Cd_{1.5}(PO_4)_2 \cdot 1.4NH_3 \cdot 3.2H_2O$ (Fig. 1, curve *1*) and products of its heating to 208 and 343°C (Fig. 1, curves *2* and *3*). As the temperature and, correspondingly, the water and ammonia loss increase, the intensity of this band decreases. In the IR spectrum of the product of heating to 392°C (Fig. 1, curve *4*), this band is ill-defined, and in the final product of heating to 710°C it is absent (Fig. 1, curve *5*). The absorption bands corresponding to bending vibrations of water and ammonia molecules are located in the range 1600–1560 cm^{-1}. In the range 1485–1360 cm^{-1}, a maximum is detected, which corresponds to bending vibrations of ammonia molecules coordinated by metal ions and forming a stable hydrogen bond with presumably possible proton transfer to the phosphate anion [21]. It should be noted that maxima observed in the range 1250–1220 cm^{-1} correspond only to symmetric bending vibrations of coordinated ammonia [22]. The absorption bands corresponding to asymmetric and symmetric stretching vibrations of the PO_4^{3-} group are located in the range 1060–735 cm^{-1}. Absorption bands at 655–540 cm^{-1} in the spectra of samples taken at elevated temperatures belong to vibrations of the P–O–P and O–P–O groups.

Thus, the IR spectra suggest that the synthesized zinc cadmium ammine aqua monophosphates contain coordinated ammonia molecules rather than ammonium ions, which is also proved by the chem-

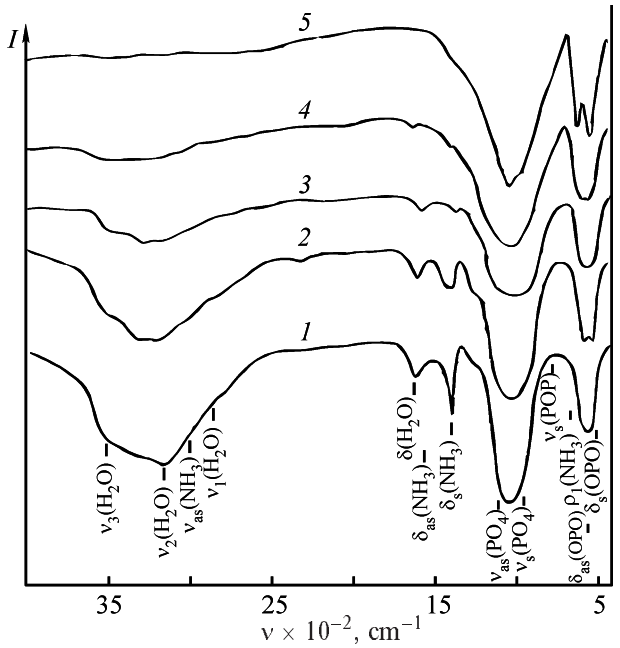


Fig. 1. IR spectra of (*1*) initial $Zn_{1.5}Cd_{1.5}(PO_4)_2 \cdot 1.4NH_3 \cdot 3.2H_2O$ and products of its heating to (*2*) 208, (*3*) 448, (*4*) 508, and (*5*) 710°C. (*I*) Intensity and (ν) wavenumber.

Table 2. Variation in the composition of zinc cadmium ammine aqua monophosphate during thermolysis

T, °C	Product composition by chemical analysis	P_2O_5 distribution, rel %		Loss, mol	
		PO_4^{3-}	$P_2O_7^{4-}$	NH_3	H_2O
15	$1.5ZnO \cdot 1.5CdO \cdot P_2O_5 \cdot 1.4NH_3 \cdot 3.2H_2O$	100	–	0	0
208	$1.5ZnO \cdot 1.5CdO \cdot P_2O_5 \cdot 0.7NH_3 \cdot 0.6H_2O$	100	–	0.70	2.60
448	$1.5ZnO \cdot 1.5CdO \cdot P_2O_5 \cdot 0.2NH_3 \cdot 0.03H_2O$	84.57	15.43	1.20	3.17
508	$1.5ZnO \cdot 1.5CdO \cdot P_2O_5 \cdot 0.1NH_3 \cdot 0.02H_2O$	89.28	10.72	1.32	3.18
710	$1.5ZnO \cdot 1.5CdO \cdot P_2O_5$	100	–	1.40	3.20

ical analysis including the molar ratio (ZnO + CdO) : P_2O_5 = 3 : 1.

The temperature ranges of the removal of volatile components from zinc cadmium ammine aqua monophosphates and the ranges of separate process steps, on the whole, coincide. Thermal transformations were studied in more detail for $Zn_{1.5}Cd_{1.5} \cdot (PO_4)_2 \cdot 1.4NH_3 \cdot 3.2H_2O$ (compound **I**) with an equimolar ratio of the metals as example.

Thermal analysis shows (Fig. 2) that the thermolysis of **I** proceeds in a wide temperature range (approximately 70–670°C) and, as follows from the DTA curve, is accompanied by endothermic effects with pronounced minima at 118, 268, and 478°C. At 504°C, an exothermic maximum superimposed on an endothermic effect is observed, which is proved, in particular, by a weight loss detected in the DTG and TG curves.

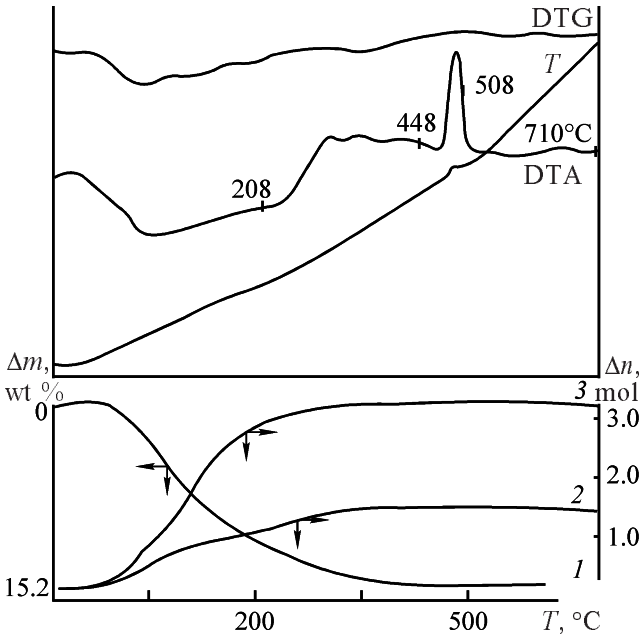


Fig. 2. Thermogravimetric curves of heating $Zn_{1.5}Cd_{1.5} \cdot (PO_4)_2 \cdot 1.4NH_3 \cdot 3.2H_2O$ at a rate of 5 deg min^{-1}. (Δm) Weight loss, (T) temperature, and (Δn) NH_3 or H_2O loss. Points in the DTA curve denote moments of sampling for X-ray diffraction analysis. (*1*) Total weight loss (TG), (*2*) NH_3 loss, and (*3*) H_2O loss.

The thermogravimetric (TG) curve shows that the weight loss of the sample is observed in the same range, 70–670°C. It was found by chemical analysis of products of heating compound **I** (Fig. 2, curves *2* and *3*) that, in the range 70–208°C, 2.6 mol of H_2O and 0.7 mol of NH_3 are removed, which corresponds to approximately half amount of ammonia and 80% of water in the initial compound. According to the chromatographic data (Table 2), phosphate in a sample taken at 208°C is entirely in the mono form PO_4^{3-}. This step of the thermolysis can be described by the overall scheme

$$[Zn_{1.5}Cd_{1.5}(NH_3)_{1.4}(H_2O)_{3.2}(PO_4)_2] \xrightarrow{60-208^\circ C} [Zn_{1.5}Cd_{1.5}(NH_3)_{0.7}(H_2O)_{0.6}(PO_4)_2] + 0.7NH_3 + 2.6H_2O.$$

Further heating of the substance to 343°C leads to the removal of certain additional amount of NH_3 and H_2O. The data of the quantitative paper chromatography (Table 2) show that, upon thermolysis performed to this temperature, monophosphate anions are partially converted to diphosphate anions. This step of transformations can be described by a combination of hydrolysis of monophosphate anion and condensation of acid monophosphate to diphosphate according to the generalized schemes

$$[Zn_{1.5}Cd_{1.5}(NH_3)_{0.7}(H_2O)_{0.6}(PO_4)_2] \xrightarrow{208-448^\circ C} [Zn_{1.5}Cd_{1.5}(NH_3)_{0.2}(H_2O)_{0.03}(PO_4)_{1.7}(P_2O_7)_{0.17}] + 0.5NH_3 + 0.6H_2O,$$

$$[Me \leftarrow OH_2 \cdots (PO_4)] \xrightarrow{208-448^\circ C} MeOH^+ + HPO_4^{2-},$$

Table 3. Crystal-chemical characteristics of final products of the thermolysis of zinc cadmium ammine aqua monophosphates

Compound	Unit cell parameters				Cell volume, Å^3
	a, Å	b, Å	c, Å	β, deg	
$Zn_{0.6}Cd_{2.4}(PO_4)_{2.0}$	9.028(6)	11.760(0)	6.113(9)	99.22	640.7(8)
$Zn_{1.2}Cd_{1.8}(PO_4)_{2.0}$	9.037(3)	11.660(7)	5.921(5)	98.88	614.7(6)
$Zn_{1.5}Cd_{1.5}(PO_4)_{2.0}$	9.044(4)	11.500(4)	5.930(0)	98.71	609.9(4)
$Zn_{1.8}Cd_{1.2}(PO_4)_{2.0}$	9.039(1)	11.517(0)	5.913(2)	98.69	608.4(9)
$Zn_{2.4}Cd_{0.6}(PO_4)_{2.0}$	8.992(9)	11.353(2)	5.934(2)	98.85	598.6(3)

$$2HPO_4^{2-} \longrightarrow P_2O_7^{4-} + H_2O.$$

On further heating to 508°C and higher temperatures, residual amounts of ammonia and water are removed from the material. The exothermic effect with a maximum at 498°C in the DTA curve (Fig. 2) coincides with the process of diphosphate decomposition (Table 2) and the onset of the zinc cadmium monophosphate crystallization (Fig. 3). In this case, the redistribution of P_2O_5 over oligomeric forms can be presented by the scheme

$$[Zn_{1.5}Cd_{1.5}(NH_3)_{0.12}(H_2O)_{0.02}(PO_4)_{1.8}(P_2O_7)_{0.1}]$$

$$\xrightarrow{508\text{–}710^\circ C} Zn_{1.5}Cd_{1.5}(PO_4)_{2.0} + 0.5NH_3 + 0.2H_2O,$$

$$[Zn_{1.5}Cd_{1.5}(NH_3)_{0.20}(H_2O)_{0.03}(PO_4)_{1.7}(P_2O_7)_{0.2}]$$

$$\xrightarrow{448\text{–}508^\circ C} [Zn_{1.5}Cd_{1.5}(NH_3)_{0.12}(H_2O)_{0.02}(PO_4)_{1.8}\cdot$$

$$(P_2O_7)_{0.1}] + 0.8NH_3 + 0.01H_2O,$$

According to X-ray phase analysis (Fig. 3), the completing stage of the thermolysis of zinc cadmium ammine aqua monophosphate, consisting in the transition from the amorphous state of the compound (20–343°C) to crystalline $Zn_{1.5}Cd_{1.5}(PO_4)_{2.0}$, requires larger energy consumption, i.e., heating to 690–710°C.

Crystal-chemical characteristics of the final products of heating the synthesized zinc cadmium ammine aqua monophosphates are given in Table 3.

All the final products of the thermolysis of zinc cadmium ammine aqua monophosphates are isostructural and crystallize in the monoclinic system. Figure 4 that their unit cell volume decreases approximately linearly (R^2 = 0.8812) with an increase in the zinc mole fraction, which agrees with the classical concept of solid solutions of substitution. This trend indirectly confirms the fact that the isolated X-ray amorphous zinc cadmium ammine aqua monophosphates are also solid solutions with practically unlimited possibility of substitution of zinc

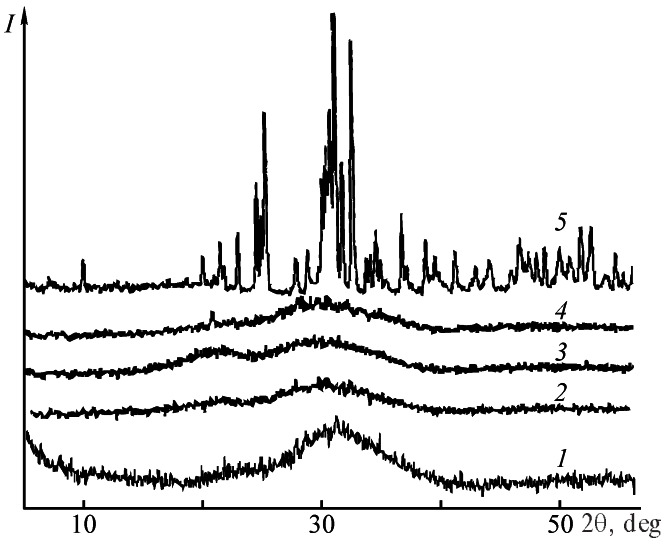


Fig. 3. Diffraction patterns of the (*1*) initial $Zn_{1.5}Cd_{1.5}\cdot(PO_4)_2\cdot 1.4NH_3\cdot 3.2H_2O$ and products of its heating to (*2*) 208, (*3*) 448, (*4*) 508, and (*5*) 710°C. (*I*) Intensity and (2θ) Bragg angle.

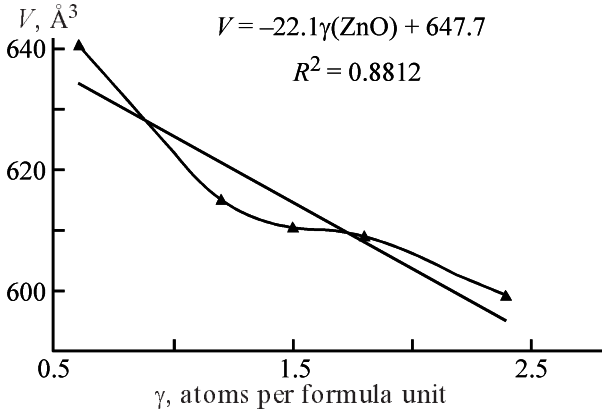


Fig. 4. Unit cell volume V of the crystal lattice of zinc cadmium monophosphates as a function of the zinc content γ.

ions for cadmium ions in equivalent crystallographic positions, as the difference in the ionic radii of the metals is insignificant (about 14%).

CONCLUSIONS

(1) The synthesized X-ray amorphous zinc cadmium ammine aqua monophosphates have the general formula $Zn_{3-x}C_x(PO_4)_2 \cdot n(NH_3) \cdot m(H_2O)$, where x = 0.6–2.4, n = 1.3–3.1, and m = 2.3–3.4. They undergo a series of thermal transformations in the temperature range 208–710°C.

(2) The compounds isolated are apparently solid solutions of substitution.

REFERENCES

1. *Neorganicheskie fosfatnye materially* (Inorganic Phosphate Materials), Kanazawa, T., Ed., Kiev: Naukova Dumka, 1998.
2. Abarbarchuk, L. M., *Cand. Sci. (Chem.) Dissertation*, Kiev, 2004.
3. Ropp, R.C., *J. Electrochem. Soc.*, 1962, vol. 109, no. 7, p. 569.
4. Nozaki, A.G. and Onta, H., *Bull. Chem. Soc. Jpn.*, 1974, vol. 47, no. 10, p. 1307.
5. Brown, J.J. and Hummel, F.A., *J. Electrochem. Soc.*, 1964, vol. 111, no. 6, p. 660.
6. Kalinin, A.A., Kabanova, G.V., and Kirillov, I.P., *Izv. Vyssh. Uchebn. Zaved., Khim. Khim. Tekhnol.*, 1965, vol. 8, no. 1, p. 88.
7. Hogarth, C.A. and Ghauri, L.A., *J. Mater. Sci.*, 1979, vol. 14, no. 7, p. 1641.
8. Bagulasankrithyan, V., Murali, K.R., Tiwari, R.A., and Rao, D.R., *J. Mater. Sci. Lett.*, 1984, vol. 3, no. 2, p. 177.
9. Calvo, C., *J. Phys. Chem. Solids*, 1963, vol. 24, no. 1, p. 141.
10. Deshmukh, S.N. and Ambardekar, D.S., *Indian J. Chem.*, 1984, vol. 23, no. 4, p. 295.
11. Szorenyi, T., Szollosy, L., and Szanka, K., *Acta Phys. Chem.*, 1974, vol. 20, no. 4, p. 371.
12. Trojan, M., *Sb. Ved. PR Vscht Pardubice*, 1986, vol. 49A, p. 213.
13. Stephens, J.S. and Calvo, C., *Can. J. Chem.*, 1967, vol. 45, no. 20, p. 2303.
14. Konstant, Z.A. and Dindune, A.P., *Fosfaty dvukhvalentnykh metallov* (Phosphates of Divalent Metals), Riga: Zinatne, 1987.
15. Voitenko, L.V., *Cand. Sci. (Chem.) Dissertation*, Kiev, 1994.
16. USSR Inventor's Certificate no. 1710503, *Byull. Izobret.*, 1992, no. 5.
17. Karnaukhov, A.I., Iosipchuk, B.V., and Kavetskii, S.V., *Ukr. Khim. Zh.*, 1990, no. 12, p. 1287.
18. *GOST* (State Standard) *20851.1–75* (*ST SEV* (COMECON Standard) *2531–80, ST SEV 2532–80, ST SEV 3369–81*), *GOST 20851.2–75–GOST 20851.4–75: Mineral Fertilizers: Methods of Analysis*, Moscow: Izd. Standartov, 1983.
19. Karpets, M.V., Milman, Y. V., Barabash, O.M., et al., *Intermetallics*, 2003, no. 11, p. 241.
20. Shchegrov, L.N., *Fosfaty dvukhvalentnykh metallov* (Phosphates of Divalent Metals), Kiev: Naukova Dumka, 1987.
21. Shevchenko, Yu.N., *Doctoral (Chem.) Dissertation*, Kiev, 1994.
22. *Atlas IK spektrov fosfatov: Dvoinye mono- i difosfaty* (Atlas of IR Spectra of Phosphates: Double Mono- and Diphosphates), Pechkovskii, V.V., Ed., Moscow: Nauka, 1990.

ISSN 1070-4272, Russian Journal of Applied Chemistry, 2008, Vol. 81, No. 9, pp. 1497–1502. © Pleiades Publishing, Ltd., 2008.
Original Russian Text © I.M. Malov, V.I. Zarembo, A.M. Syroezhko, 2008, published in Zhurnal Prikladnoi Khimii, 2008, Vol. 81, No. 9, pp. 1423–1427.

PHYSICOCHEMICAL STUDIES OF SYSTEMS AND PROCESSES

Control over Cracking of Heavy Petroleum Residue by Weak Acoustic Fields

I. M. Malov, V. I. Zarembo, and A. M. Syroezhko

St. Petersburg State Institute of Technology (Technical University), St. Petersburg, Russia

Received February 12, 2007

Abstract—Effect of weak periodic electromagnetically excited acoustic pulses with a repetition frequency of 100 to 1000 kHz on thermolysis of petroleum residue was studied. It was shown that weak acoustic fields affect the yield and quality of target products (gas, liquid, solid cracking residue).

DOI: 10.1134/S1070427208090048

Creation of innovation ways to intensify the existing processes of chemical industry is a topical task. The method of background control over heterogeneous processes [1], based on specific features of the media being controlled, makes it possible to shorten the production cycle and change the technical-and-economical parameters of the process both qualitatively and quantitatively without any significant capital expenditure or direct change in both the apparatus and technology employed.

Most of processes used in oil refining and treatment of petroleum residue are accompanied by phase transitions: evaporation and condensation, melting and crystallization, etc. Controlling the kinetics of phase transitions with chemical substances and physical fields allows optimization of the processing of the oil stock and enables modification of the properties of the products obtained. In contrast to chemical methods, the physical activation does not impair the production efficiency and extends the range within which the process parameters can be varied.

Acceleration of a phase transition is a favorable factor in dehydration, deasphalting, dewaxing, and in certain stages of coking. In thermal cracking, there occur high-temperature degradation of hydrocarbons and condensation of polyaromatic hydrocarbons, regarded as crystallization and glass formation from a petroleum solution. In the industrial technology for thermal cracking of black oils and petroleum tars (viscosity breaking), it is desirable to accelerate the thermal cracking of the heavy oil stock without any noticeable coking (to reduce the rate of formation of the solid phase via controlled decrease in the rate of thermal condensation processes). It is noteworthy that the residual oil stock of viscosity-breaking and delayed-coking installations starts to undergo partial cracking already in the stage of heating in coiled pipes of a tubular furnace. In view of the aforesaid, the present study was devoted to the effect of weak acoustic treatments on the thermal cracking of petroleum tar.

EXPERIMENTAL

The petroleum tar was taken from an AVT-6 installation at Kirishi petroleum refinery. Its parameters are listed in Table 1.

Table 1. Group composition of petroleum tar

Group components	Yield based on petroleum tar, wt %
Asphaltenes	6.4
Maltenes	93.6
Polar components (PCm):	16.6
Oils:	67.3*
paraffin–naphthene compounds	22.2*
monocycloaromatic compounds	18.6*
bicyclo- and polycycloaromatic compounds	26.5*
Resins:	32.7*
toluene	13.2*
alcohol–toluene	19.5*
Nonpolar components	83.4

* The yield of polar components is given relative to their sum taken as 100%.

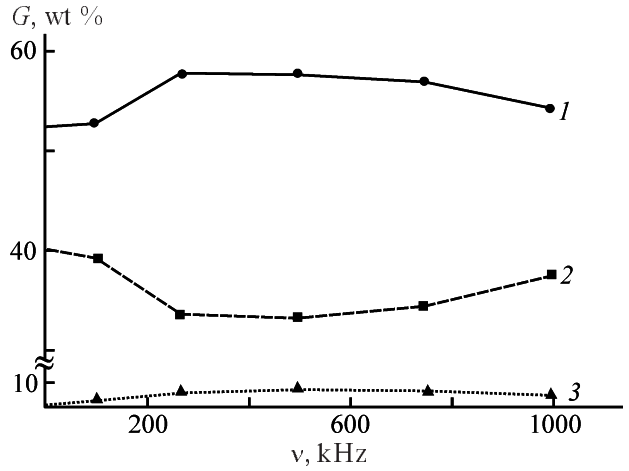


Fig. 1. Effect of weak acoustic fields on quantitative parameters of petroleum tar thermolysis. (*G*) Yield of petroleum tar thermolysis products and (ν) frequency of acoustic field. (*1*) Total yield of light distillates, (*2*) yield of the cracking residue, and (*3*) gas and loss.

The thermal cracking was performed in a heated glass reactor with mechanical agitation (ν = 45 rpm) at a thermostating temperature of 425°C and process duration of 75 min to exhaustive evaporation of the sum of liquid distillation products. A weak acoustic field with an average pulsation amplitude of 150 Pa was electromagnetically generated within the loop-antenna of a generator of electromagnetic pulses, which was brought in contact with the reactor in the zone of occurrence of petroleum tar thermolysis. The repetition frequency of weak acoustic pulses was varied in the range 100–1000 kHz [2].

The thermal cracking was performed in a heated glass reactor with mechanical agitation (ν = 45 rpm) at a thermostating temperature of 425°C and process duration of 75 min to exhaustive evaporation of the sum of liquid distillation products. A weak acoustic field with an average pulsation amplitude of 150 Pa was electromagnetically generated within the loop-antenna of a generator of electromagnetic pulses, which was brought in contact with the reactor in the zone of occurrence of petroleum tar thermolysis. The repetition frequency of weak acoustic pulses was varied in the range 100–1000 kHz [2].

The thermal cracking of petroleum tar yields gaseous and liquid products with a lower molecular mass than that of the starting raw material and solid pitch-coke-like products of thermal condensation, with a higher molecular weight. Results of balance experiments on thermal cracking of petroleum tar under the action of an acoustic field and without it are shown in Fig. 1. It is noteworthy that the most valuable product formed in thermal cracking of petroleum tar is the total liquid distillate, because its further qualified processing into motor fuel components can markedly improve the extent of petroleum processing without using high-cost methods (deasphalting and demetalation of petroleum tars) to prepare raw materials for the subsequent hydrocracking. The amount of petroleum tar formed in primary processing of West-Siberian industrial crude oil (oil distillation into fractions) is 21–23% (based on oil).

The total distillate formed in thermal cracking of petroleum tar was subjected to fractional distillation to obtain naphtha (from start of boiling to 200°C) and diesel (200–360°C) fractions. For these fractions, the density, refractive index, iodine numbers, and total sulfur content were determined by the procedures described in [3]. The qualitative composition of the fractions of the total distillate was determined by chromatography–mass spectrometry. Complex mixtures of hydrocarbons of the fractions being analyzed were separated on a 30-m-long HP-5MS capillary column coated with a nonpolar phase (polydimethylsiloxane). All the measurements were made on an Agilent 5973/6850 chromatograph–mass spectrometer.

The residence time of the raw material being cracked in the reaction zone affects, at the same temperature, the degrees of feed conversion and decomposition. It is known that competitive reactions of decomposition and condensation occur in the chosen temperature range of petroleum tar cracking. The activation energy of the condensation reactions is substantially lower than that for the decomposition reactions. Consequently, to raise the yield of decomposition products (gas, naphtha, diesel fractions) and make lower the yield of the cracking residue, it is necessary to maintain in the reaction zone a temperature sufficient for rupture of the bonds being cracked under mild process conditions as regards its duration and pressure (permanent removal of light cracking products from the reaction zone in the gas and vapor phases under atmospheric pressure).

It can be seen from Fig. 1 that the curves describing the frequency dependence of the yields of the total distillate and cracking residue show opposite trands and pass through extrema. The yield of the gas is independent, within the experimental error, of the frequency of the acoustic treatment. The optimal conditions providing the maximum yield of the total distillate (57.4%) are obtained at characteristic

frequencies in the range 270–750 kHz. In this case, the yield of light products increases by 8–10% based on the total distillate (4–5% based on converted petroleum tar). A similar behavior was observed in thermolysis of another batch of petroleum tar, taken at Kirishi refinery (repetition frequency of acoustic pulses 500 kHz, average amplitude of the sonic wave 0.15 Pa).

The acoustic pressure depends on a material chosen for the EMAP loop-antenna (copper or steel). Presumably, the optimal activated state of the system being cracked is observed in this range of sonic field frequencies. This state (which is far from the thermal equilibrium) promotes intense rupture of the weakest carbon–carbon and carbon–heteroatom (C–S, C–O, C–N) bonds of the molecules being cracked, with radicals formed. In normal alkanes with a long chain, the rupture energies of the C–C and C–H bonds somewhat decrease toward the middle of the chain. However, the former is always substantially lower than the latter. C–C bonds in cycloalkanes are less strong than those in normal alkanes. In the radical-chain process of thermal cracking of petroleum tar, paraffin, cycloparaffin, and isoparaffin hydrocarbons are easily cracked. Cracking of alkanes and cycloalkanes gives olefins in which the C–C bond in the β-position to the double bond is substantially weaker than the C–C bond in alkanes. In arenes, the C–H and C–C bonds are stronger than those in alkanes, and the bonds conjugated with the aromatic ring are weakened. In addition, weak carbon–heteroatom bonds in hybrid compounds of petroleum tar are intensely ruptured.

The ease of homolytic bond rupture in a hydrocarbon strongly depends on the stability of the radicals being formed. The final composition of the products is determined by the relative rates of interaction of the radicals being formed with the starting hydrocarbons of the feed, cracking of the radicals, cracking of the hydrocarbons, and condensation reactions yielding compounds with molecular masses exceeding those of the feed. The cracking occurs when the energy of the thermal vibration motion of molecules increases to values exceeding the bond energies. Under these conditions, there occur degradation, interaction, recombination, and condensation of fragments of the starting molecules.

The probable pathways of cracking of individual hydrocarbons belonging to different classes were analyzed in most detail in [4, 5]. Syunyaev [6] suggested that the result of cracking in a mixture of the macromolecular hydrocarbons of petroleum is

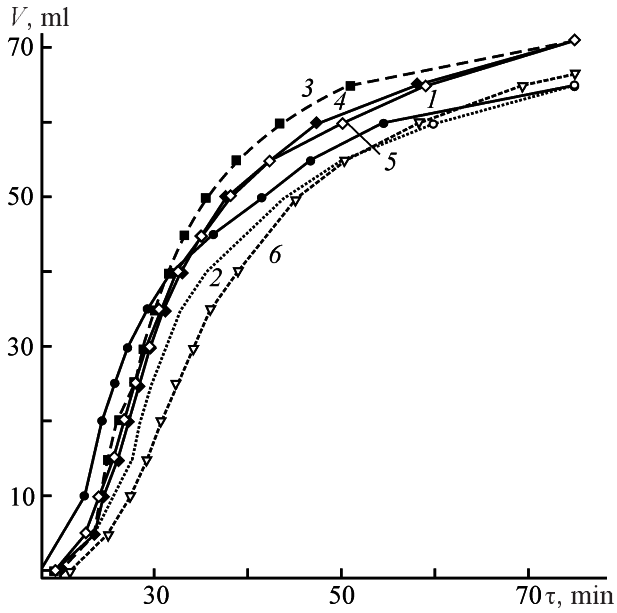


Fig. 2. Yield of the total distillate vs. the duration τ of the experiment. (V) Running volume of the total distillate. (*1*) Without acoustic treatment; (*2–6*) with acoustic treatment at a frequency (kHz): (*2*) 100, (*3*) 270, (*4*) 500, (*5*) 750, and (*6*) 1000; the same for Fig. 6.

also affected by the intermolecular interaction of molecules, a part of whose energy is expended for disaggregation of the dispersed system, rather than to cleavage of macromolecules. From this standpoint, the intensification of the thermolysis of a heavy petroleum residue is due to processing of raw materials in their active state. In this case, the optimal relationship is attained between the sizes of a solvation shell and of a complex structural unit whose core is constituted by supramolecular formations of asphaltenes. The kinetic curves representing the yield of the total distillate of the petroleum tar being cracked (Fig. 2) are S-shaped and described by the differential equation

$$d[V_i]/d\tau = k_i([V_i]_\infty - [V_i]_\tau)[V_i]_\tau, \quad (1)$$

where k_i is the constant characterizing the rate at which the limiting volume of the total distillate is reached at a fixed working frequency of the sound generator.

The whole set of experimental curves in Fig. 2 is linearized in the coordinates $\ln y$–x, where

$$y = [V_i]_\tau/([V_i]_\infty - [V_i]_\tau), \quad (2)$$

$$x = k_i[V_i]_\infty\tau, \quad (3)$$

Trend lines are plotted (Fig. 3) on the basis of

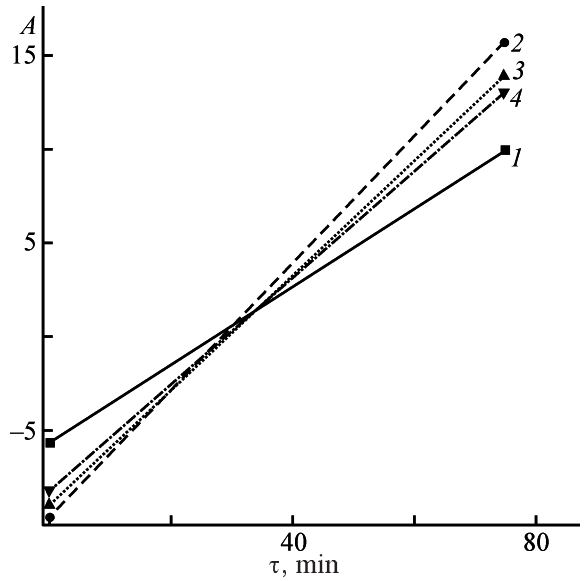


Fig. 3. Trend lines. $A = \ln [V_i/(V_{lim} - V_i)]$, where V_i is the running volume, and V_{lim}, limiting volume; (τ) time. (*1*) Without acoustic treatment; (*2–4*) with acoustic treatment at a frequency (kHz): (*2*) 270, (*3*) 500, and (*4*) 750.

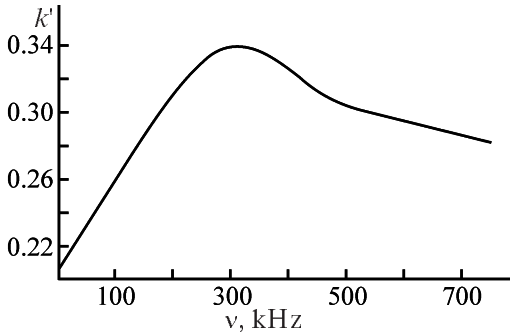


Fig. 4. Effective rate constant of thermolysis, k', vs. the acoustic treatment frequency ν.

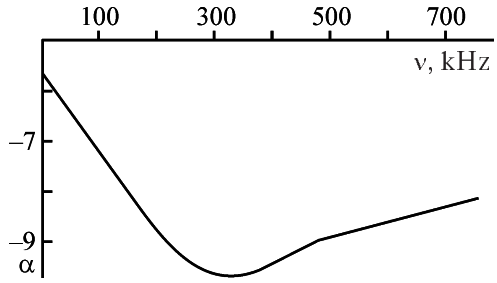


Fig. 5. Empirical parameter α as a function of the acoustic treatment frequency ν.

the converted experimental data used to find the constants of the equation

$$\ln \{[V_i]_\tau/([V_i]_\infty - [V_i]_\tau)\} = k'\tau - \alpha, \quad (4)$$

where k' is the effective rate constant of petroleum tar thermolysis (min^{-1}), and α is an empirical parameter.

Equation (4) is transformed to

$$[V_i]_\tau = \frac{[V_i]_\infty e^{k'\tau - \alpha}}{1 + e^{k'\tau - \alpha}}, \quad (5)$$

or, in the differential form, to

$$\frac{d[V_i]}{d\tau} = \frac{k'[V_i]_\infty e^{k'\tau - \alpha}}{(1 + e^{k'\tau - \alpha})^2} = \frac{k_i[V_i]^2_\infty e^{k'\tau - \alpha}}{(1 + e^{k'\tau - \alpha})^2}. \quad (6)$$

Equation (6) can be used to calculate the running volumes (concentrations) of the total distillate, gaseous products, and cracking residue and the degree of petroleum tar conversion. At an acoustic field frequency of 270 kHz, the parameters k and α (Fig. 4, 5) reach their extremal values. The empirical parameter α, which characterizes the beginning of evaporation of the total distillate, is uniquely dependent on the duration of the induction period of the radical-chain reaction by which thermolysis of petroleum tar occurs and on the related control over the nucleation of a new phase (tars start to be converted by condenation reactions to asphaltenes, and these latter, to carbenes and carboids). Presumably, it is the hindrance to this phase transition that leads to qualitative and quantitative changes in the process parameters. The thermolysis of petroleum tar involves endothermic reactions of dehydrogenation and cracking of group components, as well as exothermic reactions of synthesis, polymerization, and condensation.

During the induction period (Fig. 2), the system more actively absorbs energy (Fig. 6), with the evaporation of the total distillate beginning at higher temperatures. The effective heat conductivity of the reaction mixture varies with the controlling signal frequency, which determines the temperature mode in which the system reaches the prescribed cracking temperature.

As can be seen in Table 2, the content of total sulfur in the total distillate tends to decrease as compared with base runs of petroleum tar cracking without ultrasonic treatment. We identified 99 compounds in the naphtha fraction by chromatography–mass spectrometry. Comparative analysis of naphthas formed in thermal cracking of petroleum tar points to an increase in the content of linear alkanes (3.18%), isoparaffins (2.52%), linear olefins (1.19%), and isoolefins (1.82%) in the fraction obtained under

Table 2. Characterization of the total distillate

Parameter	Blank run	Acoustic treatment frequency, kHz				
		100	270	500	750	1000
Yield of the naphtha fraction (start of boiling–200°C), wt %	25.50	33.30	36.90	33.90	33.90	30.30
Iodine number	80.80	80.20	82.70	85.40	91.70	78.10
S_{tot}, wt %	0.44	0.41	0.33	0.36	0.35	0.39
Yield of the 200–360°C diesel fraction, wt %	45.70	43.10	47.40	39.40	52.60	53.30
Iodine number	34.80	35.50	35.50	35.70	33.50	36.10
S_{tot}, wt %	0.53	0.46	0.44	0.45	0.42	0.46
Yield of light gas oil, wt %	28.80	23.60	15.70	26.70	13.50	16.40

the action of the acoustic field. The main group of compounds unidentified in detail (15%) is represented by cycloalkenes and cycloalkanes. The fraction of aromatic compounds in the ultrasonically treated (500 kHz) naphtha fraction decreases by 5.22%, with the organoleptic properties impaired (strong unpleasant odor, poor stability). As a consequence, the boiling onset temperature and iodine numbers grow. The resulting cracking residues have a higher softening point. These substances can be used as binders for modification of starting petroleum tars to obtain compounded asphalts. A sample based on a high-melting cracking residue of field-assisted (500 kHz) thermolysis of petroleum tar produced from West-Siberian crude oil with a softening point of 214°C, modified with the starting petroleum tar (50%), satisfies in all characteristics the requirements to road asphalts of BND 60/90 brand.

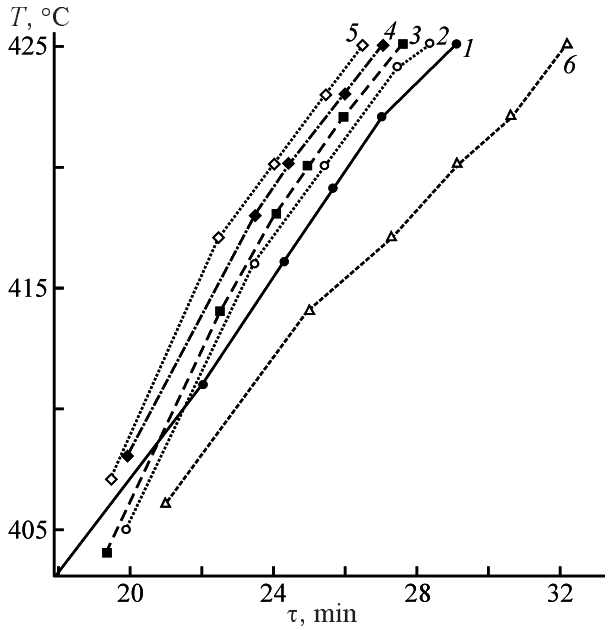


Fig. 6. Temperature T in the reaction zone as a function of time τ at fixed heating of the reactor.

The prospects for practical use of the method are quite real, and it can be implemented as a supplement to the existing technology, e.g., as an additional unit in the system for automated control over the process. There exist and are widely used ultrasonic counters–flow meters, to which an ultrasonic emitter can be added as a function. This approach does not require any additional equipment.

The induction period can be characterized at invariable output parameters of the process by an increase in the time of residence in the reaction zone. The increase in the thermal stability of an insonificated petroleum residue is a favorable factor that will make it possible to diminish coke deposits within the reaction coiled pipes of furnaces in installations for thermal cracking and delayed coking and to raise the admissible temperature of feed heating.

CONCLUSIONS

(1) Weak acoustic fields affect to a certain extent the overall process of thermal cracking of petroleum tar both in deep degradation of the starting mostly hybrid molecules of complex structure (gasification) and in their moderate decomposition.

(2) The maximum yield of the target total distillate (57.4 wt %) in thermolysis of petroleum tar at a temperature of 425°C and process duration of 75 min is obtained at an acoustic treatment frequency of 270 kHz. Under these conditions, the yields of the gas and cracking residue are 6.2 and

36.4 wt %, respectively. The yield of light products increases by 4–5%, compared to experiments on thermal cracking of petroleum tar without an acoustic treatment.

(3) The effective rate constant of formation of a liquid product in field-assisted thermolysis of petroleum tar at the optimal frequency is 1.6 times that in thermal cracking without acoustic treatment.

REFERENCES

1. Zarembo, V.I., Kolesnikov, A.A., Burnos, N.A., and Ivanov, E.V., *Tyazh. Mashinostr.*, 2005, no. 11, pp. 14–18.
2. Zarembo, V.I., Kiseleva, O.L., Kolesnikov, A.A., et al., *Neorg. Mater.*, 2004, vol. 40, no. 1, pp. 11–15.
3. Rybak, B.M., *Analiz nefti i nefteproduktov* (Analysis of Petroleum and Petroleum Products), Moscow: Gostoptekhizdat, 1962.
4. Magaril, R.Z., *Teoreticheskie osnovy termicheskikh protsessov pererabotki nefti* (Theoretical Foundations of Thermal Processes for Petroleum Refining), Moscow: Khimiya, 1976.
5. Zhorov, Yu.M., *Kinetika promyshlennykh organicheskikh reaktsii* (Kinetics of Industrial Organic Reactions), Moscow: Khimiya, 1989.
6. Syunyaev, Z.I., *Neftyanoi uglerod* (Petroleum Carbon), Moscow: Khimiya, 1980.

ISSN 1070-4272, Russian Journal of Applied Chemistry, 2008, Vol. 81, No. 9, pp. 1503–1507. © Pleiades Publishing, Ltd., 2008.
Original Russian Text © E.V. Shkol'nikov, 2008, published in Zhurnal Prikladnoi Khimii, 2008, Vol. 81, No. 9, pp. 1428–1431.

PHYSICOCHEMICAL STUDIES OF SYSTEMS AND PROCESSES

Thermodynamic Calculation of the Solubility of Solid Hydroxides of Group IIIA Elements in Water and Aqueous Media

E. V. Shkol'nikov

St. Petersburg State Academy of Forestry Engineering, St. Petersburg, Russia

Received April 10, 2008

Abstract—The effect of pH on the molar solubility of amorphous and crystalline hydroxides $M(OH)_3$ and metahydroxides MO(OH), where M is B, Al, Ga, In, or Tl, in aqueous alkaline and acidic media at 25°C was calculated thermodynamically taking into account the formation of hydroxo complexes.

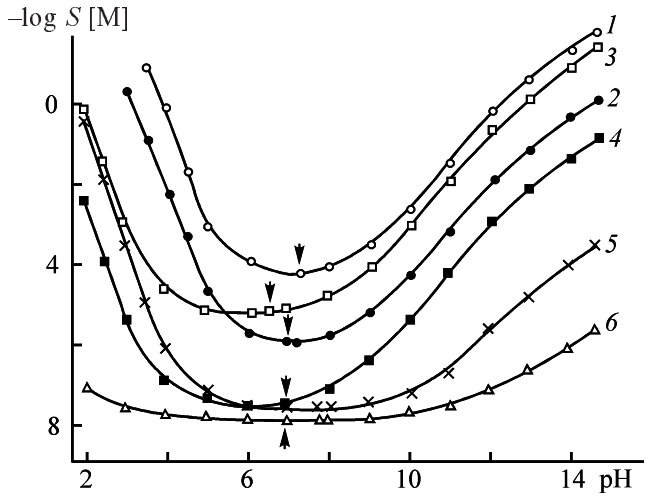
DOI: 10.1134/S107042720809005X

A thermodynamic characteristic of the amphoteric properties of solid hydroxides $M(OH)_2$ in aqueous nonoxidizing media was suggested previously [1, 2]. Of interest is the thermodynamic calculation of the effect of pH on the molar solubility of hydroxides $M(OH)_3$ and metahydroxides MO(OH), where M is a Group IIIA element, in aqueous media. The calculation results can be used for the synthesis of hydroxides and oxides and for determination of conditions of their hydrolysis, practically complete precipitation, or efficient masking of cations in the form of soluble hydroxo complexes [3–7]. The hydroxides and metahydroxides of Group IIIA elements are used in production of special glasses, enamels, and cements, in chemical analysis and synthesis, and in medicine.

The amphoteric properties of $M(OH)_3$ and MO(OH) have been studied insufficiently, and quantitative data on the solubility in aqueous media are scarce and often contradictory. Thus, according to [4–8], weak acids H_3BO_3 and HBO_2 do not have basic properties and are markedly soluble in cold water, unlike practically insoluble hydroxides of other Group IIIA elements. On the other hand, boron(III) acetate, perchlorate, and hydrosulfate can exist in the crystalline form and the acid properties of $B(OH)_3$ are attributed to the formation of hydrogen (hydroxonium) cations and hydroxo complexes $[B(OH)_4]^-$ in aqueous solution [9, 10]. Colorless solid hydroxides $Al(OH)_3$, $Ga(OH)_3$, and $In(OH)_3$ are soluble in acids and alkalis, with the acid properties of $In(OH)_3$ being weak. Freshly precipitated indium(III) hydroxide readily dissolves in dilute acids, is insoluble in dilute alkalis, and forms unstable indates in concentrated alkaline solutions [9, 10]. According to [9], gallium(III) hydroxide shows almost ideal amphoteric behavior and readily dissolves in alkalis with the formation of stable gallates $[Ga(OH)_4]^-$. At the same time, according to [7], its acid properties dominate over base properties.

Reddish brown hydroxide $Tl(OH)_3$ dissolves in acids and is easily peptized with alkalis with the formation of a sol, but it is insoluble in them and does not form thallates [9]. According to a handbook [8], the hydroxide $In(OH)_3$ is difficultly soluble and $Tl(OH)_3$ is insoluble in alkalis. At the same time, in concentrated alkaline solutions the hydrate $Tl_2O_3 \cdot mH_2O$ has very weak acid properties, forming readily hydrolyzable thallates [10]. Amphoteric hydroxides of Group IIIA elements, freshly precipitated from aqueous solutions, are X-ray amorphous gels of variable composition $M_2O_3 \cdot mH_2O$ ($m > 3$). They contain excess water of hydration, which is lost on keeping and heating with the possible formation of crystalline hydroxides, metahydroxides, and oxides of definite composition [9–11].

Four crystal modifications of $Al(OH)_3$ were identified: monoclinic (γ) and triclinic (γ') gibbsite, or hydrargillite; monoclinic bayerite (α) and triclinic nordstrandite (β). There are also two AlO(OH) modifications (rhombic boehmite and diaspor). Nordstrandite is formed on aging $Al_2O_3 \cdot mH_2O$ gels [10]. Stable gibbsite is obtained by slowly feeding CO_2 into an alkaline solution, and metastable bayerite is formed by fast precipitation [11]. Boehmite and diaspor are obtained on heating of bayerite and gibbsite. All the above modifications are components of bauxites. The chemical activity decreases in the order amorphous gel → bayerite → gibbsite →



Solubility S of solid hydroxides vs. pH of an aqueous medium at 25°C: (*1*) freshly precipitated $Al(OH)_3$, (*2*) γ-AlO(OH), (*3*) $Ga(OH)_3$, (*4*) α-GaO(OH), (*5*) $In(OH)_3$, and (*6*) $Tl(OH)_3$.

boehmite → diaspor [10]. The crystalline compounds H_3GaO_3, $In(OH)_3$, and $Tl(OH)_3$ can be obtained by precipitation from alkaline solutions [11]. Heating H_3GaO_3 to approximately 400°C yields metagallic acid $HGaO_2$ [10].

In an aqueous solution saturated with a difficultly soluble hydroxide $M(OH)_3$ or MO(OH), the heterogeneous chemical equilibria

$$M(OH)_3(cryst) \rightleftarrows M^{3+}(sol) + 3OH^-(sol),$$
$$MOOH(cryst) + H_2O(l) \rightleftarrows M^{3+}(sol) + 3OH^-(sol) \quad (1)$$

are attained, whose thermodynamic constant is given by the expression

$$K_s^0 = SP^T = a(M^{3+})a^3(OH^-) = const(T), \quad (2)$$

where $a(M^{3+})$ and $a^3(OH^-)$ are the activities of the ions (M^{3+} and OH^-).

The thermodynamic calculation of K_s^0 for equilibria (1) was performed using the method from [1]. The free energies ΔG_f^0 of formation of the ions in aqueous solutions, required for the calculation, were taken from [12] and the free energies ΔG_f^0 of formation of the solid hydroxides at 298 K, from handbooks [5, 8, 13]. The molar solubility of hydroxides, except for H_3BO_3, was calculated taking into account the ionic strength of the solution and the formation of mononuclear hydroxo complexes, using the general equation

$$S = c_M = K_s^0(f_{M^{3+}}f_{OH^-}^3)^{-1}\sum_{i=0}^{n}\beta_i[OH^-]^{i-3}, \quad (3)$$

where the constant K_s^0 characterizes heterogeneous chemical equilibrium (1); $f_{M^{3+}}$ and f_{OH^-} are the molar activity coefficients of M^{3+} and OH^- ions; $\beta_0 = 1$, β_1, β_2, β_3, and β_4 are step stability constants of the hydroxo complexes MOH^{2+}, $M(OH)_2^+$, $M(OH)_3$, and $M(OH)_4^-$, found from the averaged data [3–6].

The molar solubility of the hydroxides in 1 M NaOH solution was calculated by the simplified formula $S = 1.13K_s^0\Sigma\beta_i$.

The equilibrium concentration of free OH^- anions and the pH value of saturated aqueous solutions of the hydroxides in pure water (shown by the arrows in the figure), were found by solving the system of six equations

$$3[M^{3+}] + 2[MOH^{2+}] + [M(OH)_2^+] + [H^+] = [M(OH)_4^-] + [OH^-],$$
$$[M^{3+}][OH^-]^3 = K_s^0, \quad [H^+][OH^-] = K_w,$$
$$[MOH^{2+}] = \beta_1[M^{3+}][OH^-], \; [M(OH)_2^+] = \beta_2[M^{3+}][OH^-]^2,$$
$$[M(OH)_4^-] = \beta_4[M^{3+}][OH^-]^4 \quad (4)$$

with the use of Ferrari, Cardano, or Newton method for the obtained equation

$$(1 + K_s^0\beta_4)y^4 - (K_s^0\beta_2 + K_w)y^2 - 2K_s^0\beta_1 y - 3K_s^0 = 0, \quad (5)$$

where K_W is the autoprotolysis constant of water at 25°C, $y = [OH^-]$.

For the H_3BO_3 crystals with molecular layered structure [9–11], no thermodynamic data exists on the small triply charged boron cation exhibiting high polarizing effect. The same concerns its hydroxo complexes in aqueous solutions, except for $B(OH)_3$ and $B(OH)_4^-$. Therefore, for the molar solubility of the triclinic H_3BO_3 modification in pure water at 25°C we took the intrinsic solubility of weak boric acid [4] in the form of H_3BO_3 molecules. The latter was found from the calculation, using electrochemical data of [14], of the thermodynamic constant K_s^0 for the heterogeneous equilibrium $H_3BO_3(cryst) \rightleftarrows H_3BO_3(sol)$ in saturated aqueous solution.

The results of the calculation are given in the table ($pK_s^0 = -\log K_s^0$, s^0 is the total molar solubility of solid hydroxides in pure water and $[M(OH)_3]$, the equilibrium molarity of neutral complexes in aqueous solutions of the hydroxides at 25°C). It can be seen from the table that the pK_s^0 values calculated in this study and those taken from [4, 7] are in reasonable agreement. For a number of hydroxides, the

Thermodynamic parameters of solution of amorphous and crystalline hydroxides and metahydroxides in water and alkali at 25°C

Composition	pK_s^0		H_2O			NaOH		S, M, in 1 M NaOH	A
	calculated	data of [4, 7]	pH^0	S^0	$[M(OH)_3]$	pH_{opt}	pS_{min}		
				M					
H_3BO_3	0.07	–	3.7	0.86 ± 0.07	0.84	<–1.3	≥0.8	1.2	3.1 ± 0.5
$Al(OH)_3$*	30.80	30.70 ± 0.30	7.20	4.5×10^{-5}	4.0×10^{-5}	7.21	4.35	16	1.08×10^6
α-$Al(OH)_3$	32.0	–	7.12	2.9×10^{-6}	2.6×10^{-6}	7.21	5.54	1.05	1.08×10^6
β-$Al(OH)_3$	32.08	–	7.11	2.1×10^{-6}	1.9×10^{-6}	7.21	5.68	0.76	1.08×10^6
γ-$Al(OH)_3$	34.08	33.96	7.00	2.1×10^{-8}	1.9×10^{-8}	7.21	7.68	7.7×10^{-3}	1.07×10^6
γ'-$Al(OH)_3$	33.9	33.5	7.01	3.2×10^{-8}	2.8×10^{-8}	7.21	7.50	0.012	1.07×10^6
γ-AlOOH	32.40	–	7.07	1.0×10^{-6}	8.9×10^{-7}	7.21	6.00	0.36	1.08×10^6
α-AlOOH	34.38	–	7.00	1.0×10^{-8}	9.2×10^{-9}	7.21	7.99	3.8×10^{-3}	1.07×10^6
H_3GaO_3*	34.6	35.1	6.17	4.2×10^{-4}	4.0×10^{-4}	6.15	3.38	13**	3.5×10^6
H_3GaO_3	36.70	36.80	6.62	5.3×10^{-6}	5.1×10^{-6}	6.15	5.28	6.2	3.4×10^6
α-$HGaO_2$	39.0	39.1	6.92	2.8×10^{-8}	2.5×10^{-8}	6.15	7.58	0.031	3.3×10^6
$In(OH)_3$*	33.8	33.2	7.26	3.6×10^{-5}	3.6×10^{-5}	7.75	4.44	0.092	7.5×10^3
$In(OH)_3$	36.91	36.92	7.00	2.7×10^{-8}	2.7×10^{-8}	7.75	7.57	6.9×10^{-5}	7.4×10^3
$Tl(OH)_3$*	44.0	–	7.00	8.9×10^{-7}	8.9×10^{-7}	7.00	6.05	4.4×10^{-5}	1.5×10^2
$Tl(OH)_3$	45.90	45.89	7.00	1.2×10^{-8}	1.2×10^{-8}	7.00	7.94	5.1×10^{-7}	1.4×10^2

* Freshly precipitated amorphous.
** In 0.01 M NaOH solution.

calculation was performed for the first time. Experimental solubilities of H_3BO_3 in water at 20°C differ markedly [4, 8–11]. At the same time, they are close to the calculated value of the intrinsic solubility of boric acid in the form of neutral complexes $B(OH)_3$ (see table). The dissolution of H_3BO_3(cryst) in water is an endothermic process (ΔH_s^0 = 22.6 kJ mol^{-1} [13]). The analysis of the data from handbooks [4, 8] shows that the temperature dependence of the solubility of boric acid in water can be presented by the equation

$$\ln(S_2/S_1) = \Delta H_s^0 R^{-1}(1/T_1 - 1/T_2), \quad (6)$$

where S_1 and S_2 are the solubilities at temperatures T_1 and T_2, respectively, and R is the gas constant.

The solubility of amorphous hydroxides $M(OH)_3$, like that of hydroxides $M(OH)_2$, is considerably higher [1, 2] than that of their crystalline modifications, because dehydration and crystallization of $M_2O_3 \cdot mH_2O$ precipitates are accompanied by formation of chemically inactive oxo derivatives in which the M atoms in polynuclear hydroxo aqua complexes are bound through O bridges [3, 10]. The solubility of crystalline hydroxides markedly depends on the structure, decreasing on passing to the stable modifications γ-$Al(OH)_3$ and α-AlO(OH). The solubility of hydroxides $M(OH)_3$ and metahydroxides MO(OH) (M is Al, Ga, In, or Tl) in pure water is determined by the concentration of dissolved neutral complexes $M(OH)_3$ [from 88% in aluminum hydroxides to approximately 100% in $Tl(OH)_3$].

The tables show that aqueous saturated solutions of aluminum and indium(III) hydroxides are weakly alkaline (pH^0 7.0–7.3), those of thallium(III) hydroxide, neutral, and those of gallium(III) hydroxide, weakly acidic (pH 6.2–6.9). The isoelectric point of the dispersed system was found at pH 6.8 [9], 9.2, and 9.4 [11] for $Ga(OH)_3$, bayerite α-$Al(OH)_3$, and boehmite γ-AlO(OH), respectively.

Free M^{3+} cations are practically absent in saturated aqueous solutions (mole fraction of the cations x^0, calculated as in [1], is less than 4×10^{-6}) and dominate in strongly acidic solutions (Al^{3+} and In^{3+} at pH < 3, Ga^{3+} at pH < 2, and Tl^{3+} at pH < 1), where they can be determined by potentiometric methods.

The solubility of amphoteric aluminum, gallium, and indium hydroxides passes through a minimum as pH of the medium is varied (by adding NaOH or

$HClO_4$, see figure, curves *1–5*). For $Tl(OH)_3$, the calculation yields a wide interval of pH values in which the solubility is minimal and does not vary noticeably (see figure, curve *6*). Analysis of Eq. (3) leads to a conclusion that the minimal solubility of $M(OH)_2$ precipitates is observed at the optimal concentration of OH^- ions when neutral complexes $M(OH)_2$ dominate in solution among equilibrium species. From the condition for the maximum mole fraction $x_{M(OH)_3}$, the following equation was obtained:

$$\beta_4[OH^-]^4 - \beta_2[OH^-]^2 - 2\beta_1[OH^-] - 3 = 0. \quad (7)$$

Solving this equation by the same way as Eq. (5) yielded first $[OH^-]_{opt}$ and pH_{opt} and then S_{min}. The values of $pS_{min} = -\log S_{min}$ at 25^0C are given in the table and partly in the figure. It can be seen that the negative effect of common OH^- ions on the solubility of the hydroxides under study $[M(OH)_3]$ in alkali is absent, as in the case of $Sn(OH)_2$ and HgO [1, 2]. The analysis shows that high stability constants β_3 of the neutral complexes $M(OH)_3$ and their high mole fractions in saturated aqueous solution ($x_{M(OH)_2} \geq 0.9$) are the conditions for the absence of this effect for hydroxides $M(OH)_3$ and metahydroxides MO(OH).

For comparative quantitative estimation of the amphoteric properties of hydroxides, we used, as previously, the ratio ($A > 1$) of their molar solubilities in an alkaline medium with pH 14.7 (5 M NaOH solution) and in pure water. The amphoterism parameter A markedly depends on the structure of modifications (see table) and is determined by the chemical nature of hydroxide {ratio of total stability constants of hydroxo complexes $[M(OH)_4]^-$ and $M(OH)_3$}. The calculated values of A and of the molar solubility of stable crystalline hydroxides $M(OH)_3$ in water and in alkali decrease in the order Ga → Al → In → Tl (see table). The results of the thermodynamic calculation are consistent with the experimental data on the solubility [8–11] and with the pH values corresponding to the complete precipitation of hydroxides: 3.6–7.6, 5.2–7.8, and 4.6–11 for $Ga(OH)_3$, $Al(OH)_3$, and $In(OH)_3$, respectively [4]. According to the experimental data, the solubility of H_3BO_3 in 1 M NaOH at 25°C is higher by 40% than S^0 and is controlled by the solubility of products formed by the reaction of $Na_2B_4O_7$ and $Na[B(OH)_4]$. In a solution containing excess alkali ($c \geq 5$ M), $NaBO_2$, which is a more water-soluble component, dominates [9, 10], which agrees with the experimental determination of H_3BO_3 solubility in 5 M NaOH and of A.

The molar solubility of stable hydroxides $M(OH)_3$ in acidic medium (pH 3) decreases upon the replacement of M element in the order B → Al → Ga → In → Tl, which coincides with the order in which the M^{3+} ionic radius increases and the polarizing effect of the cation decreases. In an acidic medium (pH 3), the solubility of very weak electrolytes H_3BO_3 and $Tl(OH)_3$ is intrinsic. The solubility of gallium(III) hydroxide is determined by hydroxo complexes $GaOH^{2+}$ and by Ga^{3+} cations; that of indium(III) hydroxide, by In^{3+} cations and $InOH^{2+}$ complexes; and that of aluminum hydroxide, by free Al^{3+} cations. In a strongly acidic medium (pH < 3), the solubility of a rather weak boric acid, unlike other Group IIIA hydroxides, decreases (our experimental value in 6 M HCl with pH –1.3 at 25°C is 0.16 M, i.e., 5.4 times less than the solubility in water).

CONCLUSIONS

(1) The molar solubility of hydroxides and metahydroxides of Group IIIA elements in water is largely determined by neutral complexes $M(OH)_3$ and depends on the structure and composition, considerably decreasing on passing from the amorphous to the difficultly soluble crystalline modification. Also, the solubility in water decreases on passing from difficultly soluble and rather weak acids H_3BO_3 (pH^0 3.7) and H_3GaO_3 (pH^0 6.2–6.6) to practically insoluble very weak base $Tl(OH)_3$ ($pH^0 \sim 7$).

(2) The effect of pH on the solubility of $M(OH)_3$ hydroxides and MO(OH) metahydroxides in aqueous alkaline and acidic media at 25°C was calculated by the thermodynamic method. The amphoterism parameter $A > 1$, decreasing in the order B → Tl → In → Al → Ga, was determined. The pH values of an acidic medium, below which M^{3+} ions are not bound into hydroxo complexes, were found.

(3) The minimal solubility and the values of pH corresponding to the most complete precipitation of the amphoteric hydroxides of aluminum, gallium, indium, and thallium(III) were calculated taking into account the formation of hydroxo complexes.

REFERENCES

1. Shkol'nikov, E.V., *Zh. Prikl. Khim.*, 2004, vol. 77, no. 8, pp. 1271–1274.

2. Shkol'nikov, E.V., *Zh. Prikl. Khim.*, 2005, vol. 78, no. 11, pp. 1819–1823.
3. Fishtik, I.F., and Vataman, I.I., *Termodinamika gidroliza ionov metallov* (Thermodynamics of the Hydrolysis of Metal Ions), Chisinau: Shtiintsa, 1988.
4. Lur'e, Yu.Yu., *Spravochnik po analiticheskoi khimii* (Handbook of Analytical Chemistry), Moscow: Khimiya, 1989.
5. Lidin, R.A., Andreeva, L.L., and Molochko, V.A., *Spravochnik po neorganicheskoi khimii. Konstanty neorganicheskikh veshchestv* (Handbook of Inorganic Chemistry. Constants of Inorganic Substances), Moscow: Khimiya, 1987.
6. Nazarenko, V.A., Antonovich, V.P., and Nevskaya, E.M., *Gidroliz ionov metallov v razbavlennykh rastvorakh* (Hydrolysis of Metal Ions in Dilute Solutions), Moscow: Atomizdat, 1979.
7. Kumok, V.N., Kuleshova, O.M., and Karabin, L.A., *Proizvedenie rastvorimosti* (Solubility Product), Novosibirsk: Nauka, 1983.
8. Efimov, A.I., *Svoistva neorganicheskikh soedinenii. Spravochnik* (Properties of Inorganic Compounds. Handbook), Leningrad: Khimiya, 1983.
9. Nekrasov, B.V., *Osnovy obshchei khimii* (Fundamentals of General Chemistry), St. Petersburg, 2003, vols. 1, 2.
10. *Khimicheskaya entsiklopediya* (Chemical Encyclopedia), Knunyants, I.K., and Zefirov, N.S., Eds., Moscow: Bol'shaya Ross. Entsiklopediya, 1988, 1998, vols. 1–5.
11. Remy, H., *Lehrbuch der anorganischen Chemie*, Leipzig: Geest und Portig, 1961, vol. 2.
12. Vasil'ev, V.P., *Termodinamicheskie svoistva rastvorov elektrolitov* (Thermodynamic Properties of Electrolyte Solutions), Moscow: Vysshaya Shkola, 1982.
13. Karapet'yants, M.Kh., and Karapet'yants, M.L., *Osnovnye termodinamicheskie konstanty neorganicheskikh i organicheskikh veshchestv* (Basic Thermodynamic Constants of Inorganic and Organic Substances), Moscow: Khimiya, 1968.
14. *Spravochnik po elektrokhimii* (Handbook of Electrochemistry), Sukhotin, A.M., Ed., Leningrad: Khimiya, 1981.

ISSN 1070-4272, Russian Journal of Applied Chemistry, 2008, Vol. 81, No. 9, pp. 1508–1511. © Pleiades Publishing, Ltd., 2008.
Original Russian Text © S.V. Shikhalev, S.A. Ermakov, I.F. Reshetnikov, 2008, published in Zhurnal Prikladnoi Khimii, 2008, Vol. 81, No. 9, pp. 1432–1435.

PHYSICOCHEMICAL STUDIES OF SYSTEMS AND PROCESSES

Simulation of Nonstationary Heat Transfer in Jacketed Apparatus

S. V. Shikhalev, S. A. Ermakov, and I. F. Reshetnikov

Ural State Economical University, Yekaterinburg, Russia

Received February 18, 2008

Abstract—Nonstationary heat transfer in jacketed apparatus was studied.

DOI: 10.1134/S1070427208090061

Chemical technology and food and pharmaceutical industries widely use jacketed vessels with steam heating without an agitating device, in which heating and cooling, extraction, crystallization, dissolution, chemical reactions, etc. are performed. In most of these processes, temperatures of both heat-transfer agents and heat transfer coefficient in the apparatus vary in the course of time, i.e., the heat-transfer process occurs under nonstationary conditions.

However, designing a jacketed apparatus by the available procedures for thermal calculations, mostly based on stationary heat-transfer models, requires a longer calculation time, impairs the output capacity, and leads to a substantial energy consumption and higher steel intensity.

In particular, it was assumed in [1, 2] that the heat-transfer coefficient k is constant and the temperature of process media varies by the exponential law, which disagrees with the actual working mode of jacketed apparatus [3]. The procedure for mathematical simulation of nonstationary temperature fields of a vessel, suggested in [4], employs partial local heat-transfer coefficients, which frequently cannot be calculated using the suggested criterion equations or can be, but with a gross error. The linearized model of the heat-up mode of jacketed apparatus makes it possible to determine in an easier way the area of the heat-transfer surface and the heat-up time [3]. However, for finding the operation parameters of a jacketed apparatus (temperature and pressure of process media), which are to be known for automation of vessels or other process purposes, the linearized model should be further refined.

The difficulties encountered in thermal calculations of this equipment initiated development of a model of nonstationary heat-transfer process that would enable thermal engineering calculations of jacketed apparatus with a sufficient accuracy.

We simulated the heat-up mode of jacketed apparatus using the nonstationary heat-transfer equation [3]

$$Q = F\int_0^{\tau_h} k(\tau)[l_m(\tau) - l_l(\tau)]d\tau, \quad (1)$$

where $k(\tau)$ is the coefficient of heat transfer from the heat-carrying agent in the jacket of the apparatus to a medium being heated (W m^{-2} °C^{-1}); $t_m(\tau)$, volume-average temperature of the steam-and-gas mixture in the jacket of the apparatus (°C); $l_l(\tau)$, volume-average temperature of the medium being heated (°C); F, area of the heat-exchange surface (m^2); τ_h, heat-up time of the apparatus (s); and Q, amount of heat transferred to the product by the heat-exchange surface with area F during a time interval τ_h (J).

To solve Eq. (1), we performed a number of experiments on heating of process media in jacketed apparatus with different capacities and found the functional dependences of the thermal parameters of the heat-up mode (temperature of process media and heat-transfer coefficients) on the process duration.

As objects of our experimental studies served electric jacketed apparatus with capacities of 0.02, 0.04, and 0.06 m^3 (Fig. 1).

The temperatures of the process media and the lid in heat-up of a jacketed apparatus were measured using Chromel–Copel thermocouples with thermal electrodes 0.2 mm in diameter and automated re-

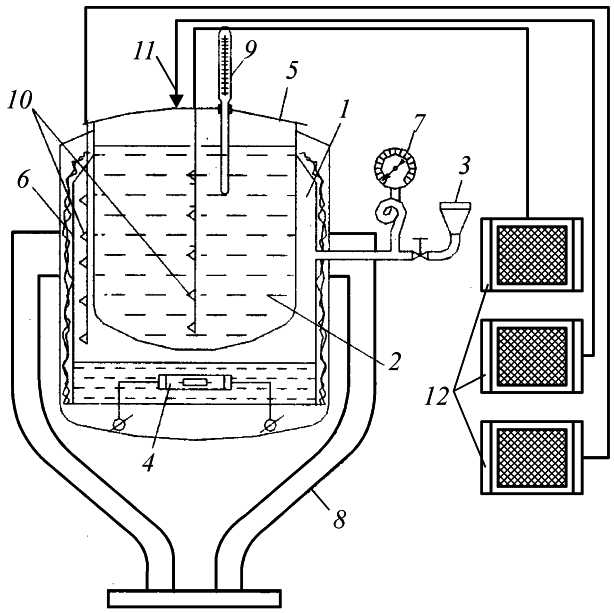


Fig. 1. Schematic of the experimental stand: (*1*) water-steam jacket, (*2*) boiling vessel, (*3*) feeding funnel, (*4*) tubular electric heaters, (*5*) cover, (*6*) insulation, (*7*) pressure gage, (*8*) console, (*9*) thermometer, (*10*) thermocouples for measuring the temperature of the working media, (*11*) thermocouple for measuring the cover temperature, and (*12*) automated multipoint potentiometer of the KSP-4 type.

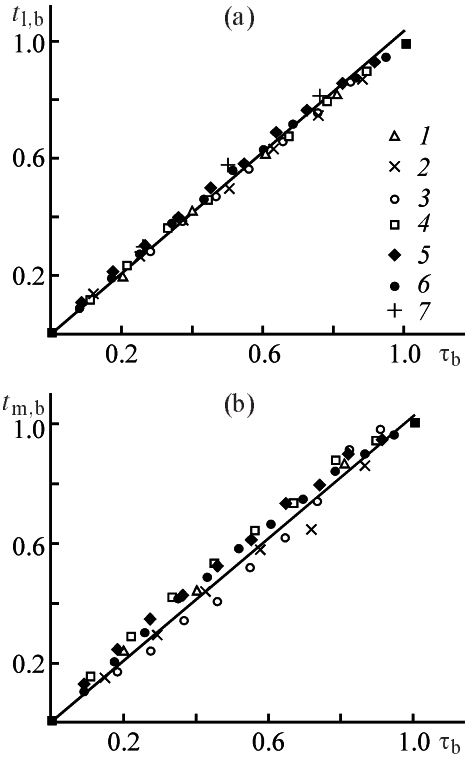


Fig. 2. Temperature of process media vs. the process duration τ_b. (a) Temperature of the product, $t_{l,b}$; and (b) temperature of the steam-and gas mixture, $t_{m,b}$. (*1*) KPE-20 (water), (*2*) KPE-40 (water), (*3*) KPE-60 (water), (*4*) KPEM-60 (10% solution of sugar), (*5*) KPEM-60 (20% solution of sugar), (*6*) KPEM-60 (5% solution of table salt), and (*7*) vessel of dairy industry [6].

cording by multipoint potentiometers of the KSP-4 type (accuracy class 0.25).

The working volume of the apparatus was filled with a rated amount of a product with an ambient temperature. As process media served solutions with different physicochemical properties: sugar solution with 10 to 20% dry substances and a 5% solution of table salt. The warming-up parameters of these solutions were compared with data on warming-up of a reference liquid (water). On switching-on the electric circuit with measuring devices and apparatus heaters, the temperatures of the technological media, heat-transfer surface, and steam-and-gas mixture in the apparatus jacket were simultaneously measured at regular intervals of time, $\Delta\tau$ = 180 s.

The local-in-time coefficient of heat transfer from the steam-and-vapor mixture to the contents of the boiling vessel was found using the relationship

$$k(\tau) = \frac{Q_{tot} - Q_{lid}}{F[t_m(\tau) - t_l(\tau)]\Delta\tau},$$

where Q_{tot} is the amount of heat transferred across the wall of the working vessel in a time τ (J), and Q_{lid}, the heat loss by the apparatus in a time $\Delta\tau$ (J).

We processed the experimental data in accordance with the recommendations of [5]. We presented the results of our experiments as graphical dependences $t_l = f(\tau)$, $t_m = f(\tau)$, and $k = f(\tau)$.

To generalize the experimental data on heat-up of jacketed apparatus, the graphical temperature dependences were plotted in the relative coordinates $t_{l,b} = f(\tau_b)$ and $t_{m,b} = f(\tau_b)$ (Fig. 2). We took as the relative temperature of the liquid

$$t_{l,b} = (t_l - t_{l,in})(t_{l,fin} - t_{l,in})^{-1}, \quad (2)$$

where t_l, $t_{l,in}$, and $t_{l,fin}$ are, respectively, the running temperature, that at the beginning of the heat-transfer process, and that at the end of the heat-up process (°C).

Similarly, we have for the relative temperature of

Testing of the linear model of heat-transfer in a jacketed apparatus

Process medium	Apparatus volume, m^3	Heat-up time τ_h, min		Error Δ, %	Temperature difference Δt_{fin} at the end of the heat-up, °C		Error Δ, %	Apparatus parameters*
		experiment	calculation by (10)		experiment	calculation by (10)		
Water	0.02	35	37.7	7.7	9.4	10.5	11.7	$F = 0.29$ m^2, $N = 3$ kW, $k_{fin} = 1276$ W m^{-2} °C^{-1}
	0.03	40.1	41.4	3.3	8.7	9	3.4	$F = 0.41$ m^2, $N = 3$ kW, $k_{fin} = 1289$ W m^{-2} °C^{-1}
	0.04	34.5	32.6	5.4	11.4	10.5	7.9	$F = 0.51$ m^2, $N = 9$kW, $k_{fin} = 1262$ W m^{-2} °C^{-1}
	0.06	45	45.6	1.4	8.7	8.9	2.3	$F = 0.75$ m^2, $N = 9$ kW, $k_{fin} = 1109$ W m^{-2} °C^{-1}
10% solution of sugar	0.05	33	36.5	10.6	8.9	10.1	13.5	$F = 0.62$ m^2, $N = 9$ kW, $k_{fin} = 1257$ W m^{-2} °C^{-1}
20% solution of sugar	0.05	39	43.4	11.4	7.7	8.7	12.9	$F = 0.62$ m^2, $N = 9$ kW, $k_{fin} = 1357$ W m^{-2} °C^{-1}
5% solution of salt	0.05	41	44.2	7.8	9.4	10.4	10.6	$F = 0.72$ m^2, $N = 9$ kW, $k_{fin} = 1025$ W m^{-2} °C^{-1}

* N is the power of electric heaters.

the steam-and-gas mixture:

$$t_{m,b} = (t_m - t_{m,in})(t_{m,fin} - t_{m,in})^{-1}, \quad (3)$$

where t_m, $t_{m,in}$, and $t_{m,fin}$ are, respectively, the running temperature, that at the beginning of the heat-transfer process, and that at the end of the heat-up process (°C).

We took as the relative time the ratio between the running time τ and the warming-up time τ_h of the contents of the boiling vessel:

$$\tau_b = \tau/\tau_h, \quad (4)$$

As can be seen in Fig. 2a, the family of points for jacketed apparatus is described with a certain accuracy (average relative error 2.9%) by the straight-line equation

$$t_{l,b} = 1.04\tau_b, \quad (5)$$

On substituting the dimensionless quantities $t_{l,b}$ and τ_b from expressions (2) and (4) into the straight-line equation (5), we obtained a correlation dependence of the temperature of the liquid in the working vessel on the heat-up time for jacketed apparatus:

$$t_l(\tau) = t_{l,in} + 1.04(t_{l,fin} - t_{l,in})\tau/\tau_h. \quad (6)$$

Similarly to (6), we obtained a correlation dependence of the temperature of the steam-and-gas mixture on the heat-up time, with a relative error of 7.9%:

$$t_m(\tau) = t_{m,in} + 1.04(t_{m,fin} - t_{m,in})\tau/\tau_h. \quad (7)$$

By plotting the dependence of the heat-transfer coefficient on the temperature difference Δt in the log–log coordinates (Fig. 3), we found an approxi-

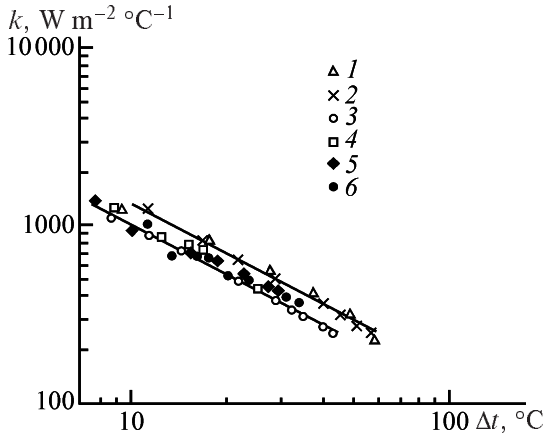


Fig. 3. Heat-transfer coefficient k vs. the temperature difference Δt. (*1*) KPE-20 (water), (*2*) KPE-40 (water), (*3*) KPE-60 (water), (*4*) KPEM-60 (10% solution of sugar), (*5*) KPEM-60 (20% solution of sugar), and (*6*) KPEM-60 (5% solution of table salt).

mate law by which k varies during the heat-up.

As can be seen in Fig. 3, the experimental data for jacketed apparatus form a family of parallel straight lines, described in the dimensionless representation by the dependence

$$k/k_{fin} = (\Delta t/\Delta t_{fin})^{-0.92}, \quad (8)$$

where k_{fin} is the heat-transfer coefficient in the final period of the heat-up (W m^{-2} °C^{-1}); Δt_{fin}, temperature difference in the final period of the heat-up (°C); and Δt, running temperature difference (°C).

The relative error of approximation of the experimental points in Fig. 3 did not exceed, on average, 5.2%.

With account of the fact that the temperature difference Δt is equal to the difference between the temperatures of the heat-carrying agents in the apparatus, dependence (8) takes the form

$$k(\tau) = k_{fin}\{[t_m(\tau) - t_l(\tau)]/(t_{m,fin} - t_{l,fin})\}^{-0.92}. \quad (9)$$

On substituting the local-in-time temperatures of media, defined by expressions (6) and (7), and the heat-transfer coefficient (9) into the nonstationary heat-transfer equation (1), we obtained a refined thermal engineering model of nonstationary heat transfer in bulk jacketed apparatus:

$$Q = 0.89Fk_{fin}\Delta t_{fin}^{0.92}(\Delta t_{in} - \Delta t_{fin})^{-1}(\Delta t_{in}^{1.08} - 1.04\Delta t_{fin}^{1.08})\tau_h, \quad (10)$$

where the subscripts "in" and "fin" correspond for all the parameters to the beginning and end of warming-up of the contents of the working vessel of the apparatus, respectively.

Our model (10) was tested against experiments on heat-up of jacketed apparatus with varied physicochemical parameters of the product and different ratios between the capacity and delivered power. The results obtained are listed in the table.

CONCLUSIONS

A nonlinear model describing the nonstationary heat-transfer process with an acceptable error was suggested. The model enables substantiated thermal engineering calculations of bulk jacketed apparatus operating in the heat-up mode.

REFERENCES

1. Gel'perin, N.I., *Osnovnye protsessy i apparaty khimicheskoi tekhnologii* (Basic Processes and Apparatus of Chemical Engineering), Moscow: Khimiya, 1981.
2. Kasatkin, A.G., *Osnovnye protsessy i apparaty khimicheskoi tekhnologii* (Basic Processes and Apparatus of Chemical Engineering), Moscow: Khimiya, 1973, 9th ed.
3. Minukhin, L.A., Shikhalev, S.V., and Reshetnikov, I.F., *Izv. Vyssh. Uchebn. Zaved., Pishch. Tekhnol.*, 2006, no. 5, pp. 56–59.
4. Tugolukov, E.N., *Khim. Prom–st.*, 2004, vol. 81, no. 2, pp. 84–92.
5. Batuner, L.M. and Pozin, M.E., *Matematicheskie metody v khimicheskoi tekhnike* (Mathematical Methods in Chemical Technology), Moscow: Khimiya, 1968.
6. Russkikh, V.M. and Filinkov, A.S., *Molochn. Prom–st.*, 2004, no. 4, pp. 53–55.

ISSN 1070-4272, Russian Journal of Applied Chemistry, 2008, Vol. 81, No. 9, pp. 1512–1517. © Pleiades Publishing, Ltd., 2008.
Original Russian Text © V.V. Samonin, M.L. Podvyaznikov, E.A. Spiridonova, A.Yu. Shevkina, 2008, published in Zhurnal Prikladnoi Khimii, 2008, Vol. 81, No. 9, pp. 1436–1441.

PHYSICOCHEMICAL STUDIES OF SYSTEMS AND PROCESSES

Effect of Surfactants on Properties of Composite Sorbents Based on Fullerene Black

V. V. Samonin, M. L. Podvyaznikov, E. A. Spiridonova, and A. Yu. Shevkina

St. Petersburg State Institute of Technology (Technical University), St. Petersburg, Russia

Received May 17, 2006

Abstract—Synthesis of composite sorbents by molding of fullerene blacks with a solution of polyacrylamide as a binder and surfactants was studied. The effect of surfactants of varied nature on the wettability of fullerene blacks and the sorption and mechanical properties of the molded products obtained was considered.

DOI: 10.1134/S1070427208090073

Composite sorbents are systems constituted by a matrix and a filler. Inorganic binders, organic polymers, metals, and carbon materials commonly serve as matrices, and both inorganic (silica gel, zeolites, active alumina) and organic (ion-exchange resins, activated carbon) sorbents, as fillers. Polymers serve as binders providing that a sorbent can be obtained as a molded product and, in particular, as pellets, blocks, and plates. Simultaneously, polymers used for molding affect the sorption and strength characteristics of the composites obtained [1, 2].

We used as a filler fullerene black (FB), which is a by-product formed in synthesis of fullerenes by combustion of graphite in an electric arc [3] and has good sorption properties [4]. In particular, the adsorption capacity for benzene from the gas phase is about 0.6–0.8 g g^{-1}, and the specific surface area determined with argon is within the range 50–250 m^2 g^{-1} and strongly depends on the conditions in which fullerenes are obtained. The content of fullerenes in the black used in the study was 4.2% ($FB_{4.2}$).

The practical use of FB as a sorbent is hindered by the fact that it is a highly dispersed material whose particle size is mostly within the range 0.5–5 μm. Therefore, it is appropriate to use this material as a component of a molded composite sorbing article. In this study, we produced a molded material from FB in the form of pellets.

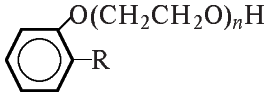
We used as a binder polyacrylamide (PAA) in the form of an aqueous gel [TU (Technical Specification) 6-01-1049–92] with the following parameters: mass fraction of the main substance, 6.1%; sedimentation rate of copper oxide, 4.2 mm s^{-1}; kinematic viscosity, 4.2 (at a 0.25% mass fraction of polyacrylamide); residual content of monomers 0.004; and that of acrylamide, 0.004. The molecular mass of PAA was about 10^6 g mol^{-1}, as determined viscometrically after Staudinger [5]. The choice of the polymer was governed by environmental and economical considerations.

The procedure used to obtain a molded material is based on mixing FB with an aqueous solution of PAA in a certain ratio. The resulting paste was molded into pellets 3 cm in diameter and 1 cm high. The molded material was kept at 20°C for two days and then was thermally treated to remove excess amounts of moisture and surfactants providing wettability of the hydrophobic FB with an aqueous solution of the hydrophilic polymer and preventing direct interaction of PAA with the active surface of FB. Molding of FB and PAA without additives markedly impairs the sorption characteristics of the resulting molded material, and the very process of mixing and molding is hindered by the hydrophobic properties of the filler.

It has been suggested previously [1] that the decrease in the sorption capacity of sorbing materials of this kind, compared to the capacity of the starting sorbent, is primarily due to blocking of the surface of the sorbent-filler by a thin (10–50 μm) PAA film formed around its particles, which hinders diffusion of adsorbate molecules to the sorbent. In addition, in the case of the filler under consideration, the functional amide groups of the polymer interact [6] with active acid centers of FB, represented by carbonyl,

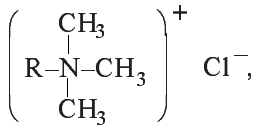
phenol, hydroxy, and other groups, whose presence is confirmed by IR spectroscopy and potentiometric titration [7]. This leads to adsorption of PAA on the FB surface and, as a result, impairs the sorption characteristics of the molded product.

To protect the surface of FB and to diminish the adsorption of the polymer on its surface in the stage of mixing of the starting products, the filler (black) is preliminarily treated with solutions of surfactants of varied structure: a nonionic surfactant (NS), Neonol-10



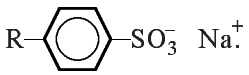
$R = C_9$, $n = 10$;

cationic surfactant (CS), quaternary ammonium compound



$R = C_{10}$–C_{16};

and anionic sufactant (AS), linear alkylbenzenesulfonate (LABS)



To determine the minimum necessary amount of a surfactant, we performed a set of experiments in which the effect of the surfactant concentration on the intensity of FB wetting was judged from the rate of FB sedimentation in aqueous solutions of surfactants. In accordance with the procedure, equal-weight portions of FB were placed in surfactant solutions with different concentrations and the same volume. After that, the time of complete FB sedimentation was determined as the time necessary for complete sedimentation of visually observed black particles in a surfactant solution, measured with a stopwatch. Figure 1 shows the resulting graphical dependences of the sedimentation time on the surfactant concentration.

Figure 1 shows that it is inexpedient to use surfactant solutions with concentrations lower than 0.8 wt %, because this impairs the stabilizing effect of a surfactant on the FB suspension, determined from the FB sedimentation rate in aqueous solutions of surfactants. At concentrations higher than 0.8 wt %, the sedimentation time of black particles becomes essentially constant, which suggests that optimal surfactant concentrations are reached.

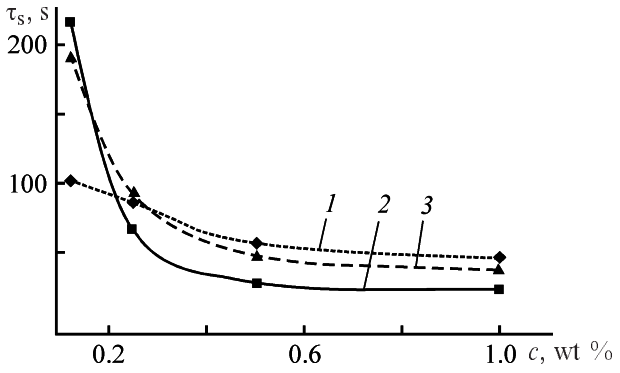


Fig. 1. Sedimentation rate of fullerene black vs. the concentration c of surfactants of varied ionic nature. (τ_s) Sedimentation time. Surfactant: (*1*) AS, (*2*) CS, and (*3*) NS.

At solution concentrations higher than 0.25 wt %, the FB sedimentation rate in a solution of the quaternary ammonium base exceeds that for other surfactants of the corresponding concentrations. This suggests that the interaction of FB with the quaternary ammonium base is more intense. At a concentration of 0.5 wt %, the time of FB wetting with an aqueous solution of CS is 1.4 and 1.5 times shorter than those for solutions of NS and CS (25, 46, and 54 s, respectively).

The interaction of a surfactant with FB is largely determined by the nature of the FB surface. It has been shown previously by means of potentiometric titration by the Boehm method [8] that the FB surface bears a large number of acid groups, whose amount substantially exceeds that for activated carbons. In all probability, the interaction of acid groups on the fullerene black surface with the quaternary ammonium groups of CS intensifies wetting processes, compared with processes associated with nonspecific interaction with AS and NS. The acceleration of the wetting of FB with CS, observed visually and recorded instrumentally, is illustrated by Fig. 1. The nature of the interaction CS groups with FB is the same as that in the FB–PAA interaction. By the nonspecific interaction we understand the adsorption due to the van der Waals interaction.

Use of surfactant solutions of concentrations higher than 2 wt % is inexpedient because such a high concentration does not make higher the wetting rate, whereas the interaction of FB with a surfactant may give rise to film effects.

In addition, surfactants affect the sorption and mechanical properties of the molded product (Table 1). The sorption properties of the materials

Table 1. Effect of surfactants on the sorption characteristics and mechanical strength of molded samples

Surfactant	W_S, $cm^3\ g^{-1}$		X, $mg\ g^{-1}$	E^{Cu}, $mg\ g^{-1}$	A_a, mg-equiv g^{-1}		S_{sp}, $m^2\ g^{-1}$	WR, %
	C_6H_6	C_2H_5OH			NaOH	$NaHCO_3$		
Initial $FB_{4.2}$	0.43	0.30	–	42	–	–	210	–
AS	0.76	0.50	141	79	5.7	5.6	185	80
CS	0.84	0.55	149	79	7.5	6.5	260	70
NS	0.68	0.44	140	55	5.6	5.5	140	75

obtained were evaluated using standard techniques by determining the following parameters: limiting volume W_S of the sorption space with respect to vapors of organic compounds [9]; specific surface area S_{sp} of samples, measured by the method of thermal desorption of argon, with data processing in terms of the Brunauer–Emmett–Teller (BET) theory (for instrumental and mathematical description, see [10]); amount A_a of acid groups, found by potentiometric titration by the Boehm method; sorption activity with respect to dyes (Methylene Blue, X) [11]; sorption activity E^{Cu} with respect to heavy metal cations, measured with a KFK-2MP photocolorimeter. The mechanical properties of the materials were evaluated by the wear resistance WR [12].

It is noteworthy that Table 1 lists results for samples obtained in the optimal conditions. The molding conditions are identical for all the samples represented in Table 1: the time of mixing of FB with a surfactant was 5 min, and that of further mixing with a PAA solution, 10 min; the mixing was performed in a paddle mixer at a treatment temperature T = 180°C and duration of 1 h.

According to the results of the study (Table 1), the composite sorbents produced by molding exhibit a sorption capacity that surpasses, in the case when CS is used, the similar characteristics of the starting material nearly twofold for benzene and ethanol, and more than 1.5-fold for copper cations. The achievable sorption capacity for copper (79 $mg\ g^{-1}$) substantially exceeds the corresponding parameter for industrial activated carbons (40–50 $mg\ g^{-1}$), determined under similar conditions. The materials are inferior in sorption capacity for Methylene Blue dye (140–149 $mg\ g^{-1}$) to industrial activated carbons OU-A (no less than 225 $mg\ g^{-1}$).

The sorption characteristics of the composite materials molded with the use of CS are better than those obtained with NS and AS both in sorption of vapors of organic compounds from the gas phase and in sorption of the organic dye and copper cations from the aqueous medium. In addition, the specific surface area substantially increases, by factors of 1.4 and 1.8, compared to the cases of AS and NS, respectively. The possible reason for such a difference in sorption properties is that the nature of a surfactant largely determines the mechanism by which PAA interacts with the black to give the corresponding structure of the sorbing material obtained. NS and AS interact with the FB surface presumably by the dispersion interaction mechanism. In the interaction of CS with the FB surface, the most probable is the interaction with active acid groups whose amount on the surface of the material is rather large (Table 1).

Thus, in the first stage of synthesis of the molded material by treatment of the starting FB with a surfactant, the wetting of the sorbent surface by water is provided by its interaction with alkyl chains. When a surfactant is mixed with the black, a film of the surfactant is formed on the surface of FB particles. The hydrophilic groups of the surfactant are directed toward the aqueous solution and the surfactant interacts with PAA (in the second stage of synthesis of the molded material) at these hydrophilic groups. It seems unlikely that the surfactant could be reoriented with its alkyl groups looking toward PAA because the hydrophobicity of the fullerene surface is very strong and exceeds that of the alkyl chain of PAA. Thus, PAA does not directly interact with the FB surface. In the subsequent thermal treatment, the surfactant is partly removed and a free space appears in the structure of the molded material, which is confirmed by the increase in the specific surface area of the sample. Owing to this free space, the sorption capacity of FB contained in the composite material for vapors of organic substances, benzene, and ethanol somewhat increases. Because the functional groups of FB remain free, its sorption capacity for copper cations, sorbed by the ion-exchange mechanism, grows. At the same time, the blocking of the FB surface by a surfactant,

with its subsequent partial removal, diminishes the interaction of PAA with the filler, which affects the strength of the molded material.

Thus, partial removal of surfactants from the pellets is an important stage of the synthesis of composite sorbents, which determines their sorption and strength properties. The temperature at which the material was treated was maintained within the range 150–200°C, which resulted in that the surfactant content of the molded sorbing material decreased to an extent sufficient for reaching its acceptable characteristics. The thermal treatment also leads to formation of interchain bonds via interaction of the amide groups of PAA [13], which provides a sufficiently high stability of the molded material against water. On raising the temperature to above 180°C, the composite sorbent being synthesized disintegrates [1], which primarily occurs because of the decomposition of the binder (PAA) and the resulting decrease in the strength of the molded material. Thus, the optimal temperature range for performing the given stage is 165–180°C. The results obtained are listed in Table 2.

It is noteworthy that the conditions in which materials of this series were synthesized differed only in agitation intensity from those in which the composite sorbents whose properties are listed in Table 1 were obtained. The latter were produced with manual agitation of the paste. It can be seen that the absolute values of the sorption characteristics of the materials slightly change, but all the main trends noted above are preserved.

The data in Table 2 suggest that, on elevating the treatment temperature, surfactants are most effectively removed from FB and the structure of the material is transformed to a certain extent and, accordingly, both the sorption capacity of the composite sorbent for benzene and ethanol vapors and the specific surface area increase.

A rather important factor affecting the filler–surfactant interaction and the properties of the sorbing material obtained is the duration of mixing of these components. Table 3 lists sorption characteristics of samples based on $FB_{4.2}$ fullerene black and obtained at different durations of mixing with a surfactant for the example of CS. The finishing thermal treatment of the composite material obtained was performed at 150°C for 1 h.

It follows from Table 3 that, on making longer the duration of FB mixing with CS, the sorption characteristics of the materials obtained are considerably improved. Upon agitation for 25 min, the sorption capacity for benzene and ethanol increases by 20 and 44%, respectively, compared with agitation for 5 min. This points to a more homogeneous distribution of the surfactant over the FB surface. In some cases, the sorption parameters of the materials obtained surpass those of the starting FB. This occurs because, in the course of interaction of fullerene materials (fullerites, fullerene blacks) with various compounds (organic solvents, water), the structure of the fullerene materials is transformed, including an increase in the porosity and sorption capacity [14, 15].

Making the agitation duration longer also leads to a substantial decrease in strength (by 20%). In all probability, this is due to a change in the meso- and

Table 2. Effect of the treatment temperature on sample properties

Type of surfactant	W_S, $cm^3\ g^{-1}$		S_{sp}, $m^2\ g^{-1}$	WR, %
	C_6H_6	C_2H_5OH		
	T = 150°C			
AS	0.52	0.43	120	80
CS	0.56	0.49	130	65
NS	0.48	0.39	90	75
	T = 180°C			
AS	0.73	0.45	180	70
CS	0.81	0.51	255	60
NS	0.65	0.41	140	70
	T = 200°C			
AS	0.76	0.47	190	65
CS	0.85	0.57	–	60
NS	0.71	0.45	–	65

Table 3. Sorption capacity, specific surface area, and wear resistance of samples produced at different durations of FB mixing with CS

τ, min	W_S, $cm^3\ g^{-1}$		S_{sp}, $m^2\ g^{-1}$	WR, %
	C_6H_6	C_2H_5OH		
5	0.52	0.53	100	70
10	0.55	0.61	115	70
15	0.58	0.88	150	65
20	0.63	0.91	195	60
25	0.67	0.95	260	55

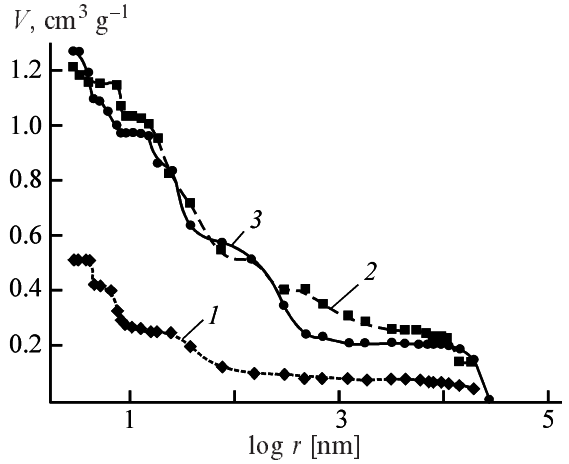


Fig. 2. Effect of the agitation duration on the pore volume V distribution with respect to pore sizes r, found by mercury porosimetry. Agitation time, min: (*1*) 5, (*2*) 15, and (*3*) 25.

macroporous structure of the composite sorbents obtained. Fig. 2 shows how the duration of FB mixing with PAA affects the pore volume distribution with respect to pore size in the composite sorbent obtained, measured by mercury porosimetry.

On raising the duration of FB mixing with CS to 15–25 min, mostly the volume of macropores (with radii of 100–30000 nm) increases, and just this circumstance impairs the strength of the product obtained. Macropores appear in the product because separate filler–binder conglomerates are formed in the course of agitation [16]. In the case in question, these are FB–PAA conglomerates whose size predetermines the size of macropores. The strength of the material decreases on passing from a homogeneous system to that constituted by a set of higher-density conglomerates.

Thus, the time of mixing of the filler and a surfactant is an important process parameter whose optimal value should be found because of its influence on the sorption and strength characteristics of the molded material.

Table 4. Sorption characteristics and strength of samples produced at different durations of FB mixing with PAA

τ, min	W_S, cm^3 g^{-1}		WR, %
	C_6H_6	C_2H_5OH	
10	0.52	0.53	70
20	0.57	0.62	65
30	0.56	0.59	60
35	0.55	0.57	50

The properties of the molded sorbents obtained are also affected by other process parameters and, in particular, by the duration of filler mixing with the binder (Table 4), which was varied in the range 10–35 min. The time of mixing with a surfactant in a mechanical paddle mixer was 5 min for all the materials; the thermal treatment was performed at 150°C for 1 h.

As follows from Table 4, the agitation duration strongly affects the strength properties of the materials obtained. As the agitation duration is raised, the wear resistance decreases from 70 to 50% (by a factor of 1.4), which is highly important for molded sorbents. On making longer the agitation duration, the sorption properties of the materials also insignificantly change, in particular, the sorption capacity for benzene and ethanol passes through a maximum. The maximum sorption capacity for ethanol was 0.62 cm^3 g^{-1} at an agitation duration of 20 min, which exceeds by 17% the same parameter for the material synthesized at an agitation duration of 10 min (at the measurement error of 3–4%). The wear resistance of this material was 65%.

Thus, it was shown that the most important stage in synthesis of composite sorbents based on FB and PAA is the additional treatment of FB with a solution of a surfactant. The strongest influence on the FB surface is exerted by the cation-active surfactant, whose use improves the sorption characteristics of the composites obtained.

Raising the thermal treatment temperature leads to an increase in the sorption capacity of the material for organic compounds from the gas phase and in the specific surface area, which possibly occurs because space is freed via partial removal of the surfactant and structural rearrangement. According to the experimental data, the optimal temperature is 160–180°C, which, on the one hand, gives a sufficiently developed porous structure and, on the other, leads to formation of a cross-linked [13] water-resistant polymer-binder.

CONCLUSIONS

(1) The possibility of obtaining high-strength molded sorbents based on fullerene black and a polymeric binder polyacrylamide was demonstrated. The key factors determining the properties of the material obtained are the conditions of mixing of the fullerene black with a surfactant and polyacrylamide and the thermal treatment of the materials.

(2) An optimization of the processes allowed preparation of composite sorbents with a wear resistance of up to 75% (relative to the initial mass of the sorbent) and a sorption capacity for organic solvent vapors of 0.7–0.8 $cm^3 g^{-1}$, which surpasses the corresponding parameters of most of industrial activated carbons.

(3) It was shown that the materials surpass commercial brands of activated carbons in sorption capacity for copper ions, but are inferior to these carbons in sorption capacity for Methylene Blue dye.

ACKNOWLEDGMENTS

The study was supported by the Russian Foundation for Basic Research (project nos. 04-03–32115 and 05-08–50240).

REFERENCES

1. Fedorov, N.F., Ivakhnyuk, G.K., Samonin, V.V., et al., *Zh. Prikl. Khim.*, 1991, vol. 64, no. 5, pp. 1054–1059.
2. Samonin, V.V., Nilova, M.I., Podvyaznikov, M.L., et al., *Sorbenty i sorbtsionnye protsessy* (Sorbents and Sorption Processes), Leningrad: Leningr. Tekhnol. Inst. im. Lensoveta, 1990, pp. 13–20.
3. Sidorov, L.N., Yurovskaya, M.A., Borshchevskii, A.Ya., et al., *Fullereny* (Fullerenes), Moscow: Ekzamen, 2005.
4. Samonin, V.V. and Slutsker, E.M., *Zh. Fiz. Khim.*, 2005, vol. 79, no. 1, pp. 100–105.
5. Braun, D., Cherdron, H., and Kern, W., *Praktikum der makromolekularen organischen Chemie*, Heidelberg: Huthig, 1971.
6. Kel'tsev, N.V. and Tesner, P.A., *Sazha: Svoistva, proizvodstvo i primenenie* (Carbon Black: Properties, Production, and Use), Moscow: Gostoptekhizdat, 1952.
7. Slutsker, E.M., Adsorption Properties of Nanostructured Carbon Materials of the Fulleroid Type, *Cand. Sci. Dissertation*, St. Petersburg, 2005.
8. Samonin, V.V. and Slutsker, E.M., *Khim. Prom–st.*, 2004, vol. 81, no. 10, pp. 534–540.
9. Boikova, G.I. and Pulerevich, M.Ya., *Izmerenie izoterm sorbtsii parov organicheskikh veshchestv na razlichnykh adsorbentakh v dinamicheskikh usloviyakh: Metodicheskie ukazaniya k laboratornym rabotam* (Measurement of Sorption Isotherms of Organic Substance Vapors on Various Adsorbents under Dynamic Conditions: Methodological Recommendations for Laboratory Works), Leningrad: Leningr. Tekhnol. Inst. im. Lensoveta, 1983.
10. Vorozhbitova, L.N., Ivakhnyuk, G.K., Samonin, V.V., et al., *Opredelenie udel'noi poverkhnosti tverdykh tel khromatograficheskim metodom: Metodicheskie ukazaniya* (Chromatographic Determination of the Specific Surface Area of Solids: Methodological Recommendations), Leningrad: Leningr. Tekhnol. Inst. im. Lensoveta, 1988.
11. *GOST* (State Standard) *4453–74: Powdered Clarifying Activated Charcoal: Technical Specification*, Moscow: Izd. Standartov, 1974.
12. *GOST* (State Standard) *16188–70: Sorbents: Method for Determining the Wear Resistance*, Moscow: Izd. Standartov, 1970.
13. Nikolaev, A.F. and Okhrimenko, G.I., *Vodorastvorimye polimery* (Water-Soluble Polymers), Leningrad: Khimiya, 1979.
14. Berezkin, V.I., Samonin, V.V., Nikonova, V.Yu., et al., Abstracts of Papers, *7th Biennial Int. Workshop in Russia "Fullerenes and Atomic Clusters,"* IWFAC'2005, St. Petersburg (Russia), June 27–July 1, 2005, p. 257.
15. Samonin, V.V., Nikonova, V.Yu., and Spiridonova, E.A., *Vliyanie obrabotki razlichnymi rastvoritelyami na poglotitel'nye svoistva fullerenov i fullerensoderzhashchikh materialov* (Effect of Treatment with Various Solvents on Absorbing Properties of Fullerenes and Fullerene-Containing Materials), available from VINITI, no. 1535-V, November 23, 2005.
16. Ur'ev, N.B., *Usp. Khim.*, 2004, vol. 73, no. 1, pp. 31–62.

ISSN 1070-4272, Russian Journal of Applied Chemistry, 2008, Vol. 81, No. 9, pp. 1518–1523. © Pleiades Publishing, Ltd., 2008.
Original Russian Text © N.P. Mustafaev, M.A. Kulieva, Yu.B. Ramazanova, K.N. Mustafaev, N.N. Novotorzhina, 2008, published in Zhurnal Prikladnoi Khimii, 2008, Vol. 81, No. 9, pp. 1442–1448.

PHYSICOCHEMICAL STUDIES OF SYSTEMS AND PROCESSES

S-Cinnamyl Esters of Thiocarbonic Acids as Additives to Lubricating Oils

N. P. Mustafaev, M. A. Kulieva, Yu. B. Ramazanova, K. N. Mustafaev, and N. N. Novotorzhina

Institute of Chemistry of Additives, National Academy of Sciences of Azerbaijan, Baku, Azerbaijan

Received August 14, 2007

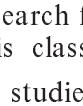
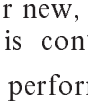
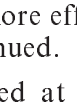
Abstract—A series of cinnamul esters of xanthic, trithiocarbonic, and dithiocarbamic acids were prepared. The optimal conditions of their synthesis were found. The cinnamyl esters were studied by thermal analysis, and the dependence of their lubricating power on the composition and structure was revealed. The tribological properties of lubricating oils with additions of cinnamyl esters of thiocarbonic acids were studied. A correlation between the structure of the esters synthesized and their antiscuff properties was found.

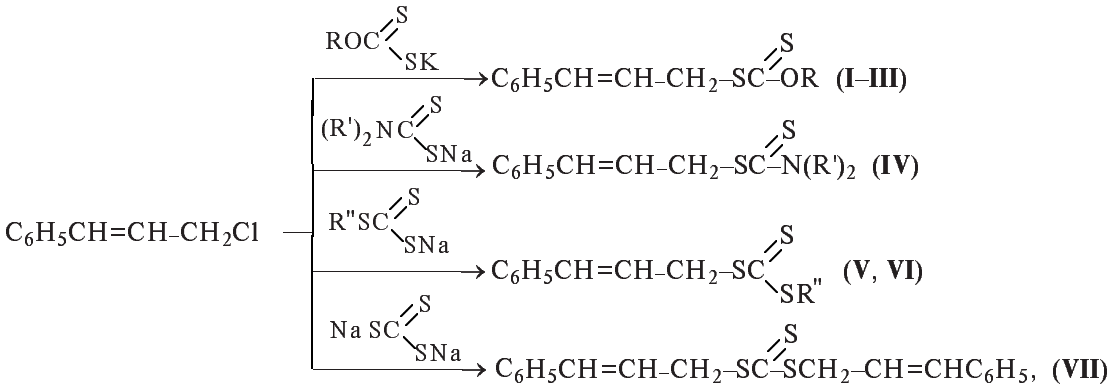
DOI: 10.1134/S1070427208090085

Improvement of machinery is often accompanied by posing more stringent requirements upon lubricating oils, which, in turn, requires the development of more effective additives. Despite enormous success in studies and application of various organic sulfur compounds as additives to lubricating oils, a systematic search for new, more effective representatives of this class is continued.

Numerous studies performed at the Institute of Chemistry of Additives on the synthesis and application of organosulfur compounds as antiscuff additives revealed high performance of various derivatives of thiocarbonic (TC) acids [1–4].

The goal of this study was to prepare derivatives of thiocarbonic (xanthic, trithiocarbonic, dithiocarbamic) acids by reactions of their salts with cinnamyl (phenylallyl) chloride; to study their lubricating properties in relation to the composition and structure; and to test the esters synthesized as antiwear and antiscuff additives to lubricating oils.

Our study is of interest from the viewpoint of predicting the optimal composition and structure of additives having the preset service properties. The choice of TC acid derivatives containing the fragments  ,  , and  based on cinnamyl chloride is governed by the presence in molecules of these esters of thione and sulfide sulfur atoms and of the phenylallyl group. All these fragments are responsible for the antiwear and antiscuff properties. Also, the required raw materials (styrene, xanthic and dithiocarbamic acid salts) are commercially available. Thiocarbonic acid derivatives were prepared by reactions of cinnamyl chloride with alkali metal salts of the corresponding acids by the scheme



where R = C_2H_5 **(I)**, *i*-C_3H_7 **(II)**, C_4H_9 **(III)**; R' = C_2H_5 **(IV)**; R" = C_4H_9 **(V)**, C_5H_{11} **(VI)**.

The known procedure for preparing cinnamyl chloride involves the reaction of styrene with formaldehyde and concentrated HCl in the presence of elemental sulfur [5]. The cinnamyl chloride yield in this procedure does not exceed 60–63%. It was shown that, in the presence of hydroquinone as an agent preventing styrene polymeriation, the cinnamyl chloride yield reaches 90%. Lyushin and Alekberova [6] suggested the following procedure for preparing cinnamyl chloride:

$$C_6H_5–CH=CH_2 + \overset{+}{C}H_2OH \rightleftarrows C_6H_5\overset{+}{C}H–CH_2–CH_2OH,$$

$$C_6H_5CH–CH_2–CH_2OH \underset{+H^+}{\overset{-H^+}{\rightleftarrows}} C_6H_5CH=CH–CH_2OH,$$

$$C_6H_5CH=CH–CH_2OH + HCl \rightarrow C_6H_5CH=CH–CH_2Cl + H_2O,$$

The reactions of cinnamyl chloride with potassium xanthates were performed in a polar solvent at 60°C and were complete in 4.5–5 h. The reaction with sodium diethyldithiocarbamate, as with xanthates, occurred smoothly in an aqueous or alcoholic solution with a noticeable heat release [7]. Dithiocarbamate was used as 50% aqueous solution.

Synthesis of trithiocarbonic acid esters was preceded by the synthesis of the starting alkali metal trithiocarbonates. From alkali metal trithiocarbonates and cinnamyl chloride we prepared both unsymmetrical and symmetrical esters of trithiocarbonic acid.

To prepare unsymmetrical trithiocarbonic acid esters, we initially prepared alkali metal alkyl trithiocarbonates by the reactions of mercaptans with carbon disulfide in the presence of an aqueous or alcoholic solution of alkali [8, 9]:

$$RSH + CS_2 + KOH \rightarrow RSC(S)SK + H_2O.$$

Then the corresponding unsymmetrical trithiocarbonic acid esters were prepared in 70–90% yield by reactions of aqueous solutions of alkyl trithiocarbonates with cinnamyl chloride [10, 11].

Sodium trithiocarbonate required for the synthesis of the symmetrical trithiocarbonic acid ester was prepared by the reaction of sodium sulfide with carbon disulfide in aqueous solution [12]:

$$Na_2S + CS_2 \rightarrow NaS–C(S)SNa.$$

Our studies showed that alkali metal alkyltrithiocarbonates and sodium trithiocarbonate are obtained in a higher yield with a strongly polar aprotic solvent, dimethylformamide. Furthermore, in dimethylformamide the second step, reaction with cinnamyl chloride, also occurs fairly readily, with a high yield of the target products. The characteristics of the synthesized esters are given in Table 1.

Cinnamyl esters of xanthic, trithiocarbonic, and dithiocarbamic acids are pale straw-colored liquids, and dicinnamyl trithiocarbonate is a yellow crystalline substance. All these compounds are readily soluble in organic solvents and lubricating oils.

The structures of the synthesized esters were confirmed by elemental analysis and by IR and ^1H NMR spectroscopy. The IR absorption spectra were recorded on a Specord-75 spectrophotometer (Carl Zeiss, Germany), and the ^1H NMR spectra, on a Varian T-60 spectrometer (60 MHz, CCl_4 solutions).

The IR spectra of cinnamyl esters of all the thiocarbonic acids contain absorption bands at 1645–1659 cm^{-1}, characteristic of the –HC=CH– bond conjugated with the aromatic ring. Strong bands at 1600–1610 cm^{-1} are due to stretching vibrations of the aromatic ring. The out-of-plane bending vibrations of the C–H bond give rise to a strong band at 695–739 cm^{-1}, characteristic of monosubstituted benzene derivatives.

In the IR spectra of xanthic acid esters, there are strong bands at 1250–1225, 1150–1090, and 1060–1030 cm^{-1}. Although all these bands belong to the R–O–C(S)– fragment, according to [13, 14], the bands at 1060–1030 cm^{-1} should be assigned to the C=S vibration, and the high-frequency bands, to the C–O stretching vibrations.

The stretching vibrations of the C=S groups in trithiocarbonates and *S*-cinnamyl diethyldithiocarbamate are manifested at 1040–1020 and 990–980 cm^{-1} (doublet), respectively. The other NCS bonds of *S*-cinnamyl diethyldithiocarbamate, characteristic of all the thioamides, are observed at 1570–1395 and 1420–1260 cm^{-1}.

The signals observed in the ^1H NMR spectra of cinnamyl esters of thiocarbonic acids (δ, ppm) are given in Table 2.

With the aim to examine the dependence of the lubricating power on the composition and structure of cinnamyl esters of thiocarbonic acids, we studied them by thermal analysis [15, 16]. As the additives operate at elevated temperatures, it was interesting

Table 1. Characteristics of cinnamyl esters of xanthic, trithiocarbonic, and dithiocarbamic acids

Compound	Yield, %	T_b, °C (P, mm Hg)	Density d_4^{20}	Refractive index n_D^{20}	Found, %/Calculated, %				
					MR_D	C	H	S	N
I	84	126–127(0.4)	1.1311	1.6184	73.39/71.77	60.22/60.46	7.80/7.92	26.75/26.90	–/–
II	90	120–125(0.4)	1.1232	1.6070	77.47/76.39	61.94/61.88	6.26/6.33	24.80/25.35	–/–
III	81	130–131(0.4)	1.1351	1.6310	83.43/81.01	63.05/63.11	6.76/6.81	24.00/24.06	–/–
IV	95	190–191(0.5)	1.1331	1.6315	83.38/83.52	63.93/63.40	7.02/7.16	23.35/24.16	5.29/5.31
V	90	–	1.1449	1.6409	88.98/88.60	59.60/59.61	6.27/6.89	34.80/34.05	–/–
VI	80	–	1.1379	1.6380	92.75/93.31	60.55/60.76	6.89/6.80	32.15/32.43	–/–
VII	87.5	T_m = 92–93	–	–	–/–	66.60/66.80	5.16/5.28	27.98/28.08	–/–

* The products were separated by liquid column chromatography.

Table 2. ^{1}H NMR spectra of cinnamyl esters of thiocarbonic acids

Compound*	Chemical shift δ, ppm						
	CH_3–C (6H)	CH_2–S	CH_2–O	C=CH–C	ArCH=C	Ar–H	N–CH_2
II	1.40	3.81	5.55	6.05	6.30	6.95	–
IV	1.25	3.99	–	6.23	6.27	7.0	3.70
VII	–	4.07	–	6.0	6.30	7.0	–

to study thermal characteristics of the synthesized compounds, both taken alone and in contact with metals, so as to evaluate their performance in the required temperature range. This would also allow estimation of their chemical activity toward metals and preliminary assessment of the performance of the compounds as antiwear and antiscuff additives to oils. The thermal analysis was performed on an OD-102T derivatograph (MOM, Hungary) in the dynamic mode at a heating rate of 5 deg min^{-1} in the temperature range 20–500°C.

Thermal analysis of the thiocarbonic acid derivatives shows that thermal transformations of the majority of compounds taken separately start above 170°C, i.e., above the oil temperature in transmission units. The dithiocarbamates and trithiocarbonates are somewhat more heat-resistant than xanthates. In the presence of metals, trithiocarbonates are more active than the other TC acid derivatives.

We found that all the TC acid derivatives are active toward metals, and their chemical activity in relation to the acid residue decreases in the order –S–C(S)SR > –S–C(S)N$(C_2H_5)_2$ ≥ –S–C(S)OR.

According to the common views [15–17], the lower the temperature of the interaction of a compound with metals and the lower the weight loss at this temperature, the more effective is the compound as an antiscuff additive. Correspondingly, the efficiency of the lubricating action of TC acid esters will vary in the same order.

EXPERIMENTAL

***S*-Cinnamyl isopropylxanthate.** To a mixture of 34.8 g (0.2 mol) of potassium isopropylxanthate in 50 ml of isopropyl alcohol, we gradually added 30.5 g (0.2 mol) of cinnamyl chloride and stirred at 60°C for 5 h. After cooling, the mixture was washed with water, dried, and subjected to vacuum distillation. Yield of *S*-cinnamyl isopropylxanthate 45.4 g (90%). *S*-Cinnamyl ethyl- and butylxanthates were synthesized similarly.

***S*-Cinnamyl butyl trithiocarbonate.** To 47 g (0.25 mol) of sodium butyl trithiocarbonate in a dimethylformamide solution, we added 38.1 g of cinnamyl chloride and stirred for 4–5 h. The mixture was washed with water, and low-boiling products were distilled off in a vacuum. The residue was purified by liquid column chromatography. Yield of *S*-cinnamyl butyl trithiocarbonate 63.5 g (90%). *S*-Cinnamyl amyl trithiocarbonate was synthesized similarly.

Table 3. Lubricating properties of thiocarbonic acid esters in liquid paraffin

Compound	Concentration in oil, %	Antiscuff characteristics, N			Wear index at a load of 392 N, duration 1 h, D_w, mm
		scuff index I_s	seize load P_s	welding load P_w	
Liquid paraffin	–	206	549	1382	0.74
I	4.76	534	1166	2930	0.78
II	5.04	528	1166	2764	0.76
III	5.32	486	1098	2450	0.73
V	5.64	583	1235	3087	0.84
VII	6.84	632	1303	3479	0.82
IV	5.3	544	1235	2930	0.79
C_7H_{15}–SC(S)–OC_4H_9	4.73	438	980	2068	0.86
C_7H_{15}–SC(S)–SC_4H_9	5.06	505	980	2450	0.88
C_8H_{17}–SC(S)–$N(C_2H_5)_2$	4.95	388	872	3068	0.80

Dicinnamyl trithiocarbonate. To 22.5 g (0.1 mol) of sodium sulfide in 20 ml of dimethylformamide, we added dropwise 8 ml of carbon disulfide and stirred for 1 h, after which we added dropwise 30.4 g (0.2 mol) of cinnamyl chloride. The mixture was heated to 60°C and stirred for 3 h. The precipitated yellow crystals were filtered off and recrystallized from isopropyl alcohol. Yield of dicinnamyl trithiocarbonate 29.9 g (87.5%).

***S*-Cinnamyl diethyldithiocarbamate.** To 45.6 g (0.2 mol) of sodium diethyldithiocarbamate trihydrate in 23 ml of water, we added 30.5 g of cinnamyl chloride and stirred at 65–70°C for 4 h. The mixture was washed with water, vacuum-dried, and distilled. Yield 50.4 g (95%).

The performance of cinnamyl esters of TC acids was examined in liquid paraffin and MS-20 oil with a four-ball friction machine according to GOST (State Standard) 9490–75. The concentration of the additives was 20 mmol per 100 g in liquid paraffin and 5% in MS-20 oil (the most frequently used concentration of antiscuff additives).

The results of studying lubricating properties of thiocarbonic acid esters as additives to liquid paraffin are given in Table 3, with the data for alkyl esters of thiocarbonic acids given for comparison.

As can be seen, all derivatives of thiocarbonic acids improve the antiscuff characteristics of liquid paraffin, with the cinnamyl esters surpassing in the antiscuff performance the related alkyl esters. High antiscuff performance of cinnamyl esters of TC acids is apparently due to the negative inductive effect of the styryl group $C_6H_5CH{=}CH{-}$. Similar effect was observed previously in studies of benzyl and allyl esters of TC acids [18]. The styryl group, like phenyl and vinyl groups, being electronegative, makes the $S{-}CH_2$ bond more polar, facilitates its heterolytic cleavage, and thus favors formation of iron sulfides mitigating the seizing process.

As follows from the comparison of cinnamyl xanthates with each other, with an increase in the length of *O*-alkyl radicals the antiscuff properties of the compounds become somewhat worse, i.e., the strength of the boundary film decreases. Relatively high antiscuff performance of short-chain xanthates may be due to higher packing density of their molecules in adsorption on a metal surface, as compared to long-chain analogs.

It can be seen that thiocarbonic acid esters surpass in the antiscuff properties xanthic and dithiocarbamic acid esters. This fact may be due to specific features of interaction of these compounds with the surface.

Thiocarbonates containing an additional sulfur atom compared to dithio acid esters provide higher concentration of useful products on friction surfaces, whereas esters of the other two thio acids partially form oxygen- and nitrogen-containing products of poor performance.

The results of 1-h tests of thiocarbonic acid esters in mineral oil solution at an axial load of 392 N might suggest that these compounds exhibit no antiwear properties, becuase the index D_w of their solutions exceeds D_w of straight liquid paraffin. However, data on the critical seize load P_s are inconsistent with this conclusion: The index P_s characterizes the strength of the boundary film, and introduction

Table 4. Lubricating properties of cinnamyl esters of thiocarbonic acids in MS-20 oil

Compound	Concentration in oil, %	Scuff index I_s	Seize load P_s	Welding load P_w	Wear index D_w, mm
		N			
MS-20 oil	–	304	784	1568	0.62
I	5.0	632	1235	3685	0.77
II	5.0	615	1235	3479	0.78
III	5.0	586	1166	3283	0.78
V	5.0	671	1303	3920	0.84
VII	5.0	715	1303	4381	0.81
IV	4.0	624	1303	3550	0.80

of TC acid esters into liquid paraffin favors formation of very strong films that withstand higher loads (872–1303 N) than do adsorption films of straight liquid paraffin (549 N). Hence, the TC acid esters do exhibit antiwear properties, which, however, are not manifested at their concentration of 20 mmol per 100 g of oil and an axial load of 392 N corresponding to a specific pressure of 2.32 GPa (232 kgf cm^{-2}).

We also examined the cinnamyl esters of TC acids as additives to MS-20 oil. The results are given in Table 4.

As can be seen, the main trends revealed with liquid paraffin were also observed with MS-20 transmission oil. The most significant difference of the samples with MS-20 oil is that their antiscuff properties are better because of higher viscosity of the initial oil.

REFERENCES

(1) The optimal conditions were found for preparing cinnamyl esters of xanthic, dithiocarbamic, and trithiocarbonic acid esters by reactions of cinnamyl chloride with alkali metal salts of the corresponding acids, with increased yields of both the starting cinnamyl chloride and thiocarbonic acid esters.

(2) All cinnamyl esters of thiocarbonic acids are chemically active toward metals; dithiocarbamates and trithiocarbonates taken separately somewhat surpass xanthates in the thermal stability. In the presence of metals, however, trithiocarbonates are more reactive than dithiocarbamates and xanthates.

(3) Lubricating properties of the synthesized esters were examined, and a correlation was revealed between their structure and antiscuff performance. All the cinnamyl esters of thiocarbonic acids exhibit high antiscuff performance and surpass in this property the esters of xanthic and dithiocarbamic acids whose performance is essentially similar. With an increase in the alkyl chain length, the seize load decreases and the antiscuff properties become worse.

REFERENCES

1. Kuliev, A.M., Kulieva, M.A., Ramazanova, Yu.B., and Shikhaliev, Sh.M., *Zh. Prikl. Khim.*, 1988, vol. 61, no. 7, pp. 1590–1596.
2. USSR Inventor's Certificate no. 1062206.
3. Kuliev, A.M., Kulieva, M.A., and Kulibekova, T.N., *Neftekhimiya*, 1985, no. 5, p. 679.
4. Mustafaev, N.P., Kulieva, M.A., and Kulibekova, T.N., *Khim. Tekhnol. Topl. Masel*, 2001, no. 2, p. 41.
5. Wichterle, O. and Cerny, J., *Chem. Listy*, 1955, vol. 49, no. 7, pp. 1038–1040.
6. Lyushin, M.M. and Alekberova, T.A., *Nauchn. Zap. Azerb. Inst. Nefti Khim.* (Baku), 1978, ser. 9, no. 5, pp. 65–68.
7. Guseinov, Kh.K., Mustafaev, N.P., Ibragimov, N.Yu., and Gasanzade, G.R., *Zh. Org. Khim.*, 1974, vol. 10, no. 7, pp. 1438–1442.
8. Codt, H.G. and Wann, R.E., *J. Org. Chem.*, 1961, vol. 26, no. 10, pp. 4047–4051.
9. US Patent 4528141.
10. USSR Inventor's Certificate no. 1082784.
11. Mustafaev, N.P., Kulieva, M.A., Efendieva, Kh.K., Novotorzhina, N.N., and Ramazanova, Yu.B., Abstracts of Papers, *II Respublikanskaya konferentsiya, posvyashchennaya 25-letiyu IKhP* (II Republican Conf. Dedicated to 25th Anniversary of the Inst. of Chemistry of Additives), Baku, 1990, p. 29.

12. Reid, E.B., *Organic Chemistry of Bivalent Sulfur*, New York: CRC, 1962.
13. Rao, C.N. and Venkatoraghavan, R., *Spectrochim. Acta*, 1962, vol. 18, pp. 541–547.
14. Bellamy, L.J., *Advances in Infrared Group Frequencies*, London: Methuen, 1968.
15. Mustafaev, N.P., Akchurina, T.Kh., Kulieva, M.A., and Ramazanova, Yu.B., *Azerb. Khim. Zh.*, 2002, no. 2, pp. 51–55.
16. Akchurina, T.Kh., Safarova, M.R., Kulieva, M.A., and Gakhramanova, G.A., *Neftepererab. Neftekhim.*, 2006, no. 11, pp. 21–25.
17. Berg, L., *Vvedenie v termografiyu* (Introduction to Thermography), Moscow: Nauka, 1969.
18. Mustafaev, N.P., Blinnikova, N.A., and Ismailov, I.P., *Khim. Tekhnol. Topl. Masel*, 1989, no. 5, pp. 19–21.

ISSN 1070-4272, Russian Journal of Applied Chemistry, 2008, Vol. 81, No. 9, pp. 1524–1527. © Pleiades Publishing, Ltd., 2008.
Original Russian Text © A.A. Gaile, G.D. Zalishchevskii, A.S. Erzhenkov, L.L. Koldobskaya, 2008, published in Zhurnal Prikladnoi Khimii, 2008, Vol. 81, No. 9, pp. 1449–1452.

PHYSICOCHEMICAL STUDIES OF SYSTEMS AND PROCESSES

Extractive Rectification of the Benzene Fraction of Reformer Naphtha Using *N*-Methylpyrrolidone–*N*-Formylmorpholine Mixtures

A. A. Gaile, G. D. Zalishchevskii, A. S. Erzhenkov, and L. L. Koldobskaya

St. Petersburg State Institute of Technology (Technical University), St. Petersburg, Russia
Kirishinefteorgsintez Production Association, Limited Liability Company, Kirishi, Leningrad oblast, Russia

Received December 28, 2007

Abstract—Extractive rectification of the benzene fraction of reformer naphtha was studied, and the relative fugacity coefficients of the heptane–benzene system in the presence of *N*-methylpyrrolidone–*N*-formylmorpholine mixtures of various compositions were determined. A synergistic effect was revealed for a mixed selective solvent containing 29–30 wt % *N*-formylmorpholine, 68–69% *N*-methylpyrrolidone, and 2–3 wt % water.

DOI: 10.1134/S1070427208090097

Previously we suggested to use a mixed selective solvent *N*-methylpyrrolidne (*N*-MP)–sulfolane, exhibiting a synergistic effect, for separation of benzene from the benzene fraction of reformer naphtha [1]. As highly selective solvent added to *N*-MP instead of sulfolane, one can use *N*-formylmorpholine (*N*-FM) which is widely applied to separation of arenes by selective rectification (Morpholane process) or extraction (Morphylex process) [2]. Advantages of *N*-FM compared to sulfolane are lower values of the boiling point, viscosity, and enthalpy of vaporization and higher solvency toward hydrocarbons [1–4]. However, the solubility of saturated hydrocarbons in *N*-FM, especially if it contains several percents of water to decrease the temperature in the lower sections of the extractive rectification and stripping towers, is limited. For example, at 80°C the solubility of hexane and heptane in *N*-FM is about 5.2 and 3.7 mol %, respectively [5]. The critical points of solution of methylcyclopentane and methylcyclohexane in *N*-FM are 130.14 and 131.61°C, respectively [6].

Thus, on the upper trays of an extractive rectification tower at pressures close to 1 atm the *N*-FM–hydrocarbons system can undergo phase separation, which will lead to a decrease in the fugacity coefficients of saturated hydrocarbons relative to arenes. Addition of *N*-MP to *N*-formylmorpholine is characterized by the following positive effects: homogenization of the system due to considerably higher solvency of *N*-MP; decrease in the process temperature due to lower boiling point of *N*-MP, which favors stabilization of π complexes of arenes with solvents; decrease in the viscosity of the system, which leads to an increase in the efficiency of trays of an extractive rectification tower.

With the aim to determine the required content of water in a mixed solvent, we found the normal boiling points of a 50 : 50 (wt %) *N*-FM–*N*-MP mixture in relation to the water content of the ternary mixture (Fig. 1).

At this composition of a mixed solvent and steam pressure of 10 atm in the stripping tower, the water content of the solvent should be about 3 wt %.

The results of benzene recovery from the benzene fraction of reformer naphtha by extractive rectification with *N*-FM and its mixtures with *N*-MP are given in Table 1.

The procedure of extractive rectification experiments was described previously [1]. In all the experiments we detected no toluene in the distillate, i.e., the degree of separation of toluene by extractive distillation with *N*-FM and its mixtures with *N*-MP is virtually 100%. The degree of separation of benzene with *N*-FM containing 3 wt % water is low: Even at a solvent to feed weight ratio of 3 : 1, the benzene concentration in the distillate exceeds 5 wt %. *N*-MP

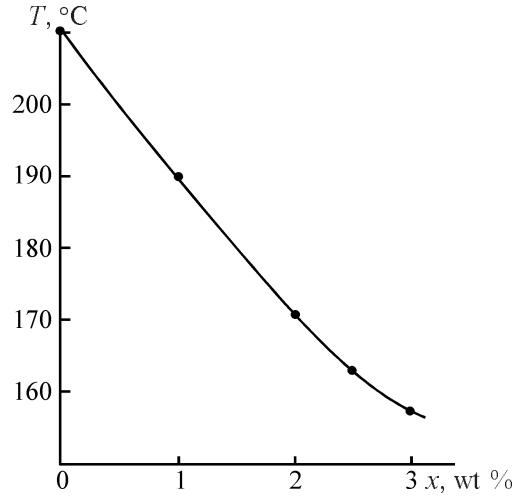


Fig. 1. Boiling point T of the mixed extractant N-FM : N-MP = 50 : 50 (wt %) as a function of its water content x.

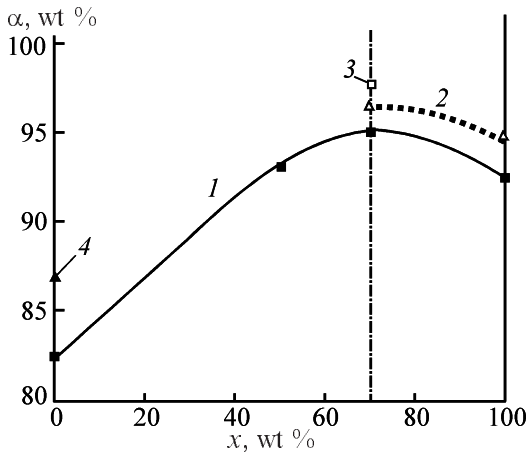


Fig. 2. Degree of arene separation α at their 99.9 wt % content in the bottoms as a function of the N-MP content in the mixed extractant. Run nos. (Table 1): (*1*) 1, 3–5; (*2*) 6, 8; (*3*) 7; and (*4*) 2.

containing 3 wt % water is more efficient, but in this case the benzene content of the distillate decreases only to 3.25 wt %. N-FM–N-MP mixtures containing 3 wt % water are still more efficient.

As seen from Fig. 2, the optimal content of N-MP in the mixed extractant at its water content of 3 wt % and extractant to feed weight ratio of 1.5 : 1 is 70 wt %.

However, even at the optimal composition of the mixed solvent, despite a synergistic effect, the arene concentration in the distillate decreases to only 2.13 wt %, or to somewhat less than 2 vol %. In principle, a decrease in the benzene concentration to this level is sufficient to meet the requirement of the maximum permissible concentration of benzene in automobile gasolines (≤1 vol %), taking into account that the distillate can be mixed with the reformer naphtha containing C_7–C_9 arenes, with isomerizates, and with other possible components containing no benzene.

In the mixed solvent of the optimal composition, relatively low-boiling N-MP prevails, which allows the water content of the ternary system to be decreased to 2 wt %. With a simultaneous increase in the mixed solvent to feed weight ratio to (2–2.5) : 1, the arene concentration in the distillate decreases to 1.65–1.07 wt % (Table 1, run nos. 6, 7). In run no. 7, the benzene concentration in the distillate decreases to a level less than 1 vol %.

The dependence of the degree of arene separation and benzene concentration in the distillate on the weight ratio of the mixed solvent of the optimal composition to the feed is shown in Fig. 3. The final temperature in the boiler of the extractive rectification tower is 160°C, which allows steam with a pressure of 10 atm to be used as heat carrier.

It should be noted that mixtures of N-MP with both N-FM and sulfolane exhibit a synergistic effect in benzene separation by extractive rectification. Addition to N-MP of approximately 15 wt % sulfolane is somewhat more efficient than addition of 30 wt % N-FM, which may be due to higher criterion of the sulfolane performance. Both recommended

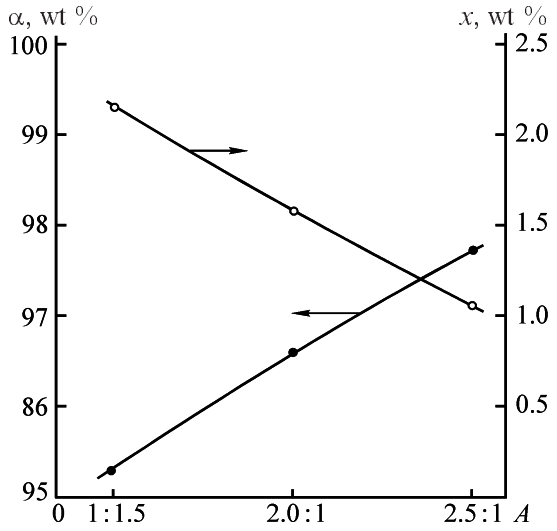


Fig. 3. Degree of arene separation α at their 99.9 wt % content in the bottoms and benzene concentration in the distillate x as functions of the mixed extractant to feed weight ratio A. Extractant: N-FM : N-MP : water = 29.4 : 68.6 : 2.0 (wt %).

Table 1. Results of benzene separation from the benzene fraction of reformer naphtha by extractive rectification with *N*-formylmorpholine and its mixtures with *N*-methylpyrrolidone

Run no.	Solvent composition, wt %			Solvent to feed weight ratio	Boiler temperature, °C	Distillate yield, wt %	Takeoff of non-aromatic hydrocarbons with distillate, wt %	Arene content, wt %		Degree of separation, wt %	
	N-FM	*N*-MP	water					distillate	bottoms	Σarenes	benzene
1	97.0	–	3.0	1.5 : 1	170	74.46	99.97	7.28	99.9	82.48	82.15
2	97.0	–	3.0	3 : 1	170	73.0	99.96	5.44	99.9	81.18	86.98
3	48.5	48.5	3.0	1.5 : 1	155	71.17	99.97	2.98	99.9	93.15	93.03
4	29.1	67.9	3.0	1.5 : 1	155	69.68	99.97	2.13	99.9	95.2	95.13
5	–	97.0	3.0	1.5 : 1	150	71.36	99.97	3.25	99.9	92.5	92.39
6	29.4	68.6	2.0	2 : 1	160	70.2	99.97	1.65	99.9	96.27	96.53
7	29.4	68.6	2.0	2.5 : 1	160	69.79	99.97	1.07	99.9	97.59	97.53
8	98.0	–	2.0	2 : 1	170	73.99	99.97	6.67	99.9	83.99	83.64

Table 2. Relative fugacity coefficients of the heptane–benzene system in the presence of selective solvents. Solvent to hydrocarbons weight ratio 2 : 1

Solvent composition, wt %			*T*, °C	Heptane content, mol %		Phase equilibrium constants		$\alpha = K_{hp}/K_b$
N-MP	*N*-FM	water		in liquid phase, X_{hp}	in vapor phase, Y_{hp}	K_{hp}	K_b	
98.0	–	2.0	98	55.20	70.8	1.28	0.65	1.97
68.6	29.4	2.0	100	53.73	72.4	1.35	0.60	2.25
49.0	49.0	2.0	103	56.49	72.1	1.27	0.64	1.98

mixtures of selective solvents allow the drawbacks of the process suggested by GTC company with Tective-100 solvent [7] to be avoided.

By circulation method, using the modified Othmer device [8], we determined the relative fugacity coefficients α of the heptane–benzene system in the presence of *N*-MP and its mixtures with *N*-FM containing 2 wt % water at a solvent to hydrocarbons weight ratio of 2 : 1 (Table 2, Fig. 4). The quantity α is maximal for the mixed selective solvent which showed the maximal activity in benzene separation by extractive rectification.

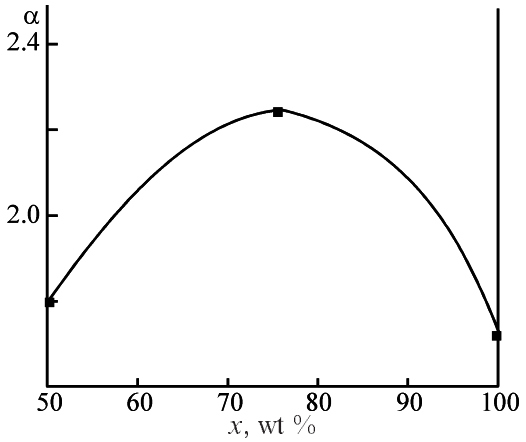


Fig. 4. Relative fugacity coefficient of the heptane–benzene system as a function of the *N*-MP content *x* in the mixed selective extractant *N*-FM–*N*-MP–water.

CONCLUSIONS

(1) The mixed selective solvent *N*-formylmorpholine–*N*-methylpyrrolidone–water containing about 30 wt % *N*-methylmorpholine and 2–3 wt % water exhibits synergistic effect in benzene separation from the benzene fraction of reformer naphtha by extractive rectification.

(2) The *N*-formylmorpholine–*N*-methylpyrrolidone mixture of optimal composition allows the benzene content to be decreased from 30–31 wt % in the feed to 1.65 wt % (about 1.25 vol %) in the distillate.

REFERENCES

1. Gaile, A.A., Zalishchevskii, G.D., Erzhenkov, A.S., and Koldobskaya, L.L., *Zh. Prikl. Khim.*, 2008, vol. 81, pp. 1296–1302.

2. Gaile, A.A., Somov, V.E., and Zalishchevskii, G.D., *Morfolin i ego proizvodnye: Poluchenie, svoistva i primenenie v kachestve selektivnykh rastvoritelei* (Morpholine and Its Derivatives: Synthesis, Properties, and Application as Selective Solvents), St. Petersburg: Khimizdat, 2007.
3. Gaile, A.A., Somov, V.E., Varshavskii, O.M., and Semenov, L.V., *Sul'folan: Svoistva i primenenie v kachestve selektivnogo rastvoritelya* (Sulfolane: Properties and Use as Selective Solvent), St. Petersburg: Khimizdat, 1998.
4. Gaile, A.A. and Zalishchevskii, G.D., *N-Metilpirrolidon: Poluchenie, svoistva i primenenie v kachestve selektivnogo rastvoritelya* (*N*-Methylpyrrolidone: Synthesis, Properties, and Use as Selective Solvent), St. Petersburg: Khimizdat, 2005.
5. Ko Min Su, Lee Sungjin, Cho Jungho, and Kim Hwayong, *J. Chem. Eng. Data*, 2002, vol. 47, no. 4, pp. 923–926.
6. Ko Min Su, Na Sangyoup, Kwon Soyoung, et al., *J. Chem. Eng. Data*, 2003, vol. 48, no. 3, pp. 699–702.
7. Gentrey, J.K., Kumar, K.S., Li, H.M., and Li, Y.H., *Khim. Tekhnol. Topl. Masel*, 2003, nos. 1–2, pp. 12–17.
8. Hala, E., Pick, I., Fried, V., and Vilm, O., *Vapour–Liquid Equilibrium*, London: Pergamon, 1958.

ISSN 1070-4272, Russian Journal of Applied Chemistry, 2008, Vol. 81, No. 9, pp. 1528–1531. © Pleiades Publishing, Ltd., 2008.
Original Russian Text © N.V. Komissarova, A.V. Bulanova, P.P. Purygin, A.V. Sokolov, 2008, published in Zhurnal Prikladnoi Khimii, 2008, Vol. 81, No. 9, pp. 1453–1456.

PHYSICOCHEMICAL STUDIES OF SYSTEMS AND PROCESSES

Correlation between the Chromatographic Retention and Physicochemical Properties of Azoles

N. V. Komissarova, A. V. Bulanova, P. P. Purygin, and A. V. Sokolov

Samara State University, Samara, Russia

Received May 14, 2008

Abstract—The chromatographic behavior of previously unknown nitrogen-containing heterocyclic compounds was studied by reversed-phase high-performance liquid chromatography. The main relationships in the retention of the compounds with variation of the acetonitrile content in the mobile phase were examined. One- and multiparameter correlations between the logarithm of the retention factor and quantities characterizing physicochemical properties of the compounds were constructed.

DOI: 10.1134/S1070427208090103

Nitrogen-containing heterocycles are a promising class of organic compounds, mainly due to their medical applications. Numerous pharmaceuticals with various pharmacological properties have been developed on the basis of these compounds. Therefore, synthesis of nitrogen-containing heterocyclic compounds with the required set of properties is a topical problem.

The development of methods allowing reliable prediction of both the physicochemical properties and the biological activity of compounds that have not yet been synthesized, as well as synthesis of new compounds with the required properties are one of the most important problems of the modern chemistry [1, 2]. This field of research is termed QSAR (Quantitative Structure–Activity Relationships), QSPR (Quantitative Structure–Property Relationships), or QSRR (Quantitative Structure–Retention Relationships).

The initial data for QSRR studies involve a set of molecular descriptors for the compounds under consideration and the retention factors obtained experimentally by HPLC. Based on these quantities, model equations are constructed, in which the parameters characterizing various descriptors of compounds are variables [3]. The QSRR model is used for predicting the retention parameters of sorbates belonging to the given class. The mathematical apparatus of this model is mainly based on the method of multidimensional statistical analysis, linear or nonlinear regression analysis [4, 5].

In this study we examined the chromatographic behavior of some previously unknown azoles by reversed-phase HPLC. The correlation dependences of the retention parameters of the compounds on their physicochemical properties were constructed. These dependences offer criteria for purposeful synthesis of compounds of this class.

EXPERIMENTAL

The compounds were analyzed under reversed-phase HPLC conditions on a Milichrom-1 microcolumn liquid chromatograph with a spectrophotometric detector (λ = 254 nm). We used an Ultrasep ES 100RP18 column (120 × 4 mm, particle diameter 4 μm) with grafted octadecyl groups. As stationary phase we used acetonitrile–water mixture with various volume ratios. Samples were prepared by dissolving crystalline substances in water and acetonitrile. The volume of the injected samples was 4 μl, at a flow rate of the mobile phase of 100 μl min^{-1}. As nonsorbable substance we used sodium nitrite.

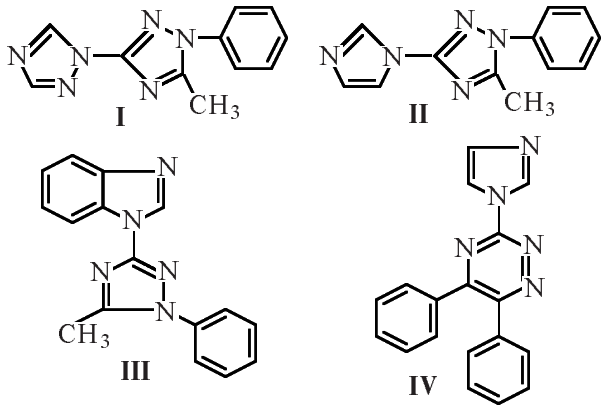
The investigration objects were previously unknown nitrogen-containing heterocyclic compounds 3-(1*H*-1,2,4-triazol-1-yl)-5-methyl-1-phenyl-1*H*-1,2,4-triazole **(I)**, 3-(1*H*-imidazol-1-yl)-5-methyl-1-phenyl-1*H*-1,2,4-triazole **(II)**, 3-(1*H*-benzimidazol-1-yl)-5-methyl-1-phenyl-1*H*-1,2,4-triazole **(III)**, and 3-(1*H*-imidazol-1-yl)-5,6-diphenyl-1,2,4-triazine **(IV)**.

Table 1. Retention factors of the compounds under consideration

Compound	Retention factor k at indicated acetonitrile : water volume ratio							
	80 : 20	70 : 30	60 : 40	50 : 50	40 : 60	30 : 70	20 : 80	10 : 90
I	0.43	0.92	0.92	0.95	1.09	1.91	3.68	4.24
II	0.59	1.04	1.08	1.45	2.27	3.00	3.93	4.37
III	1.06	1.54	2.39	4.06	4.64	5.57	5.61	6.56
IV	1.15	1.77	2.74	4.09	8.93	–	–	–

Table 2. Physicochemical properties of compounds under consideration

Compound	V, Å^3	α, Å^3	μ, C m	RM, Å^3	SA_{grid}, Å^2	M_r, g mol^{-1}
I	677.28	24.50	9.68	63.80	423.93	226.24
II	690.38	25.21	7.06	65.11	432.58	225.25
III	811.42	31.39	6.56	81.86	487.44	275.31
IV	880.35	34.45	5.08	91.51	526.16	299.33



The retention factrors of the compounds, obtained using several mobile phases, are given in Table 1.

Using the HyperChem 7.0 program, we calculated by the PM3 semiempirical method with full geometry optimization such physicochemical parameters of the compounds as molecular volume V, polarizability α, dipole moment μ, molecular refraction RM, surface area SA_{grid}, and molecular weight M_r. The values of these parameters are given in Table 2.

In reversed-phase HPLC, the retention of compounds is determined by the competition between the dispersion interaction of sorbates with the stationary phase and by donor–acceptor interaction with the mobile phase (with acetonitrile as modifier of the mobile phase). In the course of the experiment we found that the retention of the compounds under consideration strongly depends on the mobile phase composition. An increase in the fraction of the polar solvent (water) leads to an increase in the retention, which is in agreement with the retention mechanism in reversed-phase chromatography.

It is well known that, in reversed-phase chromatography, the nature of the substrate or, more accurately, of substituents in its molecule is of no less importance. Let us consider as example the retention of the compounds under consideration at an acetonitrile : water ratio in the mobile phase of 50 : 50. For example, compound **I** is characterized by the weakest retention (k = 0.95), as it is the most polar. This compound contains two triazole rings whose nitrogen atoms can enter into dipole–dipole interactions with water or acetonitrile molecules.

Compound **III** is retained more strongly than **II** (k = 4.06 and 1.45, respectively) owing to the presence of an additional phenyl, and not methyl, substituent. Presumably, the phenyl radical introduces a new π-electron system which, in turn, causes redistribution of the electron density. As a result, the compound becomes more inclined to dispersion interactions with the mobile phase.

At the same time, compounds **IV** and **II** differing in the benzimidazole and imidazole substituents have different retention constants (k = 4.09 and 1.45, respectively). The benzimidazole substituent enhances the dispersion interactions with the stationary phase owing to π electrons of the benzene ring.

In this study we obtained the correlation dependences of the retention factor on various physico-

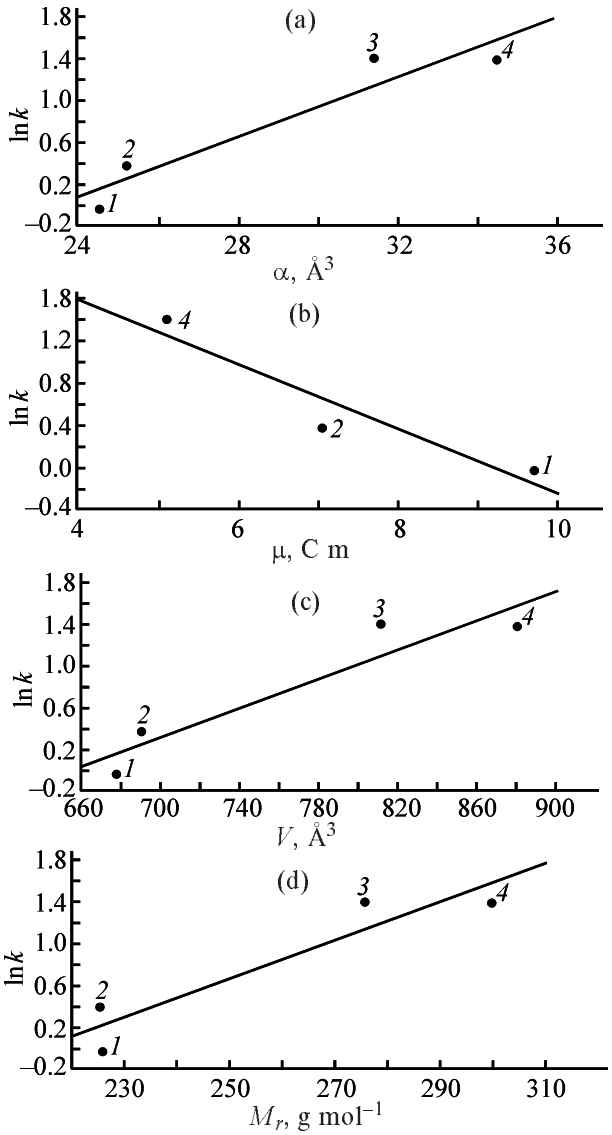


Fig. 1. Retention factor k as a function of the (a) polarizability α (r = 0.95), (b) dipole moment μ (r = –0.95), (c) molecular volume V (r = 0.94), and (d) molecular weight M_r (semilog plots). (*1–4*) Compounds **I–IV**, respectively.

chemical parameters of the compounds: polarizability, dipole moment, molecular volume, and molecular weight.

Figure 1a shows that, with an increase in the polarizability, the retention increases, which is due to enhancement of dispersion interactions with the stationary phase. Satisfactory correlation is observed between the retention of the compounds and their dipole moment (Fig. 1b). With an increase in the dipole moment of the molecule, the contribution of the orientation and induction intermolecular interactions with the mobile phase increases and hence the retention decreases. The chromatographic retention increases with an increase in the volume of the molecules (Fig. 1c). In reversed-phase HPLC, the retention increases with an increase in the molecular weight of compounds. We actually observed this trend (Fig. 1d).

Table 3. Linear multiparameter dependences for the compounds under consideration

Correlation equation	Correlation coefficient r
$\ln k = 9.14 + 1.56SA_{grid} - 0.07V$ (1)	0.98
$\ln k = 0.07 - 0.01SA_{grid} + 0.31V - 0.09E_{hydr}$ (2)	1.00
$\ln k = 0.02 + 1.18V - 0.51RM$ (3)	1.00
$\ln k = 0.07 + 0.29V - 0.06\mu$ (4)	1.00
$\ln k = 0.45 - 0.01SA_{grid} - 0.35\log P$ (5)	1.00
$\ln k = -1.29 - 0.39\alpha - 0.01M_r$ (6)	1.00
$\ln k = 0.01 + 0.66\alpha - 0.08\mu + 0.28M_r$ (7)	1.00
$\ln k = -4.91 - 0.39RM + 1.29\alpha - 0.01M_r$ (8)	1.00

Table 4. Logarithms of the calculated and experimentally obtained retention factors k ($\ln k$)

Compound	Experiment	Calculation by Eq. (1)	Calculation by Eq. (8)
I	1.41	1.32	1.31
II	0.37	0.37	0.29
III	–0.04	–0.05	–0.12
IV	1.40	1.26	1.29

The dependences we obtained have fairly high correlation coefficients. However, to enhance the predictive power of the equations in calculation of the retention factor, it is appropriate to construct multiparameter correlation dependences.

Some linear multiparameter correlations for the compounds under consideration, obtained with MS Excel 2000 program, are given in Table 3.

Low regression coefficients at some terms [e.g., –0.001 at SA_{grid} in Eq. (2)] indicate that the effect of these parameters on the retention is insignificant.

From the equations obtained, we can calculate the logarithms of the retention factors and compare them with the experimental data. The logarithms of the experimentally obtained retention factors and those calculated by Eqs. (1) and (8) are given in Table 4.

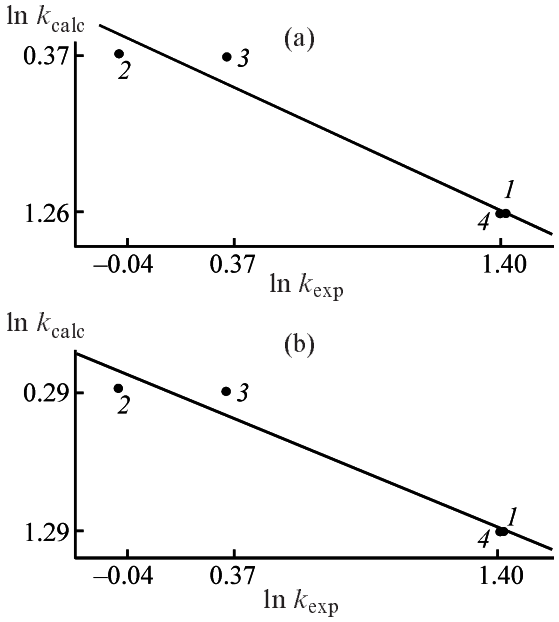


Fig. 2. Retention factor calculated by (a) Eq. (1) (r = 0.98) and (b) Eq. (2) (r = 0.99) as a function of the experimentally obtained retention factor (log–log plots).

In Figs. 2a and 2b, the experimentally obtained retention factors are plotted on the log–log scale vs. the calculated values. It can be seen that introduction of one more parameter [e.q., of V in Eq. (1)] increases the correlation coefficient. High correlation coefficients of the dependences obtained demonstrate the applicability of the QSPR approach to the compounds under consideration.

CONCLUSIONS

(1) Chromatographic behavior of previously unknown nitrogen-containing heterocyclic compounds under the conditions of reversed-phase HPLC is determined by such factors as the polarizability, dipole moment, molecular volume, and molecular weight.

(2) The linear multiparameter dependences obtained, describing the corelation between the retention and physicochemical properties of compounds, allow satisfactory prediction of the retention factors.

(3) Equations including the molecular volume, polarizability, and molecular refraction allow the most accurate prediction of the retention factors.

REFERENCES

1. Polyakova, Yu.L., Bulanova, A.V., Egorova, K.V., et al., *Izv. Ross. Akad. Nauk, Ser. Khim.*, 2000, no. 8, pp. 1401–1403.
2. Gar'kin, V.P., Kurbatova, S.V., Solovova, N.V., and Finkel'shtein, E.E., *Vestn. Samarsk. Gos. Univ., Estestvennonauchn. Ser.*, 2001, no. 2, pp. 189–193.
3. Polyakova, Yu.L., Bulanova, A.V., and Vartapetyan, R.Sh., *Izv. Ross. Akad. Nauk, Ser. Khim.*, 2001, no. 5, pp. 784–786.
4. Blinova, V.G. and Kharchevnikova, N.V., *Khim.-Farm. Zh.*, 2000, no. 4, pp. 45–50.
5. Baskin, I.I., Ait, A.O., Gal'bershtam, N.M., et al., *Dokl. Ross. Akad. Nauk*, 1997, vol. 357, no. 1, pp. 57–59.

ISSN 1070-4272, Russian Journal of Applied Chemistry, 2008, Vol. 81, No. 9, pp. 1532–1537. © Pleiades Publishing, Ltd., 2008.
Original Russian Text © A.V. Zdravkov, E.L. Aleksandrova, V.A. Aseev, N.V. Nikonorov, N.N. Khimich, 2008, published in Zhurnal Prikladnoi Khimii, 2008, Vol. 81, No. 9, pp. 1457–1462.

PHYSICOCHEMICAL STUDIES OF SYSTEMS AND PROCESSES

Formation of Organo-Inorganic Hybrid Networks in the System Consisting of Tris(2,2'-bipyridine)ruthenium Complexes and Silica

A. V. Zdravkov, E. L. Aleksandrova, V. A. Aseev, N. V. Nikonorov, and N. N. Khimich

Grebenshchikov Institute of Silicate Chemistry, Russian Academy of Sciences, St. Petersburg, Russia
Ioffe Physicotechnical Institute, Russian Academy of Sciences, St. Petersburg, Russia
St. Petersburg State University of Information Technologies, Mechanics, and Optics, St. Petersburg, Russia

Received January 13, 2008

Abstract—Organo-inorganic composites consisting of mutually linked ruthenium complexes with organic ligands and an inorganic SiO_2 network were synthesized by the sol-gel method. The luminescence and photosensitive properties of the resulting compounds were studied.

DOI: 10.1134/S1070427208090115

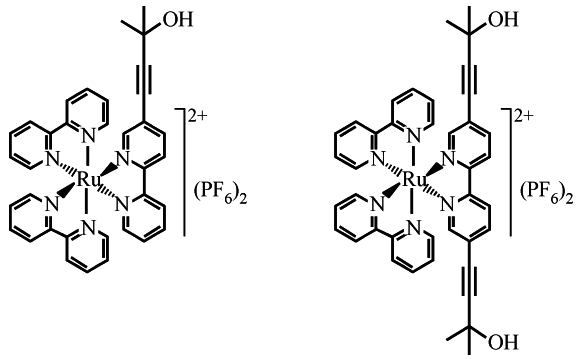
Thermally and chemically stable ruthenium(II) complexes with 2,2'-bipyridine derivatives have interesting photophysical, photochemical, and electrochemical properties. This allows them to be used for constructing photosensitive and electroluminescent devices, sensors, luminescent transducers, and catalysts [1–3]. Practical application of such structures is associated with their incorporation in a polymeric organic or inorganic matrix.

In case of organo-inorganic hybrids, the homogeneity and stability of the resulting structures is determined by the stability of the organic component of the system and by the possibility of its chemical binding with the inorganic network.

Tris(2,2'-bipyridine)ruthenium(II) complexes have unique thermal (500°C) and chemical stability: They are inert to concentrated sulfuric acid and to a 50% alkali solution [4]. The possibility of their chemical binding with an inorganic matrix by using special cross-linking agents has been shown earlier [5–8].

At the same time, further prospects for using organic complexes of transition metals, in particular, Ru^{2+}, in the form of organo-inorganic hybrids are associated with the possibility of the formation of a supramolecular organic structure based on them. In this structure, separate discrete centers of complex molecules should be connected with each other by chemical, preferentially double, bonds. An organic network synthesized in such a way opens principally new possibilities for electron movements, inaccessible for solutions of organic molecules. The most obvious method of preparing such structures is sol–gel synthesis of interpenetrating organo-inorganic hybrid networks.

To examine the basic possibility of the synthesis of such nanohybrid structures, we used ruthenium complexes containing in one of ligands substituents with triple bonds:

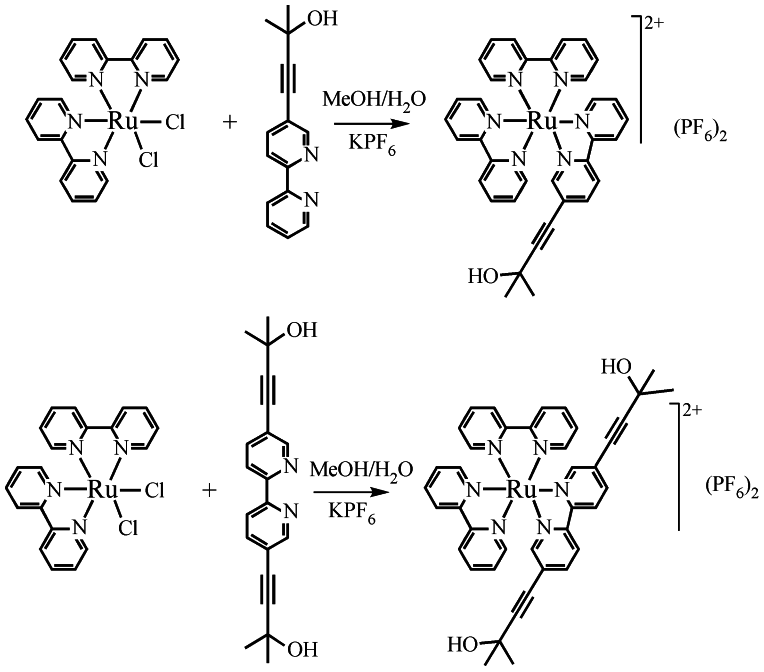


The goal of this study was to synthesize the above-mentioned complexes, to link them with each other by copolymerization with trimethoxysilicylacetylene (TMOSA), to incorporate the resulting structure into a silica matrix obtained by hydrolytic copolycondensation of tetramethoxysilane and TMOSA, and also to study physicomechanical and optical properties of the resulting materials.

EXPERIMENTAL

The ^1H and ^{13}C NMR spectra were recorded on a Bruker DPX-300 instrument, working frequencies 300.13 and 75.5 MHz, respectively, internal reference TMS. The absorption spectra were measured on an SF-56 spectrophotometer; the IR spectra, on a Bruker IFS-88 Fourier spectrometer; and the mass spectra, on an MKh5303 instrument equipped with an electrospraying ionization source (Institute of Analytical Instrument Making, Russian Academy of Sciences). The composition of reaction mixtures and purity of compounds were determined by thin-layer chromatography (TLC) on Silica gel 60 F254 and Armsorb TSKh-AN-UF 254 plates. In the synthesis we used Favorskii's carbinol and potassium hexafluorophosphate purchased from Aldrich. *cis*-[Bis-(2,2'-bipyridine)]ruthenium dichloride [9, 10], bis-(triphenylphosphine)palladium dichloride [11], copper(I) iodide [12], 5-bromo-2,2'-bipyridine, and 5,5'-dibromo-2,2'-bipyridine [13, 14] were prepared by the procedures described previously. The light sensitivity and quantum yields of photogeneration of charge carriers η were measured in the electrophotographic mode [15, 16] in the spectral range 400–800 nm at a field intensity $E = (0.1–1.0)E_0$, where E_0 is the limiting electric field strength for a material under study. The light sensitivity $S_{0.1}$ was determined by the criterion of a 10% decrease in the surface potential layer V in relation to the initial value ($\Delta V/V = 0.1$) for illumination both by a monochromatic light with a wavelength from 400 to 700 nm and with a KGM-300 halogen lamp (integral light sensitivity).

Stable tris(2,2'-bipyridine)ruthenium complexes containing triple bonds conjugated with the bipyridine system were prepared with 5-(2-hydroxyisopropylethynyl)-2,2'-bipyridine and 5,5'-bis(2-hydroxyisopropylethynyl)-2,2'-bipyridine:



For this purpose, a suspension of 500 mg of [bis-(2,2'-bipyridine)]ruthenium dichloride and 1.05 equiv of functionally substituted 2,2'-bipyridine in a mixture of 40 ml of water and 40 ml of methanol was refluxed for 2 h until the complex $bipy_2RuCl_2$ disappeared (monitoring by TLC on aluminum oxide). The resulting solution was cooled and filtered, and 2.1 equiv of potassium hexafluorophosphate in 30 ml of water was added to the filtrate. The precipitate formed was filtered off, dried, dissolved in 2 ml of acetonitrile, and reprecipitated into 20 ml of absolute diethyl ether.

[Rubipy$_2$(bipy–C≡C–CMe$_2$OH)](PF$_6$)$_2$, yield 58%. ^1H NMR spectrum [$(CD_3)_2SO$], δ, ppm: 1.39 s (6H, CH_3), 5.57 s (1H, OH), 7.55 m (6H, $1H^6 + 5H^{5,5'}$),

7.66–7.73 m (3H, $H^{6,6'}$), 7.78 d (1H, $H^{6'}$), 7.86 d (1H, H^{6}), 8.18 q (6H, $H^{4,4'}$), 8.83 t (6H, $H^{3,3'}$). ^{13}C NMR spectrum [$(CD_3)_2SO$], δ_C, ppm: 31.9 (CH_3), 64.6 (C–OH), 76.8 (C≡C), 104.1 (C≡C), 123.8, 125.0, 125.3, 125.5, 125.8, 128.7, 128.8, 128.9, 129.6, 138.9, 140.9, 151.9, 152.1, 152.3, 152.6, 152.8, 156.6, 156.8, 157.2, 157.4, 157.5. UV spectrum (CH_3CN), λ, nm (ε, 1 mol^{-1} cm^{-1}): 245 (23800), 255 (21100), 285 (68700), 401 (5800), 453 (13400). IR spectrum (KBr), ν, cm^{-1}: 3641 s, 3554 s, 3394 s, 3095 m, 3078 m, 2977 m, 2856 m, 2324 w, 2229 w (C≡C), 1604 m, 1467 s, 1369 m, 1311 m, 1271 m, 1240 m, 1166 m, 837 s, 761 s, 729 s, 557 s. Mass spectrum (solution in $CH_3CN : H_2O$ = 50 : 50, electrospray ionization): 797.11 ($[M–PF_6]^+$), 326.08 ($[M–2PF_6]^{2+}$).

[Rubipy$_2${bipy(C≡C–CMe$_2$OH)$_2$}](PF$_6$)$_2$, yield 49%. ^1H NMR spectrum [$(CD_3)_2SO$], δ, ppm: 1.38 s (6H, CH_3), 5.55 s (2H, OH), 7.51 s (2H, $H^{6,6'}$), 7.55 t (4H, $H^{5,5'}$), 7.72 d (2H, $H^{6,6'}$), 7.82 d (2H, $H^{6,6'}$), 8.20 t (6H, $H^{4,4'}$), 8.84 d (6H, $H^{3,3'}$). ^{13}C NMR spectrum [$(CD_3)_2SO$], δ_C, ppm: 31.9 (CH_3), 64.6 (C–OH), 76.8 (C≡C), 104.4 (C≡C), 118.9, 119.0, 123.9, 125.3, 125.4, 125.5, 128.8, 139.1, 140.9, 152.2, 152.7, 152.9, 156.0, 157.1, 157.5. UV spectrum (CH_3CN), λ, nm (ε, 1 mol^{-1} cm^{-1}): 255 (25300), 285 (75100), 320 (50400), 345 (32600), 401 (7600), 446 (13000), 480 (10200). IR spectrum (KBr), ν, cm^{-1}: 3626 s, 3550 s, 3394 s, 3101 s, 3076 s, 2927 s, 2864 m, 2231 (C≡C) m, 1600 s, 1471 s, 1367 m, 1274 s, 1242 s, 1168 s, 840 s, 763 s, 729 s, 557 s. Mass spectrum (solution in $CH_3CN : H_2O$ = 50 : 50, electrospray ionization): 879.15 ($[M–PF_6]^+$), 367.10 ($[M–2PF_6]^{2+}$).

According to the published data [17–22], TMOSA is prepared in two steps:

$$Si(OMe)_4 \text{ (or } SiCl_4) \rightarrow Si(OMe)_3Cl \rightarrow HC{\equiv}C{-}Si(OMe)_3.$$

Despite apparent simplicity of these transformations, this synthesis involved serious problems. Initially we thoroughly tested all the three known procedures [17–21] for preparing trimethoxychlorosilane:

$$3Si(OMe)_4 + SiCl_4 \overset{AlCl_3}{\rightleftarrows} 4Si(OMe)_3Cl,$$

$$Si(OMe)_4 + CH_3COCl \overset{AlCl_3}{\rightleftarrows} Si(OMe)_3Cl + CH_3COOMe,$$

$$SiCl_4 + 3MeOH \rightleftarrows Si(OMe)_3Cl + 3HCl.$$

The boiling points and refraction indices of thus obtained samples completely corresponded to the published values [17–21], and the elemental analysis seemed to confirm the trimethoxychlorosilane formation. However, detailed examination of their structure by NMR spectroscopy and mass spectrometry showed that the synthesized samples were mixtures containing at least three compounds: $Si(OMe)_2Cl_2$, $Si(OMe)_3Cl$, and $Si(OMe)_4$.

This result can be accounted for by closeness of their boiling points, possible formation of azeotropes, and/or disproportionation of methoxychlorosilanes on heating to boiling points.

The reaction of silicon tetrachloride with methanol appeared to be practically the most convenient. Analysis by chromatography–mass spectrometry showed that this reaction yielded a mixture of methoxychlorosilanes of the following composition (%): $Si(OMe)Cl_3$ 5, $Si(OMe)_2Cl_2$ 30, $Si(OMe)_3Cl$ 50, and $Si(OMe)_4$ 15.

The replacement of chlorine by the ethynyl group according to the known procedure [22] became the second step of the synthesis:

$$Si(OMe)_3Cl + HC{\equiv}CNa \rightarrow Si(OMe)_3C{\equiv}CH.$$

Unfortunately, here again the results were poorly reproducible and the yield of the final product was low. Variation of reaction conditions did not give a positive result. Therefore, we developed a new synthesis method using ethynylmagnesium bromide, which allowed us to considerably increase the yield of the target product:

$$Si(OMe)_3Cl + HC{\equiv}CMgBr \rightarrow Si(OMe)_3C{\equiv}CH.$$

According to the data of NMR spectroscopy, gas chromatography–mass spectrometry, and elemental analysis, the product obtained was a mixture of mono-, di-, and triethynylmethoxysilanes free from chlorine.

Attempts to separate this mixture failed. We could not increase the TMOSA content in the distillate to a value over 70%. However, this fact should not influence the formation of an organo-inorganic hybrid, as all the components contain building blocks necessary for it, namely, triple bonds and

methoxy groups, allowing organic and inorganic networks, respectively, to be formed.

Polymerization via triple bonds was carried out by the modified procedure from [23]. The initial system consisted of tetramethoxysilane (0.5 equiv), a mixture of methoxysilylacetylenes (0.5 equiv), palladium chloride (0.01 equiv), and a solution of ruthenium complexes in propionitrile. The reaction mixture was left for two days at room temperature, and then the polycondensation process was carried out. For this purpose, 4 equiv of water and 0.1 equiv of trifluoroacetic acid were added to the system.

The resulting solutions were placed in sealed polypropylene test tubes and kept at 60°C for 2 days. Then hermetic stoppers to the tubes were replaced by perforated stoppers (hole diameter about 1 mm), and crude gels were dried for 10 h at 60°C, 14 h at 75°C, 24 h at 90°C, and 24 h at 110°C. The temperature was raised at a rate of 5 deg h^{-1}. After that, the gels were placed in glass test tubes with perforated stoppers, heated to 110°CC (15 deg h^{-1}), and kept for 12 h at this temperature.

The samples were synthesized in the form of monolithic structures: disks of width 3–7 mm and diameter 15–30 mm and cylinders of length 15–30 mm and diameter 4–6 mm, and also 1–2-μm-thick films on a polymeric support. The conditions for the hydrolysis of methoxy groups of the components and for polycondensation of the formed compounds were optimized by varying the acidity of the medium in the course of the sol–gel process and by simultaneously removing the formed alcohol in the form of volatile compounds [24].

The absorption spectra of the composites practically coincide with the spectra of the initial ruthenium complexes (Fig. 1).

All the synthesized samples show strong luminescence in the region of 610–630 nm (excitation with xenon lamp radiation with λ = 450 nm). The normalized luminescence spectra of the composites (Fig. 2) contain one emission band broadened as compared to solutions. Its position depends on the concentration of the ruthenium complex in the hybrid.

The light sensitivity $S_{0.1}$ of the synthesized samples (Fig. 3) is at a level of $(1–2) \times 10^4$ cm^2 J^{-1} in

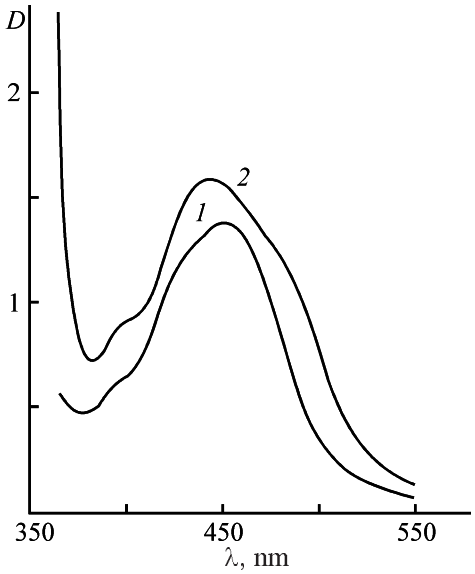


Fig. 1. Absorption spectra of ruthenium complexes. (*D*) Optical density and (λ) wavelength. Complex: (*1*) [Ru-bipy$_2$(bipy–C≡C–CMe$_2$OH)](PF$_6$)$_2$ and (*2*) [Ru-bipy$_2${bipy(C≡C–CMe$_2$OH)$_2$}](PF$_6$)$_2$; the same for Fig. 2.

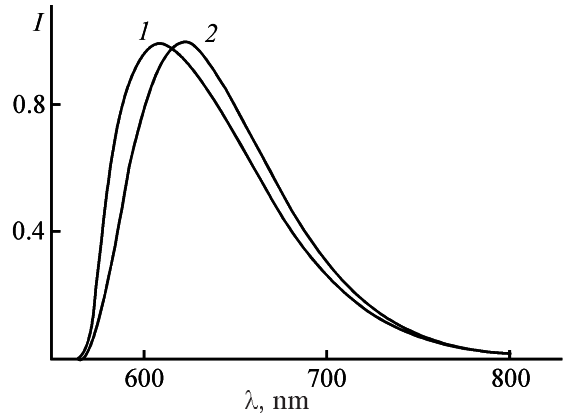


Fig. 2. Normalized luminescence spectra of composites containing various complexes. (*I*) Normalized intensity and (λ) wavelength.

the spectral range 400–550 nm; the quantum yield of charge carriers is 0.005±0.001. These values are 2–4 times higher than the analogous value found previously for composites in which ruthenium complexes are covalently bonded with the silica matrix, but are not a part of an organic network and are not bonded with each other.

An insignificant bathochromic shift in absorption spectra (~10 nm), and also a weak decrease in the intensity of absorption bands of the –C≡C– bond in the IR spectra show that the structure connecting ruthenium complexes with each other is primitive and imperfect. However, a substantial growth of

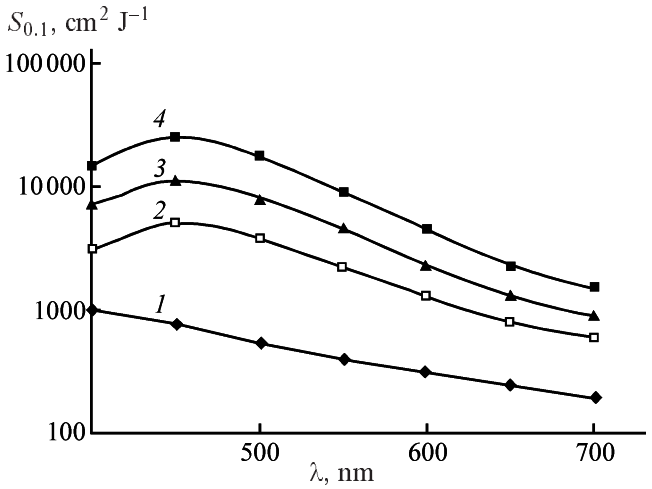


Fig. 3. Spectra of light sensitivity of composites. ($S_{0.1}$) Light sensitivity and (λ) wavelength. (*1*) Sample free of ruthenium complexes, (*2*) composite in which ruthenium complexes are not a part of a supramolecular structure [6], and (*3, 4*) composites with the ruthenium complexes under consideration: (*3*) [Rubipy$_2$(bipy–C≡C–CMe$_2$OH)](PF$_6$)$_2$ and (*4*) [Rubipy$_2${bipy(C≡C–CMe$_2$OH)$_2$}](PF$_6$)$_2$.

light sensitivity of the composites, and also a 20–40 nm long-wave shift of the emission band maximum with increasing concentration of the ruthenium complex, as compared to composites in which the components are chemically bonded with each other but are not incorporated in a supramolecular structure, suggest the formation of a supramolecular organic network linking the ruthenium complexes.

CONCLUSIONS

(1) The new organo-inorganic hybrids based on Ru(II) complexes containing substituents with triple bonds in one of ligands were synthesized.

(2) Even incomplete binding of ruthenium complexes with each other with the formation of a supramolecular structure strongly enhances the luminescence and photosensitive properties of the synthesized samples.

ACKNOWLEDGMENTS

This study was financially supported by the Russian Foundation for Basic Research (project no. 06-03-33002-a).

The authors are grateful to A.V. Novikov for performing mass-spectrometric analysis of ruthenium complexes.

REFERENCES

1. Lo, K.K.-W., Chan-Ming Ng, D., and Chung, C.-K., *Organometallics*, 2001, vol. 20, pp. 4999–5002.
2. Lo, K.K.-W., Chung, C.-K., and Zhu, N., *Chem. Eur. J.*, 2003, vol. 9, pp. 475–480.
3. Yang, J., Gordon, K., Zidon, Y., and Shapira, Y., *J. Appl. Phys.*, 2003, vol. 94, no. 10, pp. 6391–6395.
4. Seddon, A. and Seddon, K.R., *The Chemistry of Ruthenium*, Amsterdam: Elsevier, 1984.
5. Khimich, N.N., Semov, M.P., and Chepik, L.F., *Dokl. Ross. Akad. Nauk*, 2004, vol. 394, no. 5, pp. 636–638.
6. Khimich, N.N., Zdravkov, A.V., Aleksashkina, M.A., and Chepik, L.F., *Zh. Prikl. Khim.*, 2007, vol. 80, no. 3, pp. 360–365.
7. Aleksandrova, E.L., Zdravkov, A.V., Aseev, V.A., et al., *Opt. Spektrosk.*, 2007, vol. 103, no. 4, pp. 592–595.
8. Shimojima, A. and Kuroda, K., *Chem. Record.*, 2006, vol. 6, pp. 53–63.
9. Sullivan, B.P., Salmon, D.J., and Meyer, T.J., *Inorg. Chem.*, 1978, vol. 17, no. 12, pp. 3334.
10. Holder, E., Schoetz, G., Schurig, V., and Lindner E., *Tetrahedron: Asymmetry*, 2001, vol. 12, p. 2289.
11. Dangles, O., Guibe, F., and Balavoine, G., *J. Org. Chem.*, 1987, vol. 52, pp. 4984–4993.
12. *Handbuch der präparativen anorganischen Chemie*, Brauer, G., Huber, F., et al., Eds., Stuttgart: Enke, 1978, vol. 2.
13. Romero, F.M. and Ziessel, R., *Tetrahedron Lett.*, 1995, vol. 36, pp. 6471–6475.
14. Zdravkov, A.V. and Khimich, N.N., *Zh. Org. Khim.*, 2006, vol. 42, no. 8, pp. 1219–1221.
15. Aleksandrova, E.L., Goikhman, M.Ya., Kudryavtsev, V.V., et al., *Opt. Zh.*, 2001, vol. 68, no. 11, p. 67.
16. Aleksandrova, E.L., Goikhman, M.Ya., Kudryavtsev, V.V., et al., *Fiz. Tekh. Poluprovodn.*, 2002, vol. 37, no. 7, pp. 846.
17. Kalinin, I., *Dokl. Akad. Nauk SSSR*, 1940, vol. 26, p. 373.

18. Perrard, D.F., Brown, W.G., and Jonson, W.C., *J. Am. Chem. Soc*., 1946, vol. 68, pp. 70–72.

19. Goubeau, J. and Behr, U., *Z. Anorg. Chem*., 1953, vol. 272, pp. 2–9.

20. USSR Inventor's Certificate no. 1032760, 1983.

21. Corriu, R.J.P., Moreau, J.J.E., Thepot, P., and Man, M.W.C., *Chem. Mater*., 1992, no. 4, pp. 1217–1224.

22. Komarov, N.V., Yarosh, O.G., and Ivanova, Z.G., *Izv. Akad. Nauk SSSR, Ser. Khim*., 1971, nos. 4–6, p. 872.

23. Kunzler, J. and Persec, V., *J. Polym. Sci., Part A: Polym. Chem*., 1990, vol. 28, no. 5, pp. 1043–1057.

24. Khimich, N.N., Venzel', B.I., Drozdova, I.A., and Koptelova, L.A., *Zh. Prikl. Khim*., 2002, vol. 75, no. 7, pp. 1125–1130.

ISSN 1070-4272, Russian Journal of Applied Chemistry, 2008, Vol. 81, No. 9, pp. 1538–1542. © Pleiades Publishing, Ltd., 2008.
Original Russian Text © L.S. Litvinova, 2008, published in Zhurnal Prikladnoi Khimii, 2008, Vol. 81, No. 9, pp. 1463–1468.

PHYSICOCHEMICAL STUDIES OF SYSTEMS AND PROCESSES

Determination of the Retention Characteristics in Thin-Layer Chromatography Taking into Account the Actual Position of the Mobile Phase Front

L. S. Litvinova

Institute of Macromolecular Compounds, Russian Academy of Sciences, St. Petersburg, Russia

Received January 21, 2008

Abstract—To reveal the actual position of the mobile phase front, corresponding to the free volume of the layer in thin-layer chromatography, it is suggested to use a nonsorbable low-molecular-weight marker. The expressions for the capacity coefficient k', equilibrium coefficient K_d, and corrected R_f values (R'_f) were obtained taking into account the correction of the position of the mobile phase front.

DOI: 10.1134/S1070427208090127

One of the most important parameters of a chromatographic process is the capacity coefficient k':

$$k' = Q_s/Q_m, \quad (1)$$

where Q_s and Q_m are the amounts of a substance in the stationary and mobile phases, respectively. The capacity coefficient in thin-layer chromatography (TLC) can be determined as follows [1]:

$$k' = t_s/t_m, \quad (2)$$

where t_s and t_m are the residence times of a substance in the stationary and mobile phases, respectively.

A characteristic feature of TLC is that the sum $t = t_s + t_m$ is equal for all the substances being separated, whereas in column chromatography all the substances being separated have equal t_m values.

The retention in TLC is characterized by the relationship

$$R_f = X_i/L, \quad (3)$$

where X_i is the distance passed by a substance from the start and L is the distance passed by the mobile phase front from the start (see figure).

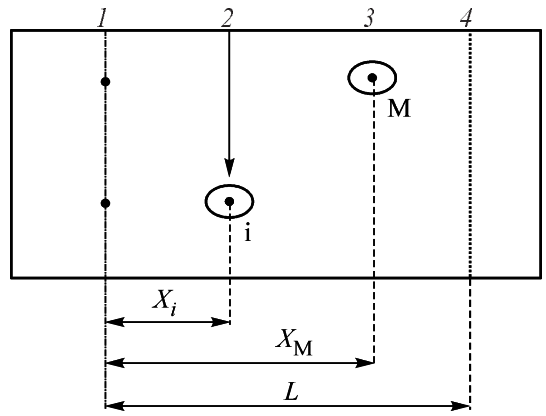
Hence, the position of the mobile phase front is the starting point in TLC. The velocity of the mobile phase motion along the plate is also judged from the front motion [2–4]. If the mobile phase vaporization from the wetted area of the sorbent layer and the adsorption of the vapor on a dry sorbent layer are excluded, then [1]

$$R_f = t_m/(t_m + t_s). \quad (4)$$

It follows from (2) and (4) that

$$k' = (1 - R_f)/R_f.$$

Determination of one of basic characteristics of a chromatographic process, k', by TLC is seemingly easy. However, the necessary conditions for experi-



Schematic representation of TLC in a saturated chromatographic chamber: (*1*) start line, (*2*) chromatographic spot of the sorbate (i), (*3*) mobile phase front found from the position of the spot of a low-molecular-weight nonsorbable ($k' = 0$) marker (M), and (*4*) observed mobile phase front.

mental determination of the capacity coefficient k' in TLC and of the true value of R_f are difficult to fulfil in practice: no vaporization of the mobile phase from the wetted area of the sorbent layer and no adsorption of the solvent vapor on the dry layer. In this ideal case, the mobile phase is spent only for filling of pores and interparticle space, and thus the solvent volume fed to the plate corresponds to the free volume.

In the course of chromatography, it is difficult to avoid uncontrollable adsorption of solvent vapor, especially if a saturated N-chamber is used or the time of solvent ascent is as long as several tens minutes. Filling of the adsorbent surface and pores with solvent molecules through the vapor phase leads to changes in the volume of the mobile phase fed to the sorvent layer at equal values of L and hence to changes in R_f. In an unsaturated S-chamber, these processes do not occur, but another problem arises: A mixed mobile phase is separated into components, forming a stepwise gradient on the plate [3]. Geiss [3] emphasizes that the R_f values commonly measured in TLC are not true quantities. Geiss believes that true R_f values can only be obtained with Vario-KS or U-chambers allowing simultaneous introduction into a solvent flow of a test sample and a reference for which $R_f = 1$. The sample and reference are applied simultaneously onto adjacent tracks in the eluent flow after a sufficient amount of the solvent passes the start line. The true R_f value (R'_f) will be determined by the ratio of the distances passed by the sample and reference.

This study is also aimed to solve the problem of determining the true values of R_f (R'_f), and also of k' and K_d in TLC and thus to improve the repeatability and reliability of the analysis results. Solving the problem requires determination of the actual mobile phase front corresponding to the free volume V_0 of the adsorbent layer. In this study we suggest to use the marker of the actual position of the front and a saturated chamber. As a marker we used a nonvolatile nonsorbable ($k' = 0$) low-molecular-weight compound to which all the pores of the adsorbent are accessible.

When a chromatographic experiment is performed on a plate with the layer cross section S, dry adsorbent weight on the working area of the layer g, specific pore volume V'_p, specific interparticle volume (volume between the adsorbent particles in the layer) V'_i, and specific free volume V'_0 ($V'_p + V'_i = V'_0$), the solvent is spent for filling of interparticle channels of the dry layer ($gV'_i = V_i$) and for pore filling ($gV'_p = V_p$).

Neglecting the vaporization of the mobile phase components from the wetted layer and vapor adsorption on the dry area of the layer, the volume gV'_0 of the solvent that filled the layer will be equal to

$$gV'_0 = g(V'_p + V'_i).$$

The front will move by the following distance:

$$L = g(V'_p + V'_i)/S.$$

The sorbate spot will move by the following distance X_i:

$$X_i = g(V'_p + V'_i)/(k' + 1)S.$$

The filling of adsorbent pores through the vapor phase regularly leads to an apparent decrease in V'_p and, correspondingly, to an increase in the front motion velocity [4]. On the contrary, the solvent vaporization from the wetted layer decreases the front motion velocity. As already noted, the vaporization processes are suppressed in a saturated N-chamber. Apparently, in the case of transfer of eluent components into the layer through the vapor phase, the solvent ascending by interparticle channels by a distance L is only partially spent for the pore filling, and its volume V is smaller than the free volume gV'_0. The distance X_i passed by the sorbate spot and the quantity R_f will also decrease, because the sorbate moves only with the solvent flow. Thus, the quantity R_f determined by a common procedure depends not only on the characteristics of the sorbent, mobile phase, and sorbate, but also on processes leading to pore filling through the vapor phase. Variation of the content of the solvent vapor in a chromatographic column leads to uncontrollable variation of R_f.

The systematic error in determining the retention parameters in TLC can be eliminated by performing the chromatography in a saturated chamber and determining the actual position of the mobile phase front with a nonvolatile nonretainable low-molecular-weight compound to which the adsorbent pores are accessible (as it is done in column chromatography for determining the free volume V_0 [5]).

The true value of R_f (R'_f) should be determined as the ratio of the distance passed by the sorbate to that passed by a nonsorbable reference (front mark-

er) that is not excluded from pores [6] (see figure):

$$R'_f = (R_f)_i/(R_f)_M = X_i/X_M,$$

where X_M is the migration distance and $(R_f)_M$ is the R_f value for the marker of the actual mobile phase front, i.e., for a nonvolatile nonretainable low-molecular-weight compound to which all the adsorbent pores are accessible. Such compounds are analogs of free volume markers in column chromatography. Note that there are no versatile compounds suitable for all adsorbents and all mobile phases. The main requirement is the solubility of the reference compound in the mobile phase, absence of adsorption (i.e., zero k' value), and absence of exclusion. Finding such substances in TLC is more difficult than in column chromatography, because they should not vaporize or sublime after a chromatographic run in the course of mobile phase evaporation.

The retention factor determined relative to the front marker corresponds to the thermodynamic value:

$$R'_f = 1/(1 + k').$$

Thus, determination of the true values of the retention factors in TLC and in liquid column chromatography is closely related to determination of the free volume. Furthermore, all the concomitant problems appear to be similar [5]. It should be noted that previously many authors suggested to correct R_f using arbitrarily chosen reference compounds [7–9]. In so doing, the only criterion for choosing the references was that the R_f values for the reference and test compounds should be close. Geiss [3] considers in detail and critically discusses methods for evaluating TLC results and for correcting R_f values. Taking into account the definition of R'_f, let us present the expressions for k' and K_d. It can be readily shown from the aforesaid that

$$k' = 1/R'_f - 1 = X_M/X_i - 1. \quad (5)$$

According to Skvortsov [10],

$$k' = (K - 1)V_p/V_0. \quad (6)$$

Taking into account expressions (10) and (11) and assuming that $V_0 = V_i + V_p$,

$$K_d = (1/R'_f - 1)(V_0/V_p) + 1 = (X_M/X_i - 1)(V_0/V_p) + 1. \quad (7)$$

As will be shown below, for Sorbfil plates used in this study $V_0/V_p = 2.08$. Hence, for Sorbfil plates

$$K_d = (2.08/R'_f - 1.08) = 2.08(X_M/X_i) - 1.08. \quad (8)$$

EXPERIMENTAL

The solvents (Reaktiv, St. Petersburg): carbon tetrachloride (pure grade), diethyl ether (pure grade), toluene (analytically pure grade), were purified by distillation. Cyclohexane (Merck, Darmstadt, Germany) of spectroscopic grade was freshly distilled. Tetrahydrofuran (THF, Reaktiv) was distilled from KOH just before use. Fullerene C_{60} (Fullerene Technologies, St. Petersburg), *meso*-tetraphenylporphyrin (TPP, Aldrich, USA), phenacetin (97%), acetanilide (sublimed), antracene (scintillation grade), and dyes (Sudan I, Cytochrome C, Anthraquinone Green (Reakhim, Shostka, Ukraine) were used without additional purification.

Thin-layer chromatography was performed on Sorbfil plates (Sorbpolimer, Krasnodar, Russia, produced before 2003) PTSKh-AF-V-UF of size 10×10 cm^2. After activation of plates by heating at 120°C for 40 min, solutions of test compounds (1.0 mg ml^{-1}, 1 μl) (anthracene in cyclohexane, dyes in CCl_4, phenacetin and acetanilide in THF) were applied onto the plate with a microsyringe (Hamilton Company, Reno, Nevada, USA) at a distance of 1 cm from the lower edge of the plate. Ascending chromatography to a height of 8 cm was performed at 20°C in an unsaturated S-chamber, a saturated N-chamber, or an unsaturated N-chamber containing 10 ml of one of the solvents (toluene, diethyl ether, THF–cyclohexane, or toluene–THF).

After a chromatographic run, the spots of the dyes and TPP were visible owing to their natural color, and the spots of the colorless compounds were visualized under a UV_{254} lamp. The quantities R_f and R'_f were determined as arithmetic mean from three runs. The determination error (relative standard deviation) under the given conditions did not exceed 5%.

The ratio V_p/V_0 was determined by impregnating the plates with water [2, 3]. From the difference in the plate weights before and after impregnation, we found the sum of the pore volume V_p and volume of interparticle space V_i per gram of the adsorbent (the plate was placed for weighing in a plastic container). The silica gel pore volume was 0.76 cm^3 g^{-1} (determined on an Auto-Pore 9200 mercury porosimeter, Coultronics, France).

To confirm experimentally the necessity of using

Table 1. Factors R_f and R'_f of dyes in S- and N-chambers (mobile phase toluene)

Chamber type	Front marker		Anthraquinone green		Sudan I		Cytochrome C	
	R_f	R'_f	R_f	R'_f	R_f	R'_f	R_f	R'_f
Front marker anthracene								
N, unsaturated	0.90	1	0.51	0.57	0.43	0.48	0.15	0.17
N, saturated	0.65	1	0.32	0.49	0.27	0.42	0.09	0.14
S, unsaturated	1	1	0.47	0.47	0.39	0.39	0.14	0.14
Front marker fullerene C_{60}								
N, unsaturated	0.93	1	0.51	0.55	0.43	0.46	0.15	0.16
N, saturated	0.70	1	0.32	0.46	0.27	0.38	0.09	0.13
S, unsaturated	1	1	0.47	0.47	0.39	0.39	0.14	0.14

Table 2. Factors R_f and R'_f of dyes in S- and N-chambers (mobile phase: THF–cyclohexane, 17 : 83 v/v, front marker fullerene C_{60})

Chamber type	C_{60}		Anthraquinone green		Sudan I		Cytochrome C	
	R_f	R'_f	R_f	R'_f	R_f	R'_f	R_f	R'_f
N, unsaturated	0.95	1	0.90	0.95	0.87	0.92	0.64	0.67
N, saturated	0.54	1	0.47	0.87	0.44	0.81	0.27	0.50
S, unsaturated	0.93	1	0.76	0.82	0.73	0.78	0.54	0.58

Table 3. Factors R_f and R'_f of phenacetin and acetanilide in S- and N-chambers (mobile phase diethyl ether, front marker *meso*-tetraphenylporphyrin)

Chamber type	TPP		Phenacetin		Acetanilide	
	R_f	R'_f	R_f	R'_f	R_f	R'_f
N, unsaturated	0.90	1	0.44	0.49	0.57	0.63
N, saturated	0.60	1	0.21	0.35	0.28	0.47
S, unsaturated	0.98	1	0.32	0.33	0.46	0.47

free volume markers in TLC, we obtained chromatograms of dyes, phenacetin, and acetanilide in one-component and mixed mobile phases. The results of the chromatography of the dyes in toluene and in THF–cyclohexane (17 : 83 v/v) are diven in Tables 1 and 2. The results of the chromatography of phenacetin and acetanilide in diethyl ether and in THF–toluene (54 : 46 v/v) are given in Tables 3 and 4. The quantities R_f and R'_f were calculated taking into account both the observed and actual (found with a marker) positions of the front. As markers we used anthracene, fullerene C_{60}, and TPP. It should be noted that acetanilide and phenacetin can also be used as markers of the actual position of the front for more polar mobile phases.

It follows from Tables 1–3 that the maximal R_f values are observed in the unsaturated N-chamber, and the minimal values, in the saturated N-chamber. As the differences in R_f range from 50 to 100%, the observed position of the mobile phase front cannot, apparently, be considered as the reference point in estimation of the mobility of chromatographic spots. It could be expected that the R'_f values obtained in different types of chromatographic chambers would coincide. However, the R'_f values obtained in saturated and unsaturated N-chambers noticeably differ.

Table 4. Statistical processing of the chromatographic data for phenacetin (P) and acetanilide (A) in a saturated N-chamber (mobile phase: toluene–THF, 46 : 54 v/v; front marker *meso*-tetraphenylporphyrin)

Run no.	Distance L, mm, from the start line to the center of spots in three replicate runs				R_f and R'_f in three replicate runs			
	L_{front}	X_{TPP}	X_P	X_A	R_f(P)	R_f(A)	R'_f(P)	R'_f(A)
1	80	55.7	33.6	35	0.42	0.438	0.603	0.628
2	80	56.5	32.8	36.6	0.41	0.458	0.580	0.648
3	80	56.7	34.8	37.8	0.435	0.472	0.614	0.667
Data processing								
$\bar{x}$ (arithmetic mean, n = 3)	80	56.3	33.7	36.47	0.422	0.456	0.599	0.648
s (standard deviation)	0	0.5	1	1.4	0.01	0.018	0.017	0.019
s_m (standard error)	0	0.3	0.6	0.8	0.007	0.010	0.010	0.011
$s/\bar{x} \times 100$		0.8	3	3.8	2.3	3.9	2.8	2.9

The lowest values of R'_f were obtained in a saturated N-chamber, and the highest values, in an unsaturated N-chamber. The probable cause is the large contribution of the mobile phase evaporation from the wetted area of the sorbent layer in an unsaturated N-chamber. Taking into account the experimental error (relative standard deviation ≤5%), the R'_f values in the S- and saturated N-chambers can be considered identical. Let us compare the reproducibility of the R_f and R'_f values of phenacetin and acetanilide, obtained in a saturated N-chamber (mobile phase toluene–THF, Table 4). As can be seen, replacement of R_f by R'_f has no effect on the standard deviation of the arithmetic mean s and on the standard error s_m.

Similarly to column chromatography, in TLC the R'_f values calculated using different markers do not coincide (Table 1). Nevertheless, the practical use of R'_f values allows the influence of conditions on the TLC retention characteristics to be largely eliminated.

CONCLUSIONS

(1) A new TLC retention characteristic, ratio of the migration distance of the sorbate to that of a front marker, a low-molecular-weight nonretainable reference compound to which all adsorbent pores are accessible, was suggested.

(2) With the aim to determine the thermodynamic parameters by thin-layer chromatography and to compare the data of thin-layer and column chromatography, formulas were suggetsted for calculating the capacity and equilibrium coefficients, involving the new retention characteristic.

(3) A formula was obtained for determining the equilibrium coefficient on Sorbfil plates.

(4) The validity of the new retention characteristic was confirmed experimentally.

REFERENCES

1. *HPTLC, High Performance Thin-Layer Chromatography*, Zlatkis, A. and Kaiser, R.E., Eds., Amsterdam: Elsevier, 1977.
2. Litvinova, L.S. and Kurenbin, O.I., *Zh. Fiz. Khim.*, 1992, vol. 66, no. 3, pp. 730–735.
3. Geiss, F., *Fundamentals of Thin Layer Chromatography (Planar Chromatography)*, Heidelberg: Huthig, 1987.
4. Guiochon, G. and Siouffi, A.J., *J. Chromatogr. Sci.*, 1978, vol. 16, no. 12, pp. 598–609.
5. Rimmer, C.A., Simmons, C.R., and Dorsey, J.G., *J. Chromatogr. A*, 2002, vol. 965, pp. 219–232.
6. Litvinova, L.S., *J. Planar Chromatogr.*, 2006, vol. 19, no. 2, pp. 171–174.
7. Dhont, J.H., Vinkenborg, C., Compaan, H., et al., *J. Chromatogr.*, 1970, vol. 47, pp. 376–381.
8. Dhont, J.H., Vinkenborg, C., Compaan, H., et al., *J. Chromatogr.*, 1972, vol. 71, pp. 283–289.
9. Van Wendel de Joode, M.D., Hindriks, H., and Lakeman, J., *J. Chromatogr.*, 1979, vol. 170, pp. 412–418.
10. Skvortsov, A. and Trathnigg, B., *J. Chromatogr. A*, 2003, vol. 1015, pp. 31–42.

ISSN 1070-4272, Russian Journal of Applied Chemistry, 2008, Vol. 81, No. 9, pp. 1543–1548. © Pleiades Publishing, Ltd., 2008.
Original Russian Text © A.V. Markova, 2008, published in Zhurnal Prikladnoi Khimii, 2008, Vol. 81, No. 9, pp. 1469–1473.

PHYSICOCHEMICAL STUDIES OF SYSTEMS AND PROCESSES

Practicability of Using Partial Condensation in Distillation

A. V. Markova

St. Petersburg Academy of Pharmaceutical Chemistry, St. Petersburg, Russia

Received January 15, 2008

Abstract—A procedure for calculation of batch distillation followed by partial condensation was developed on the basis of the suggested mathematical model. A strategy for assessing the feasibility of using this method, compared to simple distillation, was suggested. The effect of the initial conditions on the economic efficiency of the installation employed was analyzed. Numerical values of working parameters are obtained and recommendations for performing the process in the optimal mode are formulated.

DOI: 10.1134/S1070427208090139

Chemical-pharmaceutical industry widely employs simple distillation and distillation with partial condensation (also termed reflux distillation) for recovery of valuable volatiles from production waste [1]. As a rule, the distillation is performed in the batch mode in a jacketed vessel (distillation still), with heating steam or hot water commonly serving as energy carrier. When distillation is performed simultaneously with partial condensation, a partial condenser is mounted at the top of the still (Fig. 1).

Compared to simple distillation, the capital expenditure for construction of the installation becomes higher because of the appearance of an additional heat exchanger; also grow the operating costs associated with the increase in the required amount of the heat-carrying agent. Apparently, this expenditure can be justified by the more complete recovery a valuable volatile, i.e., by production of a more concentrated distillate. It is of interest in this context to find out how the degree of partial condensation affects the quality of the product being obtained and the energy parameters of operation of the installation.

The aim of this study was to find conditions in which the reflux distillation is feasible and to determine the optimal process mode.

When developing a procedure for calculating the distillation with partial condensation, we made the following assumptions. The distillation still is an ideal mixing apparatus. The vapor phase leaving the distillation still is in equilibrium with the liquid it contains. The vapor and liquid phases leaving the partial condenser are also in equilibrium. The partial condenser operates at a constant R number equal to the ratio between the mass flow rate G_{x1} of the liquid returned into the still (kg s^{-1}) and the mass flow rate G_D of the distillate (kg s^{-1}): $R = G_{x1}/G_D$ (which is provided by varying the flow rate of cooling water in the partial condenser).

With account of the assumptions made, the material balance equations for the still and partial condenser are written as follows:

$$-\mathrm{d}M_\mathrm{W}/\mathrm{d}\tau = \mathrm{d}M_\mathrm{D}/\mathrm{d}\tau = G_\mathrm{D}, \quad (1)$$

$$-\mathrm{d}(M_\mathrm{W}x_\mathrm{W})/\mathrm{d}\tau = y_1(\mathrm{d}M_\mathrm{D}/\mathrm{d}\tau) = y_1G_\mathrm{D}, \quad (2)$$

where M_W and M_D are the masses of the liquid phase in the distillation still and distillate collector, respectively (kg); x_W, mass fraction of the volatile component in the liquid phase of the distillation still; y_1, mass fraction of the volatile component in the vapor phase leaving the partial condenser; and τ, time (s).

By differentiating the left-hand part of Eq. (2) with account of (1), we obtain

$$M(\mathrm{d}x_\mathrm{W}/\mathrm{d}\tau) = (x_\mathrm{W} - y_1)G_\mathrm{D}. \quad (3)$$

The relation between the running values of y_1 and x_W can be derived from the material balance equation for the partial condenser, which has in relative flow rates the form [1]:

$$R = (y_1 - y_\mathrm{W})/(y_\mathrm{W} - x_1), \quad (4)$$

where x_1 is the mass fraction of the volatile component in the liquid phase leaving the partial condenser, and y_W, the mass fraction of the volatile

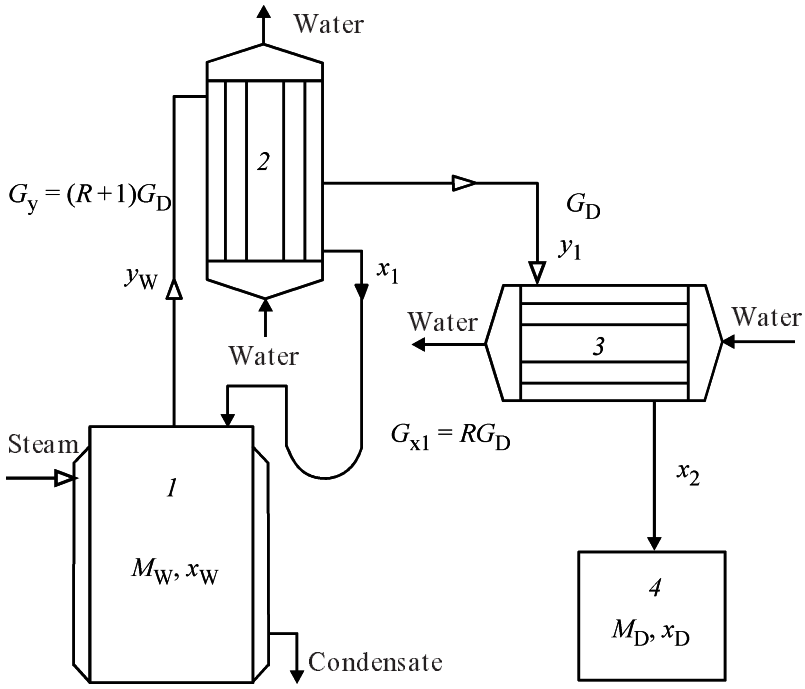


Fig. 1. Schematic of the installation for reflux distillation. (*1*) Distillation still, (*2*) partial condenser, (*3*) condenser, and (*4*) distillation collector.

component in the vapor phase leaving the still.

Using Eq. (4) and the equilibrium dependence $y_W = y^*(x_W)$, we can find, for the running value of x_W, x_1 or $y^*(x_1)$.

The heat balance equation for the still has the following form:

$$d(M_W i_W)/d\tau = q_W - G_D(R + 1)I_W + G_D R i_{x1}, \quad (5)$$

where $i_W = c_{xW}t_W$, $i_{x1} = c_{x1}t_{x1}$ are the specific enthalpies of the liquid in the still and in the liquid returned into the still after the partial condenser, respectively (kJ kg^{-1}); $I_W = c_{yW}t_W + r_{yW}$, specific enthalpy of the vapor leaving the still (kJ kg^{-1}); c_{xW}, c_{x1}, c_{yW}, specific heats of the liquid phase of composition x_W, x_1, y_W (kJ kg^{-1} K^{-1}); t_W, t_{x1}, temperatures of the liquid in the still and after the partial condenser (°C); r_{yW}, heat of vaporization of a mixture of composition y_W (kJ kg^{-1}); $q_W = KF(t_p - t_W)$, intensity of heat supply to the still (W); K, heat-transfer coefficient (W m^{-2} K^{-1}); F, heat-transfer surface area (m^2); and t_p, temperature of the heating steam (°C).

Differentiating Eq. (5) after simple rearrangements and assuming $I_W - i_{x1} \approx r_{y1}$, we can obtain the expression

$$q_W = G_D(R + 1)r_{y1} + M_W c_{xW}(dt_W/d\tau), \quad (6)$$

which can be used to estimate, with account of (3) and (4), the process duration

$$\tau = (R + 1)\int_{x_F}^{x_W} M_W r_{y1}[KF(t_p - t_W)]^{-1}(x_W - y_1)dx_W$$

$$+ \int_{t_F}^{t_W} M_W c_{x1}[KF(t_p - t_W)]^{-1}dt_W, \quad (7)$$

where the parameters with subscript F correspond to the starting mixture.

The variables in the integrands, M_W, K, r_y, and, especially, F (which is due to the decrease in the liquid level in the still), may widely vary in the course of the process and, therefore, are not taken outside the integral sign.

Equations (1), (3), (4), and (7) form the basis for calculation of the batch distillation with partial condensation. Equations (4) and (7) are solved numerically.

Preliminarily, we qualitatively analyze Eqs. (1), (3), (4), and (7) we obtained.

It follows from Eq. (4) that the composition of

the vapor phase from the partial condenser, y_1, is determined by the type of the equilibrium curve $y^*(x)$ of the binary system. Within the range x_W–x_1 the equilibrium line can be considered to be straight: $y^* = mx + b$ (b is the distribution coefficient). In this case, we obtain from (4) the following:

$$y_i = m^2(R + 1)x_W/(m + R) + b(m + mR + R)/(m + R). \quad (8)$$

Thus, at $R = 0$ (simple distillation), $y_1 = y_{1min} = mx_W + b$; at $0 < R < \infty$, Eq. (8); at $R \to \infty$, y_1 asymptotically approaches the maximum possible value: $y_1 = y_{1max} \to m^2x_W + b(1 + m)$. The quantity

$$\Delta = y_{1max}/y_{1min} = m + 1/[(m/b)x_W + 1]$$

can serve as a feasibility criterion for the method of reflux distillation. The type of the dependences $\Delta(x_W)$ for different m is shown in Fig. 2.

At low concentrations x_W, the distribution coefficient m for binary mixtures takes values $m > 1$ and the coefficient b is small. In this case, $\Delta \to m$ and the reflux distillation is efficient (Fig. 2, curves *1* and *2*).

At $m < 1$ (region of medium and high concentrations x_W), Δ approaches the line $\Delta = 1$ and even crosses it at $x_W = b/(1 - m)$. In this case, the partial condenser is inefficient and only simple distillation should be used. At other values of b, the run of the curves remains qualitatively the same.

At low concentrations of the volatile in the still, the equilibrium line can be represented as $y^* = mx$ ($m > 1$). In this case, Eqs. (1), (3), and (4) can be solved analytically. For example, the mass of the liquid in the still and its composition are related by

$$M_W = M_F x_F^c x_W^{1/c}, \quad (9)$$

and the average concentration of the final product in the distillate collector is given by

$$x_W = \frac{n^{c+1} - 1}{n^c - 1}x_W = \frac{n^{c+1} - 1}{(n^c - 1)n}x_F, \quad (10)$$

$$n = x_F/x_W.$$

In Eqs. (9) and (10), $c = (m - 1)(m + mR + R)/(m + R)$. The quantity n serves as the degree of still exhaustion. In simple distillation ($R = 0$),

$$x_{Dmin} = \frac{n^{m/(m-1)} - 1}{n^{m/(m-1)} - n}x_F.$$

In the limiting case ($R \to \infty$), the average composition of the distillate tends to the maximum value:

$$x_{Dmin} \to \frac{n^{m^2/(m^2-1)} - 1}{n^{m^2/(m^2-1)} - n}x_F.$$

The function $x_D(n)$ is plotted for the limiting cases in Fig. 3.

The region between curves *1* and *2* (Fig. 3) is that

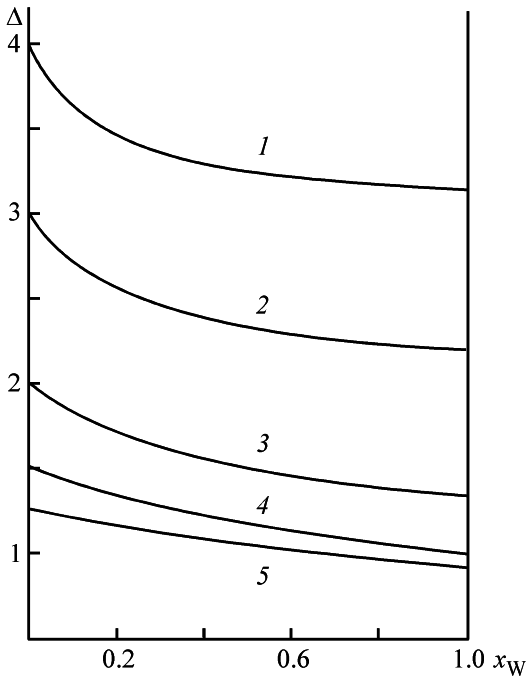


Fig. 2. Δ vs. x_W ($b = 0.5$). m: (*1*) 3, (*2*) 2, (*3*) 1, (*4*) 0.5, and (*5*) 0.25.

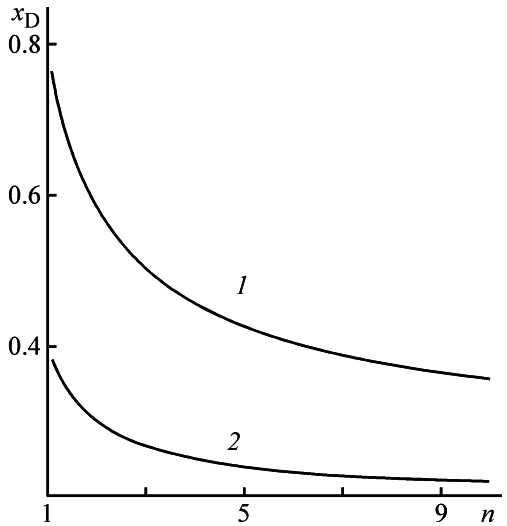


Fig. 3. Average distillate composition x_D vs. the degree n of still exhaustion ($x_F = 0.2$, $m = 2$). (*1*) $R = 0$ and (*2*) $R \to \infty$.

of working values of R. On the average, at not too strong still exhaustion, the limiting values of x_D differ by a factor of m, which confirms the feasibility of the reflux distillation at small values of x_W, characteristic of dilute solutions in the final stage of distillation. It follows from Fig. 3 that, at small n, the distillate obtained has a rather high concentration of the volatile. In further still exhaustion, the concentration of the volatile in the distillate decreases, but not so steeply as in the initial stage. This circumstance makes it possible to recover to the fullest extent the valuable component from the still at a slight deterioration of the quality of the distillate and to organize fractional collection of a distillate of high or medium quality, depending on n.

Let us consider factors determining the process duration, given by Eq. (7). The heat-exchange surface area at a variable liquid level in the still (with the surface of the partly heated bottom disregarded), $F \approx \pi Dh$, where D is the apparatus diameter (m), and h, the height of the liquid in the still (m). Taking into account that $h = 4M_W/\rho_{xW}\pi D^2$, we obtain

$$F = 4M_W/\rho_{xW}\pi D, \quad (11)$$

where ρ_{xW} is the density of the liquid in the still (kg m^{-3}).

Substituting Eq. (11) in (7), we obtain

$$\tau = (R + 1)\int_{x_F}^{x_W} D\rho_{xW}r_{y1}[4K(t_p - t_W)]^{-1}(x_W - y_1)^{-1}dx_W + \int_{t_F}^{t_W} D\rho_{xW}c_{x_W}[4K(t_p - t_W)]^{-1}dt_W. \quad (12)$$

Equation (12) gives at average values of K, t_W, and thermal parameters a simpler expression

$$\tau = (R+1)\int_{x_F}^{x_W} D\rho_{xWav}r_{y1av}[4K_{av}(t_p - t_W)_{av}]^{-1}(x_W - y_1)^{-1}dx_W + D\rho_{xWav}c_{xWav}(4K_{av})^{-1}\ln[(t_p - t_W)/(t_p - t_F)], \quad (13)$$

where the parameters with a subscript av have values averaged over the process.

Relations (12) and (13) are independent of the mass M_W of the liquid in the still. The second term in the right-hand parts of the equations, which contains the heat expended for heating the still liquid, is independent of R and is substantially smaller than the first term containing the heat of vaporization.

Calculations by Eqs. (7) and (13) show that, even at the average values K_{av}, t_{Wav}, ρ_{xWav}, c_{xWav}, and r_{y1av}, the distillation durations differ by 10–15%, with Eq. (13) yielding higher values of τ if the bottom surface is disregarded. With modern computing facilities, calculations by the more complex Eq. (7) present no difficulties, whereas Eq. (13) is well suitable for quick estimation of τ.

At small x_W, we can obtain from Eq. (13), by neglecting the second term, the following:

$$\tau = \frac{(R + 1)(m + R)}{(m - 1)(m + mR + R)}\frac{D\rho_{xWav}r_{y1av}}{4K_{av}(t_p - t_W)_{av}}\ln n. \quad (14)$$

The dependence of τ on R in Eq. (14) is virtually linear, except at very small R, and becomes less pronounced as m increases. It is also noteworthy that τ is proportional to $1/m$. Attention should also be called to the logarithmic behavior of the dependence of τ on n.

To obtain quantitative estimates, we use as input data those from an operating plant. We consider among binary mixtures the most widely occurring waste from production of extracts, aqueous–organic mixtures ethanol–water, methanol–water, and acetone–water. The mass concentration x_F of the volatile in the starting mixture was 50, 30, and 20%, and that in still bottoms, no more than 10, 5, and 2.5%, respectively. The degree of recovery of the volatile was constant (~0.9). A 5 m^3 bulk jacketed apparatus served as the distillation still. The initial charge of the starting mixture M_F = 2.6 t. The pressure of the heating steam was 2 at. The thermal properties of binary mixtures and criterion expressions for calculation of heat-transfer coefficients for jacketed apparatus were taken from [2–4].

The results of calculations made without simplifications, i.e., those by Eqs. (1), (3), (4), and (7) are presented in Figs. 4 and 5.

Figure 4 shows dependences of the concentration of the final products on the degree of partial condensation, plotted using the material balance equations (1), (3), and (4). It follows from Fig. 4 that, as expected, the efficiency of partial condensation depends on the concentration of the mixture in the still and on the separation coefficients. For example, for the system acetone–water with an initial concentration to which corresponds $m < 1$ (curve *1*), the partial condensation yields only a minor effect and is

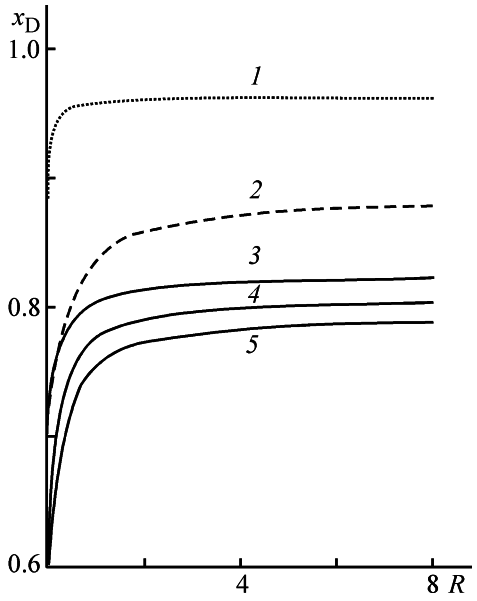


Fig. 4. Distillate concentration x_D vs. the degree of partial condensation R. (*1*) Acetone–water, x_F = 0.5; (*2*) methanol–water, x_F = 0.5; (*3*) ethanol–water, x_F = 0.5; (*4*) ethanol–water, x_F = 0.3; and (*5*) ethanol–water, x_F = 0.2; the same for Fig. 5.

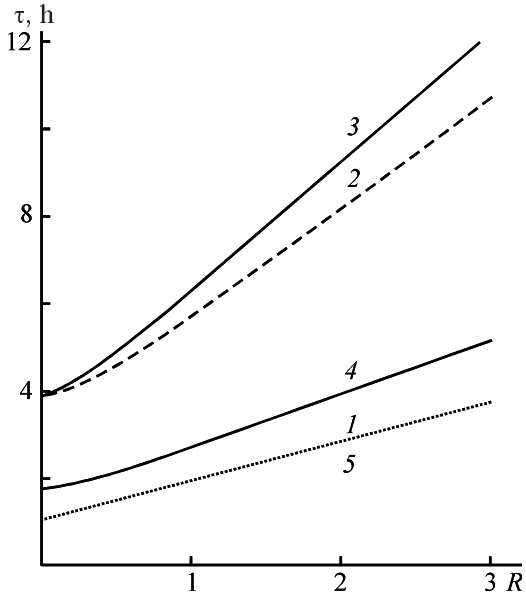


Fig. 5. Process duration τ vs. the degree of partial condensation R.

inefficient. At the same time, for the systems methanol–water (curve *2*) and ethanol–water (curve *3*) with a larger m, the partial condensation produces a certain effect. For solutions with a low initial concentration of the volatile component (curves *4*, *5*), the effect of the partial condensation is even more pronounced. In all cases, as the degree of partial condensation grows, the distillate is "saturated" with the volatile component: beginning with a certain R_{opt}, the increase in x_D is insignificant. For acetone, $R_{opt} \approx 1$ ($x_D \approx 0.96$); for methanol, $R_{opt} \approx 3$–4 ($x_D \approx 0.87$); and for ethanol, $R_{opt} \approx 2$ (x_D 0.82, 0.79, and 0.77, respectively). The expenditure for energy carriers per unit mass of the distillate is proportional to $(R + 1)$. Therefore, Fig. 4 can be interpreted as the relationship between the energy expenditure R and the distillate quality x_D.

Figure 5 shows the results obtained in calculations of the process duration. The dependences of τ on R, calculated by Eq. (7), are nearly linear. The reciprocal quantity $1/\tau$ characterizes the average output capacity of the installation.

Compared to simple distillation (R = 0), the reflux distillation of mixtures with a higher content of the volatile component in the distillation still steeply increases with R (curves *2*, *3*). In this case, it is necessary, when choosing R_{opt}, to additionally take into account the decrease in the output capacity of the installation. For mixtures with low content of the volatile in the distillation still (curves *4*, *5*), the dependence of τ on R is weaker. In this case, it is sufficient, when choosing R_{opt}, to use only material balance equations (Fig. 4). However, simple distillation should be used for separating the system acetone–water, despite the weak dependence of τ on R (Fig. 5, curve *1*).

The output capacity of the installation for reflux distillation is nearly independent of the initial mass of the feed, and other parameters (temperature of the heating steam, apparatus diameter, and thermal properties of the mixture) are related to it by a simple directly or inversely proportional dependence. Therefore, the suggested strategy for assessment of the feasibility of the reflux distillation and the procedure for choosing the optimal value of R can be regarded as general, unrelated to any particular installation.

CONCLUSIONS

(1) It is advisable to use the reflux distillation for mixtures with low concentration of a volatile component. Simple distillation should be used in the initial stage for mixtures with a high concentration. In the final stage, as the distillation still is exhausted, the partial condensation is efficient.

(2) At a degree of partial condensation $R \to \infty$,

the distillate composition asymptotically approaches the maximum limiting value.

(3) Deep exhaustion of the distillation still is not accompanied by any significant deterioration of the distillate quality.

(4) The duration of the distillation with partial condensation linearly depends on R.

(5) The choice of the optimal value of R for mixtures with low concentrations should be governed by the asymptotic nature of the $x_D(R)$ dependence; at higher concentrations, it is necessary to additionally take into account the fact that the process duration increases with R.

REFERENCES

1. Bagaturov, S.A., *Osnovy teorii i rascheta peregonki i rektifikatsii* (Fundamentals of the Theory and Calculation of Distillation and Rectification), Moscow: Khimiya, 1974, 3rd ed. rev.
2. Reid, R.G., Prausnitz, J.M., and Sherwood, T.K., *The Properties of Gases and Liquids*, New York: McGraw-Hill, 1977.
3. Kogan, V.B., Fridman, V.M., and Kafarov, V.V., *Ravnovesie mezhdu zhidkost' yu i parom* (Liquid–Vapor Equilibrium), Moscow: Nauka, 1966, books 1, 2.
4. Romankov, P.G. and Frolov, V.F., *Teploobmennye protsessy khimicheskoi tekhnologii* (Heat-Exchange Processes in Chemical Technology), Leningrad: Khimiya, 1982.

ISSN 1070-4272, Russian Journal of Applied Chemistry, 2008, Vol. 81, No. 9, pp. 1549–1553. © Pleiades Publishing, Ltd., 2008.
Original Russian Text © V.P. Yurkinskii, E.G. Firsova, O.V. Chechulina, A.M. Soboleva, 2008, published in Zhurnal Prikladnoi Khimii, 2008, Vol. 81, No. 9, pp. 1474–1478.

APPLIED ELECTROCHEMISTRY AND CORROSION PROTECTION OF METALS

Electrical Conductivity of Lithium Chloride Solutions in the System Isopropyl Alcohol–Water

V. P. Yurkinskii, E. G. Firsova, O. V. Chechulina, and A. M. Soboleva

St. Petersburg State Polytechnic University, St. Petersburg, Russia

Received April 23, 2008

Abstract—Electrical conductivity of lithium chloride solutions in the system isopropyl alcohol–water in the temperature range 290–323 K was studied. The dependences of the specific and molar electrical conductivity of the solutions on the concentration of water and lithium chloride were determined.

DOI: 10.1134/S1070427208090140

Solutions of lower aliphatic alcohols find increasing use in technology [1–3].

The physicochemical properties of alcohols strongly depend on the concentration of dissolved water in them [3–5]. Therefore, the development of an express method for the determination of water concentration in alcohol solutions is a topical problem. One of such methods is conductometric analysis [6, 7]. To develop a conductometric method for the determination of water concentration in water–alcohol solutions, it is necessary to have data on their electrical conductivity. Data on the electrical conductivity of aqueous–organic electrolytes are available from the literature. However, the effect of water concentration on this quantity is poorly understood [5].

In this study we examined the electrical conductivity of lithium chloride solutions in the system isopropyl alcohol–water in relation to the temperature and salt concentration.

EXPERIMENTAL

The study was performed in the temperature range 17–50°C. The electrical conductivity of solutions was determined conductometrically. We used a U-shaped capillary electrochemical cell (capillary diameter 1.0 mm, length 5–7 cm). The electrodes were made of nickel. The electrical resistance of solutions at a frequency of 1 kHz was measured with an automated E7-15 ac bridge. The cell was heated at a rate of 15 deg h^{-1}. In measuring the solution resistance, heating was stopped for a short time to stabilize temperature. The temperature was measured with an accuracy of ±0.1°C.

Anhydrous LiCl and isopropyl alcohol were of chemically pure grade. To remove traces of moisture, lithium chloride was additionally dried at 200°C for 4 h, placed into a hermetic container, and stored in a desiccator.

Lithium chloride solutions in isopropyl alcohol–water mixtures were prepared by mixing a calculated amount of lithium chloride or its concentrated aqueous solution (40 wt %) with isopropyl alcohol. The concentration of lithium chloride was varied in the range 0.045–0.25 M, and the concentration of water in the mixtures, from 0 to 50 vol %. In some experiments, the concentration of lithium chloride in the solutions under study was monitored by flame emission spectrophotometry.

The experimental data were used to calculate the specific electrical conductivity χ (S cm^{-1}) of solutions under study and to obtain the temperature dependences $\chi = f(T)$ and the isotherms $\chi = f(c_{LiCl})$ at varied concentration of water in a water–alcohol solution.

The specific electrical conductivities of the solutions corresponding to various temperatures and lithium chloride concentrations at a water concentration of 5.0 and 50 vol % are given in Table 1 as example.

Table 1 shows that the specific electrical conductivity increases with the lithium chloride concentration and temperature at a constant concentration of water and with the water concentration in a solution.

Table 1. Specific electrical conductivity of lithium chloride solutions in isopropyl alcohol–water mixtures at varied temperature and water concentration of 5.0 and 50 vol %

T, K	$\chi \times 10^4$, S cm^{-1}, at indicated c_{LiCl}, M (5.0 vol % H_2O)					
	0.081	0.120	0.129	0.164	0.179	0.276
290.1	4.34	5.35	5.86	6.69	7.26	8.97
295.0	4.72	5.86	6.46	7.28	7.91	9.98
300.0	5.12	6.44	7.11	7.99	8.67	11.01
302.5	5.38	6.73	7.44	8.38	9.13	11.62
306.0	5.65	7.19	7.96	8.93	9.68	12.44
310.1	6.06	7.69	8.49	9.55	10.36	13.49
312.9	6.34	8.10	8.97	10.02	10.93	14.08
318.1	6.77	8.68	9.60	10.81	11.73	15.45
320.0	6.92	8.93	9.82	11.22	12.08	15.69
322.0	7.10	9.12	10.06	11.31	12.45	16.06
T, K	$\chi \times 10^4$, S cm^{-1}, at indicated c_{LiCl}, M (50.0 vol % H_2O)					
	0.062	0.123	0.132	0.171	0.205	0.238
289.4	11.74	19.25	23.65	27.64	33.64	39.64
292.3	12.62	21.24	26.14	30.43	37.24	43.29
294.3	13.58	22.42	28.03	34.35	39.64	45.81
296.3	14.41	25.04	29.92	36.48	42.03	48.30
300.5	16.50	28.70	32.41	41.57	47.64	52.61
306.1	19.58	33.13	40.73	48.85	55.65	66.86
308.7	21.04	36.11	43.20	51.63	59.67	70.28
314.5	24.76	42.90	50.56	63.09	70.07	81.93
320.1	30.03	50.79	56.76	70.07	80.89	90.65
322.1	32.02	53.23	60.57	74.86	84.47	93.25

A typical temperature dependence of the specific electrical conductivity at varied concentration of lithium chloride in a solution at a water concentration of 2 vol % is shown in Fig. 1.

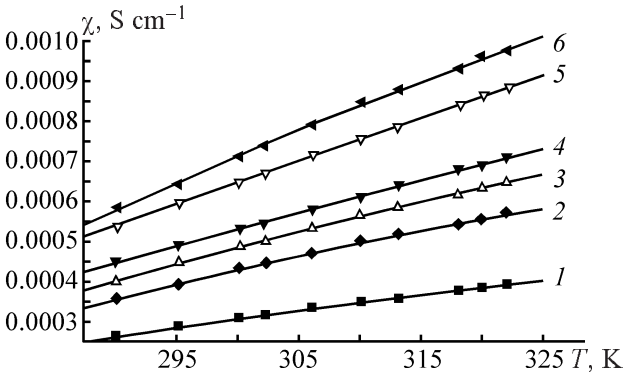


Fig. 1. Specific electrical conductivity χ vs. temperature T for lithium chloride solutions in the system isopropyl alcohol–2 vol % water at varied concentration of lithium chloride. c_{LiCl}, *M: (1)* 0.06, *(2)* 0.105, *(3)* 0.129, *(4)* 0.152, *(5)* 0.176, and *(6)* 0.228; the same for Fig. 3.

The experimental data were statistically processed by the Origin program. The correlation coefficient R and the root-mean-square deviation S were determined.

Analysis of the $\chi = f(T)$ dependences (Fig. 1) showed that, in the temperature range studied, the increase in the specific electrical conductivity with temperature is well described by a polynomial function of second degree:

$$\chi = A + B_1T + B_2T^2,$$

where A, B_1, and B_2 are constants.

The values of the polynomial coefficients are given in Table 2 for all the solutions studied.

The data of Table 2 were used to construct the isotherms of the specific electrical conductivity as a function of the lithium chloride concentration at varied concentration of water in the solutions studied. The typical $\chi = f(c_{LiCl})$ dependences corre-

Table 2. Coefficients of the polynomials for lithium chloride solutions in isopropyl alcohol–water mixtures

c_{H_2O}, vol %	c_{LiCl}, M	$\chi = A + B_1T + B_2T^2$			R	$S \times 10^6$
		A	$B_1 \times 10^5$	$B_2 \times 10^8$		
0	0.117	–0.00319	1.931	–2.643	0.998	1.119
	0.130	–0.00230	1.333	–1.629	0.996	2.183
	0.155	–0.00378	2.247	–2.942	0.998	1.566
	0.182	–0.00522	3.186	–4.507	0.996	2.796
	0.213	–0.00883	5.520	–8.196	0.997	2.483
0.5	0.063	–0.00414	2.583	–3.739	0.998	1.650
	0.095	–0.00420	2.585	–3.608	0.999	1.243
	0.118	–0.00427	2.587	–3.487	0.998	1.863
	0.131	–0.00255	1.446	–1.566	0.999	1.577
	0.182	–0.00537	3.091	–3.817	0.999	2.412
	0.234	–0.00463	2.512	–2.620	0.999	3.212
1.0	0.045	–0.00349	2.179	–3.110	0.999	1.030
	0.119	–0.00177	8.084	–2.738	0.997	3.875
	0.131	–0.00551	3.239	–4.266	0.998	2.686
	0.162	–0.00541	3.083	–3.722	0.998	3.236
	0.226	–0.0033	1.583	–9.551	0.998	3.967
2.0	0.060	–0.00315	1.862	–2.368	0.999	0.999
	0.105	–0.00803	4.849	–6.718	0.999	2.681
	0.129	–0.00537	3.088	–3.787	0.999	1.864
	0.152	–0.000038	–0.447	2.120	0.999	2.558
	0.176	–0.00248	1.010	0.106	0.999	3.426
	0.228	–0.00984	5.655	–7.127	0.999	4.521
5.0	0.081	–0.00084	0.0454	1.359	0.999	2.983
	0.120	–0.00122	0.0576	1.878	0.999	4.045
	0.129	–0.00315	1.239	0.167	0.999	4.784
	0.164	0.00026	–1.087	4.232	0.998	7.213
	0.179	0.00135	–1.892	5.774	0.999	4.483
	0.276	–0.00316	0.596	2.757	0.998	10.314
10	0.065	–0.01158	6.680	–8.791	0.995	11.077
	0.117	–0.00923	4.631	–4.290	0.998	10.167
	0.141	–0.02288	13.323	–17.971	0.996	17.542
	0.156	–0.01151	5.664	–4.988	0.997	15.544
	0.185	–0.01762	9.420	–10.619	0.997	18.182
20	0.063	–0.02367	13.770	–18.680	0.996	23.578
	0.119	–0.0363	21.294	–29.107	0.997	24.653
	0.130	–0.00482	–0.075	7.294	0.997	32.347
	0.185	–0.01801	8.442	–6.070	0.998	29.263
	0.216	–0.00408	–1.381	11.474	0.998	28.892
50	0.062	0.07465	–53.678	97.764	0.999	25.797
	0.123	0.0865	–64.719	122.675	0.998	58.703
	0.132	0.05106	–42.048	87.144	0.997	74.173
	0.171	0.05006	–43.805	94.923	0.997	91.678
	0.205	0.09257	–72.389	143.646	0.999	29.941
	0.238	0.02505	–29.308	75.910	0.995	160.35

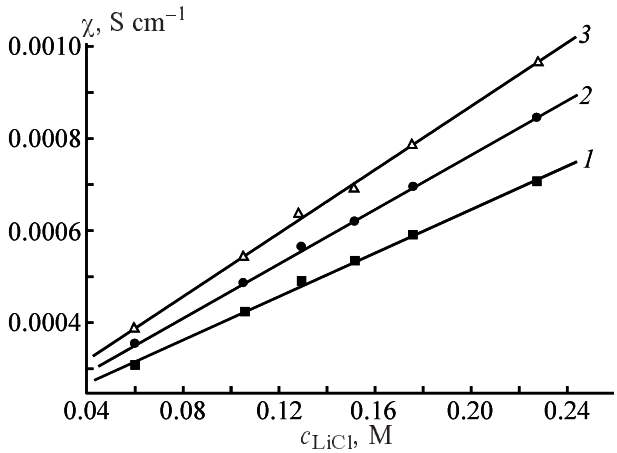


Fig. 2. Specific electrical conductivity χ of lithium chloride solutions in the system isopropyl alcohol–2 vol % water as a function of the lithium chloride concentration c_{LiCl} at various temperatures. *T*, K: (*1*) 300, (*2*) 310, and (*3*) 320; the same for Fig. 4.

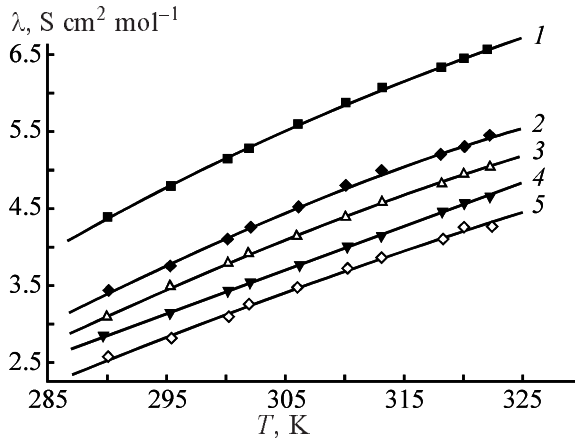


Fig. 3. Molar electrical conductivity λ vs. temperature *T* for lithium chloride solutions in the system isopropyl alcohol–2 vol % water at varied lithium chloride concentration.

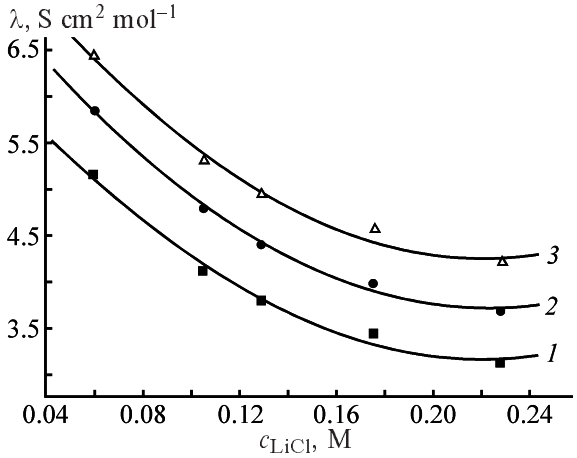


Fig. 4. Molar electrical conductivity λ of lithium chloride solutions in the system isopropyl alcohol–2 vol % water as a function of the lithium chloride concentration c_{LiCl} at various temperatures.

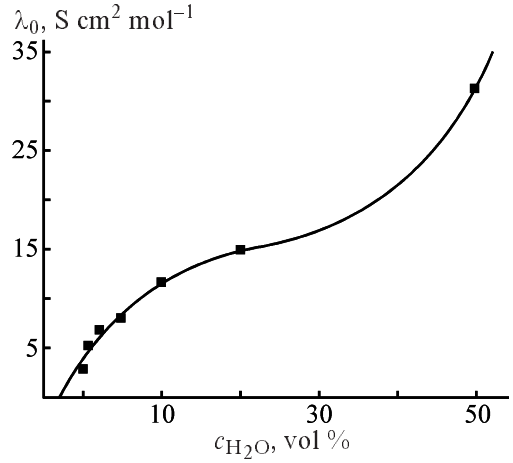


Fig. 5. Molar electrical conductivity at infinite dilution λ_0 of lithium chloride solutions in the system isopropyl alcohol–2 vol % water as a function of water concentration c_{H_2O} at 300 K.

sponding to 2 vol % water are shown in Fig. 2. We found that, for all the solutions studied, the isotherms of the specific electrical conductivity are straight lines described by the equation

$$\chi = A + Bc,$$

where c is the LiCl concentration (M), and A and B are constants.

The molar electrical conductivity of lithium chloride solutions λ was calculated and its values at infinite dilution λ_0 were determined using the values of specific electrical conductivity from Table 2.

Figure 3 shows the temperature dependences of λ, obtained at varied concentrations of lithium chloride at a water concentration of 2 vol %. The run of the $\lambda = f(T)$ curve is the same for all the solutions studied. As in the case of specific electrical conductivity, the temperature dependences for molar conductivity are nonlinear curves described by the second-degree polynomial $\lambda = A + B_1T + B_2T^2$.

Analysis of the isotherms of the molar electrical conductivity (Fig. 4) shows that, as in the case of aqueous solutions [8], in water–alcohol solutions at constant concentration of water λ decreases as the lithium chloride concentration increases. This dependence is satisfactorily described by a second-degree polynomial.

To ascertain the applicability of the Kohlrausch equation to water–alcohol solutions under study, we studied the dependence $\lambda = f(c^{1/2})$. It was found that the dependence $\lambda = f(c^{1/2})$ is linear only in solutions containing 50 vol % water. Consequently, the Kohlrausch law cannot be applied to the water–alcohol systems studied.

The dependence of λ_0 on the water concentration c_{H_2O} (vol %) in an alcohol solution at 300 K is shown in Fig. 5. As can be seen, the molar electrical conductivity at infinite dilution of lithium chloride solutions in the system isopropyl alcohol–water increases with the water concentration and is described by a third-degree polynomial:

$$\lambda_0 = 3.875 + 1.0964\,c_{H_2O} - 0.0389\,c_{H_2O}^2 + 0.00056\,c_{H_2O}^3.$$

The correlation coefficient is 0.995, and the root-mean-square deviation, 0.00057.

CONCLUSIONS

(1) The specific electrical conductivity of solution under study increases with temperature. The $\chi = f(T)$ dependence is described by a second-degree polynomial $\chi = A + B_1T + B_2T^2$.

(2) The specific electrical conductivity in the system isopropyl alcohol–water increases as the concentrations of lithium chloride and water increase. The $\chi = f(c_{LiCl})$ isotherms obtained at various concentrations of water in the solutions are linear.

(3) The molar electrical conductivity of the solutions studied was calculated. The $\lambda = f(T)$ dependence is a nonlinear curve described by a polynomial of the second degree. As the concentration of lithium chloride in the system isopropyl alcohol–water at constant concentration of water increases, the molar electrical conductivity of the solutions decreases. The isotherms $\chi = f(c_{LiCl})$ are described by a second-degree polynomial.

(4) The molar electrical conductivity of the solutions at infinite dilution λ_0 was determined. In solutions under study, λ_0 increases with water concentration, and the $\lambda = f(c_{H_2O})$ dependence is satisfactorily described by a third-degree polynomial.

REFERENCES

1. Tomilov, A.P., *Elektrokhimiya*, 2000, vol. 36, no. 2, pp. 115–116.
2. Makarov, V.V., Petrykin, V.E., Emel'yanov, V.V., et al., *Avtomob. Prom–st.*, 2005, no. 8, pp. 24–26.
3. Petrov, A.A., Bal'yan, Kh.V., and Troshchenko, A.T., *Organicheskaya khimiya* (Organic Chemistry), St. Petersburg: Ivan Fedorov, 2002.
4. Khasanshin, T.S., *Termodinamicheskie i termokhimicheskie svoistva odnoatomnykh predel'nykh spirtov: obzory po teplofizicheskim svoistvam veshchestv* (Thermodynamic and Thermochemical Properties of Monohydric Saturated Alcohols: Reviews on Thermal Properties of Substances), Moscow: Inst. Vysokikh Temperatur Ross. Akad. Nauk, 1991, no. 2 (88), pp. 3–71.
5. Janz, G.J. and Tomkins, R.P.T., *Nonaqueous Electrolytes*, Handbook, New York: Academic, 1972.
6. Khudyakova, T.A. and Kreshkov, A.P., *Konduktometricheskii metod analiza* (Conductometric Analysis), Moscow: Vysshaya Shkola, 1975.
7. Grilikhes, M.S. and Filanovskii, B.K., *Kontaktnaya konduktomeriya* (Contact Conductometry), Leningrad: Khimiya, 1980.
8. Skorchelletti, V.V., *Teoreticheskaya elektrokhimiya* (Theoretical Electrochemistry), Leningrad: Khimiya, 1974.

ISSN 1070-4272, Russian Journal of Applied Chemistry, 2008, Vol. 81, No. 9, pp. 1554–1558. © Pleiades Publishing, Ltd., 2008.
Original Russian Text © L.S. Tsybul'skaya, V.A. Kukareko, Yu.N. Bekish, T.V. Gaevskaya, A.G. Kononov, 2008, published in Zhurnal Prikladnoi Khimii, 2008, Vol. 81, No. 9, pp. 1479–1483.

APPLIED ELECTROCHEMISTRY AND CORROSION PROTECTION OF METALS

Chemical Composition, Structure, and Properties of Electrochemically Deposited Cobalt–Boron Coatings

L. S. Tsybul'skaya, V. A. Kukareko, Yu. N. Bekish, T. V. Gaevskaya, and A. G. Kononov

Research Institute of Physicochemical Problems, Belarussian State University, Minsk, Belarus
Joint Institute of Machine-Building, National Academy of Sciences of Belarus, Minsk, Belarus

Received November 2, 2007

Abstract—Polycrystalline and amorphous cobalt–boron coatings were electrochemically deposited. The effect of the boron content and heating temperature on the physicomechanical properties of the coatings was studied. A relationship between the composition, structure, and properties of the coatings was established.

DOI: 10.1134/S1070427208090152

The modern level of development of machine-building, radio electronics, and instrument making requires that new coatings should be produced with a set of valuable properties: high corrosion resistance and plasticity, low intermediate resistance and internal stresses, good solderability and ultrasonic weldability, and high microhardness and wear resistance. Such properties can be exhibited by metal–nonmetal coatings in which nickel, cobalt, and iron are used as a metallic matrix, and boron and phosphorus as a nonmetal. The best studied and practically used are nickel–boron and nickel–phosphorus coatings produced by chemical or electrochemical deposition from aqueous solutions [1, 2]. Cobalt–boron coatings have been studied to a considerably lesser extent, with the available information mostly related to structural properties and structural-phase transformations in these coatings under thermal treatment [3].

The aim of the present study was to examine the effect of the boron content and heating temperature on the physicomechanical properties of Co–B coatings: microhardness, wear resistance, internal stresses, and friction coefficient and to find the relationship between the composition, structure, and exhibited properties.

EXPERIMENTAL

Cobalt–boron coatings were electrochemically deposited onto copper and bronze surfaces in the galvanostatic mode (I = 2 A dm^{-2}) at 30°C from a solution of the following composition (M): cobalt chloride 0.8, boric acid 0.6, and a boron-containing compound 5.0×10^{-4}–1.2×10^{-1}, at pH 4. Sodium decahydro-*closo*-decaborate $Na_2B_{10}H_{10}$ served as the boron-containing compound. The film thicknesses were in the range 5–30 μm, depending on the requirements of an experiment. The amount of boron in the coatings was determined by potentiometric titration in the presence of mannitol [4]. The structure of freshly deposited and thermally treated coatings was subjected to X-ray diffraction analysis. X-ray diffraction patterns were measured on a DRON-2.0 diffractometer with monochromated CuK_α radiation in the scanning mode (scanning step 0.1 deg; time of pulse accumulation at a point, 15 s). Amorphous coatings were heated in air at 250–400°C, with keeping for 20 min. The chemical composition and surface structure of the coatings were studied by X-ray photoelectron spectroscopy (XPS) on a Q2000 spectrometer with an AlK_α X-ray source. The residual stresses were measured by the X-ray method in the inclined measurement mode [5]. The error in determining the residual stress was 50 MPa.

Tribotechnical tests of coating samples were performed on an ATVP tribometer equipped with an attachment for measuring the friction coefficient [6]. Tribotechnical characteristics of the coatings were measured under unlubricated friction conditions at a specific test load p_a = 1 MPa. Thermally treated U8 (45 HRC) steel was used as a counter body. The

microhardness was measured with a PMT-3 device under a load of 1 N with keeping for 10 s.

A chemical analysis of the coatings demonstrated that, upon introduction of sodium decahydro-*closo*-decaborate in the electrolyte solution, cobalt is codeposited with boron. As the $Na_2B_{10}H_{10}$ concentration in the electrolyte increases, the boron content of the coating grows to reach the maximum value of about 22 at. % (Fig. 1).

According to XPS data, Co–B coatings with the maximum boron content (22%) show two peaks corresponding to cobalt and boron, with the position of the first peak coinciding with the binding energy of Co $2p_{3/2}$ electrons in metallic cobalt, whereas the peak B 1*s* with a binding energy of 188.0 eV is shifted to higher energies as compared to the binding energy of electrons in elemental boron (187.3–187.5 eV [7]), which indicates that a cobalt–boron alloy is formed.

An X-ray diffraction analysis demonstrated that, in electrochemical deposition, cobalt crystallizes in the hexagonal α-modification of the metal, with unit cell parameters a = 2.5052 Å and c = 4.065 Å (reference data: a = 2.5031 Å and c = 4.0605 Å). The codeposition of cobalt and boron at boron concentrations of 4 and 6 at. % leads to an increase in the parameter c and a decrease in a (Table 1). Such a behavior of the crystal lattice constants of the cobalt coating with increasing boron concentration is presumably due to formation of an interstitial-substitutional solid solution. In this case, the decrease in the unit cell constant a is due to substitution of cobalt atoms having a large atomic radius (r_{Co} = 1.25 Å) by boron atoms with a smaller atomic radius (r_B = 0.97 Å), and the increase in c is due to accommodation of a part of boron atoms within octahedral pores of the hexagonal closest packing (hcp) of the crystal lattice. It should be noted that a large part of boron atoms substitute cobalt atoms, which is indicated by the decrease in the unit cell volume V, recorded for Co–B alloys as the boron concentration increases (Table 1). The formation of a solid solution of boron in the cobalt lattice can indirectly indicate that boron is codeposited in the elemental form. An increase in the boron content of a coating leads to strong distortions of the crystal lattice of α-Co and is accompanied by a rise in the physical broadening β of diffraction lines (Fig. 2). X-ray structural data indicate that the physical broadening is proportional to the tangent of the scattering angle. This points to the existence in the coating of long-range fields of atomic displacements,

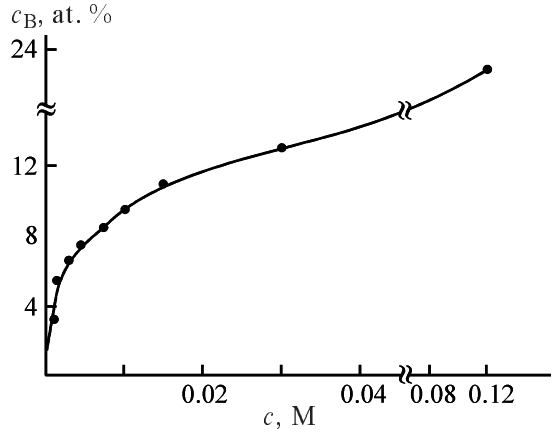


Fig. 1. Boron content c_B of the Co–B coating vs. the $Na_2B_{10}H_{10}$ concentration c in solution.

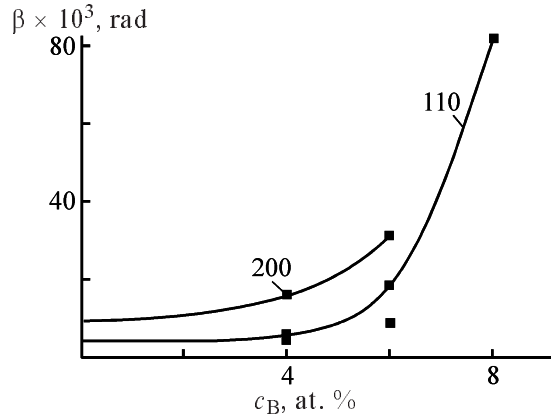


Fig. 2. Physical broadening β of the diffraction lines (110) and (200) vs. the boron content c_B of the Co–B coating.

associated with crystal lattice defects (dislocations, vacancies, impurity atoms). In this case, the strongest increase in β is observed at boron contents exceeding 6 at. %, which is presumably due to a steep rise in the density of crystal lattice defects in a Co–B coating at such concentrations of the nonmetal.

Further increase in the boron concentration in coatings from 8 to 13 at. % results in that an intermediate amorphous-crystalline structure is formed. In this case, separate broadened low-intensity dif-

Table 1. Unit cell parameters a, c, and c/a and the cell volume V for Co–B coatings

Boron content, at. %	a	c	c/a	V, Å^3
	Å			
0	2.505	4.065	1.623	22.094
4	2.502	4.069	1.626	22.064
6	2.499	4.084	1.634	22.058

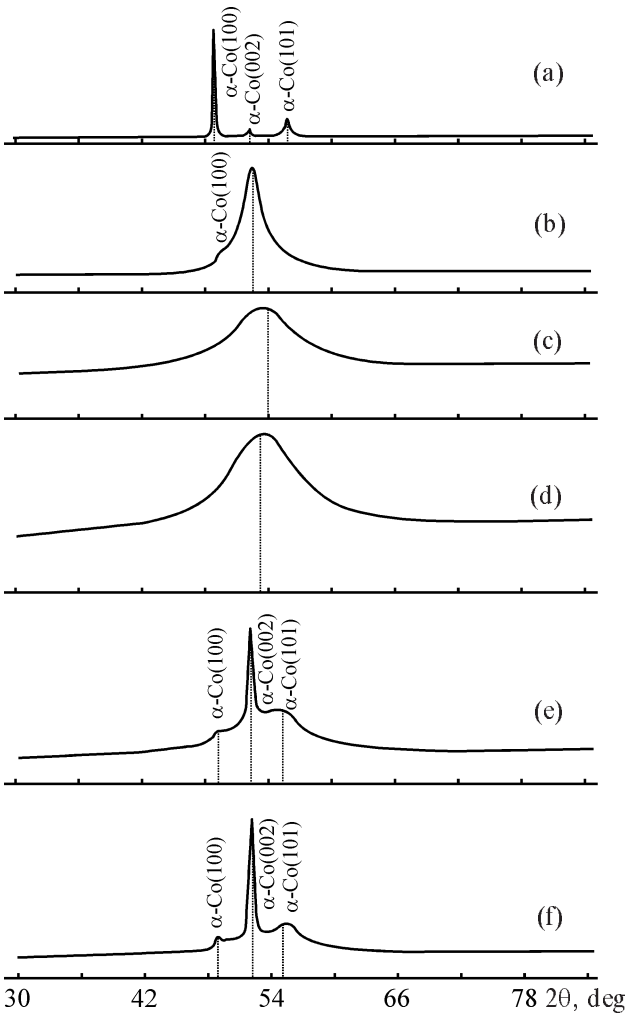


Fig. 3. Fragments of X-ray diffraction patterns of freshly deposited coatings of (a) Co and (b, c) Co–B with a boron content of (b) 8 and (c) 20 at. % and (d–f) amorphous Co–B coating (20 at. % boron) heated at different temperatures. T, °C: (d) 300, (e) 350, and (f) 400. (2θ) Bragg angle.

Table 2. Interatomic distance R_1, microhardness H_μ, and friction coefficient f in relation to the boron content of Co–B coatings

Boron content, at. %	R_1, Å	H_μ, MPa	f, rel. units
0		2300	0.5–0.6
4		3400	0.7–0.8
6		3800	0.8–0.9
8	2.496	6300	0.7–0.8
10	2.494	4700	0.5–0.6
13	2.494	5200	0.3–0.4
15	2.455	6100	0.8–0.9
20	2.446	6500	1.0–1.1

fraction lines are recorded in the diffraction patterns and a strong diffraction peak is formed at small scattering angles (Fig. 3b). Still further increase in the boron content of the coatings (to ≥15 at. %) yields an amorphous structure: broadened peaks characteristic of diffraction from amorphous materials [5] are recorded in X-ray diffraction patterns (Fig. 3c). The position of the diffraction peaks enables estimation of the interatomic distance R_1 for the first coordination sphere. R_1 was found by the Ehrenfest formula [5]

$$R_1 = 0.615\lambda/\sin\theta_{1max},$$

where λ is the wavelength of the X-ray radiation, and θ_{1max}, angular position of the first broadened diffraction peak.

The estimated values of R_1 for amorphous Co–B alloys are listed in Table 2. It can be seen that, for coatings with an amorphous-crystalline structure (boron content of 8 to 13 at. %), the shortest interatomic distance R_1 = 2.494–2.496 Å. For amorphous Co–B coatings with 15 and 20 at. % B, R_1 decreases to 2.455 and 2.446 Å, respectively. It should be noted that the interatomic distance R_1 decreases as the boron content of a coating grows (Table 2).

The results of the study demonstrate that amorphous Co–B coatings have a sufficiently high thermal stability. On their heating at 250–300°C, the diffraction pattern remains nearly unchanged and retains the type characteristic of the amorphous state of the coating (Figs. 3c, 3d). Raising the heating temperature to 350°C results in that α-Co crystals with an hcp crystal lattice (Fig. 3e) are formed in the coating. It should be noted that the 002 diffraction line has the highest intensity. This points to a preferential growth of 001 planes in the course of crystallization of an amorphous coating. The lattice constants of the crystalline phase, a = 2.511 Å and c = 4.075 Å, are close to reference data for the α-Co lattice. At the same time, the increased values of a and c indicate that boron atoms are present in octahedral voids of the α-Co lattice and distort the crystal structure. Raising the heating temperature to 400°C leads to an increase in the intensity of the diffraction lines associated with the crystalline phase, which points to further crystallization (Fig. 3f). The lattice constant c remains at about 4.072 Å, and a approaches the reference value and equals 2.506 Å.

As a rule, point defects of the crystal structure, vacancies and interstitial atoms, are responsible for macroscopic stresses in electrolytic deposits. The

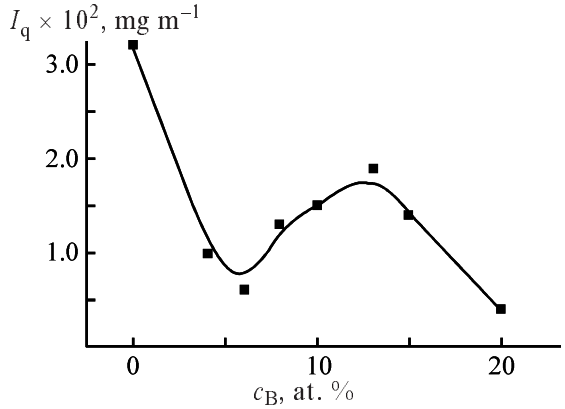


Fig. 4. Wear intensity I_q of Co–B coatings vs. their boron content c_B.

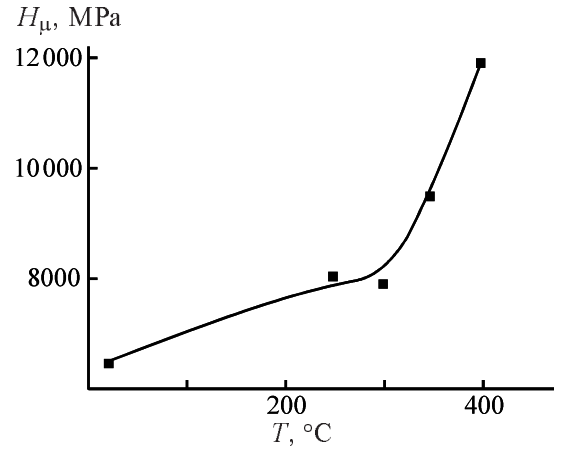


Fig. 5. Microhardness H_μ of amorphous Co–B coatings vs. the heating temperature T.

prevalent type of defects in the structure of the deposit determines the sign of these stresses. Introduction of interstitial atoms leads to a higher density of deposits and gives rise to compression stresses [8]. The estimated macroscopic stress for a Co–B alloy (6 at. % boron) is σ_ϕ = –570 MPa (compression stress), which confirms the suggestion that boron is intercalated into the α-Co crystal lattice.

The microhardness of Co–B coatings depends on their boron content in a complicated way (Table 2). Presumably, the initial rise in the microhardness, observed as the boron content of the coating increases from 4 to 8 at. %, can be understood as follows. Boron at sites of the crystal lattice of cobalt and in interstitial positions distorts its crystal lattice and makes lower the dislocation mobility, which favors strengthening of the electrochemical deposits. The substantial decrease in the microhardness for Co–B coatings with 10 at. % boron is probably due to their transition from the crystalline to amorphous–crystalline state, which is accompanied by loss of certain elements of symmetry. Steadily high values of microhardness (6100–6500 MPa) are observed for X-ray amorphous coatings.

The results of tribotechnical tests demonstrated that alloying of cobalt coatings with boron improves their wear resistance. However, the dependence of the wear intensity on the boron content is rather complicated (Fig. 4). As the boron content increases to 4 and 6 at. %, the coating wear intensity decreases by factors of 3 and 5 (Fig. 4), and the friction coefficient grows from 0.6 to 0.8–0.9 (Table 2). The high wear resistance and increased values of the friction coefficient point to a high specific work of coating wear. With an increase in the boron content in the range 8–13 at. %, the wear resistance of the coatings decreases and the intensity of their wear grows to $I_q = 1.9 \times 10^{-2}$ mg m^{-1} (Fig. 4). The friction coefficient f also decreases and reaches values of 0.3–0.4 (Table 2). As the boron content of coatings increases to 15 and 20 at. %, their wear resistance again noticeably grows and the wear intensity decreases to 0.4×10^{-2} mg m^{-1} for coatings containing 20 at. % boron (Fig. 4). The friction coefficient f = 1.0–1.1 (Table 2). Thus, the wear resistance of Co–B coatings is the lowest at boron concentrations of 10–13 at. % (Fig. 4). However, these values are higher by a factor of approximately 2 than the wear resistance of cobalt coatings. To these same boron concentrations correspond the lowest values of the friction coefficient.

As amorphous Co–B coatings are heated in the temperature range 250–300°C, their microhardness gradually grows from 6500 to 8000 MPa (Fig. 5), which indicates that crystallization nuclei are formed. Raising the heating temperature from 300 to 400°C leads to a steep rise in the microhardness, which reaches the maximum value of 12000 MPa (hardness of chromium).

As a rule, an increase in the boron content of amorphous coatings improves their thermal stability. At the same time, it is known that crystallization of amorphous materials can be caused not only by thermal heating, but also by their plastic deformation, named mechanical crystallization [9]. It can be assumed that mechanical crystallization of local parts will occur at the surface of the amorphous layer in the friction interaction (without a lubricant) of the amorphous coating with a counter body in regions of a strong plastic deformation and warming-up. The formation of crystalline regions on an amorphous substrate in friction will give rise to considerable tensile stresses at the phase boundary

because of the substantial difference between the specific atomic volumes of the amorphous and crystalline phases. It is known that the interphase deformation can make substantially lower the stability of materials against disintegration in the course of a friction interaction [10]. Therefore, the formation of crystalline regions on an amorphous substrate in the course of friction will impair the wear resistance of materials of this kind. By contrast, a higher stability of amorphous structures must lead to a better wear resistance. Thus, the lowest wear resistance in an adhesion interaction in unlubricated friction should be observed for layers with a metastable amorphous-crystalline structure with enhanced susceptibility to mechanical crystallization. This conclusion is fully confirmed by the results obtained in this study. In particular, as the threshold boron concentration leading to loss of the long-range order in the atomic arrangement is reached in alloys, the wear resistance of the coatings starts to decrease. An increase in the content of boron stabilizing the amorphous state of the materials and raising their resistance to mechanical crystallization is accompanied by a rise in the wear resistance of amorphous alloys.

CONCLUSIONS

(1) The structural-phase composition of Co–B coatings containing 4 to 22 at. % boron was studied. At a boron content lower than 8 at. %, coatings are composed of a substitutional-interstitial solid solution of boron in hexagonal α-Co; alloys with 8–13 at. % boron have an amorphous–crystalline structure; and deposits with a boron content of 15 at. % and more are X-ray amorphous.

(2) Co–B coatings with a boron concentration preceding the onset of amorphization have the optimal physicomechanical properties.

(3) Crystallization of amorphous Co–B coatings, occurring at heating temperatures of 350°C and more, improves their physicomechanical properties.

REFERENCES

1. Gaevskaya, T.V. and Tsybul'skaya, L.S., *Izv. Ross. Akad. Nauk, Materialoved.*, 2001, vol. 51, no. 6, pp. 32–39.
2. *Khimicheskoe osazhdenie metallov iz vodnykh rastvorov* (Chemical Deposition of Metals from Aqueous Solutions), Sviridov, V.V., Ed., Minsk: Universitetskoe, 1987.
3. Bekish, Yu.N., Gaevskaya, T.V., Ivashkevich, L.S., and Tsybul'skaya, L.S., *Vestsi Nats. Akad. Navuk Bel., Ser. Khim. Navuk*, 2007, no. 1, pp. 36–40.
4. Valsiuniene, J.I. and Norkus, P.K., *Tr. Akad. Nauk Lit. SSR, Ser. B*, 1972, vol. 1, no. 68, pp. 93–96.
5. Umanskii, Ya.S., Skakov, Yu.A., Ivanov, A.N., and Rastorguev, L.N., *Kristallografiya, rentgenografiya i elektronnaya mikroskopiya* (Crystallography, X-ray Diffraction Analysis, and Electron Microscopy), Moscow: Metallurgiya, 1982.
6. Karavaev, M.G. and Kukareko, V.A., *Materialy Mezhdunarodnoi nauchno-tekhnicheskoi konferentsii "Nadezhnost' mashin i tekhnicheskikh sistem"* (Proc. Int. Scientific and Technical Conf. "Reliability of Machines and Technical Systems") Minsk: Inst. Tekh. Kibernetiki, October 16–17, 2001, vol. 1, pp. 37–39.
7. *Practical Surface Analysis by Auger and X-Ray Photoelectron Spectroscopy*, Briggs, D. and Seah, M.P., Eds., New York: Wiley, 1983.
8. Povetkin, V.V., Kovenskii, I.M., and Ustinovshchikov, Yu.I., *Struktura i svoistva elektroliticheskikh splavov* (Structure and Properties of Electrolytic Alloys), Moscow: Nauka, 1992.
9. Trudeau, M., Shulz, R., and Neste, D.D. van, *Phys. Rev. Lett.*, 1990, vol. 64, pp. 99–102.
10. Kukareko, V.A., *Tren. Iznos*, 2003, vol. 24, no. 2, pp. 192–202.

ISSN 1070-4272, Russian Journal of Applied Chemistry, 2008, Vol. 81, No. 9, pp. 1559–1564. © Pleiades Publishing, Ltd., 2008.
Original Russian Text © U.V. Kharchenko, N.V. Makarenko, P.P. Safronov, A.A. Karabtsov, A.V. Kovekhova, L.A. Zemnukhova, 2008, published in Zhurnal Prikladnoi Khimii, 2008, Vol. 81, No. 9, pp. 1484–1489.

APPLIED ELECTROCHEMISTRY AND CORROSION PROTECTION OF METALS

Effect of Wastes Formed in Processing of Vegetable Raw Materials on the Corrosion of Steel in Corrosive Media

U. V. Kharchenko, N. V. Makarenko, P. P. Safronov, A. A. Karabtsov, A. V. Kovekhova, and L. A. Zemnukhova

Institute of Chemistry, Far-Eastern Branch, Russian Academy of Sciences, Vladivostok, Russia
Far-Eastern Geological Institute, Far-Eastern Branch, Russian Academy of Sciences, Vladivostok, Russia
Institute of Chemistry and Applied Ecology, Far-Eastern State University, Vladivostok, Russia

Received December 28, 2007

Abstract—Effect of liquid and dry extracts of rice, buckwheat, and sunflower husks on the corrosion of St.3 steel in water-salt and acid media was studied by gravimetric and potentiodynamic methods. The action of the extracts on the surface morphology of St.3 steel samples was examined by electron microscopy and electron microprobe analysis.

DOI: 10.1134/S1070427208090164

A search for environmentally safe complex inhibitors for corrosion protection of steels is a topical task. A promising source of raw materials for production of inhibitors of this kind are renewable wastes of annual plants, whose resources in agriculture constitute hundreds of thousands of tons annually. There is published evidence that by-products of processing of sugarcane [1], cotton plant [2], wood [3], Black sea laver [4], prickly pear [5], and wastes from food industry [6] can inhibit the corrosion of various alloys. It has also been found that the steel corrosion is decelerated by aqueous and alkaline extracts from vegetable wastes produced in processing of grain crops [7]. Inhibitors of this kind have complex and diverse chemical compositions and the mechanism of their action has practically not been studied at all.

The present study continues analysis of the integrated processing of vegetable wastes [7–14] and is concerned with the inhibiting effect of liquid and dry extracts from rice (RH), buckwheat (BH), and sunflower husks (SH) on the corrosion of St.3 low-carbon steel.

EXPERIMENTAL

We studied as inhibitor additives liquid water and acid extracts from rice, buckwheat, and sunflower husks, produced by treating weighed portions of a raw material with water or 0.1 N solution of hydrochloric acid (s : l = 1 : 10 by volume) under heating to 90°C for 1 h, with the subsequent separation of undissolved raw materials similarly to [11, 13, 14], and their dry extracts formed by evaporation of the liquid extracts on a water bath or by freeze drying [13].

The content of soluble substances in rice, buckwheat, and sunflower husks depends on the type of a raw material (Table 1). The chemical composition of water and acid extracts from RH, BH, and SH has been studied previously [8–14]. According to the data obtained, extracts from rice, buckwheat, and sunflower husks contain both organic and inorganic substances whose composition and concen-

Table 1. Content of soluble compounds in rice, buckwheat, and sunflower husks, extracted by treatment of the raw material with water and 0.1 N HCl at 90°C for 60 min (s : l = 1 : 10)

Raw material	Content of substances soluble in indicated extractant, %	
	H_2O	HCl
RH	12	13
BH	10	22
SH	6	11

Table 2. Average corrosion rates K of steel and the protective effect Z of extracts from rice, buckwheat, and sunflower husks

Raw material	Medium*	$K \pm \Delta S$,** g m^{-2} h^{-1}	Z, %
RH	NaCl + WE	0.0305 ± 0.002	54.0
	HCl + AE	0.1317 ± 0.041	94.9
BH	NaCl + WE	0.0256 ± 0.001	61.4
	HCl + AE	0.4365 ± 0.023	83.2
SH	NaCl + AE	0.0175 ± 0.005	73.6
	HCl + AE	2.5088 ± 0.062	3.5
	NaCl	0.0663 ± 0.011	
	HCl	2.5998 ± 0.051	

* WE and AE denote water and acid extracts, respectively.
** ΔS is standard deviation.

tration are determined by the type of a raw material. The main organic fractions extracted into solution in treatment of husks with water or the acid are polysaccharides, flavonoids, and organophosphorus and other substances possessing a set of various functional groups. The best studied for the time being are only the monosaccharide composition of polysaccharides in extracts from RH [10], BH [9], and SH [12] and the content of inositolhexaphosphoric acid in SH [8]. The inorganic components are represented in these solutions by ions of more than 20 metals, among which ions of potassium, calcium, magnesium, sodium, iron, zinc, and manganese predominate [8, 9, 13].

The effect of liquid extracts, whose concentration was 500 ml l^{-1}, which corresponded to a dry substance content of the extract equal to 1.2 g l^{-1}, on the corrosion rate of St.3 low-carbon steel was studied in 3% NaCl and 0.1 N HCl solutions by the gravimetric method. St.3 samples (40 × 20 × 2 mm) were preliminarily ground, degreased with acetone, and weighed on an analytical balance.

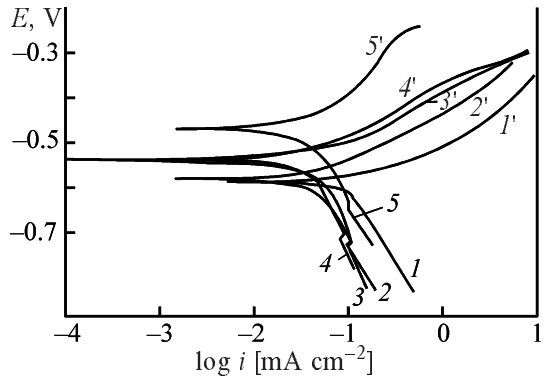


Fig. 1. (*1'–5'*) Anodic and (*1–5*) cathodic polarization curves for St.3 steel in a 3% NaCl solution containing various dry extract additives. (*E*) Potential and (*i*) current density; the same for Fig. 2. (*1, 1'*) no additive; additive: (*2, 2'*) BH, (*3, 3'*) RH, (*4, 4'*) SH, and (*5, 5'*) Diesel Guard inhibitor.

The corrosion rate K (g m^{-2} h^{-1}) was calculated by the formula

$$K = \frac{m_1 - m_2}{St}, \quad (1)$$

where m_1 and m_2 are the sample masses before and after tests (g); S, sample area (m^2); and t, time (h).

The degree of protection by vegetable extracts, Z (%), was determined by the formula

$$Z = \frac{K - K_e}{K} \times 100, \quad (2)$$

where K and K_e are the corrosion rates of St.3 steel without an additive and with addition of an extract, respectively.

Table 2 lists the results of the gravimetric studies. It can be seen that all the extracts make lower the corrosion rate. The most effective in a NaCl solution (pH 7.0) was the water extract of sunflower husks. A substantial protective effect was also produced by a water extract of buckwheat husks. However, the highest protective efficiency of all the extracts except the SH extract was manifested in an acid medium at pH 1.0. Under these conditions, the protective effect of the RH extract is as high as 94%, and that of BH extract, 83%.

A more detailed study of the inhibiting effect of the extracts was performed by measuring potentiodynamic curves with an IPC-PRO potentiostat with intellectual control (Moscow). The electrochemical measurements were made in a glass cell with an EVL-1M1 silver chloride reference electrode and a platinum auxiliary electrode. The slopes of the Tafel portions of the anodic and cathodic polarization curves, b_a and b_c, and the corrosion current density I_{cor} were calculated in the automatic mode. The hindrance coefficients of the cathodic ($\gamma_c = i_c/i_c^*$) and anodic ($\gamma_a = i_a/i_a^*$) reactions occurring in corrosion of St.3 steel were found from the polarization curves (i_c, i_a and i_c^*, i_a^* are the cathodic and anodic current densities in a medium without and with addition of an extract, respectively). The concentrations of dry extract additives and standard inhibitors was

Table 3. Corrosion-electrochemical characteristics of St.3 steel in 3% NaCl and 0.1 N HCl solutions containing dry extracts from wastes formed in processing of vegetable raw materials

Solution	E, mV	I_{cor}, μA cm^{-2}	b_a	b_c	Z, %	γ_a	γ_c
			mV				
			pH 7.0				
NaCl	–597	94	71	336			
Diesel Guard + NaCl	–477	50	286	317	46.8	62.0	1.4
RH + NaCl	–555	53	129	542	43.6	7.1	2.0
BH + NaCl	–592	43	112	341	54.2	2.9	2.2
SH + NaCl	–546	40	140	485	57.4	10.3	2.2
			pH 1.0				
HCl	–516	769	191	186			
Hexamethylene-tetramine + HCl	–521	123	174	143	84.0	3.1	4.5
RH + HCl	–521	251	166	175	67.4	2.0	1.9
BH + HCl	–520	538	195	158	30.0	1.5	1.3

0.67 g l^{-1}. Diesel Guard inhibitor, which is manufactured by Unitor (Norway) and is a mixture of organic substances on the nitrate–borate base, was used in a water–salt medium, and hexamethylenetetramine, which is an effective inhibitor of acid corrosion, in an acid medium.

The results of our potentiodynamic study of the behavior of steel in 3% NaCl and 0.1 N HCl solutions with addition of dry extracts from RH, BH, and SH confirm the gravimetric data. As follows from Fig. 1, addition of dry extracts from rice, buckwheat, and sunflower husks to a sodium chloride solution makes the overvoltage of the anodic and cathodic processes larger and the corrosion current density two times smaller (Table 3). The hindrance coefficients of the anodic and cathodic reactions point to preferential hindrance of the anodic reaction of the corrosion process.

The results obtained show (Table 3) that the protective effect of the RH, BH, and SH extracts is comparable with, and even somewhat exceeds that of the standard inhibitor Diesel Guard with respect to St.3 steel.

According to potentiometric data, additions of dry extracts also effectively diminish the corrosion rate of steel in an acid medium with pH 1.0 (Fig. 2). It should be noted here that introduction of the extracts under study into an HCl solution leads to the same hindrance of both anodic and cathodic reactions: values of the coefficients γ_a and γ_c differ only slightly (Table 3). A consequence of the identical effects of the extracts on the rate of the anodic and cathodic reactions is that there is no shift of the corrosion potential. The protective effect of the extracts in a 0.1 N HCl solution (and, especially, that of the BH extract) is weaker than that of hexamethylenetetramine (Table 3). It should be taken into account, however, that dry extracts are a mixture of organic and inorganic substances, not all of which are involved in diminishing the corrosion rate, and the concentration of the main component of the inhibitor "responsible" for the protective effect in solutions with extracts will be lower than that in a solution of pure hexamethylenetetramine in HCl.

Analysis of the data in Tables 1 and 2 shows that

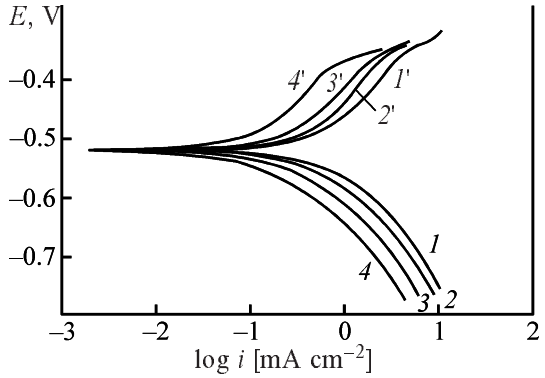


Fig. 2. (*1'–4'*) Anodic and (*1–4*) cathodic polarization curves for St.3 steel in a 0.1 N HCl solution with various extract additions. Additive: (*2, 2'*) BH, (*3, 3'*) RH, and (*4, 4'*) hexamethylenetetramine.

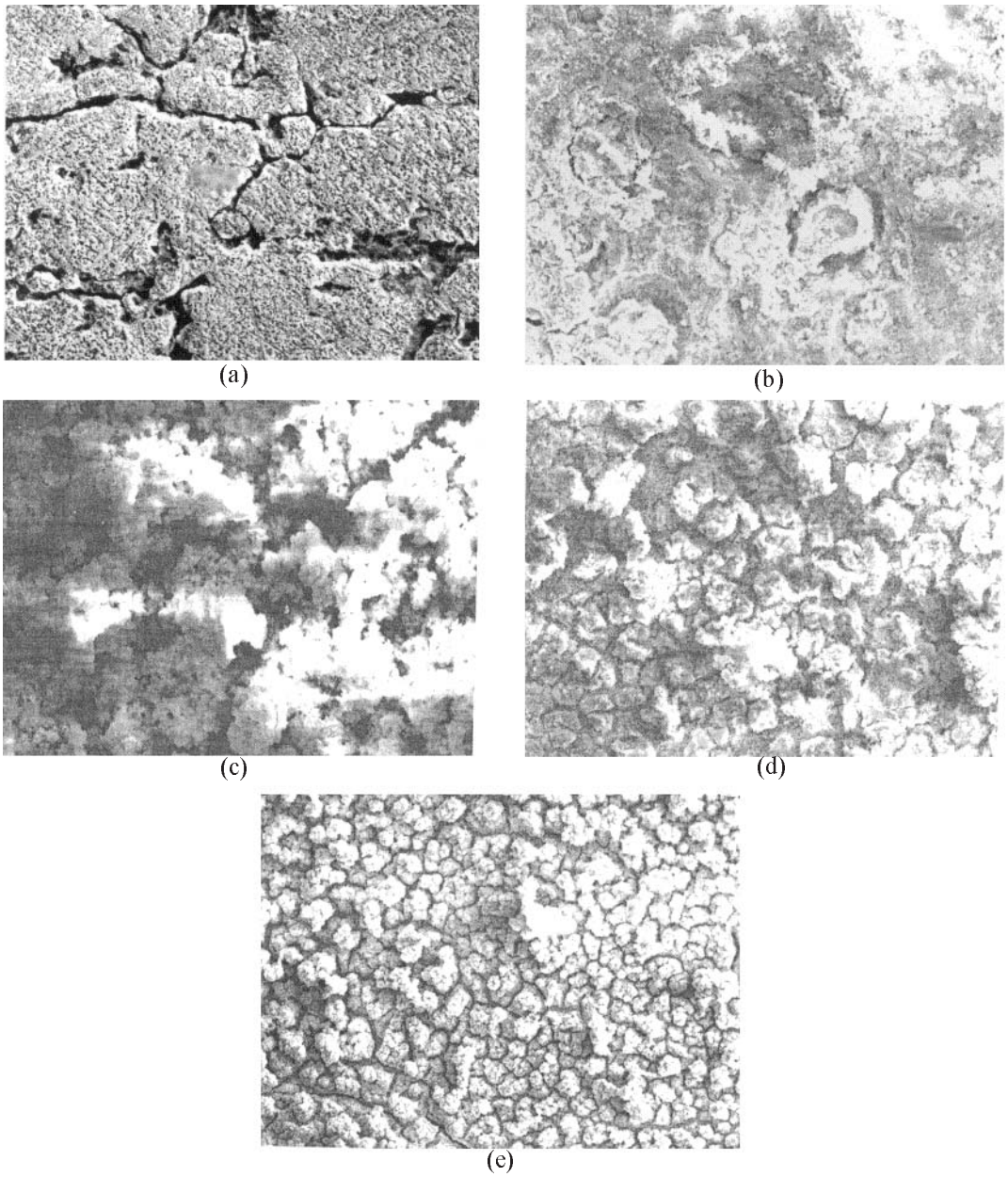


Fig. 3. Micrographs of (a) initial surface of St.3 steel and (b–e) that after corrosion tests in 3% NaCl solutions with various extract additives. (b) No additive; additive: (c) RH, (d) BH, and (e) SH.

the magnitudes Z of the protective effect, obtained using the gravimetric and potentiometric methods, are different, with the former being, as a rule, larger than the latter. This occurs because the gravimetric method determines the average corrosion rate over the entire test period, and the electrochemical method, the corrosion rate at the instant of measurement. However, the tendency toward an increase in the protective effect in water–salt and acid solutions with the extracts under study, determined by two methods, is the same: in a sodium chloride solution, the protective effect grows in the following order of water-soluble substances extracted from husks: RH < BH < SH, whereas in an HCl solution at pH 1.0, Z increases in the order SH < BH < RH.

It is known that, in the initial stage of corrosion inhibition, adsorbed films are formed on the metal surface, and, therefore, the surface morphology of St.3 steel samples was analyzed. Figure 3 shows micrographs of the St.3 steel surface before and after corrosion tests in a water–salt solution with dry

Table 4. Content of elements in corrosion products formed on the steel surface after corrosion tests in 3% NaCl solutions with dry extract additives

Solution	Content, wt %									
	Fe	O	Na	Cl	Mn	S	Si	P	Ca	Cr
NaCl	52–56	22–34	0.4–1.1	0–0.6	0–0.5	0–0.5				
RH + NaCl	39–86	6–47	1–4.8	0–1.2	0–2.4		0–1.2	2.2–6.5	0–1	
BH + NaCl	55–88	7–31	1.5–7.5			0–0.5		0.9–1.9		0.7–2.5
SH + NaCl	60–62	32–34	1.9–2.3				1.3–1.4	0–0.5	0.8–1.3	

extract additives. The surface morphology was studied using an EVO-50 XPV scanning electron microscope (LEO, Germany), and an electron microprobe analysis was made with JXA-8100 X-ray fluorescence microanalyzer (JEOL, Japan) with three wave spectrometers, additionally equipped with an INCA-250 (Oxford, UK) energy-dispersive spectrometer. St.3 samples ($10 \times 10 \times 0.4$ mm) were preliminarily ground, chemically etched, washed with water, and degreased with acetone. Then the samples were submerged in a NaCl solution with dry extract additives and kept there for four weeks.

As can be seen in the micrographs, a film composed of aggregates of various sizes is formed on the steel surface after four weeks of sample tests in solutions containing RH, BH, and SH extract additives (Figs. 3c–3e). It should also be noted that the visually densest film is formed on the steel surface in a sodium chloride solution with addition of an extract from sunflower husks. According to Table 2, the most pronounced decrease in the corrosion rate of St.3 steel is observed in the same solution. In a solution with RH additive, for which Z has the smallest value, a loose film is formed.

Corrosion pits 50–100 μm in size are formed on the surface of steel samples exposed to sodium chloride solutions without extract additives (Fig. 3b).

According to the results of X-ray fluorescence microanalysis, the films formed on the surface of steel samples after corrosion tests in a NaCl solution with dry extract additives contain a large amount of Fe and O (Table 4). In addition, the film formed on the steel surface in a NaCl solution with RH additive contains an increased amount of phosphorus (2.2 to 6.5%). Possibly, this is due to the presence of inositolhexaphosphoric acid in rice husks [8]. The elemental composition of the protective films formed on the steel surface from NaCl solutions with SH and BH is more diverse: the X-ray spectra contain, in addition to the peaks indicating that Fe, O, and Na are present in the film, peaks characteristic of S, P, Cr (for the solution with BH) and Ca, P, Si (for the solution with SH). The presence of these elements in the starting raw materials was noted in [14, 15]. The increased content of Fe and O in the films indicates that there occur corrosion processes to give corrosion products, probably in the form of Fe hydroxides and oxides. Because the corrosion process is decelerated in solutions containing extract additives, it can be assumed that extract solutions contain substances (with so far unidentified composition) that form poorly soluble complexes with Fe ions and hinder further dissolution of steel.

CONCLUSIONS

(1) A study of the corrosion of St.3 steel in 3% NaCl and 0.1 N HCl solutions containing additions of liquid and dry extracts from rice, buckwheat, and sunflower husks demonstrated that extracts produced from fruit husks of these plants behave as corrosion inhibitors.

(2) The protective effect in a sodium chloride solution (pH 7.0) with extracts from husks increases in the following order: rice husk < buckwheat husk < sunflower husk, and in a HCl solution at pH 1.0, the protective effect increases in the order: sunflower husks < buckwheat husks < rice husks.

REFERENCES

1. Ledovskikh, V.M., *Zashch. Met.*, 1987, vol. 23, no. 6, pp. 968–970.
2. Tadzhikhodzhaev, Z.A., Abumavlyanova, M.K., Tadzhikhodzhaeva, U.B., and Mivalieva, Z.Z., Abstracts of Papers, *IV Vserossiiskaya nauchnaya konferentsiya "Khimiya i tekhnologiya rastitel'nykh veshchestv"* (IV All-Russia Scientific Conf. "Chemistry and Technology of Vegetable Substances"), Syktyvkar, September 25–30, 2000, p. 459.

3. Chistokletov, V.I., Akimova, G.S., Malysheva, N.M., et al., Abstracts of Papers, *IV Vserossiiskaya nauchnaya konferentsiya "Khimiya i tekhnologiya rastitel'nykh veshchestv"* (IV All-Russia Scientific Conf. "Chemistry and Technology of Vegetable Substances"), Syktyvkar, September 25–30, 2000, p. 275.
4. Popelyukh, G.M., Talavira, L.I., Gazha, P.A., et al., *Zashch. Met.*, 1985, vol. 21, no. 5, pp. 753–755.
5. El-Etre, A.Y., *Corrosion Sci.*, 2003, vol. 45, no. 11, pp. 2485–2495.
6. Tishchenko, G.P., Vazhenin, S.F., Moiseenko, N.Yu., and Tishchenko, I.G., *Zashch. Met.*, 1990, vol. 26, no. 5, pp. 846–848.
7. RF Patent 2289639.
8. Kolzunova, L.G., Zemnukhova, L.A., Fedorishcheva, G.A., et al., *Zh. Prikl. Khim.*, 2000, vol. 73, no. 10, pp. 1644–1651.
9. Zemnukhova, L.A., Tomshich, S.V., Shkorina, E.D., and Klykov, A.G., *Zh. Prikl. Khim.*, 2004, vol. 77, no. 7, pp. 1192–1196.
10. Zemnukhova, L.A., Tomshich, S.V., Mamontova, V.A., et al., *Zh. Prikl. Khim.*, 2004, vol. 77, no. 11, pp. 1901–1904.
11. Zemnukhova, L.A., Fedorishcheva, G.A., Egorov, A.G., and Sergienko, V.I., *Zh. Prikl. Khim.*, 2005, vol. 78, no. 2, pp. 324–328.
12. Zemnukhova, L.A., Tomshich, S.V., Kovekhova, A.V., and Greben', L.Yu., *Zh. Prikl. Khim.*, 2007, vol. 80, no. 7, pp. 1200–1205.
13. Zemnukhova, L.A., Kolzunova, L.G., and Shkorina, E.D., *Zh. Prikl. Khim.*, 2007, vol. 80, no. 6, pp. 1032–1036.
14. Zemnukhova, L.A., Kovekhova, A.V., Fedorishcheva, G.A., and Barinov, N.N., *IV Mezhdunarodnyi simpozium "Khimiya i khimicheskoe obrazovanie": Sbornik nauchnykh trudov* (IV Int. Symp. "Chemistry and Chemical Education": Coll. of Scientific Works), Vladivostok: Dal'nevost. Univ., 2007, p. 178.
15. Shkorina, E.D., Composition and Integrated Processing of Buckwheat Production Wastes, *Cand. Sci. Dissertation*, Vladivostok, 2007.

ISSN 1070-4272, Russian Journal of Applied Chemistry, 2008, Vol. 81, No. 9, pp. 1565–1567. © Pleiades Publishing, Ltd., 2008.
Original Russian Text © Z.G. Gasanly, T.L. Guseinzade, 2008, published in Zhurnal Prikladnoi Khimii, 2008, Vol. 81, No. 9, pp. 1490–1492.

APPLIED ELECTROCHEMISTRY AND CORROSION PROTECTION OF METALS

Anodic Dissolution of Gallium in Solution of LiCl in Anhydrous Acetic Acid

Z. G. Gasanly and T. L. Guseinzade

Institute of Chemical Problems, National Academy of Sciences of Azerbaijan, Baku, Azerbaijan

Received June 5, 2007

Abstract—Kinetics and mechanism of the anodic dissolution of gallium in an anhydrous acetic acid medium was studied. The results obtained can be used for choosing the optimum conditions for the electrolytic refining of gallium from acetic acid solutions.

DOI: 10.1134/S1070427208090176

Study of the kinetics and mechanism of anodic dissolution of gallium is of certain interest, because low-valence ions formed in the process are the main intermediate products of gallium refining.

The study was aimed to obtain additional data on the processes occurring in the course of electrochemical oxidation of metallic gallium. The anodic dissolution of metallic gallium was studied with a rotating disc–ring electrode (RDRE) in anhydrous acetic acid, because ions of a low-valence gallium in 100% CH_3COOH are stable. The electrode (ring and disc) was made of platinum. Prior to each run, a 2-mm-thick gallium film was electrodeposited onto the disc from a gallate solution. The rotation rate of the electrode was 500 rpm, and the temperature, 25°C. Acetic acid was dehydrated by additional distillation in the presence of acetic anhydride, and lithium chloride was dried in a flow of hydrogen chloride at 150–200°C and calcined at 500°C prior to use.

The mechanism of the anodic dissolution of gallium was studied in a 0.5 M LiCl solution in 100% CH_3COOH. The results obtained are shown in Fig. 1.

As can be seen, in the course of anodic polarization of a gallium disc electrode with currents of up to $i_d \le 4.0$ mA, the anode currents i_r are observed on the ring, due to the oxidation

$$Ga^+ \rightarrow Ga^{3+} + 2e \quad (1)$$

of Ga^+ ions formed at a disc electrode by the reaction

$$Ga^0 \rightarrow Ga^+ + e. \quad (2)$$

As the ring potential E is shifted toward positive values from 300 to 900 mV, the current i_r increases and attains a limiting value at 600 mV. It follows from the anodic polarization curves obtained on a disc–ring electrode (Fig. 1) that Ga dissolution proceeds with a slight polarization and without retardation (curve *9*). The oxidation potential for Ga^+ ions at a ring electrode is attained by shifting the potential E_r by 450 mV with respect to initial

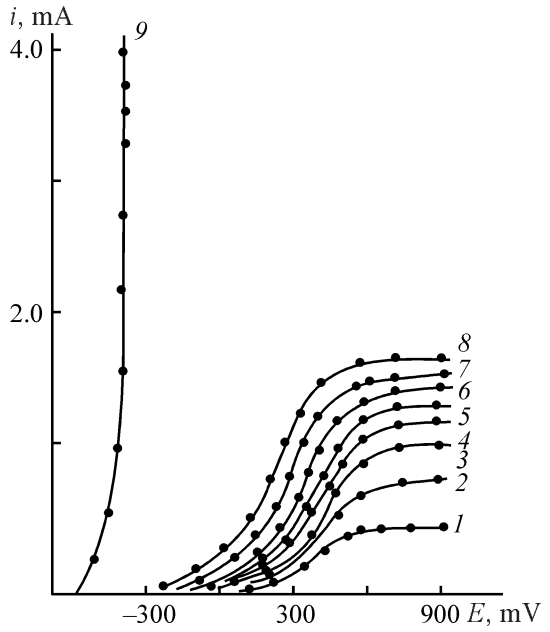


Fig. 1. Anodic polarization curves obtained at (*1*–*8*) a ring electrode and (*9*) a disc in a 0.5 N solution of LiCl in 100% CH_3COOH at varied disc current. i_d, mA: (*1*) 0.5, (*2*) 1.0, (*3*) 1.5, (*4*) 2.0, (*5*) 2.5, (*6*) 3.0, (*7*) 3.5, and (*8*) 4.0. (*i*) Current and (*E*) potential; the same for Fig. 2.

Table 1. Results of calculation and measurements on RDRE in a 0.5 M solution of LiCl in 100% CH_3COOH

I_d	i_r	i_l	i_{kin}	k_s
mA				
0.5	0.32	0.37	0.13	0.74
1.0	0.76	0.85	0.15	0.85
1.5	0.98	1.15	0.35	0.76
2.0	1.21	1.48	0.52	0.74
2.5	1.46	1.76	0.74	0.70
3.0	1.54	2.05	0.95	0.68
3.5	1.62	1.92	1.58	0.54
4.0	1.74	2.13	1.87	0.53

Table 2. Effect of temperature on the kinetic parameters of gallium ionization at RDRE in a 0.5 M solution of LiCl in 100% CH_3COOH. i_d = 2.0 mA, ω = 500 rpm

T, °C	i_r	i_l	i_{kin}	k_s
	mA			
20	1.20	1.10	0.90	0.55
25	1.24	1.23	0.77	0.62
30	1.30	1.31	0.69	0.65
35	1.40	1.36	0.64	0.68
40	1.34	1.32	0.68	0.66
45	1.26	1.28	0.72	0.64
50	1.10	1.14	0.86	0.57

value, and the limiting current is attained by shifting it by 900 mV. The results obtained show that univalent gallium cannot be electrolytically oxidized on the disc, which is in line with the data of [1–4].

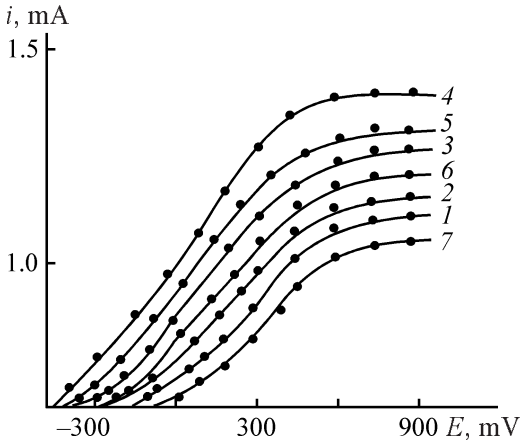


Fig. 2. Anodic polarization curves obtained at a ring electrode in a 0.5 M solution of LiCl in anhydrous acetic acid at varied temperature. T, °C: (*1*) 20, (*2*) 35, (*3*) 30, (*4*) 35, (*5*) 40, (*6*) 45, (*6*) 45, and (*7*) 50. i_d = 2.0 mA; ω = 500 rpm; the same for Fig. 3.

The kinetic parameters of the electrochemical process (i_l, i_{kin}, and k_s) of the anodic dissolution of gallium were calculated by the formulas [5]

$$i_l = n_d i_r / n_r N, \quad (3)$$

$$i_{kin} = i_d - i_l, \quad (4)$$

$$k_s = i_l / i_d, \quad (5)$$

where i_l is the current determined by the contribution of the flow of Ga^+ ions from the disc surface in the solution; i_{kin} is the current determined by the flow of Ga^+ ions spent for the disproportionation; k_s is the stability coefficient of Ga^+ ions; N is the efficiency coefficient of the rotating disc–ring electrode (0.418 in the given case); n_d and n_r are the numbers of electrons involved in the processes at disc and ring electrodes, respectively; and i_d is the disc current.

The results of the calculation are given in Table 1.

As seen from Table 1, the current i_l increases with the disc current i_d. As a result, i_{kin} increases owing to an increase in the concentration of Ga^+ ions in the bulk of the solution. The k_s values in the range of disc currents 0.0–4.0 mA do not exceed 0.85. This means that, under the given conditions, approximately 40% of univalent gallium ions do not reach the ring owing to the disproportionation

$$3Ga^+ \rightarrow 2Ga^0 + Ga^{3+}, \quad (6)$$

Reaction (6) is exothermic. With increasing temperature, its equilibrium will be shifted to the left toward the formation of Ga^+ ions. Therefore, in this study we examined the gallium ionization (i_d = 2.0 mA) in a 0.5 M LiCl solution in 100% CH_3COOH at 20, 25, 30, 35, 40, 45, and 50°C. The results obtained are given in Table 2 and Figs. 2 and 3.

The polarization curves presented in Fig. 2 show that the limiting current of the disc electrode in the temperature range 20–50°C increases (curves *1–4*). The current of the first stage, formation of Ga^+ ions, increases, reaching a maximum of 1.36 mA at 35°C, i.e., it is close to the disc current, i_{kin} = 0.64 mA, and k_s approaches 0.68 (Table 2, Fig. 3).

Consequently, at 35°C the anodic dissolution of gallium in a 0.5 M solution of LiCl in 100% CH_3COOH goes solely to the univalent state, and the Ga^+ ions are the final product of the electrode

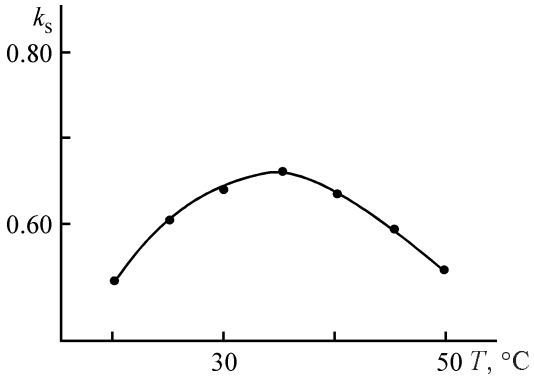


Fig. 3. Stability coefficient k_s of Ga^+ ions vs. temperature T.

reaction. In accordance with [6, 7], a decrease in the limiting current of the oxidation of Ga^+ ions and in k_s (Figs. 2, 3) at 45 and 50°C is apparently due to the increase in the rate of Ga^+ oxidation with hydrogen ions:

$$Ga^+ + 2H^+ \rightarrow Ga^{3+} + H_2. \quad (7)$$

The Ga^+ ions are unstable toward the hydrogen ions, because the standard potential of the Ga^0/Ga^{3+} couple is –0.62 V [8]. Thus, it was established that, in the course of anodic dissolution of gallium, the electrochemical ionization of gallium to Ga^+ is accompanied by subsequent disproportionation (6) with the formation of gallium ions of the highest valence and metallic gallium.

CONCLUSIONS

(1) By taking the polarization curves in a solution of LiCl in anhydrous acetic acid at a rotating disc–ring electrode, it was found that the anodic dissolution of gallium yields Ga^+ ions, which are not oxidized on the gallium disc and can be detected by the oxidation at the ring electrode.

(2) The anodic dissolution of gallium proceeds in two steps: electrochemical process and chemical disproportionation in the bulk of the electrolyte.

REFERENCES

1. Kozin, L.F., Lepesov, K.K., and Kobrand, E.E., in *Kinetika i mekhanizm elektrodnykh reaktsii* (Kinetics and Mechanism of Electrode Reactions), Alma-Ata, 1975, issue 11, pp. 3–15.
2. Kozin, L.F., and Sokol'skii, D.V., in *Elektrodnye protsessy* (Electrode Processes), Alma-Ata, 1976, issue 2, pp. 3–44.
3. Kozin, L.F., and Kobrand, E.E., *Izv. Akad. Nauk Kaz. SSR, Ser. Khim.*, 1972, no. 5, pp. 25–31.
4. Lepesov, K.K., in *Materialy II konferentsii molodykh uchenykh* (Proc. II Conf. of Young Scientists), Alma-Ata, 1974, pp. 98–99.
5. Lepesov, K.K., Kinetics and Mechanism of Ionization of Bismuth, Copper, and Indium at a Rotating Disc–Ring Electrode, *Cand. Sci. Dissertation*, Alma-Ata, 1974.
6. Egorov, A.G., and Kozin, L.F., in *Elektrodnye protsessy* (Electrode Processes), Alma-Ata, 1971, issue 2, pp. 60–72.
7. Visco, R.E., *J. Phys. Chem.*, 2003, vol. 69, pp. 202–207.
8. Sarmurzina, R.G., Egorov, A.G., and Kozin, L.F., in *Sbornik rabot po khimii* (Coll. of Works on Chemistry), Alma-Ata: Kaz. Gos. Univ., 1983, no. 3, pp. 382–394.

ISSN 1070-4272, Russian Journal of Applied Chemistry, 2008, Vol. 81, No. 9, pp. 1568–1572. © Pleiades Publishing, Ltd., 2008.
Original Russian Text © S.T. Marakaev, A.V. de Vekki, 2008, published in Zhurnal Prikladnoi Khimii, 2008, Vol. 81, No. 9, pp. 1493–1497.

ORGANIC SYNTHESIS AND INDUSTRIAL ORGANIC CHEMISTRY

Kinetics of Oxidation of Methane to Formaldehyde on $Na_4[PFeMo_{11}O_{40}]/SiO_2$

S. T. Marakaev and A. V. de Vekki

All-Russian Research Institute of Petrochemical Processes, St. Petersburg, Russia
Prikladnaya i Fundamenal'naya Khimiya Limited Liability Company, St. Petersburg, Russia

Received November 26, 2007

Abstract—The kinetics of oxidation of CH_4 to formaldehyde on the catalytic system $Na_4[PFeMo_{11}O_{40}]/SiO_2$ were studied, and a significant role of the redox potential of the CH_4–O_2 system with respect to the catalyst was shown. The density of centers participating in the reaction was determined, and dissociative competitive adsorption of methane and oxygen was established. The equation was deduced in the framework of the Langmuir–Hinshelwood theory taking into account the side conversion of formaldehyde. Possible participation of lattice oxygen in the reaction was suggested.

DOI: 10.1134/S1070427208090188

It was shown previously [1, 2] that, in oxidation of methane-containing gases with atmospheric oxygen in the presence of heteropoly compounds of the 12th series containing two ambivalent metals, it is possible to increase the conversion of methane by a factor of 2, the yield of formaldehyde by a factor of 3, and the catalyst performance by a factor of 40 in comparison with the known results.

Proceeding with studies on partial oxidation of methane, we examined the kinetics and mechanism of reaction on the $Na_4[PFeMo_{11}O_{40}]/SiO_2$ catalyst.

Oxidation was performed at 650°C in a batch reactor operating under conditions of quasiequilibrium kinetics when the methane conversion in single pass did not exceed 0.1%. In practice. the chosen operation mode means that the reactor operates under conditions of pseudozero conversion of methane. To avoid any kinetic restrictions that could be imposed by a high conversion of oxygen, we took into account the degree of methane conversion at oxygen conversion less than 20%.

The data obtained (Table 1) allow us to make the following conclusions: (1) An increase in the partial pressure of the reactants results in an increase in the reaction rate; however, the effect of methane pressure P_{CH_4} is stronger; (2) variation of P_{CH_4}/P_{O_2} does not significantly affect the selectivity of formaldehyde formation (71–77%), which depends in this case on formation of by-products, CO and CO_2 [3].

It is well known [4] that the activity of the catalysts for partial oxidation of methane is directly related to their ability to stabilize the reduced surface centers, which act as oxygen promoters in the redox cycle under the conditions of a dynamic equilibrium.

To estimate the dynamic equilibrium at the catalyst surface, we studied oxygen uptake by the surface at 650°C by the procedure described in [5] (Table 2). To analyze the data, let us introduce several designations for the catalyst surface: μ (nmol g^{-1}), number of physically reduced centers; μ_0 (nmol g^{-1}), total number of centers capable of reduction; and θ_{red}, density (fraction) of reduced centers at the surface.

Our data show that the absolute values of the partial pressure of the reactants do not affect μ, but this quantity is affected by the ratio of these parameters. For example, the number of physically reduced centers varies from 15 to 65 for P_{CH_4}/P_{O_2} ratios equal to 0.5 and 8.0, respectively, whereas in the absence of oxygen μ_0 is equal to 350 nmol g^{-1}.

To elucidate the influence of reactants on reduction of the catalyst centers, we constructed a logarithmic dependence $\ln\theta_{red} = f(\ln P)$ (Fig. 1) on the basis of data presented in Table 2.

The slopes of the curves having opposite trends show that the reaction order with respect to oxygen and methane is close to 0.5, with the order with respect to oxygen being negative. These dependences

Table 1. Influence of the partial pressure of the reactants on the rate and selectivity of formaldehyde formation in oxidation of methane on $Na_4[PFeMo_{11}O_{40}]/SiO_2$ at 650°C

Partial pressure, atm		P_{CH_4}/P_{O_2}	Conversion of CH_4/μ, %	r_{CH_4}, mol s^{-1} g^{-1}	Selectivity with respect to products, %		
methane	oxygen				CH_2O	CO	CO_2
0.09	0.18	0.5	4.5	1.0	75	19	6
0.17	0.18	1.0	4.3	1.9	76	16	8
0.35	0.18	2.0	3.5	3.3	77	18	5
0.70	0.18	4.0	3.4	6.4	74	20	6
1.04	0.18	6.0	3.7	10.0	71	20	9
1.35	0.18	7.5	3.2	11.0	71	23	6
0.41	0.05	8.0	2.9	2.8	73	22	5
0.40	0.02	20.0	2.1	2.1	75	20	5

indicate that the redox potential of the CH_4–O_2 system relative to the catalyst plays a significant role. In other words, both reactants interact with the contact surface by the redox mechanism, and the influence of the partial pressure of the reactants on the reaction rate is caused by inhibition of desorption. It is evident that the dynamic equilibrium at the catalyst surface is reached in the point of intersection of the pressure dependences of the reduced center concentration and corresponds to $\ln P = -2$ (Fig. 1).

Thus, half-order dependence of θ_{red} on P_{CH_4}/P_{O_2} evidently suggests the dissociative competitive activation of methane and oxygen molecules at the surface centers of the catalyst, and its algebraic form is as follows: $\theta_{red} = (P_{CH_4}/P_{O_2})^{0.5}$ This means that two active centers can participate in chemisorption of each reactant.

In the latter case, at inhibited desorption, the following reactions can occur at the catalyst surface:

$$CH_4 + 2\mu_1 \rightarrow CH_2O + 2\mu_2, \quad (1)$$

$$O_2 + 2\mu_2 \rightarrow 2\mu_1, \quad (2)$$

where μ_1 is the number of oxidized centers and μ_2 is the number of reduced centers.

Under the conditions of dynamic equilibrium,

$$[\mu_1] + [\mu_2] = [\mu_0]. \quad (3)$$

Then, the rate of formation of reduced centers r_{red} can be written in the form

Table 2. Influence of the partial pressure of reactants on absolute μ and fractional θ_{red} densities of reduced centers on the catalyst surface

P_{CH_4}/P_{O_2}	P_{CH_4}, atm	P_{O_2}, atm	μ, nmol g^{-1}	$\theta_{red} \times 10^2$
0.5	0.05	0.10	15	4
0.5	0.20	0.40	15	4
1.0	0.10	0.10	23	6
1.0	0.20	0.20	23	6
2.0	0.20	0.10	30	8
2.0	0.40	0.20	30	8
4.0	0.10	0.05	47	12
4.0	0.40	0.10	43	12
8.0	0.20	0.05	65	17
8.0	0.80	0.1	65	17
–	0.05	–	350	100

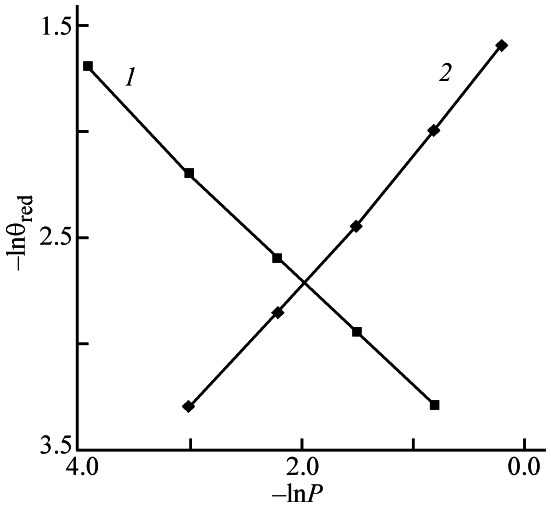


Fig. 1. Density of centers reduced at the surface θ_{red} as a function of (*1*) air and (*2*) methane pressure (log–log plots).

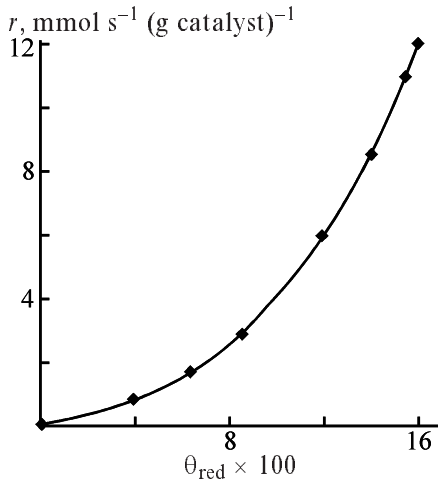


Fig. 2. Rate of methane oxidation r as a function of the fraction of centers reduced at the surface θ_{red}.

$$r_{red} = k_{red}P_{CH_4}(\mu_0 - \mu)^2. \quad (4)$$

It is well known [6] that the rate of surface diffusion of lattice oxygen ions in the SiO_2 support is negligible under the conditions of methane oxidation; however, the rate of their diffusion in phosphorus–iron–molybdenum catalyst is unknown. Based on some indirect data, it can be assumed that the catalyst fragment Mo=O donates its oxygen atom to the methyl radical to form surface methoxyl transforming into formaldehyde and methanol at elevated temperatures. At least, iron–molybdenum catalyst for oxidation of methanol into formaldehyde operates in such a way [7]. The released lattice oxygen is compensated by oxygen from the medium. However, at such a low conversion of methane (below 5%), the possible role of lattice oxygen cannot be neglected in deducing the rate equation. At the same time, the oxygen source cannot affect the rate equation since the inner balance with respect to oxygen is kept due to the compensating mechanism of its transformation. Then we assume that, under dynamic equilibrium, the rate of disappearance of reduced centers practically coincides with the rate of catalyst oxidation r_{ox}:

$$r_{ox} = k_{ox}P_{O_2}\mu^2. \quad (5)$$

Taking into account that $\theta_{red} = \mu/\mu_0$ and θ_{red} is limited by the condition $0 < \theta_{red} < 1$, the rates of reduction and oxidation of centers under dynamic equilibrium can be expressed as

$$k_{ox}P_{O_2}\mu^2\theta_{red} = k_{red}P_{CH_4}\mu_0^2(1 - \theta_{red})^2. \quad (6)$$

Solving Eq. (6) relative to θ_{red}, we obtain the following equation for the fraction (density) of reduced centers:

$$\theta_{red} = \frac{(k_{ox}/k_{red})^{0.5}(P_{CH_4}/P_{O_2})^{0.5}}{1 + (k_{ox}/k_{red})^{0.5}(P_{CH_4}/P_{O_2})^{0.5}}. \quad (7)$$

This expression corresponds to the experimental dependence $\theta_{red} = (P_{CH_4}/P_{O_2})^{0.5}$ under the condition that $k_{red}P_{CH_4}/k_{ox}P_{O_2} \ll 1$.

Treatment of data listed in Table 2 by the nonlinear regression analysis using Eq. (7) allowed estimation of k_{red}/k_{ox} at 4.5×10^{-3}. The value obtained suggests that the rate of catalyst oxidation is significantly higher than the rate of its reduction.

Since reactions (1) and (2) are irreversible, the rate of methane conversion r_{CH_4} under dynamic equilibrium should be equal to the rate of these two stages: $r_{CH_4} = r_{ox} = r_{red}$. Then, the oxidation rate can be expressed through Eqs. (4) and (5):

$$r_{CH_4} = k_{ox}P_{O_2}\mu_0^2\theta_{red}^2 = k_{red}P_{CH_4}\mu_0^2(1 - \theta_{red})^2. \quad (8)$$

The resulting dependence of the rate of methane oxidation is mathematically identical to the expression for second-order equation where one of the functions is θ_{red}. Indeed, this conclusion is confirmed by the experimental dependence shown in Fig. 2.

Substituting θ_{red} from Eq. (7) into Eq. (8) and solving these equations with respect to the oxidation rate, we obtain the following expression:

$$r_{CH_4} = \mu_0^2\frac{k_{red}P_{CH_4}}{[1 + (k_{red}P_{CH_4}/k_{ox}P_{O_2})^{0.5}]^2}. \quad (9)$$

Analyzing expression (9) from the mathematical standpoint, we can note that, at the ratio $P_{CH_4}/P_{O_2} \to \infty$, the model predicts zero reaction rate. Further, from the equation it follows that the reaction order with respect to P_{CH_4} is fractional, especially at high P_{CH_4}/P_{O_2} ratios, since with increasing methane content the degree of reduction of the catalyst surface increases. This naturally results in decreasing concentration of oxidized centers responsible for activation of methane.

The reliability of the kinetic model was confirmed by comparing the experimental and theoretical data. Nonlinear regression analysis of the curve presented

in Fig. 2 gives k_{red} and k_{ox} equal to 9×10^{7} and 4.5×10^{-3} mol s^{-1} atm^{-1}; in this case, k_{red}/k_{ox} is equal to 4.5×10^{-3}. Good agreement between the calculated and experimental data supports our kinetic model.

However, it is necessary to consider one more aspect of this problem, namely, oxygen consumption for secondary transformations of formaldehyde (to carbon oxide and carbon dioxide). According to published data [8], oxidation of CO to CO_2 proceeds at a significantly lower rate than conversion of formaldehyde to carbon oxide; therefore, we took into account one more reaction pathway:

$$CH_2O + \rho_1 \rightarrow CO + H_2O + \rho_2. \quad (10)$$

In the total rate of oxygen consumption, we considered two pathways: major and secondary, which can be described mathematically in the following way:

$$r_{O_2} = r_{CH_4}(1 + S_{CO}\alpha), \quad (11)$$

where α is the stoichiometric coefficient in reaction (10).

Continuing mathematical transformations and substitutions, we can obtain from Eq. (7) the following expression:

$$\theta_{red} = \frac{[(1+n)(k_{ox}/k_{red})]^{0.5}(P_{CH_4}/P_{O_2})^{0.5}}{1+[(1+n)(k_{ox}/k_{red})]^{0.5}(P_{CH_4}/P_{O_2})^{0.5}}, \quad (12)$$

where $n = S_{CO}\alpha$.

Substituting complete expression for θ_{red} (12) in Eq. (8), we obtain the following equation for rate of methane oxidation:

$$r_{CH_4} = \rho_2^0 \frac{k_{red}P_{CH_4}}{\{1+[(1+n)(k_{ox}/k_{red})]^{0.5}(P_{CH_4}/P_{O_2})^{0.5}\}^2}. \quad (13)$$

This expression shows not only the dependence of the reaction rate on the partial pressures of reactants but also inverse dependence of the reaction selectivity: the larger the amount of CO formed, the deeper the reduction of the catalyst surface, which results in decreased rate of the main reaction. It should be noted that the very low k_{red}/k_{ox} ratio in the examined range of P_{CH_4}/P_{O_2} is not a significant factor, since higher value of k_{ox} does not noticeably affect the reaction rate due to pseudo-first order of the reaction rate with respect to methane. On the contrary, at high P_{CH_4}/P_{O_2} ratios, the reaction rate should increase and its dependence on P_{O_2} should be insignificant. In practice this means that the concentration of sorbed methane, rather than the concentration of the oxidizing agent, becomes important. This is quite logical since the rupture of the CH_3–H bond in chemisorption of methane is the limiting stage. In addition, in formation of CH_3O the source of oxygen is presumably lattice oxygen.

Thus, it can be concluded that oxidation of methane to formaldehyde at the surface of $Na_4\cdot[PFeMo_{11}O_{40}]/SiO_2$ catalyst proceeds by a concerted mechanism involving activation of gas-phase oxygen at the surface of reduced catalyst centers and subsequent its addition to activated molecule of methane. Compensation of lattice oxygen with molecular oxygen is equally probable, especially because this process on heteropoly compounds proceeds instantaneously [9]. The latter factor suggests that the role of lattice oxygen is more significant than it was believed previously. Since completion of the lattice with oxygen is not the activated stage of the process [10], experimental consideration of its role without using special methods is difficult. In this case, one could rely on the published data [11, 12] obtained using an isotopic label. Unfortunately, these results are ambiguous because they do not allow determination of the nature of the oxygen source. In addition, based on these data, we might prefer the version of "intercalation" of molecular oxygen. However, this conclusion is not well-founded, since the content of ^{18}O in the catalyst was not determined after the reaction completion.

The only confirmation of the participation of lattice oxygen in the process is the experiment in which oxygen-free methane was passed through a catalyst bed with increased content of acting base (up to 10%). Among reaction products, traces of formaldehyde were found and the reaction quickly ceased. However, after contact of the catalyst with atmospheric oxygen, the contact activity was restored and formaldehyde was found among the reaction products again.

These data suggest that oxidation of methane can proceed, at least partially, due to participation of lattice oxygen whose consumption is compensated by oxygen from the reaction medium.

CONCLUSIONS

(1) In studying the kinetics of methane oxidation to formaldehyde, it was found that the redox poten-

tial of the CH_4–O_2 system relative to the catalyst plays a significant role, and the dissociative competitive adsorption of methane and oxygen was suggested.

(2) The reaction rate depends on the partial pressure of methane and is inversibly proportional to the reaction selectivity, due to deep reduction of the surface with carbon monoxide formed as by-product.

(3) The experimental data and especially the features of the behavior of all heteropoly compounds suggest that lattice oxygen of the heteropoly compound participates in the reaction; the vacancy formed is filled with oxygen of the reaction medium.

REFERENCES

1. Marakaev, S.T. and Vekki, A.V. de, *Neftepererab. Neftekhim.* (Moscow), 2005, no. 3, pp. 25–29.
2. Marakaev, S.T., Marakaev, T.A., and Vekki, A.V. de, *Neftepererab. Neftekhim.* (Moscow), 2004, no. 12, pp. 27–37.
3. Marakaev, S.T. and Vekki, A.V. de, *Neftepererab. Neftekhim.* (Moscow), 2005, no. 9, pp. 21–24.
4. Bielanski, A. and Haber, J., *Oxygen in Catalysis*, New York: Dekker, 1991.
5. Arena, F., Frusteri, F., and Parmaliana, A., *Appl. Catal. A: General*, 2000, vol. 197, no. 2, pp. 239–246.
6. Parmaliana, A. and Giordano, N., *J. Catal.*, 1997, vol. 167, no. 1, pp. 57–76.
7. Lebedev, N.N., *Khimiya i tekhnologiya osnovnogo organicheskogo i neftekhimicheskogo sinteza* (Chemistry and Technology of Basic Organic and Petrochemical Synthesis), Moscow: Khimiya, 1988.
8. Amiridis, M.D., Rekoshe, J.F., Dumesic, J.A., et al., *Am. Inst. Chem. Eng. J.*, 1991, vol. 37, pp. 37–92.
9. Kozhevnikov, I.V. and Matveev, K.I., *Usp. Khim.*, 1982, vol. 51, pp. 1875–1896.
10. Arena, F., Frusteri, F., and Parmaliana, A., *Am. Inst. Chem. Eng. J.*, 2000, vol. 46, no. 11, pp. 2283–2294.
11. Pak, S., Rosynec, M.P., and Lunsford, J.H., *J. Catal.*, 1997, vol. 165, no. 1, pp. 73–79.
12. Sun, Q., Hermer, R.C., and Klier, K., *Catal. Lett.*, 1992, vol. 16, no. 4, pp. 251–261.

ISSN 1070-4272, Russian Journal of Applied Chemistry, 2008, Vol. 81, No. 9, pp. 1573–1577. © Pleiades Publishing, Ltd., 2008.
Original Russian Text © S.N. Petrova, M.V. Volodarskii, S.V. Makarov, Lu Zhen Li, 2008, published in Zhurnal Prikladnoi Khimii, 2008, Vol. 81, No. 9, pp. 1498–1502.

ORGANIC SYNTHESIS AND INDUSTRIAL ORGANIC CHEMISTRY

Oxidation of Azo Dyes with Inorganic Peroxides in the Presence of Cationic Surfactants

S. N. Petrova, M. V. Volodarskii, S. V. Makarov, and Lu Zhen Li

Ivanovo State University of Chemical Technology, Ivanovo, Russia

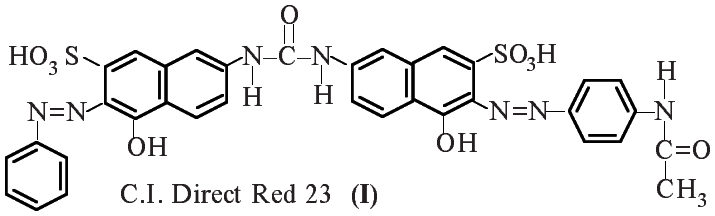
Received January 22, 2008

Abstract—Degradation of Direct Red 23, Rective Red 45, and Orange II azo dyes with hydrogen peroxide and hydroperite in the presence of cationic surfactants alkyldimethylbenzylammonium chloride (Katamin AB) and cetyltrimethylammonium chloride and without them was studied by spectrophotometry. The reactivity of the azo dyes was correlated with their chemical structure.

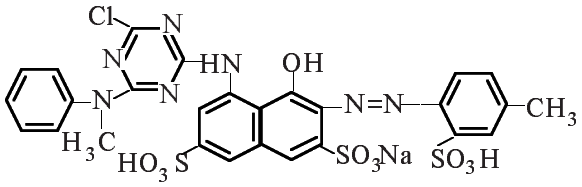
DOI: 10.1134/S107042720809019X

Azo dyes occupy the leading place in the total volume of commercially produced synthetic dyes and are widely used in various branches of industry. On the one hand, azo dyes should be resistant to various oxidants (e.g., under laundering conditions), and on the other hand, their degradation in industrial wastewater treatment is an urgent problem [1]. Also, studies of the behavior of azo dyes in redox processes in the presence of surfactants are topical [2, 3].

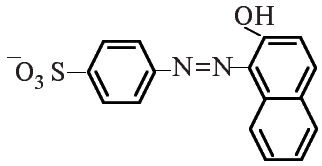
In this study we examined oxidation of commercial azo dyes Direct Red 23, Reactive Red 45, and Orange II with hydrogen peroxide and urea peroxide (hydroperite) in the presence of cationic surfactants alkyldimethylbenzylammonium chloride (Katamin AB) and cetyltrimethylammonium chloride (CTAC) and without them.



C.I. Direct Red 23 **(I)**



C.I. Reactive Red 45 **(II)**



Orange II, Aldrich **(III)**

EXPERIMENTAL

The dyes were purified by recrystallization from ethanol to constant extinction coefficient. At pH 5.9, ε was as follows ($l\,mol^{-1}\,cm^{-1}$): for dye **I**, 34300 (λ_{max} = 496 nm); for dye **II**, 24700 (λ_{max} = 542 nm); and for dye **III**, 22000 (λ_{max} = 484 nm).

Hydrogen peroxide (40% solution) was of chemically pure grade. Hydroperite was synthesized by the procedure described in [4] without adding stabilizers. The hydrogen peroxide content in hydroperite, determined by permanganatometric titration [5], was 35.2%, which corresponded to 97.2% content of $(NH_2)CO\cdot H_2O_2$. The concentrations of peroxides

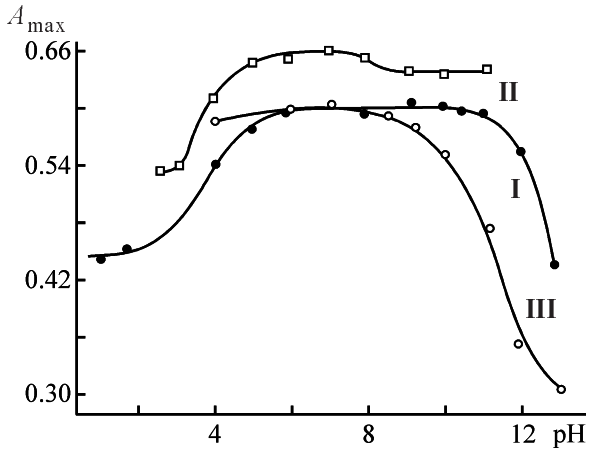


Fig. 1. Optical density A_{max} in absorption maxima of dyes **I**–**III** as a function of pH of solution. Concentration, M: **(I)** 1.75×10^{-5}, **(II)** 2.65×10^{-5}, and **(III)** 2.75×10^{-5}; 298 K.

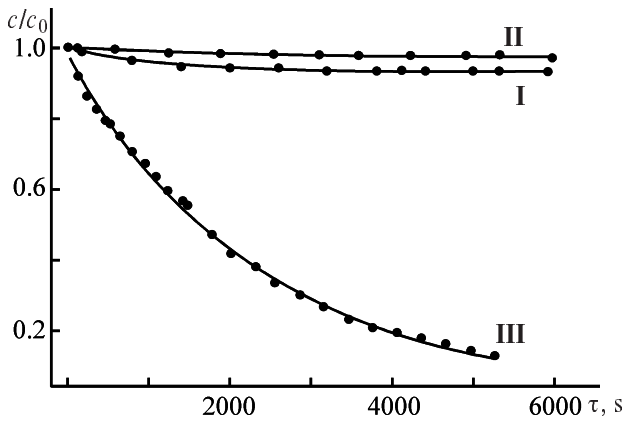


Fig. 2. Kinetic curves of oxidation of azo dyes with hydrogen peroxide. $[H_2O_2]$ = 0.05 M, 298 K, pH 11.0, initial dye concentration 3.3×10^{-5} M. (τ) Time.

are given in terms of H_2O_2.

The concentrations of Katamin AB and CTAC were determined by two-phase titration [6]. The critical micelle concentration (CMC) was determined by the maximal bubble pressure method [5] on a Rebinder installation. For both surfactants, CMC was 9.1×10^{-4} M, in agreement with the published data [7]. All surfactant solutions at the examined temperatures and concentrations were transparent, without apparent turbidity. The metal content of the detergents used, determined by atomic absorption spectroscopy on a Saturn-2 device, was as follows (%): Fe <0.00016, Cu <0.0002, and Ni <0.0002.

The absorption spectra were recorded on KFK-2 and Specord M40 devices. The concentration of the dyes was varied within $(1.6–5) \times 10^{-5}$ M.

Experiments on oxidation of Direct Red 23, Reactive Red 45, and Orange II azo dyes were performed at wavelengths of 490, 540, and 490 nm, respectively. Kinetic curves were analyzed with the OriginPro 6.0 software. The pK values of the azo dyes were determined by the standard procedure of spectrophotometric titration [8]. For azo dyes **I** and **II**, a hypsochromic shift of the electronic spectra in going from neutral to both acidic and alkaline solutions was observed (Fig. 1). For dye **I**, pK_1 3.58±0.15 and pK_2 12.30±0.12; for dye **II**, pK_1 3.81±0.09 and pK_2 8.02±0.21. For dye **III**, pK 11.22±0.11, in agreement with published data [2, 9]. In alkaline solutions, hydroxy and sulfo groups undergo ionization, and in acid solutions, amino and carbonyl groups are protonated [10, 11].

The kinetic curves of the oxidation of azo dyes with hydrogen peroxide are shown in Fig. 2. For all the three azo dyes, the reaction is first-order with respect to the dye. The reaction order with respect to hydrogen peroxide for Orange II dye is also first [12]. Figure 2 shows that the reaction rate is strongly affected by the structure of the azo dye: dye **III** is oxidized fairly readily, whereas dyes **I** and **II** under the reaction conditions are resistant to hydrogen peroxide. This trend was observed in the entire examined pH range (9.5–12.0).

Different resistance of the dyes to hydrogen peroxide is accounted for by their structural state in solution. It is known that dye **III** in aqueous solutions mainly occurs in the hydrazone form [9] and has a quinoid structure. The aromaticity of the quinoid ring is distorted, and this ring is less resistant to oxidants. Azo dye **III** is oxidized especially readily in the deprotonated form in which it occurs in alkaline solutions. It was shown previously that the pH dependence of the rate constant has a pronounced maximum at about 11.2, due to close pK values of hydrogen peroxide and the dye. Dyes **I** and **II** contain a bulky sulfo group in the *o*-position to the azo group. In these compounds, the planarity of the dye molecule is distorted and formation of the quinone hydrazone structure is hindered [10, 11].

In addition, the reaction of dyes **I** and **II** with HO_2^- is hindered by the larger, compared to **III**, number of negatively charged substituents.

Axo dyes **I** and **II** are also very resistant to such a strong oxidant as peracetic acid (PAA). Figure 3 shows the experimental kinetic curves of the oxidation of the dyes with hydrogen peroxide and PAA under similar conditions. Complete decolorization of dye solutions with peracetic acid was attained

only in 5 days. The higher reactivity of dye **I** compared to **II** is due to the presence in **I** of two carbonyl groups decreasing the mobility of the hydrogen atoms of the electron-donor NH_2 and OH groups. As a result, the dye molecule becomes more nucleophilic and more reactive toward PAA as electrophilic agent.

In industry, redox systems with azo dyes often also contain surfactants. Therefore, we examined the influence of surfactants on the behavior of azo dyes in aqueous solutions of various acidities. Experiments were performed in the presence of cationic surfactants Katamin AB and CTAC. It was shown previously that anionic and nonionic surfactants do not affect the oxidation of azo dyes [2].

Additions of Katamin AB in concentrations of $(2–2.5) \times 10^{-4}$ M to Orange II azo dye [$(2–3.5) \times 10^{-5}$ M] at pH 6.0–12.8 lead to aggregation of the dye particles. The resulting suspension of particles gradually settles, and the solution decolorizes. At pH 9.2, the aggregation and sedimentation are slow: In 3 h, the optical density decreased by 10%, and in 24 h, by 40% of the initial level. With an increase in the basicity of the medium and especially in strongly alkaline solutions, the association was faster: At pH 12.7, the optical density decreased by almost 20% in 40 min. At other concentrations of Katamin AB (above and below this interval), in the entire range of pH, aggregation and precipitation of the dye were not observed even in 100–120-h period; with CTAC, they were not observed either.

With dyes **I** and **II**, additions of Katamin AB (1×10^{-4}–2.5×10^{-3} M) in the pH range 8.0–12.5 cause formation of floccules which do not pass into the solution on stirring. The optical density of the dye solutions decreased in 40 min by 7–17% on the average, depending on the surfactant concentration and pH. With an increase in pH of solutions, the aggregation accelerated, probably owing to an increase in the concentration of the deprotonated dye species. Further experiments on the effect of surfactants on the redox processes were performed only with Orange II dye.

We found that the Bouguer–Beer law was observed in the entire examined ranges of pH and surfactant concentrations. The cationic surfactants used exert essentially equal effect on the kinetic parameters of the reaction. The reaction orders with respect to the oxidant (hydroperite) and azo dyes were the same as in the reaction without surfactant. In the presence of a surfactant, the reaction rate

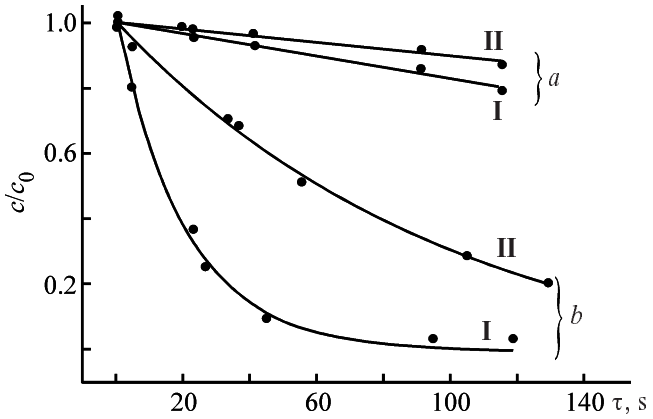


Fig. 3. Kinetic curves of oxidation of dyes **I** and **II** with (*a*) hydrogen peroxide and (*b*) peracetic acid. $[H_2O_2]$ = 0.1 M, $[CH_3COOOH]$ = 0.1 M, 298 K, pH 1.0; solvent 50% acetic acid; initial dye concentration 3.3×10^{-5} M. (τ) Time.

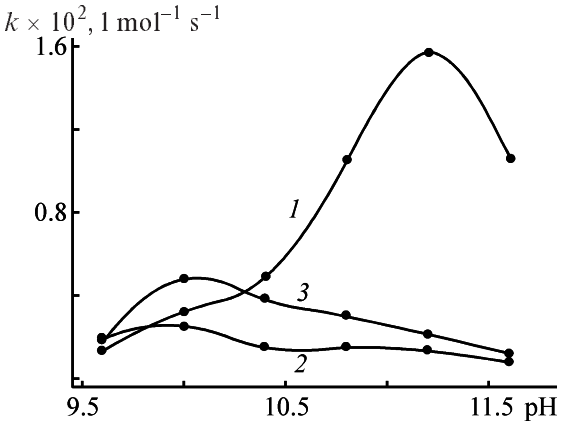


Fig. 4. pH dependence of the rate constant k of oxidation of Orange II azo dye with hydroperite at 298 K. Concentration, M: dye 2×10^{-5} and hydroperide 0.05. Surfactant (1×10^{-3} M): (*1*) none, (*2*) CTAC, and (*3*) Katamin AB.

maximum shifted to pH 10.0, and in the presence of Katamin AB the oxidation rate was slightly higher than without it (Fig. 4).

We found that the surfactant additions did not affect the reactivity of hydroperite: The concentration loss in an alkaline solution (pH 11.2) at room temperature in the presence of 1×10^{-3} M surfactant in 3 h did not exceed 5%. Hence, it can be assumed that the effect of a surfactant on the kinetics of the redox reaction is fully due to its interaction with the dye (Fig. 5). From the electronic absorption spectra of the dye in the presence of a surfactant, we calculated pK_{app} of Orange II dye (see table).

Surfactant additions alter the acid–base properties of the dye owing to formation of a dye–cationic surfactant complex. The apparent constant of for-

Influence of cationic surfactant concentration c on pK_{app} of Orange II dye

CTAC		Katamin AB	
dye : surfactant ratio (c, M)	pK_{app}	dye : surfactant ratio (c, M)	pK_{app}
0	11.22 ± 0.1	0	11.22 ± 0.1
40 : 1 (1×10^{-6})	11.22 ± 0.07	5 : 1 (5×10^{-6})	11.30 ± 0.06
4 : 1 (1×10^{-5})	11.20 ± 0.08	1 : 1 (2.5×10^{-5})	10.79 ± 0.1
1 : 1 (4×10^{-5})	10.84 ± 0.12	1 : 4 (1×10^{-4})	10.37 ± 0.12
1 : 2.5 (1×10^{-4})	10.42 ± 0.1	1 : 20 (5×10^{-4})	10.10 ± 0.07
1 : 6.5 (2.5×10^{-4})	10.05 ± 0.07	1 : 40 (1×10^{-3})	9.99 ± 0.1
1 : 25 (1×10^{-3})	9.96 ± 0.1	1 : 80 (2×10^{-3})	10.05 ± 0.08

mation of the micellar complex can be determined by the equation [13]

$$K_H^{app} = K_H(1 + K_2[M])/(1 + K_1[M]),$$

where $K_H = [HA]/[H^+][A^-]$ (quantity reciprocal to the dye dissociation constant; [HA] and $[A^-]$ are the concentrations of the protonated (acidic) and deprotonated (basic) forms of the dye; M is a surfactant micelle; $K_1 = [M–A^-][M]^{-1}[A^-]^{-1}$; $K_2 = [M–HA] \times [M]^{-1}[HA]^{-1}$; $[M–A^-]$ is the concentration of the micellar complex of a surfactant with the deprotonated form of the dye, and [M–HA] is that of the micellar complex of a surfactant with the protonated form of the dye.

The relationship between K_H^{app} and K_H depends on K_1 and K_2. Cationic surfactants are characterized by high K_a values. With an increase in the cationic surfactant concentration and hence in [M], K_H^{app} increases, and since $K_{app} = 1/K_H^{app}$, pK_{app} decreases, as also does the oxidation rate. This is characteristic of strongly alkaline solutions in which the concentration of the deprotonated form of the dye is high. In more acidic solutions (pH ≤ 10), the reaction rate, on the contrary, slightly increases owing to a decrease in the concentration of the deprotonated dye species interacting with the cationic surfactant.

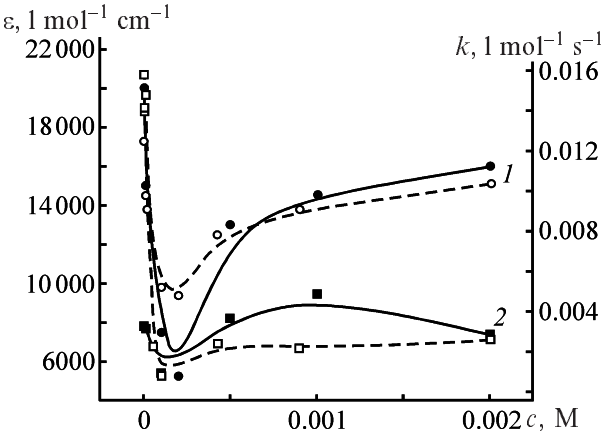


Fig. 5. (*1*) Molar extinction coefficient at λ = 490 nm ε_{490} of Orange II dye and (*2*) rate constant k of the reaction of the azo dye with hydroperite as functions of the Katamin AB concentration c at pH 10 (solid line) and 11.2 (dashed line); hydroperite concentration 0.05 M, 293 K.

CONCLUSIONS

(1) The pK values of Direct Red 23 and Reactive Red 45 azo dyes were determined.

(2) The reactivity of azo dyes in redox processes depends on their chemical structure. Bulky substituents in the *o*-position to the azo group make the dyes resistant to oxidative degradation.

(3) Addition of cationic surfactants leads to the formation of micellar complexes with Orange II dye, to a decrease in its pK_{app}, and, correspondingly, to a decrease in the rate of the dye oxidation in the presence of surfactants in strongly alkaline solutions.

REFERENCES

1. Zubareva, G.I., *Ekol. Prom–st. Ross.*, 2006, no. 2, pp. 8–10.
2. Oakes, J., Gratton, P., and Gordon-Smith, T., *Dyes Pigments*, 2000, vol. 46, pp. 169–180.
3. Menek, N., Eren, E., and Topcu, S., *Dyes Pigments*, 2006, vol. 68, pp. 205–210.
4. USSR Inventor's Certificate no. 320 485.
5. Vol'nov, I.I. and Antonovskii, V.L., *Peroksidnye proizvodnye i addukty karbonatov* (Peroxy Derivatives and Adducts of Carbonates), Moscow: Nauka, 1985.

6. *Poverkhnostno-aktivnye veshchestva: Sintez, svoistva, analiz, primenenie* (Surfactants: Synthesis, Properties, Analysis, Applications), Abramzon, A.A., Ed., Leningrad: Khimiya, 1988.
7. Patlewicz, G.Y., Rodford, R.A., Ellis, G., and Barratt, M.D., *Toxicol. in Vitro*, 2000, vol. 14, pp. 79–84.
8. Bernshtein, I.Ya. and Kaminskii, Yu.L., *Spektrofotometricheskii analiz v organicheskoi khimii* (Spectrophotometric Analysis in Organic Chemistry), Leningrad: Khimiya, 1986, 2nd ed.
9. Oakes, J. and Gratton, P., *J. Chem. Soc., Perkin Trans. 2*, 1998, pp. 1857–1864.
10. Gordon, P.F. and Gregory, P., *Organic Chemistry in Colour*, Berlin: Springer, 1983.
11. Stepanov, B.I., *Vvedenie v khimiyu i tekhnologiyu organicheskikh krasitelei* (Introduction to Chemistry and Technology of Organic Dyes), Moscow: Khimiya, 1984.
12. Volodarskii, M.V., Makarov, S.V., Kozlov, N.A., and Lu, Zh.L., *Izv. Vyssh. Uchebn. Zaved., Khim. Khim. Tekhnol.*, 2007, vol. 50, no. 10, pp. 82–85.
13. Oakes, J. and Gratton, P., *Color. Technol.*, 2003, vol. 119, pp. 91–99.

ISSN 1070-4272, Russian Journal of Applied Chemistry, 2008, Vol. 81, No. 9, pp. 1578–1582. © Pleiades Publishing, Ltd., 2008.
Original Russian Text © A.N. Khomutov, V.N. Klushin, A.V. Nistratov, 2008, published in Zhurnal Prikladnoi Khimii, 2008, Vol. 81, No. 9, pp. 1503–1507.

ORGANIC SYNTHESIS AND INDUSTRIAL ORGANIC CHEMISTRY

Rheological Properties of a Peat–Polymer Paste Used to Obtain High-Strength Granulated Activated Carbons

A. N. Khomutov, V. N. Klushin, and A. V. Nistratov

Mendeleev Russian University of Chemical Engineering, Moscow, Russia

Received January 16, 2008

Abstract—Rheological properties of a peat–polymer paste used for fabrication of high-strength granulated activated carbons were studied. A Tolstoi device was used to obtain dependences of the shear strain of a paste sample on the time of application and removal of a load at shear stresses of 2–60 kPa. These dependences make it possible to choose parameters of the rheological model of the paste and to evaluate its structural-mechanical properties.

DOI: 10.1134/S1070427208090206

Peat-based granulated activated carbons are effective in numerous sorption processes used in environment protection [1]. The most popular in the Russian market are domestic peat-based activated carbons of the SKT brand and activated carbons manufactured by NORIT company (Netherlands). Development of new peat-based activated carbons is a rather promising area in the technology of carbon adsorbents [2].

Peat is a widely occurring, readily available, and inexpensive raw material having the form of a multicomponent system with a complex colloid-chemical composition. It interacts with widely diverse organic and inorganic substances to give structures with pronounced plastic properties [3] which enable effective granulation [4]. An important quality parameter of activated carbons is their wear resistance: technologically, it determines the loss of a sorbent and its service life, and ecologically, affects the environment contamination by dustlike fractions of the sorbent, which commonly contain a wide variety of toxicants. At the same time, the strength characteristics of most of peat-based activated carbons are far from being perfect [4–7].

The technique developed for manufacture of high-strength activated carbons with a developed porous structure uses a formulation produced by mixing a viscous binder (waste thermoplastic polymer) with powdered raw materials of vegetable origin or peat. The formulation is produced in a screw apparatus [8]. The cylindrical grains of activated carbons produced by this technique (diameter 1–5 mm) are characterized at a 30–40% combustion loss by a wear resistance exceeding 95%, total porosity for water of 0.6–0.8 $cm^3 g^{-1}$, and sorption pore volume for benzene of 0.45–0.7 $cm^3 g^{-1}$ [8].

Generally speaking, the term "paste" is not strict. It can be used to name any viscous-elastoplastic (pasty) bodies, irrespective of their structure, composition, and use [9]. Reliable construction of a phenomenological model of the rheological behavior of the paste (macroscopic rheological model) requires a detailed evidence about the structure of the paste and processes occurring therein. At the same time, a knowledge of the macroscopic model of the rheological behavior of a paste can give insight into the type of its structure and processes occurring in it [10]. Phenomenological models of the rheological behavior, developed for numerous materials, make it possible to determine, using various instruments and, in particular, plastometers and viscometers, the optimal conditions of paste molding [10–14]. The molding conditions largely determine the strength properties of granulated activated carbons [6].

The mass fraction of peat in the resulting formulation [8] is many times that of the binder. Such a substance more likely belongs to peat pastes, rather than to filled polymers. The rheological properties of peat are closely related to its chemical composition, its moisture content, and presence of plasticizing additives [3, 14, 15]. Medium-watered peat (of vari-

ous brands) behaves as a Bingham liquid [14], whereas the behavior of peat with lowered moisture content is characterized, until the appearance of plastic deformations, by existence of elastic deformations. Peat with lowered moisture content mostly exhibits elastic and viscoelastic deformations. Peat with a high degree of decomposition tends to manifest plastic deformations to a greater extent than does the high-moor little-decomposed peat [3, 14].

The structure of the peat paste used to produce high-strength activated carbons in the technique suggested in [8] is apparently considerably more complex than that of the known peat pastes not only because both the binder and dispersed phase are multicomponent and the dispersed phase (peat) is a capillary-porous material, but also due to the occurrence of chemical reactions in the paste [8]. Thus, evaluation of the rheological properties of the paste under consideration is exceedingly important both for developing approaches to analysis of its structure and for determining the molding conditions. This evaluation was done using a Tolstoi device [16].

EXPERIMENTAL

Samples of freshly prepared pastes ($50 \times 20 \times 4.8$–5.5 mm) were tested on a Tolstoi plastometer with an IPG-10 mechanical plate shift indicator. A stopwatch served to measure time. The normal component of the load was zero. The tangential stresses in the course of a run were maintained within the range from 2 to 60 kPa. The time of paste keeping under a load was 900 s. The reverse deformations (after removing the load) were also measured during 900 s.

Time dependences of the relative shear strain are shown in Fig. 1. Each dependence is a generalized result of three parallel runs at a relative error of 0.7–0.85%. The general forward (under a constant load) and reverse (after removing the load) runs of the curves indicate that there are reversible and irreversible deformations of the pastes. The reverse deformations are wholly elastic-aftereffect strains (highly elastic strains) obeying the Kelvin model:

$$\Delta\gamma_{rev}(t) = \tau G_{hel}^{-1} \exp[(t_{for} - t)/\theta],$$

where $\Delta\gamma_{rev} = \gamma_0 - \gamma(t)$ is the change in the reverse-run strain; γ_0, maximum strain reached in the course of an experiment under a constant load; $\gamma(t)$, strain by instant of time t; τ, tangential stress; G_{hel}, elastic shear modulus (elasticity modulus in a Kelvin body); θ, delay time. $\theta = \mu/G_{hel}$; μ, viscosity of

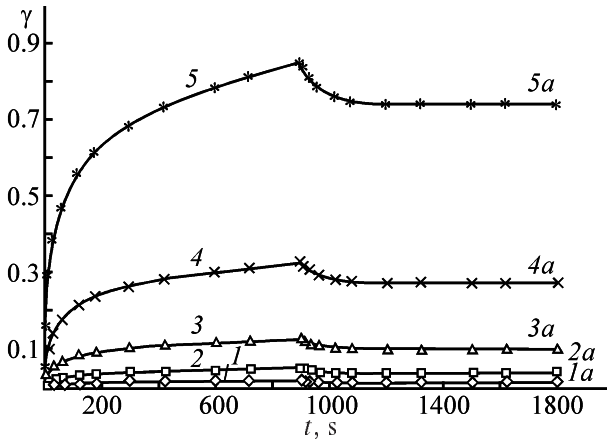


Fig. 1. Shear strain γ vs. time t. Shear stress, Pa: (*1*) 2453, (*1a*) after relieving 2453, (*2*) 4905, (*2a*) after relieving 4905, (*3*) 9810, (*3a*) after relieving 9810, (*4*) 19620, (*4a*) after relieving 19620, (*5*) 39240, and (*5a*) after relieving 39240.

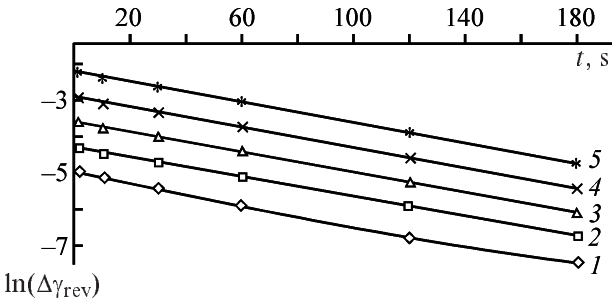


Fig. 2. Dependence of the reverse shear strain γ_{rev} on time t elapsed after relieving the load, plotted in semilog coordinates. Initial shear stress, Pa: (*1*) 2453, (*2*) 4905, (*3*) 9810, (*4*) 19620, and (*5*) 39240.

a Newton element in a Kelvin body (viscosity of the elastic aftereffect); and t_{for}, time of the forward run of a curve (time of paste exposure to a load).

This follows from Fig. 2 which shows dependences of the logarithm of reverse strains, $\ln(\Delta\gamma_{rev})$, on the time elapsed after relieving a constant load. The dependences in Fig. 2 are linear (the corresponding regression equations are given in the table). According to the data in the table, the average values of G_{hel}, θ, and μ are 362650 Pa, 69 s, and 25022920 Pa s, respectively. With account of the data obtained, the contribution of elastic strains $\gamma_{hel}(t)$ under a load can be evaluated by the formula

$$\gamma_{hel}(t) = \tau(362650)^{-1}[1 - \exp(-t/69)].$$

Figure 3 shows time dependences of the forward-run irreversible strains of the pastes, obtained in accordance with the Boltzmann superposition principle [18] by subtracting the forward-run strain of

Regression characteristics of highly elastic and irreversible strains of the paste under study [17]. Equations of the macroscopic rheological model $\ln \Delta\gamma_{rev}(t) = \ln(\tau G_{hel}^{-1}) + (900 - t)/\theta]$, $\ln \Delta\gamma_{irr}(t) = \ln C + \beta \ln \tau + n \ln t$

Shear stress, Pa	Regression equations	Correlation coefficient
2453	$\ln[\Delta\gamma_{rev}(t)] = -0.0145 \ln(900 - t) - 5.0358$	0.9959
4905	$\ln[\Delta\gamma_{rev}(t)] = -0.0140 \ln(900 - t) - 4.3129$	0.9999
9810	$\ln[\Delta\gamma_{rev}(t)] = -0.0144 \ln(900 - t) - 3.6078$	0.9997
19620	$\ln[\Delta\gamma_{rev}(t)] = -0.0145 \ln(900 - t) - 2.9088$	1
39240	$\ln[\Delta\gamma_{rev}(t)] = -0.0146 \ln(900 - t) - 2.2189$	0.9999
2453	$\ln[\Delta\gamma_{irr}(t)] = 0.2190 \ln t - 5.7807$	0.9976
4905	$\ln[\Delta\gamma_{irr}(t)] = 0.2188 \ln t - 4.7915$	0.9995
9810	$\ln[\Delta\gamma_{irr}(t)] = 0.2223 \ln t - 3.8112$	1
19620	$\ln[\Delta\gamma_{irr}(t)] = 0.2219 \ln t - 2.8120$	1
39240	$\ln[\Delta\gamma_{irr}(t)] = 0.2119 \ln t - 1.8140$	1

the Kelvin body from the total strain:

$$\gamma_{irr} = \gamma(t) - \gamma_{hel}(t),$$

where $\gamma_{irr}(t)$ is the irreversible strain by instant of time t, and $\gamma_{hel}(t) = (\tau/G_{vel})[1 - \exp(-t/\theta)]$. It can be seen that the final portions of the forward run of the flow curves are lines with a nearly constant slope.

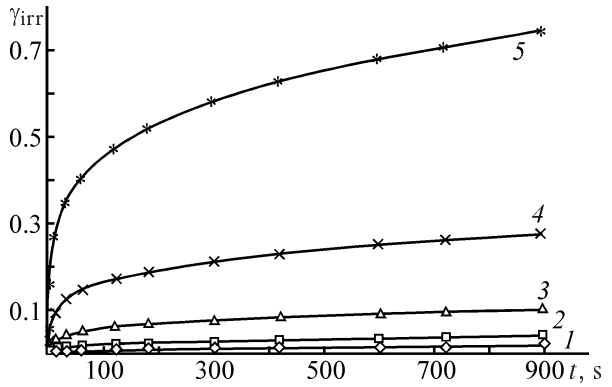


Fig. 3. Irreversible strains γ_{irr} vs. time t. Shear stress (Pa): (*1*) 2453, (*2*) 4905, (*3*) 9810, (*4*) 19620, and (*5*) 39240; the same for Fig. 4.

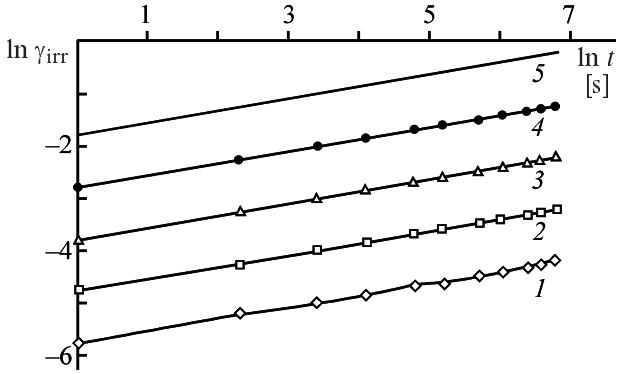


Fig. 4. Dependence of the irreversible strains γ_{irr} on time t, plotted in log–log coordinates.

However, there is no linear relationship between the slope of these portions and the applied load, and the intercepts made on the ordinate axis by straight lines coinciding with the final portions of the flow curves are smaller than the total irreversible strain at any load. Therefore, the irreversible strains are not Newtonian. At a constant load, the curves in Fig. 3 are linearized in logarithmic coordinates (Fig. 4). The corresponding regression equations $\ln[\gamma_{irr}(t)] = n \ln t + b$ are presented in the table.

The ordinate b at zero abscissa is expressed by the formula

$$b = \ln C + \beta \ln \tau$$

where $C = 4.38 \times 10^{-8}$ and $\beta = 1.43$.

The dependence obtained is in agreement with concepts of the creep theory [18, 19], and the creep function of the material under study, $\Phi(\tau, t)$, has the form corresponding to the empirical Nutting equation $\psi(\tau, t) = C\tau^{\beta} t^{p}$ [19–21], which describes the behavior of numerous polymers in the range between the brittle and vitrification points. Thus,

$$\gamma_{hel}(t) = \tau(362\,650)^{-1}[1 - \exp(-t/69)],$$

$$\gamma_{irr}(t) = \psi(\tau, t) = 4.38 \times 10^{-8} \tau^{1.43} t^{0.22}.$$

To estimate the total shear strain of a freshly prepared paste by instant of time t under the action of a constant stress τ, the following equation can be recommended:

$$\gamma(t) = \tau(362\,650)^{-1}[1 - \exp(-t/69)] + 4.38 \times 10^{-8} \tau^{1.43} t^{0.22}.$$

The resulting model of the deformation behavior of pastes enables important practical comparisons and evaluation of the structural-mechanical proper-

ties of the paste. According to the data of [3], the total shear strain γ of water–peat pastes at a tangential stress τ is equal to the sum of the initial (conditionally instantaneous) strain γ_0, elastic-aftereffect strain

$$\gamma_{hel} = \gamma_0 K \log(1 + t),$$

and irreversible plastic strain

$$\gamma_{irr} = (\tau - \tau_s)t/\mu_0,$$

where K is a constant; τ_s, limiting shear stress; and μ_0, plastic viscosity. That is,

$$\gamma = \gamma_0[1 + K\log(1 + t)] + (\tau - \tau_s)t/\mu_0.$$

The model of the rheological behavior of the peat–polymer paste, obtained in the same range of loads, differs from the model of rheological behavior of water–peat pastes in its physical essence and in the contribution of strains of each kind to the total strain. At $\tau < \tau_s = 2000–3000$ Pa, peat behaves as a elastic-viscoelastic body [3] and the paste under study manifests even at these stresses high creep strains whose contribution to the total strain is about 70–80%. At $\tau > \tau_s = 2–3$ kPa, peat flows at a constant viscosity ($\mu_0 = 10^4–10^5$ Pa s), whereas nearly instantaneous pronounced irreversible strains appear ($\Delta\gamma_{irr} = 0.1–0.3$) in the paste under study. Their buildup rate decreases to $(1–2.5) \times 10^{-4}$ s^{-1} during several tens of seconds, and the effective viscosity reaches values of $(1.6–1.9) \times 10^8$ Pa s 50–150 s after the load is applied. The calculated parameter exceeds by 3–4 orders of magnitude the plastic viscosity of peat, is 1–2 orders of magnitude lower than that of molding ceramic masses, and is at about the same level as the viscosity of melts of such polymers as polyethylene, polypropylene, and polystyrene [13]. The elastic modulus G_{hel} is smaller than the same parameter for the ceramic raw material and is the closest to the high-elasticity modulus of polymers within the range between the vitrification and flow points (nearly equal to that of polystyrene at 110–120°C) [13] or to the elasticity modulus of bakery dough [10]. The delay time θ is of the same order of magnitude as that of molding ceramic masses. The experimental plasticity index $p = 0.222$ is almost equal to the same parameter of bitumen–mineral formulations [21].

The deformation behavior of pastes under an external macroscopic load applied to a sample is based on numerous internal physical and colloid-chemical microscopic processes involving separate particles or aggregates of particles in the paste, accompanied by energy accumulation or dissipation [22]. In these two limiting cases of motion of microscopic particles, the plasticity index will be zero and unity, respectively. In the first case, the work of external forces is expended for elastic deformation leading to reversible macroscopic strains. In the second, it is expended for overcoming the internal friction in motion of separate molecules, causing irreversible macroscopic strains. The elastoplastic flow of a number of homogeneous materials (composed of identical particles) is regarded as an intermediate kind of particle motion, and the plasticity index p (power to which time is raised in the Nutting equation) corresponds to the fraction of particles executing the required displacements. The stress can be formally divided into two components causing elastic and plastic deformations. Using this approach, Rudenskii and Rudenskaya [21] suggest the following expressions for evaluating the instantaneous plastic and elastic strains:

$$\gamma_{pl}(t) = t[d\gamma(t)/dt] = p\gamma(t),$$

$$\gamma_{el}(t) = \gamma(t) - t[d\gamma(t)/dt] = (1 - p)\gamma(t).$$

According to Nechiporenko [11], the structural-mechanical type of a paste is determined by the contribution of elastic, viscoelastic, and plastic deformations developed in the paste by the instant of time $t = 1000$ s at a shear stress $\tau = 2 \times 10^6$ Pa. Estimating the contributions of elastic, viscoelastic, and plastic strains under the specified loading conditions yields relative values $\gamma_{el} = 76\%$, $\gamma_{vel} = 2.6\%$, and $\gamma_{pl} = 21.4\%$, and the paste can be attributed on these grounds to the third structural-mechanical type.

Thus, the peat–polymer paste with the above-mentioned rheological properties, intended for production of activated carbons, has, according to [8], a good moldability. In practice, with the process performed in a screw extruder with a torsion moment of 100 N m and rotation rate of 15 rpm, the paste under study can be molded at room temperature to give grains 2–6 mm in diameter. At the same time, molding of grains of about the same size from a paste in manufacture of the SKT carbon requires temperatures exceeding 60°C [23].

CONCLUSIONS

(1) The paste under study is a complex polydisperse system with interacting components; its defor-

mation properties strongly differ from those of the constituent peat and polymer. Concepts of the creep theory can be used to describe the behavior of the paste under static loads.

(2) The suggested rheological model of the paste behavior is a sum of the Kelvin and Nutting equations. The parameters of this model were determined: high-elasticity modulus 3.63×10^5 Pa; delay time 69 s; elastic-aftereffect viscosity 2.50×10^7 Pa s; and Nutting equation constants $C = 4.38 \times 10^{-8}$, $\beta = 1.43$, and $p = 0.222$.

(3) At shear stresses lower than 2–3 kPa, mostly creep deformations are observed in the paste, whereas at higher stresses, substantial irreversible deformations appear and develop with decreasing rate. The dependences of the irreversible strains on the applied stress point to a non-Newtonian type of paste flow with an effective viscosity of $(1.6–1.9) \times 10^8$ Pa s, comparable with that of polymer melts.

(4) The whole set of rheological properties of the paste under study enables its more effective molding, compared with ordinary peat pastes used in the technology of activated carbons.

REFERENCES

1. Jurgen, G., *Die Einsatzgebiete von Torfaktivkohle*, Telma, 1990.
2. Lishtvan, I.I. and Kruglitskii, O.I., *Torf. Prom–st.*, 1991, no. 4, pp. 15–23.
3. Volarovich, M.P., *Kolloid. Zh.*, 1958, no. 3, pp. 361–363.
4. Drozhalina, N.D., Yatsevich, F.S., Bulgakova, N.A., and Zhukov, V.K., *Torf. Prom–st.*, 1988, no. 8, pp. 20–22.
5. Komarov, V.S., Repina, N.S., Rat'ko, A.I., and Tomson, A.E., *Vestsi Nats. Akad. Navuk Bel., Ser. Khim. Navuk*, 2003, no. 2, pp. 12–14.
6. Mukhin, V.M., Tarasov, A.V., and Klushin, V.N., *Aktivnye ugli Rossii* (Activated Carbons of Russia), Moscow: Metallurgiya, 2000.
7. Drozhalina, N.D., *Uglerodnye molekulyarnye sita iz torfa* (Carbon Molecular Sieves Produced from Peat), Minsk: Nauka i Tekhnika, 1978.
8. Khomutov, A.N., Klushin, V.N., and Mukhin, V.M., *Sb. Nauch. Tr. Ross. Khim.-Tekhnol. Univ. im. D.I. Mendeleeva: Usp. Khim. Khim. Tekhnol.*, 2004, vol. 18, no. 6 (46), parts 1, 2, pp. 94–97.
9. *Entsiklopediya polimerov* (Encyclopedia of Polymers), Moscow: Sov. Entsiklopediya, 1974, vol. 2, p. 540.
10. Gus'kov, K.P., Machikhin, Yu.A., Machikhin, S.A., and Lunin, L.N., *Reologiya pishchevykh mass* (Rheology of Food Masses), Moscow: Pishchevaya Prom–st., 1970.
11. Nichiporenko, S.P., *Osnovnye voprosy teorii protsessov obrabotki i formovaniya keramicheskikh mass* (Basic Issues of the Theory of Processing and Molding of Ceramic Masses), Kiev: Akad. Nauk USSR, 1960.
12. Zhensa, A.V., Mathematical Simulation and Optimization of the Extrusion Molding of Water–Oxide Pastes, *Cand. Sci. Dissertation*, Moscow, 2001.
13. Lipatov, Yu.S., *Fizicheskaya khimiya napolnennykh polimerov* (Physical Chemistry of Filled Polymers), Moscow: Khimiya, 1977.
14. Kostyuk, N.S., *Fizika torfa* (Physics of Peat), Minsk: Vysheisha Shkola, 1967.
15. Fedotov, V.A., *Vodno-fizicheskie svoistva torfa* (Aqueous-Physical Properties of Peat), Minsk: Nauka i Tekhnika, 1977.
16. Tolstoi, D.M., *Kolloidn. Zh.*, 1948, no. 10, pp. 133.
17. Kruglitskii, N.N. and Lishtvan, I.I., *Fiziko-khimicheskaya mekhanika guminovykh veshchestv* (Physicochemical Mechanics of Humic Substances), Minsk: Nauka i Tekhnika, 1976.
18. Kachanov, L.M., *Teoriya polzuchesti* (Theory of Creep), Moscow: Nauka, 1960.
19. Bugakov, I.I., *Polzuchest' polimernykh materialov: Teoriya i prilozheniya* (Creep of Polymeric Materials: Theory and Applications), Moscow: Nauka, 1973.
20. Nielsen, L.E., *Mechanical Properties of Polymers and Composites*, New York: Dekker, 1974.
21. Rudenskii, A.V. and Rudenskaya, I.M., *Reologicheskie svoistva bitumov* (Rheological Properties of Bitumens), Moscow: Mosk. Avtodor. Inst., 1971, pp. 8–30.
22. *Rheology. Theory and Applications*, Eirich, F.R., Ed., New York: Academic, 1956, vol. 1.
23. *TR* (Technical Regulation) *6-16-2246–78, Manufacture of Carbons of Sulfurous–Potassium Activation*, Elektrostal: EKhMZ, 1992.

ISSN 1070-4272, Russian Journal of Applied Chemistry, 2008, Vol. 81, No. 9, pp. 1583–1591. © Pleiades Publishing, Ltd., 2008.
Original Russian Text © R.G. Romanova, A.A. Lamberov, Z.I. Shaikhutdinova, Kh.Kh. Gil'manov, R.R. Gil'mullin, 2008, published in Zhurnal Prikladnoi Khimii, 2008, Vol. 81, No. 9, pp. 1508–1516.

ORGANIC SYNTHESIS AND INDUSTRIAL ORGANIC CHEMISTRY

Thermodynamic Parameters of the Single-Stage Dehydrogenation of Isopentane to Isoprene

R. G. Romanova, A. A. Lamberov, Z. I. Shaikhutdinova, Kh. Kh. Gil'manov, and R. R. Gil'mullin

Kazan State Technological University, Kazan, Tatarstan, Russia

Received February 5, 2008

Abstract—From the results of experiments with platinum-containing catalysts operating in the steady mode, adiabatic changes in temperature in the course of 2-metylbutane dehydrogenation to monoolefins and isoprene were calculated. Dehydrogenation of 2-methylbutane and its mixtures with methylbutenes in the 500–600°C temperature range was simulated with varying the concentrations of 2-methylbutane, methylbutenes, hydrogen, and water, the conversion, and the selectivities with respect to both isoprene and methylbutenes. The most suitable reactor designs with intermediate heating of the reaction mixture were suggested.

DOI: 10.1134/S1070427208090218

The development of high-performance catalysts for dehydrogenation of isoalkanes is a priority research field today, because production of synthetic rubbers (including isoprene rubbers) is the most developed branch of petrochemical industry in Russia and other countries [1].

Single-step dehydrogenation of isoalkanes at atmospheric pressure in the presence of bimetallic platinum-containing catalysts is a promising and economically efficient process. This process surpasses in efficiency such existing processes as two-step method of isoprene preparation, one-step procedure of vacuum dehydrogenation of 2-methylbutane, and formaldehyde synthesis of isoprene [2–5]. Significant simplification of the flowsheet due to performing the process in one-step at atmospheric pressure (i.e., without any vacuum installations) is an advantage of this procedure. The catalyst is used in a fixed bed; in so doing, its high selectivity and activity are preserved. Elimination from the process scheme of the first step of dehydrogenation with a highly toxic chromium-containing catalyst will improve the working conditions and reduce the environmental hazard. Up to now, despite a number of advantages, one-stage dehydrogenation at atmospheric pressure using bimetallic catalysts is not used in commercial production. From our viewpoint, this is due to the fact that the one-step process, owing to high endothermic effect, requires supply of significant amount of heat to the reaction zone, which is unfeasible with modern installations.

The aim of this study was to calculate the thermodynamic characteristics of one-stage dehydrogenation of 2-methylbutane to methylbutenes and isoprene and to determine the type of reactor that can be used in this case.

Data on the theoretical yields of dienes in dehydrogenation of paraffin–olefin mixtures at various pressures were presented previously in [6, 7]. However, under the real experimental conditions, the catalyzate composition can strongly differ from the theoretical data for both operation (reactor type, procedures of the reagents and heat-carrier supply, etc.) and chemical (side cracking reactions, isomerization, diene transformations, etc.) reasons. To accomplish the goal of this study, we simulated on the basis of experimental data the dehydrogenation of 2-methylbutane and its mixtures with methylbutenes in a reactor with a fixed bed of platinum–aluminum–zinc catalyst.

The composition of the contact gas from dehydrogenation of isopentane in an isothermal laboratory reactor with a fixed bed of the catalyst that attained the steady operation mode is listed in Table 1. As can be seen, in one cycle of the single-stage dehydrogenation of 2-methylbutane using platinum–aluminum catalyst the yields of isoprene

Table 1. Composition of the contact gas and characteristics of the catalytic activity of bimetallic platinum–aluminum catalyst. Feed: 2-methylbutane, 98.57 wt %

Composition of contact gas and activity characteristics	Dehydrogenation temperature, °C			
	530	560	580	600
Composition, wt %:				
total C_2	0.24	0.53	0.62	0.97
CO_2 (recalculated to carbon)	0.65	1.89	2.51	4.23
total C_3	0.29	0.93	1.29	2.2
total C_4	2.03	4.32	4.91	6.03
2-methylbutane	40.95	31.62	30.91	33.67
n-pentane	1.01	0.13	0.07	0.01
methylbutenes	44.08	45.78	38.55	29.11
n-pentenes	0.82	0.95	0.6	0.28
isoprene	7.88	11.71	16.44	18.64
piperylene	0.45	0.85	1.34	1.31
cyclopentadiene	1.6	1.29	2.76	3.55
Catalytic parameter, wt %:				
yield of isoprene based on starting compound	7.99	11.88	16.68	18.91
yield of isoprene based on converted starting compound	13.68	17.49	24.30	28.72
yield of methylbutenes based on starting compound	44.62	46.34	39.01	29.66
yield of methylbutenes based on converted starting compound	76.33	68.23	56.83	54.66
conversion	58.46	67.92	68.64	65.84

and methylbutenes reach 18 and 40 wt % with the selectivity to unsaturated hydrocarbons of up to 91%.

The choice of the reactor with the fixed catalyst bed is primarily governed by the character of the occurring chemical reactions, determining adiabatic changes in temperature on passing of the feed through the catalyst bed. In this connection, we calculated adiabatic changes in temperature in the reactor for vapor-phase dehydrogenation of 2-methylbutane and its mixtures with methylbutenes.

In the general form, the adiabatic changes in temperature owing to changes in the reaction heat ΔT are determined by the following expression:

$$\Delta T_{ad} = T_{out} - T_{in} = \Sigma \Delta H_i / \Sigma (C_p)_j, \quad (I)$$

where $\Sigma \Delta H_i$ is the sum of thermal effects of chemical reactions occurring in the system (taking into account conversion of the reagent and selectivity to the final products) (kJ mol^{-1}); $\Sigma (C_p)_j$ is the sum of the heat capacities of the components (taking into account conversion of the reagent, selectivity to the final products, and heat capacity of the inert heat carrier fed to the system) (kJ mol^{-1} K^{-1}).

The following reactions occur in the system in the course of isopentane dehydrogenation.

(1) Dehydrogenation of 2-methylbutane to methylbutenes, without taking into account isomerism of the monoolefins:

$$i\text{-}C_5H_{12} \rightarrow i\text{-}C_5H_{10} + H_2. \quad (1)$$

(2) Dehydrogenation of methylbutenes (i-C_5H_{10}) to isoprene, without taking into account isomerism of the monoolefins:

$$i\text{-}C_5H_{10} \rightarrow i\text{-}C_5H_8 + H_2. \quad (2)$$

(3) Dehydrogenation of 2-methylbutane (i-C_5H_{12}) to isoprene:

$$i\text{-}C_5H_{12} \rightarrow i\text{-}C_5H_8 \text{ (isoprene)} + 2H_2. \quad (3)$$

As for thermal calculations the mechanism of a chemical reaction is of no significance, chemical transformation of 2-methylbutane into isoprene can be presented as a combination of reactions (1) and (2) with 2-methylbutane as the starting reactant.

In this case, setting certain values of the total conversion of isopentane $\alpha_{isopentane}$, selectivity of 2-methylbutane dehydrogenation to monoolefins $S_{pentene}$, and selectivity of 2-methylbutane dehydro-

Table 2. Thermodynamic characteristics of components at various temperatures

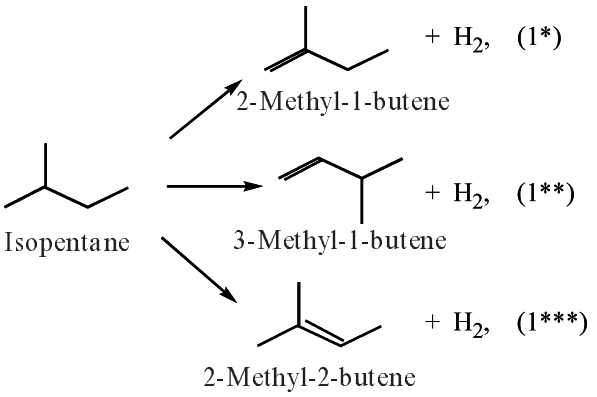
Component	Enthalpy of formation, kJ mol^{-1}	Heat capacity, J mol^{-1} K^{-1}
2-Methylbutane	$6.777\times10^{-5}T^2 - 1.345\times10^{-1}T - 1.206\times10^{2}$	$-1.756\times10^{-7}T^2 + 4.54710^{-4}T - 1.054\times10^{-3}$
2-Methyl-2-butene	$5.242\times10^{-5}T^2 - 1.126\times10^{-1}T - 1.389\times10$	$-1.410\times10^{-7}T^2 + 3.800\times10^{-4}T + 4.248\times10^{-3}$
2-Methyl-1-butene	$5.120\times10^{-5}T^2 - 1.063\times10^{-1}T - 9.285$	–
3-Methyl-1-butene	$4.475\times10^{-5}T^2 - 9.328\times10^{-2}T - 5.188$	–
Isoprene	$3.320\times10^{-5}T^2 - 6.917\times10^{-2}T + 9.326\times10$	$-1.639\times10^{-7}T^2 + 3.707\times10^{-4}T + 9.934\times10^{-3}$
Hydrogen	–	$33.066178 - 11.363417T\times10^{-3} + 11.432816(T\times10^{-3})^2 - 2.772874(T\times10^{-3})^3 - 0.158558(T\times10^{-3})^{-2}$
Water	–	$30.092 + 6.832514T\times10^{-3} + 6.793435(T\times10^{-3})^2 - 2.53448(T\times10^{-3})^3 + 0.082139(T\times10^{-3})^{-2}$

genation to isoprene $S_{isoprene}$, the amount of heat consumed in the course of the chemical reaction can be presented as follows:

$$\Delta H_{rea} = \Delta H_1\alpha_{isopentane}S_{pentene} + \Delta H_3\alpha_{isopentane}S_{isoprene},$$

where ΔH_1 and ΔH_3 are the thrmal effects of reactions (1) and (3) (kJ mol^{-1}), $\alpha_{isopentane}$ is the conversion of 2-methylbutane (fraction of unity), and $S_{pentene}$ and $S_{isoprene}$ are the molar selectivities of 2-methylbutane dehydrogenation to methylbutenes and isoprene (fraction of unity).

Since dehydrogenation of 2-methylbutane yields three major isomers of monoolefins, reaction (1) can be presented as three parallel reactions:



Now, we can identify the thermal effect of the corresponding reactions of 2-methybutane dehydrogenation to monoolefins as ΔH_1^*, ΔH_1^{**}, and ΔH_1^{***} and the selectivity of formation of the corresponding olefins as S_1^*, S_1^{**}, and S_1^{***}, after which we can transform the expression for the amount of heat consumed in dehydrogenation of 2-methylbutane to monoolefins as follows:

$$\Delta H_1^*\alpha_{isopentane}S_{pentene} = \Delta H_1^*\alpha_{isopentane}S_{pentene}S_1^* + \Delta H_1^{**}\alpha_{isopentane}S_{pentene}S_1^{**} + \Delta H_1^{***}\alpha_{isopentane}S_{pentene}S_1^{***}.$$

It should be noted the $S_1^* + S_1^{**} + S_1^{***} = 1$.

Thus, the final expression for calculation of the heat consumed in the course of chemical reactions proceeding in the system can be presented as follows:

$$\Delta H_{rea} = \Delta H_1^*\alpha_{isopentane}S_{pentene}S_1^* + \Delta H_1^{**}\alpha_{isopentane} \times S_{pentene}S_1^{***} + \Delta H_1^{***}\alpha_{isopentane}S_{pentene}S_1^{***} + \Delta H_3\alpha_{isopentane}S_{isoprene}. \quad (II)$$

It should be noted that, in our calculations of the thermal effect of dehydrogenation of methylbutenes to isoprene, we should take into account the thermal effect of isomerization of 2-methyl-2-butene to 2-methyl-1-butene and 3-methyl-1-butene.

Approximation of the second-order equations using the discrete values of the corresponding thermodynamic functions, performed in [8], allowed evaluation of the polynomial dependences of the enthalpies of formation and heat capacities of the system components, which were used in further calculations.

In the case of water and hydrogen, we used higher-order polynomial dependences published on the site of the National Institute of Standards and Technology (NIST, USA) [9], which are listed in Table 2.

Based on the given reaction conditions, a certain amount of water is added into the system to decrease the partial pressure of hydrocarbons and to compensate the endothermic effect of chemical reactions. Taking this fact into account, the heat capacity

Table 3. Thermodynamic characteristics of the system components in one-step dehydrogenation of 2-methybutane to isoprene at 600°C

Characteristic	Value
Enthalpy of formation, kJ mol^{-1}:	
2-methylbutane	–186.37
2-methyl-2-butene	–72.24
2-methyl-1-butene	–63.07
3-methyl-1-butene	–52.52
isoprene	58.18
Heat capacity, kJ mol^{-1} K^{-1}:	
2-methylbutane	0.262
2-methyl-2-butene	0.229
isoprene	0.209
hydrogen	0.0298
water	0.0397
Thermal effect of dehydrogenation to indicated compound, kJ mol^{-1}:	
2-methyl-2-butene	114.1
2-methyl-1-butene	123.3
3-methyl-1-butene	133.9
isoprene	244.6

of the flow at the reactor inlet is an additive quantity comprised of the heat capacities of the reactant (2-methylbutane or its mixture with methylbutenes), water, and excess hydrogen. Since the amount of the heat carrier is often taken as its molar excess with respect to the reagent, the specific heat capacity will be given hereinafter not on the gravimetric but on the molar scale. In this case, the heat capacity of the mixture at the reactor inlet, calculated per mole of 2-methylbutane introduced, can be presented by the expression:

$$(C_p)_{\text{inlet}} = (C_p)_{\text{isopentane}} + K_1(C_p)_{\text{water}} + K_2(C_p)_{\text{hydrogen}},$$

where $(C_p)_{\text{isopentane}}$, $(C_p)_{\text{water}}$, and $(C_p)_{\text{hydrogen}}$ are the molar heat capacities of 2-methylbutane, water, and hydrogen at the working temperature and pressure at the reactor inlet (kJ mol^{-1} K^{-1}), and K_1 and K_2 are the molar excesses of water and hydrogen with respect to 2-methylbutane at the reactor inlet (mole per mole of 2-methylbutane).

The heat capacity at the reactor outlet (or at the outlet from any reactor section) is constituted by the heat capacities of unchanged 2-methylbutane, reaction products (isomeric monoolefins, isoprene, and released hydrogen), and also water and hydrogen added to the system (heat carriers).

Thus, the heat capacity at the reactor outlet (or at the outlet from any reactor section) recalculated per mole of 2-methylbutane introduced can be presented as follows:

$$(C_p)_{\text{outlet}} = (C_p)_{\text{isopentane}}\alpha_{\text{isopentane}} + (C_p)_1^{*}\alpha_{\text{isopentane}} \times S_{\text{pentene}}S_1^{*} + (C_p)_1^{**}\alpha_{\text{isopentane}}S_{\text{pentene}}S_1^{**} + (C_p)_1^{***}\alpha_{\text{isopentane}}S_{\text{pentene}}S_1^{***} + (C_p)_{\text{hydrogen}}\alpha_{\text{isopentane}} \times S_{\text{pentene}}S_1^{*} + (C_p)_{\text{hydrogen}}\alpha_{\text{isopentane}}S_{\text{pentene}}S_1^{**} + (C_p)_{\text{hydrogen}}\alpha_{\text{isopentane}}S_{\text{pentene}}S_1^{***} + (C_p)_{\text{isoprene}} \times \alpha_{\text{isopentane}}S_{\text{isoprene}} + 2(C_p)_{\text{hydrogen}}\alpha_{\text{isopentane}}S_{\text{isoprene}} + K_1(C_p)_{\text{water}} + K_2(C_p)_{\text{hydrogen}}, \quad \text{(III)}$$

where $(C_p)_{\text{isopentane}}$, $(C_p)_1^{*}$, $(C_p)_1^{**}$, $(C_p)_1^{***}$, $(C_p)_{\text{isoprene}}$, $(C_p)_{\text{water}}$, and $(C_p)_{\text{hydrogen}}$ are the molar heat capacities of 2-methylbutane, 2-methyl-1-butene, 3-methyl-1-butene, 2-methyl-2-butene, isoprene, water, and hydrogen at working temperature and pressure at the reaction outlet (kJ mol^{-1} K^{-1}) and K_1 and K_2 are the molar excesses of water and hydrogen with respect to 2-methylbutane at the reactor inlet (mole per mole of 2-methylbutane).

Since the heat capacities of isomeric monoolefins differ insignificantly (within 1%), we used not three but only one value of the heat capacity of 2-methyl-2-butene (major isomer). In this case, expression (III) can be simplified as follows:

$$(C_p)_{\text{outlet}} = (C_p)_{\text{isopentane}}\alpha_{\text{isopentane}} + (C_p)_1^{***}\alpha_{\text{isopentane}} \times S_{\text{pentene}} + (C_p)_{\text{hydrogen}}\alpha_{\text{isopentane}}S_{\text{pentene}} + (C_p)_{\text{isoprene}} \times \alpha_{\text{isopentane}}S_{\text{isoprene}} + 2(C_p)_{\text{hydrogen}}\alpha_{\text{isopentane}}S_{\text{isoprene}} + K_1(C_p)_{\text{water}} + K_2(C_p)_{\text{hydrogen}} = (C_p)_{\text{isopentane}}\alpha_{\text{isopentane}} + (C_p)_1^{***}\alpha_{\text{isopentane}}S_{\text{pentene}} + (C_p)_{\text{isoprene}}\alpha_{\text{isopentane}}S_{\text{isoprene}} + K_1(C_p)_{\text{water}} + (C_p)_{\text{hydrogen}}(\alpha_{\text{isopentane}}S_{\text{pentene}} + 2\alpha_{\text{isopentane}}S_{\text{isoprene}} + K_2). \quad \text{(IV)}$$

The thermodynamic characteristics of the system components at 600°C, determined using the above equations, are listed in Table 3. As seen from these data, the reactions of dehydrogenation of 2-methylbutane to methylbutenes and to isoprene are strongly endothermic are require supply of heat into the reaction zone to maintain the process parameters.

Taking into account the actual experimental

results and the above theoretical reasoning, we simulated the one-step dehydrogenation of isopentane to isoprene in a reactor with a fixed catalyst bed. The dependences of adiabatic changes in temperature in the reactor is shown in Fig. 1 in relation to the dilution with steam and hydrogen under the following reaction conditions: temperature at the reactor inlet 600°C, starting reactant 2-methylbutane, 50% conversion of 2-methylbutane, and 85 and 15% selectivity to monoolefins and isoprene, respectively. The dependences of temperature changes on the dilution of the starting reactant with the heat carrier are described by a sixth-degree polynomial. As seen from Fig. 1, in the absence of the inert heat carriers (such as water and hydrogen), the adiabatic decrease in the temperature at the reaction outlet was 268°C. Water having higher heat capacity as compared to hydrogen is a more efficient heat carrier, which is confirmed by smaller adiabatic cooling at equal reactant : heat carrier ratio in the case of water.

It should be noted that, in dehydrogenation of 2-methylbutane using aluminum–platinum catalysts promoted with tin compounds, addition of hydrogen is necessary for reducing the active component. Under the laboratory conditions, the starting reactant was diluted with hydrogen to 1 : 1 ratio. The calculated data on the adiabatic changes in temperature in dehydrogenation of 2-methylbutane in relation to the water supply at the reactant : hydrogen molar ratio from 1 to 10 are plotted in Fig. 2 using data from Table 3. Under the given conditions (temperature at the reactor inlet 600°C, 50% conversion of 2-methylbutane, and 85 and 15% selectivity to monoolefins and isoprene, respectively), the calculated thermal effect was 845.45 kJ kg^{-1} reactant.

As seen from Table 4, under the laboratory conditions (temperature 600°C, reactant : hydrogen : water molar ratio 1 : 1 : 10, weight ratio 1 : 0.03 : 2.5), the adiabatic decrease in temperature was 89°C. The decrease in temperature within 20°C range (580–600°C is the optimal range for the reaction) can be attained only at dilution of the reactant with steam to 1 : 80 molar ratio (or 1 : 20 weight ratio). Such consumption of steam increases the production cost and decreases the process efficiency. Thus, in this case the use of an adiabatic vessel of the contact type is inappropriate.

One of the ways to solve the problem of strong adiabatic decrease in temperature in the reactor can be recycling, when after separation of isoprene the

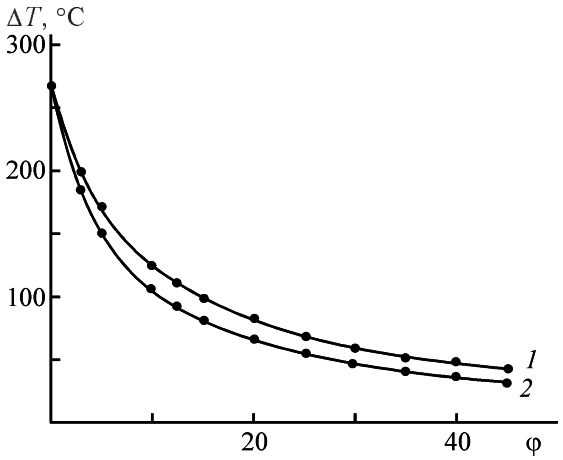


Fig. 1. Adiabatic changes in temperature in the reactor for dehydrogenation of 2-methylbutane to isoprene vs. (*1*) hydrogen : reactant and (*2*) water : reactant ratio. (ΔT) Difference between the temperatures at the reactor inlet and outlet; (φ) component ratio; the same for Fig. 2.

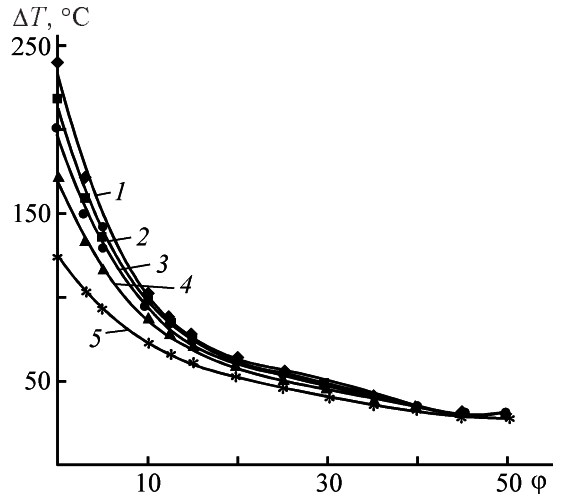


Fig. 2. Adiabatic changes in temperature in the course of 2-methylbutane dehydrogenation as function of the water supply. Reactant : hydrogen ratio: (*1*) 1 : 1, (*2*) 1 : 2, (*3*) 1 : 3, (*4*) 1 : 5, and (*5*) 1 : 10.

contact gas containing 2-methylbutane and methylbutenes is returned to the reactor. In this case, the integral thermal effect can be decreased owing to the conversion of methylbutenes. Simulation of dehydrogenation of mixtures of 2-methylbutane and methylbutenes at various selectivities to isoprene (Table 5) showed that the dilution of 2-methylbutane with methylbutenes decreases the total thermal effect and thus the difference between the temperatures at the reactor inlet and outlet.

As seen from Table 5, the selectivity of the reaction to isoprene also strongly affects the adiabatic

Table 4. Thermodynamic characteristics of 2-methylbutane dehydrogenation at various reactant : hydrogen : water ratios. Temperature 600°C, 50% conversion of 2-methylbutane, 70 and 15 wt % selectivity to methylbutenes and isoprene, respectively

Water : 2-methylbutane molar ratio	Hydrogen : 2-methylbutane molar ratio									
	0 : 1		1 : 1		3 : 1		5 : 1		10 : 1	
	ΔT, °C	ΣC,* kJ K^{-1}	ΔT, °C	ΣC,* kJ K^{-1}	ΔT, °C	ΣC,* kJ K^{-1}	ΔT, °C	ΣC,* kJ K^{-1}	ΔT, °C	ΣC,* kJ K^{-1}
0 : 1	233	3.633	209	4.046	174	4.872	148	5.698	109	7.764
3 : 1	160	5.282	148	5.690	130	6.521	115	7.347	90	9.413
5 : 1	132	6.381	124	6.794	111	7.620	100	8.446	80	10.51
10 : 1	93	9.129	89	9.542	82	10.37	76	11.20	64	13.26
15 : 1	71	11.88	69	12.29	64	13.12	61	13.94	53	16.01
20 : 1	58	14.63	56	15.04	53	15.87	51	16.69	45	18.76
25 : 1	49	17.37	48	17.79	45	18.61	43	19.44	39	21.51
30 : 1	42	20.12	41	20.54	40	31.36	38	22.19	35	24.25
35 : 1	37	22.87	36	23.28	35	24.11	34	24.94	31	27.00
40 : 1	33	25.62	32	26.03	31	26.86	31	27.68	28	29.75
45 : 1	30	28.37	29	28.78	29	29.61	28	30.43	26	32.50
50 : 1	27	31.12	27	31.53	26	32.36	25	33.18	24	35.25

* ΣC is the reduced heat capacity of the flow at the reaction inlet.

Table 5. Thermodynamic characteristics and adiabatic changes in temperature at various selectivities to isoprene and various 2-methylbutane : methylbutenes ratios. Temperature 600°C, 1 : 1 : 10 reactant : hydrogen : water molar ratio, 50% conversion of 2-methylbutane, 30% conversion of methylbutenes, 85, x, and 85 – x wt % selectivities to unsaturated hydrocarbons, isoprene, and olefins, respectively

x, wt %	2-Methylbutane : methylbutenes weight ratio				
	20 : 80	40 : 60	60 : 40	80 : 20	100 : 0
	Adiabatic change in temperature, °C				
5	64	68	72	76	80
10	65	70	75	79	84
15	66	71	77	83	89
20	67	73	80	87	83
25	67	75	83	90	98
30	68	77	85	94	102
	Total thermal effect of dehydrogenation, kJ kg^{-1} reactant				
5	598.4	638.9	679.4	719.9	760.5
10	606.9	655.9	704.9	753.9	803.0
15	615.4	672.8	730.4	787.9	845.5
20	623.9	690.0	755.9	821.9	888.0
25	632.4	706.9	781.4	855.9	930.5
30	640.9	723.9	806.9	889.9	973.0

decrease in the temperature in the reactor. However, it should be noted that the data given in Table 5 were calculated on the assumption that the degree of conversion of 2-methylbutane and methylbutenes are constant and equal to 50 and 30%, respectively. Thus, the total conversion of the mixture of 2-methylbutane and methylbutenes is 80%. At the same time, the real conversions attained in the experiments do not exceed 50%.

The experiments with catalysts that attained the

Table 6. Thermodynamic characteristics and adiabatic changes in temperature at various conversions of 2-methylbutane and methylbutenes. Temperature 600°C, reactants : hydrogen : water molar ratio 1 : 1 : 10, 18 and 67 wt % selectivity to isoprene and olefins, respectively

Conversion, %		2-methylbutane : methylbutenes weight ratio						
isopentane	isopentenes	0 : 100	20 : 80	40 : 60	50 : 50	60 : 40	80 : 20	100 : 0
Adiabatic change in temperature, °C								
0	50	100	79	59	49	39	20	0
10	40	80	67	55	49	42	30	18
20	30	60	55	50	48	46	41	37
30	20	40	43	46	47	49	52	55
40	10	20	31	41	47	52	63	73
50	0	0	19	37	46	55	73	91
Total thermal effect of dehydrogenation, kJ kg^{-1} reactant								
0	50	929.7	743.8	557.8	464.9	371.6	185.9	0
10	40	743.8	630.0	515.9	460.0	402.0	288.1	174.2
20	30	557.8	515.9	474.1	453.1	432.2	390.3	348.7
30	20	371.9	402.0	432.2	447.2	462.3	492.4	522.6
40	10	185.9	288.1	390.3	441.4	492.4	594.6	696.8
50	0	0	174.2	348.4	435.5	522.3	696.8	871.0

Table 7. Thermodynamic characteristics and adiabatic changes in temperature at various conversions of 2-methylbutane at 530–620°C. 2-Methylbutane : hydrogen : water molar ratio 1 : 1 : 12.5, 15 and 70 wt % selectivity to isoprene and methylbutenes, respectively

Process characteristic	2-Methylbutane conversion, %						
	10	20	30	40	50	60	70
Total thermal effect of reactions, kJ kg^{-1} reactants	12.2	24.4	36.6	48.8	61.0	73.2	85.4
Heat capacity of flow, T_{inlet} = 600°C, kJ K^{-1}:							
at reactor inlet	0.788	0.788	0.788	0.788	0.788	0.788	0.788
at reactor outlet	0.574	0.622	0.670	0.719	0.767	0.815	0.864
at indicated T_{inlet}, °C:							
530	16	32	48	64	80	96	112
560	16	31	47	63	79	94	110
580	15	31	46	62	78	93	109
600	15	31	46	62	77	93	108
620	15	31	46	61	77	92	108

steady operation mode showed that, with the supply of methylbutenes, the conversion was about 30%; in this case, the yield of isoprene reached 25–28% (based on the passed reactant), at the selectivity of about 80%. With the mixed reactants (2-methylbutane and methylbutenes), the yield of isoprene (based on the passed reactants) increased by 2–4% as compared to the 2-methylbutane and reached 18 wt %, with the total conversion of 40–50%. Since both 2-methylbutane and methylbutenes participate in the dehydrogenation, the conversion of each component considered separately is indefinite. The calculated thermodynamic characteristics, assuming that conversions of 2-methylbutane and methylbutenes are interrelated, are listed in Table 6. The total conversion of the reactants was taken as 50%, and the conversions of 2-methylbutane and methylbutenes were taken as x and $50 - x$, respectively.

As seen from Table 6, the integral thermal effects of the reactions decrease owing to the dehydrogenation of methylbutenes. As a result, the difference between the temperatures at the reactor inlet and outlet decreases. However, the experimental data show that, despite an increase in the isoprene yield, with increasing content of methylbutenes in the mixture the conversion and selectivity (owing to thermodynamic factors) decrease. Taking into account this fact, it should be noted that in the case of recycling it is advisable to dilute 2-methylbutane with methylbutenes up to 80 : 20–70 : 30 ratio. In this case, the adiabatic decrease in temperature varies within the 20–73°C range depending on the conversion of 2-methylbutane and methylbutenes. The catalytic experiments performed with a mixture containing 70 wt % 2-methylbutane and 30 wt % methylbutenes showed that the content of methylbutenes in the contact gas decreased by 10–12%. Hence, if we consider that the conversion of methylbutenes is 10%, then adiabatic decrease in reactor temperature will be 63 and 52°C for the mixtures containing 2-methylbutane and methylbutenes in the 80 : 20 and 60 : 40 ratios, respectively.

One of the solutions of the problem in hand is the use of a two- or three-reactor system with intermediate heating. These reactors are filled with a catalyst. The starting reactants heated to 450–500°C are fed, along with superheated steam and hydrogen in a certain ratio, to reactor 1, where dehydrogenation proceeds at 580–600°C and the conversion of 2-methylbutane is controlled so that the adiabatic decrease in the temperature in the reactor does not exceed 20–25°C. Then the contact gas from reactor 1 is transferred into a heater, where it is heated to the reaction temperature and then is fed to reactor 2.

The thermodynamic characteristics of 2-methylbutane dehydrogenation depending on the conversion are listed in Table 7. As can be seen, a less than 25°C decrease in temperature can be attained at the conversion of about 15%. Hence, to attain the total conversion of 45–50%, the dehydrogenation should be performed using at least three reactors.

CONCLUSIONS

(1) The calculated adiabatic changes in temperature in the course of dehydrogenation of 2-methylbutane to monoolefins and then to isoprene under the set conditions show that, in the optimal reaction mode, the adiabatic decrease in the reactor temperature is 89°C. The decrease in the temperature within 20–25°C range can be attained only on dilution of the starting reactants with steam to 1 : 80 molar ratio (1 : 20 weight ratio). The consumption of such amount of steam increases the product cost and decreases the process efficiency. Thus, the use of an adiabatic vessel of the contact type is not appropriate in this case.

(2) Simulation of dehydrogenation of a mixture of 2-methylbutane and methylbutenes at various selectivity to both isoprene and methylbutenes showed that the dilution of 2-methylbutane with methylbutenes decreases the total thermal effect and correspondingly the difference in temperatures at the reactor inlet and outlet. Taking into account the real conditions of operation of the aluminum–platinum catalyst, the thermodynamic parameters of the one-step dehydrogenation were evaluated. It was found that, in dehydrogenation of a mixture containing 2-methylbutane (80%) and isopentenes (20%), the adiabatic decrease in the reactor temperature should be 63°C, and for 60 : 40 isopentane : isopentenes mixture this decrease comprises 52°C. Thus, our calculations showed that one of the solutions of the problem of a strong adiabatic decrease in the reactor temperature is recycling, when after separation of isoprene the contact gas containing significant amounts of methylbutenes is returned to the reactor.

(3) A reactor with intermediate heating of the reaction mixture was suggested as the optimal solution. The thermodynamic calculations of the isopentane dehydrogenation at varied degree of conversion showed that the adiabatic decrease in temperature within 25°C can be attained at conversion of about 15% and, thus, to attain the total conversion of 45–50%, the dehydrogenation should be performed using at least three reactors.

REFERENCES

1. Busygin, V.M., Gol'manov, Kh.Kh., Lamberov, A.A., et al., *Katal. Prom–sti.*, 2005, no. 4, p. 41.
2. Buyanov, A.V. and Pakhomov, N.A., *Kinet. Katal.*, 2001, vol. 42, no. 1, p. 72.
3. Kotel'nikov, G.R., Potapov, V.A., Buyanov, R.A., and Bushin, A.N., *Issledovanie i pazrabotka tekhnologii proizvodstva monomerov i sinteticheskikh kauchukov* (Research and Development of Technologies for Production of Monomers and Synthetic Rubbers), Moscow: TsNIITEneftekhim, 1979, p. 11.

4. Pakhomov, N.A. and Buyanov, R.A., *Zh. Prikl. Khim.*, 1997, vol. 70, no. 7, p. 1133.
5. Lyu Kam Lok, Gaidai, N.A., Kiperman, S.M., and Ho Shi Tho-ang, *Kinet. Katal.*, 1995, vol. 36, no. 4, p. 558.
6. Bol'shakov, D.A., Basner, M.E., Shmulevich, E.A., et al., *Neftekhimiya*, 1974, vol. 14, no. 2, p. 180.
7. Kirpichnikov, P.A. et al., *Ravnovesie reaktsii odnostadiinogo degidrirovaniya butana v butadien i izopentana v izopren: Khimiya i tekhnologiya monomerov dlya sinteticheskogo kauchuka* (Equilibria of the One-Step Dehydrogenation of Butane to Butadiene and Isopentane to Isoprene: Chemistry and Technology of Monomers for Synthetic Rubbers), Leningrad: Khimiya, 1981, p. 72.
8. Zhorov, Yu.N., *Termodinamika khimicheskikh protsessov* (Thermodynamics of Chemical Processes), Moscow: Khimiya, 1985.
9. http://www.nist.gov. The National Institute of Standards and Technology (NIST).

ISSN 1070-4272, Russian Journal of Applied Chemistry, 2008, Vol. 81, No. 9, pp. 1592–1597. © Pleiades Publishing, Ltd., 2008.
Original Russian Text © O.N. Nikulicheva, A.P. Krysin, V.P. Fadeeva, 2008, published in Zhurnal Prikladnoi Khimii, 2008, Vol. 81, No. 9, pp. 1517–1522.

ORGANIC SYNTHESIS AND INDUSTRIAL ORGANIC CHEMISTRY

Kinetics of Thermolysis of Sterically Hindered Phenols Used as Polymeric Material Stabilizers

O. N. Nikulicheva, A. P. Krysin, and V. P. Fadeeva

Vorozhtsov Novosibirsk Institute of Organic Chemistry, Siberian Branch, Russian Academy of Sciences, Novosibirsk, Russia

Received February 14, 2008

Abstract—The thermolysis kinetics of a series of sterically hindered phenols was studied.

DOI: 10.1134/S107042720809022X

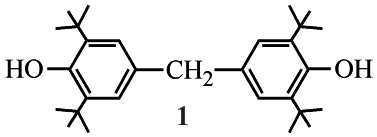
Numerous sterically hindered phenols (SHPs) have been synthesized by now. Many of them exhibit antioxidant properties and are used as additives to polymers to improve their service characteristics.

A theoretical approach to studying the performance of phenolic antioxidants consists in estimating the energy of the homolytic cleavage of the ArO–H bond [1]. These data allow conclusions on the performance of compounds used to prolong the service life of organic materials. For another important field of applied chemistry, reprocessing of stabilized polymeric materials at elevated temperatures, the decisive characeristic is their thermal oxidative degradation. The performance of thermal stabilizers for polymers is usually evaluated empirically or semiempirically [2]. In this case, the major factor is the thermal stability of the potential thermal stabilizers themselves, as it determines the temperature boundary of their applicability to stabilization of specific polymers processed in a definite temperature range.

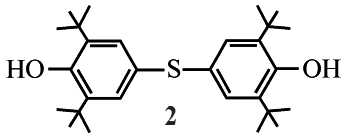
This study continues our previous kinetic studies of thermolysis of SHPs using thermal gravimetric analysis [3–5]. Here we compare the decomposition kinetics studied previously for a series of phenolic antioxidants with the data obtained for certain new compounds, to assess the performance of the new antioxidants relative to those used commercially. To solve the problem of thermal stabilization of polymers on the basis of kinetic data on SHP thermolysis, we examined in succession the following factors: stabilizer structure–thermolysis mechanism–thermal stability of the stabilizer–conditions under which this stabilizer would be the most efficient for thermal stabilization of polymer compounds.

EXPERIMENTAL

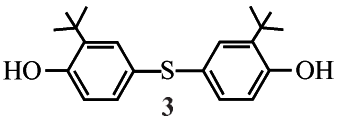
Experiments were performed with a series of compounds in which the alkyl substituents in *o*-positions of phenols, number of sulfur atoms, and structure of acid fragments of esters were varied, but the carbon core was the same (see table and structural formulas below).



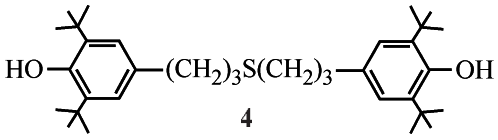
1



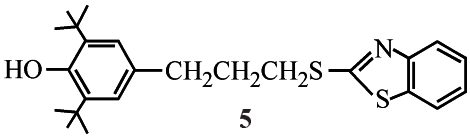
2



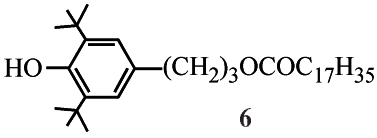
3



4



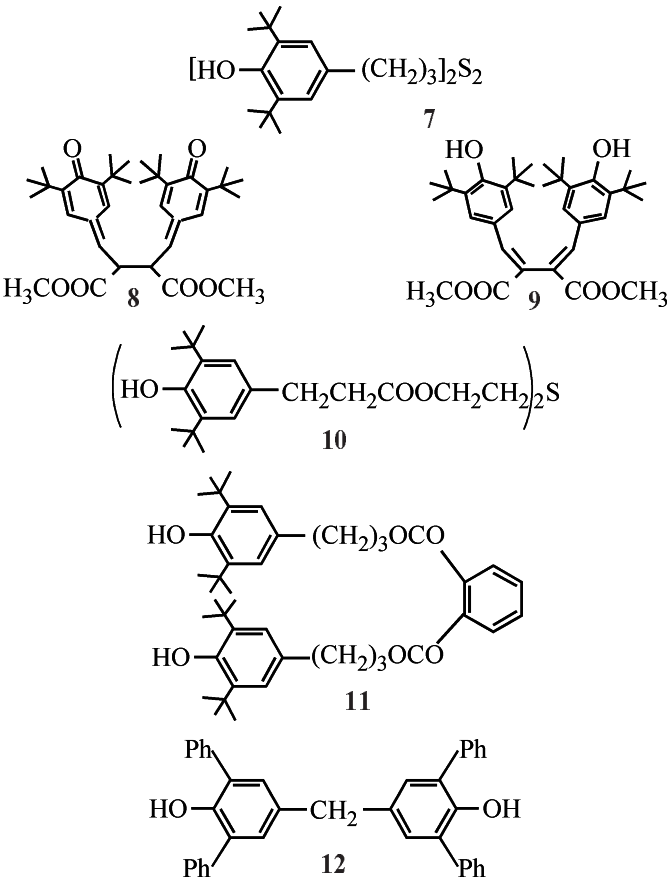
5



6

Sterically hindered phenols, their activation energies E, and preexponential factors Z

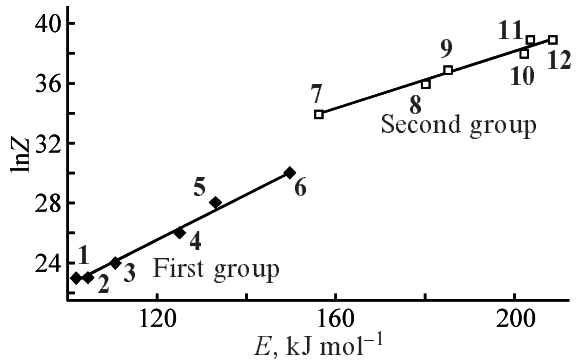
Compound	T_m, °C	E, kJ mol^{-1}	ln Z	Z, s^{-1}
4,4'-Methylenebis[2,6-bis(*tert*-butyl)phenol] (**1**)	140	102	23	1.0×10^{10}
4,4'-Thiobis[2,6-bis(*tert*-butyl)phenol] (**2**)	135	104	23	9.7×10^{9}
4,4'-Thiobis[2-(*tert*-butyl)phenol] (**3**)	110	111	24	3.3×10^{10}
4,4'-Thiobispropyl[2,6-bis(*tert*-butyl)phenol] (**4**)	73	125	26	1.7×10^{11}
4-[3-(2-Benzothiazolylthio)propyl-2,6-bis(*tert*-butylphenol) (**5**)	90	133	28	9.4×10^{11}
3-(3,5-Di-*tert*-butyl-4-hydroxyphenyl)propyl stearate (**6**)	45	150	30	8.1×10^{12}
4,4'-Dithiobispropyl[2,6-bis(*tert*-butyl)phenol] (**7**)	100	156	34	3.4×10^{14}
Dimethyl 2,3-bis[[3,5-bis(*tert*-butyl)-4-oxo-2,5-cyclohexadien-1-ylidene]methyl]butanedioate (**8**)	154	180	36	3.1×10^{15}
Dimethyl 2,3-bis[[3,5-bis(*tert*-butyl)-4-hydroxyphenyl]methylene]butanedioate (**9**)	169	184	37	9.4×10^{15}
3-Thiapentane-1,5-diyl bis[3-[3,5-bis(*tert*-butyl)-4-hydroxyphenyl]propanoate] (Irganox-1035) (**10**)	70	200	39	4.4×10^{16}
Bis[3-(3,5-di-*tert*-butyl-4-hydroxyphenyl)propyl] phthalate (Fenozan-43) (**11**)	98	203	39	5.7×10^{16}
4,4'-Methylenebis(2,6-diphenylphenol) (**12**)	195	208	39	5.2×10^{16}



Some of the compounds are already used in industry as thermal stabilizers. Particular attention was given to known unique thermal stabilizers, Fenozans (Irganoxes) (see table, compounds **10** and **11**) prepared from methyl 3-(3,5-di-*tert*-butyl-4-hydroxyphenyl)propionate (Methylox). These compounds have been successfully used for more than 30 years in thermal reprocessing of polypropylene and for stabilization of shockproof polystyrene and other polymer compounds [6]. The compounds were prepared at the Novosibirsk Institute of Organic Chemistry, Siberian Branch, Russian Academy of Sciences [3] and were characterized by NMR, elemental analysis, and liquid chromatography. The main substance content was no less than 99%.

The experiment was performed on an STA 409 PC Luxx synchronous thermal analyzer (Netzsch) allowing simultaneous recording of the sample weight change and determination of characteristic temperatures and heats of phase transitions. To study the SHP thermolysis kinetics, samples of approximately equal weight (4.0±0.2 mg) were heated in a 85-μl platinum crucible with a lid from 35 to 600°C at heating rates of 3, 5, 10, 15, and 20 deg min^{-1} in a helium atmosphere.

The sample weight loss in the course of heating can be caused by its volatilization (without changes in the chemical structure) or its decomposition into volatile fragments. As shown in [7], those phenolic stabilizers are, as a rule, volatile which have the molecular weight of 400 and lower. Low-volatile 2,6-di-*tert*-butylphenol derivatives at 280–300°C undergo rapid weight loss [3] due to thermal degradation, namely, to de-*tert*-butylation [8, 9] or deeper degradation (breakdown of the carbon core), in accordance with data for related compounds [10–12].



Correlation between the activation energy E and logarithm of the preexponential factor $\ln Z$ for compounds **1**–**12**.

To determine the kinetic parameters of thermolysis of the compounds, we used the known equation for the reaction rate constant [13]

$$k = Z\exp(-E/RT)$$

or

$$\ln k = \ln Z - E/RT,$$

where k is the reaction rate constant (mol min^{-1}); E, apparent activation energy (J mol^{-1}); Z, preexponential factor; T, temperature (K); and R, gas constant (J mol^{-1} K^{-1}).

The kinetic characteristics were calculated from the experimental thermal analysis data. We used the differential method based on the shift of the inflection point of the gravimetric curve at varied heating rate [14]. The activation energies E of the examined compounds and preexponential factors Z, calculated from the experimental data, are given in the table.

With respect to the kinetic parameters E and $\ln Z$, the compounds can be subdivided into two groups forming two straight lines in the plot of E vs. $\ln Z$ (see figure). Such results suggest the occurrence of the so-called compensation effect [15–17]:

$$\ln Z = aE + b.$$

This effect is attributed to analogies in the mechanisms of chemical processes occurring in the course of the experiment with the examined compounds [1, 18]. Subdivision of the stabilizers into two groups with respect to the kinetic characteristics suggests that the mechanisms of the thermal decomposition are similar for the compounds falling on the same straight line but essentially different for compounds of different groups [19, 20].

The products of thermal decomposition of some representatives of these two groups (e.g., compounds **1** and **7**, see table) were examined previously by gas chromatography–mass spectrometry [12, 21]. In thermolysis of compounds **1**–**6** belonging to the first group (see table and figure), initially the limiting step of the decomposition process is de-*tert*-butylation with preservation of the carbon core of the molecule [8, 9]. It is not improbable that the primary event of the process is homolytic cleavage of the ArO–OH bond [1].

The second group includes compounds **7**–**12** (see table and figure) decomposing in thermolysis into coarse reactive fragments. In the course of thermolysis in the bulk of a polymer (at high temperature), these fragments apparently enter into a chemical reaction with polymers, causing the observed significant changes in their physicochemical properties. As a rule, this leads to improvement of the service characteristics of the polymer [22–25]. Such modifying additives after introduction into a polymer and its subsequent heat treatment cannot be recovered from the polymer by extraction [26]. Since there is no principal temperature limit for the use of stabilizers, they can be used in a wide temperature range, 140–350°C. Articles fabricated from a polymer with these stabilizing modifiers have two times longer service life under a deformation load [25].

It should be noted that the assignment of a sample to the first or second group of stabilizers cannot be made solely on the basis of the molecular structure of the SHP and of the temperature at which it starts to decompose in the course of heating.

The results of the studies allow a conclusion that the kinetic characteristics of SHP thermolysis are decisive when the stabilizers are used as additives to polymers. The stabilizers characterized by E = 100–150 kJ mol^{-1} and $Z = 1\times10^{10}$–1×10^{12} s^{-1} can be used as stabilizing additives to organic substances that are not subject to large thermal loads. Stabilizers characterized by high values of the activation energy (>155 kJ mol^{-1}) and preexponential factor (~1×10^{14} s^{-1} and more, see table and figure) can be used both as stabilizing additives and stabilizing modifiers. Their new modifying property is manifested under the conditions of polymer compound reprocessing under harsh conditions. Determination of the applicability fields for each of the new phenolic antioxidants is apparently associated with elucidation of the mechanism of their thermal degradation, because determination of the thermal stability limit

for each antioxidant will allow the proper choice of the temperature and method of processing of a polymer compound with the given stabilizer. For example, in processing of polymeric materials at temperatures below 200°C, for their stabilization and modification it is appropriate to use modifiers with a low thermolysis energy [22, 23]. If higher processing temperatures are required, any modifiers can be chosen [25].

A kinetic study of the thermolysis of methylenequinone **8** and vinylphenol **9** (see table) appeared to be a connecting link between structural studies of oxidation and thermolysis products of (3,5-di-*tert*-butyl-4-hydroxyphenyl)propionic acid esters, on the one hand [10], and of a polymer stabilized with these esters, on the other hand [27]. These studies have the same goal: elucidation of the causes of extremely high performance of Irganoxes (Fenozans) used for stabilizing polypropylene against thermal oxidative degradation when it is processed at very high temperatures (240–270°C). The structure of the modified polypropylene obtained after such heat treatment contains methylenequinone fragments [28]. It became evident that the modification of polypropylene under the heat treatment conditions with Irganox-1035 stabilizer, initially introduced as additive, involves the step of transformation of Irganox-1035 from an additive into a modifier, methylenequinone. The latter, in turn, in the course of thermal decomposition generates radicals [11] reacting with compounds containing double bonds [10], which is confirmed by identification of the products of their reaction with polypropylene [28]. In the course of processing of polyethylene, polystyrene, and rubbers, Irganoxes behave as common stabilizing additives.

The absence of migration of an additive from a polymer into the environment is the decisive property in the choice of a stabilizer for polymeric compounds whose surface is subjected to the action of moisture, light, and heat. Methylenequinone **8** and vinylphenol **9** (see table and figure) showed high performance as additives for protection of polyethylene films from heat and light [28]. The results of commercial tests under the conditions of combined action of heat and seawater on polymer compounds modified with 4,4'-bis(2-*tert*-butyl-4-hydroxyphenyl) disulfide demonstrate high stability of the service properties of the article and absence of migration of the additive from the polymer [23].

CONCLUSIONS

(1) The sterically hindered phenols and their derivatives examined in this study can be subdivided into two groups with respect to the kinetic characteristics. Each group is characterized by a common thermolysis mechanism. Stabilizers with a low activation energy ($\leq$150 kJ mol^{-1}) are widely used as stabilizing additives to polymers. Their thermal degradation starts with de-*tert*-butylation. Stabilizers with the activation energy higher than 155 kJ mol^{-1} act as both stabilizing additives and modifiers. Their modifying properties are manifested only at a definite thermal action on the polymer compound and are associated with the activation energy for each stabilizing modifier.

(2) The group of modifiers consists of phenol derivatives containing chains of sulfur atoms, fragments of 1,2-diphenylethane and 2,3-diphenylsuccinic acid, and, in the case of 2,6-diphenylphenol derivatives, a methylene link. In the course of thermolysis, such compounds decompose into free radicals reacting with each other or with the polymer and thus modify and improve the service properties of the polymer.

REFERENCES

1. Roginskii, V.A., *Fenol'nye antioksidanty: Reaktsionnaya sposobnost' i effektivnost'* (Phenolic Antioxidants: Reactivity and Performance), Moscow: Nauka, 1988.
2. Gladyshev, G.P., Ershov, Yu.A., and Shustova, O.A., *Stabilizatsiya termostoikikh polimerov* (Stabilization of Heat-Resistant Polymers), Moscow: Khimiya, 1979.
3. Krysin, A.P., Nikulicheva, O.N., Fadeeva, V.P., and Chibiryaeva, E.V., Thermal Analysis of Phenolic Stabilizers for Polymeric Materials, *Preprint of the Novosibirsk Inst. of Organic Chemistry, Siberian Branch, Russian Acad. Sci.*, Novosibirsk, 1992.
4. Nikulicheva, O.N., Fadeeva, V.P., and Logvinenko, V.A., *J. Therm. Anal.*, 1995, vol. 44, pp. 329–337.
5. Nikulicheva, O.N., Fadeeva, V.P., and Logvinenko, V.A., *J. Therm. Anal.*, 1996, vol. 47, pp. 1629–1638.
6. Gurvich, Ya.A., Kumok, S.T., Lopatin, V.V., and Storikova, O.F., in *ISSN-700 X*, NIITEKhIM, 1990, no. 5.
7. Holcik, J., Korvas, M., Kassovicova, D., and Durmis, J., *Eur. Polym. J.*, 1976, vol. 12, no. 3, pp. 173–175.

8. Kun, O.B., Nogina, N.I., Ostashevskaya, L.A., et al., *Zh. Org. Khim.*, 1984, no. 12, pp. 2608–2611.
9. Saleh, S.A. and Tashtoush, H.I., *Tetrahedron*, 1998, vol. 54, pp. 14157–14177.
10. Krysin, A.P. and Titova, T.F., *Izv. Sib. Otd. Akad. Nauk SSSR, Ser. Khim.*, 1987, no. 9, issue 6, pp. 140–148.
11. Baartelik, H.J.M., Beulen, J., Bielders, G., et al., *Chem. Ind.*, 1978, no. 15, pp. 586–587.
12. Nikulicheva, O.N., Pokrovsky, L.M., Krysin, A.P., et al., *J. Therm. Anal. Calorim.*, 2000, vol. 60, pp. 157–161.
13. Pavlova, S.A., Zhuravleva, I.V., and Tolchinskii, Yu.I., *Termicheskii analiz organicheskikh i vysokomolekulyarnykh soedinenii* (Thermal Analysis of Organic and Macromolecular Compounds), Moscow: Khimiya, 1983.
14. Ozawa, T., *J. Therm. Anal.*, 1970, vol. 2, pp. 301–312.
15. Balabanov, E.I., Berlin, A.A., Parini, V.P., et al., *Dokl. Akad. Nauk SSSR*, 1960, vol. 134, pp. 1123–1127.
16. Logvinenko, V.A. and Myachina, L.I., *J. Therm. Anal.*, 1980, vol. 19, pp. 45–49.
17. Koga, N. and Tanaka, H., *Thermochim. Acta*, 1988, vol. 135, pp. 79–82.
18. Chew, W. and Harpp, D.N., *J. Org. Chem.*, 1993, vol. 58, pp. 4405–4408.
19. Logvinenko, V.A., Peshevitsky, B.I., and Gegola, O.V., *J. Therm. Anal.*, 1980, vol. 18, pp. 463–468.
20. Nikulicheva, O.N., Fadeeva, V.P., and Logvinenko, V.A., *J. Therm. Anal. Calorim.*, 1999, vol. 55, pp. 47–56.
21. Nikulicheva, O.N., Thermoanalytical and Mass-Spectrometric Methods in Studying the Thermal Stability of Sterically Hindered Phenols, *Cand. Sci. Dissertation*, Novosibirsk, 1999.
22. USSR Inventor's Certificate no. 1735326.
23. USSR Inventor's Certificate no. 1657517.
24. Gavrikova, T.Ya., Belyaeva, L.E., and Krysin, A.P., Abstracts of Papers, *Vsesoyuznaya konferentsiya* (All-Union Conf.), Yaroslavl, 1986, p. 16.
25. USSR Inventor's Certificate no. 1387361.
26. Babayan, V.G., Tarkhanova, G.P., and Baranova, A.S., *Vysokomolekulyarnye i prishivayushchiesya stabilizatory dlya elastomerov* (High-Molecular-Weight and Linking Stabilizers for Elastomers), Moscow: NIITEKhIM, 1981.
27. Volod'kin, A.A., Ershov, V.V., Gorodetskaya, N.N., et al., *Dokl. Akad. Nauk SSSR*, 1976, vol. 227, no. 4, pp. 896–899.
28. Titova, T.F., Krysin, A.P., Rusov, V.P., et al., *Plast. Massy*, 1990, no. 7, pp. 23–25.

ISSN 1070-4272, Russian Journal of Applied Chemistry, 2008, Vol. 81, No. 9, pp. 1597–1601. © Pleiades Publishing, Ltd., 2008.
Original Russian Text © Ya.I. Korenman, E.S. Rudnichenko, E.I. Mel'nikova, S.I. Niftaliev, 2008, published in Zhurnal Prikladnoi Khimii, 2008, Vol. 81, No. 9, pp. 1523–1527.

ORGANIC SYNTHESIS AND INDUSTRIAL ORGANIC CHEMISTRY

Determination of Organic Odor-Producing Substances in a Gas Mixture Using a Multisensor System

Ya. I. Korenman, E. S. Rudnichenko, E. I. Mel'nikova, and S. I. Niftaliev

Voronezh State Technological Academy, Voronezh, Russia

Received May 21, 2008

Abstract—A multisensor system based on an array of weakly selective sensors was used to determine organic odor-producing substances in gas mixture. As modifiers of electrodes of mass-metric piezoelectric resonators served polyethylene glycol esters (succinate, phthalate), tris(hydroxymethyl)aminomethane, *N*-methyl-2-pyrrolidone, polyphenyl ether, sodium nitroprusside, sulfosalicylic and ribonucleic acids, and diphenylcarbazide. For the example of a biotechnological object, true milk solution, visual "patterns" of odor-producing components were constructed. Their type is determined by the sensitivity of the sensors and is independent of the concentration of the substances under study.

DOI: 10.1134/S1070427208090231

A topical practical task of biotechnology, medicine, ecology, and security services consists in identification of odor-producing components of a gas mixture of complex composition. The odor parameters prevail in the general assessment of organoleptic characteristics.

Odor-producing substances, taken separately or in various combinations, form a characteristic odor even when present in minor amounts. The perception of this odor is due to olfactory signals caused by stimulation of nose receptors. Strong olfactory signals are produced by compounds containing the following functional groups: –OH, –CHO, –COOR, –CN, $-NR_2$, –CCl, –CBr, –SR, and –SH; the odor intensity decreases as their number in the composition of an odor-producing substance increases [1].

Lower aliphatic ketones and dicarbonyl compounds are liquids with a pungent odor. When present in small concentrations, acetylmethylcarbinol and diacetyl have a pleasant odor and are important aroma components. Carboxylic acids present in large amounts impart a forage, cheese, and rancid odors, and ethanol gives a characteristic alcoholic odor [1].

Detector devices intended for obtaining information about the qualitative and quantitative composition of an odor are known. At the same time, despite the successful solution of numerous application problems by various physicochemical methods, the only alternative are, frequently, organoleptic determinations based on subjective human perceptions [2].

In this context, an extensive work is being conducted on development of electronic sensors for odor identification [3]. The operation of these devices is based on applying a set of nonselective sensors, with the subsequent processing of their signals by methods employing modern concepts of artificial intelligence. To these methods belong the technique of substance identification by characteristic visual representations ("patterns") [4] specific to a mixture of vapors and that of multiparameter calibrations [5, 6]. In this regard, the promise shown by the method of artificial neuron networks should be noted [7, 8]. Just this approach underlies the present-day development of sensors and new detecting devices, e.g., the "electronic nose." The system is intended for odor recognition [3], its development is stimulated by the desire to simulate and, occasionally, even replace the human olfactory organ [5, 9]. First works aimed to develop a system for odor recognition were carried out in the 1960s; the concept of the "electronic nose" as an intelligent multisensor system was suggested in 1982 and became commonly accepted by the early 1990s [5].

EXPERIMENTAL

The study was carried out in order to identify individual organic odor-producing substances of

Table 1. Determination of odor-producing acids in a true milk solution (according to the chromatogram in Fig. 1a)

Acid	Retention time	Peak area, mV s^{-1}	Peak height, mV	Content, wt %
Acetic	9 min 50 s	2735	228	18.2
Butyric	11 min 32 s	11760	981	78.2
Lactic	14 min 55 s	547	23	3.6
	Σ	15042	1232	100

a biotechnological object, true milk solution obtained by ultrafiltration separation of the curd whey [10].

The main odor-producing components of the true milk solution were identified by high-performance liquid chromatography. The chromatographic conditions were as follows: 300 × 7.8 mm column, Carbo-H + 4 × 3.0 mm protective column, isocratic separation mode, 0.0025 M sulfuric acid as the mobile phase with a flow rate of 0.6 ml min^{-1}, column temperature 60°C, sample volume 20 μl.

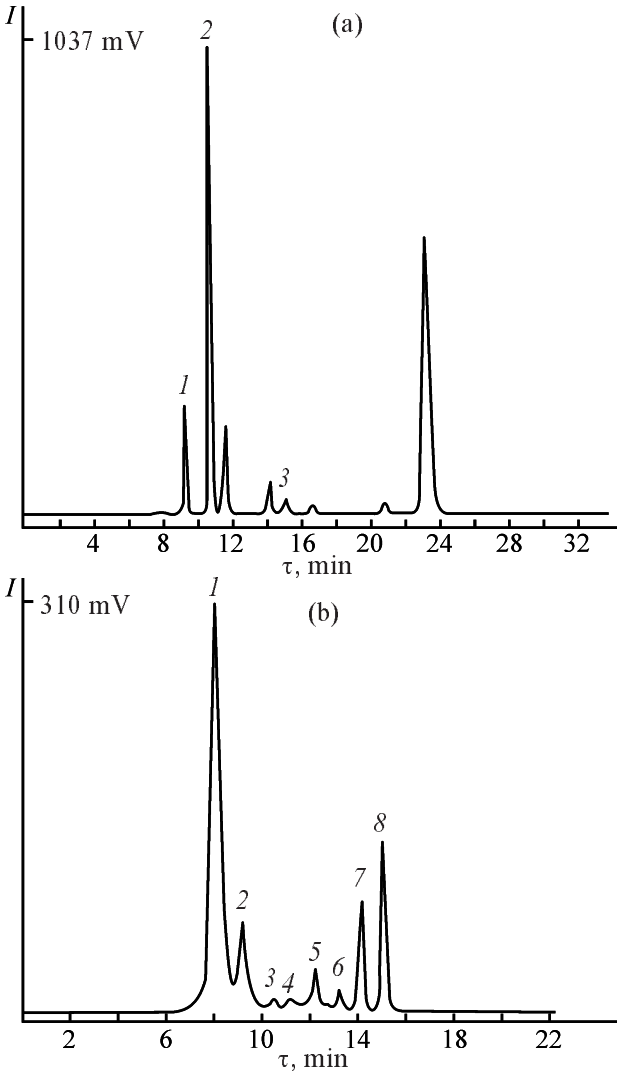


Fig. 1. Chromatogram of a true milk solution. (*I*) Signal intensity and (τ) time. Identified peaks: (a) (*1*) acetic, (*2*) butyric, and (*3*) lactic acids; (b) (*1*) ethanol, (*2*) formaldehyde, (*3*) acetaldehyde, (*4*) methyl acetate, (*5*) diacetyl, (*6*) acetylmethylcarbinol, (*7*) ethyl acetate, and (*8*) ethylal.

Substances of varied nature were identified in the gas phase of a true milk solution: acids (including volatile acetic, butyric, and lactic acids) (Fig. 1a), aldehydes (formaldehyde, acetaldehyde, ethylal), ketones (acetylmethylcarbinol, diacetyl), esters (methyl acetate, ethyl acetate), and ethanol (Fig. 1b). The identified components were quantitatively determined using the internal normalization method (Tables 1, 2).

The multisensor determination of the identified organic substances was performed under static conditions with nine piezoelectric quartz resonators. A system of the non-blow-through type provided that the results obtained were independent of the flow velocity of a sample within the cell. A multisensor detection cell fabricated from stainless steel in the form of a cylindrical vessel with a hermetically screwed cover (with panels for nine sensors circularly arranged) and a replaceable base was used. The cell casing is equipped with three pipes: (i) for sample introduction, (ii) for input of a carrier gas (air) in sorbent regeneration (bringing the sensors to the working state, removing trace amounts of substances remaining after preceding measurements), and (iii) for discharge of the carrier gas. The pipes were hermetically closed with polyurethane gaskets and pressed plugs with threaded junctions. The sensor signals were measured and processed with a nine-channel digital measuring system. The time intervals between recording of the sensor signals were 1 s. The device was connected to a computer via an RS-232 C serial interface.

Of fundamental importance is the choice of a modifier for electrodes of the mass-metric piezoelectric resonator and the optimization of the sorption conditions [11, 12]. As modifiers were studied

Table 2. Determination of odor-producing components in a true milk solution (according to the chromatogram in Fig. 1b)

Acid	Retention time	Peak area, mV s^{-1}	Peak height, mV	Content, wt %
Ethanol	8 min 31 s	6461	269	48.9
Formaldehyde	9 min 18 s	1078	645	8.2
Acetaldehyde	10 min 48 s	49	4	0.4
Methyl acetate	11 min 16 s	49	4	0.4
Diacetyl	12 min 07 s	588	25	4.4
Acetylmethylcarbinol	13 min 44 s	293	12	2.2
Ethyl acetate	14 min 11 s	1762	73	13.3
Ethylal	15 min 13 s	2938	122	22.2
	Σ	13 218	1154	100

the following substances: (1) tris(hydroxymethyl)-aminomethane, (2) *N*-methyl-2-pyrrolidone, (3) polyphenyl ether, (4) sodium nitroprusside, (5) sulfosalicylic acid, (6) ribonucleic acid, (7) diphenylcarbazide, (8) polyethylene glycol succinate, and (9) polyethylene glycol phthalate (digits in parentheses indicate the order of sensor positions in the detecting cell, Fig. 2).

The modifiers studied form thin and thickness-uniform films on the surface of electrodes of a piezoelectric resonator. These films are stable in air (are not oxidized and do not decompose) and are characterized by low volatility, considerable affinity for the sorbate, and mechanical stability (can be used for a large number of measurements on the same film). With these films, low acoustic loss is introduced into the resonant system of the sensor, which is due to use of materials that can form thickness-uniform films with a large elastic modulus on the surface of electrodes of the piezoelectric quartz resonator [10].

The optimal masses of the modifiers providing a significant signal and the minimum determination error are 10–20 μg [13, 14]. At a modifier mass smaller than 10 mg, the response of the modified piezoelectric quartz resonator is at the noise level. If the modifier mass exceeds 20 μg, the damping of oscillations in the modifier film makes lower the signal of the piezoelectric quartz resonator and leads to an increase in the determination error (Table 3).

The sorbent solvents (acetone and water) satisfied the following requirements: chemical inertness toward the sorption phases, absence of stable solvates, volatility, and high solvency.

Prior to measurements, the stability of sensor operation was checked. The stability criterion is a shift of the oscillation frequency by no more than 5 Hz in 1 min. A certain volume of vapors of the equilibrium gas phase of an odor-producing substance was injected into the multisensor detecting cell. The oscillation frequency of the sensors was recorded at intervals of 1 s by the digital measuring system and displayed on the monitor screen. Then the cell and the modifier film was regenerated by purging the system with dried laboratory air.

Substances producing a certain odor are sorbed by the modifier film, and, as a result, the frequency of characteristic oscillations of the modified piezoelectric quartz resonator changes. The analytical signal depends on the affinity of the sorbate and sorbent (determined by their nature), film mass, sorption temperature, and individual parameter of the oscillating system (resonance frequency of quartz, electrode area).

In the static conditions, the sorption of the vapor of the organic substances under study is determined by two main factors: diffusion toward the film surface and interaction with the sorbent [15]. To provide the operation speed, reversibility of sorption–desorption processes, and reproducibility of the analytical signal from the modified piezoelectric quartz resonator, only low-energy intermolecular interactions of the dipole–dipole type or donor–acceptor bonds (including hydrogen bonds) should occur in the sorbate–sorbent system. Polar molecules containing moieties with lone electron pairs (e.g., oxygen in –COOH and –CHO groups), molecules with dipole functional groups (oxygen in ethers, esters, and ketones) in their peripheral parts, and compounds with functional groups in which the electron density is concentrated on one center and is lower on another (alcohols) can exhibit, together

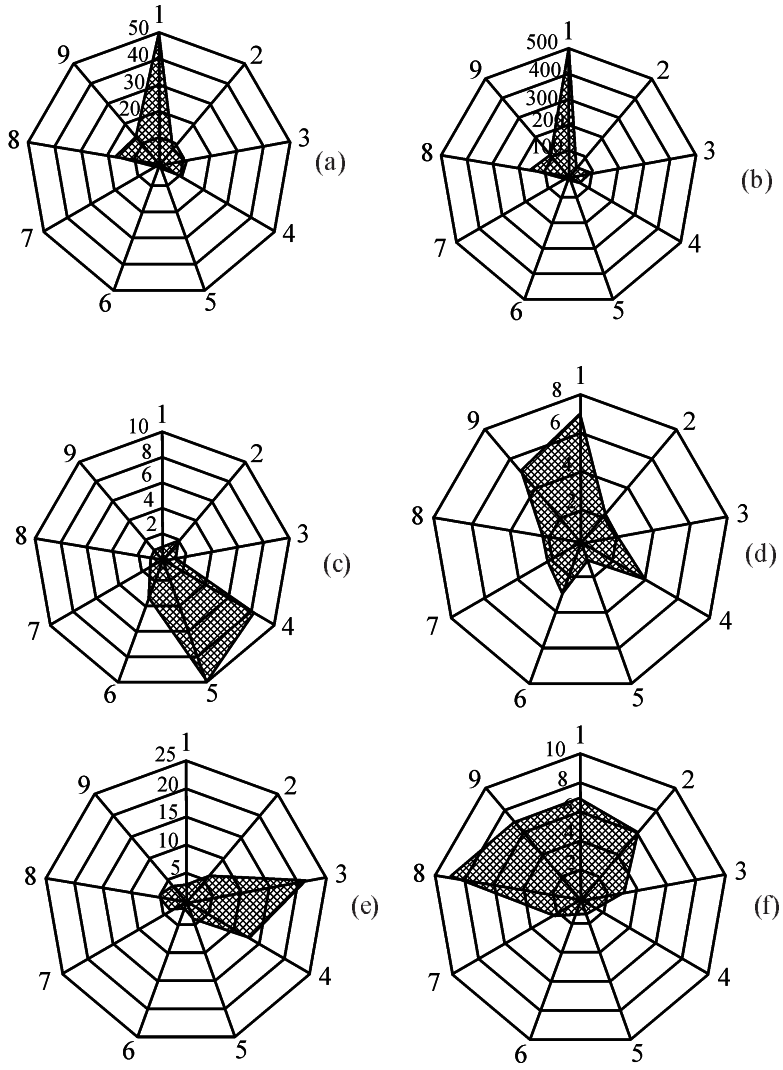


Fig. 2. "Visual patterns" of (a) butyric acid, (b) acetic acid, (c) lactic acid, (d) formaldehyde, (e) ethyl acetate, and (f) ethanol. Circularly arranged digits correspond to the order of sensor positions in the detecting cell.

Table 3. Modifiers of the electrodes of a piezoelectric quartz resonator

Sorbent	Film mass, μg
Tris(hydroxymethyl)aminomethane	9.20
Sodium nitroprusside	9.50
Sulfosalicylic acid	9.89
N-Methyl-2-pyrrolidone	10.01
Polyphenyl ether	11.27
Ribonucleic acid	12.57
Polyethylene glycol succinate	12.61
Diphenylcarbazide	12.96
Polyethylene glycol phthalate	13.55

with universal (nonspecific) intermolecular interactions, also those of directed (specific) type. The contribution of the specific interactions depends on the chemical and geometric structure of the sorbate molecule and sorbent surface and on temperature [16].

Each sensor in the multisystem is low-selective and shows cross sensitivity and selectivity in interaction with odor-producing substances toward which the sensor characteristics are different and linearly independent.

The results of multisensor determination of the odor-producing components of a true milk solution were used to construct "visual patterns" [4], lobe

diagrams of the equilibrium gas phases of individual organic odor-producing substances (Fig. 2). The shape of "visual patterns" is determined by the sensitivity of separate sensors of the multisensor system to organic odor-producing compounds and is independent of the concentration of an individual component.

Separate sensors exposed to vapors of the equilibrium gas phase exhibit the maximum response (analytical signal ΔF, Hz) in the following cases: with tris(hydroxymethyl)aminomethane and polyethylene glycol phthalate for formaldehyde; with tris(hydroxymethyl)aminomethane and polyethylene glycol esters for the alcohols studied; with tris(hydroxymethyl)aminomethane, polyphenyl ether, *N*-methyl-2-pyrroidone, and polyethylene glycol esters for acetic acid; and with polyphenyl ether and sodium nitroprusside for ethyl acetate.

If the mixture simultaneously contains formaldehyde and butyric acid, alcohols studied, or ketones, selective determination of each component is impossible.

The responses of the multisensor system were statistically processed using the method of artificial neuron networks [17, 18].

CONCLUSIONS

The shape of the visual patterns is determined by the sensitivity of separate sensors of the multisensor system toward organic odor-producing substances and is independent of the concentration of an individual component. The axis of the circular diagram corresponds to one of the nine channels of the multisensor system. In the course of sorption, the configuration of the visual pattern varies in accordance with changes in the signals of modified piezoelectric quartz resonators.

REFERENCES

1. Shidlovskaya, V.P., *Organolepticheskie svoistva moloka i molochnykh produktov: Spravochnik* (Organoleptic Properties of Milk and Dairy Products), Moscow: Kolos, 2002.
2. Zhidkov, V.E., *Nauchno-tekhnicheskie osnovy biotekhnologii al'ternativnykh variantov napitkov iz molochnoi syvorotki* (Scientific and Technological Foundation of the Technology of Alternative Variants of Drinks Produced from Lactoserum), Rostov-on-Don: Severo-Kavkazskii Nauchnyi Tsentr, 2000.
3. Kuchmenko, T.A., Method for Piezoelectric Quartz Microweighing in Gas Organic Analysis, *Doctoral Dissertation*, Saratov, 2003.
4. Kuchmenko, T.A., Strigunova, E.Yu., Shlyk, Yu.K., and Korenman, Ya.I., Abstracts of Papers, *Mezhdunarodnyi forum "Analitika i analitiki"* (Int. Symp. "Analytics and Analysts"), Voronezh, 2003, vol. 1, p. 255.
5. Vlasov, Yu.G., Legin, A.V., and Rudnitskaya, A.M., *Datch. Sist.*, 1999, no. 6, pp. 3–9.
6. Krantz-Rulcker, C., Stenbert, M., Winquist, F., and Lundstrom, In., *Anal. Chim. Acta*, 2001, vol. 426, no. 2, pp. 217–226.
7. Gao Da-Oi, *Chem. J. Chim. Univ.*, 1999, vol. 20, no. 10, pp. 1523–1527.
8. Jurs, P. and Bakken, G., *Chem. Rev.*, 2000, vol. 100, no. 7, pp. 2649–2678.
9. Kalach, A.V., Shul'gin, V.A., Yukish, V.A., and Yukish, A.V., *Datch. Sist.*, 2005, no. 7, pp. 51–52.
10. Vorob'eva, L.M., *Zh. Fiz. Khim.*, 1995, vol. 69, no. 4, pp. 668–678.
11. Kuchmenko, T.A., Semenyakina, N.V., and Korenman, Ya.I., *Zh. Prikl. Khim.*, 1999, vol. 72, no. 8, pp. 1285–1292.
12. Kuchmenko, T.A., Lisitskaya, R.P., and Korenman, Ya.I., *Zh. Anal. Khim.*, 2005, vol. 60, no. 2, pp. 198–204.
13. Kuchmenko, T.A., *Primenenie metoda p'ezokvartsevogo mikrovzveshivaniya v analiticheskoi khimii* (Application of the Method of Piezoelectric Quartz Microweighing in Analytical Chemistry), Voronezh: Voronezh. Gos. Tekhnol. Akad., 2001.
14. Kuchmenko, T.A., Korenman, Ya.I., Kudinov, D.A., and Rayakovich, L.V., *Zh. Anal. Khim.*, 2004, vol. 59, no. 12, pp. 1308–1313.
15. Semiokhin, I.A., Strakhov, B.V., and Osipov, A.I., *Kinetika khimicheskikh reaktsii* (Kinetics of Chemical Reactions), Moscow: Mosk. Gos. Univ., 1995.
16. Kiselev, A.V., *Mezhmolekulyarnye vzaimodeistviya v adsorbtsii i khromatografii* (Intermolecular Interactions in Adsorption and Chromatography), Moscow: Vysshaya Shkola, 1986.
17. Kalach, A.V., Korenman, Ya.I., and Niftaliev, S.I., *Iskusstvennye neironnye seti – vchera, segodnya, zavtra* (Artificial Neuron Networks: Yesterday, Today, and Tomorrow), Voronezh: Voronezh. Gos. Tekhnol. Akad., 2002.
18. Filaretov, G.F. and Zhitkov, A.N., *Datch. Sist.*, 1999, no. 5, pp. 2–9.

ISSN 1070-4272, Russian Journal of Applied Chemistry, 2008, Vol. 81, No. 9, pp. 1602–1607. © Pleiades Publishing, Ltd., 2008.
Original Russian Text © N.S. Novikova, E.D. Kilimenchuk, M.Yu. Yarkova, S.B. Meshkova, Z.M. Topilova, 2008, published in Zhurnal Prikladnoi Khimii, 2008, Vol. 81, No. 9, pp. 1528–1532.

ORGANIC SYNTHESIS AND INDUSTRIAL ORGANIC CHEMISTRY

Synthesis and Mesomorphism of 1,3-Benzenedicarboxylic Acid Derivatives

N. S. Novikova, E. D. Kilimenchuk, M. Yu. Yarkova, S. B. Meshkova, and Z. M. Topilova

Bogatskii Physicochemical Institute, National Academy of Sciences of Ukraine, Odessa, Ukraine

Received November 26, 2007

Abstract—4-Methoxy-1,3-benzenedicarboxylic acid esters and 4-(4-hexyloxybenzoylamino)phenyl 1,3-benzenedicarboxylate, each containing five aromatic rings, were synthesized. The influence of the structure of the synthesized banana-like compounds on their mesogenic activity was examined.

DOI: 10.1134/S1070427208090243

Much attention in chemistry of liquid crystals is given to synthesis of molecules having a bent shape, so-called banana-like molecules [1]. Such compounds can form a mesophase with ferroelectric properties and find use as components for liquid crystal displays, increasing their speed. Therefore, revealing a correlation between their structure and mesomorphic properties is a topical problem.

The central fragment of banana-like compounds is most frequently 1,3-disubstituted benzene containing the same or different functional groups. The side fragments include four to six aromatic or heteroaromatic rings linked by bridging groups (ester, azomethine, azoxy, double, or triple bond). Data on preparation of liquid crystal banana-like compounds with the amide linking group are lacking, whereas rodlike mesomorphic aromatic acid amides forming nematic and smectic phases have been reported [2]. There are data on rodlike and discotic liquid crystals forming complexes with lanthanides, e.g., on substituted Schiff bases [3, 4], β-aminovinyl ketones [5, 6], substituted diaza-18-crown-6 ethers [7]; some of such complexes exhibit luminescence properties. Complexes of lanthanides with banana-like liquid crystals have not been studied. The banana-like esters of 1,3-benzenedicarboxylic and 4-bromo-1,3-benzenedicarboxylic acids, described in the literature [8], have the structure that does not allow any complexing activity to be expected.

The goal of this study was to prepare 1,3-benzenedicarboxylic acid esters containing an amide group as the second linking fragment and 4-methoxy-1,3-benzenedicarboxylic acid esters, to examine their mesomorphism, and to evaluate their complexing power toward lanthanides.

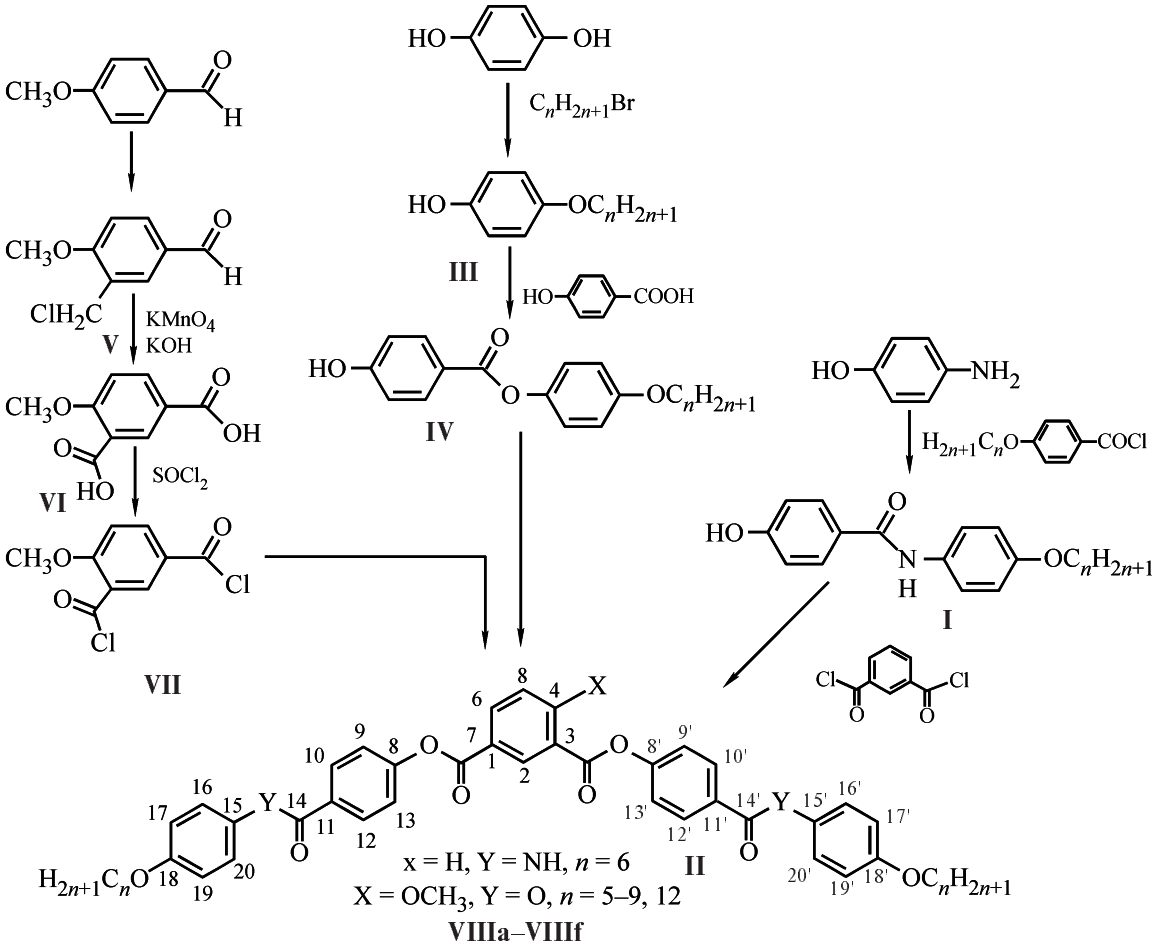
1,3-Benzendicarboxylic and 4-methoxy-1,3-benzenedicarboxylic acid derivatives were prepared by the scheme shown below.

Chlorides of 1,3-benzenedicarboxylic and alkoxybenzoic acids were prepared by the standard procedure [9] in thionyl chloride in the presence of DMF. *N*-(4-Hydroxyphenyl)-4-hexyloxybenzamide **I** was prepared by the modified procedure from [10]. Its structure was proved by mass spectrometry and IR spectroscopy ($\nu_{C=O}$ = 1680 cm^{-1}). 1,3-Bis[4-(4-hexyloxybenzoylamino)phenoxycarbonyl]benzene **II** was prepared in absolute acetone in the presence of triethylamine from isophthaloyl chloride and appropriate phenol **I**. Compound **II** shows no mesomorphic properties, has high melting point, and is very difficultly soluble in the majority of solvents.

Thus, introduction of an amide group as linker into side fragments of bent molecules negatively affects all the characteristics, including the mesogenic power. Therefore, we prepared 4-methoxy-1,3-benzenedicarboxylic acid derivatives containing exclusively ester groups in side fragments.

The starting 4-alkoxyphenols **III** were prepared by the procedure given in [11]. 4-(4-Alkoxyphenoxycarbonyl)phenols **IV** were prepared by esterification in the presence of sulfuric acid in anhydrous benzene [12]. The structures of phenols **IV** were confirmed by IR spectroscopy and mass spectrometry (Table 1).

4-Methoxy-1,3-bis[4-(4-alkoxyphenoxycarbonyl)-phenylene]benzenes **VIII** were prepared from the



corresponding phenols **IV** and 4-methoxy-1,3-benzenedicarbonyl chloride **VII** in absolute benzene in the presence of triethylamine at room temperature. The purity of compounds **VIIIa**–**VIIIf** was proved by thin-layer chromatography, and the structure, by ^{1}H NMR spectroscopy. The mesomorphic properties of the compounds were studied by polarization microscopy. The spectral and mesomorphic characteristics of 4-methoxy-1,3-benzenedicarboxylic acid diesters **VIIIa**–**VIIIf** are given in Table 2.

According to Table 2, compounds **VIIa** and **VIIIb** with short terminal alkoxy groups (n = 5, 6) and the highest homolog (**VIIIf**, n = 12) are nonmesomorphic; with the terminal heptyloxy group (compound **VIIIc**), a monotropic mesophase appears, which becomes enantiotropic for the next homologs **VIIId** and **VIIIe**.

To determine the kind of mesomorphism, along with studying the textures by polarization micros-

Table 1. Physicochemical characteristics of 4-(4-alkoxyphenoxycarbonyl)phenols **IV**

Compound	Yield, %	T_m, °C	IR spectrum, ν, cm^{-1}			M^+
			OH_{ass}	OH_{free}	$C{=}O_{ester}$	
IVa	25	163	3400	3600	1710	299
IVb	27	162	3400	3600	1700	313
IVc	69	167	3400	3600	1710	327
IVd	57	159	3360	3580	1700	341
IVe	53	152	3360	3580	1700	355
IVf	50	97	3360	3580	1705	397

Table 2. Properties of 4-methoxy-1,3-benzenedicarboxylic acid esters **VIIIa–VIIIf**

Compound	Yield, %	Found, %/Calculated, %		Empirical formula	^{1}H NMR spectrum, δ, ppm	Phase transition temperatures,* °C
		C	H			
VIIIa	60	70.7/70.8	6.3/6.2	$C_{45}H_{48}O_{11}$	0.89 t (6H, CH_3), 1.19–1.51 m (8H, CH_2), 1.7–1.86 m (4H, OCH_2CH_2), 3.95 t (4H, OCH_2), 4.07 s (3H, OCH_3), 6.93 d (4H, H-17, 19), 7.12 d (4H, H-16, 20), 7.17 d (1H, H-5), 7.38 d (2H, H-9', 13'), 7.40 d (2H, H-9, 13), 8.27 d (2H, H-10', 12'), 8.29 d (2H, H-10, 12), 8.43, 8.40 d.d (1H, H-6), 8.96 d (1H, H-2)	$Cr \underset{149.4}{\overset{156.6}{\rightleftarrows}} I$
VIIIb	58	71.2/71.4	6.6/6.7	$C_{47}H_{52}O_{11}$	0.88 t (6H, CH_3), 1.18–1.52 m (12H, CH_2), 1.7–1.85 m (4H, OCH_2CH_2), 3.95 t (4H, OCH_2), 4.07 s (3H, OCH_3), 6.94 d (4H, H-17, 19), 7.12 d (4H, H-16, 20), 7.18 d (1H, H-5), 7.38 d (2H, H-9', 13'), 7.40 d (2H, H-9, 13), 8.27 d (2H, H-10', 12'), 8.29 d (2H, H-10, 12), 8.43, 8.40 d.d (1H, H-6), 8.95 d (1H, H-2)	$Cr \underset{150.6}{\overset{153.0}{\rightleftarrows}} I$
VIIIc	64	71.7/71.5	6.8/6.9	$C_{49}H_{56}O_{11}$	0.88 t (6H, CH_3), 1.18–1.52 m (16H, CH_2), 1.7–1.86 m (4H, OCH_2CH_2), 3.95 t (4H, OCH_2), 4.08 s (3H, OCH_3), 6.93 d (4H, H-17, 19), 7.12 d (4H, H-16, 20), 7.18 d (1H, H-5), 7.38 d (2H, H-9', 13'), 7.40 d (2H, H-9, 13), 8.27 d (2H, H-10', 12'), 8.29 d (2H, H-10, 12), 8.43, 8.40 d.d (1H, H-6), 8.95 d (1H, H-2)	$Cr \underset{152.0}{\overset{158.5}{\rightleftarrows}} B_x \underset{156.3}{\rightleftarrows} I$
VIIId	67.5	72.2/72.1	7.1/7.0	$C_{51}H_{60}O_{11}$	0.88 t (6H, CH_3), 1.18–1.52 m (20H, CH_2), 1.7–1.85 m (4H, OCH_2CH_2), 3.95 t (4H, OCH_2), 4.07 s (3H, OCH_3), 6.93 d (4H, H-17, 19), 7.12 d (4H, H-16, 20), 7.18 d (1H, H-5), 7.38 d (2H, H-9', 13'), 7.40 d (2H, H-9, 13), 8.27 d (2H, H-10', 12'), 8.29 d (2H, H-10, 12), 8.43, 8.40 d.d (1H, H-6), 8.95 d (1H, H-2)	$Cr \underset{154.0}{\overset{154.0}{\rightleftarrows}} B_x \underset{167.0}{\overset{167.0}{\rightleftarrows}} I$
VIIIe	63	72.6/72.7	7.3/7.2	$C_{53}H_{64}O_{11}$	0.87 t (6H, CH_3), 1.19–1.53 m (24H, CH_2), 1.7–1.86 m (4H, OCH_2CH_2), 3.95 t (4H, OCH_2), 4.07 s (3H OCH_3), 6.94 d (4H, H-17, 19), 7.12 d (4H, H-16, 20), 7.18 d (1H, H-5), 7.38 d (2H, H-9', 13'), 7.40 d (2H, H-9, 13), 8.27 d (2H, H-10', 12'), 8.29 d (2H, H-10, 12), 8.43, 8.40 d.d (1H, H-6), 8.95 d (1H, H-2)	$Cr \underset{142.8}{\overset{148.0}{\rightleftarrows}} B_x \underset{157.1}{\overset{160.0}{\rightleftarrows}} I$
VIIIf	62	73.7/73.9	7.9/7.8	$C_{59}H_{76}O_{11}$	0.89 t (6H, CH_3), 1.18–1.52 m (36H, CH_2), 1.7–1.86 m (4H, OCH_2CH_2), 3.95 t (4H, OCH_2), 4.07 s (3H OCH_3), 6.93 d (4H, H-17, 19), 7.12 d (4H, H-16, 20), 7.18 d (1H, H-5), 7.38 d (2H, H-9', 13'), 7.40 d (2H, H-9, 13), 8.27 d (2H, H-10', 12'), 8.29 d (2H, H-10, 12), 8.43, 8.40 d.d (1H, H-6), 8.96 d (1H, H-2)	$Cr \underset{146.0}{\overset{146.0}{\rightleftarrows}} I$

* (*Cr*) Solid crystal, (*I*) isotropic liquid, and (B_x) "banana" mesophase.

copy (these textures for **VIIId** resemble a chiral smectic C* phase), we performed an X-ray diffraction study of the liquid crystal phase and differential thermal analysis [13].

In accordance with the X-ray diffraction data, the liquid crystal phase of **VIIId** is smectic, with the interlayer distance decreasing from 45.3 to 43.7 Å on cooling; the inclination angle of molecules relative

to the layer surface reaches 12°–15°.

The thermogram of **VIIId** in the heating and cooling mode is shown in Fig. 1.

The heat of the crystal → mesophase transition (first peak in the heating mode) is 30.2 J g^{-1}, and the heat of the subsequent transition to the isotropic liquid is 12.6 J g^{-1}, which is typical of ordered smectic–isotropic liquid transitions. In the course of cooling, the isotrope → mesophase transition occurs at 159.0°C (17.2 J g^{-1}), and the crystallization (with supercooling), at 141.1°C (33.4 J g^{-1}). The data obtained suggest formation of a "banana" mesophase of modification B_1 or B_2.

We found experimentally that the reaction of a terbium salt with 4-methoxy-1,3-bis[4-(4-dodecyloxyphenoxycarbonyl)phenoxycarbonyl]benzene **VIIIf** yields a complex compound with the luminescence characteristic of Tb(III) ions. The reaction was performed by mixing a solution of terbium trichloride in methanol with a solution of the ligand in benzene. The complex exhibits fairly strong *f–f* luminescence caused by transitions in the Tb(III) ion from the excited $^5D_4$ level to sublevels of the ground ^7F_j level ($j \leq 6$).

Figure 2 shows the luminescence spectrum of the Tb(III) complex with **VIIIf** in which the lanthanide ion, most probably, is coordinated by oxygen atoms of the carbonyl and methoxy groups. The spectrum shows that the most intense luminescence of the Tb(III) ions in its complex with banana-like compound **VIIIf**, as in the majority of other Tb(III) complexes, is observed at 545 nm and is due to the $^5D_4$–$^7F_5$ hypersensitive transition.

EXPERIMENTAL

The ^{1}H NMR spectra of 5–10% solutions of the compounds were recorded on a Varian VXR-300 spectrometer operating at 300 MHz. The mass spectra were taken on an MKh-1321 spectrometer using the direct inlet system at an ionizing electron energy of 70 eV and ionization chamber temperature of 220°C. The IR spectra were recorded on a Specord IR-75 spectrophotometer in $CHCl_3$ solutions and KBr pellets. The luminescence spectra were measured on an SDL-1 spectrometer. The luminescence was excited with a DRSh-250 mercury quartz lamp. The radiation with wavelengths of 313 and 365 nm was cut out with light filters. The purity of the compounds prepared was evaluated by TLC on Silufol UV-254 plates in the 5 : 2 chloroform–acetone sys-

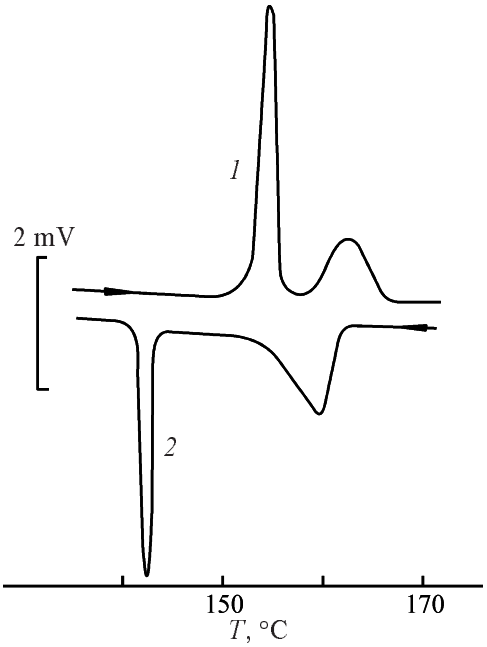


Fig. 1. DSC thermogram of 4-methoxybis-1,3-[4-(4-octyloxyphenoxycarbonyl)phenoxycarbonyl]benzene **VIIId**. (*T*) Temperature. (*1*) Heating and (*2*) cooling.

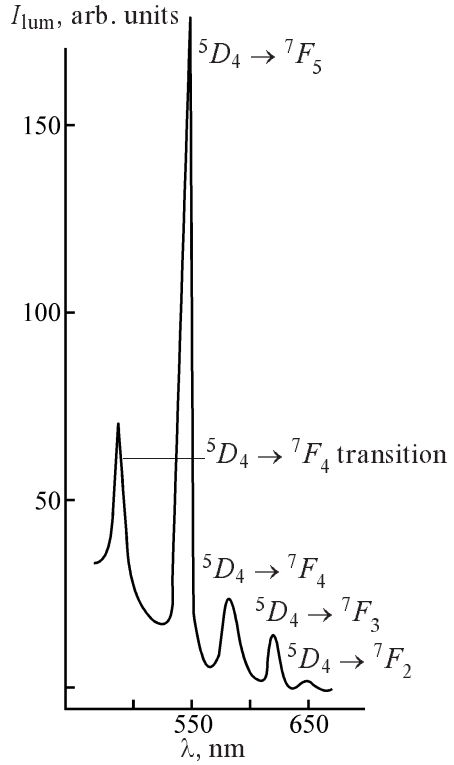


Fig. 2. Luminescence spectrum of the complex of Tb(III) with 4-methoxy-1,3-bis[4-(4-dodecyloxyphenoxycarbonyl)-phenoxycarbonyl]benzene **VIIIf**. $c_{Tb} = 1 \times 10^{-5}$, $c_{Lig} = 1 \times 10^{-4}$ M; 1 : 1.5 methanol–benzene solution. (I_{lum}) Intensity and (λ) wavelength.

tem. The spots were visualized by treatment with potassium ferricyanide and iron(III) chloride solutions. The phase transition temperatures of the compounds were determined by polarization microscopy on POLAM P-312 and Mettler TOLEDO FP 82HT microscopes (heating rate 3 deg min^{-1}).

4-Methoxy-1,3-benzenedicarboxylic acid was prepared in accordance with the procedures described in the literature; mp 270°C; published data [14, 15]: mp 270–271°C. The synthesis procedure and constants of chlorides of *p*-alkoxybenzoic and 1,3-benzenedicarboxylic acids are given in [16, 17]. 4-Dimethoxy-1,3-benzenedicarbonyl chloride (mp 79°C) was prepared in 68.7% yield by the standard procedure [9].

4-Hexyloxybenzoic acid 4-hydroxyanilide I. To a solution of 1.85 g (0.017 mol) of *p*-aminophenol in dimethylformamide (15 ml), 4 g (0.017 mol) of *p*-hexyloxybenzoyl chloride was added dropwise at room temperature. The mixture was left overnight. Then the mixture was poured into water (150 ml). The resulting crystalline precipitate was filtered off and washed with a large amount of cold alcohol. Yield 62%, mp 200–202°C. IR spectrum: $\nu_{C=O}$ 1680 cm^{-1}. Mass spectrum: M^+ 313.

Found, %: C 72.61, H 7.54, N 4.30.

Calculated, %: C 72.84, H 7.35. N 4.47.

1,3-Bis[4-(4-hexyloxybenzoylamino)phenoxycarbonyl]benzene II. To a solution of 0.812 g (0.004 mol) of isophthaloyl chloride in 8 ml of absolute acetone, we added simultaneously in portions 1.7 g (0.017 mol) of triethylamine and 2.6 g (0.0083 mol) of **I**. The mixture was refluxed for 4 h. The precipitate was filtered off, washed with water, and dried; mp 235°C. The compound is insoluble (even on heating) in alcohol, ether, chloroform, and 1 : 1 toluene–heptane mixture. The compound was refluxed in 1 : 1 acetonitrile–chloroform mixture, filtered off while hot, and dried; mp 243°C, yield 89%. IR spectrum, $\nu_{C=O}$, cm^{-1}: 1680, 1700.

Found, %: C 73.27, H 6.51, N 3.57.

Calculated, %: C 73.01, H 6.35, N 3.70.

4-Methoxybis-1,3-[4-(4-alkoxyphenoxycarbonyl)-phenoxycarbonyl]benzenes VIII. To a suspension of 0.0036 mol of phenol **IV** in 8 ml of absolute benzene, we added 0.8 ml of absolute triethylamine, after which we added dropwise a solution of 0.42 g (0.0018 mol) of chloride **VII** at 15°C and left at room temperature for 12 h. After the reaction completion (TLC monitoring), the suspension was poured onto a water (25 ml)–ice (25 g) mixture, carefully acidified with hydrochloric acid, and extracted first with ether (3 × 20 ml) and then with chloroform (3 × 20 ml). The extracts were washed with water to pH 7 and dried with anhydrous magnesium sulfate and calcium chloride. The solvents were removed under reduced pressure. The ether extract contained unchanged starting phenol **IV**. The residue after removing chloroform was recrystallized two times from a 4 : 1 alcohol–benzene mixture.

CONCLUSIONS

(1) Introduction of an amide group into side fragments of banana-like 1,3-benzenedicarboxylic acid esters leads to compounds showing no mesomorphism.

(2) Banana-like mesomorphic esters of 4-methoxy-1,3-benzenedicarboxylic acid were prepared. Their mesomorphic properties depend on the length of the terminal substituent, with the trend being similar to that observed for rodlike liquid crystals. Disappearance of the mesomorphism in the highest homolog with the terminal dodecyloxy group is due to twisting of the alkyl chain, which favors ordered packing of the molecules in a layer.

(3) The banana-like 4-methoxy-1,3-benzenedicarboxylic acid esters can be used as ligands for preparing a luminescent complex with the Tb(III) ion.

REFERENCES

1. Pelzl, G., Diele, S., and Weissflog, W., *Adv. Mater.*, 1999, vol. 11, no. 9, pp. 707–724.
2. Vora, R.A. and Gupta, R., *Mol. Cryst. Liq. Cryst.*, 1981, vol. 67, pp. 215–220.
3. Binnemans, K. and Lodewyckx, K., *Angew. Chem.*, 2001, vol. 40, no. 1, pp. 242–244.
4. Galametdinov, Yu.G., Haase, W., Malykhina, L., et al., *Chem. Eur. J.*, 2001, vol. 7, no. 1, pp. 99–105.
5. Turanova, O.A., Galyametdinov, Yu.G., and Ovchinnikov, I.V., *Izv. Ross. Akad. Nauk, Ser. Khim.*, 2001, no. 5, pp. 771–773.
6. Turanova, O.A., Turanov, A.N., Ovchinnikov, I.V., et al., *Koord. Khim.*, 2005, vol. 31, no. 10, pp. 796–800.
7. Suarez, S., Mamyla, O., Imbert, D., et al., *Chem. Commun.*, 2003, pp. 1226–1227.
8. Dehne, H., Potter, S., Sokolowski, S., et al., *Liq. Cryst.*, 2001, vol. 28, no. 8, pp. 1269–1277.

9. Weygand–Hilgetag, *Organisch-chemische Experimentierkunst*, Leipzig: Barth, 1964, 3rd ed.
10. Betnev, A.F., Abukhova, T.A., Budanov, N.A., et al., *Zh. Org. Khim.*, 1998, vol. 34, no. 1, pp. 99–102.
11. Platonova, V.A., Etingen, N.B., Petrova, G.S., et al., *Reakt. Osobo Chist. Veshch.*, 1975, no. 1, p. 27.
12. Aggarval, S.K., Bradshow, J.S., and Educhi, M., *Tetrahedron*, 1987, vol. 43, pp. 451–462.
13. Novikova, N.S., Kilimenchuk, E.D., Tolochko, A.S., et al., Abstracts of Papers, *XV Conf. on Liquid Crystals*, Zakopane, October 13–17, 2004, p. 79.
14. Quelet, R. and Allard, J., *C. R. Acad. Sci. Paris*, 1937, vol. 205, pp. 238–240.
15. Aroyan, A., *Izv. Akad. Nauk Arm. SSR*, 1962, vol. 15, no. 2, pp. 157–161.
16. Ukrainian Patent 5633.
17. Novikova, N.S., Kondrat'eva, R.V., Maksimenko, S.I., and Koval'chuk, B.A., *Dopov. Nats. Akad. Nauk Ukr.*, 2007, no. 5, pp. 138–144.

ISSN 1070-4272, Russian Journal of Applied Chemistry, 2008, Vol. 81, No. 9, pp. 1608–1611. © Pleiades Publishing, Ltd., 2008.
Original Russian Text © P.V. Plotnikova, O.L. Vlasova, A.R. Groshikova, O.A. Pisarev, E.F. Panarin, 2008, published in Zhurnal Prikladnoi Khimii, 2008, Vol. 81, No. 9, pp. 1533–1536.

MACROMOLECULAR CHEMISTRY AND POLYMERIC MATERIALS

Influence of the Molecular Weight and Structural Organization of Cationic Polyelectrolytes on Protein Flocculation

P. V. Plotnikova, O. L. Vlasova, A. R. Groshikova, O. A. Pisarev, and E. F. Panarin

St. Petersburg State Polytechnic University, St. Petersburg, Russia
Institute of Macromolecular Compounds, Russian Academy of Sciences, St. Petersburg, Russia

Received July 14, 2008

Abstract—A complex on-line procedure based on combined use of integral (spectroturbidimetry) and differential (nephelometry) light scattering methods was applied to studying the size and formation kinetics of dispersed particles in solutions containing a protein and synthetic cationic soluble polymers. The influence of pH of the medium and of the molecular weight and structural organization of polymers on the floccule size and flocculation kinetics was evaluated.

DOI: 10.1134/S1070427208090255

Native solutions of target biologically active substances (BASs) obtained after separation of mycelium from the culture broth are complex systems containing dissolved organic and inorganic impurities, colloidal particles, and suspended matter. Therefore, preparation of target products of a microbiological synthesis involves preconcentration and purification of native solutions. The extraction procedures used for this purposes involve large volumes of organic solvents (acetone, methylene chloride, butyl acetate), which makes them environmentally hazardous and leads to considerable loss of the target products [1].

Today the stability of biological liquids is controlled with water-soluble polymers of various structures, whose very small additions strongly affect the stability. Most frequently, the flocculation method is used [2]. The development of efficient flocculation procedures for biotechnology requires the development of synthetic procedures and study of properties of new soluble polymers, and also examination of molecular mechanisms of their interaction with BAS.

In this study we examined how the molecular weight and structural organization of new cationic soluble polyelectrolytes based on poly-*N,N,N,N*-trimethylmethacryloyloxyethylammonium methyl sulfate (SMS) on the floccule size and flocculation kinetics of a protein (bovine serum albumin, BSA, MW 65000 Da, pI 4.8). BSA was used as a model of impurity proteins present in native solutions of target BASs. This choice is governed by the fact that the majority of impurity proteins present in native solutions of antitumor and antibacterial antibiotics have molecular weights M 25000 Da and isoelectric points pI $\leq$ 5.5 [3].

EXPERIMENTAL

As flocculants we used cationic water-soluble polymers of various molecular weights and structural organizations, synthesized at the Institute of Macromolecular Compounds, Russian Academy of Sciences (see table). BSA was purchased from Biokhimreaktiv (now Biolar, Olaine, Latvia).

Five concentrations of flocculants (0.5, 1, 2.5, 5, 6 mg l^{-1}) were used. The BSA concentration was 1 mg ml^{-1} in all the experiments. Studies were performed in a 0.3 M ammonium acetate solution, which is an adequate model of the inorganic composition of native solutions of antibiotics.

After mixing solutions of the protein and polymer and vigorous stirring, the system became more turbid, and then the resulting insoluble complex precipitated and the solution became colorless.

The optical density of the solutions was measured on an SF-46 spectrophotometer. From the spectroturbidimetric data we calculated the wave exponent by the formula

$$n = -\partial \log \tau / \partial \log \lambda, \quad (1)$$

where n is the wave exponent; τ, turbidity of the system; and λ, incident light wavelength.

Characteristics of cationic polymers

Sample no.	Polymeric unit (polymer type)	$M \times 10^{-6}$, Da	Cationic charge, mg-equiv g^{-1}
1	Homopolymer of *N,N,N,N*-trimethylmethacryloyloxyethylammonium methyl sulfate (SMS linear)	25.5	3.5
2	Homopolymer of *N,N,N,N*-trimethylmethacryloyloxyethylammonium methyl sulfate (SMS linear)	3.1	3.5
3	Homopolymer of *N,N,N,N*-trimethylmethacryloyloxyethylammonium methyl sulfate (SMS branched)	14.0	3.5

The wave exponent is a parameter characterizing variation of the particle size. A decrease in n is indicative of an increase in the size of dispersed particles in the system [4–6]. Preliminary experiments showed that, in the visible wavelength range, the log–log plot of the optical density vs. wavelength is linear (Fig. 1). Therefore, the contribution of absorption to the light attenuation was neglected.

The kinetics of variation of the particle size was characterized by the quantity

$$A_t = n_t/n_0, \quad (2)$$

where n_t is the wave exponent at time t and n_0, wave exponent at the initial moment of time.

To measure the scattering indicatrix, we used a nephelometer allowing measurements in the angle range from 69° to 120°. As a source of linearly polarized radiation we used a He–Ne laser (λ = 632.8 nm). The polarization plane of the incident light was arranged perpendicular to the plane of recording of scattered radiation intensity. In this case, the observed scattering intensity (we measured the light scattering intensities at angles of 60° and 90°) is maximal.

In the course of experiments, we measured the quantity

$$B_t = [I(60°)/I(90°)]_t/[I(60°)/I(90°)]_0, \quad (3)$$

where $[I(60°)/I(90°)]_t$ is the ratio of light scattering intensities by particles at angles of 60° and 90° at time moment t, and $[I(60°)/I(90°)]_0$ is the ratio of the same light scattering intensities at the initial moment.

To determine the floccule size and study the flocculation kinetics, we used a complex procedure for measuring the parameters of the forming particles in liquids. In the course of developing this procedure, we found that, because of insufficient sensitivity, separate use of one of the optical methods is not informative [7]. Therefore, in this study we calculated an empirical coefficient allowing the sensitivity of each method to be enhanced:

$$C_t = B_t/A_t, \quad (4)$$

The mean effective equivalent diameter of particles at time moment t was found as follows:

$$d_{t\,\mathrm{eff}} = C_t/d_{0\,\mathrm{eff}}, \quad (5)$$

where $d_{0\,\mathrm{eff}}$ is the mean equivalent effective diameter of particles at the initial time moment [4].

It should be noted that the mean effective particle diameter is a relative quantity characterizing the kinetics of formation of the polyelectrolyte–protein dispersed phase.

Comparative analysis of the use of a single method (spectroturbidimetry) and the complex procedure showed that the complex procedure is 1.5–2.0 times more sensitive in determination of changes in the particle size with time [8].

Experimental data on flocculation of BSA with cationic polyelectrolytes at pH 3.56 (under the conditions when the ionization of carboxy groups of the

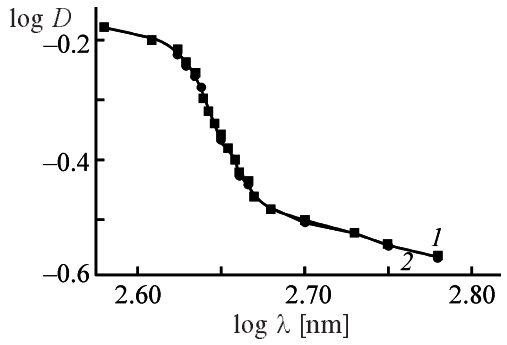


Fig. 1. log–log plot of the optical density D vs. wavelength λ.

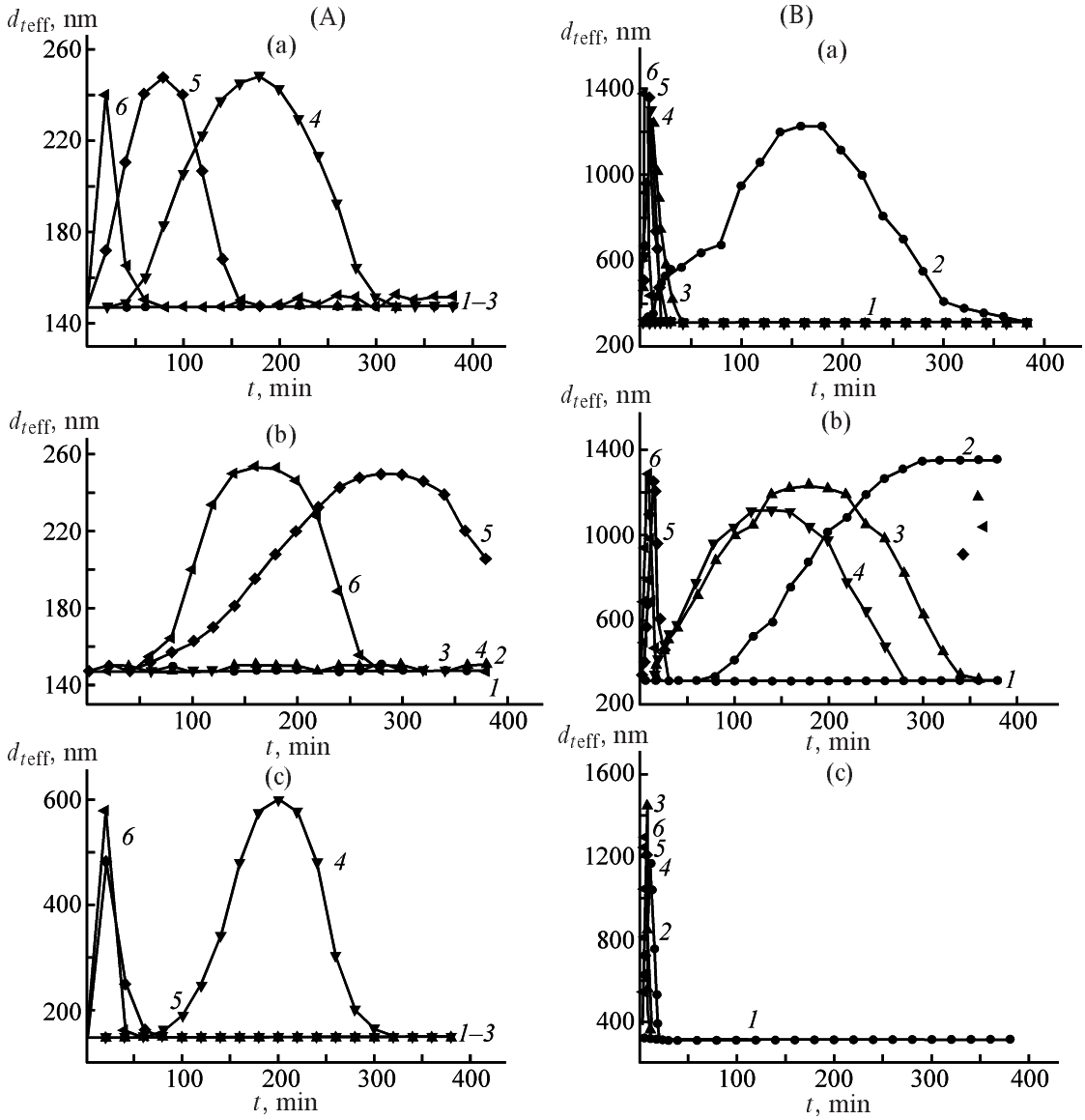


Fig. 2. Effective particle diameter d_{teff} as a function of the experiment time t at pH (A) 6.9 and (B) 9.18. Solution: (a) (*1*) BSA and (*2–6*) BSA + polymer no. 1, (b) (*1*) BSA and (*2–6*) BSA + polymer no. 2, and (c) (*1*) BSA and (*2–6*) BSA + polymer no. 3. Polymer concentration, mg l^{-1}: (*2*) 0.5, (*3*) 1, (*4*) 2.5, (*5*) 5, and (*6*) 6.

protein is suppressed and the BSA molecule bears a positive charge) showed that, for all the polymers studied, the effective particle size of the dispersed system particles was constant, about 310 nm. No floccule formation was observed. Hence, the ion–ion repulsion of positively charged amino groups of the polyelectrolytes and positively charged BSA prevented formation and growth of dispersed particles.

This conclusion is confirmed by data obtained at pH 6.9, when the degree of dissociation of carboxy groups of BSA molecules increased and the protein became negatively charged, whereas amino groups of the polyelectrolyte were still positively charged (Fig. 2A).

At this pH value, linear SMS samples of molecular weight 25.5×10^6 Da caused flocculation of dispersed particles even in concentrations of 2.5 and 5 mg l^{-1} (Fig. 2Aa). To attain the similar effect with samples of a lower molecular weight, concentrations of 5 and 6 mg l^{-1} are required (Fig. 2Ab). Furthermore, the higher-molecular-weight sample is characterized by faster flocculation kinetics. The maximal floccule size was 240–250 nm in both cases. This fact shows that the molecular weight of the linear

polyelectrolyte does not affect the size of the forming dispersed particles.

The branched SMS polymer of molecular weight 14.0×10^6 Da caused aggregation of the particles starting from a concentration of 2.5 mg l^{-1}. The effective floccule size reached 490–600 nm, and the time range of solution destabilization was 40–200 min (Fig. 2Ac). An increase in the polymer concentration to 5 and 6 mg l^{-1} led to acceleration of the flocculation.

It should be noted that the initial effective diameter of dispersed BSA micelles at pH 6.9 decreased and was about 147 nm. This may be due to the fact that, at 8.0 > pH > 4.3, the subunits of BSA molecules are in the N form and have a compact structure due to hydrophobic interactions, salt bridges, and hydrogen bonds. However, at pH < 4.3 and pH > 8.0, the N form of albumin undergoes conformational rearrangement (N–F1 in the acid range and N–B in the alkaline range). As a result, in these pH intervals the effective diameter of dispersed particles increased owing to break of interactions between their subunits [9].

Thus, the higher the molecular weight of a linear cationic polyelectrolyte, the lower concentration of this polymer is required for inducing flocculation. Apparently, the higher the molecular weight of a cationic polyelectrolyte, the higher the probability of contact of peripheral units of an adsorbed macromolecule with adjacent dispersed particles.

At the same time, the structural organization of polyelectrolytes determines the size of the dispersed particles formed and the flocculation kinetics. The linear macromolecule can simultaneously add to two particles, linking them via polymer bridges, because it has two addition sites. The branched macromolecule having several branches can add to several particles simultanepously. This fact accounts for the large effective diameter of floccules, onset of flocculation at lower concentrations, and faster flocculation kinetics with the branched polymer.

Experimental data obtained at pH 9.18 (Fig. 2B) confirm the pattern described above. The effective diameter of dispersed particles increased to 1300–1500 nm owing to unfolding of dispersed BSA micelles to the B conformation and still stronger ion–ion interaction of ionized carboxy groups of the protein and ammonium groups of cationic polyelectrolytes.

The results obtained in this study form a basis for the development of effective methods for pretreatment of native solutions of target BASs to remove impurity proteins.

CONCLUSIONS

(1) In interaction of cationic polyelectrolytes with a protein, the major driving force of floccule formation is ion–ion attraction of ionized carboxy groups of the protein and ammonium groups of polymers.

(2) An increase in the molecular weight of a linear polyelectrolyte makes lower the polymer concentration required to initiate the protein flocculation.

(3) An increase in the number of contacts of a polymeric macromolecule with a protein leads to a decrease in the time required to attain the equilibrium state in the dispersed system.

(4) At a constant pH value, the effective diameter of the forming floccules is determined by the degree of branching of the polyelectrolyte and is independent of the molecular weight of linear polymers.

REFERENCES

1. Ahuja, S., *Handbook of Bioseparation*, San Diego, CA: Academic, 2000.
2. Zapol'skii, A.K. and Baran, A.A., *Koagulyanty i flokulyanty* (Coagulants and Flocculants), Leningrad: Khimiya, 1987.
3. Flickinger, M.S. and Drew, W.C., *Encyclopedia of Bioprocess Technology*, New York: Wiley, 1999.
4. Klenin, V.I., Shchegolev, S.Yu., and Lavrushin, V.I., *Kharakteristicheskie funktsii svetorasseyaniya dispersnykh sistem* (Characteristic Light Scattering Functions of Disperse Systems), Saratov: Saratovsk. Univ., 1977.
5. Bohren, C.F. and Huffman, D.R., *Absorption and Scattering of Light by Small Particles*, New York: Wiley, 1983.
6. Artyukhov, V.G. and Putintseva, O.V., *Opticheskie metody analiza intaktnykh i modifitsirovannykh biologicheskikh sistem* (Optical Methods of Analysis of Intact and Modified Biological Systems), Voronezh: Voronezhsk. Univ., 1996.
7. Vlasova, O.L., Plotnikova, P.V., Pisarev, O.A., and Panarin, E.F., *Nauch.-Tekh. Ved. Sankt-Peterb. Gos. Univ.*, 2007, vol. 13, no. 2, pp. 32–39.
8. Vlasova, O.L., Plotnikova, P.V., Groshikova, A.R., et al., in *Materialy Mezhdunarodnoi konferentsii "Medbiotek-3"* (Proc. Int. Conf. "Medbiotek-3"), Moscow: Aviaizdat, 2006, p. 22.
9. Peters, T., *All about Albumin: Biochemistry, Genetics, and Medical Applications*, San Diego, CA: Academic, 1996.

ISSN 1070-4272, Russian Journal of Applied Chemistry, 2008, Vol. 81, No. 9, pp. 1612–1617. © Pleiades Publishing, Ltd., 2008.
Original Russian Text © V.Z. Mingaleev, V.P. Zakharov, V.M. Yanborisov, E.A. Glukhov, Yu.B. Monakov, 2008, published in Zhurnal Prikladnoi Khimii, 2008, Vol. 81, No. 9, pp. 1537–1542.

MACROMOLECULAR CHEMISTRY AND POLYMERIC MATERIALS

Activity of Butadiene Polymerization Centers at in situ Formation of Titanium Catalysts

V. Z. Mingaleev, V. P. Zakharov, V. M. Yanborisov, E. A. Glukhov, and Yu. B. Monakov

Institute of Organic Chemistry, Ufa Scientific Center, Russian Academy of Sciences, Ufa, Bashkortostan, Russia
Bashkir State University, Ufa, Bashkortostan, Russia

Received August 13, 2007

Abstract—Directional action on the activity of macromolecule propagation centers and their typical set in synthesis of stereoregular polydienes in the presence of polycentered Ziegler–Natta catalytic systems allows control over the molecular characteristics of the polymers obtained and over the service characteristics of products thereof.

DOI: 10.1134/S1070427208090267

One of the main problems of chemical kinetics is the development of a theory for calculating the kinetic parameters characterizing the specific features of a process and the possibility of its control [1]. In turn, among key parameters of diene polymerization on Ziegler–Natta catalysts is the catalytic activity of macromolecule propagation centers (ACs), numerically equal to the product of the rate constant of polymer chain propagation k_p by the AC concentration c_a.

The presently existing theoretical concepts of polymerization on Ziegler–Natta catalysts are based on the idea of polycentered nature of catalysts. In the catalytic system, there are different types of ACs differing in the chain propagation rate constants and in the probability of polymer chain termination [2, 3]. This is manifested in the presence of peak in the curve of AC distribution with respect to kinetic activity, $\psi(\ln\beta)$ (β is the probability of continuation of the polymer chain propagation) and in broad molecular-weight distribution (MWD).

The total catalytic activity in the process is determined as the sum of activities of each AC. To estimate this quantity, it is necessary to have data on the kinetics of the polymerization as a whole (concentration of active centers, degree of conversion of the monomer, rate constant of the polymer chain propagation) and the results of numerical solution of the inverse problem of MWD formation, in particular, calculation of the areas of all peaks (approximated by the Gaussian function) in the $\psi(\ln\beta)$ curve [4, 5].

At the same time, the polycentered character of Ziegler–Natta catalytic systems in polymerization of dienes makes a significant contribution to the process kinetics and molecular characteristics of polymers. This, first of all, makes necessary the calculation of the optimal set of kinetic parameters R^j_{opt} (a^j, c^j_a, k^j_p, k^j_t), where a^j is the catalytic activity of propagation centers of jth type; c^j_a, k^j_p, and k^j_t are the AC concentration, rate constant of polymer chain propagation, and rate constant of polymer chain termination on jth type of ACs, respectively. The array of such sets gives the solution of the inverse kinetic problem and allows fairly accurate determination of both conversion dependences and variation of the statistical moments of MWD in time, taking into account the presence of kinetically nonuniform centers in the system.

It should be emphasized that accurately determined and fixed value of the kinetic activity appreciably decreases the error in calculating the other kinetic parameters. Apparently, an increase in the elements constituting the set R_{opt} will lead to more detailed consideration of the polymerization process with the aim to develop procedures for control of molecular chartacteristics of polymers under industrial conditions.

Here we consider an alternative approach to calculating the total kinetic activity from the conversion

dependences of the stereospecific polymerization of butadiene and a dynamic model providing fairly accurate description of the initial portion of the kinetic curve for the case of AC formation directly in the presence of the monomer.

Polymerization was performed in toluene under the conditions excluding ingress of moisture and impurities that deactivate the catalyst. The catalyst was prepared by two procedures. In the first procedure, after mixing the solutions of a transition metal salt and an organoaluminum component, the catalytic complex was kept for 30 min at 273 K ("separate" procedure). In the second procedure, the catalyst was formed directly in the reaction mixture (in situ), i.e., an organoaluminum compound and a transition metal salt were introduced into the monomer solution in succession. The polymerization was performed with continuous stirring. The degree of conversion of the monomer was determined gravimetrically with a relative error of ≤2%.

A typical experimental dependence of the degree of the monomer conversion U on the polymerization time t in synthesis of polybutadiene in the presence of separately prepared $TiCl_4$–$Al(i\text{-}C_4H_9)_3$ is shown in Fig. 1. In the case of in situ formation of the titanium catalytic complex for butadiene polymerization, the conversion dependence becomes S-shaped with an inflection in the initial period of the process (Fig. 2). This pattern is due to the fact that the formation of Ziegler-type ACs in the course of catalyst preparation in situ occurs more slowly than with preliminary exposure of the catalyst when optimal conditions are created for the occurrence of fast alkylation processes [6, 7].

To calculate the total kinetic activity from the functional dependence of the polymer yield on the polymerization time, $U(t)$, let us present an equation for the running monomer concentration in the form

$$-dM/dt = aM, \quad (1)$$

where M is the monomer concentration and $a = \Sigma k_p^j c_a^j$ is the total activity of the catalyst.

Equation (1) is valid on the assumption that the monomer is mainly consumed in elementary chain propagation reactions and participation of the monomer in chain transfer reactions can be neglected.

By integrating Eq. (1) taking into account the initial conditions, we obtain

$$M = M_0 \exp(-at), \quad (2)$$

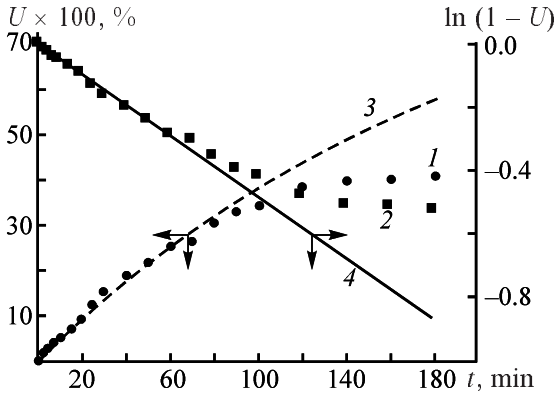


Fig. 1. Yield of polybutadiene U as a function of polymerization time t, plotted in (*1*) normal and (*2*) $\ln(1 - U)$–t coordinates. Toluene, separate procedure, [Ti] = 3 mM, M_0 = 1.5 M, Al/Ti molar ratio 1.8. (*3*, *4*) Calculated by Eqs. (4) and (5), respectively.

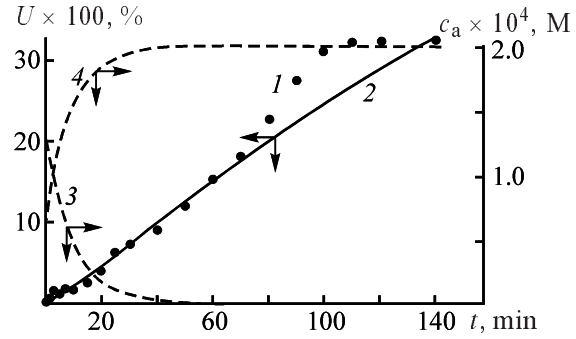


Fig. 2. Butadiene polymerization in the presence of $TiCl_4$–$Al(i\text{-}C_4H_9)_3$ (in situ procedure). Toluene, [Ti] = 3 mM, M_0 = 1.5 M, Al/Ti molar ratio 1.8. (U) Conversion. (*1*) Experimental data and (*2*) calculated by Eq. (9); (*3*, *4*) concentration of active centers c_a of the first and second types, respectively, as a function of polymerization time t.

where M_0 is the initial monomer concentration.

As the conversion, by definition, is equal to

$$U = (M_0 - M)/M_0, \quad (3)$$

from formula (2), taking into account (3), we obtain

$$U(t) = 1 - \exp(-at). \quad (4)$$

Equation (4) is the functional dependence of the conversion on time. It includes the total kinetic activity, and the total kinetic activity of macromolecule propagation centers remains constant in time. After linearization of Eq. (4),

$$\ln(1 - U) = -at, \quad (5)$$

Table 1. Activities a of the separately prepared catalytic system $TiCl_4$–OAC in polymerization of butadiene and isoprene, calculated by Eq. (5) (correlation coefficient R = 0.989–0.999)

OAC	[Ti], mM	a	a*
		min^{-1}	
Butadiene			
$Al(i\text{-}C_4H_9)_3$	3	$(4.84 \pm 0.09) \times 10^{-3}$	5×10^{-3}
	5	$(8.32 \pm 0.02) \times 10^{-3}$	8.0×10^{-3}
$Al(i\text{-}C_4H_9)_2Cl$	5	$(4.51 \pm 0.09) \times 10^{-3}$	4.1×10^{-3}
Isoprene			
$Al(i\text{-}C_4H_9)_3$	5	$(1.28 \pm 0.03) \times 10^{-2}$	1.19×10^{-2}

* Activity calculated from the polycentered model of the catalytic system [5, 11].

the kinetic activity can be found by the least-squares technique from the slope of the straight line for the initial period of the polymerization.

Equation (4) adequately describes the experimental conversion dependence of the butadiene polymerization on a separately prepared catalytic complex up to the reaction time of 60 min (25% conversion) (Fig. 1). For longer polymerization times, formula (4) gives overestimated values of conversion compared to those observed experimentally. This is apparently due to the fact that, when deducing Eqs. (4) and (5), we did not take into account the mass transfer processes decreasing the polymerization rate.

With the progress of polymerization, the solution viscosity increases and a polymer film is formed on the surface of the microheterogeneous catalyst, which considerably decreases the rate of the mass transfer of the monomer from the bulk of the reaction mixture to active centers. Stirring with a magnetic stirrer does not ensure the turbulent mode and does not efficiently lift the diffusion hindrance. At the same time, adequate description by Eq. (4) of the conversion dependence up to relatively high monomer conversion is indicative of significant contribution of the mass transfer to the reaction rate.

Also, a decrease in the observed polymerization rate due to the monomer consumption in chain transfer reactions cannot be ruled out. At the beginning of the process, the probability of the chain transfer to the monomer is high because of a large amount of unchanged butadiene. Therefore, this process should be taken into account starting from short polymerization times (low molecular weights). However, the chain trasnfer rate constant is lower by more than three orders of magnitude than the chain propagation rate constant [8]. Apparently, the influence of the monomer consumption in chain transfer reactions on the extent of deviation of the experimental conversion dependence from that calculated by Eqs. (4) and (5) is insignificant.

From the initial portions of the semilog plots, the total kinetic activity for the separately prepared catalytic complex can be determined fairly accurately (Fig. 1). By least-squares approximation of the experimental dependence $\ln(1 - U)$–t, we calculated the total kinetic activity of the propagation centers in the catalytic systems $TiCl_4$–OAC [OAC is organoaluminum compound $Al(i\text{-}C_4H_9)_3$ or $Al(i\text{-}C_4H_9)_2Cl$] in the polymerization of butadiene and isoprene (Table 1). The activity of centers of the polymer chain propagation are strongly affected by the nature of the cocatalyst (as a component of the complex catalyst) and monomer. For example, at comparable catalyst concentations, replacement of triisobutylaluminum by diisobutylaluminum chloride leads to a decrease in the activity of the catalytic system, and in the polymerization of isoprene in the presence of $TiCl_4$–$Al(i\text{-}C_4H_9)_3$ the activity of the centers is higher by an order of magnitude than in the polymerization of butadiene.

Application of Eq. (4) to describing the conversion dependence for the butadiene polymerization on a titanium catalyst prepared in situ showed that this functional dependence did not describe adequately the initial portion of the kinetic curve. To attain better agreement between the experimental and calculated data, it is appropriate to modify Eq. (4) on the basis of the simplified dynamic two-center model of the catalytic system.

Substantiation of this model for describing the initial portion of the conversion curve consists in analysis of the MWD of the polybutadiene synthesized with various procedures of catalyst formation. In the initial period of polymerization, the MWD of polybutadiene synthesized with in situ prepared catalyst is bimodal with a peak at low molecular weights (Fig. 3). With an increase in the monomer conversion, the characteristic low-molecular-weight peak disappears. Furthermore, in this case polybutadiene samples contain large amounts of the insoluble gel fraction. For example, in the interval of polymerization times of up to 30 min, the gel content is 22–26% on the average, whereas the gel fraction content in the polybutadiene synthesized with the separately

prepared catalyst is as low as 2–5%. A typical feature of cationic polymerization is the chain transfer to the polymer, resulting in cross linking and, as a consequence, in increased content of the gel fraction in the polymer [9]. These facts suggest the possibility of simultaneous occurrence of cationic (under the action of $TiCl_4$) and anionic–coordination polymerization of butadiene in the initial period of the synthesis with the titanium catalytic complex formed in situ.

It is well known [10] that $TiCl_4$ in the first step of the reaction with OAC is alkylated by the scheme typical of many Ziegler–Natta-type catalytic systems. The organotitanium compounds or their complexes formed in the process subsequently decompose with the formation of a $TiCl_3$ precipitate which, in turn, also undergoes alkylation with the formation of a bimetallic catalytic complex:

$$TiCl_4 + AlR_3 \rightarrow [TiCl_4 \cdot AlR_3] \rightarrow TiCl_3R \cdot AlR_2Cl,$$

$$TiCl_3R \cdot AlRCl_2 \rightarrow TiCl_3 \cdot AlR_2Cl + 0.5R_{-H} + 0.5R_{+H},$$

$$TiCl_3 + AlR_3 \rightarrow RTiCl_2 \cdot AlR_2Cl.$$

As $TiCl_4$ is cation-active in diene polymerization, in the initial period of the polymerization with the in situ prepared catalyst it can form an active center. With the progress of formation of the bimetallic ion–coordination polymerization catalyst, $TiCl_4$ irreversibly transforms into a catalyst–cocatalyst complex. This is indicated by an increase in the activity and stereospecificity of titanium catalysts after their exposure for 20–40 min [6, 7].

Therefore, it is appropriate to consider the transformation of a cationic AC into a coordination-type polymerization center containing a definite number of alkyl radicals, neglecting the chain termination reactions with the aim to simplify the calculations and save the computer time. For this purpose, it is necessary to solve an inverse problem of finding the AC distribution function with respect to kinetic activity from the MWD curves [3]. Figure 3 shows the result of numerical solution of the inverse problem in the form of the distribution function $\psi(\ln\beta)$ for two procedures of catalytic complex preparation. Each maximum in the $\psi(\ln\beta)$ dependence corresponds to, at least, one type of ACs. The formation of the microheterogeneous titanium catalyst in the medium of the monomer in situ leads to appearance of an AC type generating the low-molecular-weight polybutadiene fraction with the most probable molecular weight $\ln M$ = 7.1–7.8, which is not observed in preliminary exposure of the catalytic complex. Furthermore, the separately prepared catalytic system is characterized by the presence of chain propagation centers producing polybutadiene of the maximal molecular weight ($\ln M$ = 14.6–14.8) even at low conversions. Without preliminary storage of the catalyst, such centers appear only at the monomer conversion exceeding 15%.

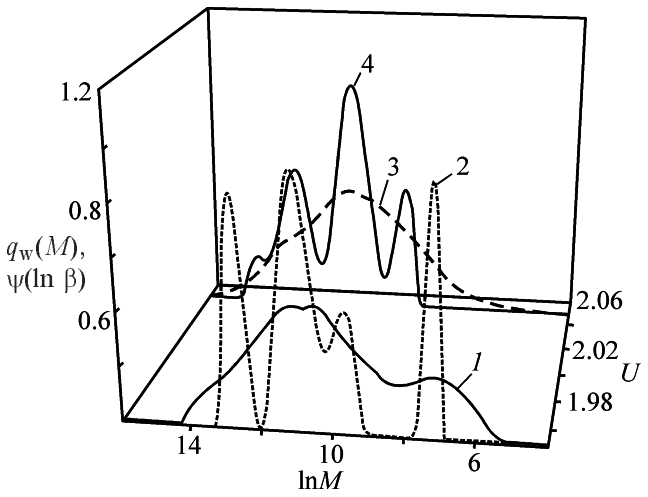


Fig. 3. (*1*, *3*) MWD–$q_w(M)$ curves and (*2*, *4*) distribution function of active centers with respect to kinetic activity $\psi(\ln\beta)$ for the (*1*, *2*) in situ and (*3*, *4*) separately prepared catalyst based on $TiCl_4$–$Al(i\text{-}C_4H_9)_3$ in polymerization of butadiene. (*U*) Conversion and (*M*) molecular weight.

Approximation of the experimental conversion dependences for the butadiene polymerization on the titanium catalyst prepared in situ, taking into account transformation of cationic ACs into coordination-type propagation centers, consists in solution of the direct kinetic problem.

In this case, the total activity of the catalytic system varies in the course of the polymerization, and Eq. (4) takes the form

$$U = 1 - \exp\left[\int_0^t a(t)\mathrm{d}t\right]. \quad (6)$$

Assuming k_p to be constant, let us relate the variation of the total activity exclusively to variation of the concentration of the transforming centers:

$$a = k_{p,1}c_{a,1}(t) + k_{p,2}c_{a,2}(t) + \delta. \quad (7)$$

Equation (7) describes the transformation of AC of the first type into that of the second type, with

Table 2. Kinetic parameters of active centers participating in the one-way transition (k = 0.1 min^{-1})

ln M	k_p	k_p^*	$c_a^0 \times 10^4$	$c_a^0 \times 10^4$*
	l mol^{-1} min^{-1}		M	
7.1–7.8	3	5.6	1.2	1.8
9.4–9.9	15	19	0.8	0.73

* Values calculated according to [5, 11].

the activities of the other types of centers being constant (δ = const). According to the concepts of formal kinetics, the differential equations describing the variation of the concentrations of ACs of the first and second types will have the form

$$\begin{aligned} dc_{a,1}/dt &= -kc_{a,1}, \\ dc_{a,2}/dt &= kc_{a,1}, \end{aligned} \tag{8}$$

where k is the rate constant of mutual transformation of propagation centers of different types.

By solving Eqs. (6)–(8) with the initial conditions that, at $t = 0$, $c_{a,1} = c_{a,1}^0$, $c_{a,2} = c_{a,2}^0$, we obtain

$$U = 1 - \exp\{c_{a,1}^0(k_{a,2} - k_{a,1})k^{-1}[1 - \exp(-kt)] - (c_{a,1}^0 + c_{a,2}^0)k_{p,2}t\}. \tag{9}$$

Equation (9) allows correct description of the initial portion of the kinetic curve with the titanium catalyst prepared in situ (Fig. 2). In so doing, we assume that, with the reaction progress, cationic centers transform into ion–coordination ACs catalyzing the stereospecific polymerization of butadiene.

Expression (9) contains a large number of unknown kinetic parameters, which leads to the instability of the solution found. To decrease the error in determining the numerical values of kinetic constants, we developed an optimization algorithm for searching for these constants in the space of five variables, consisting in minimization of the functional

$$F(x) = \Sigma[U_1^{calc} - U_1^{exp}]^2, \qquad x(c_a, k, k_{p,1}, k_{p,2}). \tag{10}$$

As a result, we found the kinetic parameters characterizing the two-center model of the catalytic system (Table 2). To check the adequacy of the model, we calculated the concentrations of the ACs participating in the transition and the corresponding propagation rate constants by the procedure based on solution of the inverse problem of MWD formation [5, 11] in which the solution is sought for using the statistical moments of MWD and the function ψ(ln β). It can be seen that the results of direct and inverse simulation of the butadiene polymerization on the titanium catalyst prepared in situ are in good agreement (Table 2). The calculations showed that the region of inflection in the kinetic curve (onset of polymerization acceleration) corresponds to flattening-out of the concentration of second-type ACs and maximal decrease in the content of first-type ACs characterized by low rate constant of the polymer chain propagation (Fig. 2).

As the polymerization is performed under the conditions excluding ingress of moisture and impurities into the reaction system, the low activity of ACs of the first (cationic) type is apparently due to the absence of the required cocatalyst (the catalyst is an aprotic acid). Furthermore, the correlation of the acidity and cationic activity of Friedel–Crafts catalysts in polymerization processes shows that $TiCl_4$ is less reactive than the $TiCl_4$–Al(i-C_4H_9)$_3$ complex, as demonstrated in [12] by the example of polymerization of 1,3-pentadiene.

Thus, in the case of separate preparation of the catalyst, the conversion dependence is well described by expression (1) to 30–40% conversions. In the process, the total catalytic activity remains constant and can be fairly accurately determined from the semilog plot. With the titanium catalyst prepared in situ, the conversion dependence is S-shaped, which may be due to transformation of cationic active centers into coordination centers with the progress of the monomer conversion.

The data we obtained indicate that it is necessary to evaluate and take into account the rate constant of the one-way transition between different types of ACs. This allows us to choose the optimal set of kinetic parameters of the reaction with the aim to develop procedures for decreasing the probability of formation of active centers initiating the cationic processes in the course of diene polymerization in the presence of Ziegler–Natta catalysts. The formation of catalytic systems in situ favors the formation of active centers producing the polymer fraction with a low molecular weight and a high content of the insoluble gel fraction. Thus, the analytical dependences given in this paper allow control of the origination of "impurity" active centers of stereospecific polymerization when the catalyst is formed in situ. As the observed process deceleration with the catalysts formed in situ is also characteristic of the

other system for ion–coordination polymerization, the suggested physicochemical interpretation of the model of active center formation seems to be the most realistic.

CONCLUSIONS

(1) Preparation of a microheterogeneous titanium catalyst in situ for butadiene polymerization favors formation of undesirable active centers initiating cationic processes, with deceleration of the rate of the ion–coordination polymerization of dienes, and producing the polymer fraction with a low molecular weight, a broad molecular-weight distribution, and a high content of the insoluble gel fraction.

(2) The suggested analytical expression allows prediction of the appearance in the reaction mixture of macromolecule propagation centers of the cationic type and estimation of the kinetic parameters of their transformation into ion–coordination-type active centers. In large-tonnage rubber production, this will allow control of the product quality by directional variation of the set of different active centers.

ACKNOWLEDGMENTS

The study was financially supported by the Russian Foundation for Basic Research (project no. 06-03-32240), Foundation for Support of Leading Scientific Schools (NSh-9342.2006.3), and Program of the Division of Chemistry and Materials Science, Russian Academy of Sciences "Development of Scientific Principles of New Chemical Technologies with Preparation of Pilot Batches of Substances and Materials."

REFERENCES

1. Berlin, Al.Al. and Vol'fson, S.A., *Kineticheskii metod v sinteze polimerov* (Kinetic Method in Polymer Synthesis), Moscow: Khimiya, 1973.
2. Sigaeva, N.N., Shirokova, E.A., Mullagaliev, I.R., et al., *Vysokomol. Soedin., Ser. A*, 2000, vol. 42, no. 8, pp. 1269–1274.
3. Monakov, Yu.B. and Sigaeva, N.N., *Vysokomol. Soedin., Ser. S,* 2001, vol. 43, no. 9, pp. 1667–1688.
4. Maksyutova, E.R., Usmanov, T.S., Spivak, S.I., et al., *Obozr. Prikl. Prom. Matem.*, 2001, vol. 8, no. 2, pp. 642–643.
5. Maksyutova, E.R., Usmanov, T.S., and Saitova, F.F., *Obozr. Prikl. Prom. Matem.*, 2002, vol. 9, no. 2, pp. 418–419.
6. Monakov, Yu.B., Rafikov, S.R., Minchenkova, N.Kh., et al., *Dokl. Akad. Nauk SSSR*, 1979, vol. 244, no. 4, pp. 918–921.
7. Natta, G. and Pasquonne, I., *Kinet. Katal.*, 1962, no. 3, pp. 805–809.
8. Mingaleev, V.Z., Zakharov, V.P., and Monakov, Yu.B., *Zh. Prikl. Khim.*, 2007, vol. 80, no. 7, pp. 1160–1164.
9. *Sinteticheskii kauchuk* (Synthetic Rubber), Garmonov, I.V., Ed., Leningrad: Khimiya, 1983.
10. Werber, F.X., Benning, S., Wszolek, W.R., et al., *J. Polym. Sci., Part A*, 1968, vol. 6, no. 4, pp. 743–755.
11. Saitova, F.F., Kinetic Nonuniformity of Active Polymerization Centers of Vanadium and Titanium Catalytic Systems and Molecular Characteristics of Polyisoprene, *Cand. Sci. Dissertation*, Ufa, 2005.
12. Monakov, Yu.B., Mullagaliev, I.R., Zakharov, V.P., et al., *Neftekhimiya*, 2001, vol. 41, no. 2, pp. 135–138.

ISSN 1070-4272, Russian Journal of Applied Chemistry, 2008, Vol. 81, No. 9, pp. 1618–1621. © Pleiades Publishing, Ltd., 2008.
Original Russian Text © D. Rashidov, U. Shoimov, Sh. Tuichiev, B.M. Ginzburg, 2008, published in Zhurnal Prikladnoi Khimii, 2008, Vol. 81, No. 9, pp. 1543–1546.

MACROMOLECULAR CHEMISTRY AND POLYMERIC MATERIALS

Influence of Fullerene C_{60} on the Structure and Mechanical Properties of Polyethylene

D. Rashidov, U. Shoimov, Sh. Tuichiev, and B. M. Ginzburg

Tajik State National University, Dushanbe, Tajikistan
Institute of Machine-Building Problems, Russian Academy of Sciences, St. Petersburg, Russia

Received April 3, 2008

Abstract—Influence of fullerene C_{60} on the structure and mechanical properties of low-density polyethylene samples cast from a melt and a solution was studied.

DOI: 10.1134/S1070427208090279

Previously we examined the influence of fullerene C_{60} additions on the mechanical properties (strength, Young's modulus, breaking elongation) of thin (10–12 μm) films of atactic poly(methyl methacrylate) (PMMA).

The choice of poly(methyl methacrylate) as the matrix was governed by the fact that its supramolecular structure is simple and uniform. The intensity of small-angle X-ray patterns of uniform inorganic and organic glasses is usually constant in the whole measurable range of scattering angles [2, 3]. Certain insignificant monotonic increase in the intensity in going to the primary beam is clearly caused by density fluctuations. Introduction of 1–5% fullerene C_{60} into PMMA films by casting from a solution containing PMMA and C_{60} had no noticeable effect on small- and wide-angle X-ray patterns. This fact suggests more or less uniform distribution of fullerene in the polymer matrix.

Introduction of fullerene into the polymer should result in formation of strong nanocomposites owing to uniform distribution of the fullerene in the matrix, the uniform size distribution of fullerene molecules, and electron-acceptor properties of fullerenes which can be considered as free radicals traps [5]. Indeed, even at 1% content of fullerene in the films, their strength increases by a factor of approximately 5.

The aim of this study was to examine the influence of small (1–10%) additions of fullerene C_{60} on the mechanical properties of the most commonly used thermoplastic, polyethylene (PE). Although the chemical composition of PE is simple, this polymer is amorphous–crystalline and has a developed morphology. Polyethylene is chemically inert and should not react with fullerene in the course of crystallization from melts and solutions. Thus, fullerene will be most likely localized in the amorphous regions of PE.

EXPERIMENTAL

Samples of low-density polyethylene [LDPE, GOST (State Standard) 16 337–77] were prepared by casting from (1) melts and (2) solutions in different solvents. The fullerene concentration was varied in the range 0–10 wt %.

In the first case, dry LDPE and C_{60} were mixed, placed in a hydraulic mold, and heated at 150°C and a pressure of 50 atm. The samples were obtained in the form of 0.2–0.3-mm plates.

In the second case, 5% solutions of LDPE in toluene and 1,2-dichlorobenzene (DCB) were prepared by heating on a water bath at 80–90°C. Then aliquots of C_{60} solutions in the same solvent were added and the mixture was stirred for a short time. The films were cast on a dry glass support heated at 80°C. The film thickness ranged from 20 to 80 μm.

To study the mechanical properties, samples in the form of a double shovel 2 or 4 mm wide, with 22-mm working part, were cut out from the films or plates. The mechanical tests were performed at 20°C on PM-1 tensile-testing machine at a moving clamp velocity of 12 mm min^{-1}. The tensile strength σ_t, breaking elongation ε_e, and initial Young's modulus E_0 were determined from the strain curves.

X-ray diffraction study of the samples was performed on DRON-2 and KRM-1 diffractometers using nickel-filtered copper radiation. The intensity of wide-angle scattering was measured on a DRON-2 diffractometer with a slit collimator. The half-width of the primary beam was 36 min. The intensity of small-angle scattering was measured on KRM-1 diffractometer with slit collimation of the primary beam. The half-width of the beam was 2.5 min. To correct the line width of the sample, the width of primary beam is usually used instead of the line width of a reference [6]. However, in this study, the width of the primary beam was not corrected since our aim was only to estimate the crystallite size. No collimation corrections were introduced for the same reason.

The measurements were performed in the transmission mode: a sample was fixed at the center of goniometer at a right angle to the primary beam. The $I_s(2\theta)$ scattering pattern was recorded. Then the sample was placed in front of the first slit and the scattering pattern of the primary beam was recorded taking into account its absorption in the sample $I_a(2\theta)$. Since the $I_a(2\theta)$ curves of all samples were similar within the limits of the experimental error, the primary beam was not normalized to the same intensity. The $I_a(2\theta)$ curve was subtracted from the $I_s(2\theta)$ curve. The experimental diffraction patterns were constructed in the form of difference curves $I(s)$ or $I(2\theta)$, where $s = 4\pi\sin\theta/\lambda$, $\varphi = 2\theta$ is scattering angle, and λ is the X-ray radiation wavelength. For small scattering angles, $s \approx 2\pi\varphi/\lambda$.

In the course of small-angle measurements, the goniometer was rotated manually. The intensity of scattered radiation at each fixed angle was measured at 1000 pulses. The relative determination error of the intensity was 3–4%.

The melting point was measured on a DSC 204F2 Netzsch calorimeter at a heating rate of 50 deg min^{-1}. The sample weight was 2–4 mg.

Representative wide-angle X-ray patterns of the initial (curve *1*) and fullerene-containing LDPE formed from a melt (curve *2*) and from a DCB solution (curve *3*) are shown in Fig. 1. As can be seen, the X-ray patterns of the initial LDPE samples are similar to those of the samples prepared from the melt and DCB solution. These patterns contain strong (110) and (200) reflections of orthorhombic lattice of PE (Fig. 1, curve *1*).

Sharp reflections of C_{60} crystallites at 2θ 10.5° and 28°–36° are observed along with (110) and (200)

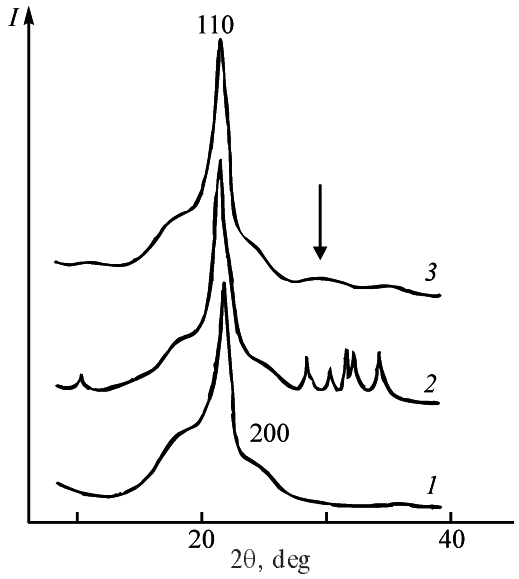


Fig. 1. Wide-angle X-ray diffraction patterns of (*1*) initial LDPE, (*2*) LDPE + 10 wt % C_{60} prepared from melt, and (*3*) LDPE + 10 wt % C_{60} prepared from DCB solution. The appearing reflection of the C_{60} lattice is indicated with an arrow. (*I*) Intensity and (2θ) Bragg angle.

reflections of LDPE on wide-angle patterns of the LDPE-C_{60} system at a fullerene concentration c = 1 wt %, prepared from the melt. At higher fullerene concentrations, the intensity of the reflections of C_{60} crystallites increases, with their radial width and location remaining the same. The intensity of the main (110) and (200) reflections of the PE matrix and their location and radial width do not change. The size of PE and C_{60} crystallites determined by the Scherrer equation [6] is 5–6 and 20–25 nm, respectively. The wide-angle X-ray diffraction patterns show that the components of the polymer compound form individual phases and C_{60} molecules are not incorporated in the crystal lattice of the matrix.

The wide-angle X-ray diffraction patterns of LDPE + C_{60} samples prepared from solutions in toluene and DCB do not change noticeably with increasing C_{60} concentration from 0 to 5 wt %. Only at c = 10 wt %, weak blurred reflections of C_{60} appear on the background of LDPE reflections (Fig. 1, curve *3*). Therefore, no ordered C_{60} aggregates are formed. According to our previous estimations [4], weak and broad C_{60} reflections are due to aggregates of no more than 100 C_{60} molecules (4–5 molecules in each direction).

Small-angle X-ray diffraction patterns of LDPE + C_{60} samples prepared from DCB solutions (samples prepared from toluene solutions are similar) are

Mechanical properties at uniaxial stretching of LDPE samples

Run no.	LDPE + C_{60} from melt				LDPE + C_{60} from toluene solution			LDPE + C_{60} from DCB solution		
	c, %	σ_t, MPa	ε_b, %	E, MPa	σ_t, MPa	ε_b, %	E, MPa	σ_t, MPa	ε_b, %	E, MPa
1	0	16	300	70	3.2	300	80	30	300	460
2	1	11.5	170	110	5.7	75	80	30	250	660
3	3	8.5	135	190	6.2	45	160	32	200	660
4	5	8.5	115	230	6.9	25	160	32	120	910
5	10	7.5	105	280	7.3	21	400	25	80	1600

shown in Fig. 2. The small-angle patterns of the samples prepared from melts are essentially similar. A common feature of small-angle patterns of all the samples is the presence of separate reflections corresponding to large spacings (16–20 nm). The intensity of the reflections at the maximum I_m changes by 20–30% with increasing fullerene concentration. Analysis of I_m changes within the framework of the two-phase model (as it was done, e.g., in [7, 8]) shows that only ~10% of fullerene penetrates in interlayer amorphous regions responsible for formation of large interplanar spacings, and the majority of fullerene molecules are concentrated in the amorphous part.

The fact that the wide-angle patterns of all polyethylene matrices are similar is consistent with similar melting points of all LDPE crystallites (106–107°C).

The results of mechanical tests of LDPE samples

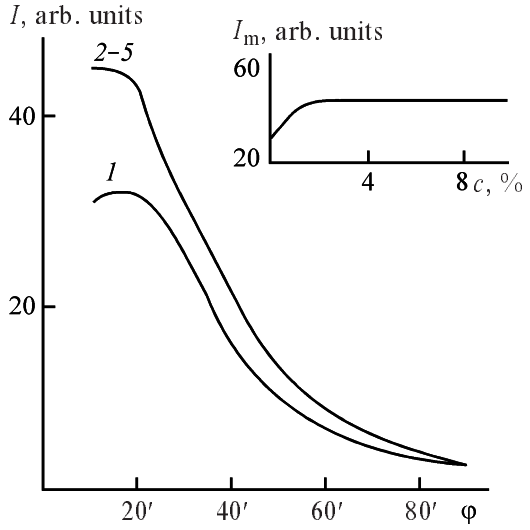


Fig. 2. Small-angle X-ray diffraction patterns of LDPE + C_{60} prepared from DCB solutions. (*I*) Intensity, (*c*) concentration, and (φ) angle. C_{60}, %: (*1*) 0, (*2*) 1, (*3*) 3, (*4*) 5, and (*5*) 10.

are presented in the table. As can be seen, the elasticity of the samples decreases (ε_b decreases) and Young's modulus E monotonically increases with increasing C_{60} concentration. The tensile strength depends on the sample type. It should be noted, however, that the mechanical properties of LDPE + C_{60} samples prepared from DCB solutions are significantly better than those of the other samples. This is probably due to high solubility of C_{60} in DCB [9] and, therefore, high uniformity of fullerene distribution in the PE matrix and dispersion of the fullerene to separate molecules and small aggregates. With an increase in the fullerene concentration, the relatively high strength (~30 MPa) of these samples is preserved, their elasticity slightly decreases, but the elastic modulus increases by a factor of more than 2.

Thus, the structure and mechanical properties of the fullerene-containing composite significantly depend on the preparation procedure and the fullerene content in the polymer matrix.

CONCLUSIONS

(1) The fullerene does not enter into low-density polyethylene crystallites and is accumulated in the amorphous parts of the matrix.

(2) Fullerene in the samples prepared from low-density polyethylene melt forms 25–30-nm crystallites, whereas in the samples prepared from solutions it is dispersed to separate molecules or small conglomerates.

(3) At uniaxial stretching of all samples, the breaking elongation decreases and the elastic modulus increases with increasing C_{60} concentration.

(4) The best mechanical properties are exhibited by the samples prepared from 1,2-dichlorobenzene solutions. With increasing fullerene concentration, their elastic modulus increases by a factor of more

than 2, with their strength preserved and elasticity slightly decreased.

ACKNOWLEDGMENTS

This study was financially supported by International Science and Technology Center (project no. T-1145) and Division of Power Engineering, Mechanical Engineering, Mechanics, and Management Processes, Russian Academy of Sciences, Program of Basic Research no. 13.

REFERENCES

1. Ginzburg, B.M., Tabarov, S.Kh., Tuichiev, Sh., and Shepelevskii, A.A., *Pis'ma Zh. Tekh. Fiz.*, 2007, vol. 33, no. 23, pp. 43–50.
2. Svergun, D.I. and Feiglin, L.A., *Rentgenovskoe i neitronnoe malouglovoe rasseyanie* (X-ray and Neutron Small-Angle Scatering), Moscow: Gos. Izd. Fiziko-Matematicheskoi Literatury, 1986.
3. Ginzburg, B.M., and Tuichiev, Sh., *J. Macromol. Sci. B: Phys.*, 2005, vol. 44, no. 4, pp. 517–530.
4. Ginzburg, B.M., Melenevskaya, E.Yu., Novoselova, A.V., et al., *Vysokomol. Soedin.*, 2004, vol. 46, no. 2, pp. 295–303.
5. Moshev, V.V. and Garishin, O.K., *Usp. Mekh.*, 2005, vol. 3, no. 2, pp. 3–36.
6. Kitaigorodskii, A.I., *Rentgenostrukturnyi analiz melkokristallicheskikh i amorfnykh tel* (X-ray Diffraction Analysis of Finely Crystalline and Amorphous Bodies), Moscow: Gos. Izd. Tekhniko-Teoreticheskoi Literatury, 1952.
7. Tuichiev, Sh., Sultanov, N., Ginzburg, B.M., and Frenkel', S.Ya., *Vysokomol. Soedin., Ser. A*, 1970, vol. 12, no. 9, pp. 2025–2035.
8. Stalevich, A.M. and Ginzburg, B.M., *J. Macromol. Sci. B: Phys.*, 2006, vol. 45, no. 2, pp. 377–394.
9. Bezmel'nitsyn, V.N., Eletskii, A.V., and Okun', M.V., *Usp. Fiz. Nauk*, 1998, no. 11, pp. 1195–1220.

ISSN 1070-4272, Russian Journal of Applied Chemistry, 2008, Vol. 81, No. 9, pp. 1622–1629. © Pleiades Publishing, Ltd., 2008.
Original Russian Text © N.M. Zabivalova, A.M. Bochek, E.N. Vlasova, B.Z. Volchek, 2008, published in Zhurnal Prikladnoi Khimii, 2008, Vol. 81, No. 9, pp. 1547–1554.

MACROMOLECULAR CHEMISTRY AND POLYMERIC MATERIALS

Preparation of Mixed Ethers by Reaction of Carboxymethyl Cellulose with Urea and Their Physicochemical Properties

N. M. Zabivalova, A. M. Bochek, E. N. Vlasova, and B. Z. Volchek

Institute of Macromolecular Compounds, Russian Academy of Sciences, St. Petersburg, Russia

Received February 1, 2008

Abstract—The conditions of preparation of mixed cellulose ethers containing carboxymethyl and amide groups by reaction with urea were examined with samples of commercial carboxymethyl cellulose and that prepared from flax cellulose as examples. The water solubility of the resulting products and their sorption activity toward copper ions were examined in relation to the amount of amide groups introduced.

DOI: 10.1134/S1070427208090280

Water-soluble cellulose compounds are widely used in various branches of engineering and also in food industry, perfumery manufacture, and medicine. Sodium salt of carboxymethyl cellulose (NaCMC) and methyl cellulose (MC) are the most widely applied cellulose compounds. They are used in oil extraction, paper, textile, and food industries, as well as in manufacture of paints and varnishes, dry building mixtures, adhesives, etc. These cellulose ethers are utilized primarily as aqueous solutions.

The application field for carboxymethyl cellulose (CMC) can be extended by its compounding with other polymers or by chemical modification.

Chemical modification of partly substituted cellulose ethers is effected either by introduction of new functional groups at free hydroxy groups of the polymer in anhydroglucose moieties or by selective modification of the already existing substituents.

Carboxymethyl cellulose amides (CMCAs) are prepared by reactions of amines with CMC chlorides [1–3] or with CMC in the H form [4]. We described previously [5] the conditions of preparation of amides of CMC based on flax and cotton cellulose by the reaction with chloroacetamide.

Cellulose compounds are produced mostly from wood and cotton cellulose. An alternative raw material can be found in large-capacity waste from flax production: short flax fibers and lignified part of pedicels (boon).

The physicochemical properties of new cellulose compounds are affected by the following factors: nature of the initial polymer, molecular weight, chemical composition, presence of concomitant substances, structural uniformity, fiber morphology, etc.

This study was aimed to elucidate the conditions of synthesis of cellulose ethers by the reaction of CMC prepared from flax and cotton fibers with urea. Vali et al. [6] and Goikhman et al. [7] described the conditions of preparation of cellulose carbamates by reaction with urea. These conditions differ from those for other cellulose compounds.

Urea can be introduced into the reaction mixture by various procedures [7]: using ammonia (introduction of biuret and urea into liquid ammonia) and without using ammonia: by impregnation of cellulose with an alkaline solution of urea, by introduction of urea in a buffer high-boiling substance where urea melts and gets uniformly spread over the surface of cellulose fibers, or by impregnation of cellulose with a solution of urea or biuret in water, DMSO, DMAA, and DMF.

Depending on the conditions, the reaction between CMC in the acid form (HCMC) and amines can yield cross-linked systems [8, 9] and mixed cellulose ethers containing amide and catboxymethyl groups [10]. Polysaccharides (starches, CMC) and urea can also be used to prepare composite materials that can be processed as a melt [11]. Such composites are obtained using an oxidizing agent (hydrogen peroxide) and a catalyst (iron chloride).

We elucidated here the conditions of synthesis of mixed cellulose ethers without oxidizing agents and

Table 1. Characteristics of the polymers used

Sample	DP_η	DS_{Na}	Water solubility, %
Purified commercial carboxymethyl cellulose NaCMC	460	0.57	99
Short flax fibers	4230	–	–
NaCMC (flax)	900	0.52	89
Repeated carboxymethylation of NaCMC (flax)	500	0.80	92

catalyst. The reaction of urea with CMC can presumably occur at carboxymethyl and hydroxy groups of the polymer and can be affected by the molecular characteristics of the polymers, the uniformity of distribution of the substituents (carboxymethyl groups), and morphological features of the cotton and flax fibers.

EXPERIMENTAL

For comparative assessment of the reactivities of the cellulose ethers we used commercial NaCMC sample obtained from cotton cellulose. For synthesis of mixed ethers of flax cellulose we synthesized in advance NaCMC samples by the technique described in [12] (Table 1). The NaCMC samples washed to remove NaOH and Cl^- were vacuum-dried at 60°C. The degree of substitution at carboxy groups was calculated using the expression [13]

$$DS_{Na} = 162n/(23 \times 100 - 80n), \quad (1)$$

where n is the Na content of the polymer, wt %; 162, molecular weight of the elementary unit of cellulose; 23, atomic weight of sodium; and 80, increment of the molecular weight of the elementary unit of cellulose upon introduction of one CH_2COONa substituent.

The Na amount was determined by conductometric back-titration of the NaCMC samples. The solubility of NaCMC and of the ethers synthesized was determined as recalculated for 1% solutions by the technique described in [14].

The initial short flax fibers contain a significant amount of concomitant polymers and mineral substances affecting the reactivity of cellulose and uniformity of distribution of substituents in the polysaccharide molecules in flax fibers. For this reason, the flax fibers were pretreated under laboratory conditions with a cooking mixture ($NaOH : Na_2S_2O_3 : H_2O$) in a nitrogen flow [15]. Such treatment removes most of the concomitant substances (hemicelluloses, lignin, pectins) from flax fibers; it causes an insignificant decrease in DP_η of the polymer and a substantial increase in the proportion of cellulose.

Table 1 shows that the degree of polymerization DP_η of NaCMC prepared from flax fibers is much higher, while DS_{Na}, lower than those of commercial NaCMC (the DP_η parameters were calculated from the viscometrically determined molecular weights).

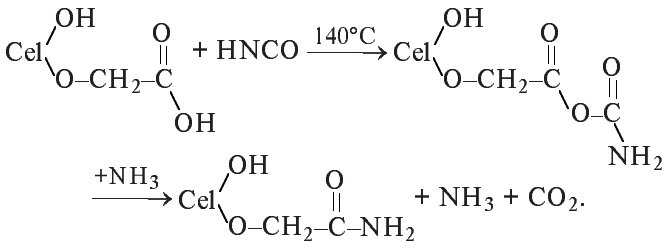
Sodium carboxymethyl cellulose was prepared by the standard technique [12], which suggests that, to increase DS_{Na} of the flax cellulose ether and its water solubility, the already synthesized NaCMC sample requires repeated carboxymethylation, which increases both its DS_{Na} and solubility in water, but simultaneously decreases DP_η of the polymer. Elucidation of the conditions of one-step synthesis of NaCMC with a higher DP requires additional research efforts [16], which is beyond the scope of this study.

Sodium carboxymethyl cellulose was converted in advance to the H form (by treating a weighed portion with 20% aqueous solution of HCl in ethanol, pH 2.0–2.5), after which the sample was washed to remove Cl^- ions to pH 7.0 and dried. The reaction was run in *o*-xylene at 140°C. The choice of *o*-xylene for the high-boiling buffer solvent was dictated by the facts that its boiling point (144.4°C) exceeds the urea decomposition temperature and that *o*-xylene is inert toward both cellulose and urea.

At 132.7°C, urea decomposes into isocyanic acid:

$$H_2N\text{–}C(O)\text{–}NH_2 \xrightarrow{140^\circ C} HN{=}C{=}O + NH_3.$$

The resulting isocyanic acid reacts with carboxymethyl goups of HCMC to form a CMC amide:

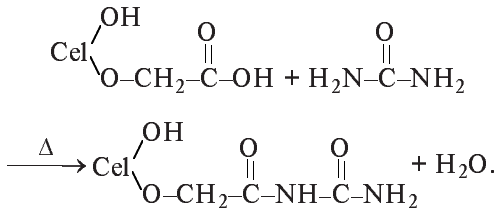


Under identical conditions (at 140°C), CMC amides were obtained by the reaction of HCMC with decylamine [10].

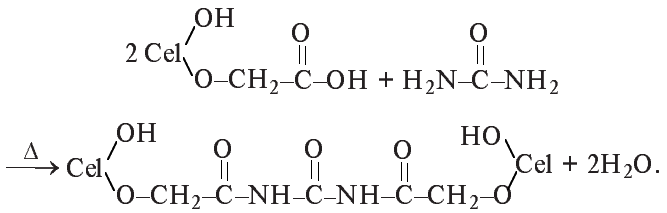
Isocyanic acid can also react with unsubstituted hydroxy groups at 140°C (preparation of cellulose carbamates) [17]:

$$Cel(OH)_3 + HN{=}C{=}O \xrightarrow{140^\circ C} Cel(OH)_{3-x}[-O-C(O)-NH_2]_x.$$

The decomposition of urea takes some time, which suggests that undecomposed urea can enter into the reaction yielding amides with elimination of water, as in the reaction of HCMC with amines (at carboxy groups) [10]:



Also possible is the reaction of urea at its two amino groups, yielding cross-linked polysaccharide macromolecules:



The necessary amount of urea was mixed with the HCMC samples at different mole fractions on a multidisperser. All the samples were mixed and ground for 30 min and then poured over with *o*-xylene. The synthesis was carried out in a glass flask at 140°C on an oil bath for different periods. The temperature was controlled with a contact thermometer. The liquor ratio in all the reactions was 13.

The resulting samples were twice washed with ethanol to remove xylene. The unchanged urea was removed by washing the samples with warm water (twice), after which they were moistened with ethanol and vacuum-dried at 40°C. A part of each sample was left in the H form, and another part was converted to the Na form (by treating with 1% NaOH solution in ethanol at 50°C for 45 min). The amount of the amide groups ($CONH_2$) in the ethers synthesized was characterized by the amount of bound nitrogen. The nitrogen content was determined by the Kjeldahl method [18]. Tables 2 and 3 present the synthesis conditions for the mixed cellulose ethers based on commercial NaCMC and that synthesized from flax fibers.

We showed previously [4] that, with increasing amount of the preliminarily introduced amine (per mole of carboxy groups) and reaction time, the proportion of bound nitrogen in the polymer tends to increase. A similar trend can be seen from Tables 2 and 3, but there are some distinctions as well. Table 2 shows that, at the 1 : 1 molar ratio and the reaction time of 2 h (experiment no. 3), the amount of bound nitrogen is at a maximum. With decreasing amount of urea preliminarily introduced into the HCMC fibers, the amount of bound nitrogen tends to decrease as a whole. At the same time, the reaction time exerts an opposite effect. For example, at the reaction time of 2 h (experiment no. 6), the amount of bound nitrogen is at a minimum. The HCMC obtained from flax fibers is also characterized by the minimal amount of bound nitrogen at the reaction time of 2 h (Table 3, run no. 5). Apparently, the reason for the observed scatter of the amounts of bound nitrogen in the mixed cellulose compounds is nonuniform distribution of urea in the fibers when the polymer was subjected to dry grinding jointly with urea and a product nonuniformly substituted over the bulk of the fibers was obtained.

Conversion of AHCMC to the Na form (needed to determine DS_{Na} and the water solubility of the samples, since HCMC is water-insoluble) by treating HCMC with an aqueous NaOH solution in ethanol causes intensive hydrolysis of the amide bonds with formation of carboxy groups [7], which results in a decrease in the amount of bound nitrogen.

It should also be noted that, with increasing amount of preliminarily introduced urea (increasing molar ratio), the amount of bound nitrogen increases to levels exceeding the theoretically possible values. For example, in the case of the reaction of isocyanic acid with carboxy groups in the CMC sample with DS_{Na} of 0.57, the theoretically possible amount of bound nitrogen is 4.3%. Table 2 shows that, for two samples (experiment nos. 2 and 3), the content of nitrogen exceeds the calculated level, which suggests that, in parallel, another reaction can also proceed, in particular, that of isocyanic acid with hydroxy groups to yield cellulose carbamates. This hypothesis will be confirmed below.

Table 2. Conditions of synthesis of mixed cellulose ethers by reaction of urea with commercial CMC and their characteristics

Run no.	Synthesis conditions		Na, %	DS_{Na}	N, %	Water solubility, %
	COOH : NH_2 molar ratio	t, h				
			AHCMC			
1	1 : 3	1			3.77	–
2	1 : 1	1			4.31	–
3	1 : 1	2			4.40	–
4	1 : 1	3			3.58	–
5	1 : 0.5	1			2.48	–
6	1 : 0.5	2			1.60	–
7	1 : 0.5	3			2.80	–
			ANaCMC			
8	1 : 3	1	2.99	0.24	1.43	88.0
9	1 : 1	1	3.57	0.29	1.36	66.5
10	1 : 1	2	2.76	0.22	1.43	89.9
11	1 : 1	3	3.01	0.24	1.29	96.0
12	1 : 0.5	1	4.42	0.37	0.94	92.0
13	1 : 0.5	2	4.29	0.36	0.51	85.2
14	1 : 0.5	3	3.99	0.33	0.59	95.2

Table 3. Conditions of synthesis of mixed cellulose ethers by reaction of urea with CMC derived from flax fibers (DS_{Na} 0.52) and their characteristics

Run no.	Synthesis conditions		Na, %	DS_{Na}	N, %	Water solubility, %
	COH : NH_2 molar ratio	t, h				
			AHCMC			
1	1 : 1	1			3.09	–
2	1 : 1	2			2.49	–
3	1 : 1	3			2.48	–
4	1 : 0.5	1			1.43	–
5	1 : 0.5	2			1.26	–
6	1 : 0.5	3			1.28	–
			ANaCMC			
7	1 : 1	1	5.03	0.43	0.71	86.5
8	1 : 1	2	4.84	0.41	0.64	87.2
9	1 : 1	3	3.74	0.30	1.40	84.6
10	1 : 0.5	1	4.32	0.36	0.99	56.0
11	1 : 0.5	2	4.54	0.38	0.78	86.0
12	1 : 0.5	3	4.6	0.39	0.64	51.0

In synthesis of mixed cellulose ethers based on flax CMC (Table 3), the amount of urea introduced into the fibers and the reaction time affect the content of bound nitrogen in a similar manner, except for the fact that the experimentally determined nitrogen content does not exceed the calculated value (for CMC with DS_{Na} of 0.52, the content of bound nitrogen arising from the reaction of isocyanic acid with carboxy groups is 3.79%). It is also seen that the content of bound nitrogen in AHCMC and ANaCMC is lower than that in the similar samples obtained with commercial CMC (cotton linter). The

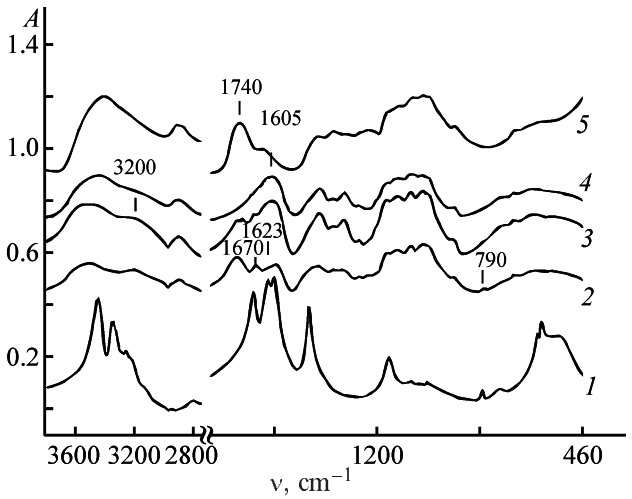


Fig. 1. IR Fourier spectra of (*1*) urea, (*2*) AHCMC, (*3*) ANaCMC, (*4*) NaCMC, and (*5*) HCMC derived from commercial CMC. (*A*) Absorption and (ν) wavenumber; the same for Fig. 2.

difference in the amount of bound nitrogen is associated with the above-mentioned presence in the initial flax fibers of other concomitant substances and the specific morphological features of the flax fibers. Presumably, the amidation in flax HCMC fibers proceeds nonuniformly and at a lower rate.

The results of chemical analysis (the amounts of bound nitrogen and carboxy groups or $DS_{Na)}$ were confirmed by IR Fourier spectroscopy. The IR absorption spectra of samples were measured on a Bruker FS-88 IR Fourier spectrometer using KBr pellets.

Figure 1 shows the IR spectra of urea, AHCMC, and ANaCMC, as well as of the initial NaCMC and HCMC. The absorption bands characteristic of purified cotton cellulose include a broad band at 3000–3700 cm^{-1} for free and hydrogen-bonded (via intra- and intermolecular hydrogen bonds) OH groups of the polymer; absorption near 2900 cm^{-1} is associated with CH_2 and CH groups of the polymers (the band at 2900 cm^{-1} of pure cellulose has approximately symmetrical shape [19]). The IR spectrum of NaCMC contains a band at 1597–1605 cm^{-1}, assigned to antisymmetric vibrations of the ionized carboxy groups COO^- [19]. Upon conversion of NaCMC to the H form, an absorption band of the COOH groups appears at 1740 cm^{-1}, as well as a shoulder at 1647 cm^{-1} [4].

Primary amides are characterized by the absorption band of the CO group at 1650–1670 cm^{-1} (amide I) and a band at 1620–1650 cm^{-1} (amide II), associated with bending vibrations of the NH_2 groups [20]. In our case, the spectrum of AHCMC contains absorption bands at 1670 and 1623 cm^{-1}. Also, an absorption band belonging to the hydrogen-bonded NH groups of the primary amide is observed at 3200 cm^{-1}. Upon conversion of AHCMC to ANaCMC, the absorption band at 1623 cm^{-1} cannot be observed because it is close to that of COO^- groups (at 1605 cm^{-1}), and the absorption band at 1670 cm^{-1} is manifested as a shoulder.

The IR spectra of cellulose carbamates contain a weak absorption band of the C=O groups at 790 cm^{-1} (bending vibrations) [7]. A stronger absorption band of the C=O groups (stretching vibrations) of cellulose carbamate at 1710–1720 cm^{-1} cannot be observed because it is obscured by the strong absorption band of the COOH groups at 1740 cm^{-1}.

Analysis of the IR spectra shows that the spectra of AHCMC contain characteristic absorption bands of amides and also an absorption band at 790 cm^{-1}. The latter confirms the above-made assumption that the hydroxy groups are also substituted, i.e., a cellulose carbamate is formed. The conversion of AHCMC to ANaCMC involves hydrolysis of the amide groups, which is responsible for the fact that the absorption band at 1670 cm^{-1} decreases in intensity. It should be noted that, during hydrolysis, the absorption band at 790 cm^{-1} virtually fully disappears. Presumably, the carbamate groups (substitution at hydroxy groups) in the samples synthesized are much less in number than the amide groups (substitution at carboxy groups).

Thus, the IR Fourier-spectroscopic results confirm the chemical and physicochemical data for the mixed cellulose ethers synthesized, which suggest the presence of carboxymethyl and amide groups in the samples. The amide groups are covalently bound to the carboxymethyl and hydroxy groups of the polymer.

Tables 2 and 3 show that the mixed cellulose ethers are only partially soluble in water. To elucidate the factors responsible for the partial solubility of ANaCMC, a sample of the mixed ether with DS_{Na} of 0.22 (Na 2.76%) and the amount of bound nitrogen N of 1.43% (Table 2, run no. 12) was preliminarily dissolved in water, and the resulting solution was filtered through a glass frit. The precipitate formed was washed with ethanol and dried, and a film was cast from the solution by the dry forming method. Figure 2 shows the IR spectra of the film and the precipitate. It is seen that these spectra differ only in the intensity of the absorption bands at 1710

and 790 cm^{-1}, which are the characteristic absorption bands of cellulose carbamates. The water-insoluble precipitate contains a large amount of carbamate groups. As known, cellulose carbamates are water-insoluble; they are well soluble in aqueous alkali solutions. Presumably, the mixed cellulose ether fraction that contains an increased amount of carbamate groups is water-insoluble.

Considering the fact that NaCMC is widely applied as aqueous solutions, we carried out comparative examination of the rheological properties of moderately concentrated (1 wt %) aqueous solutions of commercial NaCMC and of that obtained from short flax fibers (Fig. 3). The flow curves of all the systems examined are partial flow curves of non-Newtonian fluids. Based on the temperature dependences of the viscosity, we calculated the heats of activation of viscous flow E_a of the solutions, specifically for temperatures within 20–40°C. The E_a parameter for the solution of commercial NaCMC was estimated at 20.0, and for the sample based on flax fibers, at 35.0 kJ mol^{-1}. Figure 3 shows the flow curve for the solution of NaCMC that was subjected to repeated carboxymethylation to increase the DS of the cellulose ether and improve its water solubility. It is seen that the viscosity of the solution of NaCMC based on flax fibers substantially exceeds that of the solution of commercial NaCMC. The differences in the viscosity of the solutions are due to those in the molecular weight of the initial polymers.

As known, NaCMC can react with heavy metal ions [8] via carboxy groups. For example, copper, lead, zirconium, and silver salts cause precipitation of NaCMC from solution. Presumably, the appearance in the polysaccharide macromolecules of additional amide substituents containing the primary amino groups will cause an increase in the sorption activity toward polyvalent metal ions. To test this assumption, we examined the sorption activity of the mixed cellulose ethers toward Cu^{2+} ions. Figure 4 presents the kinetic curves of sorption of the copper ions with samples of commercial HCMC, AHCMC obtained thereof, and AHCMC prepared from flax (pH of the sorbate 6.3). It is seen that the maximal amount of the sorbed ions is achieved upon 30-min interaction of the polymers with the solutions of the ions. The appearance in the CMC macromolecules of amide groups (primary amino groups) causes an increase in the amount of the copper ions sorbed.

The sorption kinetic data were used for calculating the initial sorption rate and the total exchange

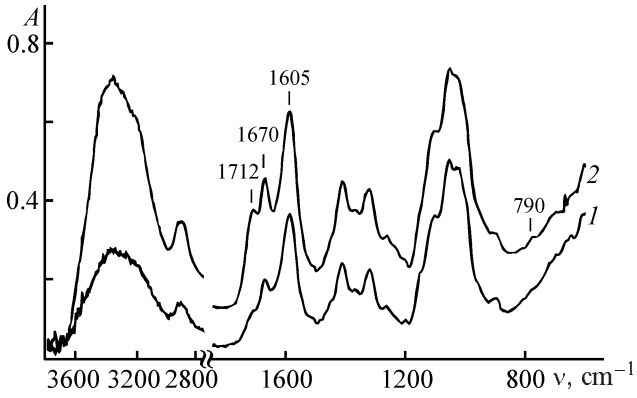


Fig. 2. IR Fourier spectra of (*1*) film obtained from an aqueous solution and (*2*) water-insoluble precipitate of ANaCMC prepared from commercial CMC.

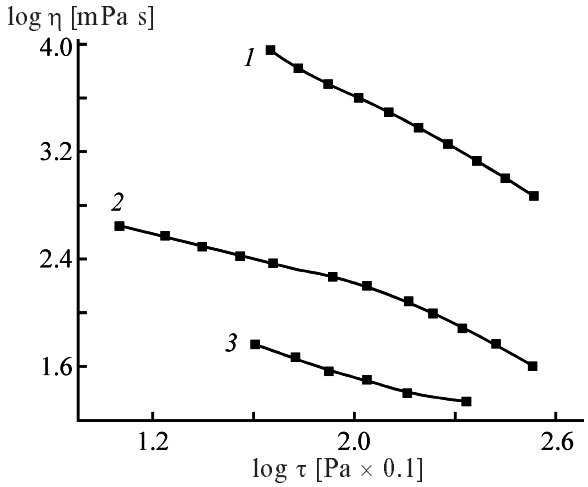


Fig. 3. Flow curves at 20°C of 1% aqueous solutions of (*1, 2*) NaCMC prepared from flax fibers with DS_{Na} of (*1*) 0.52 (DP 950) and (*2*) 0.8 (DP 500) and (*3*) commercial NaCMC (cotton) with DS_{Na} 0.57 (DP 450). (η) Viscosity and (τ) shear stress.

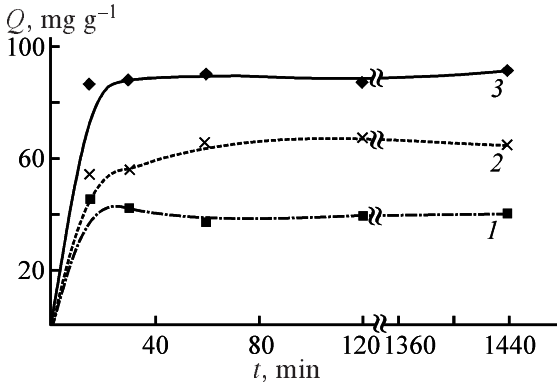


Fig. 4. Kinetic curves of sorption of the Cu^{2+} ions with (*1*) HCMC (commercial), (*2*) AHCMC (based on commercial HCMC), and (*3*) AHCMC (based on flax fibers) samples. (*Q*) Amount of copper ions sorbed and (*t*) sorption time.

Table 4. Total exchange capacity of the synthesized samples toward copper ions

Sample	Initial sorption rate, mg g^{-1} min^{-1}	TEC, meg-equiv g^{-1}
HCMC, DS_{COOH} 0.57	2.62	1.18
Commercial AHCMC, N 4.3%	3.23	2.02
Flax, AHCMC N 3.09%	5.23	2.85

capacity (TEC). The results are presented in Table 4.

It is seen that the maximal TEC is exhibited by the sample synthesized from short flax fibers. It should be noted that sorption of the Cu^{2+} ions can involve the reaction of the metal ions with carboxy groups, formation of chelate complexes, and adsorption of the ions on the fiber surface (molecular sorption via hydrogen bonding). Presumably, a higher TEC for the AHCMC sample obtained from flax is due also to adsorption on the fiber surface, which, in turn, is associated with a larger specific surface area of the flax fibers compared to the cotton fibers (0.35 for $HCMC_{cotton}$ against 0.475 cm^3 g^{-1} for $HCMC_{flax}$).

Thus, by properly choosing CMCs with different DS values and treating them with urea, it is possible to prepare carboxymethyl cellulose amides with different degrees of amidation and modified physicochemical properties. The cellulose ethers synthesized are suitable as biodegradable thickeners for various spheres of human activity, as well as sorbents for heavy metal ions.

CONCLUSIONS

(1) Mixed cellulose ethers were synthesized from commercial carboxymethyl cellulose and that obtained under laboratory conditions from flax fibers, by the reaction with urea.

(2) The cellulose compounds synthesized contain carboxymethyl and amide functional groups.

(3) The flax cellulose ethers exceed in viscosity the solutions of commercial Na salt of carboxymethyl cellulose.

(4) Introduction of amide groups into the macromolecules causes the sorption power of the mixed ethers toward copper ions to increase.

REFERENCES

1. Sun-Tun, Derevitskaya, V.A., and Rogovin, Z.A., *Vysokomol. Soedin.*, 1959, vol. 1, no. 8, pp. 1178–1183.
2. Kinstler, O.B. and Porsham, M.L., *Izv. Akad. Nauk Latv. SSR, Ser. Khim.*, 1977, no. 6, pp. 730–742.
3. Klem, D., Schnaberrauch, M., and Geschwend, G., *Wiss. Z. Friedrich Schiller Univ., Jena Naturwiss. R.*, 1985, nos. 5–6, pp. 34–39.
4. Zabivalova, N.M., Bochek, A.M., Kalyuzhnaya, L.M., et al., *Zh. Prikl. Khim.*, 2003, vol. 76, no. 12, pp. 2048–2052.
5. Zabivalova, N.M., Bochek, A.M., Vlasova, E.N., and Volchek, B.Z., *Zh. Prikl. Khim.*, 2007, vol. 80, no. 2, pp. 301–305.
6. Vali, A.I., Lazurina, L.P., and Rogovin, Z.A., *Khim. Drev.*, 1980, no. 6, pp. 22–24.
7. Goikhman, A.Sh., Irklei, V.M., Zhelevskaya, L.P., et al., *Vozmozhnost' karbamatnogo sposoba polucheniya gidrattsellyuloznylkh nitei i plenok* (Potentialities of the Procedure for Preparing Hydrated Cellulose Threads and Films Using Carbamate), Moscow: Prom–st. Khim. Volokon, 1988.
8. Petropavlovskii, G.A., *Gidrofil'nye, chastichno zameshchennye efiry tsellyulozy i ikh modifikatsiya putem khimicheskogo sshivaniya* (Hydrophilic, Partially Substituted Cellulose Ethers and Their Modification by Chemical Cross-Linking), Leningrad: Nauka, 1988.
9. Petropavlovskii, G.A., Larina, E.I., and Borisova, T.I., *Zh. Prikl. Khim.*, 1984, vol. 18, no. 3, pp. 283–292.
10. Batelaan, J.G. and Horst, P.M. van der, US Patent 6 103 885 (available from free-access patent base of the United States in Internet).
11. Karlsson, A.H., US Patent 3 961 976, 1976 (available from free-access patent base of the United States in Internet).
12. Obolenskaya, A.V., Shchegolev, V.P., Akim, G.A., et al., *Prakticheskie raboty po khimii drevesiny i tsellyulozy* (Practical Works on Wood and Cellulose Chemistry), Moscow: Lesnaya Prom–st., 1965.
13. Petropavlovskii, G.A., Vasil'eva, G.G., and Chernova, Z.D., *Zh. Prikl. Khim.*, 1974, vol. 47, no. 4, pp. 875–880.
14. *TU* (Technical Specification) *6-55-40–90* (instead of *OST* (Branch Standard) *6-05-368–80*): *Technical Grade Sodium CMC*, Vladimir, 1990.

15. *Spravochnik po khimicheskoi tekhnologii obrabotki l'nyanykh tkanei* (Reference Book on Chemical Technology of Linen Fabric Treatment), Fridlyand, G.I., Ed., Moscow: Legkaya Industriya, 1973.

16. Spasajevc, Lj.D., Majdanac, Lj.D., Petrovic, S.D., et al., *Cellulose Chem. Technol.*, 1997, vol. 31, no. 56, pp. 297–308.

17. Zimina, T.R., *Cand. Sci. Dissertation*, St. Petersburg, 1994.

18. Klimova, V.A., *Osnovnye mikrometody analiza organicheskikh soedinenii* (Principal Methods of Microanalysis of Organic Compounds), Moscow: Khimiya, 1967.

19. Zhbankov, R.G., *Infrakrasnye spektry tsellyulozy i ee proizvodnykh* (Infrared Spectra of Cellulose and Its Derivatives), Minsk: Nauka i Tekhnika, 1964.

20. Bellamy, L.J., *The Infra-Red Spectra of Complex Molecules*, London: Methuen, 1954.

ISSN 1070-4272, Russian Journal of Applied Chemistry, 2008, Vol. 81, No. 9, pp. 1630–1633. © Pleiades Publishing, Ltd., 2008.
Original Russian Text © L.V. Furda, I.G. Ryl'tsova, O.E. Lebedeva, 2008, published in Zhurnal Prikladnoi Khimii, 2008, Vol. 81, No. 9, pp. 1555–1558.

MACROMOLECULAR CHEMISTRY AND POLYMERIC MATERIALS

Catalytic Degradation of Polyethylene in the Presence of Synthetic Aluminosilicates

L. V. Furda, I. G. Ryl'tsova, and O. E. Lebedeva

Belgorod State University, Belgorod, Russia

Received May 26, 2008

Abstract—Degradation of polyethylene in the presence of synthetic amorphous aluminosilicates as catalysts to form petroleum-like hydrocarbons was studied.

DOI: 10.1134/S1070427208090292

The amount of difficultly degradable industrial and domestic wastes steadily increases. Large-tonnage wastes from polyethylene packing materials are incinerated or disposed of. However, they can be a valuable secondary raw material for chemical industry.

It is known that thermolysis of polyethylene yields lower olefins [1]. A wide range of products which are frequently characterized as petroleum-like hydrocarbons can be obtained by catalytic degradation of polyethylene. This process can be catalyzed by aluminosilicates of different compositions. Among them, zeolites are used most frequently [2–4].

Natural aluminosilicates, clays, were proposed to produce liquid hydrocarbons from polyethylene [5].

The aim of this study was to determine the features of this process in the presence of model catalysts, synthetic aluminosilicates.

It is believed that the reactive components of a clay catalyst of polyethylene thermolysis are aluminosilicates. Their catalytic activity depends on the acidity of the samples. The aluminosilicate acidity is caused by the presence of aluminum. Therefore, the catalytic activity of aluminosilicates of similar structure in polyethylene degradation should correlate with the aluminum content of the catalysts.

EXPERIMENTAL

Eight aluminosilicates with different aluminum contents and hydrated silica sample were prepared. Since the acidity of aluminosilicates increases with increasing aluminum content to 13–17 wt %, we studied the catalysts with the aluminum content in the range including this interval.

Catalysts were prepared by coprecipitation from solution. An ethanol solution of tetraethoxysilane (tetraethoxysilane : ethanol weight ratio 1 : 1) was mixed with a 6% aqueous solution of aluminum nitrate. An ammonium hydroxide solution was added to pH 9. The mixture was stirred for 1 h with a magnetic stirrer and allowed to stand for 24 h to complete precipitation. The precipitate was filtered off and calcined in a muffle furnace at 600°C. The composition and some properties of the catalysts are presented in Table 1.

The powder X-ray diffraction patterns of the catalyst samples were recorded on DRON-3 diffractometer using CuK_α radiation.

Table 1. Properties of catalysts

Sample no.	Aluminum content, wt %	Specific surface area, $m^2\ g^{-1}$	Total pore volume, $cm^3\ g^{-1}$
1	0	149	0.6
2	1.6	167	1.0
3	2.4	110	0.5
4	5.8	208	0.9
5	8.1	129	0.6
6	12.0	324	0.8
7	12.9	184	0.9
8	16.3	183	0.9
9	22.9	216	0.8

The specific surface area, pore volume, and pore size distribution were determined by low-temperature adsorption and thermal desorption of nitrogen on an ASAP-2010 unit.

The sample morphology was studied by scanning electron microscopy on a Quanta 200 3D microscope. To estimate the sample uniformity, the aluminum content of the samples was determined by energy-dispersive X-ray spectroscopy (EDX) on a spectrometer attached to the microscope. It is known that EDX allows nondestructive determination of the local composition of a sample. Three measurements in different points of the surface were performed for each sample. The results are presented in Table 2.

The surface acidity of aluminosilicate samples were estimated by the Hammett procedure.

Catalytic degradation of polyethylene was studied on a flow unit in an argon flow. The reaction mixture was prepared as follows. A weighed portion of powdered catalyst was added to heated *m*-xylene. The mixture was vigorously stirred and allowed to stand to complete evaporation of the solvent. The polyethylene : catalyst weight ratio was 3 : 1 or 5 : 1. Polyethylene films crushed to 2–3-mm particles were loaded in a quartz reactor and heated in an argon flow to 400°C. The liquid products were collected in a receiving flask.

The degree of polyethylene degradation was estimated by the gravimetric yield of liquid and solid hydrocarbons. Gaseous thermolysis products were not collected and identified.

The liquid products were analyzed by chromatography–mass spectrometry on Saturn 200 chromatograph–mass spectrometer (Varian) with an ion trap. The mixtures were separated on a 30-m quartz capillary column 0.25 mm in diameter coated with CP-Sil 8 CB stationary phase.

Our results showed that the composition and yield of polyethylene thermolysis product significantly depend on the catalyst composition. Aluminosilicates with a low aluminum content (>3 wt %) catalyzed polyethylene degradation only to solid waxy products. In this case, no liquid products are formed at both polyethylene : catalyst ratios. Liquid products are formed in the presence of aluminosilicates containing more than 5.8 wt % aluminum. It should be noted that only liquid products were observed at a polyethylene : catalyst ratio of 3 : 1. At a polyethylene : catalyst ratio of 5 : 1, polyethylene degrades to form a mixture of liquid and solid hydrocarbons. The yield of the liquid products in the presence of almost all the examined catalysts at a polyethylene : catalyst ratio of 3 : 1 is higher than that at a ratio of 5 : 1 (Table 3).

Table 2. Comparative results of chemical and energy-dispersive X-ray (EDX) analysis of the samples

Aluminum content, wt %			
chemical analysis	EDX data		
5.8	5.8	6.8	6.2
12.0	12.3	14.3	15.0
12.9	15.3	13.2	12.9
16.3	15.9	15.8	15.7
22.9	23.5	23.4	22.8

Table 3. Yield of polyethylene thermolysis products depending on the aluminum content of the catalyst

Al content, wt %	Yield of liquid products, wt %, at indicated polyethylene : catalyst ratio	
	3 : 1	5 : 1
0	0	0
1.6	0	0
2.4	0	0
5.8	69	51
8.0	48	43
12.0	50	44
12.9	57	56
16.3	69	52
22.9	49	56

The liquid products contain linear and branched isomers of C_5–C_{26} alkanes and alkenes and aromatic hydrocarbons. For example, the fraction of low-boiling C_4–C_{10} hydrocarbons (bp < 200°C) in the products obtained in the presence of aluminosilicate with 5.8 wt % aluminum content reaches 77 wt %. The olefin content in this fraction is higher by a factor of approximately 2 than that of paraffin hydrocarbons. The content of cyclic and aromatic hydrocarbon is 9 and 19 wt %, respectively. It should be noted that this fraction contains significant amounts of linear and branched heptenes (11 wt %) and xylenes (17 wt %). Among C_{11}–C_{26} hydrocarbons, paraffins prevail and virtually no olefins are detected. High content of low-boiling hydrocarbons in the liquid products makes these fractions promising as raw materials for production of gasolines and solvents.

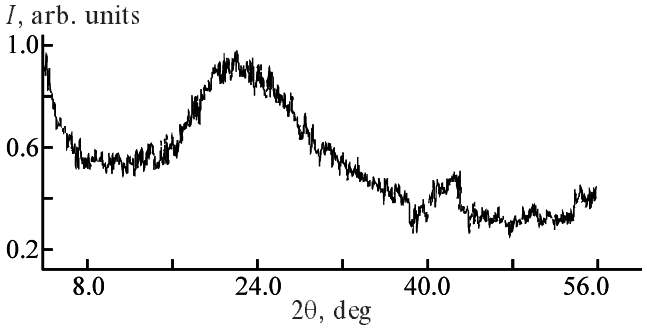


Fig. 1. X-ray diffraction pattern of aluminosilicate with 5.8 wt % aluminum content. (I) Intensity and (2θ) Bragg angle.

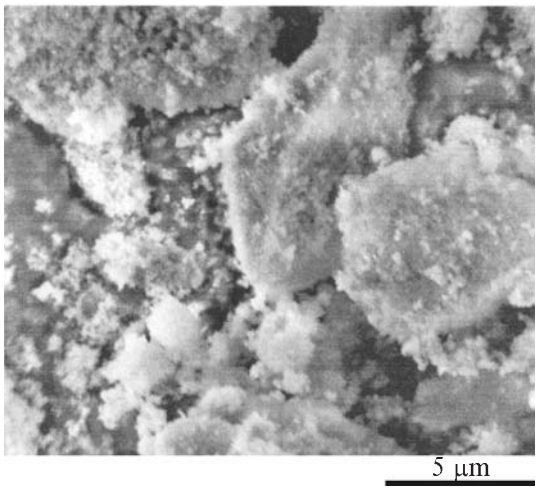


Fig. 2. Electrom micrograph of aluminosilicate with 5.8 wt % aluminum content.

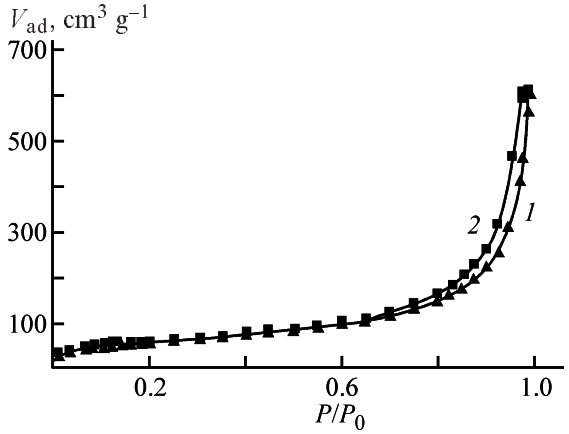


Fig. 3. Nitrogen (1) adsorption and (2) desorption isotherms on aluminosilicate with 5.8 wt % aluminum content. (V_{ad}) Adsorbed volume and (P/P_0) relative nitrogen pressure.

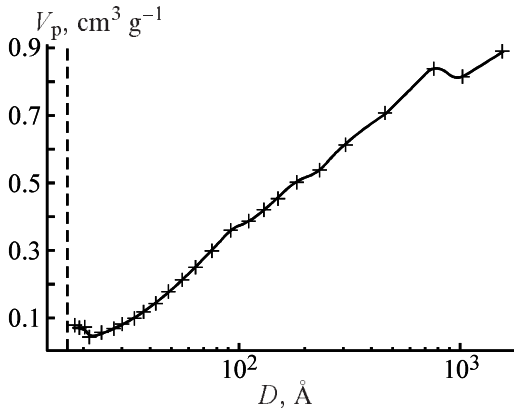


Fig. 4. Pore size distribution of aluminosilicate with 5.8 wt % aluminum content. (V_p) pore volume and (D) pore diameter.

X-ray diffraction analysis showed that all samples were X-ray amorphous. The X-ray diffraction patterns of all the samples are similar (Fig. 1). As seen from electron micrographs (magnification ×15000), the samples are characterized by a broad particle size distribution (Fig. 2).

The low-temperature nitrogen adsorption and thermal desorption isotherms for all samples are also similar (Fig. 3) and are of type IV [6]. These isotherms suggest mesoporous structure of the samples. The system in question is characterized by capillary condensation. The hysteresis loops are of type A and are typical of uniformly packed agglomerates and globules of similar size.

The pore size distribution of the aluminosilicates is rather broad. The pore size distribution of one of the examined samples is shown in Fig. 4. All samples contain significant amount of macropores.

The sample acidity was determined using appropriate indicators. All samples have acid sites affecting the color of indicators with $3.46 < pK_a < 5.0$. At the same time, only aluminosilicates that catalyze polyethylene degradation to liquid products also contain acid sites changing the color of indicators with pK_a 6.40. These sites are absent in aluminosilicates with a low aluminum content, which are inactive in polyethylene conversion to liquid products. Apparently, the behavior of aluminosilicates in polyethylene degradation depends on not only the number but also the strength of the acid sites.

CONCLUSIONS

(1) Amorphous aluminosilicates with the aluminum content exceeding 5.8 wt % are effective cata-

lysts of degradation of polyethylene waste into liquid hydrocarbons.

(2) The catalytic activity depends on not only the aluminum content but also the uniformity of aluminum distribution and the strength of acid sites of the catalyst surface.

ACKNOWLEDGMENTS

This study was financially supported by Belgorod State University (project VKG 019-07).

REFERENCE

1. Bryk, M.G., *Destruktsiya napolnennykh polimerov* (Degradation of Filled Polymers), Moscow: Khimiya, 1989.
2. Seo, Y.H., Lee K.H., and Shin, D.H., *J. Anal. Appl. Pyrol.*, 2003, vol. 70, no. 2, pp. 383–398.
3. Ali, S., Garforth, A.A., Harris, D.H., et al., *Catal. Today*, 2002, vol. 75, nos. 1–4, pp. 247–255.
4. Cardona, S.C. and Corma, A., *Appl. Catal. B: Environ.*, 2000, vol. 25, nos. 2–3, pp. 151–162.
5. RF Patent 2262520.
6. Gregg, S.J. and Sing, K.S.W., *Adsorption, Surface Area and Porosity*, London: Academic, 1982.

ISSN 1070-4272, Russian Journal of Applied Chemistry, 2008, Vol. 81, No. 9, pp. 1634–1637. © Pleiades Publishing, Ltd., 2008.
Original Russian Text © A.B. Glazyrin, M.I. Abdullin, N.A. Kochkov, R.V. Karmanov, S.T. Burtan, N.V. Shaikhutdinov, 2008, published in Zhurnal Prikladnoi Khimii, 2008, Vol. 81, No. 9, pp. 1559–1562.

MACROMOLECULAR CHEMISTRY AND POLYMERIC MATERIALS

Polymer–Asphalt Compounds Based on 1,2-Polybutadienes

A. B. Glazyrin, M. I. Abdullin, N. A. Kochkov, R. V. Karmanov, S. T. Burtan, and N. V. Shaikhutdinov

Bashkir State University, Ufa, Bashkortostan, Russia

Received April 9, 2008

Abstract—Properties of polymer–asphalt compounds containing 1,2-polybutadienes differing in the molecular weight and structure of macromolecules were examined. Introduction of syndiotactic 1,2-polybutadiene in combination with a plasticizing additive noticeably improves the main service properties of asphalts.

DOI: 10.1134/S1070427208090309

A promising way to improve the quality of road pavements is the use of asphalts in combination with various polymers. Polymer–asphalt binders (PABs), compared to common road asphalts, provide higher quality of road pavement and its longer service life.

The most widely used agents for modifying asphalts are butadiene–styrene block copolymers [1–3] which are thermoelastoplastics, i.e., they combine high elasticity with the capability to pass into a viscous-flow state at elevated temperatures, similarly to thermoplastics.

1,2-Polybutadiene produced by stereospecific polymerization of butadiene in solution is also a thermoelastoplastic [4, 5]. Its production is now being commercialized by the Russian chemical industry.

In this study we examined the effect of 1,2-polydiene on the physicomechanical properties of road asphalts.

EXPERIMENTAL

We used 1,2-polybutadienes differing in the molecular weight and structure of macromolecules: (1) high-molecular-weight syndiotactic 1,2-polybutadiene (SPB), M_n 52.6 × 10^3, degree of syndiotacticity 53%, melting point T_m 105°C, glass transition point T_g –18°C, degree of crystallinity 18%; (2) low-molecular-weight atactic 1,2-polybutadiene (LPB), M_n 8.35 × 10^3, degree of polydispersity 1.98, content of 1,2 units in macromolecules 70.5%, viscous resinous product, dropping point 54°C.

To prepare polymer–asphalt compounds, we used BND-90/130 road asphalt produced by Kichui Oil Refinery and Ufaneftekhim Joint-Stock Company. Polymer–asphalt binders were prepared by mixing the components at 140–150°C [6]. The physicomechanical properties of asphalts and polymer–asphalt binders were determined by standard procedures. As reference we used Kraton D-1101 butadiene–styrene thermoplastic widely used as PAB component in road paving.

Introduction of 2 wt % SPB into asphalt leads to a noticeable (by 14–19%) decrease in the needle penetration depth at 25 and 0°C (Table 1, Fig. 1), char-

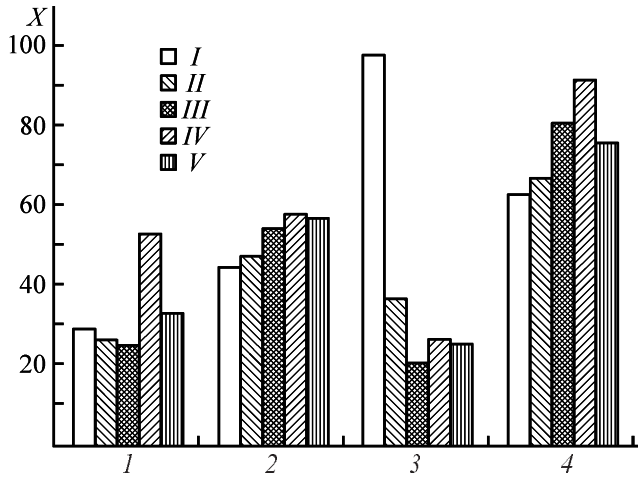


Fig. 1. Influence of composition of the asphalt compound on its properties. (*X*) Parameter value. (*1*) Needle penetration depth at 0°C, 0.1 mm units; (*2*) ring-and-ball softening point, °C: (*3*) extensibility at 25°C, cm; and (*4*) interval of working temperatures, °C. (*I*) Initial asphalt, (*II*) asphalt + 2% SPB, (*III*) asphalt + 3% SPB, (*IV*) asphalt + 3% SPB + 6% I-40A oil, and (*V*) level prescribed by [6].

Table 1. Effect of polymeric additives on asphalt properties. Polymer content of asphalt compound 2 wt %

Parameter	Initial asphalt*	Polymeric additive			Prescribed for PAB by [6]
		SPB	LPB	Kraton	
Needle penetration depth, 0.1 mm units:					
at 25°C	95.0	80.0	94.3	88.7	No less than 60
at 0°C	28.5	25.0	30.3	26.0	No less than 32
Ring-and-ball softening point, °C	43.4	46.4	45.1	48.0	No less than 56
Extensibility, cm:					
at 25°C	97.0	36.4	58.0	25.2	No less than 25
at 0°C	6.0	5.5	8.7	5.1	No less than 11
Brittle point, °C	–19.0	–20.3	–22.0	–20.1	No higher than –20
Flash point, °C	237	234	233	233	No lower than 230
Weight change after heating, %	0.70	0.04	0.06	0.02	–
Softening point change after heating, °C	2.0	2.0	1.6	2.0	No more than 5
Penetration index	–1.0	–1.0	–1.0	–0.2	From –1 to 1
Adhesion to material	Stands test	Stands test	Stands test	Stands test	Stands test with control sample no. 2
Elasticity, %:					
at 25°C	–	84	81	74	No less than 80
at 0°C	–	70	72	58	No less than 70

* BND 90/130 asphalt produced by Kichui Oil Refinery.

Table 2. Effect of plasticizers (PN-6, I-40) on properties of the polymer–asphalt compound containing 3 wt % SPB. Plasticizer content 6 wt %

Parameter	Initial asphalt*	PAB without plasticizer	PAB with PN-6	PAB with I-450
Needle penetration depth, 0.1 mm units:				
at 25°C	106	74	103	116
at 0°C	32	24	28	52
Ring-and-ball softening point, °C	44.8	53.3	52.1	56.9
Extensibility, cm				
at 25°C	102.0	20.2	21.2	26.2
at 0°C	7.2	6.8	7.8	11.0
Brittle point, °C	–23.6	–26.6	–30.8	–34.7

* BND 90/130 asphalt produced by Ufaneftekhim Joint-Stock Company.

acterizing the viscosity of the asphalt compound. The penetration also decreases on asphalt modification with Kraton polymeric product (Table 1). An increase in the viscosity of the asphalt compound in the presence of the above polymeric products is apparently due to formation of a three-dimensional polymer network in the asphalt structure.

On introducing low-molecular-weight 1,2-polybutadiene into the asphalt, the penetration index of the asphalt compounds remains essentially unchanged (Table 1). In this case, the influence of the polymeric additive on the properties of the asphalt compound is largely determined by the plasticizing effect of the polydiene.

Introduction of polymeric additives into asphalt compounds affects their softening point T_s. Introduction of 2 wt % polymeric products into asphalt increases T_s from 43.4 to 45.1–48.0°C. The increase in T_s is more significant with SPB and Kraton additives (Table 1). It should be noted that, as the SPB content in the asphalt compound is increased to 3 wt %, the softening point of PAB increases to 53.3°C, i.e., by approximately 10°C relative to the initial asphalt (Table 2, Fig. 1).

Another important parameter used for estimating the heat resistance of an asphalt compound is the dropping point T_d. As the content of 1,2-polybutadienes in asphalt is increased from 1 to 5 wt %, T_d

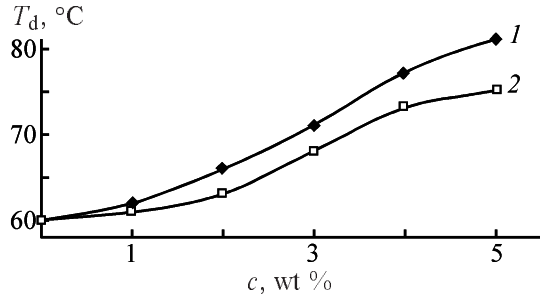


Fig. 2. Dropping point T_d of asphalt compounds as a function of the 1,2-polybutadiene content c in the asphalt. (*1*) SPB and (*2*) LPB.

regularly increases (Fig. 2). The dropping point of asphalt is affected more strongly by high-molecular-weight SPB: On adding it in an amount of 3 wt %, T_d increases by 12°C, whereas with the same amount of LPB it increases by only 7°C (Fig. 2).

On introducing polymeric additives into asphalt, the brittle point T_b characterizing the frost resistance of asphalt compound decreases by 1–3°C (Tables 1, 2).

Asphalt is a thermoplastic product showing virtually no hyperelastic properties in the service temperature range. One of parameters characterizing the plasticity of an asphalt, the extent of its structurization, is extensibility (ductility). Experiments show that the extensibility of polymer-modified asphalt compounds decreases (by a factor of 1.7–3.6 at 25°C) relative to the initial asphalt, with the effect being more significant with high-molecular-weight modifiers: SPB and Kraton (Table 1). At 0°C, binders with these polymers are also characterized by low extensibility, whereas asphalt compounds containing LPB are more ductile than the initial asphalt (Table 1).

The observed decrease in the plasticity of asphalt compounds on introducing high-molecular-weight polymeric additives should be attributed to a change in their viscoelastic properties due to formation of a three-dimensional macromolecular network and the resulting increase in the extent of asphalt structurization.

The resistance of a road pavement to dynamic loads is largely determined by elastic properties of an asphalt compound and by its resistance to reversible strains [2]. An asphalt compound can be classed with elastomers if its elasticity parameter defined as the degree of reversible tensile deformation at 0°C is no less than 70% [6]. It is important that, in contrast to the initial asphalt showing no elasticity, polymer–asphalt compounds prepared with 1,2-polybutadienes have the elasticity parameter no less than 70% (Table 1), i.e., are characterized by significant reversible deformations and hence can be classed with elastomeric products.

Thus, introduction of polymeric modifiers into SPB and LPB leads to a decrease in the plasticity characteristic of unmodified asphalt and to appearance of elasticity characteristic of amorphous polymers, which is important for making a road pavement resistant to dynamic loads.

Such parameters of asphalt compounds as the flash point, changes in the weight and softening point after heating, and penetration differ from those of the initial asphalt insignificantly and meet the requirements of the standard (Table 1).

The experimental results show that the main properties of the modified asphalt compound prepared with SPB are close to those of the asphalt compound containing Kraton D-1101 butadiene–styrene thermoelastoplastic. Introduction into the asphalt of LPB affects the properties of the asphalt compound to a lesser extent than does introduction of SPB. Nevertheless, LPB imparts to the compound certain elastic properties. The properties of asphalt compounds modified with 1,2-polybutadienes meet the requirements to PABs with butadiene–styrene block copolymers (Kraton, DST) except the penetration and extensibility at 0°C and the softening point.

Introduction into asphalts of relatively small (2–3 wt %) amounts of polybutadienes SPB and LPB yields asphalt compounds exhibiting the required elastic properties and broader, compared to the initial asphalt, set of service characteristics necessary to ensure high quality of a road pavement. To modify asphalts, it is appropriate to use high-molecular-weight syndiotactic 1,2-polybutadiene (SPB), because PABs with this additives show better characteristics than PABs with LPB.

One of the ways to improbe PAB properties, in particular, the extensibility and brittle point, is introduction into an asphalt compound of low-molecular-weight plasticizers: hydrocarbon solvents and oils [2].

We examined the effect of PN-6 aromatic solvent [TU (Technical Specification) 38.101 121 7–89] and O-40A industrial oil [GOST (State Standard) 20 799–88] on the properties of PAB containing 3 wt % SPB. Introduction of these hydrocarbons (6 wt % based on asphalt) leads to appreciable changes in the characteristics of the polymer–asphalt compound (Table 2, Fig. 1). From the viewpoint of improvement of the service properties of PAB, I-40A indus-

trial oil showed better performance as plasticizer. Introduction of I-40A oil into the polymer–asphalt compound containing SPB increased the penetration by a factor of 2.2 (at 0°C). Furthermore, the extensibility at 25 and 0°C increased by 30 and 62%, respectively, and the brittle point of PAB decreased by 8.1°C (Table 2, Fig. 1). The effect is apparently due to weakening of intermolecular interaction in the polymer–asphalt system under the action of nonpolar hydrocarbon molecules of the industrial oil.

Combined use of SPB and I-40A oil not only decreases the brittle point but also simultaneously increases the softening point of the asphalt compound (Table 2). Therefore, the service temperature range of the asphalt binder (interval between the softening and brittle points) increases by more than 20°C relative to the initial asphalt (Fig. 2) and reaches 92°C.

CONCLUSIONS

(1) The service properties of pavement bitumens can be appreciably improved by introducing high-molecular-weight syndiotactic 1,2-polybutadiene.

(2) Combined use in PAB of syndiotactic 1,2-polybutadiene and I-40A industrial oil makes its service temperature interval wider by more than 20°C compared to the initial asphalt.

(3) Polymer–asphalt compounds based on syndiotactic 1,2-polybutadiene can be recommended for practical use in road building.

REFERENCES

1. Basurmanova, I.V. and Gofman, L.M., in *Avtomobil'nye dorogi: Informatsionnyi sbornik* (Highways: Information Coll.), Informavtodor, 1996, issue 1, pp. 1–9.
2. Polymer–Asphalt Materials Based on SBS for Road Building, *Avtomobil'nye dorogi: Informatsionnyi sbornik* (Highways: Information Coll.), Informavtodor, 2002, issue 4, p. 112.
3. Gol'ts, M., *Avtomob. Dor.*, 1998, no. 7, p. 12.
4. RF Patent 2177008.
5. Glazyrin, A.B., Sheludchenko, A.V., Zaboristov, V.N., and Abdullin, M.I., *Plast. Massy*, 2005, no. 8, pp. 13–15.
6. *OST* (Branch Standard) *218.010–98: Polymer–Asphalt Road Binders with SBS-Type Block Copolymers: Technical Specification.*
7. *GOST* (State Standard) *22245–90: Viscous Petroleum Asphalts for Paving: Technical Specification.*

ISSN 1070-4272, Russian Journal of Applied Chemistry, 2008, Vol. 81, No. 9, pp. 1638–1641. © Pleiades Publishing, Ltd., 2008.
Original Russian Text © L.L. Semenycheva, E.I. Bogatova, V.V. Vins, 2008, published in Zhurnal Prikladnoi Khimii, 2008, Vol. 81, No. 9, pp. 1563–1566.

MACROMOLECULAR CHEMISTRY AND POLYMERIC MATERIALS

Copolymers of Butyl Acrylate with Vinyl Alkyl Ethers as Thickening Additives to Oils

L. L. Semenycheva, E. I. Bogatova, and V. V. Vins

Lobachevsky Nizhni Novgorod State University, Nizhni Novgorod, Russia
Sovremennye Khimicheskie Tekhnologii Private Company, Russia

Received December 28, 2007

Abstract—The possibility of preparing copolymers of butyl acrylate with vinyl butyl and vinyl isobutyl ethers with various ratios of monomeric units by radical polymerization was examined.

DOI: 10.1134/S1070427208090310

Macromolecular compounds are widely used as depressor and thickening additives to oils [1, 2]. Well-known additives based on polyalkyl methacrylates often exhibit thickening and depressor properties simultaneously [3–6]. However, the use of alkyl acrylates, in particular, polybutyl acrylate, for this purpose is restricted by their limited solubility in oils [7].

In this study, as thickeners for dioctyl sebacate (DOS), which is the base of synthetic oils [8], we suggest copolymers of butyl acrylate (BA) with vinyl isobutyl (ViBE) and vinyl butyl (VnBE) ethers. We examined the synthesis features and properties of these copolymers.

EXPERIMENTAL

We used freshly distilled ViBE and VnBE (83–84°C fraction) [9].

Butyl acrylate was purified by the procedure described in [7, 10]. The physicochemical constants of BA are in agreement with published data [10].

Azobis(isobutyronitrile) (AIBN) was purified by recrystallization from methanol [11].

The polymerization was performed at 50°C in evacuated ampules in the bulk of the monomer. The ampule was charged with a definite weighed portion of AIBN and with the comonomers: ViBE (or VnBE) and BA. The mixture was degassed by repeated freezing–pumping–thawing (~10^{-2} mm Hg).

Polymer samples were purified by reprecipitation from acetone into ethanol and then dried at reduced pressure to constant weight. The conversion was estimated gravimetrically by the dry residue [12].

The content of BA units in ViBE–BA and VnBE–BA copolymers was determined by IR spectroscopy. The composition of ViBE–BA and VnBE–BA copolymers was determined from the BA content. Studies were performed on an Infrolyum-FN-801 IR spectrometer in KBr cells (layer thickness 0.51 mm). The content of BA in the copolymer was determined with a calibration plot from the areas of the characteristic vibration band of the carbonyl group at 1727 cm^{-1}.

The molecular-weight characteristics were determined by gel permeation chromatography (GPC) on a Knauer liquid chromatography (Germany) with a Linear-2 linear column (Phenomenex, USA). An RI Detector K-2301 differential refractometer was used as detector, and chloroform was an eluent. The eluent flow rate was 1 ml min^{-1}, and the temperature, 25°C. For the calibration we used close-cut polystyrene references [13].

The kinematic viscosity of solutions of the polymers in DOS was determined with a VPZh-4 viscometer by the standard procedure [14]. The viscosity index was calculated by the procedure described in [15].

The well-known feature of butyl acrylate polymer at >30% conversion is low solubility in organic solvents, inculding oils, due to formation of the cross-linked polymer [16, 17]. To obtain an oil-soluble additive based on polybutyl acrylate, into BA polymer we introduced units of readily oil-soluble vinyl

Table 1. Results of copolymerization of BA with ViBE and VnBE, initiated with AIBN (0.15 mol %), in the bulk at 50°C

Composition of monomer mixture, mol %			Polymerization time, h	Conversion, %
BA	ViBE	VnBE		
80	20	–	0.2	90
60	40	–	10.0	85
50	50	–	11.0	67
30	70	–	8.0	49
20	80	–	38.6	36
15	85	–	36.0	28
50	–	50	11.3	71
40	–	60	12.5	60
30	–	70	8.0	43
20	–	80	38.6	34

Table 2. Results of analysis of the polymers obtained at limiting conversion from BA–VnBE (ViBE) mixtures of various compositions

Composition of monomer mixture, mol %			Conversion, %	Copolymer composition, mol %		
BA	ViBE	VnBE		BA	ViBE	VnBE
15	–	85	28	45	–	55
20	–	80	36	63	–	37
30	–	70	49	65	–	35
50	–	50	67	72	–	27
60	–	40	85	80	–	19
20	80	–	34	47	53	–
30	70	–	43	52	48	–
40	60	–	60	53	47	–
50	50	–	71	64	36	–

alkyl ethers (ViBE, VnBE) whose polymeric derivatives are also used as viscosity additives to mineral and synthetic oils [3, 4].

Copolymers of various compositions were prepared from BA–ViBE and BA–VnBE monomer mixtures at varied monomer ratio in the presence of AIBN as initiator. The results we obtained show (Table 1) that the copolymerization of BA with vinyl alkyl ethers decelerates in proportion to an increase in the ether content in the starting mixture. This is quite expectable, because it is well known that introduction of a second monomer forming a more stable radical (ether in our case) decelerates the polymerization. It is known that radical polymerization of vinyl alkyl ethers occurs difficultly, and not all compounds of this class can be involved in the process [18]. Data on homopolymerization of ViBE and VnBE and on their copolymerization with other vinyl monomers are scarce and contradictory [19–21]. Nevertheless, approximately zero relative activities of VnBE in copolymerization with BA (0, according to [21]) and relative activities of BA and ViBE in their copolymerization performed to ≤10% conversion ($r_{BA} = 5.2 \pm 1.5$, $r_{VnBE} \approx 0$, respectively), calculated by the Kelen–Tudos method [22] from the composition curve (Fig. 1) plotted on the basis of the IR data, suggest that the major fraction of both VnBE and ViBE units are incorporated in the polymer chain at deep conversions, which results in sharp deceleration of the copolymerization.

To estimate the molecular-weight characteristics, solubility, and thickening properties of copolymers, they were isolated at a conversion at which the polymerization rate starts to drastically decrease. The copolymer composition determined by IR spectroscopy appreciably differs from the composition of the monomer mixture (Table 2), which is due to different reactivities of the comonomers.

The molecular-weight characteristics indicate that, for copolymers containing up to 65% acrylate units (45 and 63%, Fig. 2, curves *1* and *2*, respectively), the molecular-weight distribution (MWD) curves are unimodal. With an increase in the content of BA units to 65%, the MWD curves tend to become bimodal (curve *3*). The bimodality is obvious in the case of the copolymer with 73% content of acrylate units (curve *4*). This fact is apparently associated with the formation of BA homopolymer along with the copolymer.

To test copolymers as additives, samples isolated at limiting conversions were dissolved in AU mineral

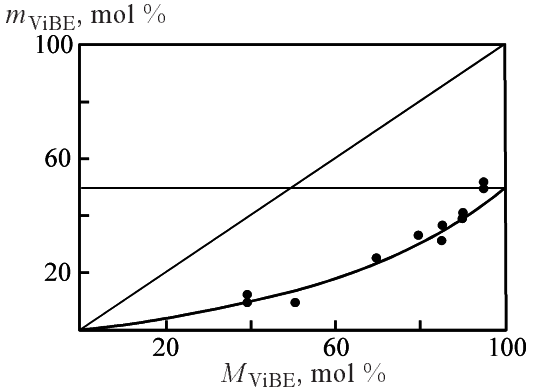


Fig. 1. Composition curve for BA–ViBE copolymer: (m_{ViBE}) content of ViBE units in the copolymer and (M_{ViBE}) content of ViBE in the monomer mixture.

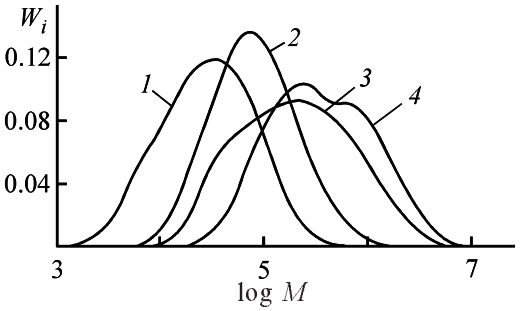


Fig. 2. Molecular-weight distribution curves for samples of BA–ViBE copolymers of compositions (mol %): (*1*) 45 : 55, (*2*) 63 : 37, (*3*) 65 : 35, and (*4*) 73 : 27. (W_i) Fraction of macromolecules with given M.

oil [8, 23] and in dioctyl sebacate (DOS), the base for synthetic oils. When added in an amount of 0.1% to the mineral base, the polymers did not dissolve even with vigorous stirring and heating. In DOS, the samples (0.1%) dissolved on heating and formed stable solutions. The viscosity of 0.1% DOS solutions of the polymers that had been isolated from monomer mixtures of various compositions was measured at 40 and 100°C in comparison with the copolymer-free sample (Table 3). For comparison, we obtained solutions of polyvinyl isobutyl ether in DOS of viscosity 3.6 cSt, attained at ~0.8% concentration of the polymer in DOS. These data indicate that ViBE–BA copolymers show a good thickening power. From the kinematic viscosities we calculated the viscosity index [14, 15]. The results are given in Table 3. As seen from the results obtained, the kinematic viscosity of solutions and viscosity indices increase in proportion with the BA content in the copolymer.

Table 3. Kinematic viscosity of 0.1 wt % solutions of VnBE (ViBE)–BA copolymers in DOS

Copolymer composition, mol %			Kinematic viscosity, cSt		Viscosity index
BA	ViBE	VnBE	40°C	100°C	
–	–	–	11.48	3.27	166
63	–	37	12.23	3.44	170
65	–	35	12.55	3.56	180
73	–	27	12.94	3.64	181
81	–	19	13.51	3.80	188
47	53	–	13.50	3.65	166
52	48	–	13.64	3.71	182
53	47	–	13.66	3.71	182
64	36	–	13.70	3.80	183

As the congealing point of DOS is very low [8], the depressor properties of the copolymers were not studied. It was shown, however, that the copolymers did not cause an increase in the congealing point.

CONCLUSIONS

(1) Copolymers of butyl acrylate with vinyl butyl and vinyl isobutyl ethers with various ratios of monomer units were prepared, and the relative activities of butyl acrylate and vinyl isobutyl ether were calculated.

(2) Copolymers of butyl acrylate and vinyl butyl or vinyl isobutyl ether are thickening additives to the base of synthetic oils, dioctyl sebacate. The effect is determined by the copolymer composition.

REFERENCES

1. Alekseev, A.P., Leonenko, V.V., and Safonov, G.A., *Khim. Tekhnol. Topl. Masel*, 2005, no. 5, pp. 39–41.
2. Kuliev, A.M., *Khimiya i tekhnologiya prisadok k maslam i toplivam* (Chemistry and Technology of Additives to Oils and Fuels), Leningrad: Khimiya, 1985.
3. Kalan, S.Z. and Radzvenchuk, I.F., *Vyazkostnye prisadki i zagushchennye masla* (Viscosity Additives and Thickening Oils), Moscow: Khimiya, 1982.
4. Arkhimedov, A.I. and Buniyatzade, I.A., *Khimiya vyazkostnykh prisadok* (Chemistry of Viscosity Additives), Baku: Elm, 1993.
5. Moikin, A.A., *Rynok Produkt. Tekhnol.*, 2006, no. 1, pp. 24–26.
6. Moikin, A.A., Valeshnyaya, T.A., and Kazantsev, O.A., *Neftepererab. Neftekhim.*, 2005, no. 7, pp. 36–39.
7. *Entsiklopediya polimerov* (Polymer Encyclopedia), Moscow: Sov. Entsiklopediya, 1976, vol. 1.
8. *Topliva, smazochnye materialy, tekhnicheskie zhidkosti: Assortiment i primenenie: Spravochnik* (Fuels, Lubricating Materials, Technical Fluids: Assortment and Use: Handbook), Shkol'nikov, V.M., Ed., Moscow: Tekhniform, 1999.
9. *Lancaster 2002–2003: Catalog of Chemicals*, 2003.
10. *Analytical Chemistry of Polymers*, part 1: *Analysis of Monomers and Polymeric Materials*, Kline, G.M., Ed., New York: Interscience, 1959.
11. *Organic Syntheses*, Blatt, A.H., Ed., New York: Wiley, 1944. Translated under the title *Sintezy organicheskikh preparatov*, Kazanskii, B.A., Ed., Moscow: Inostrannaya Literatura, 1953, vol. 4.
12. *Praktikum po khimii i fizike polimerov* (Practical

Course of Polymer Chemistry and Physics), Kurenkov, V.F., Ed., Moscow: Khimiya. 1990.

13. Moris, S., *J. Liq. Chromatogr.*, 1990, vol. 13, no. 9, pp. 1719–1721.
14. *GOST* (State Standard) *33–2000: Petroleum Products: Transparent and Opaque Liquids: Determination of Kinematic Viscosity and Calculation of Dynamic Viscosity*, Moscow: Izd. Standartov, 2001.
15. *GOST* (State Standard) *25371–97: Petroleum Products: Calculation of the Viscosity Index from the Kinematic Viscosity*, Moscow: Izd. Standartov, 2001.
16. Irzhak, V.I., Rozenberg, B.A., and Enikolopyan, N.S., *Setchatye polimery* (Network Polymers), Moscow: Nauka, 1979.
17. Odian, G., *Principles of Polymerization*, New York: McGraw-Hill, 1970.
18. Shostakovskii, M.F., *Prostye vinilovye efiry* (Vinyl Ethers), Moscow: Akad. Nauk SSSR, 1952.
19. Khomutov, A.M., *Vysokomol. Soedin.*, 1963, vol. 5, no. 8, pp. 1121–1126.
20. Arakelov, G.G., Badalyan, V.E., and Khachatryan, S.S., *Prostye vinilovye efiry: Obzornaya informatsiya* (Vinyl Ethers: Review), Ser.: *Polimerizatsionnye plastmassy* (Polymerization Plastics), Moscow: NIITEKhIM, 1979.
21. Zhurbanov, B.A., Shaikhutdinov, E.M., and Kurmanaliev, O.Sh., in *Sintez i issledovanie polimerov* (Synthesis and Study of Polymers), Alma-Ata, 1975, pp. 3–28.
22. Tudos, F., Kelen, T., Foldes Berezhnykh, T., and Turcsanyi, B., *J. Polym. Sci.*, 1977, vol. 15, pp. 3047–3074.
23. *TU* (Technical Specification) *38.1011212–89 with Revisions 1, 2, 3: AU Base Oil.*

ISSN 1070-4272, Russian Journal of Applied Chemistry, 2008, Vol. 81, No. 9, pp. 1642–1644. © Pleiades Publishing, Ltd., 2008.
Original Russian Text © A.K. Rozentsvaig, Ch.S. Strashinskii, 2008, published in Zhurnal Prikladnoi Khimii, 2008, Vol. 81, No. 9, pp. 1567–1569.

BRIEF COMMUNICATIONS

Coalescence of the Low-Boiling Dispersed Phase in a Turbulent Flow of a Cooling Emulsion

A. K. Rozentsvaig and Ch. S. Strashinskii

Kama State Engineering-Economical Academy, Naberezhnye Chelny, Tatarstan, Russia

Received May 16, 2008

Abstract—A nonlinear system of three differential equations is suggested as a model of the bubble boiling of drops of the dispersed phase. A qualitative analysis of the nature of the process of joint boiling and coalescence of drops of the dispersed phase in the overheated emulsion was made with certain simplifying assumptions.

DOI: 10.1134/S1070427208090322

Boiling of liquids is used in chemical technology both directly for heat-transfer purposes and as distillation or evaporation. There exist different concepts about the mechanism of heat transfer in boiling of a liquid. Theoretical description of the heat transfer in boiling of even homogeneous liquids is a rather complicated task [1]. This problem becomes considerably more complicated if heat transfer occurs in heterogeneous dispersed systems.

Experimental and theoretical studies of emulsions with a low-boiling dispersed phase demonstrated that they can substantially intensify the heat-transfer process as compared to any homogeneous liquid contained in an emulsion. For example, emulsions of organosilicon liquids with an aqueous dispersed phase are widely used for cooling of cutting tools and thermal treatment of metals [2, 3]. In these studies, it was found on the basis of experimental data that the emulsion is strongly overheated and the effect of boiling onset delay, $\Delta T_b = T_l - T_{sat}$, was examined [2].

The mechanism of this effects of boiling onset delay was found [3] to be related in many regards to the hydrodynamic characteristics and behavior of the dispersed phase of an emulsion. In particular, an important role in a turbulent flow can be played by the frequency of drop collision and coalescence under the action of pulsation of the continuous medium velocity. For a qualitative analysis and quantitative explanation of the heat transfer in unstable emulsions, it is necessary to consider the model of boiling of dispersed phase drops with account of their coarsening [4].

An overheated emulsion with a low-boiling dispersed phase is considered in terms of a monodisperse model approximation with a drop diameter assumed to be δ. The concentration W of the dispersed phase is low, not more than 0.5–1.5 vol %, and the overheating is sufficient for its full evaporation, which makes it possible to neglect, to a first approximation, the nature of heat-transfer processes. The influence exerted by the vapor phase formed in the boiling zone is disregarded. It is also assumed that the drops boil-up by the prescribed nucleation mechanism characterized by a constant frequency J of formation of vapor phase nuclei in a unit volume of the drops [5].

The total number N of drops of the dispersed phase in a unit volume of the emulsion decreases by the number n of boiled-up drops and by the number of drops coarsened in collisions of the $N - n$ drops remaining in the emulsion volume:

$$N = N + (dN/dt)\Delta t + 0.5\vartheta(N - n)\Delta t - (dn/dt)\Delta t, \quad (1)$$

where ϑ is the coalescence frequency of drops of the dispersed phase.

The change in the volume of the dispersed phase on passing of the boiling-up drops into the vapor phase can be written as follows:

$$N\pi\delta^3/6 = [N + (dN/dt)\Delta t][\delta + (d\delta/dt)\Delta t]^3\pi/6 - (dn/dt)(\pi/6)[\delta + (d\delta/dt)\Delta t]^3. \quad (2)$$

The number of evaporating drops in a unit volume of the overheated emulsion is determined by

the number $N - n$ of drops that had not enough time to boil-up and by the frequency J of nucleation in the unit volume of these drops, equal to v:

$$n = n + (dn/dt)\Delta t + Jv(N - n)\Delta t. \quad (3)$$

Retaining in Eqs. (1)–(3) terms containing the small quantity raised to first power, we obtain the following nonlinear system of first-order differential equations:

$$\left.\begin{aligned} d\delta/dt &= -(\delta/3N)[d(N - n)/dt], \\ d(N - n)/dt &= 0.5\vartheta(N - n), \\ dn/dt &= \vartheta v(N - n). \end{aligned}\right\} \quad (4)$$

For numerical integration of the system of equations (4), it is necessary to specify mechanisms of coalescence and nucleation, whose nature is not fully clear and requires a separate consideration under conditions of various transfer processes [6].

In order to qualitatively analyze the nature of the joint boiling and coalescence of drops of the low-boiling dispersed phase in an overheated emulsion, let us consider some analytical solutions to system (4) under certain simplifying assumptions. The frequency J at which nuclei of the vapor phase are formed in the bulk of drops of the dispersed phase is assumed to have a lower order of magnitude than the frequency ϑ of their coalescence. Accordingly, the number n of boiling-up drops is also assumed to be of a lower order of magnitude than the number N of drops of the dispersed phase. This makes it possible to reduce solution of the system of nonlinear differential equations to finding approximate solutions to each equation in the analytical form.

Integration of the second equation in system (4) on the condition $N >> n$ gives an expression for the decrease in the initial number N_0 of drops of the dispersed phase via their coalescence in collisions in a flow of the continuous phase of the emulsion under the action of a turbulent agitation [6]:

$$N(t) = N_0 \exp(-0.5\vartheta t). \quad (5)$$

The third equation can be integrated, on being represented in the form

$$(dn/dt) + nJv = NJv, \quad (6)$$

on the same assumption. Its solution was obtained on the condition that the rate dn/dt at which the number of boiling-up drops varies substantially exceeds that at which the initial number N of drops decreases:

$$n(t) = N[1 - \exp(-Jvt)]. \quad (7)$$

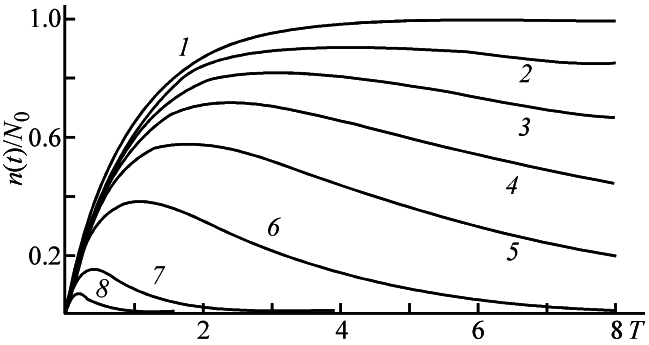
Taking into account the decrease via coalescence of drops of the dispersed phase in accordance with expression (5), we obtain the number of boiling-up drops:

$$n(t) = N_0 \exp(-0.5\vartheta t)[1 - \exp(-Jvt)]. \quad (8)$$

Multiplying both parts of the first equation of system (4) by δ^2, we can pass from drop diameters δ to drop volumes v. On substituting $d(N - n)/dt$ from the second equation of the system and taking into account the simplifying assumption, we obtain the following expression for the variation of the drop volume:

$$v(t) = v_0 \exp(-0.5\vartheta t). \quad (9)$$

This expression was not used to replace the drop volume v in formula (8) because it is preceded in this expression by the frequency J of spontaneous nucleation, whose small value is one of the basic assumptions made in this study for qualitative analysis. Their effect can be determined by numerical solution of the nonlinear system (4) of differential equations, but this requires that the mechanisms of coalescence and nucleation of drops of the dispersed phase in a turbulent flow of the emulsion should be preliminarily specified.



Relative number of boiled-up drops, $n(t)/N_0$, vs. the dimensionless time $T = Jvt$ at various values of the parameter $\lambda = \vartheta/(2Jv)$, which is the ratio between the rate of coalescence of drops of the dispersed phase and that of vapor phase nucleation in these drops. λ: (*1*) 0, (*2*) 0.02, (*3*) 0.05, (*4*) 0.1, (*5*) 0.2, (*6*) 0.5, (*7*) 2.0, and (*8*) 5.0.

The figure presents curves that show how the relative number of boiled-up drops, n/N_0, varies with

the dimensionless time $T = J\nu t$ at various ratios between the rate of coalescence and that of spontaneous formation of vapor phase nuclei, $\lambda = \vartheta/(2J\nu)$. In the absence of coalescence ($\vartheta = 0$), the number of boiled-up drops steadily increases from zero to N_0, initial number of drops of the dispersed phase. Coalescence leads to a decrease in the number of drops of the dispersed phase, involved in the boiling process, and, therefore, curves *2–8* cease to be monotonic at $\vartheta \neq 0$. As a result, the number of boiled-up drops increases to a maximum value and then steadily falls because of the decrease in the number of initial drops via coalescence.

Thus, the model expression (8) for the number of boiling-up drops indicates that there exist optimal conditions under which the maximum cooling by an emulsion via boiling of the dispersed phase can be achieved. To determine these conditions, it is necessary to find $(n/N_0)_{max}$ and $T_{max} = J\nu t_{max}$ by equating to zero the derivative of the expression in the right-hand part of formula (8). The result can be written as

$$T_{max} = \ln(1 + 1/\lambda),\ n_{max}/N_0 = (1 + \lambda)^{-1}(1 + 1/\lambda)^{-\lambda}. \quad (10)$$

This specific feature of model curves means that generalization of the drop boiling model (8), earlier derived in the study in the form of (7), gives a fuller notion of the heat exchange in emulsions with a low-boiling dispersed phase. In addition, it is in agreement with the experimentally found [2, 3] influence of the average size of drops of the dispersed phase on parameters of the heat exchange between an emulsion and a surface being cooled.

Qualitative analysis of the approximate solution of the nonlinear system (4) of differential equations shows how the coalescence of drops of the dispersed phase can account for the results obtained in experimental studies of the boiling of drops of the dispersed phase in the bulk of a high-boiling liquid [3]. This, in particular, refers to understanding of the heat-exchange mechanisms in the case of boiling delay determining the limits of the region in which the bubble mode of boiling is the most efficient.

CONCLUSIONS

(1) The model of the bubble mode of boiling of drops of the dispersed phase in a flow of a cooling emulsion, constructed with account of drop coalescence, makes substantially wider the number of factors that strongly affect the boiling onset delay and the heat-transfer efficiency.

(2) The existence of the optimal boiling conditions that can account for the boiling onset delay under conditions of coarsening of finely dispersed drops indicates that the suggested model [system of equations (4)] of the overheated emulsion with a low-boiling dispersed phase is adequate.

REFERENCES

1. Ainshtein, V.G., Zakharov, M.K., Nosov, G.A., et al., *Obshchii kurs protsessov i apparatov khimicheskoi tekhnologii: Uchebnik* (General Course of Processes and Apparatus of Chemical Technology: Textbook), Ainshtein, V.G., Ed., Moscow: Univ. Kniga, 2006, vol. 1.
2. Bulanov, N.V., *Tekh. Vys. Temp.*, 2001, vol. 39, no. 3, pp. 495–502.
3. Bulanov, N.V. and Gasanov, B.M., *Inzh.-Fiz. Zh.*, 2006, vol. 79, no. 6, pp. 81–84.
4. Rozentsvaig, A.K., *Zh. Prikl. Khim.*, 1976, vol. 49, no. 1, pp. 231–232.
5. Skripov, V.P., *Metastabil'naya zhidkost'* (Metastable Liquid), Moscow: Nauka, 1972.
6. Rozentsvaig, A.K. and Strashinskii, Ch.S., in *Proektirovanie i issledovanie tekhnicheskikh sistem: Mezhvuzovskii nauchnyi sbornik* (Design and Study of Technical Systems: Intercollegiate Coll. of Scientific Works), Naberezhnye Chelny: Inzhenerno-Ekonomicheskaya Akad., 2008, issue 11, pp. 160–164.

ISSN 1070-4272, Russian Journal of Applied Chemistry, 2008, Vol. 81, No. 9, pp. 1645–1647. © Pleiades Publishing, Ltd., 2008.
Original Russian Text © R.F. Mukhamedova, 2008, published in Zhurnal Prikladnoi Khimii, 2008, Vol. 81, No. 9, pp. 1570–1572.

BRIEF COMMUNICATIONS

Kinetics of Immobilization of 1,2,5-Trimethyl-4-dimethylphosphonopiperid-4-ol with Maleic Anhydride–Styrene Copolymer

R. F. Mukhamedova

Satpaev Kazakh National Technical University, Almaty, Kazakhstan

Received January 21, 2008

Abstract—The kinetics of interaction of biologically active piperidol with maleic anhydride–styrene copolymer was studied, and the apparent thermodynamic functions of activation of the process were determined.

DOI: 10.1134/S1070427208090334

The main pathway of intensifying the agrotechnics of cultivation of various practically important crops is the use of agents based on biologically active components immobilized on a polymeric carrier. Such polymeric forms of regulators of plant growth and development are considered today as the most promising type of new preparations. The active components of such bioadditives can be plant growth stimulants, both natural and synthetic. A series of maleic anhydride copolymers whose properties can be controlled by varying the structure of the second comonomer are widely used as polymeric carriers [1, 2].

Previously we examined systematically the synthesis and biological activity of polymers prepared by immobilization of various piperidol derivatives on maleic anhydride copolymers [3–6]. In this study we examined the kinetic features of formation of such systems.

EXPERIMENTAL

Experiments were performed with commercial maleic anhydride–styrene copolymer (Styromal) which was purified first by sublimation to remove the monomer and then by reprecipitation from cyclohexane into petroleum ether. The content of anhydride groups was 44.7%, M = 40000. As biologically active component we used 1,2,5-trimethyl-4-dimethylphosphonopiperid-4-ol (ASA, Phospinol) prepared at the Institute of Chemical Sciences, Ministry of Education and Science of the Kazakhstan Republic [7]. The compound was used without additional purification.

Dimethyl sulfoxide (DMSO) was purified by keeping for 24 h over calcium hydride, followed by double distillation under reduced pressure (100°C at 15 mm Hg), n_D^{20} 1.4766 [8]. Dimethylformamide (DMF) was purified by keeping over calcium hydride, bp 153°C, n_D^{20} 1.4269 [8].

To determine the amount of anhydride groups [9], a weighed portion of the copolymer (0.05 g) was dissolved in 10 ml of DMSO. A 0.1 N solution of morpholine in DMSO (10 ml) was added to this solution, and the mixture was allowed to stand for 2 h. A blank sample with 10 ml of DMSO and 10 ml of a 0.1 N morpholine solution in DMSO was prepared simultaneously. After 2 h, both samples were titrated with a 0.05 N solution of HCl in DMSO with an EV-74 universal pH meter.

Synthesis of polymeric esters. A three-necked flask equipped with a stirrer and a reflux condenser was charged with 0.003 mol of styrene–maleic anhydride copolymer and 10.06 ml of DMSO. After the copolymer dissolved completely (80°C), 0.003 mol of 1,2,5-trimethyl-4-dimethylphosphonopiperid-4-ol was added (reaction mixture concentration 15%). The reaction was performed at 90°C for 3 h. After the reaction completion, the polymer was precipitated into a 3 : 1 mixture of acetone and isopropyl alcohol. The precipitate was filtered off and washed with isopropyl alcohol and acetone and dried to constant weight at 50°C in a vacuum. The content of the immobilized biologically active substance (BAS) was determined by nonaqueous titration in DMSO [10].

It was noted previously [11, 12] that the use of

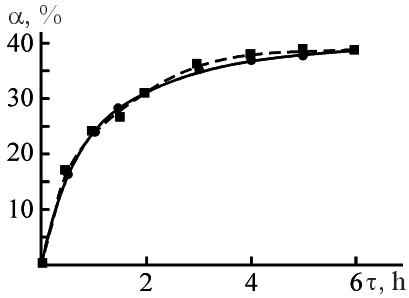


Fig. 1. Degree of completeness α of the reaction of Phospinol with Styromal as a function of reaction time τ.

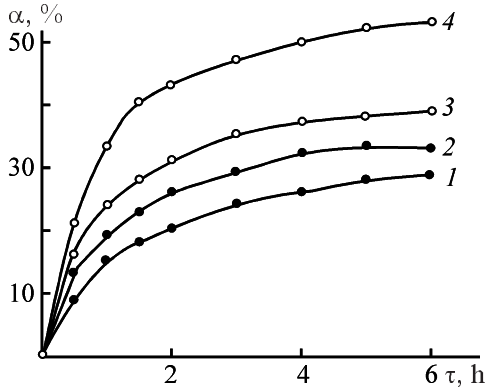


Fig. 2. Degree of completeness α of the reaction of Phospinol with Styromal as a function of reaction time τ at various temperatures. *T*, K: (*1*) 343, (*2*) 353, (*3*) 363, and (*4*) 373; the same for Fig. 3.

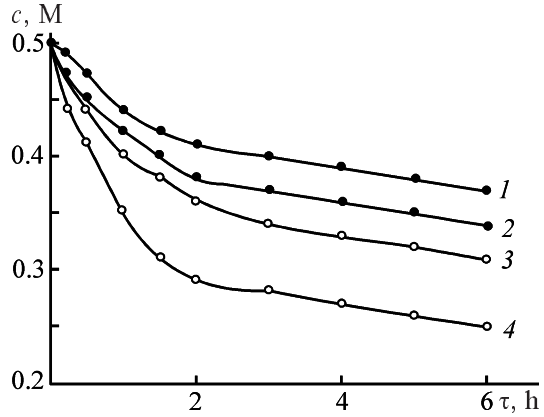


Fig. 3. Kinetic curves of Phospinol consumption in its reaction with maleic anhydride–styrene copolymer. (*c*) Phospinol concentration and (τ) time.

copolymers containing maleic anhydride with the aim of binding biologically active acids can be a very convenient and accessible procedure for preparing polymer systems exhibiting prolonged phytoactive effect. Therefore, it becomes very important to know the mechanism and kinetic features of processes by which these systems are formed. In the course of studying the reaction of the examined biologically active substances with maleic anhydride copolymers, we noted that, at certain steps of the reaction, it decelerates, and introduction of a large amount of a low-molecular-weight substance into the system does not lead to a noticeable increase in the degree of immobilization. To reveal the causes of this effect, we examined the kinetic features of the reaction.

Kinetic parameters* of the immobilization of 1,2,5-trimethyl-4-dimethylphosphonopiperid-4-ol on maleic anhydride–styrene copolymer

T, K	$k_{app} \times 10^4$, $l\,mol^{-1}\,s^{-1}$
343	1.6
353	3.1
363	5.2
373	7.6

* E_a = 63709 J mol^{-1}, $\Delta H^{\neq}$ = 60733 J mol^{-1}, $\Delta S^{\neq}$ = –34.06 J mol^{-1} K^{-1}, $\Delta G^{\neq}$ = 48000 J mol^{-1}.

For the kinetic studies we chose the temperature interval 343–373 K in which the influence of temperature on the degree of immobilization is the most noticeable.

The degree of reaction completeness was determined in parallel by two procedures: (1) from the amount of titrated unchanged anhydride groups in samples taken directly from the reaction mixture, we calculated the degree of reaction completeness and plotted it vs. reaction time (Fig. 1, solid line); (2) from the concentration of the unchanged low-molecular-weight BAS, determined by UV spectroscopy in samples taken at the same intervals as in the first case, we calculated the degree of reaction completeness and plotted it vs. reaction time (Fig. 1, dashed line).

As seen from Fig. 1, both methods gave the same degree of reaction completeness. Therefore, in the subsequent experiments were determined the degree of reaction completeness only by titration of unchanged anhydride groups.

Typical kinetic curves are shown in Figs. 2 and 3. The curves were processed by the first-, second-, and third-order equations. The kinetic curves could be linearized only in the coordinates of the second-order equation. The rate constants obtained from the slopes are given in the table.

The activation energy was determined from the Arrhenius plot $\log k$–$1/T$ (*T*, K) (Fig. 4). The result is given in the table.

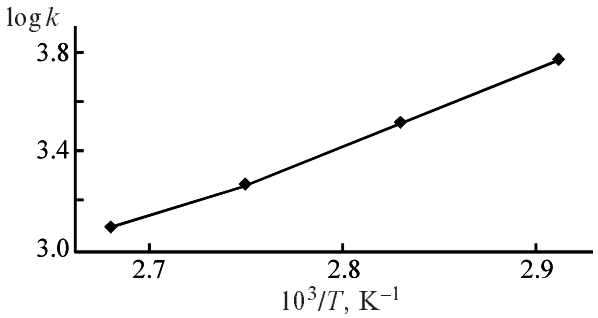


Fig. 4. Rate constant k as a function of temperature T in Arrhenius coordinates.

From the activation energy and rate constants, we determined the effective thermodynamic functions of activation of the process: enthalpy $\Delta H^{\neq}$, entropy $\Delta S^{\neq}$, and Gibbs free energy $\Delta G^{\neq}$, by the formulas $\Delta H^{\neq} = E - RT$, $\Delta G^{\neq} = H^{\neq} - TS^{\neq}$, $\Delta S^{\neq} = 4.576\log(A/T) - 49.21$.

CONCLUSION

The kinetics of immobilization of biologically active piperidol on a polymeric matrix is determined by the reaction of 1,2,5-trimethyl-4-dimethylphosphonopiperid-4-ol (Phospinol) with maleic anhydride–styrene copolymer. The activation energy and rate constants for this reaction were determined.

REFERENCES

1. Shtilman, M.I., *Polymeric Biomaterials*, Utrecht: VSP, 2003.
2. Shtil'man, M.I., *Polimery mediko-biologicheskogo naznacheniya* (Polymers for Medicobiological Purposes), Moscow: Akademkniga, 2005.
3. Zhubanov, B.A., Boiko, G.I., and Mukhamedova, R.F., Abstracts of Papers, *II Vsesoyuznoe soveshchanie "Biologicheski aktivnye polimery i polimernye reagenty dlya rastenievodstva"* (II All-Union Meet. "Biologically Active Polymers and Polymeric Reagents for Plant Cultivation"), Zvenigorod, 1991, p. 74.
4. Meirova, G., Mukhamedova, R.F., Boiko, G.I., and Zhubanov, B.A., *Izv. Nats. Akad. Nauk Resp. Kaz., Ser. Khim.*, 1993, no. 3, pp. 51–53.
5. Boiko, G.I., Mukhamedova, R.F., Lyubchenko, N.P., et al., *Vestn. Kaz. Nats. Univ. im. Al'-Farabi, Ser. Khim.*, 2007, no. 1 (45), pp. 207–211.
6. Mukhamedova, R.F., Boiko, G.I., Lyubchenko, N.P., et al., *Khim. Zh. Kaz.*, 2007, June, special issue (16), pp. 243–247.
7. RF Patent 1788725.
8. Weissberger, A. and Proskauer, E.S., *Organic Solvents. Physical Properties and Methods of Purification*, Riddick, J.A. and Toops, E.E., Eds., New York: Interscience, 1955.
9. Siggia, S. and Hanna, J.G., *Quantitative Organic Analysis via Functional Groups*, New York: Wiley–Interscience, 1979.
10. Meirova, G., Umerzakova, M.B., Mukhamedova, R.F., and Zhubanov, B.A., *Vestn. Kaz. Nats. Univ., Ser. Khim.*, 2003, no. 3 (31), pp. 231–234.
11. Shtil'man, M.I., *Soros. Obraz. Zh.*, 1998, no. 10, pp. 44–49.
12. Mukhamedova, R.F., Abstracts of Papers, *III Mezhdunarodnaya nauchno-prakticheskaya konferentsiya "Estestvenno-gumanitarnye nauki i ikh rol' v realizatsii programmy industrial'no-innovatsionnogo razvitiya Respubliki Kazakhstan"* (III Int. Scientific and Practical Conf. "Natural Sciences and Humanities and Their Role in Implementation of the Program of the Industrial and Innovation Development of the Kazakhstan Republic"), Almaty, 2007, pp. 144–145.

ISSN 1070-4272, Russian Journal of Applied Chemistry, 2008, Vol. 81, No. 9, pp. 1648–1651. © Pleiades Publishing, Ltd., 2008.
Original Russian Text © Z.F. Zoolshoev, S.A. Vesnebolotskaya, N.G. Bel'nikevich, G.K. Elyashevich, 2008, published in Zhurnal Prikladnoi Khimii, 2008, Vol. 81, No. 9, pp. 1573–1575.

BRIEF COMMUNICATIONS

Behavior of Sodium Polyacrylate Hydrogels in Copper Sulfate Solutions

Z. F. Zoolshoev, S. A. Vesnebolotskaya, N. G. Bel'nikevich, and G. K. Elyashevich

Institute of Macromolecular Compounds, Russian Academy of Sciences, St. Petersburg, Russia

Received February 19, 2008

Abstract—The behavior of hydrogels based on sodium acrylate cross-linked to different extents with *N,N'*-methylenebis(acrylamide) was examined in aqueous solutions of copper sulfate of concentrations within 0.1–0.001 M.

DOI: 10.1134/S1070427208090346

Unique physicochemical properties of polyelectrolyte hydrogels, especially the ability to substantially change their size in response to minor changes in the external conditions, attract huge researchers' interest [1–4]. High-swelling polymeric hydrogels find application in medicine, as well as in food and cosmetic industries [5–8]. The effects arising in hydrogels under the action of low-molecular-weight salts can underlie purifying and enrichment technologies.

We examined here the swelling/compression kinetics and adsorption of bivalent metal ions for sodium acrylate hydrogel contacting copper sulfate solutions in relation to the cross-linking density of the polymeric network of the hydrogel.

EXPERIMENTAL

The hydrogels were synthesized by the procedure described in [6], by radical copolymerization of completely neutralized acrylic acid with *N,N'*-methylenebis(acrylamide). The monomers were neutralized with NaOH. The concentration of the monomers in the initial solution was 25%. The cross-linking density was controlled by the amount of the cross-linking agent introduced into the copolymerization reaction (Table 1).

In the experiments we used sodium acrylate hydrogels with different cross-linking densities (1 cross-link per 100, 200, and 300 monomer units), designated as N_{100}, N_{200}, and N_{300}, respectively.

A weighed portion of the gel (~0.02 g), dried to constant weight, was placed into aqueous $CuSO_4$ solutions of different concentrations ranging from 0.001 to 0.1 M and into distilled water. The weight of the solution was 1500 times that of the gel. The degree of swelling of the gel Q was determined gravimetrically from the ratio of the weight of the swollen hydrogel to the initial weight of the dry sample. The amount of the salt bound to the hydrogel was determined on a Specord M 40 spectrophotometer by measuring the salt content in the initial solutions and in the solutions after their contact with the hydrogel.

We obtained the dependences of the degree of swelling for the hydrogels with different cross-linking densities on the $CuSO_4$ solution concentration. Also, we determined the amount of the copper ions bound to the hydrogel during its contact with the salt solution.

Figure 1 presents the kinetic curve of swelling of

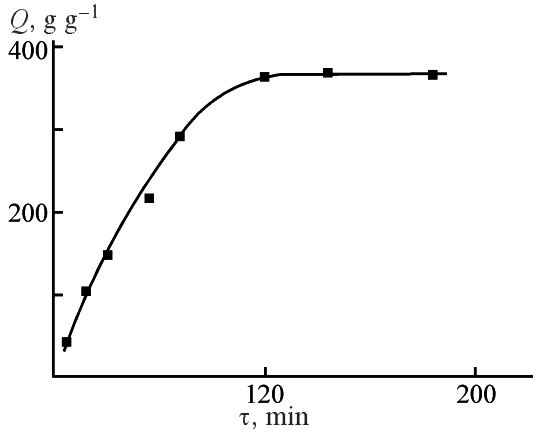


Fig. 1. Kinetic curve of swelling of sodium acrylate hydrogel in water. (Q) Degree of swelling and (τ) time.

Table 1. Amounts of the chemicals used in synthesis of the gel

Compound	Weight, g	Concentration, g mol^{-1}	Content relative to monomer, mol %
Acrylic acid	5.0	6.94×10^{-2}	100
Sodium hydroxide	2.08	5.20×10^{-2}	74.94
Methylenebis(acrylamide), cross-linking agent	0.04; 0.05; 0.10	2.32×10^{-4}	0.33; 0.50; 0.98
Tetramethylethylenediamine, inhibitor	0.0081	6.97×10^{-5}	0.10
Ammonium persulfate, initiator	0.0158	6.92×10^{-5}	0.01
Distilled water	15.0	8.32×10^{-1}	300.0

the N_{300} gel [sample] in water, which served as the basic characteristic in our experiments. It is seen that the equilibrium swelling is achieved within 100 min.

The swelling of the hydrogels was examined in copper sulfate solutions with concentrations ranging from 0.1 to 0.001 M. The equilibrium in the hydrogel–salt solution systems is achieved within 100 min as well. Figure 2 presents the measured equilibrium degrees of swelling Q in relation to the concentration of the $CuSO_4$ solution after its 120-min contact with the gel. It is seen that, with increasing salt concentration (at $c < 0.025$ M), the degree of swelling of all the hydrogels tends to sharply decrease and changes insignificantly with further increase in the salt content. As expected, the maximal Q values were observed for the hydrogel sample N_{300} (with the smallest number of cross-links). It should be noted that the degrees of swelling of the hydrogel samples with different cross-linking densities differ only for dilute salt solutions ($c <$ 0.025 M). At these concentrations, the molar ratio of the gel to salt component is 0.0002 : 0.00075. In calculation of the hydrogel concentration we took into account the total volume of the hydrogel and solution. In the actual case, the nature of the swelling process is identical to that of the hydrogel in water. The aqueous solution of copper sulfate has a dark blue color, which makes it possible to monitor its penetration inside the hydrogel. During swelling of the gel in the $CuSO_4$ solution, the copper ions penetrate inside the gel and form additional cross-links. Budtova and Navard [9] examined previously the swelling of the hydrogel based on polyacrylic acid–sodium polyacrylate system (molar ratio 0.25 : 0.75) in aqueous solutions of copper sulfate and showed that, at low salt concentrations, the metal ions diffuse into the swollen gel, which results in its more or less uniform "cross-linking" over the bulk.

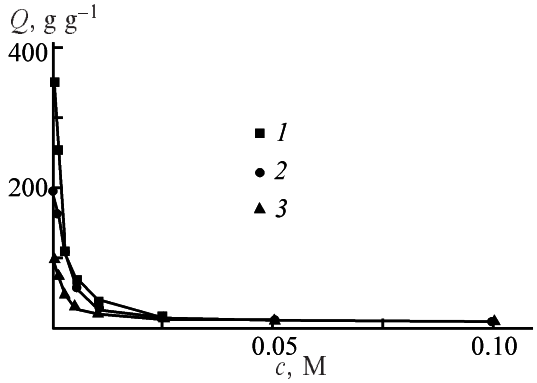


Fig. 2. Equilibrium degree of swelling Q of sodium acrylate hydrogel vs. concentration c of the $CuSO_4$ solution after 2-h contact with the gel. Sample: (*1*) N_{300}, (*2*) N_{200}, and (*3*) N_{100}.

When the gel is immersed in a salt solution of concentration $c > 0.025$ M, the degree of swelling is independent of the cross-linking density. The gel adsorbs a small amount of the solvent, whereupon its size remains unchanged. The copper ions do not fill the entire volume of the gel, since immediately after immersion of the gel into the solution, a layer preventing further penetration of the solvent inside the gel particle is formed on the surface. Hence, at high salt concentrations, the degrees of swelling for all the gel samples are approximately identical and depend only on the area of the surface contacting with the salt solution. Table 2 lists the equilibrium

Table 2. Equilibrium degrees of swelling Q of the sodium polyacrylate hydrogels with different cross-linking densities in water and copper sulfate solutions of different concentrations c_s

Cross-linking density	Q, g g^{-1}, at indicated c_s, M		
	0	0.001	0.1
N_{300}	350	250	7
N_{200}	196	163	7
N_{100}	94	71	8

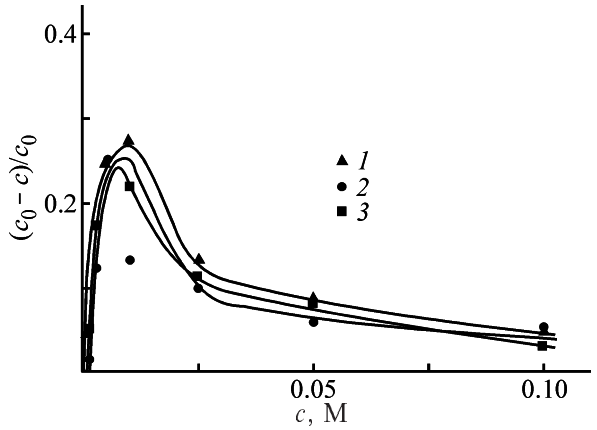


Fig. 3. Amount of copper ions sorbed by the sodium acrylate hydrogels with different cross-linking densities vs. concentration c of the $CuSO_4$ solution. (c_0, c) Copper sulfate concentrations in solution before and after the 2-h contact with the hydrogel, respectively.

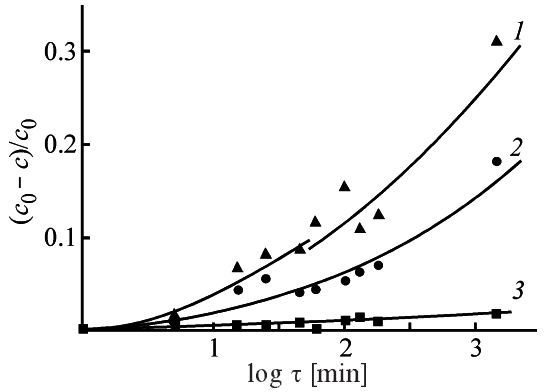


Fig. 4. Kinetic curves of sorption of copper ions with the N_{300} sodium acrylate hydrogel in copper sulfate solutions of different concentrations. (c_0, c) Copper sulfate concentrations in the solution before and after the 2-h contact with the hydrogel, respectively, and (τ) time. c, M: (*1*) 0.005, (*2*) 0.01, and (*3*) 0.1.

degrees of swelling of the sodium acrylate hydrogels with different cross-linking densities for the gel in contact with copper sulfate solutions of the maximal and minimal concentrations.

Figure 3 shows how the amounts of copper ions $(c_0 - c)/c_0$ (c_0 and c are the $CuSO_4$ concentrations in solution before and after contact with the hydrogel, respectively) sorbed by the gel samples with different cross-linking densities vary with the $CuSO_4$ solution concentration (2-h gel–solution contact) after these samples reached the equilibrium swelling. It is seen that, at the salt concentrations $c < 0.025$ M, the amount of the bound copper ions tends to increase with increasing salt concentration. With a further increase in the salt concentration in the solution, the amount of the bound ions tends to monotonically decrease. These results are fully consistent with our data on the swelling of the hydrogels (Fig. 2).

Our experiments showed that the amounts of the copper ions bound by the hydrogel are virtually identical for all the samples and independent of the cross-linking density. Presumably, the size of the insoluble copper acrylate skeleton formed on the hydrogel surface is proportional to the number of the surface carboxy groups that entered into the reaction and depends only on the area of the gel particle in contact with the salt solution. The resulting water-insoluble copper acrylate prevents further penetration of water and the ions deep inside the samples.

Figure 4 presents the kinetic curves of sorption of the ions with the hydrogel from copper sulfate solutions of different concentrations. It is seen that the rate of sorption of the ions is the higher, the lower the concentration of the solution surrounding the gel. We also found that, throughout the salt concentration range examined, the copper ions are sorbed by the hydrogel also after the equilibrium swelling was achieved.

CONCLUSIONS

(1) The degree of swelling of the hydrogels depends on the number of the cross-links only at concentrations $c < 0.025$ M, while at $c > 0.025$ M it is virtually identical for all the samples examined.

(2) When contacting the solution, the hydrogel absorbs the copper ions irrespective of the cross-linking density throughout the salt concentration range examined.

(3) The hydrogel contacting the solution absorbs the copper ions after attainment of the equilibrium swelling as well. This process is decelerated with increasing initial concentration of the copper sulfate solutions.

(4) The penetration of the copper ions inside the gel is responsible for the appearance of additional cross-links and formation on the gel surface of insoluble copper acrylate.

ACKNOWLEDGMENTS

This study was financially supported by the Russian Foundation for Basic Research (project no. 07-03-00177) and by the "Synthesis and Examination of New Polymer Systems Containing Polyconjugated Polymers and Exhibiting Semiconductor and Con-

ductor Properties" Basic Research Program of the Russian Academy of Sciences, Division of Chemistry and Materials Science, "Electroconducting and Electroactive Polymers" Direction.

REFERENCES

1. Kramarenko, E.Yu. and Khokhlov, A.R., *Vysokomol. Soedin., Ser. C*, 2006, vol. 48, no. 7, pp. 1216–1240.
2. Kramarenko, E.Yu., Khokhlov, A.R., and Yoshikawa, K., *Macromolecules*, 2000, vol. 9, pp. 249–256.
3. Filippova, O.E., *Vysokomol. Soedin., Ser. C*, 2000, vol. 42, no. 2, pp. 2328–2352.
4. Buyanov, A.L., Revelskaya, L.G., Kuznetzov, Yu.P., et al., *Appl. Pol. Sci.*, 2001, vol. 80, pp. 1452–1460.
5. Kost, J. and Langer, R., *Hydrogels in Medicine and Pharmacy*, Florida: CRC, 1987.
6. Horkay, F., Tasaki, I., and Basser, P., *Biomacromolecules*, 2000, vol. 1, pp. 84–90.
7. Tomari, T. and Doi, M., *Macromolecules*, 1995, vol. 28, pp. 8334–8343.
8. Matsuo, E.S. and Tanaka, T., *J. Chem. Phys.*, 1988, vol. 89, pp. 1695–1703.
9. Budtova, T. and Navard, P., *Macromolecules*, 1998, vol. 31, pp. 884–887.

ISSN 1070-4272, Russian Journal of Applied Chemistry, 2008, Vol. 81, No. 9, pp. 1655–1666. © Pleiades Publishing, Ltd., 2008.
Original Russian Text © G.P. Belov, 2008, published in Khimicheskaya Promyshlennost', 2008, Vol. 85, No. 3, pp. 109–121.

TECHNOLOGY OF ORGANIC AND INORGANIC CHEMISTRY

Selective Dimerization, Oligomerization, Homopolymerization and Copolymerization of Olefins with Complex Organometallic Catalysts

G. P. Belov

Institute of Chemical Physics Problems, Russian Academy of Sciences, Chernogolovka, Russia
e-mail: gbelov@cat.icp.ac.ru

Received October 10, 2007

Abstract—Review embarrasses the problems of low molecular weight olefins (ethylene and propylene) selective oligomerization to butene-1, hexene-1, octene-1, 4-methylpentene-1; selective polymerization of olefins to obtain polymers with a given molecular mass, molecular mass distribution, branching (for the polyethylene), chain structure [atactic, iso-, syndio-, gemiisotactic, stereoblock type and containing terminal vinyl and vinylidene bonds (for polypropylene)]; "live" homo- and copolymerization of olefins, and alternating copolymerization of olefins in the presence of complex organometallic catalysts.

DOI: 10.1134/S107042720809036X

Current situation issues a challenge for the scientists in academic and industrial institutes of producing monomeric, oligomeric and polymeric products with a predefined complex of physico-chemical, reological and endurance properties. For solving the problems it is necessary to know molecular mass and chain structure of the products and dependence of these parameters on the kinetic parameters of the process of their production. That is, the problem of obtaining products with predefined properties required complex approach to its solving. This in turn implies necessity of development of scientific base of creation and practical realization of highly selective processes. As the selectivity we assume, in line with the definition proposed by academician N.M. Emanuel [1], for simple reactions (in our case to the reactions of dimerization and oligomerization), "a fraction of initial substance converted into the targeted substace II," and for the reaction of polymerization, "obtaining the product with given molecular mass, molecular mass distribution and structure of the chain: concentration and character of location in the polymeric chain of side groups, content of terminal C=C groups, degree of alternation of comonomers."

Olefins (ethylene and propylene mainly) and oigomers and polymers based on them are the most large-tonnage products of petrochemical and chemical industries. The problem of effective use of olefins in the processes of di-, oligo- and polymerization at the catalysis with organometallic complex catalysts now becomes more and more significant. The main parameter defining efficiency of these processes from the viewpoint of rational using of the monomers is selectivity of oligo- and polymerization reactions_

DI- AND OLIGOMERIZATION OF OLEFINS

Ethylene dimerization. Dimerization of olefin has been initiated in the classical works by A.M. Butlerov who was first to carry out dimerization of isobutylene at the action of sulfuric acid [2]. However, till 50th of last century this method was used for the manufacturing of liquid propylene and butanes oligomers, that are applied for producing motor fuel, lubricant oil and synthetic washing means [3, 4]. Discovery by Natta and Zigler in the middle of 50th of new catalysts showing high activity and selectivity allowed in certain cases to obtain the olefins dimers and polymers with the structure that could not be achievable with the earlier known catalysts. A good example is the reaction of selective ethylene dimerization into butene-1, which has been introduced to chemical industry of Russia and some of leading countries [5–7].

Generally, reaction of ethylene dimerization can be represented as follows:

$$n C_2H_4 \rightarrow \text{butene-1} + \textit{cis-, trans-}\ (\text{butenes, hexenes, octenes}) + \text{polymer.}$$

The complex organometallic catalysts known to the moment commonly are bicomponent catalytic systems consisting of alkyl or halo derivative of a transition metal and organoaluminum compound. The most active and selective is the catalytic system of $Ti(OC_4H_9)_4$–$Al(C_3H_5)_3$ [8–14]. After modification with electron-donor compounds this system allows to perform the process of ethylene dimerization into butene-1 with the selectivity up to 98 %. As the side products are formed about 2 wt% of α-hexenes (3-methylpentene-1, 2-ethylbutene-1 and hexene-1), one tenth part of a procent of octenes and some of polymer (less than 0.01 wt%). Another feature of this process is the absence of formation in the step of the synthesis of β-olefins always formed at ethylene dimerization and oligomerization with other so far known complex organometallic catalysts.

A complex of research and development including pilot plant processing has been performed in the Division of polymers and composite materials and Laboratory of technological processes of the Institute of Physical Chemistry, Academy of Sciences of USSR, on the development of scientific base of industrial process of selective dimerization of ethylene into butene-1 at the action of catalytic system $Ti(OC_4H_9)_4$–AlR_3. These researches are protected by about 40 of Inventor Certificates within USSR and by international patents. In the Soviet Union in the beginning of 80-th first in the world were actuated two industrial installations for producing butene-1 with polymerization grade purity ("Orgsintez" in Kazan' and Budyenovsk, and "Stavropolpolymer" in Stavropol'), which provided with butene-1 two big plants in USSR and in Europe producing high density and medium density polyethylene.

Owing to increased demand for such α-olefins as butene-1, hexene-1, octene-1, and decene-1 used as copolymers at producing new sorts of polyethylene and polypropylene, it became actual development of simultaneous producing these olefins from ethylene in one process. At a first view seems that the best approach to solving this problem is improvement of the process of selective oligomerization of ethylene in the processes of ethylene tri-, tetra- and pentamerization [15–17]. Therewith, two problems should be solved in respect of the process of ethylene oligomerization:

– Narrowing the spectrum of α-olefins formed (to C_4–C_{12} instead of C_4–C_{30})

– Depressing the side reaction of isomerization of α-olefins into β-olefins.

Presence of β-olefins in the α-olefin passed to the reactor for ethylene or propylene polymerization even in micro amounts leads to substantial inhibition of polymerization, increases consumption of catalyst and generates problems of obtaining modified polyolefin with required reoligical and strength properties. Probably the problem can be solved on this pathway by application of transition metal complexes with bulky ligands [18, 19] for homogenous catalysis and gel-immobilized [20–23] or, in a general case, fixed on a support catalysts in the case of heterogenous catalysis.

Ethylene oligomerization (tri- and tetramerization of ethylene). To non-selective oligomerization of ethylene are denoted many communications and reviews (here we refer to only a small part of them) [24–29], in this communication we will consider only the problem of selective oligomerization of ethylene, namely, tri- and tetramerization of ethylene with formation of hexene-1 and octene-1, respectively.

In relatively large amount (over 1 wt%) the higher α-olefins butene-1, hexene-1 (in the ratio C_6-1 : C_4-1 = 25 : 1), octene-1, decene-1 and a series of branched decenes were detected at polymerization of ethylene with the catalytic system Cr(2-ethylhexanoate)$_3$ – polyisobutylalumoxane [30].

Accounting for a great interest to the synthesis of linear polyethylene of low density which can be obtained by copolymerization of ethylene with high α-olefins (butene-1, hexene-1, octene-1 and other), in the middle 70th researches began search for catalysts for selective oligomerization of ethylene with formation of these α-olefins. The main direction in search and development of the catalysts for selective oligomerization of ethylene to hexene-1 were and remain now as a rule the systems containing three or more components that include compounds with trivalent chromium, mono- (e.g., pyrrole and its alkyl derivatives, cyclopentadienyl compounds and other) and multidentate (e.g., triazacyclooctane, trispyrazolylmethane, diphosphazene, diphosphine, bis-diphosphine and bis-sulfanylamino derivatives) ligands and organoaluminum compounds. Recent results in the area of ethylene trimerization are considered in review

[31]. The first industrial process of producing hexene-1 by trimerization of ethylene was effected in Katar in 2003 along the join technology of Shevron and Phillips companies.

Since beginning and in particular since middle 90th of last century the search for effective catalysts for trimerization of ethylene to hexene-1 (since middle 80th these investigations were performed systematically by Phillips) began other advanced firms: in USA Amoco Co., in Japan Mitsubishi Chem. Co, Sumitomo Chem. Co., Idemitsu Kosau Co., Albemarle Co., Showa Denko Chem. Co., Mitsui Chem. Inc., and Japan Polyolefin Chem. Co. Since 2000 the number of firms that perform research and development of new catalysts for the synthesis of hexene-1 was extended.

Among effective researches we can notify the catalyst of Mitsubishi Chem. Co. based on Cr(2-ethylhexanoate)$_3$, 2,5-dimethylpyrrol, hexachloroethane and triethylaluminum at molar ratio of these components 1:6:4:40. At the temperature 105°C and ethylene pressure 50 atm was achieved catalytic activity up to 3780 kg/g_{Cr} h (at maintaining hexene-1 – ethylene molar ratio in the reactor equal to 0.5). This afforded 99.96 wt% of liquid oligomers containing up to 95.4 wt% of hexene-1 [32]. To the moment in the world patent literature were published more than 120 patents on the problem of producing hexene-1 by selective oligomerization of ethylene, predominantly by trimerization of ethylene to hexene-1.

Among the countries acquiring more than 40 patents the leading ones are USA and Japan. The countries acquiring 20 to 1 patents include SAR, Netherlands, Italy, France, Britain, Germany, China and Saudi Arabia.

The first example of effective trimerization of ethylene to hexene-1 in the presence of other transition metals is described in the communication of Pellecchia and co-authors [33] on the catalyst based on titanocene. In the presence of catalyst $CpCMe_2PhTiCl_3$ – methylalumoxane (1 : 1000) at 30 °C and ethylene pressure 0.2 MPa the rate of formation of hexene-1 achieved 22.35 kg/g_{Ti} h with selectivity on hexene-1 up to 83 wt%. Simultaneously 2.6 wt% of polyethylene was formed. Higher rate was achieved with titanocen trimethyl derivative [34].

A possibility of selective synthesis of octene-1 from ethylene was first reported by Kuhlmann and co-authors [35], who applied diphosphineamine chromium(III) complex in conjunction with β compounds of methylalumoxane. At the temperature 65°C and ethylene pressure 3 MPa was achieved the reaction rate 272.4 kg/g_{Cr} h with selectivity on octene-1 up to 70.3 wt%. More recently with the similar chromium complexes was studied effect of alkyl substituent at the nitrogen atom [36] and of organoaluminum co-catalyst both in the absence [37] and in the presence [38] of borates. It was found that polar solvent (chlorobenzene instead of toluene) increases activity and stability of catalyst, but simultaneously increases yield of decenes. For the catalytic system $Cr(C_5H_7O_2)_3$ – bis(diphosph ino)isopropylamine – methylalumoxane was shown that increase in the reaction temperature from 35 to 45°C decreases selectivity on octene-1 [39]. In [40] were applied various carbonyl chromium complexes with bis(diphosphno)amine ligands for the synthesis of cationic aluminate chromium(I) complex and was shown that it can be used as effective catalyst in the reaction of ethylene trimerization to octene-1.

Thus, we can note that there is certain success in the area of selective oligomerization of ethylene to hexene-1 and octene-1, while for the selective oligomerization of ethylene to higher α-olefins (decene-1, dodecene-1 and other) this is not achieved yet.

Propylene dimerization. Commonly, propylene dimer (4-methylpentene-1) is synthesized with heterogenous catalysts based on alkali metals. The synthesis of 4-methylpentene-1 on the complex organometalic catalysts based on decamethylmetallocene complexes $[Cp_2MCH_3(CH_8S)]^+BPh_4^-$, where M= Zr, Hf was first reported in 1990 by Teuben and coauthors [41, 42]. Besides 4-methylpentene-1 is formed also 4,6-dimethyl-1-heptene.

In 1991 Yamazaki and coauthors [43] using Cp_2MCl_2 (where M= Zr, Hf) in conjunction with methylamoxane synthesized 4-methylpentene-1 with a substantial amount of higher oligomers (C_{10} and higher). More selective propylene dimerization to 4-methylpentene-1 (up to 62 wt%) was achieved with $(\eta^5\text{-}C_5Me_4R^1)(\eta^5\text{-}C_5Me_4R^2)HfCl_2$ complex in the presence of methylalumoxane or mixture of *i*-Bu_3Al /$[Ph_3C][B(C_6F_5)_4]$ [44]. Selectivity on 4-methylpentene-1 up to 30 wt% was obtained at the propylene dimerization on the $NiBr_2$ calixarene complexes [45].

Undoubtedly interesting is selective dimerization of propylene not to branched dimer (as shown above) but to linear 1-hexene.

The table collects comparative data on activity and selectivity of transition metal complexes in the reactions of olefin di- and oligomerization.

Comparative characteristics of activity and selectivity of transition metal complexes in the reaction of dimerization and oligomerization of olefins

	I	II	III	IV	V	VI	VII	VIII		
3	Na	Mg	Al	Si	P	S	Cl			
4	K	Ca	Sc	Ti	V	Cr	Mn	Fe	Co	Ni
	Cu	Zn	Ga	Ge	As	Se	Br			
5	Rb	Sr	Y	Zr	Nb	Mo	Tc	Ru	Rh	Pd
	Ag	Cd	In	Sn	Sb	Te				
6	Cs	Ba	La	Hf	Ta	W	Re	Os	Ir	Pt

High activity, low selectivity

Moderate activity, low selectivity

Low activity and selectivity

High activity and selectivity

Low activity, high selectivity

HOMO- AND COPOLYMERIZATION OF OLEFINS

Physico-mechqanical and reological properties of polymers generally and polyolefins in particular depend on the following basic parameters:

- Molecular mass (MM)
- Molecular mass distribution (MMD)
- Degree and type of branching (B)
- crystallicity
- crystal structure
- degree of orientation, etc.

Five first parameters (MM, MMD, B, crystallicity and crystal structure) are defined by the conditions of the synthesis, while the remaining is connected with the conditions of producing certain commodity. Unfortunately, up to now have been published little works generalizing effect of all these parameters on the properties of polyolefins. The most successful attempts of consideration interconnection of these characteristics with physico-mechanical properties of amorphous, semicrystalline and crystalline polymers were made in the reviews [46, 47].

At the synthesis of polyolefins commonly not arise problem of control over MM and B. Much more difficult is solving the problem of control over MMD. MMD is the polymer characteristics which, on the one hand, reflects mechanism of polymerization, and, on the other hand, in much defines physico-mechanical and reological properties of the polymer.

The data published in literature including patent data on the control over MMD of polyolefins are extremely poor. This information commonly is an object of know-how of the firms producing polyolefins. Therefore there is no possibility to formulate any general statements on the effect of conditions on the polyolefin polydispersion. All is defined by the certain catalytic system applied in the process of polymerization, and often change in one parameter, e.g., duration of the polymerization or temperature leads to opposite results at the application of different catalytic systems.

Below are presented our attempts of generalization of the published data concerning effect of some parameters on diminishing polyethylene M_w/M_n ratio:

– decrease in concentration of the catalyst components in the system:

$(C_5H_5)_2TiCl_2$-$Al(C_2H_5)_2Cl$ [48], $(C_5H_5)_2TiCl_2$–$Al(CH_3)_2Cl$ [49];

– decrease in polymerization temperature {for the system of $(C_5H_5)_2TiCl_2$–$Al(C_2H_5)_2Cl$ in the ethyl chloride medium [48]};

– increase in polymerization temperature {for the system of $(C_5H_5)_2TiCl_2$–$Al(CH_3)_2$ in the medium of benzene [49], $TiCl_4$-$Al(C_2H_5)_2Cl$ [50], supported catalysts $TiCl_4$ on MgO [51]};

– decrease in ethylene concentration [48];

– increase in polymerization duration {for the systems of $TiCl_4$–$Al(C_2H_5)_3$ [52], $TiCl_3$–$Al(C_2H_5)_2Cl$ [53]};

– decrease in polymerization duration {for the system of $TiCl_4$–$Al(i\text{-}C_4H_9)_3$ [49, 54]};

– introducing of various additives {$(Ti(OC_4H_9)_4$ [55], $(C_6H_5)_2Mg$ [56], dienes [57]} to the system of $TiCl_4$–$Al(C_2H_5)_2Cl$.

In details was studied effect of various conditions of the polyethylene synthesis with the system of $(C_5H_5)_2TiCl_2$–$Al(C_2H_5)_2Cl$ on MMD of the product [58–67], and on basic reological and durable properties of the polymer in a wide range of MM keeping $M_w/M_n \approx 2$. Probably this is only one published example of such a systematic research.

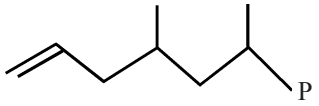
In the recent years, in principle, extended potential possibility of acquisition and detailed study of reological and durability of polyethylene, polypropylene, polybutene-1, ethylene and propylene copolymers with other α-olefins (at M_w/M_n in the range 2–3) due to application of Kaminskii catalysts [68, 69] and so-called "live" polymerization of olefins on the complex organometallic catalysts.

"Live" polymerization. Strictly controlled synthesis resulted in a given MM and narrow MMD ($M_w/M_n \sim 1.0$–1.3) can be achieved by means of "live" polymerization at anionic [70], cationic [71,72] and radical polymerization [73, 74]. A possibility of "live" polymerization of olefins (ethylene and propylene) at the action of complex organometallic catalysts has been demonstrated in the middle 80th of 20th century using vanadium catalysts [75].

To the moment, a large cycle of research on "live" polymerization of olefin has been carried out, which is considered in two reviews [76, 77]. They describe results in this area at the polymerization of ethylene and propylene as well as of norbornene, non-conjugated dienes, statistical and block-copolymerization of norbornene or cyclopentene with ethylene, propylene, dienes and polar monomers.

As is known, together with MM and MMD the polyolefin properties are defined by such a parameter as chain structure (content and type of side groups, concentration and type of terminal C=C groups). At producing polyolefins, content and type of side groups and their concentration can be commonly controlled by the conditions of the synthesis: type and concentration of co-monomer and applied catalyst. The type and concentration of C=C groups (vinyl and vinylidene) depend on the mechanism of the polymer chain termination.

Formation of terminal vinyl structures. The possibility of producing polypropylene (oligomeric, atactic) containing 92–98% of terminal vinyl structures was reported by Resconi [78]

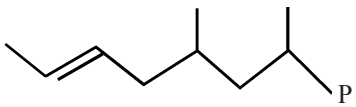


at application of the catalytic system $(CH_3C_5H_4)MCl_2$ – methylalumoxane, where M=Zr, Hf. More recently, Repo [79] informed abut the synthesis of polypropylene containing up to 90% of terminal vinyl structures in the presence of metallocenes with acetonaphthyl cyclopentadienyl substituents. The authors of this work suggest that formation of such structures is a result of β-elimination of methyl group at the chain propagation.

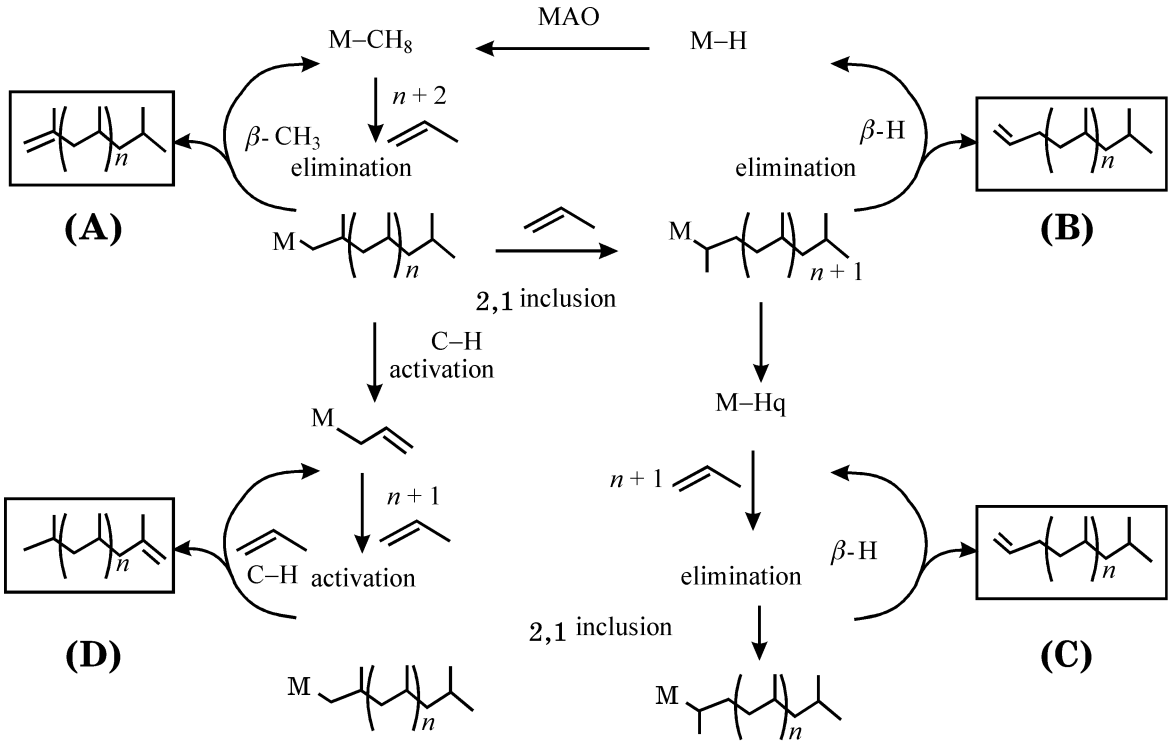
In [80] synthesis of atactic polypropylene with MM=12000-30000 and MMD≈2, containing up to 60–80% of terminal vinyl groups and with stereoregularity (mmmm pentades) up to 95% was carried out in the presence of *rac*-dimethylsilanodiyl(2-methyl-4-phenylindenyl)$ZrCl_2$ and *rac*-dimethylsilanodiyl-bis(indenyl)$Hf(CH_3)_2$ at 95–120°C. The possible pathways of formation of the terminal vinyl structures are shown in the Scheme; the pathway A is suggested as defining one.

The polymers with vinyl terminal groups can be considered as macromonomers for the reactions of binary or ternary copolymerization and also as precursors for the further functionaliztion of the macromonomer.

At the polymerization of olefins with complex organometallic catalysts, in particular with those based on metallocenes, the principal mechanism of the chain termination is β-eliminating of hydrogen leading to formation of vinylidene structures [81–83]. This mechanism leads to formation of polymer chain with vinylidene structure at the polymerization of propylene. In [84–86] was described synthesis of atactic and isotactic polypropylene containing, together with vinyl terminal groups also up to 50% of vinylidene groups.



Polymerization of α-olefins (propylene, butene-1 and other) can afford polymers with various structure of



Scheme. Formation of terminal vinyl bonds at the polymerization of α-olefins.

chain, where alkyl side groups (methyl at polymerization of propylene and ethyl at polymerization of butene-1) can occupy various positions relatively to to each other and to the main chain. Also, polymerization of α-olefins can lead to the polymer with gemiisotactic, stereoblock and atactic structures. Below we consider some of recent results on the example of propylene polymerization providing certain structure of the polypropylene formed.

Isotactic polypropylene. At the synthesis of isotactic polypropylene under the action of metallocene catalysts commonly is used *rac*-form of metallocene with C_2 sym-metry. Spaleck and coauthors [87] obtained with bis-indenyl cyrconocenes a polypropylene with M_n up to 7.3×10^5, containing 95% of isotactic pentades [mmmm] 95%, with melting point157°C. This polymer by its properties is close by its properties to the polypropylene produced by industry with heterogenous catalysts features by a narrow MM range. Mechanism of formation of isotactic polypropylene on the metallocenes with C_1 simmetry is discussed in [88].

SyndiOtactic polypropylene. At the synthesis of syndiOtactic polypropylene are applied *ansa*-metallocenes of C_s symmetry [89]. SyndiOtactic polypropylene was also synthesized on the circonium fluorenyl complexes [90, 91].

Gemiisotactic polypropylene. This type polypropylene has unusual structure with each even (or odd) CH_3 group located at one side of carbon chain while intermediate CH_3 groups are distributed statistically. Synthesis of such polypropylene is carried out in the presence of circonocenes with C_1 symmetry [88, 92].

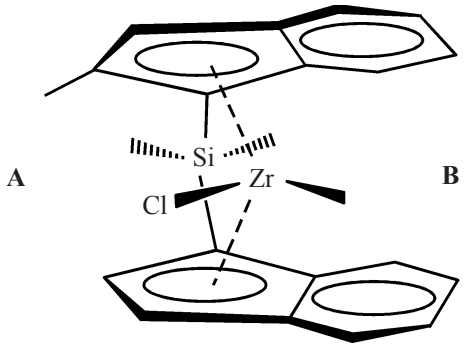
Stereoblock polypropylene. Stereoblock polypropylene was isolated by Natta by fractionation of the polypropylene obtained on the system of $TiCl_4$–AlR_3. Such polymer contains in its chain alternating isotactic and atactic blocks and has properties typical of elastomers. Commonly as the catalyst for the synthesis of stereoblock polypropylene are used so-called oscillating metallocenes, e.g., non-bridgehead bis-indenyl circonocenes with phenyl substituents in 2 position [93–97]. At the propagation of the polymer chain occurs multiple isomerization of the complex from isospecific *rac*-form into non-specific *meso*-form. Introducing of propylene molecule in the period of existence of active center in *rac*-form leqads to formation of an isotactic block. Introducing of propylene at the *meso*-form of the active center leads to an atactic block. Thus, the polymer chain growing on the oscillating active center has stereoblock structure. In the recent time appeared publications on the synthesis of stereoblock polypropylene by the method of "live" polymerization [98].

Atactic polypropylene. As compared with isotactic polypropylene, it has lower durability characteristics and lower melting point. It is well soluble in non-polar solvents, highly hydrophobic and chemically resistant. Low molecular atactic polypropylene has been synthesized on achiral and symmetrical metallocenes [99], high molecular atactic polypropylene with perfect elastomeric properties has been synthesized on a circonocene of C_{2v} symmetry $Me_2Si(Flu)_2ZrCl_2$ [100, 101] , and on phenoxyimine metallocene [102].

Polybutene-1. Isotactic polybutene-1 was first synthesized on a heterogenous catalyst $TiCl_3$, its structure was studied by D. Natta [103]. However, industrial process with this catalyst was not developed due to certain technological problems. To the moment the principal patent owner on the process of manufacturing isotactic polybutene-1 on the metallocene catalysts is Basell Polyolefine GMBE [104–107]. In Netherlands this company has facility for producing polybutene-1 with productivity 60 thousands ton per year. It is suggested that this company can be a licensiar of polybutene-1 production in the Open join stock company "Nizhnekamskneftekhim" with productivity 30-40 thousands ton per year. Isotactic polybutene-1 of different isotacticity can be produced on circonocenes of C_1 and C_2 symmetry. On the circonocenes of C_1 symmetry with indenyl ligands is formed polybutene-1 with high MM (up to 400 000). The degree of isotacticity depends on the type of substituent at the indenyl ligand [108, 109].

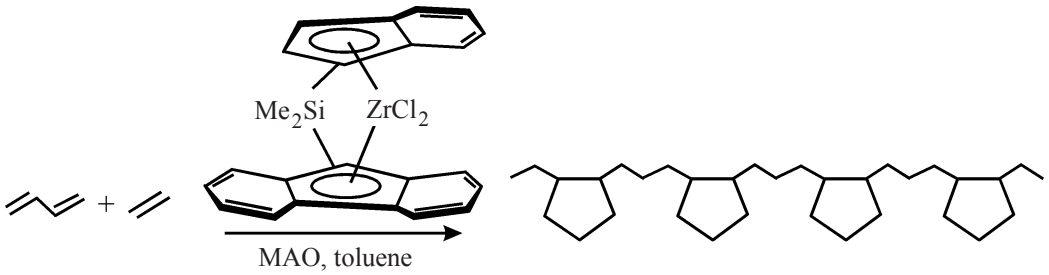
Alternating copolymerization of olefins. Synthesis of alternating copolymers as a rule is possible when the rate of homopolymerization of one of monomers is much higher than that of another, and increase in the reaction zone of concentration of less active co-monomer leads to increase in degree of alternation of the copolymers in the synthesized product. However, obtaining strictly alternating ethylene copolymers with other olefins still failed. Nevertheless, a high degree of alternation of copolymers has been achieved, at the copolymerization of ethylene with propylene [110–113] on circonium catalysts of C_1 and C_2 symmetry Et(Ind)(Flu)$ZrCl_2$, *i*-Pr(3-MeCp)Flu)$ZrMl_2$, *i*-Pr(3,4-Me_2Cp)(Flu)$ZrMe_2$; also with norbornene [114–121], octene-1 [122–125], isobutylene [126], butene-2 [127], cyclopentene [128–130], butadiene-1,3 [131] and butadiene-1,4 [132–135].

The proposed mechanism of alternation at the copolymerization of ethylene with octene-1 on the circonocene of C_1 symmetry *meso*-Me_2Si(2-MeInd)$_2ZrCl_2$ assumes [122] that the active center has two different coordination sites. One site is sterically less available (A) than another (B). Therefore one can expect that more bulky co-monomer octene-1 coordinates at the center A, while ethylene at the center B if there is significant difference in concentrations, [octene-1] >> [ethylene]



Alternating ethylene copolymer with cyclopentene with mp ~184°C has been discovered by Natta [129] in the insoluble in octane fraction of this copolymer obtained on the catalysts $VOCl_3$–$AlEt_3$, $V(acac)_3$–$AlEt_3$. More recently [130] with application of bis-phenoxyimine containing titanium catalyst were obtained atactic (Fig. 1) and sindiOtactic ethylene – cyclopentene copolymers. Fig. 2 depicts experimentally determined dependence of glass transition temperature T_g of ethylene – cyclopentene copolymers on the cyclopentene content in the copolymer.

For first time was shown a possibility of cyclocopolymerization of 1,3-butadiene with ethylene in the presence of catalytic system of Me_2Si(1-Ind)(Flu)$ZrCl_2$+ methylalumoxane in the medium of toluene at 25°C with a high degree of alternation of ethylene and cyclopentane (>90% of *trans*-1,2-cyclopentane links) [131].



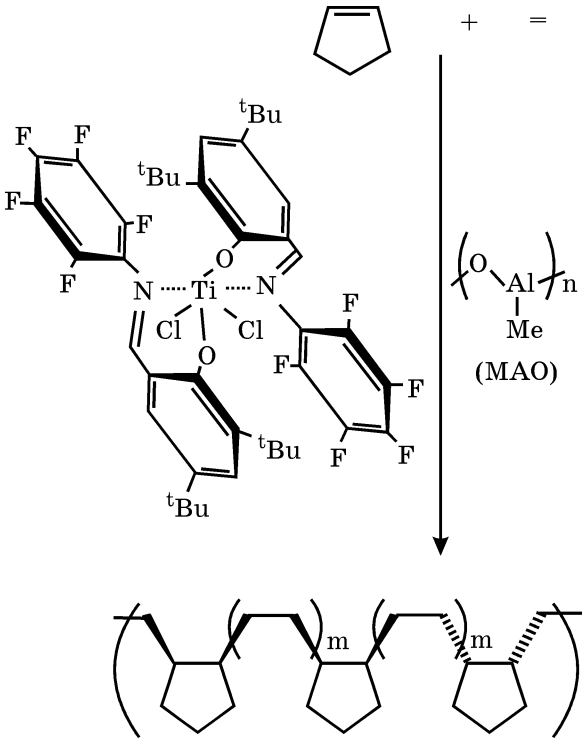


Fig. 1. Synthesis of alternating atactic cyclopentene–ethylene copolymer.

The synthesis of ethylene – 1,4-butadiene copolymers containing a fraction of alternating copolymer has been reported in [132–135].

Strictly alternating copolymers of olefins with such unusual co-monomer as carbonmonooxide wre first obtained in the middle of 80-th of the preceding century practically simultaneously by Shell firm and in the Institute of the Problems of Chemical Physics, Russian Academy of Sciences, in the presence of catalytic systems based on palladium carboxylates, mono- and bidentate phosphorus and nitrogen-containing ligands and an acid with pK <2 [136, 137]. These copolymers called polyketones represent a new generation of functional copolymers and are of certain practical significance because presence of CO group in a strict sequence after another monomeric link in the copolymer chain leads to the following:

– Increases ability of the polymer to photo- and biodestruction,

– Infinitely extends ability of modification of the copolymers by means of reactions in the polymer chain and thus obtaining new oligomeric and polymeric products with a new complex of properties,

– Admits to the polymers and compositions based on them high adhesion properties.

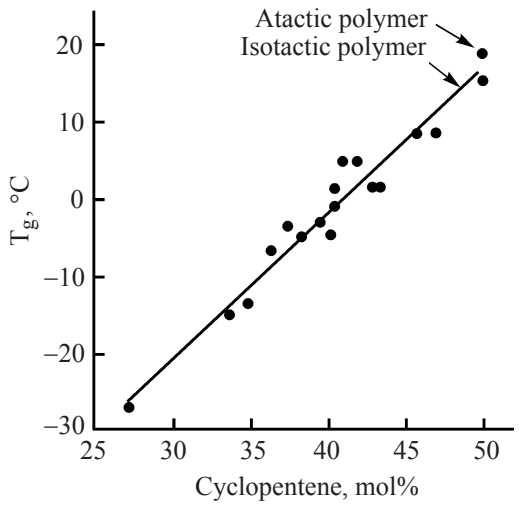


Fig. 2. Plot of glass transfer temperature T_g of cyclopentene–ethylene copolymer on the cyclopentene content in the copolymer.

The copolymer of ethylene with CO has high melting point (265°C) and can be considered as engineeric plastic. To the moment there are 16 reviews denoted to this polymer [138–153].

Analysis of the data published in patent and research literature shows that for the 50 years since discovery of complex organometallic catalysts (the Zigler – Natta catalysts and further generations) and their application in the reactions of olefins oligo- and polymerization was achieved certain success:

– in the area of selective ethylene oligomerization to butene-1, hexene-1 and octene-1 (selectivity over 70–98%) industrial processes of the synthesis of butene-1 and hexene-1 with polymerization grade purity are created,

– in the area of selective homo- and copolymerization of ethylene in the industry conditions is obtained polyethylene not only of required molecular mass (MM), branching (B) degree and type (methyl, ethyl, butyl groups), but also with a given by wideness and type (uni- and bimodal) molecular mass distribution (MMD),

– in the area of selective polymerization of propyl-ene and butene-1 are realized in the industry the processes of synthesis of isotactic and syndiotactic polypropylene, of isotactic polybutene-1,

– in the area of "live" polymerization and alternating copolymerization of olefin there are significant achievements, however, it was not yet realized in the industry, except alternating copolymerization of ethylene with carbon monoxide.

ACKNOWLEDGMENTS

This work was financially supported by Russian Foundation for Basic Research (the projects codes: 07-03-00108, 07-03-00363).

REFERENCES

1. Emanuel', N.M., *Uspekhi Khimii*, 1978, vol. 47, no. 8, p. 1326.
2. Butlerov, A.M., *Izbrannye raboty po organicheskoi khimii* (Selected Papers on Organic Chemistry), Moscow: Akad. Nauk SSSR, 1951.
3. Kuznetsov, V.I., *Razvitie issledovanii polimerizatsii nepredel'nykh soedinenii v SSSR* (Development of Investigations on the Polymerization of Unsaturated Compounds in USSR), Moscow: Akad. Nauk SSSR, 1959.
4. Paushkin, Ya.M., *Kataliticheskaya polymerizatsiya olefinov v motornoe toplivo* (Catalytic Polymerization of Olefins into Motor Fuel), Moscow: Akad. Nauk SSSR, 1955.
5. Belov, G.P., *Neftekhimiya*, 1977, vol. 17, no. 1, p. 13.
6. Belov, G.P., Dzhabiev, T.S., and Kolesnikov, I.M., *J. Mol. Catal*., 1982, vol. 14, p. 105.
7. *Neftegazovye Tekhnologii*, 1995, no. 5, p. 39.
8. Dzhabieva, Z.M., Dzhabiev, T.S., Belov, G.P., and D'yachkovskii, F.S., *Neftekhimiya*, 1975, no. 8, p. 1750.
9. Dzhabiev, T.S., Dzhabieva, Z.M., Belov, G.P., and D'yachkovskii, F.S., *Neftekhimiya*, 1976, vol. 16, no. 5, p. 706.
10. Belov, G.P., Dzhabieva, Z.M., and D'yachkovskii, F.S., in *Komplexnye metallorganicheskie katalizatory polimeriztsii olefinov* (Complex Organometallic Catalysts for Olefins Polymerization), Chernogolovka: Inst. Khim. Fiz., Akad. Nauk SSSR, 1978, No. 7, p. 119.
11. Gerasina, M.P., Brikenshtein, A.A., Belov, G.P., and D'yachkovskii, F.S., *Interuniversity Collection of Scientific Proceeding "Osnovnoi organicheskii sintez i neftekhimiya"* (General Organic Synthesis and Petrochemistry), Yaroslavl', 1978, no. 10, p. 15.
12. Belov, G.P., Dzhabieva, Z.M., and Dyachkovskii, F.S., in *Fundamental Research in Homogeneous Catalysis*, Shilov, A.E., Ed., Gordon and Breach Sci. Publ., 1986, vol. 3, p. 1015.
13. Belov, G.P., Brikenshtein, A.A., Gerasina, M.P., and D'yachkovskii, F.S., *Neftepererabotka Neftekhimiya*, 1986, no. 6, p. 14.
14. Nevzorov, V.E. and Belov, G.P., *Neftekhimiya*, 1989, vol. 29, no. 3, p. 340.
15. Fell, B., *Detergents*, 1975, no. 1, p. 3.
16. Langer, A.W., *Chem. Eng. News*, 1972, vol. 10, p. 16.
17. Brikenshtein, Kh.-M.A, Matkovskii, P.E., and Russiyan, L.N., in Komplexnye i metalloorganicheskie katalizatory polimerizatsii olefinov (Compex and Organometallic Catalysts of Olefins Polymerization), no. 7, Chernogolovka: OIKhF AN SSSR, 1978, p. 83.
18. Behr, A., Fabbee, V., Freundberg, V., and Keim, W., *Israel J. Chem*., 1986, vol. 27, no. 3, p. 277.
19. US Patent no. 4777315., 1988, *Ref. Zh. Khim.*, 17N9P, 1989.
20. Kabanov, V.A., Martynova, M.A., and Pluzhnov, S.K., *Kinetika Kataliz*, 1979, vol. 20, no. 4, p. 1012.
21. Popov, V.G. and Vasil'chenko, S.V., *Kinetika Kataliz*, 1988, vol. 29, no. 4, p. 981.
22. Cmetanyuk, V.I., Ivanyuk, A.V., and Prudnikov, A.I., *Neftekhimiya*, 2001, vol. 40, no. 1, p. 22.
23. Gyulumyan, Kh.R., Popov, V.G., Belov, G.P., Chekrii, P.S., and D'yachkovskii, F.S., Abstracts of Papers, 4-aia Vsesoyuznaia konferentsiia po kinetike geterogennykh kataliticheskikh reaktsii "Kinetika-4" (Materials of 4th All-Union Conference on the Kinetics of Heterogenous Catalytic Reactions "Kinetics-4"), Yaroslavl, 1988, p. 354.
24. Belov, G.P., *Neftekhimiya*, 1994, vol. 34, no. 2, p. 115.
25. Kurtev, K. and Tomov, A., *J. Mol. Catal.*, 1994, vol. 88, p. 141.
26. Keim, W. and Schulz, R.P., *J. Mol. Catal*., 1994, vol. 92, p. 21.
27. Wang, M., Li, R., Qian, M., Yu, X., and He, R., *J. Mol. Catal*., 2000, vol. 160, p. 337.
28. Carlini, C., Marchionna, M., Galletti, A.V.R., and Sbrana, G., *Appl. Catal., A: Gen*., 2001, vol. 206, p. 1.
29. Janak, C., *Coord. Chem. Rev*., 2006, vol. 250, p. 66.
30. Manyik, R.M., Walker, W.E., and Wilson, T.P., *J. Catal*., 1977, vol. 47, p. 197.
31. Dixon, J.T., Green, M.J., Hess, F.M., and Morgan, D.H., *J. Organometal. Chem*., 2004, vol. 689, p. 3641.
32. Araki, Y., Nakamura, H., Nanba, Y., and Okanu, T., US Patent 5856612, January 5,1999.
33. Pellecchia, C.,Papparaldo, D., Oliva, L., and Gruter, G., *Macromolecules*, 1999, Vol. 32, p. 4491.
34. Hagen, H., Kretschmer, W.P., van Buren, F.R., Hessen, B., and van Oeffelen, D.A., *J. Mol. Catal., A: Chem*., 2006, vol. 248, p. 237.
35. Bollmann, A., Blann, K., Dixon, J.T., Hess, F.M., Killian, E., Maumela, H., McGuiness, D.S., Morgan, D.H., Neveling, A., Otto, S., Overett, M., Slawin, A.M.Z., Wasserscheid, P., and Kuhlmann, S., *J. Amer. Chem. Soc*., 2004, vol. 126, p. 14712.
36. Elowe, P.R., McCann, C., Pringle, P.G., Spitzmesser, S.K., and Bercaw, J., *Organometallics*, 2006, vol. 25, p. 5255.
37. McGuiness, D.S., Rucklidge, A.J., Tooze, R.P., and Slawin, A.M.Z., *Organometallics*, 2007, vol. 26, p. 2561.
38. McGuiness, D.S., Overett, M., Tooze, R.P., Blann, K., Dixon, J.T., and Slawin, A.M.Z., *Organometallics*, 2007,

vol. 26, no. 4, p. 1108.
39. Walsh, R., Morgan, D.H., Bollman, A., and Dixon, J.T., *Appl. Catal., A: Gen*., 2006, vol. 306, p. 184.
40. Rucklidge, A.J., McGuiness, D.S., Tooze, R.P., and Slawin, A.M.Z., Pelletier, J.D.A., Hanton, M.J., Webb, P.B., *Organometallics*, 2007, vol. 26, p. 2782.
41. Eshuis, J.J.W., Tan, Y.Y., Teuben, J.H., *J. Mol. Cat*., 1990, vol. 62, p. 277.
42. Eshuis, J.J.W., Tan, Y.Y., Meetsma, A., Teuben, J.H., Renrtma, J., and Evans, G.G., *Organometallics*, 1992, vol. 11, p. 362.
43. Mise, T., Kageyama, A., Miya, S., and Yamazaki, H., *Chem. Lett*., 1991, p. 1525.
44. Suzuki, Y., Yasumoto, T., Mashima, K., and Okuda, J., *J. Amer. Chem. Soc*., 2006, vol. 128, no. 39, p. 13017.
45. Lejeune, M., Semeril, D., Jeunesse, C., Matt, D., Lutz, P., and Toupet, L., *Adv. Synt. Catal*., 2006, vol. 348, p. 881.
46. Martin, J.R., Johnson, J.F., and Cooper, A.R., *J. Macromol. Sci*., 1972, vol. 8C, no. 1, p. 57.
47. Numes, R.W., Martin, J.R., and Johnson, J.F., *Polymer Eng. Sci.,* 1982, vol. 22, no. 4, p. 205.
48. Belov, G.P., Lisitskaya, A.P., Tsvetkova, V.I, and Chirkov, N.M., *Vysokomolek. Soedin*., 1967, vol. 9A, no. 6, p. 1269.
49. Chien, J.C.W., *J. Polymer Sci*., 1963, pt. A, vol. 1, p. 1839.
50. Popov, V.P., Voropaeva, R.M., Ivanova, A.G., and Gol'denberg, A.L., *Plasticheskie Massy*, 1972, no. 5, p. 7.
51. Baulin, A.A., Shalaeva, L.F., and Ivanchev, S.S., *Dokl., Akad. Nauk SSSR*, 1976, vol. 231, no. 2, p. 413.
52. Naraba, Tsunadze, Sekikava, and Kedzoyu, *Koge Kagaku Dzassi*, 1965, vol. 68, no. 1, p. 2283.
53. Jung, K.A.. and Schnecko, H., *Macromol. Chem*., vol. 154, p. 227.
54. Taylor, W.C. and Tung, D.H., *J. Polymer Sci*., 1963, pt. B, p. 157.
55. Petrova, T., Dobrova, D., and Kostov, G., *Neft i khimiya* (Bolg.), 1971, no. 10, p. 239.
56. Petrova, T., *Europ. Polymer J*., 1976, vol. 12, no. 8, p. 571.
57. Japan Patent 50-23432; *Ref. Zh. Khim*., 1976, 1ZS287P.
58. Belov, G.P., Kaltochikhina, S.K., Atanasova, L.I., Tsvetkova, V.I, and Chirkov, N.M., *Izv. Akad. Nauk SSSR, Ser. Khim*., 1966, no. 7, p. 1275.
59. Belov, G.P., Raspopov, L.N., Lisitskaya, A.P., Tsvetkova, V.I, and Chirkov, N.M., *Vysokomolek. Soedin*., 1966, vol. 8, no. 10, p. 1852.
60. Belov, G.P., Lisitskaya, A.P., and Chirkov, N.M., *Izv. Akad. Nauk SSSR, Ser. Khim*., 1968, no. 11, p. 2650; Belov, G.P., Solov'eva, T.I., and Chirkov, N.M., *Vysokomolek. Soedin*., 1970, vol. 12B, no. 8, p. 632.
61. Belov, G.P., Solov'eva, T.I., and Gerasina, M.P., *Plasticheskie Massy*, 1970, No. 4, p. 14.
62. Belov, G.P., Belova, V.N., Raspopov, L.N., Kissin, Yu.B., Brikenshtein, A.A., and Chirkov, N.M., *Polymer J*., 1972, vol. 3, no. , 6, p. 681.
63. Raspopov, L.N.., *Cand. Sci. (Chem.) Dissertation*, Moscow: IKhF Akad. Nauk SSSR, 1970.
64. Raspopov, L.N., Belov, G.P., and Brikenshtein, Kh.-M.A., Musaelyan, I.N., Matkovskii, P.E., and Chirkov, N.M., *Plasticheskie Massy*, 1975, no. 9, p. 67.
65. Belov, G.P., Viktorova, N.L., Marikhin, V.A., Masalimov, K.T., Musaelyan, I.N., and Myasnikova, L.P., *Vysokomolek. Soedin*., 1978, vol. 20A, no. 12, p. 2694.
66. Optov, V.A., Yarlykov, B.W., Dreval, V.I., Belov, G.P., Prokhorenko, T.V., and Musaelian, I.N., *Plastics and Kautshuk*, 1979., vol. 3, p. 145.
67. Kaminsky, W., in *History of Polyolefins*, Caeng, T. and Seymour, R.B., Eds., 1986, p. 257.
68. Ewen, J.A., *J. Amer. Chem. Soc*., 1984, vol. 106, p. 6355.
70. Hsieh, H.L. and Quirk, R.P., *Anionic Polymerization: Principles and Practical Applications*, New York: Marcel Dekker; 1996.
71. Matyiaszewski, K., *Cationic Polymerizations: Mechanisms, Synthesis and Applications*, New York: Marcel Dekker, 1996.
72. Hawker, C.Y., Bosman, A.W., and Harth, E., *Chem. Rev*., 2001, vol. 101, p. 3361.
73. Kamigaito, M., Ando, T., and Sawamoto, M., *Chem. Rev*., 2001, vol. 101, p. 3689.
74. Matyiaszewski, K. and Xia, Y.H., *Chem. Rev*., 2001, vol. 101, p. 2921.
75. Doi, Y., Suzuki, S, and Soga, K., *Macromolecules,* 1986, vol. 19, no. 9, p. 2896.
76. Coates, G.V., Hustad, P.D., and Reinartz, S., *Angew. Chem., Int. Ed*., 2002, vol. 41, p. 2236.
77. Domski, G.Y., Rose, Y.M., Coates, G.W., Bolig, A.D., and Brookhart, M., *Progr. Polym. Sci*., 2007, vol. 32, p. 30.
78. Resconi, L., Piemontesi, F., Franciscono, G., Abis, L., and Fiorani, T., *J. Amer. Chem. Soc.*, 1992, vol. 114, p. 1025.
79. Repo, T., Jany, G., Hakala, K., Klinga, M., Polamo, M., Leskala, M., and Rieger, B., *J. Organomet. Chem.,* 1997, vol. 549, p. 177.
80. Weng, W., Markel, E.J., and Dekmezian, A.H., *Macromol. Rapid Commun.*, 2000, vol. 21, p. 1103; Zanghauser, F., *Organometallics*, 1994, vol. 13, p. 964.
81. Chien, J.C.W. and Wang, B.P., *J. Polymer Sci., A, Polymer Chem.*, 1990, vol. 28, p. 15.
82. Stehling, U., Diebold, J., Kristen, R., Roll, W., Brintzinger, H.H., Jungling, S., Mulhaupt, R., and Zanghauser, F., *Organometallics*, 1994, vol. 13, p. 964.
83. Kaminsky, W., Ahlers, A., Franciscono, G., Abis, L., and Fiorani, T., *Angew Chem., Int. Ed*., 1989, vol. 28, p. 1216

84. Grassi, A., Zambelli, A., Resconi, L., Albizzati, E., and Mazzocchi, R., *Macromolecules*, 1988, vol. 21, p. 617.
85. Tsutsui, T., Mizuno, A., and Kashiwa, N., *Polymer*, 1989, vol. 30, p. 428.
86. Shiono, T. and Soga, K., *Macromolecules*, 1992, vol. 25, no. 13, p. 3356.
87. Spaleck, W., Autberg, M., Aulbach, M., Bachmann, B., Doll, V., Hafka, S., Kuber, F., Rohrmann, Y., and Winter, A., in *Ziegler Catalysts*, Fink, G., Mulhaupt, R., and Brintzinger, H.H., Eds., Berlin: Springer Verlag., 1995, p. 87.
88. Miller, S.A. and Bercaw, J.E., *Organometallics,* 2006, vol. 25, no. 15, p. 3576
89. Tsvetkova, V.I., *Vysokomolek. Soedin*., 2000, vol. 42, no. 11, p. 1954.
90. Miller, S.A. and Bercaw, J.E., *Organometallics*, 2004, vol. 23, no. 8, p. 1777.
91. Miller, S.A., Hopf, A., Kaminsky, W., *et al., Polymer*, 2004, vol. 45, no. 6, p. 1815.
92. Ewen, J.A., Jones, R.L., Elder, M.J., *et al., Macromol. Chem. Phys*., 2004, vol. 205, no. 3, p. 302.
93. Coates, G.W. and Waymouth, R.M., *Science*, 1995, vol. 267, no. 5195, p. 217.
94. Bruce, M.D., Coates, G.W., Hauptmann, E., Waymouth, R.M., and Ziller, J.W., *J. Amer. Chem. Soc*., 1997, vol. 119, no. , 46, p. 11174.
95. Tsvetkova, V.I., Nedorezova, P.M., Savinov, D.V., Dubnikova, I.L., and Optov, V.A., *Vysokomolek. Soedin*., A, 1997, vol. 39, no. 3, p. 389.
96. Hu, Y., Krejchi, M.T., Shan, C.D., Myers, C.L., and Waymouth, R.M., *Macromolecules*, 1998, vol. 31, no. 9, p. 6908.
97. Nedorezova, P.M., Tsvetkova, V.I., Bravaya, N.M., Savinov, D.V., and Optov, V.A., *Vysokomolek. Soedin*., A., 2000, vol. 42, no. 6, p. 901.
98. Nishii, K., Shiono, T., and Ikeda, T., *Macromol. Rapid Commun.,* 2004, vol. 25, no. 10, p. 1029.
99. Kaminsky, W., Engehausen, R., Zoumis, K., Spaleck, W., and Rohrmann, J., *Makromol. Chem*., 1992, vol. 193, p. 1643.
100. Resconi, L., Piemontesi, F., Francoscono, G., Abis, L., and Fiorani, T., *J.Am., Chem., Soc*., 1992, vol. 114, p. 1025.
101. Resconi, L.,Jones, R.L., Rheingold, A.L., and Yap, G.P.A., *Organometallics*, 1996, Vol. 15, p. 998.
102. Weiser, M.S., Wesolek, M., and Mulhaupt, R., *J. Organomet. Chem*., 2006, vol. 691, no. 13, p. 2945.
103. Natta, G. and Corradini, P., *J. Polymer Sci*., 1956, vol. 20, p. 251.
104. Resconi, L. and Pelliconi, A., Europe Patent 1477499, 2004.
105. Resconi, L. and Guidotti, S., Europe Patent 1567565, 2005.
106. Resconi, L., Europe Patent 1753792, 2006.
107. Resconi, L. and Cascio, I., Europe Patent 1769030, 2007.
108. Resconi, L. and Camurati, I., *Macromol. Chem., Phys*., 2006, vol. 207, no. 24, p. 2257.
109. Resconi, L. and Morhard, F., Europe Patent 1765886, 2007.
110. Yin, Y., Uozumi, T., Sano, T., Teranishi, T., Soga, K., and Shiono, T., *Macromol. Rapid Commun*., 1998, vol. 19, p. 337.
111. Leclerck, M.K. and Waymouth, R.M., *Angew Chem., Int. Ed*., 1998, vol. 37, p. 922.
112. Arnadt, M., Kaminsky, W., Schauwrenold, A.M., and Weingarten, U., *Macromol. Chem*., 1998, vol. 199, p. 1135.
113. Fan, W., Leclerck, M.K., and Waymouth, R.M., *J. Amer. Chem. Soc*., 2001, vol. 123, p. 9555.
114. Harrington, B.A. and Growther, D.J., *J. Mol. Catal., A, Chem.*, 1998, vol. 128, p. 79.
115. Ruchatz, D. and Fink, G., *Macromolecules*, 1998, vol. 31, pp. 4669,4674, 4681,4684.
116. McKnight, A.L. and Waymouth, R.M., *Macromolecules*, 1999, vol. 32, p. 2816.
117. Tritto, I., Marestin, C., Boggioni, L., Sacchi, M.C., Brintzinger, H.H., and Ferro, D.R., *Macromolecules*, 2001, vol. 34, p. 5770.
118. Tritto, I., Boggioni, L., Jansen, J.C., Thorshang, K., Sacchi, M.C., and Ferro, D.R., *Macromolecules*, 2002, vol. 35, p. 616.
119. Grassi, A., Maffei, G., Milione, S., and Jordan, R.F., *Macromol. Chem. Phys*., 2001, vol. 202, p. 1239.
120. Altamura, P. and Grassi, A., *Macromolecules*, 2001, vol. 34, p. 9197.
121. Yoshida, Y., Saito, j., Mitani, M., Takagi, Y., Matsui, S., Ishii, S., Nakano, T., Kashiwa, N., and Fujita, T., *Chem. Commun*., 2002, p. 1298.
122. Uozumi, T., Miyazawa, K., Sano, T., Teranishi, T., Soga, K., and Shiono, T., *Macromol. Rapid Commun*., 1998, vol. 19, p. 883.
123. Uozumi, T., Ahn, C.H., Tomisaka, M., Jin, J., Tian, G., Sano, T., and Soga, K., *Macromol. Phys.,* 2000, vol. 201, p. 1748.
124. Hagihara, H., Murata, M., and Uozumi, I., *Macromol. Rapid., Commun*., 2001, vol. 22, p. 353.
125. Uozumi, T., Tian, G., Ahn, C.H., Jin, J.Z., Tsubaki, S., Sano, T., and Soga, K., *J. Polymer Sci., Polym. Chem*., 2000, vol. 38, p. 1844.
126. Shaffer, T.D., Canich, Y.A.M., and Squire, K.R., *Macromolecules*,1998, vol. 31, p. 5145.
127. Natta, G., Valvassori, A., Dallasta, G., Zambelli, A., Massanti, G., and Pasquon, I., *J. Amer. Chem. Soc*., 1961, vol. 83, p. 3343.
128. Natta, G., Dallasta, G., Massanti, G., Zambelli, A., Pasquon, I., and Valvassori, A., *Makromol. Chem*., 1962, vol. 54, p. 95.

129. Natta, G., Dallasta, G., Donegaui, G., and Massanti, G., *Angew Chem., Int. Ed.,* 1964, vol. 3, p. 723.
130. Fujita, G. and Coates, G.W., *Macromolecules*, 2002, vol. 35, p. 9640.
131. Choo, T.N. and Waymouth, R.M., *J. Amer. Chem. Soc*., 2003, vol. 125, p. 8970.
132. Natta, G.,Zambelli, A., Pasguon, I., and Ciampelli, F., *Macromol. Chem*., 1964, vol. 79, p. 161.
133. Furukawa, J., *Angew Macromol. Chem*., 1972, vol. 23, p. 189.
134. Furukawa, J. and Hirai, R., *J. Polymer Sci., A1*., 1972, vol. 10, p. 3027.
135. Furakawa, J. and Kobayashi, E., *Rubber Chem. Technol*., 1978, vol. 51, p. 600.
136. Drent, E., Europe Patent 121965, 1984.
137. Chepaikin, E.G., Bezruchenko, A.P., and Belov, G.P., RF Patent 1636417, 1987.
138. Sen, A., *Adv. Polym. Sci*., 1986, vol. 73/74, p. 125.
139. Sen, A., *Acc. Chem. Res.*, 1993, vol. 26, p. 303.
140. Drent, E. and Budzelaar, P.H.M., *Chem. Rev*., 1996, vol. 96, p. 663.
141. Belov, G.P., in *Polymeric Materials, Encyclopedia*, CRC Press, Inc., USA, 1996, p. 4714.
142. Drent, E., van Broekhoven, J.A.M., and Budzelaar, P., in *Applied Homogeneous Catalysis with Organometallic Compounds*, Weinheim: VCH, 1996, vol. l, p. 333.
143. Sommazzi, A. and Garbassi, G., *Progr. Polymer Sci*., 1997, vol. 22, p. 1547.
144. Belov, G.P., *Vysokomolek. Soedin*., B., 1998, vol. 40, no. 3, p. 503.
145. Nozaki, A. and Hijama, T., *J. Organomet. Chem.*, 1999, vol. 576, p. 248.
146. Belov, G.P., *Vysokomolek. Soedin*., 2001, vol. 43, no. 9, p. 1651.
147. Belov, G.P., *Kinetika Kataliz*, 2001, vol. 42, no. 3, p. 336.
148. Drent, E., Mul, W., P., and Smardijk, A.A, in *Encyclopedia of Polymer Sci. and Technol.*, Wiley & Son., Inc., 2001.
149. Bianchini, C. and Meli, A., *Coord. Chem. Rev*., 2002, vol. 225, p. 67.
150. Belov, G.P., *Izv. Russ. Akad. Nauk, Ser. Khim*., 2002, no. 9, p. 1475.
151. *Catalytic Synthesis of Alkene – Carbon Monoxide Copolymers and Cooligomers*, Sen, A., Ed., Kluwer Acad., Publ., Dordrecht: 2003.
152. Belov, G.P. and Novikova, E.V., *Uspekhi Khimii*, 2004, vol. 73, no. 3, p. 292.
153. Durand, J. and Milani, B., *Coord. Chem. Rev*., 2006, vol. 250, no. 3-4, p. 542.

ISSN 1070-4272, Russian Journal of Applied Chemistry, 2008, Vol. 81, No. 9, pp. 1667–1672. © Pleiades Publishing, Ltd., 2008.
Original Russian Text © B.B. Sadykov, N.N. Volynskova, Sh.S. Namazov, B.M. Beglov, 2008, published in Khimicheskaya Promyshlennost', 2008, Vol. 85, No. 3, pp. 127–133.

TECHNOLOGY OF ORGANIC AND INORGANIC CHEMISTRY

Technology for Manufacturing Fertilizer "Superfos" Containing Nitrogen, Phosphorus, Sulfur and Calcium

B. B. Sadykov, N. N. Volynskova, Sh. S. Namazov and B. M. Beglov

Institute of General and Inorganic Chemistry, Academy of Sciences of Republic Uzbekistan, Open Join Stock Company "Ammofos", Almalyk, Uzbekistan

Received April 2, 2008

Abstract—Technology for manufacturing a new concentrated highly effective fertilizer implemented in Join stock company "Ammofos" (Almalyk, Uzbekistan) based on the facility for the manufacturing Ammofos fertilizer is described. The technology essence is conversion of gypsum using diammonium phosphate to afford dicalcium phosphate and ammonium sulfate.

DOI: 10.1134/S1070427208090371

Until recently, the assortment of fertilizers in Uzbekistan consisted by 95% of Ammophos and by 5% of ordinary ammonized superphosphate [1]. Ammofos is produced by Almalyk join stock company "Ammofos" and by Samarkand chemical plant. This is the most concentrated nitrogen–phosphoric fertilizer (10% of N and 46% of P_2O_5) and it was applicable for all agricultural plants on the soil of any type [2]. However, its manufacturing is disadvantageous due to formation in a high scale of a side product phospho-gypsum which is pushed aside and accumulated. Producing of 1 ton of P_2O_5 as extraction phosphoric acid leads to formation of about 7 ton of phospho-gypsum [3]. Around Almalyk and Samarkand plants is accumulated 100 millions tons of this waste material.

Therefore we made efforts for utilization of this material or at least for reducing considerably its amount by means of developing conversion of gypsum in the phosphoric acid pulp into ammonium sulfate and calcium hydrogen phosphate. A possibility of such conversion follows from the data published in [4, 5]. The process essence in this case can be described by the following reaction equation

$$CaSO_4 + H_3PO_4 + 2NH_3 = CaHPO_4 + (NH_4)_2SO_4$$

In [5] was studied reaction of phospho-gypsum with ammonized solutions of diluted phosphoric acid using reagent in amounts corresponding to stoichiometry according to the above equation, under the following conditions: temperature range from 25 to 80°C, pH 6.5–9.0, reaction duration 30 to 120 min. Under the optimal conditions of the process (25°C, pH 7–8, solid–liquid ratio 1 : 2–3, duration 1 h) the phospho-gypsum conversion was 70–75%. In that study the ammonium sulfate solution was filtered, and remaining solid phase consisted of a mixture containing 75% of $CaHPO_4 \cdot 2H_2O$ and 25% of $CaSO_4 \cdot 2H_2O$.

Using pure salts, we investigated interaction of components in the systems $NH_4H_2PO_4$–$CaSO_4 \cdot 2H_2O$–H_2O, $NH_4H_2PO_4$–$(NH_4)_2HPO_4$–$CaSO_4 \cdot 2H_2O$–H_2O and $(NH_4)_2HPO_4$–$CaSO_4 \cdot 2H_2O$–H_2O as a dependence on molar ratio of the components, temperature and process duration. The lowest conversion (3.91 to 5.95%) was achieved in the system of monoammonium phosphate–gypsum dihydrate–water at the equimolar ratio of the components. The highest conversion, 93.26 and 98.33%, was achieved at 60 min interaction in the system of diammonium phosphate–gypsum dihydrate–water at the mole ratio of the components 1 : 1 and 2 : 1, respectively. We also studied the process of conversion of gypsum in real industrial phosphoric acid–gypsum pulp obtained at decomposition of washed and dried thermoconcentrate of Central Kyzylkum phosphorite with sulfuric acid in dehydrating regime [6–11]. The parent washed and dried thermoconcentrate was of the following composition (wt%): 27.26 P_2O_5; 53.36 CaO; 1.30 AI_2O_3; 0.51 Fe_2O_3; 0.61 MgO; 2.91 F 2.41 CO_2; 0.04 CI; 2.5 SO_3; 5.6 SiO_2. The sulfuric acid used was of 93% concentration. The commercial extraction phosphoric acid contained 20% of

P_2O_5, 1.9 g of SO_3 per 100 cm^3, its density was 1.23 g/cm^3. The pulp composition was controlled proceeding from the phosphorus content by adding extraction phosphoric acid. The necessity of such control is defined by the following situation. Decomposition of phosphate raw material with sulfuric acid is described by the equation:

$$Ca_5F(PO_4)_3 + 5H_2SO_4 = 5CaSO_4 + 3H_3PO_4 + HF$$

This means that the pulp contains 3 mol of phosphoric acid per 5 mol of gypsum. However, complete conversion of gypsum according to above reaction equation requires the ratio 1 : 1.

Basing on the laboratory and pilot plant research, we elaborated Specification (Technical Requirements) on the Superfos, Tsh 6.6-27:2004. The quality of Superfos four sorts should respond to those listed in Table 1.

Tables 2–9 list contents of the pulps ammonized to various pH values and of dried products for all four sorts of Superfos. Analysis was carried out according to commonly used procedures [12]. As seen from the Tables, at the ammonization of phosphoric acid–gypsum pulp to pH 8.0 the gypsum conversion at the manufacturing the product of sort A is 99.48%, sort B 92.43%, sort C 79.60% and sort D 86.12%.

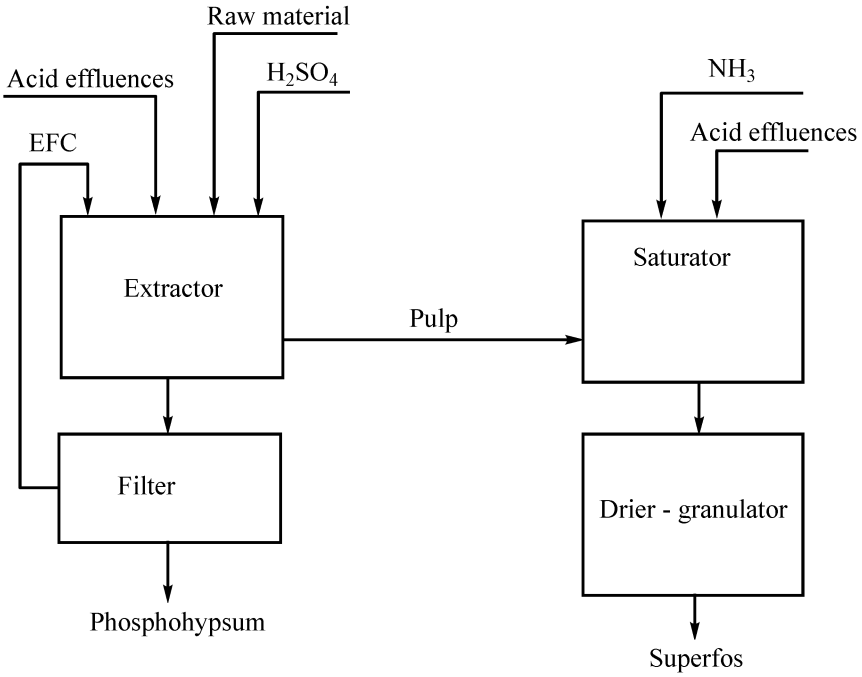
Superfos is a complex mixed fertilizer containing in its composition up to 45% of precipitate (valuable phosphoric fertilizer containing assimilable form of calcium), up to 35% of ammonium sulfate that contains 21% of nitrogen in ammonium form, 10% of mobile and

Table 1. Specification of four sorts of Superfos

No.	Characteristics	Sorts			
		A	B	C	D
1	Content of active component, not less than, %	75	67	65	60
2	Mass fraction of general phosphates, %	24 ± 1	20 ± 1	22 ± 1	20 ± 1
3	Mass fraction of water soluble phosphates in the general phosphates, ni more, %	25	25	25	25
4	Mass fraction of ammonium nitrogen, %	12 ± 1	15 ± 1	8 ± 1	10 ± 1
5	Mass fraction of magnesium, recalculated on MgO, not less than, %	0.5	1.0	2.0	2.0
6	Mass fraction of calcium, recalculated on CaO, not less than, %	14	10	12	10
7	Mass fraction of sulfur, recalculated on SO_3, not less than, %	25	22	23	21
8	Mass fraction of water, no more than, %	2.0	2.0	2.0	2.0
9	pH of 1% solution, not less than	5.5	5.5	5.5	5.5
	Granulometric composition, mass fraction of granules with the size:				
10	less than 1 mm, %	10	10	10	10
	from 1 mm to 4 mm, not less than, %	90	90	90	90
	less than 6 mm, %	100	100	100	100
11	Static strength of granules, not less than, MPa (kg/cm^2)	3.0 (30)	3.0 (30)	3.0 (30)	3.0 (30)
12	Friability, %	100	100	100	100

Table 2. Chemical composition of ammonized pulp for sort A (P_2O_5 : N = 24 : 12)

Pulp pH	Humidity of pulp, %	P_2O_5, %				CaO, %			SO_3, %		N, %	SO_3 water soluble : total, 100 %
		total	assimilable, by trilon B	assimilable, by citric acid	water soluble	total	assimilable	water soluble	total	water soluble		
5.0	53.97	11.59	10.81	11.37	7.58	8.97	3.09	2.48	13.43	5.53	3.35	41.17
5.5	53.58	11.51	10.67	11.18	6.00	8.90	5.35	2.17	13.34	10.21	3.87	76.54
6.0	53.15	11.42	10.53	11.02	5.16	8.85	6.30	1.72	13.25	11.63	4.51	87.77
6.5	52.62	11.32	10.39	10.82	4.55	8.72	7.89	0.65	13.12	12.12	5.27	92.38
7.0	52.43	11.28	10.17	10.65	4.34	8.73	8.13	0.36	13.11	12.34	5.55	94.13
7.5	52.17	11.24	10.02	10.58	3.90	8.69	8.27	–	13.05	12.62	5.80	96.70
8.0	52.07	11.21	9.94	10.44	3.78	8.66	8.54	–	13.02	12.95	6.08	99.46
8.5	51.95	11.16	9.88	10.21	3.19	8.60	8.49	–	12.90	12.88	6.20	99.84



Principal technological scheme of manufacturing Superfos.

easily assimilable by plants sulfur, and 10–15% of mono- and diammonium phosphate.

Principal technological scheme of manufacturing is shown in the figure.

Phosphoric acid–gypsum pulp from the extraction section is passed to a saturator. The pulp has following characteristics: density 1.41–1.44 g/cm^3, density of liquid phase 1.22–1.24 g/cm^3, content of P_2O_5 in the liquid phase 20%, content of SO_3 in the liquid phase 1.6–2.2 g per 100 cm^3, ratio liquid–solid 2.3–2.8. The saturator with the volume 430 m^3 is equipped with four stirrers. The saturator is feed also with acid effluences of 1.05–1.10 g/sm^3 density and the pulp is diluted to the density 1.35–1.37 g/cm^3. After dissolving, feed with ammnium is switched on. Neutralization is carried out to achieving pH 7.5–8.0, at vigorous stirring. To exclude ejection of ammonium due to high temperature of exothermal neutralization reactions, the process of ammonization is carried out stepwise to maintain temperature below 90°C. For stabilization the process of producing ammonized pulp, and for avoiding possible oversaturation with the dozing components and providing the reaction proceeding under mild regime, the neutralization is carried out on the background of mother liquor. For this purpose is provided circulation of the pulp in the saturator. From saturator the pulp is passed to a drier - granulator. The process of granulation and drying, classification and cooling the final product, purification of exhaust gas, storage and

Table 3. Chemical composition of dry products. Sort A (P_2O_5 : N = 24 : 12)

Pulp pH	P_2O_5, %				CaO, %			SO_3, %		N, %	SO_3 water soluble : total, 100 %
	total	assimilable by trilon B	assimilable by citric acid	water soluble	total	assimilable	water soluble	total	water soluble		
5.0	24.10	22.49	23.55	15.76	18.66	6.42	5.17	27.93	11.5	6.97	41.17
5.5	23.82	22.08	23.14	12.42	18.42	11.08	4.49	27.62	21.13	8.02	76.50
6.0	23.69	21.84	22.86	10.71	18.37	13.08	3.57	27.48	24.12	9.35	87.77
6.5	23.55	21.61	22.52	9.46	18.15	16.41	1.35	27.29	24.91	10.97	91.28
7.0	23.34	21.04	22.03	8.98	18.06	16.83	1.75	27.12	25.54	11.48	94.17
7.5	23.22	20.71	21.87	8.06	17.95	17.08	-	26.96	26.08	11.99	96.74
8.0	23.02	20.42	21.44	7.77	17.79	17.54	-	26.74	26.6	12.48	99.48
8.5	22.98	20.34	21.02	6.57	17.72	17.49	-	26.56	26.53	12.77	99.89

Table 4. Chemical composition of ammonized pulp. Sort B (P_2O_5 : N = 20 : 15).

Pulp pH	Humidity of pulp, %	P_2O_5, %				CaO, %			SO_3, %		N, %	SO_3 water soluble : total, 100 %
		total	assimil-able, by trilon B	assimil-able, by citric acid	water soluble	total	assimilable	water soluble	total	water soluble		
5.0	43.29	12.23	9.72	11.97	6.90	8.76	2.91	2.81	18.42	8.89	5.11	48.24
5.5	39.54	12.65	11.00	12.56	5.00	9.30	4.95	1.80	19.53	14.86	7.71	76.07
6.0	38.18	12.43	11.20	12.01	3.80	9.34	7.83	1.28	19.88	17.19	8.73	86.45
6.5	37.29	12.50	10.86	11.91	2.49	9.32	8.74	0.74	19.96	18.24	9.41	91.38
7.0	37.37	12.39	10.92	11.97	2.37	9.10	8.87	0.54	19.83	18.31	9.35	92.33
7.5	37.14	12.40	11.39	12.03	2.50	9.18	8.86	0.23	20.05	18.37	9.53	91.62
8.0	37.01	12.45	10.78	12.04	2.59	9.11	9.01	0.00	19.95	18.45	9.63	92.48
8.5	36.99	12.36	10.36	11.79	2.19	9.09	8.88	0.00	21.84	18.47	9.65	84.59

Table 5. Chemical composition of dry products. Sort B (P_2O_5 : N = 20 : 15)

Pulp pH	P_2O_5, %				CaO, %			SO_3, %		N, %	SO_3 water soluble : total, 100 %
	total	assimilable by trilon B	assimilable by citric acid	water soluble	total	assimilable	water soluble	total	water soluble		
5.0	21.57	17.14	21.11	12.17	15.44	5.13	4.96	32.51	15.67	9.01	48.20
5.5	20.92	18.19	20.78	8.27	15.38	8.19	2.98	32.31	24.6	12.76	76.14
6.0	20.11	18.11	19.43	6.14	15.11	12.67	2.07	32.17	27.8	14.12	86.42
6.5	19.93	17.31	18.99	3.97	14.87	13.93	1.18	31.88	29.11	15.01	91.31
7.0	19.78	17.43	19.11	3.78	14.53	14.17	0.87	31.73	29.27	14.93	92.25
7.5	19.73	18.12	19.14	3.97	14.61	14.09	0.37	31.83	29.17	15.16	91.64
8.0	19.76	17.11	19.11	4.11	14.47	14.31	-	31.71	29.31	15.29	92.43
8.5	19.61	16.44	18.71	3.48	14.43	14.10	-	34.69	29.32	15.31	84.52

Table 6. Chemical composition of ammonized pulp. Sort C (P_2O_5 : N = 22 : 8).

Pulp pH	Humidity of pulp, %	P_2O_5, %				CaO, %			SO_3, %		N, %	SO_3 water soluble : total, 100 %
		total	assimil-able, by trilon B	assimil-able, by citric acid	water soluble	total	assimilable	water soluble	total	water soluble		
5.0	46.85	12.62	11.41	12.49	7.15	9.75	2.92	4.54	14.75	6.25	3.63	42.37
5.5	46.34	12.65	11.47	12.64	7.07	9.84	6.07	4.35	14.65	9.50	3.92	64.85
6.0	45.78	12.73	11.36	12.59	6.57	9.91	7.24	4.14	14.35	10.40	4.32	72.47
6.5	45.26	12.68	11.43	12.65	4.07	9.84	8.20	2.08	14.65	10.74	4.64	73.31
7.0	45.19	12.66	11.41	12.58	3.85	9.86	8.27	2.05	14.62	11.05	4.72	75.58
7.5	45.06	12.63	11.40	11.87	3.52	7.50	8.37	1.63	14.62	11.37	4.78	77.77
8.0	44.95	12.61	11.38	11.94	3.44	9.57	8.36	1.35	14.42	11.48	4.79	79.62
8.5	45.03	12.43	11.27	11.95	3.66	9.54	8.32	1.20	14.40	11.53	4.74	80.09

shipping the product are carried out along the technology of manufacturing of Ammofos [2].

Reorientation of the sections of extraction phosphoric acid and of Ammofos in Almalyk join stock company "Ammofos" for manufacturing Superfos allowed:

– extension of assortment of produced fertilizers;

– increasing overall producing of mineral fertilizers with simultaneous increase of overall producing of nitrogen fertilizers based on the industrial side products;

– returning to manufacture 60% of sulfuric acid used for decomposition of phosphoric raw material, owing to conversion of phospho-gypsum;

– decreasing the norm of consumption of phosphate raw material and sulfuric acid in the step of extraction

Table 7. Chemical composition of dry products. Sort C (P_2O_5 : N = 22 : 8)

Pulp pH	P_2O_5, %				CaO, %			SO_3, %		N, %	SO_3 water soluble : total, 100 %
	total	assimilable by trilon B	assimilable by citric acid	water soluble	total	assimilable	water soluble	total	water soluble		
5.0	23.71	21.46	23.46	13.38	18.36	5.58	8.57	27.67	11.71	6.83	42.32
5.5	23.63	21.36	23.51	13.18	18.31	11.26	8.11	27.32	17.73	7.32	64.90
6.0	23.51	20.93	23.21	12.10	18.27	13.31	7.63	26.51	19.21	7.96	72.46
6.5	23.15	20.87	23.09	7.34	17.96	14.97	3.65	26.73	19.57	8.47	73.21
7.0	23.10	20.81	22.91	7.02	17.87	15.07	3.73	26.76	20.23	8.59	75.60
7.5	23.00	20.73	21.63	6.41	13.63	15.23	2.96	26.67	20.73	8.69	77.73
8.0	22.93	20.69	21.71	6.33	17.44	15.19	2.37	26.22	20.87	8.71	79.60
8.5	22.63	20.51	21.76	6.67	17.37	15.21	2.19	26.21	20.97	8.63	80.01

Table 8. Chemical composition of ammonized pulp. Sort D (P_2O_5 : N = 20 : 10)

Pulp pH	Humidity of pulp, %	P_2O_5, %				CaO, %			SO_3, %		N, %	SO_3 water soluble : total, 100 %
		total	assimil-able, by trilon B	assimil-able, by citric acid	water soluble	total	assimilable	water soluble	total	water soluble		
5.0	45.53	11.64	10.39	11.59	7.19	11.54	3.95	3.15	17.84	6.78	2.94	38.00
5.5	42.89	12.02	10.27	11.97	5.87	11.95	7.09	2.53	18.31	12.04	4.57	65.76
6.0	42.27	12.05	10.36	11.51	5.67	11.97	7.81	2.24	18.34	15.08	5.01	82.25
6.5	42.19	11.72	10.32	11.46	3.55	11.80	9.96	1.23	18.03	16.18	5.04	89.74
7.0	42.11	11.44	10.14	11.02	3.54	11.77	10.95	1.13	18.03	16.62	5.09	92.18
7.5	42.19	11.33	10.12	10.98	3.36	11.76	10.93	0.36	17.95	16.58	5.08	92.37
8.0	40.99	11.37	10.25	11.10	3.27	11.94	11.28	0.00	18.53	15.78	5.85	85.16
8.5	41.07	11.36	10.23	11.14	3.26	11.83	11.72	0.00	18.34	16.97	5.83	92.53

Table 9. Chemical composition of dry products. Sort D (P_2O_5 : N = 20 : 10)

Pulp pH	P_2O_5, %				CaO, %			SO_3, %		N, %	SO_3 water soluble : total, 100 %
	total	assimilable by trilon B	assimilable by citric acid	water soluble	total	assimilable	water soluble	total	water soluble		
5.0	21.36	18.91	21.12	13.19	21.17	7.15	5.86	32.69	12.44	5.40	38.05
5.5	21.12	17.98	20.87	10.23	20.87	12.41	4.43	32.13	21.14	8.01	65.80
6.0	20.86	17.96	19.93	9.81	20.67	13.52	3.87	31.71	26.11	8.67	82.34
6.5	20.35	17.86	19.78	6.21	20.41	17.23	2.13	31.16	27.99	8.71	89.83
7.0	19.76	17.51	19.11	6.11	20.33	18.91	1.95	31.12	28.67	8.79	92.13
7.5	19.58	17.53	18.97	5.81	20.37	18.93	0.63	31.07	28.71	8.77	92.40
8.0	19.28	17.38	18.81	5.57	20.24	19.11		31.05	26.74	9.91	86.12
8.5	19.26	17.34	18.91	5.52	20.12	19.87		31.04	28.73	9.89	92.56

in account of treatment of dehydrated pulp and repeated application of sulfuric acid;

– exclusion one of four carousel vacuum filter from the manufacturing chain;

– decreasing by over than 20% amount of phosphogypsum evacuated to tails;

– decreasing total cost of product.

REFERENCES

1. Beglov, B.M., *Khim. Prom. Segodnya* (Moscow), 2003, no. 2, pp. 25-31.
2. Dokholova, A.N., Karmyshev, V.F. and Sidorina, L.V., P*roizvodstvo i primenenie fosfatov ammoniya* (Manufacturing and application of ammonium phosphates), Moscow: Khimiya, 1986.

3. *Fosfogips i ego ispol'zovanie* (Phospho-Gypsum and Its Application), Moscow: Khimiya, 1990.
4. Panfilov, V.N., In *Fosfornye udobreniya i ikh kachestvo* (Phosphoric fertilizers and their quality). Moscow: Sel'khozgiz, 1938, pp. 176–179.
5. Kusherbekova, G.T., Kopylev, B.A., Popova, G.Ya., Moldabekov, Sh.M., and Makarova, V.F., In *Issledovanie po ochitke stochnykh vod i pererabotke otkhodov pri proizvodstve fosforsoderzhashchikh produktov i udobrenii* (Investigation on Purification of Sewages at Manufacturing of Phosphorus-Containing Products and Fertilizers), Leningrad: LenNiiGiprokhim, 1983, pp. 94-97.
6. Sadykov, B.B., Seitnazarov, A.R., and Namazov, Sh.S., Abstracts of Papers, Proceedings of Republic Scientific and Research Conference "Aktual'nye problemy khimicheskoi pererabotki fosforitov Tsentral'nykh Kyzylkumov" (Actual Problems of Chemical Treatment of the Central Kyzylkum Phosphates), Tashkent: November 23, 2006, pp. 39-43.
7. Sadykov, B.B., Reimov, A.M., and Namazov, Sh.S., Abstracts of Papers, Proceedings of Republic Scientific and Research Conference "Aktual'nye problemy khimicheskoi pererabotki fosforitov Tsentral'nykh Kyzylkumov" (Actual problems of Chemical Treatment of the Central Kyzylkum Phosphates), Tashkent: November 23, 2006, pp. 43-47.
8. Sadykov, B.B., Reimov, A.M., Namazov, Sh.S., and Beglov, B.M., *Khim. Prom*., 2006, vol. 83, no. 9, pp. 411–415.
9. Sadykov, B.B., Seitnazarov, A.R., Ibragimov, G.I., Namazov, Sh.S., and Beglov, B.M., *Khim. Prom.*, 2006, vol. 83, no. 12, p. 568–575.
10. Sadykov, B.B., Volynskova, N.V., Reimov, A.M., Namazov, Sh.S., and Beglov, B.M., Abstracts of Papers, *Regional Central Asian International Conference on the Chemical Technology*, Tashkent, June 6-8, 2007, Vol. 5, Moscow: LENAND, 2007, pp. 53–55.
11. Sadykov, B.B., Volynskova, N.V., Reimov, A.M., Namazov, Sh.S., and Beglov, B.M., *Uzbekskii Khim. Zhurn*., 2007, no. 3, pp. 61–64.Vinnik, M.M., Erbanova, L.N., Zaitsev, P.M. *et al., Metody analiza fosfatnogo syr'ya, fosfornykh i kompleksnykh udobrenii, kormovykh fosfatov* (Methods of Analysis of Phosphate Raw Material, Phosphoric and Combined Fertilizers and Feed Phosphates), Moscow: Khimiya, 1975.

ISSN 1070-4272, Russian Journal of Applied Chemistry, 2008, Vol. 81, No. 9, pp. 1673–1685. © Pleiades Publishing, Ltd., 2008.
Original Russian Text © A.A. Fedorov, Yu.S. Chekryshkin, O.V. Rudometova, Zh.A. Vnutskikh, 2008, published in Khimicheskaya Promyshlennost', 2008, Vol. 85, No. 4, pp. 163–180.

TECHNOLOGY OF ORGANIC AND INORGANIC CHEMISTRY

Application of Inorganic Compounds at the Thermal Processing of Polyvinylchloride

A. A. Fedorov, Yu. S. Chekryshkin, O. V. Rudometova, and Zh. A. Vnutskikh

Institute of Technical Chemistry, Ural Branch, Russian Academy of Sciences, Perm, Russia
e-mail: anatoly_fyodorov@mail.ru

Received March 4, 2008

Abstract—A review of publications on the effect of various inorganic additives (metals oxides, hydroxides, chlorides and carbonates) on the process of dehydrochlorination and pyrolysis at the thermal processing of polyvinylchloride (PVC). A decrease in temperature of the PVC dehydrochlorination step is noted at processing in the presence of chromium, iron, cobalt, copper and molybdenum oxides. Aluminum, titanium, circonium, cerium and lead oxides do not change temperature of beginning of PVC destruction. No effect noted of the oxides at the second step of PVC destruction.

DOI: 10.1134/S1070427208090383

Demand for plastics grows continuously due to their wide application and relatively low cost; respectively, their manufacturing and amount of side products grow. Polyvinylchloride (PVC) plays key role in the plastics industry for 40 years and remains to be the basic polymer and a source of huge amount of wastes. For example, in West Europe the amount of PVC in municipal wastes is estimated as 2 million tons per year [1].

Combustion of municipal wastes became an alternative to the technology of their concealment at the waste dump. In Japan in 2004 appeared more than 10 million ton of wastes, and approximately 40% of this amount was either concealed or combusted [2]. However, combustion leads to the liberation of substances that can bring more harm to environment than concealment or radioactive wastes. The processes of combustion whole and not controlled combustion of wastes in particular leads to formation of hazard substances, e.g., soot, smoke, benzene, dioxins, acid gases, heavy metals, aliphatic and aromatic compounds [3–6].

For the processing of wastes of synthetic polymer materials the most often is used the method of pyrolysis. However, thermal pyrolysis of PVC wastes liberates hydrogen chloride and chlorine-containing organic compounds are formed, therefore appears a problem of corrosion at the use of chlorine-contaning plastics as raw material for blast and coke furnaces at steel manufacturing [7, 8]. Chlorinated hydrocarbons can be precursors of even more toxic substances such as polychlorinated dibenzodioxines, dibenzofurans and polychlorobiphenyls [9].

Behavior of PVC at thermal decomposition has been widely studied basing on the composition of the products and kinetics of destruction [10–16]. All explorers suggest that thermal decomposition of PVC proceeds in two steps, starting with the splitting hydrogen chloride off. This process is propagated along the polymer chain and leads to formation of polyenes that are responsible for the color of the destructed polymer. In the first step, at 200–360°C, is liberated hydrogen chloride and approximately 15% of the formed therewith polyene is converted into benzene and other aromatic compounds [17, 18] via intramolecular cyclization of the polyene segments [19] with formation of cyclohexene and cyclohexadiene remaining in this step introduced to aliphatic matrix. The hydrogen chloride liberated in the first step works as a catalyst for the further reactions of decomposition [15]. In the second step, at 360–500°C, the polyene frame exerts structural decomposition leading to formation of alkylaromatic and fused aromatic compounds (toluene, naphthalene, indene, anthracene, *o*-xylene and various chlorobenzenes) together with a small amount of hydrogen chloride and benzene [17]. During this step the polymer net formed at the condensation of polyene is damaged, that promotes aromatization of cyclohexene and cyclohexadiene rings. The main reactions in the second step are *cis-trans* isomerization, aromatization and stitching [20].

Liberation of dioxins at combustion or roasting of industrial wastes belongs to the most important social problems owing to their high and various toxicity. At the combustion of PVC the amount of the forming dioxins can be diminished by maintaining combustion temperature above 800°C [21]. However, this method can be applied in the large scale installations for combusting wastes. Many studies are denoted to diminishing formation of dioxins in the process of combustion or in the systems for afterburning. Some explorers noted an effect of precursors (chlorophenol) at the formation of polychlorinated dibenzodioxins (PCDD) and polychlorinated dibenzofurans (PCDF). It has been reported that the sources of dioxin formation can be organic and inorganic chlorides (NaCl, HCl, $FeCl_3$) [22, 23]. This allows a suggestion that by removing of HCl liberated at combustion the formation of dioxins can be depressed.

To decrease amount of halogen liberated at PVC combustion two methods are known. The first one consists in diminishing of chlorine content in the recipes including PVC, by using its mixtures with other components or as copolymers not containing halogen [24].

Another method assumes application of fillers in small amounts that can bind HCl effectively. In the patent [25] has been noted that lithium-contaning compounds (LiOH and Li_2CO_3) are more effective than $CaCO_3$ for binding the formed HCl. However, LiOH is hygroscopic and is a strong base, that restricts its application as a filler for PVC. Li_2CO_3 is enough stable in air and can be used with a high content.

Also, have been patented the methods of processing the halogen-containing compounds, including solid polymer materials containing halogen, by heating them in disintegrated state and mixed with oxides or hydroxides of calcium, magnesium, or barium, that leads to formation of respective halides and carbonates [26, 27].

In the industry of plastics for long time were used various inorganic compounds for extension of functional versatility of polymers such as flash and smoke suppression. For example, metal carbonates are used as fillers at producing PVC for reducing cost of the product. Also they are used for improving resistance to aging, electric and dielectric properties, stability at saving, decrease in planting, allow to decrease content of stabilizers and increase ultimate strength of the PVC material [28–30].

At the same time, it is found that metal oxides affect composition of PVC destruction products due to formation of metal chlorides [31, 32]. Therewith, the chlorides formed from acidic oxides of transition metals accelerate thermal decomposition of PVC, in contrast to the chlorides formed from the metal oxides with basic properties [31]. The metal oxides also affect kinetics of PVC destruction decreasing or increasing liberation of hydrogen chloride [33].

In this review embarrassing publications of recent 15–20 years we attempted to reveal effect of various inorganic substances on the processes of dehydrochlorination and pyrolysis at the thermal processing of polyvinylchloride.

DERIVATIVES OF D-METALS

Investigations performed by Li [34–37] allowed to reveal effective decrease in smoke formation at the liberation of HCl by PVC in the presence of Cu_2O, MoO_3, Cu_2O/MoO_3, CuO and Fe_2O_3. At adding of these oxides in amount 4 moles of a metal per 100 moles of chlorine in PVC the smoke formation decreases by 25.1–52.0%. Copper oxides are more effective than MoO_3 and Fe_2O_3. It was established that transition metal oxides affect the process of thermal decomposition of PVC leading to decrease in mass loss and the rate of PVC mass loss, and stimulates formation of residue in the final step of combustion. Copper(I), copper(II) and iron (III) oxides show catalytic effect for the chlorine splitting off from PVC, while MoO_3 stabilizes PVC. It was concluded that transition metal oxides accelerate the process of PVC cross-linking and stabilize carbon backbone. In addition, the presence of oxides leads to changes in the composition of volatile components at combustion of PVC in a flame. The last effect was shown in [38] at the study of copper- and molybdenum-containing substances as flame- and smoke-depressors at combustion of PVC. At the dehydrochlorination of PVC at 200°C, presence of Cu_2O, CuO, $CuCl_2$, copper powder and MoO_3, but not CuCl, leads to significant acceleration of 3-chloropentane formation. 3-Chloropentane is known to alkylate benzene at 200°C in the presence of MoO_3 to form 2- and 3-pentyl isomers of benzene, but no alkylation occurs at the replacement of MoO_3 by $CuCl_2$. At the same time, $CuCl_2$ slowly chlorinates double bond of *cis*-2-pentene at 200°C. These observations confirm reliability of the mechanism with involvement of Lewis acids for the explanation of the effect of MoO_3 on the process of PVC combustion and attest the same effect of addition of copper derivatives that can play the same role. However,

in respect of application to the polymeric system there is a considerable difference in the mechanisms of the effects of MoO_3 and copper derivatives.

At the study of thermal decomposition and carbonization of PVC, PVC/Cu_2O and PVC/Cu_2O/MoO_3 in condesed phase by the method of photoemission spectroscopy [39, 40] the authors showed that the most important role at destruction and carbonization of PVC plays early cross-linking, in part, in the presence of Cu_2O catalyst. Interaction of PVC and Cu_2O along the scheme: $Cu_2O > CuCl > Cu > Cu_2O$ at elevating temperature from 20 to 500°C is confirmed experimentally.

Studies [41-44] are denoted to elucidation of the role of FeO(OH) for the depression of smoke formation at the combustion of mixtures of polymers. Study of effect of temperature in the range 500–700°C on the formation of carbon by the mixtures of polymers containing PVC showed that in the presence and in absence of FeO(OH) occurs linear dependence between the carbon yield and the temperature of carbon formation [41]. Increase in amount of chlorine and FeO(OH) in the mixtures leads to increase in the yield of carbon in the whole temperature range, but the most important factor affecting yield of carbon is actual total chlorine content in the mixtures both containing and not containing iron. A detailed study of the products of pyrolysis in air of PVC containing mixtures that include FeO(OH) as a smoke depressor was conducted [42]. Presence of iron(III) derivatives decreases considerably the concentration of aromatic and polyciclic compounds of aromatic series that are precursors in the process of smoke formation. The mechanism of smoke depression by FeO(OH) is explained by retarding reactions leading to formation of aromatic compounds. The basic iron oxide shows also stabilizing effect at the thermal decomposition of mixture of polymers [43]. It was also established that the active compound that stimulates formation of carbon by these polymer systems is iron(III) chlorooxide FeOCl [44].

Sakata and co-workers [45] at the study of catalytic action of some compounds on the destruction of a polymeric mixture containing PVC found that sorbents based on the iron oxide bind well hydrogen chloride liberated at the pyrolysis of PVC but do not affect splitting of polymers.

At the pyrolysis of PVC in the presence of cadmium and zinc chlorides was observed formation of stable complex at the double bonds of the polyene with $CdCl_2$ [46] and $H^+ZnCl_3^-$ [47].

Effect of certain metals (Fe, Zn), related oxides (Ti, Cu, Fe) and carboxylates (Zn) on the process of thermal decomposition of PVC was studied in [48]. Metals and metal oxides with large enough metal ion radius decrease temperature of beginning of hydrogen chloride splitting off probably by binding chlorine and weakening C–Cl bonds in PVC. When formation of chlorides is possible (Fe, Zn, Ca/Zn carboxylates, CuO, TiO_2) formation of HCl and benzene is dimimnished. Formation of benzene occurred in the presence of TiO_2 is a result of ease hydrogen exchange on the oxide surface that is needed for the benzene splitting off from the dehydrochlorinated PVC segment. In the presence of the studied metals and oxides the second step of thermal decomposition of PVC proceeds at lower temperature that is explainable by ease splitting of polyene chain at the contact with the metal surface or transition metal ion.

Iron oxide and its mixture with carbon that are stable toward hydrogen chloride were proposed as additives for the process of dehydrochlorination of organochlorine compounds at the obtaining of useful substances from the municipal plastic wastes containing PVC [49]. Derivatives of Fe(II) combined with Portland cement are effective at reductive dehydrochlorination of chlorine-containing organic compounds and can be applied at decomposition of pollutants [50].

Pyrolysis of PVC in the presence of Zn, Ba and Cu chlorides was studied in [51]. It was shown that metal chlorides, in particular $ZnCl_2$ and $BaCl_2$, accelerate reaction of splitting off hydrogen chloride in PVC at pyrolysis and decelerate ($ZnCl_2$ and $CuCl_2$) second step of PVC destruction occurred for pure PVC in a significant degree at 400°C. Therefore the samples containing metal chlorides as additives are characterized by a significant mass loss in the temperature range 400–500°C, therewith amount of solid residue is larger while amount of hydrocarbons with large molecular mass (over 200), condensed aromatic hydrocarbons in particular, is much less. Thus, metal chlorides can depress reaction of aromatization.

Investigation of temperature and amount of copper(II) chloride effect on the type and amount of toxic effluents at combustion of polyvinylchloride [52] showed that at combustion of pure PVC besides a significant amount of polyciclic aromatic hydrocarbons (PAH) are formed in small amounts PCDD and PCDF. Copper(II) chloride promotes formation of two latter but inhibites formation of PAH. Thus, by the opinion of the authors of [52], metal chlorides constitute one of most important factors of

increase in amount of PCDD/PCDF formed at combustion of polyvinylchloride.

Minsker and co-workers [53] at the study of oxidative destruction of PVC in the presence of metal chlorides showed that rate of this process is defined by the presence of plasticizers in the polymer. Some chlorides ($CdCl_2$, $CoCl_2$) are relatively indifferent in the reaction of PVC dehydrochlorination, other ($MnCl_2$, CuCl) activate weakly decomposition of the polymer, while $CuCl_2$, $ZnCl_2$, and $FeCl_3$ accelerate considerably thermooxidative dehydrochlorination of PVC. This effect the authors explain by changes in the kinetics of oxidation of plasticizer under the action of the metal chlorides and strengthening or weakening of catalytic effect of the chlorides on the PVC destruction.

Effect of copper, copper(II) oxide and copper(II) chloride on the thermal decomposition of PVC was studied in [54]. In the presence of copper or its derivatives, particularly of copper(II) oxide, decomposition of PVC occurs at the higher temperature and leads to the change in the nature and concentration of gaseous products. These changes are defined by the ability of copper compounds to induce cross-linking of the polymer molecules, the maximal linking occurs in the presence of copper(II) oxide. The process of linking leads to decrease in amount of aromatic hydrocarbons like benzene and increase in amount of aliphatic compounds at high temperature. In the PVC–CuO system, e.g., in the temperature range 300–600°C the total amound of liberated chlorine falls by 40% in air and by 20% in nitrogen, formation of benzene falls by more than 90% in air and in nitrogen, amount of other aromatic and chloroaromatic compounds also falls down. Increase in formation of hydrocarbons of aliphatic series together with decrease in content of aromatic hydrocarbons leads to decrease by more than 50% of amount of carbon black formed at the pyrolysis, in particular, in the PVC–CuO system, that attests more effective oxidation of the PVC carbon.

In [55] was studied effect of adding copper compounds in the mass ratio to polymer 1 : 10 on the depression of smoke formation and flame extinguishing at the pyrolysis of PVC. These additives showed good ability to depressing the smoke formation and flame extinguishing at the combustion of solid and plasticized samples of PVC. Mixed copper oxides are found more effective. At 190°C the process of PVC cross-linking is accelerated in the presence of most of additives showing no obvious dependence on their composition or on degree of copper oxidation. For the $Cu_3(MoO_4)_2(OH)_2$–$CuSnO_3$ mixture in plasticized PVC is notes synergism of these properties.

The role of various metal oxides in the thermal decomposition of polymers (PVC and PVA) and their mixtures was studied in [56]. It was shown that some oxides (Co_3O_4, Cr_2O_3, CuO, Fe_2O_3, MoO_3) decrease temperature of the first step (liberation of HCl) of destruction while the presence of other oxides (Al_2O_3, CeO_2, PbO_2, TiO_2, ZrO_2) does not affect considerably the temperature of beginning destruction. Effect of oxides in the second step of destruction (breaking of olefins) is practically absent because the difference in the temperature of breaking the olefin bonds is only ±5°C. But it was found that destruction of polymers is affected considerably by the presence of metal chlorides. Thus, the effect of metal oxides on the destruction of polymers can be explained by the formation of chlorides. The oxides containing strong Lewis acids as cations more promotes splitting off hydrogen halide. Good enough correlation occurs between the temperature of beginning of the polymer thermal decomposition stimulated by halo compound with a cation possessing Lewis acidity. This result is consistent with the earlier investigations on the destruction of vinylidene chloride polymer [57]. The reason for these phenomena consists in the fact that acidity of metal halo derivative reflects ability of its cation to the formation of complex with the polymer chlorine atoms and thus to promote the thermal decomposition. Also was noted that carbon–carbon backbones formed after first step of PVC and PVA destruction are of similar structure and that olefinic bonds remain relatively intact in the presence of oxides .

In [58] was carried out quantitative analysis of the products of pyrolysis (gaseous, liquid and residue after pyrolysis) of PVC mixed with various metal oxides including ZnO, Fe_2O_3, rare earth oxides, CaO, PbO and Al_2O_3. For the revealing ability of utilization of PVA wastes was used higher concentration of metal oxides (PVC : oxide = 2 : 1 mol/mol, one mol of PVC corresponds to one C_2H_3Cl fragment) as compared with the study of the effect of additives on the PVC flame extinguishing [59]. From this viewpoint the authors of [58] also considered binding of chlorine by oxides at the pyrolysis of the PVC–metal oxide mixtures. It was shown that ability of the used oxides to bind chlorine differ considerably in the series. Adding of ZnO leads to increase in the amoumt of the formed carbon and to decrease in amount of liquid products. A possible explanation is formation of $ZnCl_2$ which is known

as a strong Lewis acid. On the other hand, $ZnCl_2$ has high vapor pressure and therefore should be taken into account the kinetics of the chloride evaporation that is accompanied by formation of carbon. In respect of this viewpoint should be mentioned a publication [60] on the pyrolysis of mixtures of PVC with metal oxides directly in a mass-spectrometer where observed simultaneous formation of $ZnCl_2$ and benzene. The authors suggest that presence of zinc chloride affects decrease in formation of liquid products. Thus, for the PVC-ZnO system at 400°C a precursor of carbon (possibly, cross-linked hydrocarbons) is formed simultaneously with zinc chloride at the temperature below 400°C. Deceleration in the formation of liquid substances by ZnO additive points to the possibility of zinc oxide to behave as a Lewis acid.

In the case of iron(III) oxide dominates the process of its reduction and hence chlorine is liberated from PVC basically as HCl. On the other hand, at the adding Fe_2O_3 grows significantly the amount of chlorobenzene. The authors of [58] assume that formation of the latter proceeds by chlorination of benzene with involvement of $FeCl_3$ as a Lewis acid. Probably a part of the parent PVC chlorine can form iron chloride or any intermediate Cl–Fe compound on the interphase surface between melted PVC and Fe_2O_3 which promotes formation of chlorobenzene.

The authors of [61] studied a method of dechlorination of wastes containing a mixture of high density polyethylene, polypropylene, polystyrene and PVC, consisted of a series experiments with coal tar (side product at producing coke) and convertor dust (side product at producing steel consisting mainly of Fe_2O_3) in a melt and treatment with hot water. The results obtained showed that iron oxide reacts with chlorine liberated from the wastes and form water soluble iron chloride in the melt. Chlorine is dissolved in the coal tar melt that resulted in diminishing liberation of chlorine containing gas. Besides, this stimulates pyrolysis of the side products. It was shown that ca. 98% of chlorine react with Fe_2O_3 to form iron chloride which can be extracted with hot water and ca. 58% of iron chloride is bound with the melt components to form insoluble in water compound. After conducting these processes the chlorine containing plastic wastes can be used in furnace because they contain 5000 ppm or less of chlorine. Notable that for achieving such results on dehydrochlorination the Fe_2O_3/PVC ratio should be equal to 10 times or more over the stoichiometry of formation of iron chloride.

Using thermogravimetric analysis were determined parameters of the splitting off hydrogen chloride kinetics at the destruction of PVC and of PVC mixed with $ZnCl_2$ in varied ratio [62]. The values obtained are compared with those obtained by UV spectroscopic analysis in the visible region at the heating PVC film containing $ZnCl_2$. The values of apparent activation energy of the process fall with increase in the amount of $ZnCl_2$.

Horikawa and co-workers [63] while studied a possibility of regeneration of chlorine liberated at the pyrolysis of PVA used metal oxides for absorption of hydrogen chloride at 260-400°C with formation of corresponding metal chlorides. The chlorides were then roasted at 350-450°C under oxygen flow for regeneration of gaseous chlorine and oxides. Cobalt(III) oxide was found the most effective for both absorption and removing chloride ions. At the secondary application of Co_2O_3 for absorption of HCl at 300°C followed by removing Cl_2 at 400°C the amount of chloride ions bound with the cobalt oxide powder diminished to one fifth part of the amount bound with fresh oxide, that is explained by the authors by diminishing in the area of cobalt oxide surface at the repeated application.

In [64, 65] was studied composition of the product of destruction of a mixture of plastics contaned PVC and ability of chlorine removing from the products using appropriate sorbents. It was shown that at the destruction of polypropylene/PVC mixture the additives FeO(OH) and Fe_3O_4 decrease content of chlorine in the melt, and liberated chlorine becomes bound by iron compounds to form chloride. In the presence of iron(III) oxide and carbon–oxide compositions as catalysts [66] the latter is deactivated at the absorption of HCl. Therewith, iron oxide is chlorinated to form $FeCl_2$.

Sakata and co-workers studied effect of iron oxide and of composite iron oxide–carbon (Fe_2O_3–C) on the thermal and catalytic decomposition of the mixture of municipal wastes and gas oil to obtain power station fuel [67, 68]. In the process of stepwise pyrolysis at 430°C, iron(III) oxide was used as a catalyst of dechlorination. Besides was studied destruction in the presence and in the absence of alumo-silicon catalyst SiA1 at 430°C followed by dechlorination in a reactor with steady layer at 350°C. In both these processes the iron(III) showed efficiency at the sorption of both inorganic and organic chlorine-containing substances and stability toward HCl. Chlorine content in liquid products in the presence of iron(III) decreased by the factor of 12.5. A highly selective and stable catalytic system $FeCl_2/SiO_2$ was

developed for splitting off hydrogen chloride from various organochlorine compounds contained in the power station fuel obtained from plastic wastes containing PVC [69].

The catalyst Fe_2O_3–C was also applied for decomposition of brominated (9.59 wt% of Br) flame retarding composition for acrylonitrile–butadiene–styrene copolymer (the waste at the producing electric and electronic apparatuses) mixed with polypropylene, at 450°C [70] and were obtained containing no bromine liquid products that could be used as power station fuel or as initial material in oil processing.

It was shown that introducing of TiO_2 to polymer matrix leads to acceleration of photocatalytic destruction as compared with pure PVC. Therewith this additive increases amount of liberated CO_2 and H_2O, while chlorine concentration falls [71].

COMPOUNDS CONTAINING *s*- AND *p*-ELEMENTS

Aluminum oxide does not exert chlorination or reducion at the pyrolysis of PVC [58]. Catalytic action of Al_2O_3 as proposed in [48] consists in acceleration of formation and decomposition of intermediately formed cyclohexadiene that results in formation of benzene. Decrease in the presence of Al_2O_3 in liberation of gaseous products was noted. Addition of calcium oxide reduces amount of residue at the pyrolysis. This observation indicates that cross-linking of polyene chains is in a certain extent restricted. Lead oxide and oxides of rare earth elements do not affect considerably yield of liquid and gaseous products that is explainable by lower activity of these oxides in the reaction of decomposition of cyclohexadiene structures and formation of carbon. During the pyrolysis these structures are reduced or chlorinated. For example, in the presence of lead oxide, 50 to 70% of chlorine is bound to form volatile $PbCl_2$.

With the compositions containing CaO almost a half of chlorine is bound to form mixed compounds of the type of CaClOH. Lanthane oxide can bind up to 95% chlorine contained in PVC to form lanthane chlorooxide LaOCl. Taking into account a very low solubility of LaOCl in water the authors of [58] suggest that use of La_2O_3 is more reasonable for binding chlorine than CaO to form solid chlorooxide, that prevents contamination of soil. Moreover, this chlorooxide can be converted back to respective oxide and HCl by hydrolysis at high temperature that makes reasonable to use chlorine for treatment wastes containing oxides of rare earth elements with regeneration of chlorine [72, 73].

Catalytic decomposition and dechlorination of PVC mixed with polypropylene, polyethylene and polystyrene in the presence of mixed Al–Zn and Al–Mg oxide catalysts was studied by the authors of [74, 75]. At the catalytic decomposition yield of gaseous products falls sharply while amount of residue increases as compared with thermal decomposition. Such catalysts showed ability of binding HCl and increasing chlorine content in liquid products. At the application of Al–Mg catalyst the content of chlorine in the pyrolysate oil falls 4–5.6-fold depending on the mixture composition, as compared with thermal decomposition. It is established that 91–93 wt.% of chlorine is bound by the catalyst and contained in the residue, while at thermal decomposition 71–96 wt.% of chlorine contained in the sample is liberated as HCl. Application of Al–Zn catalyst reduces this value to 88-92 and 88-96 wt.%, respectively [74]. Presence of the catalyst leads to significant increase in the rate of formation of oil from wastes therewith each mixture containing PVC gives more volatile products while amount of heavy products falls that deeper catalytic decomposition. For revealing active component responsible for cracking and ability to dechlorination, the catalytic decomposition of mixtures was carried out separately with γ-Al_2O_3 and MgO prepared under the same conditions as the catalyst [75]. As shown, magnesium oxide reveals certain dechlorination action but content of liquid products remains the same, hence MgO does not show catalytic action. On the contrary, γ-Al_2O_3 showed catalytic action at the decomposition but was almost not actve in the reaction of dechlorination. Thus, the catalyst is advantageous over separate application of MgO and Al_2O_3 both for dechlorination and cracking. Study of phase composition of fresh and used catalysts showed presence of MgO and spinel $MgAl_2O_4$, while aluminum is distributed in the catalyst uniformly without formation of Al_2O_3 phase. The authors of [76] concluded the same. In the process of PVC decomposition with magnesium oxide the amount of MgO falls and increases amount of $MgCl_2$, pointing to interation of a part of MgO with the absorbed HCl. Thus, the catalyst has both acid and basic properties. Besides, it has large specific surface and higher heat capacity than MgO [76]. These results explain dual effect of the catalyst in respect of both cracking and dechlorination than MgO. Ability to promote dechlorination of Al–Zn catalyst is also much higher than of zinc and aluminum oxides separately [74].

In [77, 78] was studied sorption of hydrogen chloride by carbon-containing composite materials based on

calcium carbonate ($CaCO_3$–C), iron oxide and potassium carbonate. The sorbent $CaCO_3$–C which reacts with hydrogen chloride absorbing HCl completely during 12 h. Under optimal conditions (gas linear rate 0.18 m/sec; HCl concentration at inlet 1820 ppm; amount of sorbent 2 g; particles size 0.25 mm; gas flow 535 cm^3/min, temperature 350°C) approximately 63% of theoretical capacity of the sorbent is used. The sorbent $CaCO_3$–C was successfuls applied also for dechlorination and debromination at the pyrolysis of mixed chlorine and bromine containing plastic wastes at 430°C with formation of liquid products not containing halides.

Interaction of MgO with hydrogen chloride liberated from organochlorine compounds at the pyrolysis of PVC-containing municipal wastes was noted in [68].

At searching effective additives for increasing thermal stability of PVC, attention of investigators attracted laminated dual hydroxides (LDH) [79–82]. LDH form a group of anion-exchange substances containing laminated metal hydroxides like brusite $Mg(OH)_2$. In such compounds commonly up to one third bivalent cations (M^{2+}: Mg, Zn, Ni, Co, Fe, etc.) can be substituted by trivalent cations (M^{3+}: Al, Fe, Cr, etc.) [83–85]. Positive charges on the hydroxide layers formed at such substitution are balanced with exchanging anions in the space of intermediate layers where commonly there is some water molecules that are connected by hydrogen bonds with anions and (or) hydroxyl groups. The LDH composition can be described by a general formula $[M^{2+}_{1-x}\,M^{3+}_{x}(OH)_2]^{x+}[(A^{m-})_{x/m}\cdot nH_2O]^{x-}$, where A^{m-} is exchanged anion of CO_3^{2-}, Cl^-, SO_4^{2-} type and various organic carboxylates, sulfates and sulfonates. Fisher and co-workers [80] found that hydrogen chloride can be substantially absorbed by Mg_3ZnAl_2–LDH and they affect thermal stabilization of PVC. The authors of [81, 82] reported on significant increase in thermal stability of PVC at including MgAl–LDH–CO_3 into PVC matrix together with other organic salts such as calcium, zinc and tin stearate.

Effect of Zn, Al laminar dual hydroxides on the thermal decomposition of PVC was studied in [86]. It was found that 4 wt% LDH additive promotes the process of dehydrochlorination proceeding in the temperature range 260–300°C. The authors explain this fact by catalytic action of chlorides formed in the reaction with the liberated hydrogen chloride, as has been noted earlier [79, 80]. With zinc and aluminum chlorides the decomposition becomes autocatalytic process: they stimulate splitting hydrogen chloride off just after initiation, decrease temperature of beginning and induce reaction proceeding in narrow temperature range. This result is consistent with the data of [51] showed that introducing to the PVC matrix of 1 mol% $ZnCl_2$ increases mass loss at 250°C from 4 to 26%. As established in [59], $ZnCl_2$ catalyzes the process of splitting off chloride ion from PVC with formation of carbenium ion. The latter decomposes into alkene affording proton that couples with $ZnCl_3^-$ to afford HCl and regenerate $ZnCl_2$. Authors of [86] suggest that freshly formed $AlCl_3$ plays a role of catalyst like $ZnCl_2$ and promotes splitting hydrogen chloride off from PVC. At the same time, in the presence of LDH or products of its conversion, the chlorine occasionally isolated in polyene links or at aromatic nuclei remains intact in a significant amount as compared with pure PVC, and its splitting proceeds difficultly.

In pure PVC just after dehydrochlorination proceeds dehydrocarbonation leading to formation of various volatile hydrocarbons [51] therewith binding and cracking of the formed linear polyenes with liberation of volatile aromatic and various solid products is possible [87–89]. Cross-linking prevails in the temperature range 370–430°C, at higher temperature prevails cracking with formation of volatile aromatic compounds. It was shown that under nitrogen atmosphere the dehydrocarbonation is diminished when 4 wt% of LDH is introduced to the PVC matrix, which by opinion of the authors of [86] is connected with the catalytic effect of LDH or its products promotoing binding into dense aromatic complexes. At the use of Zn-LDH that bears function like $ZnCl_2$ [51, 59], carbonation depresses cracking, and less volatile hydrocarbons are formed. In air, in the presence of LDH at 400–550°C formation of carbonized residue becomes easier, at higher temperature occurs thermooxidation of the latter.

In the recent time are widely explored polymer–clay nanocompositese characterized by certain unique properties as compared with pure polymers and composites containing other inorganic substances [90–97]: excellent mechanical properties, high temperature of thermal deformation and thermostability, low gas penetrability, etc. Study of properties of the polymer–clay nanocomposites opens new approaches to manufacturing highly effective composites based on PVC. In [98] were studied mechanical properties and the process of stabilization of nanocomposites with montmorillonit (MMT) as an additive for obtaining PVC/MMT nanocomposite with partially intercalated structure. Wang and co-workers [99–101] synthesized

the PVC/MMT nanocomposites with non-mixied and intercalated structures and studied their thermal and mechanical properties. Results of some studies show that adding of clay particles can improve thermal stability of polymer/MMT nanocomposites, e.g., when polymeric matrix is polystyrene [102] or polymethylmetacrylate [103, 104]. Presence of MMT promotes formation of carbon and retards diffusion of volatile products of decomposition in the nanocomposites. In [105] were studied thermal properties of PVC/MMT nanocomposites synthesized by intercalative polymerization. As compared with pure PVC, the nanocomposites have slightly higher temperature of vitrification. Adding of MMT to the PVC matrix increases temperature of maximal rate of decomposition and temperature of beginning decomposition. On the nanocomposite surface is formed structure of compact carbon with the rich by carbon MMT that diminishes thermal decomposition of polymer matrix at the high temperature. Nanocomposites accelerate formation of residue and improve properties of polymer matrix. Presence of quarternary nitrogen in the nanocomposites leads to acceleration of the polymer decomposition in the initial step. It is known that thermal destruction of ammonium salt can proceed along the Hoffman mechanism [106] with formation of some H^+ and HCl catalyzing reaction of splitting off hydrogen chloride from the PVC chain. Therefore introducing of ammonium salt at the modification of PVC matrix with MMT accelerates the process of the polymer dehydrochlorination and diminishes temperature of beginning of its decomposition.

Magnesium hydroxide is used at high-temperature decomposition and as flame retarding additive to polymer materials. For improving its dispersion and compatibility with the polymer matrix it is subjected to ultrafine grinding ant treatment of its surface. The superfine magnesium hydroxide powder improves flameproof and mechanical properties of polymeric materials, but its dispergation in the polymer matrix is problematic [107, 108]. In [109] was shown that laminar dual hydroxide modified by organic compounds acts as a disperser and promotes uniform distribution of magnesium hydroxide particles throughout the PVA matrix that results in the increase by 5–18°C of thermal decomposition temperature of the nanocomposite flameproof agent.

Effect of $CaCO_3$ and Li_2CO_3 on the liberation of HCl at combustion of PVC was studied in [110]. It was found that number and size of the filler sample affect not only HCl liberation, but also capacity of absorption. Liberation of HCl can be ever more diminished at simultaneous application of $CaCO_3$ and Li_2CO_3.

In [111] was shown that adding of $CaCO_3$ to PVC at roasting diminishes considerably concentration of liberated HCl resulting in decrease of content of dioxins in the effluent gas. At the same time, high absorption capacity of $CaCO_3$ in respect of chlorine-containing aromatic compounds leads to increase in the content of PCDD and PCDF in ash. However, since beginning of application of TiO_2-photocatalyst for decomposition of dioxins and dioxin-like compounds at UV radiation or sun light [112], the dioxins contained in the ash after combustion of a material should not create problems in respect of environment saving.

Study of reaction of PVC with calcium and magnesium oxides and hydroxides [113–116] showed that the processes of thermooxidative destruction of PVC and of reactions of products of its conversion with these compounds proceeds stepwise in the temperature range 200-500°C and includes PVC dehydrochlorination followed by the reaction of hydrogen chloride formed with the metal oxide (hydroxide) and oxide (hydroxide) carbonization. Behavior of PVC mixed with calcium or magnesium derivatives differ considerably. After the step of PVC dehydrochlorination and further reaction of hydrogen chloride with calcium oxide the sample mass increases. This feature is observed at processing both in air and inert gas that allowed the authors to suggest that at this step of reaction of the products of PVC decomposition with calcium oxide are formed calcium hydroxide and carbonate. Above 500°C proceed reactions of $Ca(OH)_2$ dehydration and $CaCO_3$ decarbonization. Increase in the sample mass at the reaction of $Ca(OH)_2$ with PVC is connected with formation of calcium carbonate in this step.

Kinetics of the reaction of metal chlorides formation in the temperature range 270–350°C at mass ratio oxide(hydroxide)–PVC 2 and 3 was studied in [115, 116]. The plot of chlorine in the polymer binding has S-shape that attests acceleration of reaction of metal chloride formation in the initial period defined by autoacceleration of the process of PVC dehydrochlorination. At higher oxide(hydroxide)–PVC mass ratio the degree of binding chlorine increases, therewith the degree of chlorine in PVC binding in the mixture with CaO is higher than for PVC–MgO under any conditions.

For the period before fall in the reaction rate were calculated specific rates of formation of metal chlorides per 1 g of initial amount of PVC in the mixture.

Increase in temperature leads to increase in the rate of formation of metal chloride, therewith specific rate of chloride formation is higher for calcium chloride than for magnesium chloride. At the degree of PVC chlorine binding 20% the values of effective activation energy of the reactions of calcium and magnesium chlorides formation are respectively 92.7 ± 6.8 and 42.5 ± 1.6 kJ mol^{-1} and practically are independent of the oxide–PVC mass ratio.

The conditions of chlorine in the polymer binding into ecologically safe products were optimized. At the temperature 290–300°C, oxide(hydroxide)–PVC mass ratio equal to 3, contact duration of the forming hydrogen chloride with the solid phase particles 6 min the chlorine in PVC at the reaction with CaO and $Ca(OH)_2$ becomes bound by 99% into calcium chloride.

Effect of fillers based on calcium carbonate and aluminum hydroxide on the destruction of plasticized PVC was studied in [117]. It was found that under argon atmosphere these compounds practically do not affect destruction of rigid PVC, although they bind differently the hydrogen chloride liberated in the process of destruction of the polymer. Intensity of the oxidative destruction of the filled PVC plastics is defined mainly by the resistance of the plasticizer to oxidation. It was noted that increase in the rate of HCl elimination at the destruction of plastics mixed with aluminum hydroxide is defined in the presence of the plasticizer by increase in the catalytic action on the thermodestruction of the polymer of aluminum chloride formed at the reaction of HCl with the filler.

Effect $CaCO_3$ and dolomite on the thermal decomposition of PVC was studied in [118]. The process of PVC dehydrochlorination in the presence of metal carbonates is decelerated due to consumption of HCl with formation of chlorides. Calcium and magnesium chlorides show almost no effect on the PVC destruction. Presence of alkali earth carbonates leads to decrease in the apparent activation energy of the step of dehydrochlorination and to increase in activation energy of the second step of PVC destruction that can change the mechanism of hydrogen chloride splitting off, e.g., via formation of fused hydrocarbon structures rather than polyene in the step of dehydrochlorination. Formation of benzene is depressed by adding inorganic compounds.

To conclusion, we can note the works [119–121] denoted to the study of PVC stabilization by phosphorus and sulfur compound. In [119] was forund that reatment with phosphorus trichloride vapor increases thermooxidative stability of PVC. Reaction of PCl_3 vapor with PVC proceeds at the formed carbonyl centers with formation of phosphoroxychloride groups grafted to the polymer surface. Increase in the phosphorus concentration on the polymer surface leads to acceleration of the process of coke formation and cross-linking in the narrower temperature range.

In [120, 121] was shown that sulfur is an effective inhibitor of the process of thermooxidative dehydrochlorination of PVC and its copolymers, and under the conditions of the PVC thermal destruction shows a weak accelerating effect on the cross-linking of macromolecules. The high antioxidative power of sulfur at the destruction of plasticized polymers is defined by the significant decrease in the rate of accumulation of hydroperoxides owing totheir heterolytic decomposition at the reaction with sulfur.

CONCLUSION

Oxides. Some of oxides: Co_3O_4, Cr_2O_3, CuO, Fe_2O_3 and MoO_3 decreases temperature of the step of dehydrochlorination at the destruction of PVC, while the presence of other oxides such as Al_2O_3, CeO_2, PbO_2, TiO_2, and ZrO_2 does not affect considerably the destruction temperature. The second step of destruction (cleavage of C–C bonds in olefins) is practically not affected by oxides.

Amount of liquid products falls at the adding of metal oxides, in particular of Fe_2O_3 and ZnO. There is a correlation between the amount of liquid products and organochlorine compounds. Effect of iron(III) oxide is in line with halogenation of benzene by the Friedel–Krafts mechanism stimulated by Lewis acids of $FeCl_3$ type.

Thermal decomposition of PVC in the presence of copper or its compounds, copper(II) oxide in particular, occurs at higher temperatures with wide varied concentration of components in the gaseous products, that follows from the ability of the copper compounds to induce cross-linking of the polymer macromolecules. The process of cross-linking at high temperature leads to decrease in amount of aromatic hydrocarbons like benzene and to increase in amount of aliphatic compounds. Copper and its compounds promote effective oxidation of the PVC carbon, in particular in the case of PVC–CuO, with removing chlorine at the pyrolysis to inorganic phase.

Ability of rare earth metal oxides to bind chlorine is changed in the series $La_2O_3 > Nd_2O_3 > CeO_2$. In the presence of CeO_2 grows formation of chlorobenzene.

Mixed Al–Mg and Al–Zn oxide catalysts increase rate of PVC decomposition and amount of light hydrocarbons in liquid products, and decrease substantially content of chlorine in the latter.

Experimental results show that the oxides containing cations that are strong Lewis acids promote considerably liberation of hydrogen halide. Good enough correlation for the temperature of beginning of the polymer thermal decomposition stimulated by halo compound with the Lewis acidity of the cation of halo compound is obtained. This is explained by the fact that acidity of halo compound of a metal reflects ability of its cation to the complex formation with chlorine atoms in the polymer and thus to promote thermal decomposition.

Hydroxides. Adding of hydroxides to PVC facilitates splitting hydrogen chloride off at the temperature 270-300°C but reduces degree of the further conversion of PVC that results in high chlorine content at the polyene backbone at decomposition either in air or in an inert gas. At higher temperature, hydroxides promote formation of carbon containing substances and decrease formation of volatile hydrocarbons.

Carbonates. In the presence of carbonates the maximal temperature of hydrogen chloride splitting off at the thermal decomposition of PVC increases and the rate of mass loss decreases. Inclusion of $CaCO_3$ into PVC composition decreases considerably amount of the forming polychlorinated dibenzodioxins.

Chlorides. Adding of metal chlorides, in particular of $ZnCl_2$ and $BaCl_2$, accelerates reaction of splitting off hydrogen chloride at the pyrolysis of PVC and decreases amount of high-molecular substances. In the presence of H_2, further destruction of polyenes at high temperature is facilitated that leads to decrease in amount of solid residue. Analysis of the content of PVC pyrolysis products at different temperatures shows that regeneration of HC1 and benzene is possible when the pyrolysis temperature is below 350°C. However, copper chloride can promote formation of polychlorinated dibenzosioxins and dibenzofurans.

Thus, investigations directed to the study of catalytic role of inorganic compounds, metal oxides first of all, in the process of thermal decomposition of PVC and their effect on the content of the products of pyrolysis with systematic consideration of their acidity should be continued. Noteworthy that still no correlation was found between the amounts of certain products forming at PVC conversion and physical characteristics of inorganic additives.

ACKNOWLEDGMENTS

This work was financially supported by Russian Foundation for Basic Research, grant No. 08-03-00170.

REFERENCES

1. Zevenhoven, R., Karlsson, M., Hupa, M., and Frankenhaeuser, M., *J. Air Waste Management Assoc*., 1997, vol. 47, pp. 861–870.
2. *An Introduction to Plastic Recycling in Japan Flow of Plastic Products*, Tokyo: Plastic Waste Management Institute, 2006.
3. Everaert, K. and Baeyens, J., *Chemosphere*, 2002, vol. 46, no. 3, pp. 439–448.
4. Karasek, F.W. and Hutzinger, O., *Anal. Chem*., 1986, vol. 58, no. 6, pp. A633–A642.
5. Lanoir, D., Trouve, G., and Delfosse, L., *Waste Management*, 1998, vol. 17, no. 8, pp. 475–482.
6. McNeill, I.C., Memetea, L., and Cole, W.J., *Polym. Degrad. Stab*., 1995, vol. 49, no. 1, pp. 181–191.
7. Ogaki, Y., *J. Jap. Inst. Energ,*. 2002, vol. 81, pp. 74–80.
8. Okuwaki, A., *Polym. Degrad. Stab*., 2004, vol. 85, no. 3, pp. 981–988.
9. Christmann, W., Kasioke, D., Kloppel, K.D., Partocht, H., and Rotard, W., *Chemosphere,* 1989, vol. 19, pp. 387–392.
10. Minsker, K.S., Kolesov, S.V., and Zaikov, G.E., *Starenie i stabilizatsiya polimerov na osnove vinilkhlorida* (Aging and Stabilization of Polychlorvinyl Based Polymers), Moscow: Nauka, 1982.
11. Knimann, R. and Bockhorn, H., *Comb. Sci. Tech*., 1994, vol. 101, pp. 285–299.
12. Behnisch, J. and Zimmerman, H.J., *Therm. Anal*., 1998, vol. 33, pp. 191–196.
13. Miranda, R., Yang, J., Roy, C., and Vasile, C., *Polym. Degrad. Stab*., 1999, vol. 64, no. 1, pp. 127–144.
14. Bockhorn, H., Hornung, A., and Hornung, U., *J. Anal. Appl. Pyrol*., 1999, vol. 50, no. 2, pp. 77–101.
15. Slapak, M.Jp., van Kasteren, J.M.N., and Drinkenburg, A.A.H., *Comput. Theor. Polym. Sci*., 2000, vol. 10, no. 6, pp. 481–489.
16. Marongiu, A., Faravelli, T., Bozzano, G., Dente, M., and Ranzi, E., *J. Anal. Appl. Pyrolysis*, 2003, vol. 70, pp. 519–553.
17. Chang, E.P. and Salovey, R., *J. Polym. Sci. Polym. Chem. Ed*., 1974, vol. 12, pp. 2927–2941.
18. Guyot, A. and Bert, M., *J. Appl. Polym. Sci*., 1973, vol. 17, no. 3, pp. 753–768.
19. Starnes, W.H.Jr., *Prog. Polym. Sci*., 2002, vol. 27, no. 10, pp. 2133–2170.

20. Chatterjee, N., Basu, S., Palit, S.K., and Maiti, M.M., *J. Polym. Sci. Polym. Chem. Ed*., 1994, vol. 32, no. 7, pp. 1225–1236.
21. Horikoshi, S., Serpone, N., Hisamatsu, Y., and Hidaka, H., *Environ. Sci. Technol*., 1998, vol. 32, pp. 4010–4016.
22. Katami, T., Ohno, N., Yasuhara, A., and Shibamoto, T., *Bull. Environ. Contam. Toxicol*., 2000, vol. 64, pp. 372–376.
23. Takasuga, T., Makino, T., Tsubota, K., and Takeda, N., *Chemosphere,* 2000, vol. 40, nos. 9–11, pp. 1003–1007.
24. Sen, A.K., Mukherjee, B., Bhattacharya, A.S., Sanghi, L.K., De, P.P., and Bhowmick, A.K., *J. Appl. Polym. Sci*., 1991, vol. 43, no. 9, pp. 1673–1684.
25. Fujii Kiyotoshi, EP 0719823. A1. Chlorine–Containing Resin Composition, 07.03.1996 .
26. Chekryshkin, Yu.S, Fedorov, A.A., Shchurova, L.M., Ismagilov, Z.R., and Kerzhentsev, M. A., RF Patent 2100702. MKI6 F 23 G 7/00; *Byul. Izobr.*, 1997, no. 36.
27. Yahata, T., Tsuchiya, Y., and Toba, M., US Patent 7056483, 06.06.2006.
28. Muller, H., Gachter, R., Klemchuk, P.P., and Andreas, H., *Plastics Additives Handbook: Stabilizers, Processing Aids, Plasticizers, Fillers, Reinforcements, Colorants for Thermoplastics*, Munich: Hanser Publ., 1990, p. 523.
29. Mark, H.F., *Encyclopedia of Polymer Science and Technology*, New York: Wiley–Interscience, 1987.
30. Pan, J., Xu, H., Qi, J., Cen, J., and Ma, Z., *Polym. Degrad. Stab.,* 1991, vol. 33, no. 1, pp. 67–75.
31. Iida, T. and Goto, K., *J. Polym. Sci. Polym. Chem. Ed*., 1977, vol. 15, no. 10, pp. 2435–2440.
32. Ballistreri, A., Foti, S., Maravigna, P., Montaudo, G., and Scamporrino, E., *J. Polym. Sci. Polym. Chem. Ed*., 1980, vol. 18, no. 10, pp. 3101–3110.
33. Gupta, M.C. and Viswanath, S.G., I*nd. Eng. Chem. Res*., 1998, vol. 37, pp. 2707–2712.
34. Li, B., *Polym. Degrad. Stab.*, 2001, vol. 74, pp. 195–199.
35. Li, B., *Polym. Degrad. Stab*., 2002, vol. 78, pp. 349–356.
36. Li, B., *Polym. Degrad. Stab*., 2000, vol. 68, pp. 197–204.
37. Li, B., *Polym. Degrad. Stab.*, 2003, vol. 82, pp. 467–476.
38. Wescott, L.D., Jr., Starnes, W H., Jr., Mujsce, A.M., and Linxwiler, P A., *J. Anal. Appl. Pyrolysis*, 1985, vol. 8, pp. 163–172.
39. Tu, H. and Wang, J., *Polym. Degrad. Stab.*, 1996, vol. 54, pp. 195–203.
40. Wang, J. and Li, B., P*olym. Degrad. Stab*., 1999, vol. 63, pp. 279–285.
41. Carty, P. and White, S., *Polym. Degrad. Stab.*, 2002, vol. 75, pp. 173–184.
42. Lu, L. F., Price, D., Milnes, G.J., Carty, P., and White, S., *Polym. Degrad. Stab*., 1999, vol. 64, pp. 601–603.
43. Carty, P. and White, S., *Polym. Degrad. Stab*., 1995, vol. 47, pp. 305–310.
44. Carty, P. and White, S., *Polymer,* 1995, vol. 36, pp. 1109–1111.
45. Yanik, J., Uddin, Md. A., Ikeuchi, K., and Sakata ,Y., *Polym. Degrad. Stab*., 2001, vol. 73, pp. 335–346.
46. Khan, W. and Ahmad, Z., *Polym. Degrad. Stab*., 1996, vol. 53, pp. 243–249.
47. Manzoor, W., Yousaf ,S. M., and Ahmad, Z., *Polym. Degrad. Stab.,* 1996, vol. 51, pp. 295–299.
48. Blazsy, M. and Jakab, E., *J. Anal. Appl. Pyrolysis*, 1999, vol. 49, pp. 125–143.
49. Lingaiah, N., Uddin, Md. A., Muto, A., Imai, T., and Sakata, Y., *Fuel*, 2001, vol. 80, pp. 1901–1905.
50. Hwang, I., Park, H–J., Kang, W–H., and Park, J–Y., *J. Hazard Mater*., 2005, vol. 118, pp. 103–111.
51. Cheng, W.H. and Liang, Y.S., *J. Appl. Polym. Sci.*, 2000, vol. 77, pp. 2464–2471.
52. Wang, D.I., Xu, X.B., Zheng, M.H., and Chung, H.C., *Acta Chimica Sinica*, 2000, vol. 58, pp. 1681–1684.
53. Minsker, K.S., Abdullin, M.I., Nepochatykh, O.V., and Zueva, N.P., *Vysokomolek. Soedin*., 1987, vol. 29A, no. 11, pp. 2397–2402.
54. Grimes, S.M., Lateef, H., Jafari, A.J., and Mehta, L., *Polym. Degrad. Stab.*, 2006, vol. 91, pp. 3274–3280.
55. Starnes, W.H., Pike, R.D., Cole, J.R., Doyal, A.S., Kimlin, E.J., Lee, J.T. *et al., Polym. Degrad. Stab*., 2003, vol. 82, pp. 15–24.
56. Sivalingam, G., Karthik, R., and Madra's G., *Ind. Eng. Chem. Res*., 2003, vol. 42, pp. 3647–3653.
57. Howell, B.A. and Keeley, J.R., *Thermochim. Acta,* 1996, vol. 272, pp. 131–137.
58. Masuda, Y., Uda, T., Terakado, O., and Hirasawa, M., *J. Anal. Appl. Pyrolysis*, 2006, vol. 77, pp. 159–168.
59. Levchik, S.V. and Weil, E.D., *Polym. Adv. Technol.*, 2005, vol. 16, pp. 707–716.
60. Ballistreri, A., Montaudo, G., Puglisi, C., Scamporrino, E., and Vitalini, D., *J. Polym. Sci. Polym. Chem. Ed*., 1981, vol. 19, no. 6, pp. 1397–1408.
61. Kakuta, Y., Hirano, K., Sugano, M., and Mashimo, K., *Waste Management,* 2008, vol. 28, no. 3, pp. 615–621.
62. Ahmad, Z. and Manzoor, W., *J. Therm. Anal. Cal.,* 1992, vol. 38, no. 10, pp. 2349–2357.
63. Horikawa, S., Takai, Y., Ukei, H., Azuma, N., and Ueno, A., *J. Anal. Appl. Pyrolysis*, 1999, vol. 51, nos. 1, 2, pp. 167–179.
64. Uddin, Md. A., Sakata, Y., Shiraga, Y., Muto, A., and Murata, K., *Ind. Engng. Chem. Res.*, 1999, vol. 38, no. 4, pp. 1406–1410.
65. Shiraga, Y., Uddin, Md.A., Muto, A., Narazaki, M., and Sakata Y., *Energy Fuels,* 1999, vol. 13, no. 2, pp. 428–432.
66. Lingaiah, N., Uddin, Md.A., Muto, A., Sakata, Y., Imai, T., and Murata, K., *Appl. Catal., A,* 2001, vol. 207,

nos. 1–2, pp. 79–84.
67. Yanik J., Uddin Md.A., and Sakata Y., Energy Fuels, 2001, vol. 15, no. 1, pp. 163–169.
68. Lingaiah, N., Uddin, Md.A., Muto, A., Imai, T., and Sakata, Y., *Fuel*, 2001, vol. 80, no. 13, pp. 1901–1905.
69. Lingaiah, N., Uddin, Md.A., Morikawa, K., Muto, A., Murata, K., and Sakata, Y., *Green Chem.*, 2001, vol. 3, pp. 74–75.
70. Bhaskar, T., Murai, K., Brebu, M., Matsui, T., Uddin, Md.A., Muto, A., and Sakata, Y., *Green Chem.,* 2002, vol. 4, no. 6, pp. 603–606.
71. Cho, S.M. and Choi, W.Y., *J. Photochem. Photobiol*., *A, Chem*., 2001, vol. 143, pp. 221–228.
72. Uda, T., Jacob, K.T., and Hirasawa, M., *Science*, 2000, vol. 289, pp. 2326–2329.
73. Uda, T., *Mater. Trans*., 2002, vol. 43, no. 1, pp. 55–62.
74. Tang, C., Wang, Y.Z., Zhou, Q., and Zheng, L., *Polym. Degrad. Stab.*, 2003, vol. 81, pp. 89–94.
75. Zhou, Q., Tang, C., Wang, Y.Z., and Zheng, L. , *Fuel,* 2004, vol. 83, pp. 1727–1732.
76. Yang, X.Y., Ren, S.L., He, H., and Wang, D., *J. Mol. Catal*., 1996, vol. 10, no. 2, pp. 88–94.
77. Bhaskar, T., Matsui, T., Kaneko, J., Uddin, Md.A., Muto, A., and Sakata, Y., *Green Chem*., 2002, vol. 4, pp. 372–375.
78. Bhaskar, T., Matsui, T., Nitta, K., Uddin, Md.A., Muto, A., and Sakata, Y., *Energy Fuels*, 2002, vol. 16, no. 6, pp. 1533–1539.
79. Santamaria, E., Edge, M., Allen, N.S., Harvey, H.B., Mellor, M., and Orchison, J., *J. Appl. Polym. Sci*., 2004, vol. 93, pp. 2731–2743.
80. Ven, L., Gemert, M.L.M., Batenburg, L.F., Keern, J.J. *et al., Appl. Clay. Sci*., 2000, vol. 17, pp. 25–34.
81. Wang, X. and Zhang, Q., *Polym. Int.,* 2004, vol. 53, pp. 698–707.
82. Lin, Y.J., Li, D.Q., Evans, D.G., and Duan, X., *Polym. Degrad. Stab.*, 2005, vol. 88, pp. 286–293.
83. Cavani, F., Trifiro, F., and Vaccari, A., *Catal. Today*, 1991, vol. 11, pp. 173–301.
84. *Handbook of Layered Materials*, Braterman, P.S., Xu, Z.P., and Yarberry, F., Eds., New York: Marcel Dekker, Inc., 2004, pp. 373–474.
85. *Layered Double Hydroxides: Present and Future*, Rives, V., Ed., New York: Nova Science Publishers, Inc., 2001.
86. Xu, Z.P., Saha, S.K., Braterman, P.S., and D'Souza, N., *Polym. Degrad. Stab.*, 2006, vol. 91, pp. 3237–3244.
87. Montaudo, G. and Puglisi, C., *Polym. Degrad. Stab*., 1991, vol. 33, pp. 229–262.
88. Anthony, G.M., *Polym. Degrad. Stab.*, 1999, vol. 64, pp. 353–357.
89. Jordan, K.J., Suib, S.L., and Koberstein, J.T., *J. Phys. Chem.,* B, 2001, vol. 105, pp. 3174–3181.
90. Lee, D.C. and Jang, L.W., *J. Appl. Polym. Sci.,* 1996, vol. 61, no. 7, pp. 1117–1122.
91. Kawasumi, M., Hasegawa, N., Kato, M., Usuki, A., and Okada, A., Macromolecules, 1997, vol. 30, pp. 6333–6338.
92. Wang, S.F., Hu, Y., Song, L., Wang, Z.Z., Chen, Z.Y., and Fan, W.C., *Polym. Degrad. Stab.,* 2002, vol. 77, no. 3, pp. 423–426.
93. Chen, G.H., Yao, K.D., and Zhao, J.T., *J. Appl. Polym. Sci*., 1999, vol. 73, no. 3, pp. 425–430.
94. Lee, J.W., Lim, Y.T., and Park, O.O., *Polym. Bull*., 2000, vol. 45, no. 2, pp. 191–198.
95. Noh, M.W. and Lee, D.C., *Polym. Bull*., 1999, vol. 42, no. 5, pp. 619–626.
96. Yano, K., Usuki, A., Okada, A., Kurauchi, T., and Kamigaito, O., *J. Polym. Sci*., *Part A: Polym. Chem.*, 1993, vol. 31, no. 10, pp. 2493–2498.
97. Jeon, H.G., Jung, H.T., Lee, S.W., and Hudson, S.D., *Polym. Bull.,* 1998, vol. 41, no. 1, pp. 107–113.
98. Wan, C.Y., Qiao, X.Y., Zhang, Y., and Zhang, Y.X. , *Polym. Test*, 2003, vol. 22, no. 4, pp. 453–461.
99. Wang, D.Y., Parlow, D., Yao Q., and Wilkie, C.A., *J. Vinyl Add. Tech.,* 2001, vol. 7, no. 4, pp. 203–213.
100. Wang, D.Y., Parlow, D., Yao, Q., and Wilkie, C.A., *J. Vinyl Add. Tech*., 2002, vol. 8, no. 2, pp. 139–150.
101. Du, J.X., Wang, D.Y., Wilkie, C.A., and Wang, J.Q., *Polym. Degrad. Stab.,* 2003, vol. 79, no. 2, pp. 319–324.
102. Chen, G.M., Liu, S.H., Chen, S.J., and Qi, Z.N., *Macromol. Chem. Phys*., 2001, vol. 202, no. 7, pp. 1189–1193.
103. Blumstein, A., *J. Polym. Sci., Part A: General Papers*, 1965, vol. 3, no. 7, pp. 2665–2672.
104. Zhu, J., Start, P., Mauritz, K.A., and Wilkie, C.A., *Polym. Degrad. Stab.*, 2002, vol. 77, no. 2, pp. 253–258.
105. Gong, F., Feng, M., Zhao, C., Zhang, S., and Yang, M., *Polym. Degrad. Stab*., 2004, vol. 84, pp. 289–294.
106. Zanetti, M., Camino, G., Reichert, P., and Malhaupt, R., *Macromol. Rapid Commun.*, 2001, vol. 22, no. 3, pp. 176–180.
107. Jianping, L., Longzhen, Q., and Baojun, Q., *Nanotechnology,* 2004, vol. 15, pp. 1576–1581. 108. Jianping, L., Longzhen, Q., and Baojun, Q., *J. Crystal. Growth*, 2004, vol. 267, pp. 676–684.
109. Zhang, G., Ding, P., Zhang, M., and Qu, B., *Polym. Degrad. Stab.,* 2007, vol. 92, pp. 1715–1720.
110. Zhu, S., Zhang, Y., Zhang, Y., and Zhang, S., *Polym. Test,* 2003, vol. 22, pp. 539–543.
111. Sun, R.D., Irie, H., Nishikawa, T., Nakajima, A., Watanabe, T., and Hashimoto, K., *Polym. Degrad. Stab*., 2003, vol. 79, pp. 253–256.

112. Pelizzetti, E., Borgarello, M, Minero, C, Pramauro, E, Borgarello, E, and Serpone, N., *Chemosphere*, 1988, vol. 17, no. 3, pp. 499–510.
113. Permyakova, O.V., Fedorov, A.A., Vnutskikh, Zh.A., and Chekryshkin, Yu.S., *Vzaimodeistvie polivinilkhlorida s oksidom magniya* (Reaction of Polyvinylchloride with Magnesium Oxide), Abstracts of Papers, All–Union Conference "Technical Chemistry. Results and Perspective", Perm: June 5–9, 2006, vol. 1, pp. 360–363.
114. Permyakova, O.V., Fedorov, A.A., and Vnutskikh, Zh.A., *Vzaimodeistvie galogenorganicheskikh veshchestv s oksidami magniya i kal'tsiya* (Intraction of organogalogen compounds with magnesium and calcium oxides), Abstracts of Papers, *Int. Conference "Innovation Potential of Natural Sciences"*, Perm: Perm University, Inst. Of Natural Sciences, Perm, 2006, vol. 1, pp. 212–215.
115. Rudometova, O.V., Vnutskikh, Zh.A., Fedorov, A.A., and Chekryshkin, Yu.S., *Zh. Prikl. Khim.*, 2008, vol. 81, no. 1, pp. 108–111.
116. Rudometova, O.V., Vnutskikh, Zh.A., Fëdorov, A.A., and Chekryshkin, Yu.S., *Khim. Tekhnol*., in press (no. 8).
117. Abdullin, M.I., Ableev, V.I., Mozzhukhig, V.B., and Guzeev, V.V., *Plast. Massy,* 1990, no. 12, pp. 71–74.
118. Karayildirim, T., Yanik, J., Yuksel, M., Saglam, M., Vasile, C., and Bockhorn, H., *J. Anal. Appl. Pyrolysis*, 2006, vol. 75, pp. 112–119.
119. Trifonov, S.A., Semenova, E.Yu., and Malygin, A.A., *Zh. Prikl. Khim*., 1996, vol. 69, no. 11, pp. 1917–1920.
120. Akhmetkhanov, R.M., Nagumanova, E.I., Akhmetkhanov, R.R., and Kolesov, S.V., *Khim. Promyshlennost' Segodnya*, 2004, no. 8, p.19–21.
121. Kolesov, S.V., Akhmetkhanov, R.M., Nagumanova, E.I., Kabal'nova, N.N., and Akhmetkhanov, R.R., *Zhurn. Prikl. Khim.*, 2004, vol. 77, no. 11, pp. 1877–1879.

ISSN 1070-4272, Russian Journal of Applied Chemistry, 2008, Vol. 81, No. 9, pp. 1686–1690. © Pleiades Publishing, Ltd., 2008.
Original Russian Text © N.A. Voinov, A.N. Nikolaev, D.V. Tarovatyi, A.V. Kustov, 2008, published in Khimicheskaya Promyshlennost', 2008, Vol. 85, No. 3, pp. 142–146.

PROCESSES AND DEVICES OF CHEMICAL MANUFACTURES

Splash Type Mass Transfer on the Water Film at Downflow and Upflow

N. A. Voinov, A. N. Nikolaev, D. V. Tarovatyi, and A. V. Kustov

Siberian State Technological University, Novosibirsk, Russia

Received May 10, 2008

Abstract—Generation of droplets on a surface of the water thin film at upflow and down flow is considered. Expressions for computation of splash type mass transfer were developed.

DOI: 10.1134/S1070427208090395

Presence of droplets in gas-liquid flow at dispersion-annular stream affects heat and mass transfer parameters of a film apparatus. Despate variety of works devoted to an investigation of tear out and carry-over of the droplets from the film calculations according to the known relations give contradicting results requiring an additional analysis.

An amount of liquid entrained from the surface film at upflow in pipes with diameters ranging from 13.5 to 20 mm and with length ranging from 100 to 860 mm at gas velocity from 15 to 55 m/s and at sprinkle density from 0.3 to 3.2 m²/h computed by equation (1)

$$E = Au_g^{1.44}\Gamma^{m} l^{k} d\left(\frac{\mu}{\sigma}\right)^{0.3}, \quad (1)$$

where E is overall splash entrainment, kg /s; q is a volume density of the sprinkle, m²/h; A, m, k are coefficients depending on the volume density of the sprinkle and a channel length L: A=(17.037…20.924) × 10⁻³; m = 2.1 at q < 1.1 m²/h, m = 1.4 at q > 1.1 m²/h; k = 0.8 at L < 0.6 m, k = 0.5 at 0.6 m < L < 2.5 m, k = 0.3 at L > 2.5 m.

At deriving equation (1) the experimental data obtainrd for short pipes is used, however, that requires verifying of the value E for a dynamical equation section.

Known relation [2] for definition of the value of the splash type entrainment at upflow written as equation (2) shows that value E decreases with a gas flow rise that occurs only in a transition region of the stream:

$$E = \left[534 \log\left(\frac{\mu}{\sigma}\frac{\sigma_w}{\mu_w}\right) + 117\right] \mathrm{Re}_g^{-0.35}\, \mathrm{Re}^{\left[0.3 - 0.04\left(\frac{\mu}{\sigma}\frac{\sigma_w}{\mu_w}\right)\right]}, \quad (2)$$

E is part of the entrainment fwith respect to the total liquid flow; μ, μ_w are dynamic viscosity of the studied liquid and water, respectively, s Pa; σ, σ_w are surface tension of the studied liquid and water, respectively, N/m; $Re_g = u_g d/\nu_g$ and Re = q/ν_l – Reynolds criterion of gas and liquid; u_g is air velocity, cm/s; d is the channel diameter, cm; ν_g, ν_l are kinematic viscosity coefficient of gas and liquid, cm.

Equation (3) is used for calculation the splash-type mass transfer at the flowdown

$$E_0 = A\,\mathrm{Re}^{a}\,\mathrm{Re}_{go}^{b}, \quad (3)$$

where Re and Re_{go} is Reynolds number of liquid film and relative Reynolds number of gas, respectively, A, a, b are empirical constants depending on stream regimes of gas and film, also on a pipe diameter: A = (1.52…40) × 10⁻⁷, a = 0.29…0.97), b = 0.71…1.48. However, equation (3) can be used for computation the splash entrainment only in pipes of diameter of 25 mm.

Application of equation (4) suggested in [4] for computation of equilibrium amount of the splash entrainment on the interval of a steady stream at the upflow and the downflow is difficult because of complexity of definition of tangential stresses value depending on a dispersed phase concentration in a gas−liquid flow:

$$E_0 = 1.8\times10^{-5}\,\mathrm{Re}^{-0.26}\,\mathrm{Re}_{go}^{1.48}\,\frac{\delta}{d}\left(\frac{\tau_i}{\tau_1}\right)^{0.4}. \quad (4)$$

Here d is an internal diameter of the pipe, m; δ is average thickness of the film, m; τ_i is the tangential stress

on the interface, N/m^2 ; τ_l is a tangential stress on a pipe wall, N/m^2.

Investigation of splash entrainment in hydraulically smooth pipes made of stainless steal with the internal diameter d of 27 and 51 mm and with operation length l about 2.5 m were carried out for generalization of the known data and obtaining relation for computation of the splash type mass transfer. Air flow was ranged about 180 m^3/h at temperature from 15 to 60°C. A liquid film generation was realized with a gas jet that forms with an internal surface of the pipe an annular gap of 0.5−1.5 mm. Amount of the disperse phase on the gas flow was measured by probing like a Pitot tube [5] with an internal channel diameter 3 mm. As a boundary between continuous and disperse phases was assumed a height of regular waves that was 3 mm and overall liquid outside this boundary was assumed as the disperse phase. The probed liquid amount related to an area of the Pitot tube channel section. A summary average amount of the disperse phase over the pipe section was defined by an integration of distribution curves (Figs. 1 and 2).

The splash entertainment was computed by equation (5)

$$E_0 = G_d/G_s, \quad (5)$$

where G_d is the liquid flow in droplets, kg/s; G_s is the liquid flow input to spraying, kg/*s*.

The measuring results of the splash type mass transfer at the downflow and the upflow and the known data exhibited (Fig. 3) that value E_0 at the upflow (Fig. 3, dashed lines) was higher in comparison with the downflow.

It is caused by higher tangential stress on the interface at the upflow (τ_i/τ_l = 0.5–6) in comparison with the downflow (τ_i/τ_l = 0.1–0.9) that separates liquid from a ridges of large waves and from waves disturbing the films. There are two region of the splash type mass transfer in dependence of the gas flow. First region occurs in the transition hydrodynamic regime where the gas flow increase does not result in the considerable change of E_0 [2, 5–10]. In this case a start of the splash entertainment can be estimated [7] by Weber number analyzing thin film flows and the formation of droplets and bubbles (Fig. 3, a dotted line, for the pipe of d = 27 mm). Because of a wave structure formation on the film surface in the transition regime with the gas flow rise a height of large wave ridges decreases that results in the steady splash entrainment.

An onset of the formation of the second region of the droplet entrainment at the downflow and the upflow coincides with the transition border in the disperse–annular regime of the stream (Fig.3, the dotted lines). In this region E_0 is about $Re_{go}^{1.48}$ at the downflow, and $E_0 \sim Re_{go}^{0.6}$ at the upflow. Distinction in the values of exponent of Re_{go} is caused by laminarization of the gas−fluid flow. High concentration of the droplets at the upflow results in more suppression of a gas turbulence [11] in comparison with the downflow.

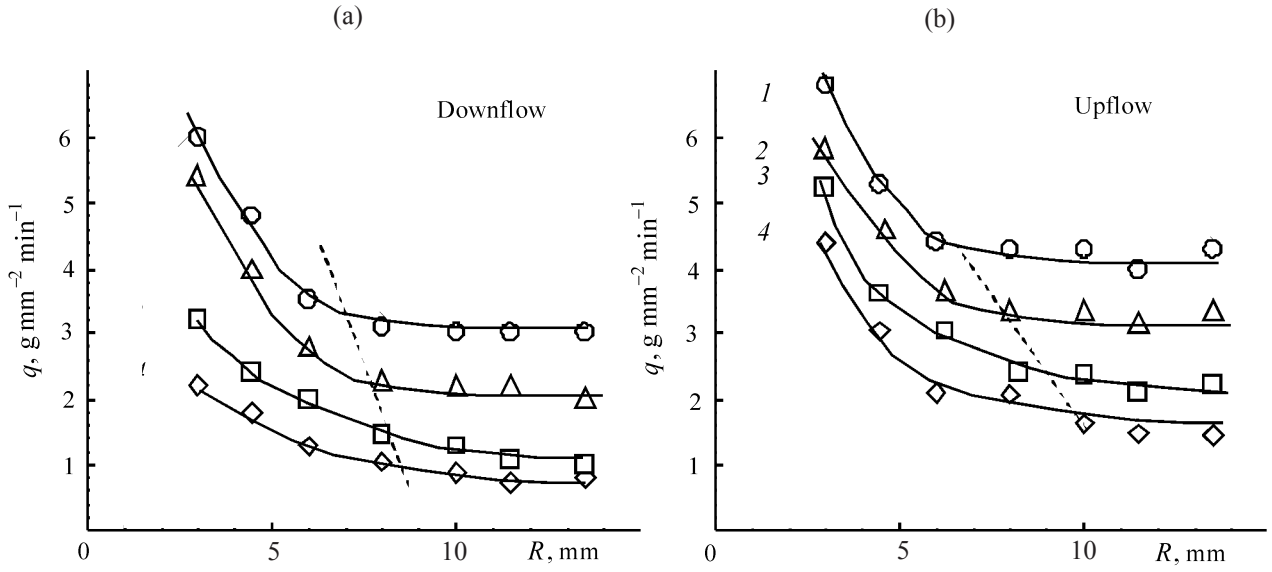


Fig. 1. Distribution of the disperse phase over the pipe section at the downflow (a) and upflow (b) of air and water at the difference Reynolds number of gas (Γ = 4.4 × 10^{-3} m^2/s, d = 27 mm, l = 1.68 m): (a) the experimental points (*1–4*) at ν_l =0.6 × 10^{-6} m^2/s: (*1*) Re_g = 42000, (*2*) 37000, (*3*) 30000, (*4*) 21000; (b) the experimental points (*1–4*) at ν_l = 1.3 × 10^{-6} m^2/s: (*1*) Re_g = 42000. (*2*) 36000, (*3*) 30000, (*4*) 21000.

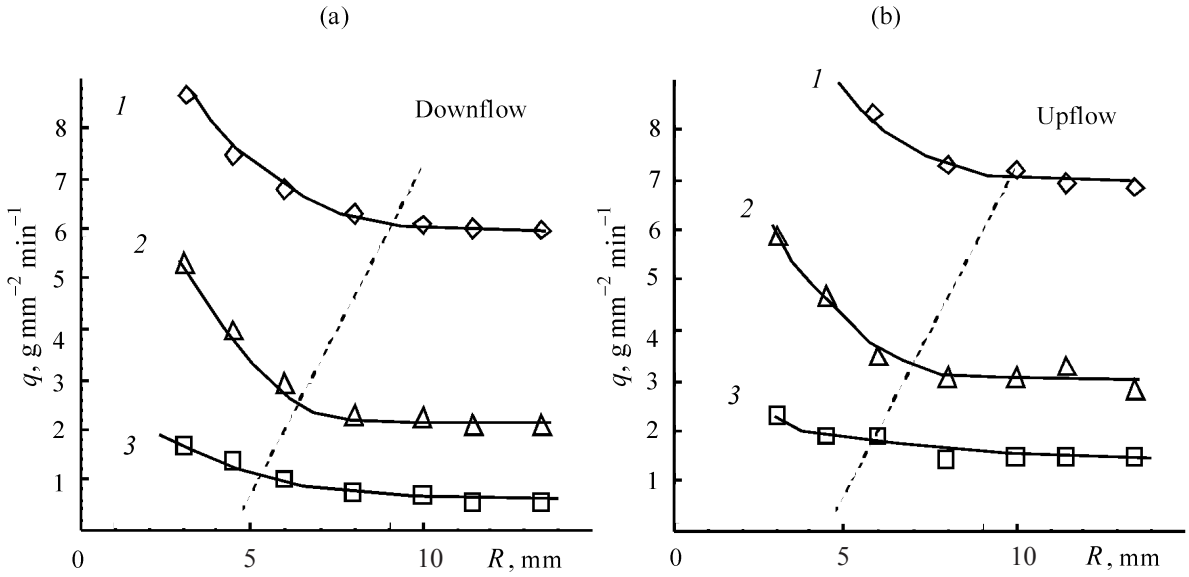


Fig. 2. Distribution of the disperse phase over the pipe section at the downflow (a) and upflow (b) of air and water at the difference spray density at $Re_g = 38000$, $d = 27$ mm, $l = 1.68$ m: (a) the experimental points (*1–3*) at $\nu_l = 0.6 \times 10^{-6}$ m²/s: (*1*) $\Gamma = 8.5 \times 10^{-3}$ m²/s, (*2*) 4.4×10^{-3}, (*3*) 2.5×10^{-3}; (b) experimental points (1–3) at $\nu_l = 1.3 \times 10^{-6}$ m²/s: (*1*) $\Gamma = 8.5 \times 10^{-3}$ m²/s, (*2*) 4.4×10^{-3}, (*3*) 2.5×10^{-3}

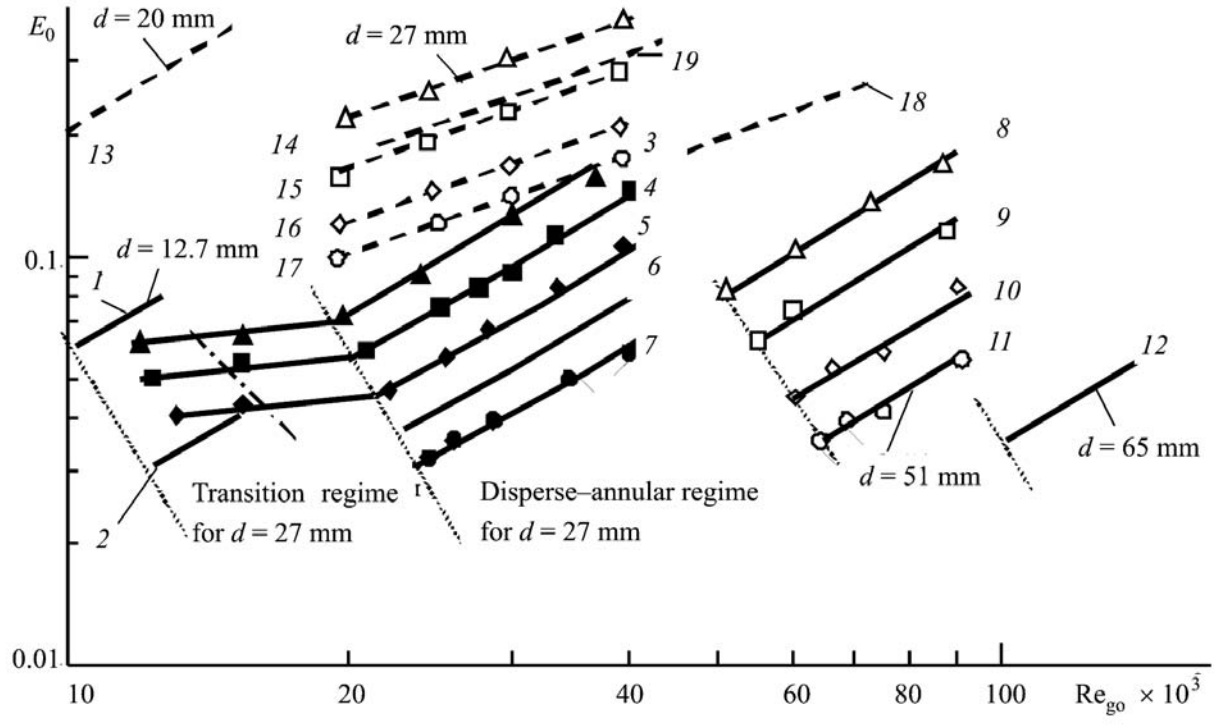


Fig. 3. Dependence of equilibrium part of E_0 on the relative Reynolds number of gas at upflow and downflow of water film and of air ($l = 1.5$–2 m), $\nu_l = (0.7$–$1.3) \times 10^{-6}$ m²/s . (*1–12*) Downflow: (*1*) Re = 8000, $d = 12.7$ mm; (*2*) 2140, $d = 12.7$, Data of [5] derived to the length 1.5 m; (*3*) 15700, $d = 27$; (*4*) 8140, $d = 27$; (*5*) 4625, $d = 27$; (*6*) 2100, $d = 25$, [3]; (*7*) 2100, $d = 27$; (*8*) 22100, $d = 51$; (*9*) 9700, $d = 51$; (*10*) 4600, $d = 51$; (*11*) 2100, $d = 51$; (*12*) 2100, $d = 65$. Computation according to equation (7): (*13–18*) Upflow (*13*) Re = 10000, $d = 20$ mm, [1]; (*14*) 10000, $d = 27$ mm; (*15*) 7200, $d = 27$; (*16*) 3700, $d = 27$; (*17*) 2100, $d = 27$; (*18*) 2020, $d = 31.75$, [8] at $l = 6.1$ m; (*19*) 2100, $d = 12.7$ mm, [5]. Points are the results of experiments performed by the authors.

Values of the coefficient C_i

The downflow					
d, mm	12.7	25	27	51	65
C_i	0.7×10^{-9}	0.28×10^{-9}	0.24×10^{-9}	0.57×10^{-10}	0.3×10^{-10}
The upflow					
d, mm	12.7	20	27	31	–
C_i	11.0×10^{-5}	0.86×10^{-5}	0.6×10^{-5}	$0.56\cdot\times10^{-5}$	–

Analysis of the experimental data in the coordination $E_0\,\mathrm{Re}_{go}^{-1.48} = f(\mathrm{Re}_l)$ at the downflow and $E_0\,\mathrm{Re}_{go}^{-0.6} = f(\mathrm{Re}_l)$ at the upflow enabled us to define an exponent of Re_l^n that have amounted $n = 0.5$ where Re_l was Reynolds number of the film on the region of the dynamic equilibrium.

$$\mathrm{Re}_l = \frac{4\mathrm{G}_n(1-E_0)}{\pi d\nu_l} \tag{6}$$

The relations for calculation of equilibrium entrainment at the disperse-annular regime are written as:

for the downflow

$$E_0 = C_i\,\mathrm{Re}^{0.5}\mathrm{Re}_{go}^{1.48}, \tag{7}$$

for upflow

$$E_0 = C_i\,\mathrm{Re}^{0.5}\mathrm{Re}_{go}^{0.6}, \tag{8}$$

where Re_{go} $(u_g - u_s)\,d/\nu_g$ is relative Reynolds number of gas; u_s is a superficial film velocity, m/s; u_g is the average gas flow, m/s.

For simplification of the computations in equations (7) and (8) Reynolds number of the liquid film can be calculated by the start the liquid flow G_s without taking into account the liquid entrainment. Analysis showed that at such data treatment $E_0 \sim \mathrm{Re}^{0.5}$.

Taking into account that on the transition border in the disperse-annular regime of the stream the value E_0 is practically the same at the constant liquid flow the values of a coefficient Ci (see the table) are defined for the pipes of different diameters.

The splash entrainment E on the start part can be calculated according to equation (9) [4] of the pipe

$$E = E_0\left[1 - \exp\left(-\frac{\mu}{u_g E_0}l\right)\right], \tag{9}$$

where an intensity of droplet entrainment from the film surface μ for obtaining experimental data was amounted to (1–20) s^{-1} and was computed by equation (10) [4]

$$\mu = c\frac{u_g}{d}E_0, \tag{10}$$

where ($c \approx 0.092$ for the downflow, $C \approx 0.055$ for the upflow).

The value μ rises with increase of Reynolds number for gas and for liquid and seems higher in 1.2–1.5 times for the upflow in comparison with the downflow.

The work is executed at a financial support of the Russian Foundation of Basas Research, the project 05-08-01367-a "Fundamental Bases of Engineering Sciences", the Ministries of Education and Sciences of the Russian Federation and the American Foundation of Civil Research and Development (CRDF) (grant P1MO002 and programs of integration researches of the Siberian Branch of the Russian Academy of Science (the project 24).

REFERENCES

1. Shcherbakov, V.N., Nikolaev, N.A., and Nikolaev, A.M., *Proceedings of Kazan. Khim. Tekhn. Inst*., 1974, no. 53, p. 120.
2. Zabrudskii, V.G., Kholpanov, L.P., Nikolaev, N.A. *et al., Izv. Vuzov., Khimiya Khim. Tekhnol*., 1976, vol. 19, no. 6, p. 963.
3. Kulov, N.N., Maksimov, V.V., Maljusov, V.A., and Zhavaoronkov, N.M., *Chem. Eng. J,* 1979, p. 183.
4. Sugak, E.V., Voinov, N.A., and Nikolaev, N.A., *Ochistka gazovykh vybrosov v apparatakh s intensivnymi, gidrodinamicheskimi rezhimami* (Gas Blowout Cleaning in Apparatus with Intense Hydrodynamic Regimes), Kazan: RITs "Shkola," 1999, 224 p.
5. Hewitt, G. and Hall-Talor, N., *Kol'tsevye dvukhfaznye techeniya* (Annular Tho-Phase Flow), Moscow: Energiya,

1974, 408 p.
6. Nikolaev, A.N., Voinov, N.A., Shcherbakov, V.N., and Nikolaev, N.A., *Teor. Osnovy Khim. Tekhnol.*, 2000, no. 2, p. 130.
7. Nigmatulin, R.I., *Dinamika mnogofaznykh sred* (Dynamic of Multiphase Media), Moscow: Nauka, 1987.
8. Gill, L.E., Hewitt, G.F., and Lacey, P.M.C., *Chem. Eng. Sci.*, 1964, vol. 19, p. 665.
9. Ueda, T. and Tanaka, T., *Bull. ISME*, 1974, vol. 17, no. 107, p. 603.
10. Ueda, T. and Nose, S., *Bull. ISME*, 1974, vol. 17, no. 107, p. 614.
11. Zakharov, L.V., Ovchinnikov, A.A., and Nikolaev, N.A., *Snizhenie treniya v dvukhfaznykh turbulent-nykh techeniyakh* (Reduction of the Friction in Two-Phase Turbulent Flows), Kazan: Izd. Novoe Znanie, 2006.

ISSN 1070-4272, Russian Journal of Applied Chemistry, 2008, Vol. 81, No. 9, pp. 1691–1696. © Pleiades Publishing, Ltd., 2008.
Original Russian Text © A.M. Kagan, L.A.Yudina, A.S. Pushnov, 2008, published in Khimicheskaya Promyshlennost', 2008, Vol. 85, No. 3, pp. 147–152.

PROCESSES AND DEVICES OF CHEMICAL MANUFACTURES

Hydraulic Resistance and Specific Surface of Irregular Nozzles

A. M. Kagan, L. A. Yudina, and A. S. Pushnov

Moscow State UIniversity of Engineering Ecology, Moscow, Russia

Received April 4, 2008

DOI: 10.1134/S1070427208090401

In hole channels various hydrodynamic regimes with precise boundaries take place at gas and fluid flows within. At Reynolds number related to the channel diameter $Re_D < 2300$ viscous forces prevailed and a pressure drop ΔP is entirely defined by a channel wall friction of the flow (here $Re_D = W_0 D/\nu$, where W_0 is the flow, m/s; D is the channel diameter, m; ν is a coefficient of kinematic viscosity, m^2/s). At Reynolds number $Re_D > 10000$ the value ΔP is characterized by inertial forces. A range of $Re_D = 2300–10000$ is transition.

Analogous hydrodynamic conditions are resulted at gas flow in channels filled by granular material or by a nozzle. However herein in distinction from the hole channels the boundaries of regimes are defined by the other values of Reynolds number and the boundaries are more diffuse.

A flow movement through the granular or nozzle layer is better to consider as the movement between the bodies filling an apparatus in many narrow curved parallel channels of variable section and form (internal problem) [1]. As a result a transfer from one hydrodynamic regime to other can not occur simultaneously within all these channels at one concrete Reynolds number [2, 3]. Thus an equivalent diameter D_{equiv} equaled to a quadrupled hydraulic radius should be accepted as characteristic linear size:

$$D_{equiv} = 4\Gamma = \frac{4F_c}{\Pi} \quad (1)$$

where: F_c is free apparatus section filled by the nozzle, m^2; Π is a perimeter of the channels in this section, m. In the nozzle layer the free section of the apparatus with the nozzle is equaled to a sumary area of the section of the channels F_c. A product F_cH gives a free volume part ε, m^3/m^3, and ΠH a specific surface S, m^2/m^3. Equation (1) is written as

$$D_{equiv} = \frac{4F_c}{\Pi} = \frac{4F_cH}{\Pi H} = \frac{4\varepsilon}{S}, \quad (2)$$

and Reynolds number that is computed with an actual gas velocity (related to a free section F: $W = V_g/F_c$) by equation (3):

$$Re_{equiv} = \frac{WD_{equiv}}{\nu} = \frac{W4\varepsilon}{\nu S} = \frac{W_0\ 4\varepsilon}{\varepsilon\ \nu\ S} = \frac{4W_0}{\nu S}, \quad (3)$$

where H is a height of the nozzle layer, m; V_g an amount of the gas, m^3/s; $W_0 = W_\varepsilon = V_g/F$ is a fictitious gas velocity (related to a total apparatus section that is not filled by nozzles: F, μ^2).

Based on experimental data [4, 5] we established that a range of Reynolds number $Re_{equiv} = 40…60$ is an upper limit of viscous flow in the apparatus filled by the nozzles of various form and $Re_{equiv} = 1200…6000$ a bottom limit of the flow regimes with the prevailing inertial forces.

We assumed that $\Delta P = f(S)$ for the nozzles since as we noted above the value ΔP is defined in the flow regime with the prevailing viscous forces by the channel wall friction of the flow.

In [6] an equation for calculation $S = f(\Delta P)$ of the granular materials of irregular shape was derived using the established relation $\varepsilon u_m = f(Re_{equiv})$. Here Euler number is $\varepsilon u_m = \Delta P \varepsilon g/HS\gamma W_0^2$; ΔP, kg/m^2; γ is the specific gas weight, kg/m^3. Ability to calculate the value S by ΔP is quite important since an exact definition of the

specific geometric surface S for the bodies of irregular shape is nontrivial.

A relation between the pressure drop and the specific surface of polymeric nozzles is considered in [7].

We attempted to establish a general relation between ΔP and the specific geometric surface of the nozzles of various shape and size at the gas flow through their layer.

A countercurrent flow of gas and fluid occurs in the nozzle layers as distinct from the granular materials where gas flows through an adsorbent or catalyst layer. Therefore now the pressure drop at two-phase movement through the nozzle is usually studied for obtaining the data required for engineering computation of a nozzle apparatus. Simultaneously the pressure drop ΔP of a not sprinkled (dry) nozzle is studied because this data contains some information about the nozzle properties.

For obtaining the target general relation data of [4, 8–23] was employed. Experimental data about the pressure drop of the dry nozzle with smooth surface of annular, semi-annular, and saddle shapes of a various construction at a value of a gas load $F_f = W_0 \gamma^{1/2} = 2.0$ were presented in Table 1. Noted value of F_f was selected because it virtually denotes the upper limit of the gas load in the nozzle apparatus. The value $F_\tau = 2.0$ for the majority annular nozzles of 50 mm size corresponds to $Re_{equiv} \sim 1600$. Also some characteristics of nozzles including the part of free volume ε and the specific geometric surface S are presented in the Table 1. Constructions of the considered nozzles are showed on the Fig. 1.

We obtained the pressure drop ΔP studying the dry nozzle for Pall ring and GIAP nozzles of 3 sizes [16–18, 23] with use of air in columns of (1) $D = 500$ m and at the height of the nozzle layer $H = 2400$ mm and (2) $D = 900$ mm at $H = 3000$ mm. Simultaneously we examined the sprinkled nozzles in the column of the same sizes for the air-water system at atmospheric pressure. Due to special techniques we provided steady start distribution of the streams: grades and wires at the input of gas flow to the nozzle layer, and multipoint spreader of liquid. Results of a hydrodynamic research of metal Pall rings of 50 mm size are presented in Fig. 3.

Results of the generalization are showed on Fig. 2. For the generalization relative values of the pressure drop were applied. On Y-axis we can see relation of hydraulic resistance of the nozzle to hydraulic resistance of metal

Experimental and calculated characteristics of the nozzles of the ring and saddle shape of the various constructions with smooth surface [4, 8–23]

Nozzle	Material	ε, m^3/m^3	S, m^2/m^3	Found		Calculated by equation (5)	
				ΔP, mm H_2O at F_f= 2.0	$\Delta P/\Delta P_{Pall\ rings}$, %	ΔP, mm H_2O at F_f=2.0	$\Delta P/\Delta P_{Pall\ rings}$, %
Ring							
Flexiring 50 μμ	metal	0.96	114.6	19.2	101	20.9	110
Beletskii 50 μμ	metal	0.95	112.0	20.0	105.2	20.5	108
Pall ring 50 μμ*)	metal	0.95	110.0	19.0	100	20.4	107
Raschig ring 50 mm	metal	0.95	110.0	19.5	103	20.4	107
Germany 50 mm	metal	0.97	106.0	20.0	105.2	18.8	99.0
Pall 50 μμ	metal	0.92	110.0	21.8	115	21.8	114.5
Ralu 50 μμ	metal	0.93	95.2	13.0	81.0	18.3	96.3
Hiflow 50 μμ	metal	0.94	83.0	11.8	62.0	15.6	82.0
Semi-ring							
GIAP 38 mm*)	metal	0.96	119	23.0	121.0	23.1	121
GIAP 50 mm*)	metal	0.96	101	17.5	92.1	18.3	96.0
GIAP 80 mm*)	metal	0.96	60.0	11.0	57.9	10.8	67.0
Hutter no. 2	metal	0.98	95.0	12.7	67	16.5	86.8
Saddle							
Intallox	polymer	0.89	126	34.2	180	26.2	138
Supertorus	polymer	0.94	114	26.6	137	21.6	114
Flexisaddle	polymer	0.89	120	31.6	166	24.5	129
Hiflow	polymer	0.94	86.4	13.0	71.0	16.2	85

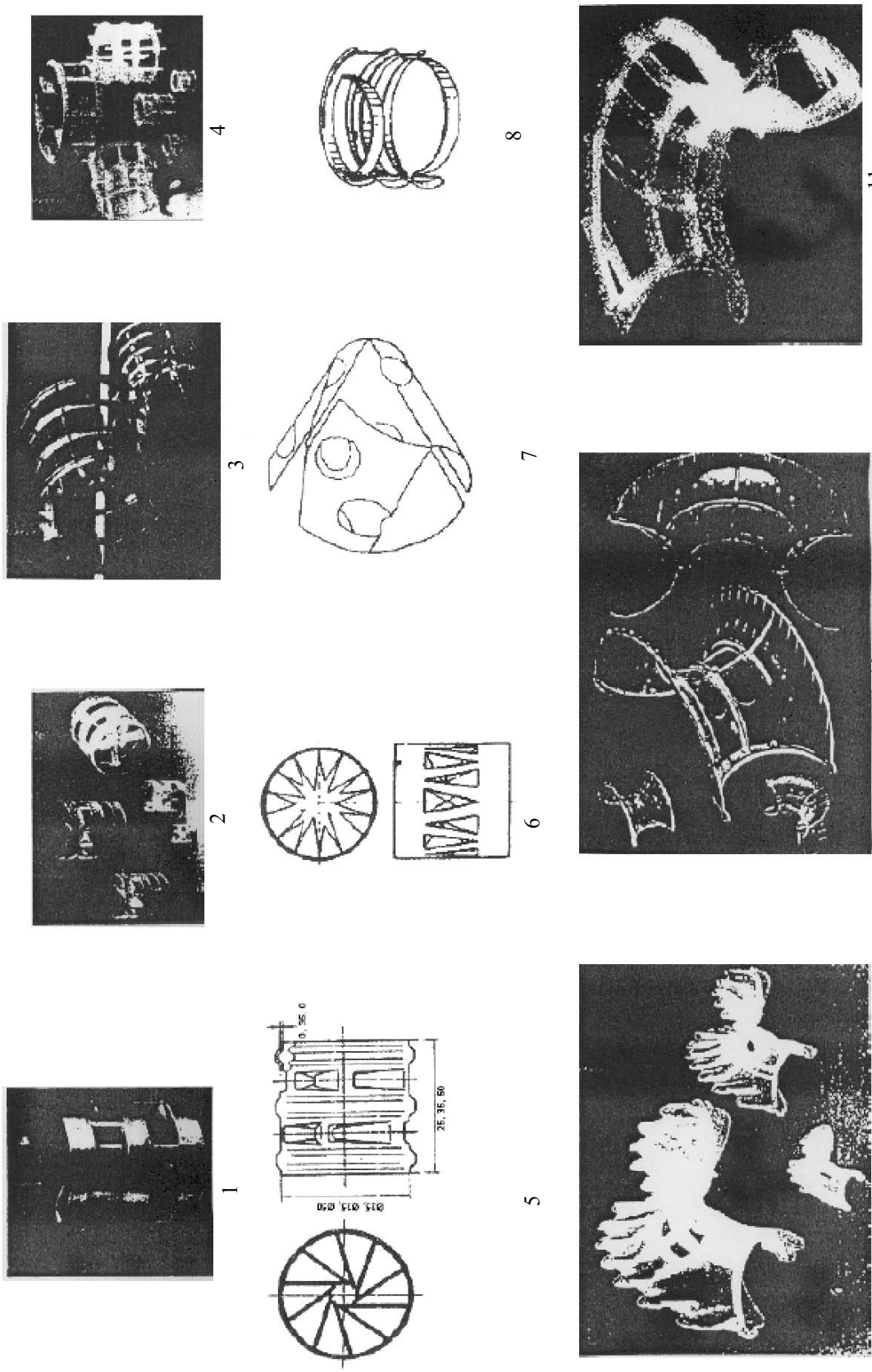


Fig. 1. Mass Transfer Nozzles: Metal: (a) ring: (1) Pall, (5) Germania, (6) Beletskii; (b) semi ring: (7) GIAP, (8) Hutter. Polymeric: (a) ring: (2) Pall, (3) Ralu, (4) Hiflow; (c) saddle: (9) Supertorus, (10) Flexisaddle, (11) Hiflow.

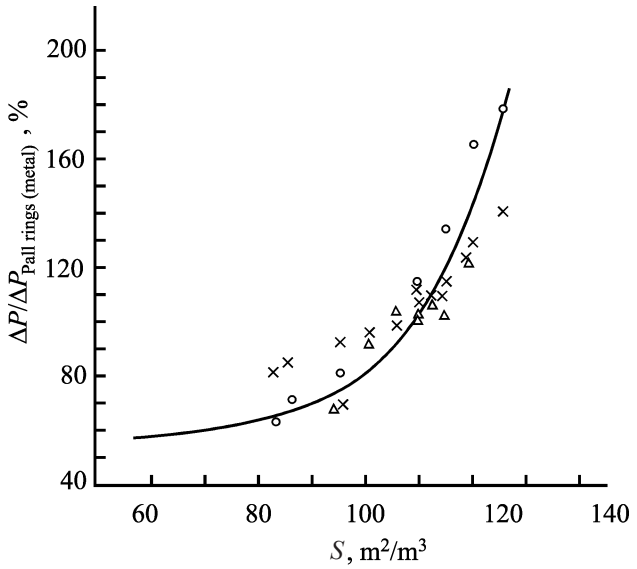


Fig. 2. A generalized dependence of the relative pressure drop $\Delta P/\ \Delta P_{\text{Pall rings}}$ on the specific surface of the smooth nozzles of various shape and size: (Δ) metal nozzles; (O) polymeruc nozzles (experimentral data); (x) calculated values according with equation (5).

Pall rings: $\Delta P/\Delta P_{\text{Pall ring}}$, %. Thus the hydraulic resistance of the metal nozzle made of Pall ring of 50 mm size as the most often on world industry was assumed as base resistance for comparison. And on the X-axis there is specific geometric surface.

Majority of the experimental points is generalized by a curve with an error no more ±12%. It reveals that at Re_e belonging to $F_f = 2$ the viscous forces prevail to a significant degree and an effect of the nozzle shape and their design features enabling stream turbulization to ΔP is not large. The curve on Fig. 3 is described by equation (4)

$$\frac{\Delta P}{\Delta P_{\text{Pall rings}}} 100 = 0.009\ S^{2.0}, \qquad (4)$$

that can be used in the range of the specific surface S = 80…125 m²/m³.

For computation of the specific surface of the granular materials by the measured pressure drop ΔP in the dry granular layer we transformed an equation suggested in [6] relative to ΔP with reference to the nozzle layers:

$$\Delta P = \frac{\left[\left(S + 18\times10^{3}\ \frac{W_0}{\nu}\right)^2 - 324\times10^{-6}\ \frac{W_0^2}{\nu}\right]\nu H\gamma W_0.}{0.09\ g\ \varepsilon^3} \qquad (5)$$

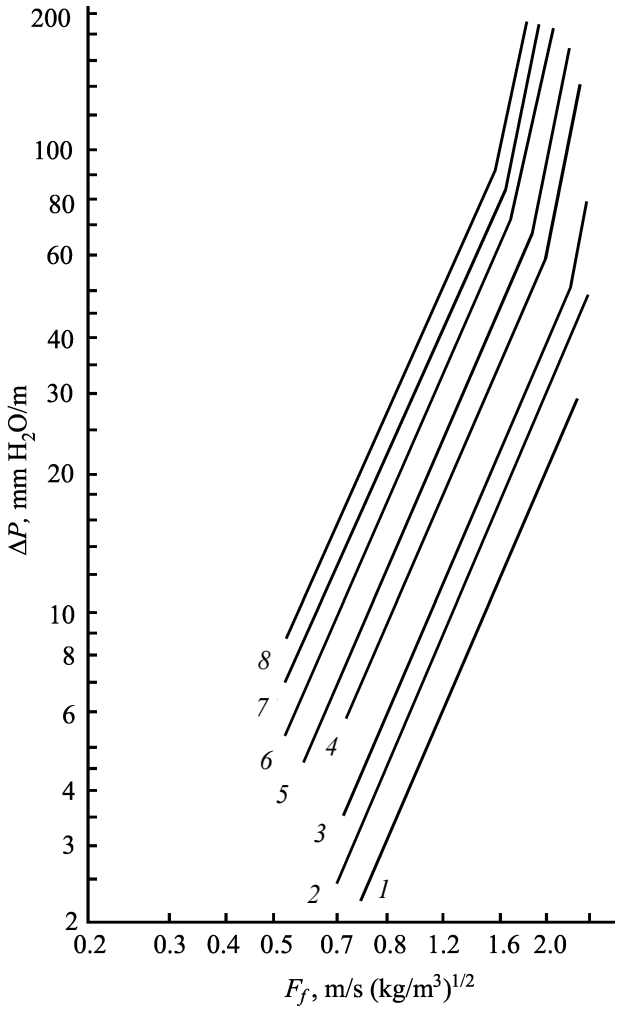


Fig. 3. Hydraulic resistance of Pall rings of 50 mm made of metal: (*1*) dry nozzle, (*2*) L_{Op} = 20 m³ m⁻² h⁻¹; (*3*) L_{Op} = 40 m³ m⁻² h⁻¹; (*4*) L_{Op} = 60 m³ m⁻² h⁻¹; (*5*) L_{Op} = 80 m³ m⁻² h⁻¹, (*6*) L_{Op} = 100 m³ m⁻² h⁻¹ (*7*) L_{Op} = 120 m³ m⁻² h⁻¹; (*8*) L_{Op} = 135 m³ m⁻² h⁻¹.

The results of computation of ΔP according to equation (5) presented in Table 1 and on Fig. 2 reveal that the experimental and calculation values of ΔP are correlated on range of ±20%. This range can be explained by errors at measurements of S and ε by various authors for the nozzles of a comlex configuration.

In [24] an analogous way is suggested for computation S of the nozzle on the base of equation $S = f(\Delta P)$ [6].

As we noted above we applied for generalization the experimental data obtained at the load $F_f = 2.0$. However the calculation exhibited that at operation with the relative hydraulic resistance, e.g. $\Delta P/\Delta P_{\text{Pall rings}}$, the curve (Fig. 2) sufficiently well describes the experimental data obtained at other loads in the range of $F_\tau = 0.5…2.0$, i.e.,

virtually in the overall range of the gas loads which are typical for industrial packed columns. Since the relation $\Delta P/\ \Delta P_{\text{Pall rings}} = f\,(S)$ sufficiently fairly correlated data about the nozzles of the various shape and size it can be suggested that this relation is universal for the nozzles of various shape. Evidently application of suggested relation $\Delta P/\Delta P_{\text{Pall rings}} = f(S)$ is of interest first for estimation of ΔP of the nozzles for which experimental data are absent due to various causes. That is in the first place the newly derived nozzles for which only the specific surface is known. Using an information about their geometric surface by the suggested curve it can be obtain a comparative estimation with Pall rings and if it is required using then the curve *1* on the Fig. 3 also a numeral value of ΔP of the dry nozzle.

The relation of hydraulic resistance of non-sprinkle nozzle made of the metal Pall rings of 50 mm size $\Delta P = f(F_f)$ is described by equation (6):

$$\Delta P = 4.9\ F_{\tau}^{2.0}\ . \qquad (6)$$

After substitution $\Delta P_{\text{Pall rings}}$ from equation (6) in (4) and then solving equation (4) relative to ΔP we obtain the relation for computing the value ΔP of any nozzle if its specific surface is known:

$$\Delta P = 4.4 \times 10^{-4}\ S^2\ W_c^2 \gamma. \qquad (7)$$

A dimension of ΔP in equations (4), (6) and (7) is mm H_2O.

Since as a rule the resistance of the dry nozzles is higher the higher is ΔP of the sprinkled nozzle the curves *2* and *3* can be used for preliminary qualitative estimation of ΔP of new nozzle at its sprinkling.

Thus, the obtained general relation enables us to execute the comparative preliminary estimation of new and known industrial nozzles on the basis of their specific surface avoiding the performance of experiments and also a search, and a comparison of experimental data obtained in various environments at different loads, temperatures, pressures etc. are quiet difficult.

A computed estimation of an effect of the nozzle design parameters: equivalent diameter, mass transfer coefficient in gas β_g and liquid phase β_*, according to equations of various authors by the example of Raschig rings is presented in [25]. From computed estimation of the effect of D_{equiv} on the β_g and β_* [25] giving contradicting results of Laptev et al. [25] included that available equations enable calculation of the transfer coefficients in the packed column at a film regime exclusively by results of the hydraulic experiments. We suggest general relation for computed estimation of ΔP and for an increase of the following accuracy of the calculation of the mass transfer coefficients in the packed columns avoiding the additional hydraulic experiments.

REFERENCES

1. Leibenzon, L.S., *Dvizhenie prirodnykh zhidkostei i gazov v poristoi srede* (Movement of Natural Liquids and Gases in Porous Medium), Moscow: Gos. Izd. Tekhniko-teoreticheskoi Literatury, 1947, 244 p.
2. Minskii, E.I., *Dokl. Akad. Nauk SSSR,* 1951, vol. 78, no. 6, p. 409.
3. Aerov, M.E., *Khim. Tekhnol. Topliv Masel*, 1962, no. 9, p. 9
4. Zhavoronkov, N.M., *Gidravlicheskie osnovy skrubbernogo protsessa i teploperedacha v skrubberakh* (Hydraulic Bases of Scrubber Process and Heat Transfer in the Scrubbers), Moscow: Sov. Nauka, 1944
5. Gelperin, I. and Kagan, A., Abstracts of Papers, *3rd Int. Heat Transfer Conference*, Chicago, 1966, p. 38
6. Gel'perin, I.I., Kagan, A.M., and Krinitsina, G.I., *Khim. Prom.,* 1977, no. 2, p. 147
7. Kagan, A.M. and Pushnov, A.S., *Khim. Prom. Segodnya*, 2006, no. 11, p. 30
8. *Flexi ring from KOCH*, Calalog: Koch Engineering, Co., 1986.
9. PNR Patent, 55193.
10. Kagan, A.M., Pal'mov, A.A., and Gel'perin, I.I., *Neregulyarnye metallicheskie nasadki dlya teplo-massoobmennykh protsessov* (Irrelular Metal Nozzles for Heat and Mass Transfer), Moscow: NIITEKhIM, 1985, 18 p.
11. Billet, R., *Packed Column Analysis and Design*, Ruhruniversitat: Bochum, 1989.
12. *Corps de Remplissage*, Catalog: Germania, 1991.
13. *In Use Around the World Tower Packing and Internal by RASCHIG*, Catalog: Raschig Gmbh, 1990.
14. *Fullkorper fur Kdonnew,* Catalog: Raschig Gmbh.
15. *Nutter Ring Random Packing*, Catalog: Nutter, Eng.
16. Gel'perin, I.I., Kagan, A.M., Dil'man, V.V., *et al.*, Abstracts of Papers, *Vsesoyuznaya konferentsiya po aerodinamike khimicheskikh apparatov* (All-Union Conf. on Aerodynamics of Chemical Devices), Severodonetsk, 1981.
17. Pal'mov, A.A., Kagan, A.M., and Gel'perin, I.I., Abstracts of Papers, *2 Vsesoyuznoe soveshchanie po, probleme "Absorbtsiya gazov"* (2nd All-Union Meeting on Gas Absorbtion), Cherkassy, 1983.
18. Pal'mov, A.A., Kagan, A.M., and Gel'perin, I.I., Abstracts of Papers, *V Vsesoyuznaya Konferentsiya po teorii i*

praktike rektifikatsii (5th All-Union Conf. on Theory and Practice of Rectification), Severodonetsk, 1984.
19. Kagan, A.M., Pal'mov, A.A., Yudina, L.A., *et al., Sb. Raboty v oblasti massoobmennykh protsessov za period 1986–90gg. po koordinatsionnomu planu golovnogo predpriyatiya* (Collected Articles on Mass Transfer for Range from 1986 to 1990 According with Parent Interproses Plan), Severodonetsk, 1989.
20. *Intolox High-Performance Separation System*, Catalog: Norton, 1987.
21. *Raudom Packing,* Catalog: Koch Engineering, Co.
22. Kolev, N., Vinkler, K. *et al.*, *Khim. Prom.,* 1986, no. 8, p. 41.
23. Kagan, A.M., Gel'perin, I.I., Dil'man, V.V. *et al., Khim. Prom*., 1992, no. 8, p. 468.
24. Makhotkin, A.F., *Teoreticheskie osnovy ochistki gazovykh vybrosov proizvodstva nitratov tsellyulozy* (Theoretical Bases of Cleaning of Gas Discharge of Cellulose Nitrate Manufacture), Monografiya, Kazan: Izd. Kazan. Iniv., 2003, 268 p.
25. Laptev, A.G., Modeli *pogranichnogo sloya i raschet teplomassoobmennykh apparatov* (Modeling the Boundary Layer and Calculation of Heat and Mass Transfer Devices), Kazan: Izd. Kazan. Univ., 2007, 500 p.

ISSN 1070-4272, Russian Journal of Applied Chemistry, 2008, Vol. 81, No. 9, pp. 1697–1698. © Pleiades Publishing, Ltd., 2008.
Original Russian Text © F.Sh. Khafizov, V.G. Afanasenko, I.F. Khafizov, A.Sh. Khaibrakhmanov, 2008, published in Khimicheskaya Promyshlennost', 2008, Vol. 85, No. 3, pp. 153–155.

PROCESSES AND DEVICES OF CHEMICAL MANUFACTURES

Main Treatment Ways of Manufacturing Water on the Local Plants

F. Sh. Khafizov, V. G. Afanasenko, I. F. Khafizov, and A. Sh. Khaibrakhmanov

State Oil-Engineering University, Sterliramak, Russia

Received October 10, 2007

Abstract—Some water treatment way of industrial water on the local plants are presented herein. An application of the suggested ways allows the treated water to reuse and to optimize operating costs.

DOI: 10.1134/S1070427208090413

Agitation is extensively used in a chemical and a related branches of industry for preparation of emulsions, suspensions, homogeneous systems, and also for enhancing the chemical, heat, and diffusive processes.

Let us consider the agitation as a way for enhancing the chemical, heat, and diffusive processes in the homo- and heterogeneous systems. These processes are applied to absorption, evaporation, extraction, and other chemical technologies because a good mixing of components provides optimum conditions for feeding the substances to a reaction area, an interphase boundary or a heat exchange surface. The enhancing of exchange processes is performed primarily due to [1]:

– increase of phase contact area;

– increase in the speed of relative movement of phases;

– use of nonsteady regimes of an interphase exchange that provide reaching high instantaneous values of mass transfer coefficients;

– executing the mass exchange in hydrodynamically unstationary conditions of the interphase surface.

Ways and selection of devices for agitation are determined by a target of agitation and an aggregate state of mixed materials. The agitation in the liquid media is extensively used in chemical industry [2].

Direct flow mixing of components for concentration equalizing on a cross sectional area normal to a velocity vector is one of the agitation ways in the fluid media. For estimation of an operation efficiency of such devices analogously to mechanic agitators the following characteristic features can be marked:

– energy loss;
– intensity or degree of the agitation;
– agitation efficiency.

ENERGY LOSS

The energy loss of a mechanical agitators is expressed by the driver power consumption that reveals the amount of spent energy for an overcoming the friction force of the agitator blades against a liquid.

In a case of the direct flow agitation a pressure drop on the agitation section of the device including the feed area, the agitator, and an area of stabilizing movement can be assumed as parameter defining the energy loss.

At the agitation of the liquid components in a pipe of the constant cross section the pressure dropped owing to hydrostatic constituent and therefore the energy loss is characterized only by the pressure drop.

THE INTENSITY OF THE AGITATION

Usually the intensity of the agitation is defined by time of reaching the given technological result or at the mechanical mixing by the speed of the agitator at a given duration of the process. The agitation intensity is the higher the smaller is the time spent for reaching of the given agitation result. The enhancing of the agitation results in the decrease of the designing devices and in an output rise. It is required from the economic point of view that the target agitation is reached in the shortest time.

A quantitative estimation of the agitation intensities of the direct flow agitators should be related to the

the given agitation result. The enhancing of the agitation results in the decrease of the designing devices and in an output rise. It is required from the economic point of view that the target agitation is reached in the shortest time.

A quantitative estimation of the agitation intensities of the direct flow agitators should be related to the geometric size of the device. Thus in the pipe of round cross section the agitation intensities can be described by a relation if the pipe diameter to the length of the mixing device section.

THE AGITATION EFFICIENCY

The agitation efficiency of the device expresses the quality of the mixing operation.

For estimation of the agitation efficiency in the general case a dispersion of concentration that is equaled to standard mean square deviation of concentration from an average concentration should be determined [1]:

$$\sigma(t) = \frac{1}{V}\int_V \sqrt{(C(t) - C_{av})^2}\,dV, \qquad (1)$$

where the average concentration is calculated in accordance with:

$$C_{av} = \frac{1}{V}\int_V C\,dV. \qquad (2)$$

For the direct flow agitators the efficiency of the mixing described by the concentration dispersion in an area normal to the velocity vector after the mixing section S:

$$\sigma(x) = \frac{1}{S}\int_S \sqrt{(C - C_{av})^2}\,dS, \qquad (3)$$

where the average concentration is calculated according to:

$$C_{av} = \frac{1}{S}\int_S C\,dS. \qquad (4)$$

A criterion of a nonuniformity in the concentration field for such devices is computed by equation (5)

$$\eta = \frac{\sigma(x)}{\sigma_{max}}, \qquad (5)$$

where

$$\sigma_{max} = \frac{|C_1 - C_{av}|Q_2 + |C_2 - C_{av}|Q_1}{Q_1 + Q_2}. \qquad (6)$$

Deriving the general criterion for the estimation of the efficiency of the direct flow agitator is complicated by considerable distinctions in physicochemical properties of the mixed components and in the requirements to the agitation efficiency for the optimum process operation. The simplest way to compare various devices is to determine a relation of the agitation efficiency to the energy loss for each device at the satisfaction of the requirements of the process to the intensity and efficiency of the agitation.

Thus selection of the apparatus that appropriates to process execution in the optimum way can be made by comparison of the basis parameters describing the direct flow agitator.

USED DESIGNATIONS

σ is the dispersion of concentration;
t is the time, s;
C is concentration in the considered point;
C_{av} is the average concentration;
V is the volume of the mixing section, m^3;
S is the cross sectional area of the apparatus, m^2;
x is the longitudinal coordinate, m;
Q_1, Q_2 are the volume flow, m^3/s.

REFERENCES

1. Sister, V.G. and Martynov, Yu.V., *Printsipy povysheniya effektivnosti teplomassoobmennykh protsessov* (Bases of Enhancing the Efficiency of the Heat and Mass Exchange), Kaluga: Izd. N. Bochkorevoi, 1998.
2. Tsibrovskii, Ya.N., *Osnovy protsessov khimicheskoi tekhnologii* (Bases of the Chemical Engineering), Leningrad: Khimiya, 1967.

ISSN 1070-4272, Russian Journal of Applied Chemistry, 2008, Vol. 81, No. 9, pp. 1699–1704. © Pleiades Publishing, Ltd., 2008.
Original Russian Text © A.G. Laptev, M.I. Farakhov, 2008, published in Khimicheskaya Promyshlennost', 2008, Vol. 85, No. 3, pp. 156–162.

PROCESSES AND DEVICES OF CHEMICAL MANUFACTURES

Model of an Aerosol Removal in Devices with Nozzles

A. G. Laptev and M. I. Farakhov

Engineering Implementation Center "Inzhekhim", Russia
e-mail: info@ingehim.ru, ingehim@kstu.ru

Received May 22, 2008

Abstract—Using stochastic model and an impulse balance in a boundary layer the equations for efficiency computation of the nozzle devices at gas scrubbing from aerosol particles were derived.

DOI: 10.1134/S1070427208090425

INTRODUCTION

The devices for the gas scrubbing from solid and liquid mechanic inclusions are important designing technological devices in chemical, gas and related branches of industry.

Dryers, furnaces, dispersers, pumps, mass and heat exchangers and many other type of equipment can not operate without effective gas scrubbing system. Variety of work conditions and targets necessitates of designing the new removal equipment and of improving their efficiency calculation. Nowadays we have accumulated some experience in solution of these problems. However despite considerable achievements in a theory and a practice of gas scrubbing a series of the problems required new solutions remain.

MATHEMATICAL MODEL

Various theoretical models of a turbulent precipitation of particles on a wall (or a liquid film) of a channels are known. In dependence on the main accepted mechanism these models are divided into five groups:

1) free-inertial subgroup that based on a conception of free inertial ejection of particles from vortexes at the wall;

2) convective inertial subgroup that associates the precipitation with inertial effects at invasion of large vortexes in a boundary layer;

3) rise migration subgroup that associates the precipitation of particles with their rise migration and inertness;

4) effective diffusion subgroup proceeding from a suggestion that a coefficient of turbulent diffusion of the particles is higher than one of a gas in the near-wall region due to the inertness;

5) turbulent migration subgroup that takes into account the turbulent migration of particles to the channel wall caused by a amplitude gradient of pulse cross component of a gas speed.

The turbulent inertial mechanism is the most significant for an experience of the gas scrubbing from a fine dispersion phase. It is assumed that in this case all particles on the distance of the length of an inertial path $l_p = \frac{u_p d_p^2 \rho_p}{18\mu_g}$ are precipitated on the wall and their initial velocity corresponds to quadratic mean velocity of turbulent pulsations $u_p = 0.9u^*$.

It should be noted that a movement of particles in crosswise direction within a flow core occurs due to the turbulent pulsations (turbulent migration mechanism) and near the wall due to decaying turbulent pulsations in the boundary layer (inertial mechanism).

An intensity of the turbulent precipitation is described by the precipitation velocity (by turbulent migration of the particles, m/s): $u_t = j/n$, that is, by amount of the particles precipitated on unit surface for unit time.

It is assumed [1, 2] that for approximate estimation of the intensity of the particle separation on the channel wall (film) concentration of the dispersed phase in the distance from the walls (out of the boundary layer) resulting from turbulent mixing is determined exclusively by the turbulent migration and diffusion.

Let us consider a derivation of the equation for computation of an efficiency of the aerosol removal for nozzle separators. Due to various ways the separation of the dispersed phase occurs when gas with the dispersed particles flows over elements of a nozzle. A film on the nozzle is formed at the liquid aerosol removal.

The turbulent migration affects the non-inertially dispersed particles in the turbulent flow. The inertially dispersed particles do not depend on lines of the liquid stream, they are not entrained by the turbulent pulsation of a medium thus their motion can be considered as rectilinear. The precipitation efficiency of the inertial dispersed particles on the nozzle is determined mainly by their geometrical size. The weak inertial particles can be divided into two groups: (1) the particles that reach the nozzle surface and precipitate in a relaxation time, and (2) the particles entraining by the gas flow. The precipitation efficiency of the second group can be estimated by the following procedure [1, 3].

Let for a time dt the gas flow with the dispersed particles pass a way $dz = u_{av}dt$ and thereby the particle concentration is changed to dn. Then an amount of particles precipitated on the nozzle is

$$dN = -V_g dn dt = -u_{av} S dn dt . \quad (1)$$

For the time dt the nozzle surface is only reached by the particles that are located at a distance not greater then $dr = u_t dt$, thus all particles in the volume dV of a cone of $2dz$ height precipitate on the wall of the section dz.

$$dN = ndV = n\,2\pi R dr dz u_{av} u_t dt^2. \quad (2)$$

If we equate right sides of the equations (1) and (2) and take into account that $V_g = u_{av}\pi R^2$ we can obtain

$$\frac{dn}{n} = -\frac{2u_t}{R}dt = -\frac{4u_t}{d}dt , \quad (3)$$

where R is a channel radius; d is a channel diameter, m.

After an integration of equation (3) with an initial condition $n = n_0$ at $t = 0$ in a range from $t = 0$ to $t = L/u_{av}$ we obtain an equation for calculation of a numerical concentration of the particles in the gas flow at a distance L:

$$n = n_0 \exp\left(-\frac{4}{du_{av}}\int_0^L u_t\, dz\right), \quad (4)$$

or at $u_t = \text{const}$

$$n = n_0 \exp\left(-\frac{4\,Lu_t}{du_{av}}\right) \approx n_0 \exp\left(-\frac{4\,u_t}{d}t_{av}\right) , \quad (5)$$

where $t_{av} \approx L/u_{av}$ is an average residence time.

A part of precipitated particles or the removal efficiency of the weak inertial particles can be expressed by a value of the efficiency of the turbulent precipitation [1, 2]

$$\eta_t = \frac{n_0 - n}{n_0} = 1 - \exp\left(-\frac{4\,Lu_t}{du_{av}}\right). \quad (6)$$

As noted in [1, 2] the exponential dependences of the removal efficiency on the channel length identical to Eq. (6) in form were obtained and used for the efficiency computation of electrostatic precipitators, centrifugal separators, plate dust collectors, Venturi scrubber and other devices with high agitation intensities. The obtained equations are in well accord with an energy theory of wet dust collecting and with results of experimental research.

DETERMINATION OF MODEL PARAMETERS

For computation of the reduced turbulent precipitation velocity $u_t^+ = \frac{u_t}{u^*}$ related to the relaxation time of the particle velocity some empiric and semi-empiric expressions can be stated.

$$\tau_r = \frac{d_p^2 \rho_p}{18\ \mu_g} = \frac{d_p^2 \rho_p}{18 \rho_g \nu_g} , \quad (7)$$

where τ_r is the relaxation time, s.

A dimensionless relaxation time is written as:

$$\tau^+ = \frac{\tau_r u_*^2}{\nu_g} . \quad (8)$$

In [1, 2] the following formulas of various authors are presented:

(1) Liu and Agarwal at $\tau^+ < 10$

$$u_t^+ = 6 \times 10^{-4} (\tau^+)^2 . \quad (9)$$

(2) Mc Coy and Hanratty

$$u_t^+ = 3.25 \times 10^{-4} (\tau^+)^2 \text{ at } \tau^+ \le 22.9, \quad (10)$$

$$u_t^+ = 0.17 \text{ at } \tau^+ > 22.9. \quad (11)$$

(3) Uzhov and Mednikov:

$$u_t^+ = 7.25 \times 10^{-4}\, k \text{ at } k \le 16.6, \quad (12)$$

$$u_t^+ = 0.2 \text{ at } k > 16.6, \quad (13)$$

where

$$k = \left[\frac{\tau_r\, u_*^2}{\nu_g} \left(1 + \frac{\tau_r\, u*}{0.05 d_{equiv}} \right)^{-1} \right]^2. \quad (14)$$

It is evident from equations (9)–(14) that the separation velocity u_t considerably depends on the dynamic velocity value $u*$ or a tangential stress $\tau_w \left(u* = \sqrt{\frac{\tau_w}{\rho_g}} \right)$.

Taking into account a presence of the aerosols in the gas flow at the movement in the channel of various forms we obtain analytically an equation for computation of the dynamic velocity. For this end we use conservative properties of the boundary layer thereby an effects of aerosols and other perturbations can be considered by a parametrical satisfaction to an impulse balance [3, 4].

In applied aero- and gas dynamics for computation of a friction resistance and a heat exchange of bodies with a various surface curvature a technique of an effective wave is employed. In this case an effect of a pressure gradient caused by the curvature of the streamline surface is taken into account by fitting the effective length if thicknesses of the energy losses of gradient and non-gradient boundary layers are equal. At the predetermined effective length characteristics of the boundary layer with the pressure gradient are calculated by appropriate formulas for a flat plate.

This approach based on known properties of conservatism of friction laws within the boundary layer at the presence of the longitudinal pressure gradient in particular on the property that a structure of a mathematical description of elementary act of transfer is invariant with respect to various perturbations and to an apparatus scale. These perturbations do not change the structure of the mathematical description of the boundary layer that enables their parametric consideration. Thus as a theoretical basis for calculation of the average value of dynamic velocity mathematical models can be used of a flat boundary layer avoiding the perturbations (e.g., Karman or Landau–Levich model) and an effect of the various perturbations (the pressure drop, a rough surface, a presence of the dispersed phase) can be considered by integral relations of the impulse balance.

An impulse flow in the turbulent boundary layer is written in a known form:

$$\tau = \rho (\nu + \nu_T) \frac{du}{dy}, \quad (15)$$

where for a turbulent exchange coefficient $\nu_T(y)$ in the viscous sublayer various power functions are used, and out of this sublayer linear functions. For example, according to three layers model a function in the following form is used:

$$\nu_T = \chi\, u_*\, y - \nu, \quad (16)$$

where $\chi = 0.4$ is Prandtl number, σ is a lateral coordinate.

From relations (15), (16) a derivative value follows:

$$\frac{du}{dy} = \frac{u_*}{\chi y}. \quad (17)$$

As it is well known an integration of equation (17) gives a logarithmic distribution of a velocity profile in the turbulent region of the boundary layer.

The tangential stress in the turbulent boundary layer is also written by an averaged values of fluctuating velocity constituents v', and $u'\tau = \rho \overline{u'v'}$.

Hence an average density of the power flow looks like $e = \rho\, u\, \overline{u'v'} = u\tau_w$.

The power flow decreases as it nears to the surface due to an energy dissipation. The derivative de/dy causes the energy dissipation in the unit volume of the medium

$$\varepsilon = \frac{de}{dy} = \tau \frac{du}{dy}. \quad (18)$$

This relation is extensively used for calculation of the dynamic velocity in the turbulent flows when application of other techniques of the calculation of $u*$ is difficult.

If we write the derivative value du/dy in equation (18) as (17) we obtain:

$$\varepsilon = \frac{\rho_g}{\chi\, y} \left(\frac{\tau}{\rho_g} \right)^{\frac{3}{2}} = \frac{\rho_g u_*^3}{\chi\, y}. \quad (19)$$

where ε is a local velocity of the energy dissipation. Evidently at some value of $y = \delta_e$ the local energy dissipation ε will coincide with an average bulk dissipation, thus $\varepsilon = \overline{\varepsilon}$ at $y = \delta_e$.

Let us use an approach from an applied aerodynamics when for determination of some effective length demanding for calculation the average tangential stress

on the surface of the complex geometry the conditions of the equality for the energy loss thicknesses of the gradient and non-gradient boundary layers are written. By this approach we determine thickness value δ_e.

From relation (19) the dynamical velocity value at $y = \delta_e$ is expressed as

$$u_* = \left(\frac{\bar{\varepsilon} \chi \delta_{equiv}}{\rho_g} \right)^{\frac{1}{3}}. \quad (20)$$

In equation (20) main parameters are a velocity of the energy dissipation $\bar{\varepsilon}$, and the thickness of the boundary layer δ_e. The average energy dissipation is found by using the pressure drop in the channels obtained experimentally taking into account the presence of the dispersed phase. An average thickness of the boundary layer is found from the impulse balance.

A resistance to the impulse transfer is written as [3, 4]:

$$\frac{1}{\gamma} = \frac{\rho_g \Delta \bar{u}_\infty}{\tau} = \int_0^{\delta_{equiv}} \frac{dy}{\nu + \nu_T(y)}. \quad (21)$$

where γ is the coefficient of the impulse transfer, m/s; $\Delta\bar{u}_\infty$ is an average driving force of the impulse transfer, m/s.

Assuming the three layers model of the turbulent boundary layer the characteristics of the turbulent transfer is written in the known form taking into account the pulsation dumping in the viscous sublayer (Dissler function):

$$\frac{\nu_T}{\nu} = (0.124\, y^+)^4 \text{ at } y^+ \le 6, \quad (22)$$

$$\frac{\nu_T}{\nu} = \frac{y}{5} \text{ at } 6 < y^+ \le 30, \quad (23)$$

$$\frac{\nu_T}{\nu} = \frac{y}{2.5} - 1 \text{ at } y^+ > 30. \quad (24)$$

Where $y^+ = yu_*/\nu$ is the dimensionless coordinate in the boundary layer.

The resistance to impulse transfer from equations (21)–(24) looks like

$$\frac{1}{\gamma} = \int_0^{\delta_1} \frac{dy}{\nu + \nu(0.124\, y^+)^4} + 5 \int_{\delta_1}^{\delta_2} \frac{dy}{u_* y} + 2.5 \int_{\delta_2}^{\delta_{equiv}} \frac{dy}{u_* y}, \quad (25)$$

where $\delta_1 = 6\nu/u_*$ is the viscous sublayer thickness, m; $\delta_2 = 30\nu/u_*$ is a buffer area thickness of the boundary layer, m.

After an integration of (25) we have obtained:

$$\gamma = \frac{u_*}{13.73 + 2.5\left(\ln\delta_{equiv} - \ln\frac{30\nu}{u_*} \right)}. \quad (26)$$

The boundary layer thickness was found using the flow relation

$$\tau = u_*^2 \rho_g = \rho_g \gamma \Delta \bar{u}_\infty, \quad (27)$$

thereof with the impulse transfer coefficient (26) the following was obtained:

$$\delta_{equiv} = \exp\left[\frac{1}{2.5}\left(\frac{\Delta\bar{u}_\infty}{u_*} - 13.76 + 2.5 \ln\frac{30\nu}{u_*} \right) \right]. \quad (28)$$

In equations (27), (28) $\Delta\bar{u}_\infty$ is the average driving force of the impulse transfer $\Delta\bar{u}_\infty = u_\infty \pm w_p$. A liquid velocity on the interphase surface of a film that is formed on the surface of a separator contact devices is bound with the film thickness and the liquid flow.

Thus set of equations (20), (28) that is solved by an iteration technique was obtained. The average value of the dynamic velocity and the thickness of the turbulent boundary layer are the solution result.

The average energy dissipation in equation (20) is written with introducing the pressure drop:

$$\bar{\varepsilon} = \frac{\Delta PS u_{av}}{V_l} = \frac{\Delta PG}{V_l \rho_g}, \quad (29)$$

Performed test of the mathematical model adequacy revealed a satisfactory agreement of the computed results to the dynamic velocity in the pipe and to the boundary layer thickness on the plate. Comparison of the results obtained with accordance to the known formulas for the pipe and the plate reveals a divergence ±(5–7)%. Therefore an obtained equation set for calculation of the dynamic velocity can be used for the flows with the various perturbations that are taken into account by keeping of the impulse balance, i.e. in the flow relation of the impulse transfer thereby the pressure drop of the apparatus operation area should be used as experimental information about the subject.

Many calculations of u_* for the nozzle separators are generalized with ±18% by a simple equation looking

like

$$u_* = 1.8\left(\frac{\varepsilon \nu_g}{\rho_g}\right)^{1/4} = 1.8\left(\frac{\Delta P u_{av} \nu_g}{L \rho_g}\right)^{1/4}. \quad (30)$$

THE CALCULATION OF THE REMOVAL EFFICIENCY

From (7), (8) and (30) we obtain the dimensionless relaxation time:

$$\tau^+ = 0.18 \frac{d_p^2 \rho_p}{(\rho_g \nu_g)^{1.5}} \sqrt{\frac{\Delta P u_{av}}{L}}. \quad (31)$$

It was established by computations that for meeting the conditions (9) ($\tau^+ < 10$) the particle size in the nozzle separator must be less than 10 μm (Fig. 1). The dimensionless relaxation time of the particles of 0.1 μm size is very small.

The velocity of the turbulent precipitation of the particles for the nozzle separators is expressed as

$$u_t = 0.36\ \text{Ч}10^{-4} \frac{d_p^4 \rho_p^2}{\nu_g^{2.75} \rho_g^{3.25}} \left(\frac{\Delta P u_{av}}{L}\right)^{\frac{5}{4}}, \quad (32)$$

where u_t was written using equation (9).

Using equation (9) we can determine the value of the removal efficiency according to equation (6) in the nozzle apparatus for small particles. We obtain:

$$\eta_t = 1 - \exp\left[1.40 \times 10^{-4} \frac{d_p^4 \rho_p^2 \Delta P^{1.25}}{\nu_g^{2.75} \rho_g^{3.25} d_{equiv}} \left(\frac{u_{av}}{L}\right)^{0.25}\right]. \quad (33)$$

The removal efficiency of large particles regarding equations (6) and (11) (or (13)) is:

$$\eta_t = 1 - \exp\left[-1.44 \frac{1}{d_{equiv}} \left(\frac{L}{u_{av}}\right)^{0.75} \left(\frac{\Delta P \nu_g}{\rho_g}\right)^{0.25}\right]. \quad (34)$$

Equations (33) and (34) enable us to quickly estimate in an explicit form an effect of regime, design features, and physical properties of the gas flow with aerosol particles to the removal efficiency in the apparatus with various nozzles.

Computed results of the removal efficiency of the small and large droplets in the apparatus with Raschig rings and Inzhekhim-2000 nozzles [3] are showed in Figs. 2–4.

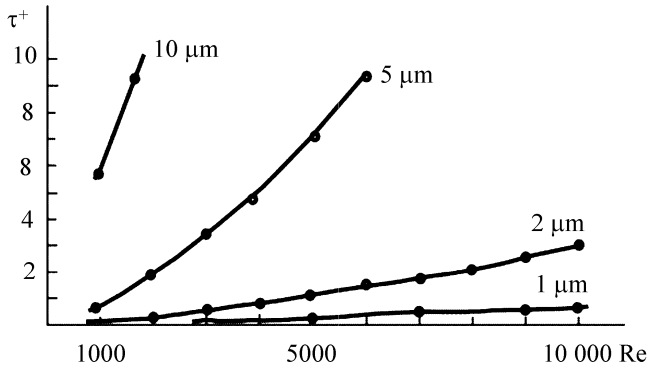


Fig. 1. A dependence of the dimensionless relaxation time on Reynolds number in the nozzle separator with Raschig rings. An operation medium is air-water droplets, d_e = 0.015 m, u_{av} = 1–10 m/s, L = 1 m.

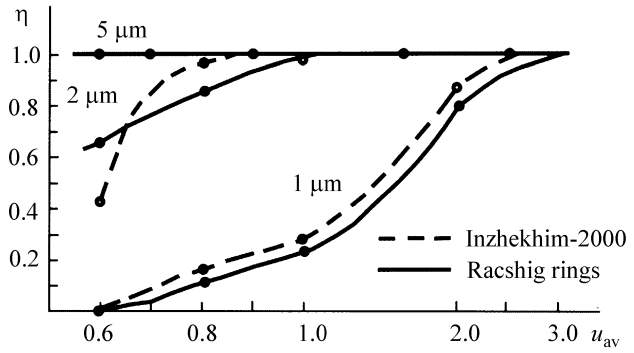


Fig. 2. Dependence of the removal efficiency on the average velocity of the gas flow for particles of a various size. A working media is air–water droplets, d_e = 0.015 m, L = 1 m.

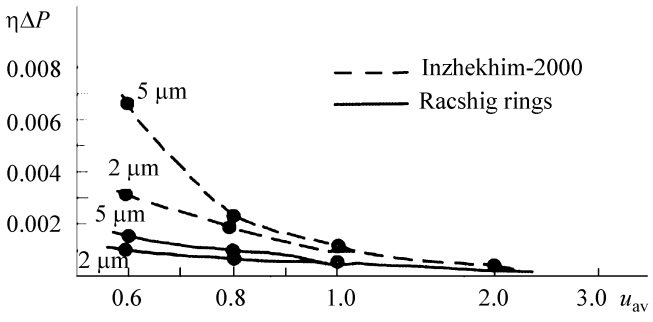


Fig. 3. A relation of the removal efficiency to hydraulic nozzle resistance in a dependence on a fictitious gas velocity.

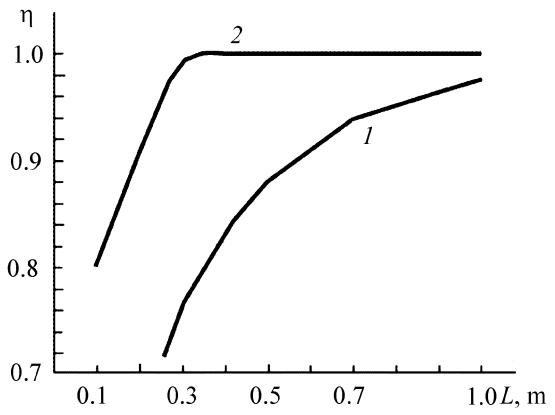


Fig. 4. Dependence of the removal efficiency on the channel length for the large droplets A working media is air, $u_{av} = 2$ m/s, $L = 0.1 \ldots 1$ m, $d_e = 0.015$ m. (*1*) swirling flow motion; (*2*) flow motion in the nozzles.

The removal efficiency in the apparatus with Inzhekhim-2000 nozzles is higher then in the apparatus with Raschig rings. Fig. 4. shows that at a swirl phase motion the removal of the dispersed phase is lower by 6–40% (in dependence on the channel length) than at the removal by the nozzles.

It should be noted that the removal efficiency of the particles with size less than 1 μm is sufficiently small. General removal efficiency of the large and small particles can be calculated in accordance with an additive equation.

The developed mathematical model of the aerosol removal enables estimating the efficiency of nozzles at an improvement and designing of the separators.

USED DESIGNATIONS

u_p is the particle velocity, m/s;
u_{av} is the average gas velocity, m/s;
u_* is the dynamic friction velocity, m/s;
d_p the particle diameter, m or μm;
ρ_p is the particle density, kg/m^3;
ρ_g is gas density, kg/m^3;
μ_g is the dynamic gas viscosity, Pa·s;
n_0 is initial concentration of the particles, 1/m^3;
d_e is equivalent channel diameter, m;
L is the channel length, m;
G is the mass gas flow, kg/s;
V_1 is the operative separator volume, m^3;
ν_g is cinematic gas viscosity, m^3/s;

REFERENCES

1. Mednikov, E.P., *Turbulentnyi perenos i osazhdenie aerozolei* (Turbulent Transfer and Precipitation of Aerosols), Moscow: Energiya, 1980, 176 p.
2. Sugak, E.V., Voinov, N.A., and Nikolaev, N.A., *Ochistka gazovykh vybrosov v apparatakh s intensivnymi gidrodinamicheskimi rezhimami* (Outburst Cleaning in Devices with Intensive Hydrodynamic Regimes), Kazan: RITs "Shkola," 1999, 222 p.
3. Laptev, A.G. and Farakhov, M.I., *Razdelenie geterogennykh sistem v nasadochnykh apparatakh* (Removal of Heterogeneous Systems in Nozzle Devices), Kazan: KGEU, 2006, 342 p.
4. Laptev, A.G., *Modeli pogranichnogo sloya i raschet teplomassoobmennykh protsessov* (Boundary Layer Model, and Heat and Mass Exchange Computation), Kazan: Izd. Kazan. Univ., 2007, 500 p.

ISSN 1070-4272, Russian Journal of Applied Chemistry, 2008, Vol. 81, No. 9, pp. 1705–1709. © Pleiades Publishing, Ltd., 2008.
Original Russian Text © F.F. Mozheiko, T.N. Potkina, I.I. Goncharik, 2008, published in Khimicheskaya Promyshlennost', 2008, Vol. 85, No. 4, pp. 193–199.

PROCESSES AND DEVICES OF CHEMICAL MANUFACTURES

Effect of Inhibitors on Corrosion Resistance of Carbon Steel in Suspensed Liquid Combined Fertilizer

F. F. Mozheiko, T. N. Potkina, and I. I. Goncharik

Institute of General and Inorganic Chemistry, Belarusian Academy of Science, Minsk, Belarus
e-mail: potkina@igic.bas-net.by

Received May 15, 2008

Abstract—Inhibitors against corrosion of metal surfaces in salt solutions, especially of carbon steel in reference 5% NaCl solution and in suspension fertilizer were selected. We examined a corrosion kinetics, effect of corrosion protection, and also a penetration and a corrosion depth in the presence of various inhibitors.

DOI: 10.1134/S1070427208090437

An efficiency of suspension liquid combined fertilizers (SLCF) is verified by a long-term scientific and practical experience in agriculture. The application of a solid mineral fertilizers does not ensure the homogeneous mixture and its uniform input in soil that leads to an excess consumption of fertilizers, decrease in crop, and an environment pollution. From the point of view expressed [1−3] main requirements to the mineral fertilizers areas follows: increase of concentration of nutrient species, input of necessary micro and macro elements in one operation, an uniform distribution over the area could be satisfied exclusively using SLCF.

We have developed a stable SLCF on the basis of a phosphorite flour, ammophos, carbamide, ammonium sulfate, calcium chloride [4]. These are saturated salt polydispersed solutions in which small particles of soluble and unsoluble salts, stabilizing agents and other materials are dispersed. Due to the presence of the solid particles and also of the concentrated salt solutions in the suspensions their abrasive and corrosion properties increase that leads to an equipment wear at manufacturing, transport, and storing of fertilizers. Despite the noted difficulties the suspensions are the most desired combined fertilizer as confirmed by the international practice.

For establishing of conditions of storage, transport, and input of the suspension fertilizers their corrosion activity schould be studied.

A sheet carbon steel that is applied in the production of bunkers, settlers, flotation devices, crystallizers, screens, cyclones etc. at a potassium chloride manufacturing [5] was selected for an examination. Samples of non-activated steel prepared in the form of 60 × 35.1 × 1 mm plates were used that were preliminary mechanically cleaned, degreased by acetone and then by hexanone, dryed, and weighted. A metal density was 7.87 g/cm^3. Corrosion examinations were carried out at room temperature in polyethylene vessels of 500 cm^3 capacity containing either 5% NaCl (a control experiment) or with addition of the corrosion inhibitors of different concentrations. All solutions were prepared using a distilled water. A weight loss of the samples was defined after removing the corrosion products. A corrosion rate was computed according to the following formula:

$$V_o = \frac{G_r - G_c}{F} 10^4 \times \frac{1}{T},$$

where G_γ is the sample weight before immersion in the solution, g; G_c is the sample weight after the corrosion during in T days; F is a sample area, cm^2; T is a number of days of inhibitor action.

A value of the corrosion protective effect of the inhibitor was computed in accordance with [6] by the formula:

$$Z = [(V_0 - V_1) / V_0] \times 100,$$

where V_0 and V_1 are corrosion rates without inhibiting additive and in its presence.

According to the state standard GOST 13819-68 a corrosion resistance is measured by a thickness of a cor-

Table 1. Results of the corrosion experiments of the carbon steel in the urea solutions with 5% NaCl at the room temperature in dependence on time (a daily agitation)

Urea concentration, %	Corrosion rate, g/(m^2 day)							Penetration, mm/year	Resistance
	days								
	7	14	21	30	35	42	Average		
–	1.44	1.42	1.29	1.26	1.24	1.26	1.32	0.061	5
2.5	1.35	1.30	1.18	1.12	1.11	1.10	1.19	0.055	5
5.0	1.13	1.12	1.03	1.06	1.03	1.04	1.07	0.049	5
10.0	1.06	1.00	0.94	0.98	0.96	0.95	0.98	0.045	4
15.0	0.84	0.89	0.85	0.87	0.86	0.90	0.87	0.040	4
20.0	0.78	0.84	0.80	0.74	0.78	0.83	0.80	0.037	4
25.0	0.78	0.88	0.84	0.81	0.79	0.81	0.82	0.038	4

Table 2. Values of the corrosion protection effect of the urea

Urea concentration, %	Corrosion protection effect in days					
	7	14	21	30	35	42
2.5	6.42	8.74	8.66	11.37	10.42	12.48
5.0	21.51	21.18	20.37	16.34	17.24	17.27
10.0	26.08	29.44	27.45	22.55	22.92	24.01
15.0	41.75	37.41	34.40	30.94	30.85	28.58
20.0	45.89	41.68	38.21	40.96	36.97	33.87
25.0	45.53	37.78	34.73	36.06	36.49	34.97

roded metal that is defined as the penetration and is expressed in mm per year. A resistance groups are used at a rough estimation, and points at more exact estimation. The metal weight loss is converted in the penetration (the depth value) according to [7] by the formula:

$$\Pi = \frac{8.76 \times K}{\gamma},$$

where Π is the penetration, mm/year; γ is the metal density, g/cm^3; K is the weight loss, g/(m^2·h).

Since the suspension combined fertilizers represents polydispersed saturated salt solutions of urea, potassium chloride, ammophos, ammonium sulfate, an influence of these components upon the carbon steel corrosion should be studied. Results of examinations on the corrosion protection of the steel by the urea are presented in Tables 1 and 2.

The obtained data shows that the urea application decreased the corrosion of the carbon steel, thus the urea reveals inhibiting action relative to the steel. However the corrosion under the action of NaCl solution preoceeds more actively in first 7−14 days and further some decrease in the rate occurs, and the corrosion rate decreases after 21 days (Table 1).

The corrosion protective effect of the urea at 25% concentration of its solutions that approximately corresponds to its content in the suspension, within 42 days on the average is 34−39.6%, within first 7 days 41.7−46%. The penetration equals to 0.041–0.045 mm/year, that is the corrosion resistance of the steel 4. The protective inhibiting action of the urea from a chloric corrosion was established earlier by a stainless steel [8]. Hence the urea use as one of the species of SLCF causes a significant decrease in the corrosion rate of the applied steel equipment at a manufacturing of the suspension fertilizer.

On the contrary a negative influence of the ammophos solutions upon steel occurs that seems unlikely on first sight since compounds of the phosphoric acid are considered as corrosion inhibitors. The ammophos is a double nitrogen phosphor fertilizer, a monoammonium phosphate with an admixture of diammonium phosphate, and compounds of the ammonium salts are as well-known to react with iron forming water insoluble ferroammonium phosphates looking like a uniform film that covers a surface of the steel plates and can be easily washed away. After first 7 days the corrosion rate in the ammophos suspension reaches 10.2−14.1 g cm^{-2} day^{-1}, hereinafter it gradually decreased. The average corrosion value in 35 days, and also the corrosion depth that in concentrated ammophos suspension reached a value of 0.504−0.512 mm/year corresponding to the low group of the metal resistance were measured. Based on the presented data an application of the ammophos as a basic solution for obtaining suspension fertilizers must be restricted.

An influence of the ammonium sulfate solutions upon the corrosion resistance of the steel results in the decrease of the corrosion rate in diluted solutions. In the concentrated solutions of the ammonium sulfate starting from 10% concentration due to decrease of an ammonium sulfate ionicity and reaction with iron ions the steel corrosion essentially falls (0.11 g/m^2 day^{-1} during 22 days).

Hence the presence of the concentrated solutions of the ammonium sulfate in the suspension combined fertilizer also promotes the corrosion protection of steel parts.

The influence of the suspension fertilizer of various compositions (1, 2, 3) upon the corrosion characteristics of the steel was studied.

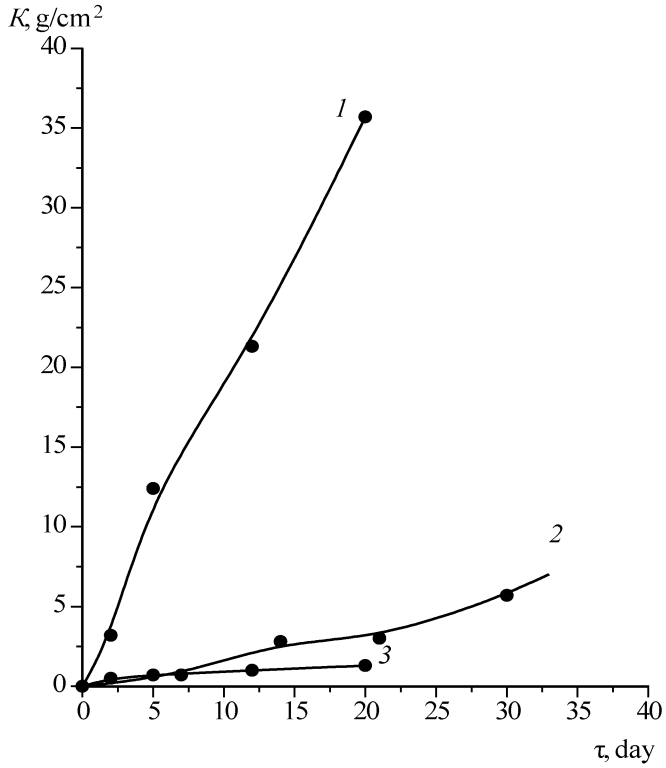
Composition of the fertilizer 1 is phosphoric flour, ammonium sulfate, ammophos, potassium sulfate in a ratio 9.6:5.6:11.3 % (by dry species). A bentonite clay used as stabilizer is 4 wt% (for all compositions).

Composition of the fertilizer 2 is phosphoric flour, urea, ammophos, potassium chloride in a ratio 10:10.7:8.8%.

Composition of the fertilizer 3 is phosphoric flour, ammonium sulfate, potassium chloride in a ratio 9.4:6.6:12.7%.

Experimental data are presented on the figure. The figure shows that the suspension including carbamide (2) is characterized by lesser corroding action on the steel. The corrosion rate in 5−7 day is 0,10 g/m^2 day. This value corresponds to the corrosion penetration of 0.005 mm/year. Thus the steel in these suspensions is considered as sufficiently resistant with the corrosion resistance of the steel 2 points.

Among the various ways of the metal corrosion protection an application of the corrosion inhibitors: (chemical compounds or their various compositions that in the sufficient concentrations can decrease the corrosion rate of metals), acquires more significance. The inhibitor action is associated with a change of a protected surface state. This can occur due to an adsorption or formation of in soluble compounds with cations of metals. These compounds reduce the active surface area of metals and increase an activation energy of the corrosion. A search of the new high effective inhibitors should be considered as an important problem although nowadays some thousands of substances and their mixtures were tasted.



Corrosion curves of the steel in the SCF of the compositions 1, 2, 3.

An effect of some inhibitors contained in liquid compositions for cold phosphatizing on a chemical corrosion of steel in chloride solutions was studied. Obtained results are presented in Tables 3 and 4.

The presented data show that all studied inhibitors excepting an ammonium molybdate reveal in either measure anticorrosive properties. Thereby the corrosion rate in the corroding solutions gradually decreased with an increase in the residence time of the samples. The best inhibitors are compounds of zinc then sodium silicate,

Table 3. An effect of a concentration of the inhibitors on the chemical resistance of the carbon steel in 5% NaCl

Inhibitor	Concentration, %	pH	Corrosion rate, g/(m^2 day)						Penetration, mm/year	Resistance
			days							
			8	15	8-15	22	15-22	average		
Na_3PO_4	0.05	9.3	4.76	3.07	1.14	2.46	1.16	2.51	0.11	6
Na_3PO_4	0.25	10.4	2.64	1.93	1.11	1.76	1.40	1.77	0.08	5
Na_3PO_4	1.0	11.9	1.08	0.92	0.73	0.95	1.02	0.94	0.043	5
$Zn(NO_3)_2$	1.0	5.9	0.3	0.15	0.27	0.24	0.42	0.22	0.01	3
Na_2SiO_3	1.0	10.5	0.71	0.60	0.51	0.46	0.21	0.50	0.02	4
$(NH_4)_2MoO_4$	1.0	5.7	3.01	1.96	1.05	2.47	3.46	2.39	0.12	6

Table 4. Values of the carbon steel corrosion protection by the action of the inhibitors in the 5% NaCl

Inhibitor	Concentration, %	Corrosion rate, g/(m^2 day), and protection effect, %					
		7		15		22	
		V_1	Z	V_1	Z	V_1	Z
Na_3PO_4	1.0	1.08	10.7	0.92	22.8	0.95	16.1
$Zn(NO_3)_2$	1.0	0.03	97.6	0.15	87.2	0.24	78.5
Na_2SiO_3	1.0	0.71	47.3	0.60	49.6	0.46	59.0
$Na_2B_4O_7$	0.25	1.23	8.40	1.23	8.30	–	–
$Na_2B_4O_7$	0.5	1.17	13.00	1.24	9.80	–	–
NaCSN	0.25	0.92	31.50	0.929	21.90	–	–
NaCSN	0.5	0.89	33.90	0.95	20.10	–	–

thiocyanates, sodium phosphate, sodium tetraborate. The corrosion penetration for zinc nitrate is 0.01 mm/year, for sodium silicate 0.02 mm/year. The positive action of the studied inhibitors was caused by both their capability to iron passivation by dissolved oxygen and their capability to form layers of corrosion products, e.g. by ferric and ferrous phosphates in Na_3PO_4 solutions or similar compounds in the sodium silicate solutions or complex compounds of iron with zinc ions. The formed layers of the corrosion products on the iron surface represent effective, anticorrosion, protective diffusive barriers. The protective effect of the corrosion, for instance of the zinc nitrate, in first 8 days of keeping of the steel in NaCl solutions is 97.6%, in sodium silicate solutions 47.3% (Table 3).

A production of inhibitors does not satisfy all industry requirements. An application of waste and inexpasive products of chemical industry is a promising way for extending the amount and decreasing the cost of the corrosion inhibitors.

A phosphate mud (IDG-1 and IDG-3) formed at the phosphatizing the metal surface before a painting was studied as inhibitors for decreasing the corrosion effect of electrolytes on the carbon steel. The zinc and iron phosphates are contained in the chemical composition of the mud. A thin dispersed steady suspension is formed in the salt solution. A presence of the zinc in the inhibitor composition permits a formation of a steady non-porous protective film of the zinc phosphate that promotes an essential decrease in the corrosion of steel devices. Values of the corrosion protective effect of the phosphate mud are presented in Table 5. The inhibitor of 1.0–1.5 wt% provides the corrosion protection 92–93%. Increased inhibitor feed is not required.

Table 5. The corrosion protection of the steel by the phosphate mud

Amount of inhibitor, mas% to NaCl	Corrosion protection effect, %				
	days				
	7	14	21	28	68
0.3	5.8	19.4	30.1	35.5	32.2
0.45	11.4	23.9	40.8	52.0	48.9
0.75	20.9	58.5	85.6	92.1	90.5
1.50	21.7	60.8	87.5	93.4	92.0
2.25	16.1	66.4	87.5	90.6	88.3
3.00	14.3	64.6	84.6	89.8	86.4
3.75	15.2	63.1	84.8	89.6	87.1

IDG-3 (a nitrite–soda melt, "Khimvolokno", Grodno, Ukraine) is a mixture of water-soluble inorganic salts crashed to grains of 10 mm size. pH number of the obtained solution is 8–9. A thin protection film that does not penetrate deep into the steel due to adsorption of nitrate and nitrite ions on the active centers is formed on the metal surface at the application of the melt of the inorganic salts as the inhibitor. An introduction of 2.5–3 wt% IDG-3 in the salt solution significantly decreases the corrosion rate of the steel devices and provides the high value of the corrosion protective effect of the inhibitor on the steel (87–92 %) (Table 6).

Table 6. The values of the corrosion protective effect of the inhibitor (the nitrite–soda melt) on the steel

Amount of inhibitor, mas% to a salt	Corrosion rate, g/(m^2 day)	Protection effect, %
–	5.52	–
0.75	3.06	44.6
1.50	1.95	64.7
2.25	0.81	85.3
2.70	0.56	89.9
3.00	0.44	92.0

The corrosion protection of a metal in result of an introduction of the inhibitor, e.g. the phosphate mud, in the fertilizer 1, is 88%. Thus, we show that the urea using as raw component of SCF, sodium silicate, or liquid glass, using in the phosphate flour manufature as a reagent, the phosphate mud (the zinc and iron phosphate), the nitrite–soda melt, the ammonium and sodium phosphates, sodium thiocyanate are the most efficient compounds studied as the inhibitors of the corrosion for an industry.

CONCLUSIONS

1. High anticorrosion effect of the urea on the steel in the presence of the chorine ions was manifested. The concentrated ammonium sulfate solutions effect similarly on the steel.

2. The phosphate mud and the nitrite–soda melt which are waste products are suggested as the corrosion inhibitors.

3. In the conducted study the carbon steel in the suspension fertilizers containing the urea reveals the sufficient resistance for employing this steel as a structural material of the equipment for the fertilizer preparation and storing without specific corrosion protection.

REFERENCES

1. Kochetkov, V.N., *Proizvodstvo i primenenie zhidkikh kompleksnykh udobrenii* (Manufactireing and Application of the Liquid Combined Fertilizers), Moscow: Agropromizdat, 1986, 296 p.
2. Briedis, P.Kh. and Birgelis, A.Ya., *Zh. Vses. Khim. Obshch. im. D.I. Mendeleeva*, 1987, vol. 32, no. 4, p. 416.
3. Postnikov, A. V. and. Efremova, L. N., *Khimiya v sel'skom khozyaistve* (Chemistry in Agriculture), 1992, no. 3, p. 28.
4. Mozheiko, F.F., Korshuk, E.F., Potkina, T.N., and Goncharik, I.I., *Doklady Nat. Akad. Nauk Belarusi*, 2007, no. 1, p. 53
5. Teterevkov, A.I. and Pechkovskii, V.V., *Oborudovanie zavodov neorganicheskikh veshchestv i osnovy proektirovaniya* (Equipment of the Neorganic Substances Manufatures and Designing Priciples), 1981, 335 p.
6. *Korrozionnaya stoikost' oborudovaniya khimicheskikh proizvodstv. Sposoby zashchity oborudovaniya ot korrozii. Spravochnoe posobie* (Corrosion Resistance of Chemical Manufacture Equipment. Methods of Corrosion Protection. Handbook), Strakan, B.V. and Sukhotin, A.M. Eds., Leningrad, Khimiya, 1987, 280 p.
7. Migai, L.L. and Taritsyna, T.A., *Korrozionnaya stoikost' materialov v khlore i ego soedineniyakh. Spravochnik* (Corrosion Resistance of Materials in Chlorine and in Its Derivatives), Moscow, Metallurgiya, 1976, 120 p.
8. Tursunova, Z.M., Sultanov, B.E. *et al., Khim. Prom*., 2003, no. 10, p. 9.

ISSN 1070-4272, Russian Journal of Applied Chemistry, 2008, Vol. 81, No. 9, pp. 1710–1712. © Pleiades Publishing, Ltd., 2008.
Original Russian Text © D.F. Suleimanov, R.N. Phatkhullin, E.V. Boev, V.G. Afanasenko, 2008, published in Khimicheskaya Promyshlennost', 2008, Vol. 85, No. 4, pp. 200–202.

PROCESSES AND DEVICES OF CHEMICAL MANUFACTURES

Main Reprocessing Ways of Industrial Waste Water on the Local Plants

D. F. Suleimanov, R. N. Phatkhullin, E. V. Boev, and V. G. Afanasenko

State Oil-Engineering University, Sterliramak, Russia

Received March 15, 2008

Abstract—Some ways of wastewater treatment on the local plants are presented. An application of the suggested ways allows reuse of the reprocessed water to reuse and the optimization of the operating costs.

DOI: 10.1134/S1070427208090449

Replacement of technologically used natural fresh water by the treated wastewater allows to avoid a deficiency of a water supply and to prevent an exhaustion of the fresh water. One of the ways is the building of recirculated system of the industrial water supply based on the reuse of the industrial water treated to fit the corresponding requirements of the process water quality.

A definite chemical composition of the water is required for each specific technological process. Hence large amount of the reprocessing ways is known.

A scheme of water treatment must provide minimum discharge of the wastewater into the onsite water, its maximum reuse in technological processes and in the recirculated systems, more complete extraction of valuable admixtures.

Local or community wastewater treatment plants are mainly emplyed in the chemical industry. The latter may include a primary (mechanical), secondary (biological), and tertiary (aftertreatment) wastewater treatment

Local wasterwater treatment plants are applied to decontaminating water immediately after a technologic outlet. The local wasterwater treatment plant is one of the steps of a technological process when as a rule the valuable admixtures are extracted, because usually regenerative processes: sedimentation, flotation, extraction, refining, adsorption, ion exchange, reverse osmosis are used.

Let us consider each of these processes.

SEDIMENTATION

Devices of periodical and continuous operation are used for removal from waste waters of the suspended substances by a settling in response to an external force such as gravity. Settlings of the periodical operation are applied in case of a small flow. They look like a metal or ferroconcrete reservoirs with conic bottom from where water is decanted through a siphon or special gutters. The settlings of continuous operation are used at the large flow. They may be vertical, horizontal, and radial. Also plate (manytier) settlings, pipe settlings with small and steep pipe slope are used [1].

A flocculation is employed for an acceleration of the sedimentation and an efficiency increase of a water clarification and a decoloration That is an enlargement of the colloid and suspended particles caused by clump ing together into flocs under action of adhesion forces. A hydrolysis and a formation of low soluble alkalis occur at a dissolution of coagulants being salts of weak bases and strong acids in water. Aluminium sulfate, ferrous sulfate, ferrous chloride, potassium alum and a mixture of ferrous sulfate and chloride are widely applied as coagulants. In the rare cases salts of magnesium, zinc, and titanium are used [2].

Significant amount of water in the sediment both in various bound states with species and in the free state is a disadvantage of this treatment.

A burial of this bulky wet mud is complicated by rapid increase of a coagulant consumption for the water treatment and conditions of its accumulation do not fit to requirements of a environmental protection. However this problem is solved by the coagulant regeneration by an acid processing that decreases the initial sediment to 15–18 vol% [4].

FLOTATION

The flotation is used for the wastewater treatment from oil waste, products of petroleum processing, fats, oils, gums, latexies, products of organic synthesis, surfactant species, dyes and others. The process is based on a specific utilization of the molecular forces causing the adhering of the suspended admixtures to the bubbles of a finely dispersed gas in water, their carrying to the upper surface, and forming a froth saturated by the separated substances [2].

A main type of devices used for the flotation is the following:

– A foam former where air, wetting and flocculated agents, and also a part of the waste waters are fed;

– A funnel-shape or cylindrical reservoir where a polluted medium slowly passes from a middle to borders of the reservoir, and the suspended particles adhered to the air bubbles are collected as the froth;

– A device for the froth removal;

The best known devices are traps of Wolf and Sawall. A starch, carboxymethyl cellulose, guar gums, polethylene amine, polydimethylaminoethylacrylate, hydrolyzed polyacrylamide are used as flocculating agents [3].

EXTRACTION

The extraction is widely applied to the cleaning from organic admixtures especially phenol waste waters of a thermal processing of the solid fuels. The extraction is available in case of high concentrations of the organic admixtures or of a cost of removed substances. An agitator-settler, and devices of column and rotation types are of commonly applied.

RECTIFICATION

Specificity of the waste water treatment by the rectification is caused by sufficiently small concentraions of the admixtures and by requirement of their practically complete removal. The difference between the rectification in columns in the presence of a superheated water steam, a rectification in the distillation columns, and azeotropic distillation should be considered . The column devices with contact items such as nozzles of various shapes, and plates with downcomer and without the latter. At the azeotropic distillation a separator where a demixing of the azeotropes occurs is added in the scheme.

ADSORPTION

The adsorption by activated carbon is one of more effective ways of the industrial water treatment containing organic admixtures that enables reacting the standard value. The following adsorbents BAU, TNK-AKhB-02,OU, KAD-Iodic, KAD ground, MS-4 are employed. Devices with blade, turbine and propeller agitators, adsorbers of a column type, single-deck adsorber, multideck adsorber with overflow pipes, adsorbers with a divided adsorbent layer are used [1].

Unfortunately the adsorption may be economically available exclusively at repeated uses of adsorbents that can be achieved either by an isolation of an adsorbed valuable substances as products or by a total destruction of compounds and their oxidation to end products: CO_2, H_2O, N_2 etc. [4].

ION EXCHANGE

The waste water treatment by the ion exchange is reduced to a binding of removed ions with forming sparringly or weakly dissociated compounds. In this case chemical reactions are practically irreversible. The ion exchange is used at heavy metals production, an isolation of compounds of a fluorine, radioactive and other elements. The following types of ionites both domestically produced and foreign are used: amberlites (US, Japan), duolites (US, France), dowexes (US), zerolites (UK), levatites, wofatites (Germany), cationites KU-1, KU-2, SG-1, KB-2, KB-4, anionites AV-16, AV-17, AN-1, AN-2F, AN-18, AN-31, EDE-10P (Russia) and others.

REVERSE OSMOSIS

The reverse ocmosis is a continuous process of a molecular separation of solutions by their filtration under pressure through semipermeable membranes that retains completely or partially molecules or ions of a dissolved substance. This process is used for an isolation of saccharides, salts, acids. The membranes of cellulose acetate processed for a water permeability by magnesium perchlorate with a polyelectrolyte film, porous carbonaceous pipes, a porous pipes made of a glass fiber, or also metal or phorphorous filters as a substrates are the most feasible. An equipment of the following types are applied to industry:

– "Filter-press" with a plate chamber filtering elements. Their main disadvantages are an insufficient specific area of a membrane surface and a large metal consumption.

– With tubular filtering elements which characterized by the insufficient specific surface and by a difficult replacement of depreciated membranes

– Filtering elements of a roll or spiral types that are noted for the large specific area of the membrane surface but also characterized by difficult mounting and replacement of the membranes.

– With membranes made of hole fibers. Their advantages are a compactness and a high output but a replacement of the damaged fibers is difficult [1].

It should be noted that an application of a regeneration ways of the treatment enable in many cases repeated use of the treated waste water in the same operation. A return in the technological process of the removed admixtures decreases a loss of a raw material, agents and products and often rises economical efficiency of the waste water treatment.

ISSN 1070-4272, Russian Journal of Applied Chemistry, 2008, Vol. 81, No. 10, pp. 1713–1716. © Pleiades Publishing, Ltd., 2008.
Original Russian Text © A.T. Belyaevskii, A.I. Nikolaev, V.B. Petrov, Yu.G. Bychenya, 2008, published in Zhurnal Prikladnoi Khimii, 2008, Vol. 81, No. 10, pp. 1585–1588.

INORGANIC SYNTHESIS AND INDUSTRIAL INORGANIC CHEMISTRY

Diagnostics of the Behavior of Apatite and Its Aggregates with Sphene in Dilute Mineral Acids

A. T. Belyaevskii, A. I. Nikolaev, V. B. Petrov, and Yu. G. Bychenya

Tananaev Institute of Chemistry and Technology of Rare Elements and Mineral Resources, Kola Scientific Center, Russian Academy of Sciences, Apatity, Murmansk oblast, Russia

Received January 22, 2008

Abstract—Behavior of monomineral fractions of apatite and sphene and their aggregates in treatment with dilute solutions of hydrochloric and sulfuric acids was studied by electron microscopy, IR spectroscopy, crystal-optical methods, and X-ray and chemical analyses. The manner in which aggregates of apatite and sphene disintegrate was for the first time visualized by electron scanning microscopy. The efficiency of purification of the apatite concentrate to remove apatite with hydrochloric and sulfuric acid solutions was examined.

DOI: 10.1134/S1070427208100017

The sphene concentrate is produced from wastes formed in dressing of apatite-nepheline ores from Khibiny deposits. The sphene concentrate is regarded as a promising raw material for production of titanium pigments [1, 2] and for use in coatings of welding electrodes [3]. Apatit Open Joint-Stock Company semi-industrially manufactures paints based on titanium dioxide produced from the sphene concentrate. Presence of phosphorus makes lower the recovery of titanium into the pigment titanium dioxide because of the precipitation of titanium phosphate, which remains in the calcium silicate product. In the technical specification for the sphene concentrate, the content of phosphorus is limited to 2 wt % in terms of P_2O_5, and in that for welding electrodes, 0.1 wt % in terms of P_2O_5 or 0.05 wt % in terms of phosphorus. The increasingly stringent requirements to the quality of welding materials necessitate a higher degree of purification of the sphene concentrate to remove phosphorus.

It has been reported [4] that sphene and apatite can form aggregates (via intergrowth of crystals of these minerals), which hinder their separation in the dressing stage. When the ore is crushed, the aggregates partly disintegrate and opened aggregates are formed, which gives reason to believe that sphene can be more fully separated from apatite by other methods. For example, a method of chemical purification, based on decomposition of apatite with mineral acids and, in particular, sulfuric acid, has been suggested for deeper purification to remove phosphorus [4, 5].

A possible obstacle to efficient purification are not-yet-opened aggregates. This hinders removal of phosphorus even upon treatment of the concentrate with rather high-concentration acids. It should be taken into account that treatment with such acids inevitably leads to decomposition of fine fractions of sphene and, accordingly, to loss of titanium. It has been suggested to use diluted (down to 10%) solutions of sulfuric, hydrochloric, and nitric acids for chemical purification of sphene and other concentrates [5].

The aim of the present study was to examine the behavior of apatite, sphene, and their aggregates in their interaction with dilute sulfuric and hydrochloric acids, which can be used in practice for optimizing the purification conditions of the sphene concentrate to remove phosphorus.

EXPERIMENTAL

The experimental procedure consisted in that narrow fractions of sphene and apatite grain size (–0.071...+0.063 mm) and aggregates of the minerals were treated with acids.[1]

[1] Monomineral fractions of sphene and apatite were sampled by V.F. Fedchenko at the Central laboratory of Apatit Open Joint-Stock Company.

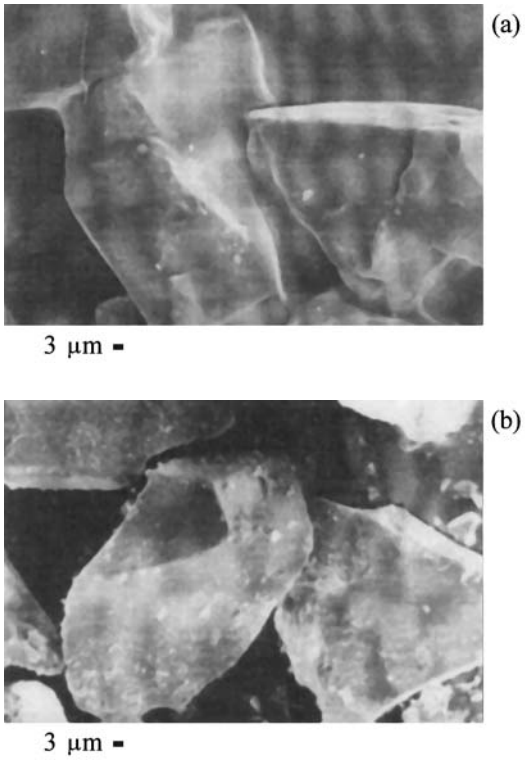


Fig. 1. Micrographs of monomineral particles of (a) sphene and (b) apatite.

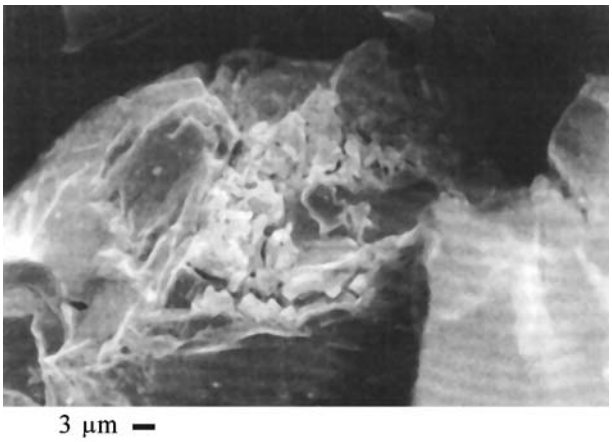


Fig. 2. Micrograph of an aggregate of sphene and apatite.

This fraction fineness was chosen because concentrates with mostly such a grain size are commonly delivered to technological processing. The largest amount of open aggregates of sphene and apatite is concentrated in the sphene concentrate with this grain size. The content of P_2O_5 in the concentrate may vary from 0.8 to 4.5 wt % [4]. Because apatite is rather easily decomposed with acids, the time of treatment of the samples at room temperature was 15 min. In separate experiments with apatite, this time was reduced to 5 min to preclude complete decomposition of apatite particles. After that, the suspension was filtered and the sediment was washed with water.

The products before and after treatment with solutions of sulfuric and hydrochloric acids with various concentrations were examined by digital scanning electron microscopy (SEM) and other techniques: X-ray phase, crystal-optical, and chemical analyses and IR spectroscopy.

With a LEO 420 SEM microscope, the magnification range was 60–30 000. This method makes it possible to trace how the morphology of mineral grains changes in the course of chemical purification of the sphene concentrate and to confirm the existence of sphene and apatite aggregates. The manner in which the aggregates disintegrate under the action of dilute acid solutions was visually represented.

The high stability of sphene against dilute acids suggests that the surface of sphene particles will not change, in contrast to that of apatite. The only exception should be aggregates of sphene and apatite crystals.

Below are presented results obtained in a study of the morphology of narrow fractions of apatite and sphene particles and their aggregates. Figure 1 shows the outward appearance of monomineral fractions of sphene (Fig. 1a) and apatite (Fig. 1b). It can be seen that sphene particles have a clear-cut faceting. It remains unchanged upon treatment with dilute sulfuric and hydrochloric acids. Apatite particles have a rough surface and there are dusty fractions produced in crushing and grinding, which form agglomerates. The agglomerates are constituted by particles less than 28 μm in size and accumulate in energy-strained regions formed at places of crystal breaking [2]. It can be seen at large magnifications that the surface of particles forming the dustlike fractions is amorphized and unstable because of the mechanical activation effect [6–8]. This surface is a product of interaction of apatite with the floating reagent and air medium in the course of crushing and flotation [8].

In the aggregates found, sphene envelops apatite. This suggests that apatite crystallizes earlier than sphene does, with sphene precipitating on the already formed apatite crystals. Figure 2 shows an aggregate of sphene and apatite. It can be seen that apatite is within a sphene crystal. Clearly, phosphorus cannot be removed without opening the crystals-aggregates.

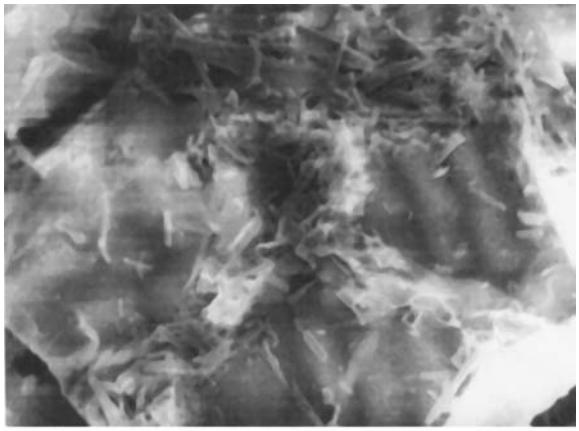


Fig. 3. Micrograph of an aggregate of sphene and apatite, treated with 5% sulfuric acid.

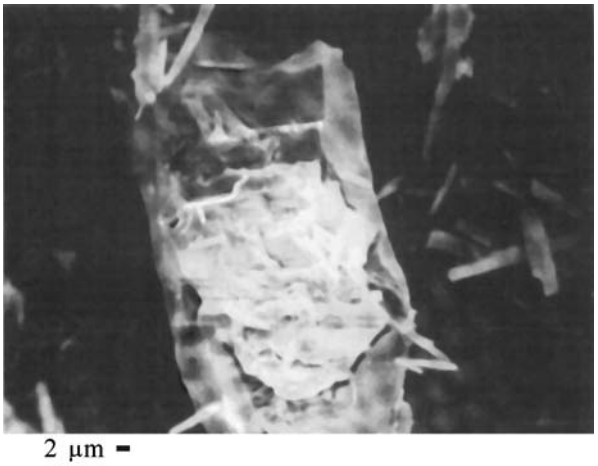


Fig. 4. Micrograph of an aggregate of sphene and apatite, treated with 2% sulfuric acid.

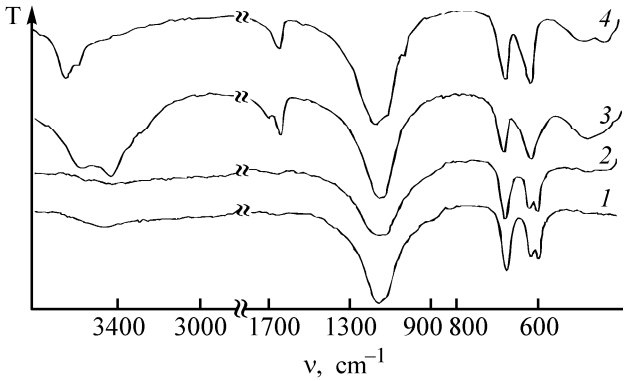


Fig. 5. IR spectra of calcium sulfate isolated in purification of the sphene concentrate. (T) Transmission and (ν) wave number. (*1*) $CaSO_4$, unwashed and dried at room temperature; (*2*) the same at 90°C; (*3*) $CaSO_4 \cdot 2H_2O$, washed and dried at room temperature; and (*4*) $CaSO_4 \cdot 0.5H_2O$, washed and dried at 90°C.

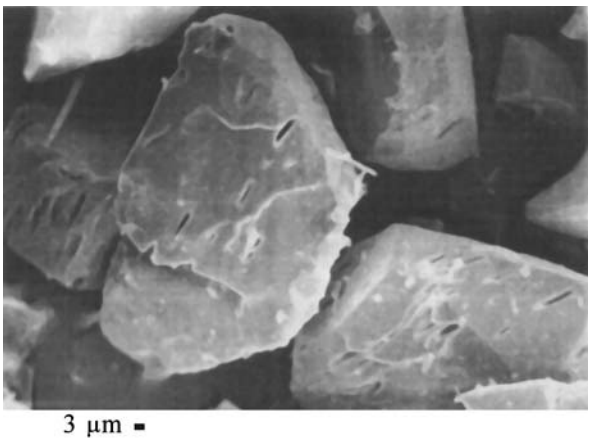


Fig. 6. Micrograph of apatite particles treated with 5% hydrochloric acid.

Figures 3 and 4 show aggregates treated with 5 and 2% sulfuric acid, respectively. Decomposition of apatite yields calcium sulfate crystals covering sphene and partly remaining within the cavern. The crystals (up to 30 μm long) contained within the cavern are strictly oriented. Probably, this occurs because the internal energy of the "mother" crystal orients calcium sulfate crystals. The chaotic arrangement of the outer crystals may be due to agitation of the suspension. Nevertheless, they are bound into druses, which points to their energetic interaction.

Figure 5 shows IR spectra of the forming calcium sulfates. Data furnished by chemical, optical, and X-ray phase analyses and by IR spectroscopy of finely dispersed precipitates isolated by hydroclassification indicate that they are formed by anhydrite, $CaSO_4$. However, washing with water and drying at room temperature and elevated temperatures (up to 90°C) result in that the precipitates are hydrated and transformed first to calcium sulfate semihydrate and then calcium sulfate dihydrate. The absorption at 3400–3700 and 1650 cm^{-1}, which is characteristic of calcium sulfate dihydrate and belongs to hydroxy groups, is observed only for washed samples.

In treatment of apatite with dilute sulfuric acid, there is no reverse formation of calcium phosphates because the main part of calcium is bound into a sulfate and the solubility product for calcium phosphates is not reached [9].

Upon treatment of apatite with 5% hydrochloric acid, the dustlike fraction nearly completely disappears (Fig. 6) and narrow deep elongated etch pits and grooves appear on the surface of the crystals.

According to the monograph [10], the etch pits and grooves are formed because the propagation direc-

tion of the etch front varies with the density of the crystal structure of apatite. In the case under consideration, their formation is facilitated by the presence of impurity elements weakening the structure of pure apatite.

Treatment of aggregates of sphene and apatite with a hydrochloric acid solution can yield calcium fluoride, but this is not observed, possibly because of the low concentration of fluorine. In contrast to the treatment of the aggregates with sulfuric acid, no new phase formation is observed in the given case.

It is noteworthy that the rate of apatite decomposition depends on the acid concentration. A decrease in this parameter within the range studied makes the rate of apatite decomposition lower. As, however, the acid concentration increases, sphene starts to decompose. This circumstance governs the choice of dilute acid solutions for chemical purification of the sphene concentrate to remove the phosphorus impurity. It is preferable to choose hydrochloric acid solutions for this purpose, because poorly soluble calcium sulfate salts, anhydrite $CaSO_4$ and gypsum $CaSO_4 \cdot 2H_2O$, are formed in the case of sulfuric acid. This contaminates the concentrate with sulfur, whose content is strictly limited by technical specifications for welding material components and leads to an increased expenditure of washing water for dissolution of calcium sulfates.

CONCLUSIONS

For a fuller removal of the apatite impurity from the sphene concentrate, it is necessary to perform its chemical purification after grinding to a grain size that provides opening of aggregates of apatite and sphene and thereby simplifies the apatite decomposition with acid solutions and diminishes the content of phosphorus to the concentrations satisfying technical specifications. It is shown that hydrochloric acid solutions are preferable for purification of the sphene concentrate to remove phosphorus and sulfur impurities.

REFERENCES

1. Gerasimova, L.G., *Pigmenty i napolniteli iz prirodnogo titansoderzhashchego syr'ya i tekhnogennykh otkhodov* (Pigments and Fillers from Natural Titanium-containing Raw Materials and Technological Wastes), Apatity: Kola Nauchn. Tsentr Ross. Akad. Nauk, 2001.
2. Gerasimova, L.G., Lazareva, I.V., Maslova, M.V., et al., *Khim. Tekhnol.*, 2004, no. 2, pp. 13–17.
3. Fedorov, S.G., Nikolaev, A.I., Brylyakov, Yu.E., et al., *Khimicheskaya pererabotka mineral'nykh kontsentratov Kol'skogo poluostrova* (Chemical Processing of Mineral Concentrates from the Kola Peninsula), Apatity: Kola Nauchn. Tsentr Ross. Akad. Nauk, 2003.
4. Motov, D.L. and Maksimova, G.K., *Sfen i ego khimicheskaya pererabotka na titanovye pigmenty* (Sphene and Its Chemical Processing to Give Titanium Pigments), Leningrad: Nauka, 1986.
5. RF Patent 2 174 561.
6. Avvakumov, E.G., *Mekhanicheskie metody aktivatsii khimicheskikh protsessov* (Mechanical Methods for Activation of Chemical Processing), Novosibirsk: Na-uka, 1986.
7. Gusev, A.I., *Nanomaterialy, nanostruktury, nanotekhnologii* (Nanomaterials, Nanostructures, and Nanotechnologies), Moscow: Fizmatlit, 2005.
8. Belyaevskii, A.T., *Sbornik nauchykh dokladov, VI Mezhdunarodnaya konferentsiya "Ekologiya i razvitie Severo-zapada Rossii"* (Proc. VI Int. Conf. "Ecology and Development of Northwestern Russia"), St. Petersburg, 2001, pp. 65–71.
9. Lidin, R.A., Andreeva, L.L., and Molochko, V.A., *Konstanty neorganicheskikh veshchestv: Spravochnik* (Constants of Inorganic Substances), Lidin, R.A., Ed., Moscow: Drofa, 2006, 2nd ed., rev., suppl.
10. Heinicke, G., *Tribochemistry*, Berlin: Akademie, 1984.

ISSN 1070-4272, Russian Journal of Applied Chemistry, 2008, Vol. 81, No. 10, pp. 1717–1721. © Pleiades Publishing, Ltd., 2008.
Original Russian Text © A.S. Brykov, V.V. Danilov, E.Yu. Aleshunina, 2008, published in Zhurnal Prikladnoi Khimii, 2008, Vol. 81, No. 10, pp. 1589–1593.

INORGANIC SYNTHESIS AND INDUSTRIAL INORGANIC CHEMISTRY

State of Silicon in Silicate and Silica-containing Solutions and Their Binding Properties

A. S. Brykov, V. V. Danilov, and E. Yu. Aleshunina

St. Petersburg State Technological Institute, St. Petersburg, Russia

Received January 5, 2008

Abstract—Relationship between the distribution of silicon atoms over connectivities in concentrated silicate and silica-containing alkaline solutions differing in chemical composition and preparation methods, on the one hand, and the binding properties of these solutions, on the other, was studied by ^{29}Si NMR spectroscopy.

DOI: 10.1134/S1070427208100029

Silicate and silica-containing alkaline solutions are important representatives of the class of air-hardenable binders: combined with various mineral fillers, they can be cured to give artificial silicate stone. For this purposes, the solutions are used in manufacture of concretes, acid-and heat-resistant articles, coatings, and many other building and special materials [1, 2].

Solutions of alkali metal silicates have a complex polymeric structure [3–5]. ^{29}Si NMR spectroscopy furnishes information about the content of silicon atoms with a particular type of nearest environment in a solution. Depending on the number of siloxane bonds (i.e., bonds with other silicon atoms via oxygen) a particular Si atom has, it can be attributed on the basis of NMR spectroscopic data to one of the following types (connectivity types): Q^0, Q^1, Q^2, Q^3, or Q^4.

In this study, we used NMR spectroscopy on ^{29}Si nuclei to examine the relationship between the distribution of silicon atoms over connectivities in concentrated silicate and silica-containing alkaline solutions differing in chemical composition and preparation methods, on the one hand, and the binding properties of these solutions, on the other.

We considered as objects of study concentrated sodium and potassium silicate solutions prepared by the autoclave method (liquid glasses) or by dissolution of hydrated sodium silicates (products of high-temperature dehydration of liquid glasses) in water under normal conditions. We also used sodium, potassium, lithium, and tetrabutylammonium (TBA) silicate solutions with a silicate modulus, i.e., molar ratio between SiO_2 and R_2O [where R = Na, K, Li, or $N(C_4H_9)_4$], of 2.8–16, produced under laboratory conditions by dissolution of colloid SiO_2 in solutions of the corresponding bases.

EXPERIMENTAL

Table 1 lists parameters of the solutions under study (type of cation R, silicate modulus n, SiO_2 concentration c_{SiO_2}, density ρ, and age τ). Solution nos. 1–5 were prepared by addition (under agitation) of distilled water and NaOH (chemically pure grade) to an industrial sodium silicate solution, sodium liquid glass [Lenstroikeramika Private Company, 32 wt % SiO_2 and 12 wt % Na_2O GOST (State Standard) 13078]. Solution no. 6 is a potassium liquid glass (Ekokhim Private Company, 23.2 wt % SiO_2 and 10.5 wt % K_2O). Solution no. 7 was prepared by dissolution in water of hydrated sodium silicate N28 [Monasil brand, Volkhovskii khimicheskii zavod Private Company, 56.0 wt % SiO_2 and 22.5 wt % Na_2O, calcination loss at 700°C 19.5 wt %, TU (Technical Specification) 2145-001-75 105 538–2005]. Solution nos. 8–13 were prepared by manual mixing of colloid silica solutions SM30 (solution nos. 8–10) and TM40 (solution nos. 11–13) with the corresponding bases (all of chemically pure grade): xLiOH · H_2O, NaOH, KOH, $N(C_4H_9)_4OH$ (30% aqueous solution) and water. The colloid solutions SM30 and TM40 (Ludox brand, Grace Davison Co.) are industrial silica dispersions with 7- and 20-nm SiO_2 particles, respectively, and SiO_2 contents of 30 and 40 wt %, respectively, stabilized with NaOH (Na^+ con-

Table 1. Parameters of silicate solutions

Solution no.	R	n	c_{SiO_2}, wt %	ρ, kg m^{-3}	pH	τ, days
1	Na	0.5	10	1.39	14.0	1
2	Na	1.5	25	1.53	14.0	30
3	Na	2.0	25	1.44	13.0	30
4	Na	2.5	25	1.38	12.4	30
5	Na	2.8	25	1.37	12.2	30
6	K	3.5	23	1.35	12.0	–
7	Na	2.7	23	1.39	11.7	3
8	Na	2.8	25	1.44	~12	30
9	K	2.8	25	1.43	12.3	30
10	Li	5	25	1.21	11.8	7
11	Li	5	25	1.25	12.1	10
12	Li	8	25	1.26	11.8	10
13	TBA	16	25	1.19	12.1	5
14	–	–	25	1.2	~9	–

tent, fractions of a percent). Solution no. 14 is a TM40 dispersion diluted with water.

All the solutions were stored in hermetically sealed plastic vessels under normal conditions. Table 1 lists the ages of the solutions by the instant of time at which their binding properties were tested and NMR spectra were measured.

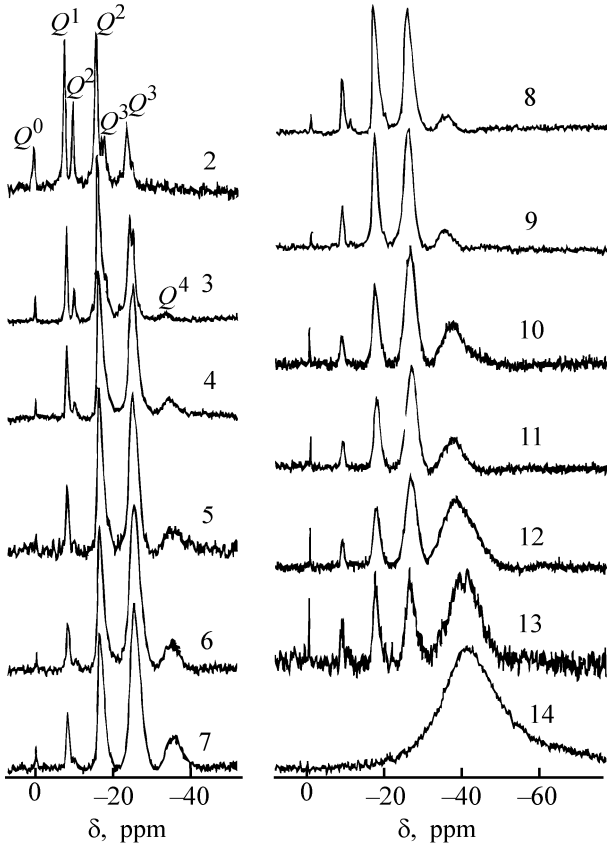


Fig. 1. NMR spectra of silicate solutions. (δ) Chemical shift. *Figures at curves* are solution numbers in Table 1.

The pH values of the solutions were measured with a pH-673.M pH-meter. The solution densities were determined pycnometrically.

^{29}Si NMR spectra of the solutions were measured with a Bruker AM500 spectrometer (99.3 MHz) in standard glass ampules. The spectra were processed using 1D WIN-NMR software (Bruker). Figure 1 shows the solution spectra after subtraction of the spectrum of a water-filled ampule in which the measurements were made. The chemical shifts of the signal are given relative to the position of the Q^0 signal. The content of silicon atoms with different connectivities Q^i (wt % relative to the total content of silicon) was determined by deconvolution and integration of the spectra obtained. The signals were assigned in accordance with the data of [3, 5], where chemical shifts for silicon atoms were presented in relation to the type of their nearest environment. The results of our calculations are shown in Fig. 2 (data from [3] are presented for solution no. 1).

To determine the binding properties, we prepared a mixture of finely ground quartz with particle size less than 100 μm and a solution under study (binder-to-filler mass ratio 0.13). From the paste obtained, we prepared cylindrical samples with a diameter and height of 2 cm by compaction under a pressure of 18 MPa. The samples were stored for 7 days under normal conditions and then their compression strength was deter-

mined. The results obtained in testing the strength of each of the silicate solutions under study are listed in Table 2.

It can be seen in Fig. 2 that, as the molar ratio between SiO_2 and R_2O in solutions becomes lower, the content of Si atoms with low connectivity (Q^0, Q^1, and Q^2) increases, whereas that of Si atoms with connectivities Q^3 and Q^4 simultaneously decreases. Apparently, these changes are due to an increase in the concentration of OH^- ions and depolymerization of large silicate ions (or dissolution of colloid particles), which occurs in this case to give monomers and low-polymer ions:

$$-\overset{|}{\underset{|}{Si}}-O-\overset{|}{\underset{|}{Si}}- + OH^- \rightleftarrows -\overset{|}{\underset{|}{Si}}- + -\overset{|}{\underset{|}{Si}}- + O^-.$$

In this case, solutions with close silicate moduli and SiO_2 concentrations have approximately the same distribution of silicon atoms over connectivities, irrespective of the preparation method.

In high-modulus solutions, a considerable part of silicon atoms have connectivity Q^4 by the time of the experiment, which indicates that the solutions contain high-polymer silica or incompletely dissolved Colloid SiO_2 particles.

Comparison of the data in Table 2 and Fig. 2 shows that the sample strength is higher in the case of low-modulus silicate solutions, in which silicon atoms with low connectivity predominate and the concentration of hydroxide ions is higher (for solution no. 1, it is necessary to take into account the lower total concentration, compared with other solutions). By contrast, colloid SiO_2 solutions and high-modulus silicate solutions, in which the fraction of Q^4 silicon atoms is high, are the least active as binders. Solutions with close distributions of silicon atoms over connectivities have approximately the same binding properties.

When silicate and silica-containing materials are used as fillers, the role of hydroxide ions contained in the binding solution consists in that the particle surface is activated via rupture of Si–O–Si bonds (here and hereinafter, it is assumed that silicon is tetravalent; however, all its four bonds are not shown in all cases for simplicity). As a result, silanol groups Si–OH and charged moieties Si–O^- are formed on the surface of filler grains. The role of silicate ions introduced with silicate binding solutions consists in that new chemical and physicochemical bonds are formed and bind filler particles to give a rigid skeleton. It can be assumed that the activity of a silicate solution toward the filler will be determined by the concentration of SiO^- and SiOH groups, which, in turn, depends on the distribution of silicon atoms in solution over connectivities Q. For example, a silicon atom of Q^1 type has one siloxane bond and, accordingly, three Si–OH or Si–O^-

Table 2. Concentrations of [SiO^-] and [SiOH] moieties in silicate solutions with different silicate moduli

Solution no.	Strength, MPa	S, M	D	[SiO^-]	[SiOH]
				M	
1	24	7.7	–	5.4	2.3
2	45	13.1	–	4.6	8.4
3	36	9.6	63.9	6.0	3.6
4	29	7.9	12.5	4.6	3.3
5	29	7.3	10.7	4.1	3.2
6	20	6.7	8.8	3.0	3.7
7	27	6.9	6.1	3.9	3.0
8	28	8.0	13.7	4.3	3.7
9	25	7.9	6.9	4.3	3.6
10	12	4.5	2.4	2.0	2.5
11	9	4.5	2.4	2.1	2.4
12	9	2.7	0.7	1.3	1.4
13	2	2.4	0.5	0.6	1.8
14	1	~0*	~0	~0	~0

* With account of silanol groups on the surface SiO_2 particles, $S \approx 0.2$ M.

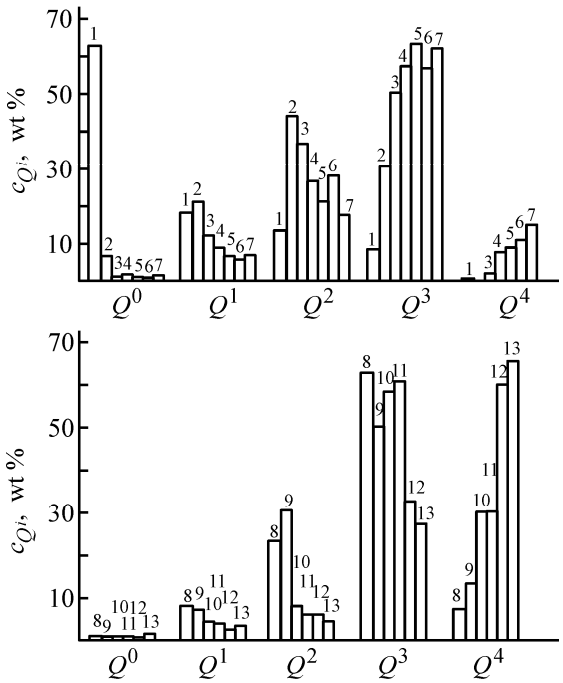
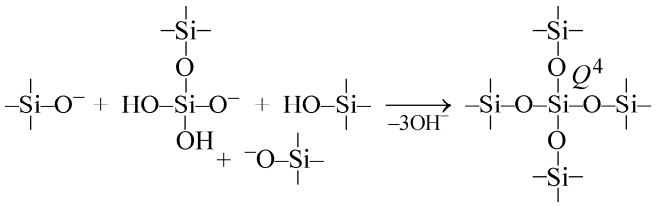


Fig. 2. Contributions of silicon atoms with different connectivities to the total silicon content of a solution. (Q^i) Connectivity of a silicon atom and (c_{Q^i}) contribution of silicon atoms with ith type of connectivity to the total silicon content of the solution. (1–13) Solution numbers in Table 1; the same for Figs. 3, 4.

bonds and can potentially form three new siloxane bonds:



Silicon atoms of Q^0, Q^2, and Q^3 types can be involved in formation of, respectively, four, two, and one siloxane bonds. The Q^4 structural units having no free $Si–O^-$ or Si–OH moieties are not involved in the formation of new siloxane bonds.

Using NMR spectroscopic data, we can calculate the total concentration S (M) of SiO^- and SiOH groups by the formula

$$S = \frac{\rho c_{SiO_2}}{10 M_{SiO_2}} \sum_{i=0}^{4} (4 - i) c_{Q^i},$$

where ρ is the solution density (g cm^{-3}); c_{SiO_2}, SiO_2 content (wt %); M_{SiO_2} = 60, molecular mass of SiO_2 (g mol^{-1}); and c_{Q^i}, content of silicon atoms with ith connectivity type (wt %) (from Fig. 2).

The calculated values of S are listed in Table 2. Apparently, S is the larger, the less structured is a silicate solution. When silica is in the form of colloid particles, S is nearly zero. In accordance with the data in Table 2, the sample strength tends to increase as S becomes larger. Thus, the value of S is a quantitative measure of the polymeric state of silicate ions and, simultaneously, determines the activity of a solution as a binder.

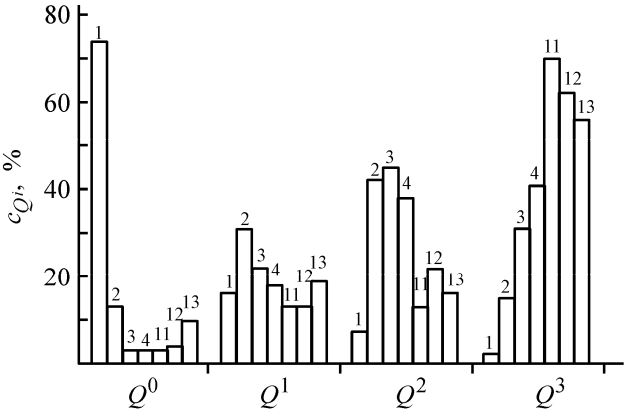


Fig. 3. Contributions of silicon atoms with different connectivities to the total concentration S of SiO^- and SiOH groups. (Q^i) Connectivity of a silicon atom and (c_{Q^i}) contribution of silicon atoms with ith type of connectivity to the total concentration S of SiO^- and SiOH groups.

Figure 3 shows for the example of several solutions under study the contributions (%) of silicon atoms with different connectivities to S, calculated by the formula

$$G_{Q^i} = \frac{(4 - i) c_{Q^i}}{\sum_{i=0}^{4} (4 - i) c_{Q^i}} \times 100.$$

It can be seen in Fig. 3 that the contribution to S from the most reactive species, Q^0 monomers, is noticeable only for low-modulus solutions (nos. 1 and 2) and insignificant in all other cases because of the low concentration of Q^0. For solutions with a modulus exceeding 2.5 (liquid glasses and high-modulus solutions), the contribution of Q^3 structural units is large: their moderate reactivity is compensated by the substantial concentration.

As the silicate modulus becomes higher, the total content of "active" silicon atoms Q^0, Q^1, Q^2, and Q^3 decreases and the fraction of "inactive" Q^4 atoms that cannot form siloxane bonds increases. Table 2 lists ratios between the amounts of active and inactive silicon atoms in the form of the quantity $D = \sum_{i=0}^{3} c_{Q^i} / c_{Q^4}$. It can be seen that the sample strength decreases as D becomes lower.

Using the obtained values of S, we separately estimate the concentrations of SiO^- moieties and silanol groups.

The silicate solutions under consideration contain three types of charged species and moieties: R^+ [R = Na, K, Li, or $N(C_4H_9)_4$], OH^-, $Si–O^-$. The concentration of charged groups $Si–O^-$ can be found on the basis of the solution electroneutrality principle: $[SiO^-] = [R^+] - [OH^-]$,

$$[R^+] = \frac{20 \rho c_{SiO_2}}{n M_{SiO_2}}, \quad [OH^-] = \frac{10^{pH - 14}}{\gamma_{OH^-}},$$

where $[R^+]$ is the cation concentration (M), and γ_{OH^-}, activity coefficient.

For solution nos. 1 and 2, the value of γ_{OH^-} was taken to be 0.26 [6]. In all other solutions, the concentration of hydroxide ions is negligible as compared with $[R^+]$ and $[SiO^-] = [R^+]$.

The concentration of silanol groups is calculated by the formula $[SiOH] = S - [SiO^-]$. It follows from the results of our calculations, listed in Table 2, that the concentrations of SiO^- and SiOH are comparable in order of magnitudewith an increase in the concentra-

tion of one type of groups not leading to a deficiency of groups of the other type.

It can be seen in Fig. 4, which shows how the stone strength depends on the product of the concentrations of the SiO^- and SiOH moieties, that the binding activity of silicate solutions grows with $[SiOH] \cdot [SiO^-]$.

It is known that siloxane bonds are formed both with silanol groups and with charged SiO^- moieties involved by the mechanism of bimolecular nucleophilic substitution S_{N_2} [7]. Accordingly, the formation rate of siloxane bonds is proportional to the product of the concentration of the groups involved in the reaction: $V \propto [SiO^-] \cdot [SiOH]$. Thus, Fig. 4 characterizes the relationship between the kinetics of formation of siloxane bonds and the formation of the stone structure.

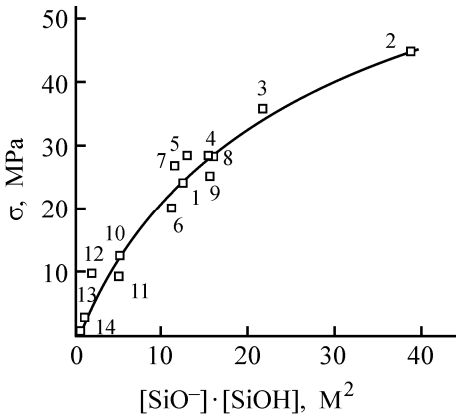


Fig. 4. Compression strength σ of silicate stone vs. the product of the concentrations of the SiO^- and SiOH moieties.

CONCLUSIONS

(1) The strength of structures formed in air curing of silicate solutions with mineral fillers increases with the product of the initial concentrations of the SiO^- and SiOH moieties contained in the solution.

(2) The concentration the SiO^- and SiOH moieties is found from the distribution of silicon atoms over connectivities, which depends on the chemical composition of a solution and is independent of the method of its preparation after the solution attains a nearly equilibrium state.

(3) In solutions with a silicate modulus exceeding 2.5, the main contribution to the formation of the stone structure is made by silicon atoms with a connectivity Q^3. At the same time, the share of inactive Q^4 silicon atoms grows as the silicate modulus becomes higher, which impairs the stone strength.

(4) The method suggested for determining the concentrations of SiO^- and SiOH groups in silicate solutions from the experimentally found (by ^{29}Si NMR spectroscopy) distribution of silicon atoms over connectivities makes it possible to prognosticate the binding properties of silicate solutions on the basis of the dependence of the strength on $[SiO^-]$ + [SiOH] or $[SiO^-] \cdot [SiOH]$.

ACKNOWLEDGMENTS

The authors are grateful to M.V. Makeev (Institute of Macromolecular Compounds, Russian Academy of Sciences) for assistance in computer processing of NMR spectra.

REFERENCES

1. Vail, J.G., *Soluble Silicates: ACS Monograch Ser.*, New York: Reinold, 1952, vols. 1, 2.
2. *Adhesion and Adhesives*, De Bruyne, N. A. and Houwink, R., Eds., Amsterdam: Elsevier, 1951.
3. Bass, J.L. and Turner, G.L., *J. Phys. Chem., B*, 1997, vol. 101, no. 50, pp. 10 638–10 644.
4. Svensson, I.L., Sjoberg, S., and Ohman, L.-O., *J. Chem. Soc., Faraday Trans. 1*, 1986, vol. 82, pp. 3635–3646.
5. Gaboriaud, F., Nonat, A., Chaumont, D., et al., *J. Phys. Chem., B*, 1999, vol. 103, no. 12, pp. 2091–2099.
6. *Kratkii spravochnik fiziko-khimicheskikh velichin* (Concise Reference Book of Physicochemical Constants), Ravdel', A.A. and Ponomareva, A.M., Eds., Leningrad: Khimiya, 1983.
7. Holmes, R.R., *Chem. Rev*., 1990, vol. 90, no. 1, pp. 17–31.

ISSN 1070-4272, Russian Journal of Applied Chemistry, 2008, Vol. 81, No. 10, pp. 1722–1724. © Pleiades Publishing, Ltd., 2008.
Original Russian Text © I.B. Zhdanovich, T.G. Rudakovskaya, V.V. Shevchuk, 2008, published in Zhurnal Prikladnoi Khimii, 2008, Vol. 81, No. 10, pp. 1594–1596.

INORGANIC SYNTHESIS AND INDUSTRIAL INORGANIC CHEMISTRY

Method for Analysis of the Porous Structure of Potassium Chloride Grains

I. B. Zhdanovich, T. G. Rudakovskaya, and V. V. Shevchuk

Institute of General and Inorganic Chemistry, National Academy of Sciences of Belarus, Minsk, Belarus

Received January 22, 2007

Abstract–-Method for determining the total porosity of potassium chloride grains is suggested. The method includes pycnometric measurements of the true and apparent densities of the grains, with kerosene used as a pycnometric liquid.

DOI: 10.1134/S1070427208100030

Grains of potassium chloride are polycrystals produced by compaction of its dispersions into plates and their subsequent crushing and classification to give the commercial fraction –4…+2 mm. In the course of compaction, potassium chloride crystals are arbitrarily oriented with respect to each other and their crystal lattices mostly do not coincide. As a consequence, numerous defects are formed at places of contact between pressed grains, become coarser via recrystallization, and thereby form the porous structure of grains, which largely determines their physicochemical and mechanical properties. The porosity enables diffusion of the surface moisture into grains, which intensifies recrystallization, impairs strength, and raises the caking of the grains.

The nature and value of the porosity depend on technological parameters of the process of grain production (stock dispersity, compaction pressure). In view of the aforesaid, it is important to determine the porosity of grains in various stages of their manufacture, which will enable control over, and wide variation of the consumer properties of grains (strength, moisture absorption, caking).

An analysis of published data demonstrated that there is no scientifically substantiated technique for determining the porosity of potassium chloride grains. Of all the known methods for analysis of the porous structure of solids, the most precise, simple, and reproducible is the liquid-type pycnometric method for porosity measurements [1–3]. Just this method served as a basis for developing a technique for determining the porosity of potassium chloride grains.

The basic parameters characterizing the porous structure of granulated potassium fertilizers is the total pore volume (total porosity) and open pore volume (open porosity). The total pore volume is constituted by the volume of open-pores connected with the outer surface of grains and that of isolated closed pores or ensembles of these.

EXPERIMENTAL

The total porosity was determined by measuring the true and apparent density of grains by the pycnometric method, with kerosene used as a pycnometric liquid. The study was performed with granulate samples from the 1st, 2nd, 3rd, and 4th sylvinite dressing plants (SDP-1–SDP-4) of Belarus'kalii Production Association, Republican Unitary Enterprise. The porosity Π_{gr} (%) of the granulate was calculated by the formula

$$\Pi_{gr} = [(\rho_p - \rho_{gr})/\rho_p] \times 100, \quad (1)$$

where ρ_p is the density of a powdered granulate (true density) (g cm^{-3}), and ρ_{gr} is the density of the granulate (apparent density) (g cm^{-3}).

To determine the true density, a weighed portion of the granulate (4–5 g) ground to a powdered state, dried to constant mass, and sieved (0.08-mm mesh) was placed in a 50-ml pycnometer, and the pycnometer was half-filled with kerosene and heated on a water bath to complete removal of air bubbles from the powder. After that the pycnometer was thermostated at 20 ± 0.1°C, the kerosene level was brought to the graduation mark, and the pycnometer was weighed.

The optimal experimental conditions were as follows: sample heating temperature 75–80°C and heating duration no less than 240 min.

The true density ρ_p of the ground granulate (powder) was calculated by the formula

$$\rho_p = P_p\rho_{ker}^{20}/(P_p + G - F), \quad (2)$$

where ρ_{ker}^{20} is the density of kerosene at 20°C (g cm^{-3}); P_p, mass of the powder (g); F, mass of the pycnometer filled with kerosene (g); and G, mass of the pycnometer with the powder and kerosene (g).

The relative determination error at a confidence probability $P = 0.95$ did not exceed ±1%.

Determining the apparent density ρ_a, which takes into account the volume of open and closed pores, consists in evaluating the geometric volume of a solid body. For samples of arbitrary shape, to which belong products formed in granulation of potassium chloride, the experimental difficulty of such an estimate consists in localization of pore boundaries on the outer surface of a sample.

In the present-day laboratory practice, the most frequently used method is insulation of the grain surface by creating a paraffin film impermeable to the pycnometric liquid (water). However, this method is highly labor-consuming; the results it yields are strongly affected by the thoroughness with which the surface is hermetically insulated and closed air bubbles are removed from the insulating coating itself.

The method of liquid pycnometry was suggested for determining the apparent density of potassium chloride grains. This technique directly measures the volume of kerosene displaced by grains submerged into the liquid.

It was found experimentally that the absorption of kerosene by the granulate is nearly zero during 24–30 h. This gives reason to believe that kerosene does not penetrate into open pores of grains, well wets their surface, and reliably localizes pore boundaries on the outer surface of the samples. Consequently, kerosene can be used as a pycnometric liquid in determining the apparent density of products formed in granulation of potassium chloride (granulate, compacted plates).

The volume of the granulate was measured with a volume meter having the form of a 400-cm^3 conical vessel with a sealed-in tube with an inner diameter of 8–10 mm and a hooked end.

The volume meter was filled with kerosene until the liquid flowed out of the tube and then a weighed sample was submerged into kerosene. The liquid displaced from the volume meter flows out in a short time (2–3 min).

Because the volume of displaced kerosene is equal to the sample volume, $V_{ker} = V_s$, the sample density ρ_s is given by

$$\rho_s = m/V_s, \quad (3)$$

where m is the mass of displaced kerosene (g).

It was found experimentally that stable values of the granulate density are obtained for sample weights of 10–40 g.

It was found that the grain densities measured for separate fractions within the range –4…+2 mm (commercial fraction) are nearly the same. The content of these fractions in the granulate is about 93%. As the granulate is ground to a grain size less than 2 mm, the pore opening occurs and, as a result, the amount of air contained within grains decreases. This reflects on the grain density, whose values approach the experimental values of true density.

The relative error in measuring the apparent density of grains was ±1% at a confidence probability $P = 0.95$.

For comparison, the apparent densities of granulate samples from for SDPs of Belarus'kalii Production Association, Republican Unitary Enterprise, were measured by the known method of insulation (waxing) of the grain surface (I) and by the suggested technique of liquid pycnometry with kerosene (II). The measurement results are listed in Table 1.

These data indicate that the KCl grain densities measured by the two methods nearly coincide.

To assess the applicability of the method suggested, the porosity of products formed in granulation at the dressing plants of Belarus'kalii Production Association, Republican Unitary Enterprise was deter-

Table 1. Apparent density of potassium chloride grains

Plant	Density of KCl grains, g cm^{-3}, found by indicated method	
	I	II
SDP-1	1.9919	1.9947
SDP-2	2.0150	2.0162
SDP-3	1.9922	1.9916
SDP-4	1.9820	1.9811

Table 2. Porous structure parameters of products formed in granulation at the dressing plants of Belarus'kalii Production Association, Republican Unitary Enterprise

Plant	Granulate			Compacted plates	
	density, g cm^{-3}		porosity, %	density ρ_{pl}, g cm^{-3}	porosity, %
	powder ρ_p	grains ρ_{gr}			
SDP-1:					
1st batch	2.1066	1.9919	5.45	–	–
2nd batch	2.1070	1.9910	5.50	–	–
SDP-2:					
1st batch	2.0949	2.0150	3.81	2.0214	3.51
2nd batch	2.0942	1.9944	4.76	–	–
SDP-3:					
1st batch	2.1011	1.9922	5.18	1.9973	4.94
2nd batch	2.1024	1.9810	5.78	–	–
SDP-4:					
1st batch	2.0561	1.9820	3.61	1.9846	3.48
2nd batch	2.0398	1.9879	2.55	–	–
Compaction conditions:					
P = 70–80 kg cm^{-2}, T = 110°C	–	–	–	1.9659	4.39
P = 80–90 kg cm^{-2}, T = 110°C	–	–	–	1.9846	3.48

mined. The study was carried out with samples of compacted plates and granulates of flotation (SDP-1–SDP-3) and halurgic (SDP-4) types.

The data in Table 2 show that the granulates from the four plants strongly differ in porosity. The lowest porosity is observed for grains of halurgic potassium chloride (SDP-4). The density of powdered grains of this type is also lower than that for flotation KCl, which is due to the absence of clayey-carbonate impurities and metal oxides. The absence of these impurities favors compaction of the halurgic potassium chloride, which reflects on the porosity of the granulate obtained.

The differences in porosity between different production batches of the granulate manufactured at the same plant indicate that granulation conditions affect their porous structure (Table 2).

The porosity of a granulate is related to that of the starting material, plates produced by roll presses. It can be seen for the example of SDP-4 that the compaction conditions of a plate determine its porosity: the plate obtained at a pressure of 80–90 kg cm^{-2} has a lower porosity than that produced at 70–80 kg cm^{-2}.

It follows from a comparison of the data in Table 2 that the porosities of the granulate and plates are in good agreement. This suggests that the method suggested can be used for determining the porosity of products formed in granulation of potassium chloride in various stages of their production. The method shows a sufficiently high precision, yields rapid results, and requires simple apparatus and, therefore, it can be used under industrial conditions of the potassium industry.

CONCLUSIONS

(1) A method was suggested for determining the total porosity of potassium chloride grains, which includes pycnometric measurements of the true and apparent densities of grains, with kerosene serving as a pycnometric liquid. Kerosene well wets the grain surface and reliably localizes pore boundaries on the outer surface of samples.

(2) It was shown that this method can be used to determine the porosity of grains in different stages of their manufacture, which will allow control over the consumer properties of products formed in granulation of potassium chloride at plants of the potassium industry.

REFERENCES

1. Cheremskoi, P.G., *Metody issledovaniya poristosti tverdykh tel* (Methods for Analysis of the Porosity of Solids), Moscow: Energoatomizdat, 1985.
2. Il'inskii, G.A., *Opredelenie plotnosti mineralov* (Determination of the Porosity of Minerals), Leningrad: Nedra, 1975.
3. Gregg, S.J. and Sing, K.S.W., *Adsorption, Surface Area and Porosity*, London: Academic, 1982.

ISSN 1070-4272, Russian Journal of Applied Chemistry, 2008, Vol. 81, No. 10, pp. 1725–1728. © Pleiades Publishing, Ltd., 2008.
Original Russian Text © O.I. Platonov, L.Sh. Tsemekhman, 2008, published in Zhurnal Prikladnoi Khimii, 2008, Vol. 81, No. 10, pp. 1597–1600.

INORGANIC SYNTHESIS AND INDUSTRIAL INORGANIC CHEMISTRY

Catalytic Conversion of COS and CS_2 under an Excess of Sulfur Dioxide

O. I. Platonov and L. Sh. Tsemekhman

Gipronikel' Institute Limited Liability Company, St. Petersburg, Russia

Received May 19, 2008

Abstract—Conversion of organosulfur components (COS and CS_2) in catalytic processing of a real reduced sulfurous gas was experimentally studied.

DOI: 10.1134/S1070427208100042

At present, about 40 million tons of sulfur is annually produced in the world in purification of discharge gases by the Claus method in natural-gas- and oil-processing industries [1]. It is prognosticated [2] that, with the environment protection regulations becoming increasingly stringent and requiring higher ecological payments, the volume of accompanying sulfur used to manufacture fertilizers will grow via utilization of metallurgical sulfurous gases. The only working technology for processing of these gases into sulfur is reduction with hydrocarbons, followed by catalytic conversion by the Claus method [3]. Because of the specific features of reduced sulfurous gas, its catalytic conversion strongly differs from that in the classical Claus technique [1, 4]. This circumstance determines the topicality of its analysis with account of parameters of a gas being processed.

A characteristic feature of the reduced gas is the increased content of organosulfur compounds (CS_2 and COS) formed from carbon introduced with the reducing agent, which predetermines the priority role of their conversion, traditionally the most difficult stage in catalytic processing by the Claus method [1, 4]. At large contents of sulfur dioxide, characteristic of the reduced sulfurous gas [5], the commonly taken into account mechanism of COS and CS_2 hydrolysis [1, 3] experiences competition from the alternative channel of conversion by reactions of sulfur dioxide reduction:

$$CS_2 + SO_2 = CO_2 + 3/nS_n, \quad (1)$$

$$2COS + SO_2 = 2CO_2 + 3/nS_n, \quad (2)$$

whose contribution can be predominant under an excess of SO_2.

The aim of our study was to experimentally analyze specific features of the conversion of organosulfur components (COS and CS_2) in catalytic processing of a reduced sulfurous gas.

EXPERIMENTAL

We performed tests in the temperature range 220–600°C on a pilot installation with a flow rate of the gas mixture equal to 0.6–0.7 standard $m^3 h^{-1}$ at Gipronikel' Institute Limited Liability Company. We studied two promising vanadium-containing catalysts: titanium oxide catalyst AOK-78-57 with a specific surface area of 145 $m^2 g^{-1}$ (extrudates 4–5 mm in diameter), manufactured by Katalizator Limited Liability Company (Novosibirsk), and a new VA-2 catalyst on an alumina support, developed at the Institute of Catalysis, Siberian Branch, Russian Academy of Sciences, and manufactured by Novomichurinsk Catalyst Plant Private Company in the form of spherical grains 4–5 mm in diameter and active surface area of no less than 240 $m^2 g^{-1}$.

The tests were made in a vertical stainless steel reactor with external electric heating (catalyst-containing cartridge with an inner diameter of 53 mm and height of 175 mm) and a catalyst charge of 0.38 dm^3. The temperature was controlled and recorded in the course of the experiments with a DT-600 digital data-acquisition device [Data Taker Pty. Ltd. (Data Electronics)]. Metran 231-01 Chromel–Alumel thermoelectric transducers (thermocouples) with a sheath diameter of 3 mm were used as temperature sensors. One of the thermocouples, buried to 4/5 of the catalyst bed height, was also used to maintain the reactor temperature; the electric power for heating the reactor and gas heater was varied using TP 403 microproc-

Gas compositions before and after conversion on the VA-2 catalyst

Gas component	Content, vol %	
	initial	at the outlet
SO_2	20.9 ± 6.5	12.5 ± 8.0
CO	<0.001	0.00 ± 0.03
H_2	3.7 ± 2.4	4.0 ± 3.2
CO_2	14.6 ± 1.9	21.5 ± 5.0
H_2S	6.1 ± 3.0	8.3 ± 7.0
COS	2.0 ± 0.97	1.2 ± 0.8
CS_2	6.2 ± 2.6	2.9 ± 2.6
CH_4	3.7 ± 2.7	3.8 ± 2.6
N_2	43.8 ± 4.4	44.9 ± 6.1

essor heat-control units manufactured by Varta Research and Production Company (St. Petersburg).

The coefficient (degree) of conversion of components of the gas mixture, η_i, was found using the formula [6]:

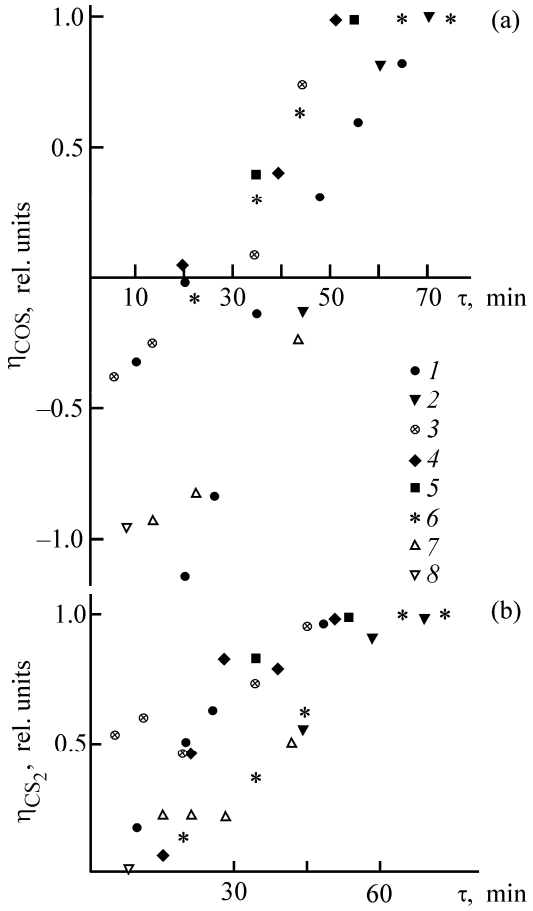


Fig. 1. Relative change in the conversion of (a) carbonyl sulfide, η_{COS}, and (b) carbon disulfide, η_{CS_2}, during tests for a time τ at different temperatures of the VA-2 catalyst. (*6*–*8*) Conversion on the AOK-78-57 catalyst. *T* (°C): (*1*, *6*) 310, (*2*) 340, (*3*, *4*) 380, (*5*) 450, and (*7*, *8*) 250.

$$\eta_i = 1 - \frac{c_i^{out} c_{N_2}^{in}}{c_i^{in} c_{N_2}^{out}}, \quad (3)$$

where c_i^{in} and c_i^{out} are the initial and final concentration of gas component i (i = H_2S, COS, SO_2), and $c_{N_2}^{in}$ and $c_{N_2}^{out}$, the initial and final concentrations of nitrogen in dried gas samples taken at, respectively, the inlet and outlet of the catalytic reactor.

The gas composition was monitored at four points of the pilot installation with an automated analytical complex based on a gas analyzer, EMG 20–1 time-of-flight mass spectrometer manufactured by METTEK Limited Liability Company (St. Petersburg), which can measure the volume concentrations of all the basic components of the gas: H_2S, SO_2, SO_3, COS, CS_2, CO, CO_2, H_2, CH_4, O_2, N_2, and Ar with a threshold sensitivity of 0.01–0.03%. The EMG 20-1 gas analyzer was calibrated against reference gas mixtures prepared at Scientific Instruments Open Joint-Stock Company and Monitoring Limited Liability Company (both from St. Petersburg).

In the course of the tests, a real sulfurous gas reduced in the homogeneous reactor of the pilot installation at a temperature of 1100°C in accordance with the promising technology for processing of metallurgical gases [7] was delivered to the inlet of the catalytic reactor (see table).

In all, the tests were made in 67 operation modes for the VA-2 catalyst and 57 modes for the AOK-78-57 catalysts. The modes differed in temperature at the same initial composition of the gas (see table) and volumetric flow rates W = 1500–1900 h^{-1}.

The results obtained in the pilot tests show that the high efficiency of conversion of organosulfur components on the catalysts under study is high. For example, this is indicated by comparison of the initial composition of the gas with that at the outlet of the catalytic reactor, found from a sample of measurements in 60 modes at a gas flow rate of 11 ± 1.1 standard dm^3 min^{-1} (W = 1600–1900 h^{-1}), also represented in the table.

It can be seen that more than a half, on average, of the organosulfur compounds (CS_2 and COS) is converted in catalytic processing of a reduced sulfurous gas. In the process, the content of carbon dioxide noticeably increases (nearly twice, on average), which points to the decisive contribution of reactions (1) and (2) of sulfur dioxide reduction to the overall conversion.

We observed a rapid variation of the activities of both the catalysts, which is manifested in that the conversion grows during the first hour after a catalyst is put into operation in the on-line mode. This effect is illustrated by Fig. 1, in which the conversion coefficients of sulfur-containing components, η_i, normalized to the maximum conversion of a given component, are arranged in order of increasing time τ elapsed from the beginning of a run. Different symbols in the figure show results of measurements in different runs, on different catalysts, and at different process temperatures.

The activity variation is manifested to the maximum extent in conversion of COS, whose relative conversion coefficient η_{COS} on the alumina catalyst VA-2 changes from –100% to 100% in 1 h (Fig. 1a). The conversion of sulfur dioxide and the overall conversion of sulfur-containing components varies qualitatively similar to η_{CS_2}. The conversion of hydrogen sulfide shows no dynamic effect.

A similar dynamic effect was observed on the titanium oxide catalyst AOK-78-57, on which the conversion of carbonyl sulfide varied under identical process conditions, e.g., at $T \approx 420$°C, from –80 to 76 rel % (Fig. 1).

The statistical scatter of values in the dynamic dependences of the conversion of both the organosulfur components, $\eta_i(\tau)$, is due to uncontrollable specific features of each run (duration of catalyst acidification) at its beginning. Nevertheless, the data scatter σ observed in different runs is noticeably smaller than the variance $\delta\eta_i(\tau)$: $3\sigma < \delta\eta_i(\tau)$, which demonstrates that the dynamic effect is revealed rather reliably.

The activities of the catalysts in CS_2 and COS conversion, determined after 1 h and more of uninterrupted operation, nearly coincide to within the experimental error, even though a tendency is observed for η_{CS_2} to somewhat exceed the conversion of carbonyl sulfide, η_{COS}, under the same conditions.

For illustration, Fig. 2 shows the average, over temperature intervals, conversions of carbonyl sulfide, η_{COS}, and carbon disulfide, η_{CS_2}, on the VA-2 catalyst as functions of temperature in the catalyst bed. The vertical portions correspond to the variances of the averages, and the horizontal portions (defined as variance) are proportional to the width ΔT of the averaging interval.

A possible reason for the appearance of the dynamic dependence of the activities of the catalysts

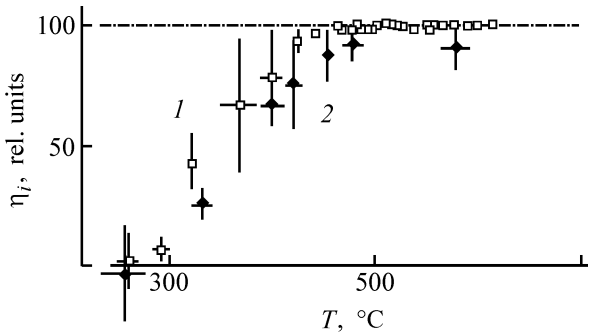


Fig. 2. Conversion η_i of (*1*) carbon disulfide and (*2*) carbonyl sulfide on the VA-2 catalyst vs. temperature T at a volumetric flow rate of 1600–1800 h^{-1}.

tested is their short-term poisoning via sulfation in the warm-up and startup of the installation with the oxygen-containing sulfurous gas. As follows from the results of our tests, the catalyst activity in conversion of organosulfur compounds, low at the beginning of a run, is completely restored during the first hour of on-line operation in the medium of a reduced gas, which contains reducing components (H_2, CO, and H_2S), but is free of oxygen. The differences in the degrees of initial sulfation of a catalyst in each startup predetermine the observed statistical scatter of the empirical values in the dynamic dependences $\eta_i(\tau)$.

As follows from the results of our experiments, CS_2 interacts with SO_2 at least in two stages, with carbonyl sulfide formed in the first of these. The only possible other intermediate in the first stage is, according to the stoichiometric balance of the overall reaction (1), sulfur oxide S_2O, as suggested by the two-stage scheme of the process [6]:

$$CS_2 + SO_2 = COS + [SO_2] = CO_2 + 1/8S_8. \quad (4)$$

In the initial period of operation of a catalyst after its sulfation, carbonyl sulfide is generated, which is manifested in large negative values of its conversion η_{COS} (Fig. 1a). Together with the simultaneously high conversion of carbon disulfide (Fig. 1b), this circumstance suggests that the second stage of carbonyl sulfide conversion is the rate-determining stage, the most sensitive to the catalyst sulfation.

An alternative explanation of the generation of carbonyl sulfide, e.g., that by interaction on the catalyst with sulfur vapor:

$$CO + 1/nS_n = COS, \quad (5)$$

would not do because of the insufficient initial concentration of carbon monoxide (see table). No con-

version of methane (also present in the starting gas), which could serve as a reactant for COS formation, was observed in our experiments within the experimental error limits.

According to the two-stage mechanism of carbon disulfide conversion by reaction (4), with the rate-determining second stage, the conversion of carbon disulfide should be more efficient than that of COS, and this, indeed, was observed in our experiments (Fig. 2). This makes it possible (at least as regards the processing of a reduced sulfurous gas) to reconsider the known paradigm [1, 4] of the more efficient conversion of COS. According to the results of this study, the conversion of organosulfur compounds under an excess of sulfur dioxide predominantly occurs via redox reactions with sulfur dioxide, of which the most efficient is that with CS_2.

The fact that the dynamic effect is observed on catalysts of different types (alumina catalyst VA-2 and titanium oxide catalyst AOK-78-57) means that the conversion of carbonyl sulfide is not directly related to the properties of the active surface, but occurs via adsorption of COS on active basic centers. By analogy with the hydrolysis process [8], the role of centers of this kind can be played by hydroxy groups, which are subject to sulfation in the presence of oxygen.

CONCLUSIONS

(1) If an excess of SiO_2 is present in the gas being processed, the conversion of organosulfur compounds predominantly occurs via their oxidation by sulfur dioxide. An intermediate formed in oxidation of carbon disulfide is carbonyl sulfide, whose further conversion is hindered by sulfation of the active centers of a catalyst. As a result, the conversion of carbon disulfide under an excess of SO_2 is more complete than that of carbonyl sulfide, which predetermines the principal characteristic feature of the catalytic processing of a reduced sulfurous gas.

(2) The experimental data obtained directly confirm for the first time the two-stage mechanism of carbon disulfide conversion by reaction (4) to give COS as an intermediate product of CS_2 conversion.

REFERENCES

1. Grunval'd, V.R., *Tekhnologiya gazovoi sery* (Technology of Gas Sulfur), Moscow: Khimiya, 1992.
2. Okura, T., Ueda, S., and Yamaguchi, K., *Sohn Int. Symp. on Sulfide Smelting, San-Diego, USA, Aug. 27–31, TMS*, 2006, vol. 8, pp. 425–431.
3. Ushakov, K.I., Eremin, O.G., Kalnin, E.I., et al., *Tsvet. Met.*, 1980, no. 2, pp. 34–37.
4. Pearson, M.J., *Hydrocarbon Proc*., 1973, vol. 52, no. 2, pp. 81–85.
5. Platonov, O.I., *Zh. Prikl. Khim*., 2007, vol. 80, no. 9, pp. 1440–1444.
6. Clark, P.D., Dowling, N.I., and Huang, M., *Appl. Catal. B: Environ*., 2001, vol. 31, pp. 107–112.
7. Diachenko, V.T., Kotukhov, S.B., Kozyrev, V.F., et al., *"Sulphur 2007," Conf. papers, Montreal, Canada, 28–31 October 2007*, London: CRU Publ. Ltd., 2007, pp. 75–82.
8. Bachelier, J., Aboulayt, A., Lavalley, J.C., et al., *Catal. Today*, 1993, vol. 17, pp. 55–62.

ISSN 1070-4272, Russian Journal of Applied Chemistry, 2008, Vol. 81, No. 10, pp. 1729–1732. © Pleiades Publishing, Ltd., 2008.
Original Russian Text © N.M. Kozhevnikova, E.P. Ermakova, 2008, published in Zhurnal Prikladnoi Khimii, 2008, Vol. 81, No. 10, pp. 1601–1604.

INORGANIC SYNTHESIS AND INDUSTRIAL INORGANIC CHEMISTRY

Synthesis and Electrical Properties of Variable-Composition Phases $Rb_{1-x}A_{1-x}R_{1+x}(MoO_4)_3$ ($0 \le x \le 0.2$; A = Mg, Mn, Co, Ni; R = Sc, Yb, Lu)

N. M. Kozhevnikova and E. P. Ermakova

Baikal Institute of Nature Management, Siberian Branch, Russian Academy of Sciences, Ulan-Ude, Buryatiya, Russia

Received February 8, 2008

Abstract—Subsolidus region of the ternary systems Rb_2MoO_4–$AMoO_4$–$R_2(MoO_4)_3$, in which variable-composition phases $Rb_{1-x}A_{1-x}R_{1+x}(MoO_4)_3$ crystallizing in the monoclinic system (space group C2) are formed, was studied. Their crystallographic parameters were calculated; temperature dependences of the electrical conductivity, dielectric constant, and dielectric loss tangent were analized.

DOI: 10.1134/S1070427208100054

In the last two decades, an intensive search has been in progress for functional materials with structural skeletons $\{[R_2(ElO_4)_3]^{p-}\}_\infty$, where R is an octahedral cation in phosphate, arsenate, molybdate, tungstate, and sulfate systems [1–8]. Promising in this regard are phases with langbeinite structure, $Sc_2(WO_4)_3$ and $K_2Mg_2(SO_4)_3$, which have bulk cavities partly filled by singly charged cations. They exhibit high conductivity by lithium, sodium, and silver ions [1]. As the radius of a cation increases, its mobility in tunnels and bulk cavities of the structure decreases, which results in a lower conductivity of the phases [4].

In a study of the systems K_2MoO_4–$AMoO_4$–$R_2(MoO_4)_3$ (A = Mg, Mn, Co, Ni; R = Sc, Yb, Lu), variable-composition phases $K_{1-x}A_{1-x}R_{1+x}(MoO_4)_3$ ($0 \le x \le 0.5$) belonging to the langbeinite structural type with a conductivity of 10^{-3} $\Omega^{-1}cm^{-1}$ were obtained [4].

The existence of structures with a considerable volume of voids and the presence of centers unpopulated by cations depend on the nature of the cations, their combination, distribution over structural positions, and population of these positions. No data on existence of the ionic conductivity in rubidium phases are available, which is probably due to a decrease in the mobility of a cation with its increasing radius.

The aim of this study was to synthesize variable-composition phases $Rb_{1-x}A_{1-x}R_{1+x}(MoO_4)_3$ and examine their electrical properties.

EXPERIMENTAL

The starting components for studying the phase formation in the systems Rb_2MoO_4–$AMoO_4$–$R_2(MoO_4)_3$ were Rb_2MoO_4, $AMoO_4$, and $R_2(MoO_4)_3$, preliminarily synthesized by the solid-phase technique from Rb_2CO_3, magnesium, nickel, cobalt, and manganese oxides, molybdenum trioxide of analytically pure grade, and scandium, ytterbium, and lutetium oxides with a content of the main component not lower than 99.99%. Oxides of divalent elements were preliminarily calcined at 650°C for 8 h; Rb_2CO_3 and MoO_3, at 400°C; and R_2O_3, in the temperature range 400–750°C. The reaction mixtures of molybdates of rubidium and di- and trivalent elements were calcined at 450–800°C with multiple intermittent grindings every 20–30 h. The time of calcination at each temperature was 120–150 h. After being annealed, the samples were slowly cooled together with a furnace. Nonequilibrium samples were additionally annealed, with the equilibrium considered to be attained if the phase composition of samples remained constant after two successive annealings. The synthesis products were identified by X-ray phase analysis in an FR-552 chamber-monochromator (Cu_{K_α} radiation, internal standard Ge). The X–ray diffraction patterns were processed using the RENTGEN software. A differential thermal analysis was performed on an MOM OD-103 derivatograph at a heating rate of 10 deg·min^{-1} and sample weight of 0.3–0.4 g.

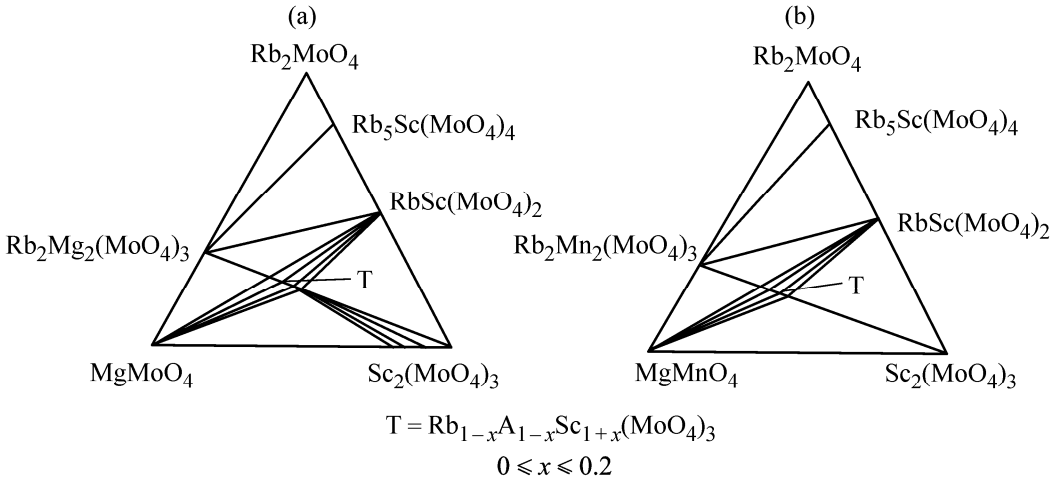


Fig. 1. Phase relationships in the systems (a) Rb_2MoO_4–$MgMoO_4$–$Sc_2(MoO_4)_3$ and (b) Rb_2MoO_4–$MnMoO_4$–$Sc_2(MoO_4)_3$ at 700°C.

Temperature dependences of conductivity σ, dielectric constant ε, and dielectric loss tangent tan δ were studied by Vest and Tallan's polarization technique [6] with densely compacted ceramic samples in the form of pellets 10 mm in diameter and 1–1.5 mm thick, with platinum electrodes. The electrodes were deposited by firing-in a platinum paste. The electrical properties were measured with an E8-4 ac bridge with a P-5025 capacitor box at a frequency of 10^3 Hz (measurement accuracy ±5%). The dc current was recorded with an E6–13A teraohmmeter at a preset voltage of 30–50 mV.

Table 1. Crystallographic and thermal characteristics of $Rb_{1-x}A_{1-x}R_{1+x}(MoO_4)_3$

Composition			*a*	*b*	*c*	*B*, deg	*V*/*Z*	mp, °C
A	R	X	Å					
Ni	Sc	0	16.246(2)	9.371(3)	9.922(1)	122.95(1)	316.7	1085
Ni	Sc	0.2	16.257(1)	9.413(1)	9.935(4)	123.05(1)	318.5	–
Ni	Lu	0	16.262(2)	9.405(3)	9.941(1)	123.16(1)	317.9	1068
Ni	Lu	0.2	16.267(3)	9.421(2)	9.953(5)	122.95(2)	319.5	–
Ni	Yb	0	16.267(2)	9.411(1)	9.969(4)	123.08(1)	319.7	1050
Ni	Yb	0.2	16.271(2)	9.428(3)	9.975(2)	123.12(2)	320.2	–
Mg	Sc	0	16.254(3)	9.386(2)	9.929(2)	122.98(2)	317.7	1070
Mg	Sc	0.2	16.305(5)	9.413(1)	9.918(5)	123.15(1)	318.6	–
Mg	Lu	0	16.248(4)	9.344(3)	9.948(3)	122.99(2)	317.8	1060
Mg	Lu	0.2	16.274(4)	9.396(2)	9.944(5)	123.06(1)	318.9	–
Mg	Yb	0	16.276(5)	9.398(1)	9.875(2)	122.72(1)	319.1	1040
Mg	Yb	0.2	16.352(3)	9.443(5)	9.827(2)	122.58(2)	320.5	-
Co	Sc	0	16.314(5)	9.435(3)	9.968(4)	123.06(1)	321.4	1020
Co	Sc	0.2	16.328(2)	9.448(2)	9.974(2)	123.11(2)	322.4	–
Co	Lu	0	16.402(1)	9.452(3)	9.979(2)	123.13(1)	324.1	1005
Co	Lu	0.2	16.417(3)	9.461(3)	9.982(3)	123.27(2)	324.2	-
Co	Yb	0	16.415(1)	9.465(3)	9.987(1)	123.19(1)	324.7	993
Co	Yb	02	16.422(4)	9.513(4)	9.992(5)	123.16(2)	326.7	-
Mn	Sc	0	16.337(5)	9.598(1)	10.023(2)	122.70(9)	330.0	970
Mn	Sc	02	16.341(2)	9.601(1)	10.027(1)	122.88(1)	331.4	–
Mn	Lu	0	16.358(4)	9.645(1)	10.019(4)	123.16(1)	331.9	960
Mn	Lu	02	16.375(3)	9.662(2)	10.021(2)	123.21(1)	332.9	–
Mn	Yb	0	16.381(4)	9.665(4)	10.081(4)	123.37(2)	333.1	945
Mn	Yb	0.2	16.484(1)	9.677(3)	10.022(2)	123.42(1)	333.7	–

The interaction in the systems Rb_2MoO_4–$AMoO_4$–$R_2(MoO_4)_3$ was examined in the subsolidus region in the temperature range 450–800°C. The study was carried out in two stages. In the first stage, an X–ray study of the phase composition of the samples corresponding to the intersection points of all cuts existing in the systems Rb_2MoO_4–$AMoO_4$–$R_2(MoO_4)_3$ enabled triangulation of the systems. In the second stage, the quasibinary cuts revealed were studied. The formation of ternary molybdates $RbAR(MoO_4)_3$ was observed in the cuts $RbR(MoO_4)_2$–$AMoO_4$ and $Rb_2A_2(MoO_4)_3$–$R_2(MoO_4)_3$ at 600–650°C (Fig. 1). The phases of variable composition $Rb_{1-x}A_{1-x}R_{1+x}(MoO_4)_3$ are formed in a plane of the triangle Rb_2MoO_4–$AMoO_4$–$R_2(MoO_4)_3$ and along the cut $RbAR(MoO_4)_3$–$R_2(MoO_4)_3$.

Samples with compositions corresponding to the quasibinary cuts were prepared with a step of 2.5–5 mol %, and those intended for refining the composition of the ternary molybdate $RbAR(MoO_4)_3$ being formed and of the homogeneity region of the variable-composition phases $Rb_{1-x}A_{1-x}R_{1+x}(MoO_4)_3$, with a step of 1 mol %. The samples were annealed at 450, 550, 600, 650, and 700°C, and those with nickel and cobalt compositions, additionally at 750 and 800°C. Single-phase samples of $Rb_{1-x}A_{1-x}R_{1+x}(MoO_4)_3$ were obtained at 700–800°C with annealing for 180–200 h. The X–ray diffraction analysis of $Rb_{1-x}A_{1-x}R_{1+x}(MoO_4)_3$ samples demonstrated that they are isostructural to each other and to the monoclinic modification of $KMgIn(MoO_4)_3$ (space group C2, $Z = 4$). The X–ray diffraction patterns of $Rb_{1-x}A_{1-x}R_{1+x}(MoO_4)_3$ were indexed in the monoclinic system, using unit cell parameters of the $KMgIn(MoO_4)_3$ single crystal [4]. They melt incongruently in the temperature range 945–1085°C (Table 1).

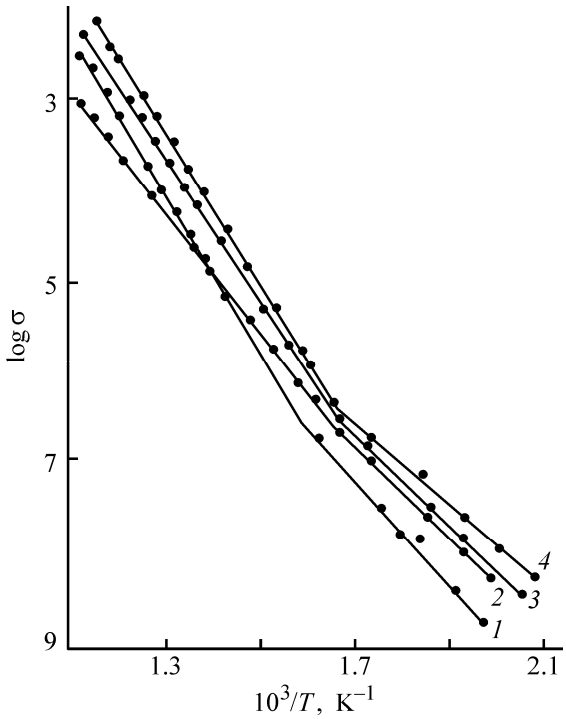


Fig. 2. Temperature dependence of the conductivity σ. (*1*) $RbMgSc(MoO_4)_3$, (*2*) $Rb_{0.8}Mg_{0.8}Sc_{1.2}(MoO_4)_3$, (*3*) $Rb_{0.8}Co_{0.8}Lu_{1.2}(MoO_4)_3$, (*4*) $Rb_{0.8}Mn_{0.8}Yb_{1.2}(MoO_4)$.

The electrical properties of $Rb_{1-x}A_{1-x}R_{1+x}(MoO_4)_3$ were examined in the temperature range 200–600°C (Figs. 2 and 3). The conductivity σ of rubidium phases varies within the range 10^{-9}–10^{-3} $\Omega^{-1}\,cm^{-1}$ (Fig. 2). They are characterized by mixed ionic-electronic conduction with predominance of the electronic component (t_e = 0.62–0.73) having an activation energy of 0.92–1.28 eV (Table 2).

Table 2. Conductivity σ of $Rb_{1-x}A_{1-x}R_{1+x}(MoO_4)_3$, electron transport numbers t_e, and activation energy E_a of conductivity

Composition			300°C		600°C		
A	R	X	$\sigma \cdot 10^8$, $\Omega^{-1}\,cm^{-1}$	t_e	$\sigma \cdot 10^3$, $\Omega^{-1}\,cm^{-1}$	t_e	E_a, eV
Ni	Sc	0.2	0.42	0.68	2.48	0.64	1.15
Ni	Sc	0.2	6.43	0.70	3.14	0.66	1.12
Mg	Sc	0	1.46	0.69	3.67	0.65	1.28
Mg	Yb	0.2	7.51	0.68	5.65	0.64	1.23
Co	Sc	0	7.55	0.69	6.13	0.67	1.05
Co	Sc	0.2	9.83	0.68	7.92	0.64	1.02
Mn	Lu	0	12.2	0.71	5.64	0.63	0.99
Mn	Lu	0.2	36.1	0.70	6.97	0.65	0.95
Mn	Yb	0	7.39	0.69	8.46	0.62	0.96
Mn	Yb	0.2	92.4	0.72	9.77	0.62	0.92

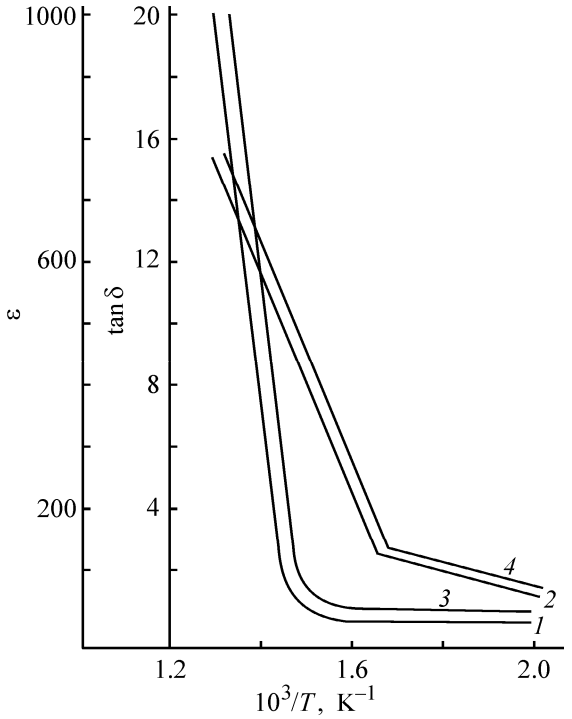


Fig. 3. Temperature dependence of (*2*, *4*) dielectric constant ε and (*1*, *3*) dielectric loss tangent for (*1*, *2*) $RbMgSc \cdot (MoO_4)_3$ and (*3*, *4*) $Rb_{0.8}Mg_{0.8}Sc_{1.2}(MoO_4)_3$.

The dielectric constant ε and the dielectric loss tangent tan δ show an exponential dependence on temperature (Fig. 3). The absence of extrema in the curves for the dielectric constant and dielectric loss tangent indicate that $Rb_{1-x}A_{1-x}R_{1+x}(MoO_4)_3$ exhibits no phase transitions and ferroelectric properties.

CONCLUSIONS

(1) Variable-composition phases $Rb_{1-x}A_{1-x}R_{1+x} \cdot (MoO_4)_3$ ($0 \le x \le 0.2$), A = Mg, Mn, Co, Ni; R = Sc, Yb, Lu were prepared by the method of solid-phase reactions from rubidium carbonate, magnesium, manganese, cobalt, nickel, scandium, lutetium, and ytterbium oxides, molybdenum trioxide, and also from molybdates of rubidium and di- and trivalent elements.

(2) The $Rb_{1-x}A_{1-x}R_{1+x}(MoO_4)_3$ samples are isostructural to each other and crystallize in the monoclinic crystal system (space group C2).

(3) The $Rb_{1-x}A_{1-x}R_{1+x}(MoO_4)_3$ samples have a mixed ionic-electronic conduction with predominance of the electronic component.

REFERENCES

1. Asabina, E.N., Pet'kov, V.I., Boguslavskii, M.V., et al., *Zh. Neorg. Khim.*, 2006, vol. 32, no. 3, pp. 1252–1260.
2. Lazoryak, B.I. and Efremov, V.A., *Zh. Neorg. Khim.*, 1987, vol. 32, no. 3, pp. 652–666.
3. Ivanov-Shits, A.K., Bykov, A.B., and Verin, I.Yu., *Kristallografiya*, 1996, vol. 41, no. 6, pp. 1060–1062.
4. Kozhevnikova, N.M. and Mosokhoev, M.B., *Troinye molibdaty* (Ternary Molybdates), Ulan-Ude: Buryat. Gos. Univ., 2000.
5. Kalinin, V.B., Stefanovich, S.Yu., and Nogai, A., *Izv. Akad. Nauk SSSR, Neorg. Mater.*, 1986, vol. 22, no. 1, pp. 107–112.
6. Vest, R.V. and Tallan, N.H., *J. Appl. Phys.*, 1965, vol. 36, no. 2, pp. 547–552.
7. Catti, M. and Stramare, S., *Solid State Ionics*, 2000, vol. 136–137, pp. 489–493.
8. Duhlev, R., *Acta Crystallogr. C.*, 1994, vol. 50, pp. 1525–1528.

ISSN 1070-4272, Russian Journal of Applied Chemistry, 2008, Vol. 81, No. 10, pp. 1733–1739. © Pleiades Publishing, Ltd., 2008.
Original Russian Text © A.E. Kravchik, Yu.A. Kukushkina, V.V. Sokolov, G.F. Tereshchenko, E.A. Ustinov, 2008, published in Zhurnal Prikladnoi Khimii, 2008, Vol. 81, No. 10, pp. 1605–1612.

PHYSICOCHEMICAL STUDIES OF SYSTEMS AND PROCESSES

Structure of Nanoporous Carbon Produced from Titanium Carbide and Carbonitride

A. E. Kravchik, Yu. A. Kukushkina, V. V. Sokolov, G. F. Tereshchenko, and E. A. Ustinov

Ioffe Physicotechnical Institute, Russian Academy of Sciences, St. Petersburg, Russia

Received June 3, 2008

Abstract—Scanning electron microscopy, X-ray diffraction and adsorption structural analyses, and helium pycnometry were used to study the structure of nanoporous carbon produced by chlorination of powdered titanium carbide and carbonitride and of titanium carbide synthesized by chemical-vapor deposition. The results obtained were used to make suggestions about the type of organization of the nanoporous structure of these materials. The evolution of the structure of nanoporous carbon was analyzed in relation to the chlorination temperature. The effect of the chlorination temperature on the structure of the nanoporous carbon obtained and on its pore volume was examined.

DOI: 10.1134/S1070427208100066

Nanoporous carbon (NPC) produced by chlorination of carbides is widely used in various fields of science and technology [1–9]. Structural studies of NPC synthesized from various carbide and carbonitride materials in the form of powders and a compact material at various thermochemical treatment (TCT) temperatures are of particular scientific and practical interest.

In this study, NPC produced from powdered TiC, $TiC_{0.44}N_{0.48}$ and pyrolytic TiC (CVD) was examined. The structure of NPC produced from TiC powder was studied in [10–13]. In [10], NPC produced from powders at chlorination temperatures of 200–1200°C was examined. It was shown that amorphous carbon with a narrow pore size distribution is formed at T = 400–600°C. Raising the synthesis temperature to above 800°C leads to a broader pore size distribution. It was shown in [11–13] that the structure of carbon produced from TiC strongly depends on synthesis temperature and presence of catalytically active metals, such as nickel, cobalt, and iron, in the reaction medium. Addition of an insignificant amount of a metal leads to formation of a turbostratic structure at temperatures as low as 800–900°C.

EXPERIMENTAL

NPC samples were synthesized from the following starting materials: titanium carbide powder (specific surface area by BET 1.3 $m^2 g^{-1}$, pycnometric density 4.87 g cm^{-3}, carbon content 19.5 wt %) by chlorination at temperatures of 400, 600, 800, 1000, 1300, and 1800°C; pyrolytic TiC (in the form of tubes 8 mm in diameter and wall thickness of up to 1.5 mm) produced by chemical vapor deposition (CVD) (pycnometric density 4.84 g cm^{-3}, carbon content 19.8 wt %); and powdered titanium carbonitride of composition $TiC_{0.44}N_{0.48}$ (specific surface area 1.5 $m^2 g^{-1}$, pycnometric density 5.42 g cm^{-3}, carbon content 8.82 wt %, and nitrogen content 11.35 wt %), produced by by chlorination at 800°C. Titanium carbide and carbonitride were charged into an electric furnace with a graphite heater directly heated by passing a current in the atmosphere of argon; chlorine was fed into the reactor heated to a prescribed temperature. The thermochemical treatment was performed in the flow-through mode [14] to complete removal of titanium from the titanium carbide lattice, as indicated by X-ray diffraction analysis (XRD) and elemental analysis by scanning electron microscopy (SEM). No residual amounts of the TiC phase and elementary titanium were found in NPC. To remove the re-sidual content of titanium chloride and chlorine, NPC was additionally dechlorinated at a temperature of 800°C in H_2 for 1 h.

The shape and size of powder particles of TiC and $TiC_{0.44}N_{0.48}$ and of NPC synthesized from powdered TiC and compact material (tube of pyrolytic TiC and NPC produced from pyrolytic TiC) was determined

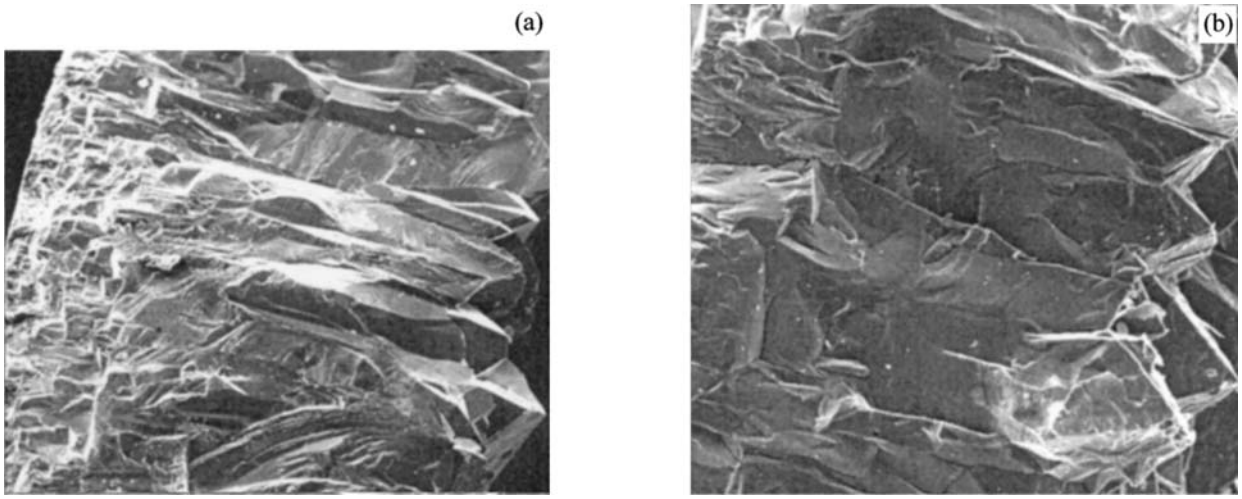


Fig. 1. Fractograms of lateral fractured surface of (a) tube composed of TiC(CVD) and (b) NPC produced from TiC(CVD).

and an elemental analysis was performed with a Quanta 200 scanning electron microscope. The structure was examined by XRD on a DRON-4 X-ray diffratometer with Co_{K_α} radiation. The pycnometric density was measured by gas pycnometry (pycnometric gas He) with a Quantachrome Ultrapycnometer 1000 device. An adsorption-structural analysis (ASA) (measurement of the adsorption–desorption of nitrogen) was performed at liquid-nitrogen temperature (–196°C) on a Micromeritics ASAP 2020 installation.

SEM studies demonstrated that powders of the starting carbide and powders subjected to thermochem-ical treatment at various temperatures have ?the same size and shape of particles?. The pyrolytic TiC has no porosity, which is indicated by results of pycnometric and metallographic studies, and, therefore, used to obtain compact NPC with a monodisperse structure. Figure 1 shows fractograms of a fractured lateral surface of tubes composed of pyrolytic TiC before chlorination (Fig. 1a) and NPC tubes produced from pyrolytic TiC after chlorination (Fig. 1b). As can be seen from these images, the shape, size, and structure of compact NPC before and after chlorination are the same. The pycnometric densities of NPC produced at 400–800°C from TiC and TiC_xN_y powders and pyrolytic TiC fall within the range 2.19–2.25 g cm^{-3}, which is close to the theoretical density of graphite (2.265 g cm^{-3}). At TCT temperatures $T \geq 1000$°C, the pycnometric density gradually decreases (Table 1), with the pore volume for nitrogen simultaneously becoming smaller. This indicates that pores inaccessible to nitrogen (to a greater extent) and helium (to a lesser extent) are formed.

Table 1. Structural parameters of NPC produced from a TiC powder at various temperatures*

T_{TCT}, °C	α, deg	q, %	d_{002}	L_a	Δa	L_c	Δd	ρ_p, g cm^{-3}
			nm					
400	34	–	–	0.9	0.005	–	–	2.19
600	28	18	0.372	1.1	0.005	–	–	2.25
800	16	21	0.370	1.2	0.004	5.8	0.011	2.25
1000	11	38	0.343	6.4	0.002	11.3	0.009	2.02
1300	8	63	0.340	8.1	0	14.2	0.008	1.97
1800	0	100	0.337	8.6	0	16.4	0.007	1.71

* α is the slope of the X-ray diffraction curve at front diffraction angles, which gives the fraction of carbon atoms in the amorphous state; q, number of hexagonal carbon monolayers in microlayers; d_{002}, average interlayer spacing between hexagonal monolayers in a microlayer; L_a, average length of a rectilinear portion of a carbon monolayer; L_c, average thickness of a microlayer; Δa and Δd, average defectiveness of monolayers in the directions a and c, respectively; and ρ_p, pycnometric density.

The structural parameters of NPC were determined using methods described in [15, 16]. An XRD analysis of the structure of NPC synthesized from TiC demonstrated that, as the TCT temperature increases, the structure of the material rather gradually changes from amorphous to paracrystalline and further to turbostratic (Table 1). It should be noted that, in the case of NPC synthesized at 400°C, hexagonal carbon monolayers do not combine into microlayers. The X-ray diffraction pattern of this material contains no (002) reflection (Fig. 2a). As the TCT temperature is raised, the fraction of the amorphous phase decreases to zero. At a TCT temperature of 1800°C, the NPC structure becomes turbostratic, with all carbon monolayers combined into microlayers (q = 100%) (Fig. 2b). The spacing between hexagonal monolayers in microlayers steadily decreases as the TCT temperature is raised and reaches a value of 0.337 nm. The average length L_a of rectilinear portions of carbon monolayers increases from 0.9 to 8.6 nm. For NPC powders produced from TiC (1800°C), in which all monolayers are combined into microlayers, the parameter L_a acquires a meaning of the length of the rectilinear portion of a carbon microlayer. As the TCT temperature is raised, the defectiveness of monolayers in the direction a decreases from 0.05 nm to zero at a temperature of 1300°C. This means that there is no curvature of carbon monolayers across a length L_a.

For NPC powders produced from TiC and subjected to TCT at 400 and 600°C, there are no (002) and (004), and (004) reflections, respectively. Therefore, it is impossible to determine L_c and Δd. The thickness L_c of microlayers is 5.8 nm in NPC produced from TiC (800°C) and increases to 16.4 nm for NPC from TiC (1800°C). The defectiveness of monolayers in the direction c substantially exceeds that in the direction a and decreases from 0.011 to 0.007 nm as the TCT temperature is raised.

The structural parameters of NPC produced from powdered $TiC_{0.44}N_{0.48}$ and compact pyrolytic TiC at 800°C coincide, to within experimental error, with those of NPC synthesized from TiC powders also at 800°C, and, therefore, these data are not presented in Table 1. The structure of NPC produced from TiC varies with the TCT temperature similarly to that of NPC from B_4C [14]. Therefore, a model suggested for NPC produced from B_4C can be adopted for NPC produced from TiC. The NPC synthesized from TiC powders at 400–1000°C contain a large amount of amorphous carbon (α = 34°–11°) with a considerable fraction of carbon monolayers (q = 0–38%). Consequently, a predominantly paracrystalline structure is formed, mostly constituted by single carbon monolayers bound to each other by linear carbine chains. Therefore, it can be stated that the pore structure of NPC synthesized at these temperatures is generated by carbon monolayers. The length and width of these layers, L_a = 0.9–1.2 nm.

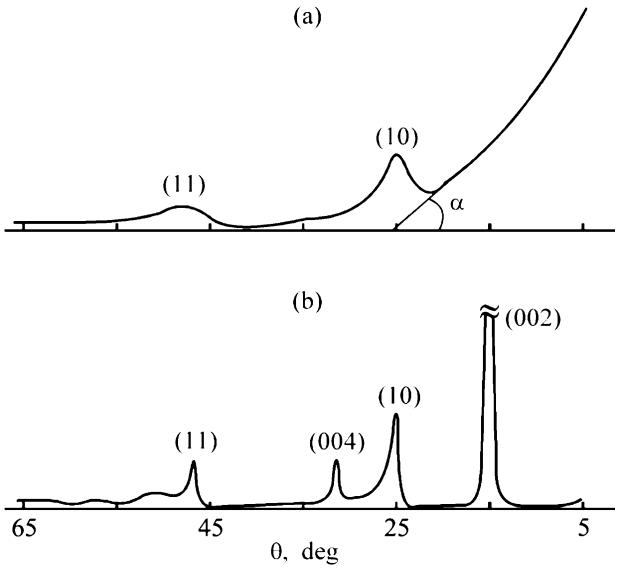


Fig. 2. X-ray diffraction patterns of NPC obtained at (a) 400 and (b) 1800°C from TiC (Co_{K_α}). (θ) Diffraction angle.

At TCT temperatures above 1300°C, the fraction of the amorphous phase decreases to zero, linear carbine chains almost disappear, and a turbostratic carbon structure is formed, with the fraction of monolayers combined into microlayers ranging from 63 to 100%. The pore structure of NPC synthesized from TiC at above 1300°C can be for the most part represented by slits formed between carbon microlayers, and, therefore, a decrease in the specific surface area and pycnometric density is observed for these materials (Table 1). The average sizes of the rectilinear regions of microlayers in NPC produced at a TCT temperature of 1800°C are as follows (nm): L_a = 8.6 and L_c = 16.4. It is apparent that an intermediate structure is formed at TCT temperatures of 1000 to 1300°C. This structure contains pores formed both by carbon monolayers and by intersection of carbon microlayers.

A study of the structure of NPC produced from TiC by high-resolution transmission electron microscopy (HRTEM) demonstrated that the structure of the material is constituted by hexagonal carbon monolayers produced at low chlorination temperatures (Fig. 3a)

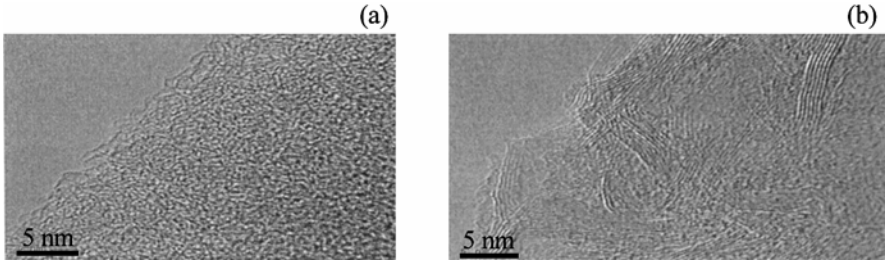


Fig. 3. HRTEM micrographs of NPC produced from α-SiC at T_{TCT} of (a) 600 and (b) 1800°C.

and by carbon microlayers formed at high chlorination temperatures (Fig. 3b).

Titanium carbide has a face-centered cubic (fcc) structure and belongs to interstitial phases formed by introduction of carbon atoms into interstitial positions of the fcc sublattice of titanium atoms. Metal atoms are arranged in densely packed layers, between which carbon layers lie. The lattice constant of TiC is 0.4328 nm. The TCT of carbides is a topochemical reaction, i.e., reaction that occurs in a narrow localized zone at the interface between a solid reagent (carbide in the case in question) and a solid product (NPC), with gradual shift of the reaction front into the carbide and its conversion into carbon. This suggestion was confirmed in chlorination of TiC produced by CVD. With account of the initial structure of TiC and of the chemical nature of the process, an NPC structure with slit-like pores should be formed.

The structure of the NPC samples under study was determined by the ASA method, using the nonlocal density functional theory (NLDFT) adapted to adsorption of nitrogen on amorphous surfaces [17–19]. The surface of ungraphitized carbon black with adsorbed nitrogen served as a reference system. It is noteworthy that the NLDFT variant developed for crystalline surface has been used until now, with graphitized carbon black chosen as a reference system in the case of activated carbons. As a rule, this choice resulted in an insufficiently accurate description of experimental isotherms of nitrogen adsorption on activated carbon and distorted the pore size distribution [18].

The suggestion that the pore wall surface has an amorphous (defective) structure considerably improves the descriptive capacity of the NLDFT and gives a more adequate pore size distribution. The working principle of the approach developed consists in that the adsorbent and adsorbed nitrogen are represented as components of a binary system and the global similarity of these components is in their disordered state. In the original theory, the adsorbate within a limited volume of a pore was understood as a gas or vapor experiencing the action of an external field created by the adsorbent. In the new variant, the adsorbent is not any more a thermodynamically inert, external with respect to the adsorbate, body whose only role is to create an adsorption field. Previously, the NLDFT has been only applied to gases, vapors, or fluids. In the NLDFT version developed in this study, a common procedure is used for the binary system constituted by a solid and a gas (vapor). Even in the case when pores have a slit-like shape, the model suggested here better describes the adsorption isotherm because of the presence of defects in the hexagonal structure of mono- and microlayers.

Particular attention was given to the inversion method used to find the differential pore distribution function from the adsorption isotherm. This problem belongs to the class of ill-posed problems because the results of analysis are rather sensitive to experimental errors. Accidental nonsignificant peaks or dips on the distribution curves are suppressed using the regularization (smoothing) method developed by Tikhonov [20]. A careful choice of the regularization parameter and of the type of the stabilizing functional made it possible to elucidate fine details of the porous structure and the effect of technological parameters on this structure. The pore width H is defined in this study as the distance between the centers of carbon atoms situated on the opposite walls. It is noteworthy that the effective pore width H–Δ (where Δ is the distance between neighboring graphenes in the graphite lattice, 0.335 nm) is used in the literature and software for instruments analyzing the porous structure by the adsorption method. Such a definition has been accepted in order to take into account only pores with width exceeding Δ, accessible to gas molecules. If, in particular, the pore wall is composed of only a single graphene, its wall thickness is considered to be equal to Δ, rather than to zero. In this study, the definition was only used

Table 2. Porous structure parameters of NPC synthesized from TiC at various temperatures*

T_{TCT},°C	V_Σ	V_1	V_2	V_3	S_Σ	S_1	S_2	S_3	H_1	H_2	H_3
	$cm^3\ g^{-1}$				$m^2\ g^{-1}$				nm		
400	0.392	0.329	0.063	–	1935	1829	106	–	0.696	1.314	–
600	0.445	0.362	0.083	–	2012	1819	193	–	0.734	1.092	–
800	0.538	0.338	0.200	–	2100	1679	421	–	0.735	1.064	–
1000	0.523	0.072	0.103	0.348	1021	375	326	320	0.734	0.981	1.713
1300	0.293	0.014	0.042	0.237	171	69	44	58	0.715	2.548	11.54
1800	0.290	0.003	0.009	0.278	62	15	8	39	0.734	2.483	18.10

* V_Σ, V_1, V_2, and V_3 are the total pore volume and volumes of the 1st, 2nd, and 3rd groups of pores; S_Σ, S_1, S_2, and S_3, the total specific surface area and specific surface areas of the 1st, 2nd, and 3rd groups of pores; H_1, H_2, and H_3, widths of the 1st, 2nd, and 3rd groups of pores, respectively.

to calculate the pore volume, because just the volume accessible to molecules of the substance being adsorbed is conventionally understood as the pore volume. However, the concept of the true, geometric pore width was used as the most adequate characteristic when analyzing the pore size distribution function.

The isotherms of nitrogen adsorption on the nanoporous carbon materials studied are shown in Fig. 4. A study of the ASA results demonstrated that, as the TCT temperature increases, the porous structure of NPC changes from microporous with high specific surface area to coarsely mesoporous with low specific surface area (Fig. 5, Table 2). For example, the isotherms of nitrogen adsorption-desorption on NPC samples synthesized at 400, 600, and 800°C show no hysteresis loop characteristic of mesoporous systems and are similar to type-I isotherms, which describe microporous systems in accordance with the IUPAC classification. A hysteresis loop appeared on the isotherm for the NPC produced at 850°C, with the fraction of mesopores equal to 21% of the total pore volume.

The pore size distribution varies with the chlorination temperature At a chlorination temperature of 400–800°C, only pores smaller than 2 nm in size (micropores) are present in NPC; at NPC synthesis temperatures of 850–1200°C, a bidisperse structure (micromesoporous) is formed; whereas chlorination at tem-

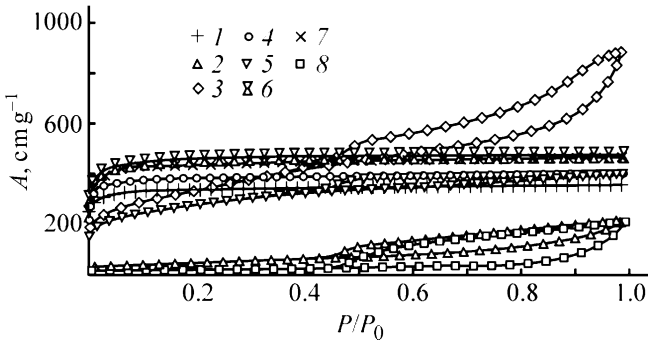


Fig. 4. Adsorption isotherms of nanoporous carbons obtained at different temperatures. (*A*) Amount of adsorbed N_2, and (P/P_0) relative pressure. Temperature (°C): (*1*) 400, (*2*) 1300, (*3*) 800 ($TiC_{0.44}N_{0.48}$), (*4*) 600, (*5*) 100, (*6*) 800 [TiC (CVD)], (*7*) 800, and (*8*) 1800.

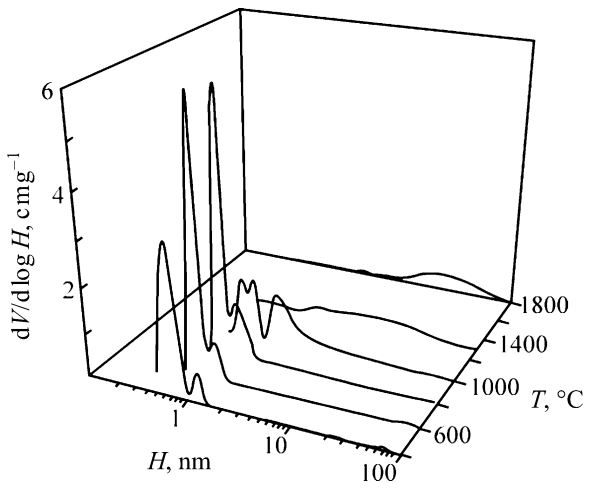


Fig. 5. Pore size distribution for NPC in relation to the TCT temperature. ($dV/d\log H$) Change in the pore volume, (*H*) pore width, and (*T*) temperature.

Table 3. Porous structure parameters of NPC synthesized from TiC and $TiC_{0.44}N_{0.48}$ at 800°C

Starting material	V_Σ	V_1	V_2	V_3	S_Σ	S_1	S_2	S_3	H_1	H_2	H_3
	$cm^3\ g^{-1}$				$m^2\ g^{-1}$				nm		
TiC	0.538	0.338	0.200	–	2100	1679	421	–	0.735	1.064	–
TiC (CVD)	0.541	0.319	0.094	0.128	2230	1710	270	250	0.715	1.008	1.314
$TiC_{0.44}N_{0.48}$	1.228	0.162	0.526	0.540	1225	684	477	64	0.956	2.008	10.10

peratures $T \geq 1300$°C yields a mesoporous structure. The isotherms of nitrogen adsorption-desorption on NPC samples synthesized at 1000, 1300, and 1800°C and NPC produced from $TiC_{0.44}N_{0.48}$ show a hysteresis loop, which indicates that mesopores are present. For NPC powders produced from TiC at 400–800°C, two groups of micropores are observed, with the following sizes (nm): 1st group, 0.70–0.74; 2nd group, 1.06–1.31 (Fig. 5, Table 2). In the temperature range specified, the volumes and specific surface areas of these two groups of micropores in the NPC obtained change only slightly.

The NPC obtained at 1000°C has already three groups of pores, with the sizes of the first two groups of pores remaining nearly the same, and the average size of pores of the third group equal to 1.71 nm (Fig. 5). The volume of micropores passes through a maximum (0.54 $cm^3\ g^{-1}$) for the NPC obtained at 800°C. Raising the temperature further, to above 800°C, leads to a decrease in the volume of micropores and to a pronounced development of mesopores. The total specific surface area and the specific surface area of micropores show the same tendency. For example, the total specific surface area first increases to 2100 $m^2\ g^{-1}$ at 800°C and then decreases as the temperature is raised further. At a TTCT of 1300°C, a mesoporous NPC structure appears. For TCT at $T \geq 1300$°C, the peaks in the region of micropores are negligible. There is a broad peak in the region of mesopores (Fig. 5) and the specific surface area decreases to 62 $m^2\ g^{-1}$. These NPC materials can be attributed to materials with a mesoporous structure.

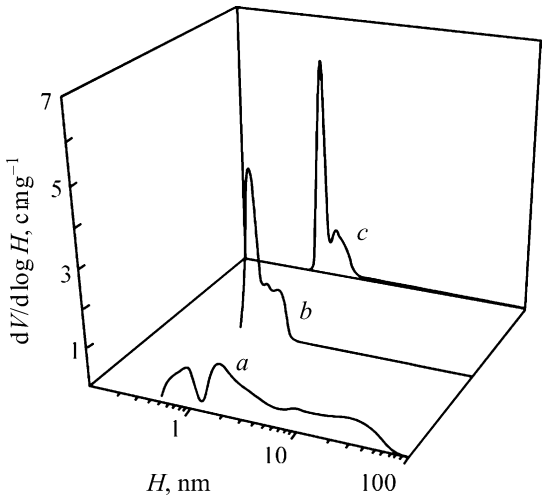


Fig. 6. Pore size distribution for NPC produced from (*a*) $TiC_{0.44}N_{0.48}$, (*b*) TiC (CVD), and (*c*) TiC (powder) in relation to the TCT temperature. ($dV/d\log H$) Change in the pore volume, and (H) pore width.

The results obtained show a good correlation with the results of XRD and refine these data. This gives reason to believe that, at TCT temperatures of 400–800°C, carbon monolayers form a microstructure with two characteristic sizes: 0.70–0.74 and 1.06–1.31 nm (on the assumption of a slit-like model). At a TCT temperature of 1000°C, carbon microlayers start to be formed, with the fraction of pores formed by monolayers becoming smaller and there appearing a new type of pores formed by spaces between microlayers. At TCT temperatures $T \geq 1300$°C, micropores formed by carbon monolayers disappear and mesopores formed by carbon microlayers remain. This yields NPC with a mesoporous structure (Fig. 5).

In this study, NPC produced from TiC powder, compact pyrolytic TiC, and $TiC_{0.44}N_{0.48}$ powder at a chlorination temperature were examined. For TiC powder and compact pyrolytic TiC, the data almost coincide (Table 3, Fig. 6). It can be stated on the basis of the results obtained that the structures of NPC produced under identical conditions are independent of the dispersity of the starting carbide, being the same even for a compact material.

The structure of the NPC produced from $TiC_{0.44}N_{0.48}$ is similar to that of the NPC synthesized from TiC (1000°C) (Figs. 5, 6). A small single peak with an average pore size of 0.96 nm is observed in the region of micropores, and two peaks (~2 and 10 nm), in the region of mesopores. The main difference between these two materials is in the volume and specific

surface area of mesopores (whose size exceeds 2 nm in accordance with the international classification by IUPAC). For example there are no mesopores at all in NPC produced from TiC (1000°C), and the volume and specific surface area of mesopores in NPC produced from $TiC_{0.44}N_{0.48}$ are 0.94 $cm^3 g^{-1}$ and 351 $m^2 g^{-1}$, respectively. The total pore volume in NPC synthesized from $TiC_{0.44}N_{0.48}$ is twice that in NPC produced from TiC (1000°C) (Tables 2, 3). This effect can be attributed to removal of titanium and nitrogen atoms from $TiC_{0.44}N_{0.48}$ by TCT. This yields lager pores.

It should also be noted that the majority of pores in NPC produced from $TiC_{0.44}N_{0.48}$ are formed by hexagonal carbon layers (q = 20%), whereas in NPC synthesized from TiC (1000°C), a substantial part of mesopores are formed by carbon microlayers (q = 38%). The fraction of micropores in NPC produced from $TiC_{0.44}N_{0.48}$ is 24%, and that in NPC synthesized from TiC (1000°C), 100%. This suggests that NPC produced from $TiC_{0.44}N_{0.48}$ belongs to materials with predominantly mesoporous structure, and NPC synthesized from TiC (1000°C), to materials with microporous structure.

CONCLUSIONS

(1) Analysis of the effect of the thermochemical treatment temperature on the structure of nanoporous carbon produced from TiC powders shows that the structure varies from paracrystalline to turbostratic. Depending on the thermochemical treatment temperature, the porous structure of nanoporous carbon varies from microporous (thermochemical treatment temperature 400–800°C) to mesoporous (thermochemical treatment temperature 1300–1800°C).

(2) The structures of nanoporous carbon produced from powdered and compact (pyrolytic) TiC at the same temperature are nearly the same. The structure of nanoporous carbon produced from $TiC_{0.44}N_{0.48}$ is predominantly mesoporous, with a large total volume of pores, including mesopores, which twice exceeds the total pore volume of nanoporous carbon synthesized from TiC.

ACKNOWLEDGMENTS

The study was in part supported by the Russian Federal Agency for Science and Innovations (grant no. 9085.2006.2). E.A.U. is grateful for the financial support to the Russian Foundation for Basic Research (grant no. 06-03-62 268).

REFERENCES

1. Fedorov, N.F., Ivakhnyuk, G.K., and Gavrilov, D.N., *Zh. Prikl.Khim*., 1982, vol. 55, no. 1, pp. 46–50.
2. Fedorov, N.F., Ivakhnyuk, G.K., and Gavrilov, D.N., *Zh. Prikl.Khim.*, 1982, vol. 55, no. 2, pp. 272–276.
3. Fedorov, N.F., *Ross. Khim. Zh.*, 1995, vol. 39, no. 6, pp. 73–83.
4. Nikitin, A. and Gogotsi, Y., *Encyclopedia of Nanosci. Nanotechnol.*, 2003, vol. 7, pp. 553–74.
5. Kravchik, A.E., *Kritich. Tehnol., Membrany*, 2003, no. 3 (19), pp. 3–12.
6. US Patent Pat. 6110335 US, C 25 B 11/12; H 01 G 4/06; H 01 G 9/00; H 01 G 9/02. *Electrode having a carbon material with a carbon skeleton network and capacitor having the same.*
7. RF Patent 2 249 876.
8. RF Patent 2 280 498.
9. Gordeev, S.K., Korchagina, S.B., Kravchik, A.E., and Tereshchenko, G.F., Abstracts of Papers, *IX Mezhdunarodnaya konferentsiya "Vodorodnoe materialovedenie i khimiya uglerodnykh nanomaterialov"* (ICHMS 2005), *Ukraina, Sudak, 5–11 sentyabrya 2005 g.* (IX Int. Conf. "Hydrogen Materials Science and Chemistry of Carbon Nanomaterials" (ICHMS 2005), Ukraine, Sudak, September 5–11, 2005), pp. 1212–1213.
10. Dashn, R.K., Chimola, J., Yushin, G., et al., *Carbon*, 2006, vol. 44, pp. 2489–2497.
11. Leis, J., Perkson, A., Arulepp, M., et al., *Carbon*, 2002, vol. 40, pp. 1559–1564.
12. Perkson, A., Leis, J., Arulepp, M., et al., *Carbon*, 2003, vol. 41, pp. 1729–1735.
13. Leis, J., Arulepp, M., Kuura, A., et al., *Carbon*, 2006, vol. 44, pp. 2122–2129.
14. Kravchik, A.E., Kukushkina, Yu.A., Sokolov, V.V., and Tereshchenko, G.F., *Carbon*, 2006, vol. 44, pp. 3263–3268.
15. Kravchik, A.E., Osmakov, A.S., and Avarbe, R.G., Zh. Prikl. Khim., 1989, vol. 62, no. 11, pp. 2430–2435.
16. Kravchik, A.E., Moshkina, T.I., and Osmakov, A.S., *Zavod. Lab*., 1986, vol. 52, no. 8, pp. 38–41.
17. Ustinov, E.A., Do, D.D., and Jaroniec, M., *Appl. Surf. Sci.*, 2005, vol. 252, pp. 548–561.
18. Ustinov, E.A., Do, D.D., and Fenelonov, V.B., *Carbon*, 2006, vol. 44, pp. 653–663.
19. Ustinov, E.A., Do, D.D., and Jaroniec, M., *Langmuir*, 2006, vol. 22, pp. 6238–6244.
20. Tikhonov, A.N. and Arsenin, V.Y., *Solutions of Ill-Posed Problems*, New York: Wiley, 1977.

ISSN 1070-4272, Russian Journal of Applied Chemistry, 2008, Vol. 81, No. 10, pp. 1740–1746. © Pleiades Publishing, Ltd., 2008.
Original Russian Text © N.I. Golovina, G.N. Nechiporenko, G.G. Nemtsev, I.N. Zyuzin, V.P. Roshchupkin, D.B. Lempert, I.V. Ovchinnikov, G.B. Manelis, 2008, published in Zhurnal Prikladnoi Khimii, 2008, Vol. 81, No. 10, pp. 1613–1619.

PHYSICOCHEMICAL STUDIES OF SYSTEMS AND PROCESSES

Control over Phase Transformations in the Crystal Lattice of Ammonium Nitrate by Modification of the System of Intermolecular Interactions via Addition of Organic Substances

N. I. Golovina, G. N. Nechiporenko, G. G. Nemtsev, I. N. Zyuzin, V. P. Roshchupkin, D. B. Lempert, I. V. Ovchinnikov, and G. B. Manelis

Institute of Problems of Chemical Physics, Russian Academy of Sciences, Chernogolovka, Moscow oblast, Russia

Received January 22, 2008

Abstract—Methods for phase stabilization of ammonium nitrate were sought for to substantially extend the application fields of this oxidizing agent in self-combustible formulations for various purposes, including the new generation of gas-generating formulations for automobile safety bags. The phase state of ammonium nitrate alloys with minor additions of organic substances with crystallographic parameters close to those of ammonium nitrate was studied.

DOI: 10.1134/S1070427208100078

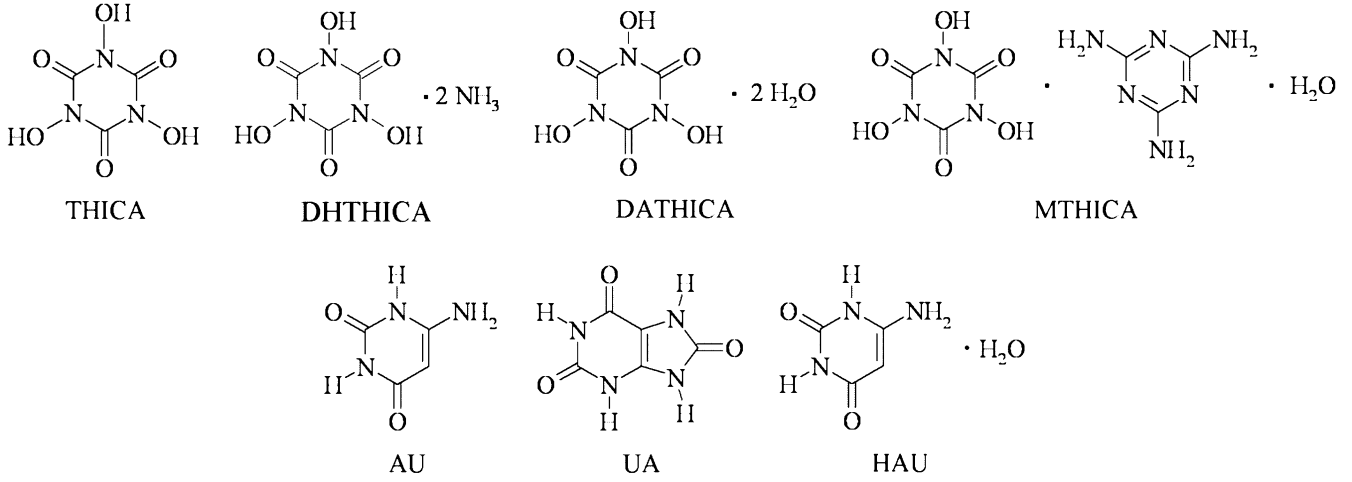
Methods for affecting the phase states and phase transformation of crystalline substances, such as introduction of minor amounts (in crystallization from solutions or melts) of modifying substances, are well known and frequently used. The modifiers can affect the phase state in different ways. They can cardinally change the phase transition points, with the thermodynamic range of existence of crystalline modifications extended or narrowed, to the point of stabilization of a substance in one of the phases. For example, ammonium nitrate (AN) can be stabilized in phase III by isomorphic introduction of potassium nitrate into its lattice. At the same time, the effect of other modifiers consists only in the influence on the phase transition kinetics, with the phase transition process substantially decelerated. Some researchers understand such a deceleration as true stabilization, rather than as the actually occurring attainment of a metastable state.

Recently, an increasing attention has been paid to the nature and mechanism of the influence exerted by modifying substances on phase states. The mechanism of the effect of isomorphic introduction of foreign cations or anions into the lattice is more or less clear. This can and must affect the energy of interionic interaction and, consequently, the phase state, too. There are examples of how substances not incorporated into the crystal lattice affect the phase state of substances. It is believed that modifiers of this kind act across the crystallite surface by entering the interblock space.

In recent years, a new group of modifying substances has been discovered. Owing to the crystallochemical similarity to AN (i.e., because of the fullest coincidence of distances between the atomic planes of a modifier with those in AN itself), these modifiers can be incorporated into its lattice. However, their effect on the phase state fundamentally differs from that of ions isomorphically introduced into the lattice [1, 2]: additional intermolecular interactions appear between the incorporated atomic planes of the modifier and the atomic planes of AN. The nature of these intermolecular interactions in the crystal lattice being modified is rather complex: it may involve changes in the electronic state of molecules or ions (to the point of electron transfer and formation of charge-transfer complexes), formation of new hydrogen bonds, and other types of chemical interactions. Performing only crystallochemical studies of the starting crystals and modifier-crystals is insufficient for understanding the nature

and mechanism of the influence exerted by substances of this kind on the phase state. Studies of UV and IR spectra, and possibly of NMR spectra, too, are necessary here, with the nature of intermolecular interactions in individual modifier substances compared with that in the lattice of an object being modified.

This communication reports on continuation and development of our previous studies [1–3]. Results obtained in an analysis of the interaction of planar molecules of unsaturated heterocycles containing carbonyl and amine (or imine) groups with the AN lattice are presented. It follows from quantum-chemical calculations that the planar nitrate anion contains an upper twice-degenerate bonding orbital of the π-type, upper nonbonding orbital of the *p*-type (lies in the plane of the anion), and lower unoccupied orbital of the π-type. the electronic structure of the nitrate ion that the anion can simultaneously act as an electron donor and electron acceptor in its possible intermolecular orbital interactions with the modifier molecule. A number of compounds were studied as modifier molecules: 1,3,5-trihydroxyisocyanuric acid (THICA) $C_3H_3N_3O_6$ (also named 1,3,5-trihydroxyhexahydro–1,3,5-triazine-2,4,6-trione), its dihydrate (DHTHICA) $C_3H_3N_3O_6 \cdot 2H_2O$, its diammonium salt (DATHICA) $C_3H_3N_3O_6 \cdot 2NH_3$, 1,3,5-trihydroxyisocyanuric acid melamine salt hydrate (MTHICA) $C_3H_3N_3O_6 \cdot C_3H_6N_6 \cdot H_2O$ (the last two salts have not been described in the literature), 4-aminouracyl (AU) $C_4H_5N_3O_2$, its monohydrate (HAU) $C_4H_5N_3O_2 \cdot H_2O$, and 2,4,6-trioxypurine (uric acid, UA) $C_5H_4N_4O_3$, suggested as an AN modifier in our previous studies [4, 5]:



Previously, [6], we have performed an X-ray diffraction analysis of DHTHICA, AU, and HAU single crystals and calculated, using the experimental data, the electronic parameters of modifier molecules in order to describe the configuration of the molecules by quantum-chemical methods. To describe the configuration of the UA molecules, we used the results of an X-ray diffraction analysis made in [7]. Our choice of the modifier molecules was governed by the fact that the molecules mentioned above are perfect electron acceptors (owing to the presence of a carbonyl group), on the one hand, and good electron donors (because of the presence of an imine group), on the other. DHTHICA crystals were chosen for an X-ray diffraction analysis; atomic coordinates furnished by the X-ray diffraction analysis were used only for the individual molecule of this acid (THICA); composites with ammonium nitrate were produced using a fine-crystalline powder of DHTHICA.

It has been shown previously as a result of a thorough search for smokeless gas-generating formulations for automobile safety bags that, possibly, one of the best combustibles to be used in pair with AN is THICA [8]. The point is that, in this composition, the low content of AN (40.4%) is combined with the low combustion point (2374 K) and low content of water in combustion products (42.9%). Unfortunately, THICA is a medium-strength acid (pH ~3 for a 10% aqueous solution) (according to the results of spectrophotometric and potentiometric measurements, p*K*(1) 5.23, p*K*(2) 6.32, and p*K*(3) 7.93 [9]). As a consequence, THICA is chemically incompatible with AN (in an attempt to fuse AN with THICA, first signs of interaction were observed at $T \approx 70$°C and decomposition at $T \approx 120$°C).

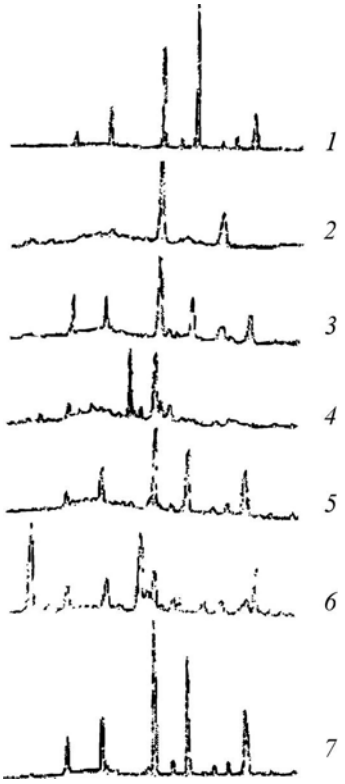


Fig. 1. X-ray diffraction patterns of polycrystalline samples. (λ Cu K_α, 2θ = 10°–50°). (*1*) Ammonium nitrate, (*2*) DATHICA, (*3*) 55.3% AN + 44.7% DATHICA alloy, (*4*) AU, (*5*) 83.8% AN + 16.2% AU, (*6*) UA, and (*7*) 70.4% AN + 29.6% UA.

In a search for THICA derivatives compatible with AN, we synthesized the previously unknown DATHICA and MTHICA. It was found that DATHICA is nearly insoluble in water and organic solvents (a unique situation for ammonium salts of organic acids). The structure of the salts was confirmed by elemental analysis and IR spectroscopy. It was shown by the DTA–TGA technique that both the salts are sufficiently thermally stable and chemically compatible with AN, and DATHICA exhibited modifying properties. Unfortunately, we could not grow single crystals of the DATHICA salt for X-ray diffraction analysis. The crystal-chemical correspondence to the structure of ammonium nitrate is characteristic of both the THICA acid and DATHICA salt.

It follows from the results of an X-ray diffraction analysis of modifier crystals that an intermolecular interaction of the N–H···O=C type, which forms infinite chains of interacting molecules in a crystal, is observed in the crystal structure of 4-aminouracyl. The configuration of the interacting molecules indicates that each modifier molecule acts as a donor of a proton and a lone electron pair of the imine nitrogen atom and as an acceptor of electrons because of the presence of a carbonyl group. It follows from ab initio quantum-chemical calculations based on the X-ray data on the molecular configuration that, being simultaneously electron donors and electron acceptors, modifier molecules form in crystals either chains or 2*D* formations with rather high intermolecular interaction energies. For example, in the structure of AU crystals, the interaction energy of a pair of molecules isolated from the chain is 18 and 10 kcal mol^{-1} before and after optimization, respectively. Such intermolecular interactions in modifier crystals can compete with the energy of the ammonium nitrate structure and be a model of the interactions occurring in the composite. The results of calculations (by GAUSSIAN-03 software) of the electronic energy in the ground singlet state for such modifier molecules as THICA, AU, and UA demonstrated that the highest occupied molecular orbitals (HOMO) of all the three molecules are weakly bonding π-type orbitals and lowest unoccupied molecular orbitals (LUMO) are also of the π-type, with the main contribution to these orbitals made by carbonyl groups and multiple C=N bonds. The LUMO are nonbonding as regards their symmetry, but weakly bonding in their orbital energy. Thus, the modifier molecules can simultaneously act as both electron donors and electron acceptors. The energies of the HOMO and, simultaneously, the energy difference (HOMO–LUMO) can be used to evaluate the acceptor capacity of the chosen three modifiers: the highest acceptor capacity is observed for the UA molecule, a lower capacity, for the AU molecule, and the lowest, for the THICA molecule.

It was demonstrated that, in the case of a crystallochemical similarity of components (modifier and AN), a certain and even, occasionally, large amount of an additive can be introduced into their alloy without any indication of the presence of this additive in the X-ray diffraction pattern of the alloy. The substance introduced into an alloy is distributed as very small clusters over separate crystalline blocks of AN, in which the interplanar spacings coincide with those in the additive. Figure 1 shows comparative X-ray diffraction data for the crystal lattices of AN, modifier substances, and the corresponding alloys.

The most characteristic reflections in the X-ray diffraction pattern of pure AN (Fig. 1, curve *1*, phase IV) to be spanned upon introduction of modifier substances are those corresponding to the interplanar spac-

ings *d* 4.906 and 3.091 Å (the second interplanar spacing is more important because it determines the distance between atomic planes in a stack of planar-parallel anions). Curve *2* in Fig. 1 is the X-ray diffraction pattern of DATHICA crystals with a strong reflection *d* 3.100 Å, and curve *3*, that of the alloy 55.3% AN + 44.7% DATHICA. The X-ray diffraction pattern of the alloy (phase IV of ammonium nitrate) represents a favorable case of an almost full coincidence of the X-ray diffraction patterns of the substances being fused. The X-ray diffraction pattern of the second additive under study, AU, is shown by curve *4* in Fig. 1. This pattern is characterized by coincidence of the interplanar spacings (4.676, 3.151, and 3.077 Å) with the corresponding closely similar spacings in the X-ray diffraction pattern of AN. However, the pattern contains a very strong reflection with *d* = 3.531 Å, which is totally absent in the diffraction pattern of ammonium nitrate in phase IV. In the diffraction pattern of the alloy 83.8% AN + 16.2% AU (Fig. 1, curve *5*), this reflection is not observed, either. Thus, 16.2% AU is fully distributed over the lattice of ammonium nitrate in phase IV. The most significant is the diffraction pattern of the modifier substance UA (Fig. 1, curve *6*). The strongest reflection (with *d* = 6.511 Å) characteristic of this substance is totally absent in the diffraction pattern of individual AN, whereas in the diffraction pattern of the alloy, this reflection appears only at the composition 70.4% AN + 29.6% UA (curve *7*) and it is very weak. Thus, in accordance with the high calculated acceptor capacity of the modifier molecule UA, the ability of this compound to be distributed over the AN lattice is the highest.

It is widely known that pure AN has five polymorphous modifications and, accordingly, shows four phase transformations: VI $\rightleftarrows$ V at –17°C, IV $\rightleftarrows$ III at +32.3°C, III $\rightleftarrows$ II at +84.2°C, and II $\rightleftarrows$ I at +125.2°C. These phase transitions strongly hinder wide use of AN in energetic formulations. The most detrimental is the transition IV $\rightleftarrows$ III (at +32.3°C). A study of the kinetics of this transition demonstrate that it occurs via total disintegration of the starting phase IV. The kinetics of the IV $\rightleftarrows$ III transition in pure ammonium nitrate in the isothermal mode was studied using the method of quantitative X-ray phase analysis of polycrystals. This was done in a specially designed temperature chamber for the DRON-2 diffractometer, which made it possible to record the variation of the phase ratio in the course of time at a constant temperature. We measured the integral intensities of the peaks corresponding to certain phases and normalized the results to an internal standard. The normalized values of the integral intensity at various fixed instants of time were related to the integral intensity at the initial instant of time. Further, kinetic curves of the degree of conversion were plotted. To construct these curves, we examined the variation of three or four reflections for the initial and final phases.

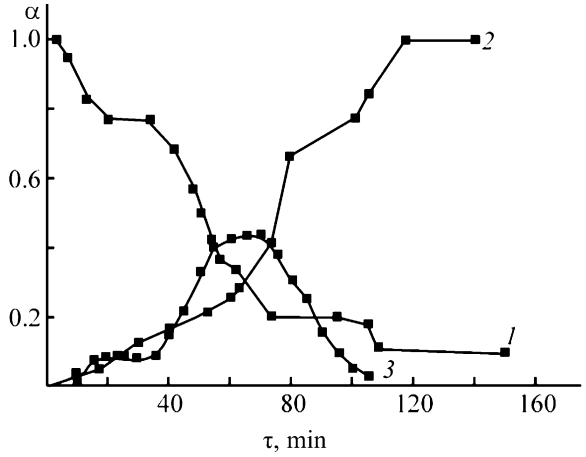


Fig. 2. Direct phase transition IV→III in ammonium nitrate (T = 33°C). (α) Fraction of a given phase relative to the initial amount of phase IV and (τ) time. (*1*) Loss of phase IV, (*2*) gain in phase III, (*3*) kinetics of formation of the intermediate phase X.

Figure 2 shows experimental data on the loss of the initial phase IV and the gain in the final phase III in the course of time at a temperature of 33°C (curves *1* and *2*, respectively). The sum of the relative amounts of the initial and final phases of AN at certain instants of time was substantially smaller than unity. This suggests that an intermediate phase X is formed (Fig. 2, curve *3*). Phase X is not observed in the experimental X-ray diffraction pattern because the substance representing this phase is distributed throughout the sample, rather than being concentrated in clusters of sufficient size, and, presumably, is situated at the interface between the initial and final phases.

Theoretical simulation of the phase transition IV $\rightleftarrows$ III with single-crystal structures gives no way of achieving this transition by minor displacements of ions. Here, a complete disintegration of the initial structure and assembly of a new structure are necessary. Therefore, the transition at +32.3°C is frequently named in the literature the point of "catastrophes." Modification of AN crystals with modifier substances represented in this communication leads to a totally new phase state of the modified product. There are no phase transitions V $\rightleftarrows$ IV and IV $\rightleftarrows$ III in these samples; however, the phase

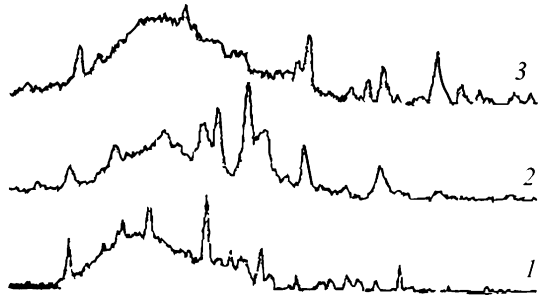


Fig. 3. X-ray diffraction patterns of polycrystalline composites ($\lambda\,Cu_{K_\alpha}$, 2θ = 10°–50°) after a temperature treatment (T = 32.3°C). Alloy: (*1*) 90% AN + 10% DATHICA, (*2*) 83.8% AN + 16.2% AU, and (*3*) 81.1% AN + 18.9% UA.

transition IV $\rightleftarrows$ II remains. The transition IV $\rightleftarrows$ II is also characteristic of pure AN samples if the transition occurs without access of moisture [10, 11].

A study of the kinetics of phase transitions in an alloy of composition 90% AN + 10% UA at temperatures of 53 and 54°C demonstrated that the sum of the initial and final phases is close to unity at any degree of conversion, i.e., the conversion of phase IV to phase II occurs directly from a crystal to crystal, nearly without formation of an intermediate X-ray-amorphous phase. Thus, modification of the product with appropriate organic additives does not lead, in the end, to the final solution of the problem of AN stabilization in the temperature range from –50 to +100°C; the stabilization of the product is limited to the temperature range from –50 to +50°C. As a result of multiple temperature treatments of alloys in the temperature range from –50 to +100°C at different humidities, the phase state of the alloys became stable; after numerous passes along the chosen temperature interval, the transition IV $\rightleftarrows$ II remained unchanged. Nevertheless, we could find conditions of an additional treatment, which consisted in prolonged keeping of samples near the temperature of "catastrophes" at an increased humidity. Such a treatment of the alloy leads to a new state of the substance, previously unknown for alloys of this kind.

Figure 3 shows X-ray diffraction patterns of alloys after their prolonged keeping near the temperature of 32.3°C. The diffraction pattern of the alloy 90% AN + 10% $C_3H_3N_3O_6 \cdot 2NH_3$ (Fig. 3, curve *1*) corresponds to the X-ray-amorphous state of the substance whose particles must be less than 100 nm in size. Even prolonged keeping of X-ray-amorphous alloy samples in a wide temperature range does not change their phase state. The most important circumstance is that the alloy samples are not recrystallized to the initial state (phase IV). X-ray studies of phase transitions in samples with a new phase state demonstrate the total absence of any phase transitions. Calorimetric studies (DTA and DSC) confirm this conclusion.

IR and UV spectroscopies were used to study the intermolecular interaction in composites of ammonium nitrate with DATHICA and AU. To preclude interaction of AN with KBr, samples for spectral studies were prepared as suspensions in Vaseline oil.

It was found that these additives strongly modify the system of hydrogen bonds in alloys with AN. We studied two compositions of AN alloys with DATHICA (44.7 and 10%). The alloy with 10% DATHICA is in the X-ray-amorphous state. IR spectral data indicate that the DATHICA additive is dispersed on the molecular dispersity level in both the composites. For example, the highest-intensity absorption band at 3236 cm^{-1} in the spectrum of the initial modifier DATHICA is observed neither in the spectrum of the alloy of the first composition (3400, 3270, 3196, 3116 cm^{-1}), nor in the spectrum of the alloy of the second composition (in which a single broad band peaked at 3400 cm^{-1} is present). These data point to a very strong interaction of modifier molecules with AN ions. The UV spectra of DATHICA and alloys of the first composition (without special treatment) differ only slightly. However, two broad bands at 240–300 nm appear in the spectrum of the alloy of the second composition (X-ray-amorphous state). Possibly, these bands are due to appearance of intermolecular orbital interactions of the type $\pi(NO_3) \rightarrow \pi^*(C{=}O)$.

The IR spectrum of the AN alloy with 16.2% AU (X-ray-amorphous state of the alloy) contain three absorption bands with comparable intensities in the range of N–H vibrations (3412, 3250, 3192 cm^{-1}), whose frequencies differ from those of the bands in the spectra of 4-aminouracyl (3416, 3396, 3176 cm^{-1}) and ammonium nitrate (3125 and 3015 cm^{-1}). The absence of a simple additivity between the spectra of the alloy and its components may indicate that there is an intermolecular interaction between the modifier molecules and ammonium nitrate ions, which changes the network of hydrogen bonds in the alloy. The IR spectrum of such an alloy, not subjected to any special treatment (not X-ray amorphous), differs from the IR spectrum of the alloy in the X-ray-amorphous state, but is not an additive sum of the spectra of the components, either. The former spectrum is dominated by the strong band

of N–H vibrations at 3180 cm^{-1}, with two weak bands observed on its wing at 3460 and 3344 cm^{-1}. It is noteworthy that a rather strong absorption band appears at 220–230 nm in the UV spectrum of the same alloy (not X-ray amorphous), but is absent in the spectrum of AU. Possibly, this occurs because there appear intermolecular orbital interactions.

EXPERIMENTAL

1,3,5-Trihydroxyisocyanuric acid and DHTHICA were synthesized by the known procedures [12, 13].

Diammonium salt of 1,3,5-trihydroxyisocyanuric acid. To a solution of 0.89 g (5mM) of THICA in 20 ml of methanol was added under agitation a solution of 1.15 g (15 mM) of ammonium acetate in 20 ml of methanol, with an abundant white precipitate formed. The mixture was agitated for 0.5 h at 40°C and for 0.5 h at 20°C. The precipitate was filtered off, washed with methanol (10 ml) and diethyl ether (10 ml), and dried in air at 70°C for 0.5 h. Yield 1.01 g (100%), decomposition point >200°C (without melting).

Found (%): C 17.30, H 4.39, N 32.45.

$C_3H_9N_5O_6$.

Calculated (%): C 17.07, H 4.30, N 33.17.

IR spectrum (KBr), ν, cm^{-1}: 3430, 3236, 3145, 2928, 1776, 1676, 1432, 1400, 1205, 1004, 985, 704. The product obtained is nearly insoluble in water and organic solvents (methanol, ethanol, acetone, DMFA, DMSO, toluene). When boiled in water, the product gradually dissolves because of the hydrolytic cleavage of the ring.

Hydrated melamine salt of 1,3,5-trihydroxyisocyanuric acid. To a solution of 0.89 g (5mM) of THICA in 20 ml of water was added under agitation a warm (~35°C) solution of 0.63 g (5 mM) of melamine in 120 ml of water, with a white precipitate formed. The mixture was cooled to 0°C and agitated at the same temperature for 0.5 h. The precipitate was filtered off, washed with ice water (20 ml), and dried in air. Yield 1.29 g (76%), decomposition point >200°C (without melting).

Found (%): C 22.71, H 3.99, N 40.23.

$C_6H_{11}N_9O_7$.

Calculated (%): C 22.44, H 3.45, N 39.25.

IR spectrum (KBr), ν, cm–1: 3532, 3500, 3400, 3125, 2930, 2870, 2700, 1712, 1672, 1630, 1504, 1440, 1384, 1344, 1212, 1180, 1008, 996, 776, 700.

Minor additions of organic substances were introduced into AN mostly by fusion at a temperature close to the melting point of AN.

The following experimental techniques were used: X-ray phase analysis (computer-controlled DRON-2 diffractometer; phase identification in transformations in the temperature range from –50 to +100°C by analysis of X-ray diffraction patterns, with preliminary calculation of theoretical diffraction patterns of polycrystals of all the phases from atomic coordinates furnished by an X-ray diffraction analysis of single crystals), DTA (MOM derivatograph, Hungary, heating rate 0.6 deg min^{-1}), UV spectroscopy on a Specord M40 spectrophotometer in the range 200–900 nm, and IR spectroscopy on a Specord IR75 spectrophotometer in the range 4000–700 cm^{-1}.

CONCLUSIONS

(1) It was found in a study of ammonium nitrate alloys with minor additions of organic substances that the phase state of the composite is affected only by additives close in crystallochemical parameters to ammonium nitrate.

(2) It was demonstrated that, for an organic substance to exert a stabilizing influence on phase states of ammonium nitrate, a modifier molecule should be an electron acceptor for creating intermolecular orbital interactions and should form new hydrogen bonds with ammonium nitrate ions.

(3) The conditions were found under which an additional temperature treatment of alloys converts them into a new X-ray-amorphous state with a stabilization temperature range from –50 to +100°C.

(4) An analysis of UV and IR spectra demonstrated that the X-ray-amorphous state of the composite is characterized by new intermolecular interactions, which are different from those in the starting components and in freshly prepared composites subjected to a temperature treatment and exposed to moisture.

REFERENCES

1. Manelis, G.B., Golovina, N.I., Lempert, D.B., et al., *7th Int. Airbag-2004. Karlsruhe, Germany*, 2004, p. 43/1.

2. Lempert, D.B., Nechiporenko, G.N., Golovina, N.I., et al., *7th Int. Airbag-2004. Karlsruhe, Germany*, 2004, p. 44/1.

3. Golovina, N.I., Nechiporenko, G.N., Nemtsev, G.G., et al., *Zh. Prikl. Khim.*, 2007, vol. 80, no. 1, pp. 25–31.

4. RF Patent 2 298 540.
5. Lempert, D.B., Manelis, G.B., Nechiporenko, G.N., et al., *10th Symp. "New Trends in Research of Energetic Materials," Pardubice, Czech Rep*., Apr. 2007, p. 728.
6. Golovina, N.I., Nechiporenko, G.N., Zyuzin, I.N., et al., *Zh. Strukt. Khim*., 2008, no. 5, pp. 942–949.
7. Ringertz, H., *Acta Cryst*., 1966, vol. 20, pp. 397–399.
8. Zyuzin, I.N. and Lempert, D.B., *Propellants, Explosives, Pyrotechnics*, 2007, vol. 32, pp. 42–44.
9. Takač, M.J.-M., Kos, I., Biruš, M., et al., *J. Mol. Struct*., 2006, vol. 782, pp. 24–26.
10. Lucas, B.W., Ahtee, M., and Hewat, A.W., *Acta Cryst*., 1979, vol. B35, pp. 1038–1041.
11. Lucas, B.W., Ahtee, M., and Hewat, A.W., *Acta Cryst*., 1980, vol. B36, pp. 2005–2008.
12. Butula, I. and Takac, M.J., *Croat. Chem. Acta*, 2000, vol. 73, pp. 569–572.
13. Hirai, N., Kagayama, T., Tatsukawa, Y., et al., *Tetrahedron Lett*., 2004, vol. 45, pp. 8277–8280.

ISSN 1070-4272, Russian Journal of Applied Chemistry, 2008, Vol. 81, No. 10, pp. 1747–1753. © Pleiades Publishing, Ltd., 2008.
Original Russian Text © V.Yu. Dolmatov, 2008, published in Zhurnal Prikladnoi Khimii, 2008, Vol. 81, No. 10, pp. 1620–1627.

PHYSICOCHEMICAL STUDIES OF SYSTEMS AND PROCESSES

Modified Method for Synthesis of Detonation Nanodiamonds and Their Real Elemental Composition

V. Yu. Dolmatov

Tekhnolog FGUP SKTB (Special Engineering Design Office, Federal State Unitary Enterprise), St. Petersburg, Russia

Received March 17, 2008

Abstract—Modified technique for synthesis of detonation nanodiamonds by exploding a charge of high explosives in a water shell is described. Reducing agents are introduced into water. Their use enables solution of a number of problems: the carbon content of nanodiamonds is raised from 90 to 96 wt %, the content of incombustible admixtures is dramatically diminished from 3 to 0.1 wt %, and the yield of detonation nanodiamonds becomes two times higher. A new method for determining the elemental composition is described and the oxidation of nanodiamonds under heating in the presence of atmospheric oxygen is analyzed.

DOI: 10.1134/S107042720810008X

Detonation-synthesis nanodiamonds (DNDs) are the only product of the nanocarbon family (fullerenes, nanotubes, carbine, globular nanocarbon, etc.) produced on the industrial scale in various countries (Russia, China, Ukraine, Belarus, Turkey).

DNDs were discovered and for the first time industrially manufactured [Altai NPO (Research and Production Association), Biisk] in Russia [1–5]. After 15–20 years of studies, researchers came to a conclusion that the optimal explosive formulation for DND synthesis is a ~50 : 50 mixture of TNT and hexogen [2, 4–9]. The synthesis is performed in a detonation chamber in a neutral gas medium in a water or ice shell [6]. At present, use of DNDs in nearly all application fields (plating, polishing, production of oils and lubricants, medicine, biology, polymer technologies, etc.) requires that the DND quality should be improved. DNDs should contain the maximum possible amount of carbon (i.e., they should have a more perfect elemental composition) and should not contain incombustible admixtures (technological contaminations: metal oxides and carbides). This study is an attempt to solve this problem.

EXPERIMENTAL

The TNT–cyclonite alloy containing 40 wt % TNT (TG 40) was exploded in a water shell in a 1-m^3 explosion chamber (charge mass 0.6 kg). The mass ratio between the explosive and water was maintained at 1 : 6; products formed in preceding detonations served as the explosion medium. Readily oxidizable reducing agents (hydrazine hydrate, urotropin, urea, ammonia) were introduced into water at a mass ratio between the explosive and a reducing agent within the range 1 : (0.1–10.0) [10, 11].

The resulting diamond-containing stock (DS, half-product of DND synthesis) was purified with dilute nitric acid at a temperature of 240°C and pressure of about 80×10^5 Pa [12].

The elemental composition of DS and DNDs was analyzed by a new method: a weighed portion of a sample was kept at temperatures of 120–140°C for (DS) or 150–180°C (for DNDs) in a vacuum at a residual pressure of 0.01–10.0 Pa for 3–5 h and then was exposed at 1050–1200°C to oxygen flowing at a rate providing complete combustion of carbon and gasification of heteroatoms (nitrogen and hydrogen) in the course of 40–50 s.

It is known [2–12] that DND particles are complex structural formations that include the following components: crystalline diamond core (75–90% of carbon atoms), transition carbon shell of complex composition around the diamond core, and surface layer of various functional groups (hydroxy, carbonyl, carboxy, amide, and methyl groups). Nitrogen is rather uniformly distributed over all of these layers.

According to [4, 13], the detonation synthesis of DND can be divided into four stages.

In the first stage, the detonation conversion of the explosive mostly occurs within the geometric limits of the charge. The use of a condensed-phase shell (water or ice) confines detonation products (DP) within the geometric dimensions of the charge for an additional time, which enables a more complete conversion of carbon into the diamond prastructure.

After the detonation process is complete, an important role is played by rapid and strong gas-dynamic cooling of DPs to preserve DNDs formed within (or outside [14]) the chemical conversion zone. Just this isoentropic expansion of gaseous explosion products is the second stage.

After reflection of the shock wave (SW) from chamber walls, the third stage of the detonation synthesis of DNDs begins: circulation of the SW and turbulent mixing of the DP with the medium within the chamber.

The maximum attained temperature of the medium within the chamber depends on the mass ratio between the explosive and the gas medium, on the composition of the latter, and on the heat capacity of the gases.

The medium heated by the explosion and confined within a cold shell is intensely cooled (fourth stage). In addition to various gaseous products (CO_2, CO, O_2, H_2, N_2, CH_4, NO, NO_2, NH_3, H_2O), the chamber contains a highly dispersed suspension of carbon particles, which have a strong radiating capacity. Therefore, the process of cooling of such a medium is characterized by combined heat transfer by convection and radiation.

The extent to which condensed carbon is preserved is determined by gas-phase reactions of its gasification by carbon dioxide and water vapor. Therefore, two competing processes occur in the chamber at a high residual temperature in the third and fourth stages: gasification of condensed carbon (primarily nondiamond carbon, which is the most chemically active) and graphitization (or amorphization [14]) of the DNDs formed.

At a constant composition and density of the explosive being exploded, it is impossible to affect the first stage of synthesis, i.e., the DND formation proper, by addition of various substances to the condensed phase enveloping the explosive charge. The processes occurring in the second stage also have hardly enough time to be affected by presence of substances in the condensed phase (water, ice), even with account of the nonideality of the gas-dynamic cooling of DPs in their expansion. By contrast, addition of more readily oxidizable substances (reducing agents) in the third stage (stage of DP turbulization), in which CO_2, H_2O, and other aggressive (under these conditions) gases mostly attack condensed carbon, strongly affects the result of the detonation synthesis. Naturally, the gas medium components (CO_2, H_2O, O_2, NO_2, N_2O_3) are primarily bound with more readily oxidizable reducing agents (in the case in question, with hydrazine, urotropin, urea, ammonia), compared with the rather difficultly oxidizable carbon and, especially, DND. Thus, it would be expected that the yield of DS and DNDs should increase, with the elemental composition of DS and DNDs changed.

In addition, presence of readily oxidizable reducing agents among the DPs also affects the fourth stage of the process by lowering the DP temperature through decomposition of a part of the reducing agent, which favors preservation of DNDs by diminishing their graphitization.

It is known from the literature [16, 17] that, in hot compaction of DNDs ($P \approx 5$–8 GPa, $\tau \approx 1500$–2000°C), volatile products firmly fixed on the DND surface are intensively desorbed. The authors of [16, 17] roughly estimated the amount of volatile admixtures at 10 wt %. Therefore, the real amount of volatile admixtures was determined and a procedure for their removal before performing an elemental analysis of DS and DNDs was developed.

Originally, a sample of a standard DS produced in explosion of TG 40 charges in a water shell (without any additives in water) was dried to constant weight under normal industrial conditions (at 120°C in contact with the atmosphere). Then the air-dry AS was dried in a vacuum (residual pressure ~10 Pa) to constant weight at 200°C (16 h). It was found that the industrial air-dry DS still contains 8 wt % volatile products, including water.

A DS sample obtained by exploding a TG 40 charge with a water shell containing hydrazine has another amount of volatile admixtures. For example, this amount was found to be 13.7 wt % by drying of such an air-dry DS at 200°C (10 Pa).

Thus, depending on the preparation conditions, DS may contain different amounts of volatile admixtures (8–13.7 wt %). This circumstance should be taken into account both in chemical purification of

DNDs contained in DS and in use of DS as a starting product in various formulations.

To determine the real amount of volatiles (including water) in DNDs after nitric acid purification [240°C, $P = (80–100) \times 10^5$ Pa], the product was preliminarily dried by the standard factory method (150°C) to constant weight in contact with the atmosphere. Then, the powder of air-dry DNDs was placed in a vacuum (residual pressure 4–5 Pa) and dried to constant weight at 200°C for 14 h. It was found that air-dry DNDs produced and dried by the standard technique contain about 10 wt % volatiles. Moreover, a sample of such "absolutely dry" DNDs, stored in a desiccator with a humidity of 86%, absorbed 20.6 wt % moisture in 4 h. Its subsequent drying in air at 20°C (relative air humidity 30–35%) for 12 h resulted in a loss of moisture, whose content was 11.8 wt %. Making the drying conditions more severe (200°C, 4–5 Pa, 12 h) led to a residual moisture content of 0.6%.

In an analysis of the elemental composition of DNDs and DS, the annealing time of these products in the atmosphere of oxygen and exposure time were substantially raised (to 1200°C and 50 s). This was necessitated by the rather high resistance of DNDs and DS to combustion and by the incomplete combustion in all the preceding studies. For example, in the known patents obtained by Altai NPO [15, 18], volatiles were not removed and the conditions of DS and DNDs combustion corresponded to combustion of organic compounds (~850–900°C, 4–5 s). This caused a strong data distortion. For DS [15], the elemental composition was as follows (wt %): C 84.0–89.0, H 0.3–1.1, N 3.1–4.3, O 2.0–7.1; incombustible admixtures 2.0–5.0 wt %. For DNDs [18], the elemental composition was the following (wt %): C 75.0–90.0, H 0.8–1.5, N 0.8–4.5, O up to 23.4.

Table 1 presents the elemental composition of DS and the amount of the main impurity interfering with its direct use: incombustible metal oxides and carbides. It can be seen that, on average, the real content of carbon (run nos. 2–10) exceeded by 6–8 wt % that described in the literature (run no. 1). The amount of hydrogen is also, on average, 3 times larger, and that of nitrogen, by contrast, 3–4 times smaller. The amount of oxygen is 3–10 times smaller.

Introduction of reducing agents lowers the amount of incombustibles by 30% in run nos. 3–10 and by a factor of 2 in run nos. 6 and 8, which makes the resulting new DS suitable for direct use in plating, finishing polishing, polymer chemistry, oil formulations, etc. In addition, such a DS is considerably more readily subject to chemical purification.

Table 1. Elemental composition of DS and yield of DS and DNDs in explosion of TG 40 charges in a water shell containing various reducing agents

Run no.	Reducing agent and mass ratio between the explosive and a reducing agent	Elemental composition of DS, wt %				Amount of incombustible admixtures in DS, wt %	Content of DNDs in DS, wt %	Yield of DS in terms of the explosive, wt %	Yield of DNDs in terms of the explosive, wt %
		C	H	N	O				
1	No additives ([15])	84.2	0.9	8.3	3.1	3.5	45.0	7.2	3.24
2	No additives (new synthesis method)	91.4	2.6	2.7	0.6	2.7	48.3	9.1	4.4
3	Hydrazine 1 : 0.1	90.2	3.3	3.0	0.4	3.1	51.1	14.4	7.36
4	Hydrazine 1 : 0.5	90.5	3.0	2.9	0.8	2.8	54.7	15.8	8.64
5	Hydrazine 1 : 2.0	90.1	3.7	3.2	0.4	2.6	53.8	16.0	8.61
6	Urotropin 1 : 0.25	94.1	1.6	2.2	0.5	1.6	51.6	12.4	6.4
7	Urotropin 1 : 0.5	91.2	3.0	2.6	0.9	2.3	51.7	12.2	6.3
8	Urotropin 1 : 1	92.7	2.8	2.8	0.3	1.4	51.9	16.3	8.46
9	Urea 1 : 0.5	90.1	3.6	3.1	0.5	2.7	51.2	14.1	7.22
10	Ammonia 1 : 0.5	91.1	3.0	2.8	0.9	2.2	51.0	13.4	6.83

Table 2. Elemental composition and purity of DNDs after nitric acid purification [12] (DS obtained with various reducing agents)

Run no.	Reducing agent and mass ratio between the explosive and a reducing agent	Elemental composition of DS, wt %				Amount of incombustible admixtures in DNDs, wt %	Content of oxidizable carbon in DNDs, wt %	Content of DNDs in the solid phase, wt %
		C	H	N	O			
1	No additives ([18])	88.5	1.1	2.2	8.2	Data unavailable		
2	No additives (from DS in Table 1, run no. 2)	93.3	1.2	2.5	1.8	1.2	1.1	97.7
3	Hydrazine 1 : 0.1	93.6	1.2	2.3	1.7	1.2	1.0	97.8
4	Hydrazine 1 : 0.5	94.4	0.4	2.5	2.3	0.4	1.1	98.5
5	Hydrazine 1 : 2.0	95.2	0.7	2.3	1.6	0.2	1.0	98.8
6	Urotropin 1 : 0.25	94.9	1.1	2.5	1.4	0.1	0.8	99.1
7	Urotropin 1 : 0.5	95.2	1.0	2.2	1.5	0.1	1.0	98.9
8	Urotropin 1 : 1	96.0	0.4	2.6	0.7	0.3	0.9	98.8
9	Urea 1 : 0.5	94.3	1.6	2.7	0.8	0.6	1.4	98.0
10	Ammonia 1 : 0.5	92.7	2.4	2.9	1.3	0.7	0.9	98.4

Although the content of DNDs in DS synthesis with the use of reducing agents increases only slightly (by 2–5 wt %), the total amount of DS increases twice, and, therefore, the yield of DNDs in terms of the starting explosive also increases by a factor of 2.

A study of the elemental composition and impurity content of DNDs produced by chemical purification of the previously described DS (run no. 2) [18] and DS synthesized by the method suggested here (run nos. 3–10) demonstrated that the amount of the main element, carbon, in run no. 2 (Table 2) is actually higher in the standard DS by approximately 5 wt %, compared with published data (Table 2, run no. 1). Introduction of reducing agents can substantially raise the amount of carbon in the DNDs to 96 wt % (run nos. 5, 8) at an appropriate type and amount of a reducing agent. Irrespective of the synthesis conditions, the amount of nitrogen varies within a narrow range, from 2.2 to 2.9 wt %, which indicates that nitrogen is rather uniformly distributed over all DND layers and is introduced into these layers already in the stage of detonation synthesis. At the same time, the amount of hydrogen and oxygen (run nos. 2–10 varies substantially (from 0.4 to 2.4 wt % and from 0.7 to 2.3 wt %, respectively. This shows that these elements are predominantly concentrated in outer layers of a DND particle and their content is strongly affected by detonation synthesis conditions. It can also be seen that the content of oxygen is very strongly overestimated by published data.

The smallest amount of incombustible admixtures is contained in DNDs synthesized in the presence of urotropin. This occurs because urotropin is a rather powerful complexing agent and binds impurity metals (Fe, Ni, Cr, Cu, etc.) into soluble complexes that are easily removed in chemical purification with nitric acid. The low content (0.1–0.3 wt %) of incombustibles (metal oxides and carbides) also enables use of these DNDs in any application field. At the same time, the content of nondiamond carbon in DNDs is rather constant, 0.8–1.4 wt %, and such an amount does not affect any DND application technology. The content of the diamond phase in purified DNDs may be as high as 99.1 wt % in terms of the solid phase of the product.

The available data on the behavior of DNDs under heating in contact with air are rather widely diverse.

For example, it was shown in [19] that, under heating in air at a rate of 10 deg min^{-1}, the DNDs manufactured by Altai NPO start to be intensively oxidized even at a temperature of 430°C, and diamond of ASM 1/0 brand (micropowder of static-synthesis diamond), at 650°C [20].

It should be noted that the content of the main substance in the DNDs manufactured by Altai NPO is

Table 3. Parameters of DS oxidation by atmospheric oxygen (derivatograph, heating rate 5 deg min^{-1})

Run no.	Type of DS (reducing agent used)	Range of the endothermic effect, °C	Range of the exothermic effect, °C, type of the effect				Temperature range of the loss of mass, °C (loss of mass, %)	
			1st	2nd	3rd	4th	slow	fast
1	DS by TU (Technical Specification) (none)	30–170	170–230; gentle	230–280; steep	280–400; gentle	430–660; gentle	170–310 (3.3)	310–660 (96.7)
2	DS-AM (ammonia)	30–170	170–210; steep	210–240; gentle	260–360; gentle	380–680; gentle	150–270 (5.0)	270–680 (95.0)
3	DS-U (urotropin)	40–190	190–385; steep	385–680	385–680	385–680	150–500 (3.3)	500–680 (96.7)
4	DS-UR (urea)	30–200	200–270; gentle	270–300; steep	300–420; gentle	450–660; gentle	130–320 (8.3)	320–660 (91.7)
5	Averaged DS	30–180	180–270	270–670	270–670	270–670	150–350 (5.0)	350–670 (95.0)

~90% and the onset temperature of intensive decomposition is presumably affected by the large amount of widely diverse impurities in DNDs.

It has been shown previously that heating of DNDs in contact with air causes an exothermic, effect with a decrease in the sample mass at a temperature as low as 250°C and intensive oxidation of carbon to an incombustible residue in the range 500–750°C [4].

However, data on DND oxidation by atmospheric oxygen under heating are scarce and information about the behavior of DS under heating in air is lacking.

Therefore, an attempt was made to thoroughly study the behavior of DS and DNDs (Tables 1, 2) obtained under various conditions under the action of high temperatures in contact with atmospheric oxygen.

On heating DS samples in air (derivatograph, heating rate 5 deg min^{-1}), a minor endothermic effect was observed in the temperature range 30–180°C (Table 3, run no. 5) as a result of desorption of water and volatiles. A set of exothermic effects is observed at temperatures higher than 180°C, which, in the end, leads to complete burning-out of DS at 670°C. These exothermic effects are due to step-by-step oxidation of nondiamond carbon. In this case, the least ordered nondiamond carbon on the very periphery of the diamond-carbon cluster burns-out first, and then, at higher temperatures, oxidation of nondiamond carbon layers closer to the diamond core begins. The DTA curve shows a large number of breaks. As a rule, there are two peaks on the DTA curve. The first of these (at 370°C) represents the oxidation of diamond-like carbon directly at the surface of the diamond core, and the second at ~610°C, the oxidation of the diamond core itself.

In the DTG curve, the loss of DS mass in the temperature range 150–350°C is ~5.0 wt %, i.e., moisture and volatiles are removed and the most disordered peripheral nondiamond carbon component of the diamond-carbon cluster is oxidized. Above ~350°C, the loss of mass rapidly increases to the point of complete burning-out of a sample.

In heating of DND samples in air (derivatograph, heating rate 10 deg min^{-1}), the endothermic effect observed at 40–200°C is due to desorption of adsorbed gases, water, and other volatiles (Table 4, run no. 7). The first, rather slow exothermic effect (200–525°C) is due to destruction of surface functional groups (~200°C) and gasification of the remaining nondiamond carbon on the surface of the diamond core in contact with atmospheric oxygen. The loss of mass by a DND sample (10–17%) corresponds just to the amount of nondiamond (X-ray-amorphous) carbon in DNDs.

At a temperature of 525°C, the diamond core of a DND particle starts to interact with atmospheric oxygen and this interaction ends in ~760°C by complete combustion of DND (peak value at 690°C).

With account of the poor quality of DNDs manufactured by Altai NPO, i.e., of the large amount of nondiamond carbon (up to 30% [18]), the onset of the exothermic effect is shifted to 120°C (Table 4, run no. 8). The large amount of incombustibles (up to 5 wt %) in UDA-B possibly exerts an inhibiting influence on the process of its oxidation and, therefore, only ~50% of a sample burns-out at 770°C.

Table 4. Parameters of ND oxidation by atmospheric oxygen (derivatograph, heating rate 10 deg min^{-1})

Run no.	Type of ND (reducing agent used)	Range of the endothermic effect, °C	Range of the exothermic effect, °C		Temperature, °C		Temperature range of the loss of mass, °C (loss of mass, %)	
			slow	fast	of maximum energy release	of complete combustion of a sample	slow	fast
1	UDD-SF by TU (Technical Specification) 05121441-275-95 (none)	140–200	200–520	520–750	660	750	140–550 (10.0)	550–750 (90)
2	UDD-TAN by TU (Technical Specification) 05121441-275-95 (none)	40–200	200–525	525–800	690	800	60–525 (10.0)	525–800 (90)
3	ND from DS-U (urotropin)		80–500	500–760	660	760	200–540 (6.7)	540–760 (93.3)
4	ND from DS-UR (urea)	40–200	200–540	540–750	700	750	240–570 (17.0)	570–750 (83)
5	ND from DS-HH (hydrazine hydrate)	40–250	250–510	510–750	720	750	160–520 (10.0)	520–750 (90)
6	DS from DS-AM (ammonia)	40–200	200–550	550–760	720	760	350–550 (10.0)	550–760 (90)
7	Averaged ND manufactured by Tekhnolog FGUP SKTB	40–200*	200–525*	525–760	690	760	185–540* (10.0)	540–760 (90)
8	UDA-B** manufactured by Altai NPO	60–120	120–510	510–700	650	–	–	570–770 (50)
9	Static-synthesis diamonds ASM 0/0.1	40–200	200–510	510–780	620	780	510–780 (100)	–
10	Natural diamond 200/240 (Yakutiya)	40–220	220–940	>940	–	–	360–810 (13.3)	810–980 (20)

* Without extreme values.

** UDA-B contains up to 30% nondiamond carbon [18].

Comparison of the oxidation parameters of DNDs (Table 4, run no. 7) and classical diamonds of static synthesis crushed to particle sizes in the range 2–100 nm (run no. 9) shows that the endo- and exothermic effects in these two kinds of diamonds are nearly identical, which points to the high quality of DNDs produced by the new method.

The minor endothermic effect observed in the temperature range 40–200°C for static-synthesis and natural diamonds is due to desorption of adsorbed water (whose amount is as large as 4 wt %).

Comparison of the oxidation processes of carbon in DS and DNDs in air shows that (naturally) DS is more readily oxidized than DND. Because of the mixed type of DS, the exothermic effects have different intensities and contain two peaks (at 370 and 610°C) for nondiamond and diamond carbon, respectively, with complete burning-out of the product at 670°C. High-intensity exothermic effects begin at temperatures as low as ~240°C.

In DNDs, the oxidation process goes smoothly, without breaks in the DTA curve; a strong exothermic effect is observed already at 525°C, with the only peak at 690°C and complete burning-out at 760°C.

As would be expected, pure DNDs are substantially more resistant to oxidation than DS.

CONCLUSIONS

(1) A modified method was developed for detonation synthesis of DNDs and DS in an aqueous medium in the presence of active reducing agents, including hydrazine, urotropin, urea, and ammonia. This method made it possible to raise the content of the main element (carbon), diminish the content of oxygen by a factor of 4 (on average), double the yield of DS and DNDs, lower the amount of incombustible admixture by a factor of 2–3, and vary the elemental composition of DNDs by choosing a reducing agent and its amount.

(2) Two distinct exothermic peaks, at 370°C (oxidation of nondiamond carbon) and 610°C (oxidation of the diamond core), were found in oxidation of new types of DS by oxygen.

(3) One distinct exothermic peak at 690°C, associated with oxidation of the diamond core, was observed in oxidation of new DNDs by atmospheric oxygen.

(4) It was found that, in contrast to the DNDs manufactured by Altai NPO, the new DNDs exhibit the endo- and exothermic effects that are nearly fully identical to those in classical static-synthesis diamonds, which points to the high quality of the new DNDs.

ACKNOWLEDGMENTS

The study was financially supported by the Federal Agency for Science and Innovations (Rosnauka) under the State contract no. 02.523.11.3003 of 16.05.2007, code 2007-3-2.3-07-02-005.

REFERENCES

1. Volkov, K.V., Danilenko, V.V., and Elin, V.I., *Fiz. Goreniya Vzryva*, 1990, vol. 26, no. 3, pp. 123–125.
2. Vereshchagin, A.L., *Detonatsionnye nanoalmazy* (Detonation Nanodiamonds), Barnaul: Altai. Gos. Tekhn. Univ., 2001.
3. Dolmatov, V.Yu., *Russ. Chem. Rev.*, 2001, vol. 70, no. 7, pp. 607–626.
4. Dolmatov, V.Yu., *Ul'tradispersnye almazy detonatsionnogo sinteza* (Ultradisperse Detonation-Synthesis Diamonds), St. Petersburg: SPb Gos. Politekhn. Univ., 2003.
5. Danilenko, V.A., *Sintez i spekanie almaza vzryvom* (Synthesis and Sintering of Diamonds by Explosion), Moscow: Energoatomizdat, 2003.
6. Dolmatov, V.Yu., *Sverkhtverd. Mater.*, 2003, no. 4, pp. 38–45.
7. Dolmatov, V.Yu., *Zh. Prikl. Khim.*, 2006, vol.79, no. 12, pp. 1937–1941.
8. Donnet, J.-B., Lemoigne, C., Wang, T.K., et al., *Bull. Soc. Chem. Fr.*, 1997, vol. 134, nos. 10–11, pp. 875–890.
9. *Ultrananocrystalline Diamond, Synthesis, Properties, and Applications*, Shenderova, O.A. and Gruen, D.M., Eds., Norwich: William Andrew, 2006.
10. Int. Patent Appl. PCT/RU 2005/000 686.
11. Int. Patent Appl. PCT/RU 2005/000 685.
12. RF Patent 2 109 683.
13. Mazanov, V.A., *Fiz. Tverd. Tela*, 2004, vol. 46, no.. 4, pp. 614–620.
14. Danilenko, V.V., *Fiz. Goreniya Vzryva*, 2005, vol. 41, no. 5, pp. 104–116.
15. US Patent 5 916 955.
16. Shulzhenko, A.A., Bochechka. A.A., Gargin, V.G., et al., *Superhard Mater.*, 1998, no. 4, pp. 46–52.
17. Nozhkina, A.V., Kolchemanov, N.A., Kardanov, A.A., and Detkov, P.Ya., *Sverkhtverd. Mater.*, 2000, no. 1, pp. 78–84.
18. US Patent 5 861 349.
19. Vereshchagin, A.L., Ul'yanova, G.M., Novoselov, V.V., and Brylyakov, P.M., *Sverkhtverd. Mater.*, 1990, no. 5, pp. 20–22.
20. Breusov, O.N., Volkov, V.M., Drobyshev, V.N., and Tatsii, V.F., *Tr. Inst. Sverkhtverd. Mater. Akad. Nauk USSR*, 1984, pp. 19–35.

ISSN 1070-4272, Russian Journal of Applied Chemistry, 2008, Vol. 81, No. 10, pp. 1754–1757. © Pleiades Publishing, Ltd., 2008.
Original Russian Text © S.M. Shilov, K.A. Gavronskaya, A.N. Levkin, V.N. Pak, 2008, published in Zhurnal Prikladnoi Khimii, 2008, Vol. 81, No. 10, pp. 1628–1632.

PHYSICOCHEMICAL STUDIES OF SYSTEMS AND PROCESSES

Molecular Layering Method Used to Sensitize Luminescence from Terbium(III) Oxide Nanoparticles in Porous Glass

S. M. Shilov, K. A. Gavronskaya, A. N. Levkin, and V. N. Pak

Herzen Russian State Pedagogical University, St. Petersburg, Russia

Received April 3, 2008

Abstract—Possibility of obtaining nanoparticles of terbium(III) oxide in a porous glass by impregnating the support with an aqueous solution of $TbCl_3$ and subsequently calcining dried samples in air at 300°C was studied. The molecular layering method was used to modify the surface of encapsulated particles with titanium oxide layers of controlled thickness.

DOI: 10.1134/S1070427208100091

Development of encapsulation methods and analysis of specific structural features of "guest" substances (intercalates) in condensed nanoporous media constitute a rapidly evolving area of research [1, 2]. The internal space of supports acts as a nanoreactor that determines the dimension specifics of processes occurring within and the properties of the materials obtained.

A series of studies in this area has been devoted to synthesis and study of properties of encapsulated phosphors [3–8]. A particular place among the supports used for this purpose is occupied by porous glasses (PGs) having high transparency and chemical resistance, combined with the possibility of purposefully controlling structural parameters and obtaining PGs both as powders and as mechanically strong articles of various configurations [9, 10]. As for intercalates providing luminescence, compounds of rare-earth elements (REE) are reasonable candidates for this function. As a rule, synthesis of luminescent materials on their basis envisages sensitization of luminescence centers by an appropriate environment. This should be done because excitation of REE cations via intrinsic absorption is insufficient both in view of the prohibition imposed by the Laport rule on *f*–*f* transitions in axially symmetric fields and due to screening of valence 4*f*-orbitals by electrons from higher-energy 5*s*- and 5*p* levels [11]. Thus, the role of the nearest environment in luminescence sensitization consists in absorption and transfer of the excitation energy to the radiative states of REE.

This study proceeds with analysis of specific features of the optical properties of REE compounds in porous glasses [6–8] by examining the possibility of sensitization of the photoluminescence (PL) from nanosize Tb_2O_3 intercalates in PGs as a result of synthesis of titanium oxide layers on their surface by the molecular layering method [12].

EXPERIMENTAL

A porous glass obtained in the form of a powder with a particle size of 0.05–0.07 mm, specific surface area S_{sp} = 80 $m^2\ g^{-1}$, pore volume V_p = 0.166 $cm^3\ g^{-1}$, and predominant pore radius r_p = 4.5 nm served as a support [10]. In the first stage, in accordance with the data of [8], terbium(III) chloride was encapsulated in the pore space of the PG by impregnating the support with a 0.8 M aqueous solution of the salt; the content of $TbCl_3$ in samples dried at 120°C was 0.12 ± 0.1 mM g^{-1}, which provided a reliably recorded luminescence [8]. The chloride species were transformed to the oxide form by calcining the $TbCl_3$-modified PG in air at 300°C. To enable further molecular layering [12], the hydroxy cover on the surface of oxide particles was restored via treatment of samples with water vapor at 180°C for 4 h. Trace amounts of adsorbed water were removed at the same temperature with a flow of dry nitrogen and then $TiCl_4$ vapor was fed into the reactor. The reaction occurring on the hydroxylated surface of particles by the scheme

$$n(\text{=Tb−OH})^{s} + TiCl_4^{g} \rightarrow (\text{=Tb−O−})_n TiCl_{4-n}^{s} + n HCl^{g},$$

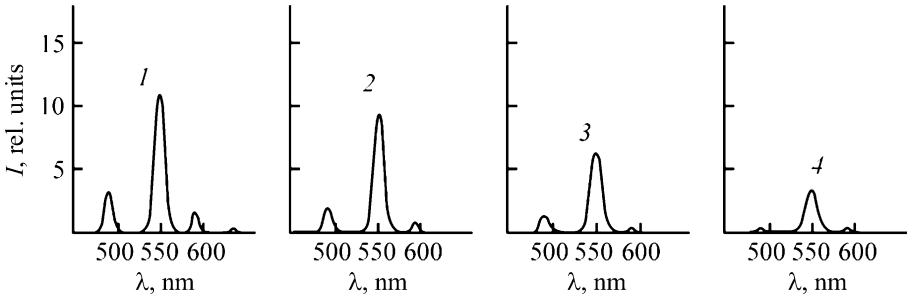


Fig. 1. (*1*) Luminescence from $TbCl_3$ particles and decrease in its intensity *I* as a result of sample calcination at 300°C for (*2*) 10, (*3*) 30, and (*4*) 60 min. (λ) Wavelength; the same for Fig. 2.

yielded a layer of chemically bound oxychloride groups of titanium(IV). The excess amount of $TiCl_4$ in the adsorbed form and the released hydrogen chloride were removed with a flow of dry nitrogen and then the samples were treated with water vapor:

$$(=Tb{-}O{-})_nTiCl^s_{4-n} + (4-n)H_2O^g \rightarrow (=Tb{-}O{-})_nTi(OH)^s_{4-n} + (4-n)HCl^g.$$

As a result, the surface of oxide particles was again covered with OH groups (now bound to titanium atoms) which could serve for further "layering." Thus, titanium oxide layers with increasing thickness (proportional to the number of cycles performed) were formed by cyclic repetition of reactions (1) and (2) [12].

Absorption spectra of modified porous glasses were recorded in reflected diffuse-scattered light, using a Specord M–40 spectrometer with a sphere photometer (pure PG as optical reference). The PL was recorded at room temperature, using an SDL-2 spectrometer with an SVD 120A mercury lamp as excitation source. To record spectra, dry powders (or those with adsorbed water) were placed in hermetically sealed quartz tubes 5 mm in diameter. The luminescence excitation spectra were recorded at the peak λ_{max} = 545 nm of the main emission band of Tb^{3+} cations. The adsorption of water by pure and modified PGs was controlled at relative vapor pressures p/p_0 = 0.1–0.8 set by the desiccator method with the use of sulfuric acid solutions.

The luminescence spectrum of encapsulated chloride particles (Fig. 1) contains, together with the main characteristic band associated with the $^5D_4 \rightarrow {}^7F_5$ transition (λ_{max} = 545 nm), low-intensity bands peaked at 490, 590, and 625 nm, associated with transitions from the lowest excited state $^5D_4$ to levels $F_{6,4,3}$ of the Tb^{3+} cation, respectively [4, 8, 11]. It should be noted that, despite the low content of $TbCl_3$ species in the support, they provide a rather bright, visually observed green emission; nevertheless, they should be converted to the oxide form to enable molecular layering reactions.

It is known that polycrystalline REE chlorides decompose to give oxides at a temperature as low as ~250°C [13]. To the decomposition of encapsulated terbium chloride in thermal treatment at 300°C of glass modified with this compound corresponds gradual decrease in the intensity of luminescence bands (Fig. 1), caused by the possible presence of OH groups on the surface of oxide nanoparticles being formed. The substantial loss of excitation energy is determined in this case by its transfer to high-frequency vibrations ν_{O-H} [11]. It is difficult to judge about the size of encapsulated particles, although it is clear that it is largely determined by pore structure parameters of the support and by the low degree of filling of its surface. For example, a simple estimate made on the assumption of a uniform distribution of the intercalate (in an amount of 0.12 mmol g^{-1}) over the internal surface of the PG (S_{sp} = 80 m^2 g^{-1}) yields approximately one formula unit per area of 1 nm^2 [8]. Thus, there is certain reason to believe that only low-dimension oxide particles with high ratio between the surface area and the volume can appear even under conditions of active aggregation in the course of thermal treatment.

The intrinsic absorption of encapsulated particles is not manifested when recording diffusion reflection spectra. This is due to the small extinction coefficients of the bands corresponding to the $4f \rightarrow 4f$ transitions of Tb^{3+} cations [11] and to the decrease in the transparence of the porous glass in the range 200–250 nm. On raising the number of modifying titanium oxide layers from 1 to 4 (see Fig. 2), the diffusion reflection spectra change, which consists in a long-wavelength shift and in an increase in the intensity of the band associated with the $2p^n(O) \rightarrow 3d(Ti)$ charge transfer from nonbonding orbitals of oxygen to titanium(IV) atoms. It

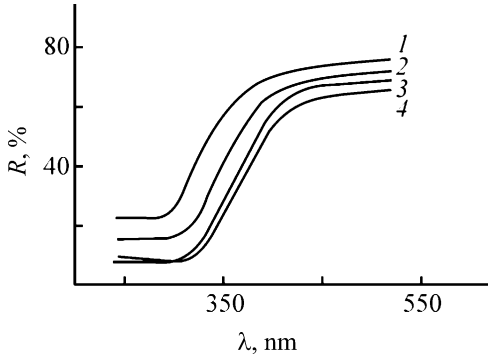


Fig. 2. Spectral distribution of the diffuse reflectance R of a porous glass with incorporated Tb_2O_3 nanoparticles after (*1*) 1, (*2*) 2, (*3*) 3, and (*4*) layering cycles.

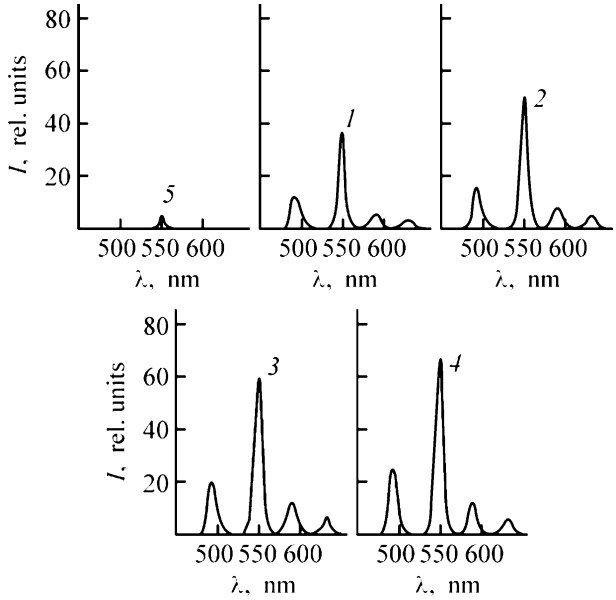


Fig. 3. (*5*) Luminescence from encapsulated Tb_2O_3 particles and its enhancement upon synthesis on their surface of (*1*) 1, (*2*) 2, (*3*) 3, and (*4*) 4 titanium oxide layers. (*I*) Intensity and (λ) wavelength; the same for Fig. 4.

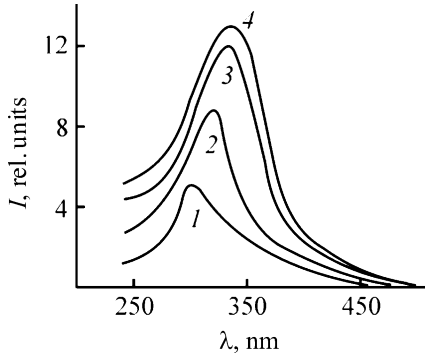


Fig. 4. Luminescence excitation spectra. *Digits at the curves*, number of titanium oxide layers synthesized.

should be noted that, in molecular layering reactions, the modifying layers are synthesized both on the hydroxylated surface of oxide nanolayers and on the free surface of PG. It is significant that, at an effective thickness of the growing titanium oxide of 3–4 monolayers, the spectra of the samples almost coincide and are close to that of the crystalline modification of TiO_2 (rutile).

The formation of =Tb–O–Ti= bonds as a result of a chemical modification of Tb_2O_3 nanoparticles is clearly manifested in luminescence spectra (Fig. 3): a substantial increase in its intensity is recorded already after the first layering cycle. Both further rise in the intensity of green emission, caused by the increase in the thickness of the oxide-sensitizer, and attainment of the maximum efficiency of its action upon synthesis of 3–4 titanium oxide layers (Fig. 3) are in good agreement with the absorption spectra of the samples under study (Fig. 2). Specific features of the sensitization are also reliably reflected in luminescence excitation spectra (Fig. 4). In this case, the increase in the thickness of the titanium oxide layer causes not only the characteristic increase in intensity, but also a pronounced long-wavelength shift in the peak positions of the bands responsible for the sensitization of luminescent centers.

The results obtained suggest that the excited states generated as a result of charge-transfer transitions $2p^n(O) \rightarrow 3d(Ti)$ in the sensitizer layers lie higher than the radiative $^5D_4$ level of the Tb^{3+} cation. The fact that this main condition is satisfied, combined with the possibility of excitation energy transfer to luminescent centers via covalent bond "channels" and the high optical absorption of titanium oxide layers in the UV spectral range, predetermine the luminescence sensitization in the systems under study.

As the thickness of titanium oxide layers synthesized by molecular layering increases, they become considerably denser and can serve as protective coatings [12]. Therefore, there is reason to believe that a titanium oxide shell present on the surface of encapsulated Tb_2O_3 particles will hinder luminescence quenching in the presence of adsorbed water. Figure 5 compares the isotherm of water adsorption by a sample exhibiting the highest emission intensity with the dependence of the intensity I of the main luminescence band on the relative humidity p/p_0. The value of I remains unchanged in a wide range of moderate vapor pressures, which points to a reliable shielding of luminescent centers from water molecules. Moreover, a minor, but reliably recorded increase in the lumines-

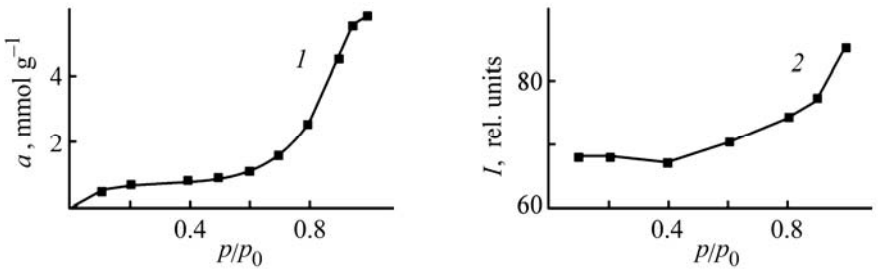


Fig. 5. (*1*) Isotherm of water adsorption *a* by the sample with the highest emission intensity and (*2*) effect of the relative humidity p/p_0 on the intensity *I* of the main band of its luminescence.

cence intensity is observed in the region of capillary condensation of water (at $p/p_0 > 0.6$). The unusual behavior of the system can be regarded, to a first approximation, as a result of luminescence activation caused by the increase in the dielectric constant of the medium [11] upon filling of the pore space by water. A similar, but clearly pronounced effect of luminescence enhancement in the presence of condensed water has been described previously for complex particles $Eu(DBM)_3 \cdot phen$ (DBM, dibenzoylmetane; phen, 1,10-phenanthroline) encapsulated in porous glass.

CONCLUSIONS

(1) It was shown that nanosize Tb_2O_3 particles are formed in a porous glass in thermal decomposition of terbium(III) chloride.

(2) Titanium oxide layers with controllable thickness were synthesized on the surface of oxide particles by the molecular layering method.

(3) It was demonstrated that Tb_2O_3 nanoparticles have a property of luminescence sensitization, which becomes more pronounced as the thickness of the modifying titanium oxide layers increases.

REFERENCES

1. Tret'yakov, Yu.D., Lukashin, A.V., and Eliseev, A.A., *Usp. Khim*., 2004, vol. 73, no. 9, pp. 974–998.
2. Bronshtein, L.M., Sidorov, S.N., and Valetskii, P.M., *Usp. Khim*., 2004, vol. 73, no. 5, pp. 542–557.
3. Maas, H., Currao, A., and Calzaferri, G., *Angew. Chem. Int. Ed.*, 2002, vol. 41, no. 14, pp. 2495–2497.
4. Bel'tyukova, S.V., Tselik, E.I., Egorova, A.V., and Teslyuk, O.I., *Zh. Prikl. Spektrosk*., 2003, vol. 70, no. 2, pp. 272–275.
5. Parra, D.F., Brito, H.F., Matos, J.D.R., and Dias, L.C., *J. Appl. Polym. Sci*., 2002, vol. 83, no. 12, pp. 2716–2726.
6. Petushkov, A.A., Shilov, S.M., Puzyk, M.V., and Pak, V.N., *Fiz. Khim. Stekla*, 2004, vol. 30, no. 4, pp. 333–336.
7. Petushkov, A.A., Shilov, S.M., Puzyk, M.V., and Pak, V.N., *Pis'ma Zh. Tekh. Fiz.*, 2006, vol. 32, no. 9, pp. 65–70.
8. Gavronskaya, K.A., Shilov, S.M., and Pak, V.N., *Zh. Prikl. Khim*., 2007, vol. 80, no. 3, pp. 366–369.
9. Enke, D., Janovski, F., and Schwieger, W., *Micropor. Mesopor. Mater.*, 2003, vol. 60, nos. 1–3, pp. 19–30.
10. Lyubavin, M.V., Burkat, T.M., and Pak, V.N., *Neorg. Mater.*, 2008, vol. 44, no. 2, pp. 248–252.
11. Poluektov, N.S., Kononenko, L.I., Efryushina, N.P., and Bel'tyukova, S.V., *Spektrofotometricheskie i lyuminestsentnye metody opredeleniya lantanoidov* (Spectrophotometric and Luminescent Methods for Determination of Lanthanides), Kiev: Naukova Dumka, 1989.
12. Malygin, A.A., *Zh. Prikl. Khim*., 1996, vol. 69, no. 9, pp. 1585–1593.
13. Stump, N.A., Schweitzer, G.K., Gibson, J.K., et al., *Appl. Spectr*., 1994, vol. 48, no. 8, pp. 937–943.

ISSN 1070-4272, Russian Journal of Applied Chemistry, 2008, Vol. 81, No. 10, pp. 1758–1763. © Pleiades Publishing, Ltd., 2008.
Original Russian Text © L.A. Kartsova, N.A. Kas'yanenko, A.V. Alekseeva, O.V. Ganzha, S.V. Paston, D.S. Ershov, 2008, published in Zhurnal Prikladnoi Khimii, 2008, Vol. 81, No. 10, pp. 1633–1638.

PHYSICOCHEMICAL STUDIES OF SYSTEMS AND PROCESSES

Electrophoretic Determination of Catechins and Examination of Their Complexing with Organic and Inorganic Compounds

L. A. Kartsova, N. A. Kas'yanenko, A. V. Alekseeva, O. V. Ganzha, S. V. Paston, and D. S. Ershov

St. Petersburg State University, St. Petersburg, Russia
Research Institute of Physics, St. Petersburg State University, St. Petersburg, Russia

Received July 17, 2007

Abstract—The biological activity of catechins, and their interaction with various inorganic [iron(III) salts] and organic (DNA, casein) compounds were examined.

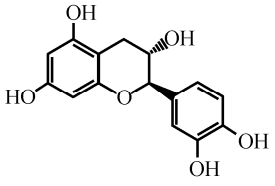
DOI: 10.1134/S1070427208100108

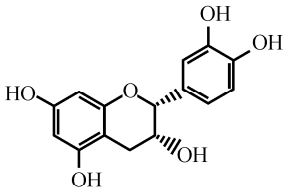
Catechins, or flavan-3-ols, are natural polyphenolic antioxidants contained in vegetables, fruits, grains, and seasonings, as well as in wine and green and black tea (in green tea, in considerably higher concentrations), coffee, and cocoa [1–3].

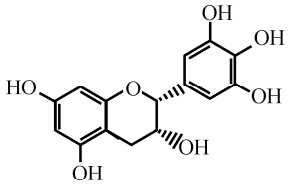
Owing to the high oxidizability of catechins, green and black tea neutralizes the action of free radicals and diminishes the damage inflicted to lipids of membranes, protein, and nucleic acids.

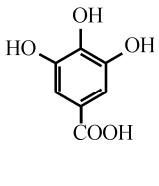
The concentration of catechins in a tea is one of its quality criteria. There exists a correlation between the total content of catechins and the total antioxidant activity of a green tea extract.

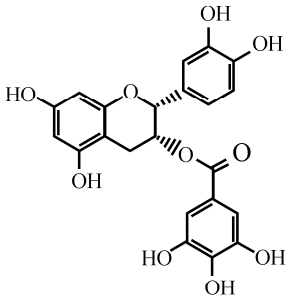
The major biologically active components of tea are flavan-3-ols [(+)-catechin, (–)-epicatechin, (–)-epigallocatechin, (–)-epicatechin gallate, (–)-gallocatechin gallate, (–)-epigallocatechin gallate] and gallic acid:

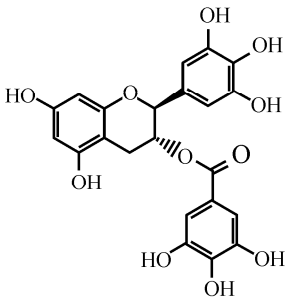

(+)-Catechin (C)

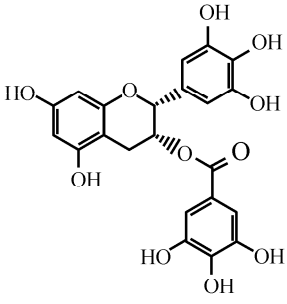

(–)-Epicatechin (EC)


(–)-Epigallocatechin (EGC)


Gallic acid (GA)


(–)-Epicatechin gallate (ECG)


(–)-Gallocatechin gallate (GCG)


(–)-Epigallocatechin gallate (EGCG)

An important property of catechins is their capacity for complexing with metal ions owing to the presence of neighboring phenolic hydroxyls, potential complexing centers, in their molecules. In tea leaves, catechins form complexes with aluminum [4], calcium, magnesium, and manganese [5] ions. This complexing ability makes these compounds suitable for determination of metal ions in biological objects [6]. These processes have been examined with model systems composed of catechins and Fe^{3+} ions [7]. Such studies are extremely important, since the biological activity of catechins is strongly dependent on the form, free or bound, in which they occur [7].

Recently, wide application in analysis of natural objects and biological fluids has been found by the method of capillary electrophoresis (CE) with an ultraviolet detector, also used for determination of polyphenolic compounds in real objects [8–11].

Earlier, we have developed a method for analysis of various brands of green and black tea by micellar electrokinetic chromatography [12]. As a micelle-forming agent served an anionic detergent, sodium dodecyl sulfate (SDS). At concentrations above 8.3 mM (critical micelle concentration), SDS molecules form micelles (pseudostationary phase). This improves the selectivity of separation relative to the capillary zone electrophoresis (CZE) owing to the distribution of analytes between the micelles and the supporting electrolyte solution.

EXPERIMENTAL

The analysis was carried out on a KAPEL' 105 capillary electrophoresis system with a spectrophotometric detector (200–400 nm). We used a quartz capillary with an external polyimide coating (inner diameter 75 μm, effective length 50 cm (total length 60 cm). The working temperature was 20°C. The detection was carried out at a wavelength of 200 nm.

Standard samples of polyphenols [(+)-catechin, (–)-epicatechin, (–)-epicatechin gallate, (–)-epigallocatechin, (–)-gallocatechin gallate, (–)-epigallocatechin gallate and gallic acid], casein, and DNA were available form Fluka and Sigma.

We used hydrochloric acid, sodium hydroxide, sodium dodecyl sulfate, sodium dihydrogen phosphate monohydrate ($NaH_2PO_4 \cdot H_2O$), disodium hydrogen phosphate dodecahydrate ($Na_2HPO_4 \cdot 12H_2O$), sodium chloride (NaCl), and iron(III) chloride (all of chemically pure grade).

To determine catechins, we used a supporting electrolyte based on 0.025 M phosphate buffer (pH 7.0) with addition of SDS in various concentrations (10, 15, 20, 25, 30 mM). The hydrodynamic sample injection was used (30 mbar, 10 s). The analytes were electro-phoretically separated at a positive polarity of +25 kV. Before analysis, the quartz capillary was washed with 1 M hydrochloric acid and distilled water for 10 min and then conditioned successively in 0.5 M sodium hydroxide solution (10 min) and distilled water (10 min). In between analyses, the capillary was washed with the working supporting electrolyte for 3 min.

To study the interaction of caseins with tea catechins, we prepared aqueous solutions of casein and epigallocatechin gallate, taken separately, in concentrations of 150 and 20 mg l^{-1}, respectively. The solution of casein (150 mg l^{-1}) served as the starting solution for preparation of less concentrated solutions of the protein.

We used a high-molecular-weight thymus DNA, whose molecular weight (11.4 MDa) was estimated from the intrinsic viscosity [η] in a 0.15 M NaCl solution: $[\eta] = 6.9 \times 10^{-4} M^{0.7}$. The optical absorption of the DNA solutions was measured on an SF-26 spectrophotometer (Russia). The DNA concentration in solution c was estimated from the UV absorption of the preliminary denaturated DNA [13]. This allowed the condition of the secondary structure of the macromolecule to be monitored before and after the experiment on the basis of the molecular extinction coefficient $E(p) = (31.3D_{260})/c_{DNA}$. We used solutions with $E(p) < 6900$ (hyperchromic effect did not exceed 5%).

The DNA solutions containing catechins in different concentrations were exposed to ^{137}Cs γ-radiation under aerobic conditions on an LMB-γ-I[1] setup at a dose rate of 2.86 krad min^{-1}. The DNA concentration c in all the irradiated solutions was 0.01 g dl^{-1}. As the UV-radiation source we used a 8 W DRB–8 lamp. The DNA solutions were irradiated in quartz cells with a thickness of 0.2 cm. The DNA concentration in all the solutions being irradiated was 0.01 g dl^{-1}. The UV-radiation intensity at a wavelength of 254 nm was 3.4×10^4 J kg^{-1} s^{-1}.

The relative viscosity η_r of the DNA solutions with different concentrations was measured in a modified low-gradient magnetic rotary viscometer [14] at different flow rate gradients g, with the subsequent extrapolation to $g = 0$. The intrinsic viscosity [η] of DNA

[1] The experiments were carried out at the Institute of Cytology, Russian Academy of Sciences, St. Petersburg.

Table 1. Change of the content of catechins in green and black tea, induced by 5% milk addition ($P = 0.95$, $n = 3$)

Analyte	Concentration,* wt %			
	green tea	green tea with addition of milk	black tea	black tea with addition of milk
EGC	1.7 ± 0.1	0.57 ± 0.06	<0.01	<0.01
EGCG	3.4 ± 0.3	0.55 ± 0.06	0.10 ± 0.01	<0.01
EC	0.83 ± 0.08	0.28 ± 0.04	0.09 ± 0.01	0.07 ± 0.01
GA	0.08 ± 0.02	0.04 ± 0.01	0.14 ± 0.02	0.06 ± 0.01
ECG	2.3 ± 0.2	0.41 ± 0.05	0.18 ± 0.03	0.11 ± 0.02

* The analyte concentrations are given as percent fractions of the weight of tea leave.

was determined by extrapolation of the concentration dependence of the reduced viscosity by the formula

$$[\eta] = \lim_{c\to 0}\left(\frac{(\eta_r - 1)_{g\to 0}}{c}\right). \quad (1)$$

The parameter [η] is proportional to the specific volume of the macromolecule. We took into account the Flory equation [15]

$$[\eta] = \Phi \frac{\left(\overline{h}_0^2\right)^{3/2}}{M}\alpha^3 = \Phi \frac{\left(LA\right)^{3/2}}{M}\alpha^3, \quad (2)$$

where $(\overline{h}_0^2)^{1/2}$ is the root-mean-square distance between the ends of the unperturbed chain; α, linear swelling coefficient of the macromolecule; Φ, Flory coefficient; *L*, hydrodynamic chain length (length of the fully extended macromolecule); *A*, average length of the statistical segment (a secuence of these rigid rod segments models the polymer chain); and *M*, molecular weight.

Based on the results of the experiments, we chose 0.025 M phosphate buffer (pH 7.0) with an SDS additive (25 mM) as the working solution for electrophoretic determination of catechins.

Under these conditions, we obtained comparative characteristic electrophoretic profiles (Fig. 1), quantitatively determinated catechins in various tea samples (Table 1), and elucidated how the detergent concentra-

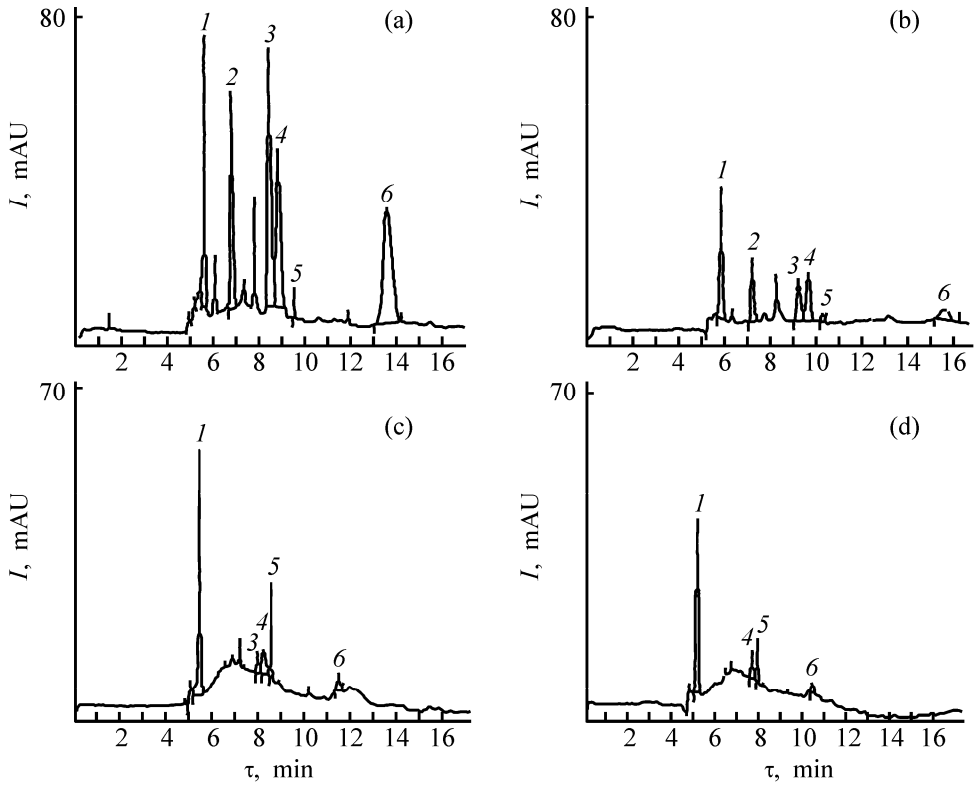


Fig. 1. Electrophoretic profiles of various tea extracts. Conditions: KAPEL' 105; supporting electrolyte: 0.025 M phosphate buffer (pH 7.0), 25 mM SDS; 25 kV; 200 nm. (*1*) Absorption intensity, and (τ) time. (a) Green tea, (b) green tea with 5% addition of milk, (c) black tea, and (d) black tea with 5% addition of milk. (*1*) Caffeine, (*2*) (–)-epigallocatechin, (*3*) (–)-epigallocatechin gallate, (*4*) (–)-epicatechin, (*5*) gallic acid, and (*6*) (–)-epicatechin gallate.

tion affects the efficiency and selectivity of separation of the biologically active components of tea (Fig. 2).

Under the optimized conditions, we examined complexing of catechins with casein and Fe^{3+} ions. As the criterion of formation of the corresponding complex served the change in the concentration of the catechins, which was monitored electrophoretically.

We examined in detail the complexing ability of flavan-3-ols for the example of (–)-epigallocatechin gallate. An increase in the proportion of casein (the basic milk protein) in the model mixture composed of EGCG (20 mg l^{-1}) and casein (3 to 15 mg l^{-1}) causes a decrease in the amount of the free form of catechin; at the casein concentration of 15 mg l^{-1} it was estimated at 1 mg l^{-1}. The content of catechins also decreased upon addition of a Fe(III) salt. We found how the concentration of (–)-epigallocatechin gallate varies with the amounts of casein (Fig. 3a) and iron(III) salt (Fig. 3b) introduced.

A similar trend was also observed in quantitative determination of catechins in various samples of green and black tea upon addition of milk (Fig. 1, Table 1).

Also, we examined the radioprotective properties of (+)-catechin and (–)-epicatechin upon exposure of the DNA molecule in solution to ionizing (gamma) and nonionizing (UV light with a wavelength of 254 nm) radiation. An adult human body contains up to 70% water, and water is involved in all the principal biochemical reactions occurring in functioning of DNA. Hence, examination of model systems, aqueous DNA solutions, provides a fairly adequate information about the biological role of various compounds. As is known, ionizing and nonionizing radiations differ in the action mechanisms toward DNA. In the former case, solutions and cells are subjected mainly to indirect action of radiation via reactions of the macromolecule with water radiolysis products, and in the latter case, to direct action, i.e., absorption of photons by the nitrogen bases of DNA [16]. In both cases, this results in disturbance of the DNA structure (single and double breaks of the complementary chains, modification, and elimination of the nitrogen bases, changes in the phosphate group). This can lead to loss of charge by DNA.

It should be noted that the radiation damage is always manifested as a decrease in the volume of the molecular coil in solution, associated with various factors mentioned above. Hence, by estimating the intrinsic viscosity of DNA, [η], proportional to its specific volume, it is possible to determine the radiation damage.

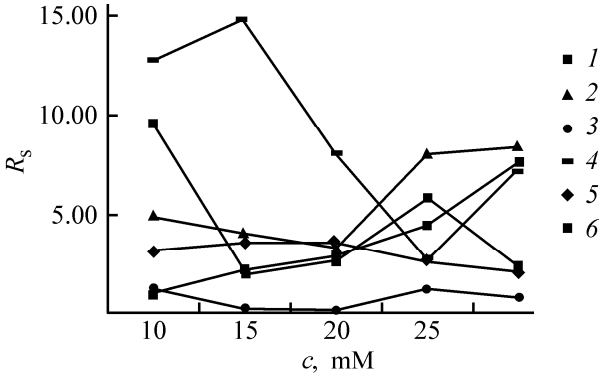


Fig. 2. Resolution coefficients R_s for the pairs of analytes vs. concentration c of SDS in the supporting electrolyte. (*1*) C/EGC, (*2*) EGC/EGCG, (*3*) EC/EGCG, (*4*) EC/GA, (*5*) GCG/ECG, (*6*) GCG/GA.

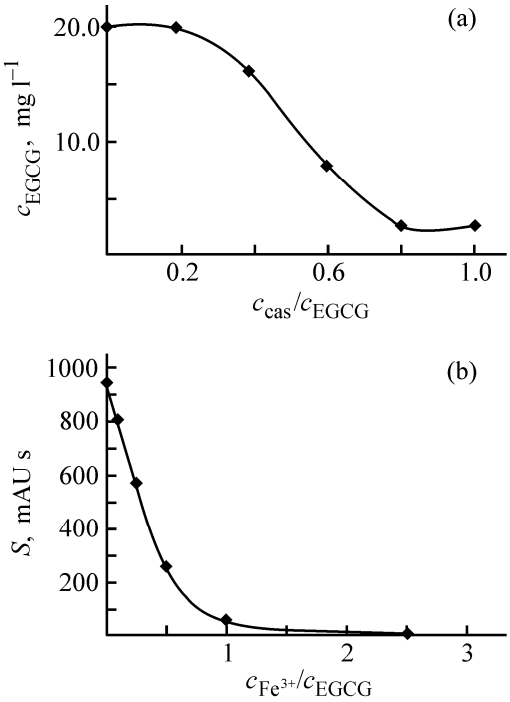


Fig. 3. Change in the concentration of (–)-epigallocatechin 3-gallate upon addition of (a) casein and (b) Fe^{3+} ions. (c_{EGCG}) Concentration of the free form of EGCG, (c_{cas}/c_{EGCG}) casein to EGCG ratio of the initial concentrations, (S) peak EGCG area, and (c_{Fe3+}/c_{EGCG}) molar concentration ratio.

It has been shown earlier that, under γ-radiation exposure of DNA solutions at up to 30 Gy doses and under UV-radiation exposure at several orders of magnitude higher doses (up to 6 ± 10^7 J kg^{-1}), the decrease in the volume of the macromolecule is not accompanied by any appreciable degradation of its secondary structure: No hyperchromic effect associated with

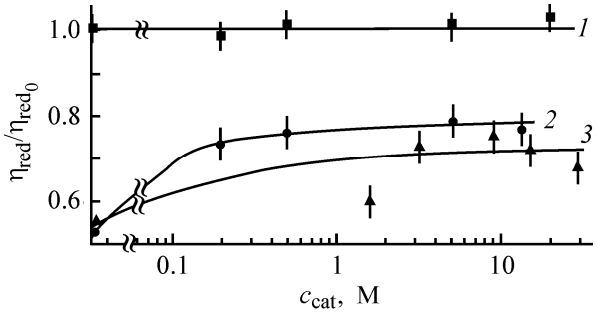


Fig. 4. Relative change in the reduced viscosity η_{red}/η_{red_0} of the DNA solution (c_{DNA}=0.005 g dl^{-1}) vs. (+)-catechin concentration c_{cat} in solution. Solution: (*1*) intact, (*2*) irradiated at a dose of 10 Gy, (*3*) UV-irradiated at a dose of 6.1 × 10^7 J (system kg)$^{-1}$.

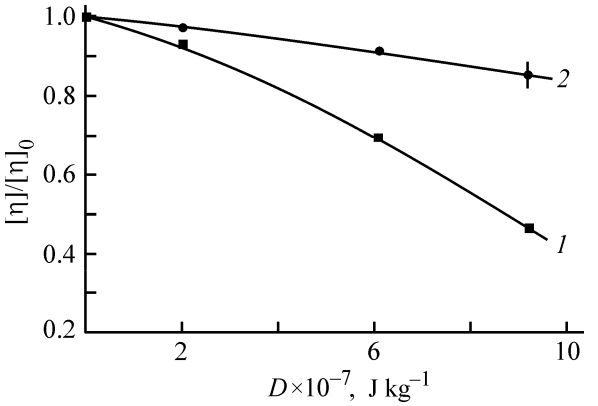


Fig. 5. Intrinsic viscosity $[\eta]/[\eta]_0$ of DNA under UV irradiation in the (*1*) absence and (*2*) presence of (+)–catechin in solution vs. irradiation dose *D*. c_{cat} = 1.3 × 10^{-3} M.

the cleavage of hydrogen bonds and stacking interaction of the bases is observed in the UV-absorption spectrum of DNA. There is no change in the flexural rigidity of the double helix, either, which also suggests that the secondary structure of DNA remains unchanged [17–19]. At high irradiation doses these parameters change, which points to a more profound modification of the structure of the macromolecule.

Table 2. Relative change in the intrinsic viscosity of DNA, induced by γ-irradiation*

γ-Radiation dose, Gy	$[\eta]/[\eta]_0 \pm 0.05$		
	$c_{cat} = 0$	$c_{(+)\text{-cat}}$=1.3×10^{-3} M	$c_{(-)\text{-epicat}}$=1.3×10^{-3} M
0	1.00	1.00	0.99
10	0.24	0.61	0.87
30	0.08	0.50	–

* $[\eta]_0$ and $[\eta]$ are the intrinsic viscosities of intact and irradiated macromolecules, respectively.

Also, we elucidated how γ-irradiation at doses of up to 30 Gy affects the DNA molecule in solutions containing various concentrations of flavanoids. Our experiment showed that the $[\eta]$ parameter of DNA tends to sharply decrease with increasing irradiation dose (Table 2). Introduction of (+)-catechin into the solution before the radiation exposure diminishes the damage. An increase in the (+)-catechin concentration up to a certain limiting value results in enhancement of the protective action (Fig. 4). An increase in the (+)-catechin concentration to above 5 × 10^{-5} M does not make this effect more pronounced.

Interestingly, this concentration of (+)-catechin is of approximately the same order magnitude as that in the standard extract of tea tree leaves (2 g of dry tea per 200 ml of boiling water after 5-min infusion). It should be noted that the presence of (+)-catechin only diminishes the γ-radiation damage, rather than provides absolute protection. Thus, our results suggest that (+)-catechin can of protect the DNA molecule against ionizing radiation. In the case of (–)-epicatechin, the radioprotective properties are even more pronounced (Table 2).

We found that, under the experimental conditions, there is no complexing between DNA and the flavan-3-ols examined. This is suggested, in particular, by the fact that the spectral characteristics of both the components in solutions containing different concentrations of DNA and catechins remain identical to those in their solutions taken separately. The volume and the optical anisotropy of the macromolecule remain unchanged. Published data [19] suggest that (+)-catechin and (–)-epicatechin do not intercalate into the double helix of DNA. Our experiment demonstrated the lack of bonding between the catechins and DNA in solution, which suggests that the examined compounds exert the radioprotective action via interception of the free radicals yielded by water radiolysis under γ-radiation exposure.

The exposure to UV light (λ = 254 nm) results in direct action on the macromolecule, rather than in water radiolysis. The wavelength we used is close to the absorption peak of DNA (260 nm) and catechins (280 nm). Despite the different mechanisms by which γ and UV radiations inflict damage, the intrinsic viscosity DNA decreases in both cases. The presence of catechin in solution partly prevents the damage to DNA as well (Fig. 5). A possible reason is that an appreciable portion of the radiation energy is absorbed by catechin, whose absorption spectrum overlaps with that of DNA.

CONCLUSIONS

(1) A micellar electrokinetic chromatographic examination revealed complexing of catechins with Fe^{3+} ions and casein.

(2) It was shown that (+)-catechin and (–)-epicatechin do not react with the DNA molecule in solution, but protect it against the radiation damage by interception of the water radiolysis products.

REFERENCES

1. Lill, G., Voit, S., Schror, K., and Weber, A.-A., *FEBS Lett.*, 2003, vol. 546. pp. 265–270.
2. Yu, H., Yin, J., and Shen, S., *Food Chem.*, 2006, vol. 95, pp. 108–115.
3. Stangl, V., Dreger, H., Stangl, K., and Lorenz, M., *Cardiovascular Research*, 2007, vol. 73, pp. 348–358.
4. Erdemoglu, S.B. and Guser, S., *Anal. Sci.*, 2005, vol. 21, pp. 1005–1008.
5. Costa, L.M., Gouveia, S.T., and Nobrega, J.A., *Anal. Sci.*, 2002, vol. 18, pp. 313–318.
6. Lian, H., Kang, Y., Yasin, A., et al., *J. Chromatogr., A.*, 2003, vol. 993, pp. 179–185.
7. Khokhar, S. and R.K.Owusu Apenten, *Food Chem.*, 2003, vol. 81, pp. 133–140.
8. Horie, H. and Kohata, K., *J. Chromatogr., A.*, 1998, vol. 802, pp. 219–223.
9. Lee, B.-L. and Ong, C.-N., *J. Chromatogr., A*, 2000, vol. 881, pp. 439–447.
10. Vaher, M. and Koel, M., *J. Chromatogr., A*, 2003, vol. 990, pp. 225–230.
11. Herreroa, M., Ibanez, E., Senorans, H., and Cifuentas, A., *J. Chromatogr., A*, 2004, vol. 1047, pp. 195–203.
12. Kartsova, L.A. and Ganzha, O.V., *Zh. Prikl. Khim.*, 2006, vol . 79, no 7, pp. 1120–1124.
13. Spirin, A.S., *Biokhimiya*, *M.*, 1958, vol. 23, pp. 656–662.
14. Frisman, E.V., Shchagina, L.V., and Vorob'ev, V.I., *Kolloidn. Zh.*, 1965, vol. 27, pp. 130–133.
15. Flory, P., *Principles of the Polymer Chemistry*, New York: Cornell Univ., 1953.
16. Kudryashev, Yu.B., *Radiatsionnaya biofizika* (Radiation Biophysics), Moscow: Fizmatlit, 2004.
17. Frisman, E.V. and Zarubina, O.P., *Dokl. Akad. Nauk SSSR*, 1988, vol. 298, no. 2, pp. 491–494.
18. Frisman, E.V. and Zarubina, O.P., *Biophys. Chem.*, 1993, vol. 46, pp. 37–46.
19. Paston, S.V. and Zyryanova, I.M., *Vestn. Sankt-Peterb. Gos. Univs., Ser. 4*, 2000, issue 1, no. 4, pp. 50–59.

ISSN 1070-4272, Russian Journal of Applied Chemistry, 2008, Vol. 81, No. 10, pp. 1764–1767. © Pleiades Publishing, Ltd., 2008.
Original Russian Text © S.G. Khaminets, L.L. Potapova, V.Z. Radkevich, Yu.G. Egiazarov, 2008, published in Zhurnal Prikladnoi Khimii, 2008, Vol. 81, No. 10, pp. 1639–1642.

PHYSICOCHEMICAL STUDIES OF SYSTEMS AND PROCESSES

Supported Metal Catalysts Based on Fibrous Carbon Material for Low-Temperature CO Oxidation

S. G. Khaminets, L. L. Potapova, V. Z. Radkevich, and Yu. G. Egiazarov

Institute of Physicoorganic Chemistry, National Academy of Sciences of Belarus, Minsk, Belarus

Received January 22, 2008

Abstract—A number of supported-metal (Pt, Pd) catalysts based on Karbopon nonwoven carbon fibers were prepared by deposition from hydrosols and by ion exchange. The catalytic activity of the catalysts in low-temperature oxidation of carbon monoxide by atmospheric oxygen was determined. Catalyst samples were studied by transmission electron microscopy.

DOI: 10.1134/S107042720810011X

Purification of air to remove carbon monoxide is an important ecological problem. The only efficient way to remove carbon monoxide from air is catalytic oxidation, and, therefore, extensive studies aimed to develop active catalysts for CO oxidation have been carried out in recent years.

The first practically used low-temperature catalyst for CO oxidation is hopcalite (mixture of copper and manganese oxides). Until recently, catalytic systems of this kind, based on transition metal oxides, have been studied and patented [1–3]. These catalysts are inexpensive and readily available, but rapidly loose activity in the presence of moisture.

Noble metals supported by thermally stable and chemically inert oxides (Al_2O_3, SiO_2) catalyze CO oxidation only at temperatures above 150°C, because, being firmly sorbed on the metal surface at low temperatures, CO hinders adsorption of oxygen [4, 5].

Catalytic systems in the form of a noble metal supported by a reducible oxide (SnO_2, MnO_2, Fe_2O_3) can work at low temperatures [6–10] and are more stable in a humid atmosphere than hopcalite. It is believed [9] that a noble metal makes lower the strength of the M–O bond in the oxide substrate, i.e., it catalyzes the reduction and reoxidation of the oxide. This generates active oxygen for the reaction of CO oxidation.

Because the efficiency of supported-metal catalysts is largely determined by the physicochemical properties of a support, the increasing interest in new types of supports is justified. In particular, a considerable attention has been given recently to carbon materials with fibrous structure. Owing to the electrical conductivity of the carbon support, the supported metal is not electron-deficient, in contrast to the case of supports of acid nature.

Previously, a number of mono- and bimetallic supported-metal catalysts based on Karbopon nonwoven carbon fibers have been synthesized and studied in the reaction of CO oxidation [11]. The catalysts were prepared by impregnation with aqueous solutions of metal salts, followed by heating and reduction. A conclusion was made that platinum-containing catalysts are the most promising for CO oxidation.

Supported-metal catalysts fabricated by the conventional impregnation method have an insufficiently high activity in CO oxidation. Therefore, it was necessary to find a way to obtain a more active catalyst.

The aim of our study was to develop a method for fabrication of an efficient catalyst for low-temperature oxidation of carbon monoxide in the form of a noble metal supported by carbon fibers.

EXPERIMENTAL

We prepared the catalyst from Karbopon carbon fibrous material manufactured by Khimvolokno Production Association (Svetlogorsk, Belarus). The mate-

rial has the following adsorption-structural characteristics: fiber diameter 5–10 μm, sorption volume for water 0.64 $cm^3\ g^{-1}$, average pore diameter 23 Å, and specific surface area S_{sp} (found from nitrogen adsorption) 780 $m^2\ g^{-1}$.

The method for deposition of metals onto supports by adsorption of metallic particles from colloid solutions (sols) is rather simple and convenient. It enables control over the size of metal particles before their deposition. At present, about ten methods for preparing metal sols are known. Of these, the chemical method consisting in treatment of a metal salt solution with a reducing agent is employed the most widely [12–14]. It should be noted that metal sols are unstable without stabilizers (surfactants or soluble polymers), whereas introduction of stabilizers, as a rule, provides stability for strongly diluted metal-containing solutions ($<10^{-3}$ M). With stabilizers used, sols may become unsuitable for fabrication of supported catalysts because either metal particles are not sorbed, or the catalysts produced are inactive due to blocking of a part of the surface by stabilizer molecules.

In view of the aforesaid, we chose sodium citrate as stabilizer for preparing hydrosols. This compound nearly does not hinder sorption of stabilized particles by the carbon fiber and, owing to its polarity, is easily removed by washing with water.

Hydrosols of platinum and palladium were obtained by reduction of aqueous solutions of platinohydrochloric acid and palladium nitrate with 10% hydrazine hydrate. Sodium citrate was used as stabilizer at a 1 : 5 molar ratio between the metal and sodium citrate. The carbon fiber was impregnated with the freshly prepared hydrosol, washed to remove the stabilizer, and dried at room temperature. The samples obtained were studied in CO oxidation both immediately after the drying and upon additional reduction in a flow of hydrogen.

Further, we prepared a number of samples of a platinum-containing catalyst by the ion exchange method. Because the number of exchange centers on the surface of the starting Karbopon is exceedingly small (exchange capacity of about 0.05 mg-equiv g^{-1}), a composite material sulfokarbopon was synthesized and used as a support.

To obtain sulfokarbopon, we grafted a styrene–divinylbenzene copolymer to the starting Karbopon by the radiation-chemical method. In doing so, we varied the composition of the grafting solution by changing the relative amounts of monomers (styrene, divinylbenzene) and a solvent (benzene, methanol) and also the irradiation dose. Karbopon plates (60 × 60 mm) were mounted vertically in a specially fabricated holder, which was placed in a glass vessel filled with the grafting solution and kept there at room temperature for 4 h. Then the solution was discharged, the vessel with the samples was placed in the channel of an RKhM-gamma-20 reactor with a ^{60}Co source, and grafting radiation-chemical copolymerization of styrene and divinylbenzene was performed. The irradiation power was 4.6 kGy h^{-1}.

After the grafting, the samples were dried at 90°C and the mass fraction of the grafted copolymer was found from the difference between the masses of the grafted and starting samples dried under identical conditions. Samples with the grafted styrene–divinylbenzene copolymer were sulfated with concentrated sulfuric acid at 115°C in the course of 3 h. After the sulfation, the samples were washed to remove H_2SO_4 to neutral reaction of the washing water and dried at room temperature. To prepare the Ba-form of sulfokarbopon, an excess amount of a 1 N $BaCl_2$ solution was passed through a column packed with the starting sulfokarbopon (H-form). The resulting sample was washed with distilled water to zero Cl^- concentration in the washing water.

The ion exchange was performed using a platinum(II) ammoniate solution and the barium form of sulfokarbopon. After the exchange, the samples were washed to remove Cl^- ions, dried, and reduced with hydrogen at 180°C. Then the catalysts were activated at 130°C by treatment with a mixture of hydrogen (3%) and air.

To obtain catalysts with different contents of the active component, we varied the number of exchange-reduction cycles.

The activity of the catalysts in oxidation of carbon monoxide was determined in a flow-through reactor at a flow rate of the reaction mixture (0.6 vol % CO in air) of 600 h^{-1}. The starting mixture and the reaction products were analyzed with a Gazokhrom chromatograph at a flow rate of the carrier gas (air) of 100 ml min^{-1}. Samples of the catalysts obtained (ultrathin sections) were examined by transmission electron microscopy on a JEM 100 CX instrument.

The results of experiments on CO oxidation in the presence of hydrosol palladium-containing samples are listed in Table 1. It can be seen that the catalytic activ-

Table 1. Content of palladium or platinum, treatment conditions of palladium- and platinum-containing catalysts produced from hydrosols and their activity in CO oxidation (0.6 vol % CO in air, $V = 600\ h^{-1}$)

Sample no.	Pd (Pt) content, %	Treatment with H_2 at 200°C	T, °C, at indicated conversion, %	
			75	100
Pd-Containing catalyst				
1	0.5	–	134	162
2	1.0	–	130	150
3	1.0	+	150	–
4	2.0	–	74	128
5	2.0	+	Inactive	
6	3.0	–	30	60
7	5.0	–	66	96
Pt-Containing catalyst				
1	0.5	+	66	68
2	2.0	+	64	80
3	3.0	+	72	78
4	5.0	–	139	160
5	5.0	+	72	90
6*	1.6	–	94	102
7*	1.8	+	87	90

* Samples obtained by metal deposition in three stages.

Table 2. Content of platinum in catalysts based on sulfokarbopon and their activity in CO oxidation [0.6 vol % CO in air, $V = 600\ h^{-1}$; activation conditions*: (I) 80°C, 1.5 h; (II) 180°C, 2 h; and (III) 110°C, 1 h]

Sample no.	Pt content, %	Number of cycles	EC of the support, mg-equiv g^{-1}	T, °C, at indicated conversion, %	
				75	100
1	1.3	1	0.6	44	72
2	2.6	2	0.6	33	64
3	2.5	4	0.3	–	30
4	5.4	5	0.6	–	16

* (I) Heating in a flow of He, (II) reduction with H_2, and (III) treatment with a mixture of H_2 (3%) and air.

ity grows as the palladium content increases to 3%, and decreases as the palladium content increases further to 5%. An additional treatment of palladium-containing catalysts with hydrogen makes their activity lower.

It is notable that, in the case of platinum-containing catalysts (Table 1), the best result is obtained for sample no. 1, which contains 0.5% metal. In contrast to palladium-containing samples, reduction of platinum-containing catalysts enhances their activity.

It can be concluded that the metal is nearly completely reduced in preparation of a palladium hydrosol. The additional treatment with hydrogen at elevated temperatures probably leads to a certain aggregation of metal clusters and to the corresponding decrease in activity. At the same time, in platinum hydrosols, a part of platinum remains in the unreduced state and additional reduction of the catalyst improves its activity.

Under the experimental conditions ($600\ h^{-1}$), the most active of the palladium- and platinum-containing samples provide the 100% conversion of carbon monoxide at 60 and 68°C, respectively [Table 1, sample nos. 6 (Pd) and 1 (Pt)]. It should be noted that the catalysts become inactive as the CO content of the reaction mixture is doubled. This indicates that the chemisorbed CO blocks the catalyst surface and the reaction becomes only possible after a part of the surface is freed for dissociative adsorption of oxygen.

As can be seen in Table 1, the samples produced by impregnation of the support with hydrosol fail to exhibit high activity in CO oxidation. The apparent reason is that rather coarse metal agglomerates are formed when these samples are synthesized. This is confirmed by an electron-microscopic analysis: the particle size is in the range 5–80 nm (Fig. 1).

Table 2 lists data for platinum-containing catalysts produced by ion exchange, with sulfokarbopon having an exchange capacity (EC) of 0.3–0.6 mg-equiv g^{-1} as a support. The content of platinum in the samples and, accordingly, their activity increases with the number of exchange-reduction cycles (sample nos. 1, 2, 4).

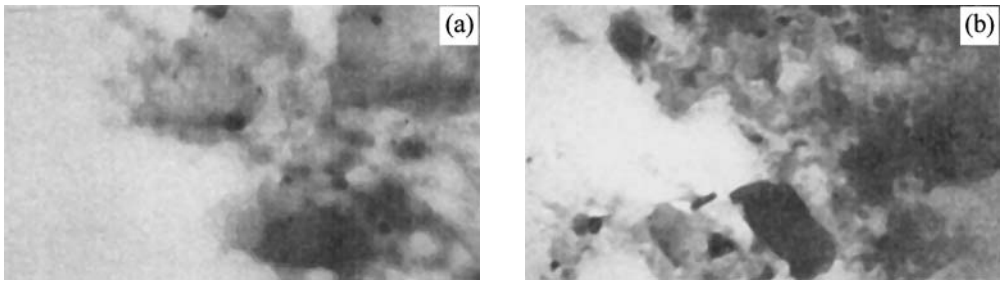


Fig. 1. Electron micrographs of catalysts produced from hydrosols. (a) 0.5% Pt/Karbopon and (b) 1.0% Pt/Karbopon.

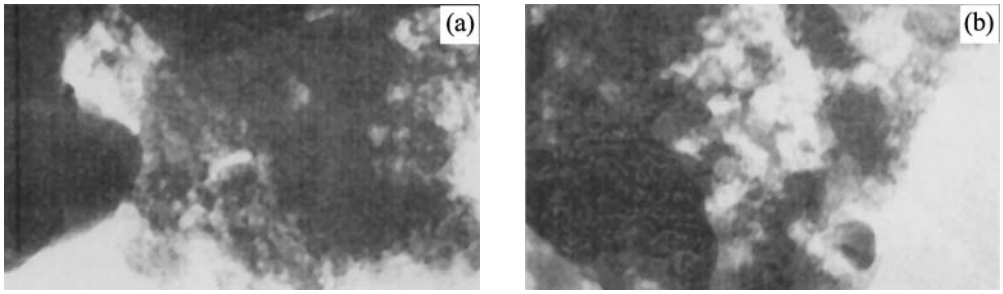


Fig. 2. Electron micrographs of an ion-exchange catalyst (5.4% Pt/sulfokarbopon).

It is notable that sample no. 3 (four exchange–reduction cycles), which contains approximately the same amount of platinum as sample no. 2 fabricated in two cycles, exhibits a substantially higher activity. Thus, the "split" deposition of the metal favorably affects the activity of the catalyst obtained.

The best result was obtained in the presence of the ion-exchange catalyst containing 5.4% Pt (Table 2, sample no. 4). The catalyst provides the 100% conversion of CO at room temperature. A study of this sample by transmission electron microscopy demonstrated that the main part of platinum in this sample is represented by clusters 1–4 nm in size (Figs. 2a, 2b).

Thus, our study demonstrated that the ion-exchange method can produce on a fibrous carbon support a sufficiently efficient platinum-containing catalyst for oxidation of carbon monoxide. It should, however, be noted that even the best of the samples obtained fail to provide a sufficiently high CO conversion in the respiratory mode (at high linear flow velocities of the gas mixture) and contain comparatively large amounts of the expensive noble metal.

CONCLUSIONS

(1) Catalyst samples produced by impregnation of a fibrous carbon support with hydrosols do not exhibit high activity in CO oxidation because of the insufficiently high dispersity of the active material.

(2) Ion-exchange samples containing highly dispersed platinum (particle size 1–4 nm) substantially exceed in activity catalysts synthesized with hydrosols. The best result is obtained in the presence of an ion-exchange sample containing 5.4% Pt. The catalyst provides a 100% conversion of CO under the experimental conditions.

REFERENCES

1. Cheng Tao, Fang Zhiyong, Hu Qixiu, et al., *Catal. Comm.,* 2007, vol. 8, p. 1167.
2. Luo Meng-Fei, Ma Jing-Meng, Lu Ji-Qing, et al., *J. Catal.*, 2007, vol. 246, p. 52.
3. Jpn. Patent Appl. 2 006 020 701.
4. Gracia, F.J., Bollmann, L., Wolf, E.E., et al., *J. Catal.*, 2003, vol. 220, p. 382.
5. Son, I.H., Shamsuzzoha, M., and Lane, A.M., *J. Catal.*, 2002, vol. 210, p. 460.
6. Hoflund, G.B., Upchurch, B.T., Schryer, D.R., et al., *J. Catal.*, 1991, vol. 129, p. 114.
7. Haruta, M., Yamada, N., Kobayashi, T., and Iijima, S., *J. Catal.*, 1989, vol. 115, p. 301.
8. Schryer, D.R., Upchurch, B.T., Van Norman, J.D., et al., *J. Catal.*, 1990, vol. 122, p. 193.
9. Hoflund, G.B. and Epling, W.S., *Rec. Res. Devel. Catal.*, 1996, vol. 1, p. 31.
10. EP Patent 0 129 406.
11. Egiazarov, Yu.G., Radkevich, V.Z., Khaminets, S.G., et al., *Vestsi Nats. Akad. Navyuk Belarusi, Ser. Khim. Navuk*, 2006, no. 3, p. 62.
12. Aiken, J.D.III, Lin, Y., and Finke, R.G., *J. Mol. Catal.*, 1999, vol. A145, nos. 1–2, p. 1.
13. Aiken, J.D.III and Finke, R.G., *Chem. Mater.*, 1999, vol. 11, no. 4, p. 1035.
14. Maksimov, G.M., Zaikovskii, V.I., Matveev, K.I., and Likholobov, V.A., *Kinet. Kataliz*, 2000, vol. 41, no. 6, p. 925.

ISSN 1070-4272, Russian Journal of Applied Chemistry, 2008, Vol. 81, No. 10, pp. 1768–1773. © Pleiades Publishing, Ltd., 2008.
Original Russian Text © V.V. Smolenskii, A.V. Novoselova, A.G. Osipenko, 2008, published in Zhurnal Prikladnoi Khimii, 2008, Vol. 81, No. 10, pp. 1643–1648.

APPLIED ELECTROCHEMISTRY AND CORROSION PROTECTION OF METALS

Electrochemical Study of the Redox Reaction Yb(III) + e ⇄ Yb(II) in a Molten LiCl–KCl Eutectic

V. V. Smolenskii, A. V. Novoselova, and A. G. Osipenko

Institute of High-Temperature Electrochemistry, Ural Branch, Russian Academy of Sciences, Yekaterinburg, Russia

Research Institute of Nuclear Reactors, Federal State Unitary Enterprise, State Scientific Center of the Russian Federation, Dimitrovgrad-10, Ul'yanovsk oblast, Russia

Received February 13, 2008

Abstract—Electrochemical process of reduction of Yb(III) ions and oxidation of Yb(II) ions in a molten LiCl–KCl eutectic in the range 723–973 K was studied by linear, cyclic, and square-wave voltammetry and zero-current potentiometry.

DOI: 10.1134/S1070427208100121

The concept of separation and transmutation is considered now as an efficient method for reducing the activity of radioactive waste. It consists in the following: recovery of long-lived fission products from spent nuclear fuel (SNF) and their incorporation into an inert (uranium-free) matrix for subsequent transmutation in appropriate reactors. Pyrochemical separation methods have a number of advantages over hydrometallurgical processes, the main of which are the high radiation hardness of salt melts and the possibility of SNF regeneration with a short cooling-off period [1–3].

Electrochemical methods, such as electrolysis, electrorefining, or reducing extraction, are used in pyrochemical processes for separation of components. The best known of these is the reprocessing of the metallic fuel of the EBR-II reactor [4]. In this process, actinides are electrochemically separated from fission products. Uranium is deposited onto a solid metallic cathode, and plutonium and minor actinides (MA), onto a liquid cadmium electrode [5].

SNF can also be regenerated by reducing extraction on liquid cathodes [6] or electrochemically on solid active electrodes [7].

The purpose of this study was to optimize the efficiency of MA separation and to minimize the content of fission products, and primarily rare earth elements, which are neutron poisons, in these actinides. To solve this problem, it is important to know electrochemical and thermodynamic properties of actinides and lanthanides. These data, obtained using various electrochemical methods for molten chlorides of alkali metals, are ambiguous in some cases [8–22].

Published information about the behavior of ytterbium compounds in chloride melts is scarce. Kinetic data on the behavior of $YbCl_3$ in the molten LiCl–KCl eutectic are entirely absent. Data on the mechanism and kinetics of reduction of trivalent ytterbium ions to the divalent state and on the thermodynamics of $YbCl_3$ formation in CsCl and NaCl–KCl melts were reported in [17, 18]. In [19] the redox potentials of the Yb(III)/Yb(II) system in the LiCl–KCl eutectic melt were measured relative to a 1 M Pt(II)/Pt(0) reference electrode, and its temperature dependence was obtained. The electrochemical behavior of Yb(III) ions on an active electrode (Ni) in the equimolar NaCl–KCl melt was studied at 973 K [20]. It was found that the reaction proceeds in two stages: in the first stage, Yb(II) ions are formed, and in the second, an electrochemical process of alloy formation takes place. The electrochemistry of ytterbium(III) in molten chlorides of alkali metals has been studied by transient methods [21]. The diffusion coefficients of Yb(III) and Yb(II) ions were calculated, and temperature dependences of Yb(III)/Yb(II) conditional standard redox potentials were found. It was assumed that the cationic composition of the solvent-salt affects the value of $E^*_{Yb(III)/Yb(II)}$. In [22], the Yb(III)/Yb(II) conditional standard redox

potentials in molten chlorides of alkali metals were estimated using a correlation between aqueous solutions and chloride melts.

The aim of the present work study was to examine the electrochemical properties of ytterbium compounds in a molten LiCl–KCl eutectic.

EXPERIMENTAL

Electrochemical experiments were carried out in a quartz cell in a glassy carbon crucible in the Ar atmosphere (H_2O <0.5 ppm and O_2 <0.1 ppm) at temperatures of 723–973 K. We used a molten LiCl–KCl eutectic mixture (Aldrich, 99.9%) as a solvent to which calculated portions of $YbCl_3$ (Merck, 99.99%) were added.

The following methods were used to analyze electrochemical processes: cyclic, linear, and square-wave voltammetry and zero-current potentiometry [23–25]. The measurements were carried out with an Autolab PGSTAT 30 (Eco-Chimie) potentiostat-galvanostat with a v.4.9 software. In some cases, a semiintegrated analysis of cyclic voltammograms was carried out with a GPES (Eco-Chimie) software.

A Godfellow tungsten wire (99.9%) 1 mm in diameter was used as a working electrode immersed into the melt to a depth of 3–10 mm. The surface area of the cathode was measured after each experiment. A rod 3 mm in diameter, made of Sofacel S.A. glassy carbon served as a counter electrode. The measurements were made relative to the standard chlorine reference electrode.

Samples for chemical analysis (about 200 mg) were taken from a salt melt and dissolved in a dilute solution of nitric acid. The concentration of ytterbium was determined with an ICP-MS instrument.

The cyclic voltammogram of the background electrolyte, obtained on a tungsten electrode at 723 K, is shown in Fig. 1. In the range of potentials under study, only waves of reduction of lithium ions and oxidation of chloride ions are observed. When ytterbium trichloride is added to the melt, a cathodic current peak at a potential of –1.762 V and an anodic peak at a potential of –1.566 V relative to the chlorine reference electrode appear in the cyclic voltammogram. Potentiostatic electrolysis at potentials of the cathodic current peak did not yield a solid phase on the electrode surface, and the working electrode did not undergo any visual changes. Similar results were obtained when

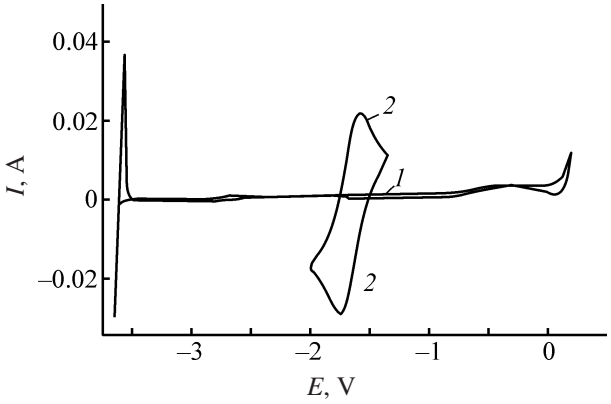


Fig. 1. Cyclic voltammograms of (*1*) background LiCl–KCl eutectic melt and (*2*) LiCl–KCl–$YbCl_3$ melt at a sweep rate of 0.1 V s^{-1} on a tungsten working electrode at 723 K. $m_{YbCl_3} = 9.41 \times 10^{-2}$ mol kg^{-1}; the same for Figs. 2–4. (*I*) current strength and (*E*) potential; the same for Fig. 2.

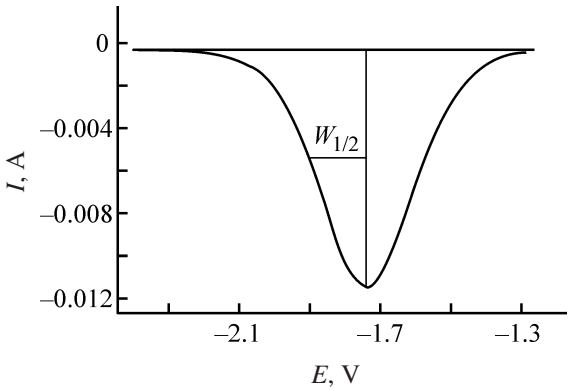


Fig. 2. Square-wave voltammogram of the LiCl–KCl–$YbCl_3$ melt at f = 12 Hz on a W working electrode at 723 K.

studying the electrochemical behavior of ytterbium (III) ions in molten CsCl [17] and in an equimolar NaCl–KCl melt [18].

We determined the number n of electrons involved in the electrode reaction by square-wave voltammetry (Fig. 2), by measuring the half-peak width $W_{1/2}$ (V) in the region in which the current peak is directly proportional to the square root of the signal frequency, according to the equation [23, 25]

$$W_{1/2} = 3.52(RT/nF), \quad (1)$$

where R, T, n, and F are the standard designations.

The calculations demonstrated that the number of electrons involved in the reduction of Yb(III) ions to Yb(II) is 1.00 ± 0.04.

These facts mean that the observed wave is related to the following redox reaction occurring in the melts

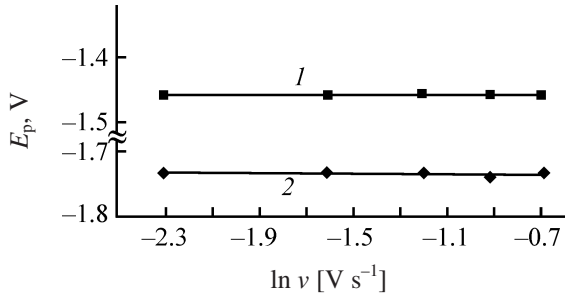


Fig. 3. Dependence of the potential E_p of (*1*) anodic and (*2*) cathodic current peaks on the logarithm of the sweep rate v for LiCl–KCl–$YbCl_3$ melt on a W working electrode at 723 K.

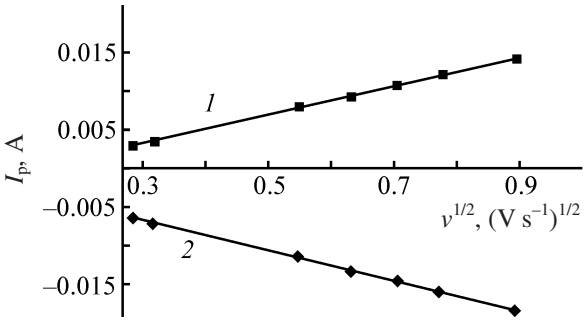


Fig. 4. Dependence of (*1*) anodic and (*2*) cathodic current peaks I_p on the square root of the sweep rate v for LiCl–KCl–$YbCl_3$ melt on a W working electrode at 723 K.

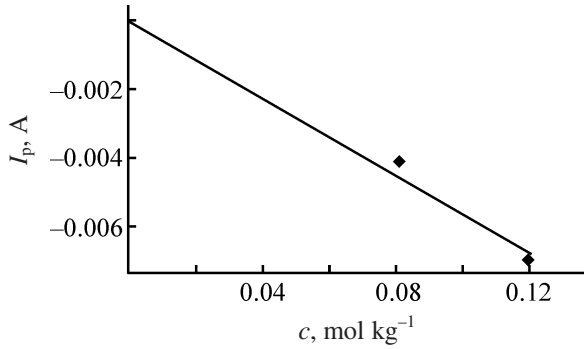


Fig. 5. Cathodic peak current I_p vs. the concentration c of $YbCl_3$ for the LiCl–KCl–$YbCl_3$ melt at 723 K.

$$\text{Yb(III)} + \text{e} \leftrightarrows \text{Yb(II)}. \quad (2)$$

It was found that the potentials of the cathodic and anodic current peaks are independent of the logarithm of the sweep rate (Fig. 3), and the currents of the cathodic and anodic peaks are directly proportional to the square root of the polarization rate in the whole range of potentials under study (Fig. 4). The current of the cathodic peak is directly proportional to the concentration of ytterbium trichloride in the melt (Fig. 5). According to the theory of linear voltammetry, the electrode processes of reduction of the trivalent ytterbium ions to the divalent state and of oxidation of Yb(II) ions to Yb(III) are reversible and are controlled by mass transfer processes.

We found using cyclic voltammetry and chronopotentiometry that the potential of reduction of divalent ytterbium ions to the metal in the molten LiCl–KCl eutectic is not reached, because it lies in the region of more negative potentials than the background decomposition voltage.

It is known [26, 27] that ions of tri- and divalent ytterbium exist in molten chlorides of alkali metals in the form of complex groups $[YbCl_6]^{3-}$ and $[YbCl_4]^{2-}$. The diffusion coefficients of $[YbCl_6]^{3-}$ ions in the molten LiCl–KCl eutectic were calculated by Randles–Shevchick equation

$$I_p = 0.446(nF)^{3/2}c_0S\left(\frac{Dv}{RT}\right)^{1/2}. \quad (3)$$

Here I_p is the peak current (A); S, surface area of the cathode (cm^2); c_0, concentration of electroactive species in the electrolyte bulk (mol cm^{-3}); D, diffusion coefficient (cm^2 s^{-1}); and v, sweep rate (V s^{-1}).

The empirical temperature dependence of the diffusion coefficients of $[YbCl_6]^{3-}$ ions is described by the Arrhenius equation [23]

$$D_{[YbCl_6]^{3-}} = D_0\exp\left(-\frac{E_a}{RT}\right) \pm \Delta. \quad (4)$$

The activation energy E_a of the diffusion process was –38.3 kJ mol^{-1}, and the preexponential factor D_0, 6.2×10^{-3} cm^2 s^{-1}.

According to the theory of linear voltammetry, the following relations are valid for a reversible electrochemical process between the cathodic (E_p^c) and anodic (E_p^a) potentials of the current peaks and the half-wave potential $E_{1/2}$:

$$E_p^c = E_{1/2} - 1.11\frac{RT}{nF}, \quad (5)$$

$$E_p^a = E_{1/2} - 1.11\frac{RT}{nF}, \quad (6)$$

$$\frac{(E_p^c - E_p^a)}{2} = E_{1/2}. \quad (7)$$

Table 1. Diffusion coefficients of $[YbCl_6]^{3-}$ ions, conditional standard potentials of the system Yb(III)/Yb(II), and the basic thermodynamic characteristics of reaction (2) in the LiCl–KCl eutectic melt

T, K	$(D_{[YbCl_6]^{3-}} \pm \Delta) \times 10^5$, $cm^2\ s^{-1}$	$E^*_{Yb(III)/Yb(II)}$, V	$-\Delta G^*_{YbCl_3}$	$-\Delta H^*_{YbCl_3}$	$-\Delta S^*_{YbCl_3}$
			kJ mol^{-1}		
723	1.0 ± 0.2	–1.662	160.93	195.96	0.036
848	2.7 ± 0.2	–1.618	159.13	195.96	0.036
973	5.4 ± 0.2	–1.574	157.33	195.96	0.036

Here,

$$E_{1/2} = E^0_{Yb(III)/Yb(II)} + \frac{RT}{nF}\ln\left(\frac{D_{Yb(II)}}{D_{Yb(III)}}\right)^{1/2} + \frac{RT}{nF}\ln\left(\frac{\gamma_{Yb(III)}}{\gamma_{Yb(II)}}\right). \quad (8)$$

It can be assumed that the activity coefficients in molten salts remain almost constant at concentrations at which the mole fractions N of depolarizer ions do not exceed the value $(3–5)\times 10^{-2}$. Introducing the conditional standard potential $E^*_{Yb(III)/Yb(II)}$, we can write the equation [28]:

$$E^*_{Yb(III)/Yb(II)} = E^0_{Yb(III)/Yb(II)} + \frac{RT}{F}\ln\left(\frac{\gamma_{Yb(III)}}{\gamma_{Yb(II)}}\right). \quad (9)$$

Assuming the diffusion coefficients of tri- and divalent ytterbium ions to be close to each other, we can take that the quantity

$$\frac{RT}{F}\ln\left(\frac{D_{Yb(II)}}{D_{Yb(III)}}\right)^{1/2}$$

is approximately zero.

In view of the aforesaid, we calculated the conditional standard redox potential $E^*_{Yb(III)/Yb(II)}$ by the equations

$$E^*_{Yb(III)/Yb(II)} = E^c_p + 1.11\frac{RT}{F}, \quad (10)$$

$$E^*_{Yb(III)/Yb(II)} = E^a_p + 1.11\frac{RT}{F}, \quad (11)$$

$$E^*_{Yb(III)/Yb(II)} = \frac{(E^c_p - E^a_p)}{2} = E_{1/2}. \quad (12)$$

The overall temperature dependence of the conditional standard redox potential (V) of the system Yb(III)/Yb(II) in the molten LiCl–KCl eutectic is described by the empirical equation

$$E^*_{Yb(III)/Yb(II)} = -(1.915 \pm 0.005) + (3.5 \pm 0.2)\times 10^{-4}T \quad (723–973\ K). \quad (13)$$

The dependence of the change in the conditional standard Gibbs energy of the redox reaction

$$YbCl_{2(s)} + 1/2Cl_{2(g)} \leftrightarrows YbCl_{3(s)} \quad (14)$$

was calculated by the formula

$$\Delta G^*_{YbCl_3} = nFE^*_{Yb(III)/Yb(II)}. \quad (15)$$

Its temperature dependence is expressed by the equation

$$\Delta G^*_{YbCl_3} = \Delta H^*_{YbCl_3} + T\Delta S^*_{YbCl_3}. \quad (16)$$

For the molten LiCl–KCl eutectic mixture this dependence has the following form (kJ mol^{-1}):

$$\Delta G^*_{YbCl_3} = -183.80 + 0.033T \pm 2.46. \quad (17)$$

The results obtained are listed in Tables 1–3 and shown in Fig. 6.

As can be seen in Tables 1 and 2, the diffusion coefficients of trivalent ytterbium ions steadily decrease as the radius of the solvent salt cation increases, which is due to a change in the stability of complex groups. As the temperature is elevated, the diffusion coefficients steadily increase.

As it was shown above, the comparatively high stability of complex ions depends on the composition

Table 2. Parameters of Eq. (4) and diffusion coefficients of $[YbCl_6]^{3-}$ ions in molten chlorides of alkali metals according to various reports

Solvent	T, K	$D \times 10^5$, $cm^2\ s^{-1}$		$-E_a$, kJ mol^{-1}	
		[17, 18], results of this study	[21]	[17, 18], results of this study	[21]
LiCl–KCl	723	1.0 ± 0.1	–	38.3	–
	848	2.7 ± 0.1	–		
	973	5.4 ± 0.1	5.3* ± 0.1		
NaCl–KCl	973	2.8 ± 0.2	2.4 ± 0.1	45.4	46.4
	1023	3.2 ± 0.2	2.7 ± 0.1		
	1073	4.1 ± 0.2	3.4 ± 0.1		
CsCl	973	0.9 ± 0.1	0.9 ± 0.1	54.4	55.6
	1023	1.2 ± 0.1	1.2 ± 0.1		
	1073	1.7 ± 0.1	1.6 ± 0.1		

* Extrapolated value.

Table 3. Conditional standard redox potential of the system Yb(III)/Yb(II) in molten chlorides of alkali metals relative to the chlorine reference electrode, according to various reports

Solvent	T, K	$E^*_{Yb(III)/Yb(II)}$, V			
		[17, 18], results of this study	[19]	[21]	[22]
LiCl–KCl	723	1.662	1.704	1.531*	1.659
	848	1.618	1.618	–	–
	973	1.574	1.532*	–	–
NaCl–KCl	973	1.671	–	1.678	1.629
	1023	1.652	–	1.662	–
	1073	1.634	–	1.646	1.551
CsCl	973	1.853	–	1.871	1.881
	1023	1.832	–	1.844	–
	1073	1.811	–	1.817	1.792

* Extrapolated value.

of the solvent salt and results in a shift of the conditional standard redox potentials to the negative region (Table 3 and Fig. 6). The results obtained agree with published data [28] on the influence of the second coordination sphere on the electrode potentials.

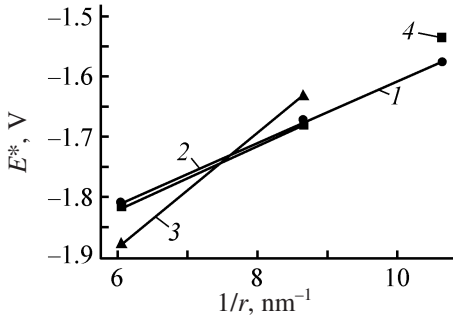


Fig. 6. Conditional standard potential E^* of the system Yb(III)/Yb(II) vs. the inverse radius $1/r$ of the cation of the solvent salt at 973 K according to various authors. (*1*) This study, (*2*) [21], (*3*) [22], and (*4*) [19].

CONCLUSIONS

(1) It was shown that the redox electrode reaction (2) in the molten LiCl–KCl eutectic is reversible in the temperature range 723–973 K and is controlled by the mass-transfer process. Its electrochemical parameters were determined and the diffusion coefficients of $[YbCl_6]^{3-}$ ions were calculated.

(2) The temperature dependence of the conditional standard potential of the system Yb(III)/Yb(II) relative to the chlorine reference electrode was obtained.

(3) The basic thermodynamic characteristics of reaction (2) in the LiCl–KCl eutectic melt were calculated and compared with the available published data.

REFERENCES

1. OCDE/NEA Report: Accelerator-driven systems (ADS) Fast Reactors (FR) in Advanced Nuclear Fuel Cycles. *A Comparative Study*, 2002.
2. Kormilitsyn, M.V., Bychkov, A.V., and Ishunin V.S., Abstract of Papers, *Int. Conf. "Pyroelectrochemical Reprocessing of Irradiated Fuel of Fast Reactors," Global 2003*, New Orleans, 2003, p. 782.
3. Smolenskii, V.V., Komarov, V.E., and Afonichkin, V.K., *Rasplavy*, 2000, no. 2, pp. 59–66.
4. Laidler, J.J., Battles, J.E., Millar, W.E., et al., *Prog. Nucl. Energy*, 1997, vol. 31, pp. 131–145.
5. Kinoshita, K., Inoue, T., Fusselman, S.P., et al., *J. Nucl. Sci. Techn.*, 1999, vol. 36, pp. 189–197.
6. Kurata, M., Sakamura, Y., and Inoue, T., *Proc. 3rd Inform. Exchange Meeting on Actinide and Fission Products Partitioning and Transmutation*, France, Cadarache, 1994, p. 407.
7. Serp, J., Allibert, M., Terrier, A.L., et al., *J. Electrochem. Soc.*, 2005, vol. 152, pp. 167–172.
8. Cordoba, G. and Caravaca, C., *J. Electroanal. Chem.*, 2004, vol. 572, pp. 145–151.
9. Bermejo, R., Castrillejo, Y., Martinez, A., and Barrado, E., Abstracts of Papers, *Int. Conf. "Back-End of the Fuel Cycle: From Research to Solution,"* Global, Paris, 2001, p. 272.
10. Castrillejo, Y., Bermejo, M.R., Diaz Arocas, P., et al., *J. Electroanal. Chem.*, 2005, vol. 579, pp. 343–358.
11. Caravaca, C., Diaz Arocas, P., Serrano, J.A., et al., *Proc. Int. Conf. 6th Inform. Exchange Meeting on Actinide and Fission Products Partitioning and Transmutation*, OCDE/NEA, 2001, pp. 625–636.
12. Martinez, A.M., Castrillejo, Y., Barrado, E., et al., *J. Electroanal. Chem.*, 1998, vol. 449, pp. 67–80.
13. Bermejo, R., Castrillejo, Y., Martinez, A., and Barrado, E., Abstracts of Papers, *Int. Conf. "Back-End of the Fuel Cycle: From Research to Solution*," Global. Paris, 2001, p. 101.
14. Fusselman, S.P., Roy, J.J., Grimmett, L.F., et al., *J. Electrochem. Soc.*, 1999, vol. 146, pp. 2573–2580.
15. Martinez, A.M., Castrillejo, Y., Pardo, R., and Haarberg, G.M., *Electrochim. Acta*, 1997, vol. 42, pp. 1869–1876.
16. Benedict, R., Goff, M., Teske, G., and Johnson, T., *J. Nucl. Sci. Techn.*, 2002, vol. 3, pp. 749–752.
17. Smolenskii, V.V., Novoselova, A.V., and Bove, A.L., *Rasplavy*, 2007, no. 6, pp. 66–72.
18. Smolenskii, V.V., Novoselova, A.V., and Bove, A.L., *Zh. Prikl. Khim.*, 2007, vol. 80, no. 10, pp. 1632–1637.
19. Johnson, K.E. and Mackenzie, J.R., *J. Electrochem. Soc.*, 1969, vol. 116, no. 12, pp. 1697–1703.
20. Guankun, L., Yexiang, T., Quichan, H., et al., *Trans. Nonferrous Met. Soc. China*, 1998, vol. 8, no. 3, pp. 516–519.
21. Kuznetsov, S.A. and Gaune-Escard, M., *Proc. 7th Int. Symp. on Molten Salts Chem. Technol. (MS 7)*, 2005, vol. 2, pp. 855–859.
22. Novoselova, A.V., Potapov, A.M., and Khokhlov, V.A., *Proc. EUCHEM Molten Salts Conf.*, 2004, pp. 270–276.
23. Bard, A.J. and Faulkner, L.R., *Electrochemical Methods: Fundamentals and Applications*, New York: John Wiley, 1980.
24. Galus, Z., *Fundamentals of Electrochemical Analysis*, London: Ellis Horwood, 1994.
25. Bret, C.M.A. and Bret, A.M.O., *Electrochemistry: Principles, Methods, and Applications*, Oxford: University, 1996.
26. Anonymous, A. (Papatheodorou, G.N.), *Progress in Molten Salt Chemistry*, Paris: Elsevier, 2000, vol. 1, pp. 65–70.
27. Novikov, G.I., Polyachenok, O.G., and Frid, S.A., *Zh. Neorg. Khim.*, 1964, vol. 9, no. 2, pp. 472–475.
28. Smirnov, M.V., *Elektrodnye potentsialy v rasplavlennykh khloridakh* (Electrode Potentials in Molten Chlorides), Moscow: Nauka, 1973.

ISSN 1070-4272, Russian Journal of Applied Chemistry, 2008, Vol. 81, No. 10, pp. 1774–1777. © Pleiades Publishing, Ltd., 2008.
Original Russian Text © M.N. Bobrov, Yu.P. Khranilov, 2008, published in Zhurnal Prikladnoi Khimii, 2008, Vol. 81, No. 10, pp. 1649–1652.

APPLIED ELECTROCHEMISTRY AND CORROSION PROTECTION OF METALS

Preparation of Compact Copper from Slurries Formed in Etching of Printed-Circuit Boards

M. N. Bobrov and Yu. P. Khranilov

Vyatka State University, Kirov, Russia

Received January 21, 2008

Abstract—Technological solutions for copper recovery in the form of a compact metal from a slurry formed in etching of printed-circuit boards as a starting material were developed.

DOI: 10.1134/S1070427208100133

In manufacture of printed-circuit boards, a copper-rich slurry is formed at the bottom of etching units. The composition of the slurry depends on that of the etching solution. The slurry formed with a copper–ammonia solution contains copper ammoniates, copper hydroxo chlorides (CHCs), and other copper salts. The high content of copper in slurries of this kind and their large volumes (several hundreds of kilograms annually for a shop of an average output capacity) make promising the recovery of copper in the form of a compact metal.

A large number of technological solutions have been developed for utilization of spent copper-ammonia etching solutions (SESs): electrochemical regeneration, including deposition of excess copper on the cathode and recycling of the etching solution into the technological process [1]; chemical conversion of SESs into CHC to be used for plant pest control [2]; high-temperature treatment of SESs with sodium hydroxide to yield copper(II) oxide as a commercial product [1]; and cementation of copper on iron shavings or iron powder from a preliminarily acidified SES to obtain a copper powder [3]. Owing to its simplicity, the last method has found wide application, although the powder it yields is contaminated with iron.

The problem of slurry utilization has been developed to a lesser extent. Mention can be made of the study [4], in which it was suggested to process the slurry into CHC to be used as an active substance in water-activated power sources. In practice, the slurry is commonly processed together with SES by the cementation method.

The goal of this study was to search for technological solutions for recovery of copper in the compact form from the slurry of copper-ammonia SESs. The total content of copper in the object under study was 40 to 47%; that of chlorine, 35%, on average; and that of ammonium nitrogen, 10 to 12 %. The concentration of copper was determined by iodometry and photocolorimetry (FKF-2 photocolorimetr); concentration of chlorine, by argentometry; and that of ammonium nitrogen, by the formalin method [5].

EXPERIMENTAL

Three procedures for copper recovery were tested experimentally. The first method included dissolution of the slurry in sulfuric acid, followed by electrolytic recovery of copper. A potentiometric titration curve for an aqueous suspension of the slurry (1.5 g of slurry per 50 ml of water) with 1% sulfuric acid is shown in Fig. 1.

Initial suspension has pH 8.5, i.e., it contains an alkaline constituent (copper ammoniates). The upper plateau on the titration curve (at pH 9–8) is due to conversion of ammonia from ammoniates into the ammonium form, and the lower plateau, to dissolution of copper hydroxo chloride by the reaction

$$2CuOHCl + H_2SO_4 \rightarrow CuSO_4 + CuCl_2 + 2H_2O. \quad (1)$$

A solution containing 15.6 g l^{-1} of copper, produced by dissolving a portion of slurry in 10% sulfuric acid (l : s = 30 : 1) , was subjected to a short-time electrolysis with a graphite anode and copper and titanium cathodes. The experiments were performed at current densities of 0.5–2 A dm^{-2}. Figure 2 shows the current efficiencies (CE) at different current densities *i*.

The presence of chlorides in the slurry results in the following. In electrolytic recovery with a copper cathode, the calculated current efficiency by copper somewhat exceeds 100%. This reason is that the surface of the copper cathode (introduced into the electrolyzer at a zero current) interacts with the chloride-containing electrolyte to give a copper monochloride film. This leads to an apparent increase in the CE by copper and to contamination of the cathode deposit. The zero-current potential of the copper electrode in the sulfuric acid solution of the slurry (E = +0.144 V relative to s.h.e.) is close to the value obtained for the equilibrium $Cu + Cl^- \rightarrow CuCl + e$ (E_0 = +0.137 V) in [6], which confirms the explanation suggested. In experiments with the titanium cathode, the CE is lower than 100%, which is due to dissolution of a part of oxygen evolved at the anode in the electrolyte and its subsequent reduction at the cathode. The presence of chlorides in the electrolyte not only contaminates the cathode copper, but also results in evolution of a certain amount of chlorine at the anode, which requires that the electrolyzer should be hermetically sealed and gives no way of using the more convenient lead anodes.

In the second of the tested procedures for copper recovery, copper ions are preliminarily sorbed from a sulfuric acid solution of the slurry onto a strongly acidic KU-2×8 cation-exchange resin. It was found that, to dissolve the slurry prior to the ion exchange, it is necessary to use a sufficiently diluted acid (about 1%). When more acidic solutions (3% and higher) are passed through the column, a breakthrough of copper ions is observed almost immediately. At a solution flow rate of 2–2.5 m h^{-1}, the dynamic exchange capacity for copper ions was 1000–1300 g-equiv m^{-3} of swollen resin.

After the sorption, the ion exchanger was regenerated with 10% sulfuric acid to obtain an eluate containing no Cl^- ions. The concentration of copper in the eluate and the degree of copper return into the eluate depend on the ratio between the volume of the regenerating solution and the mass of sorbed copper (V/m, cm^3/g). On lowering the V/m ratio from 220 to 54 cm^3/g, the copper concentration in the eluate could be raised from 3.9 to 10.8 g l^{-1} however, the degree of copper return decreased from 87 to 58%.

The low concentration of copper in the eluate gives no way of performing the electrolytic recovery at technologically acceptable current densities. The large expenditure of the acid for regeneration makes this copper recovery procedure rather economically inefficient.

The third copper recovery procedure recommended for SESs [1] is based on preliminary thermal

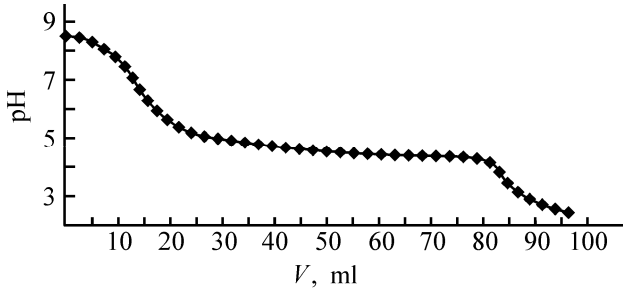


Fig. 1. Curve of pH metric titration of a slurry suspension with 1% H_2SO_4. (V) volume.

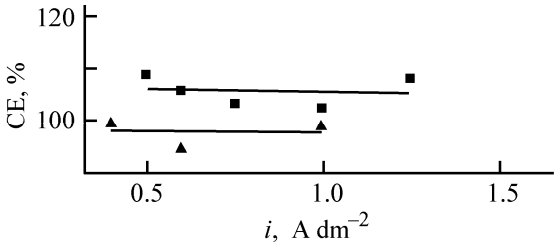


Fig. 2. Effect of the cathode material on the CE by copper. (i) Current density. Cathode: (*1*) copper and (*2*) titanium.

decomposition of ammoniate and chloride complexes of copper(II) by the reactions

$$Cu(NH_3)_2Cl_2 + 2NaOH \rightarrow CuO\downarrow + 2NH_3\uparrow + 2NaCl + H_2O, \quad (2)$$

$$CuOHCl + NaOH \rightarrow CuO\downarrow + NaCl + H_2O. \quad (3)$$

In this study, it is suggested to use this method for thermal decomposition of the slurry to obtain CuO, its dissolution in sulfuric acid, and delivery of the resulting solution to electrolysis. The experiment was performed with an aqueous suspension of the slurry at l : s = 30 : 1, to which a NaOH solution was added to adjust the pH value to 12.5–13. The mixture obtained was heated to 75–80°C. The expenditure of a 5% sodium hydroxide solution is 100–120 ml per 300 ml of the suspension. A copper oxide solution in sulfuric acid served as electrolyte.

To choose the range of the working current densities, the dependence of the limiting current density i_{lim} on the copper concentration (Fig. 3) was determined from cathodic polarization curves recorded in model solutions with a constant concentration of sulfuric acid (50 g l^{-1}) (IPC-PRO potentiostat, potential sweep rate 2 mV s^{-1}).

Various procedures can be used for electrolytic recovery from the sulfuric acid solution obtained. The first of these is based on electrolysis with a ~50% exhaustion of the electrolyte in copper. In this case, the cathode current density is constant and should not exceed

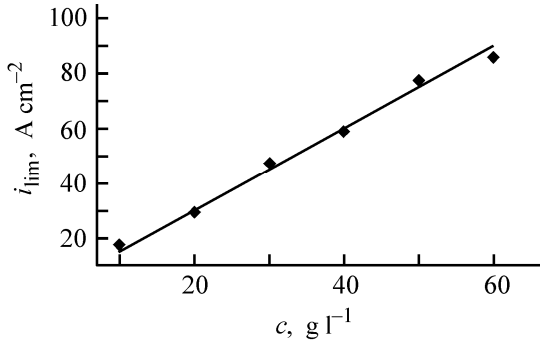


Fig. 3. i_{lim} vs. the copper concentration c.

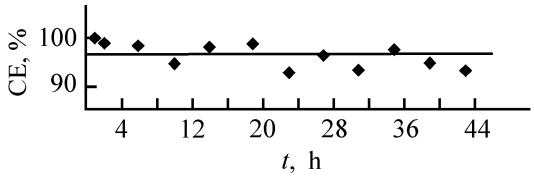


Fig. 4. Variation of the CE by copper in prolonged electrolysis. (t) Time.

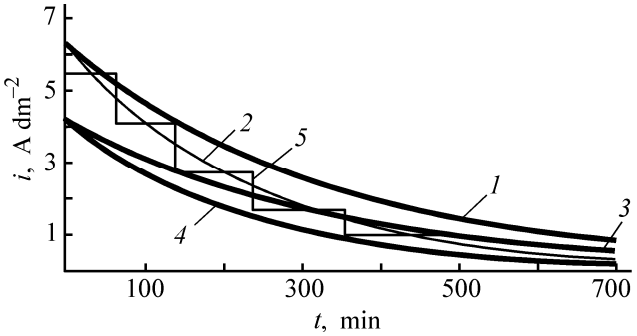


Fig. 5. Calculated working current density i in electrolytic recovery of copper from a sulfuric acid electrolyte vs. time t. (*1*) S/V = 1.5 dm^{-1}, c_0 = 60 g l^{-1}, (*2*) S/V = 2.4 dm^{-1}, c_0 = 60 g l^{-1}, (*3*) S/V = 1.5 dm^{-1}, c_0 = 40 g l^{-1}, (*4*) S/V = 2 dm^{-1}, c_0 = 40 g l^{-1}, (*5*) approximation of curve *2* (stepwise decrease in the current density).

40% of the limiting current density for the starting electrolyte to avoid formation of powdered deposits on the cathode. After about 50% of copper is recovered, a new portion of copper oxide is introduced into the electrolyte and the electrolysis is performed again. A prolonged experiment (about 40 h, with 12 corrections with respect to copper) confirmed that pure copper can be obtained at the cathode in a compact form with a high current efficiency (90–98%) (Fig. 4). According to the results of a spectral analysis (Spec-trolab optical emission spectrometer), the copper content is 99.88%.

Sulfuric acid is only consumed when the electrolyte is initially prepared, with the acid formed at the anode in the course of electrolysis used in the further process. Lead or its alloy with antimony serves as the anode material.

In another procedure for electrolytic recovery, the current density is lowered continuously or in steps in order to avoid formation of powdered deposits upon a decrease in the copper concentration. To calculate how the current density should vary with time, the following starting assumptions were made:

(1) With account of the edge effect, which can result in that spongy, and even powdered deposits can be formed at the edges of the cathode, the working current density i at each instant of time t should not exceed 70% of the limiting current density i_{lim} ($i = 0.7i_{lim}$).

(2) i_{lim} (A dm^{-2}) is proportional to the copper concentration c (g dm^{-3}) in the electrolyte. According to the experimental data of Fig. 3, $i_{lim} = 1.5c$.

(3) At the instant of time t, the copper concentration $c_t = c_0 - \Delta m/V$, where c_0 is the initial concentration (g dm^3); Δm, mass of copper deposited on the cathode in a time t (g); and V, electrolyte volume (dm^3).

(4) The loss of copper mass from the electrolyte during a time t (h) is given by the relation $\Delta m = qi_{av}St\,\mathrm{CE}$, where q is the electrochemical equivalent of copper (1.186 g (A h)$^{-1}$); i_{av}, the average current density over a time t; S, working surface area of the cathode (dm^2); and CE, current efficiency (taken to be 0.95).

With account of the above relations and accepted constants

$$i = 1.05(c_0 - 1.127i_{av}St/V). \quad (4)$$

To construct the i-vs.-t curve, Δm, i_{av}, and i were computed for reasonably short intervals of time t (Δt = 1 min). Selected results are presented in Fig. 5. The ratio S/V = 2.4 dm^3 belongs to a laboratory electrolyzer, and S/V =1.5 dm^3, to the design of an industrial installation with 42 l of electrolyte.

A laboratory experiment with a solution with an initial copper concentration of 60 g l^{-1} and a stepwise decrease in the current density (Fig. 5, curve *5*) yielded a compact deposit with a 75% degree of copper recovery without electrolyte corrections. According to the results of a spectral analysis, this copper was 99.97% pure.

CONCLUSION

Technological solutions for recovery of copper from the slurry formed in etching of printed-circuit boards in copper–ammonia solutions were experimen-

tally substantiated. These are thermal decomposition of the slurry in an alkaline medium to obtain copper(II) oxide, dissolution of copper oxide in sulfuric acid, and electrolytic recovery of copper from the solution obtained, with correction of the electrolyte with respect to copper at regular intervals of time or a stepwise decrease in the current density. The purity of the resulting copper is no less than 99.88%.

REFERENCES

1. Flerov, V.N., *Khimicheskaya tekhnologiya v proizvodstve radioelektronnykh detalei* (Chemical Technology in Manufacture of Radioelectronic Articles), Moscow: Radio i Svyaz', 1988.
2. Ivanova, V.I., Mishina, O.V., Trofimova, L.A., et al., *Gal'vanotekhn. Obrab. Poverkhn*., 1993, vol. 2, no. 4, pp. 88–89.
3. Il'in, V.A., *Khimicheskie i elektrokhimicheskie protsessy v proizvodstve pechatnykh plat. Bibliotechka gal'vanotekhnika* (Chemical and Electrochemical Processes in Manufacture of Printed-Circuit Boards, Electroplating Worker's Library), Moscow, 1994, issue 2.
4. Khranilov, Yu.P., Noskov, O.V., and Plyusnin, D.A., *Materialy IV Mezhdunarodnoi konferentsii "Fundamental'nye problemy elektrokhimicheskoi energetiki"* (Proc. IV Int. Conf. "Fundamental Problems of Electrochemical Power Engineering"), Saratov, 1999, p. 238.
5. Kreshkov, A.P., *Osnovy analiticheskoi khimii: Teoreticheskie osnovy. Kolichestvennyi analiz. Kniga vtoraya: Uchebnik dlya Vysshikh Uchebnykh Zavedenii* (Fundamentals of Analytical Chemistry: Theoretical Foundations, Quantitative Analysis; Book 2: Textbook for Higher School), Moscow: Khimiya, 1976.
6. *Spravochnik po elektrokhimii* (Handbook of Electrochemistry), Sukhotin, A.M., Ed., Leningrad: Khimiya, 1981.

ISSN 1070-4272, Russian Journal of Applied Chemistry, 2008, Vol. 81, No. 10, pp. 1778–1784. © Pleiades Publishing, Ltd., 2008.
Original Russian Text © V.K. Varentsov, S.I. Yusin, V.I. Varentsova, 2008, published in Zhurnal Prikladnoi Khimii, 2008, Vol. 81, No. 10, pp. 1653–1659.

APPLIED ELECTROCHEMISTRY AND CORROSION PROTECTION OF METALS

Dynamics of Copper Deposition from a Sulfuric Acid Solution Onto Electrically Isoconducting Electrodes Made of Fibrous Carbon Materials

V. K. Varentsov, S. I. Yusin, and V. I. Varentsova

Institute of Solid-State Chemistry and Mechanochemistry, Siberian Branch, Russian Academy of Sciences, Novosibirsk, Russia

Novosibirsk State Technical University, Novosibirsk, Russia

Received January 30, 2008

Abstract—Effect of the initial electrical conductivity of an electrically isoconducting flow-through electrode made of a fibrous carbon material on the dynamics of copper electrodeposition from a sulfuric acid solution was studied. The distribution of the copper deposit across the electrode thickness and the variation of the electrolysis parameters (copper deposition rate, current efficiency, uniformity of distribution, and mass of a deposited metal per unit mass of the fibrous carbon material) were considered.

DOI: 10.1134/S1070427208100145

Flow-through electrodes made of a fibrous carbon material (FCM) are used in various redox processes, especially in electrodeposition of metals from their low-concentration solutions for electrolytic recovery of metals or metallization of FCM fibers [1–8]. The operation efficiency of a fibrous carbon electrode (FCE) is strongly affected by the relative electrical conductivities of the liquid and solid phases of the electrode [8–14]. However, the available data give no information about the dynamics of metal electrodeposition onto FCE and variation of the deposition parameters in a wide range of electrical conductivities of the electrode and solution for various technological schemes of metal electrodeposition onto FCE (direct-flow, circulatory, circulatory with periodically increasing metal concentration in solution). Such an information is necessary for understanding the fundamental aspects of FCE operation, developing technological processes of electrolytic recovery of metals and their deposition onto FCMs, and designing electrochemical reactors with FCM electrodes.

In this study, the distribution of a deposit across the electrode thickness in the course of electrolysis and the variation of the current efficiency by the metal, deposition rate, uniformity of the metal distribution across the electrode thickness, and amount of the metal deposited on different parts of the electrode were examined in relation to the electrolysis duration for the example of copper electrodeposition from a sulfuric acid solution onto electrically isoconducting FCM electrodes with different initial electrical conductivities.

The experimental scheme simulated the process of electrolytic recovery of metals from solutions in a catching baths at plating shops [7, 8]. A similar scheme can also be applied to metallization of FCM fibers. The electrolyte (500 ml) containing (g l^{-1}): Cu 0.16, H_2SO_4 25, and $(NH_4)_2SO_4$ 80, was circulated between the vessel with a solution (catching bath) and the electrolytic cell (electrolyzer) at a rate of 0.4 cm s^{-1} in accordance with the scheme described in [5, 15]. The electrical conductivity of the solution was 0.101 S cm^{-1}.

The concentration of the me-tal ions being recovered in an electrolyzer was maintained constant within a narrow range, 0.160 ± 0.03 g l^{-1} by adding a solution (10 ml) containing (g l^{-1}): Cu 2.5, H_2SO_4 25, and $(NH_4)_2SO_4$ 80, at regular intervals of time (5–10 min), depending on the rate of copper recovery, with the total volume of the electrolyte remaining constant.

The concentration of copper ions in solution was determined by direct voltammetry on a renewable graphite microelectrode [16].

Copper was electrodeposited in the galvanostatic mode, using a B5–47 dc power supply. The electrolytic cell was described in [15]. A 6-mm thick cathode comprised five FCM layers. A platinum wire served as the anode, and a perforated titanium plate, as the current lead. The solution was delivered to an electrode with a back current lead from the back side with respect to the counter electrode. The back side of the electrode was adjacent to the perforated current lead, and its front side, was the closest to the anode. The electrode thickness was found on the basis of its possibly being assembled from five layers; it was close to the maximum possible thickness used in industry [1, 2, 7, 8].

The properties of FCMs used to assemble electrodes are listed in Table 1. When choosing the materials, the main attention was given to their electrical conductivity χ. It can be seen from the data presented that the electrical conductivities of low- and high-conductivity materials differ by more than a factor of 35. The specific reactive surface accessible to electrolysis is large and differs by less then a factor of 2 between different materials. The profiles of all the FCM fibers are irregular [2, 5], which provides close hydrodynamic conditions in the initial stage of the process.

Each of the FCM layers constituting the electrode was weighed on an analytical balance to within 0.0001 g before and after electrolysis. After electrolysis, the electrode was washed with distilled water and dried at 80°C to constant mass.

The ratio between the masses of the copper deposit and the FCE was calculated for each layer by the formula

$$\delta = m_{Cu}/m_{FCM1}.$$

and that between the total mass of the deposit and the mass of the whole FCM, by the formula

$$\Delta = \frac{\sum_{i=1}^{5} m_{Cu}}{\sum_{i=1}^{5} m_{FCM1}},$$

where m_{Cu} is the mass of the deposited metal (g), and m_{FCM1}, that of the FCM before electrolysis (g). The mass of copper deposited during the time between the delivery of two portions of an electrolyte to a solution in the course of electrolysis (cycle) was determined using the formula

$$m_{Cu} = (c^{add}_{Cu\,i} - c_{Cu\,i+1})V_{el},$$

where $c^{add}_{Cu\,i}$ (g l^{-1}) is the concentration of copper ions in solution upon addition of the adjusting electrolyte in the preceding cycle, and $c_{Cu\,i+1}$ (g l^{-1}), the concentration of copper in solution in the cycle for which the mass of the deposited metal was determined .

We also calculated the rate of copper deposition [U (mg cm^{-2} min^{-1})], current efficiency by copper in a cycle [CE (%)], and total time of electrolysis.

The uniformity of the metal distribution across the FCE thickness was evaluated by the known criterion, root-mean-square deviation [17, 18] calculated by the formulas

$$m_{Cu} = \frac{1}{5}\sum_{i=1}^{5} m_{Cu\,i},$$

$$H_{rms} = \sqrt{\frac{1}{5}\sum_{i=1}^{5} (m_{Cu\,i} - m_{Cu\,av})^2},$$

where $m_{Cu\,av}$ is the average mass of a copper deposited on the FCM layer (g), and $m_{Cu\,i}$, the mass of copper on each FCM layer (g).

All the calculations were carried out using Microsoft Office Excel 2007 software.

Copper was electrodeposited at a current density of 1500 A m^{-2} in the course of 10–460 min. The maximum time of electrolysis was limited by termination of the solution flow or by a substantial decrease in its rate because of the "clogging" of the electrode by the copper deposit. The ratio between the geometric cathode surface area and the solution volume was 0.2 m^2 : 500 l, which corresponded to a real technological process. The current density was chosen taking into account the industrial experience of application of processes with FCE in industry and the possibility of operation

Table 1. Properties of fibrous carbon materials* [2, 8]

Material	χ, S cm^{-1}	Fiber radius r, μm	S_p	S^0_p	Porosity ε
			cm^2 g^{-1}		
ANM	0.0052	6.1	2150	2500	0.96
KNM-2	0.0159	6.1	2100	2400	0.98
NTM-100	0.076	5.4	2400	3400	0.96
VINN-250	0.184	4.5	3000	4700	0.97

* S_p, S^0_p are the specific reactive surface areas accessible to electrolysis, as determined by gravimetric and electrochemical methods, respectively.

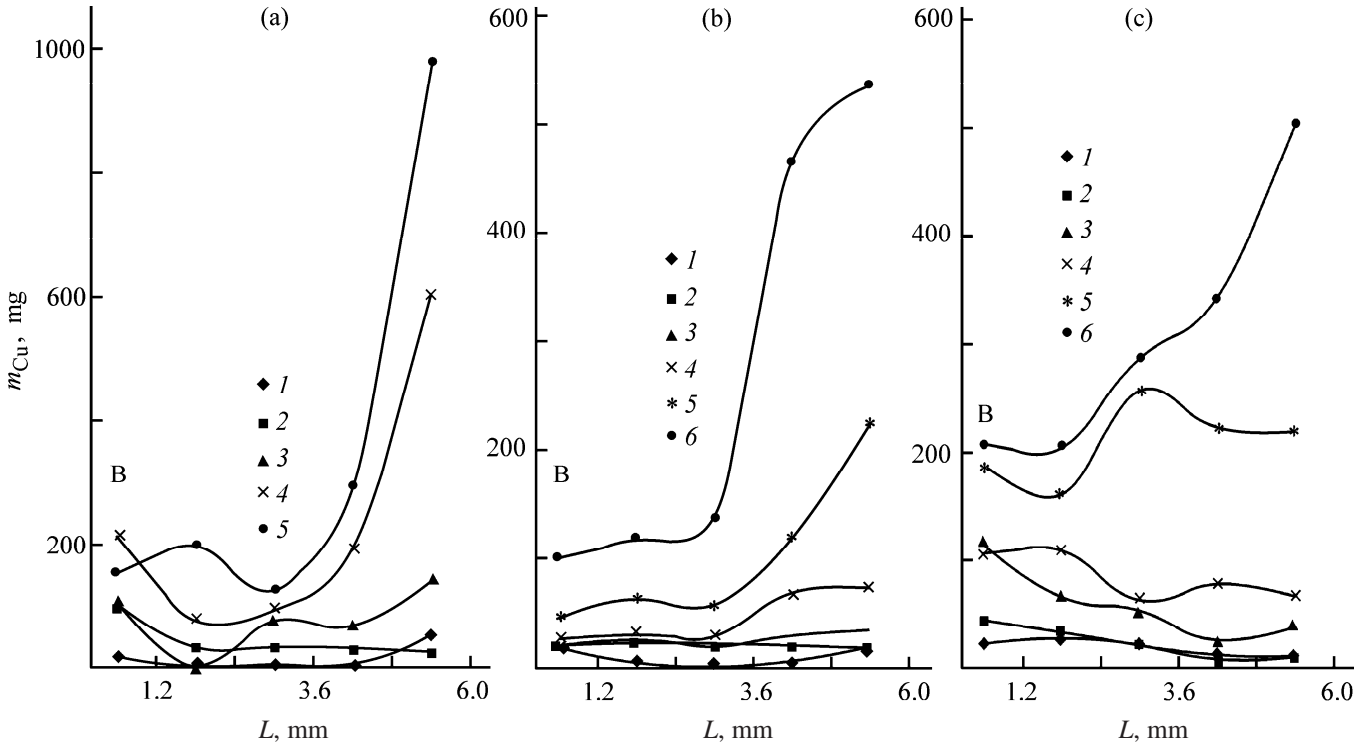


Fig. 1. Distribution of the copper deposit m_{Cu} over the electrode layers L. (B) Back side of the electrode. (a) VINN-250, (b) KNM-2, and (c) ANM. Electrolysis time (min): (a) (*1*) 35, (*2*) 70, (*3*) 240, (*4*) 360, and (*5*) 460; (b) (*1*) 10, (*2*) 20, (*3*) 35, (*4*) 60, (*5*) 180, and (*6*) 360; (c) (*1*) 20, (*2*) 35, (*3*) 75, (*4*) 120, (*5*) 300, and (*6*) 420.

of a considerable part of the electrode at the limiting diffusion current.

We now consider the results obtained on electrodes with a constant electrical conductivity across the electrode thickness and decreasing electrical conductivity of FCM.

Electrode fabricated from high-conductivity FCM (VINN-250). During the first 30 min after the beginning of electrolysis, the copper deposit is rather uniformly distributed across the electrode thickness (Fig. 1a). In the course of time, the deposit is somewhat shifted to the backside of the electrode, and more strongly, to the front side. Further increase in the electrolysis duration results in redistribution of the copper deposit across the electrode thickness to the front side of the electrode. In the central part of the electrode, the minimum (with respect to other electrode areas) amount of copper is deposited. The value of δ varies across the electrode thickness within the range 0.02–35.47. The mass ratio between copper deposited on the whole electrode and the FCM was 13.03 during the entire period of electrolysis. A similar ratio for the front part of the electrode was 35.47. Such a large amount of copper deposit on the FCM has not been obtained previously. It should be noted that the value obtained (13.03 g g^{-1} FCM) rather closely coincides with that characteristic of Cu recovery onto thinner (approximately twofold) electrodes under industrial conditions. The considerable redistribution of the copper deposit to the front side of the electrode characterizes the nonuniformity of copper distribution across the electrode thickness, which grows in the course of electrolysis and, in 460 min, results in a pronounced decrease in the flow rate of the electrolyte (root-mean-square deviation H_{rms} is 320.8).

In the course of electrolysis, the current efficiency considerably increases, from 15% (during the first 10 min of electrolysis) to 90% after 300 min of electrolysis (Fig. 2), and, accordingly, the rate of copper deposition grows from 0.6 to approximately 2.7 mg cm^{-2} min^{-1}. In the course of electrolysis, these parameters decrease by 20–25% from the maximum value. It should be noted that the manner in which the current efficiency by copper and the rate of its deposition varies with time is the same for all the materials studied.

Electrode fabricated from FCM with an electrical conductivity comparable with that of the solution (NTM-100). During the initial period (before 180 min), copper is mainly deposited on the front side of the electrode, and to a lesser extent, on its back side, with the minimum amount of copper deposited in the middle part of the electrode. Further, the mass of copper increases across the entire electrode thickness and the deposit shifts to its front side. For example, the mass ratio between copper and the FCM on the front layer reaches the highest value (37.94), with δ for the entire electrode being the lowest among all of the FCMs studied (Table 2). Therefore, the deposit is distributed the most nonuniformly across the entire electrode thickness (H_{rms} = 328.4). The manner in which the current efficiency and deposition rate vary with time is the same as that for the VINN-250 electrode. The rate of copper deposition gradually increases from 1.2 to 2.4 mg cm^{-2} min^{-1} 300 min after the beginning of electrolysis and decreases to 2.0 mg cm^{-2} min^{-1} in 420 min. Accordingly, the current efficiency increases from 40 to 80% and decreases to 60% by the end of the electrolysis, with the maximum values of CE and *U* being somewhat smaller than those for the VINN-250 electrode. The process of copper deposition is characterized by a smaller difference between the highest and lowest values of CE and *U*. During the whole time of copper deposition, the current efficiency and the deposition rate on the NTM-100 electrode are somewhat smaller than those on the VINN-250 electrode.

Electrode fabricated from FCM whose electrical conductivity is lower than that of a solution (KNM-2). In the initial period (10 min), the distribution of the copper deposit across the electrode thickness is symmetrical with respect to the middle part of the electrode, with a minimum at its center (Fig. 1b). The masses of copper deposited at the front and back sides of the electrode are nearly the same, several times that in its central part. Making the electrolysis duration longer (20–35 min) results in that the distribution of the copper deposit across the electrode thickness becomes more uniform and is further shifted to its front side. In contrast to the cases considered above, a considerable part of copper is deposited on the first and the second layers. As the amount of deposited copper increases, its distribution across the electrode thickness becomes more nonuniform (Fig. 2). In the course of electrolysis, the current efficiency linearly grows in a rather narrow range of variation of these parameters. The rate of copper deposition varies similarly. During 360 min of electrolysis, the deposition rate increases from 1.6 to 1.8 mg cm^{-2} min^{-1}, and the current efficiency by copper, accordingly, grows from 53 to 63%.

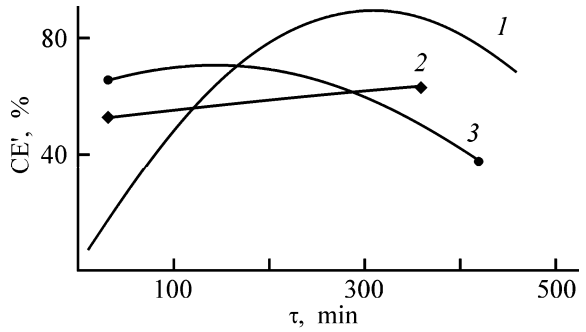


Fig. 2. Current efficiency CE by copper vs. the electrolysis duration τ for (*1*) VINN-250, (*2*) KNM-2, and (*3*) ANM.

The parameters considered above confirm the stable operation of the electrode and show that the influence exerted by the mass of the deposited copper is considerably weaker than that in copper deposition onto other FCEs. As follows from Table 2, the copper deposition rate and the current efficiency are the highest during the full electrolysis time (360 min). The more uniform distribution of copper across the electrode thickness (H_{rms} = 187.8), the higher current efficiency, and smaller changes in *U* and CE in the course of electrolysis on KNM-2 electrode apparently show that the distribution of the potential and local current densities across the electrode thickness is more uniform. The same is indicated by data on the relative mass of copper deposited per unit mass of FCM. For example, δ for the whole electrode differs only slightly from that for VINN-250 and NTM-100 and lies between them, whereas the maximum value of δ for a single layer of the KNM-2 electrode is a factor of 1.6–1.75 smaller

Table 2. Parameters of copper electrodeposition onto FCM electrodes

Material	*U*, mg min^{-1} cm^{-2}	CE', %	δ_{max} for an electrode layer	δ for the electrode	H_{rms}	τ, min
ANM	1.840	59.33	15.56	10.56	110.2	420
KNM-2	1.884	63.57	21.73	10.72	187.8	360
NTM-100	1.815	61.26	37.94	10.08	328.4	420
VINN-250	1.909	62.33	35.47	13.03	320.8	460

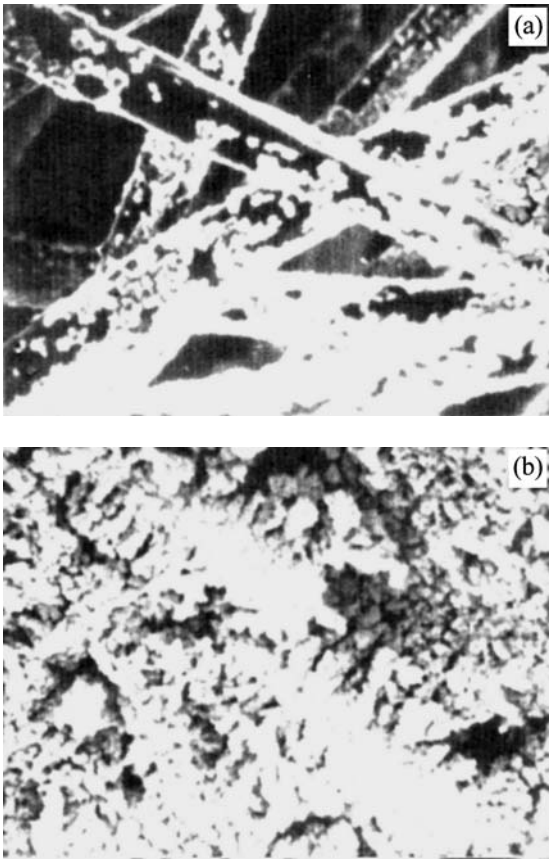


Fig. 3. Electron micrographs of FCM samples. Electrolysis duration (min): (a) 60 (×1000), and (b) 420(×350).

than that for electrodes fabricated from the above FCMs.

Electrodes fabricated from low-conductivity FCM (ANM). The dynamics of the copper distribution across the thickness of an ANM electrode in the course of electrolysis differs from that for the electrodes considered above. During a prolonged electrolysis, the copper deposit is shifted to the back side of the electrode (Fig. 1c). In the course of time, there occurs redistribution of the deposit and its shift to the front side. The current efficiency somewhat increases during 150–200 min of electrolysis, reaches the maximum value, and then decreases (Fig. 2). During the whole time of electrolysis, the integral characteristics U and CE are the lowest (1.84 mg cm^{-2} min^{-1} and 59.33%, respectively) in comparison with those of all the materials considered (Table 2). The ratio between the maximum amount of the copper deposit on a single layer of the ANM electrode (15.56) is also the smallest, but the electrode as a whole is inferior in δ only to VINN-250. Therefore, the distribution of copper across the electrode thickness at the end of the electrolysis is the most uniform (H_{rms}= 110.2).

The time dependences of the Cu distribution across the electrode thickness (Fig. 1c) and the lower U, CE, and δ values are possibly due to the "island" nature of the copper deposit on the FCM during a long electrolysis time. Therefore, the electrode as whole has no continuous current path via the deposited metal having a higher conductivity than the FCM. This suggestion can be confirmed by the shift of the copper deposit to the back side of the electrode. Apparently, the distribution of the copper deposit across the electrode thickness is affected during a rather long time by the initial ratio of the electrical conductivities of the FCM electrode and the solution.

The relative mass of copper deposited on various electrode layers does not exceed 3 g g^{-1} FCM during up to 120 min of electrolysis. Then, this ratio increases, a high-conductivity electrode is formed, and the metal deposition zone shifts to the front side. According to the previously obtained experimental data [15], a solid deposit providing a high electrical conductivity of the electrode is formed upon deposition of 1.0–2.0 g g^{-1} FCM for the case of an island structure and upon deposition of more than 0.2 g g^{-1} FCM for the case of a thin film.

The nature of copper deposition onto FCM fibers is demonstrated by the micrographs (Figs. 3a, 3b) obtained with a JSMT-20 scanning electron microscope. It can be seen that, in the initial period of electrolysis, nuclei are formed on the surface of FCM fibers, gradually grow, and merge to give a solid high-conductivity copper layer. Simultaneously, the growing metallic islands fill the space between the fibers, merge, and form additional current transport paths. All these factors lead to an increase in the electrical conductivity of some parts of the electrode and, as result, to a rise in the electrical conductivity of the electrode as a whole. The electrical conductivity of the electrode becomes considerably higher than that of the solution, which results in a shift of the copper deposit to the front side of the electrode. Apparently, the local current densities will vary in the course of electrodeposition. In the course of copper deposition, the specific reactive surface of the electrode will change, too, which will lead to a change in the mass-transfer coefficient and in the linear flow velocity of the solution. This is confirmed by the calculated values reported in [10, 19]. The results of earlier studies [2, 4, 8] demonstrate that the morphology and nature of "overgrowth" of FCM

fibers with the metal deposit depend on the electrolysis conditions, FCM type, and state of the fiber surface.

Analysis of the data in Table 2 shows that the weight of copper deposited onto the electrode and the maximum mass of the copper deposit in its single layer are in good agreement with the uniformity of the deposit distribution across the entire electrode thickness, which is reflected by the H_{rms} values. For example, the distribution of the copper deposit is the least uniform on the VINN-250 and NTM-100 electrodes (H_{rms} 320.8 and 328.4, respectively). In this case, the ratio between the mass of copper deposited on a single layer and the mass of the FCM layer is somewhat smaller for the VINN-250 electrode, compared with the NTM-100 electrode. At the same time, the ratio for the mass of copper deposited on the entire electrode is larger for the VINN-250 electrode. Rather significant is the deposition of copper onto the ANM material. The value of δ for the layer with the maximum amount of deposited copper is a factor of 2.27 lower for this material than that for VINN-250. At the same time, the value of δ for the whole electrode is only a factor of 1.14 smaller, with H_{rms} for ANM a factor of 2.91 lower than that for VINN-250.

The results of the study show that, from the standpoint of development of processes for electrolytic recovery of metals, in which a considerable amount of metal should be deposited per unit mass of the FCM at a uniform distribution of the metal across the electrode thickness, it is the most reasonable to use electrodes fabricated from a low-conductivity material of the ANM type for the chosen electrolysis conditions and design of the electrode system (back side current lead to FCM and back side delivery of the electrolyte to electrode). To provide a uniform distribution of the copper deposit across the electrode thickness in metallization of FCM fibers, it is necessary to use electrodes fabricated from a material of the KNM-2 type, whose electrical conductivity is several times lower than that of the solution.

The results presented here show, along with the previously obtained data, that the initial electrical conductivity of the electrically isoconducting FCM electrode strongly affects the dynamics of metal deposition, distribution of metal across the electrode thickness, and characteristics of the electrolysis process. For FCM electrodes with various initial electrical conductivities, the distribution of the metal across the electrode thickness can be varied, with high electrolysis characteristics preserved, by changing the electrolysis conditions and process time.

CONCLUSIONS

(1) Copper electrodeposition from a sulfuric acid solution onto electrically isoconducting flow-through electrodes with a thickness of 0.6 cm, fabricated from fibrous carbon materials with various electrical conductivities, under conditions of solution circulation through the electrode volume and by maintaining the copper concentration in solution within the range 0.160 ± 0.03 g l^{-1}) at a current density of 1500 A m^{-2} was studied.

(2) It was shown that, for all of the carbon fibrous electrodes under study, whose electrical conductivity is in the range 0.184–0.0052 S cm^{-1} (electrical conductivity of the solution, 0.101 S cm^{-1}), the copper deposit is redistributed across the electrode thickness in the course of electrolysis and the following parameters vary: current efficiency, deposition rate, uniformity of the distribution across the electrode thickness, and mass of deposited copper per mass of the fibrous carbon material, both across the electrode thickness and for the electrode as a whole.

(3) It was found that the manner in which the parameters vary in the course of copper deposition and their numerical values are determined by the initial ratio between the electrical conductivities of the solution and the electrode material.

(4) It was demonstrated that use of low-conductivity fibrous materials under the chosen electrolysis conditions with backside delivery of a solution to electrode and backside current lead provides the most uniform distribution of the copper deposit across the electrode thickness in the course of electrolysis.

REFERENCES

1. Varentsov, V.K., *Khim. Interesakh Ustoich. Razv*., 1997, vol. 5, no. 2, pp. 147–156.
2. Varentsov, V.K., *Intensifikatsiya elektrokhimicheskikh protsessov* (Intensification of Electrochemical Processes), Tomilov, A.P., Ed., Moscow: Nauka, 1988, pp. 94–118.
3. Cao, Zhu-kun, Liu, Yi-han, and Yao, Guang-chun, *Guangdong Youse Jinshu Xuebao*, 2005., vol. 15, nos. 2–3, pp. 496–500.
4. Varentsov, V.K. and Varentsova, V.I., *Khim. Interesakh Ustoich. Razv.*, 2004, vol. 12, pp. 293–302
5. Varentsov, V.K. and Varentsova, V.I., *Zh. Prikl. Khim*., 2003, vol. 76, no. 11, pp. 1788–1793.

6. Fialkov, A.S., *Uglerod: Mezhsloevye soedineniya i kompozity na ego osnove* (Carbon. Intercalation Compounds and Composites Based on Them), Moscow: Aspekt, 1997.

7. Varentsov, V.K., *Zh. Ekol. Khim.*, 1993, no. 4, pp. 335–341.

8. Varentsov, V.K., Electrochemical Processes and Apparatus with 3*D* Porous Flow-Through Electrodes for Recovery of Metals from Dilute Solutions, *Doctoral Dissertation*, Sverdlovsk, 1990.

9. Maslii, A.I. and Poddubnyi, N.P., *Elektrokhimiya*, 1978, vol. 42, pp. 149–153.

10. Maslii, A.I., Poddubnyi, N.P., and Medvedev, A.Zh., *Elektrokhimiya,* 2005, vol. 41, no. 4, pp. 452–459.

11. Maslii, A.I., Poddubnyi, N.P., and Medvedev, A.Zh., *Elektrokhimiya*, 2006, vol. 42, no. 3, pp. 286–291.

12. Koshev, A.P., Varentsov, V.K., and Gleizer, G.N., *Elektrokhimiya*,1992, vol. 28, no. 8, pp. 1128–1134.

13. Zamyatin, A.P. and Bek, R.Yu., *Elektrokhimiya*, 1980, vol. 16, no. 9, pp. 1316–1320.

14. Varentsov, V.K., Yusin, S.I., and Varentsova, V.I., Abstracts of Papers, *VII Vsesoyuznaya Nauchno-prakticheskaya konferentsiya dlya studientov i aspirantov "Khimiya i khimicheskaya kekhnologiya v 21 veke"* (VIII All-Union Sci.-Pract. Conf. for Students and Postgraduate Students "Chemistry and Chemical Technology in the XXI Century"), Tomsk, Tomsk. Polytekh. Univ., 2007, pp. 14–15.

15. Varentsov, V.K., *Sovremennye problemy tekhnicheskoi elektrokhimii. Trekhmernye protochnye elektrody* (Modern Problems of Technical Electrochemistry: 3*D* Flow-Through Electrodes), Novosibirsk, Novosib. Gos. Tekhn. Univ., 2005, part 1.

16. Kletenik, Yu.B. and Tarasova, V.A., *Izv. Sib. Otd. Akad. Nauk SSSR*, 1986, no. 5, issue 2, pp. 84–87.

17. Pugachev, V.S., *Vvedenie v teoriyu veroyatnostei* (Introduction into the Probability Theory), Moscow: Nauka, 1968.

18. Ventsel', E.S., *Teoriya veroyatnostei: Uchebnik dlya Vyssh. Uchebn. Zaved.* (The Probability Theory: Textbook for Higher Educational Institutions), Moscow: Vysshaya Shkola, 1998.

19. Koshev, A.N., Davydenko, A.A., Varentsov, V.K., and Kamburg, V.G., *Elektrokhimiya*, 1997, vol. 33, no. 1, pp. 20–25.

ISSN 1070-4272, Russian Journal of Applied Chemistry, 2008, Vol. 81, No. 10, pp. 1785–1789. © Pleiades Publishing, Ltd., 2008.
Original Russian Text © T.M. Umarova, Z.S. Dzhalolova, I.N. Ganiev, 2008, published in Zhurnal Prikladnoi Khimii, 2008, Vol. 81, No. 10, pp. 1660–1665.

APPLIED ELECTROCHEMISTRY AND CORROSION PROTECTION OF METALS

Effect of Rare-Earth Metals (Y, La, and Ce) on the Corrosion and Mechanical Properties of Aluminum–Manganese Alloy

T. M. Umarova, Z. S. Dzhalolova, and I. N. Ganiev

Nikitin Institute of Chemistry, Academy of Sciences of the Republic of Tajikistan, Dushanbe, Tajikistan

Received May 14, 2007

Abstract—Effect of some rare-earth metals (yttrium, cerium, and lanthanum) on the corrosion-electrochemical and mechanical properties of an aluminum–manganese alloy of eutectic composition (1.9% Mn) in a neutral medium was studied.

DOI: 10.1134/S1070427208100157

Aluminum–manganese alloys are a well-known construction material that is not hardenable by thermal treatment and is distinguished by high plasticity, good weldability, and high corrosion resistance. However, alloys of the AMts type are subject to pitting corrosion under certain conditions. Previously, the corrosion-electrochemical behavior of Al–Mn alloys has been studied in a wide range of concentrations [1–3].

Multicomponent systems with intermediate phases belong to the most widely used and practically important systems. The phase diagrams of these systems underlie the technology for manufacture of alloys from nonferrous metals and deformable half-products. Therefore, studying these systems and revealing the fundamental aspects of their structure is a topical task.

The aim of this study was to examine the effect of rare-earth metals (REM), such as yttrium, cerium, and lanthanum, on the corrosion-electrochemical behavior of an aluminum–manganese alloy and to analyze its mechanical properties. As a base material was chosen an alloy of eutectic composition (Al + 1.9% Mn) as a construction material with improved physicochemical properties, compared with the industrial AMts alloy.

EXPERIMENTAL

To study the corrosion-electrochemical properties of REM-containing aluminum alloys, addition alloys were prepared from A995 aluminum [GOST (State Standard) 11069–74], and alloys of prescribed compositions, from technical-grade aluminum of A8 brand (GOST 4784–74*) in an SNVL–1.301 vacuum furnace in corundum crucible in the atmosphere of argon at temperatures in the range 800–1000°C. Cylindrical rods 8 mm in diameter and 100 mm long were cast in a graphite mold from the alloys obtained. Before being submerged in an electrochemical cell, the rods were ground, polished, and degreased with ethanol.

The corrosion-electrochemical behavior of alloyed aluminum–manganese alloys was studied using the method described in [1]. The sequence of operations performed when measuring a polarization curve is schematically shown in Fig. 1. The potential sweep rate was 2 mV s^{-1}, a silver chloride electrode served as reference, and the potentials were recalculated to the standard hydrogen scale (s.h.e.). The corrosion rate K, a function of the corrosion current density i_{cor}, was found by the formula

$$K = i_{cor} k,$$

where k is the electrochemical equivalent whose numerical value for aluminum is 0.335 g $A^{-1} h^{-1}$ [4].

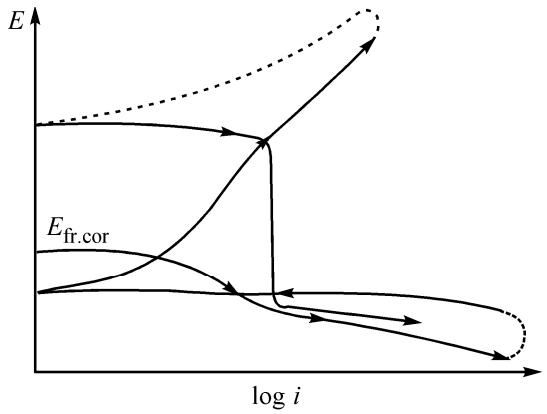


Fig. 1. Schematic of the polarization curves of the alloys under study. (E) Potential and (i) current density.

Table 1. Corrosion-electrochemical parameters of the cerium-modified Al–Mn (1.9%) alloy in a 3% NaCl solution

Ce, wt %	$-E_{fr.cor}$	$-E_{pit}$	$-E_{rpas}$	$-E_{cor}$	$-E_{pas.on}$	$-E^1_{pit}$	ΔE_{pas}	$i_{d.rpas}$	i_{cor}
	V							A m^{-2}	
–	0.620	0.39	–	0.53	0.900	0.42	0.45	0.10	0.0080
0.005	0.590	0.35	0.510	0.52	0.855	0.38	0.47	0.08	0.0075
0.01	0.600	0.35	0.510	0.52	0.850	0.37	0.44	0.07	0.0062
0.05	0.600	0.35	0.510	0.52	0.840	0.36	0.41	0.08	0.0055
0.10	0.600	0.38	0.510	0.51	0.850	0.39	0.45	0.07	0.0090
0.20	0.625	0.37	0.510	0.52	0.900	0.40	0.50	0.06	0.0095
0.50	0.625	0.36	0.515	0.53	0.970	0.40	0.55	0.05	0.0120

* $-E_{fr.cor}$, $-E_{pit}$, $-E^1_{pit}$, $-E_{rpas}$, $-E_{cor}$, and $-E_{pas.on}$ are the potentials of free-corrosion, pitting in the presence and absence of a natural oxide film on the surface, repassivation, corrosion, and passivation onset, respectively; ΔE_{pas}, passivation interval; $i_{d.rpas}$ and i_{cor}, current densities of dissolution in the repassivation region and corrosion.

Because iron is an inevitable accompanying impurity in aluminum alloys, it was of interest to preliminarily consider the joint effect of iron and manganese on the corrosion resistance of aluminum. For this purpose, alloys with a 1 : 1 manganese-to-iron ratio were prepared. With account of the free-corrosion ($E_{fr.cor}$), repassivation ($E_{r.pas}$), and corrosion (E_{cor}) potentials, it was found that the potentials of the alloys in the absence of current are in the passivation region (0.40–0.50 V). At potentials more negative than the pitting potential (E_{pit}), a uniform dissolution of the aluminum–manganese alloys is observed. At more positive potentials, oriented pits appear on the surface. The tendency of an alloy to undergo pitting corrosion can be evaluated by the difference between the pitting and repassivation potentials in a neutral medium. For the case in question, this difference is 0.6–0.9 V.

Iron affects the corrosion resistance of aluminum in diverse ways. As a rule, the effect of iron on the corrosion resistance of aluminum alloys in neutral media is slight. However, its presence in aluminum–manganese alloys leads to a tenfold increase in the corrosion rate. The key role in the corrosion behavior of the given system is played by the $FeAl_3$ phase, because the appearance of pitting is caused by just this phase.

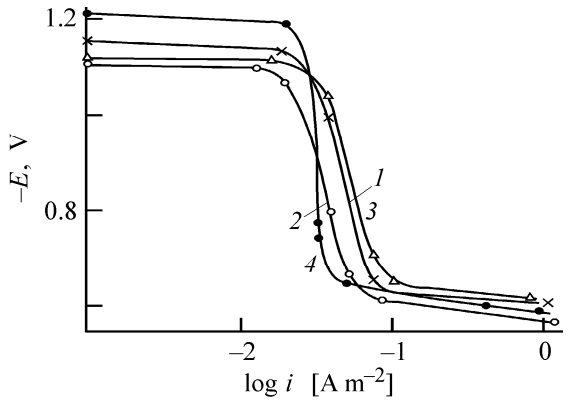


Fig. 2. Anodic polarization curves of Al–Mn (1.9%) alloys alloyed with cerium. (*E*) Potential and (*i*) current density; the same for Figs. 3, 4. Ce content (wt %): (*1*) 0.005, (*2*) 0.05, (*3*) 0.10, and (*4*) 0.50.

It is known that alloying of an aluminum alloy with cerium leads to an increase in the electrical and thermal conductivity of the alloy and improves its rollability in the hot state [5]. However, the influence exerted by cerium on the corrosion-electrochemical behavior of aluminum–manganese alloys remains to be elucidated. Therefore, the corrosion behavior of alloys of the Al–Mn–Ce system was examined in this study. Table 1 lists the results obtained in a study of alloys of this system in a 3% NaCl solution.

It should be noted that presence of manganese in an alloy results in that the aluminum grain becomes somewhat finer. Comparison of the results of the corrosion-electrochemical studies with the data of [5] demonstrates the following specific feature: as the content of cerium increases to 0.5%, the electrochemical parameters vary nonlinearly and reach the minimum values at 0.5% cerium. As the content of cerium increases, the free-corrosion potential shifts to more electronegative values. The corrosion potential E_{cor} first somewhat increases and then, at the maximum content of cerium, slightly shifts into the region of negative values. The passivation interval ΔE_{pas} of the aluminum–manganese alloy insignificantly changes within 0.10 V. It can be seen from the data in Table 1 that microalloying with cerium leads to a decrease in the corrosion rate of the aluminum–manganese alloy. The optimal, in the corrosion regard, amount of the cerium additive is 0.5%. As the content of cerium increases further, the corrosion current grows and, consequently, the corrosion resistance becomes poorer.

Figure 2 shows anodic polarization curves of an aluminum–manganese alloy alloyed with cerium

Table 2. Corrosion-electrochemical parameters of the yttrium-alloyed Al–Mn (1.9%) alloy in a 3% NaCl solution

Y, wt %	$-E_{fr.cor}$	$-E_{pit}$	$-E_{rpas}$	$-E_{cor}$	$-E_{pas.on}$	$-E^1_{pit}$	ΔE_{pas}	$i_{d.rpas}$	i_{cor}
	V							A m^{-2}	
–	0.62	0.39	–	0.530	0.90	0.42	0.45	0.10	0.0080
0.005	0.57	–	0.535	0.510	0.86	0.42	0.50	0.04	0.0050
0.01	0.57	0.38	–	0.530	0.90	0.40	0.54	0.03	0.0045
0.05	0.57	0.36	0.530	0.540	0.98	0.40	0.56	0.03	0.0060
0.10	0.58	0.37	0.520	0.540	0.96	0.40	0.52	0.02	0.0060
0.20	0.59	0.37	0.520	0.540	0.96	0.40	0.50	0.02	0.0070
0.50	0.60	0.38	0.520	0.530	0.97	0.41	0.50	0.02	0.0090

Table 3. Corrosion-electrochemical parameters of the lanthanum-alloyed Al–Mn (1.9%) alloy in a 3% NaCl solution

La, wt %	$-E_{fr.cor}$	$-E_{pit}$	$-E_{rpas}$	$-E_{cor}$	$-E_{pas.on}$	$-E^1_{pit}$	ΔE_{pas}	$i_{d.rpas}$	i_{cor}
	V							A m^{-2}	
–	0.620	0.39	–	0.530	0.900	0.42	0.45	0.10	0.008
0.005	0.61	0.39	0.51	0.520	0.800	0.35	0.43	0.10	0.006
0.01	0.60	0.38	0.51	0.520	0.800	0.40	0.45	0.08	0.005
0.05	0.60	0.36	0.51	0.525	0.800	0.44	0.36	0.08	0.0010
0.10	0.60	0.35	0.51	0.530	0.910	0.46	0.43	0.05	0.008
0.20	0.58	0.34	0.52	0.530	0.910	0.43	0.44	0.05	0.009
0.50	0.56	0.33	0.52	0.530	0.880	0.41	0.46	0.06	0.012

(up to 0.5%). It can be seen that the minimum dissolution current in the passivation region corresponds to the alloy with the maximum content of cerium (Fig. 2, curve *4*). The highest passivation-onset potential ($E_{pas.on}$) corresponds to the alloy with the maximum content of cerium. In this case, the passive region is rather stable and an increase in the content of cerium affects its width only slightly.

It is known that, owing to quite a number of properties, yttrium has found wide application in industry, metallurgy, and electronics [6]. Alloying with yttrium causes structural changes and thereby improves the mechanical properties and heat resistance of alloys. The results of a study of the corrosion-electrochemical behavior of an aluminum–manganese alloy (1.9% Mn) alloyed with yttrium are listed in Table 2.

It can be seen from Table 2 that addition of up to 0.1% yttrium to the aluminum–manganese alloy exerts an on the whole positive influence, which is due to the modification effect. The minimum corrosion currents are observed at the yttrium content in the range from 0.005 to 0.1%. The free-corrosion, pitting, repassivation, and corrosion potentials are shifted to more positive values. Alloys of this system have a rather wide and stable passivation region (ΔE_{pas} = 0.50 V). The potentials and corrosion current densities of the alloy of the system Al–Mn (1.9%)–Y (0.5%) nearly coincide with the similar parameters of the base alloy. The difference between the characteristic potentials is 0.10–0.20 V.

Figure 3 shows anodic polarization curves of an aluminum–manganese alloy of eutectic composition, alloyed with yttrium to 0.50 wt %. All the alloys of the compositions considered are well repassivated at potentials in the range 0.520–0.535 V.

It is known that intermetallic compounds (IMC) with structures of the types $ThMn_{12}$, Th_2Zn_{17}, and $LaMnAl_8$ are formed in the Al–Mn–La system. It has been found that binary compounds do not dissolve the third component [7].

Table 3 lists the results obtained in a study of the corrosion-electrochemical behavior of alloys belonging

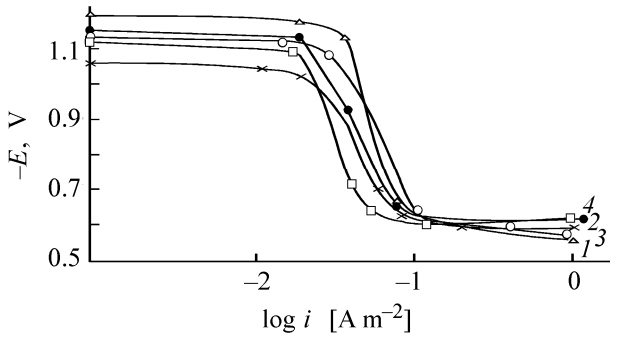


Fig. 3. Anodic polarization curves of Al–Mn (1.9%) alloys alloyed with yttrium. Y content (wt %): (*1*) 0.005, (*2*) 0.05, (*3*) 0.10, and (*4*) 0.50.

Table 4. Effect of REM (Y, La, Ce) on the mechanical properties of Al–Mn (1.9%) alloys

REM, wt %	σ_y, MPa		σ_t, MPa		δ, %		ψ, %	
	unannealed alloy	that after annealing	unannealed alloy	that after annealing	unannealed alloy	that after annealing	unannealed alloy	that after annealing
–	73.7	90.2	38.3	57.2	34.3	24.6	59.5	70.6
Y:								
0.01	72.4	88.2	44.9	58.2	40.8	30.8	52.2	–
0.05	74.9	81.2	56.1	52.6	39.1	28.7	54.1	82.9
0.10	69.1	86.8	44.2	59.3	25.0	33.4	–	69.4
0.50	61.7	82.2	41.7	60.2	10.6	30.1	78.3	92.4
La:								
0.01	70.7	88.8	43.6	56.2	36.0	20.3	50.3	84.7
0.05	70.4	87.4	45.4	49.8	29.3	18.8	61.7	90.4
0.10	68.3	90.5	44.0	60.0	19.4	22.7	70.7	86.3
0.50	77.0	87.1	41.6	59.7	31.7	23.3	58.5	78.6
Ce:								
0.01	70.5	86.7	42.7	57.8	28.0	28.9	76.9	74.8
0.05	59.8	90.8	43.6	61.8	33.5	22.4	–	93.7
0.10	70.7	90.0	41.1	61.2	35.0	35.2	54.7	95.5
0.50	72.2	83.5	41.2	59.0	32.3	30.8	67.0	94.8

to the Al–Mn (1.9%) system and alloyed with lanthanum to 0.50 wt %. It can be seen that lanthanum can shift the free-corrosion and pitting potentials to a more positive region. In this case, the corrosion potential remains nearly unchanged and the passivation interval becomes somewhat narrower. The zero-current potentials $E_{fr.cor}$ of alloys of this system are in the passive region, and, consequently, these alloys can be characterized as corrosion resistant. This conclusion is confirmed by the lower dissolution currents in the passivation region. Upon addition of lanthanum in amounts of up to 0.10%, the corrosion current decreases. And only at the maximum content of lanthanum (0.5%), the corrosion current increases and, accordingly, the corrosion rate grows.

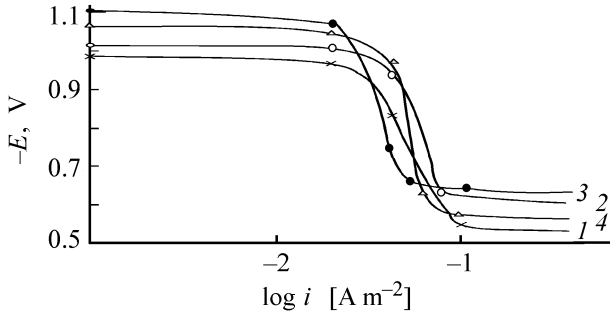


Fig. 4. Anodic polarization curves of Al–Mn (1.9%) alloys alloyed with lanthanum. La content (wt %): (*1*) 0.005, (*2*) 0.05, (*3*) 0.10, and (*4*) 0.50.

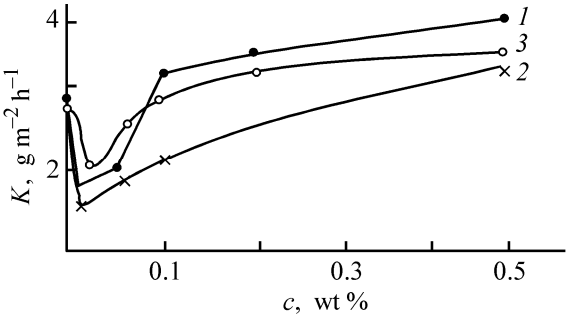


Fig. 5. Effect of the REM content *c* on the corrosion rate *K* of Al–Mn (1.9%) alloys. (*1*) Ce, (*2*) Y, and (*3*) La.

Figure 4 shows anodic polarization curves of an Al–Mn (1.9%) alloy alloyed with lanthanum, measured in a 3% NaCl solution. It can be seen that addition of lanthanum shifts the passivation-onset potential to more negative values. The alloys under study are passivated in the range 0.55–1.10 V, depending on the lanthanum content, and the currents of dissolution in the passivation region decrease as the La content increases.

Figure 5 compares dependences of the corrosion rate K (g m^{-2} h^{-1}) of an aluminum–manganese alloy in a 3% NaCl solution on the content c (wt %) of REM (Y, La, and Ce). It can be seen that all the curves are of the same type, with the minimum corrosion rate observed at a REM content of 0.01%. Further increase in the REM content leads to a rise in the corrosion rate.

The mechanical properties of the alloys were studied: ultimate tensile strength (temporal resistance

σ_t, MPa), yield point σ_y (MPa), and plasticity parameters, relative elongation δ (%) and contraction ratio ψ (%). Tests to determine the mechanical properties were performed on an R-5 tensile machine under a load of 1000–10 000 kg (GOST 1494–84). Table 4 presents the results of these tests. It can be seen that alloying with REM (Y, La, and Ce) does not improve the strength of aluminum–manganese alloys. The REM exert a stronger influence on the yield point, especially in the unannealed state. For example, the maximum value of the yield point is observed for the alloy of composition Al–Mn (1.9%)–Y (0.05%).

In the annealed state, the effect of REM is stronger for alloys alloyed with cerium and weaker for those alloyed with lanthanum. Analysis of plasticity values suggests that the relative elongation is more strongly affected by yttrium and cerium, especially for annealed alloys, and the contraction ratio ψ, by cerium in the concentration range under study.

Thus, the study of the mechanical properties of the alloys demonstrated that the aluminum–manganese alloy modified with yttrium (0.05%) and cerium or lanthanum in the concentration range 0.05–0.5 wt % can be used as a construction material with increased yield point. The effects of REM additives on the plasticity are diverse: the contraction ratio ψ increases upon alloying with 0.5% yttrium, 0.01–0.10% lanthanum, and 0.05–0.5% cerium.

CONCLUSIONS

(1) The free-corrosion potentials of the Al–Mn (1.9%)–Y (La, Ce) system are within the passivation region. Alloying of the aluminum–manganese eutectic with REM (Y, La, and Ce) shifts the $E_{fr.cor}$ and E_{pit} potentials to the region of more positive values.

(2) Alloys alloyed with cerium are repassivated at the same potential of 0.51 V (s.h.e.).

(3) The optimal content of REM (in a pure form or as a misch metal) for achieving an increased corrosion resistance of the aluminum–manganese alloy of eutectic composition is 0.01 to 0.05%. Alloys of these compositions can be recommended as a corrosion-resistant material for use in media causing the pitting corrosion.

(4) The role of REM (Y, La, and Ce) as an alloying additive to aluminum alloys consists in their modifying effect on the structure, which, on the whole, makes it possible to obtain an aluminum-based construction material with enhanced corrosion resistance.

REFERENCES

1. Karimova, T.M., Ganiev, I.N., and Krasnoyarskii, V.V., *Zh. Prikl. Khim.*, 1988, vol. 61, no. 1, pp. 51–54.
2. Umarova, T.M., Krasnoyarskii, V.V., and Ganiev, I.N., *Zh. Prikl. Khim.*, 1991, vol. 64, no. 6, pp. 1337–1341.
3. Krasnoyarskii, V.V. and Umarova, T.M., *Ekspress Informatsiya, Ser. "Zashchita ot korrozii i okhrana okruzhayushchei sredy"* (Express Information, Series "Corrosion Protection and Environment Conservation"), Moscow: VNIIOENG, 1991, issue 6, pp. 11–15.
4. Romanov, V.V., *Metody issledovaniya korrozii metallov* (Methods for Analysis of Metal Corrosion), Moscow: Metallurgiya, 1965.
5. Ershov, G.S. and Bychkov, Yu.B., *Vysokoprochnye alyuminievye splavy iz vtorichnogo syr'ya* (High-Strength Aluminum Alloys Produced from Secondary Raw Materials), Moscow: Metallurgiya, 1979.
6. Al'tovskii, R.M. et al., *Korrozionnye svoistva ittriya* (Corrosion Properties of Yttrium), Moscow: Atomizdat, 1969.
7. Bodak, O.I. and Gladyshevskii, E.I., *Troinye sistemy, soderzhashchie RZM* (REM-containing Ternary Systems), L'vov: Vishcha Shkola, 1985.

ISSN 1070-4272, Russian Journal of Applied Chemistry, 2008, Vol. 81, No. 10, pp. 1790–1795. © Pleiades Publishing, Ltd., 2008.
Original Russian Text © S.D. Kurbakov, 2008, published in Zhurnal Prikladnoi Khimii, 2008, Vol. 81, No. 10, pp. 1666–1671.

APPLIED ELECTROCHEMISTRY AND CORROSION PROTECTION OF METALS

Effect of Synthesis Conditions of Pyrocarbon Coatings on Their Corrosion Resistance in H_2SO_4–HNO_3 Oxidizing Mixture

S. D. Kurbakov

Luch Federal State Unitary Enterprise, Research Institute, Research and Production Association, Podol'sk, Moscow oblast, Russia

Received November 16, 2007

Abstract—Synthesis conditions of pyrocarbon coatings in a fluidized bed via pyrolysis of gaseous hydrocarbons from a CH_4–Ar mixture at temperatures of 1300–2000°C and from C_3H_6–Ar at 1200–1500°C were examined. The corrosion resistance of the pyrocarbon coatings in HNO_3–H_2SO_4 oxidizing mixture was studied.

DOI: 10.1134/S1070427208100169

Pyrocarbon, mostly in the form of coatings, has been of interest during many years. Having been an exclusively reactor material (protective coatings of microfuel elements of high-temperature gas-cooled nuclear reactors [1, 2]) during a long time, the material is gaining steadily expanding application areas: in the first place, these are burial of radioactive wastes, because pyrocarbon coatings show promise for prolonged insulation of a solidified waste from the corrosive effect of the environment [3], and biomedicine, including artificial heart valves [4]. Of particular importance is the role of carbon materials in heterogeneous catalytic processes [5]. The high corrosion resistance of pyrocarbon under the action of numerous chemical reagents places this material on an adequate place among protective coatings for chemical apparatus and matrices of carbon–carbon composites for various purposes [6, 7].

The aim of this study was to choose deposition conditions of pyrocarbon coatings with enhanced resistance to corrosive reagents, such as mixtures of concentrated acids HNO_3–H_2SO_4, which are intercalating agents for most of carbon-graphite materials [8].

Pyrocarbon coatings were produced on spherical zirconium carbide particles 400–600 μm in diameter in a fluidized bed via pyrolysis of gaseous hydrocarbons: from a CH_4–Ar mixture at temperatures of 1300–2000°C and C_3H_6–Ar at 1200–1500°C. The coatings were deposited in a fluidized-bed cylindrical-conical apparatus with a diameter of about 60 mm and a cone opening angle of 40°. The weight of portions of zirconium carbide particles was varied within the range 150–200 g. The overall flow rate of the gas mixture (argon with a hydrocarbon) was chosen so as to provide a bubble mode of particle fluidization (1500 ± 100 l h^{-1}).

Thus, pyrocarbon coatings obtained at 1300–2000°C from a CH_4–Ar mixture (CH_4 content ≤20 vol %) were named conditionally high-temperature (HTP) coatings, and those deposited from a C_3H_6–Ar mixture (C_3H_6 content ≤30 vol %), low-temperature (LTP).

Three basic structural elements are known for pyrocarbon coatings produced by pyrolysis: turbostratic structure, amorphous carbon, and higher-order supraatomic (supramolecular) formations [9, 10]. The main elements of the turbostratic structure are basal planes structurally similar to graphite planes. They are composed of six-membered aromatic rings (hexagons) of carbon atoms with the same interatomic distance (1.415 Å) as that in the graphite plane. A certain number of connected planes form a packet. In contrast to graphite, packets of the turbostratic structure have no mutual orientation of planes in a direction perpendicular to the *c* axis. In the strictly crystallographic sense, the packets cannot be attributed to crystallites as regards their structure, because they have no 3*D* ordering. Thus, the strict order exists for pyrocarbon only in the 2*D* plane. Nevertheless, the turbostratic pyrocarbon structure is conditionally named crystalline in the lit-

erature. According to published data [11–13], the interplanar spacings in packets of pyrocarbon crystallites are 3.36–3.44 Å, which substantially exceeds those in graphite (3.35 Å). The dimensions of turbostratic coherent scattering regions (CSR) (packets) are characterized [12, 13] by the packet thickness L_c and carbon layer width L_a:

$$L_c = 0.9\lambda/(d_{002}\cos\gamma),$$

$$L_a = 1.8\lambda/(d_{110}\cos\gamma),$$

where λ is the radiation wavelength; d_{002} and d_{110}, angular half-width of lines; and γ, Bragg angle.

Pyrocarbon coatings contain a set of packets of various sizes, and, therefore, the experimentally determined values of L_a, L_c, d_{002}, and d_{110} are statistic-average.

To characterize secondary structural formations appearing in the carbon material as a result of mutually matched stacking of carbon planes, the term "supramolecular structure," which reflects the essence of the polymeric organization of pyrocarbon, has been suggested with a rather good substantiation [9, 10].

An X-ray diffraction analysis (DRON-6 diffractometer) of the crystal structure of pyrocarbon demonstrated that the LTP and HTP coatings are polycrystalline. It was found (Fig. 1) that the interplanar spacing d_{002} of HTP coatings is weakly dependent on the deposition temperature. At 1300°C, d_{002} is independent of the CH_4 concentration, and at temperatures higher than 1800°C, a slight decrease in d_{002} is observed at CH_4 concentrations of 1–5 vol %.

For LTP coatings deposited in the range 1200–1500°C, d_{002} is independent of the deposition temperature and C_3H_6 concentration (Fig. 1). It is noteworthy that the absolute values of d_{002} substantially differ between LTP and HTP coatings.

As the deposition temperature of HTP coatings increases, the SCR dimensions L_a and L_c become larger (Fig. 2). L_a and L_c are nearly independent of the concentration. The shape of the SCR markedly changes on raising the deposition temperature. At 1500°C, the SCR diameter exceeds the SCR height, whereas at higher temperatures, the SCR changes and the L_c/L_a ratio increases.

The dimensions of the SCR of LTP coatings are independent of the deposition temperature (in the range 1200–1500°C) and C_3H_6 concentration (Fig. 2)

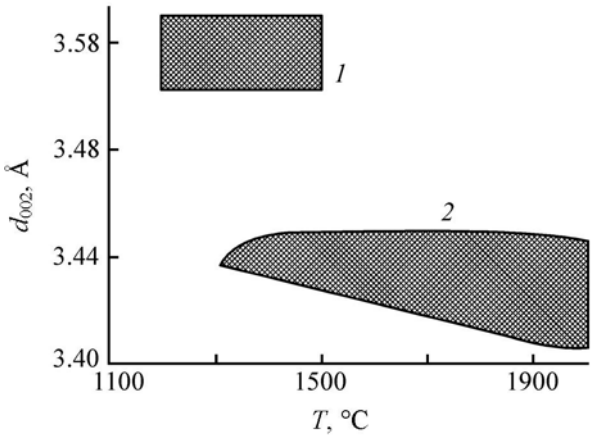


Fig. 1. Effect of the deposition temperature T on the interplanar spacing d_{002} of pyrocarbon coatings. Coating: (*1*) LTP and (*2*) HTP; the same for Figs. 2, 4.

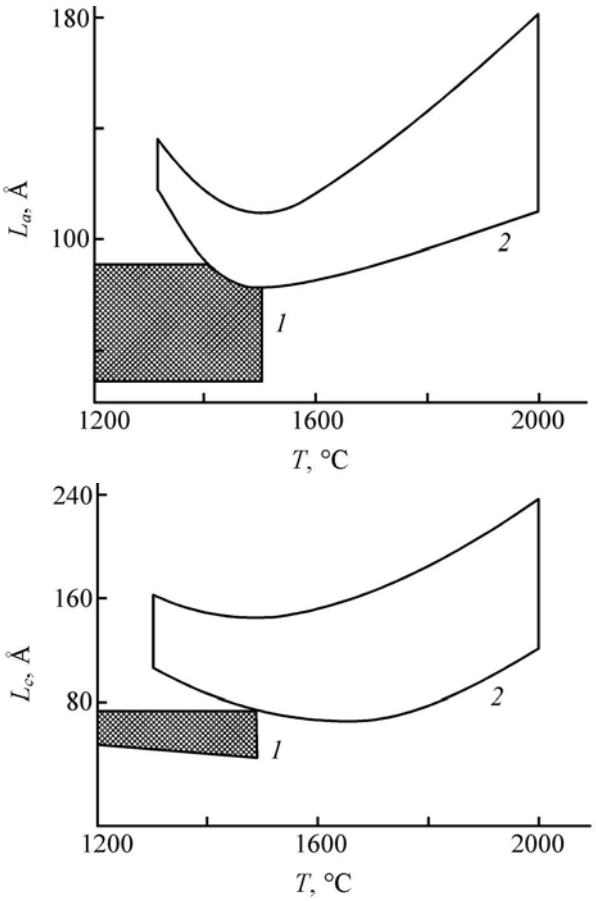


Fig. 2. Dimensions L_a and L_c of the SCR of pyrocarbon coatings vs. the deposition temperature T.

and 3–5 times smaller than those of HTP coatings. For LTP coatings, an SCR shape with $L_a > L_c$ is observed.

The chemical resistance of pyrocarbon coatings was studied under the action of a mixture of concen-

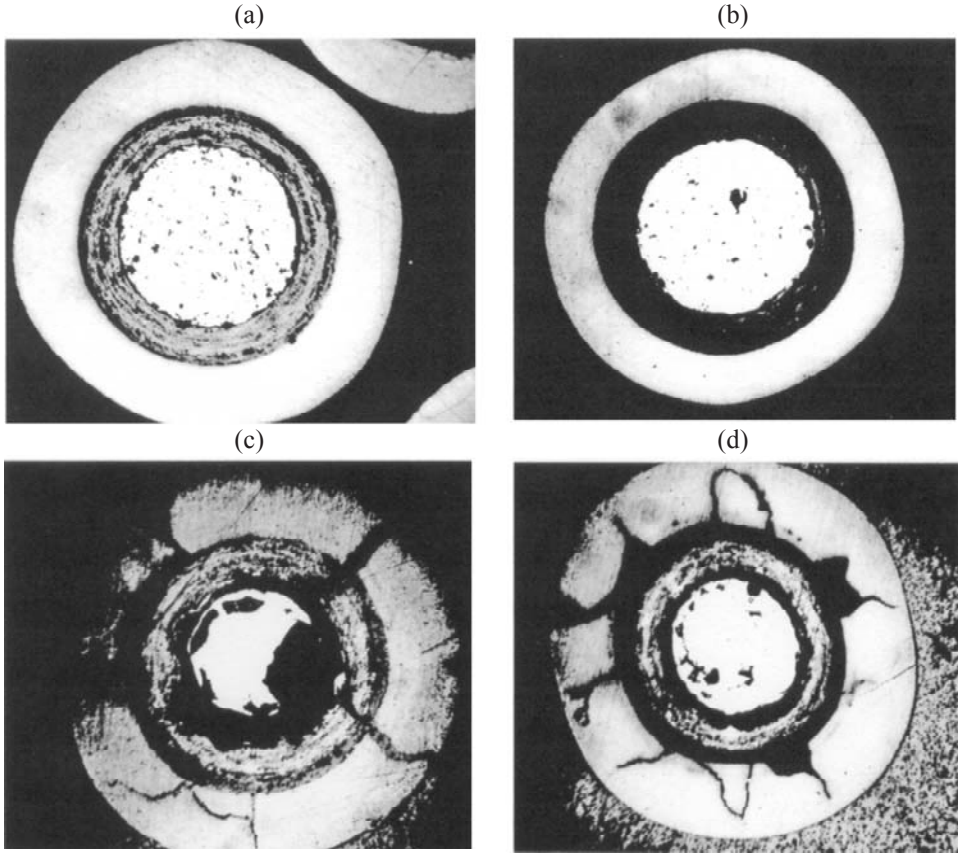


Fig. 3. Macrostructure of particles with LTP and HTP coatings after treatment with an H_2SO_4–HNO_3 oxidizing mixture. Magnification 70. Particles with a LTP layer produced from C_3H_6–Ar: (a) 10 vol % C_3H_6 and (b) 30 vol % C_3H_6; (c, d) particles with an HTP layer produced from C_3H_6. For explanations, see text.

trated acids HNO_3 and H_2SO_4. The oxidizing mixture was composed of 20 volume parts of 98% H_2SO_4 and 1 volume part of 60% HNO_3.

Pyrocarbon coatings were treated with the oxidizing mixture at a temperature of 20–25°C. Microspheres with coatings (150–450 pieces) on a stainless steel grid were placed in the oxidizing mixture and the coating surface was inspected under a microscope at regular intervals of time.

The treatment of most of batches with HTP coatings did not change the surface during the first 2–3 h. Then, particles increased in diameter by approximately 100 μm, after which the coatings cracked. It should be noted that some of samples with HTP coatings sustained a 25-h treatment with the mixture. Particles with LTP coatings did not show any visually observable changes upon an exposure exceeding 70 h. No changes in the morphology and macro-and microstructure of LTP coatings were observed, either (Figs. 3a, 3b).

Two main kinds of damage are characteristic of HTP coatings: formation of radial cracks in those cases when the optical anisotropy coefficient of pyrocarbon, found from the reflection of the plane-polarized light beam, did not exceed 1.20 and planar delamination (fragmentation) when the anisotropy coefficient exceeded 1.20 (Figs. 3c, 3d).

The stability of the coatings was judged from the appearance of first cracks on the particle surface after the beginning of the acid treatment. Figure 4a shows how the optical anisotropy of the coatings affects their resistance. It can be seen that, despite the differences in anisotropy, the LTP coatings are completely stable, whereas the stability of the HTP coating dramatically decreased as the optical anisotropy becomes higher.

The stability of the HTP coatings strongly depends on the deposition temperature (Fig. 4b): for pyrocarbon obtained at CH_4 concentration of 5–25 vol %, it decreases nearly linearly as the temperature is ele-

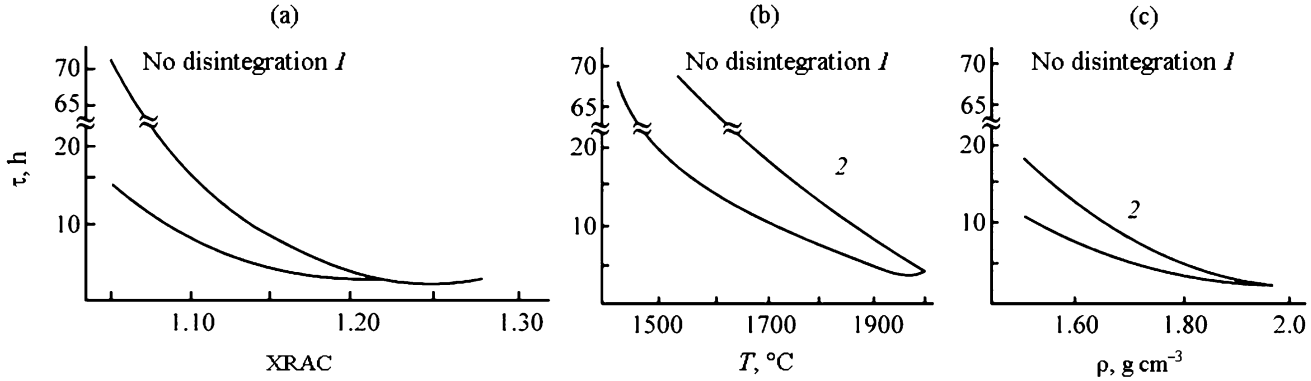


Fig. 4. Resistance of pyrocarbon coatings in an H_2SO_4–HNO_3 oxidizing mixture vs. (a) anisotropy, (b) deposition temperature T, and (c) density ρ. (τ) Time of treatment before cracking and (XRAC) X-ray anisotropy coefficient.

vated. The only exception are coatings deposited at 1500°C and a CH_4 concentration of 1.0 vol %. It should be noted that a clearly pronounced planar texture is characteristic of these coatings. The stability of HTP coatings steadily decreases as their density grows (Fig. 4c), whereas LTP coatings show no dependence of this kind.

The intercalating treatment of graphite, which leads to changes in its volume, was studied in [14]. It was demonstrated that the increase in the volume of a graphite sample upon its interaction with cesium is due to the formation of a number of layered compounds of the C_nCs type, where n = 8, 10, 24, 36, 48, 60, and 72. According to X-ray diffraction data, the process of intercalation of cesium atoms into the space between carbon layers resulted in an increase in the interlayer spacing from 3.35 to 5.94 Å.

The observed increase in the particle size upon an oxidative treatment is due to microscopic changes in pyrocarbon on the crystallite level. Powdered fragments of coatings were used in X-ray structural studies of samples before and after treatment with the oxidizing mixture. The results obtained are listed in the table.

After the treatment, the interplanar spacings d_{002} in HTP coatings (batches 13ts-4/1 and 11ts-4/1) became larger and remained somewhat increased even after coating fragments were annealed at 400°C in a flow of argon. Simultaneously, additional peaks appeared after the annealing. The corresponding interplanar spacings were 3.986 Å for both samples. The parameter d_{100} of the HTP coatings somewhat decreased after the treatment in the oxidizing mixture. The X-ray anisotropy coefficient increased for the 13ts-4/1 batch after all kinds of treatment, whereas for the 11ts-4/1 batch, it decreased from 1.322 to 1.162 after the oxidative treatment and then increased to 1.690 after the annealing. For both HTP coatings the dimensions of the SCR (L_a and L_c) increased after the oxidative and thermal treatments. For fragments of LTP coatings (2tsp batch), no changes in the crystal structure parameters was observed (see table).

In treatment of HTP coatings with the oxidizing mixture, the sulfo group of sulfuric acid can be introduced into the interplanar spacing of pyrocarbon to give the so-called graphite bisulfate. This process can be written as follows

$$nC + 3H_2SO_4 \rightarrow C_n^+[HSO_4]^-2H_2SO_4.$$

With account of the data in the table, analysis of the experimental results suggests the following pattern of structural changes in HTP coatings. In the course of treatment with the mixture of acids, boundaries of the SCR and crystalline formations are etched by nitric acid (oxidizing agent) and then sulfo groups are intercalated into the interplanar spaces of pyrocarbon. This gives rise to stresses, first in crystallites and then in crystalline formations (supramolecular organization of graphite-like carbon). These stresses tend to cleave the surface layer of the material along directions with weak bonds. When these stresses become sufficiently large, the coating suffers an irreversible deformation manifested in cracking.

In the review [15], the lowered hydrostatic compressibility of samples of a layered compound C_8Cs is attributed to a "rigidity" of the cesium bonding to carbon, caused by the strong overlapping of the wave functions of 6*s*-electrons of cesium and π-electrons of graphite along the *c* axis. Here, account should be taken of the fact that cesium is a donor intercalating agent.

Structural parameters of pyrocarbon coatings before and after a 20-h treatment with an HNO_3–H_2SO_4 oxidizing mixture and the subsequent annealing in argon at 400°C for 1 h

Parameter	Batch								
	13ts-4/1			11ts-4/1			2tsp		
	initial coating	HNO_3–H_2SO_4 treatment	annealing	initial coating	HNO_3–H_2SO_4 treatment	annealing	initial coating	HNO_3–H_2SO_4 treatment	annealing
Deposition temperture, ºC	2000	–	–	2000	–	–	1500	–	–
Hydrocarbon concentration vol %	$5CH_4$	–	–	$20CH_4$	–	–	$30C_3H_6$	–	–
d_{002}, Å	3.445	4.461	3.453* 3.986**	3.45	3.456	3.4613* 3.986**	3.562	3.562	3.562
XRAC	1.539	1.787	2.16	1.382	1.162	1.69	1.206	1.206	1.206
L_a, Å	180	350	600	130	250	480	50	50	50
L_c, Å	200	340	340	140	340	250	50	50	40
d_{100}, Å	2.133	2.125	2.127	2.136	2.125	2.127	2.08	2.08	2.08

* Ratio of 1/2 peak intensities = 206/14.

** Ratio of 1/2 peak intensities = 150/22.

The oxidizing mixture H_2SO_4–NHO_3 used in the study is an acceptor intercalating agent. The increased chemical activity of such a mixture will be primarily manifested toward unsaturated surface bonds. It is known that, for carbon-graphite materials in general and pyrocarbon in particular, produced at temperatures lower than 1500°C, the concentration of unsaturated bonds is 1.5–2 orders of magnitude higher than that for materials synthesized, e.g., at 1800–2000°C. Thus, it can be assumed that, collectivizing their "free" electrons with HNO_3, surface carbon atoms of LTP coatings create on the surface a protective layer that hinders penetration of sulfo groups to the material.

Presumably, the graphite structures of LTP coatings, with L_a of about 50 Å and L_c smaller than 80 Å, must exhibit an increased corrosion resistance with respect to the acid mixture H_2SO_4–HNO_3. In this case, the interplanar (interlayer) spacings within a packet of the pyrocarbon coating must be larger than those in graphite, i.e., 3.50 Å and more.

CONCLUSIONS

(1) It was found that high-temperature pyrocarbon coatings synthesized from a CH_4–Ar mixture at pyrolysis temperatures in the range 1300–2000°C are unstable toward the H_2SO_4–HNO_3 oxidizing mixture.

(2) It was shown that low-temperature pyrolytic coatings synthesized from a C_3H_6–Ar mixture at pyrolysis temperatures of 1200–1500°C are stable against the H_2SO_4–HNO_3 mixture, with their resistance increasing at interplanar spacings of 3.50 Å and more.

ACKNOWLEDGMENTS

The author thanks V.N. Kruglov for laborious work in X-ray structural analyses of samples and helpful discussions of the results obtained.

REFERENCES

1. Bedenig, D., *Gasgekuhlte Hochtemperaturreaktoren*, Miinchen: Karl Thiemig, 1972.
2. Bokros, J.C., *Chemistry and Physics of Carbon*, vol. 5, Walker, P.L.Jr., Ed., New York: Marcel Dekker, 1969, pp.1–216.
3. Kidd, R.W., Seifert, D.A., and Browing, M.F., *Emergent Process Meth. Hig., Technol. Ceram. Proc. Conf.,* New York, 1984, pp. 381–396.
4. Hench, L.L., *J. Am. Ceram. Soc*., 1991, vol. 74, no. 7, pp. 1487–1510.
5. Rogriguez-Reninoso, F., *Carbon*, 1998, vol. 36, no. 3, pp. 159–175.
6. Gurin, V.A., Gurin, I.V., Neklyudov, I.M., and Fursov, S.G., *Poroshk. Metall*., 2001, no. 34, pp. 1–7.
7. Kryachek, V.M., *Poroshk. Metall*., 2005, no. 1/2, pp. 8–23.
8. Leshin, V.S., Sorokina, N.E., and Avdeev, V.V., *Neorg. Mater.*, 2003, vol. 39, no. 8, pp. 964–970.
9. Mel'nichenko, V.M., Sladkov, A.M., and Nikulin, Yu.N., *Usp. Khim.,* 1982, vol. 51, no. 2, pp. 736–763.
10. Kurolenkin, E.I. and Virgil'ev, Yu.S., *Khim. Tverd. Tela*, 1980, no. 5, pp. 77–86.
11. Ubbelohde, A. R. and Lewis, F. A., *Graphite and its Crystal Compounds*, Oxford: Clarendon, 1960.
12. Fedorov, V.B., Shorshorov, M.Kh., and Khakimova, D.K., *Uglerod i ego vzaimodeistvie s metallami* (Carbon and Its Interaction with Metals), Moscow: Metallurgiya, 1978.
13. Konkin, A.A., *Uglerodnye i drugie zharostoikie voloknistye materialy* (Carbon-based and Other Heat-Resistant Materials), Moscow: Khimiya, 1974.
14. Gverdtsiteli, I.G., Kalandarashvili, A.G., Chilingarishvili, P.D., and Shartava, Sh.Sh., *Zh. Fiz. Khim*., 1975, vol. 49, no. 1, pp. 217–218.
15. Petrov, G.S., Skoropanov, A.S., and Vecher, A.A., *Usp. Khim*., 1987, vol. 56, no. 8, pp. 1233–1252.
16. Fialkov, A.S., *Uglegrafitovye materialy* (Carbon-Graphite Materials), Moscow: Energiya, 1979.

ISSN 1070-4272, Russian Journal of Applied Chemistry, 2008, Vol. 81, No. 10, pp. 1796–1802. © Pleiades Publishing, Ltd., 2008.
Original Russian Text © V.N. Esenin, L.I. Denisovich, 2008, published in Zhurnal Prikladnoi Khimii, 2008, Vol. 81, No. 10, pp. 1672–1678.

APPLIED ELECTROCHEMISTRY AND CORROSION PROTECTION OF METALS

Contact Corrosion of Metals in Aqueous and Aqueous–Glycolic Solutions

V. N. Esenin and L. I. Denisovich

Nesmeyanov Institute of Organoelement Compounds, Russian Academy of Sciences, Moscow, Russia

Received March 13, 2008

Abstract—Corrosion behavior of aluminum, steel, and cast iron both without contact and in short-circuited aluminum–steel, aluminum–cast iron, steel–cast iron, and aluminum–steel–cast iron systems in fresh water, ethylene glycol, and its aqueous solutions of various compositions containing 5 to 95 vol % fresh water was studied.

DOI: 10.1134/S1070427208100170

Designs of various machines, heat exchangers, and other technological equipment include numerous joints of articles made of metals with different electrode potentials and other electrochemical properties. Under the action of the ambient and in the absence of insulation, these joints can work as galvanic cells, which can lead to enhanced "contact" or bimetallic corrosion [1–3] of one of the metals. The main construction metals in modern liquid cooling systems and, in particular, internal combustion engines and various heat-exchange apparatus are steel, cast iron, and aluminum [4], with the role of heat-carrying agents played by aqueous or aqueous-organic formulations [5]. Despite that the problem has long been known and an ample research work has been conducted, the choice and improvement of corrosion inhibitor formulations for purely aqueous and aqueous-organic heat carrying agents remain topical because of the permanently growing integral volume of the problem and increasingly stringent requirements to the quality and, primarily, reliability of the equipment. In this context, a systematic study of the contact corrosion of the metals mentioned above in purely aqueous and agueous–glycolic media was undertaken.

Ethylene glycol (EG) and agueous–glycolic solutions were chosen as organic solvents because EG-based solutions with low content of water are used in Extreme North regions as heat-carrying agents. Also widely applied at present are fire-resistant hydraulic liquids of the HFC class according to the classification by the International Standardization Organization (ISO). These liquids contain, in addition to water (30–50%), a di- or triatomic alcohol (ethylene glycol, most frequently) [6, 7]. It should also be mentioned that EG is frequently transported in the form of 95% aqueous solutions in winter [4], and in regions with warm and moderate climate, solutions of various compositions, with high content of water in EG, are used as heat-carrying agents.

Also important is the theoretical aspect of the study, because the unsystematic nature of hinders the behavior of electrochemically different metals in aqueous-organic media of various compositions research into fundamental understanding of the specific features of the contact corrosion of metals in aqueous-organic media [8].

The aim of the present study was to elucidate the role of the organic component in the corrosion processes under consideration.

EXPERIMENTAL

Planar samples (50 × 25 × 3 mm) of St.3 steel [GOST (State Standard) 380], cast iron GH-190 [VAZ (Volga Automobile Plant) Standard 52205], and aluminum alloy AK6M2 (GOST 1583) were preliminarily polished and degreased. Water from river basins of European Russia was modeled by dissolving 148 mg dm^{-3} of anhydrous sodium sulfate, 165 mg dm^{-3} of sodium chloride, and 138 mg dm^{-3} of sodium bicarbonate in distilled water. The temperature of experiments was 20 ± 2°C.

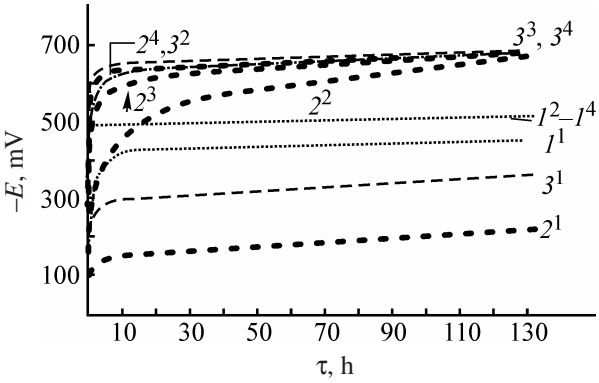


Fig. 1. Metal potentials E in the absence of contact vs. the time τ of testing in aqueous ethylene glycol solutions of various compositions (*1–3*) n. Metal: (*1*) aluminum, (*2*) steel, and (*3*) cast iron. H_2O content n (%): (*1*) 5, (*2*) 30, (*3*) 70, and (*4*) 100.

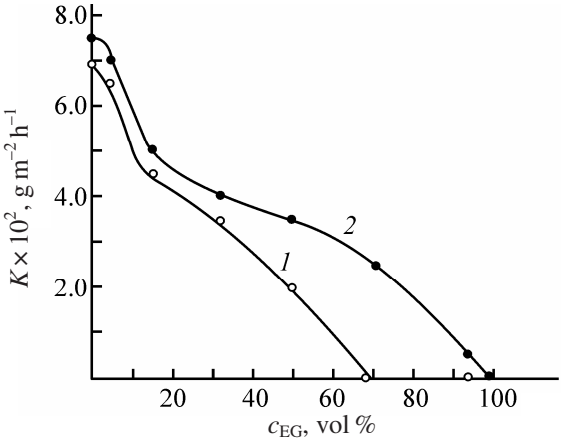


Fig. 2. Corrosion rate K of (*1*) steel and (*2*) cast iron in the absence of contact vs. the composition of aqueous ethylene glycol solutions. (c_{EG}) EG content; the same for Figs. 5–7.

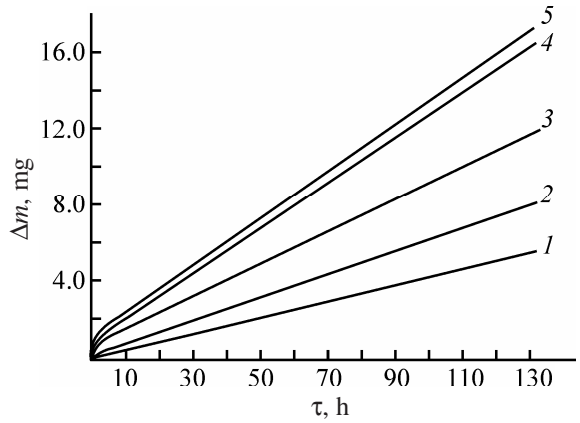


Fig. 3. Corrosion loss Δm by steel in the absence of contact vs. the time τ of testing in aqueous ethylene glycol solutions. H_2O content (%): (*1*) 50, (*2*) 70, (*3*) 85, (*4*) 95, and (*5*) 100.

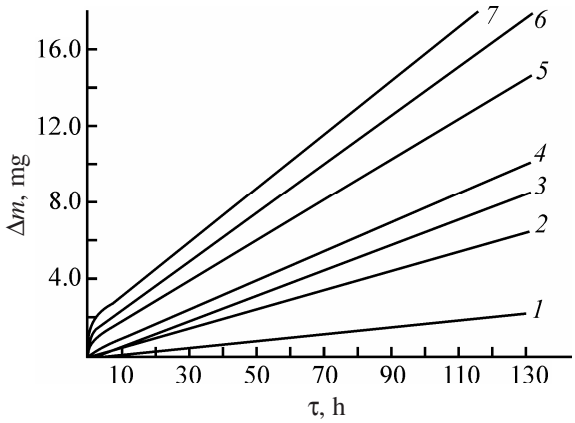


Fig. 4. Corrosion loss Δm by cast iron in the absence of contact vs. the time τ of testing in aqueous ethylene glycol solutions. H_2O content (%): (*1*) 5, (*2*) 30, (*3*) 50, (*4*) 70, (*5*) 85, (*6*) 95, and (*7*) 100.

The corrosion rate was evaluated by a change in the sample mass. The variation of the electrode potentials in the course of tests was monitored using a Shch-1413 high-input-resistance digital voltmeter relative to a silver chloride reference electrode. The electrical contact between metal plates was provided by an external low-resistance conductor. The distance between the electrodes in measurement of the electrode potentials of metals was 20–30 mm, because it has been shown previously [3] that the distance within this range has no effect on the characteristics under study.

In the absence of contact between the metals in purely aqueous and agueous–glycolic solutions, the potential of aluminum remains nearly unchanged in the course of time, and those of steel and cast iron shift to the negative region (Fig. 1), which is apparently due to gradual dissolution of these metals. This shift is the faster, the higher the water content of a solution. In the conditionally anhydrous ethylene glycol[1] and in agueous–glycolic solutions with a water content of up to 30 vol %, the mass of steel samples remained unchanged. Upon further dilution of the solutions studied, a rise in the steel dissolution rate was observed: it steadily increased with the water content and reached the maximum value on passing to the aqueous medium (Fig. 2).

In contrast to steel, cast iron starts to be corroded even upon minor additions of water (<5 vol %). However, on passing to more dilute EG solutions, the corrosion rates of cast iron and steel becomes somewhat closer (Fig. 2). According to mass change data for agueous–glycolic solutions containing EG in amounts of 50 vol % and more, the corrosion rates of steel and cast iron are constant (Figs. 3, 4). At higher water con-

[1] Water content of superior-quality EG should not exceed 0.1 wt % according to GOST 19 710.

Table 1. Initial (V_{in}) and steady-state (V_{st}) corrosion rates of steel and cast iron in purely aqueous and agueous–glycolic solutions of various compositions

Metal	Corrosion rate, g m^{-2} h^{-1}, at indicated H_2O content, vol %							
	70		85		95		100	
	V_{in}	V_{st}	V_{in}	V_{st}	V_{in}	V_{st}	V_{in}	V_{st}
Steel	0.055	0.032	0.090	0.045	0.130	0.063	0.167	0.068
Cast iron	0.070	0.041	0.100	0.051	0.135	0.064	0.185	0.074

centrations, these rates are at a maximum in the initial stage ($\tau \approx 1$–2 h), which corresponds to the also more pronounced change in the potentials of these metals (Fig. 1), and then, the corrosion rates decrease and reach the limiting value (Table 1).

By contrast, a slight increase in mass is observed for aluminum at any water : EG ratio. No traces of pitting were observed in EG and its solution containing 5% water. However, sites of local dissolution of aluminum appear as the content of water increases.

The dependence of the steel corrosion rate on the composition of the mixtures under study for the aluminum–steel and steel–cast iron pairs and for the contact polymetallic system aluminum–steel–cast iron is described by a curve similar to that obtained for individual steel samples (Fig. 5). In all the electrochemical systems studied, steel is not dissolved at water contents lower than 30%.

The rate of steel dissolution in the steel–cast iron pair decreases in a similar way, compared with the individual sample, because of the cathodic polarization of steel by cast iron and increases on passing from the contact polymetallic system aluminum–steel–cast iron to the aluminum–steel pair because of the anodic polarization by aluminum, which is not hindered in this case by the cathodic polarization by cast iron.

A more complicated situation is observed in analysis of the corrosion behavior of cast iron (Fig. 6). Minor additions of water (≤5 vol %) do not cause corrosion of cast iron in aluminum–cast iron and aluminum–steel–cast iron contact systems, but accelerate the dissolution of cast iron in the steel–cast iron pair.

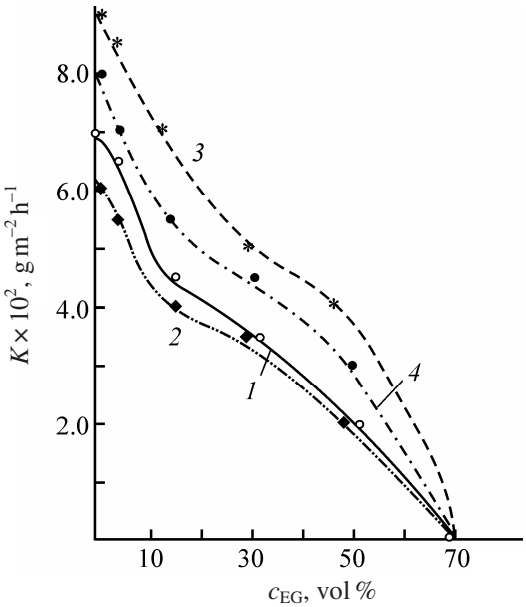


Fig. 5. Corrosion rate K of steel in the absence of contact vs. the composition of aqueous ethylene glycol solutions in various contact pairs. (*1*) Steel (without contact), (*2*) steel–cast iron, (*3*) aluminum–steel, and (*4*) polymetallic system aluminum–steel–cast iron.

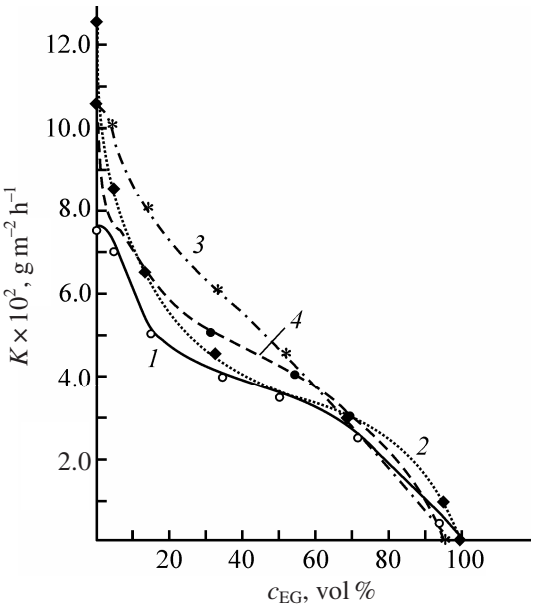


Fig. 6. Corrosion rate K of cast iron in the absence of contact vs. the composition of aqueous ethylene glycol solutions in various contact pairs. (*1*) Cast iron (without contact), (*2*) steel–cast iron, (*3*) aluminum–cast iron, and (*4*) polymetallic system aluminum–steel–cast iron.

Cast iron exhibits such a behavior because it is under cathodic protection by aluminum in concentrated EG solutions, and, in its contact with steel in the absence of aluminum, its dissolution is strongly promoted by the considerable anodic polarization by steel [9]. As the content of water increases, the corrosion rate of cast iron rapidly grows in all the contact systems studied and reaches the maximum value in the purely aqueous electrolyte. It should, however, be noted that an increase in the EG concentration from 30 to 70 vol % affects only slightly the dissolution rate of cast iron in the steel–cast iron pair (Fig. 6, curve *2*). By comparing the corrosion rates for the metals in the contact systems (K_{cont}) and for individual samples (K_{ind}), it is possible to evaluate the extent to which these contacts are hazardous by the acceleration coefficient $K_{acc} = K_{cont}/K_{ind}$ for different compositions of agueous–glycolic solutions. It can be seen in Fig. 7a that the corrosion hazard to steel in the aluminum–steel pair and in the contact polymetallic system aluminum–steel–cast iron increases with the content of EG; however, steel is not corroded in concentrated EG solutions containing 70 vol % and more [9]. The contact with cast iron is not hazardous to steel in the whole range of EG concentrations. By contrast, the acceleration coefficient for the aluminum–steel–cast iron system decreases as the EG concentration increases (Fig. 7b) and becomes zero at EG : H_2O = 95 : 5. The contact with steel is the most hazardous to cast steel in an aqueous solution: K_{acc} = 1.65. As the content of water is lowered to 70%, the acceleration coefficient decreases, passes through a minimum (K_{acc} = 1), and then again increases to reach a value of 1.4 at an EG content of 95%. In the directly opposite way varies the acceleration coefficient in the case of corrosion of cast iron in the aluminum–cast iron pair (Fig. 7b). The dependence has a maximum at an EG content of 15% and then K_{acc} steadily decreases as the EG concentration becomes higher.

The considerable difference in the corrosion behavior of cast iron from that of steel is probably due to its specific "raphitizing" selective corrosion, during which graphite inclusions uncovered upon ferrite dissolution form an increasingly developed system of microcathodes and, accordingly, accelerate the dissolution of the graphite phase to an increasing extent [9].

The high dissolution rates of steel and cast iron in solutions with high water content (Table 1) can be attributed to their surface state and its change on passing

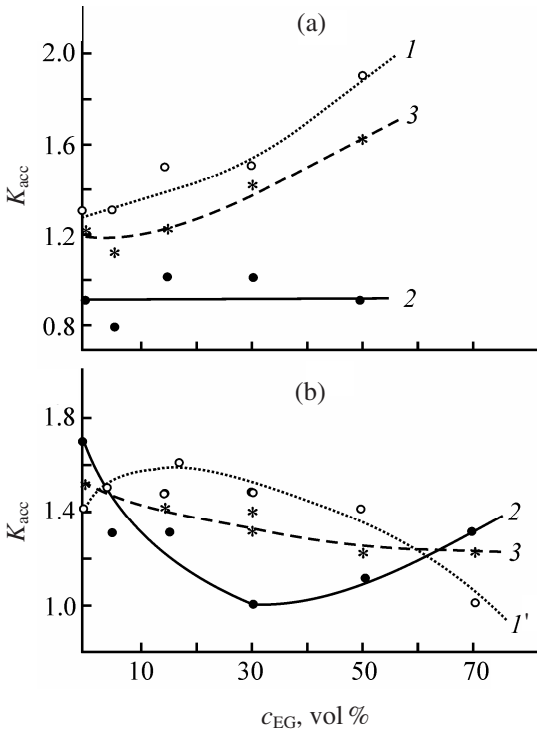


Fig. 7. Acceleration coefficient K_{acc} for (a) steel and (b) cast iron vs. the composition of aqueous ethylene glycol solutions in various contact pairs. (*1*) Steel–aluminum, (*1'*) cast iron–aluminum, (*2*) steel–cast iron, and (*3*) contact system aluminum–steel–cast iron.

from air into solution. It is known that the surface of iron, low-alloyed steels, and cast irons is covered by a thin protective film with an average thickness of 1–4 nm [10–12]. Within this "thickness," the counter gradients of the oxygen and iron concentrations are such that it is possible to state, with a certain degree of conditionality, that the composition and structure of the film pass from, approximately, Fe_2O_3 to Fe_3O_4, and further to FeO on their way to the unoxidized metal [13, 14]. The microheterogeneity of the intrinsic structure of all the three materials under study are of no independent interest in the given case. According to the preferable modern terminology, all of them belong to "mixed electrodes" in the wetted state.

Thus, in corrosion of steel in aqueous solutions, the anodic products (Fe^{3+} ions interact with hydroxide anions formed on the cathodic areas, with the subsequent oxidation of the soluble iron(II) hydroxide into the insoluble iron(III) hydroxide:

$$Fe^{2+} + 2OH^- \rightarrow Fe(OH)_2,$$

$$4Fe(OH)_2 + O_2 + 2H_2O \rightarrow 4Fe(OH)_3.$$

The formation of the insoluble $Fe(OH)_3$ does not hinder the electrochemical corrosion because rust is formed in the solution bulk, rather than on the anodic parts of the surface.

The initial corrosion rates of steel and cast iron in water and dilute EG solutions substantially exceed the steady-state values (by approximately a factor of 2.5 for water). This can be attributed to the adsorption properties of water. The primary interaction of water (having electron-donor properties) with coordination-unsaturated iron atoms yields surface complexes of the donor–acceptor type. For example, water molecules are involved in the anodic process of formation of hydrated iron ions and their transfer into solution, and the important part of this process is the donor–acceptor interaction of water with surface atoms of iron [15].

In the corrosion theory, water is commonly regarded as a reagent composed of separate molecules whose concentration in water and aqueous solutions is high and cannot control corrosion processes in metals, except corrosion under very thin films of purely aqueous electrolytes [16]. Meanwhile, according to the results of [17], liquid water is a structured system that can be regarded as an equilibrium mixture of associates and monomeric water molecules. At the same time, the interaction of water molecules with iron oxide present on the metal surface is considerably stronger than that between the molecules in their own phase. Water as an amphoteric oxide is similar to metal oxides and tends either to form compounds (hydroxides) with these oxides or to be incorporated into their crystal lattices [18].

The formation of an adsorption film of water on the surface of a solid yields dense multilayered associative structures. Owing to the formation of a network of hydrogen bonds, the structuring of water and formation of associates changes the physical properties of water [19]. This is characteristic to the greatest extent of its firmly adsorbed films. Thus, water can affect the corrosion of iron in aqueous solutions in two ways: free water molecules are a corrosion-active agent, whereas dense multilayered structures of water and, in particular, its adsorbed films can hinder the corrosion process to a certain extent via binding of separate molecules into associates and formation of a three-layer aqua-oxide-metallic surface phase [18].

The considerable decrease in the corrosion rates of steel and cast iron in aqueous ethylene glycol solutions (compared with water) is probably due to a change in the structure of the electric double layer upon adsorption of ethylene glycol. Because of the planar position on the electrode surface, ethylene glycol molecules can form a dense screening film [20], which presumably can hinder the corrosion process [21, 22]. The outer layer of iron and aluminum oxides can become thicker via incorporation of ethylene glycol molecules. As a result, a denser layer is formed and, together with the planar-oriented adsorbed layers of ethylene glycol, effectively hinders deterioration of the passive state of a metal [23].

A uniform corrosion of aluminum was observed in all of the contact systems under study in water, as well as for the aluminum–steel pair at a water concentration of 30% and for the aluminum–steel–cast iron contact polymetallic system in an agueous–glycolic solution containing 5% water. Owing to the presence of an oxide film on its surface, aluminum acted in water as a cathode with respect to both ferrous metals, with the result that the continuity of the oxide film was disturbed and aluminum dissolved via chemical interaction with water. Such a behavior of aluminum in water fundamentally differs from that in concentrated aqueous solutions of ethylene glycol, in which, in the end, aluminum undergoes anodic dissolution [9].

In anodic polarization of aluminum, its dissolution is accompanied by oxidation by water present in solution. In a solution containing 30% water, the dissolution rate somewhat exceeds the oxidation rate, whereas in a solution with 5% water, the rates of both processes are close, probably because of the high EG content, and the sensitivity of the analytical balance is insufficient for determining their difference.

The dissolution of aluminum in the steel–aluminum–cast iron contact system can probably be attributed to the considerable anodic polarization of aluminum by both steel and cast iron (Fig. 1). However, no traces of pitting corrosion were observed in any of the contact systems in the whole range of the EG concentrations used. In those cases when an increase in the mass of aluminum was observed, the nearly the same gains in mass in the aqueous electrolyte and aqueous EG solutions can probably be attributed to a low concentration of water, which is only sufficient for a discontinuous (permeable) film of a hydrated aluminum oxide $Al_2O_3 \cdot nH_2O$ ($n \geq 0$) [20, 21].

Under equilibrium conditions, a noticeable amount of coordination-bound hydroxo groups (OH^-) appears in the structure of a low-hydrated oxide. As the content of water increases, aqua groups (OH_2^-) also appear. Such an oxo-hydroxo phase can be regarded as the main

component of the passivating layer, which is in contact with both the metal and a solution under real conditions. The total thickness and the structure of the cover film are determined by the relative rates of the reaction of the metal with proton-containing fragments of water incorporated into the film and the disintegration of the film at the interface [24]. In anhydrous ethylene glycol, no changes in the mass of aluminum were observed under similar conditions. The steady-state corrosion rates of aluminum in purely aqueous and agueous–glycolic solutions containing 5 and 30% water are listed in Table 2.

Comparison of the results describing the corrosion behavior of the metals under study in purely aqueous [29] and agueous–glycolic solutions can reveal the effect of their composition on the corrosion processes. On passing from purely aqueous electrolytes to aqueous EG solutions with EG content of 5 to 95%, the corrosion rates of steel and cast iron decrease in all of the contact systems studied. It can be seen from Figs. 2, 5, and 6 that the corrosion rates of the metals steadily decrease as the EG content of an agueous–glycolic solution increases. In addition, steel does not undergo uniform corrosion in steel–aluminum and steel–cast iron contact pair or in the steel–aluminum–cast iron ternary system at a content of water in ethylene glycol lower than 30% (Figs. 2, 5). In water, aluminum acts as a cathode with respect to both ferrous metals, which led to reduction of its protective oxide film and subsequent dissolution via chemical interaction of aluminum with water. Such a behavior of aluminum in water differs from that in aqueous solutions containing 5 to 50% EG, in which it also serves as a cathode with respect to steel and cast iron and does not undergo uniform corrosion.

A somewhat different behavior was observed for aluminum in pair with steel in 50% EG, in which aluminum underwent a short-time anodic dissolution. It was found that, at 5% water in EG, aluminum behaves in all of the systems studied as an anode with respect to steel and cast iron, but undergoes anodic dissolution only in the aluminum–steel–cast iron contact system. In EG solutions containing 30% water, aluminum also anodically dissolves when in contact with steel.

As already noted, the increase in the mass of aluminum is probably due in all other cases to formation of surface films composed of hydrated aluminum oxide and iron that passed to the metal surface from solution via cathodic reduction of Fe^{2+} cations by aluminum.

Table 2. Steady-state corrosion rate V_{st} of aluminum in purely aqueous and agueous–glycolic solutions of various compositions

Contact system	H_2O content, vol %	Corrosion rate g m^{-2} h^{-1}
No contact	5	0.0
	30	0.0
	100	0.0
Aluminum–steel–cast iron	5	0.007
	30	0.0
	100	0.013
Aluminum–steel	5	0.0
	30	0.003
	100	0.012
Aluminum–cast iron	5	0.0
	30	0.0
	100	0.010

The possible explanation for the increase in the corrosion rates of steel and cast iron with the content of water in agueous–glycolic solutions is that, instead of the dense outer layers of iron oxides formed via incorporation of EG molecules [23], three-layer aqua-oxide-metallic surface phases [18, 25] start to predominate on the surface of steel and cast iron. This favors disruption of the passive state of the metals. In addition, the effect of free water molecules that are not bound yet into dense multilayered structures and, therefore, are corrosion-active agents, starts to be manifested in dilute EG solutions (5–30%) in early stages of metal corrosion. It is the interaction of monomeric water molecules with the iron surface that predetermines the high initial corrosion rate of the metals, compared with the steady-state values in these solutions and water (Fig. 3, curves *2–5*; Fig. 4, curves *4–7*).

CONCLUSIONS

(1) On passing from purely aqueous electrolytes to aqueous solutions containing 5 to 95% ethylene glycol, the corrosion rates of steel and cast iron decrease, and at a <30% content of water in ethylene glycol, steel does not undergo uniform corrosion in any of the contact systems studied.

(2) The most corrosion-hazardous contact systems in the solutions studied are the following: for steel,

aluminum–steel pair in a 50% ethylene glycol solution; for cast iron, aluminum–cast iron and steel–cast iron pairs in dilute aqueous solutions of ethylene glycol (5%); and for aluminum, all the systems under study in aqueous solutions.

(3) In all of the systems studied, aluminum behaves as a cathode in aqueous and dilute solutions of ethylene glycol, and as an anode, in solutions with high content of ethylene glycol.

(4) The difference in the behavior of the metals being tested in purely aqueous and agueous–glycolic solutions of various compositions (5–95% H_2O) is due both to the specific surface state of iron in air and to structural changes in the electric double layer upon adsorption of ethylene glycol whose molecules can form a dense screening film owing to their planar position on the electrode surface.

REFERENCES

1. Rozenfel'd, I.L., *Korroziya i zashchita ot korrozii (lokal'nye korrozionnye protsessy)* [Corrosion and Corrosion Protection (Local Corrosion Processes)], Moscow: Metallurgiya, 1970.
2. Batrakov, V.P. and Polupanov, V.L., *Elektrokhimiya*, 1975, vol. 11, no. 6, pp. 919–923.
3. Belous, V.Ya., Gurvich, L.Ya., and Zhirnov, A.D., *Zashch. Met.,* 1998, vol. 34, no. 3, pp. 266–272.
4. *GOST* (State Standard) *28 084–89*, *Low-Freezing Cooling Liquids: General Technical Specifications*, Moscow: Izd. Standartov, 1989.
5. *Korroziya pod deistviem teplonositelei, khladoa-gentov i rabochikh tel: Spravochnoe izdanie* (Corrosion under the Action of Heat-Carrying and Cooling Agents and Working Media: Reference Book), Sukhotin, A.M., Ed., Leningrad: Khimiya, 1988.
6. Sukhotin, A.M., Kazankina, A.F., and Zaretskaya, L.V., *Khim. Tekhnol. Topl. Masel*, 1977, no. 7, pp. 55–58.
7. RF Patent 2 083 646.
8. RF Patent 2 241 784.
9. Esenin, V.N. and Denisovich, L.I., *Zashch. Met*., 2007, vol. 43, no. 4, pp. 390–395.
10. Cheetham, A., Feuder, B., and Taylor, R., *J. Phys. Chem*., 1971, vol. 5, pp. 2160–2165.
11. Chen, C. and Cahan, B., *J. Electrochem. Soc*., 1982, vol. 129, no. 1, pp. 17–22.
12. Brass, A., Nelot, Z., and Aucouturier, M., *Corrosion Sci*., 1984, vol. 24, no. 1, pp. 49–56.
13. Thomas, T., Tricker, M., and Bottom, A., *J. Chem. Soc*., *Faraday. Trans. II*, 1975, vol. 71, no. 10, pp. 1708–1711.
14. Volenik, K., Cirak, T., and Seberini, M., *Br. Corros. J*., 1975, vol. 10, no. 4, pp. 196–201.
15. Gladkikh, Yu.P., Zavrazhina, V.I., Mikhailovskii, Yu.N., and Fes'kova, T.Yu., *Zashch. Met*., 1998, vol. 34, no. 3, pp. 329–331.
16. Tomashov, N.D., *Teoriya korrozii i zashchity metallov* (Theory of Corrosion and Corrosion Protection of Metals), Moscow: Akad. Nauk SSSR, 1960.
17. Sinyukov, V.V., *Voda izvestnaya i neizvestnaya* (Water Known and Unknown), Moscow: Znanie, 1987.
18. Novakovskii, V.M., *Zashch. Met*., 1994, vol. 30, no. 2, pp. 117–129.
19. Deryagin, B.V. and Churaev, N.V., *Voda v dispersnykh sistemakh* (Water in Dispersed Systems), Moscow: Khimiya, 1989, p. 6.
20. Dzhaparidze, Dzh.I., *Elektrokhimiya*, 1977, vol. 13, no. 5, pp. 668–671.
21. Kuznetsov, Yu.I., Oleinik, S.V., and Rozenfel'd, I.L., *Elektrokhimiya*, 1981, vol. 17, pp. 942–945.
22. Veselyi, S.S. and Kuznetsov, Yu.I., *Zashch. Met*., 1994, vol. 30, pp. 479–485.
23. Kuznetsov, Yu.I., Veselyi, S.S., and Oleinik, S.V., *Zashch. Met*., 1992, vol. 28, no. 1, pp. 88–95.
24. Korshunov, V.N. and Sviridova, L.I., *Elektrokhimiya*, 1991, vol. 27, no. 10, pp. 1226–1230.

ISSN 1070-4272, Russian Journal of Applied Chemistry, 2008, Vol. 81, No. 10, pp. 1803–1807. © Pleiades Publishing, Ltd., 2008.
Original Russian Text © T.G. Kyazimova, E.G. Mamedbeili, A.V. Nagiev, E.I. Suleimanova, Kh.S. Khalilov, 2008, published in Zhurnal Prikladnoi Khimii, 2008, Vol. 81, No. 10, pp. 1679–1683 .

ORGANIC SYNTHESIS AND INDUSTRIAL ORGANIC CHEMISTRY

Synthesis of Bicyclo[2.2.1]Hept-5-Enyl Methyl Esters of Haloacetic Acids

T. G. Kyazimova, E. G. Mamedbeili, A. V. Nagiev, E. I. Suleimanova, and Kh. S. Khalilov

Institute of Chemical Problems, National Academy of Sciences of Azerbaijan, Baku, Azerbaijan

Baku Institute of Petrochemical Processes, National Academy of Sciences of Azerbaijan, Baku, Azerbaijan

Received January 22, 2008

Abstract—Synthesis of norbornenyl methyl esters of a number of haloacetic acids via [4+2] cycloaddition of cyclopentadiene to allyl esters of these acids was examined. The yield and isomer composition of the synthesized compounds were examined in relation to the reaction conditions, and the best conditions for their preparation were found.

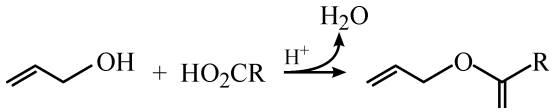
DOI: 10.1134/S1070427208100182

The structure of bicyclo[2.2.1]heptane, or norbornane, is a basis of many important natural compounds like borneal, camphor, etc. [1]. Similarly to norbornane and adamantane moieties, the norbornene moiety is a part of amines, many of which are medical preparations [2].

Significant interest in norbornene compounds also stems from their availability increased due to improvement of diene synthesis techniques. In most cases, this reaction does not involve side processes, which makes it possible to reveal factors governing the rate, direction, and equilibrium of the process with and without catalysts [3].

Halogenated functionally substituted norbornenes are good synthons for preparation of important intermediate halogenated sterically hindered phenols [4–8]. These compounds are also suitable as stanting materials for preparation of α-diketones and γ-lactones [9–12].

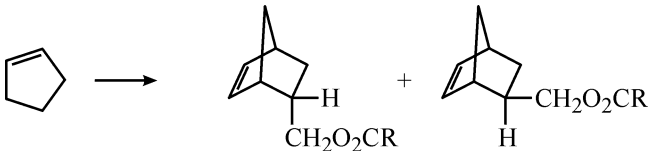
This study continues a series dedicated to synthesis of halogen-containing esters of norbornene compounds [13–16]. Here, we prepared bicyclo[2.2.1]-hept-5-enylmethyl esters of a number of haloacetic acids by the reaction of cyclopentadiene (CPD) with allyl esters of haloacetic acids **11–19**. The allyl esters **10–18** were synthesized by the well-known technique of esterification of corresponding acids **1–9** with allyl alcohol



R = CH_2Cl (**1**, **10**); $CHCl_2$ (**2**, **11**); CCl_3 (**3**, **12**); CH_2Br (**4**, **13**); $CHBr_2$ (**5**, **14**); CBr_3 (**6**, **15**); CF_3 (**7**, **16**); CH_3–CHCl (**8**, **17**); CH_2Cl–CH_2 (**9**, **18**).

Table 1 lists the physicochemical parameters of the starting allyl esters (**10–18**).

The target products (**19–27**) were prepared by [4+2] cycloaddition of CPD to allyl esters of haloacetic acids (**10–18**) by the scheme



R = CH_2Cl (**19**), $CHCl_2$ (**20**), CCl_3 (**21**), CH_2Br (**22**), $CHBr_2$ (**23**), CBr_3 (**24**), CF_3 (**25**), CH_3–CHCl (**26**), CH_2Cl–CH_2 (**27**).

The reaction was carried out at temperatures within 100–180°C in the course of 6–10 h at the diene-to-dienophile molar ratio of 1 : (1–4).

Table 1. Constants of allyl esters of haloacetic acids **10–18**

Compound	Ester	bp, °C (*P*, mm Hg)	n_D^{20}	d_D^{20}	Yield, %
10	Allyl monochloroacetate	43–44 (5)	1.4460	1.1469	85
11	Allyl dichloroacetate	63–64 (10)	1.4544	1.3496	70
12	Allyl trichloroacetate	68–69 (10)	1.4632	1.4648	75
13	Allyl monobromoacetate	73 (10)	1.4729	1.4329	65
14	Allyl dibromoacetate	66–67 (10)	1.4704	1.4500	60
15	Allyl tribromoacetate	80–82 (1)	1.5470	2.0061	45
16	Allyl trifluoroacetate	78–79	1.3364	1.1765	60
17	Allyl α-chloropropionate	81–82 (40)	1.4468	1.0868	75
18	Allyl β-chloropropionate	80–81 (40)	1.4385	1.0806	80

Table 2. Properties of bicyclo[2.2.1]hept-5-enyl methyl esters of haloacetic acids **19–27**

Compound	bp, °C (*P*, mm Hg)	n_D^{20}	d_D^{20}	Found, %			Formula	Calculated, %		
				C	H	halogen		C	H	halogen
19	91 (1)	1.4930	1.1723	59.67	6.24	17.43	$C_{10}H_{13}O_2Cl$	59.95	6.48	17.71
20	111 (2)	1.5004	1.2492	50.92	5.02	29.86	$C_{10}H_{12}O_2Cl_2$	51.06	5.11	30.21
21	107–108 (1)	1.5029	1.3243	44.14	3.88	39.08	$C_{10}H_{11}O_2Cl_3$	44.53	4.08	39.52
22	87–89 (1)	1.5077	1.3443	48.65	5.15	32.24	$C_{10}H_{13}O_2Br$	48.98	5.31	32.65
23	107–108 (2)	1.5105	1.5871	36.23	3.63	49.51	$C_{10}H_{12}O_2Br_2$	37.03	3.07	49.07
24	125–128 (3)	1.5531	1.8910	29.53	2.52	59.12	$C_{10}H_{11}O_2Br_3$	29.77	2.72	59.55
25	61–62 (10)	1.4205	1.2249	54.17	4.86	25.68	$C_{10}H_{11}O_2F_3$	54.55	5.10	25.91
26	90–91 (1)	1.4821	1.2575	61.05	6.52	14.26	$C_{11}H_{15}O_2Cl$	61.54	6.99	16.55
27	89–90 (1)	1.4852	1.2614	61.14	6.73	14.7	$C_{11}H_{15}O_2Cl$	61.54	6.99	16.55

Table 2 lists the physicochemical characteristics of the compounds synthesized.

The yield and isomer composition of adducts **19–27** were examined in relation to various reaction parameters (temperature, time, addend ratio). The results are presented in Table 3.

It is seen from Table 3 that, as the temperature increases from 100 to 160°C, the yield of adduct **19** grows from 7.4 to 56.65%. Further increase in temperature (to 180°C) causes a decrease in the yield. A possible reason is formation of a bis-adduct based on compound **19**.

The best conditions for formation of adduct **19** are as follows: temperature 140°C, reaction time 6 h, and diene : dienophile ratio 1:1.5. With increasing temperature, the *endo* selectivity of the reaction of synthesis of adduct **19** decreases from 85 to 61%, which can be associated with conversion of the *endo* isomer to a thermodynamically more advantageous *exo* isomer at a high temperature.

Under similar optimal conditions, we carried out diene condensation of CPD with other allyl esters of haloacetic acids. The yield of the adducts varied within 50.92–87.6%; the highest yield was observed for allyl tri-

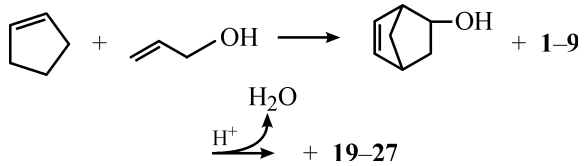
Table 3. Yield and isomer composition of esters **19–27** in relation to the conditions of the reactions of CPD with allyl esters of haloacetic acids **10–18**

Temperature	Dienophile	Diene : dienophile molar ratio	Time, h	Yield of **19–27**	Isomer ratio, %	
					endo	*exo*
100	**10**	1 : 1.5	6	7.14	95	5
120	**10**	1 : 1.5	6	19.17	85	15
140	**10**	1 : 1.5	6	55.35	79	21
160	**10**	1 : 1.5	6	56.65	71	29
180	**10**	1 : 1.5	6	52.21	61	39
140	**10**	1 : 1	6	51.41	80	20
	10	1 : 2	6	55.75	82	18
	10	1 : 3	6	56.11	81.5	18.5
	10	1 : 4	6	56.91	82	18
	10	1 : 1.5	6	55.89	78	22
	10	1 : 1.5	10	56.35	78	22
	11	1 : 1.5	6	50.92	83	17
	12	1 : 1.5	6	44.14	85	15
	13	1 : 1.5	6	48.55	83	16
	14	1 : 1.5	6	39.23	85	15
	15	1 : 1.5	6	29.67	87	13
	16	1 : 1.5	6	87.6	82	18
	17	1 : 1.5	6	61.05	78	22
	18	1 : 1.5	6	61.14	78	22

fluoroacetate **16** (87.6%), and the lowest, for allyl ester of tribromoacetic acid **15** (29.63%).

Comparative examination showed that the highest *endo* selectivity was observed in the reaction of CPD with allyl ester of tribromoacetic acid **15** (87%).

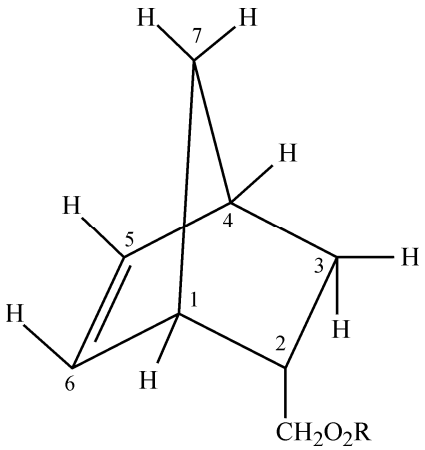
The composition and structure of the synthesized compounds **19–27** were proven by counter synthesis. First, by the technique described in [17] we carried out condensation of CPD with allyl alcohol into 2-hydroxymethylbicyclo[2.2.1]hept-5-ene **28** whose esterification with haloacetic acids by the well-known technique yielded the corresponding esters **19–27**:



All the physicochemical data obtained by both techniques for compounds **19–27** are identical.

The composition and structure of adducts **19–27** were confirmed by IR and ^{1}H NMR spectra. The IR spectra of the bicyclic esters synthesized contain characteristic signals of the C=O-group at 1730–1750 cm^{-1} and of the C–O ester group at 1000–1275 cm^{-1}. The bands of the carbon–chlorine bond are observed for chlorine-containing compounds in low-frequency spectral regions: 750, 760, 780, 760, and 770 cm^{-1} for compounds **19–21**, **7**, and **27**, respectively. The IR spectra of bromine-containing esters **22–24** contain intense bands associated with C–Br vibrations at 650–600 cm^{-1}. The ν_{C-F} band of ester **25** is observed near 1050 cm^{-1}. The absorption bands of the ethylene moiety in the norbornene ring lie at 1570–1555 and 3060–3045 cm^{-1} ($\nu_{C=C}$, ν_{C-H}).

The ^{1}H NMR spectra of esters **19–27** contain signals from protons of the double bond in the norbornene ring (H^5, H^6), manifested at 6–6.25 ppm as a multiplet, and are characterized by spin-spin coupling constants $J_{5,6}$ of 7.0 Hz. The H^3 (2H) protons give multiplet signals at high fields with a chemical shift δ of 0.7–1.2 ppm. The multiplet associated with the H^2 proton is observed at δ of 2.5 ppm and is characterized by the constant of spin-spin coupling with the H^3 proton, $J_{2,3}$ of 9.6 Hz. The H^1 and H^4 protons are chemically equivalent and give multiplet signals at δ of 2.70–2.85 ppm. The methylene protons H^8 (CH_2O group) give multiplet signals at δ of 4.15–3.95 ppm:



The isomer composition of esters **19–27** was determined by gas–liquid chromatography.

EXPERIMENTAL

The IR spectra were recorded on a UR-20 spectrophotometer at 4000–400 cm^{-1} for thin films or KBr pellets. The ^{1}H NMR spectra were measured on a BS-487B Tesla radiospectrometer (working frequency 80 MHz) for solutions in CCl_4, with HMDS as internal standard. The chromatographic analysis, as well as determination of the purity of the compounds synthesized, were carried out on an LKhM-8 MD chromatograph with a thermal-conductivity detector on a 300×0.3 cm column packed with 5% PEGS on Dinokhrom; carrier gas helium; flow rate 40 cm^3 min^{-1}; column temperature 155, and evaporator temperature 240°C.

The initial allyl esters of halogenated acetic acids **10–18** were obtained by a well-known technique via esterification in the presence of 5% H_2SO_4 as the catalyst. Upon completion of the reaction, the reaction mixture was washed with water, dried over $MgSO_4$, and distilled.

Bicyclo[2.2.1]hept-5-enyl methyl monochloroacetate 19. A mixture of 14.17 g (0.15 mole) of allyl monochloroacetate **10** and 6.6 g (0.1 mole) of freshly distilled CPD in the presence of hydroquinone was heated at 140°C for 6 h in a sealed ampule. Vacuum distillation yielded 12.69 g (55.25%) of adduct **19**, bp 95°C (1 mm Hg), n_D^{20} 1.4930, d_D^{20} 1.1723. IR spectrum, ν, cm^{-1}: 1735 (C=O), 1100 (C–O), 750 (C–Cl), 1755 (C=C). Elemental analysis:

Found, %: C 59.67; H 6.24; Cl 17.43.
Calculated, %: C 59.95; H 6.48; Cl 17.71.

2-Hydroxymethylbicyclo[2.2.1]hept-5-ene **28** was prepared by condensation of CPD with allyl alcohol by the technique described in [17]. A counter synthesis of esters **19–27** was carried out by esterficiation of bicyclic alcohol **28** with corresponding carboxylic acids **1–9** by the known technique. All the physicochemical characteristics of esters **19–27** prepared by counter synthesis are identical to the data of the same compounds obtained by condensation of CPD with esters **10–18**.

CONCLUSION

Norbornenyl methyl esters of a number of haloacetic acids were synthesized by [4+2] cycloaddition of cyclopentadiene to allyl esters of these acids. With increasing temperature, the total yield of the adducts tends to grow, and the stereoselectivity, to decrease. The best conditions for preparation of the compounds synthesized were found.

REFERENCES

1. Potapov, V.M., *Stereokhimiya* (Stereochemistry), Moscow: Khimiya, 1988.
2. Kas'yan, L.I., Tarabara, I.N., and Kas'yan, A.O., *Zh. Org. Khim.*, 2002, vol. 38, no. 1, pp. 29–35.
3. Konovalov, A.I. and Kiselev, V.D., *Izv. Ross. Akad. Nauk, Ser. Khim.*, 2003, no. 2, pp. 279–297.
4. Zhao, J., Ma, M., Wang, S., et al., *J. Nat. Prod.*, 2005, vol. 68, no. 3, pp. 691–694.
5. Wang, S., Okada, Y., Shi, H., et al., *J. Nat. Prod.*, 2005, vol. 68, no. 2, pp. 620–622.
6. Xu, N., Fan, X., Yan, X., et al., *Phytochemistry*, 2003, vol. 62, pp. 1221–1224.

7. Qribble, G.W., *J. Chem. Ed.*, 2004, vol. 81, pp. 1441–1449.
8. Khan, E.A. and Chaedhury, S., *Eur. J. Org. Chem.*, 2006, pp. 672–676.
9. Khan, E.A., Prabhudas, B., Dash, J., and Sahu, J., *J. Am. Chem. Soc.*, 2000, vol. 122, pp. 9558–9561.
10. Khan, E.A., Dash, J., Sahu, N., and Sudheer, Ch., *J. Org. Chem.*, 2002, vol. 67, pp. 3783–3789.
11. Yadav, J.S. and Sasmal, P.K., *Tetrahedron*, 1999, vol. 55, pp. 5185–5189.
12. Lapis, A.A. and Kreutz, O.C., *Tetrahedron: Asymmetry*, 2001, vol. 12, pp. 557–561.
13. Mamedov, E.G., *Zh. Prikl. Khim.*, 2004, vol. 77, no. 8, pp. 1331–1335.
14. Mamedov, E.G., *Zh. Prikl. Khim.*, 2005, vol. 78, no. 9, pp. 1377–1380.
15. Mamedov, E.G., *Zh. Org. Khim.*, 2000, vol. 36, no. 12, pp. 1785–1788.
16. Kyazimova, T.G., Zeinalov, S.B., and Mamedov, E.G., *Prots. Neftekhim. Neftepererab.*, 2007, no. 4, pp. 57–61.
17. Alder, K. and Windemuth, E., *Ber.*, 1938, vol. 71, pp. 1939–1943.

ISSN 1070-4272, Russian Journal of Applied Chemistry, 2008, Vol. 81, No. 10, pp. 1808–1812. © Pleiades Publishing, Ltd., 2008.
Original Russian Text © O.V. Platonova, Yu.G. Akhmetshin, A.A. Kossoi, M.Z. Vdovets, B.M. Laskin, A.S. Malin, A.T. Sitdikov, 2008, published in Zhurnal Prikladnoi Khimii, 2008, Vol. 81, No. 10, pp. 1684–1689.

ORGANIC SYNTHESIS AND INDUSTRIAL ORGANIC CHEMISTRY

Kinetic Model of Acylation of Diacetylethylenediamine

O. V. Platonova, Yu. G. Akhmetshin, A. A. Kossoi, M. Z. Vdovets, B. M. Laskin, A. S. Malin, and A. T. Sitdikov

Applied Chemistry, Russian Scientific Center, Federal State Enterprise, St. Petersburg, Russia

New Chemical Technologies, Limited Liability Company, St. Petersburg, Russia

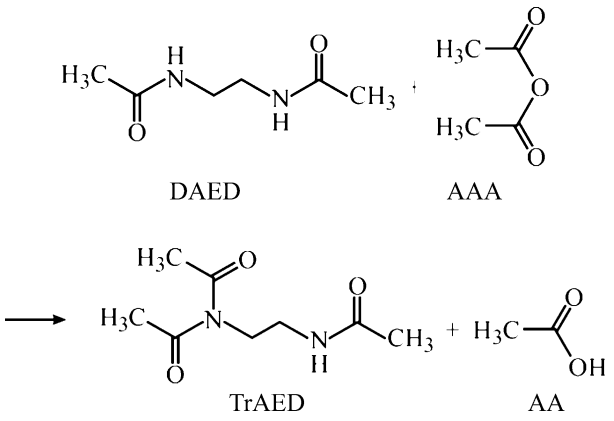
Received May 16, 2008

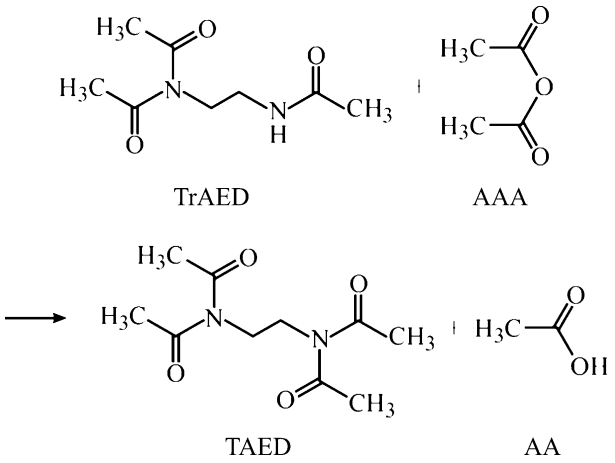
Abstract—Descriptive kinetics of synthesis of tetraacetylethylenediamine by acylation of diacetylethylenediamine with acetic acid anhydride was examined. The apparent rate constants of the process were obtained, and a mathematical model adequately describing the process was constructed.

DOI: 10.1134/S1070427208100194

In recent years, the developmental efforts in detergent chemistry have been mainly focused on a search for, and preparation of new composite systems and additives to provide a highly efficient bleaching and removal of contaminations from fabrics at as low temperatures as possible. Among such additives is tetraacetylethylenediamine (TAED), a low-temperature peroxide bleaching activator [1, 2].

Tetraacetylethylenediamine is a typical representative of the class of polyacylated aliphatic diamines, which is produced by acylation of diacetylethylenediamine (DAED) with acetic acid anhydride (AAA). The procedures for preparation of TAED were described in detail in patents [3–5], the mechanism and kinetics of the process were disregarded. At the same time, it is known that acylation of DAED into TAED involves formation of an intermediate, triacetylethylenediamine (TrAED) [6]:





Hence, for simulating the commercial process of DAED acylation, we examined the macrokinetic relationships. To this end, we carried out a series of kinetic experiments with varied DAED : AAA molar ratio (1 : 6.5; 1 : 8.5; 1 : 17) and temperature (120 and 140°C).

EXPERIMENTAL

To study the formal-kinetic aspects of DAED acylation and TAED deacylation, we used a three-necked temperature-controlled flask equipped with a mechanical stirrer, thermometer, and reflux condenser. The structure of the reaction mass was analyzed by gas–liquid chromatography on a Kristall 2000 chromatograph with a flame-ionization detector and a 30 m × 0.53 mm CPS sil-5CB capillary column in the column-temperature-programming mode (initial temperature

100°C, 5 min; heating to 240°C at a rate of 12 deg min^{-1}; final temperature 240°C, 10 min) with nitrogen as carrier gas.

The necessary amount of AAA (or AA in the case of TAED deacetylation) was placed in the flask at room temperature and heated to the desired temperature, whereupon the calculated amount of DAED (or TAED) was introduced under agitation. The instant when mixing of the reactants was complete was taken as the reaction onset time.

At regular intervals of time (15 or 30 min) during 6 h, the reaction mass was sampled and samples were placed in a cooled solvent (dioxane) used in an amount sufficient for terminating the reaction, and the reaction mass was analyzed by gas–liquid chromatography. Using test mixtures, we showed that no side reactions proceed under the chromatographic conditions. Each sample taken was subjected to at least three replicated measurements.

The derived concentration values were used for plotting the primary kinetic curves and calculating the apparent rate constant of the reaction.

The kinetic data were processed by the regression analysis procedure using Table Curve Windows V1.10 software.

Statistical processing of the measurements results was carried out by the least-squares and regression analysis procedures; the confidence interval (error corridor) was calculated under a homogeneous reproducibility condition [7].

Using the concentration values derived at different molar ratios of the reactants [DAED : AAA = 1 : (6.5–17)] and temperatures (120–140°C), we plotted the primary kinetic dependences $c = f(\tau)$, one of which is shown in Fig. 1.

An analysis of the processed experimental data (Figs. 2, 3) showed that the DAED acylation by acetic acid anhydride can be described by the pseudo-first order reaction model.

As can be seen from Fig. 3, the semilogarithmic anamorphoses are straight lines with breaks. This pattern indirectly evidences that the DAED acylation by acetic acid anhydride includes two stages. The first stage consists in the formation of TrAED, and the second, in the acylation of TrAED to TAED; the rate of the first stage exceeds that of the second stage.

Analysis of the primary experimental curves (Fig. 1) suggests that the stage of acylation of TrAED to

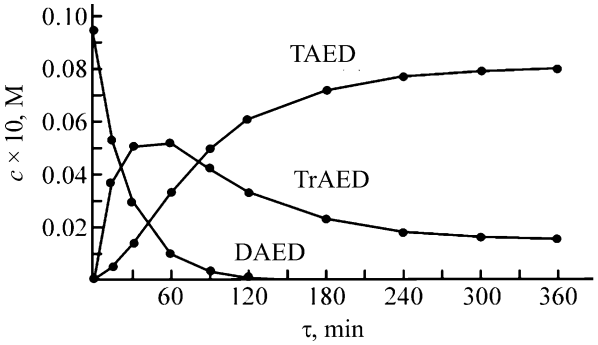


Fig. 1. Primary experimental curves of the DAED acylation by acetic acid anhydride at 140°C and initial molar ratio DAED : AAA = 1 : 8.5. (*c*) Concentration and (τ) time.

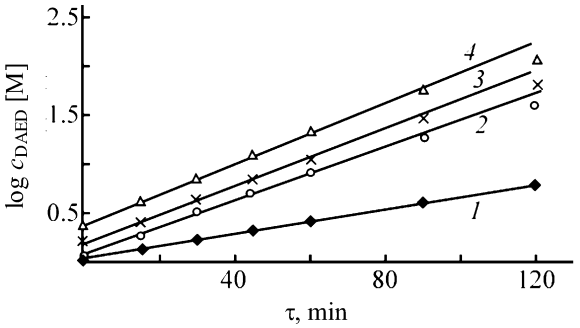


Fig. 2. Semilogarithmic plot of c_{DAED} vs. time τ. Initial molar ratio DAED : AAA, *T*, °C: (*1*) 1 : 8.5, 120; (*2*) 1 : 8.5, 140; (*3*) 1 : 6.5, 140; and (*4*) 1 : 17, 140; the same for Fig. 3.

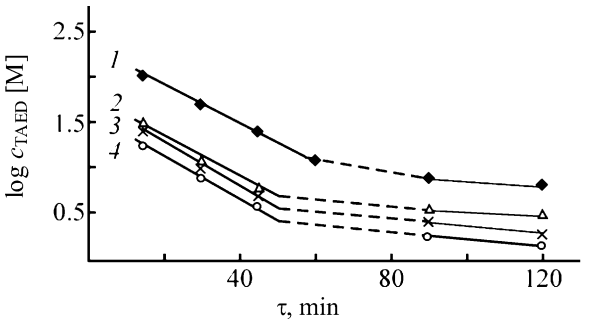


Fig. 3. Semilogarithmic plot of c_{TAED} vs. time τ.

TAED is reversible, and chemical equilibrium is eventually attained in the acylation reaction. Our experiments were carried out under nearly industrial conditions, for which reason we used 97% acetic acid anhydride. In the experiments carried out under a 8.5-fold molar excess of acetic acid anhydride over DAED, the molar ratio of the components of the DAED : AAA : AA reaction system at the initial instant of time was 1 : 8.5 : 0.4 mole, respectively. After the equilibrium was established in the system, the molar ratio of the components of the reaction mixture TrAED : TAED : AAA : AA was 0.2 : 0.8 : 6.7 : 2.2. This can

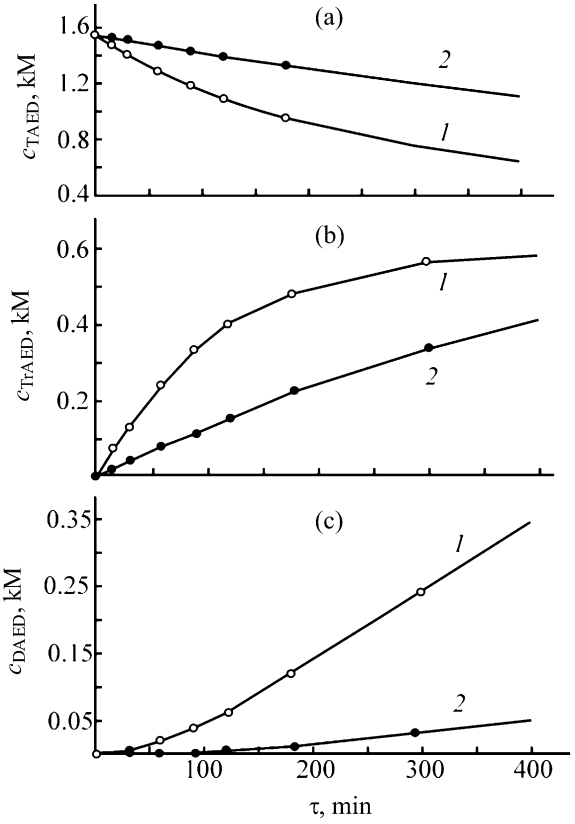


Fig. 4. Variation of the concentration c of (a) TAED, (b) TrAED, and (c) DAED with time τ. T, °C : (*1*) 125 and (*2*) 110.

be attributed to occurrence of a reverse reaction between the TAED acylation product and acetic acid formed during the reaction.

The reversibility of the reaction in the case of TrAED acylation by acetic acid anhydride was confirmed experimentally by the appearance of the peak of acetic acid anhydride in the chromatogram recorded for the reaction of TAED with acetic acid.

Thus, the DAED acylation by acetic acid anhydride is a two-stage process; the second stage of acylation of TrAED to TAED is reversible, which is responsible for the not very high (≤84%) yield of the reaction product, TAED. Naturally, each of the stages includes a series of chemical transformations. Therefore, it is expedient to describe the kinetics in terms of the concentration and yield of the target product, using the known dependences for two first-order reactions of the type

$$A \xrightarrow{k_1} B \underset{k_3}{\overset{k_2}{\rightleftarrows}} C.$$

The variation of the concentration of the substances can be described by the dependences [8]

$$a_0 = c_A + c_B + c_C,$$

$$c_A = a_0 e^{-k_1 t},$$

$$c_B = c_{B\infty} + (k_2 + k_3 - k_1)^{-1}\{a_0(k_1 - k_3)e^{-k_1 t} - [k_2 c_{B\infty} - c_{C\infty}(k_3 - k_1)]e^{-(k_2 + k_3)t}\},$$

$$c_C = c_{C\infty} - (k_2 + k_3 - k_1)^{-1} \times \{a_0 k_2 e^{-k_1 t} - [k_2 c_{B\infty} - c_{C\infty}(k_3 - k_1)]e^{-(k_2 + k_3)t}\},$$

where a_0 is the initial concentration of substance A, M; c_A, c_B, c_C, running concentrations of the initial, intermediate, and final compounds, respectively, M; and $c_{B\infty}$, $c_{C\infty}$, equilibrium concentrations of the intermediate and final compounds, respectively, M.

Analysis of the plots suggests that these dependences cannot adequately describe the experimental data. This is apparently due to the occurrence of a more complex process that cannot be described by dependences for first-order reactions.

For more detailed description of the acylation process, we performed a set of kinetic experiments on TAED deacylation by acetic acid at temperatures of 110–125°C under a significant excess of acetic acid (TAED : AA = 1 : 7). Figure 4 presents the primary experimental curves for the upper and lower limits of the temperature range examined.

A kinetic description of the DAED acylation by acetic acid anhydride is a mathematically complex procedure. Hence, we applied a special software, namely, DesK-Pro software available from Khiminform Private Company [9], used for construction of descriptive kinetic models and reactor modeling.

Descriptive kinetic models are suitable for reactions proceeding in batch, semicontinuous, or continuous reactors operating under various heating conditions and for simulation and optimization of processes.

The construction of these models requires that the initial hypothesis about the chemical nature of the reactions should be formulated, experimental data on the concentration responses be available, and basic properties of substances (thermal capacity and density as functions of temperature and molecular weight) be known.

Descriptive concentration models describe the reaction mechanism in detail. These models are based on the generalized law of mass action (GLMA) which states that the rate of a stage is proportional to the product

of the concentrations raised to arbitrary powers (orders). A special case of the law of mass action is the exact law of mass action (ELMA), in which the orders coincide with the stoichiometric coefficients.

A multi-stage reaction is described by the stoichiometric scheme

$$\sum_{i=1}^{N}(\beta_{ji}-\nu_{ji})A_{ji}=0;\quad j=1,...,M, \tag{1}$$

where the rate of jth stage is set by the expression

$$r_j=k_j\prod_{(i)}[\mathrm{A}_{ji}]^{\nu_{ji}}\quad\text{for GLMA and}$$

$$r_j=k_j\prod_{(i)}[\mathrm{A}_{ji}]^{n_{ji}}\quad\text{for ELMA;}$$

$$j=1,\ ...,\ M, \tag{2}$$

and the rate at which the concentration of ith component changes is described by the equation

$$\frac{\mathrm{d}[\mathrm{A}_i]}{\mathrm{d}t}=\sum_{(j)}(\beta_{ji}-\nu_{ji})r_j, \tag{3}$$

where ν, β are stoichiometric coefficients; r, rate of a stage, mol m^{-3} s^{-1}; k, rate constant of the stage, $k(T) = k_0\exp(-E/RT)$; k_0, pre-exponential coefficient; E, activation energy, kJ mol^{-1}; R, gas constant, J mol^{-1} K^{-1}; [A], concentration of substance A, mol m^{-3}; and t, time, s.

The model is supplemented by the appropriate initial conditions and observation model, a set of equations relating the rates of stages to the observed responses (concentration, heat or gas evolution, etc.) :

$$\frac{\mathrm{d}Q}{\mathrm{d}t}=\sum_{(j)}Q_j^{\infty}r_j;$$

$$\frac{\mathrm{d}G}{\mathrm{d}t}=\sum_{(j)}G_j^{\infty}r_j;$$

$$[A_{ji}], \tag{4}$$

where Q is the specific heat evolution, kJ mol^{-1}; Q^{∞}, specific heat effect of a stage, kJ mol^{-1}; and G^{∞}, specific final gas evolution in the stage, mol mol^{-1}.

A specific feature of complex kinetic models is that they are substantially nonlinear in the parameters. Hence, the general approach to solving the inverse kinetic problem (estimating the model parameters) is based on nonlinear optimization.

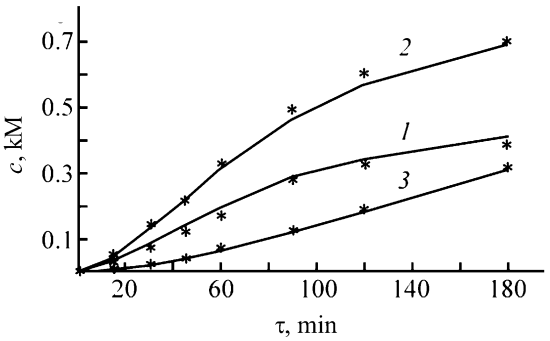


Fig. 5. Variation of the TAED concentration c with time τ. (*Line*) DesK-Pro program model and (*points*) experimental data. Initial molar ratio DAED : AAA, T, °C : (*1*) 1 : 17, 140; (*2*) 1 : 8.5, 140; and (*3*) 1 : 8.5, 120.

To solve the inverse problem means to find the kinetic parameters that best fit the experimental data. For this purpose, a certain measure of residuals between the experimental and simulated responses is minimized. Most of nonlinear optimization algorithms are based on the least-squares procedure which utilizes to this end the sum of the squared residuals. The parameter vector $\mathbf{P}_r$ is estimated by minimization of the target function SS :

$$\mathrm{SS}(\mathbf{P})=\frac{1}{2}\sum_{(i)}\left(\frac{Y_{\exp}(t_i)-Y_{\mathrm{sim}}(\mathbf{P},t_i)}{\varepsilon_i}\right)^2$$

$$\rightarrow \min = \mathrm{SS}(\mathbf{P}_r), \tag{5}$$

where SS(**P**) is the weighted sum of the squared residuals; i, experimental point number; e, experimental error at the point; and $Y_{\exp}$ and Y_{sim}, experimental and calculated responses, respectively.

The condition for the minimum SS is set by a system of the nonlinear algebraic equations

$$\frac{\partial SS(\mathbf{P})}{\partial P_j}=0;\quad j=1,...,L, \tag{6}$$

where P_j is jth component of the parameter vector.

The target function is extended by inclusion of the data derived from several multi-response experiments. Simultaneous processing of the results of several experiments and responses of varied physical nature allows use of different kind of information on the reaction and provides more adequate resulting kinetics.

A primary program processing of the experimental data (Fig. 5) showed that synthesis of TAED is satisfactorily described by the model of two successive

Rate constants and activation energies of the DAED acylation reaction

Stage no.	Activation energy E, kJ mol^{-1}	Pre-exponent, l mol^{-1} s^{-1}	Rate constants $k \times 10^{-5}$	
			120°C	140°C
1	62.3	6.02×10^3	3.2	8.1
2	87.1	2.92×10^6	0.2	1.3
3	103.3	1.69×10^8	0.8	2.8
4	112.9	2.46×10^9	0.3	1.5

reversible second-order bimolecular reactions in accordance with the general scheme.

$$\mathrm{DAED + AAA} \underset{k_3}{\overset{k_1}{\rightleftarrows}} \mathrm{TrAED + AA},$$

$$\mathrm{TrAED + AAA} \underset{k_4}{\overset{k_2}{\rightleftarrows}} \mathrm{TAED + AA}.$$

The rate constants and activation energies are listed in the table.

CONCLUSIONS

(1) Diacetylethylenediamine is acylated by acetic acid anhydride in two stages.

(2) Tetraacetylethylenediamine is deacylated by acetic acid to diacetylethylenediamine via a triacetylethylenediamine intermediate. Hence, the acylation of diacetylethylenediamine is described by successive reversible second-order equations.

(3) The formal kinetics of acylation of diacetylethylenediamine by acetic acid anhydride was examined, which allowed determination of the activation energies and the functional temperature dependences of the apparent rate constants of the reaction k_1–k_4 for two successive reversible stages of the process.

(4) The kinetic data obtained allow construction of an adequate mathematical model for industrial apparatus.

REFERENCES

1. Mazyra, L.N. and Mal'stev, V.N., *Aktivatory otbelivaniya dlya sinteticheskikh moyushchikh sredstv* (Bleaching Activators for Synthetic Detergents), Moscow : NIITEKhIM, 1989.
2. Olontsev, I.F., Grubman L.P., Khvorostinskaya, L.V., et al., *Vspomogatel'nye sredstva dlya zaklyuchitel'noi obrabotki tekstil'nykh izdelii* (Auxiliary Agents for Exhaustive Treatment of Textile Articles), Moscow: NIITEKhIM, 1988.
3. GB Patent 1 335 204.
4. DE Patent 2 118 281.
5. EP Patent 51 739.
6. Zabicky, B., *The Chemistry of Amides*, New York: Interscience, 1970.
7. Zaidel', A.N., *Elementarnye otsenki oshibok izmerenii* (Elementary Estimates of Measurement Errors), Leningrad: Akad. Nauk SSSR, 1968.
8. Rodigin, N.M. and Rodigina, E.N., *Posledovatel'nye khimicheskie* reaktsii (matematicheskii analiz i raschet) (Successive Chemical Reactions: Mathematical Analysis and Calculation), Moscow: Akad. Nauk SSSR, 1960.
9. Kossoy, A. and Akhmetshin, Yu., *Process Safety Progress*, 2007, vol. 26, no. 3, pp. 209–211.

ISSN 1070-4272, Russian Journal of Applied Chemistry, 2008, Vol. 81, No. 10, pp. 1813–1817. © Pleiades Publishing, Ltd., 2008.
Original Russian Text © A.V. Chernysheva, V.M. Chernyshev, P.V. Korolenko, V.A. Taranushich, 2008, published in Zhurnal Prikladnoi Khimii, 2008, Vol. 81, No. 10, pp. 1690–1695.

ORGANIC SYNTHESIS AND INDUSTRIAL ORGANIC CHEMISTRY

Thermodynamic and Kinetic Aspects of the Reaction of Aminoguanidine with Malonic Acid in Acidic Aqueous Solutions

A. V. Chernysheva, V. M. Chernyshev, P. V. Korolenko, and V. A. Taranushich

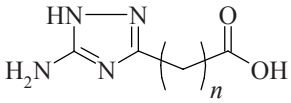
South-Russian State Technical University, Novocherkassk, Rostov oblast, Russia

Received March 25, 2008

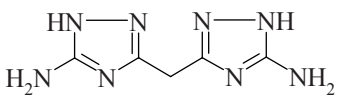
Abstract—Thermodynamic and kinetic features of the reaction of aminoguanidine with malonic acid in aqueous solutions at pH 0.5–1.3 to give mono- and diguanylhydrazides of malonic acid were examined, and the reaction mechanism was suggested.

DOI: 10.1134/S1070427208100200

The reaction of aminoguanidine (AG) with dicarboxylic acids is the synthetic route to 5-amino-1,2,4-triazole-3-carboxylic (**I**) and 5-amino-1,2,4-triazol-3-ylacetic (**II**) acids [1–3] and to bis(5-amino-1,2,4-triazol-3-yl)alkanes (**III**) [4]. These compounds are used in production of drugs and biologically active substances [5–7], dyes [8], corrosion-protecting formulations [9], and polymers [10], and also in biological studies [11]. The reactions of AG with dicarboxylic acids are usually performed in aqueous solutions. According to [1–3], the reaction occurs via formation of guanylhydrazides of the corresponding acids, which, when heated subsequently in an alkaline medium, cyclize into aminotriazoles **I–III**:



I, $n = 0$
II, $n = 1$



III

The procedure reported in [1] allows preparation of acid **I** in a yield of about 80% and is well reproducible. An experimental check of the protocols from [2, 3] showed that the yield of **II** is very sensitive to slight changes in the solution acidity and reactant ratio in the step of synthesis of malonic acid guanylhydrazide. It should be kept in mind that reactions of carboxylic acids with nitrogen nucleophiles in aqueous solutions are usually reversible, and the position of the equilibrium and the reaction rate strongly depend on the solution temperature and acidity [12–15]. Until recently, the effect of these factors on the thermodynamics and kinetics of the reactions of AG with carboxylic acids has received virtually no researchers' attention. In this study, we examined the thermodynamic and kinetic features of the reaction of AG with malonic acid (MA) in aqueous solutions at pH 0.5–1.3.

EXPERIMENTAL

Aminoguanidinium hydrocarbonate (Lancaster) contained no less than 98% main substance. The other chemicals were of analytically pure grade. Aqueous solutions were prepared using double-distilled water.

Kinetic experiments were performed in a 250-ml three-necked glass flask with a reflux condenser and a mercury thermometer. The temperature in the reactor was maintained to within ±0.5°C, using an ESR^C thermostat. The solution acidity was determined using a pH-150M with device an ESL-63-07 glass electrode and an EVL-1M3 reference electrode.

A calculated amount of aminoguanidinium hydrocarbonate was suspended in 50 ml of H_2O, after which 6 M HCl was added until the hydrocarbonate completely dissolved and the gas evolution ceased. The resulting solution was heated to the required temperature and brought to the required pH and volume of 100 ml by adding 6 M HCl and H_2O. Malonic acid was dis-

solved in 70 ml of H_2O, and the solution was heated to the required temperature and brought to the required pH and volume of 100 ml by adding 6 M HCl and H_2O. The resulting solutions of AG and MA were mixed in the reaction flask, and the time counting was started.

The AG concentration in reaction mixtures c_{AG} (M), was determined by iodatometric titration [16]. At definite time intervals, a 1-ml sample of the reaction mixture was withdrawn and dissolved in 20 ml of distilled water in a conical flask. To the resulting solution we added 30 ml of 2.5 M H_2SO_4 solution and 30 ml of 0.1 N KIO_3 solution. The flask was closed and kept for 3 min at room temperature, after which an excess amount of a saturated KI solution was added, and the released I_2 was titrated with a 0.1 N $Na_2S_2O_3$ solution. The quantity c_{AG} was calculated by the formula

$$c_{AG} = \frac{V_0 - V}{V_s} \times 0.02497,$$

where V_0 and V are the volumes of sodium thiosulfate solution spent in the blank experiment and in titration of the sample, respectively (ml), and V_s is the volume of a sample of the reaction mixture (ml).

The concentrations of guanylhydrazide (GH) c_{GH} (M) and diguanylhydrazide (DGH) c_{DGH} (M) of malonic acid were determined chromatographically after their cyclization in alkaline solution to acid **II** and bis(5-amino-1,2,4-triazol-3-yl)methane **III**, respectively. To this end, we took a 5-ml sample of the reaction mixture at definite time intervals, mixed it with 7 ml of 2 M NaOH, and heated for 30 min on a boiling water bath, after which we cooled the sample, neutralized it with concentrated HCl to pH 6–7, added 25 ml of a 0.05 M aqueous KH_2PO_4 solution, and brought the solution volume to 50 ml. The resulting sample was chromatographed on a Milikhrom-5.3 chromatograph equipped with a UV detector and an 80 × 2-mm column packed with Separon C_{18}. The mobile phase was a 0.025 M aqueous KH_2PO_4 solution; elution rate 80 μl min^{-1}, detection at a wavelength of 220 nm, sample volume 6 μl, temperature of the chromatographic column 35°C. The retention time of acid **II** was 2.9 min, and that of compound **III**, 4.0 min. The concentrations c_{GH} and c_{DGH} in the reaction mixtures were assumed to be equal to the chromatographically determined concentrations of compounds **II** and **III** after the sample treatment with an alkali. The reliability of the procedure is confirmed by the fact that the difference between the AG concentrations determined by iodatometric titration and calculated by the equation

$$c_{AG} = c_{AG0} - c_{GH} - 2c_{DGH}$$

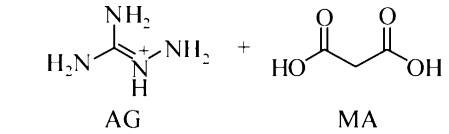
(c_{AG0} is the initial concentration of AG in the reaction mixture) did not exceed 1.6%.

The MA concentratoin c_{MA} was calculated by the formula

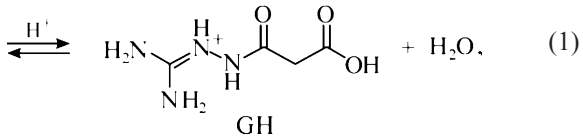
$$c_{MA} = c_{MA0} - c_{GH} - c_{DGH},$$

where c_{MA0} is the initial MA concentration.

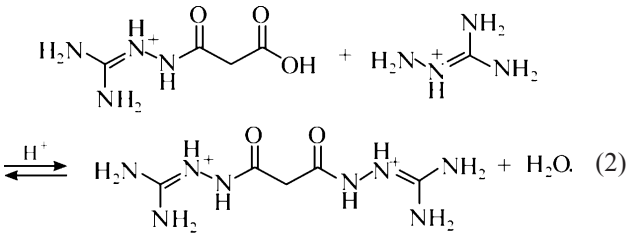
A chromatographic analysis of the reaction mixtures showed that the reaction of AG with MA involves successive formation of GH and DGH of malonic acid:



AG MA



GH (1)



DGH (2)

The equilibrium constants of the formation of GH (K_{GH}) and DGH (K_{DGH}) were calculated by the formulas

$$K_{AG} = \frac{[GH]}{[MA][AG]}, \quad (3)$$

$$K_{DGH} = \frac{[DGH]}{[GH][AG]}, \quad (4)$$

where [GH], [DGH], [MA], and [AG] are the equilibrium concentrations of the corresponding compounds, M.

It should be noted that, in acid-catalyzed reactions of carboxylic acids with nitrogen nucleophiles, e.g., amines, the position of the equilibrium and the reaction

rate are, as a rule, governed by the concentrations of the nonprotonated form of the nucleophile and nondissociated form of the acid [13]. Equations (3) and (4) should seemingly include the concentration of the nonprotonated form of AG. However, this concentration is negligible in the examined pH range, because AG is a strong base (pK_a 11.5 [17]). At the same time, it is known that, even in the protonated form, AG exhibits fairly high nucleophilicity and can react with electrophiles, because the proton in the aminoguanidinium cation is bonded to the guanidine moiety, with the lone electron pair of the amino group of the hydrazine moiety remaining free [17, 18]. Therefore, most probably, AG enters into the reaction in the form of the aminoguanidinium cation [reactions (1), (2)]. In the pH interval examined, the concentration of this form is actually equal to the analytical concentration, and specifically this quantity was taken into account in formulas (3) and (4), as well as in the further rate equations. The concentration of the nondissociated form of MA, c'_{MA}, was calculated by the equation

$$c'_{MA} = \frac{10^{-pH}}{10^{-pH} + 10^{-pK_a}} c_{MA},$$

where pK_a is equal to 2.86 [19].

The concentrations [AG], [MA], [GH], and [DGH] in Eqs. (3) and (4) were determined by analyzing the composition of the reaction mixtures afer the attainment of equilibrium. The equilibrium was attained from the sides of both forward and reverse reactions until the analyzed concentrations coincided within the experimental error. The reaction mixtures required for studying the reverse reaction were prepared by heating AG, MA, and HCl in a minimal volume of water at 60°C for 3 h. Under these conditions, the yield of guanylhydrazides was considerably higher than the equilibrium yield in dilute solutions. Then the resulting mixture was diluted with water to the required volume, and the hydrolysis of GH and DGH was studied.

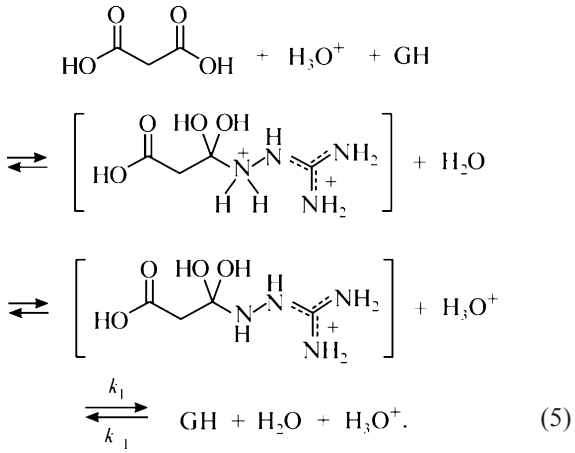
The equilibrium constants K_{GH} and K_{DGH} obtained at 50–71°C are given in Table 1. At higher temperatures, it was impossible to determine K_{GH} and K_{DGH} with acceptable reliability because of the gradual decarboxylation of MA. Varying the acidity within the interval examined did not lead to noticeable changes in K_{GH} and K_{DGH}. The good linear dependence of the logarithms of these constants on the reciprocal temperature allowed us to apply the van't Hoff isobar equation and calculate the thermal effects of the reactions of GH (1) and DGH (2) formation: $\Delta H_{GH} = -27.5 \pm 2.0$ and $\Delta H_{DGH} = -34.6 \pm 5.3$ kJ mol^{-1}. Notably, these values are close to the enthalpy of the related reaction of aniline acylation with formic acid in acidic solution (–27.5 kJ mol^{-1} [13]).

Table 1. Equilibrium constants K_{GH} and K_{DGH}

T, °C	K_{GH}	K_{DGH}
	l mol^{-1}	
50	8.9 ± 0.1	1.29 ± 0.05
60	6.1 ± 0.2	0.90 ± 0.05
63	5.4 ± 0.2	0.84 ± 0.07
71	4.9 ± 0.2	0.58 ± 0.05

To elucidate the mechanism of formation of malonic acid guanylhydrazide, we studied the kinetics of reaction (1) in the reactant concentration range 0.1–1.2 M and pH 0.5–1.3. The course of reaction (1) was monitored by variation of the AG and GH concentrations. We failed to study the kinetics of reaction (2) of DGH formation, because determination of the DGH concentration in the initial portions of the kinetic curves involved large errors due to the low degree of conversion of MA to DGH.

Because the reaction of AG with MA is similar to the reactions of carboxylic acids with amines under the conditions of acid catalysis [12–14], it is reasonable to assume that its mechanism is also similar:



The limiting step can be both the acid-catalyzed addition of AG to the carboxy group of MA with the formation of a tetrahedral intermediate (TH) and the TH

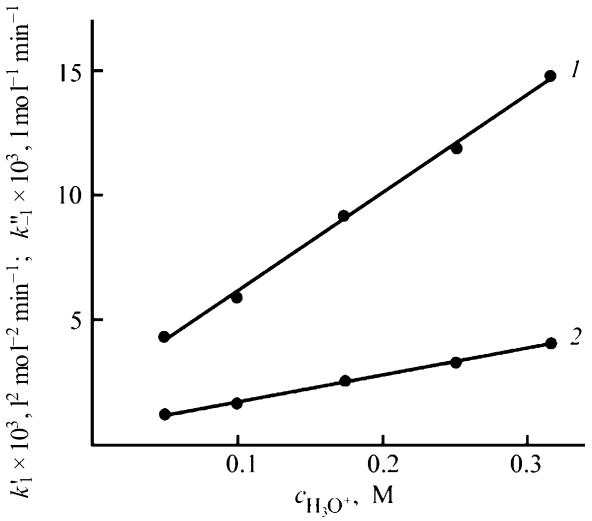


Fig. 1. Apparent rate constants of the (*1*) forward (k'_1) and (*2*) reverse (k''_{-1}) reactions at 80°C vs. the solution acidity. ($c_{H_3O^+}$) Concentration of hydroxonium ions.

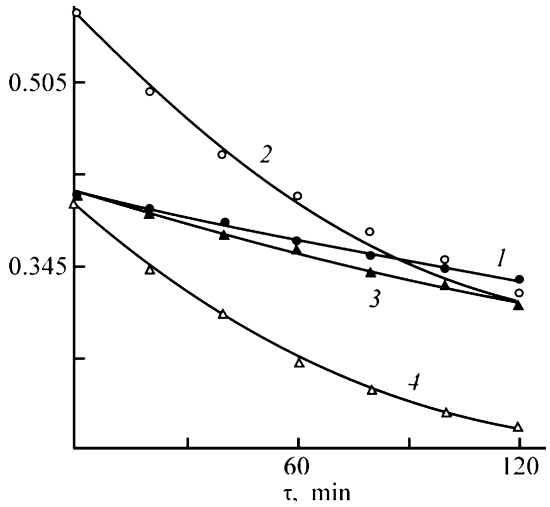


Fig. 2. Kinetic curves of AG consumption at pH 1.0. (c_{AG}) AG concentration and (τ) time. T (°C), c_{MA0} (M): (*1*) 60, 0.6001; (*2*) 80, 0.8000; (*3*) 70, 0.6004; and (*4*) 90, 0.6000. *Lines* are calculated kinetic curves, and *points*, experimental data.

dehydratoin [12–14]. In both cases, the rate of GH formation is described by the rate equation

$$\frac{dc_{GH}}{d\tau} = k_1 c_{AG} c'_{MA} c_{H_3O^+} - k_{-1} c_{GH} c'_{H_2O} c_{H_3O^+}, \qquad (6)$$

where k_1 and k_{-1} are the rate constants of the forward and reverse reactions, respectively.

As the reaction is performed in dilute aqueous solutions, it has pseudo-zero order with respect to H_2O. Therefore, the rate constant of the reverse reaction can be expressed as

$$k'_{-1} = k_{-1} c_{H_2O}.$$

At a constant pH, Eq. (6) will take the form

$$dc_{GH}/d\tau = k'_1 c_{AG} c'_{MA} - k''_{-1} c_{GH},$$

where $k'_1 = k_1 c_{H_3O^+}$ and $k''_{-1} = k_{-1} c_{H_3O^+}$ are the effective rate constants of the forward and reverse reactions, respectively.

Table 2. Rate constants k_1 and k'_{-1}

T, °C	k_1, l^2 mol^{-2} min^{-1}	k'_{-1}, l mol^{-1} min^{-1}
60	0.026 ± 0.001	0.0042 ± 0.0002
70	0.035 ± 0.003	0.0074 ± 0.0003
80	0.060 ± 0.007	0.0170 ± 0.0020
90	0.088 ± 0.004	0.0310 ± 0.0020

The constant k' was calculated by the linear least-squares method using the integral form of the rate equation for a reversible bimolecular reaction [20]:

$$\tau = \frac{1}{k'_1}\left\{\frac{1}{X_1 - X_2}\ln\left[\frac{(c_{AG_0} - X_1)(c_{AG} - X_2)}{(c_{AG_0} - X_2)(c_{AG} - X_1)}\right]\right\}, \qquad (7)$$

where X_1 and X_2 are the quantities calculated by the formulas

$$X_{1,2} = \frac{-[K_{GH}(c'_{MA} - c_{AG_0}) + 2c_{AG_0}]}{2(K_{GH} - 1)} \pm \frac{\sqrt{[K_{GH}(c'_{MA} - c_{AG_0}) + 2c_{AG_0}]^2 + 4(K_{GH} - 1)c^2_{AG_0}}}{2(K_{GH} - 1)}.$$

The rate constant of the reverse reaction k''_{-1} was obtained from the relationship $k''_{-1} = k'_1/K_{GH}$. The equilibrium constants K_{GH} at 80 and 90°C were calculated by the van't Hoff equation.

Figure 1 shows the dependence of the apparent rate constants k'_1 and k''_{-1} on the concentration $c_{H_3O^+}$. The linear dependence of k'_1 and k''_{-1} on $c_{H_3O^+}$ allows determination of the true rate constants k_1 and k'_{-1}, whose values at various temperatures are listed in Table 2.

Figure 2 shows the experimental concentrations c_{AG} and the calculated kinetic curves obtained by Eq. (7). The coincidence of the experimental and calculated data within the experimental error confirms the adequacy of the kinetic model we chose.

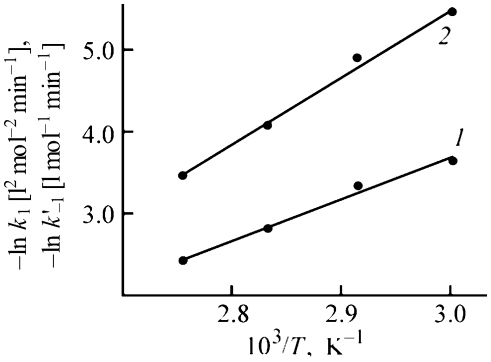


Fig. 3. Temperature dependence of the logarithms of the rate constants of the (*1*) forward (k_1) and (*2*) reverse (k'_{-1}) reactions.

The linear dependence of the logarithms of the rate constants k_1 and k'_{-1} on the reciprocal temperature (Fig. 3) allows calculation of the parameters of the Arrhenius equation $k = A\exp(-E_a/RT)$:

Rate constant	A	E_a, kJ mol^{-1}
k_1	$9.93 \pm 0.1 \times 10^4$	42.1 ± 3.0
k'_{-1}	$3.33 \pm 0.48 \times 10^8$	69.6 ± 3.5

Notably, the activation energy of hydrolysis of malonic acid guanylhydrazide is close to E_a of hydrolysis of hydroxamic acids [21] and of carboxylic acid amides and polyamides [22–24] under the conditions of acid catalysis (66–90 kJ mol^{-1}), which occur by the same mechanism. Thus, the kinetic data are consistent with the suggested mechanism of reaction (5).

The thermodynamic and kinetic data we obtained can be used for development of an improved procedure for preparing 5-amino-1,2,4-triazol-3-ylacetic acid **II** and bis(5-amino-1,2,4-triazol-3-yl)methane **III**.

CONCLUSIONS

(1) The reaction of aminoguanidine with malonic acid in acidic aqueous solutions yields not only guanylhydrazide, but also diguanylhydrazide of malonic acid. In the temperature range 50–71°C, both reactions are reversible and exothermic. The equilibrium constant of formation of malonic acid guanylhydrazide is, on the average, seven times that of formation of malonic acid diguanylhydrazide.

(2) A kinetic model was suggested for the formation of malonic acid guanylhydrazide, which adequately describes the experimental data in the range pH 0.5–1.3. The reaction of aminoguanidine with malonic acid follows the mechanism characteristic of acid-catalyzed reactions of carboxylic acids with the amine, but the role of a nucleophile in this process is played by the protonated, rather than neutral form of aminoguanidine. This fact allows synthesis of guanylhydrazides in fairly acidic media providing high reaction rate.

REFERENCES

1. Chipen, G.I. and Grinshtein, V.Ya., *Izv. Akad. Nauk Latv. SSR, Ser. Khim.*, 1965, no. 2, pp. 204–208.
2. USSR Inventor's Certificate, no. 3 204 967.
3. Kofman, T.P., Uvarova, T.A., and Kartseva, G.Yu., *Zh. Org. Khim.*, 1995, vol. 31, no. 2, pp. 271–275.
4. US Patent 2 744 116.
5. US Patent 5 990 084.
6. US Patent 6 831 177.
7. Chernyshev, V.M., Chernysheva, A.V., and Taranushich, V.A., *Zh. Prikl. Khim.*, 2006, vol. 79, no. 5, pp. 792–795.
8. US Patent 7 150 782.
9. US Patent 7 294 211.
10. Barmin, M.I., Kartavykh, V.P., Korolev, E.A., et al., *Zh. Obshch. Khim.*, 2001, vol. 71, no. 4, pp. 557–566.
11. Dervan, P.B., *Bioorg. Med. Chem.*, 2001, vol. 9, no. 9, pp. 2215–2235.
12. Brown, R.S., Bennet, A.J., and Slebocka-Tilk, H., *Acc. Chem. Res.*, 1992, vol. 25, no. 11, pp. 481–488.
13. Aman, A.M. and Brown, R.S., *J. Am. Chem. Soc.*, 1999, vol. 121, no. 19, pp. 4598–4607.
14. Bender, M.R., *Chem. Rev.*, 1960, vol. 60, no. 1, pp. 53–113.
15. Dneprovskii, A.S. and Temnikova, T.I., *Teoreticheskie osnovy organicheskoi khimii* (Theoretical Principles of Organic Chemistry), Leningrad: Khimiya, 1991.
16. Houben–Weyl, *Methoden der organischen Chemie*, vol. 2: *Analytische Methoden*, Stuttgart: Georg Thieme, 1953.
17. Koskinen, M., Mutikainen, I., Tilus, P., et al., *Monatsh. Chem.*, 1997, vol. 128, nos. 8–9, pp. 767–775.
18. Bharatam, P.V., Iqbal, P., Malde, A., and Tiwari, R., *J. Phys. Chem.* A, 2004, vol. 108, no. 47, pp. 10 509–10 517.
19. Albert, A. and Serjeant, E., *Ionization Constants of Acids and Bases. A Laboratory Manual*, New York: Wiley, 1962.
20. Lebedev, N.N., Manakov, M.N., and Shvets, V.F., *Teoriya tekhnologicheskikh protsessov osnovnogo organicheskogo i neftekhimicheskogo sinteza* (Theory of Processes of Basic Organic and Petrochemical Synthesis), Moscow: Khimiya, 1975.
21. Chung, D.Y. and Lee, E.H., *J. Ind. Eng. Chem.*, 2006, vol. 12, no. 8, pp. 962–966.
22. Williams, A., *J. Am. Chem. Soc.*, 1976, vol. 98, no. 18, pp. 5645–5651.
23. Zahn, D., *J. Phys. Chem.* B, 2003, vol. 107, no. 44, pp. 12 303–12 306.
24. Meyer, A., Jones, N., Lin, Y., and Kranbuehl, D., *Macromolecules*, 2002, vol. 35, no. 7, pp. 2784–2798.

ISSN 1070-4272, Russian Journal of Applied Chemistry, 2008, Vol. 81, No. 10, pp. 1818–1820. © Pleiades Publishing, Ltd., 2008.
Original Russian Text © N.G. Bel'nikevich, T.V. Budtova, S.A. Vesnebolotskaya, G.K. Elyashevich, 2008, published in Zhurnal Prikladnoi Khimii, 2008, Vol. 81, No. 10, pp. 1696–1698.

MACROMOLECULAR CHEMISTRY AND POLYMERIC MATERIALS

Effect of Degree of Cross-Linking of Sodium Acrylate Hydrogels on Their Swelling in Variously Acidic Solutions

N. G. Bel'nikevich, T. V. Budtova, S. A. Vesnebolotskaya, and G. K. Elyashevich

Institute of Macromolecular Compounds, Russian Academy of Sciences, St. Petersburg, Russia

Received February 19, 2008

Abstract—Swelling of sodium acrylate-based polyelectrolytic hydrogels with various degrees of cross-linking (from 300 to 50 acrylate units per cross-link) was studied over the solution pH range from 2 to 12.

DOI: 10.1134/S1070427208100212

Polyelectrolytic polymeric hydrogels based on chemically cross-linked acrylic (PAA) or methacrylic (PMAA) acid have been intensively studied in the last two decades, because of their great scientific and practical interest. In particular, such hydrogels show promise in development of new prolonged-action drug carriers. The interaction of hydrogels with low-molecular-weight electrolyte solutions has been rather well studied [1–9].

In most of these studies, the authors theoretically and experimentally examined the equilibrium in the system hydrogel–solution, as influenced by the pH, ionic strength, and nature of solvent. For systems with controlled and directed transport of drugs in human body, the drug release rate was experimentally demonstrated to be dependent not only on the pH and ionic strength of the medium, but also on such factors as the chemical structure, charge density, swelling kinetics, and degree of cross-linking of the hydrogel [1, 3]. Shefer et al. [7] studied the effect of the solution pH on the swelling of the gel based on PAA variously cross-linked with tris(4-isocyanatophenyl)methane. However, the swelling in hydrogels has not been systematically studied over wide ranges of the cross-linking density and pH.

In this study, we examined the behavior of sodium polyacrylate (Na-PAA) hydrogels with various cross-linking densities over a wide pH range in both acidic and alkaline solutions.

EXPERIMENTAL

The hydrogels were prepared by radical copolymerization of sodium acrylate with *N*,*N*'-methylenebisacrylamide as a cross-linking agent [5] and ammonium persulfate as an initiator. The monomers were completely neutralized with NaOH. The degree of cross-linking was controlled by the initial component ratio. We prepared a series of hydrogels with *N* 50, 100, 150, 200, and 300 monomer unites per cross-link. The monomer to cross-linking agent molar ratios used in the experiments are listed in the table. The monomer concentration in the initial solution was 25%. The resulting gels were thoroughly washed and vacuum-dried to constant weight.

The equilibrium degree of swelling of the hydrogels in water and acidic and alkaline solutions was determined gravimetrically to within 10%. A weighed portion of a dry gel (~0.02 g) was poured over with 30 ml of distilled water or with HCl or NaOH solutions. The initial pH was varied from 2 to 12. The hydrogel samples were allowed to stand to reach equilibrium swelling, which was monitored gravimetrically. The degree of swelling, Q, was calculated as the ratio of the weight of the swollen hydrogel to its dry weight. The solution pH was measured with an ANION-410V pH meter.

It has been demonstrated previously [10] that, at a low Na^+ concentration in the system Na-PAA–low-molecular-weight acid, no redistribution of the H^+ ions occurs between the hydrogel and the solution, so that the solution pH remains practically unchanged after contact with the hydrogel. To meet this condition in our experiments, the solution to dry gel weight ratio was 1500. In this case, the polymer concentration recalculated to the total system volume was about 10^{-5} M, and the volume fractions V_2 of the polymer in the swollen gel, calculated as

Degree of swelling of hydrogels, Q, and volume fraction of the polymer in swollen gels, V_2, at various cross-linking densities N and cross-linking agent to monomer molar ratios X

N	X	pH 2		pH 6		pH 10.6	
		Q, g g^{-1}	V_2	Q, g g^{-1}	V_2	Q, g g^{-1}	V_2
300	0.3338	59	0.016	240	0.0030	170	0.0058
200	0.5000	43	0.023	200	0.0036	160	0.0062
150	0.7400	26	0.048	150	0.0047	119	0.0083
100	0.9800	20	0.037	70	0.0100	45	0.0220
50	2.0000	13	0.071	20	0.0345	25	0.0380

$$V_2 = (1 + \rho_2 Q/\rho_1)^{-1}, \quad (1)$$

where ρ_2 and ρ_1 are the polymer and solvent densities [8], ranged from 0.003 (N 300, water) to 0.071 (N 50, pH 2) (see table).

To optimize the experimental conditions (swelling time, sample weight),we examined in preliminary experiments the swelling kinetics of Na-PAA hydrogel with N 300 at various pH values. First, we compared the swelling kinetics for the samples with the same weight, but different surface areas. Monolithic and crushed samples demonstrated different swelling kinetics, and the finer the sample, i.e., the larger its surface area, the faster the swelling kinetics. The time of establishment of equilibrium swelling in the crushed samples was lower by about an order of magnitude as compared to the monolithic sample of the same weight (2 and 24 h, respectively). In this case, the equilibrium swellability of the samples was the same. In further experiments, we used crushed gel samples. As an example, Fig. 1 shows the swelling kinetics of crushed hydrogel with N 300 at pH 4.6, 6.0, and 8.3. As an ordinate, we used the relative swelling Q_t/Q_{eq}, where Q_t and Q_{eq} are the current and equilibrium swellings, respectively. As can be seen, the equilibrium in the system is established in 2 h, irrespective of pH. Therefore, in our further experiments, the swelling time was selected to be 3 h.

The pH dependences of the equilibrium swellability Q pass through a maximum at pH 3.5–9.0. Figure 2 shows such a dependence for the hydrogel with N 300. As can be seen, the swellability is low in strongly acidic solutions, which can be attributed to replacement of Na^+ by H^+. Acrylic acid is characterized by a lower degree of dissociation as compared to Na-PAA, which results in a considerable contraction of the macromolecular chains. At low initial pH values, we observed slight increase (by 6–7%) in the equilibrium solution pH by virtue of replacement of Na^+ by H^+.

Raising the pH to 6–7 enhances swelling by a factor of 4–5. Previously, this effect has been observed for gels based on cross-linked PAA [1, 7] and copolymer of *n*-alkyl hydrogen itaconates with *N*-acrylamide [11]. Swelling of Na-PAA gels in strongly alkaline solutions is affected both by condensation of the counterions and

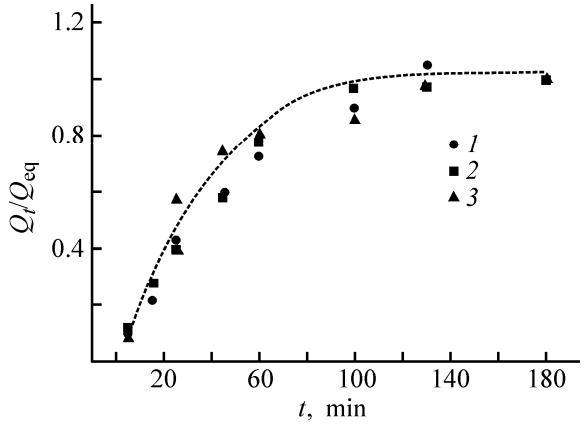


Fig. 1. Swelling kinetics of Na-PAA hydrogel. pH: (*1*) 4.6, (*2*) 6.0, and (*3*) 8.3. (Q_t) Current swelling, (Q_{eq}) equilibrium swellability, and (t) time.

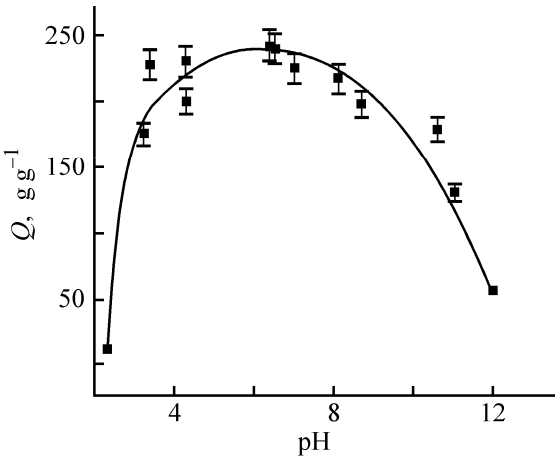


Fig. 2. pH dependence of the degree of swelling, Q, of the hydrogel with N 300.

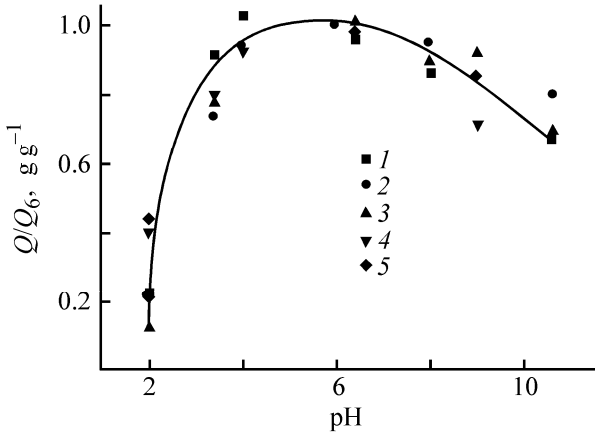


Fig. 3. pH dependence of the relative degree of swelling of the hydrogel Q/Q_6. (Q) Equilibrium degree of swelling at fixed pH and (Q_6) that at pH 6. N: (*1*) 300, (*2*) 200, (*3*) 150, (*4*) 100, and (*5*) 50.

by shielding of charges by excess Na^+ ions, suppressing polyelectrolytic swelling. In this case, the degree of swelling of the hydrogel decreases as compared to that in neutral solutions (pH 4–8), being although higher than that in acidic solutions.

At high initial pH, we observed a slight acidification of the solution [Δ(pH) <0] by no more than 6–7%. Similar results were obtained for samples with other cross-linking densities. The equilibrium swellabilities of all the hydrogels studied at pH 2.0, 6.0, and 10.6 are listed in the table. The absolute value of Q_{max} becomes about an order of magnitude lower as the distance between cross-linking sites decreases from 300 to 50 monomer units.

The pH dependence of the relative swellability Q/Q_6 (ratio of the equilibrium swelling at a fixed pH to that at pH 6) is independent of the degree of cross-linking (Fig. 3) and can be described by a common invariant curve. A similar invariant curve was obtained for the increase in the degree of swelling as a function of pH over the pH range up to pH 11 for PAA gels with various degrees of cross-linking [7]. However, no compaction of the gels in alkaline solutions was observed in this case. The invariant curve can be used as a calibration curve for preliminary estimation of changes in the size of any Na-PAA hydrogel samples with changing pH.

CONCLUSIONS

(1) pH dependences of the degree of swelling of hydrogels with various cross-linking densities (from 300 to 50 sodium acrylate units per cross-link) pass through a maximum at pH 3.5–9.0.

(2) pH dependence of the relative swellability of gels (ratio of the equilibrium swelling at a fixed pH to that at pH 6) is independent of the degree of cross-linking of hydrogels over the entire experimental pH range and can be described by a common invariant curve.

ACKNOWLEDGMENTS

The study was financially supported by the Russian Foundation for Basic Research (project no. 07-03-00 177) and Program of Basic Research of the Division of Chemistry and Materials Science of the Russian Academy of Sciences "Synthesis and Characterization of New Polymeric Systems Containing Polyconjugated Polymers and Exhibiting Semiconductor and Conducting Properties," Research Area: "Conducting and Electroactive Polymers."

REFERENCES

1. Kramarenko, E.Yu., Filippova, A.E., and Khokhlov, A.R., *Vysokomol. Soedin., Ser. C*, 2006, vol. 48, no. 7, pp. 1216–1240.
2. Filippova, O.E., *Vysokomol. Soedin., Ser. C*, 2000, vol. 42, no. 2, pp. 2328–2352.
3. Suleimenov, I.E., Budtova, T.V., and Iskakov, R.M., *Polimernye gidrogeli v farmatsevtike* (Polymeric Hydrogels in Pharmaceutics), Almaty: Inst. Khimicheskikh Nauk im. A.B. Bekturova Min. Obrazovaniya i Nauki Resp. Kazakhstan, 2004.
4. Budtova, T.V., Suleimenov, I.E., and Frenkel', S.Ya., *Zh. Prikl. Khim.*, 1997, vol. 70, no. 4, pp. 529–534.
5. Horkay, F., Tasaki, I., and Basser, P., *Biomacromolecules*, 2000, no. 1, pp. 84–90.
6. Buyanov, A.L., Revelskaya, L.G., Kuznetsov, Yu.P., and Khripunov, A.K., *J. Appl. Polym. Sci.*, 2001, vol. 80, pp. 1452–1460.
7. Shefer, A., Grodzinsky, A.J., Prime, K.L., and Bus-nel, J.-P., *Macromolecules*, 1993, vol. 26, pp. 5009–5014.
8. Molina, M.J., Gomez-Anton, M.R., and Pierola, I.F., *J. Polym. Sci., Part B.: Polym. Phys.*, 2004, no. 42, p. 2294.
9. Budtova, T.V., Belnikevich, N.G., Suleimenov, I.E., and Frenkel, S.Ya., *Polymer*, 1993, vol. 34, no. 24, pp. 5154–5156.
10. Budtova, T.V., Suleimenov, I.E., Bichutskii, D.A., and Frenkel', S.Ya., *Vysokomol. Soedin., Ser. A*, 1995, vol. 37, no. 6, pp. 1019–1023.
11. Katime, I., Velada, J.L., Novoa, R., and Diaz de Apodaca, E., *Polym. Int.*, 1996, vol. 40, pp. 281–286.

ISSN 1070-4272, Russian Journal of Applied Chemistry, 2008, Vol. 81, No. 10, pp. 1821–1830. © Pleiades Publishing, Ltd., 2008.
Original Russian Text © A.L. Aleksandrov, E.R. Badamshina, G.A. Gorbushina, A.A. Grishchuk, A.S. Dzhalmukhanova, V.V. Komratova, I.S. Kochneva, A.I. Kuzaev, V.P. Lodygina, E.V. Stovbun, T.N. Fedotova, Ya.S. Estrin, 2008, published in Zhurnal Prikladnoi Khimii, 2008, Vol. 81, No. 10, pp. 1699–1709.

MACROMOLECULAR CHEMISTRY AND POLYMERIC MATERIALS

"Dormant" Inhibitors of Urethane Type as Controllers of Temperature Modes of Styrene Polymerization

A. L. Aleksandrov, E. R. Badamshina, G. A. Gorbushina, A. A. Grishchuk, A. S. Dzhalmukhanova, V. V. Komratova, I. S. Kochneva, A. I. Kuzaev, V. P. Lodygina, E. V. Stovbun, T. N. Fedotova, and Ya. S. Estrin

Institute of Problems of Chemical Physics, Russian Academy of Sciences, Chernogolovka, Moscow oblast, Russia

Received February 28, 2008

Abstract—Urethanes based on a series of monoisocyanates and phenolic inhibitors of styrene radical polymerization, which release the initial phenolic inhibitor at elevated temperatures, were prepared and characterized. Some of these compounds meet the requirements to "dormant" inhibitors: they sharply decelerate thermally initiated high-temperature polymerization of styrene and do not noticeably affect the rate of low-temperature polymerization in the presence of an inhibiting substance. The possibility of preventing uncontrollable emergency situations by adding these compounds to the initial monomer was confirmed experimentally.

DOI: 10.1134/S1070427208100224

One of the most extensively used procedures for preparing polystyrene is polymerization in the bulk in large reactors, which is characterized by the complex behavior owing to the nonlinear dependence of the reaction rate on the temperature and reactant concentrations. The exothermic heat effect of polymerization has a positive feedback, i.e., both the reaction rate and heat release increase with temperature, which, in turn, causes further use in temperature. As a result, unstable states of the process and emergency situations arise, which are accompanied by an uncontrollable rise in the temperature of the reaction mass by tens of degrees and by a significant excess of the monomer conversion over the level permissible for the reactor.

In the commercial production of polymers, various mathematical models of the reactors are used, which allows development of automatic control systems providing the maximal productivity of the process. However, owing to the risk of uncontrollable emergency situations, the process is frequently performed under modes that are far from the optimum. Continuous polymerization of styrene is carried out in a cascade of reactors (with the volume of tens of cubic meters) to provide a gradual increase in temperature as the content of the monomer in the reaction mixture decreases [1]. The greatest danger of uncontrollable emergency situations is typical of the first reactor owing to the highest monomer concentration in the reaction mixture. Three main procedures are used to prevent the emergency with an uncontrollable temperature increase in the reactor: cooling of the reaction mixture by lowering the coolant temperature in the reactor jacket, addition of inhibitors that sharply decrease the polymerization rate, and emergency discharge of the reaction mixture into an external vessel with a solvent.

However, all the above procedures are noticeably inertial, i.e., they are characterized by slow elimination of the thermal and concentration gradients in the large reactor. Owing to the high inertia, prevention of the emergency situations in the case of local overheating may become impossible. The use of so-called "dormant" inhibitors (DIs) added to the reaction mixture before polymerization can be probably the optimal solution to this problem.

The effect of these inhibitors is as follows. A DI is inert at the polymerization temperatures. Upon an uncontrollable rise in the temperature above the permissible level, a DI exhibits the inhibition activity via its decomposition to components among which at least one component acts as a polymerization inhibitor or isomerization to give an active inhibitor. In this case, it is not necessary to supply the inhibitor to the over-

heated area because DI is uniformly distributed in the reaction mixture from the very begining.

DIs were first suggested for controlling the photoinitiated polymerization of methyl methacrylate (MMA) in the form of large blocks [2]. As DIs were studied various compounds, such as nitroso compounds, hydrazine derivatives, saturated and unsaturated halogen derivatives, nitrites, and ammonium salts, which are activated and then inhibit polymerization even at 50–60°C. However, these compounds cannot be used in the case of styrene, because its polymerization is carried out at temperatures no less than 50°C at which all the above compounds act as polymerization inhibitors lowering the process rate and molecular weight of the polymer.

As is known, phenols and polyphenols (in particular, di- and triphenols) are efficient inhibitors of radical polymerization of styrene [3–5]. The inhibiting effect of these compounds is due to the fact that propagating polystyrene radicals detach a labile hydrogen atom from the hydroxy group of the inhibitor molecule and are thereby transformed into "dead" polymer molecules. The resulting oxyphenyl radicals do not interact with the monomer and thus cannot initiate the propagation of new polymer chains. If active hydrogen in the inhibitors can be blocked so that it will be activated only at relatively high temperatures, then its reactivity with respect to the polymer radicals at lower temperatures will be suppressed.

The most appropriate blocking procedure is conversion of phenols into urethanes in the reaction with isocyanates (DI of urethane type). The reaction of urethane formation can be represented as follows:

$$RNCO + HOR' \leftrightarrows RNHC(O)OR'. \quad (1)$$

At elevated temperatures, the reaction equilibrium is shifted to the left, and the temperature at which the equilibrium concentrations of isocyanate and phenol become noticeable depends on the structure of radicals R and R' [6].

Hydrogen atoms are more strongly bound with nitrogen atoms in the urethane group than with oxygen atoms in phenols. Hence, urethanes should not exhibit significant inhibiting activity at moderate temperatures [7].

Here, we describe the synthesis of some promising DIs of the urethane type and present characteristics of the resulting compounds and data on their effect on the kinetics of styrene polymerization under the isothermal conditions and on the thermal modes under the conditions of restricted heat exchange which model parameters of the heat exchange in large-volume reactors.

EXPERIMENTAL

Styrene containing 99.9% main compound and stabilized with *p-tert*-butylpyrocatechol (0.001%) was washed to remove the inhibitor with a 10% NaOH solution (4 : 1 weight ratio). Then the monomer was washed with distilled water to neutral reaction. Washed styrene was dried over anhydrous $CaCl_2$. The dried monomer was distilled in a vacuum (44–45°C, 20 mm Hg) and stored in an argon atmosphere at –18°C. The monomer purity was determined by the kinetic method [8]. The reaction order of styrene polymerization with respect to initiator was found to be 0.5, which corresponds to the pure monomer.

Phenyl isocyanate (I-**I**), *m*-chlorophenyl isocyanate (I-**II**), *o*-chlorophenyl isocyanate (I-**III**), 2-ethylphenyl isocyanate (I-**IV**), 2,6-dimethylphenyl isocyanate (I-**V**), *o*-tolyl isocyanate (I-**VI**), and 6-chlorohexyl isocyanate (I-**VII**), all purchased from Aldrich, were distilled in a vacuum and stored in sealed glass ampules.

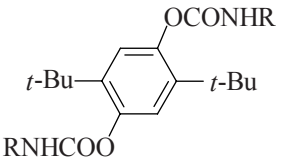
In this study, we used the following phenols: 2,5,7,8-tetramethyl-2-(4',8',12'-trimethyltridecyl)-6-chromanol (α-tocoferol) (P-**I**) purchased from Aldrich, was used without additional purification; 2,2,5,7,8-pentamethyl-6-chromanol, pure grade (P-**II**), mp 94–96°C, was recrystallized from petroleum ether; 1,2-dihydroxybenzene (pyrocatechol), pure grade (P-**III**), and 1,3-dihydroxybenzene (resorcinol), pure grade (P-**IV**), were sublimed in a vacuum at 100°C, mp 105–106 and 109–110°C, respectively; 1,4-dihydroxybenzene (hydroquinone), pure grade (P-**V**), was successively recrystallized from xylene, water, and acetonitrile, mp. 173.5–175.0°C, 1,4-dihydroxy-2,5-di-*tert*-butylbenzene (2,5-di-*tert*-butylhydroquinone), pure grade (P-**VI**), was precipitated with water from methanol and reprecipitated from ether with toluene, mp 217–219°C; and 4-*tert*-butyl-1,2-dihydroxybenzene (*p-tert*-butylpyrocatechol), pure grade (P-**VII**), was recrystallized from petroleum ether, mp 55–56°C.

Urethanes were prepared by the reaction of monoisocyanates with hydroxy compounds by reaction (1), using two standard procedures: (a) at [NCO]=[OH] at room temperature to complete consumption of

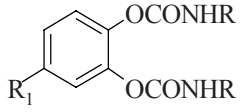
NCO groups and (b) at threefold excess of the isocyanate groups in the melt at 170°C, with subsequent distillation of excess isocyanate in a vacuum. In both procedures, the reaction was carried out in an inert gas atmosphere in the presence of 10^{-5} M urethane-forming catalyst (dibutyltin dilaurate, DBTDL). The resulting compounds were analyzed by IR spectroscopy for the reaction completeness judged from the absence of an intense absorption band at 2270 cm^{-1}, characteristic of the free isocyanate group. These compounds are crystalline compounds with mp from 20 to 271°C, except U-**IIIb** (Table 1). Urethanes were purified by recrystallization from toluene, the degree of purification was analyzed by reversed-phase chromatography.

The IR spectra were recorded on a Specord M-82 spectrophotometer: the spectra of compounds U-**Ia**–U-**Id**, U-**IIa**–U-**IIf**, and U-**IIIa**, in KBr pellets and those of compounds U-**IIIb** and U-**IIIc**, in capillary films prepared from solutions in chloroform.

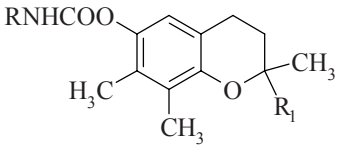
The structures of the resulting urethanes are as follows:



U-(**Ia–Id**):
R = 3-ClPh (a),
2-ClPh (b),
2-EtPh (c),
2,6-$(Me)_2$Ph (d)



U-(**IIa–IIf**):
R = Ph, R_1 = H (a);
R = Ph, R_1 = *t*-Bu (b);
R = 3-ClPh, R_1 = *t*-Bu (c);
R = 2-ClPh, R_1 = *t*-Bu (d);
R = 2-MePh, R_1 = *t*-Bu (e);
R = 6-Cl$(CH_2)_6$, R_1 = *t*-Bu (f)



U-(**IIIa–IIIc**):
R = 3-ClPh, R_1 = CH_3 (a);
R = 3-ClPh, R_1 = $[CH_2CH_2CH_2CH(CH_3)]_3CH_3$ (b);
R = 2,6-$(Me)_2$Ph, R_1 = $[CH_2CH_2CH_2CH(CH_3)]_3CH_3$ (c)

The characteristics of the urethanes prepared are listed in Table 1.

The chromatographic analysis of the initial compounds, urethanes, and diurethanes was carried out on a Milikhrom chromatograph equipped with a UV detector, using the reversed-phase procedure (2 × 80-mm column packed with Separon SGX C18, 6 μm, 5500 TP performance) with a water-methanol mixture as eluent. The optimal composition of the eluent providing determination of the maximal number of impurities at a sufficiently high resolution of the peaks was determined for each compound in the gradient mode, and analysis was carried out in the isocratic mode. Depending on the polarity of the compounds analyzed, the methanol : water ratio in the isocratic mode was varied from 30 : 70 to 90 : 10 at a flow rate of the eluent of 100 μl min^{-1}. The concentration of the compound analyzed in solution (in eluent or methanol) was up to 10 mg ml^{-1} at a sample volume of 8 μl. The detection was performed in the single- or double-wave mode at 210 and 260 nm. For preliminarily identification of the impurities (if necessary), the spectra of each chromatographic peak in the 190–360 nm range were recorded in the stopped-flow mode.

The effect of potential DIs was preliminarily evaluated from the data on the kinetics of styrene polymerization at 50–70°C with azobis(isobutyronitrile) (AIBN) initiator and at 125 and 150°C without initiator (thermal initiation), in the presence of DI and without it. The measurements were carried out in isothermal calorimeters of the Tian–Calvet type. The reaction mixture in glass ampules was thoroughly degassed, sealed, and placed in calorimeter cells [9]. The signals of the calorimeters were recorded on a computer using an E-24 analog-digital converter (ADC); the signal from the E-24 ADC was recorded using a BEG program developed by Yu.A. Sokolov.

Nonisothermal thermal modes of the styrene polymerization under the conditions of restricted heat exchange in the absence and in the presence of DI were studied on a minireactor with restricted heat removal. The monomer containing either an initiator only or the initiator and DI was degassed and poured in a vacuum into a glass ampule 30 mm in diameter, equipped with a thermocouple well. The ampule was filled with argon, sealed off, and placed in the installation preliminarily heated to the temperature of an experiment. The thermal electromotive force of the copper–constantan thermocouple, whose cold ends were placed in a Dewar vessel containing an ice–water mixture, was recorded with E-24 ADC.

Nonisothermal thermal modes of the styrene polymerization were also simulated using 1- and 8-liter metallic reactors equipped with a stirrer and modified so as to provide the conditions of restricted heat exchange; the ratio of the heat-exchange area to the volume of the reaction mixture was about 1.5 m^{-1}, whereas

Table 1. Characteristics of urethanes

Compound	Found, % / Calculated, %				Name	Empirical formula	mp, °C	IR spectrum, ν, см$^{-1}$ UR = –OC(O)NH–
	C	H	N	Cl				
U-**Ia**	62.70 63.52	5.21 5.71	7.25 5.29	14.8 13.39	2,5-Bis(*tert*-butyl)-1,4-dihydroxybenzene bis(3-chlorophenylcarbamate)	$C_{28}H_{30}Cl_2N_2O_4$	242–244	1732, 3304, 1540 (UR); 1595, 1507, 1405, 870, 811 (Ar); 2971, 2872, 1362 (CH_3)
U-**Ib**	63.09 63.52	5.20 5.71	6.0 5.29	14.66 13.39	2,5-Bis(*tert*-butyl)-1,4-dihydroxybenzene bis(2-chlorophenylcarbamate),	$C_{28}H_{30}Cl_2N_2O_4$	212–214	1742, 1721, 3306, 1526 (UR); 3040, 1595, 1492, 1395 (Ar); 2966, 2917, 2873, 1440, 1375 (CH_3)
U-**Ic**	72.87 74.39	7.50 7.80	6.60 5.42	–	2,5-Bis(*tert*-butyl)-1,4-dihydroxybenzene bis(2-ethylphenylcarbamate)	$C_{32}H_{40}N_2O_4$	201–203	1720, 1703, 3310, 1527 (UR); 3042, 1587, 1392 (Ar); 2960, 2902, 2873, 1416, 1361 (CH_3)
U-**Id**	73.50 74.39	7.47 7.80	6.94 5.42	–	2,5-Bis(*tert*-butyl)-1,4-dihydroxybenzene bis (2,6-dimethylphenylcarbamate)	$C_{32}H_{40}N_2O_4$	270–273	1720, 3287, 1519 (UR); 3045, 3029, 1595, 1485, 1394 (Ar); 2963, 2928, 2873, 1437, 1377 (CH_3)
U-**IIa**	68.36 68.96	5.04 4.63	9.65 8.04	–	1,2-Dihydroxybenzene bis(phenylcarbamate)	$C_{20}H_{16}N_2O_4$	193–196	1727, 3313, 1549, 1531 (UR); 1600, 1492, 695 (Ar);
U-**IIb**	72.28 71.27	6.28 5.98	7.68 6.93	–	4-*tert*-Butyl-1,4-dihydroxybenzene bis-(phenylcarbamate),	$C_{24}H_{24}N_2O_4$	102–104	1731, 3332, 1542 (UR); 1601, 1499, 1406, 834 (Ar); 2968, 2871, 1363 (CH_3)
U-**IIc**	61.03 60.90	4.97 4.68	6.21 5.92	15.70 14.98	4-*tert*-Butyl-1,4-dihydroxybenzene bis(3-chlorophenylcarbamate)	$C_{24}H_{22}Cl_2N_2O_4$	109–111	1719, 3334, 1541 (UR); 3048, 1611, 1505, 880 (Ar); 2961, 2937, 2863, 1460, 1361 (CH_3)
U-**IId**	59.43 60.90	4.40 4.68	6.10 5.92	15.64 14.98	4-*tert*-Butyl-1,4-dihydroxybenzene bis(2-chlorophenylcarbamate)	$C_{24}H_{22}Cl_2N_2O_4$	218–221	1752, 3326, 1531 (UR); 3047, 1595, 1510, 1407 (Ar); 2966, 2870, 1440, 1360 (CH_3)
U-**IIe**	66.47 72.20	6.02 6.53	6.80 6.48	–	4-*tert*-Butyl-1,4-dihydroxybenzene bis(2-methylphenylcarbamate)	$C_{26}H_{28}N_2O_4$	148–150	1745, 1726, 3310, 1537 (UR); 3028, 1591, 1506, 1410, 842, 812 (Ar); 2969, 2870, 1362 (CH_3)
U-**IIf**	58.12 58.89	7.62 7.83	6.20 5.72	14.65 14.49	4-*tert*-Butyl-1,4-dihydroxybenzene bis(6-chlorohexylcarbamate)	$C_{24}H_{38}Cl_2N_2O_4$	65–66	1719, 3332, 1541 (UR); 1505, 1410, 880 (Ar); 731 (C–Cl); 2959, 2936, 2862, 1467, 1361 (CH_3)
U-**IIIa**	67.43 66.75	6.21 6.16	4.40 3.89	9.84 9.85	2,2,7,8-Tetramethylchroman-6-ol 3-chlorophenylcarbamate	$C_{20}H_{22}ClNO_3$	158–160	1751, 3311, 1530 (UR); 1595, 1481, 1405, 787 (Ar); 2978, 2930, 2865, 1456, 1387 (CH_3)
U-**IIIb**	– 73.72	– 9.19	– 2.46	– 6.22	2,7,8-Trimethyl-2-(4,8,12-trimethyltridecyl)chroman-6-ol 3-chlorophenylcarbamate	$C_{35}H_{52}ClNO_3$	Waxy	1708, 3273, 1541 (UR); 3012, 1598, 1505, 1415 (Ar); 2952, 2928, 2868, 1456, 1377 (CH_2, CH_3)
U-**IIIc**	– 78.81	– 10.19	– 2.48	–	2,7,8-Trimethyl-2-(4,8,12-trimethyltridecyl)chroman-6-ol 2,6-dimethylphenylcarbamate	$C_{37}H_{57}NO_3$	19–21	1693, 3233, 1523 (UR); 3021, 1600, 1505, 1415 (Ar); 2954, 2929, 2869, 1456, 1371 (CH_2, CH_3)

for 15 m^3 industrial reactors this ratio is close to 2 m^{-1}. Experimentally, we selected the conditions at which the system passes into the high-temperature mode in the absence of DI. In the nonisothermal tests we also used AIBN initiator at a common concentration of 0.02 M.

In all the cases, unless otherwise indicated, the concentrations of the inhibitors and potential DIs were also 0.02 M.

The molecular-weight distribution (MWD) of polystyrenes was determined at 25°C on a Waters chromatograph with a refractometric detector [10] and a tetrahydrofuran eluent at 1.2 ml min^{-1} flow rate. The volume of the sample was 2 ml, and the concentration of the compound being analyzed in solution was 0.3–0.4 wt %. We used three Styrogel columns (10 × 1000 mm) calibrated using polystyrene references with a porosity of 3×10^3, 3×10^4, and 3×10^5 Å.

A distinctive feature of styrene is that it is capable of thermally initiated polymerization at a rather high temperature (above 90–100°C) [11, 12]. This means that, if the control over the process (performed at moderate temperatures in the presence of initiating substance) is lost, further polymerization and, thus, uncontrollable temperature increase can occur even after complete consumption of the initiator. Just in these cases the use of DIs may become the only way to avoid uncontrollable emergency situations.

Apparently, DIs of the urethane type can be synthesized only from such proton-donor compounds that rather effectively decelerate radical polymerization. Therefor, we estimated the inhibiting power of a series of phenols.

It should be noted that polymerization of styrene is, as a rule, accompanied by the gel effect, which is manifested in a manyfold increase in the reaction rate in the course of the process passing from the bimolecular chain termination to the diffusion-controlled stage. Transition of the polymerization to the high-temperature uncontrollable mode is the most probable just in the step of the gel effect, when the polymerization rate is the highest, whereas the intensity of the heat exchange decreases owing to the rapid increase in the viscosity of the reaction mixture [13]. Therefore, the inhibiting power of the compounds in question was evaluated using two parameters: $\varphi_0 = W_0/W_{0x}$ and $\varphi_m = W_m/W_{mx}$, where W_0 and W_{0x} are the reduced initial rates of polymerization and W_m and W_{mx} are the maximal reduced rates of polymerization (at similar conversions of the inhibitor, respectively. The parameters of the inhibiting power of phenols in styrene polymerization are listed in Table 2.

Table 2. Inhibition parameters φ_0 and φ_m of phenols in styrene polymerization

Potential inhibitor	φ_0		φ_m	
	at indicated temperature, °C			
	60	125	60	125
P-**I**	1.05	2.5	a*	20.6
P-**II**	2.03	1.5	61.2	15.2
P-**III**	2.08	1.40	26.32	3.0
P-**IV**	1.35	0.9	0.4	1.1
P-**V**	1.68	1.2	4.3	1.3
P-**VI**	b**	2.0	b**	10.0
P-**VII**	b**	1.5	b**	7.1

* Reaction is terminated at the conversion $\alpha = 0.3$.

** Strong inhibition, almost no polymerization is observed.

As can be seen, phenols P-**IV** and P-**V** do not noticeably inhibit polymerization of styrene at temperatures of 60°C and higher. Compounds P-**III**, P-**VI**, and P-**VII** more strongly inhibit the process in the case of initiated polymerization at 60°C, whereas at thermally initiated polymerization (125°C and higher) chromanols P-**I** and P-**II** are the most effective.

Based on the data on the inhibiting power of the above compounds (Table 2), we chose phenols P-**I**–P-**III**, P-**VI**, and P-**VII** for the synthesis of urethane-type DIs.

As shown above, the decomposition of urethane-type DIs with liberation of the active inhibitor should occur in a certain temperature range. We have shown previously [14] that neat urethanes based of phenols start to decompose to the initial components at a noticeable rate [reaction (1)] at temperatures higher than 200°C. Apparently, such compounds cannot be used as DIs. At the same time, as shown in [14], decomposition of these compounds with water [reactions (2)–(4)] or aliphatic alcohols [reaction (5)], especially in the presence of tin-containing organic catalysts (e.g., DBTDL), can occur at significantly lower temperatures with the release of the initial phenol. In these reactions, the isocyanates are converted into urea derivatives (reaction with water) or alkyl urethanes (reaction with alcohols), and reactions (2)–(5) are almost irreversible.

Table 3. Parameters of inhibition of styrene polymerization with urethanes at 60°C

Compound	φ_0	φ_m	Compound	φ_0	φ_m
U-**Ia**	1.11	1.43	U-**IId**	1.78	4.35
U-**Ib**	1.08	1.23	U-**IIe**	1.04	1.98
U-**Ic**	1.25	2.67	U-**IIf**	1.33	1.15
U-**Id**	1.39	2.80	U-**IIIa**	1.0	1.54
U-**IIa**	1.25	1.85	U-**IIIb**	1.1	>100*
U-**IIb**	1.11	2.56	U-**IIIc**	1.0	>100*
U-**IIc**	1.07	1.33			

* Polymerization is virtually terminated at 30–35% conversion.

$$RNHCOOAr + H_2O \rightarrow RNHCOOH + ArOH, \quad (2)$$

$$RNHCOOH \rightarrow CO_2 + RNH_2, \quad (3)$$

$$RNHCOOAr + RNH_2 \rightarrow RNHCONHR + ArOH, \quad (4)$$

$$RNHCOOAr + HOR' \rightarrow RNHCOOR' + ArOH. \quad (5)$$

Taking into account that the monomers for radical polymerization are not thoroughly dried to remove moisture, we assumed that the activation of DIs can occur, depending on their structure and operation conditions, in the acceptable temperature range.

The inhibiting activity of DIs was evaluated by two procedures. In the first procedure, we compared the isothermal kinetics of polymerization of the polymer (in particular, styrene) in the presence and absence of a compound in question. The ideal DI should not affect the process at moderate temperatures, but should decelerate polymerization at elevated temperatures.

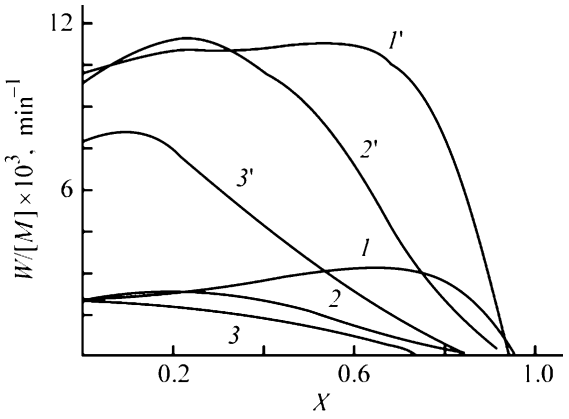


Fig. 1. Reduced rate of thermal polymerization of styrene $W/[M]$ vs. conversion X (*1*, *1'*) in the absence of additives and in the presence of urethanes (*2*) U-**IIIc**, (*3*) U-**IIIb**, (*2'*) U-**IIIa**, and (*3'*) U-**IIIb**; concentration of urethanes 2×10^{-2} M. Temperature, °C: (*1*–*3*) 125 and (*1'*–*3'*) 150.

The second procedure requires that similar comparative experiments should be performed in reactors with restricted heat exchange, in which nonisothermal modes of polymerization are provided and uncontrollable emergency situations are simulated. In this case, polymerization in the presence and absence of DIs should be performed in similar thermal modes of polymerization in a comparatively low-temperature range. In the high-temperature range, a certain decrease in temperature should be observed in styrene polymerization in the presence of DI as compared to the control experiment.

The inhibition parameters of styrene polymerization at 60°C for the urethanes prepared are listed in Table 3. As can be seen, at 60°C almost all the urethanes only slightly affect the initial and maximal rate of polymerization, except urethanes U-**IId**, U-**IIIb**, and U-**IIIc**. For example, urethane U-**IId** suppresses the gel effect and does not noticeably affect the initial polymerization rate, whereas urethanes U-**IIIb** and U-**IIIc** do not affect the initial rate and strongly inhibit polymerization at a conversion of about 30%. Nevertheless, the thermal polymerization of styrene in the presence of urethanes U-**IIIb** and U-**IIIc** was also studied.

The data on the effect of urethanes U-**IIIb** and U-**IIIc** on thermal polymerization, presented in Fig. 1, indicate that compound U-**IIIb** more effectively inhibits styrene polymerization at 125°C than does compound U-**IIIc**; it permanently decreases the polymerization rate and completely terminates the process at a 70% conversion. The inhibiting power ofprocess at urne U-**IIIb** is greater than that of U-**IIIa** at 150°C.

Our experimental data show that, at 125°C, urethanes U-**IIc** and U-**IId** do not noticeably affect the initial rate and noticeably decelerate the polymerization in the course of the process, whereas compound U-**IIa** only slightly affects the reaction rate throughout the process. Urethane U-**IIb** at elevated temperatures first significantly raises the initial rate, but after a 30% conversion is attained, it does not noticeably affect the polymerization rate. Hence, urethanes U-**IIa** and U-**IIb** are unsuitable as DIs. Compound U-**IIf** does not affect the initial rate of styrene polymerization, but it suppresses the gel effect, and the highest conversion attained in this case is 85%.

As noted above, the decomposition of urethanes with the release of the free inhibitor at temperatures

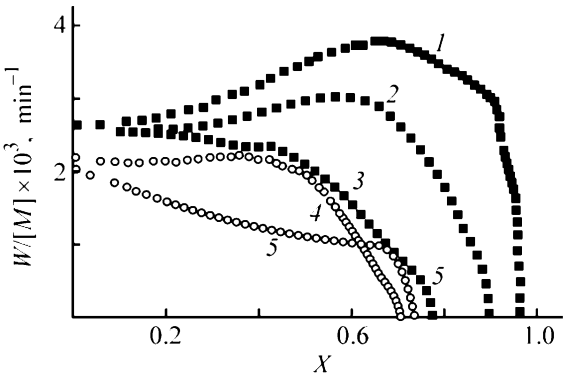


Fig. 2. Reduced rate of thermal polymerization of styrene $W/[M]$ vs. of conversion X (*1*) in the absence of additives and in the presence of (*2*) urethane U-**Id**, (*3*) inhibiting formulation based on urethane U-**Id**, (*4*) urethane U-**IIc**, and (*5*) inhibiting formulation based on urethane U-**IIc**. T = 125°C, [U] = [BuOH] = 2×10^{-2} M, [DBTDL] = 10^{-5} M.

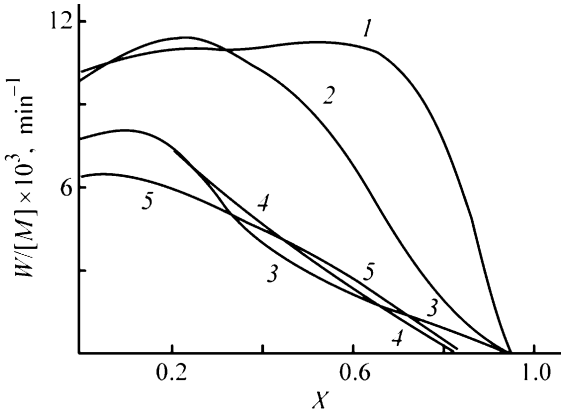


Fig. 3. Reduced rate of thermal polymerization of styrene $W/[M]$ vs. conversion X (*1*) in the absence of additives and in the presence of (*2*) urethane U-**IIIa**, (*3*) inhibiting formulation based on urethane U-**IIIa**, (*4*) urethane U-**IIe**, and (*5*) inhibiting formulation based on urethane U-**IIe**. T = 150°C, [U] = [BuOH] = 2×10^{-2} M, [DBTDL] = 10^{-5} M.

lower than 200°C proceeds at a significant rate only in the exchange reactions with proton-donor compounds and, in particular, with water and alcohols. This fact suggests that the inhibiting effect of urethanes on the styrene polymerization at 125–150°C is probably due to the exchange reactions with water present in the monomer.

The temperature at which inhibitors of the phenolic type are liberated from urethanes can be additionally lowered (i.e., the DI performance can be improved) by using the "inhibiting formulation" containing a urethane-type DI, a proton-donor compound, and a catalyst.

To confirm the above assumption, we studied the isothermal polymerization of styrene as influenced by the inhibiting compositions based on urethanes U-**Id**, U-**IIc**, U-**IIe**, and U-**IIIa**, containing *n*-butanol (BuOH) taken in equimolar amount to urethane (~0.02 M) and DBTDL (~10^{-5} M). At 60°C, these inhibiting formulations do not noticeably affect the initial rate of polymerization, but slightly diminish its maximal rate (i.e., decrease the gel effect).

The data on the inhibiting effect of some of the above formulations at 125 and 150°C (Fig. 2, curves *2* and *3*, *4* and *5*; Fig. 3, curves *2* and *3*) show that, compared to urethanes, they are actually more effective DIs of the isothermal polymerization of styrene. At the same time, under the given experimental conditions, urethane U-**IIe** exhibits the highest activity in the absence of proton donor, which does not noticeably affect the performance of this urethane (Fig. 3, curves *4*, *5*). Our special tests showed that, under the isothermal conditions in the absence of urethanes, neither *n*-butanol nor DBTDL affect the rate of styrene polymerization in the entire temperature range studied (60–150°C).

Since the MWD parameters are the decisive factors affecting the polymer properties, we studied the effect of some inhibitors and urethane-type DIs on the molecular weight (MW) of the resulting polystyrene (Table 4). As can be seen, the additives inhibiting the styrene poly-

Table 4. MWD parameters of polystyrenes prepared in the presence of some inhibitors and DIs

Additive	$M_n\times10^{-3}$	$M_w\times10^{-3}$	M_w/M_n	$M_z\times10^{-3}$	M_z/M_w
60°C (initiated polymerization)					
–	128	528	4.13	1027	1.95
P-**V**	110	290	2.64	540	1.84
P-**III**	145	313	2.15	530	1.70
P-**VII**	102	490	4.80	1093	2.23
U-**IIa**	195	422	2.15	713	1.69
U-**IIc**	177	550	3.11	1050	1.91
U-**IId**	177	560	3.16	1060	1.89
125°C (thermal polymerization)					
–	145	390	2.69	640	1.64
P-**I**	64	161	2.52	–	–
P-**VI**	34	133	3.97	276	2.07
P-**III**	102	225	2.50	453	1.77
P-**VII**	66	177	2.68	332	1.88
U-**IIa**	150	361	2.40	608	1.68
U-**IIc**	133	313	2.49	594	1.79
U-**IId**	112	295	2.63	546	1.85
U-**IIIb**	95	253	2.67	–	–

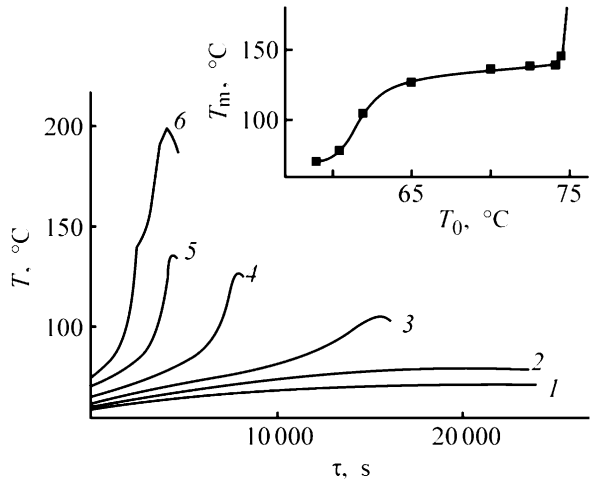


Fig. 4. Temperature curves of styrene polymerization in glass ampules in the mode of restricted heat exchange. (T) Temperature and (τ) time; the same for Figs. 5 and 6. T_0, °C: (*1*) 59, (*2*) 60.5, (*3*) 62, (*4*) 65, (*5*) 70, and (*6*) 75. In the insert: dependence of the maximal temperature T_m under the conditions of restricted heat exchange, [AIBN] = 1.1×10^{-2} M.

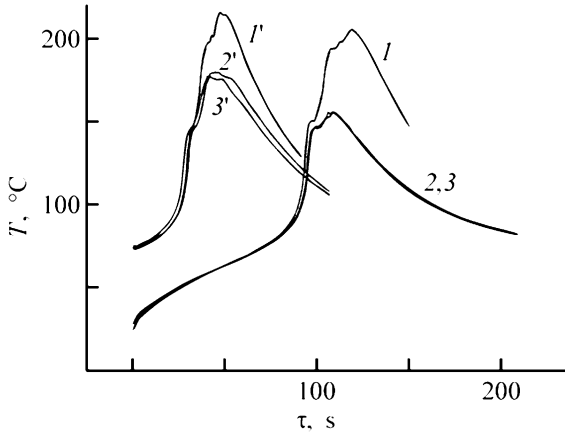


Fig. 5. Temperature curves of styrene polymerization in glass ampules in the mode of restricted heat exchange (*1*, *1*') without additives and in the presence of (*2*) urethane U-**IIIb**, (*3*) inhibiting composition based on urethane U-**IIIb**, (*2*') urethane U-**IIc**, (*3*') inhibiting composition based on urethane U-**IIc**. T_0 = 75°C, [AIBN] = 2.2×10^{-2} M, [U] = [BuOH] = 2×10^{-2} M, [DBTDL] = 10^{-5} M. (*1*'–*3*') Reaction mixture before experiment was rapidly heated to 75°C; (*1*–*3*) initial temperature of the reaction mixture was 20°C.

merization reduce the polymer MW and this effect is the most pronounced for polymerization at elevated temperatures. At 125°C, the effect of the dormant inhibitors on M_n of the resulting polystyrene is significantly weaker as compared to the initial inhibitors, and at 60°C they cause even a slight increase in the polymer molecular weight.

Thus, our experimental data on styrene polymerization under isothermal conditions suggest that urethanes U-**Id**, U-**IIc**, U-**IIe**, U-**IIf**, and U-**IIIa** or their mixtures with alcohol and a catalyst of exchange reactions can be promising DIs. However, the effect of DI can be demonstrated only in the experiments simulating uncontrollable transition of the polymerization process to the high-temperature mode.

Under the conditions of restricted heat exchange, initiated polymerization of styrene can proceed in three different modes, depending on the initial conditions. At a coolant temperature T_0 lower than a certain critical value, the process occurs in the low-temperature mode at which the difference between the temperatures of the reaction mixture and thermostat, $T - T_0$, is small and the temperature curve exhibits a flat maximum. At T_0 higher than the critical temperature, $T - T_0$ rapidly increases to tens degrees and the temperature curve is characterized by a sharp maximum. Rapid decrease in the temperature after passing the maximum is due to the consumption of the initiator and termination of initiation. This is the mode of high-temperature initiated polymerization. However, if the temperature in the reactor reaches the values providing relatively rapid thermal initiation of polymerization, the system can pass into the high-temperature mode of thermal initiation.

The thermal curves of styrene polymerization, recorded using sealed glass ampules at various T_0 on the installation with restricted heat exchange, are shown in Fig. 4. All the three modes are observed in this figure: low-temperature mode (T_0 59.0 and 60.5°C), high-temperature mode of initiated polymerization (T_0 62, 65, and 70°C), and high-temperature mode of thermal polymerization (T_0 75°C). The dependence of the maximal temperature in the ampule on T_0, which is shown in the inset, indicates that transition from one mode to another occurs in a narrow T_0 range, especially in the region of thermally initiated polymerization.

The effect of DI on the styrene polymerization was studied under the conditions nearly critical (T_0 75°C). As can be seen from Fig. 5 (curves *1*' and *2*', *3*'), which illustrates the typical results of the experiments on the effect of DI on polymerization of styrene under conditions of an uncontrollable reaction, addition of the inhibiting formulation based on urethane U-**IIc** appreciably depresses the temperature of maximal overheating of the reaction mixture in the step of thermal polymerization and does not noticeably affect the process at

lower temperatures. In this case, the degree of polymerization is significantly smaller in the presence of DI than that in its absence and the reaction mixture remains fairly fluid.

A similar behavior was observed for the inhibiting formulation based on urethane U-**IIe**. As can be seen, the kinetics of polymerization in the presence of this formulation is close to the kinetics of uninhibited polymerization at temperatures of up to 145°C. At higher temperature, polymerization sharply decelerates and the maximal temperature in the reactor decreases by 35° as compared to the uninhibited process.

Under the nonisothermal conditions, the highest performance is exhibited by urethane U-**IIIb**, which lowers the maximal temperature in the reactor by 50° at a concentration of 0.02 M as compared to the control experiment. At the same time, up to transition to the high-temperature mode, this urethane does not noticeably affect the reaction rate. Additions of BuOH and DBTDL do not appreciably affect the inhibiting activity of this DI (Fig. 5, curves *2* and *3*).

The data on the effect of the urethane-type DI on styrene polymerization, determined under the conditions of restricted heat exchange using glass ampules, were qualitatively confirmed by the experiments carried out in 1- and 8-l metallic reactors equipped with stirrers. The reactors were modified so as to provide the minimal ratio of the heat exchange surface to the volume of the reaction mixture, which allowed us to find the conditions at which the initiated polymerization passes to the high-temperature mode.

Initially we found that, at a constant coolant temperature of 90°C, the system passes to the high-temperature mode as the temperature of the reaction mixture increases to 140–150°C. However, further passing to the high-temperature mode of thermal initiation (similar to that in glass ampules) was not observed. This is probably due to a sharp increase in the heat loss through the nonthermostated inlet for the stirrer in the reaction lid. Hence, it is impossible to evaluate the DI performance under these conditions. As a result, the thermal mode of the process was changed so that after attainment of 90°C in the reactor, the temperature of the thermostat was switched to 120°C. In this case, the system passed to the high-temperature mode of thermal polymerization of styrene as the temperature of the reaction mixture increased to more than 200°C (Fig. 6, curve *1*). As a result, the degree of the monomer conversion was close to unity and the resulting mass could be unloaded from the reactor.

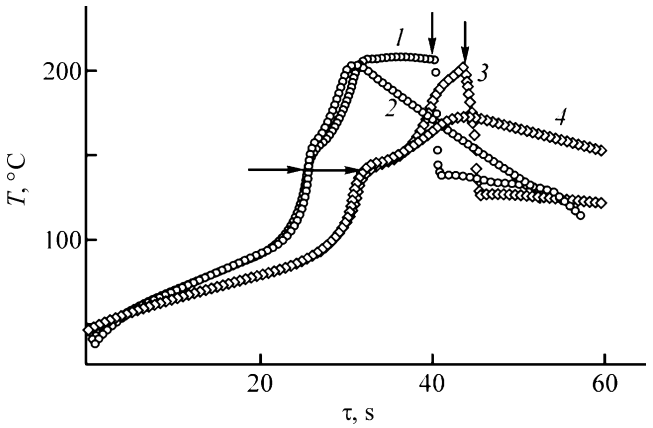


Fig. 6. Temperature curves of styrene polymerization in a 1-l metallic reactor (*1*) without additives and (*2*) in the presence of urethane U-**IIIb**, and in an 8-l metallic reactor (*3*) without additives and (*4*) in the presence of an inhibiting formulation based on urethane U-**IIIa**. (*1*, *2*) [AIBN] = 2.2×10^{-2} M, (2) [U] = 1.4×10^{-2} M; (*3*, *4*) [DIA] = 2×10^{-2} M, (*4*) [U] = [BuOH] = 1.5×10^{-2} M, [DBTDL] = 10^{-5} M. Amount of the monomer loaded, ml: (*1*, *2*) 500 and (*3*, *4*) 5000. Moments of the addition of the cold solvent in the control experiments are shown by the arrows.

Under the same conditions, we performed experiments with DI additives that were tested previously using glass ampules (Fig. 6, curve *2*). As can be seen, urethane U-**IIIb** is less efficient under the given conditions than in the case of the ampule experiments. In its presence, the rate of thermal polymerization even somewhat increases as compared to the control experiment. However, even in this case, the temperature maximum is lower by 5° than that in the control experiment, and, after attainment of the maximum, the temperature of the reaction mixture sharply decreases and the polymerization virtually terminates. The final product is fluid, and it can be discharged from the reactor without dilution with a solvent, as in the control experiment.

The results obtained for a 1-l reactor were taken into account when choosing the process modes of styrene polymerization in an 8-l reactor. This reactor was also modified to diminish the heat exchange in order to provide the possibility of attainment of the high-temperature mode of thermal polymerization. In these experiments, the temperature control unit of the thermostat was switched from 90 to 120°C when the temperature of the reaction mixture reached 150°C. The thermal modes in the course of styrene polymerization in an 8-l reactor are shown in Fig. 6 (curves *3*, *4*).

In the control experiment, when the temperature in the reactor exceeded 200°C, cold xylene was poured to lower the temperature of the reaction mixture and to

prevent uncontrollable emergency situation. Otherwise, the stirrer could be blocked and it could become impossible to unload the reaction mixture from the reactor because of the high viscosity at a conversion close to 100%. In the experiments with addition of the inhibiting formulation based on U-**IIIa**, the maximal temperature decreased by no less than 30° as compared to the control experiment, especially if we take into account that the control experiment was terminated at the temperature of the reaction mixture of 202°C, before the maximal temperature was attained.

CONCLUSIONS

(1) Dormant inhibitors of the urethane type (phenolic inhibitors blocked with isocyanates) prevent uncontrollable emergency situations in the course of styrene polymerization.

(2) In the presence of dormant inhibitors, the maximal temperature in the reactor strongly decreases and the resulting reaction mixture is a viscous mass at a conversion of about 75%, whereas in their absence the conversion reaches almost 100%.

(3) The performance of dormant inhibitors of the urethane type can be controlled by addition of proton-donor compounds accelerating liberation of the phenol inhibitor from urethane at elevated temperatures. The majority of urethanes tested do not significantly affect both the kinetics of low-temperature polymerization and the molecular-weight characteristics of the resulting polymer.

ACKNOWLEDGMENTS

The study was financially supported by the International Science and Technology Center (project no. 1529).

REFERENCES

1. Biesenberger, J.A. and Sebastian, D.H., *Principles of Polymerization Engineering*, New York: Wiley, 1983. Translated under the title *Inzhenernye problemy sinteza polimerov*, Malkin, A.Ya., Ed., Moscow: Khimiya, 1988.
2. USSR Inventor's Certificate, no. 209 742.
3. *Vinyl Polymerization*, Ham, G., Ed., New York: Dekker, 1972.
4. *Handbook of Radical Polymerization*, Matyjaszewski, K. and Davis, T.P., Eds., New York: Wiley, 2002.
5. Simonyi, M., Fitos, I., Kardos, J., et al., *J. Chem. Soc., Faraday Trans. 1*, 1977, vol. 73, no. 9, p. 1285.
6. Badamshina, E.R. and Gafurova, M.P., *Vysokomol. Soedin., Ser. C*, 2002, vol. 44, no. 9, pp. 1643-1659.
7. RF Patent 2 277 104.
8. Edel'shtein, O.A., *Cand. Sci. Dissertation*, Irkutsk, 1972.
9. Korolev, G.V. and Perepelitsina, E.O., *Vysokomol. Soedin., Ser. B*, 1977, vol. 39, no. 2, p. 338.
10. Kuzaev, A.I., *Vysokomol. Soedin., Ser. A*, 1980, vol. 22, no. 5, pp. 1146–1151.
11. Korolev, G.V., Grachev, V.P., Irzhak, V.I., et al., Abstracts of Papers, *Tret'ya Vserossiiskaya Karginskaya konferentsiya "Polimery-2004"* (3rd All-Russia Kargin Conf. "Polymers-2004"), Moscow: Mosk. Gos. Univ., 2004, vol. 2, p. 18.
12. Korolev, G.V., Grachov, V.P., Irzhak, V.I., et al., Abstracts of Papers, *40th Int. Symp. on Macromolecules "Macro-2004,"* July 4–9, 2004, p. 73.
13. Romankov, P.G. and Frolov, V.F., *Teploobmennye protsessy khimicheskoi tekhnologii* (Heat Exchange Processes of Chemical Technology), Leningrad: Khimiya, 1982.
14. Dzhalmukhanova, A.S., Badamshina, E.R., Komratova, V.V., et al., *Kinet. Katal.*, 2008, vol. 49, no. 1, pp. 57–63.

ISSN 1070-4272, Russian Journal of Applied Chemistry, 2008, Vol. 81, No. 10, pp. 1831–1836. © Pleiades Publishing, Ltd., 2008.
Original Russian Text © S.V. Kurmaz, I.S. Kochneva, V.V. Ozhiganov, A.A. Baturina, G.A. Estrina, 2008, published in Zhurnal Prikladnoi Khimii, 2008, Vol. 81, No. 10, pp. 1710–1715.

MACROMOLECULAR CHEMISTRY AND POLYMERIC MATERIALS

Synthesis and Properties of Branched Poly(Ethyl Acrylates)

S. V. Kurmaz, I. S. Kochneva, V. V. Ozhiganov, A. A. Baturina, and G. A. Estrina

Institute of Chemical Physics Problems, Russian Academy of Sciences, Chernogolovka, Moscow oblast, Russia

Received January 30, 2008

Abstract—Kinetics of radical polymerization of individual components of the ethyl acrylate–ethylene glycol dimethacrylate–chain-transfer agent system and their mixtures in toluene was studied.

DOI: 10.1134/S1070427208100236

Previously [1], we have discussed the prospects for using branched poly(methyl methacrylates) as polymers with increased molecular mobility in rigid glassy matrices (e.g., PMMA) to decelerate photochromic transformations of spiropyran. This discussion was encouraged by the increased segmental mobility of the branched macromolecules, as indicated by their glass-transition point T_g. The glass-transition point of these compounds depends on their macromolecular structure and on the content of branching and chain-transfer agent units and is lower than that of PMMA by more than 20–40°C [2]. However, our further studies showed that this level of molecular mobility of the polymer matrix is insufficient for significantly affecting the kinetics of photochromic transformation of spiropyrans.

For this purpose, linear acrylic polymers whose T_g in some cases is lower by 100°C than that of PMMA are the most suitable [3]. Branched polyacrylates are even more preferable than the linear polymers. Since these polymers are characterized by a high concentration of terminal chains and branching sites in the shell and in the core of the macromolecule [5], they can sorb molecules of a functional compound [5] (e.g., spiropyran) to form a nanocontainer, thus insulating it from the glassy matrix.

The aim of this study was to prepare branched ethyl acrylate (EA) copolymers suitable for producing sites with increased molecular mobility in organic glasses and to determine the molecular-weight distribution (MWD) and intrinsic viscosity of these copolymers and the content of residual C=C bonds in them.

EXPERIMENTAL

Branched poly(ethyl acrylates) were prepared by one-step highly efficient procedure [6] based on 3*D* radical copolymerization of EA with various multifunctional monomers [ethylene and triethylene glycol dimethacrylates (EGDM, TEGDM), 1,4-butanediol diacrylate (BDDA), and pentaerythritol triacrylate (PETA)] as branching agents. The copolymerization was controlled by 1-decanethiol (DT) as chain-transfer agent.

Monomers, EA, EGDM, TEGDM, BDDA, PETA (all Aldrich), and toluene (chemically pure grade) were used as received. Copolymerization was performed in a three-necked flask with a reflux condenser and thermometer in an argon flow for 5.5 h at T = 88°C maintained with a thermostat. The amounts of the branching agent and DT corresponded to 0.05 mol of EA. The content of the reactants in a toluene solution was approximately 20 wt %. The concentration of the initiator, 2,2'-azobis(isobutyronitrile) (AIBN), was 2×10^{-2} M.

The concentration of the branching agents and DT was varied in a wide range, with their equimolar ratio being constant. The EGDM content in EA–EGDM–DT mixtures was 2, 5, 12, and 20 mol % with respect to EA. The content of TEGDM, BDDA, and PETA in the reaction mixtures was 5, 12, and 20 mol %. After the reaction completion, the unchanged comonomers and toluene were removed in a vacuum. The polymers were dried to constant weight at T = 60°C in a vacuum.

The polymer yield determined gravimetrically was 90–95%.

The (co)polymerization kinetics of EA–EGDM–DT mixtures was studied by precision isothermal calorimetry on a DAK-1-1 calorimeter. The reaction mixture was subjected to repeated freezing–pumping–thawing and then was polymerized at T = 60°C in evacuated sealed glass ampules. The polymerization kinetics of 100 : 0 : 0, 100 : 12:0, 100 : 0 : 12, and 100 : 12 : 12 EA–EGDM–DT mixtures in toluene in the presence of 4×10^{-4} M 2,2',6,6'-tetramethylpiperidine-1-oxyl (TEMPO) was studied. The conversion *C* of C=C bonds and the reduced (co)polymerization rate *w*/[M] were calculated by the procedure described in [7] from the heats of polymerization of EA and MMA, equal to 78.7 and 58.8 kJ mol^{-1}, respectively.

The content of residual C=C bonds in the copolymers was determined by ozonolysis [8] using ADS-4M double bond analyzer. For this purpose, solutions of (co)polymers in CCl_4 were prepared. Stilbene was used as a reference compound.

The average molecular weight of the copolymers and their MWD were determined by exclusion chromatography (EC) on a Waters liquid chromatograph equipped with a differential refractometer. We used Silasorb SGH 600 and Nucleosil 300 columns connected in tandem (Set B) or a Silasorb SGH 600 column (Set A), which provide linear calibration for PS references with M ~200–(5×10^5). The columns were eluted with THF at a flow rate of 0.3 ml min^{-1}. The column temperature was 35°C. To calculate MW, we used calibration curves for the PS references. The chromatograms were recorded and treated with the aid of Millennium-32 software.

The rheological properties of linear PEA and branched EA-EGDM, EA-TEGDM, EA-BDDA, and EA-PETA copolymers were studied with an Ubbelohde viscometer. The time of toluene outflow is $t_0 \approx 70$ s. The intrinsic viscosity [η] was determined by extrapolation of the dependence of the reduced viscosity on the polymer concentration in toluene to the zero concentration. The Huggins constants *k*' were calculated from experimental [η] values and from the slope of the dependence of the reduced viscosity on the polymer concentration in the solution.

Uncontrolled propagation of polymer chains in the course of 3*D* (co)polymerization of multifunctional monomers results in intra- and intermolecular chemical cross-linking to form an insoluble cross-linked polymer [4]. To prevent cross-linking, chain-transfer agents (e.g., thiols) terminating the chain propagation by the reaction

$$R_n^{\cdot} + RSH \rightarrow R_nH + RS^{\cdot},$$

$$RS^{\cdot} + M \rightarrow RSR_n.$$

are added.

3*D* radical copolymerization (in particular, copolymerization of EA with functionalized monomers) in the presence of chain-transfer agents yields branched macromolecules with different degrees of polymerization, which increase with the content of the branching agent [9]. The formation of small rings by the reaction of the C=C bonds of adjacent chains or by intrachain interaction may interfere with branching of the polymer chains [4]. However, this process can be minimized by varying the ratio of the chain-transfer agent to the branching agent in the system.

At *T* = 20°C, the copolymers are in the hyperelastic or viscous-flow state and are soluble in many organic solvents (benzene, toluene, chloroform, acetone). Their molecular structure (content of EA and branching agent units and their distribution in the macromolecule) is determined by the monomer reactivity and the composition of the reaction mixture. For example, copolymer with a random distribution of the monomer units is formed by radical copolymerization of EA (r_1 = 0.5) with dimethacrylates (r_2 = 2) [10]. In this case, unlike diacrylates, the copolymer enriched in EGDM or TEGDM is formed in the initial steps and the copolymer containing mainly the acrylate units is formed at high monomer conversions. This, in turn, increases the chain-transfer efficiency, since the chain-transfer coefficient C_s in the case of chain termination on the acrylate radical is higher than that on the methacrylate radical [11].

The formation of branched EA copolymers in kinetically controlled. We studied first the kinetics of radical polymerization of the components of the EA–EGDM–DT system and of their mixtures in toluene. The kinetic curves of polymerization of 100 : 0 : 0, 100 : 12 : 0, 100 : 0 : 12, and 100 : 12 : 12 EA–EGDM–DT mixtures are shown in Fig. 1. It can be seen (curve *1*) that EA polymerization in toluene is accompanied by a weak gel effect (acceleration of the reaction due to a raise in the viscosity of the reaction mixture upon an increase in the monomer conversion). As a result, the termination of the propagating macroradicals becomes hindered, and the constant of chain termination

of the macromolecules decreases [4]. The reaction exhibits an autoinhibiting effect in a wide conversion range, i.e., the polymerization decelerates owing to the diffusion control of the chain propagation. Introduction of EGDM results in the conventional 3*D* radical copolymerization and inhibits the reaction which is autocatalytic (gel effect) at low conversions and autoinhibited at $C > 50\%$ (curve *2*). Introduction of DT into the re-action system shifts the gel effect to high conversions and decreases it (cf. curves *1* and *3*). The features of radical polymerization of 100 : 12 : 12 EA–EGDM–DT mixtures are described by curve *4*. The reaction is autocatalytic at $C > 30\%$ and autoinhibited at $C > 60\%$ and yields a water-soluble EA–EGDM copolymer.

The average lengths of primary polymer chains $\bar{P}$ for branched EA–BDDA and EA– PETA copolymers were calculated from the kinetic data by the equation [4]

$$\overline{P} = \frac{k_p[M_1 + M_2]}{\sqrt{w_i k_t + k_{tr}[P]}} \approx \frac{k_p[M_1 + M_2]}{k_{tr}[P]}$$

(where k_p, k_t, and k_{tr} are the rate constants of chain propagation, termination, and transfer, respectively; $[M_1]$ and $[M_2]$, the concentrations of EA and branching agent; [P], DT concentration; and w_i, initiation rate equal to approximately 10^{-6} mol l^{-1} s^{-1}) taking into account that $(w_i k_t)^{1/2} << k_{tr}[P]$. The propagation of the primary polymer chains was initiated by a single event of generation of the R_i initiator radical by the reaction $I \rightarrow R_i$. $\bar{P}$ was calculated using $C_s = k_{tr}/k_p = 1.7$. The longest primary polymer chains ($P = 12$) are formed from 100 : 5 : 5 mixtures. $\bar{P}$ for copolymers prepared in the presence of 12 and 20 mol % of BDDA and PETA and equimolar amounts of DT decreases to 6 and 4 units, respectively, which suggests shortening of the inter-cross-link segments and terminal chains.

To obtain additional information on the copolymer structure, we used the critical conversion C_{cr} (gel point) calculated by the equation of the gelation theory [4]:

$$C_{cr} = 0.5k_p[P]/k_p\Phi_{22}(0) = 0.5k_{tr}[P]/k_p 2[M_2],$$

where $\Phi_{22}(0)$ is the second moment of functional istribution of the initial monomer molecules at the instant of time $t = 0$.

The fact that C_{cr} of EA–BDDA and EA–PETA copolymers is 42.5% suggests that the high copolymer yields (which are higher by a factor of more than 2 than C_{cr}) are due to the contribution of cyclization, which shifts C_{cr} to high conversions [4]. Hence, the branched macromolecules contain cyclic fragments.

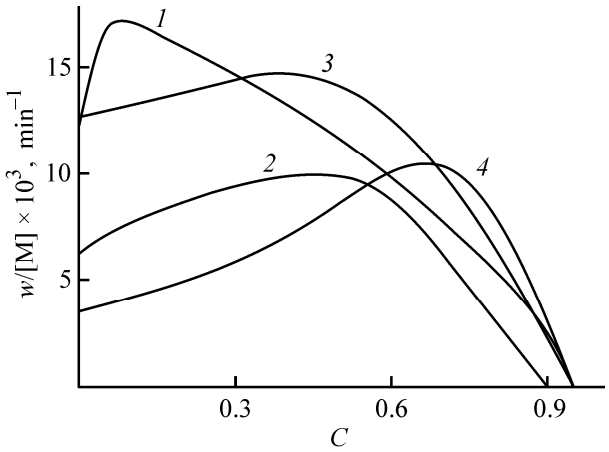


Fig. 1. Kinetic curves of polymerization of (*1*) 100 : 0 : 0, (*2*) 100 : 12 : 0, (*3*) 100 : 0 : 12, and (*4*) 100 : 12 : 12 EA–EGDM–DT mixtures in toluene. [AIBN] = 0.02 M, $T = 60°C$, [TEMPO] = 4×10^{-4} M, [toluene] = 80 wt %. (w/[M]) Reduced polymerization rate and (C) conversion.

Since the hydrodynamic volumes of linear and branched macromolecules differ, the molecular-weight parameters of the branched polymers are underestimated as compared to the absolute values calculated from the data of EC and multiple-angle light scattering. However, the MWD of branched polymers can be semiquantitatively estimated by the conventional EC method using an interferometer-reflactometer and calibration curves for linear polymers [6]. The number-average molecular weight (M_n), weight-average molecular weight (M_w), and polydispersity coefficients (M_w/M_n) of linear PEA and branched copolymers are listed in the table. MWD curves for linear PEA and branched copolymers prepared from mix-tures of different compositions are shown in Fig. 2. The MWD curve of linear PEA consisting of approximately 70 EA units is unimodal (Fig. 2, curve *1*), whereas the MWD curve (Fig. 2, curve *2*) of the copolymer prepared from a mixture of 2 mol % EGDM and DT is broadened owing to the presence of a low-molecular-weight fraction. The MWD curve of the co-polymer prepared in the presence of 12 mol % EGDM and DT is pronouncedly bimodal (Fig. 2, curve 3): the amount of the low-molecular-weight fraction is comparable to that of the high-molecular-weight fraction. M_n and M_w/M_n of the high-molecular-weight fraction ares 8×10^3 and 1.3, respectively. The molecular-weight distribution of the copolymer prepared from 20 mol % EGDM and DT is polymodal. As the EGDM content

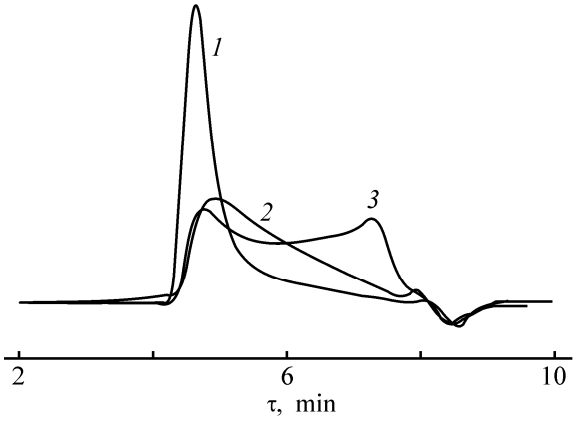


Fig. 2. MWD curves of (*1*) linear PEA and branched copolymers prepared from EA–EGDM–DT reaction mixtures of the compositions (*2*) 100 : 2 : 2 and (*3*) 100 : 12 : 12. (τ) Time.

in the reaction mixture increases from 2 to 20 mol % and hence the content of EGDM units in the copolymer grows, M_w/M_n ratio becomes larger (see table), i.e., the copolymer becomes more nonuniform in MW.

Comparison of MWD of EA–EGDM and EA–TEGDM copolymers shows that a change in the length and flexibility of the oligomeric branching agent block makes M_w and M_w/M_n of the copolymer smaller (see table). By contrast, use of BDDA as a branching agent leads to an increase in M_w and M_w/M_n of the EA–BDDA copolymers. The amount of the high-molecular-weight fraction in the MWD curves of these copolymers increases with the BDDA content in the reaction mixture from 5 to 20 mol %.

As can be seen from the table, the MWD of the copolymers depends on the content of C=C bonds in the branching agent. For example, the MWD of EA–PETA is broader than that of EA–BDDA. This fact is consistent with the data of Slark et al. [12], who showed that M_w and M_w/M_n of branched poly(methyl methacrylates) increased with the number of the functional groups of the branching agent. The number-average molecular weight (M_n) of the high-molecular-weight fraction is in the range $(13.6–21.3) \times 10^3$ and M_w/M_n, increases from 1.6 to 2.2 as PETA content becomes higher.

Thus, the MWD of the copolymers is determined by the composition of the reaction mixture, chemical structure of the branching agent, and its functionality. Our experimental data show that EA copolymers are macromolecules with different molecular weights.

Molecular weight and rheological parameters of linear and branched EA (co)polymers

(Co)polymer	Composition of EA–P*–DT mixture	MWD			[η], dl g^{-1}	k'
		$M_n \times 10^{-3}$	$M_w \times 10^{-3}$	M_n/M_w		
PEA	100 : 0 : 0	7.7	13.9	1.8	0.17	0.43
EA–EGDM	100 : 2 : 2	3.2	8.0	2.5	0.08	0.13
	100 : 5 : 5	1.9	6.8	3.6	0.06	0.13
	100 : 12 : 12	1.4	6.0	4.3	0.044	0.9
	100 : 20 : 20	1.3	7.0	5.3	0.057	0.26
EA–TEGDM	100 : 5 : 5	1.3	4.9	3.8	0.051	0.69
	100 : 12 : 12	1.3	4.6	3.5	0.048	0.32
	100 : 20 : 20	1.2	5.6	4.9	0.039	1.82
EA–BDDA	100 : 5 : 5	1.2	6.6	5.5	0.069	0.39
	100 : 12 : 12	1.6	10.0	6.3	0.054	0.89
	100 : 20 : 20	1.5	12.0	8.0	0.069	0.35
EA–PETA	100 : 5 : 5	2.5	14.3	5.7	0.061	1.02
	100 : 12 : 12	1.8	14.9	8.3	0.053	0.77
	100 : 20 : 20	1.6	31.7	19.8	0.062	1.52

* Branching agent.

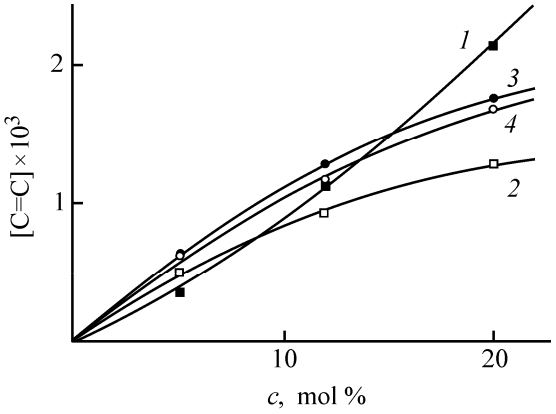


Fig. 3. Content of residual C=C bonds in 1 g of branched copolymers (*1*) EA–EGDM, (*2*) EA–TEGDM, (*3*) EA–BDDA, and (*4*) EA–PETA vs. the content *c* of the branching agent and DT.

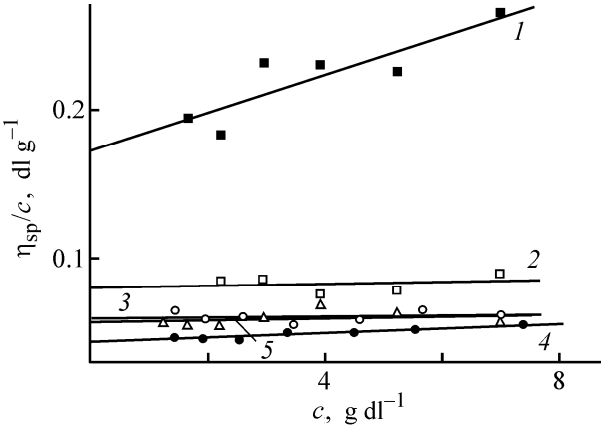


Fig. 4. Reduced viscosity η_{sp}/c vs. the concentration *c* of (*1*) linear PEA polymer and branched EA–EGDM copolymers prepared from (*2*) 100 : 2 : 2, (*3*) 100 : 5 : 5, (*4*) 100 : 12 : 12, and (*5*) 100 : 20 : 20 EA–EGDM–DT mixtures. Toluene, 20°C.

The dependence of the content of residual C=C bonds in the copolymers on the concentration of the branching agent and DT in the initial mixtures is shown in Fig. 3. The content of C=C bonds in the copolymers prepared in the presence of 20 mol % branching agent is the highest. As can be seen from Fig. 3 (curves *1*, *2*), the content of residual C=C bonds in the EA–TEGDM copolymer is a factor of 1.4 higher than that in EA–EGDM at a 5% dimethacrylate content in the reaction mixture. The content of residual C=C bonds in the EA–TEGDM copolymers prepared in the presence of 12 and 20 mol % dimethacrylates is lower than that in the corresponding EA–EGDM copolymers. This is probably due to involvement of the residual C=C bonds of TEGDM in branching and intrachain cyclization. In going from dimethacrylates to BDDA, the residual unsaturation of the copolymers grows (Fig. 3, curve *3*). As the functionality of the branching agent increases, the content of the residual C=C bonds in the copolymer (EA–PETA compared to EA–BDDA) slightly decreases.

The branching structure of copolymers can be readily confirmed by viscometry [13, 14]. The copolymer structure can be indirectly determined from the rheological properties of the copolymers and their comparison with those of the linear analogs of similar molecular weight. The typical dependences of the reduced viscosity η_{sp}/c of linear PEA and EA–EGDM copolymers of various compositions on their concentration *c* in the solution are shown in Fig. 4. These dependences were analyzed by the Huggins equation

$$\eta_{sp}/c = [\eta] + k'[\eta]^2 c,$$

where k' is the Huggins constant characterizing the thermodynamics of polymer–solvent interaction and the hydrodynamic behavior of the copolymer solutions.

We obtained the similar dependences for solutions of the other copolymers.

The intrinsic viscosities [η] and the Huggins constants k' of the copolymers examined are summarized in the table. As can be seen from the table, the rheological properties of these copolymers differ from those of the linear polymer. Since the conformation of branched copolymer macromolecules is compact, their [η] is low. In addition, the slope of the $\eta_{sp}/c = f(c)$ dependence for these copolymers suggests a weaker dependence of the reduced viscosity on the copolymer concentration (Fig. 4).

Important data on the behavior of branched copolymer in a solution were obtained from the analysis of the Huggins constants k'. As can be seen from the table, $k' < 0.5$ for linear PEA, i.e., toluene is a comparatively good solvent. Introduction of the EGDM and DT units into the macromolecule decreases k', i.e., the solvent quality becomes better. The exception is EA–EGDM copolymer (composition of the reaction mixture 100 : 12 : 12) which has $k' > 0.5$. This fact means that macromolecules of this copolymer form small dense balls in toluene, thus decreasing the viscosity of the copolymer solution. As also can be seen from the table, the interaction of EA–EGDM copolymer with the solvent varies in a wide range. The copolymer prepared in the presence of 12 mol % TEGDM is characterized by the best thermodynamic compatibility. Macromolecules of the copolymer prepared in the presence

of 20 mol % TEGDM weakly interact with the solvent. In this case, toluene becomes a bad solvent.

The branched copolymers prepared from 100 : 5 : 5 and 100 : 20 : 20 EA–BDDA–DT mixtures have similar thermodynamic affinities for toluene, whereas the interaction between the solvent and macromolecules of this copolymer prepared in the presence of 12 mol % branching agent becomes weaker. The dependence of k' on the composition of EA–PETA–DT reaction mixture is inverse. In this case, according to k', the interaction between the solvent and the branched copolymer macromolecules prepared in the presence of 12 mol % PETA and DT is the strongest.

An analysis of the experimental [η] and Huggins constants k' of EA copolymers showed no correlation between their rheological properties and the composition of the reaction mixture, the branching agent structure, and its functionality. This is due to the formation of branched copolymer by 3*D* random radical copolymerization controlled by the chain-transfer agent.

CONCLUSIONS

(1) Branched copolymers were prepared by one-step 3*D* radical copolymerization of ethyl acrylate with multifunctional comonomers of different chemical structures in toluene. The process is controlled by 1-decanethiol.

(2) The molecular-weight properties of the copolymer were determined by exclusion chromatography, and the content of residual C=C bonds in their molecules, by ozonolysis.

(3) The rheological properties of the branched copolymer in toluene were studied, the intrinsic viscosities of these solutions were measured, and the Huggins constants were calculated.

ACKNOWLEDGMENTS

This study was financially supported by the Russian Foundation for Basic Research (project no. 06-03-33 018) and by the Division of Chemistry and Materials Science, Russian Academy of Science, Program no. 8.

REFERENCES

1. Kurmaz, S.V., Kochneva, I.S., Perepelitsina, E.O., et al., *Izv. Ross. Akad. Nauk, Ser. Khim.*, 2007, no. 2, pp. 191–198.
2. Kritskaya, D.A., Kurmaz, S.V., and Kochneva, I.S., *Vysokomol. Soedin, Ser. A*, 2007, vol. 49, no. 10, pp. 1817–1827.
3. Lipatov, Yu.S., Nesterov, A.E., Gritsenko, T.M., and Veselovskii, R.A., *Spravochnik po khimii polimerov* (Handbook of Polymer Chemistry), Kiev: Naukova Dumka, 1971.
4. Korolev, G.V. and Mogilevich, M.M., *Trekhmernaya radikal'naya polimerizatsiya: Setchatye i giperrazvetvlennye polimery* (Three-Dimensional Radical Polymerization: Cross-Linked and Hyperbrached Polymers), St. Petersburg: Khimizdat, 2006.
5. Aulenta, F., Hayes, W., and Rannard S., *Eur. Polym. J.*, 2003, vol. 39, pp. 1741–1771.
6. O'Brien, N., McKee, A., Sherrington, D.C., et al., *Polymer*, 2000, vol. 41, pp. 6027–6031.
7. Berlin, A.A., Kefeli, T.Ya., and Korolev, G.V., *Poliefirakrilaty* (Polyether Acrylates), Moscow: Nauka, 1967.
8. Razumovskii, S.D. and Zaikov, G.E., *Ozon i ego reaktsii s organichekimi soedineniyami* (Ozone and Its Reactions with Organic Compounds), Moscow: Nauka, 1974.
9. Isaure, F., Cormack, P.A.G., and Sherrington, D.C., *J. Mater. Chem.*, 2003, vol. 13, pp. 2701–2710.
10. Korolev, G.V., Barurina, A.A., Berezin, M.P., and Kurmaz, S.V., *Vysokomol. Soedin., Ser. A*, 2004, vol. 46, pp. 656–667.
11. Costello, P.A., Martin, I.K., Slark, A.T., et al., *Polymer*, 2002, vol. 43, pp. 245–254.
12. Slark, A.T., Sherrington, D.C., Titterton, A., and Martin, I.K., *J. Mater. Chem.*, 2003, vol. 13, pp. 2711–2720.
13. Mori, H. and Muller, A.H.E., *Top. Curr. Chem.*, 2003, vol. 228, pp. 1–37.
14. Sato, T., Hashimoto, M., Seno, M., and Hirano, T., *Eur. Polym. J.*, 2004, vol. 40, pp. 273–282.

ISSN 1070-4272, Russian Journal of Applied Chemistry, 2008, Vol. 81, No. 10, pp. 1837–1841. © Pleiades Publishing, Ltd., 2008.
Original Russian Text © Yu.N. Pozhidaev, O.V. Lebedeva, S.S. Bochkareva, N.S. Shaglaeva, L.V. Morozova, M.G. Voronkov, 2008, published in Zhurnal Prikladnoi Khimii, 2008, Vol. 81, No. 10, pp. 1716–1720.

MACROMOLECULAR CHEMISTRY AND POLYMERIC MATERIALS

Hybrid Nanocomposites: Poly(chloromethyl-), Poly(methyl-), Poly(phenylsilsesquioxane)–Nitrogen Polybase

Yu. N. Pozhidaev, O. V. Lebedeva, S. S. Bochkareva, N. S. Shaglaeva, L. V. Morozova, and M. G. Voronkov

Irkutsk State Technical University, Irkutsk, Russia

Favorskii Institute of Chemistry, Siberian Branch, Russian Academy of Sciences, Irkutsk, Russia

Received April 17, 2008

Abstract—Formation of nanocomposites in the sol–gel systems $RSiX_3$ [R = CH_3 (**I**), C_6H_5 (**II**), X = Cl; R = $ClCH_2$ (**III**), X = OC_2H_5]–polyvinylazole [$(–CH_2–C(Y)H–)_n$, Y = pyrazolyl, imidazolyl, 4-pyridinyl, 2-methyl-5-pyridinyl], and also **I**–1-vinyl-4,5,6,7,-tetrahydroindole using was studied. The composition and structure of the resulting nanocomposites were analyzed.

DOI: 10.1134/S1070427208100248

Sol–gel technique employing tetraalkoxysilanes SiR_4 (R = OC_2H_5, OCH_3) and organic low- and high-molecular-weight compounds is being intensively developed as a method for preparing organoinorganic composite materials and, in particular, nanocomposites [1–5]. To expand the range of such materials and to improve their performance characteristics, various polymers are introduced into the sol–gel process [6–8]. An extension of this approach is use of organyltrichloro- or organyltrialkoxysilanes [$RSiX_3$; X = Cl, OCH_3, OC_2H_5; R = CH_3, C_6H_5, $CH{=}CH_2$, $(CH_2)_3NH_2$, etc.] instead of tetraalkoxysilanes, e.g., vinyltriethoxysilane, phenyltriethoxysilane, 3-aminopropyltriethoxysilane, etc. [9–11]. In this case, the structure and properties of the resulting copolymers are governed by the nature of a substituent R and by the conditions of the sol–gel process (hydrolysis of silanes) [12, 13].

For example, a specific feature of the hydrolysis product of chloromethyltriethoxysilane, poly(chloromethylsilsesquioxane) $[ClCH_2SiO_{1.5} \cdot nH_2O]_m$, is that it contain in the bulk and at the surface chloromethyl groups capable of donor–acceptor interaction with compounds basic in nature. In ethanol, a macroporous product with high content of mesopores (total volume 1.37 $cm^3\ g^{-1}$) and large specific surface area (155 $m^2\ g^{-1}$) is formed [13].

The hydrolytic polycondensation of methyltrichlorosilane in aqueous and aqueous-organic solutions is accompanied by the formation of hydrated poly(methylsilsesquioxane) $[CH_3SiO_{1.5} \cdot nH_2O]_m$. The resulting solid product is characterized by a high specific surface area (394–1204 $m^2\ g^{-1}$) and microglobular (prevalent globular size 1–2 nm) lamellar or folded structure with a highly developed system of micro- and mesopores [14, 15]. The process is rapid and gives poly(methylsilsesquioxane) in nearly 100% yield via three parallel independent mechanisms of formation of Si–O–Si groups: hetero- and homofunctional polycondensation, and generation and further transformation of silanone intermediates [16, 17].

Preparation of cross-linked phenyltrichlorosilane-based 3*D* polymers is sterically hindered by the bulky phenyl groups. Poly(phenylsilsesquioxanes) $[C_6H_5SiO_{1.5}]_m$ synthesized by any method demonstrate poor thermal stability and low solubility in water and organic solvents [13].

The goal of this study was to synthesize hybrid copolymers based on organosilicon monomers using sol–gel technique. We performed a comparative analysis of the formation, structure, and properties of nanocomposites based on $RSiX_3$ (X = CH_3, C_6H_5, CH_2Cl), on the one hand, and polyvinylazoles, on the other hand.

The following polyvinylazoles were studied: poly(1-vinylpyrazole) (PVP), poly(1-vinylimidazole) (PVI), poly(4-vinylpyridine) (PVSP), poly(2-methyl-5-vinylpyridine) (PMVP), and 1-vinyl-4,5,6,7-tetrahydroindole) (VTHI).

EXPERIMENTAL

Poly(1-vinylpyrazole), poly(1-vinylimidazole), poly(4-vinylpyridine), poly(2-methyl-5-vinylpyridine), and 1-vinyl-4,5,6,7-tetrahydroindole) were prepared using the known procedures [18–20]. Commercial chloromethyltriethoxysilane (CMTEOS), methyltrichlorosilane, and phenyltrichlorosilane were used.

An elemental analysis of reaction products was carried out on a Thermo Finnigan gas analyzer. IR spectra were recorded on an IFS-25 spectrometer using KBr pellets and Nujol mulls. ^{1}H and ^{13}C NMR spectra were recorded in $CDCl_3$ on a Bruker DPX-400 instrument (400.13 MHz) using TMS as an internal reference.

The surface structure of the organoinorganic copolymers was examined on a Philips-525M scanning electron microscope.

The specific surface area of the composites was estimated by measured the nitrogen adsorption at various temperatures and pressures in a graduated high-vacuum cell.

TG curves were recorded on a Paulik–Paulik–Erdey derivatograph (MOM, Hungary) in air at a heating rate of 5 deg min^{-1}. The maximal temperature was 700°C, and the DTA sensitivity, 1/5 to 1/10.

The sorption of Ag(I), Pd(II), and Pt(IV) on the copolymers was carried out from solutions containing 0.2–5 (mg metal) l^{-1}. Stock solutions were prepared using $AgNO_3$, $PdCl_2$, and $H_2PtCl_6 \cdot 6H_2O$ (chemically pure grade), and distilled water. The metal concentrations in solutions were determined photometrically with a KFK-2 photocolorimeter [21].

The base hydrolysis of CMTEOS in the presence of nitrogen polybases was carried out at room temperature as follows. CMTEOS (1.0 g) and 0.1 M aqueous NaOH (2.55 ml) were successively added to the nitrogen polybase (0.3 g) dissolved in ethanol (5 ml). On adding aqueous NaOH, the resulting mixture first became turbid and gel-like, and then an insoluble hybrid composite copolymer precipitated. This precipitate was multiply washed with water and vacuum-dried in a desiccator to constant weight. Carrying out the hydrolysis in alkaline medium provides a 3*D* condensation of poly(chloromethylsilsesquioxane) [12, 13], whose rigid structure makes the product insoluble in water and organic solvents and thermally stable (Table 1).

The hydrolysis of MTCS in the presence of nitrogen polybases or VTHI was performed similarly, but

Table 1. Composition and properties of composites

Copolymer	Elemental composition, %				$n : m$*	Yield, %	S_{sp}, $m^2 g^{-1}$	T_{dec}, °C
	C	H	Si	N				
$ClCH_2SiO_{1.5}$: PVP	22.55	3.52	28.84	6.64	4.2 : 1	67.7	11.3	280
$ClCH_2SiO_{1.5}$: PVI	24.86	5.12	26.16	6.48	4.0 : 1	72.4	16.8	325
$ClCH_2SiO_{1.5}$: PVSP	27.11	3.81	20.99	3.60	2.9 : 1	91.8	0.98	235
$ClCH_2SiO_{1.5}$: PMVP	35.25	4.60	18.04	4.80	1.9 : 1	78.2	1.98	270
$CH_3SiO_{1.5}$: PVP	36.21	5.82	17.55	12.41	1.4 : 1	82.2	34.7	195
$CH_3SiO_{1.5}$: PVI	36.79	7.24	11.14	13.33	0.8 : 1	84.1	17.5	274
$CH_3SiO_{1.5}$: PVSP	43.78	7.01	8.43	6.27	0.7 : 1	95.3	12.3	285
$CH_3SiO_{1.5}$: PMVP	51.58	8.97	6.64	6.74	0.5 : 1	76.4	24.7	304
$CH_3SiO_{1.5}$: $(VTHI)_2$	33.33	6.02	15.17	8.22	1.8 : 1	79.3	31.1	325
$C_6H_5SiO_{1.5}$: PVP	50.84	5.27	10.04	9.83	1 : 1	71.4	–	93**
$C_6H_5SiO_{1.5}$: PVI	43.59	5.25	17.45	4.67	3.7 : 1	69.7	–	73**
$C_6H_5SiO_{1.5}$: PVSP	39.76	5.18	20.88	6.08	1.7 : 1	60.6	–	115**
$C_6H_5SiO_{1.5}$: PMVP	51.71	6.59	8.90	3.73	2.5 : 1	65.4	–	125**

* ($n : m$) Component unit ratio ($ClCH_2SiO_{1.5}$: N-polybase, $CH_3SiO_{1.5}$: N-polybase, and $C_6H_5SiO_{1.5}$: N-polybase).

** Melting point.

without base catalysis. The hydrolysis of MTCS in accordance with Eq. (1) does not require base catalysis [12, 13], being accompanied by a considerable increase in the solution acidity as a result of formation of HCl, along with methylsilanetriol, in the first stage:

$$n\mathrm{CH_3SiCl_3} + 3n\mathrm{H_2O} \rightarrow n\mathrm{CH_3Si(OH)_3} + 3n\mathrm{HCl},$$

$$n\mathrm{CH_3Si(OH)_3} \rightarrow (\mathrm{CH_3SiO_{1.5}})_n + 1.5n\mathrm{H_2O}. \quad (1)$$

The process is rapid, and gives finely dispersed low-molecular-weight poly(methylsilsesquioxane). Such composites are stable up to 195–325°C (Table 1).

Similarly to the case of tetraethoxysilane-based systems studied previously [22], we found in this study no correlations between the hybrid copolymer composition and the basicity of the nitrogen polybase (pK^+_{BH} of 1-vinylpyr-azole, 1-vinylimidazole, 4-vinylpyridine, and 2-methyl-5-vinylpyridine is 1.7, 7.52, 5.62, and 5.67, respective-ly). In these systems, the fraction of nitrogen polybases in the composite increases in the order PVP < PVI < PVSP < PMVP. The composition of the CMTEOS-based copolymers ($\mathrm{ClCH_2SiO_{1.5}}$: N-polybase unit) is as follows: 4.2 : 1 (PVP), 4.0 : 1 (PVI), 2.9 : 1 (PVSP), and 1.9 : 1 (PMVP) (Table 1). In the MTCS-based systems, the $\mathrm{CH_3SiO_{1.5}}$: N-polybase unit ratios were 1.4 : 1 (PVP), 0.8 : 1 (PVI), 0.7 : 1 (PVSP), and 0.5 : 1 (PMVP) (Table 1).

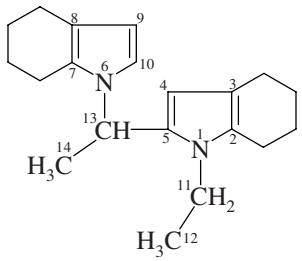
In the copolymers formed in the system phenyltrichlorosilane–nitrogen polybase, the fraction of the polybase decreases as its basicity increases. In this case, the $\mathrm{C_6H_5SiO_{1.5}}$: N-polybase unit ratios are 1 : 1 (PVP), 1.7 : 1 (PVSP), 2.5 : 1 (PMVP), and 3.7 : 1 (PVI) (Table 1).

The case with VTHI is somewhat special. In the presence of HCl, formed as a hydrolysis product of methyltrichlorosilane, VTHI tends to dimerize. As a result, the resulting composite contains VTHI dimer, but not monomeric VTHI or its polymerization product poly(1-vinyl-4,5,6,7-tetrahydroindole), and the composition of this copolymer is $\mathrm{CH_3SiO_{1.5}}$: $(\mathrm{VTHI})_2$ = 1.8 : 1.

The formation of VTHI dimer in synthesis of this composite is confirmed by the IR and ^{1}H and ^{13}C NMR spectra.

The IR spectrum of the sample under study contains pyrrole absorption bands at 690, 912, 1200, 1300, 1380, 1490, and 1540 $\mathrm{cm^{-1}}$.

The ^{1}H and ^{13}C NMR spectra of this composite show resonances typical of the dimer:



^{1}H NMR, δ, ppm: 1.77, 2.66 (cyclohexane fragment); 5.84, 6.19 (pyrrole ring); 5.17, 1.54 (=CH–CH_3). ^{13}C NMR: δ, ppm: 128.99 ($C^{2,7}$), 116.69 ($C^{3,8}$), 106.99 (C^4), 129.04 (C^5), 108.67 (C^9), 117.50 (C^{10}), 49.87 (C^{11}), 24.23 (C^{12}), 47.94 (C^{13}), 22.64 (C^{14}).

Therefore, one could suggest the following dimerization mechanism. First, HCl formed in hydrolysis reacts with 1-vinyl-4,5,6,7-tetrahydroindole to give the immonium cation. Second, electrophilic attack of the immonium cation at the pyrrole ring of the copolymer macromolecule yields VTHI dimers.

Among the MTCS-based copolymers, the composite with VTHI has the best thermal stability, highest specific surface area (Table 1), and smallest globule size (predominant particle size 86–97 nm).

Among the CMTEOS-based composites, the smallest particle size (30–50 nm) was found for the copolymers with PVP. The particle size of the corresponding copolymers with PVI is 300 nm. The products obtained in the sol–gel process with PVSP and PMVP are polydisperse crystal-like substances.

The IR spectra of all the copolymers under consideration contain strong absorption bands at 1010–1150 $\mathrm{cm^{-1}}$, typical of Si–O–Si stretching vibrations. The protonation causes a high-frequency shift of the stretching vibrations of the pyridine nitrogen from 1615 $\mathrm{cm^{-1}}$ in the initial polybases to 1650 $\mathrm{cm^{-1}}$. Weak absorption bands of the protonated pyrazole and imidazole rings are observed at 1530–1570 $\mathrm{cm^{-1}}$.

The fact that the nitrogen atoms of the heterocycles in the composites retain their chemical activity was confirmed by sorption data. The sorption activity of the copolymers of CMTEOS and MTCS with nitrogen polybases was examined with respect to Ag^+ in nitric acid solutions and to Pd(II) and Pt(IV), in HCl solutions, in which these metals exist as anionic complexes $[PdCl_4]^{2-}$ and $[PtCl_6]^{2-}$ (Table 2). Data on the static sorption capacity (SSC) and distribution coefficient D (in 1 M acid solutions) revealed no correlation between the sorption activity, polybase nature, and

Table 2. Static sorption capacity SSC and limiting sorption capacity LSC of copolymers for noble metals, and distribution coefficient *D* of noble metals between copolymers and aqueous solutions

Copolymer	SSC, mg g^{-1} / LSC, mg g^{-1}			D, cm^3 g^{-1}		
	Pd(II)	Pt(IV)	Ag(I)	Pd(II)	Pt(IV)	Ag(I)
$C1CH_2SiO_{1.5}$: PVP	225/203	580/375	152/208	1040	3750	7700
$C1CH_2SiO_{1.5}$: PVI	325/212	2050/390	–	2300	4500	–
$C1CH_2SiO_{1.5}$: PVSP	520/265	227/488	215/270	2750	1650	3930
$C1CH_2SiO_{1.5}$: PMVP	300/339	175/623	–	1900	1340	–
$CH_3SiO_{1.5}$: PVP	328/564	640/1038	480/575	860	330	5700
$CH_3SiO_{1.5}$: PVI	666/718	1280/1321	694/732	4400	1570	30 000
$CH_3SiO_{1.5}$: PVSP	1058/693	860/1274	680/706	6000	970	25 000
$CH_3SiO_{1.5}$: PMVP	803/690	850/1270	–	2500	1400	–

sorbate nature. However, the observed high sorption capacities suggest that the nitrogen donor atoms in the composites retain their complexing power. The formation of metal–nitrogen bonds is demonstrated by the appearance of the bands at 400–300 cm^{-1} in the IR spectra of the metal-saturated copolymers.

CONCLUSIONS

(1) Hydrolysis of chloromethyltriethoxysilane, methyltrichlorosilane, and phenyltrichlorosilane in the presence of poly(*N*-vinylazoles), poly(vinylpyridines), and 1-vinyl-4,5,6,7-tetrahydroindole gives organoinorganic copolymers.

(2) The resulting copolymers are characterized by high thermal and chemical stability, highly dispersed structure, and highly developed surface area.

(3) The hybrid copolymers efficiently sorb noble metal ions from acidic solution.

ACKNOWLEDGMENTS

This study was financially supported by the Russian Foundation for Basic Research (project no. 06-08-00 317).

REFERENCES

1. Khimich, N.N., Fiz. *Khim. Stekla*, 2004, vol. 30, no. 5, pp. 585–602.
2. Cazacu, M., Dragan, S., and Vlad, A., *J. Appl. Polym. Sci*., 2003, vol. 88, no. 8, pp. 2060–2067.
3. Bandyopadhyay, A., De Sarkar, M., and Bhowmick, A.K., *J. Mater. Sci*., 2005, vol. 40, no. 19, pp. 5233–5241.
4. Salesch, T., Bachmann, S., Brugger, S., et al., *Adv. Funct. Mater.*, 2002, vol. 12, no. 2, pp. 134–142.
5. Shaglaeva, N.S., Lebedeva, O.V., Pozhidaev, Yu.N., et al., *Zh. Fiz. Khim*., 2007, vol. 81, no. 3, pp. 406–409.
6. Hernandes-Pardon, G., Rojas, F, and Casta, V.M., *Nanotechnology*, 2004, vol. 15, no. 1, pp. 98–103.
7. Parvole, J., Montfort, J.-P., and Billon, L., *Macromol. Chem. Phys*., 2004, vol. 205, no. 10, pp. 1369–1378.
8. Huang, C.J., Fu, S.Y., Zhang, Y.H., et al., *Cryogenics*, 2005, vol. 45, no. 6, pp. 450–454.
9. Aparicio, M., Lecoq, E., Castro, Y., and Duran, A., *J. Sol–Gel Sci. Technol*., 2005, vol. 34, no. 3, pp. 233–239.
10. Ren, L., Wang, L., Zang, F., and Liu, P., *Polym. Mater. Sci. Technol*., 2004, vol. 20, no. 6, pp. 60–63.
11. Martos, C., Rubio, F., Rubio, J., and Oteo, J.L., *J. Sol–Gel Sci. Technol*., 2003, vol. 26, no. 1, pp. 511–516.
12. Voronkov, M.G., Mileshkevich, V.P., and Yuzhelevskii, Yu.A., *Siloksanovaya svyaz': Fizicheskie svoistva i*

khimicheskie prevrashcheniya (Siloxane Bond: Physical Properties and Chemical Transformations), Novosibirsk: Nauka, 1976.

13. Slinyakova, I.B. and Denisova, T.S., *Kremniiorganicheskie adsorbenty: Poluchenie, svoistva, primenenie* (Organosilicon Compounds: Synthesis, Characterization, and Applications), Kiev: Naukova Dumka, 1988.
14. Voronkov, M.G., Murinov, Yu.I., Pozhidaev, Yu.N., et al., *Vysokomol. Soedin., Ser. A*, 2000, vol. 42, no. 7, pp. 1175–1182.
15. Kolyadina, O.A., Murinov, Yu.I., Voronkov, M.G., and Pozhidaev, Yu.N., *Izv. Ross. Akad. Nauk. Ser. Khim.*, 2000, no. 12, pp. 2033–2035.
16. Voronkov, M.G., *Main Group Chem.*, 1998, vol. 2, no. 4, pp. 235–241.
17. Voronkov, M.G., *J. Organomet. Chem.*, 1998, vol. 557, no. 1, pp. 143–155.
18. Safronov, A.P., Tager, A.A., Voit, V.V., et al., *Vysokomol. Soedin., Ser. A*, 1988, vol. 30, no. 11, pp. 2360–2364.
19. Fuoss, R.M. and Strauss, V.P., *J. Polym. Sci.*, 1948, vol. 3, no. 1, pp. 246–253.
20. Trofimov, B.A. and Mikhaleva, A.I., *Izv. Akad. Nauk SSSR, Ser. Khim.*, 1979, issue 4, no. 12, p. 2840.
21. *Probootbiranie i analiz blagorodnykh metallov* (Sampling and Analysis of Noble Metals), Baryshnikov, I.F., Ed., Moscow: Metallurgiya, 1978.
22. Pozhidaev, Yu.N., Shaglaeva, N.S., Lebedeva, O.V., et al., *Zh. Prikl. Khim.*, 2007, vol. 80, no. 8, pp. 1346–1349.

ISSN 1070-4272, Russian Journal of Applied Chemistry, 2008, Vol. 81, No. 10, pp. 1842–1845. © Pleiades Publishing, Ltd., 2008.
Original Russian Text © I.P. Chikhacheva, V.P. Zubov, E.A. Maslova, I.V. Kurbakova, 2008, published in Zhurnal Prikladnoi Khimii, 2008, Vol. 81, No. 10, pp. 1721–1724.

MACROMOLECULAR CHEMISTRY AND POLYMERIC MATERIALS

Synthesis of Polyacetals under Microwave Irradiation

I. P. Chikhacheva, V. P. Zubov, E. A. Maslova, and I. V. Kurbakova

Lomonosov State Academy of Fine Chemical Technology, Moscow, Russia
Vernadsky Institute of Geochemistry and Analytical Chemistry, Russian Academy of Sciences, Moscow, Russia

Received November 29, 2007

Abstract—Synthesis of polyvinyl formal from a mixture of polyvinyl alcohol and formaldehyde under microwave irradiation was studied. The syntheses of polyvinyl formal under microwave irradiation and thermal treatment were compared. The yield of polyvinyl formal was examined in relation to the irradiation power, initial component concentration, and reaction time. The polyacetals were characterized by elemental analysis and IR spectroscopy.

DOI: 10.1134/S107042720810025X

One of promising approaches to development of efficient power-saving chemical processes is based on application of microwave irradiation (MWI). Therefore, the study of effects of microwave irradiation on chemical systems is an topical problem.

The published data show that microwave irradiation is an efficient technique for pretreatment of samples in analytical chemistry [1] and synthesis of low-molecular-weight organic compounds [2, 3]. The preparation of nanostructures from nanoparticles of silver, platinum, palladium, ruthenium, and other metals in the presence of polymeric stabilizers in combination with reducing agent, such as glycerol, hydrazine, dimethylformamide, and polyalcohols, has been extensively studied recently [4, 5]. It was found that, under microwave irradiation, polymeric methyl acrylate nanostructures are formed in situ from methyl acrylate monomers in the presence of silver nanoparticles [6]. The selective absorption of microwave radiation by polar components incorporated in a nonpolar polymeric matrix can improve composites. Owing to the higher efficiency of microwave heating as compared to thermal treatment, this technique can be used for dehydration of fuels (e.g., coal) [7, 8].

The number of studies concerned with the effect of microwave irradiation on foodstuffs steadily increases [9, 10]. In particular, it has been found that physicochemical characteristics of gel-like starch treated with microwave radiation strongly differ from those of thermally treated gel-like starch [11]. The problem of utilization of polymeric wastes can be solved by their microwave treatment. For example, the efficiency of decomposition and/or dehydrochlorination of polyvinyl chloride grows in the presence of components absorbing microwave radiation (activated carbon, iron) and also with increasing radiation power and irradiation time [12].

It should be noted that microwave irradiation can not only substantially accelerate slow reactions, but also make possible new processes. Therefore, the modern chemistry is characterized by growing application of microwave irradiation.

In this study, we examined the effect of microwave irradiation on synthesis of polyvinyl formal (PVF) by the reaction of polyvinyl alcohol (PVA) with formaldehyde (F). The features of PVA acetalization under these conditions are analyzed. In modern chemistry, PVF is prepared either from polyvinyl acetate or, more preferably, by heterogeneous acetalization of PVA. This reaction is commonly performed in aqueous solutions containing formaldehyde and acid catalyst (e.g., hydrochloric or sulfuric acid) at elevated temperatures in the course of several hours. The resulting insoluble product is separated, repeatedly washed, and then dried [13].

Table 1. PVF preparation under microwave treatment ([PVA] = 1.4 M, [F] = 2.0 M)

Run no.	Power, W (time, min)	$M_{PVA} \times 10^{-3}$	HCl concentration, %	PVF yield, %
1	300(5) + 800(5)	25	0.37	0
2	300(5) + 800(5)	25	0.37	18
3	300(5) + 800(5)	25	37.00	45
4	100(3) + 180(3)	25	37.00	34
5	100(3) + 180(3)	25	37.00	16
6	100(3) + 180(3)	100	0.37	0
7	100(3) + 180(1)	100	37.00	31
8	100(3) + 180(3)	100	37.00	38
9	180(3) + 300(3)	100	37.00	49
10	180(3) + 300(5)	100	37.00	57

* Closed reaction vessel.

Table 2. PVF yield under microwave treatment at different concentrations of the starting reactants [Microwave irradiation parameters: 180 W (3 min) + 300 W (3 min)]

Concentration, M		PVA : F ratio	PVF yield, %
PVA	F		
1.35	1.31	1 : 0.97	50
1.19	1.31	1 : 1.10	47
0.86	0.67	1 : 0.78	45
0.86	1.34	1 : 1.56	44
0.85	1.31	1 : 2.60	42
0.84	0.26	1 : 0.30	31
0.84	0.79	1 : 0.94	54
0.84	4.00	1 : 4.70	22
0.73	1.18	1 : 1.60	41
0.73	1.99	1 : 2.70	40
0.51	1.31	1 : 2.60	33

EXPERIMENTAL

In this study, both low- (M = 25 000) and high-molecular-weight (M = 100 000) PVA were used. Other chemicals were aqueous formaldehyde (Formalin) 40% and aqueous hydrochloric acid.

Low-molecular-weight PVA was of Laverna 16/1 brand [GOST (State Standard) 10 779–78, the acetate group content does not exceed 2%]. High-molecular-weight PVA was of Sandinil 2499M brand (Netherlands) (the acetate group content did not exceed 1%].

The PVA acetylation under microwave irradiation was carried out in a Teflon beaker at various ratios of the starting reactants.

The reaction mixture was irradiated in microwave ovens (Samsung GP90, China, 2.45 GHz; MDS-2000, CEM Corp., USA, 2.45 GHz). The resulting polymeric products were characterized by IR spectroscopy (Bruker, EGUINOX-55, Germany) and elemental analysis. The solubility of PVF in various solvents was determined both at room and elevated temperatures.

The PVF synthesis under thermal treatment was carried out as follows. An 8% aqueous solution of PVA (10 ml) was placed in a reaction flask, and then formaldehyde (2.1 ml) and concentrated acid (0.2–0.4 ml) were added. The reaction mixture was heated for 1.5 h, with the temperature gradually increasing from 60 to 90°C.

Polyacetal samples prepared under both thermal treatment and microwave irradiation were thoroughly washed with warm water (35–40°C) and then dried to constant weight. The polyacetal yield was calculated as the ratio of the weight of the final product after its contact with hot water (80°C) for 30 min to the total weight of the initial PVA and formaldehyde.

In this study, we examined how the radiation power, irradiation time, acid concentration, and molecular weight of the starting PVA affect the PVF yield. We found that MWI caused the temperature of the reaction mixture to increase to 53–55 (180 W, 3 min) or 65–70°C (300 W, 3 min). Table 1 shows that, with increasing radiation power and irradiation time, the PVF yield grows. At the irradiation time exceeding 10 min, the reaction mixture strongly warms up and is carbonized. With the HCl concentration in the reaction mixture increasing from 0.37% (pH 1.14) to concentrated HCl (pH 0.63), the PVF yield grows. It was found that the PVA molecular weight insignificantly affects the polyacetal yield.

In this study, PVF was prepared in an open reaction vessel. Under these conditions, the PVF synthesis is accompanied by gradual evaporation of the solvent (water) and increase in the reactant concentrations. As a result, the final product is formed as a swollen film. In preparing PVF in a closed reaction vessel, water formed as one of by-products is not noticeably removed from the reaction mixture. We believe that the presence of water, all other factors being the same, makes lower the PVF yield as compared to synthesis in an open reaction vessel (Table 1).

Table 3. PVF interaction with solvents at 25°C (24 h) and 85–90°C (1 h)

Solvent	Treatment method			
	thermal		MWI	
	25°C	85–90°C	25°C	85–90°C
Dioxane	w	s	w	s
DMF	w	s	w	s
Acetic acid	s	sol	s	sol
Pyridine	s	s	s	s
Benzyl alcohol	s	sol	s	sol

* (w) Weakly swelling, (s) strongly swelling, and (sol) dissolves.

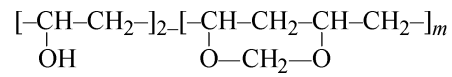
The PVF yield was examined in relation to the concentration and ratio of the starting components. Table 2 shows that, with the PVA to formaldehyde ratio varied from 1 : 0.3 to 1:6, the PVF yield is maximal when this ratio is approximately 1 : 1.5.

For comparison, PVF was also prepared by the common technique with stepwise heating of the reaction mixture: 60°C (30 min) + 75°C (30 min) + 90°C (30 min). In these experiments, the temperature of the reaction mixture was comparable to, or even higher than that in synthesis under microwave irradiation, and the reaction vessel was equipped with a reflux condenser preventing the solvent evaporation. After treatment of the reaction mixture for 1.5 h, the PVF yield was about 28%. Under these conditions, the yield remained virtually unchanged with increasing reaction time. In going to synthesis under thermal treatment in an open reaction vessel, the PVF yield changed insignificantly.

The IR spectra of PVA and formaldehyde substantially differ from the spectra of polyvinyl formal obtained under microwave or thermal treatment. The intensity of absorption bands of the hydroxo groups of polyvinylformal (3300–3600 cm^{-1}) decreases and new absorption bands at 2805 and 2885 cm^{-1} appear, presumably due to vibrations of the CH_2 groups in the O–CH_2–O fragments. Furthermore, the acetylation is accompanied by a significant change in the intensity of four absorption bands belonging to the C–O groups (1000–1200 cm^{-1}), present in the spectrum of PVA [14, 15]. It was also found that the IR spectrum of the sol prepared by extraction of PVF with hot water is almost identical to that of the initial PVA except for a weak change in the intensity of absorption bands in the range 1000–1200 cm^{-1}. This effect can be caused by the low degree of acetalization of the water-soluble fraction of polyacetal.

It is known [13] that the solubility of PVF decreases as the content of vinyl acetate groups in the starting PVA becomes lower. The solubility of PVF prepared in this study was determined in toluene, dimethylformamide, acetic acid, pyridine, benzyl alcohol, and nitrobenzene, i.e., in solvents commonly used for dissolution of polyacetals. The PVF samples were kept in these solvents either at room temperature for 24 h or at elevated temperature (85–90°C) for 1 h. Table 3 shows that the solubility of polyacetals is essentially independent of the method of their preparation. The similarity of the chemical compositions of polyacetals prepared under microwave irradiation and thermal treatment was confirmed by elemental analysis.

The carbon and hydrogen content of the polyacetals (wt %) was, respectively, 56.10–57.05 and 8.57–8.71 for samples prepared under microwave irradiation (Table 1, run no. 7) and 56.80–58.24 and 8.60–8.80 for samples prepared under thermal treatment. The calculated carbon and hydrogen content was 54.54 and 9.1% for PVA and 60 and 8% for PVF. Based on these data, we suggest the following formula of the polyacetal:



where $n = 4$ and $m = 1$.

It is known [13] that, when preparing acetals under thermal treatment, a product with a low degree of acetalization is formed. We believe that, in this case, the acetalization of PVA is deteriorated due to the fact that incompletely acetalized PVA is poorly soluble and precipitates in the form of a dense precipitate, and its further reaction with formaldehyde becomes hindered. The product with a more uniform composition can be prepared by makes larger the solid–liquid interface area. Apparently, MWI also provides some possibilities for raising the degree of acetalization.

CONCLUSIONS

(1) Polyacetals are efficiently formed under microwave irradiation of the reaction mixture containing polyvinyl alcohol and formaldehyde.

(2) At identical concentrations of the starting components and equal reaction temperatures, the yield of polyvinyl formal is 50–57% (reaction time 4–6 min) under microwave irradiation and 28–30% (reaction time 1.5 h) under thermal treatment.

(3) The yield of polyvinyl formal is maximal at a 1 : 1.5 molar ratio of polyvinyl alcohol and formaldehyde, and under microwave irradiation the reaction time decreases by a factor of 10–15 as compared to thermal treatment.

(4) Polyvinyl formal samples prepared from reaction mixtures of identical composition under microwave irradiation and thermal treatment have identical chemical composition.

REFERENCES

1. Kubrakova, I.V., *Usp. Khim*., 2002, vol. 71, no. 4, p. 327.
2. Perreux, I. and Loupy, A., *Tetrahedron*, 2001, vol. 57, p. 9199.
3. Lidstrom, P., Tierney, J., Wathey, B., and Weston, J., *Tetrahedron*, 2001, vol. 57, p. 9225.
4. Grace, A.N. and Pandian, K., One Pot Synthesis of Polymer Protected Pt, Pd, Ag and Ru Nanoparticles and Nanoprisms under Reflux and Microwave Mode of Heating in Glycerol. A Comparative Study, *Mater. Chem. Phys.* (accepted manuscript), 2007.
5. Lio, Y. And Sun, X., *Mater. Lett*., 2007, vol. 61, p. 1622.
6. Wada, Y. et al., *Polymer*, 2007, vol. 48, p. 1441.
7. Pawluezyk, J.M. et al., *Tetrahedron Lett*., 2007, vol. 48, p. 1497.
8. Seehra, M.S., Kalra, A., and Manivannan, A., *Fuel*, 2007, vol. 86, p. 829.
9. Sumnu, G., et al., *J. Food Eng*., 2007, vol. 78, p. 1382.
10. Bhattacharya, S. and Jena, R., *J. Food Eng*., 2007, vol. 78, p. 1305.
11. Palav, A. and Seetharaman, K., *Carbohydrate Polym*., 2007, vol. 67, p. 596.
12. Moriwaki, S. et al., *Appl. Therm. Eng*. 2006, vol. 26, p. 745.
13. Ushakov, S.N., *Polivinilovyi spirt i ego proizvodstvo* (Polyvinyl Alcohol and Its Production), Moscow: Akad. Nauk SSSR, 1960.
14. Dechant, J., Danz, R., Kimmer, W., et al., *Ultrarotspektroskopische Untersuchungen an Polymeren*, Berlin: Akademie, 1972.
15. *Chemical Applications of Spectroscopy*, West, W., Ed., New York: Interscience, 1956.

ISSN 1070-4272, Russian Journal of Applied Chemistry, 2008, Vol. 81, No. 10, pp. 1846–1850. © Pleiades Publishing, Ltd., 2008.
Original Russian Text © S.A. Bulgakova, S.A. Zhil'tsov, Yu.D. Semchikov, 2008, published in Zhurnal Prikladnoi Khimii, 2008, Vol. 81, No. 10, pp. 1725–1730.

MACROMOLECULAR CHEMISTRY AND POLYMERIC MATERIALS

Preparation of a Block Copolymer of Polymethyl Methacrylate with Polymethacrylic Acid by Radical Polymerization

S. A. Bulgakova, S. A. Zhil'tsov, and Yu. D. Semchikov

Research Institute of Chemistry, Lobachevsky State University, Nizhni Novgorod, Russia

Lobachevsky State University, Nizhni Novgorod, Russia

Received February 8, 2008

Abstract—Amphiphilic block copolymers of methacrylic acid with prepolymers of polymethyl methacrylate, functionalized with both silicon hydride and methacrylic terminal groups, were synthesized.

DOI: 10.1134/S1070427208100261

Recently, the interest in telechelates (polymers containing reactive terminal groups selectively reacting with functional groups of another molecule) has considerably increased. Such polymers can be used as cross-linking agents, chain extenders, and precursors for synthesis of block and graft copolymers and macromolecules with star-shaped and dendritic architecture. Macromonomers with terminal unsaturated bonds (telechelates) occupy an important place among such precursors.

The preparation of these macromonomers by radical polymerization is usually based on use of chain-transfer agents, polyfunctional initiators, or high concentrations of initiator [1–4], when side reactions of chain transfer to the initiator are absent. In the last case, azo initiators are used most frequently. Their nitrile groups are converted by hydrolysis into carboxy groups, and then, in the course of reaction of the terminal COOH groups with, e.g., glycidyl metacrylate, the polymer acquires unsaturated bonds. The same method for preparing macromonomers by radical polymerization is used with carboxyl-containing chain-transfer agents, such as iodoacetic [5], 3-mercaptopropionic [6], and thioglycolic [7, 8] acids.

Previously, we have reported [9, 10] a new versatile approach to synthesis of macromonomers via chain transfer to a tetrafunctional organosilicon hydride, dimethyldisilane, in radical polymerization of methyl methacrylate (MMA) and styrene, with the subsequent hydrosilylation of dimethacrylate with the telechelate containing terminal Si–H bonds. At the same time, in the synthesis of a block copolymer, both macromonomer and telechelate (which contains silicon hydride groups capable of chain transfer) can be used.

In this study, we examined the possibility of preparing polymethyl methacrylate (PMMA)–polymethacrylic acid (PMAA) block copolymers by radical polymerization, with PMMA precursors of both types involved.

EXPERIMENTAL

Methyl methacrylate was purified by vacuum condensation; methacrylic acid (MAA) was separated from water by repeated refreezing and distilled under reduced pressure. 1,3-Dimethacryloyloxymethyl-1,1,3,3-tetramethyldisiloxane (DMDSO) was prepared from 1,3-bis(chloromethyl)-1,1,3,3-tetramethyldisiloxane and potassium methacrylate [11]. Dimethyldisiloxane (DS) was synthesized by the method described in [12, 13]. Azobis(isobutyronitrile) (AIBN) purified by recrystallization from isopropyl alcohol (IPA) was used as initiator. Acetonitrile, toluene, and cyclohexane were used without additional purification. Methanol and dimethylformamide (DMF) were purified by the known methods [14].

Polymethyl methacrylate with a silicon hydride terminal group (prepolymer A) was prepared by radi-

cal polymerization of MMA in the bulk at 60°C in the presence of 0.005 M AIBN and 2.5 wt % DS in sealed tubes to the maximum accessible conversion of 80%, which was checked gravimetrically. The polymer prepared was purified by twofold reprecipitation from acetone into petroleum ether and dried to constant weight in a vacuum. To obtain the macromonomer (prepolymer B), DMDSO was hydrosilylated with prepolymer A dissolved in toluene (1 g in 10 ml) at 3 : 1 molar ratio at 80°C for 15 h in the presence of a 5×10^{-5} M solution of hexachloroplatinic acid in IPA (Speier catalyst). The macromonomer was isolated from the solution in toluene by solvent evaporation.

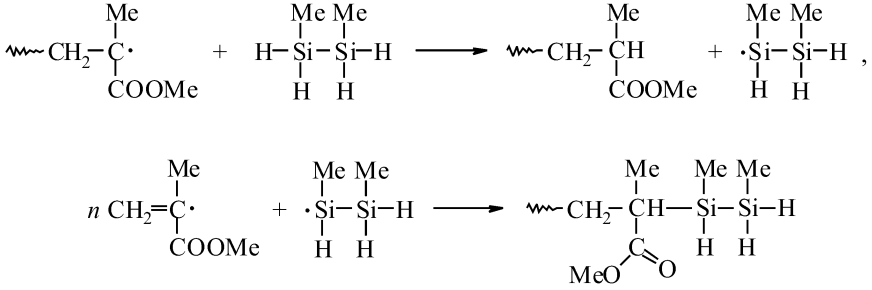
The synthesis of A-PMAA and B-PMAA block copolymers in the 50 : 50 wt % reaction mixture was performed in DMF in the presence of 0.05 M AIBN at 60°C to deep conversion. The mixtures prepared, consisting of prepolymer solution in DMF (1 g in 10 ml) and MAA, were placed in ampules, deoxygenated by threefold freezing–pumping–thawing, and sealed. After the polymerization was complete, the hybrid products obtained were purified by precipitation from solutions in DMF with diethyl ether and dried in a vacuum to constant weight. The reference PMAA sample was synthesized by radical polymerization of MAA under the same conditions as those in synthesis of block copolymers: 1 g of MAA in 10 ml of DMF, 0.05 M AIBN, 60°C.

The content of MAA units in copolymers was estimated by potentiometric titration of acid groups with a 0.1 M KOH solution in methanol on a TV-6L1 device. The molecular-mass distribution (MMD) of the polymers preliminarily methylated by the method described in [15] was determined by gel-permeation chromatography (GPC) on a Waters chromatograph (USA) with a set of five Styrogel chromatographic columns with the pore diameters of 10^5, 3×10^4, 10^4, 10^3, and 250 Å. An R-403 Waters differential refractometer was used as a detector. Tetrahydrofuran was used as an eluent. The block copolymers were fractionated in methanol with separation of the insoluble and soluble fractions.

The IR spectra of A and B prepolymer films cast on NaCl discs from solutions in chloroform were recorded on a Perkin–Elmer-577 spectrophotometer. The surface profile of polymer samples was studied with a set of Solver Pro scanning probe microscopes (NT-MDT, Zelenograd, Russia). Standard silicon cantilevers produced by NT-MDT and MicroMash (Tallinn, Estonia) with a typical curvature radius of the working part of the probe of about 10–15 nm were used. Measurements were performed in the contact and tapping modes. In the case of the tapping mode, NSG11 cantilevers (resonance frequencies 150–250 kHz) were used. The sample films were applied onto silicon plates from methanol–acetone solution.

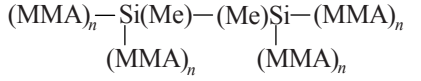
The polymeric films for determining the limiting wetting angles were prepared by dipping of quartz plates into polymer solutions in 50 : 50 vol % IPA : acetone mixtures, followed by drying in a vacuum desiccator.

Two types of PMMA precursors were used in the synthesis of PMMA–PMAA block copolymers. Prepolymer A was prepared by radical polymerization of MMA in the presence of a tetrafunctional organosilicon hydride, dimethyldisiloxane, as a chain-transfer agent:

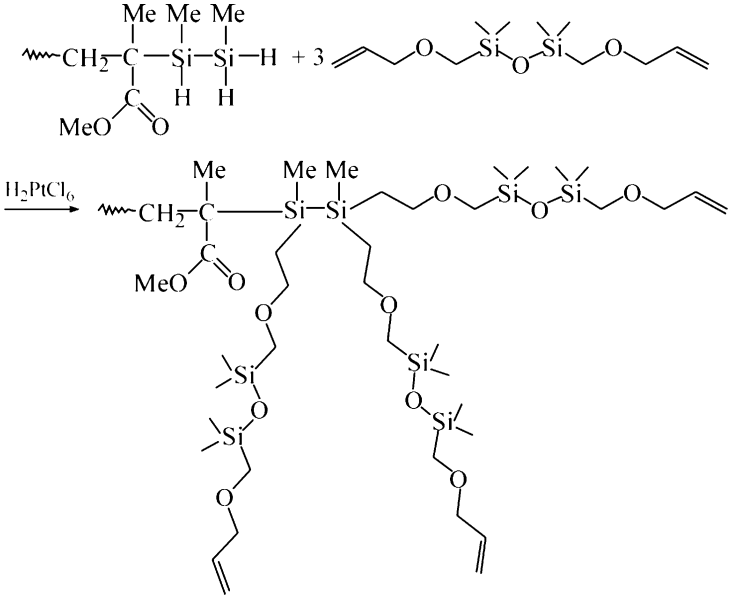


Prepolymer A

In the course of chain transfer, prepolymer A macromolecule acquires one to three terminal Si–H bonds. At the same time, the formation of completely substituted, nonfunctionalized macromolecules with the branched structure, though in substantially smaller amount, is also probable:



Therefore, in the synthesis of prepolymer B, which is a macromonomer, we proceeded from the presence of three terminal Si–H bonds in prepolymer A and performed the hydrosilylation reaction between prepolymer A and DMDSO at threefold excess of the latter:



Prepolymer B

The presence of Si-H functional groups in prepolymer A and unsaturated vinyl groups in prepolymer B is confirmed by IR spectroscopy (Fig. 1). Weak and medium bands at 2075 and 810 cm^{-1}, associated with stretching and bending vibrations of Si–H bonds, respectively, and a band at 798 cm^{-1} characteristic of the Si–Me group, in spectrum *1* and a new band at 1610 cm^{-1} due to ν(C=C) in spectrum *2* are clearly seen.

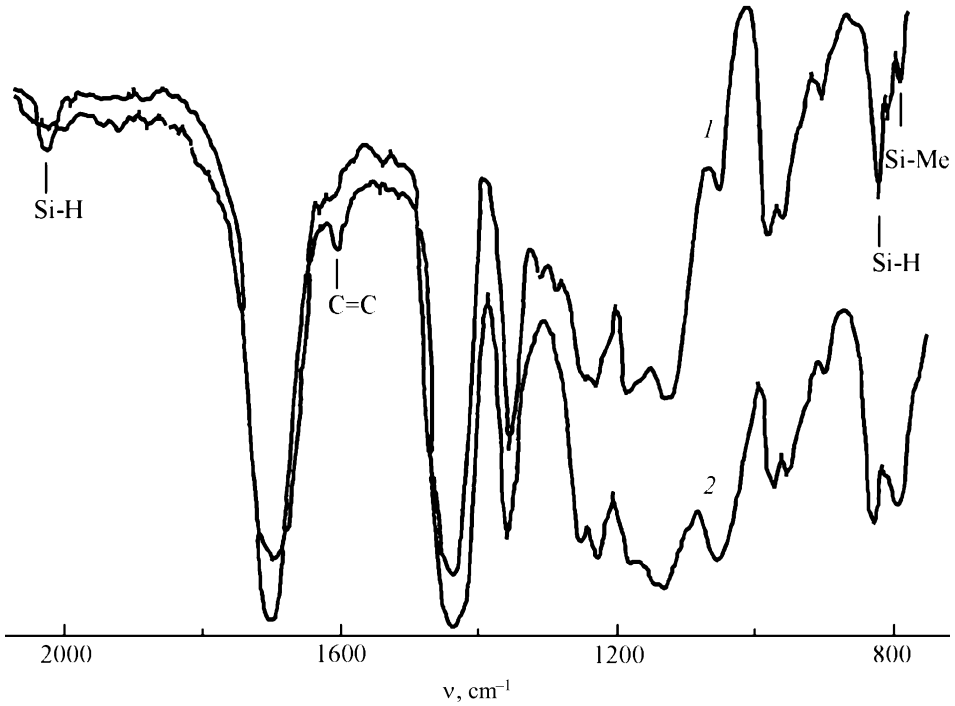


Fig. 1. IR spectra of prepolymers (*1*) A and (*2*) B. (ν) Wavenumber.

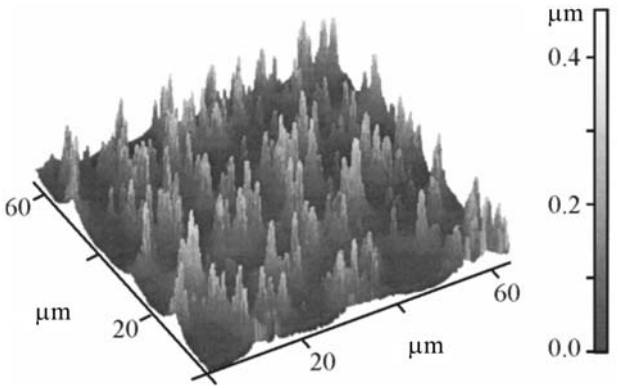


Fig. 2. AFM image of the surface of a film of A–PMAA hybrid product, first fraction.

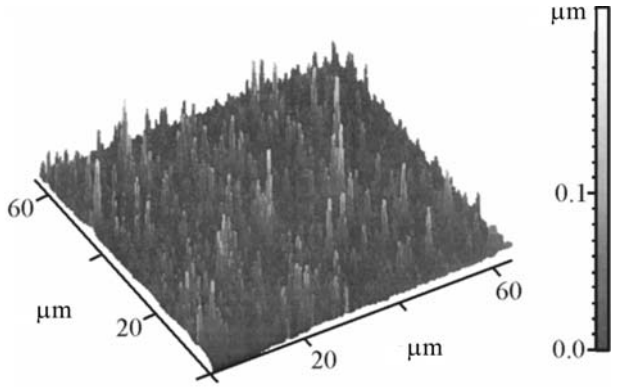
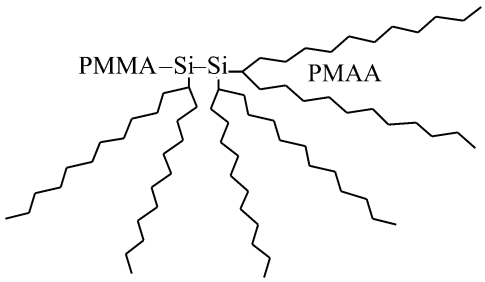


Fig. 3. AFM image of the surface of a film of B-PMAA hybrid product, second fraction.

The difference in the chemical structure of the terminal groups of prepolymers A and B suggests different mechanisms of formation of block copolymers with MAA. In the first case, due to chain transfer to the remaining three Si–H bonds, the maximum possible number of PMAA blocks grafted to prepolymer A is three. In the second case, due to addition of MAA macroradicals to prepolymer B, block copolymer B–PMAA can have six PMAA blocks, with all of its terminal unsaturated groups involved in the reaction:



The data on the synthesis of both types of block copolymers are listed in Tables 1 and 2 as characteristics of the composition and molecular weights of fractions isolated from methanol: insoluble (first fraction) and soluble (second fraction). It follows from the composition data that these fractions are not homopolymers. Since methanol is a hard precipitant for PMMA and a good solvent for PMAA, the first fraction can contain MAA, and the second fraction, MMA only in the PMMA–PMAA block copolymer. In other words, the first fraction contains the block copolymer and PMMA, and the second fraction, the block copolymer and PMAA. In systems of this kind, the supramolecular structures are formed by aggregation of blocks and macromolecules having the same chemical structure proceeds. In particular, it follows from this fact that amphiphilic block copolymers can be used as components of formulations containing a homopolymer similar to one of the blocks.

Table 1. Characteristics of the initial prepolymer A, reference sample (PMAA), and fractions of hybrid product A–PMAA

Characterisic	Pre-polymer	PMAA	A–PMAA fraction	
			first	second
Yield, wt %	–	–	45	55
MAA content, wt %	–	100	16.4	69.4
$M_w \times 10^{-3}$	51.4	32	52.0	28
$M_n \times 10^{-3}$	23.6	12	27.2	11
M_w/M_n	2.18	2.65	1.92	2.66

Table 2. Characteristics of the initial prepolymer B, reference sample (PMAA), and hybrid product B–PMAA

Character-isic	Pre-polymer	PMAA	B–PMAA fraction		
			first	second	third*
Yield, wt %	–	–	45	55	4.3
ω_{MAA}, wt %	–	100	16.4	69.4	6.3
$M_w \times 10^{-3}$	51.4	32	52.0	28	36
$M_n \times 10^{-3}$	23.6	12	27.2	11	25
M_w/M_n	2.18	2.65	1.92	2.66	1.45

* Third fraction was isolated by evaporation of the mother liquor after the precipitation of the hybrid product from DMF with diethyl ether.

Table 3. Wetting angles θ with water for polymeric films applied to quartz plates

Sample	θ, deg
Prepolymer A	62
PMAA	0
A–PMAA:	
first fraction	23
second fraction	0
B–PMAA:	
first fraction	28
second fraction	0

The surfaces of the polymeric films of the fractions separated from hybrid products A-PMAA and B-PMAA were studied. An examination of the film surface topography showed that, in almost all the cases, structures with pronounced peaks are formed. As can be seen from AFM images in Figs. 2 and 3, the height of peaks in the first fractions is several times that in the second fractions and is comprable with the contour length of the PMMA prepolymer. It follows from this fact that peaks are formed on the basis of the "crown" consisting of blocks and PMMA macromolecules of the first fraction. The wetting angles with water of the block copolymer films and films of the corresponding homopolymers are listed in Table 3. As follows from these data, drops spread on PMAA films and films of the second fractions, whereas on films of the first fractions equilibrium drops wetting the surface are formed in both cases. This fact indicates that the surface formed by peaks (bristle) is substantially enriched in blocks and macromolecules of PMMA, and the smaller wetting angles in comparison with PMMA films are caused by the admixture of PMAA blocks and probably by surface roughness, which, as a rule, gives better wetting.

CONCLUSIONS

(1) Synthesis of block-copolymers by radical polymerization proceeds through precursors with both terminal silicon hydride and unsaturated groups.

(2) Fractionation of polymethyl methacrylate–poly-methacrylic acid hybrid products with methanol gives two fractions. Each of these contains the homopolymer with the block copolymer enriched in the related block.

(3) The developed compositions containing amphiphilic block copolymers polymethyl methacrylate–poly-methacrylic acid are of interest as modifiers of the surface of polymeric materials based on polymethyl methacrylate.

REFERENCES

1. Schultz, G.O. and Milkovich, R., *J. Appl. Polym. Sci*., 1982, vol. 27, no. 12, pp. 4773–4786.
2. Rempp, P., Lutz, P., Masson, P., and Franta, E., *Makromol. Chem., Suppl*., 1984, vol. 8, no. S 19841, pp. 3–15.
3. Schultz, G.O. and Milkovich, R., *J. Polym. Sci., Polym. Chem. Ed.*, 1984, vol. 22, no. 7, pp. 1633–1652.
4. Ivanova, N.G., Ivanchev, S.S., and Domareva, N.M., *Vysokomol. Soedin., Ser. A*, 1976, vol. 18, no. 12, pp. 2788–2792.
5. Ito, K., *Prog. Polym. Sci*., 1998, vol. 23, no. 4, pp. 581–620.
6. Yamashita, Y., Ito, K., Mizino, H., and Okada, K., *Polym. J*., 1982, vol. 14, no. 4, pp. 255–260.
7. Akashi, M., Kirikihira, I., and Miyauchi, N., *Angew. Makromol. Chem*., 1985, vol. 132, no. 1, pp. 81–89.
8. Boutevin, B., Pietrasanta, Y., Taha, M., and Sarraf, T.E., *Macromol. Chem*., 1983, vol. 184, no. 12, pp. 2401–2407.
9. Bulgakova, S.A., Zhil'tsov, S.A., Dedeshina, E.A., et al., *Vestn. Univ., Khim*., 2006, issue 1(5), pp. 99–107.
10. Bulgakova, S.A., Mazanova, L.M., Semenov, V.V., and Semchikov, Yu.D., *Eur. Polym. J*., 2007, vol. 43, no. 2, pp. 644–651.
11. Merker, R.L. and Noll, J.E., *J. Org. Chem*., 1956, vol. 21, no. 12, pp. 1537–1539.
12. Kumada, M. and Tatao, K., *Adv. Organomet. Chem*., 1968, vol. 6, pp. 19–117.
13. Hengge, E., *Top. Curr. Chem*., 1974, vol. 51, pp. 1–127.
14. Weissberger, A. and Proskauer, E.S., *Organic Solvents. Physical Properties and Methods of Purification*, Riddick, J.A. and Toops, E.E., Eds., New York: Interscience, 1955.
15. Braun, D., Cherdron, H., and Kern, W., *Praktikum der Makromolekularen Organischen Chemie*, Heidelberg: Alfred Hüthig, 1971.

ISSN 1070-4272, Russian Journal of Applied Chemistry, 2008, Vol. 81, No. 10, pp. 1851–1855. © Pleiades Publishing, Ltd., 2008.
Original Russian Text © N.I. Afanas'ev, S.B. Selyanina, N.V. Selivanova, 2008, published in Zhurnal Prikladnoi Khimii, 2008, Vol. 81, No. 10, pp. 1731–1735.

MACROMOLECULAR CHEMISTRY AND POLYMERIC MATERIALS

Stabilization of the Oleic Acid–Water Emulsion with Various Kraft Lignins

N. I. Afanas'ev, S. B. Selyanina, and N. V. Selivanova

Institute of Environmental Problems of the North, Ural Branch, Russian Academy of Sciences, Arkhangelsk, Russia

Received January 30, 2008

Abstract—The influence of the initial wood species and polymolecular characteristics on the characteristics of the surface of solid-phase lignin was estimated, and the correlation of these parameters with the ability of kraft lignins to stabilize the oleic acid–water emulsion was examined. The kinetics of breakdown of emulsions stabilized with kraft lignin was studied.

DOI: 10.1134/S1070427208100273

Industrial pulp is produced today predominantly by the kraft procedure. Lignin derivatives formed in this procedure are soluble in alkalis, whereas in going to acidic solutions they pass into the solid state. Solid particles of kraft lignins have a large specific surface area (up to 20 $m^2 g^{-1}$) and contain a large number of polar groups (up to 14 mg-equiv g^{-1}) [1]. They have high sorption power with respect to many classes of substances and also efficiently stabilize oil-in-water emulsions [1, 2].

In particular, a stable lignin–tall emulsion is formed in synthesis of tall oil, by-product of kraft cellulose manufacture (Fig. 1). As shown previously [3–5], this emulsion is stabilized by kraft lignin.

It is well known [6, 7] that the stabilization mechanism of emulsions depends on hydrophilicity and lipophilicity of the solid emulsifier and, in particular, kraft lignin. Taking into account that kraft lignins recovered from liquors formed in cooking of deciduous and coniferous wood differ in topological structure and chemical composition [8, 9] and, at the same time, they are polydisperse and polyfunctional compounds, it is reasonable to expect that the nature of their surface and, accordingly, the ability to stabilize emulsions should depend on the initial wood species and also on the molecular weight and molecular-weight distribution. Although this statement is obvious, there are no published data on the behavior of fractionated lignins in the systems water-oil-lignin.

In this study, we examined the behavior of kraft birch and spruce lignins and evaluated the influence of their molecular weights on the stability of the oleic acid–water system simulating the lignin–tall emulsion.

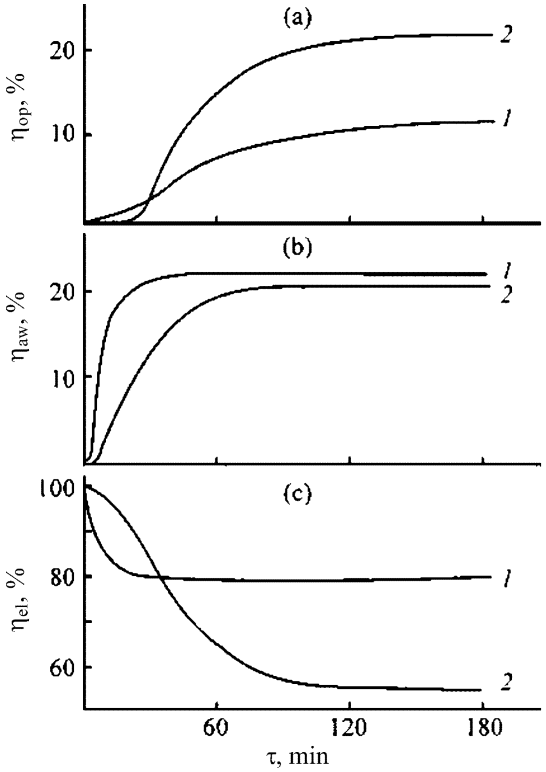


Fig. 1. Relative yields of (a) oil phase (η_{op}), (b) acidic water (η_{aw}), and (c) emulsified layer (η_{el}) vs. the settling duration τ in production of tall oil by degradation of (*1*) deciduous and (*2*) coniferous sulfate soap.

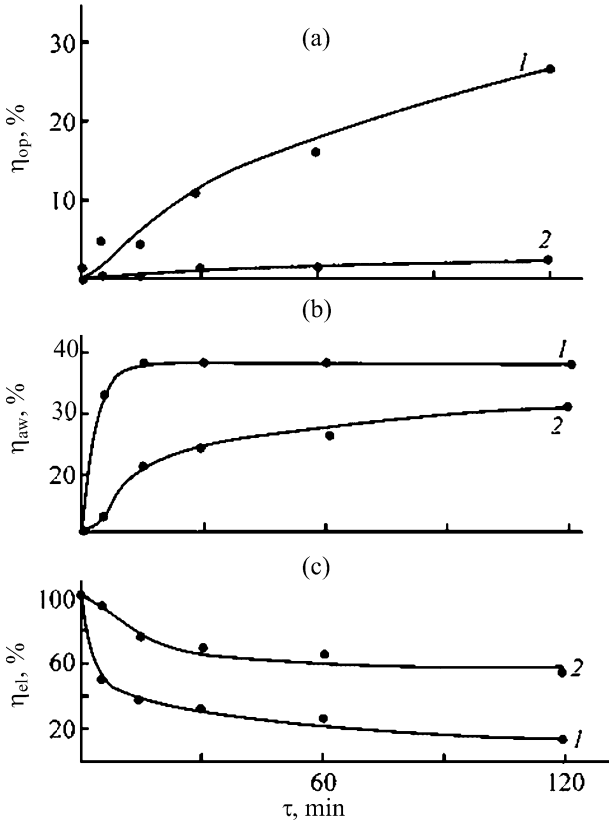


Fig. 2. 1. Relative yields of (a) oil phase (η_{op}), (b) acidic water (η_{aw}), and (c) emulsified layer (η_{el}) vs. the settling duration τ of oleic acid–water emulsion in the presence of (*1*) birch and (*2*) spruce lignins.

EXPERIMENTAL

For studies, we used the model systems prepared by successive neutralization of lignin and oleic acid (main component of tall oil) samples with a 10% solution of sodium hydroxide to pH 11. The oleic acid : water weight ratio in the system under study was 1 : 1. The amount of lignins added to the model systems was 5% relative to the weight of oleic acid. The samples were thermostated at 95 ± 2°C and treated with 30% sulfuric acid with vigorous stirring to pH 2.2–2.5. The stability of the emulsions formed was quantitatively characterized by the variation of the volume of the separated phases at certain intervals of time.

The characteristics of the lignin surface were varied by changing the initial wood species and the fractional composition of the samples.

It has been shown previously that hydrophilic–oleophilic characteristics of kraft lignin also depend on the con-tent of extractive resinous substances and precipitation pH [10]. Therefore, to study the influence of the initial wood species on the stability of emulsions we chose the lignin samples isolated by precipitation at pH 1.5 from black sulfate liquors formed in laboratory cooking of deresined spruce and birch wood.

The resulting lignin samples differ in the composition and in polymolecular and hydrophilic–oleophilic characteristics. Differences in the ratio of guaiacyl-, syringyl-, and *p*-hydroxyphenylpropane units in deciduous and coniferous lignins are manifested in a higher content of Clason lignin in the sample prepared from birch wood (93.4% in comparison with 88.2% for spruce lignin) and in a lower content of oxygen (26.2% in comparison with 31.1%); furthermore, spruce lignin has a higher molecular weight (M_w 9700) than birch lignin (M_w 2800). Adsorption of hexane vapor with spruce lignin (0.41×10^{-3} mol g^{-1}) is higher than that with birch lignin (0.29×10^{-3} mol g^{-1}) by 26%. The sorption power of birch lignin with respect to water vapor is 8.90×10^{-3} mol g^{-1}, and that of spruce lignin, 8.32×10^{-3} mol g^{-1}, i.e., it differs by 7%. This fact suggests that the hydrophilicity of birch lignin is higher.

The kinetic dependences of separation of oil (Fig. 2a) and aqueous (Fig. 2b) phases under static conditions at 80 ± 1°C and of breakdown of emulsions stabilized with birch (Fig. 2c, curve *1*) and spruce (Fig. 2c, curve *2*) lignins show that the system is more stable in the presence of spruce lignin. In both cases, breakdown of the emulsion proceeds in two stages: in the first 5–10 min, an aqueous layer is formed, and then the volume of this layer varies insignificantly. The oil layer is formed at approximately the same rate untill the equilibrium state, which is reached in the presence of spruce lignins in approximately 1 h and in the presence of birch lignins, in 1.5–2 h.

As can be seen from Fig. 2, in the presence of the more hydrophilic birch lignin, the model system is separated into layers more completely than in the presence of the higher-molecular-weight and more hydrophobic spruce lignin. The yield of the oil phase is 90% of the theoretical value in the first case and 18% in the second case.

It is well known that low-molecular-weight fractions of kraft lignins contain a larger number of phenolic hydroxyls and are more hydrophilic in comparison with the high-molecular-weight fractions [11]; therefore, the revealed relationships were studied in more detail in stabilization of the oleic acid–water emulsion with lignins differing in molecular weight. The molecular weights of lignins were determined by the gel-permeation chromatography [12]. Dimethyl sulfoxide

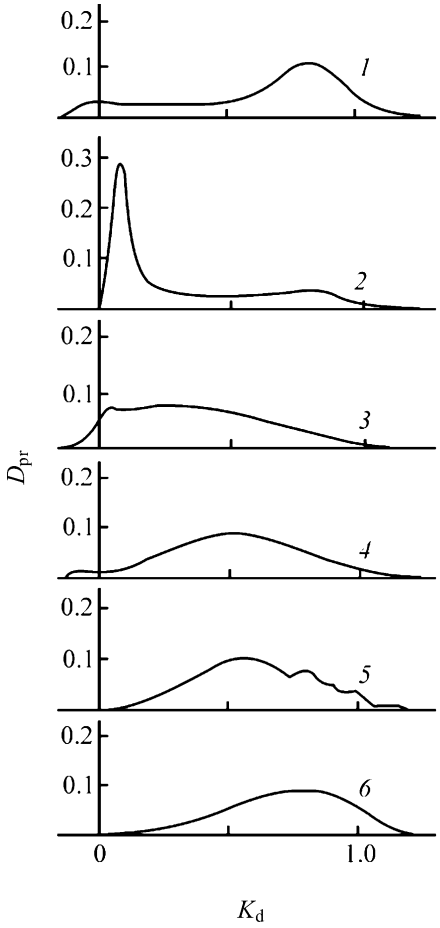


Fig. 3. Gel chromatograms of fractions of kraft birch lignin. (D_{pr}) Gravimetric concentration and (K_d) retention volume. (*1*) Nonfractionated lignin (M_w 2800); fraction: (*2*) no. 1 (M_w 36 000), (*3*) no. 2 (M_w 14 600), (*4*) no. 3 (M_w 8300), (*5*) no. 4 (M_w 4000), and (*6*) no. 5 (M_w 2400).

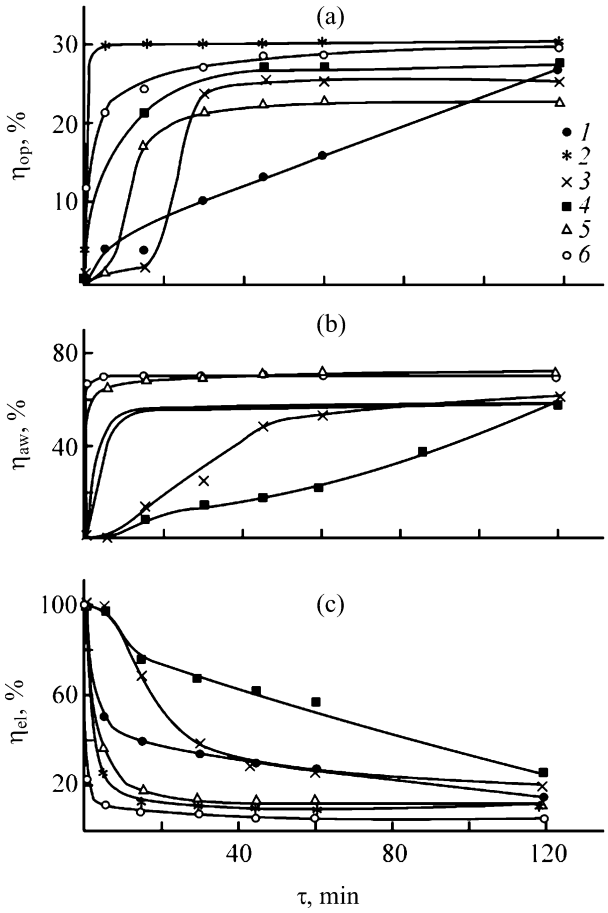


Fig. 4. Relative yield of (a) oil phase η_{op}, (b) acidic water η_{aw}, and (c) emulsified layer η_{el} vs. the settling duration τof the oleic acid–water emulsion in the presence of the (*1*) initial birch lignin and (*2–6*) fractionated lignins. Fraction: (*2*) no. 1 (M_w 36 000), (*3*) no. 2 (M_w 14 600), (*4*) no. 3 (M_w 8300), (*5*) no. 4 (M_w 4000), and (*6*) no. 5 (M_w 2400).

(freezing point 16°C) was used as an eluent. The solutions with lignin concentration of 0.5% were prepared a day before determination.

Lignin fractions prepared by fractional precipitation with benzene from a solution of birch lignin in dioxane differ significantly in the shape of chromatograms (Fig. 3). The weighted-average molecular weights of the recovered fractions vary in the range from 2400 to 36 000 and fairly completely represent the range of variation of this parameter, typical of kraft lignins [11–15].

The separation of the oleic acid–water emulsion (Fig. 4c) stabilized with lignin fraction nos. 1 (M_w 36 000) and 5 (M_w 2400) into layers is complete within 15–20 min, no. 2 (M_w 14 600) and no. 4 (M_w 4000), within 50–70 min, and no. 3 (M_w 8300), within 2 h. In this case, the highest yield of the oil phase (Fig. 4a) is observed in the presence of fractions with the lowest (M_w 2400, fraction no. 5), and highest molecular weight (M_w 36 000, fraction no. 1). With the other lignin fractions, this value is 9–13% lower.

Using the data obtained for the breakdown of the oleic acid–water emulsion in the presence of fractionated lignins, we calculated the formation rates ω of the oil layer:

$$\omega = \frac{\Delta n_i}{S\Delta\tau_i},$$

where Δn_i is an increase in the oil layer volume, mol; *S,* surface area of the phase boundary, cm^2; and $\Delta\tau_i$, time interval between measurements, min.

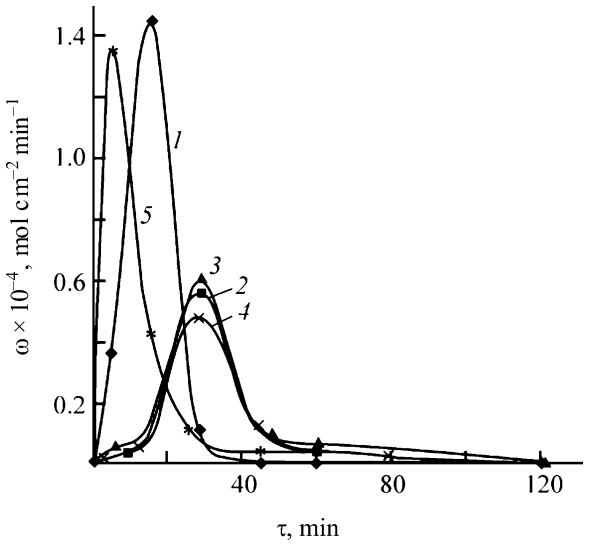


Fig. 5. Rate of oil phase separation from the emulsion, ω, vs. the settling duration τ in the presence of fractionated lignins. Fraction: (*1*) no. 1 (M_w 36 000), (*2*) no. 2 (M_w 14 600), (*3*) no. 3 (M_w 8300), (*4*) no. 4 (M_w 4000), and (*5*) no. 5 (M_w 2400).

The dependences of the rate of oil phase separation on time (Fig. 5) pass through a maximum for all the fractions. The peaks in the kinetic curves for the medium-molecular-weight fractions (4000–14 000) are observed at a settling time of 30–40 min, whereas for fraction nos. 1 and 5 (M_w 2400) they are shifted to shorter time intervals (15–20 and 3–5 min, respectively).

In interpretation of the data obtained, it should be borne in mind that lignins were recovered from the preliminary deresined wood. In addition, in estimation of the ability of lignins to stabilize oil-in-water emulsions, the differences in the composition of deciduous and coniferous tall oil and, in particular, the presence of resin acids, the specific component of the latter, were not considered. As a result, the revealed trends do not fully correspond to published results of the laboratory studies and to the practice of wood-chemical production at pulp-and-paper plants, according to which tall oil is recovered from coniferous soap more completely and faster than from deciduous soap [4, 16]. Despite this fact, the data obtained allow us to state that the breakdown of the emulsion in the presence of both deciduous and coniferous lignins proceeds in similar ways and the influence of lignins on the stability of oil–water emulsions is caused by the hydrophilic-oleophilic characteristics of their surfaces.

The relationships obtained in studying the influence of polydisperse characteristics of lignins on the stability of emulsions can be interpreted as follows. Lignins promote dispersion of oil drops in an aqueous medium. On adding fractionated lignins with a molecular weight of 4000 to 14 600, separation of the emul-sion into layers in the initial period of time becomes slower in comparison with macromolecular and low-molecular-weight fractions. Due to high hydrophobicity of the surface of solid particles surrounding the oil drop aggregates, lignins with a molecular weight of 36 000 and higher fairly rapidly pass from the aqueous phase into the oil phase. Fractions with intermediate molecular weights prevent separation of the emulsion into layers, as indicated by the broad peak and low rate of oil separation. Lignins with molecular weights lower than 4000 are more hydrophilic and, accordingly, have higher affinity for the aqueous phase. Therefore, oil drops dispersed by this fraction fairly rapidly pass into the aqueous phase and thereby provide a high rate of emulsion breakdown. In the absolute value, the rates of phase evolution for fraction nos. 1 (M_w 36 000) and 5 (M_w 2400) exceed those for the other fractions by a factor of 3.

Comparison of the peak positions and amplitudes of the rates of phase separation depending on the process duration, with the molecular weights of the samples suggests that the breakdown of the emulsion stabilized with kraft lignin proceeds in two kinetically different steps. In the first step, separation of dispersion medium (aqueous solution) predominates. In parallel, as the process develops, conditions arise for the coalescence of oil drops and formation of an oil layer with simultaneous separation of an aqueous layer. After separation of water that is not bound with lignin, the emulsion brealdown occurs only owing to the coalescence of oil drops and the process rate steadily decreases. In this case, in the course of emulsion breakdown, the low-molecular-weight fractions characterized by increased hydrophilicity will be concentrated in the aqueous phase. The hydrophobic high-molec-ular-weight fraction of lignin should have high affinity for the oil phase and, hence, should assist transfer dispersed oil particles from the emulsified layer into the oil layer. The medium-molecular-weight fractions characterized by the balance of hydrophobic and hydrophilic parts of molecules exhibit affinity for both oil and aqueous phases. The equality of hydrophilic and hydrophobic characteristics of medium-molecular-weight fractions of lignins accounts for the emulsifying effect in the oil–water–lignin systems.

CONCLUSIONS

(1) The ability of lignins to stabilize oil–water emulsions is governed by their hydrophilic–lipophilic ratio.

(2) Hydrophobic macromolecular lignins have high affinity for the oil phase and promote transfer of oil particles dispersed in water into the oil layer. Samples of medium molecular weights (M_w 4000–15 000) are characterized by the balance of hydrophilic–oleophilic characteristics. They exhibit affinity for both the oil and aqueous phases and, as a result, efficiently stabilize an oil-in-water emulsion. Hydrophilic lignins of low molecular weight ($M_w < 4000$) are concentrated in the aqueous layer, which accounts for the efficient separation of the emulsion in the presence of these lignins.

(3) The breakdown of the heterogeneous system oil–water stabilized with kraft lignin occurs in two kinetically different steps: the first fast step in which intense separation of an aqueous layer is observed and the second slow step characterized by formation of an oil layer. Separation of the dispersion medium in the first step provides conditions for coalescence of oil drops and separation of the dispersed phase to form an

REFERENCES

1. Bogomolov, B.D., Sapotnitskii, S.A., Sokolov, O.M., et al., *Pererabotka sul'fatnogo i sul'fitnogo shchelokov: uchebnoe posobie dlya vuzov* (Reprocessing of Kraft and Sulfite Liquors: A Guide for Higher School), Moscow: Lesnaya Prom–st., 1989.
2. Selyanina, S.B., Afanas'ev, N.I., Makarevich, N.A., et al., *Zh. Prikl. Khim*., 2002, vol. 75, no. 11, pp. 1910–1914.
3. Selyanina, S.B., Modernization of Procedure for Recovery of Extractive Resinous Substances of Black Sulfate Liquor, *Cand. Sci. Dissertation*, 1998.
4. Selyanina, S.B., Afanas'ev, N.I., and Makarevich, N.A., *Zh. Prikl. Khim*., 2000, vol. 73, no. 12, pp. 1986–1991.
5. Selyanina, S.B., Bogolitsyn, K.G., and Yanglyaeva, N.Zh., *Lesn. Zh*., 2000, no. 3, pp. 123–129.
6. Adamson, A.W., *Physical Chemistry of Surfaces*, New York: Wiley, 1976.
7. *Emulsion Science*, Sherman, P., Ed., London: Academic, 1968.
8. Karmanov, A.P., *Samoorganizatsiya i strukturnaya organizatsiya lignina* (Self-Organization and Structural Organization of Lignin), Yekaterinburg: Ural. Otd. Ross. Akad. Nauk, 2004.
9. Maier, L.V., A Study of Macromolecular Characteristics of Deciduous Kraft Lignin, *Cand. Sci. Dissertation*, 1998.
10. Selyanina, S.B. and Selivanova, N.V., *Zh. Pikl. Khim*., 2007, vol. 80, no. 7, pp. 1170–1174.
11. Samylova, O.A., Redox Characteristics of Lignin, *Cand. Sci. Dissertation*, 2004.
12. Sokolov, O.M., *Opredelenie molekulyarnykh mass ligninov na ul'tratsentrifuge i metodom gel'-fil'tratsii: Uchebnoe posobie* (Determination of Molecular Weights of Lignins on an Ultracentrifuge and by Gel Filtration Method: Textbook), Moscow: Lesotekh. Akad., 1978.
13. Chudakov, M.I., *Promyshlennoe ispol'zovanie lignina* (Industrial Use of Lignin), Moscow: Goslesbumizd., 1962.
14. Troyanskaya, A.F., Sokolova, A.A., and Bogomolov, B.D., *Khim. Drev*., 1985, no. 4, pp. 76–81.
15. *Lignins: Occurrence, Formation, Structure, and Reactions*, Sarkanen, K.V. and Ludwig, C.H., Eds., New York: Wiley, 1971.
16. Golovin, A.I., Trofimov, A.N., and Uzlov, G.A., *Lesokhimicheskie produkty sul'fat-tsellyuloznogo proizvodstva* (Wood-Chemical Products of Kraft Pulp Production), Moscow: VNIPIEIlesprom, 1988.

ISSN 1070-4272, Russian Journal of Applied Chemistry, 2008, Vol. 81, No. 10, pp. 1856–1859. © Pleiades Publishing, Ltd., 2008.
Original Russian Text © A.A. Beushev, V.V. Kon'shin, N.A. Chemeris, M.M. Chemeris, 2008, published in Zhurnal Prikladnoi Khimii, 2008, Vol. 81, No. 10, pp. 1736–1739.

MACROMOLECULAR CHEMISTRY AND POLYMERIC MATERIALS

Acylation of Lignocellulose Material with Aliphatic Amino Acids

A. A. Beushev, V. V. Kon'shin, N. A. Chemeris, and M. M. Chemeris

Polzunov Altai State Technical University, Barnaul, Russia

Received April 17, 2006

Abstract—A lignocellulose material was acylated with a thionyl chloride–aliphatic amino acid–trifluoroacetic acid mixture at 30–50°C with the aim to obtain cellulose esters of aliphatic amino acids.

DOI: 10.1134/S1070427208100285

Numerous cellulose esters of carboxylic acids, including mixed esters, are known [1, 2]. Studies of the synthesis of cellulose esters of amino acids have been performed for a long time [3]. The starting materials were samples of cellulose included by various procedures and cellulose alcoholate prepared by exchange of cellulose with sodium isoamylate dissolved in xylene. The acylating agents were chlorides of *N*-substituted amino acids: *N*-carbobenzoxyglycine, *N*-carbobenzoxyaminoenanthoic acid, *N*-phthalylglycine, and *N*-phthalylaminoenanthoic acid. The esters obtained contained 3.84–4.50% nitrogen. The degree of substitution with the amino acid was 1.06–1.44.

The same research team [4] developed a procedure for preparing cellulose esters of α-amino acids, based on the substitution of the residue of a sulfonic acid (*p*-toluenesulfonic, methylsulfonic) with an amino acyl residue.

A disadvantage of the above-described procedures for preparing cellulose esters of aliphatic amino acids is that they use cellulose (recovery of cellulose from wood is a time-consuming, expensive, and environmentally harmful process) or various cellulose-based included samples, and also chlorides of various *N*-substituted amino acids as acylating agents. The multistep procedure for preparing the starting reactants increases the cost of production of the final products. Preparation of cellulose esters of amino acids requires long time (from 44 to 100 h) or high temperatures (for example, the residues of methylsulfonic acids are completely substituted by glycine and alanine residues only at 155°C).

The interest in cellulose derivatives acylated with amino acids is due to their potential biological activity. It is well known that α-, β-, and γ-amino acids play a particular role in metabolism, being precursors of hormones, creatine, and energetic substrates). Recently, amino acids have found use as drugs in psychology, neurology, and oncology (glycine, β-alanine, γ-aminobutyric acid) [5].

It is known that the most active acylating agents in synthesis of mixed cellulose esters are anhydrides and chlorides of various carboxylic acids. It has been shown previously that carboxylic acid chlorides can be prepared using a thionyl chloride–carboxylic acid mixture in trifluoroacetic acid (TFAA) [6, 7]. To simplify the procedure for preparing cellulose esters of carboxylic acids, modified wood (lignocellulose material, LCM) can be used instead of cellulose [8, 9].

In this context, it seemed interesting to examine the possibility of preparing mixed cellulose esters of α-, β-, and γ-amino acids from LCM by using a mixture of thionyl chloride (TC) with aliphatic amino acid in TFAA as acylating agent. As LCM, we chose prehydrolyzed aspen wood.

EXPERIMENTAL

In the course of this study, we performed the reactions of prehydrolyzed aspen wood (LCM containing 64.8% cellulose, as determined by the Kürschner method, and 35.2% lignin, as determined by the Komarov method [10]) with aminoacetic acid (glycine), β-alanine (BAL), and γ-aminobutyric acid (GABA) in TFAA in the presence of TC, following the procedure described in [11]. Prehydrolyzed aspen wood was prepared from sawdust of size 0.40–0.75 mm, extracted with an alcohol–benzene mixture (to remove extractive substances) and treated with a 0.5–1.0% H_2SO_4 solution (to remove hemicelluloses). LCM was acylated in

a round-bottom flask into which we introduced an aliphatic amino acid and TFAA. The mixture was kept at a definite temperature, after which TC was added, and the mixture was kept at the same temperature until the aliphatic amino acid chloride was formed. To the resulting acylating mixture we added LCM.

The product obtained after the reaction was complete was a mixture of a solution of the cellulose ester with undissolved LCM particles (at a synthesis time from 1 to 5 h) or a homogeneous solution of the ester (at a synthesis time of 6 h). To isolate the product, it was precipitated into acetone, water, or ethanol (for LCM containing glycine, BAL, and GABA residues, respectively), after which it was washed and air-dried.

LCM derivatives were synthesized by the following scheme:

$$NH_2(CH_2)_nCO_2H + CF_3CO_2H + SOCl_2$$

$$\xrightarrow[-SO_2,\ -HCl]{} [NH_3(CH_2)_nCOCl]^{\oplus} + LCM\text{–}OH$$

$$\xrightarrow[-HCl,\ -CF_3CO_2H]{} NH_2(CH_2)_nC(=O)\text{–}O\text{–}LCM,$$

where n = 1–3.

An analysis of the acylated LCMs for residual lignin showed that the products were almost pure cellulose esters (lignin content 2–3%). The product yield relative to the weighed portion of the starting LCM was 70–178%, and the degree of substitution with the amino acid was 0.20–1.82.

Because the acylation of LCM with a TC–aliphatic amino acid mixture in TFAA is an example of topochemical reactions, we can calculate the rate constant by the Erofeev–Kolmogorov equation [12] which can be represented in our case in the following form:

$$\ln [-\ln(1 - \alpha)] = \ln k + n\ln \tau, \quad (1)$$

where α is the degree of conversion of hydroxy groups into ester groups; k, reaction rate constant; and τ, synthesis time.

The degree of conversion is calculated by the formula

$$\alpha = C_{OH(am)\tau}/C_{OH(am)max}, \quad (2)$$

where $C_{OH(am)\tau}$ is the amount of LCM OH groups substituted by acyl residues of amino acids by the time τ (calculated by the procedure from [13]), and $C_{OH(am)max}$ is the maximal amount of OH groups of cellulose (31.5%).

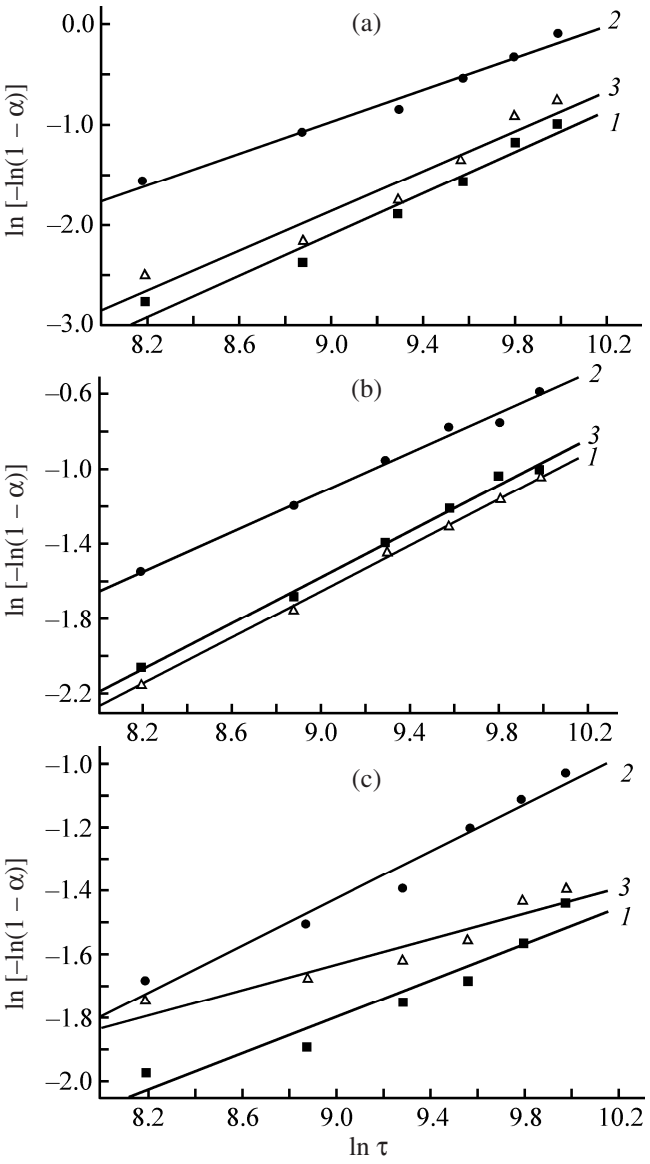


Fig. 1. Kinetic curves of the acylation of LCM with (a) glycine, (b) BAL, and (c) GABA at (*1*) 30, (*2*) 40, and (*3*) 50°C, plotted in the coordinates of the Erofeev–Kolmogorov equation. (α) Degree of polymerization and (τ) synthesis time.

The rate constant k of LCM acylation with a mixture of TC with aliphatic amino acid in TFAA, calculated by the Erofeev–Kolmogorov equation, is a dimensionless quantity. To convert the k values obtained to the rate constant K of dimension, s^{-1}, we used the Sakovich equation [12]

$$K = nk^{1/n}. \quad (3)$$

To determine k, we plotted the dependences of ln[–ln(1 – α)] on ln τ for the acylation of prehydrolyzed aspen wood with glycine, BAL, and GABA (Figs. 1a–1c).

Rate constants K of acylation of LCM with glycine, BAL, and GABA

Amino acid	pK_a	$K \times 10^5$, s^{-1}, at indicated temperature, °C		
		30	40	50
Glycine	2.36	1.70	3.14	2.15
BAL	3.55	0.58	0.92	0.59
GABA	4.23	0.07	0.11	0.08

The highest rate constant K of acylation of LCM with aliphatic amino acids in the examined temperature range (30–50°C) is observed at 40°C. The decrease in K at temperatures exceeding 40°C is due to the evaporation and decomposition of thionyl chloride. As a result, the yield of the amino acid chloride decreases. Furthermore, hydrogen chloride liberated in the process causes strong degradation of wood [14]. It should be noted that at high temperatures the product undergoes hydrolytic degradation, which leads to dissolution of LCMs acylated with amino acids and to a decrease in the yield of the target product and in the content of chemically bound nitrogen in it. To confirm the occurrence of hydrolytic degradatoin, we evaluated the degree of polymerization of cellulose isolated from LCM acylated with β-alanine.

Because the products obtained were insoluble in available solvents, we evaluated viscometrically the degree of polymerization of cellulose obtained by saponification of cellulose esters [11].

The solution viscosity was measured with an Ubbelohde viscometer at 20°C, with iron–tartaric acid–sodium complex as solvent. The viscometer was immersed in an ultrathermostat in which the temperature was maintained with an accuracy of ±0.02°C.

From the data obtained, we calculated the relative (η_{rel}) and specific (η_{sp}) viscosities:

$$\eta_{rel} = \tau/\tau_0, \quad (4)$$

$$\eta_{sp} = \eta_{rel} - 1, \quad (5)$$

where τ and τ_0 are the outflow times of the solution and solvent, respectively.

The intrinsic viscosity [η] ($cm^3\ g^{-1}$) was calculated by the formula

$$[\eta] = \frac{\eta_{sp}/c - K_1}{1 + K_2\eta_{sp}}, \quad (6)$$

where η_{sp} is the specific viscosity of the polymer solution; c, concentration of the polymer solution ($g\ l^{-1}$); and K_1 and K_2, coefficients equal to 0.25 and 0.1, respectively.

The degree of polymerization of cellulose was calculated by the Staudinger empirical equation

$$DP = \frac{[\eta]}{8.14 \times 10^{-4}}, \quad (7)$$

where [η] is the intrinsic viscosity of the polymer solution.

The degrees α of polymerization of cellulose isolated from LCM that has been acylated with β-alanine (acylation time 3 h) at various synthesis temperatures are given below:

T, °C	α
30	1150
40	800
50	450

These data show that, with increasing temperature, the degree of polymerization of cellulose derivatives acylated with BAL dereases, which confirms the occurrence of hydrolytic degradation of cellulose.

The main kinetic relationships of acylation do not change significantly in going from α- to β- and γ-amino acids.

The table shows how the rate constant K of LCM acylation correlates with pK_a of the corresponding amino acid.

It can be seen that, in going from α- to γ-amino acids at the same temperature, the rate constant of LCM acylation decreases as the strength of the amino acid becomes lower, which is in certain contradiction with published data for the acylation of cellulose with aliphatic acids in TFAA [15]. This may be due to the presence of NH_2 groups in amino acids, which presumably form additional hydrogen bonds with LCM. These bonds, in combination with the steric factor, hinder the acylation.

CONCLUSIONS

(1) In acylation of a lignocellulose material with an aliphatic amino acid–thionyl chloride–trifluoroacetic acid mitxure, cellulose esters of α-, β-, and γ-amino acids with the degree of substitution of 0.20–1.82 are formed at 30–50°C within 1–6 h.

(2) In the temperature range 30–50°C, the acylation rate is maximal at 40°C.

REFERENCES

1. Azarov, V.I., Burov, A.V., and Obolenskaya, A.V., *Khimiya drevesiny i sinteticheskikh polimerov: Uchebnik dlya vuzov* (Chemistry of Wood and Synthetic Polymers: Textbook for Higher School), St. Petersburg: Sankt-Peterb. Lesotekh. Akad., 1999.
2. *Cellulose and Cellulose Derivatives*, Bikales, N.M. and Segal, L., Eds., New York: Wiley–Interscience, 1971, part IV.
3. Lin'-Yan', Derevitskaya, V.A., and Rogovin, Z.A., *Vysokomol. Soedin.*, 1959, vol. 1, no. 1, pp. 157–161.
4. Polyakova, A.I., Derevitskaya, V.A., and Rogovin, Z.A., *Vysokomol. Soedin.*, 1961, vol. 3, no. 7, pp. 1027–1030.
5. *Kratkaya khimicheskaya entsiklopediya* (Brief Chemical Encyclopedia), Knunyants, I.L., Ed., Moscow: Sov. Entsiklopediya, 1961, vol. 1.
6. Kon'shin, V.V., Beushev, A.A., Shabalin, V.G., et al., *Izv. Vyssh. Uchebn. Zaved., Lesn. Zh.*, 2003, no. 4, pp. 92–98.
7. Shabalin, V.G., Kon'shin, V.V., Chemeris, M.M., et al., *Izv. Vyssh. Uchebn. Zaved., Lesn. Zh.*, 2004, no. 14, pp. 81–85.
8. RF Patent 2 186 784.
9. RF Patent 2 186 785.
10. Obolenskaya, A.V., El'nitskaya, Z.P., and Leonovich, A.A., *Laboratornye raboty po khimii drevesiny i tsellyulozy* (Laboratory Works on Wood and Cellulose Chemistry), Moscow: Ekologiya, 1991.
11. Protopopov, A.V., Kon'shin, V.V., and Chemeris, M.M., *Zh. Prikl. Khim.*, 2005, vol. 78, no. 10, pp. 1748–1749.
12. Rozovskii, A.Ya., *Kinetika topokhimicheskikh reaktsii* (Kinetics of Topochemical Reactions), Moscow: Khimiya, 1972.
13. Beushev, A.A., Kon'shin, V.V., Chemeris, N.A., and Chemeris, M.M., *Polzunov. Vestn.*, 2004, no. 4, pp. 34–36.
14. Strepikheev, A.A., Derevitskaya, V.A., and Slonimskii, G.L., *Osnovy khimii vysokomolekulyarnykh soedinenii* (Principles of Macromolecular Chemistry), Moscow: Khimiya, 1967.
15. Salin, B.N. and Chemeris, M.M., *Izv. Vyssh. Uchebn. Zaved., Khim. Khim. Tekhnologiya*, 1999, no. 9, pp. 16–20.

ISSN 1070-4272, Russian Journal of Applied Chemistry, 2008, Vol. 81, No. 10, pp. 1860–1862. © Pleiades Publishing, Ltd., 2008.
Original Russian Text © I.B. Sladkov, 2008, published in Zhurnal Prikladnoi Khimii, 2008, Vol. 81, No. 10, pp. 1740–1742.

BRIEF COMMUNICATIONS

Prognostication of Properties of Molecular Inorganic Fluids from the Stoichiometric Formula of a Compound

I. B. Sladkov

St. Petersburg State Polytechnic University, St. Petersburg, Russia

Received June 6, 2008

Abstract—A method is suggested for prognosticating the physicochemical properties of molecular inorganic fluids in the total absence of experimental information about the properties of a substance under study. The method makes it possible to determine quite a number of properties on the basis of only the stoichiometric formula of a compound.

DOI: 10.1134/S1070427208100297

At present, prognostication of properties of molecular inorganic fluids requires information about at least a single experimental characteristic of a substance under study, its boiling point [1, 2]. Methods for prognostication of the boiling point itself cannot be found in the literature, and, therefore, "blind" prognostication of physicochemical properties, i.e., that in the total absence of input information about the substance under study, is also impossible.

In this communication, a method for prognostication of the boiling point and a number of other properties of molecular inorganic fluids is suggested. This method doers not require any evidence about the compound under study, except its stoichiometric formula.

The first step in the development of the technique was a search for a correlation that could be used for estimating the boiling points of molecular inorganic fluids. It was found that this can be done using the correlation between two determinative criteria of thermodynamic similarity. One of these was described in detail in [3]:

$$\psi = 0.1\ln T_b - 0.122\ln V_b + 0.006, \quad (1)$$

and the other, in [4]:

$$f = \ln T_b - 1.1\ln \Pi - 4, \quad (2)$$

where T_b is the standard boiling point (K); Π, parachor ($J^{1/4}\,cm^{5/2}\,mol^{-1}$) calculated by an additive method from the stoichiometric formula of a compound [3]; and V_b, molar volume of the fluid at the boiling point ($cm^3\,mol^{-1}$).

A set of compounds, constituted by several tens of molecular inorganic compounds, was used to establish a correlation between the criteria mentioned above:

$$f = 6.8\psi + 0.21. \quad (3)$$

Relation (3) served as a basis of an iteration that enables calculation of the boiling point and quite a number of physicochemical properties of the substance. This correlation includes a set of the following formulas taken from [3, 4].

Initially, a first approximation to the boiling point T_1 ($T_1 = 200$) and molar volume of the fluid at the boiling point V_1 ($V_1 = 27\Pi$) are set.

Then, two determinative criteria of thermodynamic similarity, f and ψ, are calculated by formulas (1) and (2).

Further, the boiling point is found in a second approximation and a number of physicochemical properties are calculated:

$$T_b = \exp[6.8\psi + 1.1\ln \Pi + 4.21],$$

$$T_{cr} = 1.5\,T_b,$$

$$V_b = (-6.2f + 31.2)\Pi^{0.94},$$

$$b = 1.27V_b - 6,$$

$$P_{cr} = 1.039T_{cr}/b,$$

Table 1. Accuracy of property prognostication for ReF_6 and $SiHCl_3$

Property	Value of a property					
	ReF_6 (Π = 3.17)			$SiHCl_3$ (Π = 3.67)		
	calculation	experiment	discrepancy, %	calculation	experiment	discrepancy, %
T_b	303.3	306.9	–1	342.9	305.2	12
V_b	84.1	85.4	–2	97.3	102.8	–5
T_{cr}	455.0	479.0	–5	514.3	479.0	7
V_{cr}	228.1	230.0	–1	263.8	268.0	–2
P_{cr}	4.69	4.81	–3	4.54	4.17	9
b	100.8	103.5	–3	117.6	119.4	–1
Z_{cr}	0.283	0.278	2	0.280	0.281	–1
ΔH_b	26 600	28 300	–6	29 500	26 700	10
ρ_{293}	3.625	3.633	–0.2	1.484	1.345	10

Table 2. Effect of the error in the boiling point on the accuracy of prognostication of other properties

Substance	Calculation error (in absolute value), %								
	T_b	V_b	T_{cr}	V_{cr}	P_{cr}	b	Z_{cr}	ΔH_b	ρ_{293}
ReF_6	1	2	5	1	3	3	2	6	1
$TiCl_4$	2	1	2	1	6	5	6	1	2
NpF_6	2	5	6	2	4	2	1	4	5
$SnBr_4$	5	2	1	1	1	1	2	6	2
$PSCl_2F$	6	2	2	1	4	2	2	7	4
$SbCl_5$	9	1	5	2	3	2	1	10	3
$SiBr_4$	10	2	6	1	6	1	1	8	5
$ReCl_4O$	12	3	15	2	13	3	1	12	7
$SiHCl_3$	12	5	7	2	9	1	1	10	10
$GeCl_4$	14	4	11	2	14	3	1	13	8
$SiBrCl_3$	16	6	14	6	16	2	4	14	9

$$V_{cr} = V_1(2.69 + 0.05f),$$

$$\Delta H_b = T_1[73 + 2.09\ln(T_1M/V_b)],$$

$$Z_{cr} = P_{cr}V_{cr}/(8.314T_{cr}),$$

$$\rho_{293} = (M/V_b)[1 + 0.46(1 - 293/T_b)],$$

where T_{cr} is the critical temperature (K); V_{cr}, critical volume ($cm^3\ mol^{-1}$); P_{cr}, critical pressure (MPa); Z_{cr}, critical compressibility factor ($P_{cr}V_{cr}/RT_{cr}$); b, van der Waals constant ($cm^3\ mol^{-1}$); ΔH_b, enthalpy of evaporation at the boiling point ($J\ mol^{-1}$); M, molar mass ($g\ mol^{-1}$); and ρ_{293}, density of the fluid at 293 K ($g\ cm^{-3}$).

At the end of the iteration follows the test for the prescribed accuracy (0.1 K), $|T_b - T_1| < 0.1$. If the condition is satisfied, the calculation is terminated; otherwise, the preceding value T_1 is replaced with a new one, $T_1 = T_b$, and the calculation is repeated beginning with Eq. (1).

All the data for determining the error of prognostication of the substance property under consideration were taken from the reference book [3]. The prognostication accuracy is mostly determined by the error in determining the boiling point. Table 1 lists errors of calculation of various properties for two substances with different T_b determination errors: small (ReF_6) and large ($SiHCl_3$).

The effect of the error in prognostication of the boiling point on the calculation error for other properties is illustrated in more detail by Table 2. It can be seen from the data in Table 2 that, as the calculation error of the boiling point increases, so does that for other properties; however, the errors in calculation of

some properties (V_b, V_{cr}, Z_{cr}, b) remain comparatively small.

The precision of the method was determined on a set of 80 compounds of elements from Groups III–VIII of the Periodic system. The set included hydrides, fluorides, chlorides, bromides, iodides, mixed halides, and oxyhalides. The average (in absolute value) errors in property prognostication were the following (%): T_b 8, V_b 3, ΔH_b 10, T_{cr} 8, V_{cr} 3, P_{cr} 10, b 4, Z_{cr} 2, and ρ_{293} 5. With account of the fact that the prognosis is made without any preliminary information about the properties of a substance under study, the prognostication accuracy should be considered quite satisfactory. The data for the prognostication accuracy refer to nonpolar and weakly or moderately polar substances. For strongly polar substances (NH_3, H_2O), the prognostication error is substantially larger.

If the boiling point is known, a calculation by the same formulas [beginning with Eq. (2), but without iteration] has a two times higher accuracy.

CONCLUSION

A method for prognostication of properties of molecular inorganic fluids on the basis of only the stoichiometric formula of a compound was suggested.

REFERENCES

1. Sladkov, I.B., *Prognozirovanie fiziko-khimicheskikh svoistv veshchestv metodami teorii termodinamicheskogo podobiya* (Prognostication of Physicochemical Properties by Methods of the Theory of Thermodynamic Similarity), St. Petersburg: SPb Gos. Tekh. Univ., 1994.
2. Sladkov, I.B., *Zh. Prikl. Khim.*, 1994, vol. 67, no. 4, pp. 662–664.
3. Morachevskii, A.G. and Sladkov, I.B., *Fiziko-khimicheskie svoistva molekulyarnykh neorganicheskikh soedinenii* (Physicochemical Properties of Molecular Inorganic Compounds), St. Petersburg: Khimiya, 1996.
4. Sladkov, I.B., *Zh. Prikl. Khim.*, 2003, vol. 76, no. 12, pp. 1961–1965.

ISSN 1070-4272, Russian Journal of Applied Chemistry, 2008, Vol. 81, No. 10, pp. 1863–1864. © Pleiades Publishing, Ltd., 2008.
Original Russian Text © M.N. Gorbunova, E.A. Sazonova, 2008, published in Zhurnal Prikladnoi Khimii, 2008, Vol. 81, No. 10, pp. 1743–1744.

BRIEF COMMUNICATIONS

Sorption Ability of *N*-Vinylpyrrolidone–Trimethoxyvinylsilane Copolymers

M. N. Gorbunova and E. A. Sazonova

Institute of Technical Chemistry, Ural Branch, Russian Academy of Sciences, Perm, Russia

Received April 9, 2008

Abstract—Sorption ability of *N*-vinylpyrrolidone–trimethoxyvinylsilane copolymers was studied. Cross-linked *N*-vinylpyrrolidone–trimethoxyvinylsilane copolymers sorb Ni(II) and Cu(II) from ammonia solutions and can find use for wastewater treatment to remove these metal ions.

DOI: 10.1134/S1070427208100303

Polymeric sorbents of various classes are widely used in analysis and preconcentration of metals [1, 2]. In particular, cross-linked copolymers based on *N*-vinylpyrrolidone (VP) are used as sorbents. For example, VP–divinylbenzene copolymer is used in solid-phase extraction to determine phenoxyalkanoic acids and other herbicides in water and in the environment [3]. The copolymer of VP with 2-(vinyloxyethoxy)methylthiirane is a sulfur-containing sorbent of Ag(I) and Hg(II) ions [4]. Sorbents of a 3*D* structure, used as stabilizers for food and perfume liquids, were prepared by copolymerization of VP with triethylene glycol dimethacrylate [5, 6].

With the aim to prepare new potential sorbents, we synthesized cross-linked copolymers of *N*-vinylpyrrolidone with trimethoxyvinylsilane (TMVS) and examined their sorption activity.

EXPERIMENTAL

N-Vinylpyrrolidone (Lancaster) was dried over KOH and vacuum-distilled, with collection of the fraction with bp 65°C (1.5 mm Hg), $n_D^{20} = 1.5117$.

Trimethoxyvinylsilane (chemically pure grade) was purified by vacuum distillation, with collection of the fraction with bp 123°C, $d_4^{20} = 0.9700$, $n_D^{20} = 1.390$.

Copolymerization of VP with TMVS was performed in the bulk and in solution in a vacuum in the presence of AIBN initiator.

The pH dependence of the sorption ability of the VP–TMVS copolymer toward nonferrous and heavy metal ions was determined by the static sorption method at the initial concentration of the metal ions of 0.015 ± 0.005 M, temperature of 20 ± 2°C, polymer : salt solution ratio of 1 : 200, and phase contact time of 24 h.

Solutions of metal salts were prepared by dissolving a weighed portion of appropriate salt $CuCl_2 \cdot 2H_2O$, $NiCl_2 \cdot 6H_2O$, $Pb(NO_3)_2$, or $Sc(SO_4)_3$ in HNO_3 solutions of required concentration or in ammonia solutions. The metal concentrations in solutions were determined by complexometric titration with Na_2EDTA. The static sorption capacity for a metal, E^M, was determined from the difference between the metal concentrations in the solution before and after sorption, with an error not exceeding 5%.

VP–TMVS copolymers were prepared by radical polymerization [7].

The copolymers obtained are colorless solids soluble in ethanol, acetone, and DMSO. However, after reprecipitation and drying, the copolymers lose the solubility in organic solvents because of the formation of siloxane cross-links, in agreement with published data [8].

We examined the dependence of the sorption ability of the cross-linked VP (80 mol %)–TMVS (20 mol %) copolymer (content of active groups, according to elemental analysis, 8.64 mmol g^{-1}) toward certain transi-

Table 1. Static sorption capacity E^M and distribution coefficients K_d of nonferrous and heavy metals

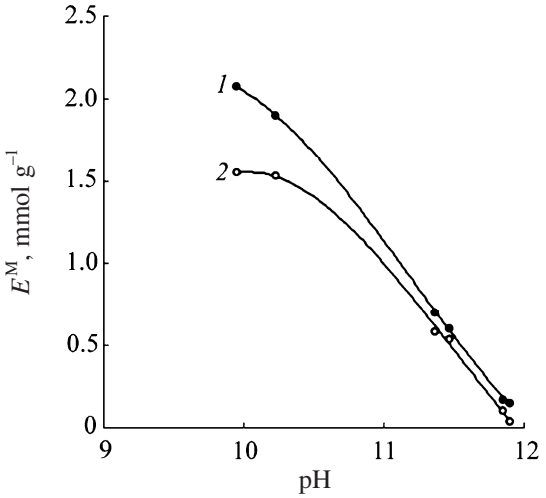
Metal	Acidity of initial solution	E^M, mmol g^{-1}	K_d, cm^3 g^{-1}
Ni(II)	pH 4.87	0.58	35.80
	pH 2.15	0.52	30.95
	0.1 M HNO_3	0.44	25.00
	1 M HNO_3	0.32	17.58
Cu(II)	pH 4.85	0.64	41.03
	pH 2.13	0.57	34.97
	0.1 M HNO_3	0.51	30.18
	1 M HNO_3	0.44	25.00
Pb(II)	pH 4.86	0.31	18.90
	pH 2.05	0.49	33.56
	0.1 M HNO_3	0.26	15.38
	1 M HNO_3	0.24	14.04
Sc(III)	pH 1.47	0.56	73.68
	pH 0.58	0.48	57.14
	pH 0.44	0.36	37.50
	1 M HNO_3	0.02	1.54

Table 2. Static sorption capacity E^M and distribution coefficients K_d of nonferrous and heavy metals in ammonia solutions

Metal	pH of initial solution	E^M, mmol g^{-1}	K_d, cm^3 g^{-1}
Ni(II)	5.78	0.96	56.47
	9.95 (0.1 M NH_3)	2.07	350.85
	11.47 (1 M NH_3)	0.60	29.13
	11.85 (3 M NH_3)	0.17	6.83
Cu(II)	5.78	0.96	77.42
	10.23 (0.1 M NH_3)	1.53	228.36
	11.37 (1 M NH_3)	0.58	35.80
	11.90 (3 M NH_3)	0.04	1.85

tion metal ions on the initial acidity of the solution (Table 1) and of that toward Cu(II) and Ni(II) ions on pH of the initial ammonia solution (figure, Table 2). We found that, with an increase in the solution acidity, the sorption ability of this polymer toward metal ions steadily decreases (Table 1) as a result of protonation of the nitrogen atom in the pyrrolidone ring.

In ammonia solutions, the sorption capacities for Cu(II) and Ni(II) and the distribution coefficients of these ions are considerably higher than those in acid solutions. With an increase in pH of ammonia solutions, the sorption capacity of the polymer with respect to Ni(II) and Cu(II) ions decreases as a result of the formation of stable metal ammine complexes in solution (figure, Table 2).



Sorption capacity E^M of cross-linked VP–TMVS copolymer for (*1*) Ni(II) and (*2*) Cu(II) as a function of pH of the initial ammonia solution.

Thus, cross-linked VP–TMVS copolymers quantitatively sorb Ni(II) and Cu(II) ions from ammonia solutions and can be used for wastewater treatment to remove these metal ions and for recovery of Cu(II) ions from ammonia solutions used in electronics production.

REFERENCES

1. Myasoedova, G.V. and Savin, S.B., *Zh. Anal. Khim.*, 1982, vol. 37, no. 3, pp. 499–502.
2. Zolotov, Yu.A. and Kuz'min, N.M., *Kontsentrirovanie mikroelementov* (Preconcentration of Microelements), Moscow: Khimiya, 1982.
3. *Peruzzi, M., Bartolucci, G., and Cioni, F., J. Chromatogr. A*, 2000, vol. 867, pp. 169–175.
4. Morozova, L.V., Mikhaleva, A.I., Golentovskaya, I.P., et al., *Zh. Prikl. Khim.*, 1990, vol. 63, no. 5, pp. 1176–1178.
5. Korshak, V.V., Zubakova, L.B., and Nikiforova, L.Ya., *Vysokomol. Soedin., Ser. B*, 1973, vol. 15, no. 6, pp. 419–421.
6. Akhnazarova, S.L., Zubakova, L.B., Pilina, I.Yu., and Ileneva, E.V., Abstracts of Papers, *Mezhdunarodnaya konferentsiya "Matematicheskie metody v khimii i khimicheskoi tekhnologii"* (Int. Conf. "Mathematical Methods in Chemistry and Chemical Technology"), Tver, 1995, part. 2, p. 96.
7. Gorbunova, M.N., Surkov, V.D., and Fedoseev, M.S., *Vysokomol. Soedin., Ser. B*, 2003, vol. 45, no. 10, pp. 1765–1768.
8. *Thompson, B.R., J. Polym. Sci.*, 1956, vol. 19, pp. 373–377.

ISSN 1070-4272, Russian Journal of Applied Chemistry, 2008, Vol. 81, No. 10, pp. 1865–1867. © Pleiades Publishing, Ltd., 2008.
Original Russian Text © A.G. Galstyan, A.I. Tarasenko, Yu.A. Shumilova, 2008, published in Zhurnal Prikladnoi Khimii, 2008, Vol. 81, No. 10, pp. 1745–1747.

BRIEF COMMUNICATIONS

Oxidation of 4-Hydroxytoluene with an Ozone–Oxygen Mixture in Acetic Acid

A. G. Galstyan, A. I. Tarasenko, and Yu. A. Shumilova

Institute of Chemical Technologies, Dal' East-Ukrainian National University, Rubezhnoe, Lugansk oblast, Ukraine

Received February 5, 2008

Abstract—Liquid-phase oxidation of 4-hydroxytoluene by ozone to 4-hydroxybenzoic acid in the presence of cobalt(II) acetate as a catalyst was studied. The optimal oxidation conditions were found.

DOI: 10.1134/S1070427208100315

4-Hydroxybenzoic acic (4-HBA) is widely used in production of drugs and pharmaceuticals, as conservant for foodstuffs, and for preparation of liquid crystal compounds [1, 2]. In industry, this acid is mainly produced by carboxylation of potassium phenolate [3] and oxidation of 4-hydroxytoluene (4-HT) with Pb, Mn, and Fe oxides [4]. The drawbacks of these procedures are the process complexity in the first case and formation of large amounts of toxic wastewater in the second case.

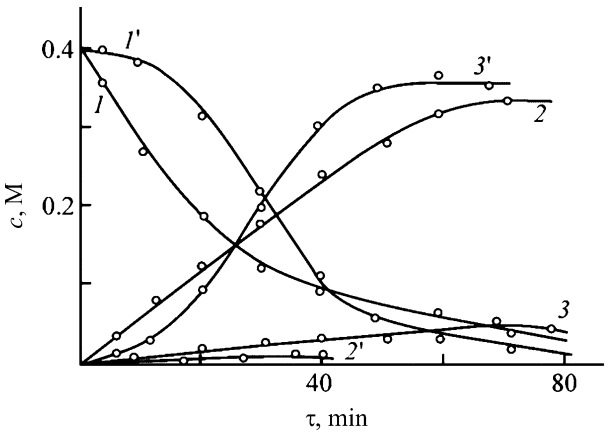
In this study we examined oxidation of 4-HT by an ozone–oxygen mixture with the aim to develop a low-waste process for 4-HBA production.

Published data on ozonation of 4-HT in acetic acid are lacking. It is only known [5–7] that, in tetrachloromethane, ozone rapidly attacks methylphenols at the lone electron pair of the OH group, which is followed by breakdown of the aromatic ring. Products of methyl group oxidation are not formed under these conditions.

The results of preliminary studies of the reaction of ozone with 4-HT in acetic acid do not differ noticeably from those described in [5–7]: The reaction rate constant at 20°C is 2.2×10^3 l mol^{-1} s^{-1}, and only aliphatic peroxides are detected in the oxidate after exhaustive oxidation of the substrate.

With the aim to protect the OH group of the 4-HT molecule from the attack by ozone, it was acylated.

The kinetic experiments showed that the reactivity of acylated 4-HT in reactions with ozone is considerably lower than that of nonacylated 4-HT, as indicated by the apparent rate constant obtained at 20°C: k_{app} = 0.74 l mol^{-1} s^{-1}. A drastic decrease in the rate constant of the reaction of ozone with 4-acetoxytoluene (4-AT), compared to 4-HT, suggests a change in the oxidation mechanism. Apparently, in this case, ozone attacks not the OH group but, in accordance with the classical concept of the reaction of ozone with alkylbenzenes [7, 8], predominantly the double bonds of the aromatic ring (86.8%) and, to a lesser extent, the methyl group (12.9%) (see figure). At 20°C, 1.15 mol of ozone is consumed per mole of 4-AT.



Variation of the concentration c of reaction mixture components in oxidaiton of 4-AT by an ozone–oxygen mixture in CH_3COOH at (*1*–*3*) 20 and (*1*'–*3*') 95°C in the presence of cobalt(II) acetate. $[4\text{-AT}]_0 = 0.4$, $[O_3]_0 = 4.8 \times 10^{-4}$, $[Co(OAc)_2] = 0.18$ M; $v_{air} = 8.3 \times 10^{-3}$ l s^{-1}. (*1*, *1*') 4-AT, (2) peroxides, (*2*') 4-ABAl, and (*3*, *3*') 4-ABA. (τ) Time.

Influence of the concentration of cobalt(II) acetate on the selectivity of 4-AT oxidation at the methyl group ($[O_3] = 4.8 \times 10^{-4}$, [4-AT] = 0.4 M; $v_{air} = 8.3 \times 10^{-3}$ l s^{-1}; $T = 95$°C)

$[Co(OAc)_2]$, M	Selectivity with respect to CH_3 group, %
0.06	43.9
0.10	58.4
0.14	71.0
0.18	87.0
0.22	87.1

The major product of 4-AT oxidation at the methyl group is 4-acetoxybenzoic acid (4-ABA) (see figure). In early steps of the oxidation, we also identified 4-acetoxybenzaldehyde (4-ABAl) whose concentration in solution does not exceed 10^{-4} M.

The selectivity of oxidation at the side chain increases on introducing into the system an oxidation catalyst, cobalt(II) acetate. Under the experimental conditions, the reaction is fast, and its major product is 4-ABA (see figure). The oxidation selectivity depends on the catalyst concentration, and, at a cobalt(II) acetate concentration of 0.18 M and temperature of 95°C, the oxidation is complete in 1 h, and the selectivity with respect to the methyl group is 87% (see table).

Selective oxidation at the methyl group in the presence of cobalt(II) acetate becomes possible as a result of two-step oxidation by ozone. Under the experimental conditions, ozone predominantly reacts with Co^{2+} [reaction (1)] ($k_1 = 9.7 \times 10^2$, $k_{AcOArCH_3 + O_3} = 0.74$ l mol^{-1} s^{-1}) to give active Co^{3+} species which involve 4-AT at a high rate [reaction (2)] in selective oxidation at the methyl group [9]:

$$Co^{2+} + O_3 + H^+ \rightarrow Co^{3+} + HO + O_2, \quad (1)$$

$$AcOArCH_3 + Co^{3+} \rightarrow AcOArCH_2 + Co^{2+} + H^+. \quad (2)$$

To ensure the occurrence of reaction (1), ozone should be continuously supplied to the oxidation system. Interruption of its supply impedes the process to the point of its complete cessation. This fact additionally confirms the assumption that the active form of the catalyst is mainly formed by reaction (1). Under the experimental conditions, the concentration of molecular oxygen in the gas mixture is one and a half orders of magnitude higher than the ozone concentration. Therefore, the acetoxybenzyl radical generated in the system [reaction (2)] reacts mainly with an oxygen molecule [reaction (3)] to form a peroxy radical which subsequently recombines [reaction (4)] to give the reaction products:

$$AcOArCH_2 + O_2 \rightarrow AcOArCH_2O_2, \quad (3)$$

$$AcOArCH_2O_2 \rightarrow \text{products}. \quad (4)$$

EXPERIMENTAL

In the experiments, we used glacial acetic acid (analytically pure grade) purified by vacuum distillation from potassium permanganate. Crystalline 4-HT was purified by repeated recrystallization from water, and liquid 4-AT, by repeated distillation. Cobalt(II) acetate (analytically pure grade) was used without additional purification.

Acylation was performed in a three-necked flask. Acetyl chloride was added dropwise at room temperature over a period of 30 min to the calculated amount of 4-HT dissolved in an equivalent amount of acetic acid. Then the reaction mixture was carefully diluted with water to a 1 : 1 ratio, with continuous stirring until the HCl evolution fully ceased. After that, the mixture was separated in a separating funnel, and the organic layer was washed with a 5% alkali solution and distilled.

The reactor (glass column with a porous partition for dispersing the ozone–air mixture) was charged with 10 ml of glacial acetic acid, 0.4 M 4-AT, and a calculated amount of the catalyst, after which the installation was thermostated and, after the ozonizer attained the steady-state operation mode, the ozone–oxygen mixture containing 4.8×10^{-4} M ozone was passed at a rate of 30 l h^{-1}.

After the oxidation was complete, the mixture was poured into water with ice (1 : 3 ratio). The precipitated 4-ABA was filtered off and dried. If necessary, 4-ABA can be readily hydrolyzed to 4-HBA. For this purpose, to 4-ABA we added 10 ml of concentrated HCl, 20 ml of water, and 4 ml of ethanol, refluxed the solution for 1 h, and then cooled it to 10°C. The 4-HBA precipitate was filtered off and dried. Yield 79% based on the loaded 4-AT.

The ozone content of the gas phase was determined spectrophotometrically from the absorption at 254–290 nm. The oxidation products in solution were identified and quantitatively determined by GLC on a chromatograph equipped with a flame ionization detector and a column 2 m long and 4 mm in diameter,

packed with Chromaton N-AW impregnated with SE-30, under the following conditions: vaporizer temperature 250°C, column temperature 180°C, flow rates, l h^{-1}: carrier gas (nitrogen) 1.8, hydrogen 1.8, air 18. As internal reference we used 4-nitrochlorobenzene.

The running concentration of 4-ABA was determined by potentiometric titration with alkali. To this end, we took from the reaction mixture a sample (0.5 ml) from which we distilled off the solvent. Then we dissolved the dry residue in 30 ml of 50% ethanol neutralized with respect to phenolphthalein and titrated it with 0.05 N NaOH.

CONCLUSIONS

(1) Noncatalytic oxidation of 4-hydroxytoluene by ozone in acetic acid occurs at a high rate predominantly at the lone electron pair of the heteroatom, without formation of products of methyl group oxidation. Acylation of the hydroxy group allows preparation under these conditions of 4-acetoxybenzoic acid in a yield of about 13%.

(2) The selectivity of 4-acetoxytoluene oxidation to 4-acetoxybenzoic acid increases to 87% at 95°C in the presence of a catalyst, cobalt(II) acetate. This acid, if necessary, can be readily hydrolyzed to 4-hydroxybenzoic acid. The yield of 4-hydroxybenzoic acid based on the loaded 4-acetoxytoluene is 79%.

REFERENCES

1. Rubtsov, M.V. and Baichikov, A.G., *Sinteticheskie khimikofarmatsevticheskie preparaty* (Synthetic Chemical Pharmaceuticals), Moscow: Meditsina, 1971.
2. JPN Patent 52-157 071.
3. *Weygand–Hilgetag, Organisch-Chemische Experimentierkunst*, Leipzig: Johann Ambrosius Barth, 1964, 3rd ed.
4. Makarova, Z.S. and Repinskaya, I.B., *Zh. Org. Khim.*, 1982, vol. 18, no. 5, pp. 1022–1026.
5. Razumovskii, S.D. and Zaikov, G.E., *Ozon i ego reaktsii s organicheskimi soedineniyami* (Ozone and Its Reactions with Organic Compounds), Moscow: Nauka, 1974.
6. *Bailey, P.S., Ozonation in Organic Chemistry: Nonolefinic Compounds*, New York: Academic, 1982, vol. 2.
7. Galstyan, G.A., Tyupalo, N.F., and Razumovskii, S.D., *Ozon i ego reaktsii s aromaticheskimi soedineniyami v zhidkoi faze* (Ozone and Its Reactions with Aromatic Compounds in the Liquid Phase), Lugansk: Vostochno-Ukr. Nats. Univ., 2004.
8. Galstyan, A.G., Sedykh, A.A., Bushuev, A.S., and Tarasenko, A.I., in *Materialy Mezhdunarodnogo simpoziuma "Nauchnye dostizheniya v organicheskoi khimii"* (Proc. Int. Symp. "Scientific Achievements in Organic Chemistry"), Sudak, 2006, p. 147.
9. Galstyan, G.A., Galstyan, T.M., and Mikulenko, L.I., *Kinet. Katal.*, 1994, vol. 35, no. 2, pp. 255–260.

ISSN 1070-4272, Russian Journal of Applied Chemistry, 2008, Vol. 81, No. 10, pp. 1868–1870. © Pleiades Publishing, Ltd., 2008.
Original Russian Text © D.A. Rozental', N.V. Maidanova, V.A. Kulikova, 2008, published in Zhurnal Prikladnoi Khimii, 2008, Vol. 81, No. 10, pp. 1748–1750.

BRIEF COMMUNICATIONS

Influence of Finely Dispersed Granite Dust on the Composition and Properties of Asphalt

D. A. Rozental', N. V. Maidanova, and V. A. Kulikova

St. Petersburg State Institute of Technology (Technical University), St. Petersburg, Russia

Received May 13, 2008

Abstract—Changes in the composition and properties of asphalt upon contact at 160°C with granite dust whose concentration in a mixture with asphalt was 40, 60, 70, and 85 wt % were examined.

DOI: 10.1134/S1070427208100327

The majority of materials based on petroleum asphalt contain mineral fillers. Their content varies from 15–20% in mastics and roofing materials to 94–96% in asphalt concrete. Although the effect of fillers on various properties of asphalts has been extensively studied [1–5], many aspects of the problem are still poorly understood.

In this study, we examined the influence exerted on the composition and properties of BDUS 70/100 asphalt by granite dust with a particle size less than 0.071 mm.

Previous studies [6, 7] has shown that, with a coarsely dispersed filler (fractions 2–3 and 3–5 mm), a part of the asphalt is adsorbed by granite. This fraction depends on the time of heating the asphalt–mineral mixture at 160°C, and the adsorption causes changes in the asphalt composition. The optimal time required to attain the adsorption equilibrium under these conditions is 3–5 h. Changes in the asphalt composition in the spaces between the filler grains consist in a decrease in the content of aromatic oils and a certain increase in the content of resins and asphaltenes. Apparently, the amount of adsorbed asphalt is proportional to the surface area of the filler and to its adsorption power.

It is known from Levchenko's studies [6, 7] that hot centrifugation (5 min, 5000 rpm) of a mixture consisting of 90 wt % granite and 10 wt % asphalt of BDUS 70/100 grade, thermostated for 5 h at 160°C, allows recovery of 16% of the introduced asphalt. Its composition and properties are listed in Table 1.

This study was performed with granite dust sieved through a 0.071-mm sieve and having the specific surface area of 1 $m^2 g^{-1}$, i.e., 10 000 $cm^2 g^{-1}$. We prepared mixtures containing 40, 60, 70, 85, and 95 wt % granite dust with asphalt of BDUS 70/100 grade. These mixtures were thermostated at 160°C for 5.5 h (4 h with stirring and 1.5 h without stirring). The results are presented in Table 2.

Table 2 shows that, with an increase in the dust content in the mixture with asphalt, its penetration considerably decreases and the softening point grows. We could not determine the softening point of the mixture

Table 1. Composition and properties of asphalt after its contact with granite

Parameter	BDUS 70/100 asphalt	
	initial	recovered
Penetration at 25°C P_{25}, 0.1 mm units	98	42
Softening point T_s, °C	44	58
Composition, wt %:		
saturated oils	12.7	12.6
aromatic oils	44.7	39.2
resins	26.6	29.9
asphaltenes	16.0	18.3

Table 2. Composition and properties of asphalt thermostated with granite dust

Asphalt	Π_{25} at 25°C, 0.1 mm units	T_s	T_b*	Composition, wt %			
		°C		saturated oils	aromatic oils	resins	asphaltenes
Initial	67	49.6	–18	15.3	41.3	24.2	19
Dust content, wt %:							
40	54	57.8	–18	15.9	40.6	24.5	19
60	39	58.2	–13	21.3	40.1	24.2	20.5
70	23	77.5	–	–	–	–	–
85	10	–	–	–	–	–	–

* (T_b) Brittle point.

Table 3. Content of granite dust in wt % and vol %

Parameter	Content, %				
Weight percentage:					
dust	40	60	70	85	95
asphalt	60	40	30	15	5
Volume percentage:					
dust	14.5	21.8	25.5	31	34.5
asphalt	60	40	30	15	5
Sum of volume percentages	74.5	61.8	55.5	46	39.5
Relative content (total = 100%):					
dust	19	35	46	67	87
asphalt	81	65	54	33	13
Dust : asphalt volume ratio	0.23	0.54	0.85	2.03	6.7

with 85% dust, because it was a set of granules of different sizes. Comparison of changes in the group composition of asphalts (Tables 1 and 2) shows that these changes are considerably more pronounced in the asphalt that was brought in contact with coarsely grained granite. This can be attributed to the limited capacity of the method for determining the component composition, suggested by VNII NP–SoyuzdorNII, as applied to mix-tures of asphalt with dust.

Dust particles having a microscopic volume and small weight are involved in the Brownian movement and are nearly uniformly distributed over the bulk of asphalt. In hexane extraction of ashpaltenes, the initial material is a mixture of asphalt with granite dust, rather than pure asphalt. In the course of the extraction, the major fraction of the adsorbed asphalt is washed out with the solvent. Therefore, the compositions of the initial asphalt and that thermostated with granite dust differ insignificantly. For the mixtures containing more than 60% dust, the analytical errors are too large.

For the convenience of the analysis of the effect exerted by the granite dust concentration on the composition and properties of asphalt, the mixture compositions were converted from wt % to vol %. The results are listed in Table 3.

It can be seen that the dust content of asphalt at weight concentrations of the dust of 40 and 60% is low: 19 and 35 vol %, respectively. Dust particles are for apart from each other and are surrounded by a solvation shell of asphalt components present in these mixtures in excess. In these mixtures, the dust particles are in the freely dispersed state and do not form a continuous structure in the bulk of asphalt.

Because the range of adhesion forces of dust particles is tens of nanometers, it whould be expected that the interaction can occur only when the particles approach each other to such a distance. Starting from a 70 wt % concentration of dust, at which the volume ratio of the dust and asphalt becomes close to unity, the dust particles can combine into a continuous framework in the bulk of the asphalt. The compound becomes a hard monolith. At a higher content of dust in the mixture with asphalt, the amount of asphalt becomes insufficient for the formation of a monolith, and

the mixture is broken to separate granules. At a 95% content of the dust, the mixture remains powdered and is only slightly black colored.

Thus, it can be concluded that, at a large specific surface area of the mineral filler and its high concentration, all the asphalt components are adsorbed. As a result, the material becomes nonmonolithic and friable. This is possible only with a finely dispersed material in which the interparticle distances are comparable with the range of the effect of the adhesion energy field. Apparently, in asphalt concrete, the voids between filler grains should be larger in size than the range of the effect of the energy field of the filler. This would allow a certain amount of asphalt to be retained in the state insignificantly differing from the initial state, with preservation of its plastic properties.

CONCLUSIONS

(1) When present in concentrations of 40 and 60 wt %, granite dust affects the asphalt composition insignificantly, but noticeably increases its softening point and decreases the penetration. At a dust concentration of 70%, a solid monolith is formed, and at 85% dust content its mixture with asphalt is broken down to separate lumps. At high concentrations of dust, it adsorbs all the asphalt components.

(2) Finely dispersed filler (in contrast to coarsely dispersed one) can form a 3*D* condensation structure in the bulk of asphalt. This is possible if dust particles approach each other to a distance comparable with the range of their adhesion energy field. A high content of dust in asphalt concrete can lead to premature destruction of the road pavement.

(3) At a dust concentration exceeding the above level, the mixture is broken down to separate particles, in the limit equal in size to dust particles. This fact indicates that, under definite conditions, all components of asphalt are adsorbed on the mineral filler.

REFERENCES

1. Koblanovskaya, A.S. and Mikhailov, V.V., *Dorozhnye bitumy* (Road Asphalts), Moscow: Transport, 1973.
2. *Bituminous Materials: Asphalts, Tars and Pitches*, Hoiberg, A.J., Ed., New York: Interscience, 1964, vol. 1.
3. Korolev, I.V., *Stroit. Mater*., 1981, no. 8, pp. 63–67.
4. Portnyagin, V.D., *Khim. Tekhnol. Topl. Masel*, 1989, no. 11, pp. 35–37.
5. Stupak, S.V., Gureev, A.A., and Kononov, V.I., *Khim. Tekhnol. Topl. Masel*, 1989, no. 1, pp. 36–38.
6. Levchenko, E.S., Rozental', D.A., and Zalishchevskii, G.D., *Zh. Prikl. Khim*., 2004, vol. 77, no. 3, pp. 521–622.
7. Levchenko, E.S., Effect of Mineral Fillers on the Properties and Composition of Asphalt, *Cand. Sci. Dissertation*, St. Petersburg, 2005.

ISSN 1070-4272, Russian Journal of Applied Chemistry, 2008, Vol. 81, No. 10, pp. 1871–1873. © Pleiades Publishing, Ltd., 2008.
Original Russian Text © I.V. Krauklish, I.Yu. Rodionov, V.A. Sirotko, 2008, published in Zhurnal Prikladnoi Khimii, 2008, Vol. 81, No. 10, pp. 1751–1753.

BRIEF COMMUNICATIONS

Conditions of Liquid Phase Formation in Operation of Fire-Extinguishing Aerosol Generators

I. V. Krauklish, I. Yu. Rodionov, and V. A. Sirotko

St. Petersburg State Institute of Technology (Technical University), St. Petersburg, Russia
Ustinov Voenmekh Baltic State Technical University, St. Petersburg, Russia

Received May 16, 2008

Abstract—Reasons for formation of the liquid phase in operation of fire-extinguishing aerosol generators were examined. The amount of the melt formed depends on the particle size and on the inclination angle and length of the cylindrical generator.

DOI: 10.1134/S1070427208100339

Fire safety is currently a pressing problem. Despite the overall decrease in the number of fires in the past three years, the total damage, according to the Emergency Ministry data, increased by more than 20%. One of the most efficient and economical means for fire control is the use of fire-extinguishing aerosol generators. However, they have certain drawbacks. In particular, formation of not only a solid, but also a liquid phase in the course of generator operation impairs the generator performance and causes additional damage to the materials being treated. The goal of this study was to elucidate the reasons for formation of the liquid phase.

Experiments were performed in a model cylindrical generator with an outer diameter of 0.85 and an inner diameter of 0.8 m, made of St.10 steel [GOST (State Standard) 8733–74]. We used two cylinders of different lengths, 0.82 and 1.64 m. Charges were prepared by dead pressing on a PSU-125 hydraulic press at a compaction pressure of 200 MPa. Charges of two types were used: with an internal channel 0.04 m in diameter and without it. The charge length in both cases was 0.20 m, and the outer diameter, 0.078 m. To protect the generators from burning-through of the side surface, the charges were twice coated with a mixture of liquid glass and iron(III) oxide. To prevent an uncontrollable increase in the combustion rate, the charge was wrapped with a 0.002-m layer of a heat-insulating material (mica).

To measure the temperature, we used standard TKhA thermocouples in a porcelain sheath [Chromel (90.5% Ni + 9.5% Cr)–Alumel (94.5% Ni + 5.5% Al, Si, Mn, Co)], 0.001 m in diameter, with the upper temperature measurement limit of 1300 K. The junctions of some of the thermocouples were fixed at hollows on the generator housing, and some of the thermocouples were inserted through apertures in the housing to record the aerosol temperature.

The model generator was tested on a special installation consisting of a computer, analog–digital converter, amplifier, and thermocouples. The installation allows on-line monitoring of changes in the temperatures of both the generator walls and the aerosol flow. Data obtained in the course of the tests were treated with a computer in the Microsoft Windows 2000 environment and were recorded using a specially developed software. The test results are listed in Table 1.

Table 1. Results of generator tests

Experimental series	Pipe length, m	Charge weight, kg	Charge length, m	T_{max}, K		Average combusiton time, s	Melt weight, wt %
				walls	aerosol		
Charge without channel	0.83	1.2	0.22	983	1083	69	5
	1.63	1.2	0.22	798	943	77	0
Double charge without channel	1.63	2.4	0.42	1118	1228	150	16
Charge with channel	1.63	1.5	0.42	943	1054	145	0

Table 2. AFC composition and energy characteristics (charge weight m_c = 2.1 kg, fuel density ρ = 994.7 kg m^{-3}, combustion velocity U_l = 0.00284 m s^{-1})

Component	Empirical formula	Content, wt %	ΔH_f^0(298.15), kJ kg^{-1}
Iditol (phenol–formaldehyde resin)	$C_{13}H_{12}O_2$	15	–2964
Dicyandiamide (DCDA)	$C_2H_4N_4$	10	221
Potassium nitrate	KNO_3	75	–4660

As the experiments showed, the amount of the melt formed in combustion of the aerosol-forming composition (AFC) in the generator depends on the extent to which the generator wall is heated, charge weight, and pipe length. To elucidate this dependence more accurately, we constructed a mathematical model of the gravity sedimentation of the liquid melt on the inner surface of the pipe of an aerosol fire extinguisher. The input data for calculating the properites of AFC combustion products and AFC energy characteristics are given in Table 2.

Thermodynamic calculations of the aerosol composition, performed according to [1], showed that the fuel composition we chose provides the combustion temperature (T = 1591 K) at which almost the whole amount of KOH, which is the main condensed product, is in the liquid state; its weight fraction Z is 0.396 (mole fraction of liquid KOH_l 0.244 and that of gaseous KOH_g 0.33×10^{-2}), i.e., the condensed phase is fully formed near the combustion surface and then undergoes only coagulation, fragmentation, and adhesion to the channel walls.

At an enthalpy of the system changed by 5%, possible fluctuations of the charge combustion temperature due to variation of the external conditions cannot significantly affect the thermodynamic characteristics of the aerosol. The condensed phase present in the aerosol is polydispersed [2].

At an initial instant of time, the condensate can fall out on a cold channel wall and even solidify. As the structure is heated to 633–678 K (melting point of KOH), the melt entrained by the gas flow will be transferred along the internal generatrix of the channel to the open end of the pipe and will be ejected to the environment in the form of coarse drops and clots.

In the suggested mechanism of deposition of the liquid melt on the channel walls, each particle of the melt is involved in two motions: to the side surface of the channel under the action of the gravitation and in the opposite direction from the channel wall under the action of the aerodynamic force.

The gravitational force acting on a particle was calculated as follows:

$$F_g = mg\cos\alpha,$$

where F_g is the force acting on a particle (N); g, free-fall acceleration; α, inclination angle of the generator axis relative to the horizon (deg); and m, particle weight (kg).

The particle weight, in turn, was calculated by the formula

$$m = V\rho_p,$$

where V is the particle volume (m^3), and ρ_p, particle density (kg m^{-3}).

The aerodynamic force acting on the particle was calculated as

$$F_a = C_y \frac{\rho W_y^2}{2} S,$$

where W_y is the particle velocity relative to the gas flow across the channel or, in other words, sedimentation velocity (m s^{-1}); ρ, gas phase density (kg m^{-3}); and S, cross-section area of the particle (m^2).

The aerodynamic resistance coefficient C_y for the turbulent flow is chosen according to [3]. The Reynolds number for the system under consideration is

$$\mathrm{Re} = \frac{\rho W_y d_z}{} > 10^4,$$

where d_z is the mean diameter of the melt particle (m) and ν is the viscosity (Pa s).

Accordingly, the aerodynamic resistance coefficient C_y will be equal to 0.4–0.5 for this system. Then the equation of the particle motion along the Y axis, determining the deposition of particles on the walls, can be written as

$$m\frac{dW_y}{dt} = mg\cos\alpha - C_y \frac{\rho W_y^2}{2} S.$$

Because the particle size is small (mean particle diameter, according to experimental data [2], is 20 μm), it can be assumed that, in motion along the X axis, $W_{xg} = W_{xm}$ (m refers to melt, and g, to gas). This

assumption will not bring about any fundamental quantitative changes to the final result and, primarily, will not affect the residence time of particles in the pipe, which is determined by the formula $\tau = L/W_x$.

Let us assume that the mean size of melt particles is d_z. Then Eq. (1) will take the form

$$\frac{dW_y}{dt} = g\cos\alpha - \frac{3}{4} C_x \rho W_y^2 \frac{1}{\rho_z d_z},$$

and the total scheme for calculation of the particle sedimentation will be as follows:

$$dx = W_x \Delta t,$$

$$dy = W_y \Delta t, \quad W_{y_i} = W_{y_{i-1}} + \left(\frac{dW_y}{dt}\right)_{i-1} \Delta t,$$

$$x + dx, \quad y = y + dy,$$

The total residence time of the aerosol in the pipe does not exceed 3 s. Therefore, to provide a sufficient calculation accuracy in the numerical integration, Δt was assumed to be 10^{-3}. To calculate the residence time of an aerosol particle in the pipe, we used the quantities calculated by the following formulas.

Generator performance (aerosol expenditure):

$$m_{as} = \rho_T F_{ch} U_l,$$

where m_{as} is the aerosol weight (kg); ρ_T, aerosol density at a current temperature (kg m^{-3}); U_l, linear velocity of combustion (m s^{-1}); and F_{ch}, charge surface area (m^2).

The charge surface area is given by

$$F_{ch} = \pi d_p^2/4.$$

The amount of the melt supplied to the fire-extinguisher pipe as a result of combustion

$$m_m = m_{as} Z,$$

where Z is the weight fraction of the melt (%).

The amount of the melt deposited on the channel walls is

$$m_{mw} = (m_m/F) dy L_x,$$

where F is the wall surface area (m^2) and L_x is the channel length.

Table 3. Melt weight in relation to the generator inclination angle and particle size

Mean particle diameter $d_z \times 10^{-6}$, m	Melt weight, kg, at indicated inclination angle of the generator, deg			
	0	30	45	60
10	1.04×10^{-2}	8.99×10^{-3}	7.34×10^{-3}	5.19×10^{-3}
20	4.13×10^{-2}	3.58×10^{-2}	2.92×10^{-2}	2.07×10^{-2}
30	0.111	8.63×10^{-2}	6.5×10^{-2}	4.6×10^{-2}
40	32.5	26	18.7	10.6
60	0.719	0.619	0.481	0.301
80	–	–	0.8	0.593
100	–	–	–	0.805

The results of a calculation of the weight of the melt formed are listed in Table 3.

CONCLUSIONS

(1) At a particle size $d_z < 10$ μm, melt is not deposited on the channel walls to any noticeable extent; with an increase in the aerosol particle size, the fraction of the melt deposited on the channel walls grows.

(2) With a decrease in the inclination angle of the fire extinguisher axis, the fraction of the melt condensing on the channel wall increases.

(3) To reduce the melt discharge along the side surface of a fire extinguisher, it can be recommended to decrease the length of the cylindrical channel and increase the inclination angle of the fire extinguisher relative to the horizon.

REFERENCES

1. *Termodinamichsekie i teplofizicheskie svoistva produktov sgoraniya: Spravochnik* (Thermodynamic and Thermal Properties of Combustion Products: Handbook), Glushko, V.P., Ed., Moscow: VINITI, 1972.
2. Rodionov, I.Yu. and Krauklish, I.V., in *Sovremennye problemy spetsial'noi tekhnicheskoi khimii: Sbornik trudov* (Modern Problems of Special Technical Chemistry: Coll. of Papers), Kazan: Kazan. Gos. Tekhnol. Univ., 2006, pp. 668–673.
3. Saltanov, G.A., *Sverkhzvukovye dvukhfaznye techeniya* (Supersonic Two-Phase Flows), Minsk: Vysheisha Shkola, 1972.

ISSN 1070-4272, Russian Journal of Applied Chemistry, 2008, Vol. 81, No. 10, pp. 1874–1876. © Pleiades Publishing, Ltd., 2008.
Original Russian Text © G.F. Nichugovskii, 2008, published in Zhurnal Prikladnoi Khimii, 2008, Vol. 81, No. 10, pp. 1754–1756.

BRIEF COMMUNICATIONS

Coulometric Determination of the Moisture Content, Using Modified Fischer Reagent with Epichlorohydrin

G. F. Nichugovskii

Prikladnaya Khimiya Russian Scientific Center, St. Petersburg, Russia

Receivd April 22, 2008

Abstract—Application of a coulometric method of water titration in the medium of a modified Fischer reagent in which epichlorohydrin is used to shift the equilibrium of sulfur dioxide oxidation by iodine was experimentally substantiated.

DOI: 10.1134/S1070427208100340

In a new modification of the Fischer reagent, it is suggested to use, instead of pyridine, epichlorohydrin (ECH), which rapidly and quantitatively reacts with HI, for shifting the equilibrium of sulfur dioxide oxidation by iodine. Certain conditions and results of using this reagent for quantitative determination of water in the volumetric titration mode, with isopropyl alcohol as solvent, have been reported previously.

Interest in the coulometric mode is caused by its two major advantages: absolute character of measurements (no calibration is required) and high sensitivity [1]. It is also important that different companies presently produce a large number of industrial coulometric installations. Apparently, coulometric titration is only possible in a conducting solution containing a certain minimal concentration of iodide ions to obtain elemental iodine at the anode. However, the suggested reagent based on ECH does not contain such a source of iodide ions. Hence, to implement a coulometric procedure, these ions should be introduced into the electrolyte in advance in the form of an appropriate salt.

EXPERIMENTAL

All the studies were performed on an experimental coulometric installation including generator and indicator units and a gas cell with a filter. For iodine indication, we used a bipotentiometric system with an additional 30 kΩ resistor in the indicator electrode circuit [2]. Preliminarily, we prepared a solution of SO_2 in ECH by passing the gas through the solvent until saturation. The SO_2 concentration was about 3 M. As a solvent for preparing the working electrolyte we used methanol with less than 0.1% moisture content. The cell was charged with 20 ml of methanol and 2–3 ml of a solution of SO_2 in ECH, after which argon dried over P_2O_5 was fed at a rate of 30–50 ml min^{-1}, and crystalline iodine was added in portions until its persistent color appeared. Initially, colored jets of an iodine solution rapidly decolorized owing to the reaction with H_2O in the immediate vicinity of the crystals, after which, with the progress of dehydration, these jets increased in length and gradually reached the surface. In the process, the indicator signal became maximal, and the potential difference at the indicator electrodes became close to zero. A similar pattern is observed with the common Fischer reagent. This fact indirectly suggests that the rate of the main chemical reaction of iodine with water in both reagents is similar.

The cathodic chamber is filled with the resulting solution containing a small excess of iodine through a filter by the principle of communicating vessels. In the course of the experiments, the solution level in the cathodic chamber should be necessarily kept below its level in the anodic chamber, to exclude ingress into the working chamber of interfering impurities accumulating in the near-cathode space.

In the first step of the studies, we used CsI as a source of iodide ions. However, its solubility in methanol in the presence of 10–20% ECH is less than 0.1 M.

Furthermore, the salt probably exists in solution mainly in the form of neutral ion pairs. Therefore, the electrolytic conductivity of the solution is relatively low: We failed to raise the generator current even to 2 mA. Characteristically, as products of the reaction of iodine with water and SO_2 in the presence of ECH are accumulated, the generator current at a given voltage noticeably increases, but no iodine generation is observed at the anode. This fact suggests accumulation in solution of methylsulfuric acid, which does not react with ECH but provides comparatively high conductivity.

Ammonium iodide NH_4I appeared to be the most efficient source of iodide ions. Its advantage is in the high solubility in methanol, which provides a high conductivity of the solution. However, due to its acidic properties, it slowly reacts with ECH, which leads to a gradual decrease in the concentration of iodide ions, and, at a certain critical level, the current efficiency of the electrochemical generation of molecular iodine becomes lower than 100% at a given current density. This critical concentration in the traditional Fischer reagent is about 0.1 M at a current density of about 10 mA cm^{-2}. Furthermore, the indicator current ceases to be proportional to the iodine concentration at very low concentration of iodide ions, and the sensitivity of the indicator system drastically decreases. Apparently, when iodide ions are fully absent, it is impossible to attain the final titratoin point, although the generator current does not change noticeably. The first sign of an irreversible change in the electrolyte composition, at which it becomes unsuitable for coulometric titration, is a well-defined increase in the results in successive analyses of the same sample. We found that this problem can be readily solved by intermittent introduction of additional amounts of NH_4I into the electrolyte.

As already noted, the main condition for applicability of the coulometric method is the 100% efficiency of titration. The simplest way to find this parameter is to perform titration of known amounts of water in accordance the introduced–found principle. To this end, we introduced with a syringe portions of a solvent with known amounts of water into a cell with the electrolyte. These amounts were calculated by a common procedure using the Faraday formula, taking into account equimolar ratio between iodine and water. Some of the results obtained are listed in Table 1.

These data show that the suggested electrolyte based on the modified Fischer reagent with ECH is quite suitable for coulometric titration of water at its content exceeding 0.01%. It is important that the stoichiometry of the reaction between the major components does not change in the process. The analytical error, as a rule, does not exceed 3 rel %. The relatively high error of the results, according to our observations, is due, firstly, to hydrodynamic flows of the catholyte and anolyte through the glass filter and, secondly, to electromigration transport of interfering products from the cathodic space into the working anodic space. Among these products, we should primarily note the di-thionite ion $S_2O_4^{2-}$ formed at the cathode by electrochem-ical reduction of SO_2 and quantitatively oxidized by iodine. In the common Fischer reagent, this process occurs with 100% efficiency. This fact served as the basis for coulometric back-titration of water [3].

Table 1. Efficiency of coulometric titration of water, using modified Fischer reagent with epichlorohydrin ($\alpha = 0.95$)

Solvent	H_2O introduced, %	H_2O found, %	Error, rel %	n
Isopropanol	–	0.052 ± 0.004	–	7
	0.48*	0.47 ± 0.06	–2.1	3
	0.80	0.78 ± 0.03	–2.5	–
DMF	–	0.218 ± 0.009	–	5
	0.38*	0.39 ± 0.02	+2.6	4
	0.78	0.79 ± 0.09	+1.3	4
Chloroform	–	0.020 ± 0.001	–	4

* Taking into account the initial moisture content.

Table 2. Efficiency of the electrochemical reduction of sulfur dioxide on a cathode in the modified Fischer reagent with epichlorohydrin ($n = 3$, $\alpha = 0.95$)

Current density, mA cm^{-2}	Time, s		t_c/t_a ratio, %
	anodic process, t_a	cathodic process, t_c	
6	200	200 ± 12	100 ± 6
10	200	196 ± 8	98 ± 4
16	200	110 ± 50	55 ± 25

We found that a similar pattern is observed in the electrolyte based on the modified reagent with ECH (Table 2). As can be seen, with an increase in the current density, the time required for the reduction of elemental iodine accumulated in the working chamber in the course of the anodic process sharply decreases. This result can be attributed to two factors: low current

Table 3. Stoichiometry of the reaction between water and iodine in modified Fischer reagent with epichlorohydrin ($\alpha = 0.95$)

Water		Iodine		$K = \frac{n_{H_2O}}{n_{I_2}}$
weight, g	*n*, mol	weight, g	*n*, mol	
0.034	0.00189	0.500	0.00197	0.96
0.022	0.00122	0.320	0.00126	0.97
0.017	0.00094	0.236	0.00093	1.01
				$K_{av} = 0.98 \pm 0.06$

efficiency by iodine at the anode (i.e., other electrochemical reactions occur along with the main reaction) and considerable electromigration transport into the working space of $S_2O_4^{2-}$ ions lowering the initial concentration of molecular iodine. Apparently, with accumulation of these ions in the cathodic space, the contribution of this process (and hence the determination error) will increase.

It is interesting that introduction into the electrolyte of chloroform, whose dielectric constant is considerably lower (4.7) than that of methanol (32.6), to a concentration of 20 vol % does not noticeably decrease the solution conductivity, but apparently improves the sensitivity of iodine indication. It is quite likely that addition of chloroform appreciably decreases the rate of the reaction of ECH with NH_4I. In this case, it is appropriate to add this amount of chloroform to the methanol-based electrolyte in advance.

The previously made conclusion that the ratio between iodine and water in the modified reagent with ECH is equimolar can be readily confirmed by direct gravimetric titration of weighed portions of pure water with crystalline iodine (Table 3). These data, as previously [4], can serve as a basis for gravimetric determination of the moisture content of substances and formulations containing up to 100% water.

CONCLUSIONS

(1) A new modification of the Fischer reagent, with epichlorohydrin used for shifting the equilibrium of the oxidation of sulfur dioxide with iodine, is suitable for coulometric titration of water, provided that ammonium iodide as a source of iodide ions is intermittently added to the methanol-based electrolyte.

(2) In the modified reagent in the presence of excess epichlorohydrin, iodine and water react in an equimolar ratio. The same ratio was confirmed by direct gravimetric titration of water with crystalline iodine.

REFERENCES

1. Nichugovskii, G.F., *Elektrokhimicheskie metody izmereniya vlazhnosti* (Electrochemical Methods for Measuring Moisture Content), St. Petersburg: Yanus, 2001.
2. Nichugovskii, G.F., *Zh. Anal. Khim.*, 1992, vol. 47, no. 7, pp. 1315– 1321.
3. Nichugovskii, G.F., *Zh. Anal. Khim.*, 1975, vol. 30, no. 12, pp. 2418– 2421.
4. Nichugovskii, G.F., *Zh. Prikl. Khim.*, 1998, vol. 71, no. 6, pp. 1036–1038.

ISSN 1070-4272, Russian Journal of Applied Chemistry, 2008, Vol. 81, No. 10, p. 1877. © Pleiades Publishing, Ltd., 2008.
Original Russian Text © Editorial board, 2008, published in Zhurnal Prikladnoi Khimii, 2008, Vol. 81, No. 10, p. 1757.

OBITUARY

Vladimir Aleksandrovich Krol' (1923–2008)

DOI: 10.1134/S1070427208100352

Vladimir Aleksandrovich Krol', a prominent scientist in the field of synthetic rubber production, doctor of chemical sciences, professor, winner of the Lenin and State Prizes, eldest staff member of the Lebedev Research Institute of Synthetic Rubber (VNIISK), died on June 7, 2008, at the age of 84, after serious sickness. A gifted man with a heroic fate passed away.

Krol' was born on November 16, 1923, in Omsk into a family of hereditary physicians. In June 1941, at the age of 17, he graduated with excellent marks from secondary school no. 37 of Omsk and hoped to continue the job of his parents. However, his destiny was different. Since the autumn of 1941, Krol' worked as a turner at a military plant in Novosibirsk. In May 1942, he volunteered into the Red Army and participated in battles. He was wounded twice (for the second time, heavily). After demobilization in the autumn of 1944, he entered the Lensovet Institute of Technology. After the second year, he passed to the University and graduated from the Chemical Faculty with honor in 1949. His specialization was organic synthesis. All the further activities of Krol' are associated with VNIISK. In 1953, he defended his Candidate's dissertation "Activity of Free Radicals in Connection with the Polymerization Process." In 1963, he became a senior researcher. Under the guidance of Prof. B.A. Dolgoplosk (Academician since 1964), Krol' actively participates in studies concerning the problem of butadiene polymerization. For a series cycle of studies on catalytic systems for the synthesis of *cis*-polybutadiene, Krol' was awarded in 1961 a Diploma of the Mendeleev All-Union Chemical Society, and for a series of papers "Development of *cis*-Polybutadiene Rubber" he, together with co-workers, received the Lebedev prize of the Presidium of the USSR Academy of Sciences. In 1967, Krol' and co-workers were awarded a Lenin Prize "For a Series of Studies on the Development of Regular Rubbers and of a Process for Their Commercial Production." The development and mastering of the production of two new kinds of rubber on a number of plants was at that time a major achievement of the Soviet science and engineering. The contribution of Krol' to this success is very large.



In 1972, Krol' very successfully defended his Doctoral (Chemistry) dissertation. It concerned the polymerization of butadiene and the development and commercial implementation of a procedure for producing SKD (*cis*-1,4-polybutadiene) rubber. In 1973, Krol' became a professor, and in 1978 he was awarded a State Prize for his studies.

From 1985 to 1989, Krol', along with heading a laboratory in VNIISK, occupied a professor's post at the Chair of Macromolecular Compounds of the Leningrad State University. He delivered the course of chemical technology of polymers and supervised diploma works. In the period from 1965 to 1990, twelve candidate's dissertations were defended under the guidance of V.A. Krol'.

Vladimir Aleksandrovich Krol' was a very good and comprehensively gifted person, a talented scientist, an excellent experimenter, and a tireless traveler. He enjoyed deserved universal esteem. Krol' spent the last period of his life in Israel, but he remained the Russian citizen and visited St. Petersburg every year.

Staff members of the Research Institute of Synthetic Rubber, colleagues, and friends

ISSN 1070-4272, Russian Journal of Applied Chemistry, 2008, Vol. 81, No. 10, p. 1878. © Pleiades Publishing, Ltd., 2008.
Original Russian Text © A.G. Morachevskii, 2008, published in Zhurnal Prikladnoi Khimii, 2008, Vol. 81, No. 10, p. 1758.

BOOK REVIEWS

Ananichev, V.A., *Ob"emnaya dilatometriya khal'kogenidnykh stekloobraznykh materialov* (Volumetric Dilatometry of Chalcogenide Glassy Materials),

St. Petersburg: Izd. Politekhnicheskogo Univ., 2007, 166 pp.

DOI: 10.1134/S1070427208100364

The discovery of semiconducting glasses by N.A. Goryunova and B.T. Kolomiets in the middle of the XX century stimulated studies of the whole set of physicochemical properties of these materials. Ananichev's book summarizes and analyzes methods and results of studying the thermal expansion of chalcogenide glasses and their melts in a wide temperature range.

The book consists of an introduction, eight chapters, and an appendix. In the brief Introduction (pp. 6–7), the author formulates the goal of the book and the problems considered. Very short Chapter 1 (pp. 8–18) presents the general relationships determining the cubic expansion coefficient of solids and liquids and, in particular, of chalcogenide glass melts. Chapter 2 (pp. 19–30) describes devices developed by V.A. Ananichev and co-workers for studying the thermal expansion of chalcogenide materials. Chapters 3 (pp. 31–72) and 4 (pp. 73–92) analyze experimental data on the thermal expansion of glasses and melts in chalcogenide and halogenide–chalcogenide systems. Chapter 5 (pp. 93–107) discusses, using specific examples, the features of isotherms expressing the composition dependence of the molar volume. It is noted that the maximal deviations from the additivity, suggesting the occurrence of ordering, in the isotherms of the molar volume of melts and glasses correspond to the compositions of compounds formed in the chalcogenide system and known from the phase diagrams. Chapter 6 (pp. 108–122) concerns the stability of chalcogenide glasses with respect to crystallization. The method of volumetric dilatometry, developed by the author, is sensitive to crystallization and furnishes useful information. Chapters 7 (pp. 123–136) and 8 (pp. 137–146) report the results of studying the vitrification of melts of chalcogenide and halogen–chalcogenide systems, obtained by volumetric dilatometry. When discussing the results, the author proceeds from the fact that chalcogenide glasses are inorganic polymers and that the trends in variation of their properties in the glass transition range are satisfactorily described in terms of the fluctuation free volume theory.

In the Appendix (pp. 147–164), the author presents tabulated data on the density of glasses and melts for nine chalcogenide systems containing arsenic. The monograph is based on original experimental studies performed by the author. V.A. Ananichev developed devices allowing chalcogenide systems to be studied in a wide temperature range with high reliability. These devices are intended for measuring the cubic expansion coefficients both for melts of chalcohenide systems in the liquid and high-viscosity states and for solid chalcogenide materials. They allow determination of the crystallization parameters and density of glasses. All these devices, protected by Inventor's Certificates, were developed on the basis of simple and available measuring devices. The book is well written, it includes ample reference material. The lists of references are given to each chapter separately. Ananichev's book is included in the series "Chemistry in the Polytechnic University." The book can be useful for a wide range of researchers dealing with physicochemical studies of both chalcogenide systems and other objects. The presentation is very intelligible. The polygraphic quality of the book is very high.

A. G. Morachevskii

ISSN 1070-4272, Russian Journal of Applied Chemistry, 2008, Vol. 81, No. 11, pp. 1879–1884. © Pleiades Publishing, Ltd., 2008.
Original Russian Text © A.F. Dresvyannikov, M.E. Kolpakov, E.V. Pronina, 2008, published in Zhurnal Prikladnoi Khimii, 2008, Vol. 81, No. 11, pp. 1761–1766.

INORGANIC SYNTHESIS AND INDUSTRIAL INORGANIC CHEMISTRY

Joint Reduction of Fe(III), Ni(II), and Co(II) Ions in Solution in Contact with Aluminum

A. F. Dresvyannikov, M. E. Kolpakov, and E. V. Pronina

Kazan State University of Technology, Kazan, Tatarstan, Russia

Received February 5, 2008

Abstract—Joint reduction of iron group metals in aqueous solutions on a dispersed aluminum matrix was studied. The powders obtained were examined by X-ray phase analysis and electron scanning microscopy.

DOI: 10.1134/S1070427208110013

The development of new generations of structural and functional materials is a topical problem. A possible way to solve this problem is variation of the composition of a system used a precursor.

It is well known that evolution of any physicochemical systems occurring under nonequilibrium conditions can lead to formation of fractal structures and nanocomposites [1]. For example, dendritic structures of frequently formed, e.g., in the course of nonequilibrium electrolytic deposition of metals and solidification of alloys under the conditions of strong supercooling, or in the course of phase decomposition. These methods can be considered as formation of nanostructures in the bulk of a matrix under the conditions of its chemical modification. This process allows the parameters of the particles in the matrix to be controlled in the step of their formation and varied in the course of material operation.

Much researchers' attention is attracted today by synthesis of metallic composites with elemental aluminum or its compounds as a matrix [2–6]. Owing to unique combination of the protective properties of surface oxide–hydroxide layers and intrinsic chemical activity, aluminum under definite conditions chemically reacts with the environment to form products exhibiting a set of specific properties [7, 8]. According to the results of numerous studies, the chemical activity of finely dispersed aluminum powders toward water and aqueous solutions of chemical compounds considerably exceeds the chemical activity of the compact metal [9, 10]. Many authors believe [7, 9, 10] that this is due to the developed surface of the powders and to the strongly defective state of the surface oxide–hydroxide coatings of the particles, and also to intense heating of the solid phase in the course of the oxidation [10]. These factors can strongly affect the extent and character of the interaction of compact and dispersed aluminum matrices with an aqueous solution containing metal ions. Of particular interest is contact deposition of iron group metals on a dispersed aluminum matrix. This process may lead to the development of powdered systems with variable composition and properties, showing promise as precursors of compact materials and coatings.

Alloys and composites based on iron and aluminum occupy a particular place among intermetallic systems promising from both theoretical and applied standpoint. They exhibit a unique set of physicochemical, mechanical, magnetic, and corrosion properties. However, iron aluminides are not still demanded by the industry because of the lack of a relatively simple and cheap procedure for their preparation. Today Fe–Al systems are prepared by mechanochemical methods which are not always efficient and are power-consuming.

It was proposed previously to prepare alloys and composites based on the Fe–Al binary system from aqueous solutions by contact exchange of metals on aluminum microparticles [11]. This process occurs in solution under normal conditions and is accompanied by the release of a large amount of heat, mainly due to ionization of aluminum. The deposition of Fe(0) from such solutions occurs in two steps: Fe(III) → Fe(II) → Fe(0), with simultaneous ionization of the aluminum

base and formation of an α-Fe layer on its surface. As a result, dendritic spherical particles with large internal cavities and pores are formed, which determines the low bulk density of the powder [11]. In the process, threadlike nuclei of submicrometer cross section can be formed in particle pores.

EXPERIMENTAL

Experiments were performed with close-cut fractions of dispersed aluminum (85 ± 15 μm, purity no less than 99.0%), with a specific surface area of 260 $cm^2\ g^{-1}$. The chemicals we used were $FeCl_3 \cdot 6H_2O$, $NiCl_2 \cdot 6H_2O$, and $CoCl_2$ (analytically pure grade). The molar ratio of the starting aluminum powder and precursor was 1.5 : 1 in all the experiments.

To study the process kinetics, we took samples at regular intervals of time and examined them by X-ray fluorescence analysis on a VRA-20L installation (Carl Zeiss) under the following conditions: LiF 200 analyzer crystal, voltage 55 kV, current 35 mA, X-ray tube with a tungsten anode, collimator 2, SZ counter, discriminator 1.0 V, and sensitivity 3×10^4–1×10^5 counts $s^{-1}\ cm^{-2}$. The degree of precursor reduction to metal was estimated from variation of the concentration of ions of the corresponding elements in solution. The experimental error was governed by the methods used and amounted to 5%.

The chronopotentiograms in a suspension of dispersed aluminum were recorded with an EPV-1 platinum electrode and an EVL-1MZ-1 silver chloride reference electrode.

The samples we obtained were analyzed with a DRON-2 X-ray diffractometer to determine their chemical and phase composition. To reduce the background from scattering of the primary X-ray beam in air, we used long-wave FeK_α radiation with a β-filter. The diffraction patterns were recorded in the following mode: voltage 30 kV, current 15 mA, recording range 2θ 10°–160°. The diffraction patterns were processed with MAUD 1.999 multifunctional software [12, 13]. As a reference for comparing the line profiles (to determine the size of coherent scattering regions and microstresses), we used annealed copper foil.

Analysis and recording of microscopic images of the initial aluminum and powders obtained were performed with a Philips SM XL-30 TMP scanning electron microscope at the following parameters: ΔE scale 10 keV (0–500), acquisition time T = 100 s, E_{probe} = 30 keV. The size of the microanalysis area was varied from 20 × 30 to 50 × 75 μm.

Electrolytic codeposition of two or several metals is of particular interest because of the mutual influence of the jointly reduced ions on the rate of electrochemical processes [14]. It is known [14–17] that, in joint reduction of Fe(II) and Ni(II) ions, the electrochemical reaction is conjugate, i.e., the rate of discharge of their ions differs from the rate at which these ions are reduced separately. It was shown in a number of papers [14, 17] that the rate of reduction of Fe(II) ions increases by a factor of almost 3 in joint electrodeposition with Ni(II). On the contrary, the rate of reduction of Ni(II) in joint deposition with Fe(II) decreases by a factor of approximately 8. In the course of nickel electrodeposition, hydrogen is released at a considerably higher rate than in joint deposition of iron and nickel, because of the lower overvoltage of hydrogen on nickel.

The experiments performed [18] suggest that the reactions of Fe(III) and Ni(II) reduction when these ions are present in solution simultaneously are conjugate, i.e., the successively occurring steps Fe(III) → Fe(II) → Fe(0) initiate the reaction Ni(II) → Ni(0).

Both conjugated reduction reactions can be adequately described by first-order rate equations

$$c(Fe^{3+}) = c_0(Fe^{3+}) \exp(-kt),$$

$$c(Ni^{2+}) = c_0(Ni^{2+}) \exp(-kt).$$

Previously, in studying joint deposition of Fe and Ni on an Al surface, we showed [18] that Ni metal is mainly deposited on the surface of the iron formed, with a certain part of iron undergoing oxidation and passing into the solution. In joint deposition of Fe(III) and Ni(II), a dark gray ferromagnetic powder is formed. The reaction is accompanied by considerable (to 373 K) heat-up of the reaction mixture. In joint deposition of Fe and Ni on Al, the powder is enriched in the less noble component [18]. The similar effect observed in electrodeposition is attributed in [19] to a shift of the metal deposition potentials when the metals are present simultaneously and to possible formation of passive films on the iron surface, preventing the deposition of Ni. Hydrogen evolution occurs simultaneously with the metal codeposition.

Similar process is observed in the Fe(III)–Co(II) system. When the cobalt and iron ions are present simultaneously, they are reduced somewhat more slowly

compared to the separate reduction. At equal content of the Fe(III) and Co(II) ions in the initial solution, the deposition of both metals is virtually simultaneous (electrolytic alloy formation), and high degrees of iron and cobalt deposition are attained (Fig. 1). Apparently, electrolytic alloy formation may take place in the course of contact exchange when the metals are deposited simultaneously. Karbasov et al. [20, 21] reported on the alloy formation in the course of contact exchange and proved the existence of various kinds of alloys by X-ray diffraction analysis and electron microscopy.

Both conjugate reactions in joint reduction of iron and cobalt can be adequately described by first-order rate equations

$$c(Fe^{3+}) = c_0(Fe^{3+}) \exp(-kt),$$

$$c(Co^{2+}) = c_0(Co^{2+}) \exp(-kt).$$

According to reference data [22], joint reduction of Fe(III), Co(II), and Ni(II) with Al to the metals is thermodynamically possible, because the redox potential of the Al(III)/Al(0) couple is more negative than those of the corresponding couples involving Fe, Co, and Ni. However, the process is stongly complicated by the presence of the natural oxide film on Al and high overvoltage of the reduction of iron ions.

Joint Fe–Ni–Co deposition is a still more complex process and is determined both by the state of the surface of dispersed Al and by the concentration of the ions of these metals in solution. Iron and cobalt are deposited at approximately equal rate, and nickel, at a somewhat lower rate (Fig. 2). In ternary solutions, iron and cobalt are deposited virtually synchronously (Fig. 2, curves *1* and *3*), but cobalt is deposited more completely (98%, against 90% for Fe). In the case of Ni, the deposition rate increases after the lapse of 90 s, at the time by which iron and cobalt have been 50% reduced. This result is consistent with the previous data on the joint deposition of iron and nickel [18].

The results of studying joint deposition of metallic iron, nickel, and cobalt showed that the reactions of the Fe(III), Ni(II), and Co(II) reduction are conjugate, i.e., the consecutive reactions with iron ions initiate the reactions with the cobalt [Co(II) → Co(0)] and nickel [Ni(II) → Ni(0)] ions. The conjugate reduction reactions can be described by first-order rate equations (Fig. 2).

Deceleration of the reduction of Ni ions in joint deposition with Fe and Co may be due to increased adsorption of hydroxy compounds on the alloy surface, compared to deposition of the individual metals. The observed deceleration of the reduction of Ni ions indicates that the discharge of the ions is not facilitated by the alloy formation. Deceleration of the ion discharge in the course of the joint reduction can be largely attributed to a change in the concentration of the ions being discharged in the electrical double layer.

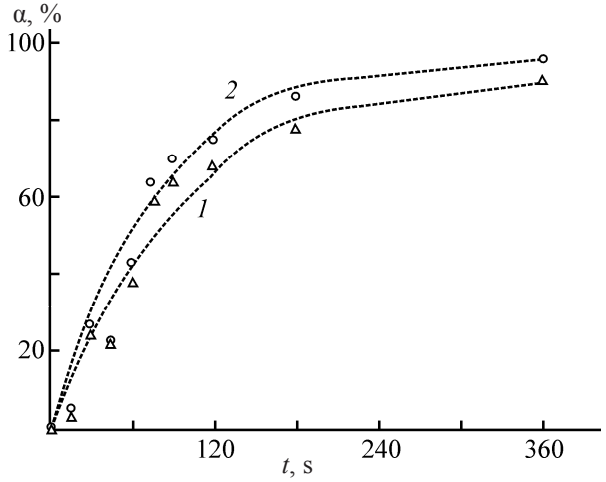


Fig. 1. Kinetic curves of joint deposition of (*1*) Fe and (*2*) Co from a 0.5 M $FeCl_3$ + 0.5 M $CoCl_2$ solution. Points refer to experimental data, and lines, to calculation; the same for Fig. 2. (α) Degree of deposition and (*t*) deposition time; the same for Fig. 2.

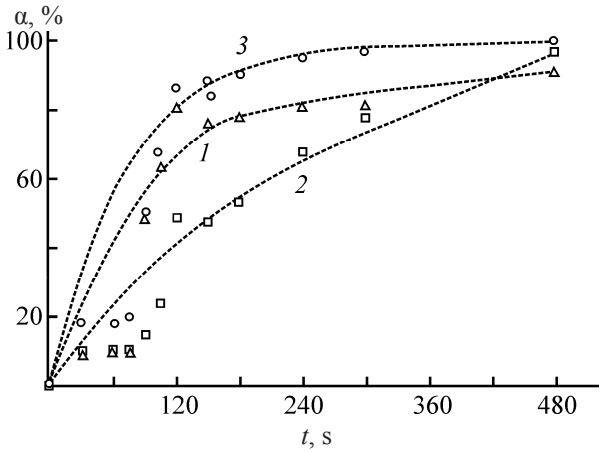


Fig. 2. Kinetic curves of joint deposition of (*1*) Fe, (*2*) Ni, and (*3*) Co from a 0.7 M $FeCl_3$ + 0.6 M $CoCl_2$ + 0.7 M $NiCl_2$ solution.

The reduction process can be illustrated by the chronopotentiograms obtained for dispersed aluminum suspended in the working solution (Fig. 3). Comparison of the chronopotentiogram (Fig. 3) obtained with a platinum electrode in the reaction mixture containing Al with the kinetic curves (Fig. 2) shows that, in the

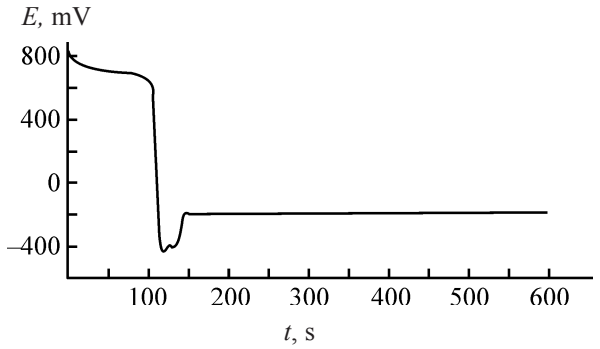


Fig. 3. Redox potential E as a function of time t in deposition of iron group metals (0.7 M $FeCl_3$ + 0.6 M $CoCl_2$ + 0.7 M $NiCl_2$).

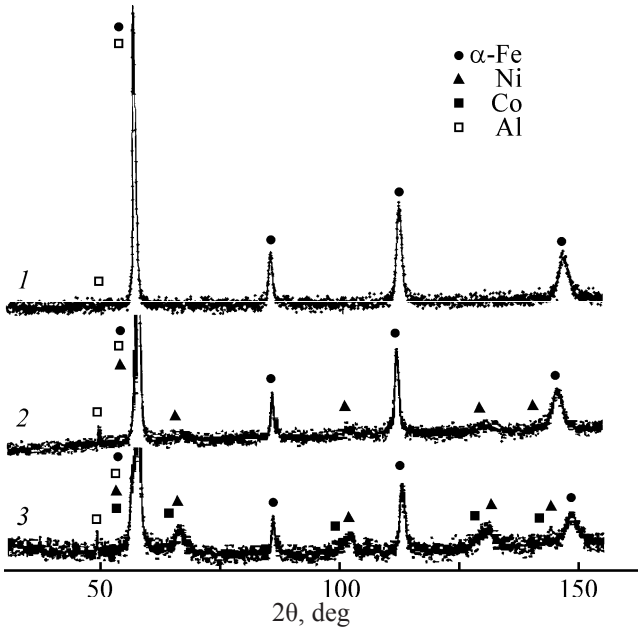


Fig. 4. Diffraction patterns of dispersed (*1*) Fe–Al, (*2*) Fe–Ni–Al, and (*3*) Fe–Ni–Co–Al samples. (2θ) Bragg angle.

course of the first 90 s, the potential smoothly decreases and the degree of metal deposition grows, also smoothly. The length of this portion of the curves strongly depends on the concentration of the starting reactants and is primarily caused by the presence of an oxide film on the aluminum particle surface. Furthermore, the potential does not decrease significantly until the nickel deposition starts. After the drop toward the negative region, the potential fairly actively shifts toward more positive values and then gets stabilized. It is known [23] that a metal being reduced can fully plug the pores of the powder, which leads to termination of the contact exchange. In the process, the electrode potential becomes close to the equilibrium potential of the more electropositive components (Fe, Ni, Co) in the solution. The chronopotentiogram (Fig. 3) indicates that the deposit fully blocks the aluminum surface. According to [20, 21], plateaus in the chronopotentiograms correspond to the formation of solid solutions or intermetallic compounds in the surface layer.

According to the results of X-ray phase analysis (Fig. 4) and local microanalysis, the powders obtained are mechanical mixtures of crystallites of iron group metals and aluminum, like the Fe–Al samples obtained previously [11, 24]. The amount of residual Al can be readily controlled by treating the powder with an alkali solution and can be reduced to tenth fractions of percent. When the powder is not kept in an alkali, an amorphous phase (probably pseudoboehmite) is detected, and with time bayerite crystals formed from metastable products of aluminum dissolution also appear [25]. In accordance with the results of X-ray structural and phase analysis and of local microanalysis, it can be concluded that the systems under consideration can be classed with substitution solid solutions with atoms of the major components (iron group elements) partially substituted in the crystal lattices by aluminum atoms. Furthermore, intermetallic phases of iron group elements are also detected. The process kinetics is strongly affected by the size and state of the surface of the aluminum particles.

Electron microscopic examination of particles taken from the solution after the metal deposition shows that they are virtually always spherical with the size similar to that of the starting Al particles (Fig. 5). This fact allows control of the properties of the synthesized particles by varying the parameters of the initial Al matrix. The presence of a large number of nuclei on the surface of coarse particles, in combination with the systems of cracks and pores, promotes the development of the metal surface, which may be very important in the possible use of such powders as heterogeneous catalysts. Furthermore, an important feature of the powders obtained is the presence of internal cavities.

It should be noted that, virtually in all the experiments, we clearly observed the formation of nanostructures in the form of whiskers (Fig. 5). However, on the surface of particles obtained in the Fe–Co system, there are also conical flaky individuals with a mean size of 100–200 nm (Fig. 5). Such a structure of the surface, in combination with the phase composition of the objects, is responsible for the specific properties of the Al–M systems (M = Fe, Ni, Co) obtained from aqueous solutions.

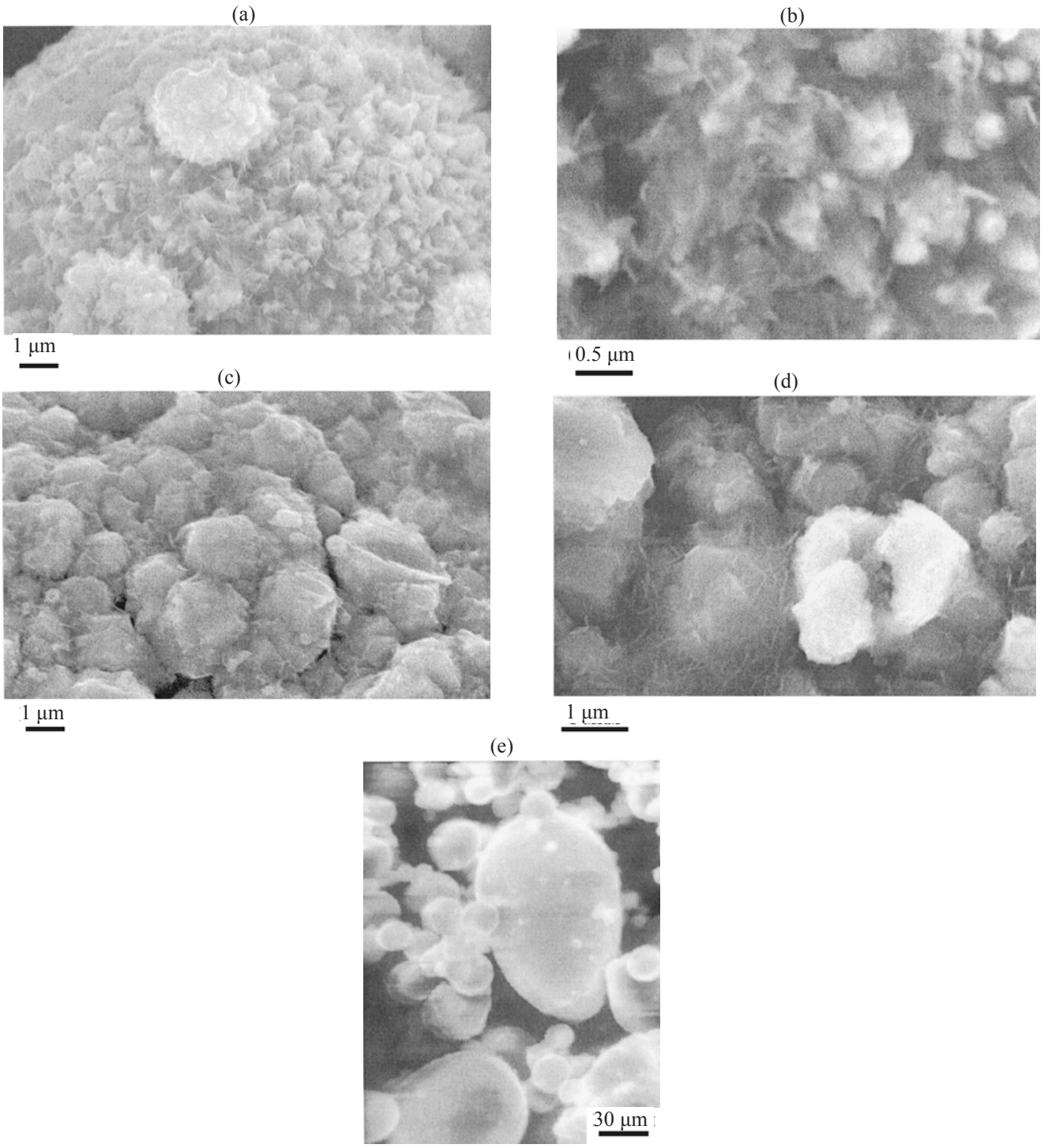


Fig. 5. Electron micrographs of disperse systems (a) Fe–Co, (b) Fe–Co–Al, (c) Fe–Co–Ni, (d) Fe–Co–Ni–Al, and (e) Al.

CONCLUSIONS

(1) Kinetic features of the formation of Fe–Co and Fe–Co–Ni deposits on dispersed aluminum matrix were elucidated.

(2) The reactions of Fe(III), Ni(II), and Co(II) reduction are conjugate and are adequately described by first-order rate equations with close rates of iron and cobalt deposition and lower rate of nickel deposition.

(3) It was found by X-ray phase analysis that the

precipitates obtained contain phases of aluminum and of individual iron group metals.

(4) Electron microscopic examination revealed nanosized whiskers and conical formations on the deposit surface.

REFERENCES

1. Tret'yakov, Yu.D., *Usp. Khim*., 2003, vol. 72, no. 8, pp. 731–763.
2. Enzo, S., Mulas, G., Delogu, F., and Principi, G., *J. Mater. Synth. Process*., 2000, vol. 8, nos. 5–6, pp. 313–318.
3. Sarkar, S. and Bansal, C., *J. Alloys Comp*., 2002, vol. 334, nos. 1–2, pp. 135–142.
4. Morris, M.A. and Morris, D.G., *Mater. Sci. Forum*, 1992, vols. 88–90, pp. 529–534.
5. Oleszak, D., Pekata, M., Jartych, E., and Zurawicz, J.K., *Mater. Sci. Forum*, 1997, vols. 269–272, pp. 643–648.
6. Grigor'eva, T.F., Barinova, A.P., and Lyakhov, N.Z., *Usp. Khim.*, 2001, vol. 70, no. 1, pp. 52–71.
7. Zhilinskii, V.V., Lokenbakh, A.K., and Liepins, L.K., *Izv. Akad. Nauk Latv. SSR, Ser. Khim*., 1986, no. 2, pp. 151–155.
8. Riegel, E.R., and Schwartz, R.D., *Anal. Chem*., 1952, vol. 24, no. 11, pp. 1803–1806.
9. Lokenbakh, A.K., Zaporina, N.A., and Liepins, L.K., *Izv. Akad. Nauk Latv. SSR, Ser. Khim*., 1981, no. 1, pp. 45–49.
10. Lyashko, A.P., Medvinskii, A.A., and Savel'ev, G.G., *Kinet. Katal*., 1990, vol. 31, no. 4, pp. 967–972.
11. Dersvyannikov, A.F., Kolpakov, M.E., and Lapina, O.A., *Zh. Prikl. Khim*., 2007, vol. 80, no. 1, pp. 9–14.
12. Matthies. S., Lutterotti. L., and Wenk, H.-R., *J. Appl. Crystallogr*., 1997, vol. 30, no. 1, pp. 31–42.
13. *The Rietveld Method*, Young, R.A., Ed., New York: Int. Union of Crystallography, 1993.
14. *Elektroliticheskoe osazhdenie splavov* (Electrolytic Deposition of Alloys), Averkin, V.A., Ed., Moscow: Mashgiz, 1961.
15. *Elektroliticheskoe osazhdenie zheleza* (Electrolytic Deposition of Iron), Zaidman, G.N., Ed., Chisinau: Shtiintsa, 1990.
16. Vagramyan, A.T. and Zhamorgortsyan, M.A., *Elektroosazhdenie metallov i ingibiruyushchaya adsorbtsiya* (Electrolytic Deposition of Metals and Inhibiting Adsorption), Moscow: Nauka, 1969.
17. Fatueva, T.A. and Vagramyan, A.T., *Dokl. Akad. Nauk SSSR*, 1959, vol. 128, no. 4, pp. 773–776.
18. Dresvyannikov, A.F. and Kolpakov, M.E., *Zashch. Met*., 2008, vol. 44, no. 1, pp. 49–57.
19. Dresvyannikov, A.F., Kolpakov, A.F., Lapina, O.A., and Shustov, V.A., *Vestn. Kazan. Tekhnol. Univ*., 2005, no. 2, pp. 70–83.
20. Karbasov, B.G., Tikhonov, K.I., Ustinenkova, L.E., and Isaev, N.N., *Elektrokhiimiya*, 1990, vol. 26, no. 5, pp. 649–651.
21. Karbasov, B.G., Ustinenkova, L.E., and Tikhonov, K.I., *Elektrokhimiya*, 1997, vol. 33, no. 5, pp. 602–604.
22. *Spravochnik po elektrokhimii* (Handbook of Electrochemistry), Sukhotin, A.M., Ed., Leningrad: Khimiya, 1981.
23. Antronov, L.I. and Donchenko, M.I., *Itogi Nauki Tekh., Ser.: Korroz. Zashch. Korroz*., 1973, vol. 2, pp. 113–170.
24. Dresvyannikov, A.F. and Kolpakov, M.E., *Mater. Res. Bull.*, 2002, vol. 37, no. 2, pp. 291–296.
25. Dresvyannikov, A.F. and Kolpakov, M.E., *Zh. Obshch. Khim*., 2005, vol. 75, no. 2, pp. 177–183.
26. Dresvyannikov, A.F. and Kolpakov, M.E., *Zh. Prikl. Khim*., 2002, vol. 75, no. 10, pp. 1602–1607.

ISSN 1070-4272, Russian Journal of Applied Chemistry, 2008, Vol. 81, No. 11, pp. 1885–1889. © Pleiades Publishing, Ltd., 2008.
Original Russian Text © O.G. Gromov, A.P. Kuz'min, G.B. Kunshina, R.M. Usmanov, E.P. Lokshin, 2008, published in Zhurnal Prikladnoi Khimii, 2008, Vol. 81, No. 11, pp. 1767–1771.

INORGANIC SYNTHESIS AND INDUSTRIAL INORGANIC CHEMISTRY

Microwave Synthesis of Barium Titanate, Strontium Zirconate, and Sodium Indium Tungstate

O. G. Gromov, A. P. Kuz'min, G. B. Kunshina, R. M. Usmanov, and E. P. Lokshin

Tananaev Institute of Chemistry and Technology of Rare Elements and Mineral Raw Materials, Kola Scientific Center, Russian Academy of Sciences, Apatity, Murmansk oblast, Russia

Received March 6, 2007

Abstract—The results of microwave (at a frequency of 2.45 GHz) synthesis of $BaTiO_3$, $SrZrO_3$, and $NaIn(WO_4)_2$ are compared with those of the common solid-phase synthesis.

DOI: 10.1134/S1070427208110025

Single-phase finely dispersed (desirably nanocrystalline) powders of barium metatitanate and strontium metazirconate are required for the production of multilayer ceramic capacitors.

Previously [1] we examined the solid-phase synthesis of powdered barium titanate with titanium oxide and oxyhydroxide and barium carbonate, nitrate, and hydroxide as starting compounds. Because the intensity of the solid-phase synthesis and the quality of the final product largely depend on the perfection of the mixture of the starting powders, this mixture was subjected to ultrasonic mechanical activation in an inert organic liquid. We found that single-phase $BaTiO_3$ containing no Ba_2TiO_4 and $BaCO_3$ impurities is formed from a mixture of titanium oxyhydroxide and barium nitrate upon treatment at 650°C for 2 h.

The drawback of this process is high content of the residual organic liquid in the filtered and dried mixture of the starting components. Calcination of such a mixture is accompanied by formation of pyrolytic carbon, and, to ensure its complete burn-out, it is necessary to increase the calcination temperature to 700–750°C, which leads to coarsening of the final product particles. The specific surface area of the samples obtained did not exceed 0.5 $m^2\ g^{-1}$. To obtain single-phase $NaIn(WO_4)_2$ by common solid-phase synthesis, a mixture of the starting compounds (WO_3, In_2O_3, Na_2CO_3) is pelletized and calcined at 950°C for 50 h [2]. It follows from the aforesaid that, to prepare these substances, it is necessary to accelerate solid-phase processes so as to decrease the calcination temperature and/or time.

Microwave heating is widely used today for accelerating various processes, including sintering, dehydration, and decomposition of salts and hydroxides [3]. Microwave radiation is a nonionizing electromagnetic radiation with a frequency from 0.3 to 30 GHz. As stipulated by the international agreement, laboratory and household microwave ovens use frequencies of 0.915 and 2.45 GHz. As shown in [4], the latter frequency is preferable for the synthesis of ceramic materials.

In microwave solid-phase synthesis, the direct reaction of powdered components occurs only if at least one of them efficiently interacts with microwaves. If the starting substances are poor microwave acceptors, a secondary acceptor is added. This additive should be chemically inert, should efficiently absorb microwave radiation, and should be readily separable from the synthesis products after the process completion.

The commonly used absorbing additive is high-purity powdered graphite (particle size about 7 μm). To perform the synthesis, a mixture of the starting compounds is pelletized, pellets are placed in a quartz test tube and covered with graphite powder, and the mixture is irradiated in a microwave oven. Owing to the high microwave susceptibility, graphite lights up and heats pellets, initiating the decomposition of nitrates or carbonates. It was found that a hot oxide mixture well interacts with microwaves, which provides rapid reaction to obtain the required product [5].

In the course of microwave heating of a sample, correct measurement of temperature is very difficult.

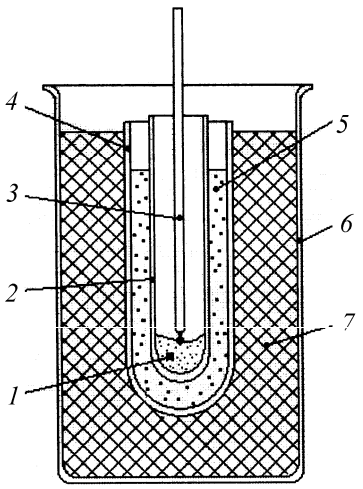


Fig. 1. Cell with a secondary heater: (*1*) initial charge, (*2, 4*) quartz test tube, (*3*) thermocouple, (*5*) WO_3, (*6*) glass beaker, and (*7*) quartz wool.

The use of common bimetallic thermocouples in microwave heating is impossible, because high-frequency electromagnetic field generates additional currents in the thermocouple and induces interference in measuring devices. Furthermore, introduction of a metallic object into the cavity alters the distribution of the microwave field power, which may lead to local overheatings. The only solution of this problem is the use of a shielded thermocouple grounded to the cavity wall. A 0.02-mm-thick platinum foil is used as a shield [6].

The aim of this study was to prepare $BaTiO_3$, $SrZrO_3$, and $NaIn(WO_4)_2$ in the form of finely dispersed powders by solid-phase microwave synthesis.

EXPERIMENTAL

The starting substances were chosen taking into account the following facts. It is known that TiO_2 and ZrO_2 are relatively poor microwave acceptors [6], whereas WO_3 absorbs microwaves very efficiently [7]. In nitrates, the high dipole moment of the nitrate ion should actively interact with a microwave field. Therefore, nitrates readily melt in their water of crystallization, and aqueous solutions always absorb microwave radiation well. Furthermore, large volume of gases released in the course of nitrate decomposition should favor disaggregation of the oxide powders being synthesized. Therefore, to prepare $BaTiO_3$ we used titanium oxyhydroxide $TiO(OH)_2$ and $Ba(NO_3)_2$; to prepare $SrZrO_3$, $ZrO(NO_3)_2{\cdot}6H_2O$ and $Sr(NO_3)_2$; and to prepare $NaIn(WO_4)_2$, we took WO_3, $Na_2WO_4{\cdot}2H_2O$, and In_2O_3.

The corresponding stoichiometric mixtures were prepared by grinding and mixing of the starting compounds in a TEFAL 6797 Magiclean household mixer. The resulting blend was charged into a quartz test tube. In first experiments, the test tube was placed in a wide glass beaker packed with quartz wool to ensure good heat insulation. The assembled cell was placed in a Samsung M192DNR microwave oven operating at 2.45 GHz, with an output power of 1 kW. The mixture temperature was measured with a Chromel–Alumel thermocouple protected with 0.04-mm-thick silver foil.

Preliminary studies showed that, in synthesis of $BaTiO_3$ or $SrZrO_3$, the mixture temperature first increased to 120–140°C and then remained essentially constant at the oven power varied from 0.3 to 1 kW. Apparently, this temperature is determined by the absorbing power of reaction mixture components and by the intensity of the heat removal from the sample surface. In the synthesis of $NaIn(WO_4)_2$, the maximal temperature of the mixture was 400°C, which was insufficient for the formation of $NaIn(WO_4)_2$.

Further experiments were performed in a cell with a secondary heater (Fig. 1). The initial charge *1* was placed in a quartz test tube *2*, which was inserted into another quartz test tube *4* packed with WO_3 (*5*). Test tube *4* was placed in a glass beaker *6* packed with quartz wool *7* as heat-insulating material. WO_3 layer *5* is intended for the primary heating of the initial charge. The mixture temperature was monitored with a thermocouple *3*. We found that the mixture temperature depends on the preset microwave oven power and on the irradiation time and can be increased to 700–900°C. Synthesis was performed in the temperature range 600–800°C. The isothermal heating time was varied from 15 min to 1 h. The final products were obtained as finely dispersed powders. The phase composition of the powders was determined by X-ray phase analysis with a DRON-2 diffractometer (CuK_α radiation, graphite monochromator, scanning rate 2 deg min^{-1}). The phases were identified using JCPDS database. The specific surface area of powdered samples was determined by thermal desorption of nitrogen with a FlowSorb II 2300 electronic laboratory device for measuring the specific surface area and porosity. The particle size was calculated by the formula

$$d = K/\Omega r,$$

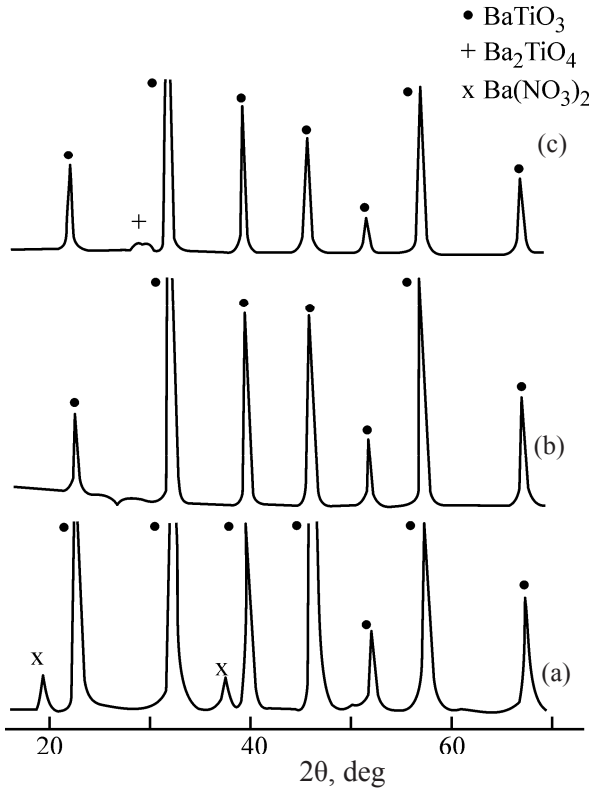


Fig. 2. Diffraction patterns of $BaTiO_3$ samples. (2θ) Bragg angle; the same for Figs. 4 and 5. Temperature (°C) and synthesis time: (a) 600, 1 h; (b) 650, 0.5 h: and (c) 720, 20 min.

where *d* is the mean particle diameter; *K*, form factor equal to 6 for spherical and cubic particles; Ω, specific surface area; and *r*, substance density.

It follows from the diffraction patterns of products obtained in synthesis of $BaTiO_3$ that (1) synthesis at 600°C for 1 h yields a product with an impurity of $Ba(NO_3)_2$, i.e., is incomplete (Fig. 2a); (2) synthesis at 650°C for 0.5 h yields single-phase $BaTiO_3$ (Fig. 2b); (3) at 720°C, the synthesis of $BaTiO_3$ is complete in 20 min, but the final product contains an impurity of Ba_2TiO_4 (Fig. 2c).

Powdered $BaTiO_3$ prepared at 650°C has a specific surface area of 2.56 $m^2\ g^{-1}$, which corresponds to a mean particle size of 380 nm.

The time–temperature dependences plotted in Fig. 3 show that microwave solid-phase synthesis of $BaTiO_3$ is more efficient than the common solid-phase synthesis from the viewpoint of both time and power consumption.

The diffraction patterns of the products obtained in synthesis of $SrZrO_3$ show that (1) synthesis at 600°C for 1 h yields $SrZrO_3$ with an impurity of $Sr(NO_3)_2$,

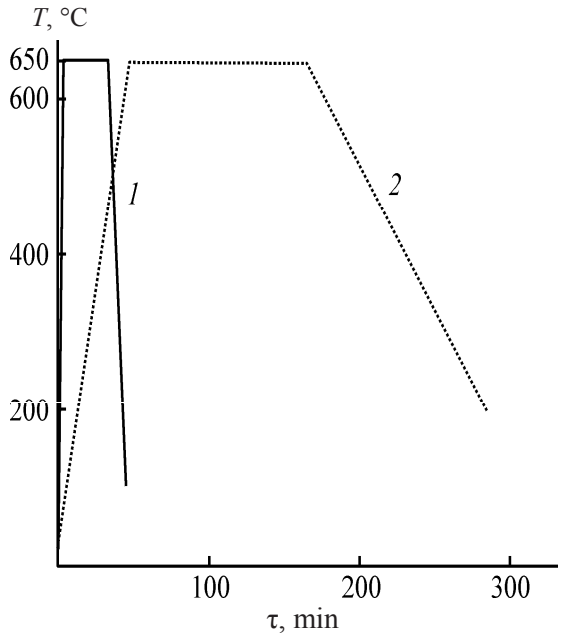


Fig. 3. Temperature *T*–time τ dependence for (*1*) microwave and (*2*) common solid-phase synthesis of $BaTiO_3$.

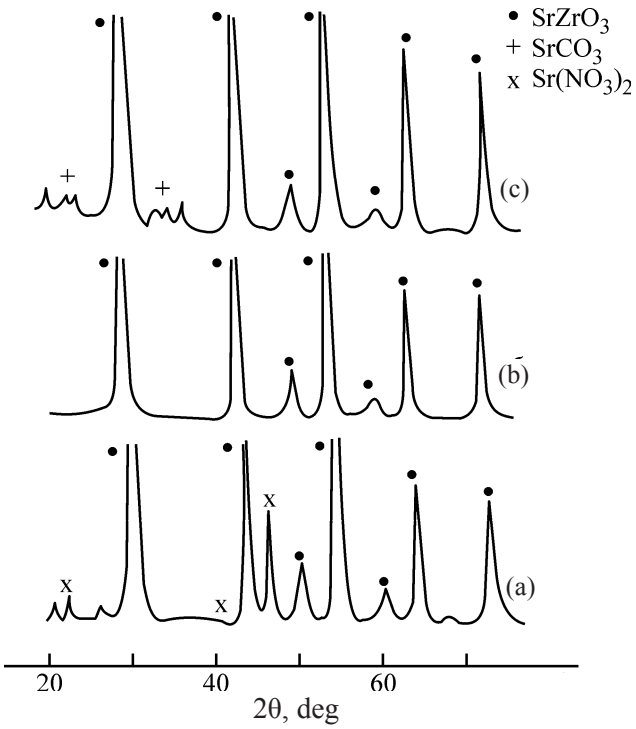


Fig. 4. Diffraction patterns of $SrZrO_3$ samples. Synthesis temperature (°C) and time: (a) 600, 1 h; (b) 650, 0.5 h; and (c) 700, 15 min.

i.e., the reaction is incomplete (Fig. 4a); (2) synthesis at 650°C for 0.5 h yields single-phase $SrZrO_3$ (Fig. 4b); (3) at 700°C, the synthesis of $SrZrO_3$ is complete in 15 min, but the final product contains an impurity of $SrCO_3$ (Fig. 4c).

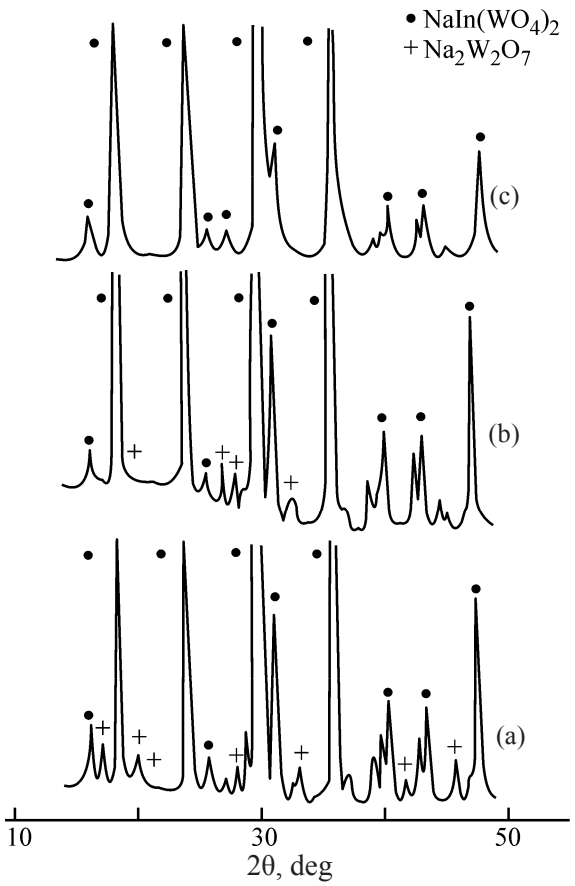


Fig. 5. Diffraction patterns of $NaIn(WO_4)_2$ samples. Synthesis conditions: (a) 600–800°C, 1 h; (b) 750°C, two steps; and (c) 750°C, 1 h, from a stoichiometric mixture of Na_2WO_4 and $In_2(WO_4)_3$.

Powdered $SrZrO_3$ prepared at 650°C has a specific surface area of 2.4 $m^2 g^{-1}$, which corresponds to a mean particle diameter of 460 nm.

The diffraction patterns of the products obtained in synthesis of $NaIn(WO_4)_2$ show that the synthesis at 600–800°C for 1 h yields $NaIn(WO_4)_2$ with an impurity of sodium tungstate $Na_2W_2O_7$ (Fig. 5a). Despite the absence of In_2O_3 reflections in the diffraction patterns, it was concluded that In_2O_3 reacted with WO_3 incompletely. To perform the synthesis with preliminary binding of WO_3 into $Na_2W_4O_{13}$, synthesis of $NaIn(WO_4)_2$ at 750°C was divided in two steps. In the first step, a stoichiometric mixture of Na_2WO_4 and WO_3 was treated for 0.5 h to obtain $Na_2W_4O_{13}$, and in the second step, a stoichiometric mixture of $Na_2W_4O_{13}$ and In_2O_3 was treated for 1 h. However, in this case also the final product contained an impurity of sodium tungstate $Na_2W_2O_7$ (Fig. 5b). It follows from these experiments that the use of WO_3, $Na_2WO_4 \cdot 2H_2O$, and In_2O_3 does not ensure preparation of single-phase $NaIn(WO_4)_2$. Therefore, we decided to replace WO_3 and In_2O_3 by indium tungstate $In_2(WO_4)_3$.

Indium tungstate was prepared by the reaction

$$3Na_2WO_4 \cdot 2H_2O(soln) + 2In(NO_3)_3 \cdot 4.5H_2O(soln) = In_2(WO_4)_3(solid) + 6NaNO_3(soln).$$

For this purpose, solutions containing equivalent amounts of $Na_2WO_4 \cdot 2H_2O$ and $In(NO_3)_3 \cdot 4.5H_2O$ were simultaneously added to a beaker with water with vigorous stirring. The $In_2(WO_4)_3$ precipitate was centrifuged off, thoroughly washed with water on the filter to remove NO_3^-, and dried at 150°C.

The diffraction pattern (Fig. 5c) of the product obtained by the treatment of a stoichiometric mixture of Na_2WO_4 and $In_2(WO_4)_3$ at 750°C for 1 h exhibits reflections of $NaIn(WO_4)_2$ only, which indicates that the product is single-phase. The specific surface area of the resulting powdered product is 1.45 $m^2 g^{-1}$, which corresponds to the mean particle size of 580 nm. At synthesis temperatures lower than 750°C, preparation of the single-phase product requires longer time of isothermal heating.

CONCLUSIONS

(1) Microwave solid-phase synthesis of complex oxides has significant advantages over the common solid-phase synthesis. It was shown by the example of $BaTiO_3$ that the time of isothermal heating required to obtain the single-phase product decreased from 2 to 0.5 h and that the specific surface area of the powder increased from 0.5 to 2.56 $m^2 g^{-1}$. Furthermore, comparison of the time–temperature dependences unambiguously indicates that the microwave process is less power- and time-consuming.

(2) Microwave solid-phase synthesis provides preparation of finely dispersed single-phase $BaTiO_3$ and $SrZrO_3$ at 650°C, at an isothermal heating time of 0.5 h.

(3) Microwave synthesis of single-phase $NaIn(WO_4)_2$ from Na_2WO_4 and $In_2(WO_4)_3$ allows the synthesis temperature to be decreased to 750°C, with 50 times shorter isothermal heating time. Furthermore, pelletizing of the initial charge becomes unnecessary.

ACKNOWLEDGMENTS

The study was financially supported by the Russian Foundation for Basic Research (project no. 06-08-00 200) and Program of Basic Research of the Presid-

ium of the Russian Academy of Sciences "Development of Methods for Preparing Chemical Substances and of New Materials."

REFERENCES

1. Gromov, O.G., Kuz'min, A.P., Kunshina, G.B., et al., *Neorg. Mater.*, 2006, vol. 42, no. 2, pp. 212–217.
2. Borisevich, A.E., Korzhik, M.V., Drobychev, G.Yu., et al., *Nucl. Instr. Meth. Phys. Res. A*, 2005, vol. 537, pp. 228–231.
3. *Microwave Processing of Materials*, Stein, D.E., Ed., Washington, DC: National Acad., 1994.
4. Cheng, J.P., Agrawal, D.K., Komarneni, S., et al., *Mater. Res. Innovat.*, 1997, no. 1, pp. 44–52.
5. Vaidhyanathan, B., Raizada, P., and Rao, K.J., *J. Mater. Sci. Lett.*, 1997, no. 16, pp. 2022–2025.
6. Vaidhyanathan, B., Singh, A.P., and Agrawal, D.K., *J. Am. Ceram. Soc.*, 2001, vol. 84, no. 6, pp. 1197–1202.
7. Rao, K.J., Vaidhyanathan, B., Ganguli, M., and Ramakrishnan, P.A., *Chem. Mater.*, 1999, no. 11, pp. 882–895.

ISSN 1070-4272, Russian Journal of Applied Chemistry, 2008, Vol. 81, No. 11, pp. 1890–1894. © Pleiades Publishing, Ltd., 2008.
Original Russian Text © V.N. Esenin and L.I. Denisovich, 2008, published in Zhurnal Prikladnoi Khimii, 2008, Vol. 81, No. 11, pp. 1772–1776.

INORGANIC SYNTHESIS AND INDUSTRIAL INORGANIC CHEMISTRY

Stability of Metallic Materials in Aqueous and Aqueous–Glycol Solutions

V. N. Esenin and L. I. Denisovich

Nesmeyanov Institute of Organometallic Compounds, Russian Academy of Sciences, Moscow, Russia

Received May 26, 2008

Abstract—The corrosion behavior of aluminum, steel, and pig iron in fresh water, ethylene glycol, and water–glycol mixtures containing 5–95 vol % fresh water in the temperature range 20–100°C was studied. The influence of temperature on the corrosion rate of the metals was examined in relation to the composition of aqueous ethylene glycol solutions.

DOI: 10.1134/S1070427208110037

This work continues our systematic studies of the corrosion of aluminum alloys, steel, and pig iron in aqueous and aqueous–glycol solutions with the aim to find how the composition of the aqueous–organic solution affects the corrosion. The choice of the metals, organic solvent, and composition of aqueous–organic solutions is governed by the fact that in modern liquid cooling systems, in particular, in internal combustion engines, in various heat-exchange apparatuses, and in hydraulic equipment the main structural materials are the above-mentioned metals. Aqueous ethylene glycol (EG) solutions of various compositions are used as heat carriers in various climatic zones of Russia. In the previous papers we reported the results of studying the corrosion of the above metals in model fresh water [1] and in aqueous EG solutions [2]. Available data on the corrosion behavior of electrochemically dissimilar metals in aqueous–alcoholic media of various compositions are scarce [3–6] and, to certain extent, contradictory. Here we report the results of examining the effect of temperature on the rate of corrosion of the above metals in aqueous and aqueous–glycol solutions. There are almost no published data [7] on this matter.

EXPERIMENTAL

Corrosion tests were performed in a temperature-controlled cell. Flat samples of St.3 steel [GOST (State Standard) 380], GH-190 pig iron (VAZ 52 205 normal), and AK6M2 aluminum alloy (GOST 1583) of size 50 × 25 × 3 mm were preliminarily polished and degreased. The corrosion rate was estimated from the sample weight loss. Experiments were performed at 20–100°C. The pH values were measured with a pH-150M pH meter. Ethylene glycol (GOST 19 710, supreme grade) was used without additional purification. Simulation of fresh water by adding into distilled water sodium sulfate, sodium chloride, and sodium hydrogen carbonate to their typical concentrations was described elsewhere [1].

Published data on the influence of temperature on the rate of metal corrosion in aqueous–glycol solutions are scarce [7]. Therefore, it seemed important to evaluate the effect of the temperature factor on the corrosion behavior of the metals under consideration. Tests of steel, pig iron, and aluminum were performed in 50% aqueous–glycol solution in the temperature range 20–100°C and in EG solutions containing 5 to 100 vol % water at 20 and 70°C. The corrosion rates of steel and pig iron at 20–90°C during the test period are constant (Fig. 1). Figure 2a shows how the temperature affects the corrosion rate of steel and pig iron. The corrosion rates of both metals sharply increase (by a factor of more than 5) in the range 20–50°C and then linearly increase up to 90°C. The temperature dependences of the rate constants of dissolution of steel and pig iron are satisfactorily linearized in the coordinates of the Arrhenius equation in the temperature range 50–90°C (Fig. 2b). From the straight lines obtained, we determined the apparent activation energies of metal dissolution in this temperature range, which amounted to 2.1 kcal mol^{-1} for steel and to 1.6 kcal mol^{-1} for pig iron.

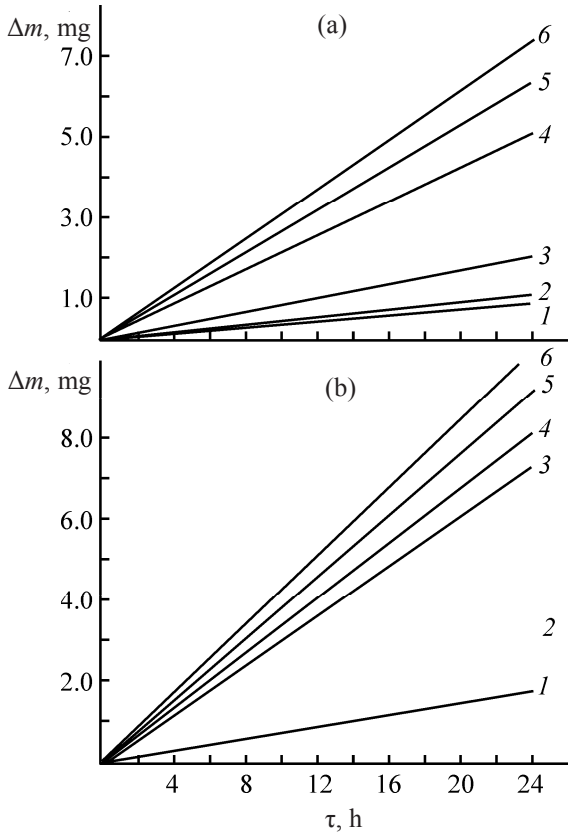


Fig. 1. Corrosion loss Δm of (a) steel and (b) pig iron as a function of testing time τ in 50% aqueous EG solution at various temperatures. T, °C: (*1*) 20, (*2*) 30, (*3*) 40, (*4*) 50, (*5*) 70, and (*6*) 90.

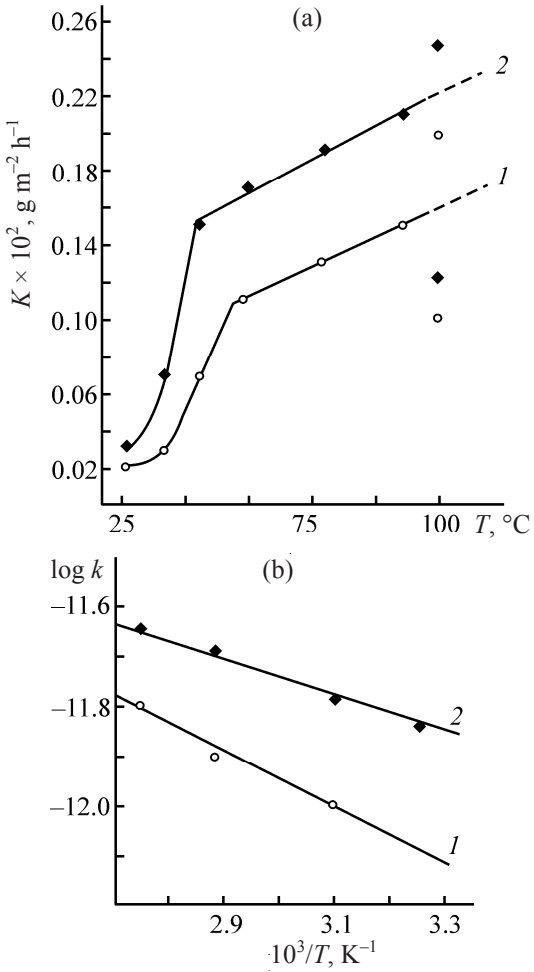


Fig. 2. Temperature dependences of the (a) corrosion rate K and (b) dissolution rate constant k (Arrhenius coordinates) of (*1*) steel and (*2*) pig iron in 50% aqueous EG solution.

At 100°C, the kinetics of dissolution of both metals is more complex: The corrosion rates of steel and pig iron samples are maximal in the initial period (τ ~2 h) and then decrease, reaching steady-state values (Fig. 3). It should be noted that these rates differ significantly from those obtained by approximation of the linear portions of the corresponding curves (Fig. 2a). In the case of aluminum samples, at all the examined temperatures, in a 50% EG solution we noted slight increase and traces of pitting corrosion. The extent of local damage of the surface increased with temperature, reaching a maximum at 50–70°C. At higher temperatures, the number of pittings decreased, and at 100°C virtually no pittings were observed.

The nonmonotonic trend in the corrosion behavior of steel and pig iron in relation to the electrolyte temperature (Fig. 2a) can be attributed to several factors. A considerable increase in the dissolution rate of both metals in the temperature range 20–50°C is apparently due to an increase in the efficiency of the diffusion steps of cathodic processes, caused by a decrease in the dynamic viscosity of the electrolyte from 5 to 1.5 cP [8, 9]. With an increase in the temperature (50–90°C), the viscosity of the aqueous–glycol solution varies less significantly (1.5–0.8 cP), and the dissolution rate of the metals starts to be controlled by formation of difficultly soluble films of secondary corrosion products hindering the diffusion processes [10]. Linear portions of the kinetic curves of the dissolution of both steel and pig iron (Fig. 2a) suggest the diffusion control of these processes. A decrease in the metal corrosion rate by a factor of more than 2 (including the disappearance of traces of pitting corrosion of aluminum) in the course of tests at 100°C is apparently due to formation of denser layers of iron and aluminum oxides, as suggested by the oxidation tint of the surface.

The kinetics of dissolution of pig iron and steel at 70°C in EG solutions is similar to that of the process at

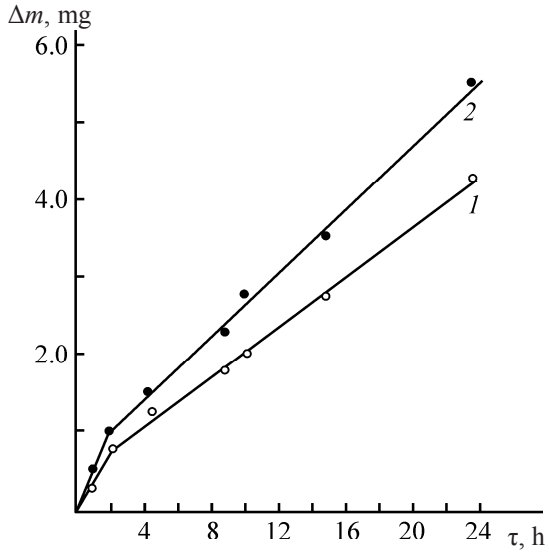


Fig. 3. Corrosion loss Δ*m* of (*1*) steel and (*2*) pig iron as a function of testing time τ in 50% aqueous EG solution at 100°C.

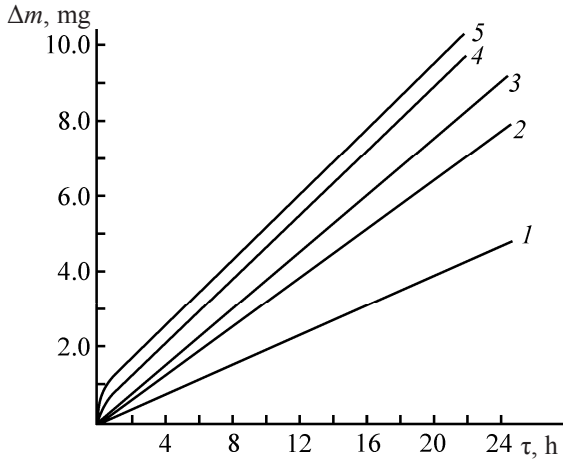


Fig. 5. Corrosion loss Δ*m* of pig iron as a function of testing time τ in aqueous EG solutions of varios compositions at 70°C. *c*(H_2O), vol %: (*1*) 5, (*2*) 30, (*3*) 50, (*4*) 75, and (*5*) 100.

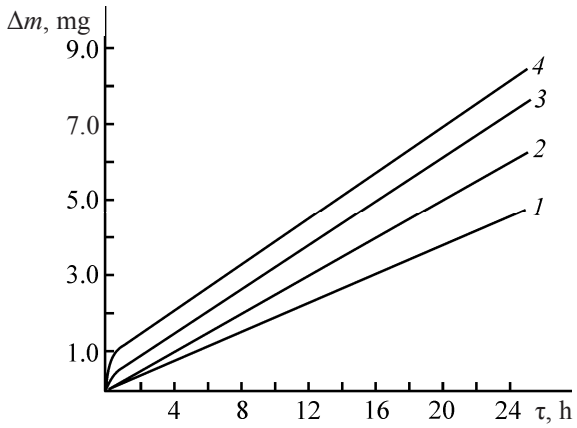


Fig. 4. Corrosion loss Δ*m* of steel as a function of testing time τ in aqueous EG solutions at 70°C. *c*(H_2O), vol %: (*1*) 30, (*2*) 50, (*3*) 75, and (*4*) 100.

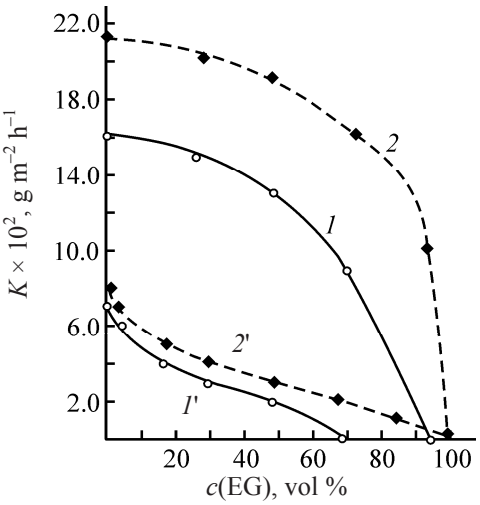


Fig. 6. Corrosion rate *K* of (*1*, *1*') steel and (*2*, *2*') pig iron as a function of the composition of aqueous–glycol solutions at (*1*, *2*) 70 and (*1*', *2*') 20°C. *c*(EG) EG concentration.

room temperature, examined previously [2]. At a water content of 5–50%, the corrosion rates are constant, and in solutions with a higher water content and in aqueous solution they are maximal in the initial period (τ ~1 h) and then become constant (Fig. 4, Table 1). The dependences of the steady-state rates of steel and pig iron corrosion at 70°C on the composition of the aqueous–glycol solution are shown in Fig. 6.

Comparison of the rates of steel and pig iron dissolution at room temperature (Fig. 6, curves *1*', *2*') and 70°C (curves *1*, *2*) reveals significant differences in the behavior of these metals. At 70°C, steel starts to dissolve at a water content slightly exceeding 5%, whereas at room temperature even at a water content of 30% steel does not undergo corrosion. At the same time, pig iron, irrespective of temperature, starts to dissolve at a very low water content (less than 5 vol %). It should also be noted that the maximal acceleration of the corrosion of both metals at 70°C, in contrast to room temperature, is observed at lower concentrations of water. An increase in the temperature leads to a decrease in the EG adsorption on the electrode surface, which disturbs the passive state of the metals. Thus, appearance of defects in the dense shielding film of

Table 1. Initial (V_{in}) and steady-state (V_{st}) rates of steel and pig iron corrosion in aqueous and aqueous–glycol solutions of various compositions at 70°C

Material	Corrosion rate, g m^{-2} h^{-1}, in EG solutions with indicated water content, vol %									
	5		30		50		75		100	
	V_{in}	V_{st}	V_{in}	V_{st}	V_{in}	V_{st}	V_{in}	V_{st}	V_{in}	V_{st}
Steel	–	0.0	–	0.092	–	0.130	0.300	0.150	0.425	0.155
Pig iron	–	0.100	–	0.167	–	0.190	0.350	0.200	0.525	0.205

Table 2. Variation of pH of 50% aqueous EG solutions in the course of tests

Test conditions	pH at indicated testing time, h					
	0	24	48	72	96	120
No stirring, no additives, no air bubbling	6.55	6.50	6.40	6.35	6.50	6.45
With pig iron plate, no stirring, no air bubbling	6.60	6.50	6.70	6.55	6.50	6.60
With pig iron plate, with air bubbling	6.50	6.35	6.50	6.45	6.60	6.55
In the presence of AIBN, with air bubbling	6.45	6.50	6.35	6.50	6.40	6.50

flat-oriented layers of adsorbed EG [11, 12] and formation of a metal aqua oxide surface phase [1, 13] occur at a lower water content of the solution.

In the case of aluminum samples, in all the examined aqueous–glycol solutions at 70°C, a slight weight gain and traces of pitting corrosion were observed. The extent of local damage of the surface increased with the EG concentration in solution. It should be noted, however, that in the individual components (EG and fresh water) we observed no pitting corrosion of the aluminum alloy.

High corrosion activity toward metals is typical of water and all water-containing liquids. According to [14, 15], in the presence of glycols many metals undergo corrosion at a considerably higher rate than in water. This fact is attributed to the corrosion activity of a mixture of organic acids (in particular, aggressive formic acid) formed by thermal oxidation of glycol. Ethylene glycol can be readily oxidized with various oxidants at relatively low temperatures. For example, potassium permanganate and periodic acid readily oxidize EG at 30–35°C to give formaldehyde and formic acid [16]. With potassium bichromate in an acid solution, EG is exhaustively oxidized to carbon dioxide [17]. Ozonation of glycols at slight heating, followed by oxidation with oxygen at 50–100°C, leads to the formation of the corresponding dicarboxylic acids. Similar reaction also occurs on treatment of aqueous–glycol solutions with nitrogen(IV) oxides [18]. Despite the fact that glycols are susceptible to autooxidation, i.e., to spontaneous oxidation with atmospheric oxygen at relatively low temperatures, an attempt to oxidize ethylene glycol at 60–95°C in a wide range of partial pressures of oxygen, in contrast to the similar reaction with diethylene glycol [19], failed [20]. Carboxylic acids were detected in EG oxidation products only after its heating at 150°C for 1000 h with continuous air bubbling [8]. However, the possibility of EG autooxidation in its aqueous solutions on contact with variable-valence metals, in particular, with iron whose soluble corrosion products efficiently initiate radical reactions [21], cannot be ruled out. The mechanism of the action of these compounds consists in acceleration of the decomposition of hydroperoxides and in an increase in the amount of free radicals participating in the chain propagation:

$$ROOH + M^{3+} \rightarrow ROO^{\cdot} + M^{2+} + H^{+},$$

$$ROOH + M^{2+} \rightarrow RO^{\cdot} + M^{3+} + OH^{-}.$$

To check the validity of this assumption, we attempted to oxidize EG in its 50% aqueous solution at the boiling point of the solution (108°C at atmospheric pressure) under various conditions. The reaction progress was monitored by variation of pH. The conditions and results of the experiments are given in Table 2.

Table 2 shows that neither the conditions favoring formation of variable-valence metal ions nor addition of 2,2'-azobis(isobutyronitrile) (AIBN) as initiator of radical reactions lead to the appearance of acidic products.

Thus, either EG is not oxidized under the experimental conditions or final products of its transformation are nonacidic products.

CONCLUSIONS

(1) A study of the corrosion behavior of aluminum, steel, and pig iron in fresh water, ethylene glycol, and its aqueous solutions showed that the corrosion rates of steel and pig iron increase with increasing temperature and water content of aqueous–glycol solutions, reaching a limit in the aqueous electrolyte.

(2) In the case of aluminum, traces of pitting corrosion appear at 30–90°C in water–glycol mixtures at any component ratios. The extent of the local damage of the metal surface increases with an increase in the ethylene glycol concentration and with temperature, reaching a maximum at 50–70°C.

(3) The apparent activation energies of steel and pig iron dissolution in the temperature range 50–90°C were estimated: 2.1 kcal mol^{-1} for steel and 1.6 kcal mol^{-1} for pig iron.

(4) Ethylene glycol in aqueous–glycol solutions is not oxidized even in the presence of initiators of radical reactions, or final products of its oxidation are not acidic.

REFERENCES

1. Esenin, V.N. and Denisovich, L.I., *Zashch. Met*., 2007, vol. 43, no. 4, pp. 390–395.
2. Esenin, V.N. and Denisovich, L.I., *Zh. Prikl. Khim*., 2008, vol. 81, no. 10, pp. 1672–1678.
3. Persiantseva, V.P., Rozenfel'd, I.L., Zorina, V.E., et al., *Zashch. Met*., 1979, vol. 15, no. 3, pp. 309–314.
4. Persiantseva, V.P., Filatov, P.G., Chechurina, O.I., et al., *Zashch. Met*., 1979, vol. 15, no. 2, pp. 154–159.
5. Kuznetsov, Yu.I., *Zashch. Met*., 1999, vol. 35, no. 3, p. 229.
6. Vigdorovich, V.I., Tsygankova, L.E., Shlykova, G.A., et al., *Khim. Prom–st*., 1973, no. 7, pp. 511–512.
7. Tseitlin, Kh.D., Zal'tsman, G.I., and Isaenko, G.I., *Khim. Prom–st*., 1979, no. 10, pp. 603–604.
8. Dyment, O.N., Kazanskii, K.S., and Miroshnikov, A.M., *Glikoli i drugie proizvodnye okisei etilena i propilena* (Glycols and Other Derivatives of Ethylene and Propylene Oxides), Moscow: Khimiya, 1976.
9. Rozenfel'd, I.L., Persiantseva, V.P., and Kuznetsov, Yu.I., *Zashch. Met*., 1970, vol. 6, pp. 677–682.
10. Kaidrikov, R.A., Zhuravlev, B.L., and Nazmieva, L.R., *Vvedenie v elektrokhimicheskuyu korroziyu metallov* (Introduction to Electrochemical Corrosion of Metals), Kazan: Kazan. Gos. Tekhnol. Univ., 2006.
11. Veselyi, S.S. and Kuznetsov, Yu.I., *Zashch. Met*., 1994, vol. 30, pp. 479–485.
12. Kuznetsov, Yu.I., Veselyi, S.S., and Oleinik, S.V., *Zashch. Met*., 1992, vol. 28, pp. 88–95.
13. Novakovskii, V.M., *Zashch. Met*., 1994, vol. 30, no. 2, pp. 117–129.
14. Bregman, J. and Boies, D., *Corrosion*, 1958, vol. 14, pp. 2756–2760.
15. Collins, H.H. and Higgens, R.I., *J. Res. Develop*., 1969, no. 7, pp. 667–671.
16. Scugupta, K., *Indian J. Chem*., 1975, vol. 13, no. 4, pp. 348–352.
17. Monick, I.A., *Alcohols*, New York: Reinhold, 1968.
18. Kaverzneva, E.D., Ivanov, V.I., and Salova, A.B., *Izv. Akad. Nauk SSSR, Otd. Khim. Nauk*, 1956, pp. 482–487.
19. Lloyd, W.G., *J. Am. Chem. Soc*., 1956, vol. 78, no. 1, pp. 72–79.
20. Lloyd, W.G., *Ind. Eng. Chem*., 1954, vol. 46, no. 11, pp. 2407–2414.
21. Emanuel', N.M., Denisov, E.T., and Maizus, Z.K., *Tsepnye reaktsii okisleniya uglevodorodov v zhidkoi faze* (Chain Reactions of Liquid-Phase Oxidation of Hydrocarbons), Moscow: Khimiya, 1965.

ISSN 1070-4272, Russian Journal of Applied Chemistry, 2008, Vol. 81, No. 11, pp. 1895–1898. © Pleiades Publishing, Ltd., 2008.
Original Russian Text © B.G. Ershov, P.A. Morozov, 2008, published in Zhurnal Prikladnoi Khimii, 2008, Vol. 81, No. 11, pp. 1777–1780.

INORGANIC SYNTHESIS AND INDUSTRIAL INORGANIC CHEMISTRY

Decomposition of Ozone in Water at pH 4–8

B. G. Ershov and P. A. Morozov

Frumkin Institute of Physical Chemistry and Electrochemistry, Russian Academy of Sciences, Moscow, Russia

Received March 4, 2008

Abstract—A systematic study of the ozone decomposition in water in the pH range 4–8 was carried out.

DOI: 10.1134/S1070427208110048

At present ozone is widely used to disinfect and oxidize impurities when preparing potable water [1–3]. It is a very strong oxidant (E^0 = 2.07 V), which is second in this regard only to the hydroxy radical (E^0 = 2.80 V) and substantially exceeds chlorine (E^0 = 1.36 V). Ozone reacts with water to give oxygen. The rate of this reaction noticeably grows as pH is raised, which is due to the catalyzing effect of hydroxide ions OH^-. The mechanism includes a chain of successive reactions yielding H_2O_2, O_3^-, and $^{\cdot}OH$ and $HO_2^{\cdot}$ radicals [4–8]. The radical products initiate chain decomposition of ozone. The disinfecting and oxidizing efficiency of ozone in water depends on its concentration, which is, in turn, determined by the rate of its decomposition. Therefore, it is important to elucidate the fundamental aspects of the kinetics of ozone decomposition in water and the effect of various factors on the rate of this process. Studies in this area have been already carried out during several decades. However, the results obtained are rather contradictory. For example, different orders of the reaction of ozone decomposition in water, including first [9, 10], first-and-a-half [11, 12], and second [13], and markedly different rate constants have been reported.

EXPERIMENTAL

Experiments were performed with triple-distilled water subjected to a preliminary treatment with ozone to decompose the possibly present organic impurities. The pH value was adjusted with $HClO_4$ and NaOH (Merck). Ozone was produced using an ozonizer (designed by LOT Limited Liability Company) with a capillary discharge chamber yielding an ozone–oxygen mixture (OOM) with a high concentration of ozone (up to 200 mg l^{-1}). The concentration of O_3 in OOM was determined with an optical UV analyzer to be approximately 166 mg l^{-1}. Solutions with a preset pH value were ozonized for 1–3 min to reach a concentration of approximately 3×10^{-4} to 8×10^{-4} M. After that, a solution was placed in hermetically sealed cylindrical glass cells connected by a sealed-in glass tube (d = 5 mm, l = 15 cm) to a quartz cell (1 × 1 × 4 cm). The concentration of ozone was measured on the basis of its absorption at the peak of the optical band at λ_{max} = 258 nm (ε = 2950 l mol^{-1} cm^{-1}) [14] with an SF-2000 spectrophotometer.

All experiments except those aimed to determine the activation energy of the reaction were carried out at 19 ± 1°C.

As can be seen in Fig. 1, the rate of ozone decomposition substantially grows as pH increases from 4 to 8. After the complete decomposition of ozone and attainment of the equilibrium with ambient air, the initial pH value of the solution is recorded. It was found that $\tau_{0.5}$ (time in which the concentration of ozone in water decreases by a factor of 2 in the course of its decomposition) depends on the initial concentration of ozone. For example, for water with pH 6.0, $\tau_{0.5}$ was 190, 330, and 600 s at ozone concentrations of 7.6×10^{-4}, 4.3×10^{-4}, and 2.4×10^{-4} M, respectively. The observed change in $\tau_{0.5}$ precisely corresponded to that expected for ozone decomposition by a second-order reaction, for which the following relation is valid:

$$\tau_{0.5} = 1/(c_0 k),$$

where c_0 is the initial concentration (M), and k is the reaction rate constant (l mol^{-1} s^{-1}).

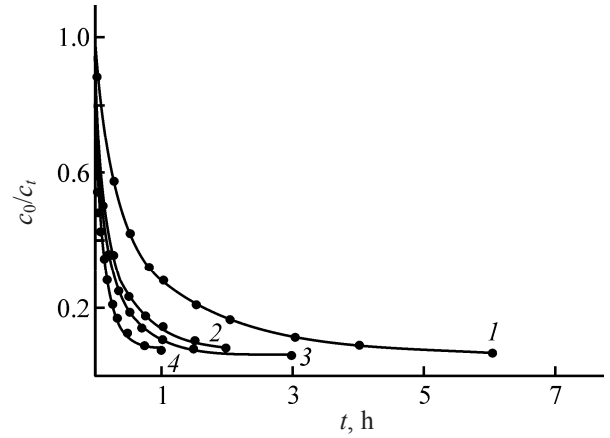


Fig. 1. Ozone decomposition in water at various pH values. (c_0, c_t) Initial and running concentrations of ozone in water and (t) time. pH: (*1*) 4.7, (*2*) 6.0, (*3*) 6.8, and (*4*) 7.9; the same for Fig. 2.

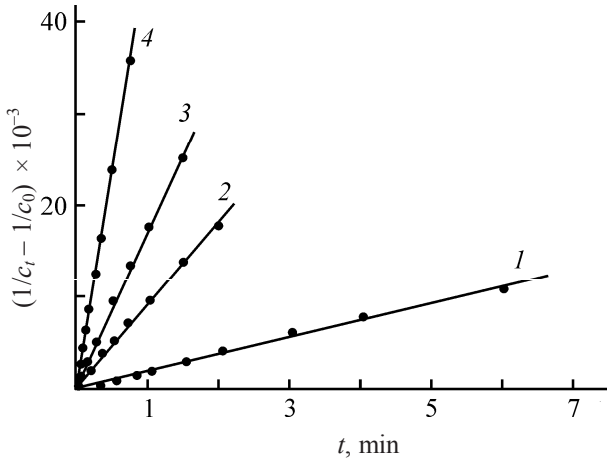


Fig. 2. Kinetic curves of ozone decomposition, plotted in the coordinates of the second-order rate equation. (c_0, c_t) Initial and running concentrations of ozone in water and (t) time.

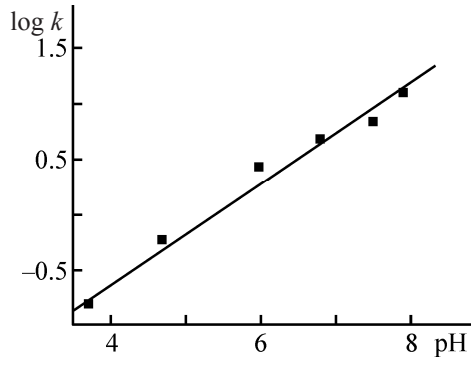


Fig. 3. Logarithm of the rate constant k vs. pH.

It is, indeed, seen that there is a strictly inversely proportional relationship between $\tau_{0.5}$ and c_0.

Figure 2 shows how the ozone decomposition kinetics depends on the pH value in the range 4–8. The process is described with high precision by a second-order rate equation

$$c_t^{-1} - c_0^{-1} = kt, \qquad (1)$$

where c_t and c_0 are the running and initial concentrations of ozone in water, and t is time.

Analysis of the kinetic dependences shows that, in all cases, the reaction order n of ozone decomposition, calculated by the least-squares method, is within the range 1.9 ± 0.2. The reaction order remains unchanged almost until the complete decomposition of ozone. This means that the mechanism is the same within the entire pH range studied. The fact that the decomposition reaction is second-order with high accuracy makes it possible to determine the reaction rate constant from the slopes of the straight lines in Fig. 2. Figure 3 shows how log k depends on pH at 19°C. In the pH range 4–8, this dependence is linear and well described by the equation

$$\log k_{(\mathrm{pH})} = \log k_{(\mathrm{pH}\,4)} + (0.49 \pm 0.03)(\mathrm{pH} - 4), \qquad (2)$$

where $k_{(\mathrm{pH})}$ is the sought-for rate constant at pH 4–8, and $k_{(\mathrm{pH}\,4)}$ is the rate constant at pH 4.0, equal to 0.2 l mol^{-1} s^{-1} (accordingly, $\log k_{(\mathrm{pH}\,4)} = -0.7$).

The decomposition of ozone is catalyzed by OH^- ions and occurs by the scheme [4–8]

$$O_3 + OH^- \rightarrow HO_2^- + O_2,$$

$$O_3 + HO_2^- \rightarrow \dot{O}_2^- + \dot{O}H + O_2,$$

$$O_3 + \dot{O}_2^- \rightarrow \dot{O}_3^- + O_2,$$

$$\dot{O}_3^- + H_2O \rightarrow \dot{O}H + OH^- + O_2.$$

The reaction of O_3 with OH^- leads to the loss of additional two molecules of ozone and regeneration of the OH^- ion. The chain process of ozone decomposition occurs as a result of reactions involving $\dot{O}H$ and $HO_2^{\cdot}$ radicals. The chain is terminated by their recombination. In [13], a second-order reaction of ozone decomposition in water was observed in the pH range 6.0–9.5. The study was carried out in the presence of 0.1–1.0 M of a borate or phosphate as a buffering additive, rather than in pure water. The values of the constants, measured at the same pH values as those in the present study, strongly depended on the additive used

and its content in solution and differed by one to two orders of magnitude. All these circumstances indicated that the additives are involved in the ozone decomposition.

The decomposition of ozone becomes faster as temperature is elevated. Figure 4 shows how the rate constant of the second-order reaction of ozone decomposition in water at pH 4.7 depends on temperature in the Arrhenius coordinates. In the temperature range 9–37°C, this dependence is described by the equation

$$k(T) = k_{19} \exp\{76.0[(T - 292)/292RT]\}, \quad (3)$$

where k_{19} is the rate constant at a temperature of 19°C, and R is the universal gas constant (8.314 J mol^{-1} K^{-1}). The activation energy of ozone decomposition was 76.0 ± 8.3 kJ mol^{-1}, which coincides within experimental error with the value of 79.5 kJ mol^{-1}, measured in [8] for ozone solutions with pH 0–4. The temperature coefficient of the reaction (reaction acceleration factor upon an increase in temperature by 10°C) is approximately 3. Thus, the results of the present study indicate that the kinetics of ozone decomposition in water is described by the equation of a second-order reaction with respect to the ozone concentration in the pH range 4–8. The linearly proportional relationship between log k and pH [Eq. (3)] makes it possible to calculate the reaction rate constants at different pH values:

pH	k, l mol^{-1} s^{-1}
4.0	0.20
4.5	0.35
5.0	0.62
5.5	1.08
6.0	1.91
6.5	3.35
7.0	5.90
7.5	10.4
8.0	15.2

It follows from the data obtained that the rate constant at 19°C grows by a factor of approximately 3 (±10%) upon an increase in pH by a single unit.

Thus, the kinetics of ozone decomposition in water is well described by the second-order reaction equation $O_3 + O_3 \rightarrow 3O_2$ and is catalyzed by hydroxide ions. The measured kinetic dependences make it possible to calculate the dynamics of concentration decrease in the course of time and evaluate the effect of pH and temperature. Potable water is disinfected with ozone concentrations on the order of 1 mg l^{-1} (or ~2 × 10^{-5} M). The time in which the ozone concentration is halved, $\tau_{0.5}$, can be calculated by Eq. (1). With the value of k at 19°C taken from the table, the values of $\tau_{0.5}$ at pH 5.0, 6.0, and 7.0 are approximately 22.2, 7.2, and 2.4 h, respectively. The time in which the ozone concentration decreases by a factor of 10 can be calculated using the equation $\tau_{0.1} = 9\tau_{0.5}$. At a temperature lower by 10°C, the time of ozone decomposition becomes approximately a factor of 3 longer, and at a 10°C higher temperature it is, accordingly, shorter by the same factor.

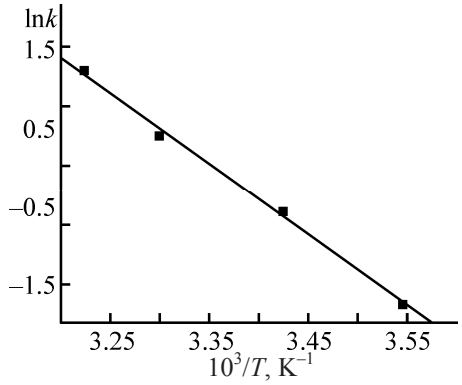


Fig. 4. Temperature dependence of the rate constant k of ozone decomposition in water (pH 4.7) in the coordinates of the Arrhenius equation.

The key factor in the ozone decomposition in water and aqueous solutions is the presence of readily oxidizable substances. This is particularly important in treatment of wastewater and process solutions with ozone. In this case, it is desired to saturate these substances with ozone to the maximum possible extent, with concentrations as high as 20–40 mg l^{-1} reached. As a result, the self-decomposition of ozone is intensified and $\tau_{0.5}$ decreases by, correspondingly, a factors of 20–40 as compared to the values presented above.

For effective decomposition of impurities (S) in aqueous solutions, it is necessary that the inequality $c_0 k << c_S k_S$ should be satisfied (here, c_0 and k are the concentration of ozone and rate constant of its self-decomposition in water; c_S and k_S, concentration of the solute and the rate constant of its interaction with ozone). If this condition is satisfied, ozone is preferentially consumed for oxidative decomposition of impurities. This relationship also makes it possible to estimate the impurity concentration at which there occurs preferential self-decomposition of ozone. It is given by the equation $c_S \le c_0(k/k_S)$. It follows from this equation that, for deeper decomposition of impurities in ozona-

tion of aqueous solutions, it is necessary to gradually lower the concentration of the dissolved gas, which also provides a decrease in its expenditure.

CONCLUSIONS

(1) In the pH range 4–8, the kinetics of ozone decomposition in water is well described by the second-order rate equation. As pH increases, the rate of ozone decomposition becomes higher.

(2) The dependence of the rate constant of ozone decomposition on pH at 19°C corresponds to Eq. (2) at $\log k_{(pH\,4)} = -0.7$. The activation energy of ozone decomposition is 76.0 ± 8.3 kJ mol^{-1}.

REFERENCES

1. Kinman, S.W.R.N., *Crit. Rev. Environ. Contr*., 1975, vol. 5, pp. 141–152.
2. Glaze, W.H. et al., *Ozone Sci. Eng*., 1987, vol. 9, no. 4, p. 335.
3. Bablon, G.P. et al., *Ozone in Water Treatment: Application and Engineering*, AWWARF, 1991.
4. Bader, H. and Hoigne, J., *J. Ozone Sci. Eng*., 1982, vol. 4, no. 4, pp. 169–176.
5. Staehelin, J. and Hoigne, J., *Environ. Sci. Technol*., 1982, vol. 16, no. 10, pp. 676–681.
6. Hoigne, J., Bader, H., Haag, W.R., and Staehelin, J., *J. Water Res*., 1985, vol. 19, pp. 993–1004.
7. Tomyasu, H., Fukutomi, H., and Gordon, G., *Inorg. Chem*., 1985, vol. 24, pp. 2962–2966.
8. Sehested, K., Corfitzen, H., Holcman, J., et al., *Environ. Sci. Technol*., 1991, vol. 25, no. 9, pp. 1589–1596.
9. Morooka, S., Ikemizu, K., and Kato, Y., *Int. Chem. Eng*., 1979, vol. 19, no. 5, pp. 650–654.
10. Teramoto, M., Imamura, S., Yatagai, N., et al., *J. Chem. Eng. Jpn.*, 1981, vol. 14, no. 5, pp. 383–388.
11. Sotelo, J.L., Beltran, F.J., Benitez, F.J., and Beltran-Heredia, J., *Ind. Eng. Chem. Res*., 1987, vol. 26, no. 10, pp. 39–43.
12. Ku, Y., Su, W.-J., and Shen, Y.-S., *Ind. Eng. Chem. Res*., 1996, vol. 35, no. 10, pp. 3369–3374.
13. Gurol, M.D. and Singer, P.C., *Environ. Sci. Technol*., 1982, vol. 16, no. 7, pp. 377–383.
14. *APHA, AWWA, WEF, Standard Methods for the Examination of Water and Wastewater*, 1988, pp. 4-137–4-139.

ISSN 1070-4272, Russian Journal of Applied Chemistry, 2008, Vol. 81, No. 11, pp. 1899–1903. © Pleiades Publishing, Ltd., 2008.
Original Russian Text © V.A. Sinyaev, E.S. Shustikova, L.V. Levchenko, R.A. Karzhaubaeva, G.A. Tokseitova, 2008, published in Zhurnal Prikladnoi Khimii, 2008, Vol. 81, No. 11, pp. 1781–1785.

INORGANIC SYNTHESIS AND INDUSTRIAL INORGANIC CHEMISTRY

Amorphous Calcium Barium Monophosphate and Its Dehydration in Air at Room Temperature

V. A. Sinyaev, E. S. Shustikova, L. V. Levchenko, R. A. Karzhaubaeva, and G. A. Tokseitova

Bekturov Institute of Chemical Sciences, Ministry of Education and Science of Kazakhstan Republic, Almaty, Kazakhstan

Received March 4, 2008

Abstract—The change in the state of chemical bonds during dehydration of amorphous calcium barium monophosphate was studied. The monophosphate was obtained by precipitation from an aqueous phosphate solution under the action of a binary solution containing simultaneously calcium and barium chlorides in the atomic ratio Ba/Ca ~0.2.

DOI: 10.1134/S1070427208110050

As a basis for new materials for medicines, amorphous calcium monophosphates (orthophosphates) close in the chemical composition to hydroxyapatite $Ca_5(PO_4)_3OH$ and to tricalcium phosphate $Ca_3(PO_4)_2$ attract growing researchers' attention [1–8]. These compounds are also of interest as precursors of technical ceramics [4]. The composition of precursors and conditions of their treatment are the main factors determining the microscopic structure of the forming ceramics. Salts of the metals that are analogs of calcium in the periodic table, namely, of magnesium, strontium, and barium, are of interest as agents for controlling the porosity of ceramics. High performance of Mg^{2+} ions as inhibitors of the crystallization of calcium phosphates has been shown in a number of studies [4, 9–15]. Later the effect of these ions on the microscopic structure of calcium phosphate ceramics was described [16, 17]. The Sr^{2+} ions are much more poorly studied [8, 18] in this respect, though the procedure for preparing strontium-containing calcium phosphate bioceramics has been described [19]. As to barium, in spite of the presence of its traces in apatites of biological origin [9, 20], the role of Ba^{2+} cations in the crystallization of calcium monophosphates is understood still more poorly.

Here we briefly describe the synthesis of amorphous calcium barium monophosphate and its transformations at room temperature.

EXPERIMENTAL

To synthesize the compounds under consideration, we used analytically pure grade sodium phosphate $Na_2HPO_4 \cdot 12H_2O$ and hydroxide NaOH, and also pharmacopoeia grade calcium and barium chlorides. 5% aqueous solutions of sodium phosphate were treated with solutions of the same concentration, containing calcium and barium chlorides in various proportions. The solutions of chlorides were added to a phosphate solution dropwise with vigorous stirring at room temperature. Preliminarily the phosphate solution was alkalized to pH 9 and was maintained at this pH level during the reaction. The precipitated substances were separated from the solution of salts by decantation, dispersed in distilled water with pH 8 taken approximately in a 10-fold excess, settled for 2–3 h, and again separated from the solution. The operation was repeated up to the absence of Cl^- ions in the wash water. The acidity of the water used for washing was adjusted with an ammonia solution. The washed products were filtered in vacuum on a Corning Nylon porous filter with a pore size of 0.2 μm.

To characterize the precipitated phosphates and to study their dehydration, we used X-ray phase and differential thermal analyses, and also IR Fourier spectroscopy. The phase analysis was carried out on a DRON-3 diffractometer with CoK_α radiation. The IR spectra were recorded on an FT-IR Nicolet 5700 spectrometer, using the attenuated total internal reflection technique on a ZnSe single crystal at a resolution of 4 cm^{-1}, measuring accuracy of ±0.5 cm^{-1}, and scan number 32. The dehydration process was monitored by recording the IR spectra with a periodicity of approximately 10 min. The thermal analysis was carried out on a Mettler Toledo TGA/SDTA 851 thermoanalyzer

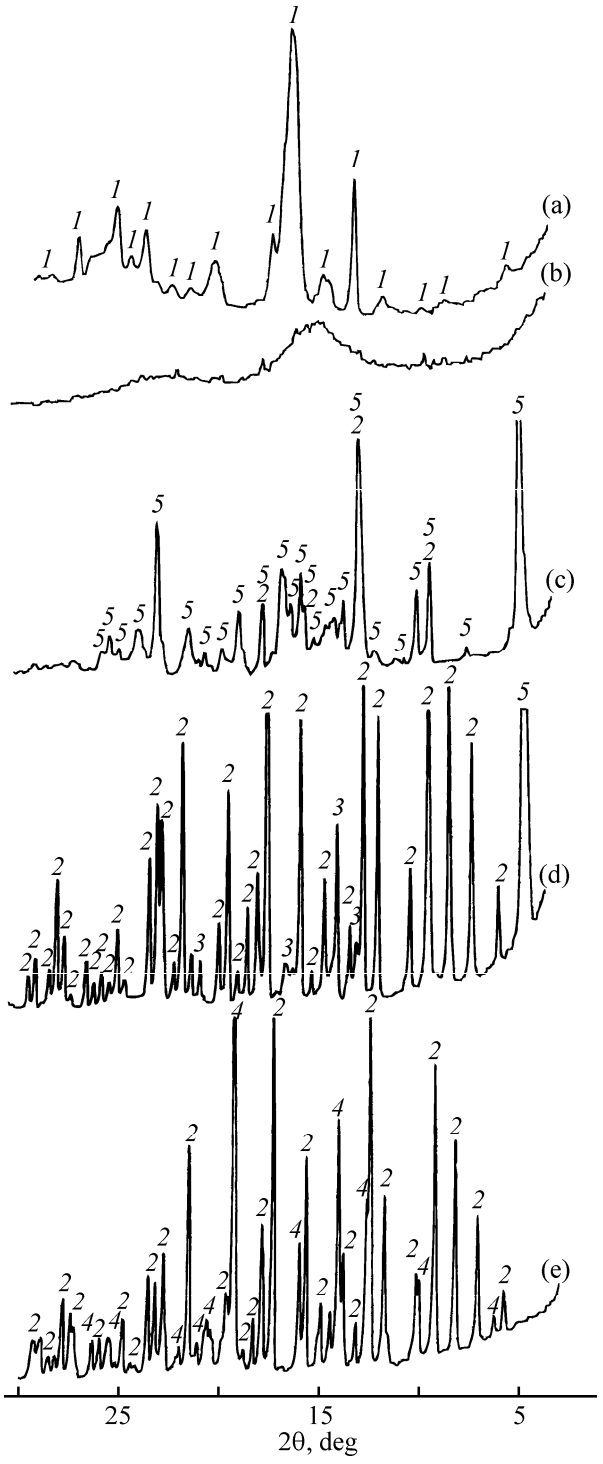


Fig. 1. Diffraction patterns of substances precipitated under the action of binary chloride solutions with various $BaCl_2$ content. (2θ) Bragg angle. $BaCl_2$ content, (mol %): (a) 0, (b) 10–20, (c) 40, (d) 60–80, and (e) 100. Individual phosphate in precipitated substances: (*1*) $Ca_5(PO_4)_3OH$, (*2*) $NaBa(PO_4)\cdot 9H_2O$, (*3*) $Ba_2Ca(PO_4)_2$, and (*4*) $Ba_3(PO_4)_2$; (*5*) not identified.

in open corundum crucibles with a weighed sample of about 100 mg at a constant temperature of 25°C.

The substances precipitated from the phosphate solution under the action of only one chloride, $CaCl_2$ or $BaCl_2$, are crystalline (Fig. 1). The calcium salt crystallizes in the form of hydroxyapatite, and the barium salt, in the form of $Ba_3(PO_4)_2$. In presence of both chlorides, either amorphous substances or a mixture of crystal phases are formed. The former appear at the Ba/Ca atomic ratio close to 1/4, which is slightly less than in the case when magnesium ions are used for the same purpose [14, 15]. At the ratio Ba/Ca > 1/4, crystalline sodium barium monophosphate $NaBa(PO_4)\cdot 9H_2O$, barium calcium monophosphate $Ba_2Ca(PO_4)_2$, and barium monophosphate $Ba_3(PO_4)_2$, usually in the form of a mixture, are formed. Among the products we have found a substance that is difficult to identify reliably. However, proceeding from Fig. 1, we can assume that it is a calcium-rich barium-containing phosphate salt.

Amorphous calcium barium phosphate (ACBP) in which components should be "intermixed" at a level close to molecular is of the greatest interest as a ceramics precursor; therefore, it became the object for the further study.

Pasty character of ACBP suggests that it is hydrated. In fact, the bands related to the main vibrations of O–H bonds in water molecules dominate in its IR spectrum in the ranges 1500–1800 and 2800–3700 cm^{-1} (Fig. 2). There is also a weak absorption at 2000–2300 cm^{-1} connected with a combination of vibrations (δ + ω)(OH) [21]. A fairly strong band at lower frequencies corresponds to the vibrations of P–O bonds in the phosphate anion PO_4^{3-} [8, 25, 26].

The comparison of the spectra of ACBP, crystalline hydroxyapatite [8], and also of amorphous calcium and calcium magnesium monophosphates described earlier [27] suggests that water in all the four substances is in the same state. However, judging from the state of P–O bonds, ACBP can be considered as a substance with less homogeneous in energy (in strength) chemical bonds and, probably, with a stronger amorphous character (Fig. 3).

Similarly to other amorphous calcium phosphates, ACBP is stable at room temperature when stored in a sealed vessel. In air it changes the consistency and rapidly erodes. The thermal analysis data show that the substance first undergoes an endothermic transformation accompanied by a weight loss at a gradually decreasing rate (Fig. 4a). After 2 h, the weight loss rate

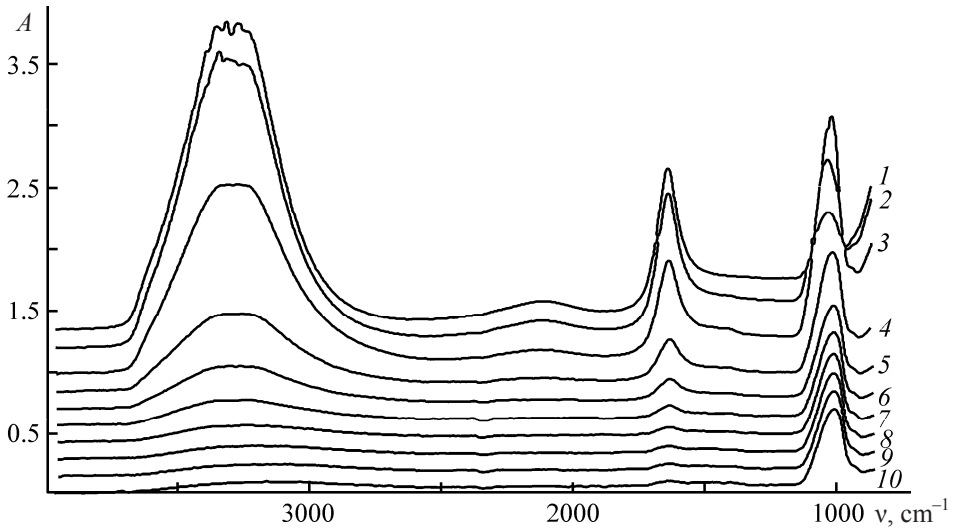


Fig. 2. Variation of the ACBP IR Fourier spectra on keeping the substance in air at room temperature for various times. (*A*) Absorbance and (ν) wavenumber; the same for Fig. 3. τ, min: (*1*) 0, (*2*) 34, (*3*) 54, (*4*) 59, (*5*) 64, (*6*) 69, (*7*) 74, (*8*) 79, (*9*) 84, and (*10*) 118.

becomes considerably lower but constant, and finally it rapidly decreases and the process stops. The shape of the TG and DTA curves indicates that the process consists of at least three steps.

The ACBP weight loss is due to dehydration. In fact, the ratio of intensities of ν(OH) and ν(PO) bands in the IR spectra of the products formed gradually decreases with time (Fig. 4b). Within 80 min, the I_{OH}/I_{PO} value reaches the lowest, though not "zero," level, suggesting retention of residual moisture in the substance. The amount of such water found from the total weight loss is close to 20%.

The dehydration should be accompanied by changes in chemical bonding in the phosphate. According to the IR spectra of the products of ACBP dehydration, despite a large water loss in the first 30–50 min, the intensities of the ν(OH) and δ(OH) bands did not decrease noticeably, whereas the intensity of the ν(PO) band appreciably increased (Fig. 4c). This is due to the fact that, in the initial dehydration step, the density of the substance increases owing to its shrinkage and hence the phosphate concentration grows. After 50 min, because of cracking and reduction of the surface area from which the spectra are recorded, all the IR bands start to rapidly weaken. After a period slightly exceeding 1 h, the values of the spectral maxima get stabilized on the same level, suggesting completion of the water removal.

In the course of ACBP dehydration, not only the intensities of bands in the IR spectra of the products but also their frequencies change. During the period of rapid weakening of all bands, the frequency of the δ(OH) band increases first smoothly, then stepwise, and finally is stabilized (Fig. 4d). As to the stronger ν(OH) maximum, it is impossible to determine reliably its frequency because the peak is smeared. Nevertheless, judging from the general profile of the spectral band, we can assert that ν(OH) behaves in the opposite way, shifting to the low-frequency region. The trend is the most significant in the period of weakening of this band. The ν(PO) band also sharply shifts to lower frequencies at the moment of a decrease in its intensity; however, after reaching a minimum its frequency again starts to grow (Fig. 4e). It is impossible to account for such a behavior simply by the progress of changes in the substance composition due to the dehydration. Therefore, we shall interpret this effect after consider-

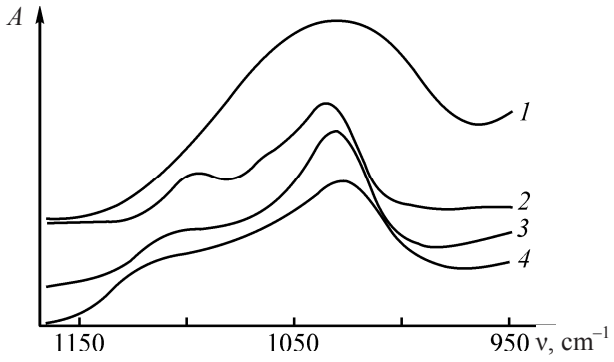


Fig. 3. Region of stretching vibrations of P–O bonds in IR Fourier spectra of (*1*) ACBP, (2) crystalline hydroxyapatite, (*3*) amorphous calcium mono–diphosphate with the molar ratio 2P/(2P + 1P) = 0.3, and (*4*) amorphous calcium magnesium monophosphate with the atomic ratio Mg/(Mg + Ca) = 0.25–0.35.

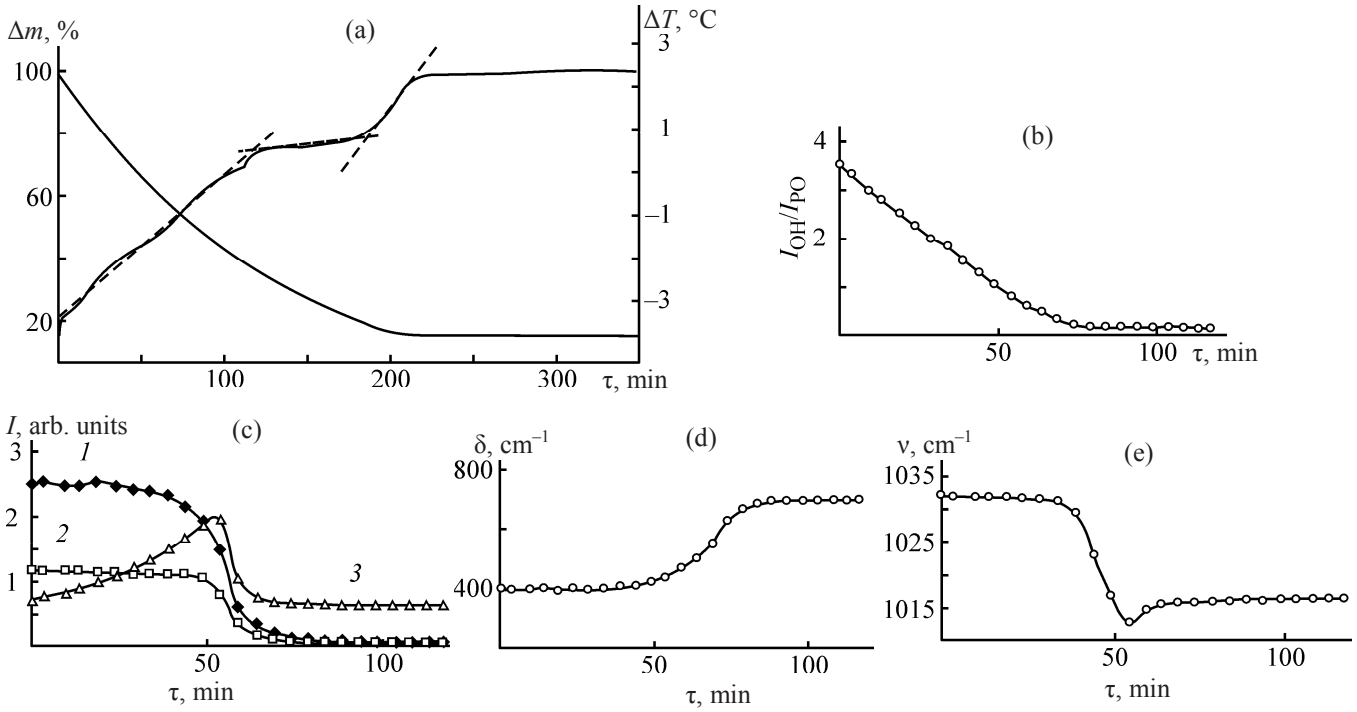


Fig. 4. Variation with time τ of (a) weight *m* and temperature *T* of ACBP sample; (b) relative intensity I_{OH}/I_{PO} of ν(OH) and ν(PO) bands; (c) intensity *I* of main bands (*1*) ν(OH), (*2*) δ(OH), and (*3*) ν(PO); (d) δ(OH) frequency; and (e) ν(PO) frequency in the IR Fourier spectra of products of dehydration in air at room temperature.

ing how the composition of dehydration products affects the state of chemical bond in ACBP.

Whereas the dynamics of the δ(OH) vibrations can be used only as an evidence of stepwise transformations in a substance in a certain dehydration step, the other two types of vibrations furnish more detailed information. The point is that the strength of chemical bonds correlates with the frequency of the corresponding stretching vibrations in the spectra. Such a dependence was used earlier to account for the shift of Raman bands of amorphous (vitreous) polyphosphates depending on their composition [28, 29]. It was concluded that, as the electronegativity of the nearest environment of phosphate anions increases, the P–O vibration frequency becomes higher and the bonds become stronger and more polar. Applying a similar approach to ACBP, we can attribute a decrease in the frequency of ν(OH) and ν(PO) bands in the spectra of the dehydration products to a decrease in the content of water as the most electronegative component. As a result, the polarizing action of the environment on PO_4^{3-} anions decreases, which results in weakening and, apparently, depolarization of the P–O bonds. Due to the same effect, O–H bonds in the molecules of residual water also become weaker, but probably more polar.

Coming back to an increase in the frequency of P–O bonds at the end of the ACBP dehydration (Fig. 4e) and using the above approach (the higher the electronegativity of the environment, the higher the vibration frequencies), we can assume that, in this step, the electronegativity of the substance does not decrease, but suddenly starts to grow. It is possible if the phosphate absorbs a component more electronegative than ACBP and water from air. Such a component can be carbon dioxide which was detected in the IR spectra of the products in final dehydration steps.

As water is removed, the shape of spectral bands also changes. In particular, the ν(OH) band becomes broader and weaker. The ν(PO) band becomes even slightly narrower when its frequency decreases, but when it is again shifted to higher frequencies, its width increases again. The broadening of bands suggests appearance of chemical bonds different from the main bonds and increase in structural disorder. Thus, it is possible that the residual moisture in ACBP is less organized than in the mother substance. Similarly, pure phosphate substance in the final step of dehydration is disordered to almost the same extent as in the initial paste, though in the products of partial dehydration P–O bonds are more uniform.

CONCLUSIONS

(1) The reaction of monophosphate anions PO_4^{3-} with Ca^{2+} and Ba^{2+} cations present in a solution simul-

taneously in the atomic ratio Ba/Ca ~0.2 yields amorphous calcium barium monophosphate. At other Ba/Ca ratios, crystalline products are precipitated.

(2) Amorphous calcium barium monophosphate contains 80% water. The substance is stable when stored in a sealed vessel, but in air it rapidly loses in three steps the main part of moisture, remaining, however, amorphous and, probably, becoming still more disordered.

(3) Dehydration leads to weakening of O–H chemical bonds in the molecules of remaining water. The P–O bonds also become weaker, but in the final dehydration step they are noticeably strengthened, possibly due to the absorption of carbon dioxide from air.

REFERENCES

1. Aoki, H., *Science and Medical Applications of Hydroxyapatite*, Tokyo: JAAS, 1991.
2. LeGeros, R.Z. and LeGeros, J.P., *An Introduction to Bioceramic*, Hench, L.L. and Wilson, J., Eds., London: World Scientific, 1993, p. 139.
3. Brown, P.W. and Constants, B., *Hydroxyapatite and Related Substances, Library Binding*, CRC, 1994.
4. *Neorganicheskie fosfatnye materialy* (Inorganic Phosphate Materials), Kanazawa, T., Ed., Kiev: Naukova Dumka, 1998.
5. Hench, L.L., *J. Am. Ceram. Soc*., 1998, vol. 81, no. 7, p. 1705.
6. Orlovskii, V.P., Komlev, V.S., and Barinov, S.M., *Neorg. Mater*., 2002, vol. 38, no. 10, p. 1159.
7. LeGeros, R.Z., Lin, S., Rohanizadeh, R., et al., *J. Mater. Sci.: Mater. Med*., 2003, vol. 14, pp. 201–209.
8. Marcovic, M., Fowler, B.O., and Tung, M.S., *J. Res. Inst. Technol*., 2004, vol. 109, pp. 553–569.
9. LeGeros, R.Z., Taheri, M.H., Quirolgico, G.B., and LeGeros, J.P., in *Proc. 2nd Int. Congr. on Phosphorus Compounds*, Boston, April 1980, pp. 89–103.
10. LeGeros, R.Z., Shirra, W.P., Miravite, M.A., and LeGeros, J.P., in *Colloques internationaux C.N.R.S*., vol. 230: *Physicochimie et cristallographie des apatites d'interet biologique*, Paris, 1973, pp. 105–115.
11. LeGeros, R.Z., *Tooth Enamel IV*, Fearnhead, R.W. and Suga, S., Eds., Amsterdam: Elsevier, 1984, pp. 32–36.
12. Harper, R.A. and Posner, A.S., *Mater. Res. Bull*., 1970, vol. 5, pp. 129–136.
13. US Patent 6 024 985, 2000.
14. Sinyaev, V.A., Shustikova, E.S., Levchenko, L.V., et al., *Zh. Prikl. Khim*., 2003, vol. 76, no. 9, pp. 1415–1418.
15. Sinyaev, V.A., Shustikova, E.S., Griggs, D., and Dorofeev, D.V., *Fiz. Khim. Stekla*, 2005, vol. 31, no. 5, pp. 924–928.
16. Sinyaev, V.A., Griggs, D.A., and Shustikova, E.S., *Khim. Zh. Kaz*., 2004, no. 1, pp. 51–62.
17. Sinyaev, V.A., Griggs, D., Dorofeev, D.V., and Tokseitova, G.A., *Khim. Zh. Kaz*., 2004, no. 2, pp. 188–194.
18. LeGeros, R.Z., Kijkowska, R., Tung, M., and LeGeros, J.P., *Tooth Enamel V*, Fearnhead, R.W., Ed., Florence, 1989, pp. 393–401.
19. Chinese Patent 1 762 897, April 4, 2006.
20. Yukhnevich, G.V., *Usp. Khim*., 1963, vol. 32, no. 11, p. 1397.
21. Millo, A., Raichlin, Y., and Katzir, A., *Appl. Spectrosc*., 2005, vol. 59, pp. 460–466.
22. Mutter, R., Mecke, R., and Luttke, W., *Z. Phys. Chem. Neue Folge*, 1959, vol. 19, pp. 83–88.
23. Plyler, E.K. and Acquista, N., *J. Opt. Soc. Am*., 1954, vol. 44, no. 6, p. 505.
24. Giguere, P.A. and Harvey, K.B., *Can. J. Chem*., 1956, vol. 34, p. 798.
25. Stutman, J.M., Termine, J.D., and Posner, A.S., *Trans. New York Acad. Sci*., 1965, ser. 2, vol. 27, no. 6, p. 669.
26. Blakeslee, K.C. and Condrate, R.A., *J. Am. Ceram. Soc*., 1971, vol. 54, no. 11, p. 559.
27. Sinyaev, V.A., Shustikova, E.S., Griggs, D., and Dorofeev, D.V., *Khim. Zh. Kaz.*, 2004, no. 2, p. 9–18.
28. Sinyaev, V.A., Karzhaubaeva, R.A., Levchenko, L.V., and Ushanov, V.Zh., *Fiz. Khim. Stekla*, 1991, vol. 17, no. 3, pp. 419–423.
29. Sinyaev, V.A. and Levchenko, L.V., *Fiz. Khim. Stekla*, 1992, vol. 18, no. 2, pp. 153–157.

ISSN 1070-4272, Russian Journal of Applied Chemistry, 2008, Vol. 81, No. 11, pp. 1904–1908. © Pleiades Publishing, Ltd., 2008.
Original Russian Text © V.A. Lebedev, V.I. Sal'nikov, V.V. Tsvetov, A.V. Bychkov, Yu.P. Savochkin, M.V. Kormilitsyn, 2008, published in Zhurnal Prikladnoi Khimii, 2008, Vol. 81, No. 11, pp. 1786–1790.

INORGANIC SYNTHESIS AND INDUSTRIAL INORGANIC CHEMISTRY

Potentialities of Low-Temperature Chlorination of Aluminum and Its Alloys with Uranium

V. A. Lebedev, V. I. Sal'nikov, V. V. Tsvetov, A. V. Bychkov, Yu. P. Savochkin, and M. V. Kormilitsyn

Ural State Technical University, State Educational Institution for Higher Professional Education, Yekaterinburg, Russia
Research Institute of Nuclear Reactors, State Scientific Center, Federal State Unitary Enterprise, Dimitrovgrad, Ul'yanovsk oblast, Russia

Received May 15, 2008

Abstract—Potentialities of low-temperature (300–500°C) chlorination to remove the aluminum cladding of fuel elements and separate uranium and aluminum were studied.

DOI: 10.1134/S1070427208110062

Fuel elements with an aluminum cladding and based on alloys with uranium and aluminum are widely used in nuclear reactors of various types. Water-based methods for processing of such fuel elements are multistage and produce a large amount of radioactive waste [1, 2].

This study is concerned with the possibility of using low-temperature chlorination of aluminum (removal of the cladding) and U–Al alloys (separation of uranium and aluminum). As prerequisites served low sublimation points of aluminum trichloride (182.7°C) and comparatively high boiling points of uranium tetrachloride (775°C) and especially uranium trichloride (1789°C).

The reaction of aluminum with chlorine $2Al + 3Cl_2 = 2AlCl_3$ is accompanied by a noticeable heat effect ($\Delta H^0_{298} = -695.85$ kJ mol^{-1}) and is characterized by a substantial negative change in the Gibbs energy ($\Delta G^0_{298} = -637.65$ kJ mol^{-1}) [3]. The thermodynamic characteristics show that the chlorination of aluminum must occur without any hindrance. However, aluminum is always covered, because of its high chemical activity, with a dense film of an oxide whose crystal lattice constants are very close to the lattice constants of aluminum itself. This provides a rather high corrosion resistance of aluminum in a wide temperature range. The reaction of chlorine with aluminum oxide becomes noticeable only at sufficiently high temperatures. For the reaction

$$Al_2O_3 + 3Cl_2 = 2AlCl_3 + 1.5O_2, \quad (1)$$

calculations of changes in the Gibbs energy on the basis of the data from [3] for temperatures of 500, 1000, and 1500 K give ΔG_r values of 156 808, 65 883, and –19 694 J mol^{-1} Al_2O_3, respectively.

It can be seen that reaction (1) becomes thermodynamically possible only at temperatures close to 1500 K. Therefore, effective chlorination of metallic aluminum with gaseous chlorine is only possible upon disintegration of the oxide film.

The aim of the study was to determine the minimum chlorination temperature of metallic aluminum, chlorination rate, extent of chlorine utilization, and completeness of uranium and aluminum separation in chlorination.

EXPERIMENTAL

The chlorination was carried out with aluminum of chemically pure grade (≥99.9%) in the form of grains ~1 cm in diameter and 0.3–0.4 cm thick, or as shavings or a foil, which had a substantially larger specific surface area than grains. As an apparatus for chlorination served a quartz or ceramic test tube tightly closed with a cover through which chlorine was introduced and volatile chlorination products, including unchanged chlorine, were removed. The breakthrough of chlorine was determined with an indicator, potassium iodide

solution, whose reaction with chlorine

$$2KI + CI_2 = 2KCl + I_2 \quad (2)$$

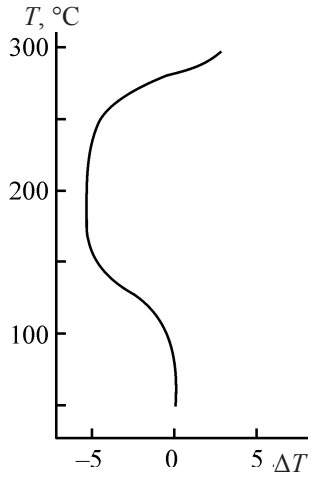
yields elemental iodine making the indicator paper brown. A weighed portion of aluminum was 5–15 g, and the charge bed height, 5–10 cm.

Chlorine was produced by electrolysis of lead chloride in a chlorine-producing unit. After being purified to remove trace amounts of moisture (bubbling through concentrated sulfuric acid) and solid dust sublimates (filtration through glass wool), chlorine was delivered via a ceramic tube into the experimental cell. The rate of chlorine supply was controlled by varying the current strength through the chlorine unit. The chlorination process was carried out with an excess of chlorine, determined from its breakthrough with the indicator, which enabled estimation of the chlorination rate.

The minimum temperature at which aluminum chlorination begins was determined using a differential thermocouple that measured the temperature difference between the exterior and interior of the chlorinator. Because the heating elements of the furnace were outside the chlorinator, the temperature of a heated chlorinator remained 5–10°C lower. The reaction of aluminum with chlorine, accompanied by a strong heat effect, results in that the negative difference between the internal and external temperatures first decreases in magnitude and then, after the chlorination is intensified and a considerable amount of heat is released, becomes positive. This was methodologically achieved by gradual heating of the furnace at a constant chlorine delivery into the chlorinator. The temperature difference ΔT was recorded with a RECORDER self-recorder. The thermogram obtained is plotted in the ΔT–T coordinates in the figure. As can be seen in the thermogram, a noticeable heat release in aluminum chlorination is observed at a temperature close to 250°C, and just this temperature is the minimum chlorination temperature.

The chlorination was mostly performed using granulated aluminum with an average grain mass of 0.4–0.6 g and surface area of about 2.5–3 cm^2. To have a larger specific surface area, aluminum foil (Table 1, run no. 10) or freshly prepared shavings (run no. 11) were used in separate experiments.

The chlorination temperature was varied from 200 to 500°C. The flow rate of chlorine delivery (in terms of the current through the chlorine unit) was within the range 2–3 A, which provided an excess of chlorine



Thermogram of aluminum chlorination.

relative to the amount consumed at the actual chlorination rate in all the experiments. The chlorination duration was 1 to 5 h. Data on the conditions and results of chlorination without preliminary treatment of the grain surface are summarized in Table 1.

As a rule, chlorination at 200–300°C fails to yield positive results: aluminum is either not chlorinated (Table 1, run nos. 1 and 2) or the chlorination rate is low and does not exceed 2 mg cm^{-2} h^{-1} (run nos. 10, 11). The best result is obtained in chlorination of freshly prepared shavings. An increase in temperature to 350–500°C raises the chlorination rate of aluminum to the maximum value of 9–12 mg cm^{-2} h^{-1}. However, no clearly pronounced temperature dependence of the chlorination rate was observed. The maximum value of 12 mg cm^{-2} h^{-1} (Table 1, run no. 4) was observed at 350°C, whereas at 450°C (run no. 8), the chlorination rate was lower, 8.2 mg cm^{-2} h^{-1}. The chlorination rate did not exhibit any pronounced dependence on the process duration, either. The best result was obtained at 350°C (Table 1, run no. 4) in a 1-h-long experiment (12 mg cm^{-2} h^{-1}), and at a duration of 4–5 h (run nos. 6, 9), the chlorination rate was two times lower.

The chlorination rate is presumably low because the oxide film is not effectively removed from the aluminum surface at the process parameters (temperature, duration) used. At the same time, an interesting type of behavior was observed: in all the runs with the highest chlorination rates, some grains (1 to 2–3 grains) lost 50 to 90% of mass, whereas parameters of all the others (15–20 grains) remained almost unchanged. Thus, the average chlorination rate is determined by chlorination of only a part of aluminum grains (~10%), with the

Table 1. Chlorination of aluminum without pretreatment of its surface

Run no.	*T*, °C	Cl feed rate, A g^{-1}	Time, h	Initial Al mass, g	Al mass loss, g		Al surface area, cm^2	Cl_2 utilization efficiency, %	Chlorination rate, mg cm^{-2} h^{-1}
					experiment	calculation			
1	200	2.5	1	13.040	–	0.838	60	–	–
2	300	2.5	2	17.924	–	1.678	70	–	–
3	350	2.5	2	13.040	1.112	1.678	60	66	9.2
4	350	3.0	1	11.472	0.600	1.007	50	60	12
5	350	3.0	1	10.872	0.333	1.007	50	32	6.7
6	350	2.0	5	11.865	1.420	3.389	50	43	5.7
7	400	2.0	1	10.977	0.213	0.678	50	31	4.2
8	450	3.0	1	10.764	0.409	1.007	50	41	8.2
9	500	2.0	4.3	11.849	1.280	2.916	50	44	5.9
10	300	3.0	1	2.306	0.062	1.007	600	6	0.1
11	300	2.0	3	7.515	1.210	2.034	200	60	2

Table 2. Chlorination of aluminum with pretreatment of its surface[a]

Run no.	*T*, °C	Cl feed rate, A g^{-1}	Time, h	Initial Al mass, g	Al mass loss, g		Al surface area, cm^2	Cl_2 utilization efficiency, %	Chlorination rate, mg cm^{-2} h^{-1}
					experiment	calculation			
1	300	2.0	1	12.524	–	0.671	60	–	–
2	350	2.0	4.08	11.215	1.254	2.74	40	45.6	7.8
3	300	3.0	0.75	12.390	0.256	0.755	55	36	6.2
4	300	3.0	1	12.116	0.519	1.007	55	53	9.4
5	300	3.0	1	11.585	0.674	1.007	55	67	12.2
6	300	2.0	1	8.339	0.055	0.671	40	8	1.3
7	370	2.0	1	8.284	0.364	0.671	40	54	7
8	400	2.0	1.3	7.920	0.570	0.873	35	66	12.5
9	300	1.3	3.8	13.422	0.352	1.678	60	21	1.5

[a] Treating solution: run no. 1, NaOH; run no. 2, $ZnSO_4$ + NaOH; run nos. 3–5, $Hg(NO_3)_2$; run nos. 6–8, $CuCl_2$; run no. 9, HCl.

chlorination rate of these grains exceeding the average value by at least an order of magnitude, i.e., it is not lower than 100 mg cm^{-2} g^{-1}. Interestingly, no chlorine breakthrough through the cell was observed in these experiments, i.e., as the intense chlorination of separate grains begins, the whole amount of passed chlorine is consumed by these grains to give aluminum chloride, which suggests that an even higher chlorination rate is possible.

The observed behavior indicates that the effective chlorination of metallic aluminum is limited by the stage of disintegration of the protective oxide film.

The following solutions were tested in decomposition of the protective film: 2 N NaOH solution, alkaline solution of zinc sulfate, and dilute (0.05 N) solutions of mercury nitrate and copper(II) chloride. The results obtained are listed in Table 2.

The stripping of the aluminum surface in alkaline solutions is based on the reaction

$$Al_2O_3 + 2NaOH = 2NaAlO_2 + H_2O, \quad (3)$$

which gives sodium aluminate well soluble in water. Prior to chlorination, aluminum grains were placed for several minutes in a 2 N NaOH solution and then

charged into the chlorinator. The chlorination was performed at 300°C. No changes in the mass of aluminum were observed. Presumably, aluminum oxide is not removed from the aluminum surface under the conditions specified.

The highest efficiency was observed in the case of triple short-time (0.5–1 min) wetting of aluminum grains with dilute solutions of mercury nitrate and copper(II) chloride.

The grains were treated with a 0.05 N $Hg(NO_3)_2$ solution three times for 0.5–1 min. Chlorination was performed after each treatment. As can be seen in Table 2, amalgamation produces a positive effect. At 300°C, the chlorination occurs at an acceptable rate, with each subsequent treatment of the aluminum surface leading to an increase in the chlorine utilization efficiency and in the chlorination intensity. The chlorination rate increased from 6.2 to 12.2 mg cm^{-2} h^{-1}, and the chlorine utilization efficiency, from 36 to 67%.

The advisability of using mercury and its salts is limited by their high toxicity. It was of interest to try other activating agents. A triple treatment of aluminum grains with a dilute copper chloride solution yielded a positive result. Upon a triple treatment, the chlorination rate at 300°C and the chlorine utilization efficiency increased from 1.3 to 12.5 mg cm^{-2} h^{-1} and from 8 to 66%, respectively.

Presence of uranium in aluminum alloys must markedly accelerate the chlorination process for two reasons. First, the fact that uranium has several stable valence states substantially accelerates delivery of the chlorinating agent to the metal surface. Uranium trichloride is stable in contact with aluminum, and uranium tetrachloride and even pentachloride, in contact with gaseous chlorine, and these uranium compounds are effective transporters of chlorine to the surface of aluminum and its alloys. Second, the protective properties of the surface oxide film are considerably impaired in the presence of uranium in aluminum.

To verify these assumptions, experiments on low-temperature chlorination of uranium–aluminum alloys were carried out. The alloys were chlorinated at 350°C in a small Alundum test tube. After chlorination for approximately 1 h, the cooled solid residue was weighed before and after the salts were removed by washing. An analysis of the resulting solutions demonstrated that they are nearly fully composed of uranium chlorides (mostly UCl_3). The conditions and results of chlorination are listed in Table 3.

Table 3. Conditions and results of the low-temperature (350°C) chlorination of uranium–aluminum alloys

Parameter	Passed quantity of electricity, A h	
	1.0	1.4
Mass of alloy, g:		
initial	1.088	0.182
after chlorination:		
before washing	1.042	0.121
after washing	0.900	0.045
Content of uranium U in alloy, %:		
initial	39.5	31.8
after washing	34.0	31.8
Mass loss, g:		
U	0.124	0.053
Al	0.064	0.072
Quantity of electricity consumed for chlorination, A h:		
U	0.042	0.018
Al	0.191	0.215
Cl_2 utilization efficiency, %	23.3	23.3
Content in fumes:		
U, mg	25.4	5.3
U, %	20	10
Al, mg	57.6	65.3
Al, %	70	92
Mass of solid residue, g:		
found from ΔP	0.142	0.076
found from difference	0.143	0.069

The contents of uranium in the starting and final, washed alloy and the differences of their masses were used to find the loss of mass by uranium and aluminum in the course of chlorination (Δm_i); the quantities of electricity required for this purposes are given by the equation $Q_i = \Delta m_i/q_i$, where q_{Al} and q_U are 0.3355 and 2.96 g A^{-1} h^{-1}, respectively; the chlorine utilization efficiency $\eta = (Q_U + Q_{Al})/Q$, where Q is the total quantity of electricity passed.

An analysis of the sublimates demonstrated that they mostly contain aluminum chloride (≥90%) and 10 to 30% uranium chlorides. The mass of the salt residue after the chlorination, found from difference of the masses of the alloy before and after its washing, almost coincides with that calculated from the difference of masses after the chlorination and sublimation of uranium (in terms of its trichloride), which additionally confirms that most of aluminum chloride is removed into sublimates.

The rate of low-temperature chlorination of uranium–aluminum alloys (200–300 mg cm^{-2} h^{-1}) substantially exceeds (by factors of tens and hundreds) the

chlorination rate of pure aluminum. Despite that the weighed portions of the alloys were small, the chlorine utilization efficiency was considerable (>20%).

The considerable loss of uranium with the fumes is presumably observed because a part of uranium is chlorinated to its tetrachloride, which has a noticeable vapor pressure. Therefore, by passing the vapor through a reducing packing (e.g., aluminum shavings), it is possible to deposit uranium trichloride reduced from the tetrachloride on this packing, with loss of uranium with the fumes precluded. It is recommended to condense aluminum chloride vapor at 240–260°C on lumps or ingots of sodium chloride to obtain molten $NaCl–AlCl_3$ mixtures containing up to 60 mol % $AlCl_3$ [4].

CONCLUSIONS

(1) The onset temperature of chlorination of pure aluminum by gaseous chlorine is close to 250°C.

(2) The existence of a dense oxide film on the metal surface results in low chlorination rates (<10 mg cm^{-2} h^{-1}) and chlorine utilization efficiencies (<20%). Upon disintegration of the oxide film at least on a part of the sample surface, the chlorination rate increases by more than an order of magnitude, with the chlorine utilization efficiency reaching 60%.

(3) The highest efficiency in disintegration of the oxide film on aluminum upon its wetting before chlorination was observed for an alkaline solution of zinc sulfate, 0.05 N solution of mercury nitrate, and 0.05 N solution of copper(II) chloride.

(4) In chlorination of solid uranium–aluminum alloys (39.5% uranium) at 350°C, the presence of uranium in an alloy provides high chlorination rates (up to 300 mg cm^{-2} h^{-1}) and high chlorine utilization efficiencies. Almost the whole amount of chlorinated aluminum and part of uranium are removed into sublimates. To preclude the loss of uranium, the gas flow should be passed through aluminum shavings reducing the volatile uranium tetrachloride to the considerably less volatile trichloride.

REFERENCES

1. Matrin, F.S. and Miles, G.L., *Chemical Processing of Nuclear Fuels*, London: Butterworth, 1958.
2. Stoller, S.M. and Richards, R.B., *Reactor Handbook*, vol. 2: *Fuel Reproceissing*, New York: Interscience, 1961, 2nd ed.
3. *Termodinamicheskie svoistva neorganicheskikh veshchestv: Spravochnik* (Thermodynamic Properties of Inorganic Substances: Reference Book), Zefirov, A.P., Ed., Moscow: Atomizdat, 1965.
4. USSR Inventor's Certificate no. 683 188.

ISSN 1070-4272, Russian Journal of Applied Chemistry, 2008, Vol. 81, No. 11, pp. 1909–1913. © Pleiades Publishing, Ltd., 2008.
Original Russian Text © S.A. Chulovskaya, S.M. Kuz'min, V.I. Parfenyuk, 2008, published in Zhurnal Prikladnoi Khimii, 2008, Vol. 81, No. 11, pp. 1791–1795.

INORGANIC SYNTHESIS AND INDUSTRIAL INORGANIC CHEMISTRY

Effect of Isopropyl Alcohol on the Granulometric and Chemical Composition of Ultradispersed Copper-Containing Powders

S. A. Chulovskaya, S. M. Kuz'min, and V. I. Parfenyuk

Institute of Solution Chemistry, Russian Academy of Sciences, Ivanovo, Russia
Ivanovo State University of Chemical Engineering, Ivanovo, Russia

Received April 12, 2008

Abstract—Possibility of obtaining nanodispersed copper-containing powders by electrochemical cathodic deposition from aqueous and water–isopropanol solutions of copper dichloride was examined.

DOI: 10.1134/S1070427208110074

In the last decade, the researchers' interest in synthesis and properties of nanosystems of varied nature has been swiftly increasing [1–3]. Nanopowders of copper and its oxides are widely used among nanostructures, and their large specific surface area and high energy content open up wide opportunities for their application in various fields of science and technology. Highly selective catalysts used in manufacture of ammonia, methanol, and caprolactam are being developed on the basis of nanopowders of copper and its compounds [4, 5]. Introduction of nanosize copper-containing powders into plastic lubricants considerably improves their tribotechnical properties and makes it possible to prolong the service life of machine and device elements owing to the slower wear of friction units [6, 7]. Nanosize copper powders intercalated into a polymeric matrix exhibit a biocide effect against a number of microbes and bacteria [8].

A still topical issue is synthesis of ultradispersed powders with required physicochemical properties. Use of electrochemical methods allows control and wide variation of the process parameters to obtain the required particle size distribution. The environmental safety of the technology for synthesis of nanosize metal-containing powders and the simplicity of the apparatus used make electrosynthesis advantageous over other methods for production of materials of this kind [9–11].

Previously, the effect of isopropyl alcohol on the cathodic reduction of ultradispersed copper-containing powders from water–isopropanol solutions of copper dichloride ($CuCl_2$) has been studied [12]. It was shown that addition of low-molecular-weight surfactants to aqueous electrolyte solutions lowers the limiting cathode current, enhances the cathodic polarization, and promotes formation of ultradispersed metal-containing deposits.

The aim of this study was to determine the chemical composition of electrodeposited ultradispersed copper-containing powders produced under various electrolysis conditions.

EXPERIMENTAL

Cathodic deposits containing ultradispersed copper and its compounds were deposited onto a preliminarily trimmed cylindrical steel cathode (working area S = 0.16 dm^2) at a constant electrode potential. Ruthenium oxide–titanium plates served as the anode. Aqueous and water–propanol solutions of copper dichloride were used as the electrolyte. The mole fraction of i-C_3H_7OH was 0.04, and the concentration of $CuCl_2$, 0.1 mol kg^{-1}. This electrolyte composition is the optimal: it corresponds to the maximum current efficiency and provides a high dispersity of the copper-containing powder [12]. The experimental installation and the synthesis procedure of ultradispersed copper-containing powders were described in detail in [13].

After the electrolysis was complete, the deposit obtained was detached from the electrode, thoroughly washed with distilled water to constant electrical con-

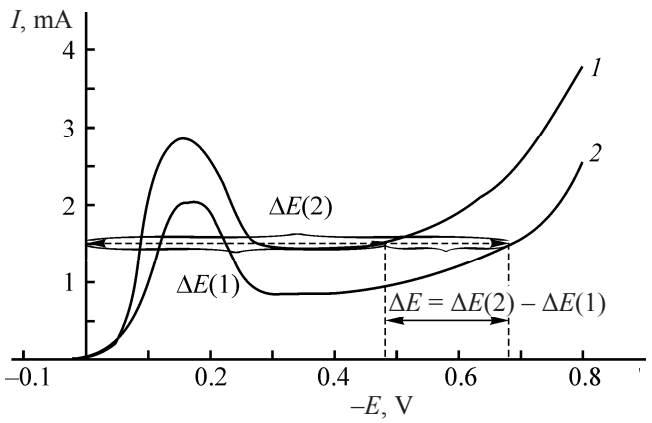


Fig. 1. Cathodic polarization characteristics of copper deposition from (*1*) aqueous and (*2*) water–isopropanol solutions of copper dichloride. *i*-C_3H_7OH mole fraction 0.04 (curve *2*), $CuCl_2$ concentration 0.1 mol kg^{-1}; the same for Figs. 4, 7. (*I*) Current strength and (*E*) potential relative to the silver chloride electrode.

ductivity of the mother liquor, and dried to powdered state.

Polarization curves of the cathodic reduction of copper were measured with a PI-50-1 potentiostat equipped with a PR-8 programming unit. The potential sweep rate was 5 mV s^{-1}. A copper disc (working area $S = 8.55 \times 10^{-4}$ dm^2) was used as the working electrode in polarization studies. A platinum electrode served as the auxiliary electrode, and a saturated silver chloride electrode, as reference.

Information about the size and shape of particles of the powders obtained was furnished by transmission electron microscopy on an EMV-100 L electron microscope in the high-resolution mode. For reliable construction of histograms characterizing the dispersion composition of the powders, electron micrographs of different parts of a sample were obtained at numerous magnifications. To determine the chemical composition, X-ray diffraction patterns of an object of study and reference sample were compared [14].

X-ray diffraction analysis was carried out on a DRON-3M diffractometer with CuK_α radiation.

The key influence on the physicochemical (including size) properties of powder particles is exerted by the electrolysis conditions and electrolyte composition. If electrolysis is performed with the maximum current density, the discharge of copper ions is diffusion-controlled, which results in the appearance and initial development of crystalline nuclei of a loose cathode deposit. Introduction of surfactants enhances the cathodic polarization and makes lower the surface energy of the powders, which leads to a higher nucleation probability. Being adsorbed on the surface of nuclei, surfactants inhibit their growth. As a result, the potential of the lateral faces of a growing crystal reaches a value sufficient for new crystalline nuclei to be formed.

Figure 1 shows results of polarization studies of the deposition of metal-containing compounds. On the plateaus in the overvoltage region ($-E \approx 0.3$–0.5 V), the current strength is independent of the voltage applied. In this case, the rate of ion delivery to the electrode surface is constant within this range and its maximum value is determined by the rate of steady-state diffusion. Introduction of an organic cosolvent into the electrolyte solution makes lower the dielectric constant and electrical conductivity of this part of the solution and, as a consequence, leads to a decrease in the limiting cathode currents and an increase in the cathodic polarization. It has been reported that, at a mole fraction of isopropyl alcohol of 0.04, the limiting cathode currents favor synthesis of highly dispersed deposits to the greatest extent [12].

The potential jump (component of the Galvani potential) caused by the preferential orientation of organic solvent dipoles adjacent to the electrode will be equal to the surface potential of the solution, –0.28 V [15] (i.e., the surface potential of neat isopropyl alcohol), for compositions with the mole fraction of isopropyl alcohol of 0.04–0.08 in the aqueous–organic mixture. It can be suggested on these grounds that the near-electrode space at the electrode/solution interface will be nearly fully composed of alcohol molecules at the alcohol mole fraction of 0.04. This hypothesis has been scientifically substantiated by Yakushevskii et al. [16], who demonstrated by using the direct immersion method that, in the water–ethanol system, the surface of the metallic electrode is fully blocked by molecules of the organic solvent. As an indirect confirmation of this fact can serve the results of [17, 18], where the surface properties of aqueous–organic electrolyte solutions were analyzed by the method of voltaic potential differences.

Addition of low-molecular-weight surfactants to aqueous electrolyte solutions makes smaller the limiting currents and raises the magnitude of the cathodic polarization $\Delta\eta$, which favors formation of highly dispersed deposits. The cathode deposit produced by electrosynthesis was a spongy formation (Fig. 2).

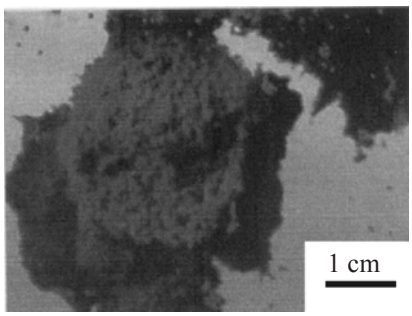


Fig. 2. Image of the spongy cathode deposit.

The results of an analysis of micrographs of the copper-containing powder produced by electrodeposition from aqueous (Fig. 3a) and water–isopropanol (Fig. 3b) solutions of 0.1 M copper dichloride are presented in the form of histograms in Fig. 4. The nanoparticle size distributions are different. In the first case, the main part (~76%) is constituted by nanosize particles (100 to 300 nm). These are mostly irregular aggregates formed by cohesion of finer particles. In the presence of *i*-C_3H_7OH, the size distribution of powder particles changes: the main part (~85%) is constituted by nanoparticles 20 to 100 nm in size. The share of coarser formations is smaller.

According to the results of an X-ray phase analysis (Fig. 5), the product obtained is multicomponent and contains unoxidized copper and copper(I, II) oxides. The structure of nanoparticles can be characterized as a druse of polycrystalline copper with an oxidized surface (Fig. 6).

The predominance of an oxide of a certain type in the powder is determined by the growth dynamics of dendrites and by the nature of the overvoltage accompanying the discharge of the metal. Powders produced from aqueous electrolytes contain a large amount of Cu and CuO. Upon addition of *i*-C_3H_7OH, the content of Cu_2O in the powder increases. This is indicated by the higher intensity of the line of cuprous oxide, with interplanar spacings d = 2.46, 2.12, 3.00, and 1.51 nm (Fig. 5).

The average particle size was calculated by the formula

$$D = k\lambda/(\beta \cos \theta),$$

where D is the crystal size; θ, Bragg angle of a reflection (deg); k, coefficient dependent on the shape of the crystal (k = 1 for spherical particles, and k = 0.9 for particles of other shapes); λ, wavelength (nm); and β, width at half-maximum of the reflection (rad).

Processing of the X-ray diffraction patterns demonstrated that the average size of copper crystallites in the copper-containing powder (50 ± 10 nm) is independent of the electrolyte composition. The average size of copper oxide (CuO and Cu_2O) crystallites is 50 ± 10 nm.

When comparing results of an X-ray diffraction analysis and electron microscopic data, it should be taken into account that X-rays are scattered on volume elements. In this case, in determining the average crystallographic size of a crystallite, a major contribution will be made by particles whose share in the total volume of a sample is the largest. The volume accounted for by particles with an average diameter d is proportional to the product of the number N of particles of this size by cubed linear size d^3.

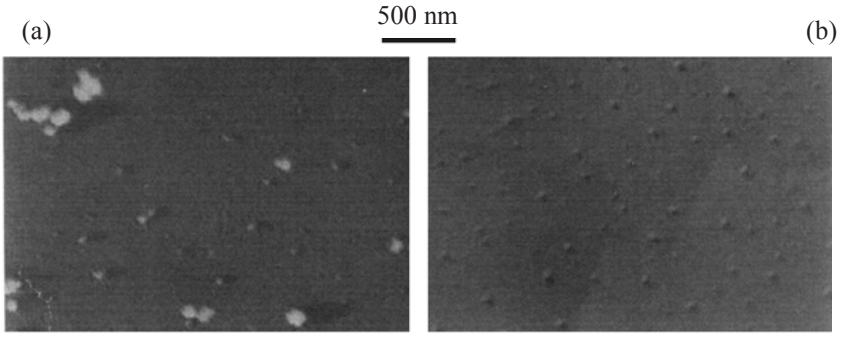


Fig. 3. Micrographs of nanosize copper-containing powders produced by electrodeposition from (a) aqueous and (b) water–isopropanol solutions of copper dichloride. *i*-C_3H_7OH mole fraction 0.04 (micrograph b), $CuCl_2$ concentration 0.1 mol kg^{-1}; the same for Fig. 5.

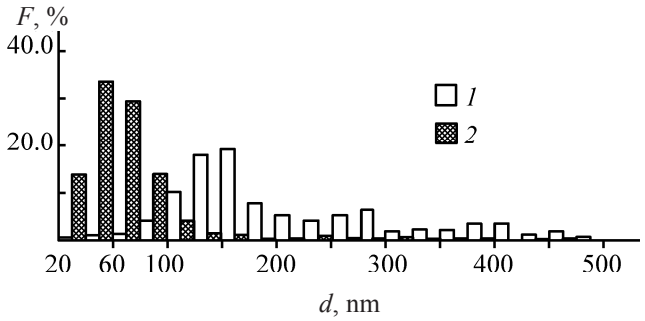


Fig. 4. Size distribution histograms of nanosize copper-containing particles in powders produced by electrodeposition from (*1*) aqueous and (*2*) water–isopropanol solutions of copper dichloride. (*F*) Fraction of particles and (*d*) particle size.

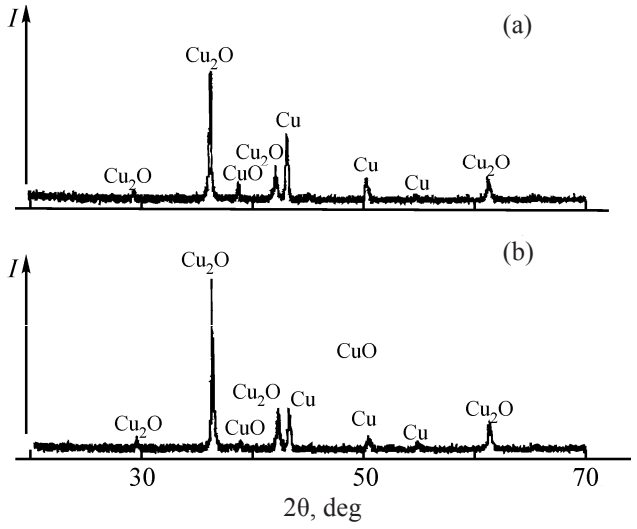


Fig. 5. X-ray diffraction patterns of nanosize copper-containing particles in powders produced by electrodeposition from (a) aqueous and (b) water–isopropanol solutions of copper dichloride. (*I*) Intensity and (2θ) Bragg angle.

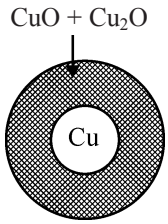


Fig. 6. Suggested structure of a nanoparticles.

In the case of spherical particles, the total volume V_d of particles with an average diameter d can be estimated using the relation

$$V_d = \pi N d^3/6.$$

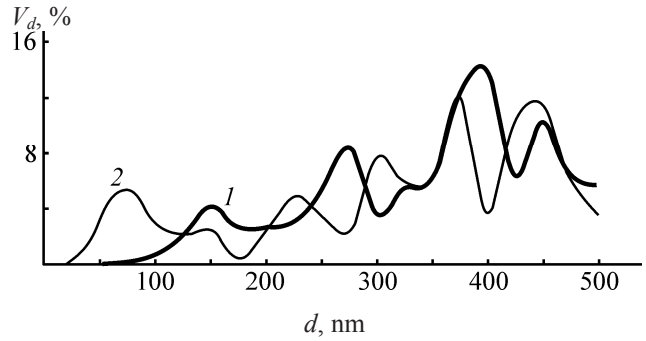


Fig. 7. Volume fraction V_d of particles corresponding to various diameters d for powders produced from (*1*) aqueous and (*2*) water–isopropanol solutions of copper dichloride.

To compare powders obtained under different conditions, the dependence of V_d on the particle size d was normalized. The total volume of particles of a powder under study (taken to be 100%) was used as the normalization parameter. The dependence of the total volume of particles in a powder on their size is shown in Fig. 7.

A characteristic feature of the dependences for powders produced from aqueous and aqueous–organic media is the appearance of periodically repeated maxima (Fig. 7). In the case of the water–isopropanol medium, the first maximum lies at 75–80 nm, which suggests that the powder contains a noticeable amount of particles composed of single crystallites. The periodicity of the maxima (70, 150, 225, 300, 375, and 450 nm) yields a sequence in which grows the number of crystallites in the cross-section of a particle. In the case of electrocrystallization from an aqueous medium, the first maximum is shifted to sizes of about 150 nm and is repeated with a period close to 120 nm, which corresponds to the sum of the average sizes of crystallites of copper and its oxide. Possibly, this occurs because the electrocrystallization of copper from aqueous solutions is accompanied by more intense oxidation processes and formation of the oxide phase, together with reduced copper. This is also indicated by the higher intensity of the reflection corresponding to copper oxide CuO in this sample.

CONCLUSIONS

(1) Introduction of isopropanol additives into the aqueous electrolyte changes both the granulometric and chemical composition of the powders obtained. Addition of isopropyl alcohol shifts the relative amounts of components in the powders obtained to-

ward a higher content of copper(I) oxide.

(2) Use of organic solvents as additives to water in electrolysis from aqueous–organic electrolyte solutions enables control over the size and chemical composition of particles constituting the powders obtained.

REFERENCES

1. Andrievskii, R.A. and Ragulya, A.V., *Nanostrukturnye materialy* (Nanostructured Materials), Moscow: Akademiya, 2005.
2. Poole, Ch.P. and Owens, F.J., *Introduction to Nanotechnology*, Wiley–Interscience, 2003.
3. Rusanov, A.I., *Zh. Obshch. Khim*., 2002, vol. 72, no. 4, pp. 532–549.
4. Semenov, V.P., *Proizvodstvo ammiaka* (Manufacture of Ammonia), Moscow: Khimiya, 1985.
5. Kolesnikov, I.M., *Kataliz i proizvodstvo katalizatorov* (Catalysis and Manufacture of Catalysts), Moscow: Tekhnika, 2004.
6. Ryabov, D.V., Matveevskii, R.M., Fuks, I.G., and Buyanovskii, I.A., *Trenie Iznos*, 1989, vol. 10, no. 6, pp. 698–705.
7. Volobuev, N.K., Danilov, V.D., and Kuznetsov, A.A., *Trenie Iznos*, 1994, vol. 15, no. 5, pp. 871–876.
8. Alekseeva, O.V., Chulovskaya, S.A., Bagrovskaya, N.A., et al., *Zhidk. Krist. Ikh Prakt. Ispol'z*., 2007, vol. 4, no. 22, pp. 84–90.
9. Chulovskaya, S.A., Balmasov, A.V., Lilin, S.A., and Parfenyuk, V.I., *Zashch. Met*., 2006, vol. 42, no. 4, pp. 430–433.
10. Sinha, A., Das, S.K., Kumar, T.V.V., et al., *J. Mater. Synth. Proc*., 1999, vol. 7, no. 6, pp. 373–377.
11. Murashova, I.B., Taushkanov, P.V., and Burkhanova, N.G., *Elektrokhimiya*, 1999, vol. 35, no. 7, pp. 835–840.
12. Chulovskaya, S.A. and Parfenyuk, V.I., *Zh. Prikl. Khim*., 2007, vol. 80, no. 6, pp. 952–955.
13. Chulovskaya, S.A., Lilin, S.A., Parfenyuk, V.I., and Girichev, G.V., *Zh. Fiz. Khim*., 2006, vol. 80, no. 2, pp. 332–335.
14. Mirkin, L.I., *Spravochnik po rentgenostrukturnomu analizu polikristallov* (Handbook of X-ray Diffraction Analysis of Polycrystals), Moscow: Fizmatizdat, 1961.
15. Parfenyuk, V.I., *Colloid J*., 2002, vol. 64, no. 5, pp. 588–596.
16. Jakuszewski, B., Partyka, S., and Przasnyski, M., *Roczn. Chem. Ann. Soc. Chim. Polon*., 1972, vol. 46, pp. 921–927.
17. Chankina, T.I. and Parfenyuk, V.I., *Zh. Fiz. Khim*., 2004, vol. 78, no. 9, pp. 1592–1595.
18. Chankina, T.I., Chulovskaya, S.A., and Parfenyuk, V.I., *Zh. Fiz. Khim*., 2004, vol. 78, no. 6, pp. 992–996.

ISSN 1070-4272, Russian Journal of Applied Chemistry, 2008, Vol. 81, No. 11, pp. 1914–1918. © Pleiades Publishing, Ltd., 2008.
Original Russian Text © T.G. Dmitrienko, I.S. Rodzivilova, 2008, published in Zhurnal Prikladnoi Khimii, 2008, Vol. 81, No. 11, pp. 1796–1801.

PHYSICOCHEMICAL STUDIES OF SYSTEMS AND PROCESSES

Adsorption Equilibria in 1,5-Diphenyl-3-selenapentane-1,5-dione–Solvent–Sorbent Systems

T. G. Dmitrienko and I. S. Rodzivilova

Technological Institute, Saratov State Technical University, Engels, Saratov oblast, Russia
Saratov Military Institute of Chemical, Biological, and Radiation Protection, Saratov, Russia

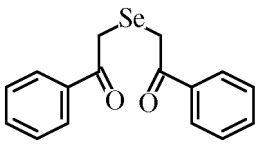
Received May 2, 2007

Abstract—Adsorption of DAFS-25 (1,5-diphenyl-3-selenapentane-1,5-dione) from dilute solutions in various solvents on various adsorbents was studied by UV spectrophotometry. The experimental data were interpreted thermodynamically by the method of excess Gibbs quantities.

DOI: 10.1134/S1070427208110086

Active development of the chemistry of 1,5-diketones is stimulated by their capability to form various heterocyclic compounds with valuable properties. The presence of a selenium heteroatom in the diketones not only strongly affects their chemical properties, but also imparts to them specific biological activity [1]. Therefore, the chemistry of these compounds attracts researchers' attention. DAFS-25 (1,5-diphenyl-3-selenapentane-1,5-dione) containing 25% Se contains a center with reducing properties. Therefore, this diketone can be considered as potential antioxidant reacting both with hydroperoxides and with organic radicals.

Today DAFS-25 is used for prophylaxis of white muscle disease, massive hepatic necrosis, and exudative diathesis [1]. It is synthesized by the reaction of acetophenone with $SeOCl_2$ [2]. After performing biological tests [2], the compound was put into commercial production. Its trade name is diacetophenonyl selenide. The compound contains two aromatic rings, which determines a specific adsorption mechanism:



1,5-Diphenyl-3-selenapentane-1,5-dione

A topical problem is the development and application to medical practice of combined enterosorbents based on two or several materials of different groups, which considerably expands the spectrum of the sorption activity and, as a result, the efficiency of the therapeutic effect of the adsorbable agent. Published data on adsorption of organoselenium compounds are virtually lacking. Dallakyan and Kiselev [3] studied the adsorption of S- and Se-containing aromatic compounds on graphitized thermal carbon black and showed that Se-containing compounds were adsorbed more strongly than their S-containing analogs, according to the atom–atom potentials. Therefore, in the development of high-quality enterosorbents, the adsorption of Se-containing 1,5-diketones on the solid surface is not only of theoretical interest but also of practical importance for the development of effective drugs.

This study concerns the adsorption of DAFS-25 from binary solutions on sorbents of various chemical nature and is aimed at further development of combined enterosorbents.

EXPERIMENTAL

For taking the adsorption isotherms, we used an HP A 8452 spectrophotometer. The optical density was recorded in the region of the absorption maximum. Using the calibration dependences of the optical density on the initial solution concentration, we determined the composition of the equilibrium solution and calculated the excess adsorption [4, 5]. The temperature was controlled with a TZh-TS-01/16-150 thermostat. As adsorbents we used calcium carbonate, silica gels ASK and MSK, NaX zeolite, and activated carbon

Physicochemical characteristics of adsorbents

Adsorbent	Micropore volume w_0, $cm^3\ g^{-1}$	Mesopore volume w_s, $cm^3\ g^{-1}$	Characteristic energy E_0, kJ mol^{-1}	Mesopore surface area S, $m^2\ g^{-1}$
SKT-2B activated carbon	0.39	0.42	25.8	43
NaX zeolite	0.320	0.342	14.2	–
Chalk, chemically precipitated $CaCO_3$	–	–	–	2.2
ASK silica gel	–	–	10.9	300

(AC), and as sorbents, diisopropyl ether (DIPE) and toluene. The choice of the adsorbents was governed by the need for examining the adsorption of DAFS-25 on both microporous and macroporous adsorbents. Interest in studying the adsorption of DAFS-25 on activated carbons is caused by the need for elucidating the mechanisms and specific features of the transfer of this compound through membranes, including biological ones. A study of the sorption kinetics will allow in the future understanding of the behavior of this agent in real biological objects and evaluation of the possibility of using activated carbons as enterosorbents.

The other demands were that the adsorbate should not chemically react with adsorbents chosen and should be infinitely soluble in the solvents chosen. Some physicochemical characteristics of the adsorbents are given in the table.

Prior to experiments, coarsely porous ASK silica gel was subjected to prolonged refluxing in HCl solution to remove iron ions, after which it was washed with distilled water to remove chloride ions and dried at 175°C in an oven to constant weight. Just before experiments, silica gel was dried for 2 h at 200°C. The concentration of OH^- groups in silica gels was 7.0–0.5 μmol m^{-2}, or 4.2–5.7 OH^- groups per 100 $Å^2$. At equal degree of hydration, the properties of the unit surface for nonporous and coarsely porous (pore size about 50 $Å^2$) silica gels coincide.

Prior to adsorption tests, activated carbon was calcined for 2 h at 120°C. Zeolite NaX was dehydrated at 500–550°C for 5 h.

Figure 1 shows the adsorption isotherms of DAFS-25 from DIPE on activated carbons, silica gels ASK and MSK, calcium carbonate, and NaX zeolite. All the adsorption isotherms in the region of dilute solutions have a similar shape. The adsorption starts to steeply increase from the very beginning. The largest excess adsorption of DAFS-25 is observed on activated carbon. On silica gels MSK and ASK and on NaX zeolite it is lower, and on calcium carbonate it is the lowest. Such features of adsorption can be attributed to the structure of the diketone molecule. In this molecule, some peripheral fragments bear high electron density (π bonds, lone electron pairs).

Fairly high values of adsorption of DAFS-25 on silica gels are caused by the presence on the surface of silanol grops ≡Si–OH capable to form hydrogen bonds with electron-donor molecules. Owing to the polarity of the OH bond, hydroxylated silica gels have local positive charges on the surface. As already noted, the properties of the unit surface for nonporous and coarsely porous (pore size about 50 $Å^2$) silica gels coincide at equal degree of hydration. Therefore, the character of adsorption of DAFS-25 on ASK and MSK is essentially similar. In this case, we can assume the adsorption due to interaction with surface hydroxy groups of silica gel with electron-donor groups which are centers of specific molecular adsorption.

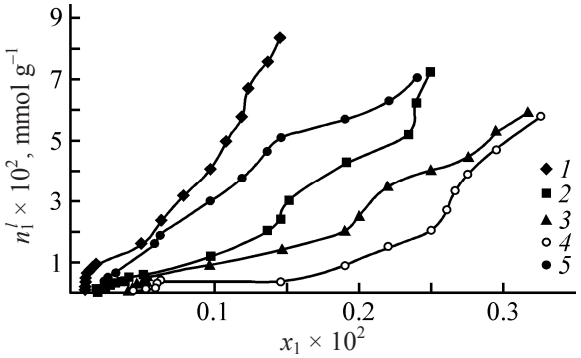


Fig. 1. Isotherms of DAFS-25 adsorption from DIPE on AC, NaX zeolite, ASK and MSK silica gels, and calcium carbonate at 298 K. (n_1^l) Amount of adsorbed DAFS-25 and (x_1) mole fraction of DAFS-25 in solution; the same for Figs. 2 and 3. (*1*) AC, (*2*) ASK, (*3*) NaX, (*4*) $CaCO_3$, and (*5*) MSK.

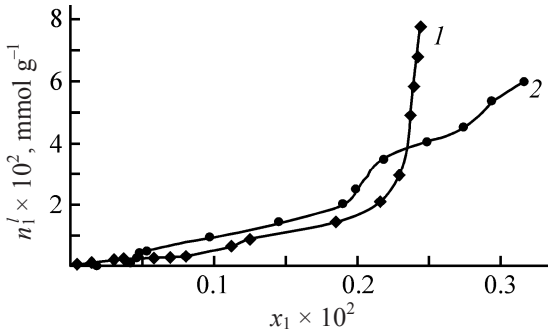


Fig. 2. Isotherms of DAFS-25 adsorption from (*1*) DIPE and (*2*) toluene on NaX zeolite at 298 K.

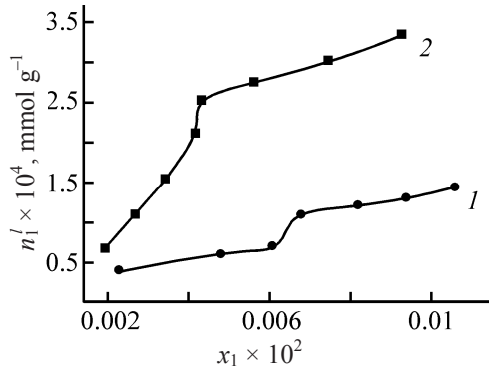


Fig. 3. Isotherms of DAFS-25 adsorption from dilute solutions in DIPE on calcium carbonate at (*1*) 293 and (*2*) 313 K.

Among possible adsorption mechanisms, chemisorption is the most probable. In this case, the polar groups of the adsorbate molecules should be oriented toward the surface, and their hydrocarbon chains, toward the solution. Presumably, a major role in the adsorption mechanism on silica gels is played by the effective volume, with carbonyl groups exerting a significant influence.

As seen from Fig. 1, the adsorption on the zeolite occurs to a considerably lesser extent than on activated carbon and silica gel. Aluminum in the zeolite is in the form of negatively charged AlO_4 tetrahedra. The compensating positive charge is localized in exchangeable cations of smaller radius. Therefore, cationized zeolites are specific molecular adsorbents of type II after Kiselev, i.e., adsorbents bearing on the surface localized positive charges (small cations) arranged near large complex anions. The presence of cations in zeolite cavities is responsible for manifestation of all the forms of adsorption interaction, from electrostatic to dispersion. As the specific features of adsorption on zeolites as heteropolar adsorbents are determined by the electrostatic interaction, it is manifested the more strongly, the more asymmetrical are adsorbate molecules. Apparently, the diketone is adsorbed on cations with the participation of the aluminosilicate framework. The diketone molecules containing peripheral electron-donor fragments are capable of strong specific interaction with zeolite cations. The major role in the process is played by localization of the electron density on specific bonds. In joint adsorption of molecules of different electronic structures, the mutual displacement is largely determined by the geometric structure.

Figure 1 shows that the adsorption isotherm on activated carbon is steeper, which is apparently due to increased adsorption potential of the micropores, compared to that of wider pores of the other adsorbents. The thin pores are filled with adsorbate molecules already at their relatively low concentration in solutions.

Analysis of the experimental isotherms of DAFS-25 adsorption from DIPE and toluene on NaX zeolite shows that, at low DAFS-25 concentrations, the adsorption is insignificant, apparently because of the competing effect of the solvent (Fig. 2).

The adsorption from toluene increases uniformly, whereas from DIPE up to the mole fraction $x_1 = 0.22$ there is a sharp bend with a characteristic increase in the excess adsorption from 2×10^{-2} to 8×10^{-2} mmol g^{-1}. The solvent effect in adsorption of DAFS-25 on ASK silica gel is manifested in that the adsorption monotonically increases with the adsorbate concentration and occurs from DIPE more actively than from toluene. These facts suggest the occurrence of the competing adsorption. On calcium carbonate at low concentrations, the adsorption isotherms have similar shape up to $x_1 = 0.2$, after which they sharply ascend. From toluene, DAFS-25 is adsorbed worse than from DIPE. Thus, on all the types of adsorbents DAFS-25 is adsorbed from DIPE better than from toluene.

The highest values of DAFS-25 adsorption from binary solutions are observed on activated carbon, which is consistent with the theory of adsorption on adsorbents of various chemical structures. The adsorption of DAFS-25 from binary solutions increases with temperature (Fig. 3). Apparently, in the adsorption system DAFS-25–calcium carbonate the interaction of solvent molecules with the adsorbent and, correspondingly, their competing effect become weaker with increasing temperature. As all the solutions are strongly dilute and the solute solubility is limited to low mole fraction, the isotherm of variation of the solution com-

position transforms into an individual isotherm of the solute adsorption, despite the possibility of the adsorption of a large amount of the solvent.

The adsorption isotherms of the DAFS-25–solvent–adsorbent systems, obtained in [4, 5], do not give a true pattern of the adsorption on the sorbent surface. Therefore, it is interesting to perform thermodynamic calculations of the adsorption equilibrium [6]. For the thermodynamic consideration of adsorption systems we used the method of excess Gibbs quantities allowing calculation of the main thermodynamic characteristics of sorption systems as a whole from the experimentally determined excess adsorption values. The change in the chemical potential of the sorbent was determined from the equation

$$-\Delta\Phi = -(\Phi x_1 - \Phi x_2) = RT \int_0^{x_1 y_1} \frac{n_1^l}{x_2 x_1 \gamma_1} \mathrm{d}(x_1 y_1),$$

where γ_1 is the activity coefficient of component 1 in the bulk of solution.

To determine the quantities $\Phi x_1 - \Phi x_2$, it is necessary to have information on the concentration dependence of the activity coefficient of bulk solution and excess adsorption n_1^l. The quantity $-\Delta\Phi$ was determined by graphical integration, namely, by calculation of the area under the curve

$$\frac{n_1^l}{x_2 x_1} = f(x).$$

The change in the free energy of the sorption system was calculated by the equation

$$\Delta G = Gx_1 - Gx_2 = -(\Phi x_1 - \Phi x_2) - \sum n_{i0}(\mu_{i0} - \mu_i),$$

where $\Phi x_1 - \Phi x_2$ is the change in the chemical potential of the sorbent, and $\mu_{io} - \mu_i$, change in the chemical potential of the bulk solution.

Figure 4 shows the concentration dependences of $\Delta\Phi$ and ΔG of the adsorption systems DAFS-25–toluene–NaX zeolite, DAFS-25–toluene–ASK silica gel, DAFS-25–toluene–activated carbon, DAFS-25–toluene–calcium carbonate, and DAFS-25–toluene–MSK silica gel. The largest values of $\Delta\Phi$ and ΔG are observed in adsorption from toluene on activated carbon, which is consistent with the excess adsorption values, and the smallest values, on calcium carbonate.

The concentration dependences of $\Delta\Phi$ and ΔG in adsorption of DAFS-25 from DIPE on NaX zeolite,

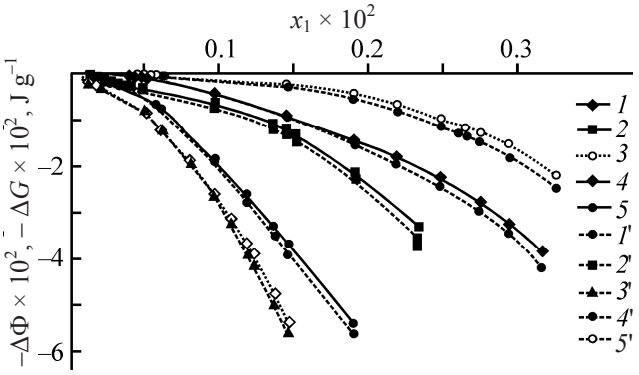


Fig. 4. Concentration dependences of the changes in the (*1*–*5*) chemical potential $\Delta\Phi$ of sorbents and (*1*'–*5*') Gibbs free energy ΔG of DAFS-25 adsorption from toluene at 298 K. (x_1) Mole fraction of DAFS-25 in solution; the same for Figs. 5 and 6. (*1*, *1*') NaX, (*2*, *2*') ASK, (*3*, *3*') AC, (*4*, *4*') $CaCO_3$, and (*5*, *5*') MSK.

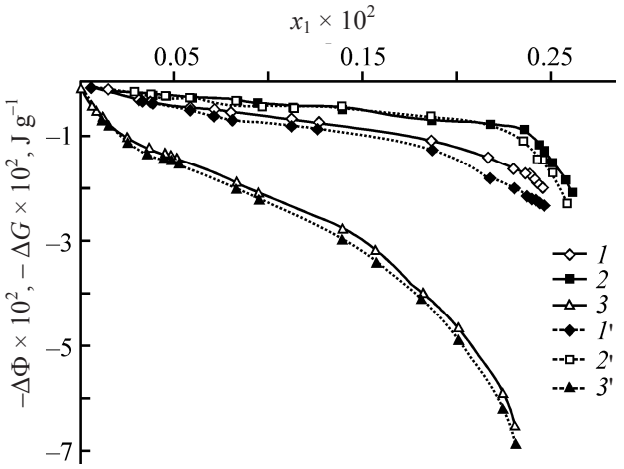


Fig. 5. Concentration dependences of the changes in the (*1*–*3*) chemical potential $\Delta\Phi$ of sorbents and (*1*'–*3*') Gibbs free energy ΔG of DAFS-25 adsorption from DIPE at 298 K. (*1*, *1*') NaX, (*2*, *2*') $CaCO_3$, and (*3*, *3*') ASK.

calcium carbonate, and ASK silica gel, shown in Fig. 5, indicate that these quantities are comparable on NaX zeolite and calcium carbonate and are considerably larger on ASK silica gel.

The thermodynamic functions allow us to trace the solvent effect more reliably. The quantities $\Delta\Phi$ and ΔG in adsorption of DAFS-25 from toluene and DIPE on ASK silica gel are plotted in Fig. 6a. They indicate that the adsorption from DIPE is higher than from toluene. On NaX zeolite, the solvent effect in adsorption of DAFS-25 is insignificant.

The concentration dependences of $\Delta\Phi$ and ΔG in adsorption of DAFS-25 on calcium carbonate (Fig. 6b) show that the adsorption is considerably more efficient

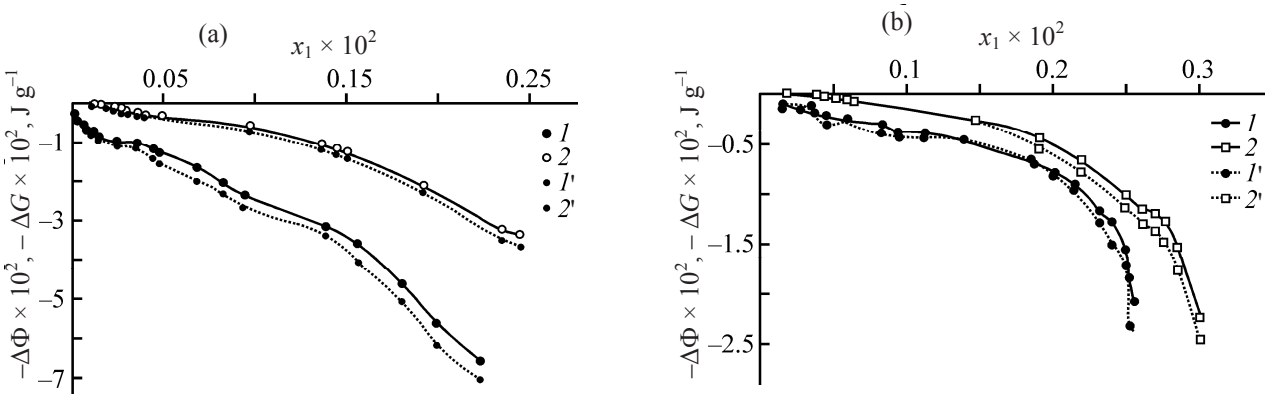


Fig. 6. Concentration dependences of the changes in the (*1*–*3*) chemical potential $\Delta\Phi$ of sorbents and (*1*'–*3*') Gibbs free energy ΔG of DAFS-25 adsorption from (*1*, *1*') DIPE and (*2*, *2*') toluene at 298 K. Adsorbent: (a) ASK silica gel and (b) $CaCO_3$.

from DIPE. The results we obtained suggest competition of the solvent with the solute for the adsorption centers of the surface. The surfaces of the adsorbents under consideration are chemically nonuniform, as they contain different centers with high and low adsorption energies and with polar and nonpolar groups.

Thus, a study of DAFS-25–solvent–adsorbent systems shows that the adsorption of DAFS-25 is the most efficient from DIPE on activated carbon. The experimental data were interpreted by the method of excess Gibbs quantities, and the concentration dependences of the chemical potential $\Delta\Phi$ and Gibbs free energy ΔG were analyzed. The character of adsorption from solutions depends not only on the properties of the bulk solution but also on the chemical nature of the surface and pore size of the sorbent.

It can be surely concluded that biologically active substances based on DAFS-25 will readily penetrate through cell membranes and, with coal used as enterosorbent, this substance and its metabolites and decay products will be sorbed or removed from the living body. The data we obtained can be used for the development of new enterosorbents with antioxidant properties, suitable for preventing poisoning with various toxicants.

CONCLUSIONS

(1) The adsorption isotherms were obtained for the systems DAFS-25–toluene–NaX zeolite, DAFS-25–toluene–ASK silica gel, DAFS-25–toluene–activated carbon, DAFS-25–toluene–calcium carbonate, DAFS-25–toluene–MSK silica gel, DAFS-25–diisopropyl ether–NaX zeolite, DAFS-25–diisopropyl ether–calcium carbonate, and DAFS-25–diisopropyl ether–ASK silica gel.

REFERENCES

1. Drevko, B.I., Chalcogen-Containing Heterocyclic Compounds Derived from 1,5-Diketones: Synthesis, Properties, and Certain Reaction Features, *Doctoral Dissertation*, Saratov, 1997.
2. Blinokhvatov, A.F., 9-R-*sym*-Nonahydro-10-oxa (chalcogena)anthracenes and 9-R-*sym*-Octahydro-10-oxonia(chalcogenonia)anthracene Salts, *Doctoral Dissertation*, Saratov, 1993.
3. Dallakyan, P.B. and Kiselev, A.V., *Zh. Fiz. Khim.*, 1985, vol. 59, no. 5, pp. 1278–1279.
4. Dmitrienko, T.G., Rodzivilova, I.S., and Drevko, B.I., in *Trudy Mezhdunarodnogo simpoziuma vostochno-aziatskikh stran po polimernym kompozitsionnym materialam i peredovym tekhnologiyam: Sbornik nauchnykh statei* (Proc. Int. Symp. of East-Asian Countries on Polymeric Composite Materials and Advanced Technologies: Coll. of Scientific Papers), Saratov: Tekhnol. Univ., Saratov. Gos. Tekh. Univ., September 20–22, 2005, pp. 185–188.
5. Dmitrienko, T.G., *Issledovanie adsorbtsii 1,5-difenil-3-selenapentadiona-1,5 iz razlichnykh rastvoritelei* (Adsorption of 1,5-Diphenyl-3-selenapentane-1,5-dione from Various Solvents), Available from VINITI, December 4, 2006, no. 1494-V2006.
6. Larionov, O.G., Chmutov, K.V., and Shayusupova, Yu.Sh., *Zh. Fiz. Khim.*, 1981, vol. 55, pp. 771–772.

ISSN 1070-4272, Russian Journal of Applied Chemistry, 2008, Vol. 81, No. 11, pp. 1919–1923. © Pleiades Publishing, Ltd., 2008.
Original Russian Text © A.V. Mamchenko, I.M. Kosygina, 2008, published in Zhurnal Prikladnoi Khimii, 2008, Vol. 81, No. 11, pp. 1802–1806.

PHYSICOCHEMICAL STUDIES OF SYSTEMS AND PROCESSES

Fluidization of Cation Exchangers with Regenerating Sulfuric Acid Solution

A. V. Mamchenko and I. M. Kosygina

Dumanskii Institute of Colloid and Water Chemistry, National Academy of Sciences of Ukraine, Kiev, Ukraine

Received April 18, 2007

Abstract—Dependences of the bed expansion of cation exchangers (weakly acidic Lewatit CNP 80 and strongly acidic KU-2×8) on the flow velocity, temperature, and concentration of the regenerating sulfuric acid solution were determined. An equation describing the dependence of the bed expansion of cation exchangers on the flow velocity, temperature, and concentration of sulfuric acid, common to the two ion exchangers, was derived, which allows a priori determination of the extent of bed expansion in regeneration of cation exchangers in the fluidization mode.

DOI: 10.1134/S1070427208110098

Regeneration of cation exchangers in a fluidized bed diminishes the threat of deposition of contaminants impairing the process efficiency onto their grains [1–3]. This primarily refers to the case of regeneration of cation exchangers with sulfuric acid, in which a solid phase of calcium sulfate can be formed on grains and in the gel phase of ion exchangers [1–7].

In this context, the aim of the study was to find a generalized dependence of the bed expansion of a cation exchanger on the linear flow velocity, temperature, and concentration of a sulfuric acid solution, which is necessary for determining the process conditions but is not available from the literature.

As objects of study we chose a weakly acidic cation exchanger Lewatit CNP 80 [5, 8] and a strongly acidic cation exchanger KU-2×8 [9]. Prior to experiments, the cation exchangers were washed first with a 2 wt % sulfuric acid solution to total absence of sodium ions in the filtrate and then with distilled water.

The experimental procedure was as follows. A temperature-controlled column was charged with 200 cm^3 of a cation exchanger. The bed height was 80–82 cm, which corresponds to the minimum admissible height of the cation exchanger charge of filters according to recommendations of manufacturers of ion-exchange materials [3–5, 8]. The temperature of the regenerating solution was varied within the range 20–60°C, which broadly overlaps the temperature range in which the regeneration process is carried out. In regeneration of the strongly acidic cation exchanger, the concentration of the sulfuric acid solution was varied within the range 2–8 wt % with a step of 2%. This concentration range corresponds to recommendations for regeneration of strongly acidic cation exchangers [4, 7, 8]. Because carboxy cation exchangers show high selectivity with respect to hardness ions in the working cycle [10–12] and to hydroxonium ions in the course of regeneration, the probability of gypsum formation in the ion exchanger bed substantially grows. Therefore, dilute sulfuric acid solutions with a concentration not exceeding 0.8% are used in the water treatment technology for regeneration of the weakly acidic cation exchanger [1–6, 8, 10, 13]. In view of this circumstance, experiments with the Lewatit CNP 80 cation exchanger were carried out with the sulfuric acid concentration in solution varied within the range 0.2–0.8 wt % with a step of 0.2%. A prepared regenerating solution with a prescribed concentration was delivered from bottom to top with an SP 311/6 peristaltic pump. The feed rate was varied so that the bed expansion was within the range 10–100% relative to the initial height, with a step of 10%. The linear flow velocity of the solution supplied was determined at a fixed bed height.

Cation exchangers in the H form show lower swelling than those in the salt form [8, 14, 15]. Therefore, the experiments were performed with the H form of the cation exchangers in order to determine the maxi-

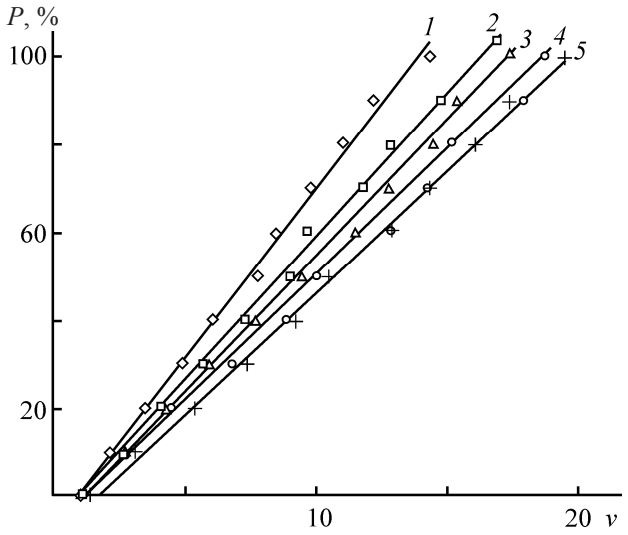


Fig. 1. Extent of bed expansion, P, of the Lewatit CNP 80 ion exchanger vs. the linear flow velocity v of the regenerating solution at different temperatures and constant concentration. Temperature, °C: (*1*) 20, (*2*) 30, (*3*) 40, (*4*) 50, and (*5*) 60.

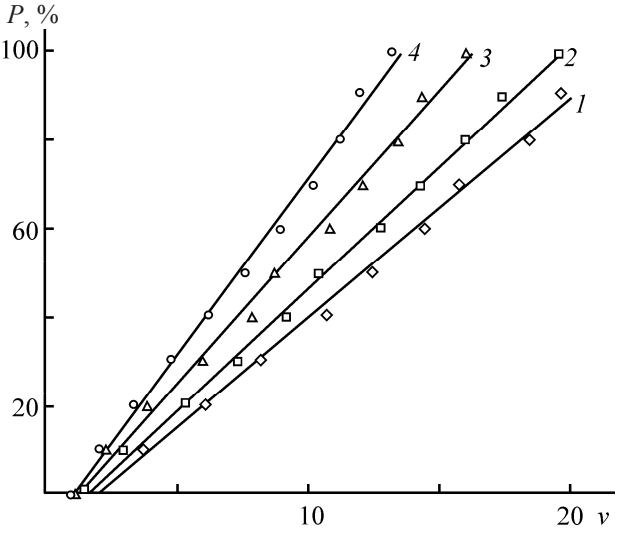


Fig. 2. Extent of bed expansion, P, of the Lewatit CNP 80 ion exchanger vs. the linear flow velocity v of the regenerating solution at different concentrations and constant temperature. Concentration, wt %: (*1*) 0.21, (*2*) 0.39, (*3*) 0.59, and (*4*) 0.81.

mum possible bed expansion in the course of their regeneration. The viscosities of sulfuric acid solutions were determined with a VPZh 2 viscometer.

Figure 1 shows as an example how the extent P of bed expansion of the Lewatit CNP 80 cation exchanger depends on the linear flow velocity v with which the regenerating solution is passed at a constant concentration c and varied temperature T. It can be seen that the extent of bed expansion of the Lewatit CNP 80 cation exchanger strongly depends on the solution temperature.

Figure 2 compares dependences of P on v for the same ion exchanger at a constant temperature T and different concentrations c. It can be seen that the extent of bed expansion of the ion exchanger also strongly depends on c. Similar results were obtained for the KU-2×8 cation exchanger.

The dependences $P = f(v)$ are affected by T and c because the densities of the solution (ρ) and ion exchanger grains (ρ_i), radius r of ion exchanger particles, and solution viscosity η vary with these parameters [16–20]. In a fixed bed, there is a free space between particles, which is characterized by the bed porosity ε_0. For identical spherical particles [18],

$$\varepsilon_0 = (V_b - V_i)/V_b = 1 - V_i/V_b = 0.44, \quad (1)$$

where V_i is the ion exchanger volume, and V_b, bed volume.

According to manufacturers' data, the ion exchangers are characterized by a comparatively uniform granulometric composition [8, 9, 21]. For example, the average diameter d_g of grains of the Lewatit CNP 80 ion exchanger is 0.48 ± 0.05 mm, and that of KU-2×8, 0.45 ± 0.1 mm [8, 9, 21]. Therefore, ε_0 was taken to be equal to the theoretical value.

In the theory [16–20], a fluidized bed is characterized by its porosity ε calculated by Eq. (1), where V_b is taken to be equal to the volume of the fluidized bed.

According to the definition of the quantities P (%) and ε, the following equation is valid:

$$P = 100(\varepsilon - \varepsilon_0)/(1 - \varepsilon). \quad (2)$$

It was shown in [16–19] that the dependence of ε on v is expressed by the Richardson–Zaki equation

$$\varepsilon^z = v/v_f, \quad (3)$$

where v_f is the linear velocity of a flow around particles (hovering velocity), and z is the exponent which is a function of the d_g/D ratio (D is column diameter) and Reynolds number $Re_t = vd_g\rho/\eta$.

The value of z for spherical particles is found using the following empirical equations [16, 19]:

$$z = 4.65 + 20d/D \text{ at } Re_t < 0.2, \quad (4)$$

$$z = (4.4 + 18d/D)Re_t^{-0.03} \text{ at } 0.2 < Re_t < 1, \quad (5)$$

$$z = (4.4 + 18d/D)\mathrm{Re}_t^{-0.1} \text{ at } 1 < \mathrm{Re}_t < 500, \quad (6)$$

$$z = 4.4\mathrm{Re}_t^{-0.1} \text{ at } 200 < \mathrm{Re}_t < 500, \quad (7)$$

$$z = 2.4 \text{ at } \mathrm{Re}_t > 500. \quad (8)$$

The calculated values of Re_t for the experimental conditions were within the range 1–80, which corresponds, according to Eq. (6), to z = 3.1–4.8.

Because a settling suspension and a fluidized bed are hydrodynamically similar [18], the velocity of a flow around particles is given by the Allen equation [22]

$$v_f = 51.53r[(\rho_i - \rho)/\rho]^{2/3}(\rho/\eta)^{1/3}. \quad (9)$$

Substitution of Eq. (9) into (3) gives the dependence of ε on v, η, ρ, r, and ρ_i:

$$\varepsilon = (v/v_i)^{1/z}\{(v/51.53r)[\rho\eta/((\rho_i - \rho)^2]^{1/3}]^{1/z}$$

$$= \{v^3\rho\eta/[51.53^3r^3(\rho_i - \rho)^2]\}^{1/3z} \equiv E. \quad (10)$$

From Eqs. (10) and (2) follows

$$P = [(E - \varepsilon_0)/(1 - E)] \times 100\%. \quad (11)$$

According to relation (11), P depends on v, η, ρ, r, and ρ_i. All the parameters, except ρ_i, are known from independent experiments, manufacturers' information [8, 9, 21], and tabulated data [23].

To find ρ_i from the dependences of $P(\varepsilon)$ on v and ρ at a given temperature T, Eq. (10) is transformed to

$$\rho_i = [\rho_1\rho_2(v_2^3\eta_2 - v_1^3\eta_1) + (\rho_1 - \rho_2)(v_1^3v_2^3\eta_1\eta_2\rho_1\rho_2)^{1/2}]$$

$$\times (v_2^3\eta_2\rho_2 - v_1^3\eta_1\rho_1)^{-1}, \quad (12)$$

where subscripts 1 and 2 correspond to two solutions with different concentrations at the same temperature.

Equation (12) was derived on the assumption that ρ_i and r are independent of c at small variations of this parameter. In addition, account was taken of the fact that, according to Eq. (10), equal values of ε and, consequently of P, too, are obtained at different v with regenerating solutions with two different concentrations c, because η and ρ of these solutions are not the same.

Equation (12) was used to calculate ρi from data obtained at close concentrations c and the same temperature T. The resulting values are close to those provided by the manufacturers [8, 21].

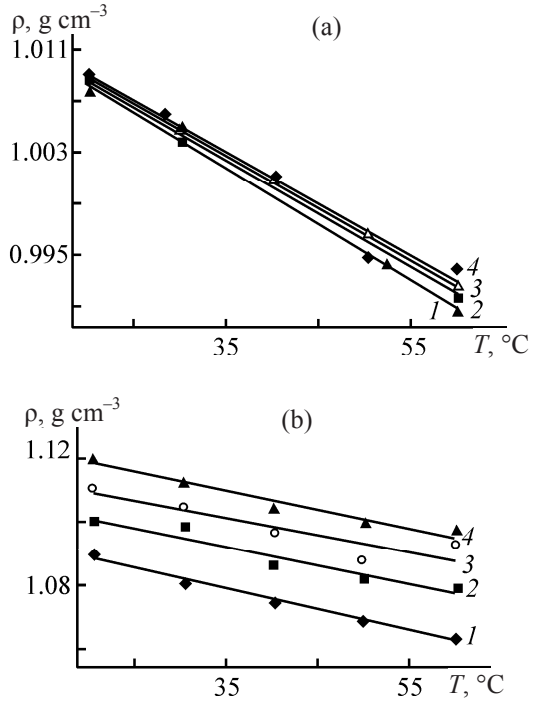


Fig. 3. Density ρ of (a) Lewatit CNP 80 and (b) KU-2×8 cation exchangers vs. temperature T of the sulfuric acid solution. Concentration, wt %: (a) (*1*) 0.21, (*2*) 0.39, (*3*) 0.59, and (*4*) 0.81; (b) (*1*) 2.06, (*2*) 4.04, (*3*) 5.93, and (*4*) 8.26.

Figures 3a and 3b shows how ρ_i varies with T. It can be seen that the dependences of ρ_i on T at different c almost coincide for the Lewatit CNP 80 cation exchanger and are markedly different for KU-2×8. Apparently, this is so because the sulfuric acid concentrations and the step of their variation differ by an order of magnitude for these two cation exchangers. The dependences are linear and are described by the equation

$$a\rho_i = dT + f. \quad (13)$$

The table lists values of the constants d and f of these dependences. It can be seen that the constants for Lewatit CNP 80 coincide at different c within the determination errors $S(d)$ and $S(f)$ (S is the standard deviation). For the KU-2×8 ion exchanger, the constant f depends on c, whereas d is constant. The fact that the density of the KU-2×8 ion exchanger increases with c is due to the nonexchange sorption of the electrolyte [24]. In the case of the Lewatit CNP 80 ion exchanger, such an effect is insignificant because of the small values of c.

If ρ_i is known, all the dependences of P on v can be represented as a generalized curve because the parame-

Constants of Eq. (13) describing the dependence of the ion exchanger density on the temperature of the regenerating solution

Ion exchanger	Regenerating agent concentration, wt %	d	$S(d)$	f	$S(f)$
Lewatit CNP 80	0	–0.0005	0.00003	1.0169	0.0014
	0.21	–0.0004	0.00004	1.0169	0.0018
	0.39	–0.0004	0.00002	1.0167	0.0008
	0.59	–0.0004	0.00001	1.0168	0.0002
	0.81	–0.0004	0.00005	1.0169	0.0021
KU-2×8	0	–0.0006	0.00010	1.0858	0.0042
	2.06	–0.0006	0.00005	1.1005	0.0021
	4.04	–0.0006	0.00010	1.1121	0.0041
	5.93	–0.0005	0.00014	1.1196	0.0061
	8.26	–0.0005	0.00007	1.1277	0.0029

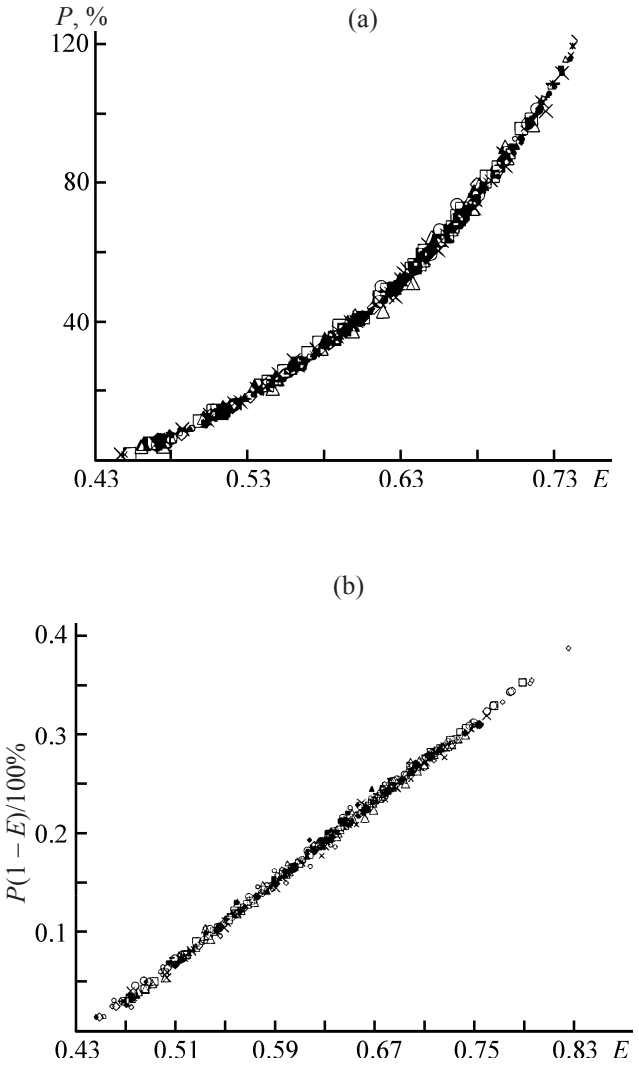


Fig. 4. Dependences of (a) P and (b) $P(1 - E)/100\%$ on E, calculated by Eq. (11). Bed expansion of a cation exchanger.

ter E in Eq. (10) can be a priori calculated. A dependence of this kind is shown in Fig. 4a. It can be seen that the dependences for the two ion exchangers merge into a single curve, in agreement with the basic assumptions of the theory.

According to Eq. (11), the dependence of $P(1 - E)/100\%$ on E should be linear and must intersect the ordinate axis at a point ε_0 at its theoretical value of –0.44, with the slope rate of the straight line equal to unity. As follows from Fig. 4b, this requirement of the theory is, indeed, satisfied. It was found from the dependence in Fig. 4b that $\varepsilon_0 = 0.43 \pm 0.003$, slope rate is 0.987 ± 0.004, and $R^2 = 0.9975 \pm 0.0011$.

CONCLUSIONS

(1) The density of an ion exchanger strongly depends on the temperature of the regenerating solution and is independent of the solution concentration at its minor variations. When the range within which the concentration varies is extended by an order of magnitude, the density of the ion exchanger grains changes only slightly.

(2) Equation (11) satisfactorily describes the dependence of the bed expansion of an ion exchanger on parameters of the regenerating solution. Consequently, if the flow velocity, temperature, concentration, density, and viscosity of the regenerating sulfuric acid solutions are known, together with dependences of the ion exchanger density on temperature and solution concentration, the bed expansion of the ion exchanger can be found in relation to the linear flow velocity of the regenerating solution.

(3) Use of this equation for calculating the bed ex-

pansion of the ion exchanger will enable a priori determination of the regeneration mode of ion exchangers in a fluidized bed, which is necessary for industrial implementation of this technology.

REFERENCES

1. Mamchenko, A.V., Yakimova, T.I., and Klimova, G.V., *Khim. Tekhnol. Vody*, 2002, vol. 24, no. 2, pp. 132–142.
2. Mamchenko, A.V., Yakimova, T.I., and Klimova, G.V., *Khim. Tekhnol. Vody*, 2001, vol. 23, no. 3, pp. 257–271.
3. Mamchenko, A.V., Yakimova, T.I., and Klimova, G.V., *Khim. Tekhnol. Vody*, 2000, vol. 22, no. 6, pp. 570–583.
4. *SNiP* (Building Standards and Regulations) *2.04.02.–84: Water Supply: Outdoors Networks and Installations*, Moscow: Stroiizdat, 1985.
5. Hellmig, R., *Dekarbonizatsiya i snizhenie zhestkosti s pomoshch'yu ionoobmennikov Levatit* (Decarbonation and Hardness Reduction with Lewatit Ion Exchangers), Kiev: Bayer, 1996.
6. Lapotyshkina, N.P. and Sazonov, R.P., *Vodopodgotovka i vodno-khimicheskii rezhim teplovykh setei* (Water Treatment and Water-Chemical Operation Mode of Heat Networks), Moscow: Energoizdat, 1982.
7. *Spravochnik khimika-energetika* (Handbook of a Chemist–Power Engineer), Gurvich, S.M., Ed., Moscow: Energiya, 1972, vol. 1.
8. *Lewatit CNP 80: Product Information*, Leverkusen: Bayer.
9. *GOST* (State Standard) *20 298–74: Ion-Exchange Resins: Cation Exchangers, Technical Specification.*
10. Mamchenko, A.V. and Stavitskii, V.V., *Khim. Tekhnol. Vody*, 2005, vol. 27, no. 1, pp. 52–68.
11. Mamchenko, A.V., Semenyuk, D.V., Kosygina, I.M., and Yakimova, T.I., *Khim. Tekhnol. Vody*, 2006, vol. 28, no. 3, pp. 222–231.
12. Mamchenko, A.V. and Klimova, G.V., *Khim. Tekhnol. Vody*, 2000, vol. 22, no. 3, pp. 232–251.
13. Mekvabishvili, T.V., Luk'yanova, N.L., and Gefter, E.L., *Khim. Tekhnol. Vody*, 1996, vol. 18, no. 3, pp. 258–269.
14. Grebenyuk, V.D. and Mazo, A.A., *Obessolivanie vody ionitami* (Water Desalination with Ion Exchangers), Moscow: Khimiya, 1980.
15. Mamchenko, A.V., Klimova, G.V., and Mogil'naya, T.O., *Khim. Tekhnol. Vody*, 2004, vol. 26, no. 1, pp. 60–77.
16. Gel'perin, N.I., Ainshtein, V.G., and Kvasha, V.B., *Osnovy tekhniki psevdoozhizheniya* (Fundamentals of Fluidization Technology), Moscow: Khimiya, 1967.
17. Protod'yakonov, I.O. and Chesnokov, Yu.G., *Gidromekhanika psevdoozhizhennogo sloya* (Hydromechanics of a Fluidized Bed), Leningrad: Khimiya, 1982.
18. Davidson, J.F. and Harrison, D., *Fluidization*, London: Academic, 1971.
19. Renganathan, T. and Krishnaiah, K., *Chem. Eng. Sci*., 2005, vol. 60, no. 10, pp. 2545–2555.
20. Lettieri, P., Saccone, G., and Cammarata, L., *Chem. Eng. Res. Des*., 2004, vol. 82, no. 8, pp. 939–944.
21. *Katalog ionitov* (Catalogue of Ion Exchangers), Cherkassy: NII Plast. Mass (NPO Plasmassy), 1989.
22. Figurovskii, N.A., *Sedimentometricheskii analiz* (Sedimentometric Analysis), Moscow: Akad. Nauk SSSR, 1948.
23. Perry, R.H., *Perry's Chemical Enginners' Handbook*, New York: McGraw-Hill, 1984.
24. Mamchenko, A.V., *Khim. Tekhnol. Vody*, 1990, vol. 12, no. 9, pp. 771–791.

ISSN 1070-4272, Russian Journal of Applied Chemistry, 2008, Vol. 81, No. 11, pp. 1924–1927. © Pleiades Publishing, Ltd., 2008.
Original Russian Text © M.I. Voronova, D.A. Kuznetsov, A.G. Zakharov, 2008, published in Zhurnal Prikladnoi Khimii, 2008, Vol. 81, No. 11, pp. 1807–1810.

PHYSICOCHEMICAL STUDIES OF SYSTEMS AND PROCESSES

Sorption of Phenol on Cellulose from Binary Aqueous–Organic Mixtures

M. I. Voronova, D. A. Kuznetsov, and A. G. Zakharov

Institute of Solution Chemistry, Russian Academy of Sciences, Ivanovo, Russia
Ivanovo State University of Chemical Technology, Ivanovo, Russia

Received December 28, 2007

Abstract—Sorption of phenol on cellulose from water–dimethyl sulfoxide and water–acetonitrile mixtures was studied. Different shape of the isotherms of phenol sorption from these mixtures is due to different character of phenol solvation in different concentration regions of water–dimethyl sulfoxide and water–acetonitrile mixtures.

DOI: 10.1134/S1070427208110104

Study and prediction of the properties of systems consisting of a polymer and an aqueous–organic solvent is necessary for solving problems related, in particular, to the development of sorbents based on composites of natural and synthetic polymers for water treatment to remove aromatic hydrocarbons and petroleum products [1–4].

To understand the nature of the interaction of low-molecular-weight liquids with a polymer, it is necessary to elucidate the physicochemical features of the interaction of a polymer with components of an aqueous–organic solution and the correlation of these features with the solution structure. The solvation effect shows a nonlinear dependence on the component ratio, owing to the fact that the solvation shell around a solute molecule or around functional groups of a polymer differs in the composition from the bulk of the binary solvent. Deviations from a thermodynamically ideal binary system arise when molecules of water and organic solvent are mixed nonhomogeneously on the level of clusters. Hence, in such nonideal binary systems the preferential solvation occurs more readily. The molecular cluster formation in binary solvents determines the solvation of solutes. This preferential solvation may be a key moment in sorption on a polymer.

In this study we examined the sorption of phenol on cellulose from water–dimethyl sulfoxide (DMSO) and water–acetonitrile (AN) mixtures.

The choice of the solvents (DMSO, AN) is governed by the fact that their mixtures with water are examples of two nonideal binary systems with different properties. It can be expected that the solvation of a solute (e.g., phenol) in these systems would be essentially different.

The shape of the composition dependences of the physicochemical properties of water–DMSO and water–AN binary mixtures indicates that the systems strongly deviate from the ideal behavior owing to various intermolecular interactions.

Certain information on intermolecular interactions in binary systems is furnished by deviations of the partial vapor pressures of mixture components over the solution from Raoult's law. If molecules in a mixture interact less strongly than those in a pure substance, the partial pressures over the solution have positive deviations from Raoult's law. It should be noted that, in the range of acetonitrile mole fractions $0.5 < x_{AN} < 0.8$, the partial pressure of both components is virtually independent of the concentration. This means that each of the molecules of the mixture interacts with molecules of the same kind more efficiently than with molecules of the other kind. This situation is possible if water molecules form three-dimensional hydrogen-bonded clusters surrounded by acetonitrile molecules. The AN molecules behave as a "solvent" and can be oriented toward water clusters owing to dipole–dipole interactions [5].

The water–DMSO system belongs to systems in which the partial pressure of one of the components (water) shows negative deviations from Raoult's law and the partial partial of DMSO shows sign-variable deviations. The latter fact suggests not only the occurrence of complex intermolecular interactions in the water–DMSO system but also variation of the mean size of associates with an increase in the DMSO mole fraction.

The cluster formation in water–DMSO and water–AN systems was studied in [5–9] using a special mass-spectrometric procedure of direct cluster isolation from a solvent mixture. The effect of additions of various substances, e.g., phenol, on the cluster composition was also examined. It is believed in [5–9] that, in water–DMSO and water–AN mixtures, phenol shows a stronger tendency to interact with the clusters already formed in the solution than with individual molecules.

According to the data of these authors, in the water–DMSO system water clusters exist only up to a concentration $x_{DMSO} < 0.07$. At $0.07 < x_{DMSO} < 0.1$, the size of water clusters sharply decreases and that of DMSO clusters increases. The same trend, though less pronounced, is observed in the range $0.1 < x_{DMSO} < 0.28$ [6]. The hydrogen bond network of water is broken, and DMSO exists in the form of dimers or "small" clusters in which the DMSO molecules are held together in the antiparallel fashion by S=O dipole–dipole interactions [6, 10]. In such dimers, the hydrophobic CH_3 groups are located on the periphery, and DMSO clusters exhibit hydrophobic properties. The hydrophobicity of DMSO in this concentration interval is confirmed by X-ray diffraction analysis [10]. In the range $0.28 < x_{DMSO} < 0.6$, the size of DMSO clusters increases, and at $x_{DMSO} > 0.6$, DMSO molecules form clusters of the same structure as in pure DMSO.

In the water–AN system, on adding AN into water in the concentration range $0 < x_{AN} < 0.2$, the number of free water molecules considerably decreases. In other words, the fraction of water clusters increases with an increase in the AN concentration. Wakisaka et al. [5, 8] believe that addition of AN to water stabilizes the hydrogen bond network of water, increasing the lifetime of large clusters. At $x_{AN} > 0.2$, a large number of AN molecules stabilize water clusters, restricting the thermal motion of water molecules owing to a strong bond network. Water clusters exist up to AN mole fraction of ~0.8, after which the hydrogen bond network is broken. At $x_{AN} > 0.8$, AN clusters consisting only of AN molecules are formed [9].

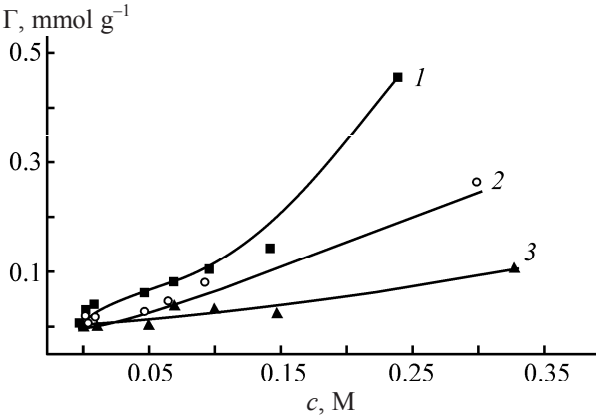


Fig. 1. Isotherms of phenol sorption Γ from water at various temperatures. (*c*) Phenol concentration; the same for Figs. 2 and 4. *T*, K: (*1*) 283, (*2*) 298, and (*3*) 313; the same for Figs. 2 and 4.

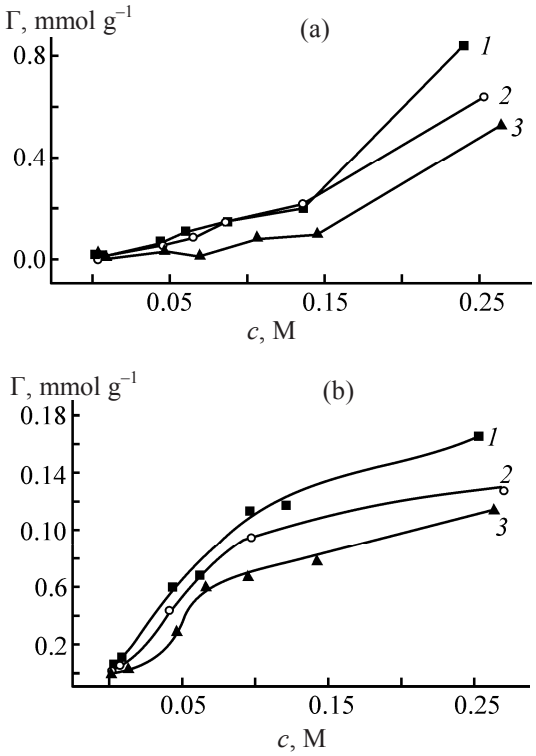


Fig. 2. Isotherms of phenol sorption Γ from water–DMSO solutions at various temperatures. x_{DMSO}: (a) 0.05 and (b) 0.3.

EXPERIMENTAL

Isotherms of phenol sorption from water and from water–DMSO and water–AN mixtures were obtained by the isothermal saturation method in the phenol concentration range 5–350 mM at 283, 288, and 313 K. To

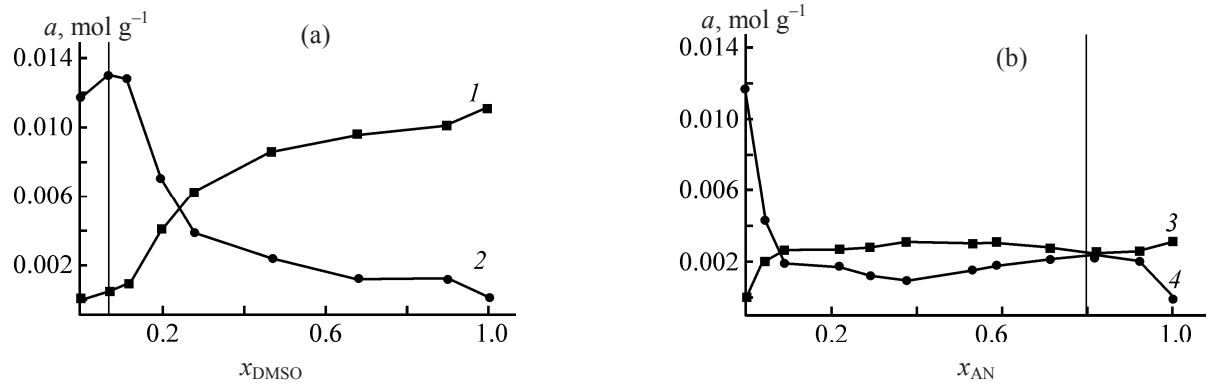


Fig. 3. Individual isotherms of adsorption a of components of water–DMSO [(*1*) DMSO and (*2*) water] and water–AN [(*3*) AN and (*4*) water] solutions on cellulose. (x_{DMSO}, x_{AN}) component mole fractions. The vertical line shows the boundary of existence of water clusters.

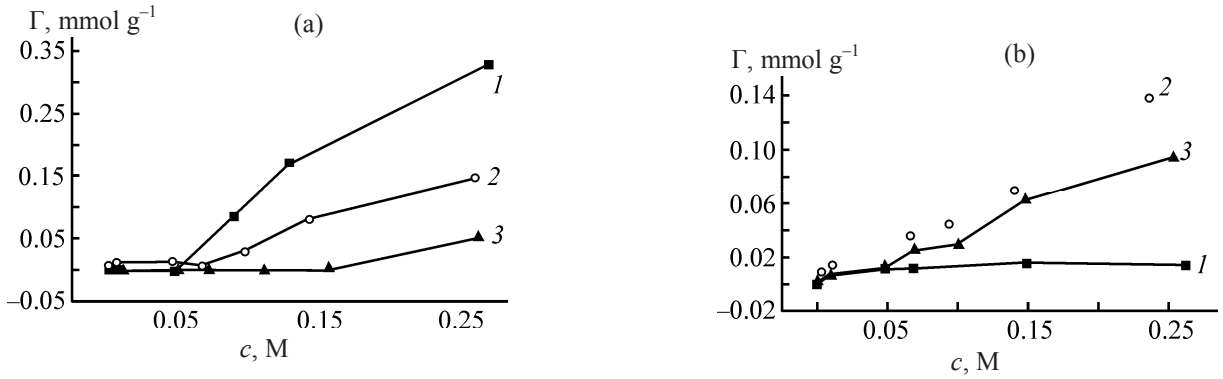


Fig. 4. Isotherms of phenol sorption from water–AN solutions at various temperatures. x_{AN}: (a) 0.05 and (b) 0.3.

a 0.8-g adsorbent sample, we added 10 ml of a phenol solution and thermostated for 48–56 h. The phenol concentration in solution before and after the adsorption was determined spectrophotometrically at λ = 271 nm. The adsorption was calculated by the formula

$$\Gamma = (c_0 - c_{eq})V/m,$$

where c_0 and c_{eq} are the initial and equilibrium concentrations of phenol (M); V, solution volume (l); and m, sample weight (g).

As adsorbent we used sulfite wood cellulose [GOST (State Standard) 3914–89].

The isotherms of phenol sorption from water and water–DMSO mixtures at three temperatures are shown in Figs. 1 and 2. It can be seen that the shapes of the sorption isotherms at x_{DMSO} = 0.05 and x_{DMSO} = 0.3 are different. At x_{DMSO} = 0.05, the shape of the sorption isotherm is similar to that obtained in pure water. The sorption value is approximately two times higher than from pure water. The isotherms of phenol sorption from the water–DMSO mixture at x_{DMSO} = 0.3 are curves with saturation. Presumably, different shape of the isotherms is due to different character of the phenol solvation in these concentration ranges of the water–DMSO mixture.

Indeed, as shown in [6], phenol at these DMSO concentrations is solvated differently. At x_{DMSO} = 0.05, phenol is mainly solvated by water clusters, and at x_{DMSO} = 0.3, by DMSO clusters, which leads to different shapes of the isotherms.

It can be seen from the previously obtained [11] individual isotherms of water and DMSO sorption on cellulose that, in the concentration range up to x_{DMSO} ~0.1, the sorption of water is larger than that from pure water (Fig. 3). The presence of a maximum at x_{DMSO} ~0.1 is associated with the existence of DMSO in the form of hydrophobic dimers. In the same concentration interval, the phenol sorption is larger than from pure water. Presumably, phenol is sorbed in the hydrated form.

A more complex pattern is observed in sorption of phenol from water–AN mixtures (Fig. 4). Sorption of

phenol from a water–AN mixture at $x_{AN} = 0.05$ decreases with increasing temperature, and at $x_{AN} = 0.03$ the temperature dependence of the sorption is anomalous: At 283 K, sorption of phenol is smaller than at 298 and 313 K.

In the concentration range $0 < x_{AN} < 0.2$, phenol mainly interacts with water clusters [8]. At $x_{AN} > 0.2$, water clusters and phenol are solvated by AN molecules, so that the water–phenol interaction is hindered. With an increase in temperature, more active thermal motion destroys the solvation shell consisting of AN molecules, and the water–phenol interaction becomes possible. Specifically this fact is responsible for an increase in the phenol sorption on cellulose at 298 K. Further increase in the temperature to 313 K leads to a decrease in the phenol sorption, which is due to the overall exothermic character of the sorption. A combination of these two factors, break of the solvation shell of molecules being adsorbed (determined by structural organization of the solution) and exothemic character of the sorption, leads to appearance of a sorption maximum at a definite temperature.

CONCLUSIONS

(1) Sorption of phenol on cellulose from water–dimethyl sulfoxide and water–acetonitrile binary mixtures is mainly determined by the hydration of phenol.

(2) Introduction of an organic component can lead both to an increase in the phenol sorption relative to the sorption from water, as in the case of the water–dimethyl sulfoxide mixture ($x_{DMSO} = 0.05$), and to a decrease in the sorption, as in the case of water–acetonitrile mixtures.

REFERENCES

1. Cowie, J.M.G. and Toporowski, P.M., *Can. J. Chem*., 1961, vol. 39, pp. 2240–2243.
2. Herrador, M.A. and Gonzalez, A.G., *Talanta*, 2002, vol. 56, pp. 769–775.
3. Belousov, V.P., Morachevskii, A.G., and Panov, M.Yu., *Teplovye svoistva rastvorov neelektrolitov: Spravochnik* (Thermal Properties of Nonelectrolyte Solutions: Handbook), Leningrad: Khimiya, 1981.
4. Lai, J.T.W., Lau, F.W., Koga, Y.K., et al., *J. Solution Chem*., 1995, vol. 24, no. 1, pp. 89–102.
5. Wakisaka, A., Shimizu, Y., Nishi, N., et al., *J. Chem. Soc., Faraday Trans*., 1992, vol. 88, no. 8, pp. 1129–1135.
6. Shin, D.N., Wijnen, J.W., Engberts, J.B.F.N., and Wakisaka, A., *J. Phys. Chem. B*, 2001, vol. 105, no. 29, pp. 6759–6762.
7. Shin, D.N., Wijnen, J.W., Engberts, J.B.F.N., and Wakisaka, A., *J. Phys. Chem. B*, 2002, vol. 106, pp. 6014–6020.
8. Wakisaka, A., Abdul-Carime, H., Yamamoto, Y., and Kiyozumi, Y., *J. Chem. Soc., Faraday Trans*., 1998, vol. 94, no. 3, pp. 369–374.
9. Wakisaka, A., Takahashi, S., and Nishi, N., *J. Chem. Soc., Faraday Trans*., 1995, vol. 91, no. 22, pp. 4063–4069.
10. Koga, Y.K., Kasahara, Y., Yoshino, K., and Nishikawa, K., *J. Solution Chem*., 2001, vol. 30, no. 10, pp. 885–893.
11. Zakharov, A.G., Voronova, M.I., Prusov, A.N., et al., *Zh. Fiz. Khim*., 2006, vol. 80, no. 8, pp. 1472–1476.

ISSN 1070-4272, Russian Journal of Applied Chemistry, 2008, Vol. 81, No. 11, pp. 1928–1932. © Pleiades Publishing, Ltd., 2008.
Original Russian Text © V.A. Ivanova, G.V. Mitrofanova, T.N. Perunkova, 2008, published in Zhurnal Prikladnoi Khimii, 2008, Vol. 81, No. 11, pp. 1811–1815.

PHYSICOCHEMICAL STUDIES OF SYSTEMS AND PROCESSES

Colloid-Chemical Properties of Sodium and Calcium Salts of α-Alkyl-Substituted Dicarboxylic Acids

V. A. Ivanova, G. V. Mitrofanova, and T. N. Perunkova

Mining Institute, Kola Scientific Center, Russian Academy of Sciences, Apatity, Murmansk oblast, Russia

Received January 16, 2008

Abstract—Surface activity and micelle formation ability in aqueous solutions of Na and Ca salts of α-alkyl-substituted dicarboxylic acids was studied in relation to the length of the hydrocarbon radical, total length of the hydrocarbon chain of the molecule, and mutual position of carboxy groups. The results obtained are compared with properties of saturated monocarboxylic and unsaturated oleic acids.

DOI: 10.1134/S1070427208110116

Previous studies have demonstrated the possibility of using α-alkyl-substituted dicarboxylic acids (DAs) as reagents-collectors for flotation of a number of sulfide-free ores. It was shown that the collecting properties of DAs depend on the composition and structure of a molecule, and primarily on the mutual position of carboxy groups. The observed changes are due to differences in their physicochemical and surface properties manifested both in the liquid phase of the flotation sludge and at water–air and water–mineral particle interfaces.

The capacity of surfactants for association in the solution bulk, determined by the critical micelle concentration (CMC), is an important parameter of colloid solutions and can characterize their capacity for structuring at the water–mineral interface in the formation of an adsorption hydrophobic layer. Properties of branched DAs are poorly understood. The available published evidence about their surface activity and micelle formation are limited to data for Na salts of DAs with 1,1- 1,2-, and 1,3-positions of carboxy groups [3, 4]. The CMC values and the relationships based on these values are contradictory and widely vary between different authors.

The aim of this study was to examine the surface activity and micelle formation ability in aqueous solutions of Na and Ca salts of a wide variety of DAs, which will make it possible to understand processes occurring in the liquid phase of the flotation sludge and to substantiate the choice of DAs with the optimal structure as collectors.

EXPERIMENTAL

Dicarboxylic acids (Table 1) of the general formula $HOOC–(CH_2)_{m-1}–CHR–COOH$ (where R is an alkyl radical, from $C_3H_7–$ to $C_{18}H_{37}–$, and m = 1–11) were synthesized by the known methods [5, 6], twice recrystallized from benzene, and identified by acid–base titration and melting points. The content of the main substance, determined by TLC and elemental analysis, was no less than 97%. The properties of DAs were compared with those of monocarboxylic saturated acids (lauric, myristic, palmitic, and stearic) and unsaturated (oleic) acid of chemically pure grade.

Solutions of Na and Ca salts of the acids mentioned above were prepared with distilled water. The Na salts were synthesized by saponification of the acids with NaOH, followed by dilution to required concentrations. Solutions of the Ca salts were prepared immediately before measurements by mixing equivalent amounts of a Na salt of the acid and $CaCl_2$ in the course of 1 min and then were thermostated at 30 or 40°C for 3 min. To prevent hydrolysis of the salts, the pH values of the solutions were maintained at 10.2–10.5.

The surface activity of the DA salts under study and the micelle formation in aqueous solutions were evaluated using isotherms of surface tension σ, measured by the Du Nouy method at solution temperatures of 30 and 40°C. As a result, the CMC values were found, adsorption isotherms were constructed, and the area per molecule of an acid in the limiting adsorption layer

Table 1. Composition and properties of the DAs under study

Acid	R	C_{n-m}-DA[a]	mp, °C	Acid number, mg KOH/g substance	
				calculated	found
Dodecylmalonic	$C_{12}H_{25}$	C_{13-1}-DA	115–117	412.0	402.0
Tridecylmalonic	$C_{13}H_{27}$	C_{14-1}-DA	109–111	392.0	391.0
Hexadecylmalonic	$C_{16}H_{33}$	C_{17-1}-DA	120–121	342.0	336.0
Octylsuccinic	C_8H_{17}	C_{10-2}-DA	78–79	529.0	524.0
Tetradecylsuccinic	$C_{14}H_{29}$	C_{16-2}-DA	103–105	357.3	354.0
Tetradecylsuccinic	$C_{16}H_{33}$	C_{18-2}-DA	99–100	328.0	330.0
Octadecylsuccinic	$C_{18}H_{37}$	C_{20-2}-DA	100–101	303.0	280.0
Tetradecylglutaric	$C_{14}H_{29}$	C_{17-3}-DA	54	342.0	329.0
Decyladipic	$C_{10}H_{21}$	C_{14-4}-DA	62–63	392.0	390.0
Tetradecyladipic	$C_{14}H_{29}$	C_{18-4}-DA	79–80	327.5	317.0
Tetradecylaselaic	$C_{14}H_{29}$	C_{21-7}-DA	80	292.0	277.0
Propylbrassilic	C_3H_7	C_{14-11}-DA	74	392.0	393.0
Octylbrassilic	C_8H_{17}	C_{19-11}-DA	68–69	315.0	301.0

[a] n is the number of carbon atoms in the total hydrocarbon chain of DA and m, the number of carbon atoms between carboxy groups.

at the water–air interface was calculated by the Shishkovskii equation [7].

It can be seen from the surface tension isotherms of solutions of Na salts of α-alkylsuccinic acid (C_{n-2}-DA), shown in Fig. 1a and characteristic of all the other DAs, that the run of the curves is typical of solutions of micelle-forming surfactants: as the concentration is raised, the surface tension first decreases and then, after the CMC is reached, takes a constant value. As in the case of other homologous series of DAs (C_{n-1}, C_{n-4}, C_{n-11}), the surface activity steadily increases as the alkyl radical R in the DA molecule becomes larger, and the total hydrocarbon chain, longer.

The surface tension isotherms of aqueous solutions of Na salts of DAs with the number of carbon atoms in the total hydrocarbon chain close to, or somewhat exceeding that in the molecule of oleic acid (C_{17}), shown in Fig. 1b, demonstrate that the Na salts of DA have at

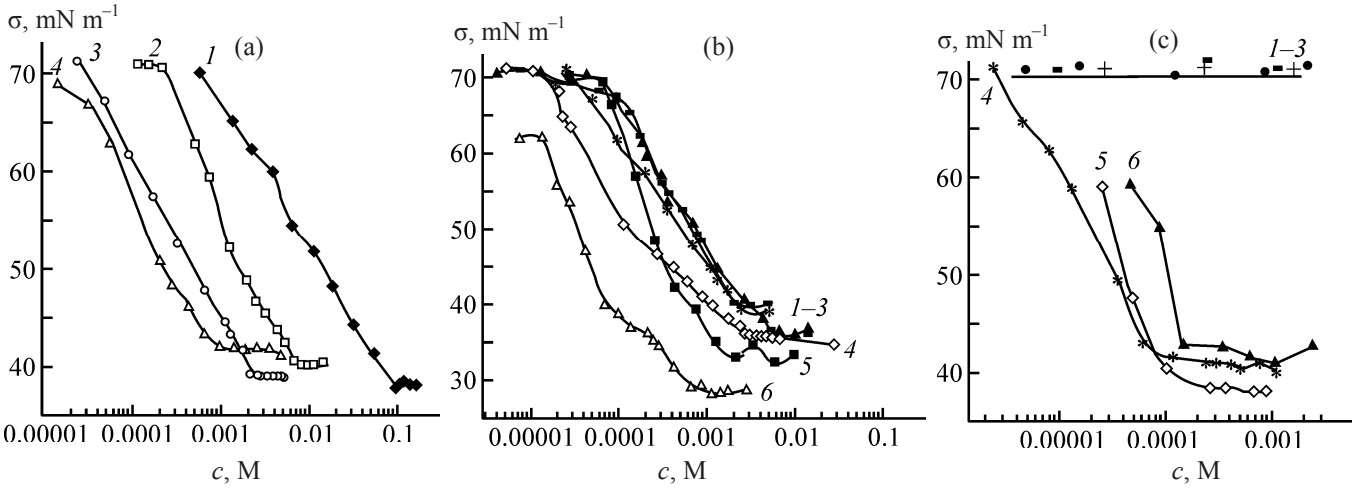


Fig. 1. Isotherms of the surface tension σ of aqueous solutions of sodium salts of (a) alkylsuccinic and (b) carboxylic acids and (c) of calcium salts of carboxylic acids at 30°C and pH 10.2–10.5. (c) DA salt concentration. Acid: (a) (*1*) C_{10-2}-DA, (*2*) C_{16-2}-DA, (*3*) C_{18-2}-DA, and (*4*) C_{20-2}-DA; (b) (*1*) C_{17-1}-DA, (*2*) C_{17-3}-DA, (*3*) C_{18-2}-DA, (*4*) C_{19-11}-DA, (*5*) C_{18-4}-DA, and (*6*) oleic; (c) (*1*) C_{17-1}-DA, (*2*) C_{18-2}-DA, (*3*) C_{17-3}-DA, (*4*) oleic, (*5*) C_{21-7}-DA, and (*6*) C_{18-4}-DA.

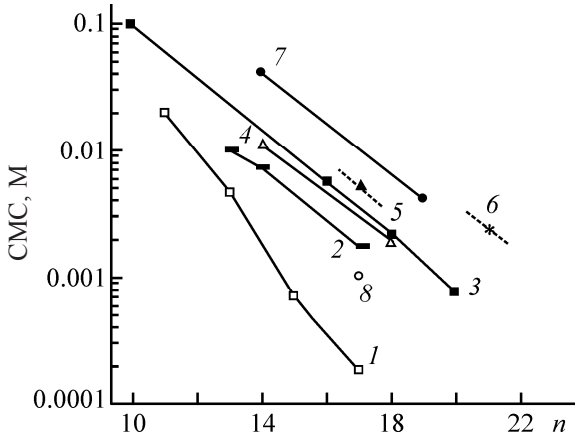


Fig. 2. Semilog plots of CMC vs. the total number n of carbon atoms in the hydrocarbon chain of sodium salts of mono- and dicarboxylic acids at (*1*) 40 and (*2–8*) 30°C, pH 10.2–10.5. Carboxylic acid: (*1*) $C_nH_{2n+1}COOH$, (*2*) C_{n-1}-DA, (*3*) C_{n-2}-DA, (*4*) C_{n-4}-DA, (*5*) C_{n-3}-DA, (*6*) C_{n-7}-DA, (*7*) C_{n-11}-DA, and (*8*) oleic.

low concentrations a noticeably weaker surface activity than sodium oleate. The minimum value of the surface tension, reached in this case, is 27–28 mN m^{-1} for sodium oleate and 38–40 mN m^{-1} for Na salts of DAs.

The CMC values found from the surface tension isotherms for Na salts of DAs are shown, in comparison with monocarboxylic acids, in Fig. 2 in the form of the known dependence on the number n of carbon atoms in the hydrocarbon chain: $\log CMC = A - Bn$. It can be seen that an increase in the length of the total hydrocarbon chain in the homologous series of DA leads, as in the case of monocarboxylic acids, to a steady decrease in the CMC.

However, the CMC of the Na salt of a DA substantially exceeds that of the Na salt of the monocarboxylic acid with the same number of carbon atoms in the hydrocarbon chain and depends on the distance between the carboxy groups. As the distance between COOH groups in the DA molecules increases within the range 1–11 carbon atoms, the micelle-forming ability passes through a maximum value presumably corresponding, in a series of acids with the same total hydrocarbon chain, to a position of the second carboxy group in the middle of the chain (Fig. 2). In this case, the carbon chains between the COOH groups and the alkyl substituent R become comparable and the molecule is branched to the greatest extent.

Table 2. Parameters A and B of the dependence $\log CMC = A - Bn$ for Na salts of carboxylic acids

Acid	A		B	
	30°C	40°C	30°C	40°C
$C_nH_{2n+1}COOH$	–	2.18	–	0.35
C_{n-1}-DA	0.56	0.78	0.20	0.20
C_{n-2}-DA	1.09	1.28	0.21	0.22
C_{n-4}-DA	0.71	0.88	0.19	0.20
C_{n-11}-DA	1.40	1.37	0.20	0.20

The DA structure can be regarded as a result of substitution of a hydrogen in the hydrocarbon chain of a saturated monocarboxylic acid with a carboxy group. In this regard, the effect of a substitution of this kind is the most pronounced for high-molecular-weight saturated acids: the solubility of Na salts of DAs steeply increases and their micelle-forming ability decreases. Comparison of the CMC of Na salts of mono- and dicarboxylic acids with 17 carbon atoms in the total chain shows (Fig. 2) that the effect of the second carboxy group on micelle formation exceeds that of the unsaturated bond (for the example of oleic acid).

The parameters A and B of the semilogarithmic dependence $\log CMC = A - Bn$, calculated from experimental data to be 2.18 and 0.35, respectively, for Na salts of dicarboxylic acids (Table 2), are in agreement with published data [3, 4]. The value obtained for the parameter B for homologous series of DA is 1.5 times lower, which is graphically manifested in the smaller slope of the $\log CMC = f(n)$ straight lines (Fig. 2). This behavior agrees with the theoretical concept about the effect of polar substituents in hydrocarbon chains of surfactants on their micelle-forming ability [4]. A shift of the carboxy group along the hydrocarbon chain of DA does not lead to any noticeable change in the parameter B.

The considerable difference of the CMC obtained for Na salts of some C_{n-1}-, C_{n-4}-, and C_{n-3}-DAs from published data [3] is presumably due to the experimental conditions and, in particular, to the pH of the solutions under study. For example, according to the data obtained, a decrease in pH from 10.2–10.5 to 9.0–9.5 causes an order-of-magnitude decrease in the CMC, which suggests noticeable hydrolysis of the salts.

The areas per DA molecule in the limiting adsorption layer at the interface are listed in Table 3. It can be seen that these values are close for DA molecules of the same homologous series (C_{n-1}-, C_{n-2}-, and C_{n-4}-DA). The exception is provided by members of the homologous series C_{n-2}-DA and C_{n-11}-DA, which have

Table 3. Area per molecule of alkyldicarboxylic acid in the surface layer

Na-DA	Area per molecule, Å^2
C_{13-1}-DA	42.0
C_{14-1}-DA	42.7
C_{17-1}-DA	43.7
C_{10-2}-DA	59.5
C_{16-2}-DA	49.5
C_{18-2}-DA	50.7
C_{20-2}-DA	49.5
C_{17-3}-DA	52.96
C_{14-4}-DA	52.1
C_{18-4}-DA	54.4
C_{21-7}-DA	59.3
C_{14-11}-DA	56.1
C_{19-11}-DA	62.4

Table 4. CMC of Ca salts of carboxylic acids

Acid	CMC, M (50°C)
Oleic	0.75×10^{-4}
C_{14-4}-DA	8.0×10^{-4}
C_{18-4}-DA	1.4×10^{-4}
C_{21-7}-DA	1.2×10^{-4}
C_{19-11}-DA	3.2×10^{-4}

a small alkyl substituent (C_3H_7, C_8H_{17}) and form loose adsorption layers because of the weak hydrophobic interaction. The area for DA molecules with close sizes of the alkyl substituent (C_{14-1}-, C_{16-2}-, C_{17-3}-, C_{18-4}-, and C_{21-7}-DA) grows with the distance between the functional groups. This behavior and comparison with the areas for monocarboxylic acids [7] indicate that DAs have the following molecular orientation in the adsorption layer: R is oriented perpendicularly to the interface, both the functional groups face the aqueous phase, and the hydrocarbon chains between these groups are parallel to the adsorbing surface. The increase in the area per C_{21-7}- and C_{n-11}-DA molecules with respect to C_{n-4}-DA is substantially smaller than it would be expected. Presumably, another possible molecular orientation takes place in these cases: similar to that of high-molecular-weight α,ω-DAs [8] in which the hydrocarbon chains between carboxy groups are bent and lie above the interface.

Figure 1c shows surface tension isotherms of aqueous solutions of Ca salts of oleic acid and DAs with comparable hydrocarbon chains, but different distances between carboxy groups. It can be seen that solutions produced by equivalent mixing of solutions of Na salts of DAs with 1,1-, 1,2-, and 1,3-positions of carboxy groups with $CaCl_2$ exhibit zero surface activity (curves *1–3*). This is accounted for by formation, similarly to first members of the homologous series of α,ω-DAs (from oxalic to glutaric), of poorly soluble complex compounds of cyclic structure with ions of alkaline-earth metals [9].

Similarly to calcium oleate, Ca salts of DAs with more than three carbon atoms between carboxy groups (C_{18-4}-, C_{21-7}-, and C_{19-11}-DA) are surface-active (Fig. 1c, curves *4–6*), with the CMC values (Table 4) an order of magnitude smaller than the CMC for their Na salts (Fig. 2).

It should be noted that opalescence was observed for each Ca salt at a premicellar concentration, and a precipitate was formed at concentrations exceeding CMC.

CONCLUSIONS

(1) For all the homologous series of dicarboxylic acids considered in the study, the parameter *B* in the logarithmic dependence of the critical micelle concentration of Na salts of α-alkyl-substituted dicarboxylic acids on the number of carbon atoms in the total hydrocarbon chain of the molecule, dependent on the decrease in the free energy per methylene group in micelle formation, is 1.5 times smaller than that for the series of saturated monocarboxylic acids.

(2) Presence of a second carboxy group in the saturated hydrocarbon chain of dicarboxylic acids makes lower the micelle-formation ability of their Na salts, compared with monocarboxylic acids.

(3) The extent of this decrease depends on the position of the carboxy group nonmonotonically, with the maximum for dicarboxylic acids with the same total chain length corresponding to the middle position of the COOH group.

(4) Presence of a second carboxy group in the hydrocarbon chain of a saturated carboxylic acid leads to a stronger decrease in the micelle-forming ability than does the unsaturated bond.

(5) Ca salts of dicarboxylic acids with 1,1–1,3-positions of carboxy groups exhibit zero surface activity at the water–air interface. At 1,4–1,11-positions of carboxy groups, Ca salts are surface-activity. Their critical micelle concentration is an order of magnitude

lower than that of the Na salts of these acids and exceeds that of calcium oleate by a factor of 2–4.

REFERENCES

1. Ivanova, V.A., Shlykova, G.A., and Mitrofanova, G.V., in *Optimizatsiya protsessov obogashcheniya mineral'nogo syr'ya: Sbornik nauchnykh trudov* (Optimization of Processes for Dressing of Mineral Raw Materials), Apatity: Kol'skii Nauchnyi Tsentr Ross. Akad. Nauk, 2000, pp. 50–68.
2. Ivanova, V.A., Mitrofanova, G.V., and Mukhina, T.N., in *Materialy Mezhdunarodnoi konferentsii "Kompleksnaya pererabotka netraditsionnogo titano-redkometall'nogo i alyumosilikatnogo syr'ya: Sovremennoe sostoyanie i perspektivy"* (Proc. Int. Conf. "Integrated Processing of Unconventional Titanium–Rare-Metal and Aluminosilicate Raw Materials: Modern State and Prospects") Apatity, April 4–8, 2006, Apatity: Kol'skii Nauchnyi Tsentr Ross. Akad. Nauk, 2006, pp. 81–85.
3. Serrano, A., Bochnia, D., and Schubert, N., *Tenside Detergents*, 1977, vol. 14, no. 2, pp. 67–73.
4. Shinoda, K., Nakagawa, T., Tamamushi, B.-I., and Isemura, Y., *Colloid Surfactants. Some Physicochemical Properties*, New York: Academic, 1963. Translated under the title *Kolloidnye poverkhnostno-aktivnye veshchestva: Fiziko-khimicheskie svoistva*, Taubman, A.B. and Markina, Z.N., Eds., Moscow: Mir, 1966, pp. 9–117.
5. Ogibin, Yu.N., Maksimova, N.G., Kondrashina, G.E., and Nikishin, G.I., *Zh. Org. Khim*., 1970, vol. 6, no. 7, pp. 1399–402.
6. *Organic Syntheses*, Blatt, A.H., Ed., New York: Wiley, 1944. Translated under the title *Sintezy organicheskikh preparatov*, Moscow: Inostrannaya Literatura, 1949, coll. 1.
7. *Praktikum po kolloidnoi khimii i elektronnoi spektroskopii* (Practical Course of Colloid Chemistry and Electronic Spectroscopy), Voyutskii, S.S. and Panich, R.M., Eds., Moscow: Khimiya, 1974.
8. Shafrin, E. and Tsisman, U., *Monomolekulyarnye sloi* (Monomolecular Layers), Taubman, A.B., Ed., Moscow: Inostrannaya Literatura, 1956, pp. 152–186.
9. Bukolov, I.E., Astakhov, K.V., Zimin, V.I., and Tairov, V.S., *Zh. Neorg. Khim*., 1962, vol. 7, no. 7, pp. 1577–1582.

ISSN 1070-4272, Russian Journal of Applied Chemistry, 2008, Vol. 81, No. 11, pp. 1933–1938. © Pleiades Publishing, Ltd., 2008.
Original Russian Text © M.V. Afonin, S.A. Simanova, N.M. Burmistrova, N.S. Panina, Yu.A. Karpov, O.A. Dal'nova, 2008, published in Zhurnal Prikladnoi Khimii, 2008, Vol. 81, No. 11, pp. 1816–1821.

PHYSICOCHEMICAL STUDIES OF SYSTEMS AND PROCESSES

Sorption Recovery of Platinum(II) and Platinum(IV) Chloro Complexes with a Heterochain Sulfur-Containing Sorbent

M. V. Afonin, S. A. Simanova, N. M. Burmistrova, N. S. Panina, Yu. A. Karpov, and O. A. Dal'nova

St. Petersburg State Institute of Technology (Technical University), St. Petersburg, Russia
State Research and Designing Institute of Rare-Metal Industry, Moscow, Russia

Received April 16, 2008

Abstract—The recovery of platinum(II) and platinum(IV) chloro complexes from hydrochloric acid and chloride solutions with a new heterochain S,N-containing sorbent, MITKhAT, was studied. The suggested mechanism of formation of platinum(II) mercapto–thio ether complexes in the course of sorption was confirmed by DFT calculations. The results of group and selective recovery of platinum metals with MITKhAT sorbent from simulated and real industrial solutions are reported.

DOI: 10.1134/S1070427208110128

Granulated and fibrous complexing S,N-containing sorbents have been widely used in the past decades for separation, preconcentration, and determination of platinum and other platinum metals (PMs) [1–3]. Early studies on the use of such sorbents, in particular, of thioamidated copolymers of cellulose with acrylonitrile (Mtilon-T) and of vinyl alcohol with acrylonitrile (MSPVS), were discussed in reviews [2–5].

For improving the procedures for sorption preconcentration of PMs, it is extremely important to know the composition and structure of complexes formed by interaction of platinum metals with functional groups of sorbents as polymeric ligands, and also to understand the effect exerted by the polymeric matrix of the sorbents on their kinetic and capacity characteristics [2, 3, 5]. As S,N-containing functional groups grafted to matrices of various sorbents used for sorption recovery of PMs, we tested diethyldithiocarbamate, thiourea, thiosemicarbazide, 8-mercaptoquinoline, and other groups. The chemical transformations occurring in the course of sorption recovery of Pd(II) with such sorbents are discussed in [6].

It was found [7] that the sorption recovery of platinum(II) chloro complexes with Tiopan-2 sorbent, which is a copolymer of acrylonitrile with grafted polyglycidyl methacrylate, containing diethyldithiocarbamate groups, is accompanied by formation in the fiber phase of platinum complexes *cis*-$[Pt(RS_2CN(C_2H_5)_2)_2Cl_2]$ in which the polymeric ligand is coordinated with Pt via sulfur atom. In sorption of platinum(II) chloro complexes with Tiopan-6 sorbent, formation of the complex *cis*-$[Pt(Rpy)_2Cl_2]$ was detected, in which the 8-mercaptoquinoline group acts as a monodentate ligand coordinated with Pt(II) via N atom. It should be noted that the reaction of platinum(II) chloro complexes with a monomeric ligand, sodium 8-quinolinethiolate (QuinS), yields bischelate complexes of the composition $[Pt(QuinS)_2]$ [8].

A study of the sorption of platinum(II) and platinum(IV) chloro complexes from hydrochloric acid and chloride solutions with a fibrous sorbent based on polyacrylonitrile modified with thiosemicarbazide (RThscH) (Glipan-1) showed that the complex $[(RThscH)_2PtCl_2]$ is formed in the fiber phase, with the polymeric ligand coordinated to the platinum atom in the bidentate fashion via N and S atoms [9, 10]. In the process, Pt(IV) is reduced to Pt(II) [10].

S,N-Containing water-soluble polyelectrolytes were suggested for the recovery of a series of platinum metals, including Pt(II) in the form of chloro complexes [11]. These agents allow quantitative recovery of $[PtCl_4]^{2-}$ from hydrochloric acid and chloride solutions containing 1–50 mM platinum. The polyelectrolytes interact with platinum(II) chloro complexes mainly

by the ion-exchange mechanism, and the forming sparingly soluble compounds have the composition $(R_4N)_2[PtCl_4]$. The possible formation of a sparingly soluble complex $[Pt(R_2S)_2Cl_2]$ in which the polymeric ligand is coordinated via S atom was noted [11].

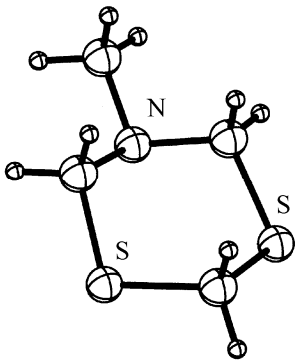
Thus, the above examples show that the interaction of platinum complexes with S,N-containing sorption materials in the course of sorption recovery depends on the nature of functional groups and matrix of the sorbent.

The preconcentration of platinum metals from process solutions and secondary raw materials for the subsequent determination of these elements by physical methods is performed, in particular, with heterochain polymeric sorbents. The matrix of such sorbents contains S and N atoms forming polymer chains in which the sorption centers and the matrix are a single whole [12–14]. Among such sorbents, the most known are those prepared by polycondensation of piperazine with formaldehyde and hydrogen sulfide [12, 13] and those containing aminoethylenepiperazine and dimethyl sulfide groups [14].

New sorbents of the polycondensation type, containing in the backbone alternating methylene and methylene sulfide groups and tertiary nitrogen atoms, have been prepared recently [15, 16]. It was found that the new S,N-containing sorbents allow recovery of microamounts of platinum group metals, gold, and silver at room temperature from solutions in dilute mineral acids in the presence of macroamounts of nickel, iron, and copper [16–19]. Procedures were developed for sorption preconcentration of platinum metals with a new S,N-containing sorbent from solutions containing macrocomponents of secondary and artificial raw materials, with the subsequent determination of PMs by atomic absorption spectrometry [16, 17]. Thiomethylation of amines as a procedure for preparing S,N-containing heterochain oligomers and polymers usually yields a mixture of products. Samples of new heterochain S,N-containing polymers KDM-2 and KPU-2 are commercially produced and used in practice [17], but for studying complexing properties of the sorbents it is preferable to use low-molecular-weight compounds.

This study concerns sorption recovery of platinum(II) and platinum(IV) chloro complexes from hydrochloric acid and chloride solutions with MITKhAT low-molecular-weight S,N-containing oligomer [15–18].

The MITKhAT sorbent, aminomethylene sulfide, contains in its chain alternating methylene and methylene sulfide groups and tertiary nitrogen atoms (~12 wt % N and ~47 wt % S). Its molecular weight is 135. It is a colorless crystalline powder stable in 6 M HCl and 3 M HNO_3:



This sorption material is insoluble in water but soluble in hydrochloric acid and chloride solutions. It was confirmed in special experiments that the sorbent does not degrade in the course of dissolution. The IR spectra of the initial sorbent before and after precipitation from hydrochloric acid solution in the range 400–3000 cm^{-1} are fully identical.

Platinum(II) and platinum(IV) chloro complexes K_2PtCl_4 and K_2PtCl_6 were prepared by well-known procedures [20]. The sorption was performed under static conditions with continuous stirring on a Unipan type 358 S laboratory shaker at room temperature in 0.1–4 M HCl and 0.1–4 M NaCl. The starting solutions were prepared by dissolving weighed portions of K_2PtCl_4 and K_2PtCl_6. The working volume of the solutions was 20 ml, and the sorbent weighed portion, 0.1 g. The platinum concentration in solutions before and after sorption was determined spectrophotometrically with tin(II) chloride [21]. The platinum concentration in the solution was varied from 1 to 60 mM. The electronic absorption spectra of solutions were measured on a Specol 11 spectrophotometer, and the IR spectra of samples, on a Shimadzu IR-435 spectrometer. The X-ray photoelectron spectra (XPS) were measured on a Perkin–Elmer PHI-5400 spectrometer with excitation by monochromatic AlK_α X-ray radiation (energy 1486.6 eV). The calculation of the atomic concentrations and resolution of separate XPS lines into components were performed by standard procedures. The binding energy was determined with an accuracy of 0.1 eV, and the quantitative analysis was made with 10% accuracy. The spectra were calibrated against C 1*s* line.

As the sorbent dissolves in hydrochloric acid and chloride solutions, actually the interaction of MITKhAT with platinum(II) and platinum(IV) chloro complexes under these conditions involves chemical reactions yielding difficultly soluble platinum compounds.

In contrast to sorption of iridium(III) and iridium(IV) chloro complexes [22], platinum chloro complexes are efficiently recovered at room temperature. Typical kinetic curves of the recovery of platinum(II) and platinum(IV) chloro complexes from 0.5 M HCl solutions at room temperature are shown in Fig. 1.

As seen from Fig. 1, the apparent equilibrium in the distribution of both platinum(II) and platinum(IV) chloro complexes between the solution and precipitate is attained at 20°C within 2.5–3 h. It is seen from the kinetic curves (Fig. 1) that 93% of platinum is recovered from a 0.5 M HCl solution (c_{Pt} = 3 mM) already in 1 h. In all the subsequent experiments, the time of contact of solutions with MITKhAT sorbent at room temperature was 3 h.

It is important that variation of the platinum concentration in solution (from 1 to 10 mM) and of the solution composition (0.1–4 M HCl and 0.1–4 M NaCl) does not noticeably affect the rate of recovery of platinum chloro complexes at room temperature. On heating the solutions to 50°C, the rate of recovery of platinum(II) and platinum(IV) chloro complexes increases by a factor of approximately 2.

The color of the products obtained after the sorption recovery depends on the platinum oxidation state. The precipitates obtained with Pt(IV) are brown, and those with Pt(II), yellow. With an increase in the metal concentration in solutions, the color becomes more intense.

Figure 2 shows that MITKhAT sorbent exhibits high sorption capacity (SC) toward platinum(II) chloro complexes, which reaches 6.5 mmol g^{-1} even at room temperature.

The steep ascent of the isotherm of recovery of platinum(II) chloro complexes shows that MITKhAT should be recommended primarily for recovering microamounts of platinum. In the range of initial platinum(IV) concentrations from 1.0 to 20 mM, platinum(IV) chloro complexes are virtually quantitatively recovered into the precipitate at room temperature (SC ~4.0 mmol g^{-1}).

The dependence of the SC on the composition and concentration of HCl and NaCl solutions is shown for platinum(II) as example (Fig. 3). In a wide range of HCl and NaCl concentrations, both the rate of Pt(II) recovery and SC remain constant.

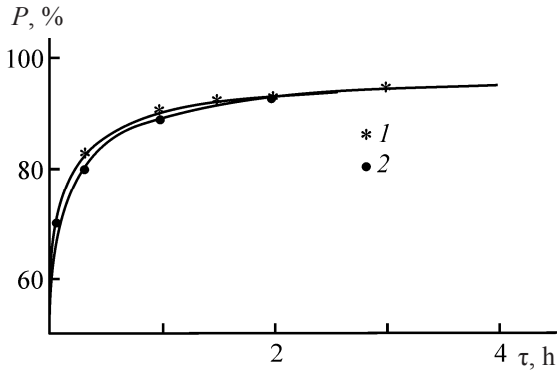


Fig. 1. Kinetic curves of the sorption of (*1*) K_2PtCl_4 and (*2*) K_2PtCl_6 with MITKhAT from 0.5 M HCl at 20°C. Platinum concentration 3 mM. (*P*) Degree of platinum recovery and (τ) time.

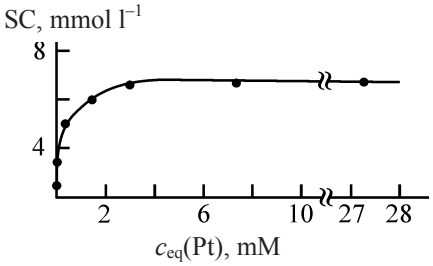


Fig. 2. Sorption capacity SC of MITKhAT sorbent in 0.5 M HCl at 20°C as a function of the equilibrium concentration c_{eq}(Pt) of Pt(II).

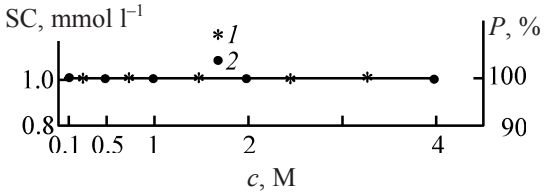


Fig. 3. Sorption capacity SC of MITKhAT sorbent for K_2PtCl_4 and K_2PtCl_6 as a function of the concentration *c* of (*1*) HCl and (*2*) NaCl. (*P*) Degree of platinum recovery.

Similar pattern is observed with platinum(IV) chloro complexes. Thus, the kinetic and capacity characteristics of MITKhAT toward platinum(II) and platinum(IV) chloro complexes are preserved in both hydrochloric acid and neutral chloride solutions.

Platinum cannot be recovered from the difficultly soluble compounds formed even by treatment with 6–10 M HCl. Platinum can be transferred into solution

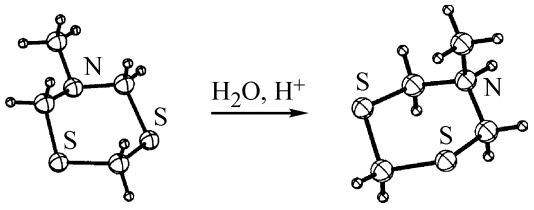
only by "wet combustion," i.e., by treatment with concentrated nitric acid or aqua regia.

The absence of any effect of the solution composition on the recovery of platinum(II) and platinum(IV) chloro complexes suggests similar mechanism of their recovery.

Elemental analysis revealed no nitrogen in the compounds isolated after the sorption of K_2PtCl_6 and K_2PtCl_4. The IR spectra of the isolated compounds differ from that of the initial sorbent in the range of ν(C=S) stretching vibrations (1450–1300 cm^{-1}) and the adjacent range of δ(CH) bending vibrations (1400–1300 cm^{-1}) [23]. Certain changes are also observed in the range of ν(C–S) stretching vibrations (700–600 cm^{-1}) [23]. In the far-IR range (400–140 cm^{-1}), the metal–halogen stretching vibration bands [24] are absent. All these facts suggest that the complexation reactions in the course of sorption recovery of platinum involve formation of Pt–S bonds.

It was shown by XPS that, after sorption of both K_2PtCl_6 and K_2PtCl_4, only Pt(II) is identified in the isolated compounds. In the spectra of the samples after recovery of both Pt(II) and Pt(IV), E_b for the Pt $4f_{7/2}$ line is 73 eV, which corresponds to Pt(II) [25, 26]. The recovery of platinum(IV) chloro complexes with MITKhAT sorbent is accompanied by reduction of Pt(IV) to Pt(II) and oxidation of sulfide sulfur to S^0 (E_b for S^0 $2p_{3/2}$ 164.0 eV) [25, 26].

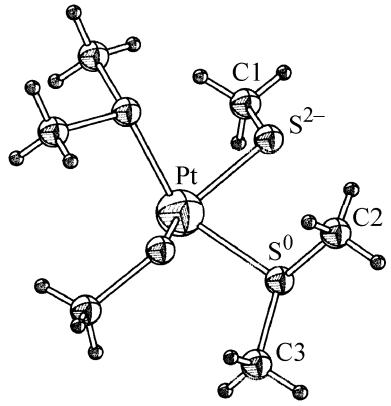
The whole set of data of elemental analysis, XPS, and IR spectroscopy indicates that the compounds isolated after sorption are mercapto–thio ether complexes of Pt(II). In hydrochloric acid solutions, the first step of the sorption involves, along with the redox reaction (in solution, with MITKhAT), also protonation of the tertiary nitrogen atom of the sorbent and formation of the onium compound by the scheme



$$2CH_3N(CH_2)_2S_2CH_2 \cdot HCl + [PtCl_4]^{2-}$$

$$\rightarrow [CH_3NH(CH_2)S_2CH_2]_2[PtCl_4].$$

The subsequent transformations involve decomposition of the onium compound, heterolytic cleavage of the C–N and C–S bonds, and inner-sphere coordination of the ligand to the Pt(II) ion with the formation of polymeric mercapto–thio ether complexes of Pt(II):



To predict the possibility of formation and the strength of platinum mercapto–thio ether complexes, we performed quantum-chemical calculations of the electronic structure of the ligand $CH_3N(CH_2)_2S_2CH_2$ (L), its protonated form $[CH_3NH(CH_2)_2S_2CH_2]^+$, and the model complex *trans*-$[Pt(DMS)_2(SCH_3)_2]$, where DMS is $S(CH_3)_2$. The calculations were performed with full geometry optimization by the DFT B3LYP method with the 6-31 G** basis set for transition metals and HW effective core potential for the Pt atom [27], using the GAMESS-2007 program package [28].

The results obtained indicate that the nitrogen atom in ligand L has an effective negative charge, whereas the S atom is charged positively: $q(N) = –0.30$ e, $q(S) = 0.13$ e. However, the electron density of the highest occupied MO (HOMO) of this ligand with an energy of –6.20 eV is concentrated on the S atom. These facts indicate that the ligand L is potentially ambidentate.

According to the Klopman's approach [29] and the Pearson's concept of hard and soft acids and bases [30], an acceptor that is a hard Lewis acid in coordination with an ambidentate ligand will "choose" the atom that bears the largest negative charge, i.e., the coordination will be charge-controlled. An acceptor that is a soft Lewis acid will "choose" in this ligand the center with the highest charge density on HOMO. The HOMO should have an energetically favorable high energy (or, in other words, low molecular ionization energy). That is, the coordination will be orbital-controlled.

From this viewpoint, the protonation of ligand L should be charge-controlled, i.e., it should occur at the

nitrogen atom bearing the largest negative charge. Calculation of the protonated ligand $[CH_3NH(CH_2)_2S_2CH_2]^+$ showed that in this species, as compared to the neutral compound, the –N–CH_2– bonds are weakened and the adjacent –CH_2–S– bonds are strengthened: $R(N–C)_L$ = 1.415, $R(N–C)_{L^+}$ = 1.526, $R(C–S)_L$ = 1.836, $R(C–S)_{L^+}$ = 1.804 Å. The Mayer bond orders n [31] are as follows: $n(N–C)_L$ = 0.89, $n(N–C)_{L^+}$ = 0.75. The calculation results demonstrate why protonation of the N atom promotes decomposition of the ligand.

Interaction of ligand L with platinum ions, which are soft Lewis acids, should be orbital-controlled: This ligand with a very low ionization energy can coordinate with Pt via S atoms whose electrons are concentrated on HOMO.

The DFT calculations of the electronic structure of the Pt(II) complexes with the $S(CH_3)^-$ and $S(CH_3)_2$ ligands simulating the decomposition products of the $CH_3NH(CH_2)_2S_2CH_2$ ligand showed that the anionic ligand $S(CH_3)^-$ is an efficient donor of the electron density. The average value of the $S(CH_3)^- \rightarrow$ metal electron transfer in the complexes under consideration is 0.77 e. Each of these ligands forms strong bonds with the central ion: The mean Mayer order of the M–$S(CH_3)^-$ bond [31] is 0.81. The $S(CH_3)_2$ ligands are also good donors. However, they donate only about 0.37 e to the metal, and the mean order of the M–$S(CH_3)_2$ bonds formed, 0.56, is lower than with the anionic ligands.

Thus, quantum-chemical calculations support the suggested scheme of the heterolytic cleavage of the C–N bonds with the formation of polymeric mercapto–thio ether complexes of Pt(II) in the course of the sorption.

The MITKhAT sorbent was tested for group recovery of metals from a model solution containing platinum metals and gold in amounts typical of an industrial process. It was found (see table) that the sorbent recovers from the solution almost 100% of Pd and Au, about 93% of Ir and Pt, and 76.5% of Rh.

MITKhAT was also tested for recovering palladium and platinum from hydrochloric acid solutions obtained in reprocessing of catalysts for exhaust gas treatment. From the solution containing (g l^{-1}) Pd 0.414, Pt 0.074, and Al 1.02, it is possible to recover 99.9 and 98.0% of Pd and Pt, respectively.

Commercial samples of S,N-containing heterochain polymers KDM-2 and KPU-2, analogs of MITKhAT, were tested for group recovery of Pt, Pd, and Rh from spent automobile catalysts after their acid breakdown, with the subsequent atomic absorption determination. Based on the results obtained, procedures were developed for sorption–atomic absorption determination of platinum metals in multicomponent samples (in the presence of Ti, Al, Zr, Sn, Co, Ni, Fe, Cu) [32].

Sorption of platinum metals from a model hydrochloric acid (3 M HCl) solution (3 h, 18°C)

Metal	Concentration in solution, μg ml^{-1}		Recovery, %
	before sorption	after sorption	
Au	4.14	0.08	98.0
Ir	4.00	0.3	92.5
Pt	10.05	0.65	93.5
Pd	53.76	0.18	99.7
Rh	12.40	2.91	76.5

CONCLUSIONS

(1) Optimal conditions were found for recovering platinum(II) and platinum(IV) chloro complexes from hydrochloric acid and chloride solutions with MITKhAT heterochain S,N-containing sorbent at room temperature. The maximal sorption capacity toward platinum(II) and platinum(IV) chloro complexes is 6.5 and 4 mmol g^{-1}, respectively.

(2) As shown by elemental analysis and by IR and X-ray photoelectron spectroscopy, the recovery of platinum(II) and platinum(IV) chloro complexes from hydrochloric acid and chloride solutions is accompanied by formation of mercapto–thio ether complexes of Pt(II).

(3) The DFT calculations of the electronic structure of aminomethylene sulfide, its protonated form, and a model Pt(II) complex, *trans*-$[Pt(DMS)_2(SCH_3)_2]$, where DMS = $S(CH_3)_2$, confirm the formation of platinum mercapto–thio ether complexes in the recovery process.

(4) Heterochain S,N-containing sorbent MITKhAT can be suggested for group recovery of platinum metals from multicomponent solutions.

ACKNOWLEDGMENTS

The authors are grateful to A.V. Shchukarev for measurement of the X-ray photoelectron spectra of samples and for assistance in their interpretation.

The study was financially supported by the departmental target program "Development of the Scientific Potential of Higher School" (RNP.2.1.1.1277) and by the Russian Foundation for Basic Research (project no. 07-03-00 597).

REFERENCES

1. Myasoedova, G.V. and Savvin, S.B., *Khelatoobrazuyushchie sorbenty* (Chelating Sorbents), Moscow: Nauka, 1984.
2. Simanova, S.A. and Kukushkin, Yu.N., *Izv. Vyssh. Uchebn. Zaved., Khim. Khim. Tekhnol*., 1985, vol. 28, pp. 3–15.
3. Simanova, S.A. and Kukushkin, Yu.N., *Izv. Vyssh. Uchebn. Zaved., Khim. Khim. Tekhnol*., 1986, vol. 29, pp. 3–14.
4. Myasoedova, G.V. and Kamozin, P.N., *Zh. Prikl. Khim*., 1994, vol. 39, no. 2, pp. 280–288.
5. Simanova, S.A. and Kukushkin, Yu.N., in *Problemy sovremennoi khimii i khimii koordinatsionnykh soedinenii* (Problems of Modern Chemistry and Coordination Chemistry), St. Petersburg: Sankt-Peterb. Gos. Univ., 1992, issue 10, pp. 41–61.
6. Simanova, S.A., Burmistrova, N.M., and Afonin, M.V., *Ross. Khim. Zh*., 2006, vol. 50, no. 4, pp. 19–25.
7. Simanova, S.A., Zamorova, I.N., Kazakevich, Yu.E., et al., *Zh. Prikl. Khim*., 1992, vol. 65, no. 9, pp. 987–1994.
8. Bankovskii, Yu.A., *Khimiya vnutrikompleksnykh soedinenii merkaptokhinolina i ego proizvodnykh* (Chemistry of Chelates of Mercaptoquinoline and Its Derivatives), Riga: Zinatne, 1978.
9. Simanova, S.A., Kuznetsova, T.V., Belyaev, A.N., et al., *Zh. Prikl. Khim*., 1999, vol. 72, no. 8, pp. 1276–1282.
10. Simanova, S.A., Knyaz'kov, O.V., Belyaev, A.N., et al., *Zh. Prikl. Khim*., 1998, vol. 71, no. 2, pp. 220–226.
11. Simanova, S.A., Tevlina, A.S., An, I.V., and Burmistrova, N.M., *Zh. Prikl. Khim*., 1992, vol. 65, no. 2, pp. 298–305.
12. Malofeeva, G.I., Petrukhin, O.M., et al., *Izv. Vyssh. Uchebn. Zaved., Khim. Khim. Tekhnol*., 1988, vol. 31, no. 5, pp. 3–14.
13. Malofeeva, G.I., Petrukhin, O.M., et al., *Zh. Anal. Khim*., 1987, vol. 42, no. 7, pp. 1204–1207.
14. Anpilogova, G.R., Aleev, R.S., et al., *Zh. Prikl. Khim*., 1995, vol. 68, no. 12, pp. 1969–1974.
15. RF Patent 2 205 237, June 8, 2001.
16. Karpov, Yu.A., Shiryaeva, O.A., and Dal'nova, Yu.S., Abstracts of Papers, *XVII Mendeleevskii s"ezd po obshchei i prikladnoi khimii* (XVII Mendeleev Congr. on General and Applied Chemistry), Kazan, September 21–26, 2003, vol. 1, p. 427.
17. Aktuganova, K.V., Karpov, Yu.A., Shiryaeva, O.A., and Dal'nova, Yu.S., *Zav. Lab. Diagn. Mater*., 2006, vol. 72, no. 6, pp. 3–9.
18. Simanova, S.A., Afonin, M.V, Aktuganova, K.V., et al., in *Razdelenie i kontsentrirovanie v analiticheskoi khimii i radiokhimii: Materialy II Mezhdunarodnogo simpoziuma (k yubileyu akademika B.F. Myasoedova)* (Separation and Preconcentration in Analytical Chemistry and Radiochemistry: Proc. II Int. Symp. (Dedicated to the Jubilee of Acad. B.F. Myasoedov)), Krasnodar, September 25–30, 2005, pp. 262–263.
19. Afonin, M.V., Simanova, S.A., Dal'nova, Yu.S., et al., Abstracts of Papers, *XVIII Mezhdunarodnaya Chernyaevskaya konferentsiya po khimii, analitike i tekhnologii platinovykh metallov* (XVIII Int. Chernyaev Conf. on Chemistry, Analytical Chemistry, and Technology of Platinum Metals), Moscow, October 9–13, 2006, vol. 1, pp. 100–101.
20. *Sintez kompleksnykh soedinenii metallov platinovoi gruppy* (Synthesis of Coordination Compounds of Platinum Group Metals), Chernyaev, I.I., Ed., Moscow: Nauka, 1964.
21. *Analiticheskaya khimiya elementov: Platinovye metally* (Analytical Chemistry of Elements: Platinum Metals), Alimarin, I.P., Ed., Moscow: Nauka, 1972.
22. Afonin, M.V., Simanova, S.A., Burmistrova, N.M., et al., Abstracts of Papers, *Vtoraya Vserossiiskaya konferentsiya "Analitika Rossii"* (Second All-Russian Conf. "Analytical Chemistry of Russia"), Krasnodar, October 7–12, 2007.
23. Bellamy, L.J., *The Infra-Red Spectra of Complex Molecules*, New York: Wiley, 1957.
24. Finch, A., Gates, K., and Radcliffe, K., *Chemical Applications of Far Infrared Spectroscopy*, London: Academic, 1970.
25. Nefedov, V.I., *Rentgenoelektronnaya spektroskopiya khimicheskikh soedinenii: Spravochnik* (X-ray Photoelectron Spectroscopy of Chemical Compounds: Handbook), Moscow: Khimiya, 1984.
26. *Handbook of X-ray Photoelectron Spectroscopy*, Perkin–Elmer, Physical Electronics Division, 1992.
27. Hay, P.J. and Wadt, W.R., *J. Chem. Phys*., 1985, vol. 82, p. 284.
28. Schmidt, M.W., Matsunaga, K.K., Nguen, K.A., et al., *J. Comput. Chem*., 1993, vol. 14, p. 1347.
29. *Chemical Reactivity and Reaction Paths*, Klopman, G., Ed., New York: Wiley–Interscience, 1974.
30. Pearson, R.G., *J. Am. Chem. Soc*., 1963, vol. 85, p. 3533.
31. Mayer, J., *Theor. Chim. Acta*, 1985, vol. 67, pp. 315–322.
32. Aktuganova, K.V., *Cand. Sci. Dissertation*, Moscow, 2006.

ISSN 1070-4272, Russian Journal of Applied Chemistry, 2008, Vol. 81, No. 11, pp. 1939–1941. © Pleiades Publishing, Ltd., 2008.
Original Russian Text © E.R. Valinurova, A.D. Kadyrova, L.R. Sharafieva, F.Kh. Kudasheva, 2008, published in Zhurnal Prikladnoi Khimii, 2008, Vol. 81, No. 11, pp. 1822–1825.

PHYSICOCHEMICAL STUDIES OF SYSTEMS AND PROCESSES

Use of Activated Carbon Materials for Wastewater Treatment to Remove Ni(II), Co(II), and Cu(II) Ions

E. R. Valinurova, A. D. Kadyrova, L. R. Sharafieva, and F. Kh. Kudasheva

Bashkir State University, Ufa, Bashkortostan, Russia

Received November 2, 2007

Abstract—The sorption activity of UVIS-AK activated carbon fiber with respect to the Co(II), Ni(II), and Cu(II) cations was studied. The possibility of using this fiber for industrial wastewater treatment to remove heavy metal ions was examined.

DOI: 10.1134/S107042720811013X

Many heavy metals exhibit high toxicity even in trace quantities and are concentrated in living bodies. In contrast to organic compounds, which undergo degradation, metals are only redistributed between natural media and are gradually accumulated in them. Therefore, further research and development of new methods for wastewater treatment to remove heavy metal ions are necessary. The most widely used methods involve precipitation of difficultly soluble heavy metal hydroxides and sulfides using appropriate reagents [1]. Such methods are simple, but involve introduction of new chemicals into the wastewater. Furthermore, the hydrated precipitates formed in the process are voluminous. Fine water purification is commonly performed with zeolites [2], cation-exchange resins [3], or activated carbons [1]. For the recovery of heavy metal ions, much promise is shown by fibrous carbon materials, as they combine filtration and sorption properties and have high specific surface area and developed porosity [4, 5].

In this study we evaluated the sorption activity of activated carbon fibers toward Co(II), Ni(II), and Cu(II) cations with the aim of its use for the treatment of wastewater contaminated with these metal ions.

EXPERIMENTAL

For the sorption of heavy metal ions, we used activated carbon fiber (ACF) of UVIS-AK brand, oxidized activated carbon fiber (OACF), and activated birch charcoal (BAU-A).

The sample of oxidized carbon fiber was prepared by refluxing ACF for 1 h in concentrated HNO_3, with the subsequent washing with double-distilled water.

The specific surface area of adsorbents S was determined by thermal desorption of nitrogen, and the limiting adsorption pore volume for ethanol vapor V_Σ, by the desiccator method [6]. The mean pore diameter r_m was calculated by the formula

$$R_m = 2 \times 10^4 V_\Sigma / S.$$

The total acidity of carbon adsorbents was determined by titration with a 0.1 N NaOH solution. The content of functional groups on the surface of carbon adsorbents was determined by the Boehm method [7] from the sorption of the solutes from 0.05 N $NaHCO_3$, Na_2CO_3, and NaOH solutions. Some characteristics of the carbon adsorbents are given in Table 1. As can be seen, the specific surface area of the sorbents is fairly high, from 660 to 1300 $m^2 g^{-1}$, with the prevalence of micropores with a mean diameter of 6–14 Å. Oxidation of the initial carbon fiber led to an increase in the micropore size by a factor of more than 2, a decrease in the specific surface area, and a considerable increase in the cation-exchange capacity.

The sorption of metal cations was performed from solutions of their chemically pure grade salts in the

Table 1. Some characteristics of carbon adsorbents

Adsorbent	S, $m^2 g^{-1}$	V_Σ, $cm^2 g^{-1}$	r_m, Å	Total acidity, mg-equiv g^{-1}
BAU-A	740–840	0.32	9	1.37
ACF	1300	0.48	6	0.97
OACF	660	0.47	14	4.26

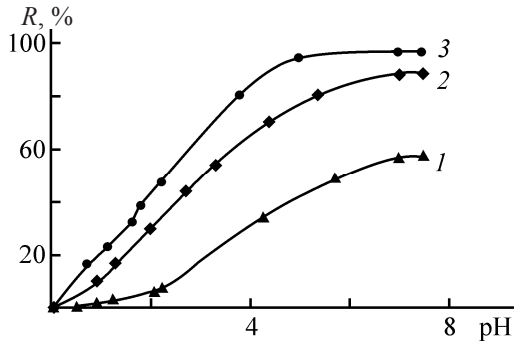


Fig. 1. pH dependence of the degree of recovery R of (*1*) Co(II), (*2*) Ni(II), and (*3*) Cu(II) ions with the carbon fiber. $C_{M^{2+}}$ = 14 mg l^{-1}, $V_{solution}$ = 25 ml, m = 0.0200 g.

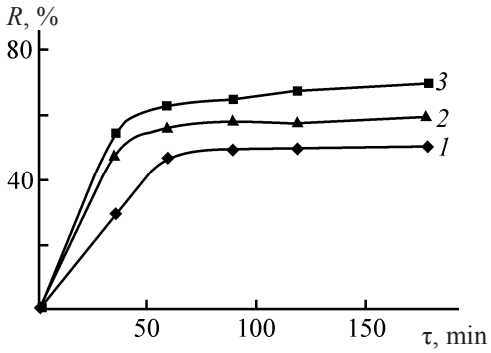


Fig. 2. Degree of recovery R of Cu^{2+} ions in the presence of Na^+ ions (600 mg l^{-1}) as a function of time τ. $C_{Co^{2+}}$ = 32 mg l^{-1}, $V_{solution}$ = 50 ml, m = 0.1000 g. ACF: (*1*) initial, (*2*) oxidized, and (*3*) impregnated with nitroso-R-salt.

static mode at room temperature with continuous stirring. Weighed portions of the adsorbents brought to constant mass (from 0.0200 to 0.1000 g) were placed in model solutions (25 ml) containing (mg l^{-1}) 6–60 cobalt(II) sulfate, 0.01–0.8 copper(II) nitrate, and 0.8–4.0 nickel(II) sulfate. The mixture was kept for a time required to attain the sorption equilibrium. The major fraction of Ni(II), Cu(II), and Co(II) cations is sorbed by the fiber within 2 h, 2.5–3 h, and no less than 1.5 days, respectively. The concentration of metal ions was determined photocolorimetrically with nitroso-R-salt for Co(II), sodium diethyldithiocarbamate for Cu(II), and dimethylglyoxime for Ni(II) [8].

Table 2. Degree of recovery R of Co(II), Ni(II), and Cu(II) ions ([Na^+] = 920 mg l^{-1})

Sorbent	R, %, without Na^+			R, %, with Na^+		
	Co^{2+}	Ni^{2+}	Cu^{2+}	Co^{2+}	Ni^{2+}	Cu^{2+}
BAU-A	30	35	83	29	35	87
ACF	41	40	98	26	30	98
OACF	100	100	93	100	100	94

One of the major factors controlling the ion exchange between an adsorbate and an adsorbent containing weakly acidic and weakly basic groups is pH of the solution. The pH was adjusted by adding small volumes of HCl and NaOH solutions. Figure 1 shows how the degree of metal ion recovery with the carbon fiber depends on the solution acidity. The Ni^{2+} and Co^{2+} ions are quantitatively recovered at pH 7 within 1.5 days and 2 h, respectively, and the Cu^{2+} ions, at pH 5–6 within 3 h. Further increase in pH is not appropriate because of the possible binding of metal cations into insoluble hydroxides and basic salts.

As wastewaters to be treated to remove heavy metal ions are usually mineralized, we examined the effect of sodium sulfate on the degree of removal of Cu^{2+}, Co^{2+}, and Ni^{2+} from water. The results of treatment to remove these metal ions from aqueous solutions containing up to 920 mg l^{-1} Na^+ ions are given in Table 2. It can be seen that the presence of sodium ions does not noticeably affect the recovery of Cu^{2+} with the carbon sorbents, whereas the recovery of Co^{2+} and Ni^{2+} cations with ACF somewhat decreases. However, in all cases OACF shows high selectivity toward heavy metal ions in the presence of sodium ions.

The selectivity of the sorption treatment with the oxidized fiber increases owing to an increase in the concentration of active acid centers responsible for the ion exchange. In particular, the concentration of carboxy groups increases by a factor of 2.5 (Table 3). Figure 2 shows the dependences of the degree of Cu^{2+} recovery from a solution containing up to 600 mg l^{-1} Na^+ on the contact time for the initial fiber, that modified with nitroso-R-salt, and that oxidized with nitric acid. As can be seen, treatment of the fiber with the reagent forming a stable complex with cobalt ions also considerably increases the efficiency and selectivity of the sorption. The complex is formed by coordination of the cobalt ion with the nitroso group atoms and phenolic oxygen. As a result, the degree of Co^{2+} recovery increases by 10%.

Figure 3 shows as example the adsorption isotherms of Cu^{2+}, obtained by the method of varied weighed portions at 25°C. The sorption isotherms on BAU and ACF have the shape described by the Langmuir equation. The shapes of the sorption isotherms are similar because of similarities in the structure of the carbon skeleton and in the surface chemistry of these adsorbents. The adsorption isotherm on the carbon fiber at a low degree of filling of the surface is steeper than that on activated carbon, which suggests

Table 3. Content of functional groups on the surface of carbon adsorbents

Adsorbent	Content of functional groups, mg-equiv g^{-1}		
	carboxy	phenolic	lactone
BAU-A	0.15	0.81	0.31
ACF	0.97	0	0
OACF	2.38	1.24	0.64

Table 4. Degree of sorption treatment of wastewater to remove Cu(II) ions

Sorbent	*R*, %
BAU-A	70
ACF	88
OACF	90

higher microporosity of the carbon fiber. Adsorption of metal ions on carbon adsorbents mainly occurs by the ion-exchange mechanism, as follows from a decrease in pH of the solution by 0.2–0.6 after the contact with the adsorbents. The total content of acidic functional groups on BAU is higher than that on ACF by a factor of 1.3 (Table 1), but the content of carboxy groups responsible for the ion exchange is lower by a factor of more than 6. This fact is, apparently, responsible for faster attainment of the sorption equilibrium of salt solutions with the fiber than with the charcoal. The sorption isotherms of metal cations on OACF are steeply ascending, which is due to considerably enhanced cation-exchange power of the fiber.

Under the optimal conditions, we performed static sorption treatment of wastewater containing up to 2.5 mg l^{-1} Cu(II), 0.02 wt % ethyl acetate, and 0.04 wt % ethanol. The results of the sorption treatment to remove Cu(II) cations are given in Table 4. The degree of removal of Cu(II) cations from water

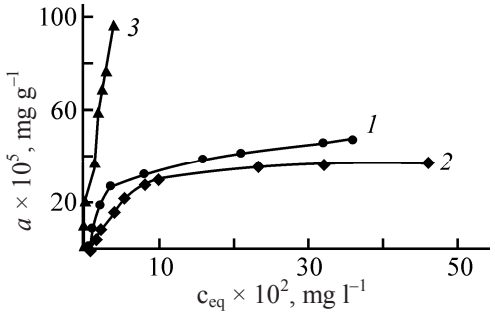


Fig. 3. Isotherms of adsorption of copper ions on (*1*) ACF, (*2*) BAU-A, and (*3*) OACF at 25°C. (*a*) Adsorption and (c_{eq}) equilibrium concentration of Cu(II) ions.

increases in the order BAU < ACF < OACF. The sample of a catalytically oxidized sulfide–alkaline wastewater containing petroleum products (25 mg l^{-1}), phenols (100 mg l^{-1}), sulfates (2300 mg l^{-1}), and Co^{2+} (20 mg l^{-1}) was treated only with ACF. After the treatment, no Co^{2+} was detected in the solution.

CONCLUSIONS

(1) Comparative estimation of the sorption activity of activated carbon fiber UVIS-AK and activated charcoal BAU-A with respect to Cu^{2+}, Co^{2+}, and Ni^{2+} ions was made. The UVIS-AK fiber exhibits higher sorption characteristics than BAU-A owing to its high permeability and higher content of active adsorption centers.

(2) The recovery of Cu^{2+}, Co^{2+}, and Ni^{2+} ions depends on pH, degree of water mineralization, and texture of carbon adsorbents (grained or fibrous).

(3) Modification of activated carbon fibers by oxidation in nitric acid appreciably enhances the efficiency of the recovery of heavy metal ions from highly mineralized water. The degree of recovery is as high as 93–94% for Cu^{2+} and 100% for Co^{2+} and Ni^{2+}.

REFERENCES

1. Rodionov, A.I., Klushin, V.N., and Sister, V.G., *Tekhnologicheskie protsessy ekologicheskoi bezopasnosti* (Processes for Environmental Safety), Kaluga: Izd. Bochkarevoi, 2000.
2. Tarasevich, Yu.I., *Prirodnye sorbenty v protsesse ochistki vody* (Natural Sorbents in Water Treatment), Kiev: Naukova Dumka, 1981.
3. Ashirov, A.N., *Ionoobmennaya ochistka stochnykh vod, rastvorov i gazov* (Ion-Exchange Treatment of Waters, Solutions, and Gases), Moscow: Khimiya, 1983.
4. Zemskova, L.A., Avramenko, V.A., Chernykh, V.V., et al., *Zh. Prikl. Khim.*, 2004, vol. 77, no. 7, pp. 1116–1119.
5. Rakitskaya, T.L., Red'ko, T.D., and Litvinskaya, V.V., *Zh. Prikl. Khim.*, 1992, vol. 65, no. 9, pp. 1977–1981.
6. Kel'tsev, N.V., *Osnovy adsorbtsionnoi tekhniki* (Fundamentals of Adsorption Technique), Moscow: Khimiya, 1976.
7. Boehm, H.P., *Carbon*, 1994, vol. 32, no. 5, pp. 759–769.
8. Lur'e, Yu.Yu., *Analiticheskaya khimiya promyshlennykh stochnykh vod* (Analytical Chemistry of Industrial Wastewaters), Moscow: Khimiya. 1984.

ISSN 1070-4272, Russian Journal of Applied Chemistry, 2008, Vol. 81, No. 11, pp. 1942–1946. © Pleiades Publishing, Ltd., 2008.
Original Russian Text © A.N. Verigin, A.V. Pelevin, 2008, published in Zhurnal Prikladnoi Khimii, 2008, Vol. 81, No. 11, pp. 1826–1830.

PHYSICOCHEMICAL STUDIES OF SYSTEMS AND PROCESSES

Rate of Energy Dissipation in Apparatus with High-Intensity Agitation

A. N. Verigin and A. V. Pelevin

St. Petersburg State Institute of Technology (Technical University), St. Petersburg, Russia

Received May 12, 2008

Abstract—Flow nature in rotary mills is considered and a mathematical description of the energy dissipation rate under high-intensity agitation is given.

DOI: 10.1134/S1070427208110141

In recent years, a considerable progress has been made in the field of basic research into the hydrodynamics and transport processes in apparatus with mechanical agitators. Studies by V.V. Kafarov, P.G. Romankov, F. Strenk, V.G. Ushakov, V.M. Barabash, N.N. Kulov, and other scientists provided insight into the physical mechanism of agitation and enabled analysis of its various aspects from the common theoretical standpoint.

However, there exists a gap between achievements in synthesis of new materials and development of technologies, on the one hand, and potentialities of their implementation on the existing equipment, on the other. This primarily refers to high-intensity processes (especially those in potentially hazardous media) and complex reactions in heterogeneous media. The increasingly stringent requirements to the quality of the products obtained entail increased requirements to the quality and rate of agitation. Just this circumstance makes important studies aimed to develop apparatus that can control the process intensity. To apparatus of this kind can be attributed rotary reactors providing a high agitation intensity.

Solving this problem requires an in-depth study of the influence exerted by the macro- and microstructure of turbulence on the fundamental aspects of agitation and efficiency of the apparatus being designed. Although the influence exerted by stable coherent formations and fractal structure of turbulent flows on transfer processes is considered in the theoretical hydrodynamics, it still has no engineering applications. In this context, studies concerned with the mechanisms of agitation in rotary apparatus at high energy dissipation rates and with application of achievements of the theoretical hydrodynamics to development of scientifically substantiated methods for their calculation remain rather topical.

The aim of our study was to examine the energy dissipation in rotary apparatus under agitation, to compare amounts of energy dissipation in laminar and turbulent agitation modes, and to select and theoretically substantiate a procedure for calculating the energy dissipation in accordance with experimental data.

Theoretical studies of transfer processes that occur under agitation in rotary apparatus have been performed using a unified approach based on the energy dissipation rate as the key parameter. A method employing elements of the theory of dissipative systems has been suggested for analyzing the fundamental aspects of energy dissipation in various hydrodynamic flow modes. An expression for calculating the energy dissipation rate in a turbulent flow can be found from the concept of the fractal nature of turbulence. Methods for experimentally estimating the fractal dimension of the energy dissipation field and determining the local rate of energy dissipation have been substantiated.

The lack of a sufficiently complete theory of turbulence makes difficult an engineering description of agitation in turbulent flows. The relations known from the literature are either purely empirical or refer to flow types rarely occurring in apparatus. It is apparent that theoretical foundations for an engineering description of turbulence in apparatus should be related both to parameters characterizing an apparatus and to pa-

rameters determining the fundamental properties of turbulence: characteristic size of turbulent pulsations, local energy dissipation rate, and fractal dimension of the dissipation field.

Theoretical studies are devoted to description of the fundamental aspects of energy dissipation in laminar, transition, and turbulent flow modes in rotary apparatus and to calculation of the power consumed for agitation on this basis.

At present, the most complete in theoretical regard and best substantiated by practical results is A.N. Kolmogorov's theory of locally isotropic turbulence. According to this theory, the turbulence is a hierarchy of vortices (i.e., perturbations or heterogeneities) of various characteristic sizes, in which vortices of a given size appear as a result of stability loss by larger vortices and "borrow" energy from these vortices, and, in turn, losing stability, give rise to pulsations of a smaller characteristic size, to which they transfer their energy. Energy passes from larger vortices to smaller pulsations, almost with zero dissipation. It can be considered that there occurs a continuous energy flow from large- to small-scale turbulent formations. This flow dissipates, i.e., the kinetic energy is transformed into heat, in the smallest-size vortices. In this case, the stationary state of the flow is provided by an external source (agitator), which continuously transfers energy to the large-scale motion. As a result of the chaotic nature of this energy transfer, the orienting effect of the medium-scale flow must become weaker in any transition to finer perturbations. Therefore, this orienting influence should not affect the turbulence properties on a sufficiently small scale. Generally speaking, the medium-scale flow and the largest vortices of real turbulent flows are anisotropic, but the statistical mode of small-scale pulsations can be considered isotropic. It is characterized by the existence of a certain averaged energy inflow (W kg^{-1}) to the largest perturbations and the equal energy dissipation into heat under the action of viscous-friction forces in the smallest perturbations. In this case, the dissipation rate is given by

$$\varepsilon \sim \nu^3/\lambda^4, \quad (1)$$

where ν is the kinematic viscosity and λ is the scale of vortices in which the energy dissipation proper occurs.

Based on dimension considerations, we can demonstrate that

$$\lambda \sim L/\mathrm{Re}^{3/4}, \quad (2)$$

where the Reynolds number $\mathrm{Re} = UL/\nu$ is expressed in terms of the characteristic velocity U and characteristic size L of the entire flow.

Relations (1) and (2) can be transformed into an equality by introducing a Reynolds number for pulsations of characteristic size λ and the corresponding velocity $U\lambda$. Then we obtain at $\lambda = [(L\mathrm{Re}_0)/\mathrm{Re}]^{3/4}$:

$$\varepsilon = \nu^3 L^{-4}(\mathrm{Re}/\mathrm{Re}_0)^{-3}. \quad (3)$$

The flow in formations of characteristic size λ is laminar and energy dissipations occurs under the action of viscous forces, with the following condition to be satisfied:

$$\varepsilon^* \sim \nu U_\lambda^3 \lambda^{-2}, \quad (4)$$

where ε^* is the local energy dissipation rate in a formation of characteristic size λ.

Converting (4) into an equality, we obtain

$$\varepsilon^* = \nu^3 \gamma \mathrm{Re}_0^2 \lambda^{-4}. \quad (5)$$

A relationship between ε^* and the energy dissipation rate ε space-averaged over the apparatus can be determined by using the concept of the fractal dimension of the energy dissipation field [1–5].

The quantity ε^* is a characteristic of the local energy dissipation, and for the flow as a whole, the following condition should be satisfied:

$$\varepsilon = \varepsilon^* N^*/N. \quad (6)$$

According to expression (6), the number N^* of formations in which the energy dissipation ε^* occurs may differ from the maximum possible number N of formations of characteristic size λ. It is apparent that $N = (L/\lambda)^3$. The value of N^* depends on the fractal dimension d of the energy dissipation field. Considering the dissipation field in a rotary apparatus to be monofractal, we can write down that $N^* = (L/\lambda)^d$. Substituting expressions for N and N^* into (6), we obtain

$$\varepsilon^* = \varepsilon(L/\lambda)^{3-d}. \quad (7)$$

Simple rearrangements can give an expression relating the energy dissipation rate to the fractal dimension

$$\varepsilon = \nu^3 L^{-4}(\gamma \mathrm{Re}^2)^{12/(17-3d)}, \quad (8)$$

where γ is the proportionality coefficient.

It can be seen from expression (8) that $\varepsilon \sim \mathrm{Re}^3$ only in the case when the fractal dimension of the dissipation field is equal to the Euclidean dimension of the field ($d = 3$), i.e., the turbulent formations of the small-

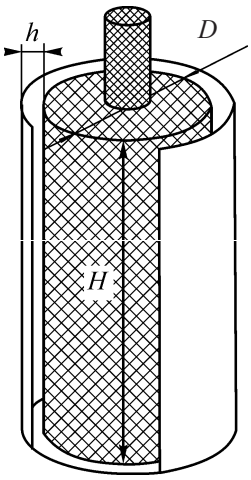


Fig. 1. Schematic of apparatus with a smooth rotor.

est size should occupy the whole flow volume. This situation rarely occurs in technological apparatus, and, therefore, the turbulence in such apparatus should be considered nonuniformly locally isotropic.

Although the thus introduced dimension d can be fractal only within a certain physical interpretation, such as capacitive (metric) dimension in the given case, rather than in the strictly mathematical understanding of this word, it is very convenient and effective for describing agitation in the apparatus under consideration.

The presently available data suggest that the fractal dimension of the energy dissipation field for flows that can be obtained in practice is within the range 2.5–3.

Let us consider two extreme cases. If $\gamma \to 1$ and $d \to 3$, i.e., the spatial scale of minimum pulsations and the corresponding Reynolds number are small. This situation corresponds to a uniform isotropic turbulence, which is observed, e.g., in a flow below a grid. If $\gamma << 1$ and $d \to 3$, the characteristic size of turbulent pulsations is large. In this case, a strongly nonuniform hydrodynamic situation is probable: a turbulent core exists, with the rest of the apparatus volume remaining laminar. Knowledge of γ and d makes it possible to judge about the structure of the turbulent flow in an apparatus. Expressions (7) and (8) enable description of transfer processes in a turbulent flow.

It was found in processing and analysis of experimental data for apparatus with different gaps that the fractal dimension d is a function of the Reynolds number:

$$D = 2 + (\mathrm{Re}/B)^n, \quad (9)$$

where B and n are found experimentally.

The suggested equations contain the quantity γ dependent on specific features of the flow in minimum turbulent pulsations. In some cases, theoretical estimation of its value is possible. In accordance with the data of [3], reasons for flow turbulization can be conditionally divided into two groups. To the first group belong specific features of the flow as a whole, which lead to loss of stability by the laminar flow at a certain critical value of the Reynolds number. From the practical standpoint, it is also necessary to take into account the effect of the existing initial fluctuations of hydrodynamic parameters in the flow, wall vibration and roughness, and chemical heterogeneity. These features constitute the second group, conditionally named the background. As shown in [2], the rather small values of the parameters characterizing the background are as important for the appearance and development of turbulence as the boundary (initial) conditions commonly taken into account in analyses of flows. In the case of a developed turbulence, when the background effects already exert no influence on the flow, a theoretical estimate of γ is possible. The value of Re_0 is 2.5, to which corresponds $\gamma = 0.16$. It would be expected that γ should be of the same order of magnitude for all types of industrially used rotors.

The main distinctive feature of rotary apparatus is the agitating device in the form of a cylindrical rotor whose diameter and height are comparable with the diameter and height of the apparatus casing. The working zone in rotary apparatus is the annular gap of width h between the casing and the surface of the rotating rotor.

We used in experiments an apparatus with a smooth rotor (Fig. 1). Its basic parameters are as follows: rotor length H 150 mm, rotor diameter D 150 mm, gap (fluid layer thickness) h = 8, 15, 18, 24, 30, 37, and 58 mm.

The parameters of the working media are listed in the table.

If the rotor of radius R rotates with angular velocity ω, then, in the case of a laminar flow, the energy dissipation rate in the annular gap is given by

$$\varepsilon = \nu(\mathrm{d}U/\mathrm{d}T)[(\mathrm{d}U - U)/(\mathrm{d}r - r)], \quad (10)$$

where U and r are the running values of the velocity and radius, respectively.

Upon rearrangements, we obtain

$$\varepsilon = \nu^3 A \mathrm{Re}^2/h^4. \quad (11)$$

The geometrical parameter A is defined as

$$A = [3(1 + h/R)^2 + 1](R + h)^2(2R + h)^{-2}. \quad (12)$$

It is known [5] that the rotary motion of a fluid in the annular gap is unstable. At $\mathrm{Re} \approx 41.3(R/h)^{0.5}$, a flow of another type is formed, constituted by toroidal vortices (Taylor vortices) regularly arranged over the length of the cylinders. At $\mathrm{Re} \approx 1000(R/h)^{0.5}$, the fluid flow becomes turbulent, but coherent structures, toroidal macrovortices remain the flow.

Let us consider qualitative features of the energy dissipation in this transition. It is suggested to use the gap width h between the casing wall and the rotor surface as the characteristic size L of the maximum pulsation when describing the turbulence in the apparatus under consideration.

From the energy dissipation standpoint, the fluid flow can be regarded as a bistable system one of whose equilibrium states corresponds to a streamline flow with a dissipation rate $\varepsilon_s(\mathrm{Re})$, and the other, to a vortex-type flow with dissipation $\varepsilon_v(\mathrm{Re})$. The streamline flow must be preserved while the whole amount of input energy can be dissipated. The appearance of a turbulence will become possible at Re_{cr}, i.e., at $\varepsilon_s(\mathrm{Re}_{cr}) = \varepsilon_v(\mathrm{Re}_{cr})$. At Reynolds numbers exceeding Re_{cr}, turbulent pulsations may appear in the medium, with a part of its volume occupied by the laminar flow, and a part by a turbulent flow. Then the dissipation rate can be represented as

$$\varepsilon = K_s\varepsilon_s(\mathrm{Re}) + K_v\varepsilon_v(\mathrm{Re}), \quad (13)$$

where K_s and K_v are the ratios of the flow volume that remained laminar (turbulent) to the whole volume of the system, which are defined as

$$K_{s(v)} = V_{v(s)}/V_\Sigma, \quad (14)$$

where $V_{v(s)}$ is the volume of the vortex-type (streamline) flow, and V_Σ, the total flow volume.

K_s and K_v are related by $K_s + K_v = 1$. Upon rearrangements, formula (13) will take the form

$$\varepsilon = K_s\varepsilon_s(\mathrm{Re}) + (1 - K_s)\varepsilon_v(\mathrm{Re}). \quad (15)$$

Having found the expression for the energy dissipation rate, we can determine the power expended for agitation:

$$N = \varepsilon\rho V_a,$$

Properties of working media (20°C)

Medium	Density, kg m^{-3}	Viscosity, m^2 s^{-1}
Water	1002	10^{-6}
Glycerol	1280	1.18×10^{-3}
Glycerol solution, 70%	1208	6.55×10^{-5}
Acetone	896	3×10^{-7}

where ρ is the density of the medium in the apparatus, and V_a is the apparatus volume.

An annular layer adjacent to the walls of the immobile cylinder (casing) must remain laminar. The power dissipated in the streamline flow can be calculated by the formula

$$\varepsilon_s = \nu^3 h^{-4} A(\mathrm{Re})^2, \quad (16)$$

and that for the vortex-type flow, by the formula

$$\varepsilon_s = \nu^3 h^{-4}(\gamma\mathrm{Re})^{12/(17-3d)}, \quad (17)$$

where ν is the kinematic viscosity of the medium being treated.

To find K_s, it was suggested to use the function of the type

$$K_s = 1 - \exp(-\mathrm{Re}/\mathrm{Re}_{cr})^m, \quad (18)$$

where Re_{cr} is the critical value of the Reynolds number (in our case, $\mathrm{Re}_{cr} = 4$), and m is an empirical coefficient equal to 1.5.

The calculated values of the energy dissipation rate are in good agreement with experimental data. The best agreement of the theory with the experiment is observed at the following values of the basic parameters: $\gamma = 0.5$, $n = 0.107$, $m = 1.5$, and $B = 2.1 \times 10^7$. The root-mean-square discrepancy between the calculation and the experiment does not exceed ±12%.

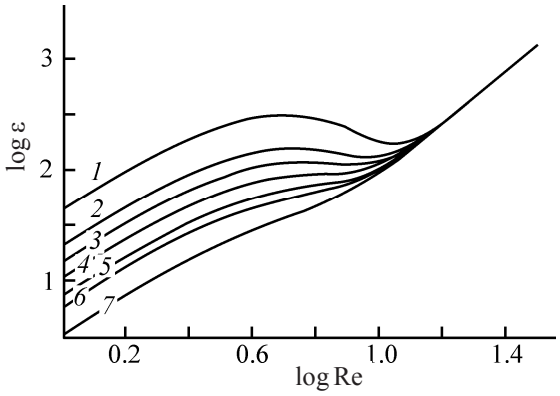


Fig. 2. Energy dissipation rate ε vs. the Reynolds number Re in the transition region. Gap width h, mm: (*1*) 58, (*2*) 37, (*3*) 30, (*4*) 24, (*5*) 18, (*6*) 15, and (*7*) 8.

The mathematical dependence we obtained enables prediction of the behavior of the system at small values of the Reynolds number in the laminar and transition flow modes (Fig. 2).

CONCLUSIONS

(1) An equation for calculating the average (over the mass of the medium in the apparatus) energy dissipation rate in the developed turbulent mode was derived.

(2) The nonuniformity of the turbulent flow can be taken into account by introducing the fractal dimension of the dissipation field.

(3) Taking into account the nonuniformity of the dissipation field by determining the corresponding fractal dimension is of use in simulation of substance and heat transfer processes in apparatus under study.

REFERENCES

1. Verigin, A.N., Ermakov, A.S., and Shashikhin, E.Yu., *Khim. Neft. Mashinostr.*, 1996, no. 3, pp. 15–316.
2. Ermakov, A.S. and Verigin, A.N., *Khim. Neft. Mashinostr.*, 1996, no. 3, pp. 13–14.
3. Verigin, A.N., Ermakov, A.S., and Shashikhin, E.Yu., *Zh. Prikl. Khim.*, 1995, vol. 68, no. 6, pp. 982–986.
4. Verigin, A.N., Ermakov, A.S., and Shashikhin, E.Yu., *Zh. Prikl. Khim.*, 1994, vol. 67, no. 9, pp. 1561–1562.
5. Ermakov, A.S., Verigin, A.N., and Romanov, N.A., *Zh. Prikl. Khim.*, 1993, vol. 66, no. 11, pp. 2520–2525.

ISSN 1070-4272, Russian Journal of Applied Chemistry, 2008, Vol. 81, No. 11, pp. 1947–1952. © Pleiades Publishing, Ltd., 2008.
Original Russian Text © V.A. Lebedev, V.I. Sal'nikov, A.V. Bychkov, Yu.P. Savochkin, M.V. Kormilitsyn, 2008, published in Zhurnal Prikladnoi Khimii, 2008, Vol. 81, No. 11, pp. 1831–1836.

APPLIED ELECTROCHEMISTRY AND CORROSION PROTECTION OF METALS

Possibility of Electrochemical Control over the Composition of Uranium–Aluminum Alloys

V. A. Lebedev, V. I. Sal'nikov, A. V. Bychkov, Yu. P. Savochkin, and M. V. Kormilitsyn

Ural State Technical University, State Educational Institution for Higher Professional Education, Yekaterinburg, Russia
Research Institute of Nuclear Reactors, State Scientific Center, Federal State Unitary Enterprise, Dimitrovgrad, Ul'yanovsk oblast, Russia

Received May 15, 2008

Abstract—Possibility of preferential dissolution of uranium or aluminum from U–Al alloys in salt electrolytes was examined by performing thermodynamic calculations and experimentally.

DOI: 10.1134/S1070427208110153

Heat-releasing fuel elements based on uranium–aluminum alloys are widely used in research and transport reactors. Fabrication and regeneration of fuel elements of this kind make necessary fine control over their composition.

Our study is concerned with the possibility of solving this problem by electrochemical methods. For this purpose, the possibility of separating uranium and aluminum in anodic dissolution of U–Al alloys in various salt electrolytes was assessed theoretically and compositions of these alloys for preferential dissolution of uranium or aluminum were determined.

The efficiency of the separation process is characterized by the separation coefficient, the quotient of the ratios between the atomic fractions of the metals M1 and M2 being separated in the electrolyte, c_1 and c_2, and in the alloy, x_1 and x_2:

$$\theta = c_1x_2/(c_2x_1). \quad (1)$$

The separation coefficients of uranium and aluminum in their anodic dissolution in various salt melts were estimated using the previously derived [1] relation

$$\ln\theta = (3F/RT)\{E^*(Al^{3+}/Al) - E^{**}[U^{3+}/U(Al)]\}, \quad (2)$$

where $E^{**}[U^{3+}/U(Al)]$ is the conditional standard potential of U–Al alloys in a certain melt, and $E^*(Al^{3+}/Al)$, the conditional standard potential of aluminum in the same melt.

$E^{**}[U^{3+}/U(Al)]$ is calculated from the conditional standard potential of uranium, $E^*(U^{3+}/U)$, and the activity coefficient of uranium in uranium-lean liquid aluminum alloys, γ_U:

$$E^{**}[U^{3+}/U(Al)] = E^*(U^{3+}/U) \times (2.3RT/3F)\log\gamma_U. \quad (3)$$

The dependence of the separation coefficient of uranium and aluminum on the composition of the salt melt and temperature was analyzed using the equation [2]

$$\Delta E_i = E_i^0 = -0.096 + 0.0897(I_i/I) + [0.029 - 0.044(I_i/I)] \times 10^{-3}T, \quad (4)$$

where I_i and I are the ionic moment of uranium or aluminum cation and that of the solvent salt [3], and E_i^0 are standard potentials of uranium and aluminum.

Equation (4) is rather precise (correlation coefficient 0.96) and convenient for analysis. Close relations were obtained for molten fluorides, chlorides, bromides, and iodides of mono-, di-, tri-, and tetravalent elements from results of both electrochemical and calorimetric measurements.

Analysis of our results and published data [4] demonstrated the possibility of calculating the conditional standard potentials E^* of the Al^{3+}/Al system in molten chloride electrolytes of arbitrary composition from the previously measured temperature dependences of the standard potential ($E^0 = -2.290 + 5.53 \times 10^{-4}T$) and ΔE_i values [Eq. (4)].

Table 1. Estimates by Eq. (9) of the separation coefficients of uranium and aluminum in various salt solvents

Solvent	I, nm^{-1}	$\ln\theta = a - b/T$		θ at indicated T, K	
		a	b	1000	1100
LiCl	14.7	10.56	4300	523	773
LiCl–KCl	10.6	11.51	6228	196	346
NaCl–KCl	8.66	12.27	7780	89	180
NaCl	10.2	11.64	6500	126	235
KCl	4.5	12.91	9089	46	104
CsCl	6.06	14.05	11 415	14	39
$MgCl_2$	27	9.44	2022	1670	2000

For mixed solvents, we found the effective ionic moment as an additive function of products of mole fractions by ionic moments of cations of individual chlorides, $I = \Sigma_i c_i I_i$. This yielded for the temperature dependence of the conditional standard potential of aluminum, E^*, the expression

$$E_2^* = -2.290 + 0.553 \times 10^{-3}T + 0.096 - 0.0897(I_2/I) - [0.029 - 0.044(I_2/I)] \times 10^{-3}T. \quad (5)$$

A similar dependence has been obtained [5] for the conditional standard potential of uranium in chloride melts:

$$E_1^* = -2.79 + 0.56 \times 10^{-3}T + 0.096 - 0.0897(I_1/I) - [0.029 - 0.044(I_1/I)] \times 10^{-3}T. \quad (6)$$

According to [1], the activity coefficient of uranium in liquid aluminum in the temperature range 934–1150 K is independent of the solution composition and varies with temperature by the equation

$$\log\gamma_U = 3.672 - 7266/T. \quad (7)$$

Substituting expressions (6) and (7) into Eq. (3), we obtain the generalized equation for calculation of the conditional standard potential of the U–Al alloy:

$$E^{**}[U^{3+}/U(Al)] = -2.31 + 0.32 \times 10^{-3}T + 0.096 - 0.0897(I_1/I) - [0.029 - 0.044(I_1/I)] \times 10^{-3}T. \quad (8)$$

By including relations (5) and (8) into Eq. (2), with account of the ionic moments of U^{3+} ($I_1 = 29.13$ nm^{-1}) and Al^{3+} ions ($I_2 = 52.13$ nm^{-1}), we obtain the generalized expression for calculation of the separation coefficients of uranium and aluminum as functions of the temperature and ionic moment I of the solvent-salt cation:

$$\ln\theta = 696/T + 8.11 - 73\,390/IT + 36/I. \quad (9)$$

The results of calculation by Eq. (9) are listed in Table 1.

Depending on the nature of the solvent salt, the separation coefficient of uranium and aluminum varies by more than two orders of magnitude. An increase in the ionic moment of the solvent-salt cations and in temperature favors more complete separation of uranium and aluminum. The maximum values of the separation coefficient are observed with molten $MgCl_2$ used as a solvent. However, pure magnesium chloride has high viscosity (469 cP), low electrical conductivity (1.58 Ω^{-1} cm^{-1}), high melting point (712°C), and increased hydrolysis susceptibility. Therefore, we used as the solvent a melt containing 20 mol % NaCl and 80 mol % $MgCl_2$ ($I = 23.64$ nm^{-1}). For this solvent, the temperature dependence of the separation coefficient has the form

$$\ln\theta = 9.63 - 2408/T, \quad \theta_{1000\,K} = 1370, \quad \theta_{1100\,K} = 1704. \quad (10)$$

EXPERIMENTAL

The anodic dissolution of an aluminum alloy with 27.4 wt % uranium was performed in purified argon at 750°C in an electrolyte composed of $MgCl_2$ + 20 mol % NaCl, with liquid aluminum electrodes as a cathode and a reference electrode. As the alloy is depleted of uranium, the anode current density was lowered from 0.03 to 0.007 A cm^{-2}. Two experiments were performed.

In the first of these, the anodic dissolution of the alloy was performed for 50% recovery of uranium in a small alundum crucible whose walls served as a diaphragm separating the catholyte from the anolyte. In the process, magnesium ions discharged at the anode to give a magnesium–aluminum alloy. At the same time, uranium and aluminum dissolving at the anode accumulated in the anolyte. As seen from Fig. 1a, this leads to a pronounced polarization of the anode.

The second mode of anodic dissolution of the same alloy for 80% recovery of uranium was performed without separation of the anode and cathode spaces. In this case, the anodic polarization became considerably weaker. A 70% amount of aluminum was dissolved with the maximum current density of 0.03 A cm^{-2}

Table 2. Results of anodic dissolution of the U–Al alloy in the $MgCl_2$ + 20 mol % NaCl electrolyte at 750°C

Mode	Anode/U weight, g		U content of anode, %		Weight loss, g/fraction, %			Amount of electricity, A h/ fraction of current, %			U recovered, %
	initial	final	initial	final	anode	U	Al	anode	U	Al	
1	1.580/0.433	1.368/0.231	27.4	16.9	0.212/100	0.202/95.3	0.010/4.7	0.098/100	0.0682/69.6	0.298/30.4	46.7
2	1.902/0.521	1.617/0.152	27.4	9.4	0.372/100	0.3688/99.14	0.0032/0.86	0.134/100	0.1245/92.9	0.0095/7.1	70.8

(Fig. 1b). The amount of dissolved uranium and aluminum was found from the total loss of mass by the anode and the quantity of passed electricity.

The final content of uranium in the alloy was confirmed by chemical analysis. The results of two experiments are listed in Table 2.

On changing the conditions of alloy dissolution, the anodic current efficiency by uranium was raised to 92.9%, the fraction of dissolved uranium increased from 95.3 to 99.1%, and the recovery of uranium from the anode alloy was 70.8%, which made it possible to lower the uranium content of the alloy from 27.4 to 9.4% (0.0116 mole fraction). According to Eq. (10), $\theta_{1023\,K} = 1445$. Substituting this value of θ and the concentrations of uranium (0.0116) and aluminum (0.9884) in the final alloy into Eq. (1), we obtain the ratio between the near-electrode concentrations of U^{3+} and Al^{3+} ions:

$$c_1/c_2 = \theta x_1/x_2 = 1445(0.0116/0.9884) = 17,$$

which is in good agreement with the experimentally obtained ratio between the fractions of current expended for dissolution of uranium and aluminum (92.9/7.1 = 13).

The results of these calculations (Table 1) indicate that the fraction of current expended for ionization of aluminum in dissolution of U–Al alloys increases as the ionic moment of the solvent-salt cation decreases, with complex ions formed in the salt melt becoming more stable. However, in all purely chloride melts, the salt phase is enriched in uranium (θ > 1).

The situation fundamentally changes on passing to mixed chloride–fluoride melts. In these melts, aluminum is in the form of complex anions AlF_4^- and AlF_6^{3-} [6], whose stability substantially exceeds that of similar complex uranium ions. For example, the instability constants of hexafluoride complexes at 1000 K are 3.2×10^{-21} for aluminum [6] and 7.8×10^{-15} for uranium [7]. As a result, preferential dissolution of aluminum from U–Al alloys becomes possible in chloride–fluoride melts. This can be done by using the three-layer method, in which the anode alloy is at the electrolyzer bottom owing to the higher density than that of aluminum, and aluminum forms the upper (third) layer floating on the electrolyte surface. For this purpose, the electrolyte density should have an intermediate value between the densities of aluminum and its alloys with uranium. Table 3 lists the densities of aluminum and uranium–aluminum alloys in relation to temperature and the uranium content. The density of the U–Al alloys was estimated by the additivity

Table 3. Density of aluminum and the U–Al alloy

T, °C	Density, g cm^{-3}					
	Al	U–Al alloy with indicated U content, wt %				
		0.1	0.5	1	2	5
700	2.37	2.38	2.44	2.52	2.66	3.10
800	2.34	2.35	2.41	2.46	2.60	3.04

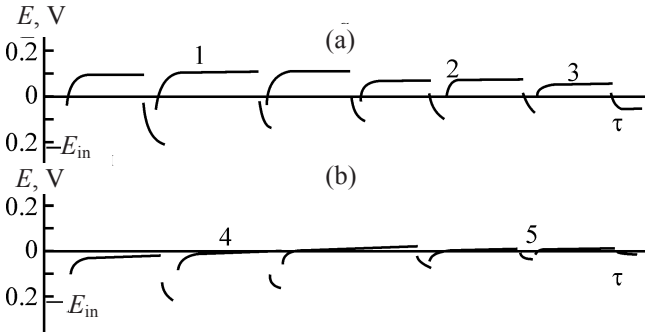


Fig. 1. Variation of the anode potential *E* under current and upon its switching-off. Current density, A cm^{-2}: (*1*) 0.02, (*2*) 0.015, (*3*) 0.01, (*4*) 0.3, and (*5*) 0.007. Mode: (a) first and (b) second.

Table 4. Conditions and results of the first set of refining of U–Al alloys at i_a = 0.5 A cm^{-2} and i_c = 0.08 A cm^{-2}

Run no.	I, A	τ, h	Anode weight loss, g		Anode weight,g/ U, wt %		Cathode weight/ U, wt %		U weight in anode, g		U weight in cathode, g		Degree of Al dissolution, %
			calculated	experimental	initial	final	initial	final	initial	final	initial	final	
1	1.5	21.3	10.722	10.818	15.954/2.57	5.036/8.24	55.710/0	66.394/≤0.005	0.407	0.415	0	<0.003	70.1
2	1.5	29.4	14.800	14.853	18.923/2.57	4.070/11.35	58.634/0	73.368/≤0.005	0.486	0.462	0	<0.004	80.4
3	1.5	29.0	14.599	14.664	17.651/2.57	2.981/15.03	56.250/0	70.801/0.004	0.454	0.448	0	0.0028	85.3

method, and that of aluminum was calculated by the formula [8]

$$d_{Al} = 2.382 - 0.000273(T - 659).$$

The three-layer refining of aluminum employs the electrolyte containing (wt %): 53–60 $BaCl_2$, 12–17 NaF, 22–24 AlF_3, and 2–4 NaCl; cryolite ratio 1.4–1.5, melting point 670–700°C, and density 2.65–2.70 g cm^{-3} at 770°C. The data in Table 3 demonstrate that this electrolyte can be used in processing of the uranium–aluminum alloy with a uranium content of no less than 3–4 wt %. To extend the concentration range, the content of barium chloride was lowered to 35–40%, and 7% lithium chloride was introduced instead of 2–4% sodium chloride to raise the electrical conductivity. The density of this electrolyte is 2.5 g cm^{-3}, and its melting point, 670°C.

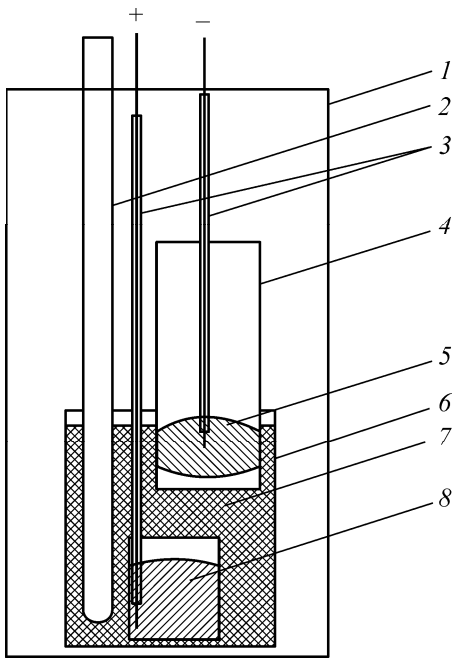


Fig. 2. Schematic of the electrolytic cell: (*1*) metallic container, (*2*) thermocouple sheath, (*3*) current leads, (*4*) alundum tube, (*5*) aluminum cathode, (*6*) alundum crucible, (*7*) electrolyte, and (*8*) U–Al alloy (anode).

The first set of experiments was performed at a current density of 0.5 A cm^{-2} at 780–800°C. The course of the process was monitored by the counter electromotive force, which included the anodic and cathodic polarizations. At the chosen ratio of the cathode and anode current densities [1 : (7–10)], the cathodic polarization is insignificant and the counter electromotive force is almost equal to the anodic polarization.

The electrolytic cell we used is schematically shown in Fig. 2. A preliminarily prepared electrolyte was melted in air in a large crucible, and then a weighed portion (15–20 g) of the U–Al alloy was placed in a small crucible and a molybdenum current lead was introduced. The cathode (aluminum) was lowered from above into the electrolyte in an alundum tube on a molybdenum rod, which served as a current lead after aluminum melted. After the required temperature was reached, a dc current from the power source was switched on. The current was monitored by readings of the stabilized power source and an ammeter. The voltage and counter electromotive force across the cell were measured with a digital voltmeter and *X–Y* self-recorder. The counter electromotive force was measured at the instant of switching-off the current. After the electrolysis, the current leads were removed and the cell was cooled to room temperature. The cathode and anode washed to remove the electrolyte were weighed and analyzed for the content of uranium by atomic-emission spectroscopy with inductively coupled plasma.

The results of these experiments are listed in Tables 4 and 5, and the manner in which the voltage and

Table 5. Conditions and results of the second set of refining of U–Al alloys at i_a = 0.5 A cm^{-2} and i_c = 0.08 A cm^{-2}

Run no.	I, A	τ, h	Anode weight loss, g		Anode weight,g/ U, wt %		Cathode weight/ U, wt %		U weight in anode, g		U weight in cathode, g		Degree of Al dissolution, %
			calculated	experimental	initial	final	initial	final	initial	final	initial	final	
1	3.9 3.0	6 6	13.894	13.886	18.543/2.57	4.657/10.1	55.167/0	68.975/≤0.005	0.476	0.470	0	<0.003	76.9
2	3.9 3.0	6 8.3	16.209	16.404	19.865/2.57	3.461/14.1	36.318/0	71.862/0.042	0.510	0.488	0	0.030	80.9

counter electromotive force vary is shown in Figs. 3 and 4.

In all the experiments, the loss of mass by the anode is larger, and that by the cathode, smaller, than those calculated from the quantity of passed electricity, which is accounted for by the noticeable corrosion of aluminum in the chloride–fluoride melt. The degree of anodic dissolution of aluminum in the first set was 70–85%, with the maximum enrichment of the anode in uranium of up to 15 wt %.

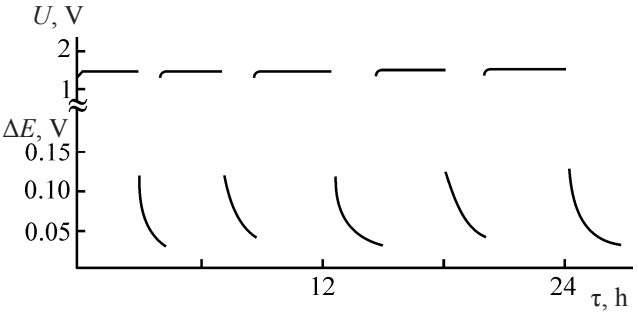


Fig. 3. Variation of the voltage U and anodic polarization ΔE in electrorefining of the U–Al alloy at a current density of 0.5 A cm^{-2}.

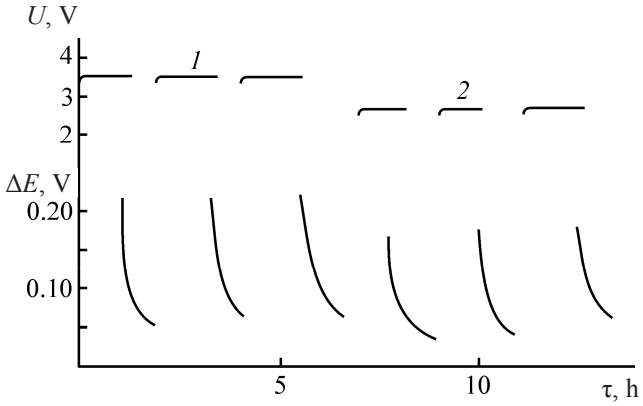


Fig. 4. Variation of the voltage U and anodic polarization ΔE in electrorefining of the U–Al alloy at a current density of (*1*) 1.3 and (*2*) 1.0 A cm^{-2}.

In the second set, the initial anode current density was raised to 1.3 A cm^{-2}, and the final current density was lowered to 1 A cm^{-2}.

It can be seen in Fig. 4 that, on raising the current density, the anode polarization increased by 0.05–0.1 V.

In the first run, uranium was hardly ionized and remained in the anode residue despite the higher anode current density. The content of uranium in the cathode product was at the sensitivity level of chemical analysis. In the second experiment at the same current densities, the degree of anodic dissolution of aluminum was raised to 80.9%. As a result, 30 mg of uranium (5.9% of the initial amount) passed to the cathodic aluminum. The reason is that the limiting current density of aluminum ionization is exceeded at the end of electrolysis because of the decrease in the anode surface area and increase in the uranium concentration in the anode.

CONCLUSIONS

(1) An equation for estimating the separation coefficients as functions of temperature and ionic moment of the solvent-salt cation was suggested.

(2) It was shown that, depending on the nature of a chloride used as a solvent, the separation coefficient varies by more than two orders of magnitude. The maximum values of the separation coefficient (2000) are observed in the $MgCl_2$ melt.

(3) Uranium was dissolved from the Al + 27.4 wt % alloy in a melt composed of 20 mol % NaCl + 80 mol % $MgCl_2$ at 750°C to a final uranium content

of 9.4 wt %. In this case, the current expended for dissolution of aluminum is 13 times smaller than that expended for dissolution of uranium, in good agreement with the theoretical estimate.

(4) The electrolyte composition and parameters of anodic dissolution of U–Al alloys in chloride–fluoride melts, with selective extraction of 80–85% of aluminum from the alloys and uranium concentration in the anode residue from 2.57 to 14–15 wt %, were substantiated.

REFERENCES

1. Lebedev, V.A., Kober, V.I., and Yamshchikov, L.F., *Termokhimiya splavov redkozemel'nykh i aktinoidnykh elementov* (Thermochemistry of Alloys of Rare-Earth and Actinide Elements), Chelyabinsk: Metallurgiya, 1989.
2. Lebedev, V.A., *Dokl. Ross. Akad. Nauk*, 1993, vol. 330, no. 5, pp. 586–589.
3. Lebedev, V.A., *Izbiratel'nost' zhidkometallicheskikh elektrodov v rasplavlennykh galogenidakh* (Selectivity of Liquid-Metal Electrodes in Molten Halides), Chelyabinsk: Metallurgiya, 1993.
4. Lebedev, V.A., Sal'nikov, V.I., and Tsvetov, V.V., *Izv. Vyssh. Uchebn. Zaved., Tsvetn. Metall.*, 2002, no. 5, pp. 10–13.
5. Lebedev, V.A., *Rasplavy*, 1994, no. 4, pp. 41–47.
6. Kudyakov, V.Ya., Smirnov, M.V., and Posokhin, Yu.V., *Koord. Khim.*, 1979, vol. 5, no. 6, pp. 821–823.
7. Smirnov, M.V., *Elektrodnye potentsialy v rasplavlennykh khloridakh* (Electrode Potentials in Molten Chlorides), Moscow: Nauka, 1973.
8. Vetyukov, M.M., Tsyplakov, A.M., and Shkol'nikov, S.N., *Elektrometallurgiya alyuminiya i magniya* (Electrometallurgy of Aluminum and Magnesium), Moscow: Metallurgiya, 1987.

ISSN 1070-4272, Russian Journal of Applied Chemistry, 2008, Vol. 81, No. 11, pp. 1953–1956. © Pleiades Publishing, Ltd., 2008.
Original Russian Text © Zh.M. Kebadze, L.Sh. Kakuriya, K.T. Ugrelidze, 2008, published in Zhurnal Prikladnoi Khimii, 2008, Vol. 81, No. 11, pp. 1837–1840.

APPLIED ELECTROCHEMISTRY AND CORROSION PROTECTION OF METALS

Synthesis of Electrolytic Manganese Dioxide on Fibrous Carbon Electrodes and Its Use in Voltaic Cells

Zh. M. Kebadze, L. Sh. Kakuriya, and K. T. Ugrelidze

Agladze Institute of Inorganic Chemistry and Electrochemistry, Tbilisi, Georgia

Received April 9, 2008

Abstract—Selected problems of electrosynthesis of manganese dioxide, with a fibrous carbon material used as anodes and cathodes, were considered. The quality of the product as a cathode material for manganese dioxide–zinc chemical power cells with an alkaline electrolyte was examined.

DOI: 10.1134/S1070427208110165

Owing to a large number of technological and economical factors, the main contribution to the saturation of the market of chemical power cells (CPCs) is made by cells of the MnO_2–Zn system (MTs cells) [1]. The best electrical characteristics among the cells of this kind are observed for those with an alkaline electrolyte [2, 3]. At the same time, they are more sensitive than salt cells to the quality (and in particular, to purity) of the active component of the cathode mixture, MnO_2 [4]. Consequently, one of ways to improve CPCs of this system is to obtain electrolytic manganese dioxide (EMD) under conditions that would provide penetration of a lesser amount of detrimental impurities into the electrosynthesis product.

Severe synthesis conditions of EMD (high temperature and acid medium) restrict the number of materials that can be used as electrode materials. At the same time, anodes and cathodes used in the industry have disadvantages: passivation under inappropriate electrolysis conditions (titanium anodes), poor mechanical stability and nonreusable nature (graphite and lead anodes), difficult fabrication and high cost (combined titanium-based anodes, steel and copper cathodes), contamination of the target process by the electrode material (most of the electrodes mentioned above, to some extent), and large size and the resulting decrease in the volume current density (graphite anodes and cathodes). Compared with other electrochemical processes, electrosynthesis of MnO_2 has low output capacity resulting from the low anode current density [5–8].

To eliminate or diminish the consequences of some of the disadvantages mentioned above, fibrous carbon materials (FCMs) have been tested as anodes and cathodes. These materials are fabricated by thermal treatment of organic fibers and petroleum products in a certain mode and are manufactured as threads, fabric, bundles, and felt [9, 10]. Such a wide range of products predetermine the broad design opportunities furnished by FCMs These materials are 85–95% composed of graphite, which leads to their good electrical conductivity, high porosity, large specific surface area, and stability in severe chemical and thermal conditions. These properties have aroused a considerable interest in use of FCMs in various fields of technology and, in particular, in applied electrochemistry [11–13]. The electrode characteristics of FCM can be improved by various, including electrochemical, methods [14, 15].

Previously, an FCM has been used in EMD synthesis only as an anode and the product obtained has been tested in MTs cells with salt electrolyte [16]. The cells were fabricated with FCM as an electrically conducting additive to the cathode mixture and as a current-lead support in electrochemical preparation of cathodes for voltaic cells [17].

EMD was synthesized with FCM anode and cathode from an acidified $MnSO_4$ solution in cylindrical electrolyzers (2 l) at a current of 1.1 A. The electrodes had the form of rectangular frames made of a nonconducting material (polypropylene) with parallel vertical lines of a bundle-like FCM. The current lead to the electrodes was provided by a pair of titanium (for the

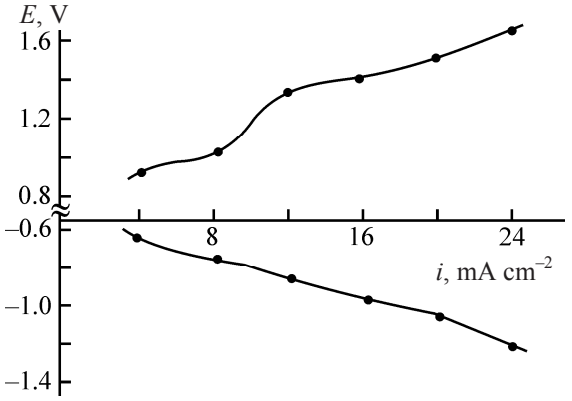


Fig. 1. (*1*) Cathodic and (*2*) anodic polarization curves measured on FCM electrodes. (*E*) Electrode potential and (*i*) current density.

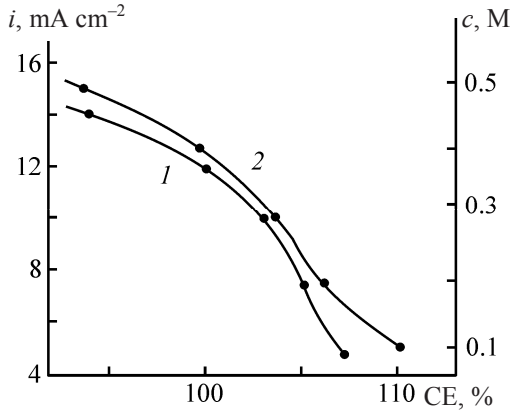


Fig. 2. (*1*) Anode current density *i* and (*2*) H_2SO_4 concentration *c* vs. current efficiency CE by EMD.

anode) and copper (for the cathode) plates. Figure 1 shows cathodic and anodic polarization curves measured on FCM electrodes under the conditions of EMD synthesis, commonly used for metallic and graphite electrodes [5, 6]: concentration (M): $MnSO_4$ 0.8 and H_2SO_4 0.25; solution temperature 94 ± 1°C. The electrode potentials were measured relative to a calomel reference electrode and recalculated to the hydrogen scale. The measurements were made after 3 h of electrolysis, when the surface area of the anode with a deposited EMD could be measured with sufficient precision. Under these conditions, the cathodic potentials of the FCM (curve *1*) lie within the range of potentials characteristic of other materials used in EMD synthesis [18] up to a current density of 11–13 mA cm^{-2} and further increase (in absolute value) to a lesser extent.

The range 16–19 mA cm^{-2} was chosen as the optimal cathode current density. Further increase in this parameter is limited by the comparatively steep rise in the voltage across the electrolyzer bath, caused by an increase in the ohmic resistance of the solution because of the high degree of its filling with the evolving hydrogen. In the case of anodic polarization, an electrode fabricated from any material becomes a MnO_2 electrode (M–MnO_2, graphite–MnO_2, FCM–MnO_2) after a solid layer of the EMD deposit is formed. Consequently, the anodic polarization curve *2* (Fig. 1) for the FCM differs only slightly from that for other materials [5]. Therefore, a principal criterion in choosing the optimal anode current density is the current efficiency (CE) by the product.

Figure 2 shows how the current efficiency by EMD depends on the anode current density at a constant solution acidity (0.25 M H_2SO_4) (curve *1*) and on the acid concentration at a constant anode current density (10 mA cm^{-2}) (curve *2*). The current efficiency by EMD has a conditional value because it is commonly calculated from the mass of a processed and dried electrolysis product containing (%): MnO_2 90–91, Mn_2O_3 up to 8, hygroscopic moisture up to 4, sulfates up to 1.3, residues insoluble in HCl up to 2, and admixtures of various metals, in trace amounts [5, 19]. The data in Fig. 2 suggest that the optimal anode current density is 9–11 mA cm^{-2}, and the optimal concentration of sulfuric acid, 0.25–0.35 M. Further decrease in the H_2SO_4 concentration is limited by the fact that the spent solution is used for leaching-out of manganese from a reduced ore concentrate, envisaged by the technology of EMD synthesis [5, 8]. Below are given parameters of EMD synthesis on FCM electrodes.

Anode current density, mA cm^{-2}	10
Cathode current density, mA cm^{-2}	17.5
Volume current density, A m^{-3}	650
Voltage, V	2.61
Temperature, °C	94 ± 1
$MnSO_4$ concentration, M	0.8
H_2SO_4 concentration, M	0.30
Current efficiency, %	103.5
Electric power expenditure, kW h kg^{-1}	1.51

It is noteworthy that the voltage across the electrolyzer bath remains unchanged in the course of time, 2.6 V. It is known [5, 7, 8] that, with cylindrical titanium anodes, the electrolysis voltage varies under the influence of three factors: thickening of the titanium oxide layer under the EMD deposit, thickening of the EMD layer, and decrease in the current density because of the increase in the anode diameter. Naturally, the first factor is unimportant for FCM, and it can be believed that the increase in the electrical resistance of

the EMD deposit layer and decrease in the polarization resistance cancel each other.

Synthesis of EMD at a volume current density of 650 A m^{-3} (calculated from the electrolyzer volume) corresponds to intensification of the process by approximately 30%. This occurs for the following reasons: titanium and combined titanium-based cylindrical anodes are 1.8–2.5 cm in diameter; graphite anodes and cathodes, 2.0–3.0 cm in diameter [5, 6, 8]; and anodes made of bundle-like FCM take the form of a cylinder 0.3 cm in diameter (in the initial stage of the process). This causes a decrease in the volume occupied by the electrodes, which makes it possible to raise the volume current density at the same interelectrode spacing. The value of one of the principal parameters of electrolysis, energy expenditure of 1.51 kW h, is rather small for the process under consideration. In contrast to the case of metallic anodes, the EMD obtained cannot be detached from FCM and, therefore, the product with the anode material was subjected to chemical processing, drying, and grinding in accordance with the production specification [5, 8, 19]. The content of FCM in the product was approximately 0.15%.

The following can be said about the economic aspect of application of nonreusable anodes and reusable cathodes fabricated from FCM. Obtaining 1 m^2 of the anode surface area in manufacture of EMD requires 21–23 kg of rod titanium (D = 2.0 cm), 22–24 kg of lead strips (4.0 × 0.4 cm), or 16–17 kg of cylindrical (D = 3.0 cm) electrode grade graphite [5, 6]. The same surface area was obtained in this study with only 74–76 g of FCM. Here is meant the FCM surface area accessible to electrochemical deposition of EMD, rather than the substantially larger true surface of FCM [9]. Although the cost of FCM exceeds that of titanium by approximately an order of magnitude, the expenditure of the former is 280 times smaller than that of the latter. According to the experiments performed, this advantage can be well utilized in engineering practice. With account of the fact that the cathode current density used is 1.75 times the anode current density, the FCM expenditure is even smaller than those of lead and graphite, by factors of 530 and 320, respectively. In the authors' opinion, an important role in determining the economic feasibility of industrial use of FCM as electrodes can be played by the improvement of the EMD obtained in this case.

The electrolytic manganese dioxide obtained on FCM was used in MTs cells with alkaline electrolyte. The aim of the experiment was to find the optimal ratio between the masses of the EMD produced under the conditions mentioned above and the carbon materials (graphite and carbon black) added to the cathode mixture of power cells to raise its electrical conductivity. A model cell intended for determining the EMD quality [20, 21] was used as the CPC of the MnO_2–Zn system with alkaline electrolyte. The composition of the dry cathode mixture corresponded to the widely occurring cylindrical power cells of this system (%): EMD 84, elemental graphite 12.5, and acetylene black 3.5. In a cell of this kind, the paste-like anode mass containing high-purity powdered zinc is taken in an excess, and, therefore, CPC parameters fully depend on the EMD quality. A 12.5 KOH solution was used as electrolyte. Eight batches of CPC were fabricated (each with four cells) with the following contents of EMD in the dry cathode mixture (wt %): batch no. 1, 75; no. 2, 78; no. 3, 81; no. 4, 84; no. 5, 87; no. 6, 90; no. 7, 93; and no. 8, 96. The mass ratio between graphite and acetylene black was the same (12.5 : 3.5) for all the batches. To obtain their electrical characteristics, the CPCs were discharged at room temperature via a constant external resistance of 20 Ω in the continuous mode to a final voltage of 0.9 V.

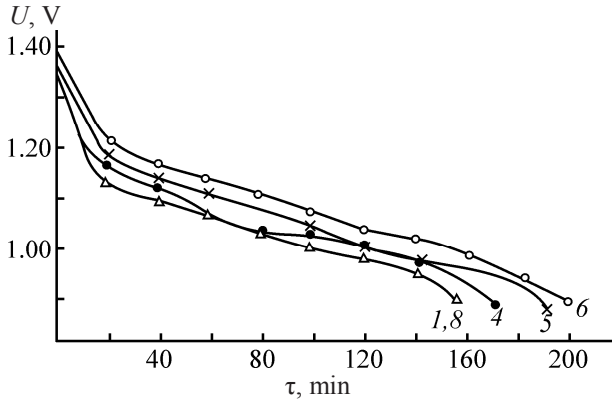


Fig. 3. Discharge curves of model MTs power cells. (U) Voltage and (τ) time. Digits at curves are numbers of power cell batches.

Figure 3 shows discharge characteristics of some batches of MTs power cells tested under the conditions specified (curves *1* and *8* almost coincide). The discharge time of the best of the cells, including that with the existing standard composition (curve *4*), corresponds to that for high-quality EMD samples [20, 21].

Figure 4 shows dependences of the electrical capacity of the power cells (curve *1*) and of the reagent utilization coefficient (RUC) (curve *2*) on the EMD content of the dry cathode mixture. It can be seen that, as the EMD content increases, the RUC first varies only

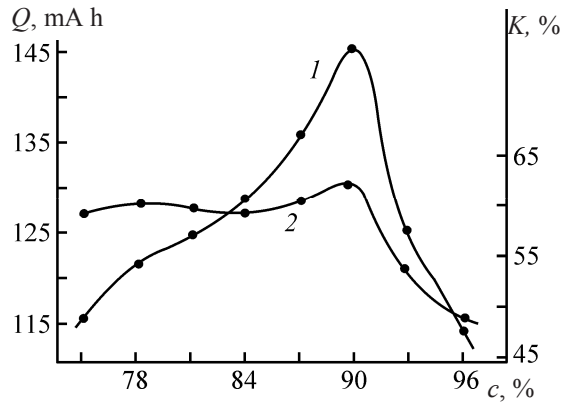


Fig. 4. (*1*) Electrical capacity Q of model MTs power cells and (*2*) reagent utilization coefficient K vs. the EMD content c of the dry cathode mixture.

slightly and the capacity of the power cells grows because the amount of the active substance (MnO_2) becomes larger. On reaching a maximum at 90% EMD, RUC steeply falls, which causes a dramatic decrease in the electrical capacity of the power cells. This is probably due to an increase in the internal resistance of the cells as a result of a decrease in the content of electrically conducting materials in the cathode mixture.

According to Figs. 3 and 4, the optimal EMD content of the dry cathode mixture is approximately 90%, which exceeds by 6% the standard value. It should be noted that, when the EMD obtained on FCM anode was tested in MTs power cells with a salt electrolyte, its optimal content was lower than the standard value [16]. It is suggested that the high quality of the EMD synthesized on FCM electrodes is due to two factors: elimination of electrode impurities (Ti, Pb, Cu, Fe) and presence of an admixture of the material of the FCM anodes in the product. If a salt electrolyte is used, the second factor is important [17]. In the case under consideration, the amount of FCM contained in the product is small, and, therefore, the purity of the EMD is of key importance in the improvement of its quality.

CONCLUSIONS

(1) Use of fibrous carbon materials as cathodes and anodes improves some technical (materials consumption, volume current density, specific electric power expenditure) parameters of MnO_2 electrosynthesis.

(2) Absence of admixtures of metallic electrode materials in electrolytic MnO_2 improves its quality as a cathode material for power cells of the MnO_2–Zn system with an alkaline electrolyte.

REFERENCES

1. Korovin, N.V., *Elektrokhim. Energet*., 2003, vol. 3, no. 4, pp. 163–168.
2. Varypaev, V.N., Dasoyan, M.A., and Nikol'skii, V.A., *Khimicheskie istochniki toka* (Chemical Power Cells), Moscow: Vysshaya Shkola, 1990.
3. *Khimicheskie istochniki toka: Spravochnik* (Chemical Power Cells: Reference Book), Korovin, N.V. and Skundin, A.M., Eds., Moscow: MEI, 2003.
4. Dam'e, V.N. and Rysukhin, N.F., *Proizvodstvo pervichnykh khimicheskikh istochnikov toka* (Manufacture of Primary Chemical Power Cells), Moscow: Energoizdat, 1981.
5. Dzhaparidze, L.N., *Elektroliticheskii dioksid margantsa* (Electrolytic Manganese Dioxide), Tbilisi: Metsniereba, 1987.
6. Preisler, E., *J. Appl. Electrochem*., 1989, vol. 19, pp. 559–565.
7. Armacanqui, M.E. and Ekern, R.J., *J. Appl. Electrochem*., 1992, vol. 22, pp. 593–595.
8. Agladze, G.R., *Elektrosintez okislitelei i elektrokhimicheskaya ochistka stochnykh vod* (Electrosynthesis of Oxidants and Electrochemical Wastewater Treatment), Tbilisi: Metsniereba, 1994.
9. Varentsov, V.K., *Intensifikatsiya elektrokhimicheskikh protsessov. Sbornik nauchnykh trudov* (Intensification of Electrochemical Processes. Coll. of Scientific Works), Moscow: Nauka, 1988, pp. 94–118.
10. *Handbook of Composites*, Lubin, G., Ed., New York: Van Nostrand Reinhold, 1982.
11. Fitzer, E., Jager, H., Popovska, N,. and Vonsturm, F., *J. Appl. Electrochem*., 1988, vol. 18, pp. 178–182.
12. Volgin, M.A., Kulikova, L.N., Konoplyantseva, N.A., et al., *Elektrokhim. Energet*., 2001, vol. 1, nos. 1–2, pp. 50–55.
13. Artem'yanov, A.P. and Sheveleva, I.V., *Zh. Prikl. Khim*., 2004, vol. 77, no. 11, pp. 1811–1814.
14. Varentsov, V.K. and Varentsova, V.I., *Elektrokhimiya*, 2001, vol. 37, no. 7, pp. 811–820.
15. Varentsova, V.I. and Varentsov, V.K., *Zh. Prikl. Khim*., 2005, vol. 78, no. 3, pp. 433–437.
16. Kebadze, Zh.M., Pruidze, V.P., Kakuriya, L.Sh., and Chakhunashvili, T.A., *Soobshch. Akad. Nauk Gruz*., 1999, vol. 160, no. 3, pp. 486–487.
17. Kebadze, Zh.M., Kakuriya, L.Sh., and Pruidze, V.P., *Elektrokhim. Energet*., 2005, vol. 5, no. 42, pp. 241–245.
18. Kebadze, Zh.M., Aneli, D.N., and Kakuriya, L.Sh., *Soobshch. Akad. Nauk Gruz*., 1991, vol. 144, no. 1, pp. 49–52.
19. *GOST SSSR* (State Standard of the USSR) *25 823–83*.
20. Chakhunashvili, T.A., Dzhaparidze, L.N., Rokva, T.V., and Shaduri, L.V., *Tr. Tekhn. Univ. Gruz*., 2002, no. 5 (444), pp. 13–14.
21. Tsagareli, G.A., Batsanadze, L.I., Shakarishvili, A.G., and Maisuradze, N.G., *Izv. Akad. Nauk Gruz*., 2006, vol. 32, nos. 1–2, pp. 315–318.

ISSN 1070-4272, Russian Journal of Applied Chemistry, 2008, Vol. 81, No. 11, pp. 1957–1962. © Pleiades Publishing, Ltd., 2008.
Original Russian Text © V.D. Tikhova, V.P. Fadeeva, M.I. Dergacheva, M.M. Shakirov, 2008, published in Zhurnal Prikladnoi Khimii, 2008, Vol. 81, No. 11, pp. 1841–1846.

ORGANIC SYNTHESIS AND INDUSTRIAL ORGANIC CHEMISTRY

Analysis of Humic Acids from Various Soils Using Acid Hydrolysis

V. D. Tikhova, V. P. Fadeeva, M. I. Dergacheva, and M. M. Shakirov

Vorozhtsov Institute of Organic Chemistry, Siberian Branch, Russian Academy of Sciences, Novosibirsk, Russia
Institute of Soil Science and Agrochemistry, Siberian Branch, Russian Academy of Sciences, Novosibirsk, Russia

Received April 23, 2008

Abstract—Structural changes in humic acids from various soils, produced by acid hydrolysis, are studied by elemental and thermal analyses and by IR and NMR spectroscopy.

DOI: 10.1134/S1070427208110177

According to the modern views of the structure of a humic acid (HA) macromolecule, it consists of two major parts, a core built by aromatic fragments interlinked by aliphatic chains and a periphery consisting of readily hydrolyzable oxygen-containing fragments such as polysaccharides, ethers, polyphenols, and amino acids. Orlov [1] noted that the terms "periphery" and "core" are not quite adequate and that it would be more correct to designate these parts as hydrolyzable and nonhydrolyzable, which, however, appears to be inconvenient, and no adequate alternative for the above-mentioned terms has been found yet.

The use of hydrolytic methods for analysis of HAs originates from routine procedures employed for analysis of complex protein molecules. However, in contrast to proteins, none of HAs ever extracted have been fully decomposed via hydrolysis. The hydrolyzates were intensively studied, including their amino acid composition [2–10], polysaccharide fraction [11–15], and other components [10, 15].

The goals of this study were to examine the changes in the composition and structure of HAs, produced by acid hydrolysis, and to compare nonhydrolyzable fractions of HAs from soils of different genesis, using such methods as elemental and thermal analyses, IR, and NMR.

EXPERIMENTAL

We studied HAs extracted from tundra soils of the Tyumen oblast [cold soils: gley podzolic sandy loam (sample no. 1) and surface-gley clay loam (sample no. 2)] and dry-steppe zone of the Altai krai [warm soils: southern chernozem (sample no. 3) and chestnut soil (sample no. 4)].

The experiments on acid hydrolysis of HAs were carried out as follows [16]. A weighed portion (about 100 mg) of a sample was heated in a specially designed flask with 2.5 ml of 6 M HCl for 18 h at 120°C (sand bath) under helium. The residue was filtered off, washed with distilled water to remove the chloride ions, and air-dried to constant weight.

Carbon, hydrogen, and nitrogen were determined on a Carlo Erba Model 1106 elemental analyzer and also using the standard C,H analysis procedure for organic substances.

To measure NMR spectra, a 20–50-mg sample was dissolved in 0.5 ml of $NaOH/D_2O$ and placed into an ampule with an outer diameter of 5 mm. The ^{13}C NMR spectra were recorded on a Bruker DRX-500 instrument operating at 125.76 MHz. To exclude the nuclear Overhauser effect, the ^{13}C NMR spectra were recorded with proton decoupling in the INVGATE mode. Tetramethylsilane (TMS) was used as external reference. The spectra were recorded at 1-s pulse delay.

The IR spectra were recorded over the range 400–4000 cm^{-1} on a Vector-22 FTIR spectrometer (Bruker) using KBr technique (1:150).

Thermal analysis was carried out on an STA 409 PC Luxx thermoanalyzer (Netzsch) in a platinum cru-

Table 1. Elemental composition

Sample no.	Ash content, %	Elemental composition, %, recalculated to ash-free sample				Elemental composition, at. %				Atomic ratio		
		C	H	N	O	C	H	N	O	H/C	C/N	O/C
Initial samples												
1	0	56.87	7.02	2.74	33.37	33.91	49.71	1.43	14.95	1.47	23.71	0.44
2	5.9	50.43	6.16	3.34	40.07	32.23	46.79	1.80	19.18	1.45	17.91	0.59
3	6.1	52.29	3.03	3.36	41.32	43.17	29.70	2.38	24.75	0.69	18.14	0.57
4	2.8	57.08	2.72	3.06	37.14	47.60	26.95	2.20	23.27	0.57	21.64	0.49
Samples after hydrolysis												
1-nhr[a]	0	66.39	7.11	1.19	25.38	38.76	49.44	0.60	11.17	1.28	64.60	0.29
2-nhr	6.33	64.59	6.05	1.74	34.40	39.44	43.91	0.88	15.76	1.11	44.82	0.40
3-nhr	0	54.62	3.27	2.26	39.85	43.58	31.03	1.53	23.85	0.71	28.48	0.55
4-nhr	0	57.16	2.52	2.45	37.87	48.57	25.41	1.84	24.18	0.52	26.40	0.50

[a] Nonhydrolyzable residue.

Table 2. Weight loss of HA samples on heating

Sample no.	Weight loss, %				Total weight loss, %	Thermal effect, $\mu V\ mg^{-1}$
	<150°C	150–400°C	400–700°C	P/C		
1	3.98	27.88	64.04	0.50	96.34	4909
1-nhr	0.5	45.66	52.94	0.87	99.45	4750
2	3.46	26.77	60.24	0.50	90.47	5213
2-nhr	1.33	27.32	59.42	0.48	87.63	5754
3	5.02	21.60	62.97	0.42	89.87	4389
4	3.13	24.18	65.77	0.41	93.17	3933
4-nhr	3.52	22.05	66.7	0.38	92.62	2141

cible in air. Samples were heated from 20 to 1000°C at a rate of 10 deg min^{-1}. The sample weight was determined to within 2 μg. The limit of intrinsic relative error of determination of the thermal effects was ±3%.

The elemental composition of the HA samples before and after hydrolysis is given in Table 1. It appears of particular significance to analyze the changes in the H/C, C/N, and O/C atomic ratios.

The H/C ratio is a significant parameter characterizing the aromaticity of humic acids. As can be seen, for chernozem and chestnut soil, hydrolysis does not affect this parameter. For the tundra soils, it slightly decreased after hydrolysis, being most strongly decreased for sample no. 2 (by more than 20%), suggesting increase in the fraction of aromatic fragments in nonhydrolyzable residue. However, in this case, the resulting H/C ratio (1.11) is still higher by a factor of 1.6 than that of HAs extracted from chernozem (0.71), suggesting a significant difference in the core structure of humic acids from tundra (cold) soils and steppe (warm) soils.

The observed considerable increase in the C/N ratio after hydrolysis, particularly, for HAs of tundra soils (by factors of 3 and 2.5 for sample nos. 1 and 2, re-

spectively), reveals that these HAs are characterized by high content of amino acid residues, which pass into solution in the course of hydrolysis along with the most part of nitrogen atoms. The remaining nitrogen is included into the heterocycles or fixed via other, stronger bonds. In HAs extracted from warm soils, the hydrolyzability of nitrogen is lower: C/N increases by a factor of 1.5 for HAs from chernozem and only 1.2 for HAs from chestnut soil.

The decrease in the relative oxygen content (O/C) after hydrolysis is observed only for HAs of tundra soils, the decrease being less pronounced as compared to that in C/N. For HAs extracted from chernozem and chestnut soils, the O/C ratio remains unchanged within the determination error. Therefore, under the experimental conditions, hydrolysis of the peptide bonds prevails over that of the ester and glycoside bonds.

No significant differences were observed between the IR spectra of HAs of steppe soils and their nonhydrolyzable residues. Furthermore, their spectra in the range 400–1800 cm^{-1} are identical to those of nonhydrolyzable residue of HAs from tundra soils. However, the IR spectra of HAs from cold and warm soils differ in the range from 1800 to 4000 cm^{-1} in that the strong bands due to stretching vibrations of methylene groups (2927 and 1854 cm^{-1}) are observed in spectra of HAs from tundra soils. Neither the intensity nor the position of these bands change after hydrolysis, evidencing the presence of the methylene chains in the nonhydrolyzable residue, i.e., in the core of HAs of tundra soils.

The DSC curves obtained in heating HAs in air are shown in Figs.1a–1c. The nonhydrolyzable residue obtained after hydrolysis of HAs of tundra soils is characterized by more distinctly pronounced low-temperature (<400°C) and high-temperature (400–700°C) thermal effects, the maximum of the high-temperature exothermic effect being shifted toward higher temperatures. For HAs of steppe soils, the low-temperature exothermic effect is no longer observed after hydrolysis, and the maximal decomposition temperature increases.

Data on the weight loss of the HA samples in the course of heating are given in Table 2. All the samples are characterized by low ash content, the total weight loss being about 90%. The periphery to core (P/C) ratio is slightly below 0.5 for HAs of steppe soils. For all HA samples studied, this ratio remains practically unchanged after hydrolysis, except for the sample of gley-podzolic soil, in which the core fraction considerably increases. The total thermal effects of decomposition of HAs of tundra soils are higher than those of HAs from steppe soils, which can be attributed to different mechanisms of oxidative decomposition of HAs of cold and warm soils.

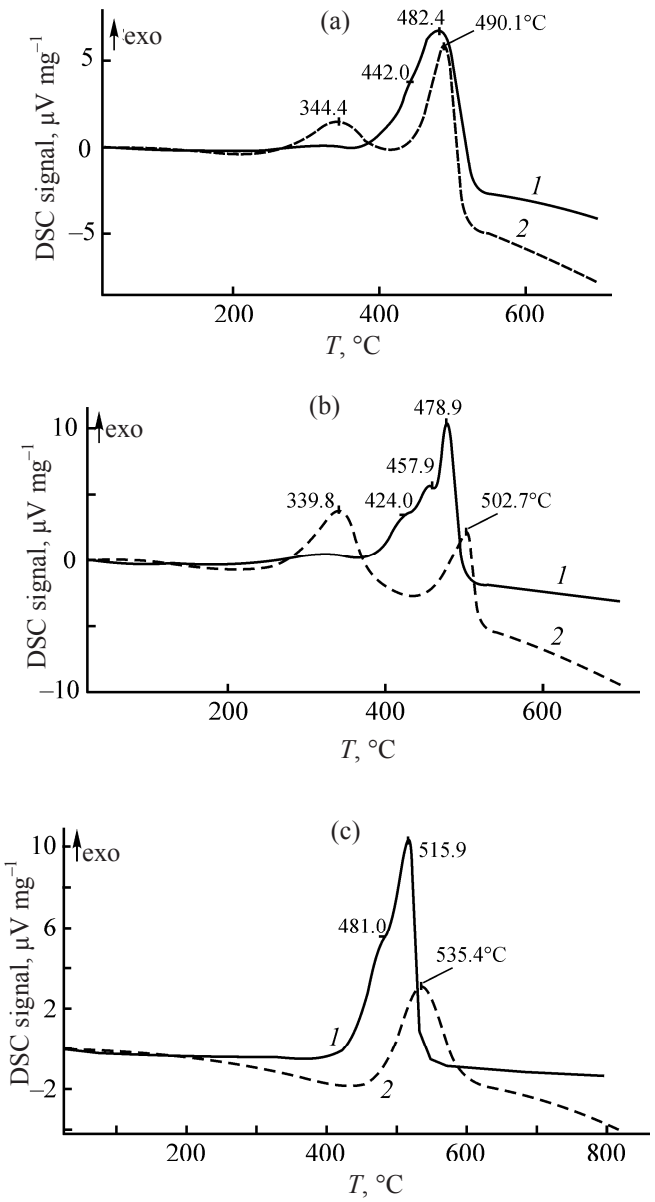


Fig. 1. DSC curves of (a) sample no. 2, (b) sample no. 1, and (c) sample no. 4: (*1*) before and (*2*) after hydrolysis. (*T*) Temperature.

Integration of ^{13}C NMR spectra in defined intervals [1] (Table 3) allows determination of the relative content of particular structural fragments of HAs (group composition) before and after hydrolysis (Fig. 2).

After recalculation of the results to the initial sam-

Table 3. Relative carbon content in structural fragments of HAs, obtained from ^{13}C NMR data

Sample no.	Carbon content, rel. %							
	carboxy (160–180 ppm)		aromatic (90–160 ppm)		polysaccharide (65–90 pm)		aliphatic (0–65 ppm)	
	initial	after hydrolysis	initial	after hydrolysis	initial	after hydrolysis	initial	after hydrolysis
1	8.5	5.6	18.5	18.1	11.3	5.0	61.6	71.3
2	6.6	6.7	17.8	23.4	17.0	7.9	58.5	61.9
3	15.4	11.6	52.9	73.6	11.2	4.5	20.5	10.3
4	17.7	14.9	65.2	72.9	5.5	2.7	11.6	9.4

ple weight and carbon content (at. %), we estimated the hydrolyzability of particular structural fragments of HAs (Table 4). As expected, the most sensitive to hydrolysis are polysaccharide fragments. Their hydrolyzability was demonstrated to be independent of the soil nature, being about 70% for both HAs of tundra soils and chernozem. Thus, about 30% of polysaccharide fragments remain in the nonhydrolyzable residue.

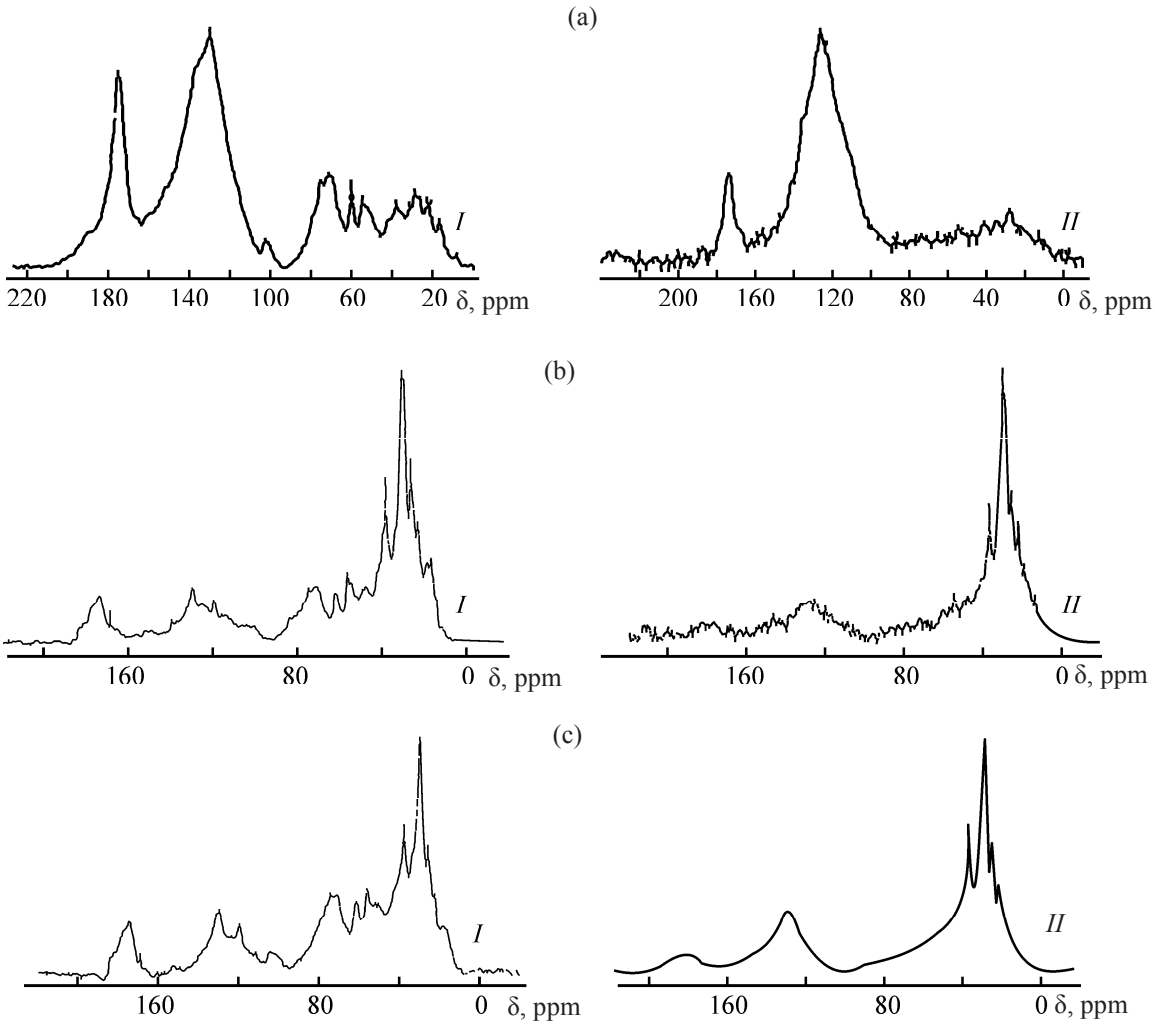


Fig. 2. ^{13}C NMR spectra of (*I*) initial HAs and (*II*) nonhydrolyzable residue after treatment with 6 M HCl. (δ) Chemical shift. Sample no.: (a) 3, (b) 1, and (c) 2.

Table. 4. Hydrolyzability of various structural fragments in HAs

Sample no.	Initial weight, mg	C, at. %	Nhr, % of initial sample weight	C_{at}, %	C_{at}, % of initial sample weight	Carboxy fragments, %		
						initial	nhr	hydrolyzed, %
1	102.4	33.91	62.6	38.76	24.26	2.9	1.4	53.1
2	98.7	32.23	58.7	39.44	23.15	2.1	1.6	26.2
3	119.9	43.17	63.3	43.58	27.59	6.7	2.2	52.2

Sample no.	Aromatic fragments, %			Polysaccharide fragments, %			Aliphatic fragments, %		
	initial	nhr	hydrolyzed, %	initial	nhr	hydrolyzed, %	initial	nhr	hydrolyzed, %
1	6.3	4.4	30.3	3.8	1.2	68.2	20.9	17.3	17.2
2	5.7	5.4	4.9	5.5	1.8	66.7	18.9	14.3	24.2
3	22.8	20.3	10.9	4.8	1.2	74.2	8.9	2.84	68.1

They are bound via ether bonds, which are stable under the experimental hydrolysis conditions.

The hydrolyzability of aromatic fragments depends on the soil kind. In this relation, the difference between two samples of tundra soils appeared to be particularly unexpected. The hydrolyzability of aromatic fragments of HAs of gley-podzolic sandy loam soil (sample no. 1) is 30%, whereas that of surface-gley clay loam soil (sample no. 2), only 5%. This value for chernozem is 11%. However, the absolute values of the loss of aromatic fragments in sample nos. 1 and 3 are very similar. It is about 2–2.5% of aromatic fragments that are bound to the macromolecule via bonds unstable under the experimental conditions.

There is a similarity in the hydrolyzability of the carboxy fragments of HAs of chernozem (sample no. 3) and gley-podzolic soil (sample no. 1): about a half of these fragments passed in the hydrolyzate (52 and 53%, respectively), in contrast to surface-gley clay loam soil (sample no. 2) initially containing small amount of carboxy fragments, and only about a quarter of them (26%) is hydrolyzed. As a result, the nonhydrolyzable residues of HAs of tundra soils contain practically equal amount (1.5%) of carboxy fragments.

The hydrolyzability of aliphatic fragments differs depending on the climatic zone. It is about 20% for tundra soils (sample nos. 1 and 2), and 70% for HAs of southern chernozem (sample no. 3).

CONCLUSIONS

(1) Under the experimental acid hydrolysis conditions, the peptide, glycoside, and ester bonds in humic acids extracted from various soils are cleaved, which affects their elemental and group composition.

(2) Hydrolyzability of the polysaccharide fragments is independent of the soil nature, while that of the aliphatic fragments depends on the climatic zone.

(3) Nonhydrolyzable fractions (core) of humic acids extracted from tundra and steppe soils differ significantly in their composition. In the core of humic acids extracted from tundra soils, aliphatic chains dominate, whereas in steppe soils, aromatic fragments prevail.

REFERENCES

1. Orlov, D.S., *Gumusovye kisloty pochv i obshchaya teoriya gumifikatsii* (Soil Humus Acids and General Theory of Humification), Moscow: Mosk. Gos. Univ., 1990.
2. Cheng, C.-N., Shufeldt, R.C., and Stevenson, F.J., *Soil Biol. Biochem*., 1975, vol. 7, no. 3, pp. 143–151.
3. Drozdova, T.V., *Geokhimiya aminikislot* (Amino Acid Geochemistry), Moscow: Nauka, 1977.
4. Dergacheva, M.I. and Zykina, V.S., *Geol. Geofiz*., 1979, no. 6, pp. 115–118.
5. Carter, P.W. and Mitterer, R.M., *Geochim. Cosmochim. Acta*, 1978, vol. 42, no. 8, pp. 1231–1238.
6. Moliner, R. and Gavilan, J.M., *Fuel*, 1981, vol. 60, no. 1, pp. 64–66.

7. Jones, D.L., Owen, A.G., and Farrar, J.F., *Soil Biol. Biochem*., 2002, vol. 34, no. 12, pp. 1893–1902.
8. Friedel, J.K. and Scheller, E., *Soil Biol. Biochem*., 2002, vol. 34, no. 3, pp. 315–325.
9. Warren, C.R., *Soil Biol. Biochem*., 2008, vol. 40, no. 4, pp. 916–923.
10. Tsutsuki, K. and Kuwatsuka, S., *Soil Sci. Plant Nutr*., 1979, vol. 25, no. 1, p. 29.
11. Tsutsuki, K. and Kuwatsuka, S., *Soil Sci. Plant Nutr*., 1978, vol. 24, no. 4, p. 547.
12. Ogner, G., *Geoderma*, 1980, vol. 23, no. 1, pp. 1–10.
13. Yamaoka, Y., *Marine Chem*., 1983, vol. 13, no. 3, pp. 227–237.
14. Tanaka, H., Homma, M., Sakagami, K., and Hamada, R., *Sci. Total Environ*., 1992, vols. 117–118, pp. 145–153.
15. Allard, B., *Geoderma*, 2006, vol. 130, nos. 1–2, pp. 77–96.
16. Orlov, D.S., Grishina, L.A., and Eroshicheva, N.L., *Praktikum po biokhimii gumusa* (Practical Course of Humus Biochemistry), Moscow: Mosk. Gos. Univ., 1969.

ISSN 1070-4272, Russian Journal of Applied Chemistry, 2008, Vol. 81, No. 11, pp. 1963–1966. © Pleiades Publishing, Ltd., 2008.
Original Russian Text © S.M. Danov, A.V. Sulimov, A.V. Sulimova , 2008, published in Zhurnal Prikladnoi Khimii, 2008, Vol. 81, No. 11, pp. 1847–1850.

ORGANIC SYNTHESIS AND INDUSTRIAL ORGANIC CHEMISTRY

Solvent Effect on Epoxidation of Allyl Chloride with Hydrogen Peroxide on Titanium-Containing Silicalite

S. M. Danov, A. V. Sulimov, and A. V. Sulimova

Dzerzhinsk Polytechnic Institute, Branch of Nizhni Novgorod State University, Dzerzhinsk, Nizhni Novgorod oblast, Russia

Received May 27, 2008

Abstract—The solvent effect on liquid-phase epoxidation of allyl chloride with an aqueous solution of hydrogen peroxide on TS-1 titanium-containing silicalite was examined. 1-Butanol, 2-butanol, 1-propanol, isopropanol, methanol, ethanol, water, acetone, methyl ethyl ketone, and 1-pentanol were tested as solvents.

DOI: 10.1134/S1070427208110189

Epichlorohydrin is an important product of basic organic synthesis. It is highly reactive owing to the presence of an epoxy group and a labile chlorine atom. Epichlorohydrin readily reacts with compounds of various classes, which allows preparation of many valuable products from it (epoxy resins, lacquers, paints, adhesives, synthetic fibers, ion-exchange resins, rubbers characterized by high oil and heat resistance and impermeability to gases). However, despite diversity of products prepared using epichlorohydrin, the major area of its application is production of epoxy resins (68% of the whole amount of epichlorohydrin produced) [1].

Today epichlorohydrin is produced on the large-tonnage scale (the annual world production exceeds 1.3 million tons [1]). In Russia, the demand for products based on epichlorohydrin increases by 4–5% annually, and the major fraction of epichlorohydrin is imported.

With the steadily growing demand for epichlorohydrin, it becomes necessary to put into operation new facilities capable of producing a competitive product. Our analysis of procedures for epichlorohydrin production [2] showed that the most promising procedure is liquid-phase oxidation of allyl chloride with hydrogen peroxide in an organic solvent on a heterogeneous catalyst, titanium-containing zeolite TS-1 [3]. However, published data on the solvent effect on the process are virtually lacking.

Here we report the results of studying the solvent effect on liquid-phase oxidation of allyl chloride with an aqueous solution of hydrogen peroxide on TS-1 titanium-containing catalyst.

In our study we used the following chemicals. Solvents: 1-butanol, 2-butanol, 1-propanol, isopropanol, methanol, ethanol, water, acetone, methyl ethyl ketone of pure or analytically pure grade, distilled and dehydrated before use; epichlorohydrin of pure grade, GOST (State Standard) 12 844–74; 33–34% hydrogen peroxide of ultrapure grade [TU (Technical Specification) 2611-069-05 807 977–2006]; and allyl chloride (TU 6-01-753–77). The catalyst, titanium-containing zeolite, was prepared by the procedure described in [3] (Ti content counting on TiO_2 3.16%). Experiments were performed on a batch laboratory installation at 30°C, allyl chloride : hydrogen peroxide molar ratio of 3.0, and solvent : allyl chloride weight ratio of 9.1. The content of the titanium-containing zeolite remained the same in all the experiments (8.0 g l^{-1}).

The reaction mixture components were analyzed by GLC on a Tsvet 500 chromatograph under the following conditions: 2000 × 3-mm metallic column; stationary phase Carbowax 6000 (15 wt % on Chromaton N-AW); flame ionization detector; carrier gas nitrogen, flow rate 50 ml min^{-1}; vaporizer and column temperatures 180 and 130°C, respectively. Hydrogen peroxide was determined by iodometric titration.

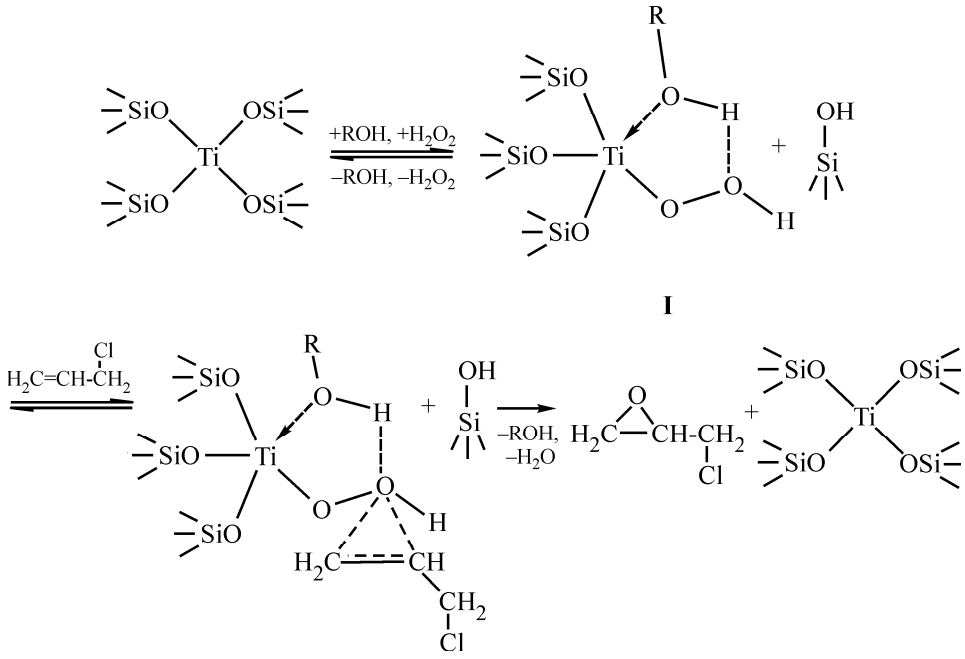
Epoxidation of allyl chloride is usually performed with aqueous solutions of hydrogen peroxide in an organic solvent. In the process, the solvent acts as a homogenizer of allyl chloride and hydrogen peroxide, providing their reaction on the surface of a solid cata-

Solvent effect on the initial rate of hydrogen peroxide conversion and on the yield of epichlorohydrin. 30°C, 8.0 g l^{-1} catalyst, catalyst : hydrogen peroxide molar ratio 3.0, solvent : allyl chloride weight ratio 9.1

Solvent	Initial rate of H_2O_2 conversion, mol l^{-1} min^{-1}, $\times 10^2$	Yield of propylene oxide at 50% conversion of H_2O_2, %
Methanol	1.61	49.6
Ethanol	0.66	45.7
Isopropanol	0.47	43.4
1-Propanol	0.37	42.4
Acetone	0.33	42.9
2-Butanol	0.29	25.9
Methyl ethyl ketone	0.16	–
1-Butanol	0.7	–
Water	0.5	–

lyst. Therefore, the solvent should meet certain requirements. It should exhibit good solvency (toward both allyl chloride and hydrogen peroxide) and be sufficiently inert under the reaction conditions. Among diverse available solvents, we chose 1-butanol, 2-butanol, 1-propanol, isopropanol, methanol, ethanol, water, acetone, methyl ethyl ketone, and 1-pentanol. The results are given in the table.

The table shows that the yield of epichlorohydrin decreases in the order methanol, ethanol, 2-propanol, acetone, 1-propanol. In the other solvents (methyl ethyl ketone, 1-butanol, 1-pentanol, water), 50% conversion of hydrogen peroxide was not attained in 180 min. Also, the solvent strongly affects the initial rate of hydrogen peroxide conversion. This solvent effect can be understood taking into account the mechanism of allyl chloride epoxidation with hydrogen peroxide in a proton-donor organic solvent on titanium-containing silicalite [4]:



Epoxidation of allyl chloride with hydrogen peroxide occurs on titanium atoms in the four-coordinate state [5] via formation of an active five-membered cyclic complex **I** in which the hydrogen peroxide molecule contains an active oxygen atom attacking the allyl chloride molecule [6].

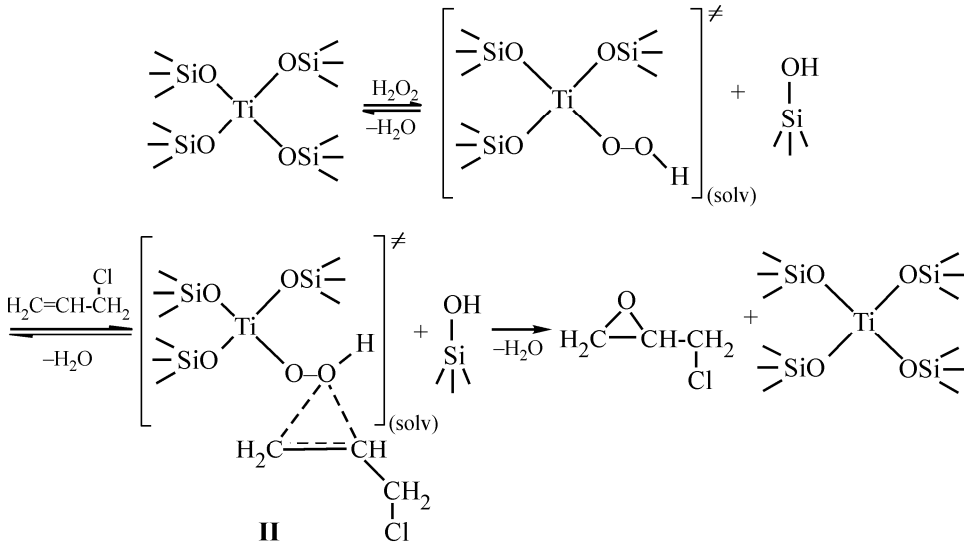
Thus, the solvent not only acts as a homogenizer of the mixture of the starting reactants but also actively participates in the stabilization of the Ti peroxo complex **I** formed by a hydrogen peroxide molecule on a titanium center of the catalyst. Such stabilization is possible owing to coordination of a solvent molecule with a titanium center and formation of a hydrogen bond with a hydrogen peroxide molecule.

It should be noted that an increase in the size of the alkyl radical R in an alcohol molecule and, correspondingly, in the size of the transition complex **I** complicates the approach of an olefin molecule to the activated complex and thus hinders the oxygen transfer. Therefore, the yield of epichlorohydrin is the highest when methanol is used as solvent. Certain authors believe [7] that, along with the steric factor, a decrease in the yield of epichlorohydrin in the series methanol, ethanol, 2-propanol, acetone, 1-propanol, 2-butanol may be due to the fact that the binding energy of the solvent molecule in the transition complex increases in the order 2-butanol, 1-propanol, acetone, 2-propanol, ethanol, methanol. This leads to a decrease in the reactivity of the five-membered complex **I** and, as a result, to a decrease in the rate of oxygen transfer from the hydrogen peroxide molecule to allyl chloride. However, this hypothesis has not yet been confirmed experimentally.

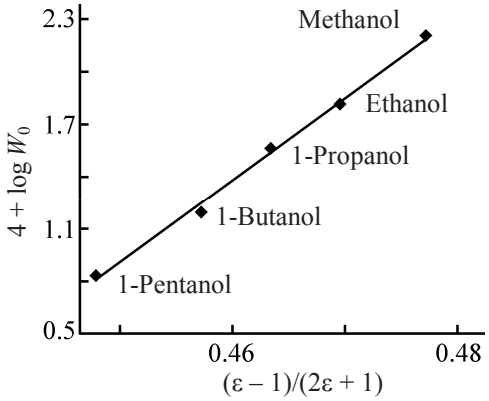
Furthermore, owing to an increase in the volume of the solvent molecule, the rate of diffusion of the solvent and reaction products in catalyst pores decreases, which leads to a decrease in the process selectivity.

Numerous studies were aimed to examine the structure of the five-membered active complex, but its structure is still unclear because of the instability of the complex consisting of a titanium atom incorporated in the framework of titanium-containing silicalite, a solvent molecule, and hydrogen peroxide [8, 9]. Attempts are made [10, 11] to elucidate the structure of the five-membered complex by quantum-chemical calculations.

It is important that complex **I** is formed only in proton-donor solvents and is not formed in aprotic solvents. However, the Ti–OOH species exists in both systems [12]. The mechanism of epoxidation of allyl chloride with hydrogen peroxide in an aprotic organic solvent on a titanium-containing zeolite is as follows:



In this case, the effect of the aprotic solvent on the epoxidation of allyl chloride can be interpreted from the standpoint of the solvent polarity. Transition states observed in the course of the reaction are characterized by certain charge separation, i.e., they are more polar than the starting reactants. This should lead to variation of the epichlorohydrin yield with variation of the solvent permittivity. The higher the solvent permittivity, the lesser the extent to which the polar transition state is stabilized by solvation and the weaker the effect of internal factors on the reaction rate. Thus, an increase in the solvent polarity facilitates the cleavage



Correlation of the initial reaction rate W_0 with the permittivity function (ε – 1)/(2ε + 1) in oxidation of allyl chloride in various solvents. 30°C, catalyst content 8.0 g l^{-1}, allyl chloride : hydrogen peroxide molar ratio 3.0, solvent : allyl chloride weight ratio 9.1.

of the peroxy bond in complex **II** and the oxygen transfer to allyl chloride. In particular, the yield of epichlorohydrin increases as the solvent polarity grows in going from acetone to methyl ethyl ketone. Similar trends are observed in proton-donor solvents. The figure shows how the initial rate of allyl chloride epoxidation correlates with the dielectric constant of the medium within the same homologous series of alcohols (methanol, ethanol, 1-propanol, 1-butanol, 1-pentanol). For solvents of different classes, it is impossible to construct a correlation between the initial rate and solvent permittivity because of the growing role of steric factors.

In view of the trends revealed for organic solvents, it could be expected that the use of water as solvent would lead to an increase in the epoxidation rate. However, despite the absence of steric hindrance caused by large molecular volume of organic solvents and high polarity (ε = 78.5) of water, it is a poor solvent for performing the process. This may be caused by the fact that the concentration of the five-membered active complex in catalyst pores will be very low because of hydrophobicity of the titanium-containing silicalite [5]. This conclusion is consistent with the fact that in other processes the catalyst also shows lower activity with water as solvent [4].

Vankelecom et al. [13] suggested to perform oxidation on titanium-containing silicalite without a solvent in a three-phase system. Unfortunately, it is difficult to judge the efficiency of such a procedure because of the lack of experimental data on epoxidation of olefins. However, it is undesirable to perform the process under such conditions because of hazard associated with the use of concentrated hydrogen peroxide solutions.

It is important that, in the synthesis of epichlorohydrin, the desired reaction can be accompanied by side reactions, in particular, by oxidation of the solvent (of methanol to formaldehyde, of ethanol to acetaldehyde, of isopropanol to acetone). It was found that the reactivity of lower alcohols increases with an increase in their molecular weight. When the experiments were performed under the same conditions, formaldehyde was not detected (trace amounts), whereas in isopropanol the yield of acetone reached several percents. Aprotic solvents (acetone, methyl ethyl ketone) do not undergo such side transformations under the reaction conditions. However, the use of acetone or other ketones as solvents is undesirable, because in the presence of hydrogen peroxide they can form dangerously explosive organic peroxides [14].

CONCLUSION

Methanol is the most suitable as solvent for epoxidation of allyl chloride with hydrogen peroxide on the commercial scale.

REFERENCES

1. http://marketpublishers.com/
2. Huanxin Gao, Gongxuan Lu, Jishuan Suo, and Shuben Li, *Appl. Catal. A: General*, 1996, vol. 138, pp. 27–38.
3. US Patent 4 410 501.
4. Clerici, M.G. and Inoallina, P., *J. Catal.*, 1993, vol. 140, pp. 71–83.
5. Danov, S.M., Sulimov, A.V., and Fedosov, A.E., *Katal. Prom–sti*., 2007, no. 6, pp. 13–17.
6. Guo Xinwen, Wang Xiangsheng, Liu Min, et al., *Catal. Lett*., 2002, vol. 81, pp. 125–131.
7. Hayashi, H., Kikawa, K., Murai, Y., et al., *Catal. Lett*., 1996, vol. 36, pp. 99–102.
8. Notari, B., *Adv. Catal*., 1996, no. 41, pp. 253–334.
9. Bellussi, G. and Rigutto, M., *Stud. Surf. Sci. Catal*., 1994, vol. 85, pp. 177–183.
10. Neurock, M. and Manzer, L.E., *Chem. Commun*., 1996, no. 10, pp. 1133–1134.
11. Vayssilov, G.N. and Van Santen, R.A., *J. Catal*., 1998, no. 175, pp. 170–174.
12. Gang Li, Jiwen Meng, Xiangsheng Wang, and Xinwen Guo, *React. Kinet. Catal. Lett*., 2004, vol. 82, pp. 73–80.
13. Vankelecom, I., Vercruysse, K., Moens, N. et al., *Chem. Commun*., 1997, no. 1, pp. 137–138.
14. Karnojitzki, V., *Les peroxides organiques*, Paris: Hermann, 1958.

ISSN 1070-4272, Russian Journal of Applied Chemistry, 2008, Vol. 81, No. 11, pp. 1972–1975. © Pleiades Publishing, Ltd., 2008.
Original Russian Text © E.G. Shushlyaeva, N.M. Polyakova, Yu.V. Suleimanova, N.V. Trukhacheva, A.I. Agafonova, G.V. Minkhaidarova, G.V. Nesyn, E.N. Cherezova, A.G. Liakumovich, 2008, published in Zhurnal Prikladnoi Khimii, 2008, Vol. 81, No. 11, pp. 1856–1860.

MACROMOLECULAR COMPOUNDS AND POLYMERIC MATERIALS

Modification of Polypropylene with Long-Chain Elastomers

E. G. Shushlyaeva, N. M. Polyakova, Yu. V. Suleimanova, N. V. Trukhacheva, A. I. Agafonova, G. V. Minkhaidarova, G. V. Nesyn, E. N. Cherezova, and A. G. Liakumovich

Kazan State University of Technology, Kazan, Tatarstan, Russia
Tomsk Polytechnic University, Tomsk, Russia

Received May 13, 2008

Abstract—Physicomechanical and rheological properties of isotactic polypropylene modified with a high-molecular-weight amorphous polymer, polyoctene, were studied. Modification of polypropylene with polyoctene allows the impact resilience and relative elongation to be increased relative to the initial polypropylene and the processing temperature to be decreased.

DOI: 10.1134/S1070427208110207

Polyolefins are the main commercial thermoplastics, thanks to a set of their valuable propertries [1]. In particular, isotactic polypropylene (PP) exhibits high strength, high wear and chemical resistance, low water vapor and gas permeability, and good dielectric characteristics. At the same time, PP is brittle, and its frost resistance is poor (–15°C). This fact significantly restricts its application area.

The PP application area can be expanded by its modification allowing preparation of composite materials with improved processing and service characteristics.

Use of plasticizing polymeric additives as PP modifiers is well known. Among such additives are rubbers (butadiene–styrene, butyl rubber, copolymers of ethylene with propylene and/or with higher α-olefins) and thermoelastoplastics (block copolymers of butadiene with styrene) [1–3]. Introduction of an elastomer into a brittle polymer yields a product that is considerably more resistant to failure than the initial polymer. The impact resilience, breaking elongation, and rupture work increase, and the material becomes less brittle. Some parameters, however, inevitably become worse: the elastic modulus and breaking tensile stress somewhat decrease, the transparency is lost, and the melt becomes more viscous. Nevertheless, all these losses are insignificant compared to the gain in the resistance to failure.

Modification of PP can be performed both in the course of the synthesis and by mixing the homopolymer with an elastomer in the melt. The latter procedure, performed in an extruder, is widely used today. The extruder acts as a reactor in which the steps of the dispersion of ingredients and a chemical reaction between them can be combined [4]. The extrusion mixing combines functionalization of the ingredients in situ and formation of block or graft copolymers on the phase boundary. These copolymers act as compatibilizers, enhancing the specific intermolecular interaction of chains and making the ingredients better compatible [5].

In this paper we analyze the results of PP modification with high-molecular-weight polyoctene (HMWPO) exhibiting elastomeric properties (HMWPO is a comb-shaped flexible-chain polymer which can itself act as compatibilizer owing to the presence of labile pendant groups).

EXPERIMENTAL

As modifier for polypropylene of 21 270D grade containing 95 wt % isotactic fraction, we used a high-molecular-weight amorphous polymer, polyoctene, prepared as described in [6]. The viscosity-average molecular weight M of polyoctene was determined viscometrically [7] in tetrahydrofuran at 20°C by the formula

$$[\eta] = 2.32 \times 10^{-4} M^{0.69},$$

where [η] is the intrinsic viscosity.

The modifier was introduced into the compound in

a Brabender mixer at 180°C for 5 ± 0.5 min. The composition of the initial PP compound modified with high-molecular-weight polyoctene was as follows (wt %):

Polypropylene of 21 270D grade	Up to 100
HMWPO	16.0
Carbon black concentrate KTU-30PP	1.4
Irganox 1010	0.2
Calcium stearate	0.1

The melt flow index (MFI) of samples was determined on a Ray–Ran extrusion plastometer in accordance with ASTM 1238 standard under the following conditions: capillary diameter 2.095 ± 0.005 mm, temperature 230°C, load 2.16 kg.

The melting and crystallization points of substances were determined by differential scanning calorimetry (DSC) on a Mettler Toledo device in the automatic mode (heating rate 20 deg min^{-1}), in accordance with ASTM D 3418 standard.

Flow curves were obtained with a Brabender plasticorder at 200°C (shear rate 228–5750 s^{-1}).

Reference samples for physicomechanical tests of the initial and modified PP were prepared by pressure casting with a Negri–Bossi machine.

The physicomechanical and thermal properties of PP and its compounds were evaluated either by standardized Russian protocols in accordance with GOST (State Standard) 26 996 or by American standards, namely: bending elastic modulus, according to ASTM D 790; Izod impact resilience, according to ASTM D 256; ultimate tensile strength at yield point and relative elongation, according to ASTM D 638.

Mixed shock-resistant plastics are composite materials consisting of a rigid matrix with a relatively high melting point and a disperse phase of an elastomer with a low glass transition point. The adhesion between the phases should be sufficiently strong, and the elastomer should be uniformly dispersed in the polymer matrix. Specific character of physicomechanical properties depends on specific features of the elastomer used [3, 8]. As crystallographic studies of polyolefins and their copolymers show [1], the use of bulky comonomer units in production of an elastomer, such as 1-octene, is more preferable than the use of propylene and 1-butene, because the latter units are inserted into crystalline formations and destroy them, whereas 1-octene units remain in amorphous regions. Therefore, the use of polyoctene as an elastomeric phase in a compound may be more efficient than the use of ethylene–propylene copolymers.

Table 1. Melting and crystallization points of modified polypropylene

HMWPO content, wt %	T_m, °C	T_{cr}, °C
0	160.0	116.0
8	159.5	117.1
14	158.5	117.2
20	157.5	116.3

As the difference between the melting point of isotactic PP and polyoctene is almost 200°C [1], it was interesting to examine the effect of HMWPO on temperature characteristis of the compound. The HMWPO content was varied from 8 to 20 wt %.

The results obtained by DSC (Table 1) show that the melting and crystallization points of PP compounds remain essentially the same.

One of important parameters for estimating the mechanical properties of the polymer is Izod impact resilience. The experimental data (Fig. 1) show that introduction of elastomeric HMWPO into the compound increases its impact resilience compared to the initial PP.

It should be noted that the impact resilience of modified samples, determined in the region of negative temperatures, increases insignificantly, whereas at room temperature the impact strength of the compound increases by a factor of almost 2 at 14 wt% and higher content of the modifier.

Along with the Izod impact resilience, the mechanical properties of PP are characterized by the stretch

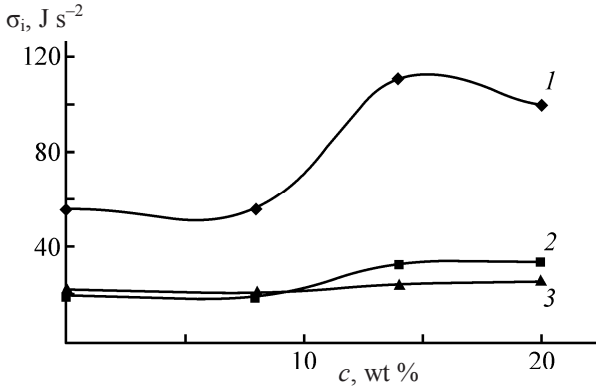


Fig. 1. Izod impact resilience σ_i as a function of the content c of HMWPO modifier in PP samples. Temperature, °C: (*1*) +23, (*2*) –20, and (*3*) –40.

Table 2. Deformation–strength properties of polypropylene–polyoctene compounds

HMWPO content, wt %	Bending elastic modulus, MPa	Ultimate tensile strength at yield point, MPa
0	1635	34
8	1170	29
14	885	24
20	666	19

diagram. At a tensile strain of a PP article, only the initial portion of the diagram is important. The "service suitability" of PP is evaluated by the yield point, i.e., by the maximum in the stretch diagram, corresponding to definite values of stress and relative elongation. The PP behavior in tensile tests is determined, according to published data, by the ratio of the crystalline and amorphous fractions in a sample. With an increase in the content of the atactic fraction playing the role of an elastomeric phase, the tensile elastic modulus decreases, the relative elongation, as a rule, increases, and the ultimate tensile strength at yield point somewhat decreases [2].

Experimental data show that this character of variation of the above characteristics is also observed with HMWPO: With an increase in the modifier content in the PP compound, the relative elongation increases (Fig. 2), and the tensile elastic modulus and the ultimate tensile strength decrease (Table 2). This is apparently associated with the elastomeric nature of the modifying additive, which can be used in production of specific articles in some branches of industry.

The effect of elastomers on the properties of the base polymer is manifested not only in the solid state but also in a melt, because the rheological properties of the melt change. For example, the viscosity associated with an increase in the hyperelastic strain appreciably increases, which is accompanied by swelling of the extrudate jet [9]. The latter fact is important for the modern high-speed casting processes. The behavior of HMWPO and PP melts is of doubtless interest in this respect.

Primary evaluation of the modifier effect on the viscosity properties of the melt was made by measuring MFI of samples at a load of 2.16 kg and a temperature of 230°C. The test results are shown in Fig. 3. It can be seen that modification of PP with elastomeric polyoctene leads to a significant increase in the melt flow index, which is apparently due to good compatibility of the components and strong plasticizing effect of the modifier.

The melt flow index of the polymer, by which the viscosity properties of melts are usually evaluated in technological practice, correspond to only one point in the flow curve in the region of relatively low shear stresses. Samples with the same MFI can strongly differ in the processing properties, owing to the sensitivity of the viscosity to the variation of the shear rate [10]. Therefore, for more complete evaluation of the rheological properties of modified PP, we used the flow curves. The results of rheological tests are given in Fig. 4.

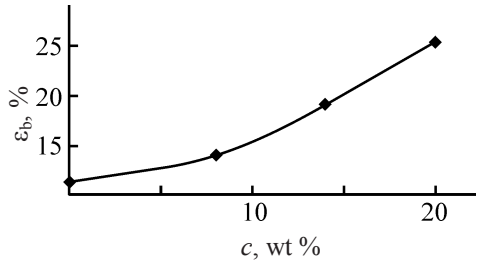


Fig. 2. Relative breaking elongation ε_b as a function of the content c of HMWPO modifier in PP samples.

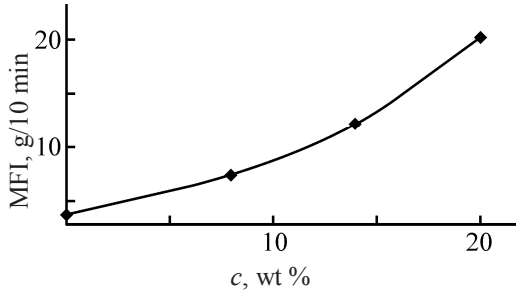


Fig. 3. Melt flow index MFI of PP melt as a function of HMWPO content c.

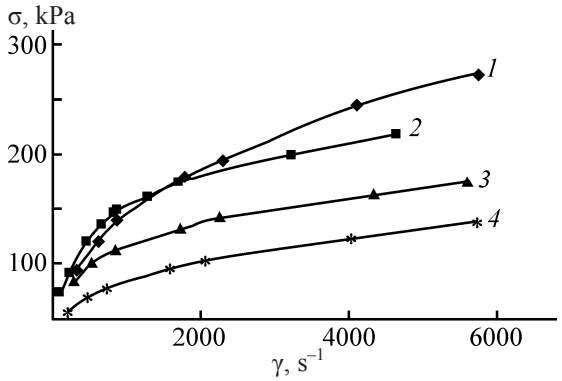


Fig. 4. PP flow curves. (σ) Shear stress and (γ) shear rate. HMWPO content, wt %: (*1*) 0, (*2*) 8, (*3*) 14, and (*4*) 20.

Table 3. Physicomechanical and thermal properties of shock- and frost-resistant polypropylene compounds

Parameter	Modifier		Method according to[a]
	HMWPO	SKEPT-50	
Melt flow index, g/10 min	20	6.4	GOST 11 645
Tensile yield point (σ_{ty}), MPa	23.0	22.2	GOST 11 262
Tensile strength (σ_t), MPa	19.6	17.4	GOST 11 262
Relative elongation at break (ε_b), %	510	380	GOST 11 262
Bending elastic modulus (E_b), MPa	1000	890	GOST 9850
Charpy impact resilience, kJ m^{-2}:			
with notching at –40°C	6.4	–	GOST 4647
without notching at –40°C	72	63	GOST 4647
Vicat softening point, °C			
at 10 N load	146	146	GOST 15 088
at 50 N load	68	–	GOST 15 088
Bending softening point, °C			
at P = 0.45 MPa	84	–	GOST 12 021
at P = 1.80 MPa	48	–	GOST 12 021
Shrinkage, %	0.9	1.2	GOST 18 616
Frost resistance, °C	–60	–60	TU 2211-065-05 796 653–2002

[a] (GOST) State Standard and (TU) Technical Specification.

Figure 4 shows that an increase in the modifier content in the compound favors a decrease in the shear stress with increasing shear rate.

Thus, analysis of the rheological properties of modified PP shows that, to intensify the PP processing, flexible-chain comb-shaped polyoctene is a promising modifier allowing not only an increase in the processing rate in production of composite materials, but also a decrease in the processing temperature.

In addition, we compared the main physicomechanical and thermal properties of 21 270 D grade polypropylene modified with polyoctene ([η] = 12.0) and of commercial frost- and shock-resistant PP modified with ternary ethylene–propylene–diene copolymer SKEPT50. The amount of modifiers in the compound was 16 wt % (Table 3).

The data we obtained show that the impact resilience and other physicomechanical characteristics of the experimental sample are no worse or appreciably better than those of the compound with SKEPT-50. At the same time, the relative elongation at break increased by 34% and MFI, by a factor of 3.

CONCLUSIONS

Polyoctene, a high-molecular-weight polymer derived from a higher α-olefin, when used as an elastomeric component of a shock- and frost-resistant polypropylene-based compound, shows certain advantages as compared to the known elastomers and quite real prospects for practical use.

REFERENCES

1. White, J.L. and Choi, D.D., *Poluolefins: Processing, Structure, Development, and Properties*, Munich: Hanser, 2005.
2. *Polipropilen* (Polypropylene), Pilipovskii, V.I. and Yartsev, I.K., Eds., Leningrad: Khimiya, 1967.
3. Bucknall, C.B., *Toughened Plastics*, London: Applied Science, 1977.
4. Prut, E.V. and Zelenetskii, A.N., *Usp. Khim.*, 2001, vol. 70, p. 72.
5. Ermakov, S.N. and Kravchenko, T.P., *Plast. Massy*, 2003, no. 12, pp. 21–26.
6. RF Patent 2 238 282.
7. *Sinteticheskie vysokomolekulyarnye materialy: Ekspress-informatsiya* (Synthetic Macromolecular Materials: Express Information), VINITI, 1992, no. 44, pp. 9–12.
8. RF Patent 2 255- 948.
9. Gorbunova, I.Yu. and Kerber, M.L., *Plast. Massy*, 2000, no. 9, pp. 7–11.
10. Ivanyukov, D.V. and Fridman, M.L., *Polipropilen (svoistva i primenenie)* (Polypropylene (Properties and Use)), Moscow: Khimiya, 1974.

ISSN 1070-4272, Russian Journal of Applied Chemistry, 2008, Vol. 81, No. 11, pp. 1976–1980. © Pleiades Publishing, Ltd., 2008.
Original Russian Text © A.V. Kulikov, A.I. Kurkin, Ya.D. Samuilov, 2008, published in Zhurnal Prikladnoi Khimii, 2008, Vol. 81, No. 11, pp. 1861–1865.

MACROMOLECULAR COMPOUNDS AND POLYMERIC MATERIALS

Influence of the Nature of Curing Agents on Properties of Polyetherurethanethiol Composites

A. V. Kulikov, A. I. Kurkin, and Ya. D. Samuilov

Kazan State Technological University, Kazan, Tatarstan, Russia

Received February 29, 2008

Abstract—The effect of the nature of curing agents on the properties of sealants based on polyetherurethanethiols was examined.

DOI: 10.1134/S1070427208110219

HS-Terminal oligomers are widely applied for preparing mastics and sealants used in machine and ship building, aviation industry, and construction [1–4]. However, preparation of such oligomers, Thiokols, is extremely hazardous for the environment. Production of 1 t of Thiokol involves formation of 60 t of highly toxic aqueous–organic salt solutions requiring utilization. Therefore, of increased interest are procedures for preparing SH-containing oligomers that do not involve formation of so large amounts of wastewater. Principally, such routes exist. For example, the reaction of polyetherdiols or –triols with diisocyanates yields preisocyanates:

$$–OH + O=C=N–R–N=C=O \rightarrow \sim O–CO–NH–R–N=C=O.$$

The reaction of preisocyanates with mercapto alcohols allows preparation of polyetherurethanethiols (PEUTs):

$$\sim O–CO–NH–R–N=C=O + HO–CH_2–CH_2–SH$$

$$\rightarrow \sim O–CO–NH–R–NH–CO–O–CH_2CH_2–SH.$$

These compounds contain terminal mercapto groups, which can be oxidized to disulfide groups or converted to metal mercaptides. In so doing, the material will be cured with the formation of a 3D structure. This procedure is environmentally clean. The PEUT synthesis process is single-step. All these advantages attract attention. However, until now, only scarce patent information concerning this approach was available, and there are virtually no data on the properties of sealants based on PEUT [5, 6].

The goal of this study was to examine the properties of sealants prepared on the basis of PEUT, in particular, to reveal the dependences of the physicomechanical properties of the vulcanizates on the nature of the curing agents, because it is well known that this factor strongly affects the properties of sealants [1–4, 7].

EXPERIMENTAL

The substances used in this study met the requirements indicated in Table 1.

Laprol used for preparing PEUT was preliminarily dried in a vacuum at a residual pressure of 2600 Pa and

Table 1. Grades of substances used[a]

Name	GOST, TU no.
Toluylene diisocyanate T-80	TU 113-03-12-17–85
Laprol 3603-2-12	TU 2226-015-10488057–94
2-Mercaptoethanol	BASF product (Germany), 99.99% main substance
Finely dispersed chalk MTD-2	TU 5743-008-05 346 453–97
Diphenylguanidine (DPH)	TU 6-14-22-269–90
Manganese dioxide	TU 6-09-01-775–90
Sodium bichromate	GOST 2651–78
Zinc oxide	GOST 202–84
Chloroparaffin KhP-470B	TU 2493-379-05 763 441–2002

[a] (TU) Technical specification and (GOST) State standard.

a temperature of 90–100°C for 4 h. Then the hydroxyl number of the dry polyether was determined in accordance with GOST (State Standard) 25 261–82. The preisocyanate was synthesized in a four-necked flask equipped with a power-driven stirrer, a thermometer, and a reflux condenser with a calcium chloride tube and a tube for introducing an inert gas (nitrogen or argon). First the dried polyether and toluylene diisocyanate (T-80 grade) were charged to the flask with stirring at 40–45°C. The reactant ratio should correspond to the HO : NCO ratio of 1 : 2. An inert atmosphere was provided by feeding nitrogen at excess pressure. The flask contents were heated to 80 ± 5°C, and this temperature was kept for no less than 2 h with stirring of the reaction medium. The reaction completion was judged from the attainment of a constant content of isocyanate groups in the reaction medium. The amount of isocyanate groups in aliquot portions was determined in accordance with TU (Technical Specification) 38.103 137–78.

Mercaptoethanol can react with isocyanates via both hydroxy and mercapto groups. When performing this step, we took into account the results of a thermodynamic analysis of the reaction of phenyl isocyanate with methanol and methyl mercaptan [8], which showed that thiourethanes at 100°C virtually completely decompose into the starting reactants, whereas urethanes remain stable at this temperature. Our experiments showed that, when this reaction step is performed at temperatures below 100°C, the reaction mixture rapidly transforms into a rubber-like mass.

The preisocyanate from the previous step was mixed with mercaptoethanol at 60–70°C. The molar ratio of the isocyanate and hydroxy groups was kept equal to 1 : 1. Then the reaction mixture temperature was increased to 100 ± 5°C, and the mixture was stirred in an inert atmosphere for no less than 6 h up to complete exhaustion of the isocyanate groups. The resulting PEUT is a viscous colorless liquid at room temperature. The content of SH groups in PEUT was determined in accordance with TU 38.103 636–87 to be 2.30 wt %. The IR spectrum of PEUT (film on KBr, Perkin–Elmer 16PC–FT-IR device) contains amide absorption bands (1720, amide I; 1540, amide II; 1280 cm^{-1}, amide III), a band of N–H stretching vibrations (3335 cm^{-1}), bands of antisymmetric and symmetric vibrations of C–H bonds in methyl and methylene groups (2960, 2940, 2970, 2860 cm^{-1}), bands of bending vibrations of C–H bonds in methylene and methyl groups (1470, 1350 cm^{-1}), a strong absorption band of C–O–C antisymmetric stretching vibrations (1150 cm^{-1}), and a weak bond of H–S stretching vibrations (2560 cm^{-1}).

Table 2. Formulas of PEUT-based compounds

Component	Content, wt proportion		
Base paste			
PEUT	20		
Chalk	55		
Chloroparaffin	15		
Curing paste	1	2	3
Sodium bichromate		0.3	
Zinc oxide			5
Manganese dioxide	2		
Chloroparaffin	2	2.0	3
Chalk	3	4.7	0.5
Water	2	2	0.5
DPH	1	1	1

The vulcanizates of PEUT-based sealants were prepared by mixing the base paste with a curing paste containing curing agents. The compositions of the base and curing pastes are given in Table 2.

To reveal the influence of the curing agent content in the sealant compound on the physicomechanical properties of the vulcanizates, we varied the relative amounts of the base and curing pastes in the compound. The preparation of the vulcanizates consisted of the following steps.

(1) Preparation of the base paste by manually mixing the components in a porcelain mortar with a putty knife, according to the formula given in Table 2.

(2) Preparation of the curing paste by manually mixing the components in a porcelain mortar with a putty knife, according to the formula given in Table 2.

(3) Preparation of vulcanizates by manually mixing the base and curing pastes in a porcelain mortar with a putty knife and keeping the compound for 1 day at room temperature and for 3 h in an oven at 70°C. The samples obtained were kept for 1 day at room temperature, and their physicomechanical parameters were determined.

The physicomechanical parameters of the vulcanizates were determined in accordance with the procedures given in TU 5772-042-05 766 764 "Building Sealant 1m." The tensile strength σ, stresses at 100 and 300% elongation σ_{100}, σ_{300}, relative elongation ε, and elongation set ε_{set} were determined with a 2166R-55 tensile-testing machine, and the Shore hardness (scale A), with a TIR hardness meter, GOST 7761–55.

The working life of sealant compounds was determined at room temperature as the time within which the compound can be uniformly applied to any surface. The water absorption of sealant vulcanizates was determined by the procedure described in [9].

We studied the vulcanization of PEUT-based sealant compounds under the action of manganese dioxide, sodium bichromate, and zinc oxide. The first two agents are oxidative curing agents, and the third is a salt-forming agent.

The use of manganese dioxide for vulcanization of oligomers with HS fragments is based on the reaction [1–4, 7]

$$2\ {\sim}SH + MnO_2 \rightarrow {\sim}S{-}S{\sim} + Mn(OH)_2. \quad (1)$$

This reaction step is catalyzed by bases. For this purpose, diphenylguanidine is added to the curing paste. The resulting white manganese(II) hydroxide is then readily oxidized to brown manganese(III) oxyhydroxide and then to manganese(IV) hydroxide [10, 11]:

$$2Mn(OH)_2 + O_2 \rightarrow 2MnO(OH) + H_2O, \quad (2)$$

$$4MnO(OH) + 6H_2O + O_2 \rightarrow 4Mn(OH)_4. \quad (3)$$

The occurrence of the last two steps requires the presence of water, which is introduced into the curing paste. Manganese(III) compounds are less powerful oxidants than Mn(IV) compounds [10]. Principally, oligomers containing HS groups could be vulcanized by catalytic amounts of manganese dioxide. However, in this case the process becomes too long, which is unacceptable. Therefore, in practice manganese dioxide is introduced into sealant compounds in increased amounts (>2 wt %). The vulcanization mainly occurs owing to the direct reaction of mercapto groups with manganese dioxide [reaction (1)]. We made experiments to determine what amounts of manganese dioxide should be introduced into PEUT-based compounds to attain the best physicomechanical parameters of the sealing agents under the common vulcanization conditions.

Bichromates are six-electron oxidants, and in the presence of water Cr(VI) compounds are readily reduced to Cr(III) compounds [11]:

$$6\ {\sim}SH + Na_2Cr_2O_7 + H_2O \rightarrow 3\ {\sim}S{-}S{\sim} + 2Na[Cr(OH)_4]. \quad (4)$$

The reaction of aromatic [12] and aliphatic [13] mercaptans with zinc oxide is a preparative route to zinc mercaptides:

$$2\ {\sim}SH + ZnO \rightarrow ({\sim}S)_2Zn + H_2O. \quad (5)$$

In the latter two cases, it was also necessary to elucidate the influence of the amount of curing agents on the properties of the sealants obtained.

The physicomechanical properties of sealants cured in the presence of curing agents of different chemical nature are given in Table 3.

As seen from the data obtained, the physicomechanical parameters of the vulcanizates in all the cases increase with an increase in the content of the curing agents in the compounds. For complete exhaustion of mercapto groups in vulcanization of the sealant compound in accordance with Eq. (1), the required content of MnO_2 is 2.63%; that of sodium bichromate [Eq. (4)], 1.51%; and that of zinc oxide [Eq. (5)], 5.30%.

The use of zinc oxide leads to formation of vulcanizates with unsatisfactory properties. Introduction into the compound of superstoichiometric amounts of zinc oxide failed to give a positive result. We believe that this fact is due to a weak oxidizing action of ZnO on SH groups.

Sodium bichromate is a more effective curing agent than manganese dioxide. Good properties of the sealants are attained when the bichromate is taken in a substantially smaller amounts relative to the stoichiometry [Eq. (4)]. This fact suggests that chromium in higher valence states can be formed from Cr(III) under the action of atmospheric oxygen. Indeed, Cr(III) compounds are oxidized with atmospheric oxygen to Cr(IV) compounds, and these reactions are catalyzed by variable-valence heavy metal ions [14, 15]. Note that an increase in the sodium bichromate concentration in the compound leads to substantial changes in the physicomechanical parameters of the vulcanizates: the tensile strength and hardness increase and the elongation set decreases. Similar trends are observed in vulcanization with manganese dioxide.

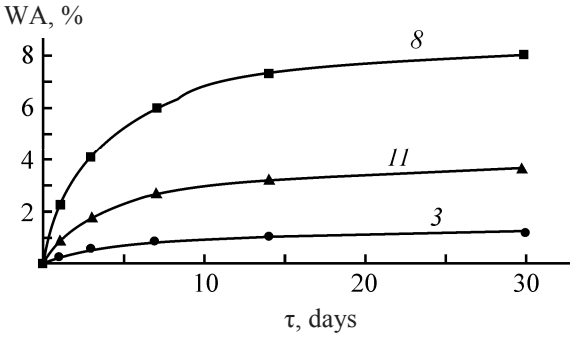
The consumer's properties of sealants are determined by their behavior toward water. Low water ab-

Table 3. Physicomechanical properties of vulcanized PEUT-based compounds

Sample no.	Vulcanizate concentration, g/100 g compound	σ	σ_{100}	σ_{300}	ε	ε_{set}	Shore hardness *A*	Working life, h
		MPa						
Manganese dioxide								
1	1.5	0.7	0.1	0.3	976	90	2	6
2	1.75	0.79	0.22	0.38	610	4	10	2.5
3	2	0.84	0.25	0.42	560	2	20	1
4	2.25	0.88	0.33	0.57	353	2	24	0.5
Sodium bichromate								
5	0.1	0.2	0.2	–	100	12	10	30
6	0.2	0.57	0.38	–	200	10	14	4
7	0.3	0.9	0.4	–	250	10	24	1
8	0.5	1.0	0.44	0.93	320	8	26	0.5
9	0.6	1.05	0.48	1.05	300	8	28	0.08
Zinc oxide								
10	2.5	0.16	0.16	–	100	10	2	40
11	5	0.25	0.18	–	250	10	12	10
12	7.5	0.4	0.2	–	280	8	12	5

sorption is the necessary condition of their practical use. Therefore, we evaluated the water absorption of the sealants. In so doing, we examined samples whose properties, from our viewpoint, are the best in the series. The results are shown in the figure.

The sealant obtained with manganese dioxide exhibits the lowest water absorption. It is two times lower than that of the common Thiokol sealants. Vulcanizates based on zinc oxide exhibit moderate water absorption. The highest water absorption is observed with the sealants vulcanized with sodium bichromate. Only in the latter case, both the curing agent and its transformation products are water-soluble. Presumably, the increased water absorption in this case is due to formation of solvation shells around species formed in transformations of sodium bichromate.



Water absorption WA of vulcanizate samples as a function of the exposure time τ. Figures at curves are sample nos. in Table 3.

Thus, sealants with acceptable service properties can be prepared on the basis of PEUT. Their production is simple and waste-free. Therefore, the new oligomers show much promise for practical use.

CONCLUSIONS

(1) Vulcanization of polyetherurethanethiol-based sealant compounds can be effected by oxidative (manganese dioxide, sodium bichromate) and condensation (zinc oxide) types. The best results are obtained with oxidative curing agents.

(2) Sodium bichromate is a more effective cross-linking agent for polyetherurethanethiol-based compounds than manganese dioxide.

(3) The water absorption of polyetherurethanethiol-based sealants depends on the nature of the curing agent used. The use of agents capable of solvation with water increases the water absorption of the vulcanizates.

REFERENCES

1. Petrie, E.M., *Handbook of Adhesives and Sealants*, New York: McGraw-Hill, 2007.
2. Uglea, C.V., *Oligomer Technology and Applications*, New York: Dekker, 1998.
3. Lucke, H., *ALIPS, Aliphatic Polysulfides: Monograph of an Elastomer: History, Economy, Chemistry, Technology*, Basel: Huthig & Wepf, 1994.
4. Averko-Antonovich, L.A., Kirpichnikov, P.A., and Smyslova, R.A., *Polisul'fidnye oligomery i germetiki na ikh osnove* (Polysulfide Oligomers and Sealants Based on Them), Leningrad: Khimiya, 1983.
5. US Patent 4 820 789.
6. US Patent 4 742 125.
7. Ramaswamy, R. and Achary, P., *J. Appl. Polym. Sci*., 1985, vol. 30, no. 9, pp. 3569–3579.
8. Samuilov, A.Ya., Zenitova, L.A., Levin, Ya.A., et al., *Vestn. Kazan. Tekhnol. Univ*., 2006, no. 2, pp. 77–80.
9. Reikhsfel'd, V.O., Erkova, L.N., and Ruban, V.L., *Laboratornyi praktikum po sinteticheskim kauchukam* (Practical Laboratory Course of Synthetic Rubbers), Leningrad: Khimiya, 1967.
10. Nekrasov, B.V., *Osnovy obshchei khimii* (Principles of General Chemistry), Moscow: Khimiya, 1973, vol. 1.
11. Chalyi, V.P., *Gidrookisi metallov* (Metal Hydroxides), Kiev: Naukova Dumka, 1972.
12. US Patent 2 413 531.
13. US Patent 2 963 434.
14. Weijden, C.H. van der and Reith, M., *Marine Chem*., 1982, vol. 11, no. 2, pp. 565–572.
15. Eary, L.E. and Ral, D., *Environ. Sci. Technol*., 1987, vol. 21, no. 12, pp. 1187–1193.

ISSN 1070-4272, Russian Journal of Applied Chemistry, 2008, Vol. 81, No. 11, pp. 1981–1986. © Pleiades Publishing, Ltd., 2008.
Original Russian Text © D.G. Lin, E.V. Vorob'eva, N.V. Marchenko, 2008, published in Zhurnal Prikladnoi Khimii, 2008, Vol. 81, No. 11, pp. 1866–1871.

MACROMOLECULAR COMPOUNDS AND POLYMERIC MATERIALS

Oxidation of Polyethylene Inhibited with a Phenolic Antioxidant under the Conditions of Contact with Metallic Zinc

D. G. Lin, E. V. Vorob'eva, and N. V. Marchenko

Skorina Gomel State University, Gomel, Belarus

Received March 25, 2008

Abstract—The inhibiting power of a phenolic antioxidant upon introduction into polyethylene contacting with metallic zinc was examined. Conditions at which zinc enhances the inhibiting effect of the antioxidant were determined, and the mechanism responsible for this effect was suggested.

DOI: 10.1134/S1070427208110220

It is well known that many variable-valence metals accelerate oxidation of noninhibited polyethylene (PE) owing to the transfer of soluble metal-containing compounds formed by contact reactions [1, 2]. These compounds exhibit high catalytic activity and transfer the oxidation process from the layer adjacent to the metal into the bulk of the polymeric material. Therefore, for successful operation of metal–polymer materials and articles containing active metals, it is necessary to ensure deactivation of the catalytic surface of metal-containing compounds which in the course of oxidative transformations migrate in a polymeric binder. One of the ways to solve this problem is introduction into a polymer of antioxidant (AO) additives. The most common of them are amine and phenolic additives. Previous studies [3–5] showed that the use of such AOs for inhibiting the oxidation of polymers that are in contact with active metals can lead to quite unexpected results. For example, Irganox 1010, an effective AO for PE, in oxidative contact of the polymer with copper (e.g., in case of a PE coating on a copper support or of PE filled with dispersed copper) is rapidly consumed, and the induction period of the oxidation (IPO) decreases by a factor of more than 7 [4, 5]. On the contrary, relatively weak amine AO, Neozon D, under the similar conditions becomes more effective, and IPO of the polymer increases [3]. Below we briefly describe the mechanism [4] of the copper effect on the inhibiting power of amine and phenolic AOs.

With a phenolic AO, the decisive factor is transfer of copper-containing compounds from the zone of adhesion contact to the bulk of the polymer [4–6]. This transfer apparently occurs even during the IPO. The transferred copper compounds catalyze the generation of primary radicals which, in turn, accelerate the AO consumption. In this step of the oxidation process, stable oxidation products (namely, carbonyl-containing compounds) are not detected yet, and, according to IR monitoring, this period can be considered as IPO. After the majority of AO is consumed, the oxidation becomes autocatalytic, and specifically this moment is fixed as the end of IPO.

Enhancement of the performance of an amine AO in the presence of copper is attributed [3, 7] to direct reaction of AO with copper (support surface or filler particles) with the formation of stable nitroxyl radicals whose inhibiting power is higher than that of the initial AO. Effective oxidation inhibitors arising in the contact zone suppress the formation and transfer of copper-containing compounds. As a result, the onset of the autocatalytic step of the oxidation process is delayed, and IPO becomes longer.

As can be seen, the use of AOs of different classes under the conditions of contact oxidation of PE on copper can lead to opposite results. Therefore, solution of the problem of suppressing the catalytic effect of active metals that are components of metal–polymer materials and of articles based on them will remain for a long time on the level of experimental search and discoveries. In this connection, we examined in this study the oxidation of PE inhibited by a phenolic AO and occurring in contact with metallic zinc.

EXPERIMENTAL

In the experiments we used powdered nonstabilized high-density PE prepared under the industrial conditions at a low pressure on complex organometallic catalysts [GOST (State Standard) 16 338–85, 20 306-005 grade). As oxidation inhibitor we used a phenolic antioxidant Irganox 1010 [pentaerythrityl tetrakis-3-(3,5-di-*tert*-butyl-4-hydroxyphenyl)propionate]. The AO was introduced into PE by wetting of the polymer powder with a solution of a dosed amount of AO in acetone (GOST 2603–79), followed by complete solvent evaporation at room temperature.

Two kinds of inhibited polymer samples were examined: PE films on a zinc support and films of PE filled with zinc powder (Ts 1 grade, GOST 18 843–73, particle size 2–7 μm). Zinc powder was introduced by mixing it with a powder of the inhibited polymer. From the binary (PE + AO) and ternary (PE + AO + ZnO) mixtures, we prepared films by hot pressing (150°C, 30 s). These films were used in the studies. Films of binary compounds were oxidized on zinc supports, and films of ternary compounds, on KBr plates (material transparent in the IR range [8]). It is known [9] that KBr is inactive with respect to PE oxidation. The samples were oxidized in air in ovens at 150 and 175°C.

As modifier for inhibited PE we also used zinc stearate [TU (Technical Specification) 6-09-17-316–96] to simulate the effect of zinc-containing compounds formed by contact oxidation of PE on zinc supports. Zinc stearate was introduced together with AO by treating the polymer powder with a solution of the modifiers in acetone. The films obtained after the solvent evaporation were then oxidized on KBr plates.

In our tests we used films of oxidized PE in which we estimated the extent of the polymer oxidation and the content of the transferred zinc in the polymer.

The extent of PE oxidation was characterized by the extinction factor, namely, by the ratio of the optical density at 1720 cm^{-1} in the IR spectra of the polymer to the film thickness in centimeters. To record the spectra of films oxidized on zinc supports, they were separated from the metallic base; films oxidized on KBr plates were subjected to IR measurements directly on the supports. The IR spectra were recorded on a Vertex 70 Fourier spectrophotometer (Bruker, Germany, 2004).

To determine the concentration of zinc transferred into the PE film in the form of compounds with polymer oxidation products, we used polarographic analysis [10]. When preparing working solutions for polarography, we used the ash residue of the polymer film oxidized on a zinc support. Ashing was performed by two-step heat treatment of the polymer samples under the conditions given in [11]. The ash residue was dissolved in a supporting electrolyte. The pH of samples was monitored with an EV-74 pH meter. The working solutions were examined with a PU-1 device using a mercury dropping electrode; the metal content of the solutions was determined from calibration plots. The results were converted to the metal concentration referred to the initial polymer weight.

Figure 1 shows data on the accumulation of carbonyl groups in PE films inhibited by Irganox 1010 and oxidized on KBr and zinc supports (curves *1*–*3*). The result was unexpected: The zinc support, promoting oxidation of nonstabilized PE, in this case acted as an additional oxidation inhibitor. The IPO of PE films oxidized on zinc appeared to be longer than that of the films contacting in the course of oxidation with an inert support, KBr. The effect of the additional suppression of the polymer oxidation on zinc depends on the polymer film thickness. With an increase in the film thickness, the support effect is enhanced and IPO increases (Fig. 1, curves *2*, *3*). The revealed effect of the zinc support on the oxidation of PE inhibited by Irganox 1010 was also observed with inhibited PE filled with zinc powder (Fig. 1b). As can be seen, introduction of zinc into the polymer makes IPO longer (Fig. 1, curves *1*, *5*–*8*).

With an increase in the concentration of the zinc filler, as well as with a decrease in the thickness of an unfilled PE film oxidized on a zinc support, IPO becomes longer. In both cases, the ratio of the surface area of the zinc support to the polymer weight increases. As a result, the effect exerted by zinc on the oxidation process becomes stronger. Apparently, a similar result can be obtained by decreasing the particle size of the zinc filler in the polymer, instead of increasing the filler concentration. In so doing, the total surface area of the filler particles and correspondingly the ratio of the filler surface area to the polymer weight will increase.

Additional prolongation of the IPO on adding dispersed zinc into inhibited PE is observed in a fairly wide range of oxidation temperatures. Figure 2 shows how IPO at 150 and 175°C depends on the concentration of the zinc filler. As can be seen, in both cases IPO of PE increases with an increase in the filler con-

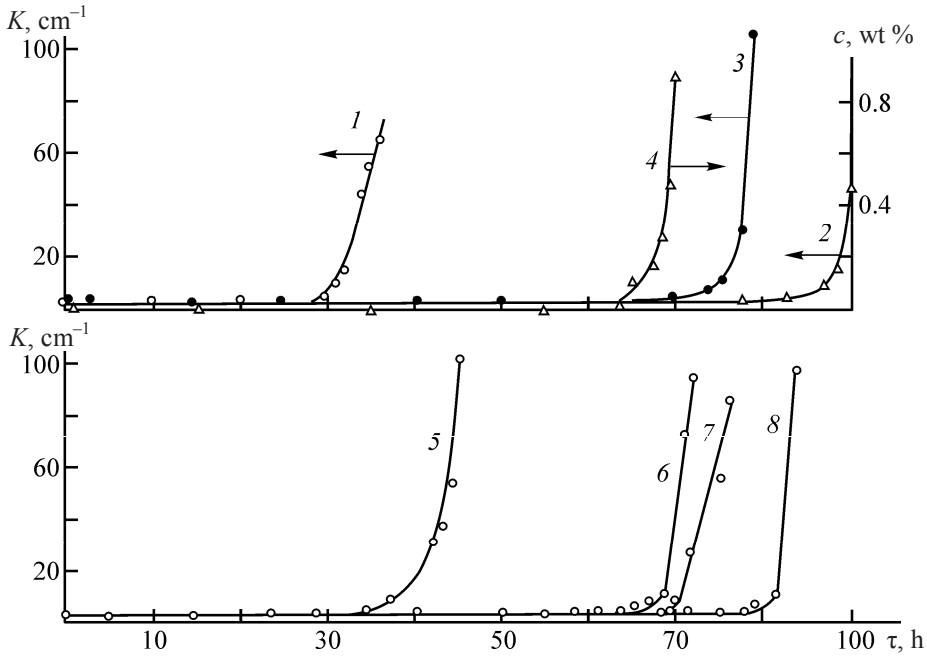


Fig. 1. Influence of the polymer oxidation time τ on (*1–3*, *5–8*) extinction factor K at 1720 cm^{-1} in the IR spectra of films and (*4*) zinc concentration c in films. Initial content of zinc powder in films, wt %: (*1–4*) 0, (*5*) 0.05, (*6*) 5, (*7*) 10, and (*8*) 15. Support: (*1*, *5–8*) KBr and (*2–4*) Zn. 150°C, 0.1 wt % Irganox 1010. Film thickness, μm: (*1*, *3–8*) 100 and (*2*) 70.

centration. On introduction of the same amount of zinc, 15 wt %, into PE inhibited by 0.1% Irganox 1010, IPO at 150 and 175°C increased by a factor of 2.5 and 2.0, respectively.

Our further experiments were aimed to elucidate the possible mechanism by which zinc enhances the efficiency of PE inhibition with Irganox 1010.

Let us first assume that, in the polymer–AO–zinc system, direct interaction of AO with the zinc support does not appreciably affect its inhibiting power. Then it can be expected that the effect of the metal support is mediated by formation of microamounts of zinc-containing compounds and their participation in redox transformations in the polymer layer adjacent to the support. In this connection, it was necessary to estimate the activity of zinc-containing compounds formed by contact thermal oxidation. Because it is difficult to isolate such compounds from the bulk of the polymer being oxidized, we performed experiments with zinc stearate simulating such compounds.

Figure 3 shows that zinc stearate catalyzes the oxidation of inhibited PE, and the higher the concentration of the additive in the polymer, the shorter the IPO. For the viscous medium of a PE melt, it can hardly be expected that direct interaction of AO and zinc stearate molecules is the decisive factor in AO transformations. Most probably, these substances in the polymer affect the oxidation process separately, each accomplishing its own functions. Being an oxidation catalyst, zinc stearate catalyzed the oxidation, whereas Irganox 1010 tends to suppress oxidation by terminating the oxidation chains. Repeated participation of the metal (zinc) ion in catalytic events leads to accelerated consumption of AO and, correspondingly, to IPO shortening.

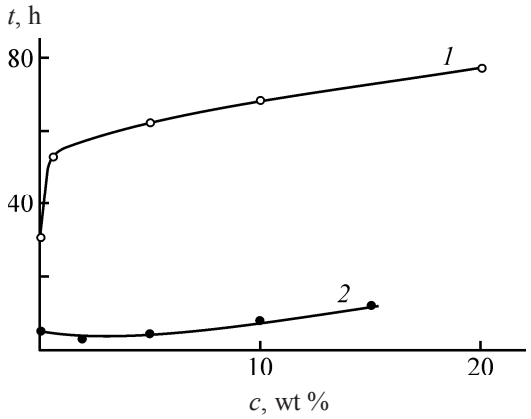


Fig. 2. Influence of the zinc powder content in the polymer c on the IPO duration t for PE films inhibited with 0.1 wt % Irganox 1010 and oxidized at (*1*) 150 and (*2*) 175°C on KBr plates. Film thickness 100 μm; the same for Figs. 3–5.

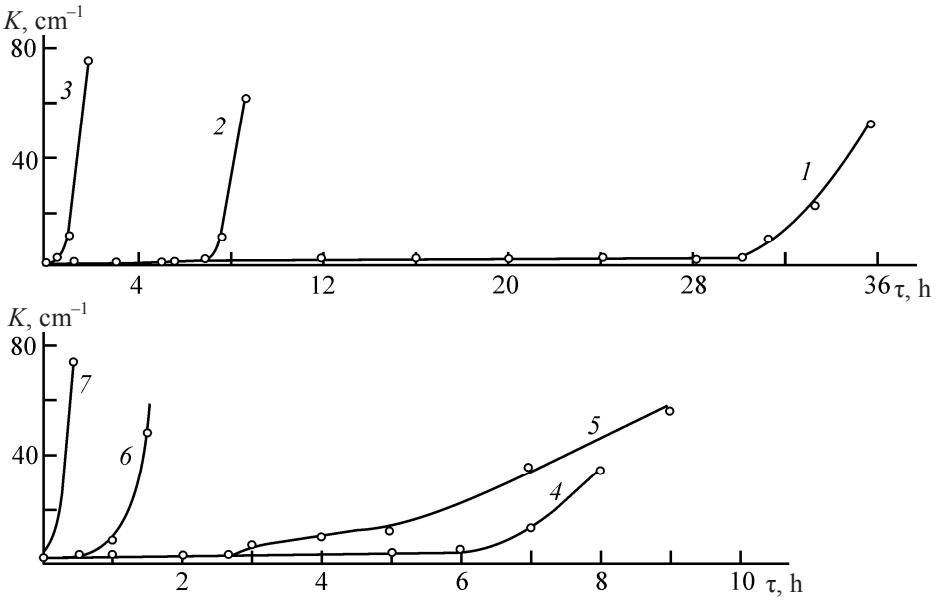


Fig. 3. Influence of the oxidation time τ of the polymer on KBr plates at (*1–3*) 150 and (*4–7*) 175°C on the extinction factor *K* at 1720 cm^{-1} in the IR spectra of PE films inhibited with 0.1 wt % Irganox 1010. Zn content in the form of metal stearate, wt %: (*1*, *4*) 0, (*5*) 0.05, (*2*, *6*) 0.5, (*7*) 1, and (*3*) 2.

Therefore, the diffusion transfer into the polymer of zinc-containing compounds formed by contact reactions should seemingly accelerate the oxidation. Actually, however, zinc enhances the inhibiting effect of Irganox 1010 introduced into the polymer. This means that, when studying the mechanism of the zinc action in inhibited PE, the consequences of the direct reaction of the metal with AO should be taken into account.

To elucidate this question, we performed the following experiments. In the first of them, we examined how the inhibiting power of Irganox 1010 changes upon its heat treatment in contact with a zinc support.

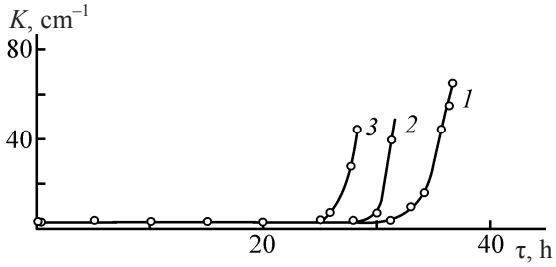


Fig. 4. Influence of the oxidation time τ of the polymer on KBr plates on the extinction factor *K* at 1720 cm^{-1} in the IR spectra of PE films inhibited with 0.1 wt % Irganox 1010. Temperature 150°C; the same for Fig. 5. Prior to introduction into the polymer, the AO was heat-treated at 123°C on the zinc surface for (*1*) 0, (*2*) 4, and (*3*) 10 h.

For this purpose, a thin (0.5 mm) layer of the AO was applied onto a zinc foil and heat-treated in air at 123°C for different times. After the heat treatment, the AO was dissolved in acetone and then introduced into PE (the Irganox 1010 concentration in the polymer was also 0.1%). Figure 4 shows that, upon heat treatment of the AO in contact with zinc support, its inhibiting power decreases. In other words, direct reaction of the initial AO with zinc cannot lead to an additional increase in IPO under the conditions of contact of inhibited PE with the metal (Fig. 4).

In the second experiment, we compared the efficiency of PE inhibition at two different modes of AO introduction into the polymer. In procedure I, the AO amount required for the inhibition was first applied onto the surface of the polymer filler, and then the filler with the antioxidant additive was introduced into the polymer. For this purpose, before introduction into the polymer, a dosed volume of the filler was wetted with a solution of AO in acetone. The resulting suspension was dried until complete evaporation of the solvent, after which the filler was mixed with the polymer powder. In this procedure, the AO distribution in the polymer was nonuniform. Virtually the whole amount of AO was on the surface of the filler particles. Naturally, in the course of the tests AO passed into the polymer melt and provided its oxidation protection. In

procedure II, a mechanical mixture of polymer and filler powders was wetted with an AO solution. After that, the solvent was evaporated and the composite obtained was used in the experiments. This procedure ensured uniform distribution of the AO in the bulk of the polymer, with only very small amount of AO deposited on the metal surface.

Figure 5 shows data on the oxidation of PE compounds prepared by procedures I and II. We found that, when the AO is introduced by procedure I, the presence of filler has virtually no effect on the heat resistance of the composite. In this case, the IPO of the samples (Fig. 5, curve *1*) is almost the same as IPO of the inhibited PE containing no zinc filler (Fig. 1, curve *1*). Hence, blocking of the filler surface with an antioxidant additive prevents participation of the metal in the additional prolongation of the IPO. Therefore, it can be assumed that the zinc surface in the course of oxidation favors regeneration of the spent AO and its reuse. If the amount of AO on the zinc surface is small and the filler surface is not blocked (procedure II), the zinc surface participates in the process more actively and IPO of the composites increases (Fig. 5, curve *2*).

Denisov et al. [12, 13] indicate that variable-valence metal ions can repeatedly terminate chains of oxidative transformations in oxidation of low-molecular-weight hydrocarbons and alcohols. The chain termination reactions occur between alcohol oxidation products and transition metal ions [13]:

$$>C(YH)OO^{\cdot} + M^{n+} \rightarrow C(YH)OO^{-} + M^{n+1},$$

$$>C(YH)OO^{\cdot} + M^{n+1} \rightarrow C{=}Y + O_2 + H^{+} + M^{n+}.$$

In the system PE–zinc–phenolic AO, such processes are quite probable. Firstly, the required substances, transition metal (Zn) and low-molecular-weight organic substance with an alcoholic group (AO), are available in the system. Secondly, multiple chain termination starts upon accumulation of the direct participants of the process: zinc ions (metal-containing compounds formed by contact reactions and zinc oxide on the surface of the support or filler) and oxidized form of AO (product of inhibitor oxidation by reactions with peroxy radicals, oxygen, and hydroperoxide [13]). This conclusion is convincingly confirmed by the following experiment.

Polyethylene films containing 0.1% Irganox 1010 were first heat-treated in air in contact with zinc supports, after which the process was terminated, and the films were separated from the supports and transferred onto KBr plates for further oxidation at the same temperature. The time of film preoxidation in contact with zinc did not exceed the IPO duration, i.e., the transition of the oxidation process to the autocatalytic step was observed only in the course of film oxidation on KBr plates. The data below show how the time of the preliminary heat treatment of the films in contact with zinc affects an increase in IPO (difference between the IPO values in combined heat treatment on zinc and KBr supports and in heat treatment on KBr plates only, without contact with zinc).

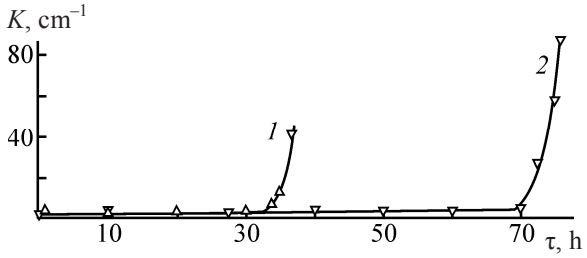


Fig. 5. Influence of the oxidation time τ of the polymer on KBr plates and procedure of the AO introduction on the extinction factor K at 1720 cm^{-1} in the IR spectra of PE films inhibited with 0.1 wt % Irganox 1010. (*1*) AO is first applied onto the surface of filler particles, which are then introduced into the polymer; (*2*) AO is uniformly introduced into a mixture of the polymer with the filler.

Influence of the time of the preliminary heat treatment of PE films in contact with zinc on an increase in IPO (PE films inhibited with 0.1% Irganox 1010, oxidation temperature 150°C, oxidation of films on KBr plates after contact with zinc)

Time of preliminary heat treatment on zinc, h	Increase in IPO, h
0.0	0.0
10.0	11.0
15.0	20.0
20.0	30.0
27.5	36.5
35.0	40.0
45.0	43.3
60.0	46.0
67.5	51.5

As can be seen, the longer the preliminary heat treatment of the films in contact with zinc, the more pronounced is an increase in IPO.

CONCLUSIONS

(1) The contact of zinc metal with polyethylene inhibited by Irganox 1010 phenolic antioxidant enhances the resistance of the polymer to thermal oxidative degradation.

(2) An increase in the performance of the phenolic antioxidant in the presence of zinc is associated with regeneration of the spent antioxidant in the presence of zinc ions. As a result, the antioxidant becomes capable of repeatedly participating in termination of oxidation chains, and the induction period of the polymer oxidation becomes longer.

REFERENCES

1. Egorenkov, N.I., Lin, D.G., and Belyi, V.A., *Dokl. Akad. Nauk SSSR*, 1972, vol. 207, no. 2, pp. 397–400.
2. Belyi, V.A., Egorenkov, N.I., and Pleskachevskii, Yu.M., *Vysokomol. Soedin., Ser. B*, 1970, vol. 12, pp. 643–644.
3. Lin, D.G. and Vorobieva, E.V., *J. Appl. Polym. Sci*., 2005, vol. 98, no. 1, pp. 401–406.
4. Lin, D.G., Vorob'eva, E.V., and Marchenko, N.V., *Zh. Prikl. Khim*., 2005, vol. 78, no. 9, pp. 1527–1532.
5. Lin, D.G., Vorob'eva, E.V., and Marchenko, N.V., *Vestsi Nats. Akad. Navuk Bel., Ser. Khim. Navuk*, 2006, no. 2, pp. 29–33.
6. Lin, D.G., Vorob'eva, E.V., and Marchenko, N.V., Abstracts of Papers, *POLIKOMTRIB 2005: Mezhdunarodnaya nauchno-tekhnicheskaya konferentsia* (POLYCOMTRIB 2005: Int. Scientific and Technical Conf.), Gomel: IMMS im. V.A. Belogo, June 18–21, 2005, pp. 236–237.
7. Lin, D.G., Vorob'eva, E.V., and Marchenko, N.V., *Zh. Prikl. Khim*., 2004, vol. 77, no. 9, pp. 1539–1542.
8. Dechant, J., Danz, R., Kimmer, W., et al., *Ultrarotspektroskopische Untersuchungen an Polymeren*, Berlin: Akademie, 1972..
9. Lin, D.G., Scinetific Principles of the Development of Lamellar Metal–Polymer Materials for Machine Building Using Thermoplastics and Elastomers, *Doctoral Dissertation*, Gomel, 1993.
10. Sviridenko, V.G., Eliseeva, I.M., and Lin, D.G., *Vysokomol. Soedin., Ser. B*, 1989, vol. 31, no. 4, pp. 885–887.
11. USSR Inventor's Certificate no. 1 226 119.
12. Denisov, E.T., *Okislenie i destruktsiya karbotsepnykh polimerov* (Oxidation and Degradation of Carbon-Chain Polymers), Leningrad: Khimiya, 1990.
13. Denisov, E.T., Sarkisov, O.M., and Likhtenshtein, G.I., *Khimicheskaya kinetika* (Chemical Kinetics), Moscow: Khimiya, 2000.

ISSN 1070-4272, Russian Journal of Applied Chemistry, 2008, Vol. 81, No. 11, pp. 1987–1991. © Pleiades Publishing, Ltd., 2008.
Original Russian Text © D.L. Starokadomskii, 2008, published in Zhurnal Prikladnoi Khimii, 2008, Vol. 81, No. 11, pp. 1872–1876.

MACROMOLECULAR COMPOUNDS AND POLYMERIC MATERIALS

Effect of the Content of Unmodified Nanosilica with Varied Specific Surface Area on Physicomechanical Properties and Swelling of Epoxy Composites

D. L. Starokadomskii

Chuiko Institute of Surface Chemistry, National Academy of Sciences of Ukraine, Kiev, Ukraine

Received January 22, 2008

Abstract—Strength characteristics of polyepoxy formulations with different contents and dispersities of Aerosil nanosilica were studied. The effect of silica on the swelling of epoxy-polymeric composite in water was examined.

DOI: 10.1134/S1070427208110232

Nanodispersed silica (NS) of the Aerosil type is a highly dispersed powder with spherical nanosize primary particles susceptible to self-aggregation. As is known, NS is capable of self-organization of its structures in polymeric matrices and affects the structure of polymeric chains, which makes it possible to improve the strength, thixotropic, and other properties of polymers. Therefore, NS is used as a filler and thickener of industrial epoxy resins in manufacture of joint fillers, glues, filled floors, and glass-reinforced plastics [1–3]. Its most readily accessible unmodified forms are frequently used in these processes. Both in practical use and in scientific studies, the problem of the influence exerted by the physical characteristics of Aerosils (specific surface area, physically adsorbed water, aggregation capacity, etc.) is frequently disregarded. In particular, not only the concentration, but also the dispersity of silica should affect the basic characteristics of the composite. Information about the nature of this influence arouses permanent interest [4–13].

In this study, we examined the possibility of controlling the physicomechanical properties and water absorption of epoxy composites by varying the concentration and specific surface area of unmodified Aerosil.

EXPERIMENTAL

Experiments were performed with an epoxy polymer based on ED-20 resin (manufactured by Ufakhimprom) with varied content of silicas A-50, A-100, A-175, A-300, and A-455 (manufactured by the Institute of Surface Chemistry, National Academy of Sciences of Ukraine; the number is the specific surface area in square meters per gram), cured by introduction of 12.5 wt % polyethylenepolyamine (PEPA) at room temperature with aftercure at 110°C for 3 h. The composites were tested in accordance with GOST (State Standard) for compression (GOST 4651–68, stubs 12 mm in diameter and 15 mm high), bending (GOST 4848–71, 2 × 25 × 80 mm plates), and shearing (GOST 17 302–71, 30-mm overlap of 10-mm-wide glass-reinforced plastic plates, layer thickness not exceeding 1 mm). The measurement error was 1–2% for compression tests and 5–10% for shearing and bending tests. Separately, the swelling of composite samples (10 × 5 × 2 mm plates) in water in the course of 100 days was studied. The swelling was evaluated by the gain in mass. Samples 1 cm in diameter and 2–3 mm thick were placed in test tubes with water. After each withdrawal, the samples were thoroughly dried with a lignin blanket and were allowed to stay for 40–50 min before weighing under normal conditions (18–22°C). Atomic-force microscopy (AFM) and scanning electron microscopy (SEM) were used to obtain images of the samples by the standard procedure. IR reflection spectra of pure powders of epoxy polymers were measured with a Nicolett instrument (USA–EU) without addition of potassium bromide.

It can be seen from the results obtained (Fig. 1) that, in some cases, minor additions of NS noticeably

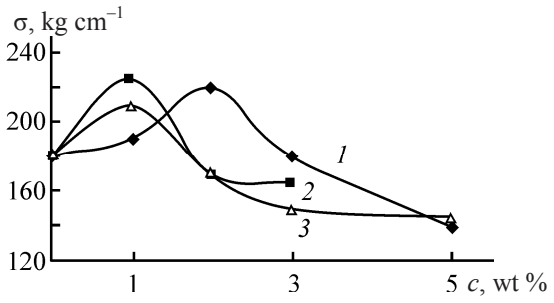


Fig. 1. Shearing strength σ of composites filled with Aerosils with different specific surface areas. (*c*) Aerosil content. (*1*) A-100, (*2*) A-175, and (*3*) A-455.

affect the physicomechanical properties of the epoxy polymer. The strongest reinforcing effect is observed for the shearing strength σ (with the composite in the form of a thin layer between plates). In the range 1–2 wt % filler, this parameter may grow by 15–25%. Further increase in the Aerosil concentration results in that σ falls. It can be concluded that its concentration strongly affects the shearing strength of the epoxy polymer in the form of a thin layer.

At the same time, the compression and bending strengths change only slightly for bulk (~1 cm^3) samples in their filling with silica. It can be seen from the table that, at best (for A-50 and A-100 NS), the increase in the compression strength does not exceed 5–10%. This weak effect is only observed within a narrow range near 1 wt %, in agreement with published data [6, 7]. Analysis of the results obtained and published data [4–12] suggests that the effect of composite strengthening upon NS introduction becomes weaker as the sample thickness grows. Possibly, this occurs because of the multiplication of bulk macroscopic defects, e.g., microcracks, heterogeneities, and air bubbles.

Compression and bending strength of composites filled with Aerosils with different specific surface areas

c, wt %	Compression strength, kg cm^{-2}				Bending strength, 10^4 kg cm^{-2}	
	A-50	A-100	A-300	A-455	A-100	A-300
0	1300	1300	1300	1300	3.3	3.3
0.1	–	–	–	–	3.4	3.3
0.5	–	–	–	–	2.9	3.0
0.7	–	–	–	–	2.8	–
1.0	1430	1340	1340	1310	2.6	3.0
1.5	–	–	–	–	2.9	–
2.0	–	1330	1300	1260	–	–
3.0	–	1360	1300	1300	–	–
5.0	–	1360	1300	1220	3.1	–

The most stable enhancing influence is exerted on the strength characteristics under study by NS with small specific surface area (with large particles): A-50, A-100, and A-175 Aerosils (see table, Fig. 1). Aerosils with large specific surface affect the strength parameters of the composite only slightly. This can be attributed to the observed effect of increasing self-aggregation and agglomeration capacity of NS at its larger specific surface area. It is also probable that, in this case, its negative effect not only on the homogeneity of the composite, but also on the structure (defect formation, loosening) of the polymer network is enhanced. It is noteworthy that the effect of an Aerosil is weakened (but not eliminated) upon modification of its surface with silanes and other organic substances (which may lead to loss of clear meaning by the notion of the specific surface area of an Aerosil).

Swelling curves are shown in Fig. 2. The negative value of the degree of smelling, *q* (%), near the beginning of the process reflects the rapid washing out that occurs immediately after a sample is submerged in water. The effect of silica on the composite swelling can be assessed as rather unambiguous. Introduction of Aerosils leads, on the whole, to a decrease in the rate and degree of swelling in water in all stages of the process. For all the composites studied (>20 samples), the swelling is 1.5–2.0%. It follows from Fig. 2 that structural changes occur even at small fillings (1 wt %). As the degree of filling grows, penetration of water molecules into the polymer network becomes increasingly difficult, which is possibly due to densification of the polymeric network upon introduction of nanoparticles. This is confirmed by SEM studies: According to Fig. 3, even upon introduction of 1 wt % Aerosil, the number of pores on the polymer surface decreases dramatically (cf. Fig. 3a).

The effect of the specific surface area on the swelling process can be estimated as comparatively insignificant. At the same time, Aerosils can be conditionally divided into two groups as regards their influence on swelling: low- and high-dispersed. As seen from Fig. 2, for the low-dispersed A-50 and A-100 (and, to a certain extent, for A-175), low concentrations (~1 wt%) of a filler do not exert any significant influence. In these cases, the swelling curves for 0 and 1 wt %

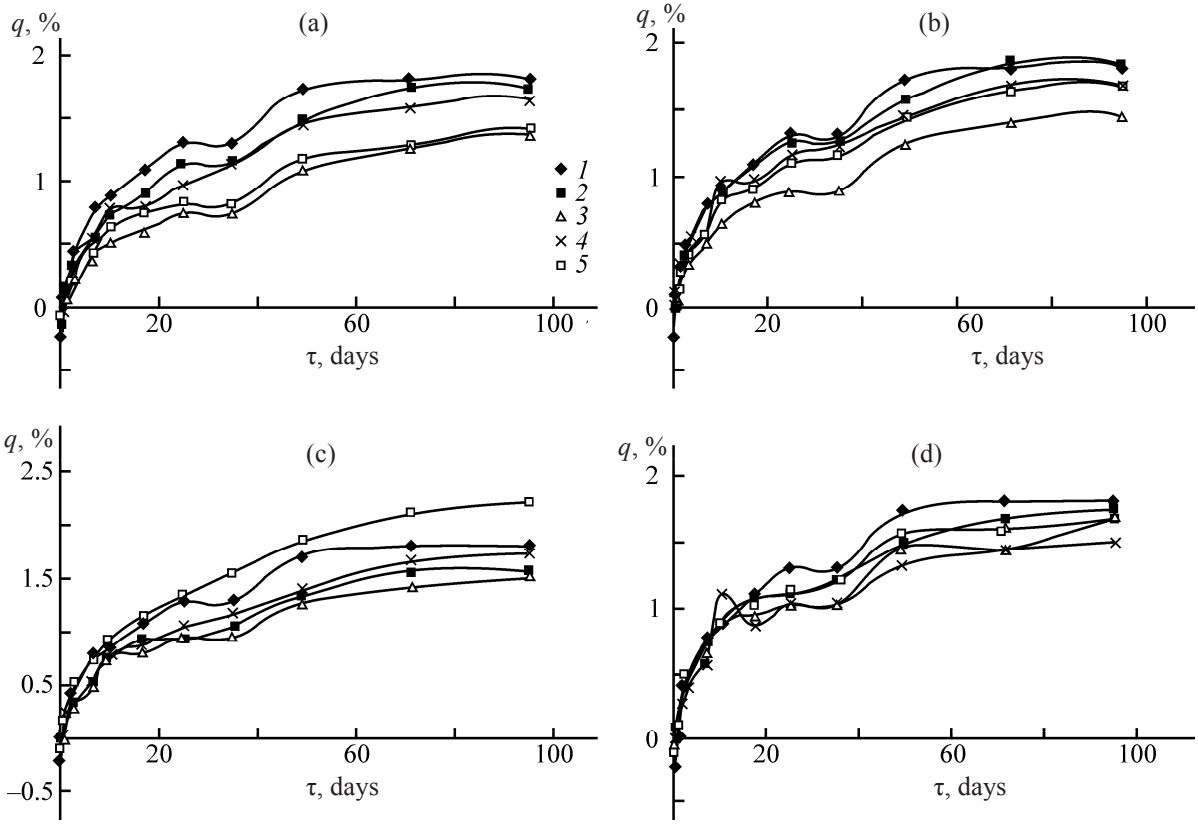


Fig. 2. Degree of swelling in water, q, of epoxy polymers with Aerosils with different specific surface areas vs. time τ. (a) A-100, (b) A-175, (c) A-300, and (d) A-455. Degree of filling, %: (*1*) 0, (*2*) 1, (*3*) 5, (*4*) 10, and (*5*) 20.

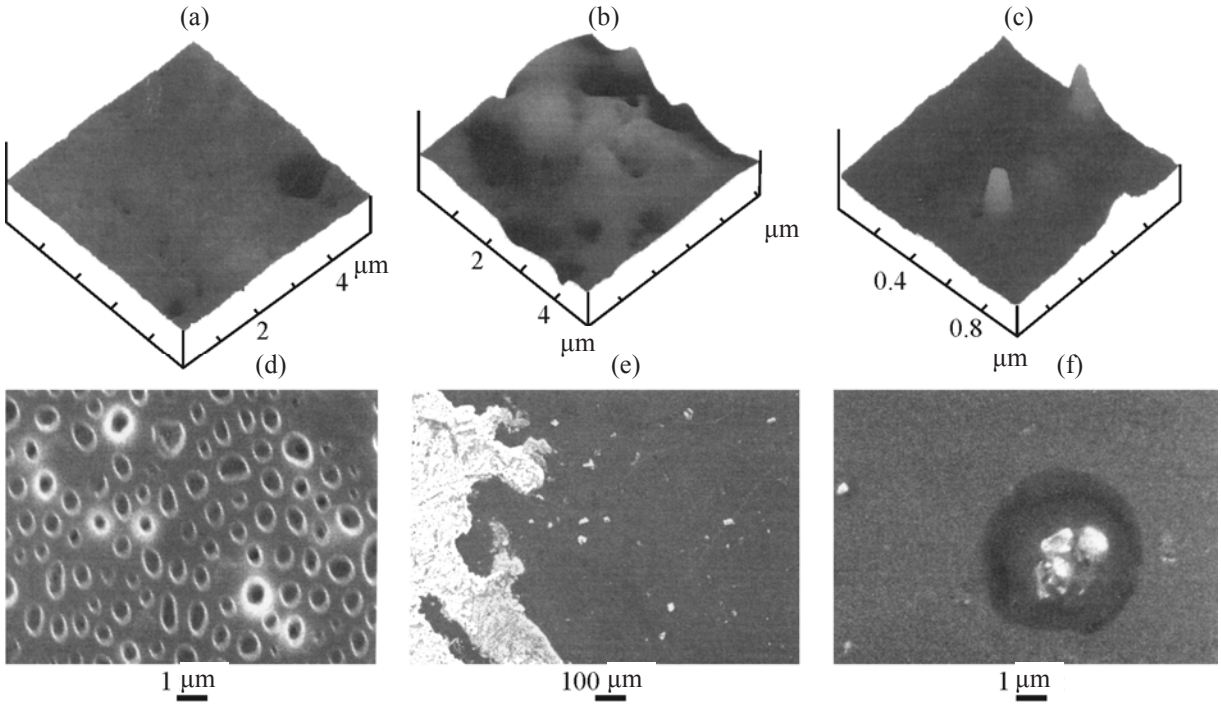


Fig. 3. AFM images of the surface of a film of an epoxy polymer (a) unfilled and (b, c) filled with 3.5 wt % A-300 Aerosil, and also SEM images of a film of an epoxy polymer (d) unfilled and (e, f) filled with 1 wt % A-100 Aerosil.

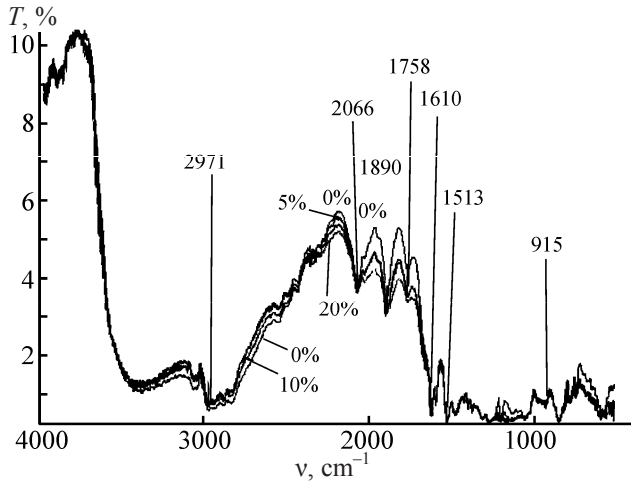


Fig. 4. IR spectra of epoxy polymers filled with 0, 5, 10, and 20 wt % A-100 Aerosil. (*T*) Transmission and (ν) wavenumber.

are very close. For the group of highly dispersed A-300 and A-455, 1 wt % of a filler has a more pronounced effect (Fig. 2).

For the low-dispersed group of Aerosils, the differences in the degree of swelling, dependent on the filler concentration, may be as large as 0.4–0.6%, i.e., approximately up to a quarter of the average degree of swelling. For the Aerosils of the highly dispersed group, these differences are substantially smaller, within the range 0.2–0.4%.

Thus, as the specific surface area of Aerosils decreases, the effect of their concentration on the swelling becomes more pronounced, with the differences in the degree of swelling being considerably less dependent on the NS concentration for highly dispersed Aerosils.

As an additional specific feature of the influence exerted by highly dispersed Aerosils can be regarded the faster saturation period, within 50–60 days. For low-dispersed aerosils, this time is substantially longer. Hence follows that the NSs of the highly dispersed group affect the composite structure to a somewhat lesser extent, whereas low-dispersed Aerosils change it so that the penetration of solvent molecules occurs during a longer time.

It was a priori assumed that there should be a more or less simple relationship between the NS concentration and degree of swelling. It was found that, most frequently, this dependence is not linear or, at least, monotonic. For example, a rather clearly pronounced correlation between the decreasing degree of swelling and increasing NS concentration is observed only for A-455 Aerosil with the largest specific surface area (i.e., smallest particles). In the other cases, the swelling nonlinearly depends on the Aerosil content and decreases near 5 wt % (Fig. 2). This means that, irrespective of the specific surface area of an NS, at its certain concentrations it can form a specific structure characterized by an increased density of the polymer network.

According to IR data (Fig. 4), introduction of unmodified NS does not change the chemical nature of the epoxy composite. All the absorption bands characteristic of epoxy polymers and (in most cases) their intensities remain unchanged even at high degrees of filling (Fig. 4). The band at 915 cm^{-1}, characteristic of oxirane groups of the epoxy resin, is almost not observed, which points to a high conversion of the composite in all cases. No changes are revealed in the intensity of the band at 1605–1610 cm^{-1}, which is standard for epoxy polymers and is characteristic of stretching vibrations ν(CH–CH) of benzene rings. True, a certain decrease is observed in the intensity of overlapping bands in the region 3100–3500 cm^{-1}, characteristic of OH groups of the polymer and adsorbed water. This may indicate that their number slightly decreases upon filling. It is noteworthy that, even at an Aerosil content of 20 wt %, its characteristic absorption band at 3750 cm^{-1}, associated with vibrations of isolated surface OH groups, is not observed. This may point to a strong physicochemical interaction (hydrogen bonds) of these groups with fragments of the polymer chain, which results in that this band disappears, or, more precisely, is shifted to lower wavelengths, to the region 3100–3500 cm^{-1} difficult for band assignment.

The data obtained suggest that regions of denser macromolecule packing, e.g., in the adsorption and orientation layer that is near-surface with respect to Aerosil particles, and a framework constituted by filler particles are formed in the filled composite [8–14]. At the same time, various defects impairing the strength characteristics are also formed. An important role in the weakening of the reinforcement effect as a result of filling may also be played by nonoptimal aggregation (e.g., clustering, rather than framework formation) and combination of particle aggregates in the polymer. The latter is frequently observed visually and is confirmed by microscopic data (Fig. 3), which can serve to make some conclusions about the structure of the epoxy

composites. For example, the AFM image (Fig. 3c) clearly shows "islets" of aggregated silica. It can be seen in smaller-scale images (Figs. 3a and 3b) that pores become coarser and sparser as a result of filling. The same effect is observed in the SEM image: Figures 3d and 3f show that pores become coarser and less in number, and islets of silica aggregates may appear in the pores. On the whole, Aerosil can form, even at small degrees of filling (1 wt %), large bodies of the intrinsic phase neighboring the polymer phase, which, in turn, includes small Aerosil aggregates (Fig. 3e).

CONCLUSIONS

(1) Addition of unmodified silica affects the strength of polymers in different ways, depending on the silica concentration and a parameter under study. A weak tendency toward an increase in the strength parameters is observed at 1–2 wt % content of Aerosil, as well as a tendency toward weakening of the effect of Aerosil on the strength parameters with its increasing specific surface area (as a result of a higher self-aggregation capacity). At the same time, introduction of nanodispersed silicas of the Aerosil type can improve the shearing strength (substantially, by 15–25%) and compression strength (insignificantly, by up to 5–10%).

(2) Changing the Aerosil concentration noticeably affects the swelling of filled epoxy polymers. In the range up to 20 wt %, filling with unmodified Aerosil makes the degree of swelling lower, with the decrease at concentrations of ~5 wt % being the most pronounced. Irrespective of their specific surface area, silicas affect the swelling in similar ways, but low-dispersed silicas (conventionally up to 200 $m^2 g^{-1}$) exert a stronger influence on the swelling (and, consequently, on the structure) of the epoxy polymer than do highly dispersed silicas.

(3) The IR spectra demonstrate that no chemical changes occur in the epoxy polymer upon introduction of unmodified Aerosils. Together with the AFM and SEM images obtained, this fact suggests that filling with unmodified nanosilica substantially changes only the physical conditions of structuring in the composite.

ACKNOWLEDGMENTS

The author is grateful to S. Golovan' (Institute of Macromolecular Compounds, National Academy of Sciences of Ukraine) for assistance in obtaining SEM images and to O. Litvin (Lashkarev Institute of Semiconductor Physics, National Academy of Sciences of Ukraine) for organizing the acquisition of AFM images of the samples. The strength tests were carried out with participation of A.G. Girchenko (Chuiko Institute of Surface Chemistry, National Academy of Sciences of Ukraine).

REFERENCES

1. Trofimov, N.N., Patrusov, V.P., and Shatskaya, K.A., *Plast. Massy*, 2005, no. 5, pp. 13–16.
2. *Handbook of Fillers and Reinforcements for Plastics*, Katz, H.S. and Milewski, J.V., Eds., New York: Van Nostrand Reinhold, 1978.
3. TEKNOS Epoxy Systems for Tank Coatings, *TEK*, 2007, no. 3 (99), p. 84.
4. Park, J.H. and Jana, S.C., *Polymer*, 2003, vol. 44, no. 7, pp. 2091–2100.
5. Mathias, L.J. and McGowen, J.A., *Polym. Composites*, 1997, vol. 18, no. 3, pp. 332–347.
6. Kim, W.G. and Ryu, J.H., *J. Appl. Polym. Sci*., 1997, vol. 65, no. 10, pp. 1975–1982.
7. Zheng, Y., Zheng, Yi., and Rong, R., *Mater. Lett*., 2003, no. 57, pp. 2940–2944.
8. Sumenkova, O.D., Osipchuk, V.S., Lebedeva, E.D., and Kononova, O.A., *Plast. Massy*, 2001, no. 3, pp. 35–37.
9. Malakhova, I.V., Bol'bukh, Yu.M., Tertykh, V.A., and Shiichuk, A.V., in *Trudy 11-i konferentsii po vysokomolekulyarnym soedineniyam* (Proc. 11th Conf. on Macromolecular Compounds), Dnepropetrovsk (Ukraine): Ukr. Derzh. Khimiko-Tekhnol. Univ., 2007, p. 148.
10. Skladanyuk, R.V. and Zakordonskii, V.P., *Vysokomol. Soedin., Ser. A*, 2005, vol. 47, no. 1, pp. 34–43.
11. Dupanov, V.O. and Ponomarenko, O.M., Abstracts of Papers, *Vseukrainskaya konferentsiya "Nanomaterialy v khimii, biologii, meditsine"* (All-Ukraine Conf. "Nanomaterials in Chemistry, Biology, and Medicine"), Kiev, 2006, pp. 11–12.
12. Gorshunov, A.V., Thermal Properties of Modified Epoxy Polymers, *Cand. Sci. Dissertation*, Kiev, 2007.
13. Sultanaev, R.M., *Plast. Massy*, 1992, no. 2, pp. 21–24.
14. *Khimiya poverkhnosti kremnezema* (Chemistry of Silica Surface), Chuiko, A.A., Ed., Kiev, 2001.

ISSN 1070-4272, Russian Journal of Applied Chemistry, 2008, Vol. 81, No. 11, pp. 1992–1996. © Pleiades Publishing, Ltd., 2008.
Original Russian Text © L.A. Nud'ga, V.A. Petrova, I.V. Gofman, I.V. Abalov, B.Z. Volchek, E.N. Vlasova, Yu.G. Baklagina, 2008, published in Zhurnal Prikladnoi Khimii, 2008, Vol. 81, No. 11, pp. 1877–1881.

MACROMOLECULAR COMPOUNDS AND POLYMERIC MATERIALS

Chemical and Structural Transformations in Chitosan Films in the Course of Storage

L. A. Nud'ga, V. A. Petrova, I. V. Gofman, I. V. Abalov, B. Z. Volchek, E. N. Vlasova, and Yu. G. Baklagina

Institute of Macromolecular Compounds, Russian Academy of Sciences, St. Petersburg, Russia

Received May 5, 2008

Abstract—Changes in the functional composition of chitosan films in the course of storage under ambient conditions were examined by conductometric titration and IR spectroscopy. The deformation–strength and thermal properties of the films were studied, and their supramolecular structure was analyzed by X-ray diffraction.

DOI: 10.1134/S1070427208110244

Chitosan film materials find growing use in medicine, as membranes of various purposes, as coatings, and as packaging films. Such films can be readily prepared by dry forming from solution in a readily available nontoxic solvent, dilute acetic acid. Installations for continuous forming with drying by air preheated to a definite temperature have been developed long ago, and therefore chitosan films can be produced in required amounts. Their cost will be chiefly determined by the market price of chitosan.

Despite such advantages as biocompatibility and bactericidal and fungicidal properties, freshly formed chitosan films have a significant drawback: They dissolve or strongly swell in aqueous media. Ways to overcome this drawback are well known: cross-linking, hydrophobization by surface treatment, and heat treatment. The first two procedures are not always acceptable, in particular, when the films are used in medicine, because of introduction of toxic substances or chemical groups. Heat treatment does not give rise to toxic products in films. Although this procedure was used in numerous studies and in practice, the chemical nature of transformations occurring in the course of heat treatment did not receive due researchers' attention until recently.

Vikhoreva and Zotkin [1–3] were the first to examine how the forming at elevated temperatures or heat treatment affects the composition of functional groups of chitosan films prepared from solutions in aliphatic carboxylic acids. They revealed a decrease in the amount of amino groups and acids depending on the solvent used and then proved by IR and NMR spectroscopy the reaction pathways: amidation and formation of Schiff bases, with the result that the films lose solubility.

The loss of the solubility of chitosan films in the course of drying at elevated temperature was noted in preparation of films for electrical engineering [4]. Later on, attention was given to the fact that the films also lose solubility in the course of prolonged storage under ambient conditions, with a simultaneous increase in the strength. This phenomenon was attributed to gradual volatilization of acetic acid used as solvent, with the amino groups of chitosan becoming free. It was interesting to examine more thoroughly the chemical nature of processes occurring in chitosan films in the course of their storage.

EXPERIMENTAL

To form films, we used chitosan prepared from crab shells, with the following characteristics: ash residue 0.35%, solubility in 2% acetic acid 99.7%, content of primary amino groups N_{am} = 8.48%, degree of deacetylation (DD) 0.98, intrinsic viscosity [η] = 9.0 dl g^{-1} (in 2% acetic acid with addition of 0.5 M NaCl), and molecular weight 200.5 kDa (calculated by the formula from [5]).

Films were formed on a glass support from 2% solutions in 2% acetic acid using a slot die and were dried under ambient conditions. The film thickness was 12 μm. Then some of the films were stored in the rolled-up state under ambient conditions, and the other films were kept in a vacuum, also at room temperature. At definite intervals (2 weeks during the first 2.5 months, 1 month during the subsequent period, maximal storage time 3 years), the amounts of primary amino groups and acetic acid in the films were determined by conductometric back-titration, the solubility in water and 2% acetic acid was evaluated, the IR spectra were taken, the deformation–strength and thermomechanical properties were determined, and the thermal gravimetric and X-ray diffraction analyses were performed.

Conductometric titration was performed with an EC 215 conductometer (Hanna Instruments, Germany). The IR spectra were recorded with a Bruker IFS-88 spectrometer (Germany).

The mechanical tests of film samples were performed in the uniaxial extension mode on a UTS 10 universal installation for mechanical tests (Germany). We determined the elastic modulus E, tensile strength σ_t, plasticity limit σ_p, and breaking elongation ε_b.

Thermomechanical tests were performed with a UMIV-3 installation in the uniaxial extension mode under the action of a constant tensile load of 0.25 MPa, with sample heating at a rate of 5 deg min^{-1}.

Thermal gravimetric analysis (TGA) was performed with a laboratory thermal balance. Samples weighing about 50 mg were heated in a self-generated atmosphere at a rate of 5 deg min^{-1}.

X-ray diffraction analysis was performed on a DRON-2 diffractometer with Ni-filtered CuK_α radiation.

Figure 1 shows how the quantitative composition of films with respect to amino groups and acetic acid varies in the course of 1-year storage. The most pronounced changes are observed in the first 50 days of storage: N_{am} decreases by a factor of 2, and acetic acid content, by 30%; the solubility decreases by a factor of 2. In the subsequent period, the content of amino groups and acetic acid decreases insignificantly, and the solubility continues to decrease: to 3.5% in 150 days and to 3% in 1 year.

The calculated AcOH/chitosan molar ratio in the forming solution (Fig. 2) is 2.74, and in the freshly

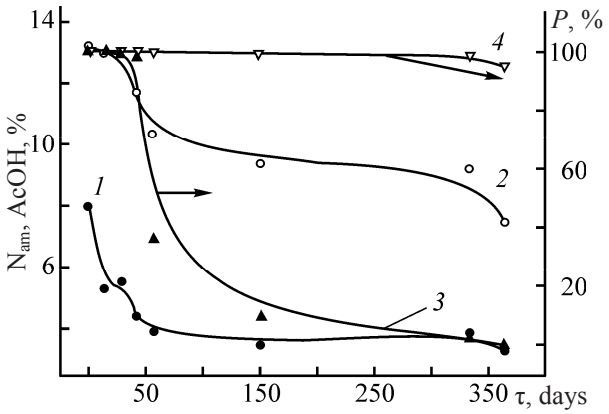


Fig. 1. Variation of the content of (*1*) primary amino groups N_{am} and (*2*) acetic acid AcOH in chitosan films and of their solubility P in (*3*) water and (*4*) 2% acetic acid in the course of storage under ambient conditions. (τ) Time; the same for Figs. 2 and 5.

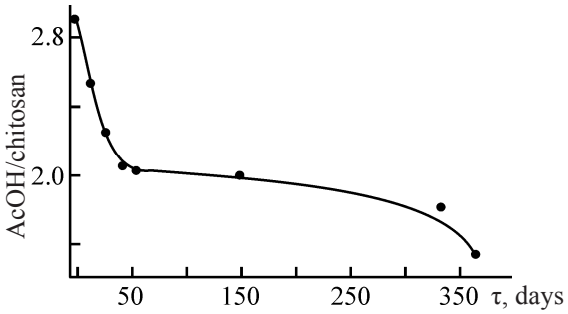


Fig. 2. Variation of the acetic acid/chitosan molar ratio in chitosan films in the course of storage under ambient conditions.

formed film after drying in air it is 2.9 (according to the results of conductometric titration). In the course of the film storage, the ratio gradually decreases to 2.0 in 150 days. Then both the ratio and the solubility in water change slowly, but by the moment of the complete loss of the solubility this ratio is still 1.5. At such an excess of the acid, the film should, seemingly, at least swell in water. The lack of swelling suggests partial conversion of the amino groups of chitosan into amide groups, i.e., reacetylation of the amino groups owing to the condensation with acetic acid. The degree of deacetylation of chitosan, calculated from the conductometric data, after 150 days of storage is 0.42 at the initial DD of 0.97, i.e., 0.55 mol of acetic acid is bound to 1 mol of chitosan units. Hence, a part of acetic acid volatilizes in the course of storage. At the same time, the films remain soluble in 2% acetic acid for a year. Hence, the remaining free amino groups provide the degree of protonation sufficient for the dissolution.

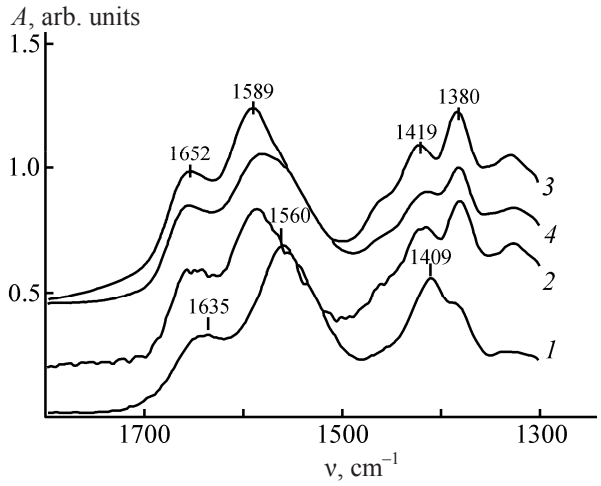


Fig. 3. IR spectra of chitosan films, (*1*) freshly prepared and stored under ambient conditions for (*2*) 2 weeks, (*3*) 2 months, and (*4*) 3 years. (*A*) Absorption and (ν) wavenumber.

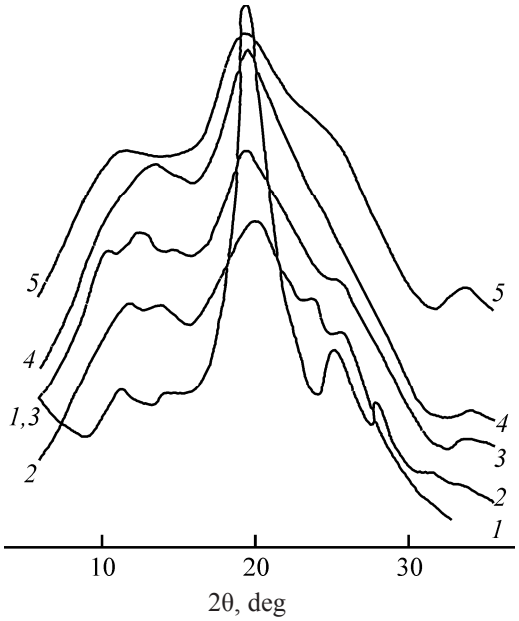


Fig. 4. X-ray diffraction patterns of (*1*) initial chitosan and chitosan films, (*2*) freshly prepared, (*3*) washed with ethanol to remove acetic acid, (*4*) heated at 120°C for 3 h, and (*5*) stored under ambient conditions for 3 years. (2θ) Bragg angle.

And only the film stored for 3 years does not dissolve in acetic acid. The DD of such film decreases to 0.20, i.e., the film material is partially deacetylated chitin.

The IR Fourier spectroscopic data confirm the quantitative results we obtained (Fig. 3). The IR spectra of the freshly formed film contain absorption bands at 1559 and 1409 cm^{-1}, corresponding to the vibrations of carboxylate groups. With an increase in the storage time, the band at 1409 cm^{-1} transforms into a shoulder but remains even in the spectrum of the film stored for 3 years. A broad band at 1559 cm^{-1} obscures the absorption bands of the amide (amide II, 1555 cm^{-1}) and amino (1560–1600 cm^{-1}) groups. Therefore, it is impossible to monitor by IR spectroscopy the variation of their amount with time. In the course of storage, the band maximum at 1559 cm^{-1} is shifted toward higher frequencies, and a shoulder at 1652 cm^{-1} (amide I) becomes more pronounced, suggesting formation of acetamide groups.

For comparison, we recorded the spectra of a freshly formed film washed with ethanol to remove acetic acid and of a film heated at 120°C for 3 h. In the IR spectrum of the washed film, the intensity of the absorption bands at 1559 and 1409 cm^{-1} considerably decreases, and in the spectrum of the heated film, the intensity of the shoulder at 1652 cm^{-1} (amide I) increases.

In the IR spectra of the films stored in a vacuum, the changes are similar to those in the spectra of the films stored in air: weakening of the absorption bands of carboxylate groups and slight increase in the intensity of the amide I band. After storage in a vacuum for 3 months, the films partially dissolve in water and fully dissolve in 2% acetic acid, i.e., atmospheric oxygen does not appreciably affect the processes occurring in the course of storage in air, at least for 3 months.

The results of X-ray diffraction analysis of chitosan films subjected to various treatments are shown in Fig. 4. The freshly formed film and the same film washed with ethanol to remove excess acetic acid give essentially similar X-ray diffraction patterns: Against the background of an amorphous halo, weak reflections are observed at 2θ 13.5° and 20° (these reflections are characteristic of the crystal structure of chitosan), and also at 2θ 24.5° and 26° (curves *1*–*3*). The diffraction patterns of the film heated at 120°C for 3 h and of that stored for 3 months (curves *4*, *5*) also have much in common: The reflections characteristic of chitosan at 2θ 13.5° and 20° are still less pronounced, and those at 2θ 24.5° and 26° are absent, which indicates that the films are more amorphous. Further distortion of the supramolecular organization may be caused by the appearance of bulky acetamide groups whose random distribution along macromolecules favors cleavage of intermolecular hydrogen bonds.

The results of determining the deformation–strength properties of films in the course of storage (see table) show no well-defined trends. Rather, they

Variation of the properties of chitosan films in the course of storage under ambient conditions

Storage time	E, GPa	σ_p	σ_t	ε_b	W	τ_1	T_1
		MPa		%		°C	
0	5.20	87	96	13	11.0	233	232
15 days	5.75	113	126	16	9.7		236
29 days	5.92	111	122	17	11.1	236	235
42 days	5.93	116	127	20	8.9		236
56 days	6.03	127	132	18	7.9	238	236
86 days	6.71	141	140	7	8.2	241	237
4 months	7.11	140	140	10	7.8	242	238
5 months	6.05	135	158	26	8.0	242	239
6 months	5.66	114	132	25	9.0	246	242
7 months	5.61	112	118	21	11.1	241	243
8 months	4.93	98	112	24	11.5	243	243
9 months	4.91	103	119	26	12.0	246	240
10 months	4.84	96	112	26	11.1	246	246
11 months	5.91	129	145	20	8.6	247	245
12 months	6.45	141	140	14	7.7	253	253
36 months	5.06	122	118	13	11.7	247	

fluctuate in a certain range, and it is impossible to correlate these fluctuations with the storage time or functional composition of the film. Only determination of the moisture content W of the films by TGA revealed certain correlations: E, σ_p, and strength characteristics (σ_t) vary in opposite directions with the moisture content (Fig. 5). At the same time, breaking elongation shows no definite trend, probably because of larger scatter of the corresponding data.

It should be particularly noted that examination of the sample stored for 3 years revealed no deterioration of the mechanical properties of the material and no appreciable changes in the qualitative characteristics of its deformation behavior.

A study of the thermal properties of the films stored for different periods showed that the shape of the DTA and TGA curves was similar for all the samples. Figure 6 shows as examples the curves for a film stored for 6 months. However, the temperature T_1 of the inflection point in the thermomechanical curves, above which the sample rigidity grows in the course of heating, gradually increases in the course of storage. This temperature corresponds to the onset of degradation processes in the material. Indeed, the temperatures T_1 are virtually identical to the parameters τ_1 determined from the TGA curves, namely, to the temperatures of 1% weight loss (Fig. 6). The parameter τ_1 tends to shift toward higher temperatures with the sample storage, which may be due to gradual transformation of amino groups into acetamide groups. Comparison of the thermomechanical curves with the TGA curves allows a conclusion that the failure of chitosan films in the course of thermomechanical tests occurs at temperatures at which the weight loss amounts to 50% and more. This means that the molecular "skeleton" capable of standing a mechanical load is preserved up to these high degrees of degradation. For films of the ma-

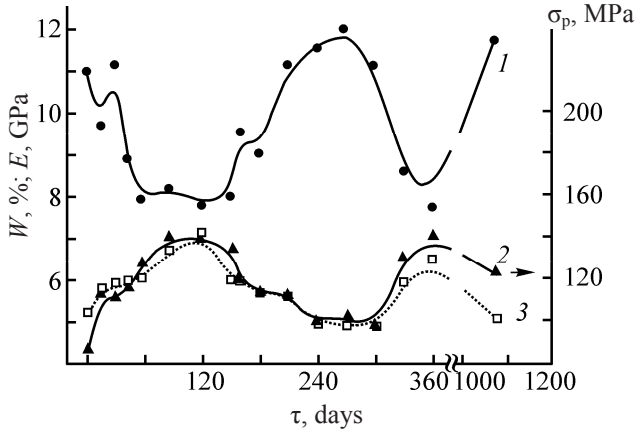


Fig. 5. Variation of the (*1*) moisture content W, (*2*) plasticity limit σ_p, and (*3*) elastic modulus E of chitosan film in the course of storage.

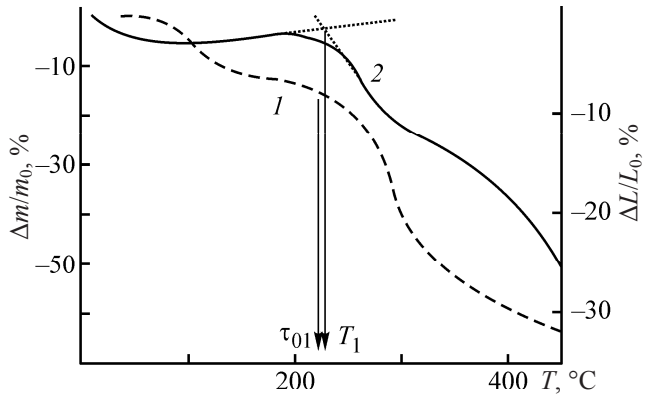


Fig. 6. (*1*) Thermomechanical ($\Delta L/L_0$) and (*2*) thermogravimetric ($\Delta m/m_0$) curves of chitosan films stored for 6 months. (*T*) Temperature.

jority of known polymeric materials, the failure on heating at the same tensile loads is observed already at 10–15% degradation.

Thus, the results we obtained show that amidation of the amino groups in chitosan films gradually occurs in the course of storage, and after storage for 3 years chitosan virtually transforms into chitin. This reaction also occurs in the course of heating the films at 120°C [1]. At the same time, formation of Schiff bases leading to cross-linking of macromolecules and characteristic of heated films is not observed, because in films stored in air excess acid preventing formation of azomethine bond is preserved. The IR spectra of the examined films do not contain a C=N bond at 1676 cm^{-1}.

The deformation–strength properties of the films in the course of prolonged storage under ambient conditions change insignificantly, and these changes are determined to a greater extent by the air humidity rather than by the storage time. The results we obtained suggest that, if a sample is stored at a constant temperature and constant humidity, prolonged storage will not affect the suitability of chitosan films as a packaging material and the properties of chitosan coatings. At the same time, the observed changes in the functional composition, especially a decrease in the amount of amino groups, can make worse the quality of films used for accelerated wound healing.

CONCLUSIONS

(1) Storage of chitosan films under ambient conditions results in slow reacetylation of amino groups. As a result, the films lose solubility in water and acetic acid.

(2) The appearance of aminoacetyl groups fully distorts the system of hydrogen bonds and leads to the film amorphization.

(3) The deformation–strength properties of films remain essentially unchanged after prolonged storage. Slight changes are due to fluctuations of the humidity of the ambient atmosphere.

(4) A DTA and TGA study of the thermal properties of the films revealed a gradual increase in the temperature of the decomposition onset with an increase in the storage time.

REFERENCES

1. Zotkin. M.A., Vikhoreva. G.A., and Kachek'yan, A.S., *Vysokomol. Soedin., Ser. A*, 2004, vol. 46, no. 2, pp. 359–363.
2. Zotkin, M.A., Vikhoreva, G.A., Smotrina, T.V., and Derbenev, M.A., *Khim. Volokna*, 2004, no. 1, pp. 14–18.
3. Zotkin, M.A., Vikhoreva, G.A., Ageev, E.P., et al., *Khim. Tekhnol*., 2004, no. 9, pp. 15–19.
4. Plisko, E.A., Nud'ga, L.A., Shabanova, N.S., et al., *Elektrotekh. Prom–st., Ser.: Khim. Fiz. Istochn. Toka*, 1971, no. 7, pp. 61–64.
5. Pogodina, N.V., Pavlov, G.M., Bushin, S.V., et al., *Vysokomol. Soedin., Ser. A*, 1986, vol. 28, no. 2, pp. 232–239.

ISSN 1070-4272, Russian Journal of Applied Chemistry, 2008, Vol. 81, No. 11, pp. 1997–2001. © Pleiades Publishing, Ltd., 2008.
Original Russian Text © I.A. Bashmakov, T.F. Tikhonova, L.V. Solov'eva, K.A. Selevich, F.N. Kaputskii, 2008, published in Zhurnal Prikladnoi Khimii, 2008, Vol. 81, No. 11, pp. 1882–1886.

MACROMOLECULAR COMPOUNDS AND POLYMERIC MATERIALS

Synthesis and Thermal Solid-Phase Transformations of Cellulose–Iron(II, III) Oxide Composite

I. A. Bashmakov, T. F. Tikhonova, L. V. Solov'eva, K. A. Selevich, and F. N. Kaputskii

Research Institute of Physicochemical Problems, Minsk, Belarus

Received June 23, 2008

Abstract—Possibility of obtaining cellulose–iron(II, III) oxide composites with various component ratios was studied. The specific magnetization of the material was determined in relation to the mass fraction of the magnetic component in the composite.

DOI: 10.1134/S1070427208110256

Development and synthesis of polymeric composites with prescribed functional (including magnetic), electrical, and other properties is a topical task for modern materials science. The undiminishing researchers' interest in composite polymeric materials is due to the fact that, in some cases, additives introduced into polymers provide a fundamental change in their properties. Because of the combination of properties of a polymer and filler, the composite as a whole becomes a new material suitable for some practical applications.

It is known that such a natural polymer as cellulose can be used to create salt-containing composites and convert them by pyrolysis into, depending on the medium, metal–carbon materials [1], fibers of refractory oxides [2], and complex oxide compounds [3], which can serve as intermediates for obtaining practically important materials.

In this study, a cellulose composite containing iron(II, III) oxide of the magnetite modification was prepared. Owing to the magnetic properties of the oxide component, the composite may find direct practical application. Some aspects of solid-phase thermal transformations of the cellulose composite in a vacuum and in air were studied.

EXPERIMENTAL

The cellulose composite with inclusion of finely dispersed iron(II, III) particles is prepared by carrying out a number of successive procedures. First, cellulose is impregnated with a solution of iron(II) sulfate and iron(III) chloride salts mixed in a 1 : 2 molar ratio, with the concentrations of the salts equal to 0.75 and 1.5 M, respectively, at a solid–liquid impregnation ratio of 2 ml g^{-1}. Then follows treatment of the salt-containing cellulose with a concentrated sodium hydroxide solution; washing of a sample with distilled water to remove the unchanged alkali, sodium chloride and sulfate formed in the reaction, and excess amount of iron oxide not fixed on the fabric; and drying. The starting cellulose was preliminarily subjected to mercerization with a 17% sodium hydroxide solution at 18°C for 30 min.

The content of iron oxide (Fe_3O_4) in the cellulose composite obtained using the above scheme was found gravimetrically after thorough washing and drying of the samples and on a Netzsch STA 449C combined thermal analyzer (Germany) by thermal gravimetric analysis (TG) from the mass of the residue formed on burning a sample in an oxygen atmosphere. In addition to measuring the mass change on the thermal analyzer, heat effects were determined by differential scanning calorimetry (DSC) on heating the samples in the temperature range from room temperature to 600°C.

The phase composition of the samples was analyzed with a DRON-3.0 X-ray diffractometer with iron-filtered CoK_α radiation (λ = 1.6208 Å). The morphology of the cellulose–Fe_3O_4 composite was analyzed by scanning electron microscopy (LEO-906 E, FRG).

The magnetic properties (specific magnetization) of samples were determined on a Faraday balance. A cotton fabric was chosen as the starting cellulose

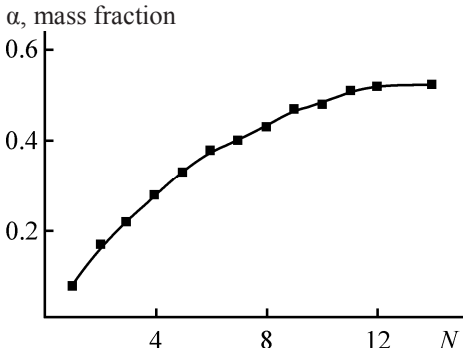


Fig. 1. Fe_3O_4 content α in the iron oxide–cellulose composite vs. the number *N* of sorption–deposition cycles.

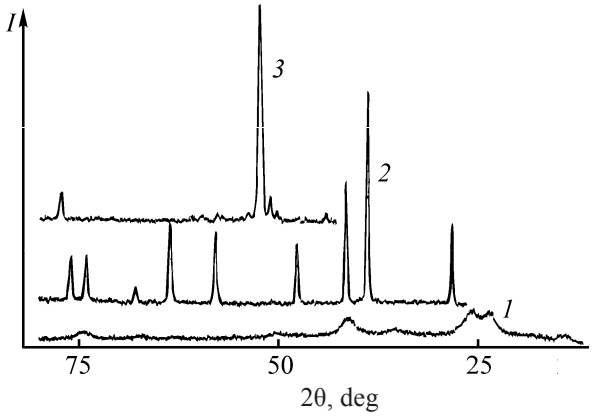


Fig. 2. X-ray diffraction patterns of (*1*) iron oxide–cellulose composite with a Fe_3O_4 mass fraction of 0.27 and of products of its thermal transformations (*2*) in air and (*3*) in a vacuum. (*I*) Signal intensity and (2θ) Bragg angle.

material. Its mercerization with a sodium alkali in the first stage was performed to impart a developed internal sorption surface. It is known that alkaline hydrolysis of a mixture of salts of bi- and trivalent iron with a molar ratio of, respectively, 1 : 2, yields Fe_3O_4 (magnetite) [4]. After impregnation of the cellulose fabric with a stoichiometric mixture of the iron salts and treatment of the iron-containing cellulose with sodium hydroxide, the gain weight due to Fe_3O_4 in a sample is about 80 wt %. However, the X-ray diffraction pattern of the sample contains only reflections at Bragg angles of 14.0°, 23.5°, and 25.3°, which are characteristic of cellulose II and appear upon treatment of natural cellulose (cellulose I) with a concentrated alkali in the first stage [5]. A similar result, lack of an X-ray diffraction evidence of the inorganic phase deposited onto the polymeric matrix, has been observed for cellulose structurally modified with 68% nitric acid and impregnated with an organic salt [3]. This fact is attributed to formation of isolated X-ray amorphous iron oxide particles within the internal system of pores and capillaries and on the fiber surface.

The amount of magnetite capable of being retained in the cellulose matrix without any noticeable washing-out and desorption was raised by performing multiple cycles of impregnation of the cotton fabric with a mixture of salts of bi- and trivalent iron, taken in a prescribed ratio, and an alkaline treatment of the salt-containing cellulose. As the number of these cycles increases, the sorption equilibrium in the system approaches saturation (Fig. 1). In this case, the maximum mass fraction of magnetite in the composite reaches 0.54. In the X-ray diffraction pattern of a sample subjected to three sorption–deposition cycles (Fig. 2, curve *1*), there appear reflections characteristic of magnetite at 2θ = 35.1°, 41.4°, 50.4°, 67.2°, and 74.1°. The average crystal size *L* found by the Scherrer formula [6] is 5.0 nm. As follows from electron micrographs (Fig. 3), magnetite deposited onto cellulose in the initial cycles rather uniformly covers fabric fibers, and only upon the saturation of the surface with magnetite, separate crystals start to be formed. The specific magnetization of the samples grows with the number of sorption–deposition cycles. As seen from the table, it reaches 14.0 A m^2 kg^{-1} at room temperatures in a magnetic field with a strength 3.97×10^5 A m^{-1}.

The cellulose–iron(II, III) composite obtained acquires magnetic properties and retains mechanical properties characteristic of cellulose, primarily elasticity and ability to take on a prescribed shape, which enables its direct use as elastic magnetic shields against electromagnetic radiation [7].

A study of the solid-phase thermal transformations of the cellulose composite in a vacuum and in air revealed a number of specific features of its thermal decomposition, compared with cellulose. The thermal treatment in a vacuum was performed at a residual pressure of 1.3 Pa with the temperature raised at a rate of 10 deg min^{-1}; after the final temperature of annealing was reached, the samples were kept under isothermal conditions for 60 min.

Our experiments showed that annealing of composite samples with varied content of Fe_3O_4 without admission of air up to temperatures of 800°C led to transformation of cellulose fibers to carbon fibers and of Fe_3O_4 particles to Fe particles. As a consequence, the specific magnetization of the samples substantially increased and exceeded by approximately an order of

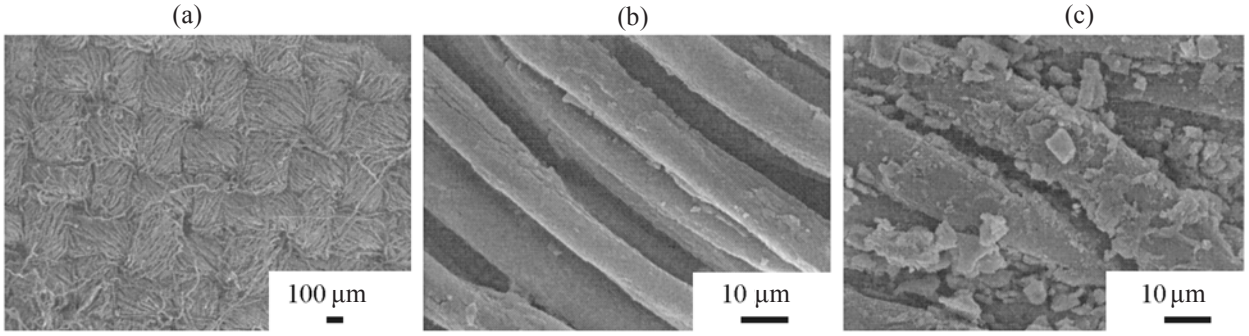


Fig. 3. SEM micrograph of iron oxide–cellulose samples. (a) General view of the composite material; Fe_3O_4 mass fraction in the composite: (b) 0.27 and (c) 0.54.

magnitude the maximum magnetization of the starting cellulose–oxide composite. The specific magnetization of the samples also grows with the number *N* of sorption–deposition cycles to reach 160.3 A m^2 kg^{-1}.

The formation of the iron phase in the carbon composite matrix is confirmed by the X-ray diffraction pattern of a sample with Fe_3O_4 mass fraction of 0.27, thermally treated in a vacuum (Fig. 2, curve *3*). Figure 2 shows that the X-ray diffraction pattern contains basic α-Fe reflections, with a crystallite size of approximately 30.0 nm. According to a calculation, the content of iron in this sample is 65 wt %. In the cellulose–iron oxide sample with a Fe_3O_4 mass fraction of 0.54, subjected to a similar treatment, the mass fraction of iron reaches 1.0. The sample composed of a purely iron phase retains the structure of the precursor composite and, upon annealing in a vacuum at 1050°C, transforms into a high-strength metallic fabric-grid. In thermal transformations of the oxide–cellulose composite in a vacuum, the iron phase is apparently formed in the same way as it does in thermal treatment of cellulose impregnated with salts of variable-valence inorganic cations, as a result of a chain of transformations: $Fe_3O_4 \rightarrow FeO \rightarrow Fe$ [8]. The procedure described in [8] is intended for synthesis of iron–carbon fibrous materials that contain approximately 10 wt % iron, exhibit important magnetic and catalytic properties, and are pyrophoric.

It should be noted that fully porous metallic fibrous structures can be produced from salt-containing cellulose [9]. However, as noted in [10], their synthesis requires a considerable change in the experimental conditions: in particular, the thermal treatment of salt-containing cellulose should be performed in the medium of ammonia decomposition products at 900–1000°C. As follows from the results obtained, by setting a certain content of Fe_3O_4 in a composite, it is possible to obtain upon its thermal treatment either an iron–carbon composite or a nearly single-phase product that is composed of α-Fe and reproduces the fabric texture of the precursor composite. The specific magnetization of the single-phase product exceeds by an order of magnitude that of the oxide–cellulose precursor composite.

The main aspects of thermal transformations of oxide–cellulose samples in air were found by analysis of their TG and DSC curves. Figure 4a shows TG curves of thermal decomposition of cellulose modified with a 17% sodium hydroxide solution. It can be seen that the thermal degradation of cellulose subjected to an activating treatment with the alkali occurs in two stages. In the first stage of intensive thermal decomposition, which involves with the main loss of mass, the tarry fraction burns out in a narrow temperature range, with the maximum of the exothermic effect at 340°C. The second, low-intensity stage of smoldering of the carbon residue ends at 520°C. The thermal decomposition of the oxide–cellulose composite almost ends at a temperature 200°C lower than that for cellulose. Accord-

Specific magnetization of the iron(II, III) oxide–cellulose composite, σ, and iron–carbon composite, σ', at room temperature at a field strength of 3.97×10^5 A m^{-1}

Number *N* of sorption–deposition cycles	σ	σ'
	A m^2 kg^{-1}	
3	9.6	95.2
8	13.7	116.4
12	14.0	160.3

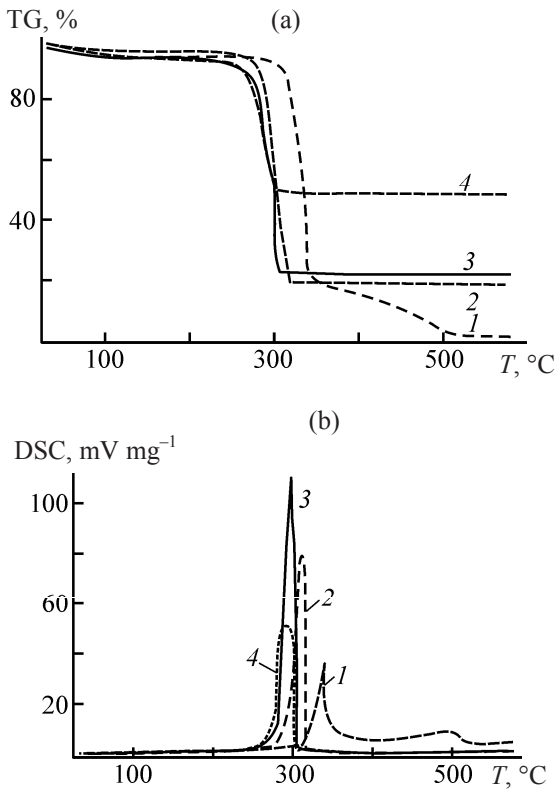


Fig. 4. (a) TG and (b) DSC curves: (*1*) cellulose activated with a 17% aqueous solution of sodium hydroxide and (*2–4*) cellulose–iron oxide composites with Fe_3O_4 mass fraction of 0.21, 0.27, and 0.54, respectively. (*T*) Temperature.

ing to the DSC data in Fig. 4b, the thermal decomposition of the composite occurs with a higher total heat release and the maximum of the exothermic effect lies at 295–313°C depending on the Fe_3O_4 content of a composite, i.e., lower than the low-temperature peak associated with the decomposition of the cellulose matrix (340°C). The second stage of the process, the smoldering of the carbon residue, is not separated by a time–temperature interval from the first stage. Apparently, the intensification of the thermal decomposition of the cellulose matrix in the composite is due not only to the catalytic effect of the filler, but also to the occurrence of the exothermic reaction

$$Fe_3O_4\ (FeO, Fe_2O_3) \rightarrow \alpha\text{-}Fe_2O_3.$$

In all probability, the metal phase is not formed in thermal decomposition of the oxide–cellulose composite in air, in contrast to the case of its thermal treatment in a vacuum. This is indicated by the fact that the X-ray diffraction pattern of an oxide–cellulose composite subjected to thermal treatment at temperatures lower than the onset temperature of the exothermic effect (260°C) contains no iron phase.

As follows from the DSC data, the magnitude of the exothermic effect, found from its area, in thermal decomposition of samples with Fe_3O_4 mass fraction of 0.21, 0.27, and 0.54 is 10 940, 13 990, and 15 730 J g^{-1}, respectively, in terms of the cellulose base, which exceeds the corresponding value for cellulose (7600 J g^{-1}). In other words, the cellulose–iron oxide composite is a more efficient energy carrier than cellulose. In this context, an attempt was made to subject the composite to thermal treatment by its initiated firing. The experiments performed demonstrated that, in initiated firing of oxide–cellulose composites with varied weight fraction of Fe_3O_4 (including the maximum mass fraction of 0.54), the cellulose base completely burns out at the combustion front to give $\alpha\text{-}Fe_2O_3$ with L = 30.0 nm according to X-ray diffraction data (Fig. 2, curve *2*). The annealed sample reproduces the texture of the starting fabric and, on being touched, crumbles without special dispersion into a dark red, loose soft, by touch, powder of anisotropic particles, microfibers. This circumstance is important, e.g., when oxides are used as pigments for polymers [10] or as synergists of fire-retardant additives to polymers [11], because, in this case, oxide microfibers arranged along chains of polymer macromolecules impair the performance characteristics of the polymer to a lesser extent than do spherical particles of oxides [12].

Thus, the oxide–cellulose composite, which is a microheterogeneous system with numerous phase boundaries, is less thermally stable than cellulose. Serving as a carrier matrix in the composite, modified cellulose fibers execute in combustion, because of the vigorous gas evolution, an additional function of a dispersant and homogenizer of the forming final degradation product, oxide stock. The thermal transformations of the composite in air are accompanied by a stronger exothermic effect than those in the case of cellulose. This circumstance enables synthesis of finely dispersed $\alpha\text{-}Fe_2O_3$ in the self-propagating combustion mode, similar to the known self-propagating high-temperature synthesis [13].

CONCLUSIONS

(1) A cellulose–iron(II, III) oxide composite material was synthesized. The material combines the magnetic properties characteristic of Fe_3O_4 with the elastic-

ity of cellulose, which enables its use as magnetic shields.

(2) The relative amounts of cellulose and Fe_3O_4 in the composite, necessary for its complete transformation in thermal treatment in a vacuum into an almost single-phase product having the form of α-Fe with the fabric texture of the precursor composite, were determined. The specific magnetization of the single-phase product is an order of magnitude higher than that of the composite.

(3) The possibility of conversion of the composite into α-Fe_2O_3 in air at the self-propagating combustion front was demonstrated.

REFERENCES

1. Ermolenko, I.N., Lyubliner, I.P., and Gul'ko, I.V., *Elementosoderzhashchie ugol'nye voloknistye materialy* (Element-Containing Fibrous Carbon Materials), Minsk: Nauka i Tekhnika, 1982.
2. Ermolenko, I.N., Ul'yanova, T.M., Vityaz', P.A., and Fedorova, I.L., *Voloknistye vysokotemperaturnye keramicheskie materialy* (High-Temperature Fibrous Ceramic Materials), Minsk: Nauka i Tekhnika, 1991.
3. Solov'eva, L.V., Bashmakov, I.A., and Kaputskii, F.N., *Vestsi Akad. Navuk Bel., Ser. Khim. Navuk*, 1994, no. 3, pp. 57–61.
4. Taketomi, S. and Tikadzumi, S., *Magnitnye zhidkosti* (Magnetic Liquids), Moscow: Mir, 1993.
5. Rogovin, Z.A., *Khimiya tsellyulozy* (Chemistry of Cellulose), Moscow: Khimiya, 1972.
6. Kropotin, O.V., Surikov, V.I., and Kalistratova, L.F., *Vestn. Omsk. Univ*., 1997, no. 3, pp. 33–34.
7. Lyn'kov, L.M., Bogush, V.A., Sen'kov, E.A., and Zavadskii, S.M., *Pis'ma Zh. Tekh. Fiz*., 2003, vol. 29, no. 15, pp. 55–60.
8. Ermolenko, I.N., Safonova, A.M., Malashevich, Zh.V., et al., *Vestsi Akad. Navuk Bel. SSR, Ser. Khim. Navuk*, 1979, no. 4, pp. 36–41.
9. UK Patent 1 183 642.
10. Bashmakov, I.A., Solov'eva, L.V., Krul', L.P., et al., *Vestn. Bel. Univ., Ser. 2*, 1997, no. 1, pp. 3–6.
11. Berlin, A.A., *Soros. Obrazov. Zh*., 1996, no. 9, pp. 57–63.
12. Vettegren', V.I., Bashkarev, A.Ya., and Suslov, M.A., *Zh. Tekh. Fiz*., 2007, vol. 77, no. 6, pp. 135–138.
13. Merzhanov, A.G. and Nersesyan, M.D., *Zh. Vses. Khim. O–va. im. D.I. Mendeleeva*, 1990, vol. 35, no. 6, pp. 700–707.

ISSN 1070-4272, Russian Journal of Applied Chemistry, 2008, Vol. 81, No. 11, pp. 2002–2007. © Pleiades Publishing, Ltd., 2008.
Original Russian Text © A.A. Lugovaya, V.M. Mikhal'chuk, V.A. Beloshenko, D.V. Gurtovoi, 2008, published in Zhurnal Prikladnoi Khimii, 2008, Vol. 81, No. 11, pp. 1887–1892.

MACROMOLECULAR COMPOUNDS AND POLYMERIC MATERIALS

Effect of Cr(III), Fe(III), Co(III), and Ni(II) Acetylacetonates on the Formation and Thermal Oxidative Degradation of Epoxy–Anhydride Polymers and Composites

A. A. Lugovaya, V. M. Mikhal'chuk, V. A. Beloshenko, and D. V. Gurtovoi

Donetsk National University, Donetsk, Ukraine
Galkin Donetsk Physicotechnical Institute, National Academy of Sciences of Ukraine, Donetsk, Ukraine

Received February 8, 2008

Abstract—The effect of Cr(III), Fe(III), Co(III), and Ni(II) acetylacetonates on epoxy–anhydride polycondensation in preparation of unmodified polymeric materials based on UP-650T epoxy resin and isomethyltetrahydrophthalic anhydride and of epoxy–siloxane hybrid composites was examined The resistance of the materials obtained to high-temperature oxidation and thermal oxidative degradation was evaluated.

DOI: 10.1134/S1070427208110268

Materials based on epoxy oligomers are widely used in industry owing a set of valuable properties: high adhesion to many materials, low shrinkage in the course of curing, good dielectric properties, chemical resistance, high strength, and low creep under a load [1]. Much attention has been given recently to a new direction in the chemistry and technology of polymeric epoxy materials, the development of hybrid composites based on epoxy resins and alkoxides of silicon, titanium, zirconium, etc. In such materials, the inorganic "phase" is formed by the sol–gel process consisting in hydrolysis of alkoxy compounds followed by polycondensation of the hydrolysis products and gelation of the system [2, 3].

The properties of epoxy–inorganic composites depend on many factors, including the procedure for curing epoxy oligomers. The most widely used procedures for forming the epoxy constituent of hybrid composites are cationic polymerization and amine curing. Studies in which dicarboxylic acid anhydrides are used for preparing epoxy–silica composites are extremely few. There are data on modification of an anhydride-curable epoxy composite material with nanodispersed silica particles [4]. Such materials exhibit enhanced heat resistance and improved mechanical properties compared to unfilled materials. Mascia and Tang [5] reported on preparation by the sol–gel procedure of keramers based on Bisphenol A epoxy resin and methylnadic anhydride.

To decrease the temperature and time of curing of unmodified epoxy–anhydride systems, various accelerators, in particular, metal acetylacetonates [6–9], are used. These agents allow preparation of materials with high dielectric properties and variation of the life of uncured composites at room temperature by varying the central atom in the chelate [9]. The most widely used are acetylacetonates of Fe(III) [9], Co(III), Co(II), Mn(III) [6, 7, 9], and Cr(III) [8]. However, as shown previously, transition metal compounds (including acetylacetonates) can both accelerate and inhibit thermal oxidative degradation of epoxy polymers [10–14]. The mechanism of the accelerating or inhibiting effect of metal acetylacetonates on thermal oxidation processes in epoxy polymers is poorly understood, and it is impossible to determine a priori what metal acetylacetonates can be used as polycondensation accelerators without decreasing the stability of the materials obtained to thermal oxidative degradation. Metal acetylacetonates were used as accelerators of reactions of dicarboxylic acid anhydrides with epoxy compounds only in simple (unmodified) systems. In preparation of hybrid composites by the sol–gel process, the system inevitably contains water, alcohols, organic solvents, and mineral acids. The presence of even small amounts

of these components and the formation of finely dispersed polysiloxane particles can affect in the general case both the curing process catalyzed by metal acetylacetonates and the heat resistance of the resulting hybrid materials.

The goal of this study is comparative evaluation of the accelerating effect of metal acetylacetonates on formation of anhydride-curable epoxy polymers and hybrid composites based on them and prepared by the sol–gel method, and also analysis of the effect exerted by metal acetylacetonates on the resistance of polymers and composites to thermal oxidative degradation and the choice of an accelerator ensuring high heat resistance of the resulting materials.

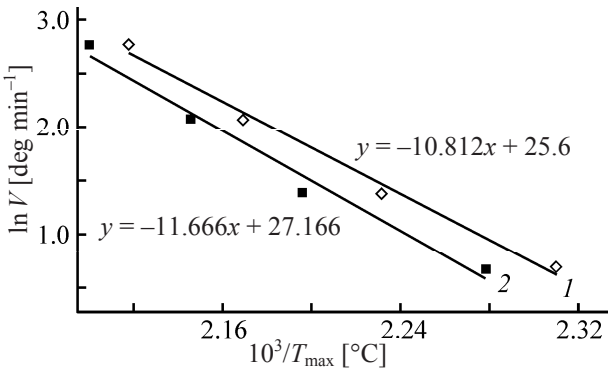


Fig. 1. Temperature of the maximum T_{max} in the DSC curves as a function of the heating rate V. $Cr(acac)_3$ catalyst; the same for Fig. 2. (*1*) Epoxy system and (*2*) hybrid system; the same for Fig. 2.

EXPERIMENTAL

As investigation objects we chose an unmodified epoxy–anhydride polymer (hereinafter, epoxy polymer) and a hybrid composite prepared by modification of the initial system by products of hydrolytic polycondensation of ethoxysilanes (hereinafter, hybrid composite). Epoxy polymers and hybrid composites were prepared on the basis of 1,1-dimethylol-3-cyclohexene triepoxide (UP-650T) and isomethyltetrahydrophthalic anhydride (*iso*-MTHPA). The curing accelerators were metal acetylacetonates $M(acac)_n$, where M = Fe(III), Co(III), Cr(III), or Ni(II), taken in an amount of 0.75 wt % relative to the epoxy resin. In preparing hybrid composites, we performed the preliminary step of the hydrolytic polycondensation of tetraethoxysilane (TEOS) and epoxypropxypropyltriethoxysilane (ES-1), taken in 2 : 1 molar ratio, in the presence of UP-65-T resin, solvent (methyl ethyl ketone, volume ratio to ethoxysilanes 1 : 2), and curing accelerator. The total content of ethoxysilanes in the initial composite was 10 wt %.

The thermograms of epoxy–anhydride polycondensation in the presence of metal acetylacetonates were recorded by differential scanning calorimetry (DSC) with a DSM-2M microcalorimeter at a heating rate of 2, 4, 8, and 16 deg min^{-1}. The sol fraction yield was determined from the weight loss of the film samples after prolonged (3 days) extraction of low-molecular-weight products with methanol. The extraction was performed at 50°C with repeated replacement of the extractant. The glass transition point of polymers and composites was determined by the thermomechanical method. Oxidation of polymeric and composite materials was performed on a gas-volumetric unit at 200°C in oxygen at a partial pressure of 1 atm. Thermogravimetric studies were performed with a Q-1500 D derivatograph (MOM, Hungary) in the dynamic mode in air at a heating rate of 10 deg min^{-1}.

All the acetylacetonates studied exert a catalytic effect on the epoxide–anhydride polycondensation in preparation of epoxy polymers and hybrid composites. With these chelates, the maximum in the DSC patterns shifts toward lower temperatures by 10 to 50°C depending on the nature of the central atom in the chelate. The temperatures of the maxima in the thermograms for the unmodified systems and hybrid composites with the same accelerator are very close. Hence, preliminary step of the hydrolytic polycondensation of ethoxysilanes and the presence of polysiloxane particles in the composites exert no significant effect on the polymerization of the organic constituent.

To evaluate the efficiency of the catalytic action of acetylacetonates, we determined from the DSC data the activation energy of curing of epoxy–anhydride polymers and composites. The dependence of the temperature of the maximum T_{max} on the heating rate V is well linearized in the coordinates $\ln V$–$1/T_{max}$ (Fig. 1). The linear correlation coefficients r vary in the range 0.9915–0.9995. This fact allowed us to calculate by the formula

$$E_a = -R\mathrm{d}(\ln V)/\mathrm{d}(1/T_{max}) \quad (1)$$

the apparent activation energy of curing of epoxy oligomers [15] in the cases of formation of epoxy polymers and hybrid compounds. The dependence of T_{max} on the heating rate is also well linearized in the coordinates

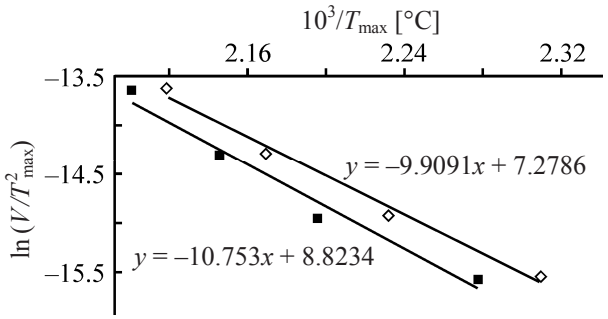


Fig. 2. Temperature of the maximum T_{max} in the DSC curves as a function of the heating rate V (deg min^{-1}) in the coordinates of the Kissinger method.

$$\ln(V/T^2_{max})–1/T_{max}$$

(Fig. 2). In this case, the activation energy was additionally calculated by the Kissinger method [16] developed for the process of cross-linking of filled epoxy polymers (Table 1). The activation energy is related to the temperature of the maximum and the heating rate by

$$E_a = –R\mathrm{d}(V/T^2_{max})/\mathrm{d}(1/T_{max}). \quad (2)$$

We found that the activation energies determined by the two methods differ by no more than 10%, which may be caused by relatively low concentration of polysiloxane particles in the composite. Counting on silicon oxide, the concentration of the products of hydrolytic polycondensation of ethoxysilanes is 3 wt %.

All the acetylacetonates used decrease by a factor of 1.3–2 the apparent activation energy of curing of epoxy–anhydride compounds and organo–inorganic hybrids. This is consistent with the published data for unmodified polymers cured in the presence of manganese and iron acetylacetonates [9]. In the systems under consideration, the most pronounced decrease in the activation energy is observed with cobalt(III) and nickel(II) acetylacetonates. Studies aimed to elucidate the mechanism of the catalytic effects of metal acetylacetonates and the factors causing differences in their activity are being continued. In this stage, it should be noted that the activation energies for the epoxy polymers and hybrid composites are approximately equal. This fact confirms the previously made assumption that the preliminary step of formation of a sol of polysiloxane particles does not appreciably affect the epoxy–anhydride polycondensation and makes it possible to compare the effect of acetylacetonates on formation of epoxy polymers and composites.

Taking into account the DSC data, we chose the optimal curing conditions allowing preparation of polymers and composites with the glass transition point as high as possible: 4 h at 160°C and 6 h at 180°C. Further increase in the curing temperature or time is not appropriate, because this may lead to the development of degradation. We obtained transparent film samples and determined their glass transition point and sol fraction content (Table 2). It can be seen that introduction of ethoxysilanes into the starting formulation decreases the glass transition point of the composites both at noncatalytic curing of the epoxy resin and at catalysis of the polycondensation with all the metal acetylaceto-

Table 1. Apparent activation energy of curing of epoxy polymers and hybrid composites, calculated by the Kissinger method

Accelerator	E_a, kJ mol^{-1}	
	epoxy polymers	hybrid composites
$Fe(acac)_3$	93	96
$Co(acac)_3$	61	60
$Ni(acac)_2$	54	59
$Cr(acac)_3$	82	90
None	123	123

Table 2. Glass transition point T_g and sol fraction content of organic and hybrid polymer films

Accelerator	Glass transition point, °C	Sol fraction content, wt %
Epoxy polymers		
$Fe(acac)_3$	149	3.4
$Co(acac)_3$	138	4.7
$Ni(acac)_2$	161	4.7
$Cr(acac)_3$	174	1.8
None	175	2.2
Hybrid composites		
$Fe(acac)_3$	135	3.5
$Co(acac)_3$	121	5.2
$Ni(acac)_2$	118	4.9
$Cr(acac)_3$	144	2.9
None	138	3.5

nates studied. The plasticizing effect of polysiloxane particles in epoxy polymers prepared by cationic polymerization and anhydride curing is due to formation of topological defects in the structure of the epoxy polymer [17, 18]. In the systems under consideration, increased defectiveness of the structure of the epoxy constituent of the composites is manifested in higher yield of the sol fraction.

Table 2 shows that the sol fraction content in epoxy polymers and in hybrid composites prepared using $Cr(acac)_3$ is lower compared to the samples prepared with the other acetylacetonates. On the whole, the glass transition points and sol fraction yields for the polymers and composites prepared with different accelerators are randomly scattered. This is apparently due to the fact that the final steps of curing of the polymeric material may be accompanied by the onset of degradation processes whose influence on the sol fraction content and glass transition point may be different and may depend on particular accelerator.

We examined the effect of Fe(III), Co(III), Cr(III), and Ni(II) acetylacetonates on the rate of high-temperature oxidation of polymeric film samples in the medium of molecular oxygen. Because of the limited solubility of acetylacetonates and the negative effect of high chelate concentrations on the resistance of unmodified films to thermal oxidative degradation [19], we chose for a detailed study epoxy polymers and hybrid composites obtained at an accelerator concentration of 0.75 wt % relative to the resin.

Typical curves of oxygen uptake by polymeric films are shown in Fig. 3. The maximal oxidation rates at 200°C, taken as a criterion of the relative stability of polymers and composites to thermal oxidative degradation, are given in Table 3. We found that the oxygen uptake by hybrid composites is slightly faster than by epoxy polymers with the same content of the polymerization accelerator in the system. This can be accounted for, firstly, by the fact that the hybrid films, compared to unmodified films, contain a larger amount of the more readily oxidizable sol fraction. Secondly, the structure of the organo-inorganic composite is more defective, which facilitates the oxygen diffusion inside the film sample. It can also be seen that all the acetylacetonates except $Fe(acac)_3$ at the given concentration exert virtually no effect on the resistance of the material to high-temperature oxidation. Higher oxidation rates for the films prepared with $Fe(acac)_3$ are due to higher activity of this compound in the decomposition of hydroperoxides (with a high yield of active radicals), which leads to considerable acceleration of the radical-chain oxidation [20].

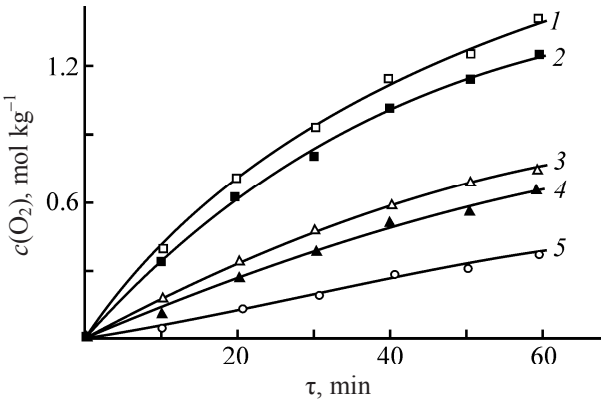


Fig. 3. Kinetic curves of oxidation of (*2*, *4*, *5*) epoxy polymers and (*1*, *3*) hybrid composites. ($c(O_2)$) Oxygen uptake and (τ) time. Accelerator: (*1*, *2*) $Fe(acac)_3$, (*3*, *4*) $Cr(acac)_3$, and (*5*) none.

As shown in [21], silica particles incorporated in epoxy polymers enhance their heat resistance as estimated from the temperatures of the onset and completion of degradation of polymer samples, temperature corresponding to maximal weight loss rate, and temperatures of 5 and 10% weight loss in the dynamic heating mode. For the systems considered in this study, we evaluated the resistance to thermal oxidative degradation by thermal gravimetric analysis (Table 4). It can be seen that introduction of all the examined acetylacetonates into unmodified epoxy–anhydride polymers decreases their heat resistance (to different extents depending on the central atom in the chelate). The less resistant to thermal oxidative degradation are the materials cured with $Fe(acac)_3$ and $Co(acac)_3$, which is due to high yield of active radicals in hydro-

Table 3. Maximal oxidation rates V_{ox} of epoxy polymers and composites

Accelerator	V_{ox}, mmol kg^{-1} s^{-1}	
	epoxy polymers	hybrid composites
$Fe(acac)_3$	0.64	0.79
$Co(acac)_3$	0.17	0.24
$Ni(acac)_2$	0.26	0.32
$Cr(acac)_3$	0.23	0.24
None	0.14	0.17

Table 4. Parameters of the heat resistance of epoxy polymers and hybrid composites, determined by derivatography[a]

Accelerator	T_{on}	T_{end}	T_5	T_{10}	T_{max}
	°C				
Epoxy polymers					
$Fe(acac)_3$	270	325	190	225	305
$Co(acac)_3$	270	325	188	220	305
$Ni(acac)_2$	272	335	205	240	320
$Cr(acac)_3$	278	340	235	250	320
None	285	352	235	264	325
Hybrid composites					
$Fe(acac)_3$	285	340	215	250	320
$Co(acac)_3$	250	325	220	242	302
$Ni(acac)_2$	275	335	220	245	315
$Cr(acac)_3$	280	348	252	274	328
None	270	345	225	248	322

[a] (T_{on}, T_{end}) Temperatures of the onset and end of degradation; (T_5, T_{10}) temperatures of 5 and 10% weight loss; (T_{max}) temperature corresponding to the maximal weight loss rate.

peroxide decomposition reactions activated by these chelates [20]. However, the use of acetylacetonates in preparation of hybrid composites allows the heat resistance to be preserved on the initial level or even enhanced. The strongest stabilizing effect is exerted by Cr(III) acetylacetonate: The temperature of 5 and 10% weight loss increases by 26–27°C.

CONCLUSIONS

(1) The examined acetylacetonates can be used as accelerators of epoxide–anhydride polycondensation in preparation of organo-inorganic composites. The apparent activation energy decreases relative to the noncatalytic process to the same extent as in curing of the unmodified polymers. The step of the hydrolytic polycondensation of ethoxysilanes and formation of a sol of polysiloxane particles exerts virtually no effect on curing of hybrid composites.

(2) At 0.75 wt % concentration of acetylacetonates relative to the resin, the high level of the heat resistance of the materials, characteristic of anhydride-cured epoxy polymers, is preserved.

(3) Among the tested catalysts for curing of epoxy–anhydride systems, the most effective is chromium(III) acetylacetonate. Epoxy polymers and hybrid composites prepared with this catalyst exhibit the best set of properties: low sol fraction content, high glass transition point, and resistance to thermal oxidative degradation.

REFERENCES

1. Zaitsev, Yu.S., Kochergin, Yu.S., Pakter, M.K., and Kucher, R.V., *Epoksidnye oligomery i kleevye kompozitsii* (Epoxy Oligomers and Adhesive Compounds), Kiev: Naukova Dumka, 1990.
2. Matejka, L., Plestil, J., and Dusek, K., *J. Non-Cryst. Solids*, 1998, vol. 226, pp. 114–121.
3. Matejka, L., Dukh, O., and Kolařik, J., *Polymer*, 2000, vol. 41, pp. 1449–1459.
4. Perminov, V.P., Modyanova, A.G., Ryabkov, Yu.I., et al., *Zh. Prikl. Khim.*, 2002, vol. 75, no. 4, pp. 650–654.
5. Mascia, L. and Tang, T., *J. Sol–Gel Sci. Technol.*, 1998, vol. 13, pp. 405–408.
6. Karkozov, V.G., Rodchenko, M.B., Nikolaev, A.F., and Emel'yanova, E.I., *Plast. Massy*, 1989, no. 1, pp. 28–29.
7. Nikolaev, A.F., Rodchenko, M.B., Karkozov, V.G., et al., *Plast. Massy*, 1989, no. 4, pp. 933–937.
8. Smith, J.D.B., *J. Appl. Polym. Sci.*, 1981, vol. 26, pp. 979–986.
9. Karkozov, V.G., Rodchenko, M.B., and Nikolaev, A.F., *Plast. Massy*, 1989, no. 1, pp. 201–203.
10. Mikhal'chuk, V.M., Kryuk, T.V., and Nikolaevskii, A.N., *Zh. Prikl. Khim.*, 1996, vol. 69, no. 6, pp. 1008–1013.
11. Mikhal'chuk, V.M., Kryuk, T.V., and Nikolaevskii, A.N., *Zh. Prikl. Khim.*, 1996, vol. 69, no. 8, pp. 1354–1358.
12. Kryuk, T.V., Mikhal'chuk, V.M., Volnyanskaya, R.I., and Nikolaevskii, A.N., *Vopr. Khim. Khim. Tekhnol.*, 2002, no. 3, pp. 73–76.
13. Kryuk, T.V., Mikhal'chuk, V.M., Volnyanskaya, R.I., and Nikolaevskii, A.N., *Ukr. Khim. Zh.*, 2002, vol. 68, no. 5, pp. 58–62.
14. Kryuk, T.V., Mikhal'chuk, V.M., Nikolaevskii, A.N., et al., *Plast. Massy*, 2001, no. 3, pp. 12–14.
15. Bershtein, V.A. and Egorov, V.M., *Differentsial'naya skaniruyushchaya kalorimetriya v fizikokhimii poli-*

merov (Differential Scanning Calorimetry in Polymer Physics and Chemistry), Leningrad: Khimiya, 1990.

16. Elegant, L., Tomi, P., Augier, G., et al., *J. Therm. Anal*., 1986, vol. 31, pp. 1351–1358.
17. Zhil'tsova, S.V., Mikhal'chuk, V.M., Petrova, E.M., et al., *Zh. Prikl. Khim*., 2007, vol. 80, no. 3, pp. 479–483.
18. Savenkova, L.A., Mikhal'chuk, V.M., Rybachenko, V.I., et al., *Vopr. Khim. Khim. Tekhnol*., 2007, no. 1, pp. 117–121.
19. Perepelitsa, A.A., Mikhal'chuk, V.M., Savina, A.A., and Zhil'tsova, S.V., *Vopr. Khim. Khim. Tekhnol*., 2007, no. 2, pp. 149–159.
20. Volnyanskaya, R.I., Mikhal'chuk, V.M., and Nikolaevskii, A.N., *Vopr. Khim. Khim. Tekhnol*., 2004, no. 1, pp. 206–209.
21. Volnyanskaya, R.I., Maneshina, L.A., and Mikhal'chuk, V.M., *Vopr. Khim. Khim. Tekhnol*., 2005, no. 5, pp. 125–129.

ISSN 1070-4272, Russian Journal of Applied Chemistry, 2008, Vol. 81, No. 11, pp. 2008–2013. © Pleiades Publishing, Ltd., 2008.
Original Russian Text © V.M. Misin, N.N. Glagolev, M.V. Misin, 2008, published in Zhurnal Prikladnoi Khimii, 2008, Vol. 81, No. 11, pp. 1893–1898.

MACROMOLECULAR COMPOUNDS AND POLYMERIC MATERIALS

Modification of Commercial Oligomers with Diphenyldiacetylene and *p*-Diethynylbenzene Polymers

V. M. Misin, N. N. Glagolev, and M. V. Misin

Emanuel' Institute of Biochemical Physics, Russian Academy of Sciences, Moscow, Russia

Received May 4, 2008

Abstract—Diphenyldiacetylene and *p*-diethynylbenzene homopolymers and copolymers exhibit high resistance to heat and thermal oxidation. Their composites with commercial oligomers were examined.

DOI: 10.1134/S107042720811027X

It is well known that substituted polyacetylenes exhibit a set of unique physicochemical properties allowing preparation on their basis of diverse materials for electronics, information recording, and catalysis [1–3]. Within the class of substituted polyacetylenes, polydiphenyldiacetylene (poly-DPD) and poly-*p*-diethynylbenzene (poly-DEB) exhibit high resistance to heat and thermal oxidative degradation [1, 4]. Furthermore, there are indications that polyconjugated polymers inhibit thermal and thermal oxidative degradation of various substances and polymeric materials [4, 5]. However, these studies dealt with samples of polyconjugated polymers that had been prepared under the conditions causing formation of defective structures of macrochains. The polymers were insoluble and contained virtually no reactive functional groups. Furthermore, the suggested procedures for preparing the polymers were difficult to implement in industry.

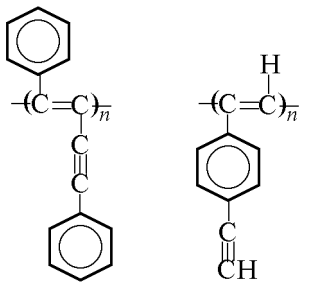
For example, in thermal polymerization of DPD in the bulk, the insoluble fraction content was as high as 61%. Macromolecules of the polymer contained both polyene and polyacene fragments [6, 7]. Polymerization of DPD in the presence of coordination initiators [6, 8, 9] led to the formation of polyenes of low molecular weight with a low conversion.

In thermal polymerization of DEB, both ethynyl groups of the monomer opened. This led to the formation of a nonmelting insoluble colored polymer of three-dimensional network structure [10]. In the presence of coordination initiators [11–16], thickly crosslinked insoluble polyphenylenes or branched oligophenylenes containing no more than 2–4 –C≡CH groups were obtained.

Later the synthesis of DPD [17] and DEB [18, 19] homopolymers and of their random copolymers [20] under mild conditions (anionic initiators, temperature lower than 60°C) allowed preparation for systematic studies of polymers in which the chains were nondefective and had proved intramolecular structure. Here we demonstrate for the first time the possibility of using these polymers for the modification of commercial oligomers of various classes.

EXPERIMENTAL

All the synthesized polyconjugated polymers were powders readily soluble in organic solvents. Thermoplastic poly-DPD and thermosetting poly-DEB had the structure of substituted polyenes. These units were also present in thermosetting random copolymers of DEB and DPD in 3 : 1 (CPL-1) and 1 : 3 (CPL-2) ratios.



Poly-DPD Poly-DEB

To prepare a carborane-containing polymer (poly-DEB-B), to a toluene solution of poly-DEB we added toluene solutions of decaborane and dimethylaniline. The reaction mixture was washed with HCl and water,

and the product was precipitated into hexane. The boron content was 20%.

Thermal gravimetric and differential thermal analyses were performed on an OD-2 derivatograph (MOM, Hungary) and a VTV-1 device (in a vacuum) with continuous heating at a rate of 5 deg min^{-1}.

When heated in air to 300°C, poly-DPD underwent virtually no changes. At 500°C, the weight loss was 18%. Above 500°C, degradation of the polymers became progressive, and at 800°C it was complete (Fig. 1).

The weight loss of poly-DEB in a vacuum was 20% at 700°C (Fig. 2). With increasing temperature, the rate of the weight loss decreased, and a significant amount of a coke residue formed. In air, poly-DEB also showed high resistance to thermal oxidation. No noticeable weight loss was observed on heating it in air to 370°C (Fig. 2a). In the DTA curve of the polymer (Fig. 2b), there was an exothermic peak at about 170°C, associated with oxidation of C≡C bonds in ethynyl groups –C≡CH. Preliminary heat treatment in a vacuum for 6 h of poly-DEB at 100 (poly-DEB-100) and 200°C (poly-DEB-200) led to a decrease and subsequent disappearance of this exothermic peak in the DTA curve. Simultaneously, in the IR spectra the vibration bands of the C≡C bonds in –C≡CH groups decreased in intensity and then disappeared.

Noticeable degradation of DPD–DEB random copolymers in air started at 350–400°C (Fig. 1). An increase in the DPD content in the copolymer led to a decrease in the extent of thermal oxidative degradation (curves *2*, *3*) owing to a decrease in the amount of readily oxidizable –C≡CH groups. The samples completely burned out at 700–750°C.

Comparison of the resistance of homo- and copolymers of DEB and DPD to thermal oxidative degradation revealed the following trend. The homopolymer poly-DEB was the least stable. With an increase in the DPD fraction in the copolymer, the resistance to thermal oxidative increased (Fig. 1), and poly-DPD appeared to be the most stable. The temperatures corresponding to 40% weight loss, $T_{40\%}$, determined from the TGA data, varied in this series of polymers from 500 to 610°C. Boron-modified poly-DEB appeared to be still more resistant to thermal oxidative degradation (Fig. 2, curve *6*). At 800°C, poly-DEB-B lost only 18% of its weight. The weight gain observed with poly-DEB-B in the range 500–600°C can be accounted for by formation of oxygen-containing boron compounds [21] and B_2O_3 [22].

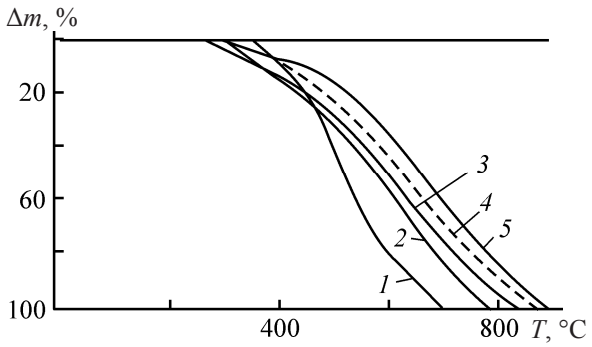


Fig. 1. TGA curves in air for DEB and DPD homo- and copolymers. (Δ*m*) Weight loss and (*T*) temperature; the same for Figs. 2 and 3. (*1*) Poly-DEB, (*2*) CPL-1, (*3*) CPL-2, (*4*) CPL-2 after vacuum thermolysis at 200°C for 6 h, and (*5*) poly-DPD.

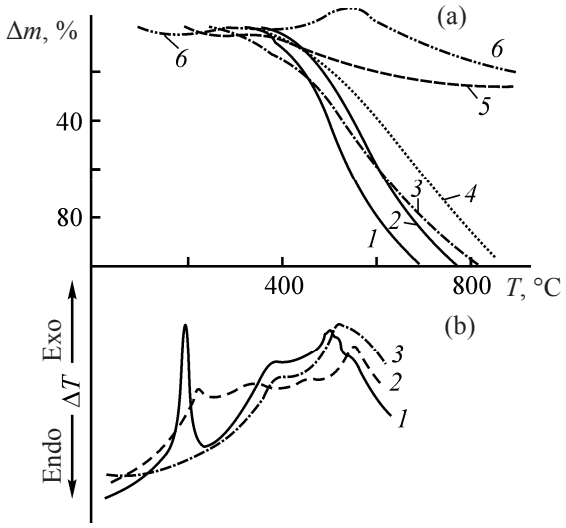


Fig. 2. (a) TGA curves (*1–4*, *6*) in air and (*5*) in a vacuum; (b) DTA curves in air. (a) (*1*) Poly-DEB, (*2*) poly-DEB-200, (*3*) CPL-2, (*4*) poly-DPD, (*5*) poly-DEB, and (*6*) poly-DEB-B; (b) (*1*) poly-DEB, (*2*) poly-DEB-100, and (*3*) poly-DEB-200.

Thus, DPD and DEB homopolymers and their copolymers exhibit high resistance to thermal and thermal oxidative degradation. Therefore, the polymers should not make a negative contribution to the degradation when used in composites with commercial oligomers.

In the production of carbon–carbon composite materials, the following procedures are used: impregnation of a fibrous carbon materials with a liquid curable resin; curing of the liquid resin to obtain a solid sam-

Table 1. Effect of additions of poly-DPD and copolymer on the yield of the pyrolyzate of EN-6 polymeric resin

Binder composition, wt %			Dry residue of binder at 250°C[a]	Yield of pyrolyzed residue[b]
DPD–DEB copolymer	poly-DPD	EN-6 resin	%	
–	–	100	96.78	29.95
10	–	90	94.21	62.80
20	–	80	92.42	55.84
30	–	70	91.23	59.61
–	10	90	94.39	44.91
–	20	80	89.41	49.66
–	30	70	93.22	50.81

[a] Heating time 2 h. [b] Pyrolysis temperature 900°C, time 10 min; the same for Table 2.

Table 2. Effect of additions of poly-DPD on the yield of the pyrolyzate of SF-010 polymeric resin

Binder composition, wt %				Dry residue of binder at 250°C	Yield of pyrolyzed residue
SF-010	furfural	*p*-TSA	poly-DPD	%	
50	50	1.0	–	66.02	49.23
45	45	0.82	10	74.39	72.41
40	40	0.72	20	72.01	66.85
35	35	0.64	30	78.43	66.49

ple; pyrolysis of the sample in the absence of oxygen, with the major fraction of the resin degrading and volatilizing and the sample becoming porous; repeated impregnation of the fibrous carbon material with a liquid resin; repetition of the impregnation–pyrolysis cycles to attain the required characteristics of the sample.

One of the main steps is pyrolysis. The larger the amount of the substance (coke residue) remaining after the pyrolysis, the smaller the number of repeated impregnation–pyrolysis cycles required. It is clear that the process is more efficient and cost-saving if the coke residue is large. Therefore, increasing the coke residue was always an important problem. To accomplish this goal, we examined the modification of widely used commercial resins.

Epoxy–novolac resin EN-6 [TU (Technical Specification) 6-05-1585–77] and novolac-type phenol–formaldehyde resin SF-010 [GOST (State Standard) 18 694–80] were modified by two procedures: in solvents (acetone, furfural) and in melts. As modifiers we used poly-DPD and DPD–DEB copolymer. The SF-010 resin was cured with *p*--toluenesulfonic acid (*p*-TSA). Then the samples of the cured modified resins were heated in a nitrogen atmosphere at various temperatures, and the amount of the remaining pyrolysis products (amount of coke residue) was determined.

Analysis of the results obtained (Tables 1, 2) showed the following: (1) introduction of 10–30 wt parts of DPD homo- and copolymer into EN-6 epoxy–novolac resin leads to the resin curing without special addition of curing agents; (2) poly-DPD is better combined with the resins in solvents with the formation of a stable composite binder; (3) introduction of 10–30 wt parts of DPD homo- and copolymer into resins increases the yield of the solid pyrolysis products by 21–33% for EN-6 resin and by 17–19% for SF-010 resin; (4) in coking of EN-6 resin, addition of the copolymer is more effective than addition of the same amount of poly-DPD; apparently; this is due to the presence in copolymer macromolecules of a large amount of reactive –C≡CH groups favoring formation of a 3D network in pyrolysis.

Thus, addition of polyconjugated polymers considerably (by 17–33%) increases the coke residue in pyrolysis of various modified commercial resins.

Table 3. Resistance of cured composite materials to thermal oxidation

Run no.	Oligoether acrylate	Content of other components, wt %				TGA data		
		poly-DEB	poly-PA	KEP-2	initiator	$T_{10\%}$	$T_{50\%}$	$T_{75\%}$
1	TGM-3	–	–	–	1.5[a]	260	350	380
2	TGM-3	6.26	–	2.0	1.5[a]	260	360	405
3	TGM-3	10.0	–	2.0	1.5[a]	280	380	430
4	TGM-3	20.0	–	2.8	1.5[a]	305	420	560
5	TGM-3	20.0	–	0.5	1.5[b]	305	420	560
6	TGM-3	20.0	–	0.5	1.5[c]	305	420	560
7	TGM-3	20.0	–	0.5	1.5[a]	305	420	560
8	TGM-3	20.0	–	0.25	1.5[a]	305	420	560
9	TGM-3	35.0	–	4.0	1.5[a]	355	485	660
10	TGM-3	45.0	–	4.0	1.5[a]	365	510	660
11	TGM-3	35.0	–	8.0	1.5[a]	335	465	630
12	OKM-2	–	–	–	1.0[a]	280	330	370
13	OKM-2	27.5	–	3.8	1.0[a]	320	420	590
14	GBK[d]	–	–	–	2.5[a]	350	410	460
15	GBK[d]	33.5	–	3.0	2.5[a]	370	575	740
16	TGM-3	–	4.7	–	1.2[a]	260	350	400
17	TGM-3	–	30.4	–	1.2[a]	260	350	400
18	TGM-3	–	30.4	4.0	1.2[a]	260	350	400
19	–	100	–	–	–	420	350	400

[a] Cumene hydroperoxide. [b] *tert*-Butyl hydroperoxide. [c] Azobis(isobutyronitrile). [d] Product of reaction of glycidyl methacrylate with boric acid.

It is known that formulations based on polyfunctional oligomeric compounds of the acrylic series exhibit poor heat resistance. Therefore, a topical problem is to enhance the heat resistance and strength of 3D polymers of various commercial oligoether acrylates at elevated temperatures. For this purpose, into the initial liquid oligoether acrylates we added 10–35 wt % poly-DEB. We also introduced oxyalkylene–organosiloxane block copolymer KEP2 as foam regulator. As references we prepared samples to which, instead of poly-DEB, we added another polyconjugated polymer, polyphenylacetylene (poly-PA), having the structure –(HC=CPh)$_n$–. It differs from the poly-DEB structure in that there are no reactive –C≡CH groups at –Ph substituents. The storage conditions and storage time for the oligoether acrylate compounds obtained were the same as for the initial oligoether acrylates. The resulting compound was cured with common radical polymerization initiators at 100–110°C. The heat resistance of the samples in air was estimated by TGA. As reference quantities in comparing the resistance of the samples to thermal oxidation we used the temperatures at which the weight loss reached 10, 50 and 75%: $T_{10\%}$, $T_{50\%}$, and $T_{75\%}$, respectively.

The results given in Fig. 3 and Table 3 allow the following conclusions: (1) addition of poly-PA does not noticeably enhance the resistance of cured TGM-3 to thermal oxidation (run nos. 16–18); (2) for all the types of oligoether acrylates studied, additions of poly-DEB in an amount of 6 wt % appreciably enhance the

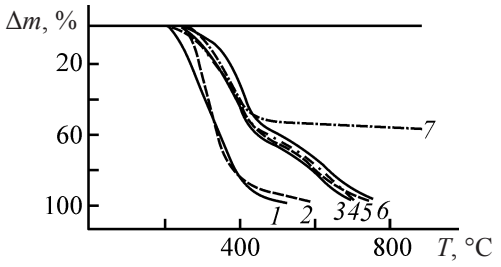


Fig. 3. DTA curves of compounds in air: (*1*) TGM-3, (*2*) OKM-2, (*3*) TGM-3 (80%) + poly-DEB (20%), (*4*) TGM-3 (64%) + poly-DEB (36%), (*5*) OKM-2 (68%) + poly-DEB (32%), (*6*) TGM-3 (68%) + poly-DEB (32%), and (*7*) TGM-3 (72%) + poly-DEB-B (28%).

Table 4. Strength properties of cured composite materials at high temperatures

Run no. in Table 3	Torque in unscrewing of screw joint, kg m, at indicated temperature, °C				
	20	150	200	250	300
1	3.0	0.38	0.12	0.10	0
2	2.9	0.6	0.19	0.12	0
3	2.7	0.92	0.38	0.18	0.05
4	3.0	1.60	0.87	0.50	0.12
5	3.0	1.62	0.87	0.50	0.12
6	3.0	1.62	0.87	0.50	0.12
7	2.5	0.94	0.25	0.38	0.06
8	2.0	0.60	0.20	0.05	0.05
9	2.5	1.25	0.58	0.63	0.25
10	2.0	0.58	0.15	0.05	0.05
11	2.5	1.25	0.58	0.63	0.25
12	3.5	0.75	0.50	0.10	0
13	2.5	0.75	0.75	0.25	0.25
14	2.5	0.75	0.25	0.30	0.12
15	2.3	0.75	0.62	0.62	0.75
16	2.5	0.30	0.10	0.05	0
17	2.4	0.25	0.10	0.05	0
18	2.4	0.90	0.20	0.65	0
19	–	–	–	–	–

heat resistance of cured oligoether acrylates in air; (3) the use of poly-DEB in an amount exceeding 35 wt % led to a considerable increase in the compound viscosity, which complicated its handling; furthermore, the strength characteristics of the cured composite materials got somewhat worse; (4) the heat resistance in air of cured oligoether acrylates increases with an increase in the amount of poly-DEB added (run nos. 3, 4, 9, 10); (5) a decrease in the sample weight loss (run nos. 2–11) relative to the reference sample (run no. 11) is the most significant at the highest temperatures: $T_{10\%}$ increased by 105°C, whereas $T_{75\%}$ increased by up to 280°C; (6) an increase in the KEP-2 content can make the resistance to thermal oxidation lower (run nos. 9, 11); (7) the type of the radical polymerization initiator does not affect the heat resistance of the cured samples (run nos. 5–7); (8) with poly-DEB-B, the weight loss by TGM-3 at 850°C was only 60%.

The compounds obtained were tested as sealants in a bolt–nut joint in simulation of high-temperature operation. For this purpose, the compounds obtained were applied to the threads, the nuts were screwed, and the compound was cured. After curing, the mean torque in unscrewing by one turn was measured. The strength tests were performed at 20, 150, 200, 250, and 300°C.

It follows from the results given in Table 4 that (1) addition of poly-PA decreases the strength characteristics of cured TGM-3 (run nos. 16–18); (2) for all the types of oligoether acrylates studied, addition of poly-DEB (10–35 wt %) enhanced the strength properties of the cured compounds; (3) an increase in the amount of poly-DEB added leads to enhancement of the strength characteristics; (4) the observed effect is more significant for TGM-3 oligomer than for OKM-2 and GBK oligomers; (5) for OKM-2 (run nos. 12, 13) and GBK (run nos. 14, 15) oligomers, no strength enhancement is observed up to 150°C, whereas at higher temperatures (200–300°C) the effect is significant.

On the whole, our results show that it is appropriate to use as modifying additive polyconjugated poly-DEB forming an additional 3D network. The modifying addition of poly-DEB enhances the resistance of all the types of oligoether acrylates studied to thermal oxidation and improves the strength properties of the cured compounds at high temperatures. Addition of poly-PA not only does not enhance the resistance of oligoether acrylate to thermal oxidation but also deteriorates the strength of the cured compounds at high temperatures.

It should be emphasized that, by varying the composition of DPD–DEB copolymers, it is possible to control their thermal oxidation resistance and thermal reactivity, and hence their modifying ability.

CONCLUSIONS

(1) Homopolymers and copolymers of phenylacetylene and *p*-diethynylbenzene exhibit high resistance to heat and thermal oxidation.

(2) The coke residue of commercial resins considerably increases upon modification of the resins with additions of polydiphenylacetylene and diphenylacetylene–*p*-diethynylbenzene copolymer.

(3) Additions of polydiethynylbenzene to oligoether acrylates enhance their resistance to thermal oxidation and the strength properties of the cured compounds at high temperatures.

(4) Polymers and copolymers of diphenyldiacetylene and *p*-diethynylbenzene can be used in industry

for improving the properties of cured polymeric materials.

REFERENCES

1. Chauser, M.G., Rodionov, Yu.M., Misin, V.M., and Cherkashin, M.I., *Usp. Khim*., 1976, vol. 45, no. 4, p. 695.
2. Misin, V.M., Kuzaev, A.I., and Misin, M.V., *Zh. Prikl. Khim*., 2006, vol. 79, no. 8, p. 1337.
3. Misin, V.M., Glagolev, N.N., and Misin, M.V., *Zh. Prikl. Khim*., 2007, vol. 80, no. 10, p. 1886.
4. Berlin, A.A. et al., *Khimiya polisopryazhennykh system* (Chemistry of Polyconjugated Systems), Moscow: Khimiya, 1972.
5. Berlin, A.A., Aseeva, R.M., Yarkina, V.P., and Kobryanskii, V.M., *Kinet. Katal*., 1970, vol. 11, p. 241.
6. Berlin, A.A., Cherkashin, M.I., Chauser, M.G., and Shifrina, R.R., *Vysokomol. Soedin., Ser. A*, 1967, vol. 9, no. 10, p. 2219.
7. Chauser, M.G., Cherkashin, M.I., Kushnerev, M.Ya., et al., *Vysokomol. Soedin., Ser. A*, 1968, vol. 10, no. 4, p. 916.
8. Teyssie, Ph. and Corn-Girard, A.C., *J. Polym. Sci*. *A*, 1964, vol. 2, p. 2849.
9. Davydov, B.E., Demidova, G.N., Nasirov, F.M., et al., *Elektrokhimiya*, 1965, no. 1, p. 876.
10. Cherkashin, M.I., Kisilitsa, P.P., and Berlin, A.A., *Izv. Akad. Nauk SSSR, Ser. Khim*., 1967, no. 11, p. 2450.
11. Sergeev, V.A., Shitikov, V.K., and Pankratov, V.A., *Usp. Khim*., 1979, vol. 48, p. 149.
12. Ermakova, V.D., Cherkashin, M.I., and Berlin, A.A., *Izv. Akad. Nauk SSSR, Ser. Khim*., 1972, no. 5, p. 1187.
13. Korshak, V.V., Sergeev, V.A., and Chernomordik, Yu.A., *Vysokomol. Soedin., Ser. B*, 1972, vol. 14, no. 12, p. 886.
14. Korshak, V.V., Sergeev, V.A., Shitikov, V.K., and Danilov, V.G., *Vysokomol. Soedin., Ser. A*, 1973, vol. 15, no. 1, p. 27.
15. Jabloner, H. and Cessna, L.C., *Am. Chem. Soc. Polym. Preprints*, 1976, vol. 17, p. 169.
16. Kirilenko, Yu.K., Plyashkevich, L.A., Perepechkina, E.P., et al., *Vysokomol. Soedin., Ser. B*, 1984, vol. 26, no. 5, p. 368.
17. Misin, V.M., Kisilitsa, P.P., Bolondaeva, N.I., and Cherkashin, M.I., *Vysokomol. Soedin., Ser. A*, 1976, vol. 18, no. 8, p. 2219.
18. Misin, V.M. and Cherkashin, M.I., *Vysokomol. Soedin., Ser. B*, 1981, vol. 23, no. 2, p. 130.
19. Glagolev, N.N., Misin, V.M., Zaichenko, N.L., and Cherkashin, M.I., *Khim. Fiz*., 1986, vol. 5, no. 7, p. 972.
20. Glagolev, N.N., Zaichenko, N.L., Kuznetsov, Yu.A., et al., *Khim. Fiz*., 1994, vol. 13, no. 11, p. 46.
21. Aksenov, K.I., Kolomiets, G.A., Golubenkova, L.I., et al., *Dokl. Akad. Nauk SSSR*, 1976, vol. 227, no. 3, p. 603.
22. Rodionov, Yu.M. and Danilov, S.I., *Dokl. Akad. Nauk SSSR*, 1986, vol. 288, no. 1, p. 143.

ISSN 1070-4272, Russian Journal of Applied Chemistry, 2008, Vol. 81, No. 11, pp. 2014–2020. © Pleiades Publishing, Ltd., 2008.
Original Russian Text © N.P. Evlampieva, M.L. Gringol'ts, I.I. Zaitseva, O.V. Okatova, T.S. Dmitrieva, P.P. Khlyabich, E.I. Ryumtsev, 2008, published in Zhurnal Prikladnoi Khimii, 2008, Vol. 81, No. 11, pp. 1899–1905.

MACROMOLECULAR COMPOUNDS AND POLYMERIC MATERIALS

Conformational Properties of Metathesis Poly(trimethylsilylnorbornene) in Solutions

N. P. Evlampieva, M. L. Gringol'ts, I. I. Zaitseva, O. V. Okatova, T. S. Dmitrieva, P. P. Khlyabich, and E. I. Ryumtsev

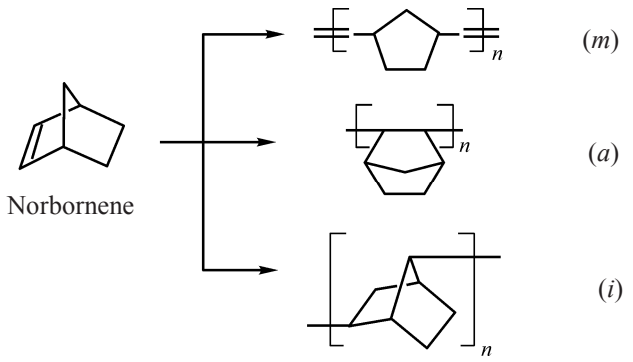
Fock Research Institute of Physics, St. Petersburg State University, St. Petersburg, Russia
Topchiev Institute of Petrochemical Synthesis, Russian Academy of Sciences, Moscow, Russia
Institute of Macromolecular Compounds, Russian Academy of Sciences, St. Peterbsurg, Russia
Research Institute of Synthetic Rubber, Federal State Unitary Enterprise, St. Petersburg, Russia

Received June 4, 2008

Abstract—The hydrodynamic and conformational properties of silicon-containing polynorbornene prepared by metathesis polymerization of 5-trimethylsilylnorbornene in the presence of Grubbs Ru carbene complex were studied by viscometry, isothermal translation diffusion, and centrifugal sedimentation. For the ten-sample homologous series of the polymer, Mark–Kuhn–Houwink relationships correlating the hydrodynamic characteristics of the molecules in toluene with their molecular weight were obtained.

DOI: 10.1134/S1070427208110281

Polymers of bicyclo[2.2.1]hept-2-ene, more commonly known as norbornene, can be prepared by various procedures, in particular, by polymerization following the metathesis (with ring opening, *m*) [1, 2] and additive [with double bond opening, *a*] [3, 4] schemes. Polymerization of norbornene by the isomerization scheme (*i*) [5, 6] is also possible:



Metathesis and additive polynorbornenes are commercial products. Both exhibit a set of practically important properties [3, 4, 7, 8]. The best studied is metathesis polymerization (the term ROMP, ring opening metathesis polymerization, is also used) of norbornenes [1, 2]. Owing to the development of highly active catalysts tolerant to functional groups: Grubbs, Schrock, Hoveyda, Grela carbine complexes [9–11], norbornenes with bulky functional groups can be successfully involved in metathesis polymerization.

It was shown recently that introduction of trimethylsilyl groups $-SiMe_3$ as side substituents into both additive and metathesis polynorbornenes substantially improves the gas-transport properties of films of these polymers compared to unmodified analogs [12, 13]. Additive poly(trimethylsilylnorbornene) (*a*-PNB-$SiMe_3$) is one of the most permeable to gases among glassy polymers. At the same time, its isomer, metathesis poly(trimethylsilylnorbornene) (*m*-PNB-$SiMe_3$), exhibits considerably lower permeability coefficients [13].



m-PNB-$SiMe_3$

In our previous study [14] we found what conformational and microstructural properties of *a*-PNB-$SiMe_3$ chains are responsible for specific morphology of films of this polymer. In this study, using hydrody-

namic methods of isothermal translation diffusion, centrifugal sedimentation, and viscometry, we examined for the first time the molecular characteristics of *m*-PNB-$SiMe_3$ and revealed its significant difference from *a*-PNB-$SiMe_3$ in molecular properties.

The specific goals of our study were as follows: (1) determination of the molecular weight (MW) of a homologous series of *m*-PNB-$SiMe_3$ samples by two independent procedures: absolute method of diffusion–sedimentation analysis [15, 16] and gel permeation chromatography [17]; (2) determination of Mark–Kuhn–Houwink relationships correlating the hydrodynamic characteristics of the macromolecules with their MW [16]; (3) determination of the equilibrium rigidity (Kuhn segment length) as a basic conformational characteristic of the polymer of a new structure; (4) simulation of *m*-PNB-$SiMe_3$ decamers by PM3 quantum-chemical semiempirical method to reveal the microstructural features of the polymer chains.

We compared the molecular conformational characteristics of silicon-substituted polynorbornenes of two types with the aim to determine why *m*-PNB-$SiMe_3$ samples are less suitable materials for gas-permeable films than their additive analogs. Our study is connected with the urgent problem of the search for new heat-resistant polymers for high-performance gas-transport membranes.

EXPERIMENTAL

In this study, the metathesis polymerization of 5-trimethylsilylnorbornene was performed for the first time in the presence of the Grubbs Ru carbene complex of the first generation, $Cl_2(PCy_3)_3Ru{=}CHPh$, which allowed variation of the molecular weight of the polymer in a wide range by varying the [Monomer]/[Cat] ratio (Table 1).The polymerization occurred at room temperature. The monomer prepared by high-temperature diene condensation of dicyclopentadiene with vinyltrimethylsilane by the procedure described in [18] was an equimolar mixture of the *exo* and *endo* isomers.

A solution of Grubbs catalyst in absolute toluene (0.04 M) was prepared in an inert atmosphere just before the polymerization. A 10-ml glass ampule equipped with a magnetic stirrer was charged under argon with a catalyst solution and with the calculated amount of the monomer. In the course of the polymerization, the solution color changed from violet to yellow-brown or pale yellow. The reaction was stopped by adding into the ampule a 3 M solution of ethyl vinyl ether in toluene, after which the oxidation inhibitor, 2,2'-methylenebis(6-*tert*-butyl-4-methylphenol), was added, and the polymer was precipitated with methanol. Then the polymer was reprecipitated from a toluene solution with methanol and vacuum-dried to constant weight. The ^{13}C NMR spectra for the sample series obtained were identical, which allowed this series to be considered as homologous. Taking into account virtually quantitative yield of the polymers, it can be concluded with confidence that they contain equal amounts of *exo*- and *endo*-monomeric units. Complex character of the spectra does not allow accurate determination of the ratio of the *cis* and *trans* double bonds. It is known, however, that polynorbornenes prepared on Ru catalysts contain, as a rule, mainly *trans* double bonds [1, 2].

Table 1. Conditions of synthesis of *m*-PNB-$SiMe_3$ samples

Sample no.	[Monomer]/[Cat], mol/mol	[Cat] × 10^4, M	Reaction time, h	Polymer yield, %
2[a]	7000	0.7	19	95
3	5000	1.6	19	92
4	3000	1.0	24	95
5	2500	3.4	0.7	98.0
6	1500	7.5	1	97.7
7	2000	3.4	0.7	99.3
8	1000	7.5	0.8	95.7
9	500	7.5	24	94.3
10	250	7.5	1	94.5

[a] Sample no. 1 was prepared under the conditions similar to those for the synthesis of sample no. 2 but with different catalytic complex; for the synthesis of sample nos. 2–10, we used the Grubbs Ru carbene complex of the same composition.

All the hydrodynamic studies of *m*-PNB-$SiMe_3$ samples were performed under similar conditions in toluene solutions at 25°C. At this temperature, the solvent had the following characteristics: density 0.863 g cm^{-3}, viscosity 0.55 cP, and refractive index 1.4945.

The viscometric measurements were performed in an Ostwald capillary viscometer with the solvent outflow time of 89.2 s. The intrinsic viscosity [η] was determined after Huggins [16] from the plot

$$[\eta] = \lim_{c \to 0}(\eta_{sp}/c), \quad (1)$$

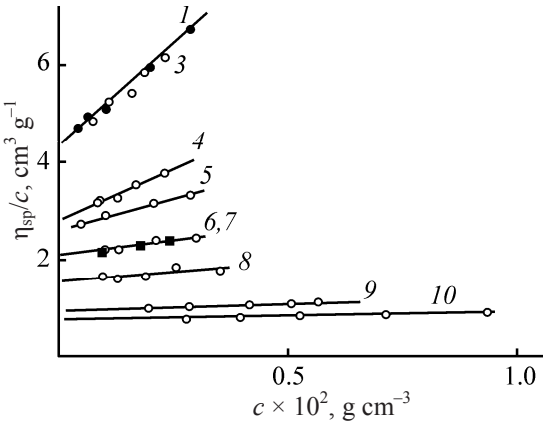


Fig. 1. Plots of η_{sp}/c vs. solution concentration c for *m*-PNB-SiMe$_3$ samples. Figures at straight lines are sample nos. in Tables 1–3.

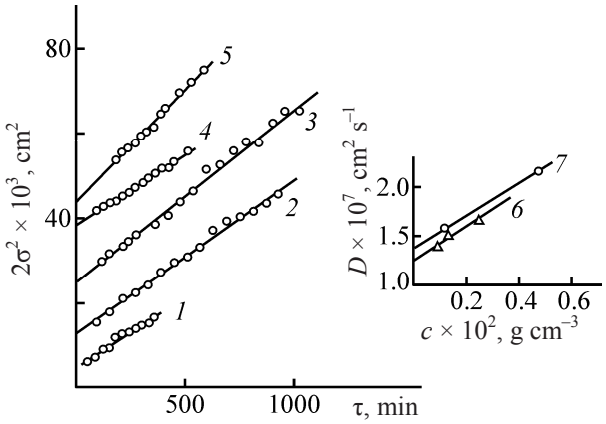
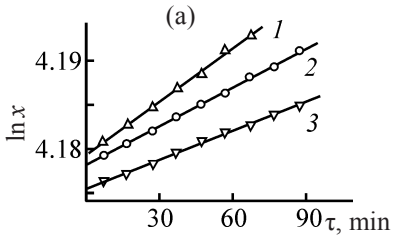


Fig. 2. Doubled variance of the diffusion curve $2\sigma^2$ as a function of time τ for sample no. 1 at solution concentrations of (*1*) 0.094, (*2*) 0.13, and (*3*) 0.248 × 10^{-2} g cm^{-3}, and for sample no. 2 at solution concentrations of (*4*) 0.0119 and (*5*) 0.475 × 10^{-2} g cm^{-3}; (*6*, *7*) concentration dependences of the diffusion coefficient *D* for sample nos. 1 and 2, respectively.



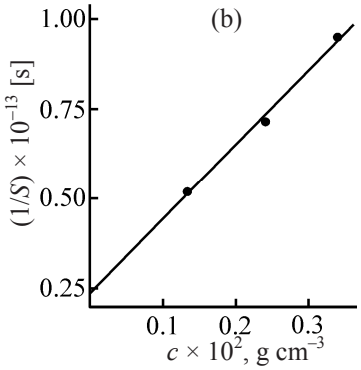


Fig. 3. (a) Logarithm of the shift of the sedimentation boundary ln x as a function of time τ at solution concentrations c of (*1*) 0.34, (*2*) 0.24, and (*3*) 0.13 × 10^{-2} g cm^{-3}; (b) the corresponding concentration dependence of the sedimentation coefficient 1/S for sample no. 4.

where $\eta_{sp} = (\eta - \eta_0)/\eta_0$ is the reduced viscosity of the solution, η and η_0 are the viscosities of the solution and solvent, and c is the polymer concentration in the solution.

For sample no. 7, we measured the temperature dependence of [η] in the range 16–35°C and determined the temperature coefficient of the viscosity $d \ln[\eta]/dT$ = 0.016. Its sign and value are typical of flexible-chain polymers [16].

The isothermal translation diffusion of polymers was studied in a Tsvetkov diffusometer [16]. The diffusion boundary was formed by layering of the solvent onto the solution and was recorded at definite intervals. The procedure is described in detail in [15, 16], and the installation parameters are given elsewhere [14].

The translation diffusion coefficients D (Fig. 2) were determined from the slope of the experimental dependences of the diffusion curve variance σ^2 on time, after which they were extrapolated to zero solution concentration c: $\lim_{c \to 0} D = D_0 + k_D c$ (Figs. 3a, 3b). For macromolecular sample nos. 1–4, we used the mean experimental value k_D = 1.75, and for the other samples in the concentration range $c[\eta] < 1$ the concentration dependence of D was not observed.

Centrifugal sedimentation of macromolecules was studied on an MOM 3180 analytical ultracentrifuge at 40 × 10^3 rpm in a two-sector cell with an artificially made concentration boundary of the layering type [15]. The ultracentrifuge was equipped with a polarization-interferometric attachment; the spar doubling value

Table 2. Hydrodynamic properties of *m*-PNB-$SiMe_3$ in toluene at 298 K

Sample no.	$[\eta] \times 10^{-2}$,[a] $cm^3\ g^{-1}$	$D_0 \times 10^7$, $cm^2\ s^{-1}$	dn/dc,[b] $cm^3\ g^{-1}$	$S_0 \times 10^{13}$, s	k_s	$M_{SD} \times 10^{-13}$, $g\ mol^{-1}$	$A_0 \times 10^{10}$ [c]
1	4.38	1.24	0.024	5.9	14.3	760	3.41
2	4.37	1.37	0.026	6.2	15.5	720	3.70
3	4.27	1.22	0.026	5.9	–	770	3.35
4	2.83	1.73	0.026	4.3	8.9	400	3.31
5	2.61	1.90	0.025	4.0	–	330	3.35
6	2.08	2.15	0.026	3.8	6.84	280	3.32
7	2.00	2.25	0.027	4.4	–	300	3.55
8	1.57	2.60	0.025	3.3	5.4	200	3.27
9	0.95	3.2	0.024	2.0	2.6	100	2.69
10	0.712	4.6	0.025	1.8	2.6	60	3.00

[a] The slopes of the experimental dependences $\eta_{sp}/c = f(c)$ [formula (1), Fig. 2] varied within 0.3–0.44.

[b] (dn/dc) Increment of the refractive index of the solution from diffusion data.

[c] Mean experimental value of the hydrodynamic invariant $A_0 = D_0(M_{SD}[\eta])^{1/3}/RT$ for the given polymer–solvent system is $(3.3 \pm 0.1) \times 10^{-10}$, which is typical of flexible-chain polymers [16].

was 0.0545 cm [15, 16]. Figure 3a shows how the logarithm of the shift of the sedimentation boundary, $\ln x$, depends on time τ for sample no. 4. From the slopes of the straight lines $\ln x = f(\tau)$, we determined the sedimentation coefficients S in the range of solution concentrations (0.18–0.55) $\times 10^{-2}$ g cm^{-3}. The sedimentation coefficients S obtained were extrapolated to zero solution concentration (Fig. 3b) in accordance with the equation $1/S = (1/S_0)(1 + k_s c)$, where S_0 is the limiting sedimentation coefficient at $c = 0$ and k_s is the concentration coefficient of the sedimentation [15, 16]. Such dependences were also obtained for the other samples, except sample nos. 3, 5, and 7, for which the coefficients S were obtained only at a single concentration and the limiting sedimentation coefficients S_0 were calculated by the above equation using k_s for sample no. 4. In the examined homologous series we revealed the dependence of k_s on MW of the polymer, which can be described by an empirical relationship $k_s = 0.965 S_0^{1.49}$.

The molecular weight of the polymers M_{SD} was determined by the Svedberg formula [15, 16]

$$M_{SD} = [RT/(1 - v\rho_0)](S_0/D_0), \quad (2)$$

where R is the universal gas constant; T, absolute temperature; $(1 - v\rho_0)$, buoyancy factor; v, specific partial volume of the polymer; and ρ_0, solvent density.

The specific partial molar volume was determined pycnometrically wth 5- and 10-ml pycnometers. The mean buoyancy factor for sample nos. 5–7 was $(1 - v\rho_0) = 0.156 \pm 0.005$.

All the hydrodynamic characteristics obtained for the examined *m*-PNB-$SiMe_3$ samples are given in Table 2.

The weight-average molecular weight M_w and polydispersity parameter M_w/M_n of *m*-PNB-$SiMe_3$ samples were determined by exclusion GPC with a Waters chromatograph equipped with styrogel columns and replaceable detection units. The sample was calibrated with polyisoprene references from the All-Russian Research Institute of Synthetic Rubber (St. Petersburg), and toluene was used as eluent. The elution rate was 1 ml min^{-1}. The GPC data for the samples studied are given in Table 3.

Decamers of *m*-PNB-$SiMe_3$ were examined by PM3 [19] semiempirical calculations using Hyperchem program [20].

As follows from the results of diffusion–sedimentation analysis (Table 2), variation of the synthesis conditions (Table 1) allowed preparation of *m*-PNB-$SiMe_3$ samples in a relatively wide (12-fold) interval of molecular weights M_{SD}, which is principally important for obtaining adequate molecular characteristics of the

Table 3. Weight-average (M_w) and number-average (M_n) molecular weights and polydispersity parameter M_w/M_n of *m*-PNB-$SiMe_3$, according to GPC data

Sample no.	$M_w \times 10^{-3}$	$M_n \times 10^{-3}$	M_w/M_n
1	813	393	2.07
2	820	404	2.03
3	779	455	1.91
5	352	204	1.71
6	329	161	2.05
9	101	55	1.79

polymer [16]. It is important that *m*-PNB-$SiMe_3$ samples, according to GPC data (Table 3), are characterized by close polydispersity parameters M_w/M_n, despite significant variations in synthesis conditions. This fact, along with spectral data, additionally confirms that the series under consideration is homologous. The mean polydispersity parameter of the samples studied is close to 2.

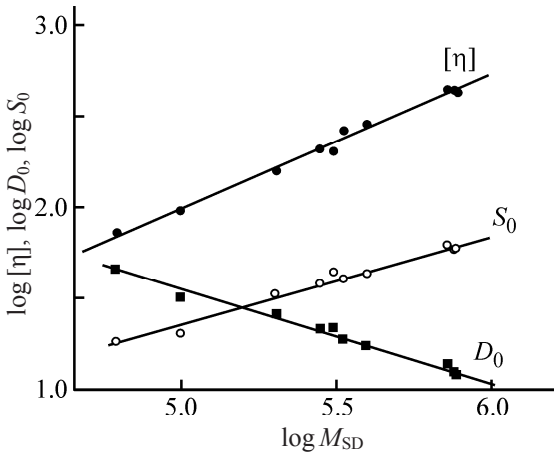


Fig. 4. Intrinsic viscosity [η] and diffusion (D_0) and sedimentation (S_0) coefficients as functoins of M_{SD} for *m*-PNB-$SiMe_3$ samples in toluene at 25°C) (log–log plots).

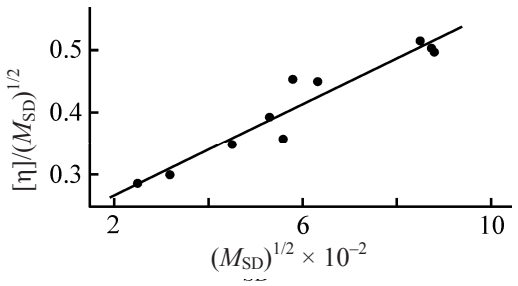


Fig. 5. Plot of [η]/$(M_{SD})^{1/2}$ vs. $(M_{SD})^{1/2}$ for the homologous series of *m*-PNB-$SiMe_3$.

Despite polydispersity, the molecular weights of *m*-PNB-$SiMe_3$ samples determined by two different methods agree with each other, as can be seen from comparison of M_{SD} (Table 2) and M_w (Table 3). This fact shows that the choice of specifically polyisoprene references for chromatograph calibration in our study was correct.

From the logarithmic plots of the intrinsic viscosity [η], D_0, and S_0 vs. M_{SD} (Fig. 4), we obtained the following Mark–Kuhn–Houwink relationships for *m*-PNB-$SiMe_3$ in toluene at 25°C:

$$[\eta] = 1.89 \times 10^{-4}(M_{SD})^{0.74\pm0.05},$$
$$D_0 = 1.11 \times 10^{-4}(M_{SD})^{-0.50\pm0.05}, \quad (3)$$
$$S_0 = 6.93 \times 10^{-16}(M_{SD})^{0.50\pm0.05}.$$

Relationships (3) are similar in the numerical coefficients and exponents to those obtained for polymers of the diene series (like polyisoprene or polybutadiene) in thermodynamically good solvents [21]. Therefore, high exponent in the equation for [η] indicates that the solvent used is thermodynamically good for *m*-PNB-$SiMe_3$ also.

In view of the latter fact, construction of the dependences $[\eta]/(M_{SD})^{1/2} = f(M_{SD})^{1/2}$, according to the Stockmayer–Fixman theory of thermodynamic properties of worm-like chains in good solvents [22], allowed us to determine the equilibrium rigidity of the *m*-PNB-$SiMe_3$ chain, $A = 21 \pm 2$ Å. This construction, in which the Kuhn segment length A is determined from the portion intercepted on the ordinate, is shown in Fig. 5. The corresponding equation of the theory [22] is given below:

$$[\eta]/M^{1/2} = \Phi_\infty(A/M_L)^{3/2} + 0.51\Phi_\infty BM^{1/2}, \quad (4)$$

where $\Phi_\infty = 2.87 \times 10^{23}$ mol^{-1} is the Flory constant for chains with strong hydrodynamic interaction, B is the numerical coefficient of the theory [22] depending on the thermodynamic quality of the solvent, A is the length of the Kuhn statistical segment, and $M_L = M_0/\lambda$ ($M_0 = 166.18$ is the molecular weight of the monomeric unit and λ is the length of its projection onto the chain propagation direction) is the molecular weight of the chain length unit, which for *m*-PNB-$SiMe_3$ at *trans* configuration of the double C=C bond and maximally stretched chain (λ = 6.2 Å) is equal to 27×10^8 g mol^{-1} cm^{-1}.

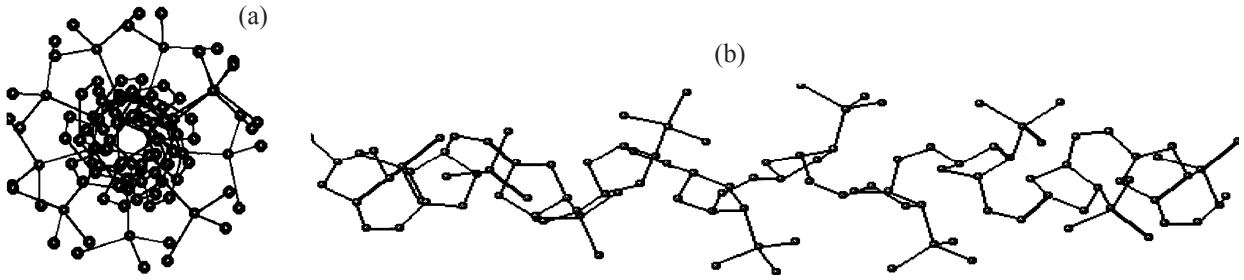


Fig. 6. PM3-optimized structure of the *exo* decamer of *m*-PNB-$SiMe_3$ containing C=C bonds in the *cis* configuration only. Projections: (a) perpendicular to $^{1}9$ axis of the helix corresponding to the conformation of the given decamer and (b) along the helix axis.

The obtained length of the Kuhn segment in *m*-PNB-$SiMe_3$ can be compared with the corresponding characteristic of the structurally related backbone of poly-2-*tert*-butylbutadiene (one double and three single C–C bonds per monomeric unit), whose equilibrium rigidity in a thermodynamically good solvent, *n*-octane, according to formula (4) is 13 Å [23]. Such comparison allows a conclusion that the presence of trimethylsilyl side substituents, which are bulkier than alkyl groups, affects the equilibrium conformational properties of chains with double C=C bonds, enhancing their rigidity. However, like poly-2-*tert*-butylbutadiene, *m*-PNB-$SiMe_3$ should be classed with typically flexible-chain polymers, as the statistical segment of these polymers contains no more than four monomeric units A/λ.

Examination of the molecular properties of *a*-PNB-$SiMe_3$ synthesized by the additive (vinyl) route of 5-trimethylsilylnorbornene polymerization, showed that the equilibrium rigidity of the chains in this polymer is considerably higher than in *m*-PNB-$SiMe_3$. The statistical Kuhn segment of *a*-PNB-$SiMe_3$ chains in toluene at 298 K is 47 Å long and consists of approximately 18 monomeric units [14]. It was also shown that the specific feature of the microstructure of *a*-PNB-$SiMe_3$ chains is their nonuniformity due to the presence of spiral fragments whose length is determined by the correlation length and hence does not exceed 47 Å. Helical segments, as the most energetically favorable, are formed and fixed in the course of *a*-PNB-$SiMe_3$ synthesis owing to steric interaction of closely located bulky trimethylsilyl groups only for regular sequences of monomeric units (e.g., head-to-tail, where the tail is the $–SiMe_3$ group). The helical fragments are randomly arranged in the chains of, on the whole, atactic *a*-PNB-$SiMe_3$, according to spectral data [13].

In the *m*-PNB-$SiMe_3$ chains, the trimethylsilyl side substituents are remote from each other, and therefore, in contrast to *a*-PNB-$SiMe_3$, they cannot cause appreciable enhancement of correlation interactions. As a result, *m*-PNB-$SiMe_3$ is two times less rigid than its additive analog.

Furthermore, as shown by quantum-chemical simulation of *m*-PNB-$SiMe_3$ decamers, helical fragments can appear only at regular repetition of the *cis* configurations of the C=C bonds (Fig. 6). With *trans* configurations only, or with alternating *trans* and *cis* configurations of C=C bonds, decamers of *m*-PNB-$SiMe_3$ take the conformation of random coils.

As the catalyst that we used for preparing *m*-PNB-$SiMe_3$ samples, according to the NMR spectra, provides incorporation of C=C bonds in the chain mainly in the *trans* configuration (~80%), it can be concluded that the microstructural nonuniformity, characteristic of the silicon-substituted additive-type polynorbornene, principally cannot be obtained in *m*-PNB-$SiMe_3$ chains. This difference in the microstructure and equilibrium rigidity of chains should lead to different morphology of *m*-PNB-$SiMe_3$ and *a*-PNB-$SiMe_3$ films and to significant difference in their gas-transport properties. Just for this reason, the gas permeability parameters given in [12] for *m*-PNB-$SiMe_3$ films are two orders of magnitude lower than those for the additive analogs.

The main conclusion following from our analysis is that the gas-transport properties of *m*-PNB-$SiMe_3$ can probably be improved by modification of the catalytic system used, with the aim to increase in the 5-trimethylsilylnorbornene polymerization product the content of C=C bonds in the *cis* configuration. The principal possibility of improving the gas-transport properties of films by this way was noted in [12, 24, 25], where other types of metathesis polymerization catalysts were used.

CONCLUSIONS

(1) With respect to hydrolytic characteristics and equilibrium rigidity of chains, the new silicon-substituted polynorbornene is a typical representative of the polydiene series.

(2) Polymerization of 5-trimethylsilylnorbornene by the metathesis route yields a more flexible (in the thermodynamic sense) polymer compared to the polynorbornene synthesized by the additive scheme. The thermodynamic equilibrium rigidity (Kuhn segment length) of the new polymer is low, about 12 ± 2 Å.

(3) Metathesis poly(trimethylsilylnorbornene) has no nanosized nonuniformities of the chain microstructure, characteristic of additive-type silicon-substituted polynorbornene, which is responsible for essential difference in the gas-transport properties of films of this polymers.

REFERENCES

1. Ivin, K.J. and Mol, J.C., *Olefin Metathesis and Metathesis Polymerization*, London: Academic, 1997.
2. *Handbook of Metathesis*, Grubbs, R.H., Ed., Weinheim: Wiley–VCH, 2003.
3. Janiak, Ch. and Lassahn, P.G., *J. Mol. Catal*., 2001, vol. 166, pp. 193–209.
4. Makovetskii, K.L., *Vysokomol. Soedin., Ser. B*, 1999, vol. 41, no. 9, pp. 1525–1543.
5. Kennedy. J.P. and Makowski, H.S., *J. Macromol. Sci. Chem*. *A*, 1967, vol. 1, pp. 345–370.
6. Gaylord, N.G., Mandal, B.M., and Martan, M., *J. Polym. Sci., Polym. Lett*., 1976, vol. 14, pp. 555–559.
7. Mol, J.C., *J. Mol. Catal. A: Chemical*, 2004, vol. 213, pp. 39–45.
8. Yamazaki, M., *J. Mol. Catal. A: Chemical*, 2004, vol. 213, pp. 81–86.
9. Buchmeiser, M.R., *Chem. Rev*., 2000, vol. 100, pp. 1565–1604.
10. Demel, S., Schoefberger, W., Slugovc, Ch., and Stelzer, F., *J. Mol. Catal*., 2003, vol. 200, pp. 11–19.
11. Schrock, R.R., *J. Mol. Catal*., 2004, vol. 213, pp. 21–30.
12. Finkelshtein, E., Bespalova, N., Portnykh, E., et al., *Polym. Sci*., 1993, vol. 35, pp. 589–593.
13. Finkelshtein, E.Sh., Makovetskii, K.L., Gringolts, M.L., et al., *Macromolecules*, 2006, vol. 39, pp. 7022–7029.
14. Evlampieva, N.P., Zaitseva, I.I., Gringol'ts, M.A., et al., *Vysokomol. Soedin*., 2008, vol. 50, no. 10, pp. 1823–1832.
15. Nefedov, P.P. and Lavrenko, P.N., *Transportnye metody v analiticheskoi khimii polimerov* (Transport Methods in Analytical Chemistry of Polymers), Leningrad: Khimiya, 1979.
16. Tsvetkov, V.N., Eskin, V.E., and Frenkel', S.Ya., *Struktura makromolekul v rastvorakh* (Structure of Macromolecules in Solutions), Moscow: Nauka, 1964.
17. Determann, H., *Gelchromatographie*, Berlin: Springer, 1967.
18. Finkelshtein, E.Sh., Makovetskii, K.L., Yampolskii, Yu.P., et al., *Macromol. Chem*., 1991, vol. 192, no. 1, p. 1.
19. Stewart, J.J.P., *J. Comp. Chem*., 1989, vol. 10, no. 2, pp. 209–220.
20. Caffery, M.L., Dobosh, P.A., and Richardson, D.M., *Laboratory Exercises Using Hyperchem*, Dainesville (USA): Hypercube, 1998.
21. *Polymer Handbook*, Brandrup, J., Immergut, E.H., and Grulke, E.A., Eds., New York: Wiley, 2003, 4th ed.
22. Stockmayer, W.H. and Fixman, M., *J. Polym. Sci. C*, 1963, no. 1, pp. 137–141.
23. Skazka, V.S., *Sedimentatsionno-diffuzionnyi analiz polimerov v rastvore* (Sedimentation–Diffusion Analysis of Polymers in Solution), Leningrad: Leningr. Gos. Univ., 1985.
24. Yampolskii, Yu., Finkelshtein, E., Makovetskii, E., et al., *J. Appl. Polym. Sci. C*, 1996, vol. 62, pp. 349–357.
25. Yampolskii, Yu., Finkelshtein, E., Makovetskii, E., et al., *J. Polym. Sci. A*, 1996, vol. 38, pp. 959–963.

ISSN 1070-4272, Russian Journal of Applied Chemistry, 2008, Vol. 81, No. 11, pp. 2021–2025. © Pleiades Publishing, Ltd., 2008.
Original Russian Text © L.U. Bazaron, S.A. Stel'makh , 2008, published in Zhurnal Prikladnoi Khimii, 2008, Vol. 81, No. 11, pp. 1906–1910.

MACROMOLECULAR COMPOUNDS AND POLYMERIC MATERIALS

Molecular-Weight Characteristics of Polyhexamethyleneguanidine Hydrochloride

L. U. Bazaron and S. A. Stel'makh

Baikal Institute of Nature Management, Siberian Branch, Russian Academy of Sciences, Ulan-Ude, Buryatia, Russia

Received November 27, 2007

Abstract—Synthesis in a hexamethylenediamine–guanidine hydrochloride melt was carried out at different monomer ratios and synthesis temperatures.

DOI: 10.1134/S1070427208110293

Polyhexamethyleneguanidine hydrochloride (PHMG) prepared by polycondensation in a hexamethylenediamine (HMDA)–guanidine hydrochloride (GHC) melt [1] is a water-soluble polymer containing amino groups, which makes it suitable as antiseptic [2], fungicide, and flocculant for removing iron from potable water [3]. Good water solubility, coupled with lack of odor and of aggressiveness towards various materials and with film formation capability, is responsible for wide application of this polymer in national economy. At the same time, the relationships in formation of the macromolecules of this polymer and its structure are poorly understood.

In this study we elucidated the conditions of formation of the PHMG macromolecules by polycondensation of bi- and trifunctional monomers and also determined the constants for the Mark–Kuhn–Houwink equation.

EXPERIMENTAL

The polycondensation reaction between bifunctional HMDA and trifunctional GHC monomers allowed changing, along with the synthesis temperature and time, the reactant ratio, from equimolar to stoichiometric. The synthesis temperature was varied from 165 to 250°C. Gembitskii et al. [4] showed that ammonia ceases to evolve 9 h after the start of the reaction, and this time was chosen as the polycondensation time. The polymers synthesized were dissolved in distilled water and filtered through a Schott filter no. 4; the resulting gel was dried in a desiccator to constant weight. The concentration of the soluble fraction of the polymer was determined by vaporization of 2 ml of the solution, followed by drying to constant weight.

Linear polymers and sol fractions of selected samples were fractionated chromatographically. To this end, we used a 1 m × 10 mm glass column packed with Sephadex-G-50. The column top was filled with 20% solution of the polymer, and the fractions were eluted with distilled water supplied until exhaustive washing of the polymer out of the column. Fractionation yielded from 10 to 15 fractions; the loss was estimated at 1.4–5%.

The intrinsic viscosities of the sol fractions were determined in a suspended-level capillary Ubbelohde viscometer [5] at the thermostat temperature of 25 ± 0.05°C**.** Because of polycationic nature, the synthesized samples exhibit the polyelectrolyte effect in viscosity measurements, i.e., a nonlinear concentration dependence of the reduced viscosity. To suppress the polyelectrolyte effect, we used NaCl solutions with different ionic strengths as solvents (Fig. 1).

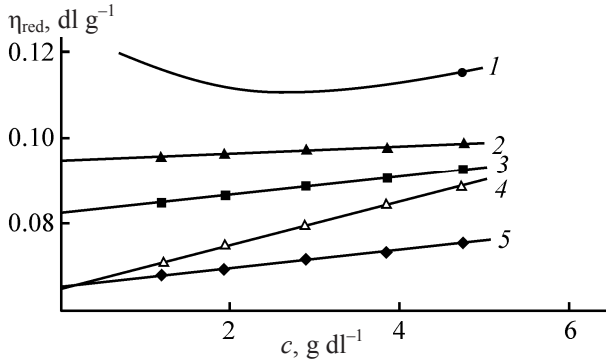
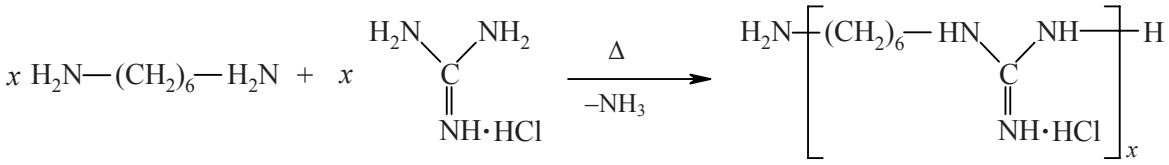


Fig. 1. Reduced viscosity $\eta_{red} = \eta_{sp}/c$, of PHMG in aqueous NaCl solutions with different ionic strengths vs. NaCl concentration c. (*1*) Pure water, (*2*) 0.2 N NaCl, (*3*) 0.3 N NaCl, (*4*) 0.4 N NaCl, and (*5*) 0.5 N NaCl.

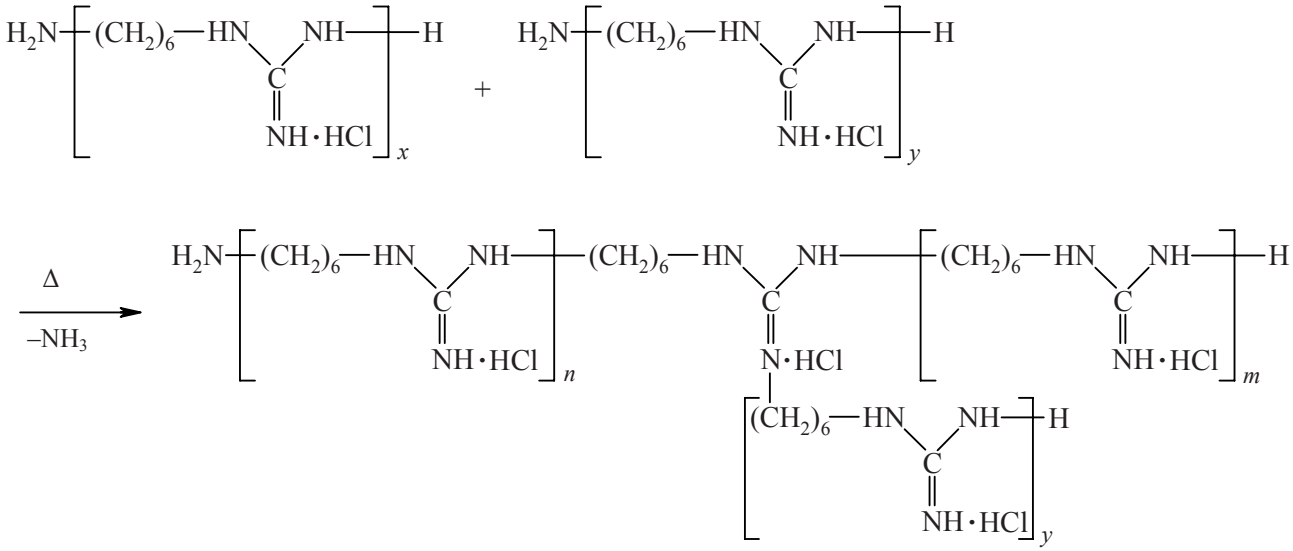
Figure 1 shows that, in 0.2 N NaCl solution, the reduced viscosity is virtually independent of the concentration; in 0.3 N NaCl solution, a positive concentration dependence is observed; and for 0.4 and 0.5 N NaCl solutions the reduced viscosities are virtually identical. In 1 N aqueous NaCl, the solution becomes turbid, which suggests precipitation of the polymer. For this reason, the solvents in our subsequent experiments were 0.3 and 0.5 N aqueous NaCl solutions, i.e., those with a minimal ionic strength at which the polyelectrolyte effect is suppressed to a sufficient extent. The viscosity was measured at concentrations within 0.5–5 g dl^{-1} for 4–6 different concentrations of the polymer in 0.3 and 0.5 N aqueous NaCl solutions. The weight-average molecular weights $\bar{M}_w$ of selected samples and selected fractions were calculated by the nonestablished equilibrium method [6] using the sedimentation data obtained in 0.3 and 0.5 N NaCl solutions on an MOM 3180 (Hungary) ultracentrifuge at a rotor temperature of 25 ± 0.1°C.

The syntheses at equimolar ratio of the reactants in argon and air at 165 ± 2°C yielded polymers with identical intrinsic viscosities, which, most likely, suggests that thermal oxidative degradation does not proceed at this temperature. The intrinsic viscosity of the polymer prepared in argon at 190°C is lower than that of the sample synthesized in air because of removal of the monomers from the argon reaction medium; for this reason, polycondensation was carried out in air. The reaction at 100°C yielded a polymer with a low intrinsic viscosity (0.029 dl g^{-1}). Therefore, we chose for our experiments the following synthesis temperatures: 165, 180, 200, and 250°C.

Formation of a linear polymer in the polycondensation reaction at the equimolar ratio of HMDA to GHC is described by the following scheme:



Since GHC is a trifunctional monomer, a branched polymer can be formed:



where $n + m + 1 = x$.

Table 1 presents the intrinsic viscosities of the linear and branched polymers, their weight-average molecular weights $\bar{M}_w$, number-average molecular weights $\bar{M}_n$, and the polydispersity index $\bar{M}_w/\bar{M}_n$. The $\bar{M}_w \times 10^{-3}$ parameters were calculated using the sedimentation data [6], and the $\bar{M}_n \times 10^{-3}$ parameters, using the mo-

Table 1. Synthesis conditions and molecular-weight characteristics of PHMG

Sample no.	GHC : HMDA	T, °C	[η], dl g^{-1}, 0.3 N NaCl	$\bar{M}_w \times 10^{-3}$	$\bar{M}_n \times 10^{-3}$	$\bar{M}_w/\bar{M}_n$	Gel content, %
1	1 : 1	165	0.042	22.8	11.4	1.9	0
2	1 : 1.05		0.050	27.7	11.8	2.1	0
3	1 : 1.10		0.056	31.4	11.7	2.5	0
4	1 : 1.125		–	–	–	–	0.30
5	1 : 1.13		0.060	–	–	–	0.72
6	1 : 1.15		0.079	91.1	–	–	33.1
7	1 : 1.20		0.064	48.5	13.8	3.6	41.1
8	1 : 1.30		0.110	–	–	–	44.9
9	1 : 1.50		0.061	56.3	–	–	44.5
10	1.05 : 1	180	0.038	17.7	9.1	1.9	0
11	1 : 1		0.054	83.1	32.1	2.8	0
12	1 : 1.05		0.054	41.0	–	–	0.43
13	1 : 1.10		0.070	95.3	–	–	5.09
14	1 : 1.15		0.066	48.1	–	–	55.7
15	1 : 1.20		0.087	–	–	–	62.1
16	1 : 1.30		0.082	66.1	–	–	50.1
17	1 : 1.50		0.042	–	–	–	66.9
18	1 : 1	200	0.061	207.7	65.4	3.7	0
19	1 : 1.03		0.154	–	–	–	0.93
20	1 : 1.05		0.150	821.0	112.9	7.3	18.0
21	1 : 1.10		0.099	182.6	–	–	60.1
22	1 : 1.15		0.060	43.1	–	–	72.2
23	1 : 1.20		0.082	–	–	–	82.9
24	1 : 1.30		0.054	–	–	–	85.0
25	1 : 1.50		–	–	–	–	90.0
26	1 : 1	250	0.142	287.7	–	–	62.6
27	1 : 1.05		0.145	1488.0	150.9	5.3	70.0
28	1 : 1.15		0.077	45.1	–	–	79.7

lecular-weight distribution curves plotted on the basis of the results of fractionation of the polymers by the technique described in [7].

Table 1 suggests that, with increasing ratio of the amounts of bifunctional to trifunctional component (HMDA/GHC = a), the intrinsic viscosities of the samples and their molecular weights tend to increase (sample nos. 1–3), and the polydispersity index also increases. An increase in temperature for sample nos. 1, 11, and 18 synthesized at equimolar ratio of the reagents (a = 1) also causes the molecular-weight characteristics to increase, which contradicts the theory of three-dimensional polycondensation proposed by Flory [8]. In the framework of this theory, the basic characteristics of the reaction products depend on the compo-

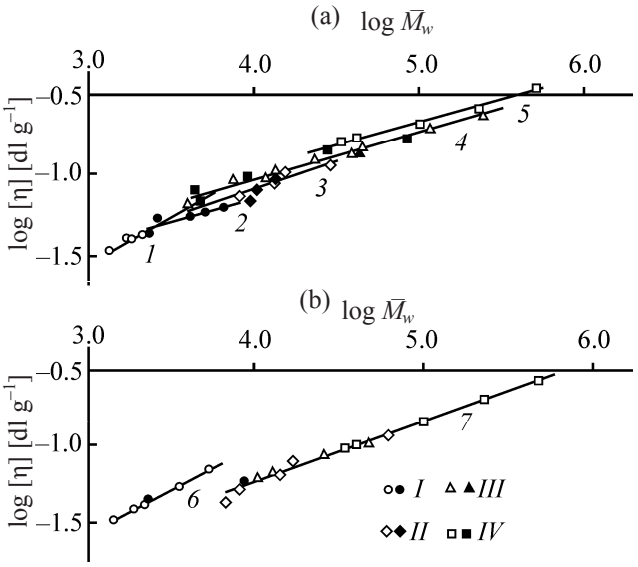


Fig 2. log–log plots for [η], vs. $\bar{M}_w$, measured in (a) 0.3 N and (b) 0.5 N aqueous NaCl solutions for the PHMG samples obtained at different temperatures and at a = 1. T, °C: (*I*) 165, (*II*) 180, (*III*) 200, and (*IV*) 250. (*1–7*) For explanations, see text.

sition only and are temperature-independent. The limiting yield of gel is also temperature-dependent. Each synthesis temperature has its corresponding limiting equilibrium amount of gel**,** which is independent of increase in the content of the bifunctional monomer. In terms of the Flory's theory, polycondensation of bi- and trifunctional monomers, taken in the stoichiometric ratio, results in 100% gelation.

The intrinsic viscosities and weight-average molecular weights of the fractions and nonfractionated polymers were used for constructing the log–log plots for the intrinsic viscosities vs. the molecular weights for two solvents, 0.3 N and 0.5 N aqueous NaCl solutions (Figs. 2a, 2b).

In Fig. 2, filled symbols correspond to the initial polymers, and hollow symbols, to the fractions of the PHMG samples. Table 2 presents the Mark–Kuhn–Houwink equation parameters corresponding to these dependences.

Figure 2 and Table 2 show that, in 0.3 N aqueous NaCl solution, the experimental points corresponding to the samples obtained at different temperatures and a = 1 fall on different straight lines (Fig. 2, straight lines *2–5*). In this solvent, the dependence of the viscosity on the molecular weight of narrow fractions tends to weaken with increasing synthesis temperature, which is typical for branched polymers. In 0.5 N NaCl, the experimental points for the PHMG samples obtained at 180, 200, and 250°C are described by a uniform dependence (Fig. 2, straight line *7*), which is not valid for the sample obtained at 165°C (Fig. 2, straight line *6*). In both solvents, the sample synthesized at 165°C (Fig. 2, straight lines *1*, *6*) exhibits an exponential dependence with the exponent lying in the range 0.5–0.8 typical for linear polymers. Thus, polycondensation of bi- and trifunctional monomers yields a linear polymer, which also contradicts the Flory theory.

Table 2. Mark–Kuhn–Houwink equation parameters for the PHMG samples, determined in aqueous NaCl solutions at four different temperatures

T, °C	a	0.3 N NaCl		0.5 N NaCl	
		$K\times10^{-3}$	α	$K\times10^{-3}$	α
165	1	0.46	0.59	0.53	0.57
180	1	2.08	0.39	1.79	0.38
200	1	4.88	0.32	1.79	0.38
250	1	8.46	0.28	1.79	0.38

CONCLUSIONS

(1) Polycondensation of hexamethylenediamine with guanidine hydrochloride in a melt at different temperatures and monomer ratios yields linear and branched polymers with different molecular weights and also cross-linked polyhexamethyleneguanidine hydrochloride samples.

(2) Polycondensation of bi- and trifunctinal monomers exhibits deviations from the Flory theory: The molecular-weight characteristics and the limiting yield of gel depend on the synthesis temperature, and the reaction gives a linear polymer.

ACKNOWLEDGMENTS

The molecular weights of the polymers were determined at the Laboratory of Physical Chemistry of Polymers, Nesmeyanov Institute of Organoelement Compounds, Russian Academy of Sciences, headed by Cand Sci. (Chem.) G.I. Timofeeva.

REFERENCES

1. Gembitskii, P.A., *Khim. Prom–st*., 1984, no. 2, p. 18.
2. Fedorova, L.S., Tsvirova, I.M., Belova, A.S., et al., *Gigiena Sanit*., 2000, no. 5, pp. 17–19.
3. Gevod, V.S., Reshetnyak, I.L., Gevod, S.V., et al., *Vopr. Khim. Khim. Tekhnol*., 2002, no. 6, pp. 161–166.
4. Gembitskii, P.A., Koryavov, Ya.I., Erusalimskii, P.M., et al., *Zh. Prikl. Khim*., 1975, vol. 48, no. 8, pp. 1833–1836.
5. Rafikov, S.R., *Vysokomol. Soedin., Ser. A*, 1959, vol. 1, no. 10, pp. 1558–1564.
6. Archibald, W.Y., *J. Appl. Phys*., 1947, vol. 18, no. 4, pp. 362–367.
7. Shatenshtein, A.I., Vyrskii, Yu.P., Pravikova, N.A., et al., *Prakticheskoe rukovodstvo po opredeleniyu molekulyarnykh vesov i molekulyarno-vesovogo raspredeleniya polimerov* (Practical Guide on Determination of Molecular Weights and Molecular-Weight Distribution of Polymers), Moscow: Khimiya, 1964.
8. Flory, P.J., *Chem. Rev*., 1947, vol. 39, no. 1, pp. 137–197.

ISSN 1070-4272, Russian Journal of Applied Chemistry, 2008, Vol. 81, No. 11, pp. 2026–2032. © Pleiades Publishing, Ltd., 2008.
Original Russian Text © S.M. Butrim, N.S. Butrim, T.D. Bil'dyukevich, T.L. Yurkshtovich, F.N. Kaputskii, 2008, published in Zhurnal Prikladnoi Khimii, 2008, Vol. 81, No. 11, pp. 1911–1917.

MACROMOLECULAR COMPOUNDS AND POLYMERIC MATERIALS

Synthesis and Physicochemical Properties of Low-Substituted Cationic Ethers of Starch

S. M. Butrim, N. S. Butrim, T. D. Bil'dyukevich, T. L. Yurkshtovich, and F. N. Kaputskii

Research Institute of Physicochemical Problems, Belarussian State University, Minsk, Belarus

Received March 27, 2008

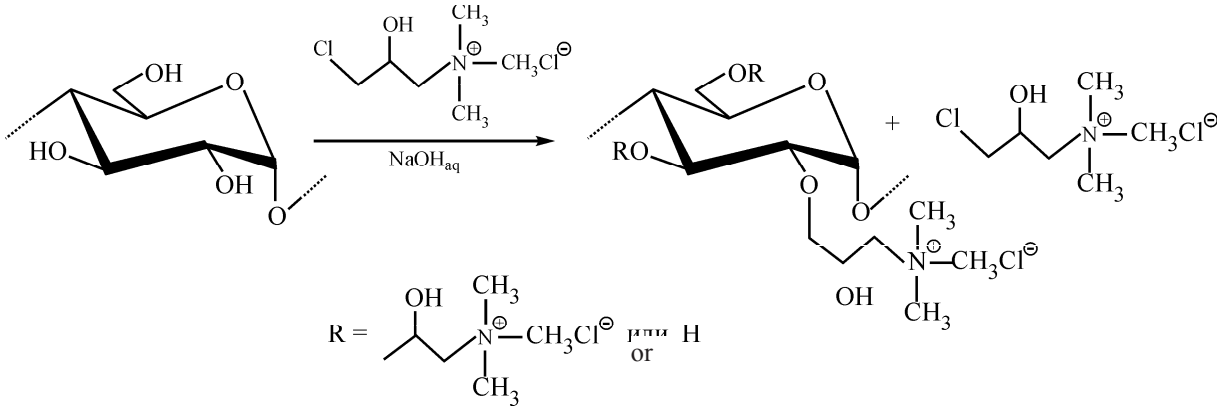
Abstract—The kinetics of the formation of cationic starch ethers under the action of 3-chloro-2-hydroxypropyltrimethylammonium chloride is studied in relation to the reactant molar ratio, temperature, and concentration of the starch suspension. Comparative data on how the content of the introduced catoinic groups depends on the origin of native starch are presented. The efficiency of starch cationization and the physicochemical properties of the synthesized samples are examined by chemical analysis, scanning electron microscopy, X-ray diffraction analysis, and thermal gravimetric analysis.

DOI: 10.1134/S107042720811030X

Starch derivatives containing cationic groups (amino, ammonium, sulfonium, phosphonium, etc.) in ether substituents are important commercial products widely used ad effective additives in pulp-and-paper, textile, cosmetic, and other industries. The most widely used are cationic starches with tertiary amino and quaternary ammonium groups in ether substituents [1], which have been efficiently used in the past decades in production of paper and cardboard to increase the retention of the fiber and filler, decrease dust formation, and enhance the surface and tearing strength of paper and its resistance to fracture [2].

Such cationic starches can be prepared by different procedures (dry, wet, extrusion), by introducing into the starch macromolecule functional groups bearing a positive charge [3–5]. The range of reagents used for this purpose is fairly wide, and the most widely used are 3-chloro-2-hydroxypropyltrimethylammonium chloride (CHPTMAC) and 2,3-epoxypropyltrimethylammonium chloride (EPTMAC).

Cationic starch ethers are prepared by the reaction of native starch (potato, corn, waxy corn, etc.) with a cationic reagent (CHPTMAC or EPTMAC) under various conditions, following the general scheme



Wet cationization procedures involve heterogeneous reactions of starch grains in a suspension and homogeneous reactions of gelatinized starch in the paste [6]. Products of these reactions should be washed and dried before use. The main requirement to the starch intended for use in paper industry is its good retention

by fiber. Depending on the degree of substitution of starch with cationic groups and its natural base, it is retained differently. As the initial substrate for cationization it is preferable to use potato starch, as it was determined experimentally that, at a degree of substitution from 0.030 to 0.040, potato starch is retained on the fiber to more than 95%, against 60% for corn starch and 50% for native starch. Cationic starch is retained and fixes adhesive particles on the fiber only at a degree of substitution higher than 0.020.

Along with these commonly used processes, there are two more methods which can be used for preparing cationic starches. For example, in the dry procedure [5], an aqueous solution of an alkali and a cationic reagent is sprayed onto starch, and then this mixture is heat-treated. The products thus obtained can be used directly, without any additional treatment.

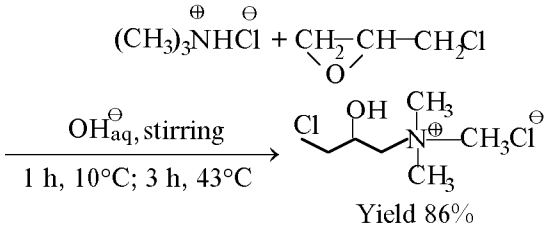
In the extrusion method, the reagent is added to a dry mixture of starch and NaOH in the course of extrusion [7, 8]. The reaction occurs under the conditions of high shear stresses and high temperatures (up to 170°C). Therefore, cationic starches prepared by this method, in contrast to other starches, are soluble in cold water, which largely facilitates manipulations with them in the course of paper and cardboard production. As in the dry procedure, extrusion cationic starches can be used directly, but in both processes the final product can contain salts, residual reagents, and by-products.

The physicochemical properties of cationic starches strongly depend on the production procedure, type of cationic groups, and degree of substitution. Variations in the properties of starches in relation to the botanical origin, cationic substituents introduced [9–12], or degree of substitution [13] are described in numerous papers. For example, Manelius et al. [9] and Vihervaara et al. [14] suggest that dry cationization of potato starch involves predominantly surface modification of the granules, whereas in wet cationization starch granules are also modified in the bulk. However, Hamunen [10] showed that the difference in the distribution of nitrogen from cationic groups in modified starches prepared by the dry and wet procedures was insignificant. Generally, in the dry procedure the native structure of starch granules strongly affects the process, in contrast to the wet procedure. In turn, the degree of crystallinity of starch was lower after dry cationization [9], but did not change noticeably after wet cationization [12, 13] compared to the crystallinity of native starch grains. Introduction of cationic groups into the structure of the polysaccharide leads to a decrease in the temperature and enthalpy of paste formation from starch granules [9, 12, 13] but increases their dispersibility and swelling [11].

In this study we examined the effect of various factors (reactant molar ratio, temperature, starch concentration in suspension, reaction time, origin of native starch) on synthesis and properties of cationic starch ethers, with 60 wt % aqueous solution of 3-chloro-2-hydroxypropyltrimethylammonium chloride synthesized by the specialy developed procedure used as cationic reagent.

EXPERIMENTAL

As investigation objects we used potato starch [GOST (State Standard) 7699–78; content, %: amylose 23.8, P 0.08, N 0.044, ash residue 0.31, moisture 12.0] and also, for comparison, corn, waxy corn, and wheat starches. All the chemicals used in this study were of chemically pure or analytically pure grade. The cationic reagent was prepared by the scheme



Yield 86%

Alkylation of starch with the cationic reagent. A 500-ml round-bottomed flask equipped with a power-driven stirrer, a dropping funnel, and a thermometer and placed on a water bath was charged with 81.0 g (0.50 mol) of starch, 200 ml of distilled water, and 25 g of NaCl (to prevent starch gelatinization in the course of the reaction). The resulting suspension was stirred at room temperature, and the required amount of a 10% aqueous NaOH solution was slowly added from a dropping funnel. In so doing, the water bath temperature was raised to the required level with continuous stirring. After that, a calculated amount of the cationic reagent was slowly added. In the course of the reaction, at definite intervals, ~10-ml samples of the suspension were withdrawn and transferred into a beaker with 200 ml of distilled water preliminarily acidified with 0.2 ml of 25% HCl. Then the precipitate of cationic starch was separated by decantation and washed on the filter with a water–isopropanol mixture (1 : 1) until the qualitative reaction for Cl^- in wash waters became negative. After that, the precipitate was washed with an additional 50-ml portion of isopropanol and dried in an oven at 50°C. The cationic starch prepared is sized in hot water. We determined by the

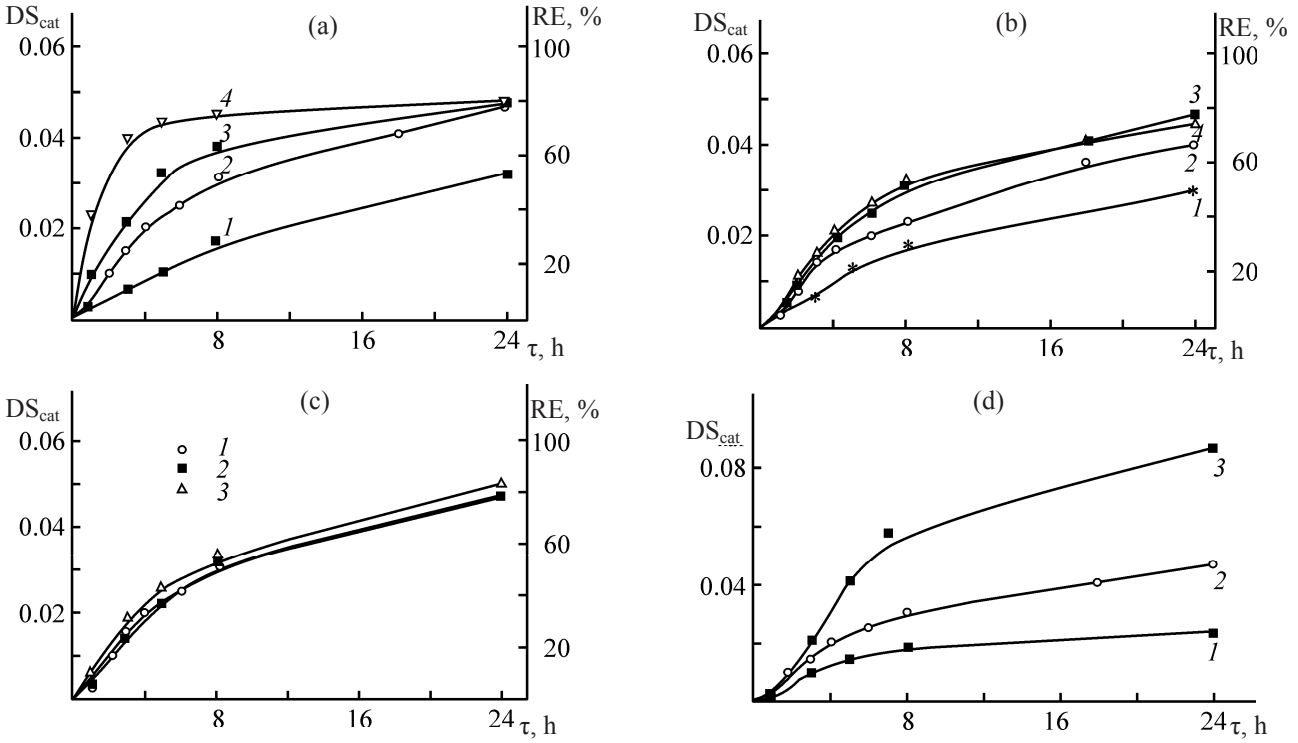


Fig. 1. Kinetic curves of cationization of potato starch. (DS_{cat}) Degree of substitution with cationic groups, (RE) reaction efficiency, and (τ) time. (a) Concentration of aqueous starch suspension 33%; molar ratios NaOH/CHPTMAC = 2.8, CHPTMAC/AGU = 0.06; temperature of reaction medium, °C: (*1*) 25, (*2*) 35, (*3*) 45, and (*4*) 55. (b) Concentration of aqueous starch suspension 33%; 35°C; molar ratio CHPTMAC/AGU = 0.06; molar ratio NaOH/CHPTMAC: (*1*) 1.6, (*2*) 2.2, (*3*) 2.8, and (*4*) 3.3. (c) 35°C: molar ratios NaOH/CHPTMAC = 2.8, CHPTMAC/AGU = 0.06; concentration of aqueous starch suspensoin, %: (*1*) 24, (*2*) 33, and (*3*) 42. (d) 35°C; concentration of aqueous starch suspension 33%; molar ratio NaOH/CHPTMAC = 2.8; molar ratio CHPTMAC/AGU: (*1*) 0.03, (*2*) 0.06, and (*3*) 0.12.

Kjeldahl method the nitrogen content N (%), and from the gain in the nitrogen content after cationization we calculated the degree of substitution DS_{cat} and the reaction efficiency RE_{cat} by the formulas

$$DS_{cat} = 162.1N_{cat}/(1401 - 151.6N_{cat}),$$

$$RE = (DS_{cat}/DS_{theor}) \times 100\%,$$

where $N_{cat} = N - N_{init}$; $DS_{theor} = n_{CHPTMAC}/n_{AGU}$; N_{cat} is the content of nitrogen introduced into starch with cationic groups (%); N, nitrogen content in cationic starch (%); N_{init}, nitrogen content in native starch (%); DS_{theor}, theoretical degree of substitution with cationic groups (2-hydroxypropyltrimethylammonium chloride groups); $n_{CHPTMAC}$, amount of CHPTMAC in the modifying agent added in the course of the reaction (mol); AGU, anhydroglucopyranose unit; and n_{AGU}, amount of starch taken for cationization (mol AGU).

The diffraction patterns were recorded with an HZG-4A X-ray diffractometer (Carl Zeiss, Jena, Germany), CuK_α radiation, Ni filter, point-by-point recording. The samples were prepared by cold pressing of the polymer in the form of monolithic round pellets 2 mm thick and 18 mm in diameter. The morphology of structural elements constituting particles of native potato starch and of the prepared samples of cationic starch was examined with an LEO 1420 scanning electron microscope (Germany). Thermal decomposition of the samples was studied on an STA 449C synchronous thermal analyzer (Netzsch, Germany) in a dynamic nitrogen atmosphere at a nitrogen feed rate of 22 cm^3 min^{-1}; heating rate 5 deg min^{-1}, sample weight 50 mg; freshly calcined aluminum oxide was used as reference.

RESULTS AND DISCUSSION

The performance of the cationic reagent was estimated by studying the kinetics of the preparation of cationic ethers of potato starch using the synthesized reagent in the temperature range 25–55°C at various molar ratios of the components and various solid-to-liquid ratios. It can be seen (Fig. 1a) that the rate of

alkylation of potato starch with 3-chloro-2-hydroxypropyltrimethylammonium chloride (main active substance in the cationic reagent) regularly increases with temperature. However, at $T > 45°C$, despite the presence of NaCl, cationization of starch leads to its gelatinization in alkaline solution, which severely complicates isolation of the final product and its washing to remove salts.

It should be noted (Fig. 1b) that, at the NaOH : CHPTMAC molar ratio in the range 2.2–3.3, the reaction rate in the initial period is essentially the same. It can also be seen that the highest rate and the highest degree of starch cationization are attained already at the NaOH/CHPTMAC molar ratio of 2.8. Hence, further increase in the amount of alkali is not appropriate. In turn, the deficiency of NaOH in the reaction mixture does not allow the desired results to be attained, even in a prolonged reaction.

We found that preparation of cationic ethers depends on the starch suspension concentration insignificantly. When this parameter was varied in the range 24–42%, at a constant stirring rate, we found no significant differences in the reaction rate and maximal degree of substitution with cationic groups (Fig. 1c).

As can be seen (Figs. 1a–1c), it is quite appropriate to use the synthesized modifying agent for preparing cationic starches, because its use allows attainment of high reaction efficiency (RE = 70–80%) which, in turn, shows that the major fraction of CHPTMAC is spent for binding with starch rather than for formation of by-products.

A strong influence on both the reaction rate and the limiting degree of substitution is exerted by the CHPTMAC/AGU molar ratio (Fig. 1d). As this ratio is increased, with the solution volume remaining constant, the CHPTMAC concentration in the solution increases. As a result, the starch alkylation rate increases. An increase in the CHPTMAC/AGU molar ratio also leads to a proportional increase in the limiting content of cationic groups in the polysaccharide.

Preliminary studies showed that introduction of a quaternary ammonium group into the anhydroglucopyranose unit of starch decreases the temperature of paste formation. Solutions prepared from modified starch are stable even at low pH values and are not prone to retrogradation, which is important for their further practical use.

Alkylation of starch with 3-chloro-2-hydroxypropyltrimethylammonium chloride in an alkaline solution

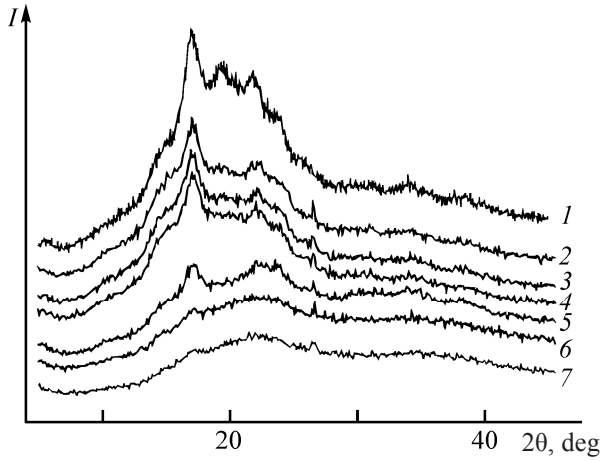


Fig. 2. Diffraction patterns of (*1*) native potato starch and (*2–7*) cationic potato starch samples differing in the cationic group content and preparation temperature. (*I*) Relative intensity and (2θ) Bragg angle. *T*, °C: (*2–5*) 35, (*6*) 45, and (*7*) 55.

can involve significant changes in the supramolecular structure of the polysaccharide, depending primarily on the process temperature. For example, the diffraction patterns shown in Fig. 2 (curves *6*, *7*) indicate that the degree of crystallinity of starch after its cationization at temperatures leading to gelatinization of starch in the reaction mixture considerably decreases, and the extent of these changes is the greater, the higher the reaction temperature. It can be seen that the main reflections characteristic of native potato starch (2θ 17.0°, 19.5°, and 22.1°) are virtually lacking in the patterns of cationic starch (Fig. 3, curves *6*, *7*) prepared at $T \geq 45°C$. As under such conditions of starch modification not only amorphous but also crystalline regions of the structure are involved in the process, the introduced 2-hydroxypropyltrimethylammonium chloride groups are, apparently, distributed fairly uniformly.

The diffraction patterns of cationic starch samples with different degrees of substitution (Fig. 2, curves *2–5*), prepared at 35°C, are characterized by the lack of the reflection at 2θ = 19.5° and the presence of well-defined peaks at about 17.0° and 22.1°. However, calculation of the relative degree of crystallinity (DC) of these cationic starches shows that DC for sample nos. 2 and 3 is higher, and for sample nos. 4 and 5, lower than that of the native starch (Table 1). Such character of changes in the degree of crystallinity of modified starch samples may be due to the fact that, in washing with a water–isopropanol mixture, the more soluble (amorphous) fraction of the modified polysaccharide remains in the filtrate. Therefore, the fraction of crystalline regions in the isolated and studied cationic

Table 1. Degrees of crystallinity (DC) of the examined samples

Sample no.	Starch sample	DC, %
1	Native potato	33.2
2	Cationic (DS_{cat} = 0.0041)	39.5
3	Cationic (DS_{cat} = 0.021)	36.5
4	Cationic (DS_{cat} = 0.047)	32.4
5	Cationic (DS_{cat} = 0.035)	28.0
6	Cationic (DS_{cat} = 0.061)	X-ray amorphous
7	Cationic (DS_{cat} = 0.045)	″

starch sometimes increases, which leads to a certain increase in DC. Also, as seen from the data obtained, by varying the cationization temperature it is possible to prepare cationic starch samples with a close content of 2-hydroxypropyltrimethyammonium chloride groups but with different degreese of crystallinity (Fig. 2, curves *4*, *7*), which can ultimately lead to differences in the physicochemical properties. The numerical values of the relative degree of crystallinity of the samples studied are given in Table 1.

As seen from Fig. 3a, granules of native potato starch are very nonuniform in the size and shape. Among them are both very small granules (d < 5 μm) of predominantly round shape and very large granules (d > 60 μm) of oval shape. The breaking effect of NaOH whose ions under definite conditions can induce the gelatinization of starch in solution is well consistent with the observed changes in the morphological structure of starch granules (Fig. 3): With an increase in the synthesis temperature, starch granules undergo more and more pronounced changes. Cavities, fractures, and folds appear in starch granules, and all these changes are enhanced with increasing temperature. For example, at 35°C, when starch cationization throughout the reaction occurs in a suspension (without gelatinization), granules of cationic starch insignificantly differ from the initial granules in the shape and size: only small cavities and surface defects are observed (Figs. 3a, 3b). At $T \geq 45$°C, in the alkaline solution, the reaction occurs under the conditions of starch gelatinization when the granules strongly swell and are destroyed. As a result, in the electron micrographs of cationic starch more significant granule defects are observed (Fig. 3c, 3d): large cavities and even through holes, as well as fine fragments of granules.

Nonisothermal thermogravimetric (TG) curves of native potato starch and three samples of cationic potato starch are shown in Fig. 4. As can be seen, introduction into starch macromolecule of 2-hydroxypropyltrimethylammonium chloride groups exerts a signifi-

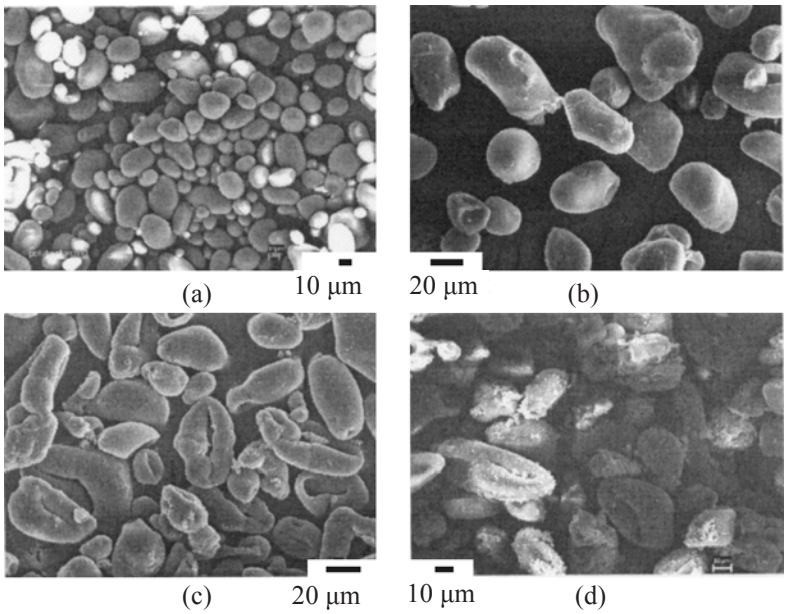


Fig. 3. Scanning electron micrographs of granules of (a) native potato starch and (b–d) cationic potato starch samples prepared at (b) 35, (c) 45, and (d) 55°C.

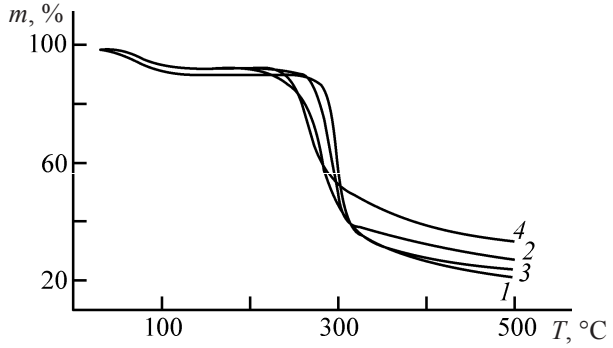


Fig. 4. TG curves of (*1*) native potato starch and (*2–4*) cationic potato starch samples prepared at various temperatures. (*m*) Sample weight and (*T*) temperature. Preparation temperature, °C: (*2*) 35 (DS_{cat} = 0.035), (*3*) 45 (DS_{cat} = 0.061), and (*4*) 55 (DS_{cat} = 0.045).

cant effect on the thermal characteristics of starch, mainly on the onset temperature and mechanism of its degradation. All the examined samples lose weight in two steps: The first step (T = 70–100°C) involves removal) of adsorbed moisture, and the second step (T = 220–287°C) involves degradation proper, with carbonization. Carbonization of all the samples of cationic starch starts at lower temperatures (Table 2) compared to native starch. As seen from Table 2, for all the cationic starches the weighed of the carbonized residue at 500°C is higher compared to the native starch, and with an increase in the content of cationic groups the carbonization temperature decreases. At the same time, the temperature at which the samples lose 50% of their weight is independent of the degree of substitution of cationic starch. Table 3 shows that the use for cationization of starches isolated from different sources allows preparation of cationic starch ethers with close degrees of substitution, i.e., the origin of native starch, other conditions being the same, affects the content of cationic groups insignificantly. The observed insignificant differences in DS_{cat} are apparently associated with differences in the molecular weight and amylose content of the initial starches.

Table 2. Quantitative characteristics of thermal degradation of starch samples[a]

Starch sample	DS_{cat}	T_{onset}	$T_{50\%}$	Residue at 500°C, %
		°C		
Potato	0	287	303	21.0
Cationic potato	0.035	267	300	26.7
	0.045	244	313	33.1
	0.061	220	292	23.1

[a] (T_{onset}, $T_{50\%}$) Temperatures of the onset of degradation (carbonization and of 50% weight loss, respectively.

Table 3. Degrees of substitution with cationic groups, obtained with various native starches. Conditions of starch cationization: 35°C, 8 h, concentration of aqueous starch suspension 33%, molar ratios NaOH/CHPTMAC = 2.8, CHPTMAC/AGU = 0.06

Initial starch	DS_{cat}
Potato	0.031
Corn	0.059
Waxy corn	0.032
Wheat	0.028

CONCLUSIONS

(1) The use of the synthesized modifying agent, 3-chloro-2-hydroxypropyltrimethylammonium chloride, allows efficient cationization of various starches.

(2) The examined conditions of starch alkylation ensure preparation of cationic starches with the preset degree of substitution (DS_{cat} = 0.01–0.06) and high reaction efficiency (RE = 80%).

(3) The structure and properties of cationic starch strongly depend on the temperature conditions of the modification of native starch.

REFERENCES

1. Solarek, D.B., *Modified Starches: Properties and Uses*, Wurzburg, O.B., Ed., Boca Raton, Florida: CRC, 1986, pp. 113–129.
2. Nachtergaele, W., *Starch/Starke*, 1989, vol. 41, pp. 27–31.
3. Radosta, S., Vorwerg, W., Ebert, A., et al., *Starch/Starke*, 2004, vol. 56, pp. 277–287.
4. Xie, F., Yu, L., Liu, H., and Chen, L., *Starch/Starke*, 2006, vol. 58, pp. 131–139.
5. Hellwing, G., Bischoff, D., and Rubo, A., *Starch/Starke*, 1992, vol. 44, pp. 69–74.
6. Ruthenberg, M.W. and Solarek, D.B., *Starch, Chemistry and Technology*, Whistler R.L., BeMiller J.N., and Paschall, E.F., Eds., San Diego, California: Academic, 1984, 2nd ed, pp. 354–364.

7. Della Valle, G., Colonna, P., and Nantes, J.T., *Starch/Starke*, 1991, vol. 43, pp. 300–307.
8. Gimmler, N. and Meuser, F., *Starch/Starke*, 1994, vol. 46, pp. 268–276.
9. Manelius, R., Buleon, A., Nurmi, K., and Bertoft, E., *Carbohydr. Res*., 2000, vol. 329, pp. 621–633.
10. Hamunen, A., *Starch/Starke*, 1995, vol. 47, pp. 215–219.
11. Liu, H., Corke, H., and Ramsden, L., *J. Agric. Food Chem*., 1999, vol. 47, pp. 2523–2528.
12. Aggarwal, P. and Dollimore, D., *Thermochim. Acta*, 1998, vol. 324, pp. 1–8.
13. Yook, C., Sosulski, F., and Bhirud, P.R., *Starch/Starke*, 1994, vol. 46, pp. 393–399.
14. Vihervaara, T., Brunn, H.H., Backman, R., and Paakkanen, M., *Starch/Starke*, 1990, vol. 42, pp. 64–68.

ISSN 1070-4272, Russian Journal of Applied Chemistry, 2008, Vol. 81, No. 11, pp. 2033–2039. © Pleiades Publishing, Ltd., 2008.
Original Russian Text © L.S. Kocheva, A.P. Karmanov, M.V. Mironov, V.A. Belyi, V.Yu. Belyaev, Yu.B. Monakov, 2008, published in Zhurnal Prikladnoi Khimii, 2008, Vol. 81, No. 11, pp. 1918–1924.

MACROMOLECULAR COMPOUNDS AND POLYMERIC MATERIALS

Straw Lignins: Hydrodynamic and Conformational Properties of the Macromolecules

L. S. Kocheva, A. P. Karmanov, M. V. Mironov, V. A. Belyi, V. Yu. Belyaev, and Yu. B. Monakov

Institute of Chemistry, Komi Scientific Center, Ural Branch, Russian Academy of Sciences, Syktyvkar, Komi Republic, Russia
Institute of Organic Chemistry, Ufa Scientific Center, Russian Academy of Sciences, Ufa, Bashkortostan, Russia

Received October 23, 2007

Abstract—The hydrodynamic and conformational properties of the macromolecules of lignins derived from *Secale sp.* rye straw and *Hordeum sp.* barley straw were examined in dimethylformamide solutions. The molecular weights, centrifugal sedimentation coefficients, translational diffusion coefficients, and intrinsic viscosities of the polymers were determined. The fractal dimensions and Mark–Kuhn–Houwink scaling indices were calculated.

DOI: 10.1134/S1070427208110311

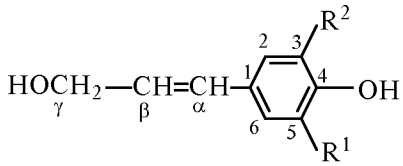
Lignins are biopolymers widely occurring in plants. As a polymer, lignin substantially differs from other macromolecular compounds, both natural and synthetic [1]. A unique feature of lignins is that their macromolecules consist of a multitude of variable microstructural units [2], which is responsible for their highly diversified topological structure. We showed earlier [3, 4] that softwood deciduous (birch, aspen) lignins can be classed with regularly branched star-shaped polymers, and the macromolecules of coniferous species (pine, larch) have a configuration corresponding to the topology of randomly branched polymers. Herbaceous lignins distinguished by extremely high species diversity received insufficient research effort, and their topological structure still remains to be elucidated.

Research activities dedicated to lignins, in particular, those of annual cereals, are urgent in view of the importance of these polymers in chemical processing of plant biomass. Specifically, the choice of technology for preparation of cellulose and other chemical products from non-woody plant materials is dictated, above all, by the structural organization and physicochemical properties of lignins.

EXPERIMENTAL

The initial plant materials were *Secale sp.* rye straw and *Hordeum sp.* barley straw (Komi Republic). Component composition of the rye straw, %: lignin 20.5, cellulose 49.0, easily hydrolyzable polysaccharides 17.4, ash 2.6. Component composition of barley straw, %: lignin 22.2, cellulose 41.3, easily hydrolyzable polysaccharides 19.5, ash 2.5. Lignin samples prepared from rye (RSL) and barley straw (BSL) were isolated by 2-h treatment with aqueous dioxane in the presence of HCl (0.7%) at the boiling temperature. The respective yields of RSL and BSL are 19 and 22% of the lignin content in the initial material (as determined by Komarov's method). Elemental composition [Hewlett–Packard analyzer (USA)]: RSL, C 58.7, H 5.5, O 35.8%; BSL, C 60.5, H 5.6, O 33.9 %. Content of methoxy groups, %: RSL 15.8, BSL 15.7. Averaged empirical formula (C_9 formula) of the monomer unit in the samples: RSL $C_9H_{10.3}O_{3.6}(OCH_3)_{1.05}$, BSL $C_9H_{10.0}O_{3.2}(OCH_3)_{1.01}$. Major absorption bands in the IR absorption spectra (Specord M-80), cm^{-1}: 3440, 1720, 1610, 1520, 1470, 1430, 1365, 1335, 1270, 1130, 1035, 840.

The macromolecules of both lignins are composed of phenylpropanoid units (PPUs) of three basic types: guaiacyl (G), syringyl (S) and *p*-coumaryl (H), linked to one another by various types of intermonomer bonds (β-O-4, α-O-4, γ-O-α, β-β, 5-5, β-5):



where R^1 = H, R^2 = H is *p*-coumaryl alcohol (H-unit); R^1 = H, R^2 = OCH_3, coniferyl alcohol (G-unit); and R^1 = OCH_3, R^2 = OCH_3, sinapyl alcohol (S-unit).

Chemical shifts of the characteristic resonance signals in the carbon spectra (^{13}C NMR, Bruker AM-300 spectrometer), ppm: G-PPE, 119.1 (C^6); S-PPE, 152.1–152.4 (C^3, C^6); H-PPE 131.4–131.5 (C^2, C^6), 160.1 (C^4).

The lignins were subjected to fractional precipitation in dioxane–benzene system. The unaccounted loss in fractionation was no larger than 5–7 %. Each fraction, as well as the nonfractionated sample, was examined by the molecular hydrodynamics method with DMF as solvent. The measurements were carried out at 298 K; η_0 0.78×10^{-2} Pa, ρ_0 0.9473 g cm^{-3}. The $\Delta n/\Delta c$ parameters for the BSL and RSL samples in DMF were estimated at 0.14–0.02.

The diffusion coefficients *D* were determined on an MOM-3180 analytical ultracentrifuge. We used the dependence of the dispersion of the concentration boundary in a two-sector polyamide cell in which an artificial boundary was formed (insert height in the beam propagation direction 12 mm). The solution–solvent boundary was recorded using standard Philpot–Svensson optical unit at the phase-contrast plate angle of 30°, rotor rotation rate of 5×10^3 rpm, and temperature of 298 K. The dispersion was calculated by the standard maximal ordinate and area method using the equation $\Delta^2 = 0.5(S/H_{max})^2\pi^{-1} = 2Dt$. The corresponding diffusion coefficients were calculated by the formula $D = (S/H_{max})^2/4\pi t$, where *S* and H_{max} are the area and the maximal ordinate of the diffusion profile, respectively. The concentration of the solutions was ca. 3×10^{-3} g cm^{-3}. We neglected the concentration dependence of the coefficients *D* in view of the dilution criterion $c[\eta] \le 1$.

The centrifugal sedimentation coefficients *S* were measured on an MOM-3180 ultracentrifuge in a two-sector polyamide cell in which an artificial boundary was formed at 48 000 rpm. The insert height was 12 mm, experiment time 50 min, and temperature 298 K. The measurements were carried out at one concentration of solutions, 3×10^{-3} g cm^{-3}. We neglected the concentration dependence of the sedimentation coefficient in view of the Debye criterion $c[\eta] \le 1$. The sedimentation coefficients were calculated by the formula

$$S = (\Delta \ln x/\Delta t)\omega,$$

where $\omega = 2\pi n$, ω is the angular rotation rate, rad s^{-1}, of rotor; *n*, centrifuge rotor rotation rate (rpm); and *x*, coordinate of the sedimentation boundary maximum.

The viscosity of the solutions was measured by the classical method in an Ostwald capillary viscometer with the solvent outflow time of 52.0 s at 298 K. The concentration of the solutions was varied within 0.02–0.08 g cm^{-3}, for which range the $c[\eta] \le 1$ and $\eta_{rel} > 1.1$ inequalities are valid. The intrinsic viscosity $[\eta]$ was calculated by the standard technique using the Huggins equation, corrected for the density of the solutions: $[\eta] = [\eta]_{meas}/\rho_0$, as substantiated by Pavlov et al. [5]. The relative error in determination of $[\eta]$ is ca. 1%.

The hydrodynamic examination of dilute solutions of lignins allows determination of the macromolecular characteristics, in particular, the molecule size, molecular weight (MW), scaling parameters, and fractal dimensions. By analogy to chemical criteria taken for lignin, Karmanov [6] introduced the macromolecular criteria according to which the basic characteristics of woody lignins as polymers include: (1) compactness of the macromolecules, responsible for their high diffusion mobility in solutions; (2) abnormally low intrinsic viscosity under normal conditions, which tends to further decrease under heating of solutions (negative temperature coefficient for $[\eta]$); (3) variability of the hydrodynamic invariants, depending on the nature and background of lignins; (4) high values and complex (random) pattern of variation of the Huggins coefficients with MW; and (5) ranking of fractal and other scaling parameters of lignins depending on the botanical origin of the plant species.

Our experimental results suggest that these criteria are also valid for nonwoody lignins of cereals, rye and barley.

The quantity M_{SD} was calculated using the experimental data for each of the lignin fractions analyzed:

$$M_{SD} = S_0RT(1 - \bar{v}\rho_0)D_0,$$

where $(1 - \bar{v}\rho_0)$ is the Archimedes buoyancy factor for the polymer–solvent system, which was estimated pycnometrically at 0.3380 and 0.3315 for RSL–DMF and BSL–DMF systems, respectively.

By contrast to high-molecular-weight fractions, for which the MW was determined with the use of Svedberg relationship, for low-molecular-weight fractions we used the equation

$$M_{D\eta} = A_0^3([D]^3[\eta])^{-1},$$

where $[D] = \eta_0 D_0/T$, and A_0 is hydrodynamic invariant estimated from the data obtained in examination of the

Table 1. Hydrodynamic and fractal parameters of RSL and BSL lignins

Fraction no.	[η], $cm^3\ g^{-1}$	$D \times 10^7$, $cm^2\ s^{-1}$	$S \times 10^3$, s	$M_{SD} \times 10^{-3}$	$M_{D\eta} \times 10^{-3}$	$A_0 \times 10^{10}$, $erg\ K^{-1}\ mol^{-1/3}$	k_H	d_f
Rye straw lignin								
1	9.5	8.9	2.9	23.9	25.4	3.1	1.08	1.81
2	8.4	10.1	2.8	20.3	19.6	3.2	1.25	1.79
3	7.3	10.9	2.65	17.8	18.0	3.1	1.00	1.79
4	6.4	12.4	2.4	14.2	13.9	3.1	1.21	1.77
5	6.0	13.3	2.3	12.7	12.0	3.2	1.13	1.75
6	5.5	13.9	2.1	11.1	11.5	3.1	1.07	1.75
7	5.3	14.7	–	–	10.1	–	1.20	1.74
8	5.2	15.2	–	–	9.3	–	1.04	1.72
9	4.5	16.6	–	–	8.2	–	0.99	1.73
10[a]	7.1	11.3	–	–	16.6	–	1.06	1.78
Barley straw lignin								
1	8.2	10.2	2.6	19.1	20.6	3.1	0.74	1.81
2	7.6	11.2	2.5	16.7	16.8	3.2	1.11	1.79
3	6.9	12.0	2.4	15.0	15.0	3.2	1.04	1.78
4	6.5	12.9	2.3	13.3	12.8	3.2	0.87	1.77
5	5.9	13.8	2.15	11.6	11.6	3.2	1.06	1.76
6	5.3	15.0	2.1	10.5	10.0	3.2	1.20	1.75
7	5.0	15.9	–	–	8.9	–	1.28	1.74
8	4.5	16.8	–	–	8.4	–	1.53	1.73
9	4.0	18.2	–	–	7.4	–	1.38	1.72
10[a]	6.8	12.3	–	–	14.1	–	0.83	1.78

[a] Nonfractionated sample.

high-molecular-weight fractions by sedimentation–diffusion analysis, $A_0 = (R[S][D]^2[\eta])^{1/3}$, $[S] = S\eta_0/(1 - \bar{\nu}\rho_0)$.

Table 1 lists the molecular weights and hydrodynamic parameters for the fractions. The molecular weight of the fractions of the examined lignins varies within $(7–25) \times 10^3$. Published data [3–6] suggest that, for dioxane lignins, the typical scaling region is $(3–5) \times 10^3$ to 30×10^3. The upper limiting value of the molecular weight is associated with the specific conditions of lignin biosynthesis in cellular shells of the plants. The low-molecular-weight fractions [MW lower than $\sim(3–5) \times 10^3$] usually are not used for conformational analysis, since a decrease in the molecular weight down to the indicated values is accompanied by escape from the scaling region, more correctly, by changing to the area where there can exist other scaling parameters. The reason is a finite value of the thermodynamic flexibility of real macromolecules.

It should be emphasized that the size and MW of the molecules of lignins derived from annual cereals RSL and BSL are comparable with those of lignins from perennial, in particular, woody plants. The macromolecules of all lignins (at least, those we examined) have fairly small hydrodynamic dimensions in any solvent known for lignin. In dilute solutions they are distinguished by small values of the translational friction coefficients, which is responsible for high values of the experimentally determined diffusion coefficients. As shown by analysis of the hydrodynamic data, the examined lignins are characterized by fairly high density of the macromolecular coils, measurable with the so-called globularity. For the RSL and BSL samples, the globularity was estimated at 20% and over, whereas

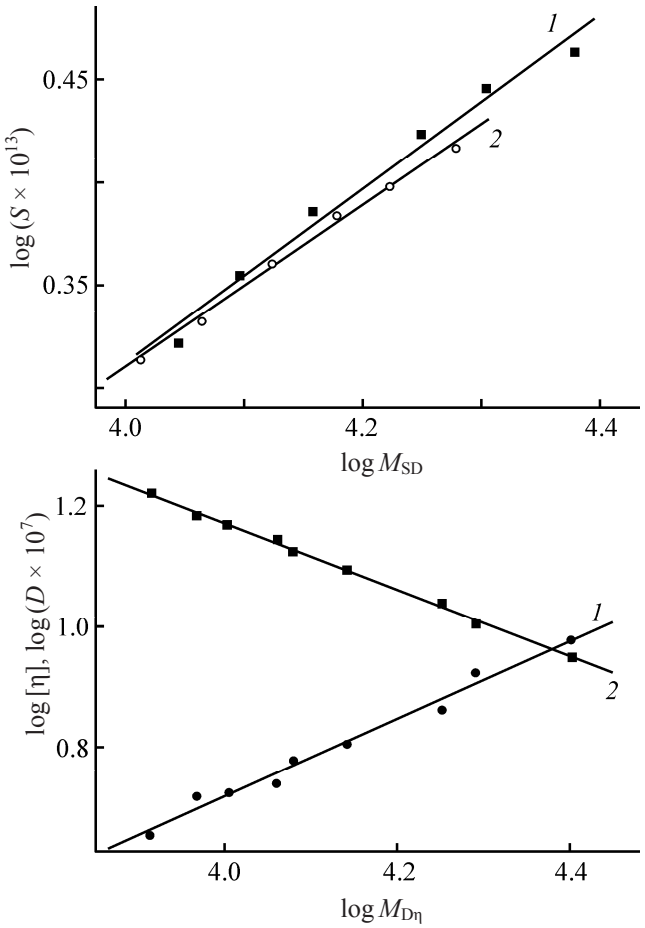


Fig. 1. Sedimentation coefficient S vs. M_{SD}, translational diffusion coefficient D vs. $M_{D\eta}$, and intrinsic viscosity [η] vs. $M_{D\eta}$ for (*1*) RSL and (*2*) BSL samples. Solvent DMF.

for typical linear flexible-chain polymers it is usually less than 10%. Another measure of compactness of the macromolecules can be found in the coefficient $q = 0.4[\eta_0]/\overline{\nu}$ [7]. The calculated q values for the RSL and BSL samples are 4.2 ± 1.5 and 3.8 ± 1.5, respectively. Synthetic linear polymers are characterized by much higher q values.

The validity of the scaling principle in the case of interest suggests the topological uniformity of the polymers, both synthetic and natural. The fact that the plots constructed in the coordinates of the Mark–Kuhn–Houwink (M–K–H) equation for lignin–DMF system are linear (Fig. 1) suggests the molecular-weight scaling of the hydrodynamic parameters for the RSL and BSL samples, which implies scale invariance of the macromolecules. The dependences for S, D, and [η] on M_{SD} can be approximated by power law equations of the M–K–H type:

$$[\eta] = K_\eta M^a,\ S = K_S M^c,\ D = K_D M^b.$$

Table 2 lists the values of scaling M–K–H indices and their corresponding K_D, K_S, K_η coefficients. In connection with analysis of the scaling indices we will note that the $|b| = (a + 1)/3 = 1 - c$ relationship is valid, which suggests that our calculations are correct and that hydrodynamic dimensions estimated from the rotational and translational friction effects reasonably agree. The values of the M–K–H parameters for RSL and BSL correspond to those of linear polymers in the conformation of a swollen nonpercolating coil**.** It should also be mentioned that these indices decrease in the following order: $a > |b| > c$, which corresponds to the trend in variation of the sensitivity of the corresponding hydrodynamic parameters to the change in the MW, typical for linear polymers.

Comparison of the values of scaling indices, in particular, of parameter a, for lignins of different origins is of interest. Certainly, it cannot but depend on the thermodynamic quality of the solvent. However, most of studies concerned with the hydrodynamic properties of lignins were carried out for systems with thermodynamically good solvents, DMF or DMSO. Karmanov [6] estimated this parameter at 0.15–0.30 and 0.5–0.65 for coniferous and deciduous lignins, respectively; for herbaceous lignins $a \geq 0.7$. For the herbaceous lignins that we examined, the index a was estimated at 0.71 ± 0.04 and 0.72 ± 0.03 for the RSL and BSL samples, respectively.

Various polymers can be characterized and compared with one another using the Tsvetkov–Klenin parameter A_0 [8], which is an invariant reflecting the probability of self-similar behavior for fractions with different molecular weights both in good solvents and θ-solvents. The differences in the A_0 values can depend

Table 2. Conformational parameters of RSL and BSL lignins

Lignin	a	c	b	K_η, cm^3 g^{-1}	K_S, s	K_D, cm^2 s^{-1}	K_θ, cm^3 g^{-1}	d_f
RSL	0.71 ± 0.04	0.42 ± 0.03	–0.58 ± 0.03	7.6×10^{-3}	4.4×10^{-15}	3.2×10^{-4}	0.25×10^{-1}	1.76/1.72
BSL	0.72 ± 0.03	0.37 ± 0.02	–0.63 ± 0.02	7.2×10^{-3}	6.6×10^{-15}	4.9×10^{-4}	0.35×10^{-1}	1.77/1.64

on the thermodynamic flexibility of the chain and, probably, should be governed by the specific features of the topological structure (all other conditions being the same). For RSL and BSL samples, this parameter was estimated at $(3.1–3.2) \times 10^{-10}$ erg K^{-1} $mol^{-1/3}$, which coincides with the available published data for A_0 in synthetic linear polymers with flexible chains. Rigid-chain polymers are characterized by higher average values of the Tsvetkov–Klenin invariant, $(3.6 \pm 0.4) \times 10^{-10}$ erg K^{-1} $mol^{-1/3}$.

By contrast to typical polymers, for lignins the invariant A_0 varies with the lignin type. The available data suggest that the parameter A_0 takes the smallest value of $\sim 2.7 \times 10^{-10}$ erg K^{-1} $mol^{-1/3}$ in the case of guaiacyl–syringyl lignin (deciduous woody species); for guaiacyl (coniferous) lignins $A_0 = (2.9–3.0) \times 10^{-10}$, and for lignins of annual plants, $A_0 \sim 3.2 \times 10^{-10}$ erg K^{-1} $mol^{-1/3}$.

A characteristic feature of lignin–solvent polymeric systems is that the Huggins coefficient k_H for them takes fairly high values, irrespective of the nature of lignin, the extraction method, and the chosen solvent. In the low-molecular-weight region, k_H randomly varies in changing from one fraction to another, typically within 1–5. Table 1 suggests that, for the BSL–DMF system, the Huggins coefficient varies within a narrow range 0.74–1.53, which, however, lies well beyond the measurement error; it is impossible to reveal any trend in variation of k_H with the MW. For the LSR–DMF system, k_H varies within 1–1.25. Of principal importance are the fractal dimensions for individual fractions of lignins, determined by the method proposed by Kozlov et al. [9], which relies on the Huggins coefficient values. Table 1 suggests that the fractal dimensions of all the fractions are virtually identical (1.76 ± 0.05) and coincide with the d_f parameter calculated with the use of the M–K–H scaling indices (Table 2). At the same time, the k_H values for fraction nos. 1 and 8 differ more than twofold. This suggests that, in the case of interest, the Huggins coefficients were reliably estimated, although it is known that the k_H values for linear polymers in good solvents typically do not exceed 0.2–0.3.

This casts doubts on the validity of a simple linear structure of the RSL and BSL lignin macromolecules, as suggested by analysis of the M–K–H scaling indices and fractal dimension d_f (Table 1). In this context, estimation of the so-called *g*-factor can be attempted. For natural polymers with complex topological and chemical structures, for which it is difficult or impossible to find a linear analog of the polymer examined, a calculation procedure was developed for estimating the *g*-factor, including the calculation of the intrinsic viscosity of a hypothetical linear macromolecule in terms of the Stockmayer–Fixman equation. By this method, the viscosity of a linear chain can be calculated by the equation

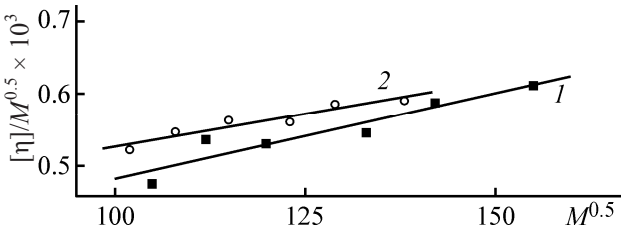


Fig. 2. Stockmayer–Fixman plot for (*1*) RSL and (*2*) BSL samples in DMF.

$$[\eta]_{lin} = K_\theta M^a,$$

where K_θ is a parameter estimated by extrapolation of the experimental data plotted in the $[\eta]/M^{0.5}$ vs. $M^{0.5}$ coordinates, and a, experimentally established M–K–H viscometric index in the solvent used.

The $[\eta]_{exp}/[\eta]_{lin}$ ratio, commonly called the g_η-factor, gives an idea of the average number of the branching sites per macromolecule. For any type of branched polymers, the g_η-factor is less than unity, and its dependence on the MW is determined by that of the number of the branching sites on MW. As shown earlier [10], with increasing MW of the fractions of randomly branched polymers the *g*-factor tends to decrease according to a certain law (provided that the configuration parameters remain unchanged), which is associated with an increase in the number of branching sites per macromolecule. For coniferous lignins, specifically this law is valid [11]. For the guaiacyl–syringyl lignins, derived from birch, aspen, white acacia, and apple-tree wood, $[\eta]_{exp}/[\eta]_{lin}$ = const; specifically, this ratio was estimated at 0.7–0.8. This allowed a presumption that the macromolecules of the abovementioned lignins are compact star-shaped structures whose hydrodynamic behavior is governed by the linear topology of the branches, no larger than 4 in number [12].

Figure 2 presents the experimental data for the examined samples, plotted in the Stockmayer–Fixman equation coordinates, which suggest $K_\theta^{RSL} = 0.25 \times 10^{-1}$ and $K_\theta^{BSL} = 0.35 \times 10^{-1}$ cm^3 g^{-1}. Using the K_θ values obtained, as well as the values of scaling index a and the molecular weight of the fractions, we determined the $[\eta]_{lin}$ values and further the desired *g*-factor values.

The calculations showed that the *g*-factors for the BSR fractions are virtually identical, 0.26; for the RSL sample the *g*-factor slightly increases with increasing MW, from 0.28 to 0.32. Our data, first, can serve as an argument in favor of branching of the RSL and BSL macromolecules, since otherwise the *g*-factor would be equal to unity; second, they allow the random (chaotic) nature of branching of the macromolecules to be unequivocally rejected, since in that case the g_η-factor should asymptotically decrease. Also, it is impossible to attribute the RSL and BSL macromolecules to comb-shaped or ladder regularly branched polymers. Based on the elimination method, we can choose the dendrimeric or star-shaped topology of the macromolecules. Indeed, certain hydrodynamic properties of dendrimers resemble those of lignins, in particular, a fairly low viscosity and the observed values of the Huggins coefficient, but the actual values of the scaling indices (Table 2) make us to reject this presumption.

As a working hypothesis we also can take a star-shaped structure of the RSL and BSL macromolecules. Actually, a number of features characteristic for star-shaped topology can be observed in our case [13], namely, the Mark–Kuhn–Houwink scaling indices typical both for linear and star-shaped polymers and compactness of the macromolecules, probably associated with the occurrence of the branching sites. It should be noted that, for single-center star-shaped macromolecules, the *g*-factor does not decrease with increasing MW and, on the contrary, should tend to increase, since the number of the branching sites remains unchanged and the degree of branching tends to decrease. If the MW of the fractions varies within a narrow range, we can expect for the *g*-factor either invariance or a weak tendency for increase, as is the case. Nevertheless, it would be premature to draw final conclusions. The analysis of the hydrodynamic behavior of real star-shaped polymers and model stars allows, as shown by Lavrenko and Vinogradova [14], estimation of the number of branches in the macromolecules. The results of calculations using the viscometric data and the estimated values of the *g*-factor allow estimation of the number of branches in the RSL macromolecules at 16, and that in BSL macromolecules, at 17. Taking into account the molecular weight of the examined lignins, we should recognize that the values obtained are unrealistically high. Thus, the presumption concerning a star-shaped structure requires sounder argumentation than that provided in this study.

Analysis of the whole set of our experimental data make us to once again resort to the concept of the linear structure of the chains, whose validity is naturally proven by the values of the scaling and fractal indices. Baranov et al. [15] showed that a linear macromolecule in a thermodynamically good solvent takes a conformation of a coil characterized by the fractal dimension of 1.67 (5/3). For the RSL sample, the fractal dimension, as averaged for the viscometric and sedimentation–diffusion data, was estimated at 1.73, and for the BSL sample, at 1.66.

As known [10], the Tsvetkov–Klenin hydrodynamic invariant for branched polymers is appreciably lower than those for linear polymers (20%). For the samples we examined, $A_0 = 3.2 \times 10^{-10}$ erg K^{-1} $mol^{-1/3}$, i.e., it coincides with that for linear flexible-chain polymers.

As found previously [6], the Stockmayer–Fixman dependences for branched macromolecules, in particular, for coniferous lignins, have a negative slope. For the polymers we examined, this dependences do not differ essentially (Fig. 2) from those for linear polymers. Among few experimental data that, to a certain extent, are inconsistent with the hypothesized linear topology of the BSL and RSL macromolecules are the Huggins coefficient values. Without overestimating the role played by this parameter which, moreover, characterizes above all the polymer–solvent interactions, rather than the topology of the polymers, we must recognize the linear structure of the macromolecules of the examined lignins as the most substantiated version.

CONCLUSIONS

The analysis of the hydrodynamic, scaling, and conformational properties of straw lignins in dimethylformamide suggests that these biopolymers can be attributed to the universal class of linear macromolecular compounds.

ACKNOWLEDGMENTS

This study was financially supported by the Russian Foundation for Basic Research (project no. 06-03-32 719).

REFERENCES

1. *Lignins, Occurrence, Formation, Structure and Reactions*, Sarkanen, K.V. and Ludwig, C.H., Eds., New York: Wily–Interscience, 1971.

2. Fengel, D. and Wegener, G., *Wood (Chemistry, Ultrastructure, Reactions)*, Berlin: Walter de Gruyter, 1984.
3. Karmanov, A.P., Belyaev, V.Yu., Marchenko, T.A., et al., *Vysokomol. Soedin., Ser. A*, 2002, vol. 44, no. 2, pp. 233–238.
4. Karmanov, A.P. and Monakov, Yu.B., *Usp. Khim*., 2003, vol. 72, no. 8, pp. 797–819.
5. Pavlov, V.M., Mikhailova, N.A., Belyaev, V.Yu., and Syutkin, V.N., *Zh. Prikl. Khim*., 1995, vol. 68, no. 2, pp. 316–319.
6. Karmanov, A.P., *Samoorganizatsiya i strukturnaya organizatsiaya lignina* (Self-Organization and Structural Organization of Lignin), Yekaterinburg: Ural. Otd. Ross. Akad. Nauk, 2004.
7. Gravitis, Ya.A. and Stoldore, I.A., *Khim. Drev*., 1977, no. 2, pp. 10–17.
8. Tsvetkov, V.N., *Zhestkotsepnye polimernye molekuly* (Rigid-Chain Polymeric Molecules), Leningrad: Nauka, 1986.
9. Kozlov, G.V., Temiraev, K.B., and Sozaev, V.A., *Zh. Fiz. Khim.*, 1999, vol. 73, no. 4, pp. 766–768.
10. Budtov, V.P., *Fizicheskaya khimiya rastvorov polimerov* (Physical Chemistry of Polymer Solutions), St. Petersburg: Khimiya, 1992.
11. Karmanov, A.P., Belyaev, V.Yu., and Monakov, Yu.B., *Vysokomol. Soedin., Ser. A*, 1995, vol. 37, no. 2, pp. 266–272.
12. Karmanov, A.P., Kuz'min, D.V., Shamshina, I.N., et al., *Vysokomol. Soedin., Ser. A*, 2004, vol. 46, no. 6, pp. 997–1004.
13. Tverdokhlebova, I.I., *Usp. Khim*., 1977, vol. 46, no. 7, pp. 1292–1301.
14. Lavrenko, P.N. and Vinogradova, L.V., *Vysokomol. Soed., Ser. A,* 2000, vol. 42, no. 7, pp. 1117–1123.
15. Baranov, V.G., Frenkel, S.Ya., and Brestkin, Yu.V., *Dokl. Akad. Nauk SSSR*, 1986, vol. 290, no. 2, pp. 369–372.

ISSN 1070-4272, Russian Journal of Applied Chemistry, 2008, Vol. 81, No. 11, pp. 2040–2042. © Pleiades Publishing, Ltd., 2008.
Original Russian Text © E.A. Venediktov, V.A. Padokhin, 2008, published in Zhurnal Prikladnoi Khimii, 2008, Vol. 81, No. 11, pp. 1925–1927.

BRIEF COMMUNICATIONS

Synthesis of Silver Nanoclusters in Starch Aqueous Solutions

E. A. Venediktov and V. A. Padokhin

Institute of Solution Chemistry, Russian Academy of Sciences, Ivanovo, Russia

Received January 21, 2008

Abstract—The capability of aqueous starch solution for reduction of Ag^+ ions and stabilization of metallic silver nanoparticles was examined. Kinetic parameters of formation of Ag nanoparticles were determined.

DOI: 10.1134/S1070427208110323

Nanodispersed silver particles have unique physicochemical and biomedical properties and are of interest for a number of fields of science, engineering, chemical engineering, and medicine [1–3].

The reducing mineralization with carbohydrates as reductants [1, 3–5] is one of methods for the synthesis of Ag nanoparticles [1–6]. The use of starch for this purpose was not reported, though there is an information on its application for stabilization of aqueous solutions of Ag nanoparticles [3–5]. At the same time, the study of starch as a reductant-stabilizer opens the way for developing environmentally safe nanocomposite materials of a wide functionality based on Ag particles [1–3].

The present work is devoted to the study of certain kinetic relationships of the synthesis of Ag nanoparticles stable in aqueous solutions using starch. As strong interaction with light is a specific feature of silver particles [1–6]; the spectrophotometric method allows reliable monitoring of their synthesis.

As model compounds we used water-soluble starch-indicator (Khimmed, Russia), silver nitrate prepared by dissolution of metallic Ag in concentrated nitric acid with its subsequent precipitation, and single-distilled water.

The order of the preparation of the starch aqueous solution was as follows. A 6-g portion of starch was dissolved in 400 ml of water with vigorous stirring in the course of 15 min at 55–80°C (the temperature region of starch gelatinization) up to the formation of a homogeneous system. Then the resulting solution was left at room temperature for 15 h. During this period, it separated into two fractions. In the experiments we used the upper, most stable, fraction of starch which could be stored in air for two weeks without visual indications of a precipitation process. Furthermore, it appeared to be the most convenient medium for the spectrophotometric study of the formation of metal particles owing to its relatively low light scattering coefficient. Then 2 ml of this solution was sampled and transferred into a 1 × 1 cm square quartz cell of total volume 4 ml, placed in a temperature-controlled chamber of a spectrophotometer. To optimize the process, after reaching the required temperature, from 0.009 to 0.18 ml of 0.028 M $AgNO_3$ solution was added to this volume with vigorous stirring for 15 s, so that the concentration of the solution became from 1.24×10^{-4} to 2.4×10^{-3} M with respect to the salt, respectively. Then electronic absorption spectra of these solutions were measured against an aqueous starch solution without $AgNO_3$ at the same temperature, using a Specord M-40 spectrophotometer. A constant temperature was maintained with an accuracy of ±0.2°C. The kinetic data were treated by the least-squares method.

It is known [4] that the concentration of a starch aqueous solution should be no less than 0.17% to stabilize silver nanoparticles. However, as preliminary experiments have shown, this starch concentration does not provide their efficient synthesis under conditions of dilute $AgNO_3$ solutions ($\leq 2.4 \times 10^{-3}$ M) and low temperatures (<50°C). Partly this problem is eliminated if a starch concentration in solution is increased to 1.5% and the solution temperature, to 50°C. However, even under these conditions the light absorption of the solution associated with the synthesis of Ag particles changes extremely slowly. Nevertheless, the aqueous solution of starch containing 2.4×10^{-3} M $AgNO_3$ appeared to be optimal for the experiments in a relatively wide temperature range.

A typical dependence of the optical density of a starch solution containing $AgNO_3$ on time is shown in Fig. 1. It is seen that an absorption band appears with a maximum in the region of 413 nm and a half-width $\lambda_{1/2}$ of ~96 nm. This band, which can be assigned to the absorption of separated Ag particles preferentially surrounded by starch molecules [5], is close in its parameters to the absorption band of Ag particles with the effective diameter d = 5.3 nm (λ_{max} = 419, $\lambda_{1/2}$ ~122 nm) [4].

According to the data from [3], there is a linear correlation between the absorption band maximum and the effective diameter of Ag particles. Using this approximation and the spectrophotometric data, we have found that the size of the obtained Ag particles does not exceed 37 nm. Thus, the presented data suggest that Ag^+ ions are mineralized in the aqueous solution of its salt in presence of starch and that nanoparticles of this metal are formed.

Published data [3] show that the reducing synthesis of silver particles is a complicated process involving, at least, reduction of metal ions and formation of clusters from its atoms. In the case under study, it is necessary to expect a complication of the kinetics of this process because it involves the formation of the aldehyde form of reducing glucose residues of this polysaccharide, as only these species have a sufficient reduction potential [7]. To find what kinetic factors affect the synthesis of Ag particles, we examined the influence of temperature on the process rate.

It is seen from Fig. 1 that the intensity of the solution absorption band grows with time, its maximum and half-width remaining practically constant at 86°C for at least the first 2 h. The same relationships can also be noted at other, lower, temperatures. The variation of the optical density of the absorption band of Ag particles in time follows a linear law; therefore, this dependence can be used for determining the initial process rate.

It is seen from Fig. 2 that the temperature dependence of the rate of formation of Ag particles is well fitted by the Arrhenius equation (r = 0.9987). The activation energy calculated from these data is 96 ± 1 kJ mol^{-1}. It significantly exceeds the activation energy of the diffusion in water (~18.8 kJ mol^{-1} [8]) and of the viscous flow of aqueous solutions of gel-like starch (~16.7 kJ mol^{-1} [9]), but is considerably lower than the activation energy of the starch hydrolysis (no less than 209 kJ mol^{-1} in highly basic media [10]). At

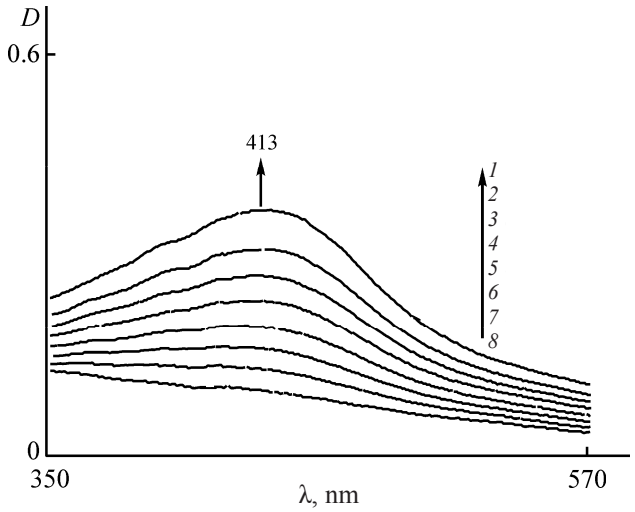


Fig. 1. Absorption spectra of a gel-like aqueous starch solution in presence of 2.4×10^{-3} M $AgNO_3$. Temperature 86°C. (*D*) Optical density and (λ) a wavelength. Process duration, min: (*1*) 1, (*2*) 7, (*3*) 13, (*4*) 19, (*5*) 26, (*6*) 33, (*7*) 39, and (*8*) 48.

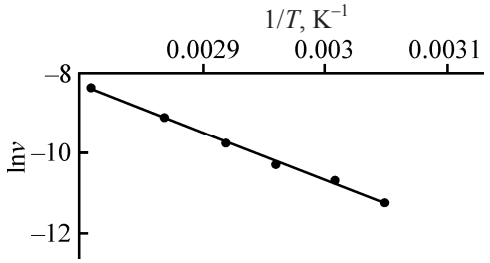


Fig. 2. Temperature dependence of initial rate v of the formation of Ag particles in starch aqueous solution ($[AgNO_3] = 2.4 \times 10^{-3}$ M).

the same time, the value we found is close to the activation energy of glucose mutarotation in water (approximately 71.1 kJ mol^{-1} [11]). It follows from the aforesaid that one of the factors controlling the formation rate of Ag particles is mutarotation of reducing residues of starch glucose.

A similar process occurs in a gel-like solution of potato starch, though less effectively. Taking into account the nature of starches, it can be accounted for by the difference in specific concentrations of glucose reducing residues.

And finally, we found that liquid-phase composites based on Ag and starch nanoparticles are stable in air for at least 1 month.

CONCLUSIONS

(1) The possibility of reducing synthesis and stabilization of silver nanoparticles in an $AgNO_3$ aqueous solution using starch was shown.

(2) One of the factors controlling the kinetics of their formation is the mutarotation of reducing glucose residues of this polysaccharide.

ACKNOWLEDGMENTS

The authors are grateful to N.E. Kochkina for the assistance in the work.

The study was financially supported by the Russian Foundation for Basic Research (project no. 06-08-01 436) and by the Federal Target Scientific and Technical Program "Research and Development in Priority Directions of the Progress of the Scientific and Technological Complex of Russia in 2007–2012" (no. 02.513.11.3229).

REFERENCES

1. *Kolloidno-khimicheskie osnovy nanonauki* (Colloid-Chemical Principles of Nanoscience), Shpak, A.P. and Ul'berg, Z.R., Eds., Kiev: Akademperiodika, 2005.
2. Poole, Ch.P., Jr. and Owens, F.J., *Introduction to Nanotechnology*, Hoboken, NJ: Wiley, 2003.
3. Krutyakov, Yu.A., Kudrinskii, A.A., Olenin, A.Yu., and Lisichkin, G.V., *Usp. Khim*., 2008, vol. 77, no. 3, p. 242–269.
4. Raveendran, P., Fu, J., and Wallen, S.L., *J. Am. Chem. Soc*., 2003, vol. 125, no. 46, pp. 13 940–13 941.
5. Božanic, D.K., Djoković, V., Blanuša, J., et al., *Eur. Phys. J. E*, 2007, vol. 22, pp. 51–59.
6. Olenin, A.Yu., Krutyakov, Yu.A., Kudrinskii, A.A., and Lisichkin, G.V., *Kolloidn. Zh*., 2008, vol. 70, no. 1, pp. 78–84.
7. Sharpenak, A.E. and Kosenko, S.A., *Praktikum po organicheskoi khimii* (Practical Works on Organic Chemistry), Moscow: Vysshaya Shkola, 1965.
8. Ermolaev, V.L, Bodunov, E.N., Sveshnikova, E.B., and Shakhverdov, T.A., *Bezyzluchatel'nyi perenos energii elektronnogo vozbuzhdeniya* (Nonradiating Transfer of Electronic Excitation Energy), Leningrad: Nauka, 1977.
9. Vashurina, I.Yu., Kochkina, N.E., and Kalinnikov, Yu.A., *Zh. Prikl. Khim*., 2006, vol. 79, no. 2, pp. 323–325.
10. Kadykova, E.L., Gubina, S.M., and Mel'nikov, B.N., *Izv. Vyssh. Uchebn. Zaved., Khim. Khim. Tekhnol*., 1991, vol. 34, no. 11, pp. 88–93.
11. Moelwyn-Hughes, E.A., *The Chemical Statics and Kinetics of Solutions*, London: Academic, 1971.

ISSN 1070-4272, Russian Journal of Applied Chemistry, 2008, Vol. 81, No. 11, pp. 2043–2044. © Pleiades Publishing, Ltd., 2008.
Original Russian Text © O.D. Chimitova, B.G. Bazarov, K.N. Fedorov, Zh.G. Bazarova, 2008, published in Zhurnal Prikladnoi Khimii, 2008, Vol. 81, No. 11, pp. 1928–1929.

BRIEF COMMUNICATIONS

Electrical Properties of Triple Molybdates $Rb_5LnHf(MoO_4)_6$

O. D. Chimitova, B. G. Bazarov, K. N. Fedorov, and Zh. G. Bazarova

Baikal Institute of Nature Management, Siberian Division, Russian Academy of Sciences, Ulan-Ude, Buryatia, Russia

Received January 21, 2008

Abstract—Triple molybdates of the compositions $Rb_5LnHf(MoO_4)_6$ (5 : 1 : 2) and $Rb_2LnHf_2(MoO_4)_{6.5}$ (2 : 1 : 4), Ln = Ce–Lu, were prepared by solid-phase reactions. The temperature dependence of the electrical conductivity of the compounds $Rb_5LnHf(MoO_4)_6$ (5 : 1 : 2) at 200–500°C was studied.

DOI: 10.1134/S1070427208110335

Increased interest in complex molybdenum oxide compounds is caused by their diverse physicochemical (piezoelectric, ferroelectric, optical, and catalytic) properties [1].

The aim of this study was to synthesize triple molybdates $Rb_5LnHf(MoO_4)_6$, Ln = Ce–Lu, and to examine their electrical conductivity.

EXPERIMENTAL

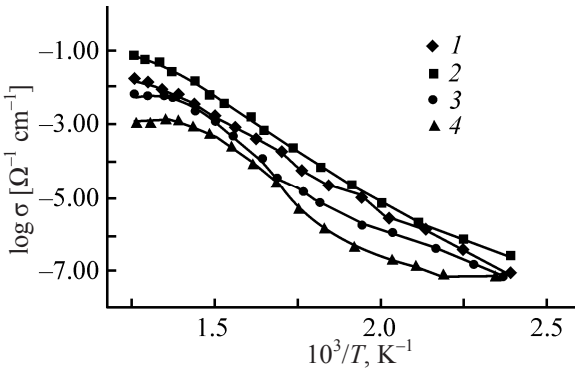
Triple molybdates of these compositions were prepared from neutral molybdates (except for cerium) by solid-phase reactions in the temperature range 500–600°C within 70–100 h. Attainment of the equilibrium was monitored by X-ray diffraction with a Bruker D8 Advance diffractometer (CuK_α radiation, graphite monochromator, interval of angles 10°–40° with a step of 0.02°).

Samples for measuring electric properties were pellets approximately 1 mm thick and 10 mm in diameter. The pellets were prepared by pressing powder samples with the subsequent annealing at a temperature of 2/3 T_m of the corresponding compound.

The temperature dependences of the conductivity σ, permittivity ε, and dielectric loss tangent tan δ were studied on a pilot installation according to the Vest–Tallan procedure [2]. The quantity σ was measured on alternating current with an E8-4 capacitance meter with the connection of a P-5025 capacitor box allowing the interval of measuring tan δ in the samples to be increased. The direct current was measured with an E6-13A teraohmmeter at fixed voltages of 30 and 60 mV. The quantity t_e was determined as the ratio of the electronic conductivity measured on direct current to the total conductivity measured on alternating current: $t_e = \sigma_{=}/\sigma_{\sim} = \sigma_e/(\sigma_e + \sigma_i)$.

We have studied the temperature dependence of the conductivity of triple molybdates in the temperature range 200–500°C. The dependence of the total conductivity of triple molybdates on reciprocal temperature in the coordinates $\log\sigma$–$10^3/T$ is shown in the figure.

The ordinate values give the conductivity at a certain temperature. We determined the activation energies of ionic and electronic conductivity E_a(i) and E_a(e) from the line slopes. The calculated activation energies of the conductivity E_a(i) and E_a(e) and the conductivities σ of triple molybdates are given in the table.



Temperature dependence of the electrical conductivity σ of (*1*) $Rb_5GdHf(MoO_4)_6$, (*2*) $Rb_5LuHf(MoO_4)_6$, (*3*) $Rb_5PrHf\cdot(MoO_4)_6$, and (*5*) $Rb_5TmHf(MoO_4)_6$.

Electrophysical properties of triple molybdates (450°C)

Compound	$\sigma \times 10^5$, Ω^{-1} cm^{-1}	E_a(i)	E_a(e)
		eV	
$Rb_5CeHf(MoO_4)_6$	1.7	0.56	
$Rb_5PrHf(MoO_4)_6$	1.2	0.60	
$Rb_5NdHf(MoO_4)_6$	1.3	0.56	
$Rb_5SmHf(MoO_4)_6$	2.1	0.58	
$Rb_5EuHf(MoO_4)_6$	1.5	0.57	
$Rb_5GdHf(MoO_4)_6$	6.7		0.50
$Rb_5TbHf(MoO_4)_6$	2.8	0.58	
$Rb_5DyHf(MoO_4)_6$	1.5	0.60	
$Rb_5HoHf(MoO_4)_6$	2.8	0.59	
$Rb_5ErHf(MoO_4)_6$	1.2	0.60	
$Rb_5TmHf(MoO_4)_6$	1.0	0.61	
$Rb_5YbHf(MoO_4)_6$	1.1	0.59	
$Rb_5LuHf(MoO_4)_6$	9.0		0.45

According to the electronic transport numbers t_e obtained, the mixed electronic-ionic conduction is observed in the samples of triple molybdates at relatively low temperatures (200–400°C). At the same time, at a higher temperature, the electrical conductivity of the molybdates containing lanthanides (Ce, Pr, Nd, Sm, Eu, Tb, Dy, Ho, Er, Tm, and Yb) is mainly ionic. The predominantly ionic character of conductivity was observed also in the previously studied triple molybdates containing lanthanide atoms, but with another ion (K^+) apparently participating in conduction [3].

It should be noted that the ionic conductivity of molybdates is independent of the ionic radii of rare-earth elements. This is attributable to the fact that the ionic radii in the series of rare-earth elements vary only slightly as their atomic weight increases. The crystal structure of the molybdates $Rb_5LnHf(MoO_4)_6$ [4] is a three-dimensional mixed framework consisting of alternating Mo tetrahedra and (Ln, Hf)O_6 octahedra sharing common O vertices. In large cavities of the framework, two types of rubidium cations are arranged, which basically determine the transport of conduction ions.

According to the electronic transport numbers t_e, preferentially electronic conduction was detected in the molybdates $Rb_5GdHf(MoO_4)_6$ and $Rb_5LuHf(MoO_4)_6$ at temperatures above 400°C. This is apparently caused by intrinsic electronic conductivity of the molybdates containing Gd and Lu atoms with the electronic configuration $4f^7 5d^1 6s^1$ and $4f^{14} 5d^1 6s^2$, respectively. According to the data of [5], the presence of the $5d^1$ levels in the electronic structure of rare-earth atoms determines the intrinsic conductivity of molybdates. The conductivities σ at 450°C of the molybdates $Rb_5GdHf(MoO_4)_6$ and $Rb_5LuHf(MoO_4)_6$ are noticeably higher than those of the other ternary molybdates exhibiting mostly ionic conductivity at the same temperatures. The fact of intrinsic electronic conductivity in the molybdates containing Gd ions is confirmed by a higher electronic conductivity found for $Gd_2Zr_3(MoO_4)_9$ as compared to double molybdates exhibiting only the impurity electronic conductivity [6].

CONCLUSIONS

(1) The triple molybdates $Rb_5LnHf(MoO_4)_6$ (Ln series except for Gd and Lu) exhibit ionic conductivity. Its value is independent of particular lanthanide.

(2) $Rb_5GdHf(MoO_4)_6$ and $Rb_5LuHf(MoO_4)_6$ exhibit predominantly electronic conductivity caused basically by the electronic configurations of Gd and Lu atoms.

REFERENCES

1. Mokhosoev, M.V. and Bazarova, Zh.G., *Slozhnye oksidy molibdena i vol'frama s elementami 1–4 grupp* (Complex Oxides of Molybdenum and Tungsten with Group 1–4 Elements), Moscow: Nauka, 1990.
2. Vest, R.W. and Tallan, N.M., *J. Appl. Phys*., 1965, vol. 36, no. 2, pp. 543–548.
3. Romanova, E.Yu., New Double and Triple Molybdates in the Systems $Ln_2(MoO_4)_3$–$Hf(MoO_4)_2$ and K_2MoO_4–$Ln_2(MoO_4)_3$–$Hf(MoO_4)_2$ (Ln = La–Lu, Y), *Cand. Sci. Dissertation*, Irkutsk, 2007.
4. Bazarov, B.G., Klevtsova, R.F., Chimitova, O.D., et al., *Zh. Neorg. Khim*., 2006, vol. 51, no. 5, pp. 866–870.
5. Tripathi, A.K. and Lal, H.V., *J. Phys. Soc. Jpn*., 1980, vol. 49, no. 5, pp. 1896–1901.
6. Tushinova, Yu.L., Phase Formation in the Systems Ln_2O_3–ZrO_2–MoO_3 (Ln = La–Lu, Y, Sc), *Cand. Sci. Dissertation*, Irkutsk, 2005.

ISSN 1070-4272, Russian Journal of Applied Chemistry, 2008, Vol. 81, No. 11, pp. 2045–2047. © Pleiades Publishing, Ltd., 2008.
Original Russian Text © A.I. Kipper, S.V. Valueva, N.A. Matveeva, 2008, published in Zhurnal Prikladnoi Khimii, 2008, Vol. 81, No. 11, pp. 1930–1931.

BRIEF COMMUNICATIONS

Determination of Parameters of Mark–Kuhn–Houwink Equations for Poly-*N*-methacryloyloxyethyl-*N*,*N*,*N*-trimethylammonium Methyl Sulfate

A. I. Kipper, S. V. Valueva, and N. A. Matveeva

Institute of Macromolecular Compounds, Russian Academy of Sciences, St. Petersburg, Russia

Received May 29, 2008

Abstract—The Mark–Kuhn–Houwink relationship was obtained for solutions of poly-*N*-methacryloyloxyethyl-*N*,*N*,*N*-trimethylammonium methyl sulfate in 1 M $NaNO_3$ from the light scattering and viscometric data. The Kuhn segment length for this polymer was estimated.

DOI: 10.1134/S1070427208110347

Molotkov et al. [1] compared two procedures for preparing water-soluble poly-*N*-methacryloyloxyethyl-*N*,*N*,*N*-trimethylammonium methyl sulfate (PDMAEM·DMS). The synthesis was performed by the radical mechanism with the Co(III)–glycine redox system and with acid-catalytic initiation. It was shown that the intrinsic viscosities [η] and molecular weights M_w of all the samples well fit in a common relationship $\log [\eta] = f(\log M_w)$. However, the range of MW did not allow the Mark-–Kuhn–Houwink (MKH) relationship $[\eta] = KM_w^a$ (where K and a are constants characterizing the specific polymer–solvent system) to be obtained reliably [2]. It should be noted that such an equation, which would allow determination of MW by the readily available viscometric method, is demanded by wide use of PDMAEM·DMS in practice and research.

In this study, we supplemented the available data by new data on viscosity and molecular weights, which allowed us to obtain the MKH relationship for a relatively wide MW range and to estimate the Kuhn segment length for this polymer.

EXPERIMENTAL

To prepare PDMAEM·DMS of a lower molecular weight, we developed a radical polymerization procedure with azobis(isobutyronitrile) (AIBN, 0.5–2 wt % relative to monomer) as polymerization initiator. The reaction was performed in ethanol or isopropanol at a monomer concentration of 10–25 mol % and a temperature of 65°C. Solutions of the initiator and monomer were prepared separately and combined at room temperature. The prepared working solution of the monomer with the initiator of the required concentration was placed in a thermostat. The reaction was performed in an argon flow with gradual heating to 65°C. After the reaction completion (18 h, ~90% conversion of the monomer), the polymer was dissolved in distilled water and purified by dialysis with a cellulose membrane. The degree of conversion was determined from the concentration of the polymer solution obtained, by weighing the dry residue. The dry polymer was isolated from the aqueous solution by freeze drying.

Viscometric measurements for determining the intrinsic viscosity [η] were performed in 1 M aqueous $NaNO_3$ at 20°C in an Ostwald viscometer with a solvent outflow time of about 100 s. The molecular weights M_w of the polymers were determined by the light scattering method with a Fica diffusometer at the wavelength of the incident vertically polarized light of 546 nm in the concentration range $c \sim (0.01–1.0) \times 10^{-2}$ g cm^{-3}; the device was calibrated against benzene. The solutions and solvent (1 M aqueous $NaNO_3$) were treated to remove dust by centrifugation at 15 000 rpm for 1.5 h. The results were processed by the Debye method taking into account asymmetry of scattering at 45° and 135° [3]. The refractive index increment dn/dc was determined with an IRF-23 refractometer. For PDMAEM·DMS in 1 M aqueous $NaNO_3$, dn/dc = 0.15 cm^3 g^{-1}.

Synthesis conditions, degree of conversion, and molecular characteristics of PDMAEM·DMS with AIBN used as polymerization initiator (65°C)

[M], wt %	AIBN, % of [M]	Solvent	τ, h	Conversion, %	[η],[a] ml g^{-1}	$M_w \times 10^{-3}$
20	1	Ethanol	18	73.3	20	95
20	1	Isopropanol	18	83.0	44	300
10	2	Ethanol	18	79.3	8	30
20	1	″	9	87.3	28	190
20	1	″	6	78.7	19	100
23	1	″	8	86.0	26	170

[a] In 1 M $NaNO_3$.

The synthesis conditions, degrees of conversion, intrinsic viscosities [η], and weight-average molecular weights M_w of PDMAEM·DMS samples obtained with AIBN initiator at 65°C are given in the table.

From the results of this study and the values of [η] and M_w for ultrahigh-molecular-weight PDMAEM·DMS samples prepared in [1] with acid-catalytic initiation, we constructed the dependence of $\log[\eta]$ on $\log M_w$ (Fig. 1). In the entire examined range of M_w, it corresponded to the MKH equation of the form

$$[\eta] = 5.24 \times 10^{-3} M_w^{0.71}.$$

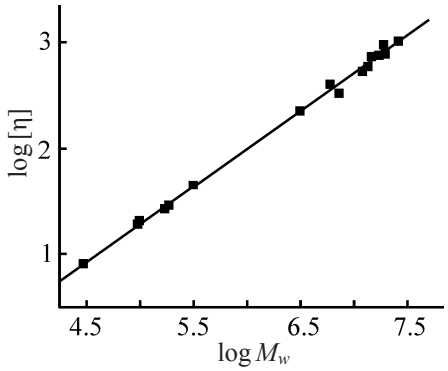


Fig. 1. Plot of $\log[\eta]$ vs. $\log M_w$ for poly-*N*-methacryloyloxyethyl-*N*,*N*,*N*-trimethylammonium methyl sulfate in 1 M $NaNO_3$.

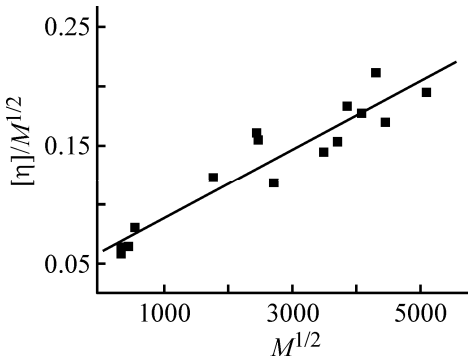


Fig. 2. Stockmayer–Fixman plot for poly-*N*-methacryloyloxyethyl-*N*,*N*,*N*-trimethylammonium methyl sulfate in 1 M $NaNO_3$.

To exclude the influence of volume effects and determine the Kuhn segment *A* of the macromolecule, we used the Stockmayer–Fixman relationship [4]

$$[\eta]/M^{1/2} = K_0 + 0.51\Phi_0 BM^{1/2} = \Phi_0(Al/M_0)^{3/2} + 0.51\Phi_0 BM^{1/2}.$$

By extrapolation of the relationship $[\eta]/M^{1/2} = f(M^{1/2})$ (Fig. 2), we obtained the Kuhn segment $A = 4.1 \pm 0.5$ nm (at the Flory coefficient $\Phi_0 = 2.51 \times 10^{23}$ mol^{-1}, length of monomeric unit projection $l = 0.252$ nm, and molecular weight of the monomeric unit of the polymer $M_0 = 283$).

The obtained Kuhn segment length *A*, despite large value, nevertheless does not allow PDMAEM·DMS to be classed with moderately rigid-chain polymers ($5 \le A \le 20$ nm, according to [5]). The exponent in the MKH equation (0.71) is also typical of flexible-chain polymers in good solvents ($a = 0.7$–0.8 [6]).

CONCLUSIONS

(1) A relationship between the intrinsic viscosity of poly-*N*-methacryloyloxyethyl-*N*,*N*,*N*-trimethylammonium methyl sulfate in 1 M $NaNO_3$ solution and its molecular weight M_w was constructed on the basis of light scattering and viscometric data. This relationship corresponds to the Mark–Kuhn–Houwink equation in the form $[\eta] = 5.24 \times 10^{-3} M_w^{0.71}$.

(2) The Kuhn segment length was estimated: $A = 4.1 \pm 0.5$ nm.

REFERENCES

1. Molotkov, V.A., Kurlyankina, V.I., Klenin, S.I., et al., *Zh. Prikl. Khim*., 2001, vol. 74, no. 6, pp. 975–979.
2. Tsvetkov, V.N., Eskin, V.E., and Frenkel', S.Ya., *Struktura makromolekul v rastvorakh* (Structure of Macromolecules in Solutions), Moscow: Nauka, 1964.
3. Eskin, V.E., *Rasseyanie sveta rastvorami polimerov i svoistva makromolekul* (Light Scattering with Polymer Solutions and Properties of Macromolecules), Leningrad: Nauka, 1986.
4. Stockmayer, W.H. and Fixman, M., *J. Polym. Sci. C*, 1963, no. 1, pp. 137–141.
5. Magarik, S.Ya., *Polyamic Acids and Polyimides: Synthesis, Transformations and Structure*, Bessonov, M.I. and Zubkov, V.A., Eds., London: CRC, 1993, pp. 281–362.
6. Budtov, V.P., *Fizicheskaya khimiya rastvorov polimerov* (Physical Chemistry of Polymer Solutions), St. Petersburg: Khimiya, 1992.

ISSN 1070-4272, Russian Journal of Applied Chemistry, 2008, Vol. 81, No. 11, pp. 2048–2049. © Pleiades Publishing, Ltd., 2008.
Original Russian Text © V.Ya. Shapkina, S.G. Krasitskaya, E.V. Lifanskii, A.G. Borovik, N.P. Shapkin, 2008, published in Zhurnal Prikladnoi Khimii, 2008, Vol. 81, No. 11, pp. 1932–1933.

BRIEF COMMUNICATIONS

Rational Use of Aluminosilicates from Primorskii Krai in Protective Coatings for Ship Building

V. Ya. Shapkina, S. G. Krasitskaya, E. V. Lifanskii, A. G. Borovik, and N. P. Shapkin

Nevel'skoi Far-Eastern Maritime University, Vladivostok, Russia
Far-Eastern State University, Vladivostok, Russia
Far-Eastern State Technical University, Vladivostok, Russia

Received July 5, 2007

Abstract—Formulations of protective polymeric coatings for sea craft, which contain natural aluminosilicates (zeolite and vermiculite from Primor'e deposits) as fillers and polyheterosiloxanes, oxides, and fluorides of some metals and mixtures of these as modifiers of binding resins, were developed.

DOI: 10.1134/S1070427208110359

It is known that polymeric coatings are widely used in ship building for corrosion protection of metals [1]. It has been shown previously that high-quality polymeric coatings can be obtained using formulations containing natural zeolite from the Chuguev deposit as a filler and polychromoorganylsiloxane as modifier of the binding polymer [2].

For a more systematic and broader-scope study of the protective properties of coatings, formulations based on perchlorovinyl (PCV) and polystyrene (PS) were developed, which contain zeolite or vermiculite as a filler and polychromophenylsiloxane, polyphenylborophenylsiloxane, iron(III) and copper(II) oxides, and antimony trifluoride as modifiers.

EXPERIMENTAL

Polymeric coatings were deposited from the formulations under study as follows: a 5% solution of polystyrene in toluene was prepared, the aluminosilicate filler was added (10, 20, 30, and 40% relative to the mass of the resin solution), and then the modifier was introduced (3% relative to the mass of the preceding solution). Prior to deposition of the coatings, St.3 steel samples were polished to remove corrosion products, degreased with toluene, and treated with a 10% sulfuric acid solution with addition of thiourea.

A polymeric coating was deposited with a brush onto a prepared and dry sample. After triple deposition, the coating was dried in air to constant mass.

The corrosion of St.3 steel was studied by submerging plates with protective coatings in seawater for a long time. At certain intervals of time, seawater was sampled and the content of iron ions was determined. The corrosion rate was also determined gravimetrically from the loss of mass by a sample, with subsequent recalculation to the corrosion depth index (mm year^{-1}) by the formula

$$\nu = \Delta m \times 10 \times 365/(\rho St),$$

where Δm is the loss of mass by a sample (g); ρ, metal density (g cm^{-3}); S, sample surface area (cm^2); and t, exposure time (days).

The interaction in the aluminosilicate–polymer system was studied by IR spectroscopy. The IR spectrum of aluminosilicate show characteristic absorption bands associated with Si–OH (3630 cm^{-1}) and OH bonds (H_2O_{assoc}) (3460–3380 cm^{-1}). The presence of bound water is also indicated by bending vibrations at 1630 cm^{-1}. In the PCV–aluminosilicate–PS systems, these bands are completely absent, which points to interactions associated with removal of water. Such an interaction enhances the cohesion of the composite and improves the coating. In the aluminosilicate–polyheterosiloxane system, the bands related to OH vibrations have a lower intensity, but do not disappear completely [2]. Probably, the interaction proceeds in this system to a lesser extent, and, accordingly, the composite is strengthened less.

The effect of the content of the filler-pigment intro-

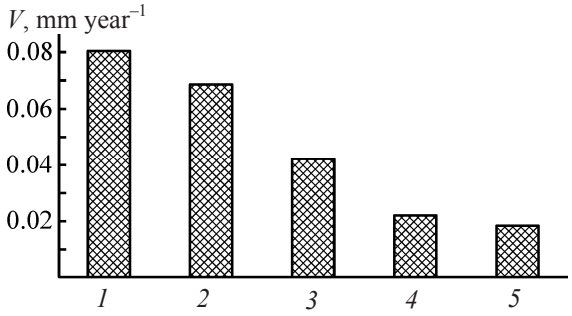


Fig. 1. Dependence of the corrosion rate V of St.3 steel in seawater on the coating composition. (*1*) No coating; coating: (*2*) PS, (*3*) PS + 10% zeolite, (*4*) PS + 20% zeolite, and (*5*) PS + 40% zeolite.

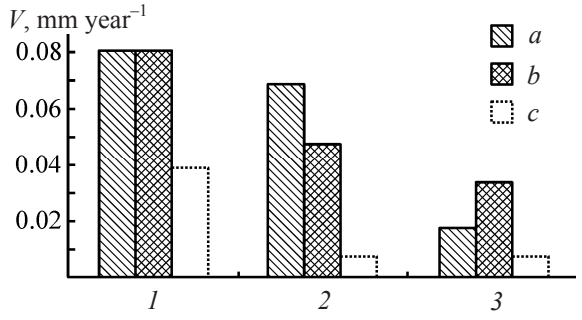


Fig. 2. Dependence of the corrosion rate V of (*a*, *b*) St.3 steel and (*c*) bronze in seawater on the nature of a polymeric binder in the coating. (*1*) No coating; coating: (*2*) (*a*) PS and (*b*, *c*) PCV; (*3*) (*a*) PS + 40% zeolite and (*b*, *c*) PCV + 40% zeolite.

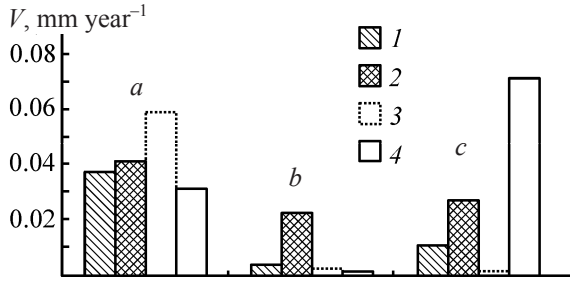


Fig. 3. Influence exerted on the corrosion rate V by addition to the coating of modifiers of various binders. Modifier: (*1*) Cu_2O + vermiculite; (*2*) Cu_2O, SbF_3, PPBPS + zeolite; (*3*) Cu_2O + zeolite; and (*4*) PPBPS + zeolite. Binder: (*a*) PCV, (*b*) PCV + PE, and (*c*) PCV + PE + PS.

duced into the coating on the corrosion rate of St.3 steel in seawater at 20°C is illustrated by Fig. 1. It can be seen that, at a zeolite content exceeding 20%, the corrosion rate remains nearly unchanged. The lowest corrosion rate was observed for the composite containing 40% zeolite. In this case, the corrosion rate decreased by a factor of 4.7, compared with the starting steel sample, whereas deposition of a filler-free polystyrene film diminished the corrosion rate by only a factor of 1.1.

Using a polystyrene coating instead of that composed of perchlorovinyl leads to an increase in the corrosion rate by a factor of 1.2. The same result was observed upon introduction of 40% zeolite. Passing from PCV to PS makes the corrosion rate 1.8 times lower. The results obtained are confirmed by Fig. 2, which points to a denser structure of the polystyrene coating with zeolite, compared with the structure of the perchlorovinyl coating with the same amount of aluminosilicate.

The influence exerted on the corrosion rate by introduction of binder modifiers, such as polyphenyl borophenyl siloxane (PPBPS), copper(II) oxide, antimony trifluoride, and mixture of antimony trifluoride, copper(I) oxide, and polyphenyl borophenyl siloxane, and also by replacement of zeolite with vermiculite is illustrated by Fig. 3.

Making the coating composition more complex results in the appearance of chemical interactions. The most pronounced effect of this interaction is observed on mixing perchlorovinyl resin and polyepoxide (PE). Also rather important is the influence of the aluminosilicate structure. The lowest corrosion rate is observed upon introduction of vermiculite, because the lamellar structure of its particles provides the highest coating density at the same modifier (CH_2O).

The highest corrosion rate was observed upon introduction of Fe_2O_3 as a filler pigment in the case of a three-component polymer mixture (PCV + PE + PS). Presumably, this is due to the effect of the polystyrene component, because the corrosion rate is substantially lower in the absence of this component.

CONCLUSION

A study of the corrosion in seawater with the coatings obtained demonstrated that introduction of zeolite and vermiculite diminishes the corrosion rate by factors of 4.5 and 10, respectively. Introduction of heterosiloxanes strongly affects the corrosion rate, which depends on the nature of an element in the heterosiloxane.

REFERENCES

1. Shapkina, V.Ya., Shchetinina, G.P., Alikovskii, A.V., et al., *Izv. Vyssh. Uchebn. Zaved., Khim. Khim. Tekhnol.*, 2001, vol. 44, no. 4, pp. 141–143.
2. Shapkin, N.P., Alikovskii, A.V., Krizhanenko, G.A., et al., *Kolloidn. Zh.*, 1988, vol. 50, no. 3, pp. 551–557.

ISSN 1070-4272, Russian Journal of Applied Chemistry, 2008, Vol. 81, No. 12, pp. 2051–2055. © Pleiades Publishing, Ltd., 2008.
Original Russian Text © V.V. Antipov, A.P. Belyaev, A.A. Malygin, V.P. Rubets, E.A. Sosnov, 2008, published in Zhurnal Prikladnoi Khimii, 2008, Vol. 81, No. 12, pp. 1937–1941.

INORGANIC SYNTHESIS AND INDUSTRIAL INORGANIC CHEMISTRY

Effect of the Substrate Nature on the Formation of Thin Titanium Dioxide Films by Molecular Layering

V. V. Antipov, A. P. Belyaev, A. A. Malygin, V. P. Rubets, and E. A. Sosnov

St. Petersburg State Technological Institute, St. Petersburg, Russia

Received July 11, 2008

Abstract—Results of structural studies of titanium dioxide films synthesized on glass, silicon, and mica substrates by molecular layering are presented. An analysis of data furnished by electron and X-ray diffraction analyses and atomic-force microscopy of the samples in different growth stages revealed the effect of the substrate nature on the structure of the titanium oxide coatings synthesized.

DOI: 10.1134/S107042720812001X

Finding the factors that affect the structure of titanium oxide films formed by molecular layering (ML) is of not only theoretical, but also practical interest. It is known that titanium dioxide finds use in optical, pigment, catalytic, sorption, etc. coatings [1–9]. Depending on the functional purpose, and important factor is the phase state of titanium dioxide, which can be in the form of anatase, rutile, and brookite.

As shown by previous studies, the substrate nature strongly affects the phase composition of the nanolayer being formed in synthesis of titanium oxide nanostructures on the surface of porous silicon and aluminum oxide particles [2, 3]. The surface of aluminum oxide favors formation of a rutile-like modification of titanium oxide, whereas on silicon dioxide, mostly an anatase-like system is produced.

A study of the properties of ML products revealed such structural-dimensional characteristics as effects of a monolayer, substrate coverage, and structural matching between the substrate surface and layer being grown [2, 7, 8]. It can be assumed that, as the thickness of a growing layer increases, the substrate will exert lesser influence on its structure, but in the initial stages of synthesis, in a thin (several monolayers) coating, the matrix is known to have the most pronounced effect (monolayer effect). In turn, the structure of the coating formed in the initial stages of synthesis, can affect that of thicker layers.

The initial stages of synthesis of titanium oxide nanolayers on the surface of semiconductor silicon and glass by the ML method, with up to 20 treatment cycles, have been studied by ellipsometry and atomic-force microscopy (AFM) [1, 7, 8, 10, 11]. At the same time, integrated studies of thicker (with several hundreds or thousands of treatment cycles, which provides film thicknesses of 100 nm and more) titanium oxide layers, their phase composition on the surface of various substrates, and the influence exerted by the matrix nature on the structure of coatings being formed have not been widely reported in scientific publications.

The aim of this study was to examine the influence exerted by the nature of the solid-phase matrix (glass, mica, silicon) on the structure of the titanium oxide layer formed on the substrate surface in molecular layering (beginning with 500 treatment cycles and more).

As substrates were used plates (20 × 20 mm) of polished sodium-calcium-silicate glass, Si(III) silicon, and mica (muscovite), treated, prior to synthesis, with a surfactant [$CH_3(CH_2)_{10}$–SO_3Na + 0.5 wt % NaOH] and then washed with distilled water and dried in a vacuum at 500 K for 15 min.

The fact that the silicon surface commonly contains a thin (up to several nanometers) layer of silicon oxide and results of an analysis of published data suggest that hydroxy groups bonded to silicon atoms are the main reaction centers on the surface of substrates treated with water and dried.

The synthesis was performed by alternate treatments of the starting matrices with $TiCl_4$ and H_2O vapors, followed by removal of the excess amount of the starting reagent and gaseous reaction products to a residual pressure in the reactor of ≤1 Pa.

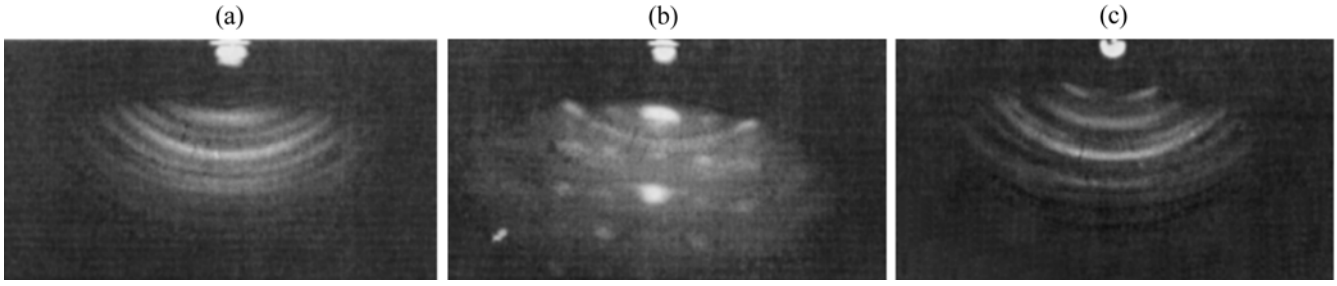


Fig. 1. Typical electron diffraction patterns of titanium oxide films after 500 ML cycles on (a) glass, (b) mica, and (c) silicon.

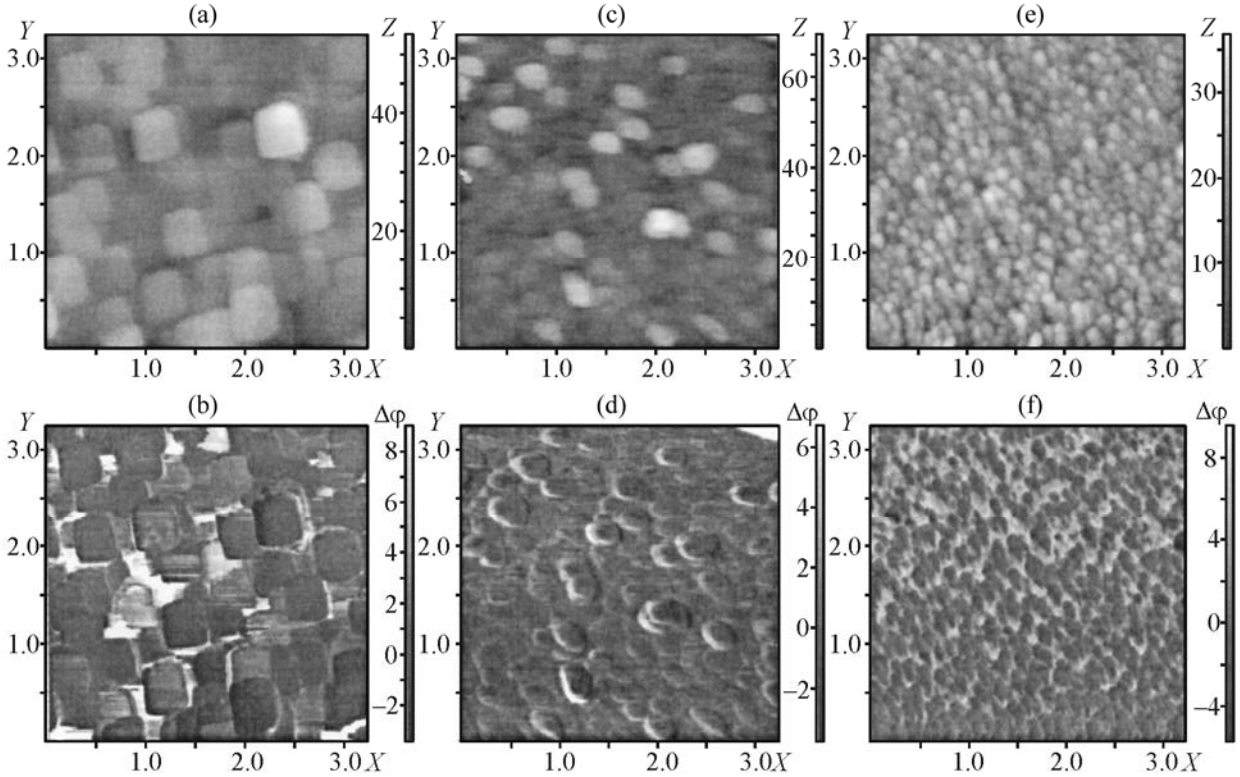


Fig. 2. AFM images of the surface of titanium oxide films after 500 ML cycles in the topographic and phase-contrast modes on (a, b) glass, (c, d) mica, and (e, f) silicon.

Each ML cycle, carried out after a preliminary evacuation of the reactor to a residual pressure of about 1 Pa, included the following stages: letting-in of a titanium chloride vapor, keeping the substrate in this vapor, pumping-out of titanium chloride and the gaseous reaction product (hydrogen chloride), letting-in water vapor, keeping the substrate in this vapor, and pumping-out of the excess amount of the reagent and gaseous reaction products. Further, the procedure was repeated for a prescribed number of times. The substrate temperature in synthesis was $T_s = 493$ K.

Titanium oxide films produced by 500–2000 cycles of molecular layering were studied.

The crystal structure of the films was analyzed with an EMR-100 electron diffractometer and Difrey DNR diffractometer.

The morphology of the titanium oxide coatings was examined with a Solver P47 Prof scanning probe microscope (NT-MDT, Russia) by the AFM method in the tapping mode in air. Samples were studied in two modes: by topographic measurements and by scanning in the phase-contrast mode, which enables evaluation of qualitative changes in the phase composition of separate areas of the sample surface by changes in the shift $\Delta\varphi$ of the amplitude-frequency characteristic of the AFM probe, caused by adhesion interactions. The main results of the study are shown in Figs. 1–5.

As follows from the electron diffraction patterns (Fig. 1), the films produced by 500 ML cycles on glass and silicon have a polycrystalline structure, and those produced on the mica surface, a crystalline structure of the "smeared texture" type.

The AFM images of the samples (Fig. 2) indicate that the surface morphology of the layer being grown strongly depends on the nature of the substrate used in synthesis. On the glass surface (Fig. 2a), titanium oxide microcrystallites of regular shape (squared at base, with a side of 350–500 nm and height of up to 15–20 nm) are formed. Despite the complete coverage of the starting substrate by TiO_2 crystallites, they are formed not only on the matrix surface, but also on lower-lying crystallites to give a coating that has a nonuniform thickness, but is solid. Scanning in the phase-contrast mode (Fig. 2b) indicates that the properties of the titanium oxide nanostructures are uniform; the differences in the image, obtained in the phase-contrast mode, are presumably due to the topographic nonuniformity of the layer being synthesized.

Performing the synthesis under the same conditions on mica (Fig. 2c) yields similar structures with a lateral size of 200 to 400 nm and height of 20 nm, which have, in contrast to those formed on glass, a rectangular shape with rounded corners. The surface image obtained in the phase-contrast mode (Fig. 2d) indicates, as in the preceding case, that the substrate is completely covered and the properties of the nanostructures formed are uniform. At the same time, the titanium oxide structures formed on mica are more closely packed than those on glass, without gaps between separate crystallites.

Synthesis on Si(III) yields on the matrix surface a solid uniform coating composed of rounded crystallites with a later size of 50–100 nm and height of 10–15 nm (Fig. 2e). In this case, scanning in the phase-contrast mode does not reveal any significant differences from the characteristics of the already considered titanium oxide coatings (Fig. 2f).

Figure 3 shows electron diffraction patterns of titanium oxide films synthesized on mica and silicon substrates after 1000 ML cycles. Comparison with the electron diffraction patterns of thinner films (Fig. 1) shows that the crystal perfection of the films becomes better in the course of synthesis. At the same time, electron diffraction analysis shows that films grown on glass retain their polycrystalline structure as the thickness increases. However, the crystal structure of the films formed on a glass substrate does change in the course of synthesis. This is indicated by Fig. 4, which shows X-ray diffraction patterns of samples in different growth stages (curves *2* and *3*) in comparison with the starting substrate (curve *1*). It follows from Fig. 4 that, in all stages, the films contain an anatase structure in addition to the amorphous phase. The crystal struc-

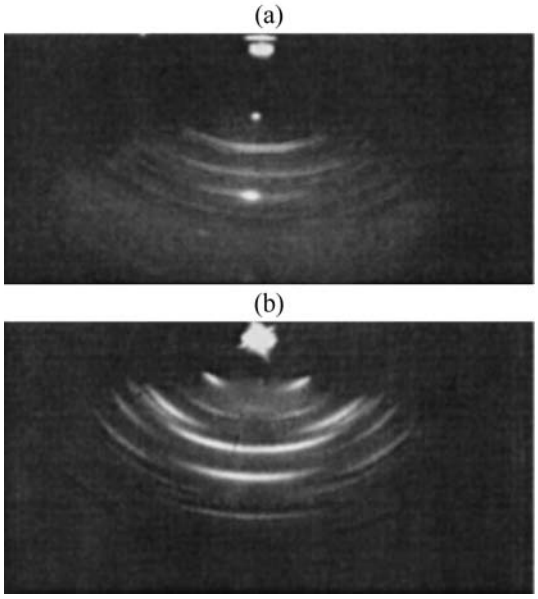


Fig. 3. Electron diffraction patterns of titanium oxide films after 1000 ML cycles on (a) mica and (b) silicon.

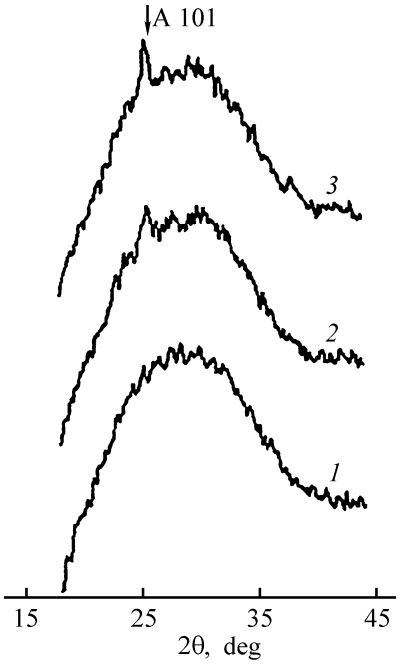


Fig. 4. X-ray diffraction patterns of (*1*) starting glass substrate and that with titanium oxide films after (*2*) 500 and (*3*) 1000 ML cycles. (2θ) Bragg angle.

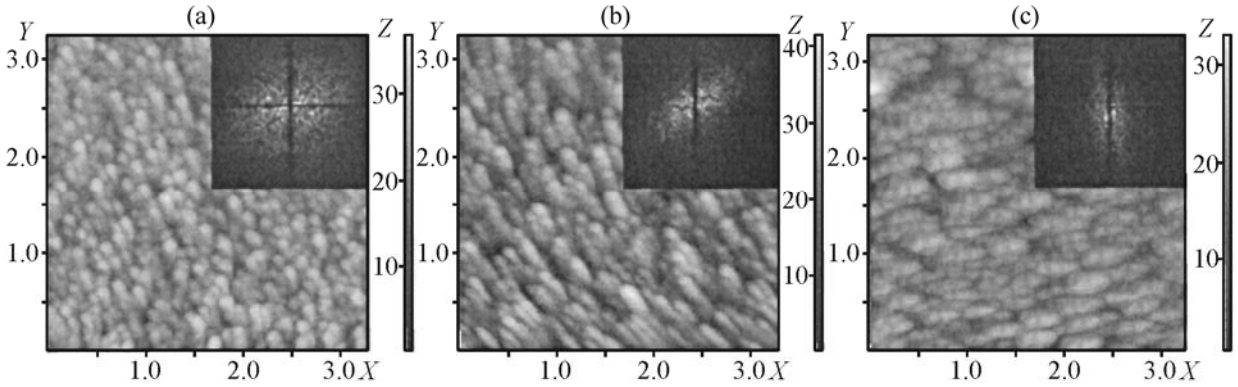


Fig. 5. AFM images of the surface of titanium oxide films on a silicon substrate after (a) 500, (b) 1000, and (c) 2000 ML cycles.

ture of anatase is oriented in the (101) direction in the film studied. In Fig. 4, the reflection from this plane is designated as A101. Its intensity grows with the film thickness.

The evolution of the surface morphology of titanium oxide films in the course of synthesis can be assessed using the data in Fig. 5, which shows AFM images of silicon samples after 500, 1000, and 2000 ML cycles. As the thickness of the film formed on Si(III) grows, the AFM images show that the shape of surface structures changes via fusion of separate closely spaced TiO_2 crystallites and the length of the final structure increases from 50–100 nm (characteristic lateral size of a separate TiO_2 crystallite in Fig. 5a) to 300–500 nm (Fig. 5c) at its almost unchanged width (50–100 nm). As the thickness of the growing titanium oxide layer increases, a texture appears in the layer after 500 ML cycles, which is clearly seen in Fourier transforms of the AFM images of the coatings under study [12].

Comparative analysis of the results obtained shows that the substrate nature strongly affects the shape and size of crystallites formed in the titanium oxide film in the course of synthesis. In going from glass, to mica, and to silicon substrates (Fig. 2), the size of the crystallites decreases and their shape changes from rather distinctly squared on glass (Fig. 2a) to squared with rounded corners on mica (Fig. 2c) and rounded on silicon (Fig. 2e). The fact that the crystallinity of the starting substrate increases in the same order suggests that a more perfect coating structure is formed on silicon already in the first monolayers and is preserved in further growth. In the case of the amorphous glass matrix, the crystallinity of the layer starts to increase only in sufficiently thick layers, when the effect of the matrix is insignificant. Mica occupies an intermediate position between the above two types of substrates.

The experimental results of this study correlate to a certain extent with data on synthesis of titanium oxide films on silicon by a method similar to the ML [13]. The authors of [13] varied the concentration of hydroxy groups on the silicon surface by their partial replacement with hydride groups, with the surface hydrophobicity thereby raised, and analyzed changes in the structure of the forming titanium oxide films. In the end, they came to a conclusion that mostly single hydroxy groups are present on a hydrophobic silicon surface and reaction (1) occurs to give finer crystallites (as in the case shown in Figs. 2e and 5); on a hydrophilic surface, the concentration of hydroxy groups is higher and the synthesis occurs predominantly by reaction (2) to give coarser crystallites (as in Figs. 2a and 2c):

$$\geq Si{-}O{-}H + Cl_2Ti(Cl)_2 \rightarrow \geq Si{-}O{-}TiCl_3 + HCl, \quad (1)$$

$$O(\geq Si{-}O{-}H)_2 + Cl_2Ti(Cl)_2 \rightarrow O(\geq Si{-}O{-})_2TiCl_2 + 2HCl. \quad (2)$$

With account of the aforesaid, it can be suggested that the growth on glass begins with the formation of an amorphous layer (compare curves *1* and *2* in Fig. 4), and then there appears a coarsely grained structure containing anatase (as indicated by A101 peak in curve *2*). In further growth, the crystallinity of this structure grows with the film thickness (as indicated by the increase in the intensity of A101 reflection with the film thickness).

The growth process on silicon begins with the appearance of fine crystals (Fig. 2e), which increase in size via fusion (Fig. 5).

CONCLUSIONS

(1) The structural study of titanium oxide films produced by molecular layering on substrates of varied nature demonstrated that the matrix nature strongly affects the size and shape of crystallites in the titanium oxide film. In passing from glass, to mica, and to silicon substrates, the crystallite sizes decrease in all stages of synthesis and their shape changes from rather distinctly squared on glass to squared with rounded corners on mica, and to rounded on silicon.

(2) In the initial stage of film formation (up to 500 molecular layering cycles), the structure of the films is largely determined by the substrate nature: an amorphous layer is formed on amorphous glass; an oriented crystalline structure, on mica; and crystalline film. on silicon.

(3) As the thickness of a film increases (to 2000 cycles of molecular layering), its crystal structure becomes more perfect.

ACKNOWLEDGMENTS

The study was in part financially supported by the Russian Foundation for Basic Research (grant nos. 07-03-00366, 07-03-120 38, 07-03-00 330, and 08-03-00 803).

The main part of the study was carried out at the Shared Center for "Chemical assembly of nanomaterials." The authors thank A.M. Abyzov for measuring X-ray diffraction patterns.

REFERENCES

1. Malkov, A.A., Sosnov, E.A., Malygin, A.A., et al., *Fiz. Khim. Stekla*, 2006, vol. 32, no. 1, pp. 100–105.
2. Malygin, A.A., Malkov, A.A., and Dubrovenskii, S.D., *Adsorption on New and Modified Inorganic Sorbents*, Dabrowski, A. and Tertykh, V.A., Eds., *Ser. "Studies in Surface Science and Catalysis,"* Amsterdam: Elsevier, 1996, vol. 99, pp. 213–237.
3. Dolgushev, N.V., Malkov, A.A., Malygin, A.A., et al., *Thin Solid Films*, 1997, vol. 293, pp. 91–95.
4. Leboda, R., Turov, V.V., Marcyniak, M., et al., *Langmuir*, 1999, vol. 15, pp. 8441–8446.
5. Gunko, V.M., Leboda, R., and Marciniak, M., *Langmuir*, 2000, vol. 16, pp. 3227–3243.
6. Leboda, R., Marciniak, M., Gunko, V.M., et al., *J. Colloid Interface Sci*., 2000, vol. 167, pp. 275–286.
7. Malygin, A.A., Ros. *Nanotekhnol*., 2007, vol. 2, nos. 3–4, pp. 87–100.
8. Malygin, A.A., *J. Industr. Eng. Chem*. (*Korean Soc. Industr. Eng. Chem.*), 2006, vol. 12, no. 1, p. 1.
9. Diebold, U., *Surf. Sci. Reports*, 2003, vol. 48, pp. 53–229.
10. Sosnov, E.S., Dorofeev, V.P., Malkov, A.A., et al., *Fiz. Tekh. Poluprovodn*. 2007, vol. 41, p. 518.
11. Ageev, D.A., Aleskovskii, V.B., Bisengaliev, R.A., et al., *Fiz. Tverd. Tela*., 1998, vol. 40, no. 5, pp. 820–821.
12. Arutyunov, P.A., Tolstikhina, A.L., and Demidov, V.N., *Zavod. Lab., Diagnost. Mater*., 1999, vol. 65, no. 9, pp. 27–37.
13. Finie, K.S., Trani, G., Short, K.T., et al., *Thin Solid Films*, 2003, vol. 440, pp. 109–116.

ISSN 1070-4272, Russian Journal of Applied Chemistry, 2008, Vol. 81, No. 12, pp. 2056–2061. © Pleiades Publishing, Ltd., 2008.
Original Russian Text © A.G. Zhigotskii, E.F. Rynda, N.A. Mishchuk, V.M. Kochkodan, A.V. Ragulya, V.P. Klimenko, M.N. Zagornyi, 2008, published in Zhurnal Prikladnoi Khimii, 2008, Vol. 81, No. 12, pp. 1942–1948.

INORGANIC SYNTHESIS AND INDUSTRIAL INORGANIC CHEMISTRY

A Study of the Photocatalytic Activity of Titanium Dioxide Nanopowders

A. G. Zhigotskii, E. F. Rynda, N. A. Mishchuk, V. M. Kochkodan, A. V. Ragulya, V. P. Klimenko, and M. N. Zagornyi

Dymanskii Institute of Colloid Chemistry and Water Chemistry, National Academy of Sciences of Ukraine, Kiev, Ukraine
Frantsevich Institute of Material Science Problems, National Academy of Sciences of Ukraine, Kiev, Ukraine

Received May 13, 2008

Abstract—Photodestruction and adsorption of dyes in aqueous suspensions of nanopowders of titanium dioxide of anatase modification was studied. The photocatalytic activity of titanium dioxide nanopowders was examined in relation to the dispersity of particles and pH of the medium.

DOI: 10.1134/S1070427208120021

Development of new optically active nanocrystalline materials and technologies of their effective application has become particularly important in recent years. This is due both to the need to search for new power sources (solar light convertes in the case in question) and to the ecological safety of the technologies employed.

Of particular scientific and applied interest in this context are studies in the field of synthesis and analysis of properties of semiconducting nanopowders, oxides of transition metals, including titanium dioxide. Owing to the excellent combination of physicochemical, optical, and catalytic properties, fields of its application are rather extensive. In particular, use of TiO_2 in heterogeneous catalytic oxidation processes for destruction of chlorine- and nitrogen-containing compounds, acids, dyes, surfactants, pesticides, and herbicides was described in [1].

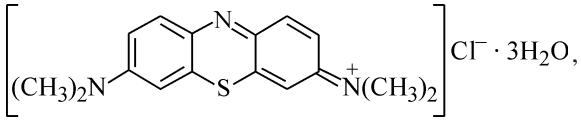
However, certain aspects of heterogeneous processes of this kind are insufficiently understood because of their multifactor and multistage nature. This is largely due to very complex chemical and structural features of the surface of TiO_2 powders, which includes basic and acidic centers, hydroxy groups, and hydroxy and oxygen radicals generated by photocatalytic processes [2]. The situation is made even more complicated in the case of nanosize TiO_2 particles having large specific surface area, mesoporous structure, and high interparticle interaction energy. Of particular interest in this case are TiO_2–dye systems with varied chemical composition and structure, which, in addition, can exhibit sensitizing properties [3].

EXPERIMENTAL

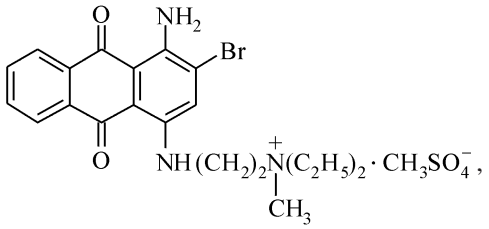
The communication reports on a study of the photocatalytic activity of TiO_2 nanopowders with different particle sizes in photodestruction of dyes of varied chemical nature and structure in aqueous solutions under UV irradiation.

As objects of study were chosen the following TiO_2 powders: of anatase crystalline modification with a particle size of 5 nm and specific surface area of 140 $m^2 g^{-1}$ (Aldrich) (TiO_2-I); of rutile modification with a particle size of <5 nm and specific surface area of 2.7 $m^2 g^{-1}$ (TiO_2-II); of anatase modification with a particle size of 20–25 nm and specific surface area of 108 $m^2 g^{-1}$, synthesized at the Institute of Material Science Problems, National Academy of Sciences of Ukraine (TiO_2-III); and a powder of AV-01-SF brand (Precheza) with a particle size of 100–120 nm and specific surface area of 15.5 $m^2 g^{-1}$ (TiO_2-IV).

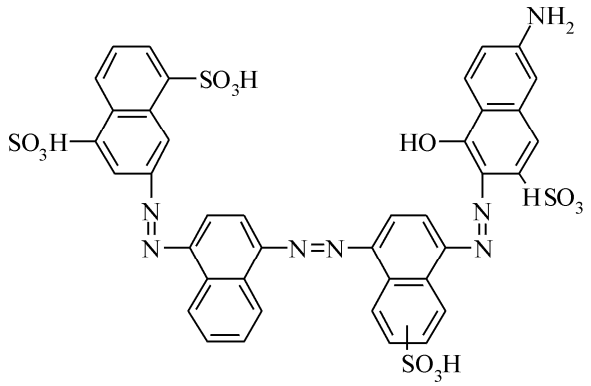
The interaction of titanium dioxide with the following dyes was studied: Methylene Blue (MB) of the thiazine series {analytically pure grade, TU (Technical Specification) 6-09-29–76 [4]}



Cationic Violet 4S (CV) of the anthraquinone series (TU 6-00-49222775-07–2001 [5])



and Direct Blue 2S polyazo dye (DB), GOST (State Standard) 22849–77 [5]



The photocatalytic activity of the TiO_2 powders was determined in 40 mg l^{-1} aqueous solutions of the dyes. The manner in which the optical density and the residual concentration of a dye in solutions vary with the type of TiO_2, pH of the medium (3.2–9.2), and duration of contact between the components (5–60 min) with and without UV irradiation was analyzed. The pH value of dye solutions was adjusted by addition of hydrochloric acid and sodium tetraborate. The optical density of the dye solutions was measured with a KFK-2MP photoelectric colorimeter at wavelengths of 540 (for CV and DB solutions) and 590 nm (for MB solutions) and solution layer thickness of 0.5 cm. The wavelengths corresponded to the absorption peaks. After being brought in contact with TiO_2 powders, the dye solutions were subjected to centrifugation at 8000 rpm for 15 min and their optical density was measured. The residual dye concentrations were found using optical density–dye concentration calibration plots obtained at the corresponding wavelengths. The UV irradiation of dye solutions and suspensions was performed using an SVD-120A high-pressure mercury lamp at an intensity of 18.9 W m^{-2} in the wavelength range 200–400 nm.

The photocatalytic activity of TiO_2 powders is mostly due to the presence of oxygen vacancies and Ti^{3+} ions in the crystal lattice and is manifested upon irradiation with photons with energies of no less than 3.0 and 3.2 eV for the rutile and anatase TiO_2 modifications, respectively. The anatase form of TiO_2 exhibits a higher activity in photoreactions [6–9]. In heterogeneous photocatalytic processes in aqueous media, electron–hole pairs are generated in TiO_2 crystals in the presence of oxygen under the action of UV light, with the subsequent formation of $O_2^{\cdot}$, $O_3^{\cdot}$, $HO^{\cdot}$, and $HO_2^{\cdot}$ radicals [1] having a strong oxidizing effect. In this case, changes in the pH of the medium can strongly affect the concentration of $HO^{\cdot}$ radicals and destruction of organic substances and, in particular, synthetic dyes.

The UV irradiation of TiO_2 suspensions in MB solutions at pH 9.2 is accompanied by an initially, during the first 5–10 min, steep and then insignificant decrease in the residual concentration of the dye (Fig. 1). The discoloration process has the highest intensity in systems containing photocatalyst nanopowders with the smallest particle size, TiO_2-I and TiO_2-III. As the particle size increases, the rate of the discoloration process becomes substantially lower. For example, for powders with particle sizes of 5 and 100–120 nm, the residual dye concentration reaches in 5 and 60 min values of 9 and 2, and 35 and 22 mg l^{-1}, respectively. The process of MB discoloration by TiO_2 nanopowders in the first 5–10 min can be attributed, in accordance with the data of [3], to zeroth-order photoreaction. A similar kinetic dependence of the residual con-

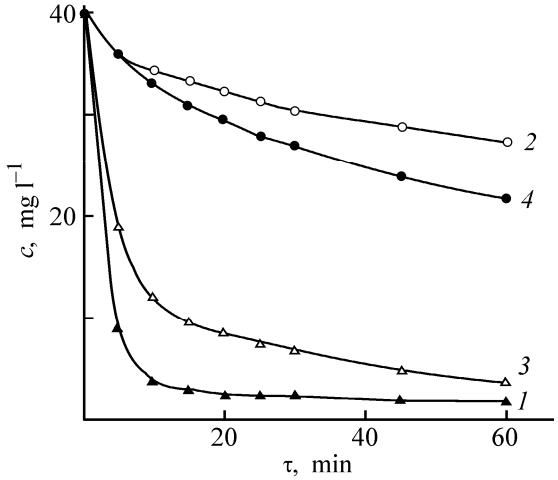


Fig. 1. Kinetics of discoloration of Methylene Blue dye solutions at pH 9.20 in suspensions containing TiO_2 powders. (*c*) Residual dye concentration in the suspensions and (τ) duration of UV irradiation; the same for Fig. 3. Sample: (*1*) TiO_2-I, (*2*) TiO_2-II, (*3*) TiO_2-III, and (*4*) TiO_2-IV; the same for Figs. 2–4.

Table 1. Residual dye concentration c and the degree G of adsorption of MB dye in TiO_2 suspensions at pH 6.1 upon UV irradiation for 10 and 60 min

Sample	c, mg l^{-1}		G, %	
	10 min	60 min	10 min	60 min
TiO_2-I	38	35	2.5	6.3
TiO_2-II	38	23	2.5	2.5
TiO_2-III	40	29	0	6.3
TiO_2-IV	35	32	12.5	15.0

centration of a fungicide, fanarimol, has been observed when the role of a photocatalyst was played by TiO_2 of P-25 brand (Degussa) with a specific surface area of 50 $m^2 g^{-1}$, which is a mixture of the anatase (70–85%) and rutile (15–30%) modifications of TiO_2 [7].

As the pH value of the MB solution is lowered to 6.1, the degree of discoloration dramatically decreases (Table 1), with this effect being characteristic of all TiO_2 powders; the relative positions of the kinetic curves is preserved, as also for dye suspensions with pH 9.2.

Because the optical density of MB solutions remains almost unchanged as pH is lowered from 9.2 to 6.1 and upon UV irradiation for 1 h, the steep decrease in the photocatalytic activity of TiO_2 powders can be attributed to changes in the properties of the photocatalyst itself, whose isoelectric point is 6.7 [10]. The adsorption of OH^- ions on the surface of TiO_2 particles makes larger their negative charge. As a result, the concentration of highly reactive $HO^{\cdot}$ radicals generated by the reaction OH^- + electron vacancy → $HO^{\cdot}$ increases, too. As the pH of TiO_2 suspensions decreases, these factors become less important and the aggregation of TiO_2 particles increases, primarily for the nanosize catalyst, which makes lower the degree of discoloration of the dye solution.

Undoubtedly, an important role is played in the mechanism of photocatalytic discoloration and destruction of a dye by adsorption of its molecules on the surface of TiO_2 particles, which is the initial event of this process. The dynamic nature of the adsorption–desorption of dye molecules and products of their destruction has the key importance for the effective course of the whole photocatalytic process.

As follows from Fig. 2, the run of the kinetic curves in the case of a dark contact of TiO_2 particles with dye solutions is similar to that for irradiated suspensions. As the size of particles decreases and their specific surface area becomes larger, the degree of dye adsorption grows. For example, for TiO_2-I, TiO_2-II, and TiO_2-IV powders brought in contact with MB solutions with pH 9.20 for 1 h, the degree of adsorption reaches values of 70, 50, and 18%, respectively, relative to the initial dye concentration. These values are substantially lower than the residual concentrations of the dye in its photocatalytic discoloration. Substantially lower degrees of MB adsorption on TiO_2 powders were observed for the suspensions at pH 6.10 (Table 1). The interaction of dye molecules with the surface of TiO_2 particles may occur as a result of electrostatic attraction between positively charged cations

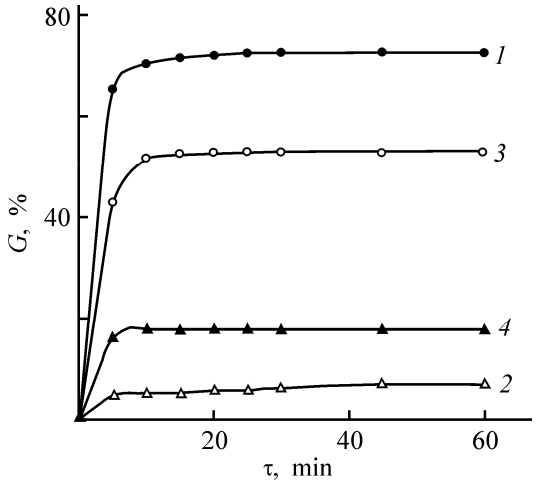


Fig. 2. Kinetics of Methylene Blue dye adsorption in suspensions containing TiO_2 powders at pH 9.20. (G) Degree of dye adsorption and (τ) adsorption duration; the same for Fig. 4.

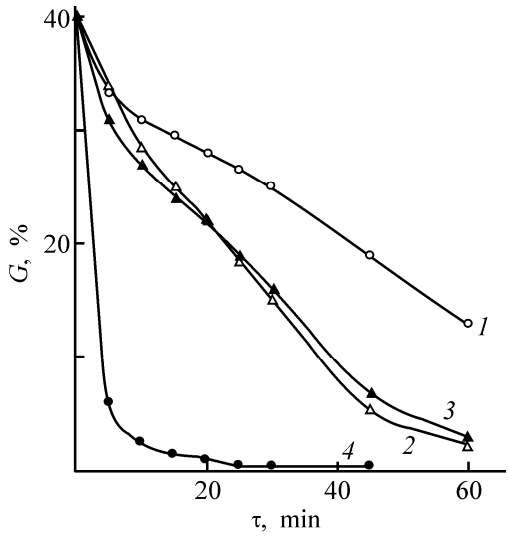


Fig. 3. Kinetics of discoloration of Cationic Violet 4S dye solutions in suspensions containing TiO_2 powders at pH 6.10.

of the dye and negatively charged TiO_2 particles and formation of π-bonds involving electrons of the conjugated system of bonds of the dye, hydrogen bonds, and van der Waals bonds [11].

Thus, there exists a direct relationship between the photocatalytic activity of TiO_2 powders, their dispersity, and adsorption of a dye on the surface of photocatalyst particles, which is noticeably manifested in the difference between the kinetic curves of discoloration of MB and carbonyl-containing CV (Table 1, Fig. 3). It should also be kept in mind that, being a comparatively strong oxidizing agent, CV itself exhibits a certain photosensitivity in the spectral range of the UV irradiation, which is expressed in a decrease in its residual concentration to 32 mg l^{-1} upon exposure for 60 min. As the solution pH increases, the coloration intensity noticeably decreases and almost completely disappears at pH 9.2.

As follows from Fig. 3, the rate of CV discoloration and destruction in TiO_2 suspensions markedly exceeds that for the thiazine dye. Noteworthy is the very high photocatalytic activity of the TiO_2-IV powder, which has the coarsest particles (100–120 nm) among TiO_2 nanopowders. This may be due to the minimum particle aggregation of this photocatalyst and to the maximum degree of adsorption of CV dye on its particles (Fig. 4). All the other TiO_2 powders also exhibit a rather high catalytic activity, compared with that in MB solutions at pH 6.1. This should be particularly emphasized for the TiO_2 powder of the rutile modification, with a particle size of less than 5 μm, for which the particle aggregation effect is the least pronounced. For example, the residual concentration of the dye in CV solutions reaches for TiO_2-I and TiO_2-II, upon 5 and 60 min of UV irradiation, values of 31 and 13 mg l^{-1} and 33 and 2.5 mg l^{-1}, respectively. In most cases, the degree of CV adsorption is smaller than that for MB, especially for the TiO_2-IV powder. Thus, the anthraquinone dye is less stable against UV irradiation as compared with the thiazine Methylene Blue.

The pH of the medium strongly affects the photocatalytic activity of TiO_2 powders. Rather important in the interaction of a dye with surface OH groups of TiO_2 is the formation of hydrogen bonds [12] involving carbonyl groups of the dye, which is accompanied by its discoloration. The nature of kinetic dependences and the absolute values of the residual concentration of the dye under UV irradiation in the course of interaction between CV and TiO_2 powder suggest the following. In given case, there is a favorable combination of the spectral sensitivity of the photoreaction of discoloration and destruction of the anthraquinone dye and the spectral excitation of the photocatalyst, which promotes high-intensity generation of electron–hole pairs and leads to an increase in their lifetime before recombination and thereby enables their involvement in the photochemical reaction.

Table 2. Residual DB dye concentration c in TiO_2 suspensions upon UV irradiation for 60 min

Sample	c, mg l^{-1}, at indicated pH		
	3.2	6.7	9.2
TiO_2-I	0.6	5/0*	35
TiO_2-II	32	29/23*	32.5
TiO_2-III	22	20/3*	34
TiO_2-IV	24	30/18*	32

* After contact in the dark between the dye solution and TiO_2 powder for 10 min and subsequent UV irradiation for 30 min.

The key role in evaluation of the catalytic activity of TiO_2 particles is played by the intrinsic photoactivity of the dye used for this purpose. As shown by studies of the photostability of the acid polyazo dye, Direct Blue 2S, its aqueous solutions are stable in the pH range studied, and only at pH 3.2 and UV irradiation, the residual concentration decreases by 10%. The nature of kinetic dependences of the residual concentration of DB in TiO_2 suspension is nearly the same as that for cationic dyes. As in the case of MB, the highest catalytic activity is exhibited by the TiO_2-I powder at any of the pH values studied (Table 2). For example, at pH 3.2 and UV irradiation duration of 60 min, the re-

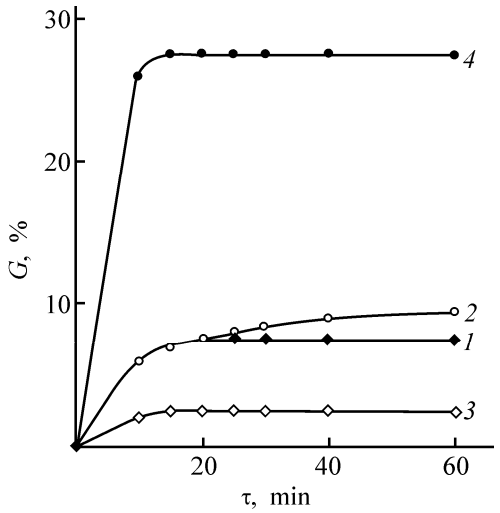


Fig. 4. Kinetics of Cationic Violet 4S dye adsorption in suspensions containing TiO_2 powders at pH 6.10.

Table 3. Residual dye concentration c and total carbon content [C] of MB and DB solutions upon UV irradiation of TiO_2-I suspensions

Suspension no.	Dye	pH	Duration of UV irradiation, min	c, mg l^{-1}	[C], mg l^{-1}
1	MB	9.2	10	4.0	6.3
2			60	2.5	7.9
3*			60 + 60	10.0	16.5
4**			60 + 60 + 60	17.5	18.6
5	DB	3.2	20	0.6	5.2
6		6.7	60	5.0	8.7

* Suspension no. 3 was produced from suspension no. 2 after a UV irradiation for 60 min, centrifugation, dispersion of the sediment in the same volume of a fresh dye solution, and UV irradiation for 60 min.

** Suspension no. 4 was produced from suspension no. 3 on performing the same procedures as those with suspension no. 2.

sidual concentration of DB reaches a value of 0.6 mg l^{-1}. In this case, the higher the dispersity of a TiO_2 powder, the stronger its catalytic activity, with this tendency becoming weaker at higher pH values and the dye discoloration being only slightly manifested at pH 9.2. In contrast to the cationic dyes, the TiO_2–DB system is characterized by a smaller difference between the residual concentrations of the dye in its discoloration via adsorption of photocatalyst particles and UV irradiation, with the correlation between these concentrations for different TiO_2 powders preserved. The degree of adsorption after a dark contact of the components for 60 min at pH 9.2 reaches a value of 70% for the TiO_2-I powder and 51% for TiO_2-III, whereas the residual concentrations of DB are 5 and 20 mg l^{-1}, respectively. This points to a considerable contribution of the adsorption of the dye to its discoloration under UV irradiation in the presence of TiO_2 powders. At the same time, the results of experiments with preliminary contact (adsorption) of the components for 10 min and subsequent UV irradiation and those with continuous UV irradiation of the suspensions for 60 min demonstrate that the residual concentration of the dye is substantially lower in the first case. These data suggest that the discoloration of the dye under UV irradiation of the suspensions studied is of dynamic nature.

A specific feature of the discoloration and destruction of DB under UV irradiation in the presence of TiO_2 powders is that this process can occur by the mechanism of photoreduction or photooxidation, as it has been observed for other azo dyes [3]. Presumably, one or the other mechanism will be observed, depending of the pH value of TiO_2 suspensions. In an aqueous medium in the presence of oxygen and low pH values, it is possible that the nitrogen atoms of nitro groups are protonated and the dye is discolored to give amines as a result of destruction of the backbone of dye molecules and oxidation by atmospheric oxygen and by ozone formed in its ionization. As the pH of the medium increases, the concentration of hydrogen ions decreases and the intensity of complexation of azo groups, dye discoloration, and destruction of dye molecules to give products with various degrees of oxidation becomes higher. Simultaneously, the negative charge of the surface of TiO_2 particles increases, the degree of ionization of acid-dye molecules grows, the electrostatic repulsion between TiO_2 particles and dye molecules becomes stronger, the adsorption decreases, and the catalytic activity of TiO_2 powders declines.

Analysis of dye solutions after the UV irradiation in the presence of TiO_2-I powder (Table 3) shows that their total carbon content markedly exceeds that corresponding to the residual concentration of a dye. This may indicate that, together with the disruption of the system of conjugated bonds, there occurs chemical destruction of the dyes to give low-molecular-weight compounds with various degrees of oxidation.

It should be kept in mind, when analyzing the results obtained, that the total carbon concentrations in the starting solutions of MB and DB are 20.6 and 20.2 mg l^{-1}, respectively. Comparison of the absolute values of the residual concentrations of the dyes and the total carbon content of solutions subjected to UV irradiation in the first 10–60 min shows that a considerable amount of volatile products is formed in photodestruction of MB and DB.

A repeated use of the TiO_2 nanopowder as a photocatalyst (suspension nos. 3 and 4) demonstrated that, in this case, the residual concentration of the dye and

the total carbon content in solution increase. The decrease in the photocatalytic activity of the TiO_2 powder in its repeated use may be due not only to "poisoning" of the catalyst, associated with blocking of active centers on the surface of its particles as a result of chemisorption of products formed in dye destruction, but also to impossibility of restoring the initial dispersity of particles of the photocatalyst in its redispersion.

Thus, the photocatalytic activity of highly dispersed TiO_2 powders in dye-containing aqueous suspensions strongly depends not only on the physicochemical properties of photocatalyst particles, but also on the chemical composition and structure of dye molecules and their mutual influence on the process of discoloration and destruction of an organic substance under UV irradiation of the system constituted by TiO_2 and an aqueous solution of a dye.

CONCLUSIONS

(1) A correlation was revealed between the kinetics of discoloration, destruction, and adsorption of a polyazo dye and thiazine and anthraquinone dyes in aqueous suspensions of titanium dioxide powders of anatase modification, with particle size of 5–120 nm.

(2) It was demonstrated that the kinetics of photodiscoloration and adsorption of aqueous solutions of the dyes studied shows the highest rate in the first 5–10 min and is largely determined by the type of interaction of their molecules with the surface of titanium dioxide particles.

(3) It was shown that the photocatalytic activity of titanium dioxide nanopowders increases with the dispersity of their particles and strongly depends on the pH of the medium, which markedly affects both the stability of synthetic dyes and the activity of titanium oxide photocatalysts.

REFERENCES

1. *Ekologicheskie aspekty sovremennykh tekhnologii okhrany vodnoi sredy* (Ecological Aspects of Modern Technologies for Protection of Water Basins), Goncharuk, V.V., Ed., Kiev: Naukova Dumka, 2005.
2. Solomon, D.H. and Howchorne, D.G., *Chemistry of Pigments and Fillers*, New York: John Wiley Sons, 1983.
3. *Khimiya sinteticheskikh krasitelei* (Chemistry of Synthetic Dye), Venkataramana, K., Ed., Leningrad: Khimiya, 1975, vol. 4.
4. Froinshtadt, D.M., *Reagenty i preparaty dlya mikroskopii* (Reagents and Preparations for Microscopy), Leningrad: Khimiya, 1980.
5. Stepanov, B.I., *Vvedenie v khimiyu i tekhnologiyu organicheskikh krasitelei* (Introduction to Chemistry and Technology of Organic Dyes), Moscow: Khimiya, 1984.
6. Sopajaree, K., Qasim, S.A., Basak, S., and Rajeshwar, K., *J. Appl. Electrochem.*, 1999, vol. 29, pp. 533–539.
7. Balansbramanian, G., Dionjsion, D., Suidan, M.T., et al., *Appl. Catal. B: Environmental*, 2004, vol. 47, pp. 73–84.
8. Bessergenev, V.G., Peretra, R.J.F., Mateus, M.C., et al., *Thin Solid Films*, 2006, vol. 503, pp. 29–39.
9. Sheng, Q., Yuan, S., Zhang, J., and Chen, F., *Microporous Mesoporous Mater.*, 2006, vol. 87, pp. 177–184.
10. Fernandez-Ibañez, P., Blanco, J., Malato, S., and de las Nieves, F.J., *Water Research*, 2003, vol. 37, pp. 3180–3188.
11. *Adsorption from Solution at the Solid/Liquid Interface*, Parfitt, G.D., Rochester, C.H., Eds., London: Academic, 1983.
12. Pimentel, G.C., *The Hydrogen Bond*, McClellan, A.L. and Pauling, L., Eds., San Francisco: Freeman, 1960.

ISSN 1070-4272, Russian Journal of Applied Chemistry, 2008, Vol. 81, No. 12, pp. 2062–2065. © Pleiades Publishing, Ltd., 2008.
Original Russian Text © A.A. Nesterov, K.S. Masurenkov, E.V. Karyukov, 2008, published in Zhurnal Prikladnoi Khimii, 2008, Vol. 81, No. 12, pp. 1949–1952.

INORGANIC SYNTHESIS AND INDUSTRIAL INORGANIC CHEMISTRY

Effect of Stock Dispersity on Properties of Ceramic Materials

A. A. Nesterov, K. S. Masurenkov, and E. V. Karyukov

Southern Federal University, Rostov-on-Don, Russia

Received January 21, 2008

Abstract—Powdered ceramic piezoelectric phases of fixed chemical composition and prescribed particle size in the range from 15 to 350 nm were obtained using a unified synthesis technique. The dependence of their electrical parameters on the granulometric composition of the stock was studied.

DOI: 10.1134/S1070427208120033

Nanopowders of ferroelectric phases can be obtained using condensation (gel-technique, cryogenic method, cooling of vapors at high supersaturations) and dispersion methods (grinding in colloid mills, thermal or mechanical impact). Despite the different types of physicochemical processes that occur when highly dispersed phase are formed, they yield highly defective particles with a considerably higher internal energy, compared with microparticles. Therefore, all the possible phase transitions in nanodispersed systems occur at lower temperatures, compared with microscopic systems. As the crystallite size decreases, the volume, symmetry, and space groups of the unit cells of the phases being synthesized change and materials on their base acquire new properties or loose those already existing [1–3].

In this study, prospects for use of nanopowders of ferroelectric phases in synthesis of ceramic piezoelectric materials were considered. Powders of phase with a perovskite structure of compositions ABO_3, $A^1_{1-x}A^2_xBO_3$, $AB^1_{1-x}B^2_xO_3$, and $A^1_{1-x}A^2_xB^1_{1-y}B^2_yO_3$ (A^1 and $A^2 = Ca^{2+}$, Sr^{2+}, Ba^{2+}, Pb^{2+}; B^1 and $B^2 = Ti^{4+}$, Zr^{4+}, Sn^{4+}, Mn^{4+}) were produced by interaction of gels of Ti(IV), Zr(IV), Sn(IV), and Mn(IV) hydroxides (Fig. 1) with oxides or hydroxides of calcium, strontium, barium, and lead [4–7]. The method enables control over the dispersity of the final crystalline product within the range from 15–20 to 2000 nm and synthesis of powders with close particle sizes. This dramatically diminishes the rate of secondary crystallization in sample sintering and thereby makes it possible to fabricate ceramics with grain sizes that begin with 50–80 nm. These specific features of the method enable assessment of the influence exerted by the size of particles of the starting powder and grains of ceramics prepared from this powder on the electrical properties of finished articles.

EXPERIMENTAL

The starting forms of Ti(IV), Zr(IV), Sn(IV), and Mn(IV) hydroxides were precipitated from nitrate solutions of compounds of these elements at 5–10°C with 10% aqueous ammonia (final pH 8). Then, Pb(II) and (or) hydroxides of alkaline-earth metals were added in a prescribed ratio. The occurrence of exchange processes in the system [between active forms of M(IV) hydroxides (Fig. 1) and M(II) oxides (hydroxides)] in the surface layer of the gel yields an intermediate amorphous reaction product [5–7]. To raise the reaction rate (renewal of the reaction zone), the suspension was ground for 1 h and dried at 80–100°C. The resulting finely dispersed powder was pelletized under a pressure of 50–70 MPa and the pallets were calcined at 300–900°C with a step of 50°C (isothermal keeping at each temperature for 1 to 10 h).

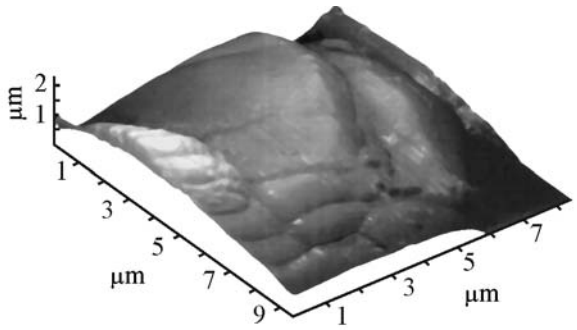


Fig. 1. Micrograph of Ti(IV) hydroxide precipitated from a nitrate solution with a 10% solution of NH_3.

Calcined samples were subjected to X-ray phase (XPA) and diffraction (XRD) analyses (DRON-2.0 diffractometer, Cu$K_{\alpha 1}$ radiation, Ni-β filter). The lattice constants were found from the (220) and (202) reflections, and sizes of the coherent-scattering regions (CSR) and microstrains ($\Delta d/d$) in the [200] direction, from the (100) and (200) reflections by the approximation method [reference and experimental diffraction profiles described by functions of the type $y = A\exp(-\alpha^2 x^2)$] [8, 9]. The rms displacements $(\bar{u}^2)^{1/2}$ of atoms from their ideal positions, caused by vacancies and interstitial atoms, were determined in the [111] and [200] directions in accordance with the pseudo-thermal multiplier $\exp[8\pi^2\bar{u}^2(\sin\theta/\lambda)^2]$ (θ is the Bragg angle, and λ, X-ray wavelength). The absolute error in determining the unit cell parameters was 0.0003 nm, and the relative error of $D_{[200]}$, $(\Delta d/d)_{[200]}$, and $(\bar{u}^2)^{1/2}$ did not exceed 15%.

The surfaces were visualized and the particle size distribution were found using a Solver Pro-M scanning probe microscope (NT-MDT).

The stocks synthesized at different temperatures by the conventional ceramic technology [1, 2] (sintering temperature 1050–1150°C, duration 2–6 h, modes monitored by the maximum density) were used to fabricate ceramic samples 10 mm in diameter and 1 mm high (Ag electrodes deposited by firing-in, polarization in silicone oil with a field of up to 50 kV cm^{-1} at 100–120°C). The electrical properties of these samples were determined in accordance with GOST (State Standard) 12370–80.

According to XPA data, the powders synthesized at 5–260°C are X-ray amorphous. The sizes of the coherent-scattering regions of cubic crystalline phases formed upon calcination of the primary amorphous product at 300–350°C for 2 h are 15–25 nm; $[(\Delta d/d)_{[200]}\times10^3 =$ 3.2 to 2.7, respectively, at $(\bar{u}^2_{[111]})^{1/2} = 0.036$–$0.039]$. The ceramic fabricated from this stock (calcination at 1100°C for 2 h) has grains with diameters of 40–60 nm (according to probe microscopy) (Figs. 2, 3), separated by wide regions of, presumably, a glassy phase. These ceramic samples have an anomalously high dielectric constant (3–5 times that of samples of the same composition, with grain sizes of several micrometers), the phase remains cubic, the material has no piezoelectric properties, the electrical conductivity of the samples widely varies, the maximum density of the ceramic does not exceed 70% of the theoretical value, and the article density cannot be raised by raising the sintering temperature and duration.

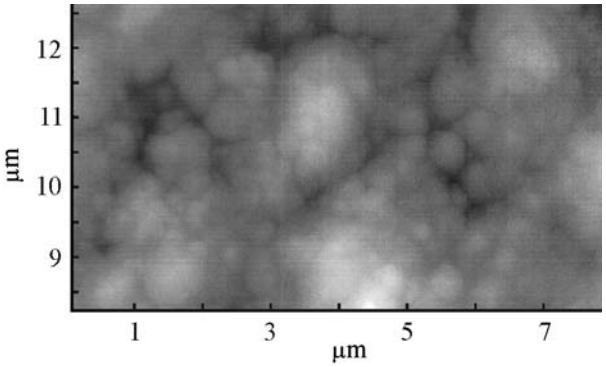


Fig. 2. Micrograph of the surface of a ceramic sample produced by the gel technique.

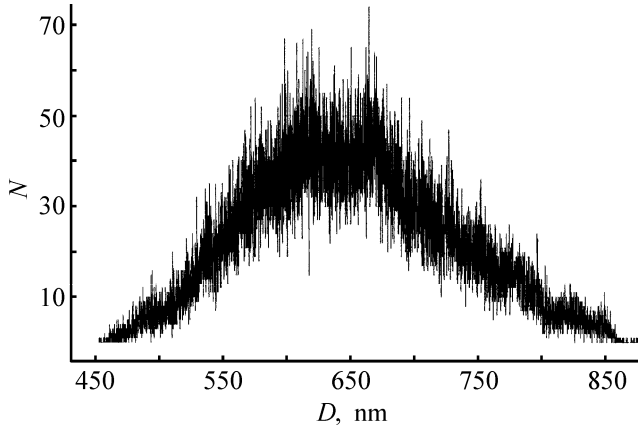


Fig. 3. Particle size distribution for the ceramic synthesized by the gel technique. (*N*) Relative number of particles and (*D*) particle diameter.

Elevating the stock synthesis temperature from 400 to 600°C leads to a gradual increase in the crystallite size, and, at a particle CSR of 70–90 nm $(\Delta d/d)_{[200]}\times10^3$ equal to 2.1 and 2.7, respectively, $(\bar{u}^2_{[111]})^{1/2} = 0.016$–$0.028]$, the cubic structure of a number of phases and solid solutions on their base ($PbTiO_3$, $BaTiO_3$, $PbZrO_3$) is transformed to a tetragonal or rhombohedral phase (Figs. 4, 5), depending on their chemical composition. These changes in the structure and size of stock particles result in that the ceramics synthesized from this stock acquire piezoelectric properties on the background of a decrease in the dielectric constant (Fig. 6).

According to probe microscopy, raising the synthesis temperature of the molding powder (up to 900°C) results in an increase in the particle size from 110 to 155 nm and, accordingly, in the grain diameter of the ceramic produced from this powder. As the grain diameter of the ceramic grows within the range 150–350 nm, its $\varepsilon^T_{33}/\varepsilon_0$ continues to decrease and the elec-

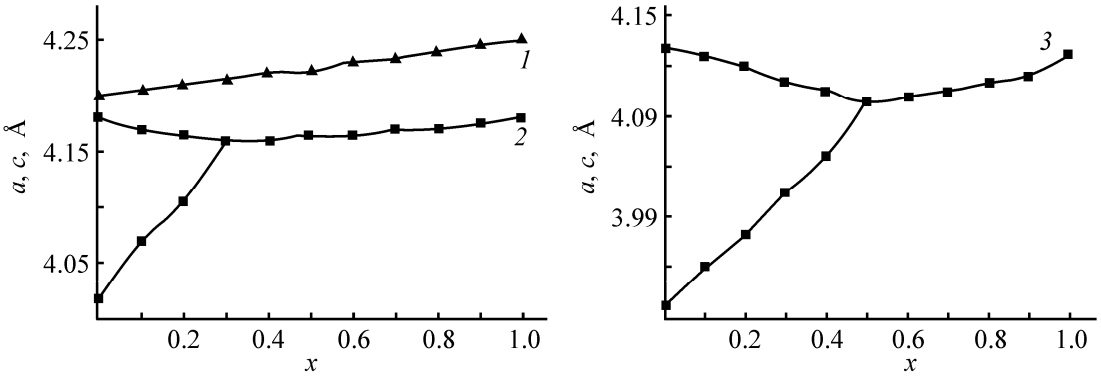


Fig. 4. Lattice constants a and c of phases of the $Ba_xPb_{1-x}Zr_xTi_{1-x}O_3$ type vs. the composition and thermal treatment conditions of a stock synthesized by the gel method. Thermal treatment duration 2 h; the same for Fig. 5. Calcination temperature (°C); (*1*) 250, (*2*) 400, and (*3*) 700; the same for Fig. 5.

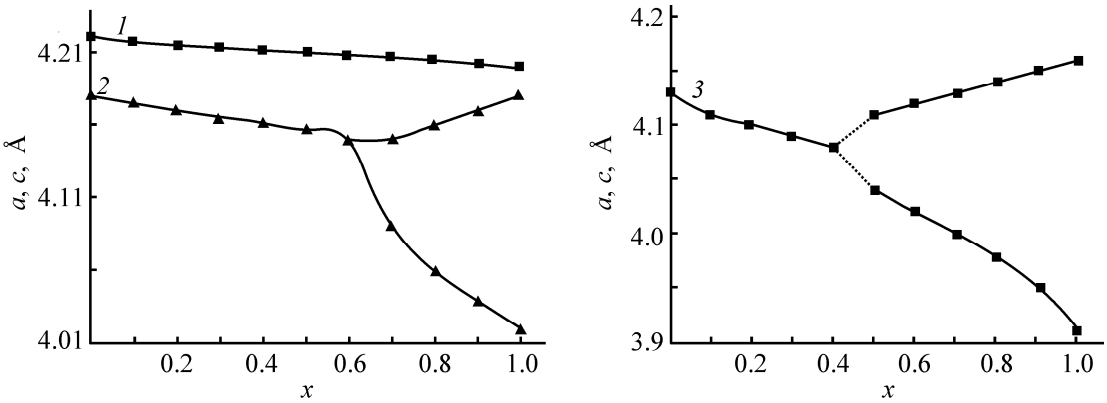


Fig. 5. Lattice constants a and c of phases of the $PbTi_xZr_{1-x}O_3$ type vs. the composition and thermal treatment conditions of a stock synthesized by the gel method.

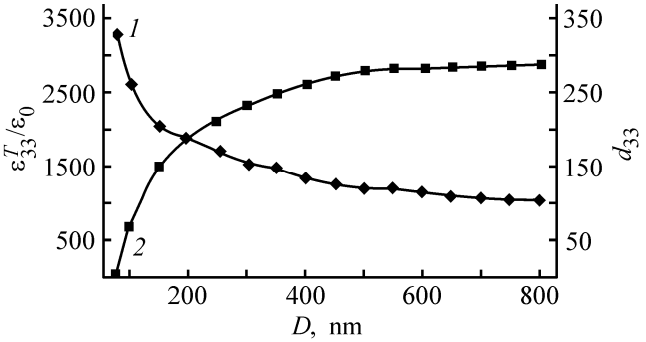


Fig. 6. Variation of the electrical properties of a ceramic sample with the average grain diameter D. (*1*) $\varepsilon_{33}^T/\varepsilon_0$ and (*2*) d_{33}.

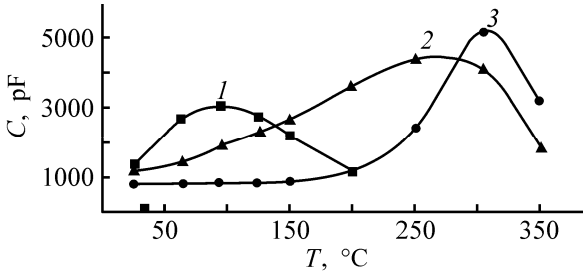


Fig. 7. Capacitance C of standard ceramic samples (h = 1 mm, d = 10 mm) vs. temperature T. Sample density is not lower than 87% of the theoretical value. Average grain size (nm): (*1*) 150, (*2*) 280, and (*3*) 600.

tromechanical coupling coefficients and piezoelectric moduli grow severalfold. Further increase in the grain size in the samples (400–600 nm) changes $\varepsilon_{33}^T/\varepsilon_0$ only slightly (tendency toward a minor decrease), whereas their K_p, K_t, and piezoelectric moduli grow by 20–30% (Fig. 6). It should also be noted that, as the grain diameter of the ceramic increases from 150 to 600 nm, the Curie point of the materials grows from 96 to 319°C (Fig. 7), in good agreement with experimental data on the decrease in $(\Delta d/d)_{[200]}$ and $(\bar{u}^2_{[111]})^{1/2}$ of the piezoelectric phase as the grain diameter becomes larger.

Analysis of the results obtained shows that the dispersity of powdered ferroelectric phases and the defectiveness of their separate particles can be rather widely varied by changing the formation conditions of the pow-

ders. An increase in the ratio between the surface area of a particle to its volume leads to a rise in the fraction of surface unit cells and, as a consequence, to a higher total energy of the system. An increase in the isobaric-isothermal potential of the phases gives rise to a number of negative, as regards the quality of piezoelectric materials, phenomena. For example, a decrease in the degree of distortion of perovskite phases makes weaker the spontaneous polarization of the samples (the factor diminishing the electromechanical coupling coefficients and piezoelectric moduli) and leads to lowering of the temperature of phase transition to the cubic modification (Curie point): e.g., at a grain size of the ceramic of less than 80 nm, the Curie point of the materials is below 0°C. In addition, the conductivity of the samples increases as the grain diameter of the ceramic decreases within the range 50–150 nm, which gives no way of performing their effective polarization. The results of the study indicate that the piezoelectric ceramic with grain sizes in the range from 200 to 800 nm is of interest from the practical standpoint. By varying the grain diameter within these limits, it is possible to fabricate materials that can effectively operate in both the reception and emission modes and articles with different temperature stabilities of separate parameters by varying the Curie point of piezoelectric phases and, consequently, to considerably extend the application fields of piezoelectric transducers fabricated from a certain phase.

CONCLUSIONS

(1) The size effect (or effect of phase defectiveness) is observed in piezoelectric materials in a wide range of granulometric compositions of the samples, which makes it possible to obtain piezoelectric ceramics with various combinations of electrical parameters from a substance of fixed composition.

(2) Of practical interest is a piezoelectric ceramic based on perovskite phases with a grain diameter in the range from 200 to 800 nm, whose piezoelectric and dielectric properties and Curie point depend on the grain size.

REFERENCES

1. Iona, F. and Shirane, G., *Ferroelectric Crystals*, Oxford: Pergamon, 1962.
2. Okazaki, K., *Ceramic Engineering for Dielectrics*, Tokyo: Gakkensya, (in Japanese), 1969.
3. Zhong, W.L., Wang, Y.G., Zang, P.L., and Qu, B.D., *Phys. Rev. B*, 1994, vol. 50, no. 2, pp. 698–703.
4. Surowiak, Z., *Molecular Quantum Acoustics*, 2000, vol. 21, pp. 267–288.
5. Nesterov, Al.An., Kupriyanov, M.F., Nesterov, An.Al., et al., *Izv. Akad. Nauk, Ser. Fiz.*, 2004, vol. 68, no. 5, pp. 711–713.
6. Nesterov, A.A., Lupeiko, T.G., and Nesterov, A.A., Trudy MNPK *"Fundamental'nye problemy p'ezoelektricheskogo priborostroeniya"* (Coll. of Works of MNPK "Fundamental Problems of Piezoelectric Instrument-building"), 1999, vol. 1, pp. 254–261.
7. Nesterov, A.A., Lupeiko, T.G., Nesterov, A.A., and Pustovaya, L.E., *Neorg. Mater.*, 2004, vol. 40, no. 12, pp. 1530–1534.
8. Kovba, L.M. and Trunov, V.K., *Rentgenofazovyi analiz* (X-ray Phase Analysis), Moscow: Mosk. Gos. Univ., 1976.
9. Surovyak, Z., Panich, A.E., and Dudkevich, V.P., *Tonkie segnetoelektricheskie plenki* (Thin Ferroelectric Films), Rostov-on-Don: Rost. Gos. Politekhn. Univ., 1994.

ISSN 1070-4272, Russian Journal of Applied Chemistry, 2008, Vol. 81, No. 12, pp. 2066–2073. © Pleiades Publishing, Ltd., 2008.
Original Russian Text © M.A. Kruglova, M.P. Yaroshenko, 2008, published in Zhurnal Prikladnoi Khimii, 2008, Vol. 81, No. 12, pp. 1953–1960.

INORGANIC SYNTHESIS AND INDUSTRIAL INORGANIC CHEMISTRY

Synthesis and Properties of Zirconium-containing Materials Produced Using Calcium Aluminates

M. A. Kruglova and M. P. Yaroshenko

NIIAP-Katalizator Limited-Liability Company, Novomoskovsk, Tula oblast, Russia

Received March 25, 2008

Abstract—Highly dispersed zirconium-alumocalcium oxide materials were synthesized with calcium aluminates. The phase composition and surface properties of the samples obtained were analyzed in relation to temperature. Texture characteristics and acid properties of the surface of the materials synthesized were examined in relation to the relative amounts of the components.

DOI: 10.1134/S1070427208120045

The expansion of the application field of zirconium oxide compounds as sorbents, supports, and catalysts for various processes [1–4] makes topical the interest in development and studies of highly dispersed systems based on ZrO_2. The key factor in application of zirconium dioxide as a component of catalysts and supports is the stabilization of its low-temperature metastable phases (amorphous, tetragonal, or cubic), to whose presence are attributed such important characteristics as the high dispersity and developed surface [5, 6] of the material. The attention of numerous researchers has been given to stabilization of the ZrO_2 structure in the low-temperature modifications by introduction of various cations: Ca^{2+}, Sr^{2+}, Ba^{2+}, Y^{3+}, La^{3+}, Fe^{3+} [7, 8], as well as Al^{3+} [9–11], in synthesis of M–Zr–O binary oxide systems. It has been noted that properties of the zirconium-containing materials synthesized depend on the preparation method and conditions. Apparently, the development of new catalytic materials containing nanosize zirconium dioxide is associated with a search for new ways of their synthesis and control over their properties.

The best presently known methods for synthesis of materials containing nanosize zirconium dioxide are the coprecipitation from metal nitrate or chloride solutions [11, 12] and the sol–gel technique using metal alkoxides [10]. Another approach to synthesis of systems of this kind may consist in that the zirconium dioxide structure is formed on the surface of solid materials under the conditions that favor interaction of the forming ZrO_2 with a carrier compound. It has been shown previously [13] that precipitation from a zirconyl nitrate solution in the presence of γ-Al_2O_3 leads to stabilization of the low-temperature phases of zirconium dioxide in the product obtained because of the interaction observed in a wide range of ZrO_2/Al_2O_3 ratios.

This study is concerned with the possibility of using calcium aluminates as a carrier compound. This compounds can serve as a "supplier" of Al^{3+} and Ca^{3+} cations for modification of the zirconium dioxide structure. At the same time, owing to their binding properties, calcium aluminates enable production of the material in various geometric configurations and sizes, with a developed surface and high mechanical strength. A specific feature of the method suggested is that, instead a solution of zirconium salts, it uses a solid hydrated zirconium oxide, which can adsorb ions produced in hydration of calcium aluminates. The combination of these factors in the synthetic procedure suggested here seems to be useful for obtaining an oxide system containing nanosize zirconium dioxide. The aim of this study was to examine the formation of the structure of zirconium dioxide in the samples synthesized and the texture characteristics of the materials obtained for their subsequent use as catalysts for methanol dehydration.

Table 1. Zirconium dioxide modifications in samples calcined at various temperatures*

Sample	ZrO_2	Calcium aluminates	Modification at indicated calcination temperature, °C						
	wt %		120	400	500	600	700	800	1000
Z	100	–	a	m, t(43)	m, t(35)	m, t(27)	m, t(19)	m, t(14)	m, t**
ZAC25	75	25	a	a	a	t(84), a	t(90), a	t(100)	t(97)
ZAC50	50	50	a	a	a	t(50), a	t(94), a	t(100)	t(97)
ZAC75	25	75	a	a	a	a	a, t	t(100)	t(100)
ZAC90	10	90	a	a	a	a	a, t	a, t	t(100)
AC	–	100	–	–	–	–	–	–	–
Mechanical mixture Z + AC	50	50	a	m, t(36)	m, t(35)	m, t(19)	m, t(19)	m, t(15)	m, t**

* ZrO_2 phases: (a) amorphous, (t) tetragonal, and (m) monoclinic.

** Trace amounts (percentage contents of the tetragonal ZrO_2 phase are given in parentheses).

EXPERIMENTAL

Zirconium-aluminocalcium samples were obtained as follows: hydrated zirconium oxide was thoroughly mixed and ground with a calculated amount of a high-alumina cement having the form of a mixture of calcium mono- and dialuminate with a $CaAl_2O_4/CaAl_4O_7$ ratio of 0.3. The mechanical mixture was mixed with a molding solution and the paste obtained was molded on a laboratory molder into extrudates, which were subjected to a humid-air treatment at a temperature of 25°C for 24 h. Then the samples were kept in water at 90°C for 3 h. The thus obtained extrudates were dried at 120°C for 5 h. The samples were calcined in air at temperatures of 300 to 1000°C. For comparison, an aluminocalcium sample containing no zirconium component was produced under similar conditions. Samples calcined at 400°C were treated with a 20% CH_3COOH solution for 30 min and then washed with water [14]. The compositions of the samples obtained are listed in Table 1.

X-ray studies were performed on DRON-3 and DRON-3m diffractometers (CuK_α radiation, with a graphite monochromator in the reflected beam). Phases were identified using the JCPDS database. The average size of coherent-scattering regions (CSR) was found from broadening of diffraction peaks by the Selyakov–Scherrer formula. The content of the tetragonal phase of zirconium dioxide was determined from the relation [15]:

$$X_t = \frac{I_t(111)}{I_m(111) + I_m(11\bar{1}) + I_t(111)},$$

where I_m and I_t are the integral intensities of the diffraction peaks associated with the monoclinic and tetragonal ZrO_2 phases.

A differential-thermal analysis (DTA) was carried out on a Q-1500D derivatograph at a heating rate of 5 deg min^{-1}. The specific surface area, pore volume, and pore size distribution were found from the low-temperature adsorption of nitrogen at 77 K on a Micrometrics ASAP 2010N instrument. The acidity of the surface of samples calcined at 400°C was examined by the method of thermally programmed desorption of ammonia (TPD NH_3)[1]. After a preliminary treatment, saturation with ammonia mixed with nitrogen, and blowing-out of the excess ammonia, the experiment was performed in a He flow at a heating rate of 8 deg min^{-1}; the evolving ammonia was recorded with a heat-conductivity detector.

According to the results of X-ray phase analyses (XPA), the resulting zirconium-aluminocalcium samples (ZAC) and the starting sample of hydrated zirconium oxide (Z) contain, after being dried at 120°C, an X-ray-amorphous zirconium oxide phase. Calcination in air at different temperatures revealed strong differences in the formation of crystallized zirconium dioxide in the samples studied. If follows from the XPA data in Table 1 that the X-ray-amorphous phase exists in the sample of individually precipitated zirconium dioxide (Z) up to 300°C, and after calcination at 400°C, the sample contains two crystalline phases: tetragonal (t-ZrO_2) and monoclinic (m-ZrO_2). As the calcination temperature is raised from 400 to 1000°C, the integral intensities of

[1] The authors thank V.V. Yushchenko for studies by the TPD NH_3 method.

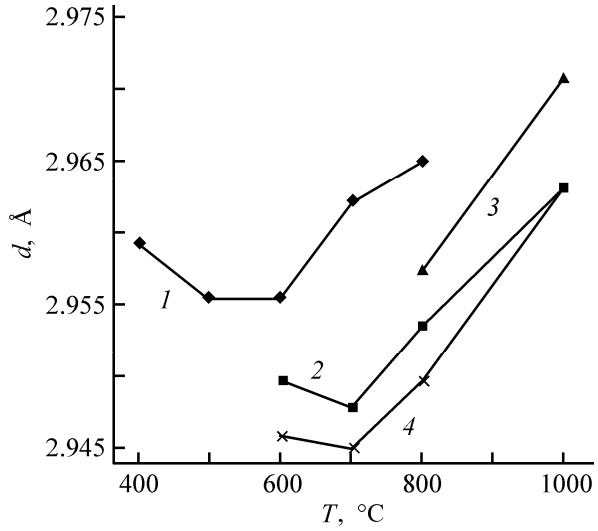


Fig. 1. Position *d* of the (111) line of t-ZrO_2 vs. calcination temperature *T* of (*1*) Z, (*2*) ZAC25, (*3*) ZAC50, and (*4*) ZAC75 samples.

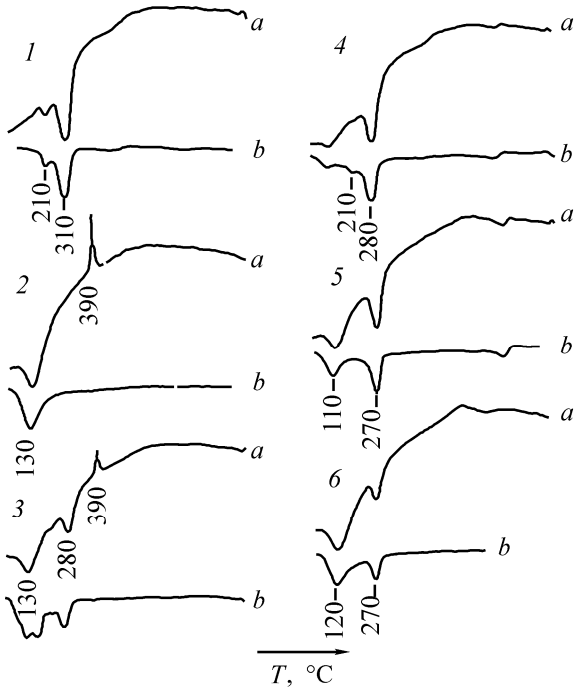


Fig. 2. Derivatograms of samples (*1*) AC, (*2*) Z, (*3*) mechanical mixture Z + AC, (*4*) ZAC75, (*5*) ZAC50, and (*6*) ZAC25. (*T*) Temperature. (*a*) DTG and (*b*) DTA.

the diffraction lines associated with t-ZrO_2 and m-ZrO_2 are redistributed, which points to transformation of the metastable low-temperature tetragonal modification of ZrO_2 to the stable monoclinic modification.

In contrast to Z, crystallization of ZrO_2 in ZAC samples was observed after calcination at 600°C and higher, with t-ZrO_2 being the only crystalline zirconium dioxide phase recorded in the whole range of calcination temperatures. An analysis of the integral intensities of the corresponding diffraction lines made it possible to evaluate the content of t-ZrO_2 in the samples studied. It was found that the crystallization onset temperature and the ratio between the crystallized and amorphous zirconium dioxide phases depend on the sample composition at certain temperatures (Table 1). For example, in ZAC25 sample, t-ZrO_2 crystallizes at 600°C by approximately 80%, whereas in ZAC50 sample, the X-ray-amorphous phase is preserved at the same temperature in an amount of up to 50%. In samples with a higher content of calcium aluminates, ZAC75 and ZAC90, only the X-ray-amorphous phase is observed under these conditions and its crystallization begins after calcination at 700°C. The fully formed t-ZrO_2 phase is observed in all ZAC samples at calcination temperatures in the range 800–1000°C. The existence of this metastable modification of ZrO_2 after treatment at so high temperatures is not characteristic of individual zirconium dioxide and can be accounted for by the presence in its structure of foreign ions that hinder the transformation of the tetragonal lattice into the monoclinic one [5].

According to X-ray data (Fig. 1), the position of the (111) line of t-ZrO_2 for ZAC samples at various temperatures noticeably differs from that in the X-ray diffraction pattern of Z sample, which can be regarded as evidence in favor of the incorporation of foreign ions into the tetragonal ZrO_2 lattice. Apparently, this results from interaction of calcium aluminates with hydrated zirconium oxide under the conditions of the synthesis.

The occurrence of such an interaction can be confirmed by comparing the results obtained for a sample of a mechanical mixture Z + AC (50 wt %) and the synthesized ZAC50 sample. The XPA data in Table 1 demonstrate that, upon calcination at 400°C, the sample of a mechanical mixture contains M-ZrO_2 and t-ZrO_2 in approximately the same ratio as that for sample Z, in contrast to ZAC50, in which the X-ray-amorphous phase is present. This is in good agreement with the DTA data. Figure 2 shows derivatograms of the samples, which demonstrate that a clearly pronounced exothermic effect at 390°C, which corresponds to ZrO_2 crystallization in Z sample, is also observed for a sample of the mechanical mixture, but is absent for ZAC50 sample and other synthesized samples containing calcium aluminates. The exothermic effect accompanying

Table 2. Phase composition of samples calcined at various temperatures*

Sample	Phase composition of samples calcined at indicated temperature, °C						
	120	400	500	600	700	800	1000
Z	a	m, t	m, t	m, t	m, t	m, t	m, t**
ZAC25	a, bayerite, gibbsite	a	a, $CaAl_4O_7$**	t, $CaAl_4O_7$, $CaCO_3$, γ-Al_2O_3	t, CaO, $CaAl_4O_7$, $CaCO_3$, γ-Al_2O_3	t, CaO, $CaAl_4O_7$, $CaCO_3$, γ-Al_2O_3	t, $CaAl_4O_7$, $\delta + \theta + \alpha$-Al_2O_3**
ZAC50	a, $CaCO_3$, bayerite, gibbsite, $CaAl_4O_7$	a, $CaCO_3$, $CaAl_4O_7$	a, $CaCO_3$, $CaAl_4O_7$	t, $CaCO_3$, $CaAl_4O_7$, γ-Al_2O_3	t, CaO, $CaAl_4O_7$, γ-Al_2O_3	t, CaO, $CaAl_4O_7$, γ-Al_2O_3	t, $CaAl_4O_7$, $\delta + \theta$-Al_2O_3
ZAC75	Gibbsite, a, $CaCO_3$, $CaAl_4O_7$, CAl,* $Ca_3Al_2(OH)_{12}$	a, $CaCO_3$, $CaAl_4O_7$, γ-Al_2O_3	a, $CaCO_3$, $CaAl_4O_7$	a, $CaCO_3$, $CaAl_4O_7$,	t, $CaAl_4O_7$, γ-Al_2O_3	t, $CaAl_4O_7$, γ-Al_2O_3, $C_{12}A_7$	t, $CaAl_4O_7$, $\theta + \alpha$-Al_2O_3
ZAC90	Gibbsite, $Ca_3Al_2(OH)_{12}$, $CaAl_4O_7$, CAl,* $CaCO_3$, $CaAl_2O_4$	a, $12CaO \cdot 7Al_2O_3$, $CaAl_4O_7$, AlOOH, γ-Al_2O_3, $CaCO_3$	a, $12CaO \cdot 7Al_2O_3$, $CaAl_4O_7$, AlOOH, $CaCO_3$, γ-Al_2O_3	a, $12CaO \cdot 7Al_2O_3$, $CaAl_4O_7$, AlOOH, $CaCO_3$, γ-Al_2O_3	a, $12CaO \cdot 7Al_2O_3$, $CaAl_4O_7$, AlOOH, $CaCO_3$, γ-Al_2O_3, t	a, t, $12CaO \cdot 7Al_2O_3$, $CaAl_4O_7$, γ-Al_2O_3, $CaCO_3$	$CaAl_4O_7$, t, CA, CaO
AC	$CaAl_4O_7$, gibbsite, $Ca_3Al_2(OH)_{12}$, CAl*	$CaAl_4O_7$, AlOOH, $12CaO \cdot 7Al_2O_3$, $CaCO_3$	$CaAl_4O_7$, $12CaO \cdot 7Al_2O_3$, Al_2O_3, $CaCO_3$	$CaAl_4O_7$, $12CaO \cdot 7Al_2O_3$, $CaCO_3$, γ-Al_2O_3	$CaAl_4O_7$, $12CaO \cdot 7Al_2O_3$, $CaCO_3$, γ-Al_2O_3	$12CaO \cdot 7Al_2O_3$, $CaAl_4O_7$, γ-Al_2O_3	$CaAl_4O_7$, CaO, $Ca(OH)_2$
Mechanical mixture Z +AC	a, gibbsite, $Ca_3Al_2(OH)_{12}$, $CaAl_4O_7$, CAl	m, t, $CaAl_4O_7$	m, t, $CaAl_4O_7$, $Ca_3Al_2(OH)_{12}$	m, t, $CaAl_4O_7$, $Ca_3Al_2(OH)_{12}$	m, t, $CaAl_4O_7$, $Ca_3Al_2(OH)_{12}$	m, t, $CaAl_4O_7$, $Ca_3Al_2(OH)_{12}$	m, t, $CaAl_4O_7$

* CAl = $Ca_4Al_2(OH)_{12}CO_3 \cdot 6H_2O$.

** Trace amounts.

the crystallization of zirconium dioxide in the ZAC system is shifted to higher temperatures and extends over a wider temperature range. This effect may be superimposed by endothermic effects corresponding to decomposition of products formed in hydration of calcium aluminates. In particular, the derivatogram of ZAC50 sample shows a pronounced endothermic effect associated with calcium carbonate decomposition (770°C), with the related loss of mass being about 4 wt %. It is noteworthy that such a pronounced endothermic effect was observed in this temperature range neither for the mechanical mixture, nor for a separately dehydrated AC, for which the loss of mass in the temperature range 600–1000°C was about 1.5–2 wt %. This points to a higher degree of dehydration (and of subsequent carbonization in air) of calcium aluminates in ZAC50 sample, compared with AC and Z + AC samples, which may result from interaction of its starting components under the synthesis conditions.

Pronounced indications that calcium aluminates interact with hydrated zirconium oxide are observed in analysis of the phase composition of products formed in hydration of the starting calcium aluminates (Table 2) It is known [16, 17] that the contact of calcium monoaluminate $CaAl_2O_4$ and dialuminate $CaAl_4O_7$ with water and atmospheric CO_2 yields phases of $Ca_3Al_2(OH)_{12}$, $Al(OH)_3$, and calcium carboaluminate $Ca_4Al_2(OH)_{12}CO_3 \cdot 6H_2O$. It is these phases, and also residual amount of $CaAl_4O_7$, that were observed in an X-ray phase analysis of uncalcined AC and Z + AC samples, with $Al(OH)_3$ present in these samples only in the form of gibbsite. In contrast to the preceding samples, the phase composition of uncalcined ZAC50 includes, in addition to the X-ray-amorphous zirconium-containing phase, a considerable amount of $CaCO_3$ and $Al(OH)_3$, represented by two modifications, bayerite and gibbsite. For ZAC50 sample, the loss of mass (related to the endothermic effect at 270 and 280°C), associated with decomposition of aluminum hydroxide, was 12.6 wt %; for Z + AC sample (with the same content of calcium aluminates, it was about 7.5 wt %.

A comparison of the XPA and DTA data demonstrated that, in the set of ZAC samples studied, the fraction of phases of aluminum hydroxide (gibbsite and bayerite) and calcium carbonate (calcite and aragonite) steadily increases as the ZrO2 content of the system is raised to 50 wt %, i.e., the presence of hydrated zirconium oxide in the samples results in a higher degree of hydration of calcium aluminates under the synthesis conditions. This may occur via removal of Ca^{2+} and $Al(OH)_4^-$ ions appearing when calcium aluminates are brought in contact with water from the reaction zone on the particle surface, which stimulates continued hydration of calcium aluminates to give phases of $Al(OH)_3$ and $Ca(OH)_2$ converted in contact with atmospheric CO_2 into $CaCO_3$.

Analysis of the phase composition of samples calcined at different temperatures (Table 2) shows, together with the above changes in structural modifications of ZrO_2, certain differences in the composition of products formed in thermolysis of the aluminocalcium component of the system. For example, the main phases in AC sample in the temperature range 400–800°C are $CaAl_4O_7$ and $12CaO \cdot 7Al_2O_3$, and also a certain amount of γ-Al_2O_3 and $CaCO_3$. ZAC50 sample containes no $12CaO \cdot 7Al_2O_3$ phase and the best represented products of hydration and thermolysis of calcium aluminates were $CaCO_3$ and γ-Al_2O_3. Upon calcination at 1000°C, the composition of AC sample is primarily represented by phases of $CaAl_2O_4$ and $CaAl_4O_7$, with trace amounts of CaO and $Ca(OH)_2$. The same phases were also observed in ZAC90 sample. However, ZAV75 and ZAC50 samples calcined at 1000°C contain, in contrast to the preceding samples, $CaAl_4O_7$ and δ-Al_2O_3 phases.

Thus, unbound CaO is observed in the final products of AC thermolysis (1000°C), whereas ZAC samples, by contrast, contain unbound Al_2O_3. Apparently, in the case of AC sample, the fraction of $CaAl_4O_7$ increases as compared with that in the initial composition, and part of calcium remains "free," in the form of CaO (or $CaCO_3$). The presence of "excess" aluminum oxide in ZAC50 sample can be attributed, taking into account that $CaAl_4O_7$ is the only observed aluminocalcium phase, to removal of a part of calcium from the sphere of the possible reactions, e.g., in the stage of hydration. This fact, as well as the above indications of an increase in the degree of hydration of the starting aluminates in uncalcined ZAC samples, indicates that hydrated zirconium oxide is involved to a certain extent in the conversion of the aluminocalcium component of the system.

In the conditions of a close contact between the surface of particles of calcium aluminates and hydrated zirconium oxide (after the molding procedure) and presence of water, the components of the ZAC system interact at the solid–liquid–solid double interface. The fact that Ca^{2+} and $[Al(OH)_4]^-$ ions are present in the liquid phase as a result of dissolution of calcium aluminates enables their involvement in the interaction

with the surface of zirconium hydroxide. On the one hand, zirconium hydroxide has a certain ability to adsorb various cations and anions and, consequently, can remove a part of ions from solution, thereby stimulating further adddissolution of calcium aluminates. On the other hand, the surface of zirconium hydroxide particles can provide additional nucleation centers for the $Al(OH)_3$ and $Ca(OH)_2$ (eventually $CaCO_3$) phases being formed in the course of hydration. The formation of phases of this kind on the surface of zirconium hydroxide particles also stimulates continued dissolution of calcium aluminates and their deeper hydration. By contrast, hydration of calcium aluminates in AC sample occurs to give a surface layer of new hydrate formations on each grain [18]. These formations hinder diffusion and thereby restrict the degree of hydration of aluminocalcium cements.

The increase in the degree of hydration of calcium aluminates, which leads to a rise in the content of hydration products, favors development of the surface of the material, and this does occur in samples of the ZAC system, with the maximum values of this parameter obtained for ZAC50 sample (Fig. 3).The specific surface area of AC sample calcined at 400°C is 88 $m^2 g^{-1}$, whereas ZAC50 sample is characterized under the same conditions by a specific surface area of 228 $m^2 g^{-1}$.

As a result of the interaction in the ZAC system, zirconium hydroxide can apparently be enriched in calcium and aluminum cations both via sorption in the initial stage of hydration and via formation on the surface of its particles of aluminum and calcium hydroxide phases, which are converted in subsequent thermolysis into the corresponding oxides, with –Zr–O–Al– and –Zr–O–Ca– bonds formed in the boundary region. Also, it is not improbable that hydrated zirconium oxide can be partly reprecipitated under the synthesis conditions, with incorporation of calcium and aluminum cations present in the reaction system. The considerable increase in the ZrO_2 crystallization point, observed in ZAC samples, and the stabilization of its tetragonal phase at high calcination temperatures may result from modification by Ca^{2+} and Al^{3+} cations of the structure of zirconium dioxide being formed. The increase in the disprosity of ZrO_2 can also be attributed to the influence of this factor.

Determination of the CSR size demonstrated (Fig. 4) that crystallites of the tetragonal ZrO_2 phase in ZAC samples at calcination temperatures in the range 600–800°C are noticeably smaller in size (6–12 nm) than those in Z sample (13–24 nm) used as a starting component in synthesis of the ZAC system.

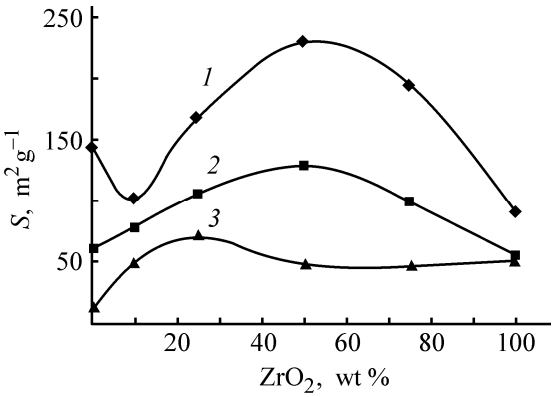


Fig. 3. Specific surface area S vs. the sample composition. (ZrO_2) Content of zirconium dioxide. Calcination temperature (°C): (*1*) 400, (*2*) 600, and (*3*) 800.

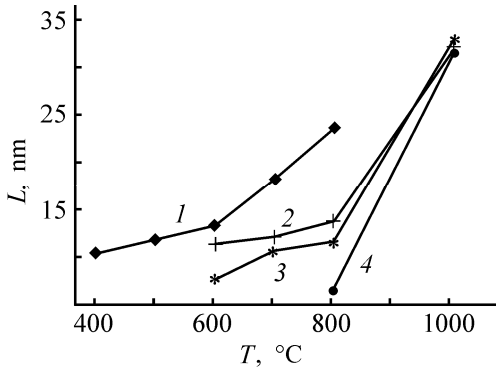


Fig. 4. CSR size L for the tetragonal ZrO_2 phase vs. the sample calcination temperature T. Sample: (*1*) Z, (*2*) ZAC25, (*3*) ZAC50, and (*4*) ZAC75.

The interaction of calcium aluminates and zirconium hydroxide under the synthesis conditions affects both the phase composition and texture characteristics of the samples obtained. It can be seen from the data in Table 3 that the pore volume increases with the ZrO_2 content of the system and reaches the maximum value (0.19 $cm^3 g^{-1}$) for ZAC50 sample. In this case, the pore size distribution markedly changes (Fig. 5). In contrast to the starting Z sample, whose pores are mostly distributed within the range 2–20 nm, ZAC samples show a considerable increase in the volume of the narrowest pores (2–3 nm) and a certain increase in that of coarse pores. The average pore diameter tended to steadily decrease as the ZrO_2 content of the ZAC system increased (from 0 to 50 wt %) and reached the maximum value for ZAC50 sample (3.36 nm), so that this sample differed in all the parameters presented above from the texture characteristics of hydrated zirconium oxide (Z) and calcium aluminates (AC), which are the starting components of the system synthesized. It is noteworthy

Table 3. Results of a study of the porous structure and acid properties of the surface of ZAC samples calcined at 400°C

Sample	Without treatment with CH_3COOH			After treatment with CH_3COOH				
	SBET, $m^2 g^{-1}$	pore volume, $cm^3 g^{-1}$	average pore diameter, nm	SBET, $m^2 g^{-1}$	pore volume, $cm^3 g^{-1}$	average pore diameter, nm	total amount of acid centers, $\mu mol\ g^{-1}$	density of acid centers, $10^{18}\ m^{-2}$
Z	144	0.19	4.75	–	–	–	86.9	0.36*
ZAC50	228	0.20	3.36	293	0.22	3.20	100.3	0.20
ZAC75	167	0.16	3.78	212	0.20	3.80	81.14	0.23
ZAC90	101	0.13	4.57	161	0.19	4.39	47.38	0.17
AC	88	0.13	4.88	143	0.20	4.68	52.6	0.21

* Data for a sample calcined at 400°C, without treatment with acetic acid.

that, because of the low content of calcium aluminates, ZAC25 sample had a mechanical strength insufficient for further study of its characteristics.

Molded grains of the samples, calcined at 400°C, were treated with an aqueous solution of acetic acid, which resulted in a 1.3–1.6-fold increase in their specific surface area (Table 3). The total pore volume of the samples increased by 20–60%. The pore size distribution preserved a bimodal shape characteristic of calcium aluminates, with the exception of ZAC50 sample, in which pores with a diameter exceeding 100 nm appeared and the volume of 2–3-nm pores decreased. The changes in the texture characteristics of the samples upon their treatment with acetic acid are due to partial dissolution of products formed in hydration of calcium aluminates. According to XPA data, the content of $CaCO_3$ and γ-Al_2O_3 phases decreased in all the samples and $12CaO \cdot 7Al_2O_3$ completely disappeared from AC and ZAC90 samples, which provided the most pronounced increase in their specific surface area and pore volume (by 60%).

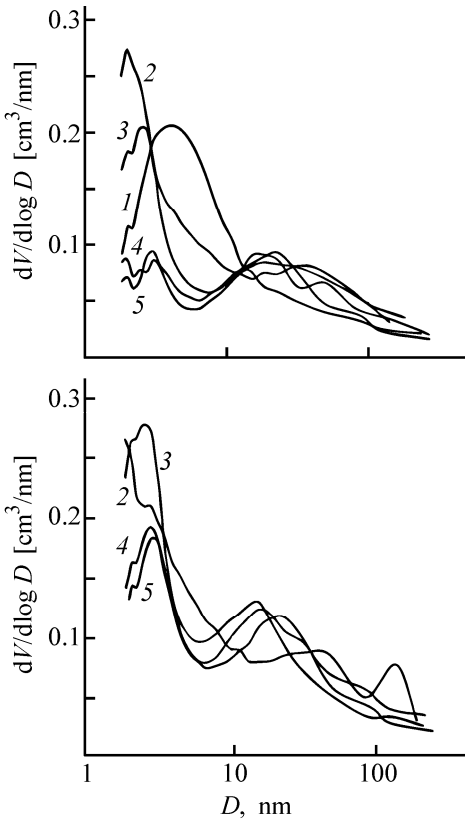


Fig. 5. Pore size distribution for samples calcined at 400°C (a) untreated and (b) treated with 20% CH_3COOH. (*V*) Pore volume and (*D*) pore size. Sample: (*1*) Z, (*2*) ZAC50, (*3*) ZAC75, (*4*) ZAC90, and (*5*) AC.

A study by the TPD NH_3 method demonstrated that the acid properties of the surface of the samples synthesized in the ZAC system and treated with acetic acid markedly differ from the surface properties of the individually synthesized zirconium dioxide (Fig. 6). As follows from the data of [13], ZrO_2 has strong acid centers, to which correspond two high-temperature desorption peaks peaked at 490 and 580°C, and a certain amount of weak acid centers manifested in ammonia desorption in the temperature range 100–400°C. For all the zirconium-containing aluminocalcium samples, the peak at 490°C, which has the highest intensity among those characteristic of ZrO_2, was completely absent in thermal desorption curves, whereas the other high-temperature peak shifted to higher temperatures (600–640°C). At the same time, the intensity of the desorption peaks in the low-temperature region, related to weak acid centers, substantially increased. According to the data obtained (Table 3), the total number of acid centers increased in the set of ZAC samples with the fraction of ZrO_2; the density of acid centers was the highest for ZAC50 and ZAC75 samples. As shown in [19], weak and medium acid centers play a key role in methanol dehydration to dimethyl ether, which suggests that the zirconium-aluminocalcium materials under consideration should exhibit a high activity and selectivity toward dimethyl ether.

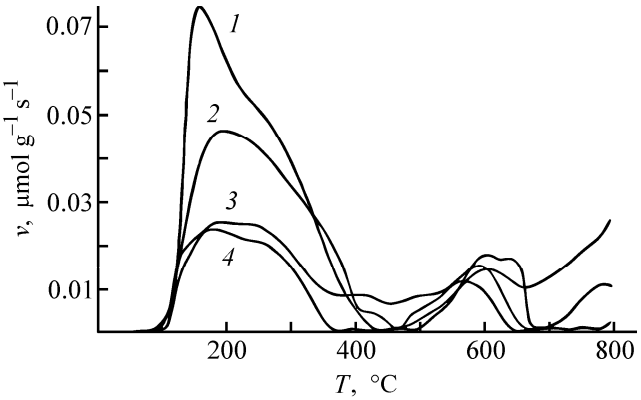


Fig. 6. Results of TPD NH_3 for samples calcined at 400°C and treated with CH_3COOH. (*v*) NH_3 desorption rate and (*T*) temperature. (*1*) ZAC50, (*2*) ZAC75, (*3*) AC, and (*4*) ZAC90.

The catalytic properties of the ZAC samples were studied in methanol dehydration. ZAC50 and ZAC75 samples exhibited an activity comparable with that of γ-Al_2O_3, successfully used in this process, and surpassed it in selectivity toward dimethyl ether.

CONCLUSIONS

(1) Materials containing nanosize zirconium dioxide stabilized in low-temperature phases, amorphous and tetragonal, were obtained using calcium aluminates. The fact that the zirconium–aluminocalcium system contains amorphous ZrO_2 up to calcination temperatures of 500–600°C and tetragonal ZrO_2 in the temperature range 600–1000°C was attributed to modification of the zirconium dioxide structure by Ca^{2+} and Al^{3+} cations. It was shown that hydrated zirconium oxide interacts with calcium aluminates in the stage of their hydration in a wide range of component ratios.

(2) It was found that the texture characteristics and acid properties of the surface of the materials synthesized are controlled by the component ratio. The largest pore volume and specific surface area are observed for a system containing 50 wt % ZrO_2. The system with 25 wt % ZrO_2 has the maximum density of acid centers.

(3) It was shown that the materials synthesized can find use as supports and catalysts. Tests of these materials in methanol dehydration demonstrated that their use as catalysts for synthesis of dimethyl ether is promising.

REFERENCES

1. Caili, S., Dehua, H., Junrong, L., et al., *J. Mol. Catal. A: Chemical*, 2000, vol. 153, pp. 139–146.
2. Ivanova, A.S., *Kinet. Kataliz*, 2001, vol. 42, no. 3, pp. 394–405.
3. Su, C., Li, J., He, D., et al., *Appl. Catal. A: General*, 2000, vol. 202, pp. 81–89.
4. Jung, K.T. and Bell, A.T., *Catal. Lett*., 2002, vol. 80, nos. 1–2, pp. 63–68.
5. Jung, K.T. and Bell, A.T., *J. Mol. Catal. A: Chemical*, 2000, vol. 163, pp. 27–42.
6. Chuah, G.K., Liu, S.H., Jaenicke, S., and Li, *J., Micropor. Mesopor. Mater.*, 2000, vol. 39, pp. 381–392.
7. Solinas, V., Rombi, E., Ferino, I., et al., *J. Mol. Catal. A: Chemical*, 2003, vols. 204–205, pp. 629–635.
8. Mims, C.A., *Catal. Lett*., 2000, vol. 68, pp. 203–208.
9. Li, G., Li, W., Zhang, M., and Tao, K., *Appl. Catal. A: General*, 2004, vol. 273, pp. 233–238.
10. Klimova, T., Rojas, M.L., Castillo, P., et al., *Micropor. Mesopor. Mater.*, 1998, vol. 20, pp. 293–306.
11. Li, G., Li, W., Zhang, M., et al., *Catal. Today*, 2004, vols. 93–95, pp. 595–601.
12. Wu, G., Sun, Yu., Li, Y.-W., et al., *J. Molec. Struct. (Theochem.)*, 2003, vol. 626, pp. 287–293.
13. Kruglova, M.A. and Yaroshenko, M.P., *Zh. Prikl. Khim.,* 2007, vol. 80, no. 9, pp. 1425–1431.
14. Golosman, E.Z., Yakerson, V.I., Mamaeva, I.A., and Boevskaya, E.A., *Kinet. Kataliz*, 1976, vol. 17, no. 2, pp. 392–398.
15. Jakubus, P., Adamski, A., Kurzawa, M., and Sojka, Z., *J. Thermal Anal. Calorimetry*, 2003, vol. 72, pp. 299–310.
16. Yakerson, V.I. and Golosman, E.Z., *Usp. Khim*., 1990, vol. 59, no. 5, pp. 778–806.
17. Golosman, E.Z., *Kinet. Kataliz*. 2001, vol. 42, no. 5, pp. 383–393.
18. *The Chemistry of Cements*, vol. 1, Taylor, H. F.W., Ed., New York: Academic, 1964.
19. Vishwanathan, V., Roh, H.-S., Kim, J.-W., and Jun, K.-W., *Catal. Lett*., 2004, vol. 96, nos. 1–2, pp. 23–28.

ISSN 1070-4272, Russian Journal of Applied Chemistry, 2008, Vol. 81, No. 12, pp. 2074–2078. © Pleiades Publishing, Ltd., 2008.
Original Russian Text © K.V. Titova, V.V. Buyanov, V.P. Nikol'skaya, O.B. Pudova, O.A. Zharkova, G.P. Karzhavina, 2008, published in Zhurnal Prikladnoi Khimii, 2008, Vol. 81, No. 12, pp. 1961–1965.

INORGANIC SYNTHESIS AND INDUSTRIAL INORGANIC CHEMISTRY

Solubility and Stability of $(NH_4)_2SO_4 \cdot H_2O_2$ in Aqueous Solutions and Change in Some Crystallographic Parameters of $(NH_4)_2SO_4$ Precipitates

K. V. Titova, V. V. Buyanov, V. P. Nikol'skaya, O. B. Pudova, O. A. Zharkova, and G. P. Karzhavina

Institute of Problems of Chemical Physics, Russian Academy of Sciences, Chernogolovka, Moscow oblast, Russia

State Research Institute of Biological Instrument Making, Federal State Unitary Enterprise, Moscow, Russia

Received February 8, 2008

Abstract—Stability of $(NH_4)_2SO_4 \cdot H_2O_2$ aqueous solutions and some structural changes in ammonium sulfate in the course of its solvation and subsequent desolvation were studied.

DOI: 10.1134/S1070427208120057

The ability of ammonium sulfate to be solvated by hydrogen peroxide was first mentioned in [1]. The composition of the peroxo solvate was found by studying the solubility of ammonium sulfate in anhydrous hydrogen peroxide and by determining the H_2O_2 content of the solid phase being crystallized [2]. In [3], the optimal conditions of synthesis, stabilization, and storage of ammonium sulfate monoperoxo solvate were reported, which provide that the sulfate retains hydrogen peroxide for more than 100 days. The fact that efficient stabilizers have been found among chemical compounds of various classes for other peroxo solvates [2] suggests that the stable state of $(NH_4)_2SO_4 \cdot H_2O_2$ can be substantially prolonged.

Ammonium sulfate peroxo solvate combines in itself an effective nitrogen fertilizer and a disinfectant in the form of coordinated hydrogen peroxide. Practical use of this compound in general disinfection science, plant growing, and, possibly, other fields requires data on its solubility and stability in aqueous solutions, because, apparently, a dry preparation is less suitable for these purposes.

This communication reports on study of the solubility and stability of $(NH_4)_2SO_4 \cdot H_2O_2$ aqueous solutions. In separate experiments, we examined precipitation of ammonium sulfate, whose X-ray diffraction patterns markedly differ in line intensity from those of the starting sulfate.

EXPERIMENTAL

Ammonium sulfate peroxo solvate was synthesized using sodium diphosphate as stabilizer [3]. Solutions for study (nearly saturated) were prepared by gradual addition of a dry solvate to water until there appeared indications of turbidity. After 24 h of keeping, no precipitate was observed. The thus obtained solutions, both undiluted and diluted to appropriate concentrations, were kept in closed polymeric containers at 20 ± 2°C. At regular intervals of time, the solutions were analyzed for the content of hydrogen peroxide by permanganatometric titration. The decomposition rate constants were calculated by the equation

$$\ln c_0/c = k(\tau - \tau_0).$$

The precipitates formed during storage of the solutions were removed, squeezed between two sheets of a filter paper, dried in air, analyzed for the content of H_2O_2, and subjected to X-ray diffraction analysis.

The X-ray diffraction patterns of powders were recorded on an ADP-2-01 diffractometer (CuK_α radiation, Ni filter) using the software for automation of data acquisition, processing, and analysis, developed for DRON X-ray diffractometers.

The values of the solubility and stability of $(NH_4)_2SO_4 \cdot H_2O_2$ in water are listed in Table 1.

As can be seen from Table 1, the decomposition of hydrogen peroxide occurs uniformly at an initial H_2O_2 concentration of 8.24% in solution at an average constant rate $k = 2.7 \pm 1.5$, which corresponds to 40.2% $(NH_4)_2SO_4 \cdot H_2O_2$, with 36.2% loss of H_2O_2 relative to the starting solution. The content of hydrogen peroxide remaining in solution is 5.34%, which makes it suitable for further use. Similar results were also obtained for a solution containing 4.66% H_2O_2.

However, the following deviation was found in a solution containing 2.51% H_2O_2. After 9 days of storage, a hardly noticeable precipitation of crystals from solution commenced, with the H_2O_2 concentration increasing from 1.96% (in 9 days) to 2.48% (in 30 days). In further storage of the solution, the amount of the precipitate became lower and the H_2O_2 concentration gradually decreased. These data were the reason why the experiments were repeated.

We prepared the second set of solutions containing 9.57 and 3.89% H_2O_2. In a solution containing 9.57% H_2O_2, the concentration of H_2O_2 started to gradually increase from the first days of storage (Table 2) and a precipitate containing 1.02% H_2O_2 was formed in 8 days. In the second solution, the hydrogen peroxide concentration also increased and a precipitate containing 1.07% H_2O_2 was formed after 8 days of storage. No other outward changes (intense gas evolution, change of solution color) were observed. The content of SO_4^{2-} in the precipitate was 71.4%, and that of NH_4^+, 26.9%. For $(NH_4)_2SO_4$, values of 72.7% and 27.3%, respectively, were calculated. Apparently, ammonium sulfate was precipitated.

The content of $(NH_4)_2SO_4$ in the first starting solution was 37.2% in terms of hydrogen peroxide. Thus, the amount of the liquid phase was (100 – 37.2)% = 62.8%. Taking into account that the solution contains 5.34% H_2O_2, the content of the aqueous solution of hydrogen peroxide is 62.8% per 37.2% ammonium sulfate.

The solubility of $(NH_4)_2SO_4$ in water is 70.1 g per 100 g water at 0°C [4] and that in anhydrous H_2O_2 at 0°C, 70.4% [2].

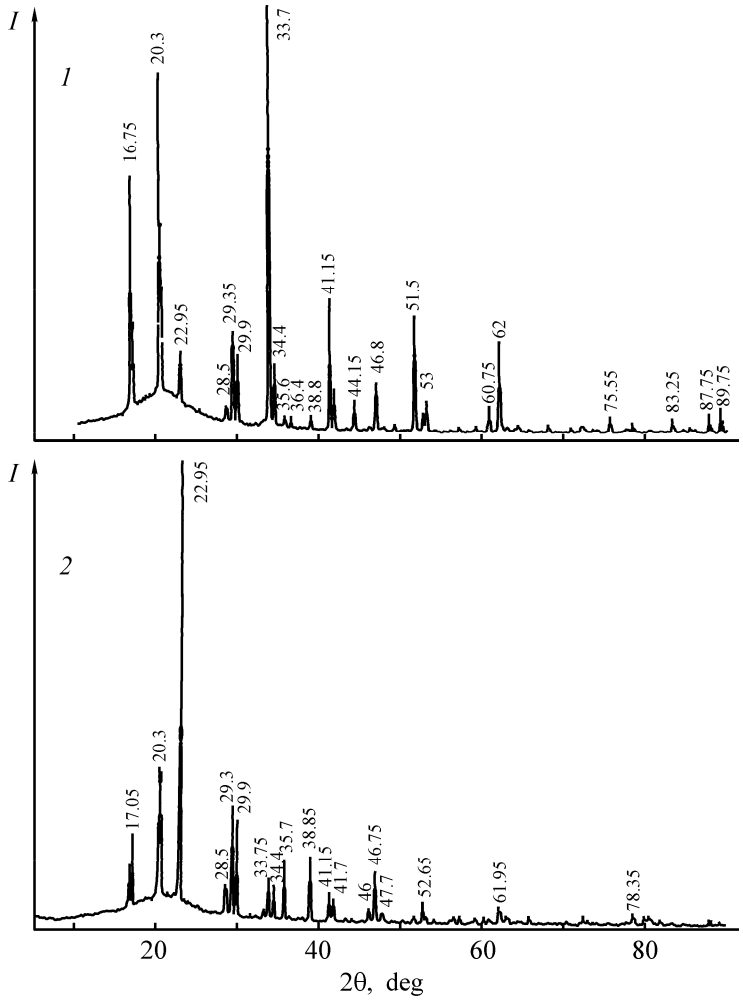
It seems unlikely that an unchanged ammonium sulfate precipitated in the initial state at such a high solubility in water and hydrogen peroxide. Because no outward changes in the system $(NH_4)_2SO_4 \cdot H_2O_2$–solvent were revealed, it is natural to suggest that ammonium sulfate precipitated in another crystalline form, which is less soluble in aqueous hydrogen peroxide.

Table 1. Solubility and stability of $(NH_4)_2SO_4 \cdot H_2O_2$ in water at 20°C

τ, days	H_2O_2 concentration in solution, %	Loss of H_2O_2, % relative to the initial amount	$k \times 10^4$, h^{-1}	H_2O_2 decomposition
0	8.24	0	0	Uniform, $k_{av} = 2.7 \pm 1.5$
1	8.13	1.3	5.6	
3	7.94	3.7	5.1	
9	7.71	6.4	3.1	
23	7.04	14.6	2.8	
30	6.81	17.4	2.6	
40	6.30	23.6	2.5	
60	5.66	31.3	2.6	
67	5.34	35.2	2.7	
0	4.46	0	0	Uniform, $k_{av} = 2.6 \pm 0.6$
3	4.32	3.1	4.4	
9	4.26	4.5	2.1	
23	3.81	14.6	2.8	
37	3.68	17.5	2.2	
53	3.49	21.8	1.9	
67	3.05	31.6	2.3	
0	2.51	0	0	Uniform, $k_{av} = 2.6 \pm 0.6$
1	2.50	0.4	0	
3	2.36	6.0	8.5	
9	1.96	21.9	11.4	
23	2.27	9.6	1.8	
30	2.48	1.2	0.17	
37	2.13	15.1	1.8	
60	1.81	27.9	2.3	

Table 2. Solubility and stability of $(NH_4)_2SO_4 \cdot H_2O_2$ at 20°C (second series of experiments)

τ, days	H_2O_2 concentration in solution, %	Loss of H_2O_2, % relative to the initial amount	$k \times 10^4$, h^{-1}	H_2O_2 content of the precipitate, %
0	9.57	0	0	1.02
1	10.10	5.53	2.2	
3	10.36	8.2	11.0	
8	11.13	16.3	7.9	
11	11.14	16.4	5.7	
18	11.66	21.8	4.6	
24	16.49	72.3	9.4	
31	15.07	57.5	6.1	
0	3.89	0	0	1.07
1	4.13	6.2	24.9	
3	4.58	17.7	22.7	
8	5.48	40.9	17.8	
11	5.77	48.3	14.9	
18	5.99	54.0	10.1	
24	18.15	46.6	26.7	



X-ray diffraction patterns of $(NH_4)SO_4$. (*I*) Intensity and (2θ) Bragg angle. (*1*) Starting sample, (*2*) Precipitate.

The results of an X-ray phase analysis demonstrate that, being identical to the starting ammonium sulfate in interplanar spacings *d*, the precipitated $(NH_4)_2SO_4$ sharply differs in relative reflection intensities I_{rel} (see figure). Therefore, the precipitate cannot be identified as the known ammonium sulfate. At the same time, it was already mentioned that the sets of interplanar spacings for these compounds are the same, which demonstrates that their lattices are identical. The unexpectedly strong differences in the relative intensities of the X-ray reflections of the starting ammonium sulfate and the precipitate initiated measurements of X-ray diffraction patterns of all the precipitates. It was shown (Table 3) that the differences we observed cannot be accounted for by measurement errors. It should be accepted as established facts that (i) the precipitate retains the unit of the starting ammonium sulfate and (ii) the lattice cell undergoes a structural change and this rearrangement is preserved upon decomposition of hydrogen peroxide. The results obtained suggest that, under the action of solvation and subsequent desolvation of hydrogen peroxide, the arrangement of atoms in the unit cell of $(NH_4)_2SO_4$ changes and differs from that in the unit cell of the known ammonium sulfate.

Table 3. Relative intensities (I_{rel}) of reflections in the X-ray diffraction patterns for starting and precipitated $(NH_4)_2SO_4$

d, Å		I_{rel}		I_{in}/I_{pr}
starting $(NH_4)_2SO_4$	precipitate	starting $(NH_4)_2SO_4$	precipitate*	
5.293	5.200	55	13 ± 3	4.2
4.75	4.375	76	35 ± 7	2.2
3.875	3.875	12	100 ± 0	0.12
2.659	2.656	100	14 ± 5	7.2

* Average over X-ray diffraction patterns of four precipitates.

Table 4. X-ray diffraction patterns of KF obtained by various methods [7]

$KF \cdot H_2O_2$ decomposition at 20°C (during more than a year)		$KF \cdot 2H_2O_2$ dehydration at 40–60°C		Heating of α-KF to 140°C		Reference [8]	
d, Å	I_{rel}	d, Å	I_{rel}	d, Å	I_{rel}	d, Å	I_{rel}
3.597	44	3.084	18	3.089	19	3.087	21
3.203	6	2.671	100	2.675	100	2.674	100
3.013	9	1.890	51	1.892	60	1.891	51
2.945	5	1.612	8	1.613	11	1.612	6
2.706	13	1.543	13	1.545	18	1.544	10
2.596	3	1.337	6	1.338	8	1.337	3
2.401	100	2.227	3	2.228	4	2.227	2
1.161	3	1.196	12	1.197	19	1.196	7
New α-form		β-form		β-form		β-form	

It should be noted that, when coordinated to certain salts, e.g., to KF, hydrogen peroxide itself undergoes the following transformation: the H–O bond forms an acute angle with the O–O bonds, which confirms the formation of an intramolecular hydrogen bond [5]. It can be suggested that, in the given case too, the change in positions of atoms in the bound H_2O_2 molecule results in displacement of other atoms within the unit cell and this rearrangement is retained after the decomposition of hydrogen peroxide, i.e., ammonium sulfate is converted to another form. It is impossible to give without additional structural studies any other explanation for the decrease in the solubility of ammonium sulfate in aqueous hydrogen peroxide, apart from the gradual conversion $(NH_4)_2SO_4(\alpha) \rightarrow (NH_4)_2SO_4(\beta)$.

The $(NH_4)_2SO_4(\alpha) \rightarrow (NH_4)_2SO_4(\beta)$ conversion and precipitation of the less soluble β-form of ammonium sulfate can be represented by the following sequence of reactions:

$$(NH_4)_2SO_4(\alpha) + H_2O_2 \rightarrow (NH_4)_2SO_4 \cdot H_2O_2, \quad (1)$$

$$(NH_4)_2SO_4 \cdot H_2O_2 + H_2O \rightarrow 2NH_4^+ + [SO_4 \cdot H_2O_2]^{2-}, \quad (2)$$

$$[SO_4 \cdot H_2O_2]^{2-} \rightarrow SO_4^{2-} + H_2O_2, \quad (3)$$

$$SO_4^{2-} + 2NH_4^+ = (NH_4)_2SO_4(\beta)\ \text{(precipitate)}. \quad (4)$$

The degree of conversion of the soluble $(NH_4)_2SO_4 \cdot H_2O_2$ into a less soluble $(NH_4)SO_4(\beta)$ is determined by the equilibrium of reaction (3), i.e., by the degree of dissociation of $[SO_4 \cdot H_2O_2]^{2-}$ anion with release of the SO_4^{2-} ion. It has been shown previously [6] that potassium fluoride peroxo solvate dissociates in aqueous solution with partial preservation of the solvated $[F...H_2O_2]^-$ ion, i.e., there exists the equilibrium

$$2KF \cdot H_2O_2 = 2K^+ + F^- + [F...H_2O_2]^- + H_2O_2. \quad (5)$$

Therefore, with account of the fact that solvated $[A...H_2O_2]^-$ ions are preserved in peroxo solvate aqueous solutions, we have that a difficultly soluble $(NH_4)SO_4(\beta)$ is precipitated when the equilibrium of reaction (3) is shifted to the right, and the soluble form, $(NH_4)_2SO_4 \cdot H_2O_2$, is preserved in the solution when the equilibrium of reaction (3) is shifted to the left. Reasons for such shifts of the equilibrium of reaction (3) remain unclear.

The suggested polymorphic conversion of ammonium sulfate, which occurs as a consequence of the coordination and subsequent release of hydrogen peroxide, is not the only example of the above conversion.

It has been shown previously [7] that another compound, potassium fluoride, undergoes a more pronounced polymorphic transformation under the action of hydrogen peroxide. It was found that, if the desolvation of $KF \cdot H_2O_2$ occurs slowly (during about a year at 20°C), the X-ray diffraction pattern is a set of bands associated with $KF \cdot 2H_2O$ formed by the reaction $2KF \cdot H_2O_2 = KF + KF \cdot 2H_2O + O_2$ and a set of bands that does not coincide with published data for KF [8] and with our data for anhydrous potassium fluoride obtained by dehydration of $KF \cdot 2H_2O_2$ or by heating of α-KF to 100–140°C (Table 4).

Table 5. Relative intensities I_{rel} of $(NH_4)_2SO_4$ precipitates at various temperatures

d, Å		I_{rel} for a chosen d					
$(NH_4)_2SO_4$	precipitate	$(NH_4)_2SO_4$ at 20°C	precipitate				Average I_{rel}
			20°C	46°C	100°C	180°C	
5.193	5.200	55	13	10	16	4	11 ± 3
4.375	4.375	76	35	22	40	17	28 ± 9
3.875	3.875	12	100	100	100	100	100 ± 0
2.659	2.656	100	14	11	11	8	11 ± 1

In this case, however, other values are observed not only for the relative intensities, but for the interplanar spacings as well. The low-temperature form, α-KF, obtained in $KF \cdot H_2O_2$ decomposition upon prolonged storage (at 20°C), is transformed to its common β-form at 100–140°C (Table 4). In the case of ammonium sulfate, the crystallographic change in I_{rel} in the precipitated sulfate is also preserved in the sulfate at higher temperatures (Table 5).

The results of this study can be understood on the assumption that hydrogen peroxide can change the structure of a solvated compound.

CONCLUSIONS

(1) Aqueous solutions of $(NH_4)_2SO_4 \cdot H_2O_2$ are rather stable in a wide range of concentrations, up to 40.2%. Such solutions containing simultaneously a fertilizing soil and disinfecting components, can be used first of all in plant growing. Owing to the full ecological safety, they are also suitable for use in general disinfection.

(2) In some cases, $(NH_4)_2SO_4$ precipitates from solution. According to tentative results of an X-ray phase analysis, this is due to the $(NH_4)_2SO_4(\alpha) \rightarrow (NH_4)_2SO_4(\beta)$ phase transition that occurs under the influence of the solvation and subsequent desolvation of the sulfate. In this case, $(NH_4)_2SO_4(\beta)$ less soluble in hydrogen peroxide is precipitated.

REFERENCES

1. Schumb, W.C., Satterfield, Ch.N., and Wentworth, R.L., *Hydrogen Peroxide*, New York: Reinhold, 1955.
2. Titova, K.V., Nikol'skaya, V.P., and Buyanov, V.V., *Koordinatsionnye soedineniya peroksida vodorova* (Coordination Compounds of Hydrogen Peroxide), Chernogolovka: Inst. Probl. Khim. Fiz. Ross. Akad. Nauk, 2000.
3. Titova, K.V., Nikol'skaya, V.P., Buyanov, V.V., and Pudova, O.B., *Zh. Prikl. Khim.*, 2007, vol. 80, no. 9, pp. 1421–1424.
4. *Spravochnik khimika* (Chemist's Handbook), Nikol'skii, B.P., Ed., Moscow: Goskhimizdat, 1951, vol. 2.
5. Titova, K.V., D'yachenko, O.A., Gritsenko, V.V., and Shilov, G.V., *Izv. Ross. Akad. Nauk. Ser. Khim.*, 1999, no. 1, pp. 38–49.
6. Titova, K.V., Nikol'skaya, V.P., Buyanov, V.V., and Pudova, O.B., *Zh. Neorg. Khim.*, 2005, vol. 50, no. 1, pp. 133–136.
7. Titova, K.V., Nikol'skaya, V.P., Buyanov, V.V., and Pudova, O.B., *Zh. Neorg. Khim.*, 2005, vol. 50, no. 4, pp. 704–706.
8. JCPDS, International Center of Diffraction Data, 1995.

ISSN 1070-4272, Russian Journal of Applied Chemistry, 2008, Vol. 81, No. 12, pp. 2079–2083. © Pleiades Publishing, Ltd., 2008.
Original Russian Text © A.G. Kasikov, A.M. Petrova, 2008, published in Zhurnal Prikladnoi Khimii, 2008, Vol. 81, No. 12, pp. 1966–1970.

INORGANIC SYNTHESIS AND INDUSTRIAL INORGANIC CHEMISTRY

Extraction of Sulfuric and Hydrochloric Acids with Macromolecular Aliphatic Alcohols of Varied Structure

A. G. Kasikov and A. M. Petrova

Tananaev Institute of Chemistry and Technology of Rare Elements and Mineral Resources, Kola Scientific Center, Russian Academy of Sciences, Apatity, Murmansk oblast, Russia

Received June 18, 2008

Abstract—Extraction of HCl and H_2SO_4 with isomers of monoatomic aliphatic alcohols C_7–C_{10} was studied. The distribution coefficients of the acids were determined in relation to their concentration in the system, length of the hydrocarbon chain of an aliphatic alcohol, and nature of an acid being extracted. It was found that the alcohol nature affects the rate of phase stratification in aqueous re-extraction of the acids.

DOI: 10.1134/S1070427208120069

Aliphatic alcohols containing 7–10 carbon atoms in the chain are a promising type of industrial oxygen-containing extractive agents that can selectively recover some elements from acid solutions with a complex salt composition [1]. There are data on application of extractive agents of the class of aliphatic alcohols to recovery of rare (Nb, Ta, Re), platinum, and noble metals (Au, Os, Ru), and also arsenic, iron, vanadium, and some other elements [1]. In extraction with aliphatic alcohols from solutions of acids, there occurs, in addition to the recovery of the target component, co-extraction of a mineral acid, and this process noticeably affects the extraction of an element. Therefore, studying the extraction of mineral acids with various aliphatic alcohols is a topical task.

By now, a considerable body of data on extraction of inorganic acids with aliphatic alcohols has been accumulated [1–14]. First reports in this field appeared in the country in the early 1960s and were devoted to analysis of the extractive properties of low-molecular-weight alcohols (amyl, butyl) [2–5], which are for the most part applicable in analytical practice. Later, researchers focused attention on higher-molecular-weight aliphatic alcohols (C_7–C_{11}) because of the possibility of their use in the technological process [6–14]. In particular, an extractive method for recovery of sulfuric acid from solutions produced at copper-nickel shops, with octanols used as extractive agents, have been developed and tested on the laboratory scale in recent years [12–14].

Most of studies failed to pay due attention to the influence exerted by the structure of aliphatic alcohols on their extracting capacity toward acids, although it is known that their extracting capacity toward some complex metalloacids strongly depends on the position of the hydroxy group [15–19]. The present study is concerned with the influence exerted by the structure of aliphatic alcohols C_7–C_{10} on the extraction of sulfuric and hydrochloric acids.

EXPERIMENTAL

As extractive agents were used higher aliphatic alcohols of domestic manufacture: 1-heptanol, 4-heptanol, 1-octanol, 2-*DL*-octanol, 1-nonanol, 2-nonanol, 4-nonanol, 1-decanol, 4-decanol, and 5-decanol of pure grade, and of foreign made: 2-heptanol and 3-heptanol of "Purum, ≥99.0% (GC)" grade and 3-octanol of "97.8 %, for synthesis" grade without additional dilution. Model acid solutions were prepared using HCl and H_2SO_4 of chemically pure grade.

The acids were extracted from their individual solutions in 0.05-l volumetric cylinders with a ground stopper at o : w = 1 : 1 and manual shaking for 5 min, which is sufficient for equilibrium to be attained in alcohol–HCl and alcohol–H_2SO_4 systems. The extraction was performed at room temperature (18 ± 2°C), and the phase stratification, with thermostating at 20 ± 1°C for 10–20 min. Experiments devoted to the effect of temperature on the extraction of acids were carried out

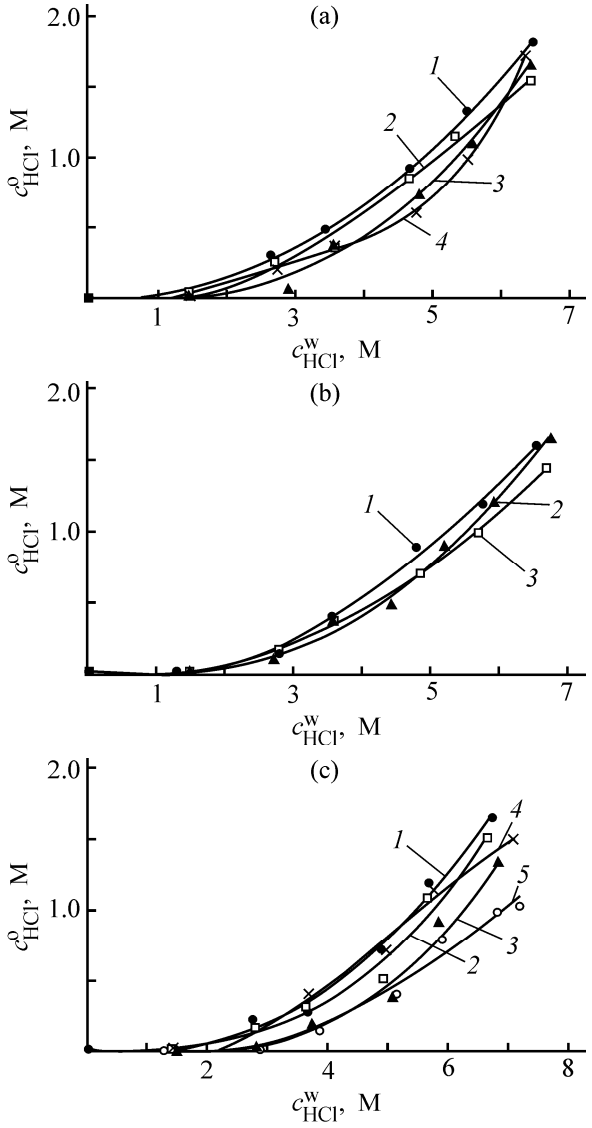


Fig. 1. Isotherms of extraction of hydrochloric acid with aliphatic alcohols C_7–C_{10} of varied structure. o : w = 1 : 1, τ = 5 min; the same for Figs. 2, 3. (c^{o}_{HCl}) Equilibrium HCl concentration in the organic phase and (c^{w}_{HCl}) equilibrium HCl concentration in the aqueous phase. (a) (*1*) Heptanol-1, (*2*) heptanol-2, (*3*) heptanol-3, and (*4*) heptanol-4; (b) (*1*) octanol-1, (*2*) octanol-2, and (*3*) octanol-3; (c) (*1*) nonanol-1, (*2*) nonanol-2, (*3*) nonanol-4, (*4*) dcanol-1, and (*5*) decanol-4; the same for Fig. 2.

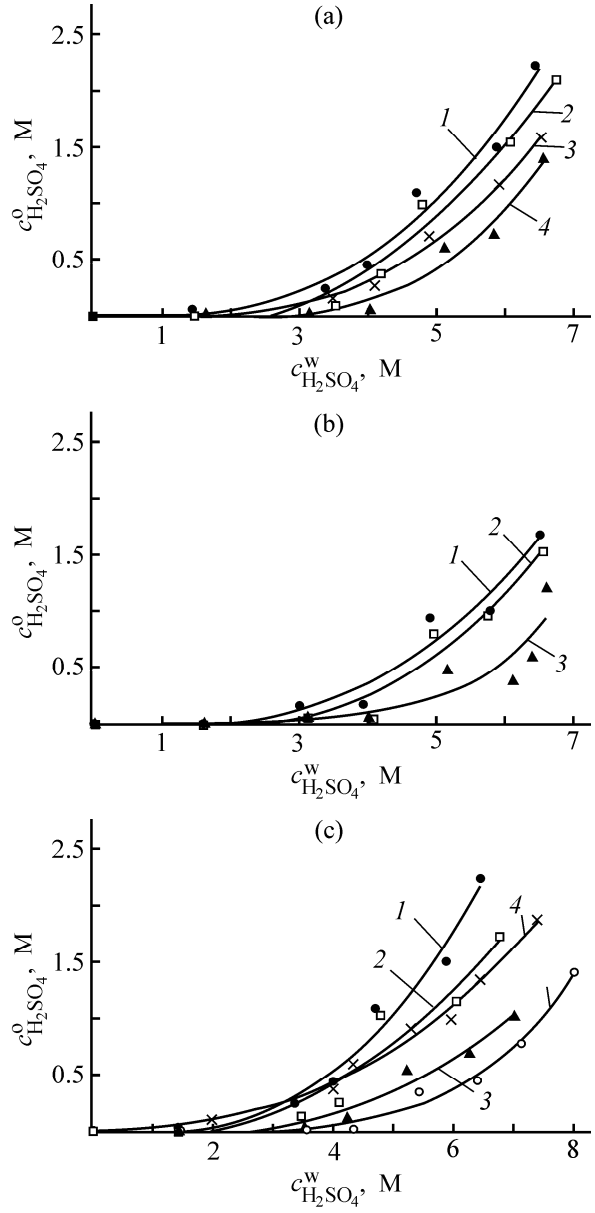


Fig. 2. Isotherms of extraction of hydrochloric acid with aliphatic alcohols C_7–C_{10} of varied structure. ($c^{o}_{H_2SO_4}$) Equilibrium H_2SO_4 concentration in the organic phase and ($c^{w}_{H_2SO_4}$) equilibrium H_2SO_4 concentration in the aqueous phase.

in a thermostated 0.25-l round-bottomed flask with a mechanical stirrer.

The acid concentrations in aqueous solutions were determined by titrimetry in the presence of phenolphthalein. The acid concentrations in the organic phase were calculated from the difference between their contents in the aqueous phase before and after extraction, with account of changes in the phase volumes. The distribution coefficients were calculated by the formula

$$D_{HX} = [c_{HX}]_{org}/[c_{HX}]_{aq}.$$

The table lists the distribution coefficients of H_2SO_4 and HCl in extraction from 3 and 6 M solutions of the acids, and Figs. 1 and 2 show extraction isotherms of these acids with isomers of aliphatic alcohols C_7–C_{10}. As can be seen in Figs. 1 and 2, the distribution curves of both acids ascend for all the alcohols studied as the acid concentration in the system becomes higher. This is natural because the extraction of

HCl and H_2SO_4 with aliphatic alcohols occurs by the hydrate-solvate mechanism [5, 9], which can be represented in the general form by the scheme

$$mH_3O^+ + nH_2O + qS_o + X^{m-} = [(H_3O^+)_m \cdot (H_2O)_n \cdot qS_o]^{m+}X^{m-},$$

where X^{m-} is the anion of an acid being extracted, and S_o, molecule of the extractive agent in the organic phase.

Apparently, in accordance with the scheme, any increase in the concentration $[H_3O^+]$ in the aqueous phase will favor a shift of the equilibrium to the right.

The extraction isotherms of HCl and H_2SO_4 with secondary and primary isomers of aliphatic alcohols with the same molecular mass differ only slightly, although the distribution coefficients in extraction of microscopic amounts (~10^{-3} M) of some elements with isomers of octyl alcohol on the background of these acids differ severalfold [15–19]. In all cases, the primary alcohols extract acids somewhat better than do secondary alcohols, despite the higher basicity of the latter [20]. Probably, the key role in the extraction of acids from rather concentrated solutions (>1 M) is played by steric hindrances that diminish the distribution coefficients in extraction with secondary alcohols whose functional group is less accessible than the OH group of primary alcohols.

As the molecular mass of the extractive agent increases, the extraction of the acids, on the whole, somewhat decreases because of the "hydrocarbon dilution effect" [7]. However, the decrease in the distribution coefficients of H_2SO_4 and HCl in the series $C_7 \rightarrow C_{10}$ is insignificant, and in some cases, this kind of behavior is not observed at all (see table). The latter presumably occurs because, as the hydrocarbon radical becomes longer, the polarity of an alcohol and its capacity for self-association decrease, and, accordingly, the number of active functional groups in the phase of the extractive agent increases [7], which partly compensates for the hydrocarbon dilution effect.

As already noted, the extraction of HCl and H_2SO_4 with aliphatic alcohols depends on the acid concentration in the system, with this dependence being pronounced for H_2SO_4. For example, HCl is extracted noticeably better than H_2SO_4 at a low acidity, and the distribution coefficients of the acids become comparable at a high acidity. Thus, the structure of aliphatic alcohol more strongly affects the extraction of H_2SO_4, compared with HCl, which is presumably due to specific forms of existence of the acids in solutions. Hydrochloric acid is a strong monobasic acid ($pK_a \approx -7$); in an aqueous solution, it is nearly completely dissociated and contains only hydrated ions H_3O^+ and Cl^- at any acidity. Sulfuric acid is weaker and, moreover, dibasic. HSO_4^- and SO_4^{2-} ions are present in sulfuric

Distribution coefficients D of the acids in extraction of H_2SO_4 and HCl with isomers of aliphatic alcohols C_7–C_{10} at various concentrations c_{in} of the starting solutions

Aliphatic alcohol	c_{in} = 3.0 M		c_{in} = 6.0 M	
	$D_{H_2SO_4}$	D_{HCl}	$D_{H_2SO_4}$	D_{HCl}
Heptanol-1	0.061	0.118	0.241	0.221
Heptanol-2	0.012	0.098	0.242	0.192
Heptanol-3	0.011	0.061	0.121	0.181
Heptanol-4	0.038	0.078	0.162	0.160
Octanol-1	0.051	0.059	0.183	0.197
Octanol-2	0.020	0.051	0.168	0.159
Octanol-3	0.023	0.042	0.079	0.177
Nonanol-1	0.033	0.080	0.220	0.185
Nonanol-2	0.021	0.061	0.182	0.156
Nonanol-4	0.013	0.008	0.110	0.120
Decanol-1	0.020	0.028	0.160	0.178
Decanol-4	0.004	0.010	0.071	0.106

acid solutions, with their relative amounts dependent on the acid concentration in solution [21]. At $c_{H_2SO_4}$ < 5–6 M, the equilibrium concentrations of HSO_4^- and SO_4^{2-} are comparable; as, however, $c_{H_2SO_4}$ increases further, HSO_4^- becomes the predominant species in solution [21]. Different ionic forms of sulfuric acid are differently extracted with aliphatic alcohols. It has been found previously that doubly charged anions are considerably more poorly extracted with alcohols, compared with those singly charged [18, 19]. Thus, the small distribution coefficients of H_2SO_4 in weakly acidic and moderately concentrated solutions can be attributed to a low concentration of the well-extractable HSO_4^- anion, as well as to the insignificant extraction of the doubly charged SO_4^{2-} anion. The higher values of $D_{H_2SO_4}$ in strongly acidic solutions, which occasionally even exceed D_{HCl}, are associated with the extraction of the singly charged HSO_4^- anion.

In addition to the aforesaid, the extraction isotherms of H_2SO_4 have a specific feature: at H_2SO_4 concentrations exceeding 4 M, the experimental values in the isotherm strongly fluctuate, which leads to considerable deviations of the corresponding points from the approximating line. Presumably, this is due to the variable composition of hydrate-solvate complexes formed in the organic phase; these complexes can contain both HSO_4^- and other ionic forms of H_2SO_4 present in strongly acid solutions. The content of water and alcohol in the complex may vary with the form being extracted, which also affects the extraction equilibrium. In addition, there are data on chemical transformations of an alcohol in extraction of H_2SO_4 [11]. An IR spectral study of sulfuric acid octanol extracts containing up to 0.9 M H_2SO_4 demonstrated that the intensity of the peak associated with the hydroxy group decreases,

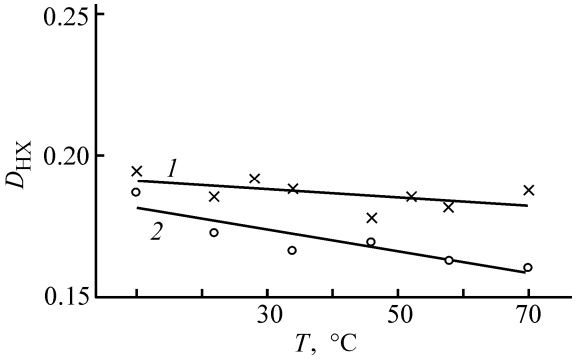


Fig. 3. Effect of temperature T on the distribution coefficients D_{HX} of sulfuric and hydrochloric acids in extraction with 2-octanol from 6.0 M solutions of the acids. (*1*) H_2SO_4, (*2*) HCl.

which is probably due to partial esterification of the alcohol to give unstable fatty alcohol sulfates, whose extracting properties differ from those of alcohols.

The effect of temperature on the extraction with aliphatic alcohols was studied for the example of H_2SO_4 and HCl recovery with 2-octanol from 6 M solutions of the acids. It follows from Fig. 3 that, for both acids, an increase in temperature leads to a certain decrease in the distribution coefficients, although the thermodynamic distribution constant is temperature-independent [6]. The authors of [6] attribute this dependence to a decrease in the degree of acid hydration in the organic phase, observed as temperature is elevated.

HCl and H_2SO_4 can be readily re-extracted from the phase of an aliphatic alcohol with distilled water. In doing so, more than 99% of an acid contained in extracts is recovered in a single stage at o : w = 1 : 1 for all the alcohols considered. It should, however, be noted that the phase stratification becomes poorer in re-extraction from extracts that are based on primary aliphatic alcohols and are concentrated in acid, as the chain length increases. For example, in re-extraction from 1-heptanol and 1-octanol containing 1.5–2 M HCl or H_2SO_4, the aqueous–organic mixture stratifies in 3–5 min, whereas in the case of concentrated acid extracts based on 1-nonanol and 1-decanol and shaking with distilled water for 5 min, the mixture turns cream-like and stratifies in 10–30 min (C_9) or in several hours (C_{10}). The stratification time depends on the type of an acid: systems containing H_2SO_4 stratify in a considerably longer time, compared with HCl. Probably, this phenomenon is due to formation of unstable solid acid-containing hydrate-solvate associates with emulsifying properties in the phase of the extractive agent upon introduction of H_2O into the extract.

In re-extraction of acids from secondary alcohols, 5–10 min was sufficient for stratification of aqueous-organic mixtures in all cases. Emulsification in re-extraction of acids with water is not characteristic of secondary aliphatic alcohols C_9–C_{10}, presumably because of their lower capacity for self-association.

CONCLUSIONS

(1) In extraction of HCl and H_2SO_4 with primary and secondary aliphatic alcohols of the C_7–C_{10} series, the extraction of HCl and H_2SO_4 mostly increases as the hydrocarbon chain becomes shorter and the concentration of the acids in the aqueous phase grows,

with the primary aliphatic alcohols extracting the acids somewhat better than secondary alcohols do.

(2) An increase in the process temperature in extraction of HCl and H_2SO_4 leads to a decrease in the distribution coefficients of the acids.

(3) Deep re-extraction of the acids from the organic phase is provided by water, with the degree of extraction in a single stage being no less than 99% at o : w = 1 : 1 in all cases.

(4) In aqueous re-extraction from concentrated extracts (1.5–2 M H_2SO_4 or HCl) based on primary alcohols, the phase stratification becomes poorer as the molecular mass of the extractive agent increases, which is not characteristic of acid extracts based on secondary alcohols.

REFERENCES

1. Nikolotova, Z.I. and Kartashova, N.A., *Spravochnik po ekstraktsii* (Handbook of Extraction), Moscow: Atomizdat, 1976.
2. Gindin, L.M., Kopp, I.F., Rozen, A.M., and Kouba, E.F., *Zh. Neorg. Khim.*, 1960, vol. 5, no. 1, pp. 139–148.
3. Grinberg, A.A. and Lozhkina, G.S., *Zh. Neorg. Khim.*, 1960, vol. 5, no. 3, pp. 738–744.
4. Zharovskii, F.G. and Mel'nik, V.F., *Zh. Neorg. Khim.*, 1961, vol. 6, no. 6, pp. 1466–1470.
5. Kopach, S. and Ezhovska-Tshebyatovska, B., *Zh. Neorg. Khim.*, 1971, vol. 16, no. 2, pp. 457–462.
6. Sergievskii, V.V., Fedyanina, L.B., and Yagodin, G.A., *Izv. Vyssh. Uchebn. Zaved., Khim. Khim. Tekhnol.*, 1979, vol. 22, no. 12, pp. 1483–1487.
7. Kopkova, E.K., Gromov, P.B., and Shchelokova, E.A., *Khim. Tekhnol.*, 2008, vol. 9, no. 3, pp. 115–120.
8. Maiorov, V.G., Baklanova, I.V., Nikolaev, A.I., and Safonova, L.A., *Zh. Prikl. Khim.*, 2000, vol. 73, no. 10, pp. 1636–1640.
9. Tyuremnov, A.V., Development of an Extraction Technology for Regeneration of Sulfuric Acid in Production of Nonferrous Metals and Titanium Dioxide, *Cand. Sci. Dissertation*, Apatity, 2004.
10. Petrova, A.M. and Kasikov, A.G., *Nauchno-tekhnicheskaya konferentsiya "Nauchno-prakticheskie problemy v oblasti khimii i khimicheskikh tekhnologii," Apatity, 8–11 aprelya 2008 g.* (Sci.-Techn. Conf. "Scientific and Practical Problems in Chemistry and Chemical Technology," Apatity, April 8–11, 2008), Apatity, 2008, pp. 90–94.
11. Tyuremnov, A.V., Kopkova, E.K., Gromov, P.B., and Shchelokova, E.A., *Vserossiiskaya nauchnaya konferentsiya "Nauchnye osnovy khimii i tekhnologii pererabotki kompleksnogo syr'ya i sinteza na ego osnove funktsional'nykh materialov," Apatity, 8–11 aprelya 2008 g.* (All-Russia Sci. Conf. "Scientific Foundations of Chemistry and Technology of Processing of Complex Raw Materials and of Synthesis of Functional Materials on Its Base," Apatity, April 8–11, 2008), Apatity, 2008, part I, pp. 186–189.
12. Kasikov, A.G., Areshina, N.S., Kudryakov, M.V., and Khomchenko, O.A., *Khim. Tekhnol.*, 2004, no. 6, pp. 25–31.
13. Sklokin, L.I., Tyuremnov, A.V., and Kalinnikov, V.T., *Khim. Tekhnol.*, 2002, no. 8, pp. 25–31.
14. RF Patent 2 159 293.
15. Baradel, A., Baradel, A., Guerriero, R., et al., *J. Metals*, 1986, no. 2, pp. 32–37.
16. Glubokov, Yu.M., Travkin, V.F., Il'in, E.G., et al., *Tsv. Metall.*, 2001, no. 10, pp. 23–27.
17. Kasikov, A.G. and Petrova, A.M., *Zh. Prikl. Khim.*, 2007, vol. 80, no. 4, pp. 689–690.
18. Petrova, A.M. and Kasikov, A.G., *XVIII Mendeleevskii s"ezd po obshchei i prikladnoi khimii* (XVIII Mendeleev Congress of General and Applied Chemistry), vol. 1., Moscow: Granitsa, 2007, p. 383.
19. Petrova, A.M. and Kasikov, A.G., *II Regional'naya konferentsiya molodykh uchenykh "Teoreticheskaya i eksperimental'naya khimiya zhidkofaznykh sistem (Krestovskie chteniya)", Ivanovo, 13–16 noyabrya 2007 g.* [II Regional. Conf. of Young Scientists "Theoretical and Experimental Chemistry of Liquid-Phase Chemistry (Krestovskie Readings)," Ivanovo, November 13–16, 2007], Ivanovo, 2007, pp. 113–114.
20. *Obshchaya organicheskaya khimiya, tom 2, Kislorodsoderzhashchie soedineniya* (General Organic Chemistry, vol. 2, Oxygen-containing Compounds), Kochetkov, N.K. and Usov, A.I., Eds., Moscow: Khimiya, 1982.
21. Robinson, R.A. and Stokes, R.H., E*lectrolyte Solutions, The Measurement and Interpretation of Conductance, Chemical Potential and Diffusion in Solutions of Simple Electrolytes*, London: Butterworth's, 1959, 2nd ed.

ISSN 1070-4272, Russian Journal of Applied Chemistry, 2008, Vol. 81, No. 12, pp. 2084–2087. © Pleiades Publishing, Ltd., 2008.
Original Russian Text © A.A. Geidarov, 2008, published in Zhurnal Prikladnoi Khimii, 2008, Vol. 81, No. 12, pp. 1971–1974.

INORGANIC SYNTHESIS AND INDUSTRIAL INORGANIC CHEMISTRY

Extractive Recovery of Gallium(III) from Acid Sulfate Solutions with Primary Amines

A. A. Geidarov

Institute of Chemical Problems, National Academy of Sciences of Azerbaijan, Baku, Azerbaijan

Received January 29, 2008

Abstract—Liquid extraction of Ga(III) ions with technical-grade aliphatic amines from sulfate media at a temperature of 20 ± 5°C was studied. The composition of the complex being extracted was determined and the equation of the reaction of Ga(III) extraction with primary amines was derived. The equilibrium constant of the reaction of gallium(III) extraction from acid sulfate solutions was found.

DOI: 10.1134/S1070427208120070

Gallium(III) is a typical scattered element and its concentration in raw materials and technological industrial products from which gallium compounds are recovered is low. Therefore, a key task of the gallium (III) technology is its primary recovery and concentration. A successful solution of this problem should be promoted by wide introduction of extractive and sorption processes previously employed for recovery, concentration, and purification of numerous rare and nonferrous metals [1–4] into the chemical technology of gallium(III). Despite that the number of studies devoted to extraction of gallium(III) is sufficient, they are mostly concerned with its recovery from alkaline media [5] and chloride solutions [6]. Information about extraction of gallium(III) from neutral and acid sulfate solutions is rather scarce. The possibility of using aliphatic amines for extraction of gallium(III) was described in [1, 2, 6–10]. Gallium(III) is recovered from acid chloride solutions via the reaction of $GaCl_4^-$ anions with the ammonium cation:

$$RNH^+_{3org} + GaCl^-_{4aq} \rightarrow RNH_3GaCl_{4org}.$$

The possibility of gallium(III) recovery from sulfate solutions with primary, secondary, and tertiary alkylamines in chloroform was first described by Shevchuk [10]. It was shown that gallium(III) can exist in the organic phase as acido complexes [$Ga(SO_4)_2^-$, $Ga(SO_4)_3^{3-}$, $Ga(SO_4)_4^{5-}$] and chloroform solutions of di-*n*-ionylamine and tri-*n*-octylamine hardly extract gallium(III) at all from acid sulfate solutions.

This communication reports on a study of the extraction of gallium(III) ions from sulfate solutions with technical-grade primary aliphatic amines.

EXPERIMENTAL

We carried out the study with the use of technical-grade mixture of primary aliphatic amines (ANPO) produced from liquid paraffins of general formula

$$CH_3(CH_2)_m—\underset{\displaystyle NH_2}{\underset{|}{CH}}—(CH_2)_n—CH_3,$$

where $m + n$ = 10 to 16 carbon atoms, manufactured by Deneprodzerzhinsk chemical combine; bp = 240–345°C, extractive agent density 0.899 g cm^{-3}, refractive index 1.51, average molecular mass 185 g mol^{-1}. Burning kerosene served as a diluent.

Our preliminary experiments demonstrated that a 5-min mixing with aqueous and organic phases by shaking is sufficient for equilibrium to be attained. The complete phase stratification is achieved in 1–3 min. The phase ratio was $V_o : V_w = 1 : 2$ in all the experiments. The content of gallium(III) in the aqueous and organic phases was found by photocolorimetry [11], and the concentration of sulfate ions in equilibrium organic phases, by gravimetry, in the form of $BaSO_4$.

We prepared the starting aqueous Ga-containing solutions [Ga(III) = 7.2×10^{-4} M] from $Ga_2(SO_4)_3 \cdot 18H_2O$ produced using the method described in [11].

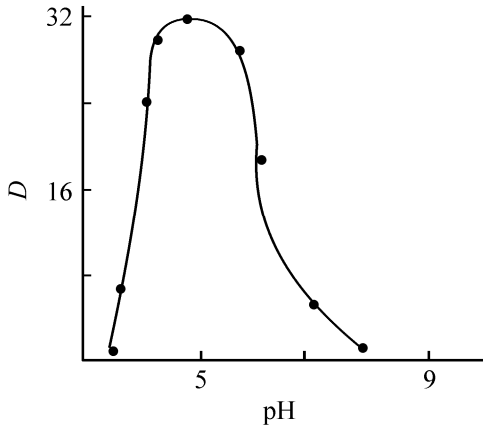


Fig. 1. Effect of the acidity of the aqueous phase on the extraction of gallium(III) ions with a 0.5 M solution of ANPO in kerosene. $c_{Ga} = 7.2 \times 10^{-4}$ M; the same for Fig. 3. (*D*) Gallium(III) distribution coefficient.

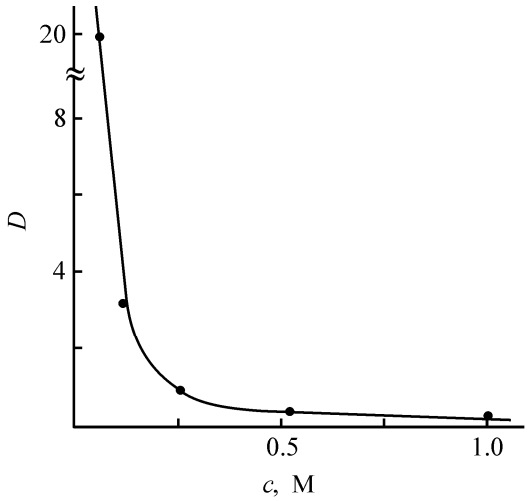


Fig. 2. Gallium(III) distribution coefficient *D* vs. H_2SO_4 concentration *c* in solution.

For this purpose, an appropriate weighed portion was dissolved under heating in water and then the solution was acidified to a required pH. IR spectra were recorded with a Specord 75-IR spectrometer in the range 400–4000 cm^{-1}.

The acidity of the aqueous phase most strongly affects the degree of gallium(III) recovery with a primary aliphatic amine (Fig. 1). It follows from the results obtained that the maximum extraction of Ga(III) ions lies in the weakly acid, nearly neutral region (pH 4–6). The maximum recovery of gallium(III), with a distribution coefficient of about 32, is observed at pH ~4.8.

In the extraction, the amine reacts with sulfuric acid in accordance with the equation $2RNH_2 + H_2SO_4 \rightarrow (RNH_3)_2SO_4$. The salt formed is distributed among the aqueous and organic phases. To study the extraction of gallium(III) from aqueous solutions, we examined the distribution of the amine salt among the aqueous and organic phases in relation to the sulfuric acid concentration. The experiments demonstrated that the ammonium salt is almost insoluble in kerosene.

Further, we studied the effect of the sulfuric acid concentration on the extraction of gallium(III) from aqueous solutions with a primary amine. It can be seen from Fig. 2 that the maximum distribution constant is observed at an H_2SO_4 concentration of 0.05 M in the starting solution. As the sulfuric acid concentration increases, the distribution coefficient of gallium(III) steeply decreases. The possible reason is that, as a result of appearance of an excess amount of sulfuric acid, H_2SO_4 is bound with ammonium ions and displaces the anion from the organic phase via competitive extraction. Ammonium sulfate is co-extracted with gallium(III) into the organic phase.

This is indicated by the results of the following experiments. The extraction was performed from a 0.05 M aqueous solution of H_2SO_4 in the absence of gallium(III), and the content of the ions in the organic phase was determined. Then, we carried out the same experiment in the presence of gallium(III). The difference between the contents of SO_4^{2-} ions in the extract was used to judge about the form of gallium being extracted, whose ions are contained in the organic phase. The experimental data are listed in the table.

Determination of the Ga^{3+}/SO_4^{2-} ratio in the extract under study

SO_4^{2-}, Ga(III)	Content, g	ν, mol
SO_4^{2-}:		
in the $Ga_2(SO_4)_3$ solution before extraction	0.0615	0.0006406
in the aqueous phase after extraction	0.009306	0.0000969
in the organic phase after extraction	0.0265	0.000276
in the organic phase after extraction from H_2SO_4	0.0156	0.0001625
in the organic phase after extraction from $Ga_2(SO_4)_3$	0.0101	0.0001052
Ga(III) in the organic phase after extraction	0.0050	0.0000717

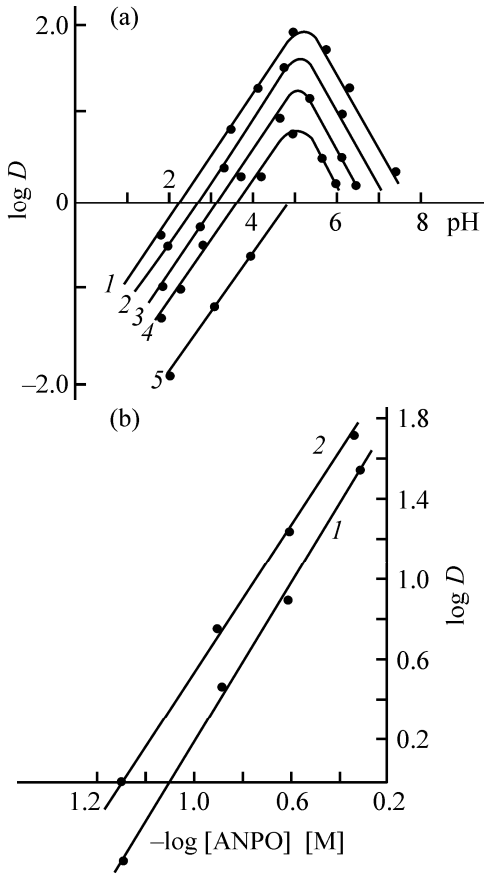


Fig. 3. Gallium(III) distribution coefficient D vs. (a) pH of the medium and (b) ANPO concentration. (a) c_{ANPO} (M): (*1*) 1, (*2*) 0.5, (*3*) 0.25, (*4*) 0.125, and (*5*) 0.05. (b) pH: (*1*) 45 and (*2*) 5.0.

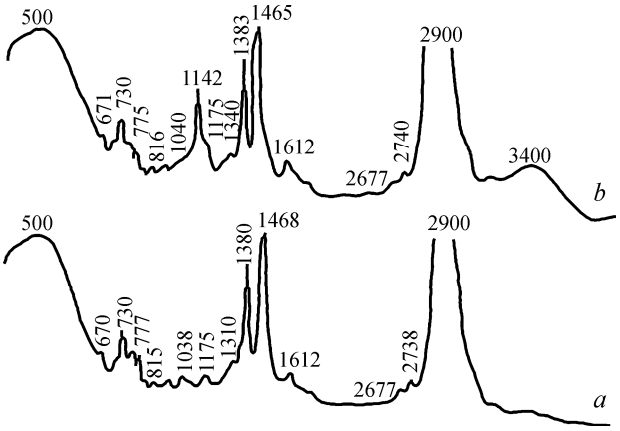


Fig. 4. IR absorption spectra. (*a*) Extractive agent and (*b*) extract.

Theoretically, it follows from the composition $Ga_2(SO_4)_3$ that 1 mg of Ga^{3+} corresponds to 2.06 mg SO_4^{2-}. The ratio experimentally found in the organic phase is 5 mg Ga^{3+} to 10.1 mg SO_4^{2-}, i.e., gallium(III) exists in the organic phase in the form of $Ga_2(SO_4)_3$.

At any of the amine concentrations studied in the organic phase, the maximum distribution coefficient corresponds to pH 4.8 (Fig. 3a).

To determine the stoichiometry of the components in the composition of the compounds being extracted, we analyzed the dependence of the distribution coefficient of gallium(III) at a constant concentration of the metal ion (0.05 g l^{-1}) and varied content of the amine in the organic solvent (Fig. 3b). In recovery of gallium (III) from weakly acid sulfate media, this dependence is represented by a straight line (Fig. 3b) with a slope approaching 2. This means that two amine molecules are associated with a single gallium(III) atom, at least within that range of amine concentrations in which the organic phase remains ideal.

To obtain additional evidence about the extractive agent and compounds being extracted, we examined their IR spectra in the range 400–4000 cm^{-1} (Fig. 4). It can be seen in Fig. 4 that the spectra of the extractive agent generally reproduce the IR spectra of a 1 M ANPO solution in kerosene, but with certain distinctions. It was demonstrated that vibrations of the following bonds appear in both the spectra: N–H (775, 1310, 3100–3200 cm^{-1}), C–N (1380 cm^{-1}), S–O (670, 1038, 1142 cm^{-1}), and O–H (1612, 3200–3700 cm^{-1}). In contrast to the IR spectrum of the reagent, the IR spectrum of the extractive agent shows a noticeable peak at around 1142 cm^{-1}, which can be attributed to stretching vibrations of the SO_4^{2-} group. The presence of a weak band in the region of deformation vibrations of water molecules (1612 cm^{-1}) can be attributed to the hygroscopic nature of the compounds studied, which is presumably due to the possibility of formation of $AmH^+\cdots OH_2$ hydrogen bonds [12].

A broad absorption band at 3100–3700 cm^{-1}, peaked at 3400 cm^{-1} and associated with deformation vibrations of OH groups of molecular water, appears in IR spectra of the extractive agent saturated with gallium(III). The absence of narrow absorption bands in the range of stretching vibrations of OH^- (3500–3700 cm^{-1}) [13] indicates that this extract contains no hydroxy groups.

In the presence of sulfuric acid, the complexation capacity of gallium(III) is manifested to a lesser extent, compared with in weakly acid sulfate media in which the $GaSO_4^+$ complex is formed [14]. Other possible sulfate acido complexes [$Ga(SO_4)_2^-$, $Ga(SO_4)_3^{3-}$, $Ga(SO_4)_4^{5-}$ are only formed in the presence of organic solvents (acetone, *n*-propanol, dioxane) [15]. Therefore, the mechanism described in the literature [10] is unlikely and

was studied for analytical purposes. We believe that gallium exists in the organic phase as $n[(RNH_3)_2SO_4] \cdot Ga_2(SO_4)_3$, as also does Fe(III) described in [2].

With account of the aforesaid, the extraction of gallium(III) from sulfuric acid solutions can be expressed by the equation

$$2Ga^{3+}_{aq} + 4(RNH_3)^{+}_{aq} + 5SO^{2-}_{4aq} \rightleftarrows 2[(RNH_3)_2SO_4] \cdot Ga_2(SO_4)_{3org},$$

with the reaction constant

$$K_{ex} = \frac{\{2[(RNH_3)_2SO_4] \cdot Ga_2(SO_4)_3\}_{org}}{[Ga^{3+}]^2_{aq}[SO^{2-}_4]^5_{aq}[(R(NH_3)_7]^4_{aq}}.$$

Based on the data obtained for the pH range 3.5–4.9, we calculated the concentration constants of gallium extraction $\log K_{ex} = 5.82 \pm 0.88$.

The fact that the calculated values of the extraction constants are invariable confirms the validity of the equation we suggested.

Gallium(III) was quantitatively re-extracted with a 1 : 1 NH_4OH ammonia solution from the organic phase, the pH value of whose equilibrium aqueous phase was 9–10, in agreement with the available recommendation for re-extraction of gallium(III) from amines [1]. In re-extraction of gallium from the organic phase with an ammonia solution, 80–85% of gallium(III) passes to the aqueous phase in a single stage.

CONCLUSIONS

(1) Ga(III) is extracted from sulfate acid solutions with primary aliphatic amines in the form of a complex compound $2[(RNH_3)_2SO_4] \cdot Ga_2(SO_4)_3$, whose composition was determined by the extraction method and analysis of the organic phase.

(2) The maximum degree of extraction is achieved in the weakly acid region at pH 4.8–5.4. Gallium(III) is quantitatively re-extracted from the organic phase with a 1 : 1 NH_4OH solution.

REFERENCES

1. Reznik, A.M., Ponomareva, E.I., Silaev, Yu.N., et al., *Protsessy ekstraktsii i sorbtsii v khimicheskoi tekhnologii galliya* (Sorption and Extraction Processes in Chemical Technology of Gallium), Alma-Ata: Nauka, 1985.
2. Good, M.L., Bryan, S.E., and Frank Juge, J. *Inorg. Chem.*, 1963, vol 2, no. 5, p. 963.
3. Bina Gupta, Niti Mudhar, Zareena Begum I, and Indu Singh, *Hydrometallurgy*, 2007, vol. 87, nos. 1–2, p. 18.
4. Pawar, S.D. and Dhadke, P.M., *J. Serb. Chem. Soc*., 2003, vol.. 68, no. 7, p. 581.
5. Turanov, A.N., Evseeva, N.K., and Karepov, B.R., *Zh. Prikl. Khim.*, 2001, vol. 74. no. 8, pp. 1269–1273.
6. Rodriguez De San Miguel, E., Aguilar, J.C., Rodriguez, M.T.J., and De Gyves, J., *Hydrometallurgy*, 2000, vol. 57, no. 2, p. 151.
7. Vainarovskaya, G.I., Gavrilov, N.I., Reznik, A.M., et al., *Izv. Vyssh. Uchebn. Zaved., Tsv. Metall.*, 1977. no. 4, p. 84.
8. *Spravochnik po ekstraktsii* (Handbook of Extraction), vol. 3, Rozen, A.M., Ed., Moscow: Atomizdat, 1978.
9. Shmidt, V.S., *Ekstraktsiya aminami* (Extraction with Amines), Moscow: Atomizdat, 1980.
10. Shevchuk, I.A. and Dubchenko, Yu.G., Available from ONIITEKhIM, 1974, Moscow, no. 164/74.Dep.
11. Busev, A.I., Tiptsova, V.G., and Ivanov, V.M., *Rukovodstvo po analiticheskoi khimii redkikh elementov* (Manual of Analytical Chemistry of Rare Elements), Moscow: Khimiya, 1978, 2ng ed.
12. Shorikov, Yu.S., Orlov, A.M., and Sinitsyn, N.M., *Khimiya ekstraktsii* (Chemistry of Extraction), Novosibirsk: Nauka, 1984, pp. 149–161.
13. Nakamoto, K., *Infrared Spectra of Inorganic and Coordination Compounds*, New York: John Wiley & Sons, 1963.
14. Tananaev, I.V. and Bol'shakova, N.K., *Zh. Neorg. Khim.*, 1962, vol. 7, no. 9, p. 2241.
15. Shishkova, L.G., *Dokl. Bolg. Akad. Nauk*, 1980, vol. 33, no. 6, p. 815.

ISSN 1070-4272, Russian Journal of Applied Chemistry, 2008, Vol. 81, No. 12, pp. 2088–2094. © Pleiades Publishing, Ltd., 2008.
Original Russian Text © E.V. Shkol'nikov, 2008, published in Zhurnal Prikladnoi Khimii, 2008, Vol. 81, No. 12, pp. 1975–1980.

PHYSICOCHEMICAL STUDIES OF SYSTEMS AND PROCESSES

Thermodynamic Characterization of the Amphotericity of Oxides and Hydroxides of Group-IIIA Elements in Aqueous Media

E. V. Shkol'nikov

St. Petersburg State Forestry Academy, St. Petersburg, Russia

Received June 11, 2008

Abstract—Dependences of the molar solubility of M_2O_3 solid oxides on the pH of aqueous media at 25°C and also the constants of acid-base equilibria in aqueous media for stable crystalline M_2O_3 oxides and for crystalline and dissolved $M(OH)_3$ hydroxides (M = In, Al, Ga, In, and Tl) were calculated by the thermodynamic method with account of the formation of hydroxo complexes.

DOI: 10.1134/S1070427208120082

Previously, the effect of pH on the molar solubility of solid hydroxides of the Group-IIIA elements in aqueous alkaline and acid media has been calculated by the thermodynamic method [1]. Of interest are a thermodynamic calculation of solubility of solid oxides M_2O_3 in water and aqueous media and calculation of acid–base equilibria [2] for oxides and hydroxides of group-IIIA elements.

Crystalline and amorphous oxides M_2O_3 are widely used in production of special glasses, ceramics, enamels, catalysts, and sorbents; in metallurgy; laser technology; radio engineering; and electronics [3–6]. Being products of a real dehydration of hydroxides, solid oxides can be obtained by heating of hydroxides and metahydroxides in an inert atmosphere. Anhydrous oxides M_2O_3 are obtained by burning elementary substances M in oxygen (ozone) and by thermal decomposition of nitrates and sulfates [4–6]. Polymeric oxides M_2O_3 form rather difficultly soluble (B_2O_3) or nearly water-insoluble amorphous and crystalline modifications whose reactivity depends on their structure and preparation method and conditions [3–7].

The amphotericity of M_2O_3 oxides has been little studied, and quantitative data on their solubility in aqueous media are rather scarce and frequently contradictory. For example, according to [5], B_2O_3 is an acid oxide, Al_2O_3 is a typical amphoteric oxide, and, in the series $Ga_2O_3 \rightarrow In_2O_3 \rightarrow Tl_2O_3$, indications of acidity become weaker, basicity increases, and solubility in acids grows. According to the data of [3, 5], the acid and basic functions of Ga_2O_3 and $Ga(OH)_3$ are exhibited approximately to the same extent, whereas according to [6, 8], the acid properties are more pronounced than the basic properties. The basic properties of $In(OH)_3$ predominate over its acid properties, and for thallium(III) hydroxide and oxide, the acid function is expressed very weakly [5]. According to [3], brown thallium(III) hydroxide and oxide are peptized by alkalis to give a sol, but do not dissolve in alkalis and form no thallates. The oxide Tl_2O_3 is obtained in the form of an amorphous powder on heating the $Tl_2O_3 \cdot mH_2O$ precipitate, and the oxide and its hydrate react with acids and do not dissolve in ammonia water and solutions of strong alkalis [4, 7]. However, hydrated thallium(III) oxide dissolves to a noticeable extent in concentrated solutions of strong alkalis to give readily hydrolyzed thallates [6].

Light yellow amorphous and yellow cubic In_2O_3 modifications react with acids under heating, but do not dissolve in dilute solutions of alkaline hydroxides [4, 6, 7]. The hydrate $In_2O_3 \cdot mH_2O$ is peptized in aqua ammonia and dissolves in acids and in concentrated solutions of strong alkalis to give unstable indates [3, 4, 6]. The oxides Ga_2O_3 and Al_2O_3 form several crystalline modifications. Moderate heating of a $Ga(OH)_3$ or GaO(OH) gel yields a metastable hexagonal α-Ga_2O_3 [4] soluble in acids and alkalis to give gallium(III) salts and gallates, respectively [6, 7]. The stable mono-

clinic modification β-Ga_2O_3 is formed as a white powder upon a stepwise heating of gallium(III) nitrate or hydroxide at 250°C and then at 600°C for 12 h [6]. After being calcined at above 600°C, Ga_2O_3 reacts with molten alkalis and ceases to be soluble in acids and aqueous-alkaline media, similarly to Al_2O_3 [4, 6, 7].

Amorphous porous oxide Al_2O_3 (aluminogel) and the tetragonal modification γ-Al_2O_3, produced by calcination of aluminum hydroxides at 550°C, are rather hygroscopic and chemically active and react with solutions of acids and alkalis [4, 6, 7]. The stable rhombohedral modification α-Al_2O_3 (corundum), produced from diaspore AlO(OH) at 500–600°C, does not react with water and reacts with solutions of acids and alkalis under heating. The reactivity and solubility of Al_2O_3 strongly decrease as its preparation temperature is raised [6]. Natural corundum and α-Al_2O_3 calcined above 1200°C are very hard, nonhydroscopic, and chemically inert under ordinary conditions [3–6].

Unlike other M_2O_3 oxides, B_2O_3 is easily vitrified and reacts with water with strong warming up [4] to give weak orthoboric acid with a limited solubility in water [1, 6]. A stable hexagonal modification of B_2O_3 is obtained by cautious heating of α-HBO_2. Boron(III) oxide and boric acids react with NaOH solutions to give $Na[B(OH)_4]$, $Na_2B_4O_7$, and $NaBO_2$ [4, 6]. Fusion of B_2O_3 and other M_2O_3 oxides with sodium oxide yields hydrolyzed oxo compounds of the $NaMO_2$ type [3–6].

Because the heterogeneous reaction

$$0.5M_2O_3(s) + 1.5H_2O(l) = M(OH)_3(g)$$

does not occur to a noticeable extent for the solid oxides under consideration ($\Delta G^0_{298} > 0$, except for boron oxide), formation of $M(OH)_3$ solid hydroxides was disregarded when calculating the solubility of oxides. In an aqueous solution saturated with the poorly soluble oxide $MO_{1.5}$ ($0.5M_2O_3$), heterogeneous chemical equilibrium (1) is attained.

$$MO_{1.5}(s) + 1.5H_2O(l) \rightleftarrows M^{3+}(sol) + 3OH^-(sol). \qquad (1)$$

Its thermodynamic constant is given, similarly to $M(OH)_3$ hydroxides [1], by the expression

$$K^0_s = SP^0 = a_{M^{3+}}\, a^3_{OH^-} = \text{const}(T),$$

where $a_{M^{3+}}$ and a_{OH^-} are the activities of M^{3+} and OH^- ions.

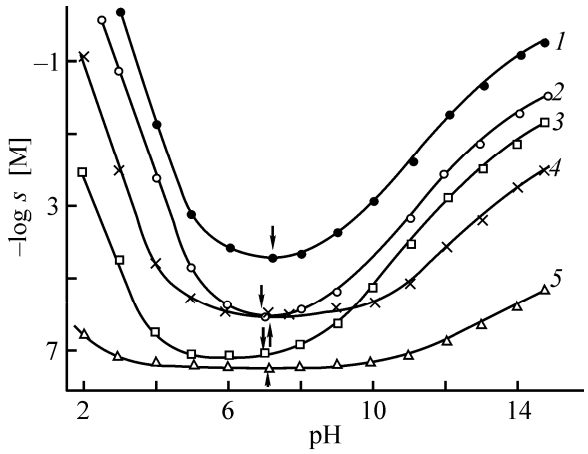


Fig. 1. Dependence of the solubility s of crystalline oxides on the pH of the aqueous medium at 25°C. (*1*) γ-Al_2O_3, (*2*) α-Al_2O_3, (*3*) β-Ga_2O_3, (*4*) In_2O_3, (*5*) Tl_2O_3.

The thermodynamic calculation of K^0_s for equilibrium (1) was performed using the procedure described in [1]. The required standard values of ΔG^0_f of ion formation in aqueous solutions were taken from [9], and values of ΔG^0_f for solid oxides at 298 K, from the reference books [7, 10, 11]. The molar solubilities of the oxides (except $BO_{1.5}$) were calculated taking into account the ionic strength of the solutions and the formation of mononuclear hydroxo complexes in accordance with the generalized equation

$$s = c_M = \frac{K^0_s}{f_{M^{3+}} f_{OH^-}} \sum_{i=0}^{n} \beta_i [OH^-]^{i-3}.$$

Here, the constant K^0_s characterizes the heterogeneous equilibrium (1); $f_{M^{3+}}$, f_{OH^-} are the molar activity coefficients of M^{3+} and OH^- ions; $\beta_0 = 1$; β_1, β_2, β_3, and β_4 are the total stability constants of MOH^{2+}, $M(OH)^+_2$, $M(OH)_3$, and $M(OH)^-_4$, found from averaged data of [8, 11–13].

The equilibrium concentration of free OH^- anions and the pH^0 values of saturated aqueous solutions of oxides in pure water (shown by arrows in Fig. 1) were found by solving a system of six equations [1], using the Ferrari, Cardano, or Newton method.

We estimated the molar solubility of the stable hexagonal modification of $BO_{1.5}$ in pure water at 25°C by using the intrinsic solubility of a rather weak orthoboric acid exothermally formed in accordance with the reaction equation [4]

$$BO_{1.5}(cr) + 1.5H_2O(l) = H_3BO_3(cr) + 38\ kJ,$$

Table 1. Thermodynamic parameters of dissolution of crystalline oxides in water and aqueous media at 25°C

Compound	K_s^0		H_2O			pH_{opt}	ρs_{min}	s, M, in 1 M NaOH	A
			pH^0	s^0	$M(OH)_3$				
	calculation	data of [14]		M					
$BO_{1.5}$	0.15	–	3.8	0.72 [13]	0.71	<–1.3	>0.9	1.01	3.1
γ-$AlO_{1/5}$	30.85	–	7.20	3.5×10^{-5}	3.2×10^{-5}	7.21	4.45	12.9	1.08×10^{6}
α-$AlO_{1.5}$	32.45	32.5	7.07	9.7×10^{-7}	8.6×10^{-7}	7.21	6.02	0.35	1.08×10^{6}
α-$GaO_{1.5}$	37.85	–	6.92	4.9×10^{-7}	4.5×10^{-7}	6.15	6.34	0.55	3.3×10^{6}
β-$GaO_{1.5}$	38.73	38.75	6.99	6.5×10^{-8}	5.9×10^{-8}	6.15	7.22	0.073	3.3×10^{6}
$InO_{1.5}^{*}$	34.30	–	7.12	1.15×10^{-5}	1.14×10^{-5}	7.75	4.94	0.029	7.4×10^{3}
$InO_{1.5}$	35.27	35.3	7.02	1.22×10^{-6}	1.21×10^{-6}	7.75	5.92	3.1×10^{-3}	7.4×10^{3}
$TlO_{1.5}^{*}$	43.7	–	7.00	1.8×10^{-6}	1.8×10^{-6}	7.00	5.75	8.8×10^{-5}	1.4×10^{2}
$TlO_{1.5}$	45.4	45.9	7.00	3.9×10^{-8}	3.9×10^{-8}	7.00	7.41	1.9×10^{-6}	1.4×10^{2}

* Amorphous powder.

with its dissolution in water being, however, an endothermic process [1, 4]. Analysis of the data from the reference book [13] shows that the temperature dependence of the solubility of the solid oxide B_2O_3 in water in the temperature range 0–100°C can be represented by the equation

$$\ln s = 9.983(\text{cr}) + 2694/T.$$

Here s is the solubility of B_2O_3 (g/100g of H_2O), and T is absolute temperature.

The graphically found standard enthalpy of dissolution, $\Delta H_s^0 = 22.4$ kJ mol^{-1}, hardly differs from the value of ΔH_s^0 for H_3BO_3 [1]. The results of our calculation are listed in Table 1, where $pK_s^0 = -\log K_s^0$, s^0 is the total molar solubility of solid oxides $MO_{1.5}$ in pure water, and $[M(OH)_3]$ is the equilibrium molarity of neutral complexes in aqueous solutions of oxides at 25°C. It is seen from Table 1 that pK_s^0 values calculated in this study satisfactorily agree with the data from [14]. For some of the oxides, the calculation was carried out for the first time. The solubility of amorphous M_2O_3 oxides, as also that of $M(OH)_3$ hydroxides [1], substantially exceeds the solubility of crystalline modifications. The solubility of these latter noticeably depends on structure and decreases on passing to the stable modifications α-Al_2O_3 and β-Ga_2O_3. The solubility of M_2O_3 oxides in pure water is determined by the content of dissolved neutral $M(OH)_3$ complexes (from 89% for aluminum oxides to approximately 100% for Tl_2O_3).

It is seen from Table 1 that saturated solutions of B_2O_3 and Ga_2O_3 in pure water are slightly acidic, those of thallium(III) are neutral, and solutions of aluminum and indium(III) oxides are weakly alkaline (pH 7.02–7.2). The isoelectric point of the dispersed system was found to be at pH 6.8 [3] and 8.0 [4], respectively, for $Ga(OH)_3$ and γ-Al_2O_3.

The calculation of the average ligand number n in the hydroxo complexes (Bjerrum function) at pH 15 gives a value of ~4 for all the oxides and hydroxides of Group-IIIA elements, which indicates that the amphotericity condition $n > 3$ is satisfied for these compounds. No thermodynamic data are available for the small B^{3+} cation with a high polarizing power and for its hydroxo complexes in aqueous solutions of B_2O_3 and H_3BO_3, with the exception of $\Delta G_{f\,298}^0$ for $B(OH)_4^-$ and $B(OH)_3$ [1, 10]. The calculated ratio of total stability constants β_4 and β_3 of these hydroxo complexes is 6×10^4, which provides that the amphotericity condition is satisfied and the homogeneous equilibrium

$$H_3BO_3(\text{sol}) + OH^-(\text{sol}) \rightleftarrows B(OH)_4^-(\text{sol})$$

is shifted to the right at pH > 9.2, with $B(OH)_4^-$ complexes formed.

The minimal solubility of M_2O_3 oxides is observed at the optimal concentration of OH^- ions, when the mole fraction of neutral $M(OH)_3$ complexes in aqueous solutions is at maximum. We found from this condition, similarly to [1], first pH_{opt} and then s_{min}. The values of $ps_{min} = -\log s_{min}$ at 25°C are listed in Table 1 and in part shown in Fig. 1, whence follows that there is no negative effect of OH^- on the solubility of both M_2O_3 oxides and $M(OH)_3$ hydroxides in alkali

[1]. Analysis shows that the conditions for the absence of this effect for oxides and hydroxides of Group-IIIA elements are the following: high values of the total stability constant β_3 of the neutral $M(OH)_3$ complex and of its mole fraction in a purely aqueous saturated solution, in contrast to, e.g., CdO, CuO, and FeO oxides with a strong negative effect of common OH^- ions [2].

For a comparative quantitative estimate of amphoterism of the oxides, we used, as before [2], the ratio ($A > 1$) of their molar solubilities in an alkaline medium with pH 14.7 (5 M NaOH solution) and in pure water. The amphotericity parameter is determined by the chemical nature of an oxide and varies over a wide range, from 3.1 for B_2O_3 to 3.3×10^6 for Ga_2O_3 (Table 1). The molar solubility of stable crystalline M_2O_3 oxides in 1 and 5 M NaOH solutions is determined by $M(OH)_4^-$ complexes and steadily decreases as the element M is replaced in the series B→Al→Ga→In→Tl coinciding with the order in which the ionic radius of M^{3+} increases in Group IIIA and the ionicity P_i of the M–O chemical bond grows from 46 (B–O) to 67% (Tl–O) in oxides, according to an estimate of P_i from Pauling's curve [5]. The solubilities of stable B_2O_3 and β-Ga_2O_3 with predominant acid properties in 5 M NaOH and 10^{-3} M $HClO_4$ are lower than those of the stable H_3BO_3 and H_3GaO_3 acids. A different relationship between the solubilities is observed in Group IIIA for other stable oxides and hydroxides with predominant basic properties.

In an acid medium with pH 3 (upon addition of $HClO_4$) the solubility of Tl_2O_3 is intrinsic [1], as also that of the very weak electrolyte $Tl(OH)_3$; the solubilities of gallium(III), indium(III), and aluminum oxides are determined, respectively, by $GaOH^{2+}$ complexes and Ga^{3+} cations, by In^{3+} cations and $InOH^{2+}$ complexes, and by free Al^{3+} cations. The molar solubility of stable $M(OH)_3$ hydroxides in the acid medium (pH 3) decreases as the element M is replaced in the following order: B→Al→Ga→In→Tl.

Despite the large value of the main amphotericity parameter A, the solubility of the stable hydroxides γ-$Al(OH)_3$, $In(OH)_3$, $Tl(OH)_3$ and the oxides In_2O_3 and Tl_2O_3 in 5 M NaOH is low (1.8, 0.03, 4×10^{-4}, 2×10^{-4}, and 1×10^{-5}, respectively) because of the small values of s^0 (Table 1) and the influence of other parameters (Fig. 2 and Table 2), which supplement the amphotericity characteristics of the hydroxides and oxides. Figure 2 shows on a logarithmic scale how the ratio of the molar solubilities of the stable crystalline oxides (hydroxides) under study in aqueous alkaline (acid) media and in pure water depends on the pH of the medium at 25°C.

Table 2. Amphotericity parameters* of stable crystalline hydroxides and oxides in aqueous media at 25°C

Compound	A	pH_b	B	C_b	C_b
γ-$Al(OH)_3$	1.07×10^6	7.6	0.5	1.0	2.8
α-$AlO_{1.5}$	1.08×10^6				
$Ga(OH)_3$	3.46×10^6	7.1	0.3	1.0	2.2
β-$GaO_{1.5}$	3.3×10^6				
$In(OH)_3$	7.39×10^3	8.9	1.9	0.8	2.5
$InO_{1.5}$	7.4×10^3				
$Tl(OH)_3$	1.42×10^2	10.5	3.5	0.5	1.2
$TlO_{1.5}$	1.4×10^2				

* $A = s(\text{pH } 14.7)/s^0$, pH_b at $s_b = s^0$, $B = pH_b - pH^0$, $C_b = |\Delta p s_b/\Delta pH|$, $C_a = \Delta p s_a/\Delta pH$.

Table 2, compiled using the data in Fig. 2, contains, in addition to A parameter, pH_b values above which the solubility s_b in alkali exceeds the solubility s^0 in water upon addition of NaOH. The lower the pH_b value, the smaller additions and the lower alkali concentrations are necessary for the solubility of a hydroxide (oxide) to start to increase as compared with the solubility in pure water. The lowest pH_b values were found for the typically amphoteric gallium and aluminum hydroxides (oxides) having the largest values of the main parameter A, and the highest pH_b values were obtained for $Tl(OH)_3$ and Tl_2O_3 with weak indications of amphotericity (Table 2). The parameter B, equal to $(pH_b - pH^0)$, determines the pH range in which $s < s^0$ is at a minimum for gallium(III) hydroxide and at a maximum for thallium(III) hydroxide and oxide upon addition of

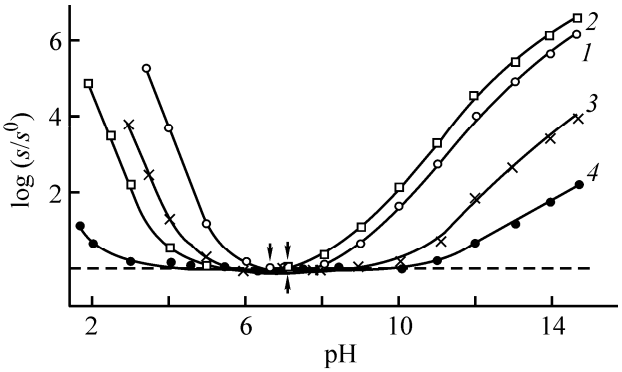


Fig. 2. Dependence of the ratio of molar solubilities of stable oxides and hydroxides in aqueous medium s and in pure water s^0 on the pH of the medium at 25°C. (*1*) α-Al_2O_3 and γ-$Al(OH)_3$, (*2*) β-Ga_2O_3 and $Ga(OH)_3$, (*3*) In_2O_3 and $In(OH)_3$, (*4*) Tl_2O_3 and $Tl(OH)_3$.

Table 3. Thermodynamic constants of heterogeneous equilibria for stable crystalline hydroxides and oxides in water (2)–(6) and in acid (7)–(9) and alkaline (10) media

Compound	pK_{298} for equilibrium								
	(2)	(3)	(4)	(5)	(6)	(7)	(8)	(9)	(10)
γ-$Al(OH)_3$	25.12	14.67	7.19	15.52	16.05	0.88	–2.85	–7.86	2.05
$Ga(OH)_3$	25.46	14.87	5.10	10.60	11.78	0.68	–2.62	–5.22	–2.21
$In(OH)_3$	26.92	16.74	7.33	19.61	17.00	2.75	–1.05	–5.05	3.01
$Tl(OH)_3$	32.52	19.51	7.24	–	18.94	5.52	4.54	3.94	4.95
H_3BO_3	–	–	0.066	9.22	9.28	–	–	–	–4.70
$BO_{1.5}$	–	–	0.13	7.41	6.52	–	–	–	–7.97
α-$AlO_{1.5}$	23.45	14.12	6.09	13.86	14.36	–0.78	–4.52	–9.52	0.39
β-$GaO_{1.5}$	27.45	16.89	7.22	12.58	13.76	2.66	–0.64	–3.24	–0.23
$InO_{1.5}$	25.05	15.07	5.92	14.51	15.36	1.11	–2.70	–6.69	1.37
$TlO_{1.5}$	32.40	19.80	7.41	–	18.40	4.97	4.00	3.39	4.41

the alkali (Fig. 2 and Table 2). The parameters C_b and C_a (Table 2) characterize the rate at which the solubility increases as the pH changes upon addition of NaOH ($pH > pH_b$) or $HClO_4$ ($pH < pH^0$). The typical amphoteric aluminum and a gallium(III) oxides and hydroxides with increased C_a and C_b parameters and with low pH_b (Table 2) readily dissolve in the amorphous state in dilute acids and alkalis [3–6]. Indium (III) oxide and hydroxide with increased C_a, B, and pH_b parameters readily dissolve in acids, but hardly do so in concentrated alkalis [3–7]. Anhydrous and hydrated thallium(III) oxides with small C_b parameter (pH 11→14), medium value of C_a parameter (pH 3→1), and increased pH_b and B are soluble in acids, but difficultly and rather poorly soluble in strongly concentrated alkalis [5, 6].

Similarly to hydroxides [1], amphoteric oxides with M–O chemical bonds close in ionicity to O–H bonds can shift the water dissociation equilibrium and add hydroxide ions or protons in aqueous media to give the corresponding ions. Therefore, we supplemented the comparative characterization of the acid-base properties of stable crystalline hydroxides and oxides with a calculation of the thermodynamic parameters ΔG^0_{298} and pK_{298} (K is the equilibrium constant) of heterogeneous reactions in a saturated aque-

$$M(OH)_3(cr) \rightleftarrows MOH^{2+}(sol) + 2OH^-(sol), \quad (2)$$

$$M(OH)_3(cr) \rightleftarrows M(OH)_2^+(sol) + OH^-(sol), \quad (3)$$

$$M(OH)_3(cr) \rightleftarrows M(OH)_3(sol), \quad (4)$$

$$M(OH)_3(cr) \rightleftarrows H^+(sol) + H_2MO_3^-(sol), \quad (5)$$

$$M(OH)_3(cr) + H_2O(l) \rightleftarrows H^+(sol) + M(OH)_4^-(sol). \quad (6)$$

The corresponding heterogeneous equilibria (2)–(6) for stable oxides differ from equilibria (2)–(6) for hydroxides in that the $M(OH)_3(cr)$ phase is replaced by two phases: $MO_{1.5}(cr) + 1.5\ H_2O(l)$. The values of pK_{298}, calculated using the data of [6–14], are listed in Table 3, which shows that, with account of equilibria (2) and (3), the basic properties are predominant and are the most pronounced for γ-$Al(OH)_3$ and α-Al_2O_3, and the least pronounced for $Tl(OH)_3$ and Tl_2O_3. According to the pK_{298} values for equilibria (5) and (6), the acid properties are characteristic of H_3BO_3 and B_2O_3, predominate over basic properties for gallium (III) hydroxide and oxide, and are the least pronounced for thallium(III) oxide and hydrated oxide. The same conclusion follows from a calculation of pK_{298} for chemical equilibria in the acid and alkaline media for stable hydroxides

$$M(OH)_3(cr) + H^+(sol) \rightleftarrows M(OH)_2^+(sol) + H_2O(l), \quad (7)$$

$$M(OH)_3(cr) + 2H^+(sol) \rightleftarrows M(OH)^{2+}(sol) + 2H_2O(l), \quad (8)$$

$$M(OH)_3(cr) + 3H^+(sol) \rightleftarrows M^{3+}(sol) + 3H_2O(l), \quad (9)$$

$$M(OH)_3(cr) + OH^-(sol) \rightleftarrows M(OH)_4^-(sol). \quad (10)$$

and for the corresponding equilibria (7)–(10) for stable oxides. It can be seen from Table 3 and Figs. 1 and 2 that boron(III) and gallium(III) oxides and hydroxides are the best soluble in alkalis, and aluminum and indium(III) oxides and hydroxides, in acids.

Table 4 lists the thermodynamic constants of basicity ($K_{b,1}$, $K_{b,2}$, and $K_{b,3}$) and acidity ($K_{a,1}$, $K_{a,2}$, and $K_{a,3}$) of $M(OH)_3$ ampholytes dissolved in water in

Table 4. Stepwise thermodynamic basicity constants $K_{b,1}$, $K_{b,2}$, $K_{b,3}$ and acidity constants $K_{a,1}$, $K_{a,2}$, $K_{a,3}$ of hydroxides in the form of neutral complexes $M(OH)_3$ dissolved in water at 25°C

Compound	$pK_{b,1}$	$pK_{b,2}$	$pK_{b,3}$	$pK_{a,1}$	$pK_{a,2}$	$pK_{a,3}$	$pK^*_{a,1}$
H_3BO_3	–	–	–	9.23	12.55	13.58	9.22
				9.22 [3]	12.3 [3]	13.4 [3]	9.15 [5]
				9.14 [4]	12.74 [4]	13.7 [4]	
				9.24 [6]	12.40 [6]	13.40 [6]	
				9.15 [13]	12.7 [13]	13.8 [13]	
$Al(OH)_3$	8.03	9.32	9.00	8.52	–	–	8.44
	8.1 [11]		9.0 [3]				
$Ga(OH)_3$	9.67	10.56	11.28	8.1	10.26	11.72	7.96
	10.7 [3]	11.4 [3]		10.3 [3]	11.7 [3]		
$In(OH)_3$	9.15	9.98	10.29	12.3	–	–	10.65
				11.7 [11]			
$Tl(OH)_3$	12.39	12.60	12.96	–	–	–	12.37
	12.2 [11]	12.4 [11]	12.7 [11]				

the form of neutral complexes. The $pK_{a,1}$ values correspond to the ionization equilibrium

$$M(OH)_3(sol) + H_2O(l) \rightleftarrows H^+(sol) + M(OH)_4^-(sol)$$

in an aqueous solution, which is rather probable for H_3BO_3 [3, 4, 6]. Along with the values calculated from the data of [8–13], Table 4 lists the pK values from [3–6, 11]. It can be seen that the inequalities $K_{a,1} > K_{b,1}$ and $K_{a,2} > K_{b,2}$ are valid not only for the weak acid H_3BO_3, but also for neutral complexes of gallium(III) hydroxide in solutions. For other dissolved $M(OH)_3$ ampholytes, the basic properties ($K_{b,1} > K_{a,1}$) predominate, being the most pronounced for $Al(OH)_3$ and the weakest for $Tl(OH)_3$.

CONCLUSIONS

(1) The molar solubility of solid oxides $MO_{1.5}$ (M is a Group-IIIA element) in water, mainly determined by neutral $M(OH)_3$ complexes, is rather low (10^{-8}–10^{-5} M at 25°C, except for $BO_{1.5}$) and depends on the composition and structure, becoming considerably lower on passing from the amorphous to the stable crystalline modification.

(2) The thermodynamic method was used to calculate the effect of pH on the solubility of solid oxides M_2O_3 in aqueous alkaline and acid media at 25°C and to find the amphotericity parameter $A > 1$, which increases in the order B→Tl→In→Al→Ga. The values of pH of an acid medium, below which M^{3+} cations are not bound into hydroxo complexes, were found.

(3) The minimum solubility and the pH values corresponding to the most complete precipitation of amphoteric aluminum, gallium, indium, and thallium(III) oxides were calculated with account of the formation of hydroxo complexes.

(4) The calculation of the thermodynamic constants of heterogeneous acid–base equilibria in aqueous media and of the stepwise basicity and acidity constants of neutral $M(OH)_3$ complexes points to the acid nature of boron oxide and hydroxide, predominance of weak acid properties over weak basic properties for gallium(III) oxide and hydroxide, and predominance of basic properties, the most pronounced for aluminum oxide and hydroxide and the weakest for thallium(III) oxide and hydroxide.

REFERENCES

1. Shkol'nikov, E.V., *Zh. Prikl. Khim.*, 2008, vol. 81, no. 9, pp. 1428– 1431.
2. Shkol'nikov, E.V., *Zh. Prikl. Khim.*, 2006, vol. 79, no. 12, pp. 1942– 1946.
3. Nekrasov, B.V., *Osnovy obshchei khimii* (Fundamentals of General Chemistry), St. Petersburg: Khimiya, 2003.
4. Remy, H., *Lehrbuch der Anorganischen Chemie*, Leipzig: Akademische Verlagsgeselschaft Geest & Portig K.-G., 1961, vol. 2.

5. Akhmetov, N.S., *Obshchaya i neorganicheskaya khimiya* (General and Inorganic Chemistry), Moscow: Vysshaya Shkola, 1988.

6. *Khimicheskaya entsiklopediya* (Chemical Encyclopedia), Knunyants, I.L. and Zefirov, N.S., Eds., Moscow: BRE, 1988–1998, vols. 1–5.

7. Efimov, A.I., Belorukova, L.P., Vasil'kova, I.V., and Chechev, V.P., *Svoistva neorganicheskikh soedinenii: Spravochnik* (Properties of Inorganic Compounds: Reference Book), Leningrad: Khimiya, 1983.

8. Nazarenko, V.A., Antonovich, V.P., and Nevskaya, E.M., *Gidroliz ionov metallov v razbavlennykh rastvorakh* (Hydrolysis of Metal Ions in Dilute Solutions), Moscow: Atomizdat, 1979.

9. Vasil'ev, V.P., *Termodinamicheskie svoistva rastvorov elektrolitov* (Thermodynamic Properties of Electrolyte Solutions), Moscow: Vysshaya Shkola, 1982.

10. Karapet'yants, M.Kh. and Karapet'yants, M.L., *Osnovnye termodinamicheskie konstanty neorganicheskikh i organicheskikh veshchestv* (Main Thermodynamic Constants of Inorganic and Organic Substances), Moscow: Khimiya, 1968.

11. Lidin, R.A., Andreeva, L.L., and Molochko, V.A., *Spravochnik po neorganicheskoi khimii: Konstanty neorganicheskikh veshchestv* (Handbook of Inorganic Chemistry: Constants of Inorganic Substances), Moscow: Khimiya, 1987.

12. Fishtik, I.F. and Vataman, I.I., *Termodinamika gidroliza ionov metallov* (Thermodynamics of Hydrolysis of Metal Ions), Kishinev: Shtiintsa, 1988.

13. Lur'e, Yu.Yu., *Spravochnik po analiticheskoi khimii* (Handbook of Analytical Chemistry), Moscow: Khimiya, 1989.

14. Kumok, V.N., Kuleshova, O.M., and Karabin, L.A., *Proizvedenie rasnvorimosti* (Solubility Product), Novosibirsk: Nauka, 1983.

ISSN 1070-4272, Russian Journal of Applied Chemistry, 2008, Vol. 81, No. 12, pp. 2095–2098. © Pleiades Publishing, Ltd., 2008.
Original Russian Text © N.M. Kozhevnikova, E.P. Ermakova, 2008, published in Zhurnal Prikladnoi Khimii, 2008, Vol. 81, No. 12, pp. 1981–1984.

PHYSICOCHEMICAL STUDIES OF SYSTEMS AND PROCESSES

A Study of Sorption of Samarium(III) Ions by Natural Clinoptilolite-containing Tuff

N. M. Kozhevnikova and E. P. Ermakova

Baikal Institute of Nature Management, Siberian Branch, Russian Academy of Sciences, Ulan-Ude, Buryatia, Russia

Received November 28, 2007

Abstract—Equilibrium and kinetics of absorption of samarium(III) ions from sulfate solutions by a natural clinoptilolite-containing tuff were studied. The kinetic parameters of the sorption process were determined.

DOI: 10.1134/S1070427208120094

Compounds of rare-earth elements (REE), and especially those of the first representatives of this series: lanthanum, cerium, neodymium, and samarium, exhibit an enhanced biological activity and are used as fertilizers [1]. Lanthanum sulfate catalyzes the fixation of atmospheric nitrogen by Azobacter in legume crops, sulfates and nitrates of neodymium and samarium are involved in humus accumulation and activate the nitrogen and carbohydrate metabolism [2, 3].

The biological activity of REE compounds can be enhanced by introduction of their ions into the zeolite matrix by the sorption technique, with natural zeolites used as sorbents [1]. It has been shown that the sorption technology is the most rational way to obtain lanthanum- and neodymium-containing microfertilizers stimulating the production process in the soil–plant system and diminishing the possible migration of microelements in soils with light granulometric composition [4, 5].

The ion-exchange properties of natural zeolites with respect to rare-earth elements are insufficiently understood; the sorption of lanthanum and neodymium ions by mordenite and clinoptilolite tuff has been studied [1, 4, 5]; data on sorption of samarium ions by natural zeolites are lacking, but are necessary for evaluating the influence exerted by the nature of REE on the equilibrium and kinetics of sorption and require a deeper analysis. This study is devoted to analysis of the sorption of samarium(III) ions from sulfate solutions by a clinoptilolite tuff in relation to the solution concentration, sorbent grain size, and solid-to-liquid mass ratio.

EXPERIMENTAL

A clinoptilolite-containing tuff with the following content of components was used (wt %): SiO_2 68.11, Al_2O_3 12.84, Fe_2O_3 1.08, FeO 0.35, Mn 0.08, P_2O_5 0.05, TiO_2 0.58, CaO 4.17, MgO 2.65, K_2O 2.47, Na_2O 2.87, CuO 0.003, F 0.002; Si/Al = 5.25. The content of the zeolite in the rock was found by X-ray diffraction analysis with PTsL-2 [6] to be about 60%.

Grain fractions with sizes of 0.25–0.5 and 1–2 mm were taken for analysis by the sieving method. The sorption equilibrium was studied under static conditions in sorption from samarium sulfate solutions in the concentration range 0.0003–0.025 M of the ion being determined at s : l ratios of 1 : 10 and 1 : 50.

The kinetic parameters were calculated from Q–τ curves, where Q is the sorbed amount of samarium ions (mmol g^{-1}) and τ is time, by the procedure reported for sorption on zeolites [7]. For the initial period of time, when sorption occurs on the sorbent surface and the process goes under the control of the outer-diffusion mechanism, the rate constant of R of the outer-diffusion process was calculate by the equation

$$R = \mathrm{d}Q/\mathrm{d}\tau(1/cK_\mathrm{d}), \quad (1)$$

where c is the concentration of the ion being exchanged in solution (M); K_d, equilibrium distribution coefficient (ml g^{-1});

$$K_\mathrm{d} = (c_0 - c_\mathrm{eq})V/c_\mathrm{eq}m, \quad (2)$$

Kinetic parameters of samarium sorption by the natural clinoptilolite-containing tuff

Solution*	τ_∞, min	$dQ/d\tau \times 10^5$, mmol g^{-1} min^{-1}	K_d, ml g^{-1}	$R \times 10^4$, s^{-1}	$B \times 10^4$, s^{-1}	$D \times 10^8$, cm^2 s^{-1}
I	1550	3.8	52.8	24.7	9.8	4.9
II	1580	3.3	46.4	23.9	10.1	5.3
III	2060	1.6	29.7	10.3	6.5	2.7

c_0 and c_{eq}, initial and equilibrium samarium ion concentrations in solution; V, solution volume (ml); and m weighed portion of the zeolite (g).

As the time of contact increases, the amount of absorbed ions is determined by the exchange rate within a sorbent grain. The effective diffusion coefficient D and the rate constant B of the inner-diffusion process, which characterize the inner-diffusion mechanism, were calculated using the relations derived for spherical particles:

$$F = \frac{Q\tau}{Q_\infty} = \frac{6\sqrt{Dr}}{r\pi}, \quad (3)$$

$$B = \pi^2 D/r^2, \quad (4)$$

where F is the degree of absorption of samarium ions, and r is the average radius of sorbent grains.

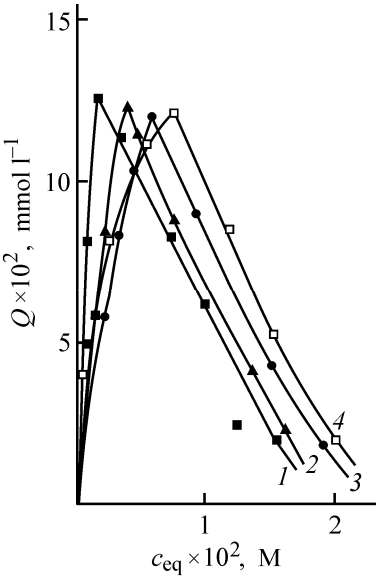


Fig. 1. Equilibrium curves of samarium sorption from $Sm_2(SO_4)_3$ solution. (Q) Sorbed amount of ions and (c_{eq}) concentration of the ion being exchanged in solution. Grain size d (mm), s : l ratio: (*1*) 0.25–0.5, 1 : 50; (*2*) 0.25–0.5, 1 : 10; (*3*) 1–2, 1 : 50; and (*4*) 1–2, 1 : 10.

The content of samarium ions was determined photometrically with arsenazo (III) [8]. The absorption capacity was calculated from the difference of the samarium ion concentrations before and after sorption, found in three parallel runs. The experimental results are listed in the table and shown in Figs. 1–3.

The equilibrium curves of samarium sorption on the clinoptilolite-containing tuff indicate that samarium is quantitatively recovered from dilute solutions (Fig. 1). With clinoptilolite grains with sizes of 1–2 mm (at s : l = 1 : 10) and 0.25–0.5 mm (at s : l = 1 : 50), samarium ions are more completely recovered at initial solution concentrations of up to 0.002 M.

As the solution concentration increases, the equilibrium curves pass through a maximum, which is followed by a decrease in the exchange capacity (EC) of the tuff. The maximum EC is 0.124–0.137 mmol g^{-1}. The appearance of the extremum in the isotherm may be due to existence in solution of intermediate reaction products to which the sorbent exhibits an increased capacity [9]. Samarium has a high capacity for complexation; in neutral and acid aqueous solutions, samarium ions are in the form of aqua complexes of the type $[Sm(H_2O)_n]^{3+}$ or $[Sm(H_2O)_nOH]^{2+}$, where n = 5–8 [10].

In samarium sulfate solutions, the formation of complexes with composition $[Sm(SO_4)_n]^{3-2n}$, where n = 1–3, was also observed. At low concentrations of sulfate ions (<0.02 M), $[SmSO_4]^+$ cations predominate [10], although anion complexes can also be formed under these conditions [4, 5, 11, 12]. Before the extremum point, aqua and hydroxo complexes of samarium are presumably sorbed, because the increased selectivity of the zeolite toward samarium ions in the initial portion of the equilibrium curve, when the ions are nearly completely absorbed, is due to the large charge carried by the ion. In [12], a mechanism of sorption of lanthanum aqua complexes on synthetic zeolite was described; the suggested mechanism is confirmed by the reversal of the sorbent selectivity toward samarium ions after their certain concentration in solution is reached. This fact is associated with a manifestation of electroselectivity, because, according to the theory [9], dilution of the solution in the solution–sorbent system shifts the equilibrium toward an increase in the sorption of an ion with a larger charge and concentration leads to full selectivity reversal.

The absorption of samarium ions is accompanied by a decrease in the solution pH by 0.7–0.9 units. The pH is 6.3 for a 0.005 M samarium sulfate solution and 6.1 for a 0.001 M solution. The grain size and the s : l

ratio affect the position of the maximum in the isotherms (Fig. 1). The maximum of EC on grains with d = 0.25–0.5 mm and s : l = 1 : 50 (Fig. 1, curve *1*) is shifted to lower equilibrium concentrations, as the grain size increases (d = 1–2 mm) at s : l = 1 : 10, the maximum lies at higher concentrations (Fig. 1, curve *4*). Thus, low solution concentrations are sufficient for reaching the highest EC on fine grains, which is important for making a rational choice of the mode of zeolite saturation with samarium ions when obtaining a modified form of the clinoptilolite-containing tuff.

It was found that a nearly equilibrium state is attained in 28 h on 0.25–0.5-mm grains and in 35 h on 1–2-mm grains, after which a certain desorption within 1.5–2.0% is observed (Fig. 2). Analysis of kinetic parameters (see table) shows that the sorption of samarium occurs under mixed-diffusion control because the rate constants of outer- (R) and inner-diffusion processes (B) are on the same order of magnitude. The run of the dependence of the degree of filling of the zeolite phase (F) on $\tau^{1/2}$ (τ is time, s), whose initial portions are linear up to high values of F (Fig. 3), points to a considerable contribution from the inner-diffusion mechanism.

An increase is observed both in the sorption rate of samarium, $dQ/d\tau$, from a dilute solution on 0.25–0.5-mm grains under the outer-diffusion control and in the equilibrium distribution coefficient K_d. The acceleration of the process is due to an increase in the dispersity of tuff grains. The values of the effective diffusion coefficient D are in agreement with those from [7]. The high values of D, compared with the data obtained for mono- and divalent metals, are accounted for by the Helfferich principle [13], according to which more mobile ions are decelerated and less mobile ions are accelerated in an exchange of a mixture of ions.

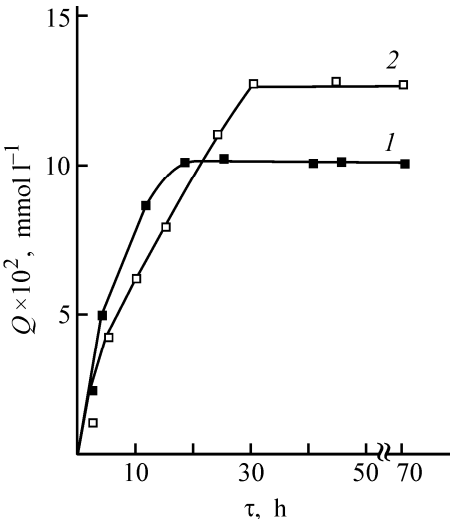


Fig. 2. Kinetic curves of samarium sorption from (*1*) 0.001 and (*2*) 0.005 M $Sm_2(SO_4)_3$ solutions by the clinoptilolite-containing tuff. (Q) Sorbed amount of ions and (τ) time. d (mm), s : l: (*1*) 0.25–0.5, 1 : 50; and (*2*) 1–2, 1 : 10; the same for Fig. 3.

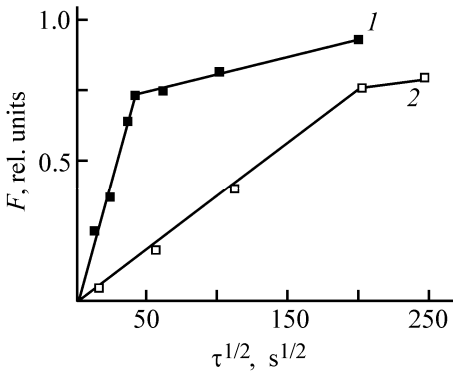


Fig. 3. F–$\tau^{1/2}$ dependence for samarium sorption from (*1*) 0.001 and (*2*) 0.005 M $Sm_2(SO_4)_3$ solutions. (F) Degree of filling of the zeolite phase and (τ) time.

CONCLUSIONS

(1) The equilibrium in the system constituted by a clinoptilolite-containing tuff and samarium(III) was studied and it was found that the sorbent can recover samarium ions from aqueous solutions. At low concentrations (<0.002 M), samarium ions are recovered quantitatively; as the concentration increases, the sorption capacity of the clinoptilolite-containing tuff becomes lower. The sorption isotherms show a maximum, which is due to the complex nature of the interaction between the components of the system.

(2) It was demonstrated that the sorption kinetics of samarium(III) ions by the natural clinoptilolite-containing tuff is controlled by the mixed-diffusion sorption mechanism. The pronounced contribution of the inner-diffusion sorption mechanism was confirmed. It was found that the rate of absorption of samarium ions from a dilute solution on 0.25–0.5-mm grains by the outer-diffusion mechanism increases and the equilibrium distribution coefficient grows as the solution concentration becomes lower.

REFERENCES

1. Mitypov, B.B., Kozhevnikova, N.M., and Abasheeva, N.E., *Agrokhimiya*, 2007, no. 8, pp. 44–47.
2. Peremolov, L.V., *Agrokhimiya*, 2007, no. 11, pp. 85–96.
3. Shung, K.H., Choi, G.S., Shin, H.S., and Lee, C.W., *J. Environ. Radioact*., 2005, vol. 3, no. 79, pp. 369–379.

4. Kozhevnikova, N.M. and Tsybikova, N.L., *Khim. Interesakh Ustoich. Razv*., 2007, vol. 15, no. 3, pp. 347–350.

5. Kozhevnikova, N.M. and Tsybikova, N.L., *Zh. Prikl. Khim*., 2008, vol. 81, no. 1, pp. 46–49.

6. Belitskii, I.A., Drobot, I.V., Valuev, G.P., et al., *Opyt ekspressnogo opredeleniya soderzhaniya tseolitov v gornykh porodakh s ispol'zovaniem portativnykh tseolitnykh laboratorii PTsL-1 i PTsL-2* (Experience of Proximate Determination of the Zeolite Content of Rock with the Use of Portable Zeolite Laboratories PTsL-1 and PTsL-2), Novosibirsk: Nauka, 1979.

7. Chelishchev, N.F., Volodin, V.F., and Kryukov, V.L., *Ionoobmennye svoistva prirodnykh vysokokremnistykh tseolitov* (Ion-Exchange Properties of Natural High-Silica Zeolites), Moscow: Nauka, 1988.

8. Jeffery, P.G., *Chemical Methods of Rock Analysis*, Oxford: Pergamon , 1970.

9. Kokotov, Yu.A., Zolotarev, P.P., and El'kin, G.E., *Teoreticheskie osnovy ionnogo obmena: Slozhnye ionoobmennye sistemy* (Theoretical Foundations of Ion Exchange: Complex Ion-Exchange Systems), Leningrad: Khimiya, 1986.

10. Komissarova, L.N., Pushkina, G.Ya., Shatskii, V.M., et al., *Soedineniya redkozemel'nykh elementov: Sul'faty, selenaty, telluraty, khromaty (Khimiya redkikh elementov)* [Compounds of Rare-Earth Elements: Sulfates, Selenates, Tellurates, Chromates (Chemistry of Rare Elements)], Moscow: Nauka, 1986.

11. Sukhno, I.V., Panyushkin, V.T., Buz'ko, V.Yu., and Artyunyan, M.M., *Zh. Neorg. Khim.*, 2003, vol. 48, no. 3, pp. 857–861.

12. Breck, D.W., *Zeolite Molecular Sieves*, New York: John Wiley & Sons, 1974.

13. Helfferich, F., *Ionenaustauscher*, Weinheim: Chemie, 1959, vol. 1.

ISSN 1070-4272, Russian Journal of Applied Chemistry, 2008, Vol. 81, No. 12, pp. 2099–2103. © Pleiades Publishing, Ltd., 2008.
Original Russian Text © G.I. Smirnov, L.M. Dimova, N.V. Chebunina, G.V. Ratovskii, L.N. Belonogova, M.T. Munkueva, 2008, published in Zhurnal Prikladnoi Khimii, 2008, Vol. 81, No. 12, pp. 1985–1990.

PHYSICOCHEMICAL STUDIES OF SYSTEMS AND PROCESSES

Ion-Exchange Properties of Tin(II) Hydrophosphates with Varied Chemical Composition and Structure

G. I. Smirnov, L. M. Dimova, N. V. Chebunina, G. V. Ratovskii, L. N. Belonogova, and M. T. Munkueva

Irkutsk State University, Irkutsk, Russia

Received February 13, 2008

Abstract—Correlation between the chemical composition, structure, and ion-exchange properties of tin(II) hydrophosphate was studied.

DOI: 10.1134/S1070427208120100

Inorganic ion exchangers of the zirconium(IV) phosphate type, characterized by high selectivity and chemical stability, are promising for separation of elements with closely similar properties and for preparation of special-purity inorganic salts. For example, it is advisable to use tin(IV) hydrophosphate for recovery of microscopic amounts of potassium from sodium salts [1]. The structure and ion-exchange capacity of this compound have been studied in sufficient detail and a correlation between these characteristics has been demonstrated [2–7]. Data on the ion-exchange properties of tin(II) phosphate are scarce and contradictory. In [8], a conclusion was made that, despite the lamellar structure and the same type of the crystal systems and space symmetry group of $Sn(HPO_4)_2 \cdot H_2O$ and $SnHPO_4$, the replacement of protons in the latter compound by other cations is impossible. At the same time, data obtained in analysis of the synthesis conditions and the ion-exchange interaction in the case of this sorbent have been reported [9, 10]. These contradictions are probably due to differences in the synthesis conditions, chemical composition, and structure of the tin(II) phosphate samples studied.

This communication reports on a study of the structural features of tin(II) hydrophosphate in sorption of elements with closely similar properties in relation to synthesis conditions.

EXPERIMENTAL

An X-ray phase analysis (XPA) (powder technique) of tin(II) phosphate samples was made on DRON-3 and DRON-3M diffractometers (CoK_α and CuK_α radiation), using the PDF database [11] for phase identification. IR spectra of samples in the form of suspensions in vacuum-treated Vaseline oil were recorded in the range 4000–400 cm^{-1} on a Specord M-80 spectrometer. A thermogravimetric analysis was performed on an MOM derivatograph (Hungary), with aluminum oxide as reference. An ion exchanger for physicochemical analysis was prepared and stored under the conditions providing the minimum contact with air. The acid–base properties of the samples were examined by potentiometric titration of separate weighed portions. The rest of the methods of study are similar to those used in [9,10].

The parameters of tin(II) hydrophosphate samples, synthesized in accordance with [10] at a varied P : Sn molar ratio in the starting products, and the distribution coefficients in sorption of alkali metal cations are listed in Table 1.

It can be seen in Table 1 that, as the P : Sn molar ratio in the starting products increases within a wide range, this ratio in the sorbents also becomes larger, and the distribution coefficients K_d of K^+, Rb^+, and Cs^+ ions first increase and then decrease. Consequently, the chemical composition of the ion exchangers strongly affects their ion-exchange properties. Under the given conditions, Na^+ ions are not sorbed. As the P : Sn ratio increases, the yield of the sorbent decreases because of a rise in the solubility of the ion exchanger being synthesized.

Table 1. Ion-exchange properties of tin(II) hydrophosphate synthesized at different P : Sn ratios [10]

Sample no.	P : Sn ratio		Sorbent yield, %	K_d		
	in starting products	in sorbent		K^+	Rb^+	Cs^+
1	1	0.65	14.65	6.7	10.0	7.2
2	2	1.32	7.42	10.1	19.1	18.4
3	4	1.53	4.17	18.2	41.6	69.4
4	6	1.69	2.57	10.1	22.1	37.3
5	15	1.91	0.92	–	–	–

* Data on the absolute mass of the ion exchanger samples synthesized under the comparable conditions.

Table 2. Interplanar spacings d/n and relative intensities I/I_0 of lines in X-ray diffraction patterns of tin(II) hydrophosphate*

Sample no. 2		Sample no. 3		Sample no. 4		Sample no. 5		$SnHPO_4$ [11]	
d/*n*, Å	I/I_0, %	*d*/*n*, Å	I/I_0, %	*d*/*n*, Å	I/I_0, %	*d*/*n*, Å	I/I_0, %	*d*/*n*, Å	I/I_0, %
6.815	100	6.815	100	6.80	100	6.820	100	6.80	100
4.566	19	4.566	19	4.566	19	4.538	19	4.562	15
3.790	12	3.787	13	3.784	21	3.776	5	3.792	12
3.728	11	3.732	22	3.734	51	3.696	4	3.731	16
3.399	97	3.392	33	3.402	40	3.400	47	3.404	35
2.997	17	2.994	38	2.991	67	2.970	8	2.997	30
2.952	25	2.948	35	2.946	85	2.938	12	2.946	40
2.820	9	2.818	22	2.820	52	2.809	3	2.820	14

* Relative intensity of the rest of the peaks is less than 10.

According to the results of an X-ray phase analysis of tin(II) phosphate sample nos. 2–5 (Table 2), all ion exchangers are crystalline compounds, and, as the P : Sn ratio increases, the intensities of the X-ray reflections become higher, i.e., the crystallinity, on the whole, grows.

Comparison with published data shows that all samples are composed of tin(II) hydrophosphate $SnHPO_4$. However, the best agreement is characteristic of ion exchanger no. 3, synthesized at P : Sn = 4. For tin(II) hydrophosphate synthesized at this P:Sn ratio, the sorption parameters are at a maximum (Table 1).

It should be noted, when comparing the XPA data for tin(II) and tin(IV) hydrophosphates, that the first ion exchanger is prepared in the crystalline form directly by low-temperature precipitation, whereas the second is amorphous upon low-temperature precipitation and crystalline samples are synthesized by high-temperature precipitation, e.g., by treating the system in boiling orthophosphoric acid [5, 6]. A submicrocrystalline structure of the X-ray amorphous tin(IV) hydrophosphate is only recorded by electron diffraction analysis [5].

The interplanar spacing in tin(II) hydrophosphate is 6.815 Å, and that in the crystalline tin(IV) phosphate, 7.8 Å. Therefore, according to the similar ion-exchange mechanism based on the ion-sieve principle, the sorption parameters of tin(II) phosphate having a lower interplanar spacing must be poorer. However, it has been found experimentally that tin(II) hydrophosphate sorbs Cs^+, Rb^+, and K^+ ions from acid solutions, whereas crystalline tin(IV) hydrophosphate does not sorb the first two ions having larger radii than the K^+ ion under the same conditions [6]. On the whole, it is probable that, despite the same monoclinic crystal system of the ion exchangers, their packing and layer

Table 3. Relative peak intensities of the IR absorption bands, A_i/A_0*

ν, cm^{-1}	A_i/A_0 for indicated sample					
	no. 1	no. 2	no. 3	no. 4	no. 5	$SnHPO_4$ [14]
540–550	0.245	0.297	0.325	0.340	0.439	0.445
580	0.046	0.184	0.195	0.246	0.318	0.418
620	0.200	0.130	0.101	0.056	0.032	0.028

* A_0 is the intensity of the band at 1015 cm^{-1}.

binding may be different and the size of channels in $Sn(HPO_4)_2$ structure will be larger than that in $SnHPO_4$. For example, for crystalline zirconium(IV) hydrophosphate, the channels in the cavity are 2.61 Å wide, which makes impossible sorption from an acid solution for ions larger than unhydrated K^+. For tin(II) hydrophosphate, the size of channels between separate oxygen atoms is 3.27 Å, and, therefore, this ion exchanger will sorb larger cations [3, 12, 13].

The IR spectra of all the tin(II) hydrophosphate samples studied (Fig. 1) show that the results obtained are, on the whole, consistent with published data for tin(II) hydrophosphate [14]. The IR spectra contain bands at 3190 and 1230 cm^{-1}, associated with stretching [ν(OH)] and deformation vibrations [δ(OH)] of the HPO_4^{2-} ion. At the same time, the spectra contain bands at 3440 and 1640 cm^{-1}, associated with vibrations of water molecules. Bands in the region 915–970 cm^{-1} correspond to vibrations of the tin–oxygen skeleton. As the P : Sn ratio increases, the crystallinity of the samples becomes higher, with sample no. 1 not only being the least crystalline, but also containing a larger amount of other impurities.

Analysis of the IR spectra of sample nos. 1–5 shows that, as the P : Sn ratio increases, the content of tin(IV) phosphate becomes lower, and that of tin(II) phosphate, higher. A comparative estimate of the amounts of tin(II) and tin(IV) in the IR spectra of the samples studied is presented in Table 3. The band at 1015 cm^{-1} served as reference.

The data of Table 3 also confirm the conclusion that Sn(II) content increases with the P : Sn ratio: the relative intensity of the 580 and 540–550-cm^{-1} bands, which characterizes the content of tin(II) hydrophosphate, increases, whereas the relative intensity of the 620-cm^{-1} band, determined by the tin(IV) content, decreases. Consequently, in synthesis of ion exchangers at a small P : Sn ratio, the known chemical reaction of Sn(II) with the acid and water to give tin(IV) probably occurs [15].

A chemical analysis of various forms of tin present in the ion exchangers under study was made with account of the high importance and probability of transition of tin to the Sn(IV) state under certain conditions. It was shown that the content of tin(IV) in sample nos. 3, 4, and 5 is 1.3, 1.1, and 0.9 wt %, respectively, and that in sample nos. 1 and 2, several times higher, with the content of this impurity in sample no. 5 being equal to that in the starting $SnCl_2 \cdot 2H_2O$. Consequently, presence of minor amounts of tin(IV) will affect only slightly the sorption properties, which confirms the previously made conclusion about the optimal value of the P : Sn ratio in the starting reagents.

The results of a thermogravimetric analysis of the ion exchangers under consideration are, on the whole, similar, with some specific features. The results of a study by the DTA method are listed in Table 4 for all the sorbent samples.

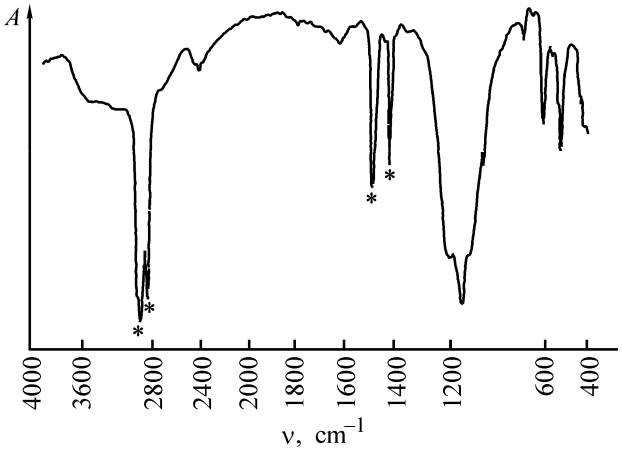


Fig. 1. IR spectra of tin(II) phosphate (sample no. 4). (*A*) Absorption and (ν) wave number. (*) IR bands of Vaseline oil.

Table 4. Results of a thermogravimetric analysis of tin(II) hydrophosphate at various P : Sn ratios

Sorbent no.	Endothermic effect			Loss of mass	
	number of effects	temperature range in which the effect is observed, °C	maximum, °C	%	mol
1	4	60–260	90	1.5	0.18
		260–360	310	0.5	0.56
		360–550	460	4.5	0.06
		550–660	570	0.5	0.06
2	2	60–250	90	2.0	0.24
		250–460	300	3.5	0.43
3	2	70–250	90	1.0	0.14
		250–480	290	5.0	0.66
4	2	60–250	90	0.5	0.06
		250–460	310	5.5	0.69
5	3	140–260	–	1.0	0.14
		240–470	300	7.0	0.89
		470–670	605	2.5	0.31

As can be seen from Table 4, the ion exchangers under study are tin(II) hydrophosphates [8, 16]. The first endothermic effect at 60–250°C corresponds to removal of occluded water, and the second endothermic effect at 260–460°C, to condensation of acid phosphate groups into $SnHPO_4$. Sample no. 1 shows endothermic effects at 360–550°C and 550–660°C, which are probably due to removal of constitution water and presence of Sn(IV) ions and other impurities. Sample no. 5 shows an endothermic effect in the high-temperature region, 470°C to 670°C, which is associated with the condensation of phosphate groups or even, according to [16], with the melting of tin(II) diphosphate. Thus, sample nos. 2–4 correspond to tin(II) hydrophosphate to the greatest extent. It is noteworthy that the amount of water in the samples studied is small (0.1 mole at the optimal P : Sn ratio of 4).

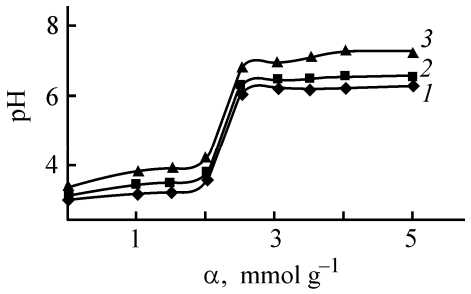


Fig. 2. Results of potentiometric titration of tin(II) phosphate. Titrant 0.1 M KOH + 0.1 M KCl. (α) Amount of OH^- per gram of sorbent. Digits at curves, sample nos. in Tables 1 and 2.

The acid–base properties of sample nos. 1–3, which differ in the P : Sn ratio to the greatest extent, were compared using potentiometric titration of their separate weighed portions. As titrants served 0.1 M KOH and 0.1 M KCl (Fig. 2).

The titration curves are identical, which points to similarity of the ion-exchange groups. The titration curves have two horizontal portions. In the first of these, K^+ ions are sorbed upon addition of KOH in amounts of up to 2 mmol g^{-1} of sorbent. The zero slope of the dependence indicates that all the released hydrogen ions are neutralized by the alkali introduced. Upon addition of 2–2.5 mmol KOH per 1 g of sorbent, pH sharply increases and, as the content of KOH is raised further (in the second horizontal portion of the curve), K^+ ions are not sorbed and excess OH^- groups favor occurrence of other reactions, e.g., hydrolysis of the ion exchanger. As follows from Table 3, the P : Sn ratio in the ion exchanger affects the maximum amount of sorbed K^+ ions only slightly.

The methods considered above were used to study the influence exerted on synthesis of tin(II) hydrophosphate by the pH of gelation, gelation duration, pH of ion exchanger washing, and concentration of orthophosphoric acid. At a pH structure gelstion equal to 0.8, the sorbent best corresponds to tin(II) hydrophosphate. All other synthesis parameters studied here af-

fect the resulting structure of the ion exchanger only slightly, and the efficiency of the ion-exchange interaction in sorption will be directly determined by the sorption parameters [10].

Consequently, the ion-exchange properties are affected by the chemical composition and structure of tin(II) phosphates. In tin(II) phosphate synthesized under the optimal conditions, the P : Sn molar ratio is 1.52. Therefore, if only phosphate-containing constituents of the ion exchangers are considered, monosubstituted tin(II) phosphates are probably present along with a disubstituted phosphate. The ratio between phosphates with different degrees of substitution will determine the P : Sn ratio in the sorbents, with other impurities also apparently present in sample no. 1.

Comparison of the data in Table 1 with the results of [5, 6, 17] shows that tin(II) hydrophosphate is of interest for separation of K^+, Rb^+, and Cs^+ ions and for purification of sodium salts to remove potassium.

CONCLUSIONS

(1) Tin(II) hydrophosphates synthesized by low-temperature precipitation, with interaction of tin(II) chloride and orthophosphoric acid, are crystalline compounds with composition $SnHPO_4$. The optimal P : Sn molar ratio in the starting reagents is 4, and the pH for maturing of the gel structure, 0.8.

(2) Tin(II) hydrophosphate exhibits ion-exchange properties related to its chemical composition and structure. The crystalline tin(II) hydrophosphate obtained sorbs Rb^+ and Cs^+ ions from acid solutions. This indicates that cavities in its structure are larger than those in crystalline tin(IV) hydrophosphate, which does not recover these ions under similar conditions.

REFERENCES

1. Smirnov, G.I., Chernyak, A.S., Kachur, N.Ya., and Ogorodnikova, A.A., *Vysokochist. Veshch*., 1989, vol. 62, no. 3, pp. 144–147.
2. Sukharev, Yu.I. and Egorov, Yu.V., *Neorganicheskie ionity tipa fosfata zirkoniya* (Zirconium Phosphate Inorganic Ion Exchangers), Moscow: Energoatomizdat, 1983.
3. *Inorganic Ion-Exchange Materials*, Clearfield, A., Ed., Roca Raton: CRC, 1982.
4. USSR Inventor's Certificate, no. 814 865.
5. Smirnov, G.I., Redchenko, A.A., Dimova, L.M., *et al*., *Zh. Prikl. Khim.,* 2000, vol. 73, no. 12, pp. 1945–1950.
6. Smirnov, G.I., Redchenko, A.A., Dimova, L.M., et al., *Izv. Vyssh. Uchebn. Zaved., Khim. Khim. Tekhnol*., 2000, vol. 43, no. 5, pp. 43–48.
7. Ratovskii, G.V., Ivanova, N.A., Smirnov, G.I., et al., *Neorg. Mater*., 1991, vol. 27, no. 7, pp. 571–575.
8. Chernorukov, N.G., Sibrika, G.F., and Zabelin, A.I., *Zh. Neorg. Khim*., 1979, vol. 24, no. 9, pp. 2333–2336.
9. Smirnov, G.I., Chebunina, N.V., and Dimova, L.M., *Vestn. Irkuts. Gos. Tekhn. Univ*., 2005, vol. 21, no. 1, pp. 106–109.
10. Smirnov, G.I., Chebunina, N.V., and Dimova, L.M., *Izv. Vyssh. Uchebn. Zaved., Khim. Khim. Tekhnol*., 2005, vol. 48, no. 9, pp. 143–145.
11. Powder Diffraction File Search Manual, Inorganic Phases, Philadelphia: Joint Committee on Powder Diffraction Standards (JCPDS), 1977.
12. Berndt, A.F. and Lamberg, R., *Acta Cryst*., 1971, vol. 27, pp. 1092–1094.
13. Yaroslavtsev, A.B., Prozorovskaya, Z.N., Chuvaev, V.F., et al., *Zh. Neorg. Khim*., 1989, vol. 34, no. 5, pp. 1188–1192.
14. Pechkovskii, V.V., Mel'nikova, R.Ya., Dzyuba, E.D., et al., *Atlas infrakrasnykh spektrov fosfatov: Ortofosfaty* (Atlas of IR Spectra of Phosphates: Orthophosphates), Moscow: Nauka, 1981.
15. Tret'yakov, Yu.D., Martynenko, L.I., Grigor'ev, A.N., and Tsivadze, A.Yu., *Neorganicheskaya khimiya. Khimiya elementov* (Inorganic Chemistry. Chemistry of Elements), Moscow: Khimiya, 2001, vol. 2.
16. Mel'nikova, R.Ya., Dzyuba, E.D., Pechkovskii, V.V., et al., *Zh. Neorg. Khim*., 1984, vol. 29, no. 9, pp. 2266–2272.
17. Smirnov, G.I., Dimova, L.M., and Redchenko, A.A., *Zh. Prikl. Khim.*, 2004, vol. 77, no. 8, pp. 1275–1278.

ISSN 1070-4272, Russian Journal of Applied Chemistry, 2008, Vol. 81, No. 12, pp. 2104–2107. © Pleiades Publishing, Ltd., 2008.
Original Russian Text © N.M. Panich, A.F. Seliverstov, B.G. Ershov, 2008, published in Zhurnal Prikladnoi Khimii, 2008, Vol. 81, No. 12, pp. 1991–1995.

PHYSICOCHEMICAL STUDIES OF SYSTEMS AND PROCESSES

Photooxidative Decomposition of Sodium Dodecyl Sulfate in Aqueous Solutions

N. M. Panich, A. F. Seliverstov, and B. G. Ershov

Frumkin Institute of Physical Chemistry and Electrochemistry, Russian Academy of Sciences, Moscow, Russia

Received July 30, 2008

Abstract—Kinetic features and the mechanism of photooxidative decomposition of sodium dodecyl sulfate in an aqueous solution under the action of pulsed short-wavelength UV light with a continuous spectrum upon introduction of hydrogen peroxide was studied.

DOI: 10.1134/S1070427208120112

Surfactants are widely used in the industry and households. They belong to the most widely occurring contaminants contained in wastewater.

An efficient way to purify wastewater to remove surfactants is their oxidative decomposition to CO_2 and H_2O. Ozone is most frequently used for this purpose (oxidation potential 2.07 V) [1]. However, ozone rather effectively oxidizes nonionogenic surfactants, but is considerably less efficient with anion-active surfactants (AAS) [2].

The hydroxy radical $^{\cdot}OH$ is a stronger and more effective oxidizing agent (oxidation potential 2.8 V). In contrast to ozone, it is not a selective oxidizing agent and equally effectively interacts with all organic substances, including surfactants [3].

After the appearance of pulsed xenon lamps with a continuous spectrum, it became possible to generate $^{\cdot}OH$ radicals in the reaction $H_2O_2 + h\nu \rightarrow 2^{\cdot}OH$ [4].

The method of photochemical oxidation in the presence of hydrogen peroxide has been used to deactivate EDTA-containing solutions [5], and the mode of nearly complete decomposition of the complexone was found.

The aim of the present study was to examine specific features of decomposition of sodium dodecyl sulfate (an AAS) in aqueous solutions by hydroxy radicals formed in H_2O_2 photolysis under irradiation with a xenon lamp.

EXPERIMENTAL

Al'fa-02 pulsed UV installation with an average electric power applied to the lamp equal to 200 W (pulse width 100 μs, pulse repetition frequency $f = 2$ Hz) was used in the experiment. Samples were irradiated in an open quartz cell with an IFP 1200 Xe lamp with a flash energy of 100 J. The cuvette with a solution was placed at a distance of 1 cm from the lamp and was cooled with an air flow in the course of irradiation. The volume of the reaction mixture was 10 ml.

The pulsed Xe lamp provides a continuous-spectrum light over the entire UV spectral range (200–400 nm). The light intensity was measured using the procedure described in [6]. The intensity I of the light flux incident on the cuvette was 3.8×10^{16} photons s^{-1}. The operation stability of the xenon lamp was monitored in the course of the study.

Sodium dodecyl sulfate (SDS, $C_{12}H_{25}OSO_2ONa$) was chosen as object of study. The aqueous solutions contained up to 100 mg of SDS per liter of a solution. The SDS concentration was found using the extraction-photometric determination with Methylene Blue by the procedure described in [7].

The degree of AAS decomposition was evaluated by measuring the chemical oxygen demand (COD) [7, 8].

The reaction course was also monitored by changes in optical spectra. The absorption spectra of the solutions in the UV and visible spectral ranges were recorded with an SF-2000 spectrophotometer in a quartz cuvette with an optical path length of 1 cm.

The hydrogen peroxide concentration in the solutions was determined from the concentration of the peroxide complex $[TiO \cdot H_2O_2]^{2+}$ [9, 10].

Figure 1 shows kinetic dependences of SDS decomposition at various initial concentrations. It can be seen that the AAS concentration almost linearly decreases in the course of irradiation. Despite the high power of the UV irradiation, the degree of decomposition is low: 20.1, 34.8, and 50.6% for SDS solutions with concentrations of 100, 50, and 25 mg l^{-1}, respectively, upon 20 min of irradiation. In the course of irradiation, the solution pH changes from 6.3 to approximately 5.0.

Figure 2 compares the kinetic dependences of SDS decomposition (100 mg l^{-1}) with and without H_2O_2 (100 mg l^{-1}). Introduction of H_2O_2 intensifies the decomposition of SDS. It almost completely decomposes after 20 min of irradiation, with about 50 mg l^{-1} of H_2O_2 consumed.

Preliminary experiments revealed that the presence of H_2O_2 in solution does not cause decomposition of SDS (8 days) if the solution is not subjected to UV irradiation.

The exposure to UV light gives rise to free $^{\cdot}OH$ radicals as a result of homolytic decomposition of H_2O_2. It is known [3] that $^{\cdot}OH$ radicals have high reactivity toward organic compounds RH of varied nature (commonly, $k_{^{\cdot}OH+RH} > 10^7$ M s^{-1}). As a result, organic compounds undergo oxidative decomposition. Thus, the oxidation in the case in question occurs in the combined mode, with an oxidizing agent (H_2O_2) and its activation with UV light.

It can be seen in Fig. 3 that the SDS decomposition rate increases with the H_2O_2 content of a solution. As a result of oxidative decomposition of SDS, the solution ceases to foam and pH changes to approximately 3–4.

Comparison of curves *1* and *2*, *4* and *5* shows that raising the initial pH value from 6.3 to 9.6 leads to a certain increase in the SDS decomposition rate.

To determine the relative qualitative composition of the aqueous solution after photooxidation, the generalized water-quality parameter, COD, was measured (Fig. 4). The irradiation of an SDS solution (100 mg l^{-1}) in the presence of 50 and 200 mg l^{-1} of H_2O_2 led to a decrease in COD, which is the more pronounced, the higher the H_2O_2 concentration. For a solution with 200 mg l^{-1} of H_2O_2, the COD decreased by 28% in 20 min after a residual SDS concentration of 0.4 mg l^{-1} was reached. This means that only 28% of SDS decomposed to CO_2 and H_2O. For a solution with 50 mg l^{-1} of H_2O_2, the decrease did not exceed 13.5% after 35 min of irradiation, with the residual SDS concentration of 7.5 mg l^{-1}.

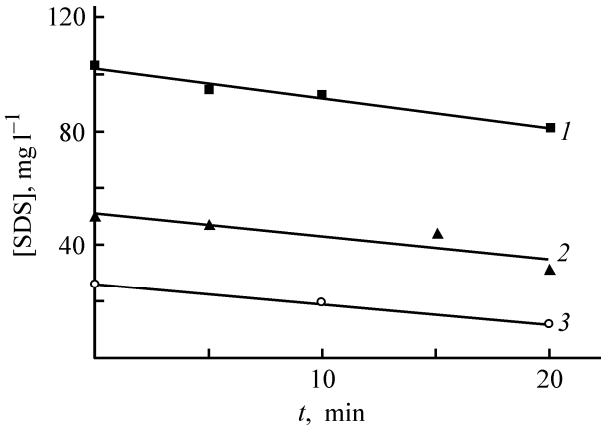


Fig. 1. SDS concentration in solution vs. the duration *t* of exposure to UV light. Initial SDS concentration (mg l^{-1}): (*1*) 25, (*2*) 50, and (*3*) 100.

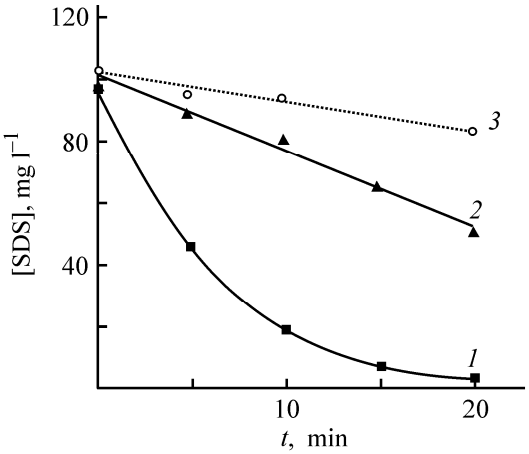


Fig. 2. Kinetic curves of decomposition of (*1*) SDS and (*2*) H_2O_2 in solutions under the action of UV light. ([SDS]) SDS concentration in solution and (*t*) duration of exposure to UV light; the same for Fig. 3. Solution composition: (*1*, *2*) SDS (100 ml g^{-1}) and H_2O_2 (100 mg l^{-1}) and (*3*) SDS (100 mg l^{-1}).

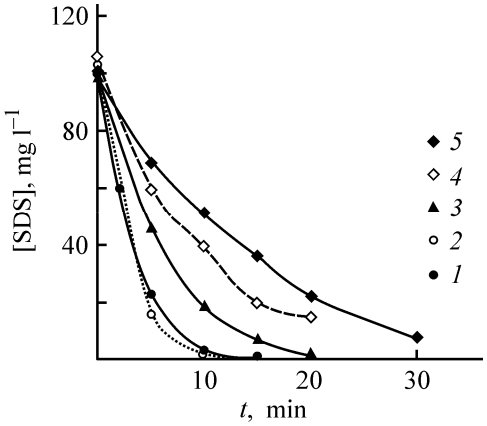


Fig. 3. Kinetic curves of SDS 100 mg l^{-1} photooxidation in solutions. H_2O_2 concentration (mg l^{-1}): (*1*, *2*) 200, (*3*) 100, and (*4*, *5*) 50. Initial pH of the solution: (*1*, *3*, *5*) 6.4 and (*2*, *4*) 9.6.

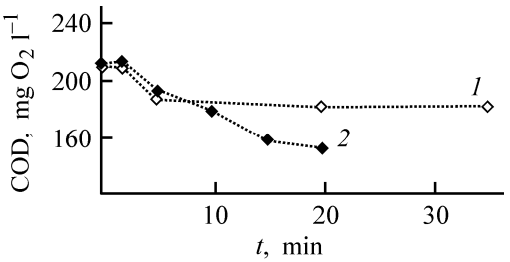


Fig. 4. COD vs. the duration t of photooxidation of an SDS solution (100 mg l^{-1}). H_2O_2 concentration (mg l^{-1}): (*1*) 50 and (*2*) 200.

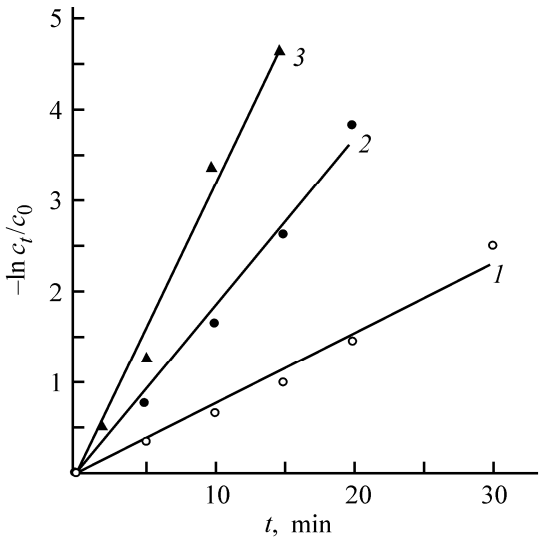


Fig. 5. Kinetic dependences of SDS decomposition in solutions, plotted in the coordinates of a first-order reaction equation. (c_0, c_t) SDS concentrations at the initial and running instants of time t. H_2O_2 concentration (mg l^{-1}): (*1*) 50, (*2*) 100, and (*3*) 200.

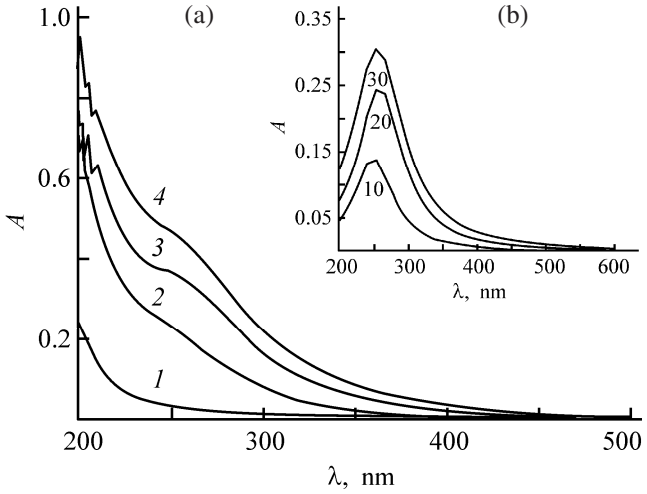


Fig. 6. (a) Absorption of SDS (100 mg l^{-1}) and H_2O_2 solutions (200 mg l^{-1}) subjected to UV irradiation and (b) absorption spectra in the spectral range 250–280 nm computed from the spectra in Fig. 6a. (A) Optical absorption and (λ) wavelength. (a) Irradiation time (min): (*1*) 0, (*2*) 10, (*3*) 20, and (*4*) 30.

It was found that the kinetics of SDS decomposition is well described by a first-order reaction equation. In accordance with this equation, the variation of the SDS concentration with time is linearized in the coordinates $-\ln(c_t/c_0)$–t, where c_0 and c_t are the SDS concentrations at the initial and running instants of time, and t is time. The experimental data well fall on the straight lines (Fig. 5), which confirms the validity of the suggested kinetic equation. The slopes of these lines were used to calculate the relative (related to the intensity of the UV light source used and experimental conditions) rate constants of SDS decomposition, k_{AAS}. The values of k_{AAS} (0.077, 0.1813, and 0.313 min^{-1} for H_2O_2 concentrations in solution of 50, 100, and 200 mg l^{-1}, respectively) almost linearly increase with the SDS concentration. This means that SDS decomposes under conditions in which $^{\cdot}OH$ radicals are generated at a constant rate proportional to the H_2O_2 concentration, because the efficiency of H_2O_2 photodecomposition is, in turn, proportional to the energy of UV light absorbed by hydrogen peroxide, i.e., to the H_2O_2 concentration in solution. This fact is confirmed by the data in Fig. 2 (curve *2*).

An analysis of the absorption spectra of SDS solutions enabled a suggestion about the possible products of its photodecomposition. Figure 6a shows absorption spectra of a solution irradiated for different times. It can be seen that the absorption spectrum of the solution changes, compared with the initial spectrum, after photooxidation.

Particularly pronounced changes are observed below 200 nm and in the range 250–280 nm. The absorption in the second range increases, which further gives rise to a new band. A computer processing of the spectra revealed a new optical absorption band peaked at 250–280 nm (Fig. 6b). It can be seen that the intensity of this band increases almost proportionally to the time of the UV irradiation. The absorption above 250 nm can be attributed to presence of carbonyl-containing oxidation products formed as a result of interaction with .OH radicals. An absorption typical of carbonyl compounds is observed at 190 nm and above 250 nm (ε_{190} = 1900 mol^{-1} cm^{-1}, ε_{280} = 1500 mol^{-1} cm^{-1}) [11]. However, quantitative characterization of the forming photoproducts by their spectra is impossible because, as it would be suggested, the composition of products containing a carbonyl group is rather complex.

In [12], products of this kind were observed upon treatment of SDS with both ozone and $^{\cdot}OH$ radicals specially generated under the action of radiation in a so-

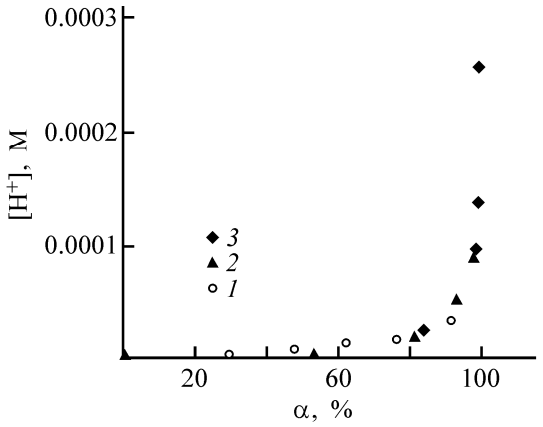


Fig. 7. Concentration of H^+ ions vs. the degree α of SDS decomposition under photooxidation. SDS concentration 100 mg l^{-1}. H_2O_2 concentration (mg l^{-1}): (*1*) 50, (*2*) 100, and (*3*) 200.

lution saturated with N_2O. It was found that $^{\cdot}OH$ radicals react with the hydrocarbon chain of SDS and oxidize carbon in this chain, with carbonyl groups randomly introduced along the entire hydrocarbon chain.

The presence of a peak at ~190 nm in spectra with a characteristic gentle slope is typical of carboxylic acids. The pH values of the solutions also point to an increase in the concentration of H^+ ions. As the exposure duration increases, the visible variation of the concentration of H^+ ions with the degree of SDS conversion in solution passes through a kind of induction period after the onset of SDS conversion and then noticeably grows (Fig. 7). Products of the carbonyl type formed in the first stage of SDS decomposition are oxidized to give carboxy-containing products in the subsequent stage.

Comparison of the data obtained (Figs. 3, 6, and 7) distinguishes two stages of the SDS decomposition. In the first stage, an almost 95% destruction of SDS occurs, which does not lead to any noticeable change in the pH of the medium. This initial period of SDS photooxidation is accompanied by splitting-off of the OSO_2ONa^- group by an SDS molecule and by loss of surface-active properties. Presumably, the role of $^{\cdot}OH$ radicals consists in this stage in the formation of carbonyl-containing intermediates. Further occurs the stage in which there exists a narrow range of SDS conversion, with the solution acidity substantially increasing as a result of the subsequent intense oxidation to give carboxy compounds. Further deeper destruction of the forming organic products, to the point of CO_2 and H_2O formation, proceeds at a considerably slower rate (Fig. 4).

CONCLUSIONS

(1) Sodium dodecyl sulfate decomposes in an aqueous solution under the action of high-intensity continuous-spectrum light emitted by a Xe lamp. The decomposition efficiency substantially increases upon addition of H_2O_2 to a solution. The decomposition kinetics of sodium dodecyl sulfate is described by a first-order equation, and the decomposition rate constant is proportional to the H_2O_2 content of the solution.

(2) In the initial stage of sodium dodecyl sulfate decomposition ($\alpha \approx 80\%$), sulfo groups are split-off and carbonyl compounds are formed, with the surface-active properties disappearing in the process. In the subsequent stage, the products of sodium dodecyl sulfate decomposition are deeply oxidized, compounds with carboxy groups are formed, and the solution acidity substantially increases.

REFERENCES

1. Goncharuk, V.V., Vakulenko, V.F., Sova, A.N., and Shvadchina, Yu.O., *Khim. Tekhnol. Vody*, 2002, vol. 24, no. 4, pp. 229–315.
2. Grachok, M.A. and Prokudina, S.A., *Khim. Tekhnol. Vody*, 1992, vol. 14, no. 2, pp. 128–132.
3. Pikaev, A.K. and Kabakchi, S.A., *Reaktsionnaya sposobnost' pervichnykh produktov radioliza vody: Spravochnik* (Reactivity of Water Radiolysis Products: Reference Book), Moscow: Energoizdat, 1982.
4. Arkhipov, V.P., Kamrukov, A.S., Kozlov, N.P., et al., *Plazmennaya tekhnika i plazmennye tekhnologii: Sbornik nauchnykh trudov Mosk. Gos. Tekh. Univ. im. N.E. Baumana* (Plasma Equipment and Plasma Technologies: Coll. of Sci. Works of Bauman State Technical University, Moscow), Moscow: Inzhener NITs, 2003, pp. 120–127.
5. Seliverstov, A.F., Ershov, B.G., Lagunova, Yu.O., et al., *Radiokhimiya*, 2008, vol. 50, no. 1, pp. 62–65.
6. Rabek, J.F., *Experimental Methods in Photochemistry and Photophysics*, Chichester: John Wiley&Sons, 1982. Translated under the title *Eksperimental'nye metody v fotokhimii i fotofizike*, Moscow: Mir, 1985, vol. 2, pp. 978–981.
7. *Unifitsirovannye metody analiza stochnykh vod* (Unified Methods for Wastewater Analysis), Lur'e, Yu.Yu., Ed., Moscow: Khimiya, 1973.
8. Dedkov, Yu.M., Kel'ina, S.Yu., and Elizarova, O.V., *Khim. Tekhnol. Vody*, 2000, vol. 22, no. 5, pp. 473–486.
9. Marczenko, Z., *Kolorymetryczne oznaczanie pierwiastkow*, Warszawa: Naukowa-techniczne, 1968.
10. Babko, A.K., Volkova, A.I., and Lisichenok, S.L., *Zh. Neorg. Khim.*, 1966, vol. 11, no. 3, pp. 478–485.
11. Sverdlova, O.V., *Elektronnye spektry v organicheskoi khimii* (Electronic Spectra in Organic Chemistry), Leningrad: Khimiya, 1985.
12. Eriksson, M., Andersson, R., and Kloo, L., *Ozone: Sci. Eng.*, 2007, vol. 29, no. 2, pp. 131–138.

ISSN 1070-4272, Russian Journal of Applied Chemistry, 2008, Vol. 81, No. 12, pp. 2108–2111. © Pleiades Publishing, Ltd., 2008.
Original Russian Text © V.V. Goncharuk, V.A. Bagrii, R.D. Chebotareva, S.Yu. Bashtan, A.V. Nanieva, 2008, published in Zhurnal Prikladnoi Khimii, 2008, Vol. 81, No. 12, pp. 1996–2000.

PROCESSES AND EQUIPMENT OF CHEMICAL INDUSTRY

Crystallization of Calcium Carbonate in Magnetic Water in the Presence of Paramagnetic Substances

V. V. Goncharuk, V. A. Bagrii, R. D. Chebotareva, S. Yu. Bashtan, and A. V. Nanieva

Dumanskii Institute of Colloid Chemistry and Water Chemistry, National Academy of Sciences of Ukraine, Kiev, Ukraine

Received July 9, 2008

Abstract—Effect of a paramagnetic substance on the crystallization of calcium carbonate in magnetic water was studied.

DOI: 10.1134/S1070427208120124

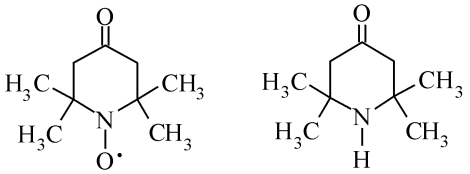
Numerous studies have been devoted to elucidation of the diminishing influence exerted by magnetic fields (MF) on the rate of scale formation on walls of heat equipment [1–4], with attempts made to explain this phenomenon on the basis of theoretical concepts. The main drawback of these studies was that the role of the experimental factor was underestimated. In this communication, we suggest a new, more perfect concept of the antiscale magnetic treatment of water, based on real experimental data.

Analysis of the scale formed on apparatus walls shows that it is mainly composed of trigonal calcite and leaf-like vaterite, whereas the needle-shaped modification of calcium carbonate, aragonite, remains in solution [5]. Having low adhesion to vessel walls and poor cohesion to each other, the needle-shaped crystals of aragonite are easily carried away by water into setting tanks, wherefrom they are periodically removed [5]. Therefore, the scale formation can be considerably diminished by forcing calcium carbonate to crystallize in the form of aragonite. Application of MF by itself promotes directed crystallization of calcium carbonate in the form of aragonite [1]. Furthermore, it has been shown [6] that the amount of aragonite sharply increases when dissolved oxygen is present in magnetic water. This fact was observed for the first time. However it remained unclear whether the observed effect is due to the paramagnetism of oxygen or to its microbubbles [2, 7] whose influence cannot be excluded a priori. As to the role of paramagnetic substances, no studies have been peerformed in this area, with the exception of an analysis of the influence exerted by ferromagnetic inclusions [4, 8, 9].

The aim of the present study was to examine the effect of paramagnetic impurities on the crystallization of calcium carbonate with and without MF application.

EXPERIMENTAL

We chose for the study paramagnetic substances of varied nature: gaseous nitrogen oxide (NO), readily water-soluble organic radical 2,2,6,6-tetramethylpiperidine-4-on-*N*-oxyl (TEMPON) (**I**), and its nonparamagnetic analogue 2,2,6,6-tetramethyl-4-piperidine (**II**), close in structure and molecular weight:



I **II**

Distilled water used to prepare solutions was preliminarily boiled to remove carbon dioxide. In the process, the pH value of distilled water increased from 5.6 to 7.0. Water was cooled to room temperature without access of air and 5 mg-equiv dm^{-3} of calcium chloride was dissolved in it. Then sodium hydrocarbonate was added with shaking until the solution pH reached a value of 8.3. During 15 min before each experiment and over the whole period of the experiment, air or argon was

bubbled through the solution. The resulting aqueous solutions were passed through a magnetic field with a strength of 60 kA m^{-1} and 75-mT remanent induction at a flow velocity of 0.15 m s^{-1}. Four pairs of permanent magnets were arranged with unlike poles on opposite sides of the hy-draulic channel at a distance of 7 mm from each other. In this arrangement, each succeeding pair of magnets repulsed from a preceding pair. The combination of a uniform magnetic field inside each pair of magnets with a "magnetic shock" in the gap between the pairs enhanced the magnetic treatment effect.

Nitrogen oxide was obtained by adding 7 M H_2SO_4 to copper shavings in a glass apparatus without access of air. For pressure equalization, the lower reaction part of the apparatus was connected by a glass tube to a separatory funnel situated in the upper part. NO was purified to remove trace amounts of NO_2 by passing the gas mixture through a Tishchenko flask filled with a 0.1 N sodium hydroxide solution. A solution under study was saturated with nitrogen oxide for 5 min, and then the NO feed was switched off. The mass concentration of TEMPON and its analogue was 5 mg l^{-1}. These concentrations of dissolved salts and a paramagnetic substance were chosen in accordance with the results of preliminary experiments as corresponding to the best manifestation of the magnetic treatment effect.

To accelerate the crystallization, we heated a glass flask with magnetic water on a water bath to 80–100°C and cooled it without access of air to room temperature. Calcium carbonate formed on heating the solution gathered in the bottom part of the flask. Upon settling of the solutions, the excess amount of water was decanted and the remaining suspension was observed and photographed with a Polyvar optical microscope equipped with a Vision video camera.

The conditions of magnetic treatment of the water type under study (arrangement of magnets and magnetic field strength, shape of the hydraulic clearance, and water flow velocity) were chosen experimentally, because it is known from the literature that the dependence of the magnetic treatment effect on these factors is of polyextremal nature and cannot be calculated.

It is known [5] that, in the absence of MF, calcium carbonate precipitates from aqueous solutions in three crystallographic modifications: calcite, vaterite, and aragonite, with predominance of calcite and vaterite. Application of a magnetic field changes the mechanism of calcium carbonate crystallization both in the presence of air (Fig. 1) and in an argon atmosphere (Fig. 2). The amount of vaterite and calcite decreases,

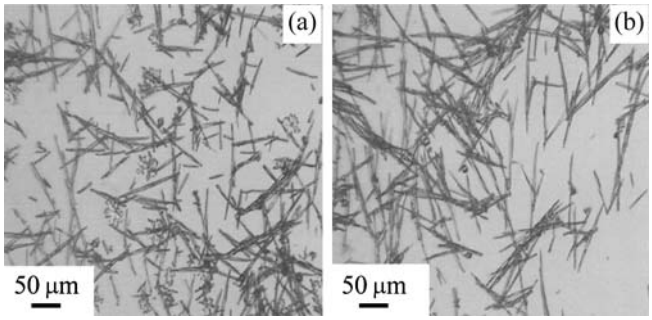


Fig. 1. Micrographs of $CaCO_3$ crystals (×140) obtained (a) without magnetic treatment and (b) with magnetic treatment of calcium hydrocarbonate water containing dissolved air.

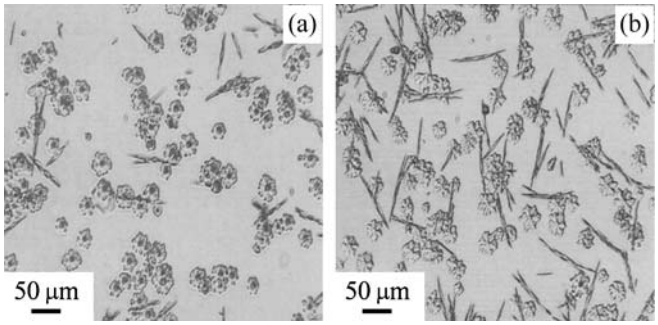


Fig. 2. Micrographs of $CaCO_3$ crystals (×140) obtained (a) without magnetic treatment and (b) with magnetic treatment of calcium hydrocarbonate water saturated with argon.

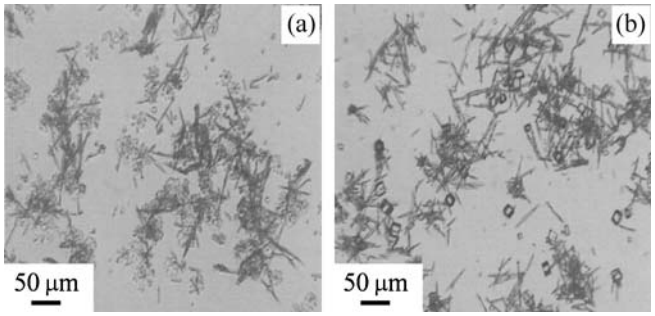


Fig. 3. Micrographs of $CaCO_3$ crystals (×140) obtained (a) without magnetic treatment and (b) with magnetic treatment of calcium hydrocarbonate water saturated with NO.

and that of aragonite increases. The larger number of aragonite crystals in air is accounted for by the presence of paramagnetic atmospheric oxygen [6], which enhances the magnetic treatment effect. The amount of needle-shaped aragonite crystals increases; the crystals become longer and thicker.

The assumption that the process of calcium carbonate crystallization is affected just by the paramagnetism of dissolved gases, rather than by their microbubble structure, was confirmed by the experiments with nitrogen oxide. Introduction of paramagnetic NO into a solution (Fig. 3a) noticeably raises the amount of

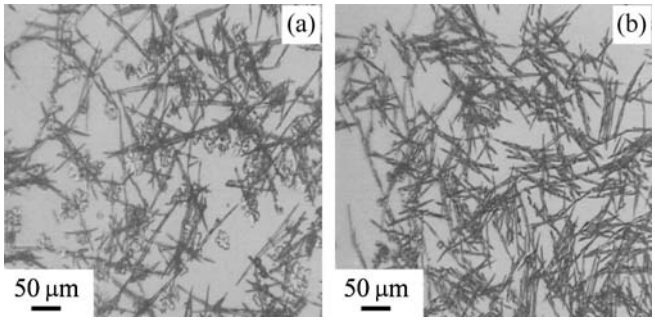


Fig. 4. Micrographs of $CaCO_3$ crystals (×140) obtained (a) without magnetic treatment and (b) with magnetic treatment of calcium hydrocarbonate water containing 5 mg l^{-1} of TEMPON.

aragonite in a precipitate, compared with control experiments in the presence of argon (Fig. 2). When MF is applied to a solution containing NO, the amount of aragonite strongly increases (Fig. 3b). In the process, leaf-like vaterite crystals completely disappear, but separate crystals of trigonal calcite appear. It can be assumed that the application of the field promotes conversion of the metastable vaterite to a more stable calcite. The slightly weaker effect of the magnetic treatment in the presence of NO (presence of calcite inclusions), compared with O_2 [6], can be attributed to the lower magnetic susceptibility of nitrogen oxide. According to the data of [10], the specific magnetic susceptibility of O_2 is 1.335 $m^3 kg^{-1}$, and that of NO, 0.62 $m^3 kg^{-1}$.

The effect of a paramagnetic substance on the process of crystallization of calcium carbonate can be explained as follows. It is known that, on applying MF, paramagnetic substances are pulled in a magnetic field and are arranged along magnetic force lines, whereas diamagnetic substances, water among them, are pushed out. Under the action of MF in the absence of a paramagnetic substance, the hydrate shells of calcium ions situated along magnetic force lines are deformed. In a water flow, partly hydrated calcium ions can approach to a distance at which the Van der Waals attraction forces exceed the electrostatic repulsion forces, and formation of crystalline nuclei becomes possible. First, short chains or planar monomolecular layers can be formed, and their further agglomeration yields a solid phase. Thus, the increased concentration of partly hydrated ions along the MF force lines is the main condition for directed crystallization of calcium carbonate in the form of needle-shaped aragonite.

There are two reasons for the enhancement of the magnetic treatment in the presence of a paramagnetic substance. On the one hand, a paramagnetic arranged along MF lines weakens the hydration of the surrounding ions. On the other hand, having an unpaired electron and an energetically nonuniform surface, the paramagnetic radical can by itself initiate the crystallization process [5]. The effect of a paramagnetic substance on the directed crystallization of calcium carbonate seems to consist in weakening of the hydration of calcium ions along the magnetic force lines. In principle, the direct crystallization of $CaCO_3$ on paramagnetic centers is not impossible, but the probability of such a process is rather small. In view of the aforesaid, we can suggest that, in a sense, the paramagnetic substance reminds in operation mechanism a catalyst, which accelerates a reaction without entering into the composition of its products. This refers to the same extent to all the paramagnetic substances studied.

The strongest influence on the directed crystallization of calcium carbonate was exerted by introduction of a paramagnetic organic radical TEMPON into a solution (Figs. 4a and 4b). Comparison of the micrographs in Figs. 3 and 4 shows that TEMPON substantially exceeds gaseous nitrogen oxide in the effect on the $CaCO_3$ crystallization. This is attributable to the difficulty of retaining gaseous NO molecules along magnetic field lines. Indeed, when a sufficient number of NO molecules join into a bubble, Archimedes forces can exceed the orienting action of MF, and the bubble will float-up to the surface of a liquid. The freed place will be primarily filled by neighboring water molecules and calcium ions, whose concentration is considerably higher than that of NO. Eventually, the labile NO molecules will displace diamagnetic water molecules and calcium ions to the periphery of the MF force lines, and the process will repeat from the very beginning. Periodic fluctuations of the paramagnetic NO somewhat diminish its influence on the process of calcium carbonate crystallization.

Fluctuations of this kind are not characteristic of the organic radical TEMPON. The crystallization of calcium carbonate occurs in more undisturbed conditions, which reflects on the properties of the resulting precipitates.

According to Fig. 4a, the precipitates of calcium carbonate formed in solution in the presence of TEMPON without magnetic treatment mainly consist of aragonite and vaterite. Trigonal calcite crystals are absent in this case. When magnetic field is applied, metastable vaterite crystals disappear and almost the whole amount of calcium carbonate crystallizes in the form of the needle-shaped aragonite (Fig. 4b). Taking into ac-

count the absence of calcite crystals in magnetic water, we can conclude that the paramagnetic radical TEMPON is as good as, or even better than, one of the strongest paramagnetic substances, molecular oxygen, in the efficiency of antiscale treatment [6].

As additional evidence in favor of our concept can serve the results of experiments with a close analogue of TEMPON, nonparamagnetic 2,2,6,6-tetramethyl-4-piperidine. According to the data obtained, calcium carbonate crystallizes in the presence of the nonparamagnetic analogue, as it also does in the case of argon, mainly in the form of leaf-like vaterite. Even though application of a magnetic field leads to a slight increase in the amount of needle-shaped aragonite, the main part of crystals retains in the leaf-like shape characteristic of vaterite.

CONCLUSIONS

The presence of paramagnetic nitrogen oxide, atmospheric oxygen, and the organic paramagnetic radical 2,2,6,6-tetramethylpiperidine-4-on-*N*-oxyl in magnetic water promotes directed crystallization of calcium carbonate in the form of a needle-shaped aragonite.

REFERENCES

1. Klassen, V.I., *Omagnichivanie vodnykh system* (Magnetic Treatment of Aqueous Systems), Moscow: Khimiya, 1978.
2. Droyaronov, A.L., *Elektron. Obrab. Mater.,* 1983, no. 2, pp. 44–47.
3. Goncharuk, V.V. and Malyarenko, V.V., *Khim. Tekhnol. Vody*, 2003, vol. 25, no. 3, pp. 213–227.
4. Evdokimov, V.V. and Manukyan, S.D., *Zh. Fiz. Khim*., 1975, vol. 49, no. 3, pp. 569–578.
5. Prisyazhnyuk, V.A., *Santekh. Vodosnab*., 2003, no. 10, pp. 26–30.
6. Goncharuk, V.V., Bagrii, V.A., Chebotareva, R.D., and Bashtan, S.Yu., *Khim. Tekhnol. Vody*, 2006, vol. 28, no. 3, pp. 311–314.
7. Margulis, M.A. and Klassen, V.I., *Elektromagnitnaya obrabotka vodnykh system v khimiko-tekhnologicheskikh protsessakh (*Electromagnetic Treatment of Aqueous Systems in Chemical-Engineering Processes), Moscow, 1982, issue 57, pp. 110–120.
8. Sandulyak, A.V. and Krivtsov, V.V., *Elektron. Obrab. Mater.*, 1983, no. 2, pp. 42–43.
9. Tebenikhin, E.F., *Bezreagentnye metody obrabotki vody v teploenergetike* (Nonchemical Methods of Water Treatment in Heat Power Engineering), Moscow: Energiya, 1977.
10. *Spravochnik khimika* (Chemist's Handbook), Nikol'skii, B.P., Ed., Leningrad: Khimiya, 1965, vol. 4, 2nd ed.

ISSN 1070-4272, Russian Journal of Applied Chemistry, 2008, Vol. 81, No. 12, pp. 2112–2117. © Pleiades Publishing, Ltd., 2008.
Original Russian Text © I.M. Lipatova, L.I. Makarova, 2008, published in Zhurnal Prikladnoi Khimii, 2008, Vol. 81, No. 12, pp. 2001–2006.

PROCESSES AND EQUIPMENT OF CHEMICAL INDUSTRY

Effect of Hydroacoustic Treatment on Chitosan Dissolution in Aqueous Acetic Acid Solutions

I. M. Lipatova and L. I. Makarova

Institute of Solution Chemistry, Russian Academy of Sciences, Ivanovo, Russia

Received May 13, 2008

Abstract—Effect of a hydroacoustic treatment in a rotary-pulsatory apparatus on the dissolution rate and the achievable limiting solubility of chitosan in aqueous acetic acid solutions of various concentrations was studied. The rheological properties of solutions produced by the conventional method and with mechanical activation were compared.

DOI: 10.1134/S1070427208120136

Chitosan is an ionogenic polysaccharide with a set of rather valuable properties. The technological convenience of chitosan, related to its solubility in weakly acid aqueous media, makes it possible to produce from this polymer microspheres, microcapsules, coupling agents, and membranes, as well as carrier matrices in manufacture of medicinal preparations. Many structurally sensitive properties of these materials and articles are preset already in the stage of preparation of starting solutions from commercial chitosans manufactured in the form of powders or scales.

The properties of chitosan solutions have been described more than once [1–4], but either the method of solution preparation was not mentioned at all, or only the dissolution duration was specified. The solvent most frequently used for chitosan is 2% acetic acid. The duration of dissolution in this solvent under laboratory conditions is 4–16 h for different samples, depending on their molecular mass and degree of deacetylation [3, 4]. It was found in a study of the solubility of various brands of chitosan [5] that all the samples studied dissolve in 1% acetic acid; however, complete dissolution was reached for some of these samples only in 24 h. In addition, we found that solutions of chitosan with a molecular mass exceeding 400 kDa are inhomogeneous because of the presence of a gel fraction, which adversely affects the quality of films formed from these solutions. With the expansion of the field of industrial application of chitosans, the problem of fast preparation of their solutions without additional filtration becomes increasingly pressing.

A rather effective method for intensification of various technological processes performed in liquid media is hydroacoustic treatment in high-speed rotary-pulsatory apparatus [6]. The main distinctive design feature of these apparatus is the presence of alternating immobile and rotating cylinders with slits. In these apparatus, the most important factors activating the liquid media being treated are ultrasonic vibrations and, accordingly, cavitation, and also high shear stresses to which the liquid is subjected in narrow (0.1–0.5 mm) gaps between the rotor and stator elements.

The aim of our study was to examine the effect of a hydroacoustic treatment in rotary-pulsatory apparatus on the dissolution rate and achievable limiting solubility of chitosan in aqueous acetic acid solutions of various concentrations. In addition, we intended to compare the rheological properties of solutions produced in the conventional way and those obtained with mechanical activation.

EXPERIMENTAL

As objects of study served three chitosan samples with M = 360 (Kh-360), 470 (Kh-470), and 500 kDa (Kh-500).[1] The degrees of deacetylation (DD) of the chitosans were 0.82, 0.79, and 0.60, respectively. In the air-dry state, the chitosans were in the form of flat scales 0.5–2 mm in size.

[1] Chitosan samples were provided by Bioprogress Private Company.

We used as solvents aqueous acetic acid solutions with an acid concentration varied within the range 0.2–2 wt %. Weighed portions of chitosans (1 g dl^{-1}) were dissolved in the aqueous acetic acid solutions at a temperature of 25°C under agitation until the process termination was analytically determined.

The thus obtained suspensions were mechanically treated in a laboratory rotary-pulsatory apparatus (RPA) in the recycle mode. The thermostated working chamber of the apparatus is formed by the rotor and stator whose cylindrical rings have rectangular channels. The average gap between the rotating and immobile members of the working chamber was 0.3 mm. The rotor rotation rate was 5000 rpm, to which corresponds a shear rate gradient of 17.4×10^4 s^{-1}. The treatment duration was varied within the range 4–40 s.

The dissolution rate of chitosans was determined by sampling the dispersion medium of the suspensions under study at regular intervals of time. The samples, transparent solutions, were analyzed for the content of chitosan by performing the reaction with Ninhydrin dye by the procedure described in [7], with the optical density of the resulting stained solutions measured on a Specol 11 spectrophotometer at a wavelength of 565 nm. Taking into account that the result of the analysis depends on the degree of deacetylation, a separate calibration plot was measured for each sample.

The content of the gel fraction in the chitosan solutions was found gravimetrically. A weighed portion of a solution was passed through preliminarily weighed sieves with 0.8×0.8-mm mesh, after which the sieves with the gel fraction they retained were again weighed and the volume fraction of the gel fraction was calculated, with the solution density taken to be 1 g cm^{-3}.

The viscosity of the solutions was determined on a Brookfield rotation viscometer (LVDV-1+) with a cylindrical rotor (6 rpm) at 25 ± 0.5°C at shear rates in the range 0.1–132 s^{-1}.

The characteristic viscosity of dissolved chitosan samples was determined at 25°C in an Ubbelohde viscometer (capillary diameter 0.73 mm) by successive dilution with 2% acetic acid. A 0.2 M solution of sodium acetate was introduced as a supporting electrolyte.

Chitosan is a polyaminosaccharide having an apparent dissociation constant of a conjugated acid, pK_a = 6.3–6.7, and dissolving in water only at pH < 6. As solvents can be used dilute solutions of monobasic organic and inorganic acids. The dissolution is preceded by protonation of NH_2 groups to give a salt adduct. Solutions are most frequently prepared using acetic acid with a concentration of 2 wt %, with the solution pH taking values of 3.3–3.6 upon complete dissolution. The so low pH values are undesirable in some cases and, in particular, in use of chitosan for immobilization of proteins and certain medicinal preparations. However, the decrease in the acid concentration strongly hinders the dissolution.

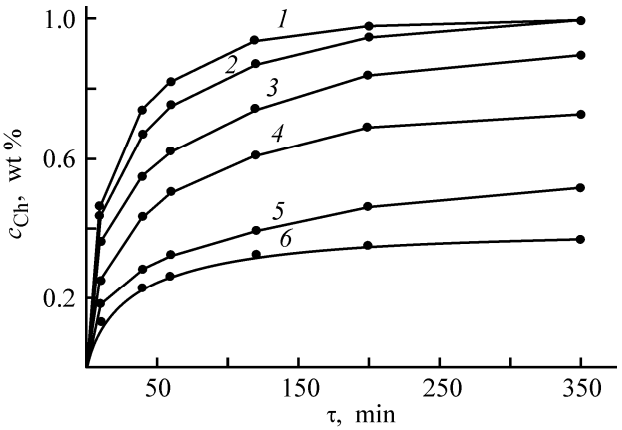


Fig. 1. Concentration c_{Ch} of Kh-360 chitosan in solution vs. the dissolution duration τ at a hydromodulus of 1 : 100. Acid concentration in solution (wt %): (*1*) 2, (*2*) 1, (*3*) 0.8, (*4*) 0.5, (*5*) 0.3, and (*6*) 0.2.

In this study, we used acetic acid solutions with concentrations of 0.2, 0.3, 0.5, 0.8, 1, and 2% as a medium for chitosan dissolution. Kinetic curves of Kh-360 chitosan dissolution in these media under ordinary conditions are shown in Fig. 1. The run of the kinetic curves indicates that the dissolution rate steeply decreases as the process duration becomes longer and the kinetic curves take a nearly horizontal position, although, according to analytical data, the process continues for several more hours until its completion.

Such a nonuniform course of the dissolution process is presumably due to structural inhomogeneity and molecular polydispersity of chitosan. The time in which the limiting concentration of chitosan is reached steadily increases as the acid concentration in the solvent decreases. For example, as indicated by analytical data and visual inspection, the process was complete in 5–6 h at acid concentrations of 1 and 2%, whereas at concentrations of 0.2 and 0.4%, the chitosan concentration in samples of the dispersion medium ceased to increase 20–22 h after introduction of chitosan into the solvent and, in this case, the solution contained a noticeable amount of undissolved particles.

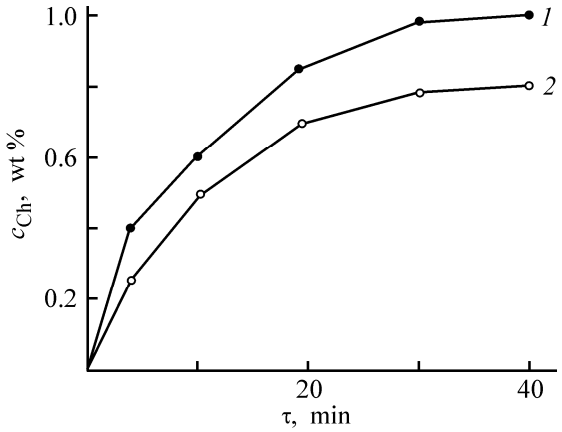


Fig. 2. Concentration c_{Ch} of Kh-360 chitosan in solution vs. the dissolution duration τ for the process performed in an RPA at a hydromodulus of 1 : 100. Acid concentration in solution (wt %): (*1*) 1 and (*2*) 0.8.

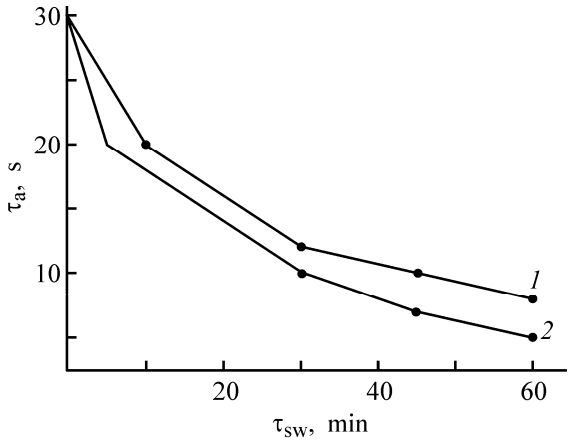


Fig. 3. Effect of the preliminary swelling time τ_{sw} on the dissolution duration τ_a of (*1*) Kh-470 and (*2*) Kh-360 chitosans in 2% acetic acid under mechanical activation in an RPA.

In the case of chitosan dissolution directly in the working chamber of RPA, sampling during treatment is impossible because of the too short process duration. To measure the rate of mechanically activated dissolution of chitosan, we prepared as many starting suspensions as the number of points to be obtained in the kinetic curve. The suspensions were activated one after another, with the treatment duration increasing each time, after which the undissolved fraction was separated and the solutions were analyzed for the content of chitosan. The kinetic curves obtained for the process of Kh-360 chitosan dissolution under hydroacoustic treatment are shown in Fig. 2 (curves *1*, *2*).

Comparison of the data in Figs. 1 and 2 points to a high efficiency of RPA application to intensification of the chitosan dissolution in the aqueous media under study. For example, a 80% dissolution of chitosan is reached under ordinary agitation by a mechanical stirrer at acid concentrations of 1 and 0.8% in 90 and 210 min, respectively, whereas in dissolution in an RPA, the same occurs in 17 and 35 s, respectively. The efficiency of mechanical activation in dissolution substantially increases if a suspension is treated in an RPA after a certain time, i.e., after a preliminary swelling of particles in the solvent, rather than immediately upon its preparation. Figure 3 shows how the time of mechanical treatment of a chitosan suspension (samples Kh-360 and Kh-470) in an RPA, necessary for complete dissolution of the polymer, becomes shorter as the time of preliminary swelling of the chitosan suspension increases.

It should be noted that, even with thermostating of the working chamber of the RPA, the solution warmed-up to 30–32°C. The heat released because of the internal friction in media being processed is apparently an additional factor that intensifies the dissolution. In this study, the duration of treatment in RPA did not exceed 40 s, because at longer durations it was impossible to preclude a considerable warming-up of the media being processed and a noticeable destruction of the polymer [8]. For Kh-500 chitosan, treatment in an RPA of a suspension without preliminary treatment does not lead to complete dissolution in 40 s. A total visually indicated dissolution is achieved only in activation of the suspension after a preliminary swelling for 2 h. In this case, too, the total process duration is substantially shorter than that in dissolution without activation. In addition, a solution obtained with mechanical activation is more homogeneous and contains no gel fraction.

The achieved effect of accelerated dissolution is accounted for by the simultaneous action of a number of factors on suspensions being processed under hydroacoustic treatment. The dissolution of solid particles in a liquid under treatment in RPA occurs simultaneously with the dispersion and, consequently, with the development of the phase-contact surface. The particles being dissolved are subjected to a multifactor treatment including turbulent pulsations of the liquid flow velocity, spherical shock waves in pulsations of cavitation bubbles, and cumulative action upon the collapse of these bubbles. Chaotic turbulent fluctuations of various layers of the liquid create strong shear stresses on the surface of a solid particle, which favors a decrease in the thickness of the diffusion layer, enhances its mobility, and provides an inflow of a fresh liquid to the surface of a particle being dissolved.

It was of interest to find whether it is possible to raise the limiting solubility of chitosan at low acetic acid concentrations by hydroacoustic treatment. According to the data of [9], the chitosan dissolution occurs at a degree of protonation equal to 0.5, i.e., 50% of amino groups are to be ionized for a macromolecule to pass into solution. According to the results of the same study, the 0.5–0.7 degree of protonation is reached only at the equimolar CH3COOH : chitosan ratio. The authors of [10] found that, irrespective of the acid concentration in the starting solutions, the residual amount of acetic acid in films formed from chitosan solutions in aqueous acetic acid is 24–27%, which corresponds to an approximately equimolar ratio between the acid and amino groups of the polymer. Upon introduction of 1 wt % chitosan into a solution, the equimolar ratio between the acid and amino groups is reached by the system at an acid concentration as low as 0.4%.

Thus, the complete dissolution can theoretically be reached at acid concentrations substantially lower than 2%, or even 1%, relative to the solution mass. As, however, follows from the experimental data obtained, only 73% of Kh-360 chitosan is dissolved even on raising the process duration to 24 h if the acid concentration is lowered to 0.5%. This result indicates that the solubility of chitosan is determined not only by the acid concentration of a solution, but, apparently, also by the degree of chemical and structural nonuniformity of a sample, i.e., by the quality of the raw material used.

Chitosan is produced by alkaline deacetylation of chitin. The incomplete course of this process is due to the presence of residual acetyl groups whose distribution in chitosan depends on the degree of crystallinity or on the relative amounts of the crystalline and amorphous regions of the starting chitosan, because the deacetylation reaction more easily proceeds in amorphous regions. The nonuniform distribution of the residual acetyl groups presumably predetermines that less soluble blocks are present in the chitosan structure, which alternate with regions of a nearly completely deacetylated polysaccharide. These latter cause a strong swelling of structural units in protonation in solution via electrostatic repulsion [11].

Under a hydroacoustic treatment, the combination of the above-mentioned factors must lead to disintegration of strongly swollen particles and to rupture of hydrogen bonds, which, in turn, must favor transfer of macromolecules with a sufficient degree of protonation to the solution. Figure 4 shows how the limiting solubility depends on the acetic acid concentration in an aqueous solution for the cases of conventional chitosan dissolution and that in the working chamber of RPA in the course of 40 s. It can be seen that, at low acid concentrations, the effect of the mechanical activation is manifested in that the limiting solubility increases, on average, by 25–45%.

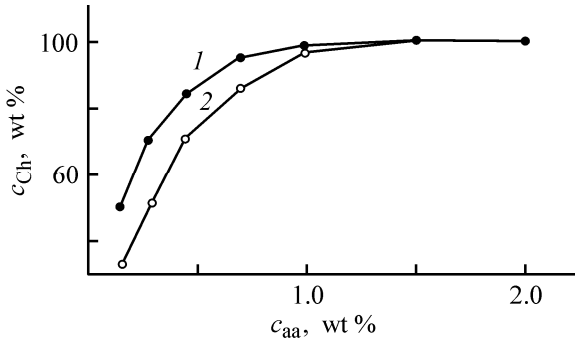


Fig. 4. Limiting solubility c_{Ch} of Kh-360 chitosan at a hydromodulus of 1 : 100 vs. the acetic acid concentration c_{aa} for the process performed (*1*) with mechanical activation in RPA and (*2*) with a mechanical stirrer at 25°C.

In mechanically activated dissolution with the use of RPA, not only the process duration changes, but also the quality of the solution obtained; in particular, the content of the gel fraction substantially decreases. Numerous publications concerned with properties of chitosan solutions do not mention presence of a gel fraction. We found that, after centrifugation of visually homogeneous solutions produced by prolonged dissolution in 2% acetic acid, their lower part with a higher viscosity can be separated by decantation. When these solutions are sieved, a viscous, gel-like part of the solution, in which spherical transparent particles ("gellites") can be seen, remains on the sieve. This primarily refers to samples with high molecular mass and low degree of deacetylation. For example, on keeping a Kh-500 sample (DD 0.6) in 2% acetic acid under periodic agitation for 18 h, complete dissolution was visually observed. However, an analysis demonstrated that the content of the gel fraction at the instant of complete visual dissolution was 11 vol %. On further keeping of the solution for additional 4 and 8 h, the content of the gel fraction decreased to 8.5 and 6.2 vol %, respectively, but it did not disappear completely even on keeping the solution for two days.

The gel fraction is present because the polymer incompletely passes into solution even at acid concentrations and process durations at which complete dissolution must occur according to published data. The rea-

Effect of hydroacoustic treatment on the duration of chitosan dissolution in 2% acetic acid and properties of the solutions obtained (c_{Ch} = 1 wt %)

Parameters of a solution	Kh-360		Kh-470	
	without activation	with RPA	without activation	with RPA
Dissolution duration	5 h	20 s	8 h	30 s
Dynamic viscosity, mPa s^{-1}	580	370	780	410
DSS	11.3	18.6	12.7	20.7
[η], dl g^{-1}	7.2	6.8	8.2	7.6
Huggins constant	0.62	0.48	0.72	0.55

sons for such a behavior are apparently related to the prehistory of a sample and to the presence of fractions with a lower degree of deacetylation. As a result, strongly swollen transparent agglomerates remain, although visual observation shows complete dissolution. Films formed from these solutions have an uneven, hummocky surface. In solutions prepared using RPA, no gel fraction was found by the method used in this study. Films formed from mechanically treated solutions are homogeneous and have a smooth surface.

It has been found previously that hydroacoustic treatment on chitosan solutions leads to a decrease in their viscosity because of the occurrence of mechanically initiated structural and chemical transformations, with a certain contribution to the observed decrease in the viscosity made by activated hydrolytic destruction of the polymer, whose extent increases with temperature [8]. In this context, a goal of the present study was to compare the rheological properties of solutions prepared by the conventional method and with mechanical activation. To evaluate the extent of mechanically initiated destruction, we measured in parallel the characteristic viscosity related to the molecular mass of the polymer. The data obtained are listed in the table.

It can be seen from the table that solutions produced by the mechanical method have a lower viscosity and are less structured than solutions prepared by ordinary dissolution. The decrease in the characteristic viscosity, indicative of the mechanical destruction of the polymer, is 5–7%. The decrease in the degree of structuring of the mechanically treated solutions is indicated by an increase in the dynamic stability of their structure (DSS), whose values were calculated using rheological data by the formula

$$DSS = (90 - \alpha)/(\alpha - 45),$$

where α is the slope rate of the linear portions of the dependences of the shear rate on shear stress, plotted in log–log coordinates.

The degree of structuring of the solutions presumably decreases via disintegration of stable aggregates of associated chitosan macromolecules in the mechanical field. The decrease in the Huggins constant, which characterizes the interaction of the polymer with the solvent, also points to a less important role of polymer–polymer contacts and increased role of polymer–solvent interactions in mechanically treated solutions. In other words, it can be stated that mechanical activation favors a more complete dissolution of chitosan.

Thus, it was shown that hydroacoustic treatment can diminish the duration of chitosan dissolution from several hours to several seconds. Solutions produced using mechanical activation are distinguished by lower viscosity and by better structural uniformity as compared with solutions of the same concentration, prepared in the conventional way. A decrease in the viscosity of chitosan solutions without any change in its concentration may be of practical interest in some cases and, in particular, for deposition of uniform films by spilling, synthesis of composite materials and impregnating solutions, and thin-layer dressing of various surfaces, and for other purposes.

CONCLUSIONS

(1) Use of hydroacoustic treatment in a rotary-pulsatory apparatus for intensification of chitosan dissolution in aqueous acetic acid solutions diminishes the process duration from several hours to 20–40 s.

(2) Mechanical activation of chitosan suspensions in acetic acid solutions with concentrations lower than 1% raises the limiting solubility of the polymer by 30–45%.

(3) Solutions produced using mechanical activation are distinguished by lower shear viscosity and molecular mass and by better structural uniformity, compared with solutions of the same concentration, prepared by the conventional method.

REFERENCES

1. Nud'ga, L.A., Petrova, V.A., Bochek, A.M., et al., *Vysokomol. Soedin. Ser. B*, 1997, vol. 39, no. 7, pp. 1232–1236.

2. Nud'ga, L.A., Bochek, A.M., Kallistov, O.V., et al., *Zh. Prikl. Khim.*, 1993, vol. 66, no. 1, pp. 198–202.

3. Sklyar, A.M., Gamzazade, A.I., Rogovina, L.Z., et al., *Vysokomol. Soedin. Ser. A*, 1981, vol. 23, no. 6, pp. 1396–1403.

4. Mironov, A.V., Vikhoreva, G.A., Kil'deeva, N.R., and Uspenskii, S.A., *Vysokomol. Soedin. Ser. B*, 2007, vol. 49, no. 1, pp. 136–138.

5. Sadovoi, V.V., Kuznetsova, T.E., and Kalashnikova, O.S., *Materialy Shestoi mezhdunarodnoi konferentsii "Sovremennye perspektivy v issledovanii khitina i khitozana"* (Proc. 6th Int. Conf. "Modern Prospects in Studies of Chitin and Chitosan"), Moscow: VNIRO, 2001, pp. 316–319.

6. Balabyshko, A.M., Zimin, A.I., and Ruzhitskii, V.P., *Gidrodinamicheskoe dispergirovanie* (Hydrodynamic Dispersion), Moscow: Nauka, 1998.

7. Lopatin, S.A., Nemtsev, S.V., and Varlamov, V.P., *Materialy Shestoi mezhdunarodnoi konferentsii "Sovremennye perspektivy v issledovanii khitina i khitozana"* (Proc. 6th Int. Conf. "Modern Prospects in Studies of Chitin and Chitosan"), Moscow: VNIRO, 2001, pp. 298–299.

8. Lipatova, I.M. and Kornilova, N.A., *Zh. Prikl. Khim.*, 2008, vol. 81, no. 5, pp. 778–782.

9. Rinaudo, M., Pavlov, G., and Desbrieres, J., *Polymer*, 1999, no. 40, pp. 7029–7032.

10. Vikhoreva, G.A., Rogovina, S.Z., Pchelko, O.M., and Gal'braikh, L.S., *Vysokomol. Soedin. Ser. A*, 2001, vol. 43, no. 6, pp. 947–951.

11. Pedroni, V.I., Schulz, P.C., Gschaider, M.E., and Andreucetti, N., *Colloid Polym. Sci.*, 2003, vol. 282, pp. 100–102.

ISSN 1070-4272, Russian Journal of Applied Chemistry, 2008, Vol. 81, No. 12, pp. 2118–2121. © Pleiades Publishing, Ltd., 2008.
Original Russian Text © M.V. Efanov, V.A. Novozhenov, N.V. Ignatova, S.V. Makarov, M.K. Kotvanova, 2008, published in Zhurnal Prikladnoi Khimii, 2008, Vol. 81, No. 12, pp. 2007–2010.

PROCESSES AND EQUIPMENT OF CHEMICAL INDUSTRY

Composite Materials Based on Acetylated Wood and Aluminum and Its Compounds

M. V. Efanov, V. A. Novozhenov, N. V. Ignatova, S. V. Makarov, and M. K. Kotvanova

Altai State University, State Educational Institution of Higher Professional Education, Barnaul, Russia
Yugra State University, State Educational Institution of Higher Professional Education, Khanty-Mansiisk, Russia

Received January 16, 2008

Abstract—The possibility of preparing new composite materials from acetylated wood and aluminum, aluminum chloride, and aluminum hydroxide as mineral fillers was examined.

DOI: 10.1134/S1070427208120148

Acylation of vegetable raw materials is an effective route of their chemical modification. Polymeric acylation products (esters of lignocarbohydrate materials) are soluble in organic solvents, exhibit hydrophobic and thermoplastic properties, and are biostable. These physicomechanical properties determine the possible applications of acylated lignocarbohydrate materials [1].

The use of acylated wood as a thermoplastic binder for preparing composite materials with mineral and wood fillers allows fabrication of boards with good physicomechanical parameters and hydrophobic properties. This is favored by the high thermoplasticity of acylated wood and its good adhesion to mineral and organic fillers [2].

Procedures have been developed for preparing esters from wood mechanochemically activated in the presence of catalysts, involving acylation of wood with a mixture of acetic anhydride with aliphatic carboxylic acid at 100–130°C for 4–6 h [3, 4]. These procedures have significant drawbacks: long process time (4–6 h), high temperature (100–130°C), and high consumption of acylating agents (3–10 mol).

The known procedure for preparing wood–mineral composite materials involves preparation of a cellulose-containing vegetable filler, its treatment with chemical additives (water glass, aluminum sulfate, calcium chloride), combination with a mineral binder (e.g., Portland cement of grade 400–500), forming of the composite, pressing, heat treatment, storage, and drying of the finished item [5]. However, the physicomechanical parameters of the resulting articles and their strength and water resistance are poor.

In this study, we prepared composite materials based on acetylated wood and aluminum and its compounds. We examined the strength properties and electrical conductivity of these materials.

EXPERIMENTAL

For activation of wood prior to the acetylation, it was subjected to cavitation pretreatment on a rotary cavitation apparatus at a rotor rotation rate of 3000 rpm. A 500-g portion of air-dry aspen sawdust (fraction 1–3 mm) was placed in a 50-l glass vessel and poured over with 8 l of water. The treatment was performed at 60°C for 30 min. Then the treated wood was filtered off with a linen filter, washed with water to neutral reaction, squeezed on the filter, and air-dried to constant weight.

The acetylation of activated aspen wood was performed as follows. A 3.0-g portion of air-dry activated sawdust was placed in a 250-ml round-bottomed flask equipped with a reflux condenser and placed on an oil bath (thermostat). Then a suspension of ammonium sulfate (20 wt % relative to wood) in 3 mol of acetic anhydride was added. The mixture was heated at 125°C for 4 h. Then the flask was cooled to room temperature, and 100 ml of distilled water was added. The mixture was filtered off on a glass frit (pore class 160) and washed with distilled water to remove acetic acid and the catalyst to neutral reaction and absence of sul-

fate ions (check with $BaCl_2$). The content of bound acetyl groups was determined by saponification of samples of acetylated wood with a 0.5 N solution of NaOH in alcohol, followed by conductometric back-titration of excess alkali with 0.5 N HCl [4]. The content of bound acetyl groups in the product obtained was 46 wt %.

The composite materials were prepared as follows. Into the matrix (acetylated aspen wood, AAW) we introduced aluminum, aluminum hydroxide, and aluminum chloride in an amount of 10–90 wt %. The resulting blends were charged into test tubes and heated for 2 h at 120°C. Then the samples of the composite materials were compacted into pellets 1 cm in diameter under a load of 15 kN (Table 1).

The phase composition of the samples was determined with a DRON-2.0 diffractometer with a cobalt anode ($\lambda Co K_{\alpha(mean)}$ = 1.7902 Å) at a rotation rate of 1 deg min^{-1} and on a X'Pert Pro diffractometer (Philips, Netherlands) with a copper anode and a nickel filter, at a tube voltage of 40 kV. The substances were identified using JCPDS data file.

The IR spectra of samples were measured on a Specord IR-82M spectrometer using KBr technique. The electrical conductivity of the polymeric composites was studied with an MO-62 dc bridge of class 0.1. Copper plates were used as electrodes, and samples of composite materials were placed between them. The limits of resistance measurements were chosen assuming that the polymer is an insulator and the filler content is varied from 10 to 90%. Accordingly, the resistance measurement range was from 10 to 10^6 Ω. The corresponding voltage was set at 36 V.

As can be seen from Table 1, the optimal content of all kinds of fillers is 30–70%. The strength of the composites reaches 21.0 MPa, which is comparable with the strength of known composites based on acetylated wood and mineral fillers [2, 5, 6].

We found that the materials have a relatively high ultimate strength, up to 21.0 MPa for the sample with Al, but the strength of the materials with aluminum chloride and aluminum hydroxide fillers is lower.

As can be seen from Table 1, composites with the same filler at its content of 70 and 90% have closely similar strengths exceeding that of unfilled AAW. Thermograms (Table 2) demonstrate a relatively high (up to 200°C) heat resistance of the composites containing 70% filles.

Table 1. Ultimate strength of composite materials based on AAW and aluminum compounds

Sample no.	Material composition	Filler content, %	Ultimate strength σ ± 0.3, MPa	Sample no.	Material composition	Filler content, %	Ultimate strength σ ± 0.3, MPa	Sample no.	Material composition	Filler content, %	Ultimate strength σ ± 0.3, MPa
1	AAW	–	12.0	7	AAW + $AlCl_3 \cdot 6H_2O$	10	16.9	12	AAW + $Al(OH)_3$	10	9.3
2	AAW + Al	10	12.7	8		30	19.6	13		30	10.9
3		30	21.0	9		50	17.3	14		50	10.4
4		50	17.2	10		70	18.3	15		70	10.7
5		70	20.5	11		90	19.3	16		90	10.8
6		90	19.5								

Table 2. Results of thermal analysis of composite samples

Composite	Peak no.	Kind of effect	T_{onset}	T_{max}	T_{final}	Weight loss, %
			°C			
AAW	1	*Exo-*	210	285	350	75
	2	*Exo-*	385	410	480	24
AAW + Al	1	*Exo-*	200	335	414	29
AAW + $AlCl_3 \cdot 6H_2O$	1	*Endo-*	64	68	79	–
	2	*Endo-*	114	134	157	–
	3	*Endo-*	164	175	186	–
	4	*Exo-*	200	246	278	81
AAW + $Al(OH)_3$	1	*Exo-*	264	321	493	72

Table 3. Results of an X-ray phase analysis of composite samples containing 90 wt % mineral filler

Composite	d, Å	I_{rel}, %	Composite	d, Å	I_{rel}, %
AAW–$Al(OH)_3$	4.90	100	AAW–Al	4.82	1
	4.30	81		2.37	100
	2.34	1		2.05	45
	1.85	9		1.44	15
	1.42	1		1.22	11

Two exothermic peaks in the range 210–480°C in the case of decomposition of the binder are due to degradation of acetylated components of aspen wood. A sample of a composite material containing aluminum chloride hydrate as a filler exhibits three endothermic peaks associated with the removal of water and cleavage of hydrogen bonds occurring as the filler complexes decompose, and also one exothermic peak with a considerable weight loss, characterizing the main degradation reactions of acetylated components of wood in the temperature range 200–278°C. The samples containing aluminum and aluminum hydroxide as fillers exhibit only one peak in the DTA curve in the temperature ranges 200–414 and 264–493°C, respectively.

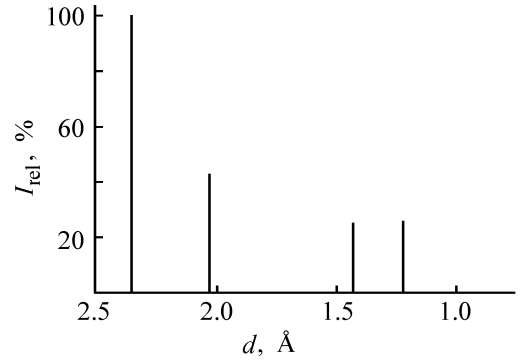


Fig. 1. X-ray diffraction pattern of a composite material based on acetylated wood with Al filler (70 wt %). (I_{rel}) Relative intensity and (d) interplanar spacing; the same for Fig. 2.

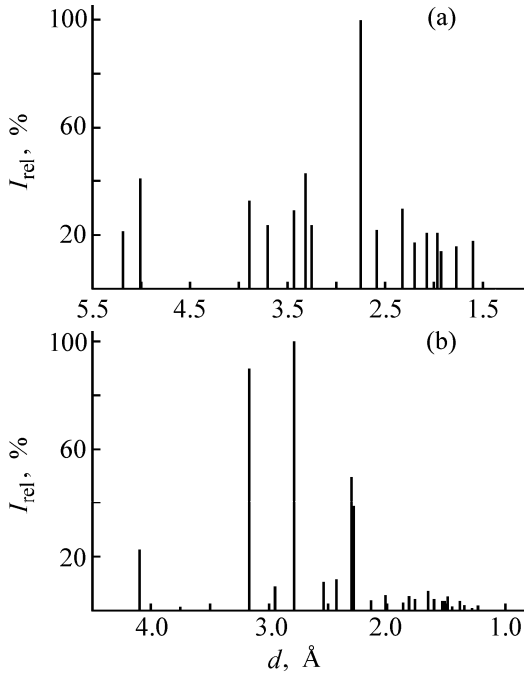


Fig. 2. X-ray diffraction patterns of a composite material based on acetylated aspen wood with aluminum chloride hydrate as filler. Filler content, wt %: (a) 70 and (b) 90.

An examination of the composite samples by X-ray phase analysis showed that the diffraction patterns of the composite material containing 70 wt % aluminum hydroxide exhibit only one reflection ($2\theta = 20.65°$) characteristic of AAW. The lack of reflections from the inorganic filler indicates that it is X-ray amorphous. The diffraction pattern of the composite material containing 90% aluminum hydroxide shows reflections from two modifications of the filler: σ-$Al(OH)_3$ (one reflection at $d = 4.30$ Å) and nordstrandite (four reflections) (Table 3).

The X-ray diffraction patterns of the materials containing 70 (Fig. 1) and 90 wt % (Table 3) Al unambiguously demonstrate the presence of the Al phase.

The AAW–$AlCl_3 \cdot 6H_2O$ composite material exhibits 16 reflections in the diffraction pattern, one of which ($d = 5.01$ Å) corresponds to AAW, and the others, to aluminum chloride hydrate (Fig. 2a).

X-ray phase analysis of the composite containing 90% $AlCl_3 \cdot 6H_2O$ (Fig. 2b) reveals the presence of two phases: aluminum chloride hydrate and AlO(OH).

The qualitative composition of the samples was determined from the characteristic IR absorption bands. The IR spectra of the materials containing aluminum chloride and hydroxide as fillers do not differ significantly from that of acetylated aspen wood.

The main absorption bands of composite components are present in all the spectra. The spectra of the samples containing 70 and 90% aluminum chloride

hydrate differ from the spectrum of unfilled AAW in that, in the range 3550–3100 cm^{-1} corresponding to vibrations of hydroxy groups, there are two bands indicative of the formation of an additional hydrogen bond between OH groups of AAW and aluminum chloride hydrate.

Conductivity measurements showed that the materials containing aluminum and aluminum hydroxide as fillers are dielectric (their resistivity exceeds 10^6 Ω cm), whereas the samples filled with aluminum chloride show weak conductivity: Their resistivity decreases to 10^5 Ω cm at a filler content of 70% and to 10^4 Ω cm at a filler content of 90%.

CONCLUSIONS

(1) Composite materials containing 30–70% acetylated wood and mineral fillers (aluminum, aluminum chloride, aluminum hydroxide) were prepared.

(2) The composites have a strength of up to 21.0 MPa, are heat-resistant up to 200°C, and can be used as finishing materials.

REFERENCES

1. Bazarnova, N.G., *Doctoral Dissertation*, Krasnoyarsk, 1999.
2. Efanov, M.V., Pershina, L.A., and Klepikov, A.G., *Plast. Massy*, 2000, no. 7, pp. 40–41.
3. RF Patent 2 143 436, *Byull. Izobret.*, 1999, no. 36.
4. Efanov, M.V., *Cand. Sci. Dissertation*, Krasnoyarsk, 1999.
5. Shcherbakov, A.S., Mel'nikova, L.V., and Gamova, I.A., *Tekhnologiya drevesnykh kompozitsionnykh materialov* (Technology of Wood Composite Materials), Moscow: Ekologiya, 1992.
6. *Prakticheskie raboty po khimii drevesiny i tsellyulozy* (Practical Works on Wood and Cellulose Chemistry), Moscow: Lesnaya Prom–st., 1965.

ISSN 1070-4272, Russian Journal of Applied Chemistry, 2008, Vol. 81, No. 12, pp. 2122–2126. © Pleiades Publishing, Ltd., 2008.
Original Russian Text © V.V. Tarasov, N.F. Kovalenko, Zhang Dongxiang, E.G. Sorokin, 2008, published in Zhurnal Prikladnoi Khimii, 2008, Vol. 81, No. 12, pp. 2011–2015.

PROCESSES AND EQUIPMENT OF CHEMICAL INDUSTRY

Removal of Compressor Oil Microdroplets from Water with a Carbon Fabric

V. V. Tarasov, N. F. Kovalenko, Zhang Dongxiang, and E. G. Sorokin

Mendeleev Russian University of Chemical Engineering, Moscow, Russia

Beijing Technological Institute, Beijing, People's Republic of China

Received June 22, 2007

Abstract—Coalescence of KHA-30 compressor oil microdroplets on a carbon fabric, aimed to remove them from air and water streams used for compressor cooling, was examined.

DOI: 10.1134/S107042720812015X

Compressors [1, 2] can be responsible for contamination of air, water, and soil with hydrocarbon oils which severely affect the hygienic characteristics of these media. This is of special relevance to finely dispersed compressor oils (COs). Oil trapping filters fail after a certain period, so that oil gets into air, water, and soils.

The removal of microscopic droplets of KHA-30 compressor oil from water, which is specifically the subject of this study, is not a simple task. This oil brand is not toxic for humans, but poses a serious threat to aquatic biota, because of the extremely low maximum permissible concentrations set for KHA-30 oil in water (0.05 mg l^{-1}). The major procedure used for removing microconcentrations from water is adsorption. However, this method, efficient for molecules, is inefficient in trapping substances in the form of micro- and nanodroplets. In this case, it seems expedient to subject water to heterogeneous hydrodynamic coagulation–coalescence (HHC) treatment to be followed by adsorption. The HHC method is highly promising for removal of microdroplets from water, as demonstrated by experiments with food fats and technical oil [3] and by simulations of this process [4–6].

Water treatment by the HHC procedure to remove oil microdroplets can also be termed adagulation [7], but this term does not cover all the processes of formation and growth of clusters, as well as detachment of the coalesced fragments of the latter. In this context, we consider two processes: 1) preparation of quasistable CO emulsions in water and 2) degradation of these emulsions. We apply the term "quasistable" to emulsions that preserve no less than 70% of the optical transparency for 1 day. The breakdown (coalescence) of emulsions can also be regarded as water treatment to remove CO microdroplets. The removal of CO emulsions can be monitored by the variation of their optical absorbance A.

Tarasov et al. have shown [8] that the kinetics of water treatment to remove oil microdroplets is described by the Eley–Rideal equation [8], modified by Tarasov [3–5]. As is known, this process is named the SV process [8]; its principal kinetic characteristic is the slope φ of the straight line $\Delta(t) = 1/A - 1/A_0$, which determines the heterogeneous coagulation rate coefficient (HCRC, s^{-1}). The heterogeneous coagulation is a first-order process with respect to the concentration of the substance in the aqueous phase, which is characterized by a variable order (ranging from unity to zero) with respect to the microdroplet concentration on the surface [3–5]. In this case, the corresponding line is described by a $\Sigma(t)$ function, namely, $\Sigma(t) = \ln(A_0/A) + (1/A - 1/A_0) = f(t)$ [3–5], where A_0 and A are the light absorbances at the onset of the process and at any other instant of time, respectively. Another variable is the degree of removal of microdroplets from the emulsion, $E = f(t)$, %.

Here, we examined the water treatment to remove KHA-30 CO microdroplets by HHC with the use of a carbon fabric.

EXPERIMENTAL

The procedure for examination of the coagulation–coalescence of compressor oil microdroplets is nearly identical to that described by us earlier [4, 5] with two essential exceptions: The reactor walls are coated with a carbon fabric layer, and the operation of the rotor with disks in the coagulator-coalescer is started and stopped with an electronic circuit. The choice of a carbon fiber fabric was due to the specific conditions of wetting of the fabric with CO (see [3–5]). The close proximity of the fabric to the walls prevents the emulsion from filtration through the carbon fabric, which, in turn, precludes the mechanism operating in filter cartridges, with all its inherent drawbacks.

The KHA-30 compressor oil has a kinematic viscosity of 28–32 $mm^2 s^{-1}$ at 50°C, or 120 $mm^2 s^{-1}$ at 25°C. Its flash point in an open crucible is 185°C, the solidification point, –38°C; and density, 905 kg m^{-3} [9].

The setup used to prepare quasistable emulsions consisted of an IKA DI25 disperser equipped with an S25N–18G sprayer and a 500 cm^3 glass vessel with a rectangular cross section. The operation of the IKA DI25 disperser is based on interruption of an emulsion stream at a frequency of 1333–4000 Hz. The disperser rotor rotation rate was fixed at 133, 158, 225, 342, and 400 s^{-1}. The emulsions were used for testing the HHC method developed (coalescence of droplets). From the hydrodynamic viewpoint, these emulsions can be regarded as homogeneous liquids, since they are sensitive solely to minor hydrodynamic pulsations [10].

Figure 1 presents as an example the number- and volume-fraction size distributions of the CO emulsion microdroplets, obtained at 133 s^{-1}. It should be noted that similar patterns were obtained for rotation rates of up to 400 s^{-1}. The particle radius determined by computer-aided photomicrography is within 0.4–7.6 μm. All the distributions are oblique (asymmetric), because they lie at the edge of the visible spectral range. At 133 s^{-1} (Fig. 1), the w(r) distribution exhibits a distinct maximum, which disappears at 158 and, the more so, at 400 s^{-1}. However, distributions the maxima are preserved in the $\alpha = f(r)$; they are observed at 0.8–1.4 μm for all the disperser rotor rotation rates used in our experiments. The volume fractions are much more sensitive to the presence of individual large particles, since they are proportional to the cubed radius. This is specifically responsible for the fact that the maxima are preserved in the $\alpha = f(r)$ distributions at all the stirring intensities used in the experiments.

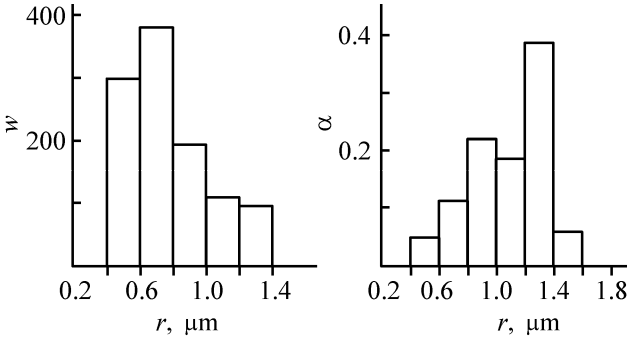


Fig. 1. Number-fraction and volume-fraction size distributions for droplets at the disperser rotor rotation frequency m=133 s^{-1} (8000×10/60 = 133.3 Hz). (w) Number, (α) volume fraction, and (r) radius of droplets.

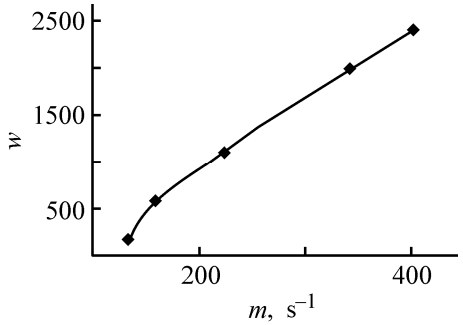


Fig. 2. Number of droplets w vs. disperser rotor rotation frequency m.

The change of the disperser rotor rotation rate m causes a nearly proportional increase in the number of droplets w (dimensionless parameter) (Fig. 2). The abscissa in Fig. 2 is the disperser rotor rotation rate m, and the ordinate, the number of the droplets, w, corresponding to the significant domain of the distribution (95% of the total area), recalculated for one image.

Importantly, not only the maxima are preserved in the $\alpha = f(r)$ distributions, but also fairly long (up to 7.6 μm) "tails" appear in the right segment of the distributions, probably due to the transverse axis vibration.

The setup for HHC treatment of water to remove microdroplets consisted of a reactor whose walls were coated with a carbon fabric, a PE–8100 stirrer with an electronic control circuit for the electric motor, a central shaft with a set of smooth polypropylene disks, and a temperature-control system (for the setup design, see [3]). There exists a direct proportionality between the CO droplet concentration in the emulsion and the light absorbance A measured on a KFK instrument. The basic kinetic parameter Δ is a function of three parameters:

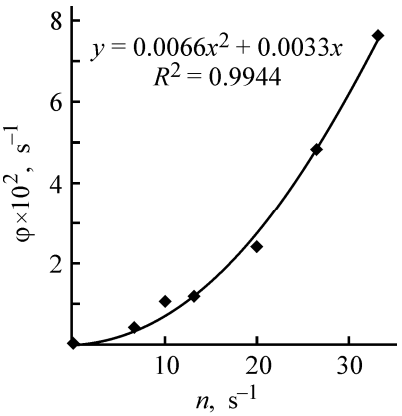


Fig. 3. Variation of the slope φ of the Δ(*t*) function with the coagulator–coalescer rotor rotation frequency *n* at a constant *m* = 225 s^{-1} (2250 Hz).

m, n, and *t*, where *m* and *n* are rotor rotation rates of the disperser and coagulator, respectively. In the case of interest, three alternatives are possible: $\Delta(t)_{m,\,n}$ = const, $\varphi(m) = \Delta(m)/t_n$ = const, and $\varphi(n) = \Delta(n)/t_m$ = const.

For all the 18 replicated experiments the $\Delta(t)_{m=225,\,n=16.7}$ function was linear with the approximation reliability factor of 0.9987. We confirmed for the first time that there exists a strict direct proportionality between the Δ(*t*) and $\Sigma(t) = \ln(A_0/A) + (1/A - 1/A_0)$ functions [3–6], the slope rate of a such function being close to unity. The approximation reliability factor for the $\Sigma = 1.1789\Delta$ equation is $R^2 = 0.9975$. Previously, this situation has been presumed, but not confirmed experimentally.

Tarasov et al.have shown [5, 6] that the Δ(*t*) function may be parabolic, $\Delta = 0.102t^2 + 0.0221t$, with the approximation reliability factor $R^2 = 0.9982$. However, the Σ(*t*) plot is represented by a straight line $\Sigma = 1.1761t$, with the approximation reliability factor $R^2 = 0.9941$ [5, 6]. Probably, this is possible only at not very large, though appreciable departures from unity of the logarithmic term of the sum (about several first ten units). As to trends in variation of the Δ(*t*) function, the function changes in the selected cases from parabolic to linear, as demonstrated and interpreted earlier [5, 6].

The $E = f(t)$ kinetic curves show that, within 2–6 min, 98–100% of compressor oil can be coagulated and even coalesced. Naturally, this specific proportion depends on the rotation rate of coagulator reactor disks.

Despite a threefold variation of the rotation frequency *m* of the disperser rotor (from 133 to 400 s^{-1}), the coagulation–coalescence rate is almost independent of *m* (see table). This is most clearly demonstrated by the microdroplet coalescence data for tri-*n*-butyl phosphate, used confirm the assumption that the microdroplet coalescence rate coefficients do not vary with *m.* The rate coefficients φ(*m*) for the CO coagulation–coalescence [4] are also listed in the table. They exhibit a weak and nonmotonic variation with *m*. It can be seen that the number of the droplets in the image varies from 166 to 2310 (nearly 14-fold). This suggests an efficient disintegration and reduction in size of the droplets. It was subsequently shown that a regular dependence of $\varphi(m) = \Delta/t$ on *m* is not observed for other objects, either. The invariance of φ(*m*) is not indicative of the kinetic control, for which φ(*m*) = const for all the rotation rates *n*.

If we accept for φ(*m*) a uniform value with a fairly large rms deviation, 0.025 ± 0.006, this can imply the invariance of φ(*m*), rather than that of the coagulation–co-alescence mechanism. In the case of a process occurring in a coagulator–coalescer, the mechanism of surface interaction with clusters becomes operative. This process is completely irreversible, and each collision of droplets with clusters results in their coalescence. In some cases, the slope of the φ(*m*) functions is zero, and in other cases, *m* tends to substantially decrease with increasing rotation rate of the disperser rotor. In the case of coalescence of the CO microdroplets, the rate-determining stage is a process characterized by a variable order (from two to unity), which results in attachment of the microdroplets attacking the surface clusters from the bulk. This stage is specifically responsible for the invariance of φ(*m*) at invariantable *n*. Hence, the size of turbulent pulsations [10] in the coagulator–coalescer bulk strongly exceeds the size of the resulting droplets. However, coalescence proceeds on the surface, rather in the volume of the coagulator–coalescer, and even minor changes in position relative to the wall coated with the fabric can be sufficient to strongly affect the behavior of droplets, which is specifically responsible for the pattern displayed in Fig. 3.

The coalescence in the coagulator–coalescer at *n* varying within 6.7–33.3 s^{-1} provides on exhaustive removal of the CO microdroplets. This result has not been achieved earlier; it suggests the irreversibility of the process. Now, the stirring intensity for the coagulator rotor with disks can be raised to ≥33.3 s^{-1} without exposing the system to a redispersion risk (Fig. 3). Even at the highest *n* values, the known maximum [11] was not achieved, which suggests complete suppres-

sion of the redispersion in the case of interest. No repeated disintegration of droplets is observed because of their high viscosity and prolonged resistance to breakdown of coalesced droplets. Apparently, it takes an appreciable time for a droplet to break down into two fragments.

The experimental $\varphi(n)$ curve at m = const = 225 s^{-1} is parabolic, $\varphi(n) = 0.0066n^2 - 0.0033n$, with the approximation reliability factor $R^2 = 0.9953$. Hence, validation of any mode should rely on variance or invariance of the process rate with respect to n, rather than on invariance of the coalescence rate coefficient φ with respect to m.

Our results suggest that the rate of coalescence of compressor oil microdroplets can be affected by introduction, in advance, of a minor amount of a diluent, such as diesel fuel (DF). The viscosity of DF at 20°C is 1.5–3.0 $mm^2 s^{-1}$, which is much lower than that of CO (140 $mm^2 s^{-1}$).

It could be expected that a decrease in viscosity would cause an increase in the coagulation–coales-cence rate coefficient $\varphi = \Delta/t$. However, even a minor decrease in viscosity caused initially a nearly fivefold decrease in the coagulation rate coefficient, and only subsequently, a minor increase in φ. A possible reason is that adding even a minor amount of diesel fuel causes a decrease in the stickiness (adhesion) of CO droplets to each other and to clusters. Therefore, the coalescence of microdroplets is decelerated by DF addition (Fig. 4).

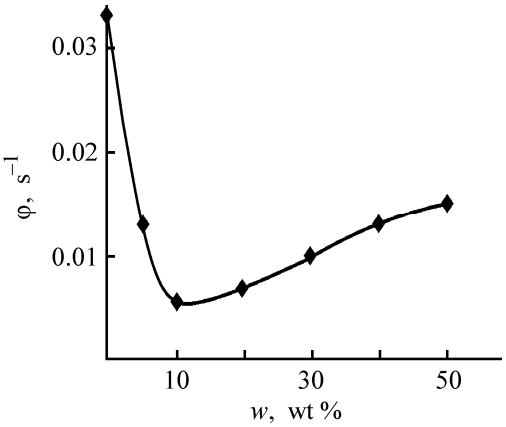


Fig. 4. Slope φ of the $\Delta(t)$ function vs. concentration w of diesel fuel additives (m = 225 s^{-1}, n = 16.7 s^{-1}).

CONCLUSIONS

(1) The coalescence of compressor oil microdroplets is an irreversible and fairly efficient process, which provides an exhaustive (nearly 100%) removal of 0.8–7.6-μm microdroplets within no longer than 480 s.

(2) An examination of the coalescence of microdroplets showed that, at invariant rotation frequency of the coagulator–coalescer rotor, the coalescence rate coefficient is nearly independent of the rotation rate of the disperser rotor. Rotation of the coagulator–coalescer rotor favors coalescence of microdroplets by a parabolic law.

(3) In the case of coalescence of compressor oil microdroplets, the rate-determining stage is a first-order process with respect to the concentration of microdroplets in the aqueous phase, which is characterized by a variable order with respect to the concentration of microdroplets on the solid surface. Adding the less viscous diesel fuel causes a nearly fivefold decrease in the rate constant coefficient of coalescence of compressor oil microdroplets.

Microdroplet coalescence rate coefficients at different disperser rotor rotation frequency m

Disperser rotor rotation frequency m, s^{-1}	CO microdroplet coalescence rate coefficient $\varphi = \Delta/t$, s^{-1}	R^2	TBP microdroplet coalescence rate coefficient $\varphi = \Delta/t$, s^{-1}	R^2
133	0.020	0.992	0.045	0.999
158	0.031	0.981	0.044	0.984
255	0.033	0.997	0.043	0.991
342	0.022	0.987	0.046	0.943
400	0.019	0.975	0.040	0.948

REFERENCES

1. Cherkasskii, V.M., Romanova, T.M., and Kaul', R.A., *Nasosy, kompressory, ventilyatory* (Pumps, Compressors, Fans), Moscow: Khimiya, 1968.
2. Frankel', M.I., *Porshnevye kompressory* (Piston Compressors), Leningrad: Khimiya, 1969.
3. Tarasov, V.V. and Shchedrova, N.I., *Nauchnaya sessiya MIFI-2007: Sbornik nauchnykh trudov* (Scientific Session of Moscow Inst. of Engineering Physics of the Year 2007: Coll. of Scientific Works), Moscow, 2007, vol. 9, pp. 154–156.
4. Tarasov, V.V., Kovalenko, N.F., Kruchinina, N.E., and Shilin, S.A., *Zh. Prikl. Khim.,* 2006, vol. 79, no. 8, pp. 1300–1304.
5. Tarasov, V.V. and Shilin, S.A., *Teor. Osn. Khim. Tekhnol.*, 2007, vol. 41, no. 2, pp. 191–196.
6. Tarasov, V.V. and Shilin, S.A., *Theor. Found. Chem. Eng.*, 2007, vol. 41, no. 2, pp. 178–183.
7. Deryagin, B.V., Churaev, N.V., and Muller, V.M., *Poverkhnostnye sily* (Surface Forces), Moscow: Nauka, 1987.
8. Tarasov, V.V., Yagodin, G.A., and Pichugin, A.A., *Kinetics of Extraction of Inorganic Substances, Itogi Nauki Tekh., Ser.: Neorg. Khim.*, Moscow: VINITI, 1984.
9. *Khimicheskii entsiklopedicheskii slovar'* (Chemical Encyclopedic Dictionary), Knunyants, I.L., Ed., Moscow: Sov. Entsiklopediya, 1983.
10. Levich, V.G., *Fizikokhimicheskaya gidrodinamika* (Physicochemical Hydrodynamics), Moscow: Akad. Nauk SSSR, 1952.
11. Tarasov, V.V., Kruchinina, N.E., Shchedrova, N.I., and Dzamashvili, S.D., *Teor. Osn. Khim. Tekhnol.*, 2006, vol. 40, no. 5, pp. 551–555.

ISSN 1070-4272, Russian Journal of Applied Chemistry, 2008, Vol. 81, No. 12, pp. 2127–2131. © Pleiades Publishing, Ltd., 2008.
Original Russian Text © Yu.A. Gorbatenko, Z.G. Rezinskikh, G.N. Lipunova, I.G. Pervova, T.I. Maslakova, P.A. Slepukhin, I N. Lipunov, 2008, published in Zhurnal Prikladnoi Khimii, 2008, Vol. 81, No. 12, pp. 2016–2020.

ORGANIC SYNTHESIS AND INDUSTRIAL ORGANIC CHEMISTRY

Synthesis and Spectroscopic Features of Iron(II) 1-Aryl-5-benzothiazol-2-ylformazanates

Yu. A. Gorbatenko, Z. G. Rezinskikh, G. N. Lipunova, I. G. Pervova, T. I. Maslakova, P. A. Slepukhin, and I. N. Lipunov

Ural State University of Forestry Engineering, Yekaterinburg, Russia

Ural State Technical University–Ural Polytechnic Institute, Yekaterinburg, Russia

Postovskii Institute of Organic Synthesis, Ural Branch, Russian Academy of Sciences, Yekaterinburg, Russia

Received June 18, 2008

Abstract—New iron(II) coordination compounds with 1-aryl-5-(benzothiazol-2-yl)formazans were prepared. Their compositions and structures were determined by electronic spectroscopy, mass spectrometry, single crystal X-ray diffraction analysis, and magnetochemical measurements.

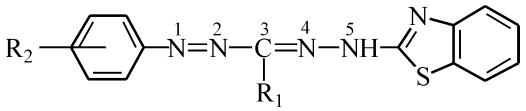
DOI: 10.1134/S1070427208120161

Iron coordination compounds with polydentate nitrogen-containing heterocyclic ligands are unique chemical systems. The specific features of their properties and structure are determined by the nature of the coordination core and by the steric arrangement of side functional groups.

Iron chelates has demonstrated good performance as effective catalysts of not only industrial (synthesis of ammonia, dehydrogenation of hydrocarbons, etc.) [1–3] but also biochemical processes [4]. Many of these compounds are characterized by exchange interactions of both ferro- (ferri-) and antiferromagnetic type, which lead under the action of certain external factors (temperature, pressure, irradiation at a definite wavelength) to transitions into a magnetically ordered state or to spin transitions $S = 5/2 \rightleftarrows S = 1/2$ [5–7] and make the iron complexes attractive objects for molecular electronics. In this context, synthesis and study of structural features of new coordination compounds of iron with ambidentate ligands are of both scientific and practical interest.

Among such ligands are, in particular, hetarylformazans, for which both bridging and chelate coordination is typical. The polydenticity and high flexibility of the formazan molecule, as well as the ability of such compounds to act as both bi-, tri-, and tetradentate ligands and also the possibility of controlling their properties through the substituent effect make them attractive for design of organometallic complexes with required stereochemistry [8, 9].

This study is concerned with synthesis of iron coordination compounds with formazans **I–V** and with the substituent effect on the composition, structure, and spin state of the metal complexes.



I–V

EXPERIMENTAL

The compounds were prepared from $FeCl_3 \cdot 6H_2O$ of analytically pure grade. 1-Aryl-5-benzothiazol-2-ylformazans were synthesized by the procedures described in [10–13]. The purity of the metal complexes was verified by TLC on Silufol UV-254 plates.

Iron 1-(4-sulfophenyl)-3-methyl-5-(benzothiazol-2-yl)formazanate (IFe). A solution of 0.3 mmol of iron (III) chloride in 15 ml of water was added dropwise with continuous stirring at 40 ± 5°C to a solution of 0.9 mmol of formazan in 100 ml of aqueous ethanol (1 : 1). The resulting mixture was stirred for 30 min and evaporated to a volume of 10 ml. The precipitate

Table 1. Elemental analyses and melting points of iron(II) formazanate complexes

Ligand	R_1	R_2	Complex	Empirical formula	T_m, °C	Found, % / Calculation, %		
						C	H	N
I	CH_3	4-SO_3H	**I**Fe	$C_{30}H_{24}N_{10}S_4O_6Fe \cdot 3H_2O$	>250	41.93 / 41.96	3.61 / 3.53	–
II	CH=CH–CH_3	H	**II**Fe	$C_{34}H_{28}N_{10}S_2Fe$	180	59.79 / 58.61	4.28 / 4.06	19.68 / 20.11
III	$CH(CH_3)_2$	H	**III**Fe	$C_{34}H_{32}N_{10}S_2Fe$	245	58.30 / 58.27	4.63 / 4.61	19.75 / 19.99
IV	$CH(CH_3)_2$	4-OCH_3	**IV**Fe	$C_{36}H_{36}N_{10}S_2O_2Fe$	190	56.45 / 56.83	4.97 / 4.78	18.06 / 18.41
V	C_6H_5	H	**V**Fe	$C_{40}H_{28}N_{10}S_2Fe$	215	62.61 / 62.52	3.64 / 3.71	18.21 / 18.18

was filtered off, washed with a small amount of distilled water, and dried in air.

Iron 1-phenyl-3-(propen-1-yl)-5-(benzothiazol-2-yl)-formazanate (IIFe). A solution of 0.3 mmol of iron(III) chloride in 15 ml of acetone was added dropwise with continuous stirring at 40 ± 5°C to a solution of 0.9 mmol of formazan in 100 ml of acetone. The resulting mixture was stirred for 30 min and evaporated to a volume of 10 ml. The precipitate was filtered off, washed with warm distilled water and ethanol, and dried in air. Iron formazanates **III**Fe, **IV**Fe, and **V**Fe were prepared similarly. The compositions of the ligands and complexes obtained are listed in Table 1.

The electronic absorption spectra of the ligands and their metal complexes in aqueous ethanol (1 : 1) for **I** or acetone for **II–V** were recorded on a Beckman UV-5260 double-beam spectrophotometer in the wavelength range 350–800 nm. The compositions of the complexes and equilibrium concentrations were determined from the plots of the optical densities of solutions vs. the volume of the salt solution added. The equivalence point corresponded to the salt solution volume required to attain the saturation. From these data, the stoichiometric composition of the complexes formed was calculated.

An elemental analysis was performed on a CHN PE2400SII automatic analyzer (Perkin–Elmer Instruments, the United States). The metal content was determined by express gravimetric analysis with a device produced by Khimlaborpribor Joint-Stock Company (Klin, Moscow oblast, Russia).

The IR spectra of the ligands and complexes obtained were recorded with a Specord 75-IR spectrophotometer in KBr pellets in the range 400–4000 cm^{-1}.

Mass spectra of iron formazanates were measured in the electron impact ionization mode on an MAT-ZPA device (Varian) with the reverse configuration in the design of magnetic and electrostatic analyzers, which allowed the spectra of metastable ions to be obtained directly. The spectra were measured under standard conditions: accelerating voltage 3 kV, cathode emission current 300 μA, and ionizing electron energy 70 eV. The samples were introduced into the ion source using the direct inlet system.

The magnetic characteristics of the compounds were measured with a Quantum Design 5-XL SQUID magnetometer in the temperature range 0–300 K in magnetic fields of strength 30 and 50 kOe.

Single-crystal X-ray diffraction analysis of complex **IV**Fe was performed at 295(2) K with an Xcalibur 3 autodiffractometric system equipped with a CCD detector. Crystals of **IV**Fe ($C_{36}H_{36}N_{10}O_2S_2Fe$, red prisms) belong to the monoclinic system. Unit cell parameters: a = 10.3951(18), b = 21.968(2), c = 15.9281(16) Å; α = 90.00°, β = 99.347(11)°, γ = 90.00°; V = 3589.0(8) $Å^3$; ρ_{calc} = 1.408 g cm^{-3}; M = 760.72; Z = 4; space group $P2(1)/n$. The experiment completeness at $\theta \le 26.38°$ was 99.5% (ω-scanning at 1° step and 10-s exposure per frame, crystal–detector distance 50 mm). A total of 7299 unique reflections were measured, including 2515 reflections with $I > 2\sigma(I)$. The absorption correction was ne-

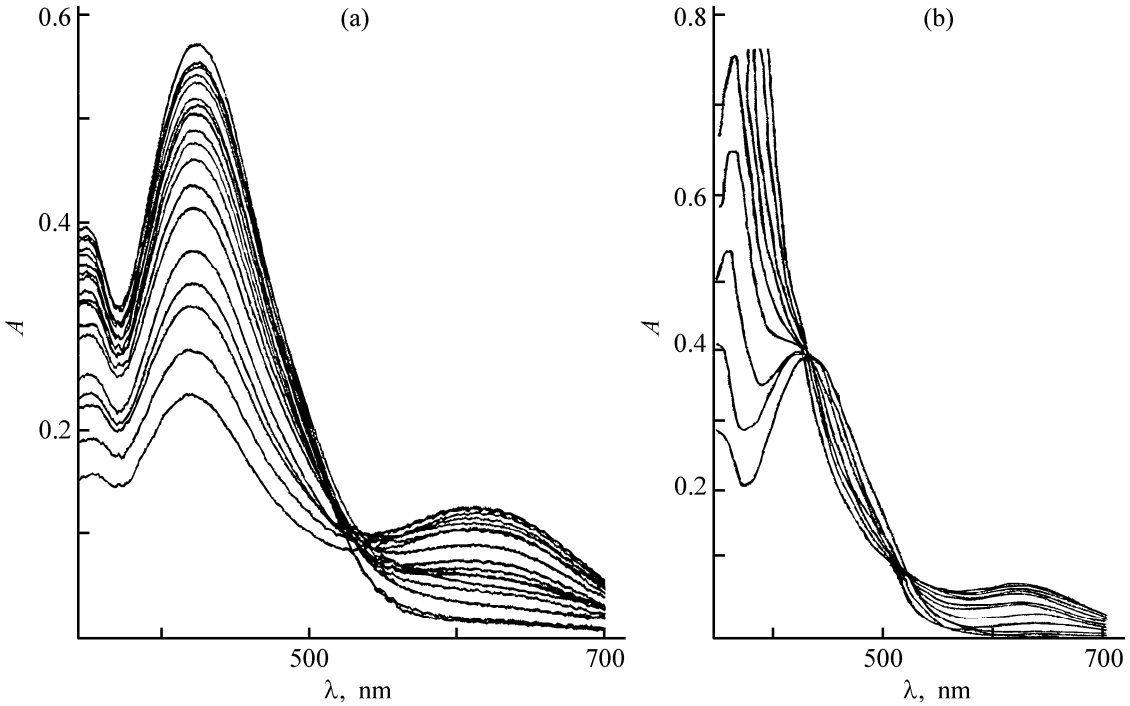


Fig. 1. Electronic spectra of formazan **IV** in acetone, recorded in the course of titration with a solution of (a) nickel(II) nitrate ([**IV**] = 2.85×10^{-5}, [$Ni(NO_3)_2$] = 10^{-3} M) and (b) iron(III) chloride ([**IV**] = 2.85×10^{-5}, [$FeCl_3$] = 1×10^{-2} M) in acetone. (*A*) Absorption and (λ) wavelength.

glected because of its insignificance (μ = 0.585 mm^{-1}). To collect and edit the experimental data and refine the unit cell parameters, we used the CrysAlis CD program [14]. The structure was solved by the direct method using the SHELX-97 program package [15]. The hydrogen atoms were placed in calculated positions and included in refinement in the rider model with dependent thermal parameters. The structure was solved by the least-squares method in the anisotropic approximation for nonhydrogen atoms and isotropic approximation for H atoms. The final divergence factors were R_1 = 0.0670, wR_2 = 0.0803 [$I > 2\sigma(I)$] at goodness-of-fit S = 0.994.

Depending on the structure of the initial formazan group, the ligands can coordinate M^{2+} and M^{3+} ions either in the tridentate fashion via N^1 and N^4 atoms of the formazan chain and nitrogen atom of the heteroring to give complexes ML_2 with a nitrogen-containing coordination core, or, if the aryl fragment contains an additional *o*-OH or *o*-COOH group, in the tridentate or tetradentate fashion to give complexes ML_2 or ML with N_xM or N_xO_yM coordination cores, depending on the synthesis conditions [8].

The variations in the mode of coordination of hetarylformazans in their complexes with metal ions, to give coordination compounds with diverse structures and properties are determined not only by the set of donor atoms in the ligand structure, but also by the electronic configuration of the central metal ion.

For example, in complexation of tridentate formazan **IV** with nickel(II) nitrate in an acetone solution, the intensity of the absorption band of the starting formazan at λ_{max} = 430 nm gradually decreases, and an absorption band of the metal complex appears at λ_{max} = 630 nm. The spectral pattern is characterized by the presence of one isobestic point, which suggests that only two formazan species are involved in the process: the starting formazan and the forming nickel(II) formazanate.

With iron(III), a metal ion with a variable oxidation state, the spectral pattern (Fig. 1) observed in the course of titration is more complicated. A decrease in the intensity of the absorption band of formazan is mainly associated with its tranformation into a product with λ_{max} < 350 nm. Apparently, formazan is oxidized into a tetrazolium salt (a well-known reaction of formazans [8]), with Fe(III) acting as oxidant. A weak absorption band appearing at 625 nm can be assigned to Fe(II) formazanate. This behavior has been already noted for complexation of some benzazolylformazans with Fe(III) and Mn(III) ions [16, 17].

The reactions of ethanol solutions of iron(III) chloride with benzothiazolylformazans **I–V** yielded

Table 2. Data furnished by electronic spectroscopy, mass spectrometry, and magnetochemical measurements for iron (II) complexes

Complex	*M*	*m/z* (*I*, %)	λ_{max}, nm	μ_{eff}, μ_B (μ^2_{eff})
IFe	858.64	–	670, 490	2.09 (4.4)
IIFe	696.72	696 (32.26)	675, 510	1.97 (3.9)
IIIFe	700.76	700 (100)	670, 520	0.22 (0.05)
IVFe	760.82	760 (100)	675, 490	0.45 (0.2)
VFe	768.78	768 (100)	680, 495	1.18 (1.4)

crystalline iron complexes **I**Fe–**V**Fe, which have, according to the analytical data (Table 1), electronic spectra, and mass spectra (Table 2), the composition L_2Fe.

For formazanate **I**Fe, we failed to detect the molecular ion and recorded only weak peaks of fragmentation ions.

In the electronic spectra of the iron-containing complexes, we observed, along with the major absorption bands at 670–680 nm, weak bands at 490–520 nm.

In the IR spectra of the iron formazanates, absorption bands assignable to ν(Fe–N) vibrations [18, 19] appear at about 745 and 500 cm^{-1}. In the IR spectra of the initial ligand, these bands are lacking.

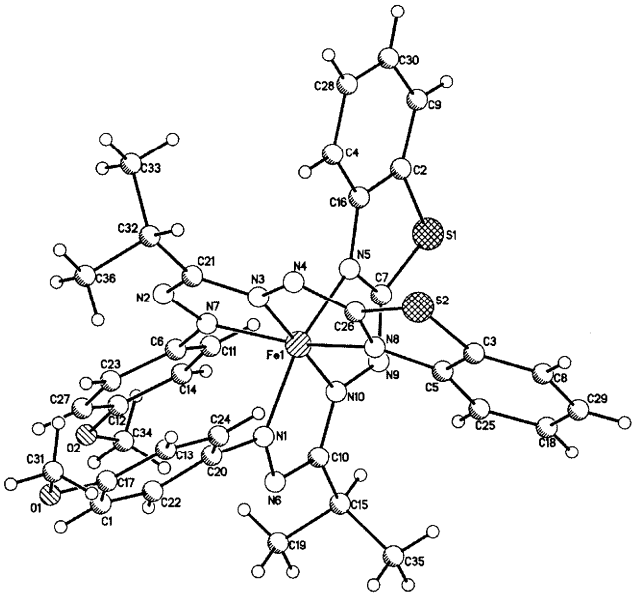


Fig. 2. Structure of iron 1-(4-methoxyphenyl)-3-isopropyl-5-(benzothiazol-2-yl)formazanate **IV**Fe. Selected bond lengths, Å: Fe(1)–N(1) 1.933(4), Fe(1)–N(5) 1.997(4), Fe (1)–N(10) 1.850(4), N(5)–C(7) 1.313(5), N(6)–N(1) 1.321 (4), N(6)–C(10) 1.364(6), N(9)–C(7) 1.346(5), N(10)–N(9) 1.366(5), N(10)–C(10) 1.332(6), N(5)–C(16) 1.373(5), C (7)–S(1) 1.745(5), C(10)–C(15) 1.500(6), N(1)–C(20) 1.411(5). Selected bond angles, deg: N(3)–Fe(1)–N(7) 79.27(18), N(3)–Fe(1)–N(8) 78.48(19), N(10)–Fe(1)–N(1) 78.80(18), N(10)–Fe(1)–N(5) 78.81(19).

The measured effective magnetic moments μ_{eff} of the metal complexes **III**Fe, **IV**Fe, and **V**Fe, containing bulky substituents in the 3-position of the formazan molecule, are as low as 0.22, 0.45, and 1.18 μ_B, respectively, which suggests formation of Fe(II) complex compounds predominantly in the low-spin (LS) state [20, 21].

For the metal complexes **I**Fe and **II**Fe containing alkyl substituents in the 3-position of the formazan molecule, μ_{eff} was 2.09 and 1.97 μ_B, respectively, which, according to [21], can be attributed to the presence of low- and high-spin (HS) iron(II) complexes and an admixture of Fe(III) complexes. Formazans with the alkyl substituent at the C^3 atom are oxidized to the tetrazolium salt somewhat more difficultly. Therefore, the probability of formation of impurity iron(III) complexes is higher.

The structure of the metal chelate core formed in complexation of formazans **I–V** with iron(III) chloride solutions was finally confirmed by single-crystal X-ray diffraction analysis for **IV**Fe as an example.

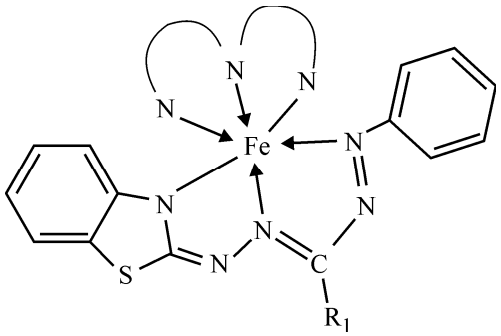
The general view of the molecule of **IV**Fe is shown in Fig. 2. The structure of **IV**Fe is, on the whole, similar to that of 1,3-diphenyl-5-(benzothiazol-2-yl) formazanate **V**Fe prepared previously [16].

The molecule of the iron complex occupies a special position on a twofold axis. Two formazan ligands are coordinated in the tridentate fashion via N^1 and N^4 atoms of the formazan chain and nitrogen atom of the heteroring to form the metal complex L_2Fe with the N_6Fe coordination core. The angle between the planes of the formazan ligands in the complex is 81.93°.

The N(8)FeN(7) (157.77°) and N(5)FeN(1) (157.66°) angles correspond to the meridional (*mer*) isomer; in the facial (*fac*) isomer this angle would be 90°. The iron coordination polyhedron is a distorted octahedron. Despite that all the vertices of the coordination polyhedron are occupied by nitrogen atoms, the Fe–N bonds noticeably differ in the length and can be subdivided into three groups, each with two bonds. The shortest Fe–N bonds, 1.850 and 1.856 Å, are formed by the N(10) and N(3) atoms occupying the vertex positions, i.e., the octahedron is compressed along the N(10)···N(3) axis. The intermediate-length Fe–N bonds, 1.933 and 1.942 Å, are formed with the N(1) and N(7) atoms, and the N(5) and N(8) atoms are the most remote from the Fe atoms: 1.997 and 2.003 Å, respectively.

The hetaryl nitrogen atom involved in the coordination behaves like an additional complexing group. The complexation leads to changes in the electronic structure of the initial ligand, which is in the amino form with the *EEZ* configuration of the formazan ring. The molecular configuration also changes significantly: in the formazanate, the ligand is in the imino form, with the open *EZE* configuration.

The above spectral data suggest that compounds **III**Fe–**V**Fe are metal complexes containing Fe(II) predominantly in the LS state with the coordination configuration similar to that in **IV**Fe:



CONCLUSION

In the course of synthesis of coordination compounds from tridentate benzothiazolylformazans and solutions of iron(III) chloride, formazan is oxidized to tetrazolium salts, iron(III) is reduced, and, as a result, iron(II) formazanates are formed with various spin states of Fe(II).

ACKNOWLEDGMENTS

The study was financially supported by the Russian Foundation for Basic Research (project nos. 06-03-08 040ofi and 07-03-12 050ofi).

REFERENCES

1. Malina, N.K., *Raznitie issledovanii v oblasti sinteza ammiaka* (Progress of Studies in the Field of Ammonia Synthesis), Moscow: Nauka, 1983.
2. Arutyunov, V.S., *Katal. Prom–sti*., 2003, no. 3, pp. 31–38.
3. Borutskii, P.N. and Podkletnova, N.M., *Katal. Prom–sti.,* 2003, no. 2, pp. 57–61.
4. Ulakhovich, N.A., *Soros. Obraz. Zh*., 1997, no. 8, pp. 27–32.
5. Lavernova, L.G., Ikorskii, V.N., Larionov, S.V., et al., *Zh. Neorg. Khim*., 1993, vol. 28, no. 9, pp. 1517–1525.
6. Stassen, A.F., Kooijman, H., Spec, A.L., et al., *Inorg. Chem*., 2002, vol. 41, no. 24, pp. 6468–6471.
7. Shvedenkov, Yu.G., Virovets, A.V., and Lavrenova, L.G., *Izv. Ross. Akad. Nauk, Ser. Khim*., 2003, no. 6, pp. 1281–1288.
8. Buzykin, B.I., Lipunova, G.N., Sysoeva, L.P., and Rusinova, L.I., *Khimiya formazanov* (Chemistry of Formazans), Moscow: Nauka, 1992.
9. Lipunova, G.N., Rusinova, L.I., and Maslakova, T.I., *Ross. Khim. Zh*., 1996, vol. 40, nos. 4–5, pp. 148–154.
10. Bednyagina, N.P. and Lipunova, G.N., *Khim. Geterotsikl. Soedin.*, 1968, no. 5, pp. 902–910.
11. Petrova, G.M., Bednyagina, N.P., Malkina, T.G., and Podchainova, V.N., *Khim. Geterotsikl. Soedin*., 1968, no. 4, pp. 709–715.
12. Lipunova, G.N., Lekomtseva, E.G., Sharova, L.I., et al., *Zh. Obshch. Khim*., 1985, vol. 55, no. 4, pp. 895–899.
13. Validuda, G.I., Lipunova, G.N., Garnovskii, A.D., et al., *Zh. Obshch. Khim*., 1986, vol. 56, no. 4, pp. 827–833.
14. CrysAlis CCD, Oxford Diffraction Ltd., Version 1.171.29.9 (release 23-03-2006 CrysAlis 171. NET).
15. Sheldrick, G.M., SHELX-97: A Software Package for the Solutions and Refinement of X-ray Data, Univ. of Göttingen (Germany), 1997.
16. Brown, D., Bogge, H., Lipunova, G.N., et al., *Inorg. Chem*., 1998, vol. 280, pp. 30–38.
17. Muller, A., Bogge, H., Diemann, E., et al., *Naturwiss.*, 1994, vol. 81, pp. 136–137.
18. Nakanishi, K., *Infrared Absorption Spectroscopy*, San Francisco: Holden-Day, 1962.
19. Nakamoto, K., *Infrared Spectra of Inorganic and Coordination Compounds*, New York: Wiley, 1963.
20. El-Sawaf, A.K., West, D.X., El-Saied, F.A., et al., *Synth. Inorg. Met.-Org. Chem*., 1997, vol. 27, no. 8, pp. 1127–1134.
21. Bushuev, M.B., Lavrenova, L.G., Ikorskii, V.N., et al., *Koord. Khim*., 2004, vol. 30, no. 4, pp. 305–311.

ISSN 1070-4272, Russian Journal of Applied Chemistry, 2008, Vol. 81, No. 12, pp. 2132–2136. © Pleiades Publishing, Ltd., 2008.
Original Russian Text © M.A. Nadzhafova, A.P. Mamedov, Dzh.Dzh. Musaev, 2008, published in Zhurnal Prikladnoi Khimii, 2008, Vol. 81, No. 12, pp. 2021–2025.

ORGANIC SYNTHESIS AND INDUSTRIAL ORGANIC CHEMISTRY

Generation of Resin–Asphaltene Substances in the Luminescent Concentrate under Irradiation

M. A. Nadzhafova, A. P. Mamedov, and Dzh. Dzh. Musaev

Institute of Petrochemical Processes, National Academy of Sciences of Azerbaijan, Baku, Azerbaijan

Received July 2, 2008

Abstract—The effect of photoirradiation on the luminescent concentrate of heavy gas oil produced by catalytic cracking (>400°C) was examined.

DOI: 10.1134/S1070427208120173

Secondary heavy petroleum residue finds limited use today. Recent studies have shown that luminescent concentrates, i.e., petroleum luminophores that are recovered from heavy gas oil produced by catalytic cracking (HGCC), can be used in various branches of science and technology. Petroleum and synthetic luminophores are widely used in luminescence flaw detection, as photosensitizers of decomposition of organic compounds, as dyes for polymeric materials, and as working substances for information recording, storage, and processing [1–3].

These processes involve, to a certain extent, the action of atmospheric oxygen, radiation, illumination, and heating on petroleum products, which leads to their diverse photochemical and thermal oxidative transformations deteriorating their quality.

The available data mainly refer to thermal oxidative transformations [4–7]. Previous studies of photochemical oxidative transformations of petroleum products have not revealed their mechanism, because they did not use appropriate low-temperature techniques allowing the rate of photochemical processes to be considerably reduced and their elementary steps to be revealed. Also, nearly no attention has been given to the problem of the contribution of one- and two-photon photochemical processes to transformations of petroleum products undergoing photochemical (in particular, photooxidative) transformations under illumination in a wide spectral range covering the UV range and a considerable part of the visible solar radiation.

Petroleum fractions thoroughly purified to remove resin–asphaltene substances (RASs) exhibit paramagnetism upon heat treatment [4–7] due to generation of RAS free radicals (FRs). However, until recently, FRs generated by photoirradiation of oils and their processing products have not been detected.

In this study, we examined the results of UV irradiation of the luminescent concentrate (LC) recovered from HGCC (>400°C). The high content of fused polycyclic aromatic hydrocarbons (PACs) efficiently absorbing light allowed preparation from this substance of multicomponent high-performance petroleum luminophores used in nontraditional (for petroleum products) branches of science and technology.

EXPERIMENTAL

The main physical methods we used were ESR, UV, and IR spectroscopy. The procedures for performing experiments and recording ESR spectra have been described previously [8]. As a light source we used a DRSh-500 mercury lamp with UFS-5 and ZhS-10 color filters. The ESR spectra were recorded with an RE-1306 radiospectrometer under the conditions of minimal saturation, using Mn^{2+} ($S = 5/2$) as a reference for the magnetic field. The IR spectra were recorded on a Specord M-80 spectrophotometer, and the UV/visible spectra, on a Specord UV Vis spectrophotometer in the range 200–700 nm at room temperature.

The LC of HGCC (>400°C) is a multicomponent substance composed of naphthene–paraffin (NPH) (57–58 wt %), polycyclic aromatic (40 wt %), and olefin (2–3 wt %) hydrocarbons. Their content was determined by fluorescence–indicator analysis (FIA) [9].

A UV study of the structural-group composition of PAHs revealed the presence of naphthalene (226 nm), anthracene (294 nm), phenanthrene (255 nm), chrysene (270 nm), 1,2-benzanthracene + 3,4-benzofluorene (295 nm), pyrene (340 nm), and perylene (430 nm) hydrocarbons, which are well-known initiators of photochemical processes [10].

Figure 1 shows how the FR concentration (in absolute units) varies with time of RAS irradiation (the ESR spectra of these radicals consist of a single line with ΔH = 0.7–0.8 mT and g-factor of ~2.0023). It can be seen that, for the LC, accumulation of radicals starts from zero. Two steps of FR accumulation are observed in the course of LC photoirradiation: the step of relatively rapid growth (~1 h) followed by the step of slow, nearly linear growth (2.5 h).

As already noted, LC consists of NPHs, PAHs, and olefins. Nevertheless, the pattern of FR generation under photoirradiation of LC is typical of RASs (Fig. 1). Therefore, it seems appropriate to examine the possible role of the initial steps of photochemical processes in RAS generation under photoirradiation for each LC component.

We assumed that PAHs in LC can photosensitize the decomposition of naphthene–paraffin hydrocarbons (NPHs), as it was observed upon addition of small amounts (10^{-7} M) of PAHs to aliphatic alcohols and liquid paraffins [11–13]. In LCs with a relatively high PAH content (~10 wt %), the concentration of RAS FRs generated in NPHs is very low, apparently because PAHs absorb the exciting light in the surface layer. The ESR spectra observed in this case are, on the whole, similar, but a new line appears (ΔH_{tot} = 2.8 mT) with signs of the hyperfine structure characteristic of $PAH^{+\cdot}$ radical cation [14].

To examine the primary and intermediate steps of photosensitized transformations in the LC under consideration, and also the role of molecular oxygen in the RAS FR generation mechanism, we studied the phototransformations of NPHs from HGCC, sensitized by PAHs from LC. As many photochemical processes in LC are extremely fast, which complicates elucidation of the phototransformation mechanism in detail because of the short lifetime of the generated excited molecules and intermediates, the photolysis was performed at –196°C.

Figure 2 shows the ESR spectra of frozen photoirradiated NPH solutions with PAH addition. A detailed analysis of the ESR spectra allowed identification of

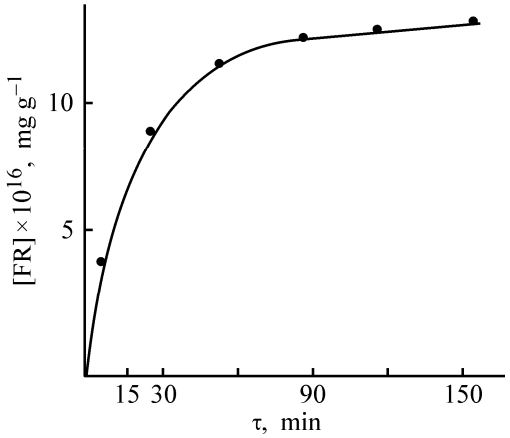


Fig. 1. Kinetic curve of a rise in the absolute concentration of RAS free radicals [FR] in the course of irradiation of LC HGCC (>400°C). (τ) Exposure time.

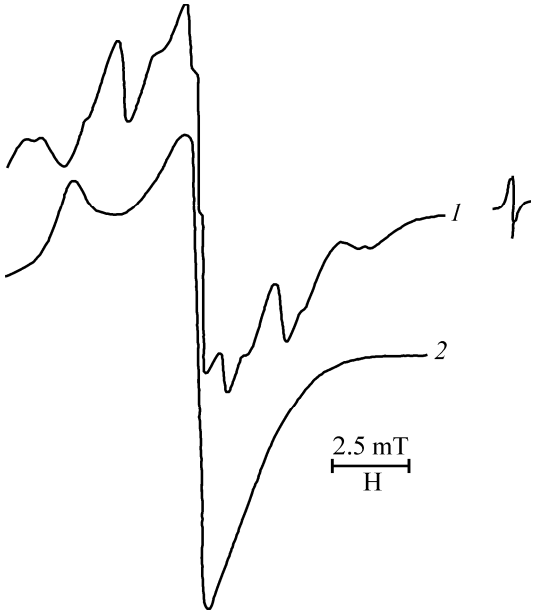


Fig. 2. ESR spectra of photoirradiated frozen (–196°C) naphthene–paraffin hydrocarbon with PAH added (10^{-7} M). Exposure time 2 h. T, °C: (*1*) –196 and (*2*) –108. To the right of curve *1* is one of the components of the ESR spectrum of atomic hydrogen.

most of the generated radicals: $R_1^{\cdot}$(–CH_2–$\dot{C}$H–CH_2–) with ΔH_{tot} = 12.5 mT, g = 2.0020; $R_2^{\cdot}$(CH_3–$\dot{C}$H–CH_2–) with ΔH_{tot} = 11.0 mT, g = 2.0018; and atomic hydrogen with ΔH_{tot} = 50 mT [14]. The other signals were not fully identified. Most likely, these are a narrow $R_3^{\cdot}$ singlet (ΔH_{tot} =1.4 mT) from phenyl-type radicals of an aromatic hydrocarbon and $R_4^{\cdot}$ signal (ΔH_{tot} = 2.8 mT) from an unresolved doublet. Overlapping with the $R_1^{\cdot}$ and $R_2^{\cdot}$ patterns, these signals distort the central components of the observed ESR spectra.

Thermal annealing of the deoxygenated samples results in a decrease in the intensity of the ESR lines, without changes in the spectrum shape. An apparent decrease in the intensity of the $R_3^{\cdot}$ is also observed in the course of solution storage under ambient conditions [11]. When the sample containing dissolved oxygen is warmed, the ESR spectrum considerably changes, starting from –108°C, and shows an asymmetric pattern characteristic of the peroxy radical $ROO^{\cdot}$, which fully decays at 17°C.

The essential role of O_2 in RAS formation has been noted in numerous papers. It was, in particular, shown [4] that the presence of oxygen in oil leads to an increase in concentration and to disproportionation of RAS radicals at a relatively low temperature (40–100°C). In the absence of oxygen, even at high temperatures (450–480°C), the radicals are not formed, which points to the important role of molecular oxygen in the mechanism of RAS generation.

Formation of RASs in LC was also observed upon slight heating (≥30°C) under conditions when the formation of excited molecules and radicals generated by photoirradiation is impossible [7]. It was shown that the necessary condition of RAS formation in the samples was the presence of molecular oxygen and a hydrocarbon.

It should be noted that there are hardly any studies in which the joint action of light and oxygen on petroleum products would be examined using methods of low-temperature photolysis. At the same time, in most cases, such an action is one of major factors affecting the properties of petroleum products, including LC [15].

Upon photoirradiation of LC with monochromatic light in the region of PAH absorption bands, no free radicals are detected. This fact suggests that the generation of radicals in the luminescent concentrate is initiated by two-photon absorption [16] by PAH molecules acting as photosensitizers, with their transition to the highly excited triplet state PAH*(T*). In this case, the energy $h\nu_1$ of the first photon may be insufficient for cleavage of the C–H and C–C[1] bonds in PAH. However, the long lifetime of the triplet excited state of molecules of aromatic compounds, such as naphthalene, phenanthrene, etc., allows absorption of one more photon $h\nu_2$ with transition to the highly excited triplet level. The excitation energy of PAH molecule (~5 eV) is in this case sufficient for cleavage of the C–H bond in an NPH and can be transferred to an NPH molecule, causing its decomposition to free radicals. Thus, simultaneous generation of alkyl radicals and H atoms from NPHs may occur by the two-photon mechanism, as it has been observed in photosensitized decomposition of organic compounds (alcohols and unsaturated paraffins) in luminescent concentrate [11–13]:

$$\begin{aligned} &\mathrm{PAH(S)} \xrightarrow{h\nu_1} \mathrm{PAH^*(S^*)} \longrightarrow \mathrm{PAH^*(T)} \\ &\xrightarrow{h\nu_2} \mathrm{PAH^*(T^*) + RH} \longrightarrow \mathrm{PAH(S) + RH^*} \\ &\longrightarrow \mathrm{PAH(S) + R^{\cdot} + H}, \end{aligned} \qquad (1)$$

where S, S* and T, T* are the ground and excited singlet and triplet states of PAH molecules, respectively.

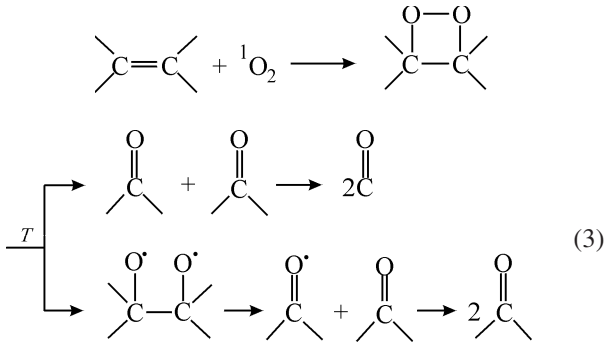
The H atoms react with hydrocarbons RH, $H + RH \rightarrow R^{\cdot} + H_2$, to form a radical $R^{\cdot}$ and a hydrogen molecule. The formation of H_2 as one of major products of chemical cleavage of oils and petroleum residues was noted in [17]. The formation of H_2 in petroleum hydrocarbons upon photolysis and radiolysis has been confirmed by gas-chromatographic analysis [18].

The radicals $R^{\cdot}$ generated in reaction (1) readily react under common conditions with molecular oxygen to form $ROO^{\cdot}$. Then the process can develop by the chain mechanism.

Polycyclic aromatic hydrocarbons initiate photochemical reactions of other LC components, olefins, which do not directly absorb UV light from the source used, but react with singlet oxygen $^1O_2$ generated by excited PAH molecules:

$$\mathrm{PAH^*(T) + {}^3O_2 \rightarrow PAH(S) + {}^1O_2}. \qquad (2)$$

It should be noted that singlet oxygen can arise only in selective excitation of PAH molecules. The same is true for dioxetanes, which are formed by reactions of olefins with $^1O_2$ and subsequently decompose thermally to form ketones or biradicals [15, 19]:



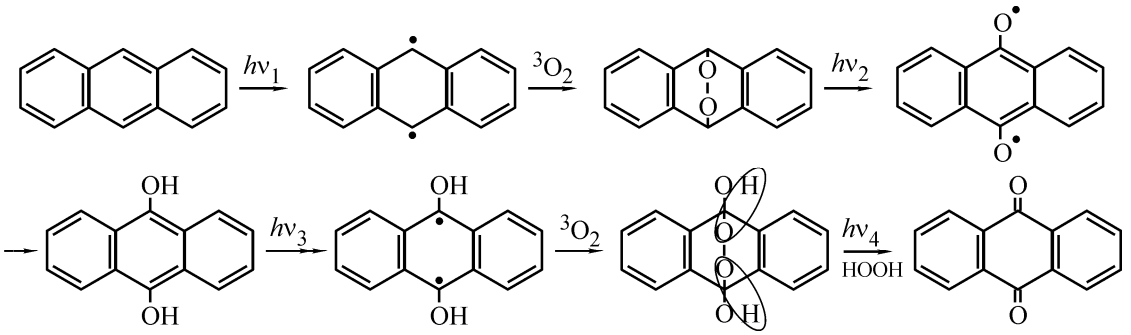
(3)

[1] Although the energy of the C–C bond is lower than that of the C–H bond, in fused aromatic systems C–H bonds are cleaved preferentially, because of the cage effect [16].

In the course of photoirradiation, the most stable LC–PAH components acting as photosensitizers in photochemical reactions also undergo, according to the IR spectra, various transformations with formation of endoperoxides (820–885 cm^{-1}), quinones (1700 cm^{-1}), and phenols (3300–3400 cm^{-1}). The formation of PAH endopexorides is associated with PAH transition from the excited singlet to triplet state:

$$PAH(S) \xrightarrow{h\nu} PAH^*(S^*) \longrightarrow PAH^*(T),$$

The reaction of PAH*(T) with molecular oxygen leads to sensitized formation of $^1O_2$ by reaction (2). The IR spectra show that the above-noted diamagnetic molecules are formed from PAHs under the action of light and molecular oxygen. The scheme of their formation (for anthracene as example) is shown below.



(4)

Anthraquinone formed in reaction (4) (along with other aromatic ketones) is also a photooxidation sensitizer. This is particularly true for LC components containing labile hydrogen (certain isoparaffins, alkylnaphthenes, etc.). In this case, anthraquinone acts as a chemical sensitizer [16].

Thus, PAHs apparently play a major role in photochemical and photooxidation reactions occurring in LC. PAHs are involved in the generation from all major LC components of a series of primary ($R_1^{\cdot}$, $R_2^{\cdot}$, $R_3^{\cdot}$, $R_4^{\cdot}$) and intermediate ($ROO^{\cdot}$) radicals and of other labile products upon irradiation with light in the UV and visible parts of the solar spectrum. These species undergo diverse transformations (oxidation, condensation) to form RASs of complex composition and structure, which have not been reliably identified yet.

Recently, Salmanova is examined [20] the dependence of the optical density of LC with 2 wt % additions of antioxidants (RASs HGCC) on the irradiation time. She showed that the presence of RASs leads to a decrease in the optical density at the carbonyl absorption wavelength (1720 cm^{-1}) throughout the irradiation period. She found that RASs of the cracking origin exerted a more efficient stabilizing effect and that the inhibiting activity of asphaltenes was higher than that of the resin.

Our results are also consistent with the results of an early study [21] which revealed generation of stable free radicals with an ESR spectrum characteristic of RASs in lubricating and motor oils under the conditions of heat treatment and oxidation with atmospheric oxygen. As stated in [21], the presence of FRs makes longer the induction period of motor oil oxidation. The autostabilization of the oil in an engine is attributed to the accumulation of FRs inhibiting the oxidation of hydrocarbons.

Thus, analysis of our and published data shows that one of the major components of heavy petroleum residue (in particular, HGCC), RASs, inhibit photosensitized photooxidative transformations of another major HGCC component, LC.

Reactions (1), (3), and (4) of photosensitized decomposition of organic compounds can find wide use in new technologies for reprocessing of petroleum raw materials into valuable petroleum intermediates for organic synthesis.

CONCLUSIONS

(1) Primary and intermediate radicals and other labile products are generated in all major components of luminescent concentrate with participation of aromatic hydrocarbons under the action of UV and visible light.

(2) Fast complex reactions involving molecular oxygen lead to oxidation and condensation of the luminescent concentrate to give resin–asphaltene substances.

REFERENCES

1. Ryabov, V.D., *Khimya nefti* (Petroleum Chemistry), Moscow: Tekhnika, 2004.
2. Akhmetov, S.A., *Fiziko-khimicheskaya tekhnologiya glubokoi pererabotki nefti* (Physicochemical Technology of Deep Oil Refining), Ufa: UGNTU, 1997.
3. *Problemy pererabotki tyazhelykh neftei* (Problems of Heavy Oil Refining), Alma-Ata: Nauka, 1980.
4. Unger, F.G. and Andreeva, L.N., *Fundamental'nye aspekty khimii nefti* (Basic Aspects of Petroleum Chemistry), Novosibirsk: Nauka, 1995.
5. Kam'yanov, V.F., Aksenov, V.S., and Titov, V.I., *Geteroatomnye komponenty neftei* (Heteroatomic Oil Components, Novosibirsk: Nauka, 1983.
6. Pokonova, Yu.V., *Khimiya vysokomolekulyarnykh soedinenii nefti* (Chemistry of Macromolecular Petroleum Compounds), Leningrad: Leningr. Gos. Univ., 1980.
7. Rustamov, M.I., Mardukhaev, V.R., and Mamedov, A.P., *Neftekhimiya*, 1991, vol. 31, no. 4, pp. 528–531.
8. Nadzhafova, M.A., Sharpatyi, V.A., and Emanuel', N.M., *Dokl. Akad. Nauk SSSR*, 1972, vol. 202, pp. 128–131.
9. Zhorov, Yu.M. and Panchenko, G.N., *Khromatografiya s lyuminestsentnym indikatorom – novyi metod gruppovogo analiza uglevodorodnykh smesei* (Chromatography with Luminescent Indicator: A New Method of Group Analysis of Hydrocarbon Mixtures), Moscow: TsNIITEneftekhim, 1969.
10. *TU* (Technical Specification) *3840294–88, Inst. Neftekhimicheskikh Protsessov Akad. Nauk Azerb. SSR.*
11. Mamedov, A.P., Nadzhafova, M.A., Salmanova, Ch.K., and Suleimanova, M.G., *Neftekhimiya*, 1996, vol. 36, no. 2, pp. 187–191.
12. Nadzhafova, M.A., *Azerb. Neft. Khoz.*, 2007, no. 6, pp. 77–85.
13. Dzhafarova, R.A., Nadzhafova, M.A., Salmanova, Ch.K., and Mamedov, A.P., *Azerb. Neft. Khoz.*, 2008, no. 4, pp. 42–45.
14. Pshezhetskii, S.Ya., Kotov, F.G., Milinchuk, V.K., et al., *EPR svobodnykh radikalov v radiatsionnoi khimii* (ESR of Free Radicals in Radiation Chemistry), Moscow: Khimiya, 1972.
15. Nadzhafova, M.A., Mamedov, A.P., Rustamov, M.I., and Salmanova, Ch.K., *Neftekhimiya*, 2003, vol. 43, no. 4, pp. 280–288.
16. Terenin, A.N., *Fotonika molekul krasitelei* (Photonics of Dye Molecules), Leningrad: Nauka, 1967.
17. Utebaev, U., Kamenskii, A.A., Mashukova, P.A., et al., *Neftepererab. Neftekhim.*, 1990, no. 11, pp. 21–24.
18. Mamedov, A.N., Dzhafarova, R.A., and Mustafaev, I.I., *Khim. Probl.*, 2005, no. 1, pp. 28–32.
19. Mamedov, A.P. and Rustamov, M.I., *Prots. Neftekhim. Neftepererab.*, 2002, vol. 3(10), pp. 47–60.
20. Salmanova, Ch.K., *Prots. Neftekhim. Neftepererab.*, 2007, vol. 5(32), pp. 3–19.
21. Shimonaev, G.S. and Zakharov, G.V., *Neftekhimiya*, 1967, vol. 7, no. 4, pp. 623–626.

ISSN 1070-4272, Russian Journal of Applied Chemistry, 2008, Vol. 81, No. 12, pp. 2137–2140. © Pleiades Publishing, Ltd., 2008.
Original Russian Text © A.V. Golounin, E.N. Marakushina, S.A. Khramenko, 2008, published in Zhurnal Prikladnoi Khimii, 2008, Vol. 81, No. 12, pp. 2026–2029.

ORGANIC SYNTHESIS AND INDUSTRIAL ORGANIC CHEMISTRY

Polycondensation of Naphthalene and Its Alkyl Derivatives

A. V. Golounin, E. N. Marakushina, and S. A. Khramenko

Institute of Chemistry and Chemical Technology, Siberian Branch, Russian Academy of Sciences, Krasnoyarsk, Russia
Krasnoyarsk Branch, Russian Engineering Company, Krasnoyarsk, Russia

Received May 23, 2008

Abstract—Polycondensation of naphthalene and its alkyl derivatives (stripping oil, 2,5-dimethylnaphthalene) in the presence of aluminum halides was performed. Under the action of an ultrasonic field on a benzene solution of naphthalene in the presence of the catalyst, intermolecular condensation and benzene addition are observed.

DOI: 10.1134/S1070427208120185

The formation of tarry by-products from aromatic hydrocarbons at elevated temperatures and in the course of alkylation in the presence of catalysts has been described in the literature [1, 2]. In some cases, tars can act as target products, rather than as contaminating components. In particular, this occurs in preparation of a binder for composite anodes in aluminum production. It seemed appropriate to examine the possibility of transformation of naphthalene and its alkyl derivatives into more complex products under the influence of catalysts and to evaluate the degree of conversion. To accelerate the condensation, we used ultrasonic activation instead of prolonged heating. Aluminum halides were tested as catalysts. It should be noted that the effect of ultrasound on fused aromatic hydrocarbons is poorly understood. It has been reported [3] that, under cavitation treatment, naphthalene undergoes cleavage with the formation of the simplest gaseous compounds.

EXPERIMENTAL

Liquid stripping oil was prepared by distillation of coal tar pitch; its boiling point is about 300°C. An ultrasonic source (UZDN-2T device, nominal power 400 W, generator working frequency 22 kHz) was immersed in a vessel with stripping oil containing 10% $AlBr_3$. In the process, the temperature of the mixture increased to 200°C. After keeping for 30 min and cooling to room temperature, the mixture solidified. To remove aluminum bromide, the mixture was poured over with water and boiled, after which it was extracted with benzene. After removing the solvent, we obtained a viscous tar. The results of its analysis by gas chromatography–mass spectrometry (GC/MS) are listed in Table 1.

We found that heating of naphthalene for 0.5 h at 180°C in the presence of 10% aluminum chloride does

Table 1. Composition of stripping oil before and after ultrasonic treatment in the presence of 10% $AlBr_3$, 0.5 h

Compound	Retention time, min	Content, %	
		before treatment	after treatment
1,2,3,4-Tetrahydro-naphthalene	9.461		5.6
Naphthalene	9.885	18.7	3.6
Isoquinoline	10.757	3.7	
Quinoline	11.149	1.0	
5-Methylquinoline	12.505	1.0	
1-Methylnaphthalene	11.680	16.1	4.2
2-Methylnaphthalene	11.935	7.5	5.2
2-Ethylnaphthalene	12.855	7.1	19.5
1-Ethylnaphthalene	13.040	2.5	
1,5-Dimethylnaphthalene	13.207	3.3	
1,3-Dimethylnaphthalene	13.418	2.7	
2,7-Dimethylnaphthalene	13.452	1.8	
2,3-Dimethylnaphthalene	13.674	1.0	
1,4-Dimethylnaphthalene	13.885	0.5	
1,4,5-Trimethylnaphthalene	14.491	0.2	
2,3,6-Trimethylnaphthalene	14.852	0.2	
1,4,6-Trimethylnaphthalene	15.089	0.1	
Fluorene	15.52	2.0	8.4
3-Ethylbiphenyl	19.51		8.9
Dibenzofuran	14.764	11.5	28.4
Acenaphthylene	13.832	8.5	
Acenaphthene	14.297	7.7	
Benz[*a*]pyrene	26.684		1.6
Perylene	28.353	Σ 97.6	0.1

Table 2. Composition of the reaction mixture obtained after ultrasonic treatment of a benzene solution of naphthalene in the presence of 10% $AlBr_3$ (air flow 200 ml min^{-1}, 60°C, 0.5 h)

Compound	MW	Yield, %
Naphthalene	128	7.7
2-Phenylacetic acid	136	18.7
Hexadecanoic acid	230	0.8
Oleic acid	284	0.7
1,4-Diphenylbutane	210	0.8
1-Phenylnaphthalene	204	4.6
1,2-Dihydro-1-phenylnaphthalene	206	0.7
1,2,3,4-Tetrahydro-1-phenylnaphthalene	208	4.7
2-Phenylnaphthalene	204	8.9
1,7-Diphenylnaphthalene	280	1.0
$1,2^1$ -Binaphthyl	254	1.5
$2,2^1$ -Binaphthyl	254	5.3
Phenanthrene	178	0.4
9,10-Diphenylphenanthrene	312	0.5
Perylene	252	0.2
$1^1,2^1,3^1,4^1$ -Tetrahydro-$1,2^1$-binaphthyl	258	2.1
9,10-Dihydrobenz[1^1, 2^1]-anthracene	278	0.5
Benz[*j*]fluoranthene	252	0.1
Benz[*k*]fluoranthene	252	0.3
Tetrahydro[*k*]fluoranthene	256	0.7
Benz[*e*]pyrene	252	0.1
Benz[*a*]pyrene	252	2.4
Tetrahydrobenz[*a*]pyrene	258	0.1
Octahydrobenz[*a*]pyrene	260	0.3

not chromatographically detectable changes. Therefore, we performed a combined cavitation-catalytic treatment of naphthalene. The procedure was as follows.

A glass beaker was charged with 1 g of naphthalene and 20 ml of benzene, after which 0.1 g of $AlBr_3$ was added. A plate-type emitter was immersed, and the UZDN-2T device was switched on. The temperature increased in the course of the treatment from 20 to 60°C. In the process, the mixture was bubbled with air for 30 min at a rate of 200 ml min^{-1}. After the treatment completion, water was added, the mixture was shaken, the aqueous solution was separated, and the tar precipitated on the beaker walls was washed out with benzene and acetone. The organic solutions were combined, dried over $CaCl_2$, filtered, and vacuum-evaporated. The yield was quantitative. To evaluate the contribution from benzene condensation to the tar formation, we subjected a solution of aluminum bromide in benzene to ultrasonic treatment. No significant amount of tar was formed upon 30-min treatment. The results of GC/MS analysis of the tar are listed in Table 2.

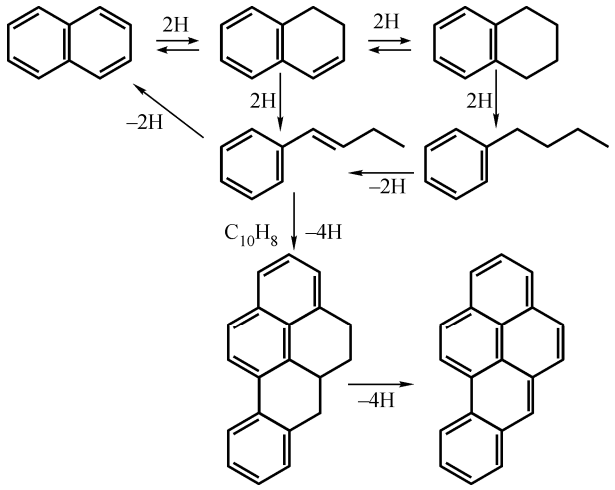
The tar composition was determined on an HP 6890A gas chromatograph equipped with an HP 5972A mass-selective detector, using NIST CSD database (275000 compounds). We used an HP-5MS quartz column, 30 m long, 0.25 mm i.d., coated with a 0.3-μm layer of 5% diphenyl–95% dimethylsiloxane copolymer.

Conditions of GC/MS analysis: initial column temperature 70°C, 4 min; linear heating at a rate of 100 deg min^{-1}; final temperature 300°C, 5 min; vaporizer temperature 280°C; sample volume 1 μl. The mass spectra were recorded with electron impact ionization (70 eV). The scanning rate was 1 scan per second, and the scanning range, 40–600 amu.

The organic compounds were identified by comparison of the experimental mass spectra with those from the NIST CSD database using the ChemStation standard system for GC/MS data processing. Polycyclic aromatic hydrocarbons (PAHs) were analyzed in the mode of selective detection of individual ions, with identification by characteristic ions and retention times, using solutions of reference substances.

According to the chromatogram, the stripping oil contained (%) naphthalene 18.7, alkylated naphthalenes 45, dibenzofuran 11.5, acenaphthene 7.6, and fluorene about 2. High-boiling carcinogenic compounds were absent (Table 1).

After the cavitation treatment, the oil composition changed considerably: The amount of naphthalene and methylnaphthalenes decreased, and di- and trimethylnaphthalenes virtually disappeared. At the same time, the amount of 2-ethylnaphthalene and dibenzofuran increased, which suggests their relative inertness under the experimental conditions. The appearance of benz[*a*]pyrene in the reaction mixture points to the occurrence of polycondensation. Apparently, benz[*a*]pyrene is



Scheme 1.

formed by a sequence of reactions involving naphthalene (Scheme 1).

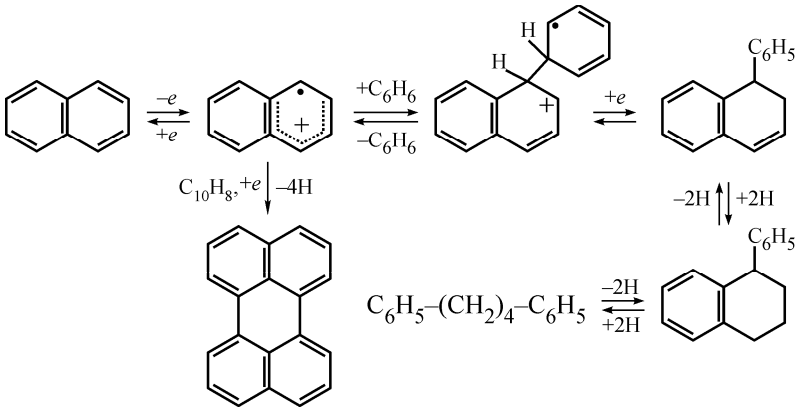
According to Scheme 1, for the formation of benz[*a*]pyrene to be formed, naphthalene should add a fragment consisting of phenyl residue and a radical with four carbon atoms. Such a fragment can be formed after hydrogenation of naphthalene to dihydronaphthalene or tetralin. The ring opening in these compounds will lead to formation of fragments required for "assembling" benz[*a*]pyrene.

If the naphthalene transformation follows this pattern, its polycondensation should lead to formation of tetrahydrobenz[*a*]pyrene and benz[*a*]pyrene. According to the chromatogram, the naphthalene tar contains more than 50 substances. The major components identified using the database on polycyclic compounds are listed in Table 2.

Indeed, heating of a benzene solution of naphthalene in the presence of $AlBr_3$ at 60°C for 0.5 h under the action of cavitation leads to formation, along with other substances, of benz[*a*]pyrene and its hydrogenated analogs: tetrahydro- and octahydrobenz[*a*]pyrenes. The occurrence of this reaction pathway is also confirmed by the detection of 1,4-diphenylbutane among reaction products.

At the same time, it should be noted that methylated naphthalenes losing methyl substituents under the conditions of acid catalysis can also be precursors of benz[*a*]pyrene. To evaluate the possibility of this route, we heated 2,5-dimethylnaphthalene with 10% aluminum chloride at 180°C for 0.5 h. By liquid chromatography, we detected among reaction products acenaphthene, 2-methylnaphthalene, benz[a]pyrene, and dibenz[*a*,*h*]anthracene (40.5, 28.1, 5.8, and 1.8%, respectively).

Along with undergoing disproportionation and condensation, naphthalene also reacts with benzene to form 1- and 2-phenylnaphthalenes, 1,2- and 1,7-diphenylnaphthalenes, and their hydrogenation products. Also, naphthalene undergoes self-condensation to form dinaphthyl and perylene. The formation of the above products can be described by Scheme 2 involving radical cations. According to Scheme 2, the reaction mixture should also contain dihydro- and tetrahydro-1-phenylnaphthalenes, which were, indeed, detected (Table 2). The formation of carboxylic acids (2-phenylacetic, hexadecanoic, oleic) is attributable to the presence of air in the reaction medium.



Scheme 2.

CONCLUSIONS

(1) Naphthalene and its methyl derivatives transform in the course of acid catalysis of the polycondensation into a complex mixture of products, some of which are carcinogenic (e.g., benz[*a*]pyrene).

(2) Ultrasonic treatment of a solution of naphthalene in benzene in the presence of aluminum halides leads to considerable tarring and formation of numerous high-molecular-weight polyaromatic derivatives.

REFERENCES

1. Thomas, Ch.A., *Anhydrous Aluminum Chloride in Organic Chemistry*, New York: Reinhold, 1941. Translated under the title *Bezvodnyi khloristyi alyuminii v organicheskoi khimii*, Moscow: Inostrannaya Literatura, 1949.
2. Olah, G.A., *Friedel–Crafts and Related Reactions*, 1963, vol. 1.
3. Morgulis, M.A., *Osnovy zvukokhimii: Khimicheskie reaktsii v akusticheskikh polyakh* (Principles of Sonochemistry: Chemical Reactions in Acoustic Fields), Moscow: Vysshaya Shkola, 1984.

ISSN 1070-4272, Russian Journal of Applied Chemistry, 2008, Vol. 81, No. 12, pp. 2141–2144. © Pleiades Publishing, Ltd., 2008.
Original Russian Text © Sh.B. Kasenova, Zh.K. Tukhmetova, A.Zh. Abil'daeva, I.M. Oskembekov, B.K. Kasenov, S.M. Adekenov, S.D. Fazylov, 2008, published in Zhurnal Prikladnoi Khimii, 2008, Vol. 81, No. 12, pp. 2030–2033.

ORGANIC SYNTHESIS AND INDUSTRIAL ORGANIC CHEMISTRY

Thermochemistry of Some Cytisine Derivatives

Sh. B. Kasenova, Zh. K. Tukhmetova, A. Zh. Abil'daeva, I. M. Oskembekov, B. K. Kasenov, S. M. Adekenov, and S. D. Fazylov

Fitokhimiya Research and Production Center, Joint-Stock Company, Ministry of Education and Science of the Republic of Kazakhstan, Karaganda, Kazakhstan

Institute of Organic Synthesis and Coal Fuel Chemistry, Limited Liability Company, Karaganda, Kazakhstan

Received June 9, 2008

Abstract—The enthalpies of solution of cytisine derivatives (phosphoric acid cytiside dimethyl ester, cytisinovinyloxyethylaminothiourea) in 96% ethanol at various dilutions were determined by isothermal calorimetry. Equations describing the dependences $\Delta H_s^0 = f(m^{1/2})$ (m is the molal concentration) were obtained. The standard enthalpies of solution, combustion, melting, and formation (at 298.15 K) of the compounds were calculated.

DOI: 10.1134/S1070427208120197

Biologically active substances (BASs) isolated from vegetable raw materials are active agents of drugs and are of particular importance for human vital functions. Revealing a correlation between the structure and physicochemical properties of BASs is of both theoretical and applied importance [1].

Calorimetry is widely used for studying the thermodynamics of biochemical processes. Particular attention is given to studies of solute–solvent interactions and elucidation of the role of hydration and solvation in biological functions of molecules [2].

Alkaloids are natural biologically active substances with base properties, which mostly occur in plants and are considerably more seldom in animal bodies. The majority of alkaloids exhibit pronounced antiarhythmic, arythmogenic, local anesthetic, spasmolytic, antiphlogistic, muscle relaxant, psychotropic, and antitoxic action [3].

Cytisine occupies a particular place among alkaloids. It was first isolated from *Cytisis laburnum* and *Thermopsis lanceolata* seeds. Today it is widely used in medicine as 0.15% aqueous solution under the name of *Cytitonium* [3–7].

Studies of thermochemical and thermodynamic properties of alkaloids as an extremely important class of biologically active substances are of theoretical and applied interest for purposeful synthesis of their derivatives and for standardization and certification of drugs based on them. For this purpose, we have previously studied the thermochemical properties of cytisine [8]. As a continuation of these studies, we calorimetrically measured the enthalpies of solution of new cytisine derivatives, phosphoric acid cytiside dimethyl ester $C_{13}H_{19}N_2O_4P$ and cytisinovinyloxyethylaminothiourea $C_{16}H_{21}N_3O_2S$, in 96% ethanol and estimated the standard heats of their formation, combustion, and melting.

The enthalpies of solution of the compounds were measured on a DAK-I-IA isothermal calorimeter (T = 25°C) at three dilutions [1 : 9000, 1 : 18 000, 1 : 36 000 (mole compound : mole solvent)]. The device characteristics are as follows: working temperature range 25–200°C, error of measuring the heat release energy within 20 μV. The calorimeter operation is based on measuring the integral thermal flux going from an ampule with substances through differentially arranged thermoelectric batteries and a massive central block of the microcalorimeter. The heat is released or absorbed in the working cell. Inside the cylindrical passive thermostat, there is a massive calorimetric unit with two calorimetric cells. The calorimetric cell consists of a sleeve and a thermostat block with vertical grooves and thermopiles arranged between them. The thermo-

Table 1. Experimental enthalpies of solution of phosphoric acid cytiside dimethyl ester in 96% ethanol at various dilutions

Dilution	$C_{13}H_{19}N_2O_4P$ sample, g	ΔH_s, J	ΔH_s^0, kJ mol^{-1}
1 : 9000	0.0028	0.2278	24.25
	0.0028	0.2250	23.95
	0.0028	0.2240	23.85
	0.0028	0.2201	23.43
	0.0028	0.2207	23.50
			$\Delta H_1^0 = 23.80 + 0.42$
1 : 18 000	0.0014	0.0781	16.63
	0.0014	0.0787	16.76
	0.0014	0.0774	16.48
	0.0014	0.0803	17.10
	0.0014	0.0785	16.71
			$\Delta H_2^0 = 16.74 + 0.28$
1 : 36 000	0.0007	0.0159	6.77
	0.0007	0.0162	6.90
	0.0007	0.0163	6.94
	0.0007	0.0164	6.98
	0.0007	0.0161	6.86
			$\Delta H_3^0 = 6.89 + 0.10$

Table 2. . Experimental enthalpies of solution of cytisinovinyloxyethylaminothiourea in 96% ethanol at various dilutions

Dilution	$C_{16}H_{21}N_3O_2S$ sample, g	ΔH_s, J	ΔH_s^0, kJ mol^{-1}
1 : 9000	0.0030	0.3218	34.24
	0.0030	0.3284	34.41
	0.0030	0.3210	34.16
	0.0030	0.3264	34.73
	0.0030	0.3208	34.14
			$\Delta H_1^0 = 34.34 + 0.30$
1 : 18 000	0.0015	0.1264	26.90
	0.0015	0.1268	26.99
	0.0015	0.1236	26.31
	0.0015	0.1288	27.41
	0.0015	0.1279	27.22
			$\Delta H_2^0 = 26.98 + 0.51$
1 : 36 000	0.0007	0.0495	22.57
	0.0007	0.0502	22.89
	0.0007	0.0507	23.12
	0.0007	0.0488	22.26
	0.0007	0.0499	22.76
			$\Delta H_3^0 = 22.72 + 0.40$

piles are welded into two differentially arranged thermoelectric batteries: measuring and compensating.

The metallic ampule with a sample was placed in the internal sleeve with a calibration heater. The sample (weighed on an analytical balance with an accuracy of 0.1 mg) was placed in a screen cup of the stopper which was then inserted into the sleeve. The sleeve with the metallic ampule and a bar was assembled. The ampule volume was 8 cm^3, and the solvent amount, 5 ml. The ampule was warmed to the experimental temperature (25°C) and introduced into the calorimetric cell. The preliminary thermostating was performed for 2 h. After the attainment of a thermal equilibrium between the calorimetric cells, monitored with a KSP-4 recorder, the "experimental zero" was set. By pressing the bar button, the stopper was ejected and the heat release energy was recorded with an IP-4 precision integrator in the automatic heat–compensation mode. The reaction course was monitored with a KSP-4 recorder.

At each dilution, we performed five replicate measurements. Their results were averaged and statistically processed. For each averaged value of ΔH_s^0, we calculated the random error using Student's test. The homogeneity of variance was checked using Cochran's test [9]. The hypothesis of the homogeneity of variance was accepted with a 5% significance level.

The device operation was checked by measuring the heat of solution of triply recrystallized KCl at 1 : 1600, 1 : 2400, and 1 : 3200 dilutions (mole salt : mole water). Our value of the mean heat of solution of KCl in water, 17640 ± 320 J mol^{-1}, is well consistent with the recommended and reference data: 17577 ± 34 [10] and 17489 ± 371 J mol^{-1} [11].

The enthalpies of solution of the cytisine derivatives in 96% ethanol at three dilutions are listed in Tables 1 and 2.

It can be seen that phosphoric acid cytiside dimethyl ester and cytisinovinyloxyethylaminothiourea dissolve in 96% ethanol with the energy absorption. The experimental values of ΔH_s^0 were extrapolated to infinite dilution using the dependence $\Delta H_s^0 \sim f(m^{1/2})$ (where m is the molal concentration) [12]. The following equations were obtained (with ΔH_s^0 in kJ mol^{-1}):

$$\Delta H_s^0 (C_{13}H_{19}N_2O_4P) = -8.58 + 677.89(m^{1/2}), \quad (1)$$

$$\Delta H_s^0 (C_{16}H_{21}N_3O_2S) = 11.51 + 461.88(m^{1/2}). \quad (2)$$

Table 3. Calculated thermodynamic characteristics of cytisine derivatives

Compound	ΔH^0_{comb}, kJ mol^{-1}			ΔH^0_m, kJ mol^{-1}	$-\Delta_f \Delta H^0_{298.15}$, kJ mol^{-1}	
	after Karash	after Frost	average		liquid	solid
$C_{13}H_{19}N_2O_4P$	7329	7793	7561	82.0	1021.6	1103.6
$C_{16}H_{21}N_3O_2S$	8637	9373	9005	97.4	593.1	690.5

From Eqs. (1) and (2), we calculated the basic thermochemical quantities, standard enthalpies of solution of $C_{13}H_{19}N_2O_4P$ and $C_{16}H_{21}N_3O_2S$ in 96% ethanol at infinite dilution. We obtained the values of –8.58 ± 0.14 and 11.51 ± 0.18 kJ mol^{-1}, respectively.

Then we estimated the standard enthalpies of combustion, melting, and formation of the compounds. It should be noted that, as the experimental data on these thermochemical characteristics of complex biologically active substances, such as cytisine derivatives, are lacking, even their estimated or calculated values are of certain theoretical and practical interest for purposefully performing chemical transformations of these compounds. Therefore, the calculations were performed by different methods, namely, by Karash's and Frost's methods which supplement each other (if contributions of certain functional groups to the heat of combustion disregarded by one method, they are taken into account by the other) [13].

The heats of combustion calculated by these two methods and their averaged values are listed in Table 3.

From the calculated heats of combustion, we calculated using the Hess law and considering the reactions

$$4C_{13}H_{19}N_2O_4P_{(l)} + 72O_{2(g)} = 52CO_{2(g)} + 38H_2O_{(l)} + 4N_{2(g)} + P_4O_{10(s)} - \Delta H^0_{comb}, \quad (3)$$

$$2C_{16}H_{21}N_3O_2S_{(l)} + 42.5O_{2(g)} = 32CO_{2(g)} + 21H_2O_{(l)} + 3N_{2(g)} + 2SO_{2(g)} - \Delta H^0_{comb}, \quad (4)$$

the standard enthalpies of formation of $C_{13}H_{19}N_2O_4P$ and $C_{16}H_{21}N_3O_2S$ in the liquid (molten) state (Table 3). It should be noted that Karash's and Frost's methods are applicable to liquid compounds only. The required data for calculating $\Delta_f H^0_{298.15}$ of $C_{13}H_{19}N_2O_4P_{(l)}$ and $C_{16}H_{21}N_3O_2S_{(l)}$ by schemes (3) and (4), except ΔH^0_{comb}, were taken from [14–17]. As both compounds are crystalline at 298.15 K, it was necessary to calculate their ΔH^0_{comb} for the solid state. For this purpose, we calculated ΔH^0_m by the Gambill equation [18]

$$\Delta H^0_m / T_m = 20.72 \times 10^{0.00324M}. \quad (5)$$

The values of ΔH^0_m of $C_{13}H_{19}N_2O_4P$ and $C_{16}H_{21}N_3O_2S$, found by Eq. (5), are listed in Table 3.

From the equations

$$\Delta_f \Delta H^0_{298.15}(C_{13}H_{19}N_2O_4P_s) = \Delta_f \Delta H^0_{298.15}(C_{13}H_{19}N_2O_4P_l) - \Delta H^0_m, \quad (6)$$

$$\Delta_f \Delta H^0_{298.15}(C_{16}H_{21}N_3O_2S_s) = \Delta_f \Delta H^0_{298.15}(C_{16}H_{21}N_3O_2S_l) - \Delta H^0_m \quad (7)$$

we calculated the standard enthalpies of formation of $C_{13}H_{19}N_2O_4P$ and $C_{16}H_{21}N_3O_2S$ in the crystalline state (Table 3).

The results obtained in this study are important for estimating the probability and direction of reactions involving related natural biologically active substances. These are primary data for inclusion into databases and reference books on thermodynamic constants of natural substances and their derivatives.

REFERENCES

1. Ur'yash, V.F., Abstracts of Papers, *Vserossiiskii nauchnyi simpozium po termokhimii i kalorimetrii* (All-Russian Scientific Symp. on Thermochemistry and Calorimetry), Nizhni Novgorod, June 1–3, 2004, pp. 32–34.
2. Abrosimov, V.K., Agafonov, A.V., Ivanov, E.V., et al., *Biologicheski aktivnye veshchestva v rastvorakh: Struktura, termodinamika, reaktsionnaya sposonost'* (Biologically Active Substances in Solutions: Structure, Thermodynamics, Reactivity), Moscow: Nauka, 2001.
3. Dzhakhangirov, F.N., Salimov B.T., Bessonova I.A., and Sultankhodzhaev, M.N., *Khim. Prirodn. Soedin.*, 1995, no. 4, p. 841.
4. Mashkovskii, M.D., *Lekarstvennye sredstva* (Drugs), Moscow: Meditsina, 1977, part 1.
5. *Gosudarstvennaya farmokopeya SSSR* (USSR State Pharmacopoeia), Moscow: Meditsina, 1968.
6. Melent'eva, G.A., *Farmatsevticheskaya khimiya* (Pharmaceutical Chemistry), Moscow: Meditsina, 1976, vol. 2.

7. Senov, P.L., *Kurs farmatsevticheskoi khimii* (Course of Pharmaceutical Chemistry), Moscow: Meditsina, 1952.
8. Kasenov, B.K., Abil'daeva, A.Zh., Kasenova, Sh.B., et al., *Zh. Prikl. Khim.*, 2004, vol. 77, no. 12, pp. 1942–1944.
9. Spiridonov, V.P. and Lopatkin, A.A., *Matematicheskaya obrabotka eksperimental'nykh dannykh* (Mathematical Processing of Experimental Data), Moscow: Mosk. Gos. Univ., 1970.
10. Mishchenko, K.P. and Poltoratskii, G.M., *Termodinamika i stroenie vodnykh i nevodnykh rastvorov elektrolitov* (Thermodynamics and Structure of Aqueous and Nonaqueous Electrolyte Solutions), Leningrad: Khimiya, 1977.
11. *Termicheskie konstanty veshchestv: Spravochink* (Thermal Constants of Substances: Handbook), Glushko, V.P., Ed., Moscow: Nauka, 1982, issue 10, part. 2.
12. Krestov, G.A., *Termodinamika ionnykh protsessov v rastvorakh* (Thermodynamics of Ionic Processes in Solutions), Leningrad: Khimiya, 1984.
13. Kazanskaya, A.S. and Skoblo, V.A., *Raschety khimicheskikh ravnovesii* (Calculations of Chemical Equilibria), Moscow: Vysshaya Shkola, 1974.
14. *Termicheskie konstanty veshchestv: Spravochink* (Thermal Constants of Substances: Handbook), Glushko, V.P., Ed., Moscow: VINITI, 1970, issue 4, part 1.
15. *Termicheskie konstanty veshchestv: Spravochink* (Thermal Constants of Substances: Handbook), Glushko, V.P., Ed., Moscow: VINITI, 1965, issue 1.
16. *Termicheskie konstanty veshchestv: Spravochink* (Thermal Constants of Substances: Handbook), Glushko, V.P., Ed., Moscow: VINITI, 1966, issue 2.
17. *Termicheskie konstanty veshchestv: Spravochink* (Thermal Constants of Substances: Handbook), Glushko, V.P., Ed., Moscow: VINITI, 1968, issue 3.
18. Viktorov, V.V., *Metody vychisleniya fiziko-khimicheskikh velichin i prikladnye raschety* (Methods for Calculating Physicochemical Quantities and Applied Calculations), Moscow: Khimiya, 1977.

ISSN 1070-4272, Russian Journal of Applied Chemistry, 2008, Vol. 81, No. 12, pp. 2145–2150. © Pleiades Publishing, Ltd., 2008.
Original Russian Text © T.E. Sukhanova, M.P. Perminova, S.V. Bronnikov, A.I. Grigor'ev, A.Ya. Volkov, G.N. Gubanova, A.A. Kutin, N. Marangoci, M. Pinteala, V. Harabagiu, B. Simionescu, 2008, published in Zhurnal Prikladnoi Khimii, 2008, Vol. 81, No. 12, pp. 2034–2039.

MACROMOLECULAR CHEMISTRY AND POLYMERIC MATERIALS

Structure and Thermal Properties of Polyrotaxanes Derived from γ-Cyclodextrin and Modified Polydimethylsiloxane

T. E. Sukhanova, M. P. Perminova, S. V. Bronnikov, A. I. Grigor'ev, A. Ya. Volkov, G. N. Gubanova, A. A. Kutin, N. Marangoci, M. Pinteala, V. Harabagiu, and B. Simionescu

Institute of Macromolecular Compounds, Russian Academy of Sciences, St. Petersburg, Russia

Petru Poni Institute of Macromolecular Chemistry, Romanian Academy, Iaşi, Romania

Received May 15, 2008

Abstract—Supramolecular inclusion complexes, polyrotaxanes, derived from γ-cyclodextrin and polydimethylsiloxane modified with terminal epoxy groups were studied. The dependence of the structure, morphology, and thermal properties of polyrotaxanes on the molecular weight of the linear polymer, molar ratio of γ-cyclodextrin and polymer, and presence of free γ-cyclodextrin in the complexes was examined.

DOI: 10.1134/S1070427208120203

Polyrotaxanes (PRots) are supramolecular inclusion complexes (SMICs) formed by macrocycles (host) strung on linear macromolecules (guest) [1–3]. Cyclodextrins (CDs), cyclic oligosaccharides consisting of *D*-glucopyranose units linked with α-1,4-glucoside bond [4], are frequently used as macrocyclic components in PRot preparation. The CD molecules have the shape of a truncated cone with a length of about 7.9 Å and inner diameter from 4.5 to 9.5 Å, depending on the number of structural units in the macroring (six, seven, or eight glucose residues in the ring; α-, β-, and γ-CD, respectively) [4, 5]. The internal hydrophobic surface of the cavity of the CD molecule can include molecules of appropriate size and functionality, whereas the external hydrophilic surface makes the resulting inclusion complex soluble in water.

PRots are usually prepared from linear components that have two hydrophilic terminal groups and a hydrophobic central part. When both components are dissolved in a polar solvent (e.g., water), the hydrophobic moiety of a linear macromolecule gets inside the CD cavity, whereas the hydrophilic moieties remain outside the cyclic components. Thus, the driving force of the complexation in this case is the hydrophobic interaction of polymer chain components with internal fragments of the macroring [2–4].

Polyrotaxanes are promising materials for various branches of technology as controllable molecular switches [2, 6, 7] and as supports for silicate materials with pH-dependent pore size [8], and also for targeted transport of medical preparations [9]. Polyrotaxanes of more complex architecture can be used for development of nanoscopic analogs of bearings, units, motors, rotors, pistons, and macroscopic ensembles consisting of centralized mechanical parts [10]. Owing to their unique properties, PRots have also been suggested as smart materials for production of sensors [11] and devices for information accumulation and storage [10, 12].

Polyrotaxanes based on γ-CD and polydimethylsiloxane (PDMS) were prepared for the first time by Harada et al. [13–15]. It was shown that, owing to the small inner diameter of its molecules (4.5 Å), α-CD cannot form inclusion complexes with PDMS macromolecules having a large cross section. At the same time, β-CD can form PRots with PDMS of low molecular weight (M_n < 700), and γ-CD can be strung on PDMS macromolecules of higher MW (up to M_n = 3300). The resulting complexes have been examined by ^{1}H and ^{13}C NMR spectroscopy, gel permeation chromatography, and IR Fourier spectroscopy [13, 15], but have not been subjected to a comprehensive structural and physicochemical study.

In this study we examined the structure, morphology, and thermal properties of PRots based on γ-CD and PDMS modified with functional epoxy groups (PDMSE) in relation to the PDMSE molecular weight, γ-CD/PDMSE molar ratio, and presence of γ-CD unbound with PDMSE.

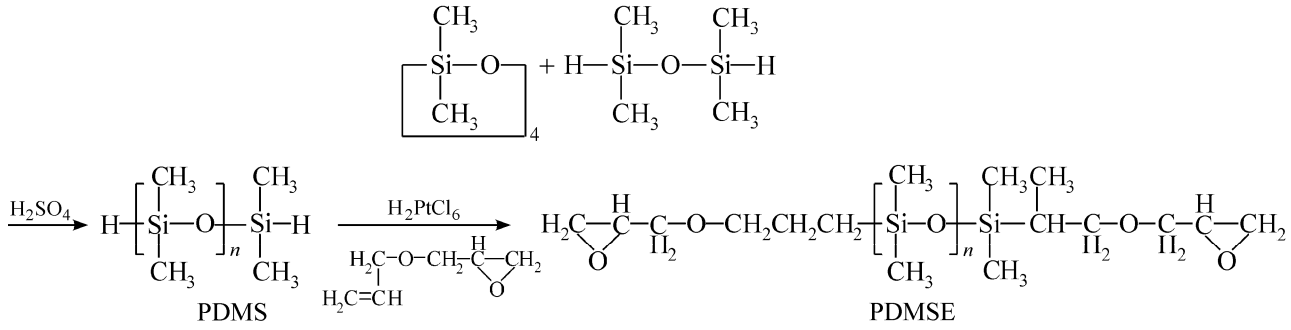
EXPERIMENTAL

The major component of the inclusion complex, linear polymer PDMSE, was prepared by two-step synthesis (Scheme 1).

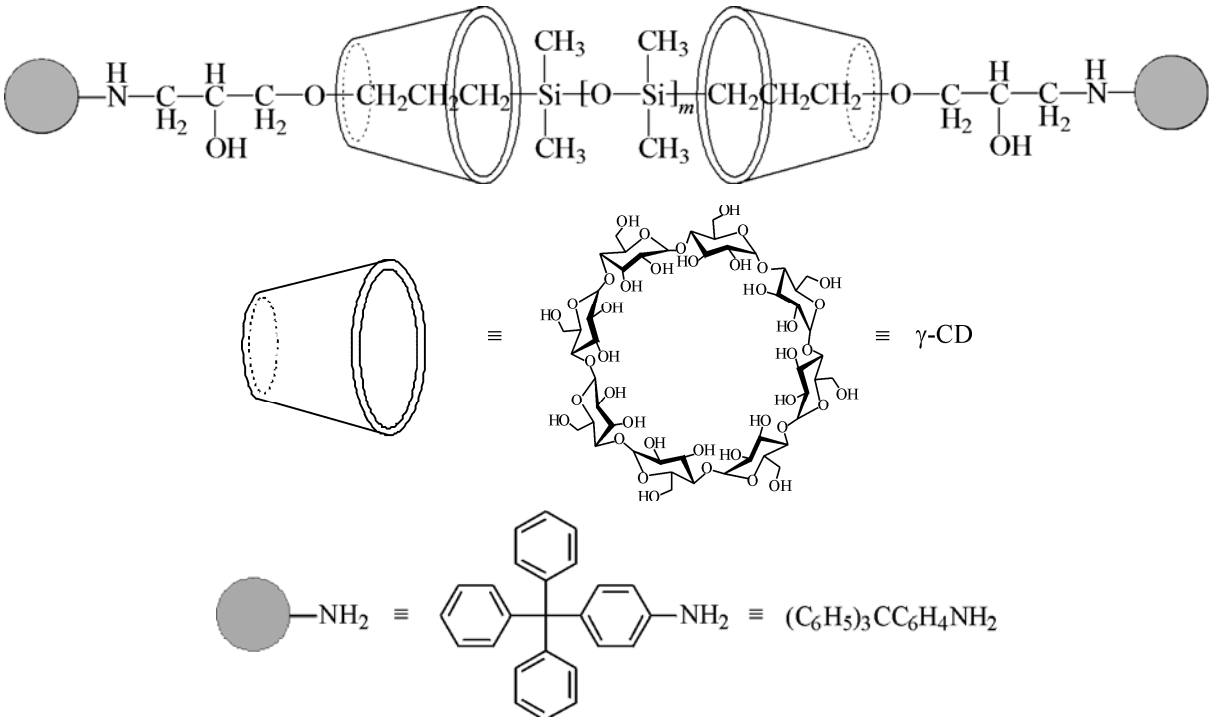
In the first step, we prepared PDMS samples of various molecular weights with the active terminal Si–H groups by the reaction of octamethylcyclotetrasiloxane with 1,1,3,3-tetramethyldisiloxane. PDMS was synthesized at room temperature within 4 h at an H_2SO_4 concentration of 2 vol %.

In the second step, PDMS dissolved in toluene (50 wt %) was brought into the hydrosilylation reaction with allyl glycidyl ether in the presence of Speier's catalyst (2% H_2PtCl_6 in isopropanol). The reaction was performed at 100–110°C for 6 h and yielded PDMSE. The precipitated polymer was purified to remove impurities and the unchanged components by heating to 150°C at 0.1 mm Hg. PDMSE samples differing in molecular weight were prepared (M_n = 1250 and 2100, according to exclusion chromatographic data).

The PRot was prepared (Scheme 2) in accordance with the data of [16, 17].



Scheme 1. PDMSE preparation.



Scheme 2. Structure of PRot derived from γ-CD and PDMSE.

Saturated solutions of γ-CD in DMF with PDMSE were stirred for 72 h at 65°C. The crude compounds PRot-1250c and PRot-2100c were prepared by reactions of the terminal epoxy groups with 4-aminophenyltriphenylmethane (8 h). The resulting suspension was poured into water, and the precipitate was filtered off, washed with ethanol, and dried for 8 h at 40°C to constant weight. To remove unchanged PDMSE, the precipitate was stirred overnight as a suspension in diethyl ether, after which it was filtered off and dried for 8 h at 40°C. Free γ-CD was removed by additional precipitation of the samples from a 50% aqueous DMF into water (samples PRot-1250p and PRot-2100p).

To study the effect of the PRot component ratio on their structure and physical properties, we examined samples with γ-CD/SiO molar ratios of 1/1.57 (PRot-1250c), 1/4.8 (PRot-1250p), 1/1.55 (PRot-2100c), and 1/4.6 (PRot-2100p). The above ratios were calculated from the ^{1}H NMR spectra per Si–O bond. It is noteworthy that, according to [13–15], the maximal γ-CD/SiO ratio for PRot derived from γ-CD and PDMS is 1.5. The characteristics of PDMSE and PRot are listed in Table 1.

X-ray diffraction studies of γ-CD and PRot were performed on a DRON-3 installation (Burevestnik Research and Production Association, Russia) in the scattering angle range 2θ = 3°–37° with Ni-filtered CuK_α radiation (λ = 1.54 Å). Thermal properties of the samples were studied with a DSM-2M differential scanning calorimeter (Special Designing Office of Instrument Making, Pushchino, Moscow oblast, Russia) at a scanning rate of 16 deg min^{-1}. Morphological studies were performed with a Tesla BS-300 scanning electron microscope (Czechia).

Figure 1 shows the X-ray diffraction patterns of hydrated samples of γ-CD, PRot-1250c, PRot-1250p, PRot-2100c, and PRot-2100p. The experimental interplanar spacings d (Å) are listed in Table 2. All the PRots examined are crystalline substances with a structure differing from that of the initial γ-CD.

Comparison of d values for the initial γ-CD used for PRot synthesis with published data shows that γ-CD has a cage-type packing arrangement [18, 19]. The crystal structures have been studied previously for inclusion complexes of γ-CD with aromatic linear polymers [19] and polyethylene oxide (PEO) [20]. It was shown that the initial hydrated inclusion complexes have a columnar-type crystal structure of molecular "necklaces" with a characteristic peak at 2θ ≈ 7.5 Å (d ≈ 12 Å) in the diffraction patterns. The crystals of the complexes have a shape of rectangular parallelepipeds and a tetragonal unit cell with the parameters $a = b = 23.75$, $c = 22.92$ Å [19] or $a = b = 16.88$, $c = 23.13$ Å [20].

Table 1. Synthesis conditions and characteristics of PDMSE and PRot samples

M_n of PDMSE	Polyrotaxane	γ-CD/SiO molar ratio	Free γ-CD, %	Yield, %
1250	PRot-1250c	1/1.6	57	–
1250	PRot-1250p	1/2.8	0	81
2100	PRot-2100c	1/1.6	58	–
2100	PRot-2100p	1/3.3	0	75

Table 2. Interplanar spacings in γ-CD and PRot samples

Sample	d, Å
γ-CD*	17.1, 14.4, 11.6, 9.40, 8.66, 7.75, 7.14, 6.31, 5.73, 5.46, 4.97, 4.73, 4.27, 4.10, 3.87, 3.59
PRot-1250c*	11.8, 7.46, 5.97, 5.62, 5.34, 4.64, 4.36, 4.09, 3.77, 3.36
PRot-1250p*	15.3, 12.0, 7.66, 6.13, 5.79, 5.48, 4.54, 4.18, 3.84, 3.42, 3.22
PRot-2100c*	15.0, 11.6, 7.59, 6.02, 5.58, 5.29, 4.59, 4.36, 4.13, 3.78, 3.38
PRot-2100p*	14.8, 10.6, 7.18, 5.98, 5.28, 4.02
PRot-2100p**	14.8, 10.5, 7.40, 6.04, 5.23, 4.10

* Experimental data. ** Calculated data.

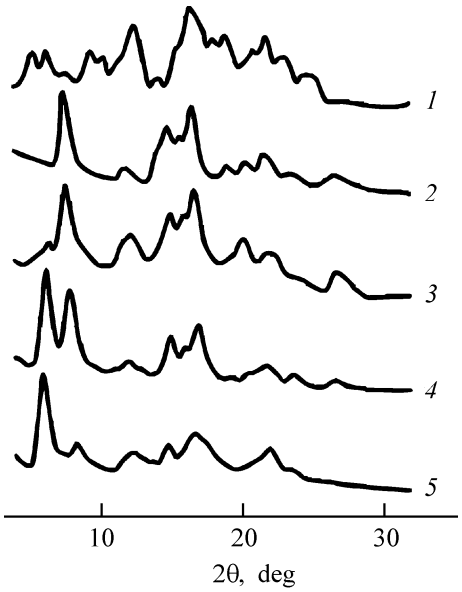


Fig. 1. X-ray diffraction patterns of (*1*) γ-CD, (*2*) PRot-1250c, (*3*) PRot-1250p, (*4*) PRot-2100c, and (*5*) PRot-2100p. (2θ) Scattering angle.

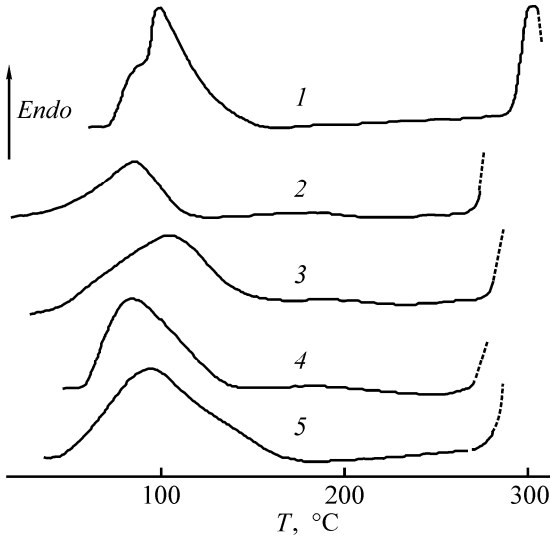


Fig. 2. DSC curves: (*1*) γ-CD, (*2*) PRot-1250c, (*3*) PRot-1250p, (*4*) PRot-2100p, and (*5*) PRot-2100c. (*T*) Temperature.

The interplanar spacings that we obtained for the complexes PRot-1250c and PRot-1250p (Table 2) well coincide with the results reported in [20]. This fact suggests that PRot-1250c and PRot-1250p have a columnar-type crystal structure with a tetragonal packing of molecular necklaces.

The diffraction pattern of the purified complex PRot-2100p (γ-CD/SiO = 1/4.6) (Fig. 1, curve *5*) differs from those of the PRot-1250c and PRot-1250p samples (Fig. 1, curves *2*, *3*) with lower molecular weights. A calculation of the interplanar spacings for PRot-2100p by formulas for quadratic lattices [21] showed good coincidence with the experimental values (Table 2) for the cubic system. Therefore, the structure of PRot-2100p can be described most adequately by the cubic lattice with unit cell parameters $a = b = c =$ 14.8 Å. Comparison of the interplanar spacings for PRot-2100c containing excess γ-CD (γ-CD/SiO = 1/1.55) (Fig. 1, curve *4*; Table 2) with the other PRot samples shows that this sample is a mixture of crystals with tetragonal and cubic packing of molecular necklaces.

Table 3. DSC data for γ-CD and PRot samples

Sample	T_{max}, °C	ΔH, J g^{-1}
γ-CD	103	237.5
PRot-1250p	95	160.0
PRot-1250c	90	224.1
PRot-2100p	85	156.0
PRot-2100c	100	206.9

Thus, the γ-CD/SiO molar ratio, molecular weight of the linear polymer PDMSE, and presence of free γ-CD in the complexes affect the crystal structure of the PRots being formed.

Figure 2 shows thermograms of γ-CD (curve *1*) and PRot (curves *2–4*), recorded in air. In the temperature range 50–170°C, γ-CD exhibits a broad endothermic peak with a shoulder in the low-temperature region, caused by dehydration of the initial γ-CD. This peak is not observed in repeated scanning of the same temperature range. Further heating leads to melting of γ-CD with simultaneous degradation. The onset of melting is observed at 280°C. Similar dependences (two endothermic effects) are observed in heating of PRot samples with different molecular weights (curves *2–4*). In the thermograms of the complexes, there is a broad endothermic peak in the range 50–150°C with a maximum at about 100°C, caused by release of bound water. As shown in [19, 20, 22], water is an important component of the complexes. It plays the role of bridges in the formation of a system of hydrogen bonds between γ-CD molecules along PRot molecular necklaces.

The enthalpies ΔH and peak temperatures T_{max} of dehydration of the systems studied are listed in Table 3. It should be noted that the enthalpy of dehydration is at a maximum for pure γ-CD. In addition, it follows from Table 3 that purification of PRot to remove γ-CD leads to a decrease in ΔH. At temperatures above 270°C, PRot melts with simultaneous decomposition.

Figure 3 shows electron micrographs of the initial γ-CD (a, b) and synthesized PRot samples (c–h). As can be seen from Fig. 3a (general view), γ-CD consists of crystalline aggregates of various shapes with a size varying in a wide range (μm): length, from 3 to 45, and width, from 2 to 12. It should be noted that both rodlike crystalline particles and platelike rhombic aggregates can be seen in the micrographs, i.e., γ-CD consists of crystals of different structures. At a higher magnification (Fig. 3b), a lamellar morphology of the majority of crystalline particles is clearly seen. A looser porous structure is observed on the surface of some particles.

Figure 3c shows a micrograph of the complex PRot-1250c containing free (unbound) γ-CD (γ-CD/SiO = 1/1.57). It can be seen that, in contrast to pure γ-CD,

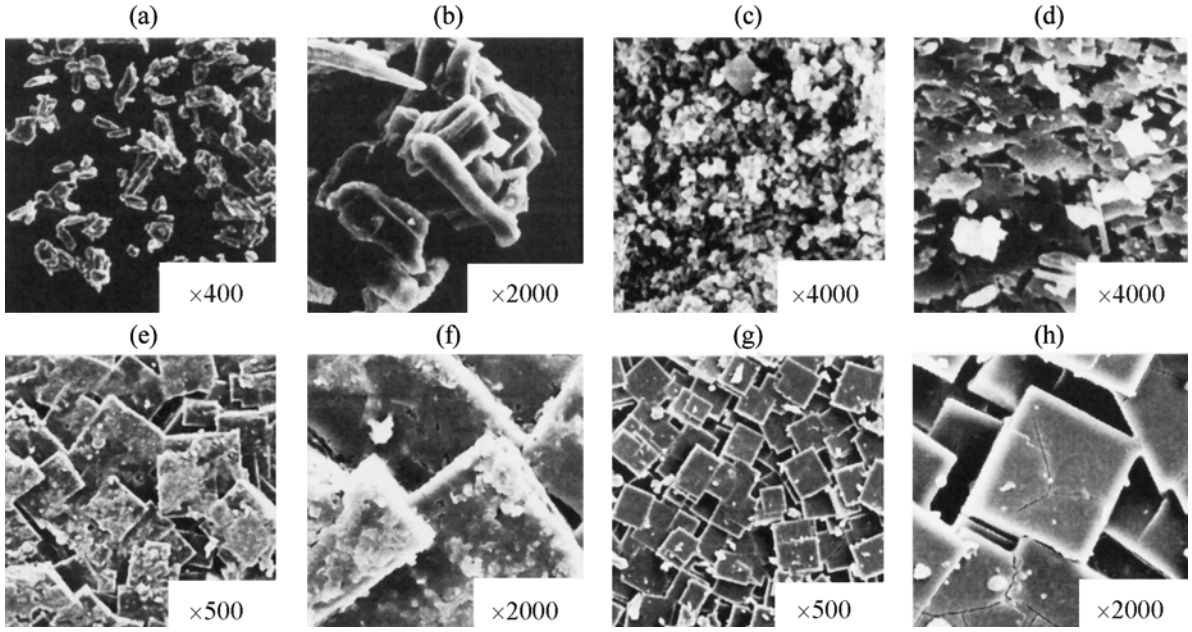


Fig. 3. Electron micrographs of (a, b) γ-CD, (c) PRot-1250c, (d) PRot-1250p, (e, f) PRot-2100c, and (g, h) PRot-2100p.

crystalline formations of the complex are close-packed and consist of small (<2 μm) aggregates having the shape of tetragonal parallelepipeds (Fig. 3c). By contrast, crystals of the purified sample PRot-1250p containing no free γ-CD (γ-CD/SiO = 1/4.8) have a lamellar morphology and consist of thin rectangular plates and a minor amount of crystals of rhombic shape (Fig. 3d). At higher magnifications, stacks of lamellas formed by self-assembling of columnar molecular necklaces of PRot can be seen.

The morphology of the complex PRot-2100c (Figs. 3e, 3f) containing excess γ-CD (γ-CD/SiO = 1/1.55) strongly differs from that of low-molecular-weight samples. The electron micrograph Fig. 3e shows that coarse crystals are formed as cubes and parallelepipeds in this case, with the face size of 30–120 μm. On the crystal surfaces, there is a thin precipitated layer apparently formed by the unchanged starting components, γ-CD and PDMSE.

Figures 3g and 3h show micrographs of the purified PRot-2100p sample (γ-CD/SiO = 1/4.6). It can be seen that, in the absence of free γ-CD, crystals are formed in the system as coarse cubes of regular shape with the face size from 20 to 100 μm. The surface of PRot-2100p crystals is clean. This fact reveals cracking of crystals (Fig. 3h), caused by dehydration of the sample in the course of preparation (evacuation) and examination in the scanning electron microscope.

It is interesting that the same crystal shape was found when [20] in studying the crystal structure and morphology of SMICs based on γ-CD and PEO with MW = 1500 and chain length of 94.7 Å. The crystals of the complex γ-CD/PEO also had the shape of rectangular parallelepipeds, but the mean face size was considerably smaller, about 15 μm.

Previously, we have studied [16] the morphology of PRots derived from PDMSE of various molecular weights and β-CD having a smaller diameter of the internal cavity compared to γ-CD. We showed that, with β-CD as a host, an increase in the molecular weight M_n of PDMSE from 1250 to 3300 makes lower the probability of formation of crystalline SMIC particles of regular shape. By contrast, in the case of the complex with γ-CD, an increase in M_n of the linear component, PDMSE, from 1250 to 2100 led to the formation of coarser and more perfect highly crystalline particles having the shape of tetragonal parallelepipeds and cubes.

CONCLUSIONS

(1) The crystal structure and morphology (packing character, crystal shape and size) of polyrotaxanes depend on the molecular weight of the linear polymer, molar ratio of γ-cyclodextrin and modified polydimethylsiloxane, and presence of free γ-cyclodextrin in the system.

(2) An increase in the molecular weight of modified polydimethylsiloxane leads to formation of polyrotaxanes in the form of coarser and well-faceted highly crystalline particles.

ACKNOWLEDGMENTS

The study was financially supported by the Russian Foundation for Basic Research (project no. 07-03-91681).

REFERENCES

1. Schill, G., *Catenanes, Rotaxanes, and Knots*, New York: Academic, 1971.
2. Panova, I.G. and Topchieva, I.N., *Usp. Khim*., 2001, vol. 70, no. 1, pp. 28–51.
3. Huang, F. and Gibson, H.W., *Prog. Polym. Sci*., 2005, vol. 30, no. 10, pp. 982–1010.
4. Szejtli, J., *Pure Appl. Chem.,* 2004, vol. 76, no. 10, pp. 1825–1832.
5. Szejtli, J., *Cyclodextrins and Their Inclusion Complexes*, Budapest: Acad. Kiado, 1988.
6. Balzani, V., Gumez-Lipez, M., and Stoddart, J.F., *Acc. Chem. Res*., 1998, vol. 31, pp. 405–411.
7. Bissell, R.A., Cordova, E., Kaifer, A.E., et al., *Nature* (London), 1994, vol. 36, pp. 133–142.
8. Han, B.H. and Antonietti, M., *Chem. Mater*., 2002, vol. 14, pp. 3477–3485.
9. Ooya, T., Eguchi, M., Ozaki, A., et al., *Int. J. Pharm*., 2002, vol. 242, pp. 47–52.
10. Hubin, T.J. and Busch, D.H., *Coord. Chem. Rev*., 2000, vol. 5, pp. 200–202.
11. Bissell, R.A., Cordova, E., Kaifer, A.E., et al., *Nature* (London), 1994, vol. 6, pp. 133–142.
12. Balzani, V., Credi, A., Raymo, F.M., et al., *Angew. Chem., Int. Ed*., 2000, vol. 39, p. 3348.
13. Okumura, H., Okada, M., Kawaguchi, Y., and Harada, A., *Macromolecules*, 2000, vol. 33, pp. 4297–4298.
14. Okumura, H., Okada, M., Kawaguchi, Y., and Harada, A., *Macromol. Rapid Commun*., 2002, vol. 23, pp. 781–785.
15. Okumura, H., Kawaguchi, Y., and Harada, A., *Macromolecules*, 2001, vol. 34, pp. 6338–6343.
16. Sukhanova, T.E., Bronnikov, S.V., Grigor'ev, A.I., et al., *Zh. Prikl. Khim.*, 2007, vol. 80, no. 7, pp. 1141–1146.
17. Marangoci, N., Farcas, A., Harabagiu, V., et al., *High Perform. Polym*., 2008, vol. 20, pp. 251–266.
18. Shuai, X., Porbeni, F.E., and Wei, M., *Macromolecules*, 2002, vol. 35, pp. 2401–2405.
19. Uyar, T., Hunt, M.A., Gracz, H.S., *Cryst. Growth Des*., 2006, vol. 6, no. 5, pp. 1113–1119.
20. Panova, I.G., Gerasimov, V.I., Kalashnikov, F.A., et al., *Vysokomol. Soedin., Ser. B*, 1998, vol. 40, no. 12, pp. 2077–2082.
21. Kachanov, N.N. and Mirkin, L.I., *Rentgenostrukturnyi analiz: Prakticheskoe rukovodstvo* (X-ray Diffraction Analysis: Practical Guide), Moscow: Mashgiz, 1960.
22. Panova, I.G., Matukhina, E.V., Popova, E.I., et al., *Vysokomol. Soedin., Ser. A*, 2001, vol. 43, no. 7, pp. 1228–1236.

ISSN 1070-4272, Russian Journal of Applied Chemistry, 2008, Vol. 81, No. 12, pp. 2151–2154. © Pleiades Publishing, Ltd., 2008.
Original Russian Text © B.A. Zhubanov, V.D. Kravtsova, R.M. Iskakov, A.A. Matnishyan, G.E. Nurumbetov, 2008, published in Zhurnal Prikladnoi Khimii, 2008, Vol. 81, No. 12, pp. 2040–2044.

MACROMOLECULAR CHEMISTRY AND POLYMERIC MATERIALS

Polymeric Composites Based on Alicyclic Polyimide and Polyaniline

B. A. Zhubanov, V. D. Kravtsova, R. M. Iskakov, A. A. Matnishyan, and G. E. Nurumbetov

Bekturov Institute of Chemical Sciences, Ministry of Education and Science of the Republic of Kazakhstan, Almaty, Kazakhstan

Yerevan Research Institute of Optical and Physical Measurements, Yerevan, Armenia

Kazakh–British Technical University, Almaty, Kazakhstan

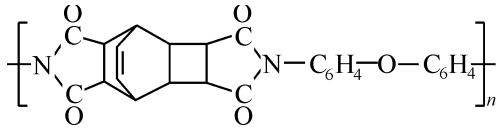
Received June 23, 2008

Abstract—Specific features of modification of an alicyclic polyimide with polyaniline were examined. The thus obtained new polymeric composites exhibit better capability for silver plating.

DOI: 10.1134/S1070427208120215

Polymeric materials, both individual polymers and multicomponent systems, attract growing researchers' interest. Modification of polymers with various low- and high-molecular-weight additives allows preparation of composites with valuable properties, making them suitable for application in microelectronics, radio engineering, and space industry [1, 2]. Of particular interest are composites of nanosize polyaniline, polypyrrole, and polythiophene, which, thanks to the high electrical conductivity and stability in redox processes have found use in high-capacity batteries; supercapacitors; corrosion-protecting, reflecting, and absorbing coatings; and power-converting and power-saving devices [3, 4]. Among conducting polymers, the most widely used are polyaniline (PANi) and its derivatives [5, 6]. Homogeneous defect-free composites with high electrical conductivity and good mechanical properties, prepared by forming PANi layers on the surface of aliphatic polymers (polyethylene, polypropylene), have been described [6–8]. It was of interest to evaluate the effect of electroactive polymers on heat-resistant polymers and, in particular, polyimides.

In this study, we examined specific features of formation and the main properties of composites based on a nanosize polyaniline and an alicyclic polyimide derived from tricyclodecenetetracarboxylic dianhydride and 4,4'-diaminodiphenyl ether:



EXPERIMENTAL

The starting compounds and solvents were purified by standard procedures. N,N'-Dimethylacetamide (DMAA) was additionally dried over 4-Å molecular sieves. Acetone, methanol, and 4,4'-diaminodiphenyl ether (DADPE), all of chemically pure grade, were used without additional purification. Polyimide (PI) was prepared in the presence of catalytic amounts of triphenyl phosphate in a DMAA solution. The polyimide was prepared in an inert atmosphere by the following procedure: A three-necked flask was charged with 13.70 g (0.05 mol) of the dianhydride, 10.00 g (0.05 mol) of DADPE, and 1.18 g (5 wt % relative to the sum of the monomers) of triphenyl phosphate, after which 70.0 ml of DMAA was added. The mixture was heated for 20 min at 70°C, after which the temperature was raised to 120°C, and the mixture was stirred for additional 4.0 h. From the resulting solution, in which, according to the IR spectra, the degree of imidization of the polymer was 94–96%, we cast films or precipitated the polymer into acetone. The products obtained were washed with two portions of acetone and dried in a vacuum oven at 80–90°C to constant weight.

The polyimide films were prepared by casting the reaction solutions or a 25% solution of the precipitated polyimide in DMAA onto glass surfaces. To remove the solvent, the films were dried at 80°C for 0.3 h, after which they were additionally heat-treated in the temperature range 80–250°C in air for 1.0 h. Silver plat-

Table 1. Some properties of alicyclic polyimide in the presence of polyaniline

Property	Polymer		PI + PANi, wt %					
	PI	PANi	0.10	0.25	0.5	1.0	1.5	2.0
η_{red} of 0.5% solution, dl g^{-1}, DMF, 25°C	1.52	0.56*	1.55	1.57	1.67	1.74	1.80	1.81
Decomposition onset temperature in air, °C	370	360	370	367	365	360	360	360
Temperature of 50% weight loss, °C	540	487	540	536	522	530	532	525
Tensile strength, MPa	140	Brittle	135	135	130	125	128	127
Elongation, %	32	–	30	28	25	23	20	18
Elastic modulus, MPa	4200	–	4200	4230	4270	4340	4380	4570

* In concentrated H_2SO_4.

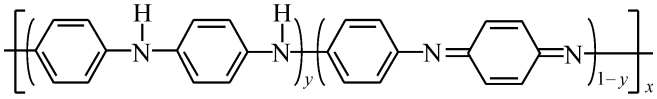
ing of the polyimide films was performed as described in [9].

Polyaniline was prepared by oxidative polycondensation of a solution of aniline in 1 M HCl with potassium persulfate [10]. The product obtained as an emeraldin salt was additionally purified by successive extraction with methanol and acetone for 24 h and treated with a 10% solution of ammonium hydroxide, after which it was dried in a vacuum oven at 50°C for 5 h. The bulk electrical conductivity of emeraldin and the emeraldin salt was 10^{-10} and 0.45 Ω^{-1} cm^{-1}, respectively. The molecular weight of the emeraldin form of PANi in concentrated sulfuric acid was 35 000. The fibril size, according to an electron-microscopic examination, was 150–220 nm [11].

The reduced viscosity was measured in an Ubbelohde viscometer at 25°C for 0.5% solutions of the polyimide in DMF and for solutions of PANi in concentrated H_2SO_4. The thermal gravimetric analysis of PI and composites was performed with a Mettler Toledo TGA SDTA device at a heating rate of 8 deg min^{-1}. The temperatures of the decomposition onset, $T_{d.o}$, and 50% weight loss for the polymers were calculated from the TG curves. The tensile strength σ_t, relative elongation l, elastic modulus E, dielectric loss tangent tan δ, relative permittivity ε, and bulk and surface resistivities ρ_v and ρ_s of 40–45-μm-thick films were measured under standard conditions [12, 13]. The electrical properties of the metal-modified films were measured in the dc mode at a field istrength of 20 mV cm^{-1}, using sputtered silver electrodes. The temperature dependence of the surface resistivity was studied in the range 25–200°C. The reflection coefficient $R(\lambda)$ was determined in the wavelength range 400–750 nm for samples with a surface area of 2.2 cm^2 on an SF-1201 spectrophotometer. The determination error was ±0.05% for ρ_v and ρ_s, and ±1% for R. The IR spectra of 3–5-μm-thick films were measured on an IR-25 device. Polymer blends with nanosize polyaniline were prepared by homogenization of 0.1–2.0 wt % PANi in a polyimide solution at 20–25°C. After settling, films were cast and dried in air for 1.0 h at 80–250°C.

The surface morphology of the composite systems was studied with a Jeol JSM-1800 scanning electron microscope (Japan) equipped with an Oxford MathScan attachment.

The first step in studying the specific features of modification of the alicyclic polyimide with the conducting polymer was to examine the effect of PANi samples of the general formula



$x = y = 0.5$

on the PI viscosity. In contrast to the known PE–PANi composite systems prepared by successive deposition of PANi layers on the surface of polyethylene films [6], composites of alicyclic polyimide and polyaniline were prepared by mechanical mixing of the starting polymers. The experimental results obtained show that the systems remain homogeneous and transparent at a PANi content of up to 2.0 wt %, and above this concentration the solution becomes turbid, the system undergoes phase separation, and high-quality films are not obtained. In the presence of conducting polymer additives, the viscosity of the PI solution somewhat increases: from 1.54 to 1.80 dl g^{-1}. The viscosity reaches a maximum in the presence of 1.5 wt % PANi and then does not change noticeably (Table 1). This fact can be attributed to the plasticizing effect of PANi, apparently leading to loosening of the structure of the initial polyimide.

As can be seen from Table 1, the thermal stability of the polyimide–polyaniline systems is relatively high and, at the PANi content examined, it is determined, on the whole, by the structure of the polyimide.

Analysis of the spectral characteristics of the polymeric system with PANi shows that the IR spectra do not change noticeably in the presence of relatively low amounts of the conducting polymer. We only observe an increase in the intensity of the absorption bands of the aromatic rings at 1500 cm^{-1} and a shift of the imide ring band from 1375 to 1385 cm^{-1}. The positions and intensities of the other bands remain essentially unchanged.

To evaluate the stability of mechanical properties of films with different PANi contents, we measured their tensile strength and elongation. As can be seen from Table 1 for unmodified PI, the mean values of σ_t and l are 140 MPa and 32%, respectively, and the elastic modulus is 4200 MPa. For the samples with PANi, these characteristics vary as follows: the tensile strength remains nearly unchanged, and the elasticity decreases (e.g., for the sample with 2% PANi, by a factor of 1.8 relative to the initial sample); the elastic modulus increases practically to 400 MPa, i.e., the system becomes appreciably more rigid. This fact, which is on the whole expected, can be attributed to structurization of the polyimide chains with a rigid PANi framework (according to [6–8], PANi is cross-linked in the temperature range 160–200°C).

The optical and electrical properties change in the presence of PANi more significantly. As can be seen from Fig. 1, as the polyaniline concentration is raised from 0.1 to 1.5 wt %, the optical reflection coefficient of the metal-plated composites increases. An evaluation of the residual silver content by TGA showed that an increase in the PANi content leads to a rise in the sorption capacity of the composite for silver ions by a factor of 1.1–1.5. It is also seen from Fig. 1 that the shape of the curve of the optical reflection coefficient of the metal-plated PI vs. wavelength (curve *1*) differs from the corresponding curves for the systems with PANi, characterized by stabilization of this parameter at λ = 550–600 nm.

On the whole, it can be noted that, as the polyaniline content of the composite is raised (within the examined range), the metal content also increases. A similar trend has been observed previously for alicyclic polyimide–poly(ethylene terephthalate) composites [14], but for the composites with the electroactive component the effect is more significant.

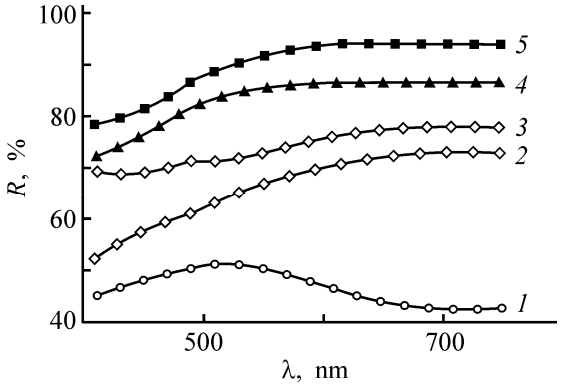


Fig. 1. Influence of the polyaniline concentration on the optical reflection coefficient R of (*1*) PI, (*2–4*) PI + PANi, and (*5*) Ag films. (λ) Wavelength. PANi concentration, wt %: (*2*) 0.1, (*3*) 0.5, and (*4*) 1.5.

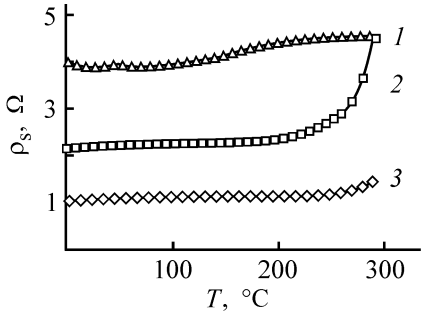


Fig. 2. Temperature dependence of the surface electrical resistivity ρ_s of (*1*) PI and (*2*, *3*) PI + PANi films. PANi concentration, wt %: (*2*) 0.5 and (*3*) 1.5.

For the metal-free polymeric composites, the bulk resistivity increases by two orders of magnitude (Table 2). Introduction of PANi into the polyimide also leads to appreciable changes in the surface resistivity of metal-plated films. Figure 2 shows that, with an increase in the polyaniline content, the surface resistivity ρ_s decreases. Thus, active properties of polyaniline are manifested not only on the surface, as noted

Table 2. Electrical properties of polymeric composites based on alicyclic polyimide and PANi

Polymer	tan δ	ε	ρ_v, Ω m
PI	0.001	2.82	$(1–3)\times10^{15}$
PI + PANi, %:			
0.5	0.003	1.30	$(2–4)\times10^{15}$
1.0	0.009	1.33	$(2–3)\times10^{14}$
1.5	0.020	1.32	$(2–3)\times10^{14}$
2.0	0.024	1.28	$(2–4)\times10^{13}$
2.5	0.030	1.30	$(2–4)\times10^{13}$
PANi	0.25–12*	1.40	222

* Depends on temperature and doping level.

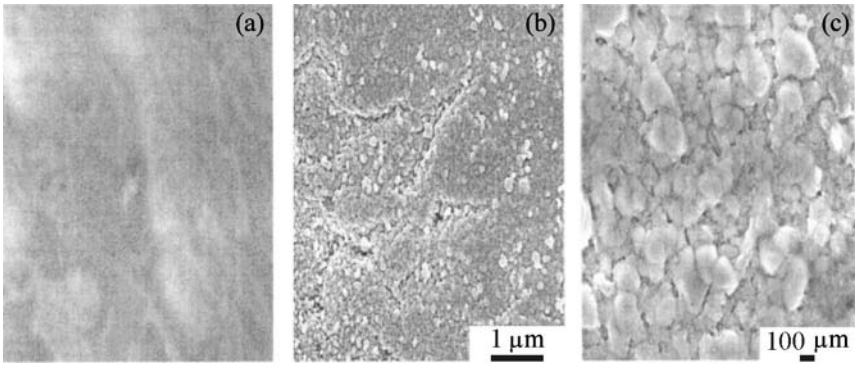


Fig. 3. Electron-microscopic images of the surface of films of (a) nonmetallized and (b, c) sliver-plated samples. (a) PI, (b) PI + Ag, and (c) PI + PANi + Ag.

in [7, 8], but also in the bulk of the polymer, i.e., these composites can be characterized by both bulk and surface conductivity.

Analysis of the properties of alicyclic polyimide + polyaniline composites shows that PANi enhances the capability of the composites for metal plating by favoring formation of larger silver clusters, compared to metal particles in the polyaniline-free polyimide (Fig. 3). It should also be noted that the thus obtained metallic layer is tightly impregnated in the polymer base, with the formation of a more uniform metal layer in the surface layer of the polyimide as compared to the individual polymer.

CONCLUSIONS

(1) Specific features of modification of the polyimide derived from tricyclodecenetetracarboxylic dianhydride and an aromatic diamine with polyaniline were examined. The components are well compatible at conducting polymer concentrations of up to 2.0 wt %.

(2) Introduction of small amounts of polyaniline leads to formation of polymeric composites with a more rigid structure, compared to the initial polyimide, and improved capability for metallization, which is reflected in the optical and electrical properties of the composites: for silver-plated films, the optical reflection coefficient increases and the surface electrical resistivity decreases.

(3) In the presence of a conducting polymer, silver clusters of larger size, compared to metal particles in the polyaniline-free polyimide, are formed.

ACKNOWLEDGMENTS

The study was financially supported by the International Science and Technology Center (project K-1117) and Program F.0354-06 of Basic Research of the Bekturov Institute of Chemical Sciences, Ministry of Education and Science of the Republic of Kazakhstan, project "Scientific Principles of the Development of New Polymer Systems and Microstructures for Medicine, Agriculture, and Electronics" (2006–2008).

REFERENCES

1. Wessling, B. and Skotheim, L., Handbook of Conducting Polymers, New York: Marcel Dekker, 1998.
2. Satheesh Kumar, K.K., Geetha, S., and Trivedi, D.C., Curr. Appl. Phys., 2006, vol. 5, no. 6, pp. 603–608.
3. MacDiarmid, A.G., Synth. Met., 2002, vol. 125, pp. 11–12.
4. Handbook of Organic Molecules and Polymers, Nalwa, H.S., Ed., Chichester: Wiley, 1997, vol. 2.
5. Genies, E.M., Boyle, A., Lapkowski, M., and Tsintavis, C., Polyaniline: A Historical Survey, Synth. Met., 1990, vol. 36, pp. 139–145.
6. Kuryndin, I.S., Mokreva, P., Terlemezyan, L., et al., Zh. Prikl. Khim., 2005, vol. 78, no. 3, pp. 484–489.
7. Rozova, E.Yu., Kuryndin, I.S., Bobrova, N.V., and Elyashevich, G.K., Vysokomol. Soedin., Ser. B, 2004, vol. 46, no. 5, pp. 923–927.
8. Hsun-Tsing Lee, Chien-Shiun Liao, and Show-An Chen, Makromol. Chem., 1993, vol. 194, pp. 2443–2452.
9. Vecherkina, E.L., Kudaikulova, S.K., Iskakov, R.M., et al., Vysokomol. Soedin., Ser. A, 2007, vol. 49, no. 2, pp. 246–253.
10. Matnishian, H.A. and Beylerian, N.M., Oxid. Com., 2005, vol. 28, no. 1, pp. 67–80.
11. Matnishyan, A.A. and Akhnazaryan, T.L., Khim. Zh. Arm., 2007, vol. 60, no. 5, pp. 801–831.
12. Gurova, T.A., *Tekhnicheskii analiz i kontrol' proizvodstva plastmass* (Technical Analysis and Monitoring of Plastics Production), Moscow: Vysshaya Shkola, 1980.
13. Metz, S., Jiguet, S., Bertsch, A., and Renaud, Ph., Lab. Chip., 2004, vol. 4, pp. 114–120.
14. Kudaikulova, S., Musapirova, S., Sarieva, R., et al., *Eur. Chem.-Technol. J.*, 2004, vol. 6, no. 1, pp. 11–16.

ISSN 1070-4272, Russian Journal of Applied Chemistry, 2008, Vol. 81, No. 12, pp. 2155–2161. © Pleiades Publishing, Ltd., 2008.
Original Russian Text © D.L. Starokadomskii, 2008, published in Zhurnal Prikladnoi Khimii, 2008, Vol. 81, No. 12, pp. 2045–2051.

MACROMOLECULAR CHEMISTRY AND POLYMERIC MATERIALS

Effect of Nanodispersed Silica (Aerosil) on the Thermal and Chemical Resistance of Photocurable Polyacrylate Compounds

D. L. Starokadomskii

Chuiko Institute of Surface Chemistry, National Academy of Sciences of Ukraine, Kiev, Ukraine

Received November 8, 2008

Abstract—The effect of filling of a photopolymeric composite based on oligoacrylates (OKM-2, TGM-3) with highly dispersed silicas (Aerosils) was examined. Thermograms recorded in the range 20–900°C were analyzed in detail. A scheme of the effect of silica on the polymer structure, accounting for the filler effect on the thermal and chemical resistance of the composites, was suggested.

DOI: 10.1134/S1070427208120227

Introduction of nanodispersed silicate particles is a commonly used method for modification of the physicochemical and mechanical characteristics of polymeric materials, as well as for thickening of polymers and for making the materials cheaper [1]. However, the effect of inorganic nanoparticles on the stability (e.g., heat resistance) of composites under the conditions of extreme external actions is not always taken into account. At the same time, natural and social calamities, becoming more and more frequent, make particularly topical the problem of enhancing the strength of composite polymeric structures.

It has been noted in numerous papers that highly dispersed particles of silica and aluminosilicates have a certain effect on the thermal degradation and chemical resistance of polymers [2–7]. In some cases, these properties of polymers change essentially [3, 4], whereas in other cases, the effect of nanoparticles is ambiguous or insignificant [2, 5]. It is still poorly understood how a silicate nanofiller can affect the thermal and chemical resistance of photocurable polyacrylates.

In this study, we examined the effect of Aerosil nanosilica samples with various specific surface areas on the resistance of photocurable polyacrylates to heat and aggressive liquids. Aerosil is a widely used filler (thickener, modifier) for polymers, and therefore elucidation of the in fluence it exerts on the thermal degradation and chemical resistance is of both scientific and practical interest. In so doing, we assumed that the decisive factors could be the specific surface area and the concentration of Aerosils.

EXPERIMENTAL

We prepared composites based on OKM-2 oligo (carbonate methacrylate) produced by the Dzerzhinsk Research Institute of Polymers, Federal State Unitary Enterprise. As photoinitiator we used benzil dimethyl ketal produced by Ciba (Switzerland). For filling of photopolymers, we used highly dispersed silicas (analogous to Aerosils produced by Degussa), of A-100, A-300, and A-455 brands (specific surface area 100, 300, and 455 $m^2 g^{-1}$, respectively), produced by the Kalush Pilot Plant (Ukra-ine). The filled composites were prepared in a dark room at ambient temperature by mixing the components weighed on an analytical balance. The compounds containing 0.6 wt % photoinitiator were applied in the form of 2–3-mm-thick layers onto a mirror glass support and cured for 5 min. The cured compounds were then milled in an Ardenna vibrator. The thermal degradation was studied with a Q-1500D derivatograph (MOM, Hungary) TG, DTG, and DTA curves recorded. The measurements were performed in the range 20–1000°C at a heating rate of 10 deg min^{-1}.

The mass spectra were measured on an MKh-7304A mass spectrometer (Selmi Joint-Stock Company) in the temperature range 20–800°C at a residual pressure of 10^{-5} mm Hg.

Table 1. Temperature characteristics of thermal oxidative degradation of photopolymeric composites based on OKM-2* (Aerosil filler)

Aerosil, wt %	Temperature, °C, of processes				Dry residue, wt %
	low-temperature		high-temperature		
	T_1/T_1^*(DTA)	t_1 (DTG)	T_2 (DTA)	t_2 (DTG)	
–	300/400	430	565	565	1.35
A-100:					
10	280/360	360	620	620	11.11
20	280/340	340	590	590	20.55
A-300:					
10	280/340	340	605	605	10.64
15	275/340	340	595	595	14.86
20	280/350	350	580	585	20.81
A-455, 20	270/340	340	575	575	19.79

* Temperature T_1^* corresponds to the maximum of the low-temperature process, and T_1, to its completion.

The stability of polymeric composites in alkaline solutions was studied using 0.1 N KOH. Samples of size 0.2 × 0.5 × 10 mm were placed in an alkaline solution. At regular intervals, during a period of 1 month, the samples were withdrawn, dried in air for 40–60 min under normal conditions, and weighed on an analytical balance. From the data obtained, we plotted the dependence of the weight loss on the time of keeping in alkali.

Table 1 and Fig. 1 show typical results obtained when studying the thermal oxidative degradation of the filler (Aerosil, Fig. 1a), unfilled photopolymer (Fig. 1b), and filled photopolymer (Fig. 1c).

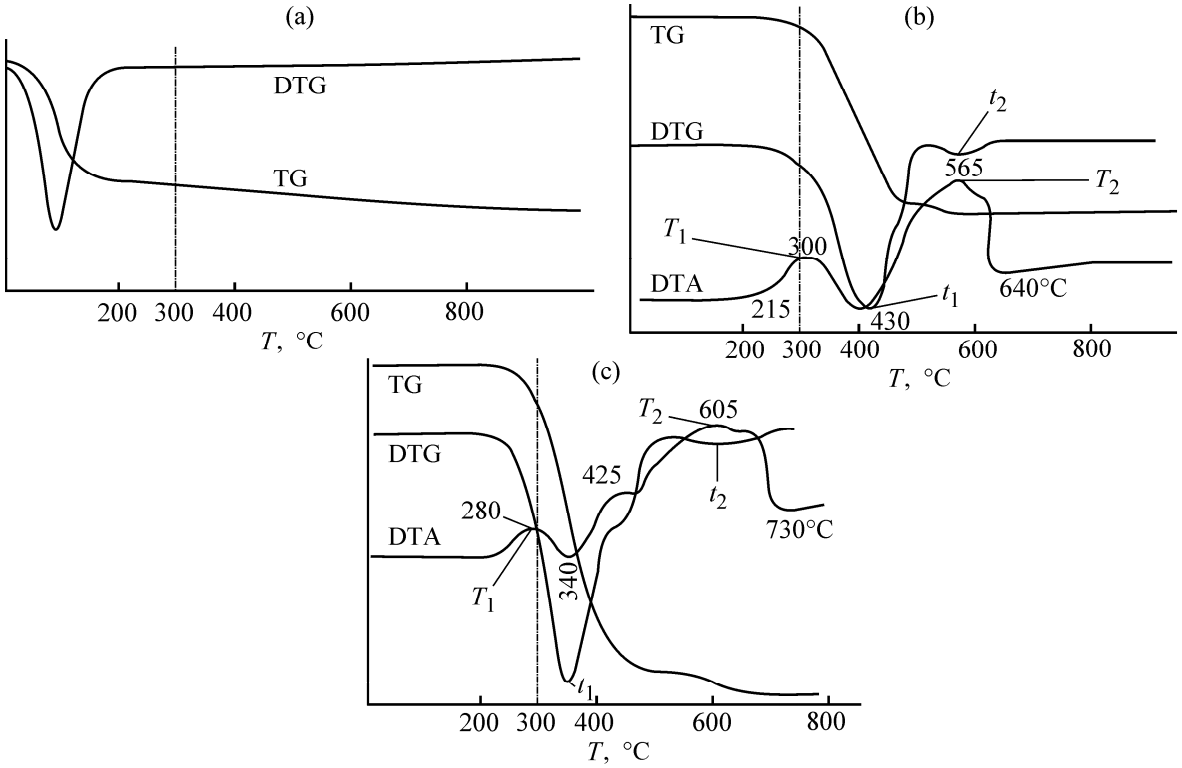


Fig. 1. Derivatograms of (a) A-300 silica, (b) cured unfilled oligo(carbonate methacrylate) (+0.6 wt % benzil dimethyl ketal), and (c) the same with 10 wt % A-300 filler. (*T*) Temperature.

It is well known that the thermogram of free unmodified Aerosil reflects only the water evaporation. This process has the highest intensity in the range 50–150°C, with the maximal weight loss rate at 100°C (Fig. 1a, DTG curve). The DTA curve corresponding to this process is, as a rule, characterized by a weak peak at 350–400°C.

Despite the considerable concentration of Aerosil (10–20 wt %), features of its thermogram are not manifested in the thermogram of the photopolymer filled with it. Apparently, the polymer surrounding silica particles shifts the water evaporation peak to higher temperatures. The filler effect was examined by comparative analysis of the experimental data before and after filling. To obtain a more objective pattern, the studies were simultaneously performed by two methods: in air (thermograms) and in a vacuum (mass spectrometry).

The unfilled polymeric compositeis, as a rule, characterized by a multistep course of thermal degradation. The TG curves of unfilled polymers, recorded in the course of heating in air, have several steps, with the corresponding extrema in the DTG and DTA curves. These features are due to various thermal oxidation processes [3, 7, 9]. The unfilled composite under consideration (Fig. 1, curve *6*; Table 1) also exhibits two extrema in the DTG curves: at $t_1 = 430$ and $t_2 = 565$°C. These extrema are due to two main types of processes giving peaks in the DTA curves at points T_1 and T_2 (Fig. 1b). Let us denote the processes occurring in the temperature range 200–450°C as low-temperature processes (with the extrema at t_1 and T_1 in the DTG and DTA curves, respectively), and the processes at temperatures above 450°C, as high-temperature processes (with extrema at t_2 and T_2 in the DTG and DTA curves, respectively).

The major fraction of the composite degrades in the low-temperature region. In the TG curve (Fig. 1b, Table 1), there is a portion of intense weight loss starting at 215°C. Its rate reaches a maximum at $t_1 = 430$°C (Fig. 1b, DTG curve). The main thermal degradation process is manifested as a peak in the DTA curve with a maximum at $T_1 \approx 300$°C (with 10% weight loss). This maximum is due to thermal oxidation of the composite. Mass-spectrometric analysis (Table 2) shows that the maximal weight loss in thermal degradation in a vacuum is observed at approximately 270°C. It follows from the mass spectra (Table 2) that, in the low-temperature process, the main thermal degradation products are water ($m/z = 18$) and carbon dioxide ($m/z = 44$).

The high-temperature process starting at 450°C is exothermic. It is accompanied by a slight weight loss and reaches the maximal intensity in the thermogram at $T_2 = 565$°C (Fig. 1b, Table 1). Recent published data also show that there may be an exothermic effect in the high-temperature region. For example, according to [3], divinylbenzene–styrene polymers also decompose in two steps, at 300–400 and 600–800°C, with the second step characterized by an exothermic effect. Bolbukh et al. [3] assign these effects, respectively, to products of primary and secondary decomposition of divinylbenzene copolymers with styrene or acrylates. As can be seen from the mass spectra we obtained, in thermal decomposition in a vacuum, the high-temperature step is ill-defined, though intensification of certain processes at 600–900°C is noticeable. As can be seen from Table 2, the major decomposition products in this case are water ($m/z = 18$) and carbon monoxide ($m/z = 28$), with the latter prevailing at high temperatures (900°C). The carbon dioxide peak, prevailing in low-tempera-ture processes (200–300°C), is not manifested at high temperatures.

After the filling, the general pattern of oxidative thermal degradation (shapes of the thermogram and mass spectra) does not change essentially. The influence of filler characteristics (concentration, specific surface area) is manifested in quantitative changes in some parameters (Fig. 1; Tables 1, 2).

Filling of the polymers under consideration with Aerosils leads in all the cases to a noticeable (by 20–50°C, i.e., by 10–15%, Table 1) shift of the exothermic effect of the low-temperature process (T_1) toward lower temperatures (DTA curve) and to a more pronounced (by 70–90°C) decrease in the temperature t_1 of the maximal rate of weight loss (DTG curve). The thermograms of samples filled with Aerosils that differ essentially in the dispersion and character of aggregation, such as A-100 and A-455, are on the whole similar. The only difference is that, as the dispersity increases, the high-temperature maximum (T_2) shifts toward still higher temperatures (Table 1).

It follows from our data that filling with Aerosils impairs the heat resistance (temperature of the maximal intensity of the primary decomposition process) of the polymeric composite. According to the data obtained, variation of the specific surface area and concentration in the range examined affects the heat resistance only slightly. An essentially similar conclusion (decrease in the heat resistance by 10°C) was made by Syrovatka et al. [2] for polyacrylate filled with another filler.

Table 2. Relative intensity I_{rel} of fragments of degrading polymer molecules, according to data of temperature-programmed mass spectrometry

m/*z*	I_{rel}, arb. units, at indicated temperature, °C, and filler content													
	155		210		235		270		400		660		910	
	0%	20%	0%	20%	0%	20%	0%	20%	0%	20%	0%	20%	0%	20%
5	0.05		0.3	0.4		1.2	0.7	0.3	0.1					
15				1.6	1.6	6.4	1.8	1.8	0.2	0.3	0.1		0.2	
16	0.2		0.5	1.1	0.9	5.3	0.9	1	0.2		0.2		0.4	
17	0.5	0.2	0.6	0.4	0.75	5	2.4	1.8	0.5		0.2	0.2	0.7	0.2
18	1.6	0.75	2.1	1.4	2.3	4.9		1.6	1.7	0.7	0.6	0.6	2.6	0.5
19						3.3				0.4	2.2			
20								0.5	0.2					
									0.7					
27			0.3	0.6	0.8	4.6	1.4		0.3					
28	0.3		1.2	2.9	1.6	>6.3	2.9			0.7	0.3	0.2	0.4	0.7
29	0.1		0.75	3.2	1.6	>6.3	3.1	4.8		0.6	0.8		4.2	0.2
30					0.3	>6.3	0.4	4.5		0.3	0.1			
31					0.2	>6.3	0.2	2.2						
32						3.4		0.8						
33						1		0.3						
39			0.2	1.6	1.2	>6.3	1.6		0.2	0.3	0.3		0.2	
40			0.1	2	0.4	>6.3	1.5	2	0.2	0.3	0.1		0.1	
43			0.3		0.9	>6.3	1.1	2	0.2	0.3	0.3		0.2	
44	0.25	0.2	1.5	5.5	1.7	>6.3	3.6	3.2	0.2	0.3				
45				2.7	0.3	>6.3	0.3	3.4		0.3				
46				0.7		>6.3		2.4						
47						6		0.8						
48						1.5								
55						0.3	0.2	0.3						
56			0.1		0.2	0.3	0.2	0.4						
57					0.1	0.5	0.1	0.4						
58				0.3	0.2	1		0.4						
59				0.2		1		0.4						
60						0.9		0.4						
61						0.3		0.2						
69					0.2	1.8	0.2							
70				0.3	0.1	1.8	0.2	0.6						
71				0.2		0.7		0.7						
72						0.5		0.6						
73						0.5		0.2						
74						0.3								
86					0.3	1.5	0.3							
87					0.1	2.7	0.1							
88				0.8	0.2	2.8		0.3						
89				0.8		1.4		0.3						
90				0.4		1		0.2						
91				0.2		0.3								
113						0.3								
114						0.3								
115						0.1								

In this case, however, both steps were observed in the temperature range 200–450°C (in our case, only the first step), and the thermal degradation was studied only by mass spectrometry.

A study of the mass spectra of the composites showed that, after filling, thermal degradation of the composites in a vacuum (apparently corresponding to the low-temperature processes in the derivatograms) have a considerably higher intensity and occurs at lower temperatures. For all the composites, the main processes start earlier and occur faster than in air (200–300°C, Table 2, against 300–500°C in air, Fig. 1). The release of thermal degradation products is the most intense at approximately 270°C from the unfilled composites and at 230°C from the filled samples (Table 2). Thus, in the case of anaerobic thermal degradation, filling with unmodified nanosilica also diminishes the heat resistance of the composite by 10–15% (Table 1).

Comparison of the mass spectra (Table 2) shows that filling makes appreciably richer the set of peaks detected in the spectrum. The decrease in the degradation temperature and the richer set of degradation products released at 200–400°C from the filled polymer are apparently due to two possible factors: decrease in the activation energy of thermal degradation due to filling and/or richer chemical composition of the polymerization products formed in the presence of the filler. The latter factor is nontrivial and inconsistent with some recent data for other fillers. For example, when an antifriction filler (probably aluminosilicate) is introduced into polyacrylate, the intensity of the release of the volatile products (the main of which are the same: H_2O, m/z = 18; CO, m/z = 28; CO_2, m/z = 44), by contrast, decreases [2]. This means that the effect of the nanodispersed filler is ambiguous and difficult to predict.

One more distinctive feature of the filled composites examined in this study is that the evolution of CO and H_2O at high temperatures (600–900°C) is considerably less pronounced than that in the unfilled composite (Table 2). This fact suggests that filling facilitates complete decomposition of the polymeric component at lower temperatures, below 400°C.

The effect of Aerosil on the high-temperature process is opposite to that on the low-temperature process. Namely, T_2 and t_2 increase. The greatest increase is observed with 10 wt % A-100 and A-300. In this case, T_2 increases by 50–60°C (by approximately 10%) relative to the unfilled composite. With a further increase in the degree of filling, T_2 decreases, but it does not reach the value observed for the unfilled sample (Table 1). This trend is the more pronounced, the larger the surface area of Aerosil (Table 1). With an increase in the silica dispersity, the "afterdegradation" temperature (T_2, t_2, Table 1) decreases to a greater extent than T_1 and t_1, i.e., filling thermodynamically facilitates the "afterdegradation," with the magnitude of this effect depending on the concentration and specific surface area of Aerosil.

The high-temperature process in thermal degradation of polymers apparently involves secondary degradation products (let us term it afterdegradation). The mass spectra (Table 2) show that, at 600–900°C, in contrast to the range 200–400°C, the filled composite gives fewer peaks. This fact points to more active "early afterdegradation" of the filled composite and suggests that, with an increase in the specific surface area of Aerosil, less ordered surface layers and denser regions are formed.

It should be noted that a dry residue (1–1.5% relative to the initial polymer weight) remains after complete degradation of even the unfilled polymer. Apparently, its presence leads to intensification of the afterdegradation at high temperatures. In filled composites, the weight of the dry residue, as a rule, corresponds to the weight of Aerosil, exceeding it by no more than 0.8% (Table 1). In all the cases, these are carbon-like formations with a size of fractions of a millimeter. This fact confirms the conclusion that filling with Aerosil favors complete degradation of the polymer in the earlier steps.

As can be seen from our results and data of [3], Aerosil strongly affects the afterdegradation processes characterized by the second extremum (T_2, t_2) in the DTA and DTG curves. It should be assumed that these processes involve more stable (compared to the amorphous part) denser structures of the polymer and its surface layers at the filler particles. Afterdegradation can also involve degradation of structurally nonuniform zones of the polymer phase, which should apparently have a higher degradation temperature than the main part of the polymer. Based on this reasoning, we can suggest a scheme of the effect of nanosilicas on the structures of network polyacrylates (based on the previously published model [8]). According to this scheme, denser surface layers of the polymer are formed around filler particles. These layers should be more resistant to degradation than inhomogeneities of the unfilled amorphous polyether acrylate.

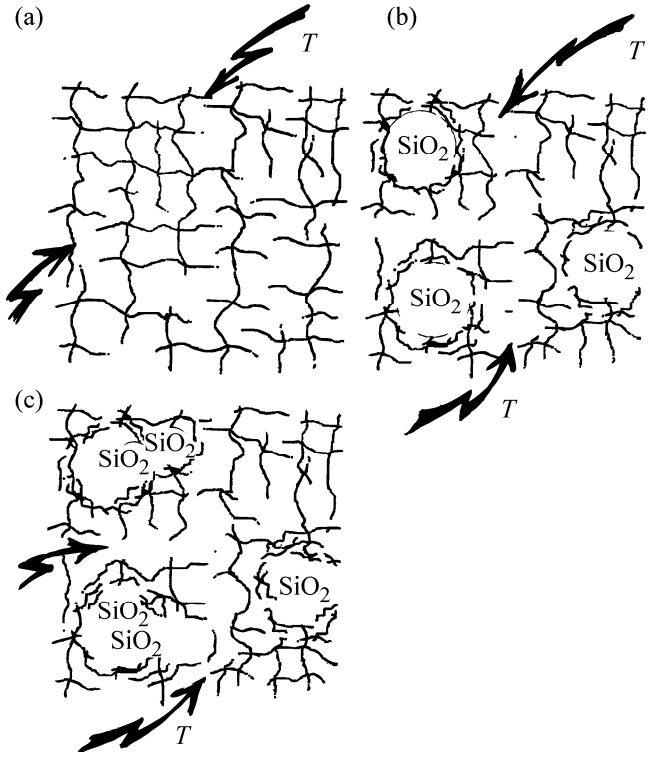


Fig. 2. Schematic illustration of the possible influence of the surface area, size, and aggregation of silica particles on the structure of a network polymer. Polymer: (a) unfilled, (b) filled with coarsely dispersed silica (A-50, A-100), and (c) filled with finely dispersed silica (A-300, A-455). Arrows symbolize the temperature effect on the polymer degradation.

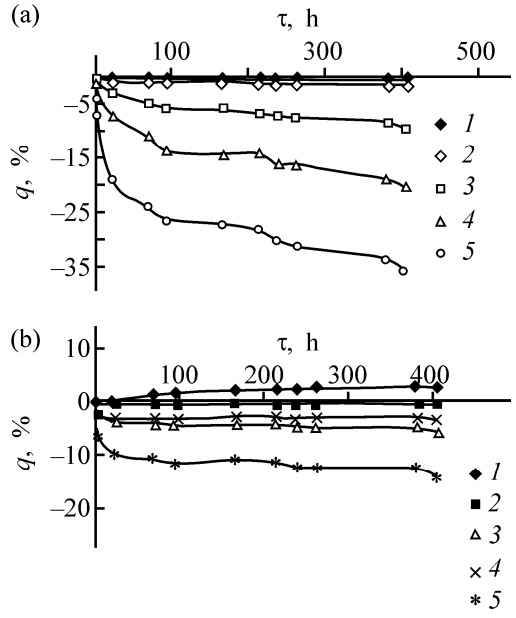


Fig. 3. Weight loss q of samples with time τ of keeping in 0.1 N KOH of composites based on (a) OKM-2 and (b) TGM-3, filled with 0–20% A-300 silica. Filler content, wt %: (*1*) 0, (*2*) 1, (*3*) 5, (*4*) 10, and (*5*) 20.

In remote areas of the adsorbed surface layer of the polymer, there are zones of increased strain of polymer chains and loose packing of macromolecules, which undergo thermal degradation first (Fig. 2, arrows). Thus, filling raises the density in the surface layer but distorts the integral structure of the network polymer, promoting appearance of breaks, loosenings, and weak regions. This leads to an increase in the temperature t_2 of the high-temperature process in the derivatograms. Apparently, the particle size (specific surface area) of silica is not a decisive factor in the formation of these loose layers; therefore, the specific surface area does not affect the temperature T_1 of primary degradation.

Variation of the filler concentration within the range 10–20 wt % also affects the amount, but not the quality of these "weak areas." This fact apparently accounts for the weak dependence of the temperature interval of the main thermal degradation process on the silica concentration. Indeed, degradation starts in weak areas irrespective of their amount (Fig. 2). The richer chemical composition of the degradation products in the case of the filled polymer can also be attributed to the formation of "weak areas" (Table 2).

Our conclusions are, on the whole, consistent with published data for other polymer–filler systems [3, 7, 9]. Bolbukh et al. [3] believe that the decrease in the activation energy of the thermal degradation of divinylbenzene–styrene or divinylbenzene–acrylate copolymers upon filling with silica containing trimethylsilyl groups is due to the formation of strained and rigid chains near the surface of Aerosil particles.

It follows from the above scheme that filling with Aerosil should also diminish the resistance of photopolyacrylate composites, e.g., in aggressive liquid media. Examination of the swelling curves for various composites in alkali solutions confirmed this conclusion. Figure 3 shows the typical curves of the weight loss with time, $q(t)$, on filling of various photopolymeric matrices with Aerosil. They demonstrate a well-defined, though not always linear (Fig. 3b), decrease in the resistance of the composite with increasing silica concentration.

From the suggested scheme and experimental data, we can make certain conclusions about the influence of the specific surface area and the concentration of Aerosil on the thermal and chemical resistance of the polymer. For example, the resistance of the composite in alkali solution strongly depends on the Aerosil concentration. The dependence may be either linear (with OKM-2) or nonlinear (with TGM-3) (Fig. 3).

In particular, of interest is the concentration of about 10 wt % at which the weight loss of the composite based on TGM-3 in alkali is lower than that with 5 and 20 wt % filler (Fig. 3).

As for the heat resistance, two cases should be considered. In the low-temperature region, there is no noticeable effect of the specific surface area of Aerosil on the temperature T_1 of primary thermal degradation: Only a slight decrease in T_1 and t_1 is observed as the surface area increases (Table 1). The Aerosil concentration affects these parameters insignificantly. In the high-temperature region (>450°C), the afterdegradation temperature ($T_2 = t_2$) strongly depends on the filling conditions: it whereases as the surface area and concentration of Aerosil decrease (Table 1). The maximal afterdegradation temperature is attained at 10 wt % filler content (Table 1), a concentration frequently mentioned in published papers. For example, according to [10], the formation of ordered supramolecular structures becomes hindered at a filler concentration exceeding 10 wt %, and according to [8], at 10 wt % filler content the polymer conversion in the composite appreciably increases. This fact suggests that the best ordered structures of surface layers, which are the most resistant to thermal degradation, are formed at a filler content of up to 10 wt %, whereas further increase in the filler concentration leads to their disordering.

CONCLUSIONS

(1) Introduction of nanosilicas into photopolymeric acrylate composites diminishes their heat resistance by 10–20%, but does not noticeably affect their thermal degradation. The effect is the stronger, the smaller the specific surface area of the silica and the lower the filler concentration (within the range examined). The decrease in the resistance to alkali solutions clearly correlates with the increase in the filler content.

(2) Upon filling of the composites, the spectrum of thermal degradation products in the temperature range 200–400°C becomes richer, and in the range 600–900°C, poorer, which indicates that the filling affects the polymer degradation at lower temperatures.

(3) The thermal degradation correlates with the level of ordering of surface layers of the polymer in the filled composite, which, in turn, is associated with the effect of nanosilica on the structures of the network polyacrylate.

REFERENCES

1. Lipatov, Yu.S., *Fiziko-khimicheskie osnovy napolneniya polimerov* (Physicochemical Principles of Polymer Filling), Moscow: Khimiya, 1991.
2. Syrovatka, L.O., Dmitrieva, T.V., and Bortnitskii, V.I., *Polim. Zh.* (Kiev), 2007, vol. 29, no. 34, pp. 301–306.
3. Bolbukh, Y.N., Tertykh, V.A., and Gawdzik, B., *J. Therm. Anal. Calorim.*, 2006, vol. 86, no. 1, pp. 125–132.
4. Yang, R., Ling, Y., Yu, J., and Wang, K., *Polym. Degrad. Stab.*, 2006, vol. 91, pp. 1651–1657.
5. Lomakin, S.M., Dubnikova, I.L., Derezina, S.M., and Zaikov, G.E., *J. Polym. Sci., Ser. A*, 2006, vol. 48, no. 1, pp. 72–84.
6. McEwlee, J., Nelmy, R., and Fadeev, A.Y., *J. Colloid Interface Sci.*, 2005, vol. 285, pp. 551–556.
7. Zapunnaya, K.V., in *Novye metody polucheniya i issledovaniya polimerov* (New Methods for Preparing and Studying Polymers), Kiev: Naukova Dumka, 1978, pp. 184–202.
8. Starokadomskii, D.L., Effect of Highly Dispersed Silica on Photopolymerization of Oligoacrylate Composites, *Cand. Sci. Dissertation*, Kiev, 2004.
9. Semko, L.S., Dzyubenko, L.S., Ogenko, V.M., and Revo, S.L., *J. Therm. Anal. Calorim.*, 2002, vol. 70, pp. 621–631.
10. Solomko, V.P., *Napolnennye kristallizuyushchiesya polimery* (Filled Crystallizing Polymers), Kiev: Naukova Dumka, 1980.

ISSN 1070-4272, Russian Journal of Applied Chemistry, 2008, Vol. 81, No. 12, pp. 2162–2165. © Pleiades Publishing, Ltd., 2008.
Original Russian Text © O.V. Zhukova, V.V. Medvedeva, Yu.D. Semchikov, 2008, published in Zhurnal Prikladnoi Khimii, 2008, Vol. 81, No. 12, pp. 2052–2055.

MACROMOLECULAR CHEMISTRY AND POLYMERIC MATERIALS

Gelation in Sodium Lignosulfonate Solutions in the Presence of a Hexavalent Chromium Salt

O. V. Zhukova, V. V. Medvedeva, and Yu. D. Semchikov

Nizhni Novgorod State Medical Academy, Nizhni Novgorod, Russia

Research Institute of Chemistry, Lobachevsky State University, Nizhni Novgorod, Russia

Lobachevsky State University, Nizhni Novgorod, Russia

Received August 5, 2008

Abstract—Gelation in the system sodium lignosulfonate–hexavalent chromium salt was studied. Isothermal phase diagrams were constructed, and the critical gelation concentrations of the polymer and cross-linking agent were determined. The time evolution of the elastic modulus of the gels was examined.

DOI: 10.1134/S1070427208120239

Raising the productivity of oil and gas wells is a pressing problem today. For this purpose, secondary and tertiary oil recovery processes are used, e.g., flooding with polymer solutions. This technique comprises injection of a polymer solution of increased viscosity through injection wells. However, injection of a polymer solution is not always an effective tool for raising the formation pressure. In this case, there is a need for systems with advanced mechanical characteristics, e.g., hydrogels, which could be prepared through gelation of the polymer via interaction of its functional groups with cross-linking agents [1].

Oil and gas industry employs various water-soluble polymers, such as polyacrylamide and its copolymers and cellulose ethers [2]. Previously, we have performed a rather thorough study of the gelation in hydroxyethyl cellulose and sodium carboxymethyl cellulose solutions, including syneresis and dynamics of viscoelastic properties of these gels, and also the effect of pH and alkali metal salts on their characteristics [3–5]. It has been shown that Sodium lignosulfonate (NaLS) is the most promising as a polymer for use in oil and gas industry [6]. Being a by-product of sulfite cellulose manufacture, this polymer is inexpensive and readily available. It forms coordination cross-linked gels in the presence of transition metal salts [7, 8]. The use of such gels in oil and gas industry facilitates solution of at least two problems, one of which is environmental (utilization of wastes from pulp-and-paper industry) and another, economic (reducing the cost of reagents for oil and gas production).

There is only limited published information on NaLS-based gels [9].

In this study, we examined the gelation in NaLS solutions in the presence of $Cr_2O_7^{2-}$ ions. The formation of such gels has been studied earlier, but therehave been no comprehensive studies because of the complexity of the process and problems arising in its practical implementation. Also the effects of alkali and alkaline-earth metal salts on the critical gelation concentration and mechanical characteristics of the resulting gels have been studied. These effects are of great practical significance in view of the fact that these salts are always present in formation water.

EXPERIMENTAL

In the study, we used commercial solid NaLS from Solikamsk Pulp and Paper Combine.

In gelation experiments, we used 40–50 wt % NaLS solution in distilled water and 10–50 wt % solutions of potassium ($K_2Cr_2O_7$) or sodium dichromate ($Na_2Cr_2O_7 \cdot 2H_2O$). Initially we prepared the gels in the presence of potassium dichromate. However, its solubility in water is only 12.5 g/100 g H_2O, which is much lower than that of the sodium salt (180.0 g/100 g H_2O, 20°C). Therefore, all the subsequent experiments were performed with sodium dichromate.

To examine the effect of alkali and alkaline earth metal salts on gelation, 0.5–3.0 M NaCl and 0.5 M $MgSO_4 \cdot 7H_2O$ were introduced into the system.

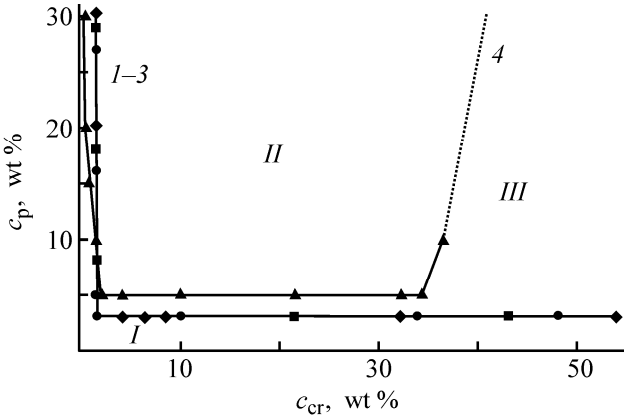


Fig. 1. c_p vs. c_{Cr} isotherm of the system NaLS–dichromate. (c_p) Polymer concentration and (c_{Cr}) sodium dichromate concentration. [NaCl], M: (*1*, *3*) 0, (*2*) 0.5, and (*4*) 3.0. [$MgSO_4 \cdot 7H_2O$], M: (*1*, *2*, *4*) 0 and (*3*) 0.5. Regions: (*I*) solutions, (*II*) gels, and (*III*) heterogeneous systems.

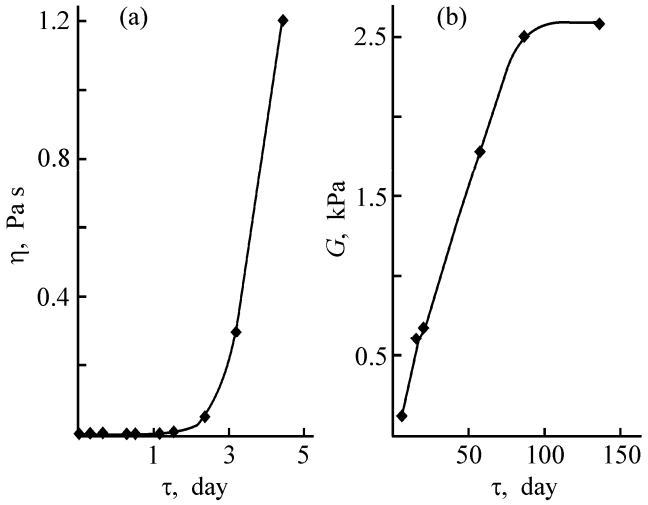


Fig. 2. (a) Viscosity η and (b) elastic modulus G vs. time τ. c_p = 10 wt %, c_{Cr} = 3.0 wt %.

The critical gelation concentrations, i.e., the minimal concentrations of the polymer and cross-linking agent that provide gelation, were fixed visually by the loss of solution flowability under gravity at the instant of turning over the vial containing the polymer and chromium salt solutions [10].

The viscous characteristics of the system before the flowability loss were measured on a BH-2 Höppler (falling ball) viscometer (Prüfgeräte–Werk Medingen, Dresden, Germany).

The elastic modulus was measured by the penetration method using spherical indenters of various radii (2–3 mm, depending on the elasticity of the gel) [11] and also by the tangential plate displacement method using a specially designed analytical balance. Following the Hertz theory, the elastic modulus of a test material is estimated in the spherical indentation case as

$$G = \frac{3}{16}\frac{F}{h^{3/2}R^{1/2}},$$

where F is the force applied to the spherical indenter of radius R, and h, indentation depth.

Experimental data on the critical gelation concentrations in the system NaLS–hexavalent chromium salt are presented in Fig. 1 as isotherms plotted in the coordinates polymer concentration vs. cross-linking agent concentration.

There are three regions in the isotherm bounded by curves corresponding to the minimal and maximal component concentrations at which gels are formed. The component concentrations in region *I* are below the critical gelation concentrations. Region *II* corresponds to formation of gels stable for a long time, and region *III*, to heterogeneous systems.

From this diagram, we estimated the critical polymer concentration (c_p = 3.0 wt %) and critical cross-linking agent concentration (c_{Cr} = 1.4 wt %) below which gelation does not occur at any concentration of the other component.

Our examination of the resulting gels revealed no visual water bleeding. In fact, however, syneresis takes place, though at a low rate: with time, the gels undergo shrinkage and compaction, keeping their shape.

Furthermore, as can be seen from Fig. 1, introduction of 0.5 M NaCl or $MgSO_4 \cdot 7H_2O$ into the system has nearly no effect on the critical polymer and cross-linking agent concentrations. However, with a simultaneous increase in the component concentrations, only two regions are found in the diagram, corresponding to solutions and gels.

Raising the NaCl concentration to 3 M leads to an increase in the critical gelation concentration with respect to the polymer to 5 wt %. Moreover, at high NaCl concentration, the range of gels is abruptly reduced, and the region of heterogeneous systems is found in the diagram, i.e., at sodium dichromate concentrations above curve *4*, no gelation occurs, but two-phase systems (solution and solid precipitate) are formed. In this case, salting-out of the polymer occurs, i.e., its solubility decreases with increasing salt concentration.

Our kinetic results show that the gelation in the system NaLS–sodium dichromate is characterized by a clearly pronounced induction period. Therefore, we measured the viscosity of the system before gelation and the elastic modulus after the loss of flowability (Fig. 2). The results show that, initially, the viscosity does not

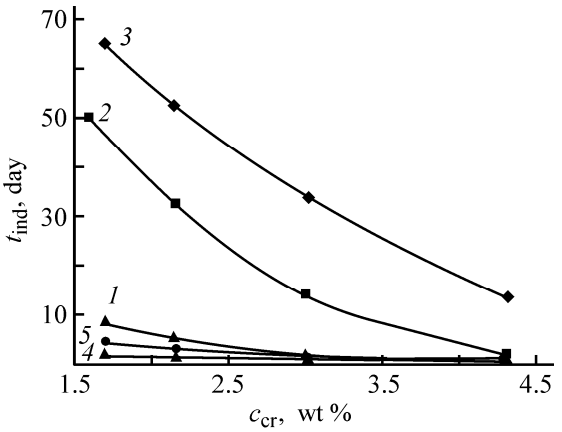


Fig. 3. Induction period t_{ind} vs. the dichromate concentration c_{Cr}. c_p, wt %: (*1*) 20.0, (*2*, *4*, *5*) 10.0, and (*3*) 5.0. [NaCl], M: (*1–3*, *5*) 0 and (*4*) 3.0. [$MgSO_4 \cdot 7H_2O$], M: (*1–4*) 0 and (*5*) 0.5.

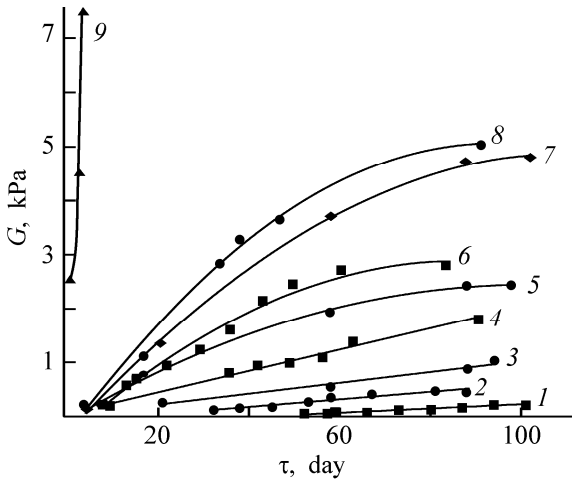


Fig. 4. Elastic modulus of the gels G vs. the time τ. c_p, wt %: (*1*, *2*, *6*) 5, (*3*, *5*, *7*, *8*) 10, and (*4*, *9*) 20. c_{Cr}, wt %: (*1*, *4*) 1.7, (*2*, *7*, *9*) 4.3, (*3*) 1.4, (*5*) 2.2, (*6*) 16.1, and (*8*) 6.5.

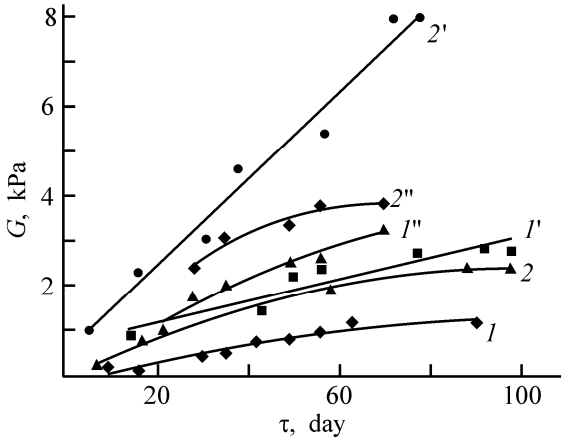


Fig. 5. Effect of alkali and alkaline-earth metal salts on the elastic modulus of the gels. c_p, wt %: (*1*, *1'*, *1"*) 5 and (*2*, *2'*, *2"*) 10. c_{Cr}, wt %: (*1*) 6.5 and (*2*) 2.2. [NaCl], M: (*1*, *2*) 0 and (*1'*, *2'*) 3. [$MgSO_4 \cdot 7H_2O$], M: (*1*, *2*) 0 and (*1"*, *2"*) 0.5.

change noticeably. Then it dramatically increases to the point of loss of flowability ($\eta \to \infty$), i.e., a gel is formed with the minimal elastic modulus (Fig. 2), which increases with time to the equilibrium value. This phenomenon can be attributed to a redox reaction between the dichromate ion and functional groups of the macromolecules, resulting in partial reduction of Cr(VI) to Cr(III). The occurrence of this reaction is confirmed by the fact that, in the course of gelation, pH changes from the acid range (pH 3.7) to the weakly alkaline range (pH 7.1).

According to the analyses in [12, 13], both Cr(III) polynuclear complexes and dichromate ions, forming cyclic structures with the guaiacyl groups of NaLS, are involved in the formation of the coordination network.

Our results show that the induction period of gelation decreases as both the polymer and the dichromate concentrations increase (Fig. 3). Addition of alkali and alkaline-earth metal salts has a more pronounced effect on the decrease of the induction period than changing in the polymer concentration. Thus, introduction of 0.5 M $MgSO_4 \cdot 7H_2O$ (Fig. 3, curve *5*) or 3.0 M NaCl (curve *4*) affects the induction period more strongly than does doubling of the polymer concentration (curves *2* and *1*).

The elastic modulus G of the gel is a rheological characteristic directly associated with the coordination network density, i.e., with the degree of structurization of the system. We studied the time evolution of G in the course of formation of gels of various compositions (Fig. 4). In all cases, the elastic modulus increases during a certain time, approaching the limiting (equilibrium) value (1–40 kPa, depending on the system composition).

Figure 4 shows that the elastic modulus of the resulting gels is controlled by the component concentrations in the system: G increases with the concentrations of the polymer (curves *1*, *3*) and dichromate (curves *1*, *5*). Deficit of both NaLS and dichromate considerably deteriorates properties of the gels: in this case, inelastic loose systems are formed.

The elastic modulus also increases upon introduction of alkali and alkaline-earth metal salts (Fig. 5). For example, addition of 3 M NaCl or 0.5 M $MgSO_4 \cdot 7H_2O$ cases an increase in G by about an order of magnitude, the effect being even more pronounced at higher polymer concentrations (Fig. 5).

Finally, our studies of the gelation in NaLS solu-

tions revealed some interesting features, which advantageously distinguish this system from those studied earlier. Gelation proceeds not instantly, but with some induction period caused by the redox reaction between the dichromate ions and macromolecules. Furthermore, addition of considerable amounts of alkali metal salts and even alkaline-earth metal salts does not interfere with the gelation; instead, it promotes formation of higher-molecular-weight gels, in contrast to the previously studied systems.

These features are important for practical appli-

CONCLUSIONS

(1) The dichromate ion is an efficient cross-linking agent for 5–30 wt % sodium lignosulfonate solutions. In this case, gels with an elastic modules G = 1–40 kPa are formed, and the gelation is characterized by clearly pronounced induction period.

(2) The elastic modulus of the resulting gels is in direct proportion to the polymer and cross-linking agent concentrations, whereas the induction period is in inverse proportion.

(3) Alkali and alkaline-earth metal salts hardly affect the critical gelation concentrations, but their addition makes the induction period several times shorter and raises the limiting (equilibrium) elastic modulus by several orders of magnitude.

REFERENCES

1. Rogers, W.F., *Composition and Properties of Oil Well Drilling Fluids*, Houston: Gulf, 1963.
2. Ibragimov, G.Z., Sorokin, V.A., and Khisamutdinov, N.I., *Khimicheskie reagenty dlya dobychi nefti* (Chemical Reagents for Oil Production), Moscow: Nedra, 1986.
3. Medvedeva, V.V. and Semchikov, Yu.D., *Vysokomol. Soedin., Ser. B*, 2001, vol. 43, no. 6, pp. 1074–1078.
4. Medvedeva, V.V., Myasnikova, L.I., and Semchikov, Yu.D., *Vysokomol. Soedin., Ser. A*, 2000, vol. 42, no. 5, pp. 840–848.
5. Medvedeva, V.V., Myasnikova, L.I., Semchikov, Yu.D., and Rogovina, L.Z., *Vysokomol. Soedin., Ser. B*, 1998, vol. 40, no. 3, pp. 492–497.
6. Chudakov, M.I., *Promyshlennoe ispol'zovanie lignina* (Industrial Application of Lignin), Moscow: Lesnaya Prom–st., 1983.
7. *Lignins: Occurrence, Formation, Structure, and Reactions*, Sarkanen, K.V. and Ludwig, C.H., Eds., New York: Wiley, 1971.
8. Sapotnitskii, S.A., *Ispol'zovanie sul'fitnykh shchelokov* (Application of Sulfite Liquors), Moscow: Lesnaya Prom–st., 1981.
9. Haiashi, A. and Goring, D.A.I., *Japan TAPPI*, 1965, vol. 154, p. 66.
10. Medvedeva, V.V., Myasnikova, L.I., Semchikov, Yu.D., and Rogovina, L.Z., *Vysokomol. Soedin., Ser. B*, 1995, vol. 37, no. 6, pp. 1040–1042.
11. Nilsen, L.E., *Mechanical Properties of Polymers and Composites*, New York: Marcel Dekker, 1974.
12. Ivnas, L. and Lingberg, P., *Acta Chem. Scand.*, 1961, vol. 15, p. 1081.
13. Migita, N., Mitsukawa, R., Nakano, J., and Ichino, M., *Japan TAPPI*, 1954, vol. 8, p. 2.

ISSN 1070-4272, Russian Journal of Applied Chemistry, 2008, Vol. 81, No. 12, pp. 2166–2168. © Pleiades Publishing, Ltd., 2008.
Original Russian Text © S.S. Ermakov, A.N. Mel'nichenko, A.A. Sheremet, 2008, published in Zhurnal Prikladnoi Khimii, 2008, Vol. 81, No. 12, pp. 2056–2058.

BRIEF COMMUNICATIONS

Evaluation of the Efficiency of Electrolysis in Cells of Various Designs in Inversion-Voltammetric Determination of Lead

S. S. Ermakov, A. N. Mel'nichenko, and A. A. Sheremet

St. Petersburg State University, St. Petersburg, Russia

Received April 9, 2008

Abstract—Efficiency of the stage of pre-electrolysis in inversion-voltammetric measurements was examined in relation to the hydrodynamic modes used.

DOI: 10.1134/S1070427208120240

The pre-electrolysis stage is a constituent of several electrochemical methods of analysis: inversion voltammetry (IVA), controlled-potential coulometry (CPC), and zero-reference combined electrochemical technique [1–3]. It is known that the electrolyte agitation efficiency strongly affects the sensitivity of the methods mentioned above, because in all of them, the deposition current is inversely proportional to the diffusion layer thickness δ, the parameter that characterizes the intensity of mass transfer.

Traditionally, IVA measurements are carried out with a rotating disk electrode (RDE), whose theory has been developed by Levich [3]. The same hydrodynamic system was employed in [1, 5, 6] in a zero-reference electrochemical method in which the pre-electrolysis efficiency is determined by the coulometric constant:

$$K = DS/(\delta V), \quad (1)$$

where D is the diffusion coefficient; S, electrode area; δ, diffusion layer thickness; and V, volume of the solution under study in the cell.

It follows from Eq. (1) that the constant K depends not only on δ, but also on the working electrode area S. The dependence of K on the volume has been studied previously [1, 6]. In the RDE method, it is not always possible to make larger the working electrode area at a fixed solution volume, which is necessary for using the zero-reference method. Another hydrodynamic model, a rotating cylindrical electrode (RCE), is possible, which allows use of large electrodes at small solution volumes [6].

The limiting diffusion current to the RDE is given by the equation [3]

$$i_d = 0.62nFc_0\omega^{0.50}\nu^{-0.167}D^{0.667}, \quad (2)$$

where n is the number of electrons involved in the electrode reaction; F, Faraday number; c_0, solution concentration in the cell; ν, kinematic viscosity; ω, angular rotation rate; and D, diffusion coefficient.

The limiting diffusion current to the RCE can be found using the equation [6, 7]

$$i_d = 0.0791nFc_0\omega^{0.70}d_i^{-0.30}\nu^{-0.344}D^{0.667}, \quad (3)$$

where d_i is the electrode diameter.

Equation (2) is satisfied for the RDE in a wide range of rotation rates [3]. For the RCE (the general scheme of the electrode is shown in Fig. 1a), there exist three fluid flow modes resulting from different electrode rotation rates.

(1) Simple laminar flow with concentric current lines, observed at low cylinder rotation rates. This flow merely sets the substance in a circular motion, without any increase in the mass-transfer rate.

(2) Flow with Taylor vortices, a cellular flow with a velocity component directed from one cylinder toward the other. This flow is also regular, laminar, and stable; it requires a higher electrode rotation rate and contributes to the mass-transfer rate.

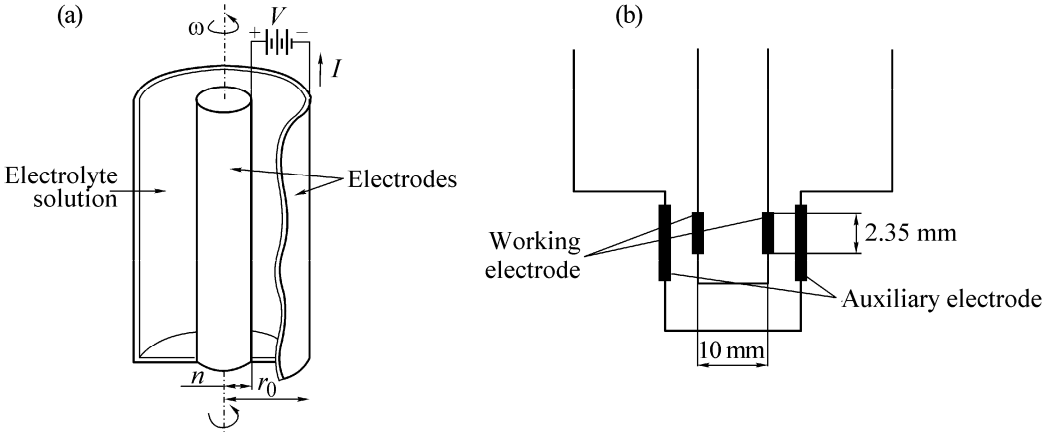


Fig. 1. (a) General scheme of a rotating cylindrical electrode and (b) schematic of the working cell: ω is the angular rotation rate of the cylindrical electrode; r, radius of the inner electrode; r_0, radius of the outer electrode; and V, voltage applied across the electrodes.

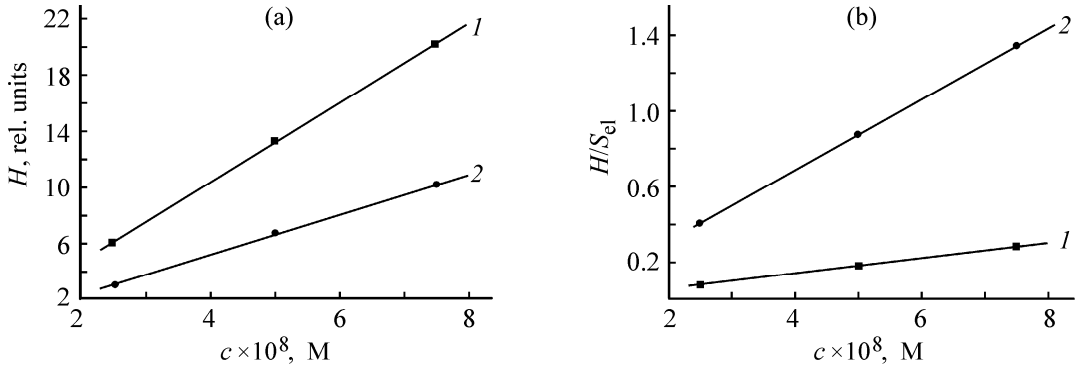


Fig. 2. (a) Height H of the ionization peak and (b) ratio between the analytical signal and the electrode area, H/S_{el}, vs. the solution concentration c in the working cell. Electrode rotation rate 1200 rpm. Electrode: (*1*) cylindrical and (*2*) disc-type; the same for Fig. 3.

(3) Turbulent flow characterized by rapid random fluctuations of velocity and pressure. Here is also included a fluctuating velocity component that is directed from one cylinder to the other and provides a substantial increase in the mass-transfer rate, which is uniform over the cylinder surface. This flow provides an effective agitation and requires the largest rotational moment.

Equation (3) is satisfied for the turbulent motion mode in a wide range of electrode rotation rates [6].

In this communication, the efficiencies of electrolysis with RDE and RCE are compared.

EXPERIMENTAL

The electrolysis efficiency was studied by the IVA method on a PLS-1 polarograph (Belarus) with an AKV-07 transducer (Akvilon NPKF, Moscow) in the ac mode. A solution of lead ions, with a concentration of 10^{-3} M, was prepared from a solution of a State standard sample (1 mg cm^{-3}) (SSS 7252–96). Solutions with concentrations of 10^{-5} and 10^{-6} M were prepared by dilution of the 10^{-3} M solution. The solutions were prepared from reagents of chemically pure and analytically pure grades and twice-distilled water. The measurements were made on a thin-film mercury-graphite electrode, with the electrode rotation rate in the accumulation stage varied from 1200 to 1800 rpm. The choice of the range of rotation rates was determined by the agitation intensity used in the IVA. All the potentials are given relative to a saturated silver chloride reference electrode. Platinum foil rolled-up in the form of a cylinder and placed along the inner wall of the lower part of the cup served as the auxiliary electrode. A solution of the following composition (M) was used as a supporting electrolyte: 1×10^{-4} $Hg(NO_3)_2 + 5 \times 10^{-2}$ HCl + 1×10^{-4} HNO_3. The preelectrolysis was carried out at a potential of –0.9 V. To satisfy the condition of a full dissolution of the metal from the amalgam, a low potential sweep rate was used (5 mV s^{-1}) [1]. The solution volume was constant (4 ml); the areas of the disc-type and cylindrical electrodes were 7.5 and 73.8 mm^2, respectively. The experiments were carried out in the quartz cell shown in Fig. 1b.

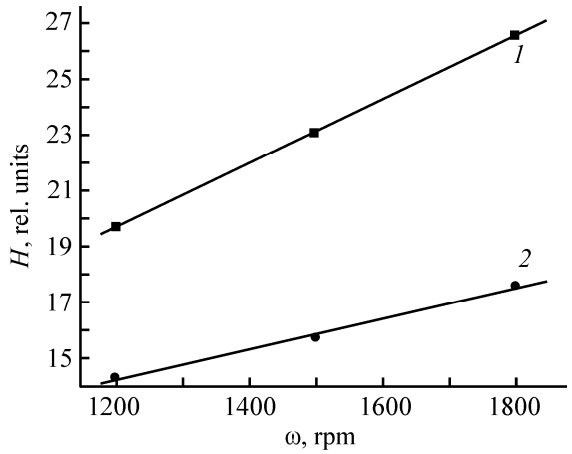


Fig. 3. Height H of the ionization peak vs. the electrode rotation rate ω.

The dependence of the current of Pb(II) dissolution from the amalgam on RDE and RCE in a solution at its different concentrations is shown in Fig. 2. The observed dependence is linear, in good agreement with Eqs. (2) and (3). The dependence of the dissolution (and, accordingly, deposition) current on the electrode rotation rate is shown in Fig. 3. At electrode rotation rates in the range 1200–1800 rpm, the dependence is almost linear in both cases and has slope rates $b_1 = 0.5$ for RDE and $b_2 = 0.7$ for RCE, also in good agreement with Eqs. (2) and (3). The value of b_2 equal to 0.7 indicates that a turbulent fluid motion occurs in the given case at the rotation rates studied.

The dependences of the currents of lead ionization from the amalgam on the rate of RDE and RCE rotation in the accumulation stage indicate that, at the electrode rotation rates within the range studied, the efficiency of electrolysis in the cell with RCE exceeds that in the cell with RDE. The efficiency of electrolysis with RCE is higher because of the larger electrode area, compared with RDE, in agreement with the data in Fig. 2b, which shows how the ratio between the height of the peak of lead ionization from the amalgam and the electrode area depends on the Pb(II) concentration in solution. The run of the dependence points to a higher efficiency of mass transfer in a cell with RDE, compared with RCE, at the electrode rotation rates within the range under study. Thus, the RDE provides a higher mass-transfer rate, compared with RCE, but the efficiency of electrolysis is higher with RCE because of its larger area at the given cell design.

CONCLUSIONS

It was shown that the efficiency of electrolysis in an electrochemical cell with a rotating cylindrical electrode exceeds that in a cell with a rotating disc electrode because of the possibility of using a larger-area cylindrical electrode at the same volume of a solution under study.

REFERENCES

1. Ermakov, S.S., Chekmeneva, E. N., and Moskvin, L.N., *Zh. Anal. Khim.*, 2007, vol. 62, no. 1, pp. 89–94.
2. Budnikov, G.K., Maistrenko, V.N., and Vyaselov, M.R., *Osnovy sovremennogo elektrokhimicheskogo analiza* (Fundamentals of Modern Electrochemical Analysis), Moscow: Mir, 2003.
3. Levich, V.G., *Fiziko-khimicheskaya gidrodinamika* (Physicochemical Hydrodynamics), Moscow: Fizmatgiz, 1959.
4. Averyaskina, E.O. and Ermakov, S.S., *Nauch. Priborostr.*, 2006, vol. 16, no. 4, pp. 97–101.
5. Sheremet, A.A. and Ermakov, S.S., *Zh. Prikl. Khim.*, 2006, vol. 79, no. 12, pp. 1970–1974.
6. Newman, J.S., *Electrochemical Systems*, Englewood Cliffs: Prentice-Hall, 1973.
7. Eisenberg, M., Tobias, C.W., and Wilke, C.R., *J. Electrochem. Soc.*, 1954, vol. 101, pp. 306–319.

ISSN 1070-4272, Russian Journal of Applied Chemistry, 2008, Vol. 81, No. 12, pp. 2169–2171. © Pleiades Publishing, Ltd., 2008.
Original Russian Text © V.V. Ivanov, V.I. Balakai, N.Yu. Kurnakova, A.V. Arzumanova, I.V. Balakai, 2008, published in Zhurnal Prikladnoi Khimii, 2008, Vol. 81, No. 12, pp. 2059–2061.

BRIEF COMMUNICATIONS

Synergistic Effect in Nickel–Teflon Composite Electrolytic Coatings

V. V. Ivanov, V. I. Balakai, N. Yu. Kurnakova, A. V. Arzumanova, and I. V. Balakai

South-Russian State Technical University (Novocherkassk Polytechnic Institute), Novocherkassk, Rostov oblast, Russia

Received March 25, 2008

Abstract—The possible synergistic effect in the manifestation of the wear resistance and antifriction properties of nickel–Teflon composite electrolytic coatings was analyzed. The results of calculations of the diagnostic properties of the coatings in terms of the "concentration-wave" model are discussed in comparison with the corresponding experimental data.

DOI: 10.1134/S1070427208120252

It is well known [1] that nickel–boron–Teflon composite electrolytic coatings (CECs) exhibit a synergistic effect: Their wear resistance and antifriction properties are better than those calculated in terms of the additive model. The synergism of the solid and lubricating components consists in that the lubricating Teflon phase is concentrated on the friction surface, thus enhancing the antifriction characteristics and wear resistance of the solid phases of the coatings, and that the coatings contain nanoparticles of certain solid phases (probably borides Ni_3B and Ni_2B). These nanoparticles have a spherical or cylindrical shape with a cross section diameter of 1.2–2.5 nm; they apparently exhibit the properties of solid lubricants [1].

To verify the assumption that nanoparticles of only low-boron nickel phases contribute to the overall synergistic effect observed with nickel–boron–Teflon CECs, we examined boron-free nickel–Teflon CECs. In this case, the possible synergism would be exclusively due to the first factor, concentration of Teflon microparticles on the friction surface.

The calculated data for the linear wear I^0_{lin} and friction coefficient f^0 of nickel–Teflon CECs in the CEC/CEC friction couple were obtained within the two-component approximation of the "concentration-wave" model [2] by the formulas:

$$I^0_{lin} = \alpha\langle I^0_{lin,\,solid}\rangle + (1-\alpha)\langle I^0_{lin,\,lub}\rangle + \delta(\langle I^0_{lin,\,solid}\rangle - \langle I^0_{lin,\,lub}\rangle), \quad (1)$$

$$f^0 = \alpha\langle f^0_{solid}\rangle + (1-\alpha)\langle f^0_{lub}\rangle - \delta(\langle f^0_{solid}\rangle - \langle f^0_{lub}\rangle), \quad (2)$$

where $\alpha = \alpha_{solid}$ and $(1-\alpha) = \alpha_{lub}$ are the volume fractions of the solid and lubricating components of CEC, respectively; $\delta = 4(1-\alpha)\alpha^2[1-k(1-k_n)]$, relative synergistic effect; k, size parameter characterizing the dispersity of the solid component of CEC: the ratio between the mean size of microparticles r_{solid} of solid phases in the surface later and the thickness of this layer Δx, i.e., $k = r_{solid}(r_{solid} + \Delta x)^{-1}$ (at $r_{solid} \to \Delta x$ $k \to 0.5$); k_n, nanostructure parameter of the solid component of CEC: the volume fraction of solid phase nanoparticles of spherical or cylindrical shape in the surface layer Δx ($0 \le k_n < 1$); $\langle I^0_{lin,\,solid}\rangle$, $\langle f^0_{solid}\rangle$, $\langle I^0_{lin,\,lub}\rangle$, and $\langle f^0_{lub}\rangle$ are the mean values of the corresponding individual characteristics in the solid and lubricating components of CEC [2].

In accordance with the data of Kryachko et al. [3], the influence of the characteristics of counterbody (CB) material (St45 steel in our case) on the CEC properties was taken into account as follows:

$$I_{lin} = I^0 + (\Delta\alpha - \Delta\delta)(I^0_{solid} - I^0_{lub}) + (\alpha + \delta)(I_{CB} - I^0_{solid}), \quad (3)$$

$$f = f^0 + (\Delta\alpha - \Delta\delta)(f^0_{solid} - f^0_{lub}) + (\alpha + \delta)(f_{CB} - f^0_{solid}), \quad (4)$$

where $\Delta\delta \cong 2\alpha(3\alpha - 2)\Delta\alpha$ is the change in the relative synergistic effect [3]; $\Delta\alpha = \alpha^* \cong (\alpha I^0_{solid} + I_{CB})\times$

Table 1. Phase composition and concentration of components of composite coatings

Coating	CEC component	Phase composition	Weight fraction	Volume fraction	α
			%		
Ni	Solid	Ni	100	100	1.00
	Lubricating	–	0	0	
Ni–Teflon	Solid	Ni	99.1	95.4	0.954
	Lubricating	Teflon	0.9	4.6	
	Solid	Ni	98.3	91.6	0.916
	Lubricating	Teflon	1.7	8.4	
	Solid	Ni	96.9	85.6	0.856
	Lubricating	Teflon	3.1	14.4	

$(I^0_{solid} + I_{CB})^{-1} - \alpha = (1 - \alpha)I_{CB}(I^0_{solid} + I_{CB})^{-1}$ is the change in the volume concentration of solid phases in going from CEC to wear products of the CEC/CB couple (for the CEC/CEC friction couple, $\Delta\alpha$ is formally equal to zero) [3]; $(\alpha + \delta) = \alpha[1 + 2\alpha(1 - \alpha)(1 + k_n)]$; I^0_{lin} and f^0 are the linear wear rate and CEC friction coefficient in the CEC/CEC friction couple, determined by formulas (1) and (2).

Composite electrolytic coatings with Teflon volume fractions of 4.6, 8.4, and 14.4% were prepared from an electrolyte of the following composition ($g\,l^{-1}$): nickel chloride hexahydrate 200–250, nickel sulfate heptahydrate 2.5–5.0, boric acid 25–40, Chloramine B 0.5–2.5, and F-4D-E (Teflon) emulsion 10–20. Electrolysis conditions: pH 1.0–5.5, temperature 18–30°C, cathode current density 0.5–9 $A\,dm^{-2}$.

From the data on the phase composition and concentration of CEC components (Table 1), using the calculation procedures described in [2, 3], we obtained the concentration dependences $I_{lin}(\alpha)$ and $f(\alpha)$ at fixed values of the parameter k_n = 0, 0.05, 0.1, 0.15, and 0.2 for the CEC/CEC and CEC/St45 friction couples.

Note that the individual characteristics of the solid and lubricating CEC components that we used in the calculations, namely, for nickel, $I_{lin,\,solid}$ = 1.1 $\mu m\,h^{-1}$, f_{solid} = 0.25; for Teflon, $I_{lin,\,lub}$ = 7.5 $\mu m\,h^{-1}$, f_{lub} = 0.03; and for St45 steel, $I_{lin,\,St45}$ = 1.2 $\mu m\,h^{-1}$, f_{St45} = 0.24, corresponded to the stationary step of the mode of dry friction of two identical materials at a specific load of 3 MPa and a friction velocity V = 0.048 $m\,s^{-1}$.

Analysis of the $I_{lin}(\alpha)$ dependences for CEP in the case of friction over the identical material showed that the minimum of the linear wear rate, 0.673 $\mu m\,h^{-1}$, at k_n = 0 is attained at α = 0.86. As the nanostructure parameter increases to 0.20, the minimum of the linear wear rate decreases to 0.401 $\mu m\,h^{-1}$ at α = 0.83. In the case of friction over St45 steel, $(I_{lin})_{min}$ = 0.520 $\mu m\,h^{-1}$ for k_n = 0 is attained at α = 0.80, and with an increase in k_n to 0.20, this value decreases to 0.356 at α = 0.75. Apparently, the observed quantitative changes in $I_{lin}(\alpha)$ dependences are due to a rise in the contribution of nickel nanoparticles to the synergistic effect of the CECs.

An analysis of the $f(\alpha)$ dependences revealed a regular decrease in the friction coefficient with an increase in the volume fraction of Teflon and decrease in f_{CB} in the entire range of α. However, the maximal synergistic effect, i.e., the maximal deviation of the dependences $f(\alpha)$ from the values calculated in terms of the corresponding additive model, is attained at α = 0.72 ± 0.02.

It should be noted that the calculated data can be used for determining the compositions of Ni–Teflon CECs with prescribed wear resistance and antifriction properties. From the same data, we can determine the optimal composition of a wear-resistant antifriction coating, i.e., a formulation with the minimal value of $(I_{lin}f)|k_n$. For example, at k_n = 0, the minimal value of this parameter is attained for CECs (friction over St45 steel) at the Teflon volume fraction of about 0.25.

Experimental data on the wear resistance of CECs in friction couples with St45 steel are in reasonable agreement with the calculated data at k = 0.5 and k_n = 0.07 (Table 2). The nanostructure parameter equal to 0.07 was used for obtaining predictable data on the other tribological characteristics of the CECs (Table 2).

Thus, the concentration-wave model with the parameters k = 0.5 and k_n = 0.07 allows satisfactory interpretation of the experimental data on the linear wear rate of Ni–Teflon CECs in friction over St45 steel and prediction of the corresponding friction coefficients. Within the framework of the model we used, the quantity $k_n > 0$ means not only a high dispersity of micro-

Table 2. Wear and antifriction properties of nickel and composite coatings in a friction couple with St45 steel

Coating	α	Linear wear rate I_{lin}, μm h^{-1}		Friction coefficient f	
		calculation	experiment	calculation	experiment
Ni	1.000	1.20	1.20	0.24	0.24
Ni–Teflon	0.954	0.782	0.79	0.217	–
	0.916	0.608	0.59	0.192	–
	0.856	0.455	0.46	0.156	–
Ni–B	1.000	1.100	1.10	0.25	0.25
Ni–B–Teflon	0.954	0.767	0.74	0.218	0.21
	0.898	0.630	0.56	0.185	0.17
	0.835	0.434	0.42	0.155	0.15

particles of Ni and γ-Fe phases, but also the presence among them of spherical or cylindrical nanofragments enhancing the effect of the CEC lubricating component.

It should be noted that the experimental data on the linear wear rate and friction coefficient for the nickel–boron–Teflon CEC, reported in [1] (Table 2), were satisfactorily described by the concentration wave model with a higher nanostructure parameter $k_n = 0.17$. In so doing, it was assumed [1] that, along with Teflon concentration on the surface of the CEC/St45 friction couple, nanoparticles of the specific shape were formed only from boron-containing phases.

The data we obtained suggest that, in nickel–boron–Teflon CECs, not only Ni_3B and Ni_2B, but also Ni and γ-Fe phases act in friction as lubricating components along with Teflon. On the whole, the role of boron-containing phases consists in that the wear resistance of the coatings is enhanced owing to their individual charactetistics I^0_{lin} and the friction coefficient of the surface decreases owing to the formation of the corresponding nanoparticles.

CONCLUSIONS

(1) Ni–Teflon composite electrolytic coatings show a synergistic effect consisting in enhancement of their wear resistance and antifriction properties, compared to the additive values.

(2) The synergism of the solid and lubricating components of the composite electrolytic coatings under consideration consists in concentration of Teflon on the wear surface, enhancing the antifriction properties and wear resistance of nickel, and in the presence of spherical or cylindrical nickel nanoparticles acting as solid lubricants.

REFERENCES

1. Ivanov, V.V., Balakai, V.I., Ivanov, A.V., and Arzumanova, A.V., *Zh. Prikl. Khim.*, 2006, vol. 79, no. 4, pp. 619–621.
2. Ivanov, V.V., Shcherbakov, I.N., Ivanov, A.V., and Bashkirov, O.M., *Izv. Vyssh. Uchebn. Zaved., Sev.-Kavk. Region, Tekh. Nauki*, 2005, no. 5, pp. 42–46.
3. Ivanov, V.V. and Shcherbakov, I.N., in *Problemy sinergetiki v tribologii, triboelektrokhimii, materialovedenii i mekhatronike: Materialy IV Mezhdunarodnoi nauchno-prakticheskoi konferentsii* (Problems of Synergism in Tribology, Triboelectrochemistry, Materials Science, and Mechatronics: Proc. IV Int. Scientific and Practical Conf.), Novocherkassk: Yuzhno-Ross. Gos. Tekh. Univ. (NPI), November 4, 2005, pp. 25–26.

ISSN 1070-4272, Russian Journal of Applied Chemistry, 2008, Vol. 81, No. 12, pp. 2172–2174. © Pleiades Publishing, Ltd., 2008.
Original Russian Text © D.S. Kalyagin, Yu.E. Ermolenko, Yu.G. Vlasov, 2008, published in Zhurnal Prikladnoi Khimii, 2008, Vol. 81, No. 12, pp. 2062–2064.

BRIEF COMMUNICATIONS

Diffusion of Tl-204 Isotope and Ionic Conductivity in Tl_4HgI_6 Membrane Material for Chemical Sensors

D. S. Kalyagin, Yu. E. Ermolenko, and Yu. G. Vlasov

St. Petersburg State University, St. Petersburg, Russia

Received October 27, 2008

Abstract—Method for solid-phase synthesis of Tl_4HgI_6 was developed and the diffusion coefficients of thallium-204 isotope were determined for this compound for the first time. Data on the ionic conductivity and diffusion of thallium ions were obtained and used to calculate the defect concentration and mobility in the thallium sublattice.

DOI: 10.1134/S1070427208120264

The topicality of this study is due to a search for new crystalline inorganic materials that would be promising as materials for ion-selective membranes for chemical sensors. Studies of the structure and transport characteristics of these materials are highly important for determining the possibility of their use in development of new sensors [1, 2]. This communication presents results obtained in measurements of the ionic conductivity and the diffusion coefficients of thallium-204 isotope in the compound Tl_4HgI_6 and data on the mobility coefficients and concentration of defects in the thallium sublattice of this compound at various temperatures.

EXPERIMENTAL

As starting substances for solid-phase synthesis of the compound Tl_4HgI_6 were chosen TlI and HgI_2 preliminarily precipitated from aqueous solutions, with $TlNO_3$, $Hg(NO_3)_2$, and KI of special-purity grade used as starting reagents. The thallium and mercury iodide salts with grain sizes $d \leq 30$ μm, dried in an inert atmosphere, were taken in the relative amounts of 80 mol % TlI + 20 mol % HgI_2, thoroughly mixed, and ground in an agate mortar to full homogeneity. The resulting mixture was placed in a steel mold and compacted into cylindrical briquettes 6 mm in diameter and 8–10 mm high at a specific pressure of 1.5 ton cm^{-2}. Then the briquettes were annealed in a dry inert atmosphere at 200°C for 3 h.

After a slow cooling, the samples were ground and again compacted to perform the second cycle of the solid-phase reaction at the same temperature (200° C). An X-ray phase analysis performed after two cycles of the solid-phase reaction demonstrated the presence of the only phase with a tetragonal unit cell (a = 9.26 Å, b = 9.45 Å, space group $P4/mnc$) corresponding to Tl_4HgI_6. For measurements of the electrical conductivity and diffusion coefficients, the resulting compound was again compacted at a residual pressure of 3 ton cm^{-2} into cylindrical samples 6 mm in diameter and 6–10 mm high.

The total electrical conductivity was measured with graphite contacts in the ac mode at frequencies of 0.3–20 kHz in the temperature range 80–200°C. The experimental setup comprised an E 8-2 resistance-capacitance bridge, F 582 zero indicator, GZ-56/1 low-frequency generator, electric furnace, and nitrogen-filled measuring cell. An analysis of the frequency dispersion of the resistance revealed an insignificant variation in the frequency range 5–20 kHz. Despite this circumstance, the conductivity data obtained were extrapolated to an infinite frequency.

Figure 1 shows temperature dependences of the electrical conductivity of Tl_4HgI_6 samples for different numbers of cycles of the solid-phase reaction. Within the experimental error, all the straight lines obtained are well reproducible both in absolute values of conductivity and in activation energies. However, all fur-

ther experiments used samples obtained after two cycles of the solid-phase reaction, because samples subjected to a single cycle contained trace amounts of unreacted thallium and mercury iodides.

Experiments aimed to estimate the electronic component of the conductivity in Tl_4HgI_6 were carried out by Wagner's polarization method in the dc mode with one reversible and one inert electrodes [3, 4]. With the method used to synthesize the Tl_4HgI_6 compound in the temperature range 80–200°C, the electronic component was 1.5–2.0 orders of magnitude lower than the total electrical conductivity. Thus, the graphical dependences log σ–T (Figs. 1, 2) with activation energy E_a eV can be assumed to represent only the ionic component σ_{ion}. It should be noted that only strict observation of the stoichiometry, well developed synthesis technology, and purity of the starting reagents make it possible to obtain the Tl_4HgI_6 compound with nearly purely ionic conductivity in the temperature range specified (80–200°C).

The adequacy of the experimental procedure and measuring techniques chosen in this study is confirmed not only by the good reproducibility of results for different numbers of cycles of solid-phase synthesis (Fig. 1), but also by their rather good agreement with data obtained by a number of other authors [5, 6] (Fig. 2).

The main part of the experimental study consisted in measuring the diffusion coefficients of thallium-204 radioactive isotope ($T_{1/2}$ = 3.78 yr, E_β = 763 keV) in the Tl_4HgI_6 ionic conductor and in comparing the results obtained in studies of the diffusion and ionic conductivity. The experiments were performed by the method of diffusion from an "infinitely" thin $TlNO_3$ layer, with the subsequent sectioning of a sample and measurements of the β-activity of ground-off layers on an end-window counter.

The diffusion annealing of the samples was performed in the temperature range 120–200°C for 900 s. The resulting linear dependences of the activity logarithm on the squared distance from the starting deposited active layer (A–x^2) are shown in Fig. 3. The experimental straight lines plotted in the coordinates log A–x^2 without any peaks of residual activity near $x \to 0$ point to diffusion from an infinitely thin layer and to the bulk nature of the process.

The diffusion coefficients were calculated using the formula for the distribution of radioactive ions in a sample for the case of diffusion from a thin layer:

$$\log A = \text{const} - (0.1086/D^*t)x^2,$$

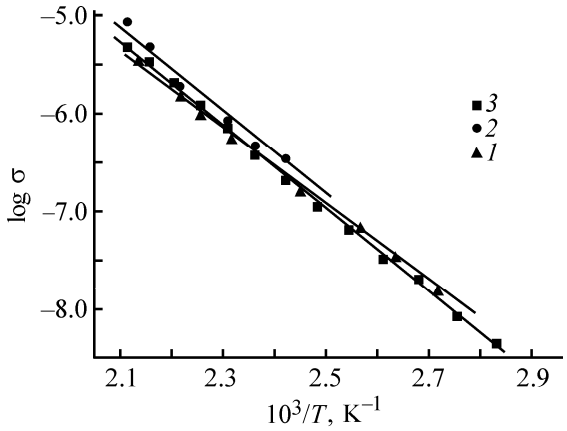


Fig. 1. Dependence of the electrical conductivity σ of Tl_4HgI_6 samples after one, two, or three cycles of the solid-phase reaction on temperature T. (*1–3*) Number of cycles of the solid-phase reaction.

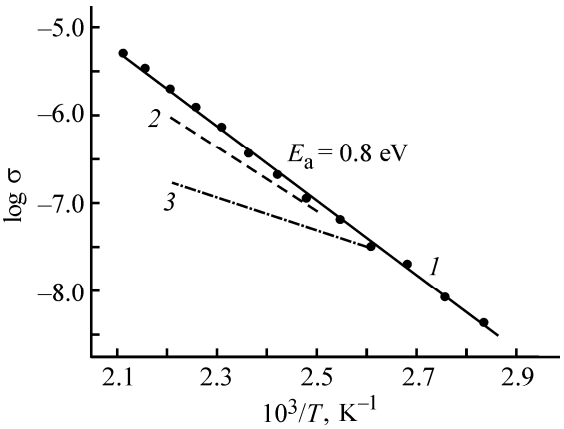


Fig. 2. Dependence of the electrical conductivity σ of Tl_4HgI_6 samples on temperature T in comparison with data of various authors. (*1*) Results of this study; published data: (*2*) [5] and (*3*) [6].

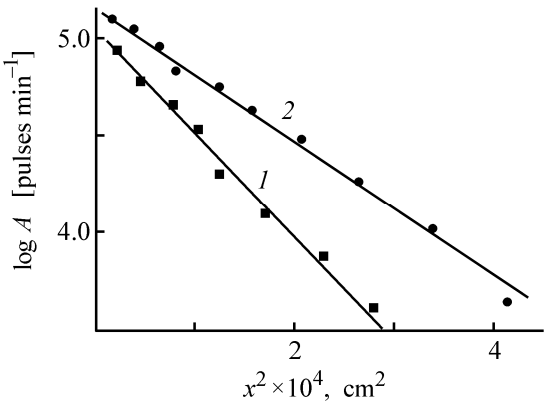


Fig. 3. Diffusion profiles of Tl_4HgI_6 samples for temperatures of (*1*) 182 and (*2*) 188°C. (*A*) Activity of a section and (*x*) distance from the active surface.

where A is the activity of a ground-off section (pulses min^{-1}); x, distance from the active surface (cm); t, time of sample annealing (s); and D^*, diffusion coefficient (cm^2 s^{-1}).

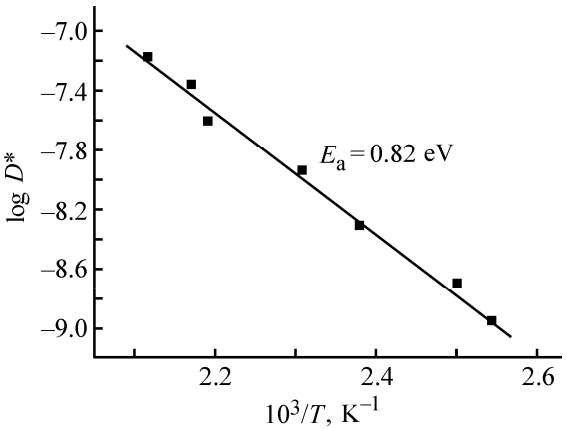


Fig. 4. Dependence of the diffusion coefficients D^* of thallium-204 isotope in the Tl_4HgI_6 compound on temperature T.

Figure 3 shows as an example the diffusion profiles for annealing temperatures of 182 and 188°C. Experiments on determining D^* were carried out for ten samples in the temperature range 120–200°C; data for seven of these are presented in Fig. 4. It is important to note that the activation energy found for diffusion of thallium ions, E_{diff} = 0.82 eV, well correlates with the activation energy of ionic conductivity, E_{cond} = 0.84 eV in Tl_4HgI_6.

The data on the diffusion of Tl-204 isotope in Tl_4HgI_6 samples can be used to calculate the mobility μ of thallium ions at various temperatures by the Nernst–Einstein equation:

$$D^*/\mu = kT/e,$$

where e is the charge of the ion (C); k, Boltzmann's constant (J deg^{-1}); μ, mobility of the ion (cm^2 V^{-1} s^{-1}); and T, absolute temperature.

For example, $\mu_1 = 5.8\times10^{-8}$ cm^2 V^{-1} s^{-1} and $\mu_2 = 1.6\times10^{-6}$ cm^2 V^{-1} s^{-1} at temperatures of 127 and 199°C, respectively.

As an additional important characteristic of the ion transport in Tl_4HgI_6 samples can serve the concentration of thallium defects in the cation sublattice, calculated from the data obtained. The total concentration of Tl^+ ions can be found ($N = 7.6\times10^{21}$ ions cm^{-3}). from the measured density of polycrystalline thallium hexaiodomercurate samples, ρ = 5.6 g cm^{-3}. Also, these concentrations can be found, e.g., for temperatures of 127 and 199°C, to be $\eta_1 = 1.1\times10^{19}$ s cm^{-3} and $\eta_2 = 1.8\times10^{19}$ s cm^{-3} on the assumption that $\sigma_{ion} = e\eta_i\mu_i$, where η is the concentration of carriers (defects).

Thus, the effective fraction of ion carriers in the temperature range in question can be estimated as (1.5–2.4) $\times10^{-3}$. The high value of the ionic component of the conductivity makes it possible to regard Tl_4HgI_6 as a promising material for chemical sensors.

CONCLUSIONS

(1) The diffusion coefficients D^* and the ionic electrical conductivity σ were found for Tl_4HgI_6 in the temperature range 80–200°C, and the concentrations of defects in the thallium sublattice and their mobilities were determined.

(2) A quantitative study of ionic transport characteristics in thallium hexaiodomercurate demonstrated the advisability of its use for development of membranes for chemical sensors for the thallium ion.

ACKNOWLEDGMENTS

The study was in part financially supported by the Russian Foundation for Basic Research (grant no. 08-03-00723).

REFERENCES

1. Bobacka, J., Ivaska, A., and Lewenstam, A., *Chem. Rev.*, 2008, vol. 108, pp. 329–351.
2. Privett, B.J., Shin, J.H., and Schoenfisch, M.H., *Anal. Chem.*, 2008, vol. 80, pp. 4499–4517.
3. West, A. R., *Solid State Chemistry and Its Applications*, Chichester: John Wiley&Sons, 1984.
4. Ivanov-Shits, A.K. and Murin, I.V., *Ionika tverdogo tela* (Solid-State Ionics), SPb. Gos. Univ., 2000, vol. 1.
5. Kennedy, J.H., Schaupp, C., Yang, Y., et al., *J. Solid State Chem.*, 1990, vol. 88, no. 2, pp. 555–563.
6. Nawaz Rafiuddin, M.S., I*onics*, 2007, vol. 13, pp. 35–40.

ISSN 1070-4272, Russian Journal of Applied Chemistry, 2008, Vol. 81, No. 12, pp. 2175–2177. © Pleiades Publishing, Ltd., 2008.
Original Russian Text © I.N. Gaidukov, L.M. Popova, 2008, published in Zhurnal Prikladnoi Khimii, 2008, Vol. 81, No. 12, pp. 2065–2067.

BRIEF COMMUNICATIONS

Preparation of Fluorinated Esters of Abietic Acid

I. N. Gaidukov and L. M. Popova

St. Petersburg State Technological University of Vegetable Polymers, St. Petersburg, Russia

Received July 28, 2008

Abstract—The reaction of abietic acid chloride with sodium salts of 1*H*,1*H*-dihydrotrifluoroethanol, 1*H*,1*H*,3*H*-trihydrotetrafluoropropanol, 1*H*,1*H*,5*H*-trihydrooctafluoropentanol, and pentafluorophenol was studied. The main reaction products are the corresponding fluorinated alkyl (aryl) abietates.

DOI: 10.1134/S1070427208120276

One of the ways to modify rosin is its esterification. The resulting products, depending on the kind of the rosin and alcohol used, show promise in production of synthetic resins, ester plasticizers, hot-melt adhesives, varnishes, paints, adhesives for food package, etc., meeting the most stringent environmental requirements. As compounds with long-chain fluoroalkyl group exhibit surface activity [1], esters of rosin and fluorinated alcohols can be valuable hydro- and oleophobizing agents for fibrous composite materials. Therefore, development of procedures for preparing such esters is a topical problem.

This work continues our studies devoted to development of new fluorinated surfactants [2, 3] and is aimed to devise of a procedure for preparing previously unknown esters of abietic acid (model compound of oleoresin rosin) and fluorinated alcohols: 1*H*,1*H*-dihydrotrifluoroethanol, 1*H*,1*H*,3*H*-trihydrotetrafluoropropanol, 1*H*,1*H*,5*H*-trihydrooctafluoropentanol, and pentafluorophenol.

Esterification of resin acids, the major component of rosin, is complicated by the steric shielding of the carboxy group located at the tertiary carbon atom [4] and by the low acidity (pK_a 6.4) [5] of compounds of this class. This results in a decrease in the rate of esterification of resin acids in the presence of common acid catalysts (H_2SO_4, H_3PO_4, etc.). Performing the esterification under harsh conditions (in the presence of aggressive acid agents and at elevated temperatures) gives rise to undesirable side reactions, such as dimerization of abietic-type acids and their disproportionation, which diminishes the yield of the target product and complicates its isolation [3]. Therefore, the reaction of resin acids with alcohols in the presence of acid catalysts is an extremely inefficient route to esters.

In some reports, alternative procedures for preparing resin acid esters have been suggested. For example, it is recommended to prepare methyl abietate by the reaction of abietic acid with diazomethane [6] or of silver abietate with methyl iodide on heating [7]. Halbrook and Lawrence [8] prepared rosin monoesters of ethylene or 1,3-propylene glycol by the reaction of rosin with ethylene or propylene oxide at elevated temperatures. The reactions of alkali metal resinates with alkyl halides also yield esters; by this route, Zandersons and Tardenaka [9] prepared glycidyl abietate. As reported by Bardyshev [4], methyl, ethyl, and phenyl abietates are formed by reactions of the corresponding alcohols with abietic anhydride. It was also noted that these reactions occur at elevated temperatures in the presence of a catalyst. Johnston [10] prepared ethyl abietate by the reaction of abietic acid chloride with ethanol.

Kryachko et al. [3] reported that esterification of abietic acid with 1*H*,1*H*,5*H*-trihydrooctafluoropentanol in the presence of *p*-toluenesulfonic acid yields 1*H*,1*H*,5*H*-trihydrooctafluoropentyl dehydroabietate, i.e., the esterification is accompanied by disproportionation of abietic acid. The same ester has been prepared by esterification of dehydroabietic acid with concentrated H_2SO_4 as catalyst [2].

In the present study, esters of abietic acid and fluorinated alcohols were prepared by reactions of sodium salts of the corresponding alcohols and abietic acid chloride synthesized as described in [4, 11–14]. The reactions between the alcoholates and acid chlo-

Analytical and NMR data for products of reactions of abietic acid chlorides with sodium salts of 1H,1H-dihydrotrifluoroethanol, 1*H*,1*H*,3*H*-trihydrotetrafluoropropanol, 1*H*,1*H*,5*H*-trihydrooctafluoropentanol, and pentafluorophenol (products **I–IV**, respectively)

Product	Reaction time, h	Product yield, %	R_f	NMR spectrum, δ, ppm		Iodine number, g I_2/g	Acid number, mg KOH/g
				^{1}H	^{19}F		
I	3	90	0.86	0.87, 1.02, 1.22, 1.26, 1.33, 2.75, 4.46, 5.37, 5.78	–72.26 (s)	154	1.5
II	6	85	0.85	0.86, 0.92, 1.01, 1.22, 1.26, 1.33, 2.87, 4.59, 4.9, 5.25–5.6, 5.78, 6.37 (t.t, $^2J_{HF}$ 52.7 Hz)	–123.6 (s), –136.4 (d)	168	35
III	6	65	0.89	0.87, 1.02, 1.22, 1.26, 1.33, 2.75, 4.75, 5.25–5.6, 5.78, 6.73 (t.t, $^2J_{HF}$ 52.7 Hz)	–119.5 (s), –124 (s), –131 (s), –138, –137.3 (d)	150	30
IV	6	60	0.79	0.85, 0.91, 1.03, 1.20, 1.21, 1.26, 2.85, 4.90, 5.37, 5.78	–170.8 (t), –165.1 (t), –161.9 (d)	168	21

ride were performed in toluene in the course of 3–6 h, at the reactant molar ratio of 1 : 1.25. The choice of the alcoholate instead of the corresponding alcohol was governed by the facts that the reaction in this case is faster and that the second product is sodium chloride, which is insoluble in toluene and can be readily removed from the reaction mixture, i.e., isolation of the desired product is simplified. The products obtained were yellow-brown resinous noncrystallizing sub-

EXPERIMENTAL

The ^{1}H and ^{19}F NMR spectra of the products were recorded on a Bruker WH-400 spectrometer (400 MHz) from 5% solutions in acetone-d_6. The chemical shifts were determined relative to internal TMS (^{1}H NMR) and trifluoroacetic acid (^{19}F NMR).

To evaluate the purity of the initial abietic acid and monitor the reaction progress, we used TLC on Silufol UV 254 plates (eluent hexane–methylene chloride–acetone, 1 : 1 : 0.5).

Abietic acid was isolated from oleoresin rosin of the Wg brand according to [6]. The solvents were purified by the standard procedures [15].

Sodium alcoholates were prepared by reactions of the corresponding fluorinated alcohols with sodium metal in ether or toluene, following the procedures described in [16–19].

Abietic acid chloride. To a solution of 5.00 g (16.5 mmol) of abietic acid in 100 ml of toluene, 0.74 g (5.5 mmol) of PCl_3 was slowly added at room temperature with stirring. The reaction mixture was stirred for 20 h, after which H_3PO_3 was filtered off. Abietic acid chloride was used immediately after preparation, without isolation.

Reaction of abietic acid chloride with sodium 1H,1H-trifluoroethylate. To 5.30 g (16.5 mmol) of abietic acid chloride in 100 ml of toluene, a suspension of 2.51 g (20.6 mmol) of sodium 1*H*,1*H*-dihydrotrifluoroethylate was added with vigorous stirring at room temperature. The mixture was stirred for 3 h, after which the NaCl precipitate was filtered off, the toluene solution was washed with water and dried over calcined $MgSO_4$, and the solvent was separated. The tarry residue was dried in a vacuum over P_2O_5. The yield of the product (**I**) was 90%.

1*H*,1*H*,3*H*-Trihydrotetrafluoropropyl (product **II**), 1*H*,1*H*,5*H*-trihydrooctafluoropentyl (product **III**), and pentafluorophenyl (product **IV**) esters of abietic acid were prepared similarly from 5.30 g (16.5 mmol) of abietic acid chloride and 3.17 g of sodium 1*H*,1*H*,3*H*-trihydrotetrafluoropropylate, 5.23 g of sodium 1*H*,1*H*,5*H*-trihydrooctafluoropentylate, and 4.24 g of sodium pentafluorophenolate, respectively; the reaction time was 6 h. The yields of fluorinated alkyl (aryl) abietates **II–IV**, evaluated by ^{1}H NMR, were 60–85% (see table).

The TLC data suggest the presence of a minor impurity of abietic acid in all the reaction mixtures. The formation of esters is also confirmed by the acid and iodine numbers of the resulting products (see table).

An NMR analysis of reaction mixtures from synthesis of **I–IV** revealed the presence of the major component, fluoroalkyl (fluoroaryl) abietate. For example, in the ^{1}H NMR spectra of **I–III**, there are multiplets with δ 4.46 (I), 4.59 (II), and 4.75 ppm (**III**), corresponding to the $-OCH_2-$ protons of the fluoroalkyl moiety. The olefinic protons in I–IV give rise to signals at 5.37, 5.78 (I), 5.25–5.6, 5.78 (**II**, **III**), and 5.37, 5.78 ppm (**IV**). In addition, in the spectra of **II** and **III** there are proton signals from terminal $-CF_2H$ groups (triplet of triplets) with δ 6.37 ($^2J_{HF}$ 52.7 Hz) (**II**) and 6.73 ppm ($^2J_{HF}$ 51.2 Hz) (**III**).

In the ^{19}F NMR spectrum of **I**, there is a single signal at –72.26 ppm, belonging to fluorine nuclei of the $-CF_3$ group. The presence of the $-^2CF_2-^3CF_2-$ group in the molecule of **II** is confirmed by the signals with δ_F –123.6 (s, $^2CF_2$) and –136.4 ppm (d, $-^3CF_2-$). In the spectrum of product **III** containing the residue of the telomeric alcohol with $n = 2$, there are the following signals: –119.5 (s, $-^2CF_2-$), –124 (s, $-^3CF_2-$), –131 ppm (s, $-^4CF_2-$), and a doublet of $-^5CF_2H$ (–138 and –137.3 ppm). For the pentafluorophenyl fragment, we observed signals from the fluorine atoms of the aromatic ring at –170.8 (γ-$C_{ar}F$), –165.1 (β-$C_{ar}F$), and –161.9 ppm (α-$C_{ar}F$).

The chemical shifts and integral intensities of the proton and fluorine signals correspond to the presumed structures of the fluorinated alkyl (aryl) abietates.

CONCLUSION

Fluorinated alkyl (aryl) abietates were prepared in 60–90% yields by the reactions of abietic acid chloride with sodium salts of 1*H*,1*H*-dihydrotrifluoroethanol, 1*H*,1*H*,3*H*-trihydrotetrafluoropropanol, 1*H*,1*H*,5*H*-trihydrooctafluoropentanol, and pentafluorophenol under mild conditions (toluene, room temperature, 3–6 h). Abietic acid does not disproportionate under these conditions.

ACKNOWLEDGMENTS

The study was financially supported by the St. Petersburg Government (project no. 3.6/04-05/19).

REFERENCES

1. *Fluorine Compounds: Modern Technology and Applications*, Ishikawa, N., Ed., Tokyo: CMC, 1987.
2. Popova, L.M. and Gaidukov, I.N., *Zh. Prikl. Khim.*, 2008, vol. 81, no. 2, pp. 338–339.
3. Kryachko, E.N., Trishin, Yu.G., and Popova, L.M., in *Materialy V Vserossiiskoi nauchnoi konferentsii "Khimiya i tekhnologiya rastitel'nykh veshchestv"* (Proc. V All-Russian Scientific Conf. "Chem-istry and Technology of Vegetable Substances"), Ufa, June 8–12, 2008, p. 171.
4. Bardyshev, I.I., *Zh. Org. Khim.,* 1999, vol. 35, no. 1, pp. 48–63.
5. Nyren, V. and Dack, E., *Acta Chem. Scand.*, 1958, vol. 12, no. 7, pp. 1516–1520.
6. Lazur'evskii, L.V., Terent'eva, I.V., and Shamshurin, A.A., *Prakticheskie raboty po khimii prirodnykh soedinenii* (Practical Works on Chemistry of Natural Compounds), Moscow: Vysshaya Shkola, 1961.
7. Krestinskii, V.N., Persiantseva, N.I., and Novak, A.A., *Zh. Prikl. Khim.*, 1939, vol. 12, no. 9, pp. 1407–1421.
8. Halbrook, N.J. and Lawrence, R.V., *Ind. Eng. Chem. Prod. Res. Develop.*, 1963, vol. 7, no. 3, pp. 183–185.
9. Zandersons, Ya.G. and Tardenaka, A.T., *Khim. Drev.*, 1983, no. 4, pp. 30–33.
10. Johnston, A.C., *Ind. Eng. Chem.*, 1929, vol. 21, no. 7, pp. 688–689.
11. Borisova, N.V., Kushnir, S.R., et al., *Khim. Rastit. Soedin.*, 2005, no. 2, pp. 21–27.
12. Kushnir, S.R., Borisova, N.V., et al., *Zh. Prikl. Khim.*, 2003, vol. 76, no. 11, pp. 1845–1847.
13. Lloyd, W.D. and Hedrick, G.W., *J. Org. Chem.*, 1963, vol. 28, no. 4, pp. 1165–1157.
14. Weygand-Hilgetag, *Organisch-chemische Experimentierkunst*, Leipzig: Johann Ambrosius Barth, 1964, 3rd ed.
15. Gordon, A.J. and Ford, R.A., *The Chemist's Companion. A Handbook of Practical Data, Techniques, and References*, New York: Wiley, 1972.
16. *Khimiya alifaticheskikh ftorsoderzhashchikh spirtov* (Chemistry of Aliphatic Fluorinated Alcohols), Krolevets, A.A., Ed., Moscow: VINITI, 1985.
17. Zinov'ev, Yu.M., Kulakova, V.N., and Soborovskii, L.Z., *Zh. Obshch. Khim.*, 1957, vol. 27, no. 9, pp. 2528–2559.
18. Gitel', P.Shch., Osipova, L.F., Solovova, O.P., and Yakubovich, A.Ya., *Zh. Obshch. Khim.*, 1969, vol. 39, no. 2, pp. 301–303.
19. Shelud'ko, E.V., *Dokl. Akad. Nauk Ukr. SSR, Ser. B*, 1980, no. 11, pp. 68–70.

ISSN 1070-4272, Russian Journal of Applied Chemistry, 2008, Vol. 81, No. 12, pp. 2178–2179. © Pleiades Publishing, Ltd., 2008.
Original Russian Text © A.V. Kurzin, A.N. Evdokimov, O.S. Pavlova, V.B. Antipina, 2008, published in Zhurnal Prikladnoi Khimii, 2008, Vol. 81, No. 12, pp. 2068–2069.

BRIEF COMMUNICATIONS

Esters of Amylose, Cellulose, and Tall Oil Fatty Acids

A. V. Kurzin, A. N. Evdokimov, O. S. Pavlova, and V. B. Antipina

St. Petersburg State Technological University of Vegetable Polymers, St. Petersburg, Russia

Received May 14, 2008

Abstract—The possibility of preparing amylose and cellulose esters by esterification and acylation with chlorides of tall oil fatty acids was examined.

DOI: 10.1134/S1070427208120288

Esters of carbohydrates and higher fatty acids (HFAs), the so-called liposaccharides, are promising and valuable nonionic surfactants used in various branches of industry and in medicine [1]. Polysaccharide esters form a particular group of liposaccharides. The main procedures for their preparation are based on acylation with HFAs under the conditions of acid or base catalysis, and also on ester interchange of alkyl esters of acids with polysaccharides [1–4].

A promising renewable source of fatty acids is tall oil, a by-product from kraft pulp production. The main components of tall oil fatty acids (TOFAs) are unsaturated C_{18} acids: oleic, linoleic, and linolenic [5]. A search for new applications of tall products is a topical problem of pulp-and-paper and resin industry. Previously, we have prepared liposaccharides from sucrose [6], xylitol [7], and tall oil fatty acids.

The goal of this study was to prepare TOFA esters of amylose and cellulose.

Use of strong Brønsted acids as acylation catalysts leads to formation of dark tarry products. A more efficient synthetic route to polysaccharide esters is the reaction of activated polymers with acid chlorides in the presence of tertiary amines.

Chlorides of higher unsaturated acids are usually prepared by treatment of the acids with phosphorus halides or thionyl chloride, but side processes occur in the latter case. For the experiments, we chose phosphorus trichloride, which is successfully used in synthesis of chlorides of higher fatty unsaturated acids, including TOFAs [8].

Among the catalysts reported in the literature for esterification of carbohydrates with HFAs, a particular place is occupied by anhydrides and chlorides of acetic acid derivatives (methoxyacetic, chloroacetic, trifluoroacetic acids). Positive results have also been obtained with free trichloroacetic acid used as catalyst (impeller).

The degree of substitution of the reaction product was calculated from the difference between the saponification number and acid number. For the amylose ester prepared with TOFA chlorides, it was 0.38, and for the ester prepared using trichloroacetic acid, 0.45. The low acid numbers (less than 1 mg KOH/g product) show that the product hardly contains any amount of starting fatty acids. The appearance of new ester bonds is also confirmed by comparison of the IR spectra of the starting amylose and its esterification products. Absorption bands characteristic of stretching vibrations of ester C=O groups (1730 cm^{-1}) and of double bonds in hydrocarbon residues of TOFAs (1680–1620 cm^{-1}) appear in the IR spectra, whereas bands of the reagents used, including C–Cl stretching vibration bands (800–600 cm^{-1}), are absent.

The polymers obtained are structurally similar to surfactants widely used today for stabilization of dispersions and control over rheological properties (Emulsan etc.) [9].

EXPERIMENTAL

TOFAs (A grade, Segezha Pulp-and-Paper Combine, Joint-Stock Company) were additionally purified by vacuum distillation, with the fraction boiling at 170–205°C/1 mm Hg collected. Bleached coniferous pulp (Kotlas Pulp-and-Paper Combine, Joint-Stock Company) was disintegrated to separate fibers. TOFA

chlorides were prepared by the reaction of the acids with phosphorus trichloride according to [7]. In our study we used edible-grade amylose and dehydrated trichloroacetic acid (chemically pure grade). Pyridine (chemically pure grade) was dried over KOH and distilled. The acid and saponification numbers were determined by the standard procedures [10]. The IR spectra of the esters were recorded on a Shimadzu FTIR-8400S spectrophotometer from Nujol mulls.

Esters of polysaccharides and TOFAs were prepared as follows.

(1) A mixture of 20 g (0.12 mol) of the polysaccharide (cellulose was preliminarily kept in 50 ml of pyridine for 2 days in a flask with a tightly ground-in stopper), 80 ml of pyridine, and 100 ml of toluene was stirred for 20 min. To this mixture, 150 ml (0.5 mol) of TOFA chlorides was added, and the mixture was heated with a reflux condenser at 55°C for 8 h. Then 100 ml of methanol was added, the mixture was filtered, and the precipitate was washed with methanol (2×50 ml) and petroleum ether (50 ml) and dried in air.

(2) Trichloroacetic acid (210 g, 1.3 mol) was mixed with 105 ml (0.36 mol) of TOFAs, after which 50 g of pyridine was added. The mixture was stirred for 20 min. To this solution, 20 g (0.12 mol) of the polysaccharide was added (cellulose was preliminarily kept in 50 ml of pyridine for 2 days in a flask with a tightly ground-in stopper), and the mixture was heated with a reflux condenser at 40°C for 8 h. Then 150 ml of methanol was added, the mixture was filtered, and the precipitate was washed with two portions of a methanol–hexane mixture (1 : 1, 50 ml) and dried in air.

The resulting amylose esters are weakly colored solid amorphous substances, and cellulose esters are pale yellowish fibrous materials.

CONCLUSION

Polysaccharides can be acylated with tall oil fatty acids or acid chlorides in the presence of pyridine or with the free acids in the presence of trichloroacetic acid.

REFERENCES

1. Zhoglo, F.A., *Zhirosakhara (Poluchenie, svoistva, primenenie*) (Liposaccharides: Preparation, Properties, Use), Moscow: Meditsina, 1975.
2. Heinze, T., Liebert, T., and Koschella, A., *Esterification of Polysaccharides*, Berlin: Springer, 2006.
3. Grass, A.T. and Feuge, R.O., *J. Am. Oil Chem. Soc*., 1962, vol. 39, no. 1, pp. 19–24.
4. Ioannidis, O.K., Pogosov, Yu.L., and Aikhodzhaev, B.I., in *Khimiya i fizikokhimiya prirodnykh i sinteticheskikh polimerov* (Chemistry and Physical Chemistry of Natural and Synthetic Polymers), Tashkent: Fan, 1964, issue 2, pp. 60–65.
5. Kogan, V.B. and Trofimov, A.N., *Poluchenie karbonovykh kislot na osnove drevesiny* (Preparation of Carboxylic Acids from Wood), Moscow: Lesnaya Prom–st., 1977.
6. Kurzin, A.V., Evdokimov, A.N., Pavlova, O.S., and Antipina, V.B., *Zh. Prikl. Khim*., 2007, vol. 80, no. 2, pp. 345–346.
7. Kurzin, A.V., Evdokimov, A.N., Pavlova, O.S., and Antipina, V.B., *Khim. Rast. Syr'ya*, 2008, no. 1, pp. 151–152.
8. Wang, S.-F., Furuno, T., and Cheng, Z., *J. Wood Sci*., 2001, vol. 47, no. 3, pp. 470–475.
9. Holmberg, K., Jönsson, B., Kronberg, B., and Lindman, B., *Surfactants and Polymers in Aqueous Solution*, Chichester: Wiley, 2003.
10. Gurova, T.A., *Tekhnicheskii kontrol' proizvodstva plastmass i izdelii iz nikh* (Technical Monitoring of Production of Plastics and Articles Thereof), Moscow: Vysshaya Shkola, 1991.

ISSN 1070-4272, Russian Journal of Applied Chemistry, 2008, Vol. 81, No. 12, pp. 2180–2182. © Pleiades Publishing, Ltd., 2008.
Original Russian Text © A.B. Shishmakov, Yu.V. Mikushina, A.S. Seleznev, O.V. Koryakova, M.S. Valova, L.A. Petrov, 2008, published in Zhurnal Prikladnoi Khimii, 2008, Vol. 81, No. 12, pp. 2070–2072.

BRIEF COMMUNICATIONS

A Carbon–Silica Composite Material Based on Powdered Cellulose: Synthesis and Properties

A. B. Shishmakov, Yu. V. Mikushina, A. S. Seleznev, O. V. Koryakova, M. S. Valova, and L. A. Petrov

Institute of Organic Synthesis, Ural Branch, Russian Academy of Sciences, Yekaterinburg, Russia

Received May 4, 2008

Abstract—A procedure was developed for preparing a carbon–silica composite by thermolysis of powdered cellulose in the presence of tetraethoxysilane. The resulting composite was studied in model processes of trimethylhydroquinone oxidation and hydrogen peroxide decomposition.

DOI: 10.1134/S107042720812029X

Carbon–mineral composite materials find growing use in various branches of science and technology [1–7]. Modification of carbon fibers with a silicon dioxide xerogel is accompanied by changes in the physicochemical (in particular, sorption) properties of the material, which expands the possibilities of its use as catalyst support, enterosorbent, hemosorbent, adsorbent for chromatography, etc. However, practical use of carbon composites is largely restricted by their relatively high cost. Therefore, a topical task is development of new methods for preparing such materials with the required set of consumer's properties from cheap and renewable raw materials. One of the most readily available materials for producing these composites is cellulose. Of most interest for this purpose is powdered cellulose, whose preparation procedures have been developed in detail [8–10], because it is characterized by higher homogeneity, compared to common (fibrous) cellulose.

The goal of this study was to prepare carbon–silica materials based on carbon fibers formed by thermolysis of powdered cellulose and to study the properties of these materials. As inorganic component, we used hydrolysis products of tetraethoxysilane (TES).

EXPERIMENTAL

Powdered cellulose (PC) was prepared by hydrolysis of kraft pulp from Baikal Pulp-and-Paper Combine [TU OP (Pilot Technical Specification) 13-027 94 88-08–91] in 2.5 N HCl at 100°C. The hydrolysis was performed for 2 h. The resulting product was washed on the filter with distilled water to neutral pH of the aqueous extract, squeezed on the vacuum filter to a moisture content of 60 wt %, and compacted into granules 4 mm in diameter, which were dried at 100°C to constant weight and impregnated with tetraethoxysilane. The PC–TES sample was placed in a desiccator in an atmosphere of NH_3 and water vapor (10% aqueous ammonia solution) and kept there to ensure TES hydrolysis. The sample was dried at 100°C. Thus, we prepared a material of the composition PC–16% SiO_2, which was subsequently subjected to thermolysis at 350°C in a reactor equipped with a hydroseal. The material was heated at a rate of 2 deg min^{-1} and kept at the final temperature for 3 h.

The yield of the solid thermolysis product was 43%. The material had the composition C–36 wt % SiO_2. The resulting composite was impregnated to saturation with TES and kept in a desiccator in an atmosphere of NH_3 and water vapor. After the hydrolysis was complete, the material was dried at 100°C. The resulting material had the composition C–46 wt % SiO_2. Then the impregnation was repeated, and the final composition was C–65 wt % SiO_2. Granules of the composite were boiled for 3 h in water, with its intermittent replacement. Figure 1 shows a micrograph of the surface of the composite obtained.

The IR spectra of the solid powder were recorded on a Perkin–Elment Spectrum One IR Fourier spec-

trometer in the range 4000–370 cm^{-1} using a diffuse reflection attachment (DRA).

The bands were assigned on the basis of data from [11]. The spectra were processed, with calculation of the band intensities, using special programs from the software supplied with the spectrometer.

Kinetic experiments on oxidation of trimethylhydroquinone (TMHQ) and decomposition of hydrogen peroxide were performed in a temperature-controlled reactor equipped with a reflux condenser. The aqueous-methanol solution (water : methanol = 1 : 1 by volume) was agitated by air bubbling. Air was fed at a rate of 2.1 $1h^{-1}$. The oxidation of TMHQ was performed at 50°C; the temperature was maintained with an accuracy of ±0.2°C. The component concentrations were as follows: substrate 66 mM, $CuCl_2 \cdot 2H_2O$ 6 mM; the amount of the composite was 0.1–0.4 g. TMHQ was quantitatively determined performed by GLC with a Chrom-4 chromatograph [12]. The decomposition of hydrogen peroxide was studied at 50°C. The initial concentration of H_2O_2 was 5.7 mM, and the amount of the composite, 0.007–0.5 g. Kinetic measurements were performed by stopping the reaction and determining the content of the starting substance.

Sorption of carbon monoxide by the composite was studied with a BI-SORBchemo-2 device. A sample was placed in a quartz reactor and heated in a helium flow to 200°C at a rate of 10 deg min^{-1}; after being kept at the final temperature for 1 h, the sample was cooled to room temperature. The pulse titration with the sorbate gas was performed. The amount of the sorbed CO was determined with a thermal conductivity detector. The CO sorption was 0.041 cm^3 per gram of C–SiO_2. The carbon matrix sorbs CO in an amount of 0.49 $cm^3\ g^{-1}$.

For comparison, we performed sorption of CO on commercial activated birch charcoal BAU-A (S_{sp} = 750 $m^2\ g^{-1}$) and on BAU-A sample subjected to a single impregnation with TES and subsequent hydrolysis as described above, BAU-A–43 wt % SiO_2. No CO sorption on the reference samples was observed. Thus, the presence of silicon dioxide in the carbon granule leads to a considerable decrease in the sorption capacity for CO, apparently, because active sorption centers become less accessible to the sorbate. The total porosity of the sample was 0.7 $cm^3\ g^{-1}$.

The carbon–mineral composite was examined by IR spectroscopy. The IR spectrum of C–SiO_2 contains an absorption band at 3647 cm^{-1}, corresponding to stretching vibrations of O–H bonds in isolated hydroxy groups; a broad band at 3385 cm^{-1}, assigned to vibrations of adsorbed water and bound OH groups; bands at 2900–2800 cm^{-1}, assigned to stretching vibrations of methylene and methyl groups (weak absorption due to incomplete hydrolysis of TES); a band at 1700 cm^{-1}, assigned to C=O vibrations in carboxy groups of the carbon matrix, formed by thermal oxidative degradation of pyranose rings of PC [13]; a band at 1593 cm^{-1}, corresponding to the superposition of the stretching bands of ethylene groups (–CH=CH–) [13] and δ_{H-O-H} (1629 cm^{-1}). It should be noted that the presence of strong bands at 1593 and 1442 cm^{-1} may also suggest the presence of conjugated –C=C– bonds in fused aromatic structures [14] arising from PC degradation. The lack of the corresponding =C–H stretching bands at 3100–3000 cm^{-1} may be due to their being obscured by the low-frequency wing of the ν_{OH} band. The peaks between 1250 and 1000 cm^{-1} are assigned to the Si–O–Si vibrations.



Fig. 1. Microstructure of the surface of the composite material (×4000).

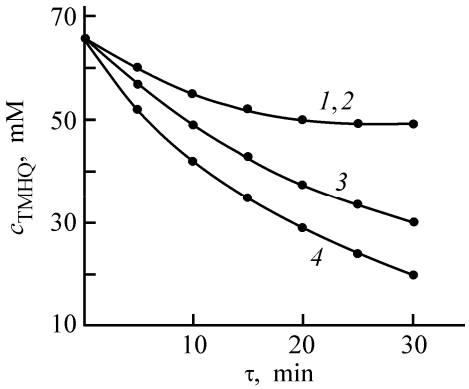


Fig. 2. Kinetic curves of oxidation of trimethylhydroquinone with atmospheric oxygen in the presence of various substances: (*1*) no substance added, (*2*) composite, (*3*) $CuCl_2$, and (*4*) $CuCl_2$ + composite. (c_{TMHQ}) Trimethylhydroquinone concentration amd (τ) time.

A study of the effect exerted by the composite on the decomposition of hydrogen peroxide showed that H_2O_2 remains stable in the presence of the composite in a wide range of substrate/C–SiO_2 ratios.

The composite material was tested in a model reaction of liquid-phase oxidation of TMHQ to trimethyl-1,4-benzoquinone. The results are shown in Fig. 2. Introduction of C–SiO_2 (sample weight 0.05–0.4 g) does not affect the course and parameters of oxidative dehydrogenation of TMHQ with atmospheric oxygen. When the reaction is performed with a catalyst, $CuCl_2 \cdot 2H_2O$, the presence of the composite leads to an increase in the TMHQ oxidation rate at the ratios of 0.15–0.2 mmol Cu^{2+}/g C–SiO_2. A previous ESR study have shown [15] that, depending on the Cu^{2+}/SiO_2 ratio, several types of Cu(II) complexes are formed in the SiO_2 phase: mononuclear complexes, Cu(II) hydroxide, and polynuclear bridged compounds. The last kind appeared to be the most reactive. Thus, the effect observed in the presence of the composite is due to complexation of Cu(II) ions with the oxide constituent of the composite, which leads to formation of the most catalytically active Cu(II) species on the surface of silicon dioxide in the examined range of Cu^{2+}/C–SiO_2 ratios.

CONCLUSIONS

(1) A granulated carbon–silica composite acting as sorbent and catalyst support was prepared by thermolysis of powdered cellulose in the presence of tetraethoxysilane.

(2) It was shown that the C–SiO_2 composite used as catalyst support in the model process of oxidative dehydrogenation of trimethylhydroquinone enhances the catalytic activity of Cu(II).

REFERENCES

1. Rachkovskaya, L.N. et al., *Izv. Sib. Otd. Akad. Nauk SSSR*, 1982, issue 5, no. 12, pp. 40–46.
2. Chernov, Yu.L., *Cand. Sci. Dissertation*, Novosibirsk, 1986.
3. Tazhkenova, G.K., Urmashev, B.A., Urazalin, A.K., et al., in *Gorenie i plazmokhimiya: Materialy II Mezhdunarodnogo simpoziuma* (Combustion and Plasmochemistry: Proc. II Int. Symp.), Almaty, 2003, pp. 214–219.
4. Tazhkenova, G.K., Ryabikin, Yu.A., Zashkvara, O.V., et al., in *Gorenie i plazmokhimiya: Materialy II Mezhdunarodnogo simpoziuma* (Combustion and Plasmochemistry: Proc. II Int. Symp.), Almaty, 2003, pp. 208–213.
5. Nikolaeva, A.F., Tazhkenova, G.K., Zhylybaeva, N.K., et al., in *Gorenie i plazmokhimiya: Materialy II Mezhdunarodnogo simpoziuma* (Combustion and Plasmochemistry: Proc. II Int. Symp.), Almaty, 2003, pp. 219–224.
6. Tazhkenova, G.K., Mansurov, Z.A., Erkasov, R.Sh., and Mansurova, R.M., in *Gorenie i plazmokhimiya: Materialy II Mezhdunarodnogo simpoziuma* (Combustion and Plasmochemistry: Proc. II Int. Symp.), Almaty, 2003, pp. 204–208.
7. Mel'gunova, E.A., Balabina, Yu.M., Shmakov, A.N., and Mel'gunov, M.S., *Zh. Fiz. Khim.*, 2003, vol. 77, no. 3, p. 510.
8. RF Patent 2 186 071.
9. Kocheva, L.S. and Karmanov, A.P., Abstracts of Papers, *II Vserossiiskaya konferentsiya "Khimiya i tekhnologiya rastitel'nykh veshchestv"* (II All-Russia Conf. "Chemistry and Technology of Vegetable Substances"), Kazan, June 24–27, 2002, p. 140.
10. Gert, E.V., Matyul'ko, A.V., Zubets, O.V., et al., *Zh. Prikl. Khim.*, 2003, vol. 76, no. 8, pp. 1375–1381.
11. Bellamy, L.J., *The Infra-Red Spectra of Complex Molecules*, New York: Wiley, 1957.
12. Kharchuk, V.G., Kolenko, I.P., Petrov, L.A., and Gus'kova, L.M., *Zh. Org. Khim.*, 1986, vol. 22, no. 11, pp. 2306–2315.
13. Smotrina, T.V., *Strukt. Din. Mol. Sist.*, 2003, no. 10, part 2, pp. 219–221.
14. Mikova, N.M., Naimushina, L.V., Chesnokov, N.V., et al., *Khim. Rast. Syr'ya*, 2001, no. 4, pp. 53–58.
15. Shishmakov, A.B., Kharchuk, V.G., Kuznetsova, O.V., et al., *Zh. Fiz. Khim.*, 2003, vol. 77, no. 4, pp. 623–628.

ISSN 1070-4272, Russian Journal of Applied Chemistry, 2008, Vol. 81, No. 12, pp. 2183–2186. © Pleiades Publishing, Ltd., 2008.
Original Russian Text © I.V. Kalinovskaya, A.G. Mirochnik, V.E. Karasev, 2008, published in Zhurnal Prikladnoi Khimii, 2008, Vol. 81, No. 12, pp. 2073–2075.

BRIEF COMMUNICATIONS

Photodegradation and Photostabilization of Europium Compounds in Polyvinyl Chloride

I. V. Kalinovskaya, A. G. Mirochnik, and V. E. Karasev

Institute of Chemistry, Far-Eastern Branch, Russian Academy of Sciences, Vladivostok, Russia

Received May 14, 2008

Abstract—The photolysis kinetics was studied, and methods were suggested for photostabilization of complexes of europium with β-diketones and europium cinnamates and quinaldates in polyvinyl chloride.

DOI: 10.1134/S1070427208120306

Preparation and study of the photochemical properties of polymeric materials doped with coordination compounds of rare-earth elements is a topical problem because of the possible applications of such materials in agriculture and medicine. The spectral characteristics and high quantum yields of fluorescence of lanthanide complexes allow their use as additives to polymeric materials [1, 2]. The thus obtained light-trans-forming polymeric materials enhance the photobiological conversion of solar light and raise the plant productivity [1, 3]. Therefore, of high importance are studies devited to preparation of photostable composites based on *f*-element compounds and organic luminophores showing strong luminescence in a wide spectrum range [4, 5]. Novel light-transforming polymeric materials with promising fluorescent and photochemical properties can be developed on the basis of these composites [6–8].

Polyvinyl chloride (PVC), a widely used polymer, exhibits high mechanical and radiation resistance and is transparent (90–95%) in the visible range [9]. However, PVC is extremely unstable when subjected to energetic actions, which nearly excludes its reprocessing and use without additional stabilization. This polymer contains a number of thermostabilizers and plasticizers, which break down a luminescent additive already in the course of preparation of the polymeric composite and initiate the photodecomposition of the luminescent additive. Therefore, photostabilization of luminophores based on europium complexes in polyvinyl chloride matrix is a topical problem [10].

In this study, we examined the kinetics of photodecomposition of luminescent europium compounds in PVC in the presence of a series of UV absorbents. As luminophores introduced into PVC we chose europium complexes that show the strongest luminescence: β-diketonates $Eu(\beta\text{-dik})_3 \cdot Phen$, where β-dik is an anion of acetylacetone (AA), thenoyltrifluoroacetone (TTA), or hexafluoroacetylacetone (HFAA); cinnamates $Eu(Cin)_3 \cdot L$, where L = H_2O, hexamethylphosphoramide (HMPA), 1,10-phenanthroline (Phen); quinaldates of monomolecular $[Eu(Qiun)_3 \cdot L$, where L = H_2O, Phen, benzimidazol-2-ylguanidine (BG)] and polymeric $\{[Eu(Quin)_3 \cdot H_2O]_n$, where Quin is anion of quinaldic acid$\}$.

As UV absorbents we chose quinaldic and cinnamic acids and the complex of europim chloride with 1,10-phenanthroline.

EXPERIMENTAL

The complexes were prepared as described in [11]. The luminescent compounds were introduced into an optically transparent polymer, polyvinyl chloride, which contained, along with commercial PVC proper, also thermostabilizers (Ba and Cd stearates), a plasticizer (dialkyl phthalate, DAP), lubricating additives (ESM soybean oil), and Ionol. The content of

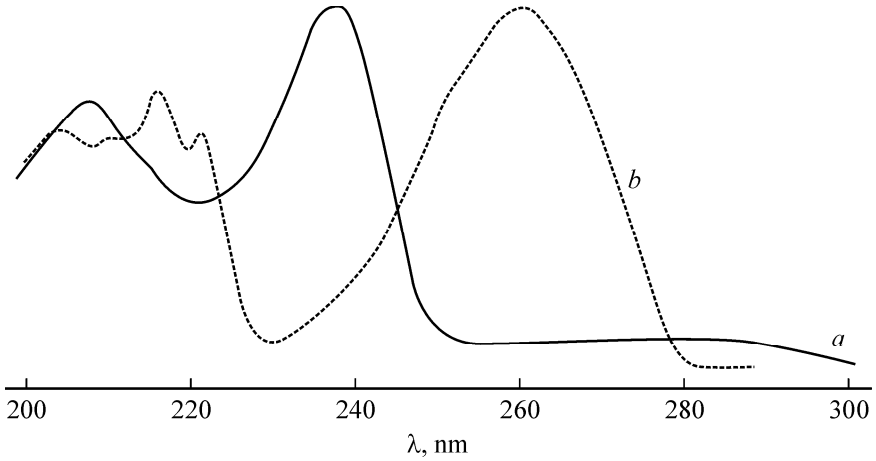


Fig. 1. Electronic absorption spectra of (*a*) quinaldic and (*b*) cinnamic acids. (λ) Wavelength.

the luminescent additive in the polymer was 0.1 wt %. The ratio of the luminophore and UV absorber in the polymer film was 1 : 1. For preparing luminescent composites, a mixture of PVC powder with the luminescent additive and UV absorber was thoroughly mixed and compacted on a hydraulic press. The electronic absorption spectra of the compounds in chloroform were recorded on an M-40 spectrometer. The luminescence spectra of polymeric compounds were recorded on an SDL-1 spectrophotometer. The polyvinyl chloride films were irradiated with the unfiltered light of a DRT-250 mercury lamp. The photodecomposition was monitored by variation of the luminescence intensity in the head line of the $^5D_0$–$^7F_2$ transition of the Eu ion with the time of the UV irradiation.

A comparative study of the absorption and luminescence spectra and photochemical properties of polymeric compounds with Eu complexes allowed us to choose the highest-intensity luminophores for further studies. Some of the examined luminophores and UV absorbers fully cease to luminesce already in the preparation step, or the intensity of their luminescence is very low. Therefore, for studying the photodegradation we chose the Eu(III) compounds that exhibited a high luminescence intensity in the polyvinyl chloride matrix.

Analysis of the spectral data shows that the composition and structure of luminescent compounds are preserved on their introduction into polyvinyl chloride. This is confirmed by the presence of a single line from the singlet $^5D_0$–$^7F_0$ transition, three Stark components assigned to the magnetic-dipole $^5D_0$–$^7F_1$ transition, and five components of the $^5D_0$–$^7F_2$ transition, as well as by only slight changes in the positions of the peak andin the distribution of the intensities of the Stark components.

Among the compounds examined, the complex of europium thenoyltrifluoroacetonate with 1,10-phenanthroline and polymeric europium quinaldate hydrate showed the strongest luminescence. Therefore, we chose these compounds for the photolysis experiments.

For photostabilization of europium complexes, we used a series of UV absorbers: cinnamic and quinaldic acids and a complex of europium chloride with 1,10-phenanthroline.

The electronic absorption spectrum of quinaldic acid is shown in Fig. 1, curve *a*. The absorption bands of the acid lie at 208–210, 240, and 282 nm. As compared to quinaldic acid, cinnamic acid shows higher extinction for some bands, i.e., it is a stronger UV absorbent (Fig. 1, curve *b*). The complex $EuCl_3 \cdot 2Phen$ has absorption bands at 220–230 and 260–270 nm.

Figure 2 illustrates the kinetics of photodecomposition of the luminescent complexes. The luminescent compounds we chose, introduced into the polyvinyl chloride film, cease to luminesce after UV irradiation for less than 1 h (Fig. 2a, curve *1*).

Introduction of quinaldic acid into the polymeric composite with $Eu(TTA)_3 \cdot Phen$ leads to a slight stabilization. The polymeric film ceases to luminesce after UV irradiation for 1.5 h (Fig. 2a, curve *2*). Cinnamic acid is a stronger UV absorbent than quinaldic acid,

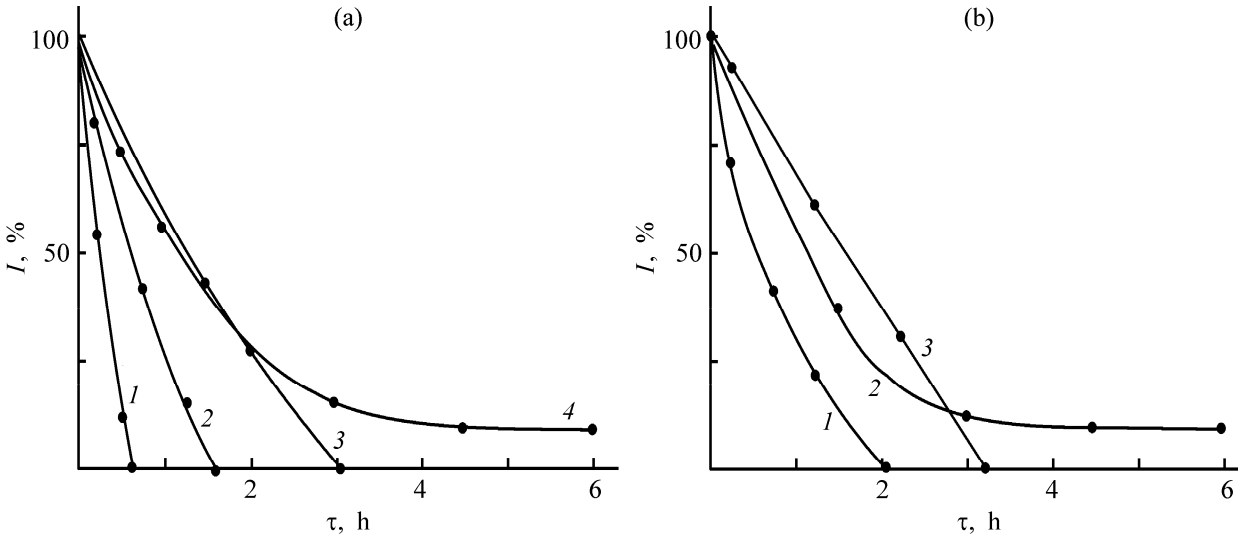


Fig. 2. Kinetic curves of photodegradation of complex compounds in the presence of UV absorbers. (*I*) Intensity and (τ) time. (a) (*1*) $Eu(TTA)_3 \cdot Phen$, (*2*) $Eu(TTA)_3 \cdot Phen + Quin$, (*3*) $Eu(TTA)_3 \cdot Phen + Cin$, and (*4*) $Eu(TTA)_3 \cdot Phen + EuCl_3 \cdot 2Phen$; (b) (*1*) $[Eu(Quin)_3 \cdot H_2O]_n$, (2) $[Eu(Quin)_3 \cdot H_2O]_n + EuCl_3 \cdot 2Phen$, and (*3*) $[Eu(Quin)_3 \cdot H_2O]_n + Cin$.

and its absorption bands cover a wider range of the spectrum. Introduction of cinnamic acid into the composites with europium thenoyltrifluoroacetonate and quinaldate hydrate leads to an increase to 3–4 h in the UV irradiation time in which the luminescence decreases to zero (Fig. 2a, curve *3*).

Figures 2a (curve *4*) and 2b (curve *2*) illustrate the kinetics of photodecomposition the complex compounds of $Eu(TTA)_3 \cdot Phen$ and $Eu(Quin)_3 \cdot H_2O$ in the presence of a UV absorbent, $EuCl_3 \cdot 2Phen$. Addition of $EuCl_3 \cdot 2Phen$ to europium β-diketonates and quinaldates results in photostabilization of the Eu^{3+} luminescence. Despite a sharp decline in the first hours, the luminescence intensity remains constant during the subsequent irradiation for a long time (>10 h).

It is well known that polyvinyl chloride degrades with the elimination of HCl molecules and formation of a polyene structure with conjugated double bonds [10]. Apparently, the release of HCl is one of the major factors leading to decomposition of both the luminophore and the UV absorbent. Hence, to provide a more efficient stabilization of the luminophore, it is necessary to choose a UV absorbent that would be more resistant to HCl, i.e., a compound inhibiting dehydrochlorination by blocking active centers of the polymer. Under certain conditions, some metal chlorides, which are usually active dehydrochlorination catalysts, inhibit the PVC degradation [10]. The presence of chloride anions in $EuCl_3 \cdot 2Phen$ as UV absorbent can make it more resistant, compared to the tested carboxylic acids (quinaldic, cinnamic), to the action of HCl released upon photoirradiation of polyvinyl chloride and can lead to stabilization of the luminophore.

CONCLUSIONS

(1) The photostabilizing effect of quinaldic acid, cinnamic acid, and complex of europium chloride with phenanthroline on the luminescence of Eu(III) in a polymeric composite was revealed. The stabilizing effect of the UV absorbents increases in the order quinaldic acid < cinnamic acid < $EuCl_3 \cdot 2Phen$.

(2) It was shown that the chlorine-containing UV absorbent $EuCl_3 \cdot 2Phen$ exerting the strongest photostabilizing effect on the examined luminophores inhibits the dehydrochlorination of polyvinyl chloride.

REFERENCES

1. Shchelokov, R.N., *Vestn. Akad. Nauk SSSR*, 1986, no. 10, pp. 50–55.
2. Karasev, V.E., *Vestn. Akad. Nauk SSSR*, 1995, no. 2, pp. 66–73.

3. Raida, V.S., Koval', E.O., Ivanitskii, A.E., et al., *Plast. Massy*, 2001, no. 12, p. 38.
4. Mirochnik, A.G., Zhikhareva, P.A. Kuryavyi, V.G., and Karasev, V.E., *Zh. Prikl. Khim*., 2004, vol. 77, no. 9, pp. 1543–1546.
5. Mirochnik, A.G., Zhikhareva, P.A., Sedakova, T.V., and Karasev, V.E., *Zh. Fiz. Khim*., 2007, no. 2, pp. 456–460.
6. Pogreb, R., Whyman, G., Musin, A., et al., *Mater. Lett*., 2006, vol. 60, no. 15, pp. 1911–1914.
7. Pogreb, R., Popov, O., Lirtsman, V., et al., *Polym. Adv. Technol.*, 2005, vol. 17, no. 1, pp. 20–25.
8. Pogreb, R., Finkelshtein, B., Shmukler, Y., and Bormarshenko, E., *Polym. Adv. Technol.*, 2004, vol. 15, no. 7, pp. 414–418.
9. Shlyapintokh, V.Ya., *Fotokhimicheskie prevrashcheniya i stabilizatsiya polimerov* (Photochemical Transformations and Stabilization of Polymers), Moscow: Khimiya, 1979.
10. Voigt, J., Die *Stabilisierung der Kunststoffe gegen Licht und Warme*, Berlin: Springer, 1966.
11. Kalinovskaya, I.V., Zadorozhnaya, A.N., Nikolenko, Yu.N., and Karasev, V.E., *Zh. Neorg. Khim*., 2006, vol. 51, no. 3, p. 505.

ISSN 1070-4272, Russian Journal of Applied Chemistry, 2008, Vol. 81, No. 12, pp. 2187–2188. © Pleiades Publishing, Ltd., 2008.
Original Russian Text © A.G. Morachevskii, I.N. Beloglazov, 2008, published in Zhurnal Prikladnoi Khimii, 2008, Vol. 81, No. 12, p. 2076.

BOOK REVIEWS

Naboichenko, S.S., Shneerson, Ya.M., Kalashnikova, M.I., and Chugaev, L.V., *Avtoklavnaya gidrometallurgiya tsvetnykh metallov* (Autoclave Hydrometallurgy of Nonferrous Metals), Naboichenko, S.S., Ed.,

Yekaterinburg: UGTU–UPI State Educational Institution, 2008, vol. 1, 376 pp.

DOI: 10.1134/S1070427208120318

In 2002, a team of authors constituted by S.S. Naboichenko, L.P. Ni, Ya.M. Shneerson, and L.V. Chugaeva published a fundamental monograph *Avtoklavnaya gidrometallurgiya tsvetnykh metallov* (Autoclave Hydrometallurgy of Nonferrous Metals) (946 pp.), which considered physicochemical foundations of hydrometallurgical processes carried out at elevated pressures and temperatures. The authors described examples of application of autoclave processes in manufacture of alumina, nickel, cobalt, zinc, copper, noble, and rare metals and discussed the instrumentation of autoclave technologies. In contrast to the single-volume first edition, the authors considered it appropriate to present the material of the second edition of the monograph in three volumes, with account of the progress made in autoclave metallurgy in recent years.

The already published first volume comprises an introduction and eight chapters grouped in two parts. The introduction (pp. 11–32) presents biographic evidence about domestic scientists who promoted the appearance and development of autoclave technologies, from N.N. Beketov (1826–1911) to B.I. Laskorin (1915–1997). The introduction also discusses the history of implementation of the autoclave technologies abroad and in Russia.

The first part of the monograph (pp. 33–179, chapters 1–4) is devoted to specific features of equilibria in hydrothermal systems that include the gaseous, liquid, and solid phases. The first chapter (pp. 33–68) presents the general principles underlying the autoclave metallurgy and considers typical solvents used in technological processes, reaction gases, and oxidizing agents. The chapter discusses methods for preparation of raw materials for autoclave leaching, various types of processes employed in leaching of sulfide raw materials (alkaline, neutral, and sulfuric acid leaching), and effect of various factors on parameters of the autoclave leaching. A special section of the first chapter considers various physicochemical methods used to study properties of hydrothermal solutions and slurries (conductometric, potentiometric, spectrophotometric methods, autoclave differential-thermal analysis, etc.)

The second chapter of the monograph (pp. 69–118) contains information necessary for a thermodynamic description of autoclave processes and potential–pH diagrams (Pourbet diagrams) for a large number of systems that are of interest for hydrometallurgical technologies. It also discusses the effect of various factors on the solubility of difficultly soluble compounds. The small third chapter (pp. 119–135) discusses the solubility of gases in various aqueous solutions. The fourth chapter (pp. 136–179) is devoted to the solubility of metal salts at elevated temperatures and considers sulfate, ammoniacal, and alkaline systems.

The second part of the first volume of the monograph (pp. 180–373, chapters 5–8) contains information about the theory of dissolution of minerals, metals, and metal alloys under the autoclave conditions, with mostly kinetic issues considered. The fifth chapter (pp. 180–277) analyzes the available published data on the dissolution of metal chalcogenides: sulfides of copper, nickel, cobalt, zinc, lead, and molybdenum; sulfides and arsenides of rare metals; selenides and tellurides of nonferrous metals. In the sixth chapter (pp. 278–334), the authors analyze the occurrence of by-processes in autoclave oxidation of sulfide concentrates. In particular, they consider the behavior of elementary sulfur and various sulfur- and oxygen-containing ions (thiosulfate and polythionate ions), specific ki-

netic features of the oxidation of pyrrhotine concentrates, and some other issues.

The seventh (pp. 335–354) and eighth (355–370) chapters are devoted to the dissolution kinetics of metals, metal alloys, and oxide materials in various media, with the effect of various factors on the process rate considered for the most part.

Each chapter is provided with a bibliographic list, with a total of 493 references. A prominent place in the whole body of the experimental material is occupied by the results of studies carried out by the authors of the monograph. The presented material is, on the whole, rather understandable; only the third chapter somewhat falls out because of a number of inaccuracies. Chapter 2 pays a considerable attention to Pourbet diagrams, but this evidence is insufficiently used in the succeeding chapters of the first volume. The polygraphic design of the monograph is very good.

A. G. Morachevskii and I. N. Beloglazov

ISSN 1070-4272, Russian Journal of Applied Chemistry, 2008, Vol. 81, No. 12, pp. 2189–2190. © Pleiades Publishing, Ltd., 2008.
Original Russian Text © G.E. Zaikov, L.L. Madyuskina, 2008, published in Zhurnal Prikladnoi Khimii, 2008, Vol. 81, No. 12, pp. 2077–2078.

INFORMATION

Bio&Polymers—New Polymer Technologies with Water Biannual Meeting of the German Chemical Society, Macromolecular Chemistry Division

DOI: 10.1134/S107042720812032X

The conference "Bio&Polymers—New Polymer Technologies with Water" (Biannual Meeting of the German Chemical Society, Macromolecular Chemistry Division) was held in Aachen from September 28 to 30, 2008.

The conference focused on the exchange of new results on the interface of classical polymer science with biological systems and on the importance of developing new water-based technologies. This includes topics ranging from "Polymers from Biomass," "Chemical and Physicochemical Transformations in Water" to the "Development of Novel Bioinspired Macromolecular Systems and Biohybrids." With the common theme expressed by the subtitle "New Polymer Technologies with Water," the Conference spanned topics starting from application-oriented research in water-based polymers to engineering polymers from biomass, and to highly specific and novel biofunctional polymers.

The limited resources of water, energy, and materials cause a growing need for new concepts in materials science and its ecological integration. Water technology and resource management are central factors not only in environmental protection, health care, and agriculture, but also in energy production and use of biomass as a material source. Within Polymer Science, this requires an adoption of a "biological view" on polymer synthesis, application, and the fate of polymer materials after use. Here, a key to the future advancement is the ability to deal with water and to take advantage of its unique properties. Due to its dielectric properties, amphoteric nature, and capacity for hydrogen bonding, water is certainly the most powerful solvent we know. It imposes enthalpic and entropic forces on other molecules that form an essential base for the richness in structure formation found in nature and the molecular functions in living systems. Hence, very topical scientific and technological challenges open up upon mastering water-based self-organization of polymers: responsiveness, switching of water solubility for water insolubility, and hybridization of synthetic components with biological systems.

The Conference program included five plenary lections and 44 presentations divided into five sessions.

Plenary lectures covered the most topical problems discussed at the Conference. The lecture presented by Dr. Stefan Marcinowski (Germany) was entitled "Renewable Raw Materials—a Novel Approach in Polymer Chemistry." J.M. Frechet (the United States) devoted his lecture to water-compatible polymer carriers for therapeutics. B.D. Ratner (the United States) entitled his lecture "Water and Biomaterials: Hydrogels, Healing and Non-Fouling." B. Rieger (Germany) reported on carbon dioxide as a building block of novel polymer architectures. Finally, R. Melhaupt (Germany) outlined data on preparation, characterization, and applications of biofunctional materials.

Session "Bioinspired Polymers" included eleven presentations covering such topics as natural polymeric composites with mechanical function, macromolecular oxidation catalysts based on miniemulsion polymerization, synthesis of bioinspired polymers, etc.

Session "Bio-medical Polymers" included presentations entitled Functionalized Nanoparticles and Nanocapsules as Markers and Nanocarriers in Biomedical Applications, Smart Hydrogels for Biomedical Applications, Injectable Biodegradable Hydrogels for Protein and Cell Delivery, Biodegradable Polymers for Biomedical Applications, Design and Function of DNA and Protein Nanoparticles, and some others.

Within the scope of Session "Polymers from Biomass", the participants discussed topical problems of production (synthesis) of polymers from biomass, including such aspects of the problem as sustainability

assessment of polymers based on renewable resources, biomass-based polyesters and polycarbonates for coating and engineering plastic applications, vegetable oils as renewable resources in polymer science, etc.

Session "Biofunctional Polymers" covered such topics as Biocompatible and Bioactive Polymers Containing Saccharide Functionality, Design and Mechanisms of Antimicrobial Polymers, Microcapsules and Nanoparticles for Controlled Delivery and Repair, Smart Nanocarriers for Bioseparation and Responsive Drug Delivery Systems, etc.

Lectures presented at Session "Waterborne Polymers" covered such topics as Synthesis of Smart Nano-Hydrogels, pH- and Temperature-Sensitive Microgels for Stimuli Controlled Emulsion Stabilization, Industrial Application of Mini-Emulsion Polymerization in the Coating Field, etc.

The Conference also included the Poster Session at which about 40 posters were presented.

The conference participants were about 100 scientists from 11 countries including Austria, China, Finland, Germany, India, Netherlands, Poland, Russia, Sweden, Switzerland, and the United States.

Generally, the Conference has demonstrated that the biopolymer research takes a great part of polymer science today.

The next Bio&Polymers Conference will be held in 2010.

G. E. Zaikov and L. L. Madyuskina

ISSN 1070-4272, Russian Journal of Applied Chemistry, 2008, Vol. 81, No. 12, pp. 2191–2198. © Pleiades Publishing, Ltd., 2008.
Original Russian Text © A.M. Kagan, L.A. Yudina, A.S. Pushnov, E.L. Urubkov, A.S. Sokolov, 2008, published in Khimicheskaya Promyshlennost', 2008, Vol. 85, No. 6, pp. 284–293.

PROCESSES AND DEVICES OF CHEMICAL MANUFACTURES

Topical Questions of Enhancing the Operation Regimes of the Packed Columns

A. M. Kagan[a], L. A. Yudina[a], A. S. Pushnov[b], E. L. Urubkov[b], and A. S. Sokolov[b]

[a]*Mendeleev Moscow Chemical Society, Moscow, Russia*
[b]*Moscow State University of Engineering Ecology, Moscow, Russia*

Received July 10, 2008

DOI: 10.1134/S1070427208120331

The packed columns are of wide use in the chemical and relative branches of industry. A nozzle packed in column is for enhancing the heat and mass transfer by an increase of a contact surface and by improving an agitation of flows.

Absorption, rectification, cooling (heating) with simultaneous contact of phases are the processes that occur in the largest scale in packed columns. Nowadays these processes are employed both as technological steps and increasingly more for solution of problems of environmental protection.

A volume of mass exchange equipment in the modern chemical industry is very large. This equipment is industry-leading (about 60%) in metal consumption. The nozzle apparatus size reaches quiet often significant value: up 100 meters in hight, and of several meters in diameter.

Thus enhancement of the nozzle column operation that can decrease their size, and, therefore, an equipment investment, and power inputs for overcoming hydraulic resistance, is the topical problem.

To the present day an application capacity of irregular nozzles prevails despite a growth in employing regular nozzles especially in a vacuum rectification. Therefore the enhancement problems of the columns with the irregular nozzles should be examined first of all.

We assume that several ways occur for intensifying the columns. First there are developments that are ready after some refining or ready for use. They are based on earlier conducted numerous studies, on present engineering designs, and also on an experience of the running plants relative to examination of the following effects: an increase of the operation gas flow, change in a management of the adsorption–desorption, use of combined nozzle devices, lowering the scale effect.

As should be expected designing new more effective construction of the main technological item, the nozzles, results in essential efficiency increase. Finally a trend that necessitates further examination is the effects of physical factors on the enhancement of the mass transfer.

In designing the apparatus with the nozzles in most of cases a value of the operation rate equaled to 60% of the rate at the point of flood w_f beginning is used as the maximum accessible operation rate w_p [1–5] since (1) w_p occurs in a region of a film regime where hydrodynamic and mass exchange characteristics are more steady; (2) an effect of the gas (vapor) flow to the hydraulic resistance of the nozzle layer ΔP increases significantly at the rates that exceed the rate of suspension beginning w_s; (3) it is required to avoid the device flood at the possible technologic regime failures (an unscheduled load increase).

The conditions noted above are considerable in the case of manual management but nowadays at computer-automated management when a given regime is supported steadily the process should be executed at the operation rate w_p more close to the value of w_f.

In accordance with Fig. 6 we suggest [6] to assign $w_p = w_n$, where w_n is point A that as rule is found in a range of 0.8–0.9 w_f, and the obtained favorable results are shown in the table. Here ΔP_{RM} is hydraulic resistance per a running meter of the nozzle layer; β_{lp} is volume mass transfer coefficient relative to the liquid phase; H is the height of the nozzle layer.

Evidently assuming $w_p = w_n = 0.885$ instead of $w_p = 0.6w_f$ and conserving the apparatus diameter D = const

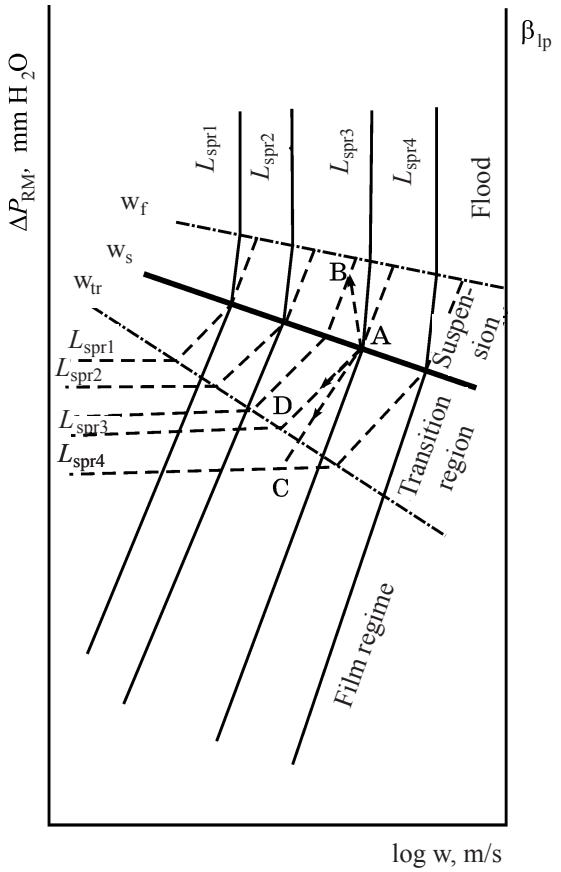


Fig. 1. Hydrodynamic and mass exchange features of a nozzle: $\Delta P_{RM} = f(w)$ and $\beta_{lp} = f(w)$.

an output can be increased to 30% and on the contrary keeping the output we can decrease the height of the nozzle layer to 24% and the diameter D to 18%.

We pictured the results of hydraulic and mass exchange studies of the nozzle characteristics on the combined diagrams (Fig. 1) that facilitated a thorough choice of the operation rate for the computation of the nozzle devices and estimation of their efficiency [7].

A significant change of the gas and liquid amount over the apparatus height caused by bleeding and feed of gas or liquid, significant temperature change, a phase transfer of the large amount of extracted components occurs sufficiently often in the nozzle columns. If in this case the apparatus diameter does not vary over the height then the noted changes on the flow amount result to increase or decrease (on the proper apparatus sections) of the gas rate and a sprinkle density. Since the apparatus diameter is computed according to the maximum loads relative to gas then lowering the rate in comparison with initial rate w_p, e.g. equaled to w_n providing the maximum value of the mass transfer coefficient β_{lp}, occurs on the sections where gas amount decreases. Also lowering the sprinkle liquid flow L_{spr} on the sections, where liquid bleeding occurs, results in increase of β_{lp}.

Therefore the column diameter should be varied over the height, if possible providing w_p = const and L_{spr} = const on the all sections of the column, to achieve maximum efficiency over the column height.

Some simplest ways of distribution of the gas and liquid flows in the apparatus of the constant and variable section are presented on Fig. 2.

According to IIa the lowering of w_p in the bottom section of the device causes a decrease of β_{lp} (in direction from A to D, Fig. 1) that leads to growth of the nozzle layer height. At the same distribution of the flows (IIb), when w_p is kept constant and L_{spr} increases in the bottom section of the apparatus, β_{lp} growths (in direction from A to B, Fig. 1). That is achieved by decrease in D at simultaneous diminishing H.

According to IIIa the lowering of L_{spr} and w_p in the top section of the apparatus (in direction from A to C) causes an essential increase of β_{lp} that leads to growth of H. A narrowing D in the top apparatus section allows supporting initial values of w_p, and L_{spr} and, therefore, the nozzle layer height.

Some technological processes necessitate presence of three or more different diameters over their height as that is presented on Fig. 2.

Evidently despite columns with different diameters over their height have more complex design their metal

The effect of increase of the operation gas velocity on an absorber size and on the absorption indices in the case of metal nozzle GIAP-N3 of 50×50 mm size at sprinkling L_f 100 $m^3 m^{-2} h^{-1}$

Gas velocity (vapor)	Indices				Change of the indices in comparison with $w_p = w_n$					Change of D at permanent gas amount, %
	w_P, $m\ s^{-1}$	ΔP_{RM}, mm H_2O	β_{lp}, h^{-1}	ΔP_{RM} : β_{lp}	w_p or output at D = const, %	ΔP, %	ΔP_{RM}, %	β_{lp}, %	H, %	
$w_p = 0.6w_f$	1.26	37.5	170	0.22	70	60.2	48.7	76.0	124	118.6
$w_p = w_n = 0.855w_f$	1,8	77	224	0,344	100	100	100	100	100	100

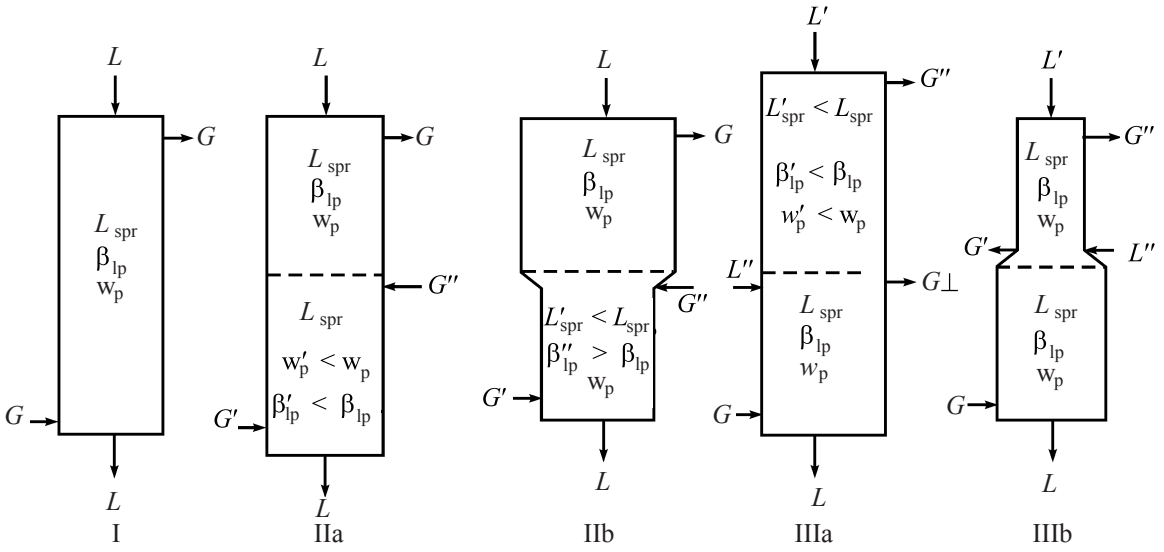


Fig. 2. The simplest ways of gas and liquid flow distribution in columns of constant or variable diameter and predicted change of apparatus size: (I) D = const, column without additional inputs and outputs of the flows; : (II) column with stepped gas input $G' + G'' = G$ (IIa: D = const, H increases, IIb: D and H in the bottom section lower), (III)) column with stepped liquid input $L' + L'' = L$ and with stepped gas output $G' + G'' = G$ (IIIa: D = const, H increases, IIIb: H = const, D deacreases in the upper section).

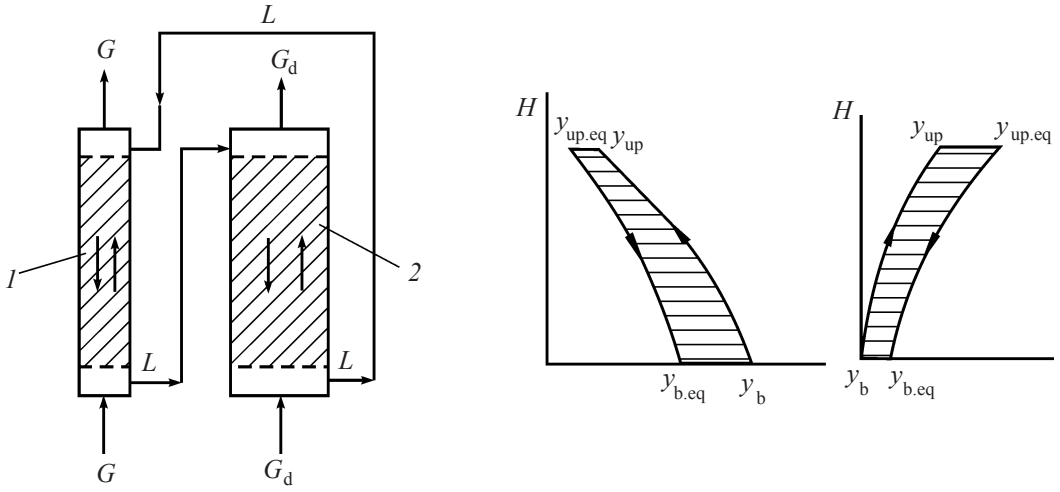


Fig. 3. Countercurrent phase movement in adsorber and in desorber: (a) scheme with countercurrent phase movement: (1) absorber, (2) desorber. G is the gas for absorption, G_d is the gas for desorption, (L) absorbent; (b) distribution of concentration over absorber height, y_{in} and y_{out} input and output concentrations of extracted component in gas, $y_{in.eq}$ and $y_{out.eq}$ input and output equilibrium concentrations. (c) the same in desorber.

consumption decreases significantly especially for adsorbers where processes are performed under high pressure. Moreover consumption of nozzles decreases.

In should be noted that the presented evident ways are already used in some industries with positive results. For example, diameter of the top section of absorber for cleaning feed gas from CO_2 in ammonia synthesis plant according to "Karsol" scheme is 2.2 m and of the bottom section, 3.4 m. And the top section of the desorber is of 4.5 m diameter, its bottom section, of 3.7 m diameter.

Placing on the different trays the nozzles of the same design but of various sizes can provide constant β_{lp} value at a single diameter of a column with variable values of flows. The small- size nozzles that are of higher efficiency should be used in the case of decrease in the gas or liquid flow.

Some advances in the efficiency of the nozzle devices can result from the combination of the nozzles of the

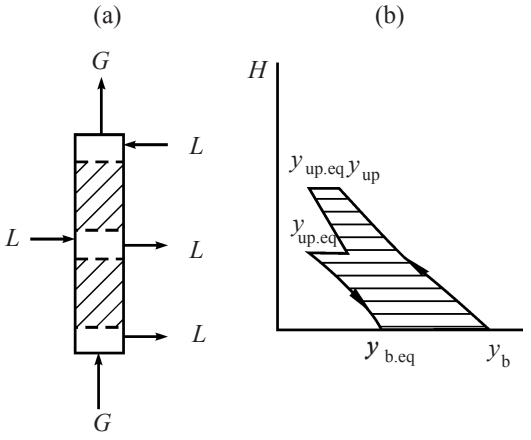


Fig. 4. Countercurrent absorber with input of live absorbent: (a) scheme of the flow movement; (b) distribution of the concentrations over absorber height.

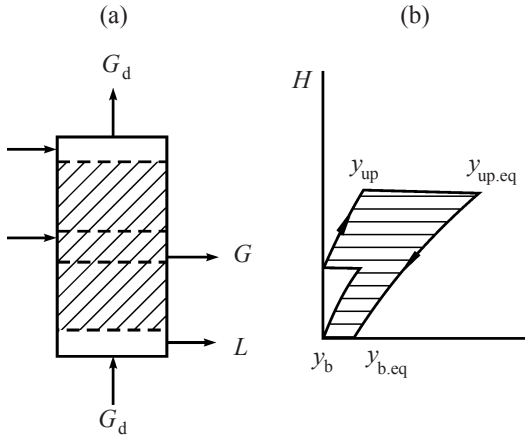


Fig. 5. Countercurrent desorber with input of live desorbent: (a) scheme of the flow movement; (b) distribution of the concentrations over absorber height.

different design. For example, an efficiency increase can be expected if the nozzle placed in the top section of the nozzle layer provides the better distribution of an inlet liquid or if a negative lengthwise mixing is lowered by a rational combination of the nozzles. In this case a target of a study is to reveal the best combination of the nozzles, a search of their optimum positional relationship, and also an optimum ratio of the layer heights made of the nozzles of different designs.

The mass transfer equation $M = \beta_{lp}\ v_{nl}\ \Delta y_{av}$, where v_{nl} is the volume of the nozzle layer reveals that an amount of a transferred substance M is defined both by value of β_{lp} and by a driving force of the process: a difference between operation and equilibrium concentration of the transferred substance (and vice versa) Δy_{av}.

Figs. 3b and 3c show the character of change of the extracted component concentration along the height nozzle layer height in the absorber and the desorber with countercurrent movement of gas and liquid according to the scheme (Fig. 3a).

Change of the concentrations over the absorber height with an additional input of a live absorbent according to the scheme (Fig. 4a) is showed on Fig. 4b.

Change of the concentrations in the desorber at an additional input of a live gas according to the scheme (Fig. 5a) is showed on Fig. 5b.

The driving force in the top section of the absorber of Fig. 4b is not practically changed in comparison with one on Fig 3b. Δy is significantly increased in the bottom section of the absorber (lower than a input point of the additional absorbent) respectively lowering a height of this section of the apparatus and the whole absorber.

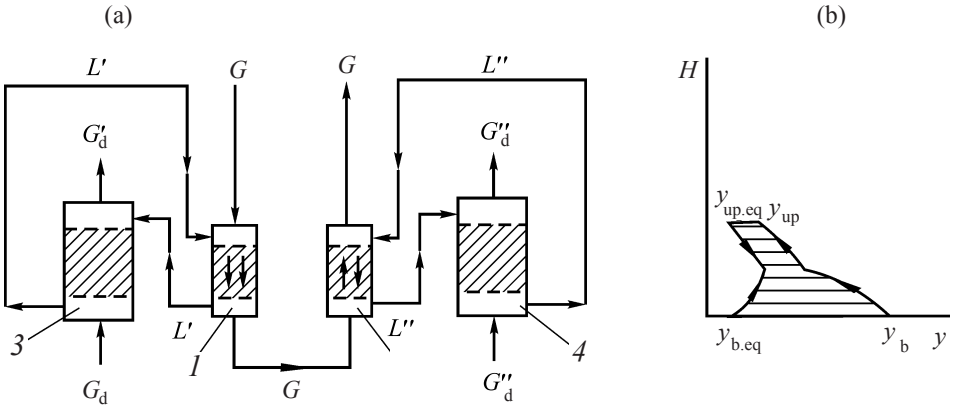


Fig. 6. Forward and countercurrent flow absorber with input of the live absorbent: (a) scheme of the absorption–desorption plant: (*1*) bottom section of absorber operating at forward flow; (*2*) upper section of absorber operating at countercurrent flow; (*3*) desorber serving to the bottom section of absorber; (*4*) desorber serving to the upper section of absorber. Ratio of the flows: $G'_d + G''_d = G$, $L' + L'' = L$. (b) Distribution of concentration over absorber height.

The additional input of the live desorbing gas in the desorber can respectively increase the driving force in its top section (Fig. 5b) and reduce the height of the whole apparatus. However an economic efficiency of such schemes where the absorbent flows and the desorbing gas are increased is doubtful though in particular cases they can be reasonable.

A number of the schemes is possible for supporting permanent values of G and L, but with a stepped input of one or another flow. An estimation of economic efficiency of the stepped inputs of gas and liquid should be carried out for each concrete case. Thereby an optimum height of the nozzle layer in a place of the additional inputs, the extracted component concentrations in the place of the inputs etc. should be determined. In this case rich facilities of the process manipulation occur for reaching the maximum performance.

Even greater lowering the apparatus size can be expected in the case of a forward movement of phases. In these apparatus operating at large gas velocities (to 10 m/s), impossible at the countercurrent movement due to the flood, the mass transfer enhances, the sizes of the devices decrease, the hydraulic resistance is significantly smaller then at the countercurrent flow [7–9]. An application of the forward flow nozzle devices is reasonable in the case when the direction of the phase movement does not significantly affect the driving force [2].

Let us consider one possible scheme of designing the forward flow in the nozzle apparatus (Fig. 6).

The forward flow occurs in the upper section of the absorber and a parallel flow of the gas and liquid phases at simultaneous feeding the live absorbent in the bottom section of apparatus takes place. However producing these two regimes of the movement in one body is difficult hence apparently both absorber and desorber should be divided in two apparatus (Fig. 6a). The height of the nozzle layer and the distribution of the concentration in the upper section of the absorber, where the countercurrent occurs, are kept approximately analogous to the picture presented on Figs. 3a and 3b. However the height of the nozzle layer on the forward flow section of the absorber decreases in comparison with the nozzle height in the same section of the absorber operating according to the schemes on Figs. 3a and 4a due to the risen driving force (let us compare Δy on the Figs. 3b, 4b, and 6b). Besides the significant increase of the value of β_{lp} in the bottom section of the apparatus that provides longer contact of each elementary volume of gas and liquid also promotes the decrease in the height of the nozzle layer. Therefore summary height of the nozzle in two absorbers (Fig. 6a) is essentially less than one in the absorber according to scheme in Fig. 3a. Also an essential decrease in the device diameter occurs in the section where the countercurrent flow takes place.

Working according this scheme the gas flow fed to each desorbers is lesser then one that feeds to desorber according to the scheme on Fig. 3a ($G'_d+G''_d = G_d$), since in both desorbers summary amount of the desorbed gas is equale to a gas amount that desorbed in one desorber in accordance with the scheme noted above. Hence supporting the permanent gas flow in the desorbers, i.e. lowering their diameter, L_{spr}, and therefore, β_{lp} increase that must result in reducing the summary height of the nozzle in two desorbers according to the scheme on Fig. 6a in comparison with the nozzle height in the desorber according to the scheme on Fig. 3a. The noted lowering of the summary nozzle height in all apparatus results in the decrease within ΔP which in certain measure



(a) (b) (c)

Fig. 7. Pall ring: (a) types of Pall ring: metal rings (flexiring, Koch Engineering Co.), (b) polymeric ring; (c) ceramic ring (Rschig Gmbh).

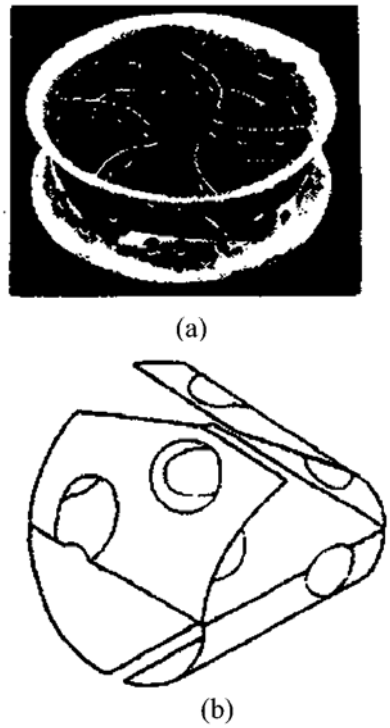


Fig. 8. Metal nozzles: (a) cascade mini-rings (Mass Transfer Inc.,), (b) semiring nozzle (GIAP-NZ) [11].

can compensate additional power consumption for the absorbent flow transfer.

We mark again that the rich facilities of the process manipulation occur for reaching the maximum performance by manipulating the values of flows, the position of the additional inputs both of the gas and of the liquid, the direction of the flow movements in apparatus, and also an engineering design of processes.

A special place in the enhancement of the nozzle apparatus efficiency must be given to development of new effective nozzles. Development of a new nozzle design with high capacity results in decrease in the diameter device, and the enhanced efficiency diminishes the height of the nozzle layer and of the whole apparatus, lower hydraulic resistance reduces the power consumption.

Some trends in the new irregular nozzle development are considered in [20, 25]. An improvement of the nozzles with the optimum shape is assumed to be the most reasonable. These are the ring and saddle nozzles [11], e.g. Pall rings, semi-ring nozzle (GIAP-NZ) (Fig. 8b), mini-ring nozzle (Fig. 8a), and saddle nozzle (Fig. 9).

Objective predicted decrease of the growth of efficiency and other parameters at the development of the new designs is noted. Consideration of the economic parameters: ease of production and low cost of mass-production is prescribed. Ways of reducing the consumption of time and resources for perfection of the new nozzle designs were considered in [21]. As first step the air blowing of single sample through an engine jet to estimate aerodynamic parameters is recommended [21]. Production of a pilot lot and its testing should begin only after required corrections of the design and reaching the optimum indices for a single nozzle constituent.

As noted above the enhancement of the mass transfer may be caused by physical factors. One of the ways, whose execution in available nozzle columns is quite possible, is producing the pressure pulsation in the gas flow that causes alternate deceleration and acceleration of the flow.

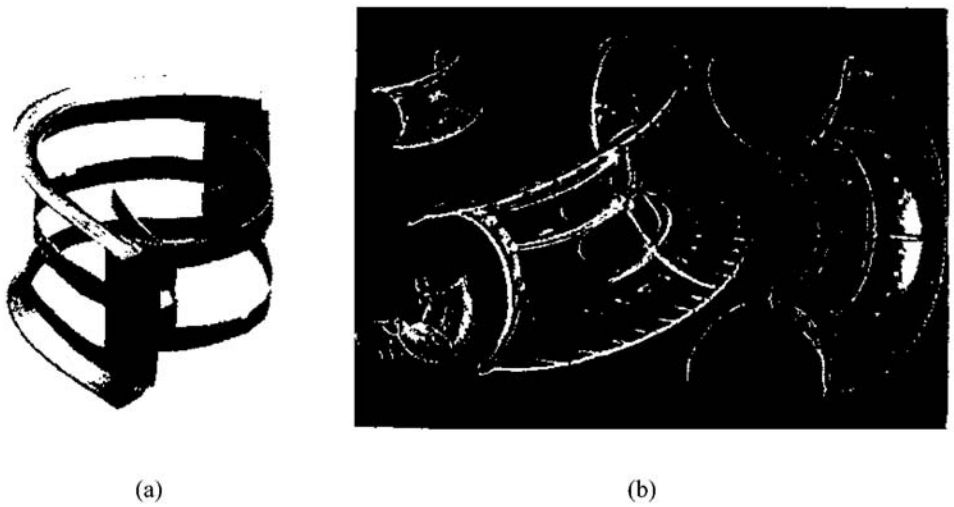


Fig. 9. Saddle nozzles: (a) metal nozzle (Norton Inc.,), (b) saddle from polymere (Flexisaddle, Koch Engineering Co.).

Effects caused by flow deceleration are analogous to an effect in a diffuser where tearing a boundary layer off a channel wall and formation of vortices occur. Under these conditions an increase in heat resistance and in the mass transfer resistance, i.e. enhancement of the heat and mass transfer, should be expected. Forming the boundary layer on the next phase occurs. However it does not finish to the point of the start of the recurring deceleration in the case of sufficiently large pulse rate. The enhanced heat and mass transfer should be expected at this stage since the boundary layer thickness is not yet large.

The longitudinal pulsation of the gas at the countercurrent two-phase movement of the flows in the nozzle apparatus must lead to an increase in the resistance to mass transfer of the boundary layer at the gas–liquid boundary. That is especially important if the processes are limited by the resistance in the gas phase. Simultaneously this pulsation must promote an additional turbulization of the liquid flowing down toward the gas over the nozzle. Thus, the physical effects of the pressure pulsation must promote the mass transfer enhancement.

The studies of the pulsation influence on the transfer efficiency mainly were conducted with respect to the heat transfer. Kosterik et al. [12] established an increase in the heat radiation coefficient of the gas α up to 50%. West et al. [13] found 60–80% increase at heating water in a pipe. Draiswamy et al. [14] established 130% increase of α at moderate value of Reynolds number (Re = 5000) and 30% increase of α at Re = 20 000.

Taking into account an analogy between heat and mass exchanges the efficiency of the mass transfer including the nozzle apparatus should be also expected as result of the pulsation. However the pressure pulsation of the flow inevitably leads to growth of the hydraulic resistance. Linke [15] examined a relation of the heat transfer growth and ΔP. He assumes that use of the pressure pulsation for enhancing the heat transfer is reasonable if a demand of device compactness prevails over one of the power consumption. However it should be taken into account that some additional power consumption is required for producing the pulsations.

A possible significant enhancement of the mass transfer in the nozzle devices, especially regarding exclusively large sizes of the absorption–desorption apparatus in some industries, necessitates an execution of a fundamental investigation on the pressure pulsation employment in mass exchange nozzle devices. Results of first such investigation reported in [22] showed, for example, that exclusively using a layer of the regular nozzle with a variable structure and geometry over a column height about 25% increase of the heat and mass exchange characteristics can be obtained. Regarding this result the studies that were performed in Moscow State University of Engineering Ecology proceed further in this direction.

Development of the new effective structured nozzles is also conducted in FGUP "Applied Chemistry" [10], and in Kazan State Energy University [26]. Sidorov et al. [24] note that a developed new nozzle in "Applied Chemistry" surpasses in the mass exchange intensity well-known nozzles of SULZER both VKH and SU.

Obviously certain effect on the mass transfer efficiency in the nozzle columns can be caused by vibration that can lead to decrease of a held liquid amount, to lowering the thickness of the gas and liquid boundary layer. The vibration like the pulsation must promote enhancement of a transversal mixing, increase in an irregular flow distribution in the transversal section of the nozzle columns and that must result in a decrease in a negative effect of the scale factor in the nozzle devices. However producing the vibration in the large dimension columns is sufficiently a difficult problem.

Other possible way of the mass transfer enhancement can be an ultrasound vibration. As in the case of the vibration the ultrasound effect is mainly studied relative to the heat transfer enhancement. Tret'yakov et al. [16] established that at heating the liquid in a pipe 30% increase of the heat radiation coefficient is defined at the one-sided effect, and 80% increase at two-sided effect of the ultrasound vibrations. Therewith the flow, physical properties of the liquid, the geometry and material of the channel, the frequency, and intensities of the vibrations produce an effect on the increase of the heat radiation coefficient α. The like results were obtained by Robinson et al. [17]. The results of an effect of the sound pulsation of ultrasonic frequency on the heat transfer under conditions of the free and forced convection were examined by Lemlich [18]. The influence of acoustic vibration in the ultrasonic range on a waste treatment was analyzed by Krivoborodova et al. [23].

Taking into account the analogy between the heat and mass transfer the positive effect of the ultrasonic vibrations also on the mass transfer in the nozzle column should be expected. Realization of the ultrasonic vibration in chemical engineering devices is possible to design. Details of such devices are discussed on [19].

We assume that the positive effect in the mass transfer also will be revealed further by other ways. Obviously that the enhancement ways of a directed movement of molecules of the extracted component both in fluid and in gas phases, and also at the phase boundary by sufficiently well examined physical phenomena, such as electromagnetic fields etc., will be found in the course of development of applied research. In the course of development of basic research, and knowledge about physical phenomena the facilities of the mass transfer enhancement will be extended.

REFERENCES

1. Shervud, T., Pigford, R., and Uilki, Ch., *Massoperedacha* (Mass Transfer), Moscow, Khimiya, 1982.
2. Ramm, V.M., *Absorbtsiya gazov* (Gas Absorption), Moscow: Khimiya, 1976, 655 p.
3. Eckert, I.S., at al., *Chem. Eng.Progr*., 1958, vol. 54, no. 1, p. 70.
4. Planovskii, A.N. and Nikolaev, P.I., *Protsessy i apparaty khimicheskoi tekhnologii* (Processes and Apparatuses of the Chemical Industry), Moscw, Khimiya, 1972, 493 p.
5. Molokanov, Yu.K., *Protsessy i apparaty neftegazopererabotki* (Processes and Appratuses), Moscow, Khimiya, 1980, 407 p.
6. Kagan, A.M, Yudina, L.A., and Pushnov, A.S., *Khim. Prom*., 2001, no. 4, pp. 46–48.
7. Postnikov, V.P., *Zh. Prikl. Khim*., 1960, vol. 33, no. 1, p. 117.
8. Dodds, W.S. and Stutzman, L.F., *AIChE Journal*, 1960, vol. 6, no. 2, p. 197.
9. Wen, S.Y. and O'Brien, E.A., *J. Chem. Eng. Data*, 1963, vol. 8, no. 1, p. 42.
10. Leont'ev, V.S and Sidorov, S.I., *Khim. Prom*., vol. 82, no. 7, 2005, p. 347.
11. Kagan, A.M., Yudina,L. A., and Pushnov, A.S., *Khim. Prom*., 2001, no. 5, p. 43
12. Kosterin, S.I., Kozhinov, I.A., and Leont'ev, A.I., *Teploenergetika*, 1959, no. 3.
13. West, F.V. and Taylor, A.T., *Chem. Eng. Progr*., 1952, vol. 48, no. 1, p. 39.
14. Draiswamy, L.K. and Patel, N.V., *Journ. Sci. Industr. Res*., 1959, vol. A18, no. 11, p. 522.
15. Linke, W., *Hufschmidtw Chem. Ingr. Technick*, 1958, vol. 30, no. 3, p. 159.
16. Tret'yakov, A.P. and Chen, Khua-Din, *Teploenergetika*, 1959, no. 11, p. 64.
17. Robinson, G.S, McClure, S.M., and Hendricks, R.T., *Amer. Ceram. Soc. Bull*., 1958, vol. 37, no. 9, p. 399
18. Lemlich, R., *Chem. Engug*., 1961, vol. 68, no. 10, p. 171.
19. Abramov, O.V. and Zubov, V.P., Abstracts of Papers, *Mezhdunarodyi simpozium "Noveishie tekhnologii i produktsiya v oblasti organicheskoi i neorganicheskoi khimii–95"* (Int. Symp. on Latest Technology and Production in Organic and Inorganic Chemistry-95), 1995, Moscw, p. 16.
20. Kagan, A.M., Pushnov, A.S., Yudina, L.A., and Chizh, K.V., *Khim. Prom*., 2007, no. 8, pp. 48–52.
21. Pushnov, A.S., Abstracts of Papers, *Vsesoyuznoe soveshchanie: Teplomassoobmennoe oborudovanie–88"* (All-Union Meeting on Heat and Mass Devices-88), Moscw: 1988, pp. 137–138.
22. Dmitrieva, G.B., Berengarten, M.G., Pushnov, A.S., Poplavskii, V.Yu., and Marshik, F., *Khim. Neftegaz. Mashinostroen*., 2006, no. 7, pp. 8–10.
23. Krivoborodova, E. G., Sister, V. G., and Karpova, E.V., *Khim. Neftegaz. Mashinostroen*., 2005, no. 12, pp. 36–38.
24. Leont'ev, V.S. and Sidorov, S.I., *Sbornik: Sovremennye napravleniya razvitiya tekhnologii i apparaturnogo oformleniya protsessov rektifikatsii v spirtovykh proizvodstvakh* (Collection: Modern Trends in Rectification of Alcohol Industry and in Its Designing), RNTs "Prikladnaya khimiya", St. Petersburg: TEZA, 2004, p. 444.
25. Kagan, A.M., Pushnov, A.S., and Ryabushenko, A.S., *Khim. Tekhnol.*, 2007, no. 5, pp. 232–240.
26. Laptev, A.G. and Farakhov, M.I., *Razdelenie geterogennykh sistem v nasadochnykh apparatakh* (Separation Of Geterogeneous System in Nozzle Apparatus), Kazan, Kazan. Gos. Energ. Univ., 2006, 342 p.

ISSN 1070-4272, Russian Journal of Applied Chemistry, 2008, Vol. 81, No. 12, pp. 2199−2206. © Pleiades Publishing, Ltd., 2008.
Original Russian Text © V.O. Yablonskii, 2008, published in Khimicheskaya Promyshlennost', 2008, Vol. 85, No. 6, pp. 300−309.

PROCESSES AND DEVICES OF CHEMICAL MANUFACTURES

Use of Regression Model of Two-Step Flotation in a Hydrocyclone for Analysis of Effects of Design and Regime Parameters on Separation Efficiency

V. O. Yablonskii

Volgograd State Engineering Iniversity, Volgograd, Russia
e-mail: pahp@vstu.ru

Received October 14, 2008

Abstract—An algorithm for a calculation of indices at separation of suspensions with non-Newtonian properties, two-step flotation in hydrocyclone with application of a regression model was developed. An analysis of an influence of governing similarity criteria that describe the suspension separation by two-step flotation in the hydrocyclone and of rheological constants of a separated media on a distribution of a recovery efficiency of solid particles from a suspension over an operation height of a hydrocyclone was carries out.

DOI: 10.1134/S1070427208120343

An extraction of suspension particles of the smallest fraction and essential increase of the separation indices may be realized by separation of a solid phase by a pressure flotation in an area of centrifugal force of a hydrocyclone. During the pressure flotation in a regime of a film flow of the highly viscous non-Newtonian fluid in the hydrocyclone the carrying of a particle−bubble group to the film surface is the limiting stage. The two-stage pressure flotation in the hydrocyclone that enables essential intensifying the process and practically complete extraction of particles of solid fraction from the suspension applied in some cases to reduce the time of carrying the particle−bubble groups to the film surface.

Several attempts were performed for developing semiempirical and empirical relations describing some points of a device hydrodynamics in well-known studies [1] on hydrocyclones. However these relations are not used in practice due to their complexity in a definition of integral indices of separation in the hydrocyclones.

It was established in [2, 3] that an amount of collisions of particles and bubbles is increased owing to the presence of the centrifugal force area, and also a dependence of the collision number on a centrifugal acceleration was indicated.

Developed calculation methods for separation of nonhomogeneous fluid systems by the flotation in the hydrocyclones [4–6] based on a solution of a differential equation for the particle−bubble movement are not utilizable for separation at the film flow of highly viscous non-Newtonian fluid in the centrifugal force area where separation is essentially enhanced.

Nowadays wide industrial implementation of the suspen-sion separation by the pressure flotation in the centrifugal force area at the film regime of the flow is hampered by the absence of a science-based algorithm of an engineering computation of such apparatus giving good results. Thus developing this algorithm is actual and practically important task.

Tasks of separation for nonhomogeneous non-Newtonian fluid system by the two stage flotation in film flow regime in a cylindrical and cylinder-conic hydrocyclones were solved in [7, 8]. Developing the algorithm on engineering computation of the hydro-cyclones for the separation of the nonhomogeneous non-Newtonian fluid systems by the two-stage flotation may be carried out on the base of results of these studies.

The hydrocyclone (Fig. 1) includes a cylinder chamber in which suspension is fed through an inlet (*1*) fixed in the upper section, and in a conic section (an angle of the conic section α) is fed tangentially at increased pressure (until 0.8 MPa). If α = 0 the hydrocyclone is cylindrical. The fed suspension flows down over the wall forming a revolving film with peripheral V_φ, axial

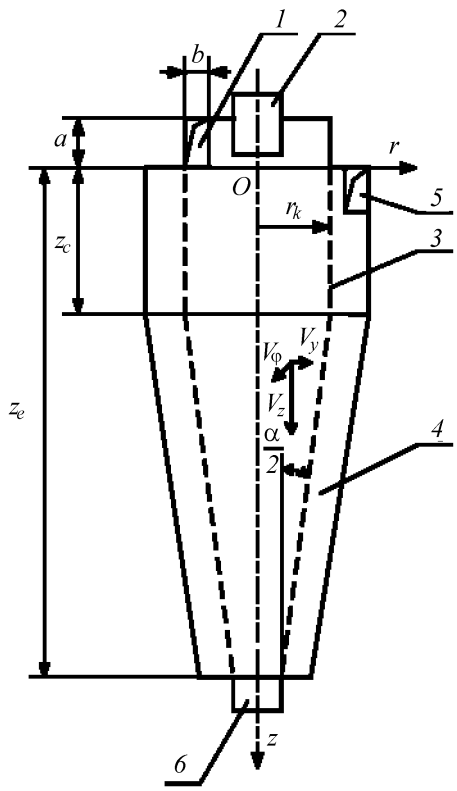


Fig. 1. Scheme of the suspension separation by the two-stage flotation in the cylinder-conic hydrocyclone: (*1*) the inlet fitting, (*2*) the upper outlet fitting, (*3*) the penetrate wall, (*4*) the manifold; (*5*) the gas feed jet, (*6*) the emptying fiitting in the bottom.

V_z, and radial V_r velocity components. An oversaturation of a solute gas and "boiling up" of the suspension are produced at decreasing the pressure to atmospheric. The particles of the solid phase move to the hydrocyclone body wall under the centrifugal force action, and the gas bubbles under the action of the buoyancy centripetal Archimedean force move towards them to the film surface. Floto groups carrying the particles of the solid phase toward the film surface in a froth layer, that is removed through the upper outlet jet (*2*) are formed on first stage of the pressure flotation at the collision of the particles of the solid phase with the gas bubbles. Besides the particles of the solid phase serve immediate centers of a formation of gas bubbles evolving at the pressure decrease that leads to essential growth of a kinetic coefficient of the pressure flotation in the first stage. The bubbles of a secondary gas input through a penetrate wall (*3*) of the hydrocyclone body from a ring manifold (*4*) to which gas is fed through the jet (*5*) with 10-fold larger diameter then the gas bubbles evolving from suspension at the pressure decrease, possess significantly larger rate of floating to the film surface than the formed particle–bubble group. In the second stage of the flotation the bubbles of the secondary gas colliding with the particle–bubble group form with them secondary group where the particle is a bridge between the bubbles [9] that quickly rush to the film surface. Since carrying the particle–bubble group to the film surface is the limiting stage [7, 8] the input of the secondary gas in the hydrocyclone through the penetrate wall leads to essential flotation enhancement. A clarified suspension is removed from the apparatus through a bottom outlet (6).

An index of quality for the separation of non-homogeneous fluid system by the two-stage flotation is a mean integral recovery efficiency of the of the solid particles S that is mean dimensionless volume part of free particles of the solid phase and the particles of the solid phase, associated in the groups in the suspension at a given film section (at $Z = const$).

With the help of the mean integral recovery efficiency of the solid particles S the effect of the governing similarity criteria and the rheological properties of the dispersion media in the efficiency of the two-stage pressure flotation in the hydrocyclone may be estimated.

The mean integral recovery efficiency of the solid particles S is calculated in accordance with equation (1):

$$S = \frac{\int_{R_K(Z)-\Delta(Z)}^{R_K(Z)} (C_p + C_{pc})\, H_p(R, Z)\, R\, dR}{C_{p0} \int_{R_K(Z)-B}^{R_K(Z)} H_{p0}(R, Z) R\, dR}.$$

Calculating according to Eq. 1 by numerical method an axial component of the velocity of the free particles and associated in group ones $H_p(R, Z)$ was assumed equaled to an axial component of the velocity of the dispersion environment $H_l(R, Z)$ since an inertia of the free particles and the particle-bubble groups in the axial direction was not taken into account [7, 8]. Relations for an approximation of the axial component of the velocity $H_l(R, Z)$ are reported in [10].

The separation by the pressure flotation in the hydrocyclone of the nonhomogeneous fluid non-Newtonian systems that can be described by an exponential equation of Ostwald-de Waele is characterized by the following governing similarity numbers [7, 8]:

$$Fr = \frac{U_0^2}{g r_k}; \quad Re_n = \frac{\rho_l r_k^n U_0^{2-n}}{k}; \quad Q_0 = \frac{a b}{\pi r_k^2};$$

$$Re_{np} = \frac{\rho_l d_p^n U_{0p}^{2-n}}{k}; \quad Re_{nc} = \frac{\rho_l d_{b1}^n U_{0c}^{2-n}}{k};$$

$$Fl_1 = \frac{A_1 c_{b1} r_k}{U_0}; \quad Fl_2 = \frac{A_2 c_{b2} r_k}{U_0}.$$

Kinetic coefficients of first and second stages of the flotation A_1 and A_2 are determined according to [7].

Let's assume that the particles of the solid phase and the bubbles of the primary phase evolved at the pressure decreasing in course of input in the hydrocyclone, and also the bubbles of the secondary gas feed through the penetrate wall of the hydrocyclone are monodisperse. If it is necessary to perform computations for the separation of polydisperse mixtures of solid particles by the two-stage flotation a given recovery efficiency S can be provided assuming a computed diameter of a solid particle equals to a particle diameter of the smallest fraction.

A distribution of the recovery efficiency of the solid particles S over the height of an operation region of the hydrocyclone at the given geometric and regime parameters of the cylinder-conic and cylindrical devices for separation of the nonhomogeneous fluid system by the two-stage flotation in the area of the centrifugal force may be simulated by an equation of regression that is written as:

$$S = \sum_{i=0}^{4} \frac{K_i + L_i[\tan(\alpha/2)]^{H_i} + M_i Fl_2^{T_i}}{Z^j}$$

$$\times Fr^{A_i} n^{B_i} Re_n^{C_i} Q_0^{D_i} Re_{np}^{E_i} Re_{nc}^{F_i} Fl_1^{G_i},$$

where $j = i$ is an exponent index of the axial coordinate Z.

Items that contain tg $2(\alpha/2)$ and Fl_2 are introduced in the regression equation additively to coefficients K_i so that errors of determination of small values of tg $(\alpha/2)$ and Fl_2 at $\alpha \to 0$ and $c_{b2} \to 0$ could not affect the accuracy of computation by the regression equation (3).

For determination of the coefficients of Eq. 3 we carried out calculation of the suspension separation by the two-stage flotation [7, 8] for the most common case in the flotation when a volume part of gas bubbles in the device is essentially higher then that of the solid particles. The calculations were conducted changing the dimensionless quantities and the rheological constants of the dispersed medium in a wide range according to a fractional factorial design [11]. Computed distribution values of the recovery efficiency S in the dependence on the coordinate Z at various values of the dimensionless quantities and the rheological constants of environment were recorded in the *SPSS* database and executing the nonlinear regression

The coefficients of the regression equation for the suspension separation by two-stage flotation in the area of the centrifugal forces into the cylinder-conic and cylindrical hydrocyclones

i	K_i	L_i	H_i	M_i	T_i	A_i
0	7.65873	−1.72606	6.23666×10^{-3}	−4.84882	-1.87667×10^{-3}	-9.76765×10^{-2}
1	2.98724×10^{1}	-2.36476×10^{1}	-6.95487×10^{-2}	-4.88105×10^{1}	-3.12019×10^{-2}	−1.16378
2	9.91094×10^{-2}	9.34876×10^{-6}	-6.37502×10^{-1}	1.48413×10^{-2}	-2.21986×10^{-1}	−1.90439
3	3.13599×10^{-1}	-2.84207×10^{-1}	-1.56100×10^{-1}	-1.36923×10^{-1}	-3.00609×10^{-1}	−1.47977
4	3.54977×10^{-3}	-3.54974×10^{-3}	-5.15890×10^{-7}	-1.65232×10^{-8}	6.54237×10^{-1}	1.35698
i	B_i	C_i	D_i	E_i	F_i	G_i
0	-4.47023×10^{-1}	4.00999×10^{-2}	-9.61696×10^{-2}	-1.57132×10^{-3}	1.87046×10^{-1}	-8.68151×10^{-3}
1	-6.32482×10^{-1}	1.19478×10^{-1}	-8.34568×10^{-2}	-6.40320×10^{-5}	-1.81784×10^{-2}	2.77762×10^{-1}
2	-8.92157×10^{-1}	7.17334×10^{-1}	−1.24394	-1.10361×10^{-2}	-1.42915×10^{-1}	5.24988×10^{-1}
3	-9.23047×10^{-1}	-1.18058×10^{-1}	−1.69124	-1.92959×10^{-2}	-2.63553×10^{-1}	7.17685×10^{-1}
4	-6.04043×10^{-1}	7.19812×10^{-1}	-7.20414×10^{-1}	-1.10506×10^{-1}	1.35304	-9.88768×10^{-1}

procedure at an iteration convergence 1×10^{-8} the coefficients of Eq. 3 were determined.

A correspondence between the values of S obtained by the simulation model [7, 8] and computed according to the regression equation (3) was evaluated with a squared correlation index $R_{squared}$ from *SPSS* [12]. Its value computed by executing a non-linear regression procedure was 0.953 and thus was evidence that the obtained regression equation described correctly the computed data. The regression coefficients of Eq. 3 are presented in the table.

At $\alpha = 0$ Eq. 3 should reduce to equation of regression for cylindrical hydrocyclone and at $Fl_2 = 0$ it should simulate single stage pressure flotation (without the secondary gas feeding). In *SPSS* instead of zero values of α and Fl_2 we have used $tg(\alpha/2) = 1 \times 10^{-7}$ and $Fl_2 = 1 \times 10^{-7}$ as no computation is possible at negative values of exponents H_i and T_i. Thus at $tg(\alpha/2) = 1 \times 10^{-7}$ in Eq. 3 we obtain the equation for simulation of the suspension separation by the two-stage pressure flotation in the cylindrical cyclone, and $Fl_2 = 1 \times 10^{-7}$ the equation for simulation of the suspension separation by the single stage pressure flotation in the cylindrical and cylinder-conic cyclones. These equations result in quiet feasible computation accuracy at given geometrical and regime parameters of the hydrocyclones.

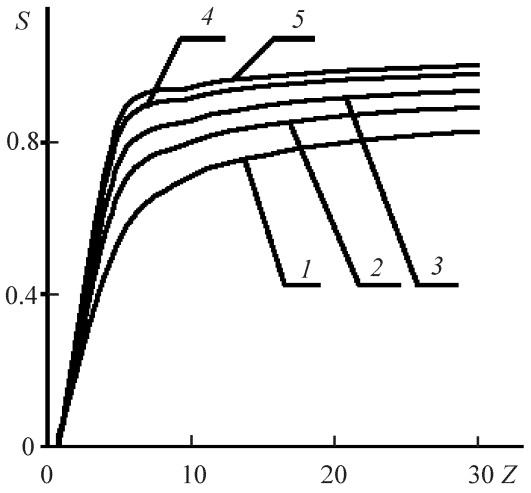


Fig. 2. A dependence of the recovery efficiency of the solid particles S by the two-stage flotation in the cylindrical hydrocyclone on Z coordinate at various values of numbers Fr; $n = 0.8$; $Re_n = 9000$; $Q = 0.12$; (*1*) $Fr = 30$, $Re_{np} = 1.27$ Ч 10^{-6}, $Re_{nc} = 7.02 \times 10^{-3}$, $Fl_1 = 1.88 \times 10^{-2}$, $Fl_2 = 1.23$; (*2*) $Fr = 50$, $Re_{np} = 4.17 \times 10^{-6}$, $Re_{nc} = 2.31 \times 10^{-2}$, $Fl_1 = 3.41 \times 10^{-2}$, $Fl_2 = 2.24$; (*3*) $Fr = 70$, $Re_{np} = 9.15 \times 10^{-6}$, $Re_{nc} = 5.07 \times 10^{-2}$, $Fl_1 = 5.05 \times 10^{-2}$, $Fl_2 = 3.32$; (*4*) $Fr = 100$, $Re_{np} = 2.10 \times 10^{-5}$, $Re_{nc} = 1.17 \times 10^{-1}$, $Fl_1 = 7.66 \times 10^{-2}$, $Fl_2 = 5.03$; (*5*) $Fr = 120$, $Re_{np} = 3.22 \times 10^{-5}$, $Re_{nc} = 1.78 \times 10^{-1}$, $Fl_1 = 9.48 \times 10^{-2}$, $Fl_2 = 6.22$.

Using MathCAD and substituting the coefficient values form the table in the non-linear regression equation (3) we performed simulation for the distribution of the recovery efficiency of the solid particles over the operating section of the hydrocyclone varying the dimensionless quantities and values of the rheological constants of a dispersed media in a wide range.

The main calculation results are shown in Figs. 2–4.

Considering a feature of the distribution of the recovery efficiency along Z coordinate two distinctive region of the curves may be notes: the region of fast growth of S where the most portion of the particles is separated and that finished at $Z = 9–12$, and the region of slow growth of S over Z. A presence of these regions is caused by the large volume part of the solid particles associated in groups that quickly floated to the film surface in the froth due to high values of peripheral component of the velocity of the dispersed media $V_{\varphi l}$. In the course of further increase of Z coordinate the volume part of the solid particles in the suspension sharply decreases as a result of removal of the particle–bubbles group in the froth, and the values of the peripheral component of the velocity $V_{\varphi l}$ decrease due to its damping towards the axial coordinate.

A length of the S fast growth region is reduced as Fr number increases from $Z = 12$ at $Fr = 30$ to $Z = 7$ at $Fr = 120$ due to the rise of the peripheral component of the velocity $V_{\varphi l}$, and the decrease in its damping aver Z coordinate [7].

Fig. 2 shows that the recovery efficiency of the solid particales S growths as Froude number increases.

An analysis of the distribution on the Fig. 2 shows that the recovery efficiency of the solid particles S grows as Froude number Fr increases because of thickening the suspension film and an increase in the peripheral velocity of the dispersed medium $V_{\varphi l}$ [7] at the rise of the radial velocity component of the solid phase, of the primary and secondary gas bubbles, and of the particle–bubble groups relative to the fluid and the their way in the radial direction at the appropriate increase in the collision number and in the kinetic coefficients of the first and second flotation stages A_1 and A_2, and groups Fl_1 and Fl_2.

A dependence of the recovery efficiency of the solid particles S by the rwo-stage flotation in the cylindrical

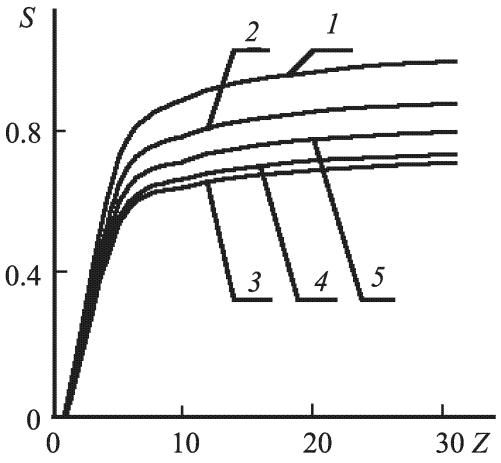


Fig. 3. A dependence of the recovery efficiency of the solid particles S by the rwo-stage flotation in the cylindrical hydrocyclone starting on the axial coordinate Z at various Re_n; n = 1.2, Fr = 200, Q = 0.04, $Re_{np} = 1.06 \times 10^{-4}$, $Re_{nc} = 5.87 \times 10^{-1}$, $Fl_1 = 1.72 \times 10^{-1}$, $Fl_2 = 1.42$; (*1*) Re_n = 500; (*2*) Re_n = 1000; (*3*) Re_n = 2000; (*4*) Re_n = 4000; (*5*) Re_n = 9000.

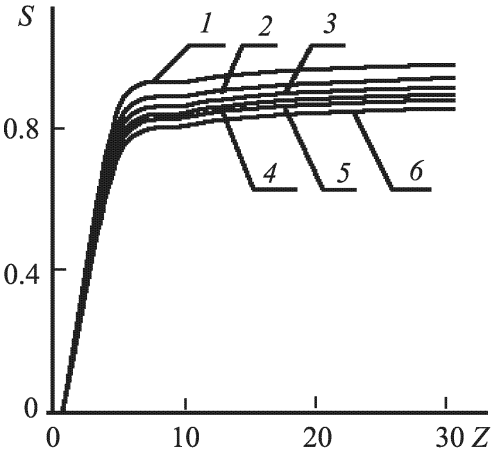


Fig. 4. The dependence of the recovery efficiency of the solid particles S by the two stage flotation in the cylindrical hydrocyclone on the axial coordinate Z at the various values of a flow dimensionless Q; n = 1, Fr = 100, Re_n = 2000, $Re_{np} = 2.10 \times 10^{-5}$, $Re_{nc} = 1.17 \times 10^{-1}$, $Fl_1 = 7.66 \times 10^{-2}$, $Fl_2 = 6.31 \times 10^{-1}$; (*1*) Q = 0.02; (*2*) Q = 0.03; (*3*) Q = 0.04; (*4*) Q = 0.05; (*5*) Q = 0.06; (*6*) Q = 0.08.

hydrocyclone starting on the axial coordinate Z at various Re_n is shown on Fig. 3.

Curves presented on Fig. 3 show that the recovery efficiency of the solid particles grows at the increase of Re_n owing to increase of the peripheral velocity component of the dispersed medium $V_{\varphi l}$ [7], rise of radial velocity component of the solid particles, of the primary and secondary gas bubbles, and the bubble–particle groups relative to the fluid and their path in the radial direction at rising collision number of the solid particles and the gas bubbles, and also of the secondary gas bubbles and the bubble–particle groups thereby the kinetic constants of the first and second flotation stages A_1 and A_2 growth and the orresponding rise in the groups Fl_1 and Fl_2.

A dependence of the recovery efficiency of the solid particles S by the two stage flotation in the cylindrical hydrocyclone on the axial coordinate Z at various values of a flow dimensionless parameter Q.

Comparing the data presented on Fig. 4 for various values of the dimensionless parameter Q we can conclude that the recovery efficiency of the solid particles S diminishes whilst the value of Q rises owing to the thickening the suspension film [7] and to the growth of the bubble–particle group path to the film surface. Hence the value of the flow dimensionless parameter Q at the hydrocyclone designing should be as small as possible small.

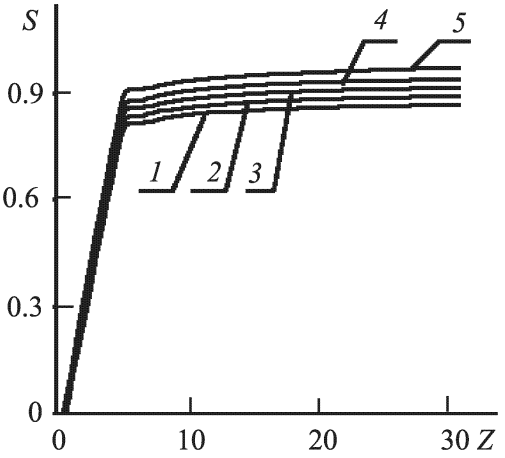


Fig. 5. Dependences of the recovery efficiency of the sold particles S by two stage flotation in the cylindrical hydrocyclone on the axial coordinate Z at the various values of a non-linearity index n; Fr = 50, Re = 4000, Q = 0.08, $Re_{np} = 4.17 \times 10^{-6}$, $Re_{nc} = 2.31 \times 10^{-2}$, $Fl_1 = 3.41 \times 10^{-2}$, $Fl_2 = 2.81 \times 10^{-1}$; (*1*) n = 0.6; (*2*) n = 0.8; (*3*) n = 1; (*4*) n = 1.2; (*5*) n = 1.3.

Fig. 5 shows dependences of the recovery efficiency of the solid particles S by two stage flotation in the cylindrical hydrocyclone on the axial coordinate Z at various values of a non-linearity index n.

Comparing the dependencies for the various value n it follows that the recovery efficiency of the solid particles S diminishes as non-Newtonian anomaly decreases (at rise of n). It is caused by damping the peripheral velocity

component of the dispersed medium $V_{\varphi l}$ towards the axial direction [7] and also by appropriate decrease in the radial velocity components of the solid particles, gas bubbles, the particle–bubble groups, and the secondary groups leading to decrease in the kinetic coefficients of the first and second flotation stages A_1 and A_2.

The obtained equation of regression well describes the computed data resulting from the simulation of the two-stage flotation in the wide range of values of the governing dimensionless criteria and the rheologic properties of dispersed medium, and also with its help constructional and regime parameters of hydrocyclones at a developing stage can be computed.

NOTIFICATION

K_i, L_i, H_i, M_i, T_i, A_i, B_i, C_i, D_i, E_i, F_i, G_i are regression coefficients;

Fr is Froude number (separation factor);

Re_n is an analogue of Reynolds number for the non-Newtonian fluids that is used to determine a flow regime of the film suspension;

Q_0 is flow dimensionless parameter;

Re_{np} is an analogue of Reynolds number that is used to determine a regime of solid particle settlement in the centrifugal force field in the non-Newtonian fluid;

Re_{nc} is an analogue of Reynolds number that is used to determine a floating regime of the particle-bubble group in the non-Newtonian fluid;

Fl_1 is number that is used to determine an efficiency of the first stage of the pressure flotation;

Fl_2 is number that is used to determine an efficiency of the secondary stage of the pressure flotation;

$H_l(R, Z) = \frac{V_{zl}}{U_0}$ is the dimensionless axial component of the fluid velocity;

$H_{l0}(R, Z) = \frac{V_{zl0}}{U_0}$ is the dimensionless axial component of the fluid velocity in the initial film section;

$H_p(R, Z) = \frac{V_{zp}}{U_0}$ is the dimensionless axial component of the free particles and of solid particles bonded in the groups;

$H_{p0}(R, Z)$ is the dimensionless axial component of the free particles of the solid phase in the initial film section;

$C_p = \frac{c_p}{c_{p0}}$ is dimensionless volume fraction of the solid particles;

C_{p0} is dimensionless volume fraction of the solid particles in the hydrocuclone inlet;

$C_{b1} = \frac{c_{b1}}{c_{p0}}$ is dimensionless volume fraction of the primary gas bubbles escaping into suspension at the pressure decrease;

$C_{b2} = \frac{c_{b2}}{c_{p0}}$ is dimensionless volume fraction of the secondary gas bubbles – feed through the penetrate porous wall of the hydrocyclone body;

C_{b10} is dimensionless volume fraction of the primary gas bubbles in the hydrocyclone inlet.

$R = \frac{r}{r_k}$ is dimensionless radial coordinate;

$R_k(Z)$ is the dimensionless body radius of the hydrocyclone that in the case if cylinder-conic hydrocyclone is piecewise-linear fuction Z defined by following relations:

$R_k(Z) = 1 \quad (Z<Z_c)$,

$R_k(Z) = 1 - (Z - Z_c)\, tg\, (\alpha/ 2) \quad (Z>Z_c)$;

$R_T(Z)$ is dimensionless radial coordinate of the most distant trajectory of the solid particles from the body wall;

$Z = \frac{z}{r_k}$ is dimensionless axial coordinate;

$Z_c = \frac{z_c}{r_k}$ is dimensionless height of the cylindrical hydrocyclone body;

$A = \frac{a}{r_k}$, $B = \frac{b}{r_k}$ is dimensionless height and wide of the hydrocyclone;

$\Delta(Z) = \frac{\delta(z)}{r_k}$ is dimensionless thickness of the suspension film;

A_1 and A_2 are kinetic coefficients of the first and secondary flotation stage, s^{-1};

n is nonlinearity index for a curve of the dispersion medium flow;

k is a thickness index, Pa/s^n;

$$U_{0p} = \left[\frac{1}{18} d_h^{n+1} (\rho_p - \rho_l) U_0^2 \frac{F(c_{p0})}{f(n) r_k k} \right]^{\frac{1}{n}}$$

is the characteristic velocity of the radial settlement of the sold particles, m/s, according to the average suspension velocity at the inlet U_0 in the case of equality of the radial coordinate value to the radius of the cylindrical hydrocyclone body r_k; is the characteristic velocity of the radial floating of the bubble–particle group, m/s, according to the average suspension velocity at the inlet U in the case of equality of the radial coordinate value to the radius of the cylindrical hydrocyclone body r_k;

$$U_{0c} = \left\{ \frac{1}{18} d_{b1}^{n-2} d_p^3 \left[\rho_l \left(1 + \left(\frac{d_{b1}}{d_p} \right)^3 \right) - \rho_p \right] \frac{U_0^2}{f(n) r_k k} \right\}^{\frac{1}{n}}$$

$\times \Phi(c_{c0})$ is coefficient that used to determine high-density movement of the solid particles computed according to equation of Prof. V.I. Sokolov;

$F(c_{p0}) = 10^{-1.82 c_{p0}}$ is coefficient that used to determine non-Newtonian properties of the dispersed medium [10];

$$f(n) = 3^{1.5(n-1)} \frac{2 + 29\ n - 22 n^2}{n(n+2)(2n+1)}$$

is a function describing a cross braking of the groups at their co-floating to the film surface computed according to Brunner equation;

Q is the suspension flow in the hydrocyclone inlet, m^3/s;

U_0 is the average speed in the hydrocyclone inlet, m/s;

V_{zl} is the axial velocity component of the dispersed medium, m/s;

V_{zl0} is the axial velocity component of the dispersed medium in the initial film section, m/s;

$V_{\varphi l}$ is the peripheral velocity component of the dispersed medium, m/s;

V_{zp} is the axial velocity component of the solid particle, m/s;

r, z is the radial and axial coordinates, m;

r_k is radius of the cylindrical hydrocyclone body, m;

ρ_p is density of the solid particles, kg/m^3;

ρ_l is density of the dispersed medium, kg/m^3;

a, b is the height and wide of the hydrocyclone inlet, m;

d_p is the particle diameter of the solid phase, m;

d_{b1} is diameter of the primary gas bubble escaped in the suspension at the pressure decrease, m;

d_{b2} – is diameter of the secondary gas bubble feed through the penetrate porous wall of the hydrocyclone body, m;

$\delta(z)$ is thickness of the suspension film, m;

z_c is cylindrical body height of the hydrocyclone, m;

α is angle of the conic section of the hydrocyclone body, deg;

c_{pc} is volume fraction of the solid particles bonded in groups, m^3/m^3;

c_p is volume fraction of the free particles of the solid phase, m^3/ m^3;

c_{p0} is volume fraction of the free particles of the solid phase in the hydrocyclone inlet, m^3/ m^3;

c_{b1} is volume fraction of the primary gas bubbles escaped in the suspension at the pressure decrease, m^3/ m^3;

c_{b2} is volume fraction of the secondary gas bubbles feed through the penetrate porous wall of the hydrocyclone body, m^3/ m^3;

c_{p0} is volume fraction of the particles of the solid phase in the hydrocyclone inlet, m^3/ m^3;

indeces: p is solid phase; c is particle–bubble group; b is gas bubbles; l dispersed medium.

REFERENCES

1. Naidenko, V.V., *Primenenie matematicheskikh metodov i EVM dlya optimizatsii i upravleniya protsessami razdeleniya suspenzii v gidrotsiklonakh* (Emploiment of Mathematical Methods for Optimization and Menagement of Suspension Separation in Hydrocyclones), Gor'kii: Volgo-Vyatsk. Kn. Izd., 1976. 287 p.
2. Orlov, S.L., Trudy instituta "VODGEO" (Proceedings of "VODGEO" Institute), Moscow, 1982, pp. 132–136.
3. Alekseev, V.I., Myasnikov, I.N., and Naidenko, V.V., *Trudy instituta "VODGEO"* (Proceedings of "VODGEO" Institute), Moscow, 1980, pp. 87–95.
4. Lagutkin, M.G. and Pavlovskii, G.V., *Khim. Prom.*, 1997, no. 8, pp. 24–26.
5. Kutepov, A.M., Lagutkin, M.G., Pavlovskii, G.V., and Mushtaev, V.I., *Teor. Osnovy Khim. Tekhnol.,* 1999, vol. 33, no. 5, pp. 571–577.

6. Khudobin, L.V. and Ryabov, G.K., *Mezhvuz. Sb. Nauch. Tr.* (Interinstitutional Collection of Scientific Works), no. 13, Penza: Penz. Politekhn. Inst., 1985, pp. 41–45.
7. Yablonskii, V.O., *Zh. Prikl. Khim.*, 2007, vol. 80, no. 3, pp. 399–406.
8. Yablonskii, V.O., *Khim. Neftegaz. Mashinostr,* 2006, no. 11, pp. 3–6.
9. Deryagin, B.V., Dukhin, S.S., and Rulev, N.N., *Mikroflotatsiya: Vodoochistka, obogashchenie* (Microflotation: Water Treatment, Concentration), Moscow: Khimiya, 1986.
10. Yablonskii, V.O., *Khim. Prom.*, 2005, vol. 82, no. 1, pp. 40–48.
11. Akhnazarova, S.L. and Kafarov, V.V., *Metody optimizatsii eksperimenta v khimicheskoi tekhnologii* (Methods of Experiment Optimization in Chemical Engineering), Moscow: "Vysshaya shkola", 1985, 327 p.
12. Byuyul', A. and Tsefel', P., *SPSS: iskusstvo obrabotki informatsii. Analiz statisticheskikh dannykh i vosstanovlenie skrytykh zakonomernostei* (SPSS: Art of Information Treatment. Analysis of Statisic Data and). SPb.: OOO, "DiaSoftYuP", 2002, 608 p.

ISSN 1070-4272, Russian Journal of Applied Chemistry, 2008, Vol. 81, No. 12, pp. 2207−2210. © Pleiades Publishing, Ltd., 2008.
Original Russian Text © Z.D. Reipnazarova, A.A. Artikov, 2008, published in Khimicheskaya Promyshlennost', 2008, Vol. 85, No. 6, pp. 310−313.

MODELING AND CALCULATION OF TECHNOLOGICAL PROCESSES

Mathematical Simulation of the Evaporation in Operation Area of a Bubble Evaporator

Z. D. Reipnazarova and A. A. Artikov

Tashkent Chemical Engineering Institute, Tashkent, Uzbekistan

Received August 15, 2008

Abstract—Simulation of evaporation in operation area of an evaporator is considered. We obtained a formalized model of this process and optimum conditions of an engineering system on the basis on the analysis.

DOI: 10.1134/S1070427208120355

Evaporation is a process in chemical engineering when concentration of process liquor increases due to evaporation of a part of a solvent.

There are surface evaporators where the heat transfers from a heat-carrier to the solution through a wall, and contact evaporators where the heat-carrier simultaneously touches the solution [1].

The contact evaporators have wide application especially due to an enhancement of a chemical fertilizers industry. A large surface of interaction between gas (heat-carrier) and liquid (solution) phases is obtained in these devices. Evaporation of solutions in them occurs without heating spirals. Thus reliability of evaporation plants rose along with their design and work simplification.

In this paper we simulate an active plant on evaporation of a pulp for computation of the optimum conditions of their operation.

In our plant suspensions are evaporated in an operation area of a bubble evaporator (BE).

We consider the operation area of the evaporator as a large system that first is divided into two subsystems: a liquid phase, and a gas phase. Besides we assume that a hydrodynamic structure of the fluid flows is as ideal mixture and then the liquid phase is a continuum where evaporation occurs (Fig. 1).

Water vapor removes from the liquid phase and transfer in a vapor phase. The gas phase is of discrete form, i.e. the gas leaving a bubbler or an exhaust into upper section of liquid, and dividing into small bubbles go up one by one.

Mainly in this case the gas phase is described by the laws of displacement of an ideal gas [3]. Generalizing a mathematical model the liquid phase can be simulated by a differential equation of the first order, and gas phase by a partial differential equation.

In this case for the liquid phase we use the heat-balance equation at non-steady state. Then a heat change of some elementary *i*th area of the liquid phase depends on a heat leaving this area of the liquid, and besides a heat of the gas

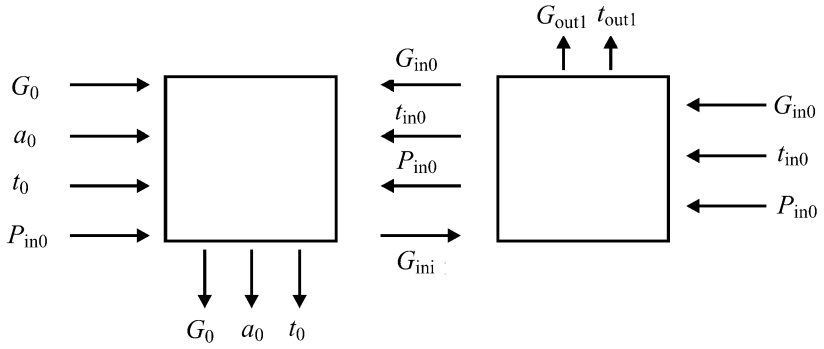


Fig. 1. Block-scheme of the evaporating process into the operation area.

phase influences this liquid. The heat-balance equation [4] for the liquid phase can be written as:

$$\frac{dQ_1}{d\tau} = q_{\text{in1}} - q_{\text{out1}} + \Delta q_i \ , \quad (1)$$

where q_{in} is heat input to the liquid; q_{out} is heat leaving the liquid; Δq_i is heat of the water vapor form.

The heat input in the elementary ith area of the liquid phase is computed by the following equation:

$$q_{\text{in1}} = G_{l0}\, c_{l0}\, t_{l0}\,, \quad (2)$$

where G_l is heat consumption by the liquid, kg/s; c_l is heat capacity of the liquid, kJ kg^{-1} K^{-1}; c_l is liquid temperature, °C.

The heat leaving the area is computed by Eq. 3.

$$q_{\text{out1}} = G_l\, c_l\, t_l\,. \quad (3)$$

An output of the water vapor can be computed by Eq. 4:

$$Q_{\text{in1}} = \Delta G_2\, I, \quad (4)$$

where I is standard enthalpy of the water vapor, kJ/kg;

As the heat is transferred by means of the gas we use a volume heat-transfer coefficient then an equation for calculation of the heat transferred by the gas phase looks as

$$\Delta q_{2i} = K \Delta V_m\, (t - t_1)\,, \quad (5)$$

where K is heat-transfer coefficient.

The heat input by the water vapor and earlier evaporated in a previous elementary area is described by equation (6).

$$\Delta q_1 = \left(\frac{1}{a_1 - 2} - \frac{1}{a_i - 1} \right) G_0\, a_0\,. \quad (6)$$

Taking into account the equation of the heat balance for the gas phase (7)

$$\frac{dQ_2}{d\tau} = q_{\text{in2}} - q_{\text{out2}} - \Delta q_i\,, \quad (7)$$

where q_{in2} is heat of the input gas and air; q_{out2} is heat of the gas removed from a furnace; Δq_i is heat that was formed in the furnace as a result of methane oxidation in the oxygen environmental, we can compute the heat input by the gas with the help of equation (8)

$$q_{\text{in2}} = G_{20}\, c_{20} t_{20}\,. \quad (8)$$

The heat removed form this elementary area can be expressed by the following equiation

$$q_{\text{out}} = G_2\ \ c_2\ t_2\,, \quad (9)$$

where G_{20}, G_2 are heat consumption of the gas and air, kg/s; c_{20}, c_2 are heat capacity of the gas and air, respectively, kJ/ kg^{-1} K^{-1}; t_{20}, t_2 are temperature of the gas and air, respectively, °C.

Thus we determine main items of the heat balance both for the liquid phase and for the vapor phase.

Assuming that at evaporation of non-volatile liquids the flow is permanent we write an equation of the mass balance

$$a_0 \cdot G_0 = a_1 \cdot G_1, \quad (10)$$

or the liquid flow in the elementary area

$$G_1 = \left(\frac{a_0}{a_1} \right) G_{10}\,. \quad (11)$$

Then an amount of the water transformed to the vapor is computed by equation (12):

$$\Delta G_i = G_{10} - G_1 = \left(\frac{1}{a_i - 1} - \frac{1}{a_i} \right) G_{10}\, a_0\,. \quad (12)$$

Boiling point is an important characteristics at the solution evaporation. In most cases accessible range of the temperature change in an ammophos industry is considered relative to an ammophos pulp. The boiling point in this case can be described by the following linear equation:

$$t = b_0 + K_{\text{t}}\, a. \quad (13)$$

Then we calculate the liquid heat in the elementary area by equation (14)

$$Q = m\, c_1\, t_1. \quad (14)$$

However the liquid weight depends on the volume and density of the liquid:

$$m = V_{\text{m}}\, S_{\text{m}}\,, \quad (15)$$

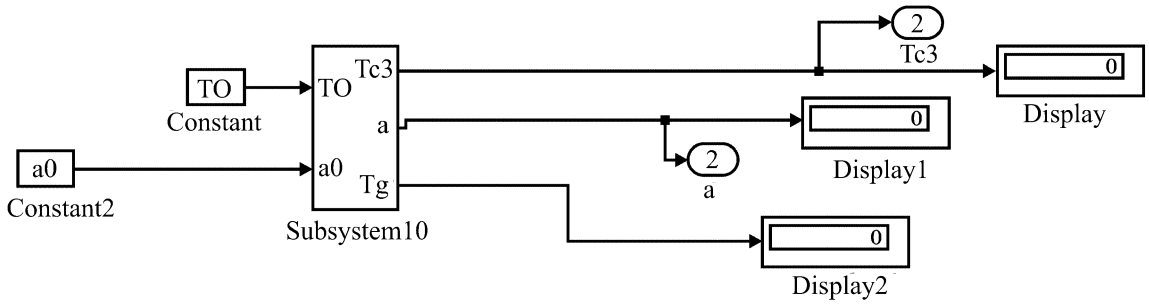


Fig. 2. One-step elementary area of the computer model for BE at ideal mixture of the flows in the liquid phase and gas displacement according to the law for ideal gas in the vapor phase.

where V_m and S_m are volume and density of the liquid, respectively.

Earlier it was established for the bubble evaporator that in the case of good operation of the bubble plant the vapor volume occupied two thirds of the device volume and the liquid phase, one third, therefore we can write equation (16)

$$V_l = \frac{1}{3} V_{ap}, \quad (16)$$

and taking into account equations (15) we can compute the heat of the liquid phase for the elementary area

$$Q = \frac{1}{3} V_{am} S_m t_1, \quad (17)$$

Substituting Eq. 13 we obtain equation (18)

$$Q = \frac{1}{3} V S_m t_1 = \frac{1}{3} V S_m (b_0 + K_t a), \quad (18)$$

and after differentiation of the heat of the elementary area we have equation (19) that described change in the concentration with respect to time.

$$\frac{dQ}{d\tau} = \frac{1}{3} V S_m K_0 \frac{d_a}{d\tau}, \quad (19)$$

Using Eq. (11) we can compute the heat removed from the elementary area

$$q_{out1} = \frac{a_0}{a_1} G_{10} c_1 t_1. \quad (20)$$

After some conversion we obtain a set of equations that characterized dynamics of processes in the liquid phase.

$$\frac{da_i}{d\tau} = \frac{3}{VpK_t}\left[G_0 c_{i-1} t_{i-1} - \frac{a_0}{a_i}\right] G_{10} c_i t_i - \left(\frac{a_0}{a_i - 1} - \frac{a_0}{a_i}\right) G_{10} I + \left(\frac{1}{a_i - 2} - \frac{1}{a_i - 1}\right) G_0 a_0 I_i + KV(t_{2i-2} - t_{i-1}), \quad (21)$$

$$t_i = (G_0 + K_t c_i), \quad (21.1)$$

$$I = (I_0 + K_i (t_2 - t_{20})), \quad (21.2)$$

$$c_1 = (c_{10} + Kc_1 (t_1 - t_{10})), \quad (21.3)$$

Computation results for the evaporation of the ammophos pulp

No.	G_{pulp}, (kg/s)	$G_{heated\ gas}$, kg/s	a_0, %	a_1, %	t_{in} of the pulp, °C	$t_{вых}$ of the gas, °C	t_{out} of the pulp, °C	Temperature in the furnace, °C
1	8.33	12.56	0.33	0.549	100	86.17	71.11	400
2	8.33	12.56	0.362	0.5881	100	88.35	73.40	400
3	8.33	11.10	0.35	0.5811	100	83.66	73.06	450
4	8.33	9.94	0.35	0.5887	100	80.61	73.43	500
5	8.33	9.94	0.362	0.6063	100	81.48	74.31	500
6	11.1	11.12	0.40	0.6095	100	86.54	74.47	500
7	11.1	11.25	0.362	0.5874	100	87.56	73.37	550
8	11.1	11.25	0.35	0.5701	100	86.72	72.50	550

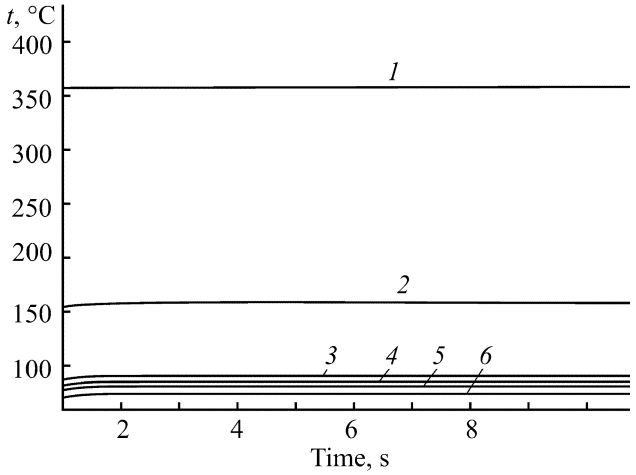


Fig. 3. Distribution of the gas temperature on liquid quasilayers in the apparatus.

where Eq. 21.1 describes the change of the concentration, Eq. 21.1 the liquid temperature in the elementary area, Eq. 21.3 the heat of vapor.

Then we developed a block-scheme for simulation of the process in the operation area on the basis of the set of equations using principles presented in [5] (Fig. 2).

Computation results on the basis of an actual plant data are presented in the table.

Numerical experiments were carried out for the initial data (no. 4): $G_1 = 8.33$ kg/s (pulp), $G_{2t} = 9.94$ kg/s (hot gas); temperature of the input pulp $t = 100°C$; initial concentration of the pulp $a_0 = 0.35$ %; the furnace temperature $t = 500°C$, heat transfer coefficient $\alpha = 9$ kJ/m^{-3} deg^{-1}. The results that depict the temperature distribution of the gas mixture along the liquid layers in the evaporator are shown in Fig. 3.

The presented mathematical model of the pulp evaporation can be used for optimum designing of new devices and for the control of this process on the actual plants.

REFERENCES

1. Taubman, E.I., *Vyparivanie* (Evaporation), Moscow, Khimiya, 1982.
2. Alabovskii, A.N., *Vyparnye apparaty pogruzhnogo goreniya* (Evaporators of Immersed Burning), Kiev, Vishcha Shkola, 1980.
3. Artikov, A.A., *Protsessy i apparaty pishchevykh proizvodstv* (Processes and Aparatuses of the Food Industry), Tashkent, Ukituvchi, 1983.
4. Kasatkin, A.G., *Osnovnye protsessy i apparaty khimicheskoi tekhnologii* (Main Processes and Apparatuses of Chemical Engineering), Moscow: Khimiya, 1971.
5. Mathworks Inc., "*Simulink User's Guide*", http://www.mathworks.com/access/helpdesk/help/toolbox/simulink/simulink.html

ISSN 1070-4272, Russian Journal of Applied Chemistry, 2008, Vol. 81, No. 12, pp. 2211–2231. © Pleiades Publishing, Ltd., 2008.
Original Russian Text © E.S. Borovinskaya, V.P. Reshetilovskii, 2008, published in Khimicheskaya Promyshlennost', 2008, Vol. 85, No. 5, pp. 217–247.

TECHNOLOGICAL PROSPECTS

Devoted to 70 years anniversary of professor V.A. Kholodnov, St. Petersburg Technological Institute

Microstructural Reactors: Concept, Development and Application

E. S. Borovinskaya[a] and V. P. Reshetilovskii[b]

[a]*St. Petersburg State Technological Institute (Technical University), St. Petersburg, Russia*
[b]*Drezden Technical University, Germany*

Received September 14, 2008

Abstract—In the recent years owing to growing necessity of raw material and energy economy and solution of ecological problems, a significant interest by the chemistry thechnologists is paid to the microsystem technology. One of directions in the development of microsystem technology is creation and application of microstructural reactors (microreactors). Currently world market proposes many samples of microstructural installations and even full-value chemical units for, in part, of organic synthesis. In Russia the microsystem technology is included to the list of priority directions of development of science and technology in 2001–2010 years.

DOI: 10.1134/S1070427208120367

The life whole sense consists in the infinite conquest of unknown, in the everlasting effort to get know more.

Emile Zola

INTRODUCTION

Microtechnology is developed in many branches of science and technology. In the recent decade have been created the microstructural units providing more effective conducting of chemical and biochemical reactions. Their performance is demonstrated in many publications [1, 2, 3–8].

An original patent has been issued in the former DDR in 1986 that protected the main principles of construction of microstructural systems and properties that they should possess for their optimal application [9]. To 1989 in the research institute Forschungszentrum Karlsruhe (Germany) has been constructed the first micro heat exchanging unity [10]. Since 1993 began analogous development in the Pacific Northwest National Laboratory (PNNL), USA [11].

In 1995, the application of microsystems for chemical and biochemical reactions has been discussed at the symposium in Mainz (Germany), that started development of microreaction technology for over the world [12]. In 1997 was arranged the first conference on microtechnology (International Conference on Micro-reaction Technology, IMRET-1), that since that time is held yearly in Europe and USA alternatively. To the year 2001 in cooperation with DECHEMA has been created industrial platform for the modeling the systems of microchemical technology (MicroChemTec) aimed at the industrial manufacturing and application of the microsystems [13].

Today the world market proposes a wide choice of microstructural units and even complete chemical installations (in part, for organic synthesis) [14]. Many companies, e.g., Ehrfeld Mikrotechnik BTS GmbH, Syrris Ltd., Micronit Microfluidics BV and others produce such units. Many research institutions and universities carry out research in this area, arrange scientific conferences and publish books and articles. In part, a great attention to the microsystem technology is paid in the Institute of Technical Chemistry of Drezden Technical University. Investigations were carried out on the enhancing efficiency of liquid phase catalytic process of phenylacetonitrile alkylation under phase transfer conditions [15, 16], and study in the area of bioreactions in the microstructural reactors [17]. In the Institute have been arranged scientific educational courses on microreactor technology in June 2006 and May 2007

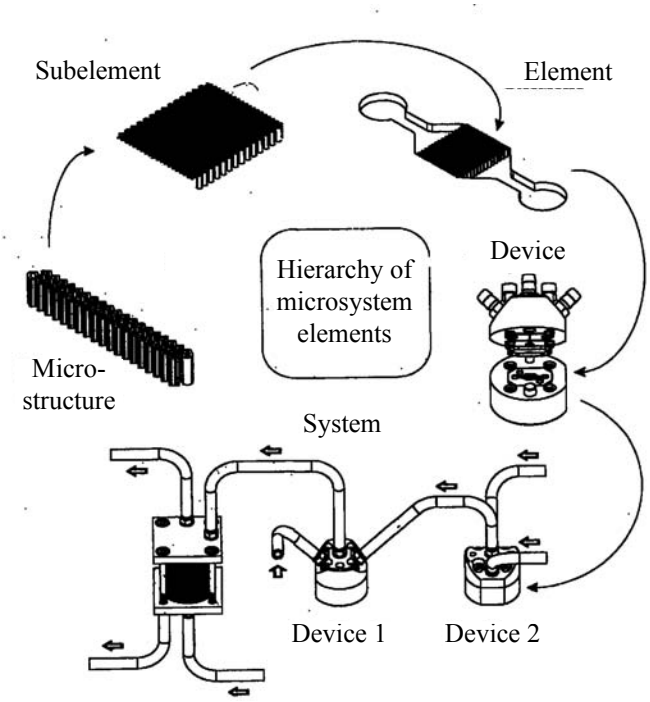


Fig. 1. Hierarchy of the elements of microsystem units on the example of micromixers [2].

(GDCh-Fortbildungskurs "Praeparative Chemie in Mikroreaktoren").

It is obvious that due to advantage of microstructural reactors in the respects of saving space, energy and material resources they will be more and more applied both for pilot installations and in general technology, under the slogan: "The reactor is as small as necessary" [1].

1. MICROSTRUCTURAL REACTORS: TERMINOLOGY

In correspondence with the widely used term "Microsystems," the term "microstructural reactor" is used for denoting a miniature system for carrying out chemical reactions, that are constructed with at lest partial application of the methods of microtechnology. The term "microstructural reactor" can be reduced to "microreactor" taking in mind that it is assumed a special microtechnology that is applied at their producing, rather than laboratory analogs of industrial reactors. The typical size of internal channels in the microstructural reactors fall to the range from microns to millimeters (Table 1). Sometimes one can meet terms "nanoreactor" or "milli/mini-reactor". These terms denotes the units with the size respectively below or higher than the above range [2].

2. STRUCTURAL HIERARCHY OF MICROREACTORS

Commonly the microreactors are produced in correspondence with the hierarchy principle, that is, they are assembled from a set of elements that includes in turn sub-elements and so on. Such approach is based on the so-called "concept of sequence" [19]. The aim of this concept is definition of various elements allowing modular producing a microsystem unit and selecting those the most often used in the installations [2].

A most miniature systems for the realization of flows, the so-called "microstructure" consist of a number of channels (Fig.1), which have the flow inlet and outlet. Single channel or a set of such channels that form a complete object is denoted as "sub-element." In some cases a sub-element can contain additional microstructures, e.g., pores [2].

A set of sub-elements combined with joined channels constructed of the same material form an "element". For increasing their input-output characteristics, the elements can be joined to form a row, e.g., a row of catalytic plates in the chamber of a gas-phase microreactor. Alternatively, identical units can be parallely connected on a plate.

Units and chambers can not work separately, that is means that they are not a microreactor till they have no body or at least upper and down plates used for the transfer of a flow to the additional units. An element becomes a unit when it is plased into a body or between two panels. A complicated system can be constructed by means of integration of severalunits in one body.

3. FUNCTIONAL CLASSIFICATION OF MICROREACTORS

By the purpose of application the microreactors can be classified as follows:

Analytical units and equipment for research

Table 1. Comparison in size of internal channels of macro-, micro-, and nano-units [2,18]

Parameter	Macro	Micro	Nano
Size range	$(1\ldots10^{-3})$ m	$(10^{-3}\ldots10^{-6})$ m	$(10^{-6}\ldots10^{-9})$ m
Measuring unit	1 mm	1 μ	1 nm
Surface area to volume ratio	100–1000 m^2/m^3	10000–50000 m^2/m^3	~100000 m^2/m^3

Some of microreactors are used presumably for analytical purposes, in biochemistry in particular, other have found application in chemical technology, although these areas obviously are very different. In view of construction of analytical and technological equipment, some of microreactors can be used in both these areas.

By the type of the processes in a microreactor they can be classified as:

Units for catalytic and non-catalytic reactions

Depending on the presence or absence of a catalyst and on the type of catalyst the microreactor construction can differ. In some systems the catalyst covers the microchannel wall, in others is applied as a powder, or can be absent at all.

Units for homogenous and heterogenous processes

Some of microreactors are specialized for homogenous, or heterogenous processes. In the first ones it is sufficient to provide well mixing of the components; the second ones should provide necessary interphase surface area.

Units for certain system types, e.g., gas–liquid,liquid–liquid, gas–gas, photochemical reactions, etc.

To provide maximal process intensification, a reactor can be developed for a certain type of the system.

Many units with micro channels have been developed in the end of 80-th for the research purposes. When one unit provided conducting several types of processes, e.g., filtration, mixing, separation and analysis in the same unit, such a system commonly had been assigned to general microanalytical type (mTAS) [20].

By analogy with technological processes, the microreactors can be classified by the type of their action, that is, a reactor can be of continuous or periodical operating. Most of used microreactors are of continuous operating.

4. DIFFERENCE BETWEEN ANALYTICAL AND REACTION SYSTEMS

Analytical systems are commonly designated for the information acquisition and estimation, e.g., analysis of water samples from a lake. Reaction systems differ from the analytical ones in that they designated for producing or processing materials or substances. For microsystems this difference vanishes because diminishing in the unit size leads to decrease in the amount of processed matter to the level of analytical systems. Such a mycrosystem can be used for fine organic synthesis and for the initial step of developing a process. In both the cases measuring technique should be applied for finding optimal parameters of the process and for testing quality of the obtainedtt product. Such measuring units are similar to analytical ones. However, they differ by the purpose of using the obtained information. In the analysis, the information obtained is the final product, e.g., determination of the ozone concentration in a certain layer of atmosphere is an important information for ecological studies. In distinct, the information obtained in the microreaction systems is used for the optimization of both laboratory synthesis and large scale complicated process. There is a significant difference between miniature analytical systems and microreactors [2].

5. PRINCIPAL ADVANTAGE OF MICROREACTORS

Despite small size of microreactors, their internal volume is too large to provide interaction of reagents on the molecular level. The main advantage of microreactors is improving the regime of flow and providing intensification of mass and heat transfer. Basically, the contribution of microreactors concerns the microscale section of chemical engineering rather than chemical aspect of reactions, reaction mechanism and kinetics.

5.1. *Diminishing of Linear Size*

Diminishing of linear size of a closed system increases respective gradient of a given parameter of process. This concerns such parameters as pressure, temperature and concentration that are the most important for conducting a process in the reactor and for data acquisition and treatment. Due to diminished linear size of the system, the moving force of mass and heat transfer or of diffusion flow per volume of surface unit increases when microreactors are applied.

These simple theoretical assumptions are confirmed by investigations in the area of mass and heat transfer. Most modern microreactors contain microchannels whose width falls to the range 50–500 μm and the wall thickness between the channel of reaction and channel of heat transfer can be diminished to the size in the range 20–50 μm which leads to increase in the heat transfer coefficient to 25000 W m^{-2}. Such value of this coefficient in the micro units at least by one order of magnitude larger than the value for commonly used heat exchange units [3]. In micromixers, the thickness of liquid layer can be diminished to the value of several tens microns and in

some cases to nanometers. As a result, the time of mixing in the micromixers falls to milliseconds and in some cases to nanoseconds [4], which is hardly available in the apparatus with stirrer or other traditional mixing units.

5.2. *Increase in the Surface–Volume Ratio*

Due to diminished linear size of microchannels the surface to volume ratio increases noticeably. As shown in Table 1, specific surface of the micrireactor channels is 50 times over than those of standard units. Besides the above mentioned advantage in heat transfer, increase in the surface area of apparatus can be used for intensification of processes, e.g., in catalytic gas phase reactors, where internal surface of the apparatus is covered by active substance.

Similar advantage of microreactors occurs in the case of multiphase processes when thickness of at least one of liquid phase layers has size of nanometers. Both theoretical and experimental investigations have confirmed that interphase surface in the microreactors are in the range 5000–30000 m^2/m^3. To the moment the best achieved interphase surface in the down draining film microreactors is 25000 m^2/m^3 [5]. For standard bubbling columns this value is below 100 m^2/m^3. In some cases, e.g., for ring regime of (two-phase) flow in microbubbling column the specific surface area can achieve approximately the same value as the surface in microchannels [6].

Due to decrease in the linear size the microreactor volume diminishes to several microliters. This difference as compared with common industrial units becomes ever more emphasized when together with diminishing in the reactor size the industrial process that includes stirring is replaced by continuous process in microreactor. In te case of organometallic reactions a receiver 6000 liters volume can be replaced by five miniature mixers several milliliters volume each [7]. Diminished volume provides the process safety and due to diminished duration of residence increases the process selectivity.

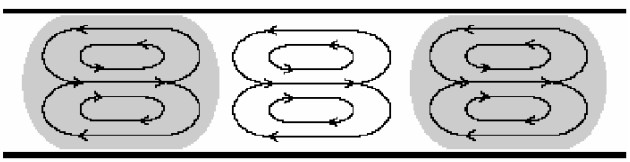


Fig. 2. Additional circular motion in a microchannel.

5.3. *Flow Regimes in Microchannels*

Another advantage of microreactors is a specific hydrodynamics of flow, which is a significant feature of microliquids. The flow is commonly laminar, directed and very symmetrical [8]. In addition, multiphase flows often demonstrate good phase separation [21]. This is connected with the formation of so-called Tailor flow ("slug-flow") in the microchannels. In this case occurs secondary circulation inside the liquid drops due to friction between the segmented liquid and microchannel wall (Fig. 2).

5.4. *Multiple Increase in the Number of Elements*

A typical feature of microstructural units is multiple repeating of basic elements (Fig. 3). They can work consecutively, as is common for the units of preliminary sampling, or being connected in parallel, with common feeding pipe, that is applied for the purposes of manufacturing [2].

In the recent time significantly extended application of combinatory strategy, beginning from the producing of drugs [22] and ending by preliminary sampling of inorganic materials, catalysts and polymers [23]. To the moment have been tested many inorganic materials and some of catalyst for their application in the microreactors [24]. For this purpose, separate sections of a microchannel were covered by a thin layer of corresponding substance using a technology of thin film covering. The investigations were carried out on the examples of standard processes with the purpose of choice of local concentration profile and therefore of given properties of materials.

However, such direct approach is restricted, especially in respect of development of new catalysts and polymers. A necessity of maintaining porosity in the first case and long reaction duration in the second are the main reasons for application standard tubular type continuously operating reactors [25].

5.5. *Versatility of Manufacturing*

In distinct to the classical industrial installations, increase in productivity of microreactors is achieved by increase in the number of units rather then in size [19]. Functional units in a microsystem, e.g., mixers, are duplicated several times. Connection of such units is achieved by using channels and sections with equal flow distribution. Increase in the number of units in a great extent provides retaining the same desired characteristics

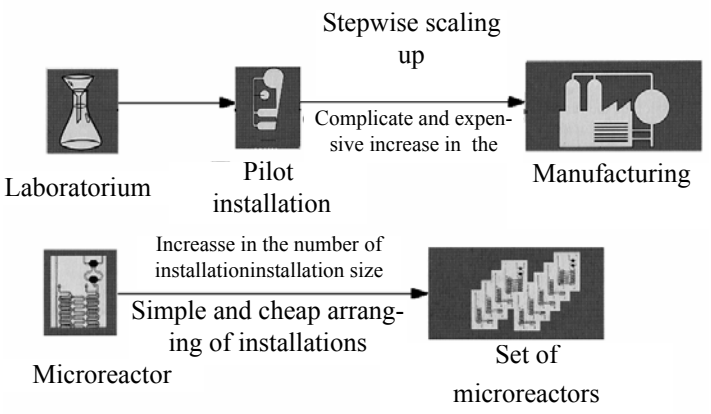


Fig. 3. A simplified scheme reflecting the principles of stepwise scaling up an industrial installation and increasing in the number of microreactors [2].

of main unit at the increase in the whole system volume [19]. In the ideal case the measuring units used in some steps of development of the process remain similar and consist of identical components. The results of application of such units have been demonstrated by comparison of efficiency of mixing in the system consisting of 10 mixers with that in one unit [26]. It should be noted also that uniformity of flow distribution is important for the productivity of general type reactors. In addition, application of great number of units allows easily change the amount of product if there is a possibility to switch on or off some units in the whole set. Such sectional projecting gives a possibility of ease modification of an installation for several reactions. By introducing changes in pipe lines, an installation can be adapted to the synthesis of various products using microreactor modules with the principle of "LEGO" system. Such flexibility is confirmed additionally by the possibility of these systems to work in a wide range of working conditions.

6. POSSIBILITY OF EXPLOITATION OF MICROREACTORS

Above mentioned fundamental advantage of microreactors allows at their application to provide the following:

– Fast transfer from research step to manufacturing at low expenses.

– Simple increase in the amount of product

– Less plant area for the manufacturing

– Less cost of transport, materials and energy

– More flexible response to the market demand

The fast transfer from research to manufacturing is possible due to the possibility of fine changing working conditions and obtaining more accurate data and information that is not available in other cases, e.g., in respect of new regimes of a process [7, 27]. In addition, simple practical aspects make application of microreactors attractive, e.g., easiness and flexibility of assembling and disassembling experimental installation, low consumption of materials and enhanced safety.

Besides the purposes of investigation, there are other potential areas of application of microreactors related to manufacturing. Now is effected production of hydrogen in miniaturized reforming installations for its further using in fuel cells. This is the most promising direction because it really requires application of light and compact microreactors.

Considering yield of product we have to note that the process productivity is connected directly with the volume of reaction system. Hence, the product cost should increase when the reactor size decreases [28]. Moreover, the ratio of amount of material needed for creating apparatus is very large for microreators because they consist of many microchannels separated by dividing walls in the apparatus. This unfavorable ratio makes supposedly unprofitable manufacturing in microreactors. However, have special aspects been revealed that either allow to increase general productivity of microreactors, or due to other factors their micro volume leads to economy in the product cost. Below are considered some of these aspects.

– Replacement of periodically loaded reactor by continuous process

– Process intensification

– Safety

– Creation of distributed manufacturing

– Ecological aspects

6.1. *Replacement of Periodical Reactor by Continuous Process, the Process Intensification*

In many cases the processes are carried out in periodical reactors, e.g., at the use of reactor with stirrer. Sometimes the reaction duration becomes too long due to slow mass and heat transfer in the system with low specific surface of contact. Continuous process in microreactor where owing to thickness of liquid layer the mass and heat transfer in microchannels is much faster leads to significant shortening of reaction duration. In addition, conversion and selectivity also can be increased, as have been described for organometallic reactions [5]. Hence, yield of the final product in microreactor can be higher than in a periodical reactor. Moreover, due to application of microreactor can be changed reaction conditions. For example, a process in a periodical reactor requiring cooling can proceed in a microreactor enough effectively without cooling.

Due to the possibility of intensification of heat transfer in micro reactor, carrying out of high temperature autothermal reactions in such reactors can lead to increased conversion [27]. Calculations show that with a technology of continuous manufacturing in microreactor the amount of catalyst for a given chemical process can be decreased approximately by the factor of 1000. Besides, by decreasing ratio between volume and cost of apparatus can be enhanced productivity of microreactors. Despite much smaller size of continuous microreactor, its advantage over traditional reactors for solving this problem becomes obvious.

6.2. Safety of Microreactors

Microreactors allow much simpler control over the process parameters (temperature, pressure, duration, etc.) due to small volume of the reaction system. Reactions proceeding at high pressure or with application of hazard chemicals proceed more safely. There are many examples of application of microreactors that demonstrate their work under the explosion safe regimes [29]. On the contrary, at classical development of a process aimed at increase in the reactor volume the work under such regimes becomes impossible. Obviously in such cases should be applied the principle of multiplicity, that is, to use several identical units while each unit remains small. The possibility to work in so-called “remote” or “hindered” regimes extends flexibility of continuous microreactors. However, for real estimation of the possibility of working in such regimes should be carried out additional investigation of model reactions.

6.3. *Creation of Distributed Manufacturing*

Currently manufacturing is carried out in big fabrics and occurs a tendency of their extension. Concerning petroleum chemistry where the essence of natural raw material is transported for treatment on large distances to the central plant where it is worked up for obtaining valuable products, then small amount and distant location of the source of raw material can lead to unprofitable manufacturing because laying of pipe or constructing of a new plant are not profitable economically. In this case manufacturing with the use of microreactors can become cheaper than application of traditional equipment. Construction and dismounting of microreactors can be carried out enough quickly and their productivity is high, in particular when the principle of multiple repeating of micro units is applied.

6.4. *Ecological Aspects*

There is an opinion that producing of microreactors requires much more energy and materials than is needed for making common continuously operating reactors due to application of stainless still, and hence they in greater extent promote environment pollution. Moreover, the time limit of application of microreactors can be shorter due to possibility of their contamination and hence they should be produced more often. Karlish and co-workers [30] have compared time limits of operation of traditional and micro reactors under the conditions of strongly exothermal organic reaction. The results of investigation showed that despite shorter time limit for the microreactors in certain processes (e.g., production of tetrahydrofuran) their application can increase yield of the targeted product and thus to decrease consumption of energy. Taking all these pluses of microreactors, one can reliably say that the necessity of often renewing in the case of microreactor plays secondary role.

7. PRINCIPAL TYPES OF MICROREACTORS

Now there are many microreactors that are used in the various types of reaction systems. Research institutes develop new technologies for producing the microsystem unities and compare them with the existing ones. All research and development in this area is directed to intensification of the processes and increase of their safety compared to traditional reactors and related economical preferences for industry.

Figure 4 depicts distribution over the types of reactions studied in laboratories. One can see that homogenous

reactions in the liquid–liquid systems are carried out most often, that is explained by their relative simplicity and by a large number of the installations for the reactions of this type.

Below we consider a construction and working principles of several microreactors for various types of reaction systems.

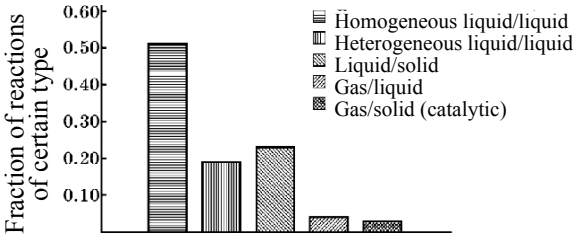


Fig. 4. Distribution over the types of the reactions carrying out in laboratories [31].

7.1. *Microreactors for Liquid Phase Processes*

In traditional reactors for liquid phase processes the components commonly are stirred by a stirrer, while in the microreactors this process in most cases is conducted through diffusion [29] which, depending on the reaction rate, can begin even in the mixer on the inlet [32].

There are different methods for mixing liquids. A simple and therefore often applied principle is the principle of multilayer [29], which is applied, e.g., in the mixers of IMM firm [29, 32] depicted in Fig. 5 and of the firm MGT, Mikroglas Technik AG [33] in Fig. 6; both companies are located in Mainz, Germany.

The specific geometry of the mixers favors so-called "focusing", that provides mixin in several milliseconds [34]. Contact of non-mixing liquids [33] or gas–liquid [35] is of more complicated nature. Various types of mixing chambers are used depending whether the flow regime is laminar or turbulent [36].

Fig. 7 depicts a mixer developed by Micronit Microfluidics BV (The Netherlands), operating on the principle of split-recombination technique. The idea of this technique is generation of multilaminar layers by splitting and recombination of liquid flows. Often due to high flow rate in such mixers is provided turbulent regime of the second stream. Thus, most of important from the practical viewpoint streams can be joined to provide a regime between laminar and turbulent ones. These additional streams in a general case are favorable for the process of mixing, but they decrease duration time and diminish a possibility of modeling the process. As compared with the counter-split mixers, the mixers of

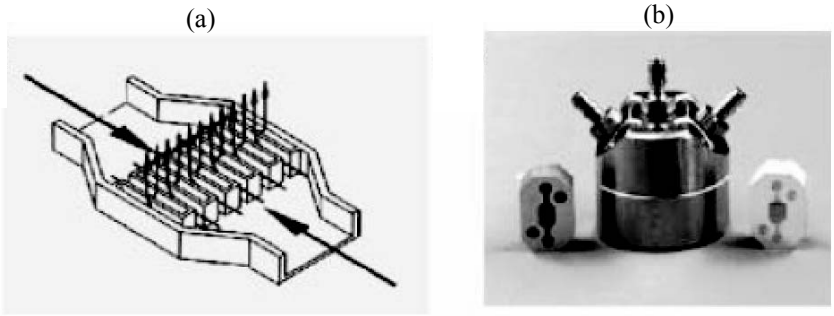


Fig. 5. Opposite gap type mixer: (a) working principle; (b) general view (made of metal and stainless steel); produced by IMM, Mainz [29].

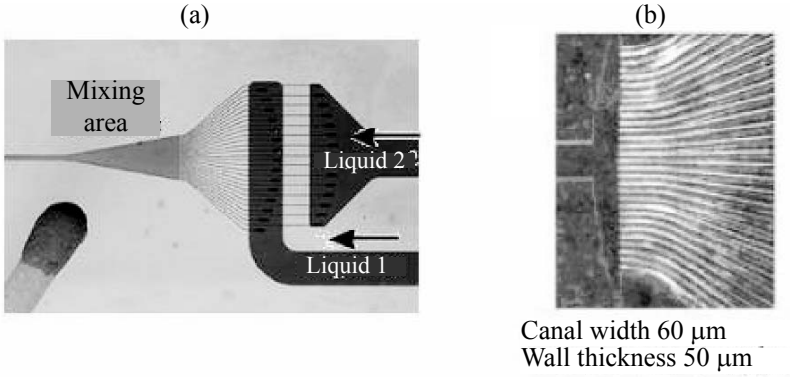


Fig. 6. A system for liquid inlet and mixing block of the opposite gap type mixer: (a) general representation; (b) details of the zones of feeding and mixing (sources: IMM, microstructure: MGT, Mikroglas Technik AG, Mainz [33]).

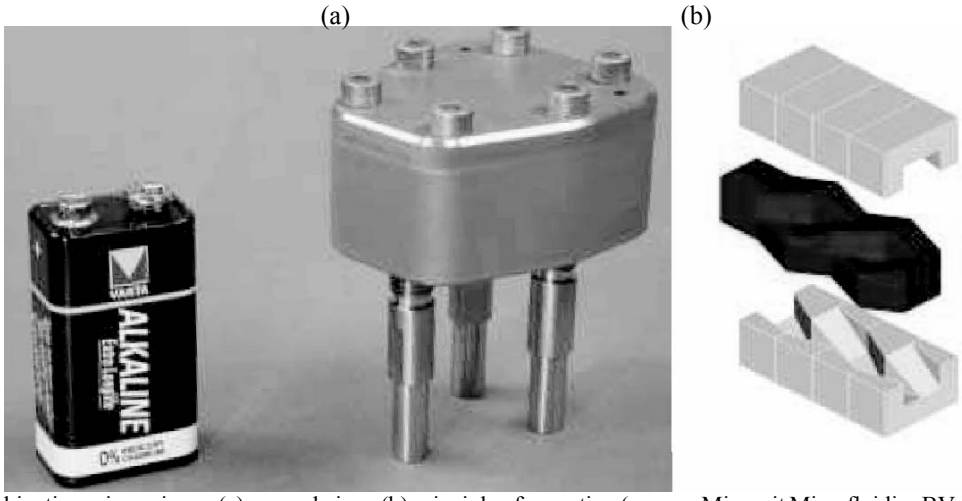


Fig. 7. Split-recombinating micromixers: (a) general view; (b) principle of operating (source: Micronit Microfluidics BV, The Netherlands [36]).

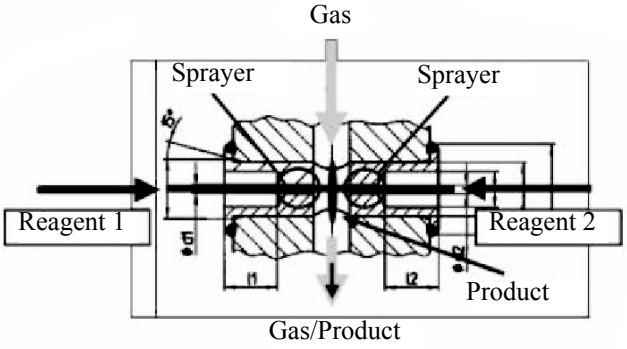


Fig. 8. Microstructural mixer (source: Synthesechemie GmbH, Heusweiler [37]).

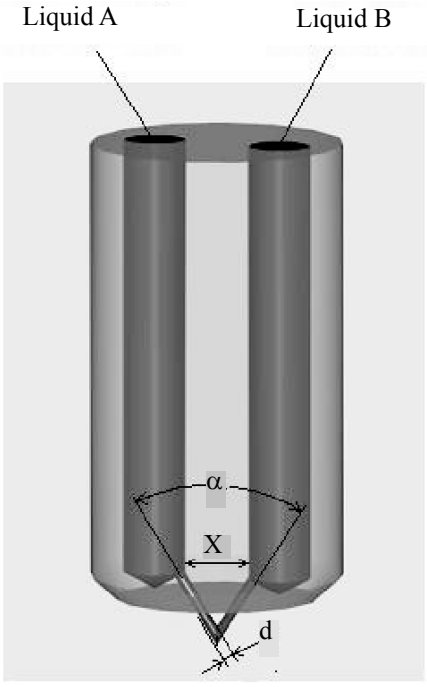


Fig. 9. Mixer of jet-collision type (source: IMM [38]).

split-recombination type can provide less pressure drop due to relatively larger internal size. Therefore the split-recombination mixers allow to work at higher rates of liquid streams that being not significant for the reliability decreases probability of depositing substances [36].

The phenomenon of turbulence is also applied at the mixing of liquids in micromixers at high stream rates. Figure 6 depicts a micro-jet mixer developed by Synthesechemie (Heusweiler, Germany) [37], where the reagents are pulverized through diamond or sapphire sprayer (with holes 60–350 m), collide in the mixer chamber and are intensively stirred. A gas input from top is responsible for removing the mixture from the chamber.

A jet-collision mixer depicted in Fig. 9 (developed by IMM) operates along the same principle [38], that is, the liquids are joined out of the mixer and are mixed in a short period.

Both the above described mixers were developed for the reaction that can lead to formation of a precipitate and as a sequence to the stoppage. Stoppage of these mixers is impossible because the reagents are stirred not in the microchannel but in open chamber and then are moved by gas flow.

To the moment a series of modular reactor systems has been developed. Figure 11 depicts a microstructural reactor (MGT, Mikroglas Technik AG), where are integrated: a mixer, a module of duration control and a cooling system [39].

More complicated microstructural reactor that has been projected by IMM for BASF is intended for two-phase reactions in a liquid-liquid system [40]. The microsystem joins three modules: mixer, duration control module and heat exchanger (Fig. 12).

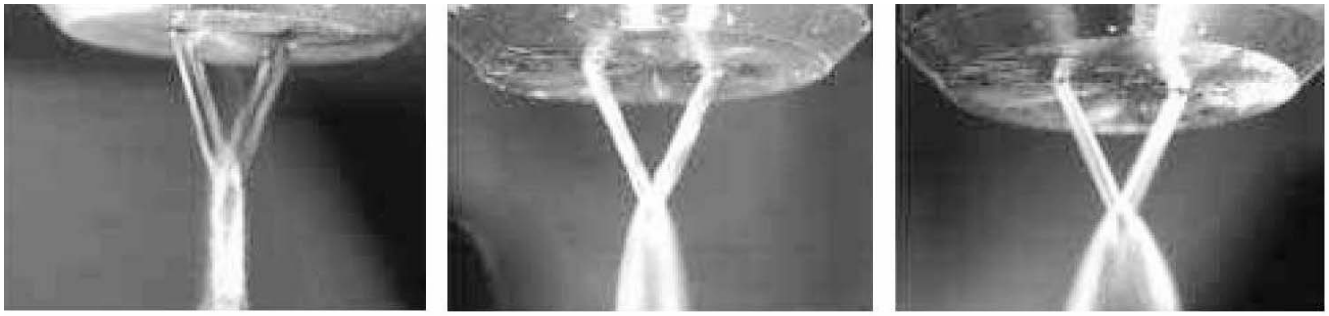


Fig. 10. Mixing regimes of the jet-collision type mixer (source: IMM).

Complete installations that include pumps, microstructural reactors, duration control modules, probes and real time analytical systems have been proposed by such producers as Cellular Process Chemistry Systems GmbH (CPC, Frankfurt), MGT Mikroglas Technik AG and IMM. Basically, these installations operate along the principle of micromixing in channel and are applied for investigations in the area of organic synthesis in laboratory.

For optimal carrying out certain chemical reaction the respective microstructural reactor installation should be assembled selectively for a given purpose. Such installations operate in many research institutions and universities in Germany.

7.2. *Microreactors for Gas–Liquid Processes*

In the recent years the interest to the investigations in the area of microreactor technique for the processes in the systems of gas–liquid increased. Two microstructural reactors for gas–liquid reactions have been developed by IMM in cooperation with other firms [41, 42]. Figure 13 depicts a principle of operation of a reactor with down draining film [41, 42]. The reactor consists of four components: bottom with integrated heat exchanger, reaction plate, seal at contact zone and a head with chamber. The central element of this microstructural reactor is reaction plate with the channels 100–1200 m width and 100–600 m depth. In the microreactor head there is a reaction channel through which the liquid drains down, that contains a rectangular gas chamber where reaction gas is passed through a distributing unit. The gas outlet hole is constructed like a gas diffuser to provide uniform distribution. Size of cooling channels depend on the width and depth of reaction channels.

To confine reaction space by the cooling volume of the reactor, the reaction plate is covered by a contact zone seal to prevent the contact with the gas in the not-cooling space.

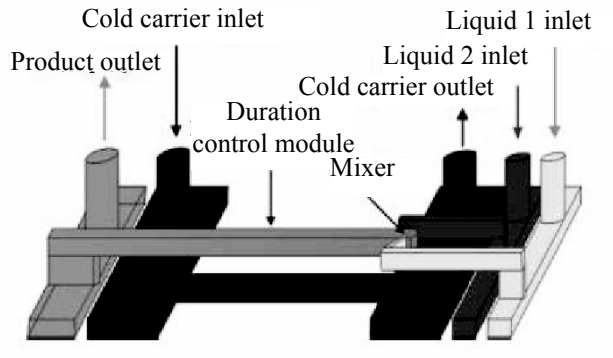


Fig. 11. Microstructural reactor with mixer, duration control module and heat exchanger (source: MGT, Mikroglas Technik AG [39]).

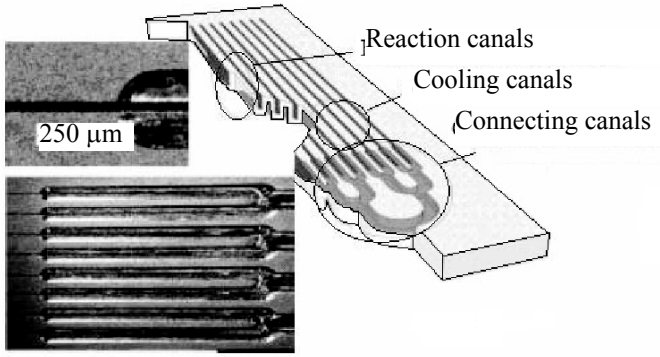


Fig. 12. Microstructural reactor with mixer, duration control module and heat exchanger (source: IMM [40]).

Figure 14 depicts a reactor with down draining film constructed of stainless steel, containing an inspection window. Good mass and heat exchange can be improved by thickening the liquid layer in microchannels. Liquid films up to 15 m thickness can have interphase space up to 20 000 m^2m^{-3}, that is approximately 10-fold over than in analogous systems, e.g., in the jet-collision type unit.

Close results have been achieved in a microbubbling column which operating principle is shown in Fig. 15 [41,

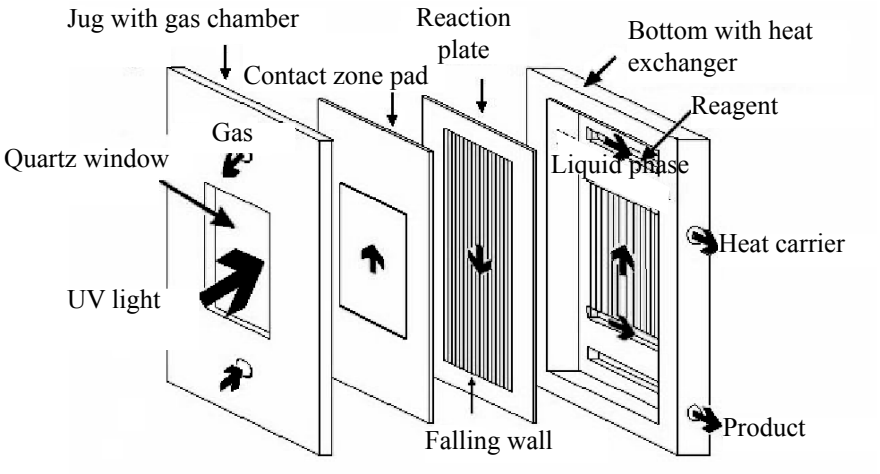


Fig. 13. Structure of the down draining film reactor (source: IMM [43]).

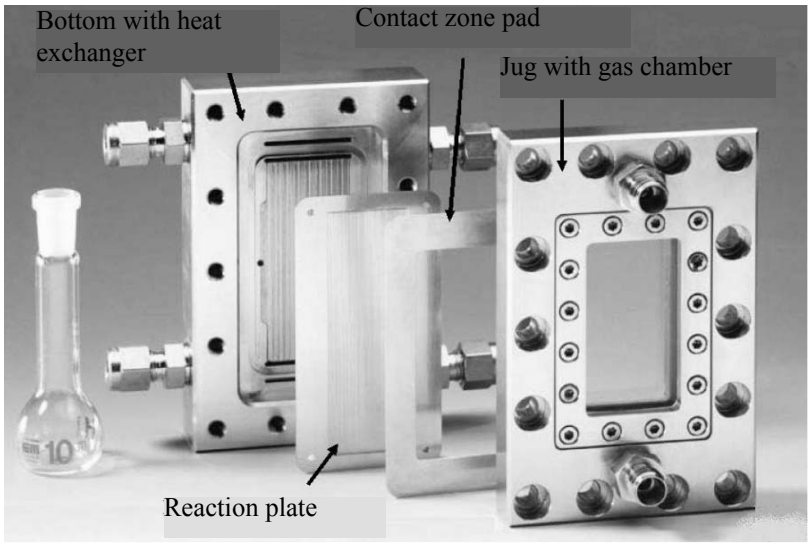


Fig. 14. Down draining film reactor with inspection window (source: IMM [43]).

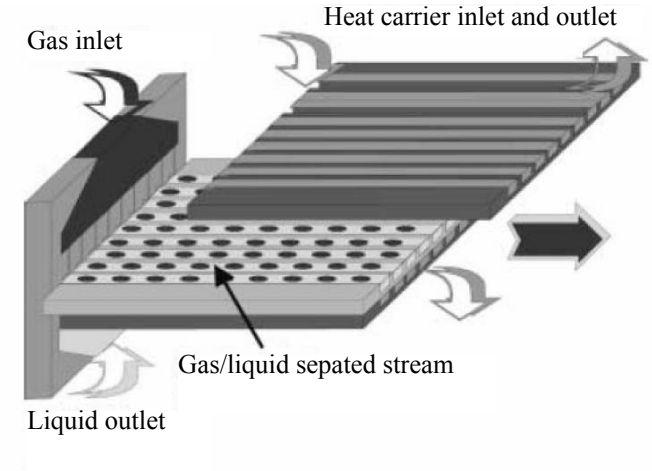


Fig. 15. Construction of microbubbling column (source: IMM [43]).

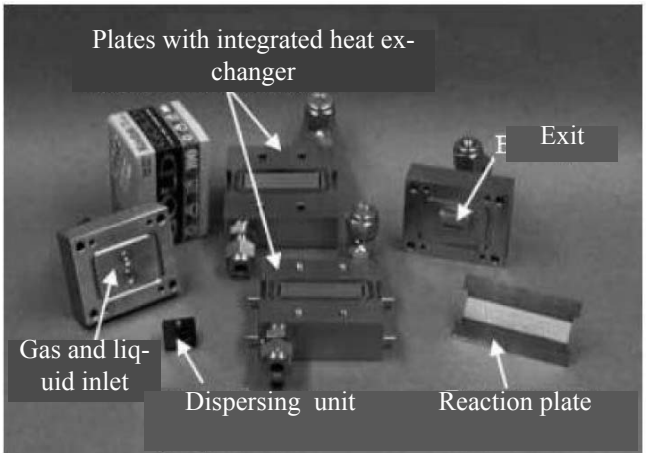


Fig. 16. Construction of microbubbling column (source: IMM [43]).

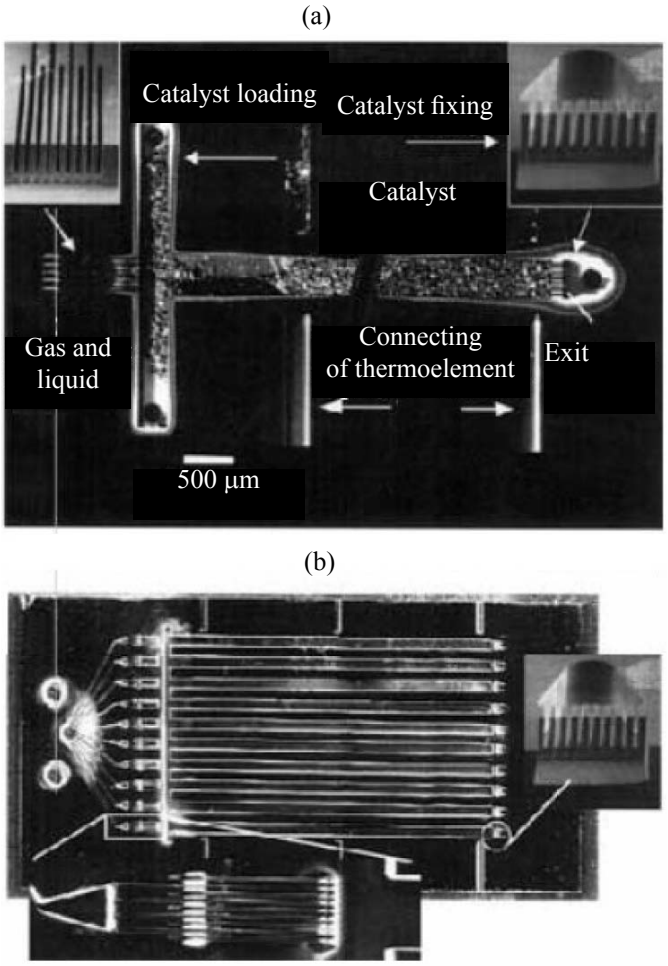


Fig. 17. Microreactor with immovable catalyst: (a) one reactor (b) ten reactors with a unit for distribution of liquid (source: MIT, Cambrige [45]).

42]. The microbubbling column is a reactor developed for providing fast contact between liquid and gas.

A central element of the microbubbling column is dispersion unit made of copper-nickel alloy. Uniform distribution of gas and liquid flows is achieved by small size of the microdispersion channels that the reagents are passed under the pressure at feeding. The channels for gas phase size is 5 m or less, for liquid phase 20 m. The channels are constructed in a metallic sheet. Effective temperature control is achieved by a heat carrier flowing through small channels as a counterflow to the reagents. Some details of the microbubbling column are shown in Fig. 16.

Figure 17 depicts a microreactor for the system of gas–liquid–solid developed in MIT (USA). Its microchannels contain powdered catalyst [44, 45]. This reactor with immovable catalyst was successfully applied for the process of hydrogenation of conjugated olefins and

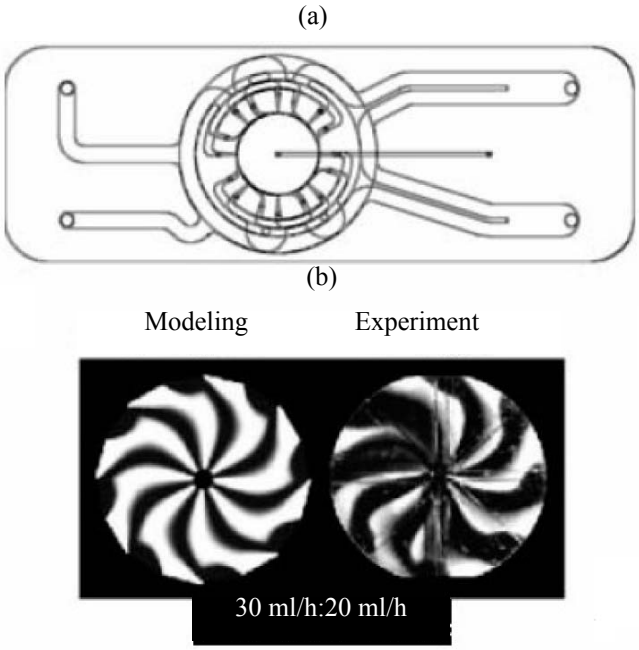


Fig. 18. Glass vortex mixer: (a) construction; (b) modeling and experiment for the liquid-liquid system (source: IMM; MGT, Microglass Technik AG [35]).

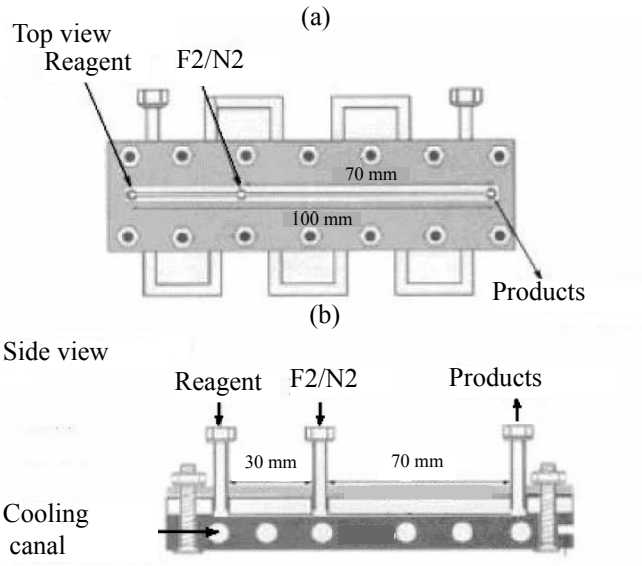


Fig. 19. Monochannel microreactor: (a) top view, (b) side view (source: University of Durham [47]).

selective oxidation of benzyl alcohol to benzaldehyde.

Figure 18 depicts a glass vortex mixer [35]. It consists of 11 equal elements that contain sprinklers of two types. A sprinkler for gas inlet is of 30 m, for liquid of 50 m width. In the reaction space for gas phase is formed a helix-like cloud, for liquid phase analogous circulating turbulent flow. Such flows are typical of the formed in two-phase mixers. In the reaction space from bubbles

(a) (b)

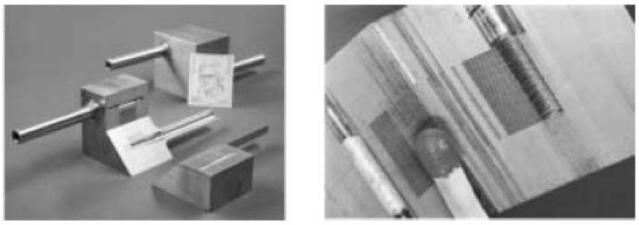


Fig. 20. Staple multiplate reactor fastened by external welding seam: (a) general view, (b) detailed photography (source: IMM).

(a) (b)

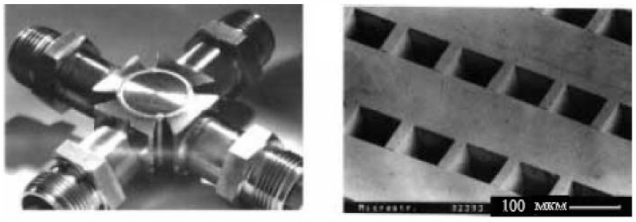


Fig. 21. Staple multiplate reactor fastened by diffusion welding: (a) general view, (b) detailed photography (source: Forschungzentrum Karlsruhe [53]).

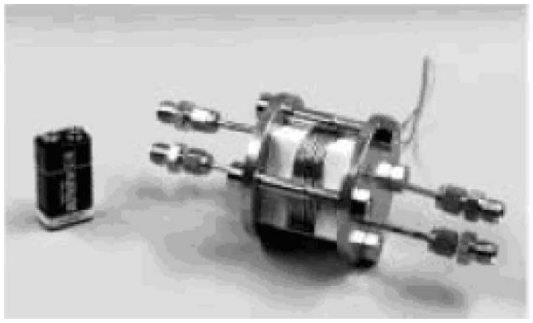


Fig. 22. Staple multiplate reactor with head (source: IMM).

and foam are formed separate bubbles that are combined together in the microchannels. Such type of reactors is appropriate for providing effective contact of catalyzed suspension with gas phase, although for this purpose the sprinkler should be extended to 150 m.

A microreactor constructed by Chamber et al. [46] is developed in particular for the strong exothermal reactions of fluorination (Fig. 19).

Liquid and gas are passed through a channel with a rate providing formation of ring type flow. Thanks to this the liquid is distributed as a thin layer on the microchannel wall while gas is passed through the middle space of the channel. Similar conditions of flow and interphase surface occur in the reactor with a down draining film.

7.3. *Microreactors for Gas Phase Reactions*

Gas phase reactions are the most studied processes in respect of application of microreactors. Even omitting economical aspect and scientific importance of such investigations, microreactors remains the most appropriate for such reactions from the viewpoint of technology. Wцrz [40] in his works affirms that the processes proceeding with a high rate and with significant heat liberation should be carried out in microreactors.

Most gas phase reactions are carried out in the presence of heterogenous catalysts , that is, a two-phase system (solid and gas) is formed, which is particularly appropriate for conducting in microreactors. In industry and in laboratory many gas phase reactions are conducted in the reactors of replacement type which by the principle of their work are analogous to microreactors. On the other side, they differ by the technology of introducing catalyst. In the replacement reactors the catalyst is commonly used in the form of balls or tablets (immobile technology) or as a well stirred dust (pseudoliquid layer). The catalyst as a thin layer on the reactor wall is applied exclusively in the microreactors. Therewith, for the fixation of the catalyst on the microchannel wall is applied technique of grounding analogous to those applied in monolithic reactors. The ground by means of wet chemical impregnation is coated by the catalyst. To the microreactors can not be placed friable materials because this leads to loss in pressure and destroys laminar regime of flow.

7.3.1. Staple multiplate reactors. The most often applied type of microreactors for the gas phase systems is a microreactor constructed of many plates assembled into staples. Each plate has parallel microchannels [48, 49]. Such plates are either fastened by external welding seam (Fig. 20) [50], or joined under end shield (Fig. 21), [51], have joining plates (Fig. 20), [52] or placed in a body (Fig. 22) [48, 49].

(a) (b)

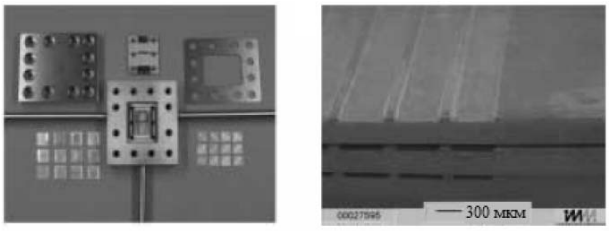


Fig. 23. Staple multiplate reactor with body, consisting of two parts: (a) construction elements; (b) zoomed view of one plate (source: IMM [2]).

When necessary, the plates can be separated into sections and mutually isolated by the sealers made of graphite or other material [52]. The body often has reinforcing screws that provide uniform pressure on the plate edges. The microstructural plates can also be joined by laser or diffusion welding [50]. The plates joined by diffusion welding should be placed into a body. Schubert and co-workers [51] have optimized the diffusion welding of the microreactor plates to provide perfect heat exchange without placing them into a body. Such configuration is quite compact one because large working surfaces are formed by joining small volumes.

A sample of such reactors is two-channel microstructural reactor that can be used for the operations with counterflows. In such reactor an exothermal reaction can be used for heating the flow of reagents. Thus, endothermic and exothermic reactions can be carried out simultaneously [52] and autothermal regime can be arraned.

Wolfart, Renken and co-authors [54] have created a microreactor that operates without microchannels. Instead of the microchannels it has a small chamber with separators that passes the flow along a constrained channel thus forming miniaturized active surfaces in each part of the chamber wall.

Among other examples of staple multiplate microreactors there are the reactors for oxidation of ammonia developed by Schouten et al. [55]. Richter et al. [48] have developed a reactor for the synthesis of ethylene oxide, Kaminos et al. [56] a reactor for methanol reforming in a steram.

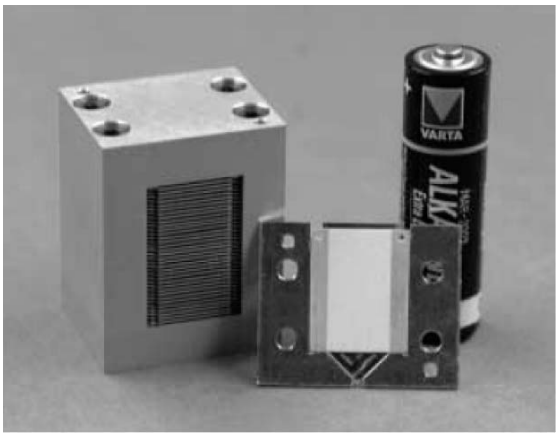


Fig. 24. Module of staple microreactor consisting of 35 plates (Source: Universitдt Chemnitz; IMM [59]).

7.3.2. Staple multiplate reactors for parallel testing of catalysts. A special form of multiplate microreactors allows parallel testing of several catalysts, each applied to certain plate. Zech and Нцnicke [57] in cooperation with IMM developed a multiplate reactor (35 plates). Central component of this installation is a capillary 300 м width that automatically collects samples from each plate (Fig. 24). More recently, Kolb et al. [58] has constructed a reactor consisting of 10 groups. Such reactor can operate consecutively or parallely, depending on the connection of its plates. In such reactor also possible to carry out optimization without changing the reactor structure and geometry of its channels.

7.3.3. A microreactor constructed of one plate and one channel. The microreactor consisting of one plate has an advantage over the staple multiplate reactors

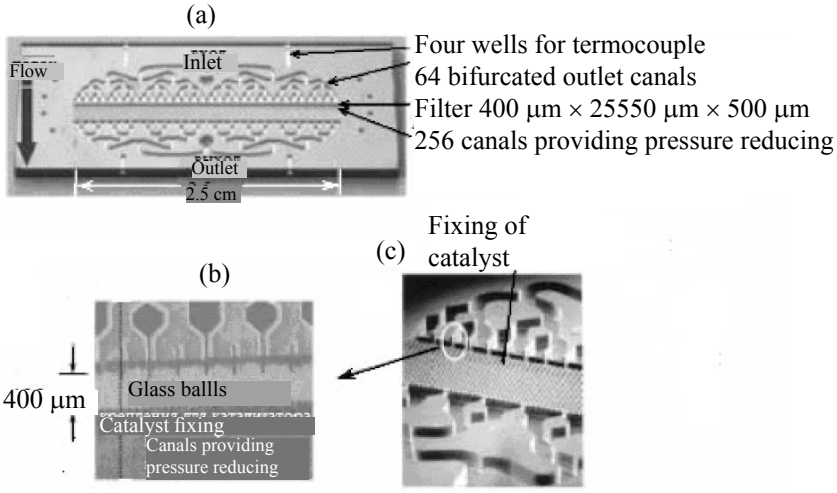


Fig. 25. Silicon microstructural reactor: (a) crtoss flow scheme; (b) microreactor filled with 50 m glass balls; (c) Microstructural reactor zoomed image obtained with an electron microscope (source: MIT [62]).

because there is no necessity of distribution between several microchannels. This special type of microreactors is created by Veser and co-authors [60]. It consists of two plates of which one contains channel and fasteners for assembling with the second plate. The plates are assembled and fastened by appropriate method.

Ajmera et al. [61] have described a monochannel microreactor that allows to use powdered catalyst and ever can work with a fabricated catalyst. The reactor has a channel of certain length where the particles are located as a bifurcated cascade to provide averaging by size and uniform flow at the both sides of the reactor.

7.3.4. Membrane type microstructural reactor. Membrane type microstructural reactors with impregnated membranes can be applied for the reactions where more favorable equilibrium conditions are provided due to continuous drain off the reaction product through a membrane wall.

Franz et al. [63] and Jensen et al. [64] have proposed a monochannel microstructural membrane type microreactor with many built in pressure and temperature probes along whole reaction zone.

The microstructural reactor is sealed at the top by hermetical membrane containing a thin film of platinum catalyst (Fig. 26). The reactor can operate at various regimes depending on the membrane material strength and ability of heat distribution. To start separation of the reaction product gas flow from the reaents the membrane should be open, that is, the plate should be removed [65].

7.3.5. Microstructural chip-reactors. Many microstructural reactors are projected using the concept and methods of manufacturing applied in microelectronics. The systems on chips commonly are formed of two or more silicon (glass) disks (Fig. 27) [63, 64]. In some cases one can meet multilayer systems where each layer possess its own function, e.g., the newest silicon microchip system developed in MIT in cooperation with DuPont, Delaware, is shown in Fig. 27 [66].

The microreactor depicted in Fig. 28 consists of two layers of borosilicate glass. Such microreactor can include one or several mixing chambers. Operating temperature in such reactor can achieve 400°C, pressure up to 100 bar. The channel length can be in the range from 332 to 676 mm depending on the modification used [67].

Among recent samples developed by Micronit Microfluidics BV (The Netherlands) is a laboratory on the microchip (Fig. 29).This system consists of the body containing a standard reactor on microchips. The body

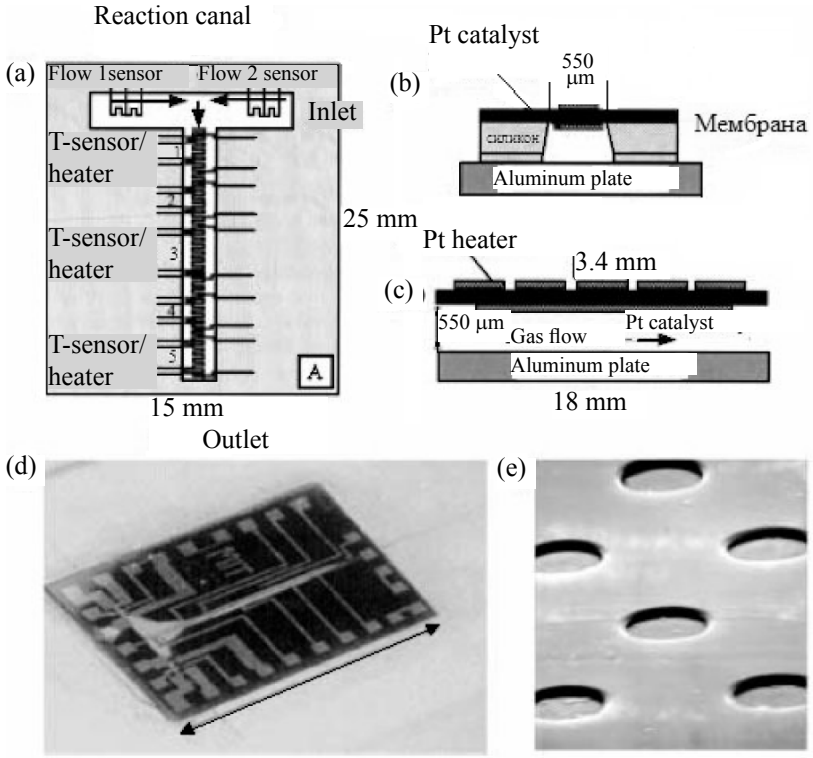


Fig. 26. Membrane type microstructural reactor : (a) top view; (b) cross section of reaction channel; (c) axial section of reaction channel; (d) microreactor general view; (e) uniformly distributed holes in the membrane (source: MIT Cambridge [45]).

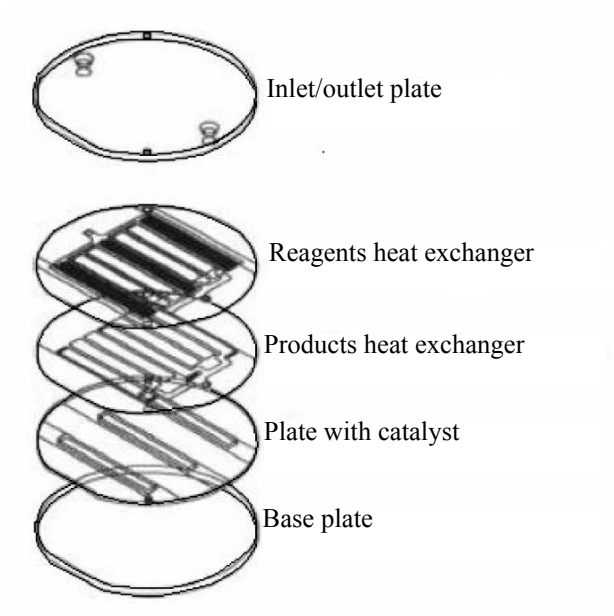


Fig. 27. Extended scheme of construction of integrated silicon reaction microsystem (source: DuPont, Delaware [66]).

provides more convenient and reliable connection of capillary tubes, has inspection window through which the processes in the reactor can be observed with a microscope. The principal advantage of the system is providing reliable operation at high pressure and ability to use various chip reactors by disassembling–assembling the installation [60].

Another interesting project of DuPont and MIT [31] is a complete microstructural installation for simultaneous conducting several reactions (Fig. 30).

Such automatized system is built basing on the principles used in microelectronics. The system block is filled with so-called mother boards analogous to those used at manufacturing computers. Each such microscheme possess microreactors, microseparators, probes and other units ("Lab on a Chip"). Inside the each mother board there is a system of microchannels that provide connection between the units. The whole system is controlled by a program which, depending on a given task can optimize the process by varying the process conditions. Due to parallel operating of the mother boards the system allows to carry out either one reaction simultaneously on several boards, or several different reactions. In the former case at the outlet of the microsystem installation the reaction product can be obtained in a higher amount.

7.3.6. The systems for fixing catalyst for gas phase reactions in microchannels. There are many techniques

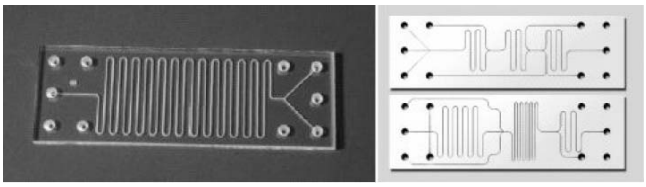


Fig. 28. Reactors on microchips (source: Micronit Microfluidics BV).

(a)



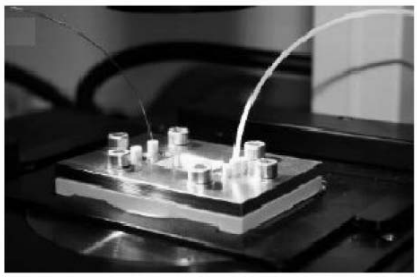


Fig. 29. Laboratory on glass microchip: (a) disassembled; (b) at the operation process (source: Micronit Microfluidics BV).

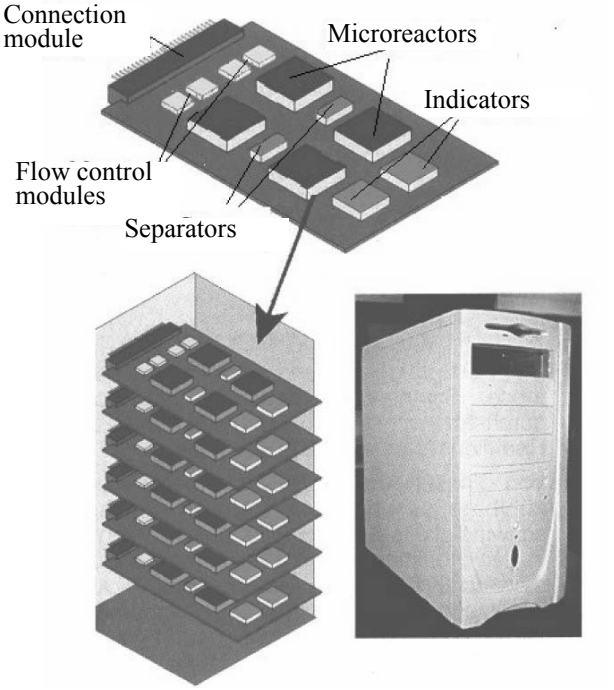


Fig. 30. A system for ssimultaneous testing of several catalysts [31].

for introducing and fixing catalyst in a microchannel. The simplest one is covering the material used for the microchannels with a layer of catalyst: then no carrier is needed for the catalyst [48, 51]. In this mode the microchannel walls act as the catalyst, but the catalyst surface is restricted to the area of the microchannel walls, that is, only small contact area is available. Therefore such type of fixing the catalyst is applied for fast reactions or for the technological processes with low rate of moving the flow along the channel.

Mostly, covering the microchannels is achieved by the method of grounding followed by wet chemical imprenation [52].

Zeolites, an important class of industrial catalysts, can be synthesized directly in the microchannel [68]. There are other types of the systems of fixing catalyst: covering with a catalyst by pulverization [63], sol-gel technique, and plasma jet electrochemical treatment [36].

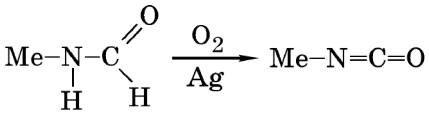
8. INDUSTRIAL APPLICATION OF MICROSTRUCTURAL REACTORS

In 1995 the microreaction technique was first applied in industrial chemical laboratories. Wцrz et al. [40, 69] have described incomplete oxidation of alcohol to aldehyde, the process that BASF developed on the industrial scale. The purpose was, on the one hand, to study a possibility of application the information obtained with the microreactors for the optimization of the process in the classical reactors, and, on the other hand, to apply the microreactors themselves for enhancing the process selectivity. Such direct comparison of the reactors allows estimate the potential of the microreactor technique for their industrial application.

8.1. *Synthesis of Methylisozyanate*

Lerou et al. [66] conducted in the DuPont laboratories a series of catalytic gas phase reactions. They studied high-temperature, dangerous, catalytic and photochemical gas phase processes. The microreactor consisted of several silicon plates assembled together. Each plate had its own function, such as heat exchanger and others. The catalyst was introduced as small particles by analogy with miniature immovable layer. On the example of synthesis of methylisocyanate from formamide in microreactor, it has been shown that conversion was the same as in traditional reactor, but selectivity was lower, due probably to not ideal temperature profile in the reaction zone [36]. The reaction scheme is shown in the Scheme 1.

Scheme 1. Synthesis of methylisocyanate from formamide [36].



To the current moment many similar investigations have been carried out. Many of them have not been published owing to their industrial significance.

Now almost each chemical firm has at least small installation related to the microreaction technique. The firms conducting fine organic syntheses are the most interested in such technology. It is expected that industrial application of microreactors will grow [70].

8.2. *Industrial Application of the Microreactor StarLam 30 (IMM)*

A recent example of successful industrial application of microreactors in the existing installation for producing chemicals was presented by Kirschneck and Tekautz (Fig. 31) [71]. The process consisted of two steps that were realized in a 10 m^3 periodical reactor. The first step is strongly exothermic, therefore the reactor should be cooled due to volatility of one reagent. The second step is endothermic, and the installation should be heated for several hours. The process is slow enough, thus productivity provided was only 1.8 ton per hour (the whole process scheme is not divulged by producer). It was decided to carry out one step in a microreactor of continuous operation, with the purpose to increase the product yield to 3.6 ton per hour.

This installation has been launched in June 2005, and after 10 months work it was studied completely in respect of corrosion. No traces of rust have been found.

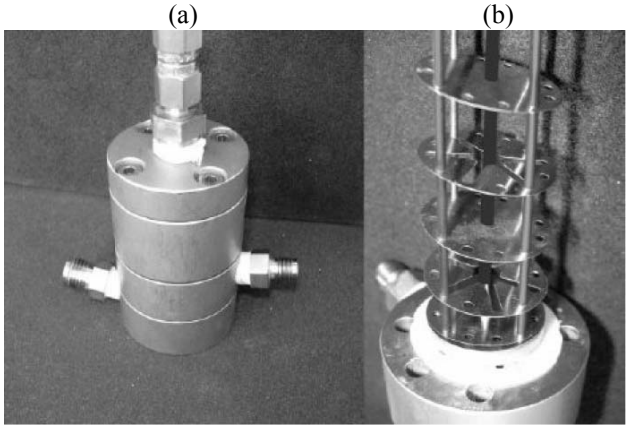


Fig. 31. Microreactor StarLam 30 produced by IMM: (a) general view, (b) inside construction [71].

The authors note a fact that control over the microreactor operations did not create any problem and that the cost of analogous reactor for periodical operations was much higher. Introduction of the microreactor led also to the economy in energetic resources for cooling because cooling was not needed in the continuously operating microreactor.

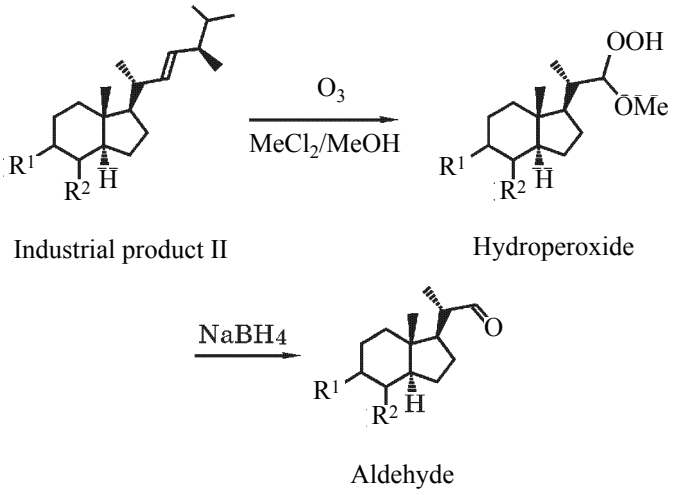
8.3. *Synthesis of Sterouids in Microreactor*

The next example of successful application of microreactors was demonstrated by Schering Company. This company performs develpment in the area of microreaction technique. One of directions of the development is seventeen steps synthesis of steroids for producing analog of Vitamin D [72]. The reaction scheme is shown in Scheme 2. Application of microreactor for this process became very actual after the explosion in DSM Fine Chemicals plant in Linz in 2004.

Commonly for this process was used a reactor of semi-continuous operation. For producing 15 kg of the product needed 13 loadings of initial mixture. It was decided to test ability of carrying out this synthesis in the reactors of three types: a microreactor with down draining film (productivity 130 g per day), a mini-reactor with down draining film (productivity 1.5 kg per day) (Fig. 32), and a mini-reactor of continuous operation (productivity 1.5 kg per day) (Fig. 33). The principal characteristics of the reactors are listed in Table 2.

It is clearly seen that the reactor of semi-continuous operations is disadvantageous as compared with other reactors both in respect of safety and by productivity. The most productive was found the microreactor with down draining film that left behind other reactors. Its productivity achieves 10 kg of steroid per day and at multiplication to whole volume 1 liter even 520 kg. This fact is explained by effective proceeding the process in account of microchannels that leads to significant increase in productivity.

Scheme 2. Synthesis of steroids for the producing of Vitamin D analog [72].



Industrial product II — Hydroperoxide — Aldehyde

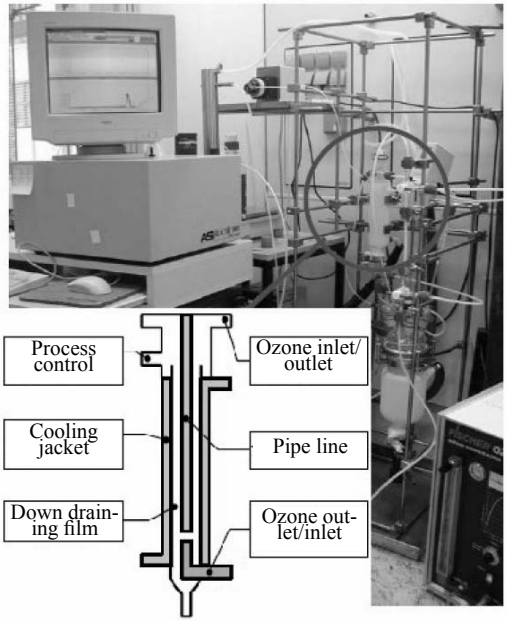


Fig. 32. Down draining film mini-reactor and its construction [72].

Table 2. Comparison of reactors for the synthesis of steroid

Parameter	Semicontinuous reactor	Down draining film microreactor	Down draining film mini-reactor	Continuous mini-reactor
Safety	–	+	+	+
Volume, l	20	0.00025	~0.150	0.150
Productivity, kg/day	15	0.13	1.5	1.5
Temperature, °C	–60	–20	–20	–20
Productivity per 1 l volume of apparatus, kg	0.75	520 (several microreactors are used)	10	10
Consumption, ml/min	-	1	12	12

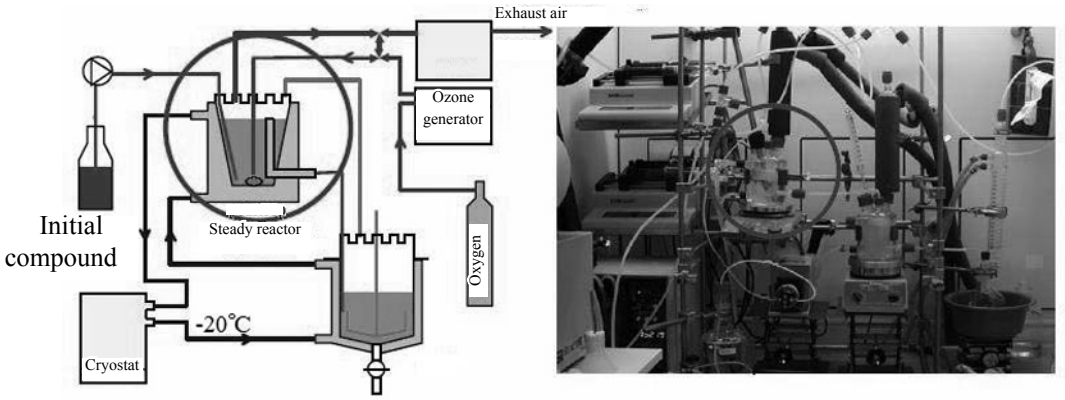


Fig. 33. Mini-reactor of continuous operation [72].

8.4. *The process of Gas Phase Propylene Epoxidation in Microreactors (Demis^T)*

Concern Degussa also leads development in the area of microreaction technique. In cooperation with other firms, research institutes and universities of Germany its researchers have developed a microstructural microreactor for the process of gas phase propylene epoxidation.

The reactor consists of special plates forming reaction chambers at butt-joining (Fig. 34). The plates can be of different length (up to 5 m) depending on the size of the apparatus. The plate internal wall is covered by catalyst. The manufacturing becomes more flexible due to modular type of this unit. Compared to the reactors commonly used for such process, this technology allows to carry out the process at higher pressure and to control the possibility of explosion. In Fig. 35 are depicted such reactors of two types: (a) laboratory unit, (b) industrial reactor.

After completing investigation, a pilot plant installation that consisted of one module and provided productivity ~1 kg of propylene oxide per hour was started up; it worked about 250 h. More recently was effected an installation consisting of three reactor modules and three evaporators, with productivity ~3 kg of propylene oxide per hour. This installation worked about 350 h in testing regime (3 periods). During the work its regime state was very stable, and was noted reproducibility of the obtained results. The catalyst that has been synthesized specially for this process showed in the pilot plant installation the same results as at the testing. The system of microstructural reactor and the new catalyst allowed obtaining results better than with all the known analogs (Fig. 36).

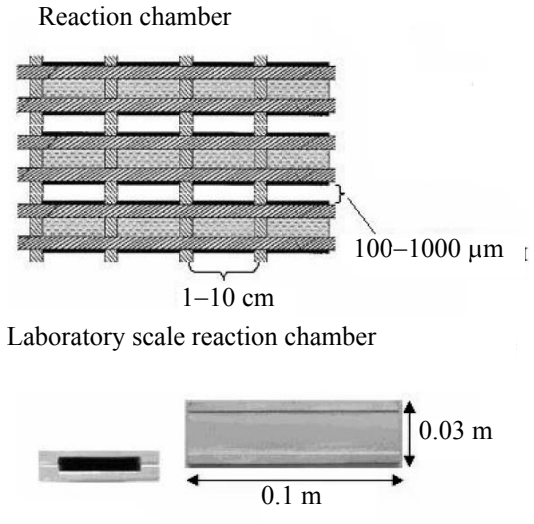


Fig. 34. Reaction chambers of microstructural reactor (source: Degussa [73]).

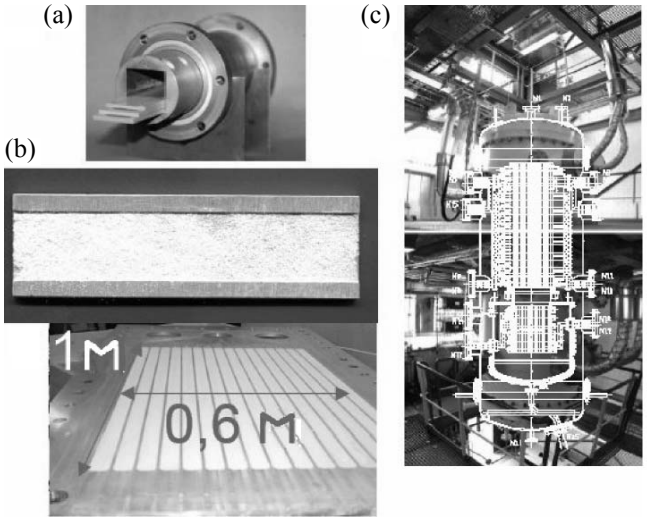


Fig. 35. (a) General view of laboratory microreactor, (b) reaction plates for industrial microstructural reactor, (c) microstructural reactor (source: Degussa [73]).

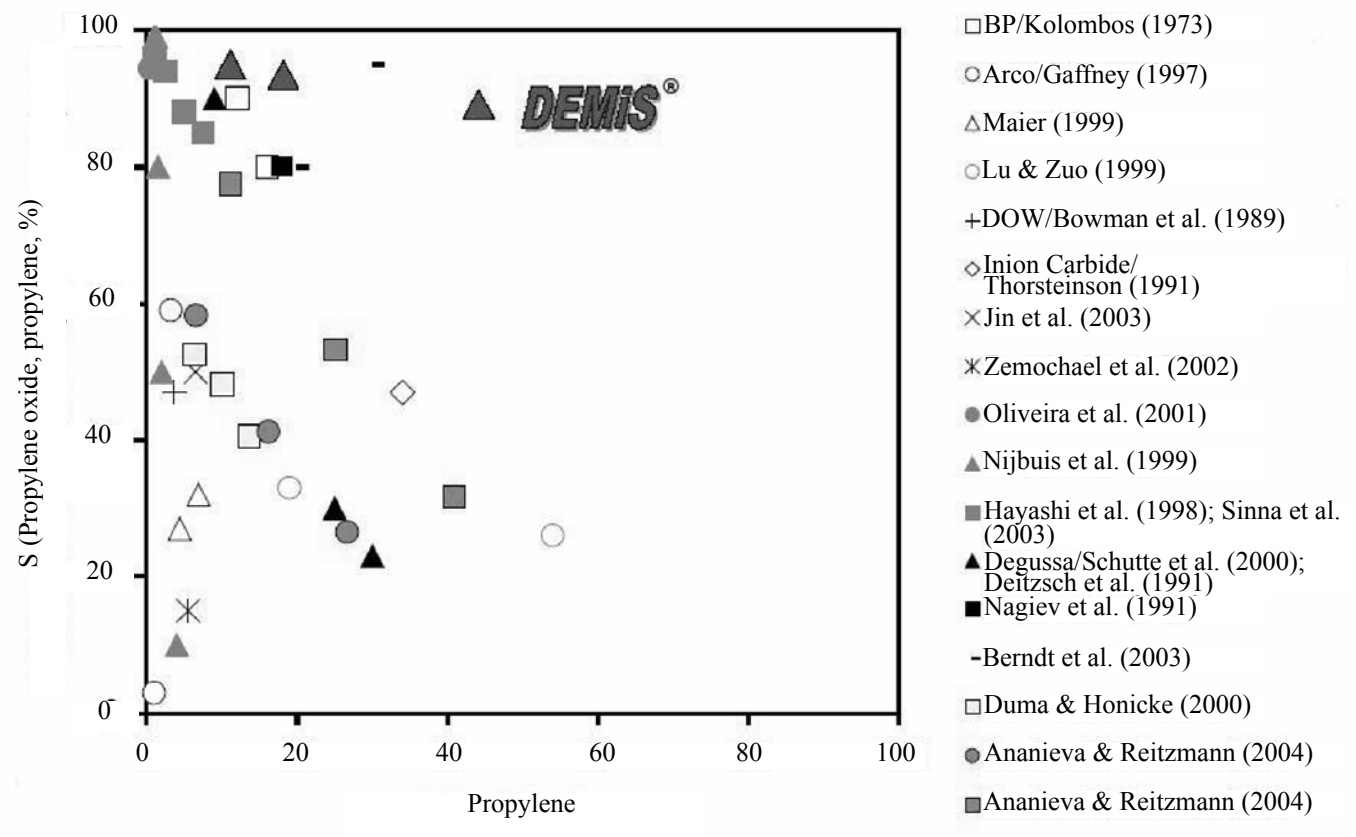


Fig. 36. Comparison of the results obtained with the pilot plant installation with the results of analogous studies by other authors (source: Degussa [73]).

CONCLUSION

In the recent years due to extension in application of microstructures in various areas of chemistry, physics, biology, materials technology, etc., began intense study of microreaction technique. In literature appear more and more examples of their industrial application. Therewith, while in the beginning of development of microreaction technique the principal works were carried out only for liquid and gas phase systems, in the recent time the technology becomes more complicated, and research and development concern also heterogenous, solid phase systems and photochemical and electrochemical reactions. A wide development concerns also so-called "Lab on a chip" systems that allow to carry out in miniature scale parallel analysis of several reactions simultaneously. Intensity of all these works is dictated by the interest of industry, because application of the microreaction technique leads to increase in the yield of final products owing to the changes in the process conditions, economy in space and energetic resources. It is ecological and economical advantage of the microreaction technique over classical reactors that explain the fact of particularly intense application of microstructural reactors in chemical technology.

Development of microreaction technique in the industrial scale still is aimed at the substitution of traditional reactors by microreaction technique in the existing industrial installations rather than at the creation of full-value microreaction systems. Therewith a principle of multiple repeated microreactors is commonly applied. Thus, we can state that modern development of microreaction technique allows to transfer "micro-approach" to the "macro-world" retaining therewith all advantages of the miniaturization.

REFERENCES

1. Freitag, A. and Dietrich, T.R., Abstracts of Papers, *Conference on Microreaction Technology: 4th International Conference on Microreaction Technology IMRET 4,* Atlanta, 2000, p. 48.
2. Ehrfeld, W., Hessel, V., and Lowe, H., *Microreactors. New Technology for Modern Chemistry*, Weinheim: Wiley-VCH, 2000, p. 2.
3. Schubert, K. et al., Abstracts of Papers, *Conference on*

Process Minituarization: 2nd International Conference on Microreaction Technology, IMRET 2m New Orleans,1998, pp. 88–95.
4. Branebjerg, J., Gravesen, P., Krog, J.P., and Nielsen, C.R., Abstracts of Papers, *The IEEE-MEMS'96*, San, Diego: CA, 1996, pp. 220–224.
5. Hessel, V., Abstracts of Papers, *Proceedings of the Conference on Microreaction, Technology: 3rd International Conference on Microreaction Technology*, IMRET 3, Berlin: Springer-Verlag, 2000, pp. 526–540.
6. Herskowits, D., Herskowits, V., and Stephan, K., *Chem. Eng. Sci*., 1990, vol. 45, pp. 1281–1287.
7. Krummradt, H., Kopp, U., and Stoldt, J., Abstracts of Papers, *Conference on Microreaction Technology: 3d International Conference on Microreaction Technology IMRET 3*, Berlin: Springer-Verlag, 2000, pp. 181-186.
8. Hessel, V. et al., Abstracts of Papers, *4th International Conference on Microreaction Technology IMRET 4*, Atlanta, 2000, pp. 174-187.
9. DD 246257, Lohder, W. and Bergmann, L., Akademie der Wissenschaften der DDR, 1986.
10. Schubert, K. et al., *Chem. Ing. Tech*., 1989, vol. 61, p. 172.
11. Wegeng, R.W., Call, C.J., and Drost, M.K., Abstracts of Papers, *American Institute of Chemical Engineers Spring National Meeting*, New Orleans, 1996, p. 1.
12. Ehrfeld, W., *DECHEMA-Monographs,* Frankfurt: DECHEMA, 1995, p. 132
13. Jahnisch, K. et al., *Angew Chem. Int. Ed.*, 2004, vol. 43, pp. 406–446.
14. Hessel, V. and Lowe, H., *Chem. Ing. Tech*., 2002, vol. 74, pp. 185–207.
15. Mammitzsch, L., Rauchle, K., Schael, F., and Reschetilowski, W., Abstracts of Papers, *1st Intern. IUPAC Conference on Green-Sustainable Chemistry,* Dresden, 2006, p. 400.
16. Borovinskaya, E.S. et al., Abstracts of Papers, *1st Intern IUPAC Conference on Green-Sustainable Chemistry*, Dresden, 2006, p. 404.
17. Borovinskaya, E.S. et al., *Experimentelle Untersuchungen und Mathematische Modellierung Chemische Processe in Microreaktoren,* Dresden, 2006, 12 p.
18. Herwig, H., *Angew Math. Mech*., 2002, vol. 82, pp. 579–586.
19. Ehrfeld, W., Hessel, V., and Haverkamp, V., *Ullmann's Encyclopedia of Industrial Chemistry,* Weinheim: Wiley-VCH, 1999, 583 p.
20. Van den Berg, A. and Bergveld, P., Abstracts of Papers, *2nd International Symposium on Miniaturized Total Analysis Systems μTAS96*, *Special Issue of Analytical Methods & Instrumentation*, Basel: AMI, 1996, pp. 9–15.
21. Cong, et al., *Angew Chem.*, 1999, vol. 111, pp. 508–512.
22. Weber, L., *Nachr. Chemi. Tech. Lab*., 1994, vol. 42. pp. 698–702.
23. Zech, T. et al., Abstracts of Papers, *3rd International Conference on Microreaction Technology IMRET 3*, Berlin: Springer-Verlag, 2000, p. 260.
24. Gong, P. et al., *Angew Chem. (Int. Ed.)*, 1999, vol. 38, pp. 484–488.
25. Senkan, S.M. and Ozturk, S., *Angew Chem*., 1999, vol. 111, p. 867.
26. Ehrfeld, W. et al., *Ind. Eng. Chem. Res*., 1999, vol. 3, pp. 1075–1082.
27. Bayer, T., Pysall, D., and Wachsen, O., Abstracts of Papers, *Conference on Microreaction Technology: 3rd International Conference on Microreaction Technology, IMRET 3*, Berlin: Springer-Verlag, 2000, pp. 165–170.
28. Rinard, I.H, Abstracts of Papers, *Process Minituarization: 2nd International Conference on Microreaction Technology*, New Orleans: AIChE, 2000, pp. 299–312.
29. Ehrfeld, W., Hessel, V., and Lowe, H, Abstracts of Papers, *4th International Conference on Microreaction Technology*, *IMRET 4*, Atlanta, 2000.
30. Kralisch, D. and Kreisel, G., *Chem. Ing. Sci*., 2007, vol. 62. pp. 1094–1100.
31. Schmalz, D., Häberl, M., Oldenburg, N., Grund, M., Muntermann, H., and Kunz, U., *Chemie Ingenieur Technik*, 2005, vol. 77, no.7, pp. 859–856.
32. Hessel, V., Hardt, S., Lowe, H., and and Schonfeld, F., *AIChE J*, 2003, vol. 49. pp. 566–577.
33. Herweck, T. et al., Abstracts of Papers, *Conference on Microreaction Technology: 5th International Conference on Microreaction Technology, IMRET 5*, Berlin: Springer-Verlag, 2001, p. 215.
34. Hessel, V. et al., Abstracts of Papers, *Conference on Microreaction Technology: 6th International Conference on Microreaction Technology, IMRET 6*, New Orleans: American, Institute of Engineers, 2002, vol. 164, p. 297.
35. Hardt, S. et al., Abstracts of Papers, *Conference on Microreaction Technology: 6rd International Conference on Microreaction Technology, IMRET 6*, New Orleans: American Institute of Engineers, 2002, vol. 164, p. 329.
36. Jahnisch, K. et al., *Angew. Chem. Int. Ed.*, 2004, vol. 43, pp. 406–446.
37. Penth, B., Abstracts of Papers, *Conference on Microreaction Technology: 5th International Conference on Microreaction Technology, IMRET 5*, Strasbourg, 2001, p. 125.
38. Werner, B. et al., Abstracts of Papers, *Conference on Microreaction Technology: 6th International Conference on Microreaction Technology, IMRET 6*, New Orleans: American Institute of Engineers, 2002, vol. 164, p. 168,
39. Loebbecke, S. et al., Abstracts of Papers, *Conference on Microreaction Technology: 6rd International Conference on Microreaction Technology, IMRET 6*, New Orleans: American Institute of Engineers, 2002, vol. 164, p. 37.

40. Worz, O. et al., *Chem. Ing. Technol.*, 2001, vol. 24. p. 138.
41. Haverkamp, V. et, al, Abstracts of Papers, *Conference on Microreaction Technology: 5th International Conference on Microreaction Technology, IMRET 5*, Berlin: Springer-Verlag, 2001, p. 202.
42. Janisch, K. et al., *J. Flourine Chem*., 2000, vol. 105, p. 117
43. Hessel, V., Abstracts of Papers, *Conference on Microreaction Technology: 3rd International Conference on Microreaction Technology, IMRET 3*, Berlin: Springer-Verlag, 2000, pp. 526–540.
44. De Mas, N. et al., Abstracts of Papers, *Conference on Microreaction Technology: 3rd International Conference on Microreaction Technology, IMRET 3*, Berlin: Springer-Verlag, 2000, p. 60.
45. Jensen, K.F., *Chem. Eng. Sci.*, 2001, vol. 56, pp. 293–303.
46. Chambers, R.D. et al., *Lab. Chip*, 2005, vol.5, pp. 1132–1139.
47. Chambers, R.D. and Spink, R. C., *Chem. Commun*., 1999, pp. 883–884.
48. Kestenbaum, H. et al., *Int. Eng. Chem. Res*., 2000, vol. 41, pp. 710–719.
49. Rebrov, E.V., de, Croon, M.H. J.M., and Schouten, J.C., *Catal. Today*, 2001, vol. 69, pp. 183–192.
50. Heinichen, H. Kleiner, *Chem. Tech*., 2001, vol. 30, p. 89.
51. Fichtner, M. et al., *Ind. Eng. Chem. Res*., 2001, vol. 40, pp. 3475-3483.
52. Liauw, M. et al., Abstracts of Papers, *Conference on Microreaction Technology: 3rd International Conference on Microreaction Technology, IMRET 3*, Berlin: Springer-Verlag, 2000. p. 224.
53. Bier, W. et al., *Am. Soc. Mech. Eng. Pap*., 1990, vol. 19, p. 189.
54. Zapf, R. et al., *Trans.Chem.,* 2003, vol. 81. p. 721.
55. Rebrov, E.V., De Croon, M.H.J.M., and Schouten, J.C., Abstracts of Papers, *Conference on Microreaction Technology: 5th International Conference on Microreaction Technology, IMRET 5*, Berlin: Springer-Verlag, 2001, p. 49.
56. Cominos, V. et al., *Chem. Eng. Res. Des*., 2005, vol. A6, pp. 626–633.
57. Zech, T., Honicke, D., Lohf, A., and Golbig, K., Abstracts of Papers, *Conference on Microreaction Technology: 3rd International Conference on Microreaction Technology, IMRET 3*, Berlin: Springer-Verlag, 2000, pp. 260–266.
58. Kolb, G. et al., Abstracts of Papers, *Conference on Microreaction Technology: 6th International Conference on Microreaction Technology, IMRET 6,* New Orleans: American Institute of Engineers, 2002, vol. 164, p. 61.
59. Zech, T. and Honicke, D., Abstracts of Papers, *Conference on Microreaction Technology: 4th International Conference on Microreaction Technology, IMRET 4*, Atlanta, 2000, p. 379.
60. Veser, G., *Chem. Eng. Sci.*, 2001, vol. 56, pp. 1265–1273.
61. Ajmera, S.K. et al., *Sens Actuators, A*, 2002, vol. 82, p. 297.
62. Ajmera, S.K. et al., Abstracts of Papers, *Conference on Microreaction Technology: 5th International Conference on Microreaction Technology, IMRET 5*, Berlin: Springer-Verlag, 2001, p. 372.
63. Franz, A.J. et al., Abstracts of Papers, *Conference on Microreaction Technology: 3rd International Conference on Microreaction Technology, IMRET 3*, Berlin: Springer-Verlag, 2000, p., 197.
64. Jensen, K.F. et al., *Micro Total Analysis Systems*, Dordrecht: Kluwer, 1998, p. 463.
65. Karnik, S.V., Hatalis, M.K., and Kothare, M.V., Abstracts of Papers, *Conference on Microreaction Technology: 5th International Conference on Microreaction Technology, IMRET 5,* Berlin: Springer-Verlag, 2001, p. 295.
66. Lerou, J. J. et al., Mycrosystem *Technology for Chemical and Biological Microreactors,* Weinheim: VHC, 1996, vol. 132, p. 51.
67. *Specification for Micronit Lab-on-a-Chip, Kit 4515, Specification for Chip-Reactor, Micronit, Microfluidics*, BV, 2006. 2 p.
68. Haswell, S.J., O'Sullivan, B., and Styring, P., *Lab. Chip*, 2001, vol. 1, p. 164.
69. Worz, O. and Jackel, K.P, *Chem. Tech*., 1997, vol. 26, pp. 130–134.
70. Felcht, U.-H., *Chem. Eng. Technol.*, 2002, vol. 25, pp. 345–346.
71. Hessel, V., Lowe, H., Muller, A., and Kolb, G., *Chemical Micro Process Engineering. Processing and Plants*, 1st ed. WILEY-VCH, Weinheim, 2005, p. 505.
72. Lovis, K., *Mikroverfahrenstechnik in der Chemischen Entwicklung bei Schering. Beispiele und Erfahrungen, Veranstaltung der Industrieplattform, Mikroverfahrenstechnik Frankfurt am Main*, DECHEMA, 31.10.2006.
73. Schirrmeister, S. and Geisselmann, A., *Erfahrungen aus der Entwicklung industrieller mikrosrtukturierter, Reaktoren fuer heterogen katalysierte Gasphasenreaktionen. Veranstaltung der Industrieplattform Mikroverfahrenstechnik*, Frankfurt am Main, DECHEMA, 31.10.2006.

ISSN 1070-4272, Russian Journal of Applied Chemistry, 2008, Vol. 81, No. 12, pp. 2232–2236. © Pleiades Publishing, Ltd., 2008.
Original Russian Text © O.I. Shapovalov, L.A. Ashkinazi, 2008, published in Khimicheskaya Promyshlennost', 2008, Vol. 85, No. 4, pp. 203–208.

ECONOMICS OF CHEMICAL INDUSTRY

Biobutanol: Biofuel of Second Generation

O. I. Shapovalov[a] and L. A. Ashkinazi[b]

[a]*Scientific and Research Institute of Hydrolysis, St. Petersburg, Russia*
[b]*Academy of Application Research, St. Petersburg, Russia*

Received June 5, 2008

DOI: 10.1134/S1070427208120379

Industrial producing of butanol began in 1916. That time was used a method of ABE fermentation (ABE abbreviates acetone, butanol and ethanol) with bacteria *Clostridia acetobutylicum*. This microorganism was first isolated by Weizman (US Patent 1 315 585), a student of Luis Paster; the microorganism produces acetone. In the time of First World War, England asked the young microbiologist to resign the right for producing by this method of acetone for further manufacturing smokeless powder cordit. This process was used up to 1920th exclusively for producing acetone. However, at the fermentation, yield of each pound of acetone is accompanied by formation of two pounds of butanol. Somebody once mixed nitrocellulose with butanol and thus obtained quickly drying lacquer. Three years later, automobile industry changed whole market completely, and to 1927 butanol became the main product of ABE process. In the time of Second World War it was used for producing synthetic rubber.

So, in the first half of 20th century biobutanol was produced from corn and molasses by fermentation. This process affords acetone, butanol and ethanol (therefore it is denoted as ABE process). However with growing demand for butanol its producing by fermentation began to fall because since 1954 the price of petroleum becomes below those of sugar because USA lost cheap sugar supply from Cuba.

Now butanol is produced starting with petroleum via hydrolysis of haloalkanes or hydration of alkenes.

Butanol can be produced from biomass and from mineral fuel. The butanol from biomass is conveniently denoted as biobutanol despite the fact that it has the same characteristics as the butanol from petroleum.

First of all, butanol is used as industrial solvent. World market for this product is estimately 350 million gallons per year, of which 220 million gallon/year is the fraction consumed by USA. Butanol can be used instead of gasoline even in higher degree than ethanol due to its physical properties, economy, safety and because it can be applied without remodeling car engine.

Progress in the area of biotechnology allows to use corn and other biomass as economically effective source of biobutanol.

The main reason that nobody know butanol as an alternative fuel is the fact that its producing has never been suggested economically reasonable. As mentioned above, this product is used mainly as industrial solvent and costs triple compared to gas. Traditional process of fermentation allows to produce from one bushel of corn (or 35 pounds of sugar) only 1.3 gallons of butanol, 0.7 gallons of acetone, 0.33 gallons of ethanol and 0.62 pounds of hydrogen. Such manufacturing of butanol can not compete with the technology of producing ethanol that yelds 2.85 gallons of the product per bushel.

The alcohol based fuel including butanol and ethanol is partially oxidized (compared to hydrocarbons) and therefore mixture for engine should be more enriched than in the case of gasoline.

As compared with ethanol, butanol can be used as a mixure with gasoline in higher proportion and thus can be used in currently working cars without modification of their system for the formation of air–fuel mixture.

The alcohol based fuel contains less energy per unit of weight or volume than gasoline and its mixture with air should be more enriched. Per one cycle of engine running, butanol liberates more pure energy than ethanol

or methanol and approximately by 10% more than gasoline.

Owing to appearance of new highly effective technologies for producing biobutanol, now butanol from corn attracts more attention of specialists than ethanol. There are several advantages of butanol over ethanol:

1. Butanol contans by 25% more energy than thanol: 110 000 Britain heat units per gallon as compared with 84 000 Britain heat units per one gallon of ethanol. Energy content of gasoline is about 115 000 Britain heat units per gallon.

2. Butanol is more safe because is evaporated six times less than ethanol and by factor 13.5 less volatile than gasoline. Its vapor pressure by Reid is 0.33 pounds per squire inch, the same characteristic of gasoline is 4.5 pounds per squire inch, of ehanol 2.0 pounds per squire inch. This makes butanol safe at its application as oxygenate, and need no significant changes in the mixture proportion at summer and winter application. Now it is used as oxygenate in the states Arizona, California and others.

3. Butanol is much less aggressive substance than ethanol and therefore it can be transported with currently used fuel pipes, while ethanol should be transported by rail way transport.

4. Bitanol can be mixed with gasoline.

5. Butanol can be used instead of gasoline, while ethanol can be used as additive to benzene with content of the latter in the mixture not less than 85% and requires significant modernization of engine. Currently predominantly are used mixtures with content of ethanol 10%.

6. Producing of butanol can simultaneously solve problems connected with the infrastructure of supplying hydrogen.

7. Butanol provides higher yield of energy (10 Wt-h/g) than ethanol (8 Wt-h/g).

8. At combustion, butanol does not produce sulfur and nitrogen oxides that is advantageous from the ecology wievpoint.

Thus, biobutanol allows to solve a part of problems retarding fast application of biofuel over the world, in part, it is compatible with existing car fuel and with infrastructure of logistics. Low vapor pressure of biobutanol and its low sensitivity to the presence of water in its mixture with gasoline extend its versatility. It can be mixed with gasoline to higher concentration than existing biofuels without modernization of engines, economically it is preferred than the mixture of ethanol with gasoline, it improves efficiency of cars in respect of fuel and increases run per a unit of consumed fuel.

Also, biobutanol can enhance productivity of ethanol–gasoline mixture, in part, in account of decreasing the effect of ethanol on the vapor pressure of the mixed fuel (a serious problem restricting wide application of ethanol).

Like ethanol, fuel biobutanol contains "green" carbon that allows decreasing emission of hotbed gases.

In USA, the fuel biobutanol as suggested can decrease dependence of the country on foreign supply of petroleum and increase development of agriculture.

Biobutanol is produced from the same raw material as ethanol: corn, sugar beet, sorghum, manioc, corn stem and other biomass, but in can replace gasoline at use in the same volume.

US patent 5 753 474 "Continuous two-step anaerobic fermentation process for producing butanol and other organic solvents using two different bacterial strains", owned by Environmental Energy Co., proposes a technology that makes producing of butanol effective and economically reasonable. Using by the company of paired bioreactors with immobilized cells of continuous application increases yield of butanol to 2.5 gallons from one bushel of corn plus gives 0.6 pounds of hydrogen as a side product.

Fermentation ABE with bacteria *Clostridium acetobutylicum* is one of the earliest processes applied to industrial fermentation for producing butanol. By the yield of product, it is second to yeast fermentation for producing ethanol. With the mentioned anaerobic microorganisms first in the world was created such branch of industry as microbiological manufacturing. One of the biggest microbiologicasl plants belonged to Commercial Solvents International company in the state Indiana. However fermentation remained a complicated and hardly controlled process at creation of new technology by Environmental Energy company.

At the typical ABE fermentation, initially *C. acetobutylicum* bacteria produce butyric, propionic, lactic and acetic acids (the step of producing acid), the pH value of the culture decreases and metabolic shift to the step of producing solvent is initiated, resulting in formation of butanol, acetone, isopropanol and ethanol.

The shift is initiated at increase in butyric acid concentration to more than 2 g/l and decrease in pH

below 5. At the commonly used ABE fermentation, yield of butanol from glucose is as low as 15%, and hardly can be achieved more than 25% (1.3 gallons per one bushel). The butanol producing is restricted because at the concentration 1.0–2.0% it blocks substantially the cell growing and can lead to cancelling fermentation. Therefore concentration of butanol in the common ABE process is not higher than 1.3%.

Efforts in the last over than 20 years allowed only to obtain butanol with concentration below 2.0% at productivity 4.46 g/l per hour and butanol yield less than 25% on the glucose weight.

Optimization of the process of ABE fermentation and synthesis of butanol via butyric acid from carbohydrates allowed considerably increase the butanol yield, productivity per volume unity and concentration. Application by Environmental Energy company of immobilized cultures *Clostridium tyrobutyricum* and *Clostridium acetobutylicum* allows to achieve optimal productivity of butanol 4.64 g/l per hour and yield 42% on the glucose weight or 2.5 gallons per bushel of corn (35 pounds of starch–lactose–sugar).

As compared with traditional ABE process, the technology of Environmental Energy company allows to avoid producing of undesirable products including acetic, lactic and propionic acids, acetone, isopropanol and ethanol, thus to save carbon and to producce only carbon dioxide, butyric acid and butanol. This process increases twice yield of butanol per bushel of corn from 1.3 to 2.5 gallons.

As compared with this process, the process of yeast fermentation for producing ethanol gives 2.5 gallons of ethanol per bushel of corn at concentration 10–15%. It is therefore ethanol was considered as the most promising candidate for alternative fuel.

The technological process patented by Environmental Energy Inc. can produce 2.5 gallons of butanol per bushel of corn, without formation of acetone and ethanol. Thus, butanol can be really nominated for using as alternative fuel. Besides, the new technology gives hydrogen as a side product that also can be applied as alternative fuel. With accounting for the hydrogen, the new technology allows to obtain by 42% more energy than traditional synthesis of ethanol, of which 25 % belongs to butanol and 18 % to hydrogen.

It is important to understand that even in the absence of technical base for application of hydrogen as the alternative source of energy, it remains to be valuable chemical product used in many subbranches of chemical industry.

Raw biomass initially is mixed with bacteria *Clostridium tyrobutyricum*, that leads to conversion of large fraction of the raw material into butyric acid and hydrogen. In the second step, the butyric acid formed is mixed with bacteria *Clostridium acetobutylicum* and is converted into butanol. This technology produces much less side products, only hydrogen, butyric acid and carbon dioxide.

This new process has been still demonstrated in laboratory scale only.

In summer 2006 the company has studied efficiency of this process on a pilot plant installation B-100 with productivity 100 gallons of butanol per week.

Theoretical calculations of specialists showed that the cost of butanol from corn will be 1.20 US dollar per gallon, excluding side hydrogen. This is comparable with the cost of producing ethanol (about 1.28 USD per gallon). Taking into account higher energetic value of butanol, this gives 105 000 Britain heat units per one dollar in the case of butanol against 84 000 Britain heat units per dollar at producing ethanol, the cost of corn is taken 2.50 dollars per bushel. For comparison, the cost of producing butanol from petroleum is about 1.35 dollars per gallon.

The process developed by Environmental Energy Inc. will become ever more effective at using agricultural by-products instead of corn: then the cost of one gallon will be 0.85 dollars.

Environmental Energy Inc. now is one of a few companies in USA that works on the creation of experimental installation for producing biobutanol which, by their opinion, can be produced from everything that grows on the globe.

Initially the Environmental Energy Inc. company is intended to arrange biobutanol manufacturing for the market of solvents, but further will produce and sale it as alternative fuel.

The company has developed and patented its own method for producing butanol by fermentation, that is more economical as compared with known petrochemical methods. This technology was developed thanks to support by federal grant of USA Ministry of Energetics in the framework of program of development small business, in cooperation with Dr. S.T. Yang, Ohio State University, who submit to the company his patented bioreactor.

Never before in the world was known any technology that could provide effective producing butanol from biomass. Therefore butanol manufactured earlier was of low concentration and its yield was lower than that of ethanol. Earlier ABE technology allowed to produce acetone, ethanol and butanol in the ratio 3 : 6 : 1, that is, from one bushel of corn it was possible to obtain 1.3 gallon of butanol (with concentration 1–2%), 0.7 gallon of acetone and 0.13 gallon of ethanol. As far as biobutanol and ethanol are produced from the same raw material, existing facilities for producing ethanol can easily be rearranged for producing biobutanol.

Companies DuPont, British Petroleum and British Sugar Corporation are intended to reassign a plant in Great Britain that produces bioethanol for manufacturing biobutanol. It is assumed that the first line of the project will produce from sugar beet 30 000 ton or 9 millions gallon of butanol per year using currently existing technology.

The difference in producing ethanol and butanol first of all is defined by features of their distillation. Therewith, both technologies use the same raw material: sugar beet, maize wheat and manioc corn, as well as straw and maize stems. As DuPont company claimed, current facilities for producing butanol can be easily rearranged for biobutanol.

On June 20, 2006 DuPont and British Petroleum (BP) announced creation of strategic partnership for development, producing and realization of next generation of biofuel. This partnership should comprise achievements of DuPont company in the area of biotechnology and great experience and know-how of BP in the area of fuel technology and market. Owing to this cooperation these companies will became world leaders in development and manufacturing of biofuel.

Since year 2003, the two companies worked jointly on the overcoming of disadvantage of existing biofuels. Now they are intended to present to world market their first jointly developed product, the biobutanol, that is planned to be introduced in Great Britain as biocomponent additive to gasoline in 2007. For organization of its producing the companies BP and DuPont cooperate with British Sugar company, a branch of Associated British Foods plc that now rearranges its first plant for producing ethanol by fermentation to the facility for producing biobutanol. At further development of respective market it is planned to create additional facilities for manufacturing this product in various countries. Now BP and DuPont in cooperation with British Sugar develop study of techno-economical validity of the project for the revealing a possibility of building in Great Britain of more powerful plants.

Initially was planned to create manufacturing of biobutanol on the ground of currently existing technologies. However, would the current research and development in the area of enhancing productivity of this process be completed successfully, in the plant will be applied the biotechnologies that allow to make efficiency of producing biobutanol comparable with that of ethanol. As a raw material is planned to use sugar cane or beet, maize, wheat and manioc, and further cellulose raw material from grace or agricultural by-products (straw and maize stems).

Biobutanol is advantageous over petroleum fuel like other types of biofuel, in part, by low emission of hotbed gases.

In April 2006 on the conference in the Illinois State University denoted to bioenergy professor Hans Blaschek, who is specialist on food microbiology in that university, has reported on a significant progress in its research on the biobutanol technology. Using patented by him genetically modified microorganism *Clostridium beijerinkii* he successfully transformed maize corn into butanol. For initiation of the fermentation process he used obtained by him genome map of this microorganism. He plans further to use result of genome analysis to produce next, more effective, generation of *C. Beijerinckii* microorganism.

C. beijerinckii has been chosen for gene mapping by USA Energy Ministry in в 2004. This research has been carried out in United Genome Institute in California.

Besides, professor Blaschek has developed grounds for the technology of synthesis butanol from gas. This butanol will be cheap and not contaminated with admixtures that are possible at application of technology based on the use of membranes.

The scientists suggests that butanol has large potential as alternative fuel because it has higher octane number than ethanol and is not mixed with moisture contained in pipe lines. Butanol also can be used as chemical raw material for producing polymers and plastics.

Increase of butanol demand leads to necessity of producing additionally 400 millions bushels of corn per year or of equivalent volume of agricultural biomass in USA, thus stimulates development of agriculture.

The scientist is planning to scale the fermentation process of producing butanol using existing strain *C. beijerinkii*, to select appropriate corn raw material and type of corn fibers for producing butanol and to create next generation of microorganisms.

In Russia first facility for producing biobutanol (biofuel of second generation) will begin to work at Spetember 2008 on the ground of Tulun hydrolysis plant. This has been confirmed at the presentation of the project on creation of new biotechnological complex on the plant. In May 2008 administration of Irkutsk region and noncommercial organization "Fuel-Energetic Union" signed the Intention Record announcing this project.

The plant stopped to work at May 2008 and soon has been claimed its bankruptcy. Note that crisis situation is characteristic of all the hydrolysis industry of Russia: all 68 hydrolysis plants were stopped, and their facilities were mostly sold out.

After transfer the packet of shares to regional ownership, the Priangar'e administration makes efforts for attracting investors to revive the plant. In early December 2007 the "Fuel-Energetic Union" has bought the plant property on the open auction. Now here is created a modern facility for manufacturing the principally new product, biobutanol, a fuel of second generation, that can be distributed at world market. The project is supported by Open join stock company "United Industrial Corporation of Defence Industry" (Oboronprom, Russia). For its realization is created Open join stock company "East Siberian Holding of Biotechnology."

New owners have planned investment 500 millions RUR and attract qualified specialists, including those formerly employed at hydrolysis plant. After initiation of the plant the number of employed will be 500 people and will be created additional jobs in agriculture and forest branch.

ISSN 1070-4272, Russian Journal of Applied Chemistry, 2008, Vol. 81, No. 4, pp. 603–608. © Pleiades Publishing, Ltd., 2008.
Original Russian Text © I.I. Obraztsova, N.K. Eremenko, 2008, published in Zhurnal Prikladnoi Khimii, 2008, Vol. 81, No. 4, pp. 565–570.

PHYSICOCHEMICAL STUDIES OF SYSTEMS AND PROCESSES

Physicochemical Modification of Nanodiamonds

I. I. Obraztsova and N. K. Eremenko

Kemerovo Branch, Institute of Solid State Chemistry and Mechanochemistry, Siberian Branch, Russian Academy of Sciences, Kemerovo, Russia

Received June 18, 2007

Abstract—Thermal modification of nanodiamonds in the atmosphere of argon and hydrogen and their chemical modification with oleum and chlorine at different temperatures were studied. The effect of the modification conditions on the catalytic activity of palladium catalysts supported by nanodiamonds in the reaction of nitrobenzene hydrogenation and on the adsorption properties of nanodiamonds with respect to benzene, chloroform, and water was analysed.

DOI: 10.1134/S107042720804006X

The increased scientific and practical interest in synthesis and study of substances in the nanostate is due to the fact that they possess new functional properties because the size of nanoparticles is in the range 10^{-9}–10^{-7} m, which is comparable with that of molecules. An object of this kind are nanodiamonds (ND) produced by detonation synthesis with explosives having a negative oxygen balance in a nonoxidative medium, which yields a carbon stock containing the diamond fraction.

The recovery and purification of ND or, as they are also named, utradispersed diamonds (UDD) can be divided into the gas- and liquid-phase methods. Oxygen and air are used in the first case, and oxidizing mixtures (H_2SO_4–HNO_3, HNO_3–$HClO_4$, HNO_3–H_2SO_4–$H_2S_2O_7$, etc.), in the second [1–4]. In the process, new functional groups are added to those already present on the UDD surface, depending on the recovery technique.

The presence of functional groups with various chemical compositions on the surface of ND predetermines their widely diverse and unique properties. Therefore, methods used to modify ND may be of key importance for various applications.

At present, nanodiamonds are used in electrodeposited metal–diamond coatings, antifriction additives, various lubricants, lubricating-cooling fluids for physical modification of ferrolacquer coatings of magnetic tapes and disks, as composite materials in polymeric films and membranes, in various rubbers, and as carriers of biological and medicinal preparations [5, 6].

Development of methods for controlling the chemical composition of the nanodiamond surface by varying the amount and nature of functional groups opens the way to their modification for creating new types of ND, including those with a multifunctional surface composition.

In this study, thermal and chemical modification of nanodiamonds was carried out in order to expand the application fields of UDD.

EXPERIMENTAL

ND recovered from a detonation diamond stock by the previously developed technique [4, 7] and additionally dried in air at 150°C was used in the study.

ND were thermally treated for 4 h in a quartz reactor similar to that used for determining carbon and hydrogen in organic compounds [8]. Argon or hydrogen served as a carrier gas. Prior to an experiment, the system was purged with carrier gas for 10 min. The released water was absorbed with anhydrone and its amount was found from the increase in the mass of this drying agent. Carbon dioxide was absorbed with a $Ba(OH)_2$ solution of a known concentration (with subsequent titration with 0.2 N HCl). The amount of the released carbon monoxide was found by its absorption with an acetone solution of palladium(II), with metallic palladium recovered and the unreacted Pd^{2+} gravimetrically determined with dimethylglyoxime [9].

Table 1. Amounts of released products in relation to the thermal treatment conditions of nanodiamonds

T, °C	Concentration, mmol g^{-1} ND				
	CO_2		H_2O		CO
	Ar	H_2	Ar	H_2	Ar
200	0.19 ± 0.01	0.30 ± 0.01	1.73 ± 0.10	2.20 ± 0.12	–
400	1.85 ± 0.07	1.00 ± 0.03	2.03 ± 0.04	3.83 ± 0.25	0.38 ± 0.02
600	7.00 ± 0.16	1.23 ± 0.03	5.60 ± 0.03	5.31 ± 0.06	4.44 ± 0.12
800	4.81 ± 0.08	0.98 ± 0.04	0.86 ± 0.03	7.53 ± 0.07	6.01 ± 0.09

To study the adsorption properties of ND, a weighed portion of ND was calcined at a prescribed temperature for 4 h, cooled in a desiccator over $CaCl_2$, weighed, and placed in a desiccator with various solvents (water, benzene, and chloroform) at 21°C. The amount of an adsorbed reagent was found from the increase in the weighed portion of ND and then the procedure was repeated many times to constant weight of the sample.

The time in which equilibrium was attained was, for all the samples, 14 days in chloroform, 28 days in water, and 21 and 2 days in benzene for samples modified in argon and hydrogen, respectively.

Samples were sulfated by boiling in oleum at 180°C for 20 h. ND were chlorinated with molecular chlorine in a flow-through quartz reactor at 400 and 600°C. Chlorine and sulfur in the samples was determined by the procedure described in [8].

Nitrobenzene was hydrogenated under an atmospheric pressure of hydrogen. The method used to synthesize palladium catalysts and nitrobenzene (NB) hydrogenation conditions were the same as those in [10], but, in some cases, the catalyst was prepared without triphenylphosphine.

IR spectra were measured on a Bruker Tensor-27 IR Fourier spectrometer with a diffuse-reflection attachment.

In thermal treatment of nanodiamonds in inert (Ar) and reducing (H_2) atmospheres, the products are formed in different relative amounts (see Table 1).

The amount of carbon dioxide formed in the inert atmosphere of argon exceeds that produced in the reducing atmosphere of hydrogen. This occurs because mainly decarbonization of various carbonyl-containing groups (=C=O, –COOH, =COH) and removal of –OH groups and adsorbed water from, the ND surface occur in Ar at temperatures below 600°C. At temperatures of 600–800°C, processes in which carbon monoxide is released start to predominate, which is accompanied by a decrease in the released amounts of CO_2 and H_2O (0.89 mmol g^{-1} ND at 800°C). The formation of CO can be attributed to interaction of carbon dioxide and water with the surface carbon of nanodiamonds. The release of CO commences in the temperature range 300–400°C and its amount increases with temperature.

In the reducing atmosphere, the modifying gas interacts with the ND surface in a different way. It can be seen that the amount of released water grows and reaches the maximum value at 800°C, whereas in the argon atmosphere, it sharply decreases.

All these phenomena are accounted for by the occurrence of reducing reactions with hydrogen on the nanodiamond surface. As it is believed by the authors of [11], hydrogen is adsorbed on the ND surface at treatment temperatures below 300°C. However, this temperature is sufficient, as also in the case of thermal desorption in a flow of Ar, for the decarbonization and dehydration processes to commence. As the modification temperature is raised further (in the range 300–600°C), hydrogen reacts with oxygen-containing groups, which results in that the amount of water released in thermal treatment below 600°C exceeds that of carbon dioxide. At temperatures of 600–800°C, hydrogen continues to react with the ND surface, which results in the maximum release of water at 800°C. The decrease in the amount of CO_2 formed in H_2 at this temperature is possibly also due to the reaction of carbon dioxide with the surface, but it is impossible to determine the amount of CO released, because, in the method used, palladium acetate is reduced by the modifying hydrogen gas to metallic palladium.

The assumptions that chemical reactions occur on the ND surface in the course of modification at various temperatures are in agreement with IR spectroscopic data obtained in this study and previously [11, 12]. The modification leads to pronounced changes in the position and intensity of absorption bands associated with carbonyl groups (see figure). Treatment at 400°C in argon shifts the peak of the band at 1730 cm^{-1} to the range 1780–1790 cm^{-1}, which indicates that –C(O)–O–C(O)– structures are formed. Modification with hydrogen gives rise to an absorption band associated with isolated –OH groups (~3680 cm^{-1}) and to absorption bands at 2938 and 2867 cm^{-1}, which point to the presence of C–H bonds at the carbon atom. The changes in the IR spectra confirm that the modification of nanodiamonds change the chemical state of their surface.

After treatment with oleum, the content of sulfur in the samples modified in hydrogen and argon was 0.26 and 0.30%, respectively. A more prolonged sulfation (up to 100 h) did not lead to any increase in the content of sulfur in the samples. Probably, these conditions are insufficient for complete sulfation of nanodiamonds; however, the IR spectra obtained after treatment with oleum clearly show a new band at 620 cm^{-1}, characteristic of sulfo groups.

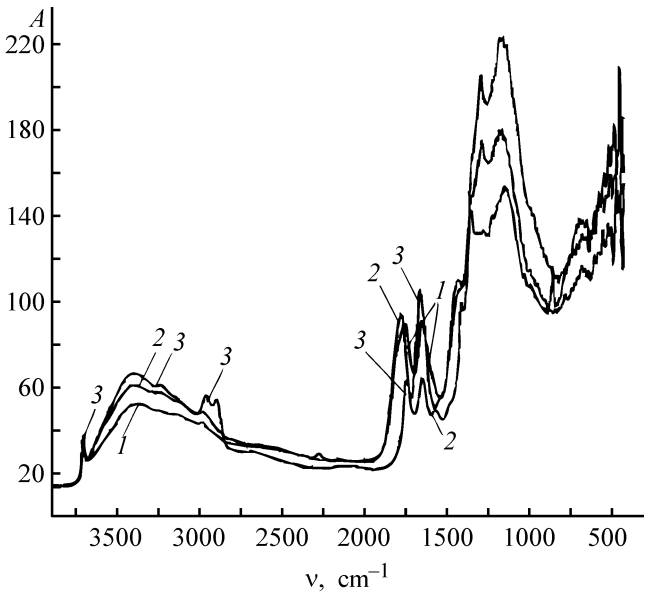
Various ND samples were chlorinated at 400 and 600°C. The results obtained are listed in Table 2.

It can be seen that chlorination of the starting sample and that modified in argon at 600°C results in that the content of chlorine increases with the chlorination temperature, whereas for samples modified in hydrogen, the content of chlorine remains constant and is independent of the ND treatment conditions and chlorination temperature.

The effect of the ND surface modification conditions on the catalytic activity of palladium catalysts supported by nanodiamonds was studied in the reaction of NB hydrogenation, chosen as the model reaction. The results obtained are listed in Table 3.

Modification of the ND surface affects the catalytic activity of nanodiamond-supported palladium catalysts in the reaction of NB hydrogenation. The relative amounts of surface groups vary with the modification conditions [13], and this circumstance is responsible for the difference in the average reaction rates. In thermal treatment, CO_2 and H_2O are removed from the surface the most easily, and phenol, ketone, and lactone groups, more difficultly [13].

As can be seen in Table 3, the highest activity is observed for the catalyst treated in a flow of argon at



IR diffuse reflection spectra of nanodiamonds. (*A*) Reflectance and (ν) wave number. (*1*) Starting sample and (*2*, *3*) that treated at 400°C with (*2*) argon and (*3*) hydrogen.

400°C (sample no. 2). As the treatment temperature is raised to 800°C, the activity of the samples modified in the atmosphere of argon somewhat falls, but remains twice that for the starting sample (sample no. 1).

Modification of nanodiamonds in the atmosphere of hydrogen (sample nos. 5–7) does not change the catalytic properties, compared with the starting ND (sample no. 1). In the case of treatment with argon, functional groups are removed and the nanodiamond surface is freed for NB adsorption, whereas in hydrogen, presumably only the chemical composition of the surface is changed (see figure).

Table 2. Effect of nanodiamond chlorination conditions on the chlorine content

ND treatment conditions	Chlorination temperature, °C	Chlorine content, %
Starting	400	11.0 ± 0.3
	600	16.0 ± 0.5
Ar, 600°C	400	8.8 ± 0.3
	600	12.0 ± 0.5
H_2, 600°C	400	10.6 ± 0.4
	600	10.6 ± 0.3
H_2, 800°C	400	10.6 ± 0.4

Table 3. Catalytic activity of catalysts produced in different support modification conditions (reaction conditions: 10 ml of ethanol, 0.3 ml of NB, weighed portion of nanodiamonds 50 mg, content of palladium 2%, temperature 40°C)

Sample no.	ND treatment conditions	W_{av},* l H_2/(g Pd min)	Sample no.	ND treatment conditions	W_{av},* l H_2/(g Pd min)
1	Starting	7.3 ± 0.2	8	600°C, oleum: Ar	13.5 ± 0.3
2	Ar: 400°C	17.5 ± 0.3	9	H_2	10.0 ± 0.2
3	600°C	16.8 ± 0.3	10	Cl_2: 400°C	13.7 ± 0.3
4	800°C	14.0 ± 0.2	11	600°C	11.0 ± 0.3
5	H_2: 400°C	4.3 ± 0.1	12	Ar, 600°C/Cl_2, 400°C	12.3 ± 0.3
6	600°C	5.3 ± 0.1	13	H_2, 600°C/Cl_2, 400°C	11.1 ± 0.2
7	800°C	6.4 ± 0.2	14	H_2, 800°C/Cl_2, 400°C	12.6 ± 0.2

* Average rate of NB hydrogenation.

Table 4. Effect of ND modification conditions on the amount of adsorption

Solvent	Adsorption, mmol g^{-1} at indicated modification temperature, °C								
	Starting ND	200	400	600	800	200	400	600	800
		Ar				H_2			
Benzene	12.3	12.6	12.7	13.2	13.6	11.4	12.1	18.7	24.9
Chloroform	13.5	14.0	14.2	14.5	14.9	14.3	14.5	14.7	15.8
Water	41.6	–	57.1	60.2	64.6	–	55.4	53.4	50.8

It can also be seen in Table 3 that modification of ND with sulfo and chloro groups makes the catalyst activity higher.

Thus, it can be concluded that the most efficient way to modify nanodiamonds is their thermal treatment in argon, which makes it possible to raise the rate of NB hydrogenation by more than a factor of 2, with ND used as a support for palladium catalysts. The nature of the support surface affects the formation of active centers in palladium catalysts and, accordingly, their catalytic activity.

A property important for various applications of nanodiamonds is their adsorption capacity. It was pointed out in [5] that UDD has a high adsorption capacity, 9 to 14 mmol g^{-1} for benzene vapor and 10.5 to 17 mmol g^{-1} for chloroform vapor, depending on a UDD brand. The adsorption properties of modified nanodiamond forms were studied. The adsorption capacity of ND for benzene, chloroform, and water vapors was determined (with an average determination error not exceeding 3 wt %). The results obtained are listed in Table 4.

It can be seen that the adsorption of chloroform is independent of the nanodiamond modification conditions and is virtually constant. Its average value is 14.55 mmol g^{-1}. The adsorption of benzene vapor on the surface of the starting nanodiamond and that modified in an inert atmosphere at various temperatures is also virtually constant, with its average value equal to 12.88 mmol g^{-1}.

Thus, the chemical composition of the ND surface (presence of functional groups of different types) weakly affects its adsorption properties. Presumably, the factor responsible for the adsorption of benzene and chloroform is the presence in a sample of sufficiently narrow pores, because nanodiamonds form stable aggregates from particles 4–5 nm in size. It should, however, be noted that the adsorption capacity for benzene vapor increases for samples modified in a flow of hydrogen, and, at the maximum thermal treatment temperature (800°C), the amount of adsorption is 24.9 mmol g^{-1}, which is more than two times the adsorption capacity of the starting ND and that modified in an inert atmosphere. Presumably, this is so because reduction reactions occur in the atmo-

sphere of hydrogen at high thermal treatment temperatures and, as a result, oxygen-containing groups are virtually absent on the nanodiamond surface and alkyl functional groups appear.

It should be noted that the maximum adsorption capacity for benzene vapor is reached in only 48 h for samples treated in a flow of hydrogen, and in 21 days for all other samples.

As can be seen in Table 4, the adsorption of water on the ND surface is two to three times that of benzene and chloroform. The adsorption capacity of samples treated in a flow of argon increases with the modification temperature and, at 800°C, exceeds that of the starting ND by a factor of 1.5. A somewhat different situation is observed for samples treated in a flow of hydrogen: the adsorption capacity slightly decreases as the sample modification temperature increases, but the amount of adsorption also exceeds that of the starting nanodiamonds. Probably, this is due to occurrence of reducing reactions in the course of thermal treatment in the atmosphere of hydrogen, with a large number of oxygen-containing groups reduced to hydrocarbon radicals at the maximum temperature (800°C). However, the adsorption capacity of samples treated in hydrogen is higher than that of the starting ND because, probably, adsorption occurs in this case at the remaining functional groups with which water forms hydrogen bonds and at active centers that appeared on the surface because of the desorption of other functional groups (amino groups, sulfo groups, etc.).

The high adsorption capacity of nanodiamonds for water can be attributed to the formation of hydrogen bonds with carboxy and hydroxy groups contained on the ND surface. Formation of strong chemical bonds between water and the ND surface is unlikely [14], which is confirmed by experiments on desorption of water from the surface with calcium chloride. Samples that absorbed water were placed in a desiccator with calcium chloride, and, after 4 days, the mass of the weighed portion of nanodiamonds took its original value. This experiment shows that a chemical interaction with the ND surface is unlikely, because chemisorption is a virtually irreversible process [15].

Thus, the higher (by a factor of 3–4.5) adsorption capacity of nanodiamonds for water, compared with chloroform and benzene, can be noted. Comparison of the amounts of adsorbed water (>100 wt %) rather unambiguously points to the physical mechanism of water adsorption in nanodiamond pores.

CONCLUSIONS

(1) Quantitative characteristics of thermal transformations of functional groups on the surface of nanodiamonds in their modification in various atmospheres were determined. It was found that a larger amount of carbon dioxide and water is released in thermal treatment of nanodiamonds in an inert atmosphere, and the maximum amount of carbon monoxide, at 800°C. In thermal treatment in a reducing atmosphere, the amount of released water exceeds that of carbon dioxide.

(2) The conditions of modification of the nanodiamond surface affect the catalytic activity of supported palladium catalysts in the reaction of nitrobenzene hydrogenation. Nanodiamonds thermally treated in the atmosphere of argon were found to be the best support for these catalysts (with the rate of nitrobenzene hydrogenation increasing by more than a factor of 2).

(3) A study of the effect of the modification conditions on the adsorption properties of nanodiamonds with respect to benzene, chloroform, and water demonstrated that the adsorption of chloroform vapor is independent of the conditions in which the nanodiamond surface is modified. The adsorption capacity for benzene vapor is independent of the modification temperature for samples treated in argon and increases with this temperature for samples treated in hydrogen. The adsorption capacity of nanodiamonds for water vapor is two to three times that for benzene and chloroform vapors.

REFERENCES

1. Vereshchagin, A.L., Ul'yanova, G.M., Novoselov, V.V., et al., *Sverkhtverd. Mater.*, 1990, no. 5, pp. 20–22.
2. RF Patent 2004491.
3. USSR Inventor's Certificate, no. 1819851.
4. Obraztsova, I.I. and Eremenko, A.N., *Zh. Prikl. Khim.*, 2003, vol. 76, no. 3, pp. 443–445.
5. Dolmatov, V.Yu., *Usp. Khim.*, 2001, vol. 70, no. 7, pp. 687–708.
6. Dolmatov, V.Yu., *Usp. Khim.*, 2007, vol. 76, no. 4, pp. 375–397.
7. RF Patent 2081821.
8. Klimova, V.A., *Osnovnye mikrometody analiza organicheskikh soedinenii* (Basic Micromethods for Analysis of Organic Compounds), Moscow: Khimiya, 1967.

9. Ginzburg, S.I., Ezerskaya, I.A., Prokof'ev, I.V., et al., *Analiticheskaya khimiya elementov: Platinovye metally: Ru, Rh, Pd, Ir, Os, Pt* (Analytical Chemistry of Elements: Platinum Metals: Ru, Rh, Pd, Ir, Os, Pt), Moscow: Nauka, 1972.
10. Obraztsova, I.I. and Efimov, O.A., *Zh. Prikl. Khim.*, 2004, vol. 77, no. 3, pp. 517–518.
11. Tapraeva, F.M., Pushkin, A.N., Epishina, N.I., et al., *Zh. Fiz. Khim.*, 1986, vol. 60, no. 7, pp. 1814–1816.
12. Kulakova, I.I., *Ross. Khim. Zh.*, 2004, vol. 48, no. 5, pp. 97–106.
13. Eremenko, A.N., Besedina, O.A., and Obraztsova, I.I., *Zh. Prikl. Khim.*, 2004, vol. 77, no. 12, pp. 1956–1959.
14. Nesmeyanov, A.N. and Nesmeyanov, N.A., *Nachala organicheskoi khimii* (Principles of Organic Chemistry), Moscow: Khimiya, 1974, book 1, p. 128, 180–181.
15. Voyutskii, S.S., *Kurs kolloidnoi khimii* (Course of Colloid Chemistry), Moscow: Khimiya, 1975.